



Acta Biochimica
Polonica

August 2025



Polskie
Towarzystwo
Biochemiczne

Acta Biochimica Polonica (ABP) | 2023-2024 Retrospective

Issue Editor

Grzegorz Węgrzyn
University of Gdańsk
Poland



frontiers | Publishing Partnerships

Acta Biochimica Polonica (ABP) | 2023-2024 Retrospective

Acta Biochimica Polonica eBook Copyright Statement

The copyright in the text of individual articles in this eBook is the property of their respective authors or their respective institutions or funders. The copyright in graphics and images within each article may be subject to copyright of other parties. In both cases this is subject to a license granted to Frontiers.

The compilation of articles constituting this eBook is the property of Frontiers.

Each article within this eBook, and the eBook itself, are published under the most recent version of the Creative Commons CC-BY licence.

The version current at the date of publication of this eBook is CC-BY 4.0. If the CC-BY licence is updated, the licence granted by Frontiers is automatically updated to the new version.

When exercising any right under the CC-BY licence, Frontiers must be attributed as the original publisher of the article or eBook, as applicable.

Authors have the responsibility of ensuring that any graphics or other materials which are the property of others may be included in the CC-BY licence, but this should be checked before relying on the CC-BY licence to reproduce those materials. Any copyright notices relating to those materials must be complied with.

Copyright and source acknowledgement notices may not be removed and must be displayed in any copy, derivative work or partial copy which includes the elements in question.

All copyright, and all rights therein, are protected by national and international copyright laws. The above represents a summary only. For further information please read Frontiers' Conditions for Website Use and Copyright Statement, and the applicable CC-BY licence.

ISSN 1734-154X
ISBN 978-2-8325-6671-8
DOI 10.3389/978-2-8325-6671-8

Generative AI statement

Any alternative text (Alt text) provided alongside figures in the articles in this eBook has been generated by Frontiers with the support of artificial intelligence and reasonable efforts have been made to ensure accuracy, including review by the authors wherever possible. If you identify any issues, please contact us.

Dear Acta Biochimica Polonica community,

It is my pleasure to present this eBook compiling the manuscripts published in Acta Biochimica Polonica in 2023 and 2024. This period was special for the journal which joined Frontiers within the Publishing Partnerships program. This collaboration has a significant impact on publishing the journal, by combining the experience and expertise of editors with the excellent editorial service provided by the publisher.

I would like to express my warm thanks to all the authors, editors, and reviewers who have been contributing to Acta Biochimica Polonica. Because of their passion, dedication and hard work it was possible to publish excellent papers in virtually all fields of biochemistry in this broadly scoped journal, devoted to all biochemical specializations, from gene expression regulation to medical biochemistry, and from basic biochemistry to immunology.

Because of the broad biochemical scope of Acta Biochimica Polonica, this collection contains papers representing a diverse range of topics, methods and research subjects. However, all of these are connected to biochemistry, as the common point of all articles included in this eBook.

After successfully joining Frontiers, we look forward to the continued growth and impact of Acta Biochimica Polonica. I invite researchers, students and all people interested in biochemistry to engage with the content of this eBook. I hope you will enjoy reading the papers which can provide a field for discussion and encourage starting new research in the fascinating field of biochemistry.

Grzegorz Węgrzyn
Editor-in-Chief

Table of contents

Basic Biochemistry

- 17 **The emergence of biological homochirality**
Agnieszka Kiliszek and Wojciech Rypniewski
- 22 **Were academic promotions in biochemistry and other research disciplines improperly controlled in Poland between 2011 and 2020?**
A response to the recently published “Who controls the national academic promotion system” article
Grzegorz Węgrzyn
- 25 **Secondary structure in polymorphic forms of alpha-synuclein amyloids**
Irena Roterman, Katarzyna Stapor, Dawid Dułak and Leszek Konieczny
- 36 **Mapping the substrate-binding subsite specificity of a *Porphyromonas gingivalis* Tpr peptidase**
Dominika Staniec, Wioletta Rut, Marcin Drąg, Michał Burmistrz, Michael Kitching and Jan Potempa
- 43 **Emerging relationship between hydrogen sulfide and ferroptosis: A literature review**
Xiaoming Gao, Ke Lu and Chong Li
- 53 **Probing the enzymatic activity and maturation process of the EcAIII Ntn-amidohydrolase using local random mutagenesis**
Joanna I. Loch, Anna Ściuk, Marta Kilichowska, Izabela Pieróg, Weronika Łukaszczyk, Katarzyna Zimowska and Mariusz Jaskolski
- 60 **Stability in biosensors derived from domain map analysis of bibliometric data**
Aleksandra Klos-Witkowska and Vasyl Martsenyuk
- 72 ***In silico* explorations of bacterial mercuric reductase as an ecofriendly bioremediator for noxious mercuric intoxications**
Muhammad Naveed, Muhammad Aqib Shabbir, Tariq Aziz, Ayesha Saleem, Rida Naveed, Ayaz Ali Khan, Taqweem Ul Haq, Metab Alharbi, Abdulrahman Alsahammari and Abdullah F. Alasmari
- 81 **Isolation and characterization of indigenous bacterial assemblage for biodegradation of persistent herbicides in the soil**
Mariam Zameer, Usaal Tahir, Sana Khalid, Nureen Zahra, Abid Sarwar, Ahsan Saidal, Tariq Aziz, Majid Alhomrani, Abdulhakeem S. Alamri, Anas S. Dabool, Manal Y. Sameeh, Amal A. Mohamed and Amnah A. Alharbi

Biochemical Physiology

- 91 **The relationship between EMG high frequency and low frequency band amplitude changes correlates with tissue inorganic phosphate levels**
Malgorzata Habich, Bartosz Pawlinski, Kamil Lorenc, Maria Sady, Katarzyna Siewruk, Piotr Zielenkiewicz, Zdzisław Gajewski, Jarosław Poznanski, Leszek Paczek and Paweł Szczesny
- 95 **The role of TGF- β in the electrotactic reaction of mouse 3T3 fibroblasts *in vitro***
Patrycja Ciesielska, Sławomir Lasota, Sylwia Bobis-Wozowicz and Zbigniew Madeja
- 108 **Anesthesia and surgery induce changes in endogenous brain protective protein (RNF146) and delirium-like behavior in aged rats**
Yubo Gao, Xu Han, Xiuhua Li, Shaling Tang, Chun Zhang, Xiaoxia Yang, Majid Alhomrani, Abdulhakeem S. Alamri, Ghulam Nabi and Xinli Ni
- 117 **Understanding mitochondrial potassium channels: 33 years after discovery**
Adam Szewczyk
- 124 **PELP1 and SRC kinase as important molecules in the estrogenmediated pathway in human testis and epididymis**
Izabela Skibińska, Mirosław Andrusiewicz, Magdalena Jendraszak, Aleksandra Żbikowska, Czesław Żaba and Małgorzata Kotwicka
- 134 **Comparison of uremic toxin removal between expanded hemodialysis and high volume online hemodiafiltrations in different modes**
Jan Biedunkiewicz, Agnieszka Zakrzewska, Sylwia Małgorzewicz, Michał Komorniczak, Katarzyna Jasiulewicz, Natalia Płonka, Agnieszka Tarasewicz, Magdalena Jankowska, Bogdan Biedunkiewicz, Alicja Dębska-Ślizień and Leszek Tylicki
- 143 **Criteria analysis for kinetics curves of initiated blood serum chemiluminescence**
Iryna Oliynyk
- 149 **Two promising natural lipopeptides from *Bacillus subtilis* effectively induced membrane permeabilization in *Candida glabrata***
Madhuri Madduri, Shivaprakash M. Rudramurthy and Utpal Roy
- 156 **Placental expression of Fatty Acid Desaturases 1, 2 and 3 in selected pregnancy pathologies**
Rafał Bobiński, Urszula Mazurek, Nikola Zmarzły, Izabela Ulman-Włodarz, Mieczysław Dutka, Monika Pizon, Wioletta Pollok-Waksmańska, Anna Pieleś, Maciej B. Hajduga, Karolina Zimmer, Jan Bujok, Celina Pająk and Tomasz Ilczak

- 164 **Synergistic effect of Dactolisib/Lys05 combination on autophagy in A549 cells**
Mohammad M. Abdelwahab, Hesham Saeed, Nefertiti El-Nikhely and Hisham A. Nematalla
- 172 **Tween 80™-induced changes in fatty acid profile of selected mesophilic lactobacilli**
Dorota Zaręba and Małgorzata Ziarno
- 187 **Endoplasmic reticulum stress involves the high glucose-induced nucleus pulposus cell pyroptosis**
Xiaochun Xiong, Ying Wu, Hengguo Long, Tianzi Liang, Wenqing Liang, Xiaogang Huang and Guijin Li

Food Biochemistry

- 194 **Investigation of microbiological safety of dry cat foods marketed in Poland**
Joanna Zięta-Wysocka, Olga Sierawska, Cansel Taskin, Agata Poniewierska-Baran, Dominika Bębnowska, Rafał Hryniewicz, Filip Lewandowski and Paulina Niedźwiedzka-Rystwej
- 201 **Hepatic Mcpip1 regulates adaptation to food restriction in mice**
Olga Mucha, Bożena Skupien-Rabian, Alicja Słota, Katarzyna Trzos, Natalia Pydyn, Bartosz Podlewski, Jolanta Jura and Jerzy Kotlinowski

Gene Expression Regulation

- 208 **Relative expression levels of growth hormone gene and growth rate in Indian major carp species**
Shahid Sherzada, Muhammad Nauman Sharif, Qurban Ali, Saeed Akram Khan, Tawaf Ali Shah, Mohamed A. M. El-Tabakh, Tariq Aziz, Ghulam Nabi, Metab Alharbi, Thamer H. Albekairi and Abdullah F Alasmari
- 215 **Isolation, preparation and investigation of leaf extracts of *Aloe barbadensis* for its remedial effects on tumor necrosis factor alpha (TNF- α) and interleukin (IL-6) by *in vivo* and *in silico* approaches in experimental rats**
Iram Khurshaid, Sobia Ilyas, Nureen Zahra, Sohail Ahmad, Tariq Aziz, Fahad Al-Asmari, Sanaa Almowallad, Rehab F. Al-Massabi, Yasmene F. Alanazi, Aminah A. Barqawi, Roaa Mohammed Tahir Kassim, Abdulhakeem S Alamri, Majid Alhomrani and Manal Y Sameeh
- 222 **Overexpressed *RAD51* promoted osteogenic differentiation by activating IGF1R/PI3K/AKT pathway in osteoblasts**
Minli Qiu, Ya Xie, Liudan Tu, Minjing Zhao, Mingcan Yang, Linkai Fang and Jieruo Gu
- 228 **Variability of plant transcriptomic responses under stress acclimation: a review from high throughput studies**
Michał Rurek and Mikotaj Smolibowski

- 249 **circROCK1 Promotes septic myocardial injury through regulating miR-96-5p/OXSR1 axis**
ZhiYu He, Lingling Xu, Xiaojun Zeng, Biqing Yang, Peiying Liu, Dunzheng Han, Hao Xue and Bihui Luo
- 257 **Timosaponin AIII attenuates precocious puberty in mice through downregulating the hypothalamic-pituitary-gonadal axis**
Lili Zhou, Yaoquan Ren, Dongmei Li, Weiwei Zhou, Chengke Li, Qiang Wang and Xiangzheng Yang
- 265 **Quercetin inhibits the expression of *MYC* and *CYP2E1* and reduces oxidative stress in the myocardium of spontaneously hypertensive rats**
Oksana Maksymchuk, Angela Shysh and Anna Kotliarova
- 271 **LncRNA MIR31HG promotes cell proliferation and invasive properties of the MCF-7 cell line by regulation of receptorinteracting serine-threonine kinase 4**
Jingwei Tang, Xiaojing Zhang, Chunchun Chen, Binbin Wang, Yansong Chen, Hao Zhang, Mengxiang Qiao, Xianfu Liu, Wei Guo and Gongsheng Jin
- 278 **Comparative analysis of A¹ and A² allele detection efficiency for bovine *CSN2* gene by AS-PCR methods**
Roman Kulibaba, Mykola Sakhatskyi and Yuriy Liashenko
- 283 **Upregulation of miR-22 alleviates oxygen–glucose deprivation/reperfusion-induced injury by targeting *Tiam1* in SH-SY5Y cells**
Jiansong Yin, Yu Wan, Jing Wang and Mei Xue
- 290 **Circ-Sirt1 promotes osteoblast differentiation by activating Sirt1 and Wnt/ β -catenin pathway**
Yuanli Li, Junlan Nie, Qing Wu, Xin Yang and Ping Jiang
- 297 **MicroRNA-221-3p promotes post-burn HUVEC proliferation, migration, and angiogenesis by regulating *CDKN1B***
Kun Miao, Fei Xie and JinGui Lin
- 303 **MALAT-1 regulates the AML progression by promoting the m6A modification of *ZEB1***
Jing Jin, Leihua Fu, Pan Hong and Weiying Feng

Immunology

- 310 **The modulation of the hexosamine biosynthetic pathway impacts the localization of CD36 in macrophages**
Karen Julissa Loaeza-Reyes, Edgar Zenteno, Eleazar Ramírez-Hernández, Roberta Salinas-Marin, Adriana Moreno-Rodríguez, Rafael Torres-Rosas, Liliana Argueta-Figueroa, Berenice Fernández-Rojas, Socorro Pina-Canseco, Alfonso E. Acevedo-Mascarúa, Alicia Hernández-Antonio and Yobana Pérez-Cervera

- 320 **Sensing antibody functions with a novel CCR8-responsive engineered cell**
Jianyu Hao, Yitong Lv, Xufeng Xiao, Lidan Li and Changyuan Yu
- 327 **Effects of Baimuxinol on the inflammation and oxidative stress of LPS-induced RAW264.7 macrophages *via* regulating the NF- κ B/I κ B α and Nrf2/ARE signaling pathway**
Yan Chen, Nan Chen, Jing Wang and Shuqing Li
- 333 **miRNA-301 As a molecule promoting necrotizing enterocolitis by inducing inflammation**
Dajun Zou, Fude Hu, Qili Zhou and Xiaoqing Xu
- 339 **Cytokine IL6, but not IL-1 β , TNF- α and NF- κ B is increased in paediatric cancer patients**
Anna Synakiewicz, Anna Stanisławska Sachadyn, Anna Owczarzak, Małgorzata Skuza and Teresa Stachowicz-Stencel
- 345 **A reverse vaccinology approach to design an mRNA-based vaccine to provoke a robust immune response against HIV-1**
Muhammad Naveed, Urooj Ali, Tariq Aziz, Muhammad Junaid Rasool, Adil Ijaz, Metab Alharbi, Mousa Essa Alharbi, Abdulrahman Alshammari and Abdullah F. Alasmari
- 357 **Prevalence of circulating antibodies against hemagglutinin of influenza viruses in epidemic season 2021/2022 in Poland**
Katarzyna Kondratiuk, Ewelina Hallmann, Karol Szymański, Katarzyna Łuniewska, Anna Poznańska and Lidia B. Brydak
- 366 ***Akkermansia muciniphila* - impact on the cardiovascular risk, the intestine inflammation and obesity**
Krzysztof Gofron, Adam Berezowski, Maksymilian Gofron, Małgorzata Borówka, Michał Dziedzic, Wojciech Kazmierczak, Maciej Kwiatkowski, Maria Gofron, Zuzanna Nowaczyk and Sylwia Małgorzewicz

Medical Biochemistry

- 373 **Relationship between chemical industrial environment and allergic skin diseases**
Shaohua Fu, Minli Gong and Guisheng Xing
- 379 **Decrease of prothrombin level during thrombolysis in acute myocardium infarction**
Daria S. Korolova, Alexander M. Parkhomenko, Volodymyr O. Chernyshenko, Tamara M. Chernyshenko, Nadiya M. Druzhyna, Olha V. Hornytska and Tetyana M. Platonova
- 384 **Relationship of gut microbiota and immunological response in obesity-related non-alcoholic fatty liver disease in children**
Pawel Czarnowski, Aldona Wierzbicka-Rucinska and Piotr Socha

- 390 **Age-related effects of fenofibrate on the hepatic expression of sirtuin 1, sirtuin 3, and lipid metabolism-related genes**
Adrian Zubrzycki, Agata Wrońska, Piotr M. Wierzbicki and Zbigniew Kmiec
- 399 **Seasonal variation of total and bioavailable 25-hydroxyvitamin D [25(OH)D] in the healthy adult Slovenian population**
Joško Osredkar, Vid Vičič, Maša Hribar, Evgen Benedik, Darko Siuka, Aleš Jerin, Urška Čegovnik Primožič, Teja Fabjan, Kristina Kumer, Igor Pravst and Katja Žmitek
- 412 **Clinical study on the difference in intestinal microecology between patients with preeclampsia and pregnant women at different stages of pregnancy**
Fan Xie, Huan Zhang, Min Peng and TingTing Jiang
- 425 **Modified Hongyu Decoction promotes wound healing by activating the VEGF/PI3K/Akt signaling pathway**
Xiang Xu, Wei-hua Yang, Zhi-wei Miao, Chun-yu Zhang, Yi-jia Cheng, Yang Chen, Jin-gen Lu and Ning He
- 436 **Chrysophanol ameliorates oxidative stress and pyroptosis in mice with diabetic nephropathy through the Kelch-like ECH-associated protein 1/nuclear factor erythroid 2-related factor 2 signaling pathway**
Xinzhu Yuan, Wenwu Tang, Changwei Lin, Hongni He and Lingqin Li
- 443 **CRISPR-Cas9 guided RNA based model for the treatment of Amyotrophic Lateral Sclerosis: A progressive neurodegenerative disorder**
Muhammad Naveed, Muhammad Aqib Shabbir, Tariq Aziz, Hafiz Muhammad Huraira, Sayyeda Fatima Zaidi, Ramsha Athar, Hassan Anwer Chattha, Metab Alharbi, Abdulrahman Alsahammari and Abdullah F. Alasmari
- 454 **Association of vitamin D with deoxyribonucleic acid (DNA) damage: A systematic review of animal and human studies**
Mayang Indah Lestari, Krisna Murti, Iche Andriyani Liberty, Zen Hafy, Violantina Linardi, Muhammad Khoirudin and Tungki Pratama Umar
- 463 **LncRNA AC093850.2 predicts poor outcomes in patients with triple-negative breast cancer and motivates tumor progression by sponging miR-4299**
Zhangbo Xu, Yongxue Gu, Ying Lei and Lili Teng
- 470 **Ellagic acid inhibits cell proliferation, migration, and invasion of anaplastic thyroid cancer cells via the Wnt/ β -catenin and PI3K/Akt pathways**
Xianglong Meng, Zhihua Cui, Hui Shi, Xiaoru Ma, Wanru Li, Xianjun Liu and Yang Jiang

- 477 **JNK promotes the progression of castration-resistant prostate cancer**
Yigeng Feng, Hongwen Cao, Dan Wang, Lei Chen, Renjie Gao and Peng Sun
- 483 **Value evaluation of serum (sdLDLc*HCYc)/HDLc ratio in the stability of intracranial arterial plaques in patients with acute cerebral infarction**
Hongyu Hao, Xing Xing, Yajing Li, Hongshan Chu, Lei Zhao, Siqi Cheng, Yang Liu, Tiankui Wang, Nan Meng and Ruisheng Duan
- 490 **β -catenin promotes resistance to trastuzumab in breast cancer cells through enhancing interaction between HER2 and SRC**
Xiaoyan Hao, Jialu Zheng, Xiaoqin Yu, Zhixin Li and Guanghui Ren
- 499 **Impact of diet modification on body mass and kidney function in patients with diabetic nephropathy: a pilot study**
Małgorzata Kaczkan, Sylwia Czaja-Stolc, Małgorzata Sikorska-Wiśniewska, Michał Chmielewski, Alicja Dębska-Ślizień and Sylwia Małgorzewicz
- 505 **Metformin promotes the normalization of abnormal blood vessels after radiofrequency ablation deficiency in hepatocellular carcinoma by microRNA-302b-3p targeting thioredoxin-interacting protein**
HaiGang Niu, ShuYing Dong, GuoMing Li, ShiLun Wu and WenBing Sun
- 515 **An mRNA-based reverse-vaccinology strategy to stimulate the immune response against *Nipah virus* in humans using fusion glycoproteins**
Muhammad Naveed, Sarmad Mahmood, Tariq Aziz, Muhammad Hammad Arif, Urooj Ali, Faisal Nouroz, Christos Zacharis, Metab Alharbi, Abdulrahman Alshammari and Abdullah F. Alasmari
- 524 **Design and development of new inhibitors against breast cancer, Monkeypox and Marburg virus by modification of natural Fisetin *via in silico* and SAR studies**
Shopnil Akash, Md. Mominur Rahman, Clara Mariana Gonçalves Lima, Talha Bin Emran, Sharifa Sultana, Sumaira Naz, Tariq Aziz, Metab Alharbi, Abdulrahman Alshammari and Abdullah F. Alasmari
- 534 **Long noncoding RNA TPTEP1 suppresses diabetic retinopathy by reducing oxidative stress and targeting the miR-489-3p/NRF2 axis**
Xinfa Wang, Xianbo Zhou, Fang Wang, Nan Zhang, Yan Zhang, Zhen Ao and Fang He
- 540 **Overexpression of miR-483-5p predicts venous thromboembolism onset in patients with lung cancer especially in high BMI cases**
Miao Zhang, Juanjuan Li, Guigang Tai, Chao Li and Hongcai Wu

- 546 **A novel ferroptosis-related gene signature associated with cuproptosis for predicting overall survival in breast cancer patients**
Xiaoyu Zhang and Qunchen Zhang
- 556 **Circ-PGPEP1 augments renal cell carcinoma proliferation, Warburg effect, and distant metastasis**
PeiRui Wang, Jin Chen, Xin Ye, RuYi Wang, Lin Chen and HanChao Zhang
- 565 **Circular RNA sirtuin-1 restrains the malignant phenotype of non-small cell lung cancer cells *via* the microRNA-510-5p/SMAD family member 7 axis**
ZiRan Zhao, HongYan Zhang, Fan Zhang, Ying Ji, Yue Peng, Fei Wang and Liang Zhao
- 574 **A case-control study in NAT2 gene polymorphism studies in patients diagnosed with acute myeloid leukemia**
Abdullah Farasani
- 579 **Discovery of a novel genetic variant in the *N-acetyltransferase2 (NAT2)* gene that is associated with bladder cancer risk**
Lina Elsalem, Ahmad Al Shatnawi, Mahmoud A Alfaqih, Ayat Alshoh, Saddam Al Demour, Ali Al-Daghmin, Omar Halalsheh, Khalid Kheirallah and Mamoun Ahram
- 587 **Alpha-Mangostin ameliorates acute kidney injury *via* modifying levels of circulating TNF- α and IL-6 in glycerol-induced rhabdomyolysis animal model**
Heba M. Eltahir, Hossein M. Elbadawy, Ali Alalawi, Ahmed J. Aldhafiri, Sabrin R.M. Ibrahim, Gamal A. Mohamed, Abdel-Gawad S. Shalkami, Mohannad A. Almikhlaifi, Muayad Albadrani, Yaser Alahmadi, Mekky M. Abouzied and Maiada H. Nazmy
- 595 **MiR-375 attenuates sorafenib resistance of hepatocellular carcinoma cells by inhibiting cell autophagy**
Dan Wang and Jingbo Yang
- 603 **Long noncoding RNA LGALS8-AS1 promotes angiogenesis and brain metastases in non-small cell lung cancer**
Jian Zhong and Bo Wang
- 612 **Clinical features and risk factors for primary Sjögren's syndrome combined with interstitial lung disease: a retrospective study**
Zhixia Yang, Hao Zhao, Lei Shan and Dan Wang
- 622 **Clinical study: the impact of goal-directed fluid therapy on volume management during enhanced recovery after surgery in gastrointestinal procedures**
Ming Gao, Minggan Chen, Gang Dai, Dengfeng Zhu and Yiting Cai

- 630 **Protective effect of tretinoin derivative and TXNRD1 protein on streptozotocin induced gestational diabetes *via* an age-rage signaling-pathway**
Wensheng Wang and Lin Wang
- 636 **Identification of AHNAK expression associated with the pathogenesis of chronic obstructive pulmonary disease by bioinformatic analysis**
Chunhui Zhang and Yu Liu
- 642 ***LINC00707* promotes multidrug resistance of ovarian cancer cells by targeting the miR-382-5p/*LRRK2* axis**
Min-Wen Zhao, Chang-Jie Lin and Jian-Ping Qiu
- 650 **Genetic association between vitamin D receptor gene and Saudi patients confirmed with Familial Hypercholesterolemia**
May Salem Al-Nbaheen
- 656 **Formononetin enhances the chemosensitivity of triple negative breast cancer *via* BTB domain and CNC homolog 1-mediated mitophagy pathways**
Shan Li, Linlian Zhu, Yufeng He and Ting Sun
- 663 **Role of albumin and prealbumin in assessing nutritional status and predicting increased risk of infectious complications during childhood cancer treatment**
Anna Milaniuk, Katarzyna Drabko and Agnieszka Chojeła
- 674 **Application of the FISH method and high-density SNP arrays to assess genetic changes in neuroblastoma—research by one institute**
Dorota Winnicka, Paulina Skowera, Magdalena Stelmach, Borys Styka and Monika Lejman
- 684 **Prevalence of poor nutrition status in multiple sclerosis patients assessed by different diagnostic tools**
Natalia Mogitko and Sylwia Małgorzewicz
- 687 **Mutational analysis of *FOLR1* and *FOLR2* genes in children with Myelomeningocele**
Nageen Hussain, Saira Malik, Tayyaba Faiz, Fiza Shafqat, Ayaz Ali Khan, Taqweem Ul Haq, Waqar Ali, Tariq Aziz, Metab Alharbi, Abdulrahman Alsahammari and Abdullah F. Alasmari
- 692 **Selected osteointegration markers in different timeframes after dental implantation: findings and prognostic value**
Emir Bayandurov, Zurab Orjonikidze, Sophio Kraveishvili, Ramaz Orjonikidze, George Ormotsadze, Sophio Kalmakhelidze and Tamar Sanikidze
- 701 **Simvastatin attenuates diabetes mellitus erectile dysfunction in rats by miR-9-5p-regulated *PDCD4***
YiMing Weng, YuanShen Mao, YanQiu Wang, YuFan Jiao, Jun Xiang and Wei Le

- 708 **Effect of artemisinin combined with allicin on improving cardiac function, fibrosis and NF- κ B signaling pathway in rats with diabetic cardiomyopathy**
Lingjuan Kong, Xiaoqing Ji, Yan Liu and YingJie Du
- 713 **Overexpression of long non-coding RNA GASL1 induces apoptosis and G₀/G₁ cell cycle arrest in human oral cancer cells**
Rui Zhang, Wanjun Tao and Lei Yu
- 719 **Vitamin D supplementation improves the therapeutic effect of mometasone on allergic rhinitis**
Minfei Guo
- 726 **Silencing circCAMSAP1 suppresses malignant behavior of endometrial cancer by targeting microRNA-370-3p/MAPK1**
Hai Feng Zhang, Cheng Cheng Cao, Cui Cui Nie and Ting Zhang
- 735 **MiR-92a regulates PTEN/Akt signaling axis to promote paclitaxel resistance in ovarian cancer cells**
Xiujuan Deng, Haigen Wu, Liping Xiong, Mouxi Wu, Jinfu Cao, Jing Liu and Wenyang Xie
- 741 **Promoting action of long non-coding RNA small nucleolar RNA host gene 4 in ovarian cancer**
Chao Liu, Shu Zhao, Zhi Xiang Lv and Xiao Juan Zhao
- 751 **Marine natural products: potential agents for depression treatment**
Xunqiang Wang, Cece Yang, Xing Zhang, Caiping Ye, Wenping Liu and Chengmin Wang
- 762 **Investigation of VEGF (rs 699947) polymorphism in the progression of Rheumatoid Arthritis (RA) and *in-silico* nanoparticle drug delivery of potential phytochemicals to cure RA**
Nageen Hussain, Mohsin Mumtaz, Muhammad Adil, Abad Ali Nadeem, Abid Sarwar, Tariq Aziz, Metab Alharbi, Abdulrahman Alsahammari, Abdullah F Alasmari and Mousa Essa Alharbi
- 770 **Circ-POLA2-mediated miR-138-5p/SEMA4C axis affects colon cancer cell activities**
YanDong Huang, QingYang Bai, HongBo Yu, YanRu Li, Hao Lu, HuiMin Kang, XueWei Shi and Kai Feng
- 777 **Hsa_circ_0023826 protects against glaucoma by regulating miR-188-3p/MDM4 axis**
Bin Qu, Jing Wang, Yan Li, XiaoWei Wu and MingYing Zhang
- 785 **Prognostic value of serum albumin level in patients with diffuse large B cell lymphoma**
Liyang Chen, Lili Pan and Tingbo Liu

- 795 **Imiquimod-induced psoriasis model: induction protocols, model characterization and factors adversely affecting the model**
Manahel Mahmood Alsabbagh
- 800 **MicroRNA-508-3p regulates the proliferation of human lung cancer cells by targeting G1 to S phase transition 1 (GSPT1) protein**
Xingyou Chen, Chen Feng, Jiliang Zha, Zihao Shen and Wei Ji
- 807 **Circular RNA METTL15/miR-374a-5p/ESCO2 axis induces colorectal cancer development**
Feng Guo, Yang Luo, GuangYao Ye and WeiJun Tang
- 816 **Recent studies on non-invasive biomarkers useful in biliary atresia – a literature review**
Anna Lew-Tusk, Marta Pęksa and Teresa Stachowicz-Stencel
- 822 **Circular RNA LPAR3 targets JPT1 via microRNA-513b-5p to facilitate glycolytic activation but repress prostate cancer radiosensitivity**
Yuan Yuan Chen, Li Ping Luo and Ke Chong Deng
- 832 **Bionics investigation of blood 25-hydroxyvitamin D in the interpretable biomechanics diagnosis of childhood anemia**
Lechi Zhang, Aijie Huang, Jingye Cai, Jiangting Hou, Hongyan Deng and Chenxiao Liu
- 838 **Hexafluoro-2-propanol represses colorectal cancer proliferation by regulating transaminases**
Zhongxin Shao, Lu Sun and Wenxin Lin
- 846 **Circular RNA CSPP1 motivates renal cell carcinoma carcinogenesis and the Warburg effect by targeting RAC1 through microRNA-493-5p**
Dong Zhang, XiaoJie Yang, QiDong Luo, DeLai Fu, HongLiang Li, Peng Zhang and Chong Tie
- 855 **MiR-96-5p is involved in permethrin-promoted proliferation and migration of breast cancer cells**
Yi Yan, Tian Wen Long, Xi Niu, Jia Fu Wang and Sheng Li
- 861 **circ_0013613 Promotes the recovery of spinal cord injury by regulating mir-370-3p/caspase1 to regulate neuronal pyroptosis**
Yong Guo, Li Ma and Zhuo Zhang
- 868 **The cadherin protein CDH19 mediates cervical carcinoma progression by regulating AKT/NF-κB signaling**
Jia Yu, Xin Sun, Yani Yu and Xiaorong Cui

- 875 Use of sertraline and agomelatine in hemodialysis patients: A case series report**
Alicja Kubanek, Mateusz Przybylak, Przemysław Paul, Anna Sylwia Kowalska, Michał Błaszczuk, Aleksandra Macul-Sanewska, Marcin Renke, Przemysław Rutkowski, Leszek Bidzan and Jakub Grabowski
- 880 Circ_PWWP2A promotes lung fibroblast proliferation and fibrosis via the miR-27b-3p/GATA3 axis, thereby aggravating idiopathic pulmonary fibrosis**
LiQing Su, Ying Nian and TianJi Zhu
- 888 The specific role of extracellular matrix metalloproteinases in the pathology and therapy of hard-to-heal wounds**
Joanna B. Trojanek
- 894 MicroRNA-1179 targets Epieregulin (EREG) regulates the proliferation and metastasis of human multiple myeloma cells**
Xiao Liu, Lan Qin, Wei Li and Fei Fei
- 899 WIF1 was downregulated in cervical cancer due to promoter methylation**
Ying Wang, Shifa Yuan, Jing Ma, Hong Liu, Lizhen Huang, Fengzhen Zhang and Xiaomei Wang
- 904 MicroRNA-196-5p targets Derlin-1 to induce autophagy in human osteosarcoma cells**
Zhenzhong Ji, Wei Chen, Song Wan, Yi Zhang and Junhua Xu
- 915 Wilforol A inhibits human glioma cell proliferation and deactivates the PI3K/AKT signaling pathway**
Zhihan Wang, Li Ren, Hao Xu, Zilong Wei and Hongjun Zeng
- 922 Resveratrol inhibits multiple organ injury in preeclampsia rat model**
Xiao Lang, Wei Liu, Qinfang Chen, Xingyu Yang, Dan Chen and Weiwei Cheng
- 927 Lipid disorders before and after successful liver transplantation**
Damian Gojowy, Joanna Urbaniec-Stompor, Joanna Adamusik, Gabriela Wójcik, Henryk Karkoszka, Robert Krol, Andrzej Wiecek and Marcin Adamczak
- 933 Circular RNA AGFG1 motivates breast cancer cell proliferation, invasion, migration, and glycolysis by controlling microRNA-653-5p/14-3-3 protein epsilon**
Liang Chen, JinXian Qian, Ying Shen and Xiang Yu
- 941 Downregulation of circular RNA 00091761 protects against heart failure after myocardial infarction via microRNA-335-3p/ ASCL4 axis**
Qian Wei, Mengni Jiang, Bin Tang, Lanlan You and Lin Zhao

- 949 **The role of USP1 deubiquitinase in the pathogenesis and therapy of cancer**
Svitlana Antonenko, Michael Zavelevich and Gennady Telegeev
- 962 **Involvement of Rictor/mTORC2/Akt/GLUT4 pathway in the regulation of energy metabolism in the gastric smooth muscle of diabetic rats**
Sun Yan, Yu-Rong Zheng, Zheng Jin, Mo-Han Zhang and Xiang-Shu Cui
- 968 **Circular RNA-AnnexinA7 accelerates cisplatin resistance in nonsmall cell lung cancer *via* modulating microRNA-545-3p to mediate Cyclin D1**
Jian Yao, Hai Yang Zhang, Shuang Gu, Jin Long Zou, Qiang Zhang and Ri Chu Qu
- 978 **Effect of 6-hydroxydopamine increase the glutathione level in SH-SY5Y human neuroblastoma cells**
Natalia Pieńkowska, Grzegorz Bartosz and Izabela Sadowska-Bartos
- 986 **NADPH oxidase 4 facilitates progression of chondrosarcoma *via* generation of reactive oxygen species**
Zheng Jun, Wang Lei, Fang Ce, Ren Wen Tao, Meng Xiang Hui and Qing Ci Nan
- 994 ***In situ* oxidative stress in patients with epiretinal membrane**
Tomasz Wilczyński, Jolanta Zalejska-Fiolka, Sabina Sapeta-Wieckowska, Monika Sarnat-Kucharczyk and Wojciech Rokicki
- 999 **Osteosarcoma's genetic landscape painted by genes' mutations**
Wiktoria Urban, Dagmara Krzystańska, Michał Piekarczyk, Jerzy Nazar and Anna Jankowska
- 1007 **MiRNA-19b-3p downregulates the endothelin B receptor in gastric cancer cells to prevent angiogenesis and proliferation**
Xiaodong Hu, Hongbing Liu and Chaoyu Li
- 1015 **Determination of modified nucleosides in the urine of children with autism spectrum disorder**
Joško Osredkar, Kristina Kumer, Teja Fabjan, Maja Jekovec Vrhovšek, Jerneja Maček, Mojca Zupan, Barbara Bobrowska-Korczak, Paulina Gątarek, Angelina Rosiak, Joanna Giebuttowicz, Geir Bjørklund, Salvatore Chirumbolo and Joanna Kałużna-Czaplińska
- 1023 **Clinical efficacy of different androgen deprivation therapies for prostate cancer and evaluation based on dynamic-contrast enhanced magnetic resonance imaging**
WenXiao Guo and MengZhu Li

- 1031 Competitive binding of circCCDC6 to microRNA-128-3p activates TXNIP/NLRP3 pathway and promotes cerebral ischemia-reperfusion defects**
ChongShu Wang, MingMing Dong, XiaoYi Zhang, XiaoYu Wang, Yan Zhao and Yunpeng Cao
- 1040 Pheochromocytoma and paraganglioma in children and adolescents**
Teresa Stachowicz-Stencel, Natalia Pasikowska and Anna Synakiewicz
- 1047 Nephro-oncology: clinical and biochemical aspects of kidney disease and cancer**
Sławomir Lizakowski, Alicja Dębska-Ślizień, Ilona Kurnatowska, Maciej J. Zaucha, Marcin Matuszewski, Beata Naumnik, Marcin Adamczak, Jerzy Chudek, Magdalena Durlak, Carla Ferrándiz-Pulido, Bartosz Foroniewicz, Ryszard Gellert, Magdalena Krajewska, Michał Nowicki, Andrzej Więcek and Jolanta Małyszko
- 1062 Knockdown of CD44 inhibits proliferation, migration, and invasiveness in hepatocellular carcinoma cells by modulating CXCR4/Wnt/ β -Catenin Axis**
Xiaojing Song, Fanghui Ding, Wei Luo, Juan Tao, Kaili Yang, Qiaoping Li and Zhitao Zhang
- 1068 MicroRNA-411-3p motivates methotrexate's cellular uptake and cytotoxicity via targeting Yin-yang 1 in leukemia cells**
HuiJing Sun, ShuGuang Zhou, ZhouSheng Yang, MingYu Meng, Yan Dai, XinYe Li and XiaoYu Chen
- 1075 Molecular and biochemical mechanisms of diabetic encephalopathy**
Igor Belenichev, Olena Aliyeva, Olena Popazova and Nina Bukhtiyarova
- 1085 Silencing lncRNA EZR-AS1 induces apoptosis and attenuates the malignant properties of lung adenocarcinoma cells**
Xianjing Yu, Lixue Wu, Zhongcui Lu, Junli Zhang and Yunfeng Zhou
- 1092 Could the lake ecosystems influence the pathogenicity of the SARS-COV-2 in the air?**
Janusz Boratyński

Plant Biochemistry

- 1100 Assessing the pharmacological and biochemical effects of *Salvia hispanica* (Chia seed) against oxidized *Helianthus annuus* (sunflower) oil in selected animals**
Tariq Aziz, Fawad Ihsan, Ayaz Ali Khan, Shafiq ur Rahman, Ghazala Yasmin Zamani, Metab Alharbi, Abdulrahman Alshammari and Abdullah F. Alasmari

- 1108 Characterization and gastroprotective effects of *Rosa brunonii* Lindl. fruit on gastric mucosal injury in experimental rats – A preliminary study**

Ejaz Ahmad, Muhammad Jahangir, Zahid Mahmood Akhtar, Tariq Aziz, Metab Alharbi, Abdulrahman Alsahammari, Abdullah F. Alasmari and Nadeem Irfan Bukhari
- 1117 Molecular cloning of glutathione reductase from *Oryza sativa*, demonstrating its peroxisomal localization and upregulation by abiotic stresses**

Pamela Chanda Roy and Gopal Chowdhary
- 1124 Evaluating the influence of *Aloe barbadensis* extracts on edema induced changes in C-reactive protein and interleukin-6 in albino rats through *in vivo* and *in silico* approaches**

Benish Rauf, Sobia Alyas, Nureen Zahra, Sohail Ahmad, Abid Sarwar, Najeeb Ullah, Tariq Aziz, Metab Alharbi, Abdulrahman Alsahammari and Abdullah F. Alasmari
- 1133 Evaluating the *in-vivo* effects of olive oil, soya bean oil, and vitamins against oxidized ghee toxicity**

Khushnuma Saleema, Tariq Aziz, Ayaz Ali Khan, Ali Muhammad, Shafiq ur Rahman, Metab Alharbi, Abdulrahman Alshammari and Abdullah F. Alasmari

The emergence of biological homochirality

Agnieszka Kiliszek and Wojciech Rypniewski✉

Institute of Bioorganic Chemistry, Polish Academy of Sciences, Poznań, Poland

The homochirality of biological molecules is one of the basic mysteries of biogenesis. The predominance of L-amino acids and D-hydrocarbons in living matter stands in contrast to the chemical principle of symmetry between enantiomers. An answer to the puzzle needs to include a plausible explanation of how the natural racemic balance was initially tipped in favor of one enantiomer and how the initial tiny excess was amplified to significant levels. It is also necessary to consider how the imbalance was sustained from returning to a thermodynamic equilibrium. This is a review of the main concepts and observations, followed by a brief discussion.

Keywords: symmetry breaking, parity violation, homochirality, monochirality, biological enantiomers, racemic compounds, conglomerates, kryptoracemate

Received: 07 July, 2023; **revised:** 25 July, 2023; **accepted:** 25 July, 2023; **available on-line:** 07 September, 2023

✉e-mail: wojtekr@ibch.poznan.pl

Abbreviations: CD, circular dichroism; TC, isothermal titration calorimetry; PVED, parity violating energy difference

The processes by which life had arisen from nonliving matter are almost certainly beyond our cognitive horizon, but we can consider the milestone events that needed to occur at the onset of life's evolution. One of them is the selection from the "primordial soup" of the enantiomers that henceforth have determined life on Earth.

The biological predominance of L-amino acids and D-sugars needs to be explained because it stands in contrast to the chemical principle of equivalence between enantiomers (Fig. 1). As a rule, the chemical synthesis of chiral compounds from nonchiral components results in a balanced mixture of enantiomers, known as racemate. This natural balance was evidently broken in the early days of life's evolution on Earth, resulting in the observed homochirality of biological molecules. By an unknown mechanism, one enantiomer outweighed its symmetric counterpart and then the initial imbalance was somehow enhanced, leading to the near exclusion of the other enantiomer. The predominance of L-amino acids and D-sugars is found in all known life forms, indicating that the initial enantioselectivity and the following enantioenhancement must have occurred at the earliest stages of life's evolution.

Several models have been proposed of how the chemical symmetry was broken. They use physical factors, both internal and external to the molecules, probabilistic effects that could break the symmetry and chemical processes that could drive chiral resolution.

The purpose of this paper is to survey only the main concepts and observations concerning enantioselectivity,

and to consider how any emerging imbalance could be sustained from returning to thermodynamic equilibrium.

Deterministic models rely on symmetry-breaking forces in nature. The natural place to look for the origin of chiral bias is the very fabric of nature, which is known to contain a chiral component. One of the fundamental forces, the weak interactions, violate parity-symmetry (Wu *et al.*, 1957). Weak interactions occur in the atomic nuclei, but their effect permeates the electronic structure, modifying its wave function and energy. Being chiral, the weak interactions should stabilize one enantiomer and destabilize the other (Fig. 2). This can possibly be detected, but there are no conclusive observations of such an effect (Avalos *et al.*, 2000). Initial theoretical calculations yielded energies of approximately 10^{-14} J/mol for simple amino acids or sugars (Tranter, 1985; Tranter, 1987; Mason & Tranter, 1985). Subsequent calculations on simple molecules indicated that the effect could be as high as 10^{-11} J/mol (Quack, 2002). This is taken as a free energy difference and corresponds to an excess of 10^6 – 10^9 molecules of one enantiomer in a mole of the racemic mixture, correlating to one molecule in $\sim 10^{15}$ – 10^{18} (Ava-

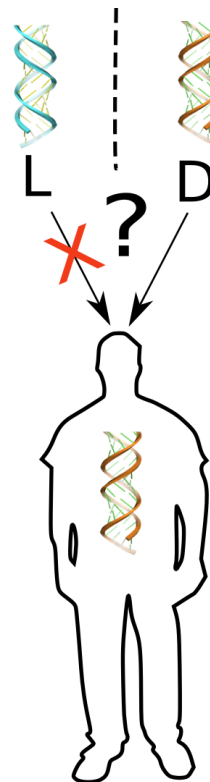


Figure 1. Biological molecules have distinct chirality. Nucleic acids and carbohydrates (sugars) have the D-configuration, while proteins have the L-configuration.

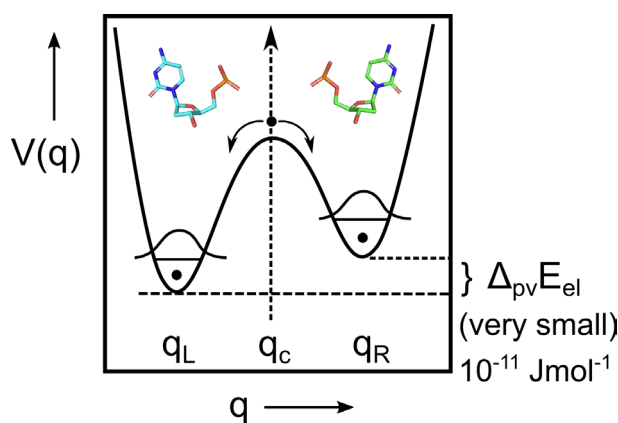


Figure 2. Parity violating weak interactions break the mirror symmetry in nature.

This is effectively demonstrated in particle physics but their effect on the stability of small chiral molecules has only been estimated. The electronic potential profile for enantiomers is not symmetric but the predicted value of the parity violating energy difference (PVED, $\Delta_{pv}E_{el}$) is very small, amounting to 10^{-11} J mol $^{-1}$.

los *et al.*, 2000). These amounts are orders of magnitude below the statistical noise level; the Poisson noise is 8×10^{11} molecules per mole (Quack, 2012). To claim that the weak forces are responsible for life's homochirality one would need to propose a mechanism *via* which this tiny difference could be amplified to give the observed imbalance in life forms.

If the inner chirality of atoms is insufficiently chiroselective, one might look for external chiral factors that could shift the balance between enantiomers in the “primordial soup”. Circularly polarized photons or spin-polarized cosmic particles have been considered, especially those produced as a result of parity-breaking weak interactions (Lee & Yang, 1956). Particles whose electric vector spirals (clockwise or counterclockwise) along their direction of motion are chiral in the same sense that screws are right- or left-handed, and when they interact with matter, they are absorbed differently by different enantiomers. It was proposed that photons resulting from β -decay should be circularly polarized and could have a stereoselective effect on organic matter (Vester *et al.*, 1959). A number of experiments were performed to verify the Vester-Ulbricht hypothesis, leading to the conclusion that this was not an effective mechanism for creating a chiral imbalance. This was reviewed in (Bonner, 2000).

To conclude, the parity-breaking weak interactions would be the best natural candidate to explain the non-parity of biological molecules, were it not for the very large energy gap between the parity violating energy difference (PVED) and the energy regime of chemical interactions. An extensive perspective on the issue of parity violation in chiral molecules and its possible role in the emergence of biological homochirality was published recently (Quack *et al.*, 2022).

Probabilistic models rely on chance events. To explain the observed homochirality of biological molecules, the models require two components: an initial breaking of the balance between enantiomers (enantioselectivity), followed by an amplification of the initial imbalance (enantioenrichment). In this scenario, the initial imbalance stems from random fluctuations at the molecular level, followed by amplification *via* asymmetric autocatalysis in which a chiral molecule assists its self-production (Mislow, 2003). Such autocatalytic reactions have been inves-

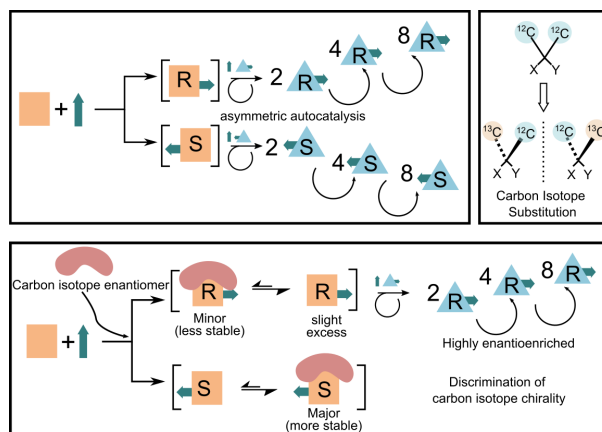


Figure 3. Scheme illustrating an autocatalytic reaction, with an “isotope enantiomer” stimulating the production of one enantiomer and inhibiting the other.

tigated by Soai and coworkers (Soai *et al.*, 1995; Soai *et al.*, 1999). Once set in motion, these self-propelling reactions could amplify a small initial imbalance between the enantiomers. One scenario that was considered involved “isotope chirality”, as the source of the initial imbalance. Isotope chirality is a result of ^{13}C substituting a ^{12}C atom in otherwise achiral organic compounds (Kawasaki *et al.*, 2009). The authors demonstrated that the presence of an isotope bestowed sufficient chirality on an achiral compound to set off enantioenrichment in an autocatalytic mechanism (Fig. 3). The question remains how to achieve the necessary initial imbalance between the “isotope enantiomers”, even a tiny one, that could then be amplified. The isotope substitution in a molecule appears to be random and therefore expected to result in a 1:1 racemic mixture.

The Soai autocatalytic reaction, using an isotopically ($^{13}\text{C}/^{12}\text{C}$) chiral molecule as the initiator, was recently used to estimate the amount of energy needed to trigger enantioselectivity (Hawbaker & Blackmond, 2019). Multiple runs of the reaction were performed at various dilutions of the initiator to assess its threshold concentration sufficient to break the balance between the produced enantiomers. The threshold enantiomeric excess for the initiator was estimated to be between 1 and 0.1% of the initiator molecule. The authors then turned to stochastic simulations to estimate the amount of energy required to break the balance between the enantiomers under autocatalytic conditions and they obtained values between 1.5×10^{-7} and 1.5×10^{-8} kJ mol $^{-1}$. This energy is five to seven orders of magnitude larger than the current estimates of PVED quoted in the previous section (Quack, 2002), confirming that the weak forces were unlikely to be the cause of biological homochirality. On the other hand, this symmetry-breaking energy threshold also is unlikely to be achieved by chance in the stochastic scenario. Thus, the probabilistic models also have a problem with delivering the necessary initial imbalance which could then be amplified *via* an autocatalytic chain reaction. Stochastic events tend to balance out, and if, by chance, an imbalance between enantiomers arises at some place, it is likely, that a compensating imbalance arises somewhere else. To circumvent this, the size of the “pool of the primordial soup” could be reduced, and then the number of possibilities would be reduced. Therefore, a fluctuation would have a better chance of not being canceled out by another fluctuation in the opposite direction. However, reducing the size of the pool

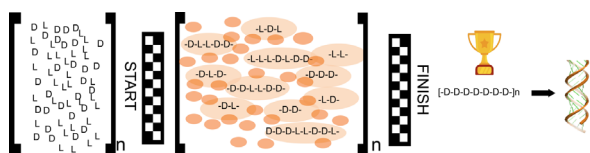


Figure 4. Chiroselective self-assembly leading to independently evolving “libraries” of polymers having different chiralities. As the populations evolve, they begin to differ. Eventually, homochiral “winner sequences” emerge from one of the libraries.

also reduces the chance of a significant fluctuation occurring in the first place.

Another approach to breaking the symmetry of the primordial racemic soup relies on the “chiroselective self-assembly” of nucleobase sequences. In this model, the chiral templates facilitate the synthesis of more oligomers of the same chirality. In time, the L- and D-libraries grow and evolve independently. Eventually, they diverge because the number of possibilities is greater than what is able to be obtained in the limited pool of resources. Eventually, “winner sequences” emerge in one of the libraries, having no symmetric equivalents in the other library (Fig. 4). Thus, homochiral seeds of biological molecules could arise (Bolli *et al.*, 1997).

CRYSTAL-BASED MODELS

Some of the proposed models for enantioselectivity and enhancement rely on crystallization. Crystals begin as seeds consisting of a small number of molecules and grow as regular lattices, often reaching macroscopic dimensions. Thus, crystallization can be considered a means to amplify interactions occurring at the molecular

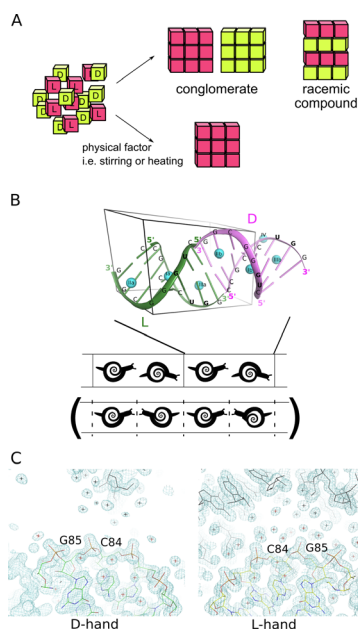


Figure 5. (A) When crystals grow from a solution of a racemate, they can be either racemic compounds (containing both enantiomers) or conglomerates (enantiomers form separate crystals). In specific cases, conglomerates can be nudged to homochirality by a physical factor (see text). (B) In racemic compounds, the enantiomers sometimes pack asymmetrically, which means that they can differ significantly in their structures and lattice contacts in the crystal (see Kiliszek *et al.*, 2021). (C) Section of electron density (blue contours) of the crystal structure reported by Kiliszek and others (Kiliszek *et al.*, 2021), showing asymmetry between the L- and D-RNA oligomers, with major differences in their interactions with the solvent and crystal lattice contacts.

level up to the macroscopic scale. Due to its amplifying effect, crystallization is analogous to autocatalysis.

A racemate can crystallize in two different ways, forming either separate crystals of L- and D-enantiomers (“conglomerates”) or crystals containing both enantiomers (“racemic compounds”) (Fig. 5A). In themselves, these crystals do not change the enantiomeric balance, but some mixtures of conglomerates can be nudged to homochirality by a physical factor, such as stirring or heating. This is possible under specific conditions. One condition is that the compound remaining in the liquid phase can undergo racemization, which enables the shifting of the balance between the L- and D-crystals (Kondepudi *et al.*, 1990). Another possibility exists for nonchiral molecules that can form chiral conglomerates (Viedma, 2005).

With racemic compounds, the main concept is that crystallization removes equal amounts of L- and D-molecules from the solution. Therefore, any initial imbalance in the quantities of the enantiomers is enhanced in the liquid phase (Klussmann *et al.*, 2006; Breslow & Levine, 2006). For this model to work, a preexisting imbalance, however small, is needed.

EXPERIMENTAL REPORTS

A number of research papers have been published that report on observations considered to be significant deviations from parity, with implications for the origin of biological homochirality. In a study published in 1999, crystals were grown from racemic solutions of sodium ammonium tartrate as well as chiral complexes of cobalt and iridium (Szabó-Nagy & Keszthelyi, 1999). The crystals were collected, dissolved and the optical activity of the resulting solution was analyzed, showing a chiral balance in the tartrate but an imbalance in the heavy metal compounds. This result indicated that from the balanced enantiomeric mixtures of the Ir and Co compounds, one enantiomer crystallized more easily than the other. This was interpreted as a sign of the parity-violating weak forces biasing the intermolecular interactions. The authors stated that “there is hope of detecting parity-violating energy difference in crystallization because macroscopic crystals consist of a large number of molecules”. Further statistical analysis showed that the asymmetry of the Ir data was significant, while the effect for Co was inconclusive; thus, it could not be ruled out that the observed effect was due to other factors (Avalos *et al.*, 2000).

A paper from 2006 describes a study of L- and D-polypeptides in solution by means of circular dichroism (CD) and isothermal titration calorimetry (ITC) (Scolnik *et al.*, 2006). Subtle differences in the helix-coil transition energies of the different enantiomers were reported. The authors argued that the tiny effect of parity-violating interactions could be amplified in the cooperative process of helix formation. They also proposed that the *ortho* spin isomers of H₂O, having a magnetic field, could have a preference for interacting with the L-polypeptides due to their magnetic component induced by the weak forces. A related work from the same research group reported differences in solubility between L- and D-tyrosine, discerned by their rate of crystallization (Shinitzky *et al.*, 2002; Deamer *et al.*, 2007). The authors suggested this was due to the energy differences originating from parity violation. This was challenged by (Goldberg, 2008), who, having performed a series of crystallization experiments, concluded that the difference “is the result of a diastere-

omeric interaction between an airborne, non-racemic, chiral influence – probably a fungal spore – and the tyrosine enantiomers, enhancing the degree of crystal nucleation of D-tyrosine over L-tyrosine”. Another critique came from (Lahav *et al.*, 2006), who repeated the crystallization experiments in their lab and observed that “samples provided by Shinitzky indeed displayed the effect he reported in his article, however, their results could not be repeated with samples obtained from other sources”; thus they concluded that the observed bias was most likely caused by impurities in the samples. In response to this, the Shinitzky group published “Comments in a Discussion”, in which they acknowledged impurities as a major problem in their experiments aimed at pinpointing a very small effect (Shinitzky & Deamer, 2008). They concluded that it would be easier to look for any parity violating effects “in bulk phases, rather than in dynamic processes such as crystallization” and referenced papers reporting a Raman spectroscopic study of L- and D-RNA oligomers in solution (Bolik *et al.*, 2007) and a CD study of L- and D-polyglutamate undergoing temperature-dependent helix-coil transitions (Kodona *et al.*, 2008). The authors of both of these papers attributed the observed differences to parity-violating weak interactions.

A more recent report describes a study of crystalline D-alanine by means of Raman scattering and neutron powder diffraction (Belo *et al.*, 2018a). The authors claimed to have observed significant differences in the hydrogen bonding in comparison with L-alanine. Their results were challenged by (Bürgi & Macchi, 2018) who raised a number of methodological objections and then stated that “the conclusions drawn by Belo *et al.* are deemed inappropriate as the data presented do not contain sufficient information to reach such a conclusion”. They added that the same objections also applied to the Raman spectroscopic study (see the paragraph above) of RNA oligomers (Bolik *et al.*, 2007). In response, Belo and others (Belo *et al.*, 2018b) denied that they had drawn any conclusions concerning the parity-violating energy difference in their original paper and added that “properties of L- and D-alanine, and the L- and D-amino acids in general, are a fascinating and important area of study for our understanding of nature, irrespective of whether they are related, or not, to the weak nuclear force and parity violation.”

A recent paper reported a crystal structure with clear differences between the L- and D-enantiomers of an RNA oligomer (Kiliszek *et al.*, 2021). The enantiomers assembled in the crystal in an asymmetric manner (Fig. 5B), made different lattice contacts and had different exposures to the water and metal ions present in the crystal (Fig. 5C). Crystals in which enantiomers are not constrained by crystallographic symmetry are known as kryptoracemates; these have been observed in small-molecule crystallography and represent *circa* 1% of structures in which enantiomers are cocrystallized (Clevens & Coquerel, 2020). These crystals could be relevant to the issue of biological enantioselectivity/deracemization because enantiomers exposed to different environments should have different stabilities. Consequently, different amounts of L- and D-molecules will remain after a certain time. Two types of such RNA-containing kryptoracemates were obtained, being mirror images of each other; therefore, in large volumes, their effects on the balance between the enantiomers should average out. However, in small volumes, with a small number of crystals, or perhaps just one crystal, the chances of a significant imbalance developing between enantiomers are greatly increased. The authors noted that this model

required no initial imbalance between the enantiomers, as both enantioselection and enantioenrichment were included in the model; the crystal lattice provided a stable asymmetric environment for the enantiomers, while crystal growth amplified the effect up to the macroscopic scale.

Another recent paper describes the crystallization of ribo-aminooxazoline, an RNA precursor, on uniformly magnetized surfaces, demonstrating a significant enantioselective effect under some conditions (Ozturk *et al.*, 2023). The authors discuss possible scenarios of enantioenrichment occurring on the surface of magnetized sedimentary rocks on the prebiotic Earth. Small magnetite particles can sediment uniformly even in the Earth’s weak magnetic field.

DISCUSSION

The formative events that defined life’s basic characteristics, including the chirality of biological molecules, are shrouded in the distant past. We may never know exactly how life developed on Earth, but we can make informed retrospective speculations based on our knowledge of life’s present form and the knowledge of universal mechanisms that govern life’s processes. The natural candidate for tipping the balance of a racemic “primordial soup” toward homochirality would be the chiral weak force, but it appears that the energy it imparts on molecules is orders of magnitude less than what is needed for a significant effect on chemical processes. Chance fluctuations have larger amplitudes locally but tend to average out over space and time. We simply do not know an enantioselective process that would deliver a significant effect. Therefore, we need a massive amplification mechanism to turn any slight, innate or transient imbalance into a dominant form. One possibility is an autocatalytic process or rather some yet unknown “series of persistent chemical and physical processes that act synergistically and stepwise” (Hawbaker & Blackmond, 2019). The other possible means of “enantioenrichment” is crystallization. Two models contain both of the required steps of enantioselection and enantioenrichment: the evolutionary model of template-based “chiroselective self-assembly” (Bolli *et al.*, 1997) and the model based on the crystallization of kryptoracemates (Kiliszek *et al.*, 2021).

The deterministic and probabilistic models are different in nature but share a common aspect: both operate on an infinitesimal scale, meaning that the probability of a significant outcome of their action is also low. Chiral resolution (enantioselection) was an unlikely event. After the racemic balance was tipped, the initial small excess of one of the enantiomers was expanded (enantioenrichment) by one of the proposed mechanisms or by some other mechanism that remains unknown. Notably, however, such an expansion, even if significant, is still insufficient to explain the persistence of the enantiomeric imbalance over time. A lasting imbalance needs a mechanism to support it. Otherwise, the system will spontaneously return to thermodynamic equilibrium, while entropy is maximized. For instance, we can envision a scenario in which a minute initial excess of one enantiomer is greatly expanded by some autocatalytic mechanism. A significant imbalance appears, but there is no reason why a corresponding autocatalytic reaction should not also occur for the other enantiomer. At best, we can get a head start in multiplying one enantiomer before the symmetric process undermines the imbalance. The

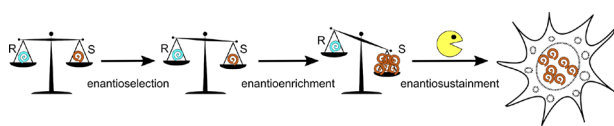


Figure 6. Result of enantioselection and enantioenrichment has to be sustained from returning to a thermodynamic equilibrium. Living organisms are well suited for maintaining a nonequilibrium thermodynamic state. It is probable that an enantioenriched solution evolved in or was engulfed by a primordial living organism or some other dissipative thermodynamic system, and thus it was stabilized.

likely result is the reestablishment of an equilibrium. To maintain an imbalance, a cascade of processes, such as the autocatalytic reaction is needed, and this is even less likely to occur than a single such event. An alternative way to maintain a thermodynamically unfavored state is to establish a lasting nonequilibrium thermodynamic system with a continuous flow of energy and matter. Life is such a system. Therefore, it is possible that the enantioselection and enantioenrichment were closely knit with the emergence of early life in which the imbalance was promptly embedded and has been sustained ever since (Fig. 6).

REFERENCES

- Avalos M, Babiano R, Cintas P, Jiménez JL, Palacios JC (2000) From parity to chirality: chemical implications revisited. *Tetrahedron: Asymmetry* **11**: 2845–2874. [https://doi.org/10.1016/S0957-4166\(00\)00265-2](https://doi.org/10.1016/S0957-4166(00)00265-2)
- Belo EA, Pereira JEM, Freire PTC, Argyriou DN, Eckert J, Bordallo HN (2018a) Hydrogen bonds in crystalline D-alanine: diffraction and spectroscopic evidence for differences between enantiomers. *IUCr* **5**: 6–12. <https://doi.org/10.1107/S2052252517015573>
- Belo EA, Pereira JEM, Freire PTC, Argyriou DN, Eckert J, Bordallo HN (2018b) Response to comment on ‘Hydrogen bonds in crystalline D-alanine: diffraction and spectroscopic evidence for differences between enantiomers’. *IUCr* **5**: 658–659. <https://doi.org/10.1107/S2052252518010321>
- Bolik S, Ru'bhausen M, Ru'bhausen R, Binder S, Schulz B, Perbandt M, Genov N, Erdmann V, Klusmann S, Betzel C (2007) First experimental evidence for the preferential stabilization of the natural D-over the nonnatural L-configuration in nucleic acids. *RNA* **13**: 1877–1880. <https://doi.org/10.1261/rna.564507>
- Bolli M, Micura R, Eschenmoser A (1997) Pyranosyl-RNA: chiroselective self-assembly of base sequences by ligative oligomerization of tetranucleotide-2',3'-cyclophosphates (with a commentary concerning the origin of biomolecular homochirality). *Chem Biol* **4**: 309–320. [https://doi.org/10.1016/S1074-5521\(97\)90074-0](https://doi.org/10.1016/S1074-5521(97)90074-0)
- Bonner WA (2000) Parity Violation and the Evolution of biomolecular homochirality. *Chirality* **12**: 114–126. [https://doi.org/10.1002/\(SICI\)1520-636X\(200012\)12:3<114::AID-CHIR3>3.0.CO;2-N](https://doi.org/10.1002/(SICI)1520-636X(200012)12:3<114::AID-CHIR3>3.0.CO;2-N)
- Breslow R, Levine MS (2006) Amplification of enantiomeric concentrations under credible prebiotic conditions. *Proc Natl Acad Sci U S A* **103**: 12979–12980. <https://doi.org/10.1073/PNAS.0605863103>
- Bürgi H-B, Macchi P (2018) Comments on ‘Hydrogen bonds in crystalline d-alanine: diffraction and spectroscopic evidence for differences between enantiomers’. *IUCr* **5**: 654–657. <https://doi.org/10.1107/S2052252518007406>
- Clevers S, Coquerel G (2020) Kryptoracemic compound hunting and frequency in the Cambridge Structural Database. *Cryst Eng Commun* **22**: 7407–7419. <https://doi.org/10.1039/D0CE00303D>
- Deamer DW, Dick R, Thiemann W, Shinitzky M (2007) Intrinsic asymmetries of amino acid enantiomers and their peptides: a possible role in the origin of biochirality. *Chirality* **19**: 751–763. <https://doi.org/10.1002/CHIR.20434>
- Goldberg SI (2008) Experimental evidence leading to an alternative explanation of why D-tyrosine sometimes crystallizes faster than its L-enantiomer. *Orig Life Evol Biosph* **38**: 149–153. <https://doi.org/10.1007/S11084-008-9123-8>
- Hawbaker NA, Blackmond DG (2019) Energy threshold for chiral symmetry breaking in molecular self-replication. *Nat Chem* **11**: 957–962. <https://doi.org/10.1038/S41557-019-0321-Y>
- Kawasaki T, Matsumura Y, Tsutsumi T, Suzuki K, Ito M, Soai K (2009) Asymmetric autocatalysis triggered by carbon isotope ($^{13}\text{C}/^{12}\text{C}$) chirality. *Science* **324**: 492–495. <https://doi.org/10.1126/SCIENCE.1170322>
- Kiliszek A, Błaszczak L, Bejger M, Rypniewski W (2021) Broken symmetry between RNA enantiomers in a crystal lattice. *Nucleic Acids Res* **49**: 12535–12539. <https://doi.org/10.1093/NAR/GKAB480>
- Kluschmann M, Iwamura H, Mathew SP, Wells DH, Pandya U, Armstrong A, Blackmond DG (2006) Thermodynamic control of asymmetric amplification in amino acid catalysis. *Nature* **441**: 621–623. <https://doi.org/10.1038/NATURE04780>
- Kodona EK, Alexopoulos C, Panou-Pomonis E, Pomonis PJ (2008) Chirality and helix stability of polyglutamic acid enantiomers. *J Colloid Interface Sci* **319**: 72–80. <https://doi.org/10.1016/J.JCIS.2007.10.063>
- Kondepudi DK, Kaufman RJ, Singh N (1990) Chiral symmetry breaking in sodium chlorate crystallization. *Science* **250**: 975–976. <https://doi.org/10.1126/SCIENCE.250.4983.975>
- Lahav M, Weissbuch I, Shavit E, Reiner C, Nicholson GJ, Schurig V (2006) Parity violating energetic difference and enantiomorphous crystals-caveats; reinvestigation of tyrosine crystallization. *Orig Life Evol Biosph* **36**: 151–170. <https://doi.org/10.1007/S11084-005-9000-7>
- Lee TD, Yang CN (1956) Question of parity conservation in weak interactions. *Phys Rev* **104**: 254–258. <https://doi.org/10.1103/PHYSREV.104.254>
- Mason SF, Tranter GE (1985) The electroweak origin of biomolecular handedness. *Proc R Soc Lond A* **397**: 45–65. <https://doi.org/10.1098/rspa.1985.0003>
- Mislow K (2003) Absolute asymmetric synthesis: a commentary. *Collect Czechoslov Chem Commun* **68**: 849–864. <https://doi.org/10.1135/CCCC20030849>
- Ozturk SF, Liu Z, Sutherland JD, Sasselov DD (2023) Origin of biological homochirality by crystallization of an RNA precursor on a magnetic surface. *Sci Adv* **9**: <https://doi.org/10.1126/SCIADV.ADG8274>
- Quack M (2002) How important is parity violation for molecular and biomolecular chirality? *Angew Chemie Int Ed* **41**: 4618–4630. <https://doi.org/10.1002/ANIE.200290005>
- Quack M (2012) Molecular parity violation and chirality: the asymmetry of life and the symmetry violations in physics. *Quantum Systems Chem Physics: Prog Methods Appl* **47**–76. https://doi.org/10.1007/978-94-007-5297-9_3
- Quack M, Seyfang G, Wichmann G (2022) Perspectives on parity violation in chiral molecules: theory, spectroscopic experiment and biomolecular homochirality. *Chem Sci* **13**: 10598–10643. <https://doi.org/10.1039/D2SC01323A>
- Scolnik Y, Portnaya I, Cogan U, Tal S, Haimovitz R, Fridkin M, Elitzur AC, Deamer DW, Shinitzky M (2006) Subtle differences in structural transitions between poly-L- and poly-D-amino acids of equal length in water. *Phys Chem Chem Phys* **8**: 333–339. <https://doi.org/10.1039/B513974K>
- Shinitzky M, Nudelman F, Barda Y, Haimovitz R, Chen E, Deamer DW (2002) Unexpected differences between D- and L-tyrosine lead to chiral enhancement in racemic mixtures. *Orig Life Evol Biosph* **32**: 285–297. <https://doi.org/10.1023/A:1020535415283>
- Shinitzky M, Deamer D (2008) Comments in a discussion: Differential rates of D- and L-tyrosine crystallization. *Orig Life Evol Biosph* **38**: 271–275. <https://doi.org/10.1007/S11084-008-9129-2>
- Soai K, Shibata T, Morioka H, Choji K (1995) Asymmetric autocatalysis and amplification of enantiomeric excess of a chiral molecule. *Nature* **378**: 767–768. <https://doi.org/10.1038/378767a0>
- Soai K, Osanai S, Kadowaki K, Yonekubo S, Shibata T, Sato I (1999) D- and L-Quartz-promoted highly enantioselective synthesis of a chiral organic compound. *J Am Chem Soc* **121**: 11235–11236. <https://doi.org/10.1021/JA993128T>
- Szabó-Nagy A, Keszthelyi L (1999) Demonstration of the parity-violating energy difference between enantiomers. *Proc Natl Acad Sci U S A* **96**: 4252–4255. <https://doi.org/10.1073/PNAS.96.8.4252>
- Tranter GE (1985) The parity-violating energy differences between the enantiomers of α -amino acids. *Chem Phys Lett* **120**: 93–96. [https://doi.org/10.1016/0009-2614\(85\)87019-6](https://doi.org/10.1016/0009-2614(85)87019-6)
- Tranter GE (1987) The enantio-preferential stabilization of D-ribose from parity violation. *Chem Phys Lett* **135**: 279–282. [https://doi.org/10.1016/0009-2614\(87\)85156-4](https://doi.org/10.1016/0009-2614(87)85156-4)
- Vester F, Ulbricht TLV, Krauch H (1959) Optische Aktivität und die Paritätsverletzung im β -Zerfall. *Naturwissenschaften* **46**: 68–68. <https://doi.org/10.1007/BF00599091>
- Viedma C (2005) Chiral symmetry breaking during crystallization: Complete chiral purity induced by nonlinear autocatalysis and recycling. *Phys Rev Lett* **94**: 065504. <https://doi.org/10.1103/PHYSREVLETT.94.065504>
- Wu CS, Ambler E, Hayward RW, Hoppe DD, Hudson RP (1957) Experimental test of parity conservation in beta decay. *Phys Rev* **105**: 1413–1415. <https://doi.org/10.1103/PHYSREV.105.1413>

Were academic promotions in biochemistry and other research disciplines improperly controlled in Poland between 2011 and 2020?

A response to the recently published “Who controls the national academic promotion system” article

Grzegorz Węgrzyn^{1,2}✉

¹Research Excellence Council, pl. Defilad 1, Warsaw, Poland; ²Department of Molecular Biology, University of Gdansk, Gdańsk, Poland

In the recently published article by Koza *et al.* (SAGE Open, 2023, 13, doi: 10.1177/21582440231177974), the authors analyzed the academic promotion system in Poland between 2011 and 2020. They concluded that “the Polish system of academic promotions in the past decade can hardly be regarded as based on pure merit”, suggesting the impropriety, based on the participation of the members of the Central Board for Degrees and Titles in panels of experts evaluating the applications. Biochemistry was provided as a research discipline in which such an “impropriety” was the most pronounced, though other disciplines were only slightly less “improperly affected”. Although the calculations presented by Koza and others (Koza *et al.*, 2023) were proper, their conclusions were affected by fundamental errors in assessing the roles of the panelists and misinterpretation of the data. The drawbacks of the interpretations of the facts and in drawing conclusions are presented and discussed in this paper, underlining the necessity of being very careful when assessing any phenomenon and concluding about any mechanism. Indeed, only very well substantiated conclusions, strongly supported by objective data, should be published. This rule is very well known in biochemistry and other exact and natural sciences, and should be mandatory in all other research disciplines.

Keywords: academic promotions, biochemistry, Poland

Received: 06 June, 2023; **accepted:** 06 June, 2023; **available on-line:** 06 June, 2023

✉e-mail: grzegorz.wegrzyn@ug.edu.pl

INTRODUCTION: THE ANALYSIS OF THE ACADEMIC PROMOTION SYSTEM IN POLAND, PERFORMED BY KOZA ET AL. (2023)

There are various systems of academic promotion operating in different countries. Their analyses might show interesting processes, and could indicate strengths and weaknesses of such systems which then could be improved.

The academic promotion system, used in Poland between 2011 and 2020, was recently analyzed by Koza and others (Koza *et al.*, 2023). The authors presented the system, based on two degrees, PhD and habilitation, and the title of professor. During the analyzed period of time, the procedures of academic promotions were over-

seen by the central (national) body called Central Board for Degrees and Titles (henceforth Central Board). In habilitation procedures, the crucial role was played by the habilitation panel, composed of the president, secretary, three reviewers, and two ordinary members. In the procedures of processing the professorship applications, the Central Board indicated five reviewers.

The analysis of the members of habilitation panels and reviewers of the professorship applications, led Koza and others (Koza *et al.*, 2023) to the conclusion that “the Polish system of academic promotions in the past decade can hardly be regarded as based on pure merit”. In their opinion, members of the Central Board were too often members of habilitation panels, and thus they “controlled a substantial majority of academic promotions beyond the PhD degree”. They also stated that they “found that this relatively small group of academics held dominant control over academic promotions by repeatedly serving on promotion panels”. The analyses presented in their article indicated that biochemistry was one of the most “affected” research disciplines, and the members of the Central Board were present in 100% habilitation panels, mostly as presidents of these panels (Supplementary Table S3 in Koza *et al.*, 2023). Nevertheless, a similar tendency was observed in most other disciplines (Koza *et al.*, 2023).

The above-mentioned conclusions might indicate that the Polish academic promotion system “is appropriated by the so-called old boys”, and that there are mechanisms “used to distribute power and prestige among those old boys”. Such conclusions are strong, but the question is whether they are substantiated. Unfortunately, the analysis of the work by Koza and others (Koza *et al.*, 2023) indicated that the authors made several fundamental errors in interpretation of the data and even in describing the system which severely influenced their conclusions, making them unsubstantiated. Below, I will present the most important errors showing the crucial problems with the above-mentioned conclusions. I suppose that as a former member of the Central Board (abbreviated by Koza and others (Koza *et al.*, 2023) as ‘CK’) and current President of the Research Excellence Council (the successor of the Central Board), I have a sufficient knowledge about the system of academic promotion in Poland and I am qualified and commissioned to professionally comment on the work analyzing this system.

MAJOR ERRORS, MISINTERPRETATIONS, AND UNSUBSTANTIATED CONCLUSIONS

Let me describe shortly the major weaknesses and drawbacks of the analyses performed by Koza and others (Koza *et al.*, 2023). First, the authors informed that: “CK members are elected by other senior academics” seemingly overlooking that the members of the Central Board were chosen by other researchers in the procedure of democratic election form all scientists with the title of professor. It should be highlighted that in each research discipline all scientists with the title of professor could cast their votes. Therefore, one should assume that they were recognized as leaders in specific research disciplines, and persons who are able to oversee the academic promotion processes objectively. In other words, they obtained the mandate of trust as scientists who were elected to ensure the correctness of the procedures. Koza and others (Koza *et al.*, 2023) did not mention that this relatively small group of persons was responsible for proposing reviewers for all habilitation and professorship procedures which was an especially hard and responsible task. If so, this may put the members of the Central Board in a different light, in contrast to the statement of Koza and others (Koza *et al.*, 2023) suggesting that they were the group of “old boys”, keeping the strong power in their hands, and acting for their own purposes. In my opinion, this is a totally improper suggestion, presented by Koza and others (Koza *et al.*, 2023). Members of the Central Board had no interest in promoting one researcher and declining application of another apart from ensuring that all requirements for the promotion are fulfilled to guarantee that academic degrees and titles were awarded to researchers having appropriate achievements. In contrast, the “old boys” model should only be valid if the members of such a group had personal interest in making specific decisions.

The errors found in the paper by Koza and others (Koza *et al.*, 2023) include even a wrong description of the habilitation panel (further used as the major model in their analyses). They wrote “Of these seven panel members, three were pre-selected by the degree-granting university: the secretary, one of the referees, and one ordinary member” which is true. However, in the next sentence they stated: “The CK selected the other four: the chair, two referees, and two ordinary members” which is an evident error, as 1 chair, 2 referees, and 2 ordinary members would mean five, not four, members selected by CK. Obviously, this error is not crucial for further analyses, but indicates imprecision and inattention of the authors in performing and describing their work.

The serious erroris, however, a lack of the information that each member of the panel had a single vote, and all these votes were equivalent during the procedure of making the final decision. In other words, after analyzing all the habilitation documents and thorough discussion during the panel meeting, the decision was based on voting of seven members of the panel, and the results dependent solely on the number of voices “for” and “against”, without any “weights of votes”, i.e. the power of each vote was exactly the same. Moreover, written evaluations, presented by reviewers, and oral opinions presented by other members, had to be seriously considered, thus, any single vote could not easily change the opinion of the whole panel. This also indicates another serious oversight of Koza and others (Koza *et al.*, 2023). The voting system determined that each member of the habilitation panel had to carefully analyze all documents submitted by the candidate and evaluate his/her achieve-

ments, irrespective of the formal function played in the panel (president, secretary, reviewer or ordinary member – the only difference was that reviewers were obligated to write formal evaluation reports, whereas other members should present their opinions during the panel meeting).

Koza and others (Koza *et al.*, 2023) strongly criticized the fact that members of the Central Board were often presidents of habilitation panels. In their opinion “This level of concentration of power is made possible by the high degree of centralization in the Polish system of academic promotions, with just a handful of influential players (or, in extreme cases, just a single individual) being in control of academic promotions in a given discipline”. In the light of the procedure described in the preceding paragraph, such a statement does not make sense, as being one of seven (equal) members of the habilitation panel it is not possible to control the academic promotion. The authors wrote “We have shown that being selected to a panel of judges is positively related to membership in a central administrative body”. Yes, this is true, and it was also reflected by the statistical analyses performed by Koza and others (Koza *et al.*, 2023). However, this fact has never been questioned or hidden. In contrast, it was a common decision of the Central Board to select their members as presidents of most of the habilitation panels. However, this was not to “control the academic promotion” in the sense of arbitrary decisions who should be promoted and who not, but to help the panels to properly analyze achievements of the candidates in the light of the obligatory rules and required criteria which should be met. Actually, this is a very responsible job which requires from the president of the panel not only high competence in the specific research discipline but also knowledge about the necessary procedures and specific criteria in the process of awarding the habilitation degree. Therefore, the statement of Koza and others (Koza *et al.*, 2023) that the role of the president of the panel is “least absorbing yet most prestigious (and influential) (...)”, as opposed to that of referee” is totally untrue. In fact, the Research Excellence Council which replaced the Central Board, decided to refrain from nominating its members as presidents in most habilitation panels. However, this resulted in many mistakes in the procedures and serious problems arising from a lack of experience and required knowledge about procedures by some presidents of panels who were not involved in works of the Council or formerly of the Central Board. Simply, some such presidents of panels were high level experts in the specific fields, however, they were not familiar with obligatory criteria and formal rules. In fact, as researchers not formally involved in the administrative procedures of the academic promotions, they were not obliged to know details of such rules during their daily work, contrary to members of the Central Board or the Council. This can be another argument for the importance of the role of the president of the panel and can corroborate the validity of the previous decision of the Central Board.

It is not my role to judge what was the reason of such a false statement described by Koza and others (Koza *et al.*, 2023), misunderstanding of the procedure or a lack of appropriate knowledge on roles of all members of the habilitation panels. Nevertheless, such a level of ignorance gives rise to serious doubts about the quality of any conclusions about the academic promotion system by the authors who either do not know or do not understand the system. The claim about the ignorance of the authors in this point is supported by

their another statement: “The secretary was a crucial role, because, despite being a glorified paper-pusher, it was the secretary’s job to make sure the procedure ran smoothly and conformed with the relevant laws and regulations”. Again, this statement is completely invalid. It is true that the secretary’s role was extremely important, not only because he/she should – like all other members of the panel – analyze and evaluate the candidate’s achievements, but also because of his/her responsibility to prepare all documents, like the protocol from the panel’s meeting and the drafts of the final resolution and its justification. However, “to make sure the procedure ran smoothly and conformed with the relevant laws and regulations” was the job of the president of the panel, not the secretary. Thus, the suggestion of Koza and others (Koza *et al.*, 2023) that the members of the Central Board selected themselves as presidents of habilitation panels to occupy the position which was “least absorbing yet most prestigious (and influential)” is totally false, as actually the president’s role was one of the hardest and most absorbing among the members of the panel. This serious error of Koza and others (Koza *et al.*, 2023) can be corroborated by another statement of these authors: “The easiest jobs were those of the chair and ordinary members, who were just additional voting members of the panel”. As I mentioned above, all members of the panel, including the president (the chair) and ordinary members, were obligated to thoroughly analyze all the documents and especially the achievements of candidates, as their votes were as strong as votes of reviewers. Saying that they “were just additional voting members of the panel” shows such a high level of ignorance of the authors about the system they analyzed that in my opinion they should never attempt to analyze it.

Another ridiculous suggestion found in the text of the article by Koza and others (Koza *et al.*, 2023) is that selecting the members of the Central Board as presidents of habilitation panels “might be related to the financial remuneration received by all panel members”. It is true that all members of the panel received financial compensation for their work (a few hundred Euro per application). However, this was just a remuneration for the extra job which had to be done, and as indicated above, this was neither easy nor quick work. Each member of the panel was obliged to analyze all achievements of the candidate which normally takes at least several hours (or even a few days in the case of a more complex or disputable application), and then a few hours for the panel meeting. Suggesting that there was “money for nothing” or “easy money” is simply absurd.

CONCLUDING REMARKS

The Polish system of academic promotions is neither easy nor perfect. It is obvious that detailed analyses of the procedures are important and can indicate points that should be improved. However, such analyses must be professional and performed with care and deep understanding the problem if one should treat them seriously. In fact, the statistical analyses performed by Koza and others (Koza *et al.*, 2023) using data from academic promotion procedures between 2011 and 2020 in Poland were correctly performed and provided some interesting results. However, the conclusions presented by the authors were highly influenced by serious errors and misinterpretation of the data. The authors ignored significant aspects of these procedures, and presented statements and conclusions which were unsubstantiated and false, at best. Therefore, the academic promotion system should be deeply analyzed but with significantly more care and with consideration of actual rules as well as roles played by researchers involved in the procedures. Biochemistry was indicated by Koza and others (Koza *et al.*, 2023) as a discipline which was the most severely affected by inadequate composition of the habilitation panels, nevertheless similar accusation was indicated for many other disciplines. However, such an incrimination appears unsubstantiated as it apparently arose from errors in data analysis and ignorance of the authors in assessing the roles of habilitation panels and their various members.

Acknowledgements

I am grateful to Ewa Bartnik, Bogusław Buszewski, Marcin Hoffmann, and Zofia Szweykowska-Kulińska for interesting discussions and important suggestions.

REFERENCE

- Koza Z, Lew R, Kulczycki E, Stec P (2023). Who controls the national academic promotion system: an analysis of power distribution in Poland. *SAGE Open* 13 (2). <https://doi.org/10.1177/21582440231177974>.

Secondary structure in polymorphic forms of alpha-synuclein amyloids

Irena Roterman¹✉, Katarzyna Stapor², Dawid Dułak³ and Leszek Konieczny⁴

¹Department of Bioinformatics and Telemedicine, Jagiellonian University, Medical College, Kraków, Poland; ²Department of Applied Informatics Silesian University of Technology, Gliwice, Poland; ³ABB Business Services Sp. z o.o. Warszawa, Poland; ⁴Chair of Medical Biochemistry, Jagiellonian University, Medical College, Kraków, Poland

Numerous Alpha-synuclein amyloid structures available in PDB enable their comparative analysis. They are all characterized by a flat structure of each individual chain with an extensive network of inter-chain hydrogen bonds. The identification of such amyloid fibril structures requires determining the special conditions imposed on the torsion angles. Such conditions have already been formulated by the Authors resulting in the model of idealised amyloid. Here, we investigate the fit of this model in the group of A-Syn amyloid fibrils. We identify and describe the characteristic supersecondary structures in amyloids. Generally, the amyloid transformation is suggested to be the 3D to 2D transformation engaging mostly the loops linking Beta-structural fragments. The loop structure introducing the 3D organisation of Beta-sheet change to flat form (2D) introduces the mutual reorientation of Beta-strands enabling the large-scale H-bonds generation with the water molecules. Based on the model of idealised amyloid we postulate the hypothesis for amyloid fibril formation based on the shaking, an experimental procedure producing the amyloids.

Keywords: secondary structure, hydrogen bonds, amyloids, alpha-synuclein, polymorphism, 3D structure, 2D structure, air-water interphase, alpha-sheet

Received: 08 April, 2023; **revised:** 25 May, 2023; **accepted:** 01 June, 2023; **available on-line:** 18 June, 2023

✉e-mail: myroterm@cyf-kr.edu.pl

Acknowledgements of Financial Support: This research was partially supported by the European Union's Horizon 2020 programme under Sano No 857533 grant, and the Sano project conducted as part of the International Research Agendas programme of the Foundation for Polish Science. Co-financed by the European Union under the European Regional Development Fund. This research was funded by Jagiellonian University Medical College grant number N41/DBS/000722.

Abbreviations: CC-0, correlation coefficient for starting structures; CC-F, correlation coefficient for residues after elimination of outstanding points; CC-β, correlation coefficient solely for β-structural forms; 2D, 3D, 2-dimensional, 3-dimensional; L-helix, left-handed helix; PDB, Protein Data Bank; RD, Relative Distance; R-helical, right-handed helix

INTRODUCTION

Alpha-synuclein (A-Syn) is a protein whose biological role and structural changes, despite advanced research, remain to be identified (Burré *et al.*, 2018). The mutations in A-Syn are considered as risk conditions (Ottolini *et al.*, 2017; Ghosh *et al.*, 2016). A large spectrum of forms of A-Syn in the context of health and disease is discussed in the paper of Lashuel and others (Lashuel *et al.*, 2013). Post-translational modifications identified in neurodegeneration in patients with Parkinson's disease concern

the aggregation propensity of A-Syn (Beyer 2006). A significant contribution of chaperones in the process of A-Syn amyloid transformation is presented in the paper of Burmann (Burmann *et al.*, 2020). There is also a certain degree of synergy between amyloid proteins, including A-Syn and Tau, especially concerning liquid-liquid phase separation (Guiney *et al.*, 2020; McDowall *et al.*, 2016). Difficulties in designing therapy arise from the complexity of the amyloid formation mechanism (Dehay *et al.*, 2015; Sivanesam & Andersen 2016). Despite the failure to recognize the amyloid transformation mechanism, analyses of the relationship between structure, function and toxicity are being conducted, focusing on the pathogenesis mechanisms of the synucleopathies phenomenon (Villar-Piqué *et al.*, 2016).

The transformation of A-Syn (described as a 'natively unfolded' monomer adopting an α-helical secondary structure only under the condition of binding to the lipid vesicles) into a highly β-structural one in the amyloid fibril is studied using many experimental techniques: ultracentrifugation, *in vitro* cell-crosslinking and scanning transmission electron microscopy (Bartels *et al.*, 2011). Adopting multivariate conformations identified under diverse conditions, including complexing to nanoscale surfaces, is treated as a potential way of targeting conformational plasticity (D'Onofrio *et al.*, 2020). The A-Syn affinity to the membrane and its ease of interaction is considered a stimulus for therapy design (Bozelli *et al.*, 2020; Kachappilly *et al.*, 2022). The concept of amyloid transformation proposed for prion proteins is also being considered (Lassen *et al.*, 2016).

Concentration-dependent transformation conditions allow the identification of the minimum concentration for fibril production (Afritska *et al.*, 2019). This observation is broadened by research on the impact of various types of interphases on the reaction process, including air-water and hydrophobic surface-water interphases (Ben-Amotz 2022; Schutzius *et al.*, 2015; Yi-Jie & Qu 2014; Eremin & Fokin 2021; Kaplaneris *et al.*, 2022; Ishiyama *et al.*, 2022; Gupta *et al.*, 2022; Cannalire *et al.*, 2022). The possibility of transformation into an amyloid form – thus rich in β-structure – as well as proteins with a high helical structure presence, is surprising in the first stages of these studies (Jayawardena *et al.*, 2017). Another example here may be A-Syn, which in 2/3 of the chain length in the WT form exhibits a helical structure, with the remainder being a loose section with random coil configuration (Ulmer *et al.*, 2005; Tuttle *et al.*, 2016). Considering the breadth of literature on experimental studies, the availability of an increasing number of amyloid structures in PDB resources makes it possible to analyse the structure of amyloid fibrils as such (Goedert *et al.*, 2017; Eisen-

Table 1. Summary of the amyloids A structures discussed in this paper (as available July 20, 2022).

The middle column shows the sections of the A-Syn chain present in a given structure. In the case of superfamily, the chain identifier is provided, thus indicating the protofibril included in the analysis. *In the case of 2N0A, only the fragment showing the fibrillar form is included.

PDB ID	Fragment	Ref.
7LC9 - F	61-98	(Xiaodan <i>et al.</i> , PDB)
6UFR	36-98	(Boyer <i>et al.</i> , 2020)]
6A6B -C	37-99	(Li <i>et al.</i> , 2018)
6OSJ	37-97	(Ni <i>et al.</i> , 2019)
7NCG	37-97	(Lövestam <i>et al.</i> , 2021)
6H6B	38-95	(Guerrero-Ferreira <i>et al.</i> , 2018)
6FLT	38-95	(Guerrero-Ferreira <i>et al.</i> , 2018)
6PEO	36-99	(Boyer <i>et al.</i> , 2020)
6PES	36-99	(Boyer <i>et al.</i> , 2020)
7NCH	14-25, 36-91	(Ni <i>et al.</i> , 2019)
7NCJ	14-25, 36-91	(Ni <i>et al.</i> , 2019)
7NCI	14-25, 36-91	(Ni <i>et al.</i> , 2019)
6XYO	14-94	(Schweighauser <i>et al.</i> , 2020)
6SSX	14-25, 36-91	(Guerrero-Ferreira <i>et al.</i> , 2019)
7NCJ	37-97	(Ni <i>et al.</i> , 2019)
7NCK	36-99	(Ni <i>et al.</i> , 2019)
6XYQ	14-94	(Schweighauser <i>et al.</i> , 2020)
6L1U	1-100	(Zhao <i>et al.</i> , 2020)
7NCA	37-97	(Ni <i>et al.</i> , 2019)
7LC9-A	46-96	(Xiaodan <i>et al.</i> , PDB)
6L4S	45-99	(Zhao <i>et al.</i> , 2020)
6LRQ	37-99	(Sun <i>et al.</i> , 2020)
6CU7	38-97	(Li <i>et al.</i> , 2018)
7L7H	36-79	(Hojjatian <i>et al.</i> , 2021)
6SST	14-25, 36-96	(Guerrero-Ferreira <i>et al.</i> , 2019)
6OSL	39-97	(Li <i>et al.</i> , 2018)
6L1T	1-100	(Zhao <i>et al.</i> , 2020)
6XYP	14-94	(Schweighauser ???)
6OSM	37-96	(Li <i>et al.</i> , 2018)
6RTB	9-24, 35-56, 62-93	(Guerrero-Ferreira <i>et al.</i> , 2019)
7E0F	50-98	(Sun <i>et al.</i> , 2020)
6CU8	43-83	(Li <i>et al.</i> , 2018)
6RTO	14-25, 36-97	(Guerrero-Ferreira 2019)
7C1D	46-96	(Sun <i>et al.</i> , 2020)
2N0A*	30-100	(Tuttle <i>et al.</i> , 2016)

berg & Sawaya 2017; Wei *et al.*, 2020). Experiments conducted in different environmental conditions indicate a significant impact on the environment, and therefore, the impact of external conditions (Ben-Amotz 2022; Sawaya *et al.*, 2021; Serpell 2000; Rana *et al.*, 2008; Lambley *et al.*, 2020).

Identification of amyloid fibril structures as consisting of chains with a planar structure requires determining the conditions that should be met in order to obtain

just such a form, additionally involving almost all C=O and H-N peptide bond groups in the construction of the hydrogen bond network. Such conditions have already been defined when constructing a model of idealised amyloid (Roterman *et al.*, 2022). The main aim of the present study is to investigate the fulfillment of the conditions formulated for idealised amyloid in the group of A-Syn amyloid fibrils. We also describe the specificity of the secondary structures in amyloids. The primary specificity of amyloid structures is the flatness (2D) of single-chain structures comprising fibrils with a high presence of the β -structure. The combination of several flat-structured chains in the β -form in a parallel chain arrangement makes it possible to engage almost all -N-H and -C=O groups of peptide bonds in the construction of inter-chain hydrogen bonds. Thus, it is possible that each amino acid – in the i -th chain – through these groups participates in the construction of two hydrogen bonds (-N-H atoms engaged in the $i-1$ -th chain and -C=O group with $i+1$ -th chain). It significantly stabilizes the fibril structure, which is observed in experiments. Such engagement is exhibited by amino acids in the helix structure – with H-bonds oriented parallelly and β -structure – with H-bonds oriented antiparallelly. However, globular proteins contain chain fragments in which H-bonds are not generated – like loops and twists in hair-pin structures (Roterman *et al.*, 2022; Roterman 1995). Additionally, the helical form introduces the structure's spatiality (3D), while in theory, the β -structure has the potential of unlimited propagation in a linear form and, in the case of β -sheet, in 2D form as a flat plate. The β -sheet structure – can be generated by different sections of the same chain with different amino acid sequences, while in the amyloid, the β -sheet is formed as a result of a combination of sections of the same sequence originating from many adjacent chains in parallel mutual orientations.

It is shown in this paper that the flat structure of the chain can be reached for β -structural fragments representing special Φ , Ψ angles with bends introduced by single R- or L-helical conformation. The identification of such an organisation in polymorphic forms of A-Syn is shown (Peng *et al.*, 2018). Two reference non-amyloid proteins: all-helical and all- β -structural – are also present in the analysis to verify the proposed model.

The role of α -sheet in amyloid construction in comparison to Beta-structural-based amyloids is also discussed (Prosswimmer & Daggett, 2022; Lee *et al.*, 2002; Trexler & Rhoades E. 2012; Balupuri *et al.* 2019, Milner-White *et al.*, 2006, Hayward & Milner-White 2021). The hypothesis of the external force field of 2D form influence of flat structure construction is presented with the main role of loops linking Beta-structural fragments of chains in native structures of proteins is presented.

Moreover, based on the already proposed model of idealised amyloid we postulate the hypothesis for amyloid fibril formation.

MATERIALS AND METHODS

Data

The structures of A-Syn amyloids (as available in PDB July 2022) analysed in this paper are provided in Table 1.

Two reference proteins are present in the analysis: the GPCR bovine rhodopsin (PDB ID 1GZM – (Li *et al.*, 2004)) mainly Alpha Up-down bundle (CATH classification 1.20.1070.10) representing the structure dominated

by helical form and a FeS cluster assembly protein SufD from *Escherichia coli* (PDB ID 2ZU0 (Wada *et al.*, 2009)) The structure of the second protein is characterised by the presence of large domain build by almost all Beta-structural form.

The torsion angle-based relationship characterizing the amyloid structures

The specificity of amyloid structures is, apart from a high presence of β structure, the flatness of every single chain, a component of the fibrils. The planarity of a polypeptide chain (i.e. its linear propagation) is provided by the rectilinear β -segments (satisfying the $\Psi = -\Phi$ condition) together with single R- α or L- α helical conformations which introduce a local bend while maintaining a flat structure. Those single helical conformations are characterized by the $\Psi \approx \Phi$ condition. This is why those two characteristics can be put in the common expression $|\Psi| = |\Phi|$ constituting the basis of the model of idealised amyloid (described in detail in (Roterman *et al.*, 2022)).

Quantification of the fit of the idealised amyloid model

The $|\Psi| = |\Phi|$ relationship of idealised amyloid is assumed here as the hypothetical criterion for amyloid structure identification. The closer to this relationship is the distribution of (Φ , Ψ) angles, the more probable the construction of a flat structure.

To enable the assessment of the degree of fit of the idealised amyloid model, the operation of replacing the Φ and Ψ values with $|\Phi|$ and $|\Psi|$ respectively is performed. This leads to a situation where all three lines are in a common position (see the illustration in Figure 3 based on the amyloidogenic fragment (30-100) of the 2N0A).

The degree of fit of chain's (Φ , Ψ) angles to the model of idealised amyloid is measured by a Pearson correlation coefficient:

$$C = \frac{\sum_{i=1}^N (x_i - \bar{x})(y_i - \bar{y})}{\sqrt{\sum_{i=1}^N (x_i - \bar{x})^2} \sqrt{\sum_{i=1}^N (y_i - \bar{y})^2}}$$

where x_i stands for $|\Phi_i|$ and y_i stands for $|\Psi_i|$.

The correlation coefficient CC for the ($|\Phi_i|$, $|\Psi_i|$) angles of residues in an analysed chain was calculated in the following cases:

For all residues in an analysed chain (coefficient marked as CC-0).

For the residues after elimination of outstanding points: i.e. by eliminating them until a value of 0.8 is reached (coefficient marked as CC-F).

For the residues participating in β -strands and satisfying the condition $|\Psi| = |\Phi|$ with a tolerance of ± 10 deg distance from $|\Psi| = |\Phi|$ line (coefficient marked as CC- β). Residues with a high CC-F coefficient value are identified as responsible for the stabilization based on a hydrogen bond network.

The described type of analysis will be used to identify the amyloid form providing the maximum proportion of residues with a conformation satisfying the condition $|\Psi| = |\Phi|$.

The polypeptide's geometry-based model

This model has already been described on many occasions (see for example Roterman 1995). Here, only the basic assumptions facilitating an interpretation of the discussed results will be recalled. The main idea is to represent

the structure of the polypeptide chain using two geometrical parameters. One of them is the curvature radius R which is low and well-defined for the helical structures and very large (theoretically infinitely large) for the β -structures (straight line for certain Φ , Ψ angles). The value of the curvature radius is the result of the mutual orientation of two neighbour peptide bond planes expressed by the angle between two peptide bond planes versus the axis defined by virtual C α -C α bonds. This angle – called the V-angle – is close to zero (parallel mutual orientation) for helical forms and close to 180 deg for the β -structure (anti-parallel mutual orientation) (Fig. 1). There is one special β -structure with a V-angle=180 deg which produces an ideal straight line (Fig. 1B).

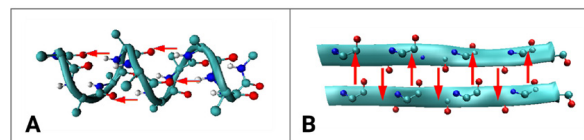


Figure 1. The hydrogen bond system (marked with red arrows): A – parallel in helical form, B – antiparallel in β -structural forms. The arrows just simply visualise the mutual orientations of hydrogen bonds.

Programs used

To visualise the 3D structures of discussed proteins the program VMD was used (<https://www.ks.uiuc.edu/Research/vmd/> accessed July 2022; Humphrey *et al.*, 1996).

RESULTS

General characteristics of secondary structures in amyloids

In this section, the general characterization of amyloid secondary structures based on the proposed earlier model of idealised amyloid will be presented,

The basic feature of amyloids is the flatness of the structure of single chains that make up the fibril. The planar amyloid structure of each polypeptide chain in a fibril is stabilized by a specific system of hydrogen bonds. In the β -structure with the $\Psi = -\Phi$ conformation (corresponding to the idealised amyloid), each amino acid participates in the construction of two hydrogen bonds with the adjacent chains. The arrangement of the chains is parallel, which causes residues from corresponding positions from adjacent chains to interact with each other. Such a structure ensures the maximum use of hydrogen bonds, thus providing much stability. Rectilinear chain segments are terminated by single residues with R- or L-helical conformation. A single residue with such a helical conformation does not disturb the planar structure, changing only the turn by introducing a bend (Fig. 2B). The presence of two residues with such a conformation introduces a three-dimensional arrangement disturbing the planarity (Roterman *et al.*, 2022).

Introducing such a single residue with helical conformation results in a change of hydrogen bond ordering. In contrast to a helical structure (which represents a parallel hydrogen bond system – see Fig. 1A), in the ideal β -structure, the arrangement of hydrogen bonds is antiparallel (Fig. 1B). A single residue with the R- or L-helical conformation introduces a local perturbation to this arrangement changing it to a parallel one.

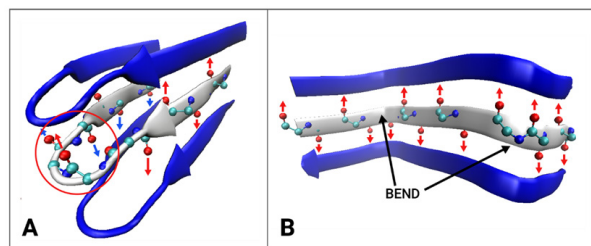


Figure 2. The β -structure propagation:

A – a hair-pin system, B – amyloid. The bend in the form of a hair-pin engages four residues with N-H and O=C groups – H-bonds system locally absent and introduces spaciousness. The one helical residue in the β -structural chain introduces a bend maintaining the flat structure of the chain and additionally continuing the system of H-bonds. The fragment presented in B is the fragment 36-53 of the A-Syn chain in amyloid form (PDB ID 2N0A)

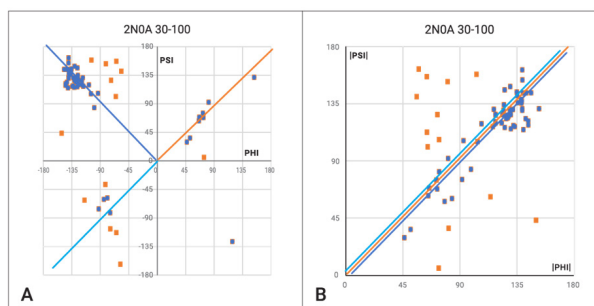


Figure 3. Ramachandran map with the superimposed (Φ , Ψ) angles from the A-Syn amyloid (A) and after transformation based on the absolute value of torsion angles (B). The points representing the residue conformations in the fibrillar sections are marked in navy blue. (30-100 aa).

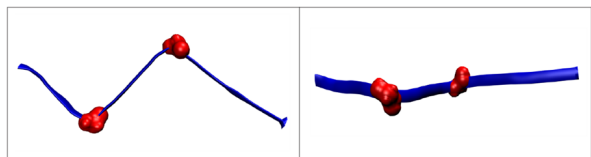


Figure 4. Section 36-53 of the A-Syn chain present in amyloid form (PDB ID 2N0A) in two perspectives. Residues marked as red – single helical conformations introducing the bend in chain propagation.

The planarity of a polypeptide chain (i.e. its linear propagation) is provided by the rectilinear β -segments (satisfying approximately the $\Psi = -\Phi$ condition) together with single helical conformations meeting the $\Psi \approx \Phi$ condition (Fig. 4).

In contrast to the above-described structure present in amyloids, changing the turn by means of hair-pins (Fig. 2A) engages more than one residue (most frequently 4 residues) and introduces spatiality. Moreover, the mutual orientation of residues in the hair-pins does not allow the formation of a hydrogen bond system in such bends.

It must be emphasized that the beta-sheet super-secondary structure in amyloids is different from the known, classical structure in other proteins. The classical beta-sheet structures are characterized by a system of hydrogen bonds binding fragments of the same chain. This allows the presence of loops, including the beta-turn (hair-pin) type, which just introduce spatiality. Beta-strand fragments in amyloids remain in one plane due to

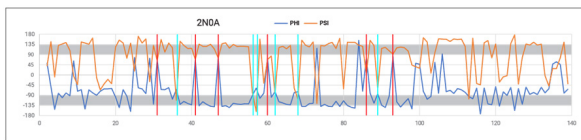


Figure 5. The profiles of Φ (red) and Ψ (navy) angles for the complete chain of A-Syn (1-140 aa) (Tuttle *et al.*, 2016). Grey lines – mark the β conformation fulfilling the $\Psi = -\Phi$ relation. Vertical lines denote positions of amino acids: red – with L- α conformation, cyan – with R- α conformation. The purpose of this picture is to visualise the differences between 30-100 aa – amyloid fragment to N- and C-terminal fragments, where the Φ , Ψ angles relation is significantly different with respect to 30-100 aa fragment.

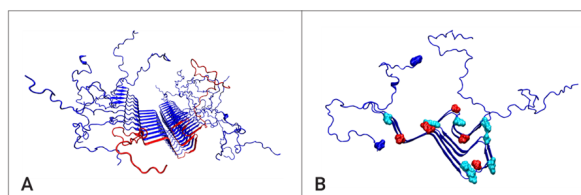


Figure 6. A-Syn structure in the amyloid form (2N0A): A – the structure of a complete fibril (chain A marked in red); B – two chains with distinguished residues representing the R- α (cyan) and L- α (red) conformation according to the identification provided in Fig. 5.

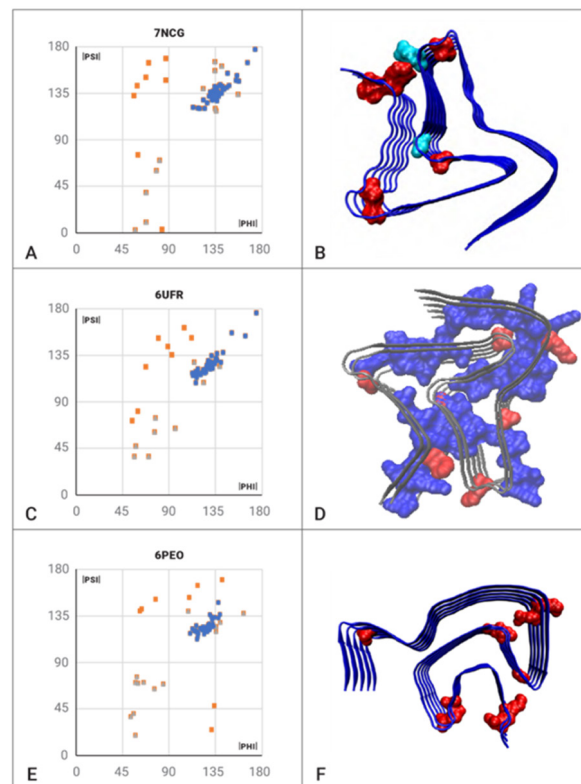


Figure 7. The plot of $|\Phi|$ versus $|\Psi|$ and 3D representation of the discussed amyloids.

The eliminated residues (by CC-F calculations) are marked in red on both the plots and 3D presentation. The points marked in blue – are the positions for residues satisfying the condition $|\Psi| = |\Phi|$ for β -structural forms. For 6UFR the residues representing the highly ordered β -structural fragments are in space-filling representation (blue).

Table 2. Summary of CC-0 and CC-F values for the set of A-Syn amyloid forms analysed in this paper.

Residue d numbers eliminated in CC-F calculation are given. The CC- β values are given to express the high fulfillment of $|\Phi| = |\Psi|$ relation. The % of residues in β -structural form for which the CC- β was calculated is given.

PDB ID	CC-0	Residues Eliminated	CC-F	% F	CC- β	% β
7LC9-F	0.815	62, 84	0.851	94	0.922	26.3
6UFR	0.722	69, 74, 85, 87	0.889	93	0.935	69.84
6A6B -C	0.687	74	0.714	98	0.964	15.8
6OSJ	0.636	44, 50, 62, 63	0.799	93	0.952	28.3
7NCG	0.580	59, 69, 84, 87, 93, 94	0.908	90	0.920	63.5
6H6B	0.577	44, 47, 58, 61, 66, 67, 75, 83, 87, 88	0.696	82	0.920	22.4
6FLT	0.564	39, 42, 73, 74, 84, 86	0.777	89	0.909	22.4
6PEO	0.559	42, 60, 61, 68, 72, 73, 85, 86, 87, 97, 98	0.946	82	0.723	63.5
6PES	0.556	42, 72, 73, 85, 87, 97, 98	0.906	89	0.785	59.3
7NCH	0.546	24, 25, 36, 37, 48, 57, 68, 83, 84	0.770	86	0.948	35.3
7NCJ-G	0.544	24, 42, 47, 48, 57, 61, 62, 68, 79, 83, 84	0.849	83	0.908	47.0
7NCI	0.507	24, 25, 36, 37, 42, 48, 57, 61, 62, 68, 78, 79, 83, 84	0.844	79	0.916	38.2
6XYO	0.500	35, 73, 83, 85	0.642	95	0.790	28.4
6SSX	0.464	59, 60, 67, 72, 73, 83, 84	0.726	90	0.928	28.7
7NCJ-A	0.451	58, 59, 68, 69, 85, 87, 90, 91	0.882	86	0.829	44.2
7NCK	0.438	43, 58, 68, 72, 74, 85, 87, 97, 98	0.857	86	0.850	45.3
6XYQ	0.436	35, 37, 42, 73, 83, 88	0.610	92	0.862	25.9
6L1U	0.435	9, 10, 24, 47, 60, 83, 99	0.616	93	0.954	20.0
7NCA	0.400	51, 52, 58, 59, 68, 69, 85, 87, 90, 91	0.909	83	0.885	55.7
7LC9-A	0.394	50, 51, 66, 67, 76	0.730	88	0.962	33.3
6L4S	0.390	50, 53, 54, 67, 72, 74, 80, 84, 90	0.679	83	0.902	30.9
6LRQ	0.372	38, 41, 46, 58, 68, 72, 85, 87, 97, 98	0.790	84	0.909	25.4
6CU7	0.367	39, 40, 67, 68, 69, 83, 84, 86, 90	0.665	85	0.916	26.6
7L7H	0.363	40, 44, 76	0.501	93	0.954	11.3
6SST	0.357	59, 60, 67, 72, 73, 83, 84	0.715	90	0.910	28.7
6OSL	0.334	43, 50, 60, 65, 66, 84, 85, 93, 94, 95	0.697	83	0.944	27.1
6L1T	0.327	3, 22, 29, 30	0.606	96	0.945	13.0
6XYP	0.310	15, 35, 37, 43, 53, 73, 74, 83, 86,	0.612	88	0.937	16.0
6OSM	0.276	38, 42, 50, 51, 52, 77, 84, 89, 94	0.626	85	0.937	20.0
6RTB	0.220	13, 36, 52, 55, 67, 68, 69, 74, 86, 87, 88	0.613	84	0.911	22.8
7E0F	0.202	52, 65, 72, 74, 79, 80, 84	0.507	85	0.894	24.4
6CU8	0.200	44, 50, 65, 67, 68	0.540	87	0.812	26.3
6RT0	0.163	43, 67, 72, 73, 83, 84, 91	0.691	90	0.888	27.3
7C1D	0.152	50, 60, 67, 72, 73, 76, 77, 83, 85, 87	0.480	80	--	1.9
2N0A (30-100)	0.528	32, 33, 34, 36, 57, 58, 59, 80, 85, 86, 87, 98	0.899	83	0.847	45.0

a turn introduced by a single R- or L-helical conformations as shown in Fig. 4. Such a radical turn allows the chain to propagate in one plane.

Figure 4 visualises the real conformation present in 36-53 fragment of A-Syn which appears to be almost ideally accordant with the proposed model of idealised amyloid. Linear propagation of β -structural fragments with single residues representing helical conformation results in a flat form with well-defined bends. The orientation of hydrogen bonds in β -fragments is antiparallel with local, parallel orientation in single helical residues.

Analysis of the fit of the idealised amyloid model 2N0A protein

In this section, the procedure of fitting the idealised amyloid model will be presented based on the reference A-Syn amyloid structure (2N0A – section 36-53). In Fig. 4, the fragments of the chain (marked as navy blue) show a rectilinear system obtained using the Phi and Psi torsion angles satisfying the relation $\Psi = -\Phi$. The residues marked in red have an α -helix conformation resulting in a turn of the chain while maintaining its flatness.

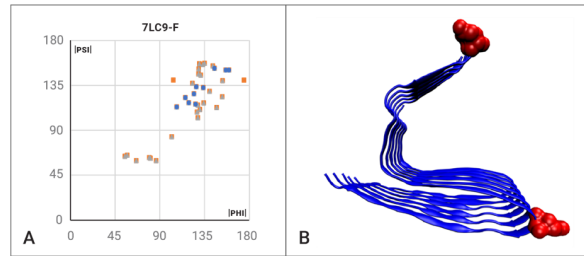


Figure 8. Presentation of the 7LC9-F amyloid with the highest CC-0 value (and the lowest number of outstanding residues). A – distribution of points representing $|\Phi|$ and $|\Psi|$. Only two residues are considered outstanding (red points). Their location in the chain is highlighted in red (space-filling) on the 3D representation (B).

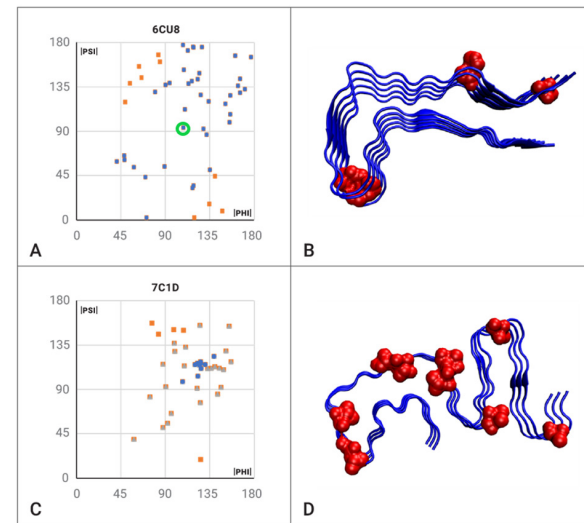


Figure 9. Examples with low CC values: A – CC-0 – all points; CC-F blue points; The circled dot is the only point satisfying the $|\Psi|=|\Phi|$. C – red points eliminated for CC-F calculation, gray points – CC-F calculation, blue points – CC- β calculation. B, D – 3D presentation of 6CU8 and 7C1D respectively with red residues – residues eliminated for CC-F calculation

The torsion angle profiles of the mentioned fragment are shown in Fig. 5. The fulfillment of relations $\Psi=\Phi$ is visible for the amyloid part (positions 30-100 aa), which is marked in gray. Within the clearly ordered and constant values of the Φ and Ψ angles for the β form, single positions with the Φ and Ψ angles corresponding to the R (cyan) and L (red) helical conformations are visible. The visualization of structures in this analysis is shown in Fig. 6.

Analysis of the structure of A-Syn amyloid forms

Table 2 provides the CC-0 and CC-F values of the chain as described in the Materials and Methods section. The values of CC- β express the status of residues satisfying the condition $|\Psi|=|\Phi|$ in relation solely to the β -structural form. The % of residues satisfying the condition for CC- β is also given to characterise the degree

of the presence of such restrictive structure in a particular protein.

Figure 9 shows examples with high values of CC-0 and CC-F arising from the location of the Φ and Ψ angles in accordance with the $\Psi=\Phi$ relationship. In a 3D visualization, these sections are represented by a rectilinear arrangement. The highlighted residues – red points – on the plots of $|\Phi|$ and $|\Psi|$ angles are residues treated as outstanding, the elimination of which results in a CC-F value > 0.8 (Table 2).

In the amyloid with PDB code 7NCG, the rectilinear β -structure sections are visible (Fig. 7B) and the corresponding locations of the $|\Phi|$ versus $|\Psi|$ plot (Fig. 7A). Items that do not satisfy the $|\Psi|=|\Phi|$ condition specified by the model are marked in red. The number of residues that do not satisfy the model is low and they do not disturb the overall form of this amyloid leaving it close to the principles of the proposed model.

A similar arrangement is identified in the case of 6URF (Fig. 7). It should be noted that this structure is characterised only by a few residues with conformations not satisfying model conditions.

The significant portion of a chain in 6PEO amyloid meets the $|\Psi|=|\Phi|$ condition, but a fairly significant scattering of several residues deviating from the model can also be observed.

The highest CC-0 value and the low number of residues deviating from the model are characteristic for amyloid 7LC9-F (Fig. 8). Eliminating only two residues results in a very high value of CC-F=0.851.

Further examples are the structures present in 6CU8 and 7C1D exhibiting the lowest CC-0 values (Fig. 9). In these two examples, no rectilinear propagation, but rather an “undulating” form is observed. This means, that the chain propagation is composed of sections with a smaller radius R . This reduction of radius applies to short sections, which, with an alternating arrangement similar to the R- and L-helical conformations, does not result in a spatial form. In this case, the hydrogen bonding arrangement is not parallel, although the deflection from the perpendicularity to the chain’s plane is compensated, resulting in maintaining the structure’s flatness.

Analysis of the structure of reference examples

Two reference proteins (Table 3) represent mainly helical and β -structural proteins. As shown in Fig. 10 their structure is highly ordered. The FeS cluster assembly of SufD from *Escherichia coli* is a protein which for the most part shows the β -structure (Banach *et al.*, 2020). The analysed fragment of this protein is limited to the beta-sheets (Fig. 10B).

The parallel orientation in the β -sheet (Fig. 10B) indicates a structural similarity to amyloids. However, the sequential β -strands represent a different sequence, while in amyloids the sequences in all neighbouring chains are identical.

The status expressed by CC- β of sequential β -strands and β -sheets reveals differences with respect to the amyloid forms discussed (Table 4). The fragments showing high accordance with the $|\Psi|=|\Phi|$ criterion (having high CC values) are accompanied by the fragments with completely opposite characteristics (low CC val-

Table 3. Characteristics of the reference proteins

PDB ID	NAME	CC-0	CC-F	CC- β	%
2ZUO	FeS cluster	0.297	0.803	0.949	28.4
1GZM	rhodopsin	0.334	0.803	0.970	2.4

Table 4. Status (CC- β) of β -strands in β -sheets (as distinguished in Fig. 10B).

The values in parentheses – denote the β -strand status for the residues representing non- β -structural Phi, Psi angles. The values given for β -sheets are calculated only for the residues belonging to the β -structural area on the Ramachandran map.

β -sheet - red		β -sheet - blue	
FRAGMENT	CC- β	FRAGMENT	CC- β
181-192	0.860 (0.501)	167-176	0.613
211-219	0.290	196-206	0.876 (0.361)
239-246	0.700	225-234	-0.012 (-0.477)
266-273	0.010	251-260	0.642 (0.263)
295-304	0.020	280-291	0.833
327-337	0.712	309-318	-0.374
357-364	0.587	341-351	-0.064
β -sheet	0.641	β -sheet	0.511

ues). The non- β -structural conformations are present in the selected fragments (values given in parentheses in Table 4). Visual analysis of two β -sheets suggests the perfect β -structural organisation (Fig. 11). However, the analysis of Phi and Psi angles reveals some residues in the lower left quarter of the Ramachandran map. Some β -strands having torsion angles typical for β -structure appear to be not organised as expected in amyloids. The differentiation of β -strands can be observed. The status of sequential β -strands in the amyloid is identical for all fragments belonging to a common β -sheet. The distribution of $|\Psi|$, $|\Phi|$ angles (Fig. 12A) identifies the large number of points satisfying the $|\Psi|=|\Phi|$ relation, however, it also shows their dispersion over the chain. The highest similarity is observed in the 181-192 fragment (marked in Fig. 12B).

The mainly-helical protein is difficult to evaluate with the $|\Phi|=|\Psi|$ criterion due to the very low presence of β -structural conformations. The distribution of Phi, Psi angles along the chain (Fig. 13) shows high accordance with the helical forms (dark lines on Fig. 13). The CC-0 for this protein is equal to 0.347, the CC-F=0.807 (the eliminated residues marked as blue dots – Fig. 13.). The number of eliminated residues constitutes 19.2% of the whole length of the chain. The linear relation between torsion angles is mostly due to the $\Psi \approx \Phi$ relation present in the helical conformation.

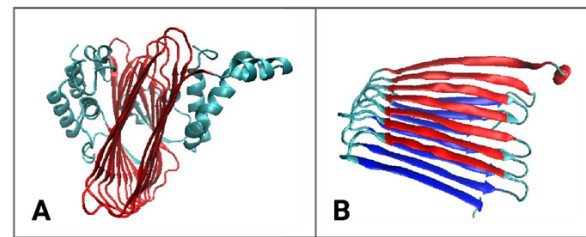
The eliminated amino acids (in the CC-F calculations) represent the unstructured fragments like loops particularly those external with respect to the surrounding membrane. The space filling presentation (Fig. 12C and 12D) distinguishes the segments satisfying to a large extent the $|\Psi|=|\Phi|$ relation, however, they belong mostly to the helical region.

The proposed hypothetical mechanism of amyloid fibril formation

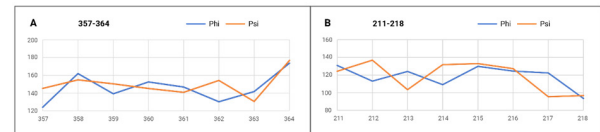
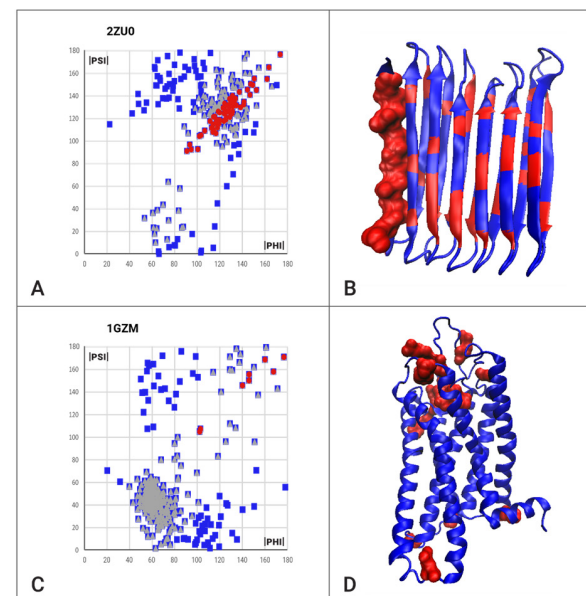
The proposed hypothesis of amyloid fibril formation presented here concerns the method and the reasons of the transformation of a 3D structure into a planar form characteristic to the amyloid structures.

We also want to refer here to the existing, different hypothesis ((Prosswimmer & Daggett, 2022; Lee *et al.*, 2002; Trexler & Rhoades, 2012; Balupuri *et al.*, 2019) of the formation of the amyloid based on the α -sheet structure as an intermediate in the aggregation process.

Shaking an aqueous solution of proteins as a laboratory technique for obtaining amyloid forms of proteins consists in increasing the presence of air-water interphase in the solution. Such a shaking process can simu-

**Figure 10. 3D structure 2ZU0**

A – chain A – with two β -sheets marked in red. B – two β -sheets marked in red and blue – N-terminal residue – marked with space filling.

**Figure 11. Phi, Psi profiles in the fragment with high (A) and low (B) correlation according to Table 4.****Figure 12. Characteristics of all- β and all-helical proteins.**

A – $|\Phi|$, $|\Psi|$ angles as they appear in the β -structural part of the protein – chain fragment selected as an aim-oriented example for the analysis of the beta-structural form of the chain. B – 3D presentation with conformations satisfying the relation $|\Psi|=|\Phi|$ – red. The space-filling – a fragment of the highest satisfaction of $|\Psi|=|\Phi|$ condition. C – $|\Phi|$, $|\Psi|$ angles as they appear in all-helical protein. D – 3D structure with amino acids satisfying the $|\Psi|=|\Phi|$ conditions distinguished by a space-filling presentation. The red dots – all $|\Phi|$, $|\Psi|$ angles to calculate CC-0, grey dots – CC-F and red – CC- β . The same colours are used in 3D presentation (red and blue).

late the conditions in a cell of a living organism. The air-water interphase has a surface structure, so it introduces an external force field with 2D characteristics.

Occasionally, a protein undergoes some conformational changes resulting in aggregation competent polypeptide chain. Such a chain, avoiding contact with air strives for maximum contact with water, which is available only on one side. The most thermodynamically favora-

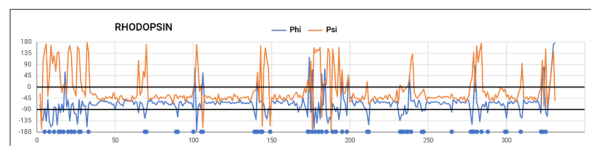


Figure 13. Profiles of Phi and Psi angles in rhodopsin. The black lines mark the range for the helical structure to visualise the closeness to the Psi=Phi relation for helical fragments. Positions not satisfying this relation are marked by blue dots on the x-axis.

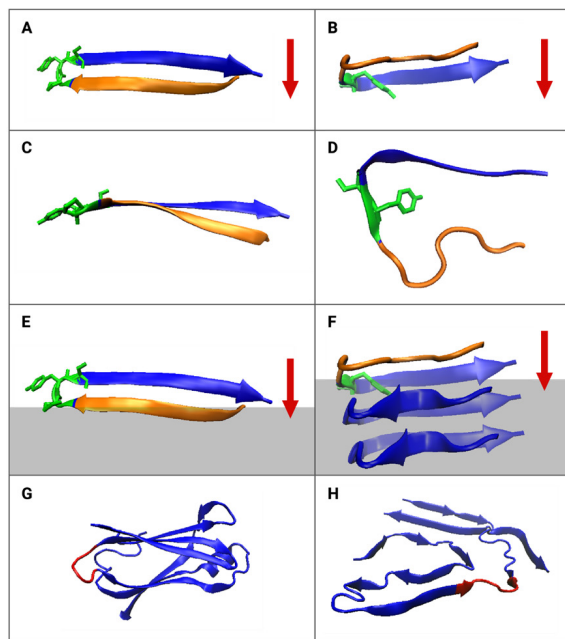


Figure 14. Structure of the transthyretin:

A, C – native form 104-125 fragment of transthyretin – green fragment loop 113-115 – different orientation – orange – residues 104 – 112. B, D – amyloid form 104-125 fragment of transthyretin – green fragment loop 113-115, orange residues – fragment 104-112. E – as in A with water phase shown in gray with orange fragment in contact with a water phase. F – as in B with water phase shown in gray – complete chain in contact with water. G – native form of transthyretin – red fragment loop 97-103. H – amyloid form of transthyretin – red fragment loop 97-103. The orientation in A, B, E and F figures is as follows: the H-bonds (red arrows) system is perpendicular to the plane of the water surface. The gray area – water, white area – air. The green fragment – the loop causing the propagation of the chain in 3D space in native form and in 2D space in the amyloid form. The red arrow crossed out on D – the H-bonds system between two fragments of the same polypeptide chain is not present. The groups participating in H-bonds are oriented perpendicularly to the paper plane on C and D.

ble situation is the formation of a system of hydrogen bonds with a planar chain where the polypeptide chain “lies” on the water surface. In this way, the backbone chain engages as many C=O and N-H groups of peptide bonds as possible in such an interaction. This explains the reason for the almost planar form of the chain in amyloid fibril.

A planar polypeptide chain formed due to the shaking finds a thermodynamically favorable opportunity to interact with another planar chain and the process of attaching the next flat chains continues until the aggregation nucleus is formed. The next phase starting from the nucleus is characterized by a rapid formation of fibrils composed of beta-sheet structures.

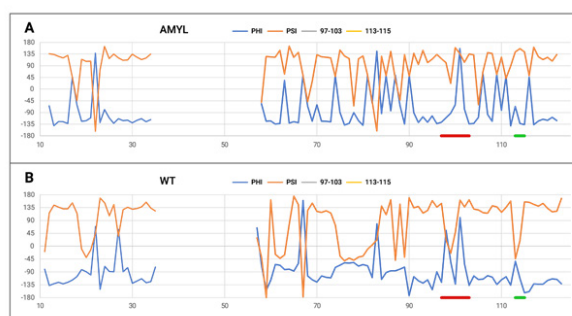


Figure 15. Profiles of Phi and Psi angles for the amyloid and WT forms of transthyretin with highlighted fragments responsible for changing the orientation of the chain propagation as shown in Fig. 14.

Amyloid transformation mainly requires conformational changes within the loops that change from 3D orientation to 2D one.

The influence of the environment on amyloid transformation with an unchanged sequence is widely recognized (Serpell, 2000). The particular form of the environment in the form of mentioned 2D interphase seems to favour the formation of the flat structure of the chains – components of amyloid fibrils.

The proposed hypothesis for amyloid fibril formation is illustrated in Fig. 14. It refers to the transthyretin (Ueda, 2022) which undergoes amyloid transformation relatively easily. A special object is a fragment of a beta-sheet identified as A (11-19), G(104-112) and H (114-124). Both the WT form (PDB ID 1DVQ (Klabunde *et al.*, 2000) and the amyloid form (PDB ID 6SDZ (Schmidt *et al.*, 2019)) are available in PDB. Another reason is the possibility to compare with the hypothesis proposed in the works (Prosswimmer & Daggett, 2022, Armen *et al.*, 2004) and based on α -sheet structure as intermediate.

Fragment beta-strand A(11-19) remains in this form in range (13-15), fragment G (104-112) changes its form to a disordered linearly propagating segment, while fragment H (114-124) remains in beta form on (118-124) fragment. The shortening of beta-stand segments can be observed.

The water-directed beta-structural fragment 104-111 can form hydrogen bonds with water molecules. The shape of the loop directs the second part of the beta-strand above the water surface, i.e. to the air zone. This is due to the orientation imposed by the loop (113-115) present in the native form of the transthyretin (green fragment in Fig. 14A and C). The same fragment after changing the conformation of the loop results in a planar structure of the entire fragment 104-124 (green fragment in Fig. 14B and D).

It should be noted that the native Beta-structure segment (104-112) changes its form to a disordered pattern, while the native-form beta-structure segment (114-124) is limited to the amyloid segment (118-124). This means that the conformational change within the loop (green fragment in Fig. 14A–D) also applies to a short fragment of the Beta-ordered segment. As a result of these changes, the structure of the entire fragment 104-124 becomes planar, allowing the generation of hydrogen bonds with water molecules along its entire length (Fig. 14E and F). The same analysis applies to loops 97-103 (Fig. 14G and H), where a change in conformation within the loop (red fragment Fig. 14G and H) allows backbone contact

(groups -C=O and -N-H of peptide bonds) with water molecules leading to the formation of hydrogen bonds with water molecules. The exact conformation changes within the discussed loops are shown in Fig. 15.

The proposed amyloid formation hypothesis relies on the 3D to 2D transformation engaging mostly the loops linking beta-structural fragments. The loops structure introducing the 3D organisation of beta-sheet change to a flat form introducing the mutual reorientation of beta-strands enabling the generation of large-scale hydrogen bonds initially with water molecules to change into an inter-chain H-bonds system in the next step.

The α -sheet structure, widely discussed in the context of amyloids (Prosswimmer & Daggett, 2022; Lee *et al.*, 2002; Trexler & Rhoades, 2012; Balupuri *et al.*, 2019) is the structure formed by amino acids with the R- and L-helical conformations alternating in the polypeptide chain. Similarly to the Beta-sheet structure, the α -sheet structure is characterized by the rectilinear form (Fig. 2 in Prosswimmer & Daggett, 2022). The distribution of Phi and Psi angles in α -sheet structures discussed in Prosswimmer & Daggett (2022) is consistent with the model assumed in this work. The difference is only quantitative. In the case of the α -sheet, the concentration of points on the Ramachandran map is significantly greater in the positions corresponding to the R- and L-helix with the presence of the Phi and Psi angles representing the β -structure in a linear relationship. In the current work, for the β forms, a much greater concentration of points on the Ramachandran map is observed. The main point is concentrated on the 3D to 2D transition. The structure discussed in (Prosswimmer & Daggett, 2022) introduces the 3D structuralisation which is not present in amyloid formation. The linear propagation of the chain in the form of Beta is the most frequently observed secondary form. The linear propagation of the chain is also possible in the form of R- followed by L-helix by turns. Such a system allows the generation of an H-bonds network. The mutual orientation of chains shall be parallel to allow propagation in fibril formation. However, the flat construction for individual chain is the most important one.

DISCUSSION

The amyloid structure of the flat form of each polypeptide chain is stabilized by a specific hydrogen bond arrangement. Each amino acid in an idealized form contributes to the construction of two hydrogen bonds with adjacent chains. The chain arrangement is parallel, causing identical residues to interact with each other in adjacent chains. The maximum use of C=O and H-N groups for the construction of hydrogen bonds is ensured by the β -structure with the $\Psi=\Phi$ conformation. A rectilinear form with C=O groups facing in the opposite direction to the H-N group of the same amino acid is an arrangement that makes maximum use of the possibilities of the hydrogen bonding structure. The rectilinear sections are terminated by single residues with R- α or L- α conformations. A single residue with such conformation does not disturb the flat structure, only changing the direction (introduction of a turn/bend). In this case, the form of arranging hydrogen bonds is changed. In a structure with the $\Psi=\Phi$ conformation, the hydrogen bond arrangement perpendicular to the plane of the chain represents an anti-parallel arrangement (if a turn is applied to the hydrogen bond).

Numerous amyloid forms of A-Syn allow tracking the structural variation of these amyloids. Among the structures satisfying the $|\Psi|=|\Phi|$ condition, there are structures showing some deviations from this condition. The deviation also provides fibrillar structures.

On the Ramachandran map presenting the distribution of radius of curvature R and V-angle (Roterman *et al.*, 2022; Roterman, 1995) the area fulfilling the $\Psi=\Phi$ condition represents the one with the highest value of R (i.e. a straight chain section). A reduction of the curvature radius R is observed moving up and down versus this line gradually introducing the arc form. If this procedure is performed stepwise (i.e. one above the $\Psi=\Phi$ line followed by one representing Φ , Ψ angles below that line), this introduces the structural form as shown in Fig. 9 for 7C1D (symmetrically located $|\Psi|$, $|\Phi|$ angles). The result of such Φ , Ψ angle combination is the sinusoidal arrangement of the chain as can be seen in 7C1D (Fig. 9) and others. The local introduction of an arc-like form in one direction is compensated by an arc form oriented in the opposite direction. In consequence, the linear propagation of the flat form can be continued. Nevertheless, this symmetrical (with respect to $|\Phi|=|\Psi|$ line) set of altered Φ and Ψ angles generates a flat arrangement, but probably with reduced stabilization derived from the hydrogen bonds (change of angle between the C=O and H-N groups in the hydrogen bonding arrangement of peptide bonds derived from adjacent polypeptides).

The condition of the presence of an R- or L-helical conformation at the turn of the chain can be satisfied in a less perfect form by a conformation with a low curvature radius R. Cyan and red lines in Fig. 5 and Fig. 6 illustrate the area with low values of V-angle and the R-radius of curvature. The presence of Φ and Ψ angles from this area satisfies the condition for obtaining a turn, although the hydrogen bond arrangement is not as perfectly ordered as in the case of Φ and Ψ angles accurately representing the R- α - or L- α -helical conformation.

The phenomenon of polymorphism in the case of amyloids is conditioned by environmental factors, as indicated by numerous experimental studies (Ben-Amotz, 2022; Schutzius *et al.*, 2015; Zuo & Qu 2014; Eremin & Fokin, 2021; Kaplaneris *et al.*, 2022; Ishiyama *et al.*, 2022; Gupta *et al.*, 2022; Cannalire *et al.*, 2022; Jayawardena *et al.*, 2017; Ulmer *et al.*, 2005; Tuttle *et al.*, 2016).

This analysis complements the detailed structural analysis of A-Syn fibrils (Roterman *et al.*, 2023) as well as the transthyretin (Roterman *et al.*, 2022), where the characteristics of fibrils were considered from the perspective of the tertiary structure and characteristics of those fibrils. Microenvironmental conditions were also indicated as the cause of structural changes in A-Syn (Candelise *et al.*, 2020; Stephens *et al.*, 2019).

The problem of describing the field in the form of 3D analyzed on a large-scale provides many forms of mathematical notation to express its presence (Cheng *et al.*, 2023).

CONCLUSIONS

The flat structure of single chains – components of amyloid fibril – is a characteristic of amyloid forms. This flatness is achieved through a β -type structure satisfying the $\Psi=\Phi$ condition resulting in a rectilinear chain propagation. Turns in chain arrangement are obtained by single residues with R- α or L- α helical conformation

(satisfying $\Psi \approx \Phi$ condition). The combination of such β -structures and single conformations allows the introduction of the general model expressed by $|\Psi| = |\Phi|$. The hypothesis introduced in this paper is to treat the presence of conformations satisfying this relation as a criterion for amyloid identification and description. The stabilization of such a form is achieved through the special hydrogen bond arrangement. In β -structured sections, the hydrogen bond arrangement is antiparallel. Each individual residue of the L- α or R- α conformation introduces a local arrangement of these bonds as parallel. Access to multiple structural forms of A-Syn amyloids reveals variation in the form of this ordering. This variation is likely a result of different environmental conditions (Roterman *et al.*, 2023). Particularly, the impact of the presence of air-water interphase (increasing this presence during shaking) is most likely indicated as a factor affecting the structuring, including the form of arranging the hydrogen bond network in amyloids.

External conditions in the form of air-water interphase also direct protein structuring to the planar form, which can be stabilized by a significantly high number of hydrogen bonds of -N-H and -C=O groups of peptide bonds. The accessibility of these groups for hydrogen bonds also includes segments that in their native form represent loops introducing 3D structuring (e.g. two parallel β -sheets) resulting in a flat structure for the entire polypeptide chain (Fig. 14G and H).

Declarations

Acknowledgements. Many thanks to Anna Śmietańska and Zdzisław Wiśniowski for technical support.

Conflicts of Interest. The authors declare no conflict of interest

REFERENCES

- Afritskaya K, Fucikova A, Shvadchak VV, Yushchenko DA (2019) α -Synuclein aggregation at low concentrations. *Biochim Biophys Acta Proteins Proteom* **1867**: 701–709. <https://doi.org/10.1016/j.bbapap.2019.05.003>
- Armen RS, DeMarco ML, Alonso DOV, Daggett V (2004) Pauling and Corey's α -pleated sheet structure may define the prefibrillar amyloidogenic intermediate in amyloid disease. *Proc Natl Acad Sci U S A* **101**: 11622–11627. <https://doi.org/10.1073/pnas.0401781101>
- Balupuri A, Choi KE, Kang NS (2019) Computational insights into the role of α -strand/sheet in aggregation of α -synuclein. *Sci Rep* **9**: 59. <https://doi.org/10.1038/s41598-018-37276-1>
- Banach M, Konieczny L, Roterman I (2020) Anti-amyloid drug design. In *From globular proteins to amyloids*. pp 215–232. Elsevier
- Bartels T, Choi JG, Selkoe DJ (2011) α -Synuclein occurs physiologically as a helically folded tetramer that resists aggregation. *Nature* **477**: 107–110. <https://doi.org/10.1038/nature10324>
- Ben-Amotz D (2022) Electric buzz in a glass of pure water. *Science* **376**: 800–801. <https://doi.org/10.1126/science.abo3398>
- Beyer K (2006) Alpha-synuclein structure, posttranslational modification and alternative splicing as aggregation enhancers. *Acta Neuropathol* **112**: 237–251. <https://doi.org/10.1007/s00401-006-0104-6>
- Boyer DR, Li B, Sun C, Fan W, Zhou K, Hughes MP, Sawaya MR, Jiang, Eisenberg DS (2020) The α -synuclein hereditary mutation E46K unlocks a more stable, pathogenic fibril structure. *Proc Natl Acad Sci U S A* **117**: 3592–3602. <https://doi.org/10.1073/pnas.1917914117>
- Bozelli JC Jr, Kamski-Hennekam E, Melacini G, Epan RM (2021) α -Synuclein and neuronal membranes: Conformational flexibilities in health and disease. *Chem Phys Lipids* **235**: 105034. <https://doi.org/10.1016/j.chemphyslip.2020.105034>
- Burmann BM, Gerez JA, Matečko-Burmann I, Campioni S, Kumari P, Ghosh D, Mazur A, Aspholm EE, Šulskis D, Wawrzyniuk M, Bock T, Schmidt A, Rüdiger SGD, Riek R, Hiller S (2020) Regulation of α -synuclein by chaperones in mammalian cells. *Nature* **577**: 127–132. <https://doi.org/10.1038/s41586-019-1808-9>

- Burré J, Sharma M, Südhof TC (2018) Cell biology and pathophysiology of α -Synuclein. *Cold Spring Harb Perspect Med* **8**: a024091. <https://doi.org/10.1101/cshperspect.a024091>
- Candelise N, Schmitz M, Thüne K, Cramm M, Rabano A, Zafar S, Stoops E, Vanderstichele H, Villar-Pique A, Llorens F, Zerr I (2020) Effect of the micro-environment on α -synuclein conversion and implication in seeded conversion assays. *Transl Neurodegener* **9**: 5. <https://doi.org/10.1186/s40035-019-0181-9>
- Cannalire R, Santoro F, Russo C, Graziani G, Tron GC, Carotenuto A, Brancaccio D, Giustiniano M (2022) Photomimetic catalyzed synthesis of amides from isocyanides: optimization, scope, and NMR studies of photocatalyst/surfactant interactions. *ACS Organic Inorganic Au* **2**: 66–74. <https://doi.org/10.1021/acsorginorgau.1c00028>
- Cheng X, Fan Z, Yao S, Jin T, Lv Z, Lan Y, Bo R, Chen Y, Zhang F, Shen Z, Wan H, Huang Y, Zhang Y (2023) Programming 3D curved mesosurfaces using microlattice designs. *Science* **379**: 1225–1232. <https://doi.org/10.1126/science.adf3824>
- Chiti F, Dobson CM (2017) Protein misfolding, amyloid formation, and human disease: a summary of progress over the last decade. *Annu Rev Biochem* **86**: 27–68. <https://doi.org/10.1146/annurev-biochem-061516-045115>
- Dehay B, Bourdenx M, Gorry P, Przedborski S, Vila M, Hunot S, Singleton A, Olanow CW, Merchant KM, Bezard E, Patskova GA, Meissner WG (2015) Targeting α -synuclein for treatment of Parkinson's disease: mechanistic and therapeutic considerations. *Lancet Neurol* **14**: 855–866. [https://doi.org/10.1016/S1474-4422\(15\)00006-X](https://doi.org/10.1016/S1474-4422(15)00006-X)
- D'Onofrio M, Munari F, Assfalg M (2020) Alpha-synuclein-nanoparticle interactions: understanding, controlling and exploiting conformational plasticity. *Molecules* **25**: 5625. <https://doi.org/10.3390/molecules25235625>
- Eisenberg DS, Sawaya MR (2017) Structural studies of amyloid proteins at the molecular level. *Annu Rev Biochem* **86**: 69–95. <https://doi.org/10.1146/annurev-biochem-061516-045104>
- Eremín DB, Fokin VV (2021) On-water selectivity switch in microdroplets in the 1,2,3-triazole synthesis from bromoethanesulfonyl fluoride. *J Am Chem Soc* **143**: 8374–8379. <https://doi.org/10.1021/jacs.1c08879>
- Ghosh D, Mehra S, Sahay S, Singh PK, Maji SK (2017) α -synuclein aggregation and its modulation. *Int J Biol Macromol* **100**: 37–54. <https://doi.org/10.1016/j.ijbiomac.2016.10.021>
- Goedert M, Eisenberg DS, Crowther RA (2017) Propagation of Tau aggregates and neurodegeneration. *Annu Rev Neurosci* **40**: 189–210. <https://doi.org/10.1146/annurev-neuro-072116-031153>
- Guerrero-Ferreira R, Taylor NM, Arteni A-A, Kumari P, Mona D, Ringler P, Britschgi M, Lauer ME, Makky A, Verasdonck J, Riek R, Melki R, Meier BH, Böckmann A, Bousset L, Stahlberg H (2019) Two new polymorphic structures of human full-length alpha-synuclein fibrils solved by cryo-electron microscopy. *Elife* **8**: e48907. <https://doi.org/10.7554/eLife.48907>
- Guerrero-Ferreira R, Taylor NM, Mona D, Ringler P, Lauer ME, Riek R, Britschgi M, Stahlberg H (2018) Cryo-EM structure of alpha-synuclein fibrils. *Elife* **7**: e36402. <https://doi.org/10.7554/eLife.36402>
- Guiney SJ, Adlard PA, Lei P, Mawal CH, Bush AI, Finkelstein DI, Aytton S (2020) Fibrillar α -synuclein toxicity depends on functional lysosomes. *J Biol Chem* **295**: 17497–17513. <https://doi.org/10.1074/jbc.RA120.013428>
- Gupta A, Vankar JK, Jadav JP, Gururaja GN (2022) Water mediated direct thioamidation of aldehydes at room temperature. *J Organic Chem* **87**: 2410–2420. <https://doi.org/10.1021/acs.joc.1c02307>
- Hayward S, Milner-White EJ (2021) Determination of amino acids that favour the α_1 region using Ramachandran propensity plots. Implications for α -sheet as the possible amyloid intermediate. *J Struct Biol* **213**: 107738. <https://doi.org/10.1016/j.jsb.2021.107738>
- Hojjatian A, Dasari AKR, Sengupta U, Taylor D, Daneshparvar N, Yeganeh FA, Dillard L, Michael B, Griffin RG, Borgnia M, Kaye R, Taylor KA, Lim KH (2021) Distinct cryo-Em structure of alpha-Synuclein filaments derived by tau. *BioRxiv* Preprint. <https://doi.org/10.1101/2020.12.31.424989>
- [https://www.ks.uiuc.edu/Research/vmd/accessed July 2022](https://www.ks.uiuc.edu/Research/vmd/accessed%20July%2022)
- Humphrey W, Dalke A, Schulten K (1996) VMD: visual molecular dynamics. *J Mol Graph* **14**: 27–28, 33–38. [https://doi.org/10.1016/0263-7855\(96\)00018-5](https://doi.org/10.1016/0263-7855(96)00018-5)
- Ishiyama T, Tahara T, Morita A (2022) Why the photochemical reaction of phenol becomes ultrafast at the air-water interface: the effect of surface hydration. *J Am Chem Soc* **144**: 6321–6325. <https://doi.org/10.1021/jacs.1c13336>
- Jayawardena N, Kaur M, Nair S, Malmstrom J, Goldstone D, Negron L, Gerrard JA, Domigan IJ (2017) Amyloid fibrils from hemoglobin. *Biomolecules* **7**: 37. <https://doi.org/10.3390/biom7020037>
- Kachapilly N, Srivastava J, Swain BP, Thakur P (2022) Interaction of alpha-synuclein with lipids. *Methods Cell Biol* **169**: 43–66. <https://doi.org/10.1016/bs.mcb.2021.12.002>
- Kaplaneris N, Vilches-Herrera M, Wu J, Ackermann L (2022) Sustainable ruthenium(II)-catalyzed C–H activations in and on H₂O. *ACS Sust Chem Engin* **10**: 6871–6888. <https://doi.org/10.1021/acssuschemeng.2c00873>

- Klabunde T, Petrassi HM, Oza VB, Raman P, Kelly JW, Sacchetti JC (2000) Rational design of potent human transthyretin amyloid disease inhibitors. *Nat Struct Biol* 7: 312–321. <https://doi.org/10.1038/74082>
- Lambley H, Schutzius TM, Poulikakos D (2020) Superhydrophobic surfaces for extreme environmental conditions. *Proc Natl Acad Sci U S A* 117: 27188–27194. <https://doi.org/10.1073/pnas.2008775117>
- Lashuel HA, Overk CR, Oueslati A, Masliah E (2013) The many faces of α -synuclein: from structure and toxicity to therapeutic target. *Nat Rev Neurosci* 14: 38–48. <https://doi.org/10.1038/nrn3406>
- Lassen LB, Reimer L, Ferreira N, Betzer C, Jensen PH (2016) Protein partners of α -synuclein in health and disease. *Brain Pathol* 26: 389–397. <https://doi.org/10.1111/bpa.12374>
- Lee H-J, Shin SY, Choi C, Lee YH, Lee S-J (2002) Formation and removal of alpha-synuclein aggregates in cells exposed to mitochondrial inhibitors. *J Biol Chem* 277: 5411–5417. <https://doi.org/10.1074/jbc.M105326200>
- Li B, Ge P, Murray KA, Sheth P, Zhang M, Nair G, Sawaya MR, Shin WS, Boyer DR, Ye S, Eisenberg DS, Zhou ZH, Jiang L (2018) Cryo-EM of full-length α -synuclein reveals fibril polymorphs with a common structural kernel. *Nat Commun* 9: 3609. <https://doi.org/10.1038/s41467-018-05971-2>
- Li J, Edwards PC, Burghammer M, Villa C, Schertler GFX (2004) Structure of bovine rhodopsin in a trigonal crystal form. *J Mol Biol* 343: 1409–1438. <https://doi.org/10.1016/j.jmb.2004.08.090>
- Li Y, Zhao C, Luo F, Liu Z, Gui X, Luo Z, Zhang X, Li D, Liu C, Li X (2018) Amyloid fibril structure of α -synuclein determined by cryo-electron microscopy. *Cell Res* 28: 897–903. <https://doi.org/10.1038/s41422-018-0075-x>
- Long H, Zheng W, Liu Y, Sun Y, Zhao K, Liu Z, Xia W, Lv S, Liu Z, Li D, He K-W, Liu C (2021) Wild-type α -synuclein inherits the structure and exacerbated neuropathology of E46K mutant fibril strain by cross-seeding. *Proc Natl Acad Sci U S A* 118: e2012435118. <https://doi.org/10.1073/pnas.2012435118>
- Lövestam S, Schweighauser M, Matsubara T, Murayama S, Tomita T, Ando T, Hasegawa K, Yoshida M, Tarutani A, Hasegawa M, Goedert M, Scheres SHW (2021) Seeded assembly *in vitro* does not replicate the structures of α -synuclein filaments from multiple system atrophy. *FEBS Open Bio* 11: 999–1013. <https://doi.org/10.1002/2211-5463.13110>
- McDowall JS, Brown DR (2016) Alpha-synuclein: relating metals to structure, function and inhibition. *Metallomics* 8: 385–397. <https://doi.org/10.1039/c6mt00026f>
- Milner-White JE, Watson JD, Qi G, Hayward S (2006) Amyloid formation may involve alpha- to beta sheet interconversion via peptide plane flipping. *Structure* 14: 1369–1376. <https://doi.org/10.1016/j.str.2006.06.016>
- Ni X, McGlinchey RP, Jiang J, Lee JC (2019) Structural insights into α -synuclein fibril polymorphism: effects of Parkinson's disease-related C-terminal truncations. *J Mol Biol* 431: 3913–3919. <https://doi.org/10.1016/j.jmb.2019.07.001>
- Ottolini D, Cali T, Szabó I, Brini M (2017) Alpha-synuclein at the intracellular and the extracellular side: functional and dysfunctional implications. *Biol Chem* 398: 77–100. <https://doi.org/10.1515/hsz-2016-0201>
- Peng C, Gathagan RJ, Lee VM (2018) Distinct α -Synuclein strains and implications for heterogeneity among α -Synucleinopathies. *Neurobiol Dis* 109(Pt B): 209–218. <https://doi.org/10.1016/j.nbd.2017.07.018>
- Prosswimmer T, Daggett V (2022) The role of α -sheet structure in amyloidogenesis: characterization and implications. *Open Biol* 12: 220261. <https://doi.org/10.1098/rsob.220261>
- Rana A, Gupta TP, Bansal S, Kundu B (2008) Formation of amyloid fibrils by bovine carbonic anhydrase. *Biochim Biophys Acta* 1784: 930–935. <https://doi.org/10.1016/j.bbapap.2008.02.020>
- Roterman I, Stapor K, Dulak D, Konieczny L (2022) The Possible mechanism of amyloid transformation based on the geometrical parameters of early-stage intermediate in silico model for protein folding. *Int J Mol Sci* 23: 9502. <https://doi.org/10.3390/ijms23169502>
- Roterman I, Stapor K, Konieczny L (2023) Structural specificity of α -synuclein amyloid. *Biomedicines* 11: 1324. <https://doi.org/10.3390/biomedicines11051324>
- Roterman I (1995) Modelling the optimal simulation path in the peptide chain folding – studies based on geometry of alanine heptapeptide. *J Theor Biol* 177: 283–288. <https://doi.org/10.1006/jtbi.1995.0245>
- Sawaya MR, Hughes MP, Rodriguez JA, Riek R, Eisenberg DS (2021) The expanding amyloid family: Structure, stability, function, and pathogenesis. *Cell* 184: 4857–4873. <https://doi.org/10.1016/j.cell.2021.08.013>
- Schmidt M, Wiese S, Adak V, Engler J, Agarwal S, Fritz G, Westermarck P, Zacharias M, Fändrich M (2019) Cryo-EM structure of a transthyretin-derived amyloid fibril from a patient with hereditary ATTR amyloidosis. *Nat Commun* 10: 5008. <https://doi.org/10.1038/s41467-019-13038-z>
- Schutzius TM, Jung S, Maitra T, Graeber G, Köhne M, Poulikakos D (2015) Spontaneous droplet trampolining on rigid superhydrophobic surfaces. *Nature* 527: 82–85
- Schweighauser M, Shi Y, Tarutani A, Kametani F, Murzin AG, Ghetti B, Matsubara T, Tomita T, Ando T, Hasegawa K, Murayama S, Yoshida M, Hasegawa M, Scheres SHW, Goedert M (2020) Structures of α -synuclein filaments from multiple system atrophy. *Nature* 585: 464–469. <https://doi.org/10.1038/s41586-020-2317-6>
- Serpell LC (2000) Alzheimer's amyloid fibrils: structure and assembly. *Biochim Biophys Acta* 1502: 16–30. [https://doi.org/10.1016/s0925-4439\(00\)00029-6](https://doi.org/10.1016/s0925-4439(00)00029-6)
- Siebert A, Rankovic M, Favretto F, Ukmar-Godec T, Strohäker T, Becker S, Zweckstetter M (2021) Interplay between tau and α -synuclein liquid-liquid phase separation. *Protein Sci* 30: 1326–1336. <https://doi.org/10.1002/pro.4025>
- Sivanesam K, Andersen NH (2016) Modulating the Amyloidogenesis of α -Synuclein. *Curr Neuropharmacol* 14: 226–237. <https://doi.org/10.2174/1570159x13666151030103153>
- Stephens AD, Zacharopoulou M, Kaminski Schierle GS (2019) The cellular environment affects monomeric α -synuclein structure. *Trends Biochem Sci* 44: 453–466. <https://doi.org/10.1016/j.tibs.2018.11.005>
- Sun Y, Hou S, Zhao K, Long H, Liu Z, Gao J, Zhang Y, Su X-D, Li D, Liu C (2020) Cryo-EM structure of full-length α -synuclein amyloid fibril with Parkinson's disease familial A53T mutation. *Cell Res* 30: 360–362. <https://doi.org/10.1038/s41422-020-0299-4>
- Sun Y, Long H, Xia W, Wang K, Zhang X, Sun B, Cao Q, Zhang Y, Dai B, Li D, Liu C (2021) The hereditary mutation G51D unlocks a distinct fibril strain transmissible to wild-type α -synuclein. *Nat Commun* 12: 6252. <https://doi.org/10.1038/s41467-021-26433-2>
- Trexler AJ, Rhoades E (2012) N-Terminal acetylation is critical for forming α -helical oligomer of α -synuclein. *Protein Sci* 21: 601–605. <https://doi.org/10.1002/pro.2056>
- Tuttle MD, Comellas G, Nieuwkoop AJ, Covell DJ, Berthold DA, Kloepper KD, Courtney JM, Kim JK, Barclay AM, Kendall A, Wan W, Stubbs G, Schwieters CD, Lee VMY, George JM, Rienstra CM (2016) Solid-state NMR structure of a pathogenic fibril of full-length human α -synuclein. *Nat Struct Mol Biol* 23: 409–415. <https://doi.org/10.1038/nsmb.3194>
- Ueda M (2022) Transthyretin: Its function and amyloid formation. *Neurochem Int* 155: 105313. doi: 10.1016/j.neuint.2022.105313
- Ulmer TS, Bax A, Cole NB, Nussbaum RL (2005) Structure and dynamics of micelle-bound human alpha-synuclein. *J Biol Chem* 280: 9595–9603. <https://doi.org/10.1074/jbc.M411805200>
- Villar-Piqué A, Lopes da Fonseca T, Outeiro TF (2016) Structure, function and toxicity of alpha-synuclein: the Bermuda triangle in synucleinopathies. *J Neurochem* 139 (Suppl 1): 240–255. <https://doi.org/10.1111/jnc.13249>
- Wada K, Sumi N, Nagai R, Iwasaki K, Sato T, Suzuki K, Hasegawa Y, Kitaoka S, Minami Y, Outten FW, Takahashi Y, Fukuyama K (2009) Molecular dynamics of Fe-S cluster biosynthesis implicated by the structure of the SufC(2)-SufD(2) complex. *J Mol Biol* 387: 245–258. <https://doi.org/10.1016/j.jmb.2009.01.054>
- Wei Z, Li Y, Cooks RG, Yan X (2020) Accelerated reaction kinetics in microdroplets: overview and recent developments. *Annu Rev Phys Chem* 71: 31–51. <https://doi.org/10.1146/annurev-physchem-121319-110654>
- Xiaodan N, Ryan PM, Jansen J, Jennifer CL (2021) Cryo-EM structure of the N-terminal alpha-synuclein truncation 41-140. *Proc Natl Acad Sci U S A* 118: (35) e2023487118. <https://doi.org/10.1073/pnas.2023487118>
- Zhao K, Li Y, Liu Z, Long H, Zhao C, Luo F, Sun Y, Tao Y, Su X-D, Li D, Li X, Liu C (2020) Parkinson's disease associated mutation E46K of α -synuclein triggers the formation of a distinct fibril structure. *Nat Commun* 11: 2643. <https://doi.org/10.1038/s41467-020-16386-3>
- Zhao K, Lim Y-J, Liu Z, Long H, Sun Y, Hu J-J, Zhao C, Tao Y, Zhang X, Li D, Li Y-M, Liu C (2020) Parkinson's disease-related phosphorylation at Tyr39 rearranges α -synuclein amyloid fibril structure revealed by cryo-EM. *Proc Natl Acad Sci U S A* 117: 20305–20315. <https://doi.org/10.1073/pnas.1922741117>
- Zuo Y-J, Jin Qu (2014) How does aqueous solubility of organic reactant affect a water-promoted reaction?. *J Organic Chem* 79: 6832–6839. <https://doi.org/10.1021/jo500733v>

Mapping the substrate-binding subsite specificity of a *Porphyromonas gingivalis* Tpr peptidase

Dominika Staniec¹, Wioletta Rut², Marcin Drąg², Michał Burmistrz¹, Michael Kitching³ and Jan Potempa^{1,4}✉

¹Department of Microbiology, Faculty of Biochemistry, Biophysics and Biotechnology, Jagiellonian University, Kraków, Poland; ²Department of Chemical Biology and Bioimaging, Wrocław University of Science and Technology, Wrocław, Poland; ³Christina Lee Brown Envirome Institute, Division of Environmental Medicine, Department of Medicine, University of Louisville, Louisville, KY, USA; ⁴Department of Oral Immunity and Infectious Diseases, University of Louisville School of Dentistry, Louisville, KY, USA

Calcium-dependent peptidases of the calpain family are widespread in eukaryotes but uncommon in prokaryotes. A few bacterial calpain homologs have been discovered but none of them have been characterized in detail. Here we present an in-depth substrate specificity analysis of the bacterial calpain-like peptidase Tpr from *Porphyromonas gingivalis*. Using the positional scanning hybrid combinatorial substrate library method, we found that the specificity of Tpr peptidase differs substantially from the papain family of cysteine proteases, showing a strong preference for proline residues at positions P2 and P3. Such a degree of specificity indicates that this *P. gingivalis* cell-surface peptidase has a more sophisticated role than indiscriminate protein degradation to generate peptide nutrients, and may fulfil virulence-related functions such as immune evasion.

Key words: proteolytic activity, calcium-dependent activity, periodontitis, calpain, virulence factor, substrate specificity

Received: 30 June, 2023; **revised:** 17 July, 2023; **accepted:** 09 November, 2023; **available on-line:** 08 December, 2023

✉ e-mail: jan.potempa@uj.edu.pl

Acknowledgements of Financial Support: grant K/PBM/000537 (to D. S.) from the National Science Center (NCN, Kraków, Poland)

Abbreviations: HyCoSul, Hybrid Combinatorial Substrate Library

INTRODUCTION

Periodontal disease is the most prevalent chronic infection in the world, affecting up to 90% of the global population (Pihlstrom *et al.*, 2005). Inflammation of the gingival tissues is caused by dysbiosis, a pathogenic shift in the microbial community (Loesche & Grossman, 2001). Chronic inflammation leads to the destruction of tooth-supporting tissues such as the gingiva, periodontal ligament, and alveolar bone (Loesche, 1996). If left untreated, periodontitis can result in tooth loss and the systemic dissemination of periodontal pathogens and/or their products (Cobb *et al.*, 2009). This increases the risk of cardiovascular disease (Friedewald *et al.*, 2009; Wegner *et al.*, 2009), rheumatoid arthritis (de Pablo *et al.*, 2009), aspiration pneumonia (Olsen & Potempa, 2014), diabetes (Chee *et al.*, 2013) and adverse pregnancy outcomes (Ide & Papanou, 2013).

The primary etiological agents of human periodontitis include *Porphyromonas gingivalis*, *Tannerella forsythia*, and *Treponema denticola* (Griffen *et al.*, 1998; Rôças *et al.*, 2001). The virulence factors these pathogens secrete include peptidases that contribute to the initiation and progres-

sion of periodontal disease (Dashper *et al.*, 2011; Potempa *et al.*, 2003). In particular, the aggressive periodontal pathogen *P. gingivalis* produces multiple proteolytic enzymes (Potempa *et al.*, 1995) that are required for important bacterial processes such as nutrient acquisition and immune evasion, driving pro-inflammatory responses within the gingival pocket. The proteolytic enzymes secreted by *P. gingivalis* include serine proteases (Nonaka *et al.*, 2014), cysteine proteases such as lysine-specific (Kgp) and arginine-specific (Rgp) gingipains (Bhagal *et al.*, 1997), PrtT protease (Tokuda *et al.*, 1998), periodontain (Nelson *et al.*, 1999) and thiol protease (Tpr) (Staniec *et al.*, 2015). Gingipains (Kgp & Rgp) account for 85% of all extracellular protease activity for *P. gingivalis* (Potempa *et al.*, 1997). Accordingly, the influence of gingipains on *P. gingivalis* virulence has been demonstrated but the role of the other peptidases remains unclear (Imamura, 2003).

Tpr is a functional cysteine peptidase encoded by the PG1055 gene (Staniec *et al.*, 2015). Distant sequence homology and calcium dependence suggest that Tpr belongs to the calpain family (EC 3.4.22.17; MEROPS family C2) of calcium-dependent cysteine peptidases produced by almost all eukaryotes and some bacteria, but not archaea (Rawlings, 2015). Calpains are ubiquitously expressed in mammalian cells and are involved in essential cellular processes such as cytoskeletal remodeling (Lebart & Benyamin, 2006), cell migration (Franco & Huttenlocher, 2005), cell differentiation (De Maria *et al.*, 2009; Garach-Jehoshua *et al.*, 1998) and apoptosis (Momeni, 2011). Gain-of-function calpain mutations are associated with muscular dystrophy (Wadosky *et al.*, 2011), rheumatoid arthritis (Morita *et al.*, 2006), Alzheimer's disease (Huang & Wang, 2001), improper platelet aggregation (Kuchay & Chishti, 2007), and Wolfram syndrome (Lu *et al.*, 2014). However, no examples of the pathological effects of prokaryotic calpain-like peptidases have been reported thus far.

Eukaryotic calpains are highly-conserved intracellular enzymes that can be assigned to the categories μ or m according to their micromolar or millimolar requirements for calcium *in vitro* (Suzuki *et al.*, 1995). Intriguingly, the specificity of both categories appears identical (Sorimachi *et al.*, 1997). The calcium-mediated regulation of proteolytic activity (Hanna *et al.*, 2008) may require cooperative interactions between several calcium binding sites, including three EF hand motifs, the negatively charged segments around the active site cleft, and an exposed acidic loop (Reverter *et al.*, 2001). However, the precise molecular mechanism is unknown. Although the physiological substrates remain poorly characterized, several

have been identified *in vitro*, including selected β -integrins (Du *et al.*, 1995), focal adhesion kinase (Cooray *et al.*, 1996), paxillin, and talin (Carragher *et al.*, 1999).

The autoprocessing and maturation of the Tpr precursor requires millimolar levels of calcium (Staniec *et al.*, 2015). This requirement prevents the premature activation of Tpr in the cytoplasm and ensures the structure is resistant to degradation by gingipains (Staniec *et al.*, 2015). The elevated expression of the *tpr* gene under nutrient-limited conditions (Lu & McBride, 1998) and the location of the enzyme in the outer membrane (Park *et al.*, 1997; Staniec *et al.*, 2015) suggest that Tpr is involved in the production of small peptides that are used as substrates for amino acid fermentation. Given that multiple physiologically relevant proteins are degraded, including key elements of the innate immune system and proteins abundant in gingival crevicular fluid, Tpr may also contribute to the pathogenesis of periodontitis (Staniec *et al.*, 2015).

A detailed analysis of Tpr substrate specificity is required to understand its contribution to the pathogenicity of *P. gingivalis*, but only a superficial characterization has been reported thus far (Staniec *et al.*, 2015). Here, we fully characterized the substrate specificity of the most active form of Tpr using Hybrid Combinatorial Substrate Library (HyCoSuL) approach to gain insight into the proteolytic mechanism and thus the function of this cell-surface peptidase.

MATERIALS & METHODS

Reagents and equipment

Isopropyl-1-thio- β -D-galactopyranoside (IPTG), ethylenediaminetetraacetic acid (EDTA), lysogeny broth (LB), L-glutathione, Tris-HCl, NaCl, dithiothreitol (DTT), sodium azide, and L-cysteine were purchased from Sigma-Aldrich. A MonoQ column was obtained from Cytiva.

Protein expression

The inactive Tpr zymogen (Tpr55) was expressed in *Escherichia coli* BL21 (DE3) cells and purified as previously described with some modifications (Staniec *et al.*, 2015). Briefly, the *PG1055* coding sequence without the signal peptide was transferred to the expression vector pGEX-6P-1, which provides the sequence for an N-terminal glutathione S-transferase (GST) tag. This construct was then introduced into electrocompetent *E. coli* BL21 cells, which were cultivated in LB at 37°C. As soon as the culture reached an optical density at 600 nm (OD_{600nm}) of 0.7, Tpr55 expression was induced by supplementing the medium with 0.5 M IPTG and incubating for a further 3 h at 37°C.

Protein purification

Transformed *E. coli* BL21 cells were harvested by centrifugation (8000×g, 20 min, 4°C) and resuspended in PBS containing 10 mM EDTA to bind any residual Ca^{2+} that would induce the premature autoprocessing of Tpr55. To recover intracellular Tpr55, the bacterial cell pellet was disrupted by sonication (60% amplitude for 5 min with 30-s pulses) and the cell debris was removed by centrifugation (18000×g, 20 min, 4°C). Tpr55 was recovered by passing the supernatant through a glutathione-Sepharose column and eluting the bound Tpr55 stepwise with increasing glutathione concentration in

elution buffer (50 mM Tris-HCl, 20 mM L-glutathione, pH 8.0).

To remove small molecular contaminants, the eluted Tpr55 was dialyzed against PreScission Protease cleavage buffer (50 mM Tris-HCl, 150 mM NaCl, 1 mM EDTA, 1 mM DTT, pH 7.0) and the GST tag was cleaved off with 40 U PreScission Protease at 4°C for 16 h. The sample was then dialyzed against 20 mM ethanolamine (pH 9.0) and applied to a MonoQ column equilibrated in dialysis buffer to separate Tpr55 from GST. Final purification was accomplished by gel filtration on a Superdex 75 column in 50 mM Tris-HCl (pH 7.6) containing 150 mM NaCl. The full-length Tpr55 was routinely purified with a yield >1 mg/L starting culture.

Proteolytically active Tpr (Tpr33) was obtained by autoprocessing the purified Tpr55 as previously described (Staniec *et al.*, 2015). Briefly, purified Tpr55 was incubated in activation buffer (50 mM Tris-HCl pH 7.6, containing 150 mM NaCl, 5 mM $CaCl_2$, 0.2% sodium azide, and 10 mM L-cysteine) for 7 h at 37°C.

Analysis of substrate specificity

Tpr33 substrate specificity was assessed using the HyCoSuL screening approach and a defined P1 library with the general structure Ac-Ala-Ala-Pro-P1-ACC, where P1 comprises one of either 19 canonical amino acids (except cysteine) or norleucine, synthesized as previously described (Kasperkiewicz *et al.*, 2015; Larsen *et al.*, 2007; Poręba *et al.*, 2014, 2017). Cleavage of the peptide substrate was detected by monitoring the release of the fluorescent label 7-amino-4-carbamoylmethylcoumarin (ACC).

To determine Tpr33 substrate specificity at the P4, P3 and P2 positions, we used a HyCoSuL with arginine fixed in P1 (Fig. 1). Each of the tetrapeptide sublibraries featured an equimolar mixture of 19 amino acids (without cysteine and methionine, but including norleucine) at two positions and one of 19 canonical amino acids plus 102 non-standard amino acids in the position selected for analysis (Fig. 1).

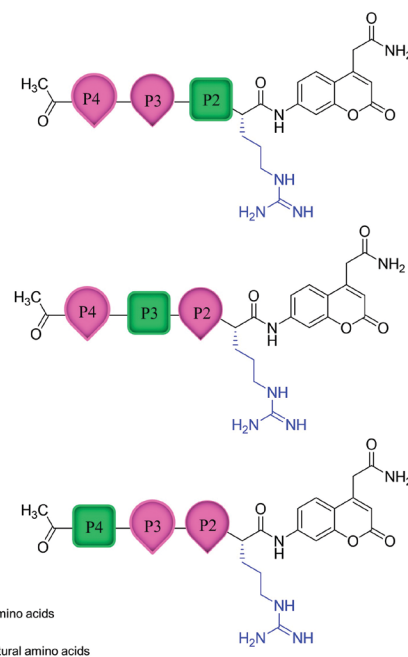


Figure 1. HyCoSuL structure.

Table 1. Kinetic parameters for selected substrates hydrolysis by Tpr33

Substrate							K_M [μM]		k_{cat} [s^{-1}]		k_{cat}/K_M [$\mu M^{-1}s^{-1}$]	
	P5	P4	P3	P2	P1	P1'						
i	Ac	Phe	Gly	Pro	Arg	ACC	150	± 1	14.3	± 1.4	96	± 9
ii	Ac	Lys	Gly	Pro	Arg	ACC	166	± 12	11.8	± 0.3	71	± 7
iii	Ac	Dap	Gly	Pro	Arg	ACC	118	± 1	14.3	± 0.1	121	± 1
iv		Ac	Idc	Pro	Arg	ACC	71	± 5	8.9	± 0.6	127	± 17
v	Ac	Gly	Idc	Cha	Arg	ACC	285	± 73	1.5	± 0.4	5.4	± 2.8
vi		NH	Idc	Cha	Arg	ACC	395	± 34	0.32	± 0.02	0.8	± 0.1
vii	Ac	Gly	Thz	Cha	Arg	ACC	711	± 42	1.12	± 0.03	1.6	± 0.1
viii		Ac	Thz	Cha	Arg	ACC	169	± 37	0.71	± 0.06	4.1	± 1.2

Tpr33 was activated by incubating 500 nM of the enzyme in activation buffer for 30 min at 37°C. To determine the enzymatic activity of Tpr33 in each sub-library, fluorescence was recorded (excitation=355 nm, emission=460 nm) 30 min after the addition of substrates. The P4, P3 and P2 sub-libraries were tested at an initial concentration of 100 μ M whereas the P1 library was tested at 10 μ M. The slope of the linear range of each curve was recorded as relative fluorescence units per second (RFU/s). Data from each sub-library were normalized to the highest RFU/s value for each specific sub-library.

Kinetic measurements

Selected substrates (Table 1) were prepared by solid phase peptide synthesis as described elsewhere (Poręba *et al.*, 2014). To determine the catalytic parameters of Tpr against these substrates, Tpr33 was titrated with the irreversible cysteine protease inhibitor E-64 as previously described (Staniec *et al.*, 2015). Peptidase activity was determined at increasing concentrations of each substrate in 50 mM Tris-HCl (pH 7.6) containing 150 mM NaCl, 5 mM CaCl_2 and 0.02% sodium azide. Velocities of substrate hydrolysis were plotted against the substrate concentration, and the k_{cat} and K_{M} values were calculated using GraphPad Prism macro.

RESULTS

Substrate specificity of the Tpr33 protease

In our previous explorative study (Staniec *et al.*, 2015) we found that Tpr33 preferentially hydrolyzes substrates containing arginine at the P1 position (nomenclature according to Schechter & Berger, 1967). Therefore, we initially investigated the amino acid preference at the S4–S2 subsites of Tpr33, followed by a more thorough interrogation of the amino acid preference at the S1 subsite. Accordingly, the P2, P3 and P4 sublibraries had arginine fixed at the P1 position (Fig. 1).

Tpr33 showed exclusive specificity for substrates that incorporated proline or alanine at the P2 position (Fig. 2A). This exclusivity was maintained when non-proteinogenic amino acids were included. None of the D stereoisomers of standard amino acids and only six of 83 non-standard amino acids resulted in hydrolysis when incorporated at the P2 position. Among these non-stand-

ard residues, only the thiazolidine-based residue L-Thz, which structurally resembles proline, resulted in hydrolysis with similar efficiency to the proline-P2 sub-library (Fig. 2B).

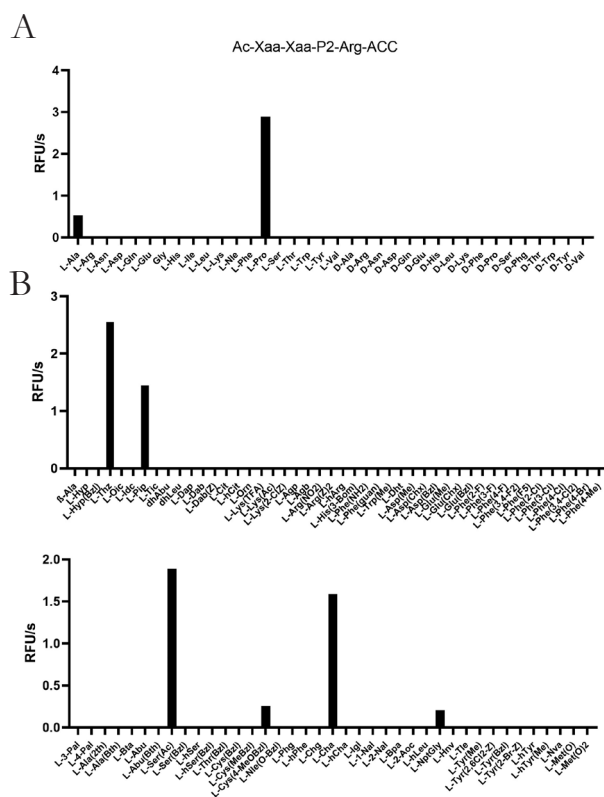


Figure 2. Specificity of Tpr33 for substrates containing canonical and non-proteinogenic amino acids at the P2 position as determined using the HyCoSuL screening approach.

The substrate preferences at position P2 were determined using a combinatorial tetrapeptide library with the general structure Ac-Xaa-Xaa-P2-Arg-ACC, where P2 represents (A) canonical or (B) non-proteinogenic amino acids and Xaa represents an equimolar mixture of 19 amino acids (all standard proteinogenic amino acids except cysteine and methionine, supplemented with norleucine). Abbreviated amino acid names are shown on the x-axis and explained in the Supplementary Materials at <https://ojps.ptbioch.edu.pl/index.php/abp/>. The y-axis shows the mean activity expressed as relative fluorescence units per second [RFU/s]. The data are means of three independent measurements.

against the best substrate containing a canonical amino acid (Fig. 4B).

Having documented the restricted substrate preference of Tpr33 at subsite S2, we reevaluated the substrate specificity at position S1 using a library containing proline fixed at P2 (Ac-Ala-Ala-Pro-P1-ACC). Tpr33 preferred arginine at position P1 in a substrate, consistent with the results of our previous explorative study (Staniec *et al.*, 2015). However, several other residues with different physicochemical characteristics were also efficiently recognized, indicating that Tpr33 has low specificity for a residue in position P1 of a substrate (Fig. 5).

Kinetic analysis of Tpr33 activity

The randomization of amino acids at certain positions in the HyCoSuL as well as cooperation between subsites may affect the efficiency of Tpr33. To validate the results generated by the HyCoSuL method, we designed and synthesized a selection of substrates and determined their kinetic parameters.

The k_{cat}/K_M value of the substrate containing the preferred canonical amino acids at each position (Ac-Phe-Gly-Pro-Arg-ACC) was $96 \mu\text{M}^{-1}$ (Table 1). A near-identical substrate containing lysine at the P4 position (Ac-Lys-Gly-Pro-Arg-ACC) had slightly inferior kinetic parameters ($k_{\text{cat}}/K_M = 71 \pm 7 \mu\text{M}^{-1}$) reflecting the lower efficiency of the Lys-P4 sub-library. Another near-identical substrate, this time containing L-Dap at the P4 position (Ac-Dap-Gly-Pro-Arg-ACC) was superior to both of the above ($k_{\text{cat}}/K_M = 121 \pm 1 \mu\text{M}^{-1}$), in agreement with the HyCoSuL library screening data. Substrates containing proline at position P3 (Ac-Idc-Pro-Arg-ACC) or glycine at the same position (Ac-Dap-Gly-Pro-Arg-ACC) shared comparable k_{cat}/K_M values, which appeared to contradict the results of the HyCoSuL screening. However, Ac-Dap-Gly-Pro-Arg-ACC is one residue longer than Ac-Idc-Pro-Arg-ACC, and longer substrates are generally better recognized by peptidases, so this may explain this apparent discrepancy. Finally, substrates with Idc (Ac-Gly-Idc-Cha-Arg-ACC and Idc-Cha-Arg-ACC) or Thz (Ac-Gly-Thz-Cha-Arg-ACC and Ac-Thz-Cha-Arg-ACC) at the P3 and Cha at P2 positions, respectively, were hydrolyzed 17–150-fold less efficiently (based on k_{cat}/K_M values) than substrates with Gly-Pro and Idc-Pro at the same positions. This contrasts with the efficiency of hydrolysis of the P2 Cha and P3 Idc/Thz sub-libraries.

Tpr33 activity against the synthetic substrates mostly agreed with the HyCoSuL screening method. Substrates with non-standard amino acids were better recognized than those containing the most preferred canonical amino acids at positions P4–P2. Furthermore, the best-recognized substrate (Ac-Idc-Pro-Arg-ACC) had the lowest K_M value. These data suggest that substrate recognition site S4 is poorly defined, resulting in weaker interactions between amino acids and the S4 pocket.

DISCUSSION

We investigated the substrate preference of the calpain-like peptidase Tpr33 at the S4–S2 subsites and reevaluated the specificity at the S1 subsite using a comprehensive library of defined and highly efficient substrates including the incorporation of non-standard amino acids. Calpain-like peptidases are widespread among eukaryotes, but homologous genes are present only in a few bacterial phyla (Rawlings, 2015). Thus far, Tpr is the only bacterial calpain-like peptidase that has been functionally characterized (Staniec *et al.*, 2015). Given the

small number of calpain-like peptidases in prokaryotes, it is not unlikely that *P. gingivalis* acquired Tpr by horizontal transfer from a mammalian host.

Like the m-calpains, a millimolar concentration of calcium is required to activate the Tpr zymogen and such concentrations are found in the extracellular fluid where Tpr is secreted. The calcium-mediated activation of Tpr prevents intracellular activation of the enzyme, which may be cytotoxic. Due to their potential cytotoxicity if left unregulated, peptidases are tightly controlled. Similar mechanisms to prevent the deleterious activity of misdirected secreted peptidases are widespread, including trypsin inhibitors produced by pancreatic cells (Hirota *et al.*, 2006).

The HyCoSuL method allowed us to explore the substrate specificity of Tpr, revealing the repertoire of physiologically accessible substrates. As previously reported for papain (Choe *et al.*, 2006) and calpain (Cuerrier *et al.*, 2005; Shinkai-Ouchi *et al.*, 2016; Tompa *et al.*, 2004), the specificity of Tpr is determined at the S2 subsite whereas S1 is much less selective, albeit with some preference for positively charged residues in all three enzymes. However, the specificity of the S2 subsite differs between Tpr, papain and calpain. Tpr strongly selects proline whereas papain prefers valine but also accepts bulky aromatic and large hydrophobic residues, and calpain accepts several medium-sized residues. The S3 subsite also shows a degree of selectivity, but again this differs between the three enzymes. All three accept proline, but Tpr also accepts bulky aromatic and small side chain residues, whereas papain prefers arginine, lysine and medium-sized side chain residues, and calpain tolerates multiple residues with dissimilar physicochemical properties while simultaneously excluding several residues. Tpr shows broad specificity for amino acid residues in position P4 in a substrate.

Peptidases play a key role in nutrient acquisition by *P. gingivalis* (Potempa & Pike, 2009). We found that Tpr is not restrictively specific at any substrate-binding subsites, but the combination of relatively high selectivity at the S2 and S3 subsites may limit the number of substrates susceptible to Tpr proteolytic activity. Such characteristics are unexpected for a digestive peptidase and suggest a more specialized role, possibly associated with the evasion of host immune defenses.

Peptidases attack the most sterically accessible regions of substrates, often cutting in loops and other unstructured regions. Proline residues are often overrepresented in such regions (Fontana *et al.*, 1986), which also tend to be functionally significant – for example, proline-rich regions are known to be involved in protein–protein interactions (Yu *et al.*, 1994). The relative preference of Tpr for proline residues at positions P2 and P3 in substrates may suggest the involvement of Tpr in the modulation of protein–protein interactions. Eukaryotic proline-specific proteases mediate cell signaling events by modulating protein–protein interactions (Dunaevsky *et al.*, 2020) and the possibility that Tpr has a similar role should be evaluated in future studies.

CONCLUSION

HyCoSuL screening revealed that the substrate specificity of Tpr is primarily determined at the S2 and S3 substrate-binding subsites, with proline being the most preferred residue in both cases. The specificity of Tpr therefore differs from that of the related eukaryotic proteases papain and calpain, and is likely to play a more

sophisticated role in bacterial physiology than indiscriminate protein degradation for the provision of nutrients, which would be facilitated by non-specific protease activity.

Declarations

Acknowledgments. We thank Paulina Kasperkiewicz-Wasilewska for providing the defined P1 library. DS was a beneficiary of the Visby Programme of the Swedish Institute. This study was supported by the grant (Preludium 2017/25/N/NZ1/00892) from Polish National Science Center (NCN) to D.S.

REFERENCES

- Bhogal PS, Slakeski N, Reynolds EC (1997) A cell-associated protein complex of *Porphyromonas gingivalis* W50 composed of Arg- and Lys-specific cysteine proteinases and adhesins. *Microbiology* (Reading) **143**: 24852495. <https://doi.org/10.1099/00221287-143-7-2485>
- Carragher NO, Levkau B, Ross R, Raines EW (1999) Degraded collagen fragments promote rapid disassembly of smooth muscle focal adhesions that correlates with cleavage of pp125(FAK), paxillin, and talin. *J Cell Biol* **147**: 619–629. <https://doi.org/10.1083/jcb.147.3.619>
- Chee B, Park B, Bartold PM (2013) Periodontitis and type II diabetes: A two-way relationship. *Int J Evid Based Healthc* **11**: 317–329. <https://doi.org/10.1111/1744-1609.12038>
- Choe Y, Leonetti F, Greenbaum DC, Lecaillon F, Bogoy M, Brömme D, Ellman JA, Craik CS (2006) Substrate profiling of cysteine proteases using a combinatorial peptide library identifies functionally unique specificities. *J Biol Chem* **281**: 12824–12832. <https://doi.org/10.1074/jbc.M513331200>
- Cobb CM, Williams KB, Gerkovitch MM (2009) Is the prevalence of periodontitis in the USA in decline? *Periodontology* **2000** **50**: 13–24. <https://doi.org/10.1111/j.1600-0757.2008.00284.x>
- Cooray P, Yuan Y, Schoenwaelder SM, Mitchell CA, Salem HH, Jackson SP (1996) Focal adhesion kinase (pp125FAK) cleavage and regulation by calpain. *Biochem J* **318**: 41–47. <https://doi.org/10.1042/bj3180041>
- Cuerrero D, Moldoveanu T, Davies PL (2005) Determination of peptide substrate specificity for mu-calpain by a peptide library-based approach: the importance of primed site interactions. *J Biol Chem* **280**: 40632–40641. <https://doi.org/10.1074/jbc.M506870200>
- Dashper SG, Seers CA, Tan KH, Reynolds EC (2011) Virulence factors of the oral spirochete *Treponema denticola*. *J Dent Res* **90**: 691–703. <https://doi.org/10.1177/0022034510385242>
- De Maria A, Shi Y, Kumar NM, Bassnett S (2009) Calpain expression and activity during lens fiber cell differentiation. *J Biol Chem* **284**: 13542–13550. <https://doi.org/10.1074/jbc.M900561200>
- de Pablo P, Chapple ILC, Buckley CD, Dietrich T. (2009) Periodontitis in systemic rheumatic diseases. *Nat Rev Rheumatol* **5**: 218–224. <https://doi.org/10.1038/nrrheum.2009.28>
- Du X, Saido TC, Tsubuki S, Indig FE, Williams MJ, Ginsberg MH (1995) Calpain cleavage of the cytoplasmic domain of the integrin subunit. *J Biol Chem* **270**: 26146–26151. <https://doi.org/10.1074/jbc.270.44.26146>
- Dunaevsky YE, Tereshchenkova VF, Oppert B, Belozersky MA, Filipova IY, Elpidina EN (2020) Human proline specific peptidases: A comprehensive analysis. *Biochim Biophys Acta* **1864**: 129636. <https://doi.org/10.1016/j.bbagen.2020.129636>
- Fontana A, Fassina G, Vita C, Dalzoppo D, Zamai M, Zamboni M (1986) Correlation between sites of limited proteolysis and segmental mobility in thermolysin. *Biochemistry* **25**: 1847–1851. <https://doi.org/10.1021/bi00356a001>
- Franco SJ, Huttenlocher A (2005) Regulating cell migration: calpains make the cut. *J Cell Sci* **118**: 3829–3838. <https://doi.org/10.1242/jcs.02562>
- Friedewald VE, Kornman KS, Beck JD, Genco R, Goldfine A, Libby P, Offenbacher S, Ridker PM, Van Dyke TE, Roberts WC (2009) The American Journal of Cardiology and Journal of Periodontology Editors' Consensus: Periodontitis and Atherosclerotic Cardiovascular Disease. *J Periodontol* **80**: 1021–1032. <https://doi.org/10.1902/jop.2009.097001>
- Garach-Jehoshua O, Ravid A, Liberman UA, Reichrath J, Glaser T, Koren R (1998) Upregulation of the calcium-dependent protease, calpain, during keratinocyte differentiation. *Br J Dermatol* **139**: 950–957. <https://doi.org/10.1046/j.1365-2133.1998.02548.x>
- Griffen AL, Becker MR, Lyons SR, Moeschberger ML, Leys EJ (1998) Prevalence of *Porphyromonas gingivalis* and periodontal health status. *J Clin Microbiol* **36**: 3239–3242. <https://doi.org/10.1128/JCM.36.11.3239-3242.1998>
- Hanna RA, Campbell RL, Davies PL (2008) Calcium-bound structure of calpain and its mechanism of inhibition by calpastatin. *Nature* **456**: 409–412. <https://doi.org/10.1038/nature07451>
- Hirota M, Ohmuraya M, Baba H (2006) The role of trypsin, trypsin inhibitor, and trypsin receptor in the onset and aggravation of pancreatitis. *J Gastroenterol* **41**: 832–836. <https://doi.org/10.1007/s00535-006-1874-2>
- Huang Y, Wang KK (2001) The calpain family and human disease. *Trends Mol Med* **7**: 355–362. [https://doi.org/10.1016/S1471-4914\(01\)00249-4](https://doi.org/10.1016/S1471-4914(01)00249-4)
- Ide M, Papapanou PN (2013) Epidemiology of association between maternal periodontal disease and adverse pregnancy outcomes—systematic review. *J Clin Periodontol* **40** (Suppl 14): S181–S194. <https://doi.org/10.1111/jcpe.12063>
- Imamura T (2003) The role of gingipains in the pathogenesis of periodontal disease. *J Periodontol* **74**: 111–118. <https://doi.org/10.1902/jop.2003.74.1.111>
- Kasperkiewicz P, Poreba M, Snipas SJ, Lin SJ, Kirchhofer D, Salvesen GS, Drag M (2015) Design of a selective substrate and activity based probe for human neutrophil serine protease 4. *PLoS One* **10**: e0132818. <https://doi.org/10.1371/journal.pone.0132818>
- Kuchay SM, Chishti AH (2007) Calpain-mediated regulation of platelet signaling pathways. *Curr Opin Hematol* **14**: 249–254. <https://doi.org/10.1097/MOH.0b013e3280ef68f8>
- Larsen KS, Østergaard H, Bjelke JR, Olsen OH, Rasmussen HB, Christensen L, Kregelund BB, Stenricke HR (2007) Engineering the substrate and inhibitor specificities of human coagulation Factor VIIa. *Biochem J* **405**: 429–438. <https://doi.org/10.1042/BJ20061901>
- Lebart MC, Benyamin Y (2006) Calpain involvement in the remodeling of cytoskeletal anchorage complexes. *FEBS J* **273**: 3415–3426. <https://doi.org/10.1111/j.1742-4658.2006.05350.x>
- Loesche WJ (1996) Microbiology of dental decay and periodontal disease. In *Medical Microbiology* 4th edn, Baron S ed, chapter 99. University of Texas Medical Branch at Galveston. <https://www.ncbi.nlm.nih.gov/books/NBK8259/>
- Loesche WJ, Grossman NS (2001) Periodontal disease as a specific, albeit chronic, infection: Diagnosis and treatment. *Clin Microbiol Rev* **14**: 727–752. <https://doi.org/10.1128/CMR.14.4.727-752.2001>
- Lu B, McBride BC (1998) Expression of the trypsin-like gene of *Porphyromonas gingivalis* is regulated by peptide nutrients. *Infect Immun* **66**: 5147–5156. <https://doi.org/10.1128/IAI.66.11.5147-5156.1998>
- Lu S, Kanekura K, Hara T, Mahadevan J, Spears LD, Oslowski CM, Martinez R, Yamazaki-Inoue M, Toyoda M, Neilson A, Blanner P, Brown CM, Semenkovich CF, Marshall BA, Hershey T, Umezawa A, Greer PA, Urano F (2014) A calcium-dependent protease as a potential therapeutic target for Wolfram syndrome. *Proc Natl Acad Sci USA* **111**: E5292–E5301. <https://doi.org/10.1073/pnas.1421055111>
- Momeni HR (2011) Role of calpain in apoptosis. *Cell J* **13**: 65–72
- Morita M, Banno Y, Dohjima T, Nozawa S, Fushimi K, Fan DG, Ohno T, Miyazawa K, Liu N, Shimizu K (2006) Mu-calpain is involved in the regulation of TNF-alpha-induced matrix metalloproteinase-3 release in a rheumatoid synovial cell line. *Biochem Biophys Res Commun* **343**: 937–942. <https://doi.org/10.1016/j.bbrc.2006.02.155>
- Nelson D, Potempa J, Kordula T, Travis J (1999) Prolyl tripeptidyl peptidase from *Porphyromonas gingivalis*. A novel enzyme with possible pathological implications for the development of periodontitis. *J Biol Chem* **274**: 9246–9252. <https://doi.org/10.1074/jbc.274.14.9246>
- Nonaka M, Shoji M, Kadowaki T, Sato K, Yukitake H, Naito M, Nakayama K. (2014) Analysis of a Lys-specific serine endopeptidase secreted via the type IX secretion system in *Porphyromonas gingivalis*. *FEMS Microbiol Lett* **354**: 60–68. <https://doi.org/10.1111/1574-6968.12426>
- Olsen I, Potempa J (2014) Strategies for the inhibition of gingipains for the potential treatment of periodontitis and associated systemic diseases. *J Oral Microbiol* **18**: 6. <https://doi.org/10.3402/jom.v6.24800>
- Park Y, Lu B, Mazur C, McBride BC (1997) Inducible expression of a *Porphyromonas gingivalis* W83 membrane-associated protease. *Infect Immun* **65**: 1101–1104. <https://doi.org/10.1128/IAI.65.3.1101-1104.1997>
- Pihlstrom BL, Michalowicz BS, Johnson NW (2005) Periodontal diseases. *Lancet* **366**: 1809–1820. [https://doi.org/10.1016/S0140-6736\(05\)67728-8](https://doi.org/10.1016/S0140-6736(05)67728-8)
- Poreba M, Szalek A, Kasperkiewicz P, Drag M (2014) Unnatural amino acids increase sensitivity and provide for the design of highly selective caspase substrates. *Methods Mol Biol* **1133**: 41–59. https://doi.org/10.1007/978-1-4939-0357-3_2
- Poreba M, Salvesen GS, Drag M (2017) Synthesis of a HyCoSuL peptide substrate library to dissect protease substrate specificity. *Nat Protoc* **12**: 2189–2214. <https://doi.org/10.1038/nprot.2017.091>
- Potempa J, Pavloff N, Travis J (1995) *Porphyromonas gingivalis*: a proteinase/gene accounting audit. *Trends Microbiol* **3**: 430–434. [https://doi.org/10.1016/s0966-842x\(00\)88996-9](https://doi.org/10.1016/s0966-842x(00)88996-9)

- Potempa J, Pike RN (2009) Corruption of innate immunity by bacterial proteases. *J Innate Immun* **1**: 70–87. <https://doi.org/10.1159/000181144>
- Potempa J, Pike R, Travis J (1997) Titration and mapping of the active site of cysteine proteinases from *Porphyromonas gingivalis* (gingipains) using peptidyl chloromethanes. *Biol Chem* **378**: 223–230. <https://doi.org/10.1515/bchm.1997.378.3-4.223>
- Potempa J, Sroka A, Imamura T, Travis J (2003) Gingipains, the major cysteine proteinases and virulence factors of *Porphyromonas gingivalis*: structure, function and assembly of multidomain protein complexes. *Curr Protein Pept Sci* **4**: 397–407. <https://doi.org/10.2174/1389203035487036>
- Rawlings ND (2015) Bacterial calpains and the evolution of the calpain (C2) family of peptidases. *Biol Direct* **10**: 66. <https://doi.org/10.1186/s13062-015-0095-0>
- Reverter D, Strobl S, Fernandez-Catalan C, Sorimachi H, Suzuki K, Bode W (2001) Structural basis for possible calcium-induced activation mechanisms of calpains. *Biol Chem* **382**: 753–766. <https://doi.org/10.1515/BC.2001.091>
- Rôças IN, Siqueira JF, Santos KRN, Coelho AM (2001) “Red complex” (*Bacteroides forsythus*, *Porphyromonas gingivalis*, and *Treponema denticola*) in endodontic infections: A molecular approach. *Oral Surg Oral Med Oral Pathol Oral Radiol Endod* **91**: 468–471. <https://doi.org/10.1067/moc.2001.114379>
- Schechter I, Berger A (1967) On the size of the active site in proteases. I. Papain. *Biochem Biophys Res Commun* **27**: 157–162
- Shinkai-Ouchi F, Koyama S, Ono Y, Hata S, Ojima K, Shindo M., duVerle D, Ueno M, Kitamura F, Doi N, Takigawa I, Mamitsuka H, Sorimachi, H (2016) Predictions of cleavability of calpain proteolysis by quantitative structure-activity relationship analysis using newly determined cleavage sites and catalytic efficiencies of an oligopeptide array. *Mol Cell Proteomics* **15**: 1262–1280. <https://doi.org/10.1074/mcp.M115.053413>
- Sorimachi H, Ishiura S, Suzuki K (1997) Structure and physiological function of calpains. *Biochem J* **328**: 721–732. <https://doi.org/10.1042/bj3280721>
- Staniec D, Ksiazek M, Thøgersen IB, Enghild JJ, Sroka A, Bryzek D, Bogyo M, Abrahamson M, Potempa J (2015) Calcium regulates the activity and structural stability of Tpr, a bacterial calpain-like peptidase. *J Biol Chem* **290**: 27248–27260. <https://doi.org/10.1074/jbc.M115.648782>
- Suzuki K, Sorimachi H, Yoshizawa T, Kinbara K, Ishiura S (1995) Calpain: novel family members, activation, and physiologic function. *Biol Chem Hoppe-Seyler* **376**: 523–529. <https://doi.org/10.1515/bchm3.1995.376.9.523>
- Tokuda M, Chen W, Karunakaran T, Kuramitsu HK (1998) Regulation of protease expression in *Porphyromonas gingivalis*. *Infect Immun* **66**: 5232–5237. <https://doi.org/10.1128/IAI.66.11.5232-5237.1998>
- Tompá P, Buzder-Lantos P, Tantos A, Farkas A, Szilágyi A, Bánóczy Z, Hudecz F, Friedrich P (2004) On the sequential determinants of calpain cleavage. *J Biol Chem* **279**: 20775–20785. <https://doi.org/10.1074/jbc.M313873200>
- Wadosky KM, Li L, Rodríguez JE, Min JN, Bogan D, Gonzalez J, Patterson C, Konegay JN, Willis M (2011) Regulation of the calpain and ubiquitin-proteasome systems in a canine model of muscular dystrophy. *Muscle Nerve* **44**: 553–562. <https://doi.org/10.1002/mus.22125>
- Wegner N, Wait R, Venables PJ (2009) Evolutionarily conserved antigens in autoimmune disease: Implications for an infective aetiology. *Int J Biochem Cell Biol* **41**: 390–397. <https://doi.org/10.1016/j.biocel.2008.09.012>
- Yu H, Chen JK, Feng S, Dalgarno DC, Brauer AW, Schreiber SL (1994) Structural basis for the binding of proline-rich peptides to SH3 domains. *Cell* **76**: 933–945. [https://doi.org/10.1016/0092-8674\(94\)90367-0](https://doi.org/10.1016/0092-8674(94)90367-0)

Emerging relationship between hydrogen sulfide and ferroptosis: A literature review

Xiaoming Gao[#], Ke Lu[#] and Chong Li[✉]

Department of Orthopedics, Affiliated Kunshan Hospital of Jiangsu University, 91 West Qianjin Road, Suzhou, Jiangsu, 215300, China

Gaseous hydrogen sulfide (H₂S) can function as a signaling molecule similar to nitric oxide or carbon monoxide under physiological conditions, ultimately exerting anti-inflammatory, anti-apoptotic, and antioxidant activities. Many studies have investigated the role of H₂S in a variety of biological contexts, and both endogenous H₂S and H₂S donors have been leveraged as tools for fundamental biomedical research, and it has been suggested that they may provide value for the design of novel therapeutic strategies in the years to come. Ferroptotic cell death is a distinct programmed cell death resulting from excessive lipid peroxidation in an iron-dependent manner, and is characterized by high levels of iron accumulation, reactive oxygen species (ROS) production, and peroxidation of cellular lipids. Several recent studies have revealed a close relationship between ferroproteins and their precursors, H₂S, and the enzymes that produce them. This review summarizes the current information pertaining to the relationship between ferroptosis and H₂S, with a particular focus on the underlying mechanisms and biological applications of this knowledge.

Keywords: Hydrogen sulfide, ferroptosis, iron, reactive oxygen species, lipid peroxidation

Received: 27 March, 2023; **revised:** 25 September, 2023; **accepted:** 03 October, 2023; **available on-line:** 07 December, 2023

✉e-mail: lichong1705@163.com

[#]These authors contributed equally to this work

Acknowledgements of Financial Support: This study was supported by the National Natural Science Foundation of China (82172441), the Scientific Research Project of Gusu School of Nanjing Medical University (GSKY20210244), the Clinical Medical Science and Technology Development Fund of Jiangsu University (JLY2021048), and the Suzhou Key Clinical Diagnosis and Treatment Technology Project (LCZX202024).

Abbreviations: H₂S, Hydrogen sulfide; CBS, cystathionine β-synthase; CSE, cystathionine γ-lyase; 3-MST, 3-mercaptopyruvate sulfurtransferase; RCD, regulated cell death; GPX4, glutathione peroxidase 4; PLP, pyridoxal 5'-phosphate; CNS, central nervous system; Hcy, homocysteine; CAT, cysteine aminotransferase; 3MP, 3-mercaptopyruvate; NADPH, nicotinamide adenine dinucleotide phosphate; NADH, nicotinamide adenine dinucleotide; GSH, glutathione; xCT, Xc-system; 5-FU, 5-fluorouracil; VSMC, vascular smooth muscle cell; HHP, high hydrostatic pressure; Nrf2, nuclear factor erythroid 2-related factor 2; COPD, chronic obstructive pulmonary disease; PFC, prefrontal cortex; ALI, acute lung injury; Fpn1, ferroportin 1; TFR1, transferrin receptor 1; miRNAs, MicroRNAs

INTRODUCTION

Hydrogen sulfide (H₂S) is a gas that can serve as a signaling intermediary and that, in mammals, it is produced by several enzymes including cystathionine β-synthase (CBS), cystathionine γ-lyase (CSE), and 3-mercaptopyruvate sulfur-transferase (3-MST) (Wang, 2012). Many recent stud-

ies have sought to elucidate the biological roles of H₂S and have demonstrated that its endogenous production is related to processes ranging from vasodilation, microbial antibiotic resistance, oxidative stress, and mitochondrial function to inflammatory activity, neuroprotection, and endoplasmic reticulum stress (Kozich *et al.*, 2019). H₂S functions as a reductant at physiological concentrations, providing protection against inflammation, oxidative stress, and apoptotic cell death (Kimura *et al.*, 2010). In plasma, endogenously derived H₂S levels are negatively correlated with oxidative stress and aging (Hine *et al.*, 2015). In addition, owing to the essential roles of H₂S in various physiological and pathological processes, its practical applications have been explored. For example, a novel fluorescent probe, Rho-HS, was developed to detect H₂S and can be used for biological imaging (Guo *et al.*, 2022). Furthermore, a surface-filled H₂S-releasing silk fibroin (SF) hydrogel was developed to achieve small-dose local administration and avoid volatile and toxic side effects (Chen *et al.*, 2022). These investigations shed light on the potential clinical application of H₂S. The production and functionality of H₂S have been identified as promising targets for the treatment of a range of conditions owing to its significant role in regulating cell death and interactions with the cell death pathway.

Multiple cell death pathways contribute to the occurrence and progression of various diseases, and H₂S plays a vital role in regulating or suppressing cell death, including necroptosis, pyroptosis, and apoptosis (Rodkin *et al.*, 2023) (Table 1). For instance, H₂S upregulates the expression of Bcl-2 and P62 (Chen *et al.*, 2022; Guo *et al.*, 2014) or downregulates NF-κB to reduce apoptosis in organ ischemia/reperfusion (Kuo *et al.*, 2013; Weirather *et al.*, 2014). Moreover, H₂S can reduce the expression of caspase-1 to exert an anti-pyroptosis effect on bone-derived macrophages and aortic endothelium (Castelblanco *et al.*, 2018; Xi *et al.*, 2016).

Ferroptosis is a subtype of regulated cell death (RCD) with features distinct from those of necrosis, autophagy, or apoptosis (Hadian & Stockwell, 2020; Jiang *et al.*, 2021). It often results from iron-dependent accumulation of toxic concentrations of lipid peroxides within cells (Rodkin *et al.*, 2023; Stockwell *et al.*, 2017), characterized by the production of high levels of lipid peroxides, accumulation of iron, and downregulation of glutathione peroxidase 4 (GPX4) (Fuhrmann & Brüne, 2022; Mahoney-Sánchez *et al.*, 2021). These characteristics offer markers that can be used to specifically detect RCD (Hadian & Stockwell, 2020). Ferroptotic cells exhibit a rounded, small morphology with intercellular separation, an intact crenulated plasma membrane, and the absence of nuclear condensation. Mitochondria in these cells often have ruptured outer membranes, increased membrane density, and shrunken or absent cristae (Liang

Table 1. Mechanisms of H₂S on different cell death in disease models.

Cell death	Character	Disease model	Mechanism	Reference
Necroptosis	Following the activation of the tumor necrosis receptor (TNFR1) by TNF α	Diabetic cardiomyopathy	Alleviated myocardial oxidative stress, necroptosis and NLRP3	(Gong <i>et al.</i> , 2022)
		Diabetic vascular complications.	p38 MAPK signaling pathway	(Lin <i>et al.</i> , 2021)
		Atherosclerosis	Attenuated the increased RIP3 expression	(Lin <i>et al.</i> , 2018)
Pyroptosis	A type of cell death culminating in the loss of plasma membrane integrity and induced by activation of so-called inflammasome sensors. These include the Nod-like receptor (NLR) family, the DNA receptor Absent in Melanoma 2 (AIM2) and the Pyrin receptor	Ischemia-reperfusion (I/R)-induced acute kidney injury (AKI)	Inhibited the NLRP3/Caspase-1 axis	(Ni <i>et al.</i> , 2021)
		Chronic obstructive pulmonary disease (COPD)	Targeted the TLR4/NF- κ B pathway	(L. Wang <i>et al.</i> , 2022)
		Nephrotoxicity caused by U exposure.	Upregulation of PI3K/AKT/mTOR pathway	(Hu <i>et al.</i> , 2023)
Apoptosis	The release of cytochrome <i>c</i> from mitochondria, regulated by a balance between proapoptotic and antiapoptotic proteins of the BCL-2 family, initiator caspases (caspase-8, -9 and -10) and effector caspases (caspase-3, -6 and -7).	Asthma	Reduced the airway inflammatory infiltrate	(Mendes <i>et al.</i> , 2019)
		Lipopolysaccharide (LPS)-induced memory impairment (MI)	Decreased c-Jun and caspase-3 levels	(Kshirsagar <i>et al.</i> , 2021)
		Myocardial reconstruction	Blocked ER stress-autophagy axis	(Li <i>et al.</i> , 2020)
		Experimental glaucoma model	Suppressed Bax, caspase-3 and p53 activations	(Erisgin <i>et al.</i> , 2019)
		Methotrexate (MTX) hepatotoxicity	Modulated IL-6/STAT3 pathway	(Fouad <i>et al.</i> , 2020)

et al., 2019). Many diseases have been linked to ferroptosis, including osteoporosis and cancer, and this form of RCD also arises in the context of reproductive system functionality and organ damage (Proneth & Conrad, 2019; Stockwell *et al.*, 2020). Ferroptosis is also associated with the efficacy of a range of therapeutic modalities, such as chemotherapy, radiotherapy, and immune checkpoint blockade treatments (Lei *et al.*, 2020). Several studies have reported the anti-ferroptosis effects of H₂S in diseases such as cardiovascular disease (Wang *et al.*, 2023; Wu *et al.*, 2023), air inflammation (Zhang *et al.*, 2020), intracerebral hemorrhage (Zhang *et al.*, 2020) and acute lung injury (ALI) (Li *et al.*, 2022). For instance, H₂S reduces ferroptosis by regulating the Nrf2-PPAR-ferroptophagy signaling pathway in PM-induced emphysema (Wang *et al.*, 2022). It also protects DOX-induced cardiotoxicity from ferroptosis by targeting the OPA3-NFS1 axis (Wang *et al.*, 2023). Overall, its functional pathways are diverse and complex.

This review provides a summary of the role of H₂S metabolism in mammals and the signaling pathways associated with H₂S-mediated ferroptosis.

ENDOGENOUS MAMMALIAN H₂S PRODUCTION

In mammals, H₂S is generated via enzymatic and nonenzymatic mechanisms (Fig. 1). Both CSE and CBS are cytosolic pyridoxal 5'-phosphate (PLP)-dependent, whereas 3-MST is a mitochondrial enzyme that functions independently of PLP (Cao *et al.*, 2019).

CBS is formed by tetramerization subunit proteins of 63 kDa in size and generates H₂S *via* the catalytic processing of L-homocysteine and L-cysteine, yielding H₂S and L-cystathionine through a mechanism comparable to its role as a component in the trans-sulfuration pathway. When L-cysteine is present, CBS mediates a β -replacement reaction to generate H₂S, while produc-

ing L-serine. An up to 23-fold higher rate of H₂S generation was observed when L-homocysteine was available compared to when only L-cysteine was available. CBS is thought to be the main producer of H₂S in the central nervous system (CNS) and is expressed throughout the brain, with the highest levels of expression in the cerebral cortex, cerebellum, and hippocampus (Zuhra *et al.*, 2020). CBS expression is also detectable in lymphocytes and organs, such as the liver, kidneys, pancreatic islets, uterus, and placenta (Kaneko *et al.*, 2006; Patel *et al.*, 2009).

Similar to CBS, CSE catalyzes the processing of homocysteine (Hcy) to produce H₂S, α -ketobutyrate, and ammonia, in addition to catalyzing the processing of L-cysteine to yield H₂S, along with ammonia and pyruvate. When L-cysteine and Hcy are present at physiological levels, CSE catalyzes the α - and β -elimination of L-cysteine to generate approximately 70% H₂S, whereas the α,γ -elimination of Hcy catalyzed by this enzyme generates only 29% of the total H₂S. However, when Hcy levels are elevated to concentrations similar to those observed in the context of hyperhomocysteinemia (HHcy), such α,γ -elimination generates approximately 90% CSE-derived H₂S, indicating that relative Hcy and L-cysteine concentrations within mammalian cells are pivotal determinants of the primary substrate utilized by this enzyme (Chiku *et al.*, 2009).

Mitochondrially localized 3-MST is an H₂S-generating enzyme that was most recently discovered. Following the initial cysteine aminotransferase (CAT)-mediated conversion of L-cysteine to 3-mercaptopyruvate (3MP), 3-MST transfers sulfur atoms from 3MP to 3-MST, resulting in persulfide generation. When a reductant such as thioredoxin is present, H₂S is released from the persulfide (Nagahara *et al.*, 1998). Regulation of CAT activity ultimately shapes the ability of 3-MST to generate H₂S. CAT inhib-

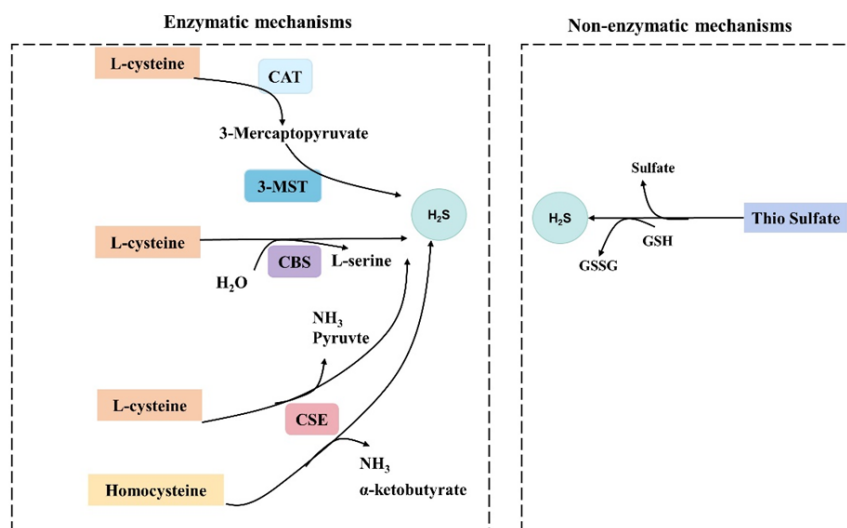


Figure 1. Endogenous generation mechanism of H₂S in cells.

The enzymatic and nonenzymatic generation pathway was presented in the above figure, in which the enzyme CBS, CSE and 3-MST play pivotal role in producing H₂S in enzymatic generation pathway, with L-cysteine being the main substrate. CAT, Cysteine aminotransferase; CBS, Cyststionine β-synthase; CSE, Cyststionine γ-lyase; GSH, glutathione; GSSG, glutathione disulfide; 3-MST, 3-mercaptopyruvate sulfurtransferase.

itors, such as aspartate, largely suppress the biosynthesis of H₂S and can therefore be leveraged as tools for pharmacological studies to explore the functional importance of H₂S generated by this enzyme (Shibuya *et al.*, 2009).

Some endogenous H₂S is also generated via the non-enzymatic chemical reduction of sulfane sulfur through the action of the ubiquitous cellular electron donor nicotinamide adenine dinucleotide (NADH), its reduced state nicotinamide adenine dinucleotide phosphate (NADPH), or other reductive equivalents (Searcy & Lee, 1998). Under these conditions, the reduction of reactive sulfur species present in polysulfides, persulfides, and thiosulfate can give rise to a range of metabolites, including H₂S (Olson *et al.*, 2013).

ENDOGENOUS H₂S AND FERROPTOSIS

In mammalian cells, the transsulfuration pathway produces H₂S as a byproduct of Hcy and cysteine processing by CSE, CBS, and 3-MST. The functional Xc-system subunit xCT (SLC7A11) is responsible for the import of cystine into cells, where it is converted into cysteine, which functions as the rate-limiting substrate necessary for the biosynthesis of glutathione (GSH) (Liu *et al.*, 2020; Stockwell *et al.*, 2017). GSH functions as a substrate for GPX4, which mitigates ferroptosis by reducing membrane phospholipid hydroperoxides to produce lipid alcohols. When xCT expression or activity is suppressed, immunotherapy- or radiotherapy-induced ferroptosis is enhanced (Lang *et al.*, 2019). The commonly utilized xCT inhibitor erastin (Era) can also activate ferroptosis, although long-term treatment with Era may contribute to enhanced cellular resistance to ferroptotic death. Moreover, Era treatment for extended periods has been shown to improve CBS and CSE expression, independently regulating ferroptosis (Liu *et al.*, 2020). Disrupting xCT activity increases both CSE and CBS expression yet significantly reduces endogenous H₂S production. The supplemental addition of the H₂S donor GYY4137 [GYY, morpholin-4-ium-4-methoxyphenyl (morpholino)

phosphinodithioate] reversed the loss of resistance to 5-fluorouracil (5-FU), which emerges upon the inhibition of xCT, highlighting the functional importance of H₂S as a mediator of xCT-associated chemoresistance activity (Chen *et al.*, 2021). Interestingly, supplementation with H₂S increased the protein levels of xCT without influencing its mRNA expression, suggesting that H₂S has a post-transcriptional regulatory effect on xCT. The H₂S axis maintains xCT stability through persulfidation of OTUB1 at cysteine 91 (Chen *et al.*, 2021). Correspondingly, xCT and the trans-sulfuration pathway have been identified as key ferroptotic regulators in cancer cells, functioning primarily by producing cysteine as a precursor for the production of the critical antioxidant glutathione (GSH). When cells are treated with both Era and AOAA, which inhibit CBS, the levels of GSH present within cells are markedly reduced, thus contributing to higher rates of ferroptosis associated with increased PTGS2 expression at the mRNA level and higher levels of MDA, which is a lipid peroxidation end-product (Marrocco *et al.*, 2017).

Hcy is an amino acid that contains sulfur and is important for methionine metabolism, gene methylation, phospholipid biosynthesis, neurotransmission, and nucleic acid biosynthesis (Shen *et al.*, 2020). Given its essential role as a mediator of Hcy transsulfuration, inhibition of CBS increases the concentration of Hcy in hepatocellular carcinoma cells, triggering ferroptosis (Wang *et al.*, 2018). Patients with excessively high levels of methionine, vitamin B12, or folic acid deficiencies can have high serum Hcy concentrations in the form of HHcy. This condition, in turn, contributes to the development of abnormal bone metabolism and mitochondrial dysfunction through oxidative stress and modification of collagen cross-linking (Levasseur, 2009). Hcy may contribute to more severe oxidative stress in nucleus pulposus cells and aggravate the induction of ferroptosis, resulting in increased lipid peroxidation, ROS production, and reduced GPX4 expression. Fer-1 is a ferroptosis inhibitor that protects nucleus pulposus cells from degeneration (Zhang *et al.*, 2020). It also reduced Hcy-induced injury

in ovarian granulosa cells in a dose-dependent manner (Shi *et al.*, 2022). Vascular smooth muscle cells (VSMCs) may become dysfunctional due to high hydrostatic pressure (HHP) levels. HHP exposure induces ferroptosis in VSMC, accompanied by high levels of ROS production, lipid peroxidation, iron accumulation, downregulation of CSE/H₂S, and suppression of GSH production (Jin *et al.*, 2022).

The transcription factor nuclear factor erythroid 2-related factor 2 (Nrf2) is a vital mediator of ferroptosis induction, and H₂S has repeatedly been shown to activate antioxidant activity mediated by Nrf2 in respiratory diseases, including rhinitis, sinusitis, conjunctivitis, acute lung injury (ALI), chronic obstructive pulmonary disease (COPD), and asthma (Han *et al.*, 2011; Khattak *et al.*, 2021). Wang *et al.* demonstrated that H₂S was capable of inhibiting ferroptosis and ferritinophagy, while this activity was impaired in mice or cells lacking Nrf2 expression, and on the other hand, the anti-ferroptosis capability of H₂S was enhanced when Nrf2 was over-expressed because the ability of H₂S to protect against injury is regulated by Nrf2 activation and PPAR- γ signaling (Y. Wang *et al.*, 2022). These results showed that the upstream of the whole protective pathway is Nrf2 because the activation of PPAR- γ and the inhibitory effects of H₂S on ferritinophagy and ferroptosis were significantly restricted when Nrf2 was knocked out, both in vivo and in vitro.

The deubiquitinating enzyme OTUB1 stabilizes proteins through specific mechanisms (Wiener *et al.*, 2012), and OTUB1 overexpression stabilizes xCT in oncogenic settings, thereby interfering with the ability of xCT to regulate ferroptotic pathways (Koppula *et al.*, 2021; Yasuhara *et al.*, 1997). Endogenous H₂S production is closely linked to interactions between xCT and OTUB1, with H₂S stabilizing xCT *via* the persulfidation of cysteine 91 of OTUB1 (Chen *et al.*, 2021).

H₂S DONORS AND FERROPTOSIS

Inorganic sulfurized salts, including NaHS and sodium sulfide (Na₂S), are among the earliest known H₂S donors and are commonly used as H₂S equivalents in research. Currently, multiple H₂S donors have been applied in various disease models and achieved remarkable effect via different signal pathways (Table 2).

C2C12 cells treated with exogenously administered NaHS could remediate abnormal redox conditions induced in response to RSL3 through the upregulation of GPX1 and GPX4, thereby normalizing lipid metabolism and mitochondrial function while also increasing acetyl-

CoA levels. NaHS also inhibits the expression and acetylation of ALOX12, thus protecting C2C12 cells from ferroptosis via the CSE/H₂S signalling pathway (Wang, Yu, *et al.*, 2021). Increased GSH content and GPX4 activity took place in response to NaHS treatment. Decreases in ROS, lipid ROS, and MDA levels have been reported in both BV2 cells and in the prefrontal cortex (PFC) of diabetic mice administered with NaHS. Mechanistically, these effects were found to be mediated by the increased expression of SLC7A11 protein in these BV2 cells or in the PFC, indicating that NaHS may act in an antidepressant-like manner *via* the upregulation of SLC7A11. NaHS can also improve PFC cysteine levels in a murine model of type 1 diabetes, resulting in upregulation of GPX4 (Wang, Wang, *et al.*, 2021), indicating that NaHS may exert its protective effect by upregulating the protein expression of SLC7A11 and cysteine levels.

In plants, bacteria, and some fungi, H₂S is converted to cysteine through sulfur assimilation. In contrast, studies have also found that the addition of Na₂S as a donor of H₂S could promote the generation of cysteine in mammalian cells in the presence of cystine. Since H₂S exists as HS⁻ in a neutral solution, disulfide compounds such as cystine can react with HS⁻ in the culture medium as well as in the cell. This study demonstrated that after the addition of Na₂S solution to the culture medium, HS⁻ was transiently generated and disappeared immediately through the reaction between HS⁻ and cystine to form cysteine persulfide and polysulfides (see Fig. 10 in Koike *et al.*, 2017). A significant increase in cystine concentration was observed after treatment with Na₂S. The mechanism by which Na₂S protects SH-SY5Y cells from MG cytotoxicity is *via* the activation of Nrf2, but not HS⁻ itself. However, this mechanism has not been verified in ferroptosis, and further investigation is needed to elucidate its molecular mechanism.

The slow-acting H₂S donor GYY4137 can release this gas for several hours (Chen *et al.*, 2016). Ferroptosis is an important component of sepsis-associated ALI, and GYY4137 has been reported to protect against ALI by alleviating oxidative stress through the removal of ROS. GYY4137 also markedly suppressed COX-2 and NOX1 expression while increasing sepsis-induced GPX4 and SLC7A11 expression, thereby inhibiting the occurrence of ferroptosis in sepsis-induced ALI (Li *et al.*, 2022).

H₂S AND IRON METABOLISM

The metabolism of iron is integral to the induction and progression of ferroptotic pathways, whereas H₂S has a complex relationship with iron metabolism. Iron is

Table 2. Summarization of current H₂S donors application in different disease models.

Disease model	H ₂ S donor	Mechanism	Reference
Myocardial fibrosis	AP39	PINK1/Parkin pathway	(Yang <i>et al.</i> , 2023)
Hypertension	NaHS	Upregulated the VSMC GSH content and cystathionine gamma-lyase (CSE)/hydrogen sulfide (H ₂ S)	(Ruxi Jin <i>et al.</i> , 2022)
Intracerebral hemorrhage (ICH)	NaHS	Improved GPX4 and SLC7A11 via the CBS/H ₂ S system	(Y. Yu <i>et al.</i> , 2023)
Retinal degenerative diseases.	NaHS	AMPK- and p62-dependent non-canonical NRF2-KEAP1 pathway	(M. Yu <i>et al.</i> , 2023)
Sepsis-induced cardiomyopathy (SIC)	NaHS	Inhibited the phosphorylation of BECN1 and increased expression levels of SLC7A11 and GPX4	(Cao <i>et al.</i> , 2022)
Beryllium disease	NaHS	Decreased the accumulation of Fe ²⁺ and lipid peroxides	(Liu <i>et al.</i> , 2023)
Sepsis-induced acute lung injury (ALI)	GYY4137	Stimulated autophagy by blocking mTOR signaling	(Jianhua Li <i>et al.</i> , 2022)

involved in H₂S production *via* non-enzymatic processes. Meanwhile, the uptake, transport, and accumulation of iron is regulated by H₂S. The interactions between H₂S and iron shape the cellular homeostasis of H₂S and define the relevant signaling crosstalk.

In addition to the enzymatic mechanisms mentioned above, non-enzymatic H₂S in eukaryotes may come from a cysteine reaction with iron and vitamin B6 or from the reduction of elemental sulfur (Kolluru *et al.*, 2013; Yang *et al.*, 2019). Nucleophilic attack by vitamin B6 on cysteine forms a cysteine-aldimine, which reacts with free or heme-bound iron to yield a quinonoid containing cysteine. Subsequently, iron ions remove the thiol group from H₂S, and the resulting de-sulfureted aldimine is hydrolyzed to produce vitamin B6, ammonia, and pyruvate.

Free iron (Fe²⁺) is taken up by the cell through ion channels or transporters, such as L-type Ca²⁺ channels on cellular membranes. H₂S is also an endogenous gaseous ATP-sensitive K⁺ (KATP) channel opener that induces vasodilation (Arif *et al.*, 2022). H₂S and iron may interact to suppress L-type Ca²⁺ channels via S-sulfhydration, as shown in mouse pancreatic β -cells (Tang *et al.*, 2013). The influx of iron into cells through L-type Ca²⁺ channels has been demonstrated in cardiomyocytes (Arif *et al.*, 2022). The inhibition of these processes by H₂S decreases the amount of iron entering the cell. Ferroporin 1 (Fpn1) and transferrin receptor 1 (TfR1) are essential regulators of iron homeostasis in most cells. Injecting NaHS *in vivo* significantly increases serum iron levels and transferrin saturation while significantly downregulating TfR1 and Fpn1 at the protein level (Zhang *et al.*, 2019). Under the influence of ferric ions, cysteine catalyzes the generation of H₂S through a protective mechanism that mitigates excessive iron concentrations by reacting with iron and generating acid-labile iron sulfide, such that excessive iron cannot cause further oxidative stress (Tang *et al.*, 2023; Yang *et al.*, 2019).

Recently, it was found that CBS is essential for iron homeostasis, and the hepatic, splenic, cardiac, and serum iron levels in CBS-deficient mice are elevated together with oxidative stress-related marker levels; mice homozygous for the knockout of CBS failed to survive for more than 4 weeks (Zhou *et al.*, 2018). Moreover, hepcidin can accelerate the degradation of Fpn1 by interacting with it, thereby reducing intracellular iron release into the systemic circulation. Upregulation of hepcidin in both the liver and systemic circulation has been reported to lead to decreased Nrf2 expression. Elevated hepcidin levels resulted in a marked decrease in Fpn1 expression and exacerbated iron retention, causing severe liver damage. An adenoviral vector was used to restore CBS expression, and this attempt was able to reverse the damaged phenotypes (Zhou *et al.*, 2018). Inflammatory cytokines such as IL-6 promote the upregulation of hepcidin via JAK-STAT3 signaling through interactions with activin B and the SMAD1/5/8 pathway. In contrast, H₂S suppresses the upregulation of hepcidin *via* JAK-STAT signaling *via* the suppression of STAT3 phosphorylation, thereby reducing IL-6 production (Zhang *et al.*, 2019). Similar findings were also reported by Xin and others who demonstrated that H₂S promoted the expression of SIRT1, stabilizing SIRT1-STAT3 interactions to reduce the acetylation of STAT3, thereby decreasing hepcidin levels (Xin *et al.*, 2016). Collectively, these results indicate that H₂S reduces hepcidin levels by acting upstream of STAT3, which provides an opportunity for further investigation. A better understanding of the mechanism underlying the regulation of STAT3 *via* H₂S may shed light on its clinical potential.

H₂S AND LIPID PEROXIDATION

Lipid peroxidation is a hallmark of ferroptosis, which results from the generation of excessive levels of ROS due to increased intracellular iron concentrations, together with the simultaneous depletion of GSH. The antioxidant enzyme GPX4 is responsible for lipid peroxide neutralization and can utilize GSH as a cofactor to preserve membrane fluidity, thus shielding the membrane against peroxidation-related damage (Su *et al.*, 2019). Inhibition of GPX4 contributes to high levels of ROS production, and its overexpression can conversely reduce ROS generation and prevent ferroptosis induction. Iron metabolism-related ROS generation is a major cause of lipid peroxidation, given that iron is required for numerous physiological processes, and excessive iron levels ultimately disrupt normal cellular function through the resultant oxidative damage, contributing to cell death (Su *et al.*, 2019).

H₂S has been reported to exhibit concentration-dependent pro- or antioxidant activities, such that plasma lipid peroxidation is suppressed and enhanced by low (10 μ M) and high (1000 μ M) concentrations of NaHS (Sun *et al.*, 2012). Sun and others found that the use of NaHS to pretreat neonatal rat cardiomyocytes resulted in the generation of lower concentrations of ROS during hypoxia/reoxygenation, and that H₂S suppressed the activity of mitochondrial complex IV while simultaneously enhancing superoxide dismutase activity (Sun *et al.*, 2012). *In vivo*, Wu and others reported that 50 μ mol/kg NaHS per day for 16 weeks with a high-fat diet prevented the increase in diet-induced lipid oxidation (Wu *et al.*, 2009), suggesting that NaHS has protective effects against lipid oxidation. H₂S is traditionally known for its toxic effects on living organisms. Current studies are still focused on cell and animal experiments, and relevant data and safety for clinical use are needed.

Hcy has been suggested to increase the severity of oxidative stress owing to the generation of free radicals through the autooxidation of excessive Hcy concentrations (Malinowska *et al.*, 2012). Yan *et al.* further reported that H₂S protected against HHcy-induced cellular injury through its antioxidant activity, leading to a 55.8% decrease in the overproduction of O₂^{•-} induced by Hcy (Yan *et al.*, 2006). Chang *et al.* found that the administration of H₂S decreased total plasma Hcy concentration and lipid peroxidation. CBS- and CSE-knocked out mice exhibit lower GSH levels and are more susceptible to oxidative stress, further confirming the link between stress and endogenous H₂S (Chang *et al.*, 2008).

Lipid metabolism is closely related to the conversion of carbohydrates into fat. The cytoplasmic hydrolysis of lipids is the first step in metabolism, resulting in the production of glycerol and fatty acids. The two compounds are then glycolyzed and β -oxidated, and H₂S regulates glycolysis and fatty acid metabolism through protein S-sulfhydration (Cheung & Lau, 2018). Activated glycolysis and the pentose phosphate pathway can increase antioxidant activity (D'Alessandro *et al.*, 2014). Exposure of clonal HepG2 hepatocyte cells to NaHS (–10–100 μ M) reduced glucose consumption and glycogen levels (Zhang *et al.*, 2013). In addition, the CSE/ H₂S pathway has recently been shown to play a key role in the regulation of glucose synthesis through pyruvate carboxylase S-sulfhydration in gluconeogenesis (Ju *et al.*, 2015).

Further details regarding the association between H₂S and ferroptotic activity are shown in Fig. 2. The interaction pathway between H₂S and ferroptosis is shown in Fig. 3.

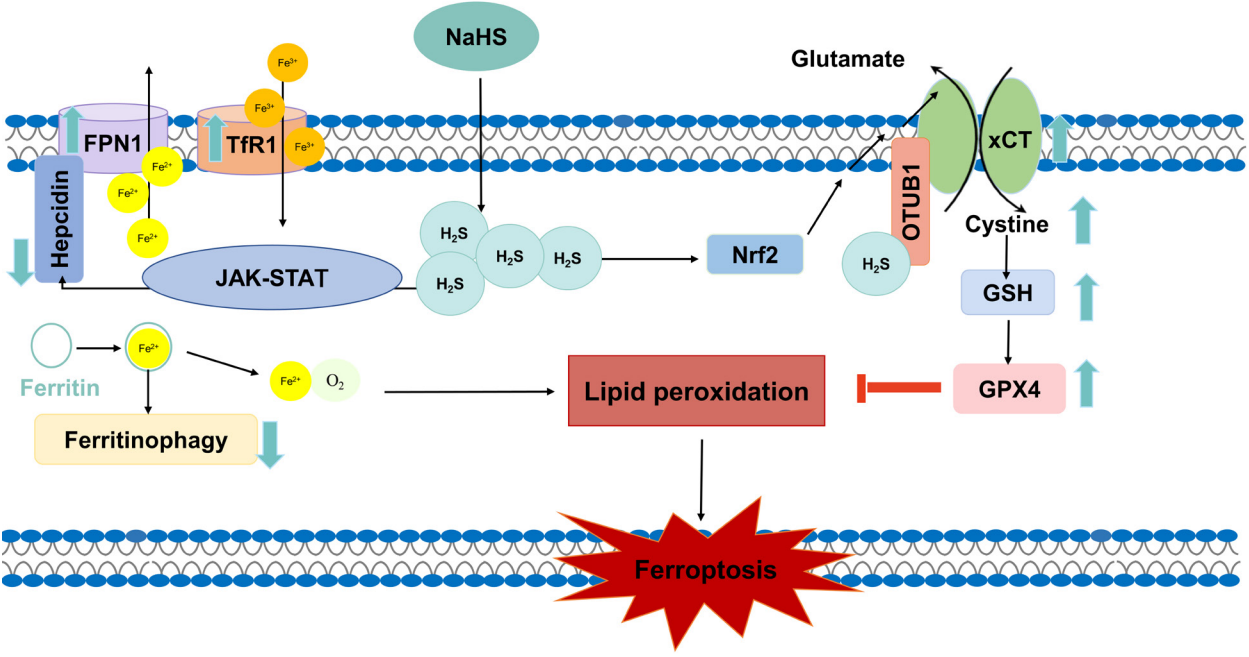


Figure 2. The effect of H₂S on ferroptosis. Cystine is imported by the Xc-system and converted into cysteine, which in turn serves as a GSH precursor. GSH is a GPX4 substrate. Both cysteine and Hcy are also substrates for the production of H₂S, and the H₂S equivalent NaHS can increase GSH levels and GPX4 activity while suppressing the activity of the lipoxygenase ALOX12, thus remediating dysregulated lipid metabolism. Overly high Fe²⁺ concentrations can contribute to ROS generation via the Fenton reaction, whereas HHcy can drive enhanced ROS production and aberrant mitochondrial functionality. HHP promoted ROS generation by suppressing CSE/H₂S expression and reducing GSH generation. TfR1 and FPN are important regulators of cellular iron homeostasis and NaHS can suppress their downregulation at the protein level. Hepcidin interacts with Fpn1 to facilitate its degradation, whereas H₂S reduces hepcidin expression via JAK-STAT signaling. The deubiquitinase OTUB1 is capable of stabilizing the xCT Xc-system subunit via cysteine 91 persulfidation. The xCT inhibitor Era, when used to treat cells for an extended period of time, upregulates CBS expression and enhances the resistance of cells to ferroptosis. In contrast, the CBS inhibitor AOA, when administered together with Era, downregulated cellular GSH levels and enhanced ferroptotic death.

H₂S AND FERROPTOSIS-ASSOCIATED MicroRNAs

MicroRNAs (miRNAs) are short RNAs of ~22 nucleotides in length that lack coding ability and function by suppressing translation and/or promoting the degradation of complementary target mRNAs. Inhibiting miR-30b-5p expression reportedly results in FPN1 and SLC7A11 upregulation in trophoblasts, while the upregulation of this mRNA under hypoxic conditions leads to the downregulation of these two genes, causing trophoblast ferroptosis (Zhang *et al.*, 2020). Members of the

miR-30 family have also been confirmed to target CSE expression, thereby directly regulating the generation of H₂S (Shen *et al.*, 2015). By targeting GPX4, miR-15a can control ferroptotic induction in colorectal cancer cells, whereas overexpression of miR-15a suppresses GPX4 expression *in vitro* and *in vivo*, resulting in elevated ROS generation, intracellular Fe²⁺ accumulation, and increased MDA levels (Liu *et al.*, 2022). Fan *et al.* found that miR-15a overexpression resulted in elevated GPX4 protein levels, with a concomitant decrease in ferroptotic induction associated with fewer severe myocardial inju-

Table 3. An overview of H₂S and ferroptosis-associated proteins and miRNAs

Protein or miRNA	Relation with H ₂ S	Relation with ferroptosis	Disease involved
Nrf2	Enhances the anti-ferritinophagy and anti-ferroptotic effects of H ₂ S	Anti-ferroptotic	COPD
OTUB1	H ₂ S maintains the stability of xCT through persulfidation of OTUB1 at cysteine 91	Stabilizes xCT	Colorectal cancer
TfR1	NaHS inhibits the downregulation of TfR1 protein expression <i>in vivo</i>	Regulates cellular iron balance	LPS
FPN1	NaHS inhibits the downregulation of Fpn1 protein expression <i>in vivo</i>	Regulates cellular iron balance	LPS
Hepcidin	H ₂ S reduces hepcidin expression	Accelerates the degradation of FPN1	Anemia of inflammation
MiR-30b-5p	Regulates H ₂ S production	Downregulates SLC7A11 and FPN1	Myocardial ischemia/reperfusion injury
MiR-15a	H ₂ S upregulates miR-15a	Positively regulates ferroptosis via directly targeting GPX4	Broiler thymus
MiR-194	Decreasing H ₂ S can downregulate miR-194	Activates the Nrf2/HO-1 signaling pathway	Cerebral injuries.

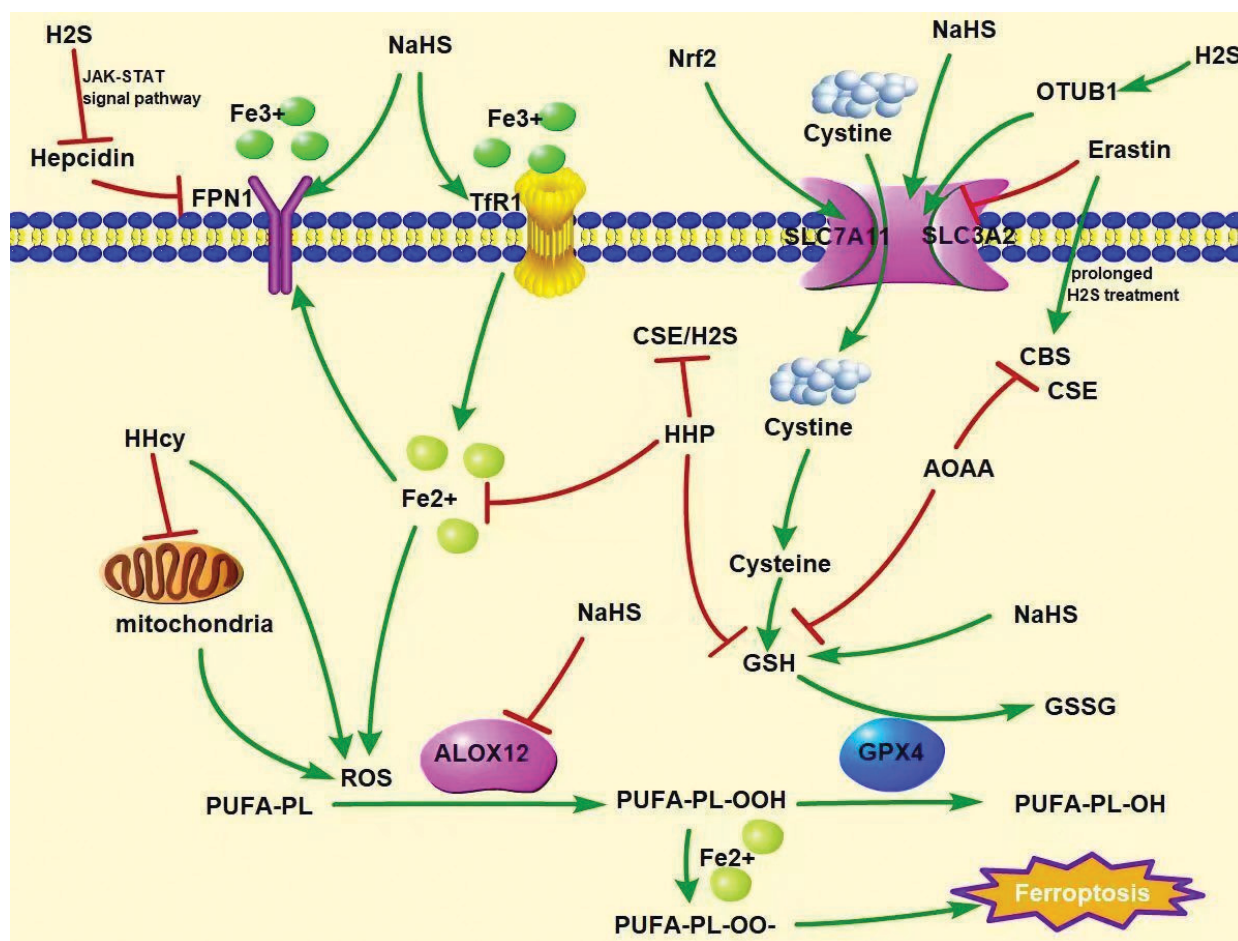


Figure 3. The pathway of H₂S interacting with ferroptosis.

NaHS is a donor of H₂S, and once entered cells, it regulates ferroptosis-associated proteins to exert protective effect. First, it can be converted into cystine, increasing the content of GSH and upregulating the activity of GPX4, resulting in reduced ferroptosis via antioxidant effect. At the same, it maintains the stability of xCT through persulfidation of OTUB1 at cysteine 91. Second, it inhibits ferroptosis and ferritinophagy via upregulating Nrf2. It reduces the expression of hepcidin via the JAK-STAT pathway, preventing the downregulation of FPN1. Thirdly, NaHS itself upregulates the expression of FPN1 and TfR1 with or without inflammation, further regulating the metabolism balance of iron *in vivo*.

ries (Fan *et al.*, 2021). Exposure to H₂S also results in miR-15a upregulation (Xueyuan *et al.*, 2021). Additional evidence suggests that miR-194 can mitigate the severity of ischemia-reperfusion injury through the inhibition of Bach1 and introduction of signaling via the Nrf2/HO-1 pathway. Therefore, miR-194 inhibition reversed these effects by reducing HO-1 and Nrf2 protein levels (Li *et al.*, 2021). Reduction in H₂S production reduces miR-194 expression and drives the deposition and realignment of collagen under diabetic conditions to attenuate fibrosis and renovascular constriction (John *et al.*, 2017). The proteins and miRNAs associated with ferroptosis are summarized in Table 3.

CLINICAL POTENTIAL APPLICATION

In cancer, the clearance of H₂S and the regulation of the enzymes involved in its pathways are essential for cancer therapy. A biocompatible fusiform iron oxide-hydroxide nano-spindles nano system (FeOOH NSs) was designed, which could be applied to magnetic resonance imaging (MRI) to monitor ferroptosis. It can efficiently scavenge endogenous H₂S by a reduction reaction to inhibit the growth of CT26 colon cancer cells (PMID:32789963). The biosafety of this nano-system has been verified in animal models for three months, indi-

cating its potential clinical translation. In addition, zinc oxide-coated virus-like silica nanoparticles (VZnO) were also tested to establish an H₂S-responding nano-system to scavenge H₂S to alleviate ferroptosis in colorectal cancer (Pan *et al.*, 2021). Additionally, fluorescent probes that can be used for selective detection of hydrogen sulfide have been developed to explore the biological and pathological effects of H₂S during ferroptosis (Di *et al.*, 2021; Guo *et al.*, 2022). The two-photon fluorescent probe (PSP) exhibited excellent photostability and two-photon imaging performance, and elevated levels of H₂S were observed during ferroptosis in tumors (Di *et al.*, 2021). Needless to say, these tools will enable a more extensive expansion of H₂S-related technologies and knowledge for broad therapeutic applications in the near future.

FUTURE DIRECTIONS

In recent decades, a broad range of physiological functions of H₂S have been gradually recognized. Accumulating evidence has indicated that H₂S plays a role in various types of cell death. However, it is still not clear whether the suppression of cell death occurs simultaneously across cell death or is more potent toward one type of cell death than the others. As a relatively new

area, the interactive mechanisms between H₂S and ferroptosis need to be further explored, and the implications of H₂S and ferroptosis interactions in various diseases, such as chronic organ fibrosis, diabetes-associated diseases, stroke, and other degenerative diseases, have not been studied. More experiments are needed to develop a safety profile and treatment regimens for H₂S in various disease models and human subjects. Currently, the time and dosage of H₂S in animal experiments are being investigated, but the results are inconsistent (Wang *et al.*, 2022; Zhang *et al.*, 2023). In addition, newly developed nanoparticles or fluorescent probes have not been applied in clinical trials and require further validation and biosafety tests. Minimizing H₂S-induced toxicities remains a challenge and H₂S associated biomarkers need to be identified for the better clinical use of H₂S.

CONCLUSION

In summary, H₂S functions as a key gastronomist closely tied to ferroptosis with the substrates, enzymes, and donors involved in the production of H₂S, all of which are related to ferroptosis. The metabolism of iron, process of lipid peroxidation, and inactivation of antioxidant systems all participate in the process of ferroptosis. H₂S can also regulate the uptake, transport, and accumulation of iron, and reduce lipid oxidation by enhancing superoxide dismutase activity and regulating glucose production. miRNAs are involved in nearly every biological process, and several miRNAs have been found to be involved in both H₂S metabolism and ferroptosis. As the interplay between H₂S and ferroptosis has only been explored in recent years, much work remains to be done to adequately understand the relationship between them. For example, additional research exploring the production, storage, and release of H₂S is needed, as are efforts to understand how H₂S affects mammals *in vivo* under a range of settings and how it shapes the process of ferroptosis.

Declarations

Acknowledgements. Not applicable.

Declaration of conflict of interest: None.

Availability of data and materials: Not applicable because this was a review article.

Author contributions: XG, KL, and CL: literature reading, data collection, and paper drafting. CL: Data analysis and revision of the paper. All the authors have read and approved the final version of the manuscript. Ethics approval and consent to participate: Not applicable because this was a review article.

Patient consent for publication: Not applicable because this is a review article.

REFERENCES

- Arif HM, Qian Z, Wang R (2022) Signaling Integration of hydrogen sulfide and iron on cellular functions. *Antioxid Redox Signal* **36**: 275–293. <https://doi.org/10.1089/ars.2021.0203>
- Cao X, Ding L, Xie ZZ, Yang Y, Whiteman M, Moore PK, Bian JS (2019) A Review of hydrogen sulfide synthesis, metabolism, and measurement: is modulation of hydrogen sulfide a novel therapeutic for cancer? *Antioxid Redox Signal* **31**: 1–38. <https://doi.org/10.1089/ars.2017.7058>
- Cao G, Zeng Y, Zhao Y, Lin L, Luo X, Guo L, Zhang Y, Cheng Q (2022) H₂S regulation of ferroptosis attenuates sepsis-induced cardiomyopathy. *Mol Med Rep* **26**. <https://doi.org/10.3892/mmr.2022.12851>
- Castellblanco M, Lugrin J, Ehrichtiou D, Nasi S, Ishii I, So A, Martinon F, Busso N (2018) Hydrogen sulfide inhibits NLRP3 inflammasome activation and reduces cytokine production both *in vitro* and in a mouse model of inflammation. *J Biol Chem* **293**: 2546–2557. <https://doi.org/10.1074/jbc.M117.806869>
- Chang L, Geng B, Yu F, Zhao J, Jiang H, Du J, Tang C (2008) Hydrogen sulfide inhibits myocardial injury induced by homocysteine in rats. *Amino Acids* **34**: 573–585. <https://doi.org/10.1007/s00726-007-0011-8>
- Chen S, Bu D, Ma Y, Zhu J, Sun L, Zuo S, Ma J, Li T, Chen Z, Zheng Y, Wang X, Pan Y, Wang P, Liu Y (2016) GYY4137 ameliorates intestinal barrier injury in a mouse model of endotoxemia. *Biochem Pharmacol* **118**: 59–67. <https://doi.org/10.1016/j.bcp.2016.08.016>
- Chen S, Guo S, Zhu J, Yue T, Guo S, Wang X, Pan Y, Liu Y, Wang P (2021) Endogenous hydrogen sulfide regulates xCT stability through persulfidation of OTUB1 at cysteine 91 in colon cancer cells. *Neoplasia* **23**: 461–472. <https://doi.org/10.1016/j.neo.2021.03.009>
- Chen X, Huang X, Liu C, Li S, Yang Z, Zhang F, Chen X, Shan H, Tao L, Zhang M (2022) Surface-fill H(2)S-releasing silk fibroin hydrogel for brain repair through the repression of neuronal pyroptosis. *Acta Biomater* **154**: 259–274. <https://doi.org/10.1016/j.actbio.2022.11.021>
- Cheung SH, Lau JYW (2018) Hydrogen sulfide mediates athero-protection against oxidative stress via S-sulphydration. *PLoS One* **13**: e0194176. <https://doi.org/10.1371/journal.pone.0194176>
- Chiku T, Padovani D, Zhu W, Singh S, Vitvitsky V, Banerjee R (2009) H₂S biogenesis by human cystathionine gamma-lyase leads to the novel sulfur metabolites lanthionine and homolanthionine and is responsive to the grade of hyperhomocysteinemia. *J Biol Chem* **284**: 11601–11612. <https://doi.org/10.1074/jbc.M808026200>
- D'Alessandro A, Amelio I, Berkens CR, Antonov A, Vousden KH, Melino G, Zolla L (2014) Metabolic effect of TAp63alpha: enhanced glycolysis and pentose phosphate pathway, resulting in increased antioxidant defense. *Oncotarget* **5**: 7722–7733. <https://doi.org/10.18632/oncotarget.2300>
- Di X, Ge C, Liu Y, Shao C, Zhu HL, Liu HK, Qian Y (2021) Monitoring hydrogen polysulfide during ferroptosis with a two-photon fluorescent probe. *Talanta* **232**: 122467. <https://doi.org/10.1016/j.talanta.2021.122467>
- Erisgin Z, Ozer MA, Tosun M, Ozen S, Takir S (2019) The effects of intravitreal H₂S application on apoptosis in the retina and cornea in experimental glaucoma model. *Int J Exp Pathol* **100**: 330–336. <https://doi.org/10.1111/iecp.12334>
- Fan K, Huang W, Qi H, Song C, He C, Liu Y, Zhang Q, Wang L, Sun H (2021) The Egr-1/miR-15a-5p/GPX4 axis regulates ferroptosis in acute myocardial infarction. *Eur J Pharmacol* **909**: 174403. <https://doi.org/10.1016/j.ejphar.2021.174403>
- Fouad AA, Hafez HM, Hamouda A (2020) Hydrogen sulfide modulates IL-6/STAT3 pathway and inhibits oxidative stress, inflammation, and apoptosis in rat model of methotrexate hepatotoxicity. *Hum Exp Toxicol* **39**: 77–85. <https://doi.org/10.1177/0960327119877437>
- Fuhrmann DC, Brüne B (2022) A graphical journey through iron metabolism, microRNAs, and hypoxia in ferroptosis. *Redox Biol* **54**: 102365. <https://doi.org/10.1016/j.redox.2022.102365>
- Gong W, Zhang S, Chen Y, Shen J, Zheng Y, Liu X, Zhu M, Meng G (2022) Protective role of hydrogen sulfide against diabetic cardiomyopathy via alleviating necroptosis. *Free Radic Biol Med* **181**: 29–42. <https://doi.org/10.1016/j.freeradbiomed.2022.01.028>
- Guo C, Liang F, Shah Masood W, Yan X (2014) Hydrogen sulfide protected gastric epithelial cell from ischemia/reperfusion injury by Keap1 s-sulphydration, MAPK dependent anti-apoptosis and NF-kappaB dependent anti-inflammation pathway. *Eur J Pharmacol* **725**: 70–78. <https://doi.org/10.1016/j.ejphar.2014.01.009>
- Guo MY, Wang W, Ainiwaer D, Yang YS, Wang BZ, Yang J, Zhu HL (2022) A fluorescent Rhodol-derived probe for rapid and selective detection of hydrogen sulfide and its application. *Talanta* **237**: 122960. <https://doi.org/10.1016/j.talanta.2021.122960>
- Hadian K, Stockwell BR (2020) SnapShot: Ferroptosis. *Cell* **181**: 1188–1188, e1181. <https://doi.org/10.1016/j.cell.2020.04.039>
- Han W, Dong Z, Dimitropoulou C, Su Y (2011) Hydrogen sulfide ameliorates tobacco smoke-induced oxidative stress and emphysema in mice. *Antioxid Redox Signal* **15**: 2121–2134. <https://doi.org/10.1089/ars.2010.3821>
- Hine C, Harputlugil E, Zhang Y, Ruckenstein C, Lee BC, Brace L, Longchamp A, Trevino-Villarreal JH, Mejia P, Ozaki CK, Wang R, Gladyshev VN, Madeo F, Mair WB, Mitchell JR (2015) Endogenous hydrogen sulfide production is essential for dietary restriction benefits. *Cell* **160**: 132–144. <https://doi.org/10.1016/j.cell.2014.11.048>
- Hu Q, Zhang R, Zheng J, Song M, Gu C, Li W (2023) Hydrogen sulfide attenuates uranium-induced kidney cells pyroptosis via up-regulation of PI3K/AKT/mTOR signaling. *J Biochem Mol Toxicol* **37**: e23220. <https://doi.org/10.1002/jbt.23220>
- Jiang X, Stockwell BR, Conrad M (2021) Ferroptosis: mechanisms, biology and role in disease. *Nat Rev Mol Cell Biol* **22**: 266–282. <https://doi.org/10.1038/s41580-020-00324-8>
- Jin R, Yang R, Cui C, Zhang H, Cai J, Geng B, Chen Z (2022) Ferroptosis due to cystathionine gamma lyase/hydrogen sulfide down-regulation under high hydrostatic pressure exacerbates VSMC dys-

- function. *Front Cell Dev Biol* 10: 829316. <https://doi.org/10.3389/fcell.2022.829316>
- John A, Kundu S, Pushpakumar S, Fordham M, Weber G, Mukhopadhyay M, Sen U (2017) GY4137, a hydrogen sulfide donor modulates miR194-dependent collagen realignment in diabetic kidney. *Sci Rep* 7: 10924. <https://doi.org/10.1038/s41598-017-11256-3>
- Ju Y, Untereiner A, Wu L, Yang G (2015) H₂S-induced S-sulhydration of pyruvate carboxylase contributes to gluconeogenesis in liver cells. *Biochim Biophys Acta* 1850: 2293–2303. <https://doi.org/10.1016/j.bbagen.2015.08.003>
- Kaneko Y, Kimura Y, Kimura H, Niki I (2006) L-cysteine inhibits insulin release from the pancreatic beta-cell: possible involvement of metabolic production of hydrogen sulfide, a novel gasotransmitter. *Diabetes* 55: 1391–1397. <https://doi.org/10.2337/db05-1082>
- Khattak S, Zhang QQ, Sarfraz M, Muhammad P, Ngowi EE, Khan NH, Rauf S, Wang YZ, Qi HW, Wang D, Afzal A, Ji XY, Wu DD (2021) The role of hydrogen sulfide in respiratory diseases. *Biomolecules* 11. <https://doi.org/10.3390/biom11050682>
- Kimura Y, Goto Y, Kimura H (2010) Hydrogen sulfide increases glutathione production and suppresses oxidative stress in mitochondria. *Antioxid Redox Signal* 12: 1–13. <https://doi.org/10.1089/ars.2008.2282>
- Koike S, Nishimoto S, Ogasawara Y (2017) Cysteine persulfides and polysulfides produced by exchange reactions with H₂S protect SH-SY5Y cells from methylglyoxal-induced toxicity through Nrf2 activation. *Redox Biol* 12: 530–539. <https://doi.org/10.1016/j.redox.2017.03.020>
- Kolluru GK, Shen X, Bir SC, Kevil CG (2013) Hydrogen sulfide chemical biology: pathophysiological roles and detection. *Nitric Oxide* 35: 5–20. <https://doi.org/10.1016/j.niox.2013.07.002>
- Koppula P, Zhuang L, Gan B (2021) Cystine transporter SLC7A11/xCT in cancer: ferroptosis, nutrient dependency, and cancer therapy. *Protein Cell* 12: 599–620. <https://doi.org/10.1007/s12328-020-00789-5>
- Kozich V, Ditroi T, Sokolova J, Krizkova M, Krijt J, Jesina P, Nagy P (2019) Metabolism of sulfur compounds in homocystinurias. *Br J Pharmacol* 176: 594–606. <https://doi.org/10.1111/bph.14523>
- Kshirsagar V, Thingore C, Gursahani M, Gawali N, Juvekar A (2021) Hydrogen Sulfide Ameliorates Lipopolysaccharide-Induced Memory impairment in mice by reducing apoptosis, oxidative, and inflammatory effects. *Neurotox Res* 39: 1310–1322. <https://doi.org/10.1007/s12640-021-00374-6>
- Kuo WW, Wang WJ, Tsai CY, Way CL, Hsu HH, Chen LM (2013) Diallyl trisulfide (DATS) suppresses high glucose-induced cardiomyocyte apoptosis by inhibiting JNK/NFκB signaling via attenuating ROS generation. *Int J Cardiol* 168: 270–280. <https://doi.org/10.1016/j.ijcard.2012.09.080>
- Lang X, Green MD, Wang W, Yu J, Choi JE, Jiang L, Liao P, Zhou J, Zhang Q, Dow A, Saripalli AL, Kryczek I, Wei S, Szeliga W, Vatan L, Stone EM, Georgiou G, Cieslik M, Wahl DR, Morgan MA, Chinnaiyan AM, Lawrence TS, Zou W (2019) Radiotherapy and immunotherapy promote tumoral lipid oxidation and ferroptosis via synergistic repression of SLC7A11. *Cancer Discov* 9: 1673–1685. <https://doi.org/10.1158/2159-8290.CD-19-0338>
- Lei G, Zhang Y, Koppula P, Liu X, Zhang J, Lin SH, Ajani JA, Xiao Q, Liao Z, Wang H, Gan B (2020) The role of ferroptosis in ionizing radiation-induced cell death and tumor suppression. *Cell Res* 30: 146–162. <https://doi.org/10.1038/s41422-019-0263-3>
- Levasseur R (2009) Bone tissue and hyperhomocysteinemia. *Joint Bone Spine* 76: 234–240. <https://doi.org/10.1016/j.jbspin.2008.11.002>
- Li Y, Liu M, Yi J, Song X, Zheng X, Liu D, Wang S, Chu C, Yang J (2020) Exogenous hydrogen sulfide inhibits apoptosis by regulating endoplasmic reticulum stress-autophagy axis and improves myocardial reconstruction after acute myocardial infarction. *Acta Biochim Biophys Sin (Shanghai)* 52: 1325–1336. <https://doi.org/10.1093/abbs/gmaa133>
- Li X, Zhang X, Liu Y, Pan R, Liang X, Huang L, Yang C (2021) Exosomes derived from mesenchymal stem cells ameliorate oxygen-glucose deprivation/reoxygenation-induced neuronal injury via transferring MicroRNA-194 and targeting Bcl1. *Tissue Cell* 73: 101651. <https://doi.org/10.1016/j.tice.2021.101651>
- Li J, Li M, Li L, Ma J, Yao C, Yao S (2022) Hydrogen sulfide attenuates ferroptosis and stimulates autophagy by blocking mTOR signaling in sepsis-induced acute lung injury. *Mol Immunol* 141: 318–327. <https://doi.org/10.1016/j.molimm.2021.12.003>
- Liang C, Zhang X, Yang M, Dong X (2019) Recent progress in ferroptosis inducers for cancer therapy. *Adv Mater* 31: e1904197. <https://doi.org/10.1002/adma.201904197>
- Lin J, Chen M, Liu D, Guo R, Lin K, Deng H, Zhi X, Zhang W, Feng J, Wu W (2018) Exogenous hydrogen sulfide protects human umbilical vein endothelial cells against high glucose-induced injury by inhibiting the necroptosis pathway. *Int J Mol Med* 41: 1477–1486. <https://doi.org/10.3892/ijmm.2017.3330>
- Lin J, Li X, Lin Y, Huang Z, Wu W (2021) Exogenous sodium hydrosulfide protects against high glucose-induced injury and inflammation in human umbilical vein endothelial cells by inhibiting necroptosis via the p38 MAPK signaling pathway. *Mol Med Rep* 23. <https://doi.org/10.3892/mmr.2020.11706>
- Liu J, Xia X, Huang P (2020) xCT: A critical molecule that links cancer metabolism to redox signaling. *Mol Ther* 28: 2358–2366. <https://doi.org/10.1016/j.ymthe.2020.08.021>
- Liu N, Lin X, Huang C (2020) Activation of the reverse transsulfuration pathway through NRF2/CBS confers erastin-induced ferroptosis resistance. *Br J Cancer* 122: 279–292. <https://doi.org/10.1038/s41416-019-0660-x>
- Liu L, Yao H, Zhou X, Chen J, Chen G, Shi X, Wu G, Zhou G, He S (2022) MiR-15a-3p regulates ferroptosis via targeting glutathione peroxidase GPX4 in colorectal cancer. *Mol Carcinog* 61: 301–310. <https://doi.org/10.1002/mc.23367>
- Liu X, Li G, Chen S, Jin H, Liu X, Zhang L, Zhang Z (2023) Hydrogen sulfide alleviates beryllium sulfate-induced ferroptosis and ferritinophagy in 16HBE cells. *J Appl Toxicol* 43: 1169–1182. <https://doi.org/10.1002/jat.4453>
- Mahoney-Sánchez L, Bouchaoui H, Ayton S, Devos D, Duce JA, Devedjian J-C (2021) Ferroptosis and its potential role in the pathophysiology of Parkinson's Disease. *Prog Neurobiol* 196: 101890. <https://doi.org/10.1016/j.pneurobio.2020.101890>
- Malinowska J, Babicz K, Olas B, Stochmal A, Oleszek W (2012) Aronia melanocarpa extract suppresses the biotoxicity of homocysteine and its metabolite on the hemostatic activity of fibrinogen and plasma. *Nutrition* 28: 793–798. <https://doi.org/10.1016/j.nut.2011.10.012>
- Marrocco I, Altieri F, Peluso I (2017) Measurement and clinical significance of biomarkers of oxidative stress in humans. *Oxid Med Cell Longev* 2017: 6501046. <https://doi.org/10.1155/2017/6501046>
- Mendes JA, Ribeiro MC, Reis Filho GJM, Rocha T, Muscará MN, Costa SKP, Ferreira HHA (2019) Hydrogen sulfide inhibits apoptosis and protects the bronchial epithelium in an allergic inflammation mice model. *Int Immunopharmacol* 73: 435–441. <https://doi.org/10.1016/j.intimp.2019.05.041>
- Nagahara N, Ito T, Kitamura H, Nishino T (1998) Tissue and subcellular distribution of mercaptopyruvate sulfurtransferase in the rat: confocal laser fluorescence and immunoelectron microscopic studies combined with biochemical analysis. *Histochem Cell Biol* 110: 243–250. <https://doi.org/10.1007/s004180050286>
- Ni J, Jiang L, Shen G, Xia Z, Zhang L, Xu J, Feng Q, Qu H, Xu F, Li X (2021) Hydrogen sulfide reduces pyroptosis and alleviates ischemia-reperfusion-induced acute kidney injury by inhibiting NLRP3 inflammasome. *Life Sci* 284: 119466. <https://doi.org/10.1016/j.lfs.2021.119466>
- Olson KR, Deleon ER, Gao Y, Hurley K, Sadauskas V, Batz C, Stoy GF (2013) Thiosulfate: a readily accessible source of hydrogen sulfide in oxygen sensing. *Am J Physiol Regul Integr Comp Physiol* 305: R592–R603. <https://doi.org/10.1152/ajpregu.00421.2012>
- Pan X, Qi Y, Du Z, He J, Yao S, Lu W, Ding K, Zhou M (2021) Zinc oxide nanosphere for hydrogen sulfide scavenging and ferroptosis of colorectal cancer. *J Nanobiotechnology* 19: 392. <https://doi.org/10.1186/s12951-021-01069-y>
- Patel P, Vatish M, Heptinstall J, Wang R, Carson RJ (2009) The endogenous production of hydrogen sulphide in intrauterine tissues. *Reprod Biol Endocrinol* 7: 10. <https://doi.org/10.1186/1477-7827-7-10>
- Proneth B, Conrad M (2019) Ferroptosis and necroinflammation, a yet poorly explored link. *Cell Death Differ* 26: 14–24. <https://doi.org/10.1038/s41418-018-0173-9>
- Rodkin S, Nwosu C, Sannikov A, Raevskaya M, Tushev A, Vasilieva I, Gasanov M (2023) The role of hydrogen sulfide in regulation of cell death following neurotrauma and related neurodegenerative and psychiatric diseases. *Int J Mol Sci* 24. <https://doi.org/10.3390/ijms241310742>
- Searcy DG, Lee SH (1998) Sulfur reduction by human erythrocytes. *J Exp Zool* 282: 310–322. [https://doi.org/10.1002/\(sici\)1097-010x\(19981015\)282:3<310::aid-jez4>3.0.co;2-p](https://doi.org/10.1002/(sici)1097-010x(19981015)282:3<310::aid-jez4>3.0.co;2-p)
- Shen Y, Shen Z, Miao L, Xin X, Lin S, Zhu Y, Guo W, Zhu YZ (2015) miRNA-30 family inhibition protects against cardiac ischemic injury by regulating cystathionine-gamma-lyase expression. *Antioxid Redox Signal* 22: 224–240. <https://doi.org/10.1089/ars.2014.5909>
- Shen W, Gao C, Cueto R, Liu L, Fu H, Shao Y, Yang WY, Fang P, Choi ET, Wu Q, Yang X, Wang H (2020) Homocysteine-methionine cycle is a metabolic sensor system controlling methylation-regulated pathological signaling. *Redox Biol* 28: 101322. <https://doi.org/10.1016/j.redox.2019.101322>
- Shi Q, Liu R, Chen L (2022) Ferroptosis inhibitor ferrostatin-1 alleviates homocysteine-induced ovarian granulosa cell injury by regulating TET activity and DNA methylation. *Mol Med Rep* 25. <https://doi.org/10.3892/mmr.2022.12645>
- Shibuya N, Tanaka M, Yoshida M, Ogasawara Y, Togawa T, Ishii K, Kimura H (2009) 3-Mercaptopyruvate sulfurtransferase produces hydrogen sulfide and bound sulfane sulfur in the brain. *Antioxid Redox Signal* 11: 703–714. <https://doi.org/10.1089/ars.2008.2253>
- Stockwell BR, Friedmann Angeli JP, Bayir H, Bush AI, Conrad M, Dixon SJ, Fulda S, Gascon S, Hatzios SK, Kagan VE, Noel K, Jiang X, Linkermann A, Murphy ME, Overholtzer M, Oyagi A,

- Pagnussat GC, Park J, Ran Q, Rosenfeld CS, Salnikow K, Tang D, Torti FM, Torti SV, Toyokuni S, Woerpel KA, Zhang DD (2017) Ferroptosis: A regulated cell death nexus linking metabolism, redox biology, and disease. *Cell* **171**: 273–285. <https://doi.org/10.1016/j.cell.2017.09.021>
- Stockwell BR, Jiang X, Gu W (2020) Emerging mechanisms and disease relevance of ferroptosis. *Trends Cell Biol* **30**: 478–490. <https://doi.org/10.1016/j.tcb.2020.02.009>
- Su LJ, Zhang JH, Gomez H, Murugan R, Hong X, Xu D, Jiang F, Peng ZY (2019) Reactive oxygen species-induced lipid peroxidation in apoptosis, autophagy, and ferroptosis. *Oxid Med Cell Longev* **2019**: 5080843. <https://doi.org/10.1155/2019/5080843>
- Sun WH, Liu F, Chen Y, Zhu YC (2012) Hydrogen sulfide decreases the levels of ROS by inhibiting mitochondrial complex IV and increasing SOD activities in cardiomyocytes under ischemia/reperfusion. *Biochem Biophys Res Commun* **421**: 164–169. <https://doi.org/10.1016/j.bbrc.2012.03.121>
- Tang G, Zhang L, Wang G, Wu L, Wang R (2013) Hydrogen sulfide-induced inhibition of L-type Ca^{2+} channels and insulin secretion in mouse pancreatic beta cells. *Diabetologia* **56**: 533–541. <https://doi.org/10.1007/s00125-012-2806-8>
- Tang Y-H, Wu L, Huang H-L, Zhang P-P, Zou W, Tang X-Q, Tang Y-Y (2023) Hydrogen sulfide antagonizes formaldehyde-induced ferroptosis via preventing ferritinophagy by upregulation of GDF11 in HT22 cells. *Toxicology* **491**: 153517. <https://doi.org/10.1016/j.tox.2023.153517>
- Wang R (2012) Physiological implications of hydrogen sulfide: a whiff exploration that blossomed. *Physiol Rev* **92**: 791–896. <https://doi.org/10.1152/physrev.00017.2011>
- Wang L, Cai H, Hu Y, Liu F, Huang S, Zhou Y, Yu J, Xu J, Wu F (2018) A pharmacological probe identifies cystathionine beta-synthase as a new negative regulator for ferroptosis. *Cell Death Dis* **9**: 1005. <https://doi.org/10.1038/s41419-018-1063-2>
- Wang Y, Wang S, Xin Y, Zhang J, Wang S, Yang Z, Liu C (2021a) Hydrogen sulfide alleviates the anxiety-like and depressive-like behaviors of type 1 diabetic mice via inhibiting inflammation and ferroptosis. *Life Sci* **278**: 119551. <https://doi.org/10.1016/j.lfs.2021.119551>
- Wang Y, Yu R, Wu L, Yang G (2021b) Hydrogen sulfide guards myoblasts from ferroptosis by inhibiting ALOX12 acetylation. *Cell Signal* **78**: 109870. <https://doi.org/10.1016/j.cellsig.2020.109870>
- Wang Y, Liao S, Pan Z, Jiang S, Fan J, Yu S, Xue L, Yang J, Ma S, Liu T, Zhang J, Chen Y (2022a) Hydrogen sulfide alleviates particulate matter-induced emphysema and airway inflammation by suppressing ferroptosis. *Free Radic Biol Med* **186**: 1–16. <https://doi.org/10.1016/j.freeradbiomed.2022.04.014>
- Wang L, Meng J, Wang C, Wang Y, Yang C, Li Y (2022b) Hydrogen sulfide attenuates cigarette smoke-induced pyroptosis through the I LR4 /NF- κB signaling pathway. *Int J Mol Med* **49**. <https://doi.org/10.3892/ijmm.2022.5112>
- Wang Y, Ying X, Wang Y, Zou Z, Yuan A, Xiao Z, Geng N, Qiao Z, Li W, Lu X, Pu J (2023) Hydrogen sulfide alleviates mitochondrial damage and ferroptosis by regulating OPA3-NFS1 axis in doxorubicin-induced cardiotoxicity. *Cell Signal* **107**: 110655. <https://doi.org/10.1016/j.cellsig.2023.110655>
- Weirather J, Hofmann UD, Beyersdorf N, Ramos GC, Vogel B, Frey A, Ertl G, Kerkau T, Frantz S (2014) Foxp3+ CD4+ T cells improve healing after myocardial infarction by modulating monocyte/macrophage differentiation. *Circ Res* **115**: 55–67. <https://doi.org/10.1161/CIRCRESAHA.115.303895>
- Wiener R, Zhang X, Wang T, Wolberger C (2012) The mechanism of OTUB1-mediated inhibition of ubiquitination. *Nature* **483**: 618–622. <https://doi.org/10.1038/nature10911>
- Wu L, Wang W, Jia X, Yang G, Duridanova D, Cao K, Wang R (2009) Pancreatic islet overproduction of H $_{2}\text{S}$ and suppressed insulin release in Zucker diabetic rats. *Lab Invest* **89**: 59–67. <https://doi.org/10.1038/labinvest.2008.109>
- Wu ZF, Yan BJ, Luo W, Gui DD, Ren Z, Ma Y, Jiang ZS (2023) Ferroptosis and hydrogen sulfide in cardiovascular disease. *Curr Med Chem* **30**: 1848–1859. <https://doi.org/10.2174/0929867329666220630144648>
- Xi H, Zhang Y, Xu Y, Yang WY, Jiang X, Sha X, Cheng X, Wang J, Qin X, Yu J, Ji Y, Yang X, Wang H (2016) Caspase-1 inflammation activation mediates homocysteine-induced Pyroptosis in endothelial cells. *Circ Res* **118**: 1525–1539. <https://doi.org/10.1161/CIRCRESAHA.116.308501>
- Xin H, Wang M, Tang W, Shen Z, Miao L, Wu W, Li C, Wang X, Xin X, Zhu YZ (2016) Hydrogen sulfide attenuates inflammatory hepcidin by reducing IL-6 secretion and promoting SIRT1-mediated STAT3 deacetylation. *Antioxid Redox Signal* **24**: 70–83. <https://doi.org/10.1089/ars.2015.6315>
- Xueyuan H, Qianru C, Zhaoyi L, Dayong T, Yu W, Yimei C, Shu L (2021) Transcriptome analysis reveals that hydrogen sulfide exposure suppresses cell proliferation and induces apoptosis through ciR-PTPN23/miR-15a/E2F3 signaling in broiler thymus. *Environ Pollut* **284**: 117466. <https://doi.org/10.1016/j.envpol.2021.117466>
- Yan SK, Chang T, Wang H, Wu L, Wang R, Meng QH (2006) Effects of hydrogen sulfide on homocysteine-induced oxidative stress in vascular smooth muscle cells. *Biochem Biophys Res Commun* **351**: 485–491. <https://doi.org/10.1016/j.bbrc.2006.10.058>
- Yang J, Minkler P, Grove D, Wang R, Willard B, Dweik R, Hine C (2019) Non-enzymatic hydrogen sulfide production from cysteine in blood is catalyzed by iron and vitamin B(6). *Commun Biol* **2**: 194. <https://doi.org/10.1038/s42003-019-0431-5>
- Yang T, Yang Q, Lai Q, Zhao J, Nie L, Liu S, Yang J, Chu C (2023) AP39 inhibits ferroptosis by inhibiting mitochondrial autophagy through the PINK1/parkin pathway to improve myocardial fibrosis with myocardial infarction. *Biomed Pharmacotherap* **165**: 115195. <https://doi.org/10.1016/j.biopha.2023.115195>
- Yasuhara N, Eguchi Y, Tachibana T, Imamoto N, Yoneda Y, Tsujimoto Y (1997) Essential role of active nuclear transport in apoptosis. *Genes Cells* **2**: 55–64. <https://doi.org/10.1046/j.1365-2443.1997.1010302.x>
- Yu M, Wang W, Dang J, Liu B, Xu J, Li J, Liu Y, He L, Ying Y, Cai J, Cheng G, Liu K (2023a) Hydrogen sulfide protects retinal pigment epithelium cells against ferroptosis through the AMPK- and p62-dependent non-canonical NRF2-KEAP1 pathway. *Exp Cell Res* **422**: 113436. <https://doi.org/10.1016/j.yexcr.2022.113436>
- Yu Y, Li X, Wu X, Li X, Wei J, Chen X, Sun Z, Zhang Q (2023b) Sodium hydrosulfide inhibits hemin-induced ferroptosis and lipid peroxidation in BV2 cells via the CBS/H2S system. *Cell Signal* **104**: 110594. <https://doi.org/10.1016/j.cellsig.2023.110594>
- Zhang L, Yang G, Untereiner A, Ju Y, Wu L, Wang R (2013) Hydrogen sulfide impairs glucose utilization and increases gluconeogenesis in hepatocytes. *Endocrinology* **154**: 114–126. <https://doi.org/10.1210/en.2012-1658>
- Zhang MW, Yang G, Zhou YF, Qian C, Mu MD, Ke Y, Qian ZM (2019) Regulating ferroportin-1 and transferrin receptor-1 expression: A novel function of hydrogen sulfide. *J Cell Physiol* **234**: 3158–3169. <https://doi.org/10.1002/jcp.27431>
- Zhang H, He Y, Wang JX, Chen MH, Xu JJ, Jiang MH, Feng YL, Gu YF (2020a) miR-30-5p-mediated ferroptosis of trophoblasts is implicated in the pathogenesis of preeclampsia. *Redox Biol* **29**: 101402. <https://doi.org/10.1016/j.redox.2019.101402>
- Zhang J, Shan H, Tao L, Zhang M (2020b) Biological effects of hydrogen sulfide and its protective role in intracerebral hemorrhage. *J Mol Neurosci* **70**: 2020–2030. <https://doi.org/10.1007/s12031-020-01608-6>
- Zhang X, Huang Z, Xie Z, Chen Y, Zheng Z, Wei X, Huang B, Shan Z, Liu J, Fan S, Chen J, Zhao F (2020c) Homocysteine induces oxidative stress and ferroptosis of nucleus pulposus via enhancing methylation of GPX4. *Free Radic Biol Med* **160**: 552–565. <https://doi.org/10.1016/j.freeradbiomed.2020.08.029>
- Zhang L, Rao J, Liu X, Wang X, Wang C, Fu S, Xiao J (2023) Attenuation of sepsis-induced acute kidney injury by exogenous H $_{2}\text{S}$ via inhibition of ferroptosis. *Molecules* **28**. <https://doi.org/10.3390/molecules28124770>
- Zhou YF, Wu XM, Zhou G, Mu MD, Zhang FL, Li FM, Qian C, Du F, Yung WH, Qian ZM, Ke Y (2018) Cystathionine beta-synthase is required for body iron homeostasis. *Hepatology* **67**: 21–35. <https://doi.org/10.1002/hep.29499>
- Zuhra K, Augsburger F, Majtan T, Szabo C (2020) Cystathionine-beta-synthase: molecular regulation and pharmacological inhibition. *Bio-molecules* **10**. <https://doi.org/10.3390/biom10050697>



OPEN ACCESS

EDITED BY
Grzegorz Węgrzyn,
University of Gdansk, Poland

REVIEWED BY
Jacek Lubkowski,
National Institutes of Health (NIH),
United States
One reviewer who chose to remain
anonymous

*CORRESPONDENCE
Joanna I. Loch,
✉ joanna.loch@uj.edu.pl

RECEIVED 25 October 2023
ACCEPTED 05 January 2024
PUBLISHED 16 January 2024

CITATION
Loch JI, Ściuk A, Kilichowska M, Pieróg I,
Łukaszczuk W, Zimowska K and
Jaskolski M (2024), Probing the
enzymatic activity and maturation
process of the EcAIII Ntn-
amidohydrolase using local
random mutagenesis.
Acta Biochim. Pol. 71:12299.
doi: 10.3389/abp.2024.12299

COPYRIGHT
© 2024 Loch, Ściuk, Kilichowska,
Pieróg, Łukaszczuk, Zimowska and
Jaskolski. This is an open-access article
distributed under the terms of the
Creative Commons Attribution License
(CC BY). The use, distribution or
reproduction in other forums is
permitted, provided the original
author(s) and the copyright owner(s) are
credited and that the original
publication in this journal is cited, in
accordance with accepted academic
practice. No use, distribution or
reproduction is permitted which does
not comply with these terms.

Probing the enzymatic activity and maturation process of the EcAIII Ntn-amidohydrolase using local random mutagenesis

Joanna I. Loch^{1*}, Anna Ściuk^{1,2}, Marta Kilichowska^{1,2},
Izabela Pieróg^{1,2}, Weronika Łukaszczuk¹, Katarzyna Zimowska¹
and Mariusz Jaskolski^{3,4}

¹Department of Crystal Chemistry and Crystal Physics, Faculty of Chemistry, Jagiellonian University, Krakow, Poland, ²Doctoral School of Exact and Natural Sciences, Jagiellonian University, Krakow, Poland, ³Institute of Bioorganic Chemistry, Polish Academy of Sciences, Poznan, Poland, ⁴Department of Crystallography, Faculty of Chemistry, Adam Mickiewicz University, Poznan, Poland

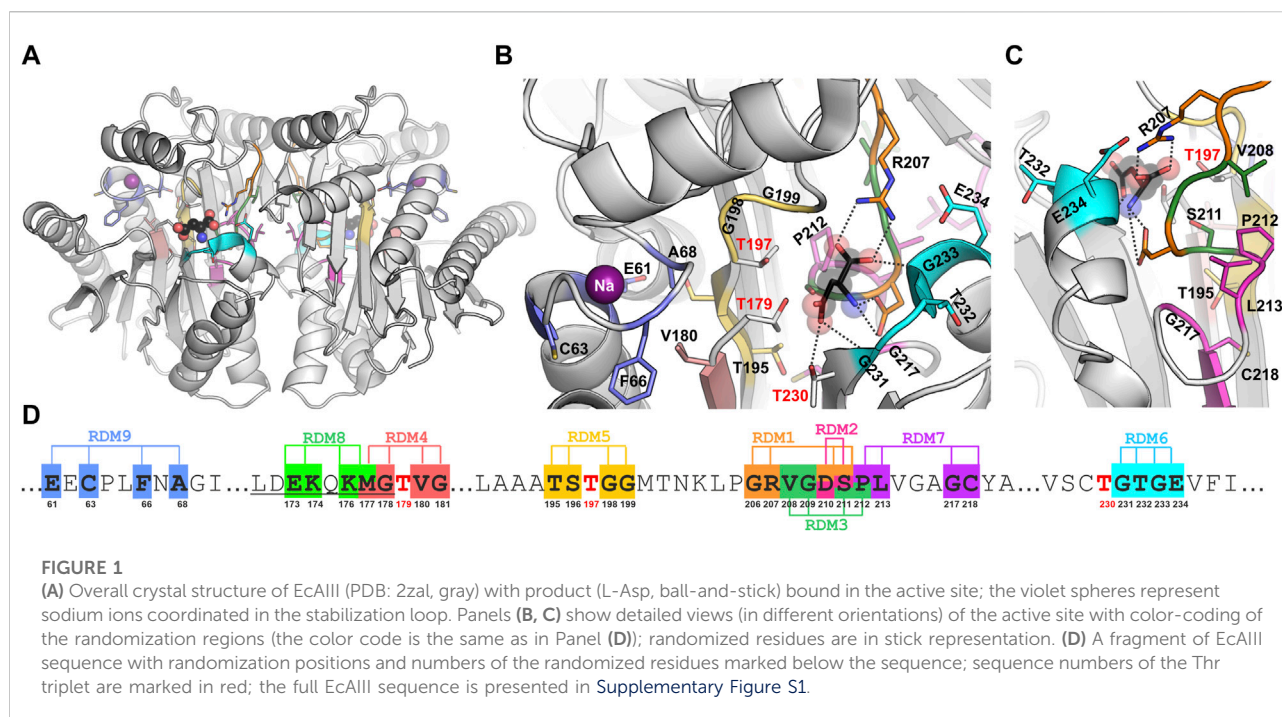
This report describes a comprehensive approach to local random mutagenesis of the *E. coli* Ntn-amidohydrolase EcAIII, and supplements the results published earlier for the randomization series RDM1. Here, random mutagenesis was applied in the center of the EcAIII molecule, i.e., in the region important for substrate binding and its immediate neighborhood (series RDM2, RDM3, RDM7), in the vicinity of the catalytic threonine triplet (series RDM4, RDM5, RDM6), in the linker region (series RDM8), and in the sodium-binding (stabilization) loop (series RDM9). The results revealed that the majority of the new EcAIII variants have abolished or significantly reduced rate of autoprocessing, even if the mutation was not in a highly conserved sequence and structure regions. AlphaFold-predicted structures of the mutants suggest the role of selected residues in the positioning of the linker and stabilization of the scissile bond in precisely correct orientation, enabling the nucleophilic attack during the maturation process. The presented data highlight the details of EcAIII geometry that are important for the autoproteolytic maturation and for the catalytic mechanism in general, and can be treated as a guide for protein engineering experiments with other Ntn-hydrolases.

KEYWORDS

L-asparaginase, Ntn-hydrolase, random mutagenesis, enzyme engineering, AlphaFold prediction

Introduction

N-terminal-nucleophile amidohydrolases (Ntn-amidohydrolases) are enzymes that hydrolyze the amide bonds of amino acids, peptides, glycopeptides, and sphingolipids (Linhorst and Lübke, 2022), using an N-terminal residue as the primary nucleophile. Ntn-amidohydrolases are produced as inactive precursors which develop their enzymatic activity in an autocatalytic cleavage maturation process that releases the nucleophilic residue (Thr, Ser, Cys) at the newly formed N-terminus of subunit β (Michalska and



Jaskolski, 2006). The *Escherichia coli* EcAIII protein is an Ntn-amidohydrolase with the L-asparaginase activity (Michalska et al., 2005). L-asparaginases are a large group of enzymes that convert L-Asn to L-Asp and ammonia. According to the most recent classification, EcAIII is a potassium-independent member of Class 2 L-asparaginases (Loch and Jaskolski, 2021; da Silva et al., 2022), formerly called plant-type L-asparaginases (Borek and Jaskólski, 2001).

The catalytic center of EcAIII is made of a threonine triplet: Thr179 (the nucleophile), Thr197, and Thr230. In the close vicinity of the triplet, other residues involved in substrate stabilization are located. Among them, the most important is Arg207, which acts as an anchor for the substrate α -carboxylate group, and Asp210, which stabilizes its amino group (Figure 1). The EcAIII molecule also features a sodium-binding (stabilization) loop, which is important for securing the proper orientation of Thr179 nucleophile (Michalska et al., 2008).

As all known Ntn-hydrolases, EcAIII requires a maturation step to develop its enzymatic activity. Upon maturation, the peptide bond between Gly178 and Thr179 is cleaved by the same Thr179 nucleophile (Michalska et al., 2008). The precursor protein is a homodimer, while the mature form of EcAIII is a dimer of two heterodimers, each comprised of subunit α and subunit β . After the autocleavage process, a flexible linker of ~20 residues remains at the C-terminal part of subunit α . The linker is naturally disordered and undergoes degradation over time (Linhorst and Lübke, 2022).

Our recent studies of the impact of random substitutions (series RDM1, Supplementary Table S1) on EcAIII performance revealed that initiation of autocatalytic cleavage is a complex and

multistep process, highly sensitive to even small changes in protein geometry and hydration pattern near the scissile Gly178-Thr179 bond (Loch et al., 2022). Following the previous run of local random mutagenesis, we performed further randomization trials to probe how the selected regions of the EcAIII molecule tolerate simultaneous multiple amino acid substitutions. Moreover, we also hoped to identify new EcAIII variant(s) with improved catalytic efficiency (k_{cat}) or substrate affinity (K_m), for potential utilization in leukemia therapy (Tosta Pérez et al., 2023).

In this work, segments of the EcAIII sequence for local random mutagenesis (Figure 1; Supplementary Table S1) were selected on the basis of crystal structure analysis. Residue randomization was carried out in the center of the EcAIII molecule, i.e., in the region important for substrate binding and its immediate neighborhood (series RDM2, RDM3, RDM7), in the vicinity of the catalytic threonine triplet (series RDM4, RDM5, RDM6), in the linker region (series RDM8) and in the sodium-binding loop (series RDM9). Although mutations usually led to inactive precursors, we were still able to identify several factors that affect the enzyme performance. Our report is one of few studies (Kim et al., 2010; Karamitros and Konrad, 2016; Xu et al., 2018; Loch et al., 2022) describing mutagenetic modification of Ntn-hydrolases.

Methods

Random mutagenesis was performed according to the QuikChange protocol with the use of the mutagenic primers

listed in [Supplementary Table S1](#). In the naming scheme applied in this work, mutants are labeled as “RDMY-X,” where X is the ordinal number of a particular bacterial colony that was screened, and Y is the number of the mutagenesis trial ([Supplementary Table S1](#); [Figure 1](#)). All SDS-PAGE gels marked with names of the mutants are presented at the end of [Supplementary Material](#) (as [Supplementary Appendix – raw experimental data](#)).

As a matrix for PCR reaction, the EcAIII sequence cloned to the pET11d (or pMCSG92) vector was used. After PCR reaction, the matrix was digested using *DpnI* enzyme (Thermo Scientific). Products of the PCR reaction were transformed to BL21 (DE3) Gold cells. Clone selection procedure, L-asparaginase activity test in cell lysate, and monitoring of autocleavage were performed according to previously described protocol ([Loch et al., 2022](#)). After monitoring of maturation by SDS-PAGE and testing for activity in cell lysate, several clones (active or inactive) were selected for plasmid DNA isolation and sequencing (Genomed SA, Poland) to check the mutations present.

Large-scale expression and purification of selected variants were performed according to previously described procedures ([Loch et al., 2022, 2023](#)). L-asparaginase activity of mutants was detected using Nessler method as describes earlier ([Janicki et al., 2023](#)). Structure prediction for selected mutants was made using AlphaFold2 (AF2) ([Jumper et al., 2021](#)) with the utilization of Amber relaxation refinement to assure the correct stereochemistry of the models.

Results and discussion

The results presented herein are a continuation and complementation of the random mutagenesis report on EcAIII published previously as the RDM1 series ([Loch et al., 2022](#)). The randomization trials RDM2 - RDM9 were performed in eight selected regions of the EcAIII sequence ([Figure 1](#); [Supplementary Figures S1, S2](#)). Screening was carried out manually for relatively small numbers of clones ([Supplementary Table S2](#)). The differences in the numbers of analyzed clones in each series were correlated with the analysis of the SDS-PAGE gels: if in a particular series a small number of clones were capable of autoprocessing, we did not continue the screening.

As the screening process was manual (not in a high-throughput mode), not all clones were submitted to sequencing due to a large number of plasmid isolations that would be too laborious for manual protocol. We decided to carry out sequencing for several clones from each series ([Supplementary Table S3](#)). The randomization trails allowed us to identify new EcAIII variants with interesting properties and to make several important observations related to the enzymatic activity of EcAIII, as well as to sequence variability observed in bacterial proteins annotated as Ntn-amidohydrolases ([Janicki et al., 2023](#)).

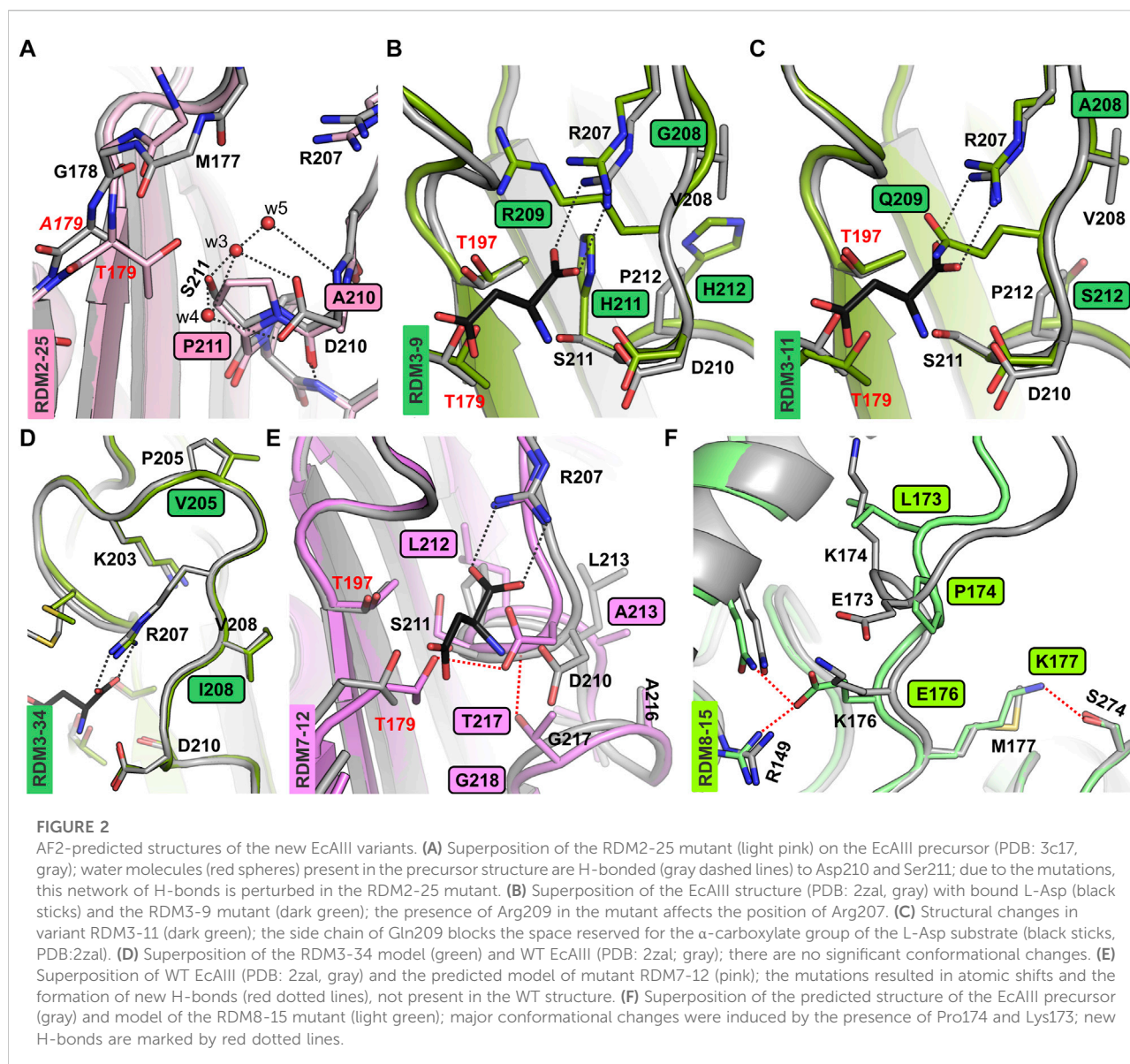
Role of residues 210 and/or 211 (RDM2 series) in EcAIII activity

In the RDM1 mutagenesis trial, four residues at the substrate binding site, namely, Gly206, Arg207, Asp210, and Ser211, were randomized ([Loch et al., 2022](#)). In the RDM1 series 64 new EcAIII variants were analyzed. Most of them were not cleaved into subunits, and those which were processed did not exhibit L-asparaginase activity. In the RDM1 variants processed to subunits α and β ([Loch et al., 2022](#)), L-Asn hydrolysis was abolished by the absence of Arg207, which is crucial for substrate binding ([Figure 1](#)). In order to analyze the behavior of new variants with intact Arg207 (and Gly206), we decided to run the mutagenesis trial RDM2, in which only Asp210 and Ser211 were randomized ([Supplementary Table S1](#)).

Screening of 33 clones of the RDM2 series showed that only 11 variants were cleaved into subunits, and among them only eight retained the L-asparaginase activity ([Supplementary Table S2](#)). Sequencing revealed that six of the active clones had the wild type (WT) sequence of EcAIII, while the two other active clones carried the mutations D210A/S211P (RDM2-25) and D210P (RDM2-27) ([Supplementary Table S3](#)). We also found in the RDM2 series three clones that were processed to subunits but did not show L-asparaginase activity during screening. We sequenced two of them, and identified the following mutations: D210A (RDM2-17) and D210A/S211V (RDM2-32) ([Supplementary Table S3](#)).

Although variants RDM2-25 and RDM2-27 were active, they had a very slow autoproteolysis rate. These observations indicate that the absence of Asp210 and/or Ser211 significantly slows down the maturation process. Although residues 210 and 211 do not seem to be directly involved in autoprocessing, as a polar residues they are part of an H-bond framework that assures the correct positioning of water molecules w3, w4, and w5 near the Gly178-Thr179 scissile bond, as visible in the crystal structure ([Michalska et al., 2008](#)) ([Figure 2A](#)). Although the AlphaFold2 models do not include water molecules, comparison of the predicted structures of mutants RDM2-25, RDM2-27, RDM2-17 and RDM2-32, and the crystal structure of the EcAIII precursor (PDB: 3c17) shows that in the absence of side chains Asp210 and/or Ser211 the correct network of water-mediated H-bonds near the nucleophilic Thr179 cannot be formed ([Figure 2A](#)). These observations can explain the slow autoproteolysis rate of the RDM2 mutants, as well as the low enzymatic performance, as Asp210 is also involved in substrate stabilization.

For the active mutants RDM2-25 and RDM2-27, large-scale expression and purification were carried out. We observed that only about ~50% of the RDM2-25 and RDM2-27 mutant proteins were processed into subunits after 48 h. When autoprocessing progressed, we observed the development of L-asparaginase activity of variants RDM2-25 and RDM2-27. As it was impossible to separate the populations of mature and immature EcAIII molecules, we were not able to



determine the kinetic parameters for preparations of partially cleaved proteins.

The data above suggest that mutations at positions 210 and 211 significantly reduce the autoprocessing rate, but mature variants develop L-asparaginase activity. On the other hand, reported earlier variants from the RDM1 series carrying similar mutations, e.g., RDM1-3, RDM1-12 or RDM1-29, did not exhibit any L-asparaginase activity at all (Loch et al., 2022). However, in the RDM1 mutants the Arg207 residue was absent, while the RDM2 mutants have intact Arg207 required as an anchor for the α -carboxylate group of the substrate. These observations indicate that the presence of Arg207 is absolutely necessary to maintain substrate affinity, while stabilization of the amino group of the substrate by a H-bond to Asp210 plays a less important role in substrate positioning.

Random mutagenesis near the substrate binding site (RDM3 and RDM7)

For the RDM3 series, the SDS-PAGE analysis showed that most of the mutants were not cleaved into subunits. The only clones that were mature and active, RDM3-12 and RDM3-19, had sequence identical to WT EcAIII. We also made attempts to sequence several other immature RDM3 clones. Unfortunately, sequencing was successful only for three mutants (Supplementary Table S3): RDM3-9, RDM3-11, and RDM3-34. These three variants were produced at large scale and purified. Although at the screening stage we did not observe autoproteolysis, the large-scale purification revealed a very slow maturation process. Nevertheless, RDM3-9 and RDM3-11,

remained enzymatically inactive, while variant RDM3-34 developed L-asparaginase activity. The predicted AF2 model of this variant did not reveal any significant conformational changes (Figure 2D), therefore, the reduced autoproteolytic efficiency of RDM3-34 has unknown origin.

Screening of the RDM3 mutants indicated that simultaneous mutations in the close neighborhood of Arg207 (positions 208, 209, 211, 212) is usually fatal for the catalytic activity of EcAIII because of conformational changes leading to incorrect positioning of the Arg207 side chain in the active site. In the RDM3 trial we randomized the highly conserved Gly209, while the rest of the mutated residues have only moderate or low conservation (Supplementary Figure S1). These observations indicate that Gly209 is important for maintaining the correct geometry of the active site. Gly209 is located very close to Arg207 and incorporation of residues with large side chains, such as Arg209 (in RDM3-9) or Gln209 (in RDM3-11) results in a positional shift of Arg207. An AF2 model of the RDM3-9 variant revealed that Arg209 and His211 strongly affect the position of Arg207, making substrate binding ineffective (Figure 2B). The predicted structure of mutant RDM3-11 revealed that Gln209 disturbs substrate binding by affecting its positioning (Figure 2C).

Most of the RDM7 clones, with randomization introduced at positions Pro212, Leu213, Gly217 and Cys218 (Figure 1), retained the ability to mature, but they lost their L-asparaginase activity. Most of active RDM7 clones (Supplementary Table S2) turned out after sequencing to be WT EcAIII. The predicted structure of inactive mutant RDM7-12 revealed a positional shift of the entire 207–217 loop, resulting in the formation of new H-bonds, the most important of which links Asp210 and Thr179 (Figure 2E). Such an interaction most probably disturbs substrate binding and affects the nucleophilic character of Thr179.

In the RDM7 series we detected a high proportion of WT sequences. A simple explanation might be an ineffective digestion of the PCR matrix by *DpnI*. However, we rather exclude this possibility as we always run control transformations in parallel. Another explanation might be that degenerated RDM7 primers with WT sequence were annealed in the PCR reaction to the DNA matrix with similar frequency as the degenerated oligonucleotides with non-complementary sequences. This observation suggest that the efficiency of random mutagenesis depends on the DNA sequence itself. In some (rare) cases, when it is not possible to produce new variants using only degenerated primers, other mutagenic approaches must be considered.

Mutagenesis in conserved sequence regions (RDM4, RDM5, RDM6 and RDM9)

SDS-PAGE analysis of clones from the RDM4, RDM5, RDM6 and RDM9 series (Supplementary Table S1) revealed

that in most cases the new EcAIII variants were incapable of splitting themselves into the α and β subunits. Absence of L-asparaginase activity was observed for all clones of RDM4 series. Plasmid sequencing revealed that selected clones in the RDM5 and RDM6 series that were active had the native WT EcAIII sequence (Supplementary Table S2). In series RDM4, RDM5 and RDM6, sequence randomization took place in the close vicinity of the conserved region of the threonine triplet (Thr179, Thr197, Thr230; Supplementary Figure S1). Mutants of the RDM9 series possessed random mutations in the conserved region of sodium-binding (stabilization) loop (Glu61, Cys63, Phe66, Ala68). In this series, the one active variant had sequence identical to WT protein (Supplementary Table S2).

These findings indicate that random mutagenesis in the highly conserved fragments of the sequence is ineffective, and it should be avoided or replaced by rational site-directed mutagenesis. However, our recent analysis of residue conservation near the catalytic triplet and the stabilization loop (Janicki et al., 2023) revealed that in bacterial EcAIII orthologs, substitutions in the Thr triplet and its close vicinity are possible but very rare. For example, the most variable position near Thr179 corresponds to Met177 in EcAIII sequence, which in other proteins can be substituted by Phe, His or Tyr, while the most mutation-prone position in the stabilization loop is Cys63 which can be replaced by Asp, Asn or Ser (Supplementary Figure S1).

Mutagenesis within the variable linker region (RDM8)

It would seem that the chance of obtaining functional EcAIII variants via random local mutagenesis depends on the sequence element that is randomized: the more conserved the designated sequence fragment (associated with a particular function), the lower the probability of obtaining functional clones. From this point of view, the most promising segment is the least-conserved fragment of the EcAIII sequence, namely the flexible Glu159-Gly178 linker immediately preceding the nucleophilic Thr179 (Supplementary Figure S1). The linker does not participate in substrate binding and L-Asn hydrolysis of the mature enzyme. The role of the linker in autoproteolysis is not clear; however, recently we reported that correct positioning of the linker is essential for efficient autocleavage of the scissile Gly178-Thr179 bond (Loch et al., 2022).

The entire linker of ~20 residues is usually not fully visible in the electron density maps, suggesting high mobility or progressive digestion. As the only available experimental model of EcAIII with part of the linker visible (residues 165–178) is the crystal structure of the T179A mutant (PDB: 3c17) (Michalska et al., 2008), we attempted to generate

AF2 models of unprocessed EcAIII. The AF2 predicted conformation of the linker was significantly different from the 3c17 crystal structure. That structure of the inactive T179A mutant showed that residues Glu173 and Lys176 might be important for the stabilization of the scissile bond (which is a part of the linker), as Lys176 is H-bonded to Glu234 and Glu173 forms a salt bridge with Arg149 (Supplementary Figure S3). These interactions were absent in the predicted model of immature WT EcAIII. Instead, we observed an H-bond between the main chain carbonyl O atom of Glu173 and nitrogen of Lys176 (Supplementary Figure S3), as well as an H-bond between the side chains of these residues.

In the RDM8 series we randomized four residues: Glu173, Lys174, Lys176 and Met177, from the linker (Supplementary Table S1). Sequencing revealed that in the RDM8 trial four out of the seven active variants had WT sequence (Supplementary Table S2). However, clones RDM8-6 and RDM8-15 (and RDM8-17) carried mutations (Supplementary Table S3). SDS-PAGE analysis showed that in variants RDM8-6 and RDM8-15 autoprocessing was rather slow, however, ultimately the proteins were converted to mature $\alpha\beta$ subunits and attained their L-asparaginase activity (as the active site region was not mutated). Variant RDM8-6 carried four mutations: E173I/K174Q/K176A/M177I. The AF2 model suggested that the K174Q substitution may lead to the creation of new H-bonds between Gln174, Gln152 and Gln19 (Supplementary Figure S3). According to the prediction, substitutions K174Q and E173I may result in a flip of the 171–173 side chains, affecting the C α backbone trace of the linker.

For the RDM8-15 variant with the E173L/K174P/K176E/M177K mutations, the AF2 model suggested that significant conformational changes may be introduced in the linker by the presence of Glu176, H-bonded to Arg149 and Gln152, and by Lys177, H-bonded to Ser274 (Figure 2F), as these interactions are absent in the AF2 model of the WT protein. According to the AF2 model, the substitution K174P of RDM8-15 also contributes to the conformational changes of the linker. The conformational changes in the linker region analyzed in this section may potentially reduce autoproteolysis rate by hampering proper orientation of the Gly178-Thr179 scissile bond for nucleophilic attack.

The results of mutagenesis in the linker region show that by modifying this part of the EcAIII sequence one can tune the efficiency of autoproteolysis without “touching” the active site. This might be important for designing new EcAIII variants with controlled maturation process. Also, designing EcAIII mutants with impaired autoproteolytic activity might be useful for crystallographic modeling of the intact linker structure, as an important step towards the elucidation of the mechanism of autoproteolytic activation.

Conclusion

This report describes a comprehensive approach to random mutagenesis of EcAIII and is a sequel to a previously published work (Loch et al., 2022). Our studies revealed that most of the new EcAIII variants had abolished or significantly reduced rate of autoprocessing, and were in consequence devoid of L-asparaginase activity. In this respect, we have demonstrated that local random mutagenesis of the EcAIII sequence is rather ineffective for designing better enzymes with increased substrate affinity. The problem lies not in the randomization itself, but is rooted in the biochemistry of Ntn-amidohydrolases. These enzymes are produced as inactive precursors and it is usually difficult to predict if the introduced mutations will affect the maturation process only, or L-Asn hydrolysis as well. Even if a given substitution could be beneficial for the ultimate substrate hydrolysis, this effect may not be observed if the same mutation is fatal to enzyme maturation. The only way to avoid such problems is to use circularly permuted genes for Ntn-amidohydrolase mutagenesis. This approach has been used only once, for the human HsAIII enzyme (Li et al., 2012).

We also predicted the role of several residues in the proper orientation of the linker and the scissile bond for autoprocessing. Moreover, we generated genes of several new active and inactive EcAIII variants that enrich the available library of EcAIII mutants (Michalska et al., 2008; Loch et al., 2022; Janicki et al., 2023). We believe that our randomization studies will help to better understand the catalytic properties of Class 2 L-asparaginases and will guide further engineering experiments with other Ntn-amidohydrolases as well as mechanistic studies (Andjelkovic et al., 2023) of the new Ntn-hydrolases.

Data availability statement

The original contributions presented in the study are included in the article/Supplementary Material, further inquiries can be directed to the corresponding author.

Ethics statement

The studies conducted with the use of Genetically Modified Microorganism (GMM) were reviewed and approved by commission on GMM at the Ministry of Climate and Environment (Poland).

Author contributions

JIL designed experiments and coordinated the experimental work, carried out mutagenesis, clone screening (RDM3,

RDM7), structure modelling, data analysis and wrote the manuscript. AS performed large scale protein expression and activity tests for purified enzymes. MK performed mutagenesis and clone screening of the RDM8 series, carried out structure modelling and participated in manuscript preparation. IP performed clone screening of the RDM2, RDM3 and RDM9 series. WL performed clone screening of the RDM2 series and analyzed the data. KZ performed clone screening of the RDM4, RDM5 and RDM6. MJ analyzed the results and wrote the manuscript. All authors contributed to the article and approved the submitted version.

Funding

Work supported by National Science Centre (Poland) grants: 2020/38/E/NZ1/00035 (Sonata Bis) and 2019/03/X/NZ1/00584 (Miniatura).

References

- Andjelkovic, M., Zinovjev, K., Ramos-Guzmán, C. A., Ruiz- Pernía, J. J., and Tuñón, I. (2023). Elucidation of the active form and reaction mechanism in human asparaginase type III using multiscale simulations. *J. Chem. Inf. Model.* 63, 5676–5688. doi:10.1021/ACS.JCIM.3C00900
- Borek, D., and Jaskólski, M. (2001). Sequence analysis of enzymes with asparaginase activity. *Acta Biochim. Pol.* 48, 893–902. doi:10.18388/abp.2001_3855
- da Silva, L. S., Doonan, L. B., Pessoa, A., de Oliveira, M. A., and Long, P. F. (2022). Structural and functional diversity of asparaginases: overview and recommendations for a revised nomenclature. *Biotechnol. Appl. Biochem.* 69, 503–513. doi:10.1002/BAB.2127
- Janicki, M., Ściuk, A., Zielezinski, A., Ruszkowski, M., Ludwików, A., Karłowski, W. M., et al. (2023). The effects of nature-inspired amino acid substitutions on structural and biochemical properties of the *E. coli* L-asparaginase EcAIII. *Protein Sci. a Publ. Protein Soc.* 32, e4647. doi:10.1002/PRO.4647
- Jumper, J., Evans, R., Pritzel, A., Green, T., Figurnov, M., Ronneberger, O., et al. (2021). Highly accurate protein structure prediction with AlphaFold. *Nature* 596, 583–589. doi:10.1038/s41586-021-03819-2
- Karamitos, C. S., and Konrad, M. (2016). Fluorescence-activated cell sorting of human L-asparaginase mutant libraries for detecting enzyme variants with enhanced activity. *ACS Chem. Biol.* 11, 2596–2607. doi:10.1021/acscchembio.6b00283
- Kim, J. H., Lee, S. C., Kyeong, H. H., and Kim, H. S. (2010). A genetic circuit system based on quorum sensing signaling for directed evolution of quorum-quenching enzymes. *ChemBioChem* 11, 1748–1753. doi:10.1002/CBIC.201000033
- Li, W., Cantor, J. R., Yogesha, S. D., Yang, S., Chantranupong, L., Liu, J. Q., et al. (2012). Uncoupling intramolecular processing and substrate hydrolysis in the N-terminal nucleophile hydrolase hASRGL1 by circular permutation. *ACS Chem. Biol.* 7, 1840–1847. doi:10.1021/cb300232n
- Linhorst, A., and Lübke, T. (2022). The human ntn-hydrolase superfamily: structure, functions and perspectives. *Cells* 11, 1592. doi:10.3390/CELLS11101592
- Loch, J. I., and Jaskólski, M. (2021). Structural aspects of L-asparaginases - a growing family with amazing diversities. *IUCr* 8, 514–521. doi:10.1107/S2052252521006011
- Loch, J. I., Klonecka, A., Kądziołka, K., Bonarek, P., Barciszewski, J., Imiolczyk, B., et al. (2022). Structural and biophysical studies of new L-asparaginase variants: lessons from random mutagenesis of the prototypic *Escherichia coli* ntn-amidohydrolase. *Acta Crystallogr. Sect. D. Struct. Biol.* 78, 911–926. doi:10.1107/s2059798322005691
- Loch, J. I., Worsztynowicz, P., Sliwiak, J., Grzechowiak, M., Imiolczyk, B., Pokrywka, K., et al. (2023). Rhizobium etli has two L-asparaginases with low sequence identity but similar structure and catalytic center. *Acta Crystallogr. Sect. D. Struct. Biol.* 79, 775–791. doi:10.1107/s2059798323005648
- Michalska, K., Brzezinski, K., and Jaskólski, M. (2005). Crystal structure of isoaspartyl aminopeptidase in complex with L-aspartate. *J. Biol. Chem.* 280, 28484–28491. doi:10.1074/jbc.M504501200
- Michalska, K., Hernandez-Santoyo, A., and Jaskólski, M. (2008). The mechanism of autocatalytic activation of plant-type L-asparaginases. *J. Biol. Chem.* 283, 13388–13397. doi:10.1074/jbc.M800746200
- Michalska, K., and Jaskólski, M. (2006). Structural aspects of L-asparaginases, their friends and relations. *Acta Biochim. Pol.* 53, 627–640. doi:10.18388/abp.2006_3291
- Tosta Pérez, M., Herrera Belén, L., Letelier, P., Calle, Y., Pessoa, A., and Farias, J. G. (2023). L-asparaginase as the gold standard in the treatment of acute lymphoblastic leukemia: A comprehensive review. *Med. Oncol.* 40, 150. doi:10.1007/s12032-023-02014-9
- Xu, G., Zhao, Q., Huang, B., Zhou, J., and Cao, F. (2018). Directed evolution of a penicillin V acylase from *Bacillus sphaericus* to improve its catalytic efficiency for 6-APA production. *Enzyme Microb. Technol.* 119, 65–70. doi:10.1016/j.enzmtec.2018.08.006

Conflict of interest

The authors declare that the research was conducted in the absence of any commercial or financial relationships that could be construed as a potential conflict of interest.

Acknowledgments

We thank Aleksandra Kusior and Agnieszka Klonecka for help with clone screening and large-scale protein expression.

Supplementary material

The Supplementary Material for this article can be found online at: <https://www.frontierspartnerships.org/articles/10.3389/abp.2024.12299/full#supplementary-material>



OPEN ACCESS

EDITED BY

Grzegorz Węgrzyn,
University of Gdansk, Poland

REVIEWED BY

Alexandra Virginia Bounegru,
Dunarea de Jos University, Romania
Masoumeh Ghalkhani,
Shahid Rajaei Teacher Training
University, Iran
Gurumurthy Hegde,
Christ University, India

*CORRESPONDENCE

Aleksandra Klos-Witkowska,
✉ aklos@ubb.edu.pl

RECEIVED 06 October 2023

ACCEPTED 05 January 2024

PUBLISHED 23 January 2024

CITATION

Klos-Witkowska A and Martsenyuk V
(2024), Stability in biosensors derived
from domain map analysis of
bibliometric data.
Acta Biochim. Pol. 71:12196.
doi: 10.3389/abp.2024.12196

COPYRIGHT

© 2024 Klos-Witkowska and
Martsenyuk. This is an open-access
article distributed under the terms of the
Creative Commons Attribution License
(CC BY). The use, distribution or
reproduction in other forums is
permitted, provided the original
author(s) and the copyright owner(s) are
credited and that the original
publication in this journal is cited, in
accordance with accepted academic
practice. No use, distribution or
reproduction is permitted which does
not comply with these terms.

Stability in biosensors derived from domain map analysis of bibliometric data

Aleksandra Klos-Witkowska* and Vasyl Martsenyuk

Department of Computer Science and Automatics, University of Bielsko-Biala, Bielsko-Biala, Poland

In the presented work, advanced methods of analysis and visualization were used to compile trends and patterns in the scientific literature. The most relevant information for the stability of biosensors was selected on the basis of clusters constructed on the basis of keywords. The most significant publications in the clusters appearing over time were analyzed. The most explosive publications were identified, i.e., those that have had the greatest impact on science in the area of the subject under study. The scientific trend in the development of biosensor stability was determined on the basis of the most frequently cited words in recent publications. A map of cooperation and networking between countries in the field of interest of the above topic was presented. Leaders were identified by country of origin.

Systematic Review Registration: <https://ubb.edu.pl>.

KEYWORDS

biosensor, stability, clusters, trends, leaders, scientometric database

Introduction

The number of scientific publications increases every year with the development of technology and the progress of civilization. Therefore, the need for a fast and accurate analysis of the literature to keep track of the development of existing research topics and emerging news in the world of science was naturally born. Previously used scientific analysis based on web reviews or studying scientific databases such as Web of Science, Scopus, PubMed allowed only retrospective analysis, i.e., chronological, recollective analysis without the ability to trace connections. Domain map analysis means the use of graph network representations of the source analysis, including the analysis of the relationships between data with the help of the choice and appropriate distance measure, clustering, mapping the relationships into graph nodes and edges. It allows us to determine the most significant resources analyzed temporal development of the area determined tendencies (Liu et al., 2020; Geng et al., 2023).

One of the most popular tools for bibliometric analysis of domain maps is CiteSpace, which is based on data mining, a process involving data extraction, pattern analysis and sorting. It is a process that can be compared to mineral processing, where the mineral must first be extracted, then cleaned and finally sorted. Data mining enables rapid predictions and classifications to be made and facilitates decision making.

CiteSpace is a Java based application designed to analyze and visualize trends and patterns in the scientific literature to present the structure and distribution of scientific

knowledge. It focuses on finding critical points in the development of a field or region, especially intellectual turning points (Xu et al., 2022; Gao et al., 2023; Zhao et al., 2023). In presented papers we used CiteSpace to group keywords and highlight results related to biosensors stability.

The analysis is based on the theoretical trend (intellectual) and the experimental trend. The intellectual trend is based on articles presenting research findings or a scientific point of view, while the experiential trend [as conceptualized by Price (1965)] is based on collections of cited articles.

The functions of the CiteSpace application are based on three central concepts:

1. The Kaliberg crack detection algorithm (Kleinberg, 2002), which is used to identify test concepts.
2. The Freeman intercentricity matrix, used to highlight potential key points
3. The Heterogeneous Network, used to map between the intellectual base and the experimental front.

Mapping can be used to identify the nature of the research front, highlight specializations and identify emerging trends over time.

The CiteSpace analysis are based on select single words or phrases of up to four keywords from titles, abstracts and article descriptions based on articles by the method LSI (Latent Semantic Indexing) related to biosensors stability.

The research is based on a surge in citation frequency. Analysis by cluster view and by temporal variation is possible. The CiteSpace tool makes it possible to follow in real time the development of new fields of knowledge and the links in the existing field of knowledge (between institutions and countries), it also gives the possibility to see the history of the emergence of a scientific question and the impact of the main discoveries on the final view. The present article analyses the stability of biosensors on the basis of experimental studies. The analysis was carried out using the CiteSpace 6.2. R4 tool, which selects the most important articles that cause the scientific development of the topic, based on the keywords that appear most frequently in the titles and abstracts. The novelty of the article is: 1) the presentation of the latest trends, the indication of the direction of research in the field of stability of biosensors, based on an advanced analysis using the CiteSpace tool, 2) the identification of the scientific leaders dealing with the studied issue, and 3) the presentation of the mutual network of scientific links between research groups coming from different countries.

Methods

Sources of data

In this paper we used the Web of Science (WoS) database as a data source and through advanced search (TS= biosensor) we

obtained 86,814 papers in the range time (01.01.1974–01.07.2023).

Figure 1 shows the number of publications in the field of biosensors from 1974 to 2022. We have chosen 2022 as the upper limit of the time frame because this is the last full calendar year in the WoS database (2023—not yet over). The graph shows a clear increase in publications over time, indicating a growing interest in biosensors, most likely related to the increase in environmental pollution (Pohrebennyk et al., 2018) and the widening range of biosensor applications [medicine (Grabowska et al., 2014), environmental protection (Klos-Witkowska, 2016), food industry (Dirpan et al., 2023) and the drive to improve existing devices to achieve even better detection quality (Laad and Ghule, 2022)]. It is worth noting the slight decrease in the number of papers published in 2020 (5,875 papers) compared to 2019 (5,902 papers), perhaps due to the impact of the COVID-19 pandemic, which was felt all over the world.

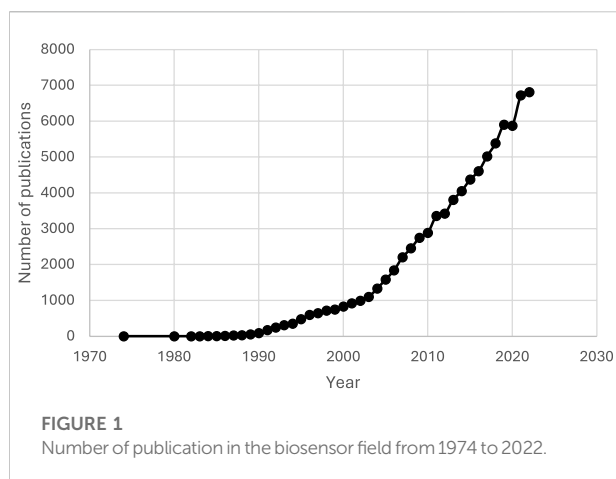
Current research is carried out in two parallel streams: experimental and theoretical.

In the experimental stream, work focuses on improving the quality of detection and the stability of the device (Klos-Witkowska and Kajstura, 2020), while the theoretical stream revolves around the development of mathematical models (Martsenyuk et al., 2021b), often using already existing solutions for this purpose (Martsenyuk et al., 2021a), also recently, the interest of scientists in combining biosensors with artificial intelligence has been noted. An extremely interesting issue is the problem of stability in biosensors, which is a very important problem not only from a scientific point of view, but also from a commercial point of view. The stability of biosensors directly translates into the longevity of use and the ability to operate the device. Therefore, following the latest scientific trends, the issue of biosensor stability was chosen to be analysed in biosensor development based on advanced analytics using CiteSpace 6.2.R4;

- (1) Identifying the most important (so called “explosive articles”) that generated the most interest among researchers based on their citability.
- (2) The most relevant keywords (most cited) in the titles and abstracts were identified and clustered, i.e., grouped according to their relevance.
- (3) The most important clusters were described.
- (4) The keywords with the highest number of citations on a time scale were visualised.
- (5) Identified scientific leaders working on stability issues in the field of biosensors and showed the network of scientific links between research groups from different countries.

Analytical method characteristics

We conducted a literature search using the following search strategy using Web of Science Advanced Search: Publication



dates were from 01.01.1974 to 01.07.2023 and search criteria were: for biosensor stability (experimental research): [TS=(biosensor)] AND [TS=(stability)] AND [TS=(empirical)] OR [TS=(experimental)] in the Web of Science Core Collection.

We created visual graphs of keyword co-occurrence, keyword clustering and scientific collaboration using CiteSpace 6.2 R4 software. We investigated the current status and trends in the stability of biosensors.

Results

Biosensor stability

Biosensors are devices that are susceptible to ageing; this phenomenon can be characterised as a decrease in signal over time.

Stability of biosensors is critical for commercial success as biosensors are now used in an increasing number of different applications. Characterisation of stability in terms of shelf life, reusability and the ability to be used continuously is inadequate, although much work has been done in this area. Stability is very important as it is a major factor affecting the operation of the device.

The mechanisms of biosensor ageing are complex and still poorly understood. However, it is known that the loss of stability of a biosensor is the sum of all changes affecting both the biological material used: for example: enzymes (Fernandez-Lopez et al., 2017), antibodies (Oyetayo et al., 2017), as well as the signal mediator (Ricci et al., 2003; Malinauskas et al., 2004) and the binding material of complexes in the matrix (Panjan et al., 2017).

The analysis presented below illustrates the current state of knowledge and trends in biosensor stability research. As shown in Figure 2, the efforts of researchers have focused on chemically modified electrodes, reduced graphene oxide, direct electron transfer, magnetic microspheres, FFT cyclic voltammetry,

poly(o-phenylenediamine), LECTIMS and optimization. The analysis presented was carried out on the basis of the most frequently occurring keywords. These were used to create the clusters shown in Figure 2.

The larger the cluster area, the more frequent the occurrence of the keyword. In the analysis carried out, the keywords are also the names of each of the most relevant clusters, those shown in Figure 2.

Thus, it can be seen that the keyword for cluster #1 (#1) is chemically modified electrode, similarly for the others: #0 reduced graphene oxide, #2 direct electron transfer, #6 magnetic microspheres, #8 fft cyclic voltameters, #10 poly(o-phenylenediamine), #11 lectins, #12 optimisation.

The dots in each cluster represent publications; the names of the most prominent can also be seen in the diagram.

The CiteSpace analysis allows us to select the most significant sentences from the publications contained in the clusters.

Thus, cluster: #0 “reduced graphene oxide” was formed on the basis of 495 publications, of which the publications (Bai et al., 2012; Dong et al., 2012; Wei et al., 2012; Xu et al., 2012; Bai et al., 2013; Wang et al., 2013; Nalini et al., 2014; Zhou et al., 2014; Li et al., 2021) are considered to be the most significant, where one can find information on the application of gold nanoparticles and the development of an amperometric biosensor based on gold nanoparticles decorated with graphene nanoparticles for the detection of clenbuterol. Also of interest are electrochemical biosensors based on hemin-modified graphene nanoplatelets for the determination of l-tyrosine levels. Au nanoparticles were used as a stabilizer.

In cluster #1 “chemically modified electrode”; among the 243 publications forming it, the publications (Arkhypova et al., 2003; Gamella et al., 2006; Mu, 2006; Rahman et al., 2006; Wang and Zhang, 2006; Du et al., 2007; Fan et al., 2007; Fanjul-Bolado et al., 2007; Di Fusco et al., 2010; Chalikian, 2016) are highlighted. The main information in this cluster concerns: the optimization of the biosensor design, as well as the influence of experimental variables such as pH, working potential and temperature on the sensor response. The research also focused on improving the analytical characteristics of the fabricated biosensor, studies of direct electron transfer reactions, optimisation of experimental conditions and substrate affinity based on the Michaelis-Menten constant. pH, working potential and temperature are known as stabilizing factors.

Cluster #2 “direct electron transfer” consists of 460 publications. The ten most important publications are Lai et al. (2008), Zhang et al. (2008), Hsu et al. (2009), Kong et al. (2009), Nenkova et al. (2009), Zhang et al. (2009), Zhu et al. (2009), Liu et al. (2010), Lu et al. (2010), and Garay (2015). They contain information on factors influencing electron transfer. These include the results of studies describing the effect of pH, the preparation of new magnetic microspheres coated with chitosan by modifying magnetic carbon-coated iron nanoparticles. The effect of gold nanoparticles on electron transfer was also investigated.

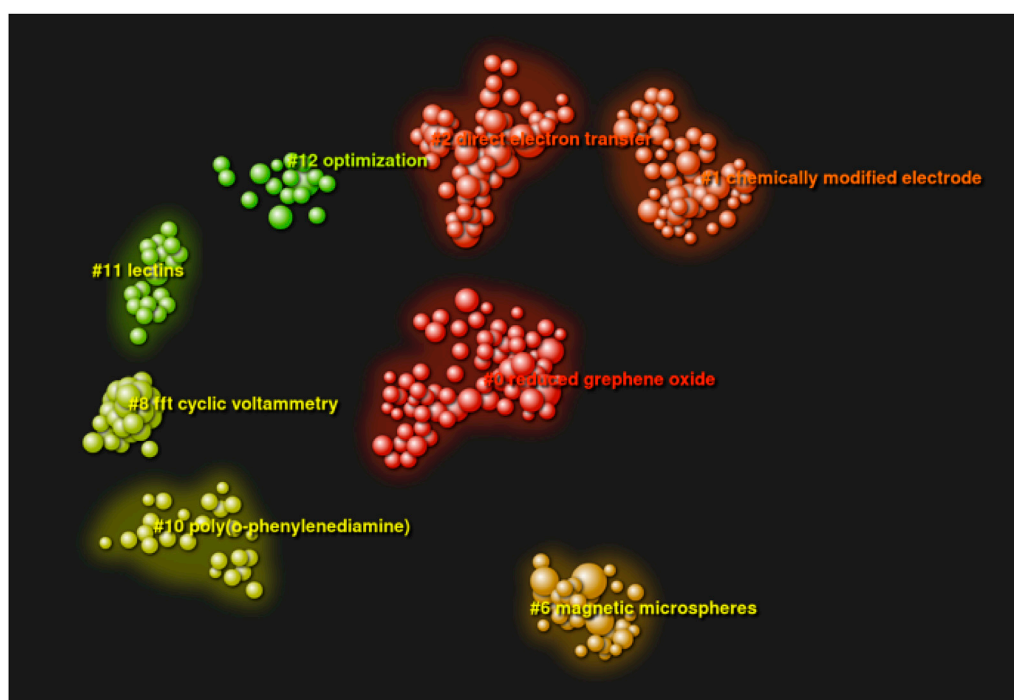


FIGURE 2
Keyword clustering analysis network.

Cluster #6 “magnetic microspheres” consists of 215 papers. The most important of these are papers (Liu et al., 2005; Tan et al., 2005; Shan et al., 2006; Fan et al., 2007; Tong et al., 2007; Liu et al., 2010; Zhen et al., 2011; Heli and Yadegari, 2014; Ltaïef et al., 2017; Villani et al., 2018) devoted to the preparation of new magnetic microspheres, control of sensor potential, detection limits and response speed from the point of view of biosensor stability.

There are 62 publications in cluster #8 “fft cyclic voltameters.” The most important are (Norouzi et al., 2010a; Norouzi et al., 2010b; Norouzi et al., 2010c; Marinov et al., 2010; Bohnenberger and Schmid, 2014; Cheraghi et al., 2017; Narwal et al., 2017; Stepashkin et al., 2018; de Oliveira et al., 2023; Kyomuhimbo et al., 2023). The key information is the application of this method to the study of: pyruvate oxidase, multiwalled carbon nanotubes immobilized on the surface of a glassy carbon electrode by means of a polymer layer of Nafion, the effect of individual components of an enzyme mixture containing gold nanoparticles, acetylcholinesterase, bovine serum albumin and glutaraldehyde on the current output of constructed acetylthiocholine biosensors. The research also included a biosensor for the detection and quantification of organophosphorus pesticides. fft cyclic voltameters allow us to investigate the stability of biosensors.

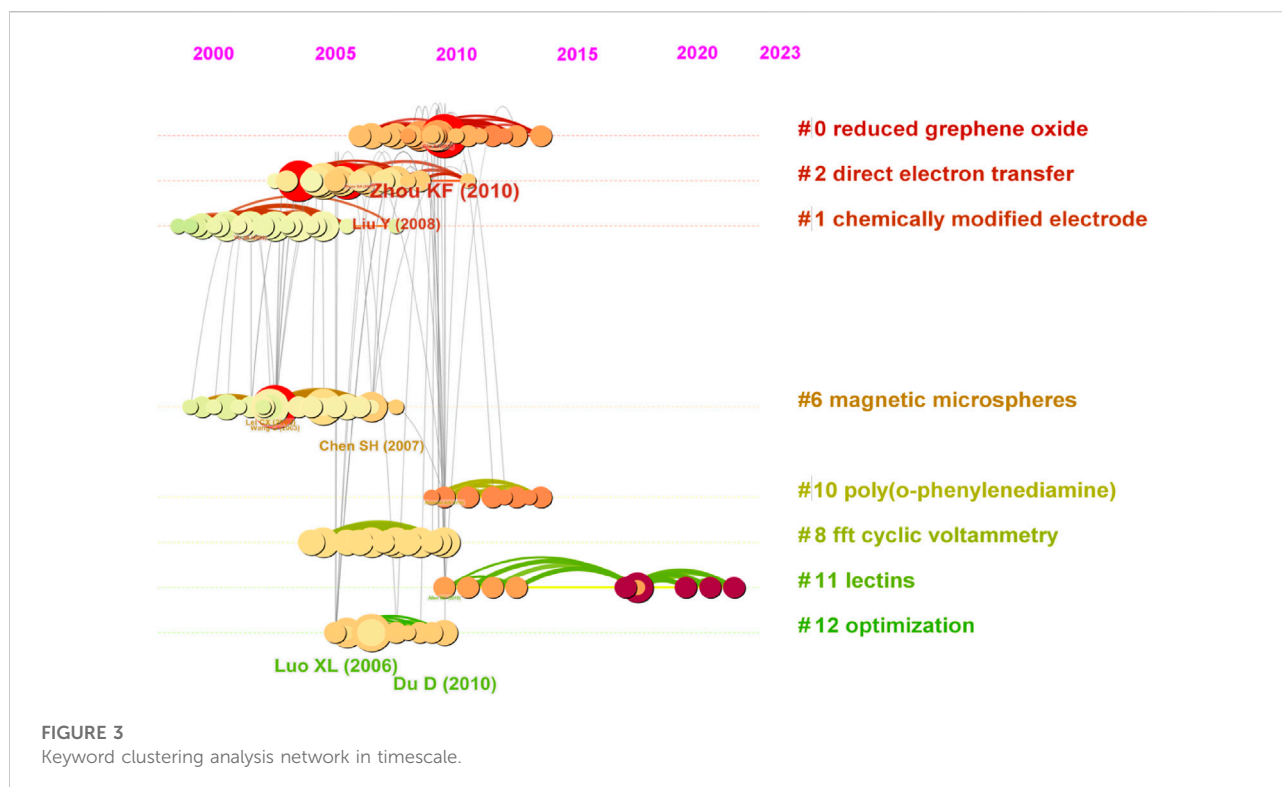
Cluster #10 “Poly(o-phenylenediamine)” was formed by 130 publications, of which the ten most important are publications (Ahammad et al., 2011; Devi et al., 2013; Zhang

et al., 2014; Dervisevic et al., 2015a; Baytak et al., 2015; Dervisevic et al., 2015b; Chen et al., 2015; Tan et al., 2015; Wang et al., 2015), while clusters #11 “Lectins” and #12 “Optimization” were formed by 65 and 163 publications, respectively. The most important for cluster #11 are Bai and Shiu (2014), Gholivand et al. (2014), Oliveira et al. (2014), Ribeiro et al. (2014), Ghanbari et al. (2019), Bravo et al. (2022), Jalalvand (2022), Tvorynska et al. (2022), Zalpour et al. (2022), Ramesh et al. (2023), while for cluster 12 (Hsu et al., 2009; Kong et al., 2009; Liu et al., 2011a; Liu et al., 2011a; Liu et al., 2011b; Pasahan et al., 2011; Yang HC et al., 2011; Yang WY et al., 2011; Makhmudiyarova et al., 2015; Rakhi et al., 2016) with information on operational stability as well as sensitivity, conductivity, detection limits, response speed, detection range, calculation of the Michaelis-Menten constant, response gain.

Diagram 3 (Figure 3) shows an analysis of the most important publications in the cluster that emerged over time. The red circles indicate the most explosive publications, i.e., those that have had the greatest impact on science. These publications were selected based on the highest number of citations of words (extracted from titles, abstracts, descriptors, and identifiers of bibliographic records) found in these publications in the presented time scale.

The time scale in the graph makes it possible to determine when the explosive publication appeared. A detailed analysis is shown in Figure 4.

Thus, in the context of the stability of biosensors, it can be seen that in 2003 there was a publication (Wang et al., 2003,



267 citations) dedicated to the amperometric biosensor of hydrogen peroxide with a sol-gel/chitosan layer as immobilization matrix, which the authors describe as the development of a new hybrid sol-gel/organic composite material based on the cross-linking of the natural polymer chitosan with (3-aryloxypropyl) dimethoxymethylsilane. This material was used to fabricate biosensors for H_2O_2 amperometry.

A composite membrane was used to immobilize horseradish peroxidase (HRP) on a gold disc electrode. The properties of the sol-gel/chitosan and sol-gel/chitosan-HRP layers were thoroughly characterized by atomic force and Fourier transform infrared microscopy. Using fluorescent tracers, the protein density in the sol-gel/chitosan was calculated to be 3.14×10^{12} molecules cm^{-2} . The developed biosensor had a fast response in less than 2 s with a linear range of 5.0×10^{-9} – 1.0×10^{-7} mol L^{-1} and a detection limit of 2×10^{-9} mol L^{-1} . The reaction showed a typical Michaelis-Menten mechanism. The activation energy of the enzymatic reaction was calculated to be 8.22 kJ mol^{-1} . The biosensor retained about 75% of its initial activity after about 60 days of storage in phosphate buffer at 4°C.

This was followed in 2004 by another publication (Wang and Wang, 2004, 415 citations) on a novel hydrogen peroxide sensor based on horseradish peroxidase immobilized on a colloidal Au-modified ITO electrode. The authors described the development of a novel method to fabricate a hydrogen peroxide sensor by immobilizing horseradish peroxidase (HRP) on a colloidal Au-modified conductive ITO glass substrate. The purified glass

substrate was first modified with (3-aminopropyl) trimethoxysilane (APTMS) to provide an interface for the deposition of colloidal Au. Next, 15 nm colloidal Au particles were chemisorbed onto the amine groups of APTMS. Finally, HRP was adsorbed onto the surface of colloidal Au. The immobilized HRP showed an excellent electrocatalytic response to hydrogen peroxide reduction. The performance and factors affecting the obtained biosensor were investigated in detail. The obtained biosensor showed a fast amperometric response (within 5 s) to H_2O_2 . The detection limit of the biosensor was $8.0 \mu\text{mol L}^{-1}$ and the linear range was from $20.0 \mu\text{mol L}^{-1}$ to 8.0 mmol L^{-1} . In addition, the obtained biosensor showed high sensitivity, good reproducibility and long-term stability.

This is an article that is particularly important for the development of the issue related to the stability of biosensors. Despite the fact that the topic of biosensor stability is developing rapidly. An analysis conducted with the help of CiteSpace showed that no explosive articles have appeared in the last 5 years, which formed the basis for further scientific issues related to the topic of stability.

The next landmark publication was a paper (Qian and Yang, 2006, 284 citations) describing a composite layer of carbon nanotubes and chitosan for the fabrication of an amperometric hydrogen peroxide biosensor. The paper described the development of a novel amperometric hydrogen peroxide biosensor based on the cross-linking of horseradish

Top 4 References with the Strongest Citation Bursts

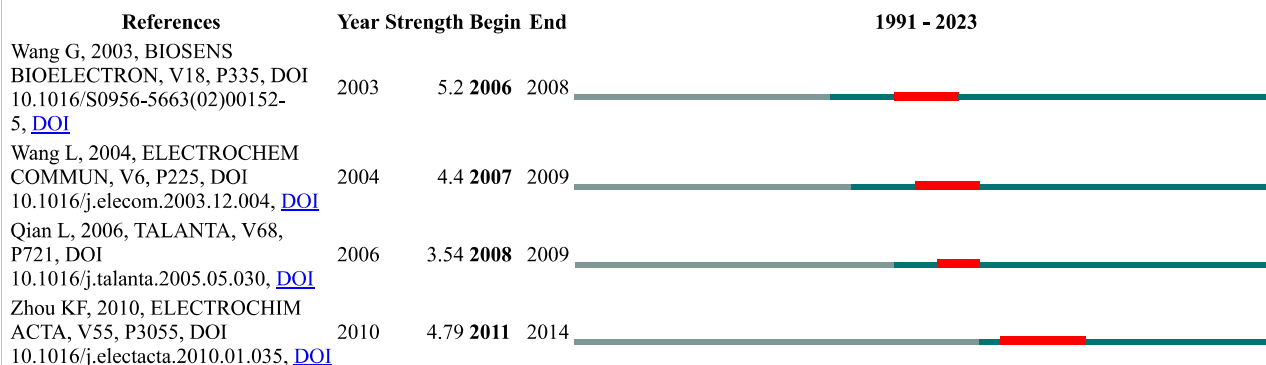


FIGURE 4

Top 4 references with the strongest citation burst.

peroxidase (HRP) with glutaraldehyde with multi-walled carbon nanotubes/chitosan (MWNTs/chitosan) coated in a composite layer on a glassy carbon electrode. The MWNTs were first dissolved in a chitosan solution. The morphology of the MWNT/chitosan composite layer was then characterised by field emission scanning electron microscopy. The results showed that the MWNTs were well soluble in chitosan and that robust layers could be formed on their surface. HRP was cross-linked with MWNTs/chitosan by glutaraldehyde to prepare a hydrogen peroxide biosensor. The enzyme electrode showed excellent electrocatalytic activity and fast response for H_2O_2 in the absence of mediator. The linear detection range of H_2O_2 (applied potential: -0.2 V) was from 1.67×10^{-5} to $7.40 \times 10^{-4}\text{ M}$ with a correction factor of 0.998. The biosensor showed good reproducibility and stability in the determination of H_2O_2 . There was no interference from ascorbic acid, glucose, citric acid and lactic acid.

The last of the four most explosive scientific publications was a paper (Zhou et al., 2010, 441 citations) on a novel hydrogen peroxide biosensor based on Au-graphene-HRP-chitosan biocomposites. The paper used graphene very effectively to construct an H_2O_2 biosensor. Graphene and horseradish peroxidase (HRP) were co-immobilised in a biocompatible chitosan (CS) polymer, and then a glassy carbon electrode (GCE) was modified with the biocomposite, followed by electrodeposition of Au nanoparticles on the surface to form an Au/Graphene/HRP/CS/GCE layer. Cyclic voltammetry showed that direct electron transfer of HRP was realized, and the biosensor had excellent performance in terms of electrocatalytic reduction towards H_2O_2 . The biosensor exhibited high sensitivity and speed. In addition, the biosensor showed good reproducibility and long-term stability.

As can be seen from the most explosive publications, the stability of biosensors is primarily related to the generation of optimal substrates (i.e., receptor layers).

The range of words considered to be the most explosive, i.e., those that appear most frequently in citations, is shown in Figure 5.

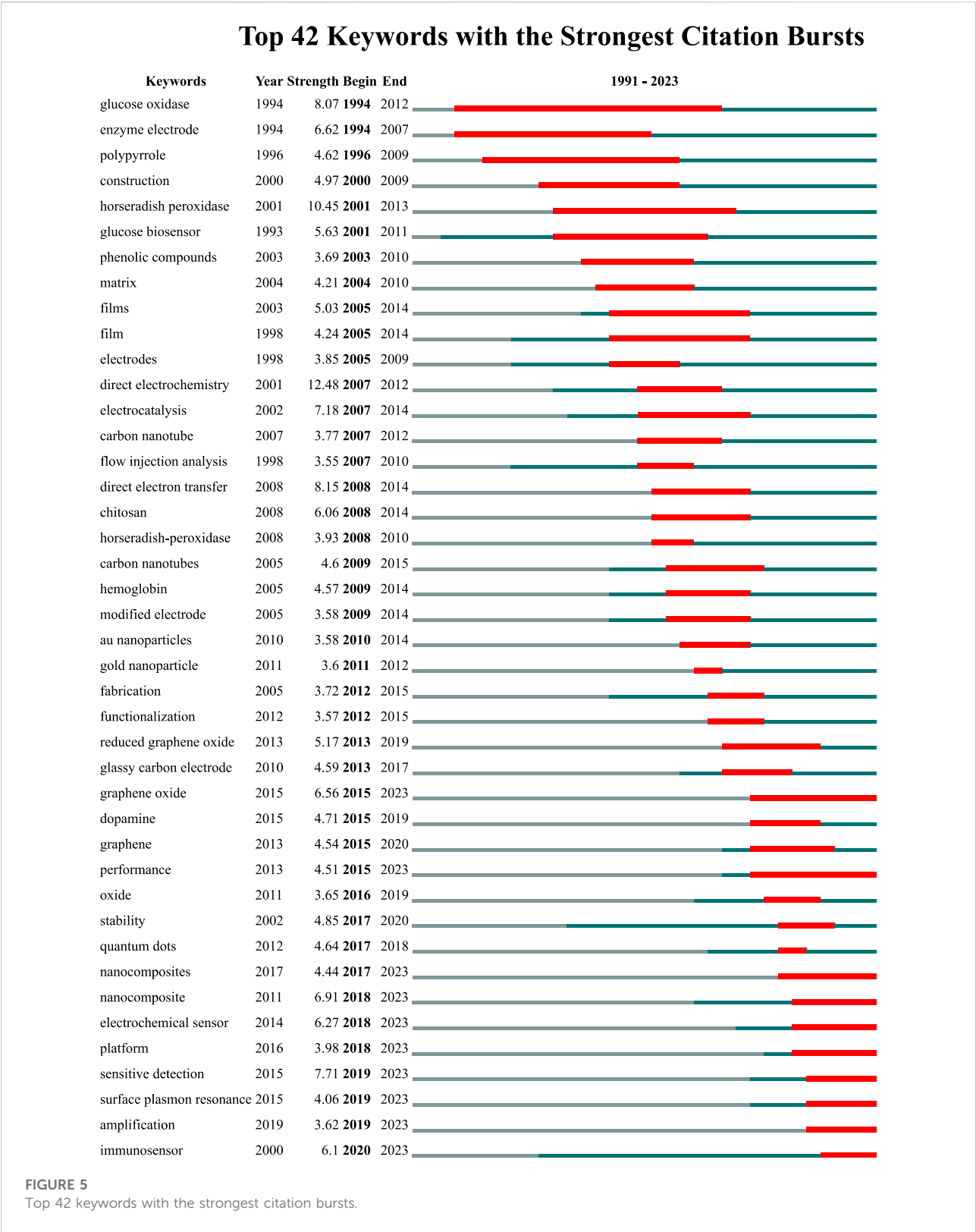
CiteSpace 6.2 R.4 software was used to highlight keywords. The tool used performed a keyword analysis, i.e., it extracted the most frequently cited words. The graph shows a time scale indicating the period of the highest citation of a given keyword. It can be seen that although the analysis covered works from 01.01.1974 to 01.07.2023, the graph shows the period from 1991 to 2023. It can be seen that the dominant keyword is “glucose oxidase,” this term has also been cited the longest, as can be seen in the figure. A similar reasoning can be applied to the other words in Figure 5.

Analyzing the entries below, the terms that deserve special attention are those that remain in quotation marks to this day. Among them we can distinguish: “Graphene oxide,” “high-performance nanocomposite,” “nanocomposites,” “electrochemical sensor,” “platform,” “sensitive detection,” “surface plasmon resonance,” “amplification” and “immunosensor.”

It can be seen that these words refer both to the substances or materials tested, e.g., non-composite, and to the test methods, e.g., “surface plasmon resonance,” but also to the type of biosensors, e.g., “immunosensor,” “electrochemical biosensor,” or to research questions, e.g., “sensitive biosensor,” “platform.”

Based on the most recent citations of keywords (the above terms are related to the stability of biosensors), we can identify scientific trends and directions of development of a given scientific issue. From the point of view of stability of biosensors, it can be seen that research is growing in the direction of electrochemical biosensors and immunosensors in search of materials that are optimal in terms of durability. The experiments mainly use surface plasmon resonance as a leading research method.

From the point of view of scientific development, international cooperation in the area of development of a



particular issue is extremely important. Cooperation between countries, institutions and authors is more likely to lead to progress in related research areas.

Figure 6 shows a map of cooperation and networking between countries in the field of biosensor stability. The analysis showed that researchers from 69 countries were

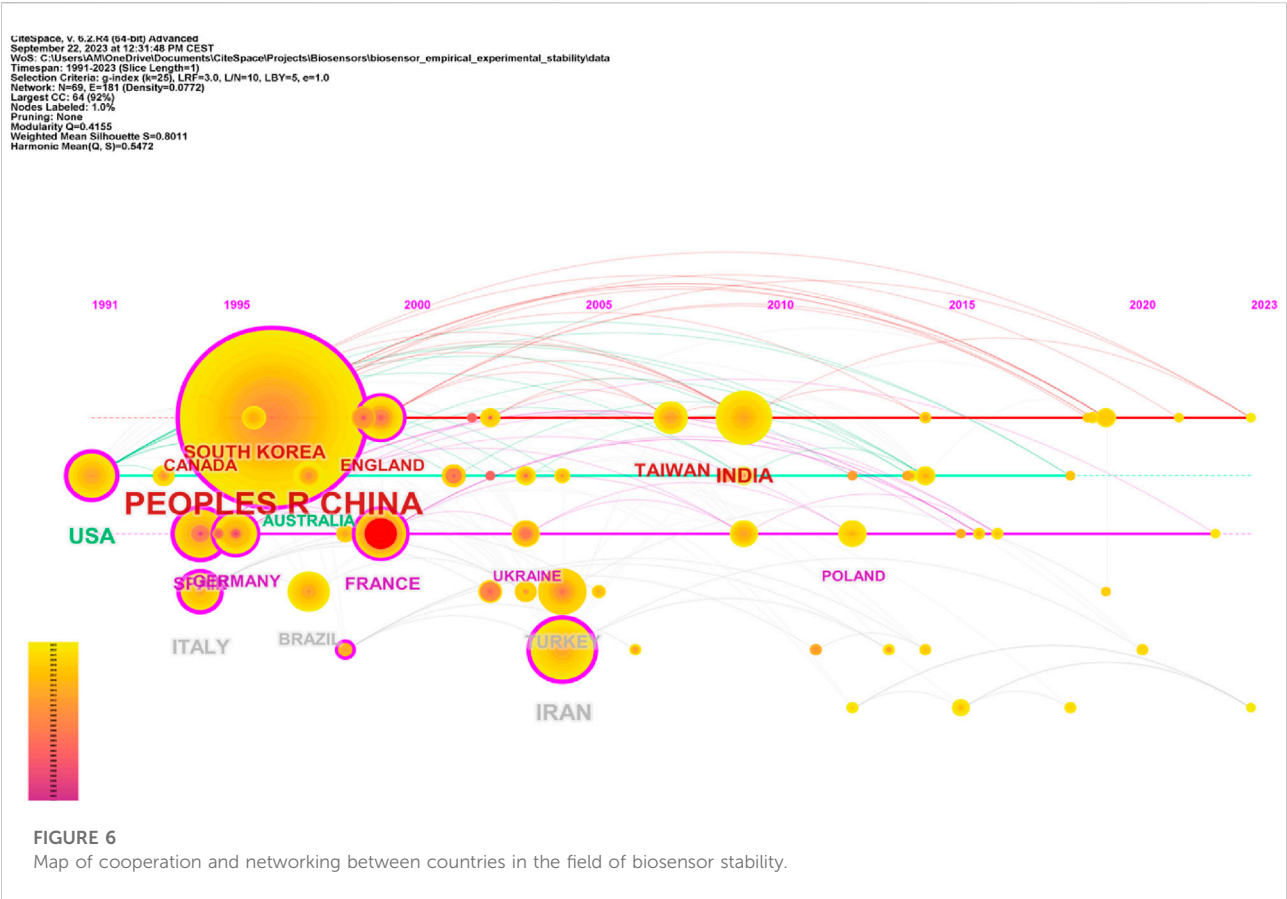


TABLE 1 Number of citations by country representative.

Citation counts	References
437	Peoples R China
70	Iran
57	United States
44	India
40	Italy
33	South Korea
28	Taiwan
25	Spain
25	France
24	Turkey

working on biosensor stability. The areas marked with circles show the citation rate of representatives of a country (the detailed number of citations of representatives of a country is presented in Table 1). In Figure 6 you can see that the larger the marked area, the higher the citation rate (the graph does not show all countries, but only those whose representatives

turned out to be the most active in terms of cited works). Thus, based on the figure below, it can be seen that the most cited works devoted to the stability of biosensors were published by representatives of China (437 citations), but also among the leaders can be distinguished representatives of: Iran (70 citations), United States (57 citations), India (44 citations), Italy (40 citations), South Korea (33 citations), Taiwan (28 citations), Spain (25 citations), France (25 citations), Turkey (24 citations). In 2012, the work of scientists from Poland was also cited.

In the diagram shown in red is the publication of the French representative (as first author) and co-authors (from the United States and Hungary), which generated the widest cooperation in the area of biosensor stability issues. This publication (Theavenot et al., 1999) is extremely important not only in terms of international cooperation, but also in terms of citations and content. The paper is dedicated to the recommendation, classification and definition of electrochemical biosensors. It contains a detailed description of guidelines for reporting biosensor response and calibration characteristics: sensitivity, working and linear concentration ranges, limits of detection and limits of quantification. You will also find information on biosensor selectivity and reliability, response time, reproducibility, stability and device lifetime.

TABLE 2 List of journals in which the most articles related to biosensors have been published.

Citation counts	References
711	Ibiosens Bioelectron
611	Anal Chem
576	Sensor Actuat B-Chem
553	Anal Chim Acta
466	Talanta
372	J Electroanal Chem
361	Electrochim Acta
359	Electroanal
344	J Am Chem Soc
304	Analyst

Table 2 presents list of journals in which the most articles related to biosensors have been published. It shows that the highest ranked item in terms of number of citations are the journals: Biosensors and Bioelectronics, Analytical Chemistry, Sensors and Actuators B: Chemical, Analytica Chimica Acta, Talanta and so forward as presented in Table 2.

Comparing the journals in which the most significant articles were published (Figure 4) with the list in which the largest number of articles related to biosensors are found (Table 2), it can be seen that the most cited articles were published in journals: Biosensors and Bioelectronics, Electrochemical Communication, Talanta and Electrochimica Acta. In the table presented (Table 2), the journal Biosensors and Bioelectronics is in the number 1 position, Talanta is in the number 5 position, Electrochimica Acta is in the number 7 position, while Electrochemical Communication is not among the top ten most cited journals.

Thus, it can be seen that there is a kind of correlation between highly cited articles and their impact on the journal’s citability, while the publications with the highest citations do not fully reflect the journal’s cutability.

Conclusion

This article presents an analysis of the stability of biosensors. This study provides a basic understanding and appreciation of biosensor stability research and shows the direction of scientific development of this topic.

Based on the CiteSpace, v.6.2.R4 tool, an analysis of trends and patterns in the scientific literature was performed. Based on the compilation of keywords, it was shown that the most frequent keywords in the analysed topic are: chemically modified electrode, reduced graphene oxide, direct electron transfer, magnetic microspheres, fft cyclic

voltammetry, poly(o-phenylenediamine), lectims, optimization.

This study identified the most important publications in the development of biosensor stability. The 42 most frequently cited words were extracted. Among them, we can distinguish: “graphene oxide,” “high-performance nanocomposite,” “nanocomposites,” “electrochemical sensor,” “platform,” “sensitive detection,” “surface plasmon resonance,” “amplification” and “immunosensor.” From these it can be seen that research is increasing towards electrochemical biosensors and immunosensors. Optimal materials in terms of durability are being sought. The experiments mainly use surface plasmon resonance and fft cyclic voltammetry as leading research methods.

A map of collaborations and transnational networks in biosensor stability showed that researchers from 69 countries were working on biosensor stability. The leaders in citability by country of origin were found to be from China.

Although the Citespace tool has significant potential and greatly facilitates analysis it has certain limitations, inconsistencies and irrelevancies.

CiteSpace analyzes the citations received through the publication of the co-citation network found in the Web of Science bibliographic database.

Web of Science indexes only part of scientific literature. Thus, all analyses, regardless of the methods and tools used, exclude many journals and books.

In the second case, the influence of a specific publication concerns studies whose results are described in publications linked by a parallel citation network, i.e., with smaller or larger thematic links. In addition, it should also be noted that keyword analysis on the basis of titles, abstracts, article descriptions based on articles related to biosensors omits important information contained in books as subsections.

However, despite the limitations of the database, which is the basis of the analysis, CiteSpace remains a very important tool for rapid retrospective and predictive analysis.

Data availability statement

The raw data supporting the conclusion of this article will be made available by the authors, without undue reservation.

Author contributions

Study conception and design: AK-W and VM; data collection: AK-W and VM; analysis: AK-W and VM; interpretation of results: AK-W and VM; draft manuscript: AK-W and VM; preparation: AK-W and VM. All authors contributed to the article and approved the submitted version.

Conflict of interest

The authors declare that the research was conducted in the absence of any commercial or financial relationships that could be construed as a potential conflict of interest.

References

- Ahammad, A. J. S., Sarker, S., and Lee, J. J. (2011). Immobilization of horseradish peroxidase onto a gold-nanoparticle-adsorbed poly(thionine) film for the construction of a hydrogen peroxide biosensor. *J. Nanosci. Nanotechnol.* 11, 5670–5675. doi:10.1166/jnn.2011.4456
- Arkhyova, V. N., Dzyadevych, S. V., Soldatkin, A. P., El'skaya, A. V., Martelet, C., and Jaffrezic-Renault, N. (2003). Development and optimisation of biosensors based on pH-sensitive field effect transistors and cholinesterases for sensitive detection of solanaceous glycoalkaloids. *Biosens. Bioelectron.* 18, 1047–1053. doi:10.1016/s0956-5663(02)00222-1
- Bai, J., Lai, Y. J., Jiang, D., Zeng, W., Xian, Y., Xiao, F., et al. (2012). Ultrasensitive electrochemical immunoassay based on graphene oxide-Ag composites for rapid determination of clenbuterol. *Analyst* 137 (18), 4349–4355. doi:10.1039/c2an35473j
- Bai, X., and Shiu, K. K. (2014). Investigation of the optimal weight contents of reduced graphene oxide-gold nanoparticles composites and their application in electrochemical biosensors. *J. Electroanal. Chem.* 720–721, 84–91. doi:10.1016/j.jelechem.2014.03.031
- Bai, X. Y., Chen, G. H., and Shiu, K. K. (2013). Electrochemical biosensor based on reduced graphene oxide modified electrode with Prussian blue and poly(toluidine blue O) coating. *Electrochimica Acta* 89, 454–460. doi:10.1016/j.electacta.2012.11.086
- Baytak, A. K., Duzmen, S., Teker, T., and Aslanoglu, M. (2015). A novel composite electrode based on tungsten oxide nanoparticles and carbon nanotubes for the electrochemical determination of paracetamol. *Mater. Sci. Eng. C* 57, 164–170. doi:10.1016/j.msec.2015.07.060
- Bohnenberger, T., and Schmid, U. (2014). Layer-by-layer approach for deposition of pure carbon nanotubes and composite films for use as electrodes in electrochemical devices. *Thin Solid Films* 565, 116–121. doi:10.1016/j.tsf.2014.05.055
- Bravo, I., Prata, M., Torrinha, A., Delerue-Matos, C., Lorenzo, E., and Morais, S. (2022). Laccase bioconjugate and multi-walled carbon nanotubes-based biosensor for bisphenol A analysis. *Bioelectrochemistry* 144, 108033. doi:10.1016/j.bioelechem.2021.108033
- Chalikian, T. (2016). Excluded volume contribution to cosolvent-mediated modulation of macromolecular folding and binding reactions. *Biophys. Chem.* 209, 1–8. doi:10.1016/j.bpc.2015.11.001
- Chen, X., Zhang, Q., Qian, C. H., Hao, N., Xu, L., and Yao, C. (2015). Electrochemical aptasensor for mucin 1 based on dual signal amplification of poly(o-phenylenediamine) carrier and functionalized carbon nanotubes tracing tag. *Biosens. Bioelectron.* 64, 485–492. doi:10.1016/j.bios.2014.09.052
- Cheraghi, S., Taher, M., Karimi-Maleh, H., and Moradi, R. (2017). Simultaneous detection of nalbuphine and diclofenac as important analgesic drugs in biological and pharmaceutical samples using a Pt/Co nanostructure-based electrochemical sensor. *J. Electrochem. Soc.* 164, B60–B65. doi:10.1149/2.0911702jes
- de Oliveira, R. H., Gonçalves, D. A., and Dos Reis, D. D. (2023). TiO₂/MWCNT/Nafion-Modified glassy carbon electrode as a sensitive voltammetric sensor for the determination of hydrogen peroxide. *Sensors* 23, 7732. doi:10.3390/s23187732
- Dervisevic, M., Cevik, E., and Senel, M. (2015a). Development of glucose biosensor based on reconstitution of glucose oxidase onto polymeric redox mediator coated pencil graphite electrodes. *Enzyme Microb. Technol.* 68, 69–76. doi:10.1016/j.enzmictec.2014.09.007
- Dervisevic, M., Custiuc, E., Cevik, E., Durmus, Z., Senel, M., and Durmus, A. (2015b). Electrochemical biosensor based on REGO/Fe₃O₄ bionanocomposite interface for xanthine detection in fish sample. *Food control* 57, 402–410. doi:10.1016/j.foodcont.2015.05.001
- Devi, R., Yadav, S., Nehra, R., and Pundir, C. (2013). An amperometric hypoxanthine biosensor based on Au@FeNPs for determination of hypoxanthine in meat samples. *Int. J. Biol. Macromol.* 62, 629–635. doi:10.1016/j.jbiomac.2013.10.009
- Di Fusco, M., Tortolini, C., Deriu, D., and Mazzei, F. (2010). Laccase-based biosensor for the determination of polyphenol index in wine. *Talanta* 81, 235–240. doi:10.1016/j.talanta.2009.11.063
- Dirpan, A., Yolanda, D., and Djalal, M. (2023). Is the use of biosensor in monitoring food quality experiencing an uplift trend over the last 30 years? a bibliometric analysis. *Heliyon* 9, e18977. doi:10.1016/j.heliyon.2023.e18977
- Dong, Y. P., Huang, L., Lei, Z. P., Chu, X. F., and Zhang, Q. F. (2012). Electrochemical biosensor of glucose based on the immobilization of glucose oxidase on a carbon microsphere modified glassy carbon electrode. *Sens. Lett.* 10, 1024–1030. doi:10.1166/sl.2012.2339
- Du, D., Ding, J. W., Cai, J., and Zhang, A. D. (2007). Determination of carbaryl pesticide using amperometric acetylcholinesterase sensor formed by electrochemically deposited chitosan. *Colloids Surfaces B Biointerfaces* 58, 145–150. doi:10.1016/j.colsurfb.2007.03.006
- Fan, Q., Shan, D., Xue, H. G., He, Y., Cosnier, S., and Cosnier, S. (2007). Amperometric phenol biosensor based on laponite clay–chitosan nanocomposite matrix. *Biosens. Bioelectron.* 22, 816–821. doi:10.1016/j.bios.2006.03.002
- Fanjul-Bolado, P., Queipo, P., Lamas-Ardizana, P. J., and Costa-Garcia, A. (2007). Manufacture and evaluation of carbon nanotube modified screen-printed electrodes as electrochemical tools. *Talanta* 74, 427–433. doi:10.1016/j.talanta.2007.07.035
- Fernandez-Lopez, L., Pedrero, S., Lopez-Carrobles, N., Gorines, B., VirgenOrtiz, J., and Fernandez-Lafuente, R. (2017). Effect of protein load on stability of immobilized enzymes. *Enzyme Microb. Technol.* 98, 18–25. doi:10.1016/j.enzmictec.2016.12.002
- Gamella, M., Campuzano, S., Reviejo, A. J., and Pingarron, J. M. (2006). Electrochemical estimation of the polyphenol index in wines using a laccase biosensor. *J. Agric. Food Chem.* 54, 7960–7967. doi:10.1021/jf061451r
- Gao, A., Yang, J., Tian, T., Wu, Y., Sun, X., Qi, N., et al. (2023). Visual analysis based on CiteSpace software: A bibliometric study of atrial myxoma. *Front. Cardiovasc. Med.* 10, 1116771. doi:10.3389/fcvm.2023.1116771
- Garay, F. (2015). How low does the oxygen concentration go within a sandwich-type amperometric biosensor? Part 2: theory for PPO biosensors. *Sensors Actuators B-Chemical* 207, 581–587. doi:10.1016/j.snb.2014.10.105
- Geng, Y., Zhang, N., and Zhu, R. (2023). Research progress analysis of sustainable smart grid based on CiteSpace. *Energy Strategy Rev.* 48, 101111. doi:10.1016/j.esr.2023.101111
- Ghanbari, K., Roshani, M., Hector, C., and Jalalvand, R. (2019). Developing an elegant and integrated electrochemical-theoretical approach for detection of DNA damage induced by 4-nonylphenol. *Heliyon* 10, 1016/j.heliyon.2019.e02755
- Gholivand, M. B., Jalalvand, A. R., and Goicoechea, H. C. (2014). Developing a novel computationally designed impedimetric pregabalin biosensor. *Electrochimica Acta* 133, 123–131. doi:10.1016/j.electacta.2014.04.017
- Grabowska, I., Malecka, K., Jarocka, U., Radecki, J., and Radecka, H. (2014). Electrochemical biosensors for detection of avian influenza virus — current status and future trends. *Acta Biochim. Pol.* 61, 471–478. doi:10.18388/abp.2014_1866
- Heli, H., and Yadegari, H. (2014). Poly(ortho-aminophenol)/graphene nanocomposite as an efficient supercapacitor electrode. *J. Electroanal. Chem.* 713, 103–111. doi:10.1016/j.jelechem.2013.12.010
- Hsu, P. Y., Lin, J. J., Wu, Y. L., Hung, W. C., and Cullis, A. G. (2009). Ultra-sensitive polysilicon wire glucose sensor using a 3-aminopropyltriethoxysilane and polydimethylsiloxane-treated hydrophobic fumed silica nanoparticle mixture as the sensing membrane. *Sensors Actuators B-Chem.* 142, 273–279. doi:10.1016/j.snb.2009.08.003
- Jalalvand, A. (2023). A novel amperometric biosensor for multi-enzymatic biosensing of triglycerides. *Sensors Int.* 4, 100206. doi:10.1016/j.sintl.2022.100206

- Kleinberg, J. (2002). "Bursty and hierarchical structure in streams," in *Proceedings of the 8th ACM SIGKDD International Conference on Knowledge Discovery and Data Mining*, 91–101.
- Klos-Witkowska, A. (2016). The phenomenon of fluorescence in immunosensors. *Acta Biochim. Pol.* 63, 215–221. doi:10.18388/abp.2015_1231
- Klos-Witkowska, A., and Kajstura, K. (2020). Effect of UV radiation applied fractionally or continuously on stability of biosensor receptor layer component. *Acta Phys. Pol. A* 138, 781–786. doi:10.12693/APhysPolA.138.781
- Kong, T., Chen, Y., Ye, Y., Zhang, K., Wang, Z., and Wang, X. (2009). An amperometric glucose biosensor based on the immobilization of glucose oxidase on the ZnO nanotubes. *Sensors Actuators B- Chem.* 138, 344–350. doi:10.1016/j.snb.2009.01.002
- Kyomuhimbo, H., Feleni, U., Haneklaus, N., and Brink, H. (2023). Recent advances in applications of oxidases and peroxidases polymer-based enzyme biocatalysts in sensing and wastewater treatment: a review. *Polymers* 15, 3492. doi:10.3390/polym15163492
- Laad, M., and Ghule, B. (2023). Removal of toxic contaminants from drinking water using biosensors: a systematic review. *Groundw. Sustain. Dev.* 20, 100888. doi:10.1016/j.gsd.2022.100888
- Lai, G. S., Zhang, H. L., and Han, D. Y. (2008). A novel hydrogen peroxide biosensor based on hemoglobin immobilized on magnetic chitosan microspheres modified electrode. *Sensors Actuators B-Chemical* 129, 497–503. doi:10.1016/j.snb.2007.08.041
- Li, X., Li, Y., Yu, P., Tong, Y., and Ye, B. (2021). A high sensitivity electrochemical sensor based on a dual-template molecularly imprinted polymer for simultaneous determination of clenbuterol hydrochloride and ractopamine. *Analyst* 146, 6323–6332. doi:10.1039/D1AN01413G
- Liu, H., Hong, R., Xiang, C., Lv, C., and Li, H. (2020). Visualization and analysis of mapping knowledge domains for spontaneous combustion studies. *Fuel* 262, 116598. doi:10.1016/j.fuel.2019.116598
- Liu, M., Wen, Y., Li, D., Yue, R., Xu, J., and He, H. (2011a). A stable sandwich-type amperometric biosensor based on poly(3,4-ethylenedioxythiophene)-single walled carbon nanotubes/ascorbate oxidase/nafion films for detection of L-ascorbic acid. *Sensors Actuators B- Chem.* 159, 277–285. doi:10.1016/j.snb.2011.07.005
- Liu, M., Wen, Y., Xu, J. K., He, H. H., Li, D., Yue, R., et al. (2011b). An amperometric biosensor based on ascorbate oxidase immobilized in poly(3,4-ethylenedioxythiophene)/multi-walled carbon nanotubes composite films for the determination of L-ascorbic acid. *Anal. Sci.* 27, 477–482. doi:10.2116/analsci.27.477
- Liu, Y., Zhang, H. L., Lai, G. S., Yu, A. M., Huang, Y. M., and Han, D. Y. (2010). Amperometric NADH biosensor based on magnetic chitosan microspheres/poly(thionine) modified glassy carbon electrode. *Electroanalysis* 22, 1725–1732. doi:10.1002/elan.200900544
- Liu, Z. M., Yang, Y., Wang, H., Liu, Y. L., Shen, G. L., and Yu, R. Q. (2005). A hydrogen peroxide biosensor based on nano-Au/PAMAM dendrimer/cystamine modified gold electrode. *Sensors Actuators B-Chemical* 106, 394–400. doi:10.1016/j.snb.2004.08.023
- Ltaïef, A. H., D'Angelo, A., Ammar, S., Gadri, A., Galia, A., and Scialdone, O. (2017). Electrochemical treatment of aqueous solutions of catechol by various electrochemical advanced oxidation processes: effect of the process and of operating parameters. *J. Electroanal. Chem.* 796, 1–8. doi:10.1016/j.jelechem.2017.04.033
- Lu, L. M., Zhang, L., Zhang, X. B., Wu, Z. S., Huan, S., Shen, G., et al. (2010). A MgO nanoparticles composite matrix-based electrochemical biosensor for hydrogen peroxide with high sensitivity. *Electroanalysis* 22, 471–477. doi:10.1002/elan.200900429
- Makhmudiyarova, N., Mudarisova, L., Meshcheryakova, E., Ibragimov, A., and Dzhebilev, U. (2015). Efficient catalytic method for the synthesis of N-aryl-substituted 1,5,3-dithiazamacroheterocycles. *Tetrahedron* 71, 259–265. doi:10.1016/j.tet.2014.11.064
- Malinauskas, A., Araminait, R., Mickevičiūt, G., and Garjonyt, R. (2004). Evaluation of operational stability of Prussian blue- and cobalt hexacyanoferrate-based amperometric hydrogen peroxide sensors for biosensing application. *Mater. Sci. Eng. C* 24, 513–519. doi:10.1016/j.msec.2004.01.002
- Marinov, I., Ivanov, Y., Gabrovska, K., and Godjevargova, T. (2010). Amperometric acetylthiocholin sensor based on acetylcholinesterase immobilized on nanostructured polymer containing gold nanoparticles. *J. Mol. Catal. B Enzym.* 62, 67–75. doi:10.1016/j.molcatb.2009.09.005
- Martsenyuk, V., Bernas, M., and Klos-Witkowska, A. (2021a). Two-strain COVID-19 model using delayed dynamic system and big data. *IEEE Access* 9, 113866–113878. doi:10.1109/ACCESS.2021.3104519
- Martsenyuk, V., Klos-Witkowska, A., Dzyadevych, S., and Sverstiuk, A. (2022). Nonlinear analytics for electrochemical biosensor design using enzyme aggregates and delayed mass action. *Sensors* 22, 980. doi:10.3390/s22030980
- Mu, S. L. (2006). Catechol sensor using poly(aniline-co-o-aminophenol) as an electron transfer mediator. *Biosens. Bioelectron.* 21, 1237–1243. doi:10.1016/j.bios.2005.05.007
- NaliniNandini, S. S., Shanmugam, S., Neelagund, S. E., Melo, J. S., and Suresh, G. S. (2014). Amperometric hydrogen peroxide and cholesterol biosensors designed by using hierarchical curtailed silver flowers functionalized graphene and enzymes deposits. *J. solid State Electrochem.* 18, 685–701. doi:10.1007/s10008-013-2305-y
- Narwal, V., Yadav, N., Thakur, M., and Pundir, C. S. (2017). An amperometric H₂O₂ biosensor based on hemoglobin nanoparticles immobilized on to a gold electrode. *Biosci. Rep.* 37. doi:10.1042/BSR20170194
- Neenkova, R., Ivanova, D., Vladimirova, J., and Godjevargova, T. (2010). New amperometric glucose biosensor based on cross-linking of glucose oxidase on silica gel/multiwalled carbon nanotubes/polyacrylonitrile nanocomposite film. *Sensors Actuators B-Chemical* 148, 59–65. doi:10.1016/j.snb.2010.05.034
- Norouzi, P., Faridbod, F., Rashedi, H., and Ganjali, M. R. (2010b). Flow injection glutamate biosensor based on carbon nanotubes and Pt-nanoparticles using FFT continuous cyclic voltammetry. *Int. J. Electrochem. Sci.* 5, 1713–1725. doi:10.1016/s1452-3981(23)15379-x
- Norouzi, P., Larijani, B., Faridbod, F., and Ganjali, M. R. (2010c). Hydrogen peroxide biosensor based on hemoglobin immobilization on gold nanoparticle in FFT continuous cyclic voltammetry flow injection system. *Int. J. Electrochem. Sci.* 5, 1550–1562. doi:10.1016/s1452-3981(23)15357-1
- Norouzi, P., Pirali-Hamedani, M., Faridbod, F., and Ganjali, M. R. (2010a). Flow injection phosphate biosensor based on PyOx-MWCNTs film on a glassy carbon electrode using FFT continuous cyclic voltammetry. *Int. J. Electrochem. Sci.* 5, 1225–1235. doi:10.1016/s1452-3981(23)15357-0
- Oliveira, T., Barroso, M., Morais, S., Araujo, M., Freire, C., de Lima-Neto, P. A., et al. (2014). Sensitive bi-enzymatic biosensor based on polyphenoloxidases-gold nanoparticles-chitosan hybrid film-graphene doped carbon paste electrode for carbamates detection. *Bioelectrochemistry* 98, 20–29. doi:10.1016/j.bioelechem.2014.02.003
- Oyetayo, O., Méndez-Lucio, O., Bender, A., and Kiefer, H. (2017). Diversity selection, screening and quantitative structure–activity relationships of osmolyte-like additive effects on the thermal stability of a monoclonal antibody. *Eur. J. Pharm. Sci.* 97, 151–157. doi:10.1016/j.ejps.2016.11.016
- Panjan, P., Virtanen, V., and Sesay, A. (2017). Determination of stability characteristics for electrochemical biosensors via thermally accelerated ageing. *Talanta* 170, 331–336. doi:10.1016/j.talanta.2017.04.011
- Pasahan, A., Koytepe, S., and Ekinci, E. (2011). Poly[tris((p-aminophenoxy) phosphineoxide)-3,3',4,4'-benzophenonetetracarboxylicdiimide] as a new polymeric membrane for the fabrication of an amperometric glucose sensor. *Int. J. Polym. Mater.* 60, 1079–1090. doi:10.1080/00914037.2011.553853
- Pohrebennyk, V., Karpinski, M., Dzhumelia, E., Klos-Witkowska, A., and Falat, P. (2018). Water bodies pollution of the mining and chemical enterprise. *SGEM Int. Multidiscip. Sci. GeoConference Expo. Proc.* 18, 1035–1042. doi:10.5593/sgem2018/5.2/S20.133
- Price, D. J. (1965). Networks of scientific papers. *Science* 149, 510–515. doi:10.1126/science.149.3683.510
- Qian, L., and Yang, X. (2006). Composite film of carbon nanotubes and chitosan for preparation of amperometric hydrogen peroxide biosensor. *Talanta* 68, 721–727. doi:10.1016/j.talanta.2005.05.030
- Rahman, M. A., Park, D. S., Chang, S. C., McNeil, C. J., and Shim, Y. B. (2006). The biosensor based on the pyruvate oxidase modified conducting polymer for phosphate ions determinations. *Biosens. Bioelectron.* 21, 1116–1124. doi:10.1016/j.bios.2005.04.008
- Rakhi, R., Nayak, P., Xia, C., and Alshareef, H. (2016). Novel amperometric glucose biosensor based on MXene nanocomposite. *Sci. Rep.* 6, 36422. doi:10.1038/srep36422
- Ramesh, M., Rajeshkumar, L., Balaji, D., and Bhuvaneshwari, V. (2023). Polymer composites for enzyme sensors. *Polym. Nanocomposite Mater. Sens. Appl.* 2023, 343–366. doi:10.1016/B978-0-323-98830-8.00019-9
- Ribeiro, F. W. M., Omari, I., Thomas, G. T., Paul, M., Williams, P. J. H., and McIndoe, J. S. (2014). Simple laccase-based biosensor for formetanate hydrochloride quantification in fruits. *Bioelectrochemistry* 95, 7–14. doi:10.1016/j.bioelechem.2013.09.005
- Ricci, F., Amine, A., Tuta, C., Ciucu, A., Lucarelli, F., Pallechi, G., et al. (2003). Prussian Blue and enzyme bulk-modified screen-printed electrodes for hydrogen peroxide and glucose determination with improved storage and operational stability. *Anal. Chim. Acta* 485, 111–120. doi:10.1016/S0003-2670(03)00403-3
- Shan, D., He, Y. Y., Wang, S. X., Xue, H. G., and Zheng, H. (2006). A porous poly(acrylonitrile-co-acrylic acid) film-based glucose biosensor constructed by electrochemical entrapment. *Anal. Biochem.* 356, 215–221. doi:10.1016/j.ab.2006.06.005

- Stepashkin, N. A., Chernenko, M., Khripun, V., Ivanov, N., and Sukhodolov, N. (2018). Electrochemical properties of Langmuir-Blodgett films containing cobalt hexacyanoferrate nanoparticles. *Thin Solid Films* 661, 1–6. doi:10.1016/j.tsf.2018.06.052
- Tan, X. C., Tian, Y. X., Cai, P. X., and Zou, X. Y. (2005). Glucose biosensor based on glucose oxidase immobilized in sol-gel chitosan/silica hybrid composite film on Prussian blue modified glass carbon electrode. *Anal. Bioanal. Chem.* 381, 500–507. doi:10.1007/s00216-004-2956-8
- Tan, X. C., Wu, J., Hu, Q., Li, X. Y., Li, P. F., Yu, H. C., et al. (2015). Electrochemical sensor for determination of chlorpyrifos based on graphene modified electrode and molecularly imprinted polymer. *Chin. J. Anal. Chem.* 43, 387–393.
- Theavenot, D., Toth, K., Durst, R., and Wilson, G. (1999). Electrochemical biosensor: recommended definitions and classification. *Pure Appl. Chem.* 71, 2333–2348.
- Tong, Z. Q., Yuan, R., Chai, Y. Q., Xie, Y., and Chen, S. H. (2007). A novel and simple biomolecules immobilization method: electro-deposition ZrO₂ doped with HRP for fabrication of hydrogen peroxide biosensor. *J. Biotechnol.* 128, 567–575. doi:10.1016/j.jbiotec.2006.12.008
- Tvorynska, S., Barek, J., and Josypczuk, B. (2022). Influence of different covalent immobilization protocols on electroanalytical performance of laccase-based biosensors. *Bioelectrochemistry* 148, 108223. doi:10.1016/j.bioelect.2022.108223
- Villani, E., Valenti, G., Marcaccio, M., Mattarozzi, L., Barison, S., GaroliCattarin, D. S., et al. (2018). Coreactant electrochemiluminescence at nanoporous gold electrodes. *Electrochimica Acta* 277, 168–175. doi:10.1016/j.electacta.2018.04.215
- Wang, G., Xu, J., Chen, H., and Lu, Z. (2003). Amperometric hydrogen peroxide biosensor with sol-gel/chitosan network-like film as immobilization matrix. *Biosens. Bioelectron.* 18, 335–343. doi:10.1016/S0956-5663(02)00152-5
- Wang, G. H., and Zhang, L. M. (2006). Using novel polysaccharide-silica hybrid material to construct an amperometric biosensor for hydrogen peroxide. *J. Phys. Chem. B* 110, 24864–24868. doi:10.1021/jp0657078
- Wang, L., and Wang, E. (2004). A novel hydrogen peroxide sensor based on horseradish peroxidase immobilized on colloidal Au modified ITO electrode. *Electrochem. Commun.* 6, 225–229. doi:10.1016/j.elecom.2003.12.004
- Wang, Y. L., Wang, Z. C., Wang, Y. P., and Li, M. G. (2015). Horseradish peroxidase immobilization on carbon nanodots/CoFe layered double hydroxides: direct electrochemistry and hydrogen peroxide sensing. *Biosens. Bioelectron.* 64, 57–62. doi:10.1016/j.bios.2014.08.054
- Wang, Z., Liu, D., Gu, H., Zhu, A. W., Tian, Y. G., and Shi, Y. (2013). NTA-modified carbon electrode as a general relaying substrate to facilitate electron transfer of SOD: application to *in vivo* monitoring of O₂– in a rat brain. *Biosens. Bioelectron.* 43, 101–107. doi:10.1016/j.bios.2012.10.071
- Wei, J. H., Qiu, J. J., Li, L., Ren, L. Q., Zhang, X. W., Chaudhuri, J., et al. (2012). A reduced graphene oxide based electrochemical biosensor for tyrosine detection. *Nanotechnology* 23, 335707. doi:10.1088/0957-4484/23/33/335707
- Xu, M. R., Zhu, J. Y., Su, H. C., Dong, J., Ai, S. Y., and Li, R. (2012). Electrochemical determination of methyl parathion using poly(malachite green)/graphene nanosheets-nafion composite film-modified glassy carbon electrode. *J. Appl. Electrochem.* 42, 509–516. doi:10.1007/s10800-012-0425-1
- Xu, Z., Zhu, Y., Hu, Y., Huang, M., Xu, F., and Wang, J. (2022). Bibliometric and visualized analysis of neuropathic pain using web of science and CiteSpace for the past 20 years. *World Neurosurg.* 162, e21–e34. doi:10.1016/j.wneu.2021.12.025
- Yang, H. C., Yuan, R., Chai, Y., Su, H., Zhuo, Y., Jiang, W., et al. (2011). Electrochemical immunosensor for human chorionic gonadotropin based on horseradish peroxidase-functionalized Prussian blue-carbon nanotubes/gold nanocomposites as labels for signal amplification. *Electrochimica Acta* 56, 1973–1980. doi:10.1016/j.electacta.2010.12.003
- Yang, W. Y., Zhou, X., Zheng, N., Li, X., and Yuan, Z. (2011). Electrochemical biosensors utilizing the electron transfer of hemoglobin immobilized on cobalt-substituted ferrite nanoparticles-chitosan film. *Electrochimica Acta* 56, 6588–6592. doi:10.1016/j.electacta.2011.04.037
- Zalpour, N., Roushani, M., and Hosseini, H. (2022). Polydopamine imprinted polymer-based tunable electrochemical synthesis of copper benzene-1, 3, 5-tricarboxylate metal-organic framework film as a hybrid dual recognition element for ultra-trace sensing of pregabalin (lyrica). *Sensors Actuators B Chem.* 370, 132418. doi:10.1016/j.snb.2022.132418
- Zhang, B. Y., Zhou, J. H., Li, S. H., Zhang, X. F., Huang, D. K., He, Y. H., et al. (2015). Hydrogen peroxide biosensor based on microperoxidase-11 immobilized on flexible MWCNTs-BC nanocomposite film. *Talanta* 131, 243–248. doi:10.1016/j.talanta.2014.07.027
- Zhang, H. L., Lai, G. S., Han, D. Y., and Yu, A. M. (2008). An amperometric hydrogen peroxide biosensor based on immobilization of horseradish peroxidase on an electrode modified with magnetic dextran microspheres. *Anal. Bioanal. Chem.* 390, 971–977. doi:10.1007/s00216-007-1748-3
- Zhang, Q. F., Chen, C., Xie, Q. J., and Liu, P. G. (2009). Electrodeposition of a biocompatible hydroxyapatite matrix to immobilize glucose oxidase for sensitive glucose biosensing. *Microchim. Acta* 165, 223–229. doi:10.1007/s00604-008-0124-0
- Zhao, X., Nan, D., Chen, C., Zhang, S., Che, S., and Kim, J. (2023). Bibliometric study on environmental, social, and governance research using CiteSpace. *Front. Environ. Sci.* 10, 1–12. doi:10.3389/fenvs.2022.1087493
- Zhen, S. H., Wang, Y., Liu, C. G., Xie, G. M., Zou, C. S., Zheng, J., et al. (2011). A novel microassay for measuring blood alcohol concentration using a disposable biosensor strip. *Forensic Sci. Int.* 207, 177–182. doi:10.1016/j.forsciint.2010.10.002
- Zhou, J., Liao, C. N., Zhang, L. M., Wang, Q. G., and Tian, Y. (2014). Molecular hydrogel-stabilized enzyme with facilitated electron transfer for determination of H₂O₂ released from live cells. *Anal. Chem.* 86, 4395–4401. doi:10.1021/ac500231e
- Zhou, K., Zhu, Y., Yang, X., Luo, J., Li, C., and Luan, S. (2010). A novel hydrogen peroxide biosensor based on Au-graphene-HRP-chitosan biocomposites. *Electrochimica Acta* 55, 3055–3060. doi:10.1016/j.electacta.2010.01.035
- Zhu, A. W., Tian, Y., Liu, H., and Luo, Y. P. (2009). Nanoporous gold film encapsulating cytochrome c for the fabrication of a H₂O₂ biosensor. *Biomaterials* 30, 3183–3188. doi:10.1016/j.biomaterials.2009.02.019

***In silico* explorations of bacterial mercuric reductase as an ecofriendly bioremediator for noxious mercuric intoxications**

Muhammad Naveed¹✉, Muhammad Aqib Shabbir¹, Tariq Aziz²✉, Ayesha Saleem¹, Rida Naveed¹, Ayaz Ali Khan³, Taqweem Ul Haq³, Metab Alharbi⁴, Abdulrahman Alsahammari⁴ and Abdullah F. Alasmari⁴

¹Department of Biotechnology, Faculty of Science and Technology, University of Central Punjab, Lahore 54590, Pakistan; ²Department of Agriculture, University of Ioannina Arta, 47100 Greece; ³Department of Biotechnology University of Malakand Chakdara, 18800 Pakistan; ⁴Department of Pharmacology and Toxicology, College of Pharmacy, King Saud University, P.O. Box 2455, Riyadh 11451, Saudi Arabia

Mercury is a major pollutant in the environment due to its high concentration in the soil. In this study, a mercuric reductase was extracted from *Pseudomonas aeruginosa*. The sequence of the enzyme was retrieved from the literature and structural homologs were identified. The protein bonded with Mercuric compounds and their interaction was briefly studied. Autodock Vina was used to perform a molecular docking with the target protein. Results showed that the sequence consists of most of the random coil 44.74% followed by α -helix and B-turns. Moreover, the protein was predicted to have a FAD/NAD(P)-binding domain. The virulence factor prediction using different approaches of Virulentpred and VICM-pred suggested that P00392 is non-toxic. Next, the mutational analyses were performed to predict the active site residues in the resulting models and to determine mutants. The results show that the enzyme is involved in the bioremediation of mercury by using in-silico techniques. Finally, molecular docking studies were conducted on the best-selected model to find the active site residues and to generate a pattern of interaction to understand the mode of action of the substrate and its catalytic activity which refers to the binding with mercury.

Keywords: Mercury, bioremediation, Mercuric reductase, heavy metals, molecular docking

Received: 10 May, 2023; **revised:** 20 July, 2023; **accepted:** 02 August, 2023; **available on-line:** 07 September, 2023

✉e-mail: dr.naveed@ucp.edu.pk (MN) iwockd@gmail.com (TA)

Acknowledgments of Financial Support: The authors greatly acknowledge and express their gratitude to the Researchers Supporting Project number (RSP2023R335), King Saud University, Riyadh, Saudi Arabia.

Abbreviations: CASTp, Computed Atlas of Surface Topography of proteins; FAD, Flavin-Adenine Dinucleotide; MSA, Multiple Sequence Alignment; NADPH, Nicotinamide adenine dinucleotide phosphate

INTRODUCTION

The proliferation of industrial waste into the environment has led to the grave predicament of heavy metal contamination which has proved to be a peril to both the biosphere and humankind. These heavy metals can accumulate in the environment from various sources (Gworek *et al.*, 2020). Soil, water and especially air can get contaminated with these heavy metal compounds and hence, it is causing disastrous impacts on our environment and health. Even at low concentrations, heavy metals including mercury, cadmium, copper, lead and

chromium are cytotoxic, carcinogenic and mutagenic in nature. The main cause of the release of such heavy metals into the environment is the utilization of non-biodegradable materials which directly affect the biosphere (Mandal & Mishra, 2023). The World Health Organization has classified four of the ten heavy metals as being of significant public health concern which includes: cadmium, arsenic, lead, and mercury (Budnik & Casteleyn, 2019).

Mercury can be produced in the atmosphere due to natural eruptions i.e., volcanoes, forest fires and weathering of rocks. Mercury can be found in a variety of forms in the inorganic state; metallic mercury, mercury vapor, mercuric salts, and mercury dioxide (Xu *et al.*, 2022). The organic state includes the mercuric compounds in which the mercury is bonded to a structure containing carbon atoms, and inorganic mercury in the form of compounds like methyl, ethyl, phenyl, or similar groups. Although the concentration of mercuric compounds in the air is less concerning, it is causing more damage to the soil. Human mercury exposure has adverse health consequences, such as headaches, insomnia, neuromuscular effects, difficulty in breathing, irritability, chest pain, stomachaches and cognitive or motor dysfunction. Mercury poisoning may also occur if the blood mercury levels exceed 100 ng/mL which will result in the malfunctioning of muscles (Duan *et al.*, 2020).

There are several conventional methods to decontaminate an environment containing mercuric compounds. An alternative method to distinctively remove this heavy metal is by utilizing a biological technique based on the use of a biological enzyme *mercuric reductase*, extracted from *Pseudomonas stutzeri* with an ecofriendly approach (Al-Ansari, 2022). Bioremediation is a safe approach that can be utilized to decontaminate our environment from these heavy metal pollutants by the use of microorganisms. Microorganisms are considered best for these types of mechanisms as they are well-known for their resistance against heavy metals. They have the potential to adopt various detoxifying mechanisms which include biomineralization, bioaccumulation and biosorption (Al-Ansari, 2022). Therefore, the aim behind opting for this topic is to use a mercury-resistant bacterium thriving in a mercuric environment and study the enzyme which is involved in the bioremediation of mercury by using in-silico techniques. Mercury-resistant *Pseudomonas stutzeri* is found in highly contaminated soil enriched with mercuric compounds. It is a gram-negative, rod-shaped, motile bacterium with greater metabolic diversity in the nature (Wan *et al.*, 2020).

In this study, *mercuric reductase* from *P. stutzeri* was selected as a candidate for further investigations (Zheng *et al.*, 2018). The sequence of mercuric reductase retrieved from literature and structural homologs was identified. Structural analysis via using bioinformatic tools was performed and validated to get good-quality protein structures and models. The protein bonded with mercuric compounds and their interaction was briefly studied. The models obtained from these strategies were further refined to remove steric clashes with other compounds. The main residue which is involved in ligand binding was determined based on the active sites and binding pockets identified in the structural homology (Bianchi *et al.*, 2012). Finally, docking studies were conducted on the best-selected model to find the active site residues and generate a pattern of interaction to understand the mode of action of the substrate and its catalytic activity which refers to the binding with mercury. Lastly, the mutational analyses were performed to predict the active site residues in the resulting models and to determine mutants. According to the study conducted, *P. stutzeri* mercuric reductase is a non-virulent protein that may be used for cheap and environmentally acceptable bioremediation of mercury (Sodhi *et al.*, 2019).

MATERIALS AND METHODS

Sequence Analysis

Sequence Retrieval

The FASTA sequence of Mercuric Reductase protein was retrieved from UniProt KB (<https://www.uniprot.org>) with the specifically allocated UniProt ID: P00392. The sequence contained a total of 561 amino acids and the annotation score 5/5 which confirmed it as a sequence of good quality and useful for all kinds of bioinformatics analysis.

Sequence Characterization

The sequence characterization was done by the prediction of Physiochemical Parameters. The computing for the physiochemical parameters of the Mercuric Reductase protein under study was performed by ExPASy-ProtParam Tool (<https://web.expasy.org/protparam>) which is an open-access online server by the Swiss Bioinformatics Resource Portal. The sequence was submitted in the FASTA format and various Physiochemical annotations like Molecular Weight, Theoretical pI, Aliphatic Index and GRAVY were calculated.

Sequence Comparison & Multiple Sequence Alignment

MSA or multiple sequence alignment is a crucial tool in understanding the interrelationships among sequences and identifying functionally important conserved regions. To detect conserved regions in the sequences, the ClustalW and MEGA version X MSA tools were utilized. Furthermore, to determine sequence homology and infer evolutionary relationships, phylogenetic analysis was performed using MEGA version X with the neighbor-joining algorithm and Poisson substitution method.

Function Prediction

The role of protein domains in protein function is essential as they often determine the protein's overall function, specificity, and interaction with other molecules. Protein domains can carry out various functions, such

as binding to DNA, RNA, or other proteins, catalyzing chemical reactions, and transporting molecules across cell membranes. By containing specific sequence motifs, domains can also be responsible for post-translational modifications such as phosphorylation, glycosylation or ubiquitination, which can alter protein activity, stability or localization. Therefore, the protein domain prediction was performed by CATH DB (<http://www.cathdb.info>) which is an online bioinformatics tool for protein domain prediction. The protein sequence was inputted in FASTA format, and the domains were predicted.

Virulence Factors Identification

Keeping in view that the protein is planned to be used as a Bioremediator, it is necessary to make sure that the protein should not be toxic or virulent (Muhammad Naveed *et al.*, 2023). Therefore, the identification of virulence factors was performed with VirulentPred (<http://bioinfo.icgeb.res.in/virulent>), that is an online server for virulent factors identification. The protein sequence was used as input and the results were obtained.

Secondary structure prediction

Secondary structure prediction was performed by PSIPRED (<http://bioinf.cs.ucl.ac.uk/psipred>) which uses position-specific matrices score that is produced by PSIBLAST to employ neural network methods (M Naveed, I Ali, *et al.*, 2023). It predicts the secondary structure of the protein sequence. In addition to identifying protein characteristics and recognizing folds, secondary structure prediction is an intermediate step in predicting three-dimensional structures (Mohamadi *et al.*, 2022).

The analysis of the secondary structure sequence was also performed by the SOPMA online tool (https://npsa.lyon.inserm.fr/cgi-bin/secpred_sopma.pl) which analyzes the number of features of secondary structure such as b-turns, a-helix and coil etc. In addition to analyzing the amino acid sequence of a given protein, this tool offers information about protein secondary structures (Buchan & Jones, 2019).

Structure Prediction

Template Recognition

The PSI-BLAST program was used to carry out a sequence similarity search against the PDB database to provide a list of results that were most similar to the query sequence to identify the template. The sequence with the highest sequence identity, the largest query coverage, and the score with the lowest e-value was chosen as the reference template. Based on the outcomes returned by BLAST, the coordinates of the template structure were obtained from the Protein Data Bank (Bekker *et al.*, 2022). The motif and domain analysis were identified by Pfam and InterProScan. InterProScan (<https://www.ebi.ac.uk/interpro/search/sequence-search>) is an online tool used to obtain the functional analysis and classify the protein sequences into the families and domains as well as binding sites (Blum *et al.*, 2021). The Pfam (<https://pfam.xfam.org/>) is a database that contains a large collection of families of proteins each represented by specific Markov models (HMMs) and modeling by multiple sequence alignment (Mistry *et al.*, 2021).

Model Generation

The homology modeling for the three-dimensional structure was performed by SWISS-MODEL (<https://>

swissmodel.expasy.org/templates/) which is a tool for automatic homology modeling and Phyre2 (<http://www.sbg.bio.ic.ac.uk/phyre2/>) which is a tool that creates 3D structures and remote homology service as well as finds binding sites in the query structure to predict the 3D structure of the mercury reductase protein (Naveed *et al.*, 2023). The best-predicted structure from each tool was chosen and was further validated for experimental analysis (Komari *et al.*, 2020; Pasaribu *et al.*, 2021).

Model Validation

The predicted structure from the two tools was further validated by performing Ramachandran plot analysis by using the PROCHECK (<http://services.mbi.ucla.edu/PROCHECK/>) via the platform of SAVES v5.0 (<http://servicesn.mbi.ucla.edu/SAVES/>) (M Naveed, N Ain, *et al.*, 2023), which outlines the stereochemical characteristics of the structures (Reddy & Rao, 2020).

Docking Studies

Interaction Analysis

Autodock Vina, a free docking engine, allows for molecular docking. This is a collection of automated docking technologies that are integrated for the prediction of the interaction of small molecules with the protein (Eberhardt *et al.*, 2021). The docking analysis of a chosen Mercuric compound was presented by Autodock Vina. Protein and ligand were first prepared, then active sites were identified, and finally a grid box was set up (by default) (Naveed *et al.*, 2023). The mercurial compound with the lowest binding energies was chosen for docking with the target protein.

Site Directed Mutagenesis

Mutant Identification

For mutation identification, four different tools were used. The I-Mutant (<http://gpcr.biocomp.unibo.it/cgi/predictors/I-Mutant3.0>) online tool was used to observe the impact of single nucleotide polymorphisms on the stability of the protein. It predicts the effect of SNPs on the tertiary structure of the protein value based on the free energy change. PHD-SNP (<http://snps.biofold.org/phd-snp/phd-snp.html>) is based on support vector machines that predict whether point mutation links with a genetic disorder or is a neutral polymorphism. It predicts the human deleterious SNPs (Mustafa *et al.*, 2020). The other mutation identification tool is SIFT (Sorting Intolerant from Tolerant) (<https://sift.bii.a-star.edu.sg/>), which employs sequence homology to predict the impact of amino acid substitution and whether it has a damaging impact on protein structure or not. It gives the probability score less than or equal to 0.05 if it is deleterious or a prediction value greater than 0.05 when it is tolerant. Another tool MuPro (<http://mupro.proteomics.ics.uci.edu/>) predicts the stability of protein decreases or increases and its effect on the protein structure (Naveed *et al.*, 2019).

Model Generation

The 3D structure of mutant mercury reductase protein was generated by using SWISS-MODEL (<http://swissmodel.expasy.org>). It is an automated tool that predicts the 3D structure of protein and generates the model based on the homology modeling (Pasaribu *et al.*, 2021; Komari *et al.*, 2020).

Model Validation

The tertiary structure was validated by the PROCHECK through which Ramachandran Plot was created for Mercuric Reductase P00391. PROCHECK checks the stereochemical property of protein and analyzes the geometry of the residues present in the protein structure. The Ramachandran Plot was analyzed based on Rama favored regions present in the plots (Reddy & Rao, 2020).

Mutant Docking Studies

Prediction Of Binding Sites

Computed Atlas of Surface Topography of proteins (CASTp) (<http://cast.engr.uic.edu>) is an online bioinformatic tool that locates, measures and delineates concave surface regions on the 3D structure of the protein. It finds out the binding pockets of protein that locate or void buried in the internal of the protein surface. It includes a flexible interactive, interface, visualization as well as on the fly calculations for the input structure (Chandran *et al.*, 2022).

Molecular Docking of the Mutants

After validating the best 3D mutant model, Autodock Vina was run to perform docking upon the protein receptor. The selective structures as ligand were taken from PubChem and were accounted for docking studies with Mercuric (Hg) compounds and complexes. Through this, the intramolecular interactions were evaluated in the final docked complex. To put it simply, PubChem is a repository for information about chemical compounds and their performance in various biological experiments (Eberhardt *et al.*, 2021; Chandran *et al.*, 2022).

RESULTS

Sequence Analysis

The protein sequence of Mercuric Reductase from *Pseudomonas aeruginosa* was obtained from UniProtKB with the UniProt ID P00392. Analysis of protein domains and motifs revealed that its function is in the

Table 1. Physiochemical characterization of the Mercuric reductase protein P00392

Number of amino acids	561
Molecular weight	58728.03
Theoretical pI	5.60
Negatively charged residues	60
Positively charged residues	48
Formula	C ₂₅₇₁ H ₄₁₇₁ N ₇₃₃ O ₇₉₆ S ₂₀
Total No. of atoms	8291
Ext. coefficient	23420
Estimated half-life	30 hours (mammalian reticulocytes, <i>in vitro</i>) >20 hours (yeast, <i>in vivo</i>) >10 hours (<i>Escherichia coli</i> , <i>in vivo</i>)
Instability index	30.67
Aliphatic index	95.40
GRAVY	0.092

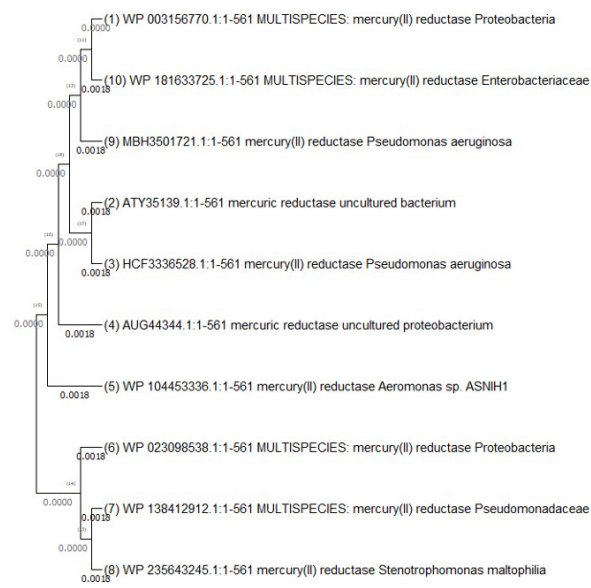


Figure 1. Phylogenetic tree of the Mercuric reductase P00392 generated by MEGA-X Neighbor-Joining Method.

reduction of mercury and that the protein family is predicted to have a FAD/NAD(P)-binding domain. Physio-chemical properties of the sequence were computed and are presented in Table 1. The instability index for P00392 was found to be 30.67, indicating its higher stability in the test tube compared to the other protein, which had a slightly higher instability index. Virulence factor prediction using different approaches of Virulentpred and VICMpred suggested that P00392 is non-toxic. Homologous sequences for P00392 were identified using BLASTp, and 10 sequences were retrieved. These sequences were suitable for multiple sequence alignment (MSA) to determine conserved regions and phylogenetic analysis to infer the evolutionary relationship. The phylogenetic tree constructed by Neighbor-Joining Method is given below in Fig. 1. A sequence similarity search was performed to search for crystal structures of the closest homologs available in the Protein Data Bank (PDB).

Table 2. Secondary structure analysis by the SOPMA tool

Alpha-helix	Extended strands	Beta turn	Random coil
35.29	19.96	0.0	44.74

Structure Predication

Secondary structure prediction

As shown in Fig. 2, the predicted secondary structure of mercury reductase protein consists of a majority of the coils as viewed by using PSI-PRED followed by a-helix. The secondary structure of a protein plays an important role in determining its stability, function, and interactions with other molecules. In the case of mercury reductase, the predominance of coils in its secondary structure suggests that it is a flexible protein that can undergo conformational changes to interact with its substrate and catalyze the reduction of mercury. The presence of alpha helices in the secondary structure also indicates that the protein may have structural stability and rigidity in certain regions. It is important to note that the predicted secondary structure is based on computational methods and may not precisely reflect the actual structure of the protein. Further experimental studies such as X-ray crystallography or NMR spectroscopy would be needed to confirm the actual secondary structure of mercuric reductase. The analysis of secondary structure by SOPMA is given in Table 2.

Secondary structure analysis was performed by SOPMA. Results show that the mercury reductase sequence

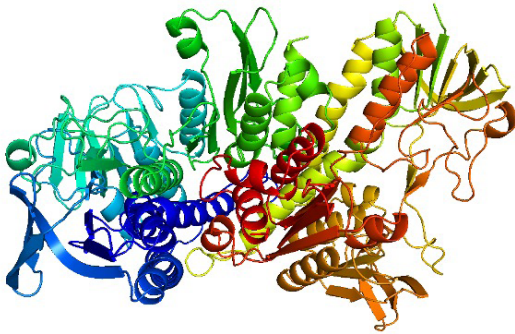


Figure 3. Predicted 3D Model of Mercuric reductase P00391 by Swiss-Model

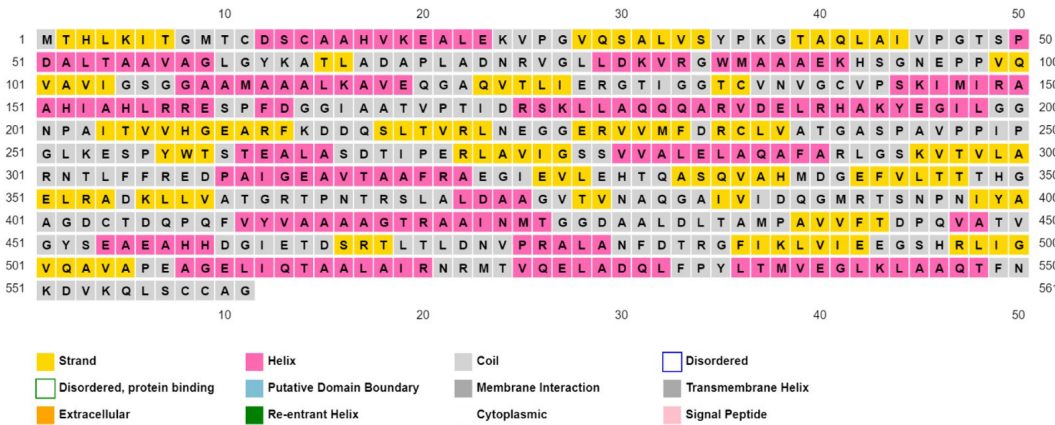


Figure 2. The predicted secondary structure of Mercuric reductase by PsiPred

Table 3. Identified mutations and classification of mutants by *in-silico* approaches

Species	Amino Acid Substituted	Mutation Position	Amino Acid Replaced	I-Mutant Results	MU-PRO Results	PHD-SNP Results	SIFT Results
Uncultured proteobacterium	L	346	M	Decrease	Decrease	Neutral	Neutral
Mercury(II) reductase (<i>P. aeruginosa</i>)	V	137	I	Decrease	Decrease	Neutral	Neutral
<i>Aeromonas</i> sp. ASNIH1	E	91	D	Decrease		Deleterious	Neutral
<i>S. maltophilia</i>	A	154	T	Decrease	Decrease	Neutral	Neutral
Mercury(II) reductase (<i>P. aeruginosa</i>)	A	114	V	Decrease	Decrease	Deleterious	Deleterious
Mercury(II) reductase (<i>C. freundii</i>)	A	192	V	Decrease	Decrease	Deleterious	Neutral
Mercury(II) reductase (<i>Burkholderia</i> sp. EMB26)	P	98	S	Decrease	Decrease	Neutral	Neutral
Mercury(II) reductase (<i>D. lacustris</i>)	L	32	M	Decrease	Decrease	Neutral	Neutral
Mercury(II) reductase (<i>S. maltophilia</i>)	V	442	A	Decrease	Decrease	Neutral	Neutral
Mercury(II) reductase (Proteobacteria)	T	240	A	Decrease	Decrease	Deleterious	Deleterious

consists of most of the random coil 44.74% followed by α -helix and B-turns as shown in Table 2.

Generation of 3D Structure

The best model generated by Swiss-Model with the highest scoring was selected for further analysis. The generated 3D structure is given below in Fig. 3. The predicted 3D structure was further validated, and the Ramachandran assessment predicted the validation score of the predicted protein model. The Ramachandran favoured regions were observed to be 92.6% that possess the protein model as stable and having good quality. Therefore, the model was valid enough to be used for various kind of bioinformatic analysis.

Site Directed Mutagenesis

The FASTA sequence of the Mercuric Reductase protein was analyzed by aligning it with the sequences of other species. The local alignment was performed by BlastP tool by NCBI, and the alignments tab accessed all the present mutations. Top 10 mutations were select-

ed, and their effects were studied by I-Mutant, MuPro, PHD-SNP and SIFT tolls. The mutants having negative effects on the structure and function of protein were further selected for the mutagenesis into the actual structure of protein so the effects could be accessed. The selected SNPs are given below in Table 3.

SNPs with negative effects were selected and using the PyMol mutagenesis was introduced into the protein structure. The mutated structure of the Mercuric Reductase protein is given below in Fig. 4. It was further utilized for interaction studies to analyze the effects of the mutated structure of protein.

Docking Studies

Interaction Analysis

Autodock Vina was used to perform molecular docking between the chosen mercuric compound and the target protein. The docked model which was selected based on the lowest binding energy retained the binding energy of -7.9 kcal/mol, predicting the more efficient binding



Figure 4. Mutated protein structure with the highlighted mutant areas.



Figure 5. A docked complex of Bis[tris(p-dimethylaminophenyl)phosphine]mercuric chloride complex with targeted protein

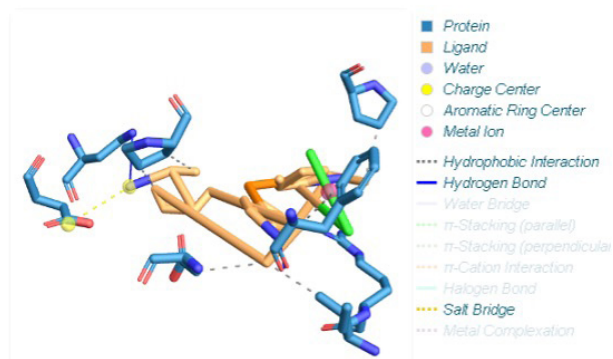


Figure 6. Interaction complex of the Mercuric reductase with Mercury compound.

with the protein. The docked Complex of Bis[tris(p-dimethylaminophenyl) phosphine] mercuric chloride complex compound with targeted protein is shown in Fig. 5.

Validation of docked complex:

Protein-ligand interaction profiler (PLIP) provided interpretation of the interaction data by estimating the bond length. As the range of hydrogen bond is between 2.7-3.3 angstroms, the three hydrogen bonds detected as 2.73, 3.19, 2.91 angstroms. Due to the slightly greater distance of bond length of van der Waals forces (3.3-4.0 angstroms) it was predicted that two van der Waals or hydrophobic bonds were present, with a length of 3.69 and 3.54 angstroms, respectively. The interaction predicted by PLIP (Protein-ligand interaction profiler) is shown in Fig. 6.

Prediction of binding sites

The analysis of active sites was performed by using CASTp online tool. This tool analyzes the proteins surface topography and measures the available surface area of the protein as a potential active site. The 3D model highlights the active sites as seen in Fig. 7.

Interaction Studies of the Mutated Mercuric Reductase

Autodock Vina was utilized to produce a mutant protein docked complex, among which the best one was chosen to make a docking complex with the maximum binding affinity of -6.6. After this, a visualizer is used to study the interactions among the ligand (*S-Mercuric-N-dansylcysteine*) and the protein (Studio, 2008). For exam-

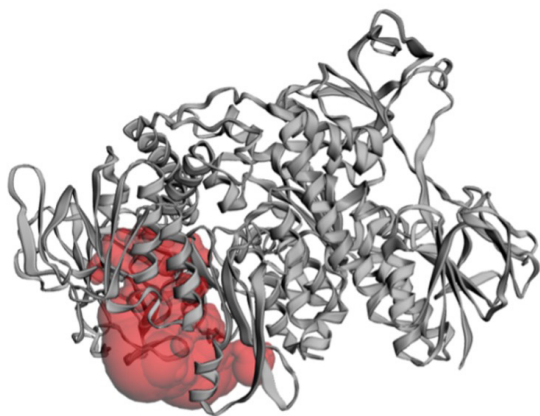


Figure 7. The 3-D structure and its active site. The red area depicts the active site, while the grey area depicts the rest of the structure as represented in cartoon style.

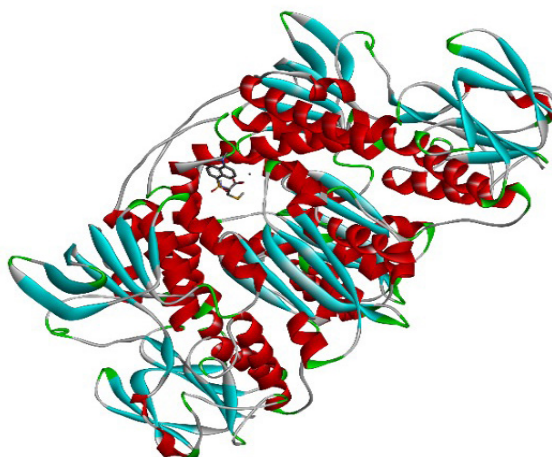


Figure 8. The docked complex of S-Mercuric-N-dansylcysteine with the targeted mutant protein.

ple; hydrogen bonds, hydrophobicity, aromaticity, charge distribution and ionizability etc., which confirmed the stability of the complex as shown in Fig. 8.

Validation of mutated docked complex:

Protein-ligand interaction profiler (PLIP) was used for the further interpretation of the interaction between the mutant protein and the ligand by measuring the bond length. According to the range, two hydrogen bonds were detected with bond length of 2.53 and 2.48 angstroms between the protein and the ligand, respectively. Moreover, one van der Waals force was detected between them with value falling in between the range; 3.99 angstroms. The interaction predicted by PLIP (Protein-ligand interaction profiler) is shown in Fig. 9.

DISCUSSION

Mercury toxicity (Hg) mainly depends on the route of exposure and the chemical form of Hg. Its most toxic form is Hg^{+2} and its non-toxic form is Hg^0 . Its accumulation in the food chain causes deleterious effects on human health (Gworek *et al.*, 2020). Lohren *et al.*, revealed the toxic effect of Hg accumulation on the central nervous system that harms the blood-brain barrier and facilitates the entrance of other toxicants to penetrate into

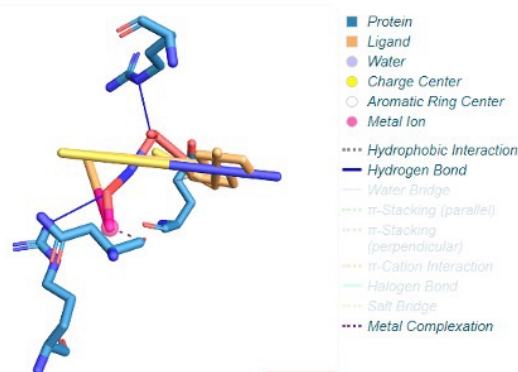


Figure 9. Interaction complex of the mutated Mercuric reductase with Mercury compound

the brain (Gworek *et al.*, 2020; Al-Ansari, 2022; Singh & Kumar, 2020).

Nowadays, the prime focus of different industries is to abolish the effect of Hg toxicity by remediation of Hg-polluted soil or water. Bacteria harbor an extensively studied Hg-detoxification mechanism, Mer operon which encodes the functional proteins for transportation (*merT*, *merP* and/or *merC*, *merF*), lysis of organomercurial compounds (*merB*), reduction of mercuric ion reductase (*merA*) and a secondary regulatory protein (*merD*) to modify toxic Hg (II) to nontoxic elemental state Hg (0) (Paria *et al.*, 2022; Nivetha *et al.*, 2023). Structural studies determined a unique fold of protein, *MerB*, which is a significant conformational transformation that occurred on the binding of the substrates as organomercurial compounds. Structural as well as computational studies revealed that aspartic acid and two cysteine residues in the active site are responsible for cleaving the carbon–mercury bond. The second enzyme, mercuric reductase (*MerA*) encoded by the *merA* gene is directly involved in the reduction of the reactive ionic form Hg (II) to the volatile form Hg (0) (Rahayu *et al.*, 2021; Somayaji *et al.*, 2022). *MerT*, a membrane-bound protein is responsible for the uptake of Hg (II) and is arranged on the *mer* operon under the control of *MerR*, a unique responsive regulator of metal. Silver and Hobman *et al.*, reveal the mercury reduction process by mercury reductase (Naguib *et al.*, 2019). The binding of Hg^{+2} to the carboxyl-terminal subunit part of Cys 557–Cys 558 of mercury reductase then quickly move towards the thiol–thiol exchange to the monomer pair of Cys 135–Cys 140. The Cys 135–Cys 140 pair is the active site that causes the reduction of Hg^{+2} into Hg^0 by the FAD cofactor that helps in the electron transport (Meyer *et al.*, 2023).

Conventional methods such as bioreactors have been used for the mercury cleanup of wastewater by up to 90%. Mercury-resistant bacteria have a major advantage as conventional practices produce a large amount of mercury load biomass (Duan *et al.*, 2020). A recent study on a non-pathogenic bacterial isolate of *Pseudomonas putida* SP-1, which volatilizes mercury by 89%, has shown the efficiency of mercury-resistant bacteria in the bioremediation process. However, case studies act as a bridge to some extent to fill the gap between field application and laboratory research. In-silico studies identify the efficacy and potential of mercury-resistant bacteria in the bioremediation of mercury toxication. The current study shows that mercury reductase is the best candidate as a bio-remediator and mercury accumulator (Gupta *et al.*, 2022; Priyadarshane *et al.*, 2022).

In a recent study, the screening of the mercury reductase calcium complex compound that results in highly competent attachment to the target protein of mercury reductase isolated from the bacteria source was done through computational analysis. Protein stability depends on the instability index. The instability index of the protein was less than 40 as shown in Table 1. Our results are consistent with the statement given by Mirzaei *et al.* where protein having a stability index of less than 40 is stable and when greater than 40 shows that protein may be unstable (Gamage *et al.*, 2019). The aliphatic index was predicted to be where a higher value of the aliphatic index shows the thermal stability of the protein. This is in line with the statement given by Sahay *et al.*, that the aliphatic index is considered a positive factor for the increase of thermostability of globular proteins. The GRAVY score was found to be positive with a 0.092 value, which indicated that mercury reductase is generally a hydrophobic protein. The reason for hydro-

phobicity may be due to the presence of large numbers of non-polar amino acids. Another study conducted by Zhou and Pang supported our results by showing that protein folding stability was mainly attributed to the hydrophobic interactions among non-polar amino acid residues. Thus, based on a few parameters of the ExPASy ProtParam, the mercury reductase could be considered a stable protein (Sharma *et al.*, 2022; Naveed *et al.*, 2022).

The mutational analysis revealed that it affects the binding sites of mercury reductase protein. The mutations identified from five tools as shown in Table 3. Docking studies have been found helpful to understand the protein–ligand interactions (Eberhardt *et al.*, 2021). The model was then generated and docking analysis of both the non-mutated protein and mutant protein shows that binding affinity energy reduces from -7.9 to 6.6 KJ/mol. The 3D structure of the mutant model generated from SWISS-MODEL shows the removal of two ligands of FAD (Flavin Adenine Dinucleotide) that were present in the non-mutated protein. As mutation T240A was introduced it acts as an active binding site as shown in the active site prediction Figure 7. The binding sites and motifs for NADPH and FAD in different *MerA* proteins vary among residues ALA, CYS, TYR, LEU, THR, PRO, SER, ASN, VAL, GLY, ALA, ASP, LYS, PHE, GLU and ARG. As the distance among binding residues of FAD and NADPH varies in microorganisms, no such correlation was observed between the protein–ligand binding affinity and binding residues (Chandran *et al.*, 2022). As a result of folding into a specific three-dimensional structure, the amino acids undergo conformational changes to perform the function they are designed to perform. Thus, the binding affinity of mutant protein reduces due to the conformational change of amino acid residues and binding active sites (Afroz *et al.*, 2023).

Engineered proteins, particularly enzymes, are being used more frequently in various industries due to their selective ligand binding, capabilities and catalytic ability as food additives. The urge to engineer or generate proteins with higher specificity, activity and stability has increased along with the number of possible applications for engineered proteins (Gupta *et al.*, 2022). As the application of protein technology develops, exploiting the potential advantages of modulating remote regions will become imperative. The present study reveals that the mutation affects the binding pockets of mercury reductase, and it acts as a mercury accumulator and candidate for bioremediation of mercury in the field of application. It is a stable protein with an applicable Ramachandran plot which validates its stability, and virulent predictions show that it is non-virulent and causes no toxicity. Protein engineering bacterial mercury reductases can produce enzymes that reduce mercury more efficiently with no toxicity, and that will function with additional contaminants (Wan *et al.*, 2020; Meyer *et al.*, 2023).

CONCLUSIONS

In conclusion, this study provides insights into the molecular and structural features of mercuric reductase. The results suggest that the protein has a stable structure and a specific function of reducing mercury. The information obtained from this study could be useful in developing strategies to bioremediate mercury-contaminated sites. Additionally, the methodology used in this study, such as homology modeling, molecular docking, and virulence factor prediction, could be applied to other proteins and enzymes to further understand their

properties and functions. Overall, this study contributes to our understanding of the biochemical and molecular mechanisms involved in the bioremediation of mercury pollution in the environment.

Declarations

Author Contributions. Conceptualization, M.A., M.N., R.N., A.S. and T.A.; methodology, M.A., M.N., R.N., A.S. and T.A.; software, M.A.; validation, A.A.S.; formal analysis, T.U.; investigation, M.A., M.N., S.R., N.U. resources, M.A. and A.A.S.; data curation, T.A.; writing—original draft preparation, T.A. and M.N.; writing—review and editing, M.A., M.N., R.N., A.S.; visualization, F.A., N.U.; supervision, T.A. and A.A.K.; project administration, A.A.S. and M.A.; funding acquisition, T.A.

Conflicts of Interest. The authors declare no conflict of interest.

REFERENCES

- Afroz L, Khan MHM, Vagdevi HM, Pari M, Shafeeulla RM, Fathima A (2023) Transition metal chelates of novel ligand bearing Isatin moiety: Synthesis, Structural characterization, Voltammetric analysis of heavy metals, Molecular docking and Biological evaluation. *J Mol Struct* **1293**: 136200. <https://doi.org/10.1016/j.molstruc.2023.136200>
- Al-Ansari MM (2022) Biodegradation of mercury by using a marine bacterium *Marinomonas* sp. RS3 and its merA gene expression under mercury stress. *Environ Res* **205**: 112452. <https://doi.org/10.1016/j.envres.2021.112452>
- Bekker G, Yokochi M, Suzuki H, Ikegawa Y, Iwata T, Kudou T, Yura K, Fujiwara T, Kawabata T, Kurisu G (2022) Protein Data Bank Japan: Celebrating our 20th anniversary during a global pandemic as the Asian hub of three dimensional macromolecular structural data. *Protein Sci* **31**: 173–186. <https://doi.org/10.1002/pro.4211>
- Bianchi V, Gherardini PF, Helmer-Citterich M, Ausiello G (2012) Identification of binding pockets in protein structures using a knowledge-based potential derived from local structural similarities. *BMC Bioinformatics* **13**: S17. <https://doi.org/10.1186/1471-2105-13-S4-S17>
- Blum M, Chang HY, Chuguransky S, Grego T, Kandasamy S, Mitchell A, Nuka G, Paysan-Lafosse T, Qureshi M, Raj S, Richardson L, Salazar GA, Williams L, Bork P, Bridge A, Gough J, Haft DH, Letunic I, Marchler-Bauer A, Mi H, Natale DA, Necci M, Orengo CA, Pandurangan AP, Rivoire C, Sigrist CJA, Sillitoe I, Thanki N, Thomas PD, Tosatto SCE, Wu CH, Bateman A, Finn RD (2021) The InterPro protein families and domains database: 20 years on. *Nucleic Acids Res* **49**: D344–D354. <https://doi.org/10.1093/nar/gkaa977>
- Buchan DWA, Jones DT (2019) The PSIPRED Protein Analysis Workbench: 20 years on. *Nucleic Acids Res* **47**: W402–W407. <https://doi.org/10.1093/nar/gkz297>
- Budnik LT, Casteleyn L (2019) Mercury pollution in modern times and its socio-medical consequences. *Sci Total Environ* **654**: 720–734. <https://doi.org/10.1016/j.scitotenv.2018.10.408>
- Chandran K, Shane DI, Zochedh A, Sultan AB, Kathiresan T (2022) Docking simulation and ADMET prediction based investigation on the phytochemical constituents of Noni (*Morinda citrifolia*) fruit as a potential anticancer drug. *In Silico Pharmacol* **10**: 14. <https://doi.org/10.1007/s40203-022-00130-4>
- Duan P, Khan S, Ali N, Shereen MA, Siddique R, Ali B, Iqbal HMN, Nabi G, Sajjad W, Bilal M (2020) Biotransformation fate and sustainable mitigation of a potentially toxic element of mercury from environmental matrices. *Arabian J Chem* **13**: 6949–6965. <https://doi.org/10.1016/j.arabjc.2020.06.041>
- Eberhardt J, Santos-Martins D, Tillack AF, Forli S (2021) AutoDock Vina 1.2.0: New docking methods, expanded force field, and python bindings. *J Chem Inf Model* **61**: 3891–3898. <https://doi.org/10.1021/acs.jcim.1c00203>
- Garage DG, Gunaratne A, Periyannan GR, Russell TG (2019) Applicability of instability index for *in vitro* protein stability prediction. *Protein Pept Lett* **26**: 339–347. <https://doi.org/10.2174/092986652666190228144219>
- Gupta N, Sundar RD V., Arunachalam S (2022) A review on the genetically engineered microbes for bioremediation of THMs namely Hg and Cr. *ECIS Trans* **107**: 11509–11531. <https://doi.org/10.1149/10701.11509ecst>
- Gworek B, Dmuchowski W, Baczewska-Dąbrowska AH (2020) Mercury in the terrestrial environment: a review. *Environ Sci Eur* **32**: 128. <https://doi.org/10.1186/s12302-020-00401-x>
- Komari N, Hadi S, Suhartono E (2020) Pemodelan protein dengan homology modeling menggunakan SWISS-MODEL. *Jurnal Jejaring Matematika dan Sains* **2**: 65–70. <https://doi.org/10.36873/jjms.2020.v2.i2.408>
- Mandal G, Mishra S (2023) A review on emerging micro and nanoplastic pollutants, heavy metals and their remediation techniques. *Nanofabrication* **8**: <https://doi.org/10.37819/nanofab.008.302>
- Meyer L, Guyot S, Chalot M, Capelli N (2023) The potential of micro-organisms as biomonitoring and bioremediation tools for mercury-contaminated soils. *Ecotoxicol Environ Saf* **262**: 115185. <https://doi.org/10.1016/j.ecoenv.2023.115185>
- Mistry J, Chuguransky S, Williams L, Qureshi M, Salazar GA, Sonnhammer ELL, Tosatto SCE, Paladin L, Raj S, Richardson LJ, Finn RD, Bateman A (2021) Pfam: The protein families database in 2021. *Nucleic Acids Res* **49**: D412–D419. <https://doi.org/10.1093/nar/gkaa913>
- Mohamadi A, Cheng T, Jin L, Wang J, Sun H, Koohi-Moghadam M (2022) An ensemble 3D deep-learning model to predict protein metal-binding site. *Cell Rep Phys Sci* **3**: 101046. <https://doi.org/10.1016/j.xcrp.2022.101046>
- Mustafa HA, Albkray AMS, AbdAlla BM, Khair MAM, Abdelwahid N, Elnasri HA (2020) Computational determination of human PPAR γ gene: SNPs and prediction of their effect on protein functions of diabetic patients. *Clin Transl Med* **9**: <https://doi.org/10.1186/s40169-020-0258-1>
- Naguib MM, Khairalla AS, El-Gendy AO, Elkhatib WF (2019) Isolation and characterization of mercury-resistant bacteria from wastewater sources in Egypt. *Can J Microbiol* **65**: 308–321. <https://doi.org/10.1139/cjm-2018-0379>
- Naveed M, Tehreem S, Mehboob MZ (2019) In-Silico analysis of missense SNPs in Human HPPD gene associated with Tyrosinemia type III and Hawkinsinuria. *Comput Biol Chem* **80**: 284–291. <https://doi.org/10.1016/j.compbiolchem.2019.04.007>
- Naveed M, Shabbir MA, Ain N, Javed K, Mahmood S, Aziz T, Khan AA, Nabi G, Shahzad M, Alharbi ME, Alharbi M, Alshammari A (2022) Chain-engineering-based *de novo* drug design against MPXVp169 virulent protein of monkeypox virus: a molecular modification approach. *Bioengineering* **10**: 11. <https://doi.org/10.3390/bioengineering10010011>
- Nivetha N, Srivarshini B, Sowmya B, Rajendiran M, Saravanan P, Rajeshkannan R, Rajasimman M, Pham THT, Shanmugam V, Rajogei E-N (2023) A comprehensive review on bio-stimulation and bio-enhancement towards remediation of heavy metals degradation. *Chemosphere* **312**: 137099. <https://doi.org/10.1016/j.chemosphere.2022.137099>
- Naveed M, Ali I, Aziz T, Ain N, Shabbir M, Javed K, Alharbi M, Alshammari A, Alasmari A, Alharbi S (2023). Halogens engineering-based design of agonists for boosting expression of frataxin protein in Friedreich's ataxia. *Eur Rev Med Pharmacol Sci* **27**: 6972–6984. https://doi.org/10.26355/eurev.202308_33269
- Naveed M, Ain N, Aziz T, Ali I, Shabbir M, Javed K, Alharbi M, Alshammari A, Alasmari A (2023). Revolutionizing treatment for toxic shock syndrome with engineered super chromones to combat antibiotic-resistant *Staphylococcus aureus*. *Eur Rev Med Pharmacol Sci* **27**: https://doi.org/10.26355/eurev.202306_32649
- Naveed M, Ain N, Aziz T, Shabbir M, Saleem A, Zafar A, Ghulam N, Alharbi M, Alshammari A, Alasmari A (2023). Side chain inset of neurogenerative amino acids to metalloproteins: a therapeutic signature for huntingtin protein in Huntington's disease. *Eur Rev Med Pharmacol Sci* **27**: 6831–6842. https://doi.org/10.26355/eurev.202307_33154
- Naveed M, Ali U, Aziz T, Rasool MJ, Ijaz A, Alharbi M, Alharbi ME, Alshammari A, Alasmari AF (2023) A reverse vaccinology approach to design an mRNA-based vaccine to provoke a robust immune response against HIV-1. *Acta Biochim Pol* **70**: 407–418. https://doi.org/10.18388/abp.2020_6696
- Paria K, Pyne S, Chakraborty SK (2022) Optimization of heavy metal (lead) remedial activities of fungi *Aspergillus penicillioideus* (F12) through extra cellular polymeric substances. *Chemosphere* **286**: 131874. <https://doi.org/10.1016/j.chemosphere.2021.131874>
- Pasaribu SA, Basyuni M, Purba E, Hasanah Y (2021) The estimated of 18.1 kDa class IV small heat shock protein (sHsp) from *Heredia brasiliensis* using of PHYRE2 and SWISS-MODEL software. *IOP Conf Ser Earth Environ Sci* **713**: 012016. <https://doi.org/10.1088/1755-1315/713/1/012016>
- Priyadarshane M, Chatterjee S, Rath S, Dash HR, Das S (2022) Cellular and genetic mechanism of bacterial mercury resistance and their role in biogeochemistry and bioremediation. *J Hazard Mater* **423**: 126985. <https://doi.org/10.1016/j.jhazmat.2021.126985>
- Rahayu HM, Putri WA, Khasanah AU, Sembiring L, Purwestri YA (2021) Indigenous *Streptomyces* spp. isolated from *Cyperus rotundus* rhizosphere indicate high mercuric reductase activity as a potential bioremediation agent. *Biodiversitas* **22**: <https://doi.org/10.13057/biodiv/d220357>
- Reddy PP, Rao UM V (2020) Homology modeling and validation of bacterial superoxide dismutase enzyme, an antioxidant. *Res*

- J Pharm Technol* **13**: 6202–6205. <https://doi.org/10.5958/0974-360X.2020.01081.1>
- Sharma P, Mondal K, Mondal KC, Thakur N (2022) Hunt for α -amylase from metagenome and strategies to improve its thermostability: a systematic review. *World J Microbiol Biotechnol* **38**: 203. <https://doi.org/10.1007/s11274-022-03396-0>
- Singh S, Kumar V (2020) Mercury detoxification by absorption, mercuric ion reductase, and exopolysaccharides: a comprehensive study. *Environ Sci Pollut Res* **27**: 27181–27201. <https://doi.org/10.1007/s11356-019-04974-w>
- Sodhi KK, Kumar M, Agrawal PK, Singh DK (2019) Perspectives on arsenic toxicity, carcinogenicity and its systemic remediation strategies. *Environ Technol Innov* **16**: 100462. <https://doi.org/10.1016/j.eti.2019.100462>
- Somayaji A, Dhanjal CR, Lingamsetty R, Vinayagam R, Selvaraj R, Varadavenkatesan T, Govarthanan M (2022) An insight into the mechanisms of homeostasis in extremophiles. *Microbiol Res* **263**: 127115. <https://doi.org/10.1016/j.micres.2022.127115>
- Wan X, Lei M, Chen T (2020) Review on remediation technologies for arsenic-contaminated soil. *Front Environ Sci Eng* **14**: 24. <https://doi.org/10.1007/s11783-019-1203-7>
- Xu H, Jia Y, Sun Z, Su J, Liu QS, Zhou Q, Jiang G (2022) Environmental pollution, a hidden culprit for health issues. *Eco-Environment Health* **1**: 31–45. <https://doi.org/10.1016/j.eehl.2022.04.003>
- Zheng R, Wu S, Ma N, Sun C (2018) Genetic and physiological adaptations of marine bacterium *Pseudomonas stutzeri* 273 to Mercury stress. *Front Microbiol* **9**: <https://doi.org/10.3389/fmicb.2018.00682>
- Studio, D. (2008). Discovery studio. *Accelrys* [2.1].

Isolation and characterization of indigenous bacterial assemblage for biodegradation of persistent herbicides in the soil

Mariam Zameer¹, Usaal Tahir¹, Sana Khalid², Nureen Zahra¹, Abid Sarwar³, Ahsan Saidal⁴, Tariq Aziz⁴✉, Majid Alhomrani⁵, Abdulhakeem S. Alamri⁵, Anas S. Dablood⁶, Manal Y. Sameeh⁷, Amal A. Mohamed⁷ and Amnah A. Alharbi⁸

¹Institute of Molecular Biology and Biotechnology, The University of Lahore, 54000, Punjab Pakistan; ²College of Earth and Environmental Sciences, University of the Punjab, Lahore, 54000, Punjab Pakistan; ³Food and Biotechnology Research Center, PCSIR Labs Complex Lahore 54600, Punjab Pakistan; ⁴Institute of Basic Medical Sciences Khyber Medical University Peshawar 25120, Pakistan; ⁵Department of Clinical Laboratory Sciences, The Faculty of Applied Medical Sciences, Taif University, Taif, Saudi Arabia; ⁶Department of Public Health, Health Sciences College Al-Leith, Umm Al-Qura University, Makkah, Saudi Arabia, 24382, Saudi Arabia; ⁷Chemistry Department, Al-Leith University College, Umm Al-Qura University, Makkah 24831, Saudi Arabia; ⁸Department of Biochemistry, Faculty of Science, University of Tabuk, Tabuk 71491, Saudi Arabia

Abstract: Extensive pesticides (herbicides) use is negatively disturbing the environment and humans. Pesticide bioremediation with eco-friendly techniques bears prime importance. This study aimed to isolate and characterize three different herbicides (metribuzin, clodinafop-propargyl, MCPA (2-methyl, 4 chlorophenoxyacetic acids) and Bromoxynil) degrading bacterial strains from agricultural fields of Punjab University, Pakistan. Among the 12 bacterial isolates, 5 were metribuzin degrading, 3 were clodinafop propargyl degrading and, 4 were MCPA and Bromoxynil degrading bacteria. Morphological, microscopic, and molecular characterization revealed that the majority of these bacterial strains were gram-negative and belonged to *Bacillus* and *Pseudomonas* genera. The isolates A6, B3, and C1 were subjected to respective herbicide degradation and the data was confirmed through GC-MS analysis. The effect of herbicide concentrations, pH, and temperature on bacterial growth was determined at OD₆₀₀. The strain A6 degraded 14.8% metribuzin out of the provided concentration of 50 ppm by following the deamination pathway. While the isolates B3 and C1 degraded 23.2% and 33.9% clodinafop, MCPA and bromoxynil, respectively, at a spiking concentration of 50ppm. The clodinafop, MCPA & Bromoxynil were metabolized into less toxic products i.e., dicarboxylic acids and 2-methyl phenol respectively, and metabolized via decarboxylation and dehalogenation mechanism. The present study evaluates the herbicides degrading bacterial strains that could potentially be used for bioremediation of agricultural contaminated sites.

Keywords: *Bacillus*, Bioremediation, GC-MS analysis, herbicides, *Pseudomonas*

Received: 28 November, 2022; **revised:** 01 February, 2023; **accepted:** 28 February, 2023; **available on-line:** 31 May, 2023

✉e-mail: iwockd@gmail.com

Acknowledgements of Financia Support: The researchers would like to acknowledge Deanship of Scientific Research, Taif University for funding this work.

Abbreviations: GCMS, Gas Chromatography Mass Spectrometry, MCPA, 2-methyl, 4 chlorophenoxyacetic acids

INTRODUCTION

Different varieties of chemicals used to repel or destroy pests including animals, insects, plants, bacteria, fungi, or other microbes; that are harmful to cultivated crops and animals are known as Pesticides (Alam *et al.*, 2018; Nawab *et al.*, 2015). They are classified according to their chemical formulation and targeted organism, but the latter is more common. Based on target organisms, these are grouped as insecticide, weedicide and fungicide, rodenticide, bactericide, etc. (Richardson *et al.*, 2019).

Pakistan is an agricultural country, and its economy greatly depends upon this sector in terms of labor participation; provision of food to the whole nation, and a primary source of foreign exchange earnings (Khan *et al.*, 2021). The share of agriculture in Gross Domestic Product (GDP) is 19.3% for the FY2020 and it is gradually shrinking in the last few decades. Different challenges like global warming, insect/pest attack, and water shortage hinder the overall potential of this sector (GOP 2020; Koondhar *et al.*, 2021). Weeds are unwanted plants that are not grown intentionally at a place and negatively impede human activities. Almost, there are 250 000 species of plants in the world; out of which approximately 8000 species i.e., 3% are considered weeds. Weeds are problematic because of their rapid growth, long-term survival, and competition with normal plant growth for sunlight, air, water, space, and soil minerals (Storkey *et al.*, 2021).

To control the growth of weeds the most extensively used form of pesticide is herbicide. Herbicides are a chemical used to eradicate or kill unwanted vegetation (weeds) that interferes with normal plant growth and restrain the overall yield of several crops (Clapp 2021; Okieimen *et al.*, 2020). Although the global use of pesticides ensures high production yield, on the other hand, it also produces high levels of environmental contamination because of their excessive use (Bakshi *et al.*, 2020). These deadly pollutants are directly exposing the trophic food web and enter into the ecosystem either by direct application, spillage, and disposal (Khan *et al.*, 2020; Lone *et al.*, 2014).

Physicochemical methods are mostly used as an alternative to chemical pesticides, which are costly because these techniques require the excavation of polluted soil

from the site of contamination and transferring it to another place for treatment. As pesticides can accumulate in food and water supplies, it is need of the time to design environmentally friendly and cost-effective technologies to replace hazardous pesticides.

Enormous biological techniques have been designed in which toxic organic pollutants are degraded by microbes (Bakshi *et al.*, 2020; Oladipo *et al.*, 2020). Bioremediation is one such technique in which naturally occurring microbes such as bacteria and fungi are used for the breakdown and removal of pollutants (Huang *et al.*, 2018). This method is relatively cheaper in comparison to physicochemical methods. Without excavating the material from the contaminated site, they have the potential to treat the polluted soil and groundwater because of this reason it requires very less energy input and preserves the soil structure which otherwise can either be disturbed by excavation (Pertile *et al.*, 2020). The present study is to focus on environment-friendly techniques for the minimization and elimination of persistent herbicide levels via biodegradation by using locally isolated bacterial strains.

MATERIALS AND METHODS

Soil Sampling

Total 9 soil samples were randomly collected at the depth of 0–12 inches from wheat fields of Punjab University located near the fishponds; where the soil had a previous history of clodinafop and MCPA & Bromoxynil applications but had never been treated with metribuzin over the last few years. The samples were taken to the laboratory, air dried at room temperature, sieved through 2 mm mesh size to remove stones and debris, and mixed thoroughly to make a composite soil sample and stored at 4°C.

Isolation and Screening of Bacterial Isolates

Four grams of soil samples were placed in 250 mL Erlenmeyer flasks containing 100 mL of mineral salt medium (Glucose 5, KH_2PO_4 0.5, K_2HPO_4 0.5, $\text{MgSO}_4 \cdot 7\text{H}_2\text{O}$ 0.2, NaCl 0.2 g/L). The stock solutions of three herbicides (metribuzin, clodinafop, and MCPA & Bromoxynil) were prepared in distilled water. Then, 100 μL of each respective herbicide stock solution providing the final concentration of 5 ppm was inoculated into the above sample medium. The samples were incubated for one week in the dark at 30°C and 160 rpm shaking. Afterwards, 10 mL of each culture medium was transferred into 90 mL of fresh mineral salt medium fortified with each of the herbicides at 10, 20, and 50 ppm by adding 200 μL , 400 μL and 1 mL of each herbicide stock solution, respectively. The samples were again incubated for 7 days at 30°C at 160 rpm in dark. After 7 days, 200 μL from each subculture was spread on L.B plates fortified with each respective herbicide at a concentration of 20 ppm. The plates were incubated for 4 days at 30°C and different bacterial colonies were observed after 4 days.

Purification of Bacterial Colonies

Morphologically different bacterial colonies were picked and streaked on L.B plates aseptically and incubated at 30°C for 24 hours to obtain pure bacterial colonies. The purified colonies were maintained on L.B slants and stored at 40°C for further use.

Identification of Bacterial Isolates

The isolated bacterial strains were identified by performing morphological analysis, gram staining technique, and 16S rRNA gene sequencing analysis.

Morphological analysis

Bacterial isolates were morphologically analyzed based on color, shape, texture, and size. Morphological analysis was carried out visually.

Gram staining

Bacterial isolates were analyzed microscopically by gram staining technique and their cell shape, size, and arrangement were determined.

Molecular identification of herbicides degrading bacterial strains

Extraction of bacterial genomic DNA. Almost 2–3 bacterial colonies from freshly grown cultures were scratched and mixed well in DNase or RNase-free water or elution buffer in sterilized Eppendorf tubes. Thermo Fisher Scientific catalogue no AM9923. The bacterial suspension was provided heat shock in boiling water for about 10 min. The tubes were then ice-cooled and centrifuged at 12000 rpm for 10 minutes. The supernatant containing the template DNA was taken carefully; its quality was observed by electrophoresis on a 1% agarose gel at 100 V and visualized under a UV-light illuminator. (Daihan Scientific Model no. Wuv-L50).

Amplification of 16S rRNA Gene and Sequencing reaction. 1.5 kb DNA fragment of 16S rRNA gene was amplified using the following set of ribotyping universal primers: forward primer 27F (5'-AGAGTTT-GATCCTGGCTCAG-3') and reverse primer 1522R (5'-AAGGAGGTGATCCA(AG)CCGCA-3') (Hasnain *et al.*, 1994; Johnson *et al.*, 1994). Reaction was carried out in 20 μL containing template DNA 5 μL , 10XPCR buffer 2 μL , 25 mM MgCl_2 2 μL , 2.5 mM dNT-Ps 2 μL , Primer-forward 2 μL , Primer-reverse 2 μL , 5 units/ μL 1 μL and ddH₂O (nuclease free) 4 μL . The template DNA was initially denatured at 94°C for 5 minutes followed by 35 cycles of denaturation at 94°C for 30 seconds, annealing of primers at 54°C for 30 seconds, and elongation at 72°C for 1 minute and 40 seconds. The PCR reaction was finally extended for 10 minutes at 72°C. The PCR was then separated on 1% agarose gel observed under a UV light illuminator. Required DNA bands were precisely cut with a sterilized surgical blade and purified from gel and sent to Korea for sequencing analysis. The sequencing analysis was performed by the dideoxy chain termination method (Sanger *et al.*, 1977).

Biodegradation of Herbicides by Soil Bacteria

Preparation of samples for GC-MS

L.B. broth (250 mL) was taken in each 1 liter flask and amended with each of the herbicide 50 ppm by adding 2 mL of each respective herbicide stock solution. The herbicides (metribuzin, clodinafop, and Bromoxynil+MCPA) fortified media were then inoculated with bacterial isolates A6, B3, and C1, respectively, aseptically and incubated for 4 days at 30°C and 160 rpm in dark. The controls contained the same herbicide concentration without bacterial culture. After 4 days, 50 mL of each sample was transferred in sterilized 50 mL falcon tubes. Samples were centrifuged at 12000 rpm for 10 minutes. The respective supernatants were collected carefully, transferred into new sterile falcon

tubes, labeled, and underwent the liquid-liquid extraction technique. For this 50 mL of each sample was placed in a glass separating funnel with equal volume (50 mL) of dichloromethane. The samples with dichloromethane were vortexed well to thoroughly mix both solvents and allowed for separation until the two distinct layers were formed. The components moved from the media phase to the dichloromethane layer. The upper layer consisting of the medium was discarded and the lower dichloromethane layer containing the components was collected from each sample carefully without any mixing with the above layer. Dichloromethane was evaporated and the final volume of each sample was adjusted with n-hexane. Final samples were then transferred in screw cap glass sterile vials and stored at 40°C until preceded for gas chromatography-mass spectrometry (GC-MS) analysis. Statistical analysis was performed to determine Pearson's correlation test between herbicide response factors and the peak areas of herbicide residues in the sample by using SPSS 16.0.

Effect of different parameters on herbicides degradation and bacterial growth

Effect of herbicides concentrations on herbicides degradation. L.B. broth (50 mL) was taken in each of the 250 mL flasks amended with different concentrations (20, 50, 80, and 100 ppm) of each of the three herbicides and inoculated with respective bacterial isolates A6, B3, and C1 under aseptic conditions. The flasks were incubated at 300°C and 160 rpm in a shaker incubator. After every 24, 48, 72, and 96 hours, the OD₆₀₀ of each treatment was measured with a mass spectrophotometer and biodegradation in terms of bacterial growth (OD₆₀₀) was noted. It is recommended to monitor the bacterial growth at 600 nm.

Effect of pH on herbicides degradation. L.B. broth (50 mL) was taken in each of the 250 mL flasks with pH values maintained at 5.0, 6.0, 7.0, and 8.0 and fortified with herbicides at a concentration of 20 ppm. The media were inoculated with respective isolates A6, B3, and C1 and incubated in dark at 300°C and 160 rpm in a shaker incubator. The OD₆₀₀ was measured every 24, 48, 72, and 96 hours with a mass spectrophotometer.

Effect of temperature on herbicides degradation. L.B. broth (50 mL) was taken in each of 250 mL Erlenmeyer flasks with each of the three herbicides at a concentration of 20 ppm and inoculated with respective bacterial isolates. These culture media were incubated at different temperatures i.e., 30, 35, and 400°C and 160 rpm in a shaker incubator. The OD₆₀₀ was measured every 24, 48, 72, and 96 hours and the biodegradation in terms of bacterial growth (OD₆₀₀) was noted.

Statistical Analysis

Statistical analysis was performed to determine the effect of different parameters on herbicide degradation with the help of a three-way Analysis of Variance (ANOVA) by using SPSS 16.0 (Wahla *et al.*, 2019; Paciani *et al.*, 2020).

RESULTS

Isolation and Screening of Herbicides Degrading Bacteria

Bacteria were isolated by inoculating an aliquot of soil sample into the mineral salt medium amended with three

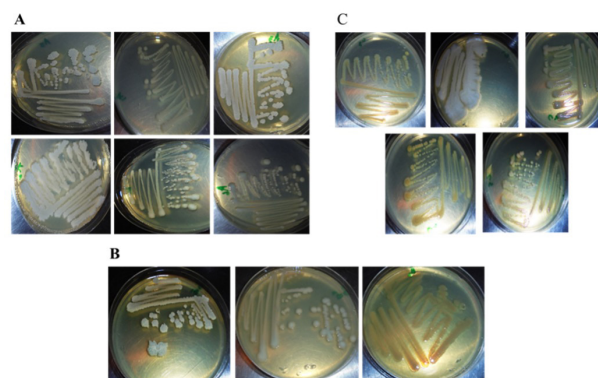


Figure 1. Morphological characteristics herbicide degrading bacteria (A, Metribuzin; B, Clodinafop; C, Bromoxynil)

different herbicides and incubated for 7 days at 30°C and 160 rpm in dark. 10mL of this cell suspension was transferred into a fresh mineral salt medium containing each of the three herbicides at 10, 20 and 50 ppm and incubated again under the same conditions as above. Morphologically different bacterial colonies were purified and stored at 4°C. A total of 14 herbicides degrading bacterial colonies were isolated from soil samples. Among these, 6 colonies (A1–A6) were found effective in degrading metribuzin; 3 colonies (B1–B3) degraded clodinafop and 5 of these bacterial colonies (C1–C6) metabolized MCPA & Bromoxynil as shown in Fig. 1 (A–C).

Identification of Herbicides Degrading Bacteria

Morphological characteristics of bacterial colonies

The morphological characters (color, shape and texture) of herbicide-degrading bacteria were observed visually. The bacterial isolates were also gram stained and their properties were observed under a light microscope.

Molecular characterization of herbicides degrading bacteria

The 16SrRNA gene of 12 herbicides degrading bacterial strains was amplified by PCR. The amplified products of the 1.5 kb fragment were purified and sequenced for further conformation (Fig. 2).

Determination of Herbicides Degradation by GC-MS Analysis

Herbicides degrading bacterial isolates were inoculated in 250 mL LB broth supplemented with 50 ppm of each herbicide to assess their biodegradation potential. Af-

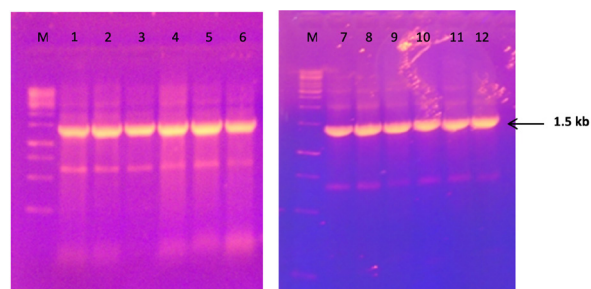


Figure 2. Amplification of 16S rRNA gene of bacterial strains. (M, DNA Marker; 10 kb 1–5 (Metribuzin degrading strains), 6–8 (Clodinafop degrading strains), 9–12, (MCPA & Bromoxynil degrading strains)

Table 1. Percentage degradation of experimental herbicides through peak areas and response factor

Sample name	Peak area of a sample	Response factor of standard	Degradation %
Metribuzin	148519263	3482815.62	14.8%
Clodinafop propargyl	5753002	149808.32	23.2%
MCPA & Bromoxynil	20651611	624497.74	33.9%

Pearson's correlation at $\alpha=0.01$ (2-tailed test) was used to identify the relationship between the response factor and % degradation for studied herbicides.

Table 2. Pearson correlations through SPSS

		Response factor	Degradation %
response factor	Pearson Correlation	1	-.748**
	Sig. (2-tailed)		.462
	N	3	3
% degradation	Pearson Correlation	-.748**	1
	Sig. (2-tailed)	.462	
	N	3	3

**Correlation is significant at the 0.01 level of significance (2-tailed)

Table 3. Variation in metribuzin concentration and optical density as a result of herbicide degradation by bacterial strain A6

Time period	Metribuzin concentration			
	20 ppm	50 ppm	80 ppm	100 ppm
Day 1	0.882	0.813	0.885	0.818
Day 2	1.804	1.78	1.77	1.705
Day 3	1.722	1.774	1.716	1.753
Day 4	1.712	1.701	1.708	1.675

Table 4. Variation in Clodinafop concentration and optical density as a result of herbicide degradation by bacterium B3

Time period	Clodinafop propargyl concentration			
	20 ppm	50 ppm	80 ppm	100 ppm
Day 1	0.405	0.447	0.491	0.147
Day 2	1.708	1.69	1.665	1.705
Day 3	1.726	1.792	1.767	1.806
Day 4	1.667	1.635	1.71	1.725

ter four days, the bacterial samples were further analyzed through gas chromatography-mass spectroscopy (GC-MS) to study possible degradative products after herbicide degradation. The results showed that metribuzin was metabolized into deaminated metribuzin by *Bacillus* sp. A6. Clodinafop propargyl, MCPA, and Bromoxynil degraded into corresponding dicarboxylic acid and 2-methyl phenol by strain C1, respectively. Pearson correlation between different herbicide response factors and the peak areas of herbicide residues in each sample was identified using SPSS 16.0 (Table 1 and 2).

Table 2 shows the resulting matrix of Pearson's correlation test which revealed that the co-efficient r is equal to -0.748 which is statistically significant at $p < 0.01$. It confirmed a strong negative correlation between the response factor and percentage degradation of all herbicides. The more the response factor; the less will be the percentage degradation.

Effect of Different Parameters on Biodegradation of Herbicide and Bacterial Growth

Effect of herbicides concentration

The herbicide biodegradation at different concentrations (20, 50, 80, and 100 ppm) was determined by measuring the optical density (OD) at 600nm (Table 3, 4, 5 and Figs 3, 4, and 5).

The metribuzin-degrading bacterium A6 showed the highest growth rate on the second and third days (48–72 h) at concentrations of 20 ppm and 50 ppm. The isolate was able to degrade metribuzin at concentrations of 20 and 50 ppm. Strain A6 showed a moderate growth pattern at (80–100 ppm) concentrations of herbicide. Whereas clodinafop degrading bacteria B3 showed almost similar growth rates at all the concentrations but the maximum clodinafop propargyl biodegradation was observed on 2nd and 3rd day with peak metabolism at the concentrations ranging from 50–100 ppm on the 3rd day. The MCPA & Bromoxynil degradation behav-

Table 5. Variation in MCPA & Bromoxynil concentration and optical density as a result of herbicide degradation by bacterial isolate C1

Time period	MCPA & Bromoxynil concentration			
	20 ppm	50 ppm	80 ppm	100 ppm
Day 1	0.902	0.81	0.757	0.842
Day 2	1.286	1.093	1.259	1.11
Day 3	1.137	1.473	1.52	1.393
Day 4	1.348	1.728	1.378	1.305

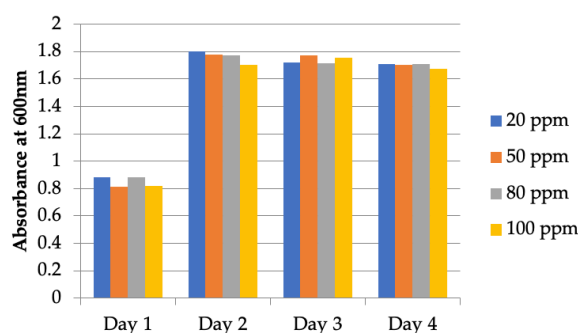


Figure 3. Growth rates of metribuzin-degrading bacteria at varying herbicide concentrations

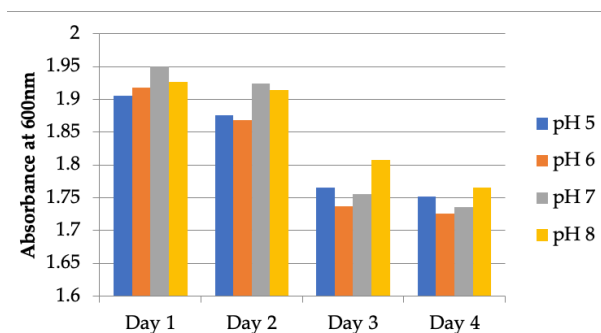


Figure 6. Growth rates of Metribuzin degrading bacteria at varying pH values

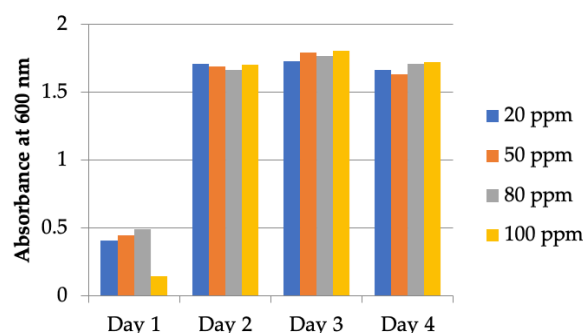


Figure 4. Growth rates of Clodinafop degrading bacteria at varying herbicide concentrations

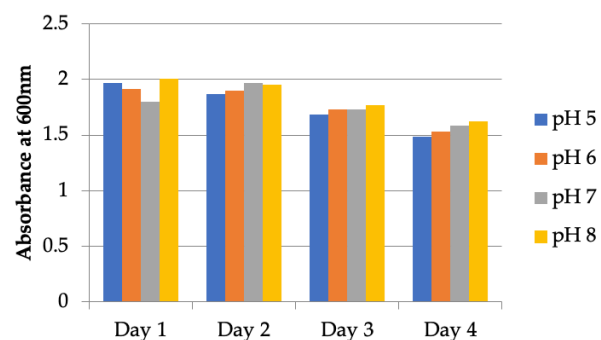


Figure 7. Growth rates of Clodinafop degrading bacteria at varying pH values

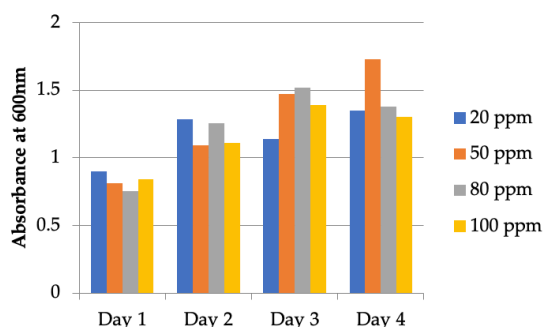


Figure 5. Growth rates of MCPA & Bromoxynil degrading bacteria at varying herbicide concentrations

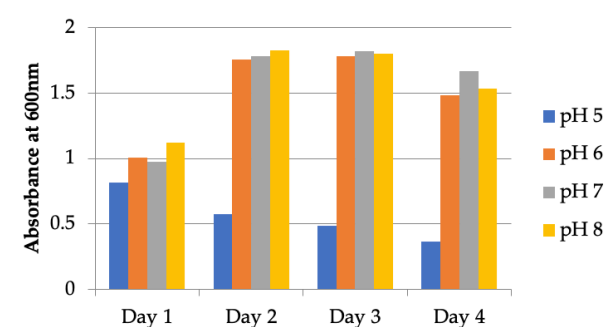


Figure 8. Growth rates of MCPA & Bromoxynil degrading bacteria at varying pH values

ior by strain C1 was a little bit different than the two herbicides i.e., the maximum degradation of MCPA & Bromoxynil was noticed on the fourth day (96 hours) at 50 ppm.

Effect of pH

The biodegradation of herbicides at different pH levels (5.0, 6.0, 7.0, and 8.0) was also studied (Tables 6, 7, 8 and Figs 6, 7, and 8). Results revealed that maximum degradation activities in terms of bacterial growth were

Table 6. Variation in pH and optical density as a result of metribuzin herbicide degradation by bacteria A6

Time period	pH			
	5.0	6.0	7.0	8.0
Day 1	1.905	1.918	1.95	1.926
Day 2	1.876	1.868	1.924	1.914
Day 3	1.765	1.737	1.756	1.807
Day 4	1.752	1.726	1.736	1.765

Table 7. Variation in pH and optical density as a result of clodinafop herbicide degradation by bacteria B3

Time period	pH			
	5.0	6.0	7.0	8.0
Day 1	1.968	1.918	1.799	2.008
Day 2	1.869	1.903	1.968	1.952
Day 3	1.683	1.729	1.732	1.768
Day 4	1.488	1.532	1.582	1.624

Table 8. Variation in pH and optical density as a result of MCPA & Bromoxynil herbicide degradation by bacteria C1

Time period	pH			
	5.0	6.0	7.0	8.0
Day 1	0.813	1.006	0.976	1.124
Day 2	0.573	1.756	1.784	1.825
Day 3	0.484	1.785	1.82	1.799
Day 4	0.367	1.483	1.667	1.533

Table 9. Variation in temperature and optical density as a result of metribuzin herbicide degradation by bacteria A6

Time period	Temperature		
	30°C	35°C	40°C
Day 1	1.05	1.55	0.871
Day 2	1.835	1.939	1.664
Day 3	1.877	1.879	1.461
Day 4	1.613	1.747	1.271

Table 10. Variation in temperature and optical density as a result of clodinafop herbicide degradation by bacteria B3

Time period	Temperature		
	30°C	35°C	40°C
Day 1	0.739	1.676	0.693
Day 2	1.221	1.957	1.348
Day 3	1.67	2.068	1.426
Day 4	1.528	1.854	1.232

observed at the end of day 1 and day 2 at pH 7.0–8.0 and minimum at pH 5.0. There was more biotic degradation in alkaline ranges of pH than in acidic.

Effect of Temperatures

The biodegradation of herbicides at different temperatures (30°C, 35°C and 40°C) was determined and the results are summarized in (Tables 9, 10, 11, and Figs 9,

10, 11). The results depicted that the optimized temperature for bacterial growth was observed at a temperature range of 35–37°C. The metribuzin degrading bacterium A6 showed maximum growth on day 2nd at 35°C and 40°C, while at 30°C maximum growth was recorded on the 3rd day. On day 4th a slight decline in bacterial growth rate was noticed at all temperatures. Almost similar trends were observed for clodinafop degrading

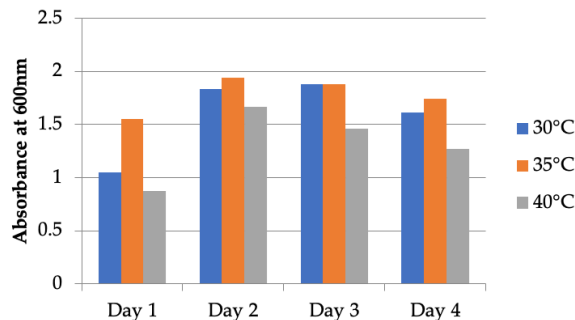
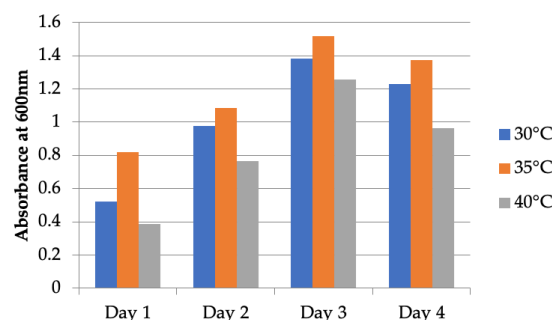
Table 11. Variation in temperature and optical density as a result of MCPA & Bromoxynil herbicide degradation by bacteria C1

Time period	Temperature		
	30°C	35°C	40°C
Day 1	0.523	0.819	0.386
Day 2	0.978	1.085	0.767
Day 3	1.382	1.516	1.258
Day 4	1.23	1.372	0.963

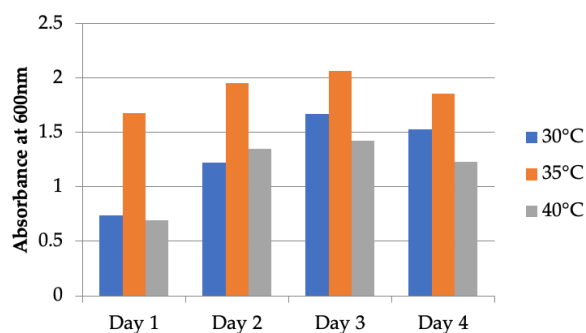
Table 12. Tests of between-subjects effects

Dependent variable: bacterial growth					
Source	Type III Sum of Squares	Df	Mean Square	F	Sig.
Herb	2.244	2	1.122	460.575	.000
Conc	.086	3	.029	11.824	.000
Time	22.610	3	7.537	3.094E3	.000
Herb* Conc	.054	6	.009	3.718	.002
Herb* Time	3.522	6	.587	240.957	.000
Conc* Time	.261	9	.029	11.917	.000
Herb* Conc* Time	.607	18	.034	13.832	.000**
Error	.234	96	.002		
Total	298.956	144			
Corrected Total	29.618	143			

**Three-way interaction is significant at 0.05 level of significance

**Figure 9. Growth rates of Metribuzin degrading bacteria at varying temperatures****Figure 11. Growth rates of MCPA & Bromoxynil degrading bacteria at varying temperatures**

at 35°C on 3rd day following a decline in growth on 4th day.

**Figure 10. Growth rates of Clodinafop degrading bacteria at varying temperatures**

bacterium B3 and Bromoxynil + MCPA degrading bacterium C1, with the maximum optical densities recorded

Statistical Analysis of the Effect of Different Parameters on Bacterial Growth

A three-way ANOVA with $\alpha=0.05$ (level of significance) was used to determine the statistically significant effect of herbicides, concentrations, and time intervals on bacterial growth. Table 12 illustrates that there is a significant effect of the three-way interaction of herbicides, concentration, and time on bacterial growth at $p<0.05$. Similarly, the effect of herbicides, pH, and time intervals on the bacterial growth also showed significant interaction at a 95% significance level i.e. $p<0.05$ as shown in Table 13. The three-way interaction of herbicides, temperature, and time intervals on bacterial growth was also statically significant at $p<0.05$ (Table 14).

Table 13. Test of between-subject effects on three-way analysis of variance

Source	Type III Sum of Squares	Df	Mean Square	F	Sig.
Herb	8.731	2	4.366	1.077E3	.000
pH	3.630	3	1.210	298.548	.000
Time	.980	3	.327	80.555	.000
Herb* pH	6.219	6	1.036	255.708	.000
Herb* Time	2.193	6	.365	90.175	.000
pH* Time	.891	9	.099	24.433	.000
Herb* pH* Time	1.340	18	.074	18.366	.000**
Error	.389	96	.004		
Total	408.869	144			
Corrected Total	24.477	143			

**Three-way interaction is significant at 0.05 level of significance

Table 14. Tests of between-subjects effects by three-way analysis of variance

Source	Type III Sum of Squares	Df	Mean Square	F	Sig.
Corrected Model	20.124 ^a	35	.575	421.673	.000
Intercept	195.606	1	195.606	1.435E5	.000
Herb	5.843	2	2.921	2.143E3	.000
Temp	4.782	2	2.391	1.753E3	.000
Time	7.105	3	2.368	1.737E3	.000
Herb* Temp	.801	4	.200	146.823	.000
Herb* Time	.812	6	.135	99.236	.000
Temp* Time	.558	6	.093	68.262	.000
Herb* Temp* Time	.223	12	.019	13.644	.000**
Error	.098	72	.001		
Total	215.828	108			
Corrected Total	20.222	107			

**Three-way interaction is significant at 0.05 level of significance

DISCUSSION

The use of chemical pesticides to reduce the pest attack on crops and to improve the yield has become routine in recent times. These hazardous chemicals are responsible for soil and groundwater contamination as they have a long persistence time and can percolate through the soil to the groundwater table and pose a serious threat to human health. There is an increasing need to identify different bioremediation approaches to degrade and detoxify these toxic pesticides. Several studies have demonstrated the use of bacteria, which can effectively degrade herbicides (Huang *et al.*, 2018). Because of its effectiveness and low cost, bioremediation appeared as the most favorable alternative treatment for the removal of agrochemicals (Arora, 2018).

In the current study, three herbicides (metribuzin, clodinafop propargyl, 2-methyl, 4-chlorophenoxyacetic acid and Bromoxynil) degrading bacterial strains were isolated and characterized. All the herbicide-degrading bacterial isolates were rod-shaped and belonged to the *Bacillus* genera. In a previous study conducted by Sehrawat and others (Sehrawat *et al.*, 2021), it was examined that pesticides in the environment are mostly mineralized and detoxified by bacterial genera like "*Bacillus* and *Pseudomonas*"

because these bacteria possess a variety of enzymes that are helpful in the degradation of toxic compounds.

Out of fourteen bacterial isolates, six were able to metabolize metribuzin. The bacterial isolate A6 was further used to study the metabolism of metribuzin herbicide and results were confirmed by GC-MS analysis. Bacterial isolate metabolized the metribuzin into the deaminated metribuzin. The results showed that the bacteria adopted the deamination pathway for sensor metribuzin degradation. The metribuzin herbicide was broken down into degradative products by the release of an amino group from the parental herbicide compound and converting it into a less toxic product i.e., deaminometribuzin. The bacterial strain A6 degraded 14.8% metribuzin out of the provided concentration of 50 ppm. In a similar study Wahla and others (Wahla *et al.*, 2019) investigated the biodegradation of two pesticides metribuzin and proflinofos by three bacterial isolates "*Pseudomonas aeruginosa*, *Staphylococcus aureus*, and *Bacillus subtilis*" and determined the effect of pH, temperature, and various carbon and nitrogen sources on degradation. The strains exhibited excellent growth at pH 6, 30°C in minimal salt broth amended with 25 mg/L pesticides containing dextrose as carbon and malt extract as nitrogen source. *Bacillus subtilis* was found active in degrading the pesticides after that *Staphylococcus aureus* and *Pseudomonas aeruginosa*.

In this study, three *Bacillus* sp. were found efficient in the metabolism of clodinafop propargyl and the bacterium B3 was further selected for biodegradation study through GC-MS analysis. The bacterial strain B3 degraded 23.2% clodinafop propargyl out of the provided concentration of 50 ppm. The isolate B3 degraded the clodinafop into corresponding acids and adopted a dehalogenation pathway for the breakdown of herbicide. The bacterium released the chloride ions from the compound, due to which the pyridyl ring underwent further degradation and broken down into the corresponding dicarboxylic acids which is an allosteric activator of acetyl co-enzyme-A decarboxylase (Singh *et al.*, 2013). *Aeromonas* sp. isolated from the crop field degraded 81.3% of clodinafop propargyl with a concentration of 80 ppm as the bacteria consumed it as a sole carbon and nitrogen source (Dong *et al.*, 2017). The formation of 4-(4-chloro-2-fluorophenoxy) phenol as a main degradative metabolite was reported. In another study conducted by Singh and others (Singh *et al.*, 2013) the degradation efficiency of clodinafop by *Pseudomonas* sp. was determined which consumed about 87.14% of herbicide out of the initial concentration of 80 ppm. The breakdown of clodinafop propargyl released chloride ion and confirmed the breakdown of CF into 4-(4-chloro-2-fluorophenoxy) phenol and clodinafop acid. The production of phenol as the metabolic product reveals the presence of esterase activity (Yuan *et al.*, 2015).

Were found to metabolize the MCPA & Bromoxynil. The strain C1 was efficient in degrading MCPA through the decarboxylation mechanism and forming 2-methyl phenol as a major degradative metabolite. (Mierzejewska *et al.*, 2016) reported three bacterial strains *Xanthomonas maltophilia*, *Pseudomonas* sp., and *Rhodococcus globerulus* that degraded 99% MCPA in non-contaminated soil and up to 61% in the contaminated soil by *Xanthomonas maltophilia*.

CONCLUSIONS

Bioremediation has become a popular environment-friendly approach for the decontamination of a heavy buildup of toxic recalcitrant compounds from the environment. Microbial degradation plays a pivotal role to endorse a clean and sustainable environment. In this study three bacterial isolates namely, A6, B3, and C1 were found efficient for degrading metribuzin, clodinafop, and Bromoxynil & MCPA herbicides respectively, and their respective degradation capacities recorded as 14.8% for metribuzin, 23.2% for clodinafop and 33.9% MCPA & Bromoxynil. The optimum temperature and pH for the biodegradation of herbicides was 35°C and pH ranging from 7.0–8.0. These bacterial strains were found efficient in the metabolism of herbicides and can be utilized for the bioremediation of polluted sites in the future.

Declarations

Supplementary Materials. The following supporting information can be downloaded: Table S1: Morphological characterization of herbicides degrading bacteria at <https://ojs.ptbioch.edu.pl/index.php/abp/>

Ethical approval. This article does not contain any studies with animals performed by any of the authors.

Data availability. All major data generated and analyzed in this study are included in this manuscript and its supplementary information files.

Conflict of interest. The authors declare no conflict of interest.

REFERENCES

- Alam MS, Gorman-Lewis D, Chen N, Safari S, Baek K, Konhauser KO, Alessi DS (2018) Mechanisms of the removal of U(VI) from aqueous solution using biochar: a combined spectroscopic and modeling approach. *Environ. Sci. Technol.* **52**: 13057–13067. <https://doi.org/10.1021/acs.est.8b01715>
- Arora NK (2018) Bioremediation: a green approach for restoration of polluted ecosystems. *Environ. Sustain.* **1**: 305–307. <https://doi.org/10.1007/s42398-018-00036-y>
- Bakshi P, Chouhan R, Sharma P, Mir BA, Gandhi SG, Landi M, Zheng B, Sharma A, Bhardwaj R (2021) Amelioration of chlorpyrifos-induced toxicity in *Brassica juncea* L. by combination of 24-epibrassinolide and plant-growth-promoting Rhizobacteria. *Biomolecules* **11**: 877. <https://doi.org/10.3390/biom110608>
- Clapp J (2021) Explaining growing glyphosate use: The political economy of herbicide-dependent agriculture. *Global Environ. Change* **67**: 102239. <https://doi.org/10.1016/j.gloenvcha.2021.102239>
- Dong W, Liu K, Wang F, Xin F, Zhang W, Zhang M, Wu H, Ma J, Jiang M (2017) The metabolic pathway of metamifop degradation by consortium ME-1 and its bacterial community structure. *Biodegradation* **28**: 181–194. <https://doi.org/10.1007/s10532-017-9787-8>
- GOP (2020) Economic survey of Pakistan 2019–2020. *Government of Pakistan*
- Hasnain S, Thomas CM (1996) Two related rolling circle replication plasmids from salt-tolerant bacteria. *Plasmid* **36**: 191–199. <https://doi.org/10.1006/plas.1996.0046>
- Huang Y, Xiao L, Li F, Xiao M, Lin D, Long X, Wu Z (2018) Microbial degradation of pesticide residues and an emphasis on the degradation of cypermethrin and 3-phenoxy benzoic acid: a review. *Molecules* **23**: 2313. <https://doi.org/10.3390/molecules23092313>
- Johnson JL (1994) In *Methods for General and Molecular Bacteriology*. Gerhardt P, Murray RGE, Wood WA, Krieg NR, eds, pp 655–700. *Am. Soc. Microbiol.* Washington DC. <https://www.ncbi.nlm.nih.gov/pmc/articles/PMC206792/pdf/jbacter00063-0002.pdf>
- Khan ZA, Koondhar MA, Khan I, Ali U, Tianjun L (2021) Dynamic linkage between industrialization, energy consumption, carbon emission, and agricultural products export of Pakistan: an ARDL approach. *Environ. Sci. Pollut. Res. Int.* **28**: 43698–43710. <https://doi.org/10.1007/s11356-021-13738-4>
- Khan SH, Pathak B (2020) Zinc oxide based photocatalytic degradation of persistent pesticides: A comprehensive review. *Environ. Nanotechnol. Monitor. Manag.* **13**: 100290. <https://doi.org/10.1016/j.enmm.2020.100290>
- Koondhar MA, Udamba EN, Cheng Y, Khan ZA, Koondhar MA, Batool M, Kong R (2021) Asymmetric causality among carbon emission from agriculture, energy consumption, fertilizer, and cereal food production – a nonlinear analysis for Pakistan. *Sustain. Energy Technol. Assess.* **45**: 101099. <https://doi.org/10.1016/j.seta.2021.101099>
- Lone AH, Raverkar K, Pareek N (2014) *In-vitro* effects of herbicides on soil microbial communities. *Bioscan* **9**: 11–16
- Mierzejewska E, Baran A, Tankiewicz M, Urbaniak M (2019) Removal and ecotoxicity of 2,4-D and MCPA in microbial cultures enriched with structurally-similar plant secondary metabolites. *Water* **11**: 1451. <https://doi.org/10.3390/w11071451>
- Hadi F, Aziz T (2015) A Mini review on lead (Pb) toxicity in plants. *J. Biol. Life Sci.* **6**: 91–101. <https://doi.org/10.5296/jbls.v6i2.7152>
- Okeimen FE, Ogeleka DF, Peretiemo-Clarke BO (2020) Ecotoxicological risk evaluation of herbicides on nontarget environmental receptors. *Environ. Ecosystem Sci. (EES)* **4**: 92–99. <https://ideas.repec.org/a/zib/zbnecs/v4y2020i2p92-99.html>
- Oladiipo AA, Gazi M, Ifebajo AO, Oladiipo AS, Ahaka EO (2020) Photocatalytic degradation of toxic pesticides: mechanistic insights. *Photocatal. Adv. Oxi. Proc. Wastewater Treat.* 93–138. <https://doi.org/10.1002/9781119631422.ch4>
- Pacciani-Mori L, Giometto A, Suweis S, Maritan A (2020) Dynamic metabolic adaptation can promote species coexistence in competitive microbial communities. *PLoS Comp. Biol.* **16**: e1007896. <https://doi.org/10.1371/journal.pcbi.1007896>
- Pertile M, Antunes JEL, Araujo FF, Mendes LW, Van Den Brink PJ, Araujo ASF (2020) Responses of soil microbial biomass and enzyme activity to herbicides imazethapyr and flumioxazin. *Sci. Rep.* **10**: 1–9. <https://doi.org/10.1038/s41598-020-64648-3>
- Richardson JR, Fitsanakis V, Westerink RH, Kanthasamy AG (2019) Neurotoxicity of pesticides. *Acta Neuropathol.* **138**: 343–362. <https://doi.org/10.1007/s00401-019-02033-9>
- Sanger F, Nicklen S, Coulson AR (1977) DNA sequencing with chain-terminating inhibitors. *Proc. Natl. Acad. Sci. U S A* **74**: 5463–5467. <https://doi.org/10.1073/pnas.74.12.5463>

- Sehrawat A, Phour M, Kumar R, Sindhu SS (2021) Bioremediation of pesticides: an eco-friendly approach for environment sustainability. *Microb. Rejuv. Poll. Environ.* Vol 25. Springer. https://doi.org/10.1007/978-981-15-7447-4_2
- Singh B (2013) Degradation of clodinafop propargyl by *Pseudomonas* sp. strain B2. *Bull. Environ. Contamin. Toxicol.* **91**: 730–733. <https://doi.org/10.1007/s00128-013-1124-2>
- Storkey J, Neve P (2018) What good is weed diversity? *Weed Res.* **58**: 239–243. <https://doi.org/10.1111/wre.12310>
- Wahla AQ, Iqbal S, Anwar S, Firdous S, Mueller JA (2019) Optimizing the metribuzin degrading potential of a novel bacterial consortium based on Taguchi design of experiment. *J. Hazard Mater.* **366**: 1–9. <https://doi.org/10.1016/j.jhazmat.2018.11.054>
- Yuan Y, Weitzel P, Schäffer A, Schmidt B (2015) Metabolic fate of the ¹⁴C-labeled herbicide clodinafop-propargyl in a sediment–water system. *J. Environ. Sci. Health B.* **50**: 533–543. <https://doi.org/10.1080/03601234.2015.1028825>

The relationship between EMG high frequency and low frequency band amplitude changes correlates with tissue inorganic phosphate levels

Malgorzata Habich^{1#}, Bartosz Pawlinski^{2#}, Kamil Lorenc², Maria Sady², Katarzyna Siewruk², Piotr Zielenkiewicz¹, Zdzisław Gajewski², Jarosław Poznanski¹, Leszek Paczek^{1,3} and Paweł Szczesny¹ ✉

¹Institute of Biochemistry and Biophysics Polish Academy of Sciences, Warsaw, Poland; ²Department of Large Animals with Clinic, Warsaw University of Life Sciences, Warsaw, Poland; ³Department of Immunology, Transplantology and Internal Diseases, Medical University of Warsaw, Warsaw, Poland

Assessing inorganic phosphate levels seems crucial in deciphering the biochemical state of organisms or tissues. The concentration of inorganic phosphate in blood is an order of magnitude smaller than in tissues and, on top of that, it is dynamically used to fill temporary gaps in tissues. This is the reason blood inorganic phosphate level is considered a poor proxy for tissue levels. Therefore, tissue biopsy seems to be the dominant method when assessing inorganic phosphate levels for instance in muscles. In this study, we attempted to derive a non-invasive biomarker for phosphate tissue levels. We analyzed surface electromyography signals taken during 31P spectroscopy of leg muscles in five adult pigs. We induced hypophosphatemia via 20 minutes-long hyperventilation. It turned out that the proportion of the amplitude of the low frequency band and the high frequency band is significantly ($p=0.002$) correlated with the relative phosphate levels. The electromyographic signal did not correlate significantly with pCO₂ levels in the blood, suggesting that the changes in the signal are a result of inorganic phosphate levels, not hyperventilation. The results might lead to the development of a real-time phosphate fluctuations measurement procedure.

Keywords: EMG, phosphate, biomarker, MRI, hyperventilation, hypocapnia

Received: 20 June, 2023; **revised:** 07 August, 2023; **accepted:** 13 September, 2023; **available on-line:** 18 October, 2023

✉e-mail: szczesny@ibb.waw.pl

[#]Both authors equally contributed to that study

Acknowledgements of Financial Support: This research was funded by The National Centre for Research and Development, grant number LIDER/028/565/L-5/13/NCBR/2014.

INTRODUCTION

Disturbance in phosphate levels is an electrolyte disorder associated with many diseases, but hypophosphatemia is more common than hyperphosphatemia. Hypophosphatemia is typically diagnosed when serum phosphate levels drop below 2.0 mg/dl. The most common causes of hypophosphatemia are infection, refeeding, and Fanconi syndrome (Saito *et al.*, 2014). It also manifests as a complication in critically ill patients in the postoperative phase, hypothermia, or trauma (Geerse *et al.*, 2010). Symptoms of hypophosphatemia are potentially life-threatening but at the same time nonspecific - it includes muscle weakness, arrhythmias, respiratory fail-

ure, hypercalciuria, and others (Assadi, 2010). The disturbance in phosphate levels is associated with increased morbidity (Felsenfeld & Levine, 2012; Sin *et al.*, 2021).

The relationship between phosphate levels in compartments is tightly regulated and complicated. As only 1% of total phosphate in the body is in the extracellular compartment, the changes of concentration in serum are dynamic and a poor indicator of total-body phosphorus level (Felsenfeld & Levine, 2012). Routine phosphate monitoring is uncommon in patients admitted to intensive care units (ICU), and hypophosphatemia is often not corrected (Berger *et al.*, 2021). 31P spectroscopy is rarely a viable solution due to equipment requirements.

As hypophosphatemia is associated with disturbances in muscle function and ATP synthesis (Pesta *et al.*, 2016), the aim of this study was to determine if muscle activity could be a non-invasive, real-time indicator of phosphate level. The studies performed on cows showed that phosphate deprivation could induce abnormalities in muscle activity that can be detected by electromyography, but there is no data about transient and immediate effects, which could have clinical implications in human studies (Pesta *et al.*, 2016; Grünberg *et al.*, 2019, 2015). The approach of combining 31P with surface EMG for studying muscle disorders and fatigue has been used many times since 1993 (Roy, 1993; Giannesini *et al.*, 2003; Rzanny *et al.*, 2006). But again, experiments using this approach did not investigate fast fluctuations of inorganic phosphate in healthy and unfatigued muscle. Our study fills this gap and might lead to the development of a novel phosphate biomarker.

MATERIALS AND METHODS

Major protocol

The experiments were approved by the II Local Ethical Committee on Animal Testing in Warsaw, Poland (permit number: 20/2015 from 23 April 2015) on behalf of the National Ethical Committees on Animal Testing. Three preliminary experiments were conducted: two animals under normo- and hyperventilation were performed outside the MRI scanner chamber and one in the MRI chamber under normoventilation (animal 0). In the main part of this study, four female healthy piglets (animals 1–4) with an average body weight of 20 kg and an average age of 2 months were first sedated with azaperone

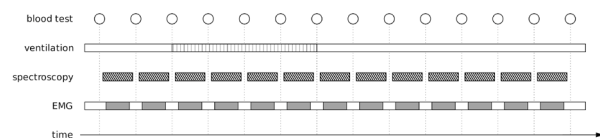


Figure 1. Schematic of the main experiment - dashed and filled rectangles indicate which fragments of data were taken into further analysis.

Additionally, the range of hyperventilation and moments of blood gasometry were shown as vertical lines and circles respectively. Each spectroscopy measurement lasted 4 min 26 seconds. The time between measurements slightly varied but the mean time between blood tests was 5 min.

(Stresnil, 3 mg/kg body weight (b.wt.), Janssen Pharmaceutica, Turnhoutseweg, Belgium). Each animal was then orotracheally intubated with an endotracheal tube and mechanically ventilated with room air. The respiration rate was set to zero (free respiration) during normoventilation and 20/min during hyperventilation. To evaluate muscle activity, the surface EMG electrodes were placed on the trapezius and triceps (front leg), and biceps femoris (rear leg) muscles. During the experiment, a swine was placed inside the MRI scanner. Each measurement lasted 4 min 26 seconds. In four cases, between the measurements, the pig's blood was drawn to evaluate gasometry. After the first two control scans, the next four were made in a hyperventilated state, followed by another seven scans under normoventilation. A schematic of the main experiment is shown in Fig. 1. The well-being of animals was closely monitored by an anesthesiologist and in case of suspected risk to animal health, the experiment was terminated. In addition to experiments with ^{31}P spectroscopy, EMG measurements for two other animals upon normo- and hyperventilation were performed outside of the MRI scanner chamber.

^{31}P MRS data analysis

^{31}P -MRS data was acquired using an MR750w 3T MRI scanner (GE Healthcare, USA) with $^{31}\text{P}/^1\text{H}$ surface coil (Rapid Biomedical, Germany). Data was acquired with parameters: TR 1s, Navg 256, spectral bandwidth 5kHz, acquisition time 102.4 ms, slice thickness 40 mm. No shimming was applied for the ^{31}P -MRS acquisition. Data were acquired before, during, and after hyperventilation. Localization was done through coil sensitivity. The coil was located on the biceps femoris. Raw data were quantified with jMRUI software (Naressi *et al.*, 2001; Stefan *et al.*, 2009) using the AMARES algorithm (Vanhamme *et al.*, 1997) according to published procedures and parametrization (de Graaf, 2019). Signal location and assignment were done for each spectrum individually to account for pH-induced changes in the spectra.

Electromyography data analysis

The electromyography record was running continuously throughout the whole experiment. Because between spectroscopy measurements the pigs were touched by a technician for blood extraction, the analysis of electromyography measurements has been made only on fragments of record that were recorded during spectroscopy. The first part of the analysis was made using the “signal” library from Python 3. The “spectrogram” function was used to create a signal spectrogram which then has been converted into dB. To extract the spectroscopy parts of the signal the sum of signal power in the 210 dB – 249 dB range has been taken and then the frag-

ments where the summed signal power went above the average for the known spectroscopy time – 4 minutes and 26 seconds – were chosen. Further signal analysis has been done using the R language “psd” library. The signal was further cleaned up, a spectrogram was created, and then the relation between high and low frequency bands was calculated according to the equation:

This approach to the analysis of EMG signals was al-

$$EMG_{score} = \Sigma_{150-400\text{Hz}}(\text{amplitude}) / \Sigma_{1-49\text{Hz}}(\text{amplitude})$$

ready used in clinical research (Allison & Fujiwara, 2002; Badier *et al.*, 1993; Krogh-Lund & Jorgensen, 1993).

Gasometry data analysis

Between ^{31}P -MRS measurements, blood samples were collected and further using a critical points analyzer RAPIDPoint 500 (Siemens, Erlangen, Germany). The measured parameters were: pH, pCO_2 (mmHg), pO_2 (mmHg), cHCO_3^- (mmol/L), BE (ecf) (mmol/L), cSO_2 (%), Na^+ (mmol/L), K^+ (mmol/L), Ca^{++} (mmol/L), Cl^- (mmol/L), cTCO_2 (mmol/L), Anion gap (mmol/L), Anion gap K^+ (mmol/L), Hct (%), cHgb (g/dL), BE (b) (mmol/L), Glucose (mg/dL), Lactate (mmol/L), Creatinine (mg/dL) (Supplementary Table 1 at <https://ojs.ptbioch.edu.pl/index.php/abp/>).

RESULTS

Hyperventilation induces hypophosphatemia in most animals

Four hyperventilated animals were put in an MRI chamber. Two measurements were done with normoventilation and then animals were hyperventilated for 4 consecutive scans (see Materials and Methods for exact protocol). Analysis of the ^{31}P -MRS signal indicates that inorganic phosphate content in muscles drops by as much as 30% after 5 steps of the experiment (about 20 minutes of hyperventilation) (Fig. 2). Not all cases had a drop in phosphate levels following hyperventilation, but when blood gasometry analysis was performed, hyperventilation robustly induces a drop in pCO_2 levels (Supplementary Fig. 1 at <https://ojs.ptbioch.edu.pl/index.php/abp/>).

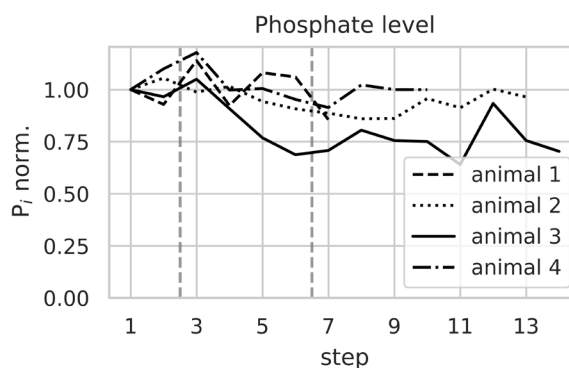


Figure 2. Inorganic phosphate levels in muscles before, during and after hyperventilation.

The total number of points per animal depended on its condition – some experiments were decided to finish earlier. Phosphate levels are normalized against the first measurement.

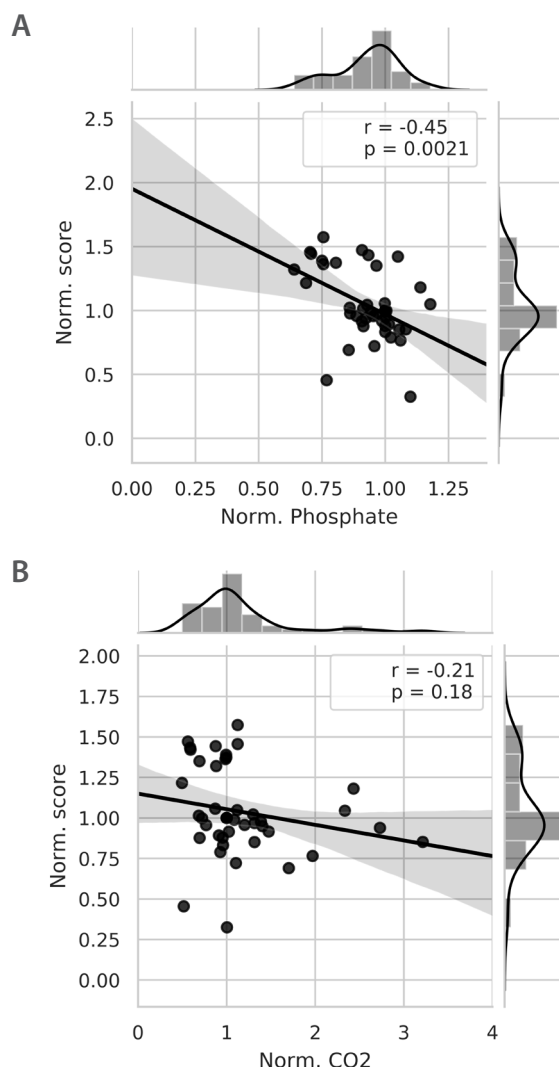


Figure 3. Correlation between EMG score (see Materials and Methods) and phosphate levels (**panel A**) and pCO₂ (**panel B**). Values on all axes were normalized against the first measurement per animal.

EMG signal correlates with inorganic phosphate but not with pCO₂ levels

The distribution of the collected EMG signal was symmetrical, and values ranged typically between -100mV and 100mV (Supplementary Fig. 2 at <https://ojs.ptbioch.edu.pl/index.php/abp/>). The ratio of the power spectrum between high and low frequencies was calculated for a window spanning 4 minutes during MRI acquisition (4 min 26 seconds). The window for EMG analysis was taken slightly smaller to remove artifacts caused by switching on/off of MRI scanning. Pearson correlation between this calculated ratio (called “normalized score”) and normalized phosphate levels is negative and significant: R is -0.45 , and the p -value is 0.002 (Fig. 3A). We made the same comparison between the score and normalized pCO₂ levels, and the Pearson test indicated an insignificant correlation (Fig. 3B). Detailed trajectories for each animal are in Supplementary Fig. 3 at <https://ojs.ptbioch.edu.pl/index.php/abp/>.

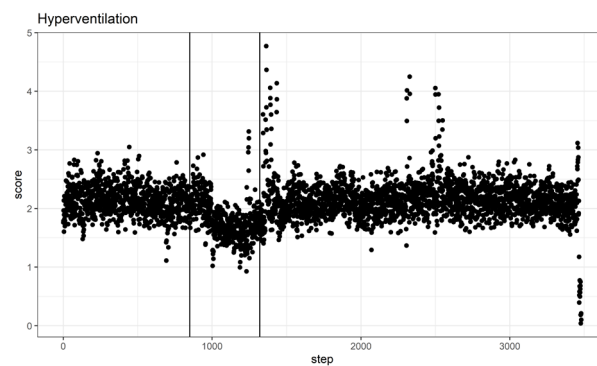


Figure 4. Experiment with hyperventilation repeated outside of the MRI chamber.

The start and end of hyperventilation are denoted as vertical lines. Dots are the EMG score calculated every 1s.

Fast reaction to hyperventilation seen in EMG

The EMG signal collected during MRI scans is, despite shielding and usage of carbon electrodes, quite noisy. We repeated the hyperventilation experiment outside of the MRI chamber. Phosphate measurement wasn't possible but the goal was to obtain a clear picture of changes in EMG following hyperventilation. It turned out that the reaction of EMG to hyperventilation is pretty fast - the changes in the EMG spectrum can be observed tens of seconds after hyperventilation is started (Fig. 4). To remove the possibility that the interaction with a ventilating machine was the cause of EMG response, another animal was put on ventilator but with respiration rate set to 12 breaths. No significant changes in EMG score (other than artifacts from body movement) were detected (Supplemental Fig. 4 at <https://ojs.ptbioch.edu.pl/index.php/abp/>).

DISCUSSION

In this study, we presented the results of an attempt to derive a non-invasive biomarker of hypophosphatemia. We showed that hyperventilation induces hypophosphatemia and that the level of inorganic phosphate in muscles correlates with changes in the power spectrum density of a surface electromyographic signal. The observed correlation is significant despite the limited number of animals used for the research.

Animals appeared healthy, but we cannot rule out pre-existing conditions (one animal needed a longer recovery time after the experiment was concluded). This could potentially explain why, not in all cases, we were able to notice hypophosphatemia.

An interesting aspect of EMG response to hyperventilation is the time needed to elicit it. MRI scans affect the EMG signal, so we could not see when exactly the EMG started to drift. Experiments outside of the MRI chamber showed that a response is faster than 30 seconds. Existing hypotheses about how hyperventilation influences phosphate levels (O'Brien & Coberly, 2003) support a fast response rate. O'Brien and Coberly proposed a model where an increased rate of glycolysis and ATP production in response to respiratory alkalosis is responsible for a sudden drop in inorganic phosphate levels. However, this study doesn't provide evidence if that is the mechanism that occurs.

REFERENCES

- Allison GT, Fujiwara T (2002) The relationship between EMG median frequency and low frequency band amplitude changes at different levels of muscle capacity. *Clin. Biomech.* **17**: 464–469. [https://doi.org/10.1016/s0268-0033\(02\)00033-5](https://doi.org/10.1016/s0268-0033(02)00033-5)
- Assadi F (2010) Hypophosphatemia: an evidence-based problem-solving approach to clinical cases. *Iran. J. Kidney Dis.* **4**: 195–201.
- Badier M, Guillot C, Lagier-Tessonier F, Burnet H, Jammes Y (1993) EMG power spectrum of respiratory and skeletal muscles during static contraction in healthy man. *Muscle Nerve* **16**: 601–609. <https://doi.org/10.1002/mus.880160605>
- Berger MM, Appelberg O, Reintam-Blaser A, Ichai C, Joannes-Boyau O, Casaer M, Schaller SJ, Gunst J, Starkopf J, ESICM-MEN section (2021) Prevalence of hypophosphatemia in the ICU – Results of an international one-day point prevalence survey. *Clin. Nutr.* **40**: 3615–3621. <https://doi.org/10.1016/j.clnu.2020.12.017>
- Felsenfeld AJ, Levine BS (2012) Approach to Treatment of Hypophosphatemia. [WWW document]. *Am. J. Kidney Dis.* **60**: 655–661. <https://doi.org/10.1053/j.ajkd.2012.03.024>
- Geerse DA, Bindels AJ, Kuiper MA, Roos AN, Spronk PE, Schultz MJ (2010) Treatment of hypophosphatemia in the intensive care unit: a review. *Crit. Care* **14**: R147. <https://doi.org/10.1186/cc9215>
- Giannesini B, Cozzone PJ, Bendahan D (2003) Non-invasive investigations of muscular fatigue: metabolic and electromyographic components. *Biochimie* **85**: 873–883. [https://doi.org/10.1016/s0300-9084\(03\)00124-x](https://doi.org/10.1016/s0300-9084(03)00124-x)
- de Graaf RA (2019) *In Vivo NMR Spectroscopy: Principles and Techniques* [WWW document]. John Wiley & Sons <https://doi.org/10.1002/9781119382461>
- Grünberg W, Scherpenisse P, Dobbelaar P, Idink MJ, Wijnberg ID (2015) The effect of transient, moderate dietary phosphorus deprivation on phosphorus metabolism, muscle content of different phosphorus-containing compounds, and muscle function in dairy cows. *J. Dairy Sci.* **98**: 5385–5400. <https://doi.org/10.3168/jds.2015-9357>
- Grünberg W, Scherpenisse P, Cohrs I, Golbeck L, Dobbelaar P, van den Brink LM, Wijnberg ID (2019) Phosphorus content of muscle tissue and muscle function in dairy cows fed a phosphorus-deficient diet during the transition period. *J. Dairy Sci.* **102**: 4072–4093. <https://doi.org/10.3168/jds.2018-15727>
- Krogh-Lund C, Jørgensen K (1993) Myo-electric fatigue manifestations revisited: power spectrum, conduction velocity, and amplitude of human elbow flexor muscles during isolated and repetitive endurance contractions at 30% maximal voluntary contraction. *Eur. J. Appl. Physiol. Occup. Physiol.* **66**: 161–173. <https://doi.org/10.1007/bf01427058>
- Naressi A, Couturier C, Devos JM, Janssen M, Mangeat C, de Beer R, Graveron-Demilly D (2001) Java-based graphical user interface for the MRUI quantitation package. *MAGMA* **12**: 141–152. <https://doi.org/10.1007/BF02668096>
- O'Brien TM, Coberly LA (2003) Severe hypophosphatemia in respiratory alkalosis. *Adv. Stud. Med.* **3**: 6
- Pesta DH, Tsigotis DN, Befroy DE, Caballero D, Jurczak MJ, Rahimi Y, Cline GW, Dufour S, Birkenfeld AL, Rothman DL, Carpenter TO, Insogna K, Petersen KF, Bergwitz C, Shulman GI (2016) Hypophosphatemia promotes lower rates of muscle ATP synthesis. *FASEB J.* **30**: 3378–3387. <https://doi.org/10.1096/fj.201600473R>
- Roy SH (1993) Combined use of surface electromyography and ³¹P-NMR spectroscopy for the study of muscle disorders. *Phys. Ther.* **73**: 892–901. <https://doi.org/10.1093/ptj/73.12.892>
- Rzanny R, Grassme R, Reichenbach JR, Scholle H-C, Kaiser WA (2006) Investigations of back muscle fatigue by simultaneous ³¹P MRS and surface EMG measurements. *Biomed. Tech.* **51**: 305–313. <https://doi.org/10.1515/BMT.2006.062>
- Saito Y, Aoki Y, Takeshita E, Saito T, Sugai K, Komaki H, Nakagawa E, Ishiyama A, Takanoha S, Wada S, Sasaki M (2014) Hypophosphatemia is a common complication in severely disabled individuals with neurological disorders and is caused by infection, refeeding and Fanconi syndrome. *Brain Develop.* **36**: 878–883. <https://doi.org/10.1016/j.braindev.2013.12.001>
- Sin JCK, King L, Ballard E, Llewellyn S, Laupland KB, Tabah A (2021) Hypophosphatemia and Outcomes in ICU: A Systematic Review and Meta-Analysis. *J. Intensive Care Med.* **36**: 1025–1035. <https://doi.org/10.1177/0885066620940274>
- Stefan D, Di Cesare F, Andrasescu A, Popa E, Lazariev A, Vescovo E, Strbak O, Williams S, Starcuk Z, Cabanas M, van Ormondt D, Graveron-Demilly D (2009) Quantitation of magnetic resonance spectroscopy signals: the jMRUI software package. *Meas. Sci. Technol.* **20**. <https://doi.org/10.1088/0957-0233/20/10/104035>
- Vanhamme L, van den Boogaart A, Van Huffel S (1997) Improved method for accurate and efficient quantification of MRS data with use of prior knowledge. *J. Magn. Reson.* **129**: 35–43. <https://doi.org/10.1006/jmre.1997.1244>



OPEN ACCESS

EDITED BY

Bożena Bruhn-Olszewska,
Uppsala University, Sweden

REVIEWED BY

Anna Polak,
Independent Researcher, Katowice,
Poland

Iga Hołyńska-Iwan,
Nicolaus Copernicus University in
Toruń, Poland

*CORRESPONDENCE

Slawomir Lasota,
✉ slawomir.lasota@uj.edu.pl
Zbigniew Madeja,
✉ z.madeja@uj.edu.pl

[†]These authors have contributed equally
to this work

RECEIVED 15 March 2024

ACCEPTED 13 June 2024

PUBLISHED 25 June 2024

CITATION

Ciesielska P, Lasota S,
Bobis-Wozowicz S and Madeja Z (2024),
The role of TGF- β in the electrotactic
reaction of mouse
3T3 fibroblasts *in vitro*.
Acta Biochim. Pol. 71:12993.
doi: 10.3389/abp.2024.12993

COPYRIGHT

© 2024 Ciesielska, Lasota, Bobis-
Wozowicz and Madeja. This is an open-
access article distributed under the
terms of the [Creative Commons
Attribution License \(CC BY\)](#). The use,
distribution or reproduction in other
forums is permitted, provided the
original author(s) and the copyright
owner(s) are credited and that the
original publication in this journal is
cited, in accordance with accepted
academic practice. No use, distribution
or reproduction is permitted which does
not comply with these terms.

The role of TGF- β in the electrotactic reaction of mouse 3T3 fibroblasts *in vitro*

Patrycja Ciesielska[†], Slawomir Lasota^{*†}, Sylwia Bobis-Wozowicz
and Zbigniew Madeja^{*}

Department of Cell Biology, Faculty of Biochemistry, Biophysics and Biotechnology, Jagiellonian
University, Kraków, Poland

Endogenous electric fields (EFs) serve as a crucial signal to guide cell movement in processes such as wound healing, embryonic development, and cancer metastasis. However, the mechanism underlying cell electrotaxis remains poorly understood. A plausible hypothesis suggests that electrophoretic or electroosmotic forces may rearrange charged components of the cell membrane, including receptors for chemoattractants which induce asymmetric signaling and directional motility. This study aimed to explore the role of Transforming Growth Factor Beta (TGF β) signaling in the electrotactic reaction of 3T3 fibroblasts. Our findings indicate that inhibiting canonical and several non-canonical signaling pathways originating from the activated TGF- β receptor does not hinder the directed migration of 3T3 cells to the cathode. Furthermore, suppression of TGF- β receptor expression does not eliminate the directional migration effect of 3T3 cells in the electric field. Additionally, there is no observed redistribution of the TGF- β receptor in the electric field. However, our studies affirm the significant involvement of Phosphoinositide 3-Kinase (PI3K) in electrotaxis, suggesting that in our model, its activation is likely associated with factors independent of TGF β action.

KEYWORDS

electric field, electrotaxis, cell migration, TGF β signaling, 3T3 fibroblasts

Introduction

The existence of endogenous electric fields in diverse anatomical locations within living organisms has been extensively documented across various research accounts [for a comprehensive overview, refer to the work of [McCaig et al. \(2005\)](#)]. These electric fields emerge from polarized ion transport across epithelial tissues, resulting in the formation of a transepithelial potential. Following the disruption of the epithelial layer, such as by injury, this potential collapses at the center of the wound, while remaining stable in distal regions where ion transport is unaffected. This creates a voltage gradient, forming a direct current electric field (dcEF) with a vector parallel to the epithelial surface, and the wound center acting as the cathode ([McCaig et al., 2009](#)). Evidence increasingly highlights the pivotal role of electric signals in guiding cell migration during processes such as wound

healing, embryonic development, and the metastasis of cancer (Djamgoz et al., 2001; McCaig et al., 2005; Zhao, 2009). This phenomenon is referred to as electrotaxis and is defined as an active directional movement toward the cathode or anode.

While electrotaxis is well-documented in various cell types, the molecular mechanisms employed by cells to sense electric fields remain largely elusive. It is hypothesized that electrophoretic or electroosmotic forces redistribute the charged components of the cell membrane, including receptors for chemoattractants. This redistribution could lead to a higher concentration of these receptors on the side of the cell facing the cathode (or anode), potentially driving asymmetric signaling that underlies directional movement (McCaig et al., 2005; Allen et al., 2013).

The role of chemoattractant receptor redistribution on the cell membrane during electrotaxis is critically important. In particular, the Epidermal Growth Factor (EGF) receptor has been identified as a key player in the electrotactic responses of various cell types, including corneal epithelial cells, keratinocytes, and breast cancer cells (Fang et al., 1999; Zhao et al., 2002; Pu et al., 2007). Small direct current electric fields not only upregulate the expression of EGF receptors but also induce their asymmetrical distribution within the cell membrane. Nevertheless, it has been proposed that the electrotaxis process depends on the redistribution of receptors specific to additional chemotactic factors such as Basic Fibroblast Growth Factor (bFGF), acetylcholine, Vascular Endothelial Growth Factor (VEGF), and Transforming Growth Factor Beta (TGF- β) (Orida and Poo, 1978; Zhao et al., 1996; Zhao et al., 1999; Zhao et al., 2012). However, the mechanism of receptor translocation does not sufficiently explain the nature of the first rapid reactions of cells to dcEF (Korohoda et al., 2000; Djamgoz et al., 2001; Zimolag et al., 2017). Another significant hypothesis posits that the mechanism underlying electrotaxis could stem from uneven activation of different ion channels within the cell membrane. Several ion channels have been implicated in the electrotactic responses of diverse cell types. These include calcium channels (Mycielska and Djamgoz, 2004), voltage-gated sodium channels (Djamgoz et al., 2001), voltage-gated potassium Kv1.2 channels (Zhang et al., 2016), inwardly rectifying potassium channels (Kir4.2) (Nakajima et al., 2015), and ion transporters such as Na, K-ATPase (NaKA) and Na⁺/H⁺ exchanger isoforms (NHE1 and 3) (Özkucur et al., 2011). Additionally, Liu et al. documented the activation of Na⁺ and K⁺ pumping modes of (Na,K)-ATPase by an oscillating electric field (Liu et al., 1990). Furthermore, large-scale screening methods identified several ion channel genes as potential key players in electrotaxis (Nakajima et al., 2015; Lasota et al., 2024).

In our previous investigation (Lasota et al., 2024), we demonstrated that in slowly migrating 3T3 cells, the response to a direct current electric field (dcEF) occurs quite swiftly, with initial signs becoming apparent after just 1 min of exposure. This strongly suggests that the primary mechanism governing the

electrotactic response is linked to the activation of ion channels rather than the translocation of cell membrane receptors. Indeed, through comprehensive screening, we identified several ion channel genes as potentially involved in 3T3-cell electrotaxis. Notably, the electrotactic response of 3T3 cells was significantly reliant on inwardly rectifying potassium channels (Kir4.2). Since inhibiting the Kir4.2 channel only diminishes the directional movement of 3T3 cells for approximately 1–2 h, followed by the reappearance of electrotaxis, we proposed a biphasic mechanism for the electrotaxis of mouse 3T3 fibroblasts. According to this model, the activation of ion channels triggers the initial rapid cellular response to an electric field, while the redistribution of membrane receptors is responsible for the sustained directionality of cell movement over the long term. Our preliminary findings indicated that the prolonged response might be attributed to the relocation of the EGF receptor in the membrane of 3T3 cells. On the other hand, we have proven the involvement of TGF β signaling in the electrotaxis of another cell type – human bronchial fibroblasts (Pavlenko et al., 2023). Building on these findings, the current study delves into the role of TGF β signaling in the long-term reaction of 3T3 fibroblasts to an electric field.

Materials and methods

Cell culture

Mouse 3T3 fibroblasts (ATCC CRL-1658) were cultured in DMEM HG (Dulbecco's Modified Eagle's Medium High Glucose) medium (Sigma–Aldrich, St. Louis, MO, United States), supplemented with 10% FBS (Fetal Bovine Serum) (Gibco, Waltham, MA, United States), penicillin (100 IU/mL), and streptomycin (100 μ g/mL) (herein referred to as the 'complete culture medium') under standard conditions at 37°C and 5% CO₂. Cells were passaged using 0.25% trypsin/EDTA (Gibco, Waltham, MA, United States) approximately every third day to maintain confluency below 80%.

Cell seeding and application of electric field

To apply a direct current electric field (dcEF) to the cells, we used a custom electrotactic chamber based on a previously described protocol with minor modifications (Sroka et al., 2018). The scheme depicting the methodology of electrotaxis examination is presented in Supplementary Figure S1. We seeded 1×10^4 cells onto a sterile $60 \times 35 \times 0.2$ mm cover glass using 400 μ L of complete culture medium, achieving a final cell density of approximately 2.5×10^3 cells/cm². Before the experiment, the second part of the observation chamber was assembled using another cover glass and two additional $60 \times 10 \times 0.2$ mm glass

pieces, connected with double-sided adhesive tape (tesa SE, Hamburg, Germany). This assembly, once completed, was filled with fresh complete culture medium or serum-free medium and inserted into an external electrotactic chamber made of PVC. Ag|AgCl electrodes (each 6 cm²) immersed in PBS were connected to a power supply. These electrodes were linked to the observation chamber using salt bridges made of glass pipes filled with agar (2% in 0.5 M KCl). Applying a dcEF with an intensity of 3 V/cm completed the setup. In the case of experiments without a dcEF, cells were seeded onto 24-well plates with glass bottoms (Eppendorf, Hamburg, Germany) in the quantity of 5×10^3 per well.

Registration and analysis of cell migration

Time-lapse imaging was conducted using integrated modulation contrast (IMC). For electrotaxis studies, a Leica DM IL LED microscope (Leica, Wetzlar, Germany) equipped with a Moticam 3.0 camera controlled by Motic Images Plus 3.0 software (both Motic, Xiamen, China) was used. For the registration in isotropic conditions (w/o dcEF), we employed a Leica DMI6000B motorized microscope with a Leica DFC360FX camera operated via LAS X 3.4 software (all Leica, Wetzlar, Germany). A temperature of 37°C was maintained inside the observation chamber using an environmental chamber and a heating unit. To offset the lack of CO₂ control, HEPES buffer (15 mM) was added to the complete culture medium before each recording session. The images were captured every 5 min for 4 h (with the cathode on the right-hand side).

Analysis of single-cell migration was performed using Hiro 1.0.0.4 software (Krecioch et al., 2015; Sroka et al., 2016; Sroka et al., 2018), where cell migration trajectories were constructed from manually identified cell centroids. To obtain circular diagrams, the initial point of each trajectory was placed in the origin of the coordinate system. The following quantitative parameters were calculated: (a) the speed of cell migration ($\mu\text{m}/\text{min}$)—the total length of the cell trajectory divided by the time of recording; (b) cell displacement (μm)—the length of the line segment from the first to the last position of a cell; (c) average directional cosine γ — γ is the angle formed by the line that connected the initial point of trajectory to subsequent cell positions and the X-axis (parallel to the vector of EF); (d) CME (Coefficient of Movement Efficiency)—representing the ratio of displacement to the total length of the cell trajectory. It approaches 1 when cell migration is persistent and decreases toward 0 when the direction of movement changes frequently.

Pharmacological modification of signaling pathways

To investigate the role of TGF β signaling in the electrotaxis of 3T3 fibroblasts, we utilized inhibitors targeting both the

canonical and noncanonical TGF- β pathways. Specifically, to block the canonical Smad-dependent signaling pathway, SB431542 (10 μM) was introduced into the complete culture medium during the preparation of the chamber. This inhibitor was applied 30 min prior to recording cell migration and was present throughout the duration of the experiment. To inhibit the noncanonical signaling pathways, the following inhibitors were added: U0126 (10 μM) for MEK1/2, SB203580 (10 μM) for p38, Y-27632 (10 μM) for ROCK, and LY-294002 (20 μM) for PI3K, following the protocol for the SB431542 inhibitor (all inhibitors from Sigma-Aldrich, St. Louis, MO, United States). In experiments without the presence of serum, the serum-free medium was additionally supplemented with TGF- β 1 at a concentration of 5 ng/mL.

Knockdown of the TGF- β receptor gene

To verify the involvement of Tgfr2 in the electrotaxis of 3T3 fibroblasts, the receptor was knocked down with a specific siRNA. Briefly, 5×10^4 cells/well were seeded into a 12-well plate the day before. Cells were transfected with 25 nM siRNA targeting mouse Tgfr2 (#AM16708, siRNA ID: 64894, Ambion, Austin, TX, United States) or non-targeting control (#AM4611, Ambion) using DharmaFECT 1 (Dharmacon, Lafayette, CO, United States) as the transfection reagent. The procedure was performed according to the manufacturer's instructions. Approximately 24 h after transfection, cells were harvested and seeded into an electrotactic chamber to allow for adherence. Electrotaxis was analyzed 24 h later as described above.

Western Blot analysis

Cells transfected with siRNA were harvested 48 h after transfection and lysed with RIPA lysis buffer (Sigma-Aldrich) supplemented with protease and phosphatase inhibitors (Thermo Fisher Scientific, Waltham, MA, United States). The lysates were then sonicated (3×10 s) with intermediate incubations on ice and centrifuged at 16,000 g for 10 min at 4°C to isolate the protein fraction. Protein concentration was measured using a BCA assay (Thermo Fisher Scientific) according to the manufacturer's instructions. Samples were then mixed with 4x Loading Protein Buffer Plus (Eux, Gdańsk, Poland) and boiled at 95°C for 5 min. 10 μg protein samples were separated by SDS-PAGE using Miniprotean TGX Gel, 4%–15% (Bio-Rad, Hercules, CA, United States) and transferred onto a polyvinylidene fluoride (PVDF) membrane using a Trans-Blot Turbo Transfer Pack Midi Format 0.2 μM PVDF (Bio-Rad) in a semi-dry transfer at 25 V, 1.3 A for 7 min in the Trans-Blot Turbo Transfer System (Bio-Rad). Membranes were incubated in 3% BSA in TBST (0.05% (v/v) Tween 20 in

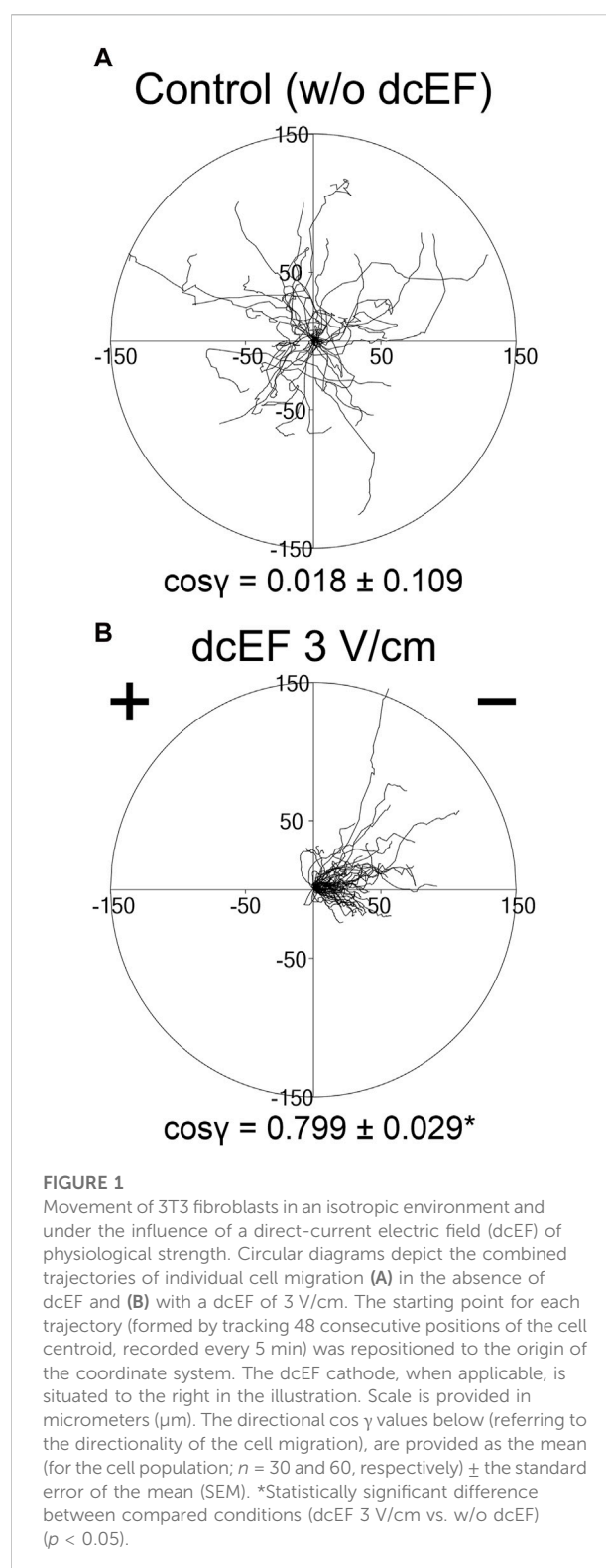
Tris-buffered saline) for 90 min to block nonspecific binding sites. The membranes were then incubated with primary antibodies against TGFBR2 (#GTX55814, GeneTex, Irvine, CA, United States) or GAPDH (#MA5-15738, Invitrogen/Thermo Fisher Scientific) as a loading control overnight at 4°C with gentle shaking. The next day, the membranes were washed three times with TBST and incubated with horseradish peroxidase (HRP)-conjugated secondary antibodies: goat anti-rabbit IgG, horse anti-mouse IgG (#7074 and #7076, respectively, both from Cell Signaling Technology, Danvers, MA, United States) in 3% BSA in TBST for 50 min at room temperature. After washing the membranes 3 times with TBST, the signal was detected with the chemiluminescent HRP substrate (Merck, Rahway, NJ, United States) in a ChemiDoc XRS + imager (BioRad). Densitometric analysis was performed using Quantity One software (Bio-Rad).

TGF- β receptor distribution

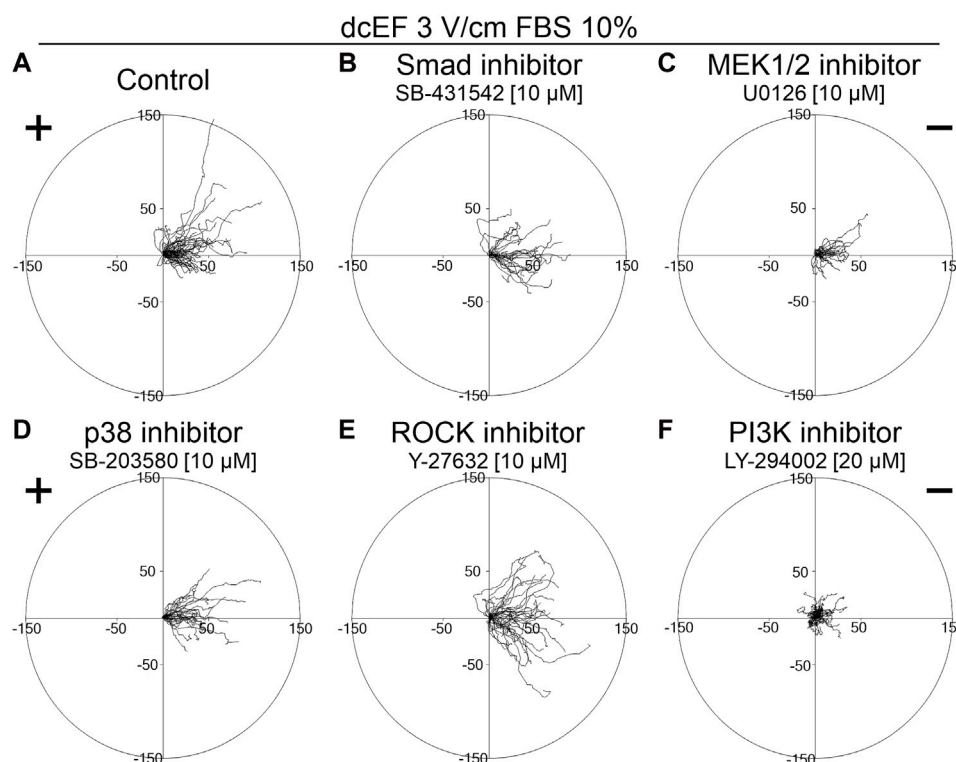
3T3 fibroblasts were seeded into a 24-well plate at a density of 2.5×10^4 cells per well and incubated overnight under standard conditions. The next day, cells were transfected in accordance with the manufacturer's protocol (Thermo Fisher Scientific, Waltham, MA, United States) using 0.75 μ L of Lipofectamine 3000 reagent and 0.5 μ g of a plasmid vector encoding the TGFBR1 (ALK5) receptor fused to an mEmerald Green fluorescent protein (Addgene, Watertown, MA, United States, #62751) for each well. Twenty-four hours post-transfection, cells were reseeded onto $60 \times 35 \times 0.2$ mm glass slides for the electrotaxis chamber as outlined in the preceding section. Given the rapid reduction in the expression of the protein, transient transfection was scheduled 48 h before the planned imaging of the receptor redistribution. Imaging was done utilizing a Leica DMI8 inverted fluorescence microscope equipped with a DFC7000 GT monochromatic CCD camera, dry HCX APO U-V-I 40x/0.75 DRY UV objective, a GFP-optimized filter set (all Leica, Wetzlar, Germany), and a CoolLED pE-4000 LED illuminator (CoolLED Ltd., Andover, Great Britain). Following the application of the electric field, as previously described, images of fluorescent cells across various fields of view were recorded. These images were then processed with ImageJ Fiji software (National Institute of Health, Bethesda, MD, United States) (Schindelin et al., 2012), i.e., the images were shading corrected and used for designation of plot profiles along lines with a thickness of 5 pixels, with the intention of reducing noise.

Statistical analysis

The statistical significance of variances in cell migration speed, cell displacement, and CME was evaluated using the



Student's t-test. In contrast, for directionality, these differences were examined using a non-parametric U-Mann-Whitney test due to the nature of this parameter and its inherent lack of a normal distribution (confirmed by the Shapiro-Wilk test). All

**FIGURE 2**

The role of TGF- β signaling in the electotaxis of 3T3 fibroblasts examined in the presence of a serum. Circular diagrams illustrating composite cell trajectories under various conditions: (A) control conditions (dcEF 3 V/cm, FBS 10%), and in the presence of (B) Smad inhibitor - SB-431542 (10 μ M), (C) MEK1/2 inhibitor - U0126 (10 μ M), (D) p38 inhibitor - SB-203580 (10 μ M), (E) ROCK inhibitor - Y-27632 (10 μ M), and (F) PI3K inhibitor - LY-294002 (20 μ M). The methodology for constructing and displaying these diagrams follows that of the previous figure (refer to Figure 1).

statistical analyses were conducted using GraphPad Prism version 8.0.1 (GraphPad Software, Boston, MA, United States), with a threshold for statistical significance set at $p < 0.05$.

Results

The impact of inhibiting canonical and non-canonical TGF- β signaling pathways on 3T3 cell electotaxis in the presence of a serum

As previously communicated, 3T3 fibroblasts in a medium with 10% FBS exhibit robust electotactic activity (Lasota et al., 2024). Indeed, as shown in Figure 1A, in the absence of an electric field, the 3T3 cells displayed random movements ($\cos \gamma = 0.018 \pm 0.109$). However, following the application of an electric field (3 V/cm), the cell migration became distinctly directional, with cells moving toward the cathode ($\cos \gamma = 0.799 \pm 0.029$) (Figure 1B).

To determine the role of TGF β in directing the migration of 3T3 cells in an electric field, we assessed the effects of inhibiting

both canonical and non-canonical signaling pathways activated by TGF β , using specific pharmacological inhibitors at concentrations validated in our previous studies (Paw et al., 2021; Pavlenko et al., 2023). As presented in Figure 2 and Figure 3D, inhibition of the canonical Smad-dependent pathway with SB431542 did not alter the electotaxis of 3T3 cells. Similarly, inhibitors of noncanonical TGF β signaling pathways, specifically MEK1/2 (U0126), p38 (SB203580), and ROCK (Y-27632), did not affect the directional migration of 3T3 cells in the electric field. However, the PI3K signaling pathway stood out as its inhibition with LY-294002 significantly reduced the directional cosine from 0.799 ± 0.029 under the control conditions to 0.347 ± 0.092 with the inhibitor present (Figure 3D; Table 1), pointing to a critical role of PI3K in migration directionality. Notably, while U0126 (MEK1/2 inhibitor) and Y-27632 (ROCK inhibitor) significantly influenced the speed of migration and cell displacement, suggesting the importance of these signaling pathways for motile activity, they did not affect the directionality of cell movement (Figure 3; Table 1). A similar effect of these inhibitors on the migration of 3T3 cells was found under control conditions without the application of an electric field (Supplementary Figure S2).

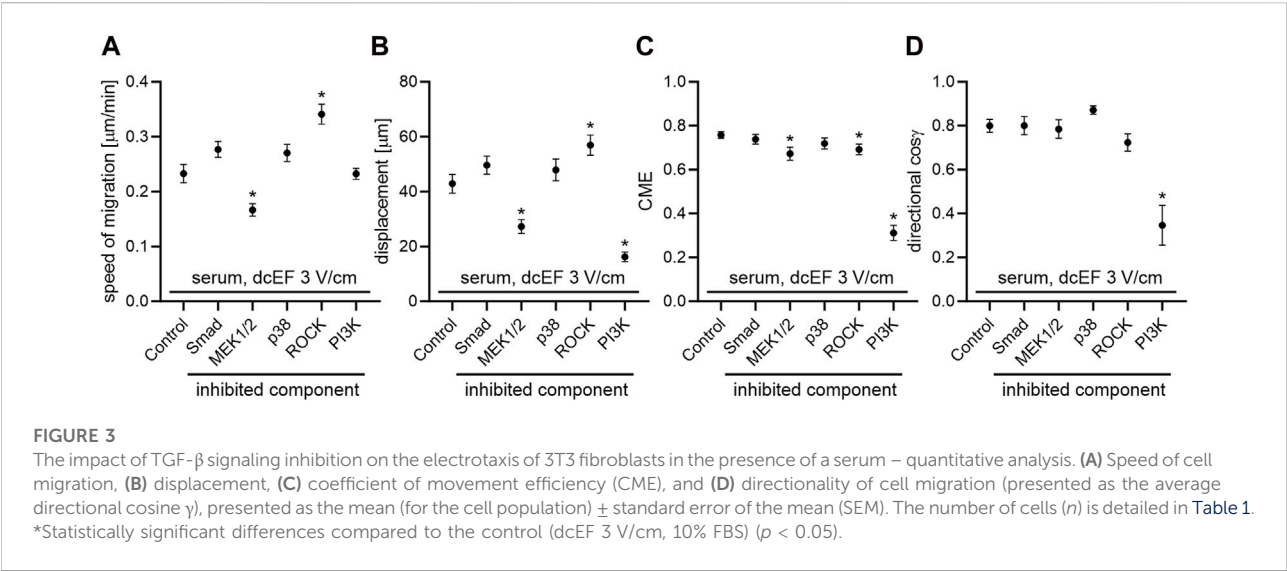


TABLE 1 The impact of TGF- β signaling inhibition on the electotaxis of 3T3 fibroblasts in the presence of a serum.

	Serum, dcEF 3 V/cm					
	Control (serum, dcEF 3 V/cm) (n = 60)	Smad inh.- SB-431542 (10 μ M) (n = 30)	MEK 1/2 inh.- U0126 (10 μ M) (n = 30)	p38 inh.- SB-203580 (10 μ M) (n = 30)	ROCK inh.- Y-27632 (10 μ M) (n = 40)	PI3K inh.- LY-294002 (20 μ M) (n = 30)
Speed of migration [μ m/min]	0.233 \pm 0.017	0.277 \pm 0.015	0.166 \pm 0.011	0.271 \pm 0.016	0.341 \pm 0.018 ^a	0.233 \pm 0.010
Displacement [μ m]	42.879 \pm 3.391	49.657 \pm 3.333	27.285 \pm 2.493 ^a	47.910 \pm 4.025	56.967 \pm 3.693 ^a	16.227 \pm 1.754 ^a
CME	0.758 \pm 0.015	0.739 \pm 0.022	0.673 \pm 0.030 ^a	0.720 \pm 0.025	0.692 \pm 0.024 ^a	0.312 \pm 0.035 ^a
Cosine γ	0.799 \pm 0.029	0.800 \pm 0.042	0.785 \pm 0.043	0.871 \pm 0.020	0.724 \pm 0.040	0.347 \pm 0.092 ^a

^aStatistically significant differences relative to control (serum, direct current electric field 3 V/cm) ($p < 0.05$).

The presented results underscore that among the TGF β -activated signaling pathways we explored, only the PI3K-dependent pathway is crucial for electotaxis. Nonetheless, given that this pathway can also be activated by additional factors within the FBS (e.g., EGF), we conducted additional experiments to investigate the impact of the tested inhibitors on the electotaxis of 3T3 cells in a serum-free medium, supplemented with exogenously added TGF β .

The impact of inhibiting canonical and non-canonical TGF- β signaling pathways on 3T3 cell electotaxis in a serum-free media

In serum-free conditions, 3T3 cells demonstrated a distinct electotactic response, migrating toward the cathode in an

electric field of 3V/cm (Figures 4A,C). The directional cosine in these conditions was only marginally lower than in the presence of 10% FBS (0.636 \pm 0.050 and 0.799 \pm 0.029, respectively). However, both the speed of cell migration and their final displacement were reduced in the absence of serum compared to conditions with 10% serum (0.169 \pm 0.006* μ m/min vs. 0.233 \pm 0.017 μ m/min and 20.098 \pm 1.364* μ m vs. 42.879 \pm 3.391 μ m, respectively). Notably, adding exogenous TGF β (5 ng/mL) did not alter the directionality of cell movement (Figure 4F), yet significantly enhanced their migration speed and final displacement (Figure 4E; Table 2).

As depicted in Figure 5 and Figure 6, in serum-free media at the presence of TGF β (5 ng/mL), SB431542, an inhibitor targeting the canonical Smad-dependent signaling pathway, did not impact the electotaxis of 3T3 cells. Similarly, inhibitors of noncanonical TGF β signaling pathways such as p38 (SB203580) and ROCK (Y-27632) exhibited no discernible

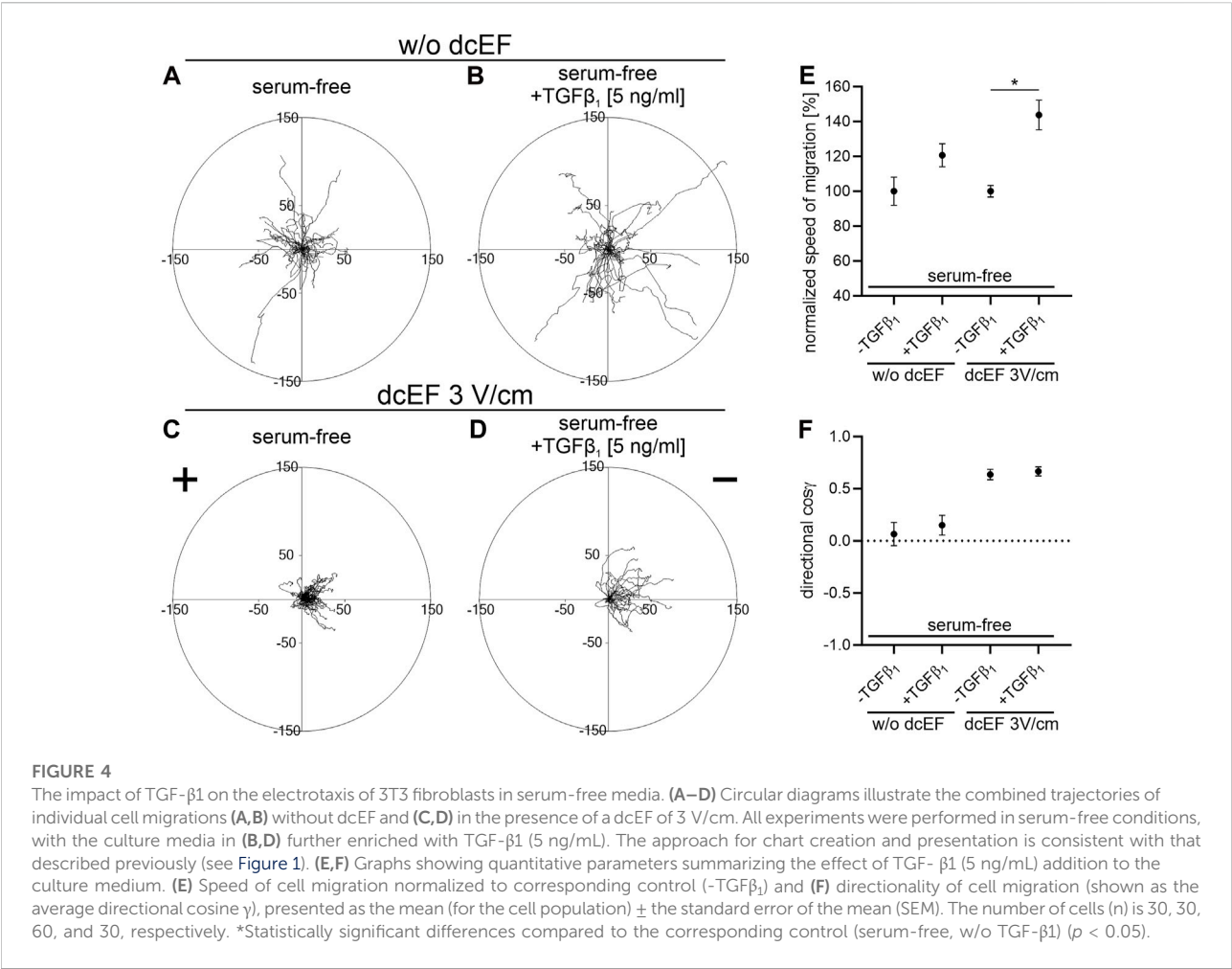


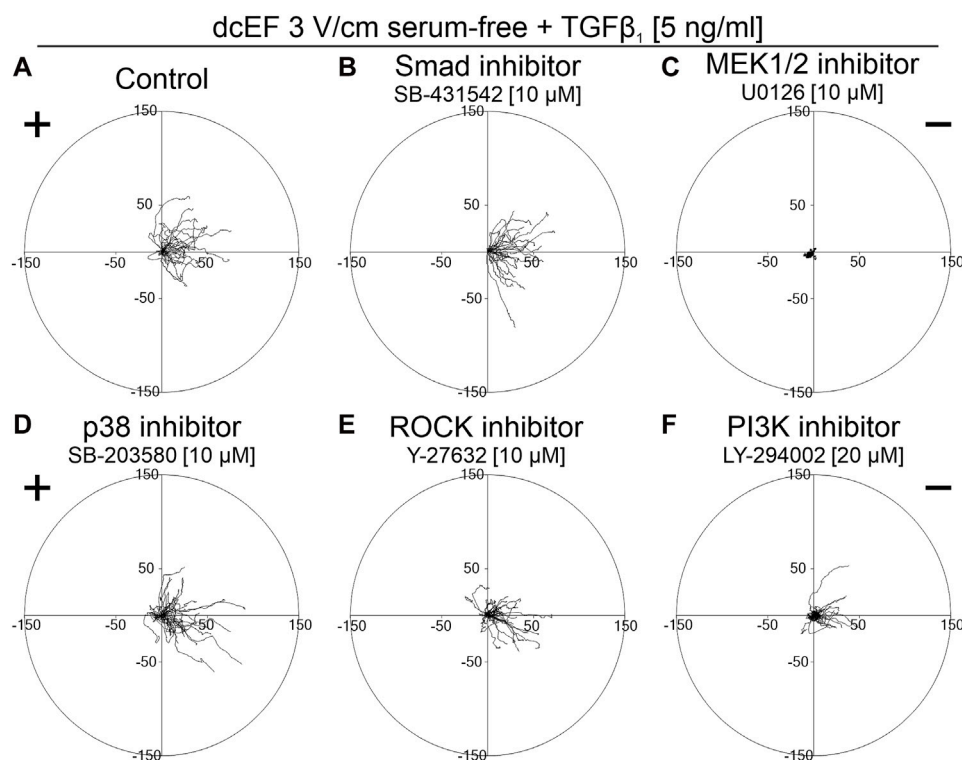
TABLE 2 The impact of TGF- β signaling inhibition on the electotaxis of 3T3 fibroblasts in the serum-free medium containing TGF- β 1.

	Serum-free + TGF β 1 (5 ng/mL), dcEF 3 V/cm				
	Control (serum-free + TGF β 1 5 ng/mL, dcEF 3 V/cm) (n = 30)	Smad inhibitor - SB-431542 (10 μ M) (n = 30)	p38 inhibitor - SB-203580 (10 μ M) (n = 40)	ROCK inhibitor - Y-27632 (10 μ M) (n = 35)	PI3K inhibitor- LY-294002 (20 μ M) (n = 30)
Speed of migration [μ m/min]	0.243 \pm 0.015	0.233 \pm 0.014	0.251 \pm 0.014	0.190 \pm 0.012 ^a	0.191 \pm 0.013 ^a
Displacement [μ m]	35.990 \pm 3.265	41.918 \pm 3.457	33.711 \pm 3.912	27.825 \pm 2.853	19.756 \pm 3.029 ^a
CME	0.608 \pm 0.030	0.736 \pm 0.029 ^a	0.518 \pm 0.039	0.586 \pm 0.035	0.396 \pm 0.044 ^a
Cosine γ	0.666 \pm 0.045	0.767 \pm 0.035	0.517 \pm 0.072	0.539 \pm 0.073	0.506 \pm 0.081

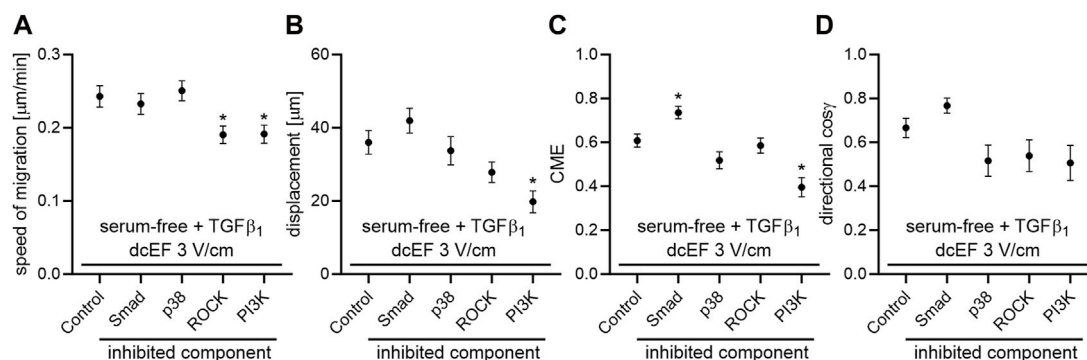
^aStatistically significant differences relative to the control (serum-free + Transforming Growth Factor Beta 1, direct current electric field 3 V/cm) ($p < 0.05$).

effect on the directional migration of 3T3 cells in the electric field. Intriguingly, even the inhibition of the PI3K signaling pathway did not significantly diminish electotaxis under these experimental conditions. It is worth emphasizing that the inhibitor of MEK1/2 (U0126) completely halted the migration

of 3T3 cells (Figure 5C). It is important to note that data from non-migrating cells were excluded from further analysis, as movement parameters could not be determined. The effects of all these inhibitors on the migration of 3T3 cells in the absence of an electric field are detailed in Supplementary Figure S3.

**FIGURE 5**

The role of TGF- β signaling in the electotaxis of 3T3 fibroblasts examined in the serum-free medium containing TGF- β_1 . Circular diagrams illustrating composite cell trajectories under various conditions: (A) control conditions (dcEF 3 V/cm, serum-free, TGF- β_1 (5 ng/mL)), and in the presence of (B) Smad inhibitor - SB-431542 (10 μ M), (C) MEK1/2 inhibitor - U0126 (10 μ M), (D) p38 inhibitor - SB-203580 (10 μ M), (E) ROCK inhibitor - Y-27632 (10 μ M), and (F) PI3K inhibitor - LY-294002 (20 μ M). The methodology for constructing and displaying these diagrams follows that of Figure 1.

**FIGURE 6**

The impact of TGF- β signaling inhibition on the electotaxis of 3T3 fibroblasts in the serum-free medium containing TGF- β_1 – quantitative analysis. (A) Speed of cell migration, (B) displacement, (C) coefficient of movement efficiency (CME) and (D) directionality of cell migration (presented as the average directional cosine γ), presented as the mean (for the cell population) \pm the standard error of the mean (SEM). The number of cells (n) is detailed in Table 2. *Statistically significant differences compared to the control (dcEF 3 V/cm, serum-free, TGF- β_1 (5 ng/mL)) ($p < 0.05$).

The obtained results suggest that although the PI3K pathway emerges as a crucial component in the response of 3T3 cells to an electric field, its activation in this context does not appear to be directly related to TGF β . Instead, it is likely associated with other factors present in the serum that stimulate this pathway.

Given that our findings do not affirm a substantial role of TGF β in driving electotaxis, we endeavoured in subsequent experiments to validate the hypothesis concerning the translocation of the TGF β receptor within the cell membrane under the influence of an applied electric field.

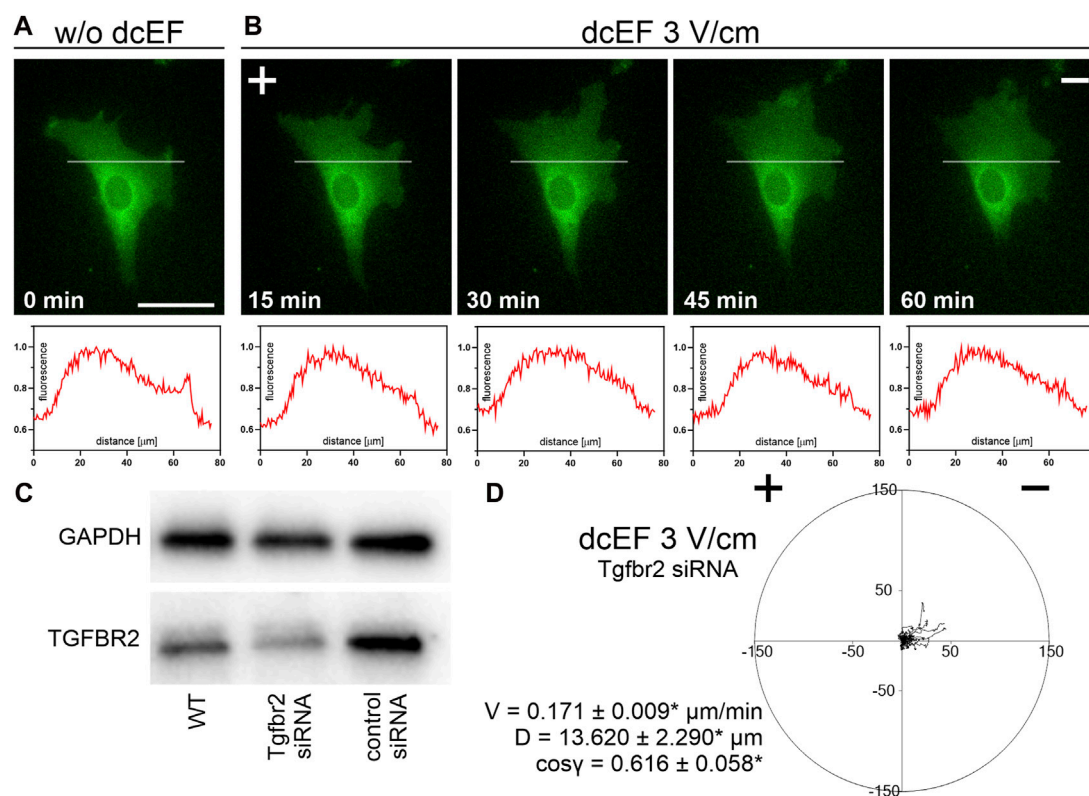


FIGURE 7

The distribution and role of TGF receptors during the electotaxis of 3T3 fibroblasts. (A,B) Fluorescence images of cells expressing TGFR1 (ALK5) fused to a fluorescent protein (green) both in the absence of an electric field (A) and following a defined period of stimulation by a dcEF of 3 V/cm (B). The scale bar in (A), representing 50 μm , applies to all images. When applicable, the dcEF's cathode is positioned on the right side of the field of view. Each image is accompanied by a corresponding plot profile that illustrates the normalized intensity of green fluorescence along the indicated white line. (C) Western blot analysis demonstrates reduced levels of TGFR2 protein in cells transfected with specific siRNA compared to wild-type cells and those transfected with non-targeting siRNA. (D) A circular diagram shows the combined migration trajectories of individual cells (with Tgfrb2 silenced) in a dcEF of 3 V/cm. The approach for diagram creation and presentation is consistent with that described in a prior figure (see Figure 1). Quantitative parameters: V – speed of cell migration, D – displacement and directional $\cos \gamma$ (referring to the directionality of cell migration), are provided as the mean (for the cell population $n = 30$) \pm the standard error of the mean (SEM). *Statistically significant differences compared to the control (dcEF 3 V/cm, 10% FBS) ($p < 0.05$).

TGF β receptor redistribution in an electric field and its implication in 3T3 fibroblast electotaxis

To test this hypothesis, we investigated the kinetics of TGF β R redistribution within the cell membrane of the 3T3 cells exposed to a direct current electric field (dcEF) of 3 V/cm, focusing on potential receptor displacement within a specified time frame. The results, illustrated in Figures 7A,B, reveal that after 15–60 min of exposure to a 3 V/cm dcEF, there was no detectable accumulation of TGF β receptors on the cathode- or anode-facing side of the cell.

As this result aligned with our earlier observations, we proceeded to investigate the impact of TGF β receptor silencing (Figure 7C) on the electotaxis of 3T3 fibroblasts in a medium containing 10% FBS. As depicted in Figure 7D, the silencing of the receptor led to only a minor reduction in the

average directional cosine, with values slightly lower than the control ($\cos \gamma = 0.616 \pm 0.058^*$ compared to 0.799 ± 0.029).

Discussion

The understanding of the intricacies of electotaxis remains incomplete, with two main hypotheses competing to explain this phenomenon. The first hypothesis predominantly concentrates on the asymmetrical activation of ion channels within the cell membrane, triggered by hyperpolarization of the cell membrane at the anodal side and depolarization at the cathodal side of the cell in response to an external electric field, or induced by mechanical effects from dcEF (Mycielska and Djamgoz, 2004; Gao et al., 2011; Allen et al., 2013). Although effective in elucidating the initial rapid responses of cells to dcEF (Korohoda et al., 2000; Djamgoz et al., 2001), this hypothesis

does not effectively explain the unclear mechanism responsible for the asymmetrical activation of these ion channels by the electric field (Mycielska and Djamgoz, 2004).

On the other hand, the second plausible hypothesis posits that electrophoretic or electroosmotic forces alter the distribution of charged components on the cell membrane, including receptors for chemoattractants. It is proposed that an increased concentration of these receptors on the side of the cell facing the cathode (or anode) triggers asymmetric signaling and directional motility (McCaig et al., 2005; Allen et al., 2013). However, this hypothesis does not fully explain the swift initial reactions of cells to dcEF (Korohoda et al., 2000; Djamgoz et al., 2001). Nevertheless, it should be acknowledged that both mechanisms, whether activation of the ion channel or receptor redistribution, are not mutually exclusive and may synergistically contribute to the process of electrotactic migration.

In our previous study (Lasota et al., 2024), we demonstrated the rapid response of 3T3 cells to a direct current electric field (dcEF), manifesting within the first minute of exposure. This response was notably reliant on inwardly rectifying potassium channels, particularly Kir4.2. Inhibiting these channels led to a transient reduction in the directional movement of 3T3 cells lasting approximately 1–2 h, followed by a reappearance of electrotaxis. We proposed a biphasic mechanism for the electrotaxis of mouse 3T3 fibroblasts, suggesting that ion channel activation underlies the initial rapid cellular response to an electric field, while the long-term maintenance of directional movement is facilitated by the redistribution of membrane receptors. Notably, we observed a distinct accumulation of EGF receptors on the side of the cell facing the cathode after 30–60 min in a dcEF (3 V/cm). Moreover, inhibition of the EGF receptor signaling pathway partially impeded the electrotaxis of 3T3 fibroblasts. Given that the relocation of EGF receptors has been established as a crucial factor in electrotaxis for various cell types (Fang et al., 1999; Zhao et al., 1999; Zhao et al., 2002), we postulated that the EGF pathway may underlie the sustained electrotactic response in 3T3 cells.

However, beyond the EGF receptor, the importance of receptor redistribution in the electrotaxis process has been suggested for additional chemotactic factors (Orida and Poo, 1978; Zhao et al., 1996; Zhao et al., 1999; Zhao et al., 2012), including Transforming Growth Factor β (TGF β). Zhao et al. (1996), Zhao et al. (1999) reported that TGF β restored cathodal-directed migration of corneal epithelial cells (CECs) under serum-free conditions. However, these studies did not examine how the inhibition of TGF β -activated signaling pathways might affect CEC electrotaxis.

Nevertheless, our research (Pavlenko et al., 2023) has shown that adult human bronchial fibroblasts respond to external electric fields by orienting themselves perpendicular to the field lines and exhibit efficient electrotaxis toward the anode.

These processes depended on both canonical and non-canonical TGF- β pathways. This observation suggested the possibility that the electrotaxis of 3T3 fibroblasts might also be dependent on TGF β .

Transforming growth factor beta (TGF- β) is a cytokine known to activate a variety of signaling pathways, leading to diverse biological effects including the stimulation of cell migration (Hao et al., 2019; Tie et al., 2022; Massagué and Sheppard, 2023). Within TGF- β -induced migratory signaling, two main types of pathways are recognized: canonical and noncanonical. The canonical pathways are Smad-dependent, where TGF- β receptor activation leads to phosphorylation and activation of Smad2 and Smad3 proteins. These phosphorylated Smad proteins then form a complex with Smad4 to move into the cell nucleus, regulating the expression of genes associated with cell migration (Costanza et al., 2017; Tie et al., 2022). On the other hand, the noncanonical MAPK pathway, comprising ERK, JNK, and p38 MAPK, can be activated by TGF- β , affecting cytoskeletal dynamics, cell adhesion, and migration. Additionally, noncanonical pathways include the Rho GTPase pathway (involving RhoA, Rac1, and Cdc42) and the PI3K/Akt pathway, each playing a role in cell migration regulation (Ridley et al., 2003; Costanza et al., 2017; Tie et al., 2022). Nevertheless, there is a lack of genetic evidence and a structural foundation supporting the notion that MAPKs and PI3K directly act as mediators in TGF- β receptor signaling. Moreover, these pathways already have established agonists which are commonly present in the microenvironment of TGF- β target cells *in vivo*, prompting inquiries into the significance of TGF- β as an activator of these pathways (Tie et al., 2022).

Unexpectedly, in our hands, inhibiting both the canonical and several non-canonical signaling pathways from the activated TGF- β receptor did not hinder the directional migration of 3T3 cells toward the cathode. Notably, the only statistically significant reduction in electrotaxis occurred with the inhibition of PI3K kinase (Figure 2; Figure 3).

This observation aligns with previous reports highlighting the essential role of PI3K activity in electrotaxis. For instance, Zhao et al. (2006) found that the genetic disruption of phosphatidylinositol-3-OH kinase- γ (PI(3)K γ) diminished electric-field-induced signaling and abolished electrotaxis of healing epithelium in response to electric signals. Similarly, Meng et al. (2011) demonstrated the significance of the PI3K pathway in the electrotaxis of neural progenitor cells (NPCs) driven by electric fields in the presence of growth factors.

However, given that PI3K activity can also be induced by additional factors in FBS (such as EGF) (Zhao et al., 2006; Meng et al., 2011), subsequent experiments were conducted to examine the influence of the tested inhibitors on the electrotaxis of 3T3 cells in a serum-free medium,

supplemented with exogenously added TGF β . This approach aimed to minimize the influence of PI3K-activating chemoattractants other than TGF β . In this simplified model, none of the inhibitors used, including LY-294002 (PI3K inhibitor), affected electrotaxis. This suggests that while PI3K plays a crucial role in the induction of directional migration of 3T3 cells in an electric field (as evidenced by the inhibition of electrotaxis in the presence of FBS after the addition of LY-294002), its activation in our experiments was probably related to the action of factors other than TGF β present in the serum. Literature reports, including our own (Zhao et al., 1996; Zhao et al., 1999; Meng et al., 2011; Lasota et al., 2024), suggest EGF as a possible activator.

The negligible effect of TGF signaling on the electrotaxis of 3T3 fibroblasts is further confirmed by the observation that the addition of TGF β in serum-free conditions does not substantially influence the directionality of cell movement (Figure 4). However, it is important to note that the presence of TGF β does induce a significant increase in the velocity of 3T3 cell movement (Figure 4E).

Our findings of TGF β 's limited role in the regulation of electrotaxis in 3T3 cells were further supported by experiments investigating the redistribution of TGF β receptors in an electric field. After 60 min in a dcEF of 3 V/cm, we did not observe any discernible accumulation of TGF β receptors on the cathode-facing side of the cells (Figure 7B). This is in line with Zhao et al. (1999), who also reported no clear asymmetry in TGF β receptor distribution under a 1.5 V/cm electric field, even after 3 h. Substantial accumulation was only noticeable after 12–16 h in the electric field. Although TGF β partially restored cathodal-directed migration of corneal epithelial cells (CECs) in a serum-free medium over a 5-h period, the mechanism responsible for the observed electrotaxis remained unclear (Zhao et al., 1999). Interestingly, the relatively low electroosmotic mobilities of the TGF β receptor also align with the theoretical model proposed by Sarkar et al. (2019). The non-involvement of TGF β in the regulation of electrotaxis in 3T3 fibroblasts was further validated through experiments where the silencing of TGF β receptors in 3T3 cells led to only a marginal reduction in the average directional cosine (Figure 7D).

By systematically inhibiting both canonical and non-canonical TGF- β signaling pathways, we demonstrated that TGF- β signaling does not play a major role in the directional migration of 3T3 fibroblasts in an electric field. The use of both serum-free and FBS-supplemented conditions further strengthens the reliability of our findings. Simultaneously, our study highlights significant insights into the role of PI3K kinase in the electrotaxis of 3T3 fibroblasts. However, our *in vitro* model has limitations, as it may not fully replicate the complex *in vivo* environment. Moreover, the findings, based on the 3T3 fibroblast cell line, may not represent the behavior of all fibroblast types. Notably, as mentioned before, we previously found that human

bronchial fibroblasts, which exhibit electrotaxis towards the anode, contrasting with the cathodal migration observed in 3T3 cells, rely on the TGF- β signaling pathways (Pavlenko et al., 2023).

While we focused on TGF- β and PI3K pathways, alternative signaling mechanisms such as ion channels and other growth factor receptors require further exploration. Our recent publication on ionic mechanisms and EGFR involvement in 3T3 electrotaxis has begun to explore these additional pathways (Lasota et al., 2024). Further investigations will focus on the dynamics of membrane receptors redistribution, aiming to validate the biphasic model proposed in our work.

Although specific *in vivo* experiments concerning the detailed cellular mechanisms of electrotaxis may be challenging, the application of electrostimulation in treating hard-to-heal wounds underscores the clinical relevance of understanding these mechanisms (Martin-Granados and McCaig, 2013). A deeper comprehension of electrotaxis could significantly enhance the efficacy of combining electrostimulation with pharmacological interventions in wound care. This integrated approach could lead to more targeted and effective treatments, paving the way for innovative therapeutic strategies in wound management.

Conclusion

Our study has shown that inhibition of both canonical and several non-canonical signaling pathways associated with the activated TGF- β receptor did not impede the directional migration of 3T3 cells to the cathode. Furthermore, silencing the expression of the TGF- β receptor failed to eliminate the directional migration of 3T3 cells in the electric field. Additionally, there was no redistribution of the TGF β receptor under electric field conditions. Nonetheless, our research confirms an important role for PI3K kinase in electrotaxis, but its activation in our model was probably related to the action of factors other than TGF β .

Data availability statement

The raw data supporting the conclusion of this article will be made available by the authors, without undue reservation.

Ethics statement

Ethical approval was not required for the studies on animals in accordance with the local legislation and institutional requirements because only commercially available established cell lines were used.

Author contributions

PC and SL contributed equally. Conceptualization: ZM, SL; methodology: ZM, SL and SB-W; validation: ZM, SL; formal analysis: PC, SL; investigation: PC, SL; resources: ZM, SB-W; data curation: ZM, SL; editing—original draft preparation: ZM, SL; writing—review and editing: ZM, SL; visualization: SL; supervision: ZM; project administration: ZM, SL; funding acquisition: ZM, SL. All authors contributed to the article and approved the submitted version.

Funding

The author(s) declare that financial support was received for the research, authorship, and/or publication of this article. This

work was supported by a grant provided by the National Science Centre, Poland, 2018/31/B/NZ3/01750.

Conflict of interest

The authors declare that the research was conducted in the absence of any commercial or financial relationships that could be construed as a potential conflict of interest.

Supplementary material

The Supplementary Material for this article can be found online at: <https://www.frontierspartnerships.org/articles/10.3389/abp.2024.12993/full#supplementary-material>

References

- Allen, G. M., Mogilner, A., and Theriot, J. A. (2013). Electrophoresis of cellular membrane components creates the directional cue guiding keratocyte galvnotaxis. *Curr. Biol.* 23, 560–568. doi:10.1016/j.cub.2013.02.047
- Costanza, B., Umelo, I. A., Bellier, J., Castronovo, V., and Turtoi, A. (2017). Stromal modulators of TGF- β in cancer. *J. Clin. Med.* 6, 7. doi:10.3390/jcm6010007
- Djamgoz, M. B. A., Mycielska, M., Madeja, Z., Fraser, S. P., and Korohoda, W. (2001). Directional movement of rat prostate cancer cells in direct-current electric field: Involvement of voltage-gated Na⁺ channel activity. *J. Cell Sci.* 114, 2697–2705. doi:10.1242/jcs.114.14.2697
- Fang, K. S., Ionides, E., Oster, G., Nuccitelli, R., and Isseroff, R. R. (1999). Epidermal growth factor receptor relocalization and kinase activity are necessary for directional migration of keratinocytes in DC electric fields. *J. Cell Sci.* 112 (Pt 12), 1967–1978. doi:10.1242/jcs.112.12.1967
- Gao, R. C., Zhang, X. D., Sun, Y. H., Kamimura, Y., Mogilner, A., Devreotes, P. N., et al. (2011). Different roles of membrane potentials in electrotaxis and chemotaxis of dictyostelium cells. *Eukaryot. Cell* 10, 1251–1256. doi:10.1128/EC.05066-11
- Hao, Y., Baker, D., and Ten Dijke, P. (2019). TGF- β -Mediated epithelial-mesenchymal transition and cancer metastasis. *Int. J. Mol. Sci.* 20, 2767. doi:10.3390/ijms20112767
- Korohoda, W., Mycielska, M., Janda, E., and Madeja, Z. (2000). Immediate and long-term galvanotactic responses of Amoeba proteus to dc electric fields. *Cell Motil. Cytoskelet.* 45, 10–26. doi:10.1002/(SICI)1097-0169(200001)45:1<10::AID-CM2>3.0.CO;2-T
- Krecioch, I., Madeja, Z., Lasota, S., Zimolag, E., and Sroka, J. (2015). The role of microtubules in electrotaxis of rat Walker carcinoma cells. *Acta Biochim. Pol.* 62, 401–406. doi:10.18388/abp.2015_1019
- Lasota, S., Zimolag, E., Bobis-Wozowicz, S., Pilipiuk, J., and Madeja, Z. (2024). The dynamics of the electrotactic reaction of mouse 3T3 fibroblasts. *Biochimica Biophysica Acta (BBA) - Mol. Cell Res.* 1871, 119647. doi:10.1016/j.bbamcr.2023.119647
- Liu, D. S., Astumian, R. D., and Tsong, T. Y. (1990). Activation of Na⁺ and K⁺ pumping modes of (Na,K)-ATPase by an oscillating electric field. *J. Biol. Chem.* 265, 7260–7267. doi:10.1016/s0021-9258(19)39108-2
- Martin-Granados, C., and McCaig, C. D. (2014). Harnessing the electric spark of life to cure skin wounds. *Adv. Wound Care* 3, 127–138. doi:10.1089/wound.2013.0451
- Massagué, J., and Sheppard, D. (2023). TGF- β signaling in health and disease. *Cell* 186, 4007–4037. doi:10.1016/j.cell.2023.07.036
- McCaig, C. D., Rajnicek, A. M., Song, B., and Zhao, M. (2005). Controlling cell behavior electrically: Current views and future potential. *Physiol. Rev.* 85, 943–978. doi:10.1152/physrev.00020.2004
- McCaig, C. D., Song, B., and Rajnicek, A. M. (2009). Electrical dimensions in cell science. *J. Cell Sci.* 122, 4267–4276. doi:10.1242/jcs.023564
- Meng, X., Arocena, M., Penninger, J., Gage, F. H., Zhao, M., and Song, B. (2011). PI3K mediated electrotaxis of embryonic and adult neural progenitor cells in the presence of growth factors. *Exp. Neurol.* 227, 210–217. doi:10.1016/j.expneurol.2010.11.002
- Mycielska, M. E., and Djamgoz, M. B. A. (2004). Cellular mechanisms of direct-current electric field effects: Galvanotaxis and metastatic disease. *J. Cell Sci.* 117, 1631–1639. doi:10.1242/jcs.01125
- Nakajima, K., Zhu, K., Sun, Y.-H., Hegyi, B., Zeng, Q., Murphy, C. J., et al. (2015). KCNJ15/Kir4.2 couples with polyamines to sense weak extracellular electric fields in galvanotaxis. *Nat. Commun.* 6, 8532. doi:10.1038/ncomms9532
- Orida, N., and Poo, M. M. (1978). Electrophoretic movement and localization of acetylcholine receptors in the embryonic muscle cell membrane. *Nature* 275, 31–35. doi:10.1038/275031a0
- Özkucur, N., Perike, S., Sharma, P., and Funk, R. H. W. (2011). Persistent directional cell migration requires ion transport proteins as direction sensors and membrane potential differences in order to maintain directedness. *BMC Cell Biol.* 12, 4. doi:10.1186/1471-2121-12-4
- Pavlenko, A., Lasota, S., Wnuk, D., Paw, M., Czyż, J., Michalik, M., et al. (2023). Bronchial fibroblasts from asthmatic patients display impaired responsiveness to direct current electric fields (dcEFs). *Biomedicine* 11, 2138. doi:10.3390/biomedicine11082138
- Paw, M., Wnuk, D., Nit, K., Bobis-Wozowicz, S., Szychowski, R., Ślusarczyk, A., et al. (2021). SB203580-A potent p38 MAPK inhibitor reduces the profibrotic bronchial fibroblasts transition associated with asthma. *Int. J. Mol. Sci.* 22, 12790. doi:10.3390/ijms222312790
- Pu, J., McCaig, C. D., Cao, L., Zhao, Z., Segall, J. E., and Zhao, M. (2007). EGF receptor signalling is essential for electric-field-directed migration of breast cancer cells. *J. Cell Sci.* 120, 3395–3403. doi:10.1242/jcs.002774
- Ridley, A. J., Schwartz, M. A., Burridge, K., Firtel, R. A., Ginsberg, M. H., Borisy, G., et al. (2003). Cell migration: Integrating signals from front to back. *Science* 302, 1704–1709. doi:10.1126/science.1092053
- Sarkar, A., Kobylkevich, B. M., Graham, D. M., and Messerli, M. A. (2019). Electromigration of cell surface macromolecules in DC electric fields during cell polarization and galvanotaxis. *J. Theor. Biol.* 478, 58–73. doi:10.1016/j.jtbi.2019.06.015
- Schindelin, J., Arganda-Carreras, I., Frise, E., Kaynig, V., Longair, M., Pietzsch, T., et al. (2012). Fiji: An open-source platform for biological-image analysis. *Nat. Methods* 9, 676–682. doi:10.1038/NMETH.2019
- Sroka, J., Krecioch, I., Zimolag, E., Lasota, S., Rak, M., Kedracka-Krok, S., et al. (2016). Lamellipodia and membrane blebs drive efficient electrotactic migration of rat Walker carcinoma cells WC 256. *PLoS One* 11, e0149133. doi:10.1371/journal.pone.0149133
- Sroka, J., Zimolag, E., Lasota, S., Korohoda, W., and Madeja, Z. (2018). Electrotaxis: cell directional movement in electric fields. *Methods Mol. Biol.* 1749, 325–340. doi:10.1007/978-1-4939-7701-7_23
- Tie, Y., Tang, F., Peng, D., Zhang, Y., and Shi, H. (2022). TGF- β signal transduction: Biology, function and therapy for diseases. *Mol. Biomed.* 3, 45. doi:10.1186/s43556-022-00109-9

Zhang, G., Edmundson, M., Telezhkin, V., Gu, Y., Wei, X., Kemp, P. J., et al. (2016). The role of Kv1.2 channel in electrotaxis cell migration. *J. Cell. Physiology* 231, 1375–1384. doi:10.1002/jcp.25259

Zhao, M. (2009). Electrical fields in wound healing-An overriding signal that directs cell migration. *Seminars Cell and Dev. Biol.* 20, 674–682. doi:10.1016/j.semcdb.2008.12.009

Zhao, M., Agius-Fernandez, A., Forrester, J. V., and McCaig, C. D. (1996). Orientation and directed migration of cultured corneal epithelial cells in small electric fields are serum dependent. *J. Cell Sci.* 109 (Pt 6), 1405–1414. doi:10.1242/jcs.109.6.1405

Zhao, M., Dick, A., Forrester, J. V., and McCaig, C. D. (1999). Electric field-directed cell motility involves up-regulated expression and asymmetric redistribution of the epidermal growth factor receptors and is enhanced by fibronectin and laminin. *Mol. Biol. Cell* 10, 1259–1276. doi:10.1091/mbc.10.4.1259

Zhao, M., Pu, J., Forrester, J. V., and McCaig, C. D. (2002). Membrane lipids, EGF receptors, and intracellular signals colocalize and are polarized in epithelial cells moving directionally in a physiological electric field. *FASEB J.* 16, 857–859. doi:10.1096/fj.01-0811fje

Zhao, M., Song, B., Pu, J., Wada, T., Reid, B., Tai, G., et al. (2006). Electrical signals control wound healing through phosphatidylinositol-3-OH kinase- γ and PTEN. *Nature* 442, 457–460. doi:10.1038/nature04925

Zhao, Z., Qin, L., Reid, B., Pu, J., Hara, T., and Zhao, M. (2012). Directing migration of endothelial progenitor cells with applied DC electric fields. *Stem Cell Res.* 8, 38–48. doi:10.1016/j.scr.2011.08.001

Zimolag, E., Borowczyk-Michalowska, J., Kedracka-Krok, S., Skupien-Rabian, B., Karnas, E., Lasota, S., et al. (2017). Electric field as a potential directional cue in homing of bone marrow-derived mesenchymal stem cells to cutaneous wounds. *Biochimica Biophysica Acta (BBA) - Mol. Cell Res.* 1864, 267–279. doi:10.1016/j.bbamcr.2016.11.011

Anesthesia and surgery induce changes in endogenous brain protective protein (RNF146) and delirium-like behavior in aged rats

Yubo Gao^{1,2#}, Xu Han^{1,3#}, Xiuhua Li^{1,3#}, Shaling Tang^{1,3}, Chun Zhang³, Xiaoxia Yang^{1,2}, Majid Alhomrani⁴, Abdulhakeem S. Alamri⁴, Ghulam Nabi⁵ and Xinli Ni¹✉

¹Department of Anesthesiology, General Hospital of Ningxia Medical University, Yinchuan, Ningxia, 750004, China; ²Department of Anesthesia and Perioperative Medicine, General Hospital of Ningxia Medical University, Yinchuan, Ningxia, 750004, China; ³Ningxia Key Laboratory of Cerebrocranial Diseases, Ningxia Medical University, Yinchuan, Ningxia, 750004, China; ⁴Department of Clinical Laboratory Sciences, The Faculty of Applied Medical Sciences, Taif University, Taif, Saudi Arabia; ⁵Institute of Nature Conservation, Polish Academy of Sciences, Kraków, 31120, Poland

Background: Postoperative delirium (POD) is a common complication after anesthesia and surgery, especially in the elderly. RNF146 has neuroprotective effects in cerebral ischemia, hypoxia, and chronic neurological diseases. However, whether RNF146 expression is related to the occurrence and development of POD remains unclear. Therefore, in this study, we aimed to determine whether RNF146 is involved in the occurrence of POD. **Methods:** (Sprague-Dawley) male rats (18 months old) were splenectomized under sevoflurane anesthesia. The cognitive function of rats at 1, 3, and 7 d after anesthesia and surgery was evaluated. Changes in the expression of neuroinflammatory cytokines, IL-6 and IL-10, and RNF146 were measured in the hippocampus in both control group (con) and anesthesia (AS) group. We examined cognitive outcomes and expression of inflammatory factors and RNF146 in con and AS mice using cluster analysis. **Results:** The cognitive ability and mobility of rats after anesthesia and surgery at day 1, 3, and 7 decreased, especially at day 3. Similarly, the expression of neuroinflammatory factors and RNF146 increased after anesthesia and surgery at day 1, 3, and 7, and the increase was highest at day 3. The clustering and correlation analysis of RNF146 expression in the hippocampi of elderly rats revealed a correlation between POD and neuroinflammation resulting from anesthesia and surgery. **Conclusion:** Anesthesia and surgery can lead to POD and neuroinflammation. The expression of RNF146 correlates with delirium and neuroinflammation caused by anesthesia and surgery.

Keywords: RNF146, anesthesia, surgery, postoperative delirium, hippocampus, neuroinflammation

Received: 25 April, 2023; **revised:** 24 May, 2023; **accepted:** 24 May, 2023; **available on-line:** 26 October, 2023

✉e-mail: xinlini6@nyfy.com.cn

#Equal contribution

Acknowledgements of Financial Support: This study was supported by the Key Research & Developing Program of Ningxia Hui Autonomous Region (2021BEG02036) and the Ningxia Natural Science Foundation Project (2020AAC03218).

Abbreviations: ANOVA, One-way analysis of variance; IL-1, 0Interleukin 10; IL-6, Interleukin 6; POD, Postoperative delirium

INTRODUCTION

With the progress of modern medicine and the aging of the population, the number of elderly patients under-

going surgery and anesthesia is increasing (H *et al.*, 2017; Lin *et al.*, 2020). Postoperative delirium (POD) is a common complication of anesthesia and surgery in elderly patients. POD is characterized by mild cognitive impairment, impaired memory, decreased ability to process information, and reduced attention accompanied by a series of negative outcomes, including changes in mood, personality, and loss of labor ability (Evered *et al.*, 2018). Having POD may result in increased morbidity and mortality, deteriorating quality of life, and causing other physical and psychological diseases, which negatively affect social stability (Carr *et al.*, 2018; Deiner *et al.*, 2017). A study reported that patients with POD were nearly twice as likely to die within 1 year within 3 months of surgery compared with patients without POD (Fodale *et al.*, 2010). According to the International Postoperative Delirium Study, the incidence of POD in elderly patients (>60 years old) is approximately 25.8% within 7 days of surgery and 10% within 3 months of surgery (Moller *et al.*, 1998). The incidence of POD within 3 months and 1 year after surgery is approximately 29% and 33.6%, respectively (Deiner *et al.*, 2017; Liu *et al.*, 2022). However, the mechanism of POD is unclear. POD occurs due to the combined action of susceptibility and predisposing factors, and aging is the only independent risk factor for the occurrence of POD (Evered *et al.*, 2018). The pathogenesis of POD is believed to be mainly caused by central nervous system inflammation (Feng *et al.*, 2017), oxidative stress (Chen *et al.*, 2020), dysregulations of the cholinergic system (Zuo *et al.*, 2018), increased neuronal apoptosis (Zhang *et al.*, 2020), and decreased neuronal regeneration and synaptic plasticity caused by amyloid deposition (Evered *et al.*, 2018). However, neuroinflammation is an important pathological basis for the occurrence of POD (Li *et al.*, 2022).

The E3 ubiquitin ligase RNF146 is present in the brain, spleen, heart, kidney, and testis (Matsumoto *et al.*, 2017). Neuronal cytoplasm mainly expresses RNF146 at a relatively high level in the cortex and hippocampus (Yang *et al.*, 2017). Studies have confirmed that RNF146 has a neuroprotective effect in cerebral ischemia, hypoxia, and chronic nervous system diseases (Kim *et al.*, 2017; Mu *et al.*, 2020) and mediates DNA damage repair through PAR-dependent ubiquitination to degrade PAR-mediated proteins (Andrabi *et al.*, 2011; Koo *et al.*, 2018). Cells overexpressing RNF146 exhibited higher survival rates after γ -irradiation (Andrabi *et al.*, 2011; Bensih *et al.*, 2023). *In vitro* and *in vivo* experiments have revealed

that RNF146 expression in nerve cells is significantly increased after exposure to low-dose *n*-methyl-D-aspartic acid (NMDA) receptor and sublethal glucose-oxygen deprivation or transient bilateral common carotid artery occlusion in mice, protecting nerve cells from injury (Belayev *et al.*, 2017; Mu *et al.*, 2020). The presence of higher RNF146 expression in the brains of patients with early Alzheimer's disease supports a neuroprotective role for RNF146 (von Rotz *et al.*, 2005). The occurrence and clinical manifestations of POD are similar to neuroinflammation-related degenerative diseases, such as Alzheimer's disease (Belayev *et al.*, 2017; Evered *et al.*, 2018). However, whether RNF146 is involved in the occurrence and development of POD is unknown. In this study, elderly rats were used to induce delirium-like behavior during anesthesia and surgery to evaluate changes in RNF146 expression in the occurrence of POD. The purpose of this paper is to investigate the changes of RNF146 expression during POD development, whether RNF146 can be a biomarker of POD development, and to improve new insights for studying the pathogenesis, treatment, and prevention of POD.

MATERIALS AND METHODS

The animal program was approved by the Animal Care and Use Committee of Ningxia Medical University Medical Center. All animal experiments were conducted following the National Institutes of Health Guidelines for the Care and Utilization of Laboratory Animals (No. 2016-124), revised in 2016.

Animals

A total of 72 healthy male SPF (Specific pathogen Free) SD rats, aged 18–20 months and weighing 450–600 g, were provided by the Laboratory Animal Center of Ningxia Medical University (IACUC Animal Use License number: SCXK (Ning) 2020-0001). The rats were randomly divided into six groups (12 animals in each group): con group 1, 3, and 7 d without exposure to anesthesia and AS group 1, 3, and 7 d after anesthesia and surgical intervention. Each cage, measuring 27.94 cm×15.24 cm×11.43 cm, contained 3–4 animals under a 12-h light–dark cycle. The rats were provided free access to food and water.

Anesthesia and Surgery

Splenectomy was performed under anesthesia with sevoflurane in the AS group. In brief, rats were anesthetized in an airtight chamber prefilled with 3% sevoflurane in 100% O₂. Anesthesia was induced by continuous inhalation of 3% sevoflurane in 100% O₂ at a rate of 1.5 L/min. As soon as the correct reflex disappeared, the rats breathed spontaneously after being fixed on the operating table. In order to maintain the depth of anesthesia, rats were given 100% pure oxygen mixed with 3% sevoflurane. Splenectomy was performed in the AS group according to the methods described in the literature (Kong *et al.*, 2017; Wang *et al.*, 2017). The operation was performed on a heating table and the temperature was maintained at 37°C. Skin disinfection was performed routinely. First, an incision of 1 cm was made, and a surgical field was created. The spleen was bluntly separated from the surrounding tissue. Then the blood vessel was ligated with 6-0 thread, and the distal blood vessel was cut after the spleen was taken out. Abdominal muscles and skin were sutured with 4-0 silk thread. The incision

was locally infiltrated with ropivacaine (1%, 1 mL), and erythromycin ointment was applied to the incision. The rats were kept at 37°C±0.5°C from anesthesia until they woke up. The entire operation was completed in 30 min, and a sine individual performed all the surgical operations. The rats in the con group were placed in the air-containing induction chamber for 30 min.

Morris water maze test

The Morris water maze (MWM) test of spatial memory and cognitive ability was performed in splenectomized rats. The MWM consists of a circular pool of 120 cm in diameter and 50 cm in height. The pool was divided into four quadrants. A circular platform with a diameter of 15 cm was fixed in the middle of the second quadrant. The platform was immersed 1 cm underwater, with a water temperature of 22°C±2°C. A camera was placed above the maze to record the rats' movements. The test included the following: (1) Positioning navigation experiment: The experiment was conducted at the same time every day, once a day for 5 consecutive days. The time for rats to find the platform was recorded as escape latency. The automatic camera system and computer analysis and processing system recorded escape latency. If the rat could not find the platform within 60 s after entering the water, it was led to the platform and allowed to stay on it for 15 s to guide its spatial learning and memory. In such cases, the escape incubation period was recorded as 100 s; (2) Space exploration experiment: The platform was removed on the second day after the positioning navigation experiment, and the rat was placed into the water facing the pool wall at the entry point of 1/2 arc in the fourth quadrant. The computer recorded the time it took the rat to reach the original platform position, the number of times it crossed the platform position, and the total swimming distance within 60 s. The samples were collected after the behavioral experiment.

IntelliCage test (automated IntelliCage testing)

The IntelliCage test (TSE Systems GmbH, Germany; <http://www.newbehavior.com>) assessed spontaneous behavior and spatial learning in rats raised in groups. After surgery, the rats in each experimental group were put in the IntelliCage box before adding water and feed and changing the padding regularly. A miniature signal transceiver was injected into the neck of the rats (used to record activity) (Wu *et al.*, 2017). The labels of each group of rats injected were input in the IntelliCage test software (IntelliCage plus). The experimental test could detect when the rats entered the corner, and the system recorded it as a "visit". Two water bottles were placed in each corner, and the system records a "nose-poke" when rats touch their noses. When a rat licks a water bottle for a drink, the system records it as a lick. The IntelliCage test was designed in four stages: (1) Free exploration: The number of corner visits and nose contacts of each rat was recorded to assess the ability of the rat to adapt to the new environment for 3 d. (2) Nose-poke learning: The times of corner visits and a nasal touch of each rat were recorded to evaluate the learning and memory ability of the rat for 5 d. POD modeling was performed after nose contact learning. (3) Position learning: The correct access ratio of each rat was recorded to evaluate the spatial position learning ability for 3 d. After the end of the learning behavior, all rats had access to all corners and vial vents. (4) Position reversal learning: the diagonal corner of the "correct" area in the previous spatial position learning stage was defined as "correct"

and the rest as “wrong.” The number of times each rat visited the correct corner was recorded to evaluate the learning ability of spatial position for 3 d.

Nesting test

The nesting experiment is used to evaluate the behavior and habits of rats. Before the experiment, each rat was placed in a new sterilized cage, facial tissue was added (the thickness of the cage was ~1.5 cm), and 10 pieces of clean, unscented tissue paper were placed in the cage (close to the side wall of the cage, and not right below the water bottle). The rectangular paper measured 10×6 cm. After the rats were put in, the cage was covered, and the room lights were turned off. The experiment generally started from 16:00 to 18:00, and all rats were placed within 1 h to reduce experimental errors. The nesting situation of the rats was scored at 24 h.

Score with reference to the literature: 1 = no obvious bite marks on the paper; 2 = partial shredding of the paper; 3 = scrap most of the paper; 4 points = flat nest can be identified; 5 = perfect nest. The experiment was double-blind, scored by more than three trained experimenters, and each experimenter's rating of a rat was evenly divided into the rat's nesting score.

Western blotting

After MWM, six animals in each group were injected with cold PBS (phosphate buffered saline) and normal saline through the cardiac vein under deep anesthesia, and their brains were quickly removed. Brain tissue was homogenized in a mixture of RIPA lysis buffers, phosphatase, and protease inhibitors and incubated in ice for 30 min. The lysates were then ultrasonicated and centrifuged at 13000×g at 4°C for 30 min. Protein samples were quantified using a BCA protein determination kit (Thermo Scientific, Waltham, MA, USA) and concentrations were determined using a spectrophotometer (MULTISKAN MK3, Thermo Scientific). Subsequently, the samples were mixed with 5× sample buffer, balanced with double distilled water, and heated at 100°C for 5 min. An equal amount of protein in each sample was separated by sodium dodecyl sulfate-polyacrylamide gel electrophoresis on a 10% gel and then electrophoretically transferred to a polyvinylidene fluoride membrane (Bio-Rad, Hercules, CA, USA). Blocking was performed with 10% skim milk in Tris-buffered saline and Tween-20 (0.1%) (TBST) for 2 h. Then the membranes were immunoblotted with primary antibodies (RNF146, 1:1000, ab2736529, Invitrogen, USA; IL-6, 1:1000, ab9324, Abcam, USA; IL-10, 1:1000, DF6894, Affinity Biosciences, China) overnight. After being incubated with secondary antibody (1:5000, anti-rabbit antibody, ab150077, Abcam), signal detection was performed by Odyssey infrared laser imaging system, followed by gray intensity analysis.

RT-PCR

Total RNA of the hippocampus was extracted using TRIzol reagent according to the manufacturer's protocol (TransGen Biotech). The reaction system was configured with a real-time quantitative PCR kit using 2 µL DNA as a template, and the reaction was amplified *in vitro* by quantitative PCR. The expression level of miR-RNF146 (internal reference GAPDH) was analyzed using the 2^{-ΔΔCT} method. The primers used for real-time fluorescent quantitative PCR are shown in Table 1. The primers and sequencing reactions were sent to Shanghai Sangong Bioengineering Co., Ltd.

ELISA

The hippocampus was homogenized with an extraction buffer containing 5 mol/L guanidine hydrochloride in 50 mmol/L Tris-HCl and a protease inhibitor cocktail containing a serine protease inhibitor AEBSF, according to the manufacturer's instructions (Jiang Lai, China). In brief, the samples were centrifuged at 16000×g for 20 min at 4°C and the supernatant was diluted from 1:2 to 1:10, added to ELISA plates coated with anti-mouse IL-6 or IL-10 antibody, respectively, and then incubated for 2 h at RT. After the samples were washed, they were incubated with 100 µL of IL-6 or IL-10 detection antibody for 1 h at RT, washed, and incubated with 100 µL of horseradish peroxidase labeled anti-rabbit antibody for 30 min at RT. Then the stop solution was added, and absorbance was measured at 450 nm with a spectrophotometer (Nanodrop2000C, ThermoScientific). The protein samples were quantified using an ELISA assay kit (Jiang Lai, China) and the concentration was determined with a spectrophotometer. The concentration of IL-6 and IL-10 was expressed in pg/mg tissues.

Immunofluorescence

All six animals in each group were deeply anesthetized with 5% chloral hydrate, infused with normal saline through the cardiac vein, and bled simultaneously in the right atrium. The animals were given 4% paraformaldehyde in 0.1 mol/L phosphate buffer (pH of 7.4) 24 h after MWM. The brain was removed and stored overnight in 4% paraformaldehyde at 4°C. Continuous 30-µm coronal sections were cut from the frozen samples using a cryoslicer (Thermo Scientific HM430, Microm, Germany). The frozen sections were warmed at RT for 30 min and washed three times with TBS for 5 min each. The sections were blocked with 5% BSA and incubated with antibodies overnight at 4°C (RNF146, 1:200, ab2736529 Invitrogen, USA; IL-6, 1:200, ab9324, Abcam, USA; IL-10, 1:200, DF6894, Affinity Biosciences, China). Then the samples were washed three times with TBS, incubated with CY3-labeled goat anti-rat IgG (H+L) (1<500) at RT for 3 h, and washed with TBS three times for 10 min each. The tablets were sealed with anti-fluorescence quenching tablets containing DAPI (4',6-diamidino-2-phenylindole) and photographed using a fluorescence microscope (The Chongqing Optical Instrument Factory). Average fluorescence intensity was analyzed using the image analysis software ImageJ1.48. The coronal plane of brain tissue in the hippocampus was included in the samples of three rats in each group for observation and analysis. The middle piece was selected to be photographed, and the average fluorescence intensity of CA1 in the hippocampus of each sample was calculated to compare differences between groups.

Statistical analysis

Data were analyzed using the SPSS21.0 software (SPSS Inc., Chicago, IL, USA). Measurement data were expressed as mean ± standard deviation (mean ± S.D.).

Table 1. Primers used for real-time fluorescent quantitative PCR

Primer name	Primer sequence (5'-3')
RNF146-sense	ATAAGAAGGCGAGTGAGACC
RNF146-anti	AGGGCAGACTGACTGGATGA
GAPDH-sense	ACAACCTTTGGCATTGTGGAA
GAPDH-anti	GATGCAGGGATGATGTTCTG

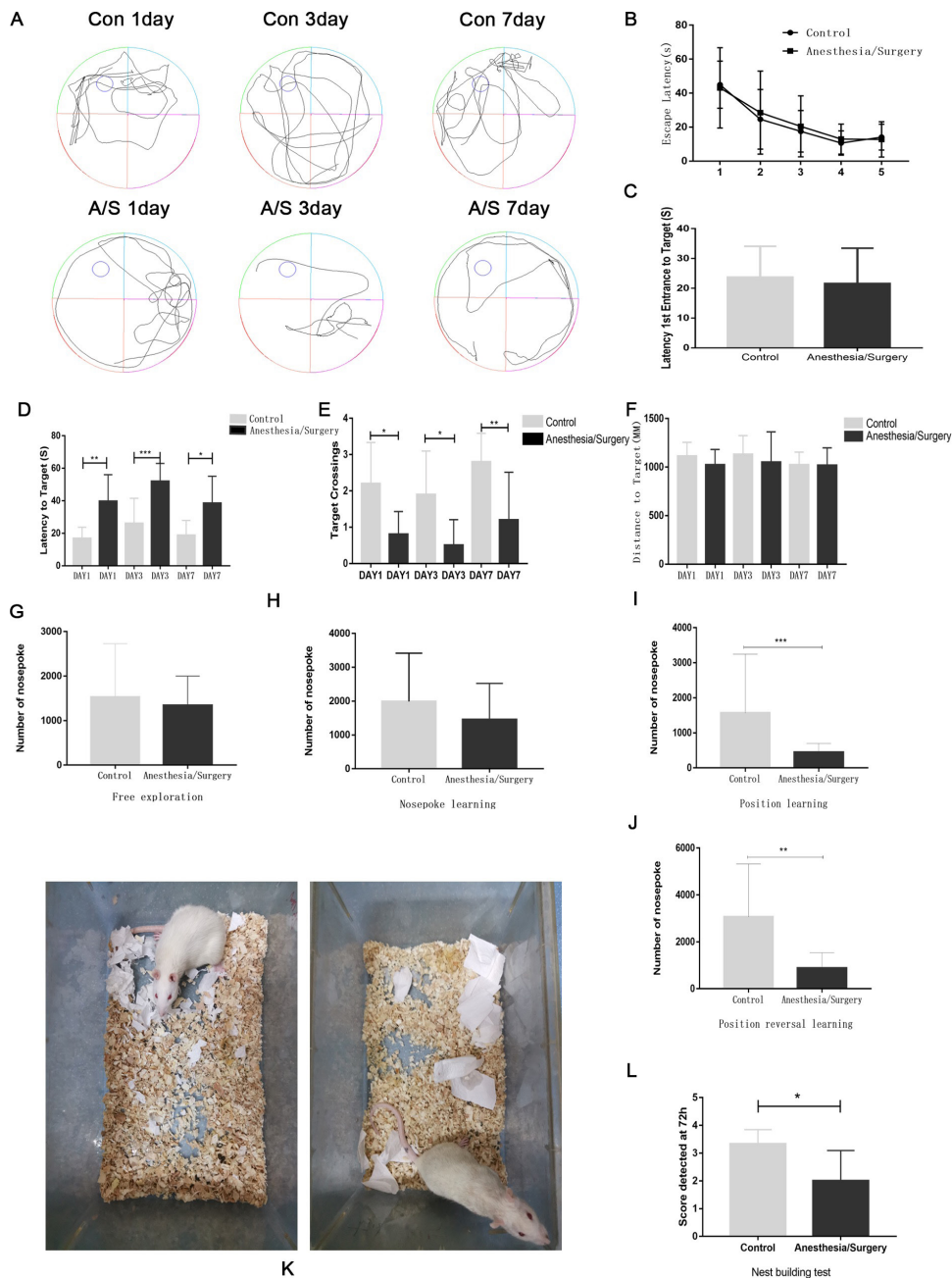


Figure 1. Behavioral changes in aged rats after anesthesia and surgery

One-way analysis of variance (ANOVA) was used to compare means between groups, SNK-q test (Student-Newman-Keuls) was used for pairwise comparison, and repeated measures analysis of variance was used for the water maze test. $P < 0.05$ was considered statistically significant, and the test level of homogeneity of variance was 0.1.

RESULTS

Learning and memory ability before anesthesia and surgery

The water maze and IntelliCage experiments were conducted to evaluate the learning and spatial memory ability of rats before anesthesia and surgery. The repre-

sentative tracking's of rats' movement in the test session were shown in Fig. 1A. During the positioning navigation stage of the water maze experiment, no statistically significant differences were observed in the learning abilities of the rats in the AS and con groups (Fig. 1B, 1C). During the free exploration and nose-poke learning stage in the IntelliCage system, no statistically significant differences were observed in the total number of corner visits and lickings between the AS and con groups (Fig. 1G, 1H). The results showed that the two groups' cognitive learning ability was the same under normal conditions. The test was performed at the end of spatial learning on day 5. The learning ability level of the two groups was the same, with no statistically significant difference (Fig. 1B). The influence of individual differences and groups on the experiment was excluded.

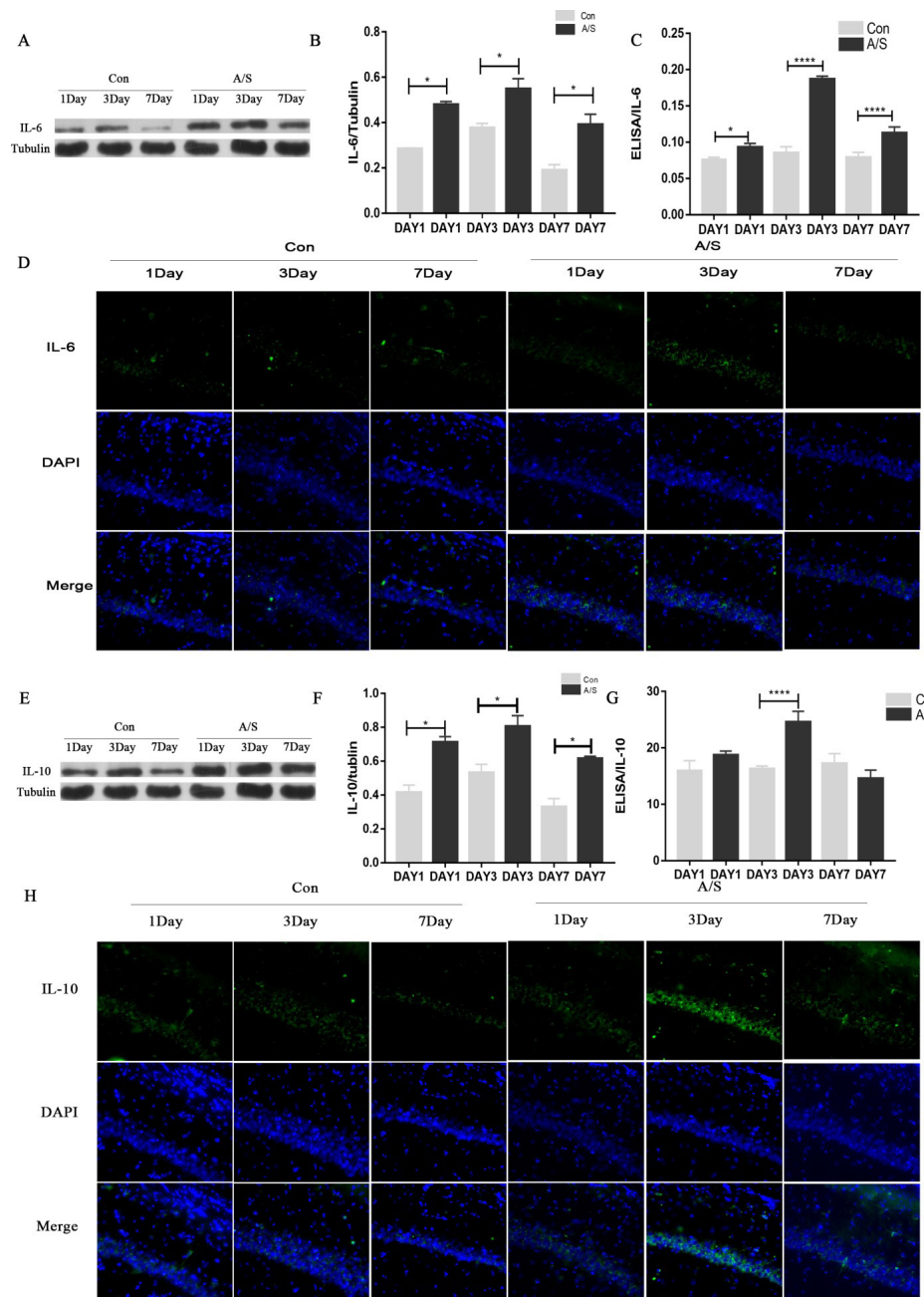


Figure 2. Neuroinflammatory response was induced in aged rats after anesthesia and surgery

Anesthesia and surgery induced decrease in learning and memory and decreased purposeful behavior.

The rats underwent behavioral evaluation after anesthesia and surgery. In the water maze experiment, compared with the con group, the escape latency of rats 1, 3, and 7 d after surgery in the AS group was longer (Fig. 1D) and the number of platform crossings was smaller (Fig. 1E). In the AS group, the escape latency time was the longest (Fig. 1D) and the number of platform crossings was the lowest (Fig. 1E) on day 3 after surgery compared with days 1 and 7 after surgery, whereas the parameters in the con group were not statistically different (Fig. 1F). During the spatial learning exploration in the IntelliCage experiment, the number of correct accesses and licks was significantly lower in the AS group than the con group (Fig. 1I), suggesting that learning and spatial memory decreased within 3 d after

the operation. In the inverse spatial learning exploration stage, the correct visits and licks of the AS group were significantly lower than those of the con group (Fig. 1J), suggesting that the learning and spatial memory ability of rats decreased within 7 d after anesthesia and operation. At the end of the experiment, the three groups of rats did not lose weight, excluding the interference of post-operative pain.

The nesting experiment was performed at the end of the water maze experiment 3 d after surgery. The con group rats tore most of the pieces of paper and the pieces were orderly stacked to build a complete nest, resulting in high nesting scores. Rats in the AS group tore a few pieces of paper, stacked a few pieces of paper or did not stack to build nests, with only embryonic nests or no nests, and the nesting scores decreased significantly (Fig. 1K). Compared with the con group, the difference

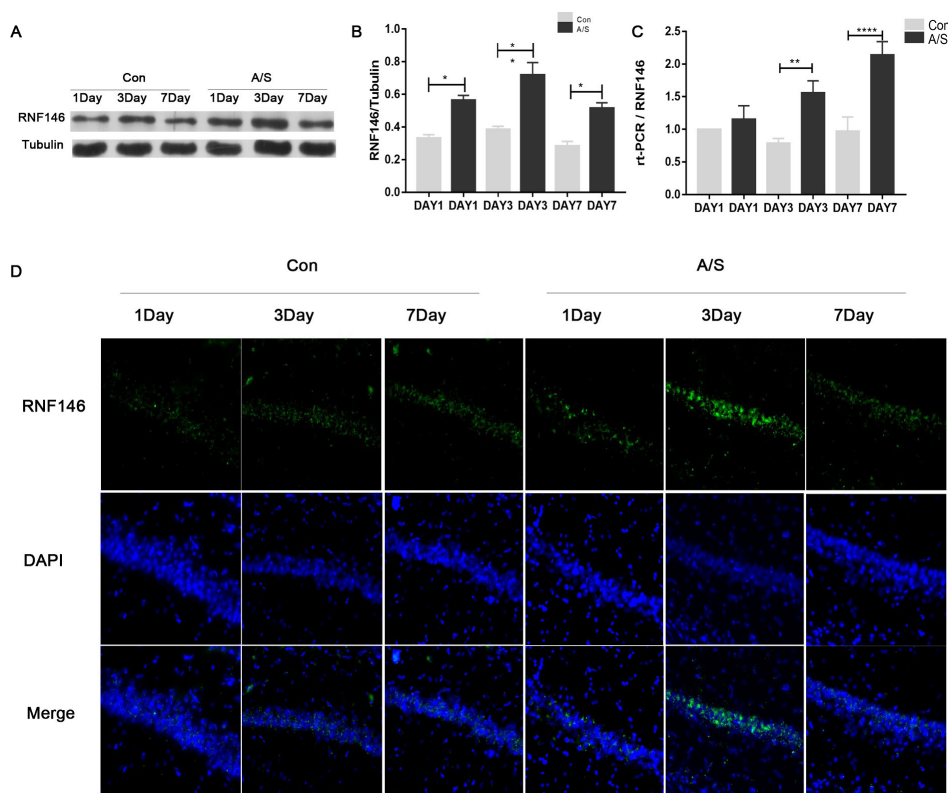


Figure 3 Expression of RNF146 in aged rats after anesthesia and surgery

was statistically significant (Fig. 1L). The results indicated that the executive function and daily activity ability of rats undergoing anesthesia and operation decreased.

Anesthesia and surgery induced changes in the levels of neuroinflammatory factors

To evaluate central nervous system inflammation in rats after anesthesia and surgery, we tested the expression of IL6 and IL-10 in the CA1 region of the hippocampus (Fig. 2A, 2E). Results from western blot analysis and immunofluorescence showed that the expression and fluorescence intensity of IL6 and IL-10 in the hippocampus of the AS group increased at 1, 3, and 7 d after surgery compared with those of the con group (Fig. 2B, 2D, 2F, 2H). In the AS group, the protein content and fluorescence intensity of IL-6 and IL-10 at 3 d after surgery were higher than those at 1 and 7 d after surgery (Fig. 2B, 2D, 2F, 2H). ELISA results were consistent with western blot and immunofluorescence tests (Fig. 2C, 2G).

Anesthesia and surgery induced changes in RNF146 expression

We detected changes in the expression of RNF146 in CA1 region after anesthesia and surgery (Fig. 3A). It shows that compared with the con group, the protein expression and fluorescence intensity of RNF146 in the hippocampus of the AS group increased 1, 3, and 7 d after surgery (Fig. 3B, 3D). Compared within the AS group, the protein expression and fluorescence intensity of RNF146 in the hippocampus of the AS group at 3 d after surgery were higher than those at 1 and 7 d after surgery. These results confirmed the high expression of RNF146 protein content and fluorescence intensity in neurons induced by anesthesia

and surgical stimulation in aged rats. The results of RT-PCR experiment showed that compared with the con group, the expression of miR-RNF146 in the hippocampus of the AS group was higher at days 1, 3, and 7 (Fig. 3C). In the AS group, miR-RNF146 in the hippocampi of rats 1 day after surgery was lower than that in rats 3 d after surgery ($p < 0.05$), and miR-RNF146 in the hippocampal region of rats 3 d after surgery was lower than that in rats 7 d after surgery (Fig. 3C).

Correlation analysis of RNF146 with behavioral and neuroinflammatory factors

Experimental data parameters were analyzed by hierarchical clustering and correlation testing. Figure 4 shows the correlation between RNF146, inflammatory cytokines IL-6, IL-10, and behavioral data. The relative expression of RNF146 was positively correlated with the relative expression of inflammatory factors IL-6 and IL-10 (Fig. 4) and was negatively correlated with the escape latency in the water maze experiment, which showed significant correlation ($p < 0.05$). It is indicating that after anesthesia/surgery, the expression of endogenous brain protective protein RNF146 is associated with hippocampus-dependent cognitive impairment and central nervous system inflammation. The expression of RNF146 was negatively correlated with the number of times that rats crossed the platform in the water maze, again demonstrating its correlation with hippocampus-dependent cognition. In addition, the correlation coefficients between RNF146 expression and cognition-related indicators in the IntelliCage system were concentrated between 0.1 and 0.4, but the correlation was not significant.

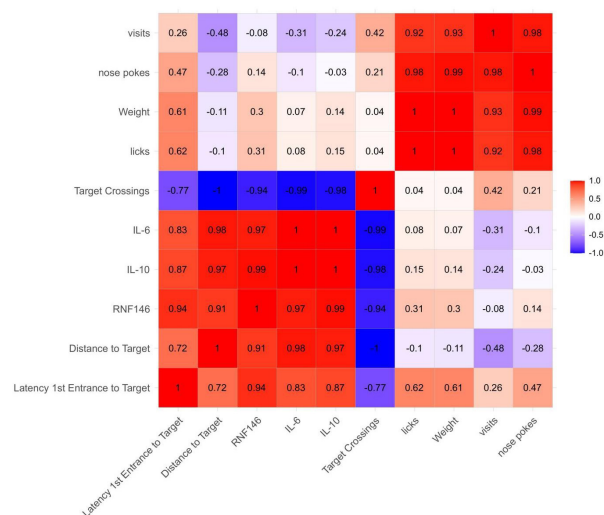


Figure 4. Heat maps of RNF146 and parameters of anesthesia and surgical induction in rats

DISCUSSION

The study investigated the involvement of RNF146 induced by anesthesia and surgery in aged rats and dissected the molecular mechanism underlying this regulation. Ho Chul Kang stated that RNF146 regulates cell survival and DNA repair by ubiquitinating PAR and blocking AIF nuclear translocation to inhibit parthanatos cell death (Kang *et al.*, 2011). In the oxygen and glucose deprivation/reoxygenation (OGD/R) model, NPD1 induces activation of the Wnt/ β -catenin pathway through upregulation of RNF146, enhanced cell survival, decreased oxidative stress markers, and a lower level of autophagy (Mu *et al.*, 2020). With reference to Ismail Nurul Iman and others (Iman *et al.*, 2021), this study combined the IntelliCage experiment and the traditional water maze experiment and nesting evaluation of elderly rats to assess learning and memory and ability to care for themselves. The findings revealed that learning and memory and ability for daily living of aged rats after anesthesia decreased on days 1, 3, and 7 after surgery, and the abnormal neurobehavioral function recovered on day 7 after surgery. Clinical evidence also shows that POD occurs mostly within 24–72 h after surgery. Most patients heal within 1 week, but some patients may develop long-term cognitive dysfunction. Animal experiment studies have shown that the appropriate time period for observing delirium-like behavior changes in rodents after anesthesia is 24–48 h, and neurobehavioral changes are the most obvious at this time. These results are consistent with our findings. Neuroinflammation causes delirium after general anesthesia in rodents (Cao *et al.*, 2010; Dong *et al.*, 2016). In animal models, the synthesis and release of proinflammatory factors can damage nerve formation and synaptic plasticity and nerve repair function (Belarbi *et al.*, 2012; Liu *et al.*, 2018). Studies have shown that anesthesia and surgery increase the level of IL-6 in the hippocampi of aged wild-type mice, resulting in cognitive dysfunction in aged mice. The use of the IL-6 antibody can improve cognitive dysfunction after peripheral trauma in aged wild-type mice. In addition, anesthesia did not affect the level of IL-6 in the hippocampi of IL-6 gene knockout rats, nor did it lead to cognitive impairment in aged IL-6 gene knockout rats, suggesting that the increase of IL-6 may be involved in

the cognitive dysfunction caused by anesthesia surgery (Dong *et al.*, 2016; Naveed *et al.*, 2022; Muhammad AS *et al.*, 2023; Waseem *et al.*, 2023). After anesthesia surgery, aged rats exhibited impaired spatial memory and significantly higher expression of inflammatory factor IL-6 within 1 and 3 d after surgery. Spatial memory is improved, and the expression of inflammatory factors is downregulated 7 d after surgery (Cao *et al.*, 2010). Studies have indicated that IL-10 is not only closely related to autoimmune diseases and infectious diseases, but also has neuroprotective effects in cerebral ischemia, hypoxia, and chronic nervous system diseases (Morris *et al.*, 2018; Sudheimer *et al.*, 2014; Wang *et al.*, 2019). Furthermore, in *in vitro* experiments, M2-type microglia produced IL-10 and TGF- β to reduce the neuronal cell damage caused by OGD, and this response was downregulated when the damage or pathogen was removed (Ahmad *et al.*, 2023; Zhao *et al.*, 2017). Li *et al.* reported that in the rat model of acute cerebral ischemia, IL-10 increased sharply 6 h after surgery, suggesting the activation of the anti-inflammatory system (Li *et al.*, 2001). In clinical studies, IL-10 in acute cerebral infarction began to rise at 24 h after surgery, reached a peak at 3 d after surgery, and then gradually decreased (van Exel *et al.*, 2002). IL-10 has similar biological activities in humans and mice (Moore *et al.*, 2001). In our study, the expressions of IL-6 and IL-10 in the hippocampi of aged rats at 1, 3, and 7 d after anesthesia were higher than that in the control group, and the expressions increased most significantly on day 3 after anesthesia. Our findings coincide with the results of other studies, suggesting that inflammatory and anti-inflammatory effects exist simultaneously in the nervous system after anesthesia and surgery.

RNF146, also known as Iduna, has two important functional regions in its N terminus: E3 ubiquitin ligase active region and PAR binding region, and the C3HC4 RING finger domain in amino acids 35–77 showed E3 ubiquitin ligase activity (Belayev *et al.*, 2017; Koo *et al.*, 2018). When glutamate excitatory toxicity, oxygen glucose deprivation, and other sublethal stimuli caused neuronal damage, RNF146 could recognize PARP1 to ubiquitinate and degrade axin/tankyrase through WWE domain-mediated PARP1, positively regulate Wnt/ β -catenin signaling pathway, and inhibit autophagy-induced death. It can reduce the excitatory toxicity of glutamate and damage of neurons induced by oxygen and sugar deprivation, and play a role in protecting neurons from damage (Mu *et al.*, 2020). In addition, RNF146 binds to apoptosis-inducing factor, a key death molecule in the parthanatos death pathway, and prevents the nuclear translocation of apoptosis-inducing factor in the mitochondria (Andrabi *et al.*, 2011). Thus, glutamate and NMDA receptor excitotoxicity-mediated cell parthanatos death is inhibited and brain protective effect is generated (Yang *et al.*, 2017). The Wnt signaling pathway plays an important role in POD. A study showed that treatment with 3.6% sevoflurane for 6 h inhibited the Wnt/ β -catenin signaling pathway, thereby increasing GSK-3 β and decreasing β -catenin. By inhibiting this pathway, sevoflurane downregulates annexin A1, thereby breaching the blood–brain barrier and inducing POD. However, it is unclear whether increasing the expression of RNF146 can activate the Wnt/ β -catenin pathway and increase the concentration of β -catenin, thus inhibiting the occurrence of POD (Hu *et al.*, 2016). However, our findings revealed that the expression of RNF146 in the hippocampi of aged rats increased 1, 3, and 7 d after surgical anesthesia, especially on day 3, when the increase was the most obvious. This change was consistent with

neurobehavioral changes and expression of neuroinflammatory factors IL-6 and IL-10 in the brain. Correlation analysis showed that the relative expression of RNF146 was positively correlated with the relative expression of inflammatory factors IL-6 and IL-10, as well as the escape latency in the water maze experiment, with the correlation coefficients being 0.90 and 0.99, respectively, and the correlation was significant.

RNF146 is an endogenous protective protein. When the body receives injury, RNF146 increases its reactivity and defends against external injury. Studies have confirmed this phenomenon. After exposure to low-dose NMDA and sublethal OGD or transient bilateral common carotid artery occlusion, the expression of RNF146 in mice nerve cells significantly increased to protect the nerve cells from injury. RNF146 may play the same role as anti-inflammatory factors such as IL-10 in the occurrence of POD.

CONCLUSION

Our findings reveal that after anesthesia and surgery, rat spatial learning and memory ability decreases and RNF146 expression increases and the level of IL-6 and IL-10 increases. Hierarchical cluster analysis showed that the expression of RNF146 was related to the degree of central nervous system inflammation and spatial learning and memory impairment. RNF146 may play a neuroprotective role similar to that of the anti-inflammatory factor IL-10. However, the mechanisms involved need to be investigated. In addition, the limitation of this study is that RNF146 was not knocked down or overexpressed in rats to verify the mechanism of action of RNF146 in POD. This will be a topic of research for the future.

Declarations

Data Sharing Statement. The datasets used and analysed during the current study are available from the corresponding author on reasonable request.

Ethics Approval and Consent to Participate. Rats were provided from the Animal Center of Ningxia Medical University (China) and all experiments were in accordance with the Regulations of Experimental Animal Administration issued by the State Committee of Science and Technology of China on May 2016.

Disclosure. The authors report no conflicts of interest in relation to this work.

REFERENCES

- Ahmad B, Muhammad Yousafzai A, Maria H, Khan AA, Aziz T, Alharbi M, Alsahamari A, Alasmari AF (2023) Curative effects of *Dianthus orientalis* against paracetamol triggered oxidative stress, hepatic and renal injuries in rabbit as an experimental model. *Separations* **10**: 182. <https://doi.org/10.3390/separations10030182>
- Andrabi SA, Kang HC, Haince JF, Lee YI, Zhang J, Chi Z, et al (2011) Iduna protects the brain from glutamate excitotoxicity and stroke by interfering with poly(ADP-ribose) polymer-induced cell death. *Nat Med* **17**: 692–699. <https://doi.org/10.1038/nm.2387>
- Andrabi SA, Kang HC, Haince JF, Lee YI, Zhang J, Chi Z, West AB, Koehler RC, Poirier GG, Dawson TM, Dawson VL (2011) Iduna protects the brain from glutamate excitotoxicity and stroke by interfering with poly(ADP-ribose) polymer-induced cell death. *Nature Med* **17**: 692–699. <https://doi.org/10.1038/nm.2387>
- Belarbi K, Jopson T, Tweedie D, Arellano C, Luo W, Greig NH, Rosi S (2012) TNF- α protein synthesis inhibitor restores neuronal function and reverses cognitive deficits induced by chronic neuroinflammation. *J Neuroinflammation* **9**: 23. <https://doi.org/10.1186/1742-2094-9-23>
- Belayev L, Mukherjee PK, Balaszczuk V, Calandria JM, Obenaus A, Khoutorova L, Hong SH, Bazan NG (2017) Neuroprotectin D1 upregulates Iduna expression and provides protection in cellular uncompensated oxidative stress and in experimental ischemic stroke. *Cell Death Differ* **24**: 1091–1099. <https://doi.org/10.1038/cdd.2017.55>
- Benish R, Sobia A, Nureen Z, Sohail A, Abid S, Najeib U, Tariq A, Metab A, Abdulrahman A, Abdullah FA (2023) Evaluating the influence of Aloe barbadensis extracts on edema induced changes in C-reactive protein and interleukin-6 in albino rats through in vivo and in silico approaches. *Acta Biochim Pol*. Epub No: 6705. https://doi.org/10.18388/abp.2020_6705
- Bin W, Siyuan L, Xipeng C, Xinghui D, Jingzhu L, Ling W, Mingshan W, Yanlin B (2017) Blood-brain barrier disruption leads to postoperative cognitive dysfunction. *Curr Neurovasc Res* **14**: 359–367. <https://doi.org/10.2174/1567202614666171009105825>
- ChunLong Z, ChunMan W, Jin L, Ting S, JiangPing Z, XinRui H, Yi Z, HuaCheng L, QingQuan L, Han L (2018) Isoflurane anesthesia in aged mice and effects of A1 adenosine receptors on cognitive impairment. *CNS Neurosci Ther* **24**: 212–221. <https://doi.org/10.1111/cns.12794>
- Deiner S, Luo X, Lin HM, Sessler DI, Saager L, Sieber FE, Lee HB, Sano M, and the Dexlirium Writing Group; Jankowski C, Bergese SD, Candiotti K, Flaherty JH, Arora H, Shander A, Rock P (2017) Intraoperative infusion of dexmedetomidine for prevention of postoperative delirium and cognitive dysfunction in elderly patients undergoing major elective noncardiac surgery: a randomized clinical trial. *JAMA Surg* **152**: e171505. <https://doi.org/10.1001/jamasurg.2017.1505>
- Evered LA, Silbert BS (2018) Postoperative cognitive dysfunction and noncardiac surgery. *Anesth Analg* **127**: 496–505. <https://doi.org/10.1213/ane.00000000000003514>
- Feng X, Valdearcos M, Uchida Y, Lutrin D, Maze M, Koliwad SK (2017) Microglia mediate postoperative hippocampal inflammation and cognitive decline in mice. *JCI Insight* **2**: e91229. <https://doi.org/10.1172/jci.insight.91229>
- Fodale V, Santamaria LB, Schifilliti D, Mandal PK (2010) Anaesthetics and postoperative cognitive dysfunction: a pathological mechanism mimicking Alzheimer's disease. *Anaesthesia* **65**: 388395. <https://doi.org/10.1111/j.1365-2044.2010.06244.x>
- Iman IN, Yusof NAM, Talib UN, Ahmad NAZ, Noraziz A, Kumar J, Mehat MZ, Jayabalan N, Muthuraju S, Stefaniuk M, Kaczmarek L, Muzaimi M (2021) The IntelliCage system: a review of its utility as a novel behavioral platform for a rodent model of substance use disorder. *Front Behav Neurosci* **15**: 683780. <https://doi.org/10.3389/fnbeh.2021.683780>
- Jiqian Z, Shasha Z, Peipei J, Yuting H, Qingqing D, Qianyun Z, Pengfei W, Zhilai Y, Lei Z, Hu L, Guanghong X, Lijian C, Erwei G, Yunjiao Z, Longping W, Xuesheng L (2020) Graphene oxide improves postoperative cognitive dysfunction by maximally alleviating amyloid beta burden in mice. *Theranostics* **10**: 11908–11920. <https://doi.org/10.7150/thno.50616>
- Kim H, Ham S, Lee JY, Jo A, Lee GH, Lee YS, Cho M, Shin HM, Kim D, Pletnikova O, Troncoso JC, Shin JH, Lee YI, Lee Y (2017) Estrogen receptor activation contributes to RNF146 expression and neuroprotection in Parkinson's disease models. *Oncotarget* **8**: 106721–106739. <https://doi.org/10.18632/oncotarget.21828>
- Koo JH, Yoon H, Kim WJ, Cha D, Choi JM (2018) Cell-penetrating function of the Poly(ADP-Ribose) (PAR)-binding motif derived from the PAR-dependent E3 ubiquitin ligase iduna. *Int J Mol Sci* **19**: 819–799. <https://doi.org/10.3390/ijms19030779>
- Li HL, Kostulas N, Huang YM, Xiao BG, van der Meide P, Kostulas V, Giedraitis V, Link H (2001) IL-17 and IFN- γ mRNA expression is increased in the brain and systemically after permanent middle cerebral artery occlusion in the rat. *Neuroimmunol* **116**: 5–14. [https://doi.org/10.1016/s0165-5728\(01\)00264-8](https://doi.org/10.1016/s0165-5728(01)00264-8)
- Liu B, Huang D, Guo Y, Sun X, Chen C, Zhai X, Jin X, Zhu H, Li P, Yu W (2022) Recent advances and perspectives of postoperative neurological disorders in the elderly surgical patients. *CNS Neurosci Ther* **28**: 470–483. <https://doi.org/10.1111/cns.13763>
- Matsumoto Y, La Rose J, Lim M, Adissu HA, Law N, Mao X, Cong F, Mera P, Karsenty G, Goltzman D, Changoor A, Zhang L, Stajkowski M, Grynias MD, Bergmann C, Rottapel R (2017) Ubiquitin ligase RNF146 coordinates bone dynamics and energy metabolism. *J Clin Invest* **127**: 2612–2625. <https://doi.org/10.1172/jci92233>
- Moller JT, Cluitmans P, Rasmussen LS, Houx P, Rasmussen H, Canet J, Rabbitt P, Jolles J, Larsen K, Hanning CD, Langeron O, Johnson T, Lauen PM, Kris-tensen PA, Biedler A, van Beem H, Fraidakis O, Silverstein JH, Beneken JE, Gravenstein JS (1998) Long-term postoperative cognitive dysfunction in the elderly ISPOCD1 study. ISPOCD investigators. International study of post-operative cognitive dysfunction. *Lancet* **351**: 857–861. [https://doi.org/10.1016/s0140-6736\(97\)07382-0](https://doi.org/10.1016/s0140-6736(97)07382-0)
- Moore KW, de Waal Malefyt R, Coffman RL, O'Garra A (2001) Interleukin-10 and the interleukin-10 receptor. *Annu Rev Immunol* **19**: 683–765. <https://doi.org/10.1146/annurev.immunol.19.1.683>
- Morris R, Kershaw NJ, Babon JJ (2018) The molecular details of cytokine signaling via the JAK/STAT pathway. *Protein Sci* **27**: 1984–2009. <https://doi.org/10.1002/pro.3519>

- Muhammad AS, Muhammad N, Shafiq UR, Noor UL, Tariq A, Metab A, Abdulrahman A, Abdullah F. A (2023) Iron oxide nanoparticles synthesis from madhuca indica plant extract, and assessment of its cytotoxic, antioxidant, anti-inflammatory and anti-diabetic properties via different nano informatics approaches. *ACS Omega*. <https://doi.org/10.1021/acsomega.3c02744>
- Nan H, Chao W, Yuxin Z, Jiying A, Chao Z, Keliang X, Yize L, Haiyun W, Yonghao Y, Guolin W (2016) The role of the Wnt/ β -catenin-Annexin A1 pathway in the process of sevoflurane-induced cognitive dysfunction. *Neurochem* **137**: 240–252. <https://doi.org/10.1111/jnc.13569>
- Nan W, Feng W, Zhe J, Zhen Z, Lian-Kun W, Chun Z, Tao S (2017) Effects of GABA(B) receptors in the insula on recognition memory observed with intel-ligace. *Behav Brain Funct* **13**: 7. <https://doi.org/10.1186/s12993-017-0125-4>
- Naveed M, Bukhari B, Aziz T, Zaib S, Mansoor MA, Khan AA, Shahzad M, Dablood AS, Alruways MW, Almalki AA, Abdulhakeem SA, Majid A (2022) Green synthesis of silver nanoparticles using the plant extract of *Acer oblongifolium* and study of its antibacterial and antiproliferative activity *via* mathematical approaches. *Molecules* **27**: 4226. <https://doi.org/10.3390/molecules27134226>
- O'Brien H, Mohan H, Hare CO, Reynolds JV, Kenny RA (2017) Mind Over Matter? The hidden epidemic of cognitive dysfunction in the older surgical patient. *Ann Surg* **265**: 677–691. <https://doi.org/10.1097/sla.0000000000001900>
- Qiong M, Hailong Z, Yingning X, Qian H, Xiao L, Wansong Z, Haibing L (2020) NPD1 inhibits excessive autophagy by targeting RNF146 and wnt/ β -catenin pathway in cerebral ischemia-reperfusion injury. *J Recept Signal Transduct Res* **40**: 456–463. <https://doi.org/10.1080/10799893.2020.1756325>
- Shou-Cai Z, Ling-Song M, Zhao-Hu C, Heng X, Wen-Qian W, Fudong L (2017) Regulation of microglial activation in stroke. *Acta Pharmacol Sin* **38**: 445–458. <https://doi.org/10.1038/aps.2016.162>
- Sudheimer KD, O'Hara R, Spiegel D, Powers B, Kraemer HC, Neri E, Weiner M, Hardan A, Hallmayer J, Dhabhar FS (2014) Cortisol, cytokines, and hippo-campal volume interactions in the elderly. *Front Aging Neurosci* **6**: 153. <https://doi.org/10.3389/fnagi.2014.00153>
- van Exel E, Gussekloo J, de Craen AJ, Bootsma-van der Wiel A, Frölich M, Westendorp RG (2002) Inflammation and stroke: the Leiden 85-Plus Study. *Stroke* **33**: 1135–1138. <https://doi.org/10.1161/01.str.0000014206.05597.9e>
- von Rotz RC, Kins S, Hipfel R, von der Kammer H, Nitsch RM (2005) The novel cytosolic RING finger protein dactylidin is up-regulated in brains of patients with Alzheimer's disease. *Eur J Neurosci* **21**: 1289–1298. <https://doi.org/10.1111/j.1460-9568.2005.03977.x>
- Waseem M, Naveed M, Rehman SU, Makhdoom SI, Aziz T, Alharbi M, Alsahamari A, Alasmari AF (2023) Molecular characterization of spa, hld, fmhA, and lukD Genes and computational modeling the multidrug resistance of *Staphylococcus* species through *Callindra harrisii* silver nanoparticles. *ACS Omega* **8**: 20920–20936. <https://doi.org/10.1021/acsomega.3c01597>
- Xianyi L, Yeru C, Piao Z, Gang C, Youfa Z, Xin Y (2020) The potential mechanism of postoperative cognitive dysfunction in older people. *Exp Gerontol* **130**: 110791. <https://doi.org/10.1016/j.exger.2019.110791>
- Xiaoting W, Kit W, Wenjun O, Sascha Rutz (2019) Targeting IL-10 family cytokines for the treatment of human diseases. *Cold Spring Harb Perspect Biol* **11**. <https://doi.org/10.1101/cshperspect.a028548>
- Xiaoxia Y, Jianhua C, Yubo G, Juan D, Xinli N (2017) Downregulation of Iduna is associated with AIF nuclear translocation in neonatal brain after hypoxia-ischemia. *Neuroscience* **346**: 74–80. <https://doi.org/10.1016/j.neuroscience.2017.01.010>
- Xue-Zhao C, Hong M, Jun-Ke W, Fang L, Bing-Yang W, A-Yong T, Ling-Ling W, Wen-Fei T (2010) Postoperative cognitive deficits and neuroinflammation in the hippocampus triggered by surgical trauma are exacerbated in aged rats. *Prog Neuropsychopharmacol Biol Psychiatry* **34**: 1426–1432. <https://doi.org/10.1016/j.pnpb.2010.07.027>
- Yeru C, Piao Z, Xianyi L, Huan Z, Jiamin M, Youfa Z, Gang C (2020) Mitophagy impairment is involved in sevoflurane-induced cognitive dysfunction in aged rats. *Aging (Albany NY)* **12**: 17235–17256. <https://doi.org/10.18632/aging.103673>
- Yuanlin D, Zhipeng X, Lining H, Yiyang Z, Zhongcong X (2016) Peripheral surgical wounding may induce cognitive impairment through interleukin-6-dependent mechanisms in aged mice. *Med Gas Res* **6**: 180–186. <https://doi.org/10.4103/2045-9912.196899>
- Yue L, Yiqing Y (2018) Emerging roles of immune cells in postoperative cognitive dysfunction. *Mediators Inflamm* **2018**: 6215350. <https://doi.org/10.1155/2018/6215350>
- Zhichao L, Youzhuang Z, Yihan K, Shangyuan Q, Jun C (2022) Neuroinflammation as the underlying mechanism of postoperative cognitive dysfunction and therapeutic strategies. *Front Cell Neurosci* **16**: 843069. <https://doi.org/10.3389/fncel.2022.843069>
- Zhong-Hong K, Xin C, Hui-Po H, Liang L, Long-Juan L (2017) The oral pretreatment of glycyrrhizin prevents surgery-induced cognitive impairment in aged mice by reducing neuroinflammation and alzheimer's-related pathology via HMGB1 inhibition. *Mol Neurosci* **63**: 385–395. <https://doi.org/10.1007/s12031-017-0989-7>
- Zyad J Carr, Theodore J Cios, Kenneth F Potter, John T Swick (2018) Does dexmedetomidine ameliorate postoperative cognitive dysfunction? a brief review of the recent literature. *Curr Neurol Neurosci Rep* **18**: 64. <https://doi.org/10.1007/s11910-018-0873-z>



OPEN ACCESS

EDITED BY

Grzegorz Węgrzyn,
University of Gdansk, Poland

REVIEWED BY

Agata Wawrzekiewicz-Jałowicka,
Silesian University of Technology,
Poland
Martin Jabůrek,
Academy of Sciences of the Czech
Republic (ASCR), Czechia
Dominika Malińska,
Polish Academy of Sciences, Poland

*CORRESPONDENCE

Adam Szewczyk,
✉ a.szewczyk@nencki.edu.pl

RECEIVED 13 April 2024

ACCEPTED 20 May 2024

PUBLISHED 28 May 2024

CITATION

Szewczyk A (2024), Understanding
mitochondrial potassium channels:
33 years after discovery.
Acta Biochim. Pol. 71:13126.
doi: 10.3389/abp.2024.13126

COPYRIGHT

© 2024 Szewczyk. This is an open-
access article distributed under the
terms of the Creative Commons
Attribution License (CC BY). The use,
distribution or reproduction in other
forums is permitted, provided the
original author(s) and the copyright
owner(s) are credited and that the
original publication in this journal is
cited, in accordance with accepted
academic practice. No use, distribution
or reproduction is permitted which does
not comply with these terms.

Understanding mitochondrial potassium channels: 33 years after discovery

Adam Szewczyk*

Laboratory of Intracellular Ion Channels, Nencki Institute of Experimental Biology, Polish Academy of Sciences, Warsaw, Poland

Mitochondrial investigations have extended beyond their traditional functions, covering areas such as ATP synthesis and metabolism. Mitochondria are now implicated in new functional areas such as cytoprotection, cellular senescence, tumor function and inflammation. The basis of these new areas still relies on fundamental biochemical/biophysical mitochondrial functions such as synthesis of reactive oxygen species, mitochondrial membrane potential, and the integrity of the inner mitochondrial membrane i.e., the passage of various molecules through the mitochondrial membranes. In this view transport of potassium cations, known as the potassium cycle, plays an important role. It is believed that K⁺ influx is mediated by various potassium channels present in the inner mitochondrial membrane. In this article, we present an overview of the key findings and characteristics of mitochondrial potassium channels derived from research of many groups conducted over the past 33 years. We propose a list of six fundamental observations and most important ideas dealing with mitochondrial potassium channels. We also discuss the contemporary challenges and future prospects associated with research on mitochondrial potassium channels.

KEYWORDS

mitochondria, potassium channels, reactive oxygen species, cytoprotection, potassium channel openers

Introduction

When investigating the fundamentals of mitochondrial function within cells, we can identify several simple cations that form the basis of many processes (Szabo and Zoratti, 2014). It is well known that the proton gradient serves as the driving force for ATP synthesis in mitochondria. The Ca²⁺ cations entering the mitochondria not only buffer the cytosolic pool of these ions but can also contribute to some physiological situations such as the mitochondrial mega-channel activation (Carraro and Bernardi, 2023; Zoratti et al., 2024). The effects of Mg²⁺ on mitochondrial functions such as energy metabolism, mitochondrial Ca²⁺ handling, and apoptosis are well established (Liu and Dudley, 2020). Mitochondrial Na⁺ have been discovered as a new second messenger regulating inner mitochondrial membrane (IMM) fluidity and reactive oxygen species (ROS) generation by respiratory chain complex III (Hernansanz-Agustín and Enríquez, 2022). In this study, we will focus on the properties and the role of K⁺ transport, via potassium channels

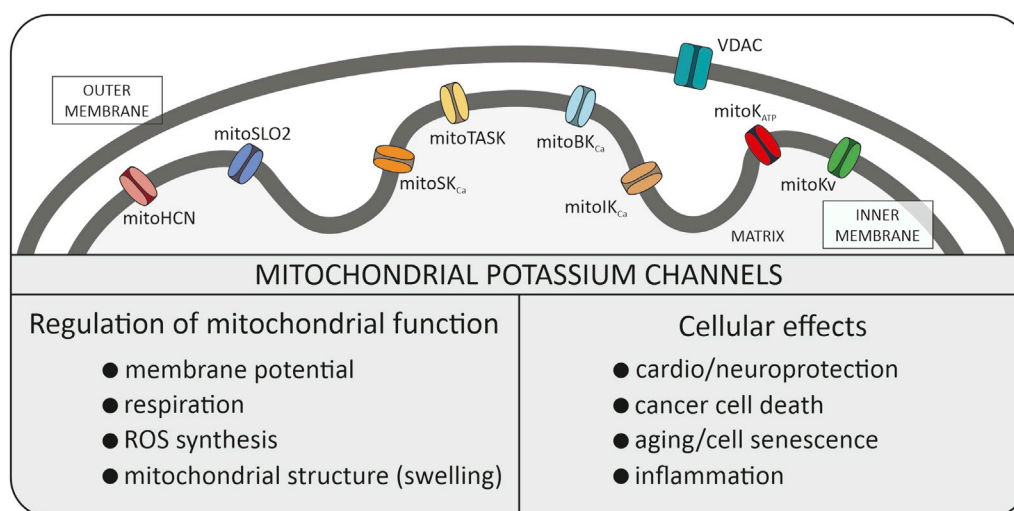


FIGURE 1

Potassium channels identified in the inner mitochondrial membrane. All these types of channels were described in the manuscript. Additionally, the biophysical role in mitochondria and physiological role within the cell is summarized. VDAC, voltage dependent anion channel (porin).

(mitoK channels) present in IMM (Szewczyk, 1996; Kicinska et al., 2000; Debska et al., 2001; O'Rourke, 2007; Singh et al., 2012; Szabo and Szewczyk, 2023) (Figure 1).

In general, proper mitochondrial function is based on the integrity of mitochondrial membranes. Peter Mitchell in his Nobel Lecture delivered in 1978 underlined the importance of the low permeability of the IMM to ions (Mitchell, 1985). Consequently, the discovery of multiple potassium channels in the IMM was for many years considered to be an experimental artifact. Nowadays, mitoK channels present in the IMM are recognized as crucial players for regulating some mitochondrial function (Kravenska et al., 2021; Szabo and Szewczyk, 2023). The mitoK channels have attracted attention for many years, especially in the context of the regulation of life/death processes in the various cell types (Garlid, 2000). For example, the activation of mitoK channels may induce cytoprotective phenomena in cardiac tissue and in neurons (O'Rourke, 2007). On the contrary, inhibition of mitoK channels may cause cell death (Checchetto et al., 2021).

In this paper, we will present what we consider to be the most significant discoveries/ideas in the field of mitoK channels over the past 33 years. These subjective, proposed by author, list of six the most important observations are as follows: 1). Discovery of mitoK channels in various tissues and identification of their molecular identity; 2). Cytoprotection (cardioprotection, neuroprotection) induced by mitoK channels activation; 3). Cancer cell death by mitoK channels inhibition; 4). Role of mitoK channels in aging/senescence/life span; 5). Interactions of mitoK channels with respiratory chain; 6). Druggability of the mitoK channels.

Mitochondrial potassium channel discovery

In 1991, an ion channel selective for K^+ was discovered in the IMM of rat liver mitochondria (Inoue et al., 1991), confirming previous findings on channels in mitochondria by Catia Sorgato (Sorgato et al., 1987). However, what significantly altered the interpretation of this experimental data was the revelation that the channel exhibited not only K^+ selectivity but also susceptibility to inhibition by ATP and the antidiabetic sulfonylurea, glibenclamide (Inoue et al., 1991). This discovery situated mitoK channels within a similar family to ATP-regulated potassium channels found in the plasma membrane of pancreatic beta-cells, cardiomyocytes, neurons, and others (Szewczyk, 1996; O'Rourke, 2007). Undoubtedly, this observation served as a pivotal starting point for numerous experiments identifying ATP-regulated mitochondrial potassium (mitoK_{ATP}) channels across various tissues, notably cardiomyocytes (Szewczyk et al., 2009; Szabo and Szewczyk, 2023). Following several years of intensive investigation across multiple laboratories into the functional role of these channels, it was demonstrated that the activation of mitoK_{ATP} channels (by potassium channel openers) induces a cardioprotective phenomenon (Liu et al., 1999; Garlid, 2000; Szteyn and Singh, 2020; Lukowski et al., 2022). Subsequently, similar findings in neural tissue suggested the involvement of these channels in neuroprotection (Busija et al., 2004; Bednarczyk, 2009). In summary, the association of mitoK_{ATP} channels with cytoprotection marked a significant milestone in the rapid development of the mitochondrial potassium channel field. Moreover, other mitoK channels

(such as large conductance calcium-activated potassium—mitoBK_{Ca} channels) were later implicated in cytoprotection across various cell types (Xu et al., 2002). Despite a plethora of observations, however, the biochemical mechanisms underlying these events remain unclear. It is probable that the indirect modulation of ROS generation by mitoK channels (via depolarization of mitochondria) contributes to this phenomenon.

In recent years, researchers have demonstrated that the family of mitoK channels constitutes one of the most numerous classes of mitochondrial channel proteins. They are also present in plants and in simple organisms (Koszela-Piotrowska et al., 2009; Matkovic et al., 2011; Laskowski et al., 2015). It includes not only mitoK_{ATP} and mitoBK_{Ca} channels but also intermediate conductance (mitoIK_{Ca}), and small conductance (mitoSK_{Ca}), voltage-regulated potassium (mitoKv1.3, mitoKv7.4) channels, mitochondrial hyperpolarization-activated cyclic nucleotide-gated (mitoHCN) channels, mitochondrial sodium-activated potassium (mitoSlo2) channel and two-pore domain potassium (mitoTASK-3) channel (Szabo and Szewczyk, 2023). The activity of potassium channels are regulated by various stimuli, such as pH, Ca²⁺ and ROS (Szabo and Szewczyk, 2023). The mitoK channels have been identified in many tissues but at the same time their number of molecules in mitochondrial membranes is relatively small compared to other mitochondrial transport proteins. Probably low density of mitoK channels and channel run down phenomenon were reasons for questioning in the 90's the presence of these channels at all.

Another issue regarding mitoK channels is the following: why is such a simple process, like K⁺ influx into a matrix, facilitated by a wide variety of potassium channels? For example, in cardiac mitochondria, six mitoK channels have been identified: mitoK_{ATP}, mitoBK_{Ca}, mitoSK_{Ca}, mitoSlo2, mitoHCN channels and mitoKv7.4 channels (Szabo and Szewczyk, 2023). What is the physiological benefit of using many different ligands and factors to regulate these channels? Probably, potassium channels present in cardiomyocyte mitochondria are activated under specific physiological circumstances (Kulawiak et al., 2021). An early event during cardiac ischemia is ATP depletion. This is followed by mitochondrial membrane depolarization. Moreover, because of ATP depletion, ion pumps cannot function, leading to an increase in the cellular Ca²⁺ concentration. The rise in Ca²⁺ during ischemia and reperfusion leads to an overload of mitochondrial Ca²⁺, during reperfusion when oxygen is reintroduced. The decrease in intracellular pH during severe ischemia promotes the imbalance of other cations and leading to cellular Na⁺ overload (Kulawiak et al., 2021). These complex changes may lead to channel activation/inhibition possibly explains why there are few potassium channels in cardiac mitochondria. Most likely, the timing of ATP, pH, Ca²⁺, and Na⁺ concentration changes is

critical to control K⁺ flux in mitochondria stabilizing structure of mitochondria.

Molecular identity of mitoK channels for many years was a mystery. Lack of molecular mitoK identity was an argument questioning the presence of potassium channels in mitochondria. Let's summarize this long way of channel molecular identity recognition. Today we believe that mitoBK_{Ca} channel is one of the splice variants of KCNMA1 (Slo1) gene (Singh et al., 2013; Galecka et al., 2021). Properties of mitoBK_{Ca} suggest that the pore-forming subunit is encoded by the same gene coding for plasma membrane BK_{Ca}. Several studies suggested that the VEDEC BK_{Ca} isoform is located in the IMM. With the mitoK_{ATP} channel there is a more complex situation. It can not be excluded that K⁺ influx is catalyzed by 2-3 various proteins in various tissues. Recently, it was shown that the pore-forming subunit of the mitoK_{ATP} channel is a product of the CCDC51 gene (Paggio et al., 2019). The mitoK_{ATP} is inhibited by the antidiabetic sulfonylurea glibenclamide. Therefore, it was speculated that the glibenclamide receptor (product of ABC8/MITOSUR gene) is an integral part of the mitoK channel. Indeed the mitoK_{ATP} channel formed by these two proteins has the established pharmacological properties of the mitoK_{ATP} channel (Paggio et al., 2019). Previous studies showed that also the ROMK2 potassium channel isoform of the renal outer medullary potassium channel could be the component of the mitoK_{ATP} channel (Bednarczyk et al., 2018; Laskowski et al., 2019). Detailed discussion on mitochondrial potassium channel molecular identity was recently reviewed (Szabo and Szewczyk, 2023).

The presence of various auxiliary β subunits in mitoBK_{Ca} channels and sulfonylurea receptors in the mitoK_{ATP} channel causes that, despite undoubted progress in the identification of channel proteins, the problem of their detailed identification is still a challenge for the future (Piwonska et al., 2008).

From cytoprotection to cell death

The mitoK channels have been described as an important player in cellular pro-life and death signaling. The activation of mitoK channels (by potassium channel openers), such as ATP-regulated or calcium-activated large conductance potassium channels, may have cytoprotective effects in cardiac or neuronal tissue (Liu et al., 1999; Busija et al., 2004). This concept was a strong driving force of studies in many laboratories. Potassium channel opener induced cytoprotection is also induced by endogenous signaling via protein kinases (Frankenreiter et al., 2017).

It has also been shown that inhibition with channel blockers of the mitochondrial Kv1.3 channel may lead to pancreatic cancer cell death (Leanza et al., 2014). But still there is an open question to what extent mitoK channels are promising drug targets in various organs and tissues? Future prospects of

the druggability concept of mitoK channels was evaluated recently (Wrzosek et al., 2020).

Searching for new functions of mitochondrial potassium channels

The putative functional roles of these channels involve alterations in mitochondrial matrix volume, mitochondrial respiration, and protonmotive force (membrane potential) (Czyz et al., 1995). Furthermore, the activity of these channels influences the generation of ROS by mitochondria (Kulawiak et al., 2008; Kulawiak et al., 2023). The activity of mitochondrial potassium channels is subject to modulation by various intrinsic signals, including Ca^{2+} concentration, membrane potential, phosphorylation, and membrane stretching (Szabo and Szewczyk, 2023).

It was demonstrated that BK_{Ca} channels are present in *Drosophila melanogaster* mitochondria, and channel mutants induce structural and functional defects in mitochondria leading to an increase in ROS (Gururaja Rao et al., 2019). It was found that the absence of BK_{Ca} channels reduced the lifespan of *Drosophila*, and overexpression of human BK_{Ca} channels in flies extends their life. This suggested a potential role of mitoK channels and ROS in regulating mitochondrial functional integrity, and lifespan (Gururaja Rao et al., 2019). Probably mito BK_{Ca} play a role in cellular senescence induced by oxidative stress (Gluchowska et al., 2023).

Mitochondrial context of potassium channel regulation

The mitochondrial respiratory chain comprises a series of complex organized redox reactions generating a protonmotive force and, consequently, ATP synthesis. Certain redox centers, such as complexes I and III of the mitochondrial respiratory chain are sources of ROS. Mitochondrial generated ROS can influence remotely the activity of mitoK channels. But there are some indications proposing an alternative, a direct mechanism for the regulation of mitoK channels by the respiratory chain.

It is well-known that mitoK channels interact with various mitochondrial proteins, some of which are involved in the respiratory chain. These observations were recently summarized (Lewandowska et al., 2024). For instance, it has been suggested that mito K_{ATP} channels interact with succinate dehydrogenase. In cardiac mitochondria, it was found that the $\beta 1$ subunit of the mito BK_{Ca} channels interacts with Cytochrome c Oxidase (COX) subunit I. Furthermore, studies have demonstrated that other respiratory chain protein complexes interact with mito BK_{Ca} channels in both cardiac and brain mitochondria. Additionally, mitochondrial tandem pore domain K^+ channels TASK-3 interact also with the respiratory

chain. A recent report revealed a similar interaction between the mitoKv1.3 channel and respiratory chain complex I (for review see Lewandowska et al., 2024).

We found that the activity of mito BK_{Ca} channels in glioblastoma cells is regulated by substrates and inhibitors of the respiratory chain (Bednarczyk et al., 2013). This study suggested that COX is a key element of this kind of channel regulation (Bednarczyk et al., 2013). Moreover, given that COX is the primary infrared-absorbing protein, it raises questions about the potential light regulation of mitoK channels (Szewczyk and Bednarczyk, 2018).

Further research will be important to clarify the functional consequences of these interactions. Undoubtedly, this form of regulation may prove to be unique for mitoK channels. The exact nature and functional implications of these interactions remain unclear. This kind of direct functional coupling between the energy generating system (respiratory chain) with the energy dissipation system (potassium channels) may lead to an interesting putative regulatory mechanism in mitochondria.

Recently other functional/structural coupling within the mitochondrial potassium channel was observed. It was found that mitochondrial potassium channel ROMK2 may interact with two lipid kinases: acylglycerol kinase (AGK) and diacylglycerol kinase ϵ (DGKE), which are localized in mitochondria (Krajewska et al., 2024). Additionally, it was found that the products of AGK and DGKE, lysophosphatidic acid (LPA) and phosphatidic acid (PA), stimulated the activity of ROMK2 potassium channels reconstituted in planar lipid bilayers (Krajewska et al., 2024).

The structure/function interplay of mitoK channels alongside other mitochondrial proteins suggests a new dimension in mitoK channels regulation. The exceptionally high membrane potential of the IMM and its potential for ROS generation may characterize significant signaling pathways within cells.

The troublesome pharmacology of mitochondrial potassium channels

In order to influence activity of various mitoK channels, numerous research groups continually explore novel compounds hoping to find molecules with high specificity for mitoK channels (Szewczyk and Marban, 1999; Augustynek et al., 2017; Leanza et al., 2019). The existing literature already reports positive protective effects on ischemia/reperfusion processes through the activation of mito K_{ATP} channels by the potassium channel opener - diazoxide, and the mito BK_{Ca} channels by potassium channel opener NS1619 and its follower NS11021 (Szewczyk et al., 2006). Nevertheless, it is noteworthy that these compounds exhibit limited specificity towards mitoK channels. Application of these substances in the micromolar concentration range unmasks a variety of side effects (Wrzosek et al., 2022). It is

important to remember that molecules with some hydrophobicity of positive charge (in physiological pH) will be accumulated by mitochondria. It is due to very high membrane potential (up to -180 mV) on the IMM, with negative polarization of the mitochondrial matrix. For example, a 10 nM drug present in cytosol could accumulate up to 10 μ M concentration in a matrix (Kowaltowski and Adbulkader, 2024). At this concentration range the probability of nonspecific interaction with some of $\sim 1,500$ mitochondrial proteins is very high. In contrast, toxins isolated from the venom of various scorpion species such as iberitoxin specifically (at low concentration) inhibit the activity of mitoBK_{Ca} channels (Augustynek et al., 2017). But application of this peptide to block mitoBK_{Ca} channels on intact cells is practically impossible.

Developing very selective channel blockers and potassium channel openers targeting mitoK channels is a significant challenge in this field. Recently it was shown that selective targeting of mitoIK_{Ca} channel (Bachmann et al., 2022), mitoTASK channel (Bachmann et al., 2021) and mitoKv channel (Severin et al., 2022) is possible.

Discussion

Over the past 33 years since the identification of the first potassium channel in the IMM, research in this field has made significant progress (Kulawiak and Szewczyk, 2022). This pathway started from identification of the mitoK channels that met with skepticism by the bioenergetics community to current research placing these channels in the phenomena of cytoprotection, cellular senescence, and neoplastic cell death. What limits further development of this field?

First, access to good pharmacology is the “dark side” of this field (Szewczyk et al., 2010; Olszewska and Szewczyk, 2013; Leanza et al., 2019). Because mitoK channels are similar to those located in plasma membranes, it is very difficult to identify pharmacological modulators specific only for mitoK channels (Szewczyk and Wojtczak, 2002; Citi et al., 2018). The unique high membrane potential of mitochondria may help to discriminate targeting of some drugs to mitoK channels (Testai et al., 2015; Wrzosek et al., 2020).

The second limiting factor for further progress is the development of new techniques to measure channel activity *in situ*, that is, within an intact cell. Majority of techniques currently applied in the studies are based on cell fractionation and mitochondria isolation (Walewska et al., 2022). By definition in this process we lose a network of signaling pathways where mitoK channels are potentially involved

(Walewska et al., 2018). Probably progress in synthesis of potassium specific fluorescent probes may solve this problem. Unfortunately, there are other potassium transport proteins in mitochondria.

The third challenge for the future involves further identifying the molecular identity of various mitoK channels. This aim will not only expand our understanding of the system but also will start new avenues of research, such as *in vitro* translation with lipid nanodiscs and the application of various biophysical techniques. Additionally, it will aid in the identification of protein neighborhoods, clarification of the import machinery, and more.

In summary, mitoK channels, considered the “younger siblings” of the potassium channels found in plasma membranes, play a crucial role in some cellular signaling pathways. The mitoK location within mitochondria, which serve as hubs for fundamental metabolic and signaling functions, highlight their significance. The author believes that the future of this field holds exciting prospects.

Author contributions

The author confirms being the sole contributor of this work and has approved it for publication.

Funding

The author(s) declare that financial support was received for the research, authorship, and/or publication of this article. Supported by the Polish National Science Centre (MAESTRO grant No. 2019/34/A/NZ1/00352).

Conflict of interest

The author declares that the research was conducted in the absence of any commercial or financial relationships that could be construed as a potential conflict of interest.

Acknowledgments

This article is dedicated to Prof. Lech Wojtczak (Nencki Institute of Experimental Biology, Warsaw), whose teachings have greatly contributed to my understanding of mitochondria, and to Prof. Michel Lazdunski (Institute of Molecular and Cellular Pharmacology CNRS, Sophia Antipolis), who introduced me to potassium channels.

References

- Augustynek, B., Kunz, W. S., and Szewczyk, A. (2017). Guide to the pharmacology of mitochondrial potassium channels. *Handb. Exp. Pharmacol.* 240, 103–127. doi:10.1007/164_2016_79
- Bachmann, M., Rossa, A., Antoniazzi, G., Biasutto, L., Carrer, A., Campagnaro, M., et al. (2021). Synthesis and cellular effects of a mitochondria-targeted inhibitor of the two-pore potassium channel TASK-3. *Pharmacol. Res.* 164, 105326. doi:10.1016/j.phrs.2020.105326
- Bachmann, M., Rossa, A., Varanita, T., Fioretti, B., Biasutto, L., Milenkovic, S., et al. (2022). Pharmacological targeting of the mitochondrial calcium-dependent potassium channel KCa3.1 triggers cell death and reduces tumor growth and metastasis *in vivo*. *Cell death Dis.* 13 (12), 1055. doi:10.1038/s41419-022-05463-8
- Bednarczyk, P. (2009). Potassium channels in brain mitochondria. *Acta Biochim. Pol.* 56, 385–392. doi:10.18388/abp.2009_2471
- Bednarczyk, P., Kicinska, A., Laskowski, M., Kulawiak, B., Kampa, R., Walewska, A., et al. (2018). Evidence for a mitochondrial ATP-regulated potassium channel in human dermal fibroblasts. *Biochim. Biophys. Acta Bioenerg.* 1859, 309–318. doi:10.1016/j.bbabi.2018.02.005
- Bednarczyk, P., Wieckowski, M. R., Broszkiewicz, M., Skowronek, K., Siemen, D., and Szewczyk, A. (2013). Putative structural and functional coupling of the mitochondrial BKCa channel to the respiratory chain. *PLoS One* 8 (6), e68125. doi:10.1371/journal.pone.0068125
- Busija, D. W., Lacza, Z., Rajapakse, N., Shimizu, K., Kis, B., Bari, F., et al. (2004). Targeting mitochondrial ATP-sensitive potassium channels—a novel approach to neuroprotection. *Brain Res. Rev.* 46, 282–294. doi:10.1016/j.brainresrev.2004.06.011
- Carraro, M., and Bernardi, P. (2023). The mitochondrial permeability transition pore in Ca^{2+} homeostasis. *Cell calcium* 111, 102719. doi:10.1016/j.ceca.2023.102719
- Checchetto, V., Leanza, L., De Stefani, D., Rizzuto, R., Gulbins, E., and Szabo, I. (2021). Mitochondrial K^+ channels and their implications for disease mechanisms. *Pharmacol. Ther.* 227, 107874. doi:10.1016/j.pharmthera.2021.107874
- Citi, V., Calderone, V., Martelli, A., Breschi, M. C., and Testai, L. (2018). Pathophysiological role of mitochondrial potassium channels and their modulation by drugs. *Curr. Med. Chem.* 25 (23), 2661–2674. doi:10.2174/0929867324666171012115300
- Czyz, A., Szewczyk, A., Nalecz, M. J., and Wojtczak, L. (1995). The role of mitochondrial potassium fluxes in controlling the protonmotive force in energized mitochondria. *Biochem. Biophysical Res. Commun.* 210, 98–104. doi:10.1006/bbrc.1995.1632
- Debska, G., Kicińska, A., Skalska, J., and Szewczyk, A. (2001). Intracellular potassium and chloride channels: An update. *Acta Biochim. Pol.* 48, 137–144. doi:10.18388/abp.2001_5120
- Frankenreiter, S., Bednarczyk, P., Kniess, A., Bork, N. I., Straubinger, J., Koprowski, P., et al. (2017). cGMP-elevating compounds and ischemic preconditioning provide cardioprotection against ischemia and reperfusion injury via cardiomyocyte-specific BK channels. *Circulation* 136, 2337–2355. doi:10.1161/CIRCULATIONAHA.117.028723
- Galecka, S., Kulawiak, B., Bednarczyk, P., Singh, H., and Szewczyk, A. (2021). Single channel properties of mitochondrial large conductance potassium channel formed by BK-VEDEC splice variant. *Sci. Rep.* 11 (1), 10925. doi:10.1038/s41598-021-90465-3
- Garlid, K. D. (2000). Opening mitochondrial K(ATP) in the heart—what happens, and what does not happen. *Basic Res. Cardiol.* 95, 275–279. doi:10.1007/s003950070046
- Głuchowska, A., Kalenik, B., Kulawiak, B., Wrzosek, A., Szewczyk, A., Bednarczyk, P., et al. (2023). Lack of activity of the mitochondrial large-conductance calcium-regulated potassium channels in senescent vascular smooth muscle cells. *Mech. Ageing Dev.* 215, 111871. doi:10.1016/j.mad.2023.111871
- Gururaja Rao, S., Bednarczyk, P., Towheed, A., Shah, K., Karekar, P., Ponnalagu, D., et al. (2019). BK_{Ca} (slo) channel regulates mitochondrial function and lifespan in *Drosophila melanogaster*. *Cells* 8, 945. doi:10.3390/cells8090945
- Hernansanz-Agustín, P., and Enríquez, J. A. (2022). Sodium in mitochondrial redox signaling. *Antioxidants Redox Signal.* 37, 290–300. doi:10.1089/ars.2021.0262
- Inoue, I., Nagase, H., Kishi, K., and Higuti, T. (1991). ATP-sensitive K^+ channel in the mitochondrial inner membrane. *Nature* 352, 244–247. doi:10.1038/352244a0
- Kicinska, A., Dbska, G., Kunz, W., and Szewczyk, A. (2000). Mitochondrial potassium and chloride channels. *Acta Biochim. Pol.* 47, 541–551. doi:10.18388/abp.2000_3977
- Koszela-Piotrowska, I., Matkovic, K., Szewczyk, A., and Jarmuszkiewicz, W. (2009). A large-conductance calcium-activated potassium channel in potato (*Solanum tuberosum*) tuber mitochondria. *Biochem. J.* 424, 307–316. doi:10.1042/BJ20090991
- Kowaltowski, A. J., and Abdulkader, F. (2024). How and when to measure mitochondrial inner membrane potentials. *Biophysical J.* S0006-3495 (24), 00176–180. doi:10.1016/j.bpj.2024.03.011
- Krajewska, M., Możajew, M., Filipek, S., and Koprowski, P. (2024). Interaction of ROMK2 channel with lipid kinases DGKE and AGK: potential channel activation by localized anionic lipid synthesis. *Biochim. Biophys. Acta Mol. Cell Biol. Lipids* 1869, 159443. doi:10.1016/j.bbalip.2023.159443
- Kravenska, Y., Checchetto, V., and Szabo, I. (2021). Routes for potassium ions across mitochondrial membranes: a biophysical point of view with special focus on the ATP-sensitive K^+ channel. *Biomolecules* 11, 1172. doi:10.3390/biom11081172
- Kulawiak, B., Bednarczyk, P., and Szewczyk, A. (2021). Multidimensional regulation of cardiac mitochondrial potassium channels. *Cells* 10, 1554. doi:10.3390/cells10061554
- Kulawiak, B., Kudin, A. P., Szewczyk, A., and Kunz, W. S. (2008). BK channel openers inhibit ROS production of isolated rat brain mitochondria. *Exp. Neurol.* 212, 543–547. doi:10.1016/j.expneurol.2008.05.004
- Kulawiak, B., and Szewczyk, A. (2022). Current challenges of mitochondrial potassium channel research. *Front. Physiol.* 13, 907015. doi:10.3389/fphys.2022.907015
- Kulawiak, B., Żochowska, M., Bednarczyk, P., Galuba, A., Stroud, D. A., and Szewczyk, A. (2023). Loss of the large conductance calcium-activated potassium channel causes an increase in mitochondrial reactive oxygen species in glioblastoma cells. *Pflugers Arch.* 475, 1045–1060. doi:10.1007/s00424-023-02833-9
- Laskowski, M., Augustynek, B., Bednarczyk, P., Żochowska, M., Kalisz, J., O'Rourke, B., et al. (2019). Single-Channel properties of the ROMK-pore-forming subunit of the mitochondrial ATP-sensitive potassium channel. *Int. J. Mol. Sci.* 20, 5323. doi:10.3390/ijms20215323
- Laskowski, M., Kicinska, A., Szewczyk, A., and Jarmuszkiewicz, W. (2015). Mitochondrial large-conductance potassium channel from *Dictyostelium discoideum*. *Int. J. Biochem. Cell Biol.* 60, 167–175. doi:10.1016/j.biocel.2015.01.006
- Leanza, L., Checchetto, V., Biasutto, L., Rossa, A., Costa, R., Bachmann, M., et al. (2019). Pharmacological modulation of mitochondrial ion channels. *Br. J. Pharmacol.* 176 (22), 4258–4283. doi:10.1111/bph.14544
- Leanza, L., Zoratti, M., Gulbins, E., and Szabo, I. (2014). Mitochondrial ion channels as oncological targets. *Oncogene* 33, 5569–5581. doi:10.1038/onc.2013.578
- Lewandowska, J., Kalenik, B., Wrzosek, A., and Szewczyk, A. (2024). Redox regulation of mitochondrial potassium channels activity. *Antioxidants* 13, 434. doi:10.3390/antiox13040434
- Liu, M., and Dudley, S. C. (2020). Magnesium, oxidative stress, inflammation, and cardiovascular disease. *Antioxidants* 9, 907. doi:10.3390/antiox9100907
- Liu, Y., Sato, T., Seharaseyon, J., Szewczyk, A., O'Rourke, B., and Marbán, E. (1999). Mitochondrial ATP-dependent potassium channels: viable candidate effectors of ischemic preconditioning. *Ann. N. Y. Acad. Sci.* 874, 27–37. doi:10.1111/j.1749-6632.1999.tb09222.x
- Lukowski, R., Cruz Santos, M., Kuret, A., and Ruth, P. (2022). cGMP and mitochondrial K^+ channels—Compartmentalized but closely connected in cardioprotection. *Br. J. Pharmacol.* 179, 2344–2360. doi:10.1111/bph.15536
- Matkovic, K., Koszela-Piotrowska, I., Jarmuszkiewicz, W., and Szewczyk, A. (2011). Ion conductance pathways in potato tuber (*Solanum tuberosum*) inner mitochondrial membrane. *Biochim. Biophys. Acta.* 1807, 275–285. doi:10.1016/j.bbabi.2010.12.001
- Mitchell, P. (1985). The correlation of chemical and osmotic forces in biochemistry. *J. Biochem.* 97, 1–18. doi:10.1093/oxfordjournals.jbchem.a135033
- Olszewska, A., and Szewczyk, A. (2013). Mitochondria as a pharmacological target: Magnum overview. *IUBMB Life* 65, 273–281. doi:10.1002/iub.1147
- O'Rourke, B. (2007). Mitochondrial ion channels. *Annu. Rev. Physiol.* 69, 19–49. doi:10.1146/annurev.physiol.69.031905.163804
- Paggio, A., Checchetto, V., Campo, A., Menabò, R., Di Marco, G., Di Lisa, F., et al. (2019). Identification of an ATP-sensitive potassium channel in mitochondria. *Nature* 572, 609–613. doi:10.1038/s41586-019-1498-3
- Piwnska, M., Wilczek, E., Szewczyk, A., and Wilczynski, G. M. (2008). Differential distribution of Ca^{2+} -activated potassium channel beta4 subunit in rat brain: Immunolocalization in neuronal mitochondria. *Neuroscience* 153, 446–460. doi:10.1016/j.neuroscience.2008.01.050
- Severin, F., Urbani, A., Varanita, T., Bachmann, M., Azzolini, M., Martini, V., et al. (2022). Pharmacological modulation of Kv1.3 potassium channel selectively

- triggers pathological B lymphocyte apoptosis *in vivo* in a genetic CLL model. *J. Exp. Clin. Cancer Res.* 41 (1), 64. doi:10.1186/s13046-022-02249-w
- Singh, H., Lu, R., Bopassa, J. C., Meredith, A. L., Stefani, E., and Toro, L. (2013). MitoBK(Ca) is encoded by the *Kcnma1* gene, and a splicing sequence defines its mitochondrial location. *Proc. Natl. Acad. Sci. U. S. A.* 110, 10836–10841. doi:10.1073/pnas.1302028110
- Singh, H., Stefani, E., and Toro, L. (2012). Intracellular BK(Ca) (iBK(Ca)) channels. *J. Physiology* 590, 5937–5947. doi:10.1113/jphysiol.2011.215533
- Sorgato, M. C., Keller, B. U., and Stühmer, W. (1987). Patch-clamping of the inner mitochondrial membrane reveals a voltage-dependent ion channel. *Nature* 330, 498–500. doi:10.1038/330498a0
- Szabo, I., and Szewczyk, A. (2023). Mitochondrial ion channels. *Annu. Rev. Biophys.* 52, 229–254. doi:10.1146/annurev-biophys-092622-094853
- Szabo, I., and Zoratti, M. (2014). Mitochondrial channels: Ion fluxes and more. *Physiol. Rev.* 94, 519–608. doi:10.1152/physrev.00021.2013
- Szewczyk, A. (1996). The ATP-regulated K⁺ channel in mitochondria: Five years after its discovery. *Acta Biochim. Pol.* 43, 713–719. doi:10.18388/abp.1996_4469
- Szewczyk, A., and Bednarczyk, P. (2018). Modulation of the mitochondrial potassium channel activity by infrared light. *Biophysical J.* 114, 43a. doi:10.1016/j.bpj.2017.11.288
- Szewczyk, A., Jarmuszkiewicz, W., and Kunz, W. S. (2009). Mitochondrial potassium channels. *IUBMB Life* 61, 134–143. doi:10.1002/iub.155
- Szewczyk, A., Kajma, A., Malinska, D., Wrzosek, A., Bednarczyk, P., Zabłocka, B., et al. (2010). Pharmacology of mitochondrial potassium channels: Dark side of the field. *FEBS Lett.* 584, 2063–2069. doi:10.1016/j.febslet.2010.02.048
- Szewczyk, A., and Marbán, E. (1999). Mitochondria: A new target for K channel openers? *Trends Pharmacol. Sci.* 20, 157–161. doi:10.1016/s0165-6147(99)01301-2
- Szewczyk, A., Skalska, J., Głab, M., Kulawiak, B., Malińska, D., Koszela-Piotrowska, I., et al. (2006). Mitochondrial potassium channels: From pharmacology to function. *Biochim. Biophys. Acta.* 1757, 715–720. doi:10.1016/j.bbabi.2006.05.002
- Szewczyk, A., and Wojtczak, L. (2002). Mitochondria as a pharmacological target. *Pharmacol. Rev.* 54, 101–127. doi:10.1124/pr.54.1.101
- Szteyn, K., and Singh, H. (2020). BKCa channels as targets for cardioprotection. *Antioxidants* 9, 760. doi:10.3390/antiox9080760
- Testai, L., Rapposelli, S., Martelli, A., Breschi, M. C., and Calderone, V. (2015). Mitochondrial potassium channels as pharmacological target for cardioprotective drugs. *Med. Res. Rev.* 35, 520–553. doi:10.1002/med.21332
- Walewska, A., Krajewska, M., Stefanowska, A., Buta, A., Bilewicz, R., Krysiński, P., et al. (2022). Methods of measuring mitochondrial potassium channels: a critical assessment. *Int. J. Mol. Sci.* 23, 1210. doi:10.3390/ijms23031210
- Walewska, A., Szewczyk, A., and Koprowski, P. (2018). Gas signaling molecules and mitochondrial potassium channels. *Int. J. Mol. Sci.* 19, 3227. doi:10.3390/ijms19103227
- Wrzosek, A., Augustynek, B., Żochowska, M., and Szewczyk, A. (2020). Mitochondrial potassium channels as druggable targets. *Biomolecules* 10, 1200. doi:10.3390/biom10081200
- Wrzosek, A., Galecka, S., Żochowska, M., Olszewska, A., and Kulawiak, B. (2022). Alternative targets for modulators of mitochondrial potassium channels. *Molecules* 27, 299. doi:10.3390/molecules27010299
- Xu, W., Liu, Y., Wang, S., McDonald, T., Van Eyk, J. E., Sidor, A., et al. (2002). Cytoprotective role of Ca²⁺-activated K_s channels in the cardiac inner mitochondrial membrane. *Science* 298, 1029–1033. doi:10.1126/science.1074360
- Zoratti, M., Biasutto, L., Parrasia, S., and Szabo, I. (2024). Mitochondrial permeability transition pore: A snapshot of a therapeutic target. *Expert Opin. Ther. Targets* 28, 1–3. doi:10.1080/14728222.2024.2306337

PELP1 and SRC kinase as important molecules in the estrogen-mediated pathway in human testis and epididymis

Izabela Skibińska¹✉, Mirosław Andrusiewicz¹, Magdalena Jendraszak¹, Aleksandra Żbikowska¹, Czesław Żaba² and Małgorzata Kotwicka¹

¹Chair and Department of Cell Biology, Poznań University of Medical Sciences, Poznań, Poland; ²Chair and Department of Forensic Sciences, Poznań University of Medical Sciences, Poznań, Poland

Background: Estrogens have pleiotropic mechanisms of action, and their cellular transduction pathways can modulate various proteins with differential tissue expression. Proline-, glutamic acid-, and leucine-rich protein 1 (PELP1) is one such protein whose role seems important. However, very little is known about the expression of modulators involved in the estrogen-mediated pathways in the tissues of the male reproductive tract. **Methods:** In this study, we obtained autopsy specimens of testis and epididymis from 13 men of Caucasian descent. Expression levels were analyzed for both estrogen receptors (*ESR1* and *ESR2*) and their co-regulators, including *PELP1* and kinase c-Src (*SRC*). **Results:** Protein expression was confirmed with western blot and immunocytochemistry techniques. The expression of both *SRC* and *PELP1* was significantly higher in the testis compared to the epididymis ($p=0.040$ and $p=0.002$, respectively). Furthermore, a significant, positive correlation was observed between *SRC* and *PELP1*, regardless of tissue type ($p<0.0001$, $R=0.78$). In the testis, *PELP1* expression positively correlated with *ESR1* expression ($p=0.0367$, $R=0.6$). **Conclusions:** Our study suggests a possible relationship between *PELP1*, *SRC*, and *ESR1* in the human testis and epididymis. This study makes a valuable contribution to the field of estrogen-mediated pathways in the male reproductive tract and describes trends of analyzed genes' expression and presence. We think our results may open some new research directions in the study of estrogen signaling in the male reproductive system.

Keywords: estrogen receptors (*ESR1* and *ESR2*); proline-, glutamic acid-, and leucine-rich protein 1 (*PELP1*); proto-oncogene tyrosine-protein kinase c-SRC (*SRC*); steroid hormones; human testis; human epididymis

Received: 14 April, 2023; **revised:** 21 April, 2023; **accepted:** 26 April, 2023; **available on-line:** 09 May, 2023

✉e-mail: iskibinska@ump.edu.pl

Acknowledgements of Financial Support: This research was funded by National Science Centre Poland, grant number UMO-2016/23/D/NZ5/02604, and PUMS funded the APC.

Abbreviations: BC, basal cells; CC, ciliated cells; Cr, concentration ratio; *ESR1*, estrogen receptor 1; *ESR2*, estrogen receptor 2; GPER, GPR30, G protein-coupled estrogen receptors; HPRT1, hypoxanthine-guanine phosphoribosyltransferase; IT, interstitial tissue; LC, Leydig Cells; MNAR, modulator of non-genomic action of estrogen receptor; nCC, non-ciliated cells; *PELP1*, proline-, glutamic acid-, and leucine-rich protein 1; Psp, primary spermatocytes; S, spermatozoa; SC, Sertoli cells; SEC, seminiferous epithelium cells; Sd, spermatids; Sg, spermatogonia; *SRC*, proto-oncogene tyrosine-protein kinase c-SRC

INTRODUCTION

The predominant paradigm concerning the influence of steroid hormones in the regulation of the male reproductive tract's functions was primarily focused on androgens such as testosterone. However, in 1990 knock-out animal models began to be extensively used and demonstrated that estrogens play an important role in male reproductive health (Carreau *et al.*, 2011a; Akingbemi, 2005; Carreau *et al.*, 2011b; Chimento *et al.*, 2020; Hess & Cooke, 2018). These commonly considered female hormones are indispensable for the proper development of certain structures within the male reproductive tract, such as the prostate, epididymis, and efferent ductules. Estrogens are synthesized in the testis, and 17 β -estradiol is highly expressed in the rete testis fluid. Studies have shown that the male reproductive tract has extensive expression of both estrogen receptors (ESRs), namely *ESR1* and *ESR2*, starting from the neonatal period through puberty to adulthood. However, expression level differs with regard to tissue type and age (Cooke *et al.*, 2017; Cunha *et al.*, 2021; Hess & Cooke, 2018). Several findings also confirmed an association between estradiol and a handful of physiological events such as erectile function, spermatogenesis, Leydig cell self-regulation, testosterone production control, and auto- and paracrine effects on germ cells (Hess & Cooke, 2018; Solakidi *et al.*, 2005; Carreau *et al.*, 2011a; Cooke *et al.*, 2017; Hammes & Levin, 2019; Lazari *et al.*, 2009). Furthermore, the identification of an aromatase function has been a tremendous breakthrough in defining the role of estrogens in males (Carreau *et al.*, 2006; Otto *et al.*, 2009; Akingbemi, 2005; Rago *et al.*, 2007; Carreau *et al.*, 2010; Aquila *et al.*, 2003) and has directed the attention of many researchers around the world to the influence on the male reproductive tract of estrogen-like compounds present in the environment (referred to as “xenoestrogens”). Previously, the idea of the potential negative influence of estrogens and their role in disrupting the function of the male reproductive system has become widespread (Rahman *et al.*, 2015; Mohamed *et al.*, 2011; Sikka & Wang, 2008; Hess *et al.*, 2011; Bertolla, 2020).

The commonly identified pathways that control the functional influence of estrogens on the tissues/cells of interest (including those in the male reproductive tract) classically involve either ESR or G protein-coupled estrogen receptors (GPER, GPR30). It cannot be excluded that recently discovered novel proteins, referred to as putative ESRs (estrogen-related receptor, saxiphilin-binding protein, ER-X, and ER-x), may play a similar role in mediating estrogen signals in males (Barut *et al.*, 2020; Li *et al.*, 2015; Eyster, 2016; Micevych & Dewing,

2011; Toran-Allerand *et al.*, 2002; Cooke *et al.*, 2017; Akingbemi, 2005). It is also essential to highlight the role of certain co-regulators in mediating estrogen signals in tissues/cells of interest. One of them is the scaffold protein proline-, glutamic acid-, and leucine-rich protein 1 (PELP1), also known as MNAR (modulator of non-genomic action of estrogen receptor). PELP1 was shown to interact not only with nuclear receptors and transcription factors (such as activator protein 1, specificity protein 1, or nuclear factor kappa B) but also with several key modulators of cell cycle progression, such as proto-oncogene tyrosine-protein, epidermal growth factor receptor, phosphoinositide-3 or c-SRC kinases (Vadlamudi & Kumar, 2007; Sareddy & Vadlamudi, 2016; Vadlamudi *et al.*, 2001). This previous literature has shown PELP1 to be an important mediator of steroid hormone regulation of cell or tissue functions. Moreover, our previous studies demonstrated that the percentage of PELP1+ sperm cells is correlated with decreasing sperm quality (Skibińska *et al.*, 2018). Also, our investigation revealed weak, negative *ESR2/PELP1* correlations in patients with abnormal sperm values. Interestingly, *SRC/PELP1* was moderately and positively correlated with all parameters within the WHO reference range in the subgroup of patients (Skibińska *et al.*, 2022). The literature has identified that SRC-mediated signaling is coordinated by binding PELP1 and ESR to SRCs SH3 and SH2 domains, which is then stabilized by the ESR-PELP1 interaction through PELP1's LXXLL motifs (Xiao *et al.*, 2019; Shupe *et al.*, 2011; Barletta *et al.*, 2004). SRC has been characterized as the downstream protein kinase of the non-classical testosterone signaling pathway involved in the release of sperm at spermiation. It cannot be excluded that close interactions between these two proteins have implications for estrogen signaling in males.

Despite the broad availability of animal models for research purposes, this is not the case for human tissues. Therefore, data regarding estrogens and estrogen-mediated pathways in humans do not currently provide clear answers concerning the presence, localization, and interactions between proteins involved in estrogen-mediated signaling. It appears crucial in determining the potential clinical repercussions of estrogens in the male reproductive tract, also in the context of impaired male fertility. Where and when estrogen and/or an estrogen/androgen balance might play a role in the development and function of the male reproductive tract needs to be determined. It is expected that with recent advances in molecular and cell biology techniques, many questions about estrogen-mediated signaling in men will be answered within the next decade. The aim of this study was to analyze the potential links between ESRs, PELP1, and SRC in human testis and epididymis, as these proteins are considered important factors involved in estrogen-mediated signaling in the male reproductive system.

MATERIALS AND METHODS

Testes tissue samples

Autopsy specimens of testis and epididymis were obtained from 13 men of Caucasian descent at the Chair and Department of Forensic Medicine of PUMS. The mean age of participants was 45±15 years (range: 23–76) with a 45% coefficient of variation. Tissues qualified for the study came from men with no significant spermatogenesis disorders. The assessment of tissues stained with the standard hematoxylin and eosin method was based

on the microscopic evaluation, accordingly to Cerilli *et al.* (Cerilli *et al.*, 2010). Each testis and epididymal caput sample was split into three fragments (equal in mass). For RT-qPCR analyses, the tissues were immersed in RNA protective medium (Englert-Golon *et al.*, 2021; Camacho-Sanchez *et al.*, 2013), and for protein isolation were placed in phosphate-buffered saline (PBS, Chem-pur; Piekary Śląskie, Poland). In both cases, the tissues were stored at –80°C until further procedures. The third portion, intended for immunohistochemistry, was fixed in 4% paraformaldehyde (Chempur; Piekary Śląskie, Poland) and processed for standard formalin-fixed paraffin-embedding.

METHODS

Nucleic acid isolation and validation

Before nucleic acid isolation, the samples were thawed to room temperature. The RNA protective medium was removed, and testis and epididymis tissue samples were patted dry with a paper towel. The tissues were immediately placed in a chilled mortar and pulverized with a pestle. Aliquots of 25 mg of tissue were immersed in 800 µL fenzol reagent to deactivate endogenous RNases (A&A Biotechnology, Gdynia, Poland). The samples were dissolved by vortexing (15 sec, 1200 rpm, room temperature) and incubated in a thermal mixer to permit complete dissociation of the nucleoproteins (5 min, 300 rpm, 56°C). Then, 200 µL of chloroform (Avantor Performance Materials Poland S.A., Gliwice, Poland) was added to each aliquot, mixed by inversion, incubated (3 min, room temperature), and centrifuged (15 min, 12000×g, 4°C). The aqueous upper phase containing total cellular RNA was carefully transferred to a new tube, avoiding transferring the interphase.

The aqueous phases were subjected to high molecular weight RNA extraction, without microRNA fractionation, using the double-column system for microRNA and RNA isolation according to the manufacturer's protocol (A&A Biotechnology, Gdynia, Poland) as described previously (Englert-Golon *et al.*, 2021). The quality, quantity, and purity of extracted RNA were analyzed as described previously (Andrusiewicz *et al.*, 2016) with the use of NanoPhotometer NP-80 (IMPLEN, München, Germany), and the integrity was evaluated by electrophoretic separation under denaturing conditions (Andrusiewicz *et al.*, 2016).

Reverse transcription and quantitative polymerase chain reaction

Three-step reverse-transcription reactions were performed as described previously (Andrusiewicz *et al.*, 2016). In brief, a mixture of 0.5 M universal oligo(d)T₁₀ primer, 1 mM random hexamer primer (Genomed; Warsaw, Poland), 1 µg RNA, and water (Thermo Fisher Scientific; Waltham, MA, USA) were incubated for 10 mins at 65°C, and samples chilled on ice. Then, 10 U transcriptase reverse transcriptase, 5 U RNasin ribonuclease inhibitor, 1× reaction buffer (Roche; Mannheim, Germany), 0.1 U/µL *E. coli* poly(A) polymerase, 100 nM adenosine triphosphate (New England BioLabs; Ipswich, MA, USA), and 100 mM deoxyribonucleotide triphosphates (Novayzm; Poznań, Poland) were added with water to a final reaction volume of 20 µL. The subsequent steps of cDNA synthesis were followed as described previously (Englert-Golon *et al.*, 2021). The cDNA was synthesized in duplicate for

each sample and subsequently served as a template for qPCR reactions. The threshold cycles mean values derived from replicated samples were used for further analysis.

To determine primer sequences and hydrolysis Universal Probe positions for *ESR1*, *PELP1*, and *SRC*, the UPL Assay Design Center was used (<http://qpcr.probefinder.com>, last accessed on September 28, 2017, product discontinued on December 30, 2020) (Skibińska *et al.*, 2018). Probe numbers and primers' sequences are as follows: *ESR1* F: CCTTCTCAAGAGAAGTATTC AAGG; R: ATTCCCACTTCGTAGCATTTG; probe #69 (Roche cat. no.: 04688686001; GenBank AC: NM_001122740.2, NM_001122741.2, NM_001385571.1, NM_001291241.2, NM_001385568.1, NM_001385572.1, NM_001385570.1, NM_001385569.1, NM_000125.4, NM_001328100.2, NM_001291230.2), *PELP1* F: CAAGGAGGAGACTCACAGGAG; R: CAAGGAGGAGACTCACAGGAG; probe #24 (Roche cat. no.: 04686985001; NM_014389.3, NM_001278241.2), and *SRC* F: GCCATGTTCACTCCGGTTT; R: CAGCGTCCTCATCTGGTTTC; probe #21 (Roche cat. no.: 04686942001; NM_005417.5). Either the forward or the reverse primers were designed for the exon-exon junction of the analyzed mRNAs. The amplicon lengths were similar. With regards to *ESR2*, we applied a ready-to-use assay (PrimePCR, qHsaCEP0052206, BioRad; Hercules, CA, USA). The hypoxanthine-guanine phosphoribosyltransferase (*HPRT1*) gene assay (UPL102079, Roche; Mannheim, Germany) was used as a reference gene.

The quantitative PCR reactions were carried out according to the MIQE guidelines (Bustin *et al.*, 2009) (Supplementary Materials: MIQE checklist and data set). All qPCR reactions were made in a total volume of 20 μ L. Standard cycling and acquisition steps were performed with adjusted and standardized reaction mixtures for Roche UPL probes in the LightCycler 2.0 glass-capillary thermal cycler (Roche Diagnostics International AG; Rotkreuz, Switzerland) (Englert-Golon *et al.*, 2021; Andrusiewicz *et al.*, 2016). The expression level of each gene, expressed as concentration ratios (Cr), was derived from reaction efficiencies (obtained from the relevant standard curves) compared with the appropriate mean of two-reaction threshold values and normalized to reference gene expression (Englert-Golon *et al.*, 2021; Skibińska *et al.*, 2018).

Western blot analysis

Tissue samples immersed in PBS were used for protein isolation, followed by western blot. After mechanical pulverization in liquid nitrogen, tissue samples were suspended by pipetting in RIPA Lysis Buffer (Merck Millipore, Darmstadt, Germany). Then, total sample extracts were shaken in an orbital shaker (1600 rpm, 60 min, 4°C) and centrifuged (14000 $\times g$, 20 min, 4°C). The supernatant was transferred into a fresh tube and centrifuged again (3000 $\times g$, 10 min, 4°C), and then the supernatant containing purified proteins was used in further analyses.

Western blot analyses were conducted as described previously (Englert-Golon *et al.*, 2021). In short, protein concentration was measured colorimetrically with Quick-Start Bradford 1 \times Dye Reagent (BioRad, Hercules, CA, USA). Protein lysates (20 μ g) diluted with Laemmli buffer (BioRad, Hercules, CA, USA) were denatured at 70°C for 10 min, loaded onto a 10% SDS-polyacrylamide gel (TGX FastCast Acrylamide Kit 10%, BioRad, Hercules, CA, USA), and separated by electrophoresis. After wet-transfer, PVDF membranes (Merck Millipore, Darmstadt,

Germany) were incubated on an orbital shaker at 200 rpm for 60 min at room temperature in TBS-T blocking buffer (TBS with 0.1% Tween-20 and 5% bovine serum albumin, pH 7.5; LabEmpire; Rzeszow, Poland). After blocking, the membranes were incubated with primary antibodies on an orbital shaker at 200 rpm overnight at 4°C. The antibodies used are as follows: anti-ESR1 (1:1000, LS-C88420, Lifespan Biosciences, Seattle, WA, USA), ESR2 (1:1000, ab3576, Abcam, Cambridge, UK), PELP1/MNAR (1:1000, A300-180A, Bethyl, Montgomery, TX, USA), SRC (1:1000 orb379229, Biorbyt, Cambridge, UK), pSRC (1:500, orb14869, Biorbyt, Cambridge, UK), and GAPDH (1:2500, sc-25778, Santa Cruz Biotechnology, Dallas, TX, USA). Subsequent visualization processing steps were performed as described previously (Englert-Golon *et al.*, 2021). Immunoreactive bands were compared with the mass standard (3-Colour Prestained Protein Marker; Blirt, Gdansk, Poland). For protein density analysis ImageJ Software version 1.53r was used (<https://imagej.nih.gov/ij/download.html>, accession date 22.04.2022). The high-resolution TIFF images obtained with G:BOX (Syngen, Cambridge, UK) from chemiluminescent-visualized western blots were converted into JPEG 255 grayscale format. A defined frame size was used to measure the optical density of analyzed proteins, the background, and the GAPDH protein as the reference. The pixel density for all data was inverted and expressed as 255 – recorded by ImageJ value. Next, the net values for analyzed proteins and controls were calculated (by subtracting the value obtained for the background). Finally, the ratios of net band values for analyzed proteins and corresponding references were obtained and expressed as optical density in arbitrary units.

Immunohistochemical protein localization

The protein localization in tissue samples was assessed using immunohistochemistry as described previously (Waligórska-Stachura *et al.*, 2017; Englert-Golon *et al.*, 2021). In brief, 3 μ m thick tissue sections were immersed in antigen retrieval solution (0.1 mM citric acid and 0.1 mM sodium citrate; pH 6.0; Avantor Performance Materials Poland S.A., Gliwice, Poland) and then microwaved, and this process repeated. Endogenous peroxidase activity was blocked in a 3% hydroperoxide solution (Avantor Performance Materials Poland S.A., Gliwice, Poland). The slides were blocked in a TBS-T blocking buffer for 60 min at room temperature. Immunohistochemical reactions were performed using the primary antibodies specified in the western blot analysis description at a 1:100 dilution in TBS-T buffer and visualized and assessed as described previously (Englert-Golon *et al.*, 2021). The specificity, dilutions and immunohistochemical reactions' conditions for positive controls were also adopted from the methodology referred above. The primary antibodies were substituted with a blocking buffer in the appropriate negative controls.

Statistical analyses

Results were evaluated using Statistica version 13.5.0 software for Windows (TIBCO Software Inc., Palo Alto, CA, USA). All continuous variables were checked for outliers. Min-Max normalization was used to describe and present the final data. All genes were analyzed for not only normalized C_r values but also gene-to-gene C_r values. Results were described by the median [interquartile range] (Me [IR]) values. The Shapiro-Wilk test was applied for the normality of continuous variables distribution assessment. The non-parametric two-tailed

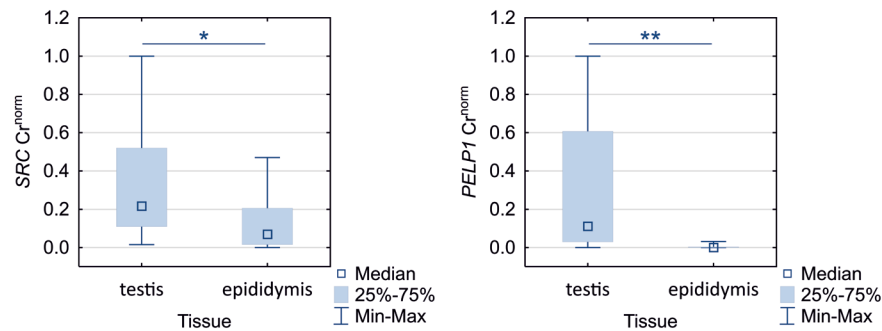


Figure 1. Normalized expression of *SRC* and *PELP1* in testis and epididymis.
* $p < 0.05$, ** $p < 0.01$ (two-tailed Mann-Whitney U test).

Mann-Whitney U test was used for statistical analyses. The Spearman rank correlation test was applied to evaluate the strength of the correlation coefficient (R). The strength of the correlation coefficient was assessed according to Guilford's classification. Data were considered statistically significant when $p < 0.05$.

RESULTS

ESRs, *PELP1* and *SRC* mRNA expression

The normalized expression level of both *SRC* and *PELP1* differ significantly between testis and epididymal tissue ($p = 0.040$ and $p = 0.002$, respectively), with both genes having higher expression levels in the testis (Fig. 1). We did not observe significant differences in the expression level of *ESR1* and *ESR2* in either testis or epididymal tissue in any of the analyzed samples ($p > 0.05$) (not shown).

With respect to the tissue of origin, both *SRC* and *PELP1* expression was significant and very strongly positively correlated in both testis and epididymis ($R = 0.66$, $p = 0.014$, and $R = 0.80$, $p = 0.0019$, respectively). Additionally, *PELP1* expression was strongly positively corre-

lated with the expression of *ESR1* in the testis ($R = 0.6$; $p = 0.0367$) (Fig. 2). We did not observe this correlation in the case of the epididymis ($p > 0.05$).

We observed a moderate positive correlation between the tissue donors' age and *ESR1* normalized expression in the testis ($R = 0.59$; $p = 0.0322$) and a moderate negative correlation of the age and *PELP1* expression in the epididymis ($R = -0.61$; $p = 0.0354$) (Fig. 3). The expression levels of other genes were not correlated with age ($p > 0.05$).

Considering the expression ratio of analyzed genes, the *ESR2/PELP1* ratio differed significantly between the testis and epididymis ($p = 0.0068$). The expression ratio was lower in the testis (Fig. 4). There was no significant difference in the expression ratios of other genes between the tissue types.

Considering tissue-origin-dependent division, *ESR1/ESR2*, *ESR1/SRC*, and *ESR1/PELP1* expression ratios were moderately and positively correlated in the testis. *ESR2/SRC* was moderately positively correlated with *ESR2/PELP1*, and strongly negatively correlated with *SRC/PELP1*. We observed very strong positive correlations of *ESR1/ESR2* with *ESR1/SRC*, *ESR1/SRC* with *ESR1/PELP1*, and *ESR2/SRC* with *ESR2/PELP1* in the epididymis. Additionally, a moderately positive

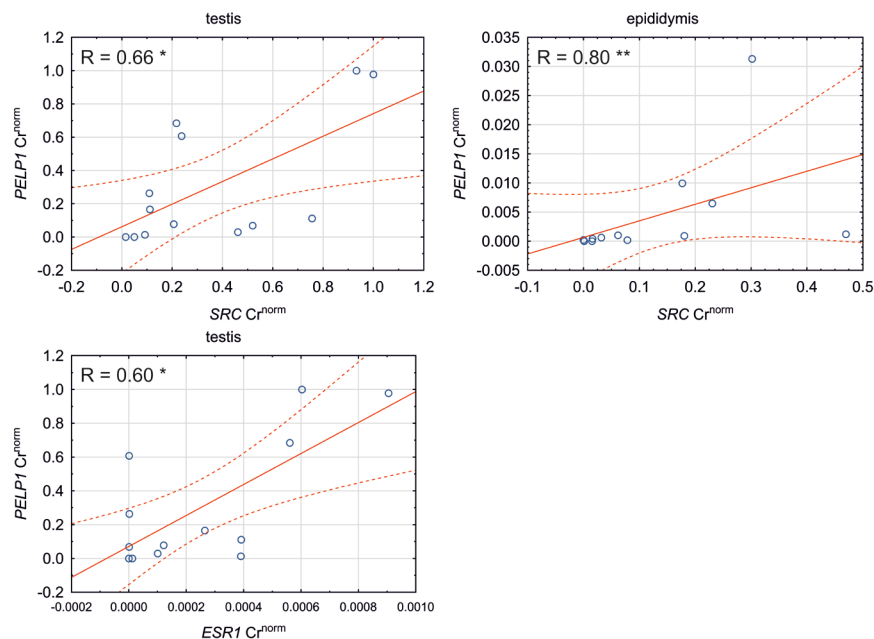


Figure 2. Dot-plot of normalized *PELP1* expression correlation with *SRC* and *ESR1* in testis and epididymis.
Spearman's rank correlation coefficient (R) is indicated as significant * $p < 0.05$, ** $p < 0.01$.

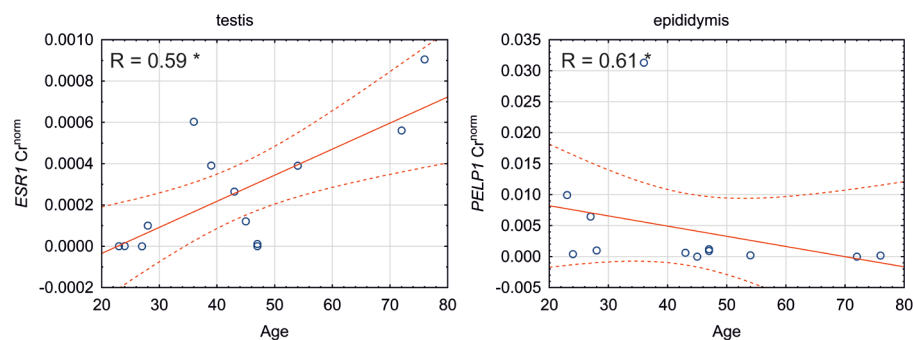


Figure 3. Dot-plot of the participants' age and correlation in testis and epididymis of *ESR1* and *PELP1* normalized expression. Spearman's rank correlation coefficient (R) is indicated as significant * $p < 0.05$.

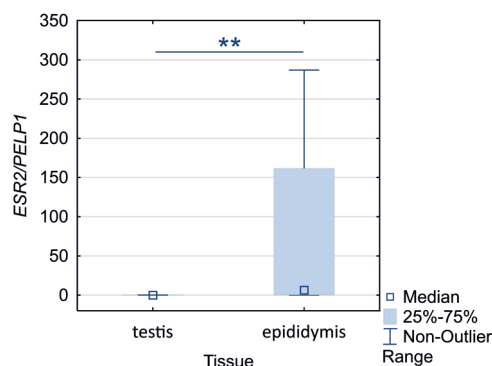


Figure 4. Normalized ratio of the expression of *ESR2/PELP1* in testis and epididymis.

** $p < 0.01$ (two-tailed Mann-Whitney *U* test).

correlation was established for the expression ratios of *ESR1/ESR2* and *ESR1/PELP1*. *ESR2/SRC* and *SRC/PELP1* in the epididymis were not correlated (Table 1).

Protein presence and localization

The presence of the analyzed proteins in the testis and epididymis was confirmed by western blotting to identify

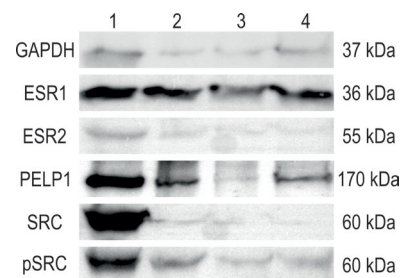


Figure 5. Western blot analysis of analyzed proteins in selected samples from different patients.

Lane 1 and 2 – testis, lane 3 and 4 – epididymis. Note that the blots displayed were cropped; see Supplementary Information for the original blots.

the presence of immunoreactive bands at the expected sizes (*ESR1*: 36 kDa; *ESR2*: 55 kDa; *PELP1*: 170 kDa; *SRC*: 60 kDa and *pSRC*: 61 kDa). The GAPDH reference protein bands (37 kDa) were present in all samples (Fig. 5).

The protein density of both *pSRC* and *PELP1* differ significantly between testis and epididymal tissue ($p = 0.015$ and $p < 0.001$, respectively), with both proteins having a higher density in the testis (Fig. 6).

Table 1. Spearman rank order correlations of the analyzed gene ratios in testis and epididymis.

Pair of Variables	Testis			Epididymis		
	N	R	<i>p</i> -value	N	R	<i>p</i> -value
<i>ESR1/ESR2</i> & <i>ESR1/SRC</i>	13	.61	.0269	9	.90	.0009
<i>ESR1/ESR2</i> & <i>ESR1/PELP1</i>	12	.58	.0479	10	.82	.0038
<i>ESR1/ESR2</i> & <i>ESR2/SRC</i>	13	-.54	.0546	9	-.33	.3807
<i>ESR1/ESR2</i> & <i>ESR2/PELP1</i>	12	-.45	.1377	10	-.04	.9074
<i>ESR1/ESR2</i> & <i>SRC/PELP1</i>	13	.25	.4154	10	-.18	.6272
<i>ESR1/SRC</i> & <i>ESR1/PELP1</i>	12	.65	.0220	10	.96	<.0001
<i>ESR1/SRC</i> & <i>ESR2/SRC</i>	13	.26	.3943	10	-.14	.7009
<i>ESR1/SRC</i> & <i>ESR2/PELP1</i>	12	.01	.9828	10	.08	.8287
<i>ESR1/SRC</i> & <i>SRC/PELP1</i>	13	-.37	.2159	10	-.39	.2600
<i>ESR1/PELP1</i> & <i>ESR2/SRC</i>	12	.15	.6331	10	.07	.8548
<i>ESR1/PELP1</i> & <i>ESR2/PELP1</i>	12	.36	.2551	11	.33	.3259
<i>ESR1/PELP1</i> & <i>SRC/PELP1</i>	12	-.39	.2081	11	-.35	.2981
<i>ESR2/SRC</i> & <i>ESR2/PELP1</i>	12	.66	.0185	11	.95	<.0001
<i>ESR2/SRC</i> & <i>SRC/PELP1</i>	13	-.86	.0001	11	-.32	.3403
<i>ESR2/PELP1</i> & <i>SRC/PELP1</i>	12	-.53	.0754	12	-.27	.3911

Legend: N, number of paired cases; R, Spearman's rank correlation coefficient; *p*-values <0.05 are indicated in bold.

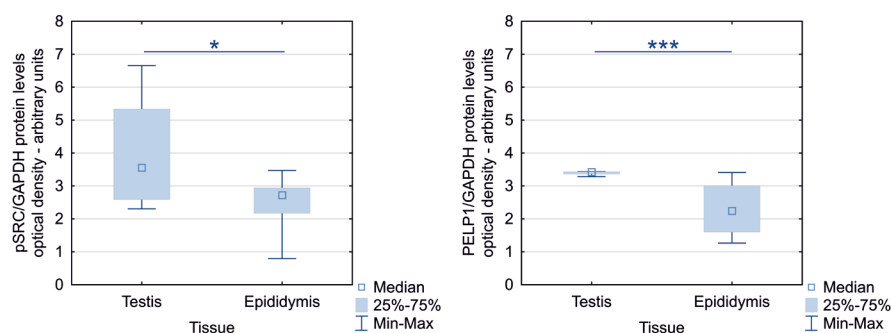


Figure 6. Protein density analysis of pSRC and PELP1 in testis and epididymis.

* $p < 0.05$, *** $p < 0.001$ (two-tailed Mann-Whitney U test).

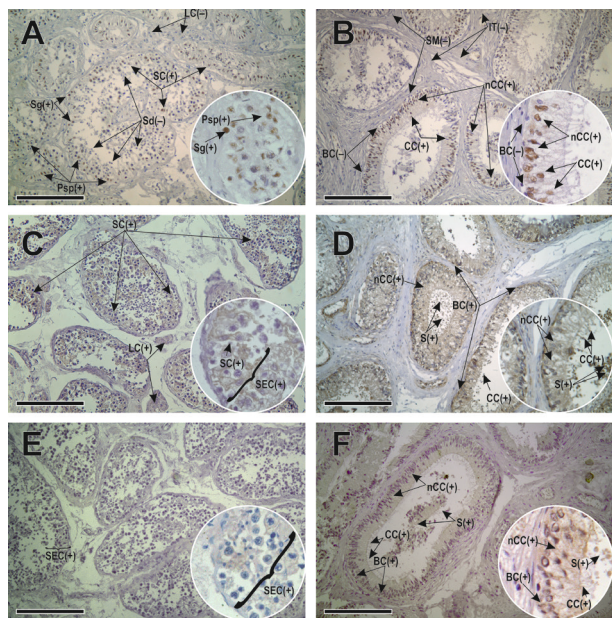


Figure 7. Immunohistochemical localization of PELP1 (A), SRC (C), pSRC (phospho-Tyr529) (E) in testis, and PELP1 (B), SRC (D), and pSRC (phospho-Tyr529) (F) in the epididymis.

Legend: BC, basal cells; CC, ciliated cells; nCC, non-ciliated cells; IT, interstitial tissue; LC, Leydig cells; Psp, primary spermatocytes; S, spermatozoa; SC, Sertoli cells; SEC, seminiferous epithelium cells; Sd, spermatids; Sg, spermatogonia. (+), positive immunostaining; (-), negative immunostaining. Scale bar: 200 μ m.

Immunohistochemical staining enabled the identification of all studied proteins in tissues of interest. The ESR1 and ESR2 expression showed similar localization as observed by other authors (Fietz *et al.*, 2014; Rago *et al.*, 2018). In the testis, ESR1 was observed in some primary spermatocytes and spermatids but not in the spermatogonia, Sertoli, or interstitial cells. The ESR2 was localized in spermatogonia, primary spermatocytes, spermatids, and Sertoli cells but not in the interstitial compartment. On the other hand, in the epididymis, ESR1 was expressed in non-ciliated cells and ESR2 in the ciliated and non-ciliated cells of the epithelium and the basal cells (Supplementary Fig. S1 at <https://ojs.ptbioch.edu.pl/index.php/abp>). We observed PELP1 localization in the Sertoli cells, primary spermatocytes, and single spermatogonia in the testis. We did not observe positive staining in Leydig cells or spermatids (Fig. 7A). In the magnification of Fig. 7A, positive immunostaining was indicated in primary spermatocytes and spermatogonia. On the other hand, SRC was extensively expressed in the cytoplasm of Sertoli cells and the cells of the seminiferous epithelium. SRC was also weakly expressed in the

cytoplasm of Leydig cells (Fig. 7C). A similar but weaker reaction was observed for the cells of the seminiferous epithelium for pSRC (Fig. 7E). In the epididymis, a strong PELP1 expression was demonstrated in the nuclei of the ciliated and non-ciliated cells of the epididymal ductal epithelium. Weak cytoplasmic staining was also observed in these cells. The vast majority of basal cells were PELP1 negative. There was no expression of PELP1 in smooth muscle cells of the ductal wall or interstitial tissue cells. In the magnification, the ciliated and non-ciliated cells were indicated (Fig. 7B). SRC was expressed in the basal cells' nuclei, spermatozoa, and the ciliated and non-ciliated cells of the epididymal ductal epithelium. In the magnification, the non-ciliated and ciliated cells and spermatozoa were indicated (Fig. 7D). A similar but slightly weaker reaction was observed in the case of pSRC (Fig. 7F).

DISCUSSION

There are distinct roles of ESRs throughout the entire reproductive tract in males. However, there is a lack of consensus on their detection and localization in the published literature (Hess *et al.*, 2021; Fietz *et al.*, 2014; Cooke *et al.*, 2017; Li *et al.*, 2015). There are several studies indicating that estrogen signaling may use a variety of different pathways where, for example, gene transcription may be induced by either direct binding of certain receptors to estrogen response elements (ERE) in the promoters of target genes or can involve transcription factor complexes that are able to activate transcription in the promoter regions of genes directly and without the use of EREs (Klinge, 2001). Conversely, an alternative non-genomic mechanism was also described. It uses other signaling pathways, such as growth factors, kinases, or associated co-regulators, which may activate ESRs in the absence of a ligand (Hess & Cooke, 2018). It was established that aromatase is expressed in human epithelial cells of ductuli efferentes and proximal caput of the epididymis. It suggests a putative role of estrogens produced locally in the epididymal function. Moreover, epididymal caput and cauda differed in ESR1 and ESR2 presence in humans and animals. Additionally, the possible involvement of ESR2 in estrogen modulation of the epididymal function is suggested, as ESR2 expression was confirmed in the epithelial cells of human epididymis indicates (Bilińska *et al.*, 2006; Carpino *et al.*, 2004a; Carpino *et al.*, 2004b; Kolasa *et al.*, 2003). Our study suggests that the specific ESR-mediated pathway in the male reproductive system might result from the different local interactions of estrogens with estrogen receptors and their co-regulators. Even though the tissues

are of the same type, we observed significant differences in the expression levels of the studied genes, especially PELP1 and SRC kinase in both mRNA and protein levels. This paper confirmed the presence of ESR1, ESR2, and their co-regulators, including PELP1 and SRC kinase, in human testis and epididymis. Furthermore, we analyzed potential links between them, as their interactions may have a particular impact on physiological phenomena in these tissues. However, further analyses exploring estrogen-mediated signaling supported by colocalization studies are essential to determine the nature of these interactions and the potential clinical repercussions of estrogens in the male reproductive tract.

Our study suggests that there may be a dependence between PELP1 and SRC in human testis. Our study established the significant differences in normalized expression levels of both SRC and PELP1 in the testis and epididymis, with significantly higher expression and protein density in the testis. Furthermore, our study indicated that SRC and PELP1 expression levels were moderately positively correlated in the testis ($R=0.66$, $p=0.014$). Moreover, PELP1 expression was positively correlated with the expression of ESR1 ($R=0.6$; $p=0.0367$). It may imply the role of ESR1 in testis, as well as the involvement of PELP1 and SRC in estrogen-mediated signaling (e.g., ligand-independent signaling to induce specific effects via ESR1). As we observed PELP1 being localized in Sertoli cells and spermatocytes, it could not be excluded that PELP1 may be involved in certain stages of spermatogenesis or may somehow modulate Sertoli cells' function in this regard.

It has been confirmed that ESR1 expression is different through certain stages of development (Hess *et al.*, 2011). In 1994, the first man lacking a functional ESR1 was reported, and subsequently, other men lacking aromatase were identified, with 13 reported cases of loss of function mutations in CYP19A1 (Cooke *et al.*, 2017). Regardless of species or investigators, ESR1 has been shown to be highly expressed in the efferent ductule epithelium, which suggests its contribution to fluid reabsorption (Fietz *et al.*, 2014). Interestingly, the most severe histopathological changes following the disruption of ESR1 function occur in the testis and efferent ductules, likely due to its high expression, which is approximately 3.5-fold greater than in the female uterus or any other

organ independent of biological sex (Fietz *et al.*, 2014). Furthermore, ESRs involvement was suggested in the development of sperm cells (Hess, 2014). We observed age-related increasing ESR1 and decreasing PELP1 expression. Due to the limited number of published papers on the topic of PELP1 expression in the male reproductive tract, and because the ESR1 and ESR2 expression alters with age (in different tissues, not only in the male reproductive tract), it would be challenging to propose strong conclusions. Considering that we analyzed the specimens from males not only of reproductive age, further studies need to be conducted to elaborate on this topic. Moreover, a recent report confirmed the ESR1 and PELP1 presence in the human reproductive tract, including in the nuclei of ciliated and non-ciliated cells for ESR1 and principal cells of proximal epididymis for PELP1 (Rago *et al.*, 2018). As our results highlight the SRC/PELP1 correlation in testis, it cannot be ruled out that these proteins may potentially be involved in ESR1-mediated processes surrounding rete fluid resorption in the testis, influence the composition of seminal fluids, or anyhow in the regulation of spermatogenesis. Interactions between PELP1-SRC-ESR1 seem feasible in the above-mentioned processes, especially due to the fact that the binding of PELP1 and ESR coordinates SRC-mediated signaling to SRC's SH3 and SH2 domains. It is known that the SRC family kinases (SFKs), including SRC (but also Yes, Fyn, and Lck among others) play a role in cell polarity, in the testis spermatogonial stem cell proliferation, cell adhesion or to influence the dynamics of the blood-testis barrier in the seminiferous epithelium. Even though the effects of c-SRC and c-Yes kinases may considerably overlap, and their action is thought to be limited to the cell matrix at the focal contacts, their role in the testis cannot be denied (Xiao *et al.*, 2013; Xiao *et al.*, 2019; Rago *et al.*, 2018). It is also suggested that SRC plays a crucial role in the 17 β -estradiol-induced translocation of estrogen receptors from the nucleus to the cell membrane (Lucas *et al.*, 2008). Furthermore, the ability of ESRs to simultaneously bind SRC and PELP1 results in the activation of a non-genomic pathway such as cSRC/MAPK-pathway, which leads to enhanced, phosphorylation-dependent ESR1 transcriptional activity (Nieto *et al.*, 2015; Barletta *et al.*, 2004).

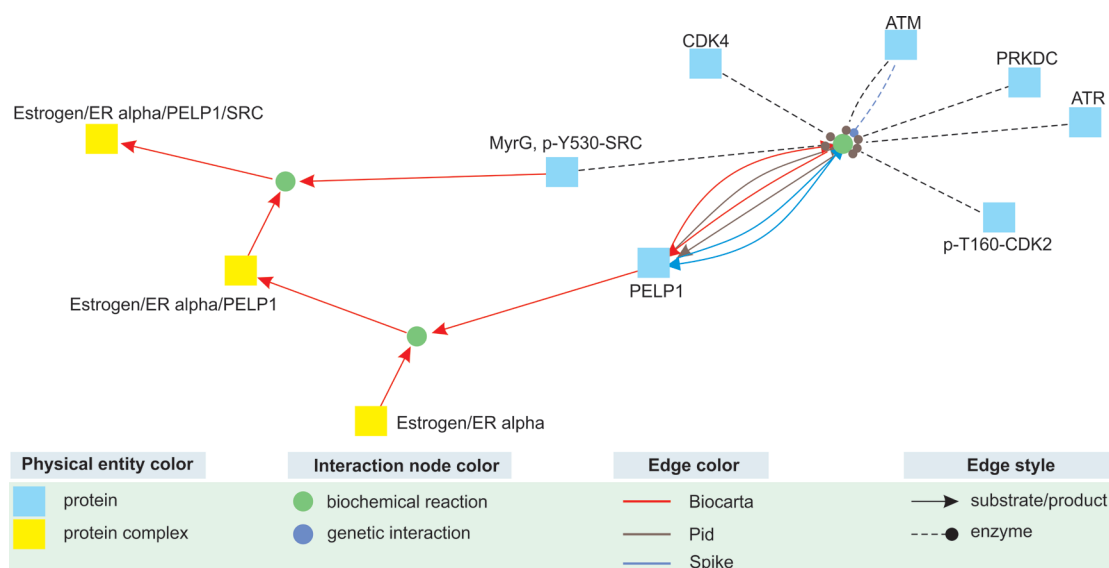


Figure 8. Map of interactions in PELP1 modulation of estrogen receptor activity (cpb.molgen.de/CPDB/cyVis).

The PELP1 biochemical interactions with other proteins are complex and involve other kinases, such as ATM, ATR, CDK2, CDK4, and PRKDC, in addition to SRC (Fig. 8). The biochemical/enzymatic reactions with these proteins directly influence PELP1 and, other protein complexes involved in estrogen signal transduction. It seems that ESR1, but not ESR2 plays a crucial role in the PELP1-mediated pathway.

Upon phosphorylation by SRC, certain cellular events may be influenced by the specific cellular localization of PELP1, SRC, and ESR1. Furthermore, it is important to mention that the extent of SRC-PELP1-ESR1 interactions in human testis may influence the availability of another estrogen receptor GPER. However, it was not analyzed in this study. These dependencies could modulate the microenvironment for spermatozoa maturation in different sites of the male reproductive tract, depending on the availability of certain receptors and their co-regulators in the tissue area of interest. It was shown that SRC phosphorylation at Tyr529 deactivates the protein function (Gonfloni *et al.*, 2000). The Tyr529 phosphorylation status is closely related to the autophosphorylation of Tyr418, which determines the SRC activity (Xiao *et al.*, 2017), leading to complex conformational changes (Gonfloni *et al.*, 2000). As a consequence SH3 domain of SRC ceases to be strongly associated with the linker of the SH2 domain and the catalytic domain and becomes more accessible to other ligands (Xiao *et al.*, 2017). Consistent with this idea would be the fact that we observed differences in the SRC and pSRC expression pattern, as this protein works bidirectionally upon phosphorylation status (Gonfloni *et al.*, 2000). Differentiated expression patterns of SRC and pSRC in testis and epididymis, observed in our study, could be reflected in the modulation of cell events, such as cell maturation and migration, mediated by other signaling pathways (Xiao *et al.*, 2017). Therefore, investigations of the molecular consequences and the role of these phenomena in the male reproductive tract should be further conducted.

Regarding ESR2 expression in the testis, *ESR2/SRC* correlated positively with *ESR2/PELP1*. Moreover, *ESR2/SRC* had a strongly negative correlation with *SRC/PELP1*. Until 2018, common knowledge regarding ESR2 indicated its ubiquitous expression in the male reproductive tract. However, more recent investigations have questioned antibody specificity for immunohistochemical localization of the receptor (Hess & Cooke, 2018), and therefore data concerning ESR2 distribution needs to be re-evaluated. Furthermore, it is worth pointing out that ESR2 knock-out animal models are more limited than ESR1 ones. Recent studies confirmed ESR2 expression only in ciliated cell nuclei of the efferent ductules and in a few epithelial layer cells in proximal epididymis (Rago *et al.*, 2018).

Additionally, it cannot be excluded that PELP1, SRC, and ESR2 also take part in maintaining the function of the efferent ductule epithelium, especially as it was reported that some of the expressed genes contain both EREs. The PELP1 function may depend on other proteins' tissue-specific availability, including ESR1, ESR2, and SRC. The expression level of these proteins may be one of the limiting elements of the entire PELP1-mediated signal transduction pathway. As shown in Figure 8, some more proteins, enzymes, and factors influence this signaling network. Our results showed a differentiated expression ratio of analyzed genes, which could result from tissue-specific availability of, e.g., transcription factors. However, since androgen response elements were also identified in this location, it is clear that a hor-

monal milieu (estrogens vs. androgens) is likely required for maintaining the proper epithelial function. For example, the testosterone metabolite 5 α -androstane-3 β -17 β -diol (3 β -diol) was shown not to bind the androgen receptor but bind ESR2 with higher affinity than it does for ESR1. Therefore it could mediate ESR2 activity in the testis and maintain epithelial function (Hess *et al.*, 2021). We speculate that SRC and PELP1 could be somehow involved in this phenomenon.

In the epididymis, we noted very strong positive correlation ratios of *ESR1/ESR2* with *ESR1/SRC* and *ESR1/SRC* with *ESR1/PELP1*. These observations could suggest SRC kinase and PELP1's more intense involvement in ESR1 function in the epididymis. Immunohistochemical staining in our study indicates strong PELP1 expression in the nuclei of the principal cells of the efferent ductules epithelium. Other studies have shown that acute morphological changes, such as epithelial degeneration, may occur due to disrupting ESR1 function in the efferent ductules. As SRC and PELP1 seem to play an important role in modulating epididymal epithelial function, it cannot be excluded that impaired SRC-PELP1 interaction caused by, for example antiestrogens, may lead to a blockage of ESR activity in the efferent ductules, and consequently to the inhibition of fluid reabsorption (Hess *et al.*, 2021). PELP1 is a scaffolding protein that enhances transcriptional activity by assembling crucial protein partners. We localized its presence in the principal cells of proximal epididymis. Thus, its function may depend on the availability of co-occurring factors in the local environment. That being said, the activity of PELP1 and other estrogen pathway-related proteins should be considered holistically (Rago *et al.*, 2018). It is worth pointing out that previous literature focuses on the exploration of *ESR1* expression patterns in the epididymis.

On the other hand, difficulties in establishing ESR2 expression are most likely caused by methodological obstacles concerning the ESR2 distribution in the male reproductive tract, and a literature review examining the expression of both ESRs in the epididymis has brought contradictory results (Cunha *et al.*, 2021; Davis & Pearl, 2019; Aprea *et al.*, 2021; Hess, 2014; Hess *et al.*, 2021). Most studies in mammals report that ESR1 distribution is species-dependent, while ESR2 expression can be found the entire length of the efferent ductules (Hess *et al.*, 2021; Hess & Cooke, 2018). Animal models have shown that ESR1 may play a prominent role in the specific cell types of the epididymis, likely during fetal development. However, the epididymal epithelium is reported to have a much lower expression of ESR1, which would likely have more significant direct estrogen and dual estrogen/androgen regulation in efferent ductules (Joseph *et al.*, 2011). Several studies suggest that estrogens play a very important role in maintaining fluid resorption by the epithelium of the efferent ductules, mostly *via* ESR1 (Joseph *et al.*, 2011; Hess *et al.*, 2011; Hess, 2014). However, recent studies have not confirmed the presence of ESR1 in the human epididymis, stating that it is ESR2 that is more prominent in this tissue (Rago *et al.*, 2018). It appears doubtful, considering several studies that have confirmed the presence of ESR1 in this tissue. There are also papers indicating that the loss of ESR2 in knock-out mice demonstrates no major effects on the development of testes, efferent ductules, and epididymis. Interestingly, important long-term effects were seen in the prostate and an increase in neonatal gonocytes, but not in the adult testis (Cunha *et al.*, 2021; Davis & Pearl, 2019; Hess, 2014; Aprea *et al.*, 2021; Hess *et al.*, 2021).

Despite the contradictory findings regarding the expression of *ESR α* in the testis and epididymis, and considering our results, we suggest that an *ESR*-*SRC*-*PELP1* relationship may be anywise important in controlling some functions of these tissues. However, our study proved the abundance of these proteins only and not their interactions. It seems that not only the level of gene expression and post-translational events influencing protein expression in a specific tissue compartment are important, but also the locally determined interaction between certain proteins and their expression ratios.

Finally, we acknowledge that our study also had some limitations. Firstly, our investigation was limited by the sample size. However, we did not find comparable data in the literature investigating the expression of modulators involved in the *ESR*-mediated pathways in the tissues of the male reproductive tract. This study was limited by sample size, so conclusions should be interpreted with caution. It is important to establish the proteins' presence, localization, and interplay with other proteins involved in estrogen-mediated signaling in a larger group. However, since these proteins have many different partners and functions, further analyses exploring estrogen-mediated signaling and/or estrogen signaling stimulation/inhibition analyses supported by colocalization studies are essential to determine the nature of these interactions and the potential clinical repercussions of estrogens in the male reproductive tract in the context of impaired male fertility.

Declarations

Acknowledgments. We would like to thank Róża Czarnecka-Cierniewska, M.Sc., and Agnieszka Sadowska, M.Sc. for technical support.

Supplementary Materials (at <https://ojs.ptbioch.edu.pl/index.php/abp>). Figure S1: Immunohistochemical localization of *ESR1* and *ESR2* in the testis and in the epididymis, Full resolution blots and MIQE checklist and data set.

REFERENCES

- Akingbemi BT (2005) Estrogen regulation of testicular function. *Reprod. Biol. Endocrinol.* **3**: 51. <https://doi.org/10.1186/1477-7827-3-51>
- Andrusiewicz M, Slowikowski B, Skibińska I, Woliński-Cholewa M, Dera-Szymanowska A (2016) Selection of reliable reference genes in eutopic and ectopic endometrium for quantitative expression studies. *Biomed. Pharmacother.* **78**: 66–73. <https://doi.org/10.1016/j.biopha.2015.12.028>
- Apra I, Nöthe-Menchen T, Dougherty GW, Raidt J, Loges NT, Kaiser T, Wallmeier J, Olbrich H, Strücker T, Kliesch S, Pennekamp P, Omran H (2021) Motility of efferent duct cilia aids passage of sperm cells through the male reproductive system. *Mol. Hum. Reprod.* **27**: <https://doi.org/10.1093/molehr/gaab009>
- Aquila S, Sisci D, Gentile M, Carpino A, Middea E, Catalano S, Rago V, Andò S (2003) Towards a physiological role for cytochrome P450 aromatase in ejaculated human sperm. *Hum. Reprod.* **18**: 1650–1659. <https://doi.org/10.1093/humrep/deg340>
- Barletta F, Wong C-W, McNally C, Komm BS, Katzenellenbogen B, Cheskis BJ (2004) Characterization of the interactions of estrogen receptor and MNAR in the activation of cSrc. *Mol. Endocrinol.* **18**: 1096–1108. <https://doi.org/10.1210/me.2003-0335>
- Barut O, Seyithanoglu M, Kucukdurmaz F, Demir BT, Olmez C, Dogan NT, Resim S (2020) Relationship between the G protein-coupled oestrogen receptor and spermatogenesis, and its correlation with male infertility. *Andrologia* **52**: <https://doi.org/10.1111/AND.13779>
- Bertolla RP (2020) Sperm biology and male reproductive health. *Sci. Reports* **2020** **10**: 1–3. <https://doi.org/10.1038/s41598-020-78861-7>
- Bilińska B, Wiszniewska B, Kosiniak-Kamysz K, Kotula-Balak M, Gancarczyk M, Hejmej A, Sadowska J, Marchlewicz M, Kolasa A, Wenda-Rózewicka L (2006) Hormonal status of male reproductive system: androgens and estrogens in the testis and epididymis. *In vivo and in vitro* approaches. *Reprod. Biol.* **6**: 43–58
- Bustin SA, Benes V, Garson JA, Hellemans J, Huggett J, Kubista M, Mueller R, Nolan T, Pfaffl MW, Shipley GL, Vandesompele J, Wittwer CT (2009) The MIQE guidelines: Minimum Information for publication of quantitative real-time PCR experiments. *Clin. Chem.* **55**: 611–622. <https://doi.org/10.1373/clinchem.2008.112797>
- Camacho-Sanchez M, Burraco P, Gomez-Mestre I, Leonard JA (2013) Preservation of RNA and DNA from mammal samples under field conditions. *Mol. Ecol. Resour.* **13**: 663–673. <https://doi.org/10.1111/1755-0998.12108>
- Carpino A, Romeo F, Rago V (2004a) Aromatase immunolocalization in human ductuli efferentes and proximal ductus epididymis. *J. Anat.* **204**: 217. <https://doi.org/10.1111/J.0021-8782.2004.00272.X>
- Carpino A, Bilińska B, Siciliano L, Maggiolini M, Rago V (2004b) Immunolocalization of estrogen receptor beta in the epididymis of mature and immature pigs. *Folia Histochem. Cytobiol.* **42**: 13–17
- Carreau S, Delalande C, Silandre D, Bourguiba S, Lambard S (2006) Aromatase and estrogen receptors in male reproduction. *Mol. Cell. Endocrinol.* **246**: 65–68. <https://doi.org/10.1016/j.mce.2005.11.021>
- Carreau S, Wolczynski S, Galeraud-Denis I (2010) Aromatase, oestrogens and human male reproduction. *Philos. Trans. R. Soc. Lond. B. Biol. Sci.* **365**: 1571–1579. <https://doi.org/10.1098/rstb.2009.0113>
- Carreau S, Bouraima-Lelong H, Delalande C (2011a) Estrogens: new players in spermatogenesis. *Reprod. Biol.* **11**: 174–93. [https://doi.org/10.1016/S1642-431X\(12\)60065-5](https://doi.org/10.1016/S1642-431X(12)60065-5)
- Carreau S, Bois C, Zanatta L, Silva FRMB, Bouraima-Lelong H, Delalande C (2011b) Estrogen signaling in testicular cells. *Life Sci.* **89**: 584–587. <https://doi.org/10.1016/j.lfs.2011.06.004>
- Cerilli LA, Kuang W, Rogers D (2010) A practical approach to testicular biopsy interpretation for male infertility. *Arch. Pathol. Lab. Med.* **134**: 1197–1204. <https://doi.org/10.5858/2009-0379-RA.1>
- Chimento A, Luca A De, Nocito MC, Avena P, Padula D La, Zavaglia L, Pezzi V (2020) Role of GPER-mediated signaling in testicular functions and tumorigenesis. *Cells* **9**: 2115. <https://doi.org/10.3390/CELLS9092115>
- Cooke PS, Nanjappa MK, Ko C, Prins GS, Hess RA (2017) Estrogens in male physiology. *Physiol. Rev.* **97**: 995–1043. <https://doi.org/10.1152/physrev.00018.2016>
- Cunha GR, Li Y, Mei C, Derpinghaus A, Baskin LS (2021) Ontogeny of estrogen receptors in human male and female fetal reproductive tracts. *Differentiation* **118**: 107–131. <https://doi.org/10.1016/j.diff.2020.10.001>
- Davis K, Pearl CA (2019) Effects of estrogen treatment on aging in the rat epididymis. *Anat. Rec. (Hoboken)*. **302**: 1447–1457. <https://doi.org/10.1002/AR.24004>
- Englert-Golon M, Andrusiewicz M, Żbikowska A, Chmielewska M, Sajdak S, Kotwicka M (2021) Altered expression of *ESR1*, *ESR2*, *PELP1* and *c-SRC* genes is associated with ovarian cancer manifestation. *Int. J. Mol. Sci.* **22**: 6216. <https://doi.org/10.3390/ijms22126216>
- Eyster KM (2016) The estrogen receptors: An overview from different perspectives. In: *Methods in Molecular Biology*, pp 1–10. Humana Press Inc. https://doi.org/10.1007/978-1-4939-3127-9_1
- Fietz D, Ratzenböck C, Hartmann K, Raabe O, Kliesch S, Weidner W, Klug J, Bergmann M (2014) Expression pattern of estrogen receptors α and β and G-protein-coupled estrogen receptor 1 in the human testis. *Histochem. Cell Biol.* **142**: 421–432. <https://doi.org/10.1007/S00418-014-1216-Z>
- Gonfloni S, Weiland A, Kretzschmar J, Superti-Furga G (2000) Cross-talk between the catalytic and regulatory domains allows bidirectional regulation of Src. *Nat. Struct. Biol.* **7**: 281–286. <https://doi.org/10.1038/74041>
- Hammes SR, Levin ER (2019) Impact of estrogens in males and androgens in females. *J. Clin. Invest.* **129**: 1818–1826. <https://doi.org/10.1172/JCI125755>
- Hess RA, Fernandes SAF, Gomes GRO, Oliveira CA, Lazari MFM, Porto CS (2011) Estrogen and its receptors in efferent ductules and epididymis. *J. Androl.* **32**: 600–613. <https://doi.org/10.2164/jandrol.110.012872>
- Hess RA (2014) Disruption of estrogen receptor signaling and similar pathways in the efferent ductules and initial segment of the epididymis. *Spermatogenesis* **4**: e979103. <https://doi.org/10.4161/2156562.2014.979103>
- Hess RA, Cooke PS (2018) Estrogen in the male: A historical perspective. *Biol. Reprod.* **99**: 27–44. <https://doi.org/10.1093/biolre/iox043>
- Hess RA, Sharpe RM, Hinton BT (2021) Estrogens and development of the rete testis, efferent ductules, epididymis and vas deferens. *Differentiation* **118**: 41–71. <https://doi.org/10.1016/j.diff.2020.11.004>
- Joseph A, Shur BD, Hess RA (2011) Estrogen, efferent ductules, and the epididymis. *Biol. Reprod.* **84**: 207–217. <https://doi.org/10.1095/biolreprod.110.087353>
- Klinge CM (2001) Estrogen receptor interaction with estrogen response elements. *Nucleic Acids Res.* **29**: 2905–2919. <https://doi.org/10.1093/nar/29.14.2905>

- Kolasa A, Wiszniewska B, Marchlewicz M, Wenda-Różewicka L (2003) Localisation of oestrogen receptors (ERalpha and ERbeta) in the human and rat epididymides. *Folia Morphol. (Warsz)*. **62**: 467–469
- Lazari MFM, Lucas TFG, Yasuhara F, Gomes GRO, Siu ER, Royer C, Fernandes SAF, Porto CS (2009) Estrogen receptors and function in the male reproductive system. *Arg. Bras. Endocrinol. Metabol.* **53**: 923–933. <https://doi.org/10.1590/s0004-27302009000800005>
- Li X, Li H, Jia L, Li X, Rahman N (2015) Oestrogen action and male fertility: Experimental and clinical findings. *Cell. Mol. Life Sci.* **72**: 3915–3930. <https://doi.org/10.1007/s00018-015-1981-4>
- Lucas TFG, Siu ER, Esteves CA, Monteiro HP, Oliveira CA, Porto CS, Lazari MFM (2008) 17Beta-estradiol induces the translocation of the estrogen receptors ESR1 and ESR2 to the cell membrane, MAPK3/1 phosphorylation and proliferation of cultured immature rat sertoli cells. *Biol. Reprod.* **78**: 101–114. <https://doi.org/10.1095/biolreprod.107.063909>
- Micevych PE, Dewing P (2011) Membrane-initiated estradiol signaling regulating sexual receptivity. *Front. Endocrinol. (Lausanne)*. **2**: 1–9. <https://doi.org/10.3389/fendo.2011.00026>
- Mohamed ESA, Park YJ, Song WH, Shin DH, You YA, Ryu BY, Pang MG (2011) Xenoestrogenic compounds promote capacitation and an acrosome reaction in porcine sperm. *Theriogenology* **75**: 1161–1169. <https://doi.org/10.1016/j.theriogenology.2010.11.028>
- Nieto L, Tharun IM, Balk M, Wienk H, Boelens R, Ottmann C, Milroy LG, Brunsfeld L (2015) Estrogen receptor folding modulates cSrc kinase SH2 interaction via a helical binding mode. *ACS Chem. Biol.* **10**: 2624–2632. <https://doi.org/10.1021/acschembio.5b00568>
- Otto C, Fuchs I, Kauselmann G, Kern H, Zevnik B, Andreasen P, Schwarz G, Altmann H, Klewer M, Schoor M, Vonk R, Fritzscheier K-H (2009) GPR30 Does not mediate estrogenic responses in reproductive organs in mice. *Biol. Reprod.* **80**: 34–41. <https://doi.org/10.1095/biolreprod.108.071175>
- Rago V, Aquila S, Panza R, Carpino A (2007) Cytochrome P450arom, androgen and estrogen receptors in pig sperm. *Reprod. Biol. Endocrinol.* **5**: 23. <https://doi.org/10.1186/1477-7827-5-23>
- Rago V, Romeo F, Giordano F, Malivindi R, Pezzi V, Casaburi I, Carpino A (2018) Expression of oestrogen receptors (GPER, ESR1, ESR2) in human ductuli efferentes and proximal epididymis. *Androl-ogy* **6**: 192–198. <https://doi.org/10.1111/andr.12443>
- Rahman MS, Kwon WS, Lee JS, Yoon SJ, Ryu BY, Pang MG (2015) Bisphenol-A affects male fertility via fertility-related proteins in spermatozoa. *Sci. Rep.* **5**: 1–9. <https://doi.org/10.1038/srep09169>
- Sareddy GR, Vadlamudi RK (2016) PELP1: Structure, biological function and clinical significance. *Gene* **585**: 128–134. <https://doi.org/10.1016/j.gene.2016.03.017>
- Shupe J, Cheng J, Puri P, Kostereva N, Walker WH (2011) Regulation of sertoli-germ cell adhesion and sperm release by FSH and non-classical testosterone signaling. *Mol. Endocrinol.* **25**: 238. <https://doi.org/10.1210/ME.2010-0030>
- Sikka SC, Wang R (2008) Endocrine disruptors and estrogenic effects on male reproductive axis. *Asian J. Androl.* **10**: 134–145. <https://doi.org/10.1111/j.1745-7262.2008.00370.x>
- Skibińska I, Andrusiewicz M, Soim M, Jendraszak M, Urbaniak P, Jędrzejczak P, Kotwicka M (2018) Increased expression of PELP1 in human sperm is correlated with decreased semen quality. *Asian J. Androl.* **20**: 425. https://doi.org/10.4103/aja.aja_11_18
- Skibińska I, Andrusiewicz M, Jendraszak M, Zbikowska A, Jędrzejczak P, Kotwicka M (2022) Expression of estrogen receptors, PELP1, and SRC in human spermatozoa and their associations with semen quality. *Hum. Cell* <https://doi.org/10.1007/S13577-022-00847-6>
- Solakidi S, Psarra A-MG, Nikolaropoulos S, Sekeris CE (2005) Estrogen receptors α and β (ER α and ER β) and androgen receptor (AR) in human sperm: localization of ER β and AR in mitochondria of the midpiece. *Hum. Reprod.* **20**: 3481–3487. <https://doi.org/10.1093/humrep/dei267>
- Toran-Allerand CD, Guan X, MacLusky NJ, Horvath TL, Diano S, Singh M, Connolly ES, Nethrapalli IS, Tinnikov AA (2002) ER-X: A novel, plasma membrane-associated, putative estrogen receptor that is regulated during development and after ischemic brain injury. *J. Neurosci.* **22**: 8391–8401. <https://doi.org/10.1523/jneurosci.22-19-08391.2002>
- Vadlamudi RK, Wang RA, Mazumdar A, Kim Y, Shin J, Sahin A, Kumar R (2001) Molecular cloning and characterization of PELP1, a novel human coregulator of estrogen receptor alpha. *J. Biol. Chem.* **276**: 38272–38279. <https://doi.org/10.1074/jbc.M103783200>
- Vadlamudi RK, Kumar R (2007) Functional and biological properties of the nuclear receptor coregulator PELP1/MNAR. *Nucl. Recept. Signal.* **5**: e004. <https://doi.org/10.1621/nrs.05004>
- Waligórska-Stachura J, Sawicka-Gutaj N, Zabel M, Andrusiewicz M, Gut P, Czarnywojtek A, Ruchala M (2017) Survivin DEX3 as a biomarker of thyroid cancers: A study at the mRNA and protein level. *Oncol. Lett.* **13**: 2437–2441. <https://doi.org/10.3892/ol.2017.5713>
- Xiao J, Gao Y, Yang F, Wang C, Xu Y, Chang R, Zha X, Wang L (2017) β 1,6 GlcNAc branches-modified protein tyrosine phosphatase alpha enhances its stability and promotes focal adhesion formation in MCF-7 cells. *Biochem. Biophys. Res. Commun.* **482**: 1455–1461. <https://doi.org/10.1016/j.bbrc.2016.12.057>
- Xiao X, Mruk DD, Cheng FL, Cheng CY (2013) C-Src and c-Yes are two unlikely partners of spermatogenesis and their roles in blood-testis barrier dynamics. *Adv. Exp. Med. Biol.* **763**: 295–317. https://doi.org/10.1007/978-1-4614-4711-5_15
- Xiao X, Yang Y, Mao B, Yan Cheng C, Ni Y (2019) Emerging role for SRC family kinases in junction dynamics during spermatogenesis. *Reproduction* **157**: R85–R94. <https://doi.org/10.1530/REP-18-0440>



OPEN ACCESS

EDITED BY

Grzegorz Węgrzyn,
University of Gdansk, Poland

REVIEWED BY

Menso Nube,
Amsterdam University Medical Center,
Netherlands
Karolina Pierzynowska,
University of Gdansk, Poland

*CORRESPONDENCE

Jan Biedunkiewicz,
✉ jbled777@gmail.com
Leszek Tylicki,
✉ leszek.tylicki@gumed.edu.pl

RECEIVED 28 August 2024

ACCEPTED 08 November 2024

PUBLISHED 29 November 2024

CITATION

Biedunkiewicz J, Zakrzewska A,
Małgorzewicz S, Komorniczak M,
Jasiulewicz K, Płonka N, Tarasewicz A,
Jankowska M, Biedunkiewicz B,
Dębska-Ślizień A and Tylicki L (2024)
Comparison of uremic toxin removal
between expanded hemodialysis and
high volume online hemodiafiltrations in
different modes.
Acta Biochim. Pol 71:13715.
doi: 10.3389/abp.2024.13715

COPYRIGHT

© 2024 Biedunkiewicz, Zakrzewska,
Małgorzewicz, Komorniczak,
Jasiulewicz, Płonka, Tarasewicz,
Jankowska, Biedunkiewicz, Dębska-
Ślizień and Tylicki. This is an open-
access article distributed under the
terms of the [Creative Commons
Attribution License \(CC BY\)](https://creativecommons.org/licenses/by/4.0/). The use,
distribution or reproduction in other
forums is permitted, provided the
original author(s) and the copyright
owner(s) are credited and that the
original publication in this journal is
cited, in accordance with accepted
academic practice. No use, distribution
or reproduction is permitted which does
not comply with these terms.

Comparison of uremic toxin removal between expanded hemodialysis and high volume online hemodiafiltrations in different modes

Jan Biedunkiewicz^{1*}, Agnieszka Zakrzewska²,
Sylvia Małgorzewicz³, Michał Komorniczak²,
Katarzyna Jasiulewicz², Natalia Płonka², Agnieszka Tarasewicz²,
Magdalena Jankowska², Bogdan Biedunkiewicz²,
Alicja Dębska-Ślizień⁴ and Leszek Tylicki^{2*}

¹Department of Anesthesiology and Intensive Therapy, Medical University of Gdansk, Gdańsk, Poland,

²Department of Nephrology, Transplantology and Internal Diseases, Medical University of Gdansk, Gdańsk, Poland, ³Department of Clinical Nutrition, Medical University of Gdansk, Gdańsk, Poland,

⁴Medical University of Gdansk, Gdańsk, Poland

Various high-efficiency hemodialysis techniques exist, including different online high- volume hemodiafiltration (HDF) modes and expanded hemodialysis (HDx) utilizing dialyzers with medium cut-off (MCO) membranes. This study aimed to evaluate the efficacy of uremic toxin removal among four modalities: (I) HDx, (II) pre-dilution HDF (PRE-HDF), (III) mixed-dilution HDF (MIX-HDF), and (IV) post-dilution HDF (POST-HDF), each applied for 1 week in a randomized order. This research was a single-center, prospective, open-label, exploratory crossover study. The reduction ratio (RR) for small molecular toxins (urea and phosphate), a middle molecular toxin (beta-2-microglobulin, β 2M), a large-middle molecular toxin (Chitinase-3-like protein 1, YKL-40), and a protein- bound uremic toxin (indoxyl sulfate, IS) was evaluated during a single mid-week dialysis session. Twelve patients were included, with an average age of 52.5 ± 15.47 years and an average dialysis duration of 42.05 ± 31.04 months. The dialysis parameters, including; post-dialysis weight, session duration, dialysate composition, blood and dialysate flow; rates, dialysate temperature, and anticoagulation dosage, were maintained consistently across all modalities. No significant differences in RR for urea, phosphate, β 2M, YKL-40, and IS were observed between the treatments. Although the highest IS clearance, though not statistically significant, was observed with POST-HDF and HDx, the differences were not substantial enough to favor any particular modality as the most effective.

KEYWORDS

dialysis, hemodialysis, uremic toxins, extended hemodialysis, protein-bound uremic toxins

Comparison of uremic toxin removal between expanded hemodialysis and high volume online hemodiafiltrations in different modes.

Biedunkiewicz et al., 2024 | Frontiers



BACKGROUND:

This study aims to compare the efficacy of uremic toxin removal between expanded hemodialysis (HDx) and high-volume online hemodiafiltration (HDF) in different modes. The research focuses on assessing the effectiveness of these methods in removing a broad spectrum of uremic toxins to determine the most efficient dialysis modality.



METHODS:

A single-center, prospective, exploratory, open-label crossover study was conducted involving 12 patients. The study compared four high-efficiency dialysis methods: HDx, pre-dilution HDF, mixed-dilution HDF, and post-dilution HDF. The reduction ratio (RR) of various uremic toxins, including small (urea, phosphate), middle (beta-2-microglobulin), large-middle molecular (YKL-40), and protein-bound toxins (Indoxyl sulfate), was measured during mid-week dialysis sessions.



RESULTS:

The study found no significant differences in the reduction ratios of urea, phosphate, beta-2-microglobulin, YKL-40, and indoxyl sulfate among the four dialysis methods. While there was a signal for better removal of YKL-40 and indoxyl sulfate with HDx, the differences were not statistically significant.



CONCLUSION:

Despite no significant differences in uremic toxin removal among the dialysis methods the potential advantages of POST-HDF and HDx, particularly in protein-bound toxin clearance were found. These findings underscore the importance of considering individual patient needs and treatment goals when selecting a dialysis modality. Further research with larger sample sizes is needed to confirm these exploratory conclusions and assess long-term clinical outcomes.

GRAPHICAL ABSTRACT

Introduction

Hemodialysis has seen substantial advancements, evolving from low-flux to high-flux membranes, which are now standard in chronic dialysis therapies (Palmer et al., 2012; Himmelfarb et al., 2020). These technological improvements have led to the development of advanced dialysis methods, such as hemodiafiltration (HDF) in pre-dilution (PRE-HDF), post-dilution (POST-HDF), and mixed-dilution (MIX-HDF) modes, as well as expanded hemodialysis (HDx) employing MCO membranes. These new methods have enhanced clearance profiles, significantly improving the removal of a wider range of uremic toxins, especially larger middle molecules, which traditional high-flux dialysis failed to eliminate effectively (Pedreros-Rosales et al., 2023; Zhang et al., 2022). The CONVINCe trial demonstrated that high-volume POST-HDF, delivering at least 23 Liters per session, was associated with a reduced risk of all-cause mortality compared to conventional high-flux hemodialysis, especially among older, non-diabetic patients with arteriovenous fistulas and no history of cardiovascular disease (Blankestijn et al., 2023). In Asian countries, PRE-HDF has also shown a potential for improved survival rates over conventional high-flux hemodialysis. A Japanese cohort study involving 5,000 patient pairs treated with either standard hemodialysis or pre-dilution HDF indicated that PRE-HDF might offer better overall and cardiovascular survival, particularly with high substitution volumes (>40.0 L per session) (Kikuchi et al., 2019).

Smaller studies have suggested HDx might improve patient quality of life and reduce symptoms such as restless leg syndrome and pruritus (Zhang et al., 2022). However, a randomized

controlled trial by Lee et al. found no significant cardiovascular differences between HDx and POST-HDF (Lee et al., 2021). HDx remains technically simple, similar to conventional hemodialysis, which makes it increasingly popular, especially in patients with high comorbidity, long dialysis duration, or who are not candidates for kidney transplantation. Although numerous studies have compared different HDF techniques or HDx with individual HDF modes, comprehensive comparisons among all high-efficiency dialysis methods are scarce (Mitchell et al., 2023; Zakrzewska et al., 2024). This study aimed to evaluate the efficacy of all available high-efficiency dialysis techniques at our center in terms of solute clearance across a broad spectrum of uremic toxins.

Materials and methods

Study design

This study was a single-center, prospective, exploratory, open-label, crossover trial. The objective was to compare the removal of uremic toxins across four high-efficiency dialysis methods: (I) HDx, (II) online pre-dilution HDF (PRE-HDF), (III) online mixed-dilution HDF (MIX-HDF), and (IV) online post-dilution HDF (POST-HDF). Patients underwent each modality for a week in a randomized sequence. The effectiveness of toxin removal was determined by calculating the reduction ratio (RR) for small molecular toxins such as urea (MW 60 Da) and phosphate (MW 95 Da); a middle molecular toxin, beta-2-microglobulin (β 2M, MW 11,800 Da); a large

middle molecular toxin, Chitinase-3-like protein 1 (YKL-40, MW 40,000 Da); and a protein-bound uremic toxin (PBUT), indoxyl sulfate (IS, MW 213 Da). Toxin reduction was evaluated during a single mid-week dialysis session. The study followed the Declaration of Helsinki's guidelines and was approved by the Medical University of Gdansk's Ethical Committee (NKBBN/479-759/2022; 18 November 2022).

Patients

Participants included adult patients with end-stage renal disease (ESRD) who had been receiving standard high-flux hemodialysis or online HDF (either pre- or postdialysis) three times per week for a minimum of 6 months. Eligible patients had a single-pool Kt/V for urea (spKt/V_{urea}) greater than 1.2, weighed between 60 and 89 kg, and had a dialysis blood flow of at least 350 mL/min through a fistula or arteriovenous catheter. Exclusion criteria included single-needle dialysis, the use of temporary non-tunneled catheters, poor compliance with dialysis procedures, hemodynamic instability during dialysis sessions, life expectancy of less than 6 months, hospitalization within the last 30 days, active inflammation or cancer, liver cirrhosis, and hypoalbuminemia (albumin <30 g/L).

Dialysis prescription and equipment

All dialysis treatments were performed using the Fresenius 5008 machine with the AutoSub Plus system (Fresenius Medical Care, Bad Homburg, Germany). Online HDF sessions were carried out with FX 100 high-flux dialyzers (surface area: 2.2 m²; UF coefficient: 73 mL/h × mmHg; Fresenius Medical Care). HDx treatments utilized Terranova 400 MCO dialyzers (surface area: 1.7 m²; UF coefficient: 48 mL/h × mmHg; Baxter, Alliston, ON, Canada). Each dialysis session lasted 4 h, with a dialysate temperature of 36.5°C. Blood flow and dialysate flow rates were set to 350 and 500 mL/min, respectively. Dry weight was verified using bioimpedance spectroscopy prior to the study. Ultrafiltration for each session was adjusted based on the patient's interdialytic weight gain and fluid intake, along with bloodline priming volume. Neither ultrafiltration nor sodium profiling was employed. The dialysate composition was: Na 138–140 mmol/L; K 2.0–3.0 mmol/L; HCO₃⁻ 32 mmol/L; Ca 1.25–1.5 mmol/L; Mg 0.5 mmol/L; Cl 110 mmol/L; glucose 1.0 g/L. Most patients (83.3%) used a potassium concentration of 2.0 mmol/L, and 91.7% used a calcium concentration of 1.25 mmol/L. Heparin was administered as a bolus and a continuous infusion according to current practices. Sterile, non-pyrogenic substitution fluid was generated online via ultrapure dialysate filtration. The AutoSub Plus system

automatically adjusted the substitution and convection rates based on pressure pulse attenuation and transmembrane pressure, optimizing ultrafiltration while preventing excessive hemoconcentration. Dialysis settings, such as post-dialysis weight, session length, dialysate composition, and anticoagulation, were kept consistent across all modalities. Medications remained unchanged throughout the study.

Monitoring of uremic toxins concentration

Blood samples for assessing toxin RR were collected before and after mid-week dialysis session. Post-dialysis sample collection was done at the dialysis session end from the arterial needle after decreasing the blood flow rate to 50 mL/min for 15s to avoid recirculation. RR of toxins was calculated by the following equation:

$$RR (\%) = \left[1 - \left(\frac{cC_{post}}{C_{pre}} \right) \right] \times 100$$

C_{pre} and *C_{post}* refer to toxin concentration of pre- and post-dialysis session, respectively while *BW_{post}* is the body weight at the end of the session. *C_{post}* was corrected for hemoconcentration as follows:

$$cC_{post} = \frac{C_{post}}{\left[1 + \left(\frac{BW}{0.2 (BW_{post})} \right) \right]}$$

Laboratory measurements

Urea and phosphate in serum were quantified using routine colorimetric methods (Abbott GmbH and Co. Wiesbaden, Germany).

Serum beta-2-microglobulin levels were determined with a reagent kit (Abbott GmbH and Co. Wiesbaden, Germany). The Alinity c β2-microglobulin reagent utilizes latex particles coated with IgG antibodies specific to human β2M, and agglutination is measured via a turbidimetric method. The detection limit was 0.110 mg/L, with an inter-assay CV of 4.1% and an intra-assay CV of 4.2%. The measurement range was 0.97–2.64 mg/L.

Serum YKL-40 (CHI3L1) was quantified using the YKL-40 Human Sandwich ELISA Kit (Thermo Fisher Scientific Inc.). This assay involves an anti-human YKL-40 antibody that binds to YKL-40 in the sample, followed by the addition of a biotin-conjugated detection antibody. The sensitivity was 10.83 pg/mL, with an assay range of 78–5,000 pg/mL, an inter-assay CV of 7.2%, and an intra-assay CV of 2.3%. Serum YKL-40 (CHI3L1) was quantified using the YKL-40 Human Sandwich ELISA Kit

TABLE 1 Characteristics of the study group.

Gender (Men/Women)	11/1
Causes of ESRD (n/%)	
Autosomal Dominant Polycystic Kidney Disease	4/33
Glomerulonephritis (primary or secondary)	3/25
Hypertensive nephropathy	2/17
Renal malformation	1/8
Interstitial nephropathy	1/8
Other	1/8
Age (years)	52.5 (15.5)
AACI (points)	4.5 (2.2)
Dialysis vintage (months)	42.5 (31.0)
Body Mass Index (kg/m ²)	23.8 (3.6)
Weight (kg)	73.7 (14.2)
spKt/V urea	1.5 (0.3)
Hemoglobin (g/dL)	10.9 (0.9)
Albumin (g/L)	33.1 (4.9)

ESRD, end-stage renal disease; AACI, Age Adjusted Charlson Comorbidity Index. Data are presents as mean (SD) or number (%).

(Thermo Fisher Scientific Inc.). This assay involves an anti-human YKL-40 antibody that binds to YKL-40 in the sample, followed by the addition of a biotin- conjugated detection antibody. The sensitivity was 10.83 pg/mL, with an assay range of 78–5000 pg/mL, an inter-assay CV of 7.2%, and an intra-assay CV of 2.3%.

Serum indoxyl sulfate (IS) levels were determined using a competitive ELISA kit (Fine Test¹). In this method, IS in the sample competes with the IS coated on the microtiter plate for the binding sites of a biotinylated detection antibody. The resulting colorimetric reaction was measured at 450 nm. The detection range for the assay was 1.563–100 ng/mL, with an intra- assay precision of 5.1% (low concentration: 3.16 ± 0.16) and inter-assay precision of 5.4%.

Statistical analysis

Continuous variables were expressed as means with standard deviations (SD), while categorical data were represented as percentages. The Shapiro–Wilk test was used to evaluate the normality of continuous variables. The Wilcoxon signed-rank test or ANOVA was utilized for repeated measures comparisons. Statistical significance was considered at $p < 0.05$. All analyses were performed using Statistica 13.3 (TIBCO Software Inc.; Palo Alto, CA, United States).

¹ <http://www.fn-test.com>

Results

Characteristics of patients

12 patients met inclusion criteria and were enrolled to the study, 11 men (92%) and 1 woman, in mean age of 52.5 ± 15.47 years. Hypertension was diagnosed in 10 (83%) patients. A description of the study group is presented in Table 1.

Dialysis parameters

Dialysis session time, blood flow rate, and dialysate flow rate were constant during all modalities. All patients achieved the minimum level of convection for high volume online HDF. Mean (standard deviation) total convection for post-HDF, pre-HDF and mix-HDF were 25.6 (3.8), 61.5 (7.2) and 47.1 (11.4) L, respectively. The arterial and venous dialysis pressure did not differ between tested treatments. Detailed delivered dialysis parameters are presented in Table 2. All patients in all sessions have achieved high-volume convection defined as ≥ 23 L of substitution fluid.

Effectiveness in the removal of toxins

No difference was seen in RR between treatments for small middle and large molecules, neither for the protein bound uremic molecule (Table 3). The best degree of IS clearance, although statistically insignificant, was obtained during POST-HD and HDX.

The impact of studied blood purification modalities on the removal of the toxins is displayed on Figure 1.

Figure 2 compares each treatment modality's capacity to remove a whole profile of molecules. Again, there was no difference between modalities.

Discussion

The main purpose of all blood purification techniques is to remove uremic toxins from the patient's blood. Our study showed no significant differences in uremic toxin removal between the compared methods of high-efficiency dialysis. Ensuring high-volume convection, i.e., 23 Liters (POST-HDF), 60 Liters (PRE) and 45 Liters (MIX-HDF) on average, these methods do not differ from each other in the clearance efficiency, nor do they differ from hemodialysis using MCO membranes.

We analyzed a broad spectrum of uremic toxins, including small-molecule toxins (urea), medium-molecule toxins ($\beta 2M$), large medium-molecule toxins (YKL-40), and toxins bound to and proteins (IS). The proposed cross-over design study excluded the influence of patient-related variability on the obtained results and ensured the same technical parameters of dialysis, including

TABLE 2 Delivered dialysis parameters during the study treatments.

	PRE-HDF	MIX-HDF	POST-HDF	HDX
Real Time min	240	240	240	240
Blood flow mL/min	350	350	350	350
Dialysate flow mL/min	500	500	500	500
Ultrafiltration L/session (SD)	2.45 (0.8)	2.29 (0.74)	2.19 (0.52)	2.33 (0.62)
Total convection L	61.5 (7.2)	47.1 (11.4)	25.6 (3.8)	NA

Note: Ultrafiltration refers to the fluid removed from the patient during the dialysis session. Total convection is the total volume of fluid moved by convection during the session, which includes both the patient's dehydration volume and the volume of replacement fluid administered.

TABLE 3 Molecules reduction ratio, according to size and treatment modality, Data expressed as means (SD).

Molecule	Size (Da)	HDF-pre	HDF-mix	HDF-post	HDx	P-value
Urea	60	0.73 (0.1)	0.72 (0.06)	0.75 (0.07)	0.72 (0.06)	0.67
Phosphate	95	0.54 (0.16)	0.56 (0.08)	0.59 (0.11)	0.56 (0.12)	0.86
Beta-2-microglobulin	11.000	0.62 (0.15)	0.69 (0.13)	0.7 (0.1)	0.67 (0.06)	0.41
YKL-40	40.000	0.31 (0.12)	0.32 (0.12)	0.32 (0.14)	0.36 (0.19)	0.92
Indoxyl sulfate	213	0.36 (0.23)	0.40 (0.17)	0.40 (0.17)	0.49 (0.17)	0.51

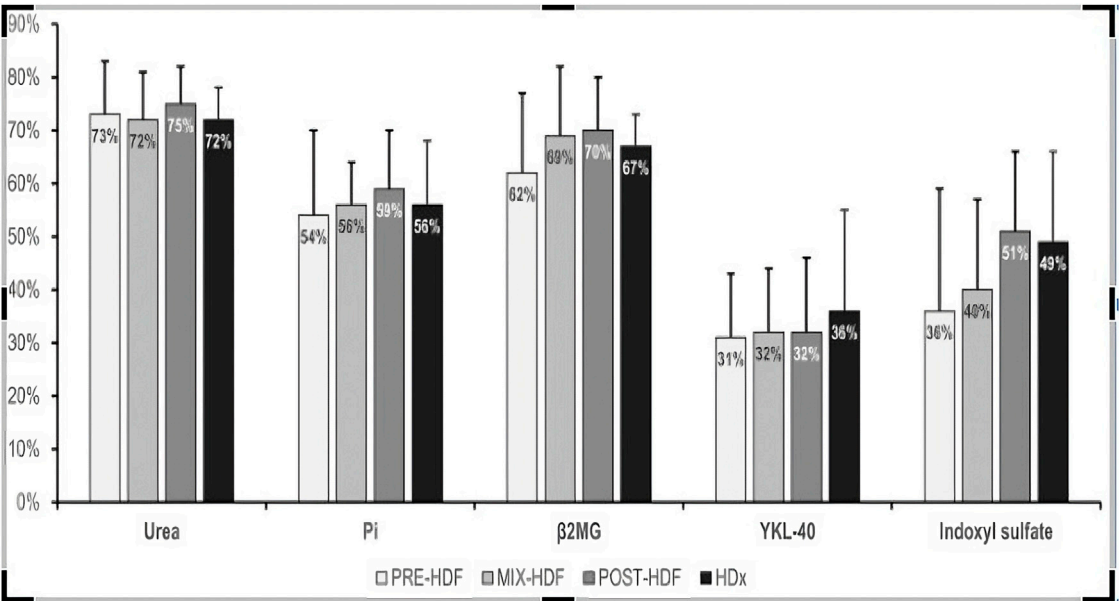


FIGURE 1
Mean reduction ratio of uremic toxins during the study treatments.

its time, blood and dialysis fluid flow rate limited bias in this regard.

The technical development of dialysis mainly resulting from the introduction of high-flux dialyzers, dialyzers with MCO

membranes and dialysis methods based on high-volume convection has led to very effective removal of most uremic toxins. This is especially true for small water-soluble compounds with low molecular mass (<500 Da) whose reduction ratio during

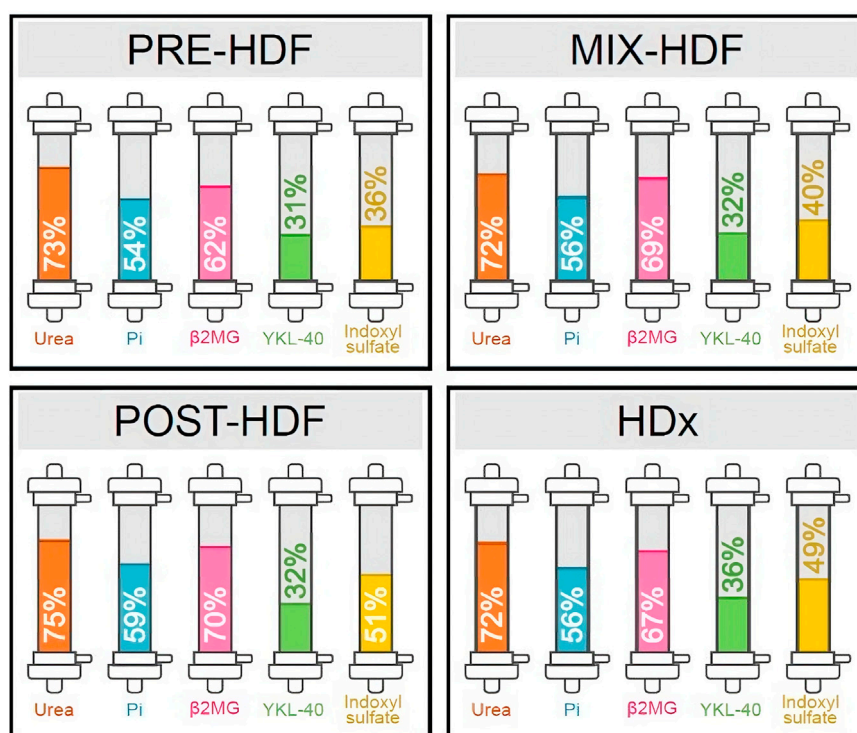


FIGURE 2

Comparative efficacy profiles of dialysis methods against specific toxins. This figure illustrates mean reduction ratio of uremic toxins during the study treatments.

the dialysis is very high for most commonly used methods. The ability to remove larger uremic toxins relies largely on the convection amount. The high-flux dialyzer, when applied in the standard hemodialysis, has a molecular mass cutoff of 25 kDa, being boosted up to 30 kDa in HDF mode. In our study, we did not show significant differences between studied treatments in the removal of urea, phosphate and β 2M. The degree of purification was high, exceeding 70% for urea. Previous studies have shown slightly better clearance rate for small molecules during POST-HDF compared to PRE-HDF, which was explained by the smaller concentration gradient of these toxins across the dialysis membrane in the later mode. These toxins are removed during dialysis primarily by the diffusion mechanism. In some studies, slightly better clearance was observed during POST-HDF compared to PRE-HDF also for medium size toxins (500–25,000 D) such as β 2M or α -1 microglobulin (Duval-Sabatier et al., 2023; Meert et al., 2008). The purification potential of MIX-HDF has been investigated only in few studies, indicating that the removal of β 2M is also slightly better than in PRE-HDF and similar to POST-HDF (Park et al., 2021; de Sequera et al., 2013). In our study, β 2M removal during PRE-HDF was the lowest among the tested methods, but the differences did not reach statistical significance. In previous studies, HDF patients in the highest β 2M tertile tended to have

lower replacement fluid volume than patients in the middle and lowest tertiles (Kanda et al., 2021). This points to an important advantage of our protocol in which all techniques were applied to the same patient. Careful selection of the study group allowed for optimal convection in each applied method. Therefore we were able to control important clinical confounders and our conclusions on comparability between single sessions of all used modalities are more reliable.

Large-middle uremic toxins (25–58 kDa) are important molecules, the accumulation of which is associated with numerous complications of chronic kidney disease and an increased risk of cardiovascular complications. They are poorly removed during hemodialysis using high-flux dialyzers; some but unsatisfactory improvement has been achieved in online HDF methods with high-volume convection (Rosner et al., 2021). The new class of MCO membranes with a large pore radius of 5 nm and high internal convection using in so called extended hemodialysis were intended to provide more efficient clearance for these toxins. Clinical studies in this area to date has yielded inconclusive results. Some studies showed better removal of large molecules involving λ free light chains and YKL-40 as compared to PRE-HDF (Kim et al., 2019), MIX-HDF (Eiamcharoenying et al., 2022), and POST-HDF (Kirsch

et al., 2017; Hadad-Arrascue et al., 2022). On the other hand, other studies do not show differences between HDx and POST-HDF in this regard (Garcia-Prieto et al., 2018; Maduell et al., 2019a). Moreover, Maduell et al. showed no differences in removal efficacy between HDx and POST-HDF analyzing the global removal score, taking into account 6 different uremic toxins (Maduell et al., 2019b). In our study, HDx showed slightly better removal of YKL-40 compared to other methods, achieving a clearance rate of 36%, though the differences were not statistically significant.

Protein-bound uremic toxins (PBUTs) like indoxyl sulfate (IS) and p-cresol sulfate are crucial prognostic markers. Elevated serum levels of these toxins are linked to cardiovascular events and contribute to vascular diseases such as arteriosclerosis, endothelial inflammation, oxidative stress, and vascular calcification (Lin et al., 2015; Opdebeeck et al., 2019). Despite their relatively small molecular weight, PBUTs are poorly cleared during conventional hemodialysis, even with high-flux dialyzers. Their removal is hindered by their strong binding to plasma albumin, as only the unbound fraction can pass through the dialysis membrane. In the kidneys, PBUTs are primarily eliminated via tubular secretion (Masereeuw et al., 2014). The efficiency of PBUT removal during hemodialysis may depend on several factors, including dialyzer size, protein loss, dialysis duration, dialysate flow rate, protein adsorption to the dialysis membrane, and the extent of PBUT-albumin dissociation during contact with the membrane (Sanchez-Ospina et al., 2024; Huang et al., 2009). There was initial hope that high-volume HDF and HDx might improve PBUT removal. However, prior studies have produced mixed results regarding whether high-volume HDF is superior to conventional HD (Abad et al., 2016; Panichi et al., 2017; Krieter et al., 2010; Snauwaert et al., 2020; van Gelder et al., 2020), and no substantial evidence has shown that HDx increases PBUT clearance (Deltombe et al., 2015; Ronco et al., 2017). No comparative studies exist that assess PBUT removal across all high-efficiency modalities. In our research, the highest IS clearance was observed with POST-HD and HDx, although the difference was not statistically significant.

The novelty of our study lies in the fact that no previous research has compared the efficacy of all forms of online HDF and HDx in a single analysis. Our study also has several strengths: 1) the crossover design was chosen to mitigate interpatient variability; 2) basic dialysis parameters were standardized across all treatment methods; 3) all HDF modalities were performed at high volumes, which is known to offer the best long-term outcomes; 4) the removal rate was adjusted for hemoconcentration during dialysis. Our findings have practical implications, suggesting that treatment selection should consider the characteristics of uremic toxins. However, we acknowledge the limitations of our study. The study population may not reflect a typical European dialysis cohort, as we only included

one woman, potentially affecting the homogeneity of the group, though the crossover design should minimize this issue. Another limitation is the small sample size, which may have prevented some differences from reaching statistical significance. Additionally, we analyzed the reduction ratio during only a single dialysis session. Future research could benefit from assessing the long-term effects of these modalities on toxin concentrations. A valuable complement to the analysis would be a comparison of the treatment effectiveness of the tested high-efficiency methods to the results obtained during standard hemodialysis. The influence of hemoconcentration on the concentration of all toxins and their reduction ration was taken into account in the study. For this purpose, toxin concentrations were corrected taking into account the change in the patient's weight during dialysis but an important limitation of the analysis is the lack of hematocrit-based hemoconcentration calculations. Considering these limitations, the findings should be viewed as exploratory.

In conclusion, this study found no significant differences in the clearance of a broad range of uremic toxins across four high-efficiency dialysis methods—PRE-HDF, MIX-HDF, POST-HDF, and HDx. While some trends were observed, particularly in PBUT removal, these differences were not substantial enough to recommend any one modality as the most effective.

Data availability statement

The raw data supporting the conclusions of this article will be made available by the authors, without undue reservation.

Ethics statement

The studies involving humans were approved by Medical University of Gdansk Ethical Committee (NKBBN/479-759/2022). The studies were conducted in accordance with the local legislation and institutional requirements. The participants provided their written informed consent to participate in this study.

Author contributions

Conceptualization, LT; methodology, JB, AZ, BB, SM, MJ, and LT; validation, MJ, SM, BB, and LT; formal analysis, LT and MK; investigation, JB, AZ, KJ, NP, MK, MJ, AT, and SM; writing—original draft preparation, JB and LT; writing—review and editing, BB, AD-S, MJ, and SM; visualization, MK; supervision, AD-S and LT. All authors contributed to the article and approved the submitted version.

Funding

The author(s) declare that no financial support was received for the research, authorship, and/or publication of this article.

References

- Abad, S., Vega, A., Quiroga, B., Arroyo, D., Panizo, N., Reque, J. E., et al. (2016). Protein-bound toxins: added value in their removal with high convective volumes. *Nefrologia* 36 (6), 637–642. doi:10.1016/j.nefro.2016.05.011
- Blankestijn, P. J., Vernooij, R. W. M., Hockham, C., Strippoli, G. F. M., Canaud, B., Hegbrant, J., et al. (2023). Effect of hemodiafiltration or hemodialysis on mortality in kidney failure. *N. Engl. J. Med.* 389 (8), 700–709. doi:10.1056/nejmoa2304820
- Deltombe, O., Van Biesen, W., Glorieux, G., Massy, Z., Dhondt, A., and Eloit, S. (2015). Exploring protein binding of uremic toxins in patients with different stages of chronic kidney disease and during hemodialysis. *Toxins (Basel)* 7 (10), 3933–3946. doi:10.3390/toxins7103933
- de Sequera, P., Albalade, M., Perez-Garcia, R., Corchete, E., Puerta, M., Ortega, M., et al. (2013). A comparison of the effectiveness of two online haemodiafiltration modalities: Mixed versus post-dilution. *Nefrologia* 33 (6), 779–787. doi:10.3265/Nefrologia.pre2013.Sep.12223
- Duval-Sabatier, A., Burtey, S., Pelletier, M., Laforet, M., Dou, L., Sallee, M., et al. (2023). Systematic comparison of uremic toxin removal using different hemodialysis modes: a single-center crossover prospective observational study. *Biomedicine* 11 (2), 373. doi:10.3390/biomedicine11020373
- Eiamcharoenying, J., Takkavatakarn, K., Chariyavilaskul, P., Susantitaphong, P., Eiam-Ong, S., and Tiranathanagul, K. (2022). Comparative effectiveness between expanded hemodialysis (hemodialysis using a medium cut-off dialyzer) and mixed-dilution online hemodiafiltration using a high-flux dialyzer in removing middle-molecule uremic toxins. *Blood Purif.* 51 (11), 923–931. doi:10.1159/000521886
- Garcia-Prieto, A., Vega, A., Linares, T., Abad, S., Macias, N., Aragoncillo, I., et al. (2018). Evaluation of the efficacy of a medium cut-off dialyzer and comparison with other high-flux dialyzers in conventional haemodialysis and online haemodiafiltration. *Clin. Kidney J.* 11 (5), 742–746. doi:10.1093/ckj/sfy004
- Hadad-Arrascue, F., Nilsson, L. G., Rivera, A. S., Bernardo, A. A., and Cabezuero Romero, J. B. (2022). Expanded hemodialysis as effective alternative to on-line hemodiafiltration: a randomized mid-term clinical trial. *Ther. Apher. Dial.* 26 (1), 37–44. doi:10.1111/1744-9987.13700
- Himmelfarb, J., Vanholder, R., Mehrotra, R., and Tonelli, M. (2020). The current and future landscape of dialysis. *Nat. Rev. Nephrol.* 16 (10), 573–585. doi:10.1038/s41581-020-0315-4
- Huang, Z., Gao, D., Letteri, J. J., and Clark, W. R. (2009). Innovation in the treatment of uremia: proceedings from the Cleveland clinic workshop: blood-membrane interactions during dialysis. *Seminars Dialysis* 22 (6), 623–628. doi:10.1111/j.1525-139x.2009.00658.x
- Kanda, E., Muenz, D., Bieber, B., Cases, A., Locatelli, F., Port, F. K., et al. (2021). Beta-2 microglobulin and all-cause mortality in the era of high-flux hemodialysis: results from the dialysis outcomes and practice patterns study. *Clin. Kidney J.* 14 (5), 1436–1442. doi:10.1093/ckj/sfaa155
- Kikuchi, K., Hamano, T., Wada, A., Nakai, S., and Masakane, I. (2019). Predilution online hemodiafiltration is associated with improved survival compared with hemodialysis. *Kidney Int.* 95 (4), 929–938. doi:10.1016/j.kint.2018.10.036
- Kim, T. H., Kim, S. H., Kim, T. Y., Park, H. Y., Jung, K. S., Lee, M. H., et al. (2019). Removal of large middle molecules via haemodialysis with medium cut-off membranes at lower blood flow rates: an observational prospective study. *BMC Nephrol.* 21 (1), 2. doi:10.1186/s12882-019-1669-3
- Kirsch, A. H., Lyko, R., Nilsson, L. G., Beck, W., Amdahl, M., Lechner, P., et al. (2017). Performance of hemodialysis with novel medium cut-off dialyzers. *Nephrol. Dial. Transpl.* 32 (1), 165–172. doi:10.1093/ndt/gfw310
- Krieter, D. H., Hackl, A., Rodriguez, A., Chenine, L., Moragues, H. L., Lemke, H. D., et al. (2010). Protein-bound uraemic toxin removal in haemodialysis and post-dilution haemodiafiltration. *Nephrol. Dial. Transplant.* 25 (1), 212–218. doi:10.1093/ndt/gfp437

Conflict of interest

The authors declare that the research was conducted in the absence of any commercial or financial relationships that could be construed as a potential conflict of interest.

- Lee, Y., Jang, M. J., Jeon, J., Lee, J. E., Huh, W., Choi, B. S., et al. (2021). Cardiovascular risk comparison between expanded hemodialysis using theranova and online hemodiafiltration (CARTOON): a multicenter randomized controlled trial. *Sci. Rep.* 11 (1), 10807. doi:10.1038/s41598-021-90311-6
- Lin, C. J., Wu, V., Wu, P. C., and Wu, C. J. (2015). Meta-analysis of the associations of p-cresyl sulfate (PCS) and indoxyl sulfate (IS) with cardiovascular events and all-cause mortality in patients with chronic renal failure. *PLoS One* 10 (7), e0132589. doi:10.1371/journal.pone.0132589
- Maduell, F., Rodas, L., Broseta, J. J., Gomez, M., Xipell, M., Guillen, E., et al. (2019a). Medium cut-off dialyzer versus eight hemodiafiltration dialyzers: comparison using a global removal score. *Blood Purif.* 48 (2), 167–174. doi:10.1159/000499759
- Maduell, F., Rodas, L., Broseta, J. J., Gomez, M., Xipell Font, M., Molina, A., et al. (2019b). High-permeability alternatives to current dialyzers performing both high-flux hemodialysis and postdilution online hemodiafiltration. *Artif. Organs* 43 (10), 1014–1021. doi:10.1111/aor.13480
- Masereeuw, R., Mutsaers, H. A., Toyohara, T., Abe, T., Jhawar, S., Sweet, D. H., et al. (2014). The kidney and uremic toxin removal: Glomerulus or tubule? *Seminars Nephrol.* 34 (2), 191–208. doi:10.1016/j.semnephrol.2014.02.010
- Meert, N., Eloit, S., Waterloos, M. A., Van Landschoot, M., Dhondt, A., Glorieux, G., et al. (2008). Effective removal of protein-bound uraemic solutes by different convective strategies: A prospective trial. *Nephrol. Dial. Transplant.* 24 (2), 562–570. doi:10.1093/ndt/gfn522
- Mitchell, C. R., Hornig, C., and Canaud, B. (2023). Systematic review to compare the outcomes associated with the modalities of expanded hemodialysis (HDx) versus high-flux hemodialysis and/or hemodiafiltration (HDF) in patients with end-stage kidney disease (ESKD). *Seminars Dialysis* 36 (2), 86–106. doi:10.1111/sdi.13130
- Opdebeeck, B., Maudsley, S., Azmi, A., De Mare, A., De Leger, W., Meijers, B., et al. (2019). Indoxyl sulfate and p-cresyl sulfate promote vascular calcification and associate with glucose intolerance. *J. Am. Soc. Nephrol.* 30 (5), 751–766. doi:10.1681/asn.2018060609
- Palmer, S. C., Rabindranath, K. S., Craig, J. C., Roderick, P. J., Locatelli, F., and Strippoli, G. F. (2012). High-flux versus low-flux membranes for end-stage kidney disease. *Cochrane Database Syst. Rev.* 2012 (9), CD005016. doi:10.1002/14651858.CD005016.pub2
- Panichi, V., Rocchetti, M. T., Scatena, A., Rosati, A., Migliori, M., Pizzarelli, F., et al. (2017). Long term variation of serum levels of uremic toxins in patients treated by post-dilution high volume on-line hemodiafiltration in comparison to standard low-flux bicarbonate dialysis: results from the REDERT study. *J. Nephrol.* 30 (4), 583–591. doi:10.1007/s40620-017-0381-2
- Park, K. S., Kang, E. W., Chang, T. I., Jo, W., Park, J. T., Yoo, T. H., et al. (2021). Mixed-versus predilution hemodiafiltration effects on convection volume and small and middle molecule clearance in hemodialysis patients: a prospective randomized controlled trial. *Kidney Res. Clin. Pract.* 40 (3), 445–456. doi:10.23876/j.krccp.21.044
- Pedrerros-Rosales, C., Jara, A., Lorca, E., Mezzano, S., Pecoits-Filho, R., and Herrera, P. (2023). Unveiling the clinical benefits of high-volume hemodiafiltration: optimizing the removal of medium-weight uremic toxins and beyond. *Toxins (Basel)* 15 (9), 531. doi:10.3390/toxins15090531
- Ronco, C., Neri, M., Lorenzin, A., Garzotto, F., and Clark, W. R. (2017). Multidimensional classification of dialysis membranes. *Contributions Nephrol.* 191, 115–126. doi:10.1159/000479260
- Rosner, M. H., Reis, T., Husain-Syed, F., Vanholder, R., Hutchison, C., Stenvinkel, P., et al. (2021). Classification of uremic toxins and their role in kidney failure. *Clin. J. Am. Soc. Nephrol.* 16 (12), 1918–1928. doi:10.2215/cjn.02660221
- Sanchez-Ospina, D., Mas-Fontao, S., Gracia-Iguacel, C., Avello, A., Gonzalez de Rivera, M., Mujika-Marticorena, M., et al. (2024). Displacing the burden: a review of

protein-bound uremic toxin clearance strategies in chronic kidney disease. *J. Clin. Med.* 13 (5), 1428. doi:10.3390/jcm13051428

Snauwaert, E., Van Biesen, W., Raes, A., Glorieux, G., Vande Walle, J., Roels, S., et al. (2020). Haemodiafiltration does not lower protein-bound uraemic toxin levels compared with haemodialysis in a paediatric population. *Nephrol. Dial. Transplant.* 35 (4), 648–656. doi:10.1093/ndt/gfz132

van Gelder, M. K., Middel, I. R., Vernooij, R. W. M., Bots, M. L., Verhaar, M. C., Masereeuw, R., et al. (2020). Protein-bound uremic toxins in hemodialysis patients relate to residual kidney function, are not influenced by convective

transport, and do not relate to outcome. *Toxins (Basel)* 12 (4), 234. doi:10.3390/toxins12040234

Zakrzewska, A., Biedunkiewicz, J., Komorniczak, M., Jankowska, M., Jasiulewicz, K., Plonka, N., et al. (2024). Intradialytic tolerance and recovery time in different high-efficiency hemodialysis modalities. *J. Clin. Med.* 13 (2), 326. doi:10.3390/jcm13020326

Zhang, Z., Yang, T., Li, Y., Li, J., Yang, Q., Wang, L., et al. (2022). Effects of expanded hemodialysis with medium cut-off membranes on maintenance hemodialysis patients: a review. *Membr. (Basel)* 12 (3), 253. doi:10.3390/membranes12030253

Criteria analysis for kinetics curves of initiated blood serum chemiluminescence

Iryna Oliynyk^{1,2}✉

¹Department of Physical and Chemical Disciplines, Lviv Medical University, Lviv, 79018, Ukraine; ²Institute of Animal Biology of NAAS, Lviv, 79034, Ukraine

The chemiluminescence (CL) methods unlike the other methods of determining free radicals (FR) allow investigating the kinetics of the derivation and recombination of radicals/antioxidants, and thus the development and attenuation of the process/processes after excitation in time. However, these methods are of limited application because the knowledge of the explored parameters is insufficient (maximum intensity and integrated area under the kinetics plot). The kinetics is studied by the CL methods and a new parameter (IR-criterion) of analysis of damping of the initiated CL dynamics has been introduced. The IR-criterion parameter: identifies the relationship between the rates of initiation and recombination of peroxide radicals in blood-serum samples; allows the full straightening of the CL curves; provides new information in the considered pathological processes; can serve as an additional universal characteristic of FR activity of blood serum in pathological processes.

Keywords: chemiluminescence, oxidation, free radicals, kinetics, IR-criteria

Received: 16 April, 2023; **revised:** 11 June, 2023; **accepted:** 16 June, 2023; **available on-line:** 07 September, 2023

✉e-mail: lakmus3041@gmail.com

Abbreviations: CL, chemiluminescence ; BS, blood serum; LPO, lipid peroxidation; FR, free radicals; OS, Oxidative Stress OS

INTRODUCTION

Causal connectivity between pathological states and lipid peroxidation has been analyzed in the scientific literature for a long time and serves as the subject of research by many scientists.

The studies are performed in several directions. Some of them are quantitative content analysis of oxidation products such as diene conjugates and malondialdehyde (Varesi *et al.*, 2022; Eggen *et al.*, 2022; Chen *et al.*, 2022). Other methods include spectral (Rubio *et al.*, 2021) and photometric analysis (Reidy *et al.*, 2023). In this case, one cannot ignore the research methods of the antioxidant status (Bojarczuk *et al.*, 2022), because antioxidants inhibit oxidation processes. All the above-mentioned methods are methods for testing the end-products of oxidation. Only the chemiluminescence methods provide opportunities to study the oxidation dynamics and branching of the oxidation chain (Mas-Bargues *et al.*, 2022). The recombination of radicals R^* , R_2^* leads to light (Damle *et al.*, 2022). The electrons of these substances are in an excited energy level during the transition to the basic state and the substance is emitting the excess energy as a photon. Exactly this emission is called CL (Li *et al.*, 2022). Studying this process can provide much informa-

tion about the processes occurring in the body (Oliynyk 2022).

Considering the benefits of the CL method highlights the following aspects

The first aspect is sensitivity. The recombination of radicals is responsible for the intensity of CL (Romodin 2022; Colowick *et al.*, 1986). Therefore recombination of radicals will determine the intensity of the glow of the process and the presence of oxidative stress (OS) in the body (Colowick *et al.*, 1986) and the CL methods are sensitive. They reveal the influence of drugs on the body and the quality of screening and monitoring therapeutic manipulation (Kohn *et al.*, 2008).

The second aspect is equally important; it is the speed of analysis. CL analyzers provide information for three minutes, and do not require expensive and specific reagents. In this case, bioliquids analysis as an estimation of the oxidative status of the whole organism is meant, not the surface CL methods of studies of a surface and local detection of problems and areas of defeat (Teruyama *et al.*, 2022; Syed *et al.*, 2021; Deepa *et al.*, 2022).

The usage of luminol and metals of variable valence greatly enhances the potential for utilizing and implementing CL methods in laboratory research. One of the applications is the investigation of the kinetics of initiated CL. The CL kinetics are initiated by adding hydrogen peroxide to the bioliquid, followed by the occurrence of glow kinetics. As with any typical laboratory analysis, such studies should have quantitative characteristics (Freyer *et al.*, 2008). There are several such characteristics identified:

- the intensity of the maximum peak I_{max} – defines the maximum concentration of peroxide radicals formed in the sample after the introduction of hydrogen peroxide;
- the area under the plot S – determines the total number of radicals formed during peroxidation processes.

These are two main features of the study. Also, there are two additional numerical characteristics of kinetics: the maximum angles of the increase and the glow recession. They characterize the maximum rates of formation and recombination of radicals (Oldham *et al.*, 2000; Rizzo *et al.*, 2022; Kaczmarek, 2011; Wang *et al.*, 2016). Yet, all these quantitative characteristics do not allow conducting a qualitative analysis without studying the kinetics curves.

The initial use of the methods of investigation of initiated CL kinetics for the analysis of lipid peroxidation was promising. However, they have not been widely introduced into diagnostic laboratory practice due to some issues:

- the variability of curves of initiated CL
- these parameters (I_{\max} , S) do not allow a quantitative diagnosis of pathology (Muller *et al.*, 2013)
- at pathological stages, these parameters often overlap
- deviation of one of them does not always indicate pathology
- getting two or more parameters in normal limits does not ensure the absence of a pathological condition.

The present article is devoted to the finding of such an additional quantitative clinical diagnostic criterion for analyzing initiated CL kinetics.

MATERIALS AND METHODS

The method of initiated CL requires using $FeSO_4$ to study blood serum. Ions of variable valence make it possible to increase the intensity of CL by oxidation chain branching. The temperature of the experiment was 38°C.

In experiments, we used fibrinogen-free BS of healthy people and also patients with different pathological processes. Blood samples for the experiments were taken in the morning on an empty stomach. The initiated H_2O_2 (2%) CL BS in the solution ($BS + FeSO_4$) (0.02 mM) + phosphate buffer) was investigated. We did not utilize any additional radiation to initiate the luminescence. The glow resulting from the chemical reaction was captured using an FEU-79 photomultiplier. The electrical signal obtained was then amplified and processed by a PC (refer to Fig. 1).

More details on the experiment methodology and equipment are available below in this article (Oliynyk, 2016; Chaichi *et al.*, 2016).

Free radical oxidation involves three stages: initiation with speed w_i , propagation, and termination (free radicals combine to form stable molecules (with radiation of excess energy) and prevent their further reaction with other molecules (without light emission)).

Overall, free radical oxidation can cause damage to cells and tissues in the body, leading to various diseases and conditions such as cancer, cardiovascular disease, and aging. Antioxidants can help to prevent or reduce the damage caused by free radicals by neutralizing them and breaking the chain reaction.

The most significant influence on the CL process with a lack of branching is introduced by the recombination of radicals. Consequently, the emission intensity is proportionate to the speed of that recombination:

$$I = \eta k [\text{radicals}]^2 \quad (1)$$

where:

η – the CL quantum efficiency

k – the constant of the speed of the peroxy radicals recombination

$[\text{radicals}]$ – the radicals concentration.

Since the recombination of FR mainly leads to radiation. Initiation is characterized by a sharp flash, and transition into the stationary condition is characterized by a decrease in the CL intensity.

In Non-Stationary mode:

$$-\frac{d[\text{radicals}]}{dt} = w_i - \eta k [\text{radicals}]^2 \quad (2)$$

where w_i is the constant of the rate of the radicals formation.

t – time moment.

We ignored all the intermediate reactions of peroxidation therefore in the future we will use the above definition.

Integration of the given formula leads to the following result:

$$\frac{1}{2\sqrt{w_i k}} \ln \frac{[\text{radicals}] \sqrt{k} + \sqrt{w_i}}{[\text{radicals}] \sqrt{k} - \sqrt{w_i}} = t \quad (3)$$

In Stationary mode, when our system stabilizes $\frac{d[\text{radicals}]}{dt} = 0$, so:

$$[\text{radicals}]_{\infty} = \sqrt{\frac{w_i}{k}} \quad (4)$$

then we get

$$\ln \frac{[\text{radicals}] + [\text{radicals}]_{\infty}}{[\text{radicals}] - [\text{radicals}]_{\infty}} = 2t\sqrt{w_i k} \quad (5)$$

substitute into (see Eqn 5):

$$\frac{I_{\infty}}{I} = \frac{[\text{radicals}]_{\infty}^2}{[\text{radicals}]^2} \quad (6)$$

the final result:

$$\ln \frac{\sqrt{I} + \sqrt{I_{\infty}}}{\sqrt{I} - \sqrt{I_{\infty}}} = 2t\sqrt{w_i k} \quad (7)$$

where:

– the time from the moment when hydrogen peroxide was introduced

I – the emission intensity for the t time moment

I_{∞} – the emission intensity at the moment when intensity becomes stationary (in our case after 70 seconds).

So in $(t, \ln \frac{\sqrt{I} + \sqrt{I_{\infty}}}{\sqrt{I} - \sqrt{I_{\infty}}})$, rectification of the initiated CL kinetics coordinates should take place.

BS is a complex heterogeneous environment and therefore the process of oxidation and recombination will be much more difficult for several reasons. Primarily, the heterogeneity and presence processes of radical hydration radicals. This will be shown in forthcoming studies on spectrum analysis during the reaction of recombination of peroxide radicals.

Note that the kinetics of fluorescence and phosphorescence spectra often exhibit similar kinetic curves. However, in the case of chemiluminescence, the glow occurs due to the recombination of free radicals, such as peroxides, which are formed as a result of a chemical reaction. The subsequent process involves relaxation to the ground state of the recombination products. In contrast, in fluorescence and phosphorescence kinetics (without observing a

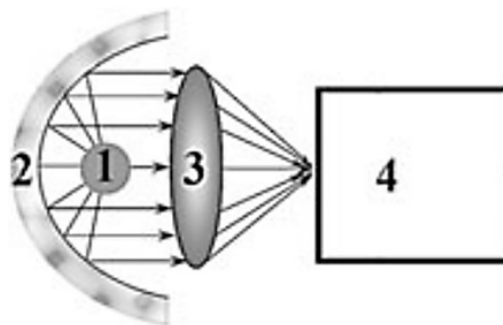


Figure 1. Chemiluminometer.

1: Suvette with the sample; 2: Parabolic mirror; 3: Collective lens; 4: Photodetector device, which includes a system of detection, amplification, conversion, analysis and signal output.

chemical reaction), only relaxation to the ground state occurs, as the molecule is excited during light irradiation of the sample. If fluorescence and phosphorescence are utilized to enhance the glow in the chemiluminescence reaction, the proposed approach carries the same significance.

All the samples of BS at pathological conditions were taken before medical treatment. The main task of this study is to refute or confirm the theory that chemiluminograms will be straightened in the specified coordinates. That the tangent of the straightening angle (IR-criterion) may vary depending on the pathology.

More than 774 chemiluminograms were analyzed, but only a few pathological conditions were selected. The criterion for choosing pathological conditions to be analyzed was an attempt to combine viral, bacterial, and fungal infections, and diseases of unknown etiology – sarcoidosis. We did not include cancer – they will be the subject of a forthcoming study.

Note: On each BS sample, we conducted a minimum of three independent parallel experiments and made an interesting discovery. When it came to I_{\max} and S , we had to discard results that deviated by more than 5% to avoid false-positive outcomes. However, for the angle tangent, such exclusion was unnecessary as the results did not differ by more than 5%. Thus, the relationship between the rates of initiation and recombination of peroxide radicals in the samples appears to be a more stable characteristic than the area under the plot and the maximum intensity of ICL. This suggests that in the analysis of $2\sqrt{w_i k}$, we have a more reliable parameter than I_{\max} and S . Nonetheless, chemiluminograms displaying a deviation of more than 5% across all these parameters were rejected since we also analyzed the average values for I_{\max} and S . Please refer to Fig. 2 for the calculation scheme.

Below we describe the division of patients suffering from different forms and diseases into six groups:

1. Active forms of pulmonary tuberculosis 14 (fourteen) people, the tuberculosis was diagnosed for the first time (disseminated forms of tuberculosis).
2. Sarcoidosis 8 (eight) people.
3. Hepatitis 21 (twenty-one) people. Viral hepatitis is not divided into subgroups. The group includes viral hepatitis of the group A, B, C.
4. Influenza 20 (twenty) people. The blood sampling was done after hospitalizing, the strain was not classified.
5. Asperhiloma 5 (five) people. Asperhiloma of the lungs was investigated against the background of pulmonary tuberculosis.
6. The control group of 51 (fifty-one) people.

RESULTS AND DISCUSSION

The differences in the results for I_{\max} and S between the control group and pathological conditions were not

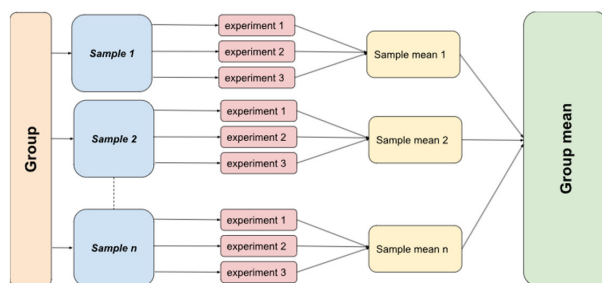


Figure 2. Scheme of conducting experiments and calculations in each group.

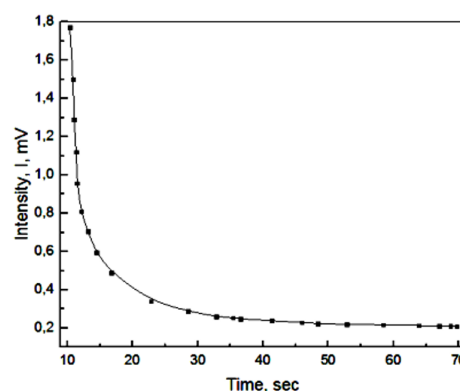


Figure 3. Typical view of a chemiluminogram of one of the samples of the control group.

always clear although these parameters were well correlated between themselves within a group.

The group correlation coefficients:

1. Active forms of pulmonary tuberculosis – 0.944
2. Sarcoidosis – 0.88
3. Hepatitis – 0.84
4. Influenza – 0.95
5. Asperhiloma – 0.76
6. Control – 0.93.

This means that within a group the parameters I_{\max} and S are interrelated. The weakest correlation between I_{\max} and S values was observed in aspergilloma. This could be due to the fungal infection and its stage, which can cause changes in the ratio between primary and secondary radicals in the middle of the group. Similar deviations were also observed in the middle of the group with sarcoidosis and hepatitis. Chemiluminescence is a highly sensitive parameter, and even the phase of the lesion can affect the relationship between I_{\max} and S values, and thus the correlation between them.

Figure 3 shows a typical view of a chemiluminogram of one of the samples of the control group. The first maximum appeared at 0.6–1 sec after the introduction of H_2O_2 . After this, the intensity of luminescence sharply decreased.

In the control group and in all pathological processes, there was no difference in the chemiluminogram view (except the group of chemiluminograms for certain types of cancer). All the chemiluminograms have an exponential character.

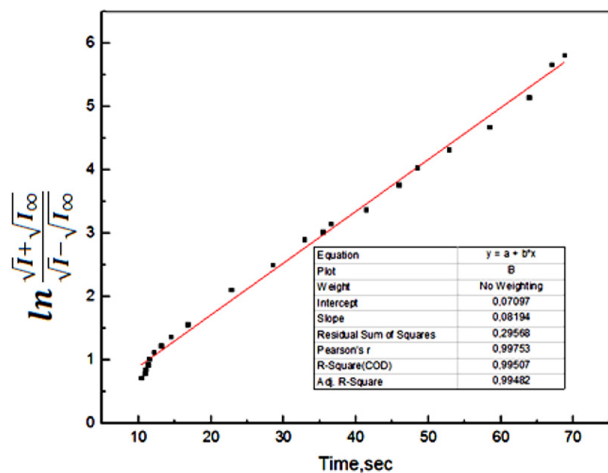
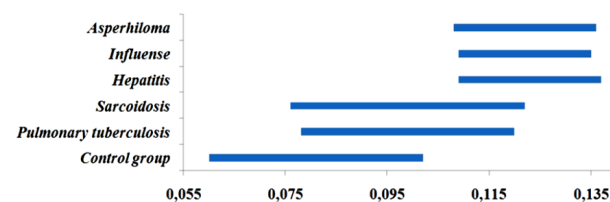
The confidence intervals of the main parameters for each pathology (the maximum intensity and the area under the plot) overlap with the confidence intervals of the parameters for the control group. This indicates selective sensitivity to the disease and low specificity of the corresponding criteria (see Table 1).

The analysis of chemiluminograms as to the coordinates $(t; \ln \frac{\sqrt{I} + \sqrt{I_{\infty}}}{\sqrt{I} - \sqrt{I_{\infty}}})$ (see Fig. 4) showed the straightening of chemiluminograms for the control group and in all pathological conditions in coordinates $(t; \ln \frac{\sqrt{I} + \sqrt{I_{\infty}}}{\sqrt{I} - \sqrt{I_{\infty}}})$.

Let's write the equation $\ln \frac{\sqrt{I} + \sqrt{I_{\infty}}}{\sqrt{I} - \sqrt{I_{\infty}}} = 2t\sqrt{w_i k}$ in the form $y = at$, where $y = \ln \frac{\sqrt{I} + \sqrt{I_{\infty}}}{\sqrt{I} - \sqrt{I_{\infty}}}$. The coefficient for the variable (angle coefficient) $a = 2\sqrt{w_i k}$, is nothing but the tangent of the angle of inclination of the straight line to the abscissa axis. The $2\sqrt{w_i k_6}$ (IR-criterion) differs from the control group under pathological conditions. Note that we have not analyzed chemiluminograms of other biological fluids; the obtained results we can design only for the blood serum tests (Table 1).

Table 1. Average measured values for different groups.

Pathological conditions	$I_{\max} \pm m$ (mV)	$S \pm m$ (mV*sec)	IR-criterion $\pm m$
Control group	1.76 \pm 0.07	18.91 \pm 1.21	0.081 \pm 0.021
Pulmonary tuberculosis	3.10 \pm 0.59	38.42 \pm 4.69	0.099 \pm 0.021
Sarcoidosis	2.72 \pm 0.57	46.98 \pm 3.85	0.099 \pm 0.023
Hepatitis	2.154 \pm 0.34	28.45 \pm 2.18	0.123 \pm 0.014
Influenza	1.946 \pm 0.37	23.84 \pm 2.22	0.122 \pm 0.013
Asperhiloma	0.677 \pm 0.08	12.73 \pm 1.14	0.122 \pm 0.014

Figure 4. Dependence of $\ln \frac{\sqrt{I} + \sqrt{I_{\infty}}}{\sqrt{I} - \sqrt{I_{\infty}}}$ on the time for the ICL curves.Figure 5. The confidence intervals of parameter $2\sqrt{w_i k_6}$.

A significant increase in the parameters I_{\max} and S relative to the control group was observed only in groups 1 (tuberculosis) (I_{\max} at 76.14% ($p < 0.05$), S at 103.17% ($p < 0.01$)) and 2 (sarcoidosis) (I_{\max} at 54.55% ($p < 0.05$), S at 147.17% ($p < 0.01$)). Such an increase indicates a significant increase of FR in the organism. We know that a quick flash is responsible for the number of primary FR formed in the organism. The primary radicals include semihions, superoxides, and nitroxides. The FR formed during the oxidation are consumed by recombination with emissions of light. Note that under the introduction of hydrogen peroxide into the samples, in the control group and in all pathologies, it was observed a significant level of CL 0.05–0.08 mV. When we came to the plateau of chemiluminograms (in the simulation, we considered this level as a steady state), this level was higher than the original level – 0.1–0.7 mV. The secondary oxidation processes that occur in the system correspond to this level. The high level of the plateau at tuberculosis and sarcoidosis indicates the significant number of secondary radicals formed in the serum samples. These radicals include hypochloride, hydroxyl radicals, and lipid radicals. The parameter S which indicates

the total number of recombinant radicals in the sample by eliminating the quanta of light is also much higher than the norm.

A large number of primary radicals is also observed with diseases such as hepatitis and influenza. $I_{\max} = 2.154$ mV – at hepatitis and 1.946 mV – at influenza, however, the situation changes when we consider the total number of radicals recombined by light emission («Hepatitis» $S = 28.45$ mV*sec, «Influence» $S = 23.84$ mV*sec). At the same time, under these pathologies we sometimes observed results falling into the normal range on these parameters.

A totally different case was with tuberculosis complicated by asperhiloma. In this case, both the number of primary radicals and secondary radicals recombined by light emission was below the norm. These effects can be caused by the four ways of reaction evolution in the sample:

1. the low level of radicals;
2. the high level of antioxidants;
3. non-radiative recombination of radicals;
4. the luminescence quenching molecules' environment.

All these four ways and mechanisms are equally possible and require further study.

The results for the angles tangents of straightening are not homogeneous. In particular – in the IR-criterion, no significant increase in tuberculosis and sarcoidosis was observed. Also, there is an overlapping of the confidence intervals in these diseases (Fig. 5).

A significant overlap of the confidence intervals is observed between tuberculosis and control groups ($p > 0.75$), and between the sarcoidosis and control groups ($p > 0.75$). At the same time, no overlapping of confidence intervals at hepatitis ($p < 0.01$), influenza ($p < 0.01$), and asperhiloma ($p < 0.01$) were found.

A significant and sustained increase of IR-criteria at influenza, hepatitis, and asperhiloma was observed, which indicates that in these diseases deviations towards the initiation/recombination of peroxide radicals occur. So, we can confidently apply this parameter as an additional criterion to improve chemiluminogram analysis in various pathological conditions, as well as the investigation of processes of free radical oxidation (FRO) and OS.

In modern biology, the activation of lipid peroxidation is considered a universal response of living systems to extreme factors. In general, the prooxidant-antioxidant status of the organism reflects the balance between the two opposite actions, namely the antioxidant properties (defence) and the formation of FR (damage). The influence of extreme factors (viruses, bacteria, xenobiotics, radiation, etc.) leads to the rejection of their balance in the prooxidant direction and the development of the so-called OS (Paulsen *et al.*, 2013). On the one hand, FRO at all stages of the course forms a series of products re-

sulting from the interaction of FR with each other and with biological macromolecules (Rahman, 2013). On the other hand, the analysis of the kinetic profile has not appeared as a universal factor in the process progress analysis. Important is the fact that the results of our investigation comply with the data published in literary sources. For example, the authors in (Wilson *et al.*, 2009) point to the fact that the FR play a significant role in the formation of lung fibrosis in pulmonary tuberculosis. This is confirmed by our results, in particular, we observed the increased levels of FR which caused an increase in both CL intensity maximum and S parameter.

For tuberculosis, the rate constants of initiation-recombination reactions are slightly different from the norm. Pulmonary tuberculosis is a serious and contagious illness that results from infection with *Mycobacterium tuberculosis*. It was studied in research the levels of free radicals, antioxidant capacity, and lipid profile in individuals who are afflicted with pulmonary tuberculosis (Vidhya *et al.*, 2019). When macrophages engulf *Mycobacterium tuberculosis*, the bacterium prevents the phagosome from maturing and fusing with lysosomes. This allows the pathogen to survive and multiply inside the phagocytic vacuoles, despite the hostile environment created by reactive oxygen and nitrogen intermediates produced by the macrophages. These highly toxic molecules, which include hydrogen peroxide, nitric oxide, and peroxynitrite, are normally produced at low levels during metabolic processes and are neutralized by antioxidant systems in the cell. However, during infection, their concentrations increase and cause damage to the cell's lipids, nucleic acids, proteins, and metal cofactors, leading to mutagenesis, necrosis, and apoptosis (Dalvi *et al.*, 2013) This may be due to a proportional increase in both the primary and secondary FR (Meulmeester *et al.*, 2022) in the body.

Sarcoidosis also causes the OS. Our results reflect an increase of the same parameters (I_{\max} and S), therefore the content of FR. Other authors (Boots *et al.*, 2009) point to the reduction of the blood serum antioxidant status. The dependence of the rate of initiation of oxidation and recombination of radicals in this case has not changed, therefore the ratio of primary and secondary radicals in this case corresponds to the norm.

Hepatitis has slightly different parameters. The significantly increased level ($2\sqrt{w_i k}$) of primary radicals against the background of reducing the secondary oxidation processes reveals the fact that the virus itself induces reactive forms of oxygen (Farinati *et al.*, 2007). So, we can predict an increase in oxidation rate constants of oxidation initiation. Furthermore, the mitochondrial dysfunction, observed in work (Moezzi *et al.*, 2022), is induced by the hepatitis C virus and decreases the oxidation of fat acids and accelerates the formation of reactive oxygen forms causing fat accumulation in the liver. This indicates that the number of secondary radicals is reduced, as well as the total number of FR, which fully confirms our results.

Influenza is also characterized by increasing of primary radicals against the background of reducing the total number of radicals in the organism. The indicator IR-criterion increased at this pathological state to which we also find the confirmation in the literature. In particular, in (Andrés *et al.*, 2022), the increase in reactive oxygen forms under this pathological condition was emphasized.

Aspergiloma was the last interesting subject of our study. Again, we observed a decrease in both primary and secondary radicals. Literature source (Ryoo *et al.*, 2009) provides an interesting fact concerning the synthe-

sis of connections based on the fermentation broth of *Aspergillus* sp. FN070449 (KCTC 26428) with antioxidant properties. So, the aspergillus infection as a complication of tuberculosis may lead to a reduction of the total number of FR. But at the same time, it increases relative to the control group, that is the ratio of primary and secondary radicals increases. The above considerations prove, that the introduced criterion, quantitatively and informatively shows the evolution of oxidative processes in the organism and can serve as an additional clinical diagnostic criterion for the quantitative analysis of chemiluminograms.

Although the analysis of chemiluminograms did not demonstrate selective specificity and sensitivity towards pathologies, it is still a useful and relevant method for evaluating the level of free radical processes in patients and monitoring their dynamics (for the purpose of assessing treatment effectiveness). Additional justification is required for the analysis of fluorescence and phosphorescence kinetics. However, preliminary analysis suggests that the fluorescence and phosphorescence kinetic curves also align within these coordinates.

CONCLUSIONS

As a result of the analysis of chemiluminograms, we introduced an additional quantitative criterion (IR-criteria/ $2\sqrt{w_i k}$). The parameter introduced displays the angle tangent of straightening chemiluminograms in the coordinates ($t; \ln \frac{\sqrt{I} + \sqrt{I_{\max}}}{\sqrt{I} - \sqrt{I_{\max}}}$). This straightening was observed in

chemiluminograms under normal conditions and in pathological processes, with the exception of with the exception of chemiluminograms characterized by two peaks. The basic assumption in the simulation was the absence of a degenerate chain FRO.

Through a comparative analysis of available publications, we found significant consistency between the data of peroxide oxidation/free radicals and obtained by us the new parameter. This suggests that this criterion can be considered a complementary and independent parameter for estimating FRO.

Therefore, the investigation of the straightening of chemiluminograms in the coordinates ($t; \ln \frac{\sqrt{I} + \sqrt{I_{\max}}}{\sqrt{I} - \sqrt{I_{\max}}}$) reveals promising perspectives for comparative monitoring of pathological states and creates a new paradigm in the study of the kinetics of initiated CL. This analysis will enable the combination of parameters such as intensity and area under the graph, providing an additional description of the rapid chemical transformations accompanied by light emission.

REFERENCES

- Andrés CMC, Pérez de la Lastra JM, Juan CA, Plou FJ, Pérez-Lebeña E (2022) The role of reactive species on innate immunity. *Vaccines* **10**: 1735. <https://doi.org/10.3390/vaccines10101735>
- Bojarczuk A, Dzitkowska-Zabielska M (2022) Polyphenol supplementation and antioxidant status in athletes: a narrative review. *Nutrients* **15**: 158. <https://doi.org/10.3390/nu15010158>
- Boots AW, Drent M, Swennen EL, Moonen HJ, Bast A, Haenen GR (2009) Antioxidant status associated with inflammation in sarcoidosis: a potential role for antioxidants. *Respir Med* **103**: 364–372. <https://doi.org/10.1016/j.rmed.2008.10.007>
- Chaichi MJ, Ehsani M. (2016) A novel glucose sensor based on immobilization of glucose oxidase on the chitosan-coated Fe_3O_4 nanoparticles and the luminol- H_2O_2 -gold nanoparticle chemiluminescence detection system. *Sensors Actuators B-Chem* **223**: 713–722. <https://doi.org/10.1016/j.SNB.2015.09.125>
- Chen HC, Chen CY, Fang YH, Hung KW, Wu DC (2022) Malondialdehyde-induced post-translational modifications in hemoglobin of

- smokers by NanoLC-NSI/MS/MS analysis. *J Proteome Res* **21**: 2947–2957. <https://doi.org/10.1021/acs.jproteome.2c00442>
- Colowick NP, Kaplan NP (1986) Bioluminescence and chemiluminescence. (1986) *Methods Enzymol* Part B. **133**: 1–649
- Dalvi SM, Patil VW, Ramraje NN, Phadtare JM, Gujarathi SU (2013) Nitric oxide, carbonyl protein, lipid peroxidation and correlation between antioxidant vitamins in different categories of pulmonary and extra pulmonary tuberculosis. *Malaysian J Med Sci* **20**: 21–30
- Damle VG, Wu K, Arouri DJ, Schirhagl R. (2022) Detecting free radicals post viral infections. *Free Radic Biol Med* **191**: 8–23. <https://doi.org/10.1016/j.freeradbiomed.2022.08.013>
- Deepa S, Ramu A, Rajendrakumar K (2022) Natural catalyst for luminol chemiluminescence: application to validate peroxide levels in commercial hair dyes. *Luminescence* **37**: 558–568. <https://doi.org/10.1002/bio.4182>
- Eggen MD, Merboth P, Neukirchner H, Glomb MA (2022) Lipid peroxidation has major impact on malondialdehyde-derived but only minor influence on glyoxal and methylglyoxal-derived protein modifications in carbohydrate-rich foods. *J Agric Food Chem* **70**: 10271–10283. <https://doi.org/10.1021/acs.jafc.2c04052>
- Farinati F, Cardin A, Bortolami M, Burra P, Russo FP, Rugge M, Guido M, Sergio A, Naccarato R (2007) Hepatitis C virus: from oxygen free radicals to hepatocellular carcinoma. *J Viral Hepatitis* **14**: 821–829. <https://doi.org/10.1111/j.1365-2893.2007.00878.x>
- Freyer W, Neacsu CC, and Raschke MB (2008) Absorption, luminescence, and Raman spectroscopic properties of thin films of benzoannulated metal-free porphyrines. *J Lumines* **128**: 661–672. <https://doi.org/10.1016/j.jlumin.2007.11.070>
- Kaczmarek M (2011) Chemiluminescence of the reaction system Ce(IV)–non-steroidal anti-inflammatory drugs containing europium(III) ions and its application to the determination of naproxen in pharmaceutical preparations and urine. *J Fluorescence* **21**: 2201–2205. <https://doi.org/10.1007/s10895-011-0923-2>
- Kohno M, Takeda M, Nivano Y, Saito R, Emoto N, Tada M, Kanazawa T, Ohuchi N, Yamada R (2008) Early diagnosis of cancer by detecting the chemiluminescence of hematoporphyrins in peripheral blood lymphocytes. *Toboku J Exp Med* **216**: 47–52. <https://doi.org/10.1620/tjem.216.47>
- Li M, Jiang R, Wang E, Xiong D, Ou T, Zhang X, Dou X. (2022) Performance evaluation of an automatic chemiluminescence immune platform for SARS-CoV-2 neutralizing antibody after vaccination in real world. *BMC Infect Dis* **22**: 157. <https://doi.org/10.1186/s12879-022-07141-8>
- Mas-Bargues C, García-Domínguez E, Borrás C (2022) Recent approaches to determine static and dynamic redox state-related parameters. *Antioxidants (Basel, Switzerland)* **11**: 864. <https://doi.org/10.3390/antiox11050864>
- Meulmeester FL, Luo J, Martens LG, Mills K, van Heemst D, Noordam R (2022) Antioxidant supplementation in oxidative stress-related diseases: what have we learned from studies on alpha-tocopherol?. *Antioxidants (Basel, Switzerland)* **11**: 2322. <https://doi.org/10.3390/antiox11122322>
- Moezzi D, Dong Y, Jain RW, Lozinski BM, Ghorbani S, D'Mello C, Wee Yong V (2022) Expression of antioxidant enzymes in lesions of multiple sclerosis and its models. *Sci Rep* **12**: 12761. <https://doi.org/10.1038/s41598-022-16840-w>
- Muller C H, Lee TK, Montañó MA (2013). Improved chemiluminescence assay for measuring antioxidant capacity of seminal plasma. *Methods Mol Biol* **927**: 363–376. https://doi.org/10.1007/978-1-62703-038-0_31
- Oldham PB, McCarroll ME, McGown LB, Warner IM. (2000). Molecular fluorescence, phosphorescence, and chemiluminescence spectrometry. *Anal Chem* **72**: 197R–209R. <https://doi.org/10.1021/a1000017p>
- Oliynyk I (2016) Limits of application of initiated chemiluminescence in monitoring of oncological process of mucous membrane of mouth and larynx. *Luminescence* **31**: 1213–1219. <https://doi.org/10.1002/bio.3093>
- Paulsen CE, Carroll KS (2013) Cysteine-mediated redox signaling: chemistry, biology, and tools for discovery. *Chem Rev* **113**: 4633–4679. <https://doi.org/10.1021/cr300163e>
- Rahman K (2007). Studies on free radicals, antioxidants, and co-factors. *Clin Interv Aging* **2**: 219–236
- Reidy E, Bottorff BP, Rosales CMF, Cardoso-Saldaña FJ, Arata C, Zhou S, Wang C, Abeleira A, Hildebrandt Ruiz L, Goldstein AH, Novoselac A, Kahan TF, Abbott JPD, Vance ME, Farmer DK, Stevens PS (2023) Measurements of hydroxyl radical concentrations during indoor cooking events: evidence of an unmeasured photolytic source of radicals. *Environ Sci Technol* **57**: 896–908. <https://doi.org/10.1021/acs.est.2c05756>
- Rizzo F (2022) Optical immunoassays methods in protein analysis: an overview. *Chemosensors* **10**: 326. <https://doi.org/10.3390/chemosensors10080326>
- Romodín LA (2022) Chemiluminescence detection in the study of free-radical reactions. Part 2. Luminescent additives that increase the chemiluminescence quantum yield. *Acta Naturae* **14**: 31–39. <https://doi.org/10.32607/actanaturae.11427>
- Rubio CP, Cerón JJ (2021) Spectrophotometric assays for evaluation of Reactive Oxygen Species (ROS) in serum: general concepts and applications in dogs and humans. *BMC Vet Res* **17**: 226. <https://doi.org/10.1186/s12917-021-02924-8>
- Ryoo IJ, Xu GH, Kim YH, Choo SJ, Ahn JS, Bae K, Yoo ID (2009) Reticulone, a novel free radical scavenger produced by *Aspergillus* sp. *J Microbiol Biotechnol* **19**: 1573–1575. <https://doi.org/10.4014/jmb.0906.06033>
- Syed AJ, Anderson JC (2021) Applications of bioluminescence in biotechnology and beyond. *Chem Soc Rev* **50**: 5668–5705. <https://doi.org/10.1039/d0cs01492c>
- Teruyama K, Naruse M, Tsuike M, Kobayashi H (2022) Novel chemiluminescent immunoassay to measure plasma aldosterone and plasma active renin concentrations for the diagnosis of primary aldosteronism. *J Hum Hypertens* **36**: 77–85. <https://doi.org/10.1038/s41371-020-00465-5>
- Varesi A, Chirumbolo S, Campagnoli LIM, Pierella E, Piccini GB, Carara A, Ricevuti G, Scassellati C, Bonvicini C, Pascale A (2022) The role of antioxidants in the interplay between oxidative stress and senescence. *Antioxidants (Basel, Switzerland)* **11**: 1224. <https://doi.org/10.3390/antiox11071224>
- Vidhya, R., Rathnakumar, K., Balu, V., Pugalendi, K. V. (2019). Oxidative stress, antioxidant status and lipid profile in pulmonary tuberculosis patients before and after anti-tubercular therapy. *Indian J Tuber* **66**: 375–381. <https://doi.org/10.1016/j.ijtb.2018.11.002>
- Wang C, Zhou C, Long Y, Cai H, Yin C, Yang Q, Xiao D (2016). An enhanced chemiluminescence bioplatfrom by confining glucose oxidase in hollow calcium carbonate particles. *Sci Rep* **6**: 24490. <https://doi.org/10.1038/srep24490>
- Wilson MS, Wynn TA (2009) Pulmonary fibrosis: pathogenesis, etiology and regulation. *Mucosal Immunol* **2**: 103–121. <https://doi.org/10.1038/mi.2008.8>



OPEN ACCESS

EDITED BY

Grzegorz Węgrzyn,
University of Gdansk, Poland

REVIEWED BY

Agnieszka Grabowiecka,
Wrocław University of Science and
Technology, Poland
Adam Junka,
Wrocław Medical University, Poland

*CORRESPONDENCE

Utpal Roy,
✉ utpalroy@gmail.com

RECEIVED 02 September 2023

ACCEPTED 05 January 2024

PUBLISHED 31 January 2024

CITATION

Madduri M, Rudramurthy SM and Roy U
(2024), Two promising natural
lipopeptides from *Bacillus subtilis*
effectively induced membrane
permeabilization in *Candida glabrata*.
Acta Biochim. Pol. 71:11999.
doi: 10.3389/abp.2024.11999

COPYRIGHT

© 2024 Madduri, Rudramurthy and Roy.
This is an open-access article
distributed under the terms of the
Creative Commons Attribution License
(CC BY). The use, distribution or
reproduction in other forums is
permitted, provided the original
author(s) and the copyright owner(s) are
credited and that the original
publication in this journal is cited, in
accordance with accepted academic
practice. No use, distribution or
reproduction is permitted which does
not comply with these terms.

Two promising natural lipopeptides from *Bacillus subtilis* effectively induced membrane permeabilization in *Candida glabrata*

Madhuri Madduri¹, Shivaprakash M. Rudramurthy² and
Utpal Roy^{1*}

¹Department of Biological Sciences, BITS Pilani K.K. Birla Goa Campus, Vasco da Gama, Goa, India,

²Department of Medical Microbiology, Medical Mycology Division, Post Graduate Institute of Medical Education and Research (PGIMER), Chandigarh, India

Candida glabrata is an important opportunistic human pathogen well known to develop resistance to antifungal drugs. Due to their numerous desirable qualities, antimicrobial lipopeptides have gained significant attention as promising candidates for antifungal drugs. In the present study, two bioactive lipopeptides (AF₄ and AF₅ m/z 1071.5 and 1085.5, respectively), coproduced and purified from *Bacillus subtilis* RLID12.1, consist of seven amino acid residues with lipid moieties. In our previous studies, the reversed phased-HPLC purified lipopeptides demonstrated broad-spectrum of antifungal activities against over 110 *Candida albicans*, *Candida non-albicans* and mycelial fungi. Two lipopeptides triggered membrane permeabilization of *C. glabrata* cells, as confirmed by propidium iodide-based flow cytometry, with PI uptake up to 99% demonstrating fungicidal effects. Metabolic inactivation in treated cells was confirmed by FUN-1-based confocal microscopy. Together, the results indicate that these lipopeptides have potentials to be developed into a new set of antifungals for combating fungal infections.

KEYWORDS

antifungal, bioactive, *Bacillus subtilis*, *Candida glabrata*, lipopeptides, membrane permeabilization

Introduction

After *Candida albicans*, the most prevalent yeast species reported to have been isolated from humans is *Candida glabrata* (*C. glabrata*). The past two and a half decades have witnessed *C. glabrata* becoming one of the most predominant *Candida* species, causing fungal infections (Chakrabarti et al., 2009; Lockhart et al., 2012; Benaducci et al., 2014; Cleveland et al., 2015; Pappas et al., 2018; Naicker et al., 2023). The reason behind this steep upward trend of *C. glabrata* infections may be associated with geographical variation and the rampant overuse of azoles (Richardson and Lass-Flörl, 2008). Given the prevalence of *C. glabrata* as the second leading cause of candidiasis infections,

including oral candidiasis, candidemia, invasive candidiasis, and urinary candidiasis (Esfandiary et al., 2012; Nash et al., 2016), it is essential to understand the alarming 40% mortality rate associated with *C. glabrata* infection underscores the seriousness of this opportunistic human pathogen, especially in immunocompromised hosts (Rodrigues et al., 2014; Mota et al., 2015; Nagayoshi et al., 2017). It has been recently reported that *C. glabrata* has developed several strategies to survive and thrive in its host cells and found ways to overcome antifungal resistance to commonly used antifungals, which also contribute to increased virulence (Pappas et al., 2018; Salazar et al., 2018). Flow cytometry (FCM) has been one of the major techniques that has successfully demonstrated its utility in determining the effect of antimycotics on yeast cells, cell membranes, or mechanisms of action when used with appropriate dye or fluorescent probes and experimental conditions (Pore, 1994). In our previous study (Ramachandran et al., 2018b), the antifungal susceptibility test (AFST) analyses of the two lipopeptides were done according to the CLSI guidelines. In this current investigation, the two lipopeptide fractions (AF₄ and AF₅) coproduced by *Bacillus subtilis* RLID 12.1 were purified, and the main objective of the study was to determine their membrane-permeabilizing effects on the yeast cell membrane and metabolic activity at two different peptide concentrations using the membrane-impermeant propidium iodide (PI) dye and two-colour FUN-1 stain.

Materials and methods

Microorganisms

The test strain *C. glabrata* ATCC 2001 was obtained from the National Culture Collection of Pathogenic Fungi (NCCPF), Post Graduate Institute of Medical Education and Research (PGIMER) Chandigarh, India and maintained as 20% glycerol stock at -80°C . The producer strain was also maintained as glycerol stock at -80°C .

Extraction and purification of antifungal compounds

For the purification of antifungal lipopeptides, cell-free supernatant (CFS) was obtained after 60 h at 30°C of incubation under stirring conditions of cells of the strain *B. subtilis* RLID 12.1. The CFS was subjected to a three-step purification that included HCl precipitation, solvent extraction using n-butanol, and silica gel (mesh size 230–400) based adsorption chromatography using proper ratios of methanol and chloroform. After the adsorption chromatography, all the collected fractions were tested for antifungal activity by spot-on-lawn assay against freshly grown *C. glabrata* cells spreading on Sabourad dextrose agar (SDA) plates. The 5 μL

aliquots of fractions which showed the clear zones of inhibition after 24 h of incubation were considered as bioactive fractions. These bioactive fractions AF₄ and AF₅ were fractionated using the reversed phased-HPLC system (Agilent Technologies, United States) at a semi-preparative scale equipped with a variable wavelength detector and an Agilent C18 column (10 mm \times 250 mm, 5 μm) (Ramachandran et al., 2018a; Ramachandran et al., 2018b). The analytical scale HPLC profiles of AF₄ and AF₅ and their m/z values are shown in Supplementary Figure S1.

Antifungal susceptibility testing (AFST) against *Candida glabrata*

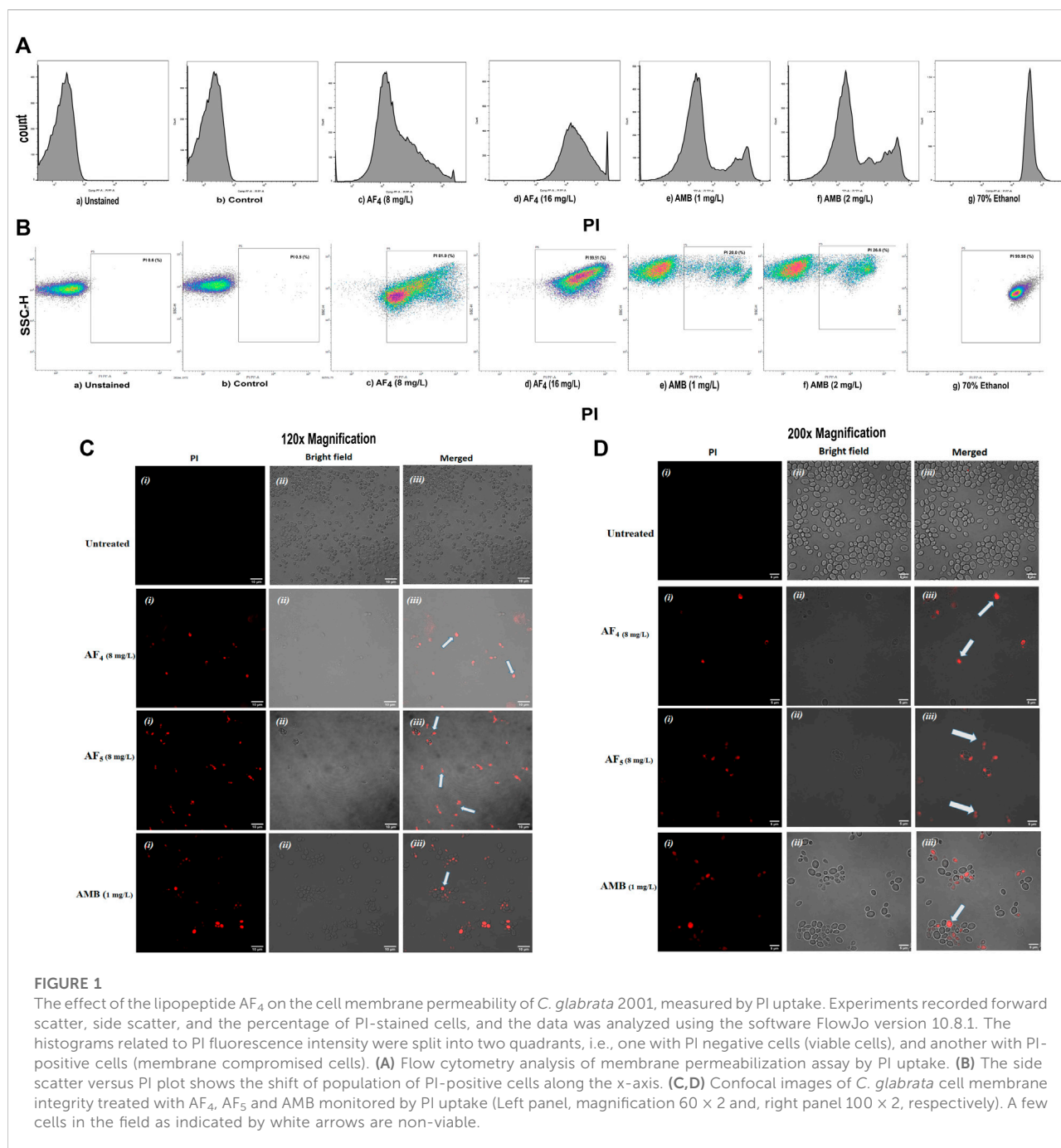
The minimum inhibitory concentrations (MICs) of the purified antifungal lipopeptides AF₄ and AF₅ were tested against *C. glabrata* ATCC 2001, according to CLSI guidelines (M27-A2) (Clinical and Laboratory Standards Institute, 2008). For antifungal assays, two-fold serial dilutions of each drug were prepared in RPMI-1640 (pH 7.0 ± 0.1) (with L-glutamine and phenol red without sodium bicarbonate) was buffered with 0.165 M MOPS (morpholinepropanesulfonic acid) (Himedia) and supplemented with 0.2% glucose. As reference yeast strain for the AFST, *C. albicans* ATCC 24433 and the positive control amphotericin B (AMB) (HiMedia, India) were used.

PI uptake assay by flow cytometry (FCM)

To study the impact of novel antifungal lipopeptides on membrane integrity, lipopeptides AF₄ and AF₅ (8 and 16 mg/L), and AMB ($\times 1$ and $\times 2$ MIC) were added to *Candida* cell suspension (1×10^6 CFU/mL) in RPMI 1640 and incubated at 37°C for 18 and 5 h, respectively, in shaking conditions (Gokahmetoglu et al., 2003; Seyedjavadi et al., 2020). Two types of controls were used in the study: negative controls consisting of untreated cells, and PI positive controls, treated with 70% ethanol for 30 min. Post-incubation, the cells were harvested, washed with $1\times$ phosphate buffered saline (PBS), and stained with PI at a concentration of 7.5 $\mu\text{g/mL}$ for 20 min. Unstained and untreated cells were sampled and analysed in the beginning. Flow cytometry analysis was performed on 30,000 events using a FACSMelody flow cytometer with a 488 nm laser line and a 586 nm filter with PI detection.

Viability (CFU) assays

Prior PI staining, aliquots of yeast cultures (both untreated and treated) were collected, serially diluted in sterile $1\times$ PBS, and plated in duplicate on SDA plates (Chaturvedi et al., 2004; Ramesh et al., 2023). The plates were incubated for 24 h at 37°C , colonies were

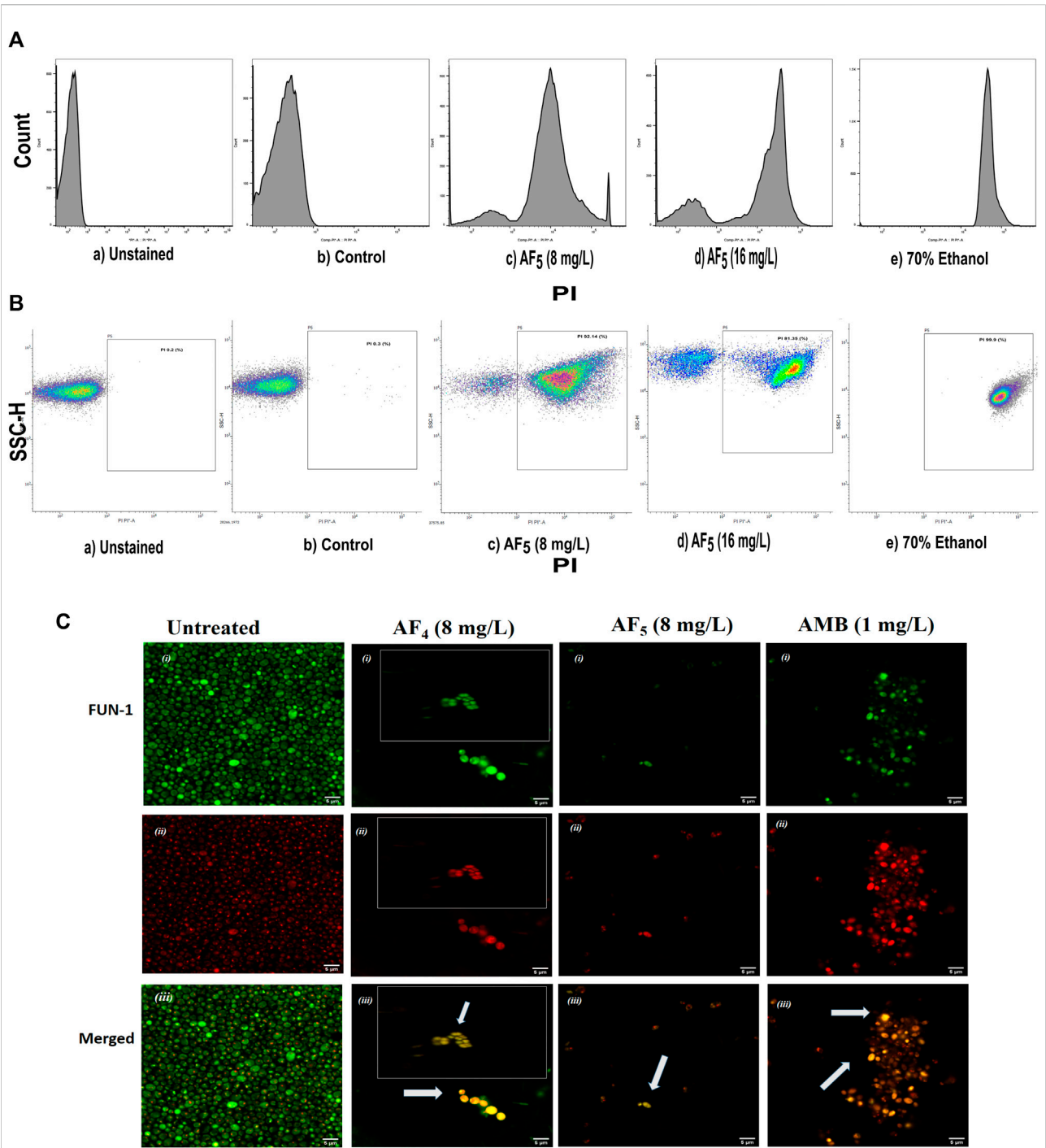


counted, and findings were represented as the percentage reduction in CFU/mL compared to the growth in the untreated sample.

Confocal laser scanning microscopy (CLSM)

The CLSM analysis was performed using PI (ThermoFisher, United States) and [2-chloro-4-(2, 3-dihydro-3-methyl-(benzol-

1, 3-thiazol-2-yl)-methylidene)-1-phenylquinolinium iodide] FUN-1 (ThermoFisher, United States) (Chan et al., 2011; Zhang et al., 2018). Cells were treated with AF₄/AF₅ (8 and 16 mg/L) for 18 h, AMB (1 mg/L) for 5 h, and untreated cells were used as control. Post-treatments, cells were harvested and resuspended in 1×PBS, following which staining with PI (7.0 µg/mL) for 20 min in the dark and washing with 1×PBS were done. FUN-1 at a final concentration of 5 µM was prepared in 10 mM glucose-HEPES (GH) buffer, and cells were incubated in (GH)



buffer with FUN-1 stain for 30 min (Pina-Vaz et al., 2001; Kwolek-Mirek and Zadrag-Tecza, 2014; Yan et al., 2019). Treated and untreated cells were imaged with an Olympus FV3000 (Japan) microscope at 60×2 and 100×2 magnifications for PI-stained cells and 100×2 for FUN-1 stained cells.

Statistical analysis

Experiments were performed in three individual times with two technical replicates. Data are presented as the means \pm SD values and, One-way ANOVA statistical analysis was done in the Graph-pad prism Software version 9.3.1.

Results and discussion

The MICs of two lipopeptides and AMB (used as the standard antifungal) against *C. glabrata* were determined to be 4 mg/L and 1 mg/L, respectively. The results agree with the previously determined MIC values (Ramchandran et al., 2018b; Ramchandran et al., 2020). To gain more insights into lipopeptides' membrane permeabilizing potential, we performed PI uptake assays using 8 mg/L ($\times 2$) and 16 mg/L ($\times 4$) MICs as determined by the AFST for *C. glabrata* ATCC 2001. FC results were expressed as the fluorescence intensity (FI) of PI-stained yeasts. AF₄ and AF₅ treatments caused cell membrane disruption in *C. glabrata* cells, as seen by the enhanced fluorescence that resulted from PI uptake. In cells treated with AMB, AF₄, AF₅, and 70% ethanol, the increase in PI-fluorescence is manifested as a distinct shift of the peak along the x-axis (Figures 1A, B) and (Figures 2A, B). The histograms pertaining to all flow cytometry assays where *C. glabrata* ATCC 2001 cells were stained with PI after being exposed to AMB for 5 h (Gokahmetoglu et al., 2003) at 1 and 2 mg/L and AF₄/AF₅ (8 and 16 mg/L) for 18 h have been shown

in Figures 1A, 2A. All the events of FC population density plots have been shown in Figures 1B, 2B.

Significant congruence was found when comparing the proportion of PI uptake with the drop in CFU/mL among AF₄ treatments. A substantial association was observed between the percentage PI uptake estimated in flow cytometry and the percentage reduction in plate counts, presented in tabular form (Table 1) to summarize the findings. Cells unexposed to lipopeptides showed very negligible fluorescence, as evidenced by the PI uptake percentage graph (Figure 3). At 8 mg/L, the AF₄-treated *C. glabrata* showed an average of 81.92% PI-positive cells and 99.90% CFU reduction, better was the observation in AF₄-(16 mg/L)-treated *C. glabrata* cells, where 99.51% PI-positive cells were noted and a CFU reduction of 99.97% recorded (Figure 3; Table 1). At 8 mg/L, the AF₅-treated *C. glabrata* showed an average of 92.14% PI-positive cells and 99.44% CFU reduction. However, AF₅-(16 mg/L)-treated *C. glabrata* cells showed 81.35% PI-positive cells, and the CFU reduction of 99.92% was recorded, indicating that AF₅ even at a 2-fold concentration, did not show more membrane permeabilization and increased fungicidal effects. This may be due to the hydrophobic aggregation of AF₅ lipopeptide at higher concentrations (Ramchandran et al., 2020). In AMB (1 and 2 mg/L)-treated cells for 5 h, only 20.02% and 26.06% PI-positive cells were detected, respectively. The increase in the fluorescence intensity percentage observed in yeast cells treated with higher AF₄ and AF₅ (8 mg/L) concentrations agreed with the positive control values, indicating potential antifungal activity. In comparison, untreated cells showed negligible fluorescence.

Candida cells exposed to AF₄/AF₅ (8 mg/L) displayed PI uptake as evident from red fluorescence, indicating cell membrane damage and hence permeabilization [Figure 1C ($\times 120$) and Figure 1D ($\times 200$)] magnifications. Since the formation of cylindrical intravacuolar structures (CIVS) needs metabolically active cells with undamaged plasma membrane, the presence of yellow-green fluorescence (Figure 2C) in FUN-1 stained cells instead of red

TABLE 1 Correlation between PI uptake percentage from flow cytometry and plate count.

Drug (concentration)	PI uptake (%)	Plate count	
		Log reduction	Reduction (%)
AF ₄ (8 mg/L)	81.92 \pm 8.7 SD	3.03	99.90 \pm 0.79 SD
AF ₄ (16 mg/L)	99.51 \pm 0.07 SD	3.64	99.97 \pm 0.59 SD
AF ₅ (8 mg/L)	92.14 \pm 6.8 SD	2.25	99.44 \pm 0.82 SD
AF ₅ (16 mg/L)	81.35 \pm 12.8 SD	3.10	99.92 \pm 2.1 SD
AMB (1 mg/L)	20.02 \pm 6.7 SD	4.12	99.99 \pm 0.53 SD
AMB (2 mg/L)	26.06 \pm 6.02 SD	4.43	99.99 \pm 0.56 SD

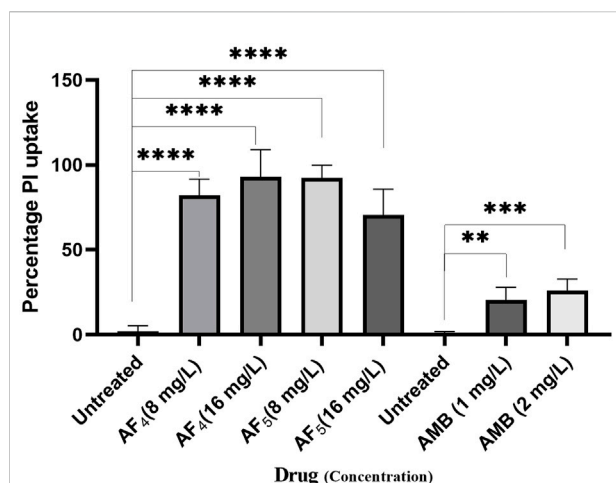


FIGURE 3

The histogram analysis in the graph shows the percentage of PI-positive *C. glabrata* cells upon (AF₄/AF₅) antifungal treatments. Ethanol-treated yeast cells exhibited a high permeability to PI (99.99% of cells stained). P-values (**** $p < 0.0001$) indicate statistically significant differences from the effects of AF₄ and AF₅-treatments and control (untreated). Statistically significant observations were made between AMB-treated cells and control used during AMB-treatments.

fluorescence in lipopeptide-treated cells clearly indicates the loss of membrane integrity, metabolic activity, and cell death (Millard et al., 1997). The cell deaths are quite evident from the log reductions of 3.03 and 3.64 CFU/mL by AF₄ (8 and 16 mg/L). In the lipopeptide-treated and AMB-treated cells CIVS were not observed. Collectively, it may be surmised that the prime targets of AF₄ and AF₅ might be the components of the cell membrane (Ramesh et al., 2023). The presence of a long acyl chain in antifungal cyclic lipopeptides such as iturin and fenzylin enables oligomer formation and subsequent insertion into the plasma membrane (Malina and Shai, 2005) and the organisation of aggregates in biological membranes triggering early membrane damage and membrane disintegration was also reported by Horn et al. (2013). The preliminary mechanism of action on the yeast cell membrane has been schematically depicted in the Supplementary Figure S2. Taken together, the results revealed that two lipopeptides demonstrated remarkable fungicidal effects on *C. glabrata* cells with enhanced cell membrane permeability, and damage. Consequently, the findings positively indicate that the lipopeptides AF₄ and AF₅ hold considerable promise as prospective antifungal agents.

References

Benaducci, T., Matsumoto, M. T., Sardi, J. C. O., Fusco-Almeida, A. M., and Mendes-Giannini, M. J. S. (2015). A flow cytometry method for testing the susceptibility of *Cryptococcus* spp. to amphotericin B. *Rev. Iberoam. Micol.* 32, 159–163. doi:10.1016/j.riam.2014.06.004

Data availability statement

The raw data supporting the conclusion of this article will be made available by the authors, without undue reservation.

Author contributions

MM was exclusively involved in the experimental works and preparing the preliminary draft. SMR oversaw the progress of the work and has been the co-principal investigator of the project. UR was involved in the logistics part, designing the experiments and revising the manuscript. All authors contributed to the article and approved the submitted version.

Funding

The investigation was funded by Science and Engineering Research Board (SERB), Govt. of India, New Delhi, India.

Conflict of interest

The authors declare that the research was conducted in the absence of any commercial or financial relationships that could be construed as a potential conflict of interest.

Acknowledgments

First author acknowledges the Science and Engineering Research Board (SERB), Govt. of India for providing the fellowship in the project (EMR/2017/000572). Authors deeply acknowledge the DST-FIST (File number DST-FIST SR/FST/LS-II/2017), Govt. of India funded FACS Facility, K.K. Birla Campus, Goa India, and the Centre for Sophisticated Instruments Facility (CSIF)-BITS Pilani K.K. Birla Campus, Goa, India for CLSM facility. Authors sincerely acknowledge the co-principal investigator of the project Arunaloake Chakrabarti (PGIMER, Chandigarh, India).

Supplementary material

The Supplementary Material for this article can be found online at: <https://www.frontierspartnerships.org/articles/10.3389/abp.2024.11999/full#supplementary-material>

Chakrabarti, A., Chatterjee, S. S., Rao, K. L. N., Zameer, M. M., Shivaprakash, M. R., Singhi, S., et al. (2009). Recent experience with fungaemia: change in species distribution and azole resistance. *Scand. J. Infect. Dis.* 41 (4), 275–284. doi:10.1080/00365540902777105

- Chan, L. L., Lyettefi, E. J., Pirani, A., Smith, T., Qiu, J., and Lin, B. (2011). Direct concentration and viability measurement of yeast in corn mash using a novel imaging cytometry method. *J. Industrial Microbiol. Biotechnol.* 38 (8), 1109–1115. doi:10.1007/s10295-010-0890-7
- Chaturvedi, V., Ramani, R., and Pfaller, M. A. (2004). Collaborative study of the NCCLS and flow cytometry methods for antifungal susceptibility testing of *Candida albicans*. *J. Clin. Microbiol.* 42 (5), 2249–2251. doi:10.1128/JCM.42.5.2249-2251.2004
- Cleveland, A. A., Harrison, L. H., Farley, M. M., Hollick, R., Stein, B., Chiller, T. M., et al. (2015). Declining incidence of candidemia and the shifting epidemiology of candida resistance in two US metropolitan areas, 2008–2013: results from population-based surveillance. *PLoS ONE* 10 (3), e0120452. doi:10.1371/journal.pone.0120452
- Clinical and Laboratory Standards Institute (CLSI) (2008). *Reference method for broth dilution antifungal susceptibility testing of yeasts. approved standard*. 3th ed. Wayne, PA: Clinical and Laboratory Standards Institute. Available at: https://clsi.org/media/1461/m27a3_sample.pdf.
- Esfandiary, M. A., Farasat, A., Rostamian, M., and Fattahy, A. (2012). Study of morphological characteristics, pathogenicity and drug resistance of *Candida glabrata* as increasing opportunistic yeast. *Eur. J. Exp. Biol.* 2 (4), 948–952.
- Gökahmetoğlu, S., Nedret Koc, A., and Patiroğlu, T. (2003). Antifungal susceptibility testing of *Candida albicans* by flow cytometry. *Empfindlichkeitsprüfung an Candida albicans mittels durchflusszytometrie. Mycoses* 46 (8), 289–293. doi:10.1046/j.1439-0507.2003.00903.x
- Horn, J. N., Cravens, A., and Grossfield, A. (2013). Interactions between fengycin and model bilayers quantified by coarse-grained molecular dynamics. *Biophysical J.* 105 (7), 1612–1623. doi:10.1016/j.bpj.2013.08.034
- Kwolk-Mirek, M., and Zdrag-Tecza, R. (2014). Comparison of methods used for assessing the viability and vitality of yeast cells. *FEMS Yeast Res.* 14 (7), 1068–1079. doi:10.1111/1567-1364.12202
- Lockhart, S. R., Iqbal, N., Cleveland, A. A., Farley, M. M., Harrison, L. H., Bolden, C. B., et al. (2012). Species identification and antifungal susceptibility testing of candida bloodstream isolates from population-based surveillance studies in two U.S. cities from 2008 to 2011. *J. Clin. Microbiol.* 50 (11), 3435–3442. doi:10.1128/JCM.01283-12
- Malina, A., and Shai, Y. (2005). Conjugation of fatty acids with different lengths modulates the antibacterial and antifungal activity of a cationic biologically inactive peptide. *Biochem. J.* 390 (3), 695–702. doi:10.1042/BJ20050520
- Millard, P. J., Roth, B. L., Thi, H. P. T., Yue, S. T., and Haugland, R. P. (1997). Development of the FUN-1 family of fluorescent probes for vacuole labeling and viability testing of yeasts. *Appl. Environ. Microbiol.* 63 (7), 2897–2905. doi:10.1128/aem.63.7.2897-2905.1997
- Mota, S., Alves, R., Carneiro, C., Silva, S., Brown, A. J., Istel, F., et al. (2015). *Candida glabrata* susceptibility to antifungals and phagocytosis is modulated by acetate. *Front. Microbiol.* 6, 919–1012. doi:10.3389/fmicb.2015.00919
- Nagayoshi, Y., Miyazaki, T., Shimamura, S., Nakayama, H., Minematsu, A., Yamauchi, S., et al. (2017). Unexpected effects of azole transporter inhibitors on antifungal susceptibility in *Candida glabrata* and other pathogenic *Candida* species. *PLoS ONE* 12 (7), e0180990. doi:10.1371/journal.pone.0180990
- Naicker, S. D., Shuping, L., Zulu, T. G., Mpembe, R. S., Mhlanga, M., Tsotetsi, E. M., et al. (2023). Epidemiology and susceptibility of *Nakaseomyces* (formerly *Candida*) *glabrata* bloodstream isolates from hospitalised adults in South Africa. *Med. Mycol.* 61 (6), myad057. doi:10.1093/mmy/myad057
- Nash, E. E., Peters, B. M., Lilly, E. A., Nover, M. C., and Fidel, P. L. (2016). A murine model of *Candida glabrata* vaginitis shows no evidence of an inflammatory immunopathogenic response. *PLoS ONE* 11 (1), e0147969. doi:10.1371/journal.pone.0147969
- Pappas, P. G., Lionakis, M. S., Arendrup, M. C., Ostrosky-Zeichner, L., and Kullberg, B. J. (2018). Invasive candidiasis. *Nat. Rev. Dis. Prim.* 4, 18026–18120. doi:10.1038/nrdp.2018.26
- Pina-Vaz, C., Sansonetty, F., Rodrigues, A. G., Costa-Oliveira, S., Tavares, C., and Martinez-De-Oliveira, J. (2001). Cytometric approach for a rapid evaluation of susceptibility of *Candida* strains to antifungals. *Clin. Microbiol. Infect.* 7 (11), 609–618. doi:10.1046/j.1198-743X.2001.00307.x
- Pore, R. S. (1994). Antibiotic susceptibility testing by flow cytometry. *J. Antimicrob. Chemother.* 34 (5), 613–627. doi:10.1093/jac/34.5.613
- Ramachandran, R., Ramesh, S., Ramkumar, S., Chakrabarti, A., and Roy, U. (2018a). Calcium alginate bead-mediated enhancement of the selective recovery of a lead novel antifungal bacillomycin variant. *Appl. Biochem. Biotechnol.* 186 (4), 917–936. doi:10.1007/s12010-018-2778-3
- Ramachandran, R., Shrivastava, M., Narayanan, N. N., Thakur, R. L., Chakrabarti, A., and Roy, U. (2018b). Evaluation of antifungal efficacy of three new cyclic lipopeptides of the class bacillomycin from *Bacillus subtilis* RLID 12.1. *Antimicrob. Agents Chemother.* 62 (1), e01457–17. doi:10.1128/AAC.01457-17
- Ramchandran, R., Ramesh, S., Aviksha, A., Thakur, R., Chakrabarti, A. R. U., and Roy, U. (2020). Improved production of two anti-*Candida* lipopeptide homologues co-produced by the wild-type *Bacillus subtilis* RLID 12.1 under optimized conditions. *Curr. Pharm. Biotechnol.* 21 (5), 438–450. doi:10.2174/1389201020666191205115008
- Ramesh, S., Madduri, M., Rudramurthy, S. M., and Roy, U. (2023). Functional characterization of a bacillus-derived novel broad-spectrum antifungal lipopeptide variant against *Candida tropicalis* and *Candida auris* and unravelling its mode of action. *Microbiol. Spectr.* 11 (2), e0158322. doi:10.1128/spectrum.01583-22
- Richardson, M., and Lass-Flörl, C. (2008). Changing epidemiology of systemic fungal infections. *Clin. Microbiol. Infect.* 14 (4), 5–24. doi:10.1111/j.1469-0691.2008.01978.x
- Rodrigues, C. F., Silva, S., and Henriques, M. (2014). *Candida glabrata*: a review of its features and resistance. *Eur. J. Clin. Microbiol. Infect. Dis.* 33 (5), 673–688. doi:10.1007/s10096-013-2009-3
- Salazar, S. B., Wang, C., Münsterkötter, M., Okamoto, M., Takahashi-Nakaguchi, A., Chibana, H., et al. (2018). Comparative genomic and transcriptomic analyses unveil novel features of azole resistance and adaptation to the human host in *Candida glabrata*. *FEMS Yeast Res.* 18 (1), 1–11. doi:10.1093/femsyr/fox079
- Seyedjavadi, S. S., Khani, S., Eslamifard, A., Ajdary, S., Goudarzi, M., Halabian, R., et al. (2019). The antifungal peptide MCh-AMP1 derived from matricaria chamomilla inhibits *Candida albicans* growth via inducing ROS generation and altering fungal cell membrane permeability. *Front. Microbiol.* 10, 3150–3210. doi:10.3389/fmicb.2019.03150
- Yan, Y., Tan, F., Miao, H., Wang, H., and Cao, Y. Y. (2019). Effect of shikonin against *Candida albicans* biofilms. *Front. Microbiol.* 10, 1085–1111. doi:10.3389/fmicb.2019.01085
- Zhang, N., Fan, Y., Li, C., Wang, Q., Leksawasdi, N., Li, F., et al. (2018). Cell permeability and nuclear DNA staining by propidium iodide in basidiomycetous yeasts. *Appl. Microbiol. Biotechnol.* 102 (9), 4183–4191. doi:10.1007/s00253-018-8906-8

Placental expression of Fatty Acid Desaturases 1, 2 and 3 in selected pregnancy pathologies

Rafał Bobiński¹, Urszula Mazurek^{2,3}, Nikola Zmarzyły⁴, Izabela Ulman-Włodarz¹, Mieczysław Dutka¹, Monika Pizon⁵, Wioletta Pollok-Waksmańska⁶, Anna Pieleś⁷, Maciej B. Hajduga¹, Karolina Zimmer¹✉, Jan Bujok¹, Celina Pająk¹ and Tomasz Ilczak⁸

¹Department of Biochemistry and Molecular Biology, Faculty of Health Sciences, University of Bielsko-Biala, Bielsko-Biala, Poland; ²Department of Molecular Biology, Faculty of Pharmaceutical Sciences in Sosnowiec, Medical University of Silesia in Katowice, Sosnowiec, Poland; ³Department of Art Therapy, The Karol Godula Upper Silesian Academy of Entrepreneurship in Chorzów, Chorzów, Poland; ⁴Department of Histology, Cytophysiology and Embryology, Faculty of Medicine, University of Technology, Zabrze, Poland; ⁵Transfusion Center Bayreuth, Bayreuth, Germany; ⁶Department of Public Health, Faculty of Health Sciences, University of Bielsko-Biala, Bielsko-Biala, Poland; ⁷Civil and Environmental Engineering Department, Faculty of Materials, University of Bielsko-Biala, Bielsko-Biala, Poland; ⁸Department of Emergency Medicine, Faculty of Health Sciences, University of Bielsko-Biala, Bielsko-Biala, Poland

Intrauterine development is a key period in human life. The foetal progress largely depends on the function of the placenta, whose responsibility is transportation and biosynthesis of fatty acids. Desaturation enzymes play a key role in placental fatty acid metabolism. Expression of genes coding for desaturases may be associated with pregnancy abnormalities. The objective of this study was to determine the transcriptional activity of the placental genes Fatty Acid Desaturases 1, 2 and 3 (*FADS* 1, 2 and 3) in women who gave birth to the infants appropriate for gestational age, large for gestational age, small for gestational age, with intrauterine growth restriction and born preterm. 34 pregnant women aged 21–37 years old participated in the study. The placental samples were taken from a site located 2–3 cm away from the umbilical cord attachment. The collected tissue sections were stored in RNAlater according to the manufacturer's protocol, until required for molecular analysis. The expression profiles of *FADS1*, *FADS2* and *FADS3* were determined with RT-qPCR. There was no difference in *FADS1* and *FADS2* expression between the groups. However, the differences in the expression of the *FADS3* were found. Analysis of the *FADS1*, *FADS2* and *FADS3* transcription showed significant differences between most of the examined groups. Our findings suggest that the transcriptional activity of *FADS* genes changes with the severity of intrauterine disorders and is associated with foetal lipid disorders linked to a greater accumulation of fat in the foetal tissues.

Keywords: placenta, foetal development, desaturases, fatty acids, gene expression

Received: 28 April, 2022; revised: 22 May, 2022; accepted: 10 October, 2022; available on-line: 18 January, 2023

✉e-mail: kzimmer@ath.bielsko.pl

Abbreviations: AA, arachidonate; AC, abdomen circumference; AGA, appropriate for gestational age; ALA, alpha-linolenic acid; BPD, bi-parietal diameter; D13D, Delta (13) Desaturase; D5D, Delta-5 Desaturase; DGLA, dihomo-gamma-linoleate; EFAs, essential fatty acids; EPA, eicosapentaenoate; ETA, eicosatetraenoate; FA, Fatty acids; *FADS1*, Fatty Acid Desaturase 1; *FADS2*, Fatty Acid Desaturase 2; *FADS3*, Fatty Acid Desaturase 3; FL, femur length; GLA, gamma-linoleate; HC, head circumference; IUGR, intrauterine growth restriction; LA, linoleic acid; L-CPUFA, long-chain polyunsaturated fatty acids; LGA, large for gestational age; MCFA, medium-chain fatty acids; PTB, preterm birth; SGA, small for gestational age

INTRODUCTION

Intrauterine foetal development is a critical period in human development. Subsequent health, susceptibility to diseases, intelligence, and many other factors are dependent on this foetal stage (Bobiński & Mikulska, 2015). The placenta plays a key role during pregnancy. It controls metabolic processes on the hormonal pathway between the organisms of the mother and child – including oxygenation and supplying the foetus with building and energy substrates (Bobiński *et al.*, 2013; Bobiński & Mikulska, 2015). Placental abnormalities lead to premature births with varying degrees of foetus malnutrition (e.g., intrauterine growth restriction, IUGR), as well as the birth of small for gestational age (SGA) or large for gestational age (LGA) babies. Fatty acids (FA) are one of the most important ingredients that determine proper intrauterine development. They are responsible for the structure of the child's nervous system, development of cell membranes, structure and function of the retina as well as fulfilling many other metabolic and structural functions (Helland *et al.*, 2003; Gale *et al.*, 2008). The diversity of FA functions results from the high heterogeneity of their structure, determined by the number of carbon atoms and the number and location of unsaturated bonds in the carbon chain. The source of FAs for the developing foetus is the mother's diet (Herrera, 2002; Cetin *et al.*, 2009a), the release of FA from deposits in maternal tissue (Prentice & Golberg, 2000), the endogenous biosynthesis of FA by the mother and later – foetal FA synthesis (Clandinin *et al.*, 1981). The placenta is primarily responsible for the maternal-foetal metabolism of FA; this includes transportation of the FA from mother to foetus, as well as placental FA biosynthesis and modification. Placental transfer is determined by numerous factors, such as the mother's health, condition of the foetus, transport efficiency of the placenta and diet during pregnancy (Cetin *et al.*, 2002; Haggarty 2002; Cetin *et al.*, 2009a). Some placental disorders can impair FA metabolism, and this may lead to intrauterine foetal developmental disorders and a predisposition to numerous diseases after birth. Changes in the activity of the enzymes responsible for the desaturation of essential fatty acids (EFAs) seem to be particularly important in the maternal-foetal homeostasis. The first of these is delta-5 desaturase (D5D) [EC 1.14.19.44], encoded by the fatty acid desaturase 1 (*FADS1*) gene.

This gene is clustered with its family members at 11q12-q13.1 (Lattka *et al.*, 2010). This desaturase plays one of the key roles in the biosynthesis of long-chain polyunsaturated fatty acids (L-CPUFA) of both the n-3 and n-6 families. D5D introduces a cis double bond at carbon 5 into dihomogamma-linoleate (DGLA) (20: 3n-6) and eicosatetraenoate (ETA) (20: 4n-3) to generate arachidonate (AA) (20: 4n-6) and eicosapentaenoate (EPA) (20: 5n-3), respectively. The second important enzyme in the biosynthesis pathway of L-CPUFA is delta-6-desaturase [EC 1.14.19.3]. It introduces a double cis bond at carbon 6 in linoleic acid (LA) (18: 2n-6) and alpha-linolenic acid (ALA) (18: 3n-3). As a result of this reaction, gamma-linoleate (GLA) (18: 3n-6) and stearidonate (18: 4n-3) are formed, respectively (GeneCards The Human Gene Database, Weizmann Institute of Science, Israel, 2020a). The third representative of desaturases is the delta (13) desaturase (D13D) enzyme (EC 1.14.19.-) encoded by the FADS3 gene. D13D introduces a cis double bond in (11E)-octadecenoate (trans-vaccenoate) at carbon 13 to generate (11E, 13Z)-octadecadienoate, likely participating in the biohydrogenation pathway of LA (GeneCards The Human Gene Database, Weizmann Institute of Science, Israel, 2020b). Under normal conditions, the activity of these enzymes remains in a delicate dynamic balance, maintaining the biosynthesis of L-CPUFA n-3 and n-6 at the appropriate level. Disturbance of enzymatic activity, which may be caused by altered transcriptional activity of FADS genes, may contribute to the loss of control over the biosynthesis of the membrane phospholipids and DHA – the key lipids for the development of the foetal nervous system (Otto *et al.*, 1997), as well as the loss of control over the metabolism of inflammatory lipids, such as prostaglandin E2, which is critical for acute inflammatory response, maintenance of epithelial homeostasis (Challis *et al.*, 2002) and metabolic disorders, such as diabetes, lipid disorders, cardiovascular diseases, etc. (Cetin *et al.*, 2002). The processes controlled by these desaturases are extremely important for the intrauterine development of the foetus, especially for the structure of its nervous system. Therefore, the aim of the study was to analyse the expression (at transcription level) of the FADS1, fatty acid desaturase 2 (FADS2), and fatty acid desaturase 3 (FADS3) genes.

MATERIALS AND METHODS

Study population

The research was conducted with the approval of the Ethics Committee in Bielsko-Biala under approval no:

2016/02/11/4. All relevant guidelines and regulations were adhered to, and informed consent was obtained in writing from all the participants. The study population consisted of 34 women who gave birth at the Provincial Specialist Hospital No. 1 in Tychy, Poland. The pregnant women were recruited for the study during their first visit to the hospital. The women were between 21 and 37 years of age. A description of the study population is provided in Table 1.

To obtain a homogeneous group of women, the following inclusion criteria were applied (Bobiński *et al.*, 2013; Waksmańska *et al.*, 2017):

- Polish nationality (excluding naturalised Polish citizens); single pregnancy; pregnancy I-III (parity considered);
- Stable socioeconomic status; married, secondary level or higher education; living in a highly industrialised urban region, both the women and their husbands having a steady job;
- Consenting to participate in the study.

The following exclusion criteria were applied (Bobiński *et al.*, 2013; Waksmańska *et al.*, 2017):

- Chronic diseases occurring before pregnancy, such as pre-gestational diabetes; pathologies during the course of pregnancy such as infections during pregnancy (any kind of infection in the perinatal period, such as fever, respiratory infections, urinary infections, etc.); miscarriages and/or premature birth resulting in the death of the child or developmental anomalies in the foetus;
- AIDS and sexually transmitted diseases;
- Adherence to a vegetarian diet, Mediterranean diet, or any other special diet;
- Lack of consent by the mother to take part in the research programme or withdrawal of consent during the study.

Women who participated in the research programme were classified into five groups according to the following criteria:

- AGA Group (AGA – appropriate for gestational age, n=9): healthy mothers, routine and uneventful pregnancy, full-term delivery neonates (bw 10–90th percentile). Age (y) 27.5±4.3; BMI (kg/m²) 22.6±4.2; delivery (week) 39.6±1.1; neonatal weight (g) 3542.1±387.7; placental weight (g) 503.4±108; mode of delivery 8n/1cs; Apgar score 9–10. AGA served as the control group.
- LGA Group (LGA – large for gestational age, n=10): healthy mothers who gave birth to large for gestational age neonates (bw>90th percentile). Age (y) 29.2±5.2; BMI (kg/m²) 35.6±4.5; delivery (week) 41.8±1.3; neonatal weight (g) 4056.8±411.2; placental weight (g) 693.3±124.9; mode of delivery 1n/8cs; Apgar score 8–9.

Table 1. Characteristics of the study population.

	AGA	LGA	SGA	IUGR	PTB
Age (Y)	27.5±4.3	29.2±5.2	29.1±5.1	25.6±5.7	27.8±4.1
BMI (kg/m ²)	22.6±4.2	35.6±4.5	23.8±4.7	37.3±7.2	23.3±4.4
Delivery (week)	39.6±1.1	41.8±1.3	38.2±1.1	34.5±1.9	36.8±1.0
Neonatal weight (g)	3542.1±387.7	4056.8±411.2	2297.5±149.9	1975.6±258.9	2398±432.8
Placental weight (g)	503.4±108	693.3±124.9	356.4±108	423.4±88.8	323.8±102
Mode of delivery	8n/1cs	1n/8cs	6n	6cs	3n
Apgar Score	9/10	8/9	9/10	6/7/8	9/10

n=natural delivery, cs=caesarean section. Apgar Score measured after 1, 3 and 5 minutes.

– SGA Group (SGA – small for gestational age, $n=6$): healthy mothers who gave birth to full-term, but small for gestational age, neonates (neonatal weight <10th percentile). Age (y) 29.1 ± 5.1 ; BMI (kg/m^2) 23.8 ± 4.7 ; delivery (week) 38.2 ± 1.1 ; neonatal weight (g) 2297.5 ± 149.9 ; placental weight (g) 356.4 ± 108 ; mode of delivery 6n; Apgar score 9–10.

– IUGR Group (IUGR – intrauterine growth restriction, $n=6$): mothers who gave birth to babies showing characteristics of intrauterine growth restriction. In this group, all ultrasound studies showed foetal growth restriction (bw <10th percentile). Age (y) 25.6 ± 5.7 ; BMI (kg/m^2) 37.3 ± 7.2 ; delivery (week) 34.5 ± 1.9 ; neonatal weight (g) 1975.6 ± 258.9 ; placental weight (g) 423.4 ± 88.8 ; mode of delivery 6cs; Apgar score 6–8.

– PTB Group (PTB – preterm birth age, $n=3$): mothers who gave birth prematurely at 32–36 weeks' gestation to neonates whose weight fell in the 10–90th percentile. Age (y) 27.8 ± 4.1 ; BMI (kg/m^2) 23.3 ± 4.4 ; delivery (week) 36.8 ± 1.0 ; neonatal weight (g) 2398 ± 432.8 ; placental weight (g) 323.8 ± 102 ; mode of delivery 3n; Apgar score 9–10.

Women eligible for the study underwent three ultrasound examinations. The first ultrasound test was performed between the 12th and 14th weeks of gestation, the second between the 20th and 22nd weeks of gestation and the third one between the 32nd and 33rd weeks of gestation.

Using ultrasound scans, the foetal weight and length were determined primarily according to the gestational age. The dimensions obtained at the 27th gestational week were crucial and determined the appropriate way to proceed with the delivery. Although usually the results of Doppler flow are not considered significant for foetuses younger than 30-weeks, this test was performed too on the foetuses at the 27th week. The foetal dimensions were taken every 6–7 days and marked on a growth chart. If the foetus was between the 10th and 3rd percentile and its gestational age was above 27 weeks further ultrasound scans were conducted to assess hypotrophy or intrauterine foetal growth inhibition (IUGR) according to the radiological criteria. The ultrasound was used to measure the standard parameters of so-called basic foetal biometry, including the bi-parietal diameter (BPD), head circumference (HC), abdomen circumference (AC), and femur length (FL). The ultrasound estimation of foetal weight and length were converted into a growth chart.

Collection of the placentas

The placental samples were collected from a site approximately 2–3 cm away from the umbilical cord attachment. For the research, we wanted to standardise the site of collection to the place where blood supply to the placenta was the highest, ensuring the highest metabolic activity and a strong RNA expression. In our opinion, taking samples from a different site would not give a full picture of the expression of the genes tested. The samples were collected immediately after birth and transported on ice to the laboratory. The transport time did not exceed one hour. The samples were then weighed, immersed in 1 ml RNAlater for 48 hours at 4°C and then snap frozen.

RT-qPCR

Collected tissue sections were stored in RNAlater according to the manufacturer's protocol (Sigma-Aldrich, St Louis, MO, USA) until required for molecular analy-

sis. Total RNA was extracted using TRIzol reagent (Invitrogen Life Technologies, Carlsbad, CA, USA) according to the manufacturer's instructions. The concentration and purity of the obtained extracts were assessed using a MaestroNano MN-913 nano-spectrophotometer (MaestroGen, Inc., USA). The expression profiles of *FADS1*, *FADS2* and *FADS3* were determined in the presence of β -actin as an endogenous control by RT-qPCR using SensiFAST SYBR No-ROX One-Step kit (Meridian Life Science Inc., Memphis, TN, USA) and Opticon DNA Engine Sequence Detector (MJ Research Inc., Watertown, MA, USA) according to the manufacturer's instructions. The reaction was carried out using primer pairs specific for the sequence of each gene tested: *FADS1* (forward: 5' ATGATTACCTTCTACGTCCG 3', reverse: 5' TCAATGTGCATGGGAATATG 3', amplicon length – 149 bp), *FADS2* (forward: 5' GATGAATCATCGTCATGG 3', reverse: 5' GTGCTCAATCTGGAAGTTAAG 3', amplicon length – 139 bp), *FADS3* (forward: 5' CAACATCTTCCACAAAGACC 3', reverse: 5' CTGGTTGTAGGGTAGGTATC 3', amplicon length – 109 bp), *ACTB* (forward: 5' TCACCCACACTGTGCCCATCTACGA 3', reverse: 5' CAGCGGAACCGCTCATTGCCAATGG 3', amplicon length – 295bp) purchased in Sigma-Aldrich (St Louis, MO, USA). The thermal profile of the RT-qPCR reaction included the following steps: reverse transcription (45°C for 10 minutes), activation of the polymerase (95°C for 2 minutes), 41 cycles consisting of denaturation (95°C for 5 seconds), annealing (60°C for 10 seconds), and elongation (72°C for 5 seconds). A standard curve was plotted for every run, based on which the Opticon DNA Engine Sequence Detector (MJ Research Inc., Watertown, MA, USA) calculated the mRNA copy numbers of studied genes in each sample. The curves were drawn based on the quantitative standard – β -actin (TaqMan DNA Template Reagent kit, Applied Biosystems, Foster City, CA, USA) at five different concentrations (400, 800, 2000, 4000, 8000 copies of *ACTB* cDNA). Each run included positive and negative controls and was completed by melting curve analysis of each sample to confirm the specificity of the reaction. The endogenous control assessment together with the melting curve analysis were the basis for including the results of the studied genes in the comparative analysis. The results are presented as the number of mRNA copies per 1 μg of total RNA.

The calculations were made in the statistical environment R ver.3.6.0, PSPP program and MS Office 2019. Parametric tests (analysis of variance ANOVA) or their non-parametric equivalents (Kruskal-Wallis test) were used to analyse the quantitative variables broken down into groups. The *T*-test and Wilcoxon pairs test were also used. The selection of tests was based on the distribution of variables, which was verified by the Shapiro-Wilk test.

There were no significant differences in β -actin mRNA copy number between the control and study groups, which indicates that β -actin can be used as an endogenous control in this experiment.

RESULTS

FADS1 and *FADS2*

After checking the assumptions of normality, a non-parametric Kruskal-Wallis test was performed to compare the median in individual groups. In terms of the *FADS1* and *FADS2* genes, the groups did not differ

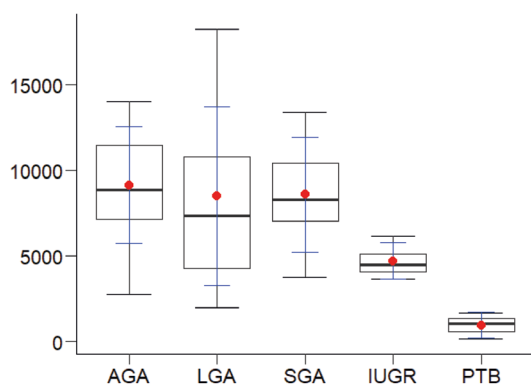


Figure 1. Box plot for *FADS3* expression.
The y-axis represents the number of mRNA copies/1 µg RNA.

significantly ($p > 0.05$). The AGA, LGA, SGA, IUGR and PTB groups were therefore similar in terms of the distribution of *FADS1* and *FADS2*.

FADS3

After checking the assumptions of normality of the distribution, it turned out to be possible to use the parametric analysis of variance ANOVA, to compare the average of the dependent variable in the individual groups. In the *FADS3* range, the groups significantly differed statistically ($p < 0.05$). Tukey's post hoc test was performed to determine the groups whose means differed significantly.

Significant statistical differences ($p < 0.05$) were observed between the following groups: AGA and IUGR, AGA and PTB, LGA and PTB, SGA and PTB, and IUGR and PTB (shown in Fig. 1). In the AGA group, the average values of *FADS3* M were: 9149.67 in the AGA group; 4713.50 for IUGR; 967.33 for PTB, 8487.60 for LGA; and 8580.83 for SGA.

In the next part of the analysis, the transcription levels of the *FADS1*, *FADS2* and *FADS3* genes were analysed within each of the research groups (AGA, LGA, SGA, IUGR, PTB) using Friedman's test and Bonferroni's post hoc test.

AGA Group

Friedman's test showed statistically significant differences ($p < 0.05$) between *FADS1*, *FADS2* and *FADS3* expression levels within the AGA group. The mean mRNA levels were M=2640.8 mRNA copies/1 µg RNA for *FADS1*, M=494.9 mRNA copies/1 µg RNA for *FADS2*, and M=9149.7 mRNA copies/1 µg RNA for *FADS3* (shown in Fig. 2).

Bonferroni's post hoc test was conducted to determine which of the comparisons between groups were statistically significant ($p < 0.05$). Such differences were detected between *FADS1* and *FADS3* and between *FADS2* and *FADS3* groups.

LGA Group

Friedman's test showed statistically significant differences ($p < 0.05$) between *FADS1*, *FADS2* and *FADS3* expression levels within the LGA group.

The mean mRNA level for *FADS1* was M=2663.2 copies/1 µg, for *FADS2* 8090.9 copies/1 µg RNA, and for *FADS3* M=8487.6 copies/1 µg RNA (shown in Fig. 3).

The Bonferroni test identified that statistically significant ($p < 0.05$) comparisons were between *FADS1* and *FADS2*, and between *FADS1* and *FADS3* groups.

SGA Group

Friedman's test showed statistically significant differences ($p < 0.05$) between *FADS1*, *FADS2* and *FADS3* expression levels within the SGA group. Tukey's post hoc test was performed to determine which of the comparisons between groups were statistically significant ($p < 0.05$). Such differences were detected between *FADS1* and *FADS3*.

The mean mRNA level for *FADS1* was M=2587.2 copies/1 µg, and M=8580.8 copies/1 µg RNA for *FADS3* (shown in Fig. 4).

IUGR Group

Friedman's test showed statistically significant differences ($p < 0.05$) between *FADS1*, *FADS2* and *FADS3* expression levels within the IUGR group.

The mean mRNA levels were M=671.8 copies/1 µg for *FADS1*, 2123 copies/1 µg RNA for *FADS2*, and

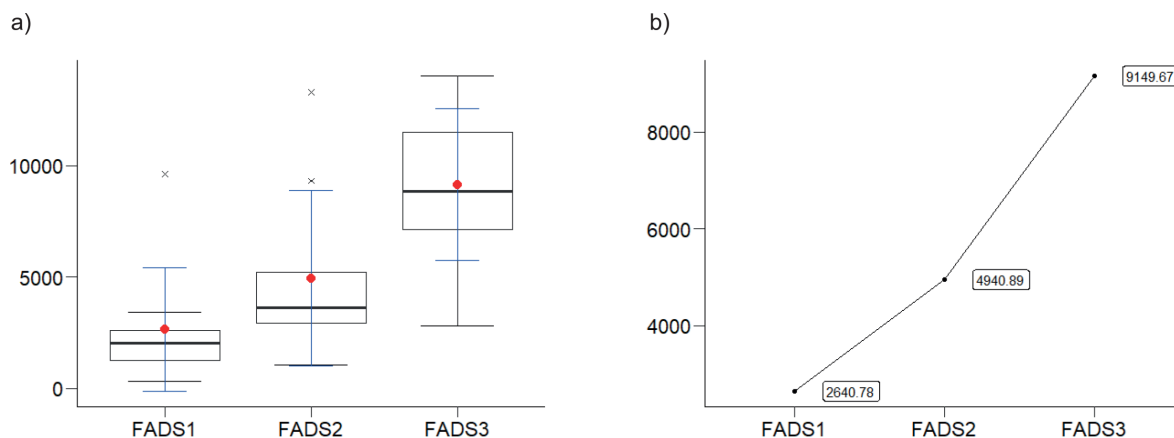


Figure 2. Expression of *FADS1*, *FADS2* and *FADS3* in the AGA group presented as:

(a) a box plot where the y-axis represents the number of mRNA copies/1 µg RNA and (b) a line graph of the average expression values, where the y-axis represents the number of mRNA copies/1 µg RNA

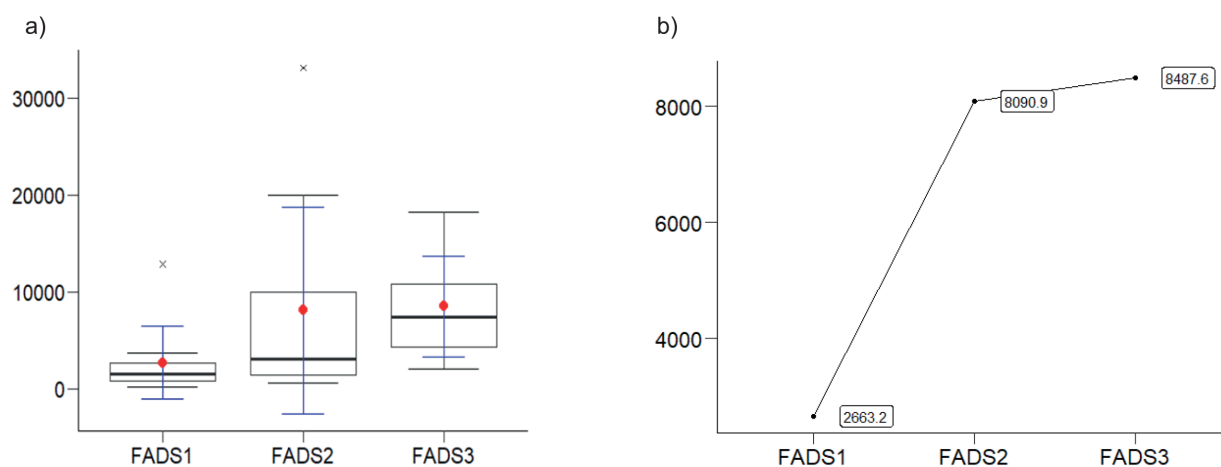


Figure 3. Expression of FADS1, FADS2 and FADS3 in the LGA group presented as:

(a) a box plot where the y-axis represents the number of mRNA copies/1 µg RNA and (b) a line graph of the average expression values, where the y-axis represents the number of mRNA copies/1 µg RNA

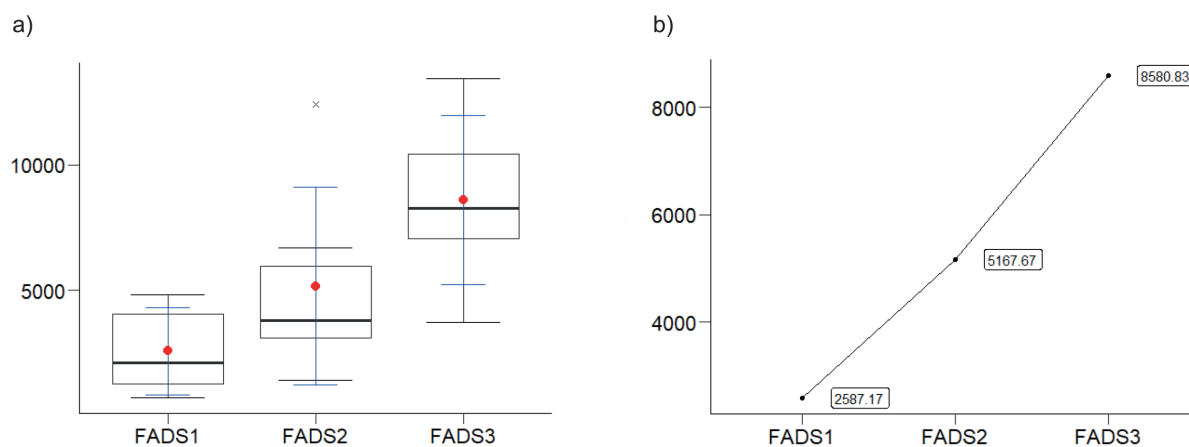


Figure 4. Expression of FADS1, FADS2 and FADS3 in the SGA group presented as:

(a) a box plot where the y-axis represents the number of mRNA copies/1 µg RNA and (b) a line graph of the average expression values, where the y-axis represents the number of mRNA copies/1 µg RNA

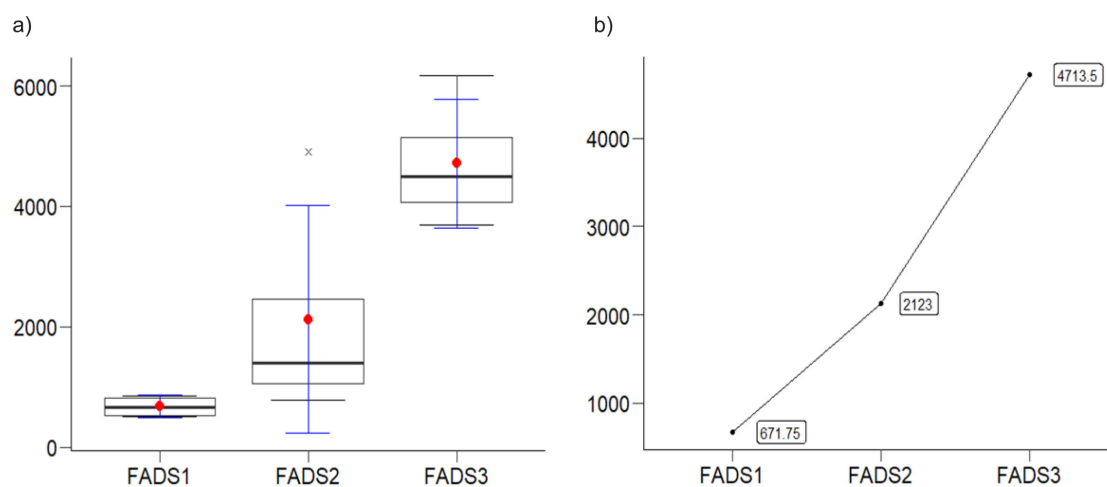


Figure 5. Expression of FADS1, FADS2 and FADS3 in the IUGR group presented as:

(a) a box plot where the y-axis represents the number of mRNA copies/1 µg RNA and (b) a line graph of the average expression values, where the y-axis represents the number of mRNA copies/1 µg RNA

for $M=4713.5$ copies/1 μg RNA for *FADS3* (shown in Fig. 5).

The Tukey's post hoc test identified that statistically significant ($p<0.05$) comparisons were between *FADS1* and *FADS3*, and between *FADS2* and *FADS3*.

PTB Group

The Friedman's test showed no statistically significant differences ($p<0.05$) between *FADS1*, *FADS2* and *FADS3* expression in the PTB group. Tukey's post hoc test confirmed there were no differences.

DISCUSSION

Fat is one of the key ingredients necessary for proper foetal development. During pregnancy, a mother's body deposits fat in an amount which corresponds approximately to the baby's weight (3500 g) (Hyttén & Chamberlain, 1974). These processes occur most vigorously in the first and second trimester and will happen even if the mother is malnourished (Prentice & Golberg, 2000; Herrera, 2002; Herrera *et al.*, 2006). In the second trimester (the anabolic period), the concentration of phospholipids, non-esterified FAs and triglycerides increases in the mother's circulation. This mechanism is associated with an insulin-dependent decrease in lipoprotein lipase activity in adipose tissue and subsequent insulin resistance. As a result of these processes, part of the accumulated fat is transferred to the foetus via the placenta. In contrast, the third trimester is a catabolic period for the mother. Increased lipolysis in the mother's adipose tissue is associated with decreased sensitivity of insulin receptors, which are hormonally controlled by progesterone, cortisol, prolactin and leptin (Cousins, 1991; Herrera *et al.*, 2006; Catov *et al.*, 2007). As a result, in comparison to the anabolic period, even greater amounts of fat, including FAs, reach the placenta. The dynamics of changes in fat content in the foetus is different from that found in the mother. First, there is no catabolic period in the foetus, and second, the anabolic period begins much later than the mother's – between 20 and 22 weeks of pregnancy. Complicated maternal-placental-foetal fat metabolism, especially of FAs and their derivatives, continues to be controlled by numerous factors, including enzymes whose expression is regulated, *inter alia*, at the level of transcription. This paper presents the analysis of expression of three genes encoding the strategic desaturases, which control the formation of n-3 and n-6 FA. In the AGA, LGA, SGA, PTB and IUGR groups that were studied, no significant differences in mRNA levels of the *FADS1* and *FADS2* were observed. This could imply that LC-PUFA biosynthesis and the function of pro- and anti-inflammatory cytokines are unaffected in neither group. However, since we have not studied the polymorphism of the *FADS1* and *FADS2* genes as a factor that could influence foetal development, this conclusion is not irrefutable. Our studies have shown differences in the placental mRNA expression level of the *FADS3*. Women who gave birth to healthy children in due time (AGA) and women who gave birth to children with only minor problems (SGA and LGA), had higher *FADS3* mRNA expression levels in the placenta than women in the PTB and IUGR (higher level of problems) groups. This result is difficult to interpret because *FADS3* and the desaturase encoded by it have not yet been sufficiently researched. It is known that *FADS3* transcriptional activity in tissues is significantly different between male and female mice and rats. *FADS3* encod-

ed desaturase can introduce a double bond into the FA chain like any other desaturase but other potential functions of the enzyme should be considered as well. Desaturases are known to perform hydroxylation (Mizutani *et al.*, 2004; Blanchard *et al.*, 2011), acetylation and epoxidation (Lee *et al.*, 1998). Substances such as etherlipid (Paltauf & Holasek, 1973), sphingolipid (Mizutani *et al.*, 2004) and cholesterol (Nusblat *et al.*, 2005) can also be substrates for desaturases. Therefore, *FADS3* potential physiological role can be broad, especially considering that D13D exists in at least three isoforms (Blanchard *et al.*, 2011). One concept that could explain the lower transcription activity of *FADS3* in the PTB and IUGR groups is the specific structure of the gene promoter. It contains target sites for NF- κ B (Szczena-Skorupa *et al.*, 2004; Yan *et al.*, 2007), MYCN (Alaminos *et al.*, 2003) and p63 protein (Blanchard *et al.*, 2011), suggesting that *FADS3* expression can be regulated by these factors. It is known that NF- κ B, MYCN and p63 are the components of intracellular pathways associated with proliferation and apoptosis. Several studies have demonstrated the relatedness of IUGR and these pathways. For example, in IUGR, the NF- κ B-regulated proangiogenic targets in foetal pulmonary artery endothelial cells are disrupted, which leads to the abnormal metabolism of extracellular matrix components and, as a result, interferes with pulmonary angiogenesis (Dodson *et al.*, 2018). In pregnancies complicated with IUGR, the processes of apoptosis in placenta are stronger than in a healthy placenta (Erel *et al.*, 2001) and a significantly higher NF- κ B expression can be observed (Aban *et al.*, 2004). It is not known why the increase in NF- κ B expression does not cause an increase in the expression of *FADS3* in the IUGR placenta; in fact, exactly the opposite is observed. Higher NF- κ B expression is accompanied by lower *FADS3* transcriptional activity. It is possible that NF- κ B inhibitors increase during IUGR, or the chromatin is remodelled in such a way that the *FADS3* promoter becomes inaccessible for NF- κ B. Changes in *FADS3* activity in the course of IUGR may also be related to the functioning of the membrane transport system, which is responsible for maintaining the correct FA ratio in the maternal (M) and foetal (F) circulation. Changes in the F/M ratio were observed in IUGR, SGA and PTB children (Cetin *et al.*, 2002; Bobiński *et al.*, 2013).

This work also analyses *FADS* genes expression within the AGA, LGA, SGA, PTB, and IUGR groups. Except for the PTB group, which had the lowest number of samples, and in which no differences in *FADS* gene expression were observed, there were differences in expression between *FADS1*, *FADS2* and *FADS3* in the remaining groups. In the LGA group there were no differences between *FADS2* and *FADS3* transcript levels. Comparing the average *FADS* mRNA expression between the AGAs and LGAs, it can be assumed that the lack of differences in the LGA group was due to an increased *FADS2* and slightly reduced *FADS3* transcript levels. LGAs are a group of children who, in addition to the increased body weight (>90 percentile), have also increased body fat. Both are involved in fat metabolism, so with the increased fat mass of the child, changes in D6D and D13D activity are highly likely, although the case of the *FADS3* gene product is surprising. It has been previously shown that the increased expression of *FADS3* in adipose tissue is characteristic of hyperlipidemia (Plaisier *et al.*, 2009). Our research shows that this is the opposite for the placenta. Perhaps, the reduced placental expression of *FADS3* in LGA pregnancies is a type of compensatory mechanism that regulates foetal fat

metabolism. From a clinical point of view, however, it would be more interesting to see a significant increase in the transcriptional activity of the *FADS2* gene encoding desaturase 6, catalysing the reactions of the n-3 and n-6 main biosynthesis pathway. One of the factors (although not studied in this research) that could affect *FADS2* expression is the pregnant woman's diet. With an ample supply of plant oils, which contain high proportion of LA, such as sunflower seed oil, safflower oil or corn oil, less DHA is produced from ALA as a result of n-6 desaturase inhibition leading to a decreased EPA biosynthesis. The n-6 FA pool then increases, which could be a risk factor for the development of LGA (Llanos *et al.*, 2005; Bobiński & Mikulska, 2015). Furthermore, it may have an influence on the metabolism of medium-chain fatty acids (MCFA), especially myristic acid (C14: 0) and lauric acid (C12: 0), which have a significant impact on the conversion of EPA to DHA (Legrand *et al.*, 2020). This, in turn, in addition to placental biosynthesis of LC-PUFA, can disturb the specified hierarchy DHA>AA>LA>ALA defining the order of transport of the acids across the placental barrier (Cetin *et al.*, 2009a; Cetin and Alvino, 2009b).

CONCLUSION

The placenta fulfils hormonal, nutritional and metabolic roles. Its task is to control the development of the foetus, but the hormonal-metabolic placental processes affect, to a large extent, also the body of a pregnant woman. Fatty acids play a key role in these mechanisms. Some of them are transported through the placental barrier, others undergo biosynthesis in the placenta. Often, placental biosynthesis involves the elongation and desaturation processes of the pre-existing FAs with shorter carbon chains, which either lack or have fewer double bonds. Desaturases are involved in these processes. This important group of enzymes maintain the balance of n-3 and n-6 FAs levels, has a significant role in the development of the nervous system and cell membranes, and affect general maternal-placental-foetal homeostasis. Our studies have shown that the transcriptional activity of the *FADS1* and *FADS2* genes remain at similar levels in the pregnancy groups we examined. It was only in the *FADS3* gene expression that the differences were discovered. *FADS3* lowest mRNA levels were observed in the placenta of women who gave birth to premature babies. In this group, also no differences were observed in the *FADS1*, *FADS2* and *FADS3* mRNA levels. In the SGA group, expression differences were observed between the *FADS3* and *FADS1* genes only. The AGA, LGA and IUGR groups had a similar expression profile, in which the *FADS3* gene had the highest and the *FADS1* gene had the lowest expression except for the difference between *FADS2* and *FADS3* expression, which was observed in AGA and IUGR, but not LGA. The IUGR group had the lowest expression of all tested genes, while maintaining differences between their expression. The largest number of differences in *FADS* mRNA levels were observed in the placenta of women who gave birth to children with a mild degree of disorder, i.e., PTB and SGA.

Considering the number of FAs undergoing maternal-placental-foetal transformation and the complexity of their metabolism, it is difficult to unequivocally interpret changes in the transcriptional activity of genes encoding desaturases in selected pregnancy pathologies. Many factors regulate these processes and one of the most im-

portant is - not studied in this work - the expression of genetic variants of the *FADS1*, *FADS2* and *FADS3*. Their analysis would provide further data for the assessment of maternal-placental-foetal FA changes, crucial for the proper development of the foetus, the emergence of metabolic or genetic risk factors and an improvement in the profile of prevention and treatment of foetal developmental abnormalities.

Declarations

Acknowledgements. Not applicable.

REFERENCES

- Aban M, Cinel L, Arslan M, Dilek U, Kaplanoglu M, Arpaci R, Dilek S (2004) Expression of nuclear factor-kappa B and placental apoptosis in pregnancies complicated with intrauterine growth restriction and preeclampsia: an immunohistochemical study. *Toboku J. Exp. Med.* **204**: 195–202. <https://doi.org/10.1620/tjem.204.195>
- Alaminos M, Mora J, Cheung NV, Smith A, Qin J, Chen L, Gerald WL (2003) Genome-wide analysis of gene expression associated with MYCN in human neuroblastoma. *Cancer Res.* **63**: 4538–4546
- Blanchard H, Legrand P, Pédrono F (2011) Fatty Acid Desaturase 3 (*Fads3*) is a singular member of the *Fads* cluster. *Biochimie* **93**: 87–90. <https://doi.org/10.1016/j.biochi.2010.03.002>
- Bobinski R, Mikulska M, Mojska M, Simon M (2013) Comparison of the fatty acid composition of maternal blood and cord blood of mothers who delivered healthy full-term babies, preterm babies, and full-term small for gestational age infants. *J. Matern. -Fetal Neonatal Med.* **26**: 96–102. <https://doi.org/10.3109/14767058.2012.722717>
- Bobinski R, Mikulska M (2015) The ins and outs of maternal-fetal fatty acid metabolism. *Acta Biochim. Pol.* **62**: 499–507. <https://doi.org/10.18388/abp.2015.1067>
- Catov JM, Patrick TE, Powers RW, Ness RB, Harger G, Roberts JM (2007) Maternal leptin across pregnancy in women with small-for-gestational-age infants. *Am. J. Obstet. Gynecol.* **196**: 558.e1–558.e8. <https://doi.org/10.1016/j.ajog.2007.01.032>
- Cetin I, Giovannini N, Alvino G, Agostoni C, Riva E, Giovannini M, Pardi G (2002) Intrauterine growth restriction is associated with changes in polyunsaturated fatty acid fetal-maternal relationships. *Pediatr. Res.* **52**: 750–755. <https://doi.org/10.1203/00006450-200211000-00023>
- Cetin I, Alvino G, Cardellicchio M (2009) Long chain fatty acids and dietary fats in fetal nutrition. *J. Physiol.* **587**: 3441–3451. <https://doi.org/10.1111/jphysiol.2009.173062>
- Cetin I, Alvino G (2009) Intrauterine growth restriction: implications for placental metabolism and transport. *Placenta* **30**: 77–82. <https://doi.org/10.1016/j.placenta.2008.12.006>
- Challis JR, Sloboda DM, Alfaidy N, Lye SJ, Gibb W, Patel FA, White WL, Newnham J (2002) Prostaglandins and mechanisms of preterm birth. *Reproduction* **124**: 1–17. <https://doi.org/10.1530/rep.0.1240001>
- Clandinin MT, Chappell JE, Heim T, Swyer PR, Chance GW (1981) Fatty acid utilization in perinatal de novo synthesis of tissues. *Early Hum. Dev.* **5**: 355–366. [https://doi.org/10.1016/0378-3782\(81\)90016-5](https://doi.org/10.1016/0378-3782(81)90016-5)
- Cousins L (1991) Insulin sensitivity in pregnancy. *Diabetes* **40**: 39–43. <https://doi.org/10.2337/diab.40.2.S39>
- Dodson RB, Powers KN, Gien J, Rozance PJ, Seedorf G, Astling D, Jones K, Crombreholme TM, Abham SH, Alvira CM (2018) Intrauterine growth restriction decreases NF-κB signaling in fetal pulmonary artery endothelial cells of fetal sheep. *Am. J. Physiol. Lung Cell. Mol. Physiol.* **315**: 348–359. <https://doi.org/10.1152/ajplung.00052.2018>
- Erel CT, Dane B, Calay Z, Kaleli S, Aydinli K (2001) Apoptosis in the placenta of pregnancies complicated with IUGR. *Int. J. Gynaecol. Obstet.* **73**: 229–235. [https://doi.org/10.1016/S0020-7292\(01\)00373-3](https://doi.org/10.1016/S0020-7292(01)00373-3)
- Gale CR, Robinson SM, Godfrey KM, Law CM, Schlottz W, O'Callaghan FJ (2008) Oily fish intake during pregnancy-association with lower hyperactivity but not with higher full-scale IQ in offspring. *J. Child Psychol. Psychiat.* **49**: 1061–1068. <https://doi.org/10.1111/j.1469-7610.2008.01908.x>
- GeneCards The Human Gene Database, Weizmann Institute of Science, Israel, 2020a. <https://www.genecards.org/cgi-bin/carddisp.pl?gene=FADS2>. Accessed 20 April 2020
- GeneCards The Human Gene Database, Weizmann Institute of Science, Israel, 2020b. <https://www.genecards.org/cgi-bin/carddisp.pl?gene=FADS3>. Accessed 20 April 2020
- Haggarty P (2002) Placental regulation of fatty acids delivery and its effect on fetal growth — a review. *Placenta* **16**: 28–38. <https://doi.org/10.1053/plac.2002.0791>

- Helland IB, Smith L, Saarem K, Saugstad OD, Drevon CA (2003) Maternal supplementation with very-long-chain n-3 fatty acids during pregnancy and lactation augments children's IQ at 4 years of age. *Pediatrics* **111**: 39–44. <https://doi.org/10.1542/peds.111.1.e39>
- Herrera E (2002) Implications of dietary fatty acids during pregnancy on placental, foetal and postnatal development — a review. *Placenta* **16**: 9–19. <https://doi.org/10.1053/plac.2002.0771>
- Herrera E, Amusquivar E, Lopez-Soldado I, Ortega H (2006) Maternal lipid metabolism and placental lipid transfer. *Horm. Res.* **65**: 59–64. <https://doi.org/10.1159/000091507>
- Hytten, F.E., Chamberlain, J.G. (ed), 1974. Weight gain in pregnancy. In *Clinical Physiology in Obstetrics*, pp 193–233. Blackwell Scientific Publication, Oxford, UK
- Lattka E, Illig T, Koletzko B, Heinrich J (2010) Genetic variants of the FADS1 FADS2 gene cluster as related to essential fatty acid metabolism. *Curr. Opin. Lipidol.* **21**: 64–69. <https://doi.org/10.1097/MOL.0b013e3283327ca8>
- Lee M, Lenman M, Banaś A, Bafor M, Singh S, Schweizer M, Nilsson R, Liljenberg C, Dahlqvist A, Gummeson PO, Sjö Dahl S, Green A, Szymme S (1998) Identification of non-heme diiron proteins that catalyze triple bond and epoxy group formation. *Science (New York, N.Y.)* **280**: 915–918. <https://doi.org/10.1126/science.280.5365.915>
- Legrand P, Catheline D, Rioux V, Durand G (2020) Lauric acid is desaturated to C12:1 n-3 by rat liver homogenate and hepatocytes. *Lipids* **37**: 569–572. <https://doi.org/10.1007/s11745-002-0934-y>
- Llanos A, Li Y, Mena P, Salem N (2005) Infants with intra uterine growth restriction have impaired formation of docosahexaenoic acid in early neonatal life: a stable isotope study. *Pediatr. Res.* **58**: 735–740. <https://doi.org/10.1203/01.PDR.0000180542.68526.A2>
- Mizutani Y, Kihara A, Igarashi Y (2004) Identification of the human sphingolipid C4-hydroxylase, hDES2, and its up-regulation during keratinocyte differentiation. *FEBS Lett.* **563**: 93–97. [https://doi.org/10.1016/S0014-5793\(04\)00274-1](https://doi.org/10.1016/S0014-5793(04)00274-1)
- Nusblat AD, Munoz L, Valcarce GA, Nudel CB (2005) Characterization and properties of cholesterol desaturases from the ciliate *Tetrahymena thermophila*. *J. Eukaryot. Microbiol.* **52**: 61–67. <https://doi.org/10.1111/j.1550-7408.2005.3279rr.x>
- Otto SJ, Houwelingen AC, Antal M, Manninen A, Godfrey K, López-Jaramillo P, Hornstra G (1997) Maternal and neonatal essential fatty acid status in phospholipids: an international comparative study. *Eur. J. Clin. Nutr.* **51**: 232–242. <https://doi.org/10.1038/sj.ejcn.1600390>
- Paltauf F, Holasek A (1973) Enzymatic synthesis of plasmalogens. Characterization of the 1-O-alkyl-2-acyl-8n-glycero-3-phosphorylethanolamine desaturase from mucosa of hamster small intestine. *J. Biol. Chem.* **248**: 1609–1615. [https://doi.org/10.1016/S0021-9258\(19\)44234-8](https://doi.org/10.1016/S0021-9258(19)44234-8)
- Plaisier CL, Horvath S, Huertas-Vazquez A, Cruz-Bautista I, Herrera MF, Tusie-Luna T, Aquilar-Salinas C, Pajukanta P (2009) A systems genetics approach implicates USF1, FADS3, and other causal candidate genes for familial combined hyperlipidemia. *PLoS Genet.* **5**: e1000642. [https://doi.org/10.1016/S0021-9258\(19\)44234-8](https://doi.org/10.1016/S0021-9258(19)44234-8)
- Prentice AM, Golberg MP (2000) Energy adaptations in human pregnancy: limits and long-term consequences. *Am. J. Clin. Nutr.* **71**: 1226–1232. <https://doi.org/10.1093/ajcn/71.5.1226s>
- Szczesna-Skorupa E, Chen CD, Liu H, Kemper B (2004) Gene expression changes associated with the endoplasmic reticulum stress response induced by microsomal cytochrome p450 overproduction. *J. Biol. Chem.* **279**: 13953–13961. <https://doi.org/10.1074/jbc.M312170200>
- Waksmańska W, Bobiński R, Ulman-Włodarz I, Pieleś A, Mikulska M (2017) The dietary composition of women who delivered pre-term and full-term infants. *Appl. Nurs. Res.* **35**: 13–17. <https://doi.org/10.1016/j.apnr.2017.02.013>
- Yan B, Yang X, Lee TL, Friedman J, Tang J, Waes CV, Chen Z (2007) Genome-wide identification of novel expression signatures reveal distinct patterns and prevalence of binding motifs for p53, nuclear factor-kappa B and other signal transcription factors in head and neck squamous cell carcinoma. *Genome Biol.* **8**: R78. <https://doi.org/10.1186/gb-2007-8-5-r78>

Synergistic effect of Dactolisib/Lys05 combination on autophagy in A549 cells

Mohammad M. Abdelwahab¹, Hesham Saeed¹✉, Nefertiti El-Nikhely¹ and Hisham A. Nematalla²

¹Department of Biotechnology, Institute of Graduate Studies and Research, Alexandria University, Alexandria, Egypt; ²Department of Pharmacology and Toxicology, Faculty of Pharmacy, Damanhour University, Damanhour, Egypt

Effective therapeutic strategies are urgently required to enhance the prognosis of patients suffering from KRAS mutations. Owing to the undruggable nature of KRAS, targeting downstream signaling pathways, namely PI3K/AKT/mTOR, shows antiproliferative and apoptotic effects. Unfortunately, targeting this pathway upregulates autophagy, contributing to reduced drug efficacy. Therefore, it was reasonable to use a combination of kinase inhibitors and autophagy inhibitors to achieve a higher therapeutic benefit. The impact of Dactolisib, a dual PI3K/mTOR inhibitor, and Lys05, a dimeric chloroquine, was tested on the survival of breast cancer MCF-7 and lung cancer A549 cells. The dose selection for the optimal effect of the Dactolisib/Lys05 combination was determined using CompuSyn software. This combinatorial effect was evaluated using various methodologies, such as expression profile analysis for autophagic, proliferative, and apoptotic markers. These effects were corroborated by ELISA, Western blot, and flow cytometry using the Annexin V-FITC apoptosis detection kit. A549 cells treated in a 2:1 ratio of Lys05 and Dactolisib demonstrated a synergistic effect on cell death, proliferation, and apoptotic gene markers, in addition to its effect on autophagic gene and protein markers, showing an enhanced effect compared to monotherapy. Therefore, the PI3K/AKT kinase inhibitor/autophagy inhibitor combination establishes higher therapeutic benefits on A549 cells compared to kinase inhibitor monotherapy.

Keywords: KRAS, autophagy, PI3K/Akt/mTOR, NSCLC, Dactolisib, Lys05

Received: 01 March, 2023; **revised:** 07 May, 2023; **accepted:** 22 May, 2023; **available on-line:** 07 September, 2023

✉e-mail: hesham25166@alexu.edu.eg

Acknowledgements of Financial Support: This paper is based on work supported by the Science, Technology & Innovation Funding Authority (STDF) under grant number 44145.

Abbreviations: ANOVA, Analysis of variance; ATG4B, Autophagy Related 4B Cysteine Peptidase; CASP3, Caspase 3; DMEM, Dulbecco's modified Eagle's medium; DMSO, Dimethyl sulfoxide; ECL, Enhanced chemiluminescence; Fa, Fraction affected; FBS, Fetal bovine serum; HPRT, hypoxanthine phosphoribosyl transferase 1; HRP, Horse Reddish peroxidase; KRAS, Kirsten Rat Sarcoma Viral Oncogene Homolog; Ki67, Proliferation index-67; LC3A, Microtubule Associated Protein 1 Light Chain 3 Alpha; LC3B, Microtubule Associated Protein 1 Light Chain 3 Beta; MTT, 3-(4,5-Dimethylthiazol-2-yl)-2,5-diphenyltetrazolium bromide; NSCLC, Non-Small Cell Lung Cancer; PI, Propidium iodide; SDS, Sodium dodecyl sulfate

INTRODUCTION

Epidemiologically, lung cancer represents the leading cause of cancer-related deaths among both men and

women (Barta *et al.*, 2019; Sun *et al.*, 2021). Our increasing understanding of cancer biology has revealed numerous causes for therapeutic failures (Rizzo, 2008). Research on signaling pathways has uncovered a complex network of cross-regulatory interactions, connecting receptors, enzymes, transducing systems, and transcription factors that regulate cell fate (Sever & Brugge, 2015).

Resistance to apoptosis, continuous proliferation, evasion from cell cycle suppressors, angiogenesis, invasion, and metastasis are the five features that characterize carcinoma (Hanahan & Weinberg, 2011). Autophagy, a further level of adaptation, is known to increase under conditions of cellular stress, particularly in cancer (Haider *et al.*, 2020; White & DiPaola, 2009).

Currently, non-small cell lung cancer (NSCLC) accounts for up to 85% of all lung cancers (El Osta *et al.*, 2019). Kirsten Rat Sarcoma Viral Oncogene Homolog (KRAS) is a gene that codes for a protein involved in cell signaling pathways. It is a well-known oncogene, meaning that mutations in the KRAS gene can contribute to the development of cancer. These mutations result in constant activation of the KRAS protein, leading to abnormal cell growth and division. KRAS mutation is among the most predominant mutations in NSCLC and shows little variation between early-stage and metastatic NSCLC (Ghimessy *et al.*, 2020; Lohinai *et al.*, 2017). The undruggable nature of KRAS, attributed to the inability to develop direct inhibitors that can effectively compete with its high affinity for GTP, and the lack of selectivity with wild-type RAS resulting in toxicity, has hindered the design of selective inhibitors targeting mutant KRAS (Chen *et al.*, 2020; Luo *et al.*, 2022). Inhibition of post-translational modifications by farnesyltransferase inhibitors has also demonstrated minimal clinical activity (Adjei *et al.*, 2003; Heymach *et al.*, 2004).

A promising approach now is to target KRAS downstream signaling pathways, particularly PI3K/AKT/mTOR, as evidence suggests their upregulation in lung cancer, promoting cell survival, growth, proliferation, and migration (Huang *et al.*, 2021). The PI3K/Akt/mTOR pathway also plays a role in tumors with other activating mutations (Yu *et al.*, 2021), and increased PI3K or Akt activity regulates mTOR activity in lung cancer (Liang *et al.*, 2019). Treatment of NSCLC cells with mTOR inhibitors has been reported to significantly decrease cancer cell proliferation (Huang *et al.*, 2021). This signaling pathway plays a crucial role in the occurrence and progression of tumors by regulating autophagy and apoptosis of tumor cells (Lee *et al.*, 2021; Zou *et al.*, 2020).

Unfortunately, targeting the PI3K/Akt/mTOR pathway with various kinase inhibitors results in the up-regulation of autophagy (Y. Liu *et al.*, 2021; Zhao *et al.*,

2015). Autophagy, as a cellular process in cancer, can both suppress and promote tumor growth, depending on the tissue and timing (Hanahan & Weinberg, 2011; Lim *et al.*, 2021). Furthermore, autophagy addiction characterizes KRAS-driven cancers, including NSCLC, as it replenishes mitochondria substrates required for acetyl-CoA synthesis (Eng *et al.*, 2016; White, 2012).

Given that the inhibition of the PI3K/Akt/mTOR pathway leads to the upregulation of autophagy, it was reasonable to consider a combination of kinase inhibitors and autophagy inhibitors to achieve a higher therapeutic benefit.

MATERIALS AND METHODS

Cell viability assay

Cancer cells MCF-7 and A549 were plated in 96-well plates at a density of 7000 cells/well in 100 µl of DMEM high glucose medium (4.5 g/L) supplemented with only 1% FBS overnight and 1% penicillin/streptomycin at 37°C and 5% CO₂. After serum starvation, cells were treated with Dactolisib (LC Laboratories, USA), and Lys05 (Sigma-Aldrich, China) at different concentrations for 48 h. For cytotoxicity assay using 3-(4,5-Dimethyl-2-thiazolyl)-2,5-diphenyl-2H-tetrazolium bromide (MTT), MTT (5 mg/mL in 1×PBS) was added to the cells and incubated for 3 h at 37°C in 5% CO₂. A volume of 100 µL of DMSO was added to the cells to solubilize the formed formazan crystals with shaking. Finally, the absorbance was measured at 490 nm and the percentage of cell viability was calculated compared to the control (Kumar *et al.*, 2018).

Identification of synergism and antagonism in drug combination

Drug concentrations used in combination studies were selected from the dose–response data for individual agents in 1% FBS starved A549 cells. Fraction affected (Fa) values were calculated as the percentage inhibition of cell viability, relative to control, as described by Chou (Chou, 2006). Synergism, additivity, or antagonism of drug combinations was identified using the Chou Talalay Combination Index (CI) method (Chou, 2006) and CompuSyn software (<http://www.combosyn.com>) based mainly on the following equation:

$$CI = (D)_1 / (D_x)_1 + (D)_2 / (D_x)_2$$

where (D)₁ and (D)₂ represent the concentrations of Drug 1 and Drug 2 in the combination that produce a Fa value of x. (D)_{x1} and (D)_{x2} represent the concentrations of Drug 1 and Drug 2 that produce the same effect (x) when applied as single agents. CI values <1, =1, and >1 indicate synergism, additivity, and antagonism, respectively.

Protein determination and analysis by Sodium dodecyl sulphate polyacrylamide gel electrophoresis (SDS-PAGE) and western blotting

Protein concentration was determined according to Bradford using bovine serum albumin as a standard (Bradford, 1976). The total protein extract (50 µg) was mixed with a 5× sample application buffer, boiled for 5 min, and resolved on 14% SDS-PAGE. LC3B was detected through western blotting using anti-LC3B monoclonal antibody (Molecular weight 17.5 KDa) (Cell signaling, USA) at a dilution of 1:1000. The sec-

ondary antibody used was goat anti-mouse IgG labeled with horse radish peroxidase (Invitrogen, USA) at a 1:1000 dilution. The nitrocellulose membrane was developed using enhanced chemiluminescence (ECL, Sigma-Aldrich, China) (Liu *et al.*, 2014). Beta-actin (ACTB) (Molecular weight 42 KDa) was used as a loading control.

Apoptosis detection by flow cytometry

Apoptosis was analyzed using Annexin V-FITC apoptosis detection kit (Miltenyi Biotec.). A549 cells were treated with Lys05, Dactolisib and the synergistic combination dose for 48 h. After incubation, cells were harvested by centrifugation, re-suspended in binding buffer, and incubated with fluorescein isothiocyanate (FITC)-labeled with Annexin V for 15 min in the dark at room temperature. Cells were then washed twice with 1×PBS and resuspended in binding buffer, propidium iodide was added, and cells were incubated for 15 min in the dark at room temperature (Lakshmanan & Batra, 2013). The stained cells were analyzed using BD FACS flow cytometer (BD Biosciences) at the flow cytometry service core facility at the Center of Excellence for Research in Regenerative Medicine and its Applications (CERRMA), Faculty of Medicine, Alexandria University.

Quantitative RT-PCR

Total RNA was isolated and purified from the treated and untreated A549 cells using TRIzol reagent (Qiagen, Germany) following the manufacturer's protocol (Rio *et al.*, 2010). The concentration and purity of RNA were determined using Nanodrop. One microgram of the total RNA was reverse transcribed into the first strand cDNA using a High-Capacity cDNA Reverse Transcription Kit (Applied Biosystems) using random hexamer primers according to the manufacturer's instructions. Quantitative real-time PCR was carried out in triplicates using Maxima SYBR Green qPCR Master Mix (ThermoFisher). Primers used were as follows: *HPRT* forward primer, 5'-TGACACTGGCAAAACAAT-3'; reverse, 5'-GGTCCTTTTCACCAGCAA-3'; *LC3A* forward primer, 5'-GGATTTTGAGGAGGGGACTC-3'; reverse, 5'-CATCTGCAAACTGAGACAGTG-3'; *ATG4B* forward primer, 5'-GCAAGTCAAAAAGCTGTCTCT-3'; reverse, 5'-CAGTCGCTCTACATCA-GAAGAA-3'; *LC3B* forward primer, 5'-CGAGA-GCAGCATCCAACCAA-3'; reverse, 5'-GAGCTGTAA-GCGCCTTCTAA-3'; *KI67* forward primer, 5'-GAG-GTGTGCAGAAAATCCAAA-3'; reverse, 5'-CTGTCC-CTATGACTTCTGGTTGT-3'; *CASP3* forward primer, 5'-TTTTTCAGAGGGGATCGTTG-3'; reverse, 5'-CG-GCCTCCACTGGTATTTTA-3'. Primers were added to the reaction mixture at a final concentration of 250 nM. The reaction was prepared in a final volume of 20 µL by mixing 5 µL of each cDNA sample (diluted 1:5), 12.5 µL of SYBR Green, 0.5 µL of each primer, and the final volume was adjusted through the addition of RNase/DNase free water. The reaction conditions used were as follows: 5 min at 95°C for 1 cycle followed by 40 cycles of 15 s at 95°C, 30 s at 58°C, and 30 s at 72°C. The specificity of each primer pair was verified by the presence of a single melting curve peak. Results were analyzed for the relative expression of mRNA normalized against hypoxanthine guanine phosphoribosyl transferase (HPRT) as a housekeeping gene. Finally, the results were analyzed, and expressed as fold change (Rao *et al.*, n.d.).

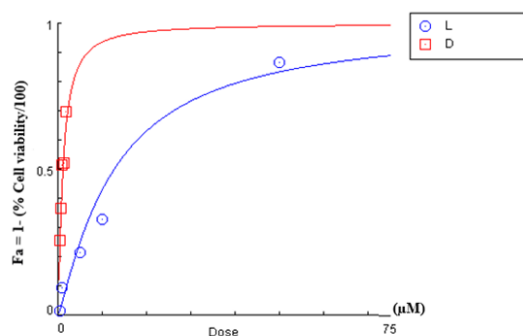


Figure 1. MTT cytotoxicity assay of Lys05 (L) and Dactolisib (D) on MCF-7.

Cells were treated with different concentrations of Lys05 and Dactolisib for 48h. Data were normalized and IC₅₀ values were 12.6 µM and 1.1 µM (n=5). The fraction affected "Fa" was calculated as $1 - (\% \text{ Cell viability}/100)$

ELISA assay

Coated 96-well strip plate has been pre-coated with target-specific capture antibody LC3A (LifeSpan Bioscience, Inc.), LC3B (LifeSpan Bioscience, Inc.) and P62/SQSTM1 (MyBioSource, Inc.). A volume of 100 µL of the samples was added to the wells and incubated for 2 hours at 37°C. The liquid was aspirated and 100 µL of Biotin-labeled antibody working solution was added and incubated for 1 hour at 37°C. The liquid was aspirated then the wells were washed 3 times with wash buffer. The HRP-Streptavidin Conjugate working solution was added and incubated for 60 minutes at 37°C. The liquid was aspirated, and wells were washed 5 times with a wash buffer. The reaction was visualized by the addition of 90 µL of TMB Substrate solution and incubated for 15–30 minutes at 37°C. The reaction was stopped with 50 µL of sulfuric acid stop solution (1N H₂SO₄) to complete the color development reaction and then the ELISA plates were measured at a wavelength of 450 nm using a micro-plate Spectrophotometer.

Statistical analysis

Data were presented as mean \pm standard deviation and were evaluated by a univariate analysis of variance (ANOVA) Tukey's multiple comparisons test at $p < 0.05$ using GraphPad Prism version 7.00, GraphPad, Software, San Diego California, USA. The IC₅₀ values and Combination analysis were conducted as described by Chou using CompuSyn software (<http://www.combosyn.com>).

RESULTS

The effect of the individual administration of dactolisib and Lys05 on MCF-7 and A549 cells

To evaluate the cell growth inhibitory effect of Dactolisib and Lys05 individually, the 3-(4,5-dimethylthiazol-2-yl)-2,5-diphenyltetrazolium bromide (MTT) assay was performed. The impact of both drugs on the survival of MCF-7 and A549 cells was examined to determine the IC₅₀ values using GraphPad Prism version 7.0 and CompuSyn software version 1.

Increasing concentrations of Dactolisib and Lys05, as well as a clear culture media (control), were administered to MCF-7 and A549 cells. Figure 1 illustrates the

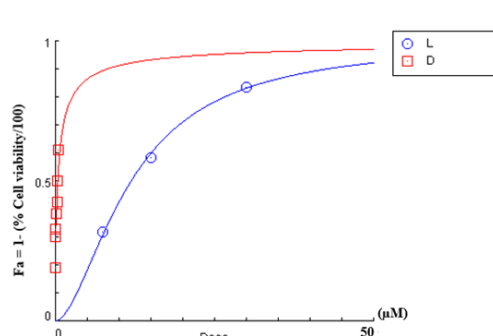


Figure 2. MTT cytotoxicity assay of Lys05 (L) and Dactolisib (D) on A549 cells.

A549 cells were treated with different concentrations of Lys05 and Dactolisib for 48h. Data were normalized and IC₅₀ values on A549 for Lys05 was 11.8 µM and for dactolisib was 0.375 µM (n=5). The fraction affected (Fa) was calculated as $1 - (\% \text{ Cell viability}/100)$

dose-dependent reduction in cell viability caused by the individual administration of Dactolisib in MCF-7 cells compared to the control (untreated cells). The cytotoxic effect of Dactolisib was observed at a concentration of 1.1 µM (n=5) in MCF-7 cells.

Similarly, Fig. 2 shows the dose-dependent reduction in cell viability caused by the individual administration of Lys05 in A549 cells compared to the control. The cytotoxic effect of Lys05 was observed at a concentration of 0.375 µM (n=5) in A549 cells.

In summary, the individual administration of Dactolisib and Lys05 resulted in a dose-dependent reduction in cell viability in MCF-7 and A549 cells, respectively. Dactolisib exhibited cytotoxic effects at concentrations of 1.1 µM (n=5) in MCF-7 cells, while Lys05 showed cytotoxic effects at concentrations of 0.375 µM (n=5) in A549 cells.

A synergistic effect results from dactolisib/Lys05 combination on A549 cells

To investigate the combined cytotoxic effect of Dactolisib and Lys05, starved A549 cells were exposed to various combination ratios. The IC₅₀ value of the 2:1 ratio (2L/1D) (0.05 µM Dactolisib + 3.19 µM Lys05)

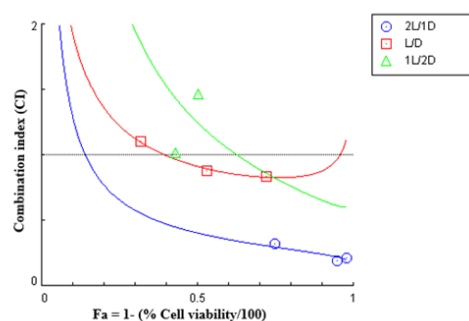


Figure 3. Combination index plot.

was determined, and it showed a significant effect below the additive line, indicating a synergistic effect. The combination index (CI) for this ratio was calculated as 0.4.

This finding suggests that the combination of Dactolisib and Lys05 at the specified ratio has a stronger cytotoxic effect on A549 cells compared to what would be expected if the effects of the two drugs were merely

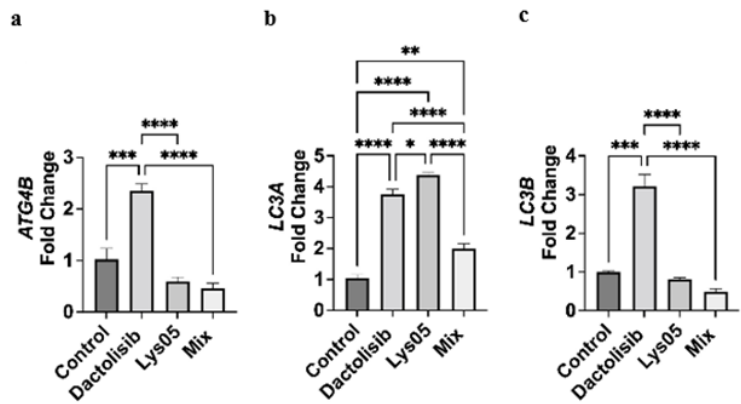


Figure 4. Expression levels of the autophagic markers. (a) *ATG4B*, (b) *LC3A* and (c) *LC3B* genes in A549 control cells, Dactolisib-treated cells (0.375 μ M), Lys05-treated cells (11.8 μ M) and mix-treated cells (0.05 μ M Dactolisib + 3.19 μ M Lys05).

additive. The synergistic effect indicates that the combination is more effective than individual treatments alone. Treatment of starved A549 cells with Lys05 plus dactolisib with various combination ratios, the IC_{50} value of the 2:1 ratio (2L/1D) (0.05 μ M Dactolisib + 3.19 μ M Lys05) showed a significant effect below the additive line, indicating a synergistic effect with combination index “CI” 0.4.

Table 1. The combination index “CI” of IC_{50} values of various combination ratios.

	Ratio		
	(2L/1D)	L/D	(1L/2D)
Combination Index: “CI”	0.4	0.91	1.2

Dactolisib and Lys05 individually and in combination altered the expression of autophagic, proliferative, and apoptotic gene markers

Using quantitative real-time PCR, the gene expression levels of the autophagic markers *ATG4B*, *LC3A*, and *LC3B* were determined. In Dactolisib-treated cells, the levels of *ATG4B*, *LC3A*, and *LC3B* were found to be elevated compared to control cells. Conversely, in Lys05-treated cells, only *LC3A* showed a significant increase in expression compared to control cells (Fig. 4a). Interestingly, in the mix-treated cells (combination of Dactolisib and Lys05), while *ATG4B* and *LC3B* were downregulated, *LC3A* exhibited a significant increase in expression compared to control cells (Fig. 4a). These results indicate that Dactolisib treatment leads to the upregulation of *ATG4B*, *LC3A*, and *LC3B*, suggesting the induction of autophagy. In contrast, Lys05 treatment primarily upregulates the expression of *LC3A*. Notably, in the mix-treated cells, the combination of Dactolisib and Lys05 resulted in the downregulation of *ATG4B* and *LC3B*, but a significant increase in *LC3A* expression compared to control cells. These findings suggest that the combination treatment may have a distinct effect on autophagic markers compared to individual treatments alone.

The expression levels of *CASP3* and *KI67* were examined in different treatment groups compared to control cells

Firstly, it was observed that *CASP3*, a marker of apoptosis, showed a considerable elevation in mix-treated cells compared to control cells (Fig. 5a). This suggests that the combination treatment of Dactolisib and Lys05 induced a higher level of *CASP3* expression, indicating an increased apoptotic response. Additionally, *CASP3* was also found to be upregulated in cells treated with Dactolisib alone and Lys05 alone, indicating that both individual treatments could induce apoptosis to some extent. Secondly, the expression *KI67*, a marker of cellular proliferation, was significantly downregulated in cells treated with Dactolisib, Lys05, and the mix of Dactolisib and Lys05 (Fig. 5b). This suggests that Dactolisib, Lys05, and the combination treatments inhibited cellular proliferation, as evidenced by the reduced expression of *KI67*. Overall, these results indicate that the mix-treated cells had a notable elevation in *CASP3* expression, indicating an enhanced apoptotic response compared to control cells. Additionally, both Dactolisib, Lys05 and the mix of Dactolisib and Lys05 resulted in the downregulation of *KI67*, suggesting inhibition of cellular proliferation.

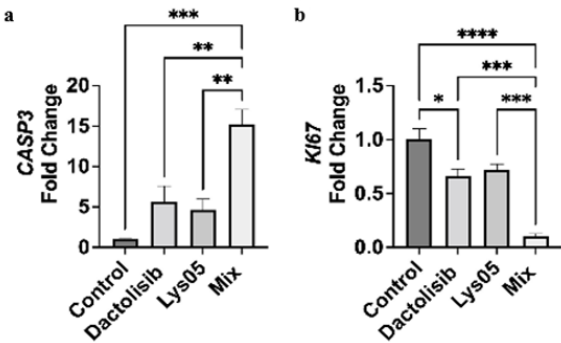


Figure 5. Expression levels of apoptotic and proliferative markers. (a) *CASP3* and (b) *KI67* genes in A549 control cells, Dactolisib-treated cells (0.375 μ M), Lys05-treated cells (11.8 μ M) and mix-treated cells (0.05 μ M Dactolisib + 3.19 μ M Lys05).

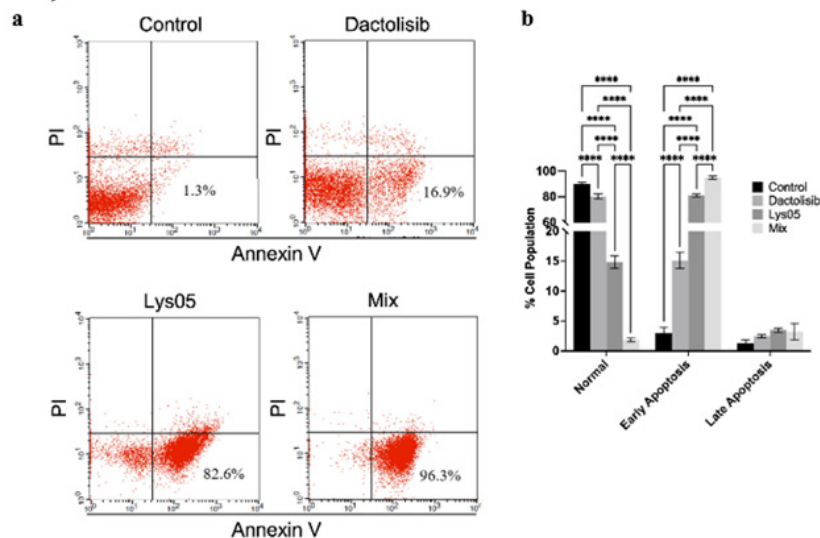


Figure 6. Apoptosis detection through flow cytometry.

(a) A549 control cells, Dactolisib-treated cells (0.375 μ M), Lys05-treated cells (11.8 μ M) and mix-treated cells (0.05 μ M Dactolisib + 3.19 μ M Lys05). Apoptosis was analyzed through double staining with Propidium iodide and Annexin V-FITC. The lower left quadrant represents control cells, the lower right quadrant represents cells in early apoptosis, the upper right quadrant represents cells in late apoptosis and the upper left quadrant represent cells in necrosis. (b) Quantitative analysis of cell population in early, late apoptosis, and necrosis in control A549 cells, Dactolisib-treated cells, Lys05-treated cells and mix-treated cells.

Dactolisib/Lys05 combination enhances killing in A549 cells

Flow cytometry was employed to evaluate the induction of apoptosis in starved A549 cells following treatment with Dactolisib, Lys05, or a combination of both. The percentage of cells undergoing early apoptosis was determined for each treatment group.

The results showed that Dactolisib treatment led to an early apoptosis percentage of 16.9%. Lys05 treatment exhibited a significantly higher early apoptosis percentage of 82.6%. Notably, when the two drugs were combined (mix), the early apoptosis percentage dramatically increased to 96.3%. In comparison, the control group of untreated A549 cells had an early apoptosis percentage of 1.3% (Fig. 6).

These findings indicate that both Dactolisib and Lys05 treatments can induce apoptosis in starved A549 cells. However, the combination of Dactolisib and Lys05

(mix) resulted in a much higher early apoptosis percentage compared to either treatment alone or the control group. This suggests a synergistic effect between Dactolisib and Lys05 in promoting apoptosis in A549 cells.

Dactolisib and Lys05 individually and in combination alter the expression of autophagic protein markers on A549 cells

The expression levels of P62/SQSTM1, LC3A, and LC3B were assessed in different treatment groups compared to control cells.

Firstly, it was found that the expression of P62/SQSTM1, a protein involved in autophagy, was significantly increased in Lys05-treated cells and mix-treated cells compared to control cells (Fig. 7a). This suggests that both Lys05 treatment and the combination treatment led to an upregulation of P62/SQSTM1 expression, indicating a potential disruption in the autophagic process.

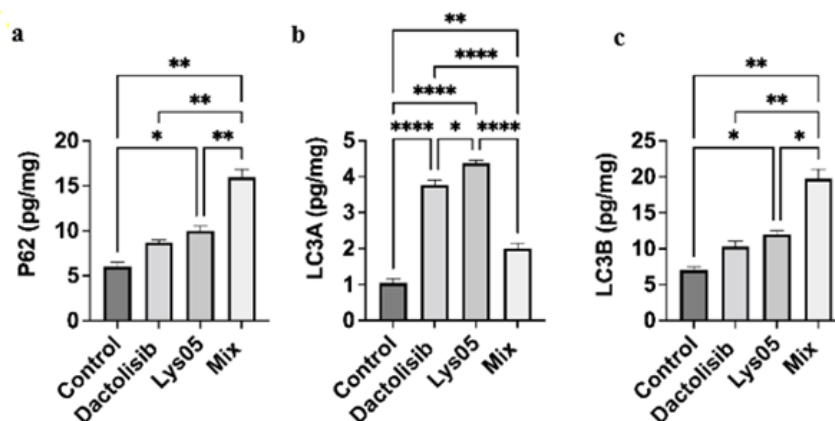


Figure 7. ELISA assay of autophagic protein markers.

(a) P62 protein, (b) LC3A protein and (c) LC3B protein on control A549 cells, Dactolisib-treated cells (0.375 μ M), Lys05-treated cells (11.8 μ M) and mix-treated cells (0.05 μ M Dactolisib + 3.19 μ M Lys05)

Secondly, the levels of LC3A, an autophagy-related protein, were significantly higher in mix-treated cells compared to control cells (Fig. 7b). This indicates that the combination treatment resulted in an increased expression of LC3A, suggesting the induction of autophagy. Similarly, LC3B showed a significant increase in expression in Lys05-treated cells (Fig. 7c). Interestingly, the same pattern was observed in cells treated with the combination of both drugs, indicating a consistent effect.

Overall, these results demonstrate that the Lys05 treatment and the combination treatment (mix) led to an upregulation of P62/SQSTM1 expression. Furthermore, the combination treatment resulted in higher levels of LC3A expression compared to control cells, while Lys05 treatment specifically increased LC3B expression. These findings suggest a potential modulation of autophagy-related proteins by the treatments, indicating a complex interplay between autophagy and the therapeutic effects of Lys05 and the combination treatment.

In the experiment, a semi-quantitative analysis of LC3B expression was conducted using Image J software. Figure 8 illustrates the results of this analysis, showing the upregulation of LC3B in Lys05-treated cells and mix-treated cells compared to the untreated control A549 cells.

The upregulation of LC3B in Lys05-treated cells and mix-treated cells suggests an increase in autophagy activity. LC3B is a well-known marker for autophagosomes, which are structures involved in the autophagy process. The upregulation of LC3B indicates an accumulation of autophagosomes, suggesting an enhancement of the autophagic response in the treated cells.

The semi-quantitative analysis performed using Image J software allows for the quantification and comparison of LC3B expression levels between different treatment groups. The results clearly demonstrate the higher expression of LC3B in Lys05-treated cells and mix-treated cells, highlighting the impact of these treatments on autophagy induction.

DISCUSSION:

Indeed, the PI3K/mTOR signaling pathway plays a crucial role in various aspects of cancer development

and progression, including cell proliferation, angiogenesis, invasion, cell survival, and motility. Dysregulation of this pathway has been frequently observed in many types of cancer, making it an attractive target for developing novel anticancer agents (Samuels *et al.*, 2004).

Targeting the PI3K/mTOR pathway has shown promise as a therapeutic approach in cancer treatment. By inhibiting specific components or key signaling molecules within this pathway, it is possible to disrupt the aberrant signaling cascade and potentially halt or slow down cancer progression (Herrera *et al.*, 2011).

Several studies have investigated the development of novel anticancer agents that target the PI3K/mTOR pathway. These agents aim to selectively inhibit the activity of specific enzymes or molecules within the pathway, thereby modulating its downstream effects on cell proliferation, angiogenesis, invasion, and survival (Herrera *et al.*, 2011).

Previously, it has been revealed that inhibition of the PI3K/mTOR pathway induces autophagy as a mechanism of cell death or drug resistance (Fujiwara *et al.*, 2007; Yang *et al.*, 2011). Therefore, the inhibition of autophagy in addition to targeting the PI3K/Akt/mTOR pathway may enhance cancer cell death.

In our study, we examined the cytotoxic effect of the two drugs on MCF-7 and A549 cells. The IC₅₀ values for each cell line were determined and presented in Fig. 1 for MCF-7 cells and Figure 2 for A549 cells. The results revealed that A549 cells exhibited greater sensitivity to the two drugs compared to MCF-7 cells.

Additionally, we investigated the effect of combining Lys05 and Dactolisib on starved A549 cells using different ratios. Among the combination ratios tested, the 2:1 ratio (2 parts Lys05 to 1 part Dactolisib) demonstrated a significant effect below the additive line, indicating a synergistic effect. The combination index (CI) value of 0.4, as shown in Figure 3, further supports the synergistic interaction between the two drugs.

Furthermore, we investigated the gene expression levels of autophagic markers, namely ATG4B, LC3A, and LC3B, using quantitative real-time PCR. ATG4B is an autophagic cysteine protease responsible for cleaving the pre-protein ATG8, specifically LC3, resulting in the formation of the non-lipidated soluble form (LC3A). The cleaved LC3A can then interact with phosphatidylethanolamine to form the lipidated form (LC3B), which is anchored to the autophagic membrane (Xia *et al.*, 2022).

Our gene expression analysis revealed significant upregulation of ATG4B, LC3A, and LC3B in Dactolisib-treated cells compared to the control cells, indicating autophagic induction (*p* values = 0.0009 for ATG4B, 0.0001 for LC3A, and 0.0003 for LC3B) (Fig. 4a, 4b, and 4c, respectively). Similarly, in Lys05-treated cells, we observed a significant upregulation of LC3A (*p* = 0.0001) (Fig. 4a) as a compensatory mechanism in response to Lys05-induced autophagic inhibition. However, ATG4B and LC3B showed obvious downregulation, suggesting autophagosome inhibition.

In mix-treated cells, we found that LC3A was significantly upregulated compared to the control cells (*p* = 0.0032) (Fig. 4a). However, both ATG4B and LC3B were downregulated, likely due to the combined effect of the two drugs. These findings indicate that the combination of Dactolisib and Lys05 exerted a significant effect on A549 cells, modulating autophagic processes through differential regulation of autophagic markers.

Furthermore, we examined the gene expression levels of a proliferative marker, KI67, and an apoptotic marker, CASP3. CASP3 is an executioner caspase involved

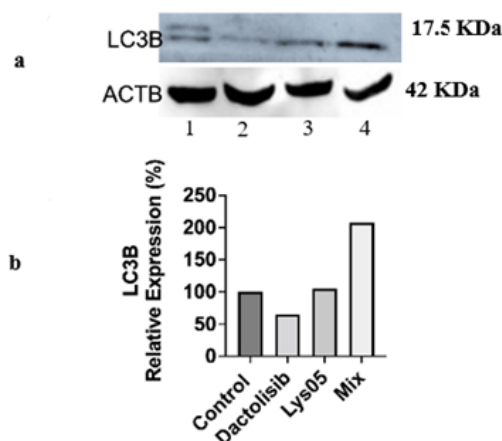


Figure 8. Western blot analysis of LC3B expression in A549 cells. After treatment with Dactolisib and Lys05 individually and in combination. (a) Lane 1 represents A549 control cells, lane 2 represents Dactolisib-treated cells (0.375 μ M), lane 3 represents Lys05-treated cells (11.8 μ M) and lane 4 represents mix-treated cells (0.05 μ M Dactolisib + 3.19 μ M Lys05). (b) Chart represents LC3B expression level.

in apoptosis that coordinates the degradation of cellular structures (Ma *et al.*, 2021). KI67 is an antigen associated with nuclear proliferation and is expressed during the growth and synthesis phases of the cell cycle (G1, S, G2, and M), but not during the resting phase (G0) (Gerdes *et al.*, 1991).

Our results demonstrated that Ki-67 was significantly downregulated in Dactolisib-treated cells and mix-treated cells compared to control cells ($p=0.0244$ and 0.0001 , respectively) (Fig. 5b). This suggests that the treatment with Dactolisib and the combination of the two drugs resulted in a suppression of proliferation in A549 cells.

In contrast, CASP3 was upregulated in Dactolisib-treated cells and Lys05-treated cells. Notably, it was significantly upregulated in mix-treated cells compared to control cells ($p=0.0007$) (Fig. 5a). These findings indicate that the combination of Dactolisib and Lys05 had a significant impact on promoting apoptosis in A549 cells.

Taken together, our results demonstrate the significant effects of the drug combination on both the proliferative and apoptotic levels in A549 cells, as evidenced by the downregulation of the proliferative marker KI67 and the upregulation of the apoptotic marker CASP3.

It is well-established that the evasion of regulated modes of cell death is a hallmark of cancer (Sharma *et al.*, 2019). In our study, we further supported our findings regarding apoptotic and proliferative levels using flow cytometry analysis. Annexin V/PI staining of A549 cells treated with dactolisib, Lys05, and the combination (Mix) revealed percentages of early apoptosis at 16.9%, 82.6%, and 96.3%, respectively (Fig. 6). In comparison, the control untreated A549 cells exhibited an early apoptosis rate of 1.3%. These results clearly demonstrate that our combination treatment has a significant effect on both proliferation and apoptosis in A549 cells.

Furthermore, to support our gene expression findings, we performed additional analyses using ELISA for p62/SQSTM1 and LC3s (MAP1-LC3A and B), and Western blot for LC3B. p62/SQSTM1 acts as a receptor for cargo destined to be degraded by autophagy, including ubiquitinated protein aggregates targeted for clearance. The p62 protein can bind to both ubiquitin and LC3, facilitating the targeting of cargo to autophagosomes for degradation (Berkamp *et al.*, 2021). LC3s (MAP1-LC3A and B) are structural proteins found in autophagosomal membranes and are widely used as biomarkers of autophagy (Koukourakis *et al.*, 2015).

Our results revealed that p62/SQSTM1 was significantly upregulated in both Lys05- and mix-treated cells ($p=0.0305$ and 0.0011 , respectively) compared to the control (Fig. 7a). This upregulation indicates autophagic inhibition. Additionally, LC3A was significantly upregulated in mix-treated cells ($p=0.0044$) (Fig. 7b). On the other hand, LC3B was significantly upregulated in Lys05-treated cells ($p=0.0482$) (Fig. 7c) due to its accumulation resulting from autophagic inhibition. Similarly, mix-treated cells exhibited the same pattern of upregulation in LC3B due to the combined effect of the two drugs ($p=0.0017$). The semi-quantified Western blot analysis of LC3B aligned with the ELISA results (Fig. 8). These findings strongly support the efficacy of our drug combination.

Considering the comprehensive findings from our study, it is evident that the combination of kinase inhibitor and autophagy inhibitor led to increased cell killing, as demonstrated by enhanced annexin V/PI staining, upregulation of the apoptotic gene marker CASP3, and downregulation of the proliferative gene marker KI67. This combination exhibited a synergistic effect on A549

cells compared to each drug used alone. Therefore, we can confidently conclude that the kinase inhibitor/autophagy inhibitor combination provides greater therapeutic benefits for A549 cells compared to monotherapy with kinase inhibitors alone. This synergistic effect has also been observed in other studies involving glioma (Cerniglia *et al.*, 2012) and malignant peripheral nerve sheath tumors (Ghadimi *et al.*, 2012), further supporting the significance of our findings.

Declarations

Conflict of interest. We declare that there is no conflict of interest regarding this article. None of the authors have any financial employment, consultancies, honoraria, stock ownership or options, expert testimony, or royalties related to this manuscript. Furthermore, we affirm that this work has not been published elsewhere, is not currently being considered for publication elsewhere, and all authors have given their consent for the submission of this manuscript.

REFERENCES

- Adjei AA, Mauer A, Bruzek L, Marks RS, Hillman S, Geyer S, Hanson LJ, Wright JJ, Erlichman C, Kaufmann SH, Vokes EE (2003) Phase II study of the farnesyl transferase inhibitor R115777 in patients with advanced non-small-cell lung cancer. *J Clin Oncol* **21**: 1760–1766. <https://doi.org/10.1200/JCO.2003.09.075>
- Barta JA, Powell CA, Wisnivesky JP (2019) Global epidemiology of lung cancer. *Ann Glob Health* **85**. <https://doi.org/10.5334/AOGLH.2419>
- Berkamp S, Mostafavi S, Sachse C (2021) Structure and function of p62/SQSTM1 in the emerging framework of phase separation. *FEBS J* **288**: 6927–6941. <https://doi.org/10.1111/FEBS.15672>
- Bradford MM (1976) A rapid and sensitive method for the quantitation of microgram quantities of protein utilizing the principle of protein-dye binding. *Anal Biochem* **72**: 248–254. [https://doi.org/10.1016/0003-2697\(76\)90527-3](https://doi.org/10.1016/0003-2697(76)90527-3)
- Cerniglia GJ, Karar J, Tyagi S, Christofidou-Solomidou M, Rengan R, Koumenis C, Maity A (2012) Inhibition of autophagy as a strategy to augment radiosensitization by the dual phosphatidylinositol 3-kinase/mammalian target of rapamycin inhibitor NVP-BEZ235. *Mol Pharmacol* **82**: 1230–1240. <https://doi.org/10.1124/mol.112.080408>
- Chen K, Shang Z, Dai AL, Dai PL (2020) Novel PI3K/Akt/mTOR pathway inhibitors plus radiotherapy: Strategy for non-small cell lung cancer with mutant RAS gene. *Life Sci* **255**. <https://doi.org/10.1016/j.lfs.2020.117816>
- Chou TC (2006) Theoretical basis, experimental design, and computerized simulation of synergism and antagonism in drug combination studies. *Pharmacol Rev* **58**: 621–681. <https://doi.org/10.1124/pr.58.3.10>
- El Osta B, Behera M, Kim S, Berry LD, Sica G, Pillai RN, Owonikoko TK, Kris MG, Johnson BE, Kwiatkowski DJ, Sholl LM, Aisner DL, Bunn PA, Khuri FR, Ramalingam SS (2019) Characteristics and outcomes of patients with metastatic kras-mutant lung adenocarcinomas: the lung cancer mutation consortium experience. *J Thorac Oncol* **14**: 876–889. <https://doi.org/10.1016/j.jtho.2019.01.020>
- Eng CH, Wang Z, Tkach D, Toral-Barza L, Ugwonalu S, Liu S, Fitzgerald SL, George E, Frias E, Cochran N, De Jesus R, McAllister G, Hoffman GR, Bray K, Lemon LA, Lucas J, Fantin VR, Abraham RT, Murphy LO, Nyfeler B (2016) Macroautophagy is dispensable for growth of KRAS mutant tumors and chloroquine efficacy. *Proc Natl Acad Sci U S A* **113**: 182–187. <https://doi.org/10.1073/PNAS.1515617113>
- Fujiwara K, Iwado E, Mills GB, Sawaya R, Kondo S, Kondo Y (2007) Akt inhibitor shows anticancer and radiosensitizing effects in malignant glioma cells by inducing autophagy. *Int J Oncol* **31**: 753–760. <https://doi.org/10.3892/IJO.31.4.753>
- Gerdes J, Li L, Schlueter C, Duchrow M, Wohlenberg C, Gerlach C, Stahmer I, Kloth S, Brandt E, Flad HD (1991) Immunobiochemical and molecular biologic characterization of the cell proliferation-associated nuclear antigen that is defined by monoclonal antibody Ki-67. *Am J Pathol* **138**: 867
- Ghadimi MP, Lopez G, Torres KE, Belousov R, Young ED, Liu J, Brewer KJ, Hoffman A, Lusby K, Lazar AJ, Pollock RE, Lev D (2012) Targeting the PI3K/mTOR axis, alone and in combination with autophagy blockade, for the treatment of malignant peripheral nerve sheath tumors. *Mol Cancer Ther*. <https://doi.org/10.1158/1535-7163.MCT-12-0015>

- Ghimessy A, Radeckzy P, Laszlo V, Hegedus B, Renyi-Vamos F, Fillinger J, Klepetko W, Lang C, Dome B, Megyesfalvi Z (2020) Current therapy of KRAS-mutant lung cancer. *Cancer Metastasis Rev* **39**: 1159–1177. <https://doi.org/10.1007/s10555-020-09903-9>
- Haider T, Pandey V, Banjare N, Gupta PN, Soni V (2020) Drug resistance in cancer: mechanisms and tackling strategies. *Pharmacol Rep* **72**: 1125–1151. <https://doi.org/10.1007/S43440-020-00138-7>
- Hanahan D, Weinberg RA (2011) Hallmarks of cancer: the next generation. *Cell* **144**: 646–674. <https://doi.org/10.1016/j.cell.2011.02.013>
- Herrera VA, Zeindl-Eberhart E, Jung A, Huber RM, Bergner A (2011) The dual PI3K/mTOR inhibitor BEZ235 is effective in lung cancer cell lines. *Anticancer Res* **31**: 849–854
- Heymach JV, Johnson DH, Khuri FR, Safran H, Schlabach LL, Yunus F, De Vore RF, De Porre PM, Richards HM, Jia X, Zhang S, Johnson BE (2004) Phase II study of the farnesyl transferase inhibitor R115777 in patients with sensitive relapse small-cell lung cancer. *Ann Oncol* **15**: 1187–1193. <https://doi.org/10.1093/ANNONC/MDH315>
- Huang L, Guo Z, Wang F, Fu L (2021) KRAS mutation: from undruggable to druggable in cancer. *Signal Transduct Target Ther* **6**: 1–20. <https://doi.org/10.1038/s41392-021-00780-4>
- Koukourakis MI, Kalamida D, Giatromanolaki A, Zois CE, Sivridis E, Pouliliou S, Mitrakas A, Gatter KC, Harris AL (2015) Autophagosome proteins LC3A, LC3B, and LC3C have distinct subcellular distribution kinetics and expression in cancer cell lines. *PLoS One* **10**. <https://doi.org/10.1371/JOURNAL.PONE.0137675>
- Kumar P, Nagarajan A, Uchil PD (2018) Analysis of cell viability by the MTT Assay. *Cold Spring Harb Protoc* **2018**: 469–471. <https://doi.org/10.1101/PDB.PROT095505>
- Lakshmanan I, Batra SK (2013) Protocol for apoptosis assay by flow cytometry using annexin V staining method. *Bio-Protoc*. e374. <http://www.bio-protocol.org/e374>
- Lee MG, Lee KS, Nam KS (2021) Arctigenin-mediated cell death of SK-BR-3 cells is caused by HER2 inhibition and autophagy-linked apoptosis. *Pharmacol Rep* **73**: 629–641. <https://doi.org/10.1007/S43440-021-00223-5>
- Liang SQ, Bührer ED, Berezowska S, Thomas, Marti M, Xu D, Froment L, Yang H, Hall SRR, Vassella E, Yang, Zhang, Kocher GJ, Amrein MA, Riether, Carsten, Ochsenbein AF, Schmid RA, Peng RW (2019) mTOR mediates a mechanism of resistance to chemotherapy and defines a rational combination strategy to treat KRAS-mutant lung cancer. *Oncogene*. <https://doi.org/10.1038/s41388-018-0479-6>
- Lim SM, Mohamad Hanif EA, Chin SF (2021) Is targeting autophagy mechanism in cancer a good approach? The possible double-edge sword effect. *Cell Biosci* **11**: 1–13. <https://doi.org/10.1186/S13578-021-00570-Z>
- Liu Y, Song A, Wu H, Sun Y, Dai M (2021) Paeonol inhibits apoptosis of vascular smooth muscle cells via up-regulation of autophagy by activating class III PI3K/Beclin-1 signaling pathway. *Life Sci* **264**: 118714. <https://doi.org/10.1016/j.lfs.2020.118714>
- Liu ZQ, Mahmood T, Yang PC (2014) Western blot: technique, theory, and troubleshooting. *NAJMS* **6**: 160. <https://doi.org/10.4103/1947-2714.128482>
- Lohinai Z, Klikovits T, Moldvay J, Ostoros G, Raso E, Timar J, Fabian K, Kovalszky I, Kenessey I, Aigner C, Renyi-Vamos F, Klepetko W, Dome B, Hegedus B (2017) KRAS-mutation incidence and prognostic value are metastatic site-specific in lung adenocarcinoma: poor prognosis in patients with KRAS mutation and bone metastasis. *Sci Rep* **7**. <https://doi.org/10.1038/SREP39721>
- Luo J, Ostrem J, Pellini B, Imbody D, Stern Y, Solanki HS, Haura EB, Villaruz LC (2022) Overcoming KRAS-mutant lung cancer. *ASCO* **42**: 1–11. https://doi.org/10.1200/EDBK_360354
- Ma X, Zhang J, Wang Z (2021) Real-time monitoring of active caspase 3 during AFB1 induced apoptosis based on SERS-fluorescent dual mode signals. *SAA* **263**. <https://doi.org/10.1016/j.saa.2021.120195>
- Rao X, Huang X, Zhou Z, Lin X (2013) An improvement of the 2[−](-delta delta CT) method for quantitative real-time polymerase chain reaction data analysis. *Biostat Bioinform Biomath* **3**: 71–85.
- Rio DC, Ares M, Hannon GJ, Nilsen TW (2010) Purification of RNA using TRIzol (TRI Reagent) *Cold Spring Harb Protoc* **5**. <https://doi.org/10.1101/PDB.PROT5439>
- Rizzo P, Osipo C, Foreman K, Golde T, Osborne B, Miele L (2008) Rational targeting of Notch signaling in cancer. *Oncogene* **27**: 5124–5131
- Samuels Y, Wang Z, Bardelli A, Silliman N, Ptak J, Szabo S, Yan H, Gazdar A, Powell SM, Riggins GJ, Willson JKV, Markowitz S, Kinzler KW, Vogelstein B, Velculescu VE (2004) High frequency of mutations of the PIK3CA gene in human cancers. *Science* **304**: 554. https://doi.org/10.1126/SCIENCE.1096502/SUPPL_FILE/SAMUELS.SOM.PDF
- Sever R, Brugge JS (2015) Signal transduction in cancer. *CSH Perspect Med* **5**. <https://doi.org/10.1101/CSHPERSPECT.A006098>
- Sharma A, Boise LH, Shanmugam M (2019) Cancer metabolism and the evasion of apoptotic cell death. *Cancers* **11**. <https://doi.org/10.3390/CANCERS11081144>
- Sun X, Li K, Zhao R, Sun Y, Xu J, Peng ZY, Song RD, Ren H, Tang SC (2021) Lung cancer pathogenesis and poor response to therapy were dependent on driver oncogenic mutations. *Life Sci* **265**. <https://doi.org/10.1016/j.lfs.2020.118797>
- Wang X, Liu J, Xie Z, Rao J, Xu G, Huang K, Li W, Yin Z (2019) Chlorogenic acid inhibits proliferation and induces apoptosis in A498 human kidney cancer cells via inactivating PI3K/Akt/mTOR signalling pathway. *J Pharm Pharmacol* **71**: 1100–1109. <https://doi.org/10.1111/JPHP.13095>
- White E (2012) Deconvoluting the context-dependent role for autophagy in cancer. *Nat Rev Cancer*. <https://doi.org/10.1038/nrc3262>
- White E, DiPaola RS (2009) The double-edged sword of autophagy modulation in cancer. *Clin Cancer Res* **15**: 5308–5316. <https://doi.org/10.1158/1078-0432.CCR-07-5023>
- Xia F, Fu Y, Xie H, Chen Y, Fang D, Zhang W, Liu P, Li M (2022) Suppression of ATG4B by copper inhibits autophagy and involves in Mallory body formation. *Redox Biol* **52**: 102284. <https://doi.org/10.1016/j.redox.2022.102284>
- Yang S, Xiao X, Meng X, Leslie KK (2011) A mechanism for synergy with combined mTOR and PI3 kinase inhibitors. *PLOS One* **6**: e26343. <https://doi.org/10.1371/JOURNAL.PONE.0026343>
- Yu X, Li Y, Jiang G, Fang J, You Z, Shao G, Zhang Z, Jiao A, Peng X (2021) FGF21 promotes non-small cell lung cancer progression by SIRT1/PI3K/AKT signaling. *Life Sci* **269**: 118875. <https://doi.org/10.1016/j.lfs.2020.118875>
- Zhao R, Chen M, Jiang Z, Zhao F, Xi B, Zhang X, Fu H, Zhou K (2015) Platycodin-D induced autophagy in non-small cell lung cancer cells via PI3K/Akt/mTOR and MAPK signaling pathways. *J Cancer* **6**: 623–631. <https://doi.org/10.7150/JCA.11291>
- Zou Z, Tao T, Li H, Zhu X (2020) MTOR signaling pathway and mTOR inhibitors in cancer: Progress and challenges. *Cell Biosci* **10**. <https://doi.org/10.1186/S13578-020-00396-1>



OPEN ACCESS

EDITED BY

Arun S. Kharat,
Jawaharlal Nehru University, India

REVIEWED BY

Margaret Lorraine Britz,
University of Tasmania, Australia
Ghada A. Mohammad,
University of Mosul, Iraq

*CORRESPONDENCE

Małgorzata Ziarno,
✉ malgorzata_ziarno@sggw.edu.pl

RECEIVED 20 March 2024

ACCEPTED 19 June 2024

PUBLISHED 04 July 2024

CITATION

Zaręba D and Ziarno M (2024), Tween
80™-induced changes in fatty acid
profile of selected
mesophilic lactobacilli.
Acta Biochim. Pol 71:13014.
doi: 10.3389/abp.2024.13014

COPYRIGHT

© 2024 Zaręba and Ziarno. This is an
open-access article distributed under
the terms of the Creative Commons
Attribution License (CC BY). The use,
distribution or reproduction in other
forums is permitted, provided the
original author(s) and the copyright
owner(s) are credited and that the
original publication in this journal is
cited, in accordance with accepted
academic practice. No use, distribution
or reproduction is permitted which does
not comply with these terms.

Tween 80™-induced changes in fatty acid profile of selected mesophilic lactobacilli

Dorota Zaręba¹ and Małgorzata Ziarno^{2*}

¹Professor E. Pijanowski Catering School Complex in Warsaw, Warsaw, Poland, ²Institute of Food Science, Department of Food Technology and Assessment, Warsaw University of Life Sciences - SGGW (WULS-SGGW), Warsaw, Poland

Fatty acid profiles are crucial for the functionality and viability of lactobacilli used in food applications. Tween 80™, a common culture media additive, is known to influence bacterial growth and composition. This study investigated how Tween 80™ supplementation impacts the fatty acid profiles of six mesophilic lactobacilli strains (*Lactocaseibacillus* spp., *Limosilactobacillus* spp., *Lactiplantibacillus plantarum*). Analysis of eleven strains revealed 29 distinct fatty acids. Tween 80™ supplementation significantly altered their fatty acid composition. Notably, there was a shift towards saturated fatty acids and changes within the unsaturated fatty acid profile. While some unsaturated fatty acids decreased, there was a concurrent rise in cyclic derivatives like lactobacillic acid (derived from vaccenic acid) and dihydrosterculic acid (derived from oleic acid). This suggests that despite the presence of Tween 80™ as an oleic acid source, lactobacilli prioritize the synthesis of these cyclic derivatives from precursor unsaturated fatty acids. Myristic acid and dihydrosterculic acid levels varied across strains. Interestingly, palmitic acid content increased, potentially reflecting enhanced incorporation of oleic acid from Tween 80™ into membranes. Conversely, cis-vaccenic acid levels consistently decreased across all strains. The observed fatty acid profiles differed from previous studies, likely due to a combination of factors including strain-specific variations and growth condition differences (media type, temperature, harvesting point). However, this study highlights the consistent impact of Tween 80™ on the fatty acid composition of lactobacilli, regardless of these variations. In conclusion, Tween 80™ significantly alters fatty acid profiles, influencing saturation levels and specific fatty acid proportions. This work reveals key factors, including stimulated synthesis of lactobacillic acid, competition for oleic acid incorporation, and strain-specific responses to myristic and dihydrosterculic acids. The consistent reduction in cis-vaccenic acid and the presence of cyclic derivatives warrant further investigation to elucidate their roles in response to Tween 80™ supplementation.

KEYWORDS

lactic acid bacteria, lactobacilli, fatty acid profile, functionality, Tween 80™

Introduction

The fatty acid composition of bacterial cells of the lactobacilli determines their survival and depends on many environmental factors (Johnsson et al., 1995; Partanen et al., 2001; Corcoran et al., 2007; Montanari et al., 2010; Li et al., 2011; Tan et al., 2012; Terraf et al., 2012; Al-Naseri et al., 2013; Hansen et al., 2015; Reitermayer et al., 2018). Corcoran et al. (2007) proved this by showing that oleic acid (C18:1,*cis*-9) and *cis*-vaccenic acid (C18:1,*cis*-11) have a protective effect on *Lactocaseibacillus rhamnosus* GG cells suspended in artificial gastric juice. These researchers have shown that only in the case of these two fatty acids, the number of bacterial cells was greater than the number of cells in the control sample. Other tested fatty acids, including stearic (C18:0), elaidic (C18:1,*trans*-9), linoleic (C18:2,*cis*-9,*cis*-12), *cis*-9,*trans*-11-octadecadienoic, and *trans*-10,*cis*-12-octadecadienoic, caused a decrease in the number of viable cells (to a level of 3.89 log CFU/mL in case of *trans*-10,*cis*-12-octadecadienoic acid and to 4.75 log CFU/mL for stearic and elaidic acids). This phenomenon can be explained by the fact that oleic (C18:1,*cis*-9) and *cis*-vaccenic (C18:1,*cis*-11) acids are the substrates for the synthesis of fatty acid in various ways required for cell survival and modification of cell membrane fluidity. Lactic acid bacteria (LAB), lactobacilli including, are equipped with the mechanisms for transforming these fatty acids in their cyclic, polyunsaturated, or conjugated forms (Henderson and McNeill, 1966; Weeks and Wakil, 1970; Partanen et al., 2001; Corcoran et al., 2007; Tan et al., 2012). Transformation of linoleic (C18:2,*cis*-9,*cis*-12) or conjugated acids to oleic acid (C18:1,*cis*-9) requires the action of specific enzymes if LAB cells lack access to external sources of oleic acid. In the absence of external oleic acid, some LAB strains may resort to this conversion pathway to maintain a certain level of oleic acid, potentially leading to a decrease in the overall protective action of these polyunsaturated fatty acids.

One of the external sources of fatty acids for bacterial cells is their living environment, including culture media. A key example is oleic acid, a fatty acid found in many natural sources. However, bacteria can also utilize oleic acid provided in the form of Tween 80™. Tween 80™ is a nonionic surfactant, commonly used in the food industry as an emulsifier, dispersant, and stabilizer. It finds application in microbiology as a common additive to media for cultivating lactobacilli (Johnsson et al., 1995; Partanen et al., 2001; Montanari et al., 2010; Li et al., 2018). It could be also employed in food fermentation processes for its beneficial effects on microbial growth and product quality (Li et al., 2018). Chemically, Tween 80™ is a synthetic molecule derived from sorbitan (a cyclic polyol) and esterified with oleic acid (C18:1,*cis*-9). This combination results in a molecule with a hydrophilic head (sorbitan) and a hydrophobic tail (oleic acid), allowing Tween 80™ to act as a surface-active agent. Tween 80™ improves the solubility and bioavailability of nutrients, promoting microbial growth and fermentation efficiency. By facilitating

nutrient uptake and metabolism, Tween 80™ can lead to higher yields of fermented products (Li et al., 2018). The combination of oleic acid (C18:1,*cis*-9) with sorbitol permits the solubility of fatty acid in aqueous solution and a uniform dispersion of particles in growth medium, thereby making it more accessible to acid bacterial cells. Corcoran et al. (2007) compared the effect of adding Tween 80™ to the survival of four strains of lactobacilli suspended in artificial gastric juice: *Lactocaseibacillus rhamnosus* GG, *Lactocaseibacillus rhamnosus* E800, *Lactocaseibacillus paracasei* subsp. *paracasei* NFBC 338, and *Ligilactobacillus salivarius* UCC 500. In each case they confirmed the protective effect of Tween 80™ on cell viability. No Tween 80™ resulted in a decrease in the number of LAB viable cells in at least two logarithmic cycles after incubation in artificial gastric juice for 90 min. The cited studies are confirmed by other references (Johnsson et al., 1995; Broadbent et al., 2014).

The most widely used methods in study cellular fatty acid (as methyl esters) of Firmicutes (including lactobacilli) is matrix-assisted laser desorption/ionization time-of-flight mass spectrometry (MALDI-TOF) based on the principle of ionization and mass analysis of molecules, and it is particularly well-suited for identifying bacteria because it can analyze intact bacterial cells rather than extracting and purifying specific molecules (Anderson et al., 2014; Foschi et al., 2017; Nacef et al., 2017). As a result of these advantages, MALDI-TOF is becoming the preferred method for the identification of lactobacilli in many laboratories. MALDI-TOF (matrix-assisted laser desorption ionization time-of-flight mass spectrometry) is another method that is increasingly being used for the study of bacterial cellular fatty acid. It is a rapid, sensitive, and easy-to-use technique that can provide accurate species identification. However, the Sherlock Microbial Identification System (by MIDI Inc.) is a reliable method for species identification, particularly for lactobacilli, and is often used in conjunction with other methods, such as sequencing, to provide a complete taxonomic profile (Brondz, 2002; Kunitsky et al., 2006; Alexander, 2012). The alternative method referred to in the statement is likely to be gas chromatography-mass spectrometry (GC-MS), which is a more sophisticated technique that can provide more detailed information about the composition of fatty acids. However, GC-MS is a more expensive and time-consuming method, so it is not always the most practical choice. MIDI is a faster and more cost-effective method, and it is often sufficient for routine identification of lactobacilli. In general, MIDI is a suitable choice for routine identification of lactobacilli when speed and cost are important, while MALDI-TOF is the more advanced method and is the best choice for routine identification and specialized applications. GC-MS is most appropriate for more detailed studies or when species identification is challenging.

This study investigates the influence of Tween 80™ (oleic acid source) supplementation in growth media on the FA profile of selected mesophilic lactobacilli strains. We aim to compare

TABLE 1 The collection of lactobacilli strains used in this study.

Species and strain (the origin)	Abbreviation
<i>Lactocaseibacillus rhamnosus</i> GG (ATCC 53103; American Type Culture Collection, United States)	Rh-GG
<i>Lactocaseibacillus rhamnosus</i> MB (Mediterranea Biotechnologies, Italy)	Rh-MB
<i>Lactocaseibacillus rhamnosus</i> ATCC 7469 (American Type Culture Collection, United States)	Rh-74
<i>Lactocaseibacillus casei</i> ATCC 393 (American Type Culture Collection, United States)	C-393
<i>Lactocaseibacillus casei</i> 431 (Chr. Hansen, Denmark)	C-431
<i>Lactocaseibacillus paracasei</i> subsp. <i>paracasei</i> MB (Mediterranea Biotechnologies, Italy)	PP
<i>Limosilactobacillus fermentum</i> ATCC 9338 (American Type Culture Collection, United States)	F-36
<i>Limosilactobacillus reuteri</i> DSM 17938 (Leibniz Institute DSMZ - German Collection of Microorganisms and Cell Cultures, Germany)	Re-P
<i>Lactiplantibacillus plantarum</i> 299v (DSM 9843; Leibniz Institute DSMZ-German Collection of Microorganisms and Cell Cultures, Germany)	P-299
<i>Lactiplantibacillus plantarum</i> NCAIM B.01149 (The National Collection of Agricultural and Industrial Microorganisms, Corvinus University of Budapest, Hungary)	P-011
<i>Lactiplantibacillus plantarum</i> NCAIM B.01834 (The National Collection of Agricultural and Industrial Microorganisms, Corvinus University of Budapest, Hungary)	P-018

their abilities to modulate FA synthesis and transformation upon incorporation of this external oleic acid (C18:1,*cis*-9) source.

Materials and methods

Materials

Eleven lactobacilli strains of the lactobacilli (Table 1) deposited in the laboratory collection in the form of monocultures freeze-dried or frozen were used in our research. Cultures of each bacterial strain were conducted in three independent experiments. First, the cultures were revived in the MRS (de Mann, Rogosa, and Sharpe) broth supplemented with Tween 80™ (Sigma-Aldrich) in portions of 50 mL (incubation at 37°C for approx. 12 h). Tween 80™ is known to influence membrane fluidity and potentially impact fatty acid synthesis in lactobacilli (Al-Naseri et al., 2013; Zotta et al., 2017b; Reitermayer et al., 2018). Subsequently, the cultures were inoculated onto the surface of three parallel MRS agar plates with Tween 80™ and three parallel MRS agar plates without Tween 80™ (in two independent replicates for each growth medium). Cultures were incubated at 37°C for 24 h under anaerobic conditions. Anaerocult™ A (Merck) was used to produce an anaerobic milieu in the anaerobic jar™ (Merck). Anaerocult™ A is recommended for the cultivation of obligatory and facultative anaerobes. To minimize growth phase variation, we carefully harvested cells for biomass collection from the defined center sector of each plate using the secondary inoculum. This ensured a representative sample of the cultured population for fatty acid analysis (Asadi et al., 2015).

The extraction of fatty acids: separating and detecting conditions of fatty acid methyl esters using GC-MS

The fatty acids were extracted from the entire bacterial biomass according to recommendations (Haack et al., 1994; Buyer, 2002; Kankaanpaa et al., 2004). Each bacterial biomass sample was prepared for analysis and analyzed in two replicates. The chromatographic separation of fatty acid methyl esters was carried out by gas chromatography coupled with mass spectrometer (GC-MS QP 2010 Shimadzu, Shimadzu Corporation, Japan) using polar column 007-23-30-0.2F (30 m × 0.25 mm × 0.20 μm; Quadrex, Quadrex Corporation, United States). The sample was injected under a split ratio of 1: 25 at the dispenser temperature equal to 230°C. The chromatographic separation was conducted in the following conditions: Initial temperature of column of 60°C, 2 min isotherm, the temperature increase of 4°C/min to 220°C, 10 min isotherm. The carrier gas was helium with a flow rate of 0.37 mL/min. The following detector conditions were used: Temperature of the ion source of 200°C, temperature of the line connecting GC with MS of 220°C, detector voltage of 1.45 kV, and quadrupole filter sweep in a range 50-400 m/z. The following standards were used for identifying fatty acids: oleic acid (Sigma Aldrich, United States), anteiso12-methyltetradecanoic acid (Sigma Aldrich, United States), 2-hydroxytetradecanoic acid (Sigma Aldrich, United States), nonadecanoic acid (Sigma Aldrich, United States), the BAME (bacterial acid methyl esters; Sigma Aldrich, United States), GLC-674 and GLC-617 (Nu-Chek-Prep., United States), and isomers of methyl esters of linoleic acid 18:2 (*cis*-9,*trans*-11 and *trans*-10,*cis*-12; Nu-Chek-Prep., United States). The composition of bacterial acid methyl

TABLE 2 The percentage fatty acids composition (mean ± SD, n = 6) in mesophilic *Lacticaseibacillus rhamnosus* strains profiles obtained from the cell cultured in a growth medium with Tween 80™ (with T80) and without Tween 80™ (no T80).

Strain symbol	<i>L. rhamnosus</i> GG		<i>L. rhamnosus</i> MB		<i>L. rhamnosus</i> ATCC 7469		<i>p-value</i>
	With T80	No T80	With T80	No T80	With T80	No T80	
C10:0	0.09 ^a ± 0.06	0.10 ^a ± 0.07	0.10 ^a ± 0.04	0.05 ^a ± 0.06	0.16 ^a ± 0.13	0.14 ^a ± 0.04	0.5612
C12:0	0.50 ^b ± 0.09	0.21 ^{ab} ± 0.13	0.58 ^b ± 0.04	0.06 ^a ± 0.02	1.03 ^{bc} ± 0.64	0.23 ^{ab} ± 0.09	0.0108
C14:0	6.62 ^c ± 0.79	4.58 ^b ± 1.27	4.50 ^b ± 0.30	2.83 ^a ± 0.19	2.86 ^a ± 0.70	2.23 ^a ± 0.49	0.0001
15:0, <i>iso</i>	0.18 ^{ab} ± 0.02	0.33 ^{bc} ± 0.10	0.12 ^a ± 0.01	0.22 ^a ± 0.01	0.16 ^a ± 0.06	0.25 ^{ab} ± 0.03	0.0036
15:0, <i>anteiso</i>	0.03 ^a ± 0.03	0.00 ^a ± 0.00	0.08 ^a ± 0.02	0.02 ^a ± 0.02	0.05 ^a ± 0.05	0.03 ^a ± 0.05	0.1106
C15:0	0.04 ^b ± 0.02	0.00 ^a ± 0.01	0.09 ^b ± 0.02	0.04 ^b ± 0.01	0.06 ^b ± 0.04	0.03 ^{ab} ± 0.05	0.0336
C16:0	35.82 ^b ± 1.54	48.51 ^d ± 2.27	30.20 ^a ± 1.95	42.09 ^c ± 0.75	28.67 ^a ± 0.48	33.86 ^b ± 0.20	0.0001
C16:1, <i>trans</i> -9	1.04 ^{ab} ± 0.11	1.93 ^c ± 0.49	0.76 ^a ± 0.09	1.88 ^{bc} ± 0.11	1.13 ^b ± 0.10	2.03 ^c ± 0.08	0.0001
C16:1, <i>cis</i> -9	1.74 ^c ± 0.12	1.69 ^{bc} ± 0.35	1.16 ^{ab} ± 0.15	1.25 ^{ab} ± 0.07	1.28 ^{ab} ± 0.13	1.10 ^a ± 0.07	0.0523
C12:0,2OH	0.22 ^a ± 0.02	0.24 ^a ± 0.08	0.22 ^a ± 0.02	0.31 ^b ± 0.03	0.25 ^a ± 0.05	0.33 ^b ± 0.04	0.0430
<i>cyc</i> C17:0, <i>cis</i> -9,10	0.10 ^{ab} ± 0.03	0.47 ^c ± 0.13	0.04 ^a ± 0.01	0.21 ^b ± 0.02	0.21 ^b ± 0.03	0.42 ^c ± 0.06	0.0001
C18:0	3.07 ^{ab} ± 0.66	4.50 ^b ± 0.29	4.16 ^b ± 1.56	7.64 ^d ± 0.26	2.81 ^a ± 0.18	6.56 ^c ± 0.24	0.0001
C18:1	0.16 ^b ± 0.02	0.00 ^a ± 0.00	0.14 ^b ± 0.07	0.00 ^a ± 0.00	0.15 ^b ± 0.07	0.00 ^a ± 0.00	0.0003
C18:1, <i>trans</i> -6	0.12 ^{ab} ± 0.02	0.25 ^c ± 0.06	0.07 ^a ± 0.01	0.17 ^b ± 0.02	0.17 ^b ± 0.03	0.34 ^d ± 0.05	0.0001
C18:1, <i>trans</i> -9	0.14 ^b ± 0.01	0.32 ^d ± 0.09	0.08 ^a ± 0.01	0.23 ^{bc} ± 0.02	0.19 ^b ± 0.04	0.41 ^e ± 0.03	0.0001
C18:1, <i>trans</i> -11	0.25 ^c ± 0.08	0.00 ^a ± 0.00	0.49 ^d ± 0.06	0.06 ^a ± 0.09	0.19 ^b ± 0.08	0.00 ^a ± 0.00	0.0001
C18:1, <i>cis</i> -6	0.23 ^a ± 0.10	0.37 ^{ab} ± 0.09	0.46 ^b ± 0.03	0.62 ^c ± 0.12	0.36 ^{ab} ± 0.09	0.84 ^d ± 0.12	0.0001
C18:1, <i>cis</i> -9	10.03 ^c ± 0.72	0.38 ^a ± 0.30	13.87 ^d ± 1.03	0.72 ^a ± 0.09	9.21 ^b ± 0.26	0.15 ^a ± 0.04	0.0001
C18:1, <i>cis</i> -11	9.49 ^a ± 0.63	13.85 ^b ± 1.73	10.10 ^a ± 0.42	20.52 ^c ± 1.12	14.36 ^b ± 0.64	20.21 ^c ± 0.82	0.0001
C18:2, <i>trans</i> -9, <i>trans</i> -12	0.01 ^a ± 0.02	0.37 ^a ± 0.72	0.03 ^a ± 0.04	0.10 ^a ± 0.02	0.06 ^a ± 0.05	0.17 ^a ± 0.05	0.1889
C18:2, <i>cis</i> -9, <i>cis</i> -12	0.05 ^{ab} ± 0.06	0.00 ^a ± 0.00	0.07 ^{ab} ± 0.02	0.00 ^a ± 0.00	0.00 ^a ± 0.00	0.00 ^a ± 0.00	0.0075
<i>cyc</i> C19:0, <i>cis</i> -9,10	15.45 ^b ± 1.94	0.23 ^a ± 0.10	21.20 ^{bc} ± 2.39	1.23 ^a ± 0.32	17.93 ^b ± 1.24	0.43 ^a ± 0.26	0.0001
<i>cyc</i> C19:0, <i>cis</i> -10,11	11.90 ^b ± 1.72	21.49 ^{d,c} ± 0.57	7.26 ^a ± 0.81	19.08 ^c ± 1.69	16.16 ^c ± 1.86	29.11 ^c ± 1.11	0.0001
18:2, <i>cis</i> -9, <i>trans</i> -11	0.92 ^{bc} ± 0.06	0.20 ^a ± 0.04	1.43 ^c ± 0.12	0.68 ^b ± 0.04	1.30 ^c ± 0.17	1.15 ^{bc} ± 0.13	0.0001
C18:2CLA_1	0.06 ^b ± 0.03	0.00 ^a ± 0.00	0.14 ^b ± 0.02	0.00 ^a ± 0.00	0.07 ^b ± 0.06	0.00 ^a ± 0.00	0.0003
18:2, <i>trans</i> -10, <i>cis</i> -12	0.82 ^b ± 0.05	0.00 ^a ± 0.00	1.16 ^b ± 0.11	0.00 ^a ± 0.00	0.48 ^b ± 0.07	0.00 ^a ± 0.00	0.0001
C18:2_CLA_2	0.09 ^b ± 0.01	0.00 ^a ± 0.00	0.14 ^b ± 0.01	0.00 ^a ± 0.00	0.06 ^{ab} ± 0.05	0.00 ^a ± 0.00	0.0001
C18:2_CLA_3	0.05 ^b ± 0.02	0.00 ^a ± 0.00	0.15 ^{bc} ± 0.01	0.00 ^a ± 0.00	0.03 ^a ± 0.03	0.00 ^a ± 0.00	0.0001
C18:2_CLA_4	0.76 ^b ± 0.09	0.00 ^a ± 0.00	1.20 ^c ± 0.13	0.00 ^a ± 0.00	0.61 ^b ± 0.19	0.00 ^a ± 0.00	0.0001
St/Lb	0.26 ^b ± 0.36	0.21 ^b ± 0.01	0.56 ^d ± 0.20	0.40 ^c ± 0.01	0.18 ^a ± 0.01	0.23 ^b ± 0.01	0.0001
O/V	1.06 ^c ± 0.01	0.03 ^a ± 0.02	1.37 ^d ± 0.01	0.04 ^a ± 0.01	0.64 ^b ± 0.01	0.01 ^a ± 0.00	0.0001
ΣU	25.96 ^b ± 2.15	19.36 ^a ± 3.87	31.45 ^d ± 2.30	26.23 ^b ± 1.70	29.66 ^c ± 2.10	26.40 ^b ± 1.40	0.0009
ΣS	74.02 ^a ± 6.28	80.66 ^a ± 5.02	68.55 ^a ± 7.20	73.78 ^a ± 3.40	70.36 ^a ± 5.50	73.62 ^a ± 2.70	0.1708
U/S	0.35 ^b ± 0.01	0.24 ^a ± 0.03	0.46 ^c ± 0.01	0.36 ^b ± 0.01	0.42 ^c ± 0.01	0.36 ^b ± 0.01	0.0001

(Continued on following page)

TABLE 2 (Continued) The percentage fatty acids composition (mean \pm SD, n = 6) in mesophilic *Lactocaseibacillus rhamnosus* strains profiles obtained from the cell cultured in a growth medium with Tween 80™ (with T80) and without Tween 80™ (no T80).

Strain symbol	<i>L. rhamnosus</i> GG		<i>L. rhamnosus</i> MB		<i>L. rhamnosus</i> ATCC 7469		<i>p</i> -value
	With T80	No T80	With T80	No T80	With T80	No T80	
Σ CLA	2.70 ^d \pm 0.26	0.20 ^a \pm 0.04	4.22 ^c \pm 0.40	0.68 ^b \pm 0.01	2.55 ^d \pm 0.60	1.15 ^c \pm 0.10	0.0001

Legend: C10:0, caproic/decanoic acid; C12:0, lauric/dodecanoic acid; C14:0, myristic/tetradecanoic acid; C15:0, iso, iso-13-methyltetradecanoic acid; C15:0, anteiso, anteiso-12-methyltetradecanoic acid; C15:0, pentadecanoic acid; C16:0, palmitic/hexadecanoic acid; C16:1, *trans*-9, palmitelaidic/*trans*-9-hexadecenoic acid; C16:1, *cis*-9, palmitoleic/*cis*-9-hexadecenoic acid; C12:0, 2OH, 2-hydroxydodecanoic acid; cycC17:0, *cis*-9, 10, *cis*-9, 10-methylenehexadecanoic acid; C18:0, stearic/octadecanoic acid; C18:1, octadecenoic acid; C18:1, *trans*-6, petroselaidic acid/*trans*-6-octadecenoic acid; C18:1, *trans*-9, elaidic acid/*trans*-9-octa-decenoic acid; C18:1, *trans*-11, *trans*-vaccenic acid/*trans*-11-octadecenoic acid; C18:1, *cis*-6, petroselinic acid/*cis*-6-octadecenoic acid; C18:1, *cis*-9, oleic/*cis*-9-octadecenoic acid; C18:1, *cis*-11, *cis*-vaccenic acid/*cis*-11-octadecenoic acid; C18:2, *trans*-9, *trans*-12, linoelaidic/*trans*-9, *trans*-12-octadecadienoic acid; C18:2, *cis*-9, *cis*-12, linoleic/*cis*-9, *cis*-12-octadecadienoic acid; cycC19:0, *cis*-9, 10, dihydrosterculic/*cis*-9, 10-methyleneoctadecanoic acid; cycC19:0, *cis*-10, 11, lactobacillic acid/*cis*-11, 12-methyleneoctadecanoic acid; 18:2, *cis*-9, *trans*-11, conjugated octadecadienoic acid; C18:2, conjugated octadecadienoic acid; 18:2_CLA_1 to _4, different isomers of CLA (their specific structures have not been determined); St/Lb, the ratio dihydrosterculic acid/lactobacillic acid; O/V, the ratio oleic acid/*cis*-vaccenic acid; S, saturated acids; U, unsaturated acids; U/S, the ratio unsaturated acids/saturated acids; Σ CLA, total sum of conjugated fatty acids.

^{a,b,c,d,e}—Means with different lowercase letters the same line indicate a significant difference at the significance level of 0.05 (Tukey HSD).

esters (BAMEs) is presented in Supplementary Table 1S. In other cases of fatty acids (including lactobacillic acid), the comparisons were made with the literature data (Brondz, 2002; Christie et al., 2007; Montanari et al., 2010). The data obtained from GC-MS was analyzed using GCMS Solution v.2.50 (Shimadzu Corporation).

Statistical analysis

The statistical analysis was carried out using the statistical program Statistica v.10. The analysis of variance (ANOVA) was employed. In this study, ANOVA was complemented by Tukey’s test, conducted at a significance level of 0.05, to scrutinize the mutual influence of the factors and identify any statistically significant differences between them. Principal components analysis (PCA) was conducted to assess the relationship between fatty acid profiles and the presence or absence of Tween 80™ in the growth medium. In this case, PCA was used to identify the main components that influenced the variation in fatty acid profiles.

Results and discussion

Lactocaseibacillus rhamnosus

The determined fatty acid profile of *L. rhamnosus* GG, *L. rhamnosus* MB, and *L. rhamnosus* ATCC 4769 cells demonstrated the presence of 29 fatty acids after the incubation on the growth medium with Tween 80™ (Table 2). The strains of *L. rhamnosus* used in our study were characterized by an intense growth on the MRS agar without Tween 80™. The character of the growth of this species’ colonies was different from other lactobacilli species used for this study. The colonies on the line of loop movement were snow-white with characteristic papules and damming, and so obtaining the

biomass required for the analysis was not difficult. Nineteen fatty acids were identified in the fatty acid profile of *L. rhamnosus* GG cells, while the presence of 21 fatty acids was noted in the case of *L. rhamnosus* MB and *L. rhamnosus* ATCC 7469 cells (Table 2).

By comparing the test strains of *L. rhamnosus* species acid, similarities were observed in the sequence fatty acid dominant in the fatty acid profile of the cells. The comparative analysis (conducted using Tukey’s test) of the share of all dominant fatty acids in the fatty acid profiles obtained from the biomass of all strains showed significant differences. The fatty acid profile of the *L. rhamnosus* GG strain was dominated (the share >10%) by palmitic (C16:0), dihydrosterculic (cycC19:0, *cis*-9,10), lactobacillic (cycC19:0, *cis*-10,11), and oleic (C18:1, *cis*-9,) fatty acids. Meanwhile, the fatty acid profile of the *L. rhamnosus* MB strain was dominated (the share >10%) by palmitic acid, dihydrosterculic acid (cycC19:0, *cis*-9,10), oleic acid, and *cis*-vaccenic fatty (C18:1, *cis*-11) acids. As for the fatty acid profile of *L. rhamnosus* ATCC 7469 strain, it was dominated by palmitic (C16:0), dihydrosterculic (cycC19:0, *cis*-9,10), lactobacillic (cycC19:0, *cis*-10,11), and *cis*-vaccenic acid (C18:1, *cis*-11) acids (the share >10%). Their contribution to the fatty acid profile changed significantly when Tween 80™ was eliminated from the growth medium. The only fatty acids whose proportion in the fatty acid profile did not change significantly were the following fatty acids: caproic (C10:0), anteiso-12-methyltetradecanoic (C15:0, anteiso), palmitoleic (C16:1, *cis*-9), and linoelaidic (C18: 2, *trans*-9, *trans*-12) fatty acids. In general, removal of Tween 80™ from the growth medium resulted in a decrease in the proportion of 14 fatty acids in the fatty acid profile, both saturated and unsaturated fatty acids, and an increase in the proportion of 11 fatty acids in the profile of fatty acids, mainly unsaturated fatty acids. Of course, these changes were not observed in every *L. rhamnosus* strains tested. Consequently, this resulted in a significant reduction in the calculated the ratio dihydrosterculic acid (cycC19:0, *cis*-9,10)/lactobacillic acid (cycC19:0, *cis*-10,11) (St/Lb ratio) with the exception for the

L. rhamnosus MB strain, the ratio oleic acid (C18:1,*cis*-9)/*cis*-vaccenic acid (C18:1,*cis*-11) (O/V ratio), and the ratio unsaturated acids/saturated fatty acids (U/S ratio). It is worth noting that removal of Tween 80™ from the growth medium resulted in a significant reduction in the proportion of total unsaturated fatty acids, including conjugated fatty acids (CLA), in the fatty acid profile, but also did not result in a complete change in the proportion of saturated fatty acids in the fatty acid profile.

Kankaanpää et al. (2004) found that *L. rhamnosus* GG cells grown with Tween 80™ contained oleic (21.5%), *cis*-vaccenic (21.8%), dihydrosterculic (23.5%), and lactobacillic (2.1%) acids as major fatty acids, along with conjugated acids at about 3%. Bacteria produce unsaturated fatty acids with various functionalities *de novo* (Zhu et al., 2019). These modifications, along with other fatty acids, increase the fluidity of the cytoplasmic membrane through their specific structures (Kaneda, 1991). The ability of the strains to synthesize *cis*-vaccenic acid and convert it to lactobacillic acid is noteworthy, with minimal *de novo* synthesis of oleic acid, especially in the absence of Tween 80™. The presence of Tween 80™ appears to inhibit the FAS system, as suggested by (Zhang et al., 2020). Our study indicates that all strains produced vaccenic acid even under anaerobic conditions, which is significant since anaerobic conditions favor the anaerobic vaccenic acid pathway. This contrasts with aerobic conditions in *L. casei* N87, which enhance growth, metabolism, and stress tolerance, influencing vaccenic acid synthesis (Ianniello et al., 2016). Refrigerated storage before biomass extraction can increase the proportion of unsaturated fatty acids (Zhu et al., 2019), which helps maintain membrane fluidity and protein activity (Santivarangkna et al., 2008; Parsons and Rock, 2013). The absence of oleic acid stimulates lactobacillic acid synthesis, while its presence increases dihydrosterculic acid levels (Kankaanpää et al., 2004). This adaptive modification in fatty acid composition helps control membrane fluidity, aiding bacterial stress defense (Beal et al., 2001; Murga et al., 2001; Montanari et al., 2010; Pawar and Aranha, 2022). Environmental factors significantly influence unsaturated fatty acid proportions in lactobacilli membranes (Zotta et al., 2017a; Fonseca et al., 2019), with oxygen availability playing a crucial role (López de Felipe, 2023). Under aerobic conditions, lactobacilli can convert palmitoleic acid to *cis*-vaccenic acid (Cronan, 2002; Schujman and Mendoza, 2008; Jimenez et al., 2023). Corcoran et al. (2007) noted a rise in certain acids in *L. rhamnosus* GG cells when exposed to oleic acid (C18:1,*cis*-9). Our research found that adding oleic acid via Tween 80™ increased dihydrosterculic acid (*cyc*C19:0,*cis*-9,10), oleic acid (C18:1,*cis*-9), and conjugated fatty acids, while reducing palmitic (C16:0) and stearic (C18:0) acids. Furthermore, *L. rhamnosus* GG, *L. rhamnosus* MB, and *L. rhamnosus* ATCC 7469 cells cultured without Tween 80™ showed lactobacillic acid (*cyc*C19:0,*cis*-10,11) dominance in

their fatty acid profiles. This difference is likely due to the lack of separation of cyclic acids in the Corcoran et al. (2007) study.

Lactocaseibacillus casei and *Lactocaseibacillus paracasei*

The identified fatty acid profile of *L. casei* 393, *L. casei* 431, and *L. paracasei* subsp. *paracasei* MB grown on MRS agar with Tween 80™ contained 29 and 27 fatty acids for *L. casei* and *L. paracasei*, respectively (Table 3). The predominant fatty acids in the fatty acid profile of the first of these strains were: palmitic acid (C16:0), dihydrosterculic acid (*cyc*C19:0,*cis*-9,10), lactobacillic acid (*cyc*C19:0,*cis*-10,11), and *cis*-vaccenic acid (C18:1,*cis*-11). Meanwhile, fatty acids such as palmitic acid, oleic acid (C18:1,*cis*-9), *cis*-vaccenic acid (C18:1,*cis*-11), and dihydrosterculic acid (*cyc*C19:0,*cis*-9,10) were found to be dominant for the fatty acid profile of *L. casei* 431. On the other hand, dominant fatty acids in the *L. paracasei* subsp. *paracasei* MB fatty acid profile included oleic acid (C18:1,*cis*-9), dihydrosterculic acid (*cyc*C19:0,*cis*-9,10), and palmitic acid (C16:0). While dihydrosterculic acid (*cyc*C19:0,*cis*-9,10) could potentially be used to differentiate between *L. casei* and *L. paracasei* subsp. *paracasei* MB, the high proportion observed in this study might be due to stress experienced by the bacteria during growth (Rouch et al., 2002; Wu et al., 2020; Klein et al., 2022). Cyclic fatty acids, including dihydrosterculic acid (*cyc*C19:0,*cis*-9,10), are known markers of stress in LAB. Further studies are needed to investigate the influence of growth conditions on the fatty acid profile of *L. paracasei* subsp. *paracasei* MB and confirm its potential as a differentiating factor. *L. casei* and *L. paracasei* grown without Tween 80™ displayed altered fatty acid profiles compared to cultures with Tween 80™. Notably, the absence of oleic acid (C18:1,*cis*-9) triggered *cis*-vaccenic (C18:1,*cis*-11) and lactobacillic acid (*cyc*C19:0,*cis*-10,11) synthesis. Total saturated fatty acids, especially iso-13-methyltetradecanoic (C15:0,iso) and stearic (C18:0) acids, increased in bacteria lacking Tween 80™, although this effect was not universal. Conversely, unsaturated fatty acid content and the U/S ratio decreased without Tween 80™. Interestingly, total CLA and St/Lb and O/V ratios also significantly declined. These changes in *L. casei* and *paracasei* are distinct from those observed previously in *L. rhamnosus*.

We observed significant differences in the proportions of saturated, unsaturated, and cyclic fatty acids compared to previous studies (Rizzo et al., 1987; Kankaanpää et al., 2004; Machado et al., 2004; Liong and Shah, 2005; Corsetti et al., 2010; Rodrigues et al., 2012). Notably, our findings revealed substantial levels of dihydrosterculic and lactobacillic acids, cyclic derivatives of oleic and vaccenic acids, respectively. These results contrast with some prior studies that may have missed these cyclic acids due to separation and detection challenges (Machado et al., 2004; Liong and Shah, 2005). For *L. casei*, our dominant fatty acids

TABLE 3 The percentage fatty acids composition (mean ± SD, n = 6) in mesophilic *Lacticaseibacillus casei* and *Lacticaseibacillus paracasei* strains profiles obtained from the cell cultured in a growth medium with Tween 80TM (with T80) and without Tween 80TM (no T80).

Strain symbol	<i>L. casei</i> ATCC 393		<i>L. casei</i> 431		<i>L. paracasei</i> subsp. <i>paracasei</i> MB		<i>p</i> -value
	With T80	No T80	With T80	No T80	With T80	No T80	
C10:0	0.16 ^c ± 0.01	0.10 ^c ± 0.03	0.01 ^a ± 0.03	0.03 ^a ± 0.08	0.05 ^{ab} ± 0.03	0.05 ^{ab} ± 0.04	0.0507
C12:0	0.70 ^b ± 0.08	0.10 ^a ± 0.03	0.80 ^{bc} ± 0.09	0.18 ^a ± 0.08	1.94 ^c ± 0.37	0.24 ^{ab} ± 0.08	0.0001
C14:0	6.29 ^c ± 0.38	3.19 ^a ± 0.10	7.92 ^d ± 0.35	4.72 ^{ab} ± 0.21	6.32 ^c ± 0.38	3.24 ^a ± 0.70	0.0001
15:0, <i>iso</i>	0.52 ^{bc} ± 0.04	0.63 ^c ± 0.03	0.70 ^{c-d} ± 0.06	0.88 ^d ± 0.03	0.12 ^a ± 0.02	0.40 ^b ± 0.06	0.0001
15:0, <i>anteiso</i>	0.06 ^a ± 0.02	0.00 ^a ± 0.00	0.07 ^{ab} ± 0.04	0.02 ^a ± 0.05	0.13 ^{ab} ± 0.03	0.05 ^a ± 0.04	0.0089
C15:0	0.06 ^a ± 0.02	0.00 ^a ± 0.00	0.09 ^{ab} ± 0.05	0.05 ^a ± 0.03	0.17 ^b ± 0.02	0.10 ^b ± 0.03	0.0003
C16:0	19.81 ^a ± 0.60	22.82 ^b ± 0.28	24.36 ^b ± 2.87	35.62 ^c ± 0.40	20.81 ^a ± 1.99	42.38 ^d ± 1.57	0.0001
C16:1, <i>trans</i> -9	2.71 ^c ± 0.14	4.50 ^c ± 0.18	1.37 ^b ± 0.19	3.18 ^{c-d} ± 0.14	0.36 ^a ± 0.12	2.49 ^c ± 0.07	0.0001
C16:1, <i>cis</i> -9	4.61 ^{bc} ± 0.22	3.89 ^b ± 0.23	5.87 ^c ± 0.26	7.11 ^d ± 0.29	1.29 ^a ± 0.06	2.59 ^{ab} ± 0.36	0.0001
C12:0,2OH	0.42 ^b ± 0.01	0.51 ^c ± 0.01	0.51 ^c ± 0.05	0.84 ^d ± 0.04	0.21 ^a ± 0.03	0.44 ^b ± 0.04	0.0001
<i>cyc</i> C17:0, <i>cis</i> -9,10	0.39 ^c ± 0.03	0.67 ^d ± 0.06	0.02 ^a ± 0.02	0.17 ^b ± 0.02	0.08 ^a ± 0.06	0.17 ^b ± 0.03	0.0001
C18:0	1.02 ^a ± 0.77	0.95 ^a ± 0.08	0.90 ^a ± 0.12	1.11 ^a ± 0.21	1.77 ^a ± 0.22	14.27 ^b ± 0.89	0.0001
C18:1	0.17 ^b ± 0.04	0.00 ^a ± 0.00	0.07 ^{ab} ± 0.05	0.00 ^a ± 0.00	0.22 ^b ± 0.06	0.00 ^a ± 0.00	0.0001
C18:1, <i>trans</i> -6	0.17 ^{bc} ± 0.01	0.24 ^d ± 0.05	0.03 ^{ab} ± 0.03	0.08 ^b ± 0.01	0.00 ^a ± 0.00	0.12 ^b ± 0.02	0.0001
C18:1, <i>trans</i> -9	0.20 ^c ± 0.02	0.32 ^d ± 0.04	0.04 ^a ± 0.01	0.13 ^b ± 0.02	0.00 ^a ± 0.00	0.12 ^b ± 0.02	0.0001
C18:1, <i>trans</i> -11	0.16 ^a ± 0.05	0.06 ^a ± 0.16	0.47 ^b ± 0.14	0.30 ^b ± 0.15	0.66 ^c ± 0.07	0.12 ^a ± 0.22	0.0018
C18:1, <i>cis</i> -6	0.25 ^a ± 0.04	0.46 ^b ± 0.05	0.26 ^a ± 0.06	0.36 ^{ab} ± 0.08	0.20 ^a ± 0.05	0.52 ^{bc} ± 0.05	0.0001
C18:1, <i>cis</i> -9	7.12 ^b ± 0.44	0.17 ^a ± 0.02	22.23 ^c ± 2.91	0.90 ^a ± 0.41	34.26 ^d ± 4.42	2.44 ^{ab} ± 0.57	0.0001
C18:1, <i>cis</i> -11	16.19 ^b ± 0.33	23.84 ^d ± 0.80	15.28 ^b ± 1.78	30.76 ^c ± 0.93	4.96 ^a ± 1.38	18.69 ^c ± 2.25	0.0001
C18:2, <i>trans</i> -9, <i>trans</i> -12	0.33 ^{bc} ± 0.02	0.55 ^{c-d} ± 0.06	0.23 ^b ± 0.04	0.49 ^c ± 0.08	0.06 ^a ± 0.04	0.25 ^b ± 0.05	0.0001
C18:2, <i>cis</i> -9, <i>cis</i> -12	0.03 ^a ± 0.01	0.00 ^a ± 0.00	0.07 ^{ab} ± 0.04	0.00 ^a ± 0.00	0.08 ^{ab} ± 0.03	0.02 ^{ab} ± 0.04	0.0098
<i>cyc</i> C19:0, <i>cis</i> -9,10	19.23 ^d ± 1.43	0.64 ^a ± 0.12	11.36 ^c ± 1.53	0.55 ^a ± 0.19	20.89 ^d ± 1.33	3.29 ^b ± 1.15	0.0001
<i>cyc</i> C19:0, <i>cis</i> -10,11	18.00 ^c ± 0.75	35.83 ^f ± 0.83	3.76 ^b ± 0.58	12.09 ^d ± 0.58	1.17 ^a ± 0.86	7.21 ^c ± 0.81	0.0001
18:2, <i>cis</i> -9, <i>trans</i> -11	0.45 ^b ± 0.05	0.19 ^a ± 0.03	1.12 ^c ± 0.16	0.25 ^{ab} ± 0.03	1.22 ^d ± 0.18	0.38 ^b ± 0.06	0.0001
C18:2CLA_1	0.04 ^{ab} ± 0.02	0.00 ^a ± 0.00	0.13 ^c ± 0.03	0.00 ^a ± 0.00	0.16 ^c ± 0.03	0.00 ^a ± 0.00	0.0001
18:2, <i>trans</i> -10, <i>cis</i> -12	0.44 ^b ± 0.04	0.00 ^a ± 0.00	0.98 ^c ± 0.14	0.00 ^a ± 0.00	1.18 ^d ± 0.11	0.09 ^a ± 0.03	0.0001
C18:2_CLA_2	0.07 ^a ± 0.02	0.13 ^b ± 0.03	0.13 ^b ± 0.02	0.07 ^a ± 0.01	0.14 ^b ± 0.02	0.06 ^a ± 0.01	0.0004
C18:2_CLA_3	0.06 ^a ± 0.03	0.19 ^b ± 0.03	0.11 ^{ab} ± 0.05	0.12 ^{ab} ± 0.01	0.15 ^{ab} ± 0.02	0.09 ^a ± 0.02	0.0025
C18:2_CLA_4	0.33 ^c ± 0.05	0.00 ^a ± 0.00	1.12 ^b ± 0.19	0.00 ^a ± 0.00	1.39 ^d ± 0.08	0.19 ^{ab} ± 0.06	0.0001
St/Lb	0.06 ^a ± 0.04	0.03 ^a ± 0.01	0.24 ^b ± 0.01	0.09 ^a ± 0.01	2.49 ^d ± 2.18	1.98 ^c ± 0.10	0.0134
O/V	0.44 ^c ± 0.01	0.01 ^a ± 0.01	1.45 ^d ± 0.02	0.03 ^a ± 0.01	7.11 ^c ± 1.13	0.12 ^b ± 0.2	0.0001
ΣU	33.33 ^b ± 1.53	34.54 ^b ± 1.68	49.51 ^d ± 6.10	43.75 ^c ± 2.16	46.33 ^c ± 6.67	28.17 ^a ± 3.83	0.0002
ΣS	66.66 ^b ± 4.14	65.44 ^b ± 1.57	50.50 ^a ± 5.79	56.26 ^a ± 1.92	53.66 ^a ± 5.34	71.84 ^c ± 5.44	0.0004
U/S	0.50 ^b ± 0.01	0.53 ^b ± 0.01	0.98 ^c ± 0.01	0.78 ^c ± 0.01	0.86 ^d ± 0.03	0.39 ^a ± 0.02	0.0001

(Continued on following page)

TABLE 3 (Continued) The percentage fatty acids composition (mean \pm SD, n = 6) in mesophilic *Lactocaseibacillus casei* and *Lactocaseibacillus paracasei* strains profiles obtained from the cell cultured in a growth medium with Tween 80TM (with T80) and without Tween 80TM (no T80).

Strain symbol	<i>L. casei</i> ATCC 393		<i>L. casei</i> 431		<i>L. paracasei</i> subsp. <i>paracasei</i> MB		<i>p</i> -value
	With T80	No T80	With T80	No T80	With T80	No T80	
Σ CLA	1.39 ^b \pm 0.21	0.51 ^a \pm 0.09	3.59 ^c \pm 0.59	0.44 ^a \pm 0.05	4.24 ^d \pm 0.44	0.81 ^a \pm 0.18	0.0001

Legend: as Table 2.
^{a,b,c,d,e,f}—Means with different lowercase letters the same line indicate a significant difference at the significance level of 0.05 (Tukey HSD).

included dihydrosterculic and lactobacillic acids, alongside palmitic acid. This aligns with the findings of Rizzo et al. (1987) who reported palmitic, octadecenoic, and cyclopropane acids as the major components in *L. casei* ATCC 393. However, some discrepancies exist, such as the presence of palmitoleic acid in Machado et al. (2004) which we did not observe. These differences could be attributed to various factors, including strain variations and growth conditions. While comparisons for *L. paracasei* subsp. *paracasei* MB were limited due to a scarcity of data specifically for this subspecies, it's important to acknowledge that the *L. casei* group taxonomy has undergone revisions in recent years. Some strains previously classified as *L. casei* may now be identified as *L. paracasei*. Future studies that incorporate a wider range of *Lactobacillus* species, including recently reclassified members of the casei group, along with standardized protocols, would offer valuable insights into the influence of growth media components on bacterial fatty acid composition.

Limosilactobacillus fermentum and *Limosilactobacillus reuteri*

The fatty acid profile of bacterial biomass of *L. fermentum* ATCC 9338 and *L. reuteri* DSM 17938 cultured on growth medium with Tween 80TM was characterized by the presence of 27 and 28 fatty acids, respectively (Table 4). We demonstrated that *L. fermentum* ATCC 9338 was characterized by the share of palmitic (C16:0), oleic (C18:1,*cis*-9), lactobacillic (*cyc*C19:0,*cis*-10,11), *cis*-vaccenic (C18:1,*cis*-11), and dihydrosterculic fatty (*cyc*C19:0,*cis*-9,10) acids, while *L. reuteri* DSM 17938 by palmitic, *cis*-vaccenic (C18:1,*cis*-11), dihydrosterculic (*cyc*C19:0,*cis*-9,10), and lactobacillic (*cyc*C19:0,*cis*-10,11) acids. Each of these strains demonstrated the ability to synthesize vaccenic and lactobacillic (*cyc*C19:0,*cis*-10,11) acids, which were in a pool of dominant fatty acids. We also demonstrated the presence of oleic acid (C18:1,*cis*-9) and its cyclic derivative, dihydrosterculic acid (*cyc*C19:0,*cis*-9,10) (Table 4). *L. fermentum* ATCC 9338 and *L. reuteri* DSM 17938 showed excellent growth on MRS agar without Tween 80TM. The fatty acid profile of the first of these strains contained 20 fatty acids, while the second strain was characterized by 22 fatty acids. Removal of Tween 80TM from the growth medium resulted in statistically significant changes in the

fatty acid profile of bacterial strains: an increase in the share of 8 fatty acids (5 unsaturated fatty acids and 3 saturated fatty acids) and a decrease in the share of 11 fatty acids (4 saturated fatty acids and 7 unsaturated fatty acids). This significantly reduced the calculated ratios of O/V and U/S, but increased the calculated St/Lb ratio. It is also worth noting that the changes observed were not the same across all bacterial strains tested, which, as with the lactobacilli strains discussed previously, allows for some differentiation.

Our study confirmed previous findings (Johnsson et al., 1995) that Tween 80TM significantly alters the fatty acid profile of *L. fermentum*. Oleic (C18:1,*cis*-9) and dihydrosterculic (*cyc*C19:0,*cis*-9,10) acids, undetectable without the surfactant, became enriched upon its addition. This effect occurred without affecting growth rate, suggesting independent processes. Furthermore, our results aligned with Rizzo et al. (1987) regarding the overall fatty acid composition of *L. fermentum*, highlighting the consistency of this profile across strains.

Taranto et al. (2006) determined the dominant fatty acid in *L. reuteri* CRL 1098 to be palmitic acid (57.7%). Our study found a similar proportion of palmitic acid (40.07%) in *L. reuteri* cells, suggesting a relatively consistent fatty acid profile for this species. Similar results were observed for stearic acid (3.86% and 3.28%, respectively) and the ratio of oleic acid (C18:1,*cis*-9) to *cis*-vaccenic acid (C18:1,*cis*-11) ratio (0.70% and 0.62%). Comparison of cyclic acids was difficult due to limitations in the cited study (Taranto et al., 2006). The ability of *L. reuteri* strains to synthesize CLA from linoleic acid (C18:2,*cis*-9,*cis*-12) has been demonstrated previously (Jenkins and Courtney, 2003; Hernandez-Mendoza et al., 2009; Macouzet et al., 2010). Our study confirmed CLA synthesis by *L. reuteri* DSM 17938 at a level comparable to other strains. The dominant CLA profile was *cis*-9,*trans*-11-octadecadienoic acid, and the strain exhibited the ability to synthesize CLA even without added oleic acid. Lactic acid bacteria possess the ability to transform unsaturated fatty acids in their conjugated form (i.e., CLA) (Kishino et al., 2002; Lin et al., 2002; Lin et al., 2003; Ogawa et al., 2005; Lin, 2006).

Lactiplantibacillus plantarum

Our study examined three strains of *L. plantarum*, all of which exhibited efficient growth on MRS agar with or without

TABLE 4 The percentage fatty acids composition (mean \pm SD, n = 6) in mesophilic *Limosilactobacillus fermentum* and *Limosilactobacillus reuteri* strains profiles obtained from the cell cultured in a growth medium with Tween 80TM (with T80) and without Tween 80TM (no T80).

Strain symbol	<i>L. fermentum</i> ATCC 9338		<i>L. reuteri</i> DSM 17938		<i>p-value</i>
Fatty acid/Medium	With T80	No T80	With T80	No T80	
C10:0	0.17 ^a \pm 0.02	0.05 ^a \pm 0.06	0.15 ^a \pm 0.09	0.13 ^a \pm 0.09	0.2550
C12:0	1.10 ^c \pm 0.12	0.12 ^a \pm 0.08	0.78 ^b \pm 0.14	0.22 ^a \pm 0.07	0.0001
C14:0	1.32 ^a \pm 0.12	1.07 ^a \pm 0.39	2.37 ^b \pm 0.23	1.39 ^a \pm 0.31	0.0022
15:0, <i>iso</i>	0.06 ^a \pm 0.01	0.04 ^a \pm 0.04	0.08 ^a \pm 0.04	0.04 ^a \pm 0.07	0.6702
15:0, <i>anteiso</i>	0.03 ^a \pm 0.00	0.03 ^a \pm 0.04	0.01 ^a \pm 0.02	0.02 ^a \pm 0.03	0.7707
C15:0	0.05 ^a \pm 0.00	0.05 ^a \pm 0.07	0.07 ^a \pm 0.02	0.06 ^a \pm 0.02	0.8983
C16:0	27.11 ^a \pm 1.97	30.28 ^a \pm 1.06	40.07 ^b \pm 1.79	46.07 ^b \pm 4.12	0.0001
C16:1, <i>trans</i> -9	1.11 ^a \pm 0.03	2.00 ^b \pm 0.10	1.94 ^{a,b} \pm 0.21	3.07 ^c \pm 0.30	0.0001
C16:1, <i>cis</i> -9	0.76 ^b \pm 0.06	0.75 ^b \pm 0.12	0.46 ^a \pm 0.02	0.44 ^a \pm 0.09	0.0515
C12:0,2OH	0.09 ^c \pm 0.01	0.05 ^b \pm 0.01	0.00 ^a \pm 0.00	0.00 ^a \pm 0.00	0.0001
<i>cyc</i> C17:0, <i>cis</i> -9,10	0.00 ^a \pm 0.00	0.05 ^a \pm 0.11	0.02 ^a \pm 0.05	0.00 ^a \pm 0.00	0.7185
C18:0	1.01 ^a \pm 0.08	1.66 ^a \pm 0.36	3.28 ^b \pm 0.60	10.66 ^c \pm 1.33	0.0001
C18:1	0.09 ^c \pm 0.01	0.00 ^a \pm 0.00	0.02 ^{a,b} \pm 0.05	0.00 ^a \pm 0.00	0.0074
C18:1, <i>trans</i> -6	0.11 ^a \pm 0.01	0.26 ^b \pm 0.02	0.10 ^a \pm 0.02	0.24 ^b \pm 0.05	0.0002
C18:1, <i>trans</i> -9	0.13 ^a \pm 0.02	0.34 ^{b,c} \pm 0.04	0.12 ^a \pm 0.01	0.26 ^b \pm 0.07	0.0004
C18:1, <i>trans</i> -11	0.34 ^a \pm 0.09	0.00 ^a \pm 0.00	0.34 ^a \pm 0.83	0.00 ^a \pm 0.00	0.5976
C18:1, <i>cis</i> -6	0.25 ^a \pm 0.02	0.55 ^{a,b} \pm 0.05	1.49 ^c \pm 0.69	1.51 ^c \pm 0.31	0.0066
C18:1, <i>cis</i> -9	18.41 ^d \pm 1.35	0.47 ^a \pm 0.17	9.07 ^c \pm 0.45	1.09 ^b \pm 1.01	0.0001
C18:1, <i>cis</i> -11	14.11 ^{a,b} \pm 0.12	22.34 ^b \pm 0.84	14.64 ^{a,b} \pm 2.90	10.26 ^a \pm 1.55	0.0002
C18:2, <i>trans</i> -9, <i>trans</i> -12	0.02 ^a \pm 0.02	0.00 ^a \pm 0.00	0.29 ^a \pm 0.70	0.01 ^a \pm 0.02	0.7046
C18:2, <i>cis</i> -9, <i>cis</i> -12	0.00 ^a \pm 0.01	0.00 ^a \pm 0.00	0.03 ^a \pm 0.04	0.07 ^a \pm 0.16	0.7029
<i>cyc</i> C19:0, <i>cis</i> -9,10	14.06 ^b \pm 0.51	0.55 ^a \pm 0.10	12.18 ^b \pm 2.80	1.45 ^a \pm 1.31	0.0001
<i>cyc</i> C19:0, <i>cis</i> -10,11	17.70 ^b \pm 0.94	39.25 ^d \pm 1.35	10.35 ^a \pm 0.58	22.09 ^c \pm 2.86	0.0001
18:2, <i>cis</i> -9, <i>trans</i> -11	0.64 ^b \pm 0.05	0.08 ^a \pm 0.01	0.68 ^b \pm 0.05	0.75 ^b \pm 0.11	0.0001
C18:2CLA_1	0.06 ^b \pm 0.01	0.00 ^a \pm 0.00	0.08 ^b \pm 0.02	0.00 ^a \pm 0.00	0.0001
18:2, <i>trans</i> -10, <i>cis</i> -12	0.67 ^c \pm 0.06	0.00 ^a \pm 0.00	0.43 ^b \pm 0.06	0.00 ^a \pm 0.00	0.0001
C18:2_CLA_2	0.05 ^b \pm 0.01	0.00 ^a \pm 0.00	0.06 ^b \pm 0.02	0.00 ^a \pm 0.00	0.0002
C18:2_CLA_3	0.04 ^a \pm 0.02	0.00 ^a \pm 0.00	0.01 ^a \pm 0.02	0.04 ^a \pm 0.05	0.2763
C18:2_CLA_4	0.52 ^c \pm 0.05	0.00 ^a \pm 0.00	0.90 ^d \pm 0.04	0.12 ^{a,b} \pm 0.13	0.0001
St/Lb	0.21 ^a \pm 0.21	0.26 ^b \pm 0.31	0.19 ^a \pm 0.18	0.26 ^b \pm 0.32	0.0001
O/V	0.92 ^b \pm 0.54	0.09 ^a \pm 0.11	0.92 ^b \pm 0.42	0.06 ^a \pm 0.07	0.0001
Σ U	37.05 ^b \pm 0.37	24.25 ^a \pm 3.59	33.01 ^b \pm 3.33	21.65 ^a \pm 5.35	0.0016
Σ S	69.21 ^a \pm 9.21	82.77 ^b \pm 13.53	64.14 ^a \pm 7.38	75.83 ^b \pm 8.91	0.0378
U/S	0.54 ^b \pm 0.08	0.30 ^a \pm 0.09	0.52 ^b \pm 0.11	0.29 ^a \pm 0.10	0.0001

(Continued on following page)

TABLE 4 (Continued) The percentage fatty acids composition (mean \pm SD, $n = 6$) in mesophilic *Limosilactobacillus fermentum* and *Limosilactobacillus reuteri* strains profiles obtained from the cell cultured in a growth medium with Tween 80TM (with T80) and without Tween 80TM (no T80).

Strain symbol	<i>L. fermentum</i> ATCC 9338		<i>L. reuteri</i> DSM 17938		<i>p</i> -value
Fatty acid/Medium	With T80	No T80	With T80	No T80	
Σ CLA	2.17 ^b \pm 0.28	0.64 ^a \pm 0.79	1.97 ^b \pm 0.27	0.49 ^a \pm 0.59	0.0001

Legend: as Table 2.

^{a,b,c,d}—Means with different lowercase letters the same line indicate a significant difference at the significance level of 0.05 (Tukey HSD).

Tween 80TM. Interestingly, the fatty acid profiles of *L. plantarum* 299v and *L. plantarum* B.01149 cultured on growth medium with Tween 80TM exhibiting profiles with 24 fatty acids, and B.01834 exhibiting a 24-fatty acid profile. Cultivation on growth medium with the addition of Tween 80TM resulted in the fatty acid profile of all three strains examined being dominated by palmitic acid (C16:0), dihydrosterculic acid, *cis*-vaccenic acid and lactobacillic acid (*cyc*C19:0,*cis*-10,11), with the involvement of the last two of these fatty acids differentiating the strains examined (Table 5). Removal of Tween 80TM from the growth medium resulted in a decrease in the share of 11 fatty acids (4 saturated and 7 unsaturated) in the fatty acid profile and an increase in the share of 9 fatty acids (6 saturated and 3 unsaturated) in the fatty acid profile. It is also worth mentioning that the overall contribution of CLA to the fatty acid profile of the tested strains was also statistically reduced due to the removal of Tween 80TM from the growth medium. As a result, the proportion of total saturated and unsaturated fatty acids in the fatty acid profile increased significantly in some bacterial strains. Instead, a significant increase in the St/Lb ratio and a significant decrease in the O/V ratio were observed.

We identified discrepancies with Johnsson et al. (1995) regarding oleic acid (C18:1,*cis*-9) and lactobacillic acid (*cyc*C19:0,*cis*-10,11) production by *L. plantarum* 2004. Our strains displayed a dominance of lactobacillic acid (11.02%–14.46%) and lower levels of oleic acid (up to 4.18%) compared to their findings. We attribute these differences to potential limitations in their methodology, such as sample size and incubation temperature. Our results for strains cultured without Tween 80TM showed a high proportion of palmitic acid (52.82%–54.78%), aligning with Rozès and Peres (1998). Both studies highlighted the prominence of C18:1 and cyclic C19:0 acids, although the specific compositions were not identical. Similarly, Russell et al. (1995) reported palmitic acid dominance, but stearic acid (C18:0) was not a major component in our analysis. These variations likely stem from differing incubation temperatures and analytical methods. Rizzo et al. (1987) identified palmitic (C16:0), *cis*-vaccenic (C18:1,*cis*-11), and cyclic C19:0 acids in *L. plantarum* ATCC 14917. However, their classification of the latter solely as lactobacillic acid (*cyc*C19:0,*cis*-10,11) might not account for all possible isomers. *L. plantarum*'s ability to produce dihydrosterculic

acid (*cyc*C19:0,*cis*-9,10), as demonstrated by Johnsson et al. (1995), supports this notion. Our findings support this notion, revealing the presence of both lactobacillic (*cyc*C19:0,*cis*-10,11) and dihydrosterculic (*cyc*C19:0,*cis*-9,10) acids. Our research confirms the ability of *L. plantarum* strains to synthesize CLA (conjugated linoleic acid) from various substrates, as reported in previous studies (Ogawa et al., 2005; Kishino et al., 2009; Corsetti et al., 2010; Rodríguez-Alcalá et al., 2011). Studies by Kishino et al. (2009) CLA levels were significantly higher in cultures supplemented with Tween 80TM (1.67%–2.21%) compared to those without (0.16%–0.19%). The two predominant CLA isomers identified (*cis*-9,*trans*-11 and *trans*-10,*cis*-12) are consistent with Rodríguez-Alcalá et al. (2011). This study highlights the variability in fatty acid profiles of *L. plantarum* strains and emphasizes the need for standardized methodologies for accurate comparisons. We confirm the prevalence of palmitic (C16:0) and C18:1/cyclic C19:0 fatty acids, with lactobacillic acid (*cyc*C19:0,*cis*-10,11) as the dominant cyclic form. Additionally, our findings support *L. plantarum*'s ability to produce CLA, with levels influenced by the presence of Tween 80TM.

Principal components analysis

Fatty acids play a crucial role in the physiology and metabolism of lactobacilli. Their composition can influence various aspects of lactobacilli growth, function, and interaction with the environment. Understanding the fatty acid profiles of lactobacilli can provide valuable insights into their metabolic capabilities and potential applications. Of course, the fatty acid composition of lactobacilli can vary significantly depending on the strain and growth conditions. Principal components analysis revealed that growth medium supplementation with Tween 80TM significantly affected the fatty acid profiles of mesophilic lactobacilli strains, particularly the share of oleic acid (C18:1,*cis*-9), *cis*-vaccenic acid (C18:1,*cis*-11), lactobacillic acid (*cyc*C19:0,*cis*-10,11), and dihydrosterculic acid (*cyc*C19:0,*cis*-9,10). In general, the values of the first two principal components of the PCA statistical analysis of 57.53% are not too high and indicate that they do not fully explain the variability of the original data set. Nevertheless, the first two principal components may be statistically significant for the variables we are interested in. The PCA gives a quick

TABLE 5 The percentage fatty acids composition (mean \pm SD, n = 6) in mesophilic *Lactiplantibacillus plantarum* strains profiles obtained from the cell cultured in a growth medium with Tween 80TM (with T80) and without Tween 80TM (no T80).

Strain symbol	<i>L. plantarum</i> 299v		<i>L. plantarum</i> B.01149		<i>L. plantarum</i> B.01834		<i>p</i> -value
Fatty acid/Medium	With T80	No T80	With T80	No T80	With T80	No T80	
C10:0	0.21 ^a \pm 0.08	0.31 ^{ab} \pm 0.09	0.29 ^a \pm 0.12	0.46 ^{bc} \pm 0.07	0.38 ^b \pm 0.07	0.52 ^c \pm 0.04	0.0057
C12:0	0.90 ^{ab} \pm 0.21	0.62 ^{ab} \pm 0.19	0.98 ^b \pm 0.50	1.00 ^{bc} \pm 0.19	1.91 ^c \pm 0.65	0.97 ^b \pm 0.15	0.0185
C14:0	2.79 ^b \pm 0.35	1.45 ^a \pm 0.35	4.21 ^c \pm 0.27	2.04 ^{ab} \pm 0.21	6.16 ^d \pm 1.92	2.70 ^b \pm 0.46	0.0002
15:0, <i>iso</i>	0.12 ^a \pm 0.02	0.27 ^b \pm 0.05	0.18 ^a \pm 0.15	0.49 ^b \pm 0.05	0.27 ^b \pm 0.06	0.45 ^c \pm 0.05	0.0003
15:0, <i>anteiso</i>	0.05 ^a \pm 0.06	0.00 ^a \pm 0.00	0.04 ^a \pm 0.05	0.02 ^a \pm 0.05	0.18 ^a \pm 0.17	0.02 ^a \pm 0.04	0.1576
C15:0	0.05 ^{ab} \pm 0.06	0.01 ^a \pm 0.03	0.05 ^{ab} \pm 0.06	0.02 ^a \pm 0.05	0.17 ^b \pm 0.10	0.01 ^a \pm 0.02	0.0472
C16:0	44.99 ^{ab} \pm 2.37	52.95 ^c \pm 1.73	41.79 ^a \pm 2.24	54.78 ^d \pm 0.87	40.11 ^a \pm 2.34	52.82 ^c \pm 0.96	0.0001
C16:1, <i>trans</i> -9	0.90 ^a \pm 0.07	1.21 ^b \pm 0.06	1.07 ^{ab} \pm 0.05	1.23 ^b \pm 0.10	1.03 ^{ab} \pm 0.07	1.40 ^c \pm 0.14	0.0002
C16:1, <i>cis</i> -9	2.31 ^b \pm 0.26	1.30 ^a \pm 0.09	2.76 ^b \pm 0.45	1.27 ^a \pm 0.14	2.73 ^b \pm 0.51	1.44 ^a \pm 0.22	0.0001
C12:0,2OH	0.08 ^a \pm 0.04	0.10 ^a \pm 0.01	0.12 ^a \pm 0.06	0.11 ^a \pm 0.01	0.03 ^a \pm 0.07	0.07 ^a \pm 0.08	0.3858
<i>cyc</i> C17:0, <i>cis</i> -9,10	0.27 ^b \pm 0.16	0.37 ^c \pm 0.04	0.16 ^a \pm 0.03	0.37 ^c \pm 0.03	0.13 ^a \pm 0.02	0.31 ^{bc} \pm 0.04	0.0046
C18:0	1.11 ^c \pm 0.43	3.23 ^b \pm 0.26	1.22 ^a \pm 0.10	4.12 ^b \pm 0.36	1.39 ^a \pm 0.17	3.58 ^b \pm 0.44	0.0001
C18:1	0.15 ^b \pm 0.04	0.00 ^a \pm 0.00	0.13 ^b \pm 0.06	0.00 ^a \pm 0.01	0.12 ^b \pm 0.02	0.00 ^a \pm 0.00	0.0001
C18:1, <i>trans</i> -6	0.14 ^a \pm 0.02	0.11 ^a \pm 0.03	0.07 ^a \pm 0.05	0.11 ^a \pm 0.02	0.10 ^a \pm 0.02	0.13 ^a \pm 0.01	0.1104
C18:1, <i>trans</i> -9	0.16 ^a \pm 0.03	0.20 ^a \pm 0.09	0.11 ^a \pm 0.05	0.16 ^a \pm 0.02	0.13 ^a \pm 0.03	0.17 ^a \pm 0.01	0.2983
C18:1, <i>trans</i> -11	0.08 ^{ab} \pm 0.02	0.00 ^a \pm 0.00	0.16 ^a \pm 0.06	0.01 ^a \pm 0.03	0.12 ^b \pm 0.06	0.00 ^a \pm 0.00	0.0006
C18:1, <i>cis</i> -6	0.14 ^a \pm 0.03	0.29 ^{ab} \pm 0.03	0.21 ^{ab} \pm 0.07	0.35 ^b \pm 0.03	0.19 ^a \pm 0.07	0.29 ^{ab} \pm 0.03	0.0015
C18:1, <i>cis</i> -9	4.03 ^c \pm 0.45	0.46 ^{ab} \pm 0.34	4.18 ^c \pm 0.52	0.11 ^a \pm 0.03	4.04 ^c \pm 0.45	0.15 ^a \pm 0.26	0.0001
C18:1, <i>cis</i> -11	12.09 ^a \pm 0.49	22.39 ^b \pm 1.60	12.96 ^a \pm 1.16	20.06 ^b \pm 0.56	12.03 ^a \pm 2.06	19.89 ^b \pm 0.85	0.0001
C18:2, <i>trans</i> -9, <i>trans</i> -12	0.00 ^a \pm 0.00	0.00 ^a \pm 0.00	0.00 ^a \pm 0.00	0.01 ^a \pm 0.02	0.00 ^a \pm 0.00	0.00 ^a \pm 0.00	0.6017
C18:2, <i>cis</i> -9, <i>cis</i> -12	0.06 ^a \pm 0.04	0.03 ^a \pm 0.07	0.00 ^a \pm 0.00	0.00 ^a \pm 0.00	0.00 ^a \pm 0.00	0.00 ^a \pm 0.00	0.1991
<i>cyc</i> C19:0, <i>cis</i> -9,10	14.76 ^b \pm 1.63	0.15 ^a \pm 0.15	16.28 ^b \pm 2.14	0.28 ^a \pm 0.06	14.91 ^b \pm 1.39	0.46 ^a \pm 0.31	0.0001
<i>cyc</i> C19:0, <i>cis</i> -10,11	12.95 ^{ab} \pm 0.62	14.39 ^{bc} \pm 0.53	11.02 ^a \pm 0.96	12.82 ^{ab} \pm 0.55	11.69 ^a \pm 2.04	14.46 ^{bc} \pm 0.91	0.0101
18:2, <i>cis</i> -9, <i>trans</i> -11	0.55 ^b \pm 0.07	0.16 ^a \pm 0.03	0.83 ^b \pm 0.20	0.18 ^a \pm 0.02	0.83 ^c \pm 0.11	0.19 ^a \pm 0.05	0.0001
C18:2CLA_1	0.00 ^a \pm 0.00	0.00 ^a \pm 0.00	0.00 ^a \pm 0.00	0.00 ^a \pm 0.00	0.00 ^a \pm 0.00	0.00 ^a \pm 0.00	0.8421
18:2, <i>trans</i> -10, <i>cis</i> -12	0.63 ^b \pm 0.08	0.00 ^a \pm 0.00	0.67 ^b \pm 0.14	0.00 ^a \pm 0.00	0.73 ^b \pm 0.11	0.00 ^a \pm 0.00	0.0001
C18:2_CLA_2	0.00 ^a \pm 0.00	0.00 ^a \pm 0.00	0.00 ^a \pm 0.00	0.00 ^a \pm 0.00	0.15 ^a \pm 0.22	0.00 ^a \pm 0.00	0.2939
C18:2_CLA_3	0.00 ^a \pm 0.00	0.00 ^a \pm 0.00	0.00 ^a \pm 0.00	0.00 ^a \pm 0.00	0.00 ^a \pm 0.00	0.00 ^a \pm 0.00	0.5747
C18:2_CLA_4	0.50 ^b \pm 0.07	0.00 ^a \pm 0.00	0.52 ^b \pm 0.13	0.00 ^a \pm 0.00	0.50 ^b \pm 0.09	0.00 ^a \pm 0.00	0.0001
St/Lb	0.09 ^a \pm 0.03	0.22 ^b \pm 0.01	0.11 ^a \pm 0.01	0.32 ^b \pm 0.01	0.12 ^a \pm 0.01	0.25 ^b \pm 0.01	0.0001
O/V	0.33 ^b \pm 0.02	0.02 ^a \pm 0.01	0.32 ^b \pm 0.01	0.01 ^a \pm 0.01	0.34 ^b \pm 0.02	0.01 ^a \pm 0.01	0.0001
Σ U	21.74 ^a \pm 1.67	26.15 ^a \pm 2.34	23.67 ^a \pm 2.94	23.49 ^a \pm 0.98	22.70 ^a \pm 3.82	23.66 ^a \pm 1.57	0.4042
Σ S	78.28 ^a \pm 6.03	73.85 ^a \pm 3.43	76.34 ^a \pm 6.68	76.51 ^a \pm 2.50	77.33 ^a \pm 9.00	76.37 ^a \pm 3.50	0.9544
U/S	0.28 ^a \pm 0.01	0.36 ^b \pm 0.02	0.31 ^{ab} \pm 0.01	0.31 ^{ab} \pm 0.01	0.29 ^a \pm 0.02	0.31 ^{ab} \pm 0.01	0.0001

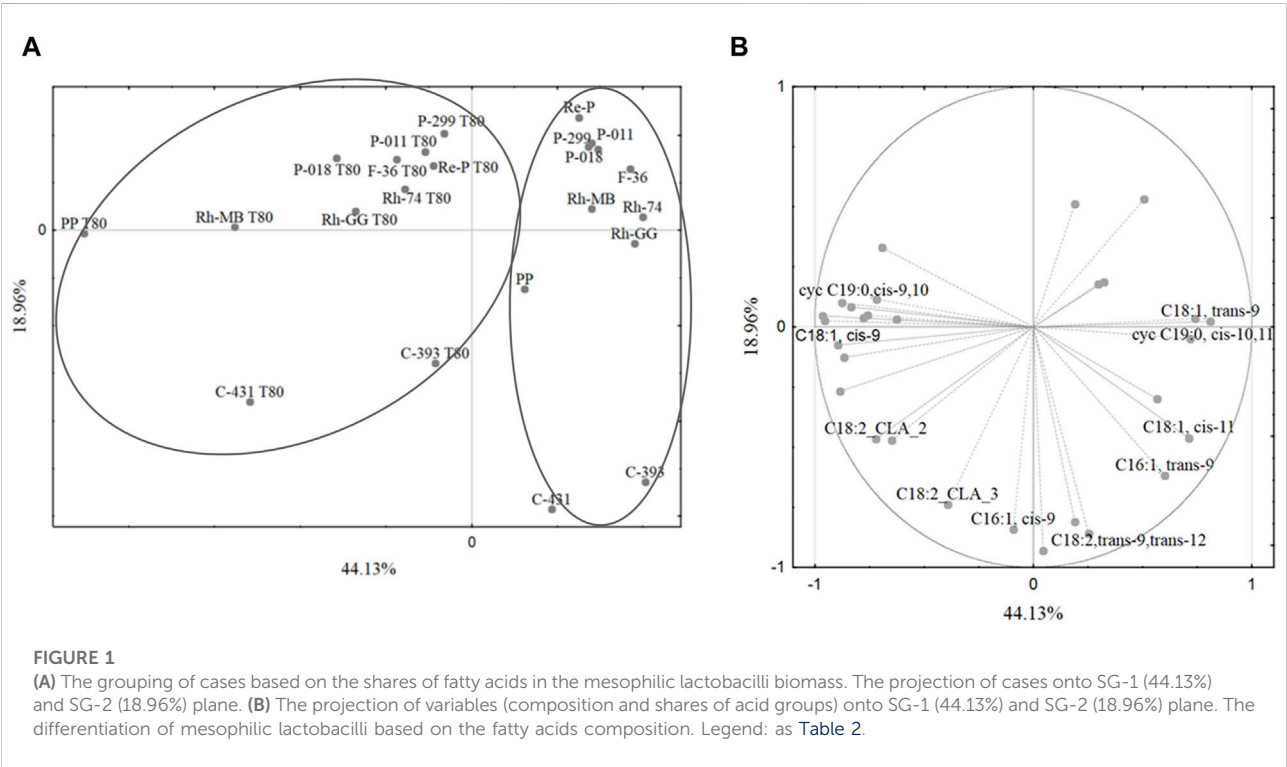
(Continued on following page)

TABLE 5 (Continued) The percentage fatty acids composition (mean \pm SD, n = 6) in mesophilic *Lactiplantibacillus plantarum* strains profiles obtained from the cell cultured in a growth medium with Tween 80TM (with T80) and without Tween 80TM (no T80).

Strain symbol	<i>L. plantarum</i> 299v		<i>L. plantarum</i> B.01149		<i>L. plantarum</i> B.01834		p-value
	With T80	No T80	With T80	No T80	With T80	No T80	
Σ CLA	1.68 ^b \pm 0.22	0.16 ^a \pm 0.03	2.02 ^c \pm 0.47	0.18 ^a \pm 0.02	2.21 ^c \pm 0.53	0.19 ^a \pm 0.05	0.0001

Legend: as Table 2.

^{a,b,c,d}—Means with different lowercase letters the same line indicate a significant difference at the significance level of 0.05 (Tukey HSD).



overview of the connection between the different factors and the samples within. It should be noted that the first main component, which is 57.53% of the model variation, divided the cases into two main groups: the fatty acid profiles obtained from the growth medium with Tween 80TM and without Tween 80TM (Figure 1A). The first principal component separated the cases into two main groups based on the growth medium with or without Tween 80TM (Figure 1A). Notably, some *L. casei* strains did not cluster together, suggesting a potential taxonomic misclassification or high variability within this group. The high share of oleic acid (C18:1,*cis*-9) and CLA was important for the separation of the bacteria cultured on the growth medium with Tween 80TM, while linoelaidic (C18:2,*trans*-9,*trans*-12), palmitelaidic (C16:1,*trans*-9), and *cis*-vaccenic (C18:1,*cis*-11) acids were important in case of growth medium without Tween 80TM (Figure 1B). This allowed for the separation of strains cultured on growth medium with Tween 80TM into two main groups: those cultured with Tween 80TM and cultured without Tween 80TM. In contrast, no significant

differentiation was observed for strains grown on the same growth medium without Tween 80TM.

Recent taxonomic revisions suggest that some *L. casei* strains might be reclassified as *L. paracasei* (Ghosh et al., 2019). Unfortunately, we could not perform phylogenetic analysis on all our strains due to the lack of a genome sequence for C-431. Despite this uncertainty, we observed distinct fatty acid profiles among the three *L. casei* strains (potentially *L. paracasei*). However, further studies with a larger and well-characterized strain collection are necessary to confirm the discriminatory power of fatty acid profiles for differentiation between these closely related species.

The exact effects of the presence of Tween 80TM in the growth medium vary depending on the type of lactobacilli, but in general, Tween 80TM can increase saturated fatty acids and reduce unsaturated fatty acids. The presence of Tween 80TM in the growth medium generally increased the proportion of lactobacillic acid (cycC19:0,*cis*-10,11) in the fatty acid profile of all lactobacilli strains. This was due to the stimulation of the

synthesis of lactobacillic acid (*cycC19:0,cis-10,11*) by lactobacilli cells in response to the absence of oleic acid (*C18:1,cis-9*) from Tween 80TM. The presence of Tween 80TM in the growth medium had a mixed effect on the proportion of myristic acid (*C14:0*) and dihydrosterculic acid (*cycC19:0,cis-9,10*) in the fatty acid profile. In some lactobacilli strains, the proportion of myristic acid and dihydrosterculic acid (*cycC19:0,cis-9,10*) increased, while in other species, the proportion of myristic acid and dihydrosterculic acid (*cycC19:0,cis-9,10*) decreased. The presence of Tween 80TM in the growth medium significantly impacts the fatty acid profile of lactobacilli, generally increased the proportion of palmitic acid in the fatty acid profile of all lactobacilli strains. This was due to the incorporation of oleic acid (*C18:1,cis-9*) from Tween 80TM into the cell membranes of lactobacilli cells, which increased the demand for saturated fatty acids to maintain the fluidity of the cell membranes. While our data suggests a decrease in *cis*-vaccenic acid (*C18:1,cis-11*) in the fatty acid profile of all lactobacilli strains, further investigation is needed to elucidate the underlying mechanisms. Existing literature suggests that Tween 80TM might suppress early fatty acids synthesis, potentially affecting *cis*-vaccenic acid (*C18:1,cis-11*) production later in the growth cycle (Jacques et al., 1980; Zotta et al., 2017b; Reitermayer et al., 2018). Future studies employing time-course experiments could provide valuable insights into the dynamics of fatty acid biosynthesis and incorporation in the presence of Tween 80TM, allowing for a more definitive understanding of potential competition or alternative pathways involved.

Conclusion

Our study investigated the influence of Tween 80TM, a widely used surfactant in culturing media, on the fatty acid profile of selected mesophilic lactobacilli strains. The fatty acid composition of mesophilic lactobacilli cells plays a crucial role in determining their membrane properties, which are essential for various cellular functions, including cell growth, motility, and stress resistance. Our study investigated the impact of Tween 80TM, a common surfactant used in bacterial culturing media, on the fatty acid profile of selected mesophilic lactobacilli strains. Tween 80TM has a significant impact on the fatty acid profile of lactobacilli. The presence of Tween 80TM in the growth medium can alter the proportion of various fatty acids, including saturated and unsaturated. The specific changes in fatty acid composition vary depending on the lactobacilli strains and species. One important aspect to consider is the role of the culturing environment in shaping the fatty acid profile of lactobacilli. Culture media can introduce external fatty acids, such as the oleic acid (*C18:1,cis-9*) present in Tween 80TM, a common additive. Notably, oleic acid originating in Tween 80TM can be incorporated into lactobacilli membranes, contributing to the complex interplay between environmental factors and bacterial fatty acid biosynthesis in shaping membrane properties.

Our results reveal that the presence of Tween 80TM in the growth medium decreases the abundance of *cis*-vaccenic acid (*C18:1,cis-11*), a key contributor to membrane fluidity. This suggests that Tween 80TM may not only act as an external fatty acid source but also potentially compete with the bacteria's own synthesis of *cis*-vaccenic acid (*C18:1,cis-11*). While competition with oleic acid (*C18:1,cis-9*) from Tween 80TM for membrane incorporation is a possibility, further investigation is needed. Existing literature suggests that Tween 80TM may initially suppress fatty acid synthesis, potentially impacting the availability of precursors for later *cis*-vaccenic acid (*C18:1,cis-11*) production. This decrease in *cis*-vaccenic acid (*C18:1,cis-11*) may lead to an increase in membrane rigidity, which could negatively impact cell growth, motility, and stress resistance.

Conversely, the addition of Tween 80TM to the growth medium had the opposite effect, increasing the proportion of *cis*-vaccenic acid (*C18:1,cis-11*), likely through precursor availability. This increase may help to maintain membrane fluidity, which is important for these cellular functions. The presence of Tween 80TM can increase the proportion of palmitic acid (*C16:0*) and lactobacillic acid (*cycC19:0,cis-10,11*). Palmitic acid is a saturated fatty acid that is involved in maintaining cell membrane structure and function. Lactobacillic acid (*cycC19:0,cis-10,11*) is a cyclopropane fatty acid that is unique to lactobacilli and is thought to play a role in their interactions with other organisms.

In conclusion, our study demonstrates that Tween 80TM significantly impact the fatty acid composition of lactobacilli. The presence of Tween 80TM can reduce the proportion of oleic acid and *cis*-vaccenic acid (*C18:1,cis-11*). Oleic acid is a major component of the cell membranes of lactobacilli, and Tween 80TM can compete with oleic acid for incorporation into the membranes. The results of our study are particularly relevant to the industrial application of mesophilic lactobacilli. These changes in fatty acid composition can in turn lead to changes in membrane properties, which could have implications for cell function.

Future studies could explore the specific mechanisms by which Tween 80TM influences fatty acid synthesis and the potential for strain-specific adaptations. Additionally, investigating the functional consequences of altered membrane fluidity on cell function would provide valuable insights for optimizing probiotic performance.

Data availability statement

The original contributions presented in the study are included in the article/Supplementary Material, further inquiries can be directed to the corresponding author.

Author contributions

MZ and DZ: data curation, conceptualization, formal analysis, visualization, writing–review and editing, and supervision. MZ: project administration, funding acquisition,

and supervision. All authors contributed to the article and approved the submitted version.

Funding

The author(s) declare that financial support was received for the research, authorship, and/or publication of this article. This research was funded by National Science Centre (NCN) in Poland, grant number N N312 121739.

Conflict of interest

The authors declare that the research was conducted in the absence of any commercial or financial

relationships that could be construed as a potential conflict of interest.

Acknowledgments

The Authors gratefully acknowledge the Institute of Food Sciences of Warsaw University of Life Sciences WULS-SGGW for supporting and providing necessary infrastructure and research stuff.

Supplementary material

The Supplementary Material for this article can be found online at: <https://www.frontierspartnerships.org/articles/10.3389/abp.2024.13014/full#supplementary-material>

References

- Alexander, M. B. (2012). Rapid fatty acid and microbial identification using the MIDI sherlock® microbial identification system. *Pharm. Regul. Aff.* 2, 1–4. doi:10.4172/2167-7689.S1.001
- Al-Naseri, A., Bowman, J. P., Wilson, R., Nilsson, R. E., and Britz, M. L. (2013). Impact of lactose starvation on the physiology of *Lactobacillus casei* GCRL163 in the presence or absence of tween 80. *J. Proteome Res.* 12 (11), 5313–5322. doi:10.1021/pr400661g
- Anderson, A. C., Sanunu, M., Schneider, C., Clad, A., Karygianni, L., Hellwig, E., et al. (2014). Rapid species-level identification of vaginal and oral *Lactobacilli* using MALDI-TOF MS analysis and 16S rDNA sequencing. *BMC Microbiol.* 14 (1), 312. doi:10.1186/s12866-014-0312-5
- Asadi, S. Z., Khosravi-Darani, K., Nikoopour, H., and Bakhoda, H. (2015). Evaluation of the effect of process variables on the fatty acid profile of single cell oil produced by *Mortierella* using solid-state fermentation. *Crit. Rev. Biotechnol.* 35, 94–102. doi:10.3109/07388551.2013.804805
- Beal, C., Fonseca, F., and Corrieu, G. (2001). Resistance to freezing and frozen storage of *Streptococcus thermophilus* is related to membrane fatty acid composition. *J. Dairy Sci.* 84 (11), 2347–2356. doi:10.3168/jds.S0022-0302(01)74683-8
- Broadbent, J. R., Oberg, T. S., Hughes, J. E., Ward, R. E., Brighton, C., Welker, D. L., et al. (2014). Influence of polysorbate 80 and cyclopropane fatty acid synthase activity on lactic acid production by *Lactobacillus casei* ATCC 334 at low pH. *J. Industrial Microbiol. Biotechnol.* 41 (3), 545–553. doi:10.1007/s10295-013-1391-2
- Brondz, I. (2002). Development of fatty acid analysis by high-performance liquid chromatography, gas chromatography, and related techniques. *Anal. Chim. Acta*, 465 (1), 1–37. doi:10.1016/S0003-2670(01)01467-2
- Buyer, J. S. (2002). Rapid sample processing and fast gas chromatography for identification of bacteria by fatty acid analysis. *J. Microbiol. Methods* 51 (2), 209–215. doi:10.1016/S0167-7012(02)00081-7
- Christie, W. W., Dobson, G., and Adlof, R. O. (2007). A practical guide to the isolation, analysis and identification of conjugated linoleic acid. *Lipids* 42 (12), 1073–1084. doi:10.1007/s11745-007-3107-8
- Corcoran, B. M., Stanton, C., Fitzgerald, G. F., and Ross, R. P. (2007). Growth of probiotic *Lactobacilli* in the presence of oleic acid enhances subsequent survival in gastric juice. *Microbiol. Read. Engl.* 153 (Pt 1), 291–299. doi:10.1099/mic.0.28966-0
- Corsetti, A., Tofalo, R., Schirone, M., Perpetuini, G., Quinto, M., and Suzzi, G. (2010). Bioconversion of linoleic acid to bioactive CLA isomers cis-9, trans-11 C18:2 and trans-10, cis-12 C18:2 by *Lactobacillus casei*- and *Lactobacillus plantarum*-group strains. *J. Biotechnol.* 150 (listopad), 338–339. doi:10.1016/j.jbiotec.2010.09.358
- Cronan, J. E. (2002). Phospholipid modifications in bacteria. *Curr. Opin. Microbiol.* 5 (2), 202–205. doi:10.1016/S1369-5274(02)00297-7
- Fonseca, F., Pénicaud, C., Tymczyszyn, E. E., Gómez-Zavaglia, A., and Passot, S. (2019). Factors influencing the membrane fluidity and the impact on production of lactic acid bacteria starters. *Appl. Microbiol. Biotechnol.* 103 (17), 6867–6883. doi:10.1007/s00253-019-10002-1
- Foschi, C., Laghi, L., Parolin, C., Giordani, B., Compri, M., Cevenini, R., et al. (2017). Novel approaches for the taxonomic and metabolic characterization of *Lactobacilli*: integration of 16S rRNA gene sequencing with MALDI-TOF MS and 1H-nmr. *PLOS ONE* 12 (2), e0172483. doi:10.1371/journal.pone.0172483
- Ghosh, S., Sarangi, A. N., Mukherjee, M., Bhowmick, S., and Tripathy, S. (2019). Reanalysis of *Lactobacillus paracasei* Lbs2 strain and large-scale comparative genomics places many strains into their correct taxonomic position. *Microorganisms* 7 (11), 487. doi:10.3390/microorganisms7110487
- Haack, S. K., Garchow, H., Odelson, D. A., Forney, L. J., and Klug, M. J. (1994). Accuracy, reproducibility, and interpretation of fatty acid methyl ester profiles of model bacterial communities. *Appl. Environ. Microbiol.* 60 (7), 2483–2493. doi:10.1128/aem.60.7.2483-2493.1994
- Hansen, M.-L. R. W., Petersen, M. A., Risbo, J., Hümmer, M., and Clausen, A. (2015). Implications of modifying membrane fatty acid composition on membrane oxidation, integrity, and storage viability of freeze-dried probiotic, *Lactobacillus acidophilus* La-5. *Biotechnol. Prog.* 31 (3), 799–807. doi:10.1002/btpr.2074
- Henderson, T. O., and McNeill, J. (1966). The control of fatty acid synthesis in *Lactobacillus plantarum*. *Biochem. Biophysical Res. Commun.* 25 (6), 662–669. doi:10.1016/0006-291X(66)90506-7
- Hernandez-Mendoza, A., Lopez-Hernandez, A., Hill, C. G., and Garcia, H. S. (2009). Bioconversion of linoleic acid to conjugated linoleic acid by *Lactobacillus reuteri* under different growth conditions. *J. Chem. Technol. Biotechnol.* 84 (2), 180–185. doi:10.1002/jctb.2021
- Ianniello, R. G., Zotta, T., Matera, A., Genovese, F., Parente, E., and Ricciardi, A. (2016). Investigation of factors affecting aerobic and respiratory growth in the oxygen-tolerant strain *Lactobacillus casei* N87. *PLOS ONE* 11 (11), e0164065. doi:10.1371/journal.pone.0164065
- Jacques, N. A., Hardy, L., Knox, K. W., and Wicken, A. J. (1980). Effect of tween 80 on the morphology and physiology of *Lactobacillus salivarius* strain IV CL-37 grown in a chemostat under glucose limitation. *Microbiology* 119 (1), 195–201. doi:10.1099/00221287-119-1-195
- Jenkins, J. K., and Courtney, P. D. (2003). *Lactobacillus* growth and membrane composition in the presence of linoleic or conjugated linoleic acid. *Can. J. Microbiol.* 49 (1), 51–57. doi:10.1139/w03-003
- Jimenez, N. R., Maarsingh, J. D., Laniewski, P., and Herbst-Kralovetz, M. M. (2023). Commensal *Lactobacilli* metabolically contribute to cervical epithelial homeostasis in a species-specific manner. *mSphere* 8 (1), e0045222–22. doi:10.1128/msphere.00452-22
- Johnsson, T., Nikkila, P., Toivonen, L., Rosenqvist, H., and Laakso, S. (1995). Cellular Fatty Acid profiles of *Lactobacillus* and *Lactococcus* strains in relation to the oleic Acid content of the cultivation medium. *Appl. Environ. Microbiol.* 61 (12), 4497–4499. doi:10.1128/aem.61.12.4497-4499.1995

- Kaneda, T. (1991). Iso- and anteiso-fatty acids in bacteria: Biosynthesis, function, and taxonomic significance. *Microbiol. Rev.* 55 (2), 288–302. doi:10.1128/mr.55.2.288-302.1991
- Kankaanpää, P., Yang, B., Kallio, H., Isolauri, E., and Salminen, S. (2004). Effects of polyunsaturated fatty acids in growth medium on lipid composition and on physicochemical surface properties of lactobacilli. *Appl. Environ. Microbiol.* 70 (1), 129–136. doi:10.1128/AEM.70.1.129-136.2004
- Kishino, S., Ogawa, J., Ando, A., Omura, Y., and Shimizu, S. (2002). Ricinoleic acid and Castor oil as substrates for conjugated linoleic acid production by washed cells of *Lactobacillus plantarum*. *Biosci. Biotechnol. Biochem.* 66 (10), 2283–2286. doi:10.1271/bbb.66.2283
- Kishino, S., Ogawa, J., Yokozeki, K., and Shimizu, S. (2009). Metabolic diversity in biohydrogenation of polyunsaturated fatty acids by lactic acid bacteria involving conjugated fatty acid production. *Appl. Microbiol. Biotechnol.* 84 (1), 87–97. doi:10.1007/s00253-009-1949-0
- Klein, D., Breuch, R., Reinmüller, J., Engelhard, C., and Kaul, P. (2022). Discrimination of stressed and non-stressed food-related bacteria using Raman-microspectroscopy. *Foods* 11 (10), 1506. doi:10.3390/foods11101506
- Kunitzky, C. J., Osterhout, G., and Sasser, M. (2006). Identification of microorganisms using fatty acid methyl ester (FAME) analysis and the MIDI Sherlock® microbial identification system. Available at: [https://www.semanticscholar.org/paper/1-1-IDENTIFICATION-OF-MICROORGANISMS-USING-FATTY-\(-Kunitzky-Osterhout/a1aa6423f0e19df3a2043f7d07cf0bc07e17918](https://www.semanticscholar.org/paper/1-1-IDENTIFICATION-OF-MICROORGANISMS-USING-FATTY-(-Kunitzky-Osterhout/a1aa6423f0e19df3a2043f7d07cf0bc07e17918).
- Li, J. Y., Zhang, L. W., Du, M., Han, X., Yi, H. X., Guo, C. F., et al. (2011). Effect of two series on growth and cis-9, trans-11 conjugated linoleic acid production of *Lactobacillus acidophilus* F0221 in the presence of bile salts. *Int. J. Mol. Sci.* 12 (12), 9138–9154. doi:10.3390/ijms12129138
- Li, Q., Lei, Y., Hu, G., Lei, Y., and Dan, D. (2018). Effects of Tween 80 on the liquid fermentation of *Lentinus edodes*. *Food Sci. Biotechnol.* 27 (4), 1103–1109. doi:10.1007/s10068-018-0339-8
- Lin, T. Y. (2006). Conjugated linoleic acid production by cells and enzyme extract of *Lactobacillus delbrueckii* ssp. *bulgaricus* with additions of different fatty acids. *Food Chem.* 94 (3), 437–441. doi:10.1016/j.foodchem.2004.11.032
- Lin, T. Y., Lin, C. W., and Wang, Y. J. (2002). Linoleic acid isomerase activity in enzyme extracts from *Lactobacillus acidophilus* and *propionibacterium freudenreichii* Ssp. *shermanii*. *J. Food Sci.* 67 (4), 1502–1505. doi:10.1111/j.1365-2621.2002.tb10312.x
- Lin, T. Y., Lin, C.-W., and Wang, Y. J. (2003). Production of conjugated linoleic acid by enzyme extract of *Lactobacillus acidophilus* CCRC 14079. *Food Chem.* 83 (1), 27–31. doi:10.1016/S0308-8146(03)00032-3
- Liong, M. T., and Shah, N. P. (2005). Acid and bile tolerance and cholesterol removal ability of *Lactobacilli* strains. *J. Dairy Sci.* 88 (1), 55–66. doi:10.3168/jds.S0022-0302(05)72662-X
- López de Felipe, F. (2023). Revised aspects into the molecular bases of hydroxycinnamic acid metabolism in *Lactobacilli*. *Antioxidants* 12 (6), 1294. doi:10.3390/antiox12061294
- Machado, M. C., López, C. S., Heras, H., and Rivas, E. A. (2004). Osmotic response in *Lactobacillus casei* ATCC 393: Biochemical and biophysical characteristics of membrane. *Archives Biochem. Biophysics* 422 (1), 61–70. doi:10.1016/j.abb.2003.11.001
- Macouzet, M., Lee, B. h., and Robert, N. (2010). Genetic and structural comparison of linoleate isomerases from selected food-grade bacteria. *J. Appl. Microbiol.* 109 (6), 2128–2134. doi:10.1111/j.1365-2672.2010.04844.x
- Montanari, C., Sado Kamdem, S. L., Serrazanetti, D. I., Etoa, F. X., and Guerzoni, M. E. (2010). Synthesis of cyclopropane fatty acids in *Lactobacillus helveticus* and *Lactobacillus sanfranciscensis* and their cellular fatty acids changes following short term acid and cold stresses. *Food Microbiol.* 27 (4), 493–502. doi:10.1016/j.fm.2009.12.003
- Murga, M. L. F., de Valdez, G. F., and Disalvo, E. (2001). Effect of lipid composition on the stability of cellular membranes during freeze–thawing of *Lactobacillus acidophilus* grown at different temperatures. *Archives Biochem. Biophysics* 388 (2), 179–184. doi:10.1006/abbi.2001.2274
- Nacef, M., Chevalier, M., Chollet, S., Drider, D., and Flahaut, C. (2017). MALDI-TOF mass spectrometry for the identification of lactic acid bacteria isolated from a French cheese: the maroilles. *Int. J. Food Microbiol.* 247 (kwiecień), 2–8. doi:10.1016/j.jfoodmicro.2016.07.005
- Ogawa, J., Kishino, S., Ando, A., Sugimoto, S., Mihara, K., and Shimizu, S. (2005). Production of conjugated fatty acids by lactic acid bacteria. *J. Biosci. Bioeng.* 100 (4), 355–364. doi:10.1263/jbb.100.355
- Parsons, J. B., and Rock, C. O. (2013). Bacterial lipids: metabolism and membrane homeostasis. *Prog. Lipid Res.* 52 (3), 249–276. doi:10.1016/j.plipres.2013.02.002
- Partanen, L., Martinen, N., and Alatossava, T. (2001). Fats and fatty acids as growth factors for *Lactobacillus delbrueckii*. *Syst. Appl. Microbiol.* 24 (4), 500–506. doi:10.1078/0723-2020-00078
- Pawar, K., and Aranha, C. (2022). *Lactobacilli* metabolites restore E-cadherin and suppress MMP9 in cervical cancer cells. *Curr. Res. Toxicol.* 3 (styczeń), 100088. doi:10.1016/j.crtox.2022.100088
- Reitermayer, D., Kafka, T. A., Lenz, C. A., and Vogel, R. F. (2018). Interrelation between Tween and the membrane properties and high pressure tolerance of *Lactobacillus plantarum*. *BMC Microbiol.* 18 (1), 72. doi:10.1186/s12866-018-1203-y
- Rizzo, A. F., Korkeala, H., and Mononen, I. (1987). Gas chromatography analysis of cellular fatty acids and neutral monosaccharides in the identification of *Lactobacilli*. *Appl. Environ. Microbiol.* 53 (12), 2883–2888. doi:10.1128/aem.53.12.2883-2888.1987
- Rodrigues, D., Rocha-Santos, T. A. P., Gomes, A. M., Goodfellow, B. J., and Freitas, A. C. (2012). Lipolysis in probiotic and synbiotic cheese: the influence of probiotic bacteria, prebiotic compounds and ripening time on free fatty acid profiles. *Food Chem.* 131 (4), 1414–1421. doi:10.1016/j.foodchem.2011.10.010
- Rodríguez-Alcalá, L. M., Braga, T., Xavier Malcata, F., Gomes, A., and Fontecha, J. (2011). Quantitative and qualitative determination of CLA produced by *Bifidobacterium* and lactic acid bacteria by combining spectrophotometric and Ag⁺-HPLC techniques. *Food Chem.* 125 (4), 1373–1378. doi:10.1016/j.foodchem.2010.10.008
- Rouch, D., Hillier, A., and Britz, M. (2002). NSLAB in cheddar: A stressful life. *Aust. J. Dairy Technol.* 57 (2), 107.
- Rozès, N., and Peres, C. (1998). Effects of phenolic compounds on the growth and the fatty acid composition of *Lactobacillus plantarum*. *Appl. Microbiol. Biotechnol.* 49 (1), 108–111. doi:10.1007/s002530051145
- Russell, N. J., Evans, R. I., ter Steeg, P. F., Hellemons, J., Verheul, A., and Abee, T. (1995). Membranes as a target for stress adaptation. *Int. J. Food Microbiol.* 28 (2), 255–261. doi:10.1016/0168-1605(95)00061-5
- Santivarangkna, C., Kulozik, U., and Foerst, P. (2008). Inactivation mechanisms of lactic acid starter cultures preserved by drying processes. *J. Appl. Microbiol.* 105 (1), 1–13. doi:10.1111/j.1365-2672.2008.03744.x
- Schujman, G. E., and de Mendoza, D. (2008). Regulation of type II fatty acid synthase in Gram-positive bacteria. *Curr. Opin. Microbiol.* 11 (2), 148–152. doi:10.1016/j.mib.2008.02.002
- Tan, W. S., Budinich, M. F., Ward, R., Broadbent, J. R., and Steele, J. L. (2012). Optimal growth of *Lactobacillus casei* in a Cheddar cheese ripening model system requires exogenous fatty acids. *J. Dairy Sci.* 95 (4), 1680–1689. doi:10.3168/jds.2011-4847
- Taranto, M. P., Perez-Martinez, G., and Font de Valdez, G. (2006). Effect of bile acid on the cell membrane functionality of lactic acid bacteria for oral administration. *Res. Microbiol.* 157 (8), 720–725. doi:10.1016/j.resmic.2006.04.002
- Terraf, M. C. L., Juárez Tomás, M. S., Nader-Macías, M. E. F., and Silva, C. (2012). Screening of biofilm formation by beneficial vaginal *Lactobacilli* and influence of culture media components. *J. Appl. Microbiol.* 113 (6), 1517–1529. doi:10.1111/j.1365-2672.2012.05429.x
- Weeks, G., and Wakil, S. J. (1970). Studies on the control of fatty acid metabolism: II. The inhibition of fatty acid synthesis in *Lactobacillus plantarum* by exogenous fatty acid. *J. Biol. Chem.* 245 (8), 1913–1921. doi:10.1016/S0021-9258(18)63185-0
- Wu, P., An, J., Chen, L., Zhu, Q., Li, Y., Mei, Y., et al. (2020). Differential analysis of stress tolerance and transcriptome of probiotic *Lactobacillus casei* Zhang produced from solid-state (SSF-SW) and liquid-state (LSF-MRS) fermentations. *Microorganisms* 8 (11), 1656. doi:10.3390/microorganisms8111656
- Zhang, G., Liu, L., and Li, C. (2020). Effects of *ccpA* gene deficiency in *Lactobacillus delbrueckii* subsp. *bulgaricus* under aerobic conditions as assessed by proteomic analysis. *Microb. Cell Factories* 19 (1), 9. doi:10.1186/s12934-020-1278-7
- Zhu, L., Zou, Q., Cao, X., and Cronan, J. E. (2019). *Enterococcus faecalis* encodes an atypical auxiliary acyl carrier protein required for efficient regulation of fatty acid synthesis by exogenous fatty acids. *mBio* 10 (3), e00577-19. doi:10.1128/mBio.00577-19
- Zotta, T., Parente, E., and Ricciardi, A. (2017a). Aerobic metabolism in the genus *Lactobacillus*: Impact on stress response and potential applications in the food industry. *J. Appl. Microbiol.* 122 (4), 857–869. doi:10.1111/jam.13399
- Zotta, T., Tabanelli, G., Montanari, C., Ianniello, R. G., Parente, E., Gardini, F., et al. (2017b). Tween 80 and respiratory growth affect metabolite production and membrane fatty acids in *Lactobacillus casei* N87. *J. Appl. Microbiol.* 122 (3), 759–769. doi:10.1111/jam.13373

Endoplasmic reticulum stress involves the high glucose-induced nucleus pulposus cell pyroptosis

Xiaochun Xiong^{1#}, Ying Wu^{2#}, Hengguo Long¹, Tianzi Liang¹, Wenqing Liang¹, Xiaogang Huang¹ and Guijin Li^{3✉}

¹Department of Orthopedics, Zhoushan Hospital of Traditional Chinese Medicine, Zhoushan, China; ²Department of Surgery, Zongrui Hospital, Beilun District, Ningbo, China; ³Department of Orthopedics, The Third Affiliated Hospital of Zhejiang Chinese Medical University, Xihu District, Hangzhou, Zhejiang 310000, China

Objective: Diabetes has been identified as a risk factor for intervertebral disc degeneration (IDD). The aim of this study is to investigate the potential mechanism underlying diabetes-related pyroptosis in nucleus pulposus (NP) cells. **Methods:** We used a high-glucose environment to mimic diabetes *in vitro* and examined the endoplasmic reticulum stress (ERS) and pyroptotic response. Furthermore, we utilized activators and inducers of ERS to explore the role of ERS in high-glucose-induced pyroptosis in NP cells. We evaluated the ERS and pyroptosis levels using immunofluorescence (IF) or RT-PCR and measured the expression of collagen II, aggrecan, and MMPs. Additionally, we used ELISA to determine the levels of IL-1 β and IL-18 in the culture medium, and CCK8 assay to test cell viability. **Results:** High-glucose conditions promoted the degeneration of NP cells and triggered ERS and pyroptosis. A high level of ERS aggravated pyroptosis, and partially suppressing ERS resisted high-glucose-induced pyroptosis and alleviated the degeneration of NP cells. Inhibiting caspase-1-based pyroptosis under high-glucose conditions helped relieve the degeneration of NP cells but did not affect ERS levels. **Conclusions:** High-glucose induces pyroptosis in NP cells via the mediation of ERS, and suppressing ERS or pyroptosis protects NP cells under high-glucose conditions.

Keywords: Nucleus pulposus cells, endoplasmic reticulum stress, high-glucose, pyroptosis

Received: 01 January, 2023; revised: 01 March, 2023; accepted: 15 April, 2023; available on-line: 12 June, 2023

✉e-mail: gkyslglj@163.com

[#]Xiaochun Xiong and Ying Wu contributed equally to this work

Acknowledgements of Financial Support: This work was supported by Zhejiang Traditional Chinese Medicine Science and Technology Project (2021ZQ048), and Zhejiang Traditional Chinese Medicine Science and Technology Project (No. 2022ZA181).

Abbreviations: ANOVA, Analysis of variance; 2-DG, 2-deoxyglucose; 2-DG6P, 2-DG-6-phosphate; CCK-8, Cell counting kit-8; DMEM, Dulbecco's modified eagle medium; ECM, Extracellular matrix; ELISA, Enzyme-linked immunosorbent assay; ER, Endoplasmic reticulum; ERS, Endoplasmic reticulum stress; IDD, Intervertebral disc degeneration; IF, Immunofluorescence; NP, Nucleus pulposus; OD, Optical density; RT-PCR, Reverse transcription-polymerase chain reaction; SPSS, Statistical Product and Service Solutions

INTRODUCTION

Low back pain is a common clinical symptom, which may or may not be accompanied by radiating pain, numbness, and muscle strength changes in the lower limbs (Chou, 2014). Intervertebral disc degeneration (IDD) is one of the leading causes of low back pain, pathologically characterized by the dysfunction of nu-

cleus pulposus (NP) cells, the degradation of extracellular matrix (ECM), and the progressive fibrosis of the intervertebral disc (Vadala *et al.*, 2015; Zhao *et al.*, 2007; Che *et al.*, 2020). In addition to age, mechanical damage, and other biomechanical risks, metabolic diseases, especially diabetes, have also been confirmed to have a strong correlation with IDD. The diffusion, distribution, and utilization of glucose play a vital role in the normal function of the intervertebral disc (Cannata *et al.*, 2020). Therefore, the imbalance in the maintenance of normal blood glucose levels in diabetic condition has become a risk factor for IDD (Agius *et al.*, 2016).

In a prospective study by Jhawar and others (Jhawar *et al.*, 2006), the relative risk factor of diabetes for lumbar disc herniation was found to be 1.52, which was higher than smoking, hypertension, and hyperlipidemia. Huang and others (Huang *et al.*, 2016) also found that diabetes duration of more than ten years is a high-risk factor for intervertebral disc herniation. Additionally, Robinson and others (Robinson *et al.*, 1998) discovered that diabetic patients have a lower content of aggrecan in their intervertebral discs compared to non-diabetic patients. Despite the strong correlation between diabetes and IDD that has been reported, the pathogenesis of IDD, especially the mechanism of high-glucose-induced IDD, has not been extensively studied.

Pyroptosis shares several morphological characteristics with apoptosis, such as nuclear condensation and chromosome DNA degradation, as well as a reliance on Caspase activation, making it easy to confuse the two (Shi *et al.*, 2017). However, they can be distinguished from one another based on their biological characteristics and molecular mechanisms. The most significant difference between pyroptosis and apoptosis is the series of inflammatory reactions that occur due to the destruction of cell membrane integrity (Fang *et al.*, 2020). Caspase-1/4/5/11 activation and the release of IL-1 β and IL-18 accompany pyroptotic cells, leading to the recruitment of more inflammatory cells and the expansion of local and systemic inflammatory responses (Toldo *et al.*, 2018).

The endoplasmic reticulum (ER) is a critical organelle responsible for protein synthesis and folding in eukaryotic cells, making it very sensitive to various stimuli. Disorders in cellular glucose metabolism can cause protein misfolding and accumulation in the ER cavity, resulting in endoplasmic reticulum stress (ERS) (Wagner & Moore, 2011). Recent studies have shown that ERS is a common feature in subjects with the development of IDD and is closely related to the activation of pyroptosis-related NLRP3 inflammasomes (Han *et al.*, 2018). Since ERS plays a role in the processes of glucose me-

Table 1. Primer sequences for RT-PCR

Gene name	Forward (5'→3')	Reverse (5'→3')
Collagen II	TGGACGATCAGCGCAAACC	GCTGCGGATGCTCTCAATCT
Aggrecan	ACTCTGGGTTTTCTGACTCT	ACACTCAGCGAGTTGTCATGG
MMP3	AGTCTTCCAATCCTACTGTTGCT	TCCCCGTCACCTCCAATCC
MMP-13	ACTGAGAGGCTCCGAGAAATG	GAACCCCGCATCTTGCTT
Caspase-4	AAGAGAAGCAACGTATGGCAGGAC	GGACAAAGCTTGAGGGCATCTGTA
Caspase-11	GGACGCCTTGTGGGAGAATG	TCAATGACCTTACACTGACGC
GADD34	ATGATGGCATGTATGTTGAGC	AACCTTGCACTGTCCTTATCAG
GRP78	CATCACGCCGTCCTATGTCG	CGTCAAAGACCGTGTCTCG
GAPDH	ACAACCTTGGTATCGTGAAGG	GCCATCACGCCACAGTTTC

RT-PCR, Reverse Transcription-Polymerase Chain Reaction

tabolism, pyroptosis, and IDD, we can experimentally explore the connection and mechanism of ERS in the high-glucose-induced pyroptosis of NP cells.

MATERIALS AND METHODS

Patient tissue collection and NP cells isolation

We recruited 9 patients (4 males, 5 females; every age: 42 years) who underwent lumbar fracture and needed discectomy. The inclusion criteria for patients is no history of the underlying disease and IDD. This research was approved by the Ethics Committee of the Zhoushan Hospital of Traditional Chinese Medicine. After cutting from patients, the disc tissue was conserved in a culture medium and shipped to the laboratory for NP cell isolation immediately.

The gelatinous NP tissue was removed from the disc, washed 3×PBS, and cut into small pieces. Then, the fragment was digested with type II collagenase (Sigma, St. Louis, MO, USA) for 6 h. After centrifuge, the cell pellets were resuspended in the DMEM low glucose medium supplemented with 10% fetal bovine serum and 1% penicillin-streptomycin (Gibco, Rockville, MD, USA). NP cells were cultured at 37°C, 5% CO₂ concentration, and 95% relative humidity. The medium was changed every three days.

NP Cells isolation and treatments

NP cells were initially cultured in low glucose DMEM (1 mg/mL), and extra glucose (Beyotime, Shanghai, China) was added to the medium to achieve a final concentration of 3, 5, 10, and 15 mg/mL. After assessing cell viability under different conditions, NP cells were cultured with 15 mg/mL glucose for three days to induce cell injury. In addition, NP cells were treated with Belnacasan (Belin, Selleck, China) to inhibit caspase-1 expression, Tunicamycin (TM, Sigma-Aldrich, St. Louis, MO, USA) to induce ERS, and 4-Phenylbutyric Acid (4-PBA, Sigma-Aldrich, St. Louis, MO, USA) to suppress ERS. Further details of the treatments are described in the Results section.

Immunofluorescence (IF)

We assessed the cellular expression of CHOP and caspase-1 using immunofluorescence (IF) staining. NP cells were seeded onto coverslips in 24-well plates at a density of 104 cells per well. After treatment, the coverslips were washed 3 times with PBS, fixed with 4%

paraformaldehyde, permeabilized with 0.1% Triton-X, and blocked with 5% bovine serum albumin (Beyotime, Shanghai, China) at room temperature. The coverslips were then incubated with primary antibodies, including Mouse monoclonal CHOP (ab11419, Abcam, Cambridge, MA, USA) and Rabbit monoclonal caspase-1 (Cell Signaling Technology, Danvers, MA, USA), overnight at 4°C. Afterwards, the cells were incubated with a rabbit monoclonal Alexa Fluor 647/mouse IgG and monoclonal Alexa Fluor 488-conjugated secondary antibody (Invitrogen, Carlsbad, CA, USA) in the dark at room temperature. The fluorescence intensity was measured using the Image-Pro Plus software.

Reverse transcription-polymerase chain reaction (RT-PCR)

We isolated total RNA from NP cells using TRIzol reagent (Invitrogen, Carlsbad, CA, USA) following the manufacturer's instructions. The RNA was then reverse-transcribed into cDNA and subjected to PCR using SYBR Green Master (TOYOBO, Osaka, Japan) following the manufacturer's instructions. The PCR primers used are listed in Table 1. The relative gene expression was normalized by the amount of GAPDH and calculated using the method of 2^{-ΔΔCt}.

Enzyme-linked immunosorbent assay (ELISA)

The contents of IL-1β and IL-18 in the culture medium were determined by the ELISA kit (ab214025, ab215539, Abcam, Cambridge, MA, USA) according to the manufacturer's instructions. The final OD values were captured using a microplate reader.

Cell counting kit-8 (CCK-8) assay

We used the CCK8 test to determine cell viability. NP cells were seeded in 96-well plates at a density of 5000/well and treated as designed. After treatments, CHs were incubated with a CCK8 kit (Beyotime, Shanghai, China) according to the manufacturer's instructions. The intensity of the CCK8 product was measured at OD of 450 nm using a microplate reader. We set the essential 1 mg/mL glucose treatment as a control group, and the other cell viability was shown relative to the control.

Glucose uptake assay

As the structure of 2-deoxyglucose (2-DG) is similar to glucose, glucose transporters take up 2-DG and

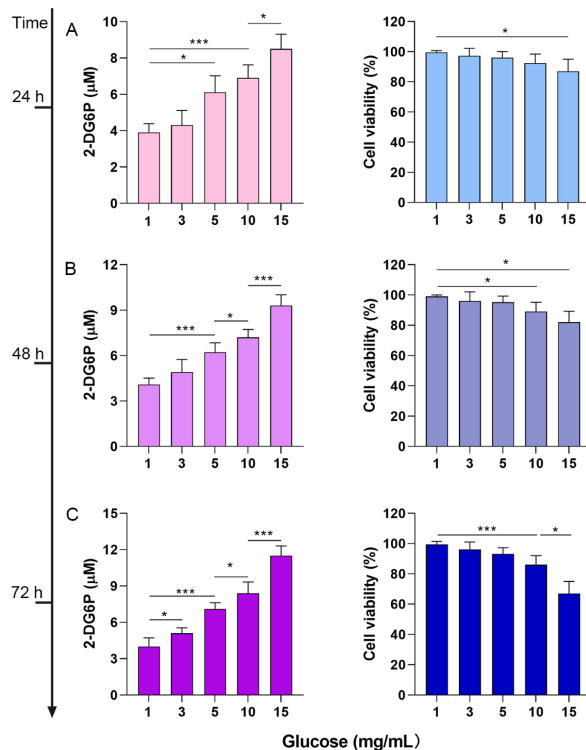


Figure 1. High-glucose injures NP cells' viability. (A) The glucose uptake and cell viability of NP cells after 24-hour culture with ranged concentration of glucose. (B) The glucose uptake and cell viability of NP cells after 48-hour culture with ranged concentration of glucose. (C) The glucose uptake and cell viability of NP cells after 72-hour culture with ranged concentration of glucose. Results are expressed as mean \pm S.D. (* P <0.05, *** P <0.001)

metabolize it to 2-DG-6-phosphate (2-DG6P). The accumulation of 2-DG6P is therefore directly proportional to glucose uptake by cells. We treated NP cells with different concentrations of glucose and 1 mM 13 C-labeled 2-DG. After collecting the metabolites with 70% methanol extraction for LC-MS/MS, we measured glucose uptake using the Glucose Uptake Assay Kit (Colorimetric) (ab136955, Abcam, Cambridge, MA, USA) following the manufacturer's instructions.

Statistical analysis

Data were expressed as mean \pm standard deviation (S.D.) of three independent experiments. All statistical analyses were performed by the Statistical Product and Service Solutions (SPSS) 22.0 software (IBM, Armonk, NY, USA) package and GraphPad Prism 8 (La Jolla, CA, USA). Unpaired one-way ANOVA was used to compare the differences among the groups. P -value <0.05 was statistically significant between groups.

RESULTS

High-glucose injures NP cells' viability

To confirm that glucose had an impact on the viability of NP cells, we cultured cells in a range of glucose concentrations and measured glucose uptake and cell viability for each condition. The culture medium was initially supplemented with 1 mg/mL glucose, and additional glucose was added to obtain final concentrations of 3/5/10/15 mg/mL. Compared to the control group, glucose uptake levels began to increase after 72 hours of culture when the glucose concentration was 3 mg/mL, and intracellular glucose uptake increased after 24 hours of culture when the glucose

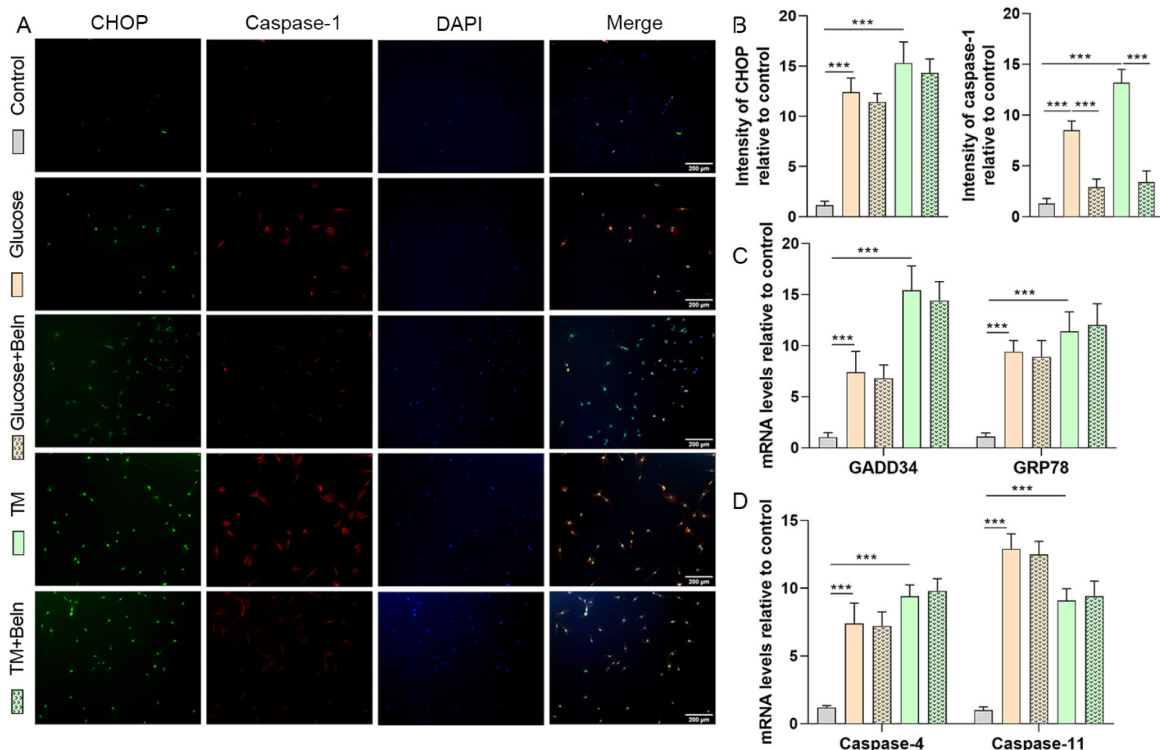


Figure 2. High-glucose induces the ERS and pyroptosis of NP cells. (A) Immunofluorescence analysis of CHOP and caspase-1 expression, and (B) quantification by ImageJ software. (C, D) RT-PCR analysis for indicated RNA expression by normalization to GAPDH expression. Results are expressed as mean \pm S.D. (*** P <0.001)

concentration was higher than 5 mg/mL (Fig. 1A–C, left). Thus, providing more soluble glucose in the medium significantly affected the glucose metabolism of NP cells. However, only the concentrations of 10 and 15 mg/mL had an impact on cell viability compared to the control, with a concentration of 15 mg/mL being more sensitive to NP cells in a short period of time (Fig. 1A–C, right).

High-glucose induces the ERS and pyroptosis of NP cells

To induce cell injury in subsequent experiments, we used a glucose concentration of 15 mg/mL, which quickly and effectively reduces the survival of NP cells. To investigate whether ERS aggravates pyroptosis, we used an ERS inducer in cell culture. NP cells were divided into five groups: 1) control: cells without any treatment, 2) glucose: cells were cultured with 15 mg/mL glucose, 3) glucose + Beln: cells were cultured with 15 mg/mL glucose and 1 nM Beln, 4) TM: cells were cultured with 5 µg/mL TM, 5) TM + Beln: cells were cultured with 5 µg/mL TM and 1 nM Beln. All cells were cultured in the indicated conditions for three days. We tested the ERS markers CHOP, GADD34, GRP78, pyroptosis markers caspase-1, caspase-4, and caspase-11 expression by IF or RT-PCR. Compared to the control, CHOP and caspase-1 were massively increased as a result of both high glucose and TM treatments (Fig. 2A, 2B). The supplement of Beln significantly reduced caspase-1 expression but did not affect the CHOP level. Additionally, the expression of GADD34, GRP78, caspase-4, and caspase-11 was also increased by the treatment of high glucose and TM, which was not affected by the supplement of Beln (Fig. 2C, 2D). Therefore, high glucose triggers the ERS and pyroptotic progress of NP cells, and ERS can trigger the pyroptosis of NP cells. The suppression of caspase-1 would not alleviate the ERS and other pyroptosis markers' expression.

Suppressing caspase-1 alleviates highglucose- induced NP cells degeneration

Continuously, we tested the cell function and pyroptosis-related inflammation under the high-glucose and ERS conditions. In addition to high glucose, TM-induced ERS also injured cell viability. However, the suppression of caspase-1

by Beln was effective in improving the cell viability in high-glucose, but not in terms of ERS (Fig. 3A). In the aspect of the secretory phenotype, high glucose influenced collagen II and aggrecan production, which can be rescued by Beln. Moreover, Beln also alleviated the ERS-caused collagen II and aggrecan downregulation (Fig. 3B). As one of the characteristics, IL-1β and IL-18 are largely synthesized and enter the intercellular substance during cell pyroptosis. Therefore, we tested the IL-1β and IL-18 content in the medium after three days' culture. The results indicated that high-glucose and ERS both raised the IL-1β and IL-18 levels, and the Beln was efficient to suppress the IL-1β and IL-18 production under both high-glucose and ERS conditions (Fig. 3C). Besides, we also analyzed the cellular MMP3 and MMP9 gene expression to value the degenerative degree of NP cells, which were all increased by glucose and TM stimulation, and the suppression of caspase-1 presented an inhibiting effect on MMP3 and MMP9 expression (Fig. 3D). Thus, Beln alleviated the pyroptosis and the resulting NP cell degeneration.

Suppressing ERS alleviates high-glucose-induced pyroptosis

We have ensured that high glucose triggered the ERS and pyroptosis; meanwhile, ERS could naturally result in pyroptosis. However, whether the high glucose aggravated the pyroptosis via the mediation of ERS remains unknown. We further applied the inhibitor of ERS in the high-glucose medium and tested the pyroptotic status. NP cells were divided into four groups, 1) control: cells without any treatments, 2) glucose: cells were cultured with 15 mg/mL glucose. 3) glucose + 4-PBA (+): cells were cultured with 15 mg/mL glucose and 1 mM 4-PBA 4) glucose + 4-PBA (++): cells were cultured with 15 mg/mL glucose and 2 mM 4-PBA. All the cells were cultured in the indicated condition for three days. The result of IF indicated that 4-PBA suppressed CHOP and caspase-1 with a dose-independence (Fig. 4A, 4B). Additionally, the expression of GADD34, GRP78, caspase-4, and caspase-11 was also decreased resulting from the presence of 4-PBA. Similarly, when the inhibitor dose increased, the efficiency became more obvious (Fig. 4C, 4D). Therefore, the 4-PBA successfully suppressed the high-glucose caused ERS and the resulting pyroptosis in NP cells.

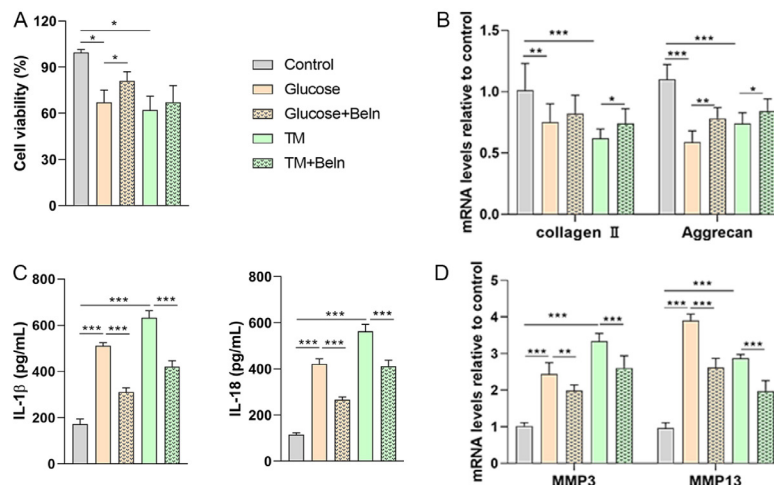


Figure 3. Suppressing caspase-1 alleviates high-glucose induced NP cell degeneration.

(A) Cell viability was determined by the CCK8 test. (B, D) RT-PCR analysis for indicated RNA expression by normalization to GAPDH expression. (C) The IL-1β and IL-18 content in the medium was tested by ELISA. Results are expressed as mean ± S.D. (* $P < 0.05$, ** $P < 0.01$, *** $P < 0.001$).

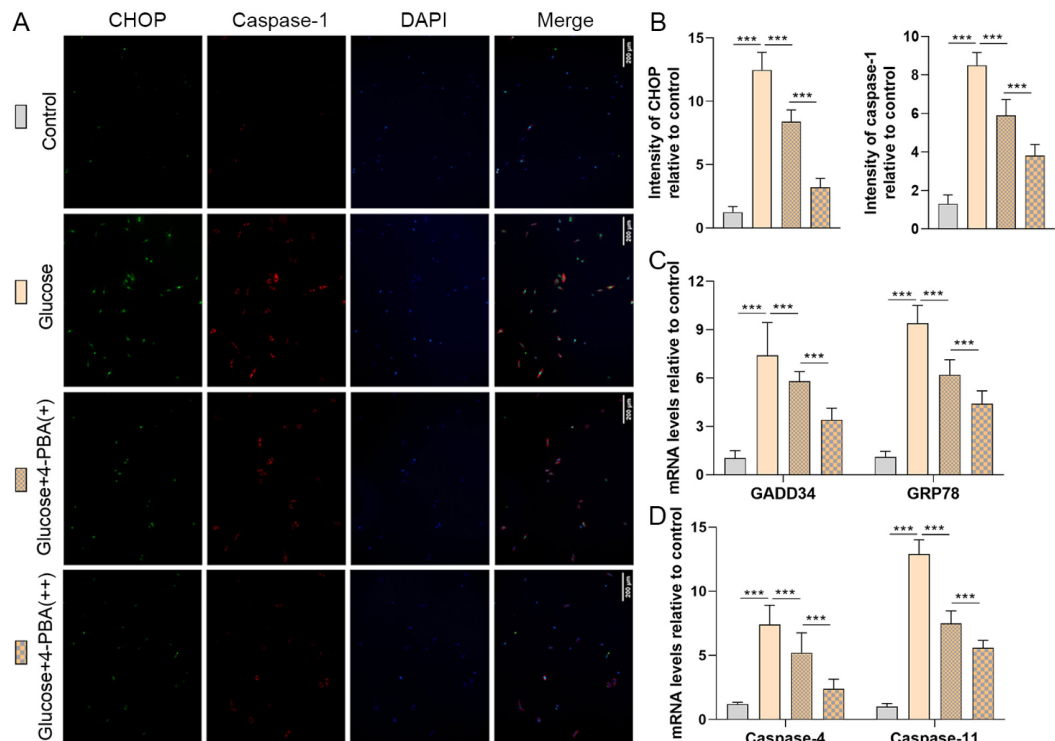


Figure 4. Suppressing ERS alleviates high-glucose induced pyroptosis.

(A) Immunofluorescence analysis of CHOP and caspase-1 expression, and (B) quantification by ImageJ software. (C, D) RT-PCR analysis for indicated RNA expression by normalization to GAPDH expression. Results are expressed as mean \pm S.D. (*** P <0.001)

Suppressing ERS alleviates high-glucose induced NP cells degeneration

In addition, the cell viability in the high-glucose environment was rescued by suppressing ERS with 4-PBA (2 mM) (Fig. 5A). Compared to the high-glucose group, collagen II and aggrecan synthesis were protected by

adding 4-PBA (2 mM) (Fig. 5B). Furthermore, 4-PBA exhibited excellent anti-inflammatory properties by dose-dependently suppressing IL-1 β and IL-18, providing further evidence that suppressing ERS alleviated pyroptosis (Fig. 5C). Finally, we tested the RNA expression of MMP3 and MMP13, which were also inhibited

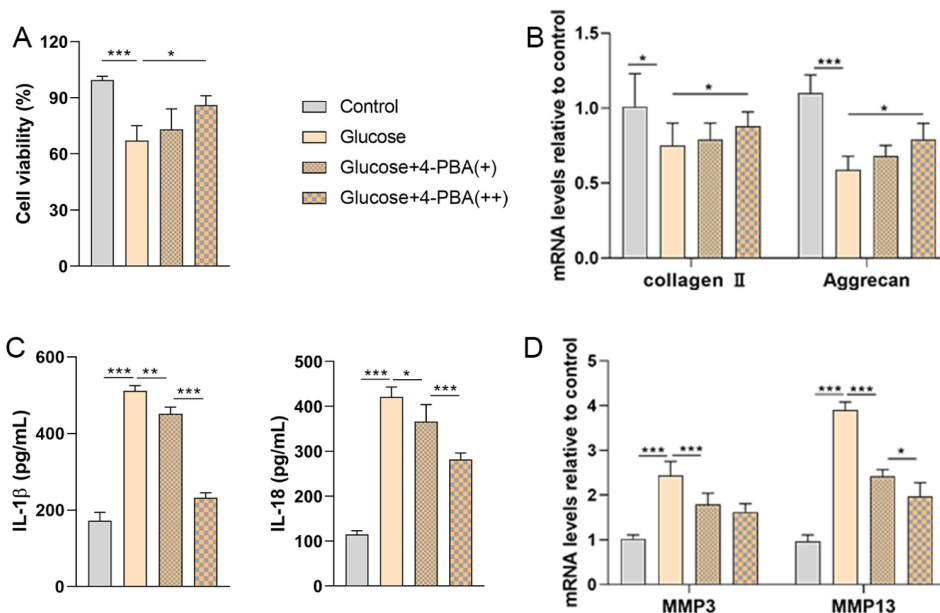


Figure 5. Suppressing ERS alleviates high-glucose induced NP cells degeneration.

(A) Cell viability was determined by the CCK8 test. (B, D) RT-PCR analysis for indicated RNA expression by normalization to GAPDH expression. (C) The IL-1 β and IL-18 content in the medium was tested by ELISA. Results are expressed as mean \pm S.D. (* P <0.05, ** P <0.01, *** P <0.001).

by 4-PBA treatment (Fig. 5D). Therefore, suppressing ERS could prevent cell degeneration.

DISCUSSION

This study investigated the current evidence that high glucose is a risk factor for pyroptosis of NP cells and explored the role of ERS in this process. Previous studies have identified various factors contributing to intervertebral disc degeneration (IDD), such as inflammation, oxidative stress, and an imbalance in extracellular matrix catabolism. The dysfunction and decreased number of NP cells are considered the main and most direct causes of IDD (Ding *et al.*, 2013). While the specific mechanism is not entirely clear, apoptosis, autophagy, and decreased cell proliferation have been implicated (Feng *et al.*, 2016). However, the role of pyroptosis in IDD remains poorly understood. Pyroptosis is a highly inflammatory programmed cell death process that is triggered by inflammasome-mediated activation of proinflammatory cysteine proteases. In contrast to apoptosis, pyroptosis is typically accompanied by the release of large amounts of IL-1 β and IL-18. Currently, caspase-1 mediates pyroptosis in the classical pathway, while the pyroptosis caused by caspase-4, 5, and 11 is defined as a non-classical pathway (Vande & Lamkanfi, 2016; Man *et al.*, 2017).

Although people are typically more familiar with the complications of diabetes affecting the heart, brain, kidneys, peripheral nerves, eyes, and feet, diabetes is also a significant risk factor for intervertebral disc disease (Fletcher *et al.*, 2002; Vijan, 2015). The high-glucose microenvironment can cause IDD due to nutritional metabolism disorder. Long-term hyperglycemia significantly alters the capillaries of the vertebral body's cartilage endplates, leading to the reduced blood supply and nutrient metabolism in the intervertebral discs (van Sloten & Schram, 2018). Additionally, the high-glucose microenvironment increases the production of advanced glycation end products (AGEs), which contribute to NP cell apoptosis (Yamamoto & Sugimoto, 2016). The combination of AGEs and their receptors results in local chronic oxidative stress and induces NP cell death. However, the role of the high-glucose microenvironment in NP cell pyroptosis remains unclear. In our study, high glucose impaired cell viability and upregulated the expression of caspase-1/4/11 and IL-1 β /18, suggesting a correlation between them. To further elucidate the potential mechanism linking them, our attention is focused on ERS.

The endoplasmic reticulum (ER) is a crucial cellular organelle responsible for synthesizing, folding, and modifying secreted proteins, regulating lipid synthesis, and maintaining intracellular calcium ion homeostasis (Wang & Kaufman, 2016). However, when the ER's normal function is impaired, ER stress (ERS) occurs. High glucose, which mimics maternal diabetes, is widely reported to be a risk factor that induces ERS in many cell types (Chen *et al.*, 2018; Hadley *et al.*, 2018; Zhang *et al.*, 2014). Consistent with previous studies, we also found that high glucose increased ERS markers in NP cells, including CHOP, GADD34, and GRP78 (Huang *et al.*, 2019). The secreted protein CHOP is a transcription factor specific to the ER, which participates in various cell activities, especially the regulation of energy metabolism, proliferation, differentiation, and apoptosis (Li *et al.*, 2014). Under normal circumstances, CHOP expression is low, but it is significantly increased when ERS occurs, which further activates downstream GADD34 and GRP78. In addition to mediating apoptosis (Oakes

& Papa, 2015; Almanza *et al.*, 2019), ERS can also lead to pyroptosis (Chou *et al.*, 2019; Cheng *et al.*, 2019). By confirming that ERS can induce pyroptosis in NP cells, we found that the pyroptotic response was activated by TM treatments (Yakin *et al.*, 2019). Furthermore, the inhibitor of ERS also played a role in suppressing high-glucose-induced pyroptosis, indicating that high glucose caused ERS in NP cells, which led to subsequent pyroptosis. Suppressing ERS is an effective strategy to alleviate high-glucose-induced pyroptosis. To determine whether suppressing pyroptosis would backwards restrain ERS, we used the caspase-1 inhibitor, which rescued cell viability, protected collagen II and aggrecan expression, and reduced IL-1 β /18 but did not affect the ERS response. Therefore, pyroptosis is a consequence of ERS, rather than the cause.

However, there are some limitations to this study. We collected only 9 intervertebral discs from patients, and this sample size may be insufficient. For the concentration and duration of glucose treatment, our *in vitro* model is a little different, with lower but longer periods of hyperglycemia. Therefore, further studies should be performed on diabetic mice *in vivo*.

In conclusion, our data indicate that high-glucose induces pyroptosis through ERS in NP cells. Suppressing ERS alleviates the pyroptotic response and reverses the degenerated NP cells under high-glucose conditions. Diabetes is involved in a variety of disease processes, and an in-depth study of the molecular mechanism of a high-glucose environment on NP cell metabolism may help us further understand diabetic IDD.

Declarations

Conflict of Interests. The authors declared no conflict of interest.

Authors' contributions. XX, YW and GL designed the study and performed the experiments, HL and TL collected the data, WL and XH analyzed the data, XX, YW and GL prepared the manuscript. All authors read and approved the final manuscript.

Availability of data and materials. The datasets used or analyzed during the current study are available from the corresponding author upon reasonable request.

REFERENCES

- Agius R, Galea R, Fava S (2016) Bone mineral density and intervertebral disc height in type 2 diabetes. *J Diabetes Complicat* **30**: 644–650. <https://doi.org/10.1016/j.jdiacomp.2016.01.021>
- Almanza A, Carlesso A, Chintia C, Creedican S, Doultinos D, Leuzzi B, Luis A, McCarthy N, Montibeller L, More S, Papaioannou A, Puschel F, Sassano ML, Skoko J, Agostinis P, de Bellerocche J, Eriksson LA, Fulda S, Gorman AM, Healy S, Kozlov A, Munoz-Pinedo C, Rehm M, Chevet E, Samali A (2019) Endoplasmic reticulum stress signalling – from basic mechanisms to clinical applications. *FEBS J* **286**: 241–278. <https://doi.org/10.1111/febs.14608>
- Cannata F, Vadala G, Ambrosio L, Fallucca S, Napoli N, Papalia R, Pozzilli P, Denaro V (2020) Intervertebral disc degeneration: A focus on obesity and type 2 diabetes. *Diabetes-Metab Res* **36**: e3224. <https://doi.org/10.1002/dmrr.3224>
- Che H, Li J, Li Y, Ma C, Liu H, Qin J, Dong J, Zhang Z, Xian CJ, Miao D, Wang L, Ren Y (2020) p16 deficiency attenuates intervertebral disc degeneration by adjusting oxidative stress and nucleus pulposus cell cycle. *Elife* **9**: e52570. <https://doi.org/10.7554/eLife.52570>
- Chen X, Shen WB, Yang P, Dong D, Sun W, Yang P (2018) High glucose inhibits neural stem cell differentiation through oxidative stress and endoplasmic reticulum stress. *Stem Cells Dev* **27**: 745–755. <https://doi.org/10.1089/scd.2017.0203>
- Cheng SB, Nakashima A, Huber WJ, Davis S, Banerjee S, Huang Z, Saito S, Sadovsky Y, Sharma S (2019) Pyroptosis is a critical inflammatory pathway in the placenta from early onset preeclampsia and in human trophoblasts exposed to hypoxia and endoplasmic re-

- ticulum stressors. *Cell Death Dis* **10**: 927. <https://doi.org/10.1038/s41419-019-2162-4>
- Chou R (2014) In the clinic. Low back pain. *Ann Intern Med* **160**: C1–C6. <https://doi.org/10.7326/0003-4819-160-11-201406030-01006>
- Chou X, Ding F, Zhang X, Ding X, Gao H, Wu Q (2019) Sirtuin-1 ameliorates cadmium-induced endoplasmic reticulum stress and pyroptosis through XBP-1s deacetylation in human renal tubular epithelial cells. *Arch Toxicol* **93**: 965–986. <https://doi.org/10.1007/s00204-019-02415-8>
- Ding F, Shao ZW, Xiong LM (2013) Cell death in intervertebral disc degeneration. *Apoptosis* **18**: 777–785. <https://doi.org/10.1007/s10495-013-0839-1>
- Fang Y, Tian S, Pan Y, Li W, Wang Q, Tang Y, Yu T, Wu X, Shi Y, Ma P, Shu Y (2020) Pyroptosis: A new frontier in cancer. *Biomed Pharmacother* **121**: 109595. <https://doi.org/10.1016/j.biopha.2019.109595>
- Feng C, Liu H, Yang M, Zhang Y, Huang B, Zhou Y (2016) Disc cell senescence in intervertebral disc degeneration: Causes and molecular pathways. *Cell Cycle* **15**: 1674–1684. <https://doi.org/10.1080/15384101.2016.1152433>
- Fletcher B, Gulanick M, Lamendola C (2002) Risk factors for type 2 diabetes mellitus. *J Cardiovasc Nurs* **16**: 17–23. <https://doi.org/10.1097/00005082-200201000-00003>
- Hadley G, Neuhaus AA, Couch Y, Beard DJ, Adriaanse BA, Vekrellis K, DeLuca GC, Papadakis M, Sutherland BA, Buchan AM (2018) The role of the endoplasmic reticulum stress response following cerebral ischemia. *Int J Stroke* **13**: 379–390. <https://doi.org/10.1177/1747493017724584>
- Han CY, Rho HS, Kim A, Kim TH, Jang K, Jun DW, Kim JW, Kim B, Kim SG (2018) FXR inhibits endoplasmic reticulum stress-induced NLRP3 inflammasome in hepatocytes and ameliorates liver injury. *Cell Rep* **24**: 2985–2999. <https://doi.org/10.1016/j.celrep.2018.07.068>
- Huang W, Han Z, Liu J, Yu L, Yu X (2016) Risk factors for recurrent lumbar disc herniation: a systematic review and meta-analysis. *Medicine* **95**: e2378. <https://doi.org/10.1097/MD.0000000000002378>
- Huang XT, Liu W, Zhou Y, Sun M, Sun CC, Zhang CY, Tang SY (2019) Endoplasmic reticulum stress contributes to NMDA-induced pancreatic beta-cell dysfunction in a CHOP-dependent manner. *Life Sci* **232**: 116612. <https://doi.org/10.1016/j.lfs.2019.116612>
- Jhawar BS, Fuchs CS, Colditz GA, Stampfer MJ (2006) Cardiovascular risk factors for physician-diagnosed lumbar disc herniation. *Spine J* **6**: 684–691. <https://doi.org/10.1016/j.spinee.2006.04.016>
- Li Y, Guo Y, Tang J, Jiang J, Chen Z (2014) New insights into the roles of CHOP-induced apoptosis in ER stress. *Acta Bioch Bioph Sin* **46**: 629–640. <https://doi.org/10.1093/abbs/gmu048>
- Man SM, Karki R, Kanneganti TD (2017) Molecular mechanisms and functions of pyroptosis, inflammatory caspases and inflammasomes in infectious diseases. *Immunol Rev* **277**: 61–75. <https://doi.org/10.1111/imr.12534>
- Oakes SA, Papa FR (2015) The role of endoplasmic reticulum stress in human pathology. *Annu Rev Pathol-Mech* **10**: 173–194. <https://doi.org/10.1146/annurev-pathol-012513-104649>
- Robinson D, Mirovsky Y, Halperin N, Evron Z, Nevo Z (1998) Changes in proteoglycans of intervertebral disc in diabetic patients. A possible cause of increased back pain. *Spine* **23**: 849–855, 856. <https://doi.org/10.1097/00007632-199804150-00001>
- Shi J, Gao W, Shao F (2017) Pyroptosis: gasdermin-mediated programmed necrotic cell death. *Trends Biochem Sci* **42**: 245–254. <https://doi.org/10.1016/j.tibs.2016.10.004>
- Toldo S, Mauro AG, Cutter Z, Abbate A (2018) Inflammasome, pyroptosis, and cytokines in myocardial ischemia-reperfusion injury. *Am J Physiol-Heart C* **315**: H1553–H1568. <https://doi.org/10.1152/ajpheart.00158.2018>
- Vadala G, Russo F, Di Martino A, Denaro V (2015) Intervertebral disc regeneration: from the degenerative cascade to molecular therapy and tissue engineering. *J Tissue Eng Regen M* **9**: 679–690. <https://doi.org/10.1002/term.1719>
- van Sloten T, Schram M (2018) Understanding depression in type 2 diabetes: a biological approach in observational studies. *F1000Res* **7**: F1000. <https://doi.org/10.12688/f1000research.13898.1>
- Vande WL, Lamkanfi M (2016) Pyroptosis. *Curr Biol* **26**: R568–R572. <https://doi.org/10.1016/j.cub.2016.02.019>
- Vijan S (2015) In the clinic. Type 2 diabetes. *Ann Intern Med* **162**: C1–C16. <https://doi.org/10.7326/AITC201503030>
- Wagner M, Moore DD (2011) Endoplasmic reticulum stress and glucose homeostasis. *Curr Opin Clin Nutr* **14**: 367–373. <https://doi.org/10.1097/MCO.0b013e32834778d4>
- Wang M, Kaufman RJ (2016) Protein misfolding in the endoplasmic reticulum as a conduit to human disease. *Nature* **529**: 326–335. <https://doi.org/10.1038/nature17041>
- Yakin M, Seo B, Rich A (2019) Tunicamycin-induced endoplasmic reticulum stress up-regulates tumour-promoting cytokines in oral squamous cell carcinoma. *Cytokine* **120**: 130–143. <https://doi.org/10.1016/j.cyto.2019.04.013>
- Yamamoto M, Sugimoto T (2016) Advanced glycation end products, diabetes, and bone strength. *Curr Osteoporosis Rep* **14**: 320–326. <https://doi.org/10.1007/s11914-016-0332-1>
- Zhang X, Yuan Y, Jiang L, Zhang J, Gao J, Shen Z, Zheng Y, Deng T, Yan H, Li W, Hou WW, Lu J, Shen Y, Dai H, Hu WW, Zhang Z, Chen Z (2014) Endoplasmic reticulum stress induced by tunicamycin and thapsigargin protects against transient ischemic brain injury: Involvement of PARK2-dependent mitophagy. *Autophagy* **10**: 1801–1813. <https://doi.org/10.4161/auto.32136>
- Zhao CQ, Wang LM, Jiang LS, Dai LY (2007) The cell biology of intervertebral disc aging and degeneration. *Ageing Res Rev* **6**: 247–261. <https://doi.org/10.1016/j.arr.2007.08.001>

Investigation of microbiological safety of dry cat foods marketed in Poland

Joanna Zięta-Wysocka^{1,2}, Olga Sierawska^{1,2}, Cansel Taskin³, Agata Poniewierska-Baran², Dominika Bębnowska², Rafał Hryniewicz², Filip Lewandowski² and Paulina Niedźwiedzka-Rystwej²

¹Doctoral School of the University of Szczecin, 70-383 Szczecin, Poland; ²Institute of Biology, University of Szczecin, 71-412 Szczecin, Poland; ³Biology Department, Faculty of Science, Ankara University, Ankara 06560, Turkey

Pets are inhabiting more and more human homes every year. In 2020, the cat population in Europe was 110 million, including 6.8 million in Poland. Dry food is the most popular dietary model for cats because of its easy storage and efficient satisfaction of pet needs. The high processing temperature of dry food reduces the chance of microbial contamination, but this can occur later, during post-production or storage in the pet's caregiver's home or, in the case of weighed foods, in the store. The purpose of this study was to investigate the microbiological safety of dry feed sold in the original manufacturer's packaging and the same feed from the same manufacturers sold in a retail store by weight. Six discriminants, presence of *Salmonella* spp., number of coliforms, number of coagulase-positive staphylococci, determination of yeast and mould counts, *Enterobacteriaceae* count, *Listeria monocytogenes* and determination of total aerobic microbial count were used for the analysis. Then, cat food was then stored for 45 days according to the manufacturer's recommendations. Based on the samples tested both after opening and after storage, it was concluded that the dry cat food analyzed posed a low microbiological risk to animals and humans.

Keywords: microbiological safety, dry cat food, pet food safety, microbiology of food, cat

Received: 11 July, 2023; **revised:** 22 October, 2023; **accepted:** 23 October, 2023; **available on-line:** 15 November, 2023

✉ e-mail: paulina.niedzwiedzka-rystwej@usz.edu.pl

Abbreviations: CFU, colony-forming unit; FEDIAF, European Pet Food Industry Federation; GMP, good manufacturing practices; MRSA, Methicillin-resistant *Staphylococcus aureus*; MKTn, Muller-Kauffmann Tetrathionate-Novobiocin; RASFF, Rapid Alert System for Food and Feed; RSV, Rappaport Vassiliadis Soya; XLD, Xylose Lysine Deoxycholate; SS, *Salmonella* Shigella; VRBL, Violet Red Bile with Lactose, VRBG, Violet Red Bile with Glucose; TAMC, total aerobic microbial count

INTRODUCTION

According to statistics presented by FEDIAF, within the European Union, 88 million households had pets and the cat population was 110 million in 2020. In Poland, there are 6.8 million cats and more than one-third of households in Poland have at least one cat (FEDIAF, 2020). By 2020, pet food sales were 21.8 billion Euros, representing 8.5 million tons of products annually. Proper feeding of animals, including cats, is essential for a healthy and long life. The development of research and access to information has increased pet owners' awareness of the quality of food provided to their pets (FE-

EDIAF, 2020). In the European Union, the Rapid Alert System for Food and Feed (RASFF, 2021) is responsible for controlling the safety of raw materials and food products. According to this organization, pet food can be a significant source of many risks, both biological, chemical, and physical (RASFF. The Rapid Alert System for Food and Feed. Annual Report, 2020). These hazards may be related to diseases and injuries that occur in pets. The foundation for maintaining nutritional safety is compositional and nutrient analyses, as well as microbiological evaluation. Despite the use of the latest dry food production methods to prevent contamination, recalls of a particular batch of products due to microbiological contamination are still evident (Kępińska-Pacelik & Biel, 2021).

Dry food is a regular part of the diet of both cats and dogs. This type of food dominates the market due to its ease of storage and efficient satisfaction of the pet's needs. It is processed at a temperature of 80–160°C (Meineri *et al.*, 2019) which significantly reduces the number of pathogenic microorganisms, however, the product may be contaminated at a later stage of production (Kazimierska *et al.*, 2021). The occurrence of pathogenic microorganisms is associated with cross-contamination and deviation from good manufacturing practices (GMP) (Meghwal *et al.*, 2017). Good microbiological quality of food is a major factor, along with the nutritional value of food, to produce healthy and safe food (Chlebicz & Śliżewska, 2018). In recent years, reports of pathogenic microorganisms (bacteria, fungi, and the toxins they produce) have accounted for about 20% of all RASFF food and feed reports, showing, in particular, the presence of *Salmonella*, *Listeria*, *Escherichia*, and others (Pigłowski, 2019).

There have been studies on the microbiological safety of dry dog food (Holda *et al.*, 2017; Kazimierska *et al.*, 2021) and livestock feeds (Hoszowski *et al.*, 2012; Kukier *et al.*, 2012) in Poland, but no studies have focused on dry cat food in Poland. Previous international studies have also focused on the study of animal foods in general (Blajet-Kosicka *et al.*, 2014; Leiva *et al.*, 2019), without distinguishing between cat and dog foods. However, it was reported that there is a need to distinguish between studies on these two species (Holda *et al.*, 2017; van Rooijen *et al.*, 2014), which differ not only in their nutritional needs but also in their behavioral patterns towards humans and other animals, which affects the possibility of infection risk.

The study aimed to evaluate dry food for adult cats, with a focus on (1) assessing their microbiological safety, (2) comparing microbiological safety in food sold in a

sealed pack and by weight, and (3) assessing their microbiological safety after 45 days.

MATERIALS AND METHODS

Materials

Microbiological analysis was performed on 6 commercially available dry, whole-food cat foods, including 5 international brands and 1 available on the local market. The criterion for the selection of a particular pet food was its availability for sale both in the form of manufacturer-sealed packages and the availability of the same food sold by weight and packaged at points of sale. All feeds were purchased from a specialized pet store located in the city of Szczecin. To obtain reliable results, five packages ($n=5$) of each feed were purchased for analysis in five replicates. Prior to purchase, the shelf life was checked and the condition of the packaging was assessed for damage that could affect the microbiological quality of the product tested. The purchased assortment for testing was divided into two groups. The first group consisted of pet food purchased in the manufacturer's original packaging. While the second group consisted of pet foods from the same manufacturers sold by weight. The weight of the finished packages ranged from 340 g to 500 g. After microbiological analysis, the tested cat food was stored for 45 days in accordance with the manufacturer's recommendations, the average shelf life of the food after opening was calculated and after that time the food was again subjected to microbiological tests.

Storage of samples for tests

In the first stage of microbiological tests, both commercial feed from the original manufacturer and feed purchased by weight (collected in sterile bags closed with string) were stored at room temperature ($18-22^{\circ}\text{C}$). In the second stage of the study (after opening the package), the shelf life of the food was 45 days.

Preparation of samples for testing

All packages were washed with alcohol before opening to exclude product contamination by microorganisms on the surface of the package. The general preparation of samples and dilutions to perform microbiological tests were carried out by the International Standard PN-EN ISO 6887-1:2017-05 "Preparation of test samples, initial suspension and decimal dilutions for microbiological examination – Part 1: General rules for the preparation of the initial suspension and decimal dilutions". Depending on the standard, 25 g or 10 g of feed was used for analysis in five replicates.

Microbiological analysis

Each sample, depending on the discriminant to be tested, was weighed accordingly and mixed with an appropriate diluent according to the standard and homogenized (time 30 seconds, speed 8 strokes/second) in Star-Blender™ Digital Homogenizator (VWR, Pennsylvania, USA).

Detection of *Salmonella* spp.

The test was performed according to the PN-EN ISO 6579-1:2017-04 standard. By mixing 25 g of the sample with 225 mL of buffered peptone water (Scharlab, Bar-

celona, Spain), a stock suspension was obtained, which was incubated at $37^{\circ}\text{C}\pm 1^{\circ}\text{C}$ for $18\text{ h}\pm 2\text{ h}$ for pre-enrichment in non-selective liquid medium. Then 0.1 mL of the obtained culture was transferred to 10 mL of Rappaport Vassiliadis Broth (RVS) medium (Scharlab, Barcelona, Spain) and 1 mL to 10 mL of Muller-Kauffmann Tetrathionate-Novobiocin (MKKTn) Broth medium (Graso, Starogard Gdański, Poland). The inoculated RVS medium was incubated at 41.5°C for $24\text{ h}\pm 3\text{ h}$, while the inoculated MKKTn medium was incubated at 37°C for $24\text{ h}\pm 3\text{ h}$. The material obtained from RVS and MKKTn cultures was seeded onto two selectively isolating media, Xylose Lysine Deoxycholate (XLD) agar (Scharlab, Barcelona, Spain) and Salmonella Shigella (SS) agar (Scharlab, Barcelona, Spain), which were incubated at 37°C for $24\text{ h}\pm 3\text{ h}$.

Number of coliforms

The test was performed according to the PN-ISO 4832:2007 standard. Pre-suspension of 1 mL obtained after mixing 10 g of the sample with 90 mL of the dilution fluid was transferred onto two sterile Petri dishes. Then about 15 mL of Violet Red Bile with Lactose (VRBL) agar medium (BioMaxima, Lublin, Poland) was added to the plate. After complete solidification, a top layer of about 5 mL of the same medium was added to obtain relatively anaerobic growth conditions. The plates were incubated at 37°C for $24\text{ h}\pm 2\text{ h}$.

Number of coagulase-positive staphylococci (CoPS), *Staphylococcus aureus*, and other species

The test was performed according to the PN-EN ISO 6888-1:2001 standard. A surface culture of 1 mL of the pre-suspension on Baird-Parker agar medium (Scharlab, Barcelona, Spain) was performed. To obtain 1 mL of the test sample, 0.33 mL of the initial suspension was inoculated onto the surface of three small agar plates (90 mm). The plates were incubated at 37°C for $24\text{ h}\pm 2\text{ h}$ and then the incubation was prolonged for another $24\text{ h}\pm 2\text{ h}$. The colonies obtained were checked by coagulase test.

Determination of yeasts and moulds counts

Dry cat food is characterized by low water activity; therefore, the PN-ISO 21527-2:2009 standard for products with water activity lower or equal to 0.95 was applied to determine the number of yeasts and moulds. Pre-suspension of 0.1 mL (10 g of the product was mixed with 90 mL of 0.1% peptone water) was inoculated onto the surface of a DG-18 agar plate (Graso, Starogard Gdański, Poland). The plates were incubated at $25^{\circ}\text{C}\pm 1^{\circ}\text{C}$ for 5 to 7 days.

Enterobacteriaceae count

The test was performed according to PN-EN ISO 21528-2:2017-08. Pre-suspension of 1 mL obtained after mixing 10 g of the sample with 90 mL of dilution fluid was applied to a sterile Petri dish. Then about 15 mL of Violet Red Bile with Glucose (VRBG) agar medium (BioMaxima, Lublin, Poland) was added to the plate. After complete solidification, a top layer of about 5 mL of the same medium was added to obtain relatively anaerobic growth conditions. The sample was performed in duplicate, according to PN-EN ISO 7218:2008/A1:2013-10. The plates were incubated at 37°C for $24\text{ h}\pm 2\text{ h}$.

Determination of total aerobic microbial count (TAMC)

The test was performed by depth culture according to the PN-EN ISO 4833-1:2013-12 standard. Pre-suspension of 1 mL was transferred to two sterile Petri dishes each and then about 15 mL of Plate Count Agar medium (BioMaxima, Lublin, Poland) was added. Observations were made after 72 hours of incubation at 30°C, under conditions that ensure the growth and multiplication of aerobic bacteria.

Listeria monocytogenes

Detection of *Listeria monocytogenes*

The test was performed according to PN-EN ISO 11290-1:2017-07. 225 mL of Semi-Fraser Broth (Graso, Starogard Gdański, Poland) was added to 25 g of product. The resulting stock suspension was incubated at 30°C for 25 h ± 1 h. Subsequently, 0.1 mL of the obtained culture was transferred to 10 mL of Fraser medium (Graso, Starogard Gdański, Poland) and a scratch culture was performed on two selective media ALOA (BioMaxima, Lublin, Poland) and Oxford (BioMaxima, Lublin, Poland). The inoculated Fraser medium was incubated at 37°C for 24 h ± 2 h, while the inoculated ALOA and Oxford media were incubated at 37°C for 24 h ± 2 h–48 h ± 2 h. The material obtained from the culture on Fraser broth was streaked onto two selective media ALOA (BioMaxima, Lublin, Poland) and Oxford (BioMaxima, Lublin, Poland), and then incubated at 37°C for 24 h ± 2 h–48 h ± 2 h.

Number of *Listeria monocytogenes*

The test was performed in accordance with PN-EN ISO 11290-2:2017-07. A surface culture of 1 mL of

the initial suspension including 10 g of sample and 90 mL of half-Fraser (Graso, Starogard Gdański, Poland) broth on ALOA (BioMaxima, Lublin, Poland) agar medium was performed. The seeded plates were incubated at 37°C for 24 h ± 2 h–48 h ± 2 h.

Calculation of results

The results were calculated and presented according to PN-EN ISO 7218:2008/A1:2013-10, using the formula:

$$N = \frac{\sum c}{V \times [n1 + (0,1 \times n2)] \times d}$$

where:

$\sum C$ – total colonies on two selected plates from two successive dilutions, of which at least one contains a minimum of 10 colonies; V – the volume of inoculum applied on each plate, in mL; n1 – number of plates obtained from the first dilution; n2 – number of plates obtained from the second dilution; d – the dilution index corresponding to the first dilution obtained.

If less than 10 colonies were obtained per plate, but the set of two plates contained at least 4 colonies, the result was calculated using the formula:

$$N = \frac{\sum c}{V \times n \times d}$$

where:

$\sum C$ – the sum of colonies counted on two plates; V – the volume of inoculum applied on each plate, in mL; n – number of plates; d – the dilution index corresponding to the first dilution obtained.

Table 1. Microbiological analysis of the tested commercial cat foods was performed after opening.

The table shows the mean obtained from 5 replicates of the analysis of one batch of feed.

No.	<i>Salmonella</i> spp. (CFU/g)	Coliforms (CFU/g)	CoPS (CFU/g)	Yeasts and moulds (CFU/g)	Enterobacteriaceae (CFU/g)	TAMC (CFU/g)	<i>L. monocytogenes</i> (CFU/g)
1a (n=5)	ND	ND	ND	ND	ND	8.3x10 ²	ND
1b (n=5)	ND	ND	ND	ND	ND	3.0x10 ¹	ND
2a (n=5)	ND	ND	ND	ND	ND	6.2x10 ²	ND
2b (n=5)	ND	ND	ND	ND	ND	1.2x10 ³	ND
3a (n=5)	ND	ND	ND	ND	ND	1.3x10 ³	ND
3b (n=5)	ND	ND	ND	ND	ND	1.0x10 ³	ND
4a (n=5)	ND	ND	ND	ND	ND	3.8x10 ³	ND
4b (n=5)	ND	ND	ND	ND	ND	8.1x10 ³	ND
5a (n=5)	ND	ND	ND	ND	ND	ND	ND
5b (n=5)	ND	ND	ND	ND	ND	5.7x10 ¹	ND
6a (n=5)	ND	ND	ND	ND	ND	ND	ND
6b (n=5)	ND	ND	ND	ND	ND	9.7x10 ²	ND

TAMC – total aerobic microbial count; a – food in original packaging; b – food purchased by weight; ND – not detected.

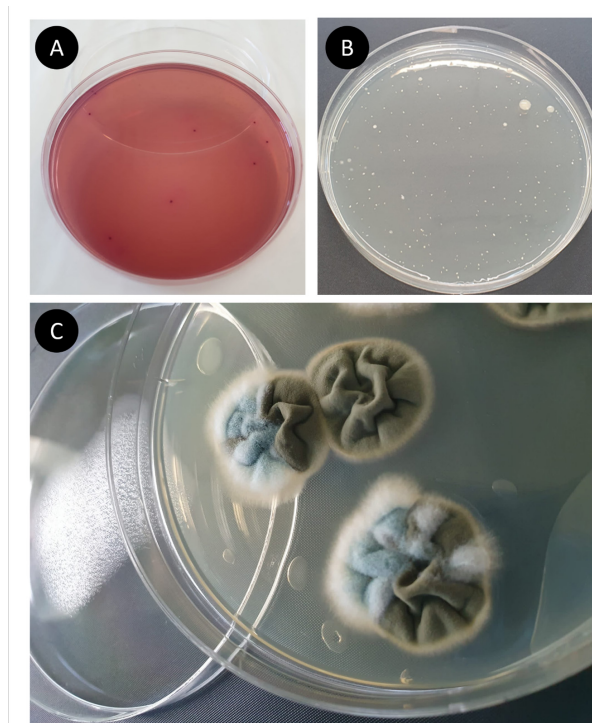


Figure 1. Example photos of culture plates showing: (A) *Enterobacteriaceae*, (B) TAMC, (C) yeasts and molds.

Statistical analysis

The statistical analysis was performed using Tibco Statistica 13.3 (StatSoft, Palo Alto, CA, USA). The values of the parameters were presented as arithmetic means. The normality of variable distributions was verified by the Shapiro–Wilk Test. Data with a normal distribution were analyzed using the Student's *t*-test and the Mann-Whitney U test was used for data with a non-normal distribution.

RESULTS

The results are presented in Table 1. For quantitative methods (coliforms, CoPS, yeasts and moulds, *Enterobacteriaceae*, TAMC, *Listeria monocytogenes*), the notation “not detected” was used for standardization when a result $<1.0 \times 10^1$ cfu/g was obtained. For the qualitative method in *Salmonella* spp. and *Listeria monocytogenes* the result was “not detection in 25g” with the laboratory's limit of detection (LOD) obtained at 5 cfu/g for *Salmonella*

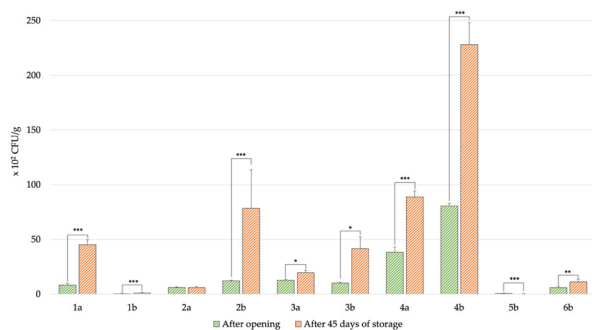


Figure 2. Comparison of total aerobic microbial count in the tested feeds. * $p \leq 0.05$; ** $p \leq 0.01$; *** $p \leq 0.0001$

spp. and 7 cfu/g, for *Listeria monocytogenes*. Therefore, no growth of coliforms, *Salmonella* spp., or CoPS, yeasts and moulds, *Enterobacteriaceae* and *Listeria monocytogenes* were observed. Typical growth of aerobic mesophilic microorganisms was obtained in 10 out of 12 samples (83%).

After 45 days of storage, tests were carried out again. No growth of *Salmonella* spp., coliforms, or CoPS was detected. Growth of yeast and moulds was observed in 3 out of 12 samples (25%, Fig. 1C). Growth of *Enterobacteriaceae* was observed in 1 out of 12 samples (8%, Fig. 1A). No growth of *Listeria monocytogenes* was observed. Detailed results are presented in Table 2. Statistical analysis was carried out to compare results from open and stored feeds. The differentiators at which changes were observed were compared: yeasts and moulds, *Enterobacteriaceae*, and TAMC. Statistical significance was then verified. For yeasts and moulds and *Enterobacteriaceae*, the samples reached a statistical difference. In the comparison of TAMC in the two groups, 9 out of 12 trials achieved a statistical difference (Fig. 2).

DISCUSSION

Although the food is processed at high temperatures that destroy microorganisms, still spore forms may be retained, and the contamination itself may occur after the production, for example during storage of the food in a retail shop or at home (FEDIAF, 2018). FEDIAF in its list of hazards during the production of dry pet food in the biological nature of hazards mentions *Aeromonas*, *Campylobacter*, *Clostridium botulinum*, *Clostridium perfringens*, *Enterobacteriaceae*, *Escherichia coli*, *Listeria monocytogenes*, *Salmonella* spp., *Staphylococcus aureus*, and moulds and yeasts including mycotoxins (FEDIAF, 2018). However, not all of them concern the finished dry food product, but also the raw materials used in its production. For this reason, the organization suggests monitoring the microbiological status by testing environmental samples obtained from surfaces not in and in contact with the product and samples of finished feeds (FEDIAF, 2018). The exact requirements for the production facility are set out in the hazard analysis and critical control points (HACCP) procedures. The procedures based on HACCP principles and other regulations stem from Regulation (EC) No 1069/2009 of 21 October 2009 and Commission Regulation (EU) No 142/2011 of 25 February 2011 (Osinski *et al.*, 2014). These include many areas related to pet food production. In terms of microbiological safety. The regulation sets out the following standards that a product must meet after production: the product must be packaged in packaging which is protected against the intrusion of microorganisms, and 5 samples of the product tested for *Salmonella* spp. in 25 g must not show the presence of these bacteria ($n=5$, $c=0$, $m=0$, $M=0$). The result for *Enterobacteriaceae* is considered satisfactory if the number of bacteria in all samples does not exceed 10 cfu/g (m) or in two samples the result is between 10 and 300 cfu/g (c) if, in the remaining samples, the value obtained does not exceed 10 cfu/g. The result is considered abnormal if the number of bacteria in one or more samples equals or is greater than 300 cfu/g (M) – ($n=5$, $c=2$; $m=10$; $M=300$ in 1 g) (European Commission, 2011).

Particularly after 2012, when there were two major outbreaks of human salmonellosis in the US caused by contaminated pet food products, attention was directed toward this pathogen (Chen *et al.*, 2019). Actually, in most previous studies conducted on dry commercial pet

Table 2. Microbiological analysis of the tested commercial cat foods was performed after 45 days of storage.
The table shows the mean obtained from 5 replicates of the analysis of one batch of feed.

No.	<i>Salmonella</i> sp. (CFU/g)	Coliforms (CFU/g)	CoPS (CFU/g)	Yeasts and moulds (CFU/g)	Enterobacteriaceae (CFU/g)	TAMC (CFU/g)	<i>L. monocytogenes</i> (CFU/g)
1a (n=5)	ND	ND	ND	2.2x10 ³	ND	4.5x10 ³	ND
1b (n=5)	ND	ND	ND	1.4x10 ²	ND	1.1x10 ²	ND
2a (n=5)	ND	ND	ND	ND	ND	6.0x10 ²	ND
2b (n=5)	ND	ND	ND	ND	ND	1.4x10 ⁴	ND
3a (n=5)	ND	ND	ND	ND	ND	2.0x10 ³	ND
3b (n=5)	ND	ND	ND	ND	ND	4.2x10 ³	ND
4a (n=5)	ND	ND	ND	ND	ND	8.9x10 ³	ND
4b (n=5)	ND	ND	ND	ND	6.5x10 ³	2.3x10 ⁴	ND
5a (n=5)	ND	ND	ND	ND	ND	ND	ND
5b (n=5)	ND	ND	ND	ND	ND	ND	ND
6a (n=5)	ND	ND	ND	ND	ND	ND	ND
6b (n=5)	ND	ND	ND	2.3x10 ³	ND	1.1x10 ³	ND

TAMC – total aerobic microbial count; a – food in original packaging; b – food purchased by weight; ND – not detected.

foods, no *Salmonella* sp. was reported, which is consistent with the results of our study (Holda *et al.*, 2017; Kazimierska *et al.*, 2021; Leiva *et al.*, 2019; Nemser *et al.*, 2014; Taymaz *et al.*, 2022; Yang *et al.*, 2016). As the pathogen causes a dangerous disease, salmonellosis, this is good news. In 2020, 5470 cases of *Salmonella* spp. infection was reported in Poland. The chance of infection occurs through human-to-human transmission, animal-to-human transmission, also through contaminated food or drinking water (Milczarek *et al.*, 2022). Cases of the spread of *Salmonella* spp. from cats to other animals and humans have been described. In cats, salmonellosis is mainly manifested by acute enteritis (diarrhea, vomiting, fever, inappetence, abdominal pain, dehydration, lethargy) that may progress to septicemia. Conjunctivitis, neutropenia, excessive salivation, fever without diarrhea, and uterine infections may also be among the usual clinical signs of the disease. Uterine infections are particularly important for pregnant cats because they can cause, stillbirths, weak offspring or abortions, which can be caused, for example, by *S. typhimurium* and *S. enteritidis* causing acute inflammation of the stomach and intestines, which as it progresses affects the development of the fetus in pregnant animals (Kurja, 2023). In addition to the possibility of *Salmonella* spp. infection through consumption of contaminated food, outdoor cats are particularly at risk, as they may become infected by preying on birds weakened by salmonellosis (Söderlund *et al.*, 2019) or drinking water from sources that are not controlled, such as puddles (Kozak *et al.*, 2003).

In our study, no growth of coliforms was noted in any sample. This is consistent with previous studies on dry pet food (Holda *et al.*, 2017; Kazimierska *et al.*, 2021; Leiva *et al.*, 2019; Nemser *et al.*, 2014). This is important

for animal foods because the consumption of food with pathogenic coliforms by a cat can cause food poisoning. In the case of coliforms, the bacteria can also be transmitted from the cat to humans. It is most commonly transmitted by direct contact with the animal or its excreta, especially in the case of a cut or open wound. In humans, symptoms of infection with pathogenic coliforms include food poisoning, flu-like symptoms, fever, abdominal cramps, and diarrhea (Srikullabutr *et al.*, 2021).

In our study, no growth of CoPS was noted in any sample. However, they are known to cause disease in livestock and pets, such as methicillin-resistant strains of *S. aureus* (MRSA). In addition, it has been determined that MRSA can contaminate food in food processing plants and slaughterhouses, with its major presence occurring in meat products, the stuff from which pet food is made. The infection can spread from animal to human. MRSA causes infections in humans such as acne, food poisoning, ear infections and septicemia. In cats, MRSA infection leads to food poisoning and pustular dermatitis (Algammal *et al.*, 2020). Domesticated animals, cats and dogs, are defined as environmental sources of CoPS (Velázquez-Guadarrama *et al.*, 2017).

It was assumed that the number of yeasts and moulds exceeding 10⁴ cfu/g indicates the poor microbiological quality of food and levels exceeding the recommended limits to ensure hygienic quality (Kazimierska *et al.*, 2021). No yeast or mould growth was observed in the feeds tested after opening. However, they developed after 45 days of storage in 3 of the 12 samples (25%). The highest value was 1.32x10³ cfu/g, which is within the suggested microbiological quality value. The presence of yeast and mould in pet food has been reported previously (Kazimierska *et al.*, 2021; Leiva *et al.*, 2019). In

the case of yeast and moulds, the greatest risk is posed by mycotoxins. However, the presence of moulds does not always clearly indicate product contamination with mycotoxins. Specific conditions are needed for the production of toxins (Janik *et al.*, 2020). Mycotoxins may contaminate the product both during production (if the food contains cereals) and outside this stage, e.g. during improper storage of the product. However, there is no legislation in Poland setting a maximum level for these in cat food (Blajet-Kosicka *et al.*, 2014). Mycotoxins can cause adverse effects, in the worst cases even cancer. While analyzing pet food with a cereal content of 6% or more, data were obtained showing a very high presence of mycotoxins in dry food. and cat food was more contaminated than dog food. Among mycotoxins, cats may be more sensitive to the effects of trichothecenes and fumonisins (Macías-Montes *et al.*, 2020). Symptoms of trichothecenes poisoning include immune system disorders loss of appetite, vomiting, diarrhea, ataxia, and gastrointestinal bleeding. Fumonisin, on the other hand, can be responsible for lack of appetite, and blindness. depression, ataxia, and even liver and kidney cancer (Blajet-Kosicka *et al.*, 2014).

The number of microorganisms able to grow and form colonies in the solid medium after incubation under aerobic conditions at 30°C in the samples we tested is shown in Fig. 1B. Compared to other studies conducted on dry animal foods (Holda *et al.*, 2017; Kazimierska *et al.*, 2021), this is not an outlier. TAMB standards for dry pet food are not specified in the guides for pet food manufacturers in Europe and the US (FEDIAF, 2018; Food and Drug Administration, 2022). Thus in animal feeds this value should not exceed 10⁶ cfu/g (Kukier *et al.*, 2012), because an increase in the total number of mesophilic aerobic microorganisms may increase the probability of pathogenic microorganisms and their toxic metabolites in the product (Kazimierska *et al.*, 2021). Our testing for mesophilic aerobic microorganisms resulted in an acceptable level of 10⁴ cfu/g.

As in our study, no *Listeria monocytogenes* were found in dry pet food in earlier studies (Bilung *et al.*, 2018; Kazimierska *et al.*, 2021; Nemser *et al.*, 2014). In cats, the disease caused by *L. monocytogenes*, listeriosis, is rare. When infected, it can involve the whole organism, skin wounds, encephalomyelitis, and lymphadenitis (Elbert & Rissi, 2021).

The tested feeds were distinguished by a high level of microbiological safety. Despite the demonstrated increase in the number of microorganisms in tests conducted after 45 days of storage, it is worth emphasizing that this number still remained within acceptable limits in accordance with applicable standards. Carrying out analyzes on feed stored in a manner not recommended by the manufacturer has a significant potential to obtain additional data. Such activities may provide more detailed information on the impact of non-recommended storage on the microbiological quality of feed and possible health and food safety consequences.

Declarations

Acknowledgment. We would like to thank Agata Kulinska, MSc for her invaluable technical assistance and support.

Funding. Not applicable.

Conflict of Interest. The authors declare that they have no competing interests.

Code or data availability. The datasets generated during and/or analyzed during the current study are

available from the corresponding author upon reasonable request.

Authors' Contributions. Conceptualization, J.Z.-W. and P.N.-R.; methodology, O.S., J.Z.-W. and P.N.-R.; software, D.B., R.H., F.L.; validation, O.S., J.Z.-W., C.T., A.P.-B., D.B., R.H., and P.N.-R.; formal analysis, J.Z.-W., and P.N.-R.; investigation, O.S., J.Z.-W., C.T., and P.N.-R.; resources, O.S., J.Z.-W., A.P.-N., D.B., R.H. and P.N.-R.; data curation, O.S., J.Z.-W., A.P.-N., D.B., R.H., F.L. and P.N.-R.; writing – original draft preparation, O.S., J.Z.-W.; writing – review and editing, A.P.-B., D.B., R.H., F.L. and P.N.-R.; visualization, A.P.-B., and R.H.; supervision, P.N.-R.; project administration, P.N.-R.; funding acquisition, P.N.-R. All authors have read and agreed to the published version of the manuscript.

Animal Ethics. The study did not require ethics approval.

Consent to participate. Not applicable.

Consent for publication. Not applicable.

REFERENCES

- Algammal AM, Hetta HF, Elkelish A, Alkhalifah DHH, Hozzein WN, Batiha GES, El Nahhas N, Mabrok MA (2020) Methicillin-resistant *Staphylococcus aureus* (MRSA): One health perspective approach to the bacterium epidemiology, virulence factors, antibiotic-resistance, and zoonotic impact. *Infect Drug Resist* 13: 3255–3265. <https://doi.org/10.2147/IDR.S272733>
- Bilung LM, Ulok V, Tesfamariam FM, Apun K (2018). Assessment of *Listeria monocytogenes* in pet food. *Agric Food Secur* 7: 23. <https://doi.org/10.1186/s40066-018-0175-3>
- Blajet-Kosicka A, Kosicki R, Twarużek M, Grajewski J (2014) Determination of moulds and mycotoxins in dry dog and cat food using liquid chromatography with mass spectrometry and fluorescence detection. *Food Addit Contam Part B Surveill* 7: 302–308. <https://doi.org/10.1080/19393210.2014.933269>
- Carter ME, Quinn PJ (2000) Salmonella infections in dogs and cats. In *Salmonella in Domestic Animals*, Wray C, Wray A eds, pp 231–244. CAB International. <https://doi.org/10.1079/9780851992617.0231>
- Chen CH, Yin HB, Upadhyay A, Brown S, Venkitanarayanan K (2019) Efficacy of plant-derived antimicrobials for controlling *Salmonella* Schwarzengrund on dry pet food. *Int J Food Microbiol* 296: 1–7. <https://doi.org/10.1016/j.ijfoodmicro.2019.02.007>
- Chlebicz A, Śliżewska K (2018) Campylobacteriosis, Salmonellosis, Yersiniosis, and Listeriosis as zoonotic foodborne diseases: a review. *Int J Environ Res Public Health* 15: E863. <https://doi.org/10.3390/ijerph15050863>
- Elbert JA, Rissi DR (2021) Systemic *Listeria monocytogenes* infection and concurrent pleural mesothelioma in a cat. *J Vet Diagn Invest* 33: 120–123. <https://doi.org/10.1177/1040638720966321>
- European Commission. (2011) Commission Regulation (EU) No 142/2011 of 25 February 2011 implementing Regulation (EC) No 1069/2009 of the European Parliament and of the Council laying down health rules as regards animal by-products and derived products not intended for human consumption and implementing Council Directive 97/78/EC as regards certain samples and items exempt from veterinary checks at the border under that Directive.
- FEDIAF (2018) Guide to Good Practice for the Manufacture of Safe Pet Foods. https://fediaf.org/images/FEDIAF_Safety_Guide_Febuary_2018_online.pdf
- FEDIAF (2020) Facts & Figures 2020 *European Overview*
- Finley R, Reid-Smith R, Weese JS, Angulo FJ (2006) Human health implications of salmonella-contaminated natural pet treats and raw pet food. *Clin Infect Dis* 42: 686–691. <https://doi.org/10.1086/500211>
- Food and Drug Administration (2022) FDA's Regulation of Pet Food. FDA. <https://www.fda.gov/animal-veterinary/animal-health-literacy/fdas-regulation-pet-food>
- Holda K, Głogowski R, Hac-Szymańczuk E, Wiczuk W (2017) Comprehensive microbiological evaluation of dry foods for growing dogs marketed in Poland. *Ann Warsaw Univ Life Sci* 56: 81–89. <https://doi.org/10.22630/AAS.2017.56.1.10>
- Janik E, Niemcewicz M, Ceremuga M, Stela M, Saluk-Bijak J, Siadkowski A, Bijak M (2020) Molecular aspects of mycotoxins – a serious problem for human health. *Int J Mol Sci* 21: 8187. <https://doi.org/10.3390/ijms21218187>
- Kazimierska K, Biel W, Witkiewicz R, Karakulska J, Stachurska X (2021) Evaluation of nutritional value and microbiological safety in commercial dog food. *Vet Res Commun* 45: 111–128. <https://doi.org/10.1007/s11259-021-09791-6>

- Kępińska-Pacelik J, Biel W (2021) Microbiological hazards in dry dog chews and feeds. *Animals (Basel)* **11**: 3. <https://doi.org/10.3390/ani11030631>
- Kozak M, Horosova K, Lasanda V, Bilek J, Kyselova, J (2003) Do dogs and cats present a risk of transmission of salmonellosis to humans? *Bratisl Lek Listy* **104**: 323–328
- Kukier E, Goldsztejn M, Grenda T, Krzysztof K, Wasyl D, Hoszowski A (2012) Microbiological quality of compound feed used in Poland. *J Vet Res* **56**: 349–354. <https://doi.org/10.2478/v10213-012-0061-x>
- Kuria JKN (2023) Salmonellosis in food and companion animals and its public health importance. *IntechOpen*. <https://doi.org/10.5772/intechopen.109324>
- Leiva A, Molina A, Redondo-Solano M, Artavia G, Rojas-Bogantes L, Granados-Chinchilla F (2019) Pet food quality assurance and safety and quality assurance survey within the Costa Rican pet food industry. *Animals (Basel)* **9**: 980. <https://doi.org/10.3390/ani9110980>
- Macías-Montes A, Rial-Berriel C, Acosta-Dacal A, Henríquez-Hernández LA, Almeida-González M, Rodríguez-Hernández Á, Zumbado M, Boada LD, Zaccaroni A, Luzardo OP (2020) Risk assessment of the exposure to mycotoxins in dogs and cats through the consumption of commercial dry food. *Sci Total Environ* **708**: 134592. <https://doi.org/10.1016/j.scitotenv.2019.134592>
- Meghwal M, Heddurshetti U, Biradar R (2017) Good manufacturing practices for food processing industries: Principles and practical applications. In *Food Technology: Applied Research and Production Techniques*, Meghwal M, Goyal MR, Kaneria MJ eds, pp 3–28. Apple Academic Press. <https://doi.org/10.1201/9781315365657-1>
- Meineri G, Peiretti PG, Tassone S, Candellone A, Longato E, Russo N, Pattono D, Prola L (2019) Nutritional value of extruded dog food with mechanically separated chicken meat or meat by-products (Preprints). <https://doi.org/10.20944/preprints201901.0189.v1>
- Milczarek M, Sadkowska-Todys M, Czarkowski MP, Kitowska W (2019) Salmonellosis in Poland in 2017 *Przegl Epidemiol* **73**: 463–477. <https://doi.org/10.32394/pe.73.44> (in Polish)
- Nemser SM, Doran T, Grabenstein M, McConnell T, McGrath T, Pamboukian R, Smith AC, Achen M, Danzeisen G, Kim S, Liu Y, Robeson S, Rosario G, McWilliams Wilson K, Reimschuessel R (2014) Investigation of *Listeria*, *Salmonella*, and toxigenic *Escherichia coli* in various pet foods. *Foodborne Pathog Dis* **11**: 706–709. <https://doi.org/10.1089/fpd.2014.1748>
- Osinski Z, Kwiatek K, Sieradzki Z (2014) Current veterinary requirements for the domestic animals foods *Żywie Wet* **89**: 10. <http://agro.icm.edu.pl/agro/element/bwmeta1.element.agro-42be7d6d-7ad0-4967-bd20-7d215ee60855> (in Polish)
- Pigłowski M (2019) Pathogenic and non-pathogenic microorganisms in the rapid alert system for food and feed. *Int J Environ Res Public Health* **16**: 477. <https://doi.org/10.3390/ijerph16030477>
- RASFF (2020) The Rapid Alert System for Food and Feed. *Annual Report – 2020*. European Union.
- RASFF (2021) The Rapid Alert System for Food and Feed. *Annual Report 2020*. European Union.
- Söderlund R, Jernberg C, Trönberg L, Pääjärvi A, Ågren E, Lahti E (2019) Linked seasonal outbreaks of *Salmonella* Typhimurium among passerine birds, domestic cats and humans, Sweden, 2009 to 2016. *Eurosurveillance* **24**: 1900074. <https://doi.org/10.2807/1560-7917.ES.2019.24.34.1900074>
- Srikullabutr S, Sattasathuchana P, Kerdsin A, Thengchaisri N (2021) Prevalence of coliform bacterial contamination in cat drinking water in households in Thailand. *Vet World* **14**: 721–726. <https://doi.org/10.14202/vetworld.2021.721-726>
- Taymaz E, Morgan G, Schmidt V, Pinchbeck G, Williams N (2022) A two-part study: A survey of dog owners' feeding preferences and the subsequent microbiological analysis of raw and non-raw dog food for the prevalence of *Escherichia coli*, *Enterobacter* and *Salmonella* spp. BSAVA Library. <https://www.bsavalibrary.com/content/chapter/10.22233/9781913859114.Ch200>
- Velázquez-Guadarrama N, Olivares-Cervantes AL, Salinas E, Martínez L, Escorcia M, Oropeza R, Rosas I (2017) Presence of environmental coagulase-positive staphylococci, their clonal relationship, resistance factors and ability to form biofilm. *Rev Argent Microbiol* **49**: 15–23. <https://doi.org/10.1016/j.ram.2016.08.006>
- Yang Q, Domesle KJ, Wang F, Ge B (2016) Rapid detection of *Salmonella* in food and feed by coupling loop-mediated isothermal amplification with bioluminescent assay in real-time. *BMC Microbiol* **16**: 112. <https://doi.org/10.1186/s12866-016-0730-7>

Hepatic Mcpip1 regulates adaptation to food restriction in mice

Olga Mucha¹, Bożena Skupien-Rabian^{2&}, Alicja Słota^{1#&}, Katarzyna Trzosa^{1#}, Natalia Pydyn¹, Bartosz Podlewski¹, Jolanta Jura¹ and Jerzy Kotlinowski¹✉

¹Jagiellonian University, Faculty of Biochemistry, Biophysics and Biotechnology, Department of General Biochemistry, Kraków, Poland; ²Jagiellonian University, Malopolska Centre of Biotechnology, Proteomics and Mass Spectrometry Core Facility, Kraków, Poland

Monocyte-chemoattractant protein-induced protein 1 (MCP1P1, or Regnase-1) is an endoribonuclease that degrades translationally active mRNA molecules. MCP1P1 is mostly known for its anti-inflammatory actions, but it is also an important regulator of adipogenesis and lipid metabolism. Its overexpression impairs adipogenesis by reducing mRNA levels of C/EBP β and PPAR γ , key transcription factors regulating this process. Although adipocytes overexpressing MCP1P1 are characterised by impaired glucose uptake, the function of MCP1P1 in hepatocyte metabolism remains unknown. In this study, conditional deletion of *Zc3h12a* in murine liver epithelial cells was used to characterise the role of *Mcpip1* in adaptation to 24-hour food restriction. We found that *Mcpip1* deficiency in liver epithelial cells (*Mcpip1^{fl/fl}Alb^{Cre}* mice) resulted in higher blood glucose levels in response to fasting in comparison to *Mcpip1^{fl/fl}* counterparts. Hepatic proteome analysis showed 26 down-regulated and 117 up-regulated proteins in *Mcpip1^{fl/fl}Alb^{Cre}* animals that were involved in cellular adhesion, extracellular matrix and metabolic processes. In conclusion, our studies provide new insight into the hepatic function of *Mcpip1* and its involvement in metabolic control.

Keywords: MCP1P1, liver, fasting, feeding, food restriction

Received: 27 April, 2023; **revised:** 28 July, 2023; **accepted:** 21 September, 2023; **available on-line:** 06 November, 2023

✉e-mail: j.kotlinowski@uj.edu.pl

#current affiliation: Jagiellonian University, Doctoral School of Exact and Natural Sciences, Kraków, Poland
#equal contribution as a second author

Acknowledgements of Financial Support: This work was supported by a research grant from the National Science Centre, Poland, No. 2017/27/B/NZ5/01440 to JK.

Abbreviations: DAVID, Database for Annotation, Visualization and Integrated Discovery; FDR, false discovery rate; HSCs, hepatic stellate cells; MCP1P1, Monocyte-chemoattractant protein-induced protein 1; NAFLD, Non-alcoholic fatty liver disease

INTRODUCTION

Both humans and animals adjust their metabolism to an excess or deficiency of food and the liver plays a central role in these processes. During the shift from a feeding to a fasting state, hepatic production of glucose and ketone bodies increases, with concomitant glycogen depletion and triacylglycerol accumulation (Goldstein & Hager, 2015). In contrast, a meal containing carbohydrates stimulates hepatic glucose uptake and glycolysis and repletes glycogen stores. Fatty acid synthesis is induced, while β -oxidation and ketogenesis are inhibited (Moore *et al.*, 2012). As a result, high-energy stores are replenished both in hepatocytes and adipocytes, main-

taining metabolic homeostasis during periods of feeding and fasting (Geisler *et al.*, 2016).

Monocyte-chemoattractant protein-induced protein 1 (MCP1P1), encoded by the *ZC3H12A* gene, is mostly known for its anti-inflammatory properties. It is an endoribonuclease that degrades mRNA, pre-miRNA, and viral RNA molecules. The broad spectrum of MCP1P1 targets includes IL-1 β (Mizgalska *et al.*, 2009), IL-6 (Matsushita *et al.*, 2009) and IL-2 (Li *et al.*, 2012). MCP1P1 was also shown to regulate glucose and lipid metabolism and its hepatic levels are reduced in humans suffering from Non-alcoholic fatty liver disease (NAFLD) (Pydyn *et al.*, 2023). MCP1P1 inhibits adipogenesis *in vitro* by reducing the levels of key transcription factors, including C/EBP β (Lipert *et al.*, 2017). Additionally, adipocytes that overexpress the MCP1P1 protein are characterised by a lower level of the insulin receptor Glut4 and impaired glucose uptake (Losko *et al.*, 2020).

In this study, we aimed to analyse the role of hepatic *Mcpip1* in murine adaptation to fasting. We performed mass spectrometry analysis of whole-liver lysates from *Mcpip1^{fl/fl}* and *Mcpip1^{fl/fl}Alb^{Cre}* mice that were fasted for 24 h, followed by functional annotation and enrichment analysis of differentially expressed proteins. We demonstrated that *Mcpip1* is involved in the regulation of metabolic pathways, including glyoxylate and dicarboxylate metabolism or the pentose phosphate pathway. Our studies provide new insight into the hepatic function of *Mcpip1* and its involvement in metabolic control.

MATERIAL AND METHODS

Animals and genotyping

The study used 10-week-old female control *Zc3h12a^{lox/lox}* mice (designed as *Mcpip1^{fl/fl}*) and *Mcpip1* liver epithelial cell-specific knockout mice (designed as *Mcpip1^{fl/fl}Alb^{Cre}*). Deletion of *Mcpip1* protein in *Mcpip1^{fl/fl}Alb^{Cre}* mice was present in liver epithelial cells (hepatocytes and cholangiocytes). Its level in whole liver tissue was only partially reduced (Kotlinowski *et al.*, 2021). The animals were genotyped as previously described (Kotlinowski *et al.*, 2021). In brief, DNA was extracted from tail tissue using a KAPA Mouse Genotyping Kit (KAPA Biosystems) according to the manufacturer's instructions. Genotyping for loxP insertion was performed by PCR using the following primers: GCCTTCCTGATCCTATTG-GAG (wild-type), GAGATGGCGCAGCGCAATTAAT (knockout), and GCCTCTTGTCACCTCCCTCCTCC (common). Genotyping for *AlbCre* tg/+ was conducted with the following primers: TGCAACATCATCATG-CACAC (wild-type), GAAGCAGAAGCTTAGGAA-

GATGG (mutant), and TTGGCCCCCTTACCATAACTG (common). The animals were housed under SPF conditions in ventilated cages in a temperature-controlled environment with a 14-h light/10-h dark cycle. The mice were randomly divided into 'fed' and 'fasted' groups at 10 weeks of age. Mice from the fed group received food and water *ad libitum*, whereas the animals enrolled in the 'fasted' group were placed into cages containing only water for 24 hours. On the following day, all animals were sacrificed, and blood and liver were collected. All animal procedures were conducted in accordance with the Guide for the Care and Use of Laboratory Animals (Directive 2010/63/EU of the European Parliament) and carried out under a licence from the 2nd Local Institutional Animal Care and Use Committee in Krakow (study no. 272/2017).

Blood analysis

All blood tests were measured by an automated analyser (Arkray) according to the manufacturer's instructions.

Protein isolation and western blot

Liver samples were lysed using RIPA buffer (25 mM Tris-HCl; pH 7.6; 150 mM NaCl, 1% sodium deoxycholate and 0.1% SDS) with Complete Protease Inhibitor Cocktail (Roche) and PhosSTOP Phosphatase Inhibitor Cocktail (Roche). A bicinchoninic acid assay was used to assess protein concentration, and 25 µg of proteins were separated on a 10% SDS/PAGE polyacrylamide gel. After wet transfer to PVDF membranes (Millipore), the membranes were blocked in 5% skim milk and then incubated overnight with primary antibodies at 4°C. On the following day, the membranes were washed and incubated with a secondary antibody for 1 h at room temperature. Chemiluminescence was detected after 5 min of incubation with ECLTM Select Western Blotting Detection Reagent (GE Healthcare) in a ChemiDoc chemiluminescence detector (Bio-Rad). The following antibodies were used: rabbit anti-MCPIP1 (1:2000; GeneTex), rabbit anti-PPAR γ (1:1000; Cell Signaling), mouse anti- β -actin (1:4000; Sigma), peroxidase-conjugated anti-rabbit (1:30 000; Cell Signaling) and peroxidase-conjugated anti-mouse (1:20 000; BD).

LC-MS/MS analysis and data processing

Liver fragments were homogenised in lysis buffer (7M urea, 2M thiourea, 4% CHAPS and 30 mM Tris; pH 7.5) using a CTFE/stainless steel pestle. Then, dithiothreitol was added at a concentration of 50 mM and the tissue homogenates were sonicated in a Bioruptor Pico (Diagenode) (15 cycles of 30 s ON/30 s OFF). After this step, the samples were centrifuged and supernatants were collected. Protein concentration was measured by Bradford assay and the samples (100 µg) were prepared for LC-MS/MS analysis using a filter-aided sample preparation (FASP) protocol (Wiśniewski *et al.*, 2009). The LC-MS/MS analysis was performed on a Q Exactive mass spectrometer (Thermo Fisher Scientific) coupled with a nanoHPLC (UltiMate 3000 RSLCnano System, Thermo Fisher Scientific), as previously described (Zacchini *et al.*, 2021). The acquired data were processed using MaxQuant software (version 1.6.7.0) (Tyanova *et al.*, 2016a) and searched with the integrated Andromeda search engine (Cox *et al.*, 2011) against the SwissProt database restricted to *Mus musculus* taxonomy (17 038 sequences; downloaded on 7 July 2020). The false discovery rate

(FDR) for the peptide and protein identification was set to 1%. The match between runs algorithm was enabled, and label-free quantification (LFQ) was carried out. The MaxQuant output table was further processed with the use of Perseus (version 1.6.5.0) (Tyanova *et al.*, 2016b). The protein groups identified in the decoy database, contaminants and proteins only identified by site were filtered out. The LFQ intensities were log2-transformed. Student's t-test with the permutation-based FDR set to 1% was used to reveal changes between the mutant and wild-type mice. The statistical analysis was performed for the protein groups that had a minimum of 4 valid LFQ intensity values in both animal groups. The final list of differences contained proteins identified based on at least 2 peptides with a significance threshold *q* value of <0.01 and fold change cutoffs of 1.3 and -1.3.

All proteins selected from mass spectrometry analysis are named according to UniProt nomenclature. A PCA graph, volcano plot and hierarchical clustering were prepared with the Perseus platform (version 1.6.5.0) (Tyanova *et al.*, 2016b). Functional annotation was performed using either the Database for Annotation, Visualization and Integrated Discovery (DAVID) (Huang *et al.*, 2009a; Huang *et al.*, 2009b) tools or STRING tools (Szklarczyk *et al.*, 2023). The results were further visualised using a free online platform for data analysis and visualisation: <https://www.bioinformatics.com.cn/en>.

The mass spectrometry data were deposited to the ProteomeXchange Consortium (Vizcaino *et al.*, 2014) via the MassIVE repository with the dataset identifier PXD041676.

RNA isolation and real-time PCR

Total RNA from livers was isolated using FenoZol (A&A Biotechnology), followed by spectrophotometric measurement of RNA concentration using a NanoDrop 1000 (Thermo Fisher Scientific). For reverse transcription, 1 µg of total RNA, oligo(dT) 15 primer (Promega) and M-MLV reverse transcriptase (Promega) were used. Real-time PCR was carried out using SYBR Green Master Mix (A&A Biotechnology) and a QuantStudio Real-Time PCR System (Applied Biosystems). Gene expression was normalized to *Ef2*, and then the relative transcript level was quantified by the 2^{- $\Delta\Delta$ Ct} method. The primer sequences (Sigma) are listed in Table S1 in the Supplementary Material at <https://ojs.ptbioch.edu.pl/index.php/abp/>.

Statistical analysis

The results are expressed as means \pm SEM. One-way ANOVA with Tukey's post hoc test was applied for the comparison of multiple groups, and Student's t-test for two-group comparisons. The *p*-values are marked with asterisks in the charts (**p*<0.05, ***p*<0.01 and ****p*<0.001).

RESULTS

Biochemical characterisation of 'fed' and 'fasted' Mcpip1^{fl/fl}Alb^{Cre} mice

Deletion of *Mcpip1* in liver epithelial cells leads to hepatomegaly, previously described in male mice (Kotlinowski *et al.*, 2021). As shown in Table 1, the female *Mcpip1*^{fl/fl}Alb^{Cre} animals were also characterised by larger livers and higher liver/body ratios in comparison to the *Mcpip1*^{fl/fl} controls (Table 1). There were no differences

Table 1. Biochemical characteristics of Mcpip1^{fl/fl} and Mcpip1^{fl/fl}Alb^{Cre} mice

	Fed		Fasted	
	Mcpip1 ^{fl/fl}	Mcpip1 ^{fl/fl} Alb ^{Cre}	Mcpip1 ^{fl/fl}	Mcpip1 ^{fl/fl} Alb ^{Cre}
Animal mass (g)	21.92±0.33	21.96±0.60	18.50±0.79###	18.23±0.39###
Liver mass (g)	0.969±0.023	1.229±0.113*	0.774±0.035 ^{p=0.09}	0.985±0.018*,#
Liver/body ratio	0.045±0.001	0.056±0.004**	0.042±0.001	0.054±0.001**
Cholesterol (mmol/L)	1.70±0.14	1.77±0.16	1.70±0.10	1.68±0.10
HDL (mmol/L)	0.86±0.07	0.93±0.09	0.82±0.05	0.78±0.02
LDL (mmol/L)	0.20±0.02	0.24±0.02	0.16±0.01	0.14±0.01##
Triglycerides (mmol/L)	0.89±0.09	0.71±0.05	0.81±0.07	0.88±0.16
AST (U/L)	73.3±12.7	77.5±9.1	97.2±13.2	124.5±20.7
ALT (U/L)	30.3±6.6	35.2±5.0	21.9±3.2	31.8±6.9
Glucose (mmol/L)	6.53±0.37	6.49±0.49	3.36±0.23###	4.22±0.31*,###

Data are presented as means ± S.E.M. Data were compared using one-way ANOVA with Tukey's post hoc test, **p*<0.05, ***p*<0.01 vs Mcpip1^{fl/fl} and #*p*<0.05, ##*p*<0.01, ###*p*<0.001 vs counterparts from the fed group.

es in serum biochemical markers – cholesterol, HDL, LDL, triglycerides, AST, ALT and glucose – between the two groups. After 24 h of food restriction, all mice lost weight and had lower serum glucose concentrations in comparison to their fed counterparts. In the fasted group, the Mcpip1^{fl/fl}Alb^{Cre} animals had higher glucose concentrations than the age-matched Mcpip1^{fl/fl} controls,

which may suggest better adaptation to food restriction (Table 1).

Proteomic analysis revealed metabolic pathways to be affected by the lack of Mcpip1 in fasted mice

In order to investigate how Mcpip1 deletion in liver epithelial cells affects murine adaptation to fasting, we

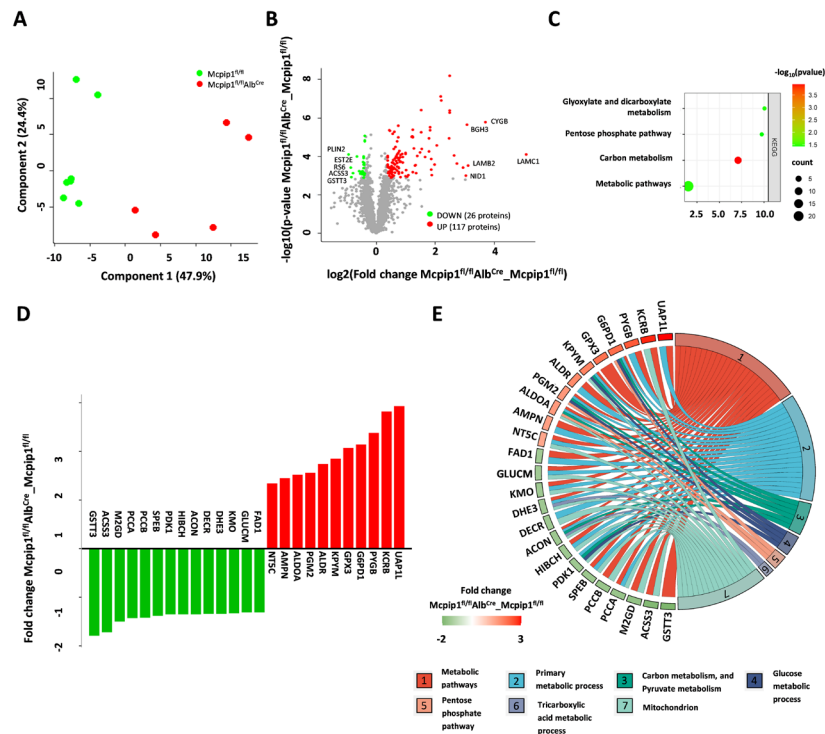


Figure 1. Metabolic pathways are affected by fasting conditions in the Mcpip1^{fl/fl}Alb^{Cre} animals compared to the control animals (A) Substantial experimental group separation visualised by principal component analysis (PCA); (B) Differentially expressed proteins presented on volcano plot (shows the relationship between the fold changes (log₂(FC)) and the level of significance (-log₁₀(p-value)). Significance was marked (green – down-regulated proteins, red – up-regulated proteins) using a q-value of <0.01 and a fold change (FC) of >1.3 or <-1.3; (C) Bubble chart plotted by <https://www.bioinformatics.com.cn/en> showing enriched themes within KEGG metabolism-related pathways (results from DAVID functional annotation tool; default settings); the colour of the dots represent the significance of the enrichment; size is related to the number of changed proteins; the y-axis is the fold enrichment parameter; (D) Bar chart representing fold change for the differentially expressed protein related to metabolic processes (plotted by <https://www.bioinformatics.com.cn/en>); (E) Chord diagram showing the most enriched biological processes (GO terms/ KEGG pathways) with their differentially expressed proteins. green-red scale represents the fold change (plotted by <https://www.bioinformatics.com.cn/en>).

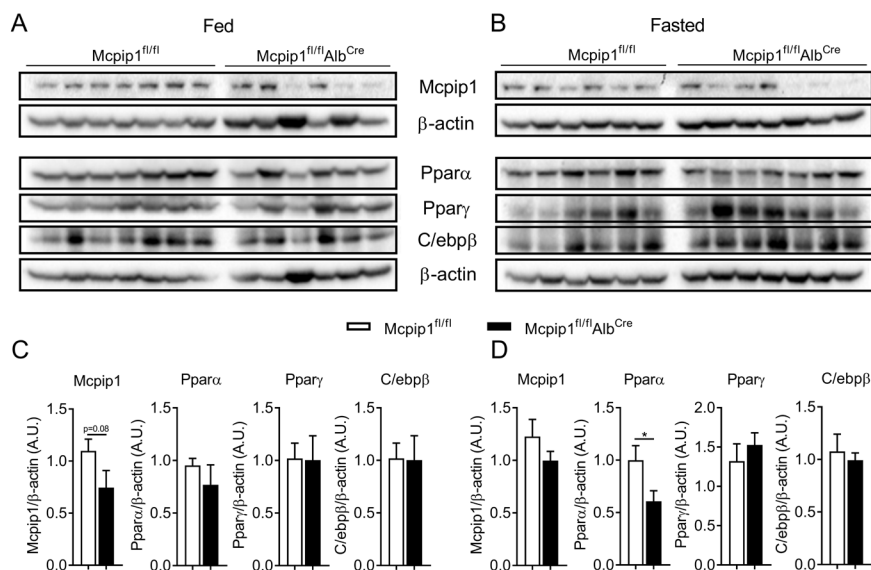


Figure 2. Levels of transcription factors regulating metabolism in livers

(A) Western blot analysis and (C) Densitometric quantification of Mcpip1, Ppara, Pparg and C/ebpβ levels in the livers collected from Mcpip1^{fl/fl} control and Mcpip1^{fl/fl}Alb^{Cre} knockout animals fed *ad libitum*; (B) Western blot analysis and (D) densitometric quantification of Mcpip1, Ppara, Pparg and C/ebpβ levels in the livers collected from Mcpip1^{fl/fl} control and Mcpip1^{fl/fl}Alb^{Cre} knockout animals after 24 h of fasting; graphs show the means + S.E.Ms; n=6–7; *p<0.05.

performed a mass spectrometry experiment utilising the label-free (LF) method. The analysis showed satisfactory separation of the groups and 143 differentially expressed proteins (Fig. 1A, Table S2 at <https://ojs.ptbioch.edu.pl/index.php/abp/>), 26 and 117 of which were potentially down-regulated and up-regulated, respectively, in the Mcpip1^{fl/fl}Alb^{Cre} animals (Fig. 1B, Table S2 at <https://ojs.ptbioch.edu.pl/index.php/abp/>). Among the most down-regulated proteins in Mcpip1^{fl/fl}Alb^{Cre} mice, we identified perilipin 2 (PLIN2), pyrethroid hydrolase Ces2e (EST2E), 40S ribosomal protein S6 (RS6), acyl-CoA synthetase short-chain family member 3, mitochondrial (ACSS3) and glutathione S-transferase theta-3 (GSTT3) (Fig. 2B, green dots). Cytochrome (CYGB), transforming growth factor-beta-induced protein ig-h3 (BGH3), laminin subunit beta-2 (LAMB2), laminin subunit gamma-1 (LAMC1) and nidogen-1 (NID1) were the most up-regulated upon Mcpip1 deletion (Fig. 2B, red dots).

In the next step, we used DAVID bioinformatics resources for functional annotation and enrichment analysis of differential proteins. We were able to distinguish several enriched biological themes among gene ontology terms and KEGG pathways (Supplementary Fig. 1A at <https://ojs.ptbioch.edu.pl/index.php/abp/>). A substantial number of the identified processes were related to cellular adhesion, the cytoskeleton and the extracellular matrix. Among the less affected, but still significant, we observed themes such as angiogenesis, glutathione metabolism, cell migration and proliferation. Interestingly, we also showed several processes related to the metabolic pathways that were enriched, including glyoxylate and dicarboxylate metabolism, the pentose phosphate pathway and carbon metabolism (Fig. 1C). The hierarchical clustering of proteins associated with metabolism confirmed the observed differences (Supplementary Fig. 1B at <https://ojs.ptbioch.edu.pl/index.php/abp/>), which were then demonstrated on the bar graph using the corresponding fold change (FC) (Fig. 1D). Fourteen and 11 proteins were significantly down-regulated and up-

regulated, respectively, with an FC higher than 2 for 5 proteins: UDP-N-acetylhexosamine pyrophosphorylase-like protein 1 (UAP1L), creatine kinase B-type (KCRB), glycogen phosphorylase, brain form (PYGB), glucose-6-phosphate 1-dehydrogenase (G6PD1) and glutathione peroxidase 3 (GPX3). A more thorough analysis of those 25 proteins using the STRING software tool for known and predicted protein–protein interactions was performed and visualised on a chord diagram (Fig. 1E). As a result, we graphically demonstrated the distribution of the proteins significantly changed in our analysis within several metabolism-related themes, including the primary metabolic process, carbon and pyruvate metabolism, the glucose metabolic process, the pentose phosphate pathway, the tricarboxylic acid metabolic process and mitochondrion localisation.

Evaluation of metabolic pathways that regulate glucose and lipid turnover in the livers of Mcpip1^{fl/fl} and Mcpip1^{fl/fl}Alb^{Cre} mice

It was already shown, that the MCP1 protein influences lipid metabolism by regulating C/ebpβ and Pparg transcription factors (Lipert *et al.*, 2014). Since the turnover of lipids is a key adaptation to fasting, we also tested these proteins in the livers of control and food-restricted animals. The Mcpip1^{fl/fl}Alb^{Cre} mice in the fed group were characterised by lower hepatic Mcpip1 in comparison to their Mcpip1^{fl/fl} counterparts, but there were no differences in the levels of Ppara, Pparg or C/ebpβ (Fig. 2A, C). Upon fasting, hepatic Mcpip1 deletion led to a reduction of Ppara, but the other protein levels did not change (Fig. 2B, D). In the next step, we tested whether changes in protein levels resulted from different amounts of their transcripts, which might be directly regulated by Mcpip1 *via* its RNase activity. Under fed conditions, Mcpip1 deletion did not affect glycolysis (*Pkm*) – neither glycogenolysis (*Pygb*, *Pgm2*), fatty acid metabolism (*Cpt1a*, *Fabp4*, *Acox1* and *Lcad*) nor keton bodies production (*Hmgcs2*) (Fig. 3A–F). There

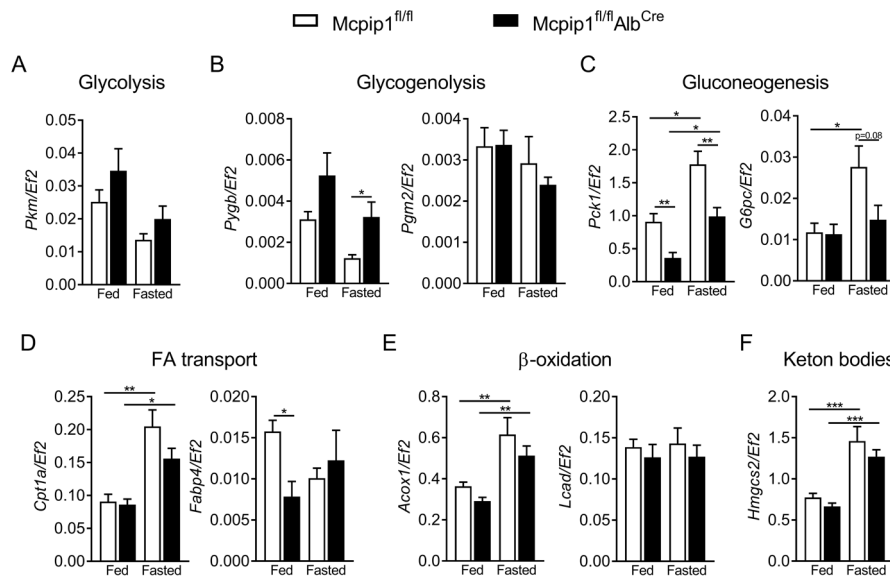


Figure 3. Hepatic Mcpip1 deletion in Mcpip1^{fl/fl}Alb^{Cre} mice impairs gluconeogenesis after 24 h of fasting

Expression of key enzymes regulating (A) glycolysis (*Pkm* – pyruvate kinase), (B) glycogenolysis (*Pygb* – glycogen phosphorylase; *Pgm2* – Phosphoglucomutase-2), (C) gluconeogenesis (*Pck1* – phosphoenolpyruvate carboxykinase 1; *G6pc* – glucose-6-phosphatase), (D) fatty acid transport (*Cpt1a* – carnitine palmitoyltransferase 1A; *Fabp4* – fatty acid binding protein 4), (E) β -oxidation (*Acox1* – peroxisomal acyl-coenzyme A oxidase 1; *Lcad* – acyl-CoA dehydrogenase, long chain) and (F) ketone body production (*Hmgcs2* – 3-hydroxy-3-methylglutaryl-CoA synthase 2); graphs show the means + S.E.Ms; n=6–7; * p <0.05; ** p <0.01; *** p <0.001

was only a reduction in *Pck1* expression in the livers of Mcpip1^{fl/fl}Alb^{Cre} mice that were fed *ad libitum* (Fig. 3C). After 24 h of fasting, Mcpip1 deletion led to increased expression of *Pygb*-encoding glycogen phosphorylase, which catalyses the phosphorylase of glycogen to yield glucose 1-phosphate (Fig. 3B). In the livers of Mcpip1^{fl/fl}Alb^{Cre} mice, the expression of *Pck1* and *G6pc*-encoding phosphoenolpyruvate carboxykinase 1 and glucose-6-phosphatase, respectively, was reduced in comparison to the Mcpip1^{fl/fl} animals in the fasted group (Fig. 3C). Similarly to fed conditions, there were no changes in the expression of the other genes tested (Fig. 3).

DISCUSSION

The demonstration that Mcpip1^{fl/fl}Alb^{Cre} mice have higher serum glucose levels after food deprivation, is a major finding of this study. During fasting, hepatic glucose production relies on either glycogen breakdown or gluconeogenesis from glycerol, amino acids or TCA cycle intermediates. According to a study by Geisler *et al.*, for the first 8 hours of fasting, the serum glucose level is balanced by depletion of the hepatic glycogen content. When the duration of fasting exceeded 8 h, the researchers observed increases in hepatic gluconeogenic potential (phosphoenolpyruvate carboxykinase activity and mRNA expression) from TCA cycle intermediates (Geisler *et al.*, 2016). In line with these data, after fasting we observed increased expression of phosphoenolpyruvate carboxykinase 1 (*Pck1*) and glucose-6-phosphatase catalytic subunit (*G6pc*) – key gluconeogenic enzymes – in the livers of Mcpip1^{fl/fl} mice. Although fasting did not induce *Pck1* or *G6pc* in Mcpip1^{fl/fl}Alb^{Cre} livers, these mice had a higher serum glucose level than their Mcpip1^{fl/fl} counterparts.

According to the literature, glycogenolysis is the first adaptation to fasting and is followed by a metabolic shift toward gluconeogenesis, β -oxidation and ketogenesis – which were all observed in our experimental model. For

example, the activation of β -oxidation and ketogenesis, mediated *via* induction of *Cpt1* and *Hmgcs2*, respectively, was detected after only 12 h of food deprivation (Vilà-Brau *et al.*, 2011; Monsénégro *et al.*, 2012). In line with these results, *Hmgcs2* knockdown completely eliminates the increase in serum β -OH butyrate upon fasting (Hepler *et al.*, 2016). Although proteomic analysis did not give us a clear answer as to why Mcpip1^{fl/fl}Alb^{Cre} mice adapt better to fasting than Mcpip1^{fl/fl} mice, we detected a few differentially expressed proteins involved in metabolic control. As shown in Fig. 1, the liver proteome of Mcpip1^{fl/fl}Alb^{Cre} mice significantly differed from their Mcpip1^{fl/fl} counterparts when it comes to proteins involved in carbon, pyruvate and glucose metabolism, together with the pentose phosphate pathway and the tricarboxylic acid process. Perilipin 2 (PLIN2) was the most strongly down-regulated liver protein among them in the knockout animals.

Perilipin 2 belongs to a family of lipid droplet coat proteins that have emerged as physiological regulators of lipid accumulation in many tissues, including adipose and liver tissue (Ducharme & Bickel, 2008). It is constitutively located on the lipid droplet surface and has no lipolytic function, but it can block lipases, limiting triglyceride hydrolysis. Thus, the low level of perilipin 2 in Mcpip1^{fl/fl}Alb^{Cre} livers might facilitate triglyceride catabolism (LL *et al.*, 2007; Bell *et al.*, 2008). It was also shown that PLIN2 is the predominant lipid droplet coat protein in hepatocytes in humans and rodents subjected to NAFLD induced by a high-fat diet (Imai *et al.*, 2007). Mice with whole-body PLIN2 knockout are resistant to obesity, adipose tissue inflammation and liver steatosis when fed a high-fat diet for 12 weeks (McManaman *et al.*, 2013). Similarly, PLIN2 liver-specific ablation in mice alleviates diet-induced hepatic steatosis, inflammation, non-alcoholic steatohepatitis and liver fibrosis (Najt *et al.*, 2016; DJ *et al.*, 2019). Thus, perilipin 2 is a potentially valuable molecular target for future studies.

A growing body of evidence shows that MCP1 is involved in the regulation of metabolism. Its overexpression impairs adipogenesis by reducing mRNA levels of C/EBP β and PPAR γ , key transcription factors regulating this process (Lipert *et al.*, 2014). Later studies showed that MCP1-overexpressing adipocytes exhibit lower levels of the proteins involved in lipid and carbohydrate metabolism, and up-regulation of the proteins involved in cellular organisation and movement (Losko *et al.*, 2018). Adipocytes overexpressing MCP1 are additionally characterised by impaired glucose uptake due to a lower level of insulin receptor, reduced insulin-induced Akt phosphorylation and depleted Glut4 (Losko *et al.*, 2020). The level of MCP1 is also lower in the adipose tissue of obese subjects and in patients suffering from NAFLD (Losko *et al.*, 2018; Pydyn *et al.*, 2023). In line with these data, fatty liver disease induced by a high-fat diet in C57BL/6J mice was followed by a reduced hepatic level of Mcp1 (Pydyn *et al.*, 2019). However, quite surprisingly, Mcp1^{fl/fl}Alb^{Cre} mice on a high-fat diet for 12 weeks were not susceptible to the development of fatty liver disease. Liver fat content did not change significantly in comparison to age-matched Mcp1^{fl/fl} controls (Pydyn *et al.*, 2021).

Mcp1 was recently described as an important regulator of hepatic homeostasis, in both physiological and pathophysiological conditions. Sun and others (Sun *et al.*, 2018) described the protective role of Mcp1 in mice subjected to liver ischemia/reperfusion injury. Hepatocyte-specific Mcp1 gene knockout and transgenic mice demonstrated that Mcp1 functions to ameliorate liver damage, reduce inflammation, prevent cell death and promote regeneration. As we previously reported, the deletion of Mcp1 in Mcp1^{fl/fl}Alb^{Cre} mice led to the development of primary biliary cholangitis symptoms. In the livers of these animals, intrahepatic bile ducts displayed proliferative changes with inflammatory infiltration, bile duct destruction and fibrosis leading to cholestasis (Kotlinowski *et al.*, 2021). Massive fibrosis was already detected in young, 6-week-old Mcp1^{fl/fl}Alb^{Cre} mice. Thus, the high amount of fibrosis-related or extracellular matrix proteins in the liver upon fasting was not surprising to us. Since Mcp1 is an endoribonuclease, it is possible that some of the mRNAs encoding these proteins are direct targets of Mcp1. In the future, it would be interesting to test whether Mcp1 binds and digests transcripts encoding the proteins involved in the remodeling of the ECM other than MMP9 (Szukala *et al.*, 2021).

Out of 10 the most strongly up-regulated proteins, 9 were related to fibrosis. Cytoglobin (Cygb) was induced 13.1 times. In 2001 cytoglobin was discovered in hepatic stellate cells (HSCs), and it was later demonstrated to be an important regulator of HSC O₂ homeostasis under hypoxic conditions (Kawada *et al.*, 2001; Yoshizato *et al.*, 2016). Upon deletion of the *Cygb* gene in mice, hepatic O₂ homeostasis was disrupted, leading to the activation of HSCs and liver fibrosis (Yoshizato *et al.*, 2016). Cytoglobin inhibits HSC activation by maintaining its quiescent state. However, its induction in Mcp1^{fl/fl}Alb^{Cre} livers does not reduce liver fibrosis in these mice, which is demonstrated by the significant overexpression of ECM-related proteins. On the contrary, in our model cytoglobin induction may result from disturbed liver homeostasis, i.e. fibrosis or inflammatory infiltration, which are both characteristic of Mcp1^{fl/fl}Alb^{Cre} mice (Kotlinowski *et al.*, 2021). In fact, cytoglobin induction was already reported after long-term thioacetamide-induced liver fibrosis (Thi Thanh Hai *et al.*, 2018).

In summary, we demonstrated that hepatic deletion of Mcp1 led to higher serum glucose concentration in mice subjected to fasting. For future studies, it would be interesting to concentrate on the liver and serum metabolome to better understand the role of Mcp1 in metabolic homeostasis.

REFERENCES

- Bell M, Wang H, Chen H, McLenithan JC, Gong D-W, Yang R-Z, Yu D, Fried SK, Quon MJ, Londres C, Sztalryd C (2008) Consequences of lipid droplet coat protein downregulation in liver cells: abnormal lipid droplet metabolism and induction of insulin resistance. *Diabetes* **57**: 2037–45. <https://doi.org/10.2337/db07-1383>
- Cox J, Neuhauser N, Michalski A, Scheltema RA, Olsen J V, Mann M (2011) Andromeda: a peptide search engine integrated into the MaxQuant environment. *J. Proteome Res.* **10**: 1794–805. <https://doi.org/10.1021/pr101065j>
- DJ O, AE L, ES B, RH M, J M, FG LR, JL M (2019) Perilipin-2 promotes obesity and progressive fatty liver disease in mice through mechanistically distinct hepatocyte and extra-hepatocyte actions. *J. Physiol.* **597**: <https://doi.org/10.1113/JP277140>
- Ducharme NA, Bickel PE (2008) Lipid droplets in lipogenesis and lipolysis. *Endocrinology* **149**: 942–9. <https://doi.org/10.1210/en.2007-1713>
- Geisler CE, Hepler C, Higgins MR, Renquist BJ (2016) Hepatic adaptations to maintain metabolic homeostasis in response to fasting and refeeding in mice. *Nutr. Metab. (Lond)*. **13**: 62. <https://doi.org/10.1186/s12986-016-0122-x>
- Goldstein I, Hager GL (2015) Transcriptional and chromatin regulation during fasting – the genomic era. *Trends Endocrinol. Metab.* **26**: 699–710. <https://doi.org/10.1016/j.tem.2015.09.005>
- Hepler C, Foy CE, Higgins MR, Renquist BJ (2016) The hypophagic response to heat stress is not mediated by GPR109A or peripheral β -OH butyrate. *Am. J. Physiol. Regul. Integr. Comp. Physiol.* **310**: R992–R998. <https://doi.org/10.1152/ajpregu.00513.2015>
- Hodges NJ, Innocent N, Dhanda S, Graham M (2008) Cellular protection from oxidative DNA damage by over-expression of the novel globin cytoglobin *in vitro*. *Mutagenesis* **23**: 293–298. <https://doi.org/10.1093/mutage/gen013>
- Huang DW, Sherman BT, Lempicki RA (2009a) Systematic and integrative analysis of large gene lists using DAVID bioinformatics resources. *Nat. Protoc.* **4**: 44–57. <https://doi.org/10.1038/nprot.2008.211>
- Huang DW, Sherman BT, Lempicki RA (2009b) Bioinformatics enrichment tools: paths toward the comprehensive functional analysis of large gene lists. *Nucleic Acids Res.* **37**: 1–13. <https://doi.org/10.1093/nar/gkn923>
- Imai Y, Varela GM, Jackson MB, Graham MJ, Crooke RM, Ahima RS (2007) Reduction of hepatosteatosis and lipid levels by an adipose differentiation-related protein antisense oligonucleotide. *Gastroenterology* **132**: 1947–1954. <https://doi.org/10.1053/j.gastro.2007.02.046>
- Kawada N, Kristensen DB, Asahina K, Nakatani K, Minamiyama Y, Seki S, Yoshizato K (2001) Characterization of a stellate cell activation-associated protein (STAP) with peroxidase activity found in rat hepatic stellate cells. *J. Biol. Chem.* **276**: 25318–25323. <https://doi.org/10.1074/jbc.M102630200>
- Kotlinowski J, Hutsch T, Czyzowska-Cichon I, Wadowska M, Pydyn N, Jaszal A, Kij A, Dobosz E, Lech M, Miekus K, Pośpiech E, Fu M, Jura J, Koziel J, Chlopicki S (2021) Deletion of Mcp1 in Mcp1^{fl/fl}Alb^{Cre} mice recapitulates the phenotype of human primary biliary cholangitis. *Biochim. Biophys. Acta – Mol. Basis Dis.* **1867**: <https://doi.org/10.1016/j.bbdis.2021.166086>
- Li M, Cao W, Liu H, Zhang W, Liu X, Cai Z, Guo J, Wang X, Hui Z, Zhang H, Wang J, Wang L (2012) MCP1 down-regulates IL-2 expression through an ARE-independent pathway. *PLoS One* **7**: e49841. <https://doi.org/10.1371/journal.pone.0049841>
- Lipert B, Węgrzyn P, Sell H, Eckel J, Winiarski M, Budzynski A, Matlok M, Kotlinowski J, Ramage L, Malecki M, Wilk W, Mitus J, Jura J (2014) Monocyte chemoattractant protein-induced protein 1 impairs adipogenesis in 3T3-L1 cells. *Biochim. Biophys. Acta – Mol. Cell Res.* **1843**: 780–788. <https://doi.org/10.1016/j.bbamer.2014.01.001>
- Lipert B, Wilamowski M, Gorecki A, Jura J (2017) MCP1, alias Regnase-1 binds and cleaves mRNA of C/EBP β . *PLoS One* **12**: e0174381. <https://doi.org/10.1371/journal.pone.0174381>
- LL L, AG O-F, EB G, WJ B, DA B (2007) Adipocyte differentiation-related protein reduces the lipid droplet association of adipose triglyceride lipase and slows triacylglycerol turnover. *J. Lipid Res.* **48**: <https://doi.org/10.1194/JLR.M700359-JLR200>
- Losko M, Lichawska-Cieslar A, Kulecka M, Paziewska A, Rumieniczak I, Mikula M, Jura J (2018) Ectopic overexpression of MCP1 impairs adipogenesis by modulating microRNAs. *Biochim. Biophys. Acta* **1865**: 186–195. <https://doi.org/10.1016/j.bbamer.2017.09.010>

- Losko M, Dolicka D, Pydyn N, Jankowska U, Kedracka-Krok S, Kulecka M, Paziewska A, Mikula M, Major P, Winiarski M, Budzynski A, Jura J (2020) Integrative genomics reveal a role for MCP1P1 in adipogenesis and adipocyte metabolism. *Cell. Mol. Life Sci.* **77**: 4899–4919. <https://doi.org/10.1007/s00018-019-03434-5>
- Matsushita K, Takeuchi O, Standley DM, Kumagai Y, Kawagoe T, Miyake T, Satoh T, Kato H, Tsujimura T, Nakamura H, Akira S (2009) Zc3h12a is an RNase essential for controlling immune responses by regulating mRNA decay. *Nature* **458**: 1185–1190. <https://doi.org/10.1038/nature07924>
- McManaman JL, Bales ES, Orlicky DJ, Jackman M, MacLean PS, Cain S, Crunk AE, Mansur A, Graham CE, Bowman TA, Greenberg AS (2013) Perilipin-2-null mice are protected against diet-induced obesity, adipose inflammation, and fatty liver disease. *J. Lipid Res.* **54**: 1346–1359. <https://doi.org/10.1194/jlr.M035063>
- Mizgalska D, Wegrzyn P, Murzyn K, Kasza A, Koj A, Jura J, Jarzab B, Jura J (2009) Interleukin-1-inducible MCP1P protein has structural and functional properties of RNase and participates in degradation of IL-1beta mRNA. *FEBS J.* **276**: 7386–7399. <https://doi.org/10.1111/j.1742-4658.2009.07452.x>
- Monsénégó J, Mansouri A, Akkaoui M, Lenoir V, Esnous C, Fauveau V, Tavernier V, Girard J, Prip-Buus C (2012) Enhancing liver mitochondrial fatty acid oxidation capacity in obese mice improves insulin sensitivity independently of hepatic steatosis. *J. Hepatol.* **56**: 632–639. <https://doi.org/10.1016/j.jhep.2011.10.008>
- Moore MC, Coate KC, Winnick JJ, An Z, Cherrington AD (2012) Regulation of hepatic glucose uptake and storage in vivo. *Adv. Nutr.* **3**: 286–294. <https://doi.org/10.3945/an.112.002089>
- Najt CP, Senthivayagam S, Aljazi MB, Fader KA, Olenic SD, Brock JRL, Lydic TA, Jones AD, Atshaves BP (2016) Liver-specific loss of Perilipin 2 alleviates diet-induced hepatic steatosis, inflammation, and fibrosis. *Am. J. Physiol. Gastrointest. Liver Physiol.* **310**: G726–G738. <https://doi.org/10.1152/ajpgi.00436.2015>
- Okina Y, Sato-Matsubara M, Matsubara T, Daikoku A, Longato L, Rombouts K, Thanh Thuy LT, Ichikawa H, Minamiyama Y, Kadota M, Fujii H, Enomoto M, Ikeda K, Yoshizato K, Pinzani M, Kawada N (2020) TGF- β 1-driven reduction of cytoglobin leads to oxidative DNA damage in stellate cells during non-alcoholic steatohepatitis. *J. Hepatol.* **73**: 882–895. <https://doi.org/10.1016/j.jhep.2020.03.051>
- Pydyn N, Kadluczka J, Kus E, Pospiech E, Losko M, Fu M, Jura J, Kotlinowski J (2019) RNase MCP1P1 regulates hepatic peroxisome proliferator-activated receptor gamma via TXNIP/PGC-1alpha pathway. *Biochim. Biophys. Acta Mol. Cell Biol. Lipids* **1864**: 1458–1471. <https://doi.org/10.1016/j.bbalip.2019.06.006>
- Pydyn N, Żurawek D, Koziel J, Kus E, Wojnar-Lason K, Jaształ A, Fu M, Jura J, Kotlinowski J (2021) Role of Mcp1p1 in obesity-induced hepatic steatosis as determined by myeloid and liver-specific conditional knockouts. *FEBS J.* **288**: 6563–6580. <https://doi.org/10.1111/febs.16040>
- Pydyn N, Kadluczka J, Major P, Hutsch T, Belamri K, Malczak P, Radkowiak D, Budzynski A, Miekus K, Jura J, Kotlinowski J (2023) Hepatic MCP1P1 protein levels are reduced in NAFLD patients and are predominantly expressed in cholangiocytes and liver endothelium. *Hepatol. Commun.* **7**: e0008. <https://doi.org/10.1097/HC9.0000000000000008>
- Sun P, Lu Y-X, Cheng D, Zhang K, Zheng J, Liu Y, Wang X, Yuan Y-F, Tang Y-D (2018) Monocyte chemoattractant protein-induced protein 1 targets hypoxia-inducible factor 1 α to protect against hepatic ischemia/reperfusion injury. *Hepatology* **68**: 2359–2375. <https://doi.org/10.1002/hep.30086>
- Szklarczyk D, Kirsch R, Koutrouli M, Nastou K, Mehryary F, Hachilif R, Gable AL, Fang T, Doncheva NT, Pyysalo S, Bork P, Jensen LJ, von Mering C (2023) The STRING database in 2023: protein-protein association networks and functional enrichment analyses for any sequenced genome of interest. *Nucleic Acids Res.* **51**: D638–D646. <https://doi.org/10.1093/nar/gkac1000>
- Szukała W, Lichawska-Cieslar A, Pietrzycka R, Kulecka M, Rumieniczek I, Mikula M, Chlebicka I, Konieczny P, Dziedzic K, Szeptowski JC, Fontemaggi G, Rys J, Jura J (2021) Loss of epidermal MCP1P1 is associated with aggressive squamous cell carcinoma. *J. Exp. Clin. Cancer Res.* **40**: 391. <https://doi.org/10.1186/s13046-021-02202-3>
- Thi Thanh Hai N, Thuy LTT, Shiota A, Kadono C, Daikoku A, Hoang DV, Dat NQ, Sato-Matsubara M, Yoshizato K, Kawada N (2018) Selective overexpression of cytoglobin in stellate cells attenuates thioacetamide-induced liver fibrosis in mice. *Sci. Rep.* **8**: 17860. <https://doi.org/10.1038/s41598-018-36215-4>
- Tyanova S, Temu T, Cox J (2016a) The MaxQuant computational platform for mass spectrometry-based shotgun proteomics. *Nat. Protoc.* **11**: 2301–2319. <https://doi.org/10.1038/nprot.2016.136>
- Tyanova S, Temu T, Sinitcyn P, Carlson A, Hein MY, Geiger T, Mann M, Cox J (2016b) The Perseus computational platform for comprehensive analysis of (prote)omics data. *Nat. Methods* **13**: 731–40. <https://doi.org/10.1038/nmeth.3901>
- Vilá-Brau A, De Sousa-Coelho AL, Mayordomo C, Haro D, Marrero PF (2011) Human HMGCS2 regulates mitochondrial fatty acid oxidation and FGF21 expression in HepG2 cell line. *J. Biol. Chem.* **286**: 20423–30. <https://doi.org/10.1074/jbc.M111.235044>
- Vizcaíno JA, Deutsch EW, Wang R, Csordas A, Reisinger F, Ríos D, Dienes JA, Sun Z, Farrah T, Bandeira N, Binz PA, Xenarios I, Eisenacher M, Mayer G, Gatto L, Campos A, Chalkley RJ, Kraus HJ, Albar JP, Martínez-Bartolomé S, Apweiler R, Omenn GS, Martens L, Jones AR, Hermjakob H (2014) ProteomeXchange provides globally coordinated proteomics data submission and dissemination. *Nat. Biotechnol.* **32**: 223–6. <https://doi.org/10.1038/nbt.2839>
- Wiśniewski JR, Zougman A, Nagaraj N, Mann M (2009) Universal sample preparation method for proteome analysis. *Nat. Methods* **6**: 359–62. <https://doi.org/10.1038/nmeth.1322>
- Yoshizato K, Thuy LTT, Shiota G, Kawada N (2016) Discovery of cytoglobin and its roles in physiology and pathology of hepatic stellate cells. *Proc. Jpn. Acad. Ser. B Phys. Biol. Sci.* **92**: 77–97. <https://doi.org/10.2183/pjab.92.77>
- Zacchini F, Heber MF, Arena R, Radczuk N, Jankowska U, Ptak GE (2021) Perturbations of the hepatic proteome behind the onset of metabolic disorders in mouse offspring developed following embryo manipulation. *Theriogenology* **171**: 119–129. <https://doi.org/10.1016/j.theriogenology.2021.05.022>

Relative expression levels of growth hormone gene and growth rate in Indian major carp species

Shahid Sherzada¹✉, Muhammad Nauman Sharif², Qurban Ali³, Saeed Akram Khan¹, Tawaf Ali Shah⁴, Mohamed A. M. El-Tabakh⁵, Tariq Aziz⁶✉, Ghulam Nabi⁷, Metab Alharbi⁸, Thamer H. Albekairi⁸ and Abdullah F Alasmari⁸

¹Department of Zoology, Government College University Lahore, Pakistan; ²Centre of Excellence in Molecular Biology, University of the Punjab, Lahore, Pakistan; ³Department of Plant Breeding and Genetics, University of the Punjab, Lahore, Pakistan; ⁴Department of Biotechnology, University of Okara, Punjab, Pakistan; ⁵Zoology Department, Faculty of Science, Al-Azhar University, Cairo, Egypt; ⁶Laboratory of Animal Health, Food Hygiene and Quality, Department of Agriculture, University of Ioannina, 47132 Arta, Greece; ⁷Institute of Nature Conservation Polish Academy of Sciences Krakow Poland; ⁸Department of Pharmacology and Toxicology, College of Pharmacy, King Saud University, Riyadh 11451, Saudi Arabia

The phenomenon of growth is a leading factor for aquaculture success. The uneven growth of major Indian carps (*Labeo rohita*, *Catla catla*, and *Cirrhinus mrigala*) is a serious issue in fish culture from an economic point of view. The growth hormone (GH) gene is crucial for selection in commercially cultivated fish species for better growth and production. Indian major carp (*L. rohita*, *C. catla*, and *C. mrigala*) are commonly cultured in Pakistan. The GH expression was examined using qPCR to understand growth in fish species better. Muscle tissue samples ($n=480$) from 160 individuals of the same age were collected from three species (*L. rohita*, *C. catla*, and *C. mrigala*). Individuals were divided into two groups (high-weight and low-weight groups), cultured under normal conditions. The housekeeping gene β -actin validated GH expression in fast and slow-growing fishes from the same species. Results showed that GH expression varies across species and fish specimens that overweight their counterpart feature have higher GH expression. A selection for overweight fish in the aquaculture breeding systems is preferable as those fish could inherit their genomics to the future cohort, enhancing production, and commercial profit for farmers. Comprehensive research about different growth genes and the environmental aspects that influence fish growth is mandatory. No work has been reported regarding the growth gene analysis of fish from Pakistan. This report was Pakistan's first and baseline study regarding growth analysis of main culturable fish species at the molecular level.

Keywords: *Labeo rohita*, *Cirrhinus mrigala*, *Catla catla*, Growth hormone, Beta-actin gene, Q-PCR

Received: 02 June, 2023; **revised:** 20 September, 2023; **accepted:** 02 November, 2023; **available on-line:** 14 November, 2023

✉ e-mail: shahid.sherzada@gcu.edu.pk (SS); iwocdk@gmail.com (TA)

Acknowledgments: Authors are thankful to the Researchers Supporting Project number (RSPD2023R568), King Saud University, Riyadh, Saudi Arabia.

Abbreviations: cDNA, complementary DNA; GH, growth hormone; RT-PCR, reverse transcriptase Polymerase Chain Reaction

INTRODUCTION

Pakistan is blessed with fish fauna and water resources, but only nine species (7 warm and 2 cold water) are commercially cultured. Moreover, only carp culture is carried out through extensive farming depending on

natural water resources. Among polyculture, carp polyculture systems primarily consisting of major carps (*Labeo rohita*, *Catla catla*, and *Cirrhinus mrigala*) are more prevalent due to their high growth rate and ability to adapt in captive conditions (FAO, 2016; Wasim, 2007). Aquaculture success is mainly dependent on the maximum growth and production of fish. Vertebrate growth is regulated by several genes and various morphological characters (Dunham, 2011). The growth expression is correlated with a screening of candidate genes involved in the growth and selection of fish species. Higher fish growth is essential for boosting the aquaculture industry (Khan *et al.*, 2023; Canestro *et al.*, 2013). The role of the GH is extensively studied in many fishes like Mandarin fish (*Siniperca chuatsi*; Yi *et al.*, 2015), Nile tilapia (*Tilapia nilotica*; Tanamati *et al.*, 2015), Tench (*Tinca tinca*; Kocour *et al.*, 2011), Ganges Jewfish (*Nibea coibor*; Zhang *et al.*, 2009), and Mandarin fish (*Siniperca chuatsi*; Tian *et al.*, 2014). In recent years, marker-assisted growth selection has been employed in the aquaculture and livestock sector for better performance (Ling *et al.*, 2023; Biswas *et al.*, 2003; Pal *et al.*, 2004; De Faria *et al.*, 2006).

Fish growth is a key feature for many fish biologists regarding fish production and the selective breeding program of many economically significant fish species (Gjedrem *et al.*, 2012; Hulata, 2001). Growth is a quantitative trait controlled by many genes (Mullis, 2005) and environmental factors (Mackay, 2001; Moriyama *et al.*, 2000). The GH, growth hormone receptor (GHR), insulin-like growth factors (IGF), and myostatin (MSTN) genes are observed in tamed animals and aquaculture species. Among them, GH is the main regulator of postnatal development. Moreover, it is also associated with strengthening anabolic functions such as protein interaction, cell growth, and muscle development (Reinecke *et al.*, 2005). In addition to hormone-flagging procedures, it participates in other pathways that make its physiology challenging to understand (Vairamani *et al.*, 2017). The primary genes that control fish growth have been studied using various experimental methods. Research on such fish ranges from those whose growth has been retarded through starvation during gametogenesis to those whose growth has been accelerated through refeeding after starvation, GH-transgenesis, or domestication. These studies also discovered a complicated association among factors that control growth and other biological processes. Moreover, it is also

Table 1. Feeding and water quality monitoring data during tissue sampling.

Seed Rearing Stage				Production Stage	
Total Age: 19 Months	Jun–Aug	Aug–Nov	Dec–Jan	February	March–October
Feed (CP level %)	Rice polish CP 14	Supreme feed CP 24	Partial feeding: Low temperature CP 26	Partial feeding: Low temperature CP 26	Supreme feed CP 31
*DO (ppm)	5.5–6.5	5.5–6.5	6.0–7.0	6.5–8.5	5.2–7.5
Temperature (°C)	29–32	27–29.5	19–23	20–25	24–31
pH	6.8–8.7	7.9–9.2	8.6–9.5	8.2–9.4	7.4–8.8
Salinity(ppt)	<0.09	<0.09	<0.09	<0.09	<0.09
*TDS (ppm)	1900–2300	2100–2500	2300–2590	2295–2476	2340–2700
Ammonia (ppm)	0.012–0.024	0.018–0.03	0.03–0.041	0.025–0.039	0.028–0.065

*DO, dissolved oxygen; *TDS, total dissolved solid

revealed that many somatotrophic genes such as *GH*, *GHR*, and insulin-like growth factors *IGFs* are more expressed in fast-growing fishes, i.e., rainbow trout (*Oncorhynchus mykiss*) (Devlin *et al.*, 2013) and regulate muscle growth (Sheridan & Hagemeister, 2010).

GH is secreted by somatotrophic cells and comprises a single-chain polypeptide of about 22kDa. It plays a vital role in metabolic processes, i.e., reproductive and immune systems and seawater adaptability. Moreover, it is also involved in problems related to appetite and food conversion (Rajesh & Majumdar, 2007; Canosa *et al.*, 2007). Previously DNA and cDNA sequences of the *GH* have been well studied in various economically important fish species like *Cyprinus carpio* (Chiou *et al.*, 1990), *Protopterus annectens* (May *et al.*, 1999), *Cynoglossus semilaevis* (Ma *et al.*, 2012), and *Pelteobagrus fulvidraco* (Li *et al.*, 2017). The total length of the *GH* was almost 3–4kb and its structures differed in different fishes. The *GH* genome in some fishes consists of 5 exons and 4 introns; in other fish species, it was 6 exons and 5 introns (Chiou *et al.*, 1990; Li *et al.*, 2017). The current study was undertaken to determine the differential expression levels of the *GH* in fast and slow-growing fish species of Indian major carps (*Labeo rohita*, *Catla catla*, and *Cirrhinus mrigala*), which are commonly cultured in Pakistan.

MATERIALS AND METHODS

Sample Collection for Growth Expression Analysis

A total of 480 fish individuals (*Labeo rohita*/n=160, *Cirrhinus mrigala*/n=160, and *Catla catla*/n=160) of similar age were collected from the Umer Fish Farm, located at District Rajanpur, Pakistan. The capturing and experiments on fish species were conducted following relevant institutional, national, and international guidelines and legislation. Out of 160 muscle tissue samples (Skeletal Muscle, 5 g) from each fish species, 80 samples were captured from extremely high-weight fishes (≥ 1.3 ; ≥ 2 and ≥ 0.9 Kg) and 80 from extremely low-weight fishes (≤ 0.5 ; ≤ 1 and ≤ 0.5 kg) from *L. rohita*, *C. catla*, and *C. mrigala*, respectively. Fish samples were collected in a centrifuge tube (1.5 ml), containing RNA later solution. Samples were stored immediately in liquid nitrogen and then at -80°C for later analysis. During sampling, feeding and water quality data were continuously collected (Table 1).

Total RNA isolation and cDNA synthesis

Total RNA isolation from the muscle tissue sample was carried out using TRIzol reagent (Life Technologies cat no. 15596026). Samples were ground in liquid nitrogen using a pre-chilled mortar and pestle. The homogenate of muscle tissue samples was made in a 2.0 ml microcentrifuge tube with 1.5 mL of TRIzol® reagent and incubated for 5 minutes at room temperature. After shaking strongly for 30–40 seconds, 200 μL of chloroform was added per 1 ml of TRIzol® reagent and the content was mixed vigorously for 15 seconds and incubated at room temperature for 10 minutes followed by centrifugation for 5 minutes at 13000 rpm (at 4°C). As a result of centrifugation, three distinctive layers were formed consisting of the upper colorless, middle whitish layer and bottom dark layer. The upper clear phase containing nucleic acid was transferred to another nuclease-free 2.0 ml Eppendorf tube and 750 μL of pre-chilled isopropanol was added to precipitate the RNA and incubated for 10 minutes at room temperature followed by centrifugation. To clean the RNA pellet, 750 μL of 75% ethanol was used and centrifuged again at 13000 rpm (at 4°C) for 15 minutes (2 \times) by discarding the upper content. The RNA pellet was air-dried by incubating at room temperature for 10 minutes. The air-dried RNA samples were resuspended in 30 μL DEPC water and immediately stored at -70°C . The quality and quantity of the isolated RNA were determined by using Spectrophotometer ND 1000 NanoDrop® and the Size of RNA was determined by 1.5 % gel electrophoresis (Fig. 1).

Synthesis of complementary DNA (cDNA)

The cDNA was synthesized using the Revert Aid First-Strand cDNA synthesis kit (Thermo Fisher Sci-

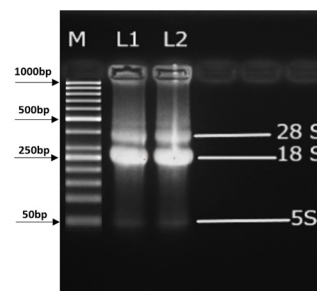


Figure 1. Confirmation of RNA by gel electrophoresis (1.5%)

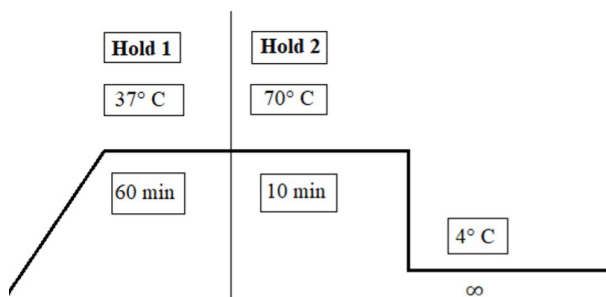


Figure 2. Thermal conditions for cDNA synthesis

entific, cat no. 1622). 1 µg of total RNA template isolated from each fish sample was used to synthesize cDNA. The reaction mixture for cDNA synthesis contained 10 pm of random hexamer primers, 1.2 µl of RNA (1 µg) and nuclease-free DEPC treated water was used to make a final volume of 11 µl. PCR tube containing the cDNA mixture was centrifuged for 5–10 seconds. The reaction mixture was incubated at 70°C for 5 minutes and tubes were immediately placed on ice. After that 4.0 µl of 5x reaction buffer, 1.0 µl (20 units) of ribonuclease inhibitor, and 2.0 µl of dNTPs mixture (40 mM) were supplemented. The reaction mixture was incubated for 5 minutes at 37°C and 2.0 µl (40 units) of reverse transcriptase (MMuLV) was supplemented. The final reaction mixture of 20 µl was finally incubated at 37°C for 60 minutes. The cDNA reaction mixture was additionally incubated at 70°C for 10 minutes to break the reaction. The obtained cDNA product was immediately placed on ice. The thermal profile of the reaction is shown below.

Table 2. RT-PCR primers selection

Gene	Primers	Sequence of primers	Product size
GH	GH-F	ATAACGACTCCCTGCCACTG	125 bp
	GH-R	CCTGTGTCATGTCCTCTTG	
β-actin	β-actin-F	ACCCACACTGTGCCATCTACG	146 bp
	β-actin-R	ATTTCCTCTCGCTGTGGTGG	

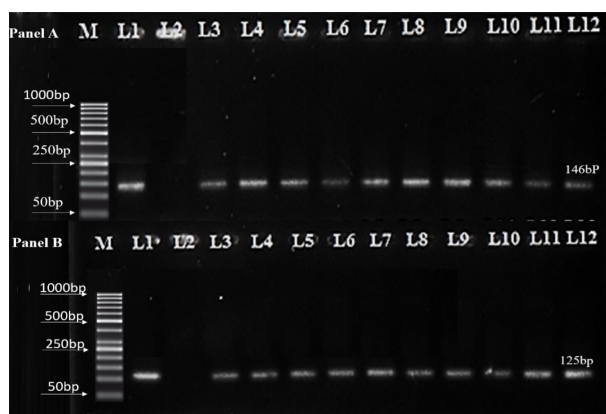


Figure 3. Primer's optimization for RT-PCR.

Panel (A) Beta-actin amplification (fragments=146bp: L3-L12); M=Marker (50bp); L1=Positive control; L2=Negative control. Panel (B) Growth hormone gene (GH) amplification (fragments=125bp: L3-L12); M=Marker (50bp); L1=Positive control; L2=Negative Control.

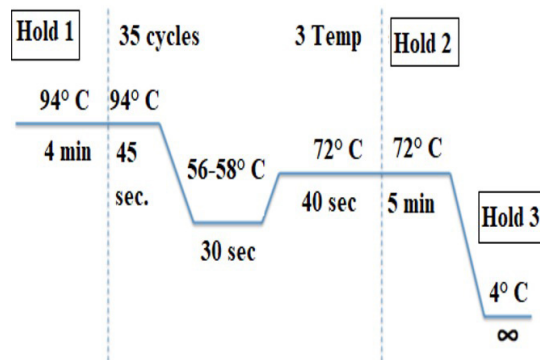


Figure 4. RT-PCR Amplification thermal conditions to amplify targeted genes

Primer Designing and Optimization

Primer Express 3.0 software was used to design primers for the *GH* and housekeeping genes (*β-actin*). The *β-actin* was selected as an internal control for precise validation of qPCR (Table 2). Both primers (*GH* and *β-actin*) were optimized using certain qPCR conditions. The results of the optimized protocol were assessed by the gel documentation system (Fig. 3).

Amplification of targeted genes by reverse transcriptase Polymerase Chain Reaction (RT-PCR)

Real-time PCR was used to quantify differential *GH* expression of fishes with the highest and lowest weight under uniform pond conditions. The RT-PCR process was accomplished using PikoReal™ Q-PCR to quantify selected samples. Amplification of the targeted genes was carried out using gene-specific primers (Table 2) and DreamTaq Green PCR Master mix 2x (Thermo Fisher Scientific, cat no. K1081). The PCR reaction contained 10 µ-L of DreamTaq Green PCR master mix, 0.8 µ-L template cDNA and 0.4 µ-L of both forward and reverse primers (10 µ-mol) added to PCR tube (0.2 mL) and nuclease-free water to a final volume of 20 µ L. The PCR thermal conditions were; preliminary incubation for 4 minutes at 94°C, 30 cycles of amplifications with denaturation at 94°C for 45 seconds, primer binding at 56–58°C for 30 seconds and amplification at 72°C for 40 seconds and then ending extension for 5 minutes at 72°C (Fig. 4). The 2– $\Delta\Delta C_T$ mode was selected to assess *GH* expression (Livak & Schmittgen, 2001).

Data analysis

Data were coded and entered using the statistical package SPSS (IBM SPSS Statistics V.22). The data were checked for satisfying parametric test assumptions, and continuous variables were tested for normality using Shapiro-Wilk and Kolmogorov-Smirnov tests. Data were presented as mean and standard deviation. A student *t*-test was conducted for experimental groups, while a Tukey pairwise comparison was conducted in MiniTab V14 for post-hoc analysis. The *P*-value was considered significant at <0.05 . Data was visualized when possible, using R studio V 2022.02.4.

RESULTS

In this study, we observed significant differences in body weights between high-weight and low-weight groups of similar ages in all three fish species (Fig. 5).

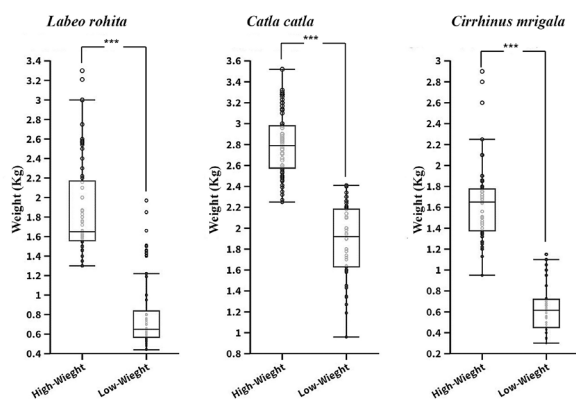


Figure 5. Box and whisker plot of observed weight for investigated fish species.

Data undergoes an independent sample t-test, after being evaluated for normality. NS=non-significant; * <0.05 ; ** <0.01 ; *** <0.001 .

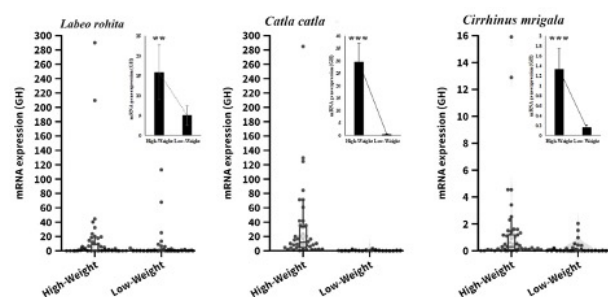


Figure 6. Comparative analysis of differential growth hormone gene expression (GH) among three fish species having a High-Weight and Low-Weight group.

Data undergoes the Mann-Whitney U test, after being evaluated for normality. NS=non-significant; * <0.05 ; ** <0.01 ; *** <0.001 .

Differential GH Analysis

Labeo rohita

Average values of GH expression and body weight of selected fish samples were utilized to determine the relationship between GH expression and body weight. Larger body weight fishes (1.88 ± 0.50 kg) have significantly higher GH expression relative to lower body weight fishes (0.83 ± 0.38 kg) (Fig. 6).

Catla catla

Similar to *Labeo rohita*, individuals having high body weight (80 ± 0.30 Kg) had significantly higher GH expression than lower body weight individuals (Fig. 6).

Cirrhinus mrigala

Like the other two fish species, *Cirrhinus mrigala* expressed GH significantly higher in higher body weight fishes (1.65 ± 0.36 Kg) as compared to lower body weight fishes (0.65 ± 0.25 ; Fig. 6).

We found a very surprising correlation between GH expression and the body weight of selected fish species (Fig. 7). The analysis revealed a statistically significant positive correlation between body weight and gene expression for both groups of low and high body weight fish. The strength of association was greater in the high-weight groups compared to the low-weight groups for all three species. For *L. rohita*, the correlation coefficient was 0.965 and 0.729 for the high and low-weight groups,

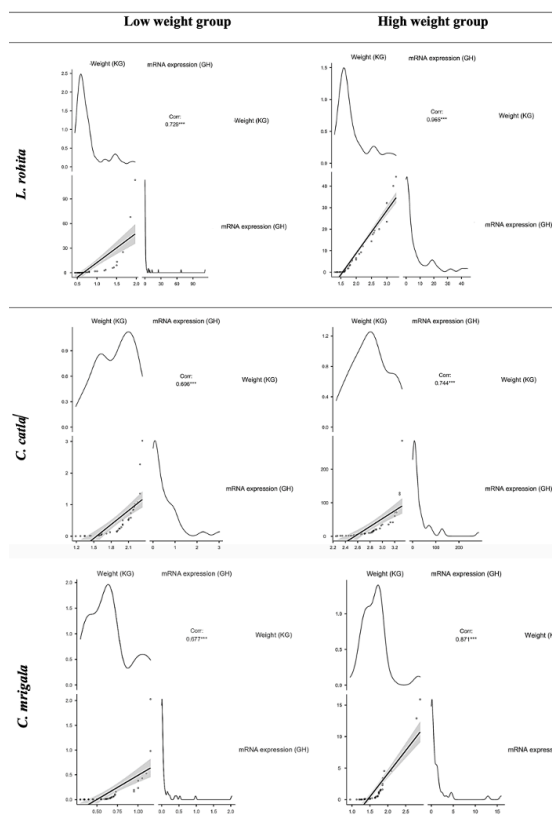


Figure 7. Correlation coefficient between observed fish weight in low and high weight groups and the gene expression values of GH hormone

NS=non-significant; * <0.05 ; ** <0.01 ; *** <0.001

respectively. Similarly, for *C. catla* the correlation coefficients were 0.744 and 0.696, and for *C. mrigala* they were 0.871 and 0.677 for the high and low-weight groups, respectively. In summary, the degree of correlation between body size and gene expression intensified as body weight increased for all species.

The analysis revealed a statistically significant positive correlation between body weight and gene expression for both groups of fish with low and high body weight. The strength of association was greater in the high-weight groups compared to the low-weight groups for all three species. For *L. rohita*, the correlation coefficient was 0.965 and 0.729 for the high and low weight groups, respectively. Similarly, for *C. catla* the correlation coefficients were 0.744 and 0.696, and for *C. mrigala* they were 0.871 and 0.677 for the high and low weight groups, respectively. In summary, the degree of correlation between body size and gene expression intensified as body weight increased for all species.

DISCUSSION

Growth in vertebrates is mainly controlled by GH, a vital gene influencing growth physiology (Quik *et al.*, 2010; Clayton *et al.*, 2010). Indian major carp species (*Labeo rohita*, *Catla catla*, *Cirrhinus mrigala*) are widely cultured in Asia. GH might directly or indirectly affect the growth mechanism of these economically important fish species. We therefore investigated the connection of GH expression with the growth characteristics of carp species. In recent years, GH association with growth traits

has been studied well in domestic animals (An *et al.*, 2011; Sugita *et al.*, 2014) and poultry (Xu *et al.*, 2007; Wu *et al.*, 2012). The GH is the chief controller of IGF-I production in fry, fingerling, and adult fishes. Studies reported that injecting GH boosts the expression of IGF-I in salmon, (Duguay *et al.*, 1994), rainbow trout (Shamblott *et al.*, 1995), and gilthead sea bream (Duguay *et al.*, 1996), zebrafish (Maures *et al.*, 2002). The IGF-I mRNA levels in plasma or serum and its expression in tissues also confirmed its dependency on GH as observed in goldfish (Marchant & Moroz, 1993), salmonids (Moriyama *et al.*, 1995) and tilapia (Kajimura *et al.*, 2001).

We reported that GH expression varies in high and low-body-weight fish species of Indian major carp. The variable expression of growth-related genes has also been observed in fish and other animals in previous scientific studies (Carnevali *et al.*, 2006; Filby & Tyler, 2007; Opazo *et al.*, 2017). In fish, somatic growth is accelerated at the juvenile stage while it slows down during the adult stage as fish utilizes its energy for gonadal development and sexual maturation (Le Gac *et al.*, 1993; Chen *et al.*, 2018). In the present study, fish with the same age class and different body weights exhibit high GH expression as fish weight increases. Differences in recorded body weight of fish within the same age group could rely on stress factors, that can minimise fish growth and production. This stress may be caused due to internal factors (stocking density, fish species' competition for space and food) or external factors (low water quality) (Karakatsouli *et al.*, 2008). If the stress factor is negated, then the role of the gene can be observed and explained well in experimental fishes, which enlightens the present study findings. Considering this scenario, present cultured fishes undergo uniform culturing conditions by following good feeding practices and healthy water quality management so that possible genetic effects on fish growth can be assessed effectively. The differential expression level of GH in three fish species defined that fish growth rates are different concerning GH content in muscle tissue. Similar observations were recorded in red spotted grouper (*Epinephelus akaara*) regarding expression analysis of growth genes like GH, GHR, and IGF1 from fish tissue (Mun *et al.*, 2019).

A direct relationship was noticed between body weight and GH expression in *L. rohita*, which depicts that expression of the GH increases or decreases with the gradual increase or decrease in body weight of fish samples. GH-mRNA expression was found higher in a high-weight group while lower in low-weight populations, similar to those mentioned for crucian carp *C. auratus* (Zhong *et al.*, 2012); European sea bass (*Dicentrarchus labrax*), which had a significantly higher GH-mRNA expression in fast-growing as compared to slow-growing fish samples (Carnevali *et al.*, 2006). However, such differential GH-mRNA expression level was not obvious in zebrafish, *Danio rerio* (Opazo *et al.*, 2017). Similar to *L. rohita*, we found the same findings for *C. catla*. Results of GH expression concerning the body weight of *C. catla* fish samples were very interesting as we found the same high per unit expression of GH with respect to a gradual increase in weight in higher body weight fishes. Such kind of growth pattern may reflect some ongoing interconnected morphological as well as physiological changes inside the body of *C. catla*. In contrast, a low level of GH expression was reported in high-body weight fish of Nile Tilapia (*Oreochromis niloticus*), which may be compensated by expression in some other tissues of the fish body (Aboukila *et al.*, 2021). The low level of GH expression may depict its low synthesis from the

pituitary due to the influence of endocrine and environmental aspects correlated with the body physiology, suggesting that GH expression in fish is a very complicated phenomenon (Tymchuk *et al.*, 2009).

A direct correlation was also identified between body weight and GH expression in collected *C. mrigala*. Such results indicated a higher chance of reciprocal effect of GH expression in low-body-weight fish than in the high-body-weight group. A previous study on GH expression analysis of red-spotted grouper revealed that GH-mRNA expression was slightly higher in higher body weight samples than in moderate and slow-growing samples (Mun *et al.*, 2019). Likewise, in *C. mrigala* GH expression results, a marine water fish named gilthead sea bream (*Sparus aurata*) possessed similar influential growth patterns of GH on high and low-weight fish tissues (Perez-Sanchez *et al.*, 1994). Comparing GH expression among high and low body weight Indian major carp species revealed that GH expression varies from species to species in these fishes, however, it follows a similar trend with increasing or decreasing body weight. Certain other vital growth genes and various ambient environmental factors important for fish's body development and growth may cause current variation in expression results. The intricate phenomenon of the endocrine system in fishes reveals that the growth pattern with respect to hormonal state is very complex. This pattern gradually fluctuates among fresh and marine water fish species. More research in this area is necessary to properly understand growth governing endocrinology in fish.

CONCLUSION

Our research focused on *Labeo rohita*, *Catla catla*, and *Cirrhinus mrigala*, which are major Indian carp species commonly cultured in Pakistan. The uneven growth of these species is a significant challenge in aquaculture, impacting economic outcomes. The growth hormone (GH) gene is pivotal in selecting fish with superior growth and production potential in aquaculture. By validating GH expression using the housekeeping gene β -actin, we discovered that GH expression varies not only among species but also within the same species based on weight, with better-weight fish exhibiting higher GH expression levels. The significance of our findings lies in their potential application within the aquaculture sector in Pakistan. Selecting and breeding better-weight fish, which demonstrate higher GH expression can lead to improved production outcomes and increased profitability for farmers. Furthermore, this study represents the first molecular-level analysis of growth genes in fish species from Pakistan, making it a baseline study for future research in this region.

Declarations

Ethical Approval. It has been confirmed that the experimental sample, including the collection of fish blood samples, complied with relevant institutional, national, and international guidelines and legislation with appropriate approval from the Ethical Review Committee of the Department of Zoology, Government College University Lahore, Pakistan (Approval ID: Fish2570). It has been confirmed that the study was reported following the Guidelines for the Use of Fishes in Research (AFS 2014).

Competing interests. There are no competing interests regarding the publication of this manuscript.

Funding. Currently, no funding is available.

Availability of data and materials. All data generated or analyzed during the study are included in the manuscript.

REFERENCES

- Aboukila RS, Hemeda SAE, El Nahas AF, Abd El Naby WSH (2021) Molecular characterization of GHR1 gene and expression analysis of some growth-related genes in *Oreochromis niloticus*. *Adv Anim Vet Sci* **9**: 1025–1033. <https://doi.org/10.17582/journal.aavs/2021/9.7.1025.1033>
- An X, Wang L, Hou J, Li G, Song Y, Wang J, Yang M, Cui Y, Cao B (2011) Novel polymorphisms of goat growth hormone and growth hormone receptor genes and their effects on growth traits. *Mol Biol Rep* **38**: 4037–4043. <https://doi.org/10.1007/s11033-010-0522-3>
- Bhatta S, Iwai T, Miura T, Higuchi M, Maugars G, Miura C (2013) Differences between male and female growth and sexual maturation in tilapia (*Oreochromis mossambicus*). *Kathm Univ J Sci Eng Techn* **8**: 57–65. <https://doi.org/10.3126/kuset.v8i2.7326>
- Biswas TK, Bhattacharya TK, Narayan AD, Badola S, Kumar P, Sharma A (2003) Growth hormone gene polymorphism and its effect on birth weight in cattle and buffalo. *Anim Breed Genet* **16**: 494–497. <https://doi.org/10.5713/ajas.2003.494>
- Canestro C, Albalat R, Irimia M, Garcia-Fernandez J (2013) Impact of gene gains, losses and duplication modes on the origin and diversification of vertebrates. *Semin Cell Dev Biol* **24**: 83–94. <https://doi.org/10.1016/j.semcdb.2012.12.008>
- Canosa LF, Chang DR, Peter RE (2007) Neuroendocrine control of growth hormone in fish. *Gen Comp Endocrinol* **151**: 1–26. <https://doi.org/10.1016/j.ygcen.2006.12.010>
- Carnevali O, Vito LD, Sulipizio R, Gioacchini G, Olivetto I, Silvi S, Cresci A (2006) Growth improvement by probiotic in European sea bass juveniles (*Dicentrarchus labrax*) with particular attention to IGF-1, myostatin and cortisol gene expression. *Aquac* **258**: 430–438. <https://doi.org/10.1016/j.aquaculture.2006.04.025>
- Chen JJ, Cao M, Zhang A, Shi M, Tao B, Li Y, Wang Y, Zhu Z, Trudeau VL, Hu W (2018) Growth hormone overexpression disrupts reproductive status through actions on leptin. *Front Endocrinol* **9**: 131. <https://doi.org/10.3389/fendo.2018.00131>
- Chiou CS, Chen HT, Chang WC (1990) The complete nucleotide sequence of the growth-hormone gene from the common carp (*Cyprinus carpio*). *Biochim Biophys Acta* **1087**: 91–94. [https://doi.org/10.1016/0167-4781\(90\)90126-m](https://doi.org/10.1016/0167-4781(90)90126-m)
- Clayton PE, Indraneel B, Philip GM, Andrew GR (2010) Growth hormone, the insulin-like growth factor axis, insulin and cancer risk. *Nat Rev Endocrinol* **7**: 11–24. <https://doi.org/10.1038/nrendo.2010.171>
- Contreras-Sanchez WM, Schreck CB, Fitzpatrick MS, Pereira CB (1998) Effects of Stress on the Reproductive Performance of Rainbow Trout (*Oncorhynchus mykiss*). *Biol Reprod* **58**: 439–447. <https://doi.org/10.1095/biolreprod58.2.439>
- De-Santis C, Jerry DR (2007) Candidate growth genes in finfish—Where should we be looking? *Aquac* **272**: 22–38. <https://doi.org/10.1016/j.aquaculture.2007.08.036>
- De-Faria DA, Guimaraes SEF, Lopes PS, Pires AV, Paiva SR, Sollero BP, Wenceslau AA (2006) Association between G316A growth hormone polymorphism and economic traits in pigs. *Genet Mol Biol* **29**: 634–640. <https://doi.org/10.1590/s1415-47572006000400010>
- Devlin RH, Sakhrani D, White S, Overturf K (2013) Effects of domestication and growth hormone transgenesis on mRNA profiles in rainbow trout (*Oncorhynchus mykiss*). *J Anim Sci* **91**: 5247–5258. <https://doi.org/10.2527/jas.2013-6612>
- Duguay SJ, Lai-Zhang J, Steiner DF, Funkenstein B, Chan SJ (1996) Developmental and tissue-regulated expression of IGF-I and IGF-II mRNAs in *Sparus aurata*. *J Mol Endocrinol* **16**: 123–132. <https://doi.org/10.1677/jme.0.0160123>
- Duguay SJ, Swanson P, Dickhoff WW (1994) Differential expression and hormonal regulation of alternatively spliced IGF-I mRNA transcripts in salmon. *J Mol Endocrinol* **12**: 25–37. <https://doi.org/10.1677/jme.0.0120025>
- Dunham RA (2011) Aquaculture and fisheries biotechnology: Genetic approaches. CABI Publishing, Wallingford, UK, pp 495. <https://doi.org/10.1079/9781845936518.0000>
- FAO (2016) IFAD. The State of Food Insecurity in the World 2015. Meeting the 2015 international hunger targets: taking stock of uneven progress. 2015. Rome. <https://doi.org/10.3945/an.115.009936>
- Filby AL, Tyler CR (2007) Cloning and characterization of cDNAs for hormones and/or receptors of growth hormone, insulin-like growth factor-I, thyroid hormone, and corticosterone and the gender-, tissue-, and developmental specific expression of their mRNA transcripts in fathead minnow (*Pimephales promelas*). *Gen Comp Endocrinol* **150**: 151–163. <https://doi.org/10.1016/j.ygcen.2006.07.014>
- Gjedrem T, Robinson N, Rye M (2012) The importance of selective breeding in aquaculture to meet future demands for animal protein: a review. *Aquac* **350**: 117–129. <https://doi.org/10.1016/j.aquaculture.2012.04.008>
- Hulata G (2001) Genetic manipulations in aquaculture: a review of stock improvement by classical and modern technologies. *Genetica* **111**: 155–173. <https://doi.org/10.1023/a:1013776931796>
- Kajimura S, Uchida K, Yada T, Riley LG, Byatt JC, Collier RJ, Aida K, Hirano T, Grau EG (2001) Stimulation of insulin-like growth factor-I production by recombinant bovine growth hormone in Mozambique tilapia, *Oreochromis mossambicus*. *Fish Physiol Biochem* **25**: 221–230. <https://doi.org/10.1023/a:1022268811599>
- Karakatsoulis N, Papoutsoglou SE, Pizzonia G, Tsatsos G, Tsopelakos A, Chadio S, Kalogiannis D, Polissidis A, Papadopoulou-Daifoti Z (2008) Effects of light spectrum on growth and physiological status of gilthead seabream *Sparus aurata* and rainbow trout *Oncorhynchus mykiss* reared under recirculating system conditions. *Aquac Eng* **36**: 302–309. <https://doi.org/10.1016/j.aquaeng.2007.01.005>
- Khan BN, Ullah H, Ashfaq Y, Hussain N, Atique U, Aziz T, Alharbi M, Albekairi TH, Alasmari AF (2023) Elucidating the effects of heavy metals contamination on vital organ of fish and migratory birds found at fresh water ecosystem. *Heliyon* **9** (2023) e20968. <https://doi.org/10.1016/j.heliyon.2023.e20968>
- Kocour M, Kohlmann K (2011) Growth hormone gene polymorphisms in Tench, *Tinca tinca*. *Aquac* **310**: 298–304. <https://doi.org/10.1016/j.aquaculture.2010.10.006>
- Le Gac F, Blaise O, Fostier A, Le Bail PY, Loir M (1993) Growth hormone (GH) and reproduction a review. *Fish Physiol Biochem* **11**: 219–232. <https://doi.org/10.1007/BF00004569>
- Li MJ, Liu WS, Luo W, Zhang XQ, Zhu WL, Wang J, Liao LY, Li GH (2017) Polymorphisms and their association with growth traits in the growth hormone gene of yellow catfish, *Pelteobagrus fulvidraco*. *Aquac* **469**: 117–123. <https://doi.org/10.1016/j.aquaculture.2016.11.028>
- Ling L, Liu Y, Zhang X, Aziz T, Shahzad M, Sameeh MY, Wang Y, Cai C, Zhu Y (2023). Effect of *Flammulina velutipes* polysaccharides on the physicochemical properties of catfish surimi and myofibrillar protein oxidation during frozen storage. *Front Nutr* **10**: 1268580. <https://doi.org/10.3389/fnut.2023.1268580>
- Livak KJ, Schmittgen TD (2001) Analysis of relative gene expression data using real-time quantitative PCR and the 2(-Delta Delta C(T)) method. *Methods* **25**: 402–408. <https://doi.org/10.1006/meth.2001.1262>
- Ma Q, Liu S, Zhuang Z, Lin L, Sun Z, Liu C, Ma H, Su Y, Tang Q (2012) Genomic structure, polymorphism and expression analysis of the growth hormone (GH) gene in female and male half smooth tongue sole (*Cynoglossus semilaevis*). *Gene* **493**: 92–104. <https://doi.org/10.1016/j.gene.2011.11.015>
- Mackay TF (2001) The genetic architecture of quantitative traits. *Annu Rev Genet* **35**: 303–39. <https://doi.org/10.1146/annurev.genet.35.102401.090633>
- Marchant TA, Moroz BM (1993) In vitro effects of insulin-like growth factors and related peptides on the uptake of [35S]- sulfate from the goldfish (*Carassius auratus*). *Fish Physiol Biochem* **11**: 393–400. <https://doi.org/10.1007/bf00004589>
- Maures T, Chan SJ, Xu B, Sun H, Ding J, Duan C (2002) Structural, biochemical, and expression analysis of two distinct insulin-like growth factor I receptors and their ligands in zebrafish. *Endocrinol* **143**: 1858–1871. <https://doi.org/10.1210/endo.143.5.8768>
- May D, Alrubaian J, Patel S, Dores RM, Rand-Weaver M (1999) Studies on the GH/SL gene family: cloning of African lungfish (*Protopterus annectens*) growth hormone and somatolactin and toad (*Bufo marinus*) growth hormone. *Gen Comp Endocrinol* **113**: 121–135. <https://doi.org/10.1006/gcen.1998.7185>
- Milla S, Wang N, Mandiki, SNM, Kestemont P (2009) Corticosteroids: Friends or foes of teleost fish reproduction? *Comp Biochem Phys* **153**: 242–251. <https://doi.org/10.1016/j.cbpa.2009.02.027>
- Moriyama, S, Dickhoff, WW, Plisetskaya, EM (1995) Isolation and characterization of insulin-like growth factor-I from rainbow trout, *Oncorhynchus mykiss*. *Gen Comp Endocrinol* **99**: 221–229. <https://doi.org/10.1006/gcen.1995.1105>
- Moriyama S, Ayson GF, Kawauchi H (2000) Growth regulation by insulin-like growth factor-I in fish. *Biosci Biotech Bioch* **64**: 1553–1562. <https://doi.org/10.1271/bbb.64.1553>
- Mun SH, You JH, Oh HJ, Lee CH, Baek HJ, Lee YD, Kwon JY (2019) Expression patterns of growth-related genes in juvenile red spotted grouper (*Epinephelus akaara*) with different growth performance after size grading. *Dev Reprod* **23**: 35–42. <https://doi.org/10.12717/DR.2019.23.1.035>
- Mullis PE (2005) Genetic control of growth. *Eur J Endocrinol* **152**: 11–31. <https://doi.org/10.1530/eje.1.01797>
- Opazo R, Valladares L, Romero J (2017) Comparison of gene expression patterns of key growth genes between different rate growths in zebrafish (*Danio rerio*) siblings. *Lat Am J Aquat Res* **45**: 766–775. <https://doi.org/10.3856/vol45-issue4-fulltext-12>
- Pal A, Chakravarty AK, Bhattacharya TK, Joshi BK, Sharma A (2004) Detection of polymorphism of growth hormone gene for the analysis of relationship between allele type and growth traits in Karan

- fries cattle. *Asian-australas J Anim Sci* **17**: 1334–1337. <https://doi.org/10.5713/ajas.2004.1334>
- Perez-Sanchez, J, Marti-Palanca, H, Le Bail, PY (1994) Seasonal changes in circulating growth hormone (GH), hepatic GH-binding and plasma insulin-like growth factor-I immunoreactivity in a marine fish, gilthead sea bream, *Sparus aurata*. *Fish Physiol Biochem* **13**: 199–208. <https://doi.org/10.1007/bf00004358>
- Purohit GK, Mahanty A, Mohanty BP, Mohanty S (2016) Evaluation of housekeeping genes as references for quantitative real-time PCR analysis of gene expression in the murrel *Channa striata* under high-temperature stress. *Fish Physiol Biochem* **42**: 125–135. <https://doi.org/10.1007/s10695-015-0123-0>
- Quik EH, Van Dam PS, Kenemans JL (2010) Growth hormone and selective attention: A review. *Neurosci Biobehav Rev* **34**: 1137–1143. <https://doi.org/10.1016/j.neubiorev.2010.01.001>
- Rio DC, Mi A, Hannon GJ, Nilsen TW (2010) Purification of RNA using TRIzol (TRI reagent). *Cold Spring Harb Protoc* pp 5439. <https://doi.org/10.1101/pdb.prot5439>
- Reinecke M, Bjornsson BT, Dickhoff WW, McCormick SD, Navarro I, Power DM, Gutierrez J (2005) Growth hormone and insulin-like growth factors in fish: where we are and where to go. *Gen Comp Endocrinol* **142**: 20–24. <https://doi.org/10.1016/j.ygcen.2005.01.016>
- Rajesh R, Majumdar KC (2007) A comparative account of the structure of the growth hormone encoding gene and genetic interrelationship in six species of the genus *Labeo*. *Fish Physiol Biochem* **33**: 311–333. <https://doi.org/10.1007/s10695-007-9164-3>
- Shamblott MJ, Cheng CM, Bolt D, Chen TT (1995) Appearance of insulin-like growth factor mRNA in the liver and pyloric ceca of a teleost in response to exogenous growth hormone. *Proc Natl Acad Sci USA* **92**: 6943–6946. <https://doi.org/10.1073/pnas.92.15.6943>
- Sugita H, Ardiyanti A, Yokota S, Yonekura S, Hirayama T, Shoji N, Yamauchi E, Suzuki K, Katoh K, Roh SG (2014) Effect of single nucleotide polymorphisms in gh gene promoter region on carcass traits and intramuscular fatty acid compositions in Japanese black cattle. *Livest Sci* **165**: 15–21. <https://doi.org/10.1016/j.livsci.2014.04.026>
- Sheridan MA, Hagemaster AL (2010) Somatostatin and somatostatin receptors in fish growth. *Gen Comp Endocrinol* **167**: 360–365. <https://doi.org/10.1016/j.ygcen.2009.09.002>
- Tanamati F, Da Silva SCC, Rodriguez MDPR, Schuroff GP, Do Nascimento CS, Del Vesco AP, Gaparino E (2015) GHR and IGF-I Gene expression and production characteristics associated with GH gene polymorphism in Nile Tilapia. *Aquac* **435**: 195–199. <https://doi.org/10.1016/j.aquaculture.2014.09.033>
- Tian C, Yang M, Lv L, Yuan Y, Liang X, Guo W, Song Y, Zhao C (2014) Single nucleotide polymorphisms in growth hormone gene and their association with growth traits in *Siniperca chuatsi*. *Int J Mol Sci* **15**: 7029–7036. <https://doi.org/10.3390/ijms15047029>
- Tymchuk WE, Beckmen B, Devlin RH (2009) Altered expression of growth hormone/insulin-like growth factor – axis hormones in domesticated fish. *Endocrinol* **150**: 1809–1816. <https://doi.org/10.1210/en.2008-0797>
- Vairamani K, Merjanah L, Casano-Sancho P, Sanli ME, David A, Metherell LA, Savage MO, Sanchez del Pozo J, Backeljauw PF, Rosenfeld RG Aisenberg J (2017) Novel dominant-negative GH receptor mutations expands the spectrum of GHI and IGF-I deficiency. *J Endocr Soc* **1**: 345–358. <https://doi.org/10.1210/js.2016-1119>
- Wasim MP (2007) Issues, growth and instability of inland fish production in Sindh (Pakistan): Spatial – Temporal Analysis. *Pakistan Economic and Social Review* 203–230
- Wu Y, Pan AL, Pi JS, Pu YJ, Du JP, Liang ZH, Shen J (2012) One novel SNP of growth hormone gene and its associations with growth and carcass traits in ducks. *Mol Bio Rep* **39**: 8027–8033. <https://doi.org/10.1007/s11033-012-1649-1>
- Xu SH, Bao WB, Huang J, Cheng JH, Shu JT, Chen GH (2007) Polymorphic analysis of intron 2 and 3 of growth hormone gene in duck. *Hereditas* **29**: 438–442. <https://doi.org/10.1360/yc-007-0438>
- Yi TL, Fang L, Liang XF, Sun LF, Li J, Luo XN, Guo WJ, Dou, YQ, Sun, J (2015) Characterization of microsatellite markers and their correlations with growth traits in mandarin fish (*Siniperca chuatsi*). *Genet Mol Res* **14**: 8926–8934. <https://doi.org/10.4238/2015.August.7.1>
- Zhang D, Shao Y, Jiang S, Li J, Xu X (2009) *Nibeia Coibor* Growth hormone gene: its phylogenetic significance, microsatellite variation and expression analysis. *Gen Comp Endocrinol* **163**: 233–241. <https://doi.org/10.1016/j.ygcen.2009.03.030>
- Zhong H, Zhou Y, Liu S, Tao S, Long Y, Liu Z, Zhang C, Duan W, Hu J, Song C, Liu Y (2012) Elevated expressions of GH/IGF axis genes in triploid crucian carp. *Gen Comp Endocrinol* **178**: 291–300. <https://doi.org/10.1007/s11033-010-0522-3>

Isolation, preparation and investigation of leaf extracts of *Aloe barbadensis* for its remedial effects on tumor necrosis factor alpha (TNF- α) and interleukin (IL-6) by *in vivo* and *in silico* approaches in experimental rats

Iram Khurshaid¹, Sobia Ilyas¹, Nureen Zahra¹✉, Sohail Ahmad², Tariq Aziz³✉, Fahad Al-Asmari⁴, Sanaa Almowallad⁵, Rehab F. Al-Massabi⁵, Yasmene F. Alanazi⁵, Aminah A. Barqawi⁶, Roaa Mohammed Tahir Kassim⁷, Abdulhakeem S Alamri⁸, Majid Alhomrani⁸ and Manal Y Sameeh⁶

¹Institute of Microbiology and Biotechnology The University of Lahore, Pakistan; ²Department of Poultry Production, University of Veterinary and Animal Sciences, Lahore, Pakistan; ³Department of Agriculture University of Ioannina Arta, Greece; ⁴Department of Food Science and Nutrition, College of Agriculture and Food Sciences, King Faisal University, P.O. Box 400, Al-Ahsa, Saudi Arabia; ⁵Department of Biochemistry, Faculty of Sciences, University of Tabuk, Tabuk 71491, Saudi Arabia; ⁶Department of Chemistry, Al-Leith University College, Umm Al-Qura University, Makkah 21955, Saudi Arabia; ⁷Umm Al-Qura University, College of Science, Department of Biology, Makkah, Saudi Arabia; ⁸Department of Clinical Laboratory Sciences, The Faculty of Applied Medical Sciences, Taif University, P.O. Box 11099, Taif 21944, Saudi Arabia

Aloe barbadensis is a stemless plant with a length of 60–100 cm with juicy leaves which is used for its remedial and healing properties in different suburbs of various countries. The present study was conducted to investigate the effect of *A. barbadensis* leaf extract (aqueous and ethanolic) in yeast induced pyrexia and acetic acid induced writhing in rat model to evaluate the antipyretic biomarkers and its phytochemical screening with computational analysis. For analgesic activity model 60 Albino rats (160–200 kg) were divided into four groups. Of the 4 groups, control consisted of 6 rats (Group I) treated with normal saline, standard comprised of 6 rats treated with drug diclofenac (Group II). Experimental groups consisted of 48 rats, treated with *A. barbadensis* ethanolic and aqueous leaf extracts at doses of 50 mg/kg, 100 mg/kg, 200 mg/kg, and 400 mg/kg (Group III, IV). For antipyretic activity group division was same as in analgesic activity. All groups were treated the same as in the analgesic activity except for the second group which was treated with paracetamol. In both antipyretic and analgesic activity at the dose of 400 mg/kg, group III showed significant inhibition. TNF- α and IL-6 showed significant antipyretic activity at a dose of 400 mg/kg. For molecular docking aloe emodin and cholestanol were used as ligand molecules to target proteins Tnf- α and IL-6. Acute oral toxicity study was performed. There was no mortality even at the dose of 2000 mg/kg. Quantitative and qualitative phytochemical screening was performed for the detection of various phytochemicals. Hence, *A. barbadensis* leaf extracts can be used in the form of medicine for the treatment of pain and fever.

Keywords: induced pyrexia, pain, antipyretic biomarkers, *in-silico*, *in vivo*, *Aloe barbadensis*

Received: 05 May, 2023; **revised:** 10 October, 2023; **accepted:** 22 October, 2023; **available on-line:** 08 November, 2023

✉ e-mail: iwocdk@gmail.com (TA); naureen.zahra@imbb.uol.edu.pk (NZ)

Acknowledgements of Financial Support: This research was funded by the Deanship of Scientific Research (DSR) at King Faisal University (under Ambitious Researcher Track) with project no. GRANT 4601

Abbreviations: COX-1 and COX-2, Cyclooxygenase 1 and 2; IL-6, interleukin 6; NSAIDs, Nonsteroidal Anti-Inflammatory drugs; TNF- α , tumor necrosis factor alpha

INTRODUCTION

An unpleasant signal that something hurts, which is basically a complex experience that differs greatly from person to person, is called pain. We can also define pain as a somatic sense of severe discomfort, a sign of a disorder and physical injury or even emotional sorrow. The body's defense mechanisms depend largely on pain which also serves as a rapid warning system that instructs the motor neurons in the central nervous system to prevent physical harm. There are two categories of pain: acute and chronic pain (Kumar *et al.*, 2015). NSAIDs reduce pain by blocking the formation of prostaglandins, which is accomplished by decreasing the activity of the enzyme Cyclooxygenase 1 and 2 (COX-1 and COX-2) (PG) (Hayat *et al.*, 2023; Naveed *et al.*, 2023; Waseem *et al.*, 2023; Aqib *et al.*, 2023; Naveed *et al.*, 2022a; Naveed *et al.*, 2022b; Ayesha *et al.*, 2022; Liet *et al.*, 2009). Fever is a common component of inflammation in animals, and it amplifies the host's reaction. The hypothalamus generally regulates fever, but certain bacterial or viral illnesses can promote the formation of pyrogens, substances that effectively alter the hypothalamic “thermostat setting” to raise body temperature and cause fever. Endogenous or exogenous pyrogens are both possible (Walter *et al.*, 2016). Infection, tissue injury, inflammation or other disease conditions can cause pyrexia or fever. Among the most common symptoms of these conditions is an increase in the production of cytokines, such as Interleukin-1, Interleukin-6, interferon, and tumor necrosis factor among others. PGE2 synthesis is boosted by the cytokines because they stimulate the arachidonic acid pathway. To elevate body temperature PGE2 activates the hypothalamus, which causes it to increase heat production while minimizing heat loss (Ahmad B *et al.*, 2023; Mathew *et al.*, 2021).

Thousands of people around the world, mostly in developing nations, depend on herbal medication for their health. Traditional and complementary medicine practitioners have extensive experience in the inhibition, diagnosis, and management of a wide range of disorders including infectious diseases, allergies, and hypertension (Hamid *et al.*, 2023; Ammara *et al.*, 2023; Ejaz Ahmad

et al., 2023; Ahmad *et al.*, 2023; Rauf *et al.*, 2023; Nayakudya *et al.*, 2020; Sajjad *et al.*, 2014). *Aloe barbadensis* is one of the most popular plant these days and it is attracting a lot of scientific attention. The use of this plant may be traced all the way back to the Babylonian era. It grows in warm areas and is unable to survive in freezing temperatures. According to WHO estimates, traditional medicines are being used by up to 80% of the population. *A. barbadensis* is a stemless plant with a length of 60–100 cm with juicy leaves (Sana *et al.*, 2023; Aziz *et al.*, 2023a; Hena *et al.*, 2023; Wajid *et al.*, 2023; Nureen *et al.*, 2023; Gul *et al.*, 2023). On several plants, *A. barbadensis* bears thick green leaves with white dots on the lower and upper surface of the stem. In Ayurveda, ghririkumari is defined as an *A. barbadensis* being a blood cleanser, anti-inflammatory, uterine tonic, laxative, diuretic, spermatogenic and fever reliever (Saleem *et al.*, 2023; Aziz *et al.*, 2023b; Narjis *et al.*, 2023; Zawar *et al.*, 2023a; Farooq *et al.*, 2022).

Many phytochemicals, vitamins, minerals, and antioxidants are found in the plant. A class of substances known as phytochemicals (derived from the Greek word “phyto,” which literally means “plant”) are physiologically active molecules found in minute amounts in plants that are not recognized as nutrients, but which appear to protect against degenerative diseases (Zawar *et al.*, 2023b; Tayyaba *et al.*, 2023; Zawar *et al.*, 2023c; Dalia *et al.*, 2017). Molecular docking is a computer simulation technique for predicting the form of a receptor-ligand complex, in which the receptor is a protein, or a nucleic acid molecule (DNA or RNA) and the ligand is a small molecule or another protein; the receptor and ligand are both proteins. Also known as simulation-based prediction, it is a technique for forecasting the location of a ligand in an expected or pre-defined binding site (Ahmad *et al.*, 2023; Bermen *et al.*, 2000).

MATERIALS AND METHODS

Collection of samples and their extracts

A. barbadensis leaves were collected, aqueous and ethanolic extract was prepared by cold maceration method (Singh *et al.*, 2010).

Albino rats

Albino rats (160–200 g) of both sexes were purchased from the animal home for the experiment. Rats were kept in polypropylene cages at the University of Lahore animal house. Rats were fasted before being used in the experiments. After that they were given distilled water and balanced feed.

Groups and treatment schedule

In group I, rats were treated with distilled water 10ml/kg. In analgesic and antipyretic activity in group II rats were treated with diclofenac and paracetamol 100 mg/kg. In group III and IV rats were treated with different quantities of *A. barbadensis* ethanolic and aqueous leaf extracts.

Steps

Fever induced by yeast.

All the groups were injected with yeast below the nape of neck to induce fever after 21 hours, and the

highest temperature was 101.58 Fahrenheit. Control rats were injected with normal saline, group II, the rats were treated with a dose of paracetamol, while group III and IV rats were treated with the different concentrations of ethanolic and aqueous leaf extracts of *A. barbadensis*. The body temperature (rectum) of rats was measured with digital thermometer after the equal time intervals until fourth hour.

Analgesic activity model

All groups were treated the same as in the analgesic activity except the second group which was treated with diclofenac.

Procedure

Writhing induced by acetic acid

By the injection of acetic acid, the writhing process began in rats. It was injected to determine the potential of leaf extract of *A. barbadensis* in pain process. But 1 hour before the experiment, rats in group I were injected with normal saline (10 ml/kg) intraperitoneally. In group II, the rats were treated with a dose of diclofenac 100 mg/kg. While in groups III and IV the rats were treated with different concentrations of ethanolic and aqueous leaf extracts of *A. barbadensis* at a dose of 50, 100, 200, and 400 mg/kg. For counting the writhes, a stopwatch was used. The rats were placed into different cages during activity.

Acute oral toxicity study

Acute oral toxicity study was carried out using a protocol as described by Srinivasan *et al* (2018).

Qualitative phytochemical analysis of *Aloe barbadensis*

Qualitative and quantitative phytochemical analysis of *A. barbadensis* was done by standard protocol (Usman *et al.*, 2020).

In silico antipyretic and analgesic activity of *A. barbadensis*

For *in-silico* investigation, various software of bioinformatics was used to support *A. barbadensis* antipyretic and analgesic activity. Chemskech, chimera, pymol, pyrx, depth residue, and discovery studio were the computational tools used.

Data analysis

Data were analyzed using PROC GLM in SAS software (version 9.1).

RESULTS

Ethanolic and aqueous extracts of *A. barbadensis*

In this study, the potential of *A. barbadensis* leaf extracts at different doses were observed against rat models. The difference between the groups of rats treated with extracts and the control group was at a significant level. All groups showed a remarkable increase in temperature after being injected with yeast. Group I showed a marked increase in temperature after 1–4 hrs of injection. Meanwhile, experimental groups treated with *A. barbadensis* leaf extracts reduced the temperature from 1 to 4 hours as compared to group I. The improvement was more pronounced at fourth hour in a dose depend-

Table 1. Inhibition (%) of pain by ethanolic and aqueous extracts of *A. barbadensis* and diclofenac on acetic acid induced pain in rats

Treatment	Ethanolic	Aqueous
Control	18.83±0.40	18.83±0.40
Standard	7.36±0.91 (61%)	7.36±0.91 (61%)
Treated at dose 50mg/kg	17.00±0.41 (9%)	17.75±0.95 (-5%)
Treated at dose 100mg/kg	15.25±0.48 (19%)	16.5±0.29 (12%)
Treated at dose 200mg/kg	12.25±0.75 (34%)	13±0.91 (30%)
Treated at dose 400mg/kg	6.50±1.04 (65%)	9.75±0.63 (48%)
p-value	<0.0001	<0.0001

ent manner. Within the experimental groups, *A. barbadensis* leaf ethanolic extract (group III) showed the most pronounced effect as compared to *A. barbadensis* leaf aqueous extracts (group IV). Interleukin-6 and TNF- α concentrations in the plasma were increased as a result of yeast injection. In both ethanolic and aqueous extracts TNF- α and IL-6 marker values differ considerably between treatment groups. Effect of *A. barbadensis* leaf extracts on IL-6 and TNF- α in group III and IV indicated a significant decrease in pyrexia in comparison to control (Fig. 1 and Table 1).

Analgesic activities

In analgesic activity, all groups showed a significant increase in pain which was induced with acetic acid.

Group I showed the most evident increase in pain after injection. While group III and IV treated with *A. barbadensis* leaf extracts reduced the temperature as compared to group I.

The acute toxicity results showed that the ethanolic extracts had a high safety profile as neither death nor signs related with toxicity were observed at the highest dose level (2000 mg/kg orally) in the rats. Rats did not show any change in their gross behavior or associated stereotypical symptoms as shown in Table 2.

Qualitative phytochemical screening of aqueous and ethanol gel extracts of *A. barbadensis*

The results of qualitative phytochemical screening of the aqueous and ethanol gel extracts of *A. barbadensis*

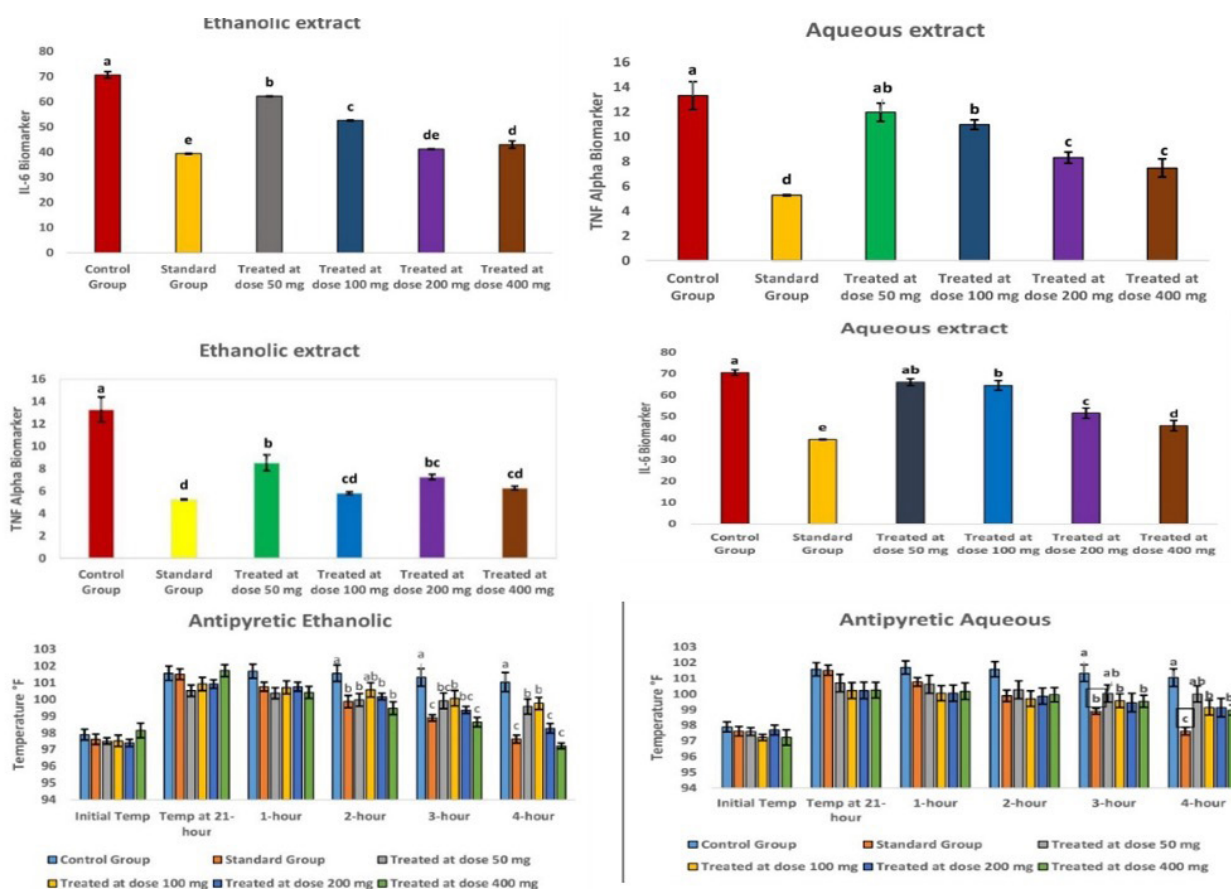


Figure 1. TNF Alpha and IL-6 showing significant upregulation and downregulation and temperature of rats (F°) at 1–4 hours post yeast injection in group I, II, III and IV

Table 2. Effect of acute toxicity by ethanolic extracts of *A. barbadensis* and normal saline in rats

Treatment	Control	Dose A	Dose B	Dose C	p-value
AST (μL)	7.40 ^c ±1.21	35.40 ^b ±8.78	243.20 ^a ±7.74	11.40 ^c ±1.36	< 0.0001
ALT(μL)	9.80 ^c ±2.08	34.00 ^b ±7.09	53.60 ^a ±7.59	13.60 ^c ±1.57	< 0.0001
Alkp_v	44.60 ^b ±7.31	70.80 ^b ±10.27	154.40 ^a ±9.52	56.40 ^b ±8.79	< 0.0001
Bilurobin (mg/dl)	1.68 ^a ±0.16	1.50 ^a ±0.25	1.88 ^a ±0.49	0.36 ^b ±0.12	0.0091
Total protein (g/dl)	7.46 ^a ±0.27	5.24 ^b ±0.63	7.12 ^a ±0.43	4.56 ^b ±0.70	0.0032
Albumin (pg/dl)	3.20 ^{ab} ±0.29	3.32 ^{ab} ±0.36	4.42 ^a ±0.76	2.04 ^b ±0.36	0.0247

Superscripts on different means within row differ significantly at $p \leq 0.05$. Dose A=500 mg/kg; Dose B=1000 mg/kg; Dose C=2000 mg/kg

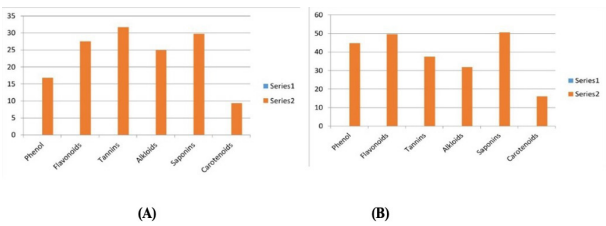


Figure 2. Qualitative phytochemical screening of the aqueous and ethanol gel extracts of *Aloe barbadensis*

Table 3. Qualitative phytochemical screening of the aqueous and ethanol gel extracts of *Aloe barbadensis*

S/N	Phytochemical components	Ethanoic extract	Aqueous extract
1	Tannins	+	+
2	Saponins	+	+
3	Anthraquinones	+	-
4	Glycosides	+	+
5	Alkaloids	-	+
6	Flavonoids	+	+
7	Phenolics	+	+
8	Steroids	-	-
9	Terpenoids	-	-

showed the presence of tannins, saponins, phenolics and flavonoids. Proteins were present in ethanolic extract but absent in aqueous extract while glycosides and alkaloids were present in aqueous extract but absent in ethanolic extract. Terpenoids and steroids were absent in both extracts (Table 3).

Quantitative phytochemical screening showed that ethanolic extract showed a high quantity of phytochemicals as compared to aqueous extract. These bioactive chemicals are important in medicine because they have anti-inflammatory, anti-diabetic, analgesic, anti-oxidant, and antipyretic properties (Fig. 2).

In-silico studies

The objective of the in-silico analysis is to study the potential of phytochemicals to target the cytokine TNF-Alpha and Il-6 protein, hence, showing its antipyretic and analgesic activity. The molecular binding score of the phytochemicals of *A. barbadensis* and the stand-

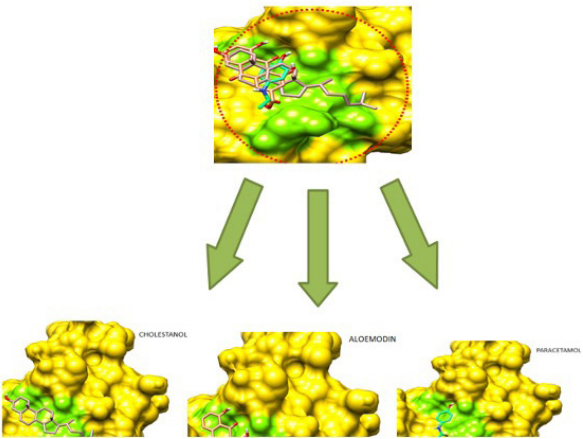


Figure 3. IL-6 and ligand molecules aloe emodin, cholestanol and paracetamol.

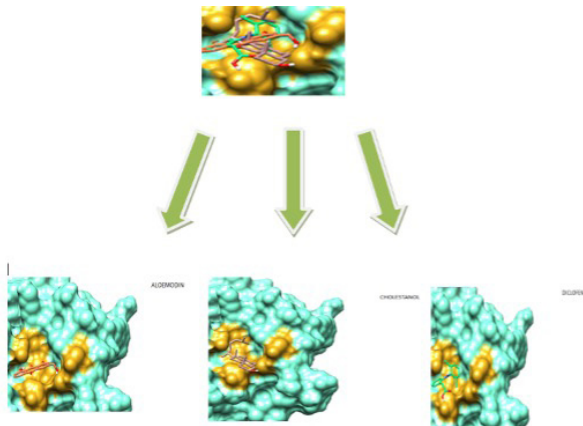


Figure 4. IL-6 and ligand molecules aloe emodin, cholestanol and diclofenac

ard drug paracetamol against target TNF-Alpha protein and IL-6 was -4.2 and -5.9 kcal/mol and -6 while the cholestanol showed the highest score amongst the three (Fig. 3 and Fig. 4).

DISCUSSION

This study was conducted to evaluate the medicinal prospective of *Aloe barbadensis* ethanolic and aqueous leaf extracts against pain and fever. The presence of distinct chemical ingredients was recognized during phytochemical screening of aqueous and ethanolic ex-

tracts of *A. barbadensis*. Previous studies reported that several endogenous pyrogens, including prostaglandin, interleukin-1, interleukin-6, interleukin-8, tumour necrosis factor- α , and macrophage protein-1 to induce fever. Tumor necrosis factor and phospholipase A2 may activate prostaglandin production. Brewer's yeast causes pathogenicity by inducing TNF- α and prostaglandin production (Riditid *et al.*, 2008).

In the present study, fever was significantly ($p < 0.05$) reduced in group III and IV in a dose dependent manner. The higher the dose (400 mg/kg) the greater was inhibition of fever. Brewer's yeast intravenously causes pyrexia by increasing the synthesis of prostaglandins. It is a beneficial test for determining the antipyretic activity of plant materials as well as synthetic medications (Khan *et al.*, 2009). Antipyretic efficacy could be mediated by inhibiting prostaglandin synthesis, similar to how paracetamol works by inhibiting cyclo-oxygenase enzyme activity. Pyrexia is caused by a variety of mediators and inhibiting these mediators has an antipyretic effect. Results of another study were concurrent with our findings (Safari *et al.*, 2016; Okokon *et al.*, 2010; Demoze A *et al.*, 2020; S Alyas *et al.*, 2023; Ghosh *et al.*, 2015; Velázquez-González *et al.*, 2014). Previous studies revealed that antipyretic activity of these extracts could potentially be due to the presence of alkaloids. Prostaglandins, which are involved in pyrexia, are known to be targeted by flavonoids. As a result, the presence of flavonoids in *A. barbadensis* aqueous leaf extract may contribute to its antipyretic activity (Hussain *et al.*, 2022; Safari *et al.*, 2016).

The medicinal ability of ethanolic and aqueous leaf extract of *A. barbadensis* was evaluated against pain. A system of sensory neurons and neural afferent pathways that selectively respond to potentially unpleasant, tissue-damaging stimuli support the sense of pain. The myelinated A delta and unmyelinated C fibres, which are found in skin nerves and in deep somatic and visceral regions, are most responsive to painful stimuli. The primary afferent nociceptors are these pain receptors (Okokon *et al.*, 2010). In this study, fever was remarkably decreased in group III and IV in a dose dependent manner. Endogenous substances, such as bradykinins, serotonin, progesterone, histamine, and substance P are released when acetic acid is exposed to a painful stimulus. The abdominal constriction reaction is thought to be mediated by local peritoneal receptors. Therapy has been linked to levels of PGE2 and PGF2 in peritoneal fluids as well as lipoxygenase products. Previous studies confirmed that the chemo sensitive nociceptors of rats were activated by intraperitoneal dose of acetic acid, resulting in abdominal writhing (Apu *et al.*, 2012; Ara *et al.*, 2010; Zulfikar *et al.*, 2010). The findings of this study are congruent with another study (Ghosh *et al.*, 2015).

The phytochemicals found in the ethanolic and aqueous extracts of *A. barbadensis* may be responsible for the analgesic effects shown in this investigation. The ethanolic extracts may have functioned in a similar way to NSAIDs by inhibiting the COX pathway metabolically. The cyclooxygenase and lipoxygenase pathways, which are important for peripheral nociception, have been revealed to be inhibited by flavonoids (Velázquez-González *et al.*, 2014). Previous studies reported that flavonoids reduce prostaglandin production by reducing prostaglandin synthase's action. Prostaglandin production, which is implicated in pain perception via an opiodergic mechanism, has been shown to be targeted by flavonoids (Lenard *et al.*, 2023; Panda *et al.*, 2009). Flavonoids lower intracellular calcium levels through inhibiting N-methyl-D-aspartate (NMDA) receptor activation.

The nitric oxide synthase enzyme and phospholipase A2 activity are lowered, leading to a reduction in NO and prostaglandin formation (Ara *et al.*, 2010; Valdes *et al.*, 2023). Previous studies reported that analgesic properties have been attributed to tannins, alkaloids, and steroidal substances. Terpenoids have also been linked to antinociceptive properties via inhibiting thrombocyte aggregation and interfering with pain signaling processes (Ali *et al.*, 2012). Acute toxicity was also performed to evaluate possible adversative effect of repetitive extract's administration to rats at different doses. Our study was correlated with a previous study (Paul *et al.*, 2018; Devaraj *et al.*, 2011).

CONCLUSIONS

Qualitative phytochemical study showed that the crude extract of *A. barbadensis* showed the presence of alkaloid, saponins, flavonoid, terpenoids, tannins, anthraquinones, phenols and steroids. The presence of phytochemicals, such as polyphenols and flavonoids in plants, reduces the risk of chronic diseases and increases the ability of biological systems to trap highly reactive free radical species. Its antipyretic and analgesic action is attributed to the presence of these polyphenols. The results of phytochemical screens were identical to those discovered by other researchers, including alkaloids, saponins, tannins, flavonoids, and steroids.

Declarations

Ethical Approval. The ethical approval for this study was provided Molecular Biology and Biotechnology Bioethical, Biosafety and Biosecurity Committee, The University of Lahore under Ref no: CRiMM/22/Research /146 dated 02/12/2022.

Competing interests. The authors declare no conflict of interest.

Availability of data and materials. All the data has been included in the manuscript.

REFERENCES

- Ahmad B, Muhammad Yousafzai A, Maria H, Khan AA, Aziz T, Alharbi M, Alsahammari A, Alasmari AF (2023) Curative effects of dianthus orientalis against paracetamol triggered oxidative stress, hepatic and renal injuries in rabbit as an experimental model. *Separations* **10**: 182. <https://doi.org/10.3390/separations10030182>
- Ahmad E, Jahangeer M, Mahmood Akhtar Z, Aziz T, Alharbi M, Alsahammari A, Alasmari AF, Irfan Bukhari N (2023) Characterization and gastroprotective effects of *Rosa brunonii* Lindl. fruit on gastric mucosal injury in experimental rats – A preliminary study. *Acta Biochim Pol* **70**: 633–641. https://doi.org/10.18388/abp.2020_6772
- Ali K, Ashraf A, Nath Biswas N (2012) Analgesic, anti-inflammatory and anti-diarrheal activities of ethanolic leaf extract of *Typhonium trilobatum* L. Schott. *Asian Pac J Trop Biomed* **2**: 722–726. [https://doi.org/10.1016/S2221-1691\(12\)60217-2](https://doi.org/10.1016/S2221-1691(12)60217-2)
- Alyas S, Habib B, Shafique T, Zahid B, Hayat S, Ilyas A, Ahmad S, Khan R (2023) Anti-inflammatory, antipyretic and analgesic activities of chloroform extract of *Aloe barbadensis* miller in albino rats. *Res J Biol Sci* **1**: 208. <https://doi.org/10.54112/bsrj.v2023i1.208>
- Ammara A, Sobia A, Nureen Z, Sohail A, Abid S, Aziz T, Nahaa MA, Rewaa SJ, Ahellah MJ, Nouf SAA, Nehad AS, Manal YS, Amnah AA, Majid A, Abdulhakeem SA, Anas SD, Saad A (2023) Revolutionizing the effect of *Azadirachta indica* extracts on edema induced changes in C-reactive protein and interleukin-6 in albino rats: *in silico* and *in vivo* approach. *Eur Rev Med Pharmacol Sci* **27**: 5951–5963. https://doi.org/10.26355/eurrev_202307_32947
- Apu AS, Hossain F, Rizwan F, Bhuyan SH, Matin M, Jamaluddin AT (2012) Study of pharmacological activities of methanol extract of *Jatropha gossypifolia* fruits. *J Basic Clin Pharm* **4**: 20–24. <https://doi.org/10.4103/0976-0105.109404>
- Ara Arzumand, Saleh-e-In M, Ahmed NU, Ahmed M, Abul M (2010) Phytochemical screening, analgesic, antimicrobial and anti-oxidant

- activities of bark extracts of *Adenantharpavonina* L. (Fabaceae). *Adv Nat Appl Sci* 4: 352–360.
- Aysha S, Muhammad A, Muhammad N, Syeda IM, Modasrah M, Tariq A, Ayaz AK, Muhammad S, Metab A, Abdulrahman A (2022) HPLC and GC-MS Quantification of phytoconstituents from *T. vulgaris* eliciting the potential of bioactive compounds by executing multiple *in-vitro* and *in vivo* biological activities inducing functionalized capabilities on COX-1, COX-2 and gastric cancer genes computationally. *Molecules* 27: 8512. <https://doi.org/10.3390/molecules27238512>
- Aziz T, Ihsan F, Ali Khan A, Ur Rahman S, Zamani GY, Alharbi M, Alshammari A, Alasmari AF (2023) Assessing the pharmacological and biochemical effects of *Salvia hispanica* (Chia seed) against oxidized *Helianthus annuus* (sunflower) oil in selected animals. *Acta Biochim Pol* 70: 211–218. <https://doi.org/10.18388/abp.2020.6621>
- Aziz T, Nadeem AA, Sarwar A, Perveen I, Hussain N, Khan AA, Daudzai Z, Cui H, Lin L (2023) Particle nanoarchitectonics for nanomedicine and nanotherapeutic drugs with special emphasis on nasal drugs and aging. *Biomedicine* 11: 354. <https://doi.org/10.3390/biomedicine11020354>
- Berman HM, Westbrook J, Feng Z, Gilliland G, Bhat TN, Weissig H, Bourne PE (2000) The protein data bank. *Nucleic Acids Res* 28: 235–242. <https://doi.org/10.1093/nar/28.1.235>
- Dalia ISM, Jaime LC, Raquel S, Ana SS (2017) *Aloe vera*: Ancient knowledge with new frontiers. *Trend Food Sci Tech* 61: 94–102. <https://doi.org/10.1016/j.tifs.2016.12.005>
- Demoze A, Tesfay HK, Gebrehiwot GT (2020) Antibacterial and antifungal activities of the leaf exudate of *Aloe megalacantha* baker. *Int J Microbiol* 2020: 8840857. <https://doi.org/10.1155/2020/8840857>
- Devaraj A, Karpagam T (2011) Evaluation of anti-inflammatory activity and analgesic effect of *Aloe vera* leaf extract in rats. *Int Res J Pharm* 2: 103–110
- Ejaz A, Muhammad J, Nadeem IB, Abid S, Tariq A, Metab A, Abdulrahman A, Abdullah FA (2023) Isolation, structure elucidation & antidiabetic potential of *Rosa brunonii* L. fruit – fight diabetes with natural remedies. *J Chil Chem Soc* 68: 5887–5894. <https://www.jcchems.com/index.php/JCCHEMS/article/view/2355/603>
- Farooq S, Shaheen G, Asif HM, Aslam MR, Zahid R, Rajpoot SR, Jabbar S, Zafar F (2022) Preliminary phytochemical analysis: *in-vitro* comparative evaluation of anti-arthritis and anti-inflammatory potential of some traditionally used medicinal plants. *Dose Response* 20: 15593258211069720. <https://doi.org/10.1177/15593258211069720>
- Ghosh AK, Banerjee M, Mandal TK, Mishra A, Bhowmik MK (2015) A study on analgesic efficacy and adverse effects of *Aloe vera* in wistar rats. *Pharmacologyonline* 1: 1098–1108
- Gul R, Rahmatullah Q, Ali H, Bashir A, Ayaz AK, Tariq A, Metab A, Abdulrahman A, Abdullah FA (2023) Phytochemical, antimicrobial, radical scavenging and *in-vitro* biological activities of *Tenacium stocksianum* leaves. *J Chil Chem Soc* 68: 5748–5754. <https://doi.org/10.4067/S0717-97072023000105748>
- Hena Z, Mohsin S, Shafiq UR, Zafar I, Ayaz AK, Tariq A, Waqar A, Ghazala YZ, Saeed A, Muhammad S, Metab A, Abdulrahman A (2023) Assessing the effect of walnut (*Juglans regia*) and olive (*Olea europaea*) oil against the bacterial strains found in gut microbiome. *24. Prng Nutrit*. <https://doi.org/10.23751/pn.v24i3.13311>
- Hamid M, Salar U, Rashid Y, Azim MK, Khan KM, Naz S, Aziz T, Alharbi M, Alshammari A, Alasmari FA (2023) Determining the 3-substituted coumarins inhibitory potential against the HsIV protease of *E. coli*. *Eur Rev Med Pharmacol Sci* 27: 9169–9182. <https://doi.org/10.26355/eurrev.202310.33945>
- Hussain A, Attique F, Naqvi SAR, Ali A, Ibrahim M, Hussain H, Zafar F, Iqbal RS, Ayub MA, Assiri M, Imran M, Ullah S (2022) Nanoformulation of *Curcuma longa* root extract and evaluation of its dissolution potential. *ACS Omega* 8: 1088–1096. <https://doi.org/10.1021/acsomega.2c06258>
- Khan I, Nisar M, Ebad F, Nadeem S, Saeed M, Khan H, Ahmad, Z (2009) Anti-inflammatory activities of Sieboldogenin from *Smilax china* Linn. experimental and computational studies. *J Ethnopharmacol* 121: 175–177. <https://doi.org/10.1016/j.jep.2008.10.009>
- Kumar S, Vandana UK, Agrwal D, Hansa J (2015) Analgesic, anti-inflammatory and anti-pyretic effects of *Azadirachtaindica* (Neem) leaf extract in albino rats. *Int J Sci Res* 4: 713–721. <https://www.ijsr.net/archive/v4i8/SUB157156.pdf>
- Lenard S, Jhuly W, Lacerda F, Mariana SM, Akbar A, Leonardo GV, Paulo TS Junior, Barbara S, Bellete MA, Soares Lucas CC, Vieira, Olivia MS (2023) Metabolomics analysis of *Combretum lanceolatum* roots in the presence of its endophytic fungi *J Braz Chem Soc* 34: 234–241. <https://dx.doi.org/10.21577/0103-5053.20220103>
- Li W, Lian YY, Yue WJ, Yang Q, Yue Q, Meng QG, Zhao CB (2009) Experimental study of COX-2 selective and traditional non-steroidal anti-inflammatory drugs in total hip replacement. *J Int Med Res* 37: 472–478. <https://doi.org/10.1177/147323000903700223>
- Mathew AA, Asirvatham R, Tomy DV (2021) Cardioprotective effect of *Marsdenia tenacissima* and *Sansevieria roxburghiana* in doxorubicin-induced cardiotoxicity in rats *in vivo*: the role of dresgenin and lupeol. *Turk J Pharm Sci* 18: 271–281. <https://doi.org/10.4274/tjps.galenos.2020.27880>
- Naveed M, Bukhari B, Aziz T, Zaib S, Mansoor MA, Khan AA, Shahzad M, Dabool AS, Alruways MW, Almalki AA, Alamri AS, Alhomrani M (2022) Green synthesis of silver nanoparticles using the plant extract of *Acer oblongifolium* and study of its antibacterial and antiproliferative activity via mathematical approaches. *Molecules* 27: 4226. <https://doi.org/10.3390/molecules27134226>
- Naveed M, Batool H, Rehman SU, Javed A, Makhdoom SI, Aziz T, Mohamed AA, Sameeh MY, Alruways MW, Dabool AS, Almalki AA, Alamri AS, Alhomrani M (2022) Characterization and evaluation of the antioxidant, antidiabetic, anti-inflammatory, and cytotoxic activities of silver nanoparticles synthesized using *Brachycton populus* leaf extract. *Processes* 10: 1521. <https://doi.org/10.3390/pr10081521>
- Narjis K, Najeeb U, Abid S, Tariq A, Metab A, Abdulrahman A (2023) Isolation and identification of protease producing bacillus strain from cold climate soil and optimization of its production by applying different fermentation conditions. *Appl Ecol Environ Res* 21: 3391–3401. http://doi.org/10.15666/aecr/2104_33913401
- Naveed M, Makhdoom SI, Rehman SU, Aziz T, Bashir F, Ali U, Alharbi M, Alshammari A, Alasmari AF (2023) Biosynthesis and mathematical interpretation of zero-valent iron NPs using *Nigella sativa* seed tincture for indemnification of carcinogenic metals present in industrial effluents. *Molecules* 28: 3299. <https://doi.org/10.3390/molecules28083299>
- Nureen Z, Tahira F, Muhammad H, Basit Z, Abid S, Tariq A, Metab A, Abdulrahman A, Abdullah FA (2023) *In-vitro* and *in-silico* analysis of anti-inflammatory, analgesic, and anti pyretic activities of *Citrus paradisi* leaf extract. *J Chil Chem Soc* 68: 5813–5821. <https://www.jcchems.com/index.php/JCCHEMS/article/view/2335/595>
- Hayat P, Khan I, Rehman A, Jamil T, Hayat A, Rehman MU, Ullah N, Sarwar A, Alharbi AA, Dabool AS, Daudzai Z, Alamri AS, Alhomrani M, Aziz T (2023) Myogenesis and analysis of antimicrobial potential of silver nanoparticles (AgNPs) against pathogenic bacteria. *Molecules* 28: 637. <https://doi.org/10.3390/molecules28020637>
- Nyakudya TT, Tshabalala T, Dangarembizi R, Erlwanger KH, Ndhala AR (2020) The potential therapeutic value of medicinal plants in the management of metabolic disorders. *Molecules* 25: 2669. <https://doi.org/10.3390/molecules25112669>
- Okonok JE, Nwafor PA (2010) Antiinflammatory, analgesic and antipyretic activities of ethanolic root extract of *Croton zambesicus*. *Pak J Pharm Sci* 23: 385–392. PMID: 20884451
- Paul S, Chakraborty AK, Modak D, Sen A, Bhattacharjee S (2018) *In vivo* and *in silico* investigations of the toxicological and analgesic properties of unprocessed Aloe vera gel in experimental rat models. *Arch Biol Sci* 70: 727–735. <https://doi.org/10.2298/ABS180524036P>
- Rauf B, Alyasi S, Zahra N, Ahmad S, Sarwar A, Aziz T, Alharbi M, Alshammari A, Alasmari AF (2023) Evaluating the influence of *Aloe barbadensis* extracts on edema induced changes in C-reactive protein and interleukin-6 in albino rats through *in vivo* and *in silico* approaches. *Acta Biochim Pol* 70: 425–433. <https://doi.org/10.18388/abp.2020.6705>
- Riditid W, Saewong C, Reanmongkol W, Wongnawa M (2008) Antinociceptive activity of the methanolic extract of *Kaempferia galanga* Linn. in experimental animals. *J Ethnopharmacol* 118: 225–230. <https://doi.org/10.1016/j.jep.2008.04.002>
- Safari VZ, Kamau JK, Nthiga PM, Ngugi MP, Orinda G, Njagi EM (2016) Antipyretic, anti-inflammatory and analgesic activities of aqueous leaf extract of *Aloe volkensii* in albino mice. *J Appl Res Med Aromat Plants* 5: 1–7. <https://doi.org/10.4172/2167-0412.1000240>
- Saleem K, Aziz T, Ali Khan A, Muhammad A, Ur Rahman S, Alharbi M, Alshammari A, F Alasmari A (2023) Evaluating the *in-vitro* effects of olive oil, soya bean oil, and vitamins against oxidized ghee toxicity. *Acta Biochim Pol* 70: 305–312. <https://doi.org/10.18388/abp.2020.6549>
- Sana, Ur Rahman S, Zahid M, Khan AA, Aziz T, Iqbal Z, Ali W, Khan FF, Jamil S, Shahzad M, Alharbi M, Alshammari A (2022) Hepatoprotective effects of walnut oil and *Caralluma tuberculata* against paracetamol in experimentally induced liver toxicity in mice. *Acta Biochim Pol* 69: 871–878. <https://doi.org/10.18388/abp.2020.6387>
- Shabbir MA, Naveed M, Rehman SU, Ain NU, Aziz T, Alharbi M, Alshammari A, Alasmari AF (2023) Synthesis of iron oxide nanoparticles from *Madhuca indica* plant extract and assessment of their cytotoxic, antioxidant, anti-inflammatory, and anti-diabetic properties via different nanoinformatics approaches. *ACS Omega* 8: 33358–33366. <https://doi.org/10.1021/acsomega.3c02744>
- Sajjad A, Subhani Sajjad (2014) Aloe vera: An ancient herb for modern dentistry. A literature review. *J Dental Surgery* 14: 1–6. <https://doi.org/10.1155/2014/210463>
- Singh M, Kumar V, Singh I, Gauttam V, Kalia AN (2010) Anti-inflammatory activity of aqueous extract of *Mirabilis jalapa* Linn. leaves. *Pharmacognosy Res* 2: 364–367. <https://doi.org/10.4103/0974-8490.75456>
- Srinivasan P, Vijayakumar S, Kothandaraman S, Palani M (2018) Anti-diabetic activity of quercetin extracted from *Phyllanthus emblica* L.

- fruit: *In silico* and *in vivo* approaches. *J Pharm Anal* **8**: 109–118. <https://doi.org/10.1016/j.jpha.2017.10.005>
- Tayiba G, Mahmood UH, Najeeb U, Abid S, Muhammad HF, Tariq A, Alharbi M, Alsahammari A, Alasmari AF (2023) Optimization of pyoverdine pigment biosynthesis conditions from a locally isolated strain of *Pseudomonas aeruginosa*. *Biomass Conv Bioref*. <https://doi.org/10.1007/s13399-023-04855-w>
- Usman RB, Adamu M, Isyaku IM, Bala HA (2020) Quantitative and qualitative phytochemicals and proximate analysis of Aloe vera (*Aloe barbadensis miller*). *Int J Adv Sci Eng Inform Tech* **6**: 95–104. <https://doi.org/10.13140/RG.2.2.16689.12643>
- Valdes O, Ali A, Carrasco-Sánchez V, Cabrera-Barjas G, Duran-Lara E, Ibrahim M, Ahmad S, Moreno R, Concepción O, de la Torre AF, Abrar M, Morales-Quintana L, Abril D (2023) Ugi efficient synthesis of novel N-alkylated lipopeptides, antimicrobial properties and computational studies in *Staphylococcus aureus* via MurD antibacterial target. *Comput Biol Chem* **106**: 107932. <https://doi.org/10.1016/j.compbiolchem.2023.107932>
- Velázquez-González C, Carriño-Cortés R, Gayosso de Lucio JA, Ortiz MI, De la O Arciniega M, Altamirano-Báez DA, Ángeles LJ, Bautista-Ávila M (2014) Antinociceptive and anti inflammatory activities of *Geranium bellum* and its isolated compounds. *BMC Complement Altern Med* **14**: 506. <https://doi.org/10.1186/1472-6882-14-50>
- Wajid AS, Muhammad SA, Mujaddad UR, Azam H, Abid S, Tariq A, Alharbi M, Alsahammari A, Alasmari AF (2023) *In-vitro* evaluation of phytochemicals, heavy metals and antimicrobial activities of leaf, stem and roots extracts of *Caltha palustris* var. *alba* *J Chil Chem Soc* **68**: 5807–5812. <http://doi.org/10.4067/S0717-97072023000105807>
- Waseem M, Naveed M, Rehman SU, Makhdoom SI, Aziz T, Alharbi M, Alsahammari A, Alasmari AF (2023) Molecular characterization of *spa*, *bld*, *fmbA*, and *lukD* genes and computational modeling the multidrug resistance of *Staphylococcus* species through *Callindra harisii* silver nanoparticles. *ACS Omega* **8**: 20920–20936. <https://doi.org/10.1021/acsomega.3c01597>
- Walter EJ, Hanna-Jumma S, Carraretto M, Forni L (2016) The pathophysiological basis and consequences of fever. *Crit Care* **20**: 200. <https://doi.org/10.1186/s13054-016-1375-5>
- Zawar H, Muhammad AR, Muhammad J, Abid S, Abad AN, Sumaira N, Tariq A, Metab A, Abdulrahman A, Abdullah FA (2023) Green synthesis of silver nanoparticles prepared by leaves extract of *trigonilla foenum-graecum* and its antibacterial potential against *Escherichia coli* and *Pseudomonas aeruginosa*. *Biomass Conv Bioref*. <https://doi.org/10.1007/s13399-023-04852-z>
- Zawar H, Muhammad J, Abid S, Najeeb U, Tariq A, Metab A, Abdulrahman AL (2023) Synthesis and characterization of silver nanoparticles mediated by the *Mentha piperita* leaves extract and exploration of its antimicrobial activities. *J Chil Chem Soc* **68**. <https://www.jc-chems.com/index.php/JCCEMS/article/view/2313/609>
- Zawar H, Muhammad J, Abid S, Najeeb U, Tariq A, Metab A, Abdulrahman AL (2023) Synthesis of silver nanoparticles by aqueous extract of *Zingiber officinale* and their antibacterial activities against selected species. *Polish J Chem Tech* **25**: 23–30. <https://doi.org/10.2478/pjct-2023-0021>

Overexpressed *RAD51* promoted osteogenic differentiation by activating IGF1R/PI3K/AKT pathway in osteoblasts

Minli Qiu, Ya Xie, Liudan Tu, Minjing Zhao, Mingcan Yang, Linkai Fang and Jieruo Gu✉

Department of Rheumatology, The Third Affiliated Hospital of Sun Yat-Sen University, 600 Tianhe Road, Tianhe District, Guangzhou, 510630, China

Background: Osteoporosis (OP) is a skeleton disease induced by imbalance between osteoblast and osteoclast. Osteogenic differentiation of osteoblasts is of great importance, and the regulatory mechanisms are urgent to be studied. **Methods:** Differentially expressed genes were screened from microarray profile related to OP patients. The dexamethasone (Dex) was used to induce osteogenic differentiation of MC3T3-E1 cells. MC3T3-E1 cells were exposed to microgravity environment to mimic OP model cells. Alizarin Red staining and alkaline phosphatase (ALP) staining were used to evaluate the role of *RAD51* in osteogenic differentiation of OP model cells. Furthermore, qRT-PCR and western blot were applied to determine expression levels of genes and proteins. **Results:** *RAD51* expression was suppressed in OP patients and model cells. Alizarin Red staining and ALP staining intensity, the expression of osteogenesis-related proteins including runt-related transcription factor 2 (Runx2), osteocalcin (OCN), and collagen type I alpha1 (COL1A1) were increased by over-expressed *RAD51*. Furthermore, *RAD51* related genes were enriched in IGF1 pathway, and up-regulated *RAD51* activated IGF1 pathway. The effects of oe-*RAD51* on osteogenic differentiation and IGF1 pathway were attenuated by IGF1R inhibitor BMS754807. **Conclusions:** Overexpressed *RAD51* promoted osteogenic differentiation by activating IGF1R/PI3K/AKT signaling pathway in OP. *RAD51* could be a potential therapeutic marker for OP.

Keyword: osteoporosis, osteogenic differentiation, *RAD51*, IGF1R/PI3K/AKT

Received: 21 October, 2021; revised: 11 January, 2022; accepted: 21 March, 2022; available on-line: 16 January, 2023

✉e-mail: gujieruo@163.com

Acknowledgements of Financial Support: This study was supported by National Natural Science Foundation of China, No.82071587.

Abbreviations: BMD, bone mineral density; OP, Osteoporosis;

main treatment for OP. However, the emerging side effects neutralized the clinical outcome. For instance, bisphosphonates may lead to mandibular osteonecrosis; hormones are associated with an increased risk of cardiovascular disease; the composition of traditional Chinese medicine is complex and its efficacy is not exact. Therefore, it is of great significance to find safer and more effective treatments (Miller, 2016; Liu *et al.*, 2018).

The basic process of bone formation is divided into bone formation and bone resorption, which are reflected as the dynamic balance between osteoblasts and osteoclasts at the cellular level (Chen *et al.*, 2018; Li *et al.*, 2019). The processes of osteogenic and osteoclastic differentiation are influenced by a variety of cytokines, cellular signaling pathways, and intercellular communication (Muruganandan *et al.*, 2020; Yang *et al.*, 2020). In recent years, the researches have attached great attention to on its complex molecular biological mechanism

Gene therapy, as a rising therapeutic method in recent years, can be targeted for gene defects and diseased tissues of diseases, direct to the lesions, with little side effects (Shan *et al.*, 2019; Fei *et al.*, 2020; Gu *et al.*, 2020; Bonnet *et al.*, 2019). The human *RAD51* gene located at 15q15.1 has been found to be aberrant expressed in OP through microarray analyses. The *RAD51* protein interacts with the ssDNA-binding protein replication protein A (RPA) and *RAD52*, and is involved in DNA homologous pairing and chain transfer (Bonilla *et al.*, 2020; Wasling & Esashi, 2021). Studies have shown that *RAD51* is abnormally expressed in breast cancer (Cruz *et al.*, 2018), cervical cancer (Sun *et al.*, 2020), pancreatic cancer (Zhang *et al.*, 2019), prostate cancer (Maranto *et al.*, 2018), esophageal cancer (Wang *et al.*, 2019), and is associated with poor prognosis (Zhang *et al.*, 2019; Zhang *et al.*, 2019; Xue, *et al.*, 2019). What's more, bone marrow mesenchymal stem cell (BMMSC)-derived exosomes restore radiation-induced bone loss by alleviating DNA and oxidative stress damage (Zuo *et al.*, 2019). Hence, we suspected that *RAD51* may be a novel target for OP.

Thereby, this study aimed to elucidate the regulatory mechanisms of *RAD51* in osteogenic differentiation. These findings may help to uncover newfound diagnostic biomarkers for OP.

MATERIALS AND METHODS

Bioinformatics

A microarray profile GSE100609 associated with genes of Indian post menopausal female and non-OP post menopausal female was downloaded from the Gene Expression Omnibus (GEO) database (<http://www.>

INTRODUCTION

Osteoporosis (OP) has become one of the epidemic diseases affecting people's quality of life due to its diverse etiology and complex molecular mechanism. OP is characterized by decreased bone mass, destroyed microstructure of bone tissue, increased bone brittleness, as well as high rate of fracture (Lupsa & Insogna, 2015).

Currently, bone mineral density (BMD) is the accepted gold standard for the diagnosis of OP, but due to its low sensitivity, many patients with potential fracture risk will be missed (Lupsa & Insogna, 2015; Black & Rosen, 2016). At present, systemic drug therapy is the

ncbi.nlm.nih.gov/geo). R language was used to analyse the dataset, then limma package was applied to identify all differentially expressed genes (DGEs) of OP group ($n=4$) and non-osteoporotic group ($n=4$). Finally DGEs in this study were screened under the standard of $P<0.05$ and $|\log_2FC| \geq 1.5$, and the heatmap was drawn by heatmap package. Pearson correlation and KEGG analysis were also carried out to analyse DGEs.

Subjects

Total number of 80 volunteers (healthy controls, $n=40$; OP patients, $n=40$) in this study were from The Third Affiliated Hospital of Sun Yat-Sen University. All the volunteers have signed the informed consent. This study was approved by Ethics Committee of The Third Affiliated Hospital of Sun Yat-Sen University. Fasting blood was collected for the follow-up experimental studies.

Isolation of human monocytes

Peripheral blood samples were collected from patients with osteoporotic fractures in the case group and healthy controls, and monocytes were obtained by density gradient centrifugation using sodium citrate anticoagulation tube (Histopaque-1077; Sigma, New Jersey, USA). Then monocytes were incubated at 37°C under 5% CO_2 in a humidified atmosphere with DMEM (pH 7.2).

Cell culture

Osteoblastic MC3T3-E1 cells were purchased from the Cell Bank of the Chinese Academy of Sciences (Shanghai, China). MC3T3-E1 cells were incubated in α -MEM medium (Gibco, Grand Island, USA) containing 10% fetal bovine serum (FBS, Gibco, Grand Island, USA) in 5% CO_2 at 37°C .

OP model cell establishment

2D Rotating Wall Vessel Bioreactor (RWVB) clinostat was used to simulate microgravity. 1×10^5 of MC3T3-E1 cells were seeded on cell climbing pieces. 1×10^5 MC3T3-E1 cells were seeded on coverslips. After culture for 24 h, the climbing pieces were placed in a box 12.5 mm away from the rotational axis. After the air bubbles were removed, the chambers were fixed in the clinostat and rotated around a horizontal axis at 28 rpm for 15 min. The vertical rotation groups were used as controls. The rotation process was taken at 37°C under 5% CO_2 .

Induction of osteogenic differentiation

Osteoblastic MC3T3-E1 cells were seeded into 6-well plates at a density of 5×10^4 cells per well, and cultured with 100 nM dexamethasone (Dex; Sigma, Merck, USA), 10 nM beta-glycerophosphate (Sigma, Merck, USA) along with 50 mg/mL ascorbic acid (Sigma, Merck, USA). The mixed medium were replenished every 3 days. Cells treated with Dex was deemed as negative control (NC), and microgravity stimulated cells treated with Dex were named as OP group.

Cell transfection

To detect the role of *RAD51* in osteogenic differentiation, over-expressed *RAD51* (oe-*RAD51*) vector (GenePharma, Shanghai, China) was transfected into OP model cells using Lipofectamine3000 (Invitrogen, Carlsbad, USA) according to instruction manuals. The transfection efficiency was verified by qRT-PCR.

qRT-PCR

Total RNA was isolated from blood sample, monocytes, and MC3T3-E1 cells by Trizol method (Takara, Kyoto, Japan) and measured at the absorbance of 260 nm (NanoDrop 2000; Thermo Fisher, MA, USA). Then, quantified RNA were converted into complementary DNA by the reverse transcription kit (TaKaRa, Kyoto, Japan) according to manufacturer's protocols. RT-PCR was then performed using Power SYBR® Green PCR Master Mix (Takara) on the ABI StepOnePlus System (Applied Biosystems, Warrington, UK). GAPDH was used as a housekeeping gene. The relative mRNA expressions were calculated using the $2^{-\Delta\Delta Ct}$ method. Primer sequences were listed in Table 1.

Table 1. Primer sequences

Primer	Sequence
RAD51	forward 5'-TGGGTTTCACCACTGCAACT-3'
	reverse 5'-AAACATCGCTGCTCCATCCA-3'
Runx2	forward 5'-TAAGATGGGAGGGCGTGAGA-3'
	reverse 5'-GTCGAGAGGATGAAGGAGCG-3'
OCN	forward 5'-CACTCCTCGCCCTATTGGC-3'
	reverse 5'-CCCTCTGCTTGGACACAAAG-3'
COL1A1	forward 5'-TGGATACTGGGAGGGTGAGG-3'
	reverse 5'-CCCTTACCTGAGATGGGGGA-3'
GAPDH	forward 5'-CGAGCCACATCGCTCAGACA-3'
	reverse 5'-GTGGTGAAGACGCCAGTGGGA-3'

Alizarin red staining and alkaline phosphatase (ALP) staining

OP model cells were seeded into 12-well plates, and fixed with 4% paraformaldehyde (Sigma, New Jersey, USA) for 15 min, then washed with PBS for three times. For alizarin red staining, cells were washed with distilled water, and incubated with 0.5% solution of alizarin red solutions for 30 min at room temperature. Afterwards, the relative values of alizarin red staining were measured at 560 nm using a microplate reader (ELX808; BioTek). The readings of all samples were normalized to the alizarin red staining intensity. For ALP staining, an ALP Staining Kit (Beyotime, Nantong, China) was used after the cells were washed with distilled water for three times. The stained cells were photographed by a microscope (Zeiss, Oberkochen, Germany), and calculated at the absorbance of 562 nm using microplate reader (BioTek, Winooski, USA).

Western blot assay

OP model cells were lysed in a RIPA lysis buffer (Beyotime, Nantong, China) for 30 min at 4°C . The supernate was harvested by centrifuging at $12000 \times g$ for 5 min at 4°C . The proteins were separated by 10% SDS-PAGE and transferred to polyvinylidene fluoride membranes (Millipore, MA, USA). Then the membranes were blocked with 5% skimmed milk for 1 h, and then incubated with primary antibodies, such as anti-Runx2 (1/1000, ab236639), anti-OCN (1/1000, ab133612), anti-COL1A1 (1/1000, ab34710), anti-IGF1R (1/1000, ab182408), and anti-p-IGF1R (1/1000, ab39398), anti-PI3K (1/1000, ab32089), anti-p-PI3K (1/1000, ab182651), anti-AKT (1/10000, ab179463),

anti-p-AKT (1/1000, ab38449), and GADPH (1/1000, ab8245) at 4°C overnight, and then with secondary antibody (1/5000, ab6721) for 1 h at room temperature. The Infrared Imaging System (LI-COR, Lincoln, USA) was used to scan and analyze the images. All antibodies were purchased from Abcam company (Cambridge, England).

Statistical analysis

Statistical analysis was performed with GraphPad Prism 8.3 (GraphPad, San Diego, USA). All data were expressed as mean \pm S.D. Statistical comparisons were performed by using the student's t-test between two groups and one-way ANOVA followed by Tukey's test for multiple groups. *P* values less than 0.05 were considered as statistically significant.

RESULTS

RAD51 expression was decreased in OP

Firstly, we identified prominently expressed DEGs through the bioinformatic analysis, and the results showed that total number of 107 genes were abnormally down-regulated genes and 42 up-regulated, compared with healthy controls, among which *RAD51* expression was most significantly suppressed (Fig. 1A). To further verify the roles of *RAD51* in OP, we determined the expression of *RAD51* in blood samples of OP patients. As shown in Fig. 1B, the mRNA expression of *RAD51* was significantly decreased in blood samples of OP patients compared with healthy controls (Fig. 1B). Furthermore, *RAD51* expression levels were also downregulated in isolated monocytes of patients with OP (Fig. 1C).

Osteogenic differentiation of OP model cells was weakened

Then, Dex was used to induce osteogenic differentiation of MC3T3-E1 cells, and osteogenic differentiation ability of OP model cells were measured. After microgravity stimulation, both alizarin red and ALP intensity of MC3T3-E1 cells were dramatically decreased, indicating that mineralization levels of OP model cells were declined (Fig. 2A–B). Meanwhile, both protein and mRNA expression levels of osteogenesis-related proteins including Runx2, OCN, and COL1A1 were markedly suppressed in OP model cells (Fig. 2C–E). Furthermore, *RAD51* was also suppressed in OP model cells (Fig. 2F). Hence, osteogenic differentiation of OP model cells was significantly weakened.

Up-regulated *RAD51* promoted osteogenic differentiation of OP model cells

Next, whether *RAD51* could modulate osteogenic differentiation of MC3T3-E1 cells was investigated. After *RAD51* was prominently up-regulated in MC3T3-E1 cells transfected with overexpressed *RAD51* vectors (Fig. 3A), alizarin red staining and ALP staining intensity of OP model cells were dramatically increased (Fig. 3B), so did the mRNA and protein expression levels of Runx2, OCN, and COL1A1 (Fig. 3C–D).

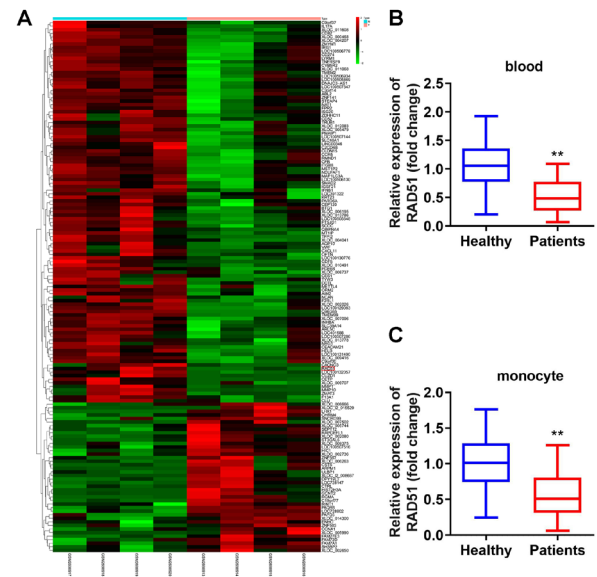


Figure 1. *RAD51* was suppressed in OP.

(A) heatmap consisting of post menopausal female and non-OP post menopausal female genes. The red represents the up-regulated genes and the green represents the down-regulated genes. *RAD51* expression detected by qRT-PCR of (B) blood and (C) monocytes of OP patients compared with healthy controls. ***P*<0.01. OP: osteoporosis.

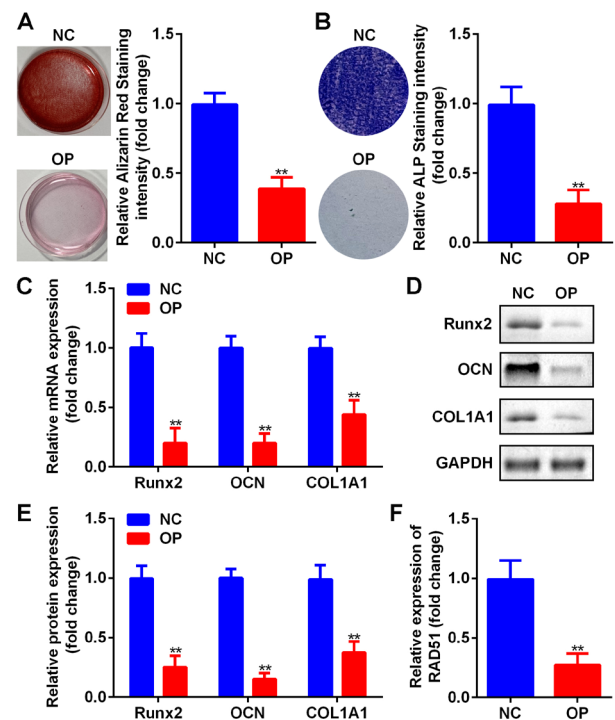


Figure 2. Osteoblast differentiation of OP model cells.

(A) Alizarin red staining images and intensity of MC3T3-E1 cells before and after microgravity stimulation. (B) ALP staining images and intensity of MC3T3-E1 cells before and after microgravity stimulation. (C) mRNA expression levels of Runx2, OCN, and COL1A1 in OP model cells measured by qRT-PCR. (D) Protein bands of Runx2, OCN, and COL1A1 in OP model cells measured by western blot. (E) Protein quantitative analysis of Runx2, OCN, and COL1A1. (F) *RAD51* expression detected by qRT-PCR of OP model cells compared with control cells. ***P*<0.01.

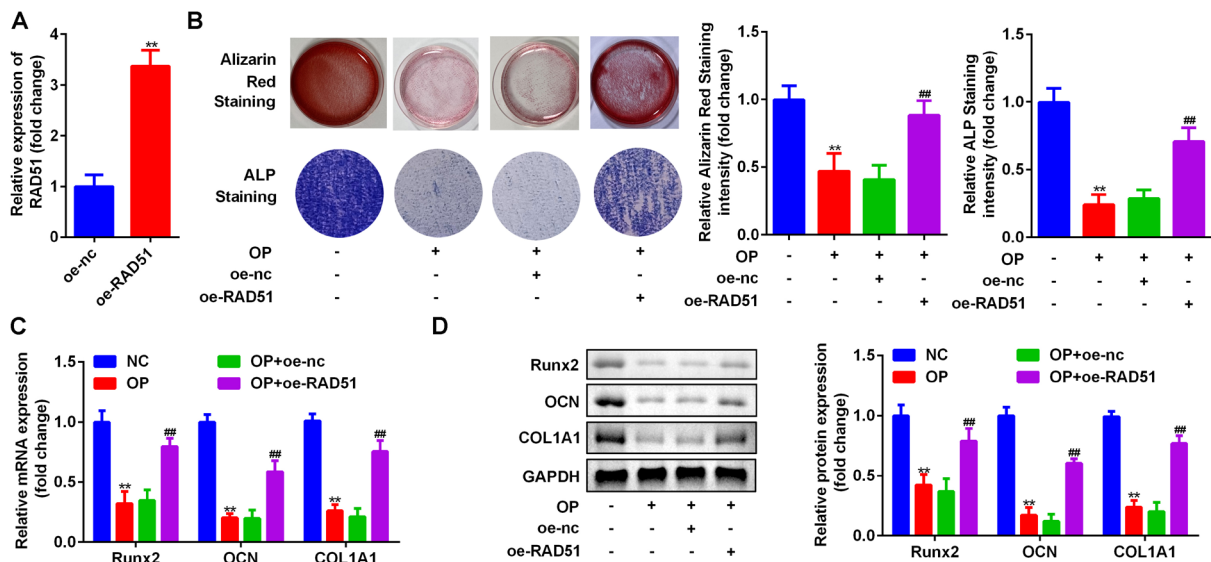


Figure 3. Up-regulated *RAD51* promoted osteogenic differentiation of OP model cells.

(A) Transfection efficiency of *RAD51* detected by qRT-PCR. (B) Alizarin red staining and ALP images and intensity of OP model cells transfected with oe-*RAD51* vectors. (C–D) Expression levels of Runx2, OCN, and COL1A1 measured by qRT-PCR and western blot of OP model cells. ** $P < 0.01$, compared with oe-nc and NC group. ## $P < 0.01$, compared with OP+ oe-nc group. oe: overexpressed.

Over-expressed *RAD51* promoted osteogenic differentiation of OP model cells by activating IGF1R/PI3K/AKT signaling pathway

Subsequently, molecular mechanism of *RAD51* regulating osteoporosis was then studied. Pearson correlation analysis between *RAD51* expression levels and other genes expression levels suggested that most aberrant expressed genes identified were positively related to *RAD51* (Fig. 4A). Subsequently, KEGG analysis demonstrated that genes related to *RAD51* were enriched in ten pathways, including IGF1 pathway, EGF receptor signaling pathway, C-MYB transcription factor network and so on. (Fig. 4B). Interestingly, downstream proteins in IGF1 pathway including phosphorylated IGF1R, PI3K, and AKT were up-regulated induced by oe-*RAD51*, suggesting the activation of IGF1R/PI3K/AKT signaling pathway (Fig. 5A). Meanwhile, alizarin red and ALP stained cells as well as expression of Runx2, OCN, and COL1A1 were markedly increased after *RAD51* was overexpressed in OP model cells (Fig. 5B–D). Furthermore, BMS754807, an IGF1R inhibitor, attenuated the effects of oe-*RAD51* on mineral intensity and ALP activity number and the expression of Runx2, OCN, and COL1A1 (Fig. 5B–D).

DISCUSSION

OP has become one of the epidemic diseases affecting people's quality of life due to its diverse etiology and complex molecular mechanisms (Black & Rosen, 2016). In our study, *RAD51* was down-regulated in OP patients as well as OP model cells. Over-expressed *RAD51* promoted osteoblast differentiation by activating IGF1R/PI3K/AKT signaling pathway.

Recently evidence suggested that various aberrant expressed genes are involved in osteogenesis. For instance, osteogenic differentiation can be inhibited by blocking the correlation between RANKL and its only known receptor RANK (Bonnet *et al.*, 2019). Likewise, SOST secreted sclerostin to promote bone formation, thus alleviating the progression of OP (Shan *et al.*, 2019; Weivoda *et al.*, 2017). Our data suggested that *RAD51* was down-regulated in both OP patients and OP model cells.

Over the past decade, specific biochemical markers associated with metabolic bone disease have been identified and described to determine whether there is an imbalance in bone metabolism by measuring biochemical markers of bone turnover (Greenblatt *et al.*, 2017; Szulc, 2018). Our

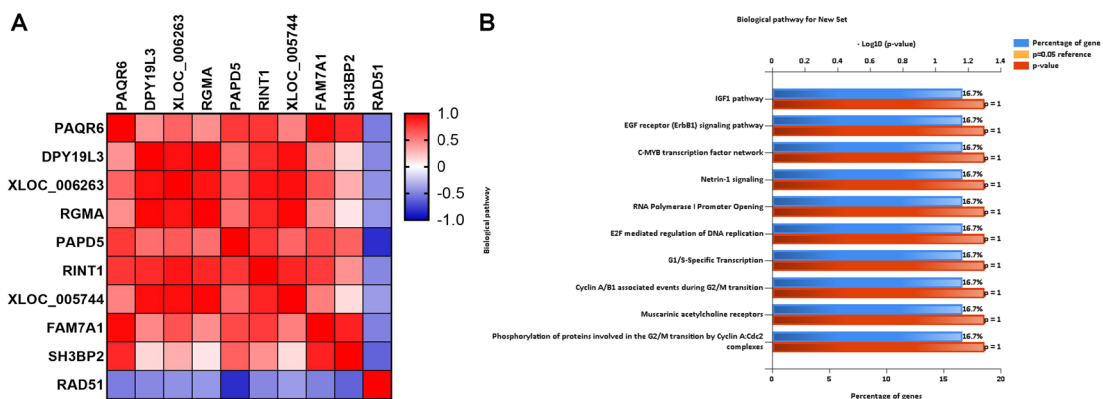


Figure 4. *RAD51* related genes were enriched in several pathways.

(A) Pearson correlation analysis between *RAD51* gene and other genes related with OP. (B) KEGG analysis of enriched genes associated with *RAD51* gene.

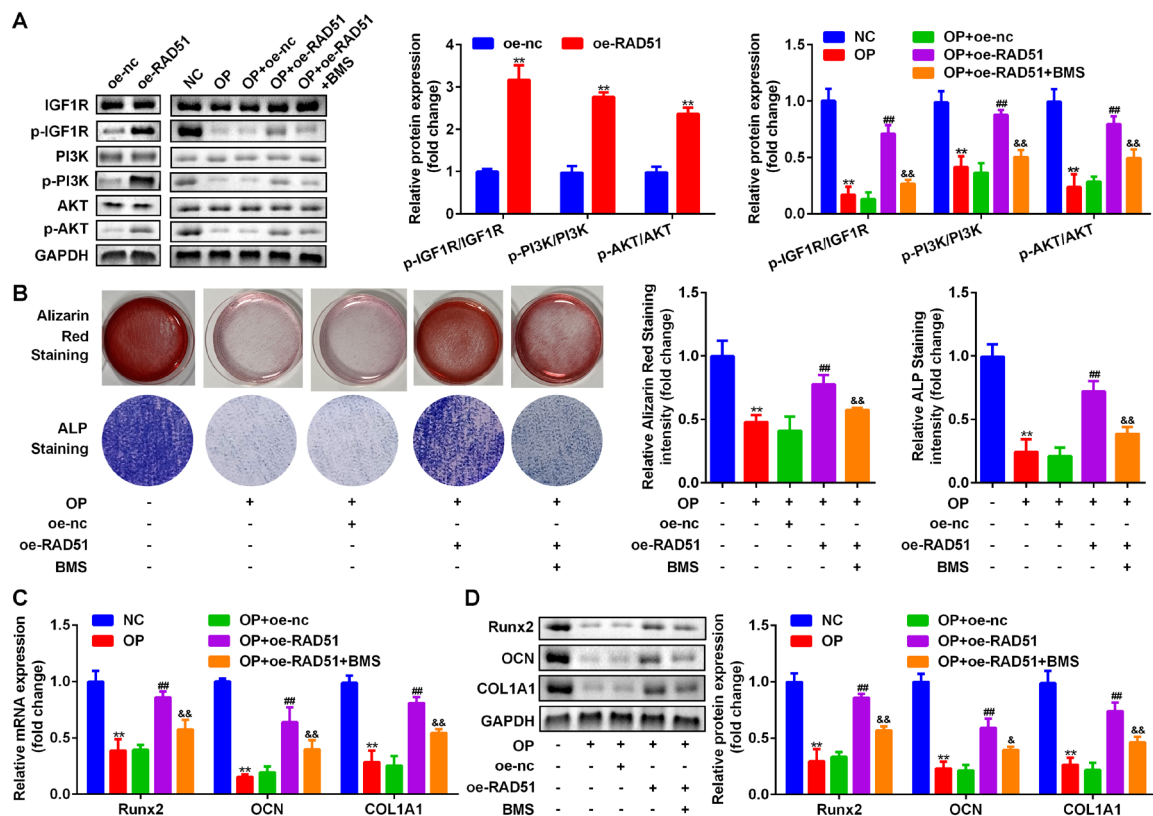


Figure 5. Over-expressed *RAD51* promoted osteogenic differentiation of OP model cells by activating IGF1R/PI3K/AKT signaling pathway.

(A) Protein expression of IGF1R, PI3K, AKT and their phosphorylated types measured by western blot assay. (B) Alizarin red staining and ALP staining images and intensity of OP model cells. (C) mRNA expression levels of Runx2, OCN, and COL1A1 measured by qRT-PCR. (D) Protein bands and quantitative analysis of Runx2, OCN, and COL1A1 measured by western blot. ** $P < 0.01$, compared with oe-nc and NC group. ## $P < 0.01$, compared with OP+ oe-nc group. & $P < 0.05$, && $P < 0.01$, compared with OP+ oe-RAD51 group.

study showed that osteogenic differentiation was promoted as represented by higher Runx2, OCN and COL1A1 secretion. Runx2, OCN and COL1A1 were biochemical markers of OP widely studied in various studies. Runx2 is an osteoblast differentiation specific transcription factor which can regulate the transcription of many genes, and is significant for the differentiation of stromal cells into osteoblast lineage (Komori, 2018). Besides, Runx2 is reported to promote secretion of proteins including OPN, OCN, and collagen type I alpha1 (Yin *et al.*, 2019; Lu *et al.*, 2019; Komori, 2020). Furthermore, bone matrix mineralization is recognized as an indicator of osteogenic differentiation (Li *et al.*, 2018). In present study, the osteogenic differentiation, and the expression of *RAD51* of MC3T3-E1 cells was significantly suppressed by microgravity treatment. What's more, up-regulated *RAD51* promoted osteogenic differentiation of OP model cells, which was in line with previous studies (Shan *et al.*, 2019; Bonnet *et al.*, 2019; Weivoda *et al.*, 2017).

IGF-1 is known to play an anabolic role in bone (Fraser *et al.*, 2018). Decreased IGF-1 levels are associated with an increased risk of bone fragility and fracture (Yan *et al.*, 2016). IGF1R is a homodimer of two protein subunits consisting of α and β chains, and is associated with bone and glucose metabolism and is a key mediator of glucose and bone metabolism disorders (Xian *et al.*, 2012). The conformation of IGF1R is altered by binding to the ligand IGF-1, which is then fully activated by ligand-independent autophosphorylation. This induces phosphorylation of various substrates, such as insulin receptor substrates and Shc proteins, and triggers specific signaling cascades, such

as the PI3K/AKT and Ras/MAPK pathways (Yoshida & Delafontaine, 2020; Vitiello *et al.*, 2019).

In recent years, many studies have explored the influence of some factors on BMMSC through PI3K/AKT signaling pathway (Shen *et al.*, 2019). For instance, macrophage MSR1 contributed to osteogenic differentiation of BMMSC through PI3K/AKT pathway (Zhao *et al.*, 2020). Fang *et al.* found that calyculin stimulates the osteogenic differentiation of rat calvarial osteoblasts by activating the IGF1R/PI3K/Akt signaling pathway (Fang *et al.*, 2019). Furthermore, our data demonstrated that the activation of IGF1R/PI3K/AKT signaling pathway induced by over-expressed *RAD51* was suppressed by IGF1R inhibitor, so did the osteogenic differentiation. These results indicated that up-regulated *RAD51* promoted osteogenic differentiation via activating IGF1R/PI3K/AKT signaling pathway.

CONCLUSION

In a word, overexpressed *RAD51* promoted osteogenic differentiation of osteoblasts via activating IGF1R/PI3K/AKT signaling pathway.

Declarations

Acknowledgments. Not Applicable.

Ethical approval. This study protocol was approved by the Ethics Committee of The Third Affiliated Hospital of Sun Yat-Sen University.

Informed consent. Informed consent was obtained from all individual participants included in the study.

REFERENCES

- Black DM, Rosen CJ (2016) Clinical Practice. Postmenopausal Osteoporosis. *N Engl J Med* **74**: 254–262. <https://doi.org/10.1056/NEJMc1513724>
- Bonilla B, Hengel SR, Grundy MK, Bernstein KA (2020) RAD51 gene family structure and function. *Annu Rev Genet* **54**: 25–46. <https://doi.org/10.1146/annurev-genet-021920-092410>
- Bonnet N, Bourgoin L, Biver E, Douni E, Ferrari S (2019) RANKL inhibition improves muscle strength and insulin sensitivity and restores bone mass. *J Clin Invest* **129**: 3214–3223. <https://doi.org/10.1172/JCI125915>
- Chen X, Wang Z, Duan N, Zhu G, Schwarz EM, Xie C (2018) Osteoblast-osteoclast interactions. *Connect Tissue Res* **59**: 99–107. <https://doi.org/10.1080/03080207.2017.1290085>
- Cruz C, Castroviejo-Bermejo M, Gutiérrez-Enríquez S, Llop-Guevara A, Ibrahim YH, Gris-Oliver A, Bonache S, Moranchó B, Bruna A, Rueda OM, Lai Z, Polanska UM, Jones GN, Kristel P, de Bustos L, Guzman M, Rodríguez O, Grueso J, Montalbán G, Caratú G, Mancuso F, Fasani R, Jiménez J, Howat WJ, Dougherty B, Vivancos A, Nuciforo P, Serres-Créixams X, Rubio IT, Oaknin A, Cadogan E, Barrett JC, Caldas C, Baselga J, Saura C, Cortés J, Arribas J, Jonkers J, Diez O, O'Connor MJ, Balmaña J, Serra V (2018) RAD51 foci as a functional biomarker of homologous recombination repair and PARP inhibitor resistance in germline BRCA-mutated breast cancer. *Ann Oncol* **29**: 1203–1210. <https://doi.org/10.1093/annonc/mdy099>
- Fang Y, Xue Z, Zhao L, Yang X, Yang Y, Zhou X, Feng S, Chen K (2019) Calycosin stimulates the osteogenic differentiation of rat calvarial osteoblasts by activating the IGF1R/PI3K/Akt signaling pathway. *Cell Biol Int* **43**: 323–332. <https://doi.org/10.1002/cbin.11102>
- Fei Q, Li X, Lin J, Yu L, Yang Y (2020) Identification of aberrantly expressed long non-coding RNAs and nearby targeted genes in male osteoporosis. *Clin Interv Aging* **15**: 1779–1792. <https://doi.org/10.2147/CIA.S271689>
- Frazer J, Lie D, Bartlett P, McGrath JJ (2018) Insulin-like Growth Factor 1 (IGF-1) as a marker of cognitive decline in normal ageing: A review. *Ageing Res Rev* **42**: 14–27. <https://doi.org/10.1016/j.arr.2017.12.002>
- Greenblatt MB, Tsai JN, Wein MN (2017) Bone turnover markers in the diagnosis and monitoring of metabolic bone disease. *Clin Chem* **63**: 464–474. <https://doi.org/10.1373/clinchem.2016.259085>
- Gu Z, Xie D, Huang C, Ding R, Zhang R, Li Q, Lin C, Qiu Y (2020) MicroRNA-497 elevation or LRG1 knockdown promotes osteoblast proliferation and collagen synthesis in osteoporosis via TGF-beta1/Smads signalling pathway. *J Cell Mol Med* **24**: 12619–12632. <https://doi.org/10.1111/jcmm.15826>
- Komori T (2020) Molecular mechanism of Runx2-dependent bone development. *Mol Cells* **43**: 168–175. [10.14348/molcells.2019.0244](https://doi.org/10.14348/molcells.2019.0244)
- Komori T (2018) Runx2, an inducer of osteoblast and chondrocyte differentiation. *Histochem Cell Biol* **149**: 313–23. <https://doi.org/10.1007/s00418-018-1640-6>
- Li J, Li X, Liu D, Hamamura K, Wan Q, Na S, Yokota H, Zhang P (2019) eIF2alpha signaling regulates autophagy of osteoblasts and the development of osteoclasts in OVX mice. *Cell Death Dis* **10**: 921. <https://doi.org/10.1038/s41419-019-2159-z>
- Li X, Zheng Y, Zheng Y, Huang Y, Zhang Y, Jia L, Li W (2018) Circular RNA CDR1as regulates osteoblastic differentiation of periodontal ligament stem cells via the miR-7/GDF5/SMAD and p38 MAPK signaling pathway. *Stem Cell Res Ther* **9**: 232. <https://doi.org/10.1186/s13287-018-0976-0>
- Liu GF, Wang ZQ, Liu L, Zhang BT, Miao YY, Yu SN (2018) A network meta-analysis on the short-term efficacy and adverse events of different anti-osteoporosis drugs for the treatment of postmenopausal osteoporosis. *J Cell Biochem* **119**: 4469–4481. <https://doi.org/10.1002/jcb.26550>
- Lu X, Lu J, Zhang L, Xu Y (2019) Effect of ANGPTL7 on proliferation and differentiation of MC3T3-E1 cells. *Med Sci Monit* **25**: 9524–9530. <https://doi.org/10.12659/MSM.918333>
- Lupsa BC, Insogna K (2015) Bone health and osteoporosis. *Endocrinol Metab Clin North Am* **44**: 517–530. [10.1016/j.ecl.2015.05.002](https://doi.org/10.1016/j.ecl.2015.05.002)
- Maranto C, Udhane V, Hoang DT, Gu L, Alexeev V, Malas K, Cardenas K, Brody JR, Rodeck U, Bergom C, Iczkowski KA, Jacobsohn K, See W, Schmitt SM, Nevalainen MT (2018) STAT5A/B Blockade sensitizes prostate cancer to radiation through inhibition of RAD51 and DNA repair. *Clin Cancer Res* **24**: 1917–1931. <https://doi.org/10.1158/1078-0432.CCR-17-2768>
- Miller PD (2016) Management of severe osteoporosis. *Expert Opin Pharmacother* **17**: 473–488. <https://doi.org/10.1517/14656566.2016.124856>
- Muruganandan S, Ionescu AM, Sinal CJ (2020) At the crossroads of the adipocyte and osteoclast differentiation programs: future therapeutic perspectives. *Int J Mol Sci* **21**: 2277. <https://doi.org/10.3390/ijms21072277>
- Shan Y, Wang L, Li G, Shen G, Zhang P, Xu Y (2019) Methylation of bone SOST impairs SP7, RUNX2, and ERalpha transactivation in patients with postmenopausal osteoporosis. *Biochem Cell Biol* **97**: 369–374. <https://doi.org/10.1139/bcb-2018-0170>
- Shen WC, Lai YC, Li LH, Liao K, Lai HC, Kao SY, Wang J, Chuong CM, Hung SC (2019) Methylation and PTEN activation in dental pulp mesenchymal stem cells promotes osteogenesis and reduces oncogenesis. *Nat Commun* **10**: 2226. <https://doi.org/10.1038/s41467-019-10197-x>
- Sun H, Fan G, Deng C, Wu L (2020) miR-4429 sensitized cervical cancer cells to irradiation by targeting RAD51. *J Cell Physiol* **235**: 185–193. <https://doi.org/10.1002/jcp.28957>
- Szulc P (2018) Bone turnover: Biology and assessment tools. *Best Pract Res Clin Endocrinol Metab* **32**: 725–738. <https://doi.org/10.1016/j.beem.2018.05.003>
- Vitiello PP, Cardone C, Martini G, Ciardiello D, Belli V, Matrone N, Barra G, Napolitano S, Della Corte C, Turano M, Furia M, Troiani T, Morgillo F, De Vita F, Ciardiello F, Martinelli E (2019) Receptor tyrosine kinase-dependent PI3K activation is an escape mechanism to vertical suppression of the EGFR/RAS/MAPK pathway in KRAS-mutated human colorectal cancer cell lines. *J Exp Clin Cancer Res* **38**: 41. <https://doi.org/10.1186/s13046-019-1035-0>
- Wang J, Che W, Wang W, Su G, Zhen T, Jiang Z (2019) CDKN3 promotes tumor progression and confers cisplatin resistance via RAD51 in esophageal cancer. *Cancer Manag Res* **11**: 3253–3264. <https://doi.org/10.2147/CMAR.S193793>
- Wassong IE, Esashi F (2021) RAD51: Beyond the break. *Semin Cell Dev Biol* **113**: 38–46. <https://doi.org/10.1016/j.semedb.2020.08.010>
- Weivoda MM, Youssef SJ, Oursler MJ (2017) Sclerostin expression and functions beyond the osteocyte. *Bone* **96**: 45–50. <https://doi.org/10.1016/j.bone.2016.11.024>
- Xian L, Wu X, Pang L, Lou M, Rosen CJ, Qiu T, Crane J, Frassica F, Zhang L, Rodriguez JP, Jia X, Yakar S, Xuan S, Efstratiadis A, Wan M, Cao X (2012) Matrix IGF-1 maintains bone mass by activation of mTOR in mesenchymal stem cells. *Nat Med* **18**: 1095–10101. <https://doi.org/10.1038/nm.2793>
- Xue Y, Tong L, LiuAnwei Liu F, Liu A, Zeng S, Xiong Q, Yang Z, He X, Sun Y, Xu C (2019) Tumorinfiltrating M2 macrophages driven by specific genomic alterations are associated with prognosis in bladder cancer. *Oncol Rep* **42**: 581–594. <https://doi.org/10.3892/or.2019.7196>
- Yan J, Herzog JW, Tsang K, Brennan CA, Bower MA, Garrett WS, Sartor BR, Aliprantis AO, Charles JF (2016) Gut microbiota induce IGF-1 and promote bone formation and growth. *Proc Natl Acad Sci U S A* **113**: E7554–E7563. <https://doi.org/10.1073/pnas.1607235113>
- Yang JX, Xie P, Li YS, Wen T, Yang XC (2020) Osteoclast-derived miR-23a-5p-containing exosomes inhibit osteogenic differentiation by regulating Runx2. *Cell Signal* **70**: 109504. <https://doi.org/10.1016/j.cellsig.2019.109504>
- Yin N, Zhu L, Ding L, Yuan J, Du L, Pan M, Xue F, Xiao H (2019) MiR-135-5p promotes osteoblast differentiation by targeting HIF1AN in MC3T3-E1 cells. *Cell Mol Biol Lett* **24**: 51. <https://doi.org/10.1186/s11658-019-0177-6>
- Yoshida T, Delafontaine P (2020) Mechanisms of IGF-1-mediated regulation of skeletal muscle hypertrophy and atrophy. *Cells-Basel* **9**: 1970. <https://doi.org/10.3390/cells9091970>
- Zhang X, Ma N, Yao W, Li S, Ren Z (2019) RAD51 is a potential marker for prognosis and regulates cell proliferation in pancreatic cancer. *Cancer Cell Int* **19**: 356. <https://doi.org/10.1186/s12935-019-1077-6>
- Zhao SJ, Kong FQ, Jie J, Li Q, Liu H, Xu AD, Yang YQ, Jiang B, Wang DD, Zhou ZQ, Tang PY, Chen J, Wang Q, Zhou Z, Chen Q, Yin GY, Zhang HW, Fan J (2020) Macrophage MSR1 promotes BMSC osteogenic differentiation and M2-like polarization by activating PI3K/AKT/GSK3beta/beta-catenin pathway. *Theranostics* **10**: 17–35. <https://doi.org/10.7150/thno.36930>
- Zuo R, Liu M, Wang Y, Li J, Wang W, Wu J, Sun C, Li B, Wang Z, Lan W, Zhang C, Shi C, Zhou Y (2019) BM-MSC-derived exosomes alleviate radiation-induced bone loss by restoring the function of recipient BM-MSCs and activating Wnt/beta-catenin signaling. *Stem Cell Res Ther* **10**: 30. <https://doi.org/10.1186/s13287-018-1121-9>



OPEN ACCESS

EDITED BY
Maurycy Daroch,
Peking University, China

REVIEWED BY
Małgorzata Ryngajtto,
Lodz University of Technology, Poland
Agnieszka Zmienko,
Polish Academy of Sciences, Poland

*CORRESPONDENCE
Michał Rurek,
✉ rurek@amu.edu.pl

RECEIVED 26 July 2024
ACCEPTED 15 October 2024
PUBLISHED 25 October 2024

CITATION
Rurek M and Smolibowski M (2024)
Variability of plant transcriptomic
responses under stress acclimation: a
review from high throughput studies.
Acta Biochim. Pol. 71:13585.
doi: 10.3389/abp.2024.13585

COPYRIGHT
© 2024 Rurek and Smolibowski. This is
an open-access article distributed
under the terms of the Creative
Commons Attribution License (CC BY).
The use, distribution or reproduction in
other forums is permitted, provided the
original author(s) and the copyright
owner(s) are credited and that the
original publication in this journal is
cited, in accordance with accepted
academic practice. No use, distribution
or reproduction is permitted which does
not comply with these terms.

Variability of plant transcriptomic responses under stress acclimation: a review from high throughput studies

Michał Rurek* and Mikołaj Smolibowski

Department of Molecular and Cellular Biology, Institute of Molecular Biology and Biotechnology,
Faculty of Biology, Adam Mickiewicz University, Poznań, Poland

Plant transcriptomes are complex entities shaped spatially and temporally by a multitude of stressors. The aim of this review was to summarize the most relevant transcriptomic responses to selected abiotic (UV radiation, chemical compounds, drought, suboptimal temperature) and biotic (bacteria, fungi, viruses, viroids) stress conditions in a variety of plant species, including model species, crops, and medicinal plants. Selected basic and applicative studies employing RNA-seq from various sequencing platforms and single-cell RNA-seq were involved. The transcriptomic responsiveness of various plant species and the diversity of affected gene families were discussed. Under stress acclimation, plant transcriptomes respond particularly dynamically. Stress response involved both distinct, but also similar gene families, depending on the species, tissue, and the quality and dosage of the stressor. We also noted the over-representation of transcriptomic data for some plant organs. Studies on plant transcriptomes allow for a better understanding of response strategies to environmental conditions. Functional analyses reveal the multitude of stress-affected genes as well as acclimatory mechanisms and suggest metabolome diversity, particularly among medicinal species. Extensive characterization of transcriptomic responses to stress would result in the development of new cultivars that would cope with stress more efficiently. These actions would include modern methodological tools, including advanced genetic engineering, as well as gene editing, especially for the expression of selected stress proteins *in planta* and for metabolic modifications that allow more efficient synthesis of secondary metabolites.

KEYWORDS

acclimation, differentially expressed genes, plant transcriptome, RNA-seq, stress response

Introduction

Higher plants, known as vascular or telome plants (Tracheophyta), appeared during plant evolution back in the Palaeophytic era. They are characterized by the development of tissues that distribute water, mineral compounds, and photosynthesis products, and the dominance of the sporophyte (Kenrick and Crane, 1997; Forster et al., 2007). Due to the sessile life cycle,

higher plants respond adequately to unfavorable conditions at multiple levels, including transcriptomic one (Morris et al., 2018).

The plant transcriptome is a complete pool of various RNA molecules (mRNA, rRNA, tRNA, as well as numerous ncRNAs) belonging to the translated fraction of the genome that responds to its environment (Imadi et al., 2015). Transcriptomics belongs to key “omics” studies that link genomic and proteomic “worlds” by analyses of RNA, a biopolymer with a central role in the transfer of genetic information and regulation of gene expression. Transcriptomics shows a more universal status than other “omics” disciplines. It offers complex and deep insights into studying gene expression in whole plants or plant organs/tissues; factors that regulate the transcriptome spatially and temporally can also be characterized (Alkan et al., 2011; Lowe et al., 2017; Zhang, 2019; Athanasopoulou et al., 2021). Moreover, plant genome assembly is more complex and expensive compared to RNA sequencing (RNA-seq), and when a reference genome is absent, the transcriptome can be used to assess plant overall transcriptional activity. Transcriptomics also allows for the quantification of low-abundance transcripts or their structural variants and estimation of the correlation of gene expression with biological traits. Additionally, the transcriptome outperforms the genome, allowing the characterization of genes related to therapeutic compound biogenesis (Wang et al., 2009). However, transcriptomics seems to be inappropriate for identifying genes with large impacts on adaptive responses to the environment due to a small number of genes with large impacts on fitness. When only transcriptomics is used to identify genes underlying environmental adaptations, constitutively expressed regulatory genes that play a major role in setting tolerance limits are often over-represented (Evans, 2015). Other disadvantages are serious challenges in analysing large datasets, as they demand a lot of bioinformatic tools, and most importantly, costs of sequencing (discussed below). The transcriptomic data may also contain noise enhanced by technical variations and batch effects resulting from inter-sample differences that were not rooted in the experimental design (Sprang et al., 2022).

Tissue-specific transcriptomics offer particularly valuable information on the underlying molecular processes that govern tissue-specific functions; furthermore, specific genes and regulatory mechanisms that display unique roles in diverse tissues can be better characterized (Booth et al., 2022). Droplet single cell RNA-seq (with most prominent platforms, including 10x Genomics) and spatial RNA-seq (with microdissection, spatial imaging and spatial coding approaches) allow the possibility of getting insight into the heterogeneity of tissue transcriptomes, to identify cell types and markers, and to analyse gene and regulatory networks under developmental and environmental factors. Their strengths include, for instance, the availability of spatial information and high resolution performance (Cervantes-Pérez et al., 2022; Chen et al., 2023; Wang et al., 2024).

The recent and prompt development of high-throughput RNA-seq platforms with a subsequent decrease in sequencing

costs, as well as data meta-analyses, advanced on plant transcriptome studies (Tyagi et al., 2022). Currently, third-generation sequencing, including SMRT (single-molecule real-time) and Nanopore sequencing allows to obtain longer sequence reads, which challenged transcriptomic analyses. Long read sequencing is accurate and allows detection of alternative splicing events. SMRT sequencing employs sequencing by synthesis, linking of chemical groups to reduce background noise and is based on properties of zero-mode waveguides. In SMRT protocol, there is no need for amplification. SMRT sequencing was used by Pacific Biosciences of California (PacBio) platform. Nanopore platform is based on electrical signal sequencing and offers particularly long reads (Li et al., 2018; Ma L. N. et al., 2019; Huang et al., 2021). However, Illumina RNA-seq is still the most preferred sequencing platform in quantitative analyses (Supplementary Table S1).

The study of tissue-specific changes in gene expression under stress is instrumental in the development of strategies to improve plant response under environmental conditions (Berkowitz et al., 2021; Tyagi et al., 2022). In previous years, some reviews focused on methodological advances in plant transcriptomics (Schliesky et al., 2012; Tyagi et al., 2022; Chen et al., 2023; Wang et al., 2024). Species-specific omics analyses characterized the relevance of transcription factors (TFs), hormones, translational reprogramming and epigenetic level, as well as phenotypic and physiological levels in stress response (Singh et al., 2016; Ahmad, 2022; Bhat et al., 2022; Hu et al., 2022; Kourani et al., 2022; Son and Park, 2023; Tu et al., 2023). Some studies also focused on the roles of non-coding RNA in stress response (Yu et al., 2019; Jin et al., 2024). However, an updated review discussing transcriptomic responses to various stress conditions assayed by high-throughput approaches from various plant species is currently needed.

In this paper, the diversity of transcriptomic responses to various stressors, both abiotic (including chemical treatments, UV radiation, drought, cold and heat) and biotic (fungal, bacterial, and viral/viroid infections) ones, will be presented, and the results will be discussed in tissue/developmental and temporal contexts, reflecting the transcriptomic dynamicity. We will focus on current studies employing high-throughput analyses, for instance, RNA-seq from various experimental platforms, as well as microarrays. We will also summarise the transcriptomic responses of not only the model but also useful crop and medicinal species, which can be used for the development of future stress-resistant cultivars by genetic and metabolic engineering (Figure 1).

Alterations in plant transcriptomes during abiotic stress

Stress conditions can be defined as internal and external cues that affect the efficiency of physiological, metabolic, and

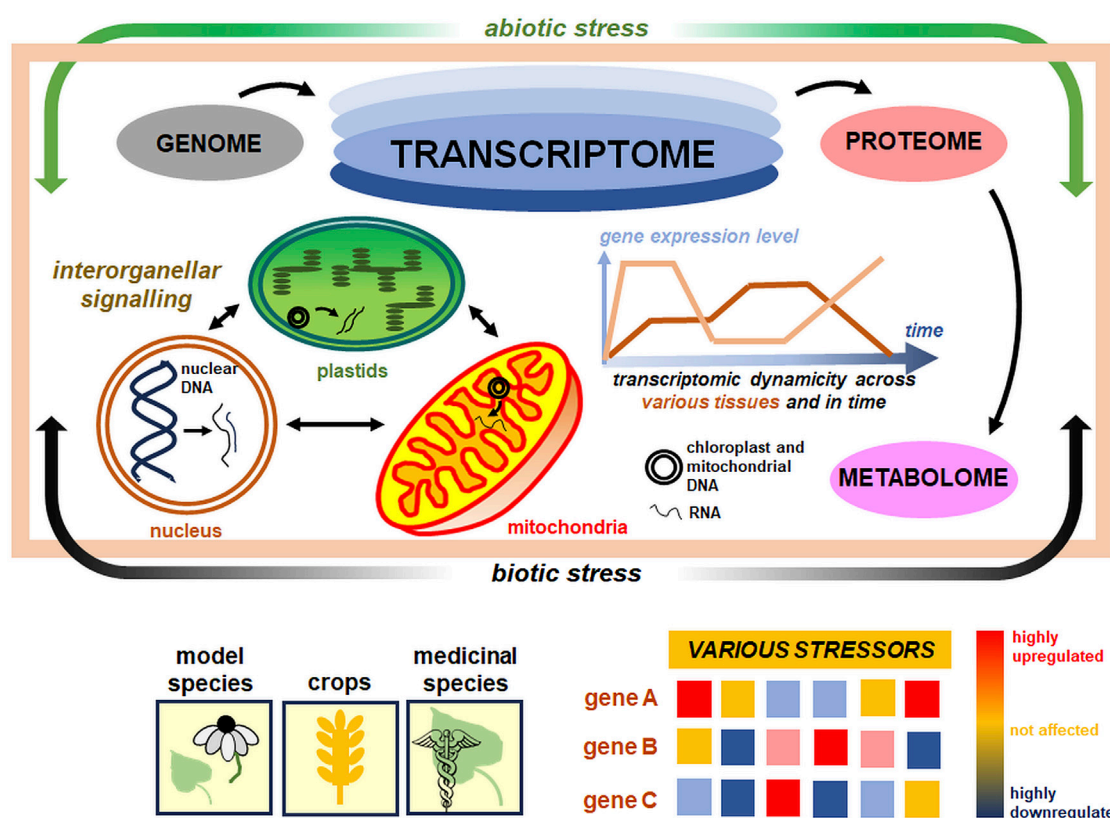


FIGURE 1

Plant transcriptome as a central stress-responsive entity in the cell. The plant transcriptome is a highly dynamic structure in plant cells (bluish ovals at the top). It links genomic, proteomic, and metabolomic levels, responding on a multidimensional scale, across various tissues, and along time (the center). The response of plant nuclear and organellar transcriptomes is also shaped by a number of factors, including abiotic and biotic stressors (green and black arrows encompassing the light brown central rectangle), which affect the differential expression pattern of various gene sets (bottom). For proper organellar biogenesis under stress acclimation, inter-organellar signaling between actively transcribed nuclear, plastid, and mitochondrial genomes is indispensable (small arrows within marked organelles on the panel in the center and to the left). The diversity of transcriptomes from model, crop, and medicinal species (bottom) under selected stress conditions was discussed in this paper. More details in the text.

molecular plant processes, leading to a reduction in the efficiency of energy-to-biomass conversion. They can be divided into abiotic and biotic ones (Umar et al., 2021).

Abiotic stress results from the action of multiple physical or chemical stimuli (Gull et al., 2019; Wang et al., 2020). A comparison of the plethora of enriched functional terms representing numerous genes and transcription factors (TFs) responsive to various abiotic stressors from RNA-seq studies is shown in Figure 2 and additional quantitative details on genes affected by abiotic stress from high-throughput transcriptomic studies are also given in Supplementary Table S1, where details on stress treatments and the respective references to the literature are also shown. The experimental studies discussed in this review showed the huge variability of the gene response under those conditions, even between similar treatments. However, the stress response involves not only functional terms/TFs common for all abiotic stressors discussed here (representing differentially

expressed genes [DEGs] for photosynthetic genes or genes controlling secondary metabolite biosynthesis as well as MYB TFs), but also specific ones for each treatment; they were also presented in Venn diagrams, although depending on the stressor (Figure 2). Leaves, which are involved in the metabolism of carbon skeletons and the capture of photosynthetic energy, belong to plant organs particularly affected by unfavorable environmental conditions. However, studies on the impact of stress on leaf tissues, contrary to roots, are still underrepresented (Berkowitz et al., 2021).

UV radiation and chemical treatments

Variability of Arabidopsis leaf tissue transcriptomic responses under UV radiation, as well as under chemical treatments [e.g., antimycin A, 3-amino-1,2,4-triazole, methyl

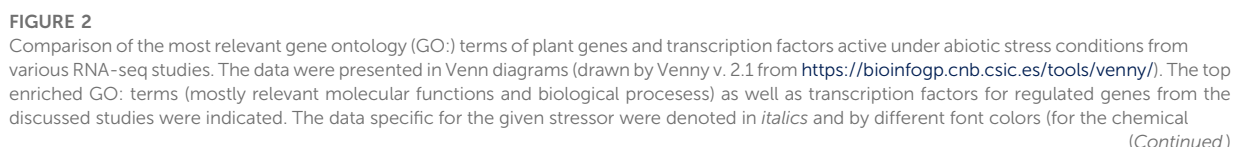


FIGURE 2 (Continued)

treatment and UV radiation in blue, for drought in brown, for cold and freeze in green and for heat stress in red). GO: terms and transcription factors common for responses to all abiotic stressors were displayed within yellow text boxes. More details in the text.

viologen, and salicylic acid (SA)] was characterized by Berkowitz et al. (2021). Responses of leaf tissues to these stressors were complex; for example, UV-affected genes were expressed mainly in the vasculature and epidermis. Treatment with 3-amino-1,2,4-triazole and SA downregulated genes for photosynthetic proteins in all tissues of Arabidopsis, while methylviologen upregulated the genes for the PS subunits, and UV radiation downregulated the photosynthetic genes in epidermis and upregulated them in mesophyll. Arabidopsis genes for oxidoreductase activity, porphyrin metabolism, plastid organization, and carbohydrate metabolism regulation were also affected by UV-B. Interestingly, Arabidopsis genes for proteins for chlorophyll biogenesis, protein folding, oxidoreductase and ligase genes, and glyceraldehyde-3-phosphate dehydrogenase were differentially regulated between UV-A and UV-B treatments. Tissues studied also showed distinct mitochondrial responses to antimycin A, which affected the expression pattern of respiratory genes, general oxidoreductase activity genes, glutathione transferase, as well as genes related to Ser/Thr kinase activity and membrane transport (Berkowitz et al., 2021).

Among DEGs upregulated in *Vaccinium corymbosum*, genes involved in plant hormone signal transduction were significantly enriched after 1 h, followed by genes involved in phenylpropanoid biosynthesis after 3 h, and genes involved in the flavonoid anthocyanin pathway after 6 h of exposure to UV-B. These results suggest that phytohormone-related genes contribute to the primary response to UV-B radiation. However, the highest number of DEGs appeared among *V. corymbosum* plants exposed to UV-B treatment for 24 h. Genes involved in proanthocyanidin and flavanol biosynthesis (*PAL1*, *ACL2*, *CHS*, *CHI3*, *VcFLS* and *VcUFGT*) were upregulated by UV, and their expression level lasted a long time after 24 h of treatment (Song et al., 2022). These DEGs resembled Arabidopsis genes affected by radiation (Berkowitz et al., 2021). Common genes for UV-B response in Arabidopsis and *Pachycladon cheesemanii* included genes for amino acid, vitamin, pigment, and secondary compound metabolism (Dong, 2024).

The impact of UV-B radiation on the transcriptome of *Glycyrrhiza uralensis*, a potent medicinal species, was investigated by Zhang et al. (2018). Participation of amino acid metabolism and enzymes in secondary metabolite pathways in the response to radiation at five different time points was suggested. Genes for various amino acid metabolic pathways were differentially enriched depending on UV-B duration, however, DEGs for enzymes of cysteine and methionine metabolism were mainly enriched in all treatments.

Polygonum cuspidatum, a medicinal plant species used in traditional Chinese medicine, exhibits numerous medicinal applications (Ke et al., 2023). The impact of UV-C radiation on the transcriptome of *Polygonum cuspidatum* leaves was studied by Liu et al. (2019); more DEGs (including more downregulated genes) were involved in shorter radiation response. Furthermore, this was accompanied by an increased concentration of resveratrol (the most important stilbene phytoalexin polyphenolic compounds) in the leaves of *P. cuspidatum*. Resveratrol used in the nutraceutical industry exhibits anticancer and anti-ageing properties. Under UV-C radiation, upregulated DEGs coded enzymes involved in proanthocyanidin and flavanol biosynthesis, however, chalcone synthase (*CHS*) gene was downregulated. Furthermore, MYB, bHLH, and ERF TFs appeared to be potential regulators of resveratrol biosynthesis genes. These results will help to find more practical applications of resveratrol synthesis (Liu et al., 2019). Upregulation of PAL, C4H, 4CL, and STS enzymes by means of genome editing may be positively associated with the resveratrol levels (Hasan and Bae, 2017).

Under high light treatment (with the enhanced UV radiation) of ginseng (*Panax ginseng*), another medicinal species, affected DEGs in the leaf transcriptome were mostly involved in various metabolic pathways and in the stress response. Stress-responsive functions were enriched among 33% of the upregulated DEGs, and the high light intensity and/or ROS response was associated with another 6% of the affected DEGs (Jung et al., 2020).

Lettuce (*Lactuca sativa*) grown under greenhouse conditions usually contains a lower level of ascorbic acid (ASC), an essential antioxidant nutrient for human health, compared to field-grown plants. To investigate the effect of radiation on ASC level in plants, lettuce plants were treated with various UV-B doses. Numerous DEGs were identified within lowly and highly radiated plants (Zhou et al., 2023). It was suggested that the expression of MIOX (for myo-inositol oxygenase, a key enzyme in the myo-inositol pathway), APX, and MDHAR may contribute to the indirect increase in the level of ASC induced by UV-B radiation (Lorence et al., 2004).

In general, plant transcriptomic responses to UV and chemical compound treatments were specifically enriched in genes for amino acid biosynthesis, ascorbate and glutathione metabolism, kinase activity, membrane transport, mitochondrial electron transport proteins, organellar ribosome biogenesis and seed development (Zhang et al., 2018; Liu et al.,

2019; Berkowitz et al., 2021; Song et al., 2022; Zhou et al., 2023; Dong, 2024). Interestingly, as shown on the Venn diagram, ERF proteins belong to TFs active under chemical treatment and UV radiation (Figure 2).

Water deficiency (drought)

As drought belongs to factors that affect the largest part of crop productivity, the analysis of multiple molecular responses by omics studies would allow characterising the mechanisms of drought in crops that result in the search for stress-resistant cultivars (Verma et al., 2013; Shanker et al., 2014).

Analysis of sweet potato (*Ipomoea batatas*) transcriptome in drought allowed identification of various upregulated genes for ABA, ethylene, and JA biosynthesis, indicating the relevance of hormonal signaling in a water deficit. Genes for ABI phosphatase and Ca^{2+} -ATPase were severely altered, while genes for SA synthesis appeared not affected (Zhu et al., 2019). Also in chickpea (*Cicer arietinum*) numerous genes for AP2-EREBP, bHLH, bZIP, C3H, MYB, WRKY or MADS TFs that regulate signaling regulation, secondary metabolism, or transition to the generative phase were involved in drought acclimation (Kumar et al., 2019). The transcriptomic response of *Phoebe bournei*, a Chinese wood species, to drought also used DEGs for plant hormone signal transduction in addition to genes for redox homeostasis (*POD*, *SOD*, and *CAT*), phenylpropanoid, flavonoid and porphyrin biosynthesis, starch and sucrose metabolism, chlorophyll *a/b* binding proteins, and genes for numerous TFs from 25 families (Li et al., 2022).

Recent investigation of transcriptomes of two rice (*Oryza sativa*) cultivars that varied with stress resistance revealed that genes for hormone signaling (in line with Kumar et al., 2019; Zhu et al., 2019; Li et al., 2022 studies), LEA proteins, proteins related to redox homeostasis and NAC and ZIP TFs played crucial roles in developing drought tolerance (Tyagi et al., 2023). Additionally, in the transcriptome of *Medicago falcata* seedlings, DEGs for hormone signaling (ABA biosynthesis, JA biosynthesis), nucleic acid helicases, and diverse genes for RNA polymerases and DNA repair proteins were enriched. In contrast, gibberellin biogenesis genes were antagonistically expressed compared to ABA-related genes (except for the *GID1* gene). Numerous TFs were also affected (Miao et al., 2015).

In *Ceratostigma plantagineum*, a resurrection species, studied by Xu et al. (2021), affected DEGs encoded proteins also active in hormone signaling, and in photosynthesis, stress response, amino acid catabolism, sucrose and fatty acid biogenesis, RNA processing and regulation, energy metabolism (distinctive in mild drought), protein modification and transport, and membrane organization. Those data indicate the flexibility of primary and secondary metabolism in water shortage and re-watering, using, among others, an alternative respiratory pathway, the C3-CAM switch, and the GABA shunt. During

global reanalysis of the *Glycine max* transcriptome, DEGs for proteins for hormone signaling, cell division, cell cycle, cell wall organization, stress responses, signal transduction, and regulation of gene expression, were regulated by progressing drought (De Oliveira-Busatto et al., 2022).

Mild drought-affected Arabidopsis genes code proteins that participate in ABA signaling, ROS biogenesis, response to osmotic stress, and also in cell wall remodelling and cell growth, among which multiple genes were previously not associated with drought-responsive mechanisms. Hormone signaling genes for PYRABACTIN RESISTANCE/ ABA receptors, two ACC oxidases and four ethylene response factors were downregulated and protein phosphatases 2C, HAB proteins, some ABA-responsive element-binding factors as well as some their target genes were all upregulated. Cell wall-loosening expansins, pectin lyases were also upregulated (Clauw et al., 2015). These data, which allowed insight into the transcriptomic landscape of six Arabidopsis accessions in drought, were further re-analysed by Benny et al. (2019), who underlined the importance of hydrogen peroxide, water deprivation, salinity, osmotic stress, and ABA-responsive proteins among upregulated genes. Transcriptomic analysis of rapeseed (*Brassica napus*), another representative of Brassicaceae, revealed that upregulated DEGs were related to the response to water deprivation, ABA signaling, osmotic stress, and other abiotic stimuli and lipid metabolism, as well as cutin, suberin, and wax biogenesis, fatty acid degradation, and secondary compound metabolism (Fang et al., 2022).

The multitude of various TFs was associated with the response to drought of *Dendrobium sinense*, an endemic species (Zhang et al., 2021). DEGs coded proteins for carbohydrate derivative and nucleotide binding, ATPase and oxidoreductase activity, pectin metabolism, and multiple TFs. Interestingly, more DEGs participated in a mild drought response, where detrimental downregulation prevailed (Zhang et al. (2021). Furthermore; Xia et al. (2024) broadened the analysis of *Dendrobium* drought responses by three additional species; the highest count of DEGs appeared in *D. fimbriatum*. Multiple DEGs among various *Dendrobium* species were involved in carbon metabolism and anthocyanin biosynthesis. Noticeable differences in the expression level of the *PEPC* gene (for phosphoenolpyruvate carboxylase) were associated with CAM and improved drought tolerance.

Artemisia annua, a medicinal species, is a potent worldwide source of artemisinin, an antimalarial compound. Attempts have been made to significantly increase artemisinin yield, and stress tolerance engineering would be one of such strategies. Drought response of *A. annua* leaf transcriptome employed many DEGs, including those coding for Δ -1-pyrroline-5-carboxylate synthetase, aquaporins, glyceraldehyde-3-phosphate dehydrogenase, LEA proteins, HSPs, glyoxalase I, glutathione-S-transferase, PR proteins, Ca^{2+} -dependent protein kinases, as well as

proteins involved in ethylene and oxylipin biosynthesis as well as NAC and MYB-related TFs (Vashisth et al., 2018).

Transcriptomes of two wheat (*Triticum aestivum*) varieties with contrasting drought resistance were compared; in stress resistant cultivars, the drought response involved genes for the synthesis of secondary metabolites and important transcription coregulators and TFs (Kumar et al., 2018).

Growth regulator 5-aminolevulinic acid (ALA) has been used to alleviate drought in grapevine (*Vitis vinifera*), by increasing antioxidative responses (Yang et al., 2023). Chlorophyll metabolism and photosynthetic apparatus were primarily affected by ALA, which uses synergistic mechanisms to alleviate drought. In the presence of ALA, alterations in the expression pattern of DEGs for chlorophyll biogenesis and Rubisco-related genes played an important role that allowed ALA to maintain cell homeostasis under water scarcity.

Little was known about the combined action of drought and cold on the plant transcriptome. Sharma et al. (2018) provided a comparative study of the impact of both stressors on the Arabidopsis transcriptome by meta-analysis of publicly available transcriptomic data. Responsive DEGs encoded proteins related to photosynthesis, respiratory burst, hormone response, signal transduction, and water deprivation, as well as some stress-specific genes. Furthermore, at least 43 diverse TFs were expressed in both treatments. Coolen et al. (2016) analysed Arabidopsis plants under drought combined with biotic treatments. The water deficit alone increased expression level of DEGs coding for proteins responding to oxygen-containing compounds and cell wall biogenesis. As the drought progressed, the more pronounced were the alterations in gene profiles. Each of the stressors induced specific expression profiles over time. In sequential stress application, Arabidopsis displayed transcriptome profiles similar to those of the second treatment, regardless of the nature of the first stressor. Overall, this study highlights the importance of stress signatures in identifying key molecular responses that act between various response pathways.

In general, hormone signaling pathways belong to the common terms for UV treatment (as discussed above; Figure 2; Song et al., 2022) and drought (Figure 2; Miao et al., 2015; Sharma et al., 2018; Kumar et al., 2019; Zhu et al., 2019; Fang et al., 2022; Li et al., 2022). The transcriptomic response in drought specifically affects a multitude of genes involved in alternative respiratory pathways, aminoacid catabolism and carbohydrate metabolism, developmental processes, DNA metabolism, kinase binding, membrane organisation, postranslational modifications, protein turnover, regulation of protein synthesis, RNA processing, and stress response. It is also specifically regulated by a particularly broad variety of TFs and transcriptional coactivators of various families (Figure 2; Kumar et al., 2018; Kumar et al., 2019; Benny et al., 2019; Zhu et al., 2019; Xu et al., 2021; De Oliveira-Busatto et al., 2022; Yang et al., 2023; Xia et al., 2024).

Elevated temperature (heat stress)

Elevated temperature affects cereal productivity, particularly male generative organ development and pollen maturation and viability (Young et al., 2004; Asseng et al., 2011; Wu et al., 2015). Heat stress leads to an increase in the level of reactive oxygen species (ROS) and a simultaneous decrease in ROS scavenger activity, leading to biomolecular damage and apoptosis (Bita and Gerats, 2013; Guan et al., 2013). *Chrysanthemum* leaf transcriptomes were analyzed in heat with or without melatonin (to alleviate the consequences of heat treatment; Xing et al., 2021). Heat alone resulted in massive downregulation of DEGs. In contrast, heat combined with melatonin increased expression level of several DEGs. Melatonin affected *HSF* and *HSP*, starch and sucrose metabolism, cell signaling, chlorophyll, flavonoid, carotenoid biosynthesis genes, and genes for various TFs.

Comparison of microspore transcriptomes under heat in two tomato (*Solanum lycopersicum*) cultivars with contrasting stress tolerance revealed among upregulated DEGs at least 11 *HSP* genes. Increased expression of the *HSP* and *APX* genes pinpoints the key role of antioxidant enzymes in the heat response (Frank et al., 2009). Valdés-López et al. (2016) studied dynamics of root hair transcriptome in soybean (*G. max*) subjected to heat at various time points. Responsive genes were classified into 10 functional modules regulated by a few TFs. In general, heat affected the expression pattern of DEGs for protein folding genes, but also for genes coding proteins for chromatin remodeling, and lipid and ATP synthesis, indicating for the importance of controlling water/nutrient intake by roots and the relevance of maintaining high ATP level under heat response.

Rice leaf transcriptome under thermal shift was studied by Rashid et al. (2020). Multiple genes were affected for the abiotic stress response and metabolite biosynthesis. Among the DEGs affected, only a few photosynthetic/ OXPHOS genes as well as some genes for glycolytic enzymes were present. Chen and Li (2017) investigated *Brachypodium distachyon* leaf transcriptome in heat. Affected DEGs coded proteins that participate in alternative RNA splicing, spliceosome, and PS biogenesis, indicating an increased extent of such events in response to high temperature in order to synthesize protein isoforms alleviating heat detrimental effects.

To describe thermotolerance and protective mechanisms against thermal stress in desert species, the *Rhizya stricta* transcriptome, the evergreen shrub, was analysed at elevated temperature. Upregulated genes coded HSPs, chaperones, UDP-glycosyltransferase, aquaporins and transparent protein *testa 12*, suggesting the distinctness of thermotolerance in leaves of *Rhizya stricta*, which is controlled primarily by improving protein folding and preventing protein degradation (Obaid et al., 2016). *HSP* genes and genes for flavonoid biosynthesis were upregulated in leaves of three tea cultivars (*Camellia sinensis*), important medicinal species, under heat (Huang et al., 2024).

Studied cultivars differed in stress tolerance and exhibited mainly upregulated DEGs under heat acclimation, however, among the affected DEGs in all cultivars, the genes for photosynthetic activity were the most notable. In heat-tolerant cultivars at elevated temperatures, genes for proteins containing the chaperone domain, including universal stress proteins (USPs), small heat shock protein sHSP18.1, chaperonin-like protein 2 (CLP2), and the LEA5 protein were preferentially expressed. Additionally, the level of flavonols increased in heat-tolerant varieties, accompanied by increased expression of *FLS* genes. Therefore, in accordance with Obaid et al. (2016), Xing et al. (2021) and Frank et al. (2009) reports, the study by Huang et al. (2024) highlights the importance of chaperones and secondary metabolism in the heat response.

Heat stress often acts simultaneously with water deficit. Mikołajczak et al. (2023) focused on investigating the impact of heat stress, drought, and their joining effects on transcriptome of barley (*Hordeum vulgare*) flag leaves. In medium-sized leaves, short heat stress (similarly to drought) affected multiple genes, regardless of the duration of the stress. However, under longer heat and drought, more DEGs were affected in large leaves. Investigated stressors affected mainly the *LEA* and *HSP* genes. Overall, Mikołajczak et al. (2023) provided novel data on the molecular mechanisms of barley flag leaf that determine the response to drought and heat. Furthermore, according to Mahalingam et al. (2022), the number of DEGs increased in barley heads in the stress-tolerant genotype as heat progressed. Heat response involved genes for transporter proteins, and ABA response, and resulted in differential expression of *LEA* genes in stress-sensitive genotype. In contrast, genes for nonspecific lipid transfer proteins and carbonate dehydratase were enriched in a stress-tolerant cultivar. Heat with drought resulted in a notable increase in DEG number only in the stress-sensitive cultivar. In particular, at least 900 TFs controlled transcriptional reprogramming in two barley cultivars in all treatments.

Cellular signalling, including hormone signaling, is particularly important in multiple treatments, when heat is combined with other stressors. Martin et al. (2021) pointed out the broadening range of DEGs affected by double treatment (heat and drought) of *Lolium temulentum*, which encoded proteins for cell signaling, cell cycle, organellar biogenesis, binding, transport, oxidoreductase and antioxidative activity, as well as chaperones and multiple TFs. When heat stress acted together with an elevated level of CO₂, detrimental effects were only partially alleviated by deregulation of primary and secondary metabolism genes in flag leaves of durum wheat (*Triticum durum*) flag leaves. Most affected DEGs coded proteins involved also in cellular signaling but also in stress response and nucleic acid metabolism. In particular, genes upregulated by CO₂ were often downregulated by heat (they coded, among others, photosynthetic and OXPHOS proteins, proteins for hormone signaling, enzymes of lipid and amino acid metabolism and the glutathione-ascorbate cycle, nucleic acid

metabolism, and transport proteins (Vicente et al., 2019). Suzuki et al. (2016) investigated the impact of heat and salinity on Arabidopsis transcriptome. DEGs regulated by heat and salt stress were enriched in genes coded proteins for ABA signaling, stress response, developmental processes, protein metabolism, and DNA-dependent transcription. However, in heat, DEGs for ABA-responsive proteins, glyoxylase 17 and catalase, among others, appeared to be responsive, indicating the importance of the antioxidative response.

Arabidopsis leaf transcriptome under various stress conditions (salinity, osmotic stress, and heat) was also investigated by Sewelam et al. (2020). Of all these treatments, elevated temperature appeared to have the most notable effect on transcriptomic profiles. DEGs affected by heat covered induction of eleven *HSP* genes, late embryogenesis abundant (LEA) proteins, receptor-like kinases (RLKs), glutathione S-transferases, genes for carbohydrate binding, UDP-galactosyltransferases, membrane transporters, and programmed cell death (PCD), and genes for WRKY TFs. However, heat treatment repressed several cell cycle genes, ribosomal protein genes, and genes involved in DNA synthesis and repair. In particular, osmotic stress and heat acted antagonistically, while double treatment largely reprogrammed the gene expression pattern. Heat in combination with salinity and osmotic stress also induced numerous mitochondrial genes, presumably as a compensatory response to excessive protein degradation (Rurek et al., 2018).

In general, multiple stress treatment (including heat) in plant transcriptomes results in different and distinct transcriptomic responses under single treatments. In particular, although drought often accompanies heat, those stressors result in the upregulation of different gene sets in various plant species (Mahalingam et al., 2022; Mikołajczak et al., 2023). The transcriptomic response to heat stress specifically engages DEGs for cellular signaling (particularly in multiple stress treatments and under melatonin supplementation; Suzuki et al., 2016; Vicente et al., 2019; Martin et al., 2021; Xing et al., 2021), and also genes for chromatin remodelling, DNA synthesis, endopeptidase activity, heat response, regulation of protein phosphorylation and dephosphorylation, RNA metabolism, spliceosome biogenesis, transcription regulation, volatile compound biosynthesis as well as AP2/EREBP, C2H2, G2-like, GRAS, HSF, MADS-box and RWP-RK TFs (Figure 2; Frank et al., 2009; Obaid et al., 2016; Suzuki et al., 2016; Valdés-López et al., 2016; Chen and Li, 2017; Rurek et al., 2018; Vicente et al., 2019; Rashid et al., 2020; Sewelam et al., 2020; Martin et al., 2021; Xing et al., 2021; Mahalingam et al., 2022; Mikołajczak et al., 2023; Huang et al., 2024).

Low temperature (cold, freeze)

Similarly to heat, also cold treatment and freeze result in plant growth and development aberrations, as well as direct

inhibition of metabolic reactions. Due to the limited osmosis, cell dehydration and oxidative stress occur simultaneously with other detrimental responses. Most plants can gain tolerance to ice formation by gradually being exposed to reduced (non-freezing) temperatures under cold acclimation (Chinnusamy et al., 2007). In general, genes for the early cold response encoded a wide variety of TFs that regulate other gene expression (Gull et al., 2019).

Signal transduction and hormone signaling appeared also to be important for the low-temperature response. Amur vine (*Vitis amurensis*) transcriptomic response under cold used DEGs that encode proteins for signal transduction, transcription regulation, and alternative splicing. At least 38 major families of TFs (with 326 genes for TFs) involved in the regulation of cold response were detected, including several previously uncharacterized TF families homologous to Arabidopsis proteins (e.g., HAP2, ABI3VP1, ARF, PLATZ, LIM, atypical HD and MYB factors, BBR-BPC, zinc Dof, C3H-type I, EIL, GARP G2-like and Trihelix). Genes for CBL-interacting protein kinases participating in signal transduction were upregulated (Xu et al., 2014). Du et al. (2017) analysed the cold response of *Agropyron mongolicum* ABA receptors and upregulated genes for bZIP and NAC TFs. Most DEGs participated in carbohydrate metabolism, hormonal and phosphatidylinositol signaling, as well as biogenesis of numerous secondary metabolites. Also, the cold response of *M. falcata* focused on phytohormone and nodulation signaling, revealing some similarities with the drought replies; however, *ABF1*, *GID1*, and *AUX* genes were downregulated. Interestingly, *GH3* auxin-responsive gene was extensively upregulated in cold (similarly to *DIMI1*, but contrary to *DIMI2* and *DIMI3*, all of which encode important nodulation factors). Furthermore, at least 16 genes for MYB and 12 genes for NAC TFs were induced by cold, indicating their participation in cold tolerance (Miao et al., 2015). The transcriptomic response to cold in two rape cultivars (*Brassica rapa*) cultivars, varying with stress tolerance, also involved DEGs coding proteins for plant hormone signal transduction (MAPK signaling pathway) and also for photosynthesis, phenylpropanoid biosynthesis, lipid binding, plant-type cell wall, positive regulation of circadian rhythm, abaxial cell fate specification and basal TFs (Ma L. et al., 2019).

Arabidopsis chilling response covered almost half of expressed genes (Calixto et al., 2018; Liu et al., 2022). Cold response also involved genes for plant hormone signaling, but also for glucosinolate biosynthesis, transporter proteins, long ncRNA, RNA splicing, and spliceosome biogenesis, as well as multiple TFs from 52 families. Cold downregulated photosynthetic genes and short cold-induced quickly responding DEGs coding proteins for chloroplast organisation, ribosome biogenesis, and rRNA processing, which may activate cold tolerance. On the contrary, long cold affected DEGs for the cell response to hypoxia, fatty acid and flavonoid biosynthesis, as well as redox homeostasis and diverse *HSP* genes (Liu et al.,

2022). Massive alternative splicing events occurred in the first few hours of cold treatment, including mobilisation of cold-responsive TFs, splicing factors, and selected RNA-binding proteins (Calixto et al., 2018). Interestingly, in *P. cheesemanii*, contrary to Arabidopsis, the cold response employed genes for glucosinolate metabolism. For Arabidopsis and *P. cheesemanii*, genes for wound-like circadian clock, as well as for secondary metabolite biogenesis, responded under the early cold response (Dong et al., 2023).

Cheng et al. (2019) described the effects of *MeTCP4* (a specific cassava [*Manihot esculenta*] TF) overexpression in Arabidopsis plants during cold stress. Affected genes were classified as stress-responsive under all tested conditions, to DNA binding and TF activity in control, and to oxidoreductase, peroxidase, and antioxidative activity under cold treatment. Analysis of transcriptomic response of leaves of *Lavandula angustifolia* to cold revealed DEGs coding for photosynthetic proteins among affected genes. The most important functions of DEGs were also associated with the decreased stomatal conductance, ROS scavenging, and the development of cold tolerance. In general, these findings may allow for further engineering of cold tolerance in *L. angustifolia* to improve its medicinal potential, as this species is a source of aromatic compounds in traditional Chinese medicine (Li L. et al., 2023). In the leaf transcriptome of another medicinal species, *A. annua*, cold induced a multitude of genes for kinases, peroxidases, ABA biosynthesis, LEA and LEA-like proteins, various desaturases, glyoxalase I family protein, proteins for oxylipin and polyamine biosynthesis, Δ -1-pyrroline-5-carboxylate synthetase, NAC and MYB TFs (Vashisth et al., 2018).

Important metabolic regulations occur in plant organelles under cold acclimation. Naydenov et al. (2010) investigated the mitochondrial and nuclear transcriptomes of germinated wheat (*T. aestivum*). The upregulated genes encoded mitochondrial proteins, including Mn superoxide dismutase (SOD) and alternative oxidase (AOX); however, the level of expression of nuclear genes essential for mitochondrial biogenesis was visibly reduced. This indicates a fine-tuning of gene expression between mitochondrial and nuclear transcriptomes, executed by anterograde and retrograde signaling, affected by stress conditions.

On the whole, the cold response of plant transcriptomes specifically employs DEGs involved in abaxial cell fate specification, lipid binding, nucleic acid metabolism, post-translational modifications, protein degradation, regulation of transcription, and biomolecule transport. Cold response also specifically mobilizes a variety of TFs, including BBR-BPC, C3H-type I, EIL, GARP G2-like, HAP, LIM, NIN-like, PcG, PLATZ, TUB, and WHIRLY proteins (Figure 2; Naydenov et al., 2010; Xu et al., 2014; Miao et al., 2015; Du et al., 2017; Calixto et al., 2018; Vashisth et al., 2018; Cheng et al., 2019; Gull et al., 2019; Ma L. et al., 2019; Liu et al., 2022; Dong et al., 2023; Li L.

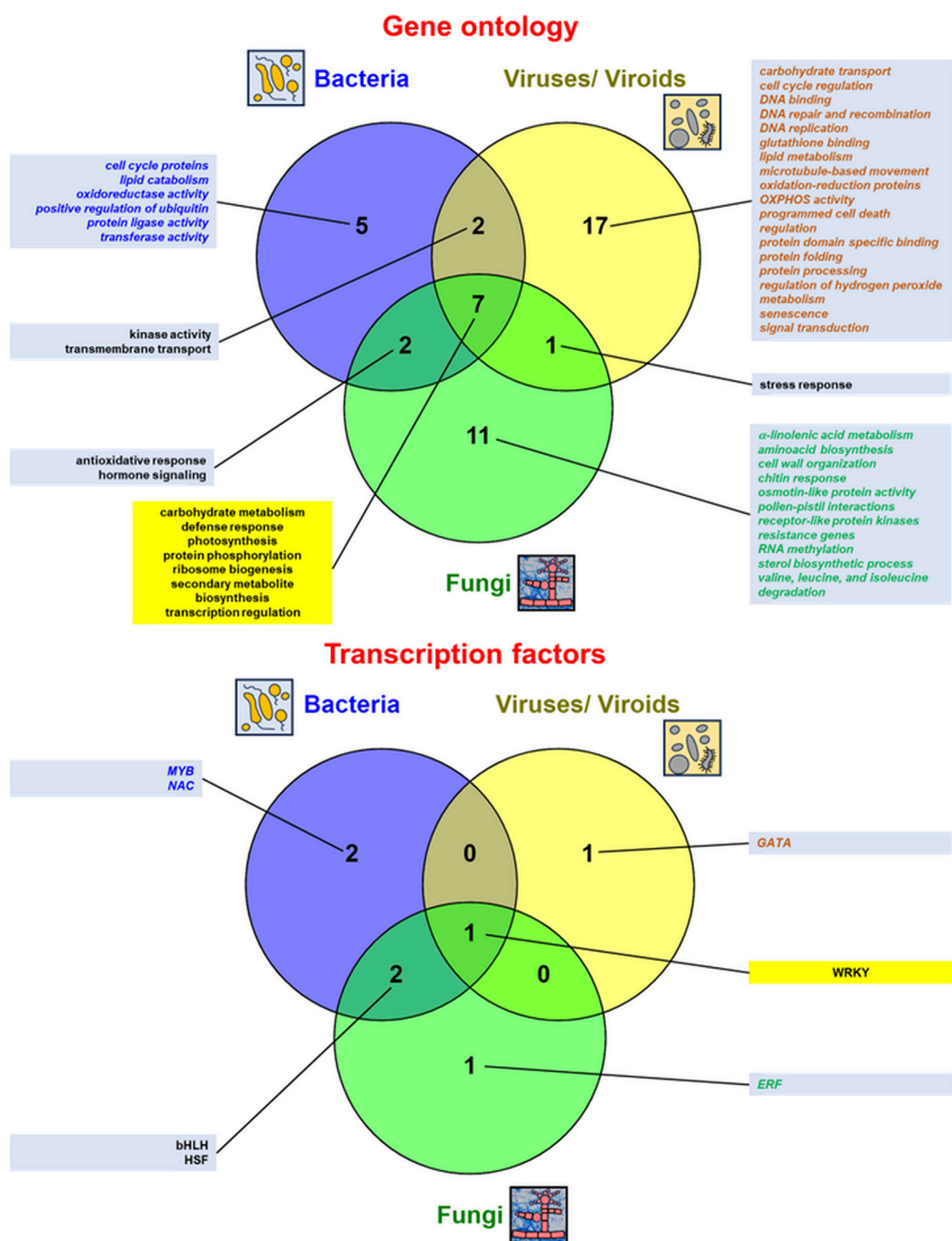


FIGURE 3
Comparison of the most relevant gene ontology (GO) terms of plant genes and transcription factors active under biotic stress conditions from various RNA-seq studies. The data were presented in Venn diagrams (drawn by Venny v. 2.1 from <https://bioinfogp.cnb.csic.es/tools/venny/>). The top enriched GO terms (mostly relevant molecular functions and biological processes) as well as transcription factors for regulated genes from the discussed studies were indicated. The data specific for the given stressor were denoted in *italics* and by different font colors (for bacterial (Continued)

FIGURE 3 (Continued)

infections in blue, for virus/viroid infections in brown and for fungal infections in green). GO: terms and transcription factors common for responses to all abiotic stressors were displayed within yellow text boxes. More details in the text.

et al., 2023). Hormone signalling is also affected by the cold response in numerous studies, including members of *Fabaceae* and *Brassicaceae* (Miao et al., 2015; Du et al., 2017; Vashisth et al., 2018; Gull et al., 2019; Ma L. et al., 2019; Liu et al., 2022).

Plant transcriptomic responses under biotic stress

Under global climate alterations, crop species are gradually exposed to increasing biotic stress. The findings discussed below may help develop plant cultivars that are highly resistant to fungal, bacterial and virus infections. To cope with biotic stress, plants have developed defensive responses precisely induced by pathogen attack (Verma et al., 2013). Plant cells contain plasma membrane receptors, which recognize pathogen-associated molecular patterns (PAMP). Subsequently, PAMP-triggered immunity (PTI) usually stops the infection before it spreads throughout the plant. Due to the constant combat between pathogens and their victims, pathogens can neutralize PTI by secreting special effector proteins into the cytosol. In response, plants developed the ability to detect microorganisms by effector-triggered immunity (ETI). Interactions between intracellular receptors designed to recognize effector molecules produced by pathogens and effectors trigger a complex network of cell responses to achieve infection resistance (McDowell and Dangel, 2000). To protect against pathogens, plants use an “oxidative outbreak” that initiates a hypersensitive response (HR) limiting the pathogen spread (Sato et al., 2010).

A comparison of the multitude of enriched functional terms representing numerous genes and transcription factors (TFs) that respond to various biotic stressors (fungal, bacterial, and virus/viroid infections) from RNA-seq studies is shown in Figure 3 and further quantitative details on genes affected by abiotic stress from high-throughput transcriptomic studies are also given in Supplementary Table S1, where details on various biotic treatments and references from the respective literature were given. Fungal, bacterial, and virus/ viroid infections involve common DEGs for carbohydrate metabolism, defence response, photosynthesis, protein phosphorylation, ribosome biogenesis, secondary metabolite biosynthesis, and transcription regulation. Biotic stress influence also expression pattern of genes for hormone signaling/ signal transduction (more details below). All conditions of biotic stress mobilize WRKY factors responding to pathogen infection (Figure 3). Interestingly, terms for photosynthesis and secondary

metabolite biosynthesis overlap with those for abiotic stress response; however, most functional terms and TFs in biotic infections differ from those of abiotic stressors (Figures 2, 3).

Fungal infections

Pathogenic fungi can be divided into biotrophic, necrotrophic, and hemibiotrophic species (biotrophic in their early stages and necrotrophic in their later stages of the life cycle). Analysis of transcriptome of pumpkin leaves (*Cucurbita moschata*) infected with powdery mildew (*Blumeria graminis*) 24 and 48 h after the infection onset showed a downregulation of multiple DEGs, including genes coding for resistance to powdery mildew and various TFs for ethylene signaling. Numerous host photosynthetic genes were also regulated. Upregulation of photosynthetic genes after 48 h of infection was associated with the appearance of initial fungal hyphae, which was also shown in infected wheat (*T. aestivum*) (Guo et al., 2018).

The transcriptomes of wheat leaves infected with powdery mildew (*Erysiphe* species) and striped rust (*Puccinia striiformis*) were analysed by Zhang et al. (2014). In powdery mildew infection, DEGs coded proteins for α -linolenic acid metabolism, as well as phenylpropanoid, flavonoid, phenylalanine, tyrosine and tryptophan biosynthesis. However, striped rust upregulated DEGs for photosynthetic proteins and proteins for ubiquinone biosynthesis. These results indicate the participation of different genes in response to various fungi (Zhang et al., 2014). Coolen et al. (2016) investigated Arabidopsis transcriptome under infection of the necrotrophic fungus, *Botrytis cinerea*, alone or in combination with drought. DEGs responding to chitin, defence response, incompatible interactions, and RNA methylation were upregulated, and photosynthetic ones were deregulated up to 1 day after infection. Massive upregulation of core DEGs coding proteins that respond to oxygen-containing compounds according to the impact of drought. Kumar et al. (2022) compared two transcriptomic data sets of maize (*Zea mays*) silk infected with different fungal species. Set A contained data for silk samples affected by *F. graminearum* and *U. maydis*, while set B contained data from samples infected with *F. verticillioides* and *Trichoderma atroviride*. Interestingly, only 21 DEGs were found in all variants tested. Among these DEGs, peroxidase genes that control the lengthening of the germ tube to protect maize kernels from fungal disease were upregulated. The differential expression pattern was also found for the osmotin-like protein gene, which

improves host defense and immune defense against stress, and for genes coding the receptor-like protein kinase subfamily. These genes appeared to be upregulated under infection with *Fusarium verticillioides*, *Fusarium graminearum*, and *Ustilago maydis* and downregulated when samples infected with *T. atroviride*.

Generally, host DEGs specifically regulated during fungal infections code proteins related to α -linolenic acid metabolism, amino acid biosynthesis, cell wall organization, chitin response, osmotin-like protein activity, pollen-pistil interactions, receptor-like protein kinases, resistance genes, RNA methylation, sterol biosynthesis process, as well as valine, leucine, and isoleucine degradation. SA signaling is believed to be mainly involved in resistance to biotrophic and hemibiotrophic pathogens. On the contrary, JA and ethylene signaling appeared to be indispensable for necrotrophic resistance (Pieterse et al., 2009; Guo et al., 2018). In addition, ERF belong to main TFs specifically regulating gene expression of plant host under fungal infections (Figure 3; Zhang et al., 2014; Coolen et al., 2016; Guo et al., 2018; Kumar et al., 2022).

Bacterial infections

Analysis of rice (*Oryza indica*) infected with *Xanthomonas oryzae* revealed multiple upregulated genes that encode proteins involved in signal transduction, carbohydrate metabolism, and transcription regulation. On the contrary, the downregulated genes encoded TFs and proteins necessary for lipid catabolism, oxidative burst, and cell cycle (Kottapalli et al., 2007). Furthermore, analysis of the transcriptome of tomato (*Solanum lycopersicon*) infected with *Clavibacter michiganensis* allowed the identification of upregulated genes that encode proteins that also participated in hormonal signaling, but also in protein phosphorylation, and the plant defense response (including numerous TFs, such as WRKY, NAC, HSF, and CBP60). Resistance gene analogues (RGA) that included *RLK* genes were also upregulated. Exogenous treatment with SA resulted in induction of genes for WRKY TFs, therefore, SA-driven gene expression resulted in improved quality of the plant immune response (Yokotani et al., 2021).

Analysis of transcriptomes of rice (*O. sativa*) cultivars resistant and susceptible to infection with *Xanthomonas oryzae*, which causes a cereal disease called bacterial leaf streak (BLS), revealed more DEGs among the infection-susceptible cultivar. Upregulations of genes encoding proteins involved in secondary metabolism, as well as participation of selected WRKY, NAC, MYB, and bHLH TFs in plant response to bacterial infection were notable (Lu et al., 2020). Deng et al. (2023) study on resistant (“IBL2353”) and susceptible (“Ohio88119”) tomato (*S. lycopersicum*) cultivars infected by *C. michiganensis* identified new gene families that participate in antibacterial defense. The key role of WRKY TFs in this

process was revealed. At least 25 genes for proteins associated with the plant defense response and *WAKL20* gene (for the wall-associated receptor kinase similar to wall 20 and the only member of the WAKS subfamily that participates in innate resistance to pathogens) were upregulated in “IBL2353” cultivar. Viral-induced silencing of *WAKS20* gene in the “IBL2353” cultivar resulted in the appearance of susceptibility to *C. michiganensis* infection, suggesting an important role for the *WAKS20* gene in antibacterial defense (Deng et al., 2023).

In general, plant host genes specifically affected by bacterial infections code proteins related to the cell cycle, lipid catabolism, oxidoreductase activity, and positive regulation of ubiquitin protein ligase activity as well as transferase activity. Hormone signaling is also important for the antibacterial response of host plants (Kottapalli et al., 2007; Yokotani et al., 2021). Additionally, the host response to bacterial infections specifically mobilizes MYB and NAC TFs (Figure 3; Kottapalli et al., 2007; Lu et al., 2020; Yokotani et al., 2021; Deng et al., 2023).

Viral and viroid infections

Plant transcriptomes also respond to the plethora of viral and viroids, which may leave their genome fragments within the host genome/transcriptome (Jo et al., 2018; Mifsud et al., 2022; Raza and Wu, 2022). The enriched functional terms for genes affected by viral and viroid infections are presented in Figure 3 and the summary of quantitative data from discussed experimental reports is available in Supplementary Table S1. Most viral proteins interact with host proteins, which promote the appearance of symptoms. Plants counteract this initial symptom development by using adaptive immunity; defense hormones are also active, resulting in hampering of virus biogenesis (Malavika et al., 2023).

Viroids are among the smallest and most infectious pathogens of crops, having short ssRNA genomes. They can affect host genes whose products participate in defense response, phytohormone signaling, cell wall modification, photosynthesis, secondary metabolism, transport, gene expression, and protein modification (Joubert et al., 2022).

Tobacco transcriptomes (*Nicotiana tabacum*) infected with seven genotypes of tobacco etch potyvirus (TEV) varying in fitness were compared. Host genes (including those for hormone signaling and RNA silencing-mediated pathways of plant defense) whose expression was correlated with the fitness level of TEV were examined (Cervera et al., 2018). The relevance of hormone signaling and signal transduction in the host response under virus attack was also pinpointed by other reports. Recently, Li Z. et al. (2023) focused on the analysis of antiviral response of bottle gourd (*Lagenaria siceraria*) under cucumber green mottle mosaic virus (CGMMV) infection. Affected DEGs were involved in the biosynthesis of secondary metabolites, hormone signal transduction (JA biogenesis), plant-pathogen interactions, and

carbohydrate metabolism. Méndez-López et al. (2023) investigated the impact of the pandemic infection of the Pepino mosaic virus (PepMV) on two tomato cultivars. The SGSTU38 protein belongs to PepMV-specific susceptibility factors. The transcriptomes of healthy and virus-infected knocked out plants (*gstu38*) were examined. When *gstu38* plants were compared with healthy wild-type plants, some key stress-related genes (including those for WRKY TFs) were upregulated and genes for intracellular signal transduction proteins, various TFs, HSP70, and proteins involved in sugar metabolism and transport were downregulated. Among DEGs affected in both tomato cultivars, genes for peroxidases, various kinases, RNA binding proteins, resistance proteins, PDH, DNA repair, recombination proteins, and chaperonins and GATA TFs were also notable. Furthermore, the rice transcriptome was assayed during *planta* overexpression of the OsNF-YA protein displaying antiviral defense against rice stripe virus (RSV) and Southern rice blackstreaked dwarf virus (SRBSDV). Interestingly, the expression pattern of genes for JA biogenesis was decreased in plants overexpressing NF-YA under viral infection, due to interference between the NF-YA protein and TFs that regulate JA signaling (Tan et al., 2022). On the other hand, Arabidopsis cabbage leaf curl virus (CaLCuV) infection triggered the SA-dependent pathogen response and induced the expression of genes involved in PCD, genotoxic stress, DNA repair, and cell cycle (Ascencio-Ibáñez et al., 2008). Signal transduction is also crucial when plant viruses could alter host plant traits so that they modify their insect behavior. When *Myzus persicae* aphids were foraging in Arabidopsis and *Camelina sativa* plants, cauliflower mosaic virus (CaMV) infection appeared more severe than turnip yellows virus (TuYV) and affected DEGs that encode proteins for photosynthesis, oxidation reduction proteins, microtubule-based movement, as well as enzymes for JA, ethylene, and glucosinolate biogenesis. TuYV infection in Arabidopsis plants resulted in alterations in DEGs for carbohydrate transport, defence and stress response proteins (Chesnais et al., 2022).

Zhu et al. (2018) investigated the impact of cucumber mosaic virus (CMV) infection on hot pepper (*Capsicum annuum*) transcriptome. Affected genes were involved in stress and defence response, and plant-pathogen interactions. DEGs for chitinase, pathogenesis-related protein (PR), tobacco mosaic virus resistance protein (TMV), WRKY TFs, and jasmonate ZIM-domain protein, were upregulated after inoculation. Intron retention for WRKY23 transcripts indicated a deep reprogramming in alternative splicing pattern under viral infection.

Zhou et al. (2019) studied transcriptomes of tomato (*S. lycopersicum*) plants grown from neutron-irradiated seeds and infected with tomato yellow leaf curl virus (TYLCV). Transcriptomes of plants grown from presoaked seeds were highly altered compared to those developed from dry seeds. Various doses of neutron irradiation affected the expression pattern of various DEGs. At least regulated DEGs that were

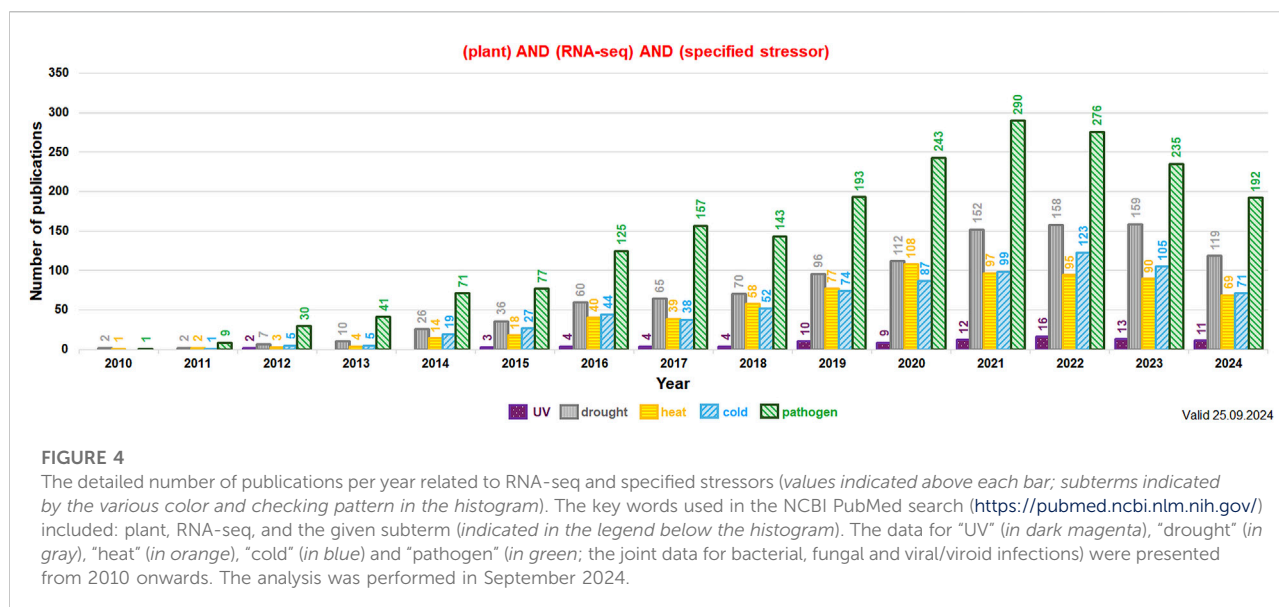
common for all irradiated mutants encoded proteins for metabolism, transport, binding and responses to various stimuli, photosynthesis, and transcription. Spanò et al. (2020) applied the RNA sequence to study the transcriptomic profiles of tomato cultivars varying with resistance level, as well as their graft combinations, exposed to potato virus Y recombinant strain. Graft wounding and virus Y infection had various impacts on the tomato transcriptome, depending on genotype.

Roy et al. (2023) have used 3'RNA-seq to identify transcriptomic alterations in *N. benthamiana* plants infected by two strains of grapevine fanleaf virus (GFLV). During appearance of peak vein clearing symptom at 7 days post-inoculation (dpi), the genes involved in the immune response, gene regulation, and secondary metabolite production were over-represented. In other stages, DEGs related to chitinase activity, hypersensitive response, and transcriptional regulation were notable. Previously, Medzihradsky et al. (2019) investigated the transcriptomic reprogramming in the shoot apical meristem of *Nicotiana benthamiana* plants infected with Cymbidium ringspot virus (CymRSV). Upregulated genes coded proteins indispensable for cell defense, and downregulated DEGs were related to DNA replication and organization, shoot meristem development and plasmodesmata functions.

On the whole, plant host genes specifically affected under virus and viroid infections are related with carbohydrate transport, cell cycle regulation, DNA binding, DNA repair and recombination, DNA replication, glutathione binding, lipid metabolism, microtubule-based movement, oxidation-reduction proteins, OXPHOS activity, programmed cell death regulation, protein domain specific binding, protein folding and processing, regulation of hydrogen peroxide metabolism, senescence as well as signal transduction (with hormone signaling, highlighting relevance of JA signaling in host antiviral defence, e.g., Chesnais et al., 2022; Tan et al., 2022; Li Z. et al., 2023). Among TFs specifically mobilized under virus/viroid infection, GATA proteins were discernible (Figure 3; Ascencio-Ibáñez et al., 2008; Cervera et al., 2018; Zhu et al., 2018; Medzihradsky et al., 2019; Zhou et al., 2019; Spanò et al., 2020; Chesnais et al., 2022; Tan et al., 2022; Li Z. et al., 2023; Méndez-López et al., 2023; Roy et al., 2023).

Discussion

Transcriptomic datasets, together with proteomic and metabolomic analyses, belong to the valuable and prospective components of modern systems biology in the functional network study (Figure 1; Cramer et al., 2011). In plant cells, in addition to the transcriptome being a product of nuclear genome expression, plastid and mitochondrial transcriptomes are also present (Barkan and Goldschmidt-Clermont, 2000; Daniell et al., 2016; Rurek, 2016; Rurek et al., 2018; Best et al., 2020a). They are dynamically shaped by multiple factors at



multiple levels of biological diversity (Zhu, 2002; Wang et al., 2020). Studies on plant transcriptomes, which participate in stress response, may thus allow for better understanding how plants properly react to changing environmental conditions (Zhu, 2002).

Plant stress studies employing RNA-seq

Extensive research on the plant transcriptome is being developed at various levels. Transcriptomic data can be acquired both from differential expression studies in tissue/organs or even from single cells, and modern RNA-seq approaches. From 2010 the number of experimental reports on RNA-seq and stress response among diverse plant species increased almost exponentially. In total, between 2010 and 2024 at least 4,710 plant studies related to RNA-seq and UV, drought, cold, heat and pathogen response were published (Figure 4; the data valid to 25 September 2024). This indicates the growing interest of these topics in plant molecular biology. Interestingly, reports on pathogen attack and drought using RNA-seq dominate in number from at least 2014 and those for temperature treatments (cold, heat) are generally in the third place in each year indicated (Figure 4).

Similarities and differences in transcriptomic response under various stressor conditions

The plant transcriptomic response depends greatly on the quality of the stressor and its duration, leading to metabolic

flexibility (Supplementary Table S1; Wang et al., 2020; Xu et al., 2021; De Oliveira-Busatto et al., 2022). Commonly regulated genes under the action of almost all abiotic stressors often encode proteins for the photosynthetic apparatus and enzymes for secondary metabolism; interestingly, limited TFs (MYB mostly) overlap for all abiotic stressors (Figure 2).

In contrast, all conditions of biotic stress employ a large number of DEGs that represent a particularly broad landscape of enriched functional terms. DEGs for carbohydrate metabolism, defence response, protein modifications, ribosome biogenesis, transcription regulation, and secondary metabolism overlap both for bacterial, virus/viroid infections and for fungal infections across a plethora of host species (Figure 3). Furthermore, the WRKY proteins belong to universal TFs that regulate gene expression in biotic stress.

In general, photosynthesis and secondary metabolite biosynthesis belong to commonly enriched functional categories for all stress treatments discussed here.

From abiotic stressors, drought and heat stress employ the highest number of specific terms for these stressors (twelve and eleven terms, respectively, Figure 2). Drought stress appeared to be particularly detrimental at the transcriptomic level (Kumar et al., 2019; Zhu et al., 2019; Tyagi et al., 2023). Chemical treatments and UV as well as cold/freeze stress resulted in a lower quantity of terms specific to DEGs affected under action of those stressors. Furthermore, double stress treatments led to highly specific responses, sometimes increasing the number of DEGs (Zhou et al., 2019; Sewelam et al., 2020; Martin et al., 2021). It should be underlined that highly specific TFs from different families regulate gene expression under each abiotic stress conditions (with the highest number of TFs participating in drought and cold and freeze). Therefore, the most harmful

stressors employ particularly numerous TFs within adaptive responses (Figure 2; Mahalingam et al., 2022).

Regarding biotic stress, virus and viral infections employ DEGs for host proteins with broadening functional categories that are specific only to those stressors. Less quantities of functional GO terms were also observed from the data representing fungal and bacterial infections (comparing with virus infections) were also notable. Genes for hormone signaling appeared to be important for both bacterial and fungal infections, and DEGs for signal transduction proteins were notably over-represented in virus/viroid infections (Figure 3). Overall, such a pattern differs from the one for abiotic stress treatments, where only a limited number of common GO terms for all treatments was evident (Figure 2). Furthermore, distinct TFs specifically regulate host gene expression under various biotic stressors, with MYB/NAC proteins mainly for bacterial infections and GATA and ERF factors for virus/virus and fungal infections, respectively (Figure 3).

As shown in Supplementary Table S1, stress-sensitive cultivars engage more DEGs in their stress responses; however, these patterns are highly tissue dependent (Mahalingam et al., 2022). Plant responses to biotic stress indicated the challenging importance of plant-microorganism interactions, which can generally influence stress tolerance (Rivero et al., 2022).

Future outlines

From the data discussed within the present review, few conclusions for future actions can be presented. Hopefully, they will increase both the quantity and quality of the data. First, more organellar transcriptomes for important crop species should be analysed to better understand the responses of the plastome and mitogenome to stress and their relevance in plant developmental steps. Furthermore, due to the peculiar under-representation of transcriptomic data on stress in some plant organs, future studies should improve such biases (Best et al., 2020a; Best et al., 2020b; Berkowitz et al., 2021).

Most of the transcriptomic data discussed here came from plant material grown under controlled conditions. Therefore, field experiments that test the variations of multiple stress responses are still awaited. Additionally, both the complexity of plant viromes and impact of the plant microbiome on stress response at the transcriptional level should be widely investigated (Jo et al., 2018; Mifsud et al., 2022; Raza and Wu, 2022).

Due to the importance of DEGs for secondary metabolite synthesis in the analysed data, it would also be important (1) to

investigate further the biogenesis of active compounds, (2) to better understand how metabolic pathways contribute to various stress acclimation strategies, and (3) to develop new more stress-resistant cultivars after genetic and metabolic engineering of medicinal and crop plant species. These actions should include modern methodological tools, for example, genetic engineering and gene editing, as well as metabolome engineering (Singh et al., 2016; Yan et al., 2020; Guo et al., 2021; Kumar et al., 2023; Dong, 2024).

Author contributions

MR and MS contributed to the conception and design of the paper. MR conceived the idea for the review, supervised submission, reviewed and edited first manuscript draft. MR and MS compiled the literature and wrote first manuscript draft. MR prepared all figures and the Supplementary Material. All authors contributed to the article and approved the submitted version.

Funding

The author(s) declare that financial support was received for the research, authorship, and/or publication of this article. Supported by the Excellent Initiative – Research University (ID-UB) program at the Adam Mickiewicz University, Poznań and KNOW RNA Research Center at Adam Mickiewicz University, Poznań, grant no. 01/KNOW2/2014.

Acknowledgments

We would like to thank colleagues from our Institute for the valuable remarks during the preparation of the manuscript.

Conflict of interest

The authors declare that the research was conducted in the absence of any commercial or financial relationships that could be construed as a potential conflict of interest.

Supplementary material

The Supplementary Material for this article can be found online at: <https://www.frontierspartnerships.org/articles/10.3389/abp.2024.13585/full#supplementary-material>

References

- Ahmad, M. (2022). Genomics and transcriptomics to protect rice (*Oryza sativa* L.) from abiotic stressors: pathways to achieving zero hunger. *Front. Plant Sci.* 13, 1002596. doi:10.3389/fpls.2022.1002596
- Alkan, C., Sajjadian, S., and Eichler, E. E. (2011). Limitations of next-generation genome sequence assembly. *Nat. Methods* 8, 61–65. doi:10.1038/nmeth.1527
- Ascencio-Ibáñez, J. T., Sozzani, R., Lee, T.-J., Chu, T.-M., Wolfinger, R. D., Cella, R., et al. (2008). Global analysis of *Arabidopsis* gene expression uncovers a complex array of changes impacting pathogen response and cell cycle during geminivirus infection. *Plant Physiol.* 148, 436–454. doi:10.1104/pp.108.121038
- Asseng, S., Foster, I., and Turner, N. C. (2011). The impact of temperature variability on wheat yields. *Glob. Change Biol.* 17, 997–1012. doi:10.1111/j.1365-2486.2010.02262.x
- Athanasopoulou, K., Boti, M. A., Adamopoulos, P. G., Skourou, P. C., and Scorilas, A. (2021). Third-generation sequencing: the spearhead towards the radical transformation of modern genomics. *Life* 12, 30. doi:10.3390/life12010030
- Barkan, A., and Goldschmidt-Clermont, M. (2000). Participation of nuclear genes in chloroplast gene expression. *Biochimie* 82, 559–572. doi:10.1016/S0300-9084(00)00602-7
- Benny, J., Pisciotto, A., Caruso, T., and Martinelli, F. (2019). Identification of key genes and its chromosome regions linked to drought responses in leaves across different crops through meta-analysis of RNA-Seq data. *BMC Plant Biol.* 19, 194. doi:10.1186/s12870-019-1794-y
- Berkowitz, O., Xu, Y., Liew, L. C., Wang, Y., Zhu, Y., Hurgobin, B., et al. (2021). RNA-seq analysis of laser microdissected *Arabidopsis thaliana* leaf epidermis, mesophyll and vasculature defines tissue-specific transcriptional responses to multiple stress treatments. *Plant J.* 107, 938–955. doi:10.1111/tpj.15314
- Best, C., Mizrahi, R., and Ostersetzer-Biran, O. (2020a). Why so complex? The intricacy of genome structure and gene expression, associated with angiosperm mitochondria, may relate to the regulation of embryo quiescence or dormancy—intrinsic blocks to early plant life. *Plants* 9, 598. doi:10.3390/plants9050598
- Best, C., Sultan, L. D., Murik, O., and Ostersetzer, O. (2020b). Insights into the mitochondrial transcriptome landscapes of two Brassicales plant species, *Arabidopsis thaliana* (var. Col-0) and *Brassica oleracea* (var. botrytis). *Endocyt. Cell Res.* 30, 16–38.
- Bhat, K. A., Mahajan, R., Pakhtoon, M. M., Urwat, U., Bashir, Z., Shah, A. A., et al. (2022). Low temperature stress tolerance: an insight into the omics approaches for legume crops. *Front. Plant Sci.* 13, 888710. doi:10.3389/fpls.2022.888710
- Bitá, C. E., and Gerats, T. (2013). Plant tolerance to high temperature in a changing environment: Scientific fundamentals and production of heat stress-tolerant crops. *Front. Plant Sci.* 4, 273. doi:10.3389/fpls.2013.00273
- Booth, M. W., Breed, M. F., Kendrick, G. A., Bayer, P. E., Severn-Ellis, A. A., and Sinclair, E. A. (2022). Tissue-specific transcriptome profiles identify functional differences key to understanding whole plant response to life in variable salinity. *Biol. Open* 11, bio059147. doi:10.1242/bio.059147
- Calixto, C. P. G., Guo, W., James, A. B., Tzioutziou, N. A., Entizne, J. C., Panter, P. E., et al. (2018). Rapid and dynamic alternative splicing impacts the *Arabidopsis* cold response transcriptome. *Plant Cell* 30, 1424–1444. doi:10.1105/tpc.18.00177
- Cervantes-Pérez, S. A., Thibivilliers, S., Tennant, S., and Libault, M. (2022). Review: challenges and perspectives in applying single nuclei RNA-seq technology in plant biology. *Plant Sci.* 325, 111486. doi:10.1016/j.plantsci.2022.111486
- Cervera, H., Ambrós, S., Bernet, G. P., Rodrigo, G., and Elena, S. F. (2018). Viral fitness correlates with the magnitude and direction of the perturbation induced in the host's transcriptome: the tobacco etch potyvirus—tobacco case study. *Mol. Biol. Evol.* 35, 1599–1615. doi:10.1093/molbev/msy038
- Chen, C., Ge, Y., and Lu, L. (2023). Opportunities and challenges in the application of single-cell and spatial transcriptomics in plants. *Front. Plant Sci.* 14, 1185377. doi:10.3389/fpls.2023.1185377
- Chen, S., and Li, H. (2017). Heat stress regulates the expression of genes at transcriptional and post-transcriptional levels, revealed by RNA-seq in *Brachypodium distachyon*. *Front. Plant Sci.* 7, 2067. doi:10.3389/fpls.2016.02067
- Cheng, Z., Lei, N., Li, S., Liao, W., Shen, J., and Peng, M. (2019). The regulatory effects of *MeTCP4* on cold stress tolerance in *Arabidopsis thaliana*: A transcriptome analysis. *Plant Physiol. Biochem.* 138, 9–16. doi:10.1016/j.plaphy.2019.02.015
- Chesnais, Q., Golyaev, V., Velt, A., Rustenholz, C., Brault, V., Pooggin, M. M., et al. (2022). Comparative plant transcriptome profiling of *Arabidopsis thaliana* Col-0 and *Camelina sativa* var. *celine* infested with *Myzus persicae* aphids acquiring circulative and noncirculative viruses reveals virus- and plant-specific alterations relevant to aphid feeding behavior and transmission. *Microbiol. Spectr.* 10, e0013622. doi:10.1128/spectrum.00136-22
- Chinnusamy, V., Zhu, J., and Zhu, J.-K. (2007). Cold stress regulation of gene expression in plants. *Trends Plant Sci.* 12, 444–451. doi:10.1016/j.tplants.2007.07.002
- Clauw, P., Coppens, F., De Beuf, K., Dhondt, S., Van Daele, T., Maleux, K., et al. (2015). Leaf responses to mild drought stress in natural variants of *Arabidopsis*. *Plant Physiol.* 167, 800–816. doi:10.1104/pp.114.254284
- Coolen, S., Proietti, S., Hickman, R., Davila Olivas, N. H., Huang, P., Van Verk, M. C., et al. (2016). Transcriptome dynamics of *Arabidopsis* during sequential biotic and abiotic stresses. *Plant J.* 86, 249–267. doi:10.1111/tpj.13167
- Cramer, G. R., Urano, K., Delrot, S., Pezzotti, M., and Shinozaki, K. (2011). Effects of abiotic stress on plants: a systems biology perspective. *BMC Plant Biol.* 11, 163. doi:10.1186/1471-2229-11-163
- Daniell, H., Lin, C.-S., Yu, M., and Chang, W.-J. (2016). Chloroplast genomes: diversity, evolution, and applications in genetic engineering. *Genome Biol.* 17, 134. doi:10.1186/s13059-016-1004-2
- Deng, S., Li, Z., Liu, X., Yang, W., and Wang, Y. (2023). Comparative transcriptome analysis reveals potential genes conferring resistance or susceptibility to bacterial canker in tomato. *Horticulturae* 9, 242. doi:10.3390/horticulturae9020242
- De Oliveira-Busatto, L. A., De Almeida, R. M. C., Weber, R. L. M., Favero, D., Bredemeier, C., Da Silva Giordano, C. P., et al. (2022). The soybean Transcriptogram allows a wide genome-to-single-gene analysis that evinces time-dependent drought response. *Plant Mol. Biol. Rep.* 40, 1–27. doi:10.1007/s11105-021-01297-4
- Dong, H. (2024). Application of genome editing techniques to regulate gene expression in crops. *BMC Plant Biol.* 24, 100. doi:10.1186/s12870-024-04786-2
- Dong, Y., Gupta, S., Wargent, J. J., Putterill, J., Macknight, R. C., Gechev, T. S., et al. (2023). Comparative transcriptomics of multi-stress responses in *Pachycladon cheesemanii* and *Arabidopsis thaliana*. *Int. J. Mol. Sci.* 24, 11323. doi:10.3390/ijms241411323
- Du, J., Li, X., Li, T., Yu, D., and Han, B. (2017). Genome-wide transcriptome profiling provides overwintering mechanism of *Agropyron mongolicum*. *BMC Plant Biol.* 17, 138. doi:10.1186/s12870-017-1086-3
- Evans, T. G. (2015). Considerations for the use of transcriptomics in identifying the 'genes that matter' for environmental adaptation. *J. Exp. Biol.* 218, 1925–1935. doi:10.1242/jeb.114306
- Fang, S., Zhao, P., Tan, Z., Peng, Y., Xu, L., Jin, Y., et al. (2022). Combining physio-biochemical characterization and transcriptome analysis reveal the responses to varying degrees of drought stress in *Brassica napus* L. *Int. J. Mol. Sci.* 23, 8555. doi:10.3390/ijms23158555
- Forster, B. P., Heberle-Bors, E., Kasha, K. J., and Touraev, A. (2007). The resurgence of haploids in higher plants. *Trends Plant Sci.* 12, 368–375. doi:10.1016/j.tplants.2007.06.007
- Frank, G., Pressman, E., Ophir, R., Althan, L., Shaked, R., Freedman, M., et al. (2009). Transcriptional profiling of maturing tomato (*Solanum lycopersicum* L.) microspores reveals the involvement of heat shock proteins, ROS scavengers, hormones, and sugars in the heat stress response. *J. Exp. Bot.* 60, 3891–3908. doi:10.1093/jxb/erp234
- Guan, Q., Lu, X., Zeng, H., Zhang, Y., and Zhu, J. (2013). Heat stress induction of *miR398* triggers a regulatory loop that is critical for thermotolerance in *Arabidopsis*. *Plant J.* 74, 840–851. doi:10.1111/tpj.12169
- Gull, A., Ahmad Lone, A., and Ul Islam Wani, N. (2019). "Biotic and abiotic stresses in plants," in *Abiotic and biotic stress in plants*. Editor A. Bosco de Oliveira (London, United Kingdom: IntechOpen Limited). doi:10.5772/intechopen.85832
- Guo, J., Huang, Z., Sun, J., Cui, X., and Liu, Y. (2021). Research progress and future development trends in medicinal plant transcriptomics. *Front. Plant Sci.* 12, 691838. doi:10.3389/fpls.2021.691838
- Guo, W.-L., Chen, B.-H., Chen, X.-J., Guo, Y.-Y., Yang, H.-L., Li, X.-Z., et al. (2018). Transcriptome profiling of pumpkin (*Cucurbita moschata* Duch.) leaves

infected with powdery mildew. *PLoS ONE* 13, e0190175. doi:10.1371/journal.pone.0190175

Hasan, M., and Bae, H. (2017). An overview of stress-induced resveratrol synthesis in grapes: perspectives for resveratrol-enriched grape products. *Molecules* 22, 294. doi:10.3390/molecules22020294

Hu, J., Cai, J., Xu, T., and Kang, H. (2022). Epitranscriptomic mRNA modifications governing plant stress responses: Underlying mechanism and potential application. *Plant Biotechnol. J.* 20, 2245–2257. doi:10.1111/pbi.13913

Huang, F., Lei, Y., Duan, J., Kang, Y., Luo, Y., Ding, D., et al. (2024). Investigation of heat stress responses and adaptation mechanisms by integrative metabolome and transcriptome analysis in tea plants (*Camellia sinensis*). *Sci. Rep.* 14, 10023. doi:10.1038/s41598-024-60411-0

Huang, N., Nie, F., Ni, P., Luo, F., Gao, X., and Wang, J. (2021). NeuralPolish: A novel Nanopore polishing method based on alignment matrix construction and orthogonal Bi-GRU networks. *Bioinformatics* 37, 3120–3127. doi:10.1093/bioinformatics/btab354

Imadi, S. R., Kazi, A. G., Ahanger, M. A., Gucel, S., and Ahmad, P. (2015). Plant transcriptomics and responses to environmental stress: an overview. *J. Genet.* 94, 525–537. doi:10.1007/s12041-015-0545-6

Jin, X., Wang, Z., Li, X., Ai, Q., Wong, D. C. J., Zhang, F., et al. (2024). Current perspectives of lncRNAs in abiotic and biotic stress tolerance in plants. *Front. Plant Sci.* 14, 1334620. doi:10.3389/fpls.2023.1334620

Jo, Y., Lian, S., Chu, H., Cho, J. K., Yoo, S.-H., Choi, H., et al. (2018). Peach RNA viromes in six different peach cultivars. *Sci. Rep.* 8, 1844. doi:10.1038/s41598-018-20256-w

Joubert, M., Van Den Berg, N., Theron, J., and Swart, V. (2022). Transcriptomics advancement in the complex response of plants to viroid infection. *Int. J. Mol. Sci.* 23, 7677. doi:10.3390/ijms23147677

Jung, J. H., Kim, H.-Y., Kim, H. S., and Jung, S. H. (2020). Transcriptome analysis of *Panax ginseng* response to high light stress. *J. Ginseng Res.* 44, 312–320. doi:10.1016/j.jgr.2018.12.009

Ke, J., Li, M.-T., Xu, S., Ma, J., Liu, M.-Y., and Han, Y. (2023). Advances for pharmacological activities of *Polygonum cuspidatum* - A review. *Pharm. Biol.* 61, 177–188. doi:10.1080/13880209.2022.2158349

Kenrick, P., and Crane, P. R. (1997). *The origin and early diversification of land plants: a cladistic study*. Washington, DC: Smithsonian Institution Press.

Kottapalli, K. R., Rakwal, R., Satoh, K., Shibato, J., Kottapalli, P., Iwahashi, H., et al. (2007). Transcriptional profiling of *indica* rice cultivar IET585 (Ajaya) infected with bacterial leaf blight pathogen *Xanthomonas oryzae pv oryzae*. *Plant Physiol. Biochem.* 45, 834–850. doi:10.1016/j.plaphy.2007.07.013

Kourani, M., Mohareb, F., Rezwani, F. I., Anastasiadi, M., and Hammond, J. P. (2022). Genetic and physiological responses to heat stress in *Brassica napus*. *Front. Plant Sci.* 13, 832147. doi:10.3389/fpls.2022.832147

Kumar, A., Kanak, K. R., Arunachalam, A., Dass, R. S., and Lakshmi, P. T. V. (2022). Comparative transcriptome profiling and weighted gene co-expression network analysis to identify core genes in maize (*Zea mays* L.) silks infected by multiple fungi. *Front. Plant Sci.* 13, 985396. doi:10.3389/fpls.2022.985396

Kumar, J., Gunapati, S., Kianian, S. F., and Singh, S. P. (2018). Comparative analysis of transcriptome in two wheat genotypes with contrasting levels of drought tolerance. *Protoplasma* 255, 1487–1504. doi:10.1007/s00709-018-1237-x

Kumar, M., Chauhan, A. S., Kumar, M., Yusuf, M. A., Sanyal, I., and Chauhan, P. S. (2019). Transcriptome sequencing of chickpea (*Cicer arietinum* L.) genotypes for identification of drought-responsive genes under drought stress condition. *Plant Mol. Biol. Rep.* 37, 186–203. doi:10.1007/s11105-019-01147-4

Kumar, M., Prusty, M. R., Pandey, M. K., Singh, P. K., Bohra, A., Guo, B., et al. (2023). Application of CRISPR/Cas9-mediated gene editing for abiotic stress management in crop plants. *Front. Plant Sci.* 14, 1157678. doi:10.3389/fpls.2023.1157678

Li, L., Liang, Y., Liu, Y., Sun, Z., Liu, Y., Yuan, Z., et al. (2023). Transcriptome analyses reveal photosynthesis-related genes involved in photosynthetic regulation under low temperature stress in *Lavandula angustifolia* Mill. *Front. Plant Sci.* 14, 1268666. doi:10.3389/fpls.2023.1268666

Li, X., Liu, L., Sun, S., Li, Y., Jia, L., Ye, S., et al. (2022). Leaf-transcriptome profiles of *phoebe bournei* provide insights into temporal drought stress responses. *Front. Plant Sci.* 13, 1010314. doi:10.3389/fpls.2022.1010314

Li, Y. M., Li, S. X., Li, X. S., and Li, C. Y. (2018). Transcriptome studies with the third-generation sequencing technology. *Life Sci. Instrum.* 16, 114–121.

Li, Z., Tang, Y., Lan, G., Yu, L., Ding, S., She, X., et al. (2023). Transcriptome and metabolome analyses reveal that jasmonic acids may facilitate the infection of cucumber green mottle mosaic virus in bottle gourd. *Int. J. Mol. Sci.* 24, 16566. doi:10.3390/ijms242316566

Liu, Y., Cai, Y., Li, Y., Zhang, X., Shi, N., Zhao, J., et al. (2022). Dynamic changes in the transcriptome landscape of *Arabidopsis thaliana* in response to cold stress. *Front. Plant Sci.* 13, 983460. doi:10.3389/fpls.2022.983460

Liu, Z., Xu, J., Wu, X., Wang, Y., Lin, Y., Wu, D., et al. (2019). Molecular analysis of UV-C induced resveratrol accumulation in *Polygonum cuspidatum* leaves. *Int. J. Mol. Sci.* 20, 6185. doi:10.3390/ijms20246185

Lorence, A., Chevone, B. L., Mendes, P., and Nessler, C. L. (2004). *myo* -inositol oxygenase offers a possible entry point into plant ascorbate biosynthesis. *Plant Physiol.* 134, 1200–1205. doi:10.1104/pp.103.033936

Lowe, R., Shirley, N., Bleackley, M., Dolan, S., and Shafee, T. (2017). Transcriptomics technologies. *PLoS Comput. Biol.* 13, e1005457. doi:10.1371/journal.pcbi.1005457

Lu, L., Yang, D., Tang, D., Li, S., and Chen, Z. (2020). Transcriptome analysis of different rice cultivars provides novel insights into the rice response to bacterial leaf streak infection. *Funct. Integr. Genomics* 20, 681–693. doi:10.1007/s10142-020-00744-x

Ma, L., Coulter, J. A., Liu, L., Zhao, Y., Chang, Y., Pu, Y., et al. (2019). Transcriptome analysis reveals key cold-stress-responsive genes in winter rapeseed (*Brassica rapa* L.). *Int. J. Mol. Sci.* 20, 1071. doi:10.3390/ijms20051071

Ma, L. N., Yang, J. B., Ding, Y. F., and Li, Y. K. (2019). Research progress on three generations sequencing technology and its application. *China Anim. Husb. Vet. Med.* 46, 2246–2256. doi:10.16431/j.cnki.1671-7236.2019.08.007

Mahalingam, R., Duhan, N., Kaundal, R., Smertenko, A., Nazarov, T., and Bregitzer, P. (2022). Heat and drought induced transcriptomic changes in barley varieties with contrasting stress response phenotypes. *Front. Plant Sci.* 13, 1066421. doi:10.3389/fpls.2022.1066421

Malavika, M., Prakash, V., and Chakraborty, S. (2023). Recovery from virus infection: plant's armory in action. *Planta* 257, 103. doi:10.1007/s00425-023-04137-9

Martin, R. C., Kronmiller, B. A., and Dombrowski, J. E. (2021). Transcriptome analysis of *Lolium temulentum* exposed to a combination of drought and heat stress. *Plants* 10, 2247. doi:10.3390/plants10112247

McDowell, J. M., and Dangel, J. L. (2000). Signal transduction in the plant immune response. *Trends Biochem. Sci.* 25, 79–82. doi:10.1016/S0968-0004(99)01532-7

Medzihradsky, A., Gyula, P., Sós-Hegedűs, A., Szittya, G., and Burgián, J. (2019). Transcriptome reprogramming in the shoot apical meristem of CymRSV-infected *Nicotiana benthamiana* plants associates with viral exclusion and the lack of recovery. *Mol. Plant Pathol.* 20, 1748–1758. doi:10.1111/mpp.12875

Méndez-López, E., Donaire, L., Gosálvez, B., Díaz-Vivancos, P., Sánchez-Pina, M. A., Tilsner, J., et al. (2023). Tomato SIGSTU38 interacts with the PepMV coat protein and promotes viral infection. *New Phytol.* 238, 332–348. doi:10.1111/nph.18728

Miao, Z., Xu, W., Li, D., Hu, X., Liu, J., Zhang, R., et al. (2015). *De novo* transcriptome analysis of *Medicago falcata* reveals novel insights about the mechanisms underlying abiotic stress-responsive pathway. *BMC Genomics* 16, 818. doi:10.1186/s12864-015-2019-x

Mifsud, J. C. O., Gallagher, R. V., Holmes, E. C., and Geoghegan, J. L. (2022). Transcriptome mining expands knowledge of RNA viruses across the plant kingdom. *J. Virol.* 96, e0026022–22. doi:10.1128/jvi.00260-22

Mikołajczak, K., Kuczyńska, A., Krajewski, P., Kempa, M., and Nuc, M. (2023). Transcriptome profiling disclosed the effect of single and combined drought and heat stress on reprogramming of genes expression in barley flag leaf. *Front. Plant Sci.* 13, 1096685. doi:10.3389/fpls.2022.1096685

Morris, J. L., Puttick, M. N., Clark, J. W., Edwards, D., Kenrick, P., Pressel, S., et al. (2018). The timescale of early land plant evolution. *Proc. Natl. Acad. Sci. U.S.A.* 115, E2274–E2283. doi:10.1073/pnas.1719588115

National Center for Biotechnology Information (2024). National Center for Biotechnology Information. Available at: <https://pubmed.ncbi.nlm.nih.gov/> (Accessed September 25, 2024).

Naydenov, N. G., Khanam, S., Siniauskaya, M., and Nakamura, C. (2010). Profiling of mitochondrial transcriptome in germinating wheat embryos and seedlings subjected to cold, salinity and osmotic stresses. *Genes Genet. Syst.* 85, 31–42. doi:10.1266/ggs.85.31

Obaid, A. Y., Sabir, J. S. M., Atef, A., Liu, X., Edris, S., El-Domyati, F. M., et al. (2016). Analysis of transcriptional response to heat stress in *Rhazya stricta*. *BMC Plant Biol.* 16, 252. doi:10.1186/s12870-016-0938-6

- Pieterse, C. M. J., Leon-Reyes, A., Van der Ent, S., and Van Wees, S. C. M. (2009). Networking by small-molecule hormones in plant immunity. *Nat. Chem. Biol.* 5, 308–316. doi:10.1038/nchembio.164
- Rashid, F. A. A., Crisp, P. A., Zhang, Y., Berkowitz, O., Pogson, B. J., Day, D. A., et al. (2020). Molecular and physiological responses during thermal acclimation of leaf photosynthesis and respiration in rice. *Plant, Cell & Environ.* 43, 594–610. doi:10.1111/pce.13706
- Raza, A., and Wu, Q. (2022). “Diagnosis of viral diseases using deep sequencing and metagenomics analyses,” in *Plant virology*. Editors A. Wang and Y. Li (New York, NY: Springer US), 225–243. doi:10.1007/978-1-0716-1835-6_22
- Rivero, R. M., Mittler, R., Blumwald, E., and Zandalinas, S. I. (2022). Developing climate-resilient crops: improving plant tolerance to stress combination. *Plant J.* 109, 373–389. doi:10.1111/tjp.15483
- Roy, B. G., DeBlasio, S., Yang, Y., Thannhauser, T., Heck, M., and Fuchs, M. (2023). Profiling plant proteome and transcriptome changes during grapevine fanleaf virus infection. *J. Proteome Res.* 22, 1997–2017. doi:10.1021/acs.jproteome.3c00069
- Rurek, M. (2016). Participation of non-coding RNAs in plant organelle biogenesis. *Acta Biochim. Pol.* 63, 653–663. doi:10.18388/abp.2016_1346
- Rurek, M., Czołpińska, M., Pawłowski, T., Krzesiński, W., and Spizewski, T. (2018). Cold and heat stress diversely alter both cauliflower respiration and distinct mitochondrial proteins including OXPHOS components and matrix enzymes. *Int. J. Mol. Sci.* 19, 877. doi:10.3390/ijms19030877
- Sato, M., Tsuda, K., Wang, L., Coller, J., Watanabe, Y., Glazebrook, J., et al. (2010). Network modeling reveals prevalent negative regulatory relationships between signaling sectors in Arabidopsis immune signaling. *PLoS Pathog.* 6, e1001011. doi:10.1371/journal.ppat.1001011
- Schliesky, S., Gowik, U., Weber, A. P. M., and Bräutigam, A. (2012). RNA-seq assembly – are we there yet? *Front. Plant Sci.* 3, 220. doi:10.3389/fpls.2012.00220
- Sewelam, N., Brilhaus, D., Bräutigam, A., Alseekh, S., Fernie, A. R., and Maurino, V. G. (2020). Molecular plant responses to combined abiotic stresses put a spotlight on unknown and abundant genes. *J. Exp. Bot.* 71, 5098–5112. doi:10.1093/jxb/eraa250
- Shanker, A. K., Maheswari, M., Yadav, S. K., Desai, S., Bhanu, D., Attal, N. B., et al. (2014). Drought stress responses in crops. *Funct. Integr. Genomics* 14, 11–22. doi:10.1007/s10142-013-0356-x
- Sharma, R., Singh, G., Bhattacharya, S., and Singh, A. (2018). Comparative transcriptome meta-analysis of Arabidopsis thaliana under drought and cold stress. *PLoS ONE* 13, e0203266. doi:10.1371/journal.pone.0203266
- Singh, S., Parihar, P., Singh, R., Singh, V. P., and Prasad, S. M. (2016). Heavy metal tolerance in plants: role of transcriptomics, proteomics, metabolomics, and ionomics. *Front. Plant Sci.* 6, 1143. doi:10.3389/fpls.2015.01143
- Son, S., and Park, S. R. (2023). Plant translational reprogramming for stress resilience. *Front. Plant Sci.* 14, 1151587. doi:10.3389/fpls.2023.1151587
- Song, Y., Ma, B., Guo, Q., Zhou, L., Lv, C., Liu, X., et al. (2022). UV-B induces the expression of flavonoid biosynthetic pathways in blueberry (*Vaccinium corymbosum*) calli. *Front. Plant Sci.* 13, 1079087. doi:10.3389/fpls.2022.1079087
- Spanò, R., Ferrara, M., Montemurro, C., Mulè, G., Gallitelli, D., and Mascia, T. (2020). Grafting alters tomato transcriptome and enhances tolerance to an airborne virus infection. *Sci. Rep.* 10, 2538. doi:10.1038/s41598-020-59421-5
- Sprang, M., Andrade-Navarro, M. A., and Fontaine, J.-F. (2022). Batch effect detection and correction in RNA-seq data using machine-learning-based automated assessment of quality. *BMC Bioinformatics* 23, 279. doi:10.1186/s12859-022-04775-y
- Suzuki, N., Bassil, E., Hamilton, J. S., Inupakutika, M. A., Zandalinas, S. I., Tripathy, D., et al. (2016). ABA is required for plant acclimation to a combination of salt and heat stress. *PLoS ONE* 11, e0147625. doi:10.1371/journal.pone.0147625
- Tan, X., Zhang, H., Yang, Z., Wei, Z., Li, Y., Chen, J., et al. (2022). NF-YA transcription factors suppress jasmonic acid-mediated antiviral defense and facilitate viral infection in rice. *PLoS Pathog.* 18, e1010548. doi:10.1371/journal.ppat.1010548
- Tu, M., Du, C., Yu, B., Wang, G., Deng, Y., Wang, Y., et al. (2023). Current advances in the molecular regulation of abiotic stress tolerance in sorghum via transcriptomic, proteomic, and metabolomic approaches. *Front. Plant Sci.* 14, 1147328. doi:10.3389/fpls.2023.1147328
- Tyagi, A., Kumar, S., and Mohapatra, T. (2023). Biochemical, physiological and molecular responses of rice to terminal drought stress: transcriptome profiling of leaf and root reveals the key stress-responsive genes. *J. Plant Biochem. Biotechnol.* doi:10.1007/s13562-023-00865-x
- Tyagi, P., Singh, D., Mathur, S., Singh, A., and Ranjan, R. (2022). Upcoming progress of transcriptomics studies on plants: an overview. *Front. Plant Sci.* 13, 1030890. doi:10.3389/fpls.2022.1030890
- Umar, O., Ranti, L., Abdulbaki, A., Bola, A., Abdulhamid, A., and Biola, M. (2021). “Stresses in plants: biotic and abiotic,” in *Current trends in wheat research*. Editor Mahmood-ur-Rahman Ansari (London, United Kingdom: IntechOpen Limited). Available at: www.intechopen.com/chapters/79012.
- Valdés-López, O., Batek, J., Gomez-Hernandez, N., Nguyen, C. T., Isidra-Arellano, M. C., Zhang, N., et al. (2016). Soybean roots grown under heat stress show global changes in their transcriptional and proteomic profiles. *Front. Plant Sci.* 7, 517. doi:10.3389/fpls.2016.00517
- Vashisth, D., Kumar, R., Rastogi, S., Patel, V. K., Kalra, A., Gupta, M. M., et al. (2018). Transcriptome changes induced by abiotic stresses in *Artemisia annua*. *Sci. Rep.* 8, 3423. doi:10.1038/s41598-018-21598-1
- Verma, S., Nizam, S., and Verma, P. K. (2013). “Biotic and abiotic stress signaling in plants,” in: *Stress signaling in plants: genomics and proteomics perspective, volume 1*. Editors M. Sarwat, A. Ahmad, and M. Abidin (New York, NY: Springer New York), 1, 25–49. doi:10.1007/978-1-4614-6372-6_2
- Vicente, R., Bolger, A. M., Martínez-Carrasco, R., Pérez, P., Gutiérrez, E., Usadel, B., et al. (2019). *De novo* transcriptome analysis of durum wheat flag leaves provides new insights into the regulatory response to elevated CO₂ and high temperature. *Front. Plant Sci.* 10, 1605. doi:10.3389/fpls.2019.01605
- Wang, H., Xu, Y., Zhang, Z., Zhang, G., Tan, C., and Ye, L. (2024). Development and application of transcriptomics technologies in plant science. *Crop Des.* 3, 100057. doi:10.1016/j.crope.2024.100057
- Wang, X., Li, N., Li, W., Gao, X., Cha, M., Qin, L., et al. (2020). Advances in transcriptomics in the response to stress in plants. *Glob. Med. Genet.* 07, 030–034. doi:10.1055/s-0040-1714414
- Wang, Z., Gerstein, M., and Snyder, M. (2009). RNA-seq: a revolutionary tool for transcriptomics. *Nat. Rev. Genet.* 10, 57–63. doi:10.1038/nrg2484
- Wu, L., Taohua, Z., Gui, W., Xu, L., Li, J., and Ding, Y. (2015). Five pectinase gene expressions highly responding to heat stress in rice floral organs revealed by RNA-seq analysis. *Biochem. Biophysical Res. Commun.* 463, 407–413. doi:10.1016/j.bbrc.2015.05.085
- Xia, K., Wu, Q., Yang, Y., Liu, Q., Wang, Z., Zhao, Z., et al. (2024). Drought stress induced different response mechanisms in three Dendrobium species under different photosynthetic pathways. *Int. J. Mol. Sci.* 25, 2731. doi:10.3390/ijms25052731
- Xing, X., Ding, Y., Jin, J., Song, A., Chen, S., Chen, F., et al. (2021). Physiological and transcript analyses reveal the mechanism by which melatonin alleviates heat stress in Chrysanthemum seedlings. *Front. Plant Sci.* 12, 673236. doi:10.3389/fpls.2021.673236
- Xu, W., Li, R., Zhang, N., Ma, F., Jiao, Y., and Wang, Z. (2014). Transcriptome profiling of *Vitis amurensis*, an extremely cold-tolerant Chinese wild *Vitis* species, reveals candidate genes and events that potentially connected to cold stress. *Plant Mol. Biol.* 86, 527–541. doi:10.1007/s11103-014-0245-2
- Xu, X., Legay, S., Sergeant, K., Zorzan, S., Leclercq, C. C., Charton, S., et al. (2021). Molecular insights into plant desiccation tolerance: Transcriptomics, proteomics and targeted metabolite profiling in *Craterostigma plantagineum*. *Plant J.* 107, 377–398. doi:10.1111/tjp.15294
- Yan, J., Qian, L., Zhu, W., Qiu, J., Lu, Q., Wang, X., et al. (2020). Integrated analysis of the transcriptome and metabolome of purple and green leaves of *Tetragonia hemsleyana* reveals gene expression patterns involved in anthocyanin biosynthesis. *PLoS ONE* 15, e0230154. doi:10.1371/journal.pone.0230154
- Yang, Y., Xia, J., Fang, X., Jia, H., Wang, X., Lin, Y., et al. (2023). Drought stress in ‘Shine Muscat’ grapevine: Consequences and a novel mitigation strategy–5-aminolevulinic acid. *Front. Plant Sci.* 14, 1129114. doi:10.3389/fpls.2023.1129114
- Yokotani, N., Hasegawa, Y., Sato, M., Hirakawa, H., Kouzai, Y., Nishizawa, Y., et al. (2021). Transcriptome analysis of *Clavibacter michiganensis* subsp. *michiganensis*-infected tomatoes: a role of salicylic acid in the host response. *BMC Plant Biol.* 21, 476. doi:10.1186/s12870-021-03251-8
- Young, L. W., Wilen, R. W., and Bonham-Smith, P. C. (2004). High temperature stress of *Brassica napus* during flowering reduces micro- and megagametophyte fertility, induces fruit abortion, and disrupts seed production. *J. Exp. Bot.* 55, 485–495. doi:10.1093/jxb/erh038
- Yu, Y., Zhang, Y., Chen, X., and Chen, Y. (2019). Plant noncoding RNAs: Hidden players in development and stress responses. *Annu. Rev. Cell Dev. Biol.* 35, 407–431. doi:10.1146/annurev-cellbio-100818-125218
- Zhang, C., Chen, J., Huang, W., Song, X., and Niu, J. (2021). Transcriptomics and metabolomics reveal purine and phenylpropanoid metabolism response to drought stress in *Dendrobium sinense*, an endemic orchid species in Hainan island. *Front. Genet.* 12, 692702. doi:10.3389/fgene.2021.692702

Zhang, H. (2019). The review of transcriptome sequencing: principles, history and advances. *IOP Conf. Ser. Earth Environ. Sci.* 332, 042003. doi:10.1088/1755-1315/332/4/042003

Zhang, H., Yang, Y., Wang, C., Liu, M., Li, H., Fu, Y., et al. (2014). Large-scale transcriptome comparison reveals distinct gene activations in wheat responding to stripe rust and powdery mildew. *BMC Genomics* 15, 898. doi:10.1186/1471-2164-15-898

Zhang, X., Ding, X., Ji, Y., Wang, S., Chen, Y., Luo, J., et al. (2018). Measurement of metabolite variations and analysis of related gene expression in Chinese liquorice (*Glycyrrhiza uralensis*) plants under UV-B irradiation. *Sci. Rep.* 8, 6144. doi:10.1038/s41598-018-24284-4

Zhou, H., Yu, L., Liu, S., Zhu, A., Yang, Y., Chen, C., et al. (2023). Transcriptome comparison analyses in UV-B induced AsA accumulation of *Lactuca sativa* L. *BMC Genomics* 24, 61. doi:10.1186/s12864-023-09133-7

Zhou, Y., Cho, W. K., Byun, H., Kil, E., Bak, S., Moon, D., et al. (2019). Transcriptome profiles of tomato plants after neutron irradiation and infection with TYLCV. *Physiol. Plant.* 165, 427–441. doi:10.1111/ppl.12913

Zhu, C., Li, X., and Zheng, J. (2018). Transcriptome profiling using Illumina- and SMRT-based RNA-seq of hot pepper for in-depth understanding of genes involved in CMV infection. *Gene* 666, 123–133. doi:10.1016/j.gene.2018.05.004

Zhu, H., Zhou, Y., Zhai, H., He, S., Zhao, N., and Liu, Q. (2019). Transcriptome profiling reveals insights into the molecular mechanism of drought tolerance in sweetpotato. *J. Integr. Agric.* 18, 9–23. doi:10.1016/S2095-3119(18)61934-3

Zhu, J.-K. (2002). Salt and drought stress signal transduction in plants. *Annu. Rev. Plant Biol.* 53, 247–273. doi:10.1146/annurev.arplant.53.091401.143329

Glossary

ABA	abscisic acid	CXIP	CAX-interacting protein
ABI3VP1	ABSCISIC ACID INSENSITIVE 3 VIVIPAROUS 1	CymRSV	Cymbidium ringspot virus
ABF	ABSCISIC ACID RESPONSIVE ELEMENT-BINDING FACTOR	DEGs	differentially-expressed genes
ACC	1-aminocyclopropane-1-carboxylic oxidase	DIMI	DIMINUTO
ALA	5-aminolevulinic acid	Dof	DNA-binding with one finger
AOS	allene oxide synthase	EIL	ethylene insensitive-like
AOX	alternative oxidase	ER	endoplasmic reticulum
AP	APETALA	EREBP	ethylene-responsive element binding protein
APX	ascorbate peroxidase	ERF	ethylene response factor
ARF	auxin response factor	ETI	effector-triggered immunity
ARID	AT-rich interactive domain	FLS	flavonol synthase
ASC	L-ascorbic acid	FRS	FAR1-RELATED SEQUENCE
AUX	auxin receptor	FT	FLOWERING LOCUS T
BBR-BPC	Barley B Recombinant/Basic PentaCysteine	G2-like	GOLDEN2-LIKE
BIM	BES1-INTERACTING MYC-LIKE	GABA	γ-aminobutyric acid
bHLH	basic helix–loop–helix	GARP	GOLDEN2, ARR-B and Psr1 superfamily
BLS	bacterial leaf streak	GFLV	grapevine fanleaf virus
BPM	BTB/POZ and MATH domain-containing protein	GH3	Gretchen Hagen3
BT	BTB and TAZ domain protein	GID	GA-INSENSITIVE DWARF
bHLH	basic helix-loop-helix	GRAS	GIBBERELLIC-ACID INSENSITIVE, REPRESSOR of GAI and SCARECROW
bZIP	basic (region) leucine zipper	GRF	growth regulating factor
CaLCuV	cabbage leaf curl virus	GSTU	glutathione S-transferase belonging to the <i>tau</i> class
CAM	crassulacean acid metabolism	HAB	HYPERSENSITIVE TO ABSCISIC ACID
CaMV	cauliflower mosaic virus	HAP	CCAAT-box binding protein
CAT	catalase	HD	homeodomain
CBP	calmodulin-binding protein	HLH	helix-loop-helix
CDP	CAAT displacement protein (transcriptional repressor)	HR	hypersensitive response
CGMMV	cucumber green mottle mosaic virus	HSF	heat shock factor
C2H	zinc finger protein	HSP	heat shock protein
C3H	zinc finger CCCH domain-containing protein	JA	jasmonic acid
C4H	4-cinnamate hydroxylase	LEA	late-embryogenesis abundant
CHI	chalcone isomerase	LHC	light-harvesting complex
CHS	chalcone synthase	LIM	homeobox transcription factor
4CL	4-coumarate: CoA ligase	LOX	lipoxygenase
Clp	caseinolytic protease	MADS	MINICHROMOSOME MAINTENANCE 1/AGAMOUS/DEFICIENS/SERUM RESPONSE FACTOR
CLP	chaperonin-like protein	MAPK	mitogen-associated protein kinase
CMV	cucumber mosaic virus	MDHAR	monodehydroascorbate reductase
CRISPR/Cas	clustered regularly interspaced short palindromic repeats/CRISPR-associated	MIOX	<i>myo</i> -inositol oxygenase
CRK	cysteine-rich receptor-like kinase	MYB	myeloblastosis

NAC	no apical meristem/ATAF1/cup-shaped cotyledon	WUS	WUSCHEL
NF-Y	nuclear factor Y	ZIM	zinc-finger inflorescence meristem
NIN	nodule inception	ZIP	leucine zipper
OXPHOS	oxidative phosphorylation		
PAL	phenylalanine ammonia-lyase		
PAMP	pathogen-associated molecular pattern		
PCD	programmed cell death		
PcG	Polycomb group		
PDH	proline dehydrogenase		
PEPC	phosphoenolpyruvate carboxylase		
PepMV	pepino mosaic virus		
PLATZ	plant AT-rich sequence and zinc-binding protein		
POD	peroxidase		
PR	pathogen-related		
PS	photosystem		
PTI	PAMP-triggered immunity		
RGA	resistance gene analogue		
RLK	receptor-like kinase		
ROS	reactive oxidative species		
RR	response regulator		
RSV	rice stripe virus		
RWP-RK	transcription factor with RWPxRK motif		
SA	salicylic acid		
SBP	SQUAMOSA-PROMOTER BINDING PROTEIN		
SOD	superoxide dismutase		
SMRT	single-molecule real-time		
SRBSDV	Southern rice blackstreaked dwarf virus		
STS	stilbene synthase		
TCP	bHLH DNA-binding domain		
TEV	tobacco etch potyvirus		
TF	transcription factor		
TMV	tobacco mosaic virus		
TUB	Tubby family of bipartite transcription factors		
TuYV	turnip yellows virus		
TYLCV	tomato yellow leaf curl virus		
UFGT	UDP-glucose:flavonoid 3-O-glucosyltransferase		
USP	universal stress protein		
WAKL	wall-associated receptor kinase-like		
WAKS	wall-associated kinases		
WRKY	transcription factor family		
WT	wild type		

circROCK1 Promotes septic myocardial injury through regulating miR-96-5p/OXSR1 axis

ZhiYu He¹, Lingling Xu¹, Xiaojun Zeng¹, Biqing Yang², Peiying Liu¹, Dunzheng Han¹, Hao Xue³ and Bihui Luo¹✉

¹Department of cardiovascular, The First Affiliated Hospital of Guangzhou Medical University, Guangzhou City, Guangdong Province, 510120, China; ²Stroke Center of Guangzhou Panyu Central Hospital, Guangzhou City, Guangdong Province, 511486, China; ³Department of Cardiovascular, Meizhou People's Hospital, Meizhou City, Guangdong Province, 514011, China

Objective: A recent high-throughput sequencing showed that circular RNA Rho-associated kinase 1 (circROCK1) is abnormally highly expressed in sepsis, but whether it is involved in sepsis development remains unclear. The objective of this study was to investigate the biological function of circROCK1 in sepsis-induced myocardial injury and reveal its potential downstream molecular mechanism. **Methods:** Real-time reverse transcriptase-polymerase chain reaction was applied to detect circROCK1 and miR-96-5p expressions in the serum of septic patients. Spearman correlation analysis examined the correlation between circROCK1 and the clinicopathological characteristics of septic patients. The Cecal puncture and ligation (CLP) method was used to establish an *in vivo* sepsis model. circROCK1 and miR-96-5p expressions in mice were modified by injection of lentivirus or oligonucleotide. The left ventricular systolic pressure, left ventricular end-diastolic pressure, and the maximum increase/decrease rate of left ventricular pressure were checked. ELISA was applied to detect inflammatory factors levels as well as myocardial injury markers levels. Hematoxylin and eosin staining was performed to observe pathological changes in myocardial tissues, and Western blot examined phosphorylated nuclear factor (NF)-κB and oxidative stress-responsive 1 (OXSR1) expression. Dual luciferase reporter experiment was conducted to confirm the targeting relationship between circROCK1, OXSR1, and miR-96-5p. **Results:** circROCK1 and OXSR1 were highly expressed in sepsis and miR-96-5p was under-expressed. circROCK1 was positively correlated with serum creatinine, C-reactive protein, procalcitonin, and sequential organ failure assessment scores in septic patients. Silencing circROCK1 could improve the diastolic and systolic function of CLP mice, as well as myocardial damage, reduce myocardial tissue edema and necrosis, and inhibit inflammatory factor level and phosphorylated NF-κB expression. Down-regulating miR-96-5p promoted myocardial injury in CLP mice. Silencing circROCK1 and miR-96-5p inhibited and promoted OXSR1 expression, respectively. Both circROCK1 and OXSR1 had a targeting relationship with miR-96-5p. **Conclusion:** CircROCK1 promotes myocardial injury in septic mice by regulating the miR-96-5p/OXSR1 axis, and it can be used as a potential target for treating septic myocardial dysfunction.

Keywords: CircROCK1, OXSR1, miR-96-5p, sepsis, myocardial injury

Received: 08 November, 22; revised: 28 April, 2023; accepted: 26 May, 2023; available on-line: 18 September, 2023

✉e-mail: luobihui73@cmu.edu.cn

Acknowledgements of Financial Support: Medical Science and Technology Research Foundation of Guangdong Province of China (A2021028). Science and Technology Plan Foundation of Guangzhou, 202201010855. National Innovation and Entrepreneurship Training Program for College Students (2021A018). College Students' Science and Technology Innovation Cultivation Fund Project of Guangdong Province (pdjh2022b0429). College Students' Science and Technology Innovation Project of Guangzhou Medical University, 2021A018.

Abbreviations: circROCK1, circular RNA Rho-associated kinase 1; CLP, Cecal puncture and ligation; MOF, multiple-organ failure; OXSR1, oxidative stress-responsive 1

INTRODUCTION

Sepsis is an acute systemic infection caused by a variety of bacteria invading the blood circulation. The main clinical manifestations are rapid onset, fever, tachypnea, shivers, hepatosplenomegaly, etc. (Stanski & Wong, 2020; Rubio *et al.*, 2019). In severe cases, septic shock and multiple-organ failure (MOF) may occur (Lelubre and Vincent 2018). Sepsis has a high morbidity and mortality rate, especially for those with weakened immune systems, and about 50% of patients with sepsis require admission to an intensive care unit (Salomão *et al.*, 2019). Among common complications of sepsis, cardiac dysfunctions, such as myocardial injury and depression (Yang *et al.*, 2023), are characterized by impaired myocardial contractility and ejection fraction, with mortality up to 70% (Li *et al.*, 2013; Settergren & Henareh, 2014; Bansal *et al.*, 2023). Sepsis triggers a systemic inflammatory response that activates the body's immune system and releases a variety of inflammatory mediators. These inflammatory mediators cause damage to cardiomyocytes and induce apoptosis (Zhou *et al.*, 2022; Zhen *et al.*, 2022). Therefore, exploring the potential molecular mechanism of sepsis-induced myocardial injury is essential for promoting the survival rate of patients with sepsis-induced myocardial injury.

Circular RNA (circRNA) is formed under special and selective shearing. Unlike linear RNA, circRNA is basically derived from the exons or introns of its parent gene (Kristensen *et al.*, 2018; Memczak *et al.*, 2013). Based on a recent genome-wide analysis of non-coding RNA, in comparison with healthy individuals, more than 80% of septic patients showed differential expression. These molecules act in innate cell immunity, mitochondrial function, and apoptosis (Nie *et al.*, 2020). As a non-coding RNA, circRNA recently has been considered to have a vital relationship with sepsis occurrence and development. CircRNA is involved in regulating multi-

ple-organ injury in septic patients, like lung (Zou *et al.*, 2020), kidney (Shi *et al.*, 2020), and liver injury (Xiong *et al.*, 2021). Circular RNA Rho-associated kinase 1 (circROCK1) is an essential member of the circRNA family and has been shown to be differentially expressed in sepsis (Bao *et al.*, 2019). However, it is not clear whether it has an impact on septic myocardial injury.

This work investigated serum circROCK1 expression level and its clinical effect on septic patients. The effect of circROCK1 on myocardial function and myocardial inflammation in sepsis was investigated *in vivo* by establishing a mouse model by cecal puncture and ligation (CLP). The results revealed that circRNA promoted myocardial injury in sepsis by sponging miR-96-5p to mediate oxidative stress-responsive 1(OXSR1) expression.

METHODS

Clinical samples

Healthy people (n=37) were randomly selected from the health examination center of The First Affiliated Hospital of Guangzhou Medical University. From September 2018 to January 2020, blood samples were obtained from patients with sepsis (n=44) and septic shock (n=19) at The First Affiliated Hospital of Guangzhou Medical University. The diagnosis of sepsis or septic shock is based on the International Guidelines for the Management of Sepsis and Septic Shock: 2016. This research was approved by The First Affiliated Hospital of Guangzhou Medical University Institutional Ethics Committee. All subjects and their families had signed the informed consent form.

Diagnostic criteria

Sepsis is diagnosed in reference to *International Guidelines for the Management of Sepsis and Septic Shock: 2016*, with a Sequential Organ Failure Assessment (SOFA) score of more than 2. Patients diagnosed with sepsis who required adequate volumetric resuscitation and sustained hypotension with pressors to maintain arterial pressure of 65 mmHg or higher and serum lactate levels greater than 2 mmol/L (18 mg/dL) were identified as having septic shock.

Exclusion criteria

Exclusion criteria: (1) Under 18 years old; (2) MOF caused by other non-infectious factors; (3) Autoimmune diseases treated with steroids or immunosuppressive therapy; (4) Complications with other diseases that affect blood coagulation; (5) Malignant tumors; (6) Complications with other diseases that may affect this study results; (7) Immunosuppressive drug treatment within the last three months.

Clinical data collection

Clinical information was recorded, including age, gender, body mass index (BMI), and SOFA score. Additionally, Quzhou People's Hospital clinical laboratory provided routine blood test results (serum creatinine [Scr], white blood cells, albumin, C-reactive protein [CRP], and procalcitonin [PCT]).

Septic animal model establishment

C57BL/6 mice (25±5 g) were kept in cages in a temperature-controlled room with a 12-hour light/dark cycle

and a free diet and water. Twenty-four mice were allocated into the sham group (n=12) and the CLP group (n=12) to evaluate the survival rate within 48 hours after surgery. The survival rate of mice after CLP was measured every 2 h for 48 h.

In the following experiment, another 72 mice were used, 12 of which underwent sham surgery and the rest received CLP. These mice were allocated into 5 groups (n=12 for each): Sham group (CLP without ligation and puncture on the cecum), CLP group (CLP surgery), sh-circROCK1 group (injection with 5×10⁷ sh-circROCK1 lentiviral vector particles via tail vein one week before CLP), sh-NC group (injection with 5×10⁷ sh-NC lentiviral vector particles via tail vein one week before CLP), miR-96-5p antagomir group (injection with 10 µg miR-96-5p antagomir via tail vein one week before CLP), and NC antagomir group (injection with 10 µg NC antagomir via tail vein one week before CLP). sh-circROCK1/NC lentiviral vectors and miR-96-5p/NC antagomir were provided by GenePharma (China). The cardiac function of mice was monitored 12 h after CLP, myocardial tissue and serum samples were collected from 6 mice in each group, and myocardial tissues from the remaining 6 mice were stained with hematoxylin and eosin (HE). miR-96-5p antagomir sequence: 5'-TAACACTGTCTGGTAACGATGT-3'.

CLP procedures: Midline laparotomy was performed, and a 3 cm dissection was performed to expose the cecum. At the site designated for high severity, the cecum was ligated with a 4-0 silk thread and pierced at two sites 1 cm apart with a 20-gauge needle. The cecum was then gently pressed to squeeze a small drop of feces. After laparotomy, all mice were resuscitated by subcutaneous injection of normal saline (37°C, 50 ml/kg). The sham operation was performed with the same procedure but without ligation and puncture of the cecum.

Heart function detection

All mice were anesthetized by intraperitoneal administration of pentobarbital sodium 12 hours after CLP. The right carotid artery was exposed, from where a catheter was inserted into the left ventricle. A multi-channel data acquisition and processing system (RM6240BD, Chengdu Instrument) was utilized to monitor left ventricular systolic pressure (LVSP) and maximum rate of increase/decrease in left ventricular pressure ($\pm dp/dt_{max}$).

Enzyme-linked immunosorbent assay (ELISA)

The myocardial homogenate was centrifuged, and the supernatant was collected. Tumor necrosis factor (TNF)- α , interleukin (IL)-6, and IL-1 β levels were measured using ELISA kits. Creatine kinase-MB (CK-MB, E006-1-1) and cardiac troponin I (cTnI, H149-2) content in serum were measured. All kits were purchased from Nanjing Jiancheng Bioengineering Institute.

HE staining

The myocardial tissue of mice was fixed with 4% paraformaldehyde, embedded in paraffin, and cut into 4 µm slices. The slices were deparaffinized with xylene, infiltrated with gradient alcohol, and stained with HE. At last, the tissue structure was observed microscopically.

Table 1. RT-qPCR primer sequences

Genes	Primer sequence (5'-3')
GAPDH	Forward: 5'-ATGGGGAAGGTGAAGGTCG-3'
	Reverse: 5'-TTACTCCTTGAGGCCATGTG-3'
U6	Forward: 5'-CTCGCTTCGGCAGCACATATACT-3'
	Reverse: 5'-ACGCTTCACGAATTTGCGTGC-3'
CircROCK1	Forward: 5'- TCCCAATGCTGCCCCAAAGCC -3'
	Reverse: 5'- GGTTCTGCTCCCCATCACTCCA -3'
miR-96-5p	Forward: 5'- ATGCTTTCTCAACTTGTGG -3'
	Reverse: 5'- TCACCGCTCTTGCCGTCACA -3'
OXSR1	Forward: 5'- AAAGACGTTTGTGGCACCC -3'
	Reverse: 5'- GCCCCTGTGGCTAGTTCAAT -3'

Real-time reverse transcriptase-polymerase chain reaction (RT-qPCR)

Total RNA in mouse myocardial tissue and human serum samples was isolated using TRIzol RNA extraction reagent (Invitrogen, USA). PrimerScript real-time kit (TAKARA, Japan) was applied for reverse transcription. Finally, RT-qPCR was detected by SYBR Premix Ex Taq™ II reagent and ABI PRISM 7000 (Applied Biosystems, USA). Using U6 and glyceraldehyde-3-phosphate dehydrogenase (GAPDH) as internal references for miRNA and mRNA, respectively, relative gene expression was calculated by $2^{-\Delta\Delta C_t}$. The primer sequence was shown in Table 1.

Western blot

Total protein in the myocardial homogenate was extracted using a protein extraction kit (Beyotime, China), and later a bicinchoninic acid kit (Nanjing Jiancheng Bioengineering Institute) was utilized to determine the protein concentration. Next, the protein was loaded for electrophoresis, and protein gel was transferred to a polyvinylidene fluoride membrane (Millipore, USA), which was sealed with 0.1% Tween-20 in Tris-buffered saline (5% skim milk) at room temperature for 1 hour, and later combined with the primary antibody p-NF- κ B p65 (ab86299, Abcam), NF- κ B p65 (#8242, Cell Signaling), OXSR1 (H00009943-M09, Abnova), and GAPDH (ab181602, Abcam) overnight at 4°C. Next, the membrane was incubated with horseradish peroxidase-conjugated goat anti-rabbit immunoglobulin G (ab205718, Abcam) to evaluate protein immunoreactivity. The density of

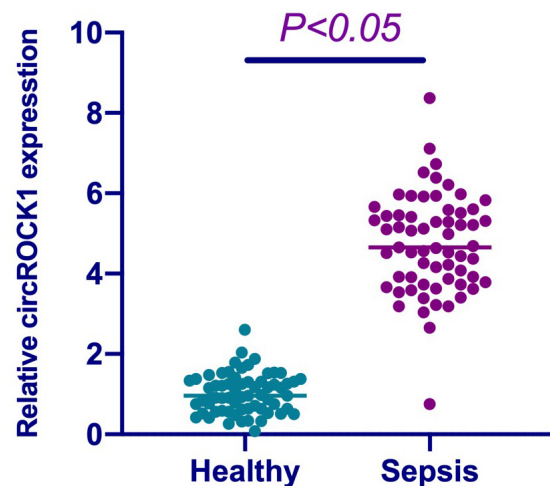


Figure 1. circROCK1 is highly expressed in sepsis.

Note: RT-qPCR to detect circROCK1 expression in the serum of normal subjects and patients with sepsis. The data were expressed as mean \pm S.D., and the Student's *t*-test was applied.

protein bands was analyzed by Image-Pro Plus version 6.0 (Media Cybernetics, USA).

Dual luciferase reporter experiment

The circROCK1 or OXSR1 3'untranslated region sequence containing miR-96-5p binding site was inserted into the pmirGLO vector (Promega, USA), and the wild type (WT) luciferase reporter plasmids were named circROCK1-WT and OXSR1-WT. After the binding sites were mutated, mutant type (MUT) luciferase plasmids (circROCK1-MUT and OXSR1-MUT) were constructed. HEK293 cells were transfected into 48-well plates at 3×10^4 cells/well and transfected with 2 μ L of plasmids and 100 nM miR-96-5p mimic or mimic-NC (GenePharma, China). After 48-hour transfection, the dual luciferase reporter system (Promega; E1910) was utilized to detect firefly and renilla luciferase activities.

Data analysis

Values expressed as mean \pm standard deviation (S.D.) were analyzed by GraphPad Prism software 8.01 (GraphPad Software, USA). The Student's *t*-test was applied to compare two groups. Spearman correlation analysis examined the relationship between circROCK1 and the clinicopathological characteristics of septic patients. * $P < 0.05$ was considered statistically significant.

Table 2. Clinicopathological characteristics of subjects

Parameters	Healthy subjects (n = 37)	Septic patients (n = 63)
Age (years)	57.64 \pm 6.27	53.78 \pm 4.93
Gender (male/female)	male (14)/female (23)	male (39)/female (24)*
BMI (kg/m ²)	21.27 \pm 0.79	20.98 \pm 1.07
Scr (mg/dL)	0.91 \pm 0.17	1.54 \pm 0.24*
Albumin (g/L)	42.97 \pm 4.78	31.47 \pm 3.59*
WBC ($\times 10^9$ /L)	8.49 \pm 2.03	17.56 \pm 4.12*
CRP (mg/L)	11.04 \pm 2.39	47.83 \pm 8.83*
PCT (ng/mL)	0.79 \pm 0.12	8.74 \pm 2.41*
SOFA score	–	3.97 \pm 1.24

Note: Scr: serum creatinine; WBC: white blood cells; CRP: C-reactive protein; PCT: procalcitonin; SOFA: sequential organ failure assessment. Data expressed as mean \pm S.D., combined with student's *t*-test or chi-square test; in contrast to healthy subjects, * $P < 0.05$.

Table 3. The correlation between circROCK1 and clinicopathological characteristics of sepsis

Parameters	circROCK1 low expression (n = 31)	circROCK1 high expression (n = 32)	P	R
Age (years)	54.32±5.79	56.43±3.87	0.478	0.237
Gender (male/female)	male (18)/female (13)	male (15)/female (17)	0.327	0.379
BMI (kg/m ²)	19.72±0.84	20.37±0.77	0.782	0.113
Scr (mg/dL)	1.22±0.13	1.94±0.36	< 0.001	0.639
Albumin (g/L)	31.37±2.78	29.25±4.03	0.174	-0.335
WBC (×10 ⁹ /L)	15.79±3.47	17.63±4.55	0.264	0.341
CRP (mg/L)	39.84±6.29	54.27±5.91	<0.001	0.749
PCT (ng/mL)	5.74±1.63	10.93±2.80	<0.001	0.538
SOFA score	2.69±0.74	5.27±0.63	<0.001	0.673

Note: Scr: serum creatinine; WBC: white blood cells; CRP: C-reactive protein; PCT: procalcitonin; SOFA: sequential organ failure assessment. Data expressed as mean ± S.D., combined with student's *t*-test and spearman correlation analysis.

RESULTS

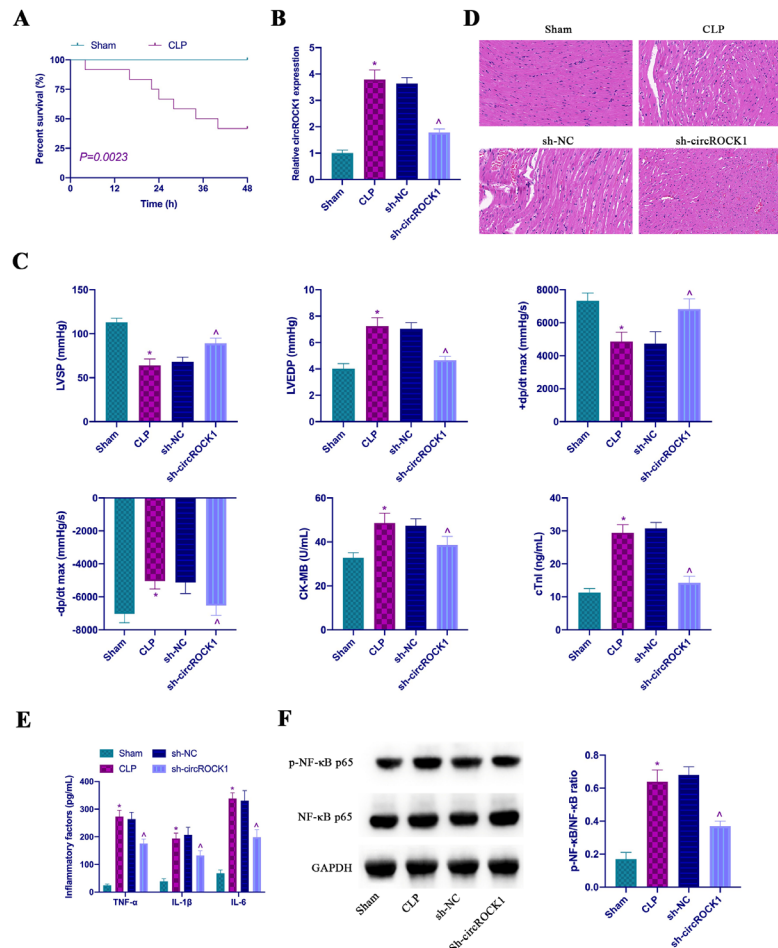
Clinical and pathological characteristics of subjects

37 healthy subjects (14 males, 23 females, average age: 57.64±6.27 years old) and 63 septic patients (39 males, 24 females, average age: 53.78±4.93 years old) were recruited. The clinicopathological characteristics of the two groups were detailed in Table 2. There were no significant

differences in age or BMI between healthy subjects and sepsis patients. There were significant differences in gender, Scr, albumin, white blood cells, CRP, and PCT.

circROCK1 is highly expressed in sepsis and is related to sepsis clinicopathology

circROCK1 in sepsis was examined. circROCK1 expression in the serum of septic patients was higher than that in healthy subjects (Fig. 1). The clinicopathological

**Figure 2 Silencing circROCK1 improved myocardial injury in septic mice.**

Note: (A) Survival rate of CLP mice within 48 hours; (B) RT-qPCR to detect circROCK1 expression in mouse myocardial tissue; (C) Cardiac function indexes LVSP, LVEDP, +dp/dt_{max} and -dp/dt_{max} and serum cTnI and CK-MB levels; (D) HE staining of mice myocardial tissue; (E) ELISA to detect TNF-α, IL-1β, and IL-6 levels in mice myocardial tissue; (F) Western blot to detect phosphorylated NF-κB expression in mice myocardial tissue; the data were expressed as mean ± S.D. (n=6) and compared by Student's *t*-test. In comparison with the Sham group, * $P<0.05$; in comparison with the sh-NC group, $^{\wedge}P<0.05$.

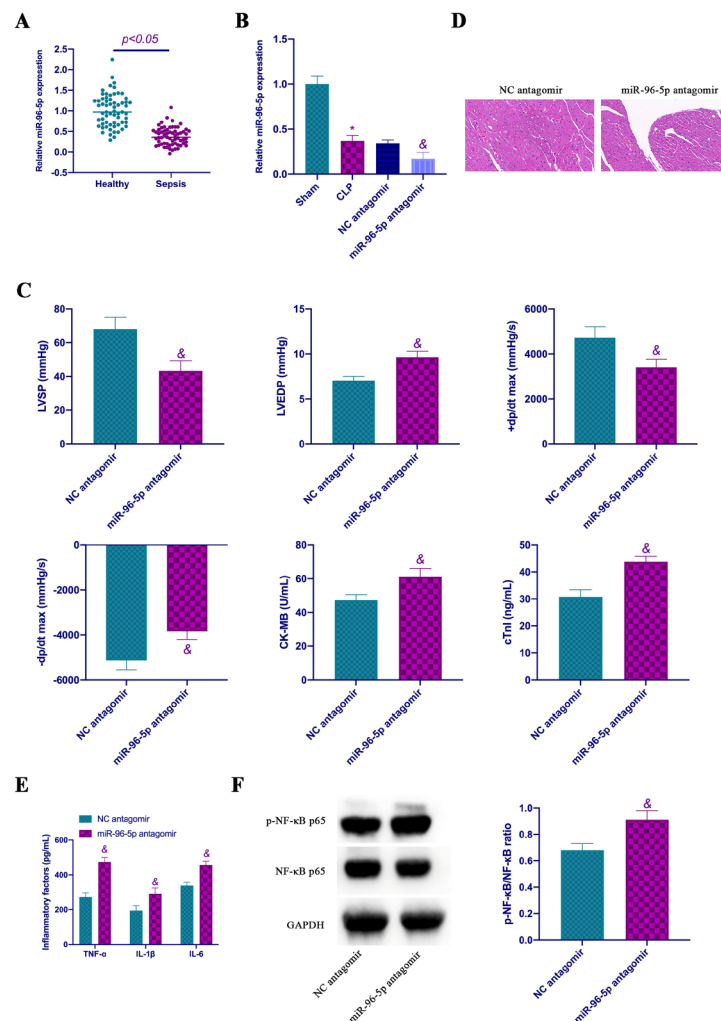


Figure 3. Silencing miR-96-5p promotes myocardial injury in septic mice.

Note: (A) RT-qPCR to detect serum miR-96-5p expression in healthy subjects and septic patients; (B) RT-qPCR to detect miR-96-5p expression; (C) Mice cardiac function indexes LVSP, LVEDP, +dp/dt_{max} and -dp/dt_{max} as well as serum cTnI and CK-MB levels; (D) HE staining of mice myocardial tissue; (E) ELISA to detect TNF-α, IL-1β, and IL-6 levels in mice myocardial tissue; (F) Western blot to detect phosphorylated NF-κB expression in mice myocardial tissues; the data were expressed as mean ± S.D. (n=6) and compared by Student's *t*-test. In comparison with the NC antagonist group, * $P < 0.05$.

relationship between circROCK1 and sepsis was subsequently examined. circROCK1 was positively correlated with Scr, CRP, PTC, and SOFA scores in sepsis (Table 3).

Silencing circROCK1 improved myocardial injury in septic mice

A CLP mouse model was established to further examine the role of circROCK1 in sepsis. First, the survival rate of CLP mice within 48 hours was evaluated. The survival rate of CLP mice within 48 hours after surgery was 41.2%, while the mice in the Sham group did not die (Fig. 2A). After CLP, circROCK1 expression in the myocardial tissue of mice was elevated; after sh-circROCK1 injection, circROCK1 expression was reversed (Fig. 2B). Later the cardiac function of the mice was checked. After CLP, LVSP and +dp/dt_{max} were reduced, while -dp/dt_{max}, LVEDP, cTnI, and CK-MB were elevated. After sh-circROCK1 injection, the changes in the above indicators were reversed (Fig. 2C). HE staining revealed that myocardial necrosis and interstitial

edema appeared in the myocardial tissue of CLP mice, and these pathological changes were attenuated after silencing circROCK1 (Fig. 2D). Additionally, CLP surgery elevated inflammatory factors TNF-α, IL-1β, and IL-6 levels in the myocardial tissue of mice. After silencing circROCK1, inflammatory factor levels were reduced (Fig. 2E). Western blot results implied that CLP elevated phosphorylated NF-κB expression in mouse myocardial tissue. After silencing circROCK1, phosphorylated NF-κB expression was reduced (Fig. 2F). Based on these findings, silencing circROCK1 improves myocardial injury in septic mice.

Silencing miR-96-5p promoted myocardial injury in septic mice

In this work, miR-96-5p was under-expressed in the serum of septic patients (Fig. 3A). Subsequently, miR-96-5p in CLP mice was down-regulated by injection of miR-96-5p antagonist (Fig. 3B). Next, the impact of miR-96-5p on myocardial injury in septic mice was examined. After down-regulating miR-96-5p, LVSP and

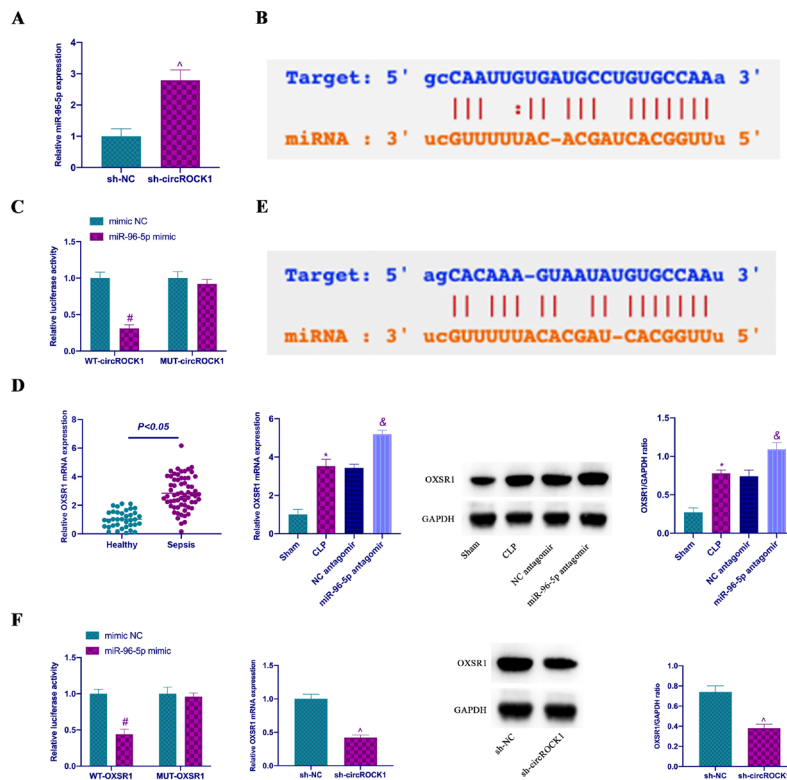


Figure 4. circROCK1 acts as a miR-96-5p sponge in sepsis to mediate OXSR1 expression.

Note: (A) RT-qPCR to detect miR-96-5p expression in mice myocardial tissues; (B) <http://starbase.sysu.edu.cn/> to query circROCK1 and miR-96-5p potential binding sites; (C) Dual luciferase reporter experiment to verify the targeting relationship between circROCK1 and miR-96-5p; (D) RT-qPCR and western blot to detect OXSR1 expression in mice myocardial tissue; (E) <http://starbase.sysu.edu.cn/> to query OXSR1 and miR-96-5p potential binding sites; (F) Dual luciferase reporter experiment to confirm the targeting relationship between miR-96-5p and OXSR1; (G) RT-qPCR and western blot to examine OXSR1 expression mice myocardial tissues; data were expressed as mean \pm S.D. (n=6) and compared by student's t-test. In comparison with the Sham group, * $P < 0.05$; in comparison with the sh-NC group, $\Delta P < 0.05$; in comparison with the NC antagonist group, $\& P < 0.05$; in comparison with the mimic NC group, $\# P < 0.05$.

+dp/dt_{max} decreased, whereas -dp/dt_{max}, LVEDP, cTnI, and CK-MB elevated in CLP mice (Fig. 3C). HE staining indicated that down-regulating miR-96-5p aggravated myocardial necrosis and edema in CLP mice (Fig. 3D). Additionally, down-regulating miR-96-5p further elevated inflammatory factors TNF- α , IL-1 β , and IL-6 in the myocardial tissue of CLP mice and promoted phosphorylated NF- κ B expression (Figs. 3E, F).

circROCK1 acted as a miR-96-5p sponge in sepsis to mediate ROCK1 expression

After silencing circROCK1, miR-96-5p expression in CLP mice was elevated (Fig. 4A). It is speculated that circROCK1 is available to target miR-96-5p expression. CircROCK1 and miR-96-5p have a targeting relationship on <http://starbase.sysu.edu.cn/> (Fig. 4B). Next, a dual luciferase reporter experiment was conducted to further examine the targeting relationship between circROCK1 and miR-96-5p. WT-circROCK1 reduced the luciferase activity in the miR-96-5p mimic group, whereas MUT-circROCK1 had no impact (Fig. 4C). This indicates that circROCK1 competitively binds miR-96-5p in sepsis. OXSR1 has been found to be highly expressed in sepsis and has an important relationship with sepsis development. In this work, OXSR1 expression was elevated in septic patients compared with healthy controls as well as in CLP mouse myocardial tissue compared with the Sham group. After down-regulating miR-96-5p, OXSR1 expression was further elevated (Fig. 4D). Given that, OXSR1 may be a potential target gene of miR-96-

5p. On the <http://starbase.sysu.edu.cn/>, it was found that OXSR1 and miR-96-5p had potential binding sites (Fig. 4E). Based on dual-luciferase findings, WT-OXSR1 could reduce miR-96-5p luciferase activity, while MUT-OXSR1 had no impact on it (Fig. 4F). Additionally, silencing circROCK1 can inhibit OXSR1 expression in the myocardial tissue of CLP mice (Fig. 4G). These findings indicate that OXSR1 is the target gene of miR-96-5p and is regulated by circROCK1.

DISCUSSION

In recent years, sepsis incidence has risen year by year, but the specific mechanism that affects septic organ injury is still not clear (Font *et al.*, 2020; L'Heureux *et al.*, 2020). In this work, our team found that circROCK1 was highly expressed in the serum of septic patients and indicated a positive correlation with Scr, CRP, PTC, and SOFA scores in sepsis. Additionally, knocking down circROCK1 improved septic myocardial injury by enhancing myocardial contractility, reducing myocardial tissue necrosis and edema, as well as inhibiting the activation of NF- κ B signaling pathway and downstream inflammatory factor expression. In terms of mechanism, circROCK1 silencing can ameliorate myocardial injury in sepsis mainly through competitive binding of miR-96-5p-mediated OXSR1 expression.

The CLP mouse model has been widely applied in basic research on sepsis. After CLP, the mice presented myocardial inhibition and inflammatory injury, mainly

including decreased LVSP and $+dp/dt_{\max}$ and elevated $-dp/dt_{\max}$, LVEDP, cTnI, CK-MB, and inflammatory factors. These findings are in line with previous studies (Gao *et al.*, 2021; Liu *et al.*, 2020), revealing that CLP is available to induce severe myocardial dysfunction.

Various circRNAs can regulate inflammatory responses in sepsis, which is vital for understanding sepsis inflammation development. For example, circ_0114428 regulates sepsis-induced renal inflammatory injury by targeting miR-495-3p/cereblon axis (He *et al.*, 2021). The circRNA circVMA21 improves lipopolysaccharide-induced acute kidney injury by targeting the miR-199a-5p/Neuropilin-1 axis in sepsis (Li *et al.*, 2021). This work found for the first time that circROCK1 can reduce septic myocardial tissue inflammation mainly by inhibiting NF- κ B phosphorylation. NF- κ B is an essential inflammatory signaling pathway, which acts in the process of cellular inflammation and immune response (Lawrence 2009; Pflug & Sitcheran, 2020).

Organ failure is a common feature of sepsis (Joffre *et al.*, 2020; Black *et al.*, 2020). In recent years, studying the role of circRNA in protecting cardiac function has become a research hotspot. Recently, Qiu and others (Qiu *et al.*, 2021) found that circHIPK3 regulates cardiomyocyte autophagy and apoptosis stimulated by hypoxia/reoxygenation via miR-20b-5p/autophagy related 7 axis. Additionally, Cheng and others (Cheng *et al.*, 2020) found that circular RNA POSTN promotes myocardial infarction-induced myocardial injury and cardiac remodeling through regulating miR-96-5p/Bcl-2/adenovirus E1B 19kDa interacting protein 3 axis. In our research, knocking down circROCK1 improved myocardial function and inflammatory injury in septic mice. It is worth noting that circROCK1 has been found to be highly expressed in septic lung tissue, so we speculate that circRNA also has a similar impact on sepsis and other organ failures.

In further research on the mechanism, based on the bioinformatics website and dual luciferase reporter system, circROCK1 was directly bound to miR-96-5p to elevate OXSR1 expression. miR-96-5p regulates the NF- κ B signaling pathway to reduce the severe response of neonatal sepsis (Chen *et al.*, 2020), which is the same as our findings. Furthermore, miR-96-5p also improved myocardial function in septic mice. This may be because miR-96-5p can reduce the release of systemic inflammatory cytokines in septic mice. OXSR1 is an essential immunomodulator in the body, which is differentially expressed in cancer, hypertension (Frame *et al.*, 2019; Puleo *et al.*, 2020), as well as neurological diseases (Frame *et al.*, 2019). A recent report revealed that overexpressing OXSR1 can improve acute kidney injury induced by sepsis (Qin *et al.*, 2019). Previous studies have shown that abnormal expression of the miR-96-5p/OXSR1 axis plays an important role in acute lung injury (Wu *et al.*, 2022). This suggests that the miR-96-5p/OXSR1 axis may also be involved in other organ injuries induced by sepsis, such as liver and intestine. We speculate that OXSR1 is also involved in the process of septic organ injury. This needs to be explored in subsequent studies. In this article, OXSR1 was also highly expressed in sepsis-induced myocardial injury.

In conclusion, our findings show that circROCK1 is highly expressed in sepsis and is correlated with clinicopathological characteristics. In terms of mechanism, circROCK1 promotes septic myocardial dysfunction by acting as a miR-96-5p sponge to mediate OXSR1 expression.

Declarations

Acknowledgments. Not applicable.

Declaration of Conflicting Interests. The author(s) declared no potential conflicts of interest with respect to the research, authorship, and/or publication of this article.

REFERENCES

- Bansal M, Mehta A, Machanahalli Balakrishna A, Kalyan Sundaram A, Kanwar A, Singh M, Vallabhajosyula S (2023) Right ventricular dysfunction in sepsis: an updated narrative review. *Shock* **59**: 829–837. <https://doi.org/10.1097/shk.0000000000002120>
- Bao X, Zhang Q, Liu N, Zhuang S, Li Z, Meng Q, Sun H, Bai J, Zhou X, Tang L (2019) Characteristics of circular RNA expression of pulmonary macrophages in mice with sepsis-induced acute lung injury. *J Cell Mol Med* **23**: 7111–7115. <https://doi.org/10.1111/jcmm.14577>
- Black LP, Puskas MA, Smotherman C, Miller T, Fernandez R, Guirgis FW (2020) Time to vasopressor initiation and organ failure progression in early septic shock. *J Am Coll Emerg Physicians Open* **1**: 222–230. <https://doi.org/10.1002/emp2.12060>
- Chen X, Chen Y, Dai L, Wang N (2020) MiR-96-5p alleviates inflammatory responses by targeting NAMP1 and regulating the NF- κ B pathway in neonatal sepsis. *Biosci Rep* **40**. <https://doi.org/10.1042/bsr20201267>
- Cheng N, Wang MY, Wu YB, Cui HM, Wei SX, Liu B, Wang R (2020) Circular RNA POSTN promotes myocardial infarction-induced myocardial injury and cardiac remodeling by regulating miR-96-5p/BNIP3 axis. *Front Cell Dev Biol* **8**: 618574. <https://doi.org/10.3389/fcell.2020.618574>
- Font MD, Thyagarajan B, Khanna AK (2020) Sepsis and Septic Shock – Basics of diagnosis, pathophysiology and clinical decision making. *Med Clin North Am* **104**: 573–585. <https://doi.org/10.1016/j.mcna.2020.02.011>
- Frame AA, Puleo F, Kim K, Walsh KR, Faudoa E, Hoover RS, Wainford RD (2019) Sympathetic regulation of NCC in norepinephrine-evoked salt-sensitive hypertension in Sprague-Dawley rats. *Am J Physiol Renal Physiol* **317**: F1623–F1636. <https://doi.org/10.1152/ajprenal.00264.2019>
- Gao H, Ma H, Gao M, Chen A, Zha S, Yan J (2021) Long non-coding RNA GAS5 aggravates myocardial depression in mice with sepsis via the microRNA-449b/HMGB1 axis and the NF- κ B signaling pathway. *Biosci Rep* **41**. <https://doi.org/10.1042/bsr20201738>
- He Y, Sun Y, Peng J (2021) Circ_0114428 regulates sepsis-induced kidney injury by targeting the miR-495-3p/CRBN axis. *Inflammation* **44**: 1464–1477. <https://doi.org/10.1007/s10753-021-01432-z>
- Joffre J, Hellman J, Ince C, Ait-Oufella H (2020) Endothelial responses in sepsis. *Am J Respir Crit Care Med* **202**: 361–370. <https://doi.org/10.1164/rccm.201910-1911TR>
- Kristensen LS, Hansen TB, Veno MT, Kjems J (2018) Circular RNAs in cancer: opportunities and challenges in the field. *Oncogene* **37**: 555–565. <https://doi.org/10.1038/onc.2017.361>
- L'Heureux M, Sternberg M, Brath L, Turlington J, Kashiouris MG (2020) Sepsis-induced cardiomyopathy: a comprehensive review. *Curr Cardiol Rep* **22**: 35. <https://doi.org/10.1007/s11886-020-01277-2>
- Lawrence T (2009) The nuclear factor NF-kappaB pathway in inflammation. *Cold Spring Harb Perspect Biol* **1**: a001651. <https://doi.org/10.1101/cshperspect.a001651>
- Lelubre C, Vincent JL (2018) Mechanisms and treatment of organ failure in sepsis. *Nat Rev Nephrol* **14**: 417–427. <https://doi.org/10.1038/s41581-018-0005-7>
- Li X, Li R, Gong Q, Shi D, Song L, Song Y (2021) Circular RNA circVMA21 ameliorates lipopolysaccharide (LPS)-induced acute kidney injury by targeting the miR-199a-5p/NRP1 axis in sepsis. *Biochem Biophys Res Commun* **548**: 174–181. <https://doi.org/10.1016/j.bbrc.2021.02.028>
- Li Y, Ge S, Peng Y, Chen X (2013) Inflammation and cardiac dysfunction during sepsis, muscular dystrophy, and myocarditis. *Burns Trauma* **1**: 109–121. <https://doi.org/10.4103/2321-3868.123072>
- Liu JJ, Li Y, Yang MS, Chen R, Cen CQ (2020) SP1-induced ZFAS1 aggravates sepsis-induced cardiac dysfunction via miR-590-3p/NLRP3-mediated autophagy and pyroptosis. *Arch Biochem Biophys* **695**: 108611. <https://doi.org/10.1016/j.abb.2020.108611>
- Memczak S, Jens M, Elefsinioti A, Torti F, Krueger J, Rybak A, Maier L, Mackowiak SD, Gregersen LH, Munschauer M, Loewer A, Ziebold U, Landthaler M, Kocks C, le Noble F, Rajewsky N (2013) Circular RNAs are a large class of animal RNAs with regulatory potency. *Nature* **495**: 333–338. <https://doi.org/10.1038/nature11928>
- Nie MW, Han YC, Shen ZJ, Xie HZ (2020) Identification of circRNA and mRNA expression profiles and functional networks of vascu-

- lar tissue in lipopolysaccharide-induced sepsis. *J Cell Mol Med* **24**: 7915–7927. <https://doi.org/10.1111/jcmm.15424>
- Pflug KM, Sitcheran R (2020) Targeting NF- κ B-Inducing Kinase (NIK) in immunity, inflammation, and cancer. *Int J Mol Sci* **21**. <https://doi.org/10.3390/ijms21228470>
- Puleo F, Kim K, Frame AA, Walsh KR, Ferdaus MZ, Moreira JD, Comsti E, Faudoa E, Nist KM, Abkin E, Wainford RD (2020) Sympathetic regulation of the NCC (Sodium Chloride Cotransporter) in Dahl salt-sensitive hypertension. *Hypertension* **76**: 1461–1469. <https://doi.org/10.1161/hypertensionaha.120.15928>
- Qin Y, Wang G, Peng Z (2019) MicroRNA-191-5p diminished sepsis-induced acute kidney injury through targeting oxidative stress responsive 1 in rat models. *Biosci Rep* **39**. <https://doi.org/10.1042/bsr20190548>
- Qiu Z, Wang Y, Liu W, Li C, Zhao R, Long X, Rong J, Deng W, Shen C, Yuan J, Chen W, Shi B (2021) CircHIPK3 regulates the autophagy and apoptosis of hypoxia/reoxygenation-stimulated cardiomyocytes via the miR-20b-5p/ATG7 axis. *Cell Death Discov* **7**: 64. <https://doi.org/10.1038/s41420-021-00448-6>
- Rubio I, Osuchowski MF, Shankar-Hari M, Skirecki T, Winkler MS, Lachmann G, La Rosée P, Monneret G, Venet F, Bauer M, Brunkhorst FM, Kox M, Cavaillon JM, Uhle F, Weigand MA, Flohé SB, Wiersinga WJ, Martin-Fernandez M, Almansa R, Martín-Loeches I, Torres A, Giamarellos-Bourboulis EJ, Girardis M, Cossarizza A, Netea MG, van der Poll T, Scherag A, Meisel C, Schefold JC, Bermejo-Martin JF (2019) Current gaps in sepsis immunology: new opportunities for translational research. *Lancet Infect Dis* **19**: e422–e436. [https://doi.org/10.1016/s1473-3099\(19\)30567-5](https://doi.org/10.1016/s1473-3099(19)30567-5)
- Y-Hassan S, Settergren M, Henareh L (2014) Sepsis-induced myocardial depression and takotsubo syndrome. *Acute Card Care* **16**: 102–109. <https://doi.org/10.3109/17482941.2014.920089>
- Salomão R, Ferreira BL, Salomão MC, Santos SS, Azevedo LCP, Brunialti MKC (2019) Sepsis: evolving concepts and challenges. *Braz J Med Biol Res* **52**: e8595. <https://doi.org/10.1590/1414-431x20198595>
- Shi Y, Sun CF, Ge WH, Du YP, Hu NB (2020) Circular RNA VMA21 ameliorates sepsis-associated acute kidney injury by regulating miR-9-3p/SMG1/inflammation axis and oxidative stress. *J Cell Mol Med* **24**: 11397–11408. <https://doi.org/10.1111/jcmm.15741>
- Stanski NL, Wong HR (2020) Prognostic and predictive enrichment in sepsis. *Nat Rev Nephrol* **16**: 20–31. <https://doi.org/10.1038/s41581-019-0199-3>
- Wu W, Zhong W, Xu Q, Yan J (2022) Silencing of long non-coding RNA ZFAS1 alleviates LPS-induced acute lung injury by mediating the miR-96-5p/OXSR1 axis in sepsis. *Am J Med Sci* **364**: 66–75. <https://doi.org/10.1016/j.amjms.2022.03.008>
- Xiong H, Wang H, Yu Q (2021) Circular RNA circ_0003420 mediates inflammation in sepsis-induced liver damage by downregulating neuronal PAS domain protein 4. *Immunopharmacol Immunotoxicol* **43**: 271–282. <https://doi.org/10.1080/08923973.2021.1887212>
- Yang Y, Lei W, Qian L, Zhang S, Yang W, Lu C, Song Y, Liang Z, Deng C, Chen Y, Tian Y and Zhao H (2023) Activation of NR1H3 signaling pathways by psoralidin attenuates septic myocardial injury. *Free Radic Biol Med* **204**: 8–19. <https://doi.org/10.1016/j.freeradbiomed.2023.04.006>
- Zhen G, Liang W, Jia H, Zheng X (2022) Melatonin relieves sepsis-induced myocardial injury via regulating JAK2/STAT3 signaling pathway. *Minerva Med* **113**: 983–989. <https://doi.org/10.23736/s0026-4806.20.06626-4>
- Zhou B, Zhang J, Chen Y, Liu Y, Tang X, Xia P, Yu P, Yu S (2022) Puerarin protects against sepsis-induced myocardial injury through AMPK-mediated ferroptosis signaling. *Aging (Albany NY)* **14**: 3617–3632. <https://doi.org/10.18632/aging.204033>
- Zou Z, Wang Q, Zhou M, Li W, Zheng Y, Li F, Zheng S, He Z (2020) Protective effects of P2X7R antagonist in sepsis-induced acute lung injury in mice via regulation of circ_0001679 and circ_0001212 and downstream Pln, Cdh2, and Nprl3 expression. *J Gene Med* **22**: e3261. <https://doi.org/10.1002/jgm.3261>

Timosaponin AIII attenuates precocious puberty in mice through downregulating the hypothalamic-pituitary-gonadal axis

Lili Zhou¹✉, Yaoquan Ren², Dongmei Li², Weiwei Zhou², Chengke Li¹, Qiang Wang¹ and Xiangzheng Yang¹

¹Pediatrics Department, Beijing University of Chinese Medicine Shenzhen Hospital at Longgang, Shenzhen, China; ²Pediatrics Department, Gansu Provincial Hospital of Traditional Chinese Medicine, Lanzhou, China

Precocious puberty (PP) has increasingly become a social concern. This study aimed to investigate the effect of timosaponin AIII (TAIII) on the precocious puberty and its possible mechanisms in mice. Four groups of mice consisting of controls that received saline or TAIII, a model that received leptin to induce precocious puberty (PP), and leptin+TAIII (the leptin model treated with TAIII) were used to determine the effect of TAIII on PP. Pathological and cytological examinations were conducted to investigate the signs and onset of PP and the development of reproductive organs. The level of serum luteinizing hormone (LH), follicle stimulating hormone (FSH) and estradiol (E2) were determined using enzyme-linked immunosorbent assay (ELISA). The expression of genes related to the hypothalamic-pituitary-gonadal axis (HPGA) was assessed using qRT-PCR and Western blotting. Bone mineral density (BMD) was determined using high resolution peripheral quantitative computed tomography. In mice treated with leptin, earlier vaginal opening and estrus were observed, as well as the increased ovarian and uterine weight, total uterine cross-sectional size, number of corpora lutea, and elevated serum sex hormone levels and HPGA expression. On the other hand, TAIII treatment delayed the vaginal opening and vaginal estrus to 32.1 and 37.5 days after birth, and delayed the development of reproductive organs, leading to significantly smaller uterus and ovary size, less corpora lutea and low BMD ($P<0.05$). In addition, the serum levels of LH, FSH and E2 were significantly reduced ($P<0.05$) and so was the expression of HPGA and leptin genes ($P<0.05$). Our experimental data demonstrated that TAIII has activity against leptin-induced PP activity and may attenuate PP by reducing reproductive hormones and deactivating the hypothalamic-pituitary-gonadal axis through downregulating leptin expression.

Keywords: precocious puberty; herbal medicine; triterpenoid; serum hormone; gene expression

Received: 05 August, 2022; **revised:** 30 December, 2022; **accepted:** 16 January, 2023; **available on-line:** 16 March, 2023

✉e-mail: lilizhou22@yeah.net

Abbreviations: ANOVA, analysis of variance; CPP, central PP; E2, estradiol; ELISA, enzyme-linked immunosorbent assay; FSH, follicle stimulating hormone; GRP54, G protein-coupled receptor 54; HE, hematoxylin-eosin; HPGA, hypothalamic-pituitary-gonadal axis; KISS1, KISSpeptin-1; LH, luteinizing hormone; PCR, polymerase chain reaction; PP, precocious puberty; PVDF, polyvinylidene fluoride; qRT-PCR, real-time quantitative reverse transcription PCR; TAIII, timosaponin AIII; VE, vaginal estrus; VO, vaginal opening

INTRODUCTION

Precocious puberty (PP) is a growth and developmental disorder that manifests as early onset of secondary sexual characteristics, occurring before the age of 8 and 9 years in girls and boys (Bradley *et al.*, 2020; Yang *et al.*, 2021). The incidence of precocious puberty is growing and the age of puberty onset gradually decreases, largely due to the change of lifestyles (Kim *et al.*, 2015). Clinical signs such as premature breast and pubic hair development, together with determination of bone age, pelvic echography and hormone tests are among the routine procedures to diagnose central (gonadotropin-releasing hormone (GnRH)-dependent) PP (CPP) and peripheral (GnRH-independent) PP (PPP) (Antoniazzi & Zamboni, 2004; Neely & Crossen, 2014). Due to the early onset of puberty, children with PP develop earlier and grow shorter, due to shorter time of bone growth and subsequently shorter stature (Censani *et al.*, 2019) because the activation of the hypothalamic-pituitary-gonadal axis (HPGA) results in the release of gonadotropins that induces the development of puberty and promotes bone maturation (Cheuiche *et al.*, 2021). In addition, PP can cause a series of psychological and physiological problems, which may also be associated with diseases, obesity, overweight and other environmental factors (Chae *et al.*, 2021; Sitruk-Ware *et al.*, 1986). At the molecular level, PP has been found to up- and down-regulate hundreds of proteins that potentially impact numerous metabolic pathways (Wang *et al.*, 2021). In recent years, the age of PP onset trends to decrease and PP has become an important social issue, particularly for girls, who have the condition 10 times more often than boys, and their families (Cesario & Hughes, 2007).

Long-acting gonadotropin-releasing hormone analogs have revolutionized the treatment of CPP, resulting in the stabilization of pubertal progression, a reduced growth velocity, and a decreased bone age advancement (Cheuiche *et al.*, 2021). However, questions remain regarding their optimal use in CPP and other conditions. Although most cases of precocious sexual maturation are gonadotropin-dependent and currently assumed to be idiopathic, there are mutations in genes involved in pubertal development, such as MKRN3 and DLK1, which may require different treatment options. Additional studies are needed to address key areas related to the psychosocial effects of CPP and their alterations due to the use of gonadotropin-releasing hormone analogs (Carel *et al.*, 2009).

In East Asia, herbal medicines are used for the treatment of PP (Liu *et al.*, 2016). Traditional Chinese medicine Zhimu is made from the roots of *Anemarrhena*

rhena asphodeloides and is an important member of the herbal medicines that have activity against PP. For example, Zhibaidihuang decoction made with *A. asphodeloides*, *Rehmannia glutinosa*, *Cornus officinalis*, peony bark, yam, *Poria cocos* and *Alisma orientalis* was found to alleviate PP by reducing the levels of serum hormone FSH, LH and E₂ (Xu & Qiu, 2007; Yu *et al.*, 2014). Sarsasapogenin, a steroidal sapogenin, is a main active ingredient in Zhimu (Bao *et al.*, 2007) and was found to have anti-PP activity through inhibiting the HPGA (Hu *et al.*, 2020a). In addition, pharmacological studies have shown that sarsasapogenin also has activities against thrombosis, Alzheimer's disease, tumor, inflammation, and depression (Han *et al.*, 2018; Wang *et al.*, 2014). Timosaponin AIII (TAIII), a triterpenoid, is also a main ingredient in *A. asphodeloides* extract with a number of pharmacological activities (Lin *et al.*, 2020). However, little is known about its activity against PP although decoctions made with *A. asphodeloides* are shown to be effective to attenuate PP (Xu & Qiu, 2007; Yu *et al.*, 2014).

The aim of this study was to investigate the therapeutic effect of TAIII on PP and its possible mechanisms by measuring serum sex hormone levels and expression of KISS1/GPR54 genes in mouse model of PP.

MATERIALS AND METHODS

Animals and treatments

Female C57BL mice, female, aged 2 weeks and weighing 12±1.1g, were purchased from the Laboratory Animal Center, Yanjiang Biotech, Shanghai, China. The animals were housed in groups of three in plastic box cages kept in pathogen-free animal rooms at 25°C and 42% humidity with 12-h light (06:00–18:00) and dark (18:00–06:00) cycles and *ad libitum* access to chow and drinking water. At the completion of experiments, mice were euthanized by carbon dioxide asphyxiation and tissues were isolated for subsequent analysis. Carbon dioxide was supplied at a flow rate of 20% of the cage volume per minute (5L/min). The death after exposure to carbon dioxide was confirmed after careful assessment of cardiac arrest. The study was carried out in compliance with the ARRIVE guidelines. The animal experimental protocols procedures were approved by the Institutional Animal Care and Use Committee of Beijing University of Chinese Medicine Shenzhen Hospital, Shenzhen, China.

The animals were randomly divided into controls (saline and TAIII), model (leptin), and TAIII (leptin+TAIII) groups with 16 mice in each group. At the age of 20 days, the mice were subcutaneously injected daily with leptin at 2 µg/g body weight (cat. no. 177404-21-6, Guangjian Pharmaceuticals, Shenzhen, China) in 100 µl saline with 0.1% DMSO *i.p.* at 09:00–10:00 hours during the light cycle as described previously (Ahima *et al.*, 1997) (model) and additionally TAIII at 10 µg (100 µl) per g body weight (cat. no. HY-N0810, MedChemExpress LLC, Shanghai, China) was administered to mice by gavage (TAIII group). Before use, TAIII was dissolved in 0.1% DMSO to 10 µg/µl to keep as a stock solution and stored at –20°C. Controls were injected with 100 µl saline or TAIII containing 0.1% DMSO. From the age of 25 days, the vaginal opening (VO) was checked daily. For the mice with VO, vaginal smear was checked every morning and the onset of vaginal estrus (VE) was determined as described previously (Nelson *et al.*, 1990).

Detection of serum hormone levels

Blood samples were collected from the abdominal aorta, and centrifuged at 4°C to obtain serum, which was stored at –20°C before analysis. Serum LH (ab72838, 1:2000), FSH (ab21011, 1:2000) and E₂ (ab100969, 1:2000) levels were determined using ELISA kits according to the supplier's instructions (abcam, Shanghai, China) with a Accuris SmartReader 96 (Labrepco, PA, USA). All assessments were repeated three times.

Pathological examination

The uterus and ovary samples were immediately isolated after the last blood samples were taken. The uterus and ovaries were isolated, weighed and fixed in 10% formalin, embedded in paraffin, sectioned and stained with hematoxylin-eosin (HE). To measure the size of uterus and ovary, the sections were pictured at 40× magnification, the edge of uterine was traced and grided with 100×100 point-grid using CAST software (v.2.0). The numbers of points falling on the cross section of the whole uterus and endometrium were counted and used to calculate the area through the built-in area conversion system in the software.

Bone densitometry

The tibias of the right hind limb were isolated and fixed in 70% ethanol after removing the surrounding tissue. The tibial samples were longitudinally scanned using high resolution peripheral quantitative computed tomography (HR-pQCT) to display the morphology of the proximal tibia. HR-pQCT scans were performed 3.0 mm and 12.0 mm below the epiphysis line for determination of the cancellous and compact bone density.

qRT-PCR

Total RNA was extracted using Beyozol reagent (cat. no. R0011, Beyotime, Beijing China) from the hypothalamus tissues isolated from the brain according to the supplier's instructions and quantified using a UV spectrophotometer. The RNA was converted to cDNA using BeyoRT first strand cDNA kit (cat. no. D7166, Beyotime). Real-time PCR amplification and quantification were carried out using BeyoFast SYBR Green One-Step qRT-PCR Kit (cat. no. D7268s, Beyotime) on the ProFlex™ PCR Systems (Thermo Fisher, USA). The cycle parameters consisted of initial denaturation at 96°C for 10 min, followed by 45 cycles of denaturation at 95°C for 10 s, annealing at 55°C for 15 s, and extension at 60°C for 60 s. β-actin gene was used as the internal standard, the 2^{–ΔΔC_t} method was used to calculate the relative expression level of genes (Livak & Schmittgen, 2001). Primers for the PCR were synthesized at Huada Gene Inc., Shanghai and the sequences were:

KISS1

forward, 5'-GATGTCTGCGACCTGAGTCCC,

reverse, 5'-AGGCATTAACGAGTTCCTGGG;

GPR54

forward, 5'-GCGGCCACAGATGTCACTTT and

reverse, 5'-AGGTGGGCAGCGGATAGA;

GnRH

forward, 5'-GGAGCTCTGGAACGTCTGATT,

reverse, 5'-CAGCGTCAATGTCACTACG,

gonadotropin releasing hormone receptor (GnRHR)

forward, 5'-CAGGACCCACGCAAACTACA,

reverse, 5'-GGGAGTCCAGCAGATGACAA,

leptin

forward, 5'-GCTGTGCCCATCCAAAAAGTCC,

Table 1. Weight and size of the ovaries and uterus and number of corpora lutea in mice treated with leptin and TAIII.

Group	No. animals	Ovarian weight (mg)	Uterine weights (mg)	Total uterine cross-sectional area (mm ²)	Endometrial cross-sectional area (mm ²)	No. corpora lutea
Control (Saline)	6	15.8±1.21	25.8±2.91	0.45±0.05	0.20±0.02	0
TAIII	6	15.2±1.11	25.5±2.11	0.48±0.06	0.20±0.02	0
Leptin	6	22.4±2.21*	40.3±4.99*	1.05±0.08*	0.55±0.03*	5.48±0.75*
Leptin+TAIII	6	18.8±1.81#	27.8±2.01#	0.65±0.06#	0.35±0.04#	1.28±0.25#

Data were presented as mean±standard deviation. *and #*P*<0.05 compared to controls (saline and TAIII) and leptin treatment, respectively, using one-way ANOVA.

reverse, 5'-CCCAGGAATGAAGTCCAAACCG and β -actin

forward, 5'-CATTGCTGACAGGATGCAGAAGG, reverse, 5'-TGCTGGAAGGTGGACAGTGAGG.

All reactions were repeated three times.

Western blot

Western blot analysis was performed to assess the expression of the KISS1 and GRP54 genes. The brain tissues were lysed in RIPA buffer (Thermo Fisher Scientific, USA) with protease inhibitors according to the supplier's instructions. Proteins in the lysates were quantitated using BAC protein quantification kit (Thermo Fisher Scientific) according to manufacturer's instructions. After boiling at 100°C for 5 min, 50 μ g denatured proteins were subjected to each lane of 12% polyacrylamide gel electrophoresis (SDS-PAGE), and transferred to PVDF membranes. The KISS1 and GRP54 proteins were detected by incubating the membranes with antibodies against KISS1 (ab226786, 1:1500, Abcam, US), GRP54 (ab108606, 1500, Abcam), GnRH (ab281844, 1:1500, Abcam), GnRHR (ab183079, 1:1500, Abcam), leptin (ab219260, 1:1200, Abcam) and β -actin (as internal reference, ab179467, 1:1500, Abcam) and horseradish peroxidase conjugated IgG (H + L) (ZB-2301, 1:2000, ZSbio, Beijing). The immunoreactive bands were visualized using chemiluminescent substrate (ab5801, Abcam) in the dark according to the supplier's protocols and quantified using Quantity one (v4.62) analysis software (General Electric, UK).

Statistical analysis

Microsoft Excel (IBM, USA) with statistical add-in was used for statistical analysis of experimental data. The measurement data were compared among and between groups were conducted using one-way analysis of variance (ANOVA) and *t*-test, respectively, and the data were expressed as mean \pm standard deviation (m \pm S.D.). *P*<0.05 was regarded as statistically significant.

RESULTS

TAIII postpones VO and VE

From day 25, all mice were checked for VO. For controls (saline or TAIII containing 0.1% DMSO-treated mice), VO occurred similarly at 32.4±1.96 and 32.6±1.86 days after birth. In leptin-treated mice, VO occurred at 29.47±1.26 days, which was significantly earlier than in controls (*P*<0.05). The VO occurred at 32.18±2.26 days in mice receiving leptin+TAIII, which was significantly later than for those receiving leptin treatment alone (*P*<0.05), suggesting that TAIII postpones leptin-induced

PP. Similarly, VE occurred earlier in leptin-treated mice (34.8±2.74) as compared with controls (38.0±2.61 and 37.5±2.22) and was delayed in leptin+TAIII-treated mice (37.5±2.47) as compared with leptin-treated mice (Fig. 1). Leptin+TAIII-treated mice looked and behaved normally as compared with saline-, TAIII- and leptin-treated mice, during the experimental period.

TAIII delays sexual development

No difference was observed between the controls (saline or TAIII alone) in sexual development. Compared with the controls, leptin facilitated the development of ovaries and uterus, resulting in increased weight and size of these organs (*P*<0.05, Table 1). However, treatment with TAIII hindered this effect, as the sizes of ovaries and uterus were significantly reduced (*P*<0.05, Table 1), with lower ovarian weight (18.8 *vs* 22.4mg), uterine weight (27.8 *vs* 40.3mg), smaller total uterine cross-sectional area (0.65 *vs* 1.05 mm²) and smaller endometrial cross-sectional area (0.35 *vs* 0.55 mm²) as compared with leptin-treated mice (*P*<0.01, Table 1), although they were still larger than in the controls. Leptin treatment also resulted in the early development of corpora lutea, while leptin+TAIII treatments significantly reduced the number of corpora lutea as compared to the leptin-treated mice (*P*<0.01, Table 1).

TAIII reduces BMD

Bone development was similar between the controls (saline or TAIII alone) (Table 2). After leptin treatment, mice had significantly higher BMD, TBD and CBD as compared with controls (Table 2). TAIII treatment sig-

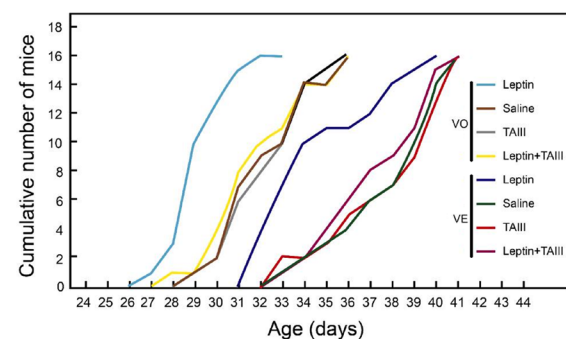


Figure 1. Onset of puberty in leptin-, saline- and TAIII-treated female mice.

The mice were weaned at 21 d, housed in groups of three under 12 h light (06:00–18:00) and dark (18:00–06:00) cycles, and allowed ad libitum access to chow and water. They were injected with recombinant mouse leptin, 2 μ g/g body weight, saline vehicle, 100 μ l i.p., or leptin plus TAIII, 10 μ g/g body weight once a day at 10:00–11:00 hours until day 42. *n*=15 per group.

Table 2. Bone mineral density, trabecular bone density and cortical bone density in mice treated with leptin and TAIII.

Group	No. animals	Bone mineral density (mg/cm ²)	Trabecular bone density (mg/cm ²)	Cortical bone density (mg/cm ²)
Control (saline)	6	340.5±2.21	180.5±1.24	540.5±4.14
Control (TAIII)	6	342.5±2.21	183.5±1.54	537.5±3.24
Leptin	6	410.5±3.23*	230.1±1.94*	680.5±5.04*
Leptin+TAIII	6	380.2±1.11#	210.8±2.11#	650.2±3.31

Data were presented as mean ± standard deviation. *and #*P*<0.05 compared to controls (saline and TAIII) and leptin treatment, respectively, using one-way ANOVA.

Table 3. Serum luteinizing hormone (LH), follicle stimulating hormone (FSH) and estradiol (E₂) levels in mice treated with leptin and TAIII.

Group	No. animals	LH (ng/ml)	FSH (ng/ml)	E ₂ (pg/ml)
Control (saline)	6	5.8±0.91	22.4±3.91	25.2±2.6
TAIII	6	5.7±0.61	21.4±3.56	24.7±2.4
Leptin	6	12.4±1.21*	39.3±4.99*	55.7±7.6*
Leptin+TAIII	6	7.8±0.81#	27.8±3.01#	±4.3 #

Data were presented as mean ± standard deviation. *and #*P*<0.05 compared to controls (saline and TAIII) and leptin treatment, respectively, using one-way ANOVA.

nificantly decreased BMD, TBD but not CBD in leptin-treated mice (Table 2).

TAIII reduces LH, FSH and E₂ levels

Next, we investigated the changes of several serum hormones that are related to PP development. The results showed that LH, FSH and E₂ levels were similar between controls (saline or TAIII alone) (Table 3). However, compared with the controls, the hormone levels were increased significantly after leptin treatment (*P*<0.01, Table 3). On other hand, TAIII administration reduced the levels of these hormones significantly as compared with leptin-treated mice (*P*<0.01, Table 3), although they were still higher than the controls.

TAIII downregulates the expression of KISS1, GPR54, GnRH and GnRHR

qRT-PCR and Western blot analyses showed that the expression of KISS1, GPR54, GnRH and GnRHR at both mRNA and protein levels was significantly upregulated in leptin treated mice (Fig. 2) but not in TAIII treated mice, as compared with control mice (saline-treated). Leptin+TAIII treatment significantly downregulated the expression of the four genes compared to leptin treatment (Fig. 2).

TAIII downregulates the expression of leptin

Since leptin is involved in GnRH secretion from hypothalamic neurons (Burcelin *et al.*, 2003), we assessed leptin gene expression in brain tissue. qRT-PCR and Western blot analysis showed that both mRNA and protein levels of leptin were not affected by either TAIII or leptin treatment, as compared with saline treatment (Fig. 3). However, both mRNA and protein levels of leptin were significantly reduced in leptin-treated mice after TAIII treatment (Fig. 3) the control, TAIII- or leptin-alone treated mice.

DISCUSSION

PP is a developmental disorder in children caused by early activation and hyperfunction of the HPGA axis.

Our experimental data showed that leptin could induce PP in mice, manifesting with earlier VO and VE and increased BMD. TAIII delayed leptin-induced sexual development acceleration, as evidenced by reduced sex hormone production and decreased expression of the genes encoding HPGA components: KISS1, GPR54, GnRH and GnRHR. TAIII also reduced BMD, TBD, and leptin expression in the leptin-treated mice. These findings indicate that TAIII is one of the active ingredients in *A. asphodeloides* preparations that confers anti-PP activity.

Puberty is a complex developmental process, which is affected by a variety of genetic and endocrine factors. To investigate the therapeutic effect of TAIII, we constructed murine model of PP using leptin and measured the progress of sexual maturation using several indexes such as VO, VE and BMD. VO and VE are external signs of the initiation of female sexual development, and are also used as the criteria for judging the onset of puberty (Zhou & Li, 2014). After leptin treatment, VO and VE were accelerated, and BMD was increased, as compared with the controls (saline or TAIII). Furthermore, pathological and biochemical analysis showed that the ovarian and uterus development was enhanced and serum hormone levels were increased in the leptin-treated mice as compared with control, confirming that the leptin treatment induced PP in mice. This is consistent with the results obtained in a previous study showing that leptin could facilitate the onset of puberty in female mice (Ahima *et al.*, 1997). On other hand, TAIII treatment delayed VO and VE, reduced BMD and delayed the sexual organ developments in the leptin-treated mice, indicating that TAIII attenuates leptin-induced PP. The crude preparations of *A. asphodeloides* are used as herbal medicine for PP (Xu & Qiu, 2007; Zhou & Li, 2014), it would be interesting to investigate whether this purified compound from *A. asphodeloides* is also able to alleviate PP in humans. Recent study shows that leptin communicates metabolic information with the brain neurons that control reproduction using GABAergic circuitry, resulting in releasing of GnRH from hypothalamic neurons (Burcelin *et al.*, 2003) and puberty onset (Egan *et al.*, 2017). In rats, the model of PP is established using da-

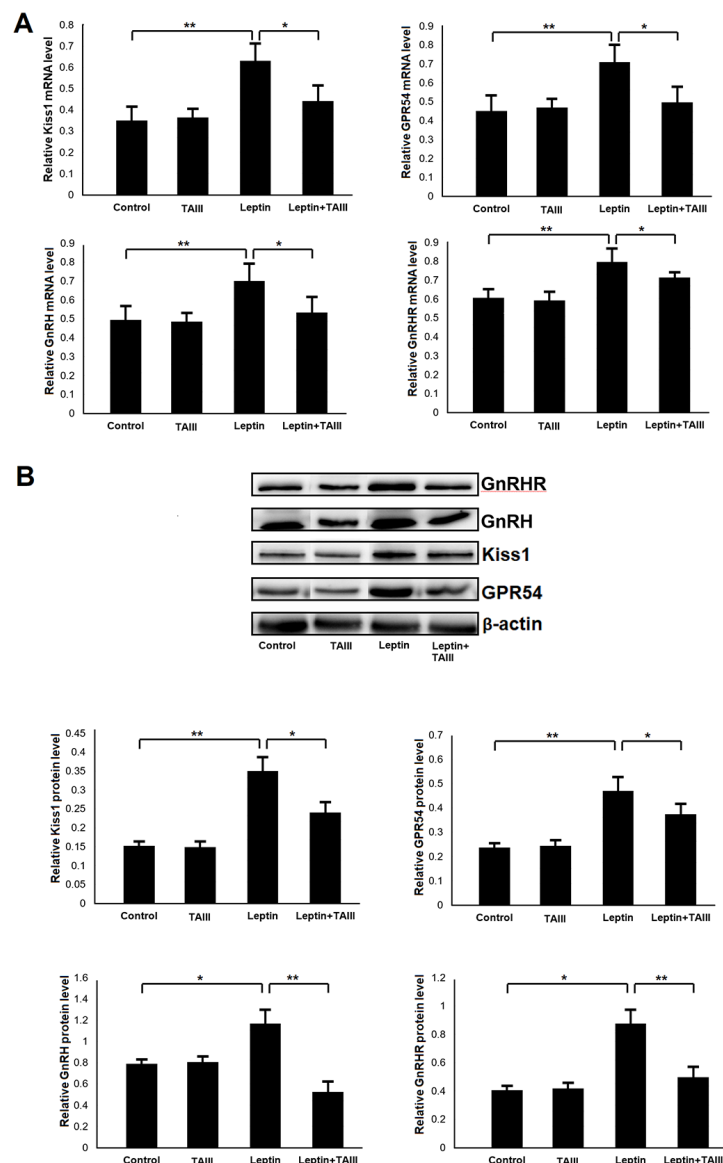


Figure 2. mRNA and protein expression of KISS1 and GPR54 after leptin and TAIII treatment.

qRT-PCR and Western blot analyses were performed using mRNA and protein extracted from the tissues of mice treated with leptin and TAIII for 15 days. (A) Relative mRNA levels, (B) upper panel: representative Western blots, lower panel: relative protein levels. All assays were triplicated. One-way ANOVA was performed to compare the difference among the groups. *, ** $P < 0.05$ and < 0.01 , respectively.

nazol, a drug that can rapidly activate the HPGA leading to increased expression of KISS1 and GRP45 and onset of PP (Park *et al.*, 2021).

To further investigate the mechanisms underlying TAIII-mediated anti-PP activity, we profiled the changes of several serum hormones that are related to PP. In females, LH and FSH are synthesized in the anterior pituitary gland and the levels of LH and FSH exhibit rhythmic changes throughout the menstrual or estrous cycle and have an important influence on development of puberty, gonads, and reproductive function. Premature secretion of LH and FSH leads to the early gonad activation and development of secondary sexual traits (Coss, 2018). E_2 is a steroid hormone secreted in the ovaries and is involved in the regulation of the estrous and menstrual reproductive cycles in female (Park *et al.*, 2006; Siemieniuch *et al.*, 2010). E_2 receptors are distributed in the uterus, breast and ovary. They function to promote the maturation of sexual organs (Hewitt & Korach, 2018). Earlier secretion of E_2 and other sex hormones acceler-

ate bone maturation, resulting in shortened bone growth cycle and reduced bone mineral density (Khosla & Monroe, 2018; Manolagas *et al.*, 2002). Therefore, LH, FSH, E_2 and GnRH stimulation test have been used as intuitive clinical indexes to diagnose PP (Yeh *et al.*, 2021).

Our data showed that LH, FSH and E_2 were increased following leptin treatment as compared to the controls, which is consistent with the symptoms of PP, and the increases observed in other PP models (Park *et al.*, 2021). However, after TAIII treatment, the levels of LH, FSH and E_2 in leptin-treated mice were decreased significantly, suggesting that TAIII is able to modulate the synthesis and/or secretion of these hormones, although the exact mechanisms of this modulation remain unclear. In parallel with the hormone levels, the signs of sexual development in leptin-treated mice, such as ovarian and uterus weight and size, and corpora lutea number, were reduced after TAIII treatment, further confirming that TAIII has activity against puberty onset. While hormones have been shown to play important role in sexual (Park *et*

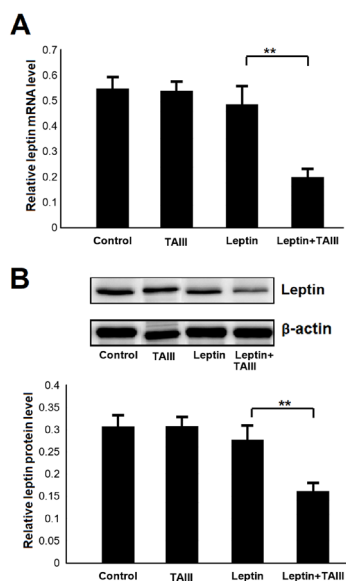


Figure 3. Leptin mRNA and protein levels in mice treated with leptin and TAIII.

qRT-PCR and Western blot analyses were performed using mRNA and protein extracted from the tissues of mice treated with leptin and TAIII for 15 days. **(A)** Relative mRNA levels, **(B)** upper panel: representative Western blots, lower panel: relative protein levels. All assays were triplicated. One-way ANOVA was performed to compare the difference among the groups. ** $P < 0.01$.

al., 2006; Siemieniuch *et al.*, 2010; Miyakoshi, 2004) and bone development (Miyakoshi, 2004; Olney, 2003), the causal relationship between the reduced hormone levels, reproductive organ development and bone development needs to be further investigated to better understand the model of action of TAIII.

The hypothalamus secretes GnRH, which triggers the anterior pituitary to release FSH and LH that act on the gonads (ovaries) to secrete E2, forming the HPGA axis (Lockett *et al.*, 1977). KISS1 was discovered as a novel human malignant melanoma metastasis-suppressor gene in melanoma cells on chromosome 6 (Lee *et al.*, 1996). KISS1 expression is significantly upregulated in pubertal rats (Kuohung & Kaiser, 2006) and may be induced by estrogenic mycotoxin (Yang *et al.*, 2016). GPR54 is a member of G protein-coupled receptors in the rhodopsin family and is expressed in brain regions (pons, midbrain, thalamus, hypothalamus, hippocampus, amygdala, cortex, frontal cortex, and striatum), as well as in peripheral regions (liver and intestine) (Lee *et al.*, 1999). Although the actual role of the KISS-1/GPR54 system in the timing of puberty onset remains unexplored, the activation of the gonadotrophic axis at puberty represents the final point of a complex sex developmental cascade for reproductive capacity. KISS1 and its receptor GPR54 are important for puberty onset. The levels of KISS1 and GPR54 mRNA in the thalamus are elevated at puberty onset and they could stimulate GnRH neurons to trigger various pathways engaged in the onset of puberty (Kuohung & Kaiser, 2006). In PP rat, serum sex hormone concentrations are closely related to GnRH mRNA levels, while the synthesis and release of GnRH and GnRHR are regulated by KISS-1/GPR54. Early activation of KISS1/GPR54 could activate the production of GnRH in the neurons, and subsequently the HPGA axis, resulting in accelerated sexual development (Dedes, 2012; Song *et al.*, 2017). Our data showed that mRNA and protein expression of KISS1 and GPR54, as well as

GnRH and GnRHR, in serum, was significantly upregulated after the leptin treatment, which was reversed by concomitant TAIII treatment. In rat model of PP, increased KISS1 and GPR54 expression was also observed following danazol treatment. However, GPR54 expression was not affected by sarsasapogenin, another active ingredient from *A. asphodeloides*, although it has anti-PP activity (Hu *et al.*, 2020b). Apparently, the molecular mechanism of action of sarsasapogenin is different from the mechanism of action of TAIII, which downregulated KISS1 and GPR54 expression elevated by leptin treatment, suggesting that TAIII may exert anti-PP activity through the KISS1/GPR54 system.

As an adipocyte-derived hormone, leptin stimulates the secretion of gonadotropins from the pituitary and hence play important roles in pubertal development and maintenance of reproductive function (Dehpour *et al.*, 1976; Tezuka *et al.*, 2002). It regulates development and is a permissive factor for the initiation of human puberty, but not the only stimulator of puberty initiation (Terasawa & Fernandez, 2001). The difference in body fat quantity can affect leptin concentration to regulate the expression of genes related to obesity (Hu *et al.*, 2001). Through informing brain centers about the amount of fat stored in the body, leptin exerts various regulatory functions especially associated with energy intake and metabolism, including controlling the activity of the hypothalamic-pituitary-adrenal (HPA) axis (Roubos *et al.*, 2012). Our analysis showed that after TAIII treatment, leptin mRNA and protein levels were reduced in the brain of leptin-treated mice. This might generate signals leading to reduced HPGA activities, including decreased KISS1, GPR54, GnRH and GnRHR expression, and consequently reduced serum hormone levels, reduced BMD, and postponed PP (Antoniazzi & Zamboni, 2004). However, the impact of TAIII on leptin level in the blood was not assessed and should be investigated further. It is also noted that leptin protein level in the brain remained unchanged in leptin-treated mice compared to untreated mice. The exact reasons for this are unclear. It is likely that the subcutaneously injected leptin might need leptin receptor as a transporter to enter the brain via choroid plexus (Lynn *et al.*, 1996) due to the blood-brain barrier, or it might be diluted/partially degraded after injection. While leptin treatment was reported to cause PP (Ahima *et al.*, 1997), which is confirmed in the present study, no increase in brain leptin level observed in the leptin-treated mice suggests that leptin may signal outside of the brain to regulate gene expression in the brain indirectly.

Our assessment showed that endogenous leptin expression was only reduced in leptin and TAIII-treated animals, but not in control, TAIII, or leptin treated animals. There might be several mechanisms for this. TAIII might be bound/alterd/activated by the injected leptin to downregulate the expression of leptin in the brain. Since the concentration of injected leptin was likely much higher than endogenous leptin in the blood (Odle *et al.*, 2014), TAIII could act as concentration-dependent antagonist of leptin to inhibit the expression of leptin, resulting in differential outcomes in leptin-treated animals and untreated animals. This hypothesis should be further tested to verify the relationship between TAIII concentration and leptin expression level. For example, ligand-binding assays could be used to investigate the molecular interaction between TAIII and leptin to better explain the results observed in the present study.

Although TAIII has been shown to have multiple pharmacological targets, including VEGFR, XIAP,

BMI1, mTOR, NF- κ B, COX-2 and MMPs, the way it impacts gene expression of these targets is still unclear (Lin *et al.*, 2020). It is possible that TAIH may bind to regulatory sequences or targeting microRNAs that subsequently impact the expression of the target genes. Ligand binding assays, immunoprecipitation, compound-target binding assays and *in silico* predictions of herbal compound target may be designed to gain insight on the physical interactions between the molecule and cellular targets for better exploration of its anti-PP activity.

Taken together, our work demonstrated that TAIH is an active ingredient of *A. asphodeloides* preparation that counteracts PP. It downregulates the expression of KISS1, GPR54, GnRH, GnRHR and leptin, reduces the levels of serum LH, FSH, E₂, and delays BMD and sexual development in leptin-induced PP murine models. However, since this is a single dose study with model animals, the optimal efficacy and dose for PP control have not been determined. The safety profiles of this compound need to be determined and the therapeutic effects need to be further verified in other animal models and eventually in human subjects in order to develop it into a clinically applicable agent. Meanwhile, chemical modifications or screening of analogs may be carried to improve the efficacy and safety of this compound for clinical use.

Declarations

Ethics approval: the Institutional Animal Care and Use Committee of Beijing University of Chinese Medicine Shenzhen Hospital, Shenzhen, China.

Patient consent for publication: n/a.

Availability of data and material: The datasets used during the current study are available from the corresponding author on reasonable request.

Competing interests: The authors declare that they have no competing interests.

Funding: This study did not receive any specific fund from public and private sector.

Authors' contributions: LZ and XY designed the study. LZ, YR, QW and XY collected the data and performed analysis. LZ, DL, WZ, CL, and XY drafted the manuscript. All authors read and approved the final version of manuscript.

Acknowledgements: none

REFERENCES

- Ahima RS, Dushay J, Flier SN, Prabakaran D, Flier JS (1997) Leptin accelerates the onset of puberty in normal female mice. *J Clin Invest* **99**: 391–395. <https://doi.org/10.1172/JCI119172>
- Antoniazzi F, Zamboni G (2004) Central precocious puberty: current treatment options. *Paediatr Drugs* **6**: 211–231. <https://doi.org/10.2165/00148581-200406040-00002>
- Bao W, Pan H, Lu M, Ni Y, Zhang R, Gong X (2007) The apoptotic effect of sarsasapogenin from *Anemarrhena asphodeloides* on HepG2 human hepatoma cells. *Cell Biol Int* **31**: 887–892. <https://doi.org/10.1016/j.cellbi.2007.02.001>
- Bradley SH, Lawrence N, Steele C, Mohamed Z (2020) Precocious puberty. *BMJ* **368**: l6597. <https://doi.org/10.1136/bmj.l6597>
- Burcelin R, Thorens B, Glauser M, Gaillard RC, Pralong FP (2003) Gonadotropin-releasing hormone secretion from hypothalamic neurons: stimulation by insulin and potentiation by leptin. *Endocrinology* **144**: 4484–4491. <https://doi.org/10.1210/en.2003-0457>
- Carel JC, Eugster EA, Rogol A, Ghizzoni L, Palmert MR; ESPE-LWPES GnRH Analogs Consensus Conference Group; Antoniazzi F, Berenbaum S, Bourguignon JP, Chrousos GP, Coste J, Deal S, de Vries L, Foster C, Heger S, Holland J, Jahnukainen K, Juul A, Kaplowitz P, Lahlou N, Lee MM, Lee P, Merke DP, Neely EK, Oostdijk W, Phillip M, Rosenfield RL, Shulman D, Styne D, Tauber M, Wit JM (2009) Consensus statement on the use of gonadotropin-releasing hormone analogs in children. *Pediatrics* **123**: e752–e762. <https://doi.org/10.1542/peds.2008-1783>
- Censani M, Feuer A, Orton S, Askin G, Vogiatzi M (2019) Changes in body mass index in children on gonadotropin-releasing hormone agonist therapy with precocious puberty, early puberty or short stature. *J Pediatr Endocrinol Metab* **32**: 1065–1070. <https://doi.org/10.1515/jpem-2019-0105>
- Cesario SK, Hughes LA (2007) Precocious puberty: a comprehensive review of literature. *J Obstet Gynecol Neonatal Nurs* **36**: 263–274. <https://doi.org/10.1111/j.1552-6909.2007.00145.x>
- Chae HW, Na JH, Kwon A, Kim HS, Lee YM (2021) Central precocious puberty may be a manifestation of endocrine dysfunction in pediatric patients with mitochondrial disease. *Eur J Pediatr* **180**: 425–432. <https://doi.org/10.1007/s00431-020-03804-3>
- Cheuiche AV, da Silveira LG, de Paula LCP, Lucena IRS, Silveiro SP (2021) Diagnosis and management of precocious sexual maturation: an updated review. *Eur J Pediatr* **180**: 3073–3087. <https://doi.org/10.1007/s00431-021-04022-1>
- Coss D (2018) Regulation of reproduction via tight control of gonadotropin hormone levels. *Mol Cell Endocrinol* **463**: 116–130. <https://doi.org/10.1016/j.mce.2017.03.022>
- Dedes I (2012) Kisspeptins and the control of gonadotrophin secretion. *Syst Biol Reprod Med* **58**: 121–128. <https://doi.org/10.3109/19396368.2011.651555>
- Dehpour AR, Ghaffarpour F, Hosseinzadeh K, Khoyi MA (1976) Effect of denervation and cocaine on the response of isolated rat vas deferens to noradrenaline and methoxamine (Proceedings). *Br J Pharmacol* **58**: 280P
- Egan OK, Inglis MA, Anderson GM (2017) Leptin signaling in AgRP neurons modulates puberty onset and adult fertility in mice. *J Neurosci* **37**: 3875–3886. <https://doi.org/10.1523/JNEUROSCI.3138-16.2017>
- Han FY, Song XY, Chen JJ, Yao GD, Song SJ (2018) Timosaponin AIII: A novel potential anti-tumor compound from *Anemarrhena asphodeloides*. *Steroids* **140**: 125–130. <https://doi.org/10.1016/j.steroids.2018.09.014>
- Hewitt SC, Korach KS (2018) Estrogen Receptors: New Directions in the New Millennium. *Endocr Rev* **39**: 664–675. <https://doi.org/10.1210/er.2018-00087>
- Hu FB, Chen C, Wang B, Stampfer MJ, Xu X (2001) Leptin concentrations in relation to overall adiposity, fat distribution, and blood pressure in a rural Chinese population. *Int J Obes Relat Metab Disord* **25**: 121–125. <https://doi.org/10.1038/sj.ijo.0801480>
- Hu K, Sun W, Li Y, Zhang B, Zhang M, Guo C, Chang H, Wang X (2020a) Study on the mechanism of sarsasapogenin in treating precocious puberty by regulating the HPG axis. *Evid Based Complement Alternat Med* **2020**: 1978043. <https://doi.org/10.1155/2020/1978043>
- Hu K, Sun W, Li Y, Zhang B, Zhang M, Guo C, Chang H, Wang X (2020b) Study on the mechanism of sarsasapogenin in treating precocious puberty by regulating the HPG axis. *Evid Based Complement Alternat Med* **2020**: 1978043. <https://doi.org/10.1155/2020/1978043>
- Khosla S, Monroe DG (2018) Regulation of bone metabolism by sex steroids. *Cold Spring Harb Perspect Med* **8**: <https://doi.org/10.1101/cshperspect.a031211>
- Kim SH, Huh K, Won S, Lee KW, Park MJ (2015) A Significant increase in the incidence of central precocious puberty among Korean girls from 2004 to 2010. *PLoS One* **10**: e0141844. <https://doi.org/10.1371/journal.pone.0141844>
- Kuohung W, Kaiser UB (2006) GPR54 and KiSS-1: role in the regulation of puberty and reproduction. *Rev Endocr Metab Disord* **7**: 257–263. <https://doi.org/10.1007/s11154-006-9020-2>
- Lee DK, Nguyen T, O'Neill GP, Cheng R, Liu Y, Howard AD, Coulombe N, Tan CP, Tang-Nguyen AT, George SR, O'Dowd BF (1999) Discovery of a receptor related to the galanin receptors. *FEBS Lett* **446**: 103–107. [https://doi.org/10.1016/S0014-5793\(99\)00009-5](https://doi.org/10.1016/S0014-5793(99)00009-5)
- Lee JH, Miele ME, Hicks DJ, Phillips KK, Trent JM, Weissman BE, Welch DR (1996) KiSS-1, a novel human malignant melanoma metastasis-suppressor gene. *J Natl Cancer Inst* **88**: 1731–1737. <https://doi.org/10.1093/jnci/88.23.1731>
- Lin Y, Zhao WR, Shi WT, Zhang J, Zhang KY, Ding Q, Chen XL, Tang JY, Zhou ZY (2020) Pharmacological activity, pharmacokinetics, and toxicity of timosaponin AIII, a natural product isolated from *Anemarrhena asphodeloides* bunge: A review. *Front Pharmacol* **11**: 764. <https://doi.org/10.3389/fphar.2020.00764>
- Liu Z, Guo F, Wang Y, Li C, Zhang X, Li H, Diao L, Gu J, Wang W, Li D, He F (2016) BATMAN-TCM: a bioinformatics analysis tool for molecular mechanism of traditional Chinese medicine. *Sci Rep* **6**: 21146. <https://doi.org/10.1038/srep21146>
- Livak KJ, Schmittgen TD (2001) Analysis of relative gene expression data using real-time quantitative PCR and the 2(-Delta Delta C(T)) Method. *Methods* **25**: 402–408. <https://doi.org/10.1006/meth.2001.1262>
- Lockett FC, Rothfeld B, Mecklenburg R, Sagar V (1977) Detection of bone trauma after cardiopulmonary resuscitation. *Md State Med J* **26**: 78–79
- Lynn RB, Cao GY, Considine R, Hyde TM, Caro JF (1996) Autoradiographic localization of leptin binding in the choroid plexus of

- ob/ob and db/db mice. *Biochem Biophys Res Commun* **219**: 884–889. <https://doi.org/10.1006/bbrc.1996.0328>
- Manolagas SC, Kousteni S, Jilka RL (2002) Sex steroids and bone. *Recent Prog Horm Res* **57**: 385–409. <https://doi.org/10.1210/rp.57.1.385>
- Miyakoshi N (2004) Effects of parathyroid hormone on cancellous bone mass and structure in osteoporosis. *Curr Pharm Des* **10**: 2615–2627. <https://doi.org/10.2174/1381612043383737>
- Neely EK, Crossen SS (2014) Precocious puberty. *Curr Opin Obstet Gynecol* **26**: 332–338. <https://doi.org/10.1097/GCO.0000000000000099>
- Nelson JF, Karelus K, Felicio LS, Johnson TE (1990) Genetic influences on the timing of puberty in mice. *Biol Reprod* **42**: 649–655. <https://doi.org/10.1095/biolreprod42.4.649>
- Odle AK, Haney A, Allensworth-James M, Akhter N, Childs GV (2014) Adipocyte versus pituitary leptin in the regulation of pituitary hormones: somatotropes develop normally in the absence of circulating leptin. *Endocrinology* **155**: 4316–4328. <https://doi.org/10.1210/en.2014-1172>
- Olney RC (2003) Regulation of bone mass by growth hormone. *Med Pediatr Oncol* **41**: 228–234. <https://doi.org/10.1002/mpo.10342>
- Park JY, Pillingier MH, Abramson SB (2006) Prostaglandin E2 synthesis and secretion: the role of PGE2 synthases. *Clin Immunol* **119**: 229–240. <https://doi.org/10.1016/j.clim.2006.01.016>
- Park SC, Trinh TA, Lee WY, Baek JY, Lee S, Choi K, Ha J, Kim CE, Kang KS, Lee HL (2021) Effects of estrogen inhibition formula herbal mixture for danazol-induced precocious puberty in female rats: an experimental study with network pharmacology. *Integr Med Res* **10**: 100708. <https://doi.org/10.1016/j.imr.2020.100708>
- Roubos EW, Dahmen M, Kozicz T, Xu L (2012) Leptin and the hypothalamo-pituitary-adrenal stress axis. *Gen Comp Endocrinol* **177**: 28–36. <https://doi.org/10.1016/j.ygcen.2012.01.009>
- Siemieniuch MJ, Bowolaksono A, Skarzynski DJ, Okuda K (2010) Ovarian steroids regulate prostaglandin secretion in the feline endometrium. *Anim Reprod Sci* **120**: 142–150. <https://doi.org/10.1016/j.anireprosci.2010.02.020>
- Sitruk-Ware R, de Lignieres B, Mauvais-Jarvis P (1986) Progestogen treatment in post-menopausal women. *Maturitas* **8**: 95–100. [https://doi.org/10.1016/0378-5122\(86\)90015-0](https://doi.org/10.1016/0378-5122(86)90015-0)
- Song W, Li K, Sun C, Xue J (2017) Kisspeptin permits the sexual development of female rats with normal and precocious puberty but is not a trigger for it. *Neuro Endocrinol Lett* **38**: 422–428
- Terasawa E, Fernandez DL (2001) Neurobiological mechanisms of the onset of puberty in primates. *Endocr Rev* **22**: 111–151. <https://doi.org/10.1210/edrv.22.1.0418>
- Tezuka M, Irahara M, Ogura K, Kiyokawa M, Tamura T, Matsuzaki T, Yasui T, Aono T (2002) Effects of leptin on gonadotropin secretion in juvenile female rat pituitary cells. *Eur J Endocrinol* **146**: 261–266. <https://doi.org/10.1530/eje.0.1460261>
- Wang C, Chen Q, Yuan K, He M, Zhu J, Fang Y, Hu J, Yan Q (2021) The first central precocious puberty proteomic profiles revealed multiple metabolic networks and novel key disease-associated proteins. *Aging (Albany NY)* **13**: 24236–24250. <https://doi.org/10.18632/aging.203676>
- Wang Y, Dan Y, Yang D, Hu Y, Zhang L, Zhang C, Zhu H, Cui Z, Li M, Liu Y (2014) The genus *Anemarrhena* Bunge: A review on ethnopharmacology, phytochemistry and pharmacology. *J Ethnopharmacol* **153**: 42–60. <https://doi.org/10.1016/j.jep.2014.02.013>
- Xu W, Qiu Z (2007) Effect of Zhibaidihuang Decoction on hormone level of idiopathic central precocious puberty. *J Trad Chinese Med* **48**: 335–336. <https://doi.org/10.3321/j.issn:1001-1668.2007.04.018>
- Yang L, Jiang M, Yu R, Hu R, Xiong F, Li J (2021) A case report of precocious puberty related to Rett syndrome and a literature review. *Pharmazie* **76**: 559–561. <https://doi.org/10.1691/ph.2021.1747>
- Yang R, Wang YM, Zhang L, Zhao ZM, Zhao J, Peng SQ (2016) Prepubertal exposure to an oestrogenic mycotoxin zearalenone induces central precocious puberty in immature female rats through the mechanism of premature activation of hypothalamic kisspeptin-GPR54 signaling. *Mol Cell Endocrinol* **437**: 62–74. <https://doi.org/10.1016/j.mce.2016.08.012>
- Yeh SN, Ting WH, Huang CY, Huang SK, Lee YC, Chua WK, Lin CH, Cheng BW, Lee YJ (2021) Diagnostic evaluation of central precocious puberty in girls. *Pediatr Neonatol* **62**: 187–194. <https://doi.org/10.1016/j.pedneo.2020.12.001>
- Yu CH, Liu PH, Van YH, Lien AS, Huang TP, Yen HR (2014) Traditional Chinese medicine for idiopathic precocious puberty: A hospital-based retrospective observational study. *Complement Ther Med* **22**: 258–265. <https://doi.org/10.1016/j.ctim.2014.01.002>
- Zhou SS, Li P (2014) Effects of NELL2 on the regulation of GnRH expression and puberty in female rats. *Genet Mol Res* **13**: 6672–6682. <https://doi.org/10.4238/2014.August.28.12>

Quercetin inhibits the expression of *MYC* and *CYP2E1* and reduces oxidative stress in the myocardium of spontaneously hypertensive rats

Oksana Maksymchuk¹✉, Angela Shysh² and Anna Kotliarova²

¹Institute of Molecular Biology and Genetics, Department of Molecular Oncogenetics, National Academy of Sciences of Ukraine, Kyiv 03143, Ukraine; ²Bogomoletz Institute of Physiology, Department of General and Molecular Pathophysiology, National Academy of Sciences of Ukraine, Kyiv 01024, Ukraine

Oxidative stress is one of the most important pathological processes in chronic heart failure caused by hypertension. These processes involve MYC-regulated mechanisms, including the induction of CYP2E1 as a potent prooxidant factor. In this work, we used qPCR, Western blot analysis, and biochemical markers of oxidative stress to investigate the ability of quercetin to inhibit oxidative stress by modulating MYC expression. We studied spontaneously hypertensive rats (SHRs) in which the onset of cardiac pathology was observed at least at 4 months of age and the development of pathology occurred during life up to 22 months of age. Wistar rats were used as normotensive controls. We observed overexpression of the transcription factor MYC ($p=0.0024$) in the myocardium of SHRs compared to normotensive controls, and an increased expression of MYC-target gene, *CYP2E1*, ($p=0.0001$) in the old SHR group compared to young SHRs. This probably contributed significantly to the development of oxidative stress in the cardiac tissue of old SHRs. We demonstrated that long-term treatment of old SHRs with quercetin resulted in dramatic inhibition of MYC ($p=0.0000$), and a significant decrease in CYP2E1 ($p=0.0001$) expression and CYP2E1 protein levels ($p=0.0136$). This probably contributed significantly to the decrease in lipid peroxidation ($p=0.0000$). Quercetin was also able to activate antioxidant activity, resulting in a significant improvement in the prooxidant-antioxidant balance in the heart. In turn, the elimination of oxidative stress could contribute to a decrease in blood pressure ($p=0.0000$) and relative heart weight ($p=0.0071$) in quercetin-treated old SHRs compared to the untreated old SHR group.

Keywords: CYP2E1, hypertension, MYC, myocardium, oxidative stress, quercetin

Received: 12 October, 2022; **revised:** 23 November, 2022; **accepted:** 12 December, 2022; **available on-line:** 02 February, 2023

✉e-mail: o.v.maksymchuk@imbg.org.ua, mksusha@gmail.com

Acknowledgements of Financial Support: This study was funded by the National Research Foundation of Ukraine under the project "Support for Research of Leading and Young Scientists" (No. 20220.02/0332).

Abbreviations: cDNA, complementary deoxyribonucleic acid; CHF, chronic heart failure; CYP2E1 (*CYP2E1*), protein (gene) of cytochrome P450 2E1; GAPDH, glyceraldehyde-3-phosphate dehydrogenase; H₂O₂, hydrogen peroxide; LPO, lipid peroxidation; MYC (*MYC*), protein (gene) of bHLH transcription factor; NADH, nicotinamide adenine dinucleotide (reduced form); qPCR, quantitative polymerase chain reaction; RNA, ribonucleic acid; ROS, reactive oxygen species; SHR, spontaneously hypertensive rat; SOD, superoxide dismutase

INTRODUCTION

Hypertension is one of the most common pathologies of the cardiovascular system, characterized by chronic high blood pressure. This is one of the main factors in the development of chronic heart failure (CHF). Hypertension leads to functional overload of the myocardium (Nolly *et al.*, 2015), which significantly increases the risk of arrhythmias, stroke, and myocardial infarction.

It is known that in cardiac pathologies, the expression of genes regulating energy metabolism in the myocardium changes significantly (Kodde *et al.*, 2007). This is favored by the strong activation of some transcription factors, including MYC (Ahuja *et al.*, 2010). MYC-mediated metabolic changes have been associated with the preservation of cardiac function under stressors (Ahuja *et al.*, 2010). MYC directly regulates glucose metabolism and mitochondrial biogenesis in cardiomyocytes and is an important regulator of energy metabolism in the heart. Activation of MYC has been shown to promote the development of myocardial hypertrophy and functional overload in response to pathological conditions (Ahuja *et al.*, 2010). In turn, increased expression of MYC causes the induction of transcription of many genes, including *CYP2E1* (cytochrome P450 2E1) (Guan *et al.*, 2019). CYP2E1 is one of the major sources of cellular (especially mitochondrial) reactive oxygen species (ROS). CYP2E1 is a potent prooxidant factor in the cell, an increase in its expression leads to an intensification of peroxide processes and the development of oxidative stress, resulting in oxidative damage to cellular structures, mainly biomembranes (Zhang *et al.*, 2011; Guan *et al.*, 2019). This affects the functionality of the plasma membrane (permeability, electrical conductivity, receptor function, etc.). Mitochondrial membrane damage contributes to the initiation of apoptosis (Zhang *et al.*, 2011). Moreover, *CYP2E1* is one of the genes that control mechanotransduction, mitochondrial energy metabolism, redox balance, and myocardial extracellular matrix function (Guan *et al.*, 2019). It has been shown that an increase in CYP2E1 contributes significantly to myocardial energy supply under overload and stress conditions. On the other hand, overexpression of CYP2E1 leads to the initiation of pathological mechanisms in the myocardium, including oxidative stress and stress-associated pathological processes (Guan *et al.*, 2019).

It has been shown that a diet enriched with quercetin has a beneficial effect on the cardiovascular system. Some molecular mechanisms of the cardioprotective effects of this bioflavonoid have already been described. In particular, quercetin may prevent the development

of cardiac hypertrophy, oxidative stress, etc. (Yan *et al.*, 2013; Ghafouri-Fard *et al.*, 2021). The positive cardioprotective properties of quercetin suggest that this bioflavonoid could be used for therapeutic purposes (Larson *et al.*, 2010; Patel *et al.*, 2018). Research into the detailed molecular mechanisms of action of quercetin remains important. This is necessary for the identification of new molecular targets for the treatment of various heart diseases. In this work, we investigated the effect of long-term consumption of quercetin on the expression levels of *MYC* (as an important transcription factor in cardiac pathology) and *MYC*-regulated *CYP2E1* (as a major factor for oxidative stress). Prooxidant and antioxidant processes were also investigated in the myocardium of spontaneously hypertensive rats (SHRs) as a model of hypertension in the elderly (Reckelhoff *et al.*, 2006).

MATERIAL AND METHODS

Animals

Adult male rats (Wistar – normotensive rats and SHRs – Spontaneously hypertensive rats) were provided by Bogomoletz Institute of Physiology NAS of Ukraine (Kyiv, Ukraine). Spontaneously hypertensive rats have been used as a well-established model for genetic hypertension and age-related left ventricle dysfunction. The study involved 20 animals, which were divided into four experimental groups: five young Wistar rats (aged 4 months), five young SHRs (aged 4 months), five old SHRs (aged 22 months), and five old SHRs (aged 22 months) treated with quercetin. The old SHRs were administered quercetin ($\geq 95.0\%$, PhytoLab, Sigma-Aldrich, Germany) once daily in the morning via oral gavage at a dose of 50 mg/kg bw per day for 30 days. The group of young Wistar animals was used as a normotensive control. A noninvasive method of tail artery blood pressure measurement using the Sphygmomanometer S-2 (“HSE”, Germany) was used. The experimental rats were decapitated at the end of the experiment under sodium pentobarbital anesthesia (60 mg/kg bw).

All manipulations of laboratory animals were performed in accordance with the European Convention for the Protection of Vertebrate Animals Used for Experimental and Other Scientific Purposes (Strasbourg, 1986). The protocol was approved by the Local Committee on Bioethics (registration number: 0114U007233).

Oxidative stress markers

Levels of lipid peroxidation (LPO), catalase, and superoxide dismutase (SOD) in heart tissue were determined as previously described (Maksymchuk *et al.*, 2015). The level of LPO was determined in heart homogenates by assessing the level of malondialdehyde (MDA). Catalase activity in heart homogenates was measured by hydrogen peroxide (H_2O_2) degradation. SOD was determined using nicotinamide adenine dinucleotide and phenazine methosulfate reagents for the reduction of nitro-blue tetrazolium salt to blue-colored formazan. MDA values were expressed as μmol per milligram of protein. Enzyme activity values were expressed as U/mg protein (one unit of catalase activity means the amount of enzyme that degrades 1 μmol of H_2O_2 per minute, one unit of SOD activity – the amount of enzyme that oxidizes 1 nmol NADH per minute).

Determination of target gene expression levels by quantitative PCR (qPCR)

RNA isolation from rat heart tissue and cDNA synthesis were performed using the GeneJET RNA purification kit and the Maxima H Minus cDNA Synthesis master mix (ThermoSci), respectively. The qPCR was performed using 5x Hot FirePol EvaGreen qPCR Supermix (Solis Biodynes) according to the manufacturer's protocol. The specific primers were used in qPCR to quantify gene expression of *MYC* (forward primer: CAACGTCCTTGGAACGTCAGA, reverse primer: CTCGCCGTTTCCTCAGTAAG) (Barathidasan *et al.*, 2013), *CYP2E1* (forward primer: TGAAAAAGCCCAAGGAACACC, reverse primer: TGTGCTGGTGGTCTCAGTTC) and *GAPDH* (forward primer: CTACCCACGGCAAGTTCAAC, reverse primer: CCAGTAGACTCCACGACATAC) (Cabiati *et al.*, 2012). *GAPDH* expression was used for normalization. Results are expressed in relative units.

Western blot analysis and protein measurement

Preparation of heart samples for Western blot analysis and measurement of CYP2E1 protein levels were performed as previously described (Maksymchuk *et al.*, 2015). CYP2E1 was detected using rabbit anti-CYP2E1 antibodies (Sigma-Aldrich, USA). GAPDH (loading control) was identified using mouse anti-GAPDH antibodies (Sigma-Aldrich, USA). After treatment of the membranes with secondary antibodies (Sigma-Aldrich, USA), chemiluminescence detection was performed according to the manufacturer's instructions. Western blots were visualized and calculated using the ChemiDoc XRS + system with Image Lab software (Bio-Rad, USA). Relative protein levels were calculated by comparing CYP2E1 levels with GAPDH levels and expressed as relative units.

Statistical analysis

Statistical analysis was performed using Status software (<http://status-please.herokuapp.com>). Data were tested for normal distribution using the Shapiro-Wilk test. The Tukey HSD test was used for multiple comparisons. Differences in means between groups were tested with the one-way ANOVA and the *t*-test. Statistically significant results were considered at $p < 0.05$. Results are expressed as mean \pm standard deviation (S.D.).

RESULTS

Blood pressure and body weight of animals

In this work, we studied the physiological parameters of adult male Wistar and SHR rats. We showed that the average blood pressure in the group of young Wistar rats (Table 1) corresponded to physiologically normal values for age (Novelli *et al.*, 2007). Therefore, we defined this group of rats as a normotensive control group. We found a significant increase in blood pressure in young SHRs at 4 months of age (22%, $p = 0.0000$) compared to normotensive animals of the same age (Table 1). We also found an increase (42%, $p = 0.0021$) in relative heart weight in young hypertensive rats compared to young normotensive rats (Table 1). This could be one of the signs of cardiac hypertrophy that may develop in chronic hypertension (Kahan & Bergfeldt, 2005). We demonstrated that the parameters studied in the hypertensive animals increased, even more, when they reached the

Table 1. Physiological parameters of experimental animals

Animal groups	Blood pressure, mmHg	Body weight, g	Heart weight, g	Relative heart weight, %
young Wistar	129±4.2	353.4±10.19	0.839±0.034	0.237±0.015
young SHR	158±5.7*	270.6±18.35	0.912±0.133	0.337±0.047*
old SHR	185±6.1*	391.0±26.39	1.628±0.362	0.414±0.079
old SHR/Quercetin	149±4.2*	444.4±29.16	1.262±0.095	0.284±0.015*

Values are means±S.D., n=5 rats in each group. * $p \leq 0.001$ compared to the Wistar group, # $p \leq 0.001$ compared to the young SHR group, * $p \leq 0.001$ compared to the old SHR group (One-way ANOVA)

Table 2. Oxidative stress markers in the heart of experimental animals

Animal groups	Catalase, U/mg	Superoxide dismutase, U/mg	Malondialdehyde, $\mu\text{mol/mg}$
young Wistar	96.37 ± 6.51	2.94 ± 0.27	5.9 ± 0.42
young SHR	68.94 ± 10.12*	2.07 ± 0.12*	8.64 ± 0.64*
old SHR	54.45 ± 9.34#	1.52 ± 0.14#	12.13 ± 0.87#
old SHR /Quercetin	107.32 ± 17.67*	2.93 ± 0.07*	8.68 ± 0.26*

Values are means ± S.D., n=5 rats in each group. * $p \leq 0.001$ compared to the Wistar group, # $p \leq 0.05$ compared to the young SHR group, * $p \leq 0.001$ compared to the old SHR group (One-way ANOVA)

age of 22 months. We found an increase in blood pressure (17%, $p=0.0001$) and relative heart weight (23%, $p=0.0995$) in old SHRs compared to the group of young SHRs (Table 1).

Treatment of old hypertensive rats with quercetin resulted in a reduction in blood pressure (20%, $p=0.0000$) and relative heart weight (32%, $p=0.0071$) compared to untreated old SHRs. Thus, quercetin treatment contributed to the return of these indicators to the level of young SHRs (Table 1).

Oxidative stress markers in the heart of animals

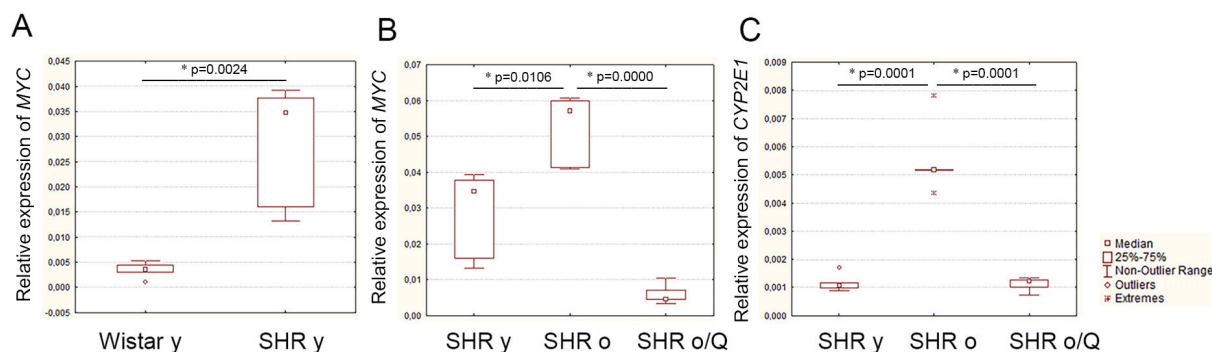
It is well known that oxidative stress is one of the most important pathological processes in CHF caused by chronic hypertension (Rodrigo *et al.*, 2011). In this work, we found evidence of oxidative stress in the heart of SHRs. A significant decrease in the activities of the antioxidant enzymes catalase (29%, $p=0.0009$) and SOD (30%, $p=0.0002$) was observed in young SHRs compared to age-matched normotensive controls. At the same time, we found an increase in MDA content (45%, $p=0.0000$), which may indicate a dramatic intensification of peroxide processes (Table 2). It should be noted that significant changes in these parameters were observed in

the heart of the old hypertensive rats in comparison with the young SHR group: a decrease in the activities of the antioxidant enzymes (catalase, 21%, $p=0.0467$; SOD, 27%, $p=0.0002$) and an increase in MDA content (40%, $p=0.0001$) (Table 2).

Treatment of old hypertensive rats with quercetin significantly improved the prooxidant-antioxidant balance and caused an increase in the activity of antioxidant enzymes: catalase (1.9-fold, $p=0.0004$) and SOD (2-fold, $p=0.0000$). At the same time, the MDA level decreased by 29% ($p=0.0000$) compared to untreated old hypertensive animals (Table 2). It should be noted that the prooxidant-antioxidant balance also improved compared to the young SHR group (Table 2).

MYC expression level in the myocardium

It is well known that MYC controls transcriptional regulation of cardiac metabolism and mitochondrial biogenesis in response to pathological stress (Ahuja *et al.*, 2010). In this work, a large increase (8-fold, $p=0.0024$) in the expression of MYC was observed in the myocardium of young SHRs compared to the age-matched normotensive control (Fig. 1a). It should be noted that the expression of this transcription factor in hypertensive rats contin-

**Figure 1. Gene expression in the myocardium of experimental rats.**

(A) MYC expression in the myocardium of young rats. (B) MYC and (C) CYP2E1 expression in the myocardium of spontaneously hypertensive rats. Wistar y – normotensive young rats, SHR y – spontaneously hypertensive young rats, SHR o – spontaneously hypertensive old rats, SHR o/Q – spontaneously hypertensive old rats treated with quercetin, * p -values <0.05 were considered statistically significant, (A) Student's t -test, (B) and (C) One-way ANOVA, n=5 in each group

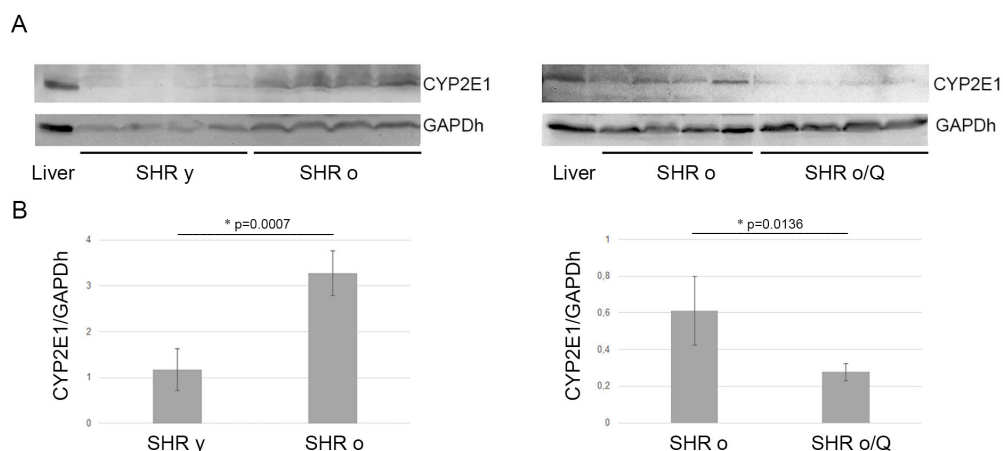


Figure 2. CYP2E1 protein levels in the heart of experimental rats.

(A) Western blot analysis of total heart lysates probed with specific anti-CYP2E1 antibodies. GAPDH is a loading control. (B) Quantification of Western blotting results. *SHR y* – spontaneously hypertensive young rats, *SHR o* – spontaneously hypertensive old rats, *SHR o/Q* – spontaneously hypertensive old rats treated with quercetin, *Liver* – a total liver lysate (as a reference control). **p*-values <0.05 were considered statistically significant, Student's *t*-test. Means \pm S.D., *n*=4 in each group

ues to increase throughout life. We found that the expression of *MYC* was higher (1.9-fold, $p=0.0106$) in the myocardium of old SHRs than in the group of young SHRs (Fig. 1b).

Treatment of old SHRs with quercetin resulted in a significant decrease (8.7-fold, $p=0.0000$) in myocardial *MYC* expression compared to the group of untreated old SHRs (Fig. 1b). Thus, the expression of this transcription factor was much lower than in the group of young hypertensive rats (Fig. 1b).

CYP2E1 expression and protein levels in the myocardium

Since *CYP2E1* is under *MYC*-dependent transcriptional control, modulation of *MYC* could cause a change in *CYP2E1* expression. We found a significant increase in *CYP2E1* gene expression (4.8-fold, $p=0.0001$) (Fig. 1c) as well as protein content (2.8-fold, $p=0.0007$) in the heart of old hypertensive rats compared to the young SHR group (Fig. 2).

Quercetin treatment resulted in a significant decrease in *CYP2E1* expression (4.9-fold, $p=0.0001$), which was accompanied by a decrease in protein content (2.2-fold, $p=0.0136$) in the heart of the old hypertensive rats compared to the group of untreated old SHRs (Fig. 1c and 2).

DISCUSSION

Despite modern optimal therapies, mortality of patients with cardiovascular pathology (coronary heart diseases, myocardial infarction etc.) caused by hypertension remains high. Detailed study of the pathogenesis of heart disease is necessary to prevent and correct pathological changes in the myocardium, improve the quality of life of patients, and prolong their lives. It is known that in a normal physiological state, mitochondrial fatty acid oxidation is the main source of energy production in the myocardium. In heart failure, the level of this oxidation often decreases, while glycolytic pathways become more prominent, ultimately leading to contractile dysfunction. Chronic hypertension has been shown to be one of the

key factors in such pathological processes (Oh & Cho, 2020). In this work, we investigated the development of cardiac pathology using a model of spontaneously hypertensive rats. We found a steady increase in blood pressure even in young SHRs compared with normotensive animals of the same age and sex. An increase in relative heart weight was also noted in young SHRs, which may be a sign of cardiac hypertrophy. It is well known that chronic hypertension may contribute to the development of oxidative stress, one of the major pathological processes leading to structural and functional damage of the myocardium in the development of CHF (Rodrigo *et al.*, 2011; Mei *et al.*, 2015). We also found evidence of an imbalance between prooxidants and antioxidants, which may indicate the development of oxidative stress in the heart of young SHRs. Thus, the data obtained may indicate the onset of pathological processes in the heart of young hypertensive animals. These processes continued and are exacerbated during the life of the animals.

Significant metabolic changes have been shown to occur in the myocardium during hypertension-induced cardiac overload. Changes in the expression of key transcription factors (including *MYC*) that regulate metabolic genes in cardiomyocytes lead to transient adaptation of the myocardium to stress and also initiate pathological processes (Ahuja *et al.*, 2010; Guan *et al.*, 2019). We found strong activation of *MYC* expression in the myocardium of young hypertensive animals compared to normotensive controls. It should be noted that this activation further increased during life in hypertensive rats. It has been shown that *MYC* is expressed at a very low level in the adult heart under normal physiological conditions. However, in response to cardiac overload, the expression of *MYC* increases sharply (Xiao *et al.*, 2001). In particular, it has been shown that the expression of *MYC* was significantly increased in the myocardium of spontaneously hypertensive animals and was associated with cardiac hypertrophy and atherosclerosis (Negoro *et al.*, 1988). In our work, we also demonstrated an increase in *MYC* expression that was accompanied by an increase in relative heart weight. Such activation of *MYC* in adult myocardium was found to increase glucose uptake and utilization, reduce fatty acid oxidation by downregulat-

ing PPAR α , and induce mitochondrial biogenesis. As a result, the function of the left ventricle remains normal despite hypertrophic changes (Ahuja *et al.*, 2010). Thus, in young hypertensive rats, we found evidence of pathological processes and a sharp increase in the expression of *MYC*, which persisted and increased until 22 months of age.

In turn, the increased expression of *MYC* may be a key factor in the induction of transcription of many genes, including *CYP2E1* in the myocardium (Guan *et al.*, 2019). We have demonstrated a significant increase in *CYP2E1* expression as well as protein content in the myocardium of old hypertensive animals compared to young SHR. It has been reported that *CYP2E1* expression levels may change significantly during the development of myocardial hypertrophy in various models of heart failure. Such an increase in *CYP2E1* expression has previously been demonstrated in hypertension and acute myocardial injury, and a key factor might be the upregulation of *MYC* (Guan *et al.*, 2019). Clearly, increased expression of *CYP2E1*, a potent prooxidant factor, may be one of the most important reasons for the development of oxidative stress (Pang *et al.*, 2021) in the myocardium, for which we found evidence in our experiment. It has been shown previously that altered expression of *CYP2E1* may be a marker of various pathophysiological factors and conditions in the myocardium. Increased expression of *CYP2E1* plays several pathophysiological roles in the heart, including oxidative stress and apoptosis, as well as involvement in energy production and supply pathways to meet the increased energy demands of the heart under pathological conditions (Zhang *et al.*, 2011; Guan *et al.*, 2019). Therefore, an increase in *CYP2E1* expression in the early stages of heart failure development may be an adaptation of the myocardium to the conditions of altered energy exchange pathways, ensuring the preservation of the contractile function of the heart. On the other hand, oxidative stress, which may be caused by increased *CYP2E1* expression, is one of the crucial pathological mechanisms in the development of heart disease (Guan *et al.*, 2019; Pang *et al.*, 2021).

Thus, increased expression of *MYC* could lead to activation of *CYP2E1* expression, which is associated with the development of oxidative stress and other pathological processes in the myocardium. We hypothesize that modulation of *MYC* expression level in the myocardium may help to inhibit the development of the above pathological processes (including oxidative stress) caused by hypertension. This conjecture was tested in our study. A natural agent such as quercetin was chosen as a modulatory agent because this agent has cardioprotective properties and can prevent the development of *CYP2E1*-induced oxidative stress (Larson *et al.*, 2010; Yan *et al.*, 2013; Maksymchuk *et al.*, 2017; Ghafouri-Fard *et al.*, 2021).

We found that treatment with quercetin resulted in a significant decrease in *MYC* expression in old SHR compared to untreated old SHR and young SHR. This bioflavonoid has been shown to modulate multiple signaling pathways, including activation of PPAR (Yan *et al.*, 2013), resulting in downregulated *MYC* expression. In addition, quercetin has been found to directly inhibit the expression of *MYC* by binding to the regulatory region of the corresponding gene (Tawani *et al.*, 2017). It has been shown that inhibition of *MYC* can significantly inhibit myocardial hypertrophic growth (Ahuja *et al.*, 2010). In this work, we also showed a significant decrease in relative heart weight, which may be a consequence of the downregulation of this transcription factor. Since

MYC induces *CYP2E1* (Guan *et al.*, 2019), suppression of *MYC* could lead to a decrease in *CYP2E1* expression, which contributes to a decrease in *CYP2E1* protein content in the heart. This is exactly the effect we observed in the myocardium of animals treated with quercetin. We also noted some normalization of the balance between pro- and antioxidants in the heart, i.e., a decrease in the level of LPO and an increase in the activity of antioxidant enzymes. A decrease in the expression of *CYP2E1* (as a potent prooxidant factor) could lead to a decrease in LPO levels (Pang *et al.*, 2021). Moreover, the quercetin molecule can directly inhibit the activity of *CYP2E1* by blocking the active site of the enzyme (Östlund *et al.*, 2017). At the same time, this bioflavonoid can scavenge radicals and activate the expression of antioxidants (de Lacerda Alexandre *et al.*, 2021). It also contributes to the antioxidant effect of quercetin in the myocardium. It is known that quercetin can lower blood pressure and hypertrophy by reducing the manifestations of oxidative stress (Larson *et al.*, 2010; de Lacerda Alexandre *et al.*, 2021). We observed a similar effect in old-treated hypertensive rats.

CONCLUSION

Oxidative stress is one of the most important pathological processes in chronic heart failure caused by hypertension. These processes involve *MYC*-regulated mechanisms, including the induction of *CYP2E1* as a potent prooxidant factor. We observed overexpression of the transcription factor *MYC* in the myocardium of SHR compared to normotensive controls, and an increased expression of the *MYC*-target gene, *CYP2E1*, in the old SHR group compared to young SHR. This probably contributed significantly to the development of oxidative stress in the cardiac tissue of old SHR. We demonstrated that long-term treatment of old SHR with quercetin resulted in dramatic inhibition of *MYC*, and a significant decrease in *CYP2E1* expression and *CYP2E1* protein levels. This probably contributed significantly to the decrease in lipid peroxidation. Quercetin was also able to activate antioxidant activity, resulting in a significant improvement in the prooxidant-antioxidant balance in the heart. In turn, the elimination of oxidative stress could contribute to a decrease in blood pressure and relative heart weight in quercetin-treated old SHR compared to the untreated old SHR group.

Statements and Declarations

Conflict of Interest. The authors declare that the research was conducted in the absence of any commercial or financial relationships that could be construed as a potential conflict of interest.

Author contributions. OM and AS contributed equally to this work and share the first authorship. OM and AS made substantial contributions to the conception and design, acquisition, and analysis of the data, and participated in the critical review of the manuscript for important intellectual content. OM performed the Western-blot analysis and RT-PCR. AS and AK examined markers of oxidative stress and performed a statistical analysis. The first draft of the manuscript was written by OM. All authors contributed to the revision of the manuscript, read and approved the submitted version.

Acknowledgments. The authors thank Lahuta T., Zhukovska A. and Lapikova-Bryginska T. for their help in obtaining RNA samples. The authors also thank Academic Proofreading (<https://www.academicproofreading.com>).

uk/) for their significant contribution to the English language editing of the manuscript.

Data Availability Statement. All relevant data is contained within the article. The original contributions presented in the study are included in the article, further inquiries can be directed to the corresponding author.

Ethical Approval. All manipulations with laboratory animals were performed in accordance with the European Convention for the Protection of Vertebrate Animals Used for Experimental and Other Scientific Purposes (Strasbourg, 1986). The protocol was approved by the Local Committee on Bioethics (registration number: 0114U007233).

REFERENCES

- Ahuja P, Zhao P, Angelis E, Ruan H, Korge P, Olson A, Wang Y, Jin ES, Jeffrey FM, Portman M, MacLellan WR (2010) Myc controls transcriptional regulation of cardiac metabolism and mitochondrial biogenesis in response to pathological stress in mice. *J Clin Invest* **120**: 1494–1505. <https://doi.org/10.1172/JCI38331>
- Barathidasan R, Pawaiya RS, Rai RB, Dhama K (2013) Upregulated Myc expression in N-methyl nitrosourea (MNU)-induced rat mammary tumours. *Asian Pac J Cancer Prev* **14**: 4883–4889. <https://doi.org/10.7314/apjcp.2013.14.8.4883>
- Cabiati M, Raucci S, Caselli C, Guzzardi MA, D'Amico A, Prescimone T, Giannessi D, Del RS (2012) Tissue-specific selection of stable reference genes for real-time PCR normalization in an obese rat model. *J Mol Endocrinol* **48**: 251–260. <https://doi.org/10.1530/JME-12-0024>
- de Lacerda Alexandre JV, Viana YIP, David CEB, Cunha PLO, Albuquerque AC, Varela ALN, Kowaltowski AJ, Facundo HT (2021) Quercetin treatment increases H₂O₂ removal by restoration of endogenous antioxidant activity and blocks isoproterenol-induced cardiac hypertrophy. *Naunyn-Schmiedeberg's Arch Pharmacol* **394**: 217–226. <https://doi.org/10.1007/s00210-020-01953-8>
- Ghafouri-Fard S, Shoorci H, Khanbabapour Sasi A, Taheri M, Aya-tollahi SA (2021) The impact of the phytotherapeutic agent quercetin on expression of genes and activity of signaling pathways. *Biomed Pharmacother* **141**: 111847. <https://doi.org/10.1016/j.biopha.2021.111847>
- Guan F, Yang X, Li J, Dong W, Zhang X, Liu N, Gao S, Wang J, Zhang L, Lu D (2019) New molecular mechanism underlying Myc-mediated cytochrome P450 2E1 upregulation in apoptosis and energy metabolism in the myocardium. *J Am Heart Assoc* **8**: e009871. <https://doi.org/10.1161/JAHA.118.009871>
- Kahan T, Bergfeldt L (2005) Left ventricular hypertrophy in hypertension: its arrhythmogenic potential. *Heart* **91**: 250–256. <https://doi.org/10.1136/hrt.2004.042473>
- Kodde IF, van der Stok J, Smolenski RT, de Jong JW (2007) Metabolic and genetic regulation of cardiac energy substrate preference. *Comp Biochem Physiol A Mol Integr Physiol* **146**: 26–39. <https://doi.org/10.1016/j.cbpa.2006.09.014>
- Larson AJ, Symons JD, Jalili T (2010) Quercetin: A treatment for hypertension? a review of efficacy and mechanisms. *Pharmaceuticals (Basel)* **3**: 237–250. <https://doi.org/10.3390/ph3010237>
- Maksymchuk O, Shysh A, Chashchyn M, Moibenko O (2015) Dietary omega-3 polyunsaturated fatty acids alter fatty acid composition of lipids and CYP2E1 expression in rat liver tissue. *Int J Vitam Nutr Res* **85**: 322–328. <https://doi.org/10.1024/0300-9831/a000296>
- Maksymchuk O, Shysh A, Rosohatska I, Chashchyn M (2017) Quercetin prevents type 1 diabetic liver damage through inhibition of CYP2E1. *Pharmacol Rep* **69**: 1386–1392. <https://doi.org/10.1016/j.pharep.2017.05.020>
- Mei Y, Thompson MD, Cohen RA, Tong X (2015) Autophagy and oxidative stress in cardiovascular diseases. *Biochim Biophys Acta* **1852**: 243–251. <https://doi.org/10.1016/j.bbdis.2014.05.005>
- Negoro N, Inariba H, Inoue T, Kanayama Y, Takeda T (1988) Expression of c-myc proto-oncogene in hearts and cultured smooth muscle cells of spontaneously hypertensive rats. *J Hypertens Suppl* **6**: S128–S130. <https://doi.org/10.1097/00004872-198812040-00037>
- Nolly MB, Pinilla AO, Ennis IL, Cingolani HE, Morgan PE (2015) Cardiac hypertrophy reduction in SHR by specific silencing of myocardial Na⁺/H⁺ exchanger. *J Appl Physiol* (1985) **118**: 1154–1160. <https://doi.org/10.1152/jappphysiol.00996.2014>
- Novelli EL, Diniz YS, Galhardi CM, Ebaid GM, Rodrigues HG, Mani F, Fernandes AA, Cicogna AC, Novelli Filho JL (2007) Anthropometrical parameters and markers of obesity in rats. *Lab Anim* **41**: 111–119. <https://doi.org/10.1258/00236770779399518>
- Oh GC, Cho HJ (2020) Blood pressure and heart failure. *Clin Hypertens* **26**: 1. <https://doi.org/10.1186/s40885-019-0132-x>
- Östlund J, Zlabek V, Zamaratskaia G (2017) *In vitro* inhibition of human CYP2E1 and CYP3A by quercetin and myricetin in hepatic microsomes is not gender dependent. *Toxicology* **381**: 10–18. <https://doi.org/10.1016/j.tox.2017.02.012>
- Pang S, Dong W, Liu N, Gao S, Li J, Zhang X, Lu D, Zhang L (2021) Diallyl sulfide protects against dilated cardiomyopathy via inhibition of oxidative stress and apoptosis in mice. *Mol Med Rep* **24**: 852. <https://doi.org/10.3892/mmr.2021.12492>
- Patel RV, Mistry BM, Shinde SK, Syed R, Singh V, Shin HS (2018) Therapeutic potential of quercetin as a cardiovascular agent. *Eur J Med Chem* **155**: 889–904. <https://doi.org/10.1016/j.ejmech.2018.06.053>
- Reckelhoff JF, Ilescu R, Yanes L, Fortepiani L (2006) 83 – Models of hypertension in aging. In *Handbook of Models for Human Aging*. Conn PM ed, pp 999–1009. Academic Press. <https://doi.org/10.1016/B978-012369391-4/50084-9>
- Rodrigo R, González J, Paoletto F (2011) The role of oxidative stress in the pathophysiology of hypertension. *Hypertens Res* **34**: 431–440. <https://doi.org/10.1038/hr.2010.264>
- Tawani A, Mishra SK, Kumar A (2017) Structural insight for the recognition of G-quadruplex structure at human c-myc promoter sequence by flavonoid Quercetin. *Sci Rep* **7**: 3600. <https://doi.org/10.1038/s41598-017-03906-3>
- Xiao G, Mao S, Baumgarten G, Serrano J, Jordan MC, Roos KP, Fishbein MC, MacLellan WR (2001) Inducible activation of c-Myc in adult myocardium *in vivo* provokes cardiac myocyte hypertrophy and reactivation of DNA synthesis. *Circ Res* **89**: 1122–1129. <https://doi.org/10.1161/hh2401.100742>
- Yan L, Zhang JD, Wang B, Lv YJ, Jiang H, Liu GL, Qiao Y, Ren M, Guo XF (2013) Quercetin inhibits left ventricular hypertrophy in spontaneously hypertensive rats and inhibits angiotensin II-induced H9C2 cells hypertrophy by enhancing PPAR-γ expression and suppressing AP-1 activity. *PLoS One* **8**: e72548. <https://doi.org/10.1371/journal.pone.0072548>
- Zhang W, Lu D, Dong W, Zhang L, Zhang X, Quan X, Ma C, Lian H, Zhang L (2011) Expression of CYP2E1 increases oxidative stress and induces apoptosis of cardiomyocytes in transgenic mice. *FEBS J* **278**: 1484–1492. <https://doi.org/10.1111/j.1742-4658.2011.08063.x>

LncRNA MIR31HG promotes cell proliferation and invasive properties of the MCF-7 cell line by regulation of receptor-interacting serine-threonine kinase 4

Jingwei Tang, Xiaojing Zhang, Chunchun Chen, Binbin Wang, Yansong Chen, Hao Zhang, Mengxiang Qiao, Xianfu Liu, Wei Guo and Gongsheng Jin✉

Department of Surgical Oncology, the First Affiliated Hospital of Bengbu Medical College, Changhuai Road, Bengbu 233000, Anhui, China

LncRNA MIR31HG is involved in many types of cancers, while its roles in breast cancer are still unknown. The current study aimed to explore the function of LncRNA MIR31HG in breast cancer and the underlying mechanisms. Stable expression cell lines were constructed by using lentivirus particles. MTT assay was used to determine cell viability. Wound healing and Transwell assay were used to determine cell migration and invasion, respectively. The changes in biomarkers were determined by using qPCR-PCT and Western blotting, respectively. BALB/c nude mice were used to generate a xenograft mouse model. MIR31HG regulated cell proliferation, migration and invasion in MCF7 cells. Besides, MIR31HG regulated N-Cadherin, Vimentin, and E-Cadherin. MIR31HG positively regulated receptor-interacting serine-threonine kinase 4 (RIPK4), as supported by the fact that knockdown of MIR31HG suppressed RIPK4, and the knockdown of RIPK4 did not affect MIR31HG. Additionally, we found that RIPK4 regulated cell proliferation, migration and invasion in MCF7 cells. The changes in RIPK4 regulated N-Cadherin, Vimentin, and E-Cadherin. Consistently, *in vivo* studies showed that the knockdown of MIR31HG or RIPK4 reduced tumor size in xenograft animal models. The roles of LncRNA MIR31HG in breast cancer were associated with its regulatory effects against RIPK4.

Keywords: Breast cancer, LncRNA, cell proliferation, MIR31HG, RIPK4

Received: 15 May, 2023; revised: 26 August, 2023; accepted: 25 October, 2023; available on-line: 08 December, 2023

✉e-mail: jgs197381@163.com

Acknowledgements of Financial Support: The study was supported by the Key projects of natural science research in universities in Anhui Province (KJ2021A0716).

Abbreviations: FBS, fetal bovine serum; lncRNAs, long non-coding RNAs; MIR31HG, microRNA-31 host gene; NF-κB, nuclear factor kappa B; RIPK4, receptor-interacting serine-threonine kinase 4; shNC, shRNAs; STAT3, signal transducer and activator of the transcription 3

INTRODUCTION

Breast cancer is known as the most common cancer in women, which accounts for about 12.5% of all cancer cases in the world (Ferlay *et al.*, 2021; Lei *et al.*, 2021). Approximately 2.3 million newly diagnosed breast cancer cases were reported with around 685,000 breast cancer-related deaths in 2020 (Ferlay *et al.*, 2021; Lei *et al.*, 2021; Lima *et al.*, 2021). Breast cancer can be divided into non-invasive or pre-invasive (also termed intraductal carcinoma) and invasive types, where the invasive type accounts

for 70~80% of all cases (Matsuno *et al.*, 2007; Sharma *et al.*, 2010). In patients with early stage breast cancer, a 99% of 5-year survival rate can be achieved in patients with localized non-metastasis breast cancer with proper treatment (Page, 2003; Sharma *et al.*, 2010). However, breast cancer can spread to other tissues including liver, lung, bone, and brain tissues. When tumor metastasis occurs, the 5-year survival rate is only 29% (Matsuno *et al.*, 2007; Page, 2003). Therefore, diagnosis of breast cancer in the early stage is crucial for the treatment of breast cancer and the improvement of the survival rate.

The roles of long non-coding RNAs (lncRNAs) have been implicated in many types of cancers such as lung cancer, hepatoma, colorectal cancer, breast cancer, etc. (Fang & Fullwood, 2016; Hauptman & Glavač, 2013). LncRNAs are involved in a series of cellular events such as cell proliferation, migration and invasion, and genetic stability, in part, by the regulation of various genes (Fang & Fullwood, 2016; Spizzo *et al.*, 2012). Moreover, lncRNAs are also known as functional transcripts, which are associated with tumor progression and metastasis (Spizzo *et al.*, 2012; Zhang *et al.*, 2013). Targeting lncRNAs becomes a promising strategy for cancer therapy (Zhang *et al.*, 2013). LncRNA microRNA-31 host gene (MIR31HG) was identified as an oncogene in twelve different types of cancers including bladder cancer, head and neck cancer, osteosarcoma, cervical cancer, gastric cancer, etc. (Wei *et al.*, 2022). Besides, the changes of MIR31HG can also be used as a prognosis biomarker for patients with digestive system cancer (Zhou *et al.*, 2020). However, it is still unclear whether MIR31HG is involved in breast cancer. Therefore, this study aims to determine the role of MIR31HG in breast cancer and its molecular mechanisms.

A receptor-interacting serine-threonine kinase (RIPK) 4 is known to be associated with epidermal homeostasis and development by the regulation of cell-cell adhesion (Oberbeck *et al.*, 2019; Xu *et al.*, 2020). It also acts as a transcriptional target of TP63 and plays important roles in transcriptional factor- nuclear factor kappa B (NF-κB) activation (Liu *et al.*, 2018; Xu *et al.*, 2020). Recently, the roles of RIPK4 in cancer have drawn much attention from scientists (Li *et al.*, 2021; Liu *et al.*, 2015; Liu *et al.*, 2021). In 2015, Liu and colleagues have reported that the RIPK4 can be used as a prognostic and diagnostic biomarker for patients with cervical cancer (Liu *et al.*, 2015). In 2021, Li and colleagues have found that RIPK4 regulates cell migration and metastasis in hepatoma by the regulation of signal transducer and activator of the transcription 3 (STAT3) signaling pathway (Li *et al.*, 2021). However, the roles of RIPK4 are still unknown. Herein,

the roles of MIR31HG in breast cancer *in vitro* and *in vivo* were clarified in our study.

MATERIALS AND METHODS

Antibody and reagents

Antibodies against Vimentin, E-Cadherin, N-Cadherin, and GADPH were obtained from Cell Signaling Technology (Danvers, MA). Antibodies against RIPK4 and Ki67 were obtained from Thermo Fisher Scientific (Waltham, MA). Predesigned shRNAs targeting MIR31HG and RIPK4, control shRNAs (shNC), and other chemicals were purchased from Sigma-Aldrich (St. Louis, MO).

Cell culture and cell viability

Breast cancer cell line MCF7 was purchased from the ATCC (Rockville, MD). The cells were cultured in recommended medium with 10% fetal bovine serum (FBS) and penicillin/streptomycin (100 U/ml) under 37°C with 95% humidity and 5% CO₂. MTT assay was used to determine cell viability. In brief, MTT solution (5 mg/mL, 10 µL) was added and incubated for another 2 h. Next, DMSO (100 µL) was used to dissolve the purple formazan crystal followed by shaking for 30 sec. Next, the plate was read under a wavelength of 570 nm with a reference wavelength of 630 nm.

Construction of stable cell lines

To construct stable MIR31HG and RIPK4 knock-down cell lines, MCF7 cells were transfected with MIR31HG shRNA (Targeting sequence: GCTGCTGATGACGTAAAGT), RIPK4 shRNA (Targeting sequence: CGTTCGTTTCTCGTTGCCTAA) or empty vector (shNC) lentivirus as previously described. After 72 h, a medium containing puromycin (2 µg/mL) was added and incubated for another 72 h for the selection of the cells. To construct MIR31HG and RIPK4 overexpressing cell lines, pcDNA MIR31HG, pcDNA RIPK4, or empty plasmid containing shNC sequence was used to construct pLKO.1 plasmid followed by the generation of lentivirus. Puromycin (2 µg/mL) was used for the selection of stable overexpressing cell lines.

Cell invasion and wound healing assays

Cell invasion assay was determined by using Transwell chamber. In the upper chamber, the cells were seeded and cultured with a serum-free medium. In the lower chamber, a medium containing 10% FBS was added. After 72 h, cells that were in the lower chamber were stained. Five random fields were selected, and the number of cells were counted. In the wound healing assay, cells were seeded into a 6-well plate. When 80–90% confluence was observed, a sterile tip (1 mm width, 200 µL) was used to scratch the cell monolayer. After 72 h, cells were observed by using a microscope, and wound healing rate was calculated. The Transwell chamber was purchased from BD (Franklin Lakes, NJ, USA).

Western blotting assay

Protein samples were extracted from the cells by using cold RIPA buffer (1% phenylmethanesulfonyl fluoride) and qualified by using BCA assay. Protein samples were loaded on a 10% SDS page followed by transferring onto the PVDF membrane. After that, the mem-

brane was blotted with 5% non-fat milk for 1 h at room temperature. The primary antibodies were added and incubated overnight at 4°C. After that, the secondary antibodies conjugated with HRP were added and blotted for another 2 h at room temperature. A chemiluminescence substrate was added, and the protein intensity was compared to the internal control GADPH.

qRT-PCR

Total RNAs were extracted by using the phenol-chloroform method. In this study, the sequences of primers were described below.

TAP-1 forward primer: 5'-GCCCACTACCACGTCAAGAT-3', and reverse primer: 5'-TTCACCATGATGTGCAGGAT-3'; MIR31HG forward primer: 5'-GTTTCTGGTCCATACCGTGTGGTT-3', and reverse primer: 5'-CTTGAATGAATCCTCTGTCTCC-3'; GADPH forward primer: 5'-TCAACGACCACTTTGTCAAGCTCA-3', and reverse primer: 5'-GCTGGTGGTCCAGGGGCTTACT-3'. A reverse transcription reaction was then performed by using real-time PCR kits (Takara Bio Inc, San Jose, CA).

MCF7 Xenograft animal model

BALB/c nude mice (age 4–6 weeks) were purchased from GemPharmatech (Nanjing, China) and kept in specific pathogen-free facilities. In this study, animal procedures were approved by the First Affiliated Hospital of Bengbu Medical College. Mice were subcutaneously injected with MCF7 cells (MIR31HG-KD, MIR31HG-OE, or MCF7) at a density of 5×10⁶ cells, and tumor size was measured once a week in accordance with a formula: tumor volume=length×width²/2.

Data analysis

The results were represented as means ± standard deviation (S.D.). A significant difference was obtained by using GraphPad prism 7 based on either one-way or two-way ANOVA test followed with a post hoc test. When a *p*-value was smaller than 0.05, the statistical significance was decided.

RESULTS

MIR31HG regulated cell proliferation in MCF7 cells

Our results showed an elevation of MIR31HG in MIR31HG-OE cells and a reduction of MIR31HG in the MIR31HG-KD cells, indicating the successful construction of MIR31HG stable cell lines (Fig. 1A). MTT assay showed that cell proliferation was significantly increased in the MIR31HG-KD cells, whereas cell proliferation was diminished in the MIR31HG-OE cells (Fig. 1B). Consistently, we found that Ki67 decreased in the MIR31HG-KD cells. Interestingly, the protein expressions of Ki67 were enhanced in the MIR31HG-OE cells (Fig. 1C).

MIR31HG regulated wound healing and cell invasion

The effects of MIR31HG on cell migration and invasion were then determined. We observed a decrease in the closure rate and a reduction in the invaded cell numbers in the MIR31HG-KD cells, whereas an elevation in closure rate and invaded cell numbers was observed in the MIR31HG-OE cells (Fig. 2A and B). Additionally, overexpression of MIR31HG enhanced the protein ex-

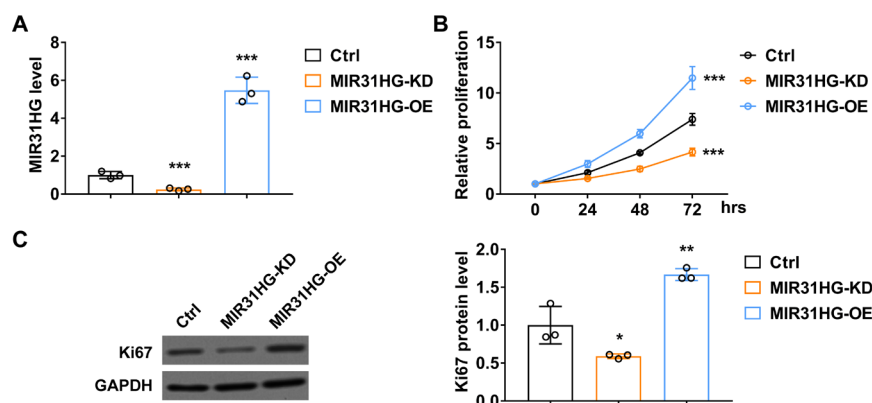


Figure 1. MIR31HG regulated the proliferation of MCF7 cells.

(A) qRT-PCR was used to determine the mRNA levels of MIR31HG in control (Ctrl), MIR31HG knockdown (KD), and MIR31HG overexpressing (OE) MCF7 cells. (B) MTT assay was used to determine the cell proliferation in control, MIR31HG-KD, and MIR31HG-OE MCF7 cells. (C) Western blotting was used to determine the protein levels of Ki67 in control, MIR31HG-KD, and MIR31HG-OE MCF7 cells (n=3).

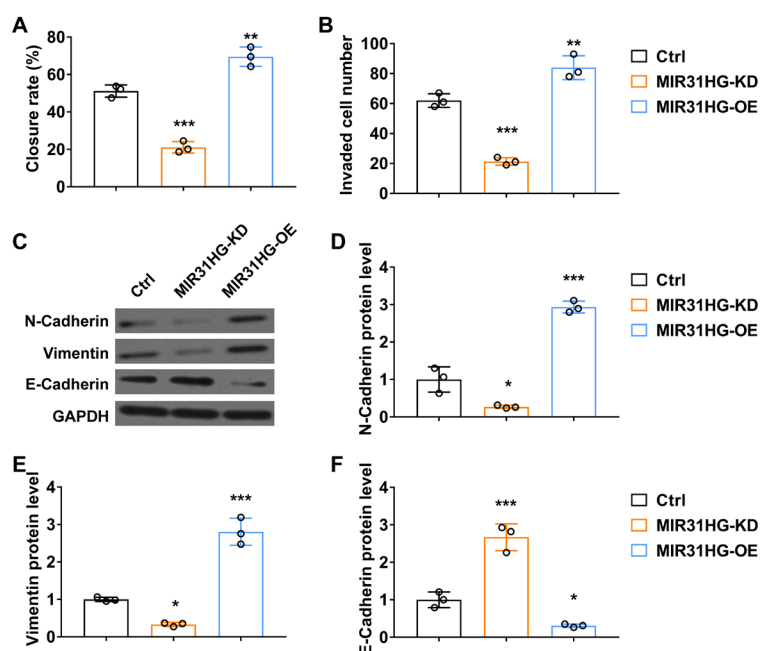


Figure 2. MIR31HG regulated the migration and invasion of MCF7 cells.

(A) A wound healing assay was used to determine the closure rate of control, MIR31HG-KD, and MIR31HG-OE MCF7 cells. (B) The invasion assay was used to determine the numbers of invaded cells in control, MIR31HG-KD, and MIR31HG-OE MCF7 cells. (C–F) Western blotting was used to determine the protein levels of EMT-related markers including N-Cadherin (C and D), Vimentin (C and E), and E-Cadherin (C and F) in control, MIR31HG-KD, and MIR31HG-OE MCF7 cells (n=3).

pressions of N-Cadherin and Vimentin, whereas knockdown of MIR31HG suppressed the protein expressions of N-Cadherin and Vimentin in MCF7 cells (Fig. 2C–E). Moreover, overexpression of MIR31HG suppressed the protein expressions of E-Cadherin, whereas knockdown of MIR31HG enhanced the protein expressions of E-Cadherin (Fig. 2C and F).

MIR31HG regulated the levels of RIPK4

We further determined the impact of MIR31HG on RIPK4 in MCF7 cells. An elevation of RIPK4 in the MIR31HG-KD cells, and a reduction of RIPK4 was observed in the MIR31HG-OE cells (Fig. 3A and B). Next, we successfully constructed RIPK-KO and RIPK-OE cells (Fig. 3D). Interestingly, no significant change of MIR31HG was found among RIPK-KO, RIPK-OE, and control MCF7 cells (Fig. 3C). We also found that a

reduction in RIPK4 in the RIPK-KO cells, whereas an elevation of RIPK4 was observed in the MIR31HG-OE cells both at the mRNA and protein levels (Fig. 3D and E). These results indicate that MIR31HG regulated the levels of RIPK4 in MCF7 cells.

RIPK4 mediated cell proliferation in breast cancer cells

We determined the effects of RIPK4 on cell proliferation. Our results showed that cell proliferation was enhanced in the MIR31HG-KD cells as compared to the MIR31HG-OE cells (Fig. 4A). Consistently, we found that Ki67 decreased in the MIR31HG-KD cells. Interestingly, Ki67 increased in the MIR31HG-OE cells (Fig. 4B).

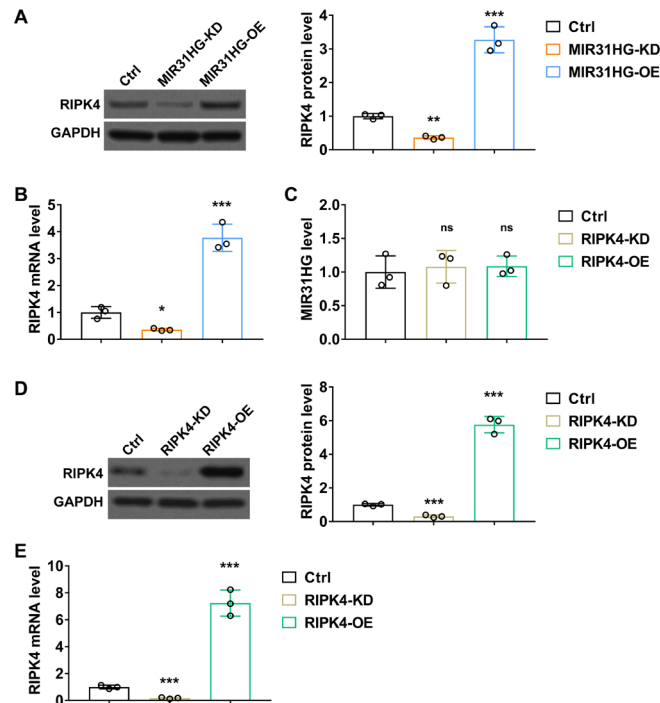


Figure 3. MIR31HG regulated the levels of RIPK4 in MCF7 cells.

(A–B) Western blotting and qRT-PCR were used to determine the protein (A) and mRNA (B) levels of RIPK4 in control, MIR31HG-KD, and MIR31HG-OE MCF7 cells. Besides, (C) the mRNA levels of MIR31HG were determined in control, RIPK4 knockdown (KD), and RIPK4 overexpressing (OE) MCF7 cells. (D–E) The protein and mRNA levels of RIPK4 in control, RIPK4-KD, and RIPK4-OE MCF7 cells (n=3).

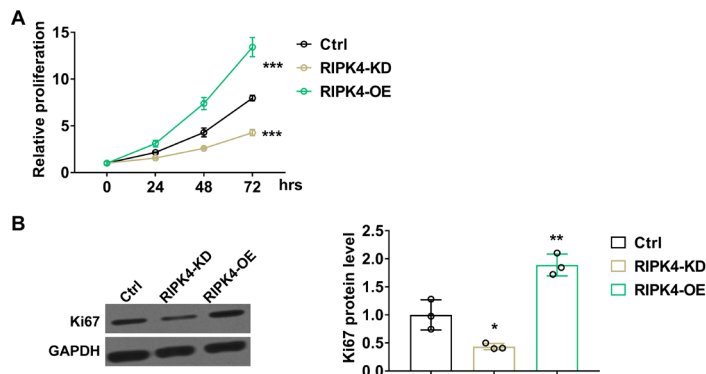


Figure 4. RIPK4 mediated the proliferation of breast cancer cells *in vitro*.

(A) MTT assay was used to determine cell viability of control, RIPK4-KD, and RIPK4-OE MCF7 cells (B) Western blotting was used to determine the protein levels of Ki67 in control, RIPK4-KD, and RIPK4-OE MCF7 cells (n=3).

RIPK4 regulated cell migration and invasion

Moreover, we investigated the impact of RIPK4 change on cell migration and invasion. A decrease in closure rate as well as a reduction in invaded cell numbers were observed in the RIPK4-KD cells, whereas both closure rate and invaded cell numbers were increased in RIPK4-OE cells (Fig. 5A and B). Additionally, overexpression of RIPK4 increased N-Cadherin and Vimentin, whereas knockdown of RIPK4 suppressed N-Cadherin and Vimentin (Fig. 5C–E). Moreover, overexpression of RIPK4 suppressed E-Cadherin, whereas knockdown of RIPK4 increased E-Cadherin (Fig. 5C and F).

Knockdown of MIR31HG or RIPK4 repressed MCF7 tumor growth in mice

To confirm the observations *in vitro*, we observed the effects of MIR31HG or RIPK4 knockdown on tumor

growth in the animal cancer xenograft model. Interestingly, we found that tumor size was significantly reduced in the MIR31HG-KD and RIPK4-KD groups (Fig. 6A). The protein expressions of Ki67 were also significantly decreased in the MIR31HG-KD and RIPK4-KD groups (Fig. 6B). These results indicate that the knockdown MIR31HG or RIPK4 suppressed tumor growth *in vivo*. Next, we investigated the levels of Epithelial-to-mesenchymal transition (EMT)-related biomarkers. A reduction of N-Cadherin and Vimentin was observed in the MIR31HG-KD and RIPK4-KD group as compared to the control group (Fig. 6C–E). Besides, an elevation of E-Cadherin was observed in the MIR31HG-KD and RIPK4-KD group (Fig. 6F), suggesting the regulatory effects of MIR31HG and RIPK4 on EMT.

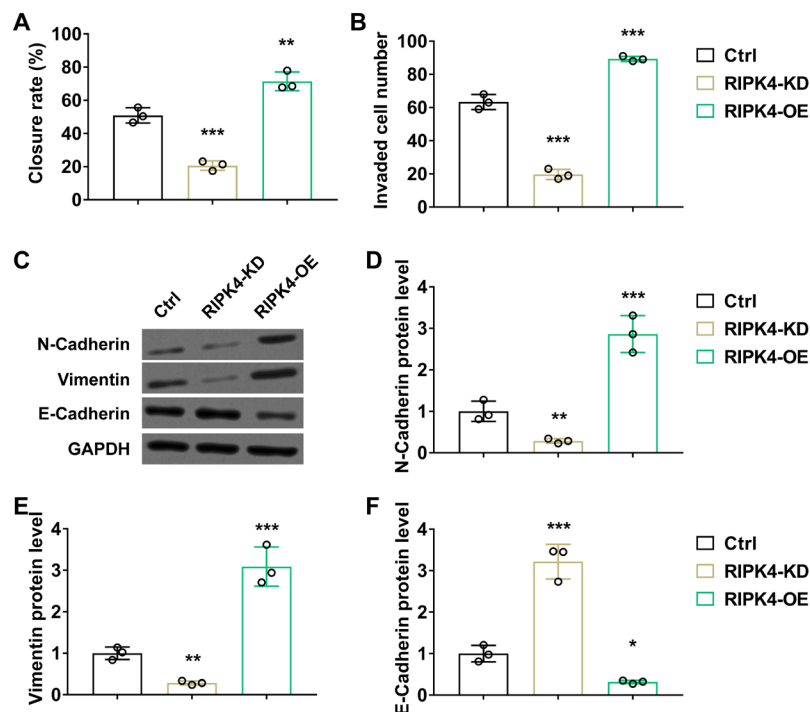


Figure 5. RIPK4 regulated the migration and invasion of MCF7 cells.

(A) A wound healing assay was used to determine the closure rate of control, RIPK4-KD, and RIPK4-OE MCF7 cells. (B) Invasion assay was used to count the numbers of the invaded cells of control, RIPK4-KD, and RIPK4-OE MCF7 cells. (C-F) Western blotting was used to determine the protein levels of EMT-related markers including N-Cadherin (C and D), Vimentin (C and E), and E-Cadherin (C and F) in control, RIPK4-KD and RIPK4-OE MCF7 cells (n=3).

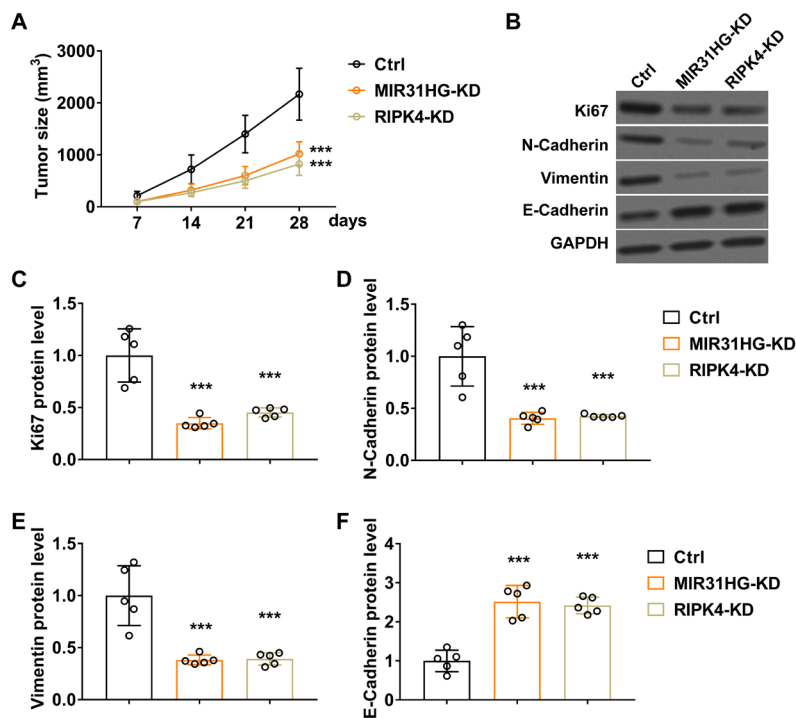


Figure 6. Knockdown of MIR31HG or RIPK4 repressed MCF7 tumor growth in mice.

(A) Tumor size was measured in the xenograft mice of the control, MIR31HG-KD, and RIPK4-KD MCF7 group. (B-F) Western blotting was used to determine the protein levels of Ki67 (C), N-Cadherin (D), Vimentin (E), and E-Cadherin (F; n=5 mice).

DISCUSSION

This study revealed the roles of MIR31HG in the MCF7 breast cancer cell lines and breast cancer xeno-

graft mouse model. MIR31HG promoted cancer growth by regulating a series of cellular events including cell proliferation, migration and invasion. Additionally, the roles of MIR31HG in breast cancer were associated

with its regulatory effects against EMT, as suggested by the changes in N-Cadherin, Vimentin, and E-Cadherin that were observed in these MIR31HG overexpressing or knockdown cell lines. Underlying mechanism studies identified RIPK4 as a downstream target of MIR31HG, as supported by MIR31HG positively regulating the levels of RIPK4, whereas knockdown of RIPK4 did not significantly affect MIR31HG. These results suggested that MIR31HG might serve as an oncogenic gene in breast cancer by its regulatory effects against RIPK4.

MIR31HG is involved in cancer occurrence and progression (Wei *et al.*, 2022). Moreover, the alteration of MIR31HG is observed in twenty types of cancers (Wei *et al.*, 2022). For instance, Zheng and colleagues reported that MIR31HG promotes cell proliferation and invasion in lung cancer (Zheng *et al.*, 2019). The downregulation of MIR31HG is associated with the alteration of EMT in non-small cell lung cancer. In another study, the overexpression of MIR31HG is associated with a low overall survival rates and advanced tumor, node, and metastasis stage in patients with bladder cancer (Wu *et al.*, 2019). More recently, Ko and colleagues demonstrated that the overexpression of MIR31HG is associated with poor disease-free survival rate in patients with pancreatic ductal adenocarcinoma (Ko *et al.*, 2022). These results suggested the oncogenic roles of MIR31HG in cancer. However, it is still unclear whether MIR31HG promoted tumor growth in breast cancer. Herein, our study reported the roles of MIR31HG in breast cancer. Consistently, our results revealed that the overexpression of MIR31HG promoted cancer cell growth and invasion in MCF7 cells as well as tumor growth in the cancer xenograft mouse model.

EMT is frequently observed in breast tumor invasion and metastasis (Ye *et al.*, 2017). Moreover, the activation of EMT is linked with drug resistance in breast cancer (Kotiyal & Bhattacharya, 2014). Previous studies indicated the regulatory effects of MIR31HG on EMT in many types of cancers (Zheng *et al.*, 2019). For instance, MIR31HG is known to promote EMT in pancreatic cancer cells induced by the transforming growth factor β and to induce EMT phenotype in non-small lung cancer cells (Ko *et al.*, 2022). Therefore, we explored whether the roles of MIR31HG in breast cancer were associated with EMT. Interestingly, our data suggested that overexpression of MIR31HG increased the protein levels of N-Cadherin and Vimentin, whereas changes in MIR31HG regulated these EMT-related biomarkers in MCF7 cells and breast tumor tissues.

The roles of MIR31HG in cancers are associated with its regulatory effects on various biological processes, signaling pathways, and proteins (Ko *et al.*, 2022; Wei *et al.*, 2022; Zheng *et al.*, 2019). For instance, MIR31HG promotes non-small cell lung cancer growth, in part, by regulating Wnt/ β -catenin signaling pathways (Zheng *et al.*, 2019). Another study revealed that MIR31HG is upregulated in colorectal tumor tissues and associated with proteins relevant to glycolysis (ex. hexokinase 2 and glucose transporter 1) and angiogenesis (ex. vascular endothelial growth factor A and tissue inhibitor matrix metalloproteinase 1) (Wang *et al.*, 2022). Wang and colleagues reported that MIR31HG promotes tumor growth in head and neck cancer via its regulation of hypoxia-inducible factor A and cyclin-dependent kinase inhibitor p21 (Wang *et al.*, 2018). Our study found the role of MIR31HG in breast cancer, at least partly, by regulating RIPK4. Interestingly, we found RIPK4 served as a downstream target of MIR31HG, since changes in MIR31HG regulated the levels of RIPK4, whereas the

knockdown of RIPK4 did not significantly affect the levels of MIR31HG.

RIPK4 is involved in many types of cancers by affecting a series of biological functions and signaling transduction proteins (Li *et al.*, 2021; Qi *et al.*, 2018). For instance, Li and colleagues reported that RIPK4 inhibits hepatoma cancer cell invasion and metastasis by the regulation of STAT3 signaling pathways (Li *et al.*, 2021). As an immune regulatory biomarker, the abnormal expressions of RIPK4 are observed in many types of cancers including gynecologic cancer, melanoma, cervical squamous cell carcinoma, etc. (Liu *et al.*, 2015; Liu *et al.*, 2021; Madej *et al.*, 2021). Liu and colleagues observed that an elevation of RIPK4 in cervical squamous cell carcinoma is correlated to poor overall survival rate, and knockdown of RIPK4 suppresses cell migration and invasion (Liu *et al.*, 2015). In this study, we identified RIPK4 as a downstream target of MIR31HG in breast cancer. RIPK4 regulated cell proliferation, invasion, and migration as well as EMT-related biomarkers. Consistently, *in vivo* studies showed that the knockdown of RIPK4 reduced tumor size in cancer xenograft animal models. These results suggested that targeting RIPK4 might be a good strategy for breast cancer therapy.

CONCLUSION

MIR31HG positively regulates cell proliferation, invasion and migration, and EMT. In addition, MIR31HG positively regulates RIPK4, as supported by the fact that changes in MIR31HG affect RIPK4, whereas RIPK4 knockdown does not affect MIR31HG. Consistently, *in vivo* studies showed that the knockdown of MIR31HG or RIPK4 reduces tumor size in tumor xenograft animal models. These data suggest that the roles of lncRNA MIR31HG in breast cancer are associated with its regulatory effects against RIPK4.

Declarations

Disclosure of potential conflicts of interest. The authors declare that they have no competing interests.

Ethical Approval. The animal procedures were approved by the First Affiliated Hospital of Bengbu Medical College. This study was performed in strict accordance with the NIH guidelines for the care and use of laboratory animals (8th edition, NIH).

Data availability statement. The raw data supporting the conclusions of this article will be made available on request to the corresponding author by email, as requested by our department.

Consent for publication. Current study is available from the corresponding author on reasonable request.

REFERENCES

- Fang Y, Fullwood MJ (2016) Roles, functions, and mechanisms of long non-coding RNAs in cancer. *Genomics Proteomics Bioinformatics* **14**: 42–54. <https://doi.org/10.1016/j.gpb.2015.09.006>
- Ferlay J, Colombet M, Soerjomataram I, Parkin DM, Piñeros M, Znaor A, Bray F (2021) Cancer statistics for the year 2020: An overview. *Int. J. Cancer* **149**: 778–789. <https://doi.org/10.1002/ijc.33588>
- Hauptman N, Glavač D (2013) Long non-coding RNA in cancer. *Int. J. Mol. Sci.* **14**: 4655–4669. <https://doi.org/10.3390/ijms14034655>
- Ko C-C, Hsieh Y-Y, Yang P-M (2022) Long non-coding RNA MIR31HG promotes the transforming growth factor β -induced epithelial-mesenchymal transition in pancreatic ductal adenocarcinoma cells. *Int. J. Mol. Sci.* **23**: 6559. <https://doi.org/10.3390/ijms23126559>
- Kotiyal S, Bhattacharya S (2014) Breast cancer stem cells, EMT and therapeutic targets. *Biochem. Biophys. Res. Commun.* **453**: 112–116. <https://doi.org/10.1016/j.bbrc.2014.09.069>

- Lei S, Zheng R, Zhang S, Wang S, Chen R, Sun K, Zeng H, Zhou J, Wei W (2021) Global patterns of breast cancer incidence and mortality: A population-based cancer registry data analysis from 2000 to 2020. *Cancer Commun.* **41**: 1183–1194. <https://doi.org/10.1002/cac2.12207>
- Li H, Luo D, Huttad L, Zhang M, Wang Y, Feng J, Ding Y, Han B (2021) RIPK4 suppresses the invasion and metastasis of hepatocellular carcinoma by inhibiting the phosphorylation of STAT3. *Front Mol Biosci* 582. <https://doi.org/10.3389/fmolb.2021.654766>
- Lima SM, Kehm RD, Terry MB (2021) Global breast cancer incidence and mortality trends by region, age-groups, and fertility patterns. *EClinicalMedicine* **38**: 100985. <https://doi.org/10.1016/j.eclim.2021.100985>
- Liu D-Q, Li F-F, Zhang J-B, Zhou T-J, Xue W-Q, Zheng X-H, Chen Y-B, Liao X-Y, Zhang L, Zhang S-D (2015) Increased RIPK4 expression is associated with progression and poor prognosis in cervical squamous cell carcinoma patients. *Sci. Rep.* **5**: 1–13. <https://doi.org/10.1038/srep11955>
- Liu JY, Zeng QH, Cao PG, Xie D, Chen X, Yang F, He LY, Dai YB, Li JJ, Liu XM, Zeng HL, Zhu YX, Gong L, Cheng Y, Zhou JD, Hu J, Bo H, Xu ZZ, Cao K (2018) RIPK4 promotes bladder urothelial carcinoma cell aggressiveness by upregulating VEGF-A through the NF- κ B pathway. *Br. J. Cancer* **118**: 1617–1627. <https://doi.org/10.1038/s41416-018-0116-8>
- Liu S, He L, Sheng C, Su R, Wu X, Sun Y, Xi X (2021) Overexpression of RIPK4 predicts poor prognosis and promotes metastasis in ovarian cancer. *BioMed Res Int* **2021**. <https://doi.org/10.1155/2021/6622439>
- Madej E, Ryszawy D, Brożyna AA, Czyz M, Czyz J, Wolnicka-Glubisz A (2021) Deciphering the functional role of RIPK4 in melanoma. *Int. J. Mol. Sci.* **22**: 11504. <https://doi.org/10.3390/ijms222111504>
- Matsuno RK, Anderson WF, Yamamoto S, Tsukuma H, Pfeiffer RM, Kobayashi K, Devesa SS, Levine PH (2007) Early-and late-onset breast cancer types among women in the United States and Japan. *Cancer Epidemiol. Biomarkers Prev.* **16**: 1437–1442. <https://doi.org/10.1158/1055-9965.EPI-07-0108>
- Oberbeck N, Pham VC, Webster JD, Reja R, Huang CS, Zhang Y, Roose-Girma M, Warming S, Li Q, Birnberg A, Wong W, Sandoval W, Kömüves LG, Yu K, Dugger DL, Maltzman A, Newton K, Dixit VM (2019) The RIPK4–IRF6 signalling axis safeguards epidermal differentiation and barrier function. *Nature* **574**: 249–253. <https://doi.org/10.1038/s41586-019-1615-3>
- Page DL (2003) Special types of invasive breast cancer, with clinical implications. *Am. J. Surg. Pathol.* **27**: 832–835. <https://doi.org/10.1097/00000478-200306000-00016>
- Qi ZH, Xu HX, Zhang SR, Xu JZ, Li S, Gao HL, Jin W, Wang WQ, Wu CT, Ni QX, Yu XJ, Liu L (2018) RIPK4/PEBP1 axis promotes pancreatic cancer cell migration and invasion by activating RAF1/MEK/ERK signaling. *Int. J. Oncol.* **52**: 1105–1116. <https://doi.org/10.3892/ijo.2018.4269>
- Sharma GN, Dave R, Sanadya J, Sharma P, Sharma K (2010) Various types and management of breast cancer: an overview. *J. Adv. Pharm. Technol. Res.* **1**: 109. PMID: 22247839
- Spizzo R, Almeida ME, Colombatti A, Calin GA (2012) Long non-coding RNAs and cancer: a new frontier of translational research? *Oncogene* **31**: 4577–4587. <https://doi.org/10.1038/nc.2011.621>
- Wang J, Liu B, Cao J, Zhao L, Wang G (2022) MIR31HG Expression predicts poor prognosis and promotes colorectal cancer progression. *Cancer Manag. Res.* **16**: 1973–1986. <https://doi.org/10.2147/CMAR.S351928>
- Wang R, Ma Z, Feng L, Yang Y, Tan C, Shi Q, Lian M, He S, Ma H, Fang J (2018) LncRNA MIR31HG targets HIF1A and P21 to facilitate head and neck cancer cell proliferation and tumorigenesis by promoting cell-cycle progression. *Mol. Cancer* **17**: 1–6. <https://doi.org/10.1186/s12943-018-0916-8>
- Wei Y, Zhai Y, Liu X, Jin S, Zhang L, Wang C, Zou H, Hu J, Wang L, Jiang J, Shen X, Pang L (2022) Long non-coding RNA MIR31HG as a prognostic predictor for malignant cancers: A meta- and bioinformatics analysis. *J. Clin. Lab. Anal.* **36**: e24082. <https://doi.org/10.1002/jcla.24082>
- Wu S, Nitschke K, Heinkele J, Weis CA, Worst TS, Eckstein M, Porubsky S, Erben P (2019) ANLN and TLE2 in muscle invasive bladder cancer: a functional and clinical evaluation based on *in silico* and *in vitro* data. *Cancers (Basel)* **211**: 1840. <https://doi.org/10.3390/cancers11121840>
- Xu J, Wei Q, He Z (2020) Insight into the function of RIPK4 in keratinocyte differentiation and carcinogenesis. *Front. Oncol.* **10**: 1562. <https://doi.org/10.3389/fonc.2020.01562>
- Ye X, Brabletz T, Kang Y, Longmore GD, Nieto MA, Stanger BZ, Yang J, Weinberg RA (2017) Upholding a role for EMT in breast cancer metastasis. *Nature* **547**: E1–E3. <https://doi.org/10.1038/nature22816>
- Zhang H, Chen Z, Wang X, Huang Z, He Z, Chen Y (2013) Long non-coding RNA: a new player in cancer. *J. Hematol. Oncol.* **6**: 1–7. <https://doi.org/10.1186/1756-8722-6-37>
- Zheng S, Zhang X, Wang X, Li J (2019) MIR31HG promotes cell proliferation and invasion by activating the Wnt/ β -catenin signaling pathway in non-small cell lung cancer. *Oncol. Lett.* **17**: 221–229. <https://doi.org/10.3892/ol.2018.9607>
- Zhou Y, Fan Y, Zhou X, Mou A, He Y, Wang F, Liu Y (2020) Significance of lncRNA MIR31HG in predicting the prognosis for Chinese patients with cancer: a meta-analysis. *Biomark. Med.* **14**: 303–316. <https://doi.org/10.2217/bmm-2019-0145>

Comparative analysis of A¹ and A² allele detection efficiency for bovine CSN2 gene by AS-PCR methods

Roman Kulibaba¹✉, Mykola Sakhatskyi¹ and Yuriy Liashenko²

¹National University of Life and Environmental Sciences of Ukraine, Kyiv, Ukraine; ²Institute of Animal Science, the National Academy of Agrarian Sciences of Ukraine, Kharkiv, Ukraine

This study was aimed at conducting a comparative analysis of the efficiency in genotyping cattle by beta-casein locus using the allele-specific PCR methods. The results of the study have demonstrated the necessity to optimize the protocol for the use of AS-PCR to detect alleles A¹ and A². It was found that the use of non-optimized PCR protocols led to the genotyping errors, manifested regarding beta-casein locus (CSN2). The impossibility of using the touchdown PCR as an optimization instrument for AS-PCR was proven. The elaborated typing protocols were used to study the genetic structure of the cattle populations of different breeds, reared in Ukraine – Ukrainian Red-and-White dairy, Ukrainian Black-and-White dairy (two populations), and Charolais. It was found that locus CSN2 was polymorphic in all the cattle populations. The frequencies of allele A² varied within 0.34–0.91 depending on the population of the animals, which may be conditioned by the specificities in the selection work. No deviation from the Hardy-Weinberg equilibrium was found in any investigated population of cattle.

Key words: β-casein, allele, gene, polymorphism, cattle, population

Received: 22 October, 2022; **revised:** 04 January, 2023; **accepted:** 05 January, 2023; **available on-line:** 11 February, 2023

✉e-mail: romankx37@gmail.com

Abbreviations: ACRS-PCR, artificially created restriction site polymerase chain reaction; AS-PCR, allele-specific polymerase chain reaction; bp, base pair; BW, Ukrainian Black-and-White dairy breed; DNA, deoxyribonucleic acid; Fis, Wright's fixation index; He, expected heterozygosity; Ho, observed heterozygosity; PCR, polymerase chain reaction; Pop, population; RW, Ukrainian Red-and-White dairy breed

INTRODUCTION

The genetic structure analysis for the experimental populations of cattle is among the routine tasks of genetics and marker-associated selection in cattle breeding (Wakchaure *et al.*, 2015). However, along with such widely known qualitative trait loci as kappa casein, prolactin, beta-lactoglobulin, leptin, etc., related to the expression of productive traits of animals, in a few recent years, there has been a steady interest in the beta-casein gene, the allelic variants of which are related to the parameters of milk quality (Cieślińska *et al.*, 2019; Sebastiani *et al.*, 2022; Jiménez-Montenegro *et al.*, 2022). A¹ and A² belong to one of the best-studied and promising allele systems of beta-casein from the standpoint of applied genetics of cattle (Antonopoulos *et al.*, 2021). As shown in numerous studies, various forms of beta-casein are associated with a number of human pathological states which makes the CSN2 gene a relevant research object

in the context of the production performance of different dairy cattle breeds (Summer *et al.*, 2020; Bisutti *et al.*, 2022; De Vitte *et al.*, 2022). Alleles A¹ and A² differ by the presence of a specific amino acid in position 67 of the beta-casein molecule (Sebastiani *et al.*, 2020). In the case of form A¹, it is histidine, and as for A² – proline (Thiruvengadam *et al.*, 2020). Different forms of protein (beta-casein) are determined by the mutation in the CSN2 gene, in position 304 (GenBank, NM_181008) – by the presence of adenine for allele A¹ and cytosine for allele A² (Dai *et al.*, 2016; Kay *et al.*, 2021). The replacement of nitrogenous bases in DNA does not relate to the restriction site for endonucleases which necessitated the elaboration of alternative typing methods for alleles at the CSN2 locus. One of the most common methods is ACRS-PCR (Artificially Created Restriction Site), using TaqI and DdeI as restriction endonucleases (Lien *et al.*, 1992; McLachlan, 2006). The alternative elaborated variant was found in the methods of allele-specific PCR (AS-PCR), real-time probes for PCR, etc. (Manga *et al.*, 2010; Rahimi *et al.*, 2015; Gigliotti *et al.*, 2021; Ristanic *et al.*, 2022). Sequencing is conducted in some cases, but regardless of its efficiency, at this stage, it is not always reasonable for routine large-scale population studies (Dai *et al.*, 2016). The genotyping of cattle by alleles A¹ and A² at the beta-casein locus is conducted in different regions of the world which demonstrates the increasing interest in this problem (Zepeda-Batista *et al.*, 2015; Vougiouklaki *et al.*, 2020; Ivanković *et al.*, 2021). In recent years, the interest in genotyping cattle from different breeds has been noted in Ukraine, which is confirmed by a number of publications (Ladyka *et al.*, 2020; Ladyka *et al.*, 2021).

The availability of rather a large spectrum of different typing methods for beta-casein alleles leads to the need for a comparative analysis of their efficiency, which is especially relevant if similar methodological approaches are applied. Compared to other methods of differentiating beta-casein alleles, allele-specific PCR is one of the most promising technologies due to its low cost, speed, and accuracy (Pabitra *et al.*, 2022). However, this matter has a number of additional complications, related to the specificities of conducting the amplification and analysis of genotyping results, which, considering the promising nature of using AS-PCR as the main instrument in large-scale studies, substantiates the need for the analysis of different critical constituents of the method.

The analysis of a number of publications demonstrated that in many instances of using the AS-PCR method for typing of CSN2 alleles, the issues of PCR protocol optimizations are ignored during routine analyses (Ramkaran *et al.*, 2017; Raja *et al.*, 2021; Adoligbe *et al.*, 2022). However, the analysis shows that there is rather a high risk of inaccurate genotyping which, first of all, is caused

Table 1. The methods, primer nucleotide structure, and melting temperature.

Method	Primer	Sequence	T _m , °C	Source
ACRS-PCR	Ddel F	ccttctttccaggatgaactccagg	64.6	McLachlan (2006)
	Ddel R	gagtaagaggaggatgtttgtggaggctct	69.6	
AS-PCR 854 bp	854 F	gcccatgatgagagaagtggagg	62.2	Keating <i>et al.</i> (2008)
	854 R (A ¹)	gatgtttgtggaggctgttat	59.8	
	854 R (A ²)	gatgtttgtggaggctgttag	60.8	
	IGBR	agactggagcagaggcagag	60.1	
AS-PCR 244 bp	IGBhF (A ¹)	cttcctggggcccatcca	63.1	Ganguly <i>et al.</i> (2013)
	IGBpF (A ²)	cttcctggggcccatccc	64.6	

by the simple replication of the methods, described in the scientific literature. First and foremost, it is related to the specificities of amplification programs for different AS-PCR methods (Gaudet *et al.*, 2009). Inaccurate genotyping may lead to a false interpretation of the obtained genetic structure parameters of the experimental groups of animals which distorts the results of the population studies completely. In addition, the genotyping of the cattle individuals is one of the demanded commercial services for the tasks of further selection and for the purpose of obtaining A2 milk, which is an additional indication of the need for maximization of the accuracy and reproducibility of the typing procedure (Park *et al.*, 2021).

Therefore, the aim of our studies is to conduct a comparative analysis of the efficiency of cattle genotyping by beta-casein gene using the methods of allele-specific PCR.

MATERIAL AND METHODS

The studies were conducted in the Laboratory of Molecular and Genetic Studies at the Department of Animal Biology, the National University of Life and Environmental Sciences of Ukraine. To study the efficiency of genotyping by *CSN2* locus, the cows of the Ukrainian Black-and-White dairy breed were used as a model object.

DNA was extracted using the commercial set of reagents “DNA-sorb-B” (Amplisense, RF) according to the manufacturer’s recommendations. Hair follicles were used as a source of biological material.

The genotyping of cattle was conducted using the methods of AS-PCR (as the methods under investigation) and ACRS-PCR (as a control method of genotyping).

The primers, presented in Table 1, were used for the amplification of exon 7 of the *CSN2* gene.

The following amplification program was used for the ACRS-PCR method: 1 cycle – denaturation at 94°C; 35 cycles – denaturation at 94°C, 30 s, annealing at 60°C, 30 s, elongation – 72°C, 30 s. The size of restriction fragments was 121 bp for allele A¹; 86 and 35 bp for allele A².

T_m Calculator (Thermo Fisher Scientific) based on Allawi & SantaLucia’s thermodynamics method (Allawi & SantaLucia, 1997) was used to calculate the temperatures of annealing primers.

In both cases of applying the AS-PCR method, the amplification protocol was optimized according to the following schemes:

The variations of the annealing temperature of primers (from 55°C to 68°C with 1°C interval).

The number of intermediate steps of the second stage of PCR (from two to ten with one step interval).

The duration of the intermediate steps of the second stage of PCR (from 15 to 120 s with 15 s. interval).

Touchdown PCR protocol (Korbie & Mattick, 2008).

PCR was conducted using MiniAmp™ Thermal Cycler (Thermo Fisher Scientific) and the commercial reagent kit “DreamTaq PCR Master Mix” (Thermo Scientific). The volume of the final reaction mixture was 10 µl. The final concentration of primers in the reaction mixture was 0.2 µM.

The electrophoretic separation of the amplification/restriction products involved the use of 3% agarose gel for the ACRS-PCR method and 2% – while using the allele-specific PCR.

The visualization of DNA fragments in the gel was conducted using ethidium bromide in the ultraviolet spectrum (312 nm). The molecular mass marker GeneRuler 50 bp (Thermo Scientific) was used to determine the size of the amplified/restriction fragments.

The object of the study was the populations of cows of different breeds, reared in Ukraine: Ukrainian Red-and-White dairy breed (n=38), Ukrainian Black-and-White dairy breed (two populations from different farms and regions of Ukraine – n=31 and n=100, respectively), Charolais (n=29).

The results of the individual genotyping of the animals were used to estimate the main genetic structure parameters: the frequencies of genotypes and alleles, observed (H_o) and expected (H_e) heterozygosity, the Wright’s fixation index (F_{is}), the correspondence to the Hardy-Weinberg genetic equilibrium by the method of χ^2 . The estimation of genetic structure parameters was conducted using Popgen32 Version 1.32 (Yeh *et al.*, 2000).

RESULTS AND DISCUSSIONS

The use of standard amplification programs for AS-PCR, described in the scientific literature, allowed for differentiating between alleles A¹ and A² of the beta-casein locus of cattle. To conduct the comparative analysis of the efficiency of genotyping the cattle by the beta-casein locus for the purpose of the amplification of the experimental fragment of *CSN2*, only the animals, homozygous by allele A² (A²A²) were used, whose genotype had previously been determined using the ACRS-PCR (Ddel) method (McLachlan, 2006). The variation in the temperature regimes (PCR parameters) led to a considerable change in the genotyping results. Figure 1 presents the electrophoregram for the amplification products of

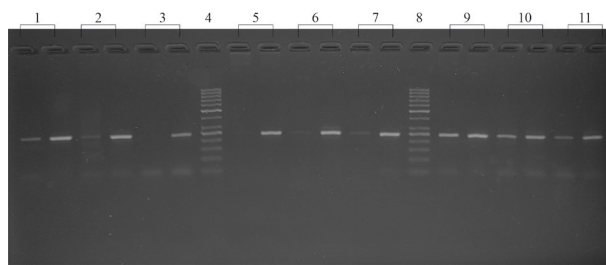


Figure 1. Different PCR protocols for the amplification of CSN2 fragment using the primers of AS-PCR 244 bp. 1–11, numbers of the samples; 4, 8, molecular mass marker GeneRuler 50 bp; 1–3, annealing temperature for oligonucleotides, 58°C; 5–7, annealing temperature for oligonucleotides, 62°C; 9–10, Touchdown PCR.

the fragment of the *CSN2* gene using the AS-PCR 244 bp.

In the case of genotype A¹A¹, the electrophoregram shows the DNA fragment of 244 bp only in the well, corresponding to allele A¹, for genotype A²A² – only in the well, corresponding to allele A²; as for the heterozygous genotype, the amplified fragments are found in both wells. The use of different amplification programs led to significant variations in PCR efficiency. In this case, a critical moment is the selection of optimal parameters for amplification protocols of the experimental fragments. This variation can be implemented into the general program both *via* temperature and the introduction of the intermediate cycles. In our studies, we have used a wide spectrum of annealing temperatures – from 58 to 69°C (with one-degree interval), the Touchdown PCR method, and two additional cycles for the second stage of PCR, one of which was optimized for the annealing temperature for the first (forward) primer, and the other – for the second (reverse) one. The theoretical analysis of the annealing temperatures demonstrated the differences of several degrees between the used primers (under 4°C). The study results were used to set optimal temperatures for both inner cycles.

Figure 1 shows the results of applying three different PCR protocols for the amplification of *CSN2* fragment using primers for AS-PCR 244 bp. All the samples in the presented electrophoregram are related to genotype A²A², but the results of typing differ considerably.

The decrease in the annealing temperature below the minimal theoretically estimated temperature for primers (Table 1) leads to the reduction in the specificity of the method – allele A¹ is amplified in the samples (samples 1, 2, 6, 7). The maximal decrease in the annealing temperature values practically leads to the coincidence in the staining intensity for the amplified fragments of alleles A¹ and A². In its turn, the use of the Touchdown PCR method results in the amplification of all the possible variants of alleles in each sample (samples 9–11), which is a reason for their false interpretation as heterozygous individuals A¹A².

The use of the optimal values of the annealing temperature and the number of cycles allowed for a maximal decrease in the concentration of “unused” primers (to increase the amplification efficiency to the maximum), in case of preserving the high specificity of the reaction and in case of complete absence of non-specific PCR products. In this case, two cycles with different annealing temperatures are used: 67°C – 10 cycles; 65°C – 25 cycles. The final optimal protocol, which ensured the successful genotyping of the cattle, is as follows: 1 cycle – denaturation at 94°C for 5 min; 10 cycles – denaturation at 94°C for 30 s, annealing at 67°C for 30 s,

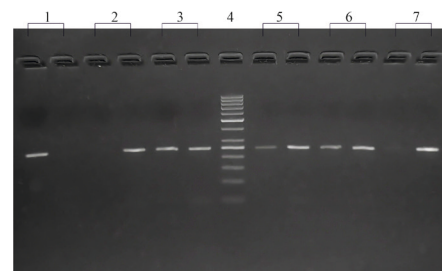


Figure 2. The results of typing the cattle individuals by AS-PCR 244 bp method using the optimized amplification protocol. 1, A¹A¹; 2, 7, A²A²; 3, 5, 6, A¹A²; 4, molecular mass marker GeneRuler 50 bp.

elongation at 72°C for 30 s; 25 cycles – denaturation at 94°C for 30 s, annealing at 65°C for 30 s, elongation at 72°C for 30 s.

However, even in the case of optimal parameters, some samples may still have the fragment, remarkable for the second allele, which may be explained by a close value of the annealing temperatures for allele-specific primers (IGBhF A¹ and IGBpF A²), as well as a number of additional potential factors – the differences in the values of the initial concentration of the DNA under analysis, the type of the used enzyme (different modified forms of Taq-polymerase), the concentrations of primers, etc. In this case, we used the primers in the concentration of 0.2 μM, which allowed obtaining the maximally vivid and unambiguous picture in each case of genotyping the animals of *Bos taurus* by *CSN2* locus. In general, when the method of allele-specific PCR is used, there is still a possibility for the amplification of the non-specific allele in a sufficiently wide range. If the luminosity intensity is insufficient regarding the second fragment, one can make a conclusion about the amplification of the non-specific allele (Fig. 1, samples 2 and 7). In the ideal system (under maximally possible amplification efficiency), the luminosity intensity of different fragments (A¹ and A²) in the case of heterozygous samples will be the same, as both variants are present in the initial DNA in the equivalent number. In case of the insufficient luminosity of one of the specific fragments, two assumptions are possible: either the phenomenon of non-specific amplification or the presence of inhibitors in a specific sample. Then the algorithm of targeted testing of “problematic” samples should be applied based on the alternative method (ACRS-PCR), which is actually ignored by different researchers. In addition to the above, it is reasonable to have regular “blind testing” of the samples using the alternative method (ACRS-PCR).

Regardless of the present difficulties, the application of the optimized (described above) PCR protocol ensured the successful genotyping for the animals of *Bos taurus* by alleles A¹ and A² (Fig. 2).

The results of the typing were entirely confirmed by the ACRS-PCR method (DdeI), the coincidence of geno-types, found by both methods, was 100%.

The application of the described methodological approaches allowed for obtaining similar results while using the AS-PCR 854 bp method as well. In this case, the optimal results, which ensure unambiguous identification of *CSN2* alleles, were also obtained using the two-stage PCR algorithm. The values of the annealing temperature for primers were considerably different from the ones, presented in other scientific works (Keating *et al.*, 2008; Rahimi *et al.*, 2015).

The best result was obtained using the following amplification program – the use of two cycles on the second stage

Table 2. The genetic structure parameters of different cattle populations.

Breed	Genotype frequency			Allele frequency		H_e	F_{is}	χ^2 test
	A ¹ A ¹	A ¹ A ²	A ² A ²	A ¹	A ²			
RW	0.13	0.61	0.26	0.43	0.57	0.49	-0.24	2.06
BW (pop 1)	0.42	0.48	0.1	0.66	0.34	0.45	-0.07	0.201
BW (pop 2)	0.12	0.49	0.39	0.37	0.63	0.47	-0.04	0.34
Charolais	0	0.17	0.83	0.09	0.91	0.16	-0.06	0.24

RW, Ukrainian Red-and-White dairy breed; BW (pop 1), Ukrainian Black-and-White dairy breed (Population 1); BW (pop 2), Ukrainian Black-and-White dairy breed (Population 2); H_e , expected heterozygosity; F_{is} , Wright's fixation index

of PCR with different annealing temperatures: 66°C – 10 cycles; 64°C – 25 cycles (Fig. 3). The final optimal protocol, which ensured the successful genotyping of the cattle, is as follows: 1 cycle – denaturation at 94°C for 5 min; 10 cycles – denaturation at 94°C for 30 s, annealing at 66°C for 30 s, elongation at 72°C for 30 s; 25 cycles – denaturation at 94°C for 30 s, annealing at 64°C for 30 s, elongation at 72°C for 30 s. The amplification was conducted without the final elongation stage (stage 3). The obtained results of typing are completely confirmed by the ACRS-PCR (DdeI) method and are in complete correlation with the results of using AS-PCR 244 bp. The coincidence of genotypes between all the used methods of typing was 100 %.

Therefore, the study results directly demonstrate the need for a thorough selection of amplification parameters while using the allele-specific PCR for the genotyping of cattle by beta-casein locus. The identity of the typing results for two different primer systems for AS-PCR demonstrates the commonality of the methodological approaches in solving the task of enhancing the specificity, reproducibility, and efficiency of amplifying alleles A¹ and A². The obtained results can be used for large-scale routine genotyping of individuals of different cattle breeds by allelic variants of the beta-casein gene.

The above-mentioned methodological approaches were used to determine the genetic structure parameters of the cattle population of different breeds, reared in Ukraine (Table 2).

The study results demonstrated that the beta-casein locus is related to polymorphous ones in all the experimental populations. The animals with all the possible genotypes were found in each experimental population except for Charolais.

The maximal value for allele A² frequency was found in the Charolais population, which may be determined by the fact of its origin. Charolais are meat cattle, so, taking into consideration the descent of allele A¹ from the European dairy cattle breeds, the minimal number

of heterozygotes A¹A² in the population (5 out of 29) is absolutely reasonable. Homozygotes A¹A¹ are entirely absent in this population.

The analysis of the genetic structure of the populations of dairy cows shows the following picture: two populations of Ukrainian Black-and-White breed from different farms demonstrate significant differences regarding the values of allele frequencies. For instance, in population 2 there is a prevalence of allele A² frequency, while in population 1, the situation is diametrically opposite – there is a significant prevalence of allele A¹ frequency (practically two-fold). At the same time, the values of the observed (H_o) and expected (H_e) heterozygosity in both populations are very similar. The obtained study results allow for the assumption that the observed picture is related to the specificities of the selection work with this breed at each farm and to the degree of “Holsteinization”, used in breeding to enhance the parameters of dairy performance of cattle. The study results confirm the data for the distribution of allelic frequencies obtained in the analysis of the Holsteinized Black-and-White cattle, reared in Latvia (Smiltina *et al.*, 2018). This assumption is also indirectly confirmed by the actual presence of allele A¹ (with different frequency) in the populations of Holstein cattle in different regions of the world (Yamada *et al.*, 2021; Ivanković *et al.*, 2021; Bisutti *et al.*, 2022).

In its turn, the insignificant domination of allele A² frequency was noted for the population of the Ukrainian Red-and-White breed, with the two-fold prevalence of the number of homozygotes A²A² over A¹A¹. The excess of heterozygous animals was also noted in this population of cows (24%). The data about the distribution of allelic frequencies in the populations of Black-and-White and Red-and-White dairy breeds are confirmed by the results of other authors obtained for these breeds in other countries (Ehrmann *et al.*, 1997; Kamiński *et al.*, 2006).

It should be noted that no deviation from the Hardy-Weinberg genetic equilibrium was found in any cattle population under study.

CONCLUSIONS

The application of the above-described methodological approaches to the optimization of PCR methods allows for efficient genotyping of the animals (A¹ and A² allele detection) on the background of current advantages of AS-PCR before the alternative variants – low material-technical and time expenditures under completely comparable efficiency.

To achieve the maximal efficiency of the amplification, it is recommended to use the modified PCR protocol, including the two-step second stage with the following values of the annealing temperatures for primers: for AS-PCR 244 bp – 67°C (10 cycles) and 65°C (25 cycles); for AS-PCR 854 bp – 66°C (10 cycles) and 64°C (25 cycles).

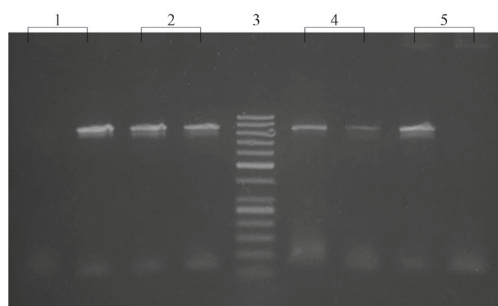


Figure 3. The results of typing the cattle individuals by AS-PCR 854 bp method using the optimized amplification protocol. 1, A²A², 2, A¹A², 5, A¹A¹, 3, molecular mass marker GeneRuler 50 bp.

The use of the touchdown PCR method as the instrument for optimization of AS-PCR protocols is not efficient for the primer systems under investigation and leads to genotyping mistakes.

To control the specificity of the amplification of the experimental CSN2 gene fragment, it is recommended to use the alternative method (ACRS-PCR) via both so-called analyses of “problematic samples” and blind typing from the sampling frame.

Declarations

Acknowledgments. None.

Conflicts of Interest. The authors declare no conflict of interest.

REFERENCES

- Adoligbe CM, Akpo SG, Adido S, MPo M, Zoclanclounon A, Mantip S, Akpo Y, Farougou S (2022) Distribution of the beta-casein gene variants in three cattle breeds reared in Benin. *J Agri Sci* **14**: 86–94. <https://doi.org/10.5539/jas.v14n2p86>
- Allawi HT, SantaLucia J (1997) Thermodynamics and NMR of internal G-T mismatches in DNA. *Biochemistry* **36**: 10581–10594. <https://doi.org/10.1021/bi962590c>
- Antonopoulos D, Vougiouklaki D, Laliotis GP, Tsironi T, Valasi I, Chatzilazarou A, Halvatiotis P, Houhoula D (2021) Identification of polymorphisms of the CSN2 gene encoding β -casein in Greek local breeds of cattle. *Vet Sci* **8**: 257. <https://doi.org/10.3390/vet-sci8110257>
- Bisutti V, Pegolo S, Giannuzzi D, Mota FM, Vanzin A, Toscano A, Trevisi E, Marsan PA, Brasca M, Cecchinato A (2022) The β -casein (CSN2) A2 allelic variant alters milk protein profile and slightly worsens coagulation properties in Holstein cows. *J Dairy Sci* **105**: 3794–3809. <https://doi.org/10.3168/jds.2021-21537>
- Cieślńska A, Fiedorowicz E, Zwierchowski G, Kordulewska N, Jarmolowska B, Kostyra E (2019) Genetic polymorphism of β -casein gene in Polish Red Cattle – preliminary study of A1 and A2 frequency in genetic conservation herd. *Animals (Basel)* **9**: 377. <https://doi.org/10.3390/ani9060377>
- Dai R, Fang Y, Zhao W, Liu S, Ding J, Xu K, Yang L, He C, Ding F, Meng H (2016) Identification of alleles and genotypes of beta casein with DNA sequencing analysis in Chinese Holstein cow. *J Dairy Res* **83**: 312–316. <https://doi.org/10.1017/S0022029916000303>
- De Vitte K, Kerziane S, Klementavičiūtė J, De Vitte M, Mišeikienė R, Kudlinskienė I, Čepaitė J, Dilbėnė V, Stankevičius R (2022) Relationship of β -casein genotypes (A1A1, A1A2 and A2A2) to the physicochemical composition and sensory characteristics of cows' milk. *J Appl Anim Res* **50**: 161–166. <https://doi.org/10.1080/09712119.2022.2046005>
- Ehrmann S, Bartenschlager H, Geldermann H (1997) Quantification of gene effects on single milk proteins in selected groups of dairy cows. *J Anim Breed Genet* **114**: 121–132. <https://doi.org/10.1111/j.1439-0388.1997.tb00499.x>
- Ganguly I, Kumar S, Gaur GK, Singh U, Kumar A, Kumar S, Mann S, Sharma A (2013) Status of β -casein (CSN2) Polymorphism in Frieswal (HF X Sahiwal Crossbred) cattle. *Int J Biotechnol Bioeng Res* **4**: 249–256
- Gaudet M, Fara AG, Beritognolo I, Sabatti M (2009) Allele-specific PCR in SNP genotyping. *Methods Mol Biol* **578**: 415–424. https://doi.org/10.1007/978-1-60327-411-1_26
- Gigliotti R, Hiromi Okino C, Azevedo BT, Gutmanis G, Katiki LM, Oliveira MC, Filho AEV (2021) Novel LNA probe-based assay for the A1 and A2 identification of β -casein gene in milk samples. *Food Chem: Mol Sci* **3**: 100055. <https://doi.org/10.1016/j.fochms.2021.100055>
- Ivanković A, Pećina M, Ramljak J, Pašić V (2021) Genetic polymorphism and effect on milk production of CSN2 gene in conventional and local cattle breeds in Croatia. *Mljekarstvo* **71**: 3–12. <https://doi.org/10.15567/mljekarstvo.2021.0101>
- Jiménez-Montenegro L, Alfonso L, Mendizabal JA, Urrutia O (2022) Worldwide Research Trends on Milk Containing Only A2-Casein: A Bibliometric Study. *Animals* **12**: 1909. <https://doi.org/10.3390/ani12151909>
- Kamiński S, Ruś A, Cieślńska A (2006) A note on frequency of A1 and A2 variants of bovine beta casein locus in Polish Holstein bulls. *J Anim Feed Sci* **15**: 195–98. <https://doi.org/10.22358/JAFS/66892/2006>
- Kay SIS, Delgado S, Mittal J, Eshraghi RS, Mittal R, Eshraghi AA (2021) Beneficial Effects of Milk Having A2 β -Casein Protein: Myth or Reality? *J Nutr* **151**: 1061–1072. <https://doi.org/10.1093/jn/nxaa454>
- Keating A, Smith T, Ross R, Cairns M (2008) A note on the evaluation of a beta-casein variant in bovine breeds by allele-specific PCR and relevance to β -casomorphin. *Irish J Agri Food Res* **47**: 99–104
- Korbic DJ, Mattick JS (2008) Touchdown PCR for increased specificity and sensitivity in PCR amplification. *Nature Protocols* **3**: 1452–1456. <https://doi.org/10.1038/nprot.2008.133>
- Ladyka V, Pavlenko Y, Sklyarenko Y (2021) β -casein gene polymorphism use in terms of brown dairy cattle preservation. *Arch Zootec* **70**: 88–94
- Ladyka VI, Sklyarenko YI, Pavlenko YM (2020) Analysis of complex genotypes of beta- and kappa casein of bulls of dairy breeds. *Anim Breed Genet* **60**: 99–109. <https://doi.org/10.31073/abg.60.13>
- Lien S, Alestrom P, Klungland H, Rogne S (1992) Detection of multiple β -casein (CASB) alleles by amplification created restriction sites (ACRS). *Anim Genet* **23**: 333–338. <https://doi.org/10.1111/j.1365-2052.1992.tb00155.x>
- Manga I, Dvorak J (2010) TaqMan allelic discrimination assay for A1 and A2 alleles of the bovine CSN2 gene. *Czech J Anim Sci* **55**: 307–312. <https://doi.org/10.17221/89/2009-CJAS>
- McLachlan CN (2006) *Breeding and milking cows for milk free of β -casein A1*. United States Patent 7094949
- Pabitra MH, Maruf TM, Mony SI, Ebnat R, Hoque MR, Bhuiyan MSA (2022) Molecular characterization and A1/A2 genotyping of casein beta gene in zebu and crossbred cattle of Bangladesh. *Czech J Anim Sci* **67**: 318–326. <https://doi.org/10.17221/206/2021-CJAS>
- Park YW, Haenlein GFW (2021) A2 Bovine milk and caprine milk as a means of remedy for milk protein allergy. *Dairy* **2**: 191–201. <https://doi.org/10.3390/dairy2020017>
- Rahimi Z, Gholami M, Rahimi Z, Yari K (2015) Evaluation of beta-casein locus for detection of A1 and A2 alleles frequency using allele specific PCR in native cattle of Kermanshah, Iran. *Biharean Biologist* **9**: 85–87
- Raja A, Rajendran R, Ganapathi P (2021) Detection of A1 and A2 alleles at beta-casein locus in Bargur and Umblachery (Indian Zebu) cattle breeds by allele-specific PCR. *Indian J Anim Res* **B-4273**: 1–5. <https://doi.org/10.18805/IJAR.B-4273>
- Ramkaran, Ganguly A, Gera S, Kumar S, Magotra A, Kumar A, Sheoran M (2017) Status of β casein gene in Hardhenu crossbred cattle. *Haryana Vet* **56**: 1–4
- Ristanic M, Niksic A, Niketic M, Jelisc S, Rajkovic M, Glavinic U, Stanimirovic Z (2022) Use of allele specific PCR to investigate the presence of β -casein polymorphism in Holstein-Friesian cows. *Veterinarski Glasnik* **76**: 17–24. <https://doi.org/10.2298/VE-T-G1211125004R>
- Sebastiani C, Arcangeli C, Ciullo M, Torricelli M, Cinti G, Fisichella S, Biagetti M (2020) Frequencies evaluation of β -casein gene polymorphisms in dairy cows reared in central Italy. *Animals* **10**: 252. <https://doi.org/10.3390/ani10020252>
- Sebastiani C, Arcangeli C, Torricelli M, Ciullo M, D'avino N, Cinti G, Fisichella S, Biagetti M (2022) Marker-assisted selection of dairy cows for β -casein gene A2 variant. *Italian J Food Sci* **34**: 21–27. <https://doi.org/10.15586/ijfs.v34i2.2178>
- Smiltina D, Grislis Z (2018) Molecular genetics analysis of milk protein gene polymorphism of dairy cows and breeding bulls in Latvia. *Agronomy Res* **16**: 900–909. <https://doi.org/10.15159/AR.18.084>
- Summer A, Di Frangia F, Marsan AP, De Noni I, Malacarne M (2020) Occurrence, biological properties and potential effects on human health of β -casomorphin 7: Current knowledge and concerns. 2020. *Crit Rev Food Sci Nutr* **60**: 3705–3723. <https://doi.org/10.1080/10408398.2019.1707157>
- Thiruvengadam M, Venkidasamy B, Thirupathi P, Chung IM, Subramanian U (2020) β -Casomorphin: A complete health perspective. *Food Chem* **337**: 127765. <https://doi.org/10.1016/j.foodchem.2020.127765>
- Vougiouklaki D, Antonopoulos D, Alexeli S, Houhoula D (2020) Identification of polymorphisms of gene CSN2 of β casein in Greek cow breeds (Holstein) by restriction fragment length polymorphism. *J Agri Sci* **12**: 32–39. <https://doi.org/10.5539/jas.v12n11p32>
- Wakchaure R, Ganguly S, Praveen PK, Kumar A, Sharma S, Mahajan T (2015) Marker assisted selection (MAS) in animal breeding: a review. *J Drug Metab Toxicol* **6**: e127. <https://doi.org/10.4172/2157-7609.1000e127>
- Yamada A, Sugimura M, Kuramoto T (2021) Genetic polymorphism of bovine beta-casein gene in Japanese dairy farm herds. *Anim Sci J* **92**: e13644. <https://doi.org/10.1111/asj.13644>
- Yeh FC, Yang R, Boyle TJ, Ye Z, Xiyan JM (2000) *PopGene32*, Microsoft Windows-based freeware for population genetic analysis, version 1.32. Mol Biol Biotechnol Centre, Univ. Alberta, Edmonton, Alberta, Canada
- Zepeda-Batista JL, Alarcon-Zuniga B, Ruiz-Flores A, Nunez-Dominguez R, Ramirez-Valverde R (2015) Polymorphism of three milk protein genes in Mexican Jersey cattle. *Electronic J Biotechnol* **18**: 1–4. <https://doi.org/10.1016/j.ejbt.2014.10.002>

Upregulation of miR-22 alleviates oxygen–glucose deprivation/reperfusion-induced injury by targeting Tiam1 in SH-SY5Y cells

Jiansong Yin[#], Yu Wan[#], Jing Wang and Mei Xue✉

Department of Neonatology, The Affiliated Changzhou No.2 People's Hospital of Nanjing Medical University, Changzhou 213200, Jiangsu, China

MicroRNA-22 (miR-22) has been reported to exert a neuroprotective effect. However, the specific role and mechanism of miR-22 in ischemia/reperfusion (I/R)-induced brain injury are still not known well. In this study, we evaluated whether miR-22 participates in I/R-induced neuronal injury and the potential mechanism by using an oxygen-glucose deprivation/reperfusion (OGD/R) model *in vitro*. Our results showed that miR-22 was significantly down-regulated in SH-SY5Y cells suffering from OGD/R. Up-regulation of miR-22 by its specific mimic could protect SH-SY5Y cells against OGD/R-induced injury. The luciferase reporter assay demonstrated that T-cell lymphoma invasion and metastasis 1 (Tiam1) was a direct target of miR-22. MiR-22 mimic obviously inhibited Tiam1 expression in OGD/R-exposed SH-SY5Y cells. Tiam1 siRNA could attenuate OGD/R-induced SH-SY5Y cell injury. In addition, Tiam1 siRNA reduced the activation of Ras-related C3 botulinum toxin substrate 1 (Rac1) in OGD/R-exposed SH-SY5Y cells, and up-regulation of Rac1 activity could attenuate the neuroprotective effect of miR-22 up-regulation. Furthermore, OGD/R exposure led to increased methylation of miR-22, and the demethylating agent 5-Aza-dC significantly up-regulated miR-22 expression and inhibited Tiam1 expression and Rac1 activation. Taken together, our results demonstrated that DNA methylation-mediated miR-22 down-regulation aggravated I/R-induced neuron injury by promoting the activation of Tiam1/Rac1 signals. Our findings provide a deeper understanding of I/R-induced brain injury and suggest that miR-22 may be a promising therapeutic target for this disease.

Keywords: miR-22, Tiam1, Rac1, neuronal injury

Received: 29 January, 2022; **revised:** 22 June, 2022; **accepted:** 11 May, 2023; **available on-line:** 06 September, 2023

✉e-mail: xmjswjchi@163.com

[#]These authors contributed equally to the manuscript

Acknowledgements of Financial Support: This work was supported by grants from Changzhou Sci&Tech Program (CJ20210086).

Abbreviations: OGD/R, oxygen–glucose deprivation/reperfusion; I/R, ischemia/Reperfusion; HIBD, hypoxic-ischemic brain damage; MSC-exos, Mesenchymal stem cells-derived exosomes; PUMA, P53 upregulated modulator of apoptosis; GEF, Guanine nucleotide-exchange factor; Rac1, Ras-related C3 botulinum toxin substrate 1; Tiam1, T-cell lymphoma invasion and metastasis 1; NMDAR, N-methyl-D-aspartate (NMDA) receptor

INTRODUCTION

Neuron dysfunction and/or death serves a pivotal function in the development and progression of brain-related diseases, such as Parkinson's disease, ischemic stroke and neonatal ischemic hypoxic brain damage (HIBD), which is caused by oxygen deprivation in the

infant's brain (Khoshnam *et al.*, 2017; Koehn *et al.*, 2020; Liu *et al.*, 2020a; Salamon *et al.*, 2020). The neuronal cell was susceptible to injury or death by various pathophysiological factors (Khoshnam *et al.*, 2017; Koehn *et al.*, 2020; Liu *et al.*, 2020a; Salamon *et al.*, 2020). Ischemia is characterized by an insufficient oxygen supply and serves as the main cause of the aggravation of cerebral injury. The treatment for cerebral ischemia usually involves the restoration of blood flow as quickly as possible. However, this can entail secondary injury to the ischemic area, referred to as 'ischemia/reperfusion' (I/R) injury (Ryou and Mallet, 2018). However, the molecular mechanisms underlying I/R-induced neuronal injury are not entirely clear.

It is demonstrated that miRNAs played an important role in I/R-induced injury in various tissues, including brain tissue (Cai *et al.*, 2021; Duan *et al.*, 2019; Kuai *et al.*, 2021; Liu *et al.*, 2020b). Previous studies have reported that miR-22 played a protective role in myocardial injury (Du *et al.*, 2016; Zhang *et al.*, 2019). Up-regulation of miR-22 was shown to protect the cerebra against I/R injury (Wang *et al.*, 2020). A recent study discovered that mesenchymal stem cells-derived exosomes (MSC-exos) alleviated I/R-induced brain injury by transferring miR-22 to neurons (Zhang *et al.*, 2021b). Jiao *et al.* reported that enhanced miR-22 expression reversed I/R-induced apoptosis in PC12 cells (Jiao *et al.*, 2020). These findings indicated that miR-22 might provide a potential neuroprotective effect. However, the neuroprotective mechanism of miR-22 in I/R-induced injury is far from fully elucidated.

Ras-related C3 botulinum toxin substrate 1 (Rac1), a Rho-related small GTPase, is ubiquitously expressed throughout the brain (Stankiewicz and Linseman, 2014). Rac1 has been implicated in oxygen-glucose deprivation (OGD)/reperfusion (OGD/R)-induced pathways responsible for neuronal injury, neuronal degeneration, and cognitive dysfunction (Chen *et al.*, 2020; Li *et al.*, 2021). The precise spatial and temporal regulation of Rac1 activation depends on its upstream regulators, the guanine nucleotide exchange factors (GEFs) (Marei and Malliri, 2017). T-cell lymphoma invasion and metastasis 1 (Tiam1) is a Rac1-specific GEF, which is stimulated by N-methyl-D-aspartate (NMDA) receptor (NMDAR) activation in a Ca²⁺-dependent manner (Tolias *et al.*, 2005). Previous studies demonstrated that Tiam1-mediated Rac1 activation in hippocampal and cortical neurons mediates differential spine shrinkage in response to OGD (Blanco-Suarez *et al.*, 2014). However, whether Tiam1-mediated Rac1 activation is involved in OGD/R-induced neuronal injury remains unknown. Tiam1 was demonstrated to be a target gene of miR-22 in various cells (Li *et al.*, 2013; Li *et al.*, 2012) and endometrial Tiam1/Rac1 signal was shown to be negatively regulated by miR-22

(Ma *et al.*, 2015). Therefore, it is worthwhile to explore whether Tiam1/Rac1 signal is involved in protective effect of miR-22 against I/R-induced neuronal injury.

In vitro OGD/R is a widely accepted experimental model of *in vivo* I/R-induced neuronal injury (Zhang *et al.*, 2021a). In this study, we investigated the effect of miR-22 on I/R-induced neuronal injury and its mechanism by using an OGD/R model in SH-SY5Y cells. Our results showed that miR-22 was down-regulated in SH-SY5Y cells. Enforced miR-22 expression could inhibit Tiam1 expression and suppress Rac1 activation, thus contributing to SH-SY5Y cell protection against I/R-induced injury. Furthermore, we also found that methylation of the miR-22 gene promoter suppressed its expression in OGD/R-exposed SH-SY5Y cells.

MATERIALS AND METHODS

Cell culture and OGD/R induction

The SH-SY5Y human neuroblastoma cell line was purchased from Zhong Qiao Xin Zhou Biotechnology Co., Ltd (Shanghai, China). Cells were grown in MEM/F12 (1:1 mixture) supplemented with supplemented with 10% heat inactivated fetal bovine serum, 1% sodium pyruvate, 1% L-alanyl-L-glutamine, and 1% penicillin/streptomycin at 37°C in a humidified atmosphere with 5% CO₂. For neuronal differentiation, SH-SY5Y cells were cultured for 3 days in MEM/F12 medium containing 10 µM retinoic acid and 1% FBS, followed by culturing for a further 3 days with 50 ng/mL brain-derived neurotrophic factor and 2 mmol/L glutamine in MEM/F12 medium containing 1% FBS. For OGD/R induction, SH-SY5Y cells were cultured in glucose-free MEM/F12 under the conditions of 95% N₂, 5% CO₂ and 37°C for 4 h. Thereafter, the cells were then cultured in normal DMEM for 24 h of reoxygenation under normoxic condition. SH-SY5Y cells cultured in DMEM containing glucose under normoxic condition served as a control.

Cell transfection

The miR-22 mimic and its negative control, Tiam1 siRNA and control siRNA were purchased from Genepharma (Shanghai, China) and transfected into SH-SY5Y cells using lipofectamine 2000 (Invitrogen) according to the manufacturer's manual. The expression of target genes was determined after 24 h of transfection and cells were used in further experiments. Sequences of the miR-22 mimic, and its negative control (NC) were as follows: miR-22 sense, 5'-AAGCUGCCAGUUGAAGAA CUGU-3' and antisense, 5'-AGUUCUUAACUGGC AGCUUUU-3'; and NC sense, 5'-UUCUCCGAACGU GUCACGUTT-3' and antisense, 5'-ACGUGACACGUU CGGAGAATT-3'. Sequences of Tiam1 siRNA were as follows: GCGAGCUUUAAGAAGAAAT (sense) and UUUCUUCUUAAGCUCGCGGT (antisense). Scrambled siRNA was used as a negative control in all experiments.

CCK-8 assay

The cell viability of SH-SY5Y cells was measured by CCK-8 assay. SH-SY5Y cells were seeded into 96-well plates (5×10³/well) and treated as described in the text. At the end of treatment, CCK-8 solution (10 µL/well, Chemicon, Temecula, CA, USA) was added to the cultured cells for 2 h incubation at 37°C. The absorbance

(OD) at 450 nm was measured using an ELx-800 microplate reader (Bio-Tek Inc., Winooski, VT, USA).

Hoechst staining

SH-SY5Y cells were seeded onto coverslips in 6-well plates (5×10³/well) and treated as described in the text. At the end of treatment, cells were fixed with 4% paraformaldehyde for 30 min, then stained with Hoechst 33258 (5 µg/mL) for 20 min at room temperature. After washing with PBS, the cells were observed and photographed under a fluorescence microscope.

Luciferase reporter assay

The wild-type Tiam1 3'-UTR and mutant-type Tiam1 3'-UTR were cloned into the pGL3 basic luciferase reporter vector (Promega, Madison, WI, USA). SH-SY5Y cells were transfected in 24-well plates with miR-22 agomir and WT Tiam1 3'-UTR or miR-22 agomir and Mut Tiam1 3'-UTR respectively using Lipofectamine 2000 (Invitrogen) according to the manufacturer's protocol. After 48 h of transfection, the cells were harvested, and the luciferase activity was measured using a Dual-Luciferase Reporter Gene Assay kit (Promega). Renilla luciferase activity was used to normalize the firefly luciferase intensity.

Western blot

At the end of treatment, total proteins were extracted from SH-SY5Y cells using RIPA lysis buffer (Beyotime Biotechnology, Shanghai, China). Proteins were separated by SDS-PAGE and transferred onto polyvinylidene fluoride (PVDF) membranes (Millipore, USA). After blocking with 5% milk for 1 h at room temperature, the membranes were incubated overnight at 4°C with primary antibodies specific to Tiam1, Rac1, Bcl-2, Bax, Bad and GAPDH (all 1:1000; Cell Signaling Technology, Danvers, MA, USA). The membranes were then incubated with secondary antibodies (1:2000, anti-rabbit; 1:5000, anti-mouse) at room temperature for 1 h. The blots were visualized with an enhanced chemiluminescence kit (Pierce; Thermo Fisher Scientific, Inc.). Image J software was used to analyze the band density.

Pull-Down Assay

Pull-down assay was used to detect Rac1 activity and performed as described previously (Stahle *et al.*, 2003). Briefly, after treatments, equal volumes of total cellular protein were incubated with GST-PBD beads captured on MagneGST glutathione particles (Promega, Madison, WI) for 1 h at 4°C. The particles were then resuspended in SDS and subjected to immunoblotting analysis by using an anti-Rac1 antibody.

Lactate dehydrogenase (LDH) activity detection

At the end of treatment, the supernatants of SH-SY5Y cells were collected and the contents of LDH were measured by an LDH detection kit (Nanjing Jiancheng Bioengineering Institute, Jiangsu, China) according to the manufacturer's manual. Absorbance values were read at 450 nm using an ELx-800 microplate reader (Bio-Tek Inc., Winooski, VT, USA).

RT-qPCR

Total RNA was extracted from SH-SY5Y cells using RNAeasy™ Small RNA Isolation Kit (Beyotime,

Shanghai, China) according to the manufacturer's manual. cDNAs were synthesized using the OneStep PrimeScript miRNA cDNA Synthesis Kit (Takara Biotechnology, Dalian, China). Quantitative real-time PCR was performed with an ABI 7300 system (Applied Biosystems, USA) using BeyoFast™ SYBR Green qPCR Mix (Beyotime). The relative gene expression level of miR-22 was normalized to U6 and calculated using the $2^{-\Delta\Delta C_t}$ method. Primers used for RT-qPCR were listed as follows: U6 small nuclear RNA was used as internal reference, with upstream: 5'-GGAACAGAGAAGATTA GC-3', and downstream: 5'-TTGGAATCACGAATTCG-3'. miR-22 upstream: 5'-TGACAACCGTTTTTGACTG-3' and downstream: 5'-TACTGTTTTGAAAATCGTT-3'.

Methylation specific PCR (MSP)

The genomic DNA was extracted and purified by the Genomic DNA Extraction Kit (TaKaRa, Dalian, China). Bisulfite treatment and conversion of DNA for methylation analysis were performed using the EZ-96 DNA Methylation Kit (Zymo Research, Irvine, CA, USA). The PCR reaction conditions were as follows: 98°C for 4 min, 40 cycles of 98°C for 30 s, 56°C for 30 s, and 72°C for 30 s, and then 72°C for 10 min. The PCR products were electrophoresed in 3% agarose gel.

Statistical analysis

SPSS 16.0 statistics software (SPSS, Chicago, IL) was used for statistical analysis. The data were presented as the mean \pm standard deviation (S.D.). Significant differences were determined using One-way ANOVA. $P < 0.05$ was considered statistically significant.

RESULTS

OGD/R down-regulated miR-22 expression, up-regulated Tiam1 expression and Rac1 activation in SH-SY5Y cells

As shown in Fig. 1A, the expression level of miR-22 was decreased time-dependently in SH-SY5Y cells after OGD/R treatment. The results of the western blot assay revealed that the expression level of Tiam1 was significantly increased after treatment for 12 h or 24 h with OGD/R (Fig. 1B). The activity of Rac1 was obviously increased, while the total Rac1 expression remained unchanged during OGD/R treatment (Fig. 1B).

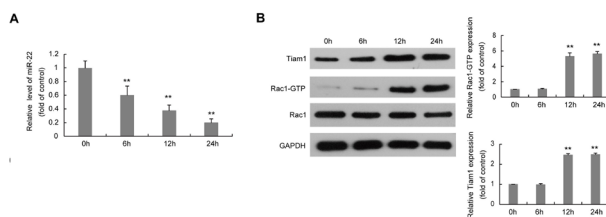


Figure 1. The effects of OGD/R exposure on the activation of Rac1 and the expression levels of miR-22 and Tiam1 in SH-SY5Y cells.

SH-SY5Y cells were exposed to OGD/R for the indicated times, and then the expression level of miR-22 was detected by qRT-PCR (A), the expression levels of Tiam1 and Rac1 were measured by western blot, Rac1 activation (Rac1-GTP) was determined by pull-down assay and analyzed by western blot (B). ** $P < 0.01$ compared with 0 h group.

Up-regulation of miR-22 protected SH-SY5Y cells against OGD/R-induced injury

To elucidate the effect of miR-22 down-regulation on OGD/R-induced neuronal injury, SH-SY5Y cells were transfected with miR-22 mimic, which obviously up-regulated the expression level of miR-22 in OGD/R-exposed SH-SY5Y cells (Fig. 2A). CCK-8 assay showed that miR-22 mimic notably elevated the viability of SH-SY5Y cells under OGD/R condition (Fig. 2B). Hoechst staining showed that miR-22 mimic significantly reduced the number of apoptotic cells in OGD/R-exposed SH-SY5Y cells (Fig. 2C). In addition, OGD/R treatment significantly increased the expression levels of Bax and cleaved caspase-3, and reduced the expression level of Bcl-2 in SH-SY5Y cells (Fig. 2D). However, the expression levels of these proteins were notably reversed after treatment with miR-22 mimic in OGD/R-exposed SH-SY5Y cells (Fig. 2D). Furthermore, miR-22 mimic markedly reduced the content of LDH from OGD/R-exposed SH-SY5Y cells (Fig. 2E). These data indicated that up-regulation of miR-22 protected SH-SY5Y cells against OGD/R-induced injury.

MiR-22 alleviated OGD/R-induced injury by directly targeting Tiam1 in SH-SY5Y cells

To investigate the protective mechanism of miR-22, we analyzed its potential targets using TargetScan and

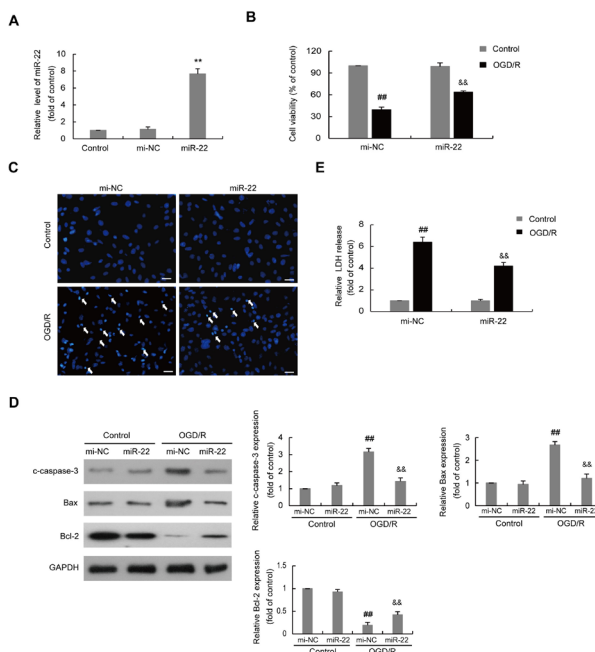


Figure 2. The effect of miR-22 mimics on OGD/R-induced SH-SY5Y cell injury.

(A) The expression level of miR-22 was measured by qRT-PCR in OGD/R-exposed SH-SY5Y cells with negative control mimic (mi-NC) or miR-22 mimic (miR-22) transfection, or without transfection (control). (B) Cell viability was measured by CCK-8 assay in SH-SY5Y cells with mi-NC or miR-22 transfection under normal (control) or OGD/R conditions. (C) Apoptosis was measured by Hoechst staining in SH-SY5Y cells with mi-NC or miR-22 transfection under normal or OGD/R conditions. Scale bar 100 μ m. (D) The levels of apoptosis-related proteins were measured by western blot in SH-SY5Y cells with mi-NC or miR-22 transfection under normal (control) or OGD/R conditions. (E) LDH release was determined by ELISA assay in SH-SY5Y cells with mi-NC or miR-22 transfection under normal (control) or OGD/R conditions. ** $P < 0.01$ compared with mi-NC group; ## $P < 0.01$ compared with mi-NC + control group; && $P < 0.01$ compared with mi-NC + OGD/R group.

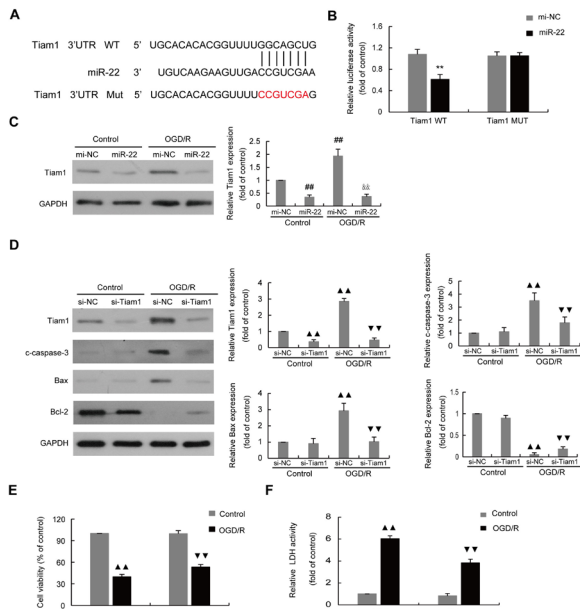


Figure 3. MiR-22 protected SH-SY5Y cells against OGD/R-induced injury by directly targeting Tiam1.

(A) 3'-UTR of Tiam1 and its putative binding sites in miR-22. (B) The luciferase activity for binding of miR-22 to 3'-UTR of Tiam1 was measured by luciferase reporter assay in SH-SY5Y cells. (C) The protein level of Tiam1 was measured by western blot in SH-SY5Y cells with negative control mimic (mi-NC) or miR-22 mimic (miR-22) transfection under normal (control) or OGD/R conditions. (D) The protein levels of Tiam1 and apoptosis-related proteins were measured by western blot in SH-SY5Y cells with negative control siRNA (si-NC) or Tiam1 siRNA (si-Tiam1) transfection under normal (control) or OGD/R conditions. (E) Cell viability was measured by CCK-8 assay in SH-SY5Y cells with si-NC or si-Tiam1 transfection under normal (control) or OGD/R conditions. (F) LDH release was determined by ELISA assay in SH-SY5Y cells with si-NC or si-Tiam1 transfection under normal (control) or OGD/R conditions. ** $P < 0.01$ compared with mi-NC + Tiam1 WT group; ## $P < 0.01$ compared with mi-NC + control group; ** $P < 0.01$ compared with mi-NC + OGD/R group; ▲ $P < 0.01$ compared with control + si-NC group; ▼ $P < 0.01$ compared with OGD/R + si-NC group.

miRDB. Tiam1 was selected for further study as it was predicted to be a potential target of miR-22 by using the two software and was demonstrated to be involved in the regulation of hippocampal neuronal vulnerability to OGD/R (Blanco-Suarez *et al.*, 2014). The possible binding sites between miR-22 and Tiam1 were presented in Fig. 3A. Luciferase reporter assay illustrated that miR-22 mimic notably inhibited the luciferase activity of Tiam1 harboring wild type (WT) 3'UTR, but it had no effect on the luciferase activity of Tiam1 with a mutant type (Mut) 3'UTR (Fig. 3B). Moreover, OGD/R treatment led to a significant increased expression level of Tiam1, which was reversed by the miR-22 mimic (Fig. 3C). These data suggest that Tiam1 is a direct target of miR-22 under the OGD/R condition.

To examine whether Tiam1 is involved in the protective effect of miR-22, SH-SY5Y cells were transfected with Tiam1 siRNA, which markedly inhibited Tiam1 expression in OGD/R-exposed SH-SY5Y cells (Fig. 3D). OGD/R-induced up-regulation of Bax and cleaved caspase-3, and down-regulation of Bcl-2 were reversed by Tiam1 siRNA in SH-SY5Y cells (Fig. 3D). Tiam1 siRNA obviously increased the viability of SH-SY5Y cells under OGD/R condition (Fig. 3E). Tiam1 siRNA also significantly inhibited LDH release in OGD/R-exposed SH-SY5Y cells (Fig. 3F). The above data indicated that miR-

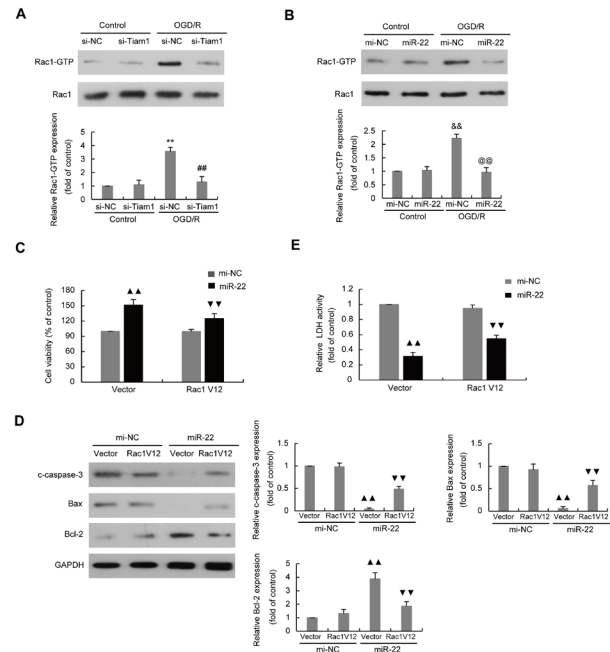


Figure 4. The effect of Rac1 V12 over-expression on the protective effect of miR-22 over-expression during OGD/R-induced injury.

(A) Rac1 activation was measured by pull-down assay in SH-SY5Y cells with negative control siRNA (si-NC) or Tiam1 siRNA (si-Tiam1) transfection under normal (control) or OGD/R conditions. (B) Rac1 activation was measured by pull down assay in SH-SY5Y cells with negative control mimic (mi-NC) or miR-22 mimic (miR-22) transfection under normal (control) or OGD/R conditions. (C–E) After transfection of empty plasmid (vector) or the plasmid containing constitutively active form of Rac1 (Rac1-V12) in mi-NC or miR-22 overexpressed SH-SY5Y cells, cell viability, the levels of apoptosis-related proteins and LDH release were determined by CCK-8 assay (C), western blot (D) and ELISA assay (E), respectively. ** $P < 0.01$ compared with control + si-NC group; ## $P < 0.01$ compared with OGD/R + si-NC group; §§ $P < 0.01$ compared with control + mi-NC group; §§ $P < 0.01$ compared with OGD/R + mi-NC group; ▲ $P < 0.01$ compared with vector + mi-NC group; ▼ $P < 0.01$ compared with vector + mi-22 group.

22 alleviated OGD/R-induced injury by directly targeting Tiam1 in SH-SY5Y cells.

Rac1 activation reversed the protective effect of miR-22 up-regulation on OGD/R-induced injury in SH-SY5Y cells

As Tiam1 is a specific guanine nucleotide-exchange factor (GEF) of Rac1, the involvement of Rac1 in the protective mechanism of miR-22 was then investigated. As shown in Fig. 4A, Tiam1 siRNA significantly inhibited OGD/R-induced Rac1 activation in SH-SY5Y cells. OGD/R-induced Rac1 activation was also inhibited by miR-22 mimic (Fig. 4B). MiR-22 overexpression significantly elevated cell viability, inhibited LDH release, Bax and cleaved caspase-3 expression, and up-regulates Bcl-2 expression in OGD/R-exposed SH-SY5Y cells (Fig. 4C–4E). However, these parameters were reversed by transfection of Rac1-V12, an active mutant of Rac1 (Fig. 4C–4E). These results suggested that Rac1 activation reversed the protective effect of miR-22 up-regulation on OGD/R-induced injury in SH-SY5Y cells.

Methylation of the miR-22 gene promoter suppressed its expression in SH-SY5Y cells under OGD/R condition

To investigate the underlying mechanism of miR-22 down-regulation in SH-SY5Y cells after OGD/R expo-

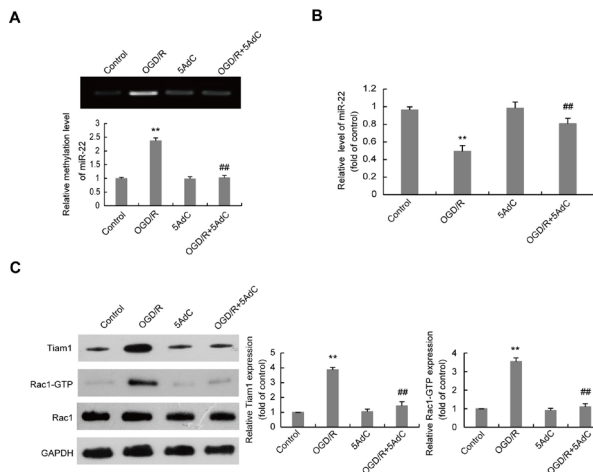


Figure 5. Methylation of the miR-22 gene promoter inhibited miR-22 expression under OGD/R condition.

(A) The methylation level of miR-22 in OGD/R-exposed SH-SY5Y cells with or without 5-Aza-dC (5Aza-dC) treatment was analyzed by MSP analysis. (B) The expression level of miR-22 in OGD/R-exposed SH-SY5Y cells with or without 5-Aza-dC (5Aza-dC) treatment was examined by RT-qPCR. (C) The level of Tiam1 expression and Rac1 activation in OGD/R-exposed SH-SY5Y cells with or without 5-Aza-dC (5Aza-dC) treatment were determined by western blot and pull down assay, respectively. ** $P < 0.01$ compared with control group; ## $P < 0.01$ compared with OGD/R group.

sure, the methylation level of the miR-22 gene promoter was measured. As shown in Fig. 5A, OGD/R exposure led to increased methylation of miR-22, which was reversed by treatment with 5-Aza-dC, a demethylating agent. 5-Aza-dC treatment also obviously up-regulated the level of miR-22 in OGD/R-exposed SH-SY5Y cells (Fig. 5B). Moreover, the increased Tiam1 expression and Rac1 activation in OGD/R-exposed SH-SY5Y cells were significantly inhibited by 5-Aza-dC treatment (Fig. 5C). These results suggested that methylation of the miR-22 gene promoter suppressed its expression in SH-SY5Y cells under OGD/R condition.

DISCUSSION

MicroRNAs have been demonstrated to work as critical factors in various brain injuries (Song *et al.*, 2019; Suofu *et al.*, 2020; Zhao *et al.*, 2020). Previous studies have indicated that up-regulation of miR-22 could protect neuron against I/R-induced injury (Wang *et al.*, 2020). Recently, MSC-exos-derived miR-22 was shown to attenuate I/R-induced brain (Zhang *et al.*, 2021b). However, the specific mechanism of miR-22 in I/R-induced neuronal injury is far from clear nowadays. In this study, we constructed an OGD/R model of SH-SY5Y cells and found that the level of miR-22 was decreased. Up-regulation of miR-22 could protect SH-SY5Y cells against OGD/R-induced injury. Our results suggest that miR-22 plays a protective role in OGD/R-induced neuronal injury.

The potential neuroprotective mechanism of miR-22 was then explored by searching for its target gene with targetscan and miRDB. Our results showed that the expression of Tiam1 was negatively correlated with miR-22 and was a potential target of miR-22. Tiam1 was demonstrated to be the target of miR-22 in several types of cells, such as NK/T cells, colon cancer cells and ovarian cancer cells (Huang *et al.*, 2016; Li *et al.*, 2013; Li *et al.*,

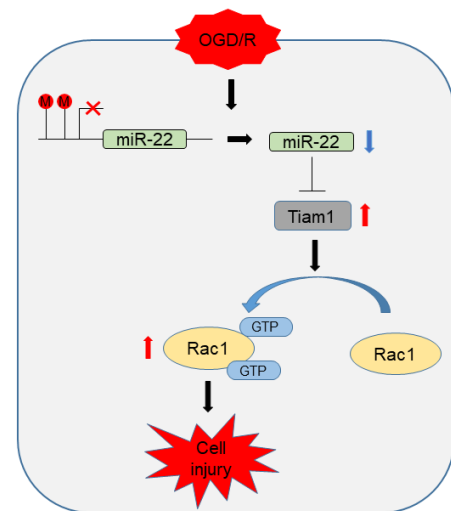


Figure 6. Schematic illustration of OGD/R-induced SH-SY5Y cell injury via the miR-22/Tiam1/Rac1 signaling pathway.

2012). In the present study, luciferase report assay and western blot assay indicated that Tiam1 is a direct target of miR-22 in OGD/R-exposed SH-SY5Y cells. Furthermore, Tiam1 siRNA could obviously attenuate OGD/R-evoked injury in SH-SY5Y cells. These results suggested that miR-22 overexpression alleviated OGD/R-induced injury by directly targeting Tiam1 in SH-SY5Y cells. MiR-22 was shown to exert its neuroprotective function by regulating PI3K/AKT signaling pathway in cerebral I/R rats (Wang *et al.*, 2020). Jiao *et al.* (Jiao *et al.*, 2020) reported that miR-22 protects PC12 cells from OGD/R-evoked injury by targeting the p53 upregulated modulator of apoptosis (PUMA). Recently, it is demonstrated that MSC-exos-derived miR-22 attenuated OGD/R-evoked injury by inhibiting KDM6B expression in rat primary cortical neurons (Zhang *et al.*, 2021b). These findings, together with our results, indicated that miR-22 exerts neuroprotective effects by different downstream targets, which depend on cell type. It will be interesting to determine whether the reported targets of miR-22 are involved in our system and their crosstalk with Tiam1.

Tiam1 is known best as a specific GEF for Rac1 activation (Chapelle *et al.*, 2020; Kurdi *et al.*, 2016; Yue *et al.*, 2021). Previous studies showed that Tiam1 mediates an OGD-induced increase in Rac1 activity in hippocampal neurons (Blanco-Suarez *et al.*, 2014; Smith *et al.*, 2017). Furthermore, Rac1 activation was demonstrated to play an important role in I/R-induced injury in different tissues, including brain tissue (Chen *et al.*, 2020; Li *et al.*, 2017; Liang *et al.*, 2018; Liu *et al.*, 2019; Su *et al.*, 2019). Therefore, we speculated that miR-22 exerts its neuroprotective function by inhibiting Tiam1-mediated Rac1 activation. Our results showed that Rac1 activity was obviously increased in OGD/R-exposed SH-SY5Y cells. Tiam1 siRNA and miR-22 agomir could markedly inhibit OGD/R-induced Rac1 activation. Moreover, Rac1-V12, an active mutant of Rac1, could significantly attenuate the inhibitory effect of miR-22 up-regulation on OGD/R-evoked injury. These data indicated that miR-22 exerts its neuroprotective function on OGD/R-evoked injury by inhibiting Tiam1-mediated Rac1 activation in SH-SY5Y cells.

The key factors that reduced miR-22 expression in our system were then investigated. It is demonstrated that the CpG island methylation in promoter regions is key to miRNAs expression (Chhabra, 2015; Glaich *et al.*,

2019). Moreover, DNA-methylation was shown to play an important role in I/R-induced brain injury (Deng *et al.*, 2019; Jin *et al.*, 2021; Tang and Zhuang, 2019; Zeng *et al.*, 2020). Thus, we investigated whether the decreased miR-22 expression in OGD/R-exposed SH-SY5Y cells is due to DNA-methylation in its promoter. Our results showed that the methylation level of the CpG island in the miR-22 promoter was significantly increased after OGD/R exposure. 5-Aza-dC treatment could obviously up-regulated miR-22 expression in OGD/R-exposed SH-SY5Y cells. Furthermore, Tiam1 expression and Rac1 activity were significantly inhibited by 5-Aza-dC treatment in OGD/R-exposed SH-SY5Y cells. These results suggested that DNA-methylation in OGD/R-exposed SH-SY5Y cells led to a decreased miR-22 expression and increased Tiam1 expression and Rac1 activation, thereby promoting neuronal injury.

In conclusion, our study demonstrated that DNA-methylation of miR-22 causes miR-22 down-regulation, which results in Tiam1 up-regulation and Rac1 activation in OGD/R-exposed SH-SY5Y cells, therefore leading to cell injury (Fig. 6). MiR-22 up-regulation plays a neuroprotective role in OGD/R-exposed SH-SY5Y cells, which is partly via directly targeting Tiam1 to inhibit Rac1 activation. Although additional *in vivo* studies are needed to verify our findings, our study provides a new insight into the protective effects of miR-22 against I/R-induced brain injury and warrants further study of DNA methylation-mediated silencing of miR-22 may serve as a potential therapeutic strategy for I/R-induced brain injury.

Declarations

Competing interests. The authors declare that they have no competing interests.

Ethical approval. Not applicable.

Statement of Informed Consent. Not applicable.

Availability of data and materials. The datasets used during the present study are available from the corresponding author upon reasonable request.

Authors' contributions. Jiansong Yin wrote the manuscript, performed the experiments and analyzed the experimental data, Yu Wan performed the experiments and analyzed the experimental data, Jing Wang analyzed the experimental data, Mei Xue edited the manuscript and supervised the study. All authors read and approved the final manuscript.

REFERENCE

Blanco-Suarez E, Fiuza M, Liu X, Chakkarapani E, Hanley JG (2014) Differential Tiam1/Rac1 activation in hippocampal and cortical neurons mediates differential spine shrinkage in response to oxygen/glucose deprivation. *J Cereb Blood Flow Metab* **34**: 1898–1906. <https://doi.org/10.1038/jcbfm.2014.158>

Cai Q, Gao ML, Huang LS, Pan LH (2021) lncRNA H19/miRNA-1: Another potential mechanism for treating myocardial ischemia-reperfusion injury. *Int J Cardiol* **322**: 57. <https://doi.org/10.1016/j.ijcard.2020.10.054>

Chapelle J, Baudino A, Torelli F, Savino A, Morellato A, Angelini C, Saleme V, Centonze G, Natalini D, Gai M, Poli V, Kahne T, Turco E, Defilippi P (2020) The N-terminal domain of the adaptor protein p140Cap interacts with Tiam1 and controls Tiam1/Rac1 axis. *Am J Cancer Res* **10**: 4308–4324. <https://www.ajcr.us/ISSN:2156-6976/ajcr0143948>

Chen X, Zhang S, Shi P, Su Y, Zhang D, Li N (2020) MiR-485-5p promotes neuron survival through mediating Rac1/Notch2 signaling pathway after cerebral ischemia/reperfusion. *Curr Neurovasc Res* **17**: 259–266. <https://doi.org/10.2174/1567202617666200415154822>

Chhabra R (2015) miRNA and methylation: a multifaceted liaison. *ChemBiochem* **16**: 195–203. <https://doi.org/10.1002/cbic.201402449>

Deng GX, Xu N, Huang Q, Tan JY, Zhang Z, Li XF, Wei JR (2019) Association between promoter DNA methylation and gene expression in the pathogenesis of ischemic stroke. *Aging (Albany NY)* **11**: 7663–7677. <https://doi.org/10.18632/aging.102278>

Du JK, Cong BH, Yu Q, Wang H, Wang L, Wang CN, Tang XL, Lu JQ, Zhu XY, Ni X (2016) Upregulation of microRNA-22 contributes to myocardial ischemia-reperfusion injury by interfering with the mitochondrial function. *Free Radic Biol Med* **96**: 406–417. <https://doi.org/10.1016/j.freeradbiomed.2016.05.006>

Duan C, Cao Z, Tang F, Jian Z, Liang C, Liu H, Xiao Y, Liu L, Ma R (2019) miRNA-mRNA crosstalk in myocardial ischemia induced by calcified aortic valve stenosis. *Aging (Albany NY)* **11**: 448–466. <https://doi.org/10.18632/aging.101751>

Glaich O, Parikh S, Bell RE, Mekahel K, Donyo M, Leader Y, Shayevitch R, Sheinboim D, Yannai S, Hollander D, Melamed Z, Lev-Maor G, Ast G, Levy C (2019) DNA methylation directs microRNA biogenesis in mammalian cells. *Nat Commun* **10**: 5657. <https://doi.org/10.1038/s41467-019-13527-1>

Huang H, Fan L, Zhan R, Wu S, and Niu W (2016) Expression of microRNA-10a, microRNA-342-3p and their predicted target gene Tiam1 in extranodal NK/T-cell lymphoma, nasal type. *Oncol Lett* **11**: 345–351. <https://doi.org/10.3892/ol.2015.3831>

Jiao H, Chen R, Jiang Z, Zhang L, Wang H (2020) miR-22 protect PC12 from ischemia/reperfusion-induced injury by targeting p53 upregulated modulator of apoptosis (PUMA). *Bioengineered* **11**: 209–218. <https://doi.org/10.1080/21655979.2020.1729321>

Jin D, Wei W, Song C, Han P, Leng X (2021) Knockdown EZH2 attenuates cerebral ischemia-reperfusion injury via regulating microRNA-30d-3p methylation and USP22. *Brain Res Bull* **169**: 25–34. <https://doi.org/10.1016/j.brainresbull.2020.12.019>

Khoshtam SE, Winlow W, Farzaneh M, Farbood Y, Moghaddam HF (2017) Pathogenic mechanisms following ischemic stroke. *Neural Sci* **38**: 1167–1186. <https://doi.org/10.1007/s10072-017-2938-1>

Koehn LM, Chen X, Logsdon AF, Lim YP, Stonestreet BS (2020) Novel neuroprotective agents to treat neonatal hypoxic-ischemic encephalopathy: inter-alpha inhibitor proteins. *Int J Mol Sci* **21**: 9193. <https://doi.org/10.3390/ijms21239193>

Kuai F, Zhou L, Zhou J, Sun X, Dong W (2021) Long non-coding RNA THRIL inhibits miRNA-24-3p to upregulate neuropilin-1 to aggravate cerebral ischemia-reperfusion injury through regulating the nuclear factor kappaB p65 signaling. *Aging (Albany NY)* **13**: 9071–9084. <https://doi.org/10.18632/aging.202762>

Kurdi AT, Bassil R, Olah M, Wu C, Xiao S, Taga M, Frangieh M, Buttrick T, Orent W, Bradshaw EM, Khoury SJ, Elyaman W (2016) Tiam1/Rac1 complex controls Il17a transcription and autoimmunity. *Nat Commun* **7**: 13048. <https://doi.org/10.18632/aging.202762>

Li B, Song Y, Liu TJ, Cui YB, Jiang Y, Xie ZS, Xie SL (2013) miRNA-22 suppresses colon cancer cell migration and invasion by inhibiting the expression of T-cell lymphoma invasion and metastasis 1 and matrix metalloproteinases 2 and 9. *Oncol Rep* **29**: 1932–1938. <https://doi.org/10.3892/or.2013.2300>

Li H, Luo Y, Liu P, Liu P, Hua W, Zhang Y, Zhang L, Li Z, Xing P, Zhang Y, Hong B, Yang P, Liu J (2021) Exosomes containing miR-451a is involved in the protective effect of cerebral ischemic preconditioning against cerebral ischemia and reperfusion injury. *CNS Neurosci Ther* **27**: 564–576. <https://doi.org/10.1111/cns.13612>

Li J, Liang S, Jin H, Xu C, Ma D, Lu X (2012) Tiam1, negatively regulated by miR-22, miR-183 and miR-31, is involved in migration, invasion and viability of ovarian cancer cells. *Oncol Rep* **27**: 1835–1842. <https://doi.org/10.3892/or.2012>

Li T, Qin JJ, Yang X, Ji YX, Guo F, Cheng WL, Wu X, Gong FH, Hong Y, Zhu XY, Gong J, Wang Z, Huang Z, She ZG, Li H (2017) The ubiquitin E3 ligase TRAF6 exacerbates ischemic stroke by ubiquitinating and activating Rac1. *J Neurosci* **37**: 12123–12140. <https://doi.org/10.1523/JNEUROSCI.1751-17.2017>

Liang H, Huang J, Huang Q, Xie YC, Liu HZ, Wang HB (2018) Pharmacological inhibition of Rac1 exerts a protective role in ischemia/reperfusion-induced renal fibrosis. *Biochem Biophys Res Commun* **503**: 2517–2523. <https://doi.org/10.1016/j.bbrc.2018.07.009>

Liu W, Huang J, Doycheva D, Gamdzyk M, Tang J, and Zhang JH (2019) RvD1 binding with FPR2 attenuates inflammation via Rac1/NOX2 pathway after neonatal hypoxic-ischemic injury in rats. *Exp Neurol* **320**: 112982. <https://doi.org/10.1016/j.expneurol.2019.112982>

Liu Y, Zhu C, Guo J, Chen Y, Meng C (2020a) The Neuroprotective Effect of irisin in ischemic stroke. *Front Aging Neurosci* **12**: 588958. <https://doi.org/10.3389/fnagi.2020.588958>

Liu Z, Liu Y, Zhu Y, Gong J (2020b) HOTAIR/miRNA-1/Cx43: A potential mechanism for treating myocardial ischemia-reperfusion injury. *Int J Cardiol* **308**: 11. <https://doi.org/10.1016/j.ijcard.2019.12.019>

Ma HL, Gong F, Tang Y, Li X, Li X, Yang X, Lu G (2015) Inhibition of endometrial Tiam1/Rac1 signals induced by miR-22 up-regulation leads to the failure of embryo implantation during the implantation window in pregnant mice. *Biol Reprod* **92**: 152. <https://doi.org/10.1095/biolreprod.115.128603>

- Marei H, Malliri A (2017) GEFs: Dual regulation of Rac1 signaling. *Small GTPases* **8**: 90–99. <https://doi.org/10.1080/21541248.2016.1202635>
- Ryou MG, Mallet RT (2018) An *in vitro* oxygen-glucose deprivation model for studying ischemia-reperfusion injury of neuronal cells. *Methods Mol Biol* **1717**: 229–235. https://doi.org/10.1007/978-1-4939-7526-6_18
- Salamon A, Zadori D, Szpisjak L, Klivenyi P, Vecsei L (2020) Neuroprotection in Parkinson's disease: facts and hopes. *J Neural Transm (Vienna)* **127**: 821–829. <https://doi.org/10.1007/s00702-019-02115-8>
- Smith KR, Rajgor D, Hanley JG (2017) Differential regulation of the Rac1 GTPase-activating protein (GAP) BCR during oxygen/glucose deprivation in hippocampal and cortical neurons. *J Biol Chem* **292**: 20173–20183. <https://doi.org/10.1074/jbc.M117.796292>
- Song Y, Li Z, He T, Qu M, Jiang L, Li W, Shi X, Pan J, Zhang L, Wang Y, Zhang Z, Tang Y, Yang GY (2019) M2 microglia-derived exosomes protect the mouse brain from ischemia-reperfusion injury via exosomal miR-124. *Theranostics* **9**: 2910–2923. <https://doi.org/10.7150/thno.30879>
- Stahle M, Veit C, Bachfischer U, Schierling K, Skripczynski B, Hall A, Gierschik P, Giehl K (2003) Mechanisms in LPA-induced tumor cell migration: critical role of phosphorylated ERK. *J Cell Sci* **116**: 3835–3846. <https://doi.org/10.1242/jcs.00679>
- Stankiewicz TR, Linseman DA (2014) Rho family GTPases: key players in neuronal development, neuronal survival, and neurodegeneration. *Front Cell Neurosci* **8**: 314. <https://doi.org/10.3389/fncel.2014.00314>
- Su Q, Liu Y, Lv XW, Ye ZL, Sun YH, Kong BH, Qin ZB (2019) Inhibition of lncRNA TUG1 upregulates miR-142-3p to ameliorate myocardial injury during ischemia and reperfusion via targeting HMGB1- and Rac1-induced autophagy. *J Mol Cell Cardiol* **133**: 12–25. <https://doi.org/10.1016/j.jmcc.2019.05.021>
- Suofu Y, Wang X, He Y, Li F, Zhang Y, Carlisle DL, Friedlander RM (2020) Mir-155 knockout protects against ischemia/reperfusion-induced brain injury and hemorrhagic transformation. *Neuroreport* **31**: 235–239. <https://doi.org/10.1097/WNR.0000000000001382>
- Tang J, Zhuang S (2019) Histone acetylation and DNA methylation in ischemia/reperfusion injury. *Clin Sci (Lond)* **133**: 597–609. <https://doi.org/10.1042/CS20180465>
- Tolias KF, Bikoff JB, Burette A, Paradis S, Harrar D, Tavazoie S, Weinberg RJ, Greenberg ME (2005) The Rac1-GEF Tiam1 couples the NMDA receptor to the activity-dependent development of dendritic arbors and spines. *Neuron* **45**: 525–538. <https://doi.org/10.1016/j.neuron.2005.01.024>
- Wang X, Shi C, Pan H, Meng X, Ji, F (2020) MicroRNA-22 exerts its neuroprotective and angiogenic functions via regulating PI3K/Akt signaling pathway in cerebral ischemia-reperfusion rats. *J Neural Transm (Vienna)* **127**: 35–44. <https://doi.org/10.1007/s00702-019-02124-7>
- Yue Y, Zhang C, Zhao X, Liu S, Lv X, Zhang S, Yang J, Chen L, Duan H, Zhang Y, Yao Z, Niu W (2021) Tiam1 mediates Rac1 activation and contraction-induced glucose uptake in skeletal muscle cells. *FASEB J* **35**: e21210. <https://doi.org/10.1096/fj.202001312R>
- Zeng M, Zhen J, Zheng X, Qiu H, Xu X, Wu J, Lin Z, Hu J (2020) The role of DNA methylation in ischemic stroke: a systematic review. *Front Neurol* **11**: 566124. <https://doi.org/10.3389/fneur.2020.566124>
- Zhang BF, Chen J, Jiang H (2019) LncRNA H19 ameliorates myocardial ischemia-reperfusion injury by targeting miR-22-3P. *Int J Cardiol* **278**: 224. <https://doi.org/10.1016/j.ijcard.2018.11.017>
- Zhang L, Wang Y, Pan RL, Li Y, Hu YQ, Xv H, Zhu C, Wang X, Yin JW, Ma KT, Zhao D (2021a) Neuritin attenuates oxygen-glucose deprivation/reoxygenation (OGD/R)-induced neuronal injury by promoting autophagic flux. *Exp Cell Res* **407**: 112832. <https://doi.org/10.1016/j.yexcr.2021.112832>
- Zhang Y, Liu J, Su M, Wang X, Xie, C (2021b) Exosomal microRNA-22-3p alleviates cerebral ischemic injury by modulating KDM6B/BMP2/BMF axis. *Stem Cell Res Ther* **12**: 111. <https://doi.org/10.1186/s13287-020-02091-x>
- Zhao J, Li L, Fang G (2020) Salvianolic acid A attenuates cerebral ischemia/reperfusion injury induced rat brain damage, inflammation and apoptosis by regulating miR-499a/DDK1. *Am J Transl Res* **12**: 3288–3301. <https://www.ajtr.org/ISSN:1943-8141/AJTR0105946>

Circ-Sirt1 promotes osteoblast differentiation by activating Sirt1 and Wnt/ β -catenin pathway

Yuanli Li¹, Junlan Nie², Qing Wu¹, Xin Yang¹ and Ping Jiang¹✉

¹Department of Orthopedics, Affiliated Hospital of North Sichuan Medical College, Sichuan, 637000, P. R. China; ²Department of Operating Room, Affiliated Hospital of North Sichuan Medical College, Sichuan, 637000, P. R. China

Osteoporosis, a bone disease common in the elderly, results in bone loss and damage to bone microstructure. Sirtuin 1 (Sirt1), belongs to Sirtuin family, is involved in regulating bone quality. Circ-Sirt1 is one of the transcripts of Sirt1 host gene. Here, the involvement of circ-Sirt1 was determined in bone disease for the first time, proposing that circ-Sirt1 can activate the Wnt/ β -catenin pathway to promote osteogenesis differentiation. This study was aimed to elucidate the potential function of Circ-Sirt1 and Sirt1 regulatory loop in the differentiation of bone marrow mesenchymal stem cells (BMSCs). The differentiation of bone marrow mesenchymal stem cells was detected by ALP, alizarin red staining and qPCR. The dual luciferase reporter assay was applied to reveal the interaction between RNAs. The result showed that Sirt1 promoted osteogenic differentiation of BMSCs. Circ-Sirt1, derived from Sirt1, acted as miR-132 and miR-212 sponge, and up-regulated the expression of Sirt1. Furthermore, Sirt1-mediated circ-Sirt1 promoted osteogenic differentiation. Finally, we unveiled that Circ-Sirt1 facilitates osteogenic differentiation by activating the Wnt/ β -catenin pathway. In conclusion, our data suggested that Circ-Sirt1 elevates osteogenic differentiation via miR-132/212/Sirt1 and Wnt/ β -catenin pathway.

Key word: Circ-Sirt1, Osteoporosis, Wnt/ β -catenin pathway, mesenchymal stem cells (BMSCs)

Received: 18 November, 2021; revised: 17 June, 2022; accepted: 26 November, 2022; available on-line: 25 February, 2023

✉e-mail: 43954680@qq.com

Abbreviations: BMSCs, bone marrow mesenchymal stem cells; CircRNA, Circular RNA; DPSCs, Dental pulp stem cells; NC, negative control; Sirt1, Sirtuin 1

INTRODUCTION

Osteoporosis is a systemic bone disease which has serious complications in elderly people especially elderly females. It is caused by functional disproportion between osteoblasts and osteoclasts (Liu *et al.*, 2020; Zhang *et al.*, 2020). Osteoblasts, responsible for bone formation, are not terminally differentiated. However, these osteoblasts can eventually differentiate into osteocytes through physiological activities such as proliferation, secretion of protein, and calcification (Chen *et al.*, 2019; Chu *et al.*, 2020). Inhibition of the growth and physiological activities of osteoblasts can cause numerous bone diseases, including osteoporosis, osteoarthritis, rheumatoid arthritis and osteogenesis imperfecta (Dadras *et al.*, 2020; Edwards *et al.*, 2013). Therefore, clarifying the regulatory mechanism of osteoblast differentiation and proliferation may pos-

sibly provide novel and effective treatment strategies for osteoporosis.

Sirt1 is a nicotinamide adenine dinucleotide (NAD⁺) dependent class 3 histone deacetylases which has been demonstrated as regulating lifespan in several model organisms (Koga *et al.*, 2015). Sirt1 plays an important role in the physiological activities of bone tissue. It has been revealed that Sirt1 regulates SOX2 to maintain the self-renewal and pluripotency of BMSCs (Yoon *et al.*, 2014). Whereas, another study reported that Sirt1 knockout mice shows a low bone mass phenotype, but the specific signaling pathway has not been elucidated (Feng *et al.*, 2016). Wnt is a type of secreted protein that is rich in cysteine. It is well known that Wnt/ β -catenin signaling pathway affects the differentiation balance of BMSCs in bone tissue. Meanwhile, it is also established that Sirt1 is involved in TNF- α -stimulated osteogenic differentiation of human Dental pulp stem cells (DPSCs) through Wnt/ β -catenin signal (Zainabadi *et al.*, 2017). As core target of cellular aging, energy metabolism and bone metabolism, Sirt1 is known to play significant role in the pathogenesis of osteoporosis. In this study, we sought to investigate the function and mechanism of Sirt1 in regulating BMSCs differentiation.

Recently, the role of non-coding RNA in osteoporosis has been gradually discovered. Circular RNA (CircRNA) is a new type of non-coding RNA that has regulatory abnormalities in a variety of cancers, frequently involving different carcinogenic processes (Lou *et al.*, 2020). CircRNA is a covalent closed loop structure formed by back-splicing of pre-mRNA without 5' and 3' ends (Salzman *et al.*, 2013).

With comparison of linear exosomes, the high stability of them is manifested *in vivo* with main existing in the cytoplasm and classification of exosomes (Li *et al.*, 2018). Previous studies have affirmed the typical modulation of homologous mRNAs via circRNAs as nuclear transcriptional regulators, platforms for RNA-binding proteins, or cytoplasmic microRNA sponges (Li *et al.*, 2015). Using the CircBase database, it was found that Sirt1 host gene may produce 11 circRNAs. However, the function and mechanism of circRNA derived from the Sirt1 host gene is still unclear in the bone related diseases, and the role of Circ-Sirt1 in the regulation of Wnt/ β -catenin signaling pathway has not been fully explored.

In this study, it was found that Circ-Sirt1 derived from the Sirt1 gene promotes the expression of Sirt1 by competing with miR-132/212, and activates the Wnt/ β -catenin signaling pathway to accelerate the differentiation of bone marrow mesenchymal stem cells. Therefore, Circ-Sirt1 may serve as a new biomarker and therapeutic target in bone related diseases.

MATERIAL AND METHODS

Cell culture and treatment

BMSCs (Riken Cell Bank, cell line RCB2154, Tsukuba, Japan) were cultured in α -MEM medium supplemented with 10% fetal bovine serum (FBS, Gibco, USA) and 100 U/ml penicillin, and 100 mg/ml streptomycin sulfate, under 5% CO₂ and 37°C. Ascorbic acid (50 mg/mL), dexamethasone (0.1 mg/mL) and sodium glycerophosphate (10 mM) (Sigma-Aldrich, St. Louis, MI) were applied in the culture medium to stimulate the differentiation of osteoblasts.

RNA extraction and qPCR detection

Total RNA was extracted from BMSCs using TRNzol reagent (TIANGEN Biotech, Beijing, China) according to the manufacturer's instructions. Reverse transcription kit (TIANGEN Biotech, Beijing, China) was applied to generate cDNA from total RNA. RNA concentration was determined by NanoDrop spectrophotometer (TIANGEN Biotech, Beijing, China). Real-time qPCR was conducted by using FastFire qPCR PreMix (TIANGEN Biotech, Beijing, China). Primer sequences used in this study were listed in Table 1.

ALP activity and ALP staining

To detect the osteogenic differentiation, BMSCs were cultured in osteogenic differentiation induction medium for 21 days. ALP activity was determined using an Alkaline Phosphatase Assay Kit (Beyotime, Beijing, China) by following the manufacturer's instructions.

Alizarin red staining

First, the osteogenic differentiation was induced in BMSCs for 21 days, which were then fixed the cells with 4% paraformaldehyde, and stained with 1% Alizarin Red S (Beyotime, Beijing, China) for 30 minutes. After

washing with PBS for 3 times, the cells were visualized, and images were captured under an inverted microscope (Olympus Corporation, Japan). The alizarin red staining was quantified using Image J.

Luciferase reporter assay

The 3'UTR of circ-Sirt1 or Sirt1 containing miR-132 or miR-212 binding sites was amplified by PCR, cloned into the pgl3 promoter vector of Xba I (circ-Sirt1 WT or Sirt1 WT). The mutant sequence was cloned into pgl3 promoter vector to construct circ-Sirt1 MUT or Sirt1 MUT. Twenty-four hours before transfection, cells were trypsinized (2×10^5 cells/mL) and then plated on 24-well plates. The above plasmids together with Renilla (pRLTK) plasmid, miR-132 mimics, miR-212 mimics, negative control (NC) mimics plasmids were transfected into cells using Lipofectamine 2000 (Invitrogen). After 6 h, the medium was replaced with serum-containing medium, and 48 h after transfection, cells were collected to detect dual-luciferase activity using dual-luciferase assay system (Promega, USA). The relative luciferase activity was calculated from the ratio of firefly to Renilla luciferase signals.

RNA pull down assay

The MagCapture™ RNA Pull Down Kit (whatman, England) was applied for RNA pull-down assay. In brief, BMSCs were washed with precooled PBS, and then incubated with beads and biotinylated miR-132/212 probes for 1 hour. Western blot analysis was used to detect proteins.

Western Blot

Total protein was extracted from BMSCs using RIPA buffer containing 1mM Phenylmethylsulfonyl fluoride (PMSF). BCA kit (Beyotime, Beijing, China) was applied to determine protein concentration. The protein was separated using SDS-PAGE (10% or 12%), and then transferred to PVDF membrane (Millipore, Danvers, MA, USA), and then incubated with primary antibodies Sirt1 (1:1000; ab110304; Abcam), β -catenin (1:1000; ab32572; Abcam), Lamib B1 (1:1000; ab16048; Abcam), β -Tubulin (1:1000; ab6046; Abcam) at 4°C overnight. Later, membranes were washed, and incubated with respective secondary antibodies HRP (anti-rabbit IgG, 1:5000, Cell Signaling Technology, Inc., MA, USA). Finally, the membranes were exposed using ECL system (Beyotime, Beijing, China), and protein bands were analyzed using Quantity One software.

Statistical analyses

Data were analyzed with Graphpad Prism 8 software and expressed as mean \pm S.D. One-way ANOVA followed up with a post hoc test was performed for multiple group comparisons. T test was used for comparison between the two groups. $P < 0.05$ was considered as statistically significant.

RESULT

Sirt1 promotes BMSCs differentiation

Firstly, it was observed that the mRNA expression of Sirt1 was gradually increased during the differentiation of BMSCs (Fig. 1A), indicating that Sirt1 might play vital role in the differentiation of BMSCs. To evaluate the function of Sirt1 in BMSCs, pcDNA3.1-Sirt1 was used to over-ex-

Table 1. The sequences of Primer were provided.

Primer sequence		
Sirt1	Forward	5'-TAGCCTTGTCAGATAAGGAAGGA-3'
	Reverse	5'-ACAGCTTCACAGTCAACTTTGT-3'
Runx2	Forward	5'-TGGTTACTGTCATGGCGGGA-3'
	Reverse	5'-TCTCAGATCGTTGAACCTTGCTA-3'
OCN	Forward	5'-CACTCCTCGCCCTATTGGC-3'
	Reverse	5'-CCCTCCTGCTTGGACACAAAG-3'
OPN	Forward	5'-CTCCATTGACTCGAACGACTC-3'
	Reverse	5'-CAGGTCTGCGAACTTCTTAGAT-3'
MiR-132	Forward	5'-ACACTCCAGCTGGGTAACAGTCTACAGCA-3'
	Reverse	5'-TGGTGTCTGGAGTCG-3'
MiR-212	Forward	5'-ACACTCCAGCTGGGTAACAGTCTCAGTC-3'
	Reverse	5'-TGGTGTCTGGAGTCG-3'
U6	Forward	5'-CTCGCTTCGGCAGCACA-3'
	Reverse	5'-AACGCTTCACGAATTTGCGT-3'
Circ-Sirt1	Forward	5'-TATGACACTGTGGCAGATTG-3'
	Reverse	5'-TTTCATCACCGAACAGAAGG-3'

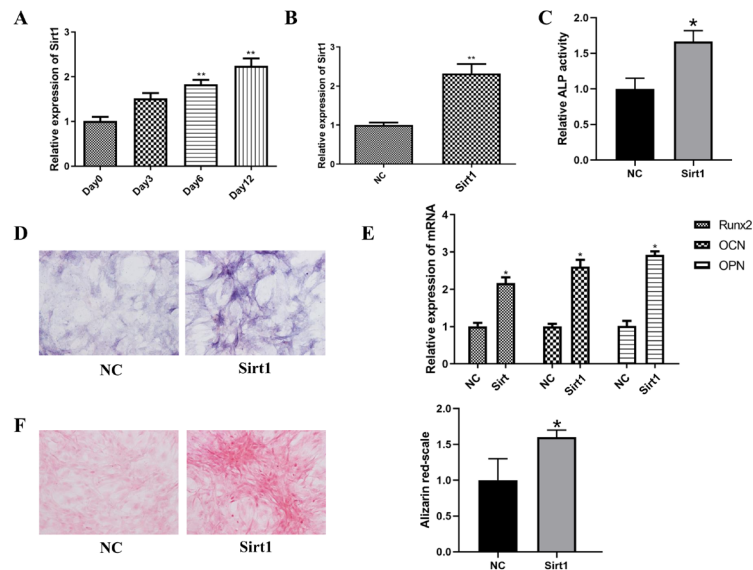


Figure 1. Sirt1 promotes BMSCs differentiation.

(A) The relative expression of Sirt1 in the differentiation of BMSCs was detected by qRT-PCR on the 3rd, 6th and 12th day. (B) The qRT-PCR was used to detect the overexpression efficiency 24 hours after Sirt1 transfection. (C) After overexpression of Sirt1 for 24 hours, the relative activities of alkaline phosphatase in BMSCs were measured with the ALP kit. (D) Sirt1 was overexpressed in BMSCs for 24 hours and stained with ALP. (E) After overexpression of Sirt1 in BMSCs, qRT-PCR was used to detect the mRNA levels of Runx2, OCN and OPN. (F) Sirt1 overexpressed in BMSCs for 24 hours was stained with alizarin red. All results are expressed as mean \pm S.D., n=3. * P <0.05, ** P <0.01

press Sirt1 (Fig. 1B). Interestingly, over-expression of Sirt1 apparently increased ALP activity and ALP staining intensity in BMSCs as shown in Fig.1C-D. Moreover, osteogenic markers Runx2, OCN and OPN were obviously elevated *via* upregulation of Sirt1 (Fig. 1E). Alizarin red staining showed that BMSCs overexpressing Sirt1 was more likely to develop calcified nodules (Fig. 1F). These data indicated that Sirt1 facilitated osteoblastic differentiation in BMSCs. To study the effect of Sirt1 on Wnt/ β -catenin signaling pathway, Western Blot experiment found that β -catenin in

cytoplasm and nucleus was also detected after knockdown of Sirt1, affirming that β -catenin in cytoplasm was elevated, while in nucleus was reduced. To further confirm that Sirt1 promoted the nuclear translocation of β -catenin, immunofluorescence experiments was conducted, finding that the immunocytochemical strength of β -catenin in the nucleus of si-Sirt1 group was declined. In short, Sirt1 activates the Wnt/ β -catenin pathway to facilitate the nuclear translocation of β -catenin during the osteogenic differentiation of BMSCs (Attached Fig. 1B, C), suggesting that Sirt1 accelerates

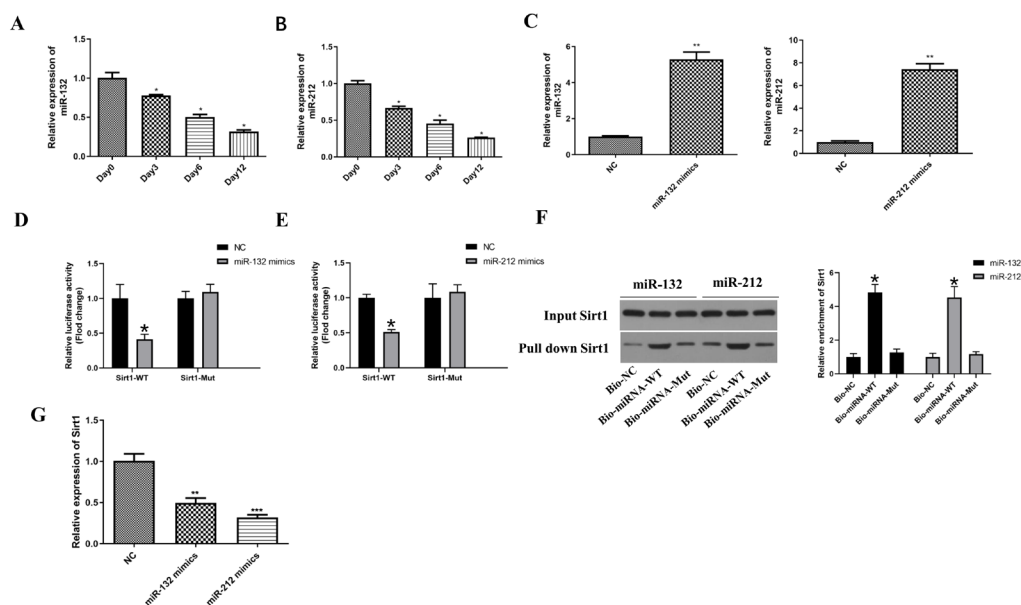


Figure 2. Sirt1 is the direct target of miR-132/212.

(A, B) Relative level of miR-132/212 during BMSCs differentiation on the 0, 3rd, 6th and 12th day was detected through qRT-PCR. (C) miR-132/212 was overexpressed in BMSCs for 24 hours, and the overexpression efficiency was detected by qRT-PCR. (D, E) Effects of Sirt1 luciferase activity were detected by transfection of miR-132/212 mimic in BMSCs for 24 hours. (F) RNA pull down detected Sirt1 level by incubating with bio-miR-132/212 (WT or Mut) for 24 hours. (G) The effect of overexpression of miR-132/212 for 24 hours on Sirt1 expression in BMSCs was detected by qRT-PCR. All results are expressed as mean \pm S.D., n=3. * P <0.05, ** P <0.01

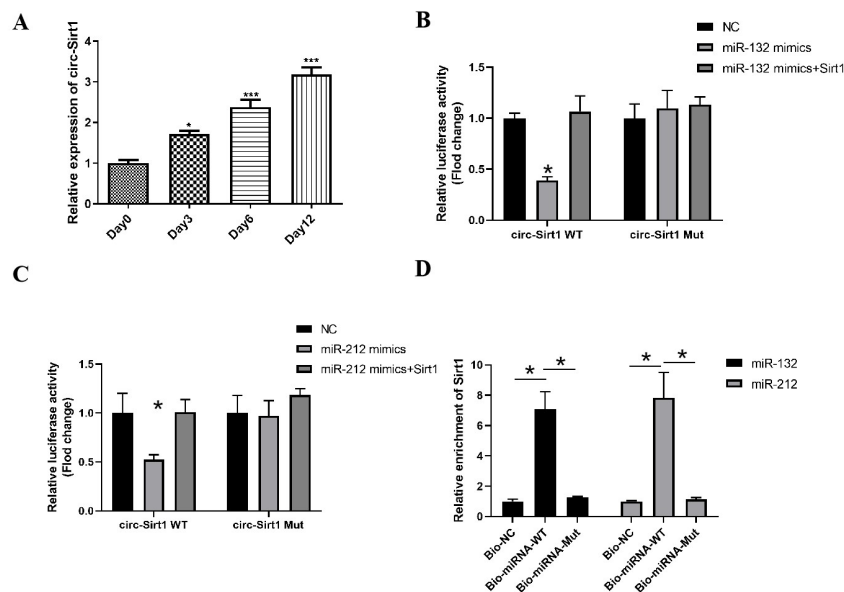


Figure 3. The miR-132/212 are sponged by circ-Sirt1.

(A) Relative expression of circ-Sirt1 in BMSC differentiation on the 0, 3rd, 6th and 12th day was detected through qRT-PCR. (B, C) The luciferase activities of WT and Mut circ-Sirt1 were detected 24 hours after overexpression of miR-132/212. (D) RNA pull down detected circ-Sirt1 level by incubating with bio-miR-132/212 (WT or Mut) for 24 hours. All results are expressed as mean \pm S.D., $n=3$. * $P<0.05$, ** $P<0.01$

osteogenic differentiation of BMSCs through the Wnt/ β catenin pathway.

MiR-132/212 binds to Sirt1 in BMSCs

Next, the binding of upstream miRNAs to Sirt1 was explored. The relative expression of miR-132/212 was decreased during osteogenic differentiation of BMSCs in a time-dependent manner (Fig. 2A–B). Then, miR-132/212 mimics was used to increase the expression of miR-132/212 in BMSCs (Fig. 2C). In order to further investigate the interaction of miR-132/212 and Sirt1, miR-132/212 mimics or mimics-NC was co-transfected with wt-Luc-Sirt1 or mut-Luc-Sirt1 in BMSCs. Our results showed that overexpression of miR-132/212 can clearly inhibit the luciferase activity of Sirt-WT, while overexpression of miR-132/212 had no effect on the relative luciferase activity of Sirt1-MUT in BMSCs (Fig. 2D–E). In addition, RNA pull down assay showed that biotinylated miR-132/212-WT clearly pull down the Sirt1 mRNA, while miR-132/212-MUT did not (Fig. 2F). Finally, it was revealed that miR-123/212 up-regulation apparently reduced the expression of Sirt1 (Fig. 2G). Thus, it was concluded that miR-132/212 reduced the expression of Sirt1 by directly targeting the Sirt1 3'UTR.

MiR-132/212 is sponged by circ-Sirt1 in BMSCs

It was previously reported that miR-132 and miR-212 are sponged by circ-Sirt1 in vascular smooth muscle cells (VSMCs) (Kong *et al.*, 2019). The detection for circRNAs candidates from Sirt1 host genes in the human genome was conducted. Meanwhile, the identification of three circRNAs (hsa_circ_0093883, hsa_circ_0093887, hsa_circ_0093890) from Sirt1 host genes was exposed in human BMSCs (attached Fig. 1A). The up-regulation of Sirt1 *via* circ-Sirt1 was assured in BMSCs by sponging miR-132/212. As shown in Fig. 3A, it was found the elevation of circ-Sirt1 during osteogenic differentiation of BMSCs in a time-dependent manner. It was further determined that the ectopic expression of miR-132/212 reduced the relative luciferase activity of circ-Sirt1-WT,

while Sirt1 overexpression further enhanced it. Whereas, similar experimental conditions had not affected the relative luciferase activity of MUT-circ-Sirt1 (Fig. 3B–C). RNA pull down assay manifested that circ-Sirt1 was clearly pulled down *via* biotinylated miR-132/212-WT, while not affected *via* miR-132/212-MUT (Fig. 3D). Taken together, these results indicated that miR-132/212 was sponged by circ-Sirt1 in BMSCs.

Sirt1 plays an essential role in circ-Sirt1-promoted osteoblastic differentiation

To further examine the effect of Sirt1 in circ-Sirt1 dependent BMSCs differentiation, sh-Sirt1 was applied to transfect BMSCs. Our results showed that silencing of Sirt1 reduced the stimulatory effects of up-regulatory circ-Sirt1 on ALP activity and staining intensity as shown in Fig. 4A–B. Moreover, silencing of Sirt1 also restored the expression of Runx2, OCN and OPN upregulation as induced by circ-Sirt1 upregulation (Fig. 4C–E). These data suggested that Sirt1 played an essential role in the BMSC differentiation as regulated by circ-Sirt1.

Circ-Sirt1 promotes BMSCs differentiation by activating Wnt/ β -catenin pathway

Finally, it was investigated whether the Wnt/ β -catenin pathway mediated circ-Sirt1 dependent BMSCs differentiation, finding that β -catenin was apparently declined via silencing of circ-Sirt1 in the nucleus, while an opposite trend manifested in the cytoplasm (Fig. 5A). The detection results of TOP/FOP Flash showed that silencing of circ-Sirt1 obviously reduced the TOP luciferase activity in BMSCs (Fig. 5B), indicating that silencing circ-Sirt1 inhibited Wnt/ β -catenin pathway. Finally, it was found that WIF-1 (Wnt/ β -catenin pathway inhibitor) treatment obviously reduced the stimulatory effects of circ-Sirt1 up-regulation on osteogenic differentiation of BMSCs in Fig. 5C–H. In summary, these results indicated that circ-Sirt1 up-regulates Sirt1 through miR-132/212, and activates Wnt/ β -catenin pathway to promote BMSCs differentiation.

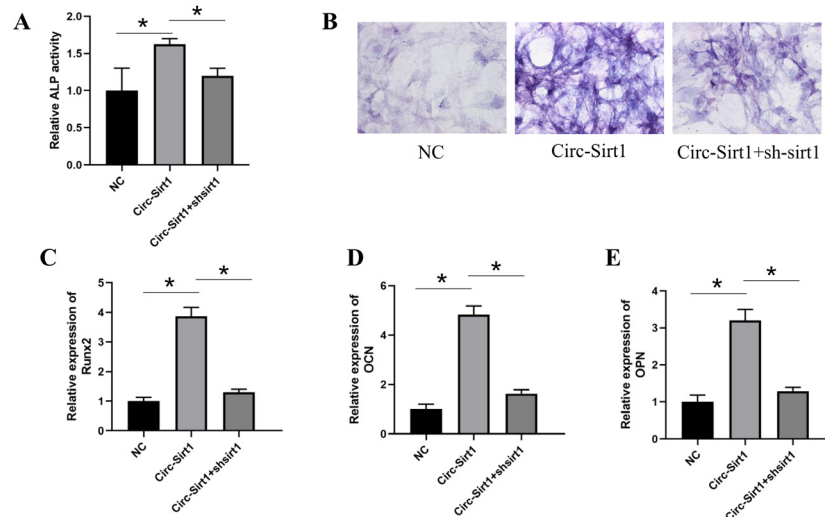


Figure 4. Sirt1 is essential in Circ-Sirt1-induced BMSC differentiation.

(A, B) The ALP activity and ALP staining of BMSCs were detected 24 hours after transfection of circ-Sirt1 and sh-Sirt1. (C–E) The mRNA levels of osteogenic differentiation marker were detected 24 hours after transfection of circ-Sirt1 and sh-Sirt1. All results are expressed as mean \pm S.D., $n=3$. * $P<0.05$, ** $P<0.01$.

DISCUSSION

In this study, it was uncovered that Circ-Sirt1 promoted osteoblast differentiation by activating Sirt1 and Wnt/ β -catenin pathway (Fig. 6). It has been determined

that Sirt1 is widely involved in the physiological activities of bone tissue, and the biological functions of bone cells (Qu *et al.*, 2020). Inhibition of Sirt1 accelerates the acetylation and ubiquitination of SOX2, and represses the osteogenic differentiation of BMSCs. In current study, the

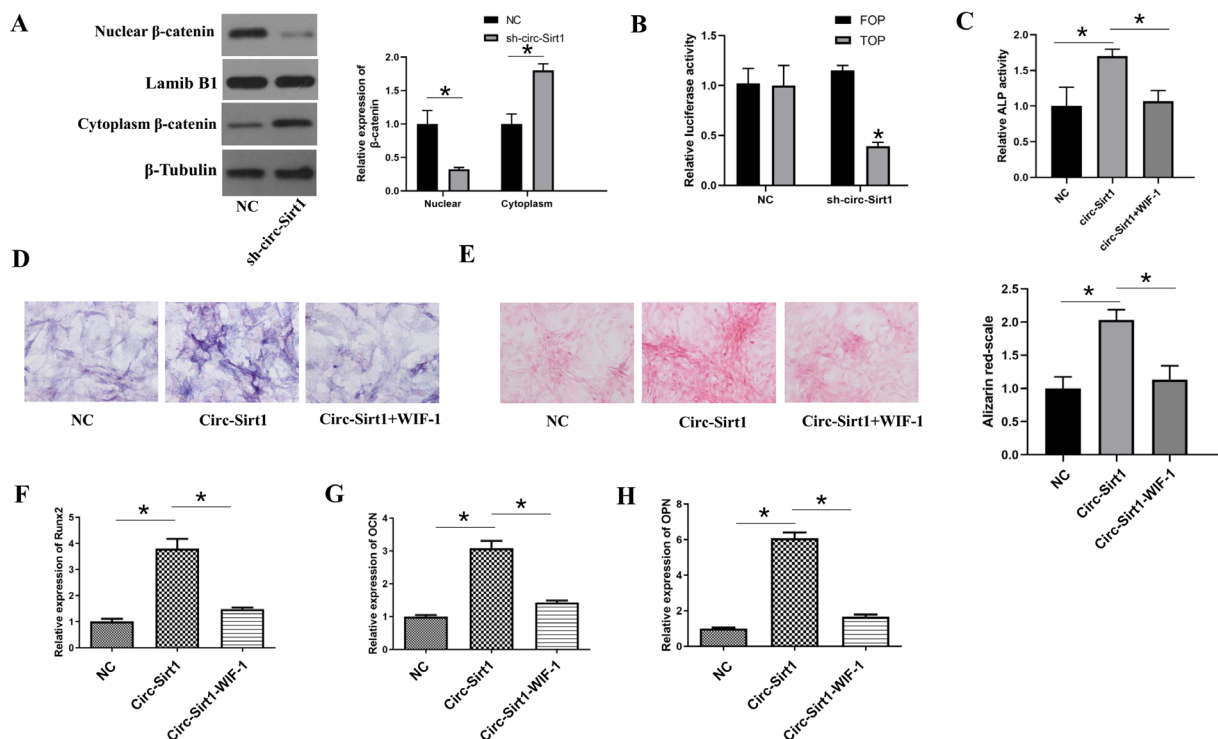


Figure 5. Circ-Sirt1 regulates BMSC differentiation via regulate Wnt/ β -catenin pathway.

(A) Relative expression of nuclear β -catenin and cytoplasm β -catenin were detected by Western blot 24 hours after transfection of sh-circ-Sirt1 in BMSCs. (B) The relative activity of TOP and FOP luciferase were detected 24 hours after transfection of sh-circ-Sirt1 in BMSCs. (C–D) ALP activity and ALP staining were detected in BMSCs treated with circ-Sirt1 and WIF-1 for 24 hours. E. Alizarin red was detected in BMSCs treated with circ-Sirt1 and WIF-1 for 24 hours. (F–H) The mRNA levels of osteogenic differentiation marker were detected in BMSCs treated with circ-Sirt1 and WIF-1 for 24 hours. All results are expressed as mean \pm S.D., $n=3$. * $P<0.05$, ** $P<0.01$.

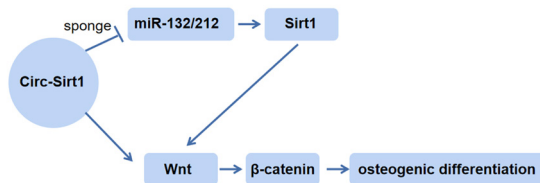


Figure 6. Schematic diagram of circ-Sirt1 activating Wnt/ β -catenin signaling pathway through direct and indirect mechanisms

role and molecular mechanism of Sirt1 was explored in BMSCs differentiation, affirming that Sirt1 was elevated with BMSCs differentiation. Moreover, miR-132 and miR-212 restrain the Sirt1 dependent BMSCs differentiation.

Increasing evidence showed that host genes can be regulated by circRNA which are formed by non-classical splicing. For example, circGFRA1 regulates GFRA1 in breast cancer by sponging miR-34a (Bai *et al.*, 2018). Similarly, CircFBLIM1 promotes HCC progression by sponging miR-346 (He *et al.*, 2017). It has been studied that Circ-Sirt1 enhances Sirt1 expression through sequence-specific interaction with miR-132/212 binding in Vascular smooth muscle cells. Therefore, the study was aimed to investigate if Circ-Sirt1, spliced from Sirt1, could sponge miR-132/212 to up-regulate Sirt1 in BMSCs. Sirt1 and miR-132/212 have been closely associated with human aging and Alzheimer's disease (Hernandez *et al.*, 2016). However, the function of miR-132/212 in osteoporosis remains ambiguous. In this study, it was confirmed that circ-Sirt1 can sponge miR-132/212 as the ceRNA of Sirt1. Circ-Sirt1 promoted BMSCs differentiation, and the silencing of Sirt1 inhibited the stimulatory effects of circ-Sirt1 on the differentiation of BMSCs.

Previous studies reported that Sirt1 could trigger the Wnt/ β -catenin pathway (Hwang *et al.*, 2015). β -catenin, the core molecule of Wnt/ β -catenin pathway, is widely implicated with osteoblast differentiation and proliferation (Feng *et al.*, 2020). demonstrated that microRNA-378 inhibits osteogenesis and bone formation damage of BMSC by inactivating the Wnt/ β -catenin signaling pathway (Wang *et al.*, 2021). Whereas, miR-130a-3p regulates Wnt/ β -catenin pathway to induce osteogenic differentiation among adipose stem cells (Yang *et al.*, 2020). Additionally, a study has manifested the participation of Sirt1 in osteoblast differentiation through Wnt/ β -catenin signaling in endodontic stem cells. The first detection of β -catenin in cytoplasm and nucleus in this study was conducted after Sirt1 knockdown, affirming up-regulation of β -catenin in cytoplasm and decline in nucleus. Furthermore, the promotion of the nuclear translocation of β -catenin via Sirt1 was determined. Moreover, elevation of β -catenin in the cytoplasm and reduction in the nucleus via down-regulation of circ-Sirt1 were founded. Briefly, our experimental results demonstrated that circ-Sirt1 elevates BMSCs differentiation by activating Wnt/ β -catenin signaling pathway.

In summary, our study demonstrated that circ-Sirt1 up-regulates Sirt1 as a sponge for miR-132/212, and activates the Wnt/ β -catenin pathway to promote osteoblastic differentiation of BMSCs, suggesting that circ-Sirt1 may be associated with bone formation. Circ-Sirt1 activates the Wnt/ β -catenin signaling pathway through direct and indirect mechanisms, respectively. However, the direct and indirect effects of circ-Sirt1 are performed on Wnt/ β -catenin signaling pathway, and of them which is

the main way remains to be further studied. The possible application of circ-Sirt1 in clinic needs further study. Clinical samples and in vivo experiments will be further explored with the permission of experimental conditions later. Overall, these findings provide novel directions and insights into potential osteoporosis therapeutics.

Declarations

Acknowledgments. Not applicable.

Funding Statements. Not applicable.

Conflict of interest. All authors declare no conflict of interest

REFERENCE

- Bai N, Peng E, Qiu X, Lyu N, Zhang Z, Tao Y, Li X, Wang Z (2018) circFBLIM1 act as a ceRNA to promote hepatocellular cancer progression by sponging miR-346. *J Exp Clin Cancer Res* 37: 172. <https://doi.org/10.1186/s13046-018-0838-8>.
- Chen PC, Liu JF, Fong YC, Huang YL, Chao CC, Tang CH (2019) CCN3 Facilitates Runx2 and osterix expression by inhibiting miR-608 through PI3K/Akt signaling in osteoblasts. *Int J Mol Sci* 20. <https://doi.org/10.3390/ijms20133300>.
- Chu Y, Gao Y, Yang Y, Liu Y, Guo N, Wang L, Huang W, Wu L, Sun D, Gu W (2020) β -catenin mediates fluoride-induced aberrant osteoblasts activity and osteogenesis. *Environ Pollut* (Barking, Essex: 1987). 265 (Pt A): 114734. <https://doi.org/10.1016/j.envpol.2020.114734>.
- Dadras M, May C, Wagner JM, Wallner C, Becerikli M, Dittfeld S, Serschnitzki B, Schilde L, Guntermann A, Sengstock C, Köller M, Seybold D, Gefßmann J, Schildhauer TA, Lehnhardt M, Marcus K, Behr B (2020) Comparative proteomic analysis of osteogenic differentiated human adipose tissue and bone marrow-derived stromal cells. *J Cell Mol Med* 24: 11814–11827. <https://doi.org/10.1111/jcmm.15797>.
- Edwards JR, Perrien DS, Fleming N, Nyman JS, Ono K, Connelly L, Moore MM, Lwin ST, Yull FE, Mundy GR, Eleftheriou F (2013) Silent information regulator (Sir)T1 inhibits NF- κ B signaling to maintain normal skeletal remodeling. *J Bone Mineral Res* 28: 960–969. <https://doi.org/10.1002/jbmr.1824>.
- Feng G, Zheng K, Song D, Xu K, Huang D, Zhang Y, Cao P, Shen S, Zhang J, Feng X, Zhang D (2016) SIRT1 was involved in TNF- α -promoted osteogenic differentiation of human DPSCs through Wnt/ β -catenin signal. *In Vitro Cell Dev Biol Anim* 52: 1001–1011. <https://doi.org/10.1007/s11626-016-0070-9>.
- Feng L, Zhang JF, Shi L, Yang ZM, Wu TY, Wang HX, Lin WP, Lu YF, Lo JHT, Zhu DH, Li G (2020) MicroRNA-378 suppressed osteogenesis of MSCs and impaired bone formation via inactivating Wnt/ β -catenin signaling. *Mol Therapy Nucleic Acids* 21: 1017–1028. <https://doi.org/10.1016/j.omtn.2020.07.018>.
- He R, Liu P, Xie X, Zhou Y, Liao Q, Xiong W, Li X, Li G, Zeng Z, Tang H (2017) circGFRA1 and GFRA1 act as ceRNAs in triple negative breast cancer by regulating miR-34a. *J Exp Clin Cancer Res* 36: 145. <https://doi.org/10.1186/s13046-017-0614-1>.
- Hernandez-Rapp J, Rainone S, Goupil C, Dorval V, Smith PY, Saint-Pierre M, Vallée M, Planel E, Droit A, Calon F, Cicchetti F, Hébert SS (2016) microRNA-132/212 deficiency enhances A β production and senile plaque deposition in Alzheimer's disease triple transgenic mice. *Sci Rep* 6: 30953. <https://doi.org/10.1038/srep30953>.
- Hwang JH, Cha PH, Han G, Bach TT, Min do S, Choi KY (2015) Euodia sutchuenensis Dode extract stimulates osteoblast differentiation via Wnt/ β -catenin pathway activation. *Exp Mol Med* 47: e152. <https://doi.org/10.1038/emmm.2014.115>.
- Koga T, Suico MA, Shimasaki S, Watanabe E, Kai Y, Koyama K, Omachi K, Morino-Koga S, Sato T, Shuto T, Mori K, Hino S, Nakao M, Kai H (2015) Endoplasmic reticulum (ER) stress induces sirtuin 1 (SIRT1) expression via the PI3K-Akt-GSK3 β signaling pathway and promotes hepatocellular injury. *J Biol Chem* 290: 30366–3074. <https://doi.org/10.1074/jbc.M115.664169>.
- Kong P, Yu Y, Wang L, Dou YQ, Zhang XH, Cui Y, Wang HY, Yong YT, Liu YB, Hu HJ, Cui W, Sun SG, Li BH, Zhang F, Han M (2019) circ-Sirt1 controls NF- κ B activation via sequence-specific interaction and enhancement of SIRT1 expression by binding to miR-132/212 in vascular smooth muscle cells. *Nucleic Acids Res* 47: 3580–3593. <https://doi.org/10.1093/nar/gkz141>.
- Li X, Yang L, Chen LL (2018) The biogenesis, functions, and challenges of circular RNAs. *Mol Cell* 71: 428–442. <https://doi.org/10.1016/j.molcel.2018.06.034>.
- Li Y, Zheng Q, Bao C, Li S, Guo W, Zhao J, Chen D, Gu J, He X, Huang S (2015) Circular RNA is enriched and stable in exosomes:

- a promising biomarker for cancer diagnosis. *Cell Res* **25**: 981–984. <https://doi.org/10.1038/cr.2015.82>.
- Liu Z, Li C, Huang P, Hu F, Jiang M, Xu X, Li B, Deng L, Ye T, Guo L (2020) CircHmbox1 targeting miRNA-1247-5p is involved in the regulation of bone metabolism by TNF- α in postmenopausal osteoporosis. *Frontiers Cell Develop Biol* **8**: 594785. <https://doi.org/10.3389/fcell.2020.594785>.
- Lou J, Hao Y, Lin K, Lyu Y, Chen M, Wang H, Zou D, Jiang X, Wang R, Jin D, Lam EW, Shao S, Liu Q, Yan J, Wang X, Chen P, Zhang B, Jin B (2020) Circular RNA CDR1as disrupts the p53/MDM2 complex to inhibit gliomagenesis. *Mol Cancer* **19**: 138. <https://doi.org/10.1186/s12943-020-01253-y>.
- Qu B, He J, Zeng Z, Yang H, Liu Z, Cao Z, Yu H, Zhao W, Pan X (2020) MiR-155 inhibition alleviates suppression of osteoblastic differentiation by high glucose and free fatty acids in human bone marrow stromal cells by upregulating SIRT1. *Pflugers Archiv* **472**: 473–480. <https://doi.org/10.1007/s00424-020-02372-7>.
- Salzman J, Chen RE, Olsen MN, Wang PL, Brown PO (2013) Cell-type specific features of circular RNA expression. *PLoS Genet* **9**: e1003777. <https://doi.org/10.1371/journal.pgen.1003777>.
- Wang K, Zhao Z, Wang X, Zhang Y (2021) BRD4 induces osteogenic differentiation of BMSCs via the Wnt/ β -catenin signaling pathway. *Tissue Cell* **72**: 101555. <https://doi.org/10.1016/j.tice.2021.101555>.
- Yang S, Guo S, Tong S, Sun X (2020) Exosomal miR-130a-3p regulates osteogenic differentiation of Human Adipose-Derived stem cells through mediating SIRT1/Wnt/ β -catenin axis. *Cell Prolifer* **53**: e12890. <https://doi.org/10.1111/cpr.12890>.
- Yoon DS, Choi Y, Jang Y, Lee M, Choi WJ, Kim SH, Lee JW (2014) SIRT1 directly regulates SOX2 to maintain self-renewal and multipotency in bone marrow-derived mesenchymal stem cells. *Stem Cells* (Dayton, Ohio) **32**: 3219–3231. <https://doi.org/10.1002/stem.1811>.
- Zainabadi K, Liu CJ, Caldwell ALM, Guarente L (2017) SIRT1 is a positive regulator of *in vivo* bone mass and a therapeutic target for osteoporosis. *PLoS One* **12**: e0185236. <https://doi.org/10.1371/journal.pone.0185236>.
- Zhang L, Xie H, Li S (2020) LncRNA LOXL1-AS1 controls osteogenic and adipocytic differentiation of bone marrow mesenchymal stem cells in postmenopausal osteoporosis through regulating the miR-196a-5p/Hmga2 axis. *J Bone Mineral Metabol* **38**: 794–805. <https://doi.org/10.1007/s00774-020-01123-z>.

MicroRNA-221-3p promotes post-burn HUVEC proliferation, migration, and angiogenesis by regulating CDKN1B

Kun Miao, Fei Xie and JinGui Lin✉

Department of Hand and Foot Microsurgery, Fuzhou Second Hospital Affiliated to Xiamen University, Fuzhou City, Fujian Province, 350000, China

Background and objective: Previous studies have shown that miR-221-3p plays an important role in vascular remodeling, but it is unclear whether it contributes to angiogenesis after burn injury. The purpose of this study was to investigate the effect of miR-221-3p on angiogenesis in HUVECs after burn injury and to reveal its underlying molecular mechanism. **Methods:** The burn HUVECs model was established by heat treatment. Plasmid or oligonucleotide transfection altered the expression of miR-221-3p and CDKN1B in HUVECs. MTT, colony formation, Transwell, flow cytometry, and tube formation experiments were applied to assess the proliferation, migration, apoptosis, cell cycle, and tube formation capacity of HUVECs. miR-221-3p, CDKN1B, Ki-67, and PCNA expression was assessed by RT-qPCR or Western blot. The dual-luciferase reporter assay verified the targeting relationship between miR-221-3p and CDKN1B. **Results:** miR-221-3p was lowly expressed and CDKN1B was highly expressed in burn HUVECs. Overexpression of miR-221-3p promoted the proliferation, migration, and tube formation ability of burn HUVECs and inhibited apoptosis and the proportion of cells in the G0/G1 phase, whereas overexpression of CDKN1B had the opposite effect. Knockdown of miR-221-3p further inhibited the angiogenic capacity of burn HUVECs, but this effect was reversed by knockdown of CDKN1B. Mechanistically, miR-221-3p targeted CDKN1B. **Conclusion:** miR-221-3p improves the angiogenesis of burn HUVECs by targeting CDKN1B expression, and the miR-221-3p/CDKN1B axis may serve as a potential molecular target for future burn therapy.

Keywords: microRNA-221-3p, CDKN1B, Burn; Human umbilical vein endothelial cells, Angiogenesis

Received: 28 March, 2022; **revised:** 11 July, 2023; **accepted:** 23 September, 2023; **available on-line:** 22 November, 2023

✉ e-mail: jingui17441@outlook.com

Abbreviations: BCA, Bicinchoninic acid; CDKN1B, Cyclin-dependent kinase inhibitor 1B; cDNA, Complementary DNA; DMEM, Dulbecco's Modified Eagle's Medium; ECL, Enhanced chemiluminescent; EDTA, Ethylene diamine tetra acetic acid; FITC, Fluorescein isothiocyanate; GAPDH, Glyceraldehyde 3-phosphate dehydrogenase; HUVECs, human umbilical vein endothelial cells; JAK-STAT, Janus kinase-signal transducer and activator of transcription; miRNA, MicroRNA; MTT, 3-(4,5-dimethylthiazol-2-yl)-2,5-diphenyltetrazolium bromide; MUT, Mutant type; OD, Optical density; PBS, Phosphate buffered saline; PCNA, Proliferating cell nuclear antigen; PI, Propidium iodide; PI3KR, Phosphatidylinositol 3-kinase, regulatory subunit 1; PVDF, Polyvinylidene difluoride; RIPA, Radio-Immunoprecipitation Assay; RT-qPCR, Reverse transcription quantitative polymerase chain reaction; S.D., Standard deviation; siRNA, Small interfering RNA; 3' UTR, 3' untranslated region; vWF, Von Willebrand factor; WT, Wild type

INTRODUCTION

Burn is one of the top ten causes of death in the world, killing more than 200 000 patients each year. In addition to a significant economic burden, burn injuries have a higher risk of developing mental illness (Haagsma *et al.*, 2016). Severe burn injuries can affect various organs and systems of the body, and their severity is related to the surface area and depth of burn throughout the body, but even relatively minor burn injury can still be life-threatening and life-altering (Kanitakis *et al.*, 2011). The core problem of burn injury is the loss of vascular integrity, the destruction of physiological barriers, and the edema caused by increased interstitial pressure (Edgar *et al.*, 2011). One of the key points of burn injury treatment is to maintain the blood volume, supply blood to the organs, and accelerate the exchange of skin and important nutrients, such as oxygen (Gelfand, Donelan, and Burke 1983). Vascular damage caused by burn injury can easily cause tissue edema around the wound or even systemic (van Baar *et al.*, 2006). Therefore, post-burn angiogenesis is an important factor for a good outcome of the disease.

MicroRNA (miRNA) is a class of conservative non-coding microRNA molecules consisting of about 22 nucleotides, which can regulate gene expression (Johnson *et al.*, 2019). With the development of next-generation sequencing technology, the research on the function and mechanism of miRNA has become increasingly in-depth, and there are also more studies on miRNA targeting mRNA in the treatment of vascular-related diseases. For example, miR-342-3p/-5p has significant anti-inflammatory and pro-angiogenic effects when targeting pannexin-2 down-regulation (Ray *et al.*, 2020); miR-210 can inhibit the apoptosis of arteriosclerotic occlusive vascular endothelial cells through JAK-STAT (Yue *et al.*, 2019) and miR-125b can limit the formation of the vascular lumen through translation inhibition of VE-cadherin (Muramatsu *et al.*, 2013). This study focused on a miRNA with an important role in vascular remodeling, named miR-221-3p. miR-221-3p has also been studied to mediate vascular remodeling in perivascular adipose tissue-derived extracellular vesicles (Li *et al.*, 2019) and regulate the dysfunction of diabetic retinal microangiopathy (Wang *et al.*, 2020). However, it is unclear whether miR-221-3p plays a role in vascular remodeling after burn injury.

Preliminary experiments found that miR-221-3p was abnormally low expressed in the serum of burn injury patients. It was speculated that miR-221-3p may have a similar role in the process of vascular remodeling after burn injury. Therefore, this work focused on exploring the effects of miR-221-3p on the proliferation, migration, tube formation, apoptosis, and cell cycle of HU-

VECs in the burn environment, and revealed its potential downstream molecular mechanisms.

MATERIALS AND METHODS

Serum from burn injury patients

Ten burn injury patients (burns area $\geq 50\%$) in Fuzhou Second Hospital Affiliated to Xiamen University were enrolled, including 6 males and 4 females, aged 18–55 years. Venous blood (10 mL) was collected within 24 h before regular anti-shock treatment and centrifuged at 4°C to obtain the supernatant which was then stored at -80°C . Normal serum from 10 healthy volunteers was recruited as a control group. This study was approved by the Ethics Committee of Fuzhou Second Hospital Affiliated to Xiamen University (ethical number: 2015061129s), and written informed consent was obtained from all participants.

Heat treatment

HUVECs (BeNA, Beijing, China) were identified by STR typing. HUVECs were seeded in Petri dishes for 48 h, harvested into 15 mL centrifuge tubes, and immersed in a circulating water bath at 52°C for 3 min. The cells in the control group were placed in a 37°C water bath for 3 min. Heat-treated cells were re-seeded in Petri dishes and further incubated at 37°C . Cells were then harvested after 6 h of heat treatment.

Cell culture and transfection

Heat-treated HUVECs were grown to 80% confluence in an endothelial cell culture medium (Sciencell, USA) with 5% fetal bovine serum, 0.05% penicillin-streptomycin (Thermo Fisher Scientific, USA). Then, HUVECs were detached with 0.25% trypsin, added with a culture medium to terminate the detachment, and prepared for a cell suspension (1×10^5 cells/mL). Flow cytometry confirmed the positive expression of CD31 and VWF in the purchased HUVECs (Supplementary Fig. 1 at <https://ojs.ptbioch.edu.pl/index.php/abp/>).

HUVECs with a cell density of 1×10^5 cell/mL were inoculated into 96-well plates (100 μL /well), and 10% fetal bovine serum (Thermo Fisher) was added and incubated for 24 h. miR-221-3p-mimic, miR-221-3p-inhibitor, mimic/inhibitor-negative control (mimic/inhibitor-NC), small interfering RNA (siRNA) targeting CDKN1B (si-CDKN1B), si-NC, pCDNA-CDKN1B, and pcDNA 3.1 were purchased from Shanghai GenePharma. The reagent was transfected into HUVECs instantaneously according to the manufacturer's instructions for Lipofectamine 2000 (Thermo Fisher). After incubation for 48 h, the transfection efficiency was detected by RT-qPCR and western blot.

MTT method

After transfection, every 4×10^4 HUVECs in each well on the 96-well plates were combined with 20 μL of MTT solution (Sigma, USA) at 0 h, 24 h, 48 h, and 96 h. Then, the samples were further cultured for 3 h, centrifuged at 4°C for 15 min, and dissolved by adding 150 μL of dimethyl sulfoxide solution (Sigma). Finally, optical density (OD)₄₉₀ nm was measured (Zhang *et al.*, 2022).

Colony formation method

HUVECs were cultured at 700 cells/well on the 6-well plates with the culture medium changed every

3 days. The culture was terminated when macroscopic clonal clusters appeared. Then, colonies were fixed with 4% paraformaldehyde (Leagene, Beijing, China) at 1 mL/well for 40 min, stained with crystal violet solution (Leagene) at 1 mL/well for 20 min, and counted (Zhang *et al.*, 2021).

Transwell experiment

A total of 2×10^4 HUVECs suspended in a serum-free DMEM (Thermo Fisher Scientific) were added to the upper chamber of the transwell plate, and 800 μL of endothelial cell culture medium and 10% fetal bovine serum were added to the lower chamber. HUVECs after 48-h culture were dyed with crystal violet solution for 20 min and counted under a microscope (Wang *et al.*, 2022).

Flow cytometry detection

Apoptosis was assessed according to Annexin V-FITC Apoptosis Detection Kit (ThermoFisher, USA). The log-phase growing HUVECs were digested with EDTA-free trypsin, washed once with pre-cooled PBS, centrifuged at low speed for 15 min at 4°C , and centrifuged once again. After discarding the supernatant, 5 μL of Annexin V-FITC and PI were added for 10 min, and finally, 500 μL of Annexin V binding buffer was supplemented to detect cell apoptosis by flow cytometry (He *et al.*, 2021).

Cell cycle was assessed by the Propidium Iodide Flow Cytometry Kit (Abcam, USA). HUVECs were first digested with trypsin to obtain a single cell suspension, fixed with 66% ethanol for 2 h at 4°C , and centrifuged at $500 \times g$ for 5 min. The cell pellet was resuspended in prepared $1 \times \text{PI} + \text{RNase}$ Staining solution for 20 min at 37°C in the dark and loaded into a flow cytometer.

RT-qPCR detection

Total RNA was extracted with Trizol reagent (Thermo Fisher Scientific), reverse-transcribed into cDNA with the reverse transcription kit (Thermo Fisher Scientific). All primers were synthesized by Sangon (Shanghai, China). Taking U6 and GAPDH as the internal references, miR-221-3p and CDKN1B expression was calculated by the $2^{-\Delta\Delta\text{CT}}$ method (Miao *et al.*, 2020).

Western blot

Protein lysates were harvested by adding RIPA (Merck, Germany) and the concentration was examined by a BCA kit (Enzyme-Linked Biotechnology, Shanghai, China). Proteins were separated by protein electrophoresis on sodium dodecyl sulfate-polyacrylamide gel (Thermo Fisher Scientific) and transferred to PVDF membranes for reaction with CDKN1B (1:1000, sc-1641), Ki67 (1:1000, ab92742), PCNA (1:1000, sc-56) and GAPDH (1:1000, ab8245), together with goat anti-rabbit secondary antibody (1:5000, 7074). ECL solution (GlpBio, USA)-developed bands were tested to analyze the gray value (Lu & Huang, 2021).

Luciferase reporter gene assay

Prediction from the website <https://starbase.sysu.edu.cn> shows that miR-221-3p has a binding site for CDKN1B. Wild-type and mutant CDKN1B sequences containing the miR-221-3p binding site were cloned into the PGL4 luciferase reporter vector (Promega). The above luciferase reporter vector and miR-221-3p mimic and mimic-NC were then co-transfected into HUVECs using Lipofectamine 2000 (Invitrogen). The cells were collected 48 h after trans-

fection, and the luciferase activity was detected according to the instructions of the luciferase activity detection kit (Promega). Renilla luciferase activity was considered as a reference for signal intensity (Dong *et al.*, 2021).

In vitro HUVECs tube formation model

Matrigel (Merck, Germany) was added to the center of the μ -slide well plate and left for 15 min. Cell suspension (50 μ L, 3×10^4 /mL) was centrifuged, washed twice with serum-free DMEM, and centrifuged again. Cells were resuspended in 50 μ L endothelial cell culture medium (containing 10% burn serum or 10% control serum) and added to μ -slide well plates. Images were taken in 5 fields of view 6 h later and analyzed by Image-pro Plus 6.0 software (Stefanini *et al.*, 2009).

Statistical analysis

All data were analyzed using SPSS 21.0. Data were presented as mean \pm standard deviation (S.D.). Two groups were compared by Student's *t*-test while multiple groups were compared by One-way ANOVA. All functional experiments were run in triplicate. Results were plotted using GraphPad Prism 7.0 software. $P < 0.05$ indicated statistical significance.

RESULTS

Abnormally low expression of miR-221-3p in burn environment

miR-221-3p Expression was decreased in the serum of burn injury patients (Fig. 1A). Subsequently, miR-221-3p expression was found to be reduced in heat-treated HUVECs (Fig. 1B).

Overexpression of miR-221-3p restores the angiogenic capacity of burn-injured HUVECs

miR-221-3p-mimic Was transfected into burn-injured HUVECs. miR-221-3p-mimic promoted miR-221-3p ex-

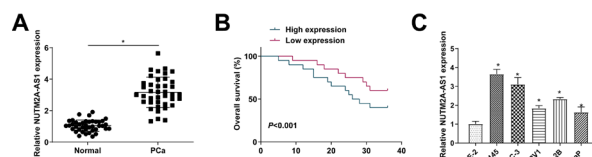


Figure 1. miR-221-3p and CDKN1B signatures in HUVECs

(A) RT-qPCR to detect miR-221-3p in the serum of healthy subjects and burns patients; (B) RT-qPCR to detect miR-221-3p in the normal and heat-treated HUVECs. Data are presented as mean \pm S.D. * $P < 0.05$.

pression in burn-injured HUVECs (Fig. 2A). MTT assay and colony formation assays showed that heat treatment inhibited the proliferation and clonogenic ability of HUVECs, while overexpression of miR-221-3p alleviated this phenomenon (Fig. 2B, C). Transwell assay indicated that heat treatment inhibited the migration ability of HUVECs, whereas the migration ability of HUVECs was increased after overexpression of miR-221-3p (Fig. 2D). Western blot reported that heat treatment decreased the expression of the proliferation proteins Ki-67 and PCNA in HUVECs, whereas overexpression of miR-221-3p prevented this change (Fig. 2E, F). Flow cytometry demonstrated that heat treatment increased the apoptotic rate of HUVECs and arrested cells in G0/G1 phase, while overexpression of miR-221-3p alleviated this phenomenon (Fig. 2G, H). Tube formation experiments manifested that heat treatment reduced the angiogenic capacity of HUVECs, but overexpression of miR-221-3p increased tube formation in HUVECs (Fig. 2I).

Targeted regulation of CDKN1B by miR-221-3p

Subsequently, the potential downstream target genes of miR-221-3p were explored. miRNAs can often bind to the 3' UTR of mRNA to regulate their expression (Yang *et al.*, 2021). Through the bioinformatics prediction website <https://starbase.sysu.edu.cn>, it was found that miR-221-3p had a binding site with CDKN1B (Fig. 3A). The luciferase reporter gene assay

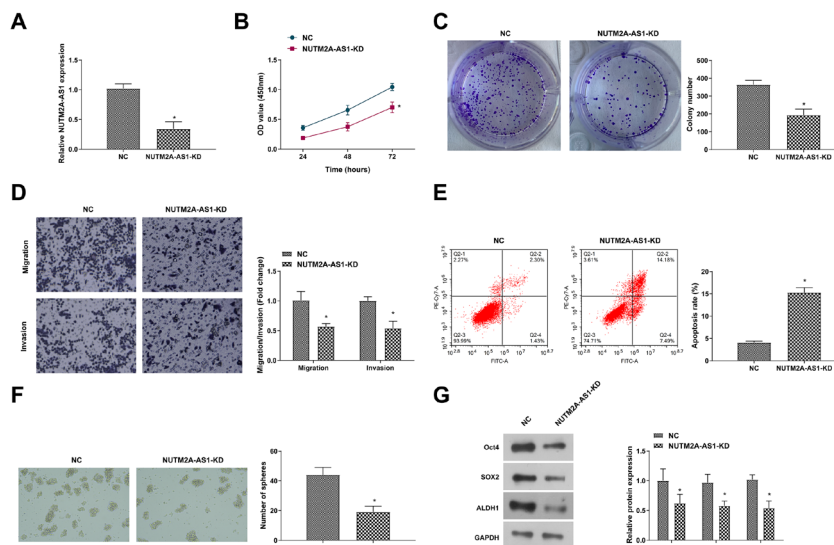


Figure 2. Overexpression of miR-221-3p restores the angiogenic capacity of burn-injured HUVECs

miR-221-3p-mimic was transfected into burn-injured HUVECs to upregulate miR-221-3p. (A) RT-qPCR to detect miR-221-3p in HUVECs; (B) MTT assay to detect the proliferation of HUVECs; (C) Clone formation assay to evaluate the clonogenic ability of HUVECs; (D) Transwell assay to detect the migration of HUVECs; (E-F) Western blot to measure Ki-67 and PCNA; (G-H) Flow cytometry to determine apoptosis and cell cycle; (I) Tube formation assay to assess the tube-forming ability of HUVECs; data are expressed as mean \pm S.D. * $P < 0.05$.

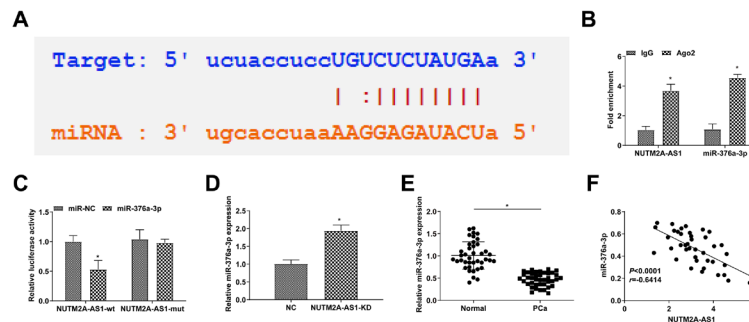


Figure 3. Targeted regulation of CDKN1B by miR-221-3p

(A) The binding region of miR-221-3p and CDKN1B on <https://starbase.sysu.edu.cn>; (B) Luciferase activity of cells after co-transfection; (C) RT-qPCR and Western blot to detect CDKN1B in burn-injured HUVECs; (D) RT-qPCR and Western blot to detect the effect of overexpression of miR-221-3p on CDKN1B expression; data are expressed as mean \pm S.D. * $P < 0.05$.

results verified the binding relationship between the two. The co-transfection of WT-CDKN1B and miR-221-3p-mimic reduced luciferase activity, but that of MUT-CDKN1B and miR-221-3p-mimic had no effect on luciferase activity (Fig. 3B). In burn-injured HUVECs, an abnormal increase in CDKN1B expression (Fig. 3C) was determined. Furthermore, overexpression of miR-221-3p suppressed CDKN1B expression (Fig. 3D).

Overexpression of CDKN1B enhances the inhibitory effect of burn on HUVECs angiogenesis

Subsequently, pcDNA-CDKN1B was transfected into burn-injured HUVECs to explore the role of CDKN1B. pcDNA-CDKN1B increased CDKN1B expression in HUVECs (Fig. 4A). Functional experiments verified that overexpression of CDKN1B further inhibited the proliferation and colony ability of burn-injured HUVECs, decreased the number of migrating cells, suppressed Ki-67 and PCNA protein expression, promoted cell apoptosis, blocked cells at G0/G1 phase, and reduced the number of tube formations (Fig. 4B–I).

miR-221-3p Targets CDKN1B expression to improve angiogenesis in burn-injured HUVECs

A functional rescue experiment was implemented to probe the regulatory role of the miR-221-3p/CDKN1B axis in burn-injured HUVECs. The transfection designs were as follows: Inhibitor-NC+si-NC, miR-221-3p-inhibitor+si-NC and miR-221-3p-inhibitor + si-CDKN1B. The results presented that miR-221-3p inhibitor promoted CDKN1B expression, while si-CDKN1B reversed this effect (Fig. 5A). Functional experiments manifested that after transfection of miR-221-3p-inhibitor, cell proliferation and cloning abilities were attenuated (Fig. 5B, C), the number of migrating cells was reduced (Fig. 5D), and Ki67 and PCNA protein expressions were reduced (Fig. 5E, F), the apoptotic rate was promoted, cells in G0/G1 phase were increased (Fig. 5G, H), and tube-forming ability was impaired (Fig. 5I), and these effects were reversed by knockdown of CDKN1B.

DISCUSSION

Burn injury damages the body caused by thermal exposure, radiation, and chemical or electrical contact, which

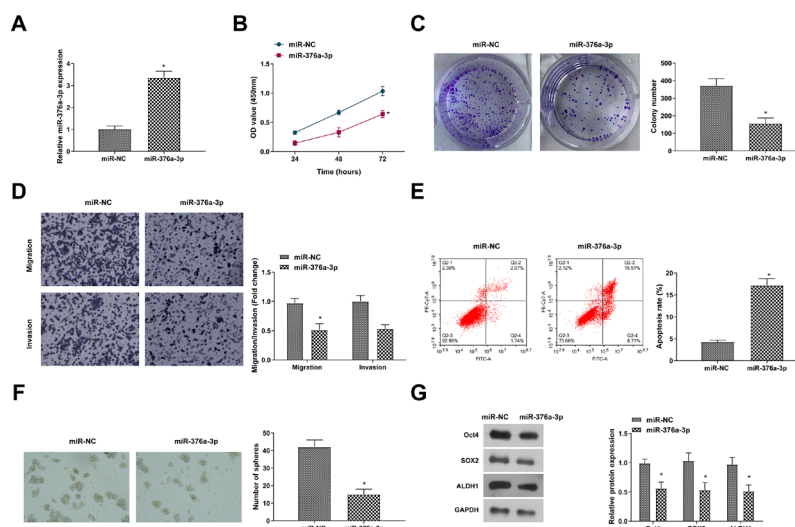


Figure 4. Overexpression of CDKN1B enhances the inhibitory effect of burn on HUVECs angiogenesis

pcDNA-CDKN1B was transfected into burn HUVECs to upregulate CDKN1B expression. (A) RT-qPCR and Western blot to detect CDKN1B in HUVECs; (B) MTT assay to detect the proliferation of HUVECs; (C) Clone formation assay to evaluate the clonogenic ability of HUVECs; (D) Transwell assay to detect the migration of HUVECs; (E–F) Western blot to measure Ki-67 and PCNA; (G–H) Flow cytometry to determine apoptosis and cell cycle; (I) Tube formation assay to assess the tube-forming ability of HUVECs; data are expressed as mean \pm S.D. * $P < 0.05$.

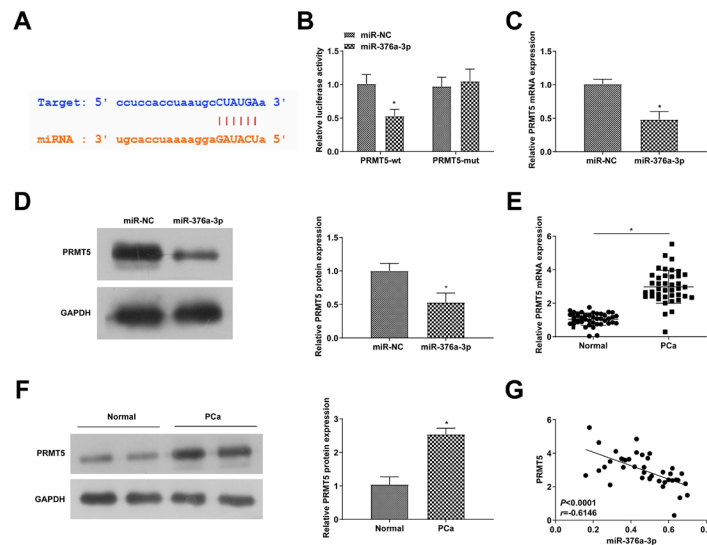


Figure 5 miR-221-3p targets CDKN1B expression to improve angiogenesis in burn-injured HUVECs
miR-221-3p-inhibitor and si-CDKN1B were co-transfected into burn-injured HUVECs (A) RT-qPCR and Western blot to detect CDKN1B in HUVECs; (B) MT assay to detect the proliferation of HUVECs; (C) Clone formation assay to evaluate the clonogenic ability of HUVECs; (D) Transwell assay to detect the migration of HUVECs; (E–F) Western blot to measure Ki-67 and PCNA; (G–H) Flow cytometry to determine apoptosis and cell cycle; (I) Tube formation assay to assess the tube-forming ability of HUVECs; data are expressed as mean \pm S.D. * $P < 0.05$.

induce activation of peripheral nerve fibers, initiating a sustained hypersensitivity response to thermal and mechanical stimuli (Laycock *et al.*, 2013). The consequences of burns are severe, with a high mortality rate and common in low- and middle-income countries (Atwell *et al.*, 2020). With the development of science and technology, there have been many studies on gene technology treatment for burn injury (Zhang *et al.*, 2021). Bioinformatics analysis has identified 43 miRNAs as potential regulators of early burn injury response among which miR-212-3p is down-regulated in dermal interstitial fluid (Foessel *et al.*, 2021). In addition to post-burns pain management, psychological counseling, scar healing, etc., post-burns angiogenesis is the basis of many burn treatment principles (Eyuboglu *et al.*, 2018). The physiological basis of tissue edema and body fluid extravasation after burn injury is the change of vascular permeability which is one of the main manifestations of vascular endothelial cell damage (Tian *et al.*, 2015).

Belonging to miRNAs family which affects physiological processes (Amponsah *et al.*, 2017), miR-221 is located in the p11.3 region of the X chromosome and is involved in the physiological regulation of hematopoiesis and angiogenesis (Liu *et al.*, 2009). In vascular endothelial cells, miR-221 acts on CDKN1B and PI3KR1 and inhibits endothelial cell biological functions (Celic *et al.*, 2017). In human aortic endothelial cells, miR-221-3p carries the ability to block the production of peroxisome proliferator-activated receptor λ coactivator 1 α , leading to mitochondrial dysfunction and apoptosis (Xue *et al.*, 2015). The present study found that miR-221-3p has a positive role in vascular remodeling after burn injury. Overexpression of miR-221-3p promoted the proliferation of HUVECs by reducing the ratio of HUVECs in the G0/G1 phase, thereby mediating HUVECs migration and tube formation, which will benefit the angiogenic capacity of HUVECs in the burn environment. Cell cycle changes are important for the proliferation of HUVECs. When cells are arrested in the G0/G1 phase, the proliferation of HUVECs is inhibited and their tube-forming ability is

reduced (Cota Teixeira *et al.*, 2019; Zhang *et al.*, 2013). Several studies have demonstrated the role of miRNAs in regulating the cell cycle and proliferation of HUVECs, such as miRNAs including miR-182-5p (Su *et al.*, 2021), miR-20b (Dong *et al.*, 2020). This study speculated that the regulation of miR-221-3p on the cell cycle of HUVECs will affect the ability of vascular remodeling, and the effect of miR-221-3p on the cell cycle of HUVECs needs to be further explored in subsequent studies.

CDKN1B is located on chromosome 12p 13 and has a promoting regulatory role in tumors (Kim *et al.*, 2015), such as osteosarcoma (Gao *et al.*, 2022). As a downstream target gene of miR-221, CDKN1B can promote the proliferation of vascular smooth muscle cells in the neovascular intima (Medina *et al.*, 2008). MiR-221-3p/CDKN1B axis can regulate the proliferation and cell cycle of HUVECs after burn injury, and further influence cellular migration and tube formation ability. It is worth noting that this study only validated the role of the miR-221-3p/CDKN1B axis in angiogenesis in an *in vitro* model and could be explored in future animal burn injury models. In addition, there are few reports on the regulatory mechanism of ncRNAs in burn injury, and the regulatory mechanism of ncRNAs is crucial in vascular remodeling, skin recovery and other processes. Therefore, it is necessary to further explore the changes and mechanisms of ncRNAs in burn injury.

In conclusion, this work confirmed that miR-221-3p affects the proliferation, migration, cell cycle, apoptosis, and tube formation of burn-injured HUVECs by regulating CDKN1B. MiR-221-3p/CDKN1B axis may be of interest in future burn treatments.

REFERENCES

- Amponsah PS, Fan P, Bauer N, Zhao Z, Gladkich J, Fellenberg J, Herr I (2017) microRNA-210 overexpression inhibits tumor growth and potentially reverses gemcitabine resistance in pancreatic cancer. *Cancer Lett* **388**: 107–117. <https://doi.org/10.1016/j.canlet.2016.11.035>
- Atwell K, Bartley C, Cairns B, Charles A (2020) The epidemiologic characteristics and outcomes following intentional burn injury at a

- Atwell K, Bartley C, Cairns B, Charles A (2020) The epidemiologic characteristics and outcomes following intentional burn injury at a

- regional burn center. *Burns* 46: 441–446. <https://doi.org/10.1016/j.burns.2019.08.002>
- Celic T, Metzinger-Le Meuth V, Six I, Massy ZA, Metzinger L (2017) The miR-221/222 Cluster is a key player in vascular biology via the fine-tuning of endothelial cell physiology. *Curr Vasc Pharmacol* 15: 40–46. <https://doi.org/10.2174/1570161114666160914175149>
- Cota Teixeira S, Silva Lopes D, Santos da Silva M, Cordero da Luz FA, Cirilo Gímenes SN, Borges BC, Alves da Silva A, Alves Martins F, Alves Dos Santos M, Teixeira TL, Oliveira RA, de Melo Rodrigues Avila V, Barbosa Silva MJ, Elias MC, Martin R, Vieira da Silva C, Knölker HJ (2019) Pentachloropseudilin impairs angiogenesis by disrupting the actin cytoskeleton, integrin trafficking and the cell cycle. *Chembiochem* 20: 2390–2401. <https://doi.org/10.1002/cbic.201900203>
- Dong C, Fan B, Ren Z, Liu B, Wang Y (2021) CircSMARCA5 Facilitates the progression of prostate cancer through miR-432/PDCD10 axis. *Cancer Biother Radiopharm* 36: 70–83. <https://doi.org/10.1089/cbr.2019.3490>
- Dong F, Dong S, Liang Y, Wang K, Qin Y, Zhao X (2020) miR-20b inhibits the senescence of human umbilical vein endothelial cells through regulating the Wnt/ β -catenin pathway via the TXNIP/NLRP3 axis. *Int J Mol Med* 45: 847–857. <https://doi.org/10.3892/ijmm.2020.4457>
- Edgar DW, Fish JS, Gomez M, Wood FM (2011) Local and systemic treatments for acute edema after burn injury: a systematic review of the literature. *J Burn Care Res* 32: 334–347. <https://doi.org/10.1097/BCR.0b013e31820ab019>
- Eyuboglu AA, Uysal CA, Ozgun G, Coskun E, Markal Ertas N, Haberal M (2018) The effect of adipose derived stromal vascular fraction on stasis zone in an experimental burn model. *Burns* 44: 386–396. <https://doi.org/10.1016/j.burns.2017.08.016>
- Foessel I, Haudum CW, Vidakovic I, Prassl R, Franz J, Mautner SI, Kainz S, Hofmann E, Obermayer-Pietsch B, Birngruber T, Kotzbeck P (2021) miRNAs as Regulators of the early local response to burn injuries. *Int J Mol Sci* 22. <https://doi.org/10.3390/ijms22179209>
- Gao LF, Jia S, Zhang QM, Xia YF, Li CJ, Li YH (2022) MicroRNA-802 promotes the progression of osteosarcoma through targeting p27 and activating PI3K/AKT pathway. *Clin Transl Oncol* 24: 266–275. <https://doi.org/10.1007/s12094-021-02683-w>
- Gelfand JA, Donelan M, Burke JF (1983) Preferential activation and depletion of the alternative complement pathway by burn injury. *Ann Surg* 198: 58–62. <https://doi.org/10.1097/0000658-198307000-00011>
- Haagsma JA, Graetz N, Bolliger I, Naghavi M, Higashi H, Mullany EC, Abera SF, Abraham JP, Adofu K, Alsharif U, Ameh EA, Ammar W, Antonio CA, Barrero LH, Bekele T, Bose D, Brazinova A, Catalá-López F, Dandona R, Dandona R, Dargan PI, De Leo D, Degenhardt L, Derrett S, Dharmaratne SD, Driscoll TR, Duan L, Petrovich Ermakov S, Farzadfar F, Feigin VL, Franklin RC, Gabbe B, Gosselin RA, Hafezi-Nejad N, Hamadeh RR, Hajar M, Hu G, Jayaraman SP, Jiang G, Khader YS, Khan EA, Krishnaswami S, Kulkarni C, Lecky FE, Leung R, Lunevicius R, Lyons RA, Majdan M, Mason-Jones AJ, Matzopoulos R, Meaney PA, Mekonnen W, Miller TR, Mock CN, Norman RE, Orozco R, Polinder S, Pourmalek F, Rahimi-Movaghar V, Refaat A, Rojas-Rueda D, Roy N, Schwebel DC, Shaheen A, Shahraz S, Skirbekk V, Soreide K, Soshnikov S, Stein DJ, Sykes BL, Tabb KM, Temesgen AM, Tenkorang EY, Theadom AM, Tran BX, Vasankari TJ, Vavilala MS, Vlassov VV, Woldeyohannes SM, Yip P, Yonemoto N, Younis MZ, Yu C, Murray CJ, Vos T (2016) The global burden of injury: incidence, mortality, disability-adjusted life years and time trends from the Global Burden of Disease study 2013. *Inj Prev* 22: 3–18. <https://doi.org/10.1136/injuryprev-2015-041616>
- He J, Chu Z, Lai W, Lan Q, Zeng Y, Lu D, Jin S, Xu H, Su P, Yin D, Chu Z, Liu L (2021) Circular RNA circHERC4 as a novel oncogenic driver to promote tumor metastasis via the miR-556-5p/CTBP2/E-cadherin axis in colorectal cancer. *J Hematol Oncol* 14: 194. <https://doi.org/10.1186/s13045-021-01210-2>
- Johnson T, Zhao L, Manuel G, Taylor H, Liu D (2019) Approaches to therapeutic angiogenesis for ischemic heart disease. *J Mol Med (Berl)* 97: 141–151. <https://doi.org/10.1007/s00109-018-1729-3>
- Kanitakis J, Kyamidis K, Toussinas A, Tsoitis G (2011) Pure apocrine nevus: immunohistochemical study of a new case and literature review. *Dermatology* 222: 97–101. <https://doi.org/10.1159/000323000>
- Kim TH, Lee HH, Chung SH, Park J, Lee A (2015) Expression of p27 and Jun activation domain-binding protein 1 in endometriosis. *Arch Gynecol Obstet* 292: 377–381. <https://doi.org/10.1007/s00404-015-3642-0>
- Laycock H, Valente J, Bantel C, Nagy I (2013) Peripheral mechanisms of burn injury-associated pain. *Eur J Pharmacol* 716: 169–178. <https://doi.org/10.1016/j.ejphar.2013.01.071>
- Li X, Ballantyne LL, Yu Y, Funk CD (2019) Perivascular adipose tissue-derived extracellular vesicle miR-221-3p mediates vascular remodeling. *Faseb J* 33: 12704–12722. <https://doi.org/10.1096/fj.201901548R>
- Liu X, Cheng Y, Zhang S, Lin Y, Yang J, Zhang C (2009) A necessary role of miR-221 and miR-222 in vascular smooth muscle cell proliferation and neointimal hyperplasia. *Circ Res* 104: 476–487. <https://doi.org/10.1161/circresaha.108.185363>
- Lu YH, Huang ZY (2021) Global identification of circular RNAs in imatinib (IM) resistance of chronic myeloid leukemia (CML) by modulating signaling pathways of circ_0080145/miR-203/ABL1 and circ_0051886/miR-637/ABL1. *Mol Med* 27: 148. <https://doi.org/10.1186/s10020-021-00395-z>
- Medina R, Zaidi SK, Liu CG, Stein JL, van Wijnen AJ, Croce CM, Stein GS (2008) MicroRNAs 221 and 222 bypass quiescence and compromise cell survival. *Cancer Res* 68: 2773–2780. <https://doi.org/10.1158/0008-5472.Can-07-6754>
- Miao X, Xi Z, Zhang Y, Li Z, Huang L, Xin T, Shen R, Wang T (2020) Circ-SMARCA5 suppresses colorectal cancer progression via downregulating miR-39-3p and upregulating ARID4B. *Dig Liver Dis* 52: 1494–1502. <https://doi.org/10.1016/j.dld.2020.07.019>
- Muramatsu F, Kidoya H, Naito H, Sakimoto S, Takakura N (2013) microRNA-125b inhibits tube formation of blood vessels through translational suppression of VE-cadherin. *Oncogene* 32: 414–421. <https://doi.org/10.1038/onc.2012.68>
- Ray SL, Coulson DJ, Yeoh MLY, Tamara A, Latief JS, Bakhshab S, Weaver JU (2020) The role of miR-342 in vascular health: study in subclinical cardiovascular disease in mononuclear cells, plasma, inflammatory cytokines and PANX2. *Int J Mol Sci* 21. <https://doi.org/10.3390/ijms21197217>
- Stefanini MO, Wu FT, Mac Gabhann F, Popel AS (2009) The presence of VEGF receptors on the luminal surface of endothelial cells affects VEGF distribution and VEGF signaling. *PLoS Comput Biol* 5: e1000622. <https://doi.org/10.1371/journal.pcbi.1000622>
- Su G, Sun G, Lv J, Zhang W, Liu H, Tang Y, Su H (2021) Hsa_circ_0004831 downregulation is partially responsible for atorvastatin-alleviated human umbilical vein endothelial cell injuries induced by ox-LDL through targeting the miR-182-5p/CXCL12 axis. *BMC Cardiovasc Disord* 21: 221. <https://doi.org/10.1186/s12872-021-01998-4>
- Tian KY, Liu XJ, Xu JD, Deng J, Wang G (2015) Propofol inhibits burn injury-induced hyperpermeability through an apoptotic signal pathway in microvascular endothelial cells. *Braz J Med Biol Res* 48: 401–407. <https://doi.org/10.1590/1414-431x20144107>
- van Baar ME, Essink-Bot ML, Oen IM, Dokter J, Boxma H, van Beeck EF (2006) Functional outcome after burns: a review. *Burns* 32: 1–9. <https://doi.org/10.1016/j.burns.2005.08.007>
- Wang C, Lin Y, Fu Y, Zhang D, Xin Y (2020) MiR-221-3p regulates the microvascular dysfunction in diabetic retinopathy by targeting TIMP3. *Pflugers Arch* 472: 1607–1618. <https://doi.org/10.1007/s00424-020-02432-y>
- Wang N, Guo Y, Song L, Tong T, Fan X (2022) Circular RNA intracellular transport 80 facilitates endometrial cancer progression through modulating miR-545-3p/FAM98A signaling. *J Gynecol Oncol* 33: e2. <https://doi.org/10.3802/jgo.2022.33.e2>
- Xue Y, Wei Z, Ding H, Wang Q, Zhou Z, Zheng S, Zhang Y, Hou D, Liu Y, Zen K, Zhang CY, Li J, Wang D, Jiang X (2015) MicroRNA-19b/221/222 induces endothelial cell dysfunction via suppression of PGC-1 α in the progression of atherosclerosis. *Atherosclerosis* 241: 671–681. <https://doi.org/10.1016/j.atherosclerosis.2015.06.031>
- Yang L, Zhou YN, Zeng MM, Zhou N, Wang BS, Li B, Zhu XL, Guan QL, Chai C (2021) Circular RNA Circ-0002570 accelerates cancer progression by regulating VCAN via MiR-587 in gastric cancer. *Front Oncol* 11: 733745. <https://doi.org/10.3389/fonc.2021.733745>
- Yue JN, Li WM, Hong WZ, Yang J, Zhu T, Fang Y, Fu WG (2019) MiR-210 inhibits apoptosis of vascular endothelial cells via JAK-STAT in arteriosclerosis obliterans. *Eur Rev Med Pharmacol Sci* 23 (Suppl 3): 319–326. <https://doi.org/10.26355/eurev.201908.18663>
- Zhang D, Zhang Y, Zhang X, Zhai H, Sun X, Li Y (2021) Circ_0046600 promotes hepatocellular carcinoma progression via up-regulating SERBP1 through sequestering miR-1258. *Pathol Res Pract* 228: 153681. <https://doi.org/10.1016/j.prp.2021.153681>
- Zhang L, Zhang W, Zuo Z, Tang J, Song Y, Cao F, Yu X, Liu S, Cai X (2022) Circ_0008673 regulates breast cancer malignancy by miR-153-3p/CFL2 axis. *Arch Gynecol Obstet* 305: 223–232. <https://doi.org/10.1007/s00404-021-06149-w>
- Zhang P, Xu X, Hu X, Wang H, Fassett J, Huo Y, Chen Y, Bache RJ (2013) DDAH1 deficiency attenuates endothelial cell cycle progression and angiogenesis. *PLoS One* 8: e79444. <https://doi.org/10.1371/journal.pone.0079444>
- Zhang T, Zhang R, Xu B, Zhang M, Zhang Q, Li N, Qiu Y, Chen D, Xu K, Xiao J, Zhang N, Fang Q (2021) Spinal endomorphins attenuate burn-injury pain in male mice by inhibiting p38 MAPK signaling pathway through the mu-opioid receptor. *Eur J Pharmacol* 903: 174139. <https://doi.org/10.1016/j.ejphar.2021.174139>

MALAT-1 regulates the AML progression by promoting the m6A modification of ZEB1

Jing Jin, Leihua Fu, Pan Hong and Weiyang Feng✉

Department of Hematology, Shaoxing People's Hospital, Shaoxing City, Zhejiang Province, China

Metastasis-associated lung adenocarcinoma transcript 1 (MALAT-1) is abnormally upregulated in various human cancers. However, the role of MALAT-1 in acute myeloid leukemia (AML) remains unclear. This study investigated the expression and function of MALAT-1 in AML. MTT assay was used to determine cell viability, qRT-PCR was applied to determine the RNA levels. Western blot was performed to detect the protein expression. Flow cytometry was conducted to measure cell apoptosis. RNA pull-down assay was carried out to detect the interaction between MALAT-1 and METTL14. RNA FISH assay was performed to determine the localization of MALAT-1 and METTL14 in AML cells. Our results have revealed the key role of MEEL14 and m6A modification in AML. Besides, MALAT-1 was significantly up-regulated in AML patients. MALAT-1 knockdown inhibited the proliferation, migration and invasion of AML cells, and induced cell apoptosis; additionally, MALAT-1 binding to METTL14 promoted the m6A modification of ZEB1. Besides, ZEB1 overexpression partially reversed the effect of MALAT-1 knockdown on the cellular functions of AML cells. Taken together, MALAT-1 promoted the aggressiveness of AML through regulating m6A modification of ZEB1.

Keywords: AML, MALAT1, MEEL14, m6A, ZEB1

Received: 11 November, 2021; **revised:** 30 December, 2021; **accepted:** 04 January, 2022; **available on-line:** 22 February, 2023

✉e-mail: fengweiyang1996@163.com

Acknowledgements of Financial Support: Zhejiang Provincial Medical and Health Research Project 2021KY363 and Young Innovative Talents Project of Zhejiang Health Science and Technology Plan 2022RC078.

Abbreviations: AML, acute myeloid leukemia; MALAT-1, metastasis-associated lung adenocarcinoma transcript 1; lncRNAs, long non-coding RNAs; m6A, N6-methyladenosine; ZEB1, the zinc finger E-box binding homeobox 1; EMT, epithelial-mesenchymal transition; PI, propidium iodide

INTRODUCTION

Acute myeloid leukemia (AML) is a malignant disease of myeloid hematopoietic stem/progenitor cells (Cai & Levine, 2019). Before maturation, leukemic cells abnormally proliferate and accumulate in bone marrow and blood, causing loss of hematopoietic function (Acheampong *et al.*, 2018; Mueller *et al.*, 2018). AML is highly popular among adults, accounting for more than 30 percents of all leukemia cases worldwide (Zimta *et al.*, 2019). Current studies have shown that chromosome abnormalities, uncontrolled gene expression, and non-coding RNA such as long non-coding RNAs (lncRNAs) could promote acute myeloid leukemia (Mer *et al.*, 2018; Wang *et al.*, 2019). Clinically, the AML recuperation rate is less than 45%, while 50% relapse and

the late survival rate is only at about 10% (Pan *et al.*, 2017). Because of the poor prognosis of AML, it is of great importance to identify new markers and therapeutic targets for AML.

lncRNA is a category of transcripts larger than 200bp and lacks protein-coding function (Yang *et al.*, 2019). Recent studies have illustrated the crucial roles of the lncRNAs in cell proliferation, survival, apoptosis, and differentiation (Ferre *et al.*, 2016; Ju *et al.*, 2019). However, most lncRNAs underlying mechanisms are yet to be studied. The lncRNA MALAT-1 is involved in the development of various tumors (Zhang *et al.*, 2017; Liu *et al.*, 2019; He *et al.*, 2019). Previous studies have confirmed that the overexpression of MALAT-1 can promote the invasion and migration of lung cancer, cervical cancer, and ovarian cancer (Xia *et al.*, 2018; Guo *et al.*, 2018; Yu *et al.*, 2019). It is also an essential marker for the early prognosis of lung adenocarcinoma, gastrointestinal cancer, and B-cell lymphomas (Li *et al.*, 2016; Xu *et al.*, 2018). However, the underlying mechanism of MALAT-1 in AML is not clear.

N6-methyladenosine (m6A) is the most accustomed mRNA modification; this modification affects all steps of RNA metabolism (Yu *et al.*, 2018). Emerged evidence showed that m6A is involved in cancer progression and proliferation; it is also engaged in cancer stem cells' maintenance and differentiation (Sun *et al.*, 2019). However, the mechanism of m6A in AML remains to be studied.

The zinc finger E-box binding homeobox 1 (ZEB1) leads to epithelial-mesenchymal transition (EMT) and confers properties of 'stemness', such as self-renewal in cancer. ZEB1 is involved in myogenesis (Postigo & Dean, 1999), neuronal development and differentiation (Wang *et al.*, 2019), gastrulation (Funahashi *et al.*, 1993), and T fine cell development (Higashi *et al.*, 1997). Copious evidence suggests that ZEB1 regulates stem cell self-renewal in cancer (Brabletz & Brabletz, 2010). Although ZEB1 is a renowned regulator of the expression of different stem cell/cancer-related transcription factors such as BMI1, KLF4, and SOX2, the deletion of ZEB1 promotes cell differentiation during the development of embryonic CNS (Singh *et al.*, 2016) and skeletal muscle (Li *et al.*, 2017). The comprehensive role of ZEB1 in normal stem cell progression remains unclear.

In the present study, we explored the underlying mechanism of MALAT-1 in AML. We found that the expression of MALAT-1 was significantly up-regulated in AML patients, and MALAT-1 promoted the m6A modification of ZEB1 through binding with METTL14, thereby promoting the proliferation and inhibiting the apoptosis of AML cells.

MATERIALS AND METHODS

Patient samples

40 AML patients and 40 healthy controls were recruited from Ningbo First Hospital. Among the AML patients, male: 26, female: 14; age: 35.21 ± 6.14 ; physical activity state score, 0-1: 27, 2-4: 13; Type, M1: 3; M2: 5; M3: 11; M4: 13; M5: 6; M6: 2. The peripheral blood was collected and stored in liquid nitrogen immediately until needed. The patients who received chemotherapy or radiotherapy were excluded from this study. This study was approved by the Research Ethics Committee of Ningbo First Hospital 20190126, January 26th, 2019, and each patient has signed an informed consent form.

Cell culture and transfection

The human bone marrow stromal cell line HS-5 and human AML cell lines HL60 and THP-1 were obtained from the Cell Bank of the Chinese Academy of Science (Shanghai, China). All cells were maintained in RPMI-1640 medium (Hyclone, Logan, UT, USA) and were supplemented with 10% fetal bovine serum (FBS, Hao Yang Bio) in a humidified atmosphere of 5% CO₂ at 37°C. The MALAT-1 overexpression plasmids, si-MALAT1, si-METTL14, and ZEB1 overexpression plasmids were synthesized by GenePharma (Shanghai, China). Lipofectamine 2000 (Invitrogen, USA) was used for cell transfection following the manufacturers' instructions.

Quantitative real-time RCR (qRT-PCR)

The RNA was extracted from HS-5, HL60, and THP-1 cells using TRIzol reagent (nitrogen source). The cDNA was synthesized using a reverse-transcription kit (TRAGEN). The real-time quantitative PCR was conducted on 20ng of cDNA by SYBR Green mixture (Shanghai Yisheng) and GAPDH was used as an internal control. The primer sequences are as follows:

MALAT1:

Forward 5'-AGGCGTTGTGCGTAGAGGA-3',

reverse 5'-GGATTTTTACCAACCACTCGC-3';

ZEB1:

Forward 5'-GATGATGAATGCGAGTCAGATGC-3',

reverse 5'-ACAGCAGTGTCTTGTGTGTGT-3'.

MTT assay

MTT assay was used to determine the HL60 and THP-1 cells' viability. 1×10^4 cells were seeded into 96-well plates. Next, we added 16 μ L/well MTT solution (5 mg/mL, Sigma) and incubated for 4 h at 37°C. The cell viability was determined by a microplate reader (Bio-Tek, Winooski, USA) at 570 nm.

Cell apoptosis assay

Annexin V-FITC Apoptosis Detection kit (YEASEN, Shanghai) was used to evaluate cell apoptosis. In brief, after treating HL60 and THP-1 cells for 72h, the cells were washed using PBS; Then, the cells were mixed with the binding buffer, Annexin V-FITC and propidium iodide (PI) and were incubated in dark for 15 min. The apoptotic rates were determined using flow cytometry (BD).

Transwell

The transwell assay was performed to detect the cell invasion, while transwell without Matrigel was performed to analyze the cell migration. About 0.6 mL Complete medium was added into lower chambers. Then, the cells were added into the upper chambers. After incubating for 48 h, the non-migrated and non-invaded cells were removed with a swab. The 4% paraformaldehyde was used to immobilize the cells on the bottom surface and 0.1% crystal violet was used to stain the cells. A light microscope was used to observe the cells.

RNA FISH

The RNA FISH probe for MALAT1 and METTL14 was purchased from Biosearch Technologies (Novato, CA, USA) and used to visualize RNA in the interchromatin granule clusters. Hybridizations were performed according to the manufacturer's instructions. Briefly, slides were hybridized overnight with 50 pmol probe in 20 μ L hybridization buffer, washed in RNase-free PBS, dehydrated in ethanol, post-fixed in 1% paraformaldehyde (Life Technologies, Darmstadt, Germany) in PBS, and treated for 2 min with 0.1% Triton-X100 (Serva, Heidelberg, Germany).

RNA immunoprecipitation

RNA experiments were performed using a Magna RIP RNA-Binding Protein Immunoprecipitation Kit (Millipore, USA) according to the manufacturer's instructions.

Western blotting

HL60 and THP-1 cells were placed in an ice-cold lysis buffer for 30 min (Beyotime). The supernatants were collected by centrifugation at 14000 r/min for 20 min at 4°C. Protein concentration was calculated with a BCA Kit (Pierce, USA). Then the protein was separated with 10% SDS-PAGE and transferred onto PVDF membranes. Afterwards, the membranes were blocked in 5% non-fat milk; next, the membranes were incubated with primary antibodies: anti-ZEB1 (1:1000), anti-METTL14 (1:1000), and anti-METTL3 (1:1000) (Boster Biological Technology, China) overnight at 4°C. On the next day, the membranes were incubated with the HRP-labeled secondary antibodies (Abcam, Shanghai) and treated with BeyoECL Plus (Beyotime, China). The bands were visualized using CC-D camera (Bio-Rad, USA).

RNA pull-down

RNA pull-down assay was performed to confirm whether METTL14 or METTL3 can be pulled down by MALAT-1 in HL60 and THP-1 cells. The biotin-labeled METTL14 and METTL3 were transcribed with the Biotin RNA Labeling Mix (Roche) and T7 RNA polymerase (Roche). After 2d of transfection, cells were lysed and then mixed with biotin-labeled METTL14 and METTL3 and streptavidin agarose magnetic beads at 4°C for 1 h. Western blot was used to detect the protein levels of the retrieved Ago2.

Statistical analysis

Data were analyzed using SPSS17.0 software (SPSS, Inc.) and expressed as mean \pm S.D. One-way ANOVA followed by Duncan's post hoc test was used to evaluate the differences among groups. The differences between the two groups were analyzed by Student's *t*-test. $P < 0.05$ was defined as significant.

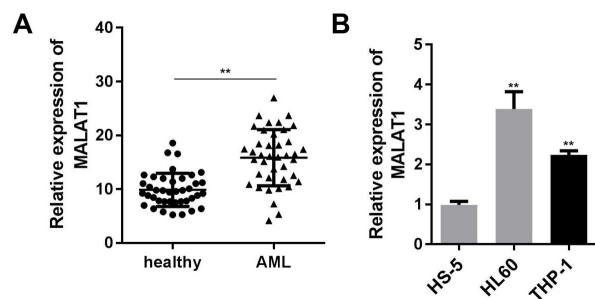


Figure 1. MALAT1 was upregulated in AML patients and AML cell lines.

(A) The expression of MALAT1 in serum samples from AML patients and healthy volunteers. (B) The expression of MALAT1 in AML in the human bone marrow stromal cell line HS-5 and human AML cell lines HL60 and THP-1. ** $P < 0.01$ vs HS-5.

RESULTS

lnc-MALAT-1 was up-regulated in AML patients and cells

Firstly, we collected serum samples from 40 healthy participants and 40 AML patients, and then examined the expression of MALAT-1 in serum by RT-qPCR method. The expression level of MALAT-1 in the serum of patients with AML was significantly higher than normal controls ($P < 0.05$; Fig. 1A). It was consistent with in vitro assay, the expression of MALAT-1 in HL60 and THP-1 cells were significantly increased compared with HS-5 cells ($P < 0.05$; Fig. 1B).

MALAT-1 knockdown inhibited proliferation of AML cells

To explore the role of MALAT-1 in AML, HL60, and THP-1 cells were transfected with si-MALAT-1 or MALAT-1 overexpression plasmids, and then we examined the effects of MALAT-1 on cell proliferation. Results, in Fig. 2A, revealed that compared with the si-NC group the expression of MALAT-1 was significantly reduced after transfection with si-MALAT1. Compared with the vector group, the expression of MALAT-1 was remarkably promoted after transfection with MALAT1 overexpression plasmids ($P < 0.01$). As shown in Fig. 2B–C, knockdown of MALAT-1 significantly suppressed the cell viability of HL60 and THP-1, whereas overexpression MALAT-1 remarkably promoted the AML cell viability ($P < 0.05$).

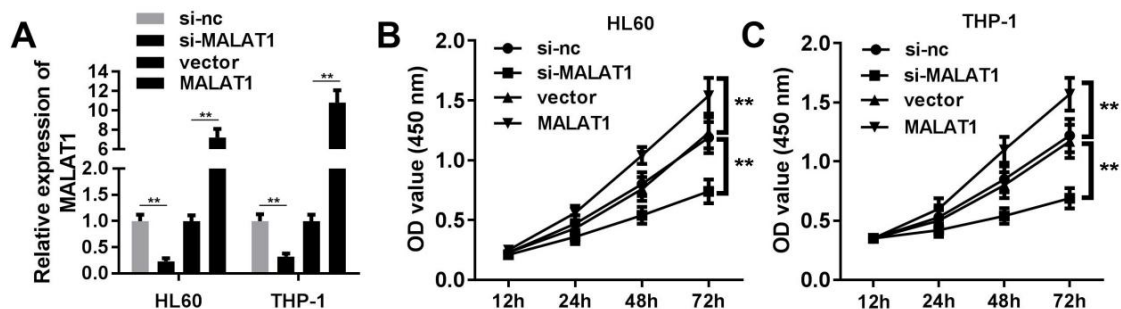


Figure 2. Effects of MALAT1 on proliferation of AML cells.

(A) After AML cells were transfected with si-MALAT1 or MALAT1 for 48 h, the transfection efficiency was evaluated by qRT-PCR. (B and C) MTT assay was conducted to determine cell proliferation in HL60, and THP-1 cells transfected with si-MALAT1 or MALAT1. ** $P < 0.01$.

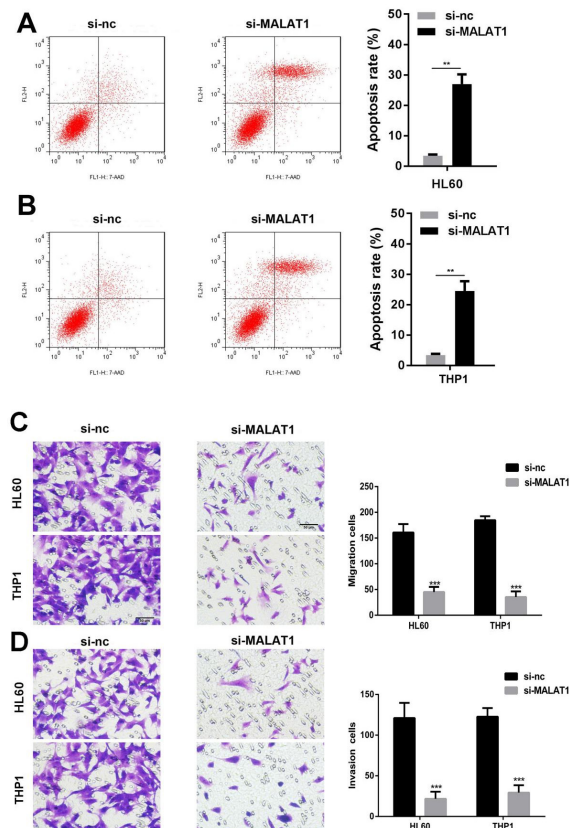


Figure 3. Effects of MALAT1 knockdown on apoptosis of AML cells.

After HL60 and THP-1 cells were transfected with si-MALAT1 or MALAT1 for 48 h, cell apoptosis (A–B), migration (C) and invasion (D) were evaluated by flow cytometry assay. ** $P < 0.01$. *** $P < 0.001$.

MALAT-1 knockdown promoted AML cells apoptosis

To further explore the function of MALAT-1 in AML, after HL60 and THP-1 cells transfection with si-MALAT-1 or MALAT-1 overexpression plasmids, we examined the effects of MALAT-1 on cell apoptosis, migration, and invasion. Flow cytometry results showed that compared with the si-NC group, the apoptosis of HL60 and THP-1 cells was significantly increased in si-MALAT1 group ($P < 0.05$; Fig. 3A–B). Besides, the results of Transwell exhibited that compared with the si-NC group, the migration and invasion abilities of the HL60 and THP-1 cells were significantly decreased in

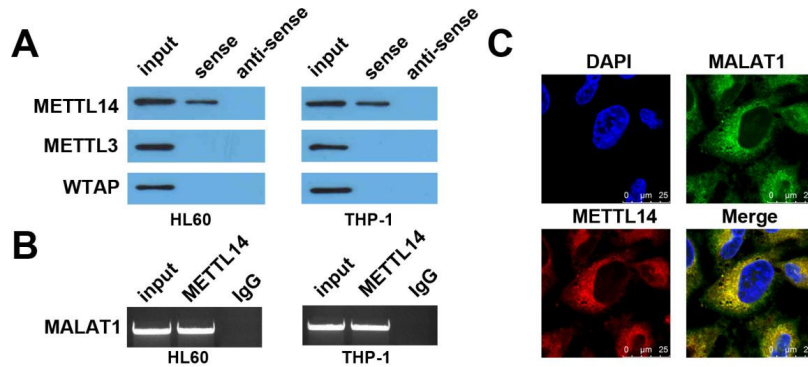


Figure 4. MALAT1 bound with METTL14 in AML cells.

(A) RNA pull-down assay. (B) RNA immunoprecipitation assay. (C) MALAT1 and METTL14 location detecting by RNA FISH in AML cells.

the si-MALAT1 group ($P < 0.05$; Fig. 3C–D). These data revealed that MALAT1 knockdown promoted AML cell apoptosis and inhibited AML cell migration and invasion.

METTL14 bound with MALAT-1

m6A Modification affects almost all steps of RNA metabolism, including lncRNA. Therefore, RNA pull-down assay, RIP experiment, and RNA FISH were used to verify whether m6A binds with MALAT-1. The results of the RNA pull-down assay verified the interaction between MALAT-1 and METTL14 (Fig. 4A). Furthermore, METTL14 directly bound with MALAT-1 (Fig. 4B). Similarly, RNA FISH results also confirmed the mutual binding of MALAT-1 and METTL14 (Fig. 4C). Taken together, these data confirmed that METTL14 bound with MALAT-1.

MALAT-1 regulated m6A modification of ZEB1

Previous research has shown that mRNA translation is regulated by lncRNA and m6A modification. Therefore, we explored the effects of MALAT-1 and m6A modification on ZEB1 expression. In Fig. 5A, ZEB1 produced significant m6A methylation modification in both AML cells, compared with the control group.

MALAT-1 knockdown remarkably reduced the enrichments of ZEB1 in HL60 and THP-1 cells ($P < 0.05$; Fig. 5B). As shown in Fig. 5C, overexpression of MALAT-1 significantly promoted the enrichments of ZEB1 compared with the control group. However, these changes would be partly reversed in the MALAT-1+si-METTL14 group ($P < 0.05$; Fig. 5C). After transfection with MALAT-1 overexpression plasmids or si-METTL14, we detected the expression of ZEB1 in AML cells. Results showed that the expression levels of ZEB1 were promoted by MALAT-1 overexpression plasmids, compared with the control group. The expression levels of ZEB1 were significantly reduced by MALAT-1+si-METTL14 compared with the MALAT-1+si-NC group ($P < 0.05$; Fig. 5C). As shown in Fig. 5D, after transfection with MALAT-1 overexpression plasmids, the stability of ZEB1 expression was promoted, compared with the vector+si-NC group, which was partly reversed by si-METTL14 (Fig. 5D). Overexpressed MALAT-1 promoted the protein expression of ZEB1 compared with the vector+si-NC group, while the protein expression of ZEB1 was decreased in the MALAT-1+si-METTL14 group compared with the MALAT-1+si-NC group ($P < 0.05$; Fig. 5E).

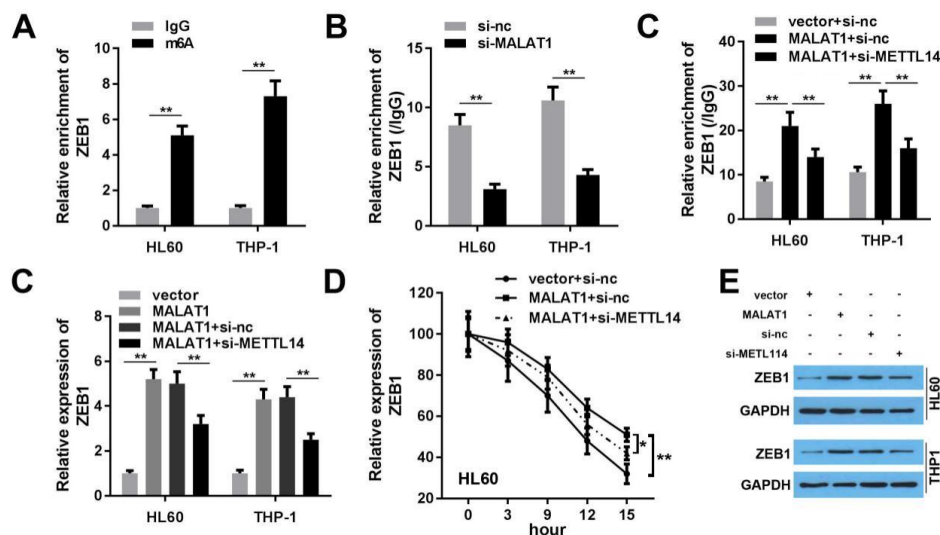


Figure 5. Effects of MALAT1 and METTL14 on ZEB1.

(A) ZEB1 produces m6A modification in AML cells. (B) After AML cells were transfected with si-MALAT1, the enrichment of ZEB1 was evaluated by qRT-PCR. (C) After AML cells were transfected with MALAT1 or si-METTL14, the enrichment and expression of ZEB1 was evaluated by qRT-PCR. (D) The stability of ZEB1. (E) The protein expression of ZEB1. ** $P < 0.01$.

Overexpression ZEB1 alleviated the effects of MALAT-1 knockdown on cellular function AML cells

To further explore the role of MALAT-1 and ZEB1, a rescue experiment was conducted in AML cells. As presented in Fig 6A, MALAT-1 knockdown significantly reduced the expression of ZEB1 compared with the vector+si-NC group, the expression levels of ZEB1 were promoted by ZEB1 overexpression plasmids compared with si-MALAT-1+si-NC group ($P<0.05$; Fig. 6A). Knockdown MALAT-1 significantly reduced cell viability of HL60 and THP-1 cells, whereas overexpression of ZEB1 remarkably reversed the effect of MALAT-1 knockdown ($P<0.05$; Fig. 6B). Knockdown of MALAT-1 significantly induced the apoptosis of HL60 and THP-1 cells, whereas overexpression of ZEB1 reversed the effect of MALAT-1 knockdown ($P<0.05$; Fig. 6C). What is more, knockdown of MALAT-1 significantly decreased the migration and invasion of the HL60 and THP-1 cells, whereas overexpressed ZEB1 remarkably reversed the effect of MALAT-1 knockdown on the migration and invasion of AML cells ($P<0.05$; Fig. 6D–E).

DISCUSSION

In this study, MALAT-1 was significantly upregulated in patients compared with the healthy control group. Besides, MALAT-1 knockdown inhibited HL60 and THP-1 cells' proliferation, migration, and invasion abilities, and promoted the apoptosis of HL60 and THP-1 cells.

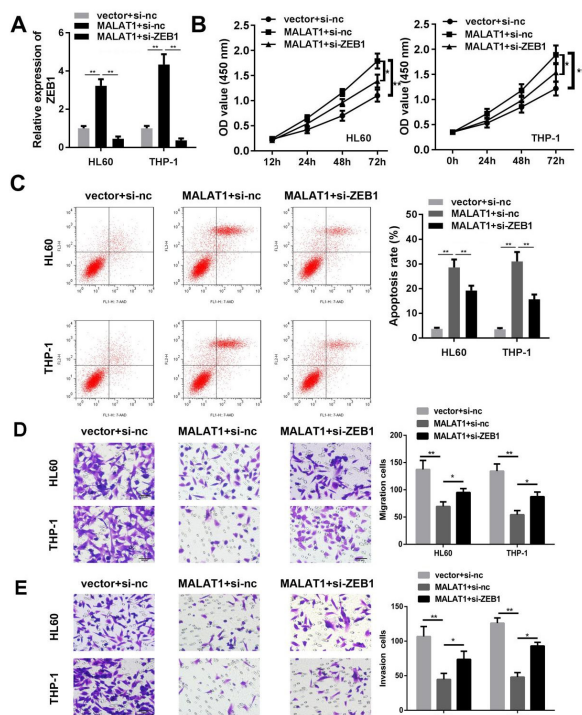


Figure 6. Knockdown ZEB1 reversed the effect of MALAT1 on AML cells.

(A) After AML cells were transfected with MALAT1 or si-ZEB1 for 48 h, the expression of ZEB1 was detected by qRT-PCR. (B) MTT assay was conducted to determine cell proliferation in HL60, and THP-1 cells transfected with MALAT1 or si-ZEB1. (C) After HL60 and THP-1 cells were transfected with MALAT1 or si-ZEB1 for 48 h, cell apoptosis was evaluated by flow cytometry assay. (D–E) After HL60 and THP-1 cells were transfected with MALAT1 or si-ZEB1 for 48 h, Transwell assay was performed to detect the migration and invasion. * $P<0.05$, ** $P<0.01$.

Moreover, MALAT-1 promoted m6A methylation modification of ZEB1 by binding with METTL14, thereby enhancing the proliferation, migration, and invasion ability of AML cells.

MALAT-1 is a highly methylated lncRNA that is often abnormally upregulated in human cancer tissues (YiRen *et al.*, 2017; Shen *et al.*, 2019). Recently, abnormal expression of MALAT-1 can be a diagnostic marker for multiple myeloma at early stage (Hu *et al.*, 2018). Additionally, the abnormally high expression of lncRNA-MALAT-1 was associated with the poor prognosis of AML patients (Huang *et al.*, 2017). However, MALAT-1 knockout enhances cytarabine chemosensitivity of AML cells (Hu *et al.*, 2019). These findings suggest that MALAT-1 may function as an oncogene in AML. In this study, MALAT-1 was up-regulated in AML clinical samples and cells. Moreover, knockdown of MALAT-1 reduced AML cells' viability, migration, and invasion, and induced cells' apoptosis, which is a key "player" in the occurrence and development of AML. Nevertheless, the underlying molecular mechanisms remain unclear.

The m6A methylation modification mediates the 0.3–0.5% adenosine modification in human cell mRNA, and the main complexes responsible for the m6A modification of mRNAs are METTL3 and METTL14 (Ianniello *et al.*, 2019). The study found that METTL14 was over-expressed in AML, which was consistent with previous studies (Vu *et al.*, 2017; Barbieri *et al.*, 2017). Overexpression of METTL14 promotes the proliferation of AML cells, while knockout of METTL14 promotes AML cell apoptosis (Weng *et al.*, 2018). Barbieri *et al.* reveal that METTL14 is a crucial gene regulating the survival of AML and maintain leukemia stem cells (Weng *et al.*, 2018). These results prove the oncogenic role of METTL14 in AML. In this study, MALAT-1 bound with methyltransferase METTL14, which suggests the possibility of m6A modification in AML cells.

ZEB1 is the primary regulator of EMT-related signal pathways related to cancer stem cells' growth, survival, and metastasis. For example, up-regulating ZEB1 improves the migration ability of HCC cells (Wang *et al.*, 2020). ZEB1 is highly expressed in AML patients and can be a marker for early diagnosis and prognosis of AML (Shousha *et al.*, 2019). However, ZEB1 knockout reduces the invasiveness of leukemia stem cells (Stavropoulou *et al.*, 2016). However, the reason that ZEB1 was overexpressed in AML cells is still unclear. In this study, we found that ZEB1 was rich in m6A level in AML cells. Additionally, MALAT-1 interacted with METTL14 to promote m6A modification of ZEB1, which induced the up-regulation of ZEB1 in AML cells. Besides, overexpression of ZEB1 promoted proliferation, migration, and invasion, and suppressed the apoptosis of AML cells.

In conclusion, MALAT-1 was overexpressed in AML. MALAT-1 bound with METTL14 to promote the m6A modification of ZEB1, which promoted the proliferation, migration, and invasion of AML cells. This might provide a new effective therapeutic strategy for the treatment of AML.

Declarations

Declaration of Competing Interest. No conflict of interest exists in the submission of this manuscript, and manuscript is approved by all authors for publication.

Acknowledgments. Not applicable.

Data Availability Statement. The datasets used and analyzed during the current study are available from the corresponding author on reasonable request.

Authors' contributions. All authors participated in the design, interpretation of the studies, and analysis of the data, and review of the manuscript; LHF and PH conducted the experiments; JJ wrote the manuscript; WYF provided the idea.

REFERENCES

- Acheampong DO, Adokoh CK, Asante DB, Asiamah EA, Barnie PA, Bonsu DOM, Kyei F (2018) Immunotherapy for acute myeloid leukemia (AML): a potent alternative therapy. *Biomed Pharmacother* **97**: 225–232. <https://doi.org/10.1016/j.biopha.2017.10.110>
- Barbieri I, Tzelepis K, Pandolfini L, Shi J, Millan-Zambrano G, Robson SC, Aspris D, Migliori V, Bannister AJ, Han N, De Braekeleer E, Ponstingl H, Hendrick A, Vakoc CR, Vassiliou GS, Kouzarides T (2017) Promoter-bound METTL3 maintains myeloid leukaemia by m(6) A-dependent translation control. *Nature* **552**: 126–131. <https://doi.org/10.1038/nature24678>
- Brabletz S, Brabletz T (2010) The ZEB/miR-200 feedback loop – a motor of cellular plasticity in development and cancer? *EMBO Rep* **11**: 670–677. <https://doi.org/10.1038/embor.2010.117>
- Cai SF, Levine RL (2019) Genetic and epigenetic determinants of AML pathogenesis. *Semin Hematol* **56**: 84–89. <https://doi.org/10.1053/j.seminhematol.2018.08.001>
- Ferre F, Colantoni A, Helmer-Citterich M (2016) Revealing protein-lncRNA interaction. *Brief Bioinform* **17**: 106–116. <https://doi.org/10.1093/bib/bbv031>
- Funahashi J, Sekido R, Murai K, Kamachi Y, Kondoh H (1993) Delta-crystallin enhancer binding protein delta EF1 is a zinc finger-homodomain protein implicated in postgastrulation embryogenesis. *Development* **119**: 433–446. <https://doi.org/10.1242/dev.119.2.433>
- Guo C, Wang X, Chen LP, Li M, Li M, Hu YH, Ding WH, Wang X (2018) Long non-coding RNA MALAT1 regulates ovarian cancer cell proliferation, migration and apoptosis through Wnt/beta-catenin signaling pathway. *Eur Rev Med Pharmacol Sci* **22**: 3703–3712. https://doi.org/10.26355/eurrev.201806_15249
- He B, Peng F, Li W, Jiang Y (2019) Interaction of lncRNA-MALAT1 and miR-124 regulates HBx-induced cancer stem cell properties in HepG2 through PI3K/Akt signaling. *J Cell Biochem* **120**: 2908–2918. <https://doi.org/10.1002/jcb.26823>
- Higashi Y, Moribe H, Takagi T, Sekido R, Kawakami K, Kikutani H, Kondoh H (1997) Impairment of T cell development in deltaEF1 mutant mice. *J Exp Med* **185**: 1467–1479. <https://doi.org/10.1084/jem.185.8.1467>
- Hu N, Chen L, Wang C, Zhao H (2019) MALAT1 knockdown inhibits proliferation and enhances cytarabine chemosensitivity by upregulating miR-96 in acute myeloid leukemia cells. *Biomed Pharmacother* **112**: 108720. <https://doi.org/10.1016/j.biopha.2019.108720>
- Hu Y, Lin J, Fang H, Fang J, Li C, Chen W, Liu S, Ondrejka S, Gong Z, Reu F, Maciejewski J, Yi Q, Zhao JJ (2018) Targeting the MALAT1/PARP1/LIG3 complex induces DNA damage and apoptosis in multiple myeloma. *Leukemia* **32**: 2250–2262. <https://doi.org/10.1038/s41375-018-0104-2>
- Huang JL, Liu W, Tian LH, Chai TT, Liu Y, Zhang F, Fu HY, Zhou HR, Shen JZ (2017) Upregulation of long non-coding RNA MALAT-1 confers poor prognosis and influences cell proliferation and apoptosis in acute monocytic leukemia. *Oncol Rep* **38**: 1353–1362. <https://doi.org/10.3892/or.2017.5802>
- Ianniello Z, Paiardini A, Fatica A (2019) N(6)-Methyladenosine (m(6)A): A promising new molecular target in acute myeloid leukemia. *Front Oncol* **9**: 251. <https://doi.org/10.3389/fonc.2019.00251>
- Ju C, Liu R, Zhang YW, Zhang Y, Zhou R, Sun J, Lv XB, Zhang Z (2019) Mesenchymal stem cell-associated lncRNA in osteogenic differentiation. *Biomed Pharmacother* **115**: 108912. <https://doi.org/10.1016/j.biopha.2019.108912>
- Li G, Luo W, Abdalla BA, Ouyang H, Yu J, Hu F, Nie Q, Zhang X (2017) miRNA-223 upregulated by MYOD inhibits myoblast proliferation by repressing IGF2 and facilitates myoblast differentiation by inhibiting ZEB1. *Cell Death Dis* **8**: e3094. <https://doi.org/10.1038/cddis.2017.479>
- Li J, Wang J, Chen Y, Li S, Jin M, Wang H, Chen Z, Yu W (2016) LncRNA MALAT1 exerts oncogenic functions in lung adenocarcinoma by targeting miR-204. *Am J Cancer Res* **6**: 1099–1107
- Liu P, Li X, Cui Y, Chen J, Li C, Li Q, Li H, Zhang X, Zu X (2019) LncRNA-MALAT1 mediates cisplatin resistance via miR-101-3p/VEGF-C pathway in bladder cancer. *Acta Biochim Biophys Sin (Shanghai)* **51**: 1148–1157. <https://doi.org/10.1093/abbs/gmz112>
- Mer AS, Lindberg J, Nilsson C, Klevebring D, Wang M, Gronberg H, Lehmann S, Rantalainen M (2018) Expression levels of long non-coding RNAs are prognostic for AML outcome. *J Hematol Oncol* **11**: 52. <https://doi.org/10.1186/s13045-018-0596-2>
- Mueller BU, Seipel K, Bacher U, Pabst T (2018) Autologous transplantation for older adults with AML. *Cancers (Basel)* **10**: 9. <https://doi.org/10.3390/cancers10090340>
- Pan JQ, Zhang YQ, Wang JH, Xu P, Wang W (2017) lncRNA co-expression network model for the prognostic analysis of acute myeloid leukemia. *Int J Mol Med* **39**: 663–671. <https://doi.org/10.3892/ijmm.2017.2888>
- Postigo AA, Dean DC (1999) Independent repressor domains in ZEB regulate muscle and T-cell differentiation. *Mol Cell Biol* **19**: 7961–7971. <https://doi.org/10.1128/MCB.19.12.7961>
- Shen F, Zheng H, Zhou L, Li W, Xu X (2019) Overexpression of MALAT1 contributes to cervical cancer progression by acting as a sponge of miR-429. *J Cell Physiol* **234**: 11219–11226. <https://doi.org/10.1002/jcp.27772>
- Shousha WG, Ramadan SS, El-Said AS, Abdelmonem AE, Abbas MA (2019) Expression and clinical significance of SNAI1 and ZEB1 genes in acute myeloid leukemia patients. *Mol Biol Rep* **46**: 4625–4630. <https://doi.org/10.1007/s11033-019-04839-y>
- Singh S, Howell D, Trivedi N, Kessler K, Ong T, Rosmaninho P, Raposo AA, Robinson G, Roussel MF, Castro DS, Solecki DJ (2016) Zeb1 controls neuron differentiation and germinal zone exit by a mesenchymal-epithelial-like transition. *Elife* **5**: e12717. <https://doi.org/10.7554/eLife.12717>
- Stavropoulou V, Kaspar S, Brault L, Sanders MA, Juge S, Moretini S, Tzankov A, Iacovino M, Lau IJ, Milne TA, Royo H, Kyba M, Valk PJM, Peters AHFM, Schwaller J (2016) MLL-AF9 Expression in hematopoietic stem cells drives a highly invasive AML expressing EMT-related genes linked to poor outcome. *Cancer Cell* **30**: 43–58. <https://doi.org/10.1016/j.ccr.2016.05.011>
- Sun T, Wu R, Ming L (2019) The role of m6A RNA methylation in cancer. *Biomed Pharmacother* **112**: 108613. <https://doi.org/10.1016/j.biopha.2019.108613>
- Vu LP, Pickering BF, Cheng Y, Zaccara S, Nguyen D, Minuesa G, Chou T, Chow A, Saletore Y, MacKay M, Schulman J, Famulare C, Patel M, Klimek VM, Garrett-Bakelman FE, Melnick A, Carroll M, Mason CE, Jaffrey SR, Kharas MG (2017) The N(6)-methyladenosine (m(6)A)-forming enzyme METTL3 controls myeloid differentiation of normal hematopoietic and leukemia cells. *Nat Med* **23**: 1369–1376. <https://doi.org/10.1038/nm.4416>
- Wang H, Xiao Z, Zheng J, Wu J, Hu XL, Yang X, Shen Q (2019) ZEB1 Represses neural differentiation and cooperates with CTBP2 to dynamically regulate cell migration during neocortex development. *Cell Rep* **27**: 2335–2355. e6. <https://doi.org/10.1016/j.celrep.2019.04.081>
- Wang JD, Zhou HS, Tu XX, He Y, Liu QF, Liu Q, Long ZJ (2019) Prediction of competing endogenous RNA coexpression network as prognostic markers in AML. *Aging (Albany NY)* **11**: 3333–3347. <https://doi.org/10.18632/aging.101985>
- Wang M, Yang Y, Yang J, Yang J, Han S (2020) circ_KIAA1429 accelerates hepatocellular carcinoma advancement through the mechanism of m(6)A-YTHDF3-Zeb1. *Life Sci* **257**: 118082. <https://doi.org/10.1016/j.lfs.2020.118082>
- Weng H, Huang H, Wu H, Qin X, Zhao BS, Dong L, Shi H, Skibbe J, Shen C, Hu C, Sheng Y, Wang Y, Wunderlich M, Zhang B, Dore LC, Su R, Deng X, Ferchen K, Li C, Sun M, Lu Z, Jiang X, Marcucci G, Mulloy JC, Yang J, Qian Z, Wei M, He C, Chen J (2018) METTL14 inhibits hematopoietic stem/progenitor differentiation and promotes leukemogenesis via mRNA m(6)A modification. *Cell Stem Cell* **22**: 191–205. e9. <https://doi.org/10.1016/j.stem.2017.11.016>
- Xia C, Liang S, He Z, Zhu X, Chen R, Chen J (2018) Metformin, a first-line drug for type 2 diabetes mellitus, disrupts the MALAT1/miR-142-3p sponge to decrease invasion and migration in cervical cancer cells. *Eur J Pharmacol* **830**: 59–67. <https://doi.org/10.1016/j.ejphar.2018.04.027>
- Xu Y, Zhang X, Hu X, Zhou W, Zhang P, Zhang J, Yang S, Liu Y (2018) The effects of lncRNA MALAT1 on proliferation, invasion and migration in colorectal cancer through regulating SOX9. *Mol Med* **24**: 52. <https://doi.org/10.1186/s10020-018-0050-5>
- Yang Z, Jiang S, Shang J, Jiang Y, Dai Y, Xu B, Yu Y, Liang Z, Yang Y (2019) LncRNA: Shedding light on mechanisms and opportunities in fibrosis and aging. *Ageing Res Rev* **52**: 17–31. <https://doi.org/10.1016/j.arr.2019.04.001>
- YiRen H, YingCong Y, Sunwu Y, Keqin L, Xiaochun T, Senrui C, Ende C, XiZhou L, Yanfan C (2017) Long noncoding RNA MALAT1 regulates autophagy associated chemoresistance via miR-23b-3p sequestration in gastric cancer. *Mol Cancer* **16**: 174. <https://doi.org/10.1186/s12943-017-0743-3>
- Yu J, Chen M, Huang H, Zhu J, Song H, Zhu J, Park J, Ji SJ (2018) Dynamic m6A modification regulates local translation of mRNA in axons. *Nucleic Acids Res* **46**: 1412–1423. <https://doi.org/10.1093/nar/gkx1182>
- Yu W, Ding J, He M, Chen Y, Wang R, Han Z, Xing EZ, Zhang C, Yeh S (2019) Estrogen receptor beta promotes the vasculogenic

- mimicry (VM) and cell invasion *via* altering the lncRNA-MALAT1/miR-145-5p/NEDD9 signals in lung cancer. *Oncogene* **38**: 1225–1238. <https://doi.org/10.1038/s41388-018-0463-1>
- Zhang TH, Liang LZ, Liu XL, Wu JN, Su K, Chen JY, Zheng QY, Huang HZ, Liao GQ (2017) Long non-coding RNA MALAT1 interacts with miR-124 and modulates tongue cancer growth by targeting JAG1. *Oncol Rep* **37**: 2087–2094. <https://doi.org/10.3892/or.2018.6688>
- Zimta AA, Tomuleasa C, Sahnoune I, Calin GA, Berindan-Neagoe I (2019) Long non-coding RNAs in myeloid malignancies. *Front Oncol* **9**: 1048. <https://doi.org/10.3389/fonc.2019.01048>



OPEN ACCESS

EDITED BY

Paulina Niedźwiedzka-Rystwej,
University of Szczecin, Poland

REVIEWED BY

Agnieszka Wnuk,
Maj Institute of Pharmacology-Polish
Academy of Sciences, Poland
Jiayu Yu,
City of Hope National Medical Center,
United States

*CORRESPONDENCE

Yobana Pérez-Cervera,
✉ yobanper@gmail.com

[†]PRESENT ADDRESS

Liliana Argueta-Figueroa,
CONAHCYT—Tecnológico Nacional de
México, Instituto Tecnológico de
Toluca, Metepec, México

RECEIVED 19 March 2024

ACCEPTED 06 June 2024

PUBLISHED 08 July 2024

CITATION

Loaeza-Reyes KJ, Zenteno E,
Ramírez-Hernández E, Salinas-Marin R,
Moreno-Rodríguez A, Torres-Rosas R,
Argueta-Figueroa L, Fernández-Rojas B,
Pina-Canseco S, Acevedo-Mascarúa AE,
Hernández-Antonio A and Pérez-
Cervera Y (2024), The
modulation of the hexosamine
biosynthetic pathway impacts the
localization of CD36 in macrophages.
Acta Biochim. Pol. 71:13004.
doi: 10.3389/abp.2024.13004

COPYRIGHT

© 2024 Loaeza-Reyes, Zenteno,
Ramírez-Hernández, Salinas-Marin,
Moreno-Rodríguez, Torres-Rosas,
Argueta-Figueroa, Fernández-Rojas,
Pina-Canseco, Acevedo-Mascarúa,
Hernández-Antonio and Pérez-
Cervera. This is an open-access article
distributed under the terms of the
[Creative Commons Attribution License](#)
(CC BY). The use, distribution or
reproduction in other forums is
permitted, provided the original
author(s) and the copyright owner(s) are
credited and that the original
publication in this journal is cited, in
accordance with accepted academic
practice. No use, distribution or
reproduction is permitted which does
not comply with these terms.

The modulation of the hexosamine biosynthetic pathway impacts the localization of CD36 in macrophages

Karen Julissa Loaeza-Reyes^{1,2}, Edgar Zenteno³,
Eleazar Ramírez-Hernández³, Roberta Salinas-Marin⁴,
Adriana Moreno-Rodríguez⁵, Rafael Torres-Rosas¹,
Liliana Argueta-Figueroa^{1,6†}, Berenice Fernández-Rojas¹,
Socorro Pina-Canseco², Alfonso E. Acevedo-Mascarúa¹,
Alicia Hernández-Antonio¹ and Yobana Pérez-Cervera^{1,2*}

¹Centro de Estudios en Ciencias de la Salud y la Enfermedad, Facultad de Odontología, Universidad Autónoma Benito Juárez de Oaxaca, Oaxaca, Mexico, ²Centro de Investigación Multidisciplinaria Facultad de Medicina-UNAM-UABJO, Universidad Autónoma Benito Juárez de Oaxaca, Oaxaca, Mexico, ³Departamento de Bioquímica, Facultad de Medicina, Universidad Nacional Autónoma de México, Mexico City, Mexico, ⁴Laboratorio de Glicobiología Humana y Diagnóstico Molecular, Centro de Investigación en Dinámica Celular, Instituto de Investigación en Ciencias Básicas y Aplicadas, Universidad Autónoma del Estado de Morelos, Cuernavaca, Mexico, ⁵Facultad de Ciencias Químicas, Universidad Autónoma Benito Juárez de Oaxaca, Oaxaca, Mexico, ⁶CONAHCYT – Facultad de Odontología, Universidad Autónoma Benito Juárez de Oaxaca, Oaxaca, Mexico

CD36 is a type 2 cell surface scavenger receptor expressed in various tissues. In macrophages, CD36 recognizes oxidized low-density lipoprotein (ox-LDL), which promotes the formation of foam cells, the first step toward an atherosclerotic arterial lesion. CD36 possesses a variety of posttranslational modifications, among them N-glycosylation and O-GlcNAc modification. Some of the roles of these modifications on CD36 are known, such as N-linked glycosylation, which provides proper folding and trafficking to the plasma membrane in the human embryonic kidney. This study aimed to determine whether variations in the availability of UDP-GlcNAc could impact Rab-5-mediated endocytic trafficking and, therefore, the cellular localization of CD36. These preliminary results suggest that the availability of the substrate UDP-GlcNAc, modulated in response to treatment with Thiamet G (TMG), OSMI-1 (O-GlcNAcylation enzymes modulators) or Azaserine (HBP modulator), influences the localization of CD36 in J774 macrophages, and the endocytic trafficking as evidenced by the regulatory protein Rab-5, between the plasma membrane and the cytoplasm.

KEYWORDS

CD36 localization, O-GlcNAcylation, hexosamine biosynthetic pathway, vesicular traffic, environment of cells

Introduction

Human CD36 is a class B scavenger receptor localized to the plasma membrane that is widely expressed in immune cells like macrophages, monocytes, dendritic cells and subsets of T and B cells, and non-immune cells, such as platelets, immature erythrocytes adipocytes, myocytes, specialized epithelial cells, and microvascular endothelial cells. Its ligands include endogenously derived ligands such as apoptotic cells, cholesterol esters, fatty acids, oxidatively modified lipoproteins, glycosylated proteins, and amyloid-forming peptides (Luiken et al., 2016; Chen et al., 2022). Similarly, CD36 is a pattern recognition receptor for molecular patterns presented by various pathogens on phagocytic cells, binds, and mediates phagocytosis (Patel et al., 2004; Baranova et al., 2008; Silverstein and Febbraio, 2009).

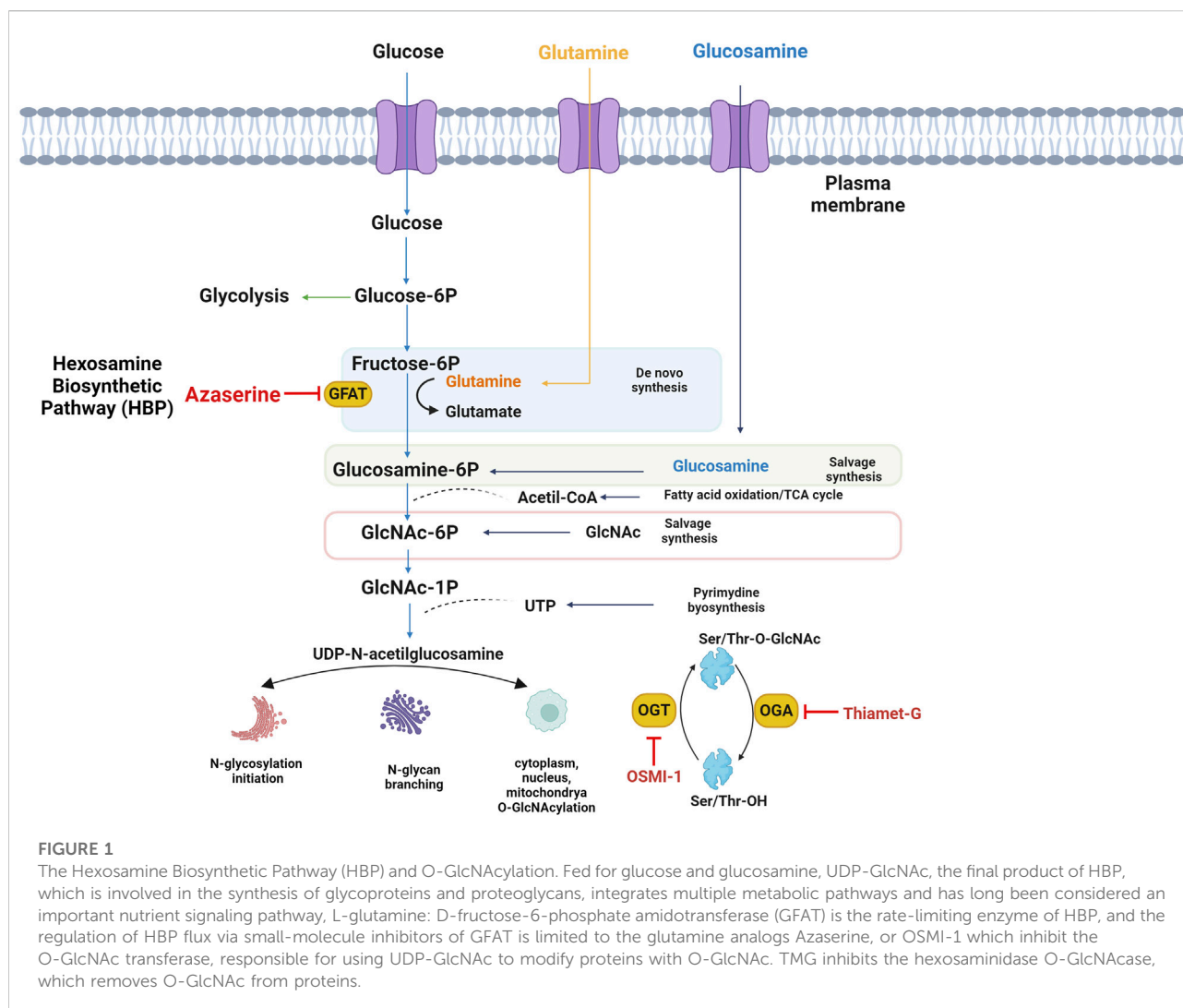
The endocytic system of eukaryotic cells embraces a complex network of membrane compartments, each of which fulfills a specific set of tasks in cargo sorting, distribution, and catabolism (Barbero et al., 2002). Rab GTPases organize the endocytic pathway into a mosaic of biochemically and functionally distinct membrane domains; they are involved in vesicle trafficking and endocytic and exocytic processes (Rink et al., 2005). Rab5 recruits different effector proteins that oligomerize within a membrane domain enriched in PI(3)P (Christoforidis et al., 1999). Rab5, Rab4, and Rab11 occupy distinct membrane domains that are sequentially traversed by recycling cargo. Cargo destined for degradation is first internalized into Rab5 domains in early endosomes (Yuan and Song, 2020) and later appears in Rab7 domains in late endosomes (Mukhopadhyay et al., 1997).

Short-term (minutes) regulation of cellular fatty acid uptake rate occurs by reversible intracellular recycling (vesicular traffic) of CD36 from an endosomal storage compartment to the plasma membrane. Long-term regulation of cellular fatty acid uptake occurs via changes in CD36 gene transcription, mediated, among others, by fatty acid-induced PPAR activation, HIF-1, and C/EBP α (Glatz and Luiken, 2018). CD36 expression is regulated at both the transcriptional and posttranslational levels; the regulation differs between different cell types. Post-translational modifications (PTMs) modulate partner-to-partner interactions and are responsible for protein function. A single PTM or a combination of PTMs modifies the local conformation of a region or domains of a protein and offers different interaction surfaces. Therefore, a protein can interact with many partners, changing its localization, stability, interaction with other partners, and, ultimately, its activities (Vercouter-Edouart et al., 2015). The evidence concerning PTMs of CD36 suggests that these modifications impact protein function in a tissue-specific way; for more details, see the reviews (Shu et al., 2022; J.J. Luiken et al., 2016).

In addition, CD36 is heavily N-linked glycosylated (Mori et al., 2012), which is the cause for the increase in molecular mass to 88 kDa. N-glycosylation of membrane and secretory proteins

impacts proper folding and trafficking to the plasma membrane and enhances their stability (Hoosdally et al., 2009). N-glycosylation occurs in the endoplasmic reticulum (ER) and refers to the attachment of the oligosaccharide N-acetylglucosamine (GlcNAc) to the side chain of Asparagine (Asn) through a β -1N linkage of a protein molecule—N-glycans impact the structure and function of some eukaryotic proteins (Reilly et al., 2019). The endoplasmic reticulum and the Golgi apparatus synthesize glycolipids, glycoproteins, and glycans utilizing UDP-GlcNAc, which is synthesized through the Hexosamine Biosynthetic Pathway (HBP).

A small portion of UDP-GlcNAc acts as a versatile substrate pool for reversible post-translational modifications known as O-GlcNAc. This process, which occurs in the cytoplasm, mitochondria, and nucleus, shares common features with phosphorylation. O-GlcNAcylation and phosphorylation target serine or threonine residues, leading to a dynamic interplay as they compete for the same or adjacent sites (Leney et al., 2017). Furthermore, O-GlcNAcylation engages in intricate crosstalk with other PTMs, such as acetylation, methylation, ubiquitination, and proteolysis, offering a myriad of combinations that give rise to diverse protein isoforms in the human proteome (Leutert et al., 2021). Moreover, protein O-GlcNAcylation is very sensitive to the availability of uridine di-phospho-N-acetylglucosamine, the GlcNAc donor for O-GlcNAcylation, and a downstream metabolite of glucose; therefore, O-GlcNAcylation is often referred to as a nutrient sensor in cells (Hardivillé and Hart, 2014). A single N-acetylglucosamine group is attached to the serine and threonine residues of target proteins by O-GlcNAc transferase. In contrast, the enzyme O-GlcNAcase manages the removal of this group (Fisi et al., 2017) (Figure 1). OGT interacts with several intracellular proteins and O-GlcNAcylation to modify proteins associated with various human diseases such as cancer, neurodegenerative and cardiovascular diseases (Nie and Yi, 2019). Rescue metabolites such as glucosamine and N-acetylglucosamine are used to modulate flux through the hexosamine pathway, and pharmacological agents or anti-metabolites have been used to alter activity and/or substrate for research purposes or therapeutic benefit. Since GFAT1 catalyzes the main step in the *de novo* synthesis of HBP, many studies have used inhibitors of this enzyme, which are mainly glutamine analogs as cytotoxic antimetabolites of glutamine, Azaserine is used to study glutamine-dependent metabolic pathways (Van Cura et al., 2023). OSMI-1 has been identified as a permeable Hogt inhibitor. OSMI-1 binds to the active site of hOGT and inhibits the enzyme with an IC₅₀ value of 2.7 μ M *in vitro* (Ju Kim, 2020). On the other hand, Thiamet G is a stable sugar-based inhibitor of the OGA enzyme with excellent inhibitory efficacy (K_i = 21 nM) and good selectivity over human lysosomal β -hexosaminidase (Liu et al., 2017). The effect of glycosylations on the CD36 protein is unclear, but our study shows preliminary



results on the localization of CD36 in response to UDP-GlcNAc levels, using HBP pathway and O-GlcNAcylation modulators.

Materials and methods

Cell culture

The J774.2 mouse bone marrow-derived macrophage cell line was maintained. In RPMI-1640 medium supplemented with 10% fetal bovine serum (FBS) and 1% antibiotic penicillin-streptomycin at 37°C in 5% CO₂.

Western blot

J774 macrophages were cultured in 6-well plates (9.6 cm²), at 1.2×10^6 cells to confluence for 1, 8, and 12 h in RPMI

1640 medium supplemented with 1% FBS, in the presence or absence of 10 μM of TMG (SML0244 Sigma), 50 μM OSMI-1 (SML1621 Sigma) or 0.5 μM Azaserine (A4142 Sigma). The concentrations of the HBP modulators were taken from the following references: OSMI-1 (Ortiz-Meoz et al., 2015), Azaserine (Rajapakse et al., 2009), and TMG (Wani et al., 2017). Cells were then washed with ice-cold PBS and lysed with buffer 50 mM Tris-HCl (pH 8), 137 mM NaCl, 10% (v/v) glycerol, 1% (v/v) Triton, 50 mM NaF, 10 mM disodium β-glycerophosphate, 1 mM Na₃VO₄, and protease inhibitor cocktail tablets (ROCHE) supplemented with 100 μM PUGNAc (A7229 Sigma) and 4 μM TMG (SML0244 Sigma), to preserve the O-GlcNAcylation state of the proteins during the extraction procedure. The quantification of protein content was determined using the BCA Protein Assay Kit (Thermo Scientific™ 23225), according to the manufacturer's instructions. Forty μg of total protein was resolved by a 10% reduction SDS-PAGE using Tris-Glycine gels and transferred to

nitrocellulose membranes (GE Healthcare) at constant amperage (10 V for 14 h). The transfer efficiency and equal loading were verified using Ponceau red staining (17435103 Thermo Scientific). Membranes were first saturated for 60 min with 5% (m/v) nonfat dry milk in Tris-buffered saline (TBS)-Tween buffer [15 mM Tris-HCl, 140 mM NaCl, and 0.05% Tween 20 (vol/vol), pH 8.0]. We used mouse monoclonal anti-O-GlcNAc (RL2, ab2739) at a dilution of 1:1,000, and rabbit polyclonal anti- β -actin (4967 Cell Signaling) at a dilution of 1:1,000 was used as a loading control. After incubation with appropriate antibodies, the bands were visualized using enhanced chemiluminescence reagents (ECL Select, Amersham) and detected with a chemiluminescence ImageQuant™ 500.

Signal density quantification by ImageJ

All western blots were performed independently in triplicate. The obtained images were analyzed by ImageJ software. First, they were converted to 8-bit format, then each “O-GlcNAc protein profile was individually selected and circumscribed with the rectangular ROI selection and “gels” function, followed by quantification of the peak area of the obtained histograms. For more details on the configuration of “gel analyzer options,” see supplementary materials. Data were acquired as arbitrary area values, and the differences in the expression between groups were normalized to β -actin. All data are presented as the means \pm standard deviation for all performed repetitions. Statistically significant differences among three or more groups were analyzed by one-way analysis of variance, followed by Tukey's *post hoc* analysis. *, **, ***, $p < 0.05$, $p < 0.001$, $p < 0.0001$, respectively, ns non-significant.

Immunofluorescence

J774 cells were grown on a Chamber Slide System (Thermo Fisher Scientific) for 12 h in 1% FBS in the absence or presence of TMG [10 μ M], OSMI-1 [50 μ M], or Azaserine [0.5 μ M]. Cells were washed with Phosphate-buffered saline (PBS), fixed with 4% cold methanol for 20 min, and then washed with PBS. Non-specific binding sites were blocked with IgG-free 2% bovine serum albumin (BSA, Thermo Fisher Scientific) for 30 min at room temperature. Slides were washed and incubated with primary antibody (anti-CD36) diluted 1:200 in PBS with 1% albumin overnight at 4°C in a humidity chamber. Slides were washed with TBS and incubated with a second primary antibody (anti-O-GlcNAc) diluted 1:100, and Rab-5 (E6N8S Cell Signaling) diluted 1:100, for 90 min in a dark humidity chamber. Then, the chambers were washed with PBS 3 times for 5 min. We

incubated the secondary antibodies (Alexa 488-conjugated anti-mouse and Alexa 594-conjugated anti-rabbit) diluted 1:100 at room temperature for 60 min in a dark humidity chamber. Slides were washed, stained, and sealed with Fluoroshield with DAPI-mounting medium (Sigma-Aldrich) and coverslipped. Images were obtained with a Cytation 5 imaging reader.

Signal fluorescence quantification by ImageJ

First, images were converted to 16 bits and freehand selected to draw on the circumference of the cells; 10 cells were randomly selected per image in 4 independent experiments. The “measure” function was used to obtain an average fluorescence intensity. Statistically significant differences between groups were analyzed by one-way analysis of variance, followed by Tukey's *post hoc* analysis. *, **, ***, $p < 0.05$, $p < 0.001$, $p < 0.0001$, respectively, ns non-significant.

Signal fluorescence colocalization by ImageJ

Images were converted to 8-bit and analyzed with the JACoP plug-in of the ImageJ software (2006.02.01). The JACoP colocalization plug-in primarily uses statistics to assess the relationship between fluorescence intensities (Bolte and Cordelières, 2006), using Pearson correlation coefficients that measure the strength of the linear relationship between two variables, the gray values of fluorescence intensity pixels of green and red image pairs, this is mostly done using correlation coefficients that measure the strength of the linear relationship between two variables, in this case the gray values of fluorescence intensity pixels of green and red image pairs. Subsequently, statistically significant differences between groups were analyzed by one-way analysis of variance, followed by Tukey's *post hoc* analysis. *, **, ***, $p < 0.05$, $p < 0.001$, $p < 0.0001$, respectively, ns non-significant.

Results

O-GlcNAcylation protein levels respond according to the time treatment with modulators

To analyze the effect of TMG, OSMI-1, and Azaserine on the levels of O-GlcNAcylated proteins, we treated J774 macrophages in the presence of 10 μ M TMG as the optimal dose, 50 μ M OSMI-1, or 0.5 μ M Azaserine, the signal detected in the blot was

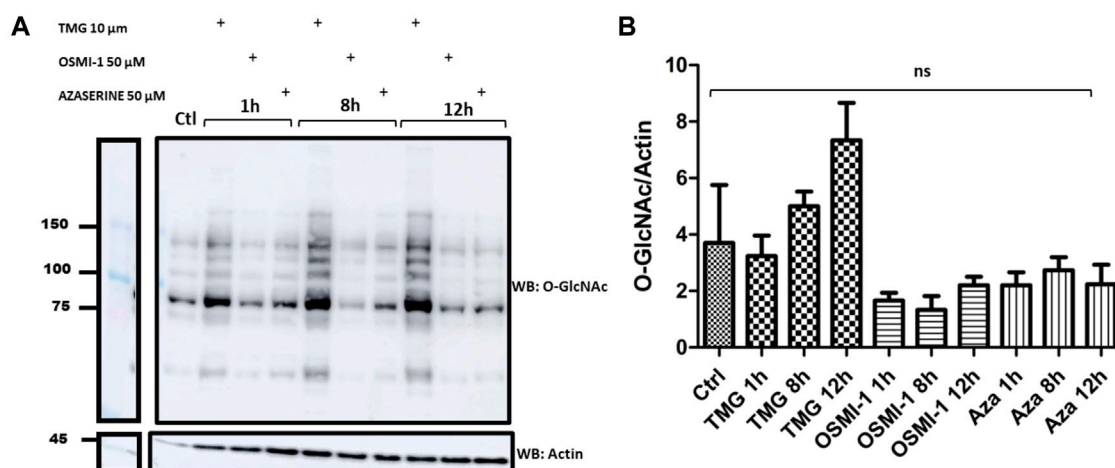


FIGURE 2

Western Blots of the profile of O-GlcNAcylated proteins in J774 macrophages. (A) O-GlcNAc profile in cells without stimulation (control), in the presence or absence of TMG (10 μ M), OSMI-1 (50 μ M), or Azaserine (0.5 μ M), during 1, 8 and 12 h. We incubated Western Blots with anti-O-GlcNAc and anti-actin (as a loading control). (B) The effect of TMG, OSMI-1, and Azaserine treatment on O-GlcNAc/actin protein expression is observed. Graphs represent the means \pm 3 independent experiments. Statistical analysis was performed using a one-way analysis of variance followed by Tukey's *post hoc* test. *, **, ***, $p < 0.05$, $p < 0.001$, $p < 0.0001$, respectively, ns non-significant.

measured by densitometry (Figure 2A), shows O-GlcNAc profile proteins in response to treatments; we noticed that when J774 cells were treated with TMG at 8 and 12 h, they had a tendency to exhibit more O-GlcNAcylation compared to the control. OSMI-1 and Azaserine did not show variations between treatment times, otherwise a better response was observed at 12 h of TMG treatment; after these results, we decided to perform the next experiments at 12 h.

CD36 protein colocalization with O-GlcNAc and Rab-5

To explore the effects of TMG, OSMI-1, and Azaserine treatment on the cellular distribution of CD36, J774 cells were examined using immunofluorescence, and we evaluated the colocalization using Pearson correlation with the JACoP plugin of the ImageJ software. In control cells, CD36 and Rab-5 show a large distribution in intracellular compartments. The increase in UDP-GlcNAc availability under TMG treatment shows a wide distribution to intracellular compartments and areas with increased staining of CD36, which colocalizes with Rab-5, located near the plasma membrane (yellow arrows). Treatment with the OSMI-1 and Azaserine generated a redistribution of CD36 from the cytoplasm to the surface (white arrows). CD36 and Rab-5 colocalization showed a significant decrease in Pearson correlation after treatment with OSMI-1 and Azaserine ($p < 0.05$) (see supplementary materials). These results suggest that CD36 trafficking is sensitive to the environmental status of UDP-GlcNAc.

Discussion

To evaluate the effect of modulators TMG, OSMI-1, and Azaserine on O-GlcNAc protein levels, we treated J774 macrophages. The effects of increased/decreased O-GlcNAcylation levels, depending on the treatment with the aforementioned modulators, were evaluated using an anti-O-GlcNAc antibody (R12). The treatment with OSMI-1 and Azaserine demonstrated a non-significant reduction of O-GlcNAcylated proteins, because their formation depends on the availability of UDP-GlcNAc as a substrate (Rajapakse et al., 2009; Olivier-Van Stichelen et al., 2012; Chiaradonna et al., 2018).

An increase in global O-GlcNAcylation levels was observed when J774 cells were treated with TMG, for 8 and 12 h (Figure 2). Immunofluorescence staining showed significant changes in the mean fluorescence intensity of O-GlcNAcylation after Azaserine treatment ($p < 0.0001$), and we observed a tendency to decrease O-GlcNAcylation after treatment with OSMI-1. We significantly increased O-GlcNAcylation levels by applying TMG treatment ($p < 0.0001$) (Figures 3A, B). These results confirm the function of the modulators. CD36 and O-GlcNAc showed high correlation rates with the control, and we detected no changes between the treatments compared to the control (Figure 3C).

Subsequently, we evaluated whether the availability of UDP-GlcNAc could impact the localization of CD36. We assessed the localization of CD36 by immunofluorescence; J774 macrophages were treated with TMG, OSMI-1, and Azaserine for 12 h. Under

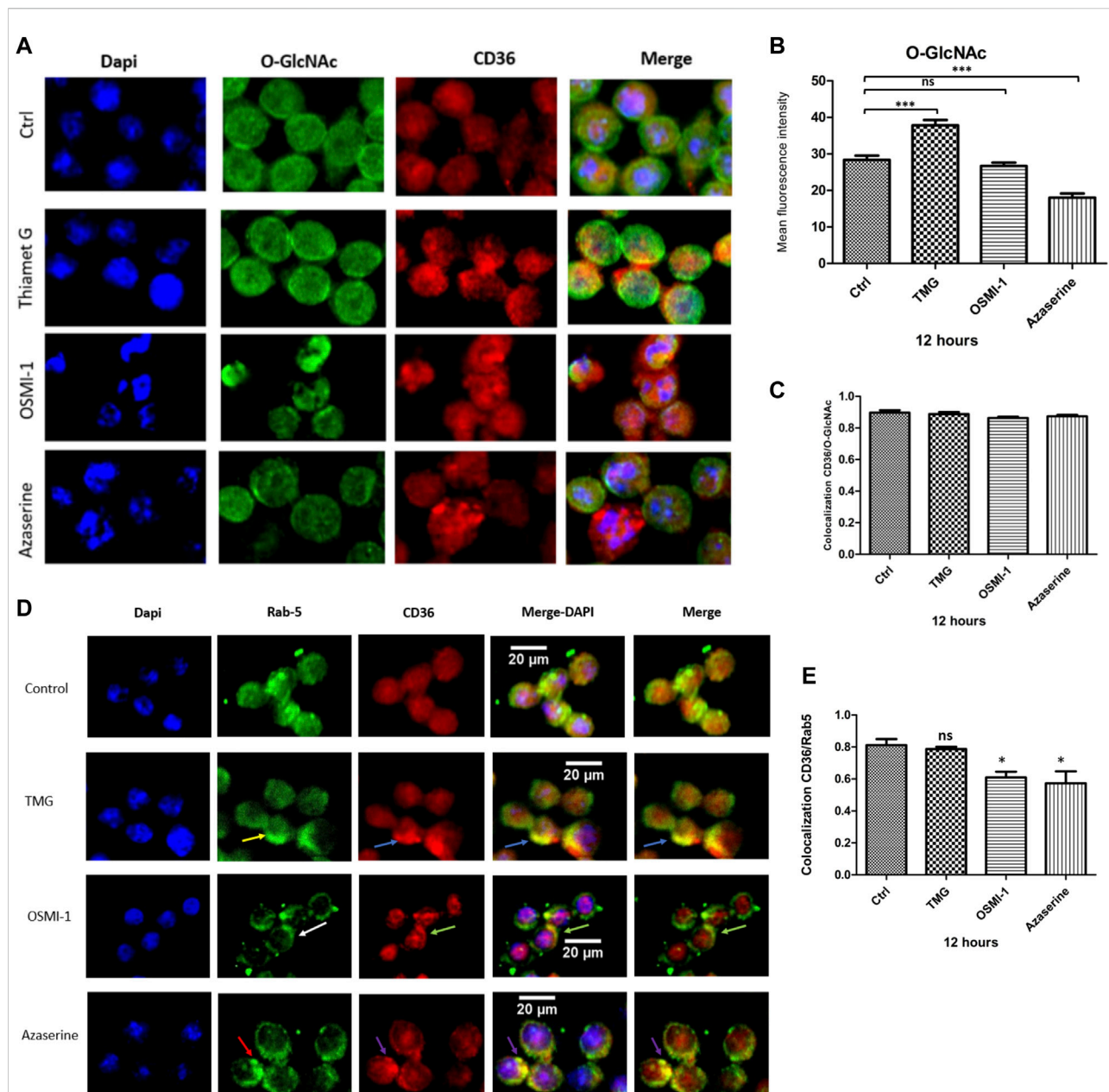


FIGURE 3

CD36 protein colocalization with O-GlcNAc and Rab-5. Macrophages were cultured with RPMI medium either in the presence or absence of TMG, OSMI-1, or Azaserine for 12 h and processed for immunofluorescence, as described in the materials and methods section. (A) Representative images of immunofluorescence staining for O-GlcNAc (green), CD36 (red), and merged with cell nuclei (blue). (B) Histograms represent the means \pm SE from four independent experiments of mean fluorescence intensity of O-GlcNAcylation levels (green), with different treatments of TMG, OSMI-1, and Azaserine for 12 h. (C) The graph represents the means \pm SE from four independent experiments to measure the Pearson correlation of CD36 and O-GlcNAc colocalization, using the JACoP plug-in of the ImageJ software. (D) Representative images of immunofluorescence staining for cell nuclei (blue), Rab-5 (green), and CD36 (red), merged with DAPI and Rab-5/CD36. (E) Bar graphs represent the means \pm SE from four independent experiments of Pearson correlation of Rab-5/CD36 colocalization using the JACoP plug-in in ImageJ. * Significant as compared with untreated controls ($p < 0.05$), using ANOVA followed by Tukey's *post hoc* test, *, **, ***, $p < 0.05$, $p < 0.001$, $p < 0.0001$, respectively, ns; non-significant.

basal conditions, a wide and even distribution of CD36 was observed, both in the cytoplasm and in the plasma membrane. Proteins bound to the Rab-5 antibody were observed predominantly close to the plasma membrane (yellow arrows)

and still present in the cytoplasm, probably in intracellular vesicles. When macrophages were treated with TMG, CD36 was observed to be increased in specific areas close to the plasma membrane (blue arrows), although we obtained non-

significant changes compared to control, in colocalization results. On the other hand, after OSMI-1 treatment, CD36 and Rab-5 tended to redistribute close to the plasma membrane (white and green arrows, respectively). Treatment with Azaserine also redistributed CD36 (red arrows) and Rab-5 (purple arrows) to the plasma membrane (Figure 3D). The colocalization between CD36 and Rab-5 showed a significant decrease with OSMI-1 and Azaserine treatment (Figure 3E).

One study suggested that the N-glycosylations present in CD36 are responsible for the increase of CD36 to the membrane and the β -oxidation of oleate in rat hearts after treatment with N-acetylglucosamine (feeder of the hexosamine pathway), which would therefore increase the levels of UDP-GlcNAc favoring the levels of N-glycosylation (Lauzier et al., 2011). Alternatively, another modification involved in the recruitment of CD36 to the plasma membrane may be O-GlcNAc, as demonstrated by Laczy, when perfusing mouse hearts with N-acetylglucosamine, where the binding of CD36 to OGT was increased, improving fatty acid absorption (Laczy et al., 2011). Our results suggest that the O-GlcNAc modification may play a role in the recruitment of CD36 to the macrophage membrane following treatment with TMG. TMG inhibits the OGA enzyme, thereby increasing O-GlcNAcylation levels. After this treatment, CD36 is predominantly found near the plasma membrane predominantly, after this treatment.

There is evidence that both N-glycosylation and O-GlcNAc modification can contribute to the regulation of membrane trafficking. These modifications depend on the concentration of UDP-GlcNAc, generated by the HBP, through the intervention of several metabolites, such as glucose, glutamine, ATP, and Acetyl-CoA, depending on the environmental conditions, which are increasingly considered central regulators that affect cellular physiology (Bond and Hanover, 2015). The control of membrane trafficking can result from the direct modification of the receptor with O-GlcNAc or through the O-GlcNAcylation of other proteins that regulate endocytic trafficking processes, for example, modifying coat proteins involved in membrane fusion and fission (Guo et al., 2014), or proteins involved in clathrin-mediated endocytosis (Guo et al., 2014; Rahmani et al., 2019).

The decrease in colocalization suggests a redistribution of CD36 close to the plasma membrane after OSMI-1 and Azaserine treatment. This evidence also suggests that CD36 localization may be influenced by the nutrient availability of the cell, which determines the level of UDP-GlcNAc through the flux of the HBP. As mentioned, there are many examples that demonstrate the regulation of membrane trafficking through post-translational modifications; however, much remains to be discovered about the details of these mechanisms. One study that evaluated the impact of O-GlcNAc levels on cellular metabolism and energy homeostasis involved AMPK, a heterotrimeric complex signaling protein with many targets that regulate a wide range of cellular processes. AMPK

upregulates catabolism, inactivates anabolism, and modulates endocytic traffic (Li and Chen, 2019). AMPK phosphorylation increases and ameliorates autophagic flux after inhibiting O-GlcNAcylation. Jin L et al. suggest that O-GlcNAcylation behaves like a regulator of AMPK activity (Jin et al., 2020).

Pathogen recognition, antigen presentation, and macrophage homeostasis are mediated by various receptors, including mannose and scavenger receptors. It has been reported that these receptors co-localize with Rab5 (Mukherjee et al., 2002), and IL-4/PGE2 stimulation significantly increases the expression of the mannose receptor, Rab5, and the Rab5 GEF Rin in mouse bone marrow-derived macrophages (Wainszelbaum et al., 2006). The recycling of CD36 from endosomes to the plasma membrane and *vice versa* is regulated by different families of proteins, adapter proteins (Scales et al., 1999), and Rab-GTPases, which regulate the binding of coat proteins to CD36-enriched areas, leading to the generation of a vesicle that moves through the filaments of the cytoskeleton to its target membrane (Glatz and Luiken, 2018). The Ras superfamily of GTPases is extensively modified by posttranslational modifications like prenylation, phosphorylation, and ubiquitination (Shinde and Maddika, 2018), which facilitate their membrane attachment and determine their subcellular localization and function; phosphorylation could trap the GDP-bound Rab either in the cytosol or at the membrane (Konstantinopoulos et al., 2007). In Hep3B cells, hyper O-GlcNAc modification regulates Rab3A, which attenuates the tumor suppressor effect of Rab3A on hepatocellular carcinoma (HCC) metastasis (Wu et al., 2018). Rab11, another traffic membrane regulator, is also modified by O-GlcNAc (Zhong et al., 2015). The evidence above suggests that glycosylations influence vesicular traffic by directly modifying membrane receptors like CD36 and impacting proteins involved in vesicular traffic, like Rab proteins.

The structure and function of receptors and vesicular trafficking regulatory proteins are mediated by modifications such as glycosylation, that are sensitive to metabolic conditions and impact different physiological contexts, health, and disease. The complexity of glycosylation on CD36 needs to be supported by further research. The structural variation presented by N-glycans is regulated by the modulation in the expression profile and activity of glycosyltransferases and glycosidases, leading to specific N-glycosylation structures in each cell type (Croset et al., 2012; Butler and Spearman, 2014). Direct glycosylation or phosphorylation of glycosyltransferases promotes their activity (Agrawal et al., 2014). Furthermore, glycosyltransferases and glycosidases and/or the availability of their specific substrates also modulate the glycosylation profile (Paneque et al., 2023). Then, the modulation of N-glycosylation is regulated at the transcriptional and post-translational levels and by the availability of substrates, revealing the complexity of regulating N-glycosylation (Esmail and Manolson, 2021). Nutrient availability regulates cellular O-GlcNAcylation levels by determining the amount of UDP-GlcNAc and modulating the

levels of OGT, OGA, and their respective adapter proteins and substrates. Similarly, the activity of the OGT enzyme is regulated by the nutritional conditions of the cell. In response to systemic changes in the metabolic state (through hormonal signals) (Yang and Qian, 2017), specific adapter proteins intervene to O-GlcNAcylate a specific substrate, leading to the activation of key cellular pathways, such as suppression of anabolism, stimulation of gluconeogenesis and ketogenesis, and activation of thermogenesis (Yang and Qian, 2017). This study modified the availability of a single substrate, UDP-GlcNAc, a variable within a complex network that regulates glycosylations. Further investigation using CD36 mutants at specific glycosylation sites may provide more compelling results for understanding its biological effects in folding, maturation, trafficking, secretion, and function.

These results are intended to set a pattern to continue discovering the impact of glycosylations on macrophage functions related to CD36. There are some questions to be addressed, such as whether aberrant modification of these glycosylations could uniquely influence localization, similarly influence inflammatory functions and lipid uptake, or disrupt the physiological conditions of macrophages. Our results suggest that UDP-GlcNAc is available for influx into CD36 and Rab-5 redistribution between the cytoplasm and cell surface.

Limitations of the study

1. Dependence on Specific Modulators: The conclusions of this study rely heavily on the effects of specific chemical modulators (Thiamet G, OSMI-1, and Azaserine) on the HBP. The observed responses may be specific to these compounds and may not fully represent the natural physiological regulation of O-GlcNAcylation. Hence, gene manipulations of OGT, OGA, GFAT, and CD36, will be required in addition to the use of agonists/antagonists of CD36.
2. *In vitro* Model: While the J774 macrophage cell line is a valuable tool, it limits the applicability of the findings to *in vivo* systems, where the cellular environment and interactions are more complex. The results obtained *in vitro* may not fully translate to *in vivo* contexts due to differences in the cellular microenvironment and systemic factors, underscoring the need for further research in this area.
3. Single Time-Point Analysis: Although necessary, the study's focus on specific time points (e.g., 12 h post-treatment) to assess the effects of modulation on protein O-GlcNAcylation and localization may miss transient changes and dynamic processes at other time intervals. A more comprehensive time-point analysis could provide a more nuanced understanding of these processes.
4. Limitations of Quantitative Analysis: The methods used to quantify O-GlcNAcylation levels and protein localization, such as densitometry of Western blots and fluorescence intensity measurements in immunofluorescence, have

inherent limitations in precision and reproducibility. These methods are heavily dependent on the linearity and sensitivity of the detection systems and may not accurately reflect subtle changes in O-GlcNAcylation or protein distribution. Other loading controls, such as β -tubulin or clathrin, may be considered in future studies.

5. Lack of Direct Evidence for Mechanistic Pathways: While the study discusses the potential mechanisms by which O-GlcNAcylation affects protein function and localization, it needs more direct experimental evidence linking specific O-GlcNAcylation changes to observed functional outcomes. Molecular studies or genetic interventions that directly alter O-GlcNAcylation sites on CD36 may provide more conclusive evidence of causality.
6. Generalizability of Findings: The findings are derived from a single type of immune cell (macrophages) and may not be generalizable to other cell types involved in the immune response, such as T cells, B cells, or dendritic cells, which may have different O-GlcNAcylation dynamics and functional responses.

Data availability statement

The original contributions presented in the study are included in the article/supplementary material, further inquiries can be directed to the corresponding author.

Ethics statement

Ethical approval was not required for the studies on animals in accordance with the local legislation and institutional requirements because only commercially available established cell lines were used.

Author contributions

Conceptualization and experimental procedures, KJL-R and YP-C; experimental procedures, E-RH; supervision and critical revision, EZ, and YP-C; critical revision of the manuscript, RS-M, AM-R, RT-R, LA-F, B-FR, SP-C, and AEA-M.

Funding

The author(s) declare that financial support was received for the research, authorship, and/or publication of this article. This research was funded by Consejo Nacional de Humanidades Ciencias y Tecnologías (CONAHACYT), CB 2017-2018, Project Grant Number A1-S-39534 and benefiting KJL-R through grant number: CVU 660789.

Conflict of interest

The authors declare that the research was conducted in the absence of any commercial or financial relationships that could be construed as a potential conflict of interest.

References

- Agrawal, P., Kurcon, T., Pilobello, K. T., Rakus, J. F., Koppolu, S., Liu, Z., et al. (2014). Mapping posttranscriptional regulation of the human glycome uncovers microRNA defining the glycode. *Proc. Natl. Acad. Sci.* 111 (11), 4338–4343. doi:10.1073/pnas.1321524111
- Baranova, I. N., Kurlander, R., Bocharov, A. V., Vishnyakova, T. G., Chen, Z., Remaley, A. T., et al. (2008). Role of human CD36 in bacterial recognition, phagocytosis, and pathogen-induced JNK-mediated signaling. *J. Immunol.* 181 (10), 7147–7156. doi:10.4049/jimmunol.181.10.7147
- Barbero, P., Bittova, L., and Pfeffer, S. R. (2002). Visualization of Rab9-mediated vesicle transport from endosomes to the trans-Golgi in living cells. *J. Cell Biol.* 156 (3), 511–518. doi:10.1083/jcb.200109030
- Bolte, S., and Cordelières, F. P. (2006). A guided tour into subcellular colocalization analysis in light microscopy. *J. Microsc.* 224 (Pt 3), 213–232. doi:10.1111/j.1365-2818.2006.01706.x
- Bond, M. R., and Hanover, J. A. (2015). A little sugar goes a long way: The cell biology of O-GlcNAc. *J. Cell Biol.* 208 (7), 869–880. doi:10.1083/jcb.201501101
- Butler, M., and Spearman, M. (2014). The choice of mammalian cell host and possibilities for glycosylation engineering. *Curr. Opin. Biotechnol.* 30, 107–112. doi:10.1016/j.copbio.2014.06.010
- Chen, Y., Zhang, J., Cui, W., and Silverstein, R. L. (2022). CD36, a signaling receptor and fatty acid transporter that regulates immune cell metabolism and fate. *J. Exp. Med.* 219 (6), e20211314. doi:10.1084/jem.20211314
- Chiaroni, F., Ricciardiello, F., and Palorini, R. (2018). The nutrient-sensing hexosamine biosynthetic pathway as the hub of cancer metabolic rewiring. *Cells* 7 (6), 53. doi:10.3390/cells7060053
- Christoforidis, S., McBride, H. M., Burgoyne, R. D., and Zerial, M. (1999). The Rab5 effector EEA1 is a core component of endosome docking. *Nature* 397 (6720), 621–625. doi:10.1038/17618
- Croset, A., Delafosse, L., Gaudry, J. P., Arod, C., Glez, L., Losberger, C., et al. (2012). Differences in the glycosylation of recombinant proteins expressed in HEK and CHO cells. *J. Biotechnol.* 161 (3), 336–348. doi:10.1016/j.jbiotec.2012.06.038
- Esmail, S., and Manolson, M. F. (2021). Advances in understanding N-glycosylation structure, function, and regulation in health and disease. *Eur. J. Cell Biol.* 100 (7–8), 151186. doi:10.1016/j.ejcb.2021.151186
- Fisi, V., Miseta, A., and Nagy, T. (2017). The role of stress-induced O-GlcNAc protein modification in the regulation of membrane transport. *Oxidative Med. Cell. Longev.* 2017, 1–15. doi:10.1155/2017/1308692
- Glatz, J. F. C., and Luiken, J. J. F. P. (2018). Dynamic role of the transmembrane glycoprotein CD36 (SR-B2) in cellular fatty acid uptake and utilization. *J. Lipid Res.* 59 (7), 1084–1093. doi:10.1194/jlr.R082933
- Guo, B., Liang, Q., Li, L., Hu, Z., Wu, F., Zhang, P., et al. (2014). O-GlcNAc-modification of SNAP-29 regulates autophagosome maturation. *Nat. Cell Biol.* 16 (12), 1215–1226. doi:10.1038/ncb3066
- Hardivillé, S., and Hart, G. W. (2014). Nutrient regulation of signaling, transcription, and cell physiology by O-GlcNAcylation. *Cell metab.* 20 (2), 208–213. doi:10.1016/j.cmet.2014.07.014
- Hoosdally, S. J., Andress, E. J., Wooding, C., Martin, C. A., and Linton, K. J. (2009). The human scavenger receptor CD36: Glycosylation status and its role in trafficking and function. *J. Biol. Chem.* 284 (24), 16277–16288. doi:10.1074/jbc.M109.007849
- Jin, L., Yuan, F., Dai, G., Yao, Q., Xiang, H., Wang, L., et al. (2020). Blockage of O-linked GlcNAcylation induces AMPK-dependent autophagy in bladder cancer cells. *Cell. Mol. Biol. Lett.* 25, 17. doi:10.1186/s11658-020-00208-x
- Ju Kim, E. (2020). O-GlcNAc transferase: structural characteristics, catalytic mechanism and small-molecule inhibitors. *ChemBioChem* 21 (21), 3026–3035. doi:10.1002/cbic.202000194
- Konstantinopoulos, P. A., Karamouzis, M. V., and Papavassiliou, A. G. (2007). Post-translational modifications and regulation of the RAS superfamily of GTPases as anticancer targets. *Nat. Rev. Drug Discov.* 6 (7), 541–555. doi:10.1038/nrd2221

Acknowledgments

We thank the Biochemistry Department of Universidad Nacional Autónoma de México, Mexico City, Mexico, for their technical support.

- Laczy, B., Fülöp, N., Onay-Besikci, A., Des Rosiers, C., and Chatham, J. C. (2011). Acute regulation of cardiac metabolism by the hexosamine biosynthesis pathway and protein O-GlcNAcylation. *PloS one* 6 (4), e18417. doi:10.1371/journal.pone.0018417
- Lauzier, B., Merlen, C., Vaillant, F., McDuff, J., Bouchard, B., Beguin, P. C., et al. (2011). Post-translational modifications, a key process in CD36 function: Lessons from the spontaneously hypertensive rat heart. *J. Mol. Cell. Cardiol.* 51 (1), 99–108. doi:10.1016/j.yjmcc.2011.04.001
- Leney, A. C., El Atmioui, D., Wu, W., Ovaa, H., and Heck, A. J. R. (2017). Elucidating crosstalk mechanisms between phosphorylation and O-GlcNAcylation. *Proc. Natl. Acad. Sci. U. S. A.* 114 (35), E7255–E7261. doi:10.1073/pnas.1620529114
- Leutert, M., Entwistle, S. W., and Villén, J. (2021). Decoding post-translational modification crosstalk with proteomics. *Mol. Cell. Proteomics* 20, 100129. doi:10.1016/j.mcpro.2021.100129
- Li, Y., and Chen, Y. (2019). AMPK and autophagy. *Adv. Exp. Med. Biol.* 1206, 85–108. doi:10.1007/978-981-15-0602-4_4
- Liu, Y., Ren, Y., Cao, Y., Huang, H., Wu, Q., Li, W., et al. (2017). Discovery of a low toxicity O-GlcNAc transferase (OGT) inhibitor by structure-based virtual screening of natural products. *Sci. Rep.* 7 (1), 12334. doi:10.1038/s41598-017-12522-0
- Luiken, J. J., Chanda, D., Nabben, M., Neumann, D., and Glatz, J. F. (2016). Post-translational modifications of CD36 (SR-B2): implications for regulation of myocellular fatty acid uptake. *Biochimica Biophysica Acta (BBA) - Mol. Basis Dis.* 1862 (12), 2253–2258. doi:10.1016/j.bbadis.2016.09.004
- Mori, M., Kimura, H., Iwamura, Y., Arai, S., and Miyazaki, T. (2012). Modification of N-glycosylation modulates the secretion and lipolytic function of apoptosis inhibitor of macrophage (AIM). *FEBS Lett.* 586 (20), 3569–3574. doi:10.1016/j.febslet.2012.08.017
- Mukherjee, K., Parashuraman, S., Krishnamurthy, G., Majumdar, J., Yadav, A., Kumar, R., et al. (2002). Diverting intracellular trafficking of Salmonella to the lysosome through activation of the late endocytic Rab7 by intracellular delivery of muramyl dipeptide. *J. Cell Sci.* 115 (Pt 18), 3693–3701. doi:10.1242/jcs.00034
- Mukhopadhyay, A., Funato, K., and Stahl, P. D. (1997). Rab7 regulates transport from early to late endocytic compartments in *Xenopus* oocytes. *J. Biol. Chem.* 272 (20), 13055–13059. doi:10.1074/jbc.272.20.13055
- Nie, H., and Yi, W. (2019). O-GlcNAcylation, a sweet link to the pathology of diseases. *J. Zhejiang Univ. Sci. B* 20 (5), 437–448. doi:10.1631/jzus.B1900150
- Olivier-Van Stichelen, S., Guinez, C., Mir, A. M., Perez-Cervera, Y., Liu, C., Michalski, J. C., et al. (2012). The hexosamine biosynthetic pathway and O-GlcNAcylation drive the expression of β -catenin and cell proliferation. *Am. J. Physiology. Endocrinol. metabolism* 302 (4), E417–E424. doi:10.1152/ajpendo.00390.2011
- Ortiz-Meoz, R. F., Jiang, J., Lazarus, M. B., Orman, M., Janetzko, J., Fan, C., et al. (2015). A small molecule that inhibits OGT activity in cells. *ACS Chem. Biol.* 10 (6), 1392–1397. doi:10.1021/acscchembio.5b00004
- Paneque, A., Fortus, H., Zheng, J., Werlen, G., and Jacinto, E. (2023). The hexosamine biosynthesis pathway: regulation and function. *Genes* 14 (4), 933. doi:10.3390/genes14040933
- Patel, S. N., Serghides, L., Smith, T. G., Febbraio, M., Silverstein, R. L., Kurtz, T. W., et al. (2004). CD36 mediates the phagocytosis of *Plasmodium falciparum*-infected erythrocytes by rodent macrophages. *J. Infect. Dis.* 189 (2), 204–213. doi:10.1086/380764
- Rahmani, S., Defferrari, M. S., Wakarchuk, W. W., and Antonescu, C. N. (2019). Energetic adaptations: metabolic control of endocytic membrane traffic. *Traffic (Copenhagen, Den.)* 20 (12), 912–931. doi:10.1111/tra.12705
- Rajapakse, A. G., Ming, X. F., Carvas, J. M., and Yang, Z. (2009). The hexosamine biosynthesis inhibitor azaserine prevents endothelial inflammation and dysfunction under hyperglycemic condition through antioxidant effects. *Am. J. Physiology. Heart circulatory physiology* 296 (3), H815–H822. doi:10.1152/ajpheart.00756.2008

- Reily, C., Stewart, T. J., Renfrow, M. B., and Novak, J. (2019). Glycosylation in health and disease. *Nat. Rev. Nephrol.* 15 (6), 346–366. doi:10.1038/s41581-019-0129-4
- Rink, J., Ghigo, E., Kalaidzidis, Y., and Zerial, M. (2005). Rab conversion as a mechanism of progression from early to late endosomes. *Cell* 122 (5), 735–749. doi:10.1016/j.cell.2005.06.043
- Scales, S. J., Gomez, M., and Kreis, T. E. (2000). Coat proteins regulating membrane traffic. *Int. Rev. Cytol.* 195, 67–144. doi:10.1016/s0074-7696(08)62704-7
- Shinde, S. R., and Maddika, S. (2018). Post translational modifications of Rab GTPases. *Small GTPases* 9 (1-2), 49–56. doi:10.1080/21541248.2017.1299270
- Shu, H., Peng, Y., Hang, W., Nie, J., Zhou, N., and Wang, D. W. (2022). The role of CD36 in cardiovascular disease. *Cardiovasc. Res.* 118 (1), 115–129. doi:10.1093/cvr/cvaa319
- Silverstein, R. L., and Febbraio, M. (2009). CD36, a scavenger receptor involved in immunity, metabolism, angiogenesis, and behavior. *Sci. Signal.* 2, re3. doi:10.1126/scisignal.272re3
- Van Cura, D., Ng, T. L., Huang, J., Hager, H., Hartwig, J. F., Keasling, J. D., et al. (2023). Discovery of the azaserine biosynthetic pathway uncovers a biological route for α -diazooester production. *Angewandte Chemie Int. ed. Engl.* 62 (28), e202304646. doi:10.1002/anie.202304646
- Vercoutter-Edouart, A. S., El Yazidi-Belkoura, I., Guinez, C., Baldini, S., Leturcq, M., Mortuaire, M., et al. (2015). Detection and identification of O-GlcNAcylated proteins by proteomic approaches. *Proteomics* 15 (5-6), 1039–1050. doi:10.1002/pmic.201400326
- Wainszelbaum, M. J., Proctor, B. M., Pontow, S. E., Stahl, P. D., and Barbieri, M. A. (2006). IL4/PGE2 induction of an enlarged early endosomal compartment in mouse macrophages is Rab5-dependent. *Exp. Cell Res.* 312 (12), 2238–2251. doi:10.1016/j.yexcr.2006.03.025
- Wani, W. Y., Ouyang, X., Benavides, G. A., Redmann, M., Cofield, S. S., Shacka, J. J., et al. (2017). O-GlcNAc regulation of autophagy and α -synuclein homeostasis; implications for Parkinson's disease. *Mol. Brain* 10 (1), 32. doi:10.1186/s13041-017-0311-1
- Wu, W., Zheng, X., Wang, J., Yang, T., Dai, W., Song, S., et al. (2018). O-GlcNAcylation on Rab3A attenuates its effects on mitochondrial oxidative phosphorylation and metastasis in hepatocellular carcinoma. *Cell death Dis.* 9 (10), 970. doi:10.1038/s41419-018-0961-7
- Yang, X., and Qian, K. (2017). Protein O-GlcNAcylation: Emerging mechanisms and functions. *Nat. Rev. Mol. Cell Biol.* 18 (7), 452–465. doi:10.1038/nrm.2017.22
- Yuan, W., and Song, C. (2020). The emerging role of Rab5 in membrane receptor trafficking and signaling pathways. *Biochem. Res. Int.* 2020, 1–10. doi:10.1155/2020/4186308
- Zhong, J., Martinez, M., Sengupta, S., Lee, A., Wu, X., Chaekady, R., et al. (2015). Quantitative phosphoproteomics reveals crosstalk between phosphorylation and O-GlcNAc in the DNA damage response pathway. *Proteomics* 15 (2-3), 591–607. doi:10.1002/pmic.201400339



OPEN ACCESS

EDITED BY

Grzegorz Wegrzyn,
University of Gdansk, Poland

REVIEWED BY

Mark Charles Glassy,
University of California, San Diego,
United States

*CORRESPONDENCE

Changyuan Yu,
✉ yucy0101@outlook.com
Lidan Li,
✉ cncd_lilidan@163.com

RECEIVED 04 October 2023

ACCEPTED 29 March 2024

PUBLISHED 29 April 2024

CITATION

Hao J, Lv Y, Xiao X, Li L and Yu C (2024),
Sensing antibody functions with a novel
CCR8-responsive engineered cell.
Acta Biochim. Pol. 71:12185.
doi: 10.3389/abp.2024.12185

COPYRIGHT

© 2024 Hao, Lv, Xiao, Li and Yu. This is
an open-access article distributed
under the terms of the Creative
Commons Attribution License (CC BY).
The use, distribution or reproduction in
other forums is permitted, provided the
original author(s) and the copyright
owner(s) are credited and that the
original publication in this journal is
cited, in accordance with accepted
academic practice. No use, distribution
or reproduction is permitted which does
not comply with these terms.

Sensing antibody functions with a novel CCR8-responsive engineered cell

Jianyu Hao¹, Yitong Lv¹, Xufeng Xiao², Lidan Li^{3*} and
Changyuan Yu^{1*}

¹College of Life Science and Technology, Beijing University of Chemical Technology, Beijing, China,
²Jiangsu Key Laboratory of Phylogenomics and Comparative Genomics, Jiangsu Normal University,
Xuzhou, China, ³National Clinical Research Center for Infectious Diseases, Shenzhen Third People's
Hospital, The Second Affiliated Hospital of Southern University of Science and Technology,
Shenzhen, China

Human chemokine receptor 8 (CCR8) is a promising drug target for immunotherapy of cancer and autoimmune diseases. Monoclonal antibody-based CCR8 targeted treatment shows significant inhibition in tumor growth. The inhibition of CCR8 results in the improvement of antitumor immunity and patient survival rates by regulating tumor-resident regulatory T cells. Recently monoclonal antibody drug development targeting CCR8 has become a research hotspot, which also promotes the advancement of antibody evaluation methods. Therefore, we constructed a novel engineered customized cell line HEK293-cAMP-biosensor-CCR8 combined with CCR8 and a cAMP-biosensor reporter. It can be used for the detection of anti-CCR8 antibody functions like specificity and biological activity, in addition to the detection of antibody-dependent cell-mediated cytotoxicity and antibody-dependent-cellular-phagocytosis. We obtained a new CCR8 mAb 22H9 and successfully verified its biological activities with HEK293-cAMP-biosensor-CCR8. Our reporter cell line has high sensitivity and specificity, and also offers a rapid kinetic detection platform for evaluating anti-CCR8 antibody functions.

KEYWORDS

monoclonal antibody, CCR8, engineered cell line, functional evaluation, HEK293-cAMP-biosensor-CCR8

Introduction

Chemokine (C-C motif) receptor 8 (CCR8) is a chemokine receptor principally expressed on regulatory T cells (Treg) (Miller et al., 1990; Vila-Caballer et al., 2019). CCR8 is preferentially expressed in lymphoid organs and participates in the recruitment of Tregs and Th2 cells to inflammatory and tumor sites (Miller et al., 1990; Zingoni et al., 1998; Gombert et al., 2005). CCR8 is a promising drug target for immunotherapy of cancer and autoimmune diseases. Compared to normal tissues, CCR8 is upregulated in rectal cancer, melanoma, gastric cancer, metastatic brain cancer, and metastatic liver cancer, especially in Tregs cells of breast cancer (Agarwal et al., 2013; Cao et al., 2016; Saito

et al., 2017; Hughes and Nibbs, 2018; Kuehnemuth et al., 2018; Li et al., 2018; Wiedemann et al., 2019). More than 30% of Tregs are activated in the presence of CCL1 (Chemokine (C-C motif) ligand 1) in human peripheral blood cells causing the expression of CCR8 upregulation (Yeh et al., 2015; Barsheshet et al., 2017; Xu et al., 2017). In recent years, monoclonal antibodies have been successfully developed as targeted therapies for various inflammatory diseases and cancers (Weiner et al., 2010; Scott et al., 2012; Grilo and Mantalaris, 2019). Tregs with CCR8 were found to be sensitive to the effects of monoclonal antibodies (mAbs), which may have a significant impact on the immune response (García-Domínguez et al., 2021). Many CCR8 monoclonal antibodies have been produced by hybridomas to explore their biological function and cancer immunotherapy (Villarreal et al., 2018).

Various assays were performed to evaluate the properties of the antibody. The biological activities could be measured by Enzyme-linked immunosorbent assay (ELISA) (Suárez et al., 2016).

The biological functions of mAbs could be measured by ELISA (Xiao and Isaacs, 2012; Waritani et al., 2017). Western blot is a widely used analytical technique in molecular biology and immunogenetics that detects specific proteins or antibodies, which was used to detect the biological function, thermal stability, and purity of antibodies (Mahmood and Yang, 2012; Ma et al., 2019).

However, these approaches are time- and solvent-consuming and often involve several complicated procedures. BIAcore could be utilized to indicate the retention of antigen binding and specificity, but it requires costly instrumentation and specialized reagents (Hutchinson, 1995). In this study, we developed a novel CCR8 response engineered cell to achieve rapid dynamic detection of antibody specificity and biological activity. First, we constructed a cAMP signaling pathway regulated by G protein-coupled receptors in HEK293 cells by lentiviral infection. The anti-CCR8 antibodies regulate the level of intracellular cAMP after binding to cell surface receptors, which characterizes the specificity and biological activity of anti-CCR8 antibodies. Compared with ELISA and complex flow cytometers, the operation of the experiment becomes more convenient with the CCR8 response engineered cell sensing system. Our detection platform can be completed in 6 h and dynamically evaluates intracellular cAMP levels. Our reporter cell line has high sensitivity and specificity and also offers a rapid kinetic detection platform for evaluating antibody functions.

Materials and methods

All of the oligonucleotides used in this work were synthesized by Genewiz. (Suzhou, China). Forskolin was obtained from MedChemExpress (Shanghai, China). jetPRIME was from Polyplus (Franch) and CCL1 was purchased from R&D

Systems (Minnesota, United States). SP2/0 and HEK293T were purchased from Procell (Hubei, China). The engineered cell lines, Jurkat-NFAT-Luc2-CD16a-V158, Jurkat-NFAT-Luc2-CD32a-V158, BXPC-3-CCR8, CHO-K1-cyno-CCR8, CHO-K1-CCR8 and HEK293T-CCR8 used in this work were constructed in our previous research.

Construction of the HEK293-cAMP-biosensor-CCR8

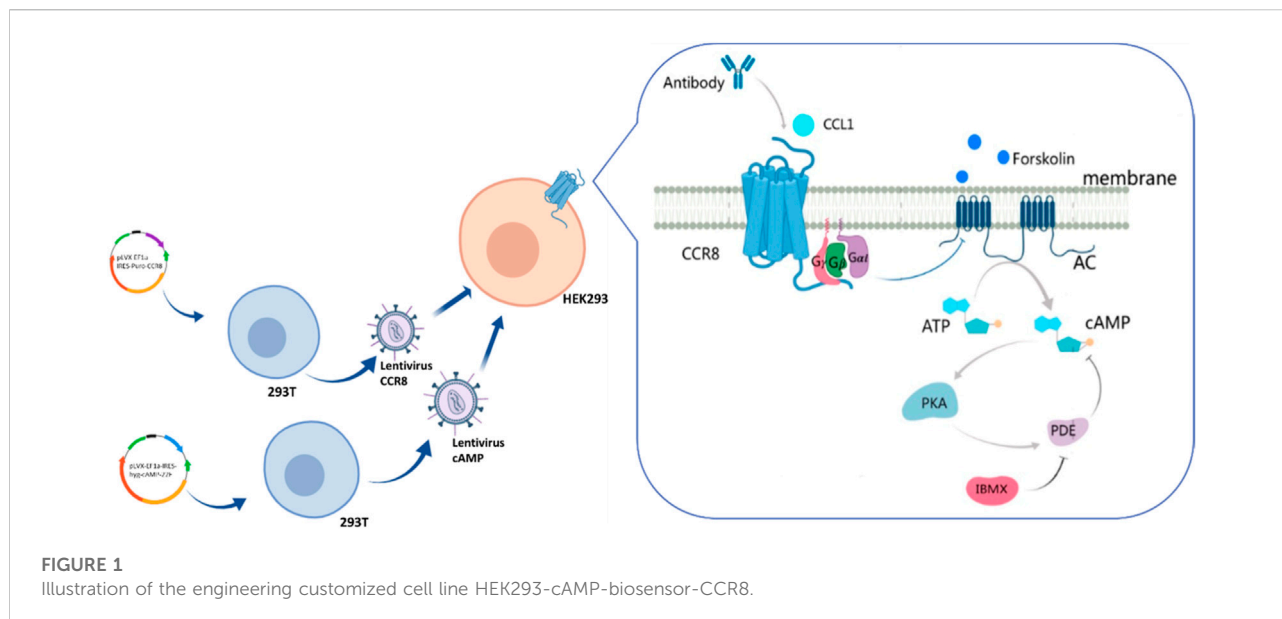
The DNA coding sequences for CCR8 and cAMP biosensors were cloned into the vector pLVX to generate the pLVX-IRES-hyg-cAMP-22F and pLVX-EF1a-IRES-puro-CCR8 vectors. Lentiviral particles were produced in HEK293T cells by transient co-transfection with the helper plasmids PSPAX2 and PMD2G using jetPRIME. HEK293T was cultured in RPMI1640 supplemented with 10% fetal bovine serum and incubated at 37°C in a humidified atmosphere of 5% CO₂/95% air for 48 h. The virus was collected and concentrated after 12 h and resuspended in a medium to obtain the lentiviral particles. The method of lentiviral infection was used to gradually integrate the foreign genes cAMP-biosensor and CCR8 into the target cell HEK293T. HEK293T-cAMP-biosensor-CCR8 was cultured in RPMI1640 medium supplemented with 9 µg/mL Puromycin, 100 µg/mL Hygromycin B and 10% fetal bovine serum and incubated at 37°C in a humidified atmosphere of 5% CO₂/95% air. After antibiotic killing, gene overexpression efficiencies were verified by Glosensor cAMP and flow cytometer.

Validation of the HEK293-cAMP-biosensor-CCR8

Cells were collected after digestion with 0.25% trypsin-EDTA and seeded at a density of 20,000 cells per well in a 96-well opaque assay plate. These cells were cultured in a CO₂-independent medium supplemented with Glosensor cAMP Reagent and 10% fetal bovine serum and incubated at 37°C in a humidified atmosphere of 5% CO₂/95% air for 2 h. 0.1 mL of CCL1 (1 ng/mL) was added to the assay plate and incubated in dark conditions for 0.5 h. After adding 0.01 mL of Forskolin (1 µM), luminescence signals were measured using the BMG CLARIO star.

Flow cytometry (FACS)

Homogenous cells of HEK293-cAMP-Biosensor-CCR8 were collected after digestion with 0.25% trypsin-EDTA and seeded at a density of 20,000 cells per well in a 96-well assay plate. PE Anti-human CD198 antibody was added at 1 µg/mL



and the cells were incubated at 4°C in dark conditions for 1 h with Anti-human-CD198 (CCR8). After cleaning with PBS, data were acquired with a flow cytometer (Luminex Corporation, Inc.) and analyzed using FlowJo.

Antibody validation by enzyme-linked immunosorbent assay (ELISA)

BXPC-3-CCR8 cells were collected after digestion with 0.25% trypsin-EDTA and seeded at a density of 20,000 cells per well in a 96-well assay plate. After the cells were fixed and washed with PBS, the 22H9 antibody was added at a 10-fold dilution of 20 µg/mL as the starting concentration. Mouse serum (971) was used as a positive control, and the unrelated antibody IgG isotype was used as a negative control. HRP-conjugated anti-mouse IgG was incubated as a secondary antibody. ELISA signals were measured using the TMB Substrate Reagent Set (BD Bioscience, San Diego, United States).

Antibody-dependent cell-mediated cytotoxicity (ADCC) and antibody-dependent-cellular-phagocytosis (ADCP) assays

Cells were collected after digestion with 0.25% trypsin-EDTA and seeded at a density of 10,000 cells per well in a 96-well opaque assay plate and then co-cultured with Jurkat-NFAT-Luc2-CD16a V158 and Jurkat-NFAT-Luc2-CD32a V158. 22H9 was added at a maximum concentration of 10 µg/mL at a 10x dilution and incubated

for 6 h, followed by the addition of 50 µL luciferase substrate; luminescence signals were measured using the BMG CLARIO star.

Results and discussion

As shown in Figure 1, the DNA coding sequences for CCR8 and the cAMP biosensor were cloned into the pLVX vector. Lentiviral particles were produced in HEK-293T cells by transient co-transfection with the helper plasmids PSPAX2 and PMD2G using jetPRIME. Lentiviral infection was employed to gradually integrate the foreign genes encoding the cAMP biosensor and CCR8 into the target HEK293 cells. CCR8 is currently recognized as the sole receptor for CCL1 (Korbecki et al., 2020). Upon binding and activation of CCR8 by CCL1, intracellular Gαi proteins are recruited. These Gαi proteins inhibit the activation of adenylate cyclase (AC), leading to a decrease in intracellular cAMP levels (Wang et al., 2020). Antibodies that specifically bind to CCR8 can hinder the activation of CCR8 by CCL1, resulting in an increase in intracellular cAMP concentrations. Intracellular cAMP concentrations can serve as an indicator of antibody bioactivity.

Forskolin, a potent activator of AC, is known to increase the production of intracellular cAMP (Alasbahi and Melzig, 2012; Sapio et al., 2017). First, the cAMP biosensor vector was transfected into HEK-293 cells. To confirm the successful construction of the HEK293-cAMP-biosensor cell line, Forskolin was utilized to stimulate intracellular cAMP production, and its concentration was measured using the Glosensor cAMP reagent. As the concentration of Forskolin

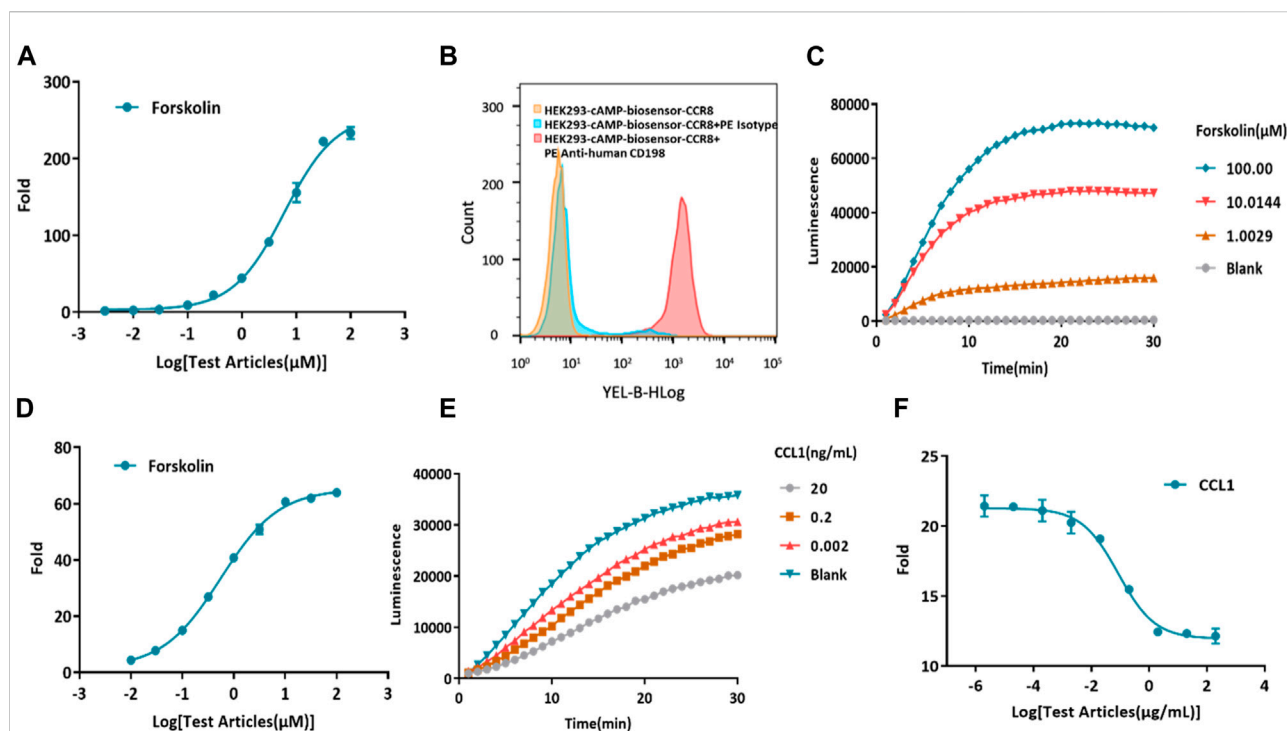


FIGURE 2

Construction of a model for kinetic detection of the HEK293-cAMP-biosensor-CCR8 reporter cell line. (A) Activation of forskolin on the HEK293-cAMP-Biosensor. The intracellular cAMP levels display a dose-dependent increase as the concentration of Forskolin also increases. The Y-axis "Fold" represents the multiple of the dosing group versus the blank group. (B) Flow cytometry measurements of CCR8 mAb binding on the homogeneous cell clone HEK293-cAMP-Biosensor-CCR8 1B1 reporter cell line. (C,D) Kinetics of the HEK293-cAMP-Biosensor-CCR8 reporter cell line upon treatment with different concentrations of Forskolin. The cAMP signal value progressively increases as the concentration of Forskolin also increases. (E,F) Kinetics of intracellular cAMP levels in the HEK293-cAMP-Biosensor-CCR8 reporter cell line treated with different concentrations of CCL1 and Forskolin (1 μ M). The cAMP signal value gradually decreases as the concentration of CCL1 increases.

increased, intracellular cAMP levels also increased, indicating the successful establishment of the HEK293-cAMP-biosensor cell line (Figure 2A). Single-cell clones were generated for the HEK293-cAMP-biosensor-CCR8 cells. The expression of CCR8 in the target cells was verified by flow cytometry analysis (Supplementary Figure S2). Based on the results of flow cytometry and functional assays, the homogeneous cell clone 1B1 was selected for further experiments. Flow cytometry analysis showed a single peak, indicating specific binding of the CCR8 monoclonal antibody to cell surface CCR8 expression (Figure 2B). A 30-min kinetic assay was performed to examine the cAMP signaling pathways in the cells (Figure 2C; Supplementary Figure S1A), and the data from the 10-minute time point were chosen for analysis (Figure 2D). With increasing concentrations of Forskolin, the intracellular cAMP levels exhibited a corresponding increase. These results suggested the successful construction of the HEK293-cAMP-biosensor-CCR8 reporter cell line. Furthermore, based on the findings in Figures 2A, D, forskolin concentration of 1 μ M was selected for the subsequent experiments. CCL1 was added at a concentration of 200 ng/mL, at a 10x dilution with nine test concentrations. After incubation in the dark for 0.5 h, kinetic detection was performed using 1 μ M Forskolin (Figures 2E, F;

Supplementary Figure S1B). This established a kinetic detection platform capable of measuring intracellular cAMP levels.

A total of 10 female Balb/c mice, aged 6–8 weeks, were immunized by injecting CCR8 mRNA (10 μ g/mouse) into the inner thigh muscle of the hind leg. Antibody titers in the blood were assessed by tail cutting (Supplementary Figure S3). Splenocytes were then electrofused with SP2/0 cells to generate a hybridoma cell line. Flow cytometry and enzyme-linked immunosorbent assay (ELISA) were employed to evaluate the binding activity of the monoclonal hybridoma cell supernatant (Supplementary Figures S4, S5). The optimal antibody, 22H9, was selected for further experiments.

The functionality of the new anti-CCR8 antibody, 22H9, was assessed using the HEK293-cAMP-biosensor-CCR8 reporter cell line. In this system, varying concentrations of 22H9, CCL1, and Forskolin were co-incubated to observe the kinetics (Figure 3A; Supplementary Figure S1C). The results indicated that the HEK293-cAMP-biosensor-CCR8 reporter system exhibited remarkable sensitivity, even at low antibody concentrations. As the antibody concentration increased, the inhibitory effect of CCL1 on the cAMP signaling pathway decreased, leading to an increase in the induction factor (Figure 3B). We hypothesized that

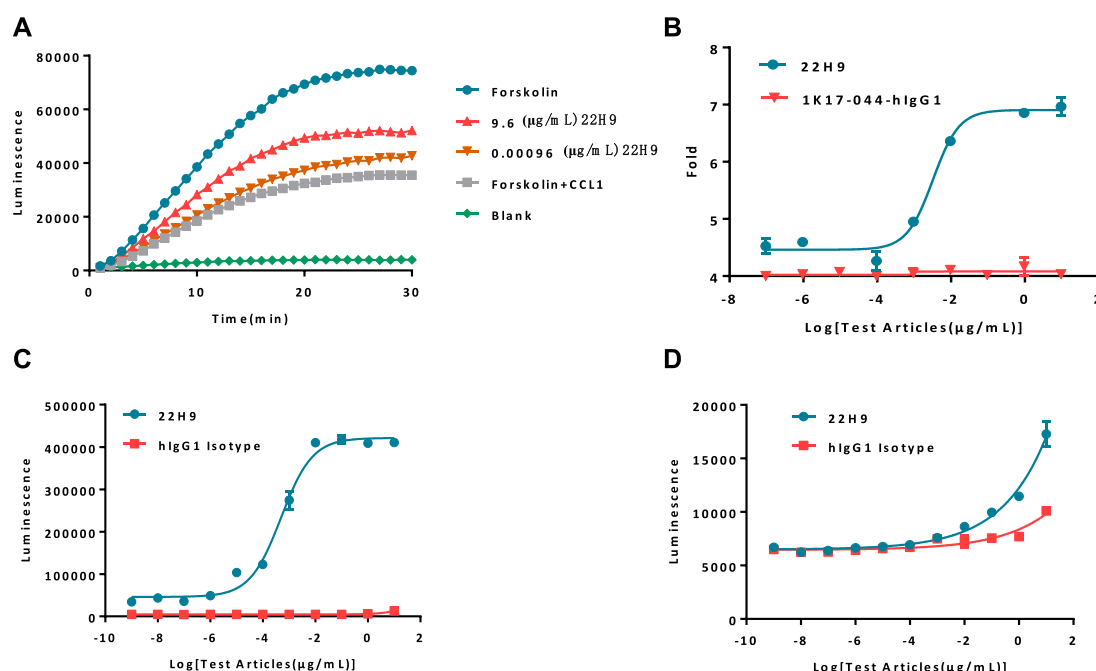


FIGURE 3

Report cell line evaluation of antibody activity. (A) Kinetics of antibodies blocking the binding of CCL1. As the concentration of the antibody increases, the cAMP signal value exhibits a corresponding increase. (B) Fold response of the antibody blocking the binding of CCL1. (C) Antibody-dependent cell-mediated cytotoxicity activity against HEK293-cAMP-Biosensor-CCR8. (D) Antibody-dependent-cell-phagocytosis activity against HEK293-cAMP-Biosensor-CCR8.

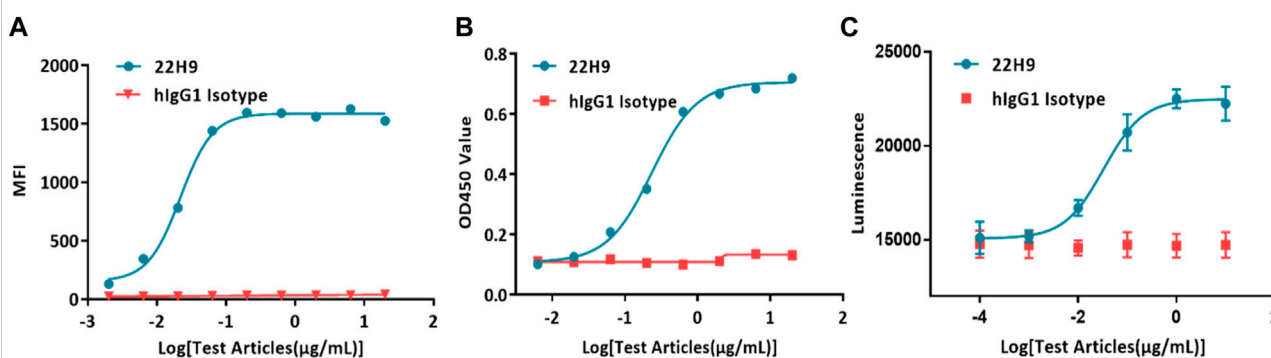


FIGURE 4

Demonstration of the specificity and biological activity of the 22H9 antibody. (A) Binding of the 22H9 antibody to HEK293T-CCR8 by flow cytometry. (B) Binding of the 22H9 antibody to HEK293T-CCR8 by ELISA. (C) Antibody blocking the binding of CCL1 to HEK293-cAMP-Biosensor-CCR8.

this antibody binds to the CCR8 receptor on the cell surface and effectively blocks the activation of the chemokine CCL1. To evaluate the ADCC and ADCP activity of 22H9, we utilized the Jurkat-NFAT-Luc2-CD16a-V158 and Jurkat-NFAT-Luc2-CD32a-V158 reporter cell lines, respectively. As depicted in Figures 3C, D, the anti-CCR8 antibody 22H9 bound to its target on the surface of the HEK293-cAMP-biosensor-

CCR8 cells, thereby activating ADCC and ADCP. The luminescence intensity increased with higher antibody concentrations, allowing the detection of the biological activity of 22H9. Our engineered cell line proves useful for evaluating antibody activity.

Typically, antibody binding activity is assessed using flow cytometry or ELISA. In the case of the new anti-CCR8

antibody 22H9, its binding capacity was characterized by measuring fluorescence values. The EC₅₀ values, as determined by flow cytometry (Figure 4A) and ELISA (Figure 4B), were 0.0218 µg/mL and 0.236 µg/mL, respectively. However, these methods are time-consuming, require the use of solvents, and involve several complicated steps. Alternatively, the binding activity of antibodies can be evaluated using the HEK293-cAMP-biosensor-CCR8 reporter system. In this system, 22H9 binds to CCR8, blocking the binding activity of CCL1. Upon the addition of forskolin, luminescence increases. Different concentrations of the antibody elicit different responses, with an EC₅₀ value of 0.0332 µg/mL (Figure 4C). Compared to traditional methods using an inherent Luciferase reporter gene system, the reporter cell system developed in this study exhibits high sensitivity and can effectively characterize the specificity of anti-CCR8 antibodies.

Conclusion

In summary, we have successfully constructed a reporter cell line that regulates the cAMP signaling pathway through the CCR8 protein receptor. The anti-CCR8 antibody can specifically bind to the cell surface G protein-coupled receptor CCR8 to block the binding of the chemokine CCL1 to CCR8. The specificity and biological activity of antibodies are demonstrated by intracellular cAMP levels. In this study, we constructed reporter cell lines to provide a rapid dynamic detection platform for the specificity and biological activity of CCR8 antibodies.

Data availability statement

The original contributions presented in the study are included in the article/supplementary material, further inquiries can be directed to the corresponding authors.

References

- Agarwal, M., He, C., Siddiqui, J., Wei, J. T., and Macoska, J. A. (2013). CCL11 (eotaxin-1): a new diagnostic serum marker for prostate cancer. *Prostate* 73, 573–581. doi:10.1002/pros.22597
- Alasbahi, R. H., and Melzig, M. F. (2012). Forskolin and derivatives as tools for studying the role of cAMP. *Pharmazie* 67, 5–13. doi:10.1691/ph.2012.1642
- Barsheshet, Y., Wildbaum, G., Levy, E., Vitenshtein, A., Akinseye, C., Griggs, J., et al. (2017). CCR8+FOXP3+ Treg cells as master drivers of immune regulation. *Proc. Natl. Acad. Sci. U. S. A.* 114, 6086–6091. doi:10.1073/pnas.1621280114
- Cao, Q., Wang, N., Qi, J., Gu, Z., and Shen, H. (2016). Long non-coding RNA-GAS5 acts as a tumor suppressor in bladder transitional cell carcinoma via regulation of chemokine (C-C motif) ligand 1 expression. *Mol. Med. Rep.* 13, 27–34. doi:10.3892/mmr.2015.4503
- García-Domínguez, M., González-Rodríguez, S., Hidalgo, A., Baamonde, A., and Menéndez, L. (2021). Kappa-opioid receptor-mediated thermal analgesia evoked by the intrathecal administration of the chemokine CCL1 in mice. *Fundam. Clin. Pharmacol.* 35, 1109–1118. doi:10.1111/fcp.12685
- Gombert, M., Dieu-Nosjean, M.-C., Winterberg, F., Bunemann, E., Kubitz, R. C., Da Cunha, L., et al. (2005). CCL1-CCR8 interactions: an Axis mediating the recruitment of T cells and langerhans-type dendritic cells to sites of atopic skin inflammation. *J. Immunol.* 174, 5082–5091. doi:10.4049/jimmunol.174.8.5082
- Grilo, A. L., and Mantalaris, A. (2019). The increasingly human and profitable monoclonal antibody market. *Trends Biotechnol.* 37, 9–16. doi:10.1016/j.tibtech.2018.05.014
- Hughes, C. E., and Nibbs, R. J. B. (2018). A guide to chemokines and their receptors. *FEBS J.* 285, 2944–2971. doi:10.1111/febs.14466
- Hutchinson, A. M. (1995). Evanescent wave biosensors - real-time analysis of biomolecular interactions. *Mol. Biotechnol.* 3, 47–54. doi:10.1007/BF02821334
- Korbecki, J., Grochans, S., Gutowska, I., Barczak, K., and Baranowska-Bosiacka, I. (2020). Cc chemokines in a tumor: a review of pro-cancer and anti-cancer properties of receptors ccr5, ccr6, ccr7, ccr8, ccr9, and ccr10 ligands. *Int. J. Mol. Sci.* 21, 7619. doi:10.3390/ijms21207619

Ethics statement

The studies involving animal subjects were reviewed and approved by College of Life Science and Technology, Beijing University of Chemical Technology (Ethical number: 2021068).

Author contributions

JH: analysis and interpretation of results; YL and XX: data collection and draft manuscript preparation; CY and LL: conceptualization and supervision. All authors contributed to the article and approved the submitted version.

Funding

The author(s) declare(s) financial support was received for the research, authorship, and/or publication of this article. This work was supported by the National Natural Science Foundation of China (Grant No. 82174531) and the Shenzhen Fund for Guangdong Provincial High-level Clinical Key Specialties (No. SZGSP010).

Conflict of interest

The authors declare that the research was conducted in the absence of any commercial or financial relationships that could be construed as a potential conflict of interest.

Supplementary Material

The Supplementary Material for this article can be found online at: <https://www.frontierspartnerships.org/articles/10.3389/abp.2024.12185/full#supplementary-material>

- Kuehnemuth, B., Piseddu, I., Wiedemann, G. M., Lauseker, M., Kuhn, C., Hofmann, S., et al. (2018). CCL1 is a major regulatory T cell attracting factor in human breast cancer. *BMC Cancer* 18, 1278. doi:10.1186/s12885-018-5117-8
- Li, Z., Chan, K., Qi, Y., Lu, L., Ning, F., Wu, M., et al. (2018). Participation of cd1 in snail-positive fibroblasts in colorectal cancer contribute to 5-fluorouracil/paclitaxel chemoresistance. *Cancer Res. Treat.* 50, 894–907. doi:10.4143/crt.2017.356
- Ma, H., Ó'Fágáin, C., and O'Kennedy, R. (2019). Unravelling enhancement of antibody fragment stability – role of format structure and cysteine modification. *J. Immunol. Methods* 464, 57–63. doi:10.1016/j.jim.2018.10.012
- Miller, M. D., Wilson, S. D., Dorf, M. E., Seunanez, H. N., O'Brien, S. J., and Krangel, M. S. (1990). Sequence and chromosomal location of the I-309 gene. Relationship to genes encoding a family of inflammatory cytokines. *J. Immunol.* 145, 2737–2744. doi:10.4049/jimmunol.145.8.2737
- Saito, M., Sejima, H., Naito, T., Ushirogawa, H., Matsuzaki, T., Matsuura, E., et al. (2017). The CC chemokine ligand (CCL) 1, upregulated by the viral transactivator Tax, can be downregulated by minocycline: possible implications for long-term treatment of HTLV-1-associated myelopathy/tropical spastic paraparesis. *Virology J.* 14, 234. doi:10.1186/s12985-017-0902-6
- Sapio, L., Gallo, M., Illiano, M., Chiosi, E., Naviglio, D., Spina, A., et al. (2017). The natural cAMP elevating compound forskolin in cancer therapy: is it time? *J. Cell. Physiology* 232, 922–927. doi:10.1002/jcp.25650
- Scott, A. M., Wolchok, J. D., and Old, L. J. (2012). Antibody therapy of cancer. *Nat. Rev. Cancer* 12, 278–287. doi:10.1038/nrc3236
- Suárez, I., Salmerón-García, A., Cabeza, J., Capitán-Vallvey, L. F., and Navas, N. (2016). Development and use of specific ELISA methods for quantifying the biological activity of bevacizumab, cetuximab and trastuzumab in stability studies. *J. Chromatogr. B* 1032, 155–164. doi:10.1016/j.jchromb.2016.05.045
- Vila-Caballer, M., González-Granado, J. M., Zorita, V., Abu Nabah, Y. N., Silvestre-Roig, C., del Monte-Monge, A., et al. (2019). Disruption of the CCL1-CCR8 axis inhibits vascular Treg recruitment and function and promotes atherosclerosis in mice. *J. Mol. Cell. Cardiol.* 132, 154–163. doi:10.1016/j.jmcc.2019.05.009
- Villarreal, D. O., L'Huillier, A., Armington, S., Mottershead, C., Filippova, E. V., Coder, B. D., et al. (2018). Targeting CCR8 induces protective antitumor immunity and enhances vaccine-induced responses in colon cancer. *Cancer Res.* 78, 5340–5348. doi:10.1158/0008-5472.CAN-18-1119
- Wang, C., Xu, R., Wang, X., Li, Q., Li, Y., Jiao, Y., et al. (2020). Spinal CCL1/CCR8 regulates phosphorylation of GluA1-containing AMPA receptor in postoperative pain after tibial fracture and orthopedic surgery in mice. *Neurosci. Res.* 154, 20–26. doi:10.1016/j.neures.2019.05.003
- Waritani, T., Chang, J., McKinney, B., and Terato, K. (2017). An ELISA protocol to improve the accuracy and reliability of serological antibody assays. *MethodsX* 4, 153–165. doi:10.1016/j.mex.2017.03.002
- Weiner, L. M., Surana, R., and Wang, S. (2010). Monoclonal antibodies: versatile platforms for cancer immunotherapy. *Nat. Rev. Immunol.* 10, 317–327. doi:10.1038/nri2744
- Wiedemann, G. M., Röhrle, N., Makeschin, M. C., Fessler, J., Endres, S., Mayr, D., et al. (2019). Peritumoral CCL1 and CCL22 expressing cells in hepatocellular carcinomas shape the tumour immune infiltrate. *Pathology* 51, 586–592. doi:10.1016/j.pathol.2019.06.001
- Xiao, Y., and Isaacs, S. N. (2012). Enzyme-linked immunosorbent assay (ELISA) and blocking with bovine serum albumin (BSA)-not all BSAs are alike. *J. Immunol. Methods* 384, 148–151. doi:10.1016/j.jim.2012.06.009
- Xu, Y., Dong, X., Qi, P., Ye, Y., Shen, W., Leng, L., et al. (2017). Sox2 communicates with Tregs through CCL1 to promote the stemness property of breast cancer cells. *Stem Cells* 35, 2351–2365. doi:10.1002/stem.2720
- Yang, P. C., and Mahmood, T. (2012). Western blot: technique, theory, and trouble shooting. *North Am. J. Med. Sci.* 4, 429. doi:10.4103/1947-2714.100998
- Yeh, C.-R., Hsu, I., Song, W., Chang, H., Miyamoto, H., Xiao, G.-Q., et al. (2015). Fibroblast ERα promotes bladder cancer invasion via increasing the CCL1 and IL-6 signals in the tumor microenvironment. *Am. J. cancer Res.* 5, 1146–1157.
- Zingoni, A., Soto, H., Hedrick, J. A., Stoppacciaro, A., Storlazzi, C. T., Sinigaglia, F., et al. (1998). Cutting edge: the chemokine receptor CCR8 is preferentially expressed in Th2 but not Th1 cells. *J. Immunol.* 161, 547–551. doi:10.4049/jimmunol.161.2.547

Effects of Baimuxinol on the inflammation and oxidative stress of LPS-induced RAW264.7 macrophages *via* regulating the NF- κ B/I κ B α and Nrf2/ARE signaling pathway

Yan Chen¹, Nan Chen¹, Jing Wang² and Shuqing Li¹✉

¹Department of critical care, Taizhou Hospital of traditional Chinese Medicine, Taizhou, Jiangsu, China; ²Department of emergency, Taizhou Hospital of traditional Chinese Medicine, Taizhou, Jiangsu, China

Baimuxinol (BAI) is a sesquiterpenoid compound isolated from agarwood. This study aimed to investigate the specific mechanism of BAI on the inflammation as well as oxidative stress of RAW264.7 cells induced by lipopolysaccharide (LPS). The proliferation and cell viability were detected with EdU and MTT assay. The levels of inflammatory factors and antioxidant-related indexes were determined with corresponding kits. The qRT-PCR and western blot assays were performed to detect the expression of the related genes. We found that compared with the control group, cell viability and proliferation of the RAW264.7 cells was increased in the LPS group, while it was decreased in the BAI groups. In addition, in the LPS group, the contents of TNF- α , IL-1 β , IL-6, ROS, MDA, PC and 8-OHdG were increased, the activities of T-SOD and CAT were decreased in comparison with the control group. It was reversed after BAI treatment. Finally, we confirmed that the NF- κ B/I κ B α signaling pathway is inhibited and the Nrf2/ARE signaling pathway is activated after BAI treatment. BAI relieved inflammation and oxidative stress of RAW264.7 macrophages induced by LPS through regulating the NF- κ B/I κ B α and Nrf2/ARE signaling pathway, which provided a novel insight for the therapy of sepsis.

Keywords: Baimuxinol, oxidative stress, lipopolysaccharide, proliferation, viability

Received: 11 February, 2022; **revised:** 16 March, 2022; **accepted:** 01 November, 2022; **available on-line:** 11 February, 2023

✉e-mail: chenqy_yan@163.com

Acknowledgements of Financial Support: The study was supported by Taizhou TCM science and technology development project(TZ202203)

Abbreviations: BAI, Baimuxinol; CAT, catalase; HO-1, heme oxygenase-1; IL-1 β , interleukin 1 β ; IL-6, interleukin 6; LPS, lipopolysaccharide; MDA, malondialdehyde; PC, protein carbonyl; ROS, reactive oxygen species; SOD, superoxide dismutase; TNF- α , tumor necrosis factor α

INTRODUCTION

Sepsis is a systemic inflammatory response syndrome, which refers to organ dysfunction caused by host response disorder. It is a serious life-threatening disease, not only has a high incidence rate and mortality but also takes up a lot of medical resources (Arefian *et al.*, 2017). In 2016, the global medical community redefined sepsis, pointing out that sepsis is a fatal organ dysfunction due to the infection (Singer *et al.*, 2016). At present, despite the advances in antibiotic therapy (Alhashem *et al.*, 2017), mechanical therapy (Zampieri *et al.*, 2017), maintaining blood glucose balance (Dellinger *et al.*, 2008) and other

treatment methods, severe sepsis is still the main cause of death. In addition, in the process of an inflammatory response, macrophages recognize pathogen/injury-related molecular patterns such as lipopolysaccharide (LPS) through toll-like receptor 4 (TLR4) and other pattern recognition receptors expressed on their cell membrane and then activate downstream signaling pathways, such as NF- κ B and MAPKs (Lancaster *et al.*, 2018). Many studies have confirmed that NF- κ B is closely related to inflammation (McDaniel *et al.*, 2016; Zaidi *et al.*, 2018). The p65/p50 NF- κ B usually binds to I κ B α and exists in the cytoplasm (McDaniel *et al.*, 2016). In response to an inflammatory reaction, I κ B α will be phosphorylated and isolated from the NF- κ B subunit. Free NF- κ B transported to the nucleus and acted as a transcription factor, eventually leads to the secretion of inflammatory factors such as IL-6, IL-1 β and TNF- α (Liang *et al.*, 2018).

Additionally, there is the interaction between inflammatory response and oxidative stress, the role of oxidative stress in uncontrolled inflammatory diseases has been gradually concerned (Tian *et al.*, 2017). Oxidative stress refers to the imbalance of the redox system in the body under the attack of harmful stimulating factors. Excessive reactive oxygen species (ROS) destroy the antioxidant function and lead to the inflammatory response (Newsholme *et al.*, 2018; Forrester *et al.*, 2018). Studies have found that Nrf2/ARE signaling pathway is closely related to oxidative stress in sepsis (Li *et al.*, 2018). When oxidative stress occurs, Nrf2 will enter into the nucleus and interact with ARE to regulate the levels of downstream antioxidant genes, including heme oxygenase-1 (HO-1), catalase (CAT) and superoxide dismutase (SOD). Therefore, up-regulation of Nrf2 expression and activation of ARE-related antioxidant protein can improve oxygenation, inhibit oxidative stress response and alleviate sepsis injury (Wu *et al.*, 2020).

Eaglewood, also known as *Aquilaria Sinensis* (Lour.) Spreng. is a famous traditional Chinese medicine in China. It has the functions of Xiangqi Zhitong, Wenzhong Zhou, Naqi Pingchuan. Clinically, it is commonly used in the treatment of chest and abdominal distension and pain, stomach cold and vomiting hiccup, kidney deficiency and dyspnea, etc. The main active components of Eaglewood are 2-(2-phenylmethyl) chromones and sesquiterpenes. Many studies have found eaglewood extract has anti-inflammatory and antioxidant effects (Zhou *et al.*, 2008; Lin *et al.*, 2013). Baimuxinol (BAI) is a sesquiterpenoid compound isolated from agarwood. However, as far as we know, there are very limited studies on the pharmacological effects of BAI.

Therefore, in the present study, we aimed to explore the effects of BAI on the proliferation and levels of inflammatory factors and antioxidant-related indexes of RAW264.7 cells stimulated by LPS. We hypothesized that BAI may alleviate LPS induced inflammation and oxidative stress *via* regulating the NF- κ B/I κ B α and Nrf2/ARE signaling pathway.

MATERIAL AND METHOD

Cell culture

RAW264.7 cells from leukemic mice were provided by the cell bank of Shanghai Chinese Academy of Sciences and cultured in high glucose DMEM medium containing 20% fetal bovine serum. 1% penicillin-streptomycin double-antibody was added to the medium. Then the cells were digested with 0.25% trypsin EDTA, passaged in 1:2, and cultured in a 5% CO₂ incubator at 37°C.

Groups

The cells were divided into Control group (CON), Lipopolysaccharide group (LPS, cultured with 50 mg/L LPS), Low baimuxinol group (L+BAI, cultured with 50 mg/L LPS+10 nM baimuxinol), Middle baimuxinol group (M+BAI, cultured with 50 mg/L LPS+50 nM baimuxinol), High baimuxinol group (H+BAI, cultured with 50 mg/L LPS+100 nM baimuxinol). Then the cells were cultured in a 5% CO₂ incubator at 37°C for 24 hours.

MTT

The cells were placed into 96-well plates (2×10⁴ cells/well). The MTT reagent was added to the cells after incubation for 24 h. Then the cells were cultured with dimethyl sulfoxide. Finally, the absorbance was measured at 490 nm by a microplate reader.

5-ethynyl-2-deoxyuridine (EdU) Assay

The trypsin was added to the logarithmic phase cells, and resuspended in a complete medium to obtain cell suspensions, then the cells were placed into a 96-well plate (2×10⁴ cells/well) and cultured at 37°C in an atmosphere of 5% CO₂, with the cell concentration adjusted to 2000 cells/well. The proliferation ability was measured with a Cell-Light EdU DNA Cell Proliferation Kit (RiboBio, Guangzhou, China) according to the instructions of the manufacturer.

Determination of inflammatory factors antioxidant related indexes

The contents of tumor necrosis factor α (TNF- α), interleukin 1 β (IL-1 β), interleukin 6 (IL-6), malondialdehyde (MDA), 8-hydroxy-2'-deoxyguanosine (8-OHdG), protein carbonyl (PC) and ROS, and CAT and total superoxide dismutase (T-SOD) activities of the cells were determined by the corresponding kits provided by Nanjing Jiangcheng Bioengineering Institute (Nanjing, China).

Quantitative real-time polymerase chain reaction (qRT-PCR)

The RNA was extracted with TRIzol® (Thermo Fisher Scientific, MA, USA). The transcript RT Kit (TIANGEN Biotech, Beijing, China) was conducted to reverse

the RNA to cDNA. The mRNA expressions of the target genes were determined with a miScript SYBR Green PCR Kit (Qiagen, Germany) on a 7900 Real-Time PCR System. Reaction conditions: 95°C, 30 s; 95°C, 5 s, 40 cycles; 60°C, 30 s; 95°C, 15 s; 60°C, 30; 95°C, 15 s. The 2^{- $\Delta\Delta$ Ct} method was performed to analyze the relative mRNA expressions. GAPDH was selected as the housekeeping gene. The primers used for qPCR were as follows: IL-6, For: TCCAGTTGCCTTCTTGGGAC, Rev: AGA-CAGGTCTGTTGGGAGTG; IL-1 β , For: GAAATGCCACCTTTTGACAGTG and Rev: TG-GATGCTCTCATCAGGACAG; TNF- α , For: AGC-CGATGGGTGTACCTTG, Rev: ATAGCAAATCG-GCTGACGGT.

Western blot

The protein of the cells was lysed with RIPA buffer (Beyotime Biotechnology), and the concentration was detected using the BCA method (Beyotime Biotechnology). The protein samples (give concentration=20 μ g) were separated by 12% SDS-PAGE, transferred to the PVDF membrane (Millipore) and blocked in TBS (50 mmol/l Tris-HCL [PH7.6], 150mmol/l NaCl) containing 0.1% Tween-20 (TBS-T) and 5% non-fat milk powder for 2 hr. Then the PVDF membranes were incubated with the primary antibody (Nrf2, 1:1000 dilution; HO-1, 1:1000 dilution; NF- κ B, 1:1000 dilution; p-NF- κ B, 1:1000 dilution; I κ B α , 1:1000 dilution; p-I κ B α , 1:1000 dilution; GAPDH, 1:500 dilution; Abcam Trading Co. Ltd., Shanghai) at 4°C overnight. The incubation product was further incubated with a secondary antibody (1:2000 dilution) for 1.5h. Finally, the blot was colored with ECL, and then exposed by LAS4000 chemiluminescence imaging analyzer for gray analysis.

Statistical analysis

All data were expressed as mean \pm S.D. SPSS22.0 software was performed for statistical analyses. One way analysis of variance (ANOVA) with a Tukey's post hoc test was used for comparison among groups. *P*<0.05 indicated significant difference.

RESULTS

BAI suppressed the viability of the RAW264.7 cells

First, we determined the effect of BAI on the viability of the RAW264.7 cells. The molecular structure of CEP was shown in Fig. 1A. Compared with the CON group, the viability of the cells in the LPS group was significantly increased. After BAI treatment, the viability of the cells was dramatically decreased (Fig. 1B). In addition, the proliferation of the cells was significantly increased after LPS treatment and BAI inhibited the growth of the cells in a dose-dependent manner (Fig. 1C–D).

BAI decreased the levels of inflammatory factors in the RAW264.7 cells

To accurately explore the role of the BAI on the inflammatory response. We analyzed the TNF- α , IL-1 β and IL-6 levels of the cells. As shown in Fig. 2, in the LPS group, the levels of TNF- α , IL-1 β and IL-6 were markedly up-regulated in comparison with the CON group. In comparison with the LPS group, the TNF- α , IL-1 β and IL-6 levels were markedly decreased in L-BAI, M-BAI and H-BAI groups in a dose-dependent manner.

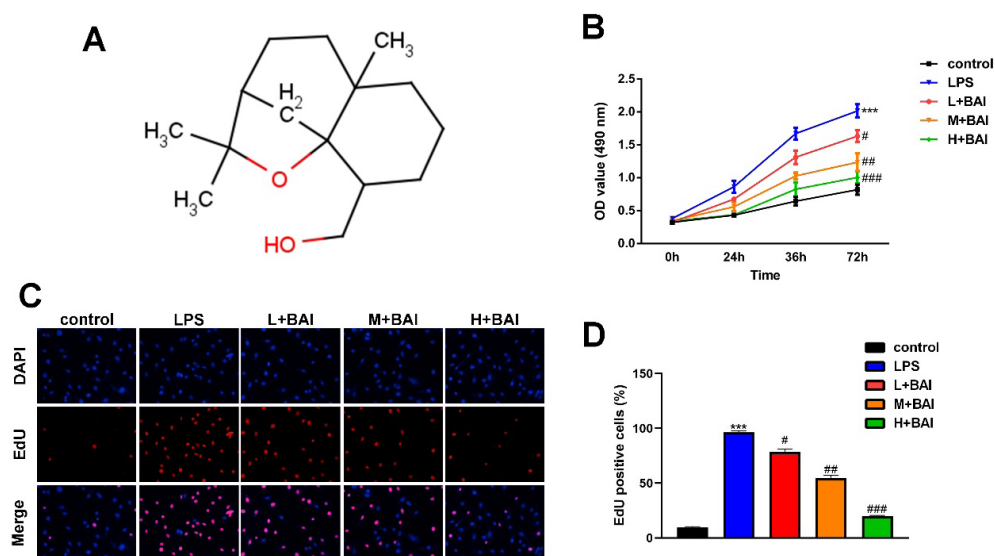


Figure 1. Role of BAI in the viability of RAW264.7 cells induced by LPS.

(A) Molecular structure formula of BAI. (B) The viability of the cells was detected with MTT. (B–D) The proliferation of the cells was detected by EdU. Notes: control, normal cells; LPS, normal cells + 50 mg/L LPS; L+BAI, normal cells + 50 mg/L LPS+10 nM baimuxinol; M+BAI, normal cells + 50 mg/L LPS+50 nM baimuxinol; H+BAI, normal cells + 50 mg/L LPS+100 nM baimuxinol. *** $P < 0.001$, vs. control group; # $P < 0.05$, ## $P < 0.01$, ### $P < 0.001$ vs. LPS group.

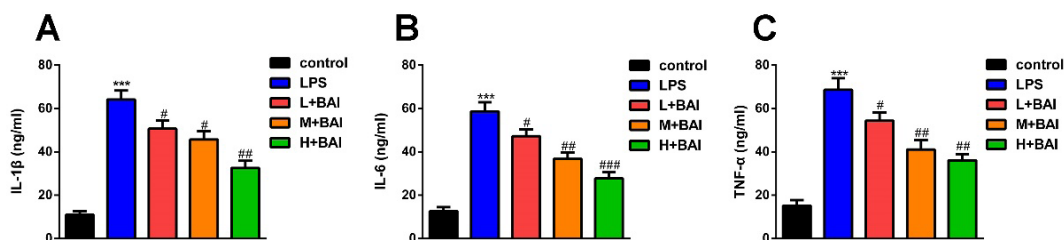


Figure 2. Role of BAI in the levels of TNF- α , IL-1 β and IL-6 in RAW264.7 cells induced by LPS.

The levels of IL-1 β (A), IL-6 (B) and TNF- α (C) in RAW264.7 cell was detected after LPS and BAI treatment. Notes: Control, normal cells; LPS, normal cells + 50 mg/L LPS; L+BAI, normal cells + 50 mg/L LPS+10 nM baimuxinol; M+BAI, normal cells + 50 mg/L LPS+50 nM baimuxinol; H+BAI, normal cells + 50 mg/L LPS+100 nM baimuxinol. *** $P < 0.001$, vs. control group; # $P < 0.05$, ## $P < 0.01$, ### $P < 0.001$ vs. LPS group.

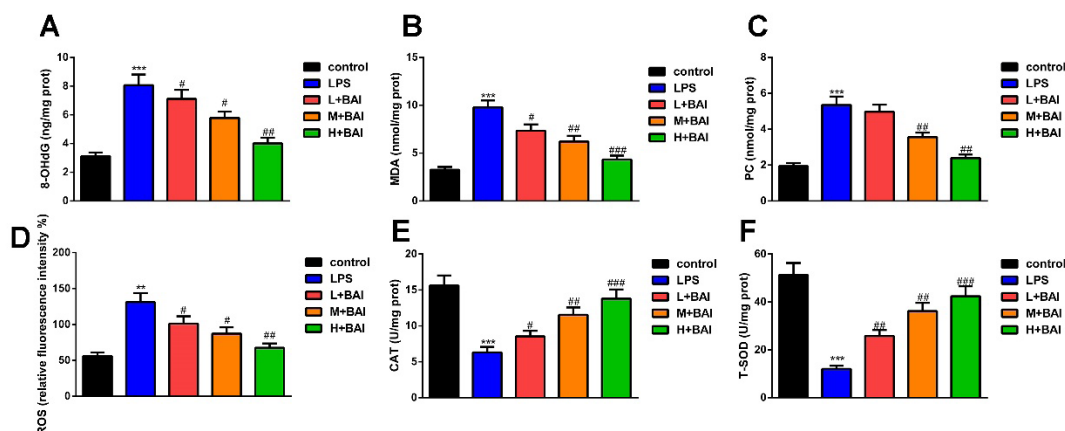


Figure 3. Role of BAI in the antioxidant function of RAW264.7 cells induced by LPS.

(A) The levels of 8-OHdG (A), MDA (B), PC (C), ROS (D), CAT (E) and T-SOD (F) in RAW264.7 cell was detected after LPS and BAI treatment. Notes: Control, normal cells; LPS, normal cells + 50 mg/L LPS; L+BAI, normal cells + 50 mg/L LPS+10 nM baimuxinol; M+BAI, normal cells + 50 mg/L LPS+50 nM baimuxinol; H+BAI, normal cells + 50 mg/L LPS+100 nM baimuxinol. ** $P < 0.01$, *** $P < 0.001$, vs. control group; # $P < 0.05$, ## $P < 0.01$, ### $P < 0.001$ vs. LPS group.

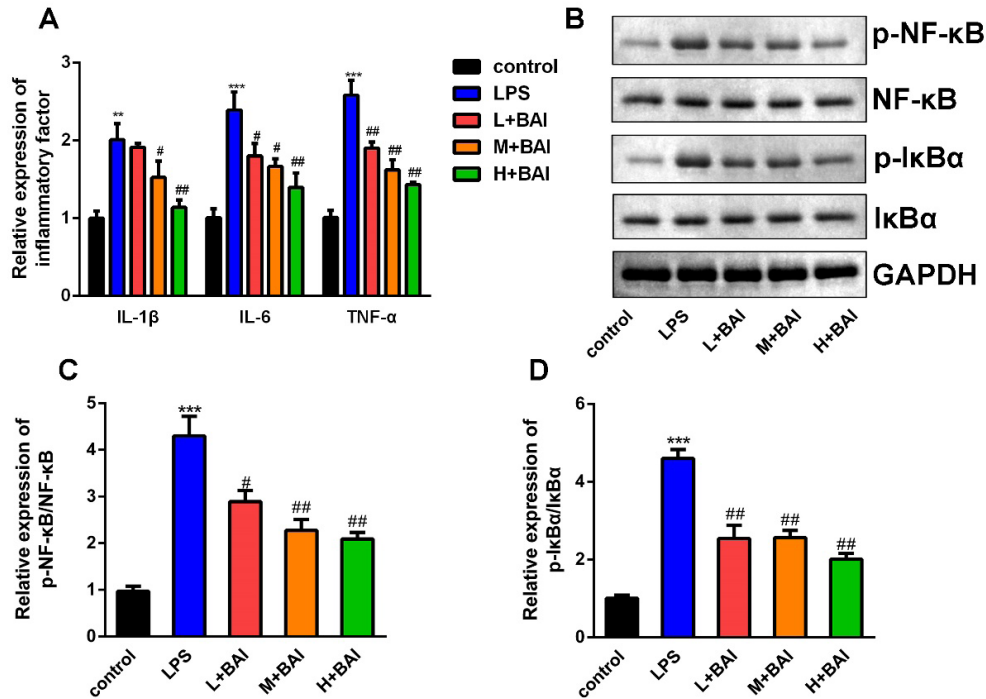


Figure 4. Role of BAI in the mRNA levels of inflammatory factors and NF- κ B/I κ B α signaling pathway in RAW264.7 cells induced by LPS.

(A) The mRNA expressions of TNF- α , IL-1 β and IL-6 were measured with qRT-PCR. (B–D) The protein expressions of p-NF- κ B, NF- κ B, p-I κ B α and I κ B α were detected with western blot. Notes: Control, normal cells; LPS, normal cells + 50 mg/L LPS; L+BAI, normal cells + 50 mg/L LPS+10 nM baimuxinol; M+BAI, normal cells + 50 mg/L LPS+50 nM baimuxinol; H+BAI, normal cells + 50 mg/L LPS+100 nM baimuxinol. *** P <0.01, **** P <0.001, vs. control group; # P <0.05, ## P <0.01 vs. LPS group.

BAI relieved the oxidative stress of the RAW264.7 cells

Subsequently, we explore the effects of BAI on the antioxidant capacity of the RAW264.7 cells. As shown in Fig. 3, in the LPS group, the concentrations of the ROS, MDA, PC and 8-OHdG were dramatically up-regulated, and the T-SOD and CAT activities were significantly down-regulated in comparison with the control

group. BAI reversed the effects of LPS on the levels of ROS, MDA, PC, 8-OHdG, T-SOD and CAT in a dose-dependent manner.

BAI suppressed the NF- κ B/I κ B α signaling pathway

Next, we analyzed the role of BAI in mRNA expressions of inflammatory factors and NF- κ B/I κ B α signal-

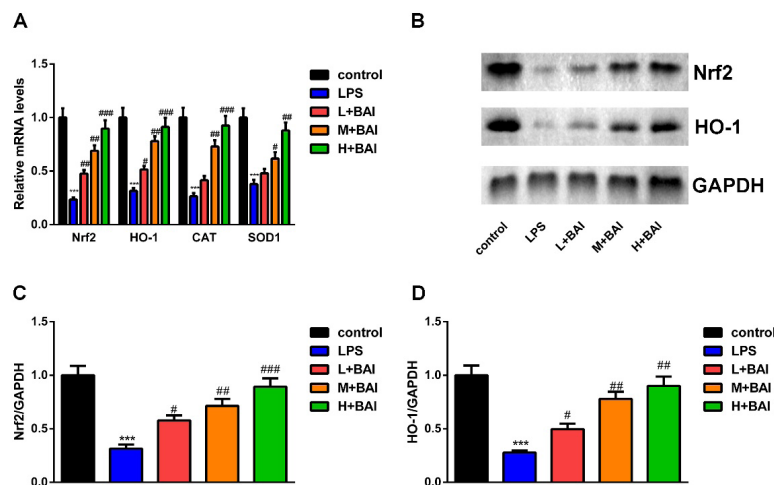


Figure 5. Role of BAI in the Nrf2/ARE signaling pathway in RAW264.7 cells induced by LPS.

(A) The mRNA expressions of Nrf2, HO-1, CAT and SOD1 were detected by qRT-PCR. (B–D) The protein expressions of Nrf2 and HO-1 were measured by western blot. Notes: Control, normal cells; LPS, normal cells + 50 mg/L LPS; L+BAI, normal cells + 50 mg/L LPS+10 nM baimuxinol; M+BAI, normal cells + 50 mg/L LPS+50 nM baimuxinol; H+BAI, normal cells + 50 mg/L LPS+100 nM baimuxinol. *** P <0.001, vs. control group; # P <0.05, ## P <0.01, ### P <0.001 vs. LPS group.

ing pathway. In the LPS group, the mRNA expressions of TNF- α , IL-1 β and IL-6 were markedly up-regulated in comparison with the control group. Compared with the LPS group, the TNF- α , IL-1 β and IL-6 mRNA expressions were markedly down-regulated in L-BAI, M-BAI and H-BAI groups in a dose-dependent manner (Fig. 4A). In addition, in comparison with the control group, the protein expressions of p-NF- κ B and p-I κ B α in the LPS group were markedly up-regulated. BAI treatment significantly down-regulated the protein expressions of p-NF- κ B and p-I κ B α in a dose-dependent manner (Fig. 4B–D).

BAI suppressed the Nrf2/ARE signaling pathway

Finally, the role of BAI in the Nrf2/ARE signaling pathway was explored. We found the mRNA expressions of Nrf2, HO-1, CAT and SOD1 were significantly decreased after LPS treatment, while BAI significantly increased the Nrf2, HO-1, CAT and SOD1 mRNA expressions in a dose-dependent manner (Fig. 5A). Additionally, the protein expressions of Nrf2 and HO-1 were increased in the LPS group in comparison with the control group. BAI markedly up-regulated the protein expressions of Nrf2 and HO-1 (Fig. 5B–D).

DISCUSSION

At present, the theory of uncontrolled inflammatory response and oxidative stress are major factors for the pathogenesis of sepsis. In the current study, we found BAI can reverse the excessive proliferation of RAW264.7 cells caused by LPS. Additionally, BAI could relieve inflammation and oxidative stress by regulating the NF- κ B/I κ B α and Nrf2/ARE signaling pathway.

Macrophages is one of the main cells that participated in inflammation. Stimulated by LPS, macrophages could induce the secretion of inflammatory factors, such as IL-1 β , IL-6, TNF- α and so on, and then produce a clinical inflammatory response (Cotran *et al.*, 1999). Excessive inflammation is the major factor in many chronic diseases, including autoimmune diseases and neurodegenerative diseases. Therefore, inhibition of excessive inflammatory response is an effective method for the therapy of chronic diseases (Tabas *et al.*, 2013). TNF- α and IL-1 β are the initiating factors in inflammatory mediators cascade reaction (Johnson *et al.*, 2015). Among them, TNF- α is a pro-inflammatory cytokine in regulating immune cells. It can induce fever and apoptosis by producing IL-1 β and IL-6 and then induce inflammation. The abnormal content of TNF- α leads to the occurrence of many diseases (Wang *et al.*, 2020; Yosefifard *et al.*, 2019; Johnson *et al.*, 2015). IL-6 is a multifunctional cytokine that regulates immune, inflammatory and other physiological processes (Unver *et al.*, 2018). The expression of IL-6 is positively regulated by LPS and IL-1 β . In the present study, we confirmed that BAI decreases the production and mRNA expression of LPS induced pro-inflammatory cytokines (TNF- α , IL-1 β and IL-6) in a dose-dependent manner, suggesting BAI has potential anti-inflammatory activity. Previous studies have confirmed that eaglewood or its extract has an anti-inflammatory function. Lin and coworkers found that the ethanol extract of eaglewood leaf has an obvious anti-inflammatory effect on capillary dilation, hyperpermeability, exudation and edema in the early stage of inflammation (Lin *et al.*, 2013). Wu *et al.* showed that the extract of eaglewood can inhibit inflammation by down-regulating the expression of COX-2 and iNOS in the immune sig-

nal pathway (Wu *et al.*, 2012). These results were similar to ours and indicated that the extract of eaglewood has an effective anti-inflammatory effect. Therefore, we speculate that BAI, a sesquiterpenoid isolated from eaglewood, maybe a key anti-inflammatory compound.

To further explore the mechanism of BAI, we analyzed the protein expression of the NF- κ B/I κ B α signaling pathway. NF- κ B is critically the control center to regulate inflammatory response (Tak *et al.*, 2001). NF- κ B usually binds to I κ B in cells in the form of inactive complexes. Once I κ B is degraded, NF- κ B dimer will transfer to the nucleus and start the transcription of the target gene. A previous study has confirmed that NF- κ B can mediate the proliferation, differentiation and production of inflammatory factors of various immune cells (Hayden *et al.*, 2011). In this study, the proliferation ability of the cells was dramatically promoted by LPS, and after treatment of BAI, the over-proliferation of macrophages RAW264.7 was decreased. In addition, we found that LPS activates the NF- κ B/I κ B α signaling pathway and BAI inhibited it in a dose-dependent manner. Our findings indicated that the inhibitory effect of BAI on over-proliferation may be realized by NF- κ B/I κ B α inhibiting signal pathway. However, the specific mechanism needs to be further explored.

In addition, ROS is an important product of oxidative stress. When the body or cells are stimulated by endogenous or exogenous harmful substances, the antioxidant capacity will be destroyed, which results in a large amount of accumulated ROS and other oxides. Excessive ROS induces cell damage and promotes the occurrence of inflammatory reactions (Bae *et al.*, 2017). On the other hand, inflammatory cells release many active substances in the inflammatory site, which will also lead to the aggravation of oxidative stress (Kumar *et al.*, 2018). In sepsis, a large number of pro-inflammatory factors and the host's anti-inflammatory factors are released to induce the production of ROS, which leads to the imbalance of oxidation-reduction state in the body, causes oxidative stress reaction, and finally damages tissue cells and organ systems (Prauchner *et al.*, 2017). Previous studies have shown that various plant extracts can relieve oxidative damage in sepsis, such as curcumin (Zhong *et al.*, 2016) resveratrol (Aydin *et al.*, 2016), etc. In the current study, we also confirmed that BAI reduces the excess ROS induced by LPS. Furthermore, excessive ROS can lead to protein, lipid and DNA damage (Aitken, 2017), which was also be confirmed in this study that the MDA, PC and 8-OHdG levels are increased after LPS treatment. It implied that the cells lipid peroxidation, protein and DNA damage occur in the cells. It is worth noting that all these are relieved after BAI treatment. Nrf2/ARE signaling pathway is one of the most important protection systems against oxidative stress. When cells are exposed to oxidative stress, Nrf2 is recognized and combined with the DNA motif (GCTGAGTCA) on ARE, which starts the transcription of antioxidant genes, and then leads to the expression of antioxidants and related enzymes, such as HO-1 (Shaw *et al.*, 2020). Interestingly, we demonstrated that expressions of Nrf2 and HO-1 are up-regulated after BAI treatment, which indicated that BAI may improve the antioxidant function *via* the Nrf2/ARE signaling pathway.

To sum up, our results confirmed that BAI can effectively alleviate the inflammatory response and oxidative stress induced by LPS through regulating the NF- κ B/I κ B α and Nrf2/ARE signaling pathway. However, there are some limitations in this paper, such as we do not have *in vivo* experiments for validation because the con-

ditions do not permit. Also we hope to validate it on multiple cells in future studies. In conclusion, this study is the first to confirm that BAI has antioxidant and anti-inflammatory functions. Our findings provide a theoretical basis for the clinical application of eaglewood and a new method for the treatment of sepsis.

REFERENCES

- Aitken RJ (2017) Reactive oxygen species as mediators of sperm capacitation and pathological damage. *Mol Reprod Develop* **84**: 1039–1052. <https://doi.org/10.1002/mrd.22871>
- Alhashem F, Tiren-Verbeet NL, Alp E, Doganay M (2017) Treatment of sepsis: What is the antibiotic choice in bacteremia due to carbapenem resistant Enterobacteriaceae? *World J Clin Cases* **5**: 324–332. <https://doi.org/10.12998/wjcc.v5.i8.324>
- Arefian H, Heublein S, Scherag A, Brunkhorst FM, Younis MZ, Moerer O, Fischer D, Hartmann M (2017) Hospital-related cost of sepsis: A systematic review. *J Infect* **4**: 107–117. <https://doi.org/10.1016/j.jinf.2016.11.006>
- Aydın S, Şahin TT, Bacanlı M, Taner G, Başaran AA, Aydın M, Başaran N (2016) Resveratrol protects sepsis-induced oxidative DNA damage in liver and kidney of rats. *Balkan Med J* **33**: 594–601. <https://doi.org/10.5152/balkanmedj.2016.15516>
- Bae H, Jeong CH, Cheng WN, Hong K, Seo HG, Han SG (2017) Oxidative stress-induced inflammatory responses and effects of N-acetylcysteine in bovine mammary alveolar cells. *J Dairy Res* **84**: 418–425. <https://doi.org/10.1017/S002202991700067X>
- Cotran RS, Kumar V (1999) *Robbins pathologic basis of disease*. W.B. Saunders
- Dellinger RP, Levy MM, Carlet JM, Bion J, Parker MM, Jaeschke R, Reinhart K, Angus DC, Brun-Buisson C, Beale R, Calandra T, Dhainaut JF, Gerlach H, Harvey M, Marini JJ, Marshall J, Ranieri M, Ramsay G, Sevransky J, Thompson BT, Townsend S, Vender JS, Zimmerman JL, Vincent JL; International Surviving Sepsis Campaign Guidelines Committee; American Association of Critical-Care Nurses; American College of Chest Physicians; American College of Emergency Physicians; Canadian Critical Care Society; European Society of Clinical Microbiology and Infectious Diseases; European Society of Intensive Care Medicine; European Respiratory Society; International Sepsis Forum; Japanese Association for Acute Medicine; Japanese Society of Intensive Care Medicine; Society of Critical Care Medicine; Society of Hospital Medicine; Surgical Infection Society; World Federation of Societies of Intensive and Critical Care Medicine (2008) Surviving Sepsis Campaign: international guidelines for management of severe sepsis and septic shock: 2008. *Crit Care Med* **36**: 296–327. <https://doi.org/10.1097/01.CCM.0000298158.12101.41>
- Forrester SJ, Kikuchi DS, Hernandez MS, Xu Q, Griendling KK (2018) Reactive oxygen species in metabolic and inflammatory signaling. *Circ Res* **122**: 877–902. <https://doi.org/10.1161/CIRCRESA-HA.117.311401>
- Hayden MS, Ghosh S (2011) NF- κ B in immunobiology. *Cell Res* **21**: 223–244. <https://doi.org/10.1038/cr.2011.13>
- Johnson ZI, Schoepflin ZR, Choi H, Shapiro IM, Risbud MV (2015) Disc in flames: Roles of TNF- α and IL-1 β in intervertebral disc degeneration. *Eur Cells Mat* **30**: 104–117. <https://doi.org/10.22203/ecm.v030a08>
- Kumar S, Gupta E, Kaushik S, Kumar SV, Mehta SK, Jyoti A (2018) Evaluation of oxidative stress and antioxidant status: Correlation with the severity of sepsis. *Scand J Immunol* **87**: e12653. <https://doi.org/10.1111/sji.12653>
- Lancaster GI, Langley KG, Berglund NA, Kammoun HL, Reibe S, Estevez E, Weir J, Mellett NA, Pernes G, Conway JRW, Lee MKS, Timpson P, Murphy AJ, Masters SL, Gerondakis S, Bartonicek N, Kaczorowski DC, Dinger ME, Meikle PJ, Bond PJ, Febbraio MA (2018) Evidence that TLR4 is not a receptor for saturated fatty acids but mediates lipid-induced inflammation by reprogramming macrophage metabolism. *Cell Metab* **27**: 1096–1110.e5. <https://doi.org/10.1016/j.cmet.2018.03.014>
- Li Y, Feng Y, Liu X, Li Y, Zhu H, Sun M, Li P, Liu B, Yang H (2021) Songorine promotes cardiac mitochondrial biogenesis via Nrf2 induction during sepsis. *Redox Biol* **38**: 101771. <https://doi.org/10.1016/j.redox.2020.101771>
- Liang H, Yang X, Liu C, Sun Z, Wang X (2018) Effect of NF- κ B signaling pathway on the expression of MIF, TNF- α , IL-6 in the regulation of intervertebral disc degeneration. *J Musculoskelet Neur Interact* **18**: 551–556. PMID: 30511959
- Lin H, Li H, Mei Q (2013) Comparative study on anti-inflammation activity between chinese eaglewood leaves and chinese eaglewood. *Chinese Arch Trad Chinese Med* **3**: 548–549 (in Chinese). <https://doi.org/10.13193/j.archctcm.2013.03.102.linhz.055>
- McDaniel DK, Eden K, Ringel VM, Allen IC (2016) Emerging roles for noncanonical NF- κ B signaling in the modulation of inflammatory bowel disease pathobiology. *Inflam Bowel Dis* **22**: 2265–2279. <https://doi.org/10.1097/MIB.0000000000000858>
- Newsholme P, Cruzat VF, Keane KN, Carlessi R, de Bittencourt PIH (2016) Molecular mechanisms of ROS production and oxidative stress in diabetes. *Biochem J* **473**: 4527–4550. <https://doi.org/10.1042/BCJ20160503C>
- Prauchner CA (2017) Oxidative stress in sepsis: Pathophysiological implications justifying antioxidant co-therapy. *Burns* **43**: 471–485. <https://doi.org/10.1016/j.burns.2016.09.023>
- Shaw P, Chattopadhyay A (2020) Nrf2-Are signaling in cellular protection: Mechanism of action and the regulatory mechanisms. *J Cell Physiol* **235**: 3119–3130. <https://doi.org/10.1002/jcp.29219>
- Singer M, Deutschman CS, Seymour CW, Shankar-Hari M, Annane D, Bauer M, Bellomo R, Bernard GR, Chiche JD, Coopersmith CM, Hotchkiss RS, Levy MM, Marshall JC, Martin GS, Opal SM, Rubenfeld GD, van der Poll T, Vincent JL, Angus DC (2016) The third international consensus definitions for sepsis and septic shock (Sepsis-3). *JAMA* **315**: 801–810. <https://doi.org/10.1001/jama.2016.0287>
- Tabas I, Glass CK (2013) Anti-inflammatory therapy in chronic disease: challenges and opportunities. *Science* **39**: 166–172. <https://doi.org/10.1126/science.1230720>
- Tak PP, Firestein GS (2001) NF- κ B: a key role in inflammatory diseases. *J Clin Invest* **107**: 7–11. <https://doi.org/10.1172/JCI11830>
- Tian T, Wang Z, Zhang J (2017) Pathomechanisms of oxidative stress in inflammatory bowel disease and potential antioxidant therapies. *Oxid Med Cell Longev* **2017**: 4535194. <https://doi.org/10.1155/2017/4535194>
- Unver N, McAllister F (2018) IL-6 family cytokines: Key inflammatory mediators as biomarkers and potential therapeutic targets. *Cytokine Growth Factor Rev* **41**: 10–17. <https://doi.org/10.1016/j.cytogfr.2018.04.004>
- Wang Y, Che M, Xin J, Zheng Z, Li J, Zhang S (2020) The role of IL-1 β and TNF- α in intervertebral disc degeneration. *Biomed Pharmacother* **131**: 110660. <https://doi.org/10.1016/j.biopha.2020.110660>
- Wu Q, Liu LT, Wang XY, Lang ZF, Meng XH, Guo SF, Yan B, Zhan T, Zheng HZ, Wang HW (2020) Lycium barbarum polysaccharides attenuate kidney injury in septic rats by regulating Keap1-Nrf2/Are pathway. *Life Sci* **242**: 117240. <https://doi.org/10.1016/j.lfs.2019.117240>
- Yoseffard M, Vaezi G, Malekiran AA, Faraji F, Hojati V (2019) A randomized control trial study to determine the effect of melatonin on serum levels of IL-1 β and TNF- α in patients with multiple sclerosis. *Iran J Allergy Asthma Immunol* **8**: 649–654. <https://doi.org/10.18502/ijaa.v18i6.2177>
- Zaidi D, Wine E (2018) Regulation of nuclear factor kappa-light-chain-enhancer of activated B cells (NF- κ B) in inflammatory bowel diseases. *Frontiers Pediatr* **6**: 317. <https://doi.org/10.3389/fped.2018.00317>
- Zampieri FG, Mazza B (2017) Mechanical ventilation in sepsis: A reappraisal. *Shock (Augusta, Ga.)* **47** (1S Suppl 1): 41–46. <https://doi.org/10.1097/SHK.0000000000000702>
- Zhong W, Qian K, Xiong J, Ma K, Wang A, Zou Y (2016) Curcumin alleviates lipopolysaccharide induced sepsis and liver failure by suppression of oxidative stress-related inflammation via PI3K/AKT and NF- κ B related signaling. *Biomed Pharmacother* **83**: 302–313. <https://doi.org/10.1016/j.biopha.2016.06.036>
- Zhou M, Wang H, Suolangjiba, Kou J, Yu B (2008) Antinociceptive and anti-inflammatory activities of *Aquilaria sinensis* (Lour.) Gilg. Leaves extract. *J Ethnopharmacol* **117**: 345–350. <https://doi.org/10.1016/j.jep.2008.02.005>

miRNA-301 As a molecule promoting necrotizing enterocolitis by inducing inflammation

Dajun Zou, Fude Hu, Qili Zhou and Xiaoqing Xu✉

Department of Pediatric Surgery, Affiliated Hospital of Chengde Medical College, 36 Nanyingzi Street, Chengde, Hebei, 067000. P.R. China

Objective: Necrotizing enterocolitis (NEC) is a devastating inflammatory disease with high morbidity and mortality, mainly affecting premature infants. This study aimed to explore the role of miRNA-301a in the pathogenesis of NEC. **Methods:** The differentially expressed miRNAs and mRNAs were screened by collating RNA-Seq data from the GEO database of intestinal tissue samples. The differential miRNA-mRNAs regulatory network was constructed based on functional enrichment analysis. Newborn BALB/c mice were used to establish the NEC model. Haematoxylin and eosin staining was used to assess intestinal damage. The levels of IL-8 and TNF- α in mouse serum were evaluated by ELISA. qRT-PCR was used to detect the expression of miRNA-301a in intestinal tissues. **Results:** Bioinformatics analysis showed that miRNA-301a was involved in intestinal lesions. Intestinal tissue damage was reduced and serum levels of the inflammatory cytokines IL-8 and TNF- α were lower in NEC model mice treated with miRNA-301a antagonists. The level of miRNA-301a in intestinal tissues of NEC model mice was significantly higher than in the control group and miRNA-301a antagonists treated group. **Conclusion:** miRNA-301a plays an important role in the pathogenesis of NEC by promoting inflammation, and is a potential therapeutic target of NEC.

Keywords: necrotizing enterocolitis; miRNA-301a; bioinformatics analysis; inflammation

Received: 16 April, 2023; **revised:** 18 September, 2023; **accepted:** 19 October, 2023; **available on-line:** 28 November, 2023

✉ e-mail: xiaoqingxu0419@163.com

Acknowledgements of Financial Support: This work was supported by the Hebei Medical Science Research Project (20210287).

Abbreviations: IBD, inflammatory bowel disease; NEC, necrotizing enterocolitis

INTRODUCTION

Despite decades of studies on necrotizing enterocolitis (NEC), NEC continues to be the most prevalent surgical condition that crises the lives of newborns (Meister *et al.*, 2020). Among very low birth weight infants, the prevalence of NEC ranges from 5% to 10%, and more than 50% of patients with NEC require surgery. Furthermore, the mortality rate of NEC treated by surgery ranges from 30% to 50% (Flahive *et al.*, 2020; Bell *et al.*, 2021). Hence, it is urgent to explore effective and reliable biomarkers for early identification of infants at risk of progression to improve the prognosis of NEC.

MicroRNAs (miRNAs) are a family of highly conserved RNAs, ranging in size from 19 to 24 nucleotides, and regulate the 3'-untranslated region of target mRNA transcripts (Chen *et al.*, 2013). In recent years, substantial

progress has been achieved in understanding the role of diverse miRNAs in human diseases, including NEC (Cai *et al.*, 2022; Donda *et al.*, 2022). MiRNA-124 has been identified to facilitate NEC by targeting ROCK1 and promoting inflammatory cell infiltration in intestinal cells (Yin *et al.*, 2019). The increased expression of miRNA-141-3p could attenuate NEC damage to intestinal tissues by targeting MNX1 (Chen *et al.*, 2020). In addition, miRNA-301a facilitated intestinal mucosal inflammation by inducing IL-17A and TNF- α in inflammatory bowel disease (IBD) and colorectal cancer (He *et al.*, 2016). However, the role of miRNA-301a in NEC remains unclear.

In this study, a miRNA-mRNA regulatory network was successfully established by bioinformatics analysis and key miRNAs were screened based on this network. Next, a neonatal mouse NEC model was successfully established and the expression of miRNA-301a in the intestinal tissues and the levels of inflammatory factors TNF- α and IL-8 in the serum of mice were examined.

MATERIALS AND METHODS

Source of sample

MRNA and miRNA microarray data of intestinal tissue samples were gathered from GEO Datasets. GSE115513 includes 31 normal and 30 diseased intestinal tissue samples. GSE184093 includes 9 normal and 9 diseased intestinal tissue samples. The datasets were analysed by using PERL 5.30.2 (<https://www.PERL.org/>). The two datasets were sorted in the order of normal and experimental groups to acquire mRNA and miRNA data.

Differentially expressed miRNAs and mRNAs

The differentially expressed miRNAs and mRNAs were filtered by using the LIMMA package in the R software (<https://rstudio.com/>, version 3.6.2). The filtering criteria were set as $|\log_2(\text{fold change})| > 1$ and FDR (False Discovery Rate) < 0.05 . The "pheatmap" in R (3.6.2) was then applied to create differential volcano maps of the filtered differentially expressed mRNAs and miRNAs, respectively.

Identification of miRNA targets and construction of miRNA-mRNA regulatory network

The target genes of 222 differential miRNAs were predicted by using the gene function analysis tool FunRich (3.1.3) (<http://www.funrich.org/>). The differentially expressed mRNAs were crossed with the target genes of the miRNAs to generate the shared mRNAs and corresponding miRNAs, and the regulatory network was visualised using Cytoscape (3.7.2) (<https://cytoscape.org/re>

lease_notes_3_7_2.html) to produce the miRNA-mRNA regulatory network.

GO and KEGG enrichment analyses

To further elucidate the biological functions of target genes in the regulatory network, GO (<https://geneontology.org/docs/go-enrichment-analysis/>) and KEGG enrichment analyses (<https://www.genome.jp/kegg/pathway.html>) of differential mRNAs were conducted with a screening condition of $p < 0.05$ and $q < 0.05$ and all outcomes were presented as bar graphs using the Bioconductor plugin in R software (Gao *et al.*, 2018).

Mice

Seventy-five newborn and pathogen-free BALB/c mice (7–10 days old) were obtained from the Animal Research Centre of Chengde Medical College (Chengde, China). All mice were housed at 28–30°C and 45–65% humidity for 12 hours on a light/dark cycle. This study was approved by the Animal Care and Use Committee of the Affiliated Hospital of Chengde Medical College (Approved No. 000134, date 2020-6-17). Mice were randomized into three groups ($n=25$ mice per group): the NEC group, the control group, and the NEC+anti-miRNA-301a group.

Neonatal mouse NEC model

The neonatal mouse NEC model was established as described previously (Nolan *et al.*, 2021). Mice in the NEC and NEC+anti-miRNA-301a groups ($n=25$) were fed Esbilac puppy formulae, which was complemented by bacteria cultured from the faeces of infants with severe NEC (12.5 μ l of faecal slurry in 1 ml of formula). Briefly, a syringe filled with formulae was attached to a peripherally inserted central catheter (PICC) line. Next, the PICC line was gently introduced into the mouse's stomach by using forceps. Then the formulae were slowly dispensed into the stomach, and the PICC line was slowly withdrawn from the oral cavity (Nolan *et al.*, 2021). Mice were fed every 3 hours and after 3 feeds were placed under 5% O_2 + 95% N_2 for 10 minutes of stress to induce NEC. The feeding volume was 0.1 ml and gradually increased to 0.25 ml. The animals were sacrificed by decapitation on Day 5. For NEC+anti-miRNA-301a group, the mice were orally administered miRNA-301a antagonist (sequence mGmCmUmUmGmAmCmAmAmUmAmCmUmAmUmUmGmCmAmCmUmG, Genecreate LTD, Wuhan, China) following the manufacturer's manual once a day, starting at the beginning of NEC induction (Day 0) and continuing to Day 5.

Haematoxylin and eosin (H&E) staining

The intestinal tissues were dissected and washed with PBS at 4°C and fixed with 4% paraformaldehyde, paraffin-embedded, sectioned at 5 μ m and stained with haematoxylin and eosin (H&E). The intestinal damage was analysed under a microscope with a 40x lens by two independent pathologists, who scored it double-blind according to published criteria (Zhang *et al.*, 2020).

MiRNA/mRNA isolation and reverse transcription

According to the manufacturer's instructions, TRIzol reagent (Invitrogen) was used to isolate total RNA from the intestinal tissues of the mice. Total RNA (2

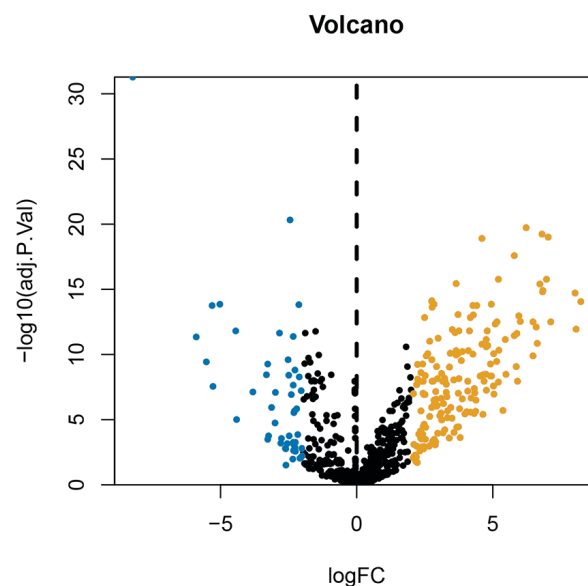


Figure 1. Volcanic map of differentially expressed miRNAs (orange represents upregulated miRNAs, blue represents downregulated miRNAs, and black represents miRNAs without a significant difference in expression).

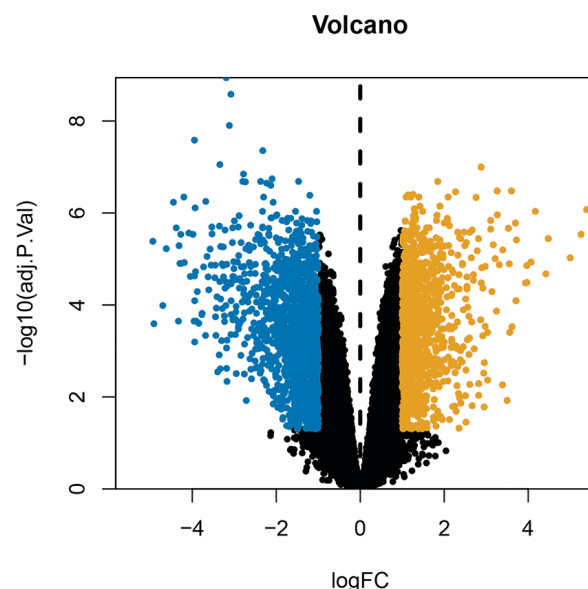


Figure 2. Volcanic map of differentially expressed mRNAs (orange represents upregulated mRNAs, blue represents downregulated mRNAs, and black represents mRNAs without a significant difference in expression).

μ g) was used to generate cDNA by utilizing the Prime Script RT reagent kit (Takara, Tokyo, Japan).

qRT-PCR

QRT-PCR was undertaken by using SYBR Premix Ex Taq II (Perfect Real Time) (Takara, Tokyo, Japan). The gene-specific primers were purchased from Applied Biosystems (Foster City, CA, USA) with following sequences: U6: 5'-CTCGCTTCGGCAGCACA-3' and 5'-AACGCTTCACGAATTTGCGT-3', miRNA-301a: 5'-GGCAGTGAATAGTATTGT-3' and 5'-TG-TGTCGTGGAGTCG-3'. U6 was used as an internal control for miR-301a expression. All experiments were in triplicates.

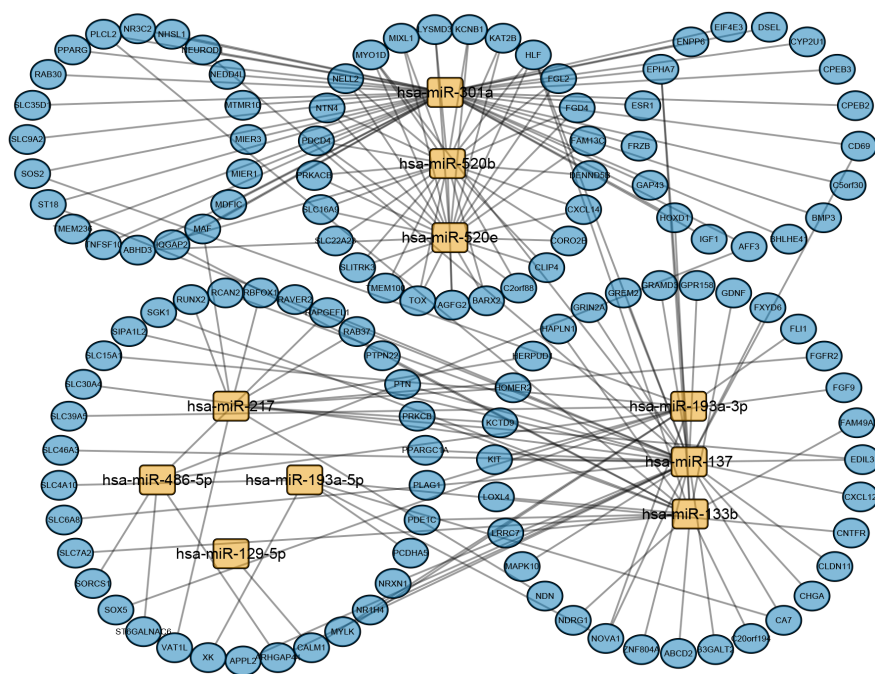


Figure 3. The miRNA-mRNA regulatory network (ellipses represent mRNAs, squares represent miRNAs, orange represents upregulated expression, blue represents downregulated expression, and connected lines represent targeted relationships).

ELISA

Serum was taken from all groups of mice. Paired ELISA kits for IL-8 and TNF- α (all from Enzyme Linked Biotechnology Co., Ltd., Shanghai, China) were used to evaluate the concentrations of IL-8 and TNF- α in the serum of the mice from each group. The optical density (OD) values of each well were recorded at 450 nm by a microplate reader.

Statistical analysis

Data were analysed by using SPSS 25.0 statistical software and expressed as mean \pm standard deviation. The

differences were considered to be statistically significant at $p < 0.05$.

RESULTS

Differentially expressed miRNAs and mRNAs

After processing the dataset, a total of 222 differential miRNAs were screened, of which 172 miRNAs were highly expressed and 50 miRNAs were lowly expressed. Similarly, we obtained 2584 differential mRNAs, of which 1155 mRNAs were up-regulated and 1429 mR-

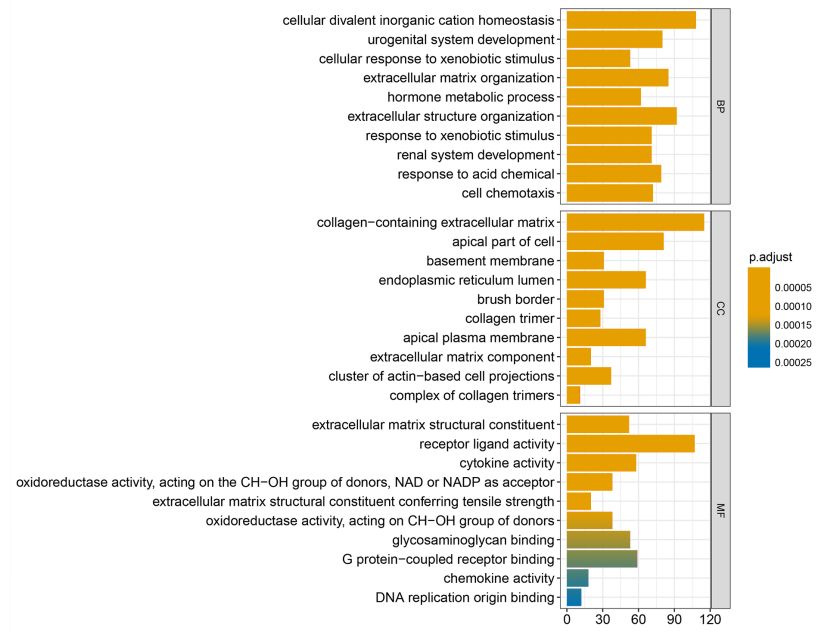


Figure 4. GO enrichment analysis of differentially expressed mRNAs.

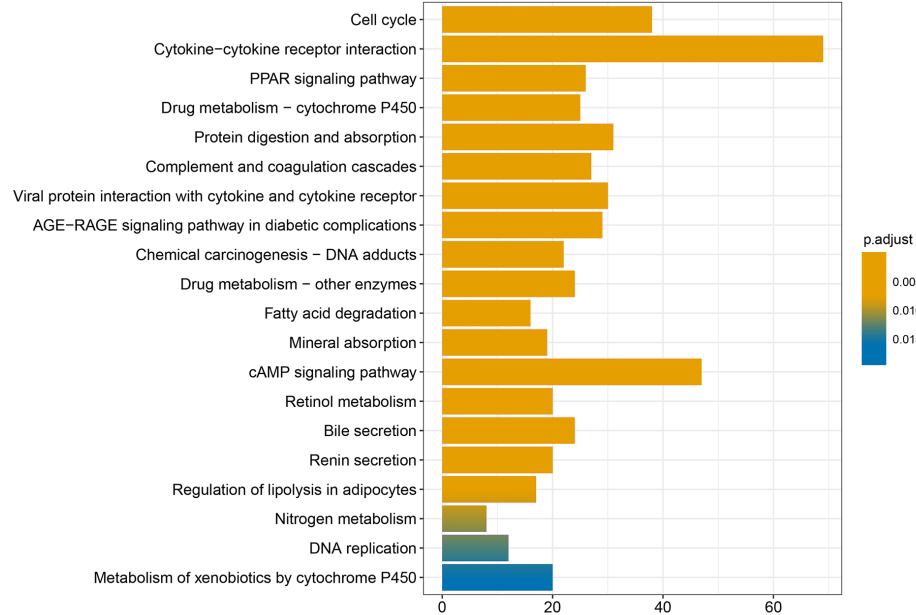


Figure 5. KEGG enrichment analysis of differentially expressed mRNAs.

NAs were down-regulated. The volcanoes of the differential miRNAs and mRNAs were subsequently mapped using R software (Figs 1 and 2).

Construction of miRNA-mRNA network and functional enrichment analysis

The FunRich (3.1.3) was used to predict the target genes of 222 differential miRNAs and a total of 2908 target genes were identified. The miRNA-mRNA regulatory network was then mapped using Cytoscape software (Fig. 3). The regulatory network showed that miRNA-301a regulated a greater number of mRNAs. We performed GO and KEGG enrichment analysis on 2584 different mRNAs using R language with $p < 0.05$ and $q < 0.05$ as screening conditions (Figs 4 and 5).

miRNA-301a antagonist reduced histological damage in NEC mice

We successfully established the NEC model using a previously published protocol (Nolan *et al.*, 2021) (Fig. 6A). During the experiments, two mice died both in the control and in NEC+anti-miRNA-301a groups, while three mice died in the NEC group. The difference in mortality among the three groups was not statistically significant ($p > 0.05$). At the end of the experiments, the intestinal tissues of the mice in the NEC group showed a bluish-black colour compared to those of the mice in the control group. However, after treatment with the miRNA-301a antagonist, the degree of intestinal tissue necrosis in mice was significantly reduced (Fig. 6B).

The average histological score of the mice in the NEC group was 3.12 ± 0.72 , while the scores of the control

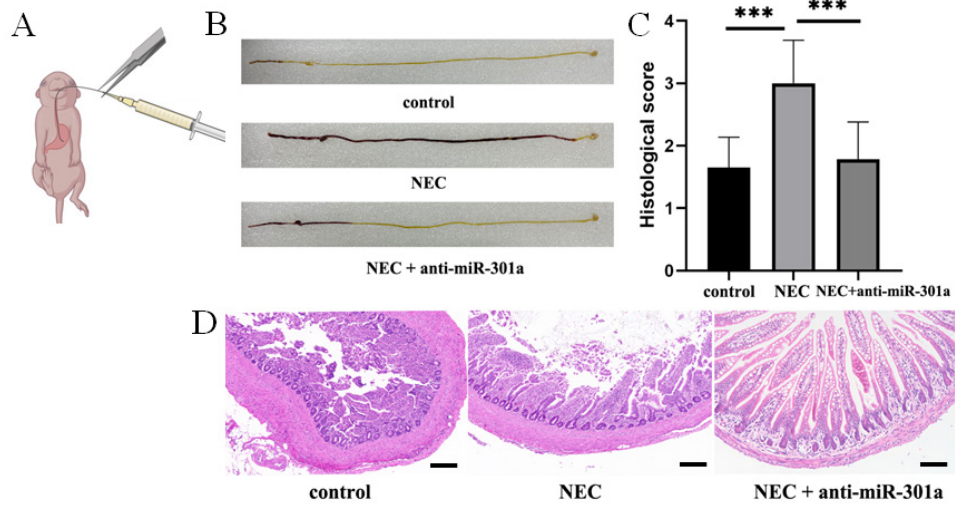


Figure 6. Inhibition of miRNA-301a ameliorated histological damage of NEC mice. (A) Illustration of the delivery of NEC formulae to neonatal mice. (B) Representative gastrointestinal images of the different groups of mice. (C) H&E staining was used to evaluate the severity of tissue damage in different groups of mice (n=5) Mann-Whitney U-test. *** $p < 0.001$. (D) Representative histological images of the terminal ileum in different groups of mice. Scale bar: 10 μ m.

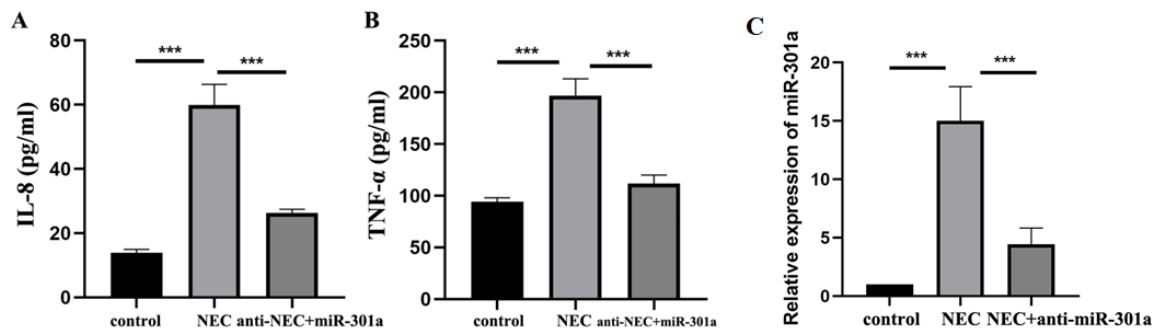


Figure 7. Inhibition of miRNA-301a reduced serum levels of inflammatory factors in NEC mice (n=5)

(A) Serum levels of IL-8 in different groups of mice. (B) Serum levels of TNF-α in different groups of mice. (C) Expression levels of miRNA-301a in intestinal tissues of different groups of mice. All experiments were in triplicates. *** $p < 0.001$.

group were typically < 2 points ($p < 0.05$). After treatment with miRNA-301a antagonist, the average histological score was 1.78 ± 0.60 , and the inflammation grade was significantly reduced ($p < 0.05$; Fig. 6C, D).

miRNA-301a antagonist reduced serum levels of IL-8 and TNF-α in NEC mice

The serum level of IL-8 was 13.95 ± 1.05 pg/ml in the control group and 59.93 ± 6.41 pg/ml in the NEC group ($p < 0.05$). However, posttreatment with the miRNA-301a antagonist reduced IL-8 level to 26.23 ± 1.22 pg/ml ($p < 0.05$ compared to the NEC group; Fig. 7A).

Furthermore, the serum level of TNF-α was 94.16 ± 3.92 and 197.04 ± 16.19 in the control and NEC groups ($p < 0.05$), respectively, and was 111.51 ± 8.62 in mice that received miRNA-301a antagonist treatment ($p < 0.05$ compared to the NEC group; Fig. 7B).

In addition, qRT-PCR showed that the expression level of miRNA-301a increased in the intestinal tissues of the NEC group ($p < 0.05$ compared to the control group), but decreased in NEC mice treated with miRNA-301a antagonist ($p < 0.05$ compared to the NEC group; Fig. 7C).

DISCUSSION

NEC is the main catastrophic cause of death in surviving premature infants. The pathogenesis of NEC as well as potential strategies for NEC prevention and treatment remain elusive, although it is evident that the inflammatory cascade plays an important role in the development of NEC (Niño *et al.*, 2016; Liu *et al.*, 2019). In this study, we successfully established an NEC mouse model to explore the role of miRNA-301a in the pathogenesis of NEC, and we proved the association between high expression of miRNA-301a and increased severity of NEC. In addition, our study revealed that high expression of miRNA-301a promoted the release of inflammatory factors IL-8 and TNF-α.

Numerous studies have proven that non-coding RNAs regulate inflammation through a variety of pathways (Zhou *et al.*, 2021; Yang & Ge, 2018). miRNA-301a was highly expressed in peripheral blood mononuclear cells and inflamed mucosa of patients with active IBD and may promote TNF-α production by targeting SNIP1, ultimately facilitating the pathogenesis of IBD (He *et al.*, 2016). miRNA-301a also inhibited the expression of BTG1, thereby reducing the integrity of the epithelium, promoting inflammation of the mouse colon and stimulating tumorigenesis (He *et al.*, 2017). In this

study we found that the pathological inflammation of the mouse intestinal tissue was reduced after we treated NEC mice with miRNA-301a antagonist, indicating that miRNA-301a plays an important role in the inflammatory progression of NEC.

For newborns with NEC, IL-8, IL-10, and TNF-α can be used as biomarkers for early diagnosis (Seliga-Siwecka & Kornacka, 2013). Combined analysis of IFN-γ-inducible protein 10 and TNF-α showed a specificity of 80% and a sensitivity of 90% (Weissenbacher *et al.*, 2013). In this study, we focused on TNF-α and IL-8, and found that the serum levels of inflammatory cytokines IL-8 and TNF-α were reduced after we treated NEC mice with miRNA-301a antagonist, suggesting that miRNA-301a may be a potential therapeutic target for NEC. In future studies, we need to examine other pro-inflammatory interleukins such as IL-1, IL-6 and IL-10 (Fu *et al.*, 2023).

Studies have shown that microRNAs play an important role in energy metabolism, immune regulation, homeostasis, cell apoptosis, cell proliferation and differentiation (Qi *et al.*, 2022; Zhong *et al.*, 2018; Zhang *et al.*, 2022; Liu *et al.*, 2022; Dai *et al.*, 2022; Chen *et al.*, 2021). Interference with these key cell functions can lead to an increase in apoptosis and inflammation and a decrease in repair capacity, which may be crucial in the pathogenesis of NEC (Premkumar *et al.*, 2014; Ng *et al.*, 2015). To further explore the potential mechanism of miRNA-301a in promoting NEC, we need to identify target genes of miRNA-301a that mediate the effects of miRNA-301a on cell proliferation, apoptosis, inflammation, metabolism and autophagy involved in the progression of NEC.

In conclusion, although further studies are necessary to confirm the role of miRNA-301a in MEC, our results provide the first evidence that miRNA-301a plays an important role in the pathogenesis of NEC by promoting inflammation, and is a potential therapeutic target of NEC.

Declarations

Availability of data and material. All data and materials are included in this manuscript.

Competing interests. The authors have no conflict of interest.

Authors' contributions. XX designed and supervised the study. DZ, FH and QZ performed the experiments and analyzed the data. All authors read and approved the final manuscript.

REFERENCES

- Bell RL, Withers GS, Kuypers FA, Stehr W, Bhargava A (2021) Stress and corticotropin releasing factor (CRF) promote necrotizing enterocolitis in a formula-fed neonatal rat model. *PLoS One* **16**: e0246412. <https://doi.org/10.1371/journal.pone.0246412>
- Cai L, Lai D, Gao J, Wu H, Shi B, Ji H, Tou J (2022) The role and mechanisms of miRNAs in neonatal necrotizing enterocolitis. *Front Pediatr* **10**: 1053965. <https://doi.org/10.3389/fped.2022.1053965>
- Chen CZ, Schaffert S, Fragoso R, Loh C (2013) Regulation of immune responses and tolerance: the microRNA perspective. *Immunol Rev* **253**: 112–128. <https://doi.org/10.1111/imr.12060>
- Chen H, Zeng L, Zheng W, Li X, Lin B (2020) Increased expression of microRNA-141-3p improves necrotizing enterocolitis of neonates through targeting MNX1. *Front Pediatr* **8**: 385. <https://doi.org/10.3389/fped.2020.00385>
- Chen X, Zhang H, Li L, Chen W, Bao T, Li B (2021) miR-5100 mediates migration and invasion of melanomatous cells *in vitro* via targeting SPINK5. *J Comp Mol Sci Genet* **1**: 14–23. Retrieved from <https://mbgm.journals.publicknowledgeproject.org/index.php/mbgm/article/view/1395>
- Dai D, Li B, Su Y, Li L, Fang X, Chen Y, Wang Y, Xu W (2022) Aminophylline inhibits the expression of inflammatory factors in airway smooth muscle cells under hypoxia through miR-138-5p/HIF1A axis. *J Comp Mol Sci Genet* **1**: 15–20. Retrieved from <https://mbgm.journals.publicknowledgeproject.org/index.php/mbgm/article/view/2240>
- Donda K, Bose T, Dame C, Maheshwari A (2022) The impact of microRNAs in neonatal necrotizing enterocolitis and other inflammatory conditions of intestine: a review. *Curr Pediatr Rev* **19**: 5–14. <https://doi.org/10.2174/1573396318666220117102119>
- Flahive C, Schlegel A, Mezzoff EA (2020) Necrotizing enterocolitis: updates on morbidity and mortality outcomes. *J Pediatr* **220**: 7–9. <https://doi.org/10.1016/j.jpeds.2019.12.035>
- Fu J, Chen R, Zhang Z, Zhao J, Xia T (2023) An inflammatory-related genes signature based model for prognosis prediction in breast cancer. *Oncol Res* **31**: 157–167. <https://doi.org/10.32604/or.2023.027972>
- Gao X, Chen Y, Chen M, Wang S, Wen X, Zhang S (2018) Identification of key candidate genes and biological pathways in bladder cancer. *PeerJ* **6**: e6036. <https://doi.org/10.7717/peerj.6036>
- He C, Shi Y, Wu R, Sun M, Fang L, Wu W, Liu C, Tang M, Li Z, Wang P, Cong Y, Liu Z (2016) miR-301a promotes intestinal mucosal inflammation through induction of IL-17A and TNF- α in IBD. *Gut* **65**: 1938–1950. <https://doi.org/10.1136/gutjnl-2015-309389>
- He C, Yu T, Shi Y, Ma C, Yang W, Fang L, Sun M, Wu W, Xiao F, Guo F, Chen M, Yang H, Qian J, Cong Y, Liu Z (2017) MicroRNA 301A Promotes intestinal inflammation and colitis-associated cancer development by inhibiting BTG1. *Gastroenterology* **152**: 1434–1448. e15. <https://doi.org/10.1053/j.gastro.2017.01.049>
- Liu J, Li Y, Feng Y, Pan L, Xie Z, Yan Z, Zhang L, Li M, Zhao J, Sun J, Hong L (2019) Patterned progression of gut microbiota associated with necrotizing enterocolitis and late onset sepsis in preterm infants: a prospective study in a Chinese neonatal intensive care unit. *PeerJ* **7**: e7310. <https://doi.org/10.7717/peerj.7310>
- Liu Y, Wang M, Deng T, Liu R, Ning T, Bai M, Ying G, Zhang H, Ba Y (2022) Exosomal miR-155 from gastric cancer induces cancer-associated cachexia by suppressing adipogenesis and promoting brown adipose differentiation via C/EBP β . *Cancer Bio Med* **19**: 1301–1314. <https://doi.org/10.20892/j.issn.2095-3941.2021.0220>
- Meister AL, Doheny KK, Travagli RA (2020) Necrotizing enterocolitis: It's not all in the gut. *Exp Biol Med (Maywood)* **245**: 85–95. <https://doi.org/10.1177/1535370219891971>
- Ng PC, Chan KY, Leung KT, Tam YH, Ma TP, Lam HS, Cheung HM, Lee KH, To KF, Li K (2015) Comparative MiRNA expression profiles and molecular networks in human small bowel tissues of necrotizing enterocolitis and spontaneous intestinal perforation. *PLoS One* **10**: e0135737. <https://doi.org/10.1371/journal.pone.0135737>
- Niño DF, Sodhi CP, Hackam DJ (2016) Necrotizing enterocolitis: new insights into pathogenesis and mechanisms. *Nat Rev Gastroenterol Hepatol* **13**: 590–600. <https://doi.org/10.1038/nrgastro.2016.119>
- Nolan LS, Gong Q, Hofmeister HN, Good M (2021) A protocol for the induction of experimental necrotizing enterocolitis in neonatal mice. *STAR Protoc* **2**: 100951. <https://doi.org/10.1016/j.xpro.2021.100951>
- Premkumar MH, Sule G, Nagamani SC, Chakkalakal S, Nordin A, Jain M, Ruan MZ, Bertin T, Dawson B, Zhang J, Schady D, Bryan NS, Campeau PM, Erez A, Lee B (2014) Argininosuccinate lyase in enterocytes protects from development of necrotizing enterocolitis. *Am J Physiol Gastrointest Liver Physiol* **307**: G347–G354. <https://doi.org/10.1152/ajpgi.00403.2013>
- Qi L, Xu X, Li B, Chang B, Wang S, Liu C, Wu L, Zhou X, Wang Q (2022) Dihydroartemisinin ameliorates palmitate-induced apoptosis in cardiomyocytes via regulation on the miR-133b/Sirt1 axis. *Biocell* **46**: 989–998. <https://doi.org/10.32604/biocell.2022.018014>
- Seliga-Siwecka JP, Kornacka MK (2013) Neonatal outcome of preterm infants born to mothers with abnormal genital tract colonisation and chorioamnionitis: a cohort study. *Early Hum Dev* **89**: 271–275. <https://doi.org/10.1016/j.earlhumdev.2012.10.003>
- Weissenbacher T, Laubender RP, Witkin SS, Gingelmaier A, Schiessl B, Kainer F, Frieske K, Jeschke U, Dian D, Karl K (2013) Diagnostic biomarkers of pro-inflammatory immune-mediated preterm birth. *Arch Gynecol Obstet* **287**: 673–685. <https://doi.org/10.1007/s00404-012-2629-3>
- Yang T, Ge B (2018) miRNAs in immune responses to *Mycobacterium tuberculosis* infection. *Cancer Lett* **431**: 22–30. <https://doi.org/10.1016/j.canlet.2018.05.028>
- Yin Y, Qin Z, Xu X, Liu X, Zou H, Wu X, Cao J (2019) Inhibition of miR-124 improves neonatal necrotizing enterocolitis via an MYPT1 and TLR9 signal regulation mechanism. *J Cell Physiol* **234**: 10218–10224. <https://doi.org/10.1002/jcp.27691>
- Zhang J, Wang C, Guo Z, Da B, Zhu W, Li Q (2021) miR-223 improves intestinal inflammation through inhibiting the IL-6/STAT3 signaling pathway in dextran sodium sulfate-induced experimental colitis. *Immun Inflamm Dis* **9**: 319–327. <https://doi.org/10.1002/iid3.395>
- Zhang T, Wang J, Wang D, Xu K, Wu L, Wang X, Wang W, Deng L, Liang J, Lv J, Hui Z, Zhou Z, Feng Q, Xiao Z, Chen D, Wang J, Wang L, Bi N (2022) The time-series behavior of systemic inflammation-immune status in predicting survival of locally advanced non-small cell lung cancer treated with chemoradiotherapy. *J Natl Cancer Center* **2**: 33–40. <https://doi.org/10.1016/j.jncc.2021.11.003>
- Zhong L, Simard MJ, Huot J (2018) Endothelial microRNAs regulating the NF- κ B pathway and cell adhesion molecules during inflammation. *FASEB J* **32**: 4070–4084. <https://doi.org/10.1096/fj.201701536R>
- Zhou J, Ji X, Wang Y, Wang X, Mao Y, Yang Z (2021) Long intergenic noncoding RNAs differentially expressed in *Staphylococcus aureus*-induced inflammation in bovine mammary epithelial cells. *Biocell* **45**: 1033–1044. <https://doi.org/10.32604/biocell.2021.015586>

Cytokine IL6, but not IL-1 β , TNF- α and NF- κ B is increased in paediatric cancer patients

Anna Synakiewicz¹✉, Anna Stanislawska Sachadyn², Anna Owczarzak³, Malgorzata Skuza⁴ and Teresa Stachowicz-Stencel¹

¹Department of Pediatrics, Hematology and Oncology, Medical University of Gdansk, Gdańsk, Poland; ²Department of Molecular Biotechnology and Microbiology, Gdansk University of Technology; ³Department of Clinical Nutrition, Medical University of Gdansk, Gdańsk, Poland; ⁴Individual Medical Practice, Gdynia, Poland

Cytokines are responsible for maintaining homeostasis as cell growth, differentiation, migration and apoptosis mediators. They play a pivotal role in immune responses to inflammatory reactions. In oncological diseases, the cross-talk between cells of the immunological system and cells of the tumour microenvironment is led by cytokines. Also, the overproduction of cytokines may change the tumour microenvironment and stimulate tumour development and growth. To test whether pro-inflammatory cytokines or associated with them transcription factor levels are changed in a group of 53 paediatric cancer patients, serum levels of IL-1 β , IL-6, TNF- α and NF- κ B were assessed and compared to measures in 25 healthy controls. Increased levels of IL-6 were found among patients in active oncological treatment ($P=0.002$) but not among patients whose treatment was completed. Our data suggest that IL6, but not IL-1 β , TNF- α and NF- κ B, is elevated as a result of the immune response in the microenvironment around the tumour and in blood cancers, among patients who were not infected at the time of blood collection. Thus, IL6 levels might serve as a potential biomarker of oncohematological diseases.

Keywords: cytokines, cancer, interleukins, biomarker, pediatric neoplasm

Received: 12 February, 2023; revised: 15 March, 2023; accepted: 25 March, 2023; available on-line: 12 April, 2023

✉e-mail: anna.synakiewicz@gumed.edu.pl

Acknowledgements of Financial Support: Funding support was provided from ST 02-0008/07

Abbreviations: ATGL, adipose triglyceride lipase; BAFF, B-cell activating factor; CAFs, cancer-associated fibroblasts; ER, estrogen receptor; HER2, human epidermal growth factor receptor 2; IL-1, interleukin 1; IL-1 α , interleukin 1 α ; IL-1 β , interleukin 1 β ; IL-6, interleukin 6; TNF- α , tumour necrosis factor α ; IL-8, interleukin 8; ILs, interleukins; MAPK, mitogen-activated protein kinase; NF- κ B, nuclear factor kappa B; NIK, NF- κ B-inducing kinase; NK, natural killers; ROS, reactive oxygen species; TAMs, tumour associated macrophages; TME, tumour microenvironment; TRAF2/3, TNF receptor-associated factor 2/3; VEGF, vascular endothelial growth factor

INTRODUCTION

Cytokines are intercellular protein mediators which regulate many processes, including cell growth, differentiation, migration and apoptosis. They play a crucial role in immune responses to inflammatory reactions and, generally, are responsible for maintaining homeostasis. In the case of a healthy person, they are present locally in tissues or body fluids in relatively small amounts. High

activity in low concentrations is a characteristic feature in certain pathological states.

These molecules are produced by many types of cells and may cause numerous reactions. Inversely, various groups of cytokines may play the same role. In addition, the source of cytokines may affect its final response, and even cause the opposite effect.

Cytokines create a complicated network of stimulation and inhibition processes (Jansen *et al.*, 2022). Interleukins (ILs) were the first described growth and differentiation regulators expressed by leukocytes. With further studies, other factors were discovered in terms of cytokines, and it is now known that there are more than 50 interleukins and additional proteins (Brocker *et al.*, 2010). Interleukins are divided according to their origin and functions, specifically to pro-inflammatory, proangiogenic, chemotactic or hematopoietic. Specific surface receptors are necessary for proper cytokine effect by increasing or decreasing its influence on cell metabolism.

The role of cytokines in malignant proliferation is widely studied. It is well known that the neoplastic process is associated with uncontrolled cell division and disturbances in metabolic regulation. Cancer cells are much better consumers of nutritional substances than normal tissue components due to their rapid growth. It includes amino acids, lipids, protein or glucose metabolism and its influence on the tumour microenvironment. The expression of adipose triglyceride lipase (ATGL) may be downregulated in some cancers and may be associated with glycolytic processes typical for most malignant tumours (Pan *et al.*, 2013).

Moreover, tumour cells may adapt by metabolic reprogramming (Tang *et al.*, 2021). Rapidly growing tumour mass requires new blood vessels, and angiogenesis takes place. But it is insufficient, and hypoxia is another process in this situation. Tumour cells use more likely energy from aerobic glycolysis and glutaminolysis or fatty acids, which is known as Warburg effect. Such a process may be connected with oncogene activation such as Myc, Ras, or inactivation of the p53 suppressor gene and some metabolic damage (Koppenol *et al.*, 2011; Cairns *et al.*, 2011). All these processes influence signal transmission and have an impact on immunometabolism in cancer. Cytokines play a role as mediators between cells of the immunological system and cells of the tumour microenvironment. Cancer cell – intrinsic and extrinsic signalling is needed for progression and invasion of the neoplastic process (Briukhovetska D *et al.*, 2021).

Cytokines play different roles in uninhibited proliferation processes, such as paracrine and autocrine factors, proangiogenic agents, survival factors of neoplastic cells

and other elements that affect invasiveness and distant metastasis formation.

The role of the immune system, and thus the influence of cytokines in malignancies, cannot be overestimated. Inflammation, primarily chronic, and oxidative stress mediate different kinds of malignancies. Most of the studies on that correlation were collected from colon cancer patients who primarily have Crohn's disease (Monteleone *et al.*, 2012; Klampfer L, 2011; Borowczak *et al.*, 2022). Pro-inflammatory cytokines, such as IL-1 β , IL-6 or TNF- α play a key role in proliferative diseases, and their overproduction may change the tumour micro-environment and stimulate tumour development. Also, activation of transcription factors such as NF- κ B is involved in various cellular processes in neoplasms. This factor can inhibit apoptosis as well as enhance angiogenesis. Thus, it may play a role in developing both haematological neoplasms and solid tumours.

We have attempted to answer the question if changes in the level of the determined substances can serve as an early marker of neoplastic disease or be a prognostic marker of the outcome.

MATERIALS AND METHODS

Patients

Paediatric cancer patients, including patients with haematological malignancies and solid tumours, who were diagnosed and treated in the Department of Paediatrics, Haematology and Oncology, Medical University of Gdansk, Poland, were enrolled in the study. Twenty-five patients, between 1 and 18 years of age (mean age 8.04 years, median age six years), were during treatment, and twenty-eight patients, between 3 and 18 years of age (mean age 9.79 years, median age eleven years) were after treatment.

Inclusion criteria

We included children between 1 month and 18 years of age with confirmed neoplastic disease. The patients showed no signs of infection.

Control group

Twenty-five healthy children were recruited during routine medical checkup (14 males and 11 females), aged between 3 and 17 years (mean age 12.24 years, median age 14 years).

Laboratory analysis

Peripheral blood was collected from the patients during and after successful treatment; the average duration of treatment was about two years.

Measurements of IL-1 β , IL-6 and TNF- α were assessed using R&D Systems Quantikine ELISA Kits (Minneapolis, MN, USA) and NF- κ B using Nuclear Factor Kb P65 (NFKB P65), ELISA Kit (My BioSource, San Diego CA, USA). All assays were performed according to the procedure provided by the manufacturer. All analyses were performed in the laboratory of the Department of Clinical Nutrition Medical University of Gdansk, Poland.

Statistical analyses

The Wilcoxon rank-sum test was used to assess differences in subjects' age (years) and in levels of NF- κ B (μ mol/L), TNF- α (pg/mL), IL-6 (pg/mL) and IL-1 β (pg/mL) between patients before treatment, patients during treatment, patients after treatment and healthy controls. The distributions of NF- κ B, TNF- α , IL-6 and IL-1 β were skewed as assessed by Kolmogorov-Smirnov test. Tests were two-tailed, and P-values ≤ 0.05 were considered statistically significant. Means and standard deviations, medians and 25th–75th percentiles were given for continuous variables. Statistical analyses were calculated using SAS 9.4 (NC, USA). XLStat (Addinsoft) programme was used to generate plots.

RESULTS

The study population consisted of 25 patients during treatment, 28 patients after treatment and 25 healthy controls (Table 1). Those groups did not differ significantly in age at the time of blood collection. A slightly

Table 1. Characteristics of study population.

		Patients during treatment	Patients after treatment	Healthy controls
*Age (years)	Mean, St Dev	8.04, 5.87	9.79, 4.63	12.24, 4.69
	(N)	(25)	(28)	(25)
	Median (q1-q3)	6 (3–14)	11 (6–12.5)	14 (9–16)
Sex	Females	8 (32%)	12 (42.86%)	11 (44%)
	Males	17 (68%)	16 (57.14%)	14 (56%)
Diagnosis	acute lymphoblastic leukemia	8 (32%)	3 (10.71%)	
	non-Hodgkin lymphoma	1 (4%)	1 (3.57%)	
	neuroblastoma	2 (8%)	14 (50%)	
	rhabdomyosarcoma	4 (16%)	2 (7.14%)	
	Wilms tumor	–	2 (7.14%)	
	retinoblastoma	–	1 (3.57%)	
	Hodgkin lymphoma	6 (24%)	5 (17.86%)	
	osteosarcoma	2 (8%)	–	
	Langerhans cell histiocytosis	2 (8%)	–	

*P=0.178 for a difference in age between patients during treatment vs. patients after treatment. *P=0.014 for a difference in age between patients during treatment vs. controls. *P=0.052 for a difference in age between patients after treatment vs controls

Table 2. Comparison of NF- κ B, TNF- α , IL-6, IL-1 β levels from patients before or after treatment and healthy controls.

		Patients during treatment	Patients after treatment	Healthy controls	P^{*1}	P^{*2}	P^{*3}
NF- κ B	Mean, StDev	1.83, 1.66	2.57, 1.92	2.78, 2.91	0.092	0.273	0.618
	(μ mol/L) (N)	(25)	(28)	(25)			
	Median (q1-q3)	1.42 (0.7-3.12)	1.71 (1.15-3.82)	1.45 (1.03-3.16)			
TNF- α	Mean, StDev	1.62, 1.45	1.32, 0.92	1.04, 0.64	0.624	0.109	0.154
	(pg/mL) (N)	(25)	(28)	(25)			
	Median (q1-q3)	1.38 (0.59-1.85)	0.98 (0.78-1.69)	0.90 (0.71-1.07)			
IL-6	Mean, StDev	6.34, 4.13	2.32, 2.55	2.75, 3.45	0.0002	0.002	0.563
	(pg/mL) (N)	(25)	(28)	(25)			
	Median (q1-q3)	6.16 (2.07-10.55)	1.27 (0.65-2.85)	1.19 (0.91-2.35)			
IL-1 β #	Mean, StDev	0.1, 0.0709	0.10, 0.12	0.07, 0.06	0.203	0.116	0.950
	(pg/mL) (N)	(23)	(28)	(25)			
	Median (q1-q3)	0.09 (0.05-0.14)	0.05 (0.03-0.11)	0.06 (0.03-0.09)			

*Wilcoxon ranked-sum test; ¹patients during treatment vs. patients after treatment; ²patients during treatment vs. controls; ³patients after treatment vs. controls; # two outlying values: 2.49, 6.08 pg/mL were removed from analyses

higher proportion of males were included in each group; males constituted 68% of patients, 57.14% of survivors and 56% of healthy subjects. More patients than survivors were diagnosed with acute lymphoblastic leukaemia (32% *vs.* 10.71%), while more survivors were diagnosed with neuroblastoma (50% *vs.* 8%). Among survivors, two patients were diagnosed with Wilms tumour; one person was diagnosed with retinoblastoma. Among patients, two were diagnosed with osteosarcoma and two with Langerhans cell histiocytosis.

Levels of IL-1 β , IL-6 or TNF- α and NF- κ B were measured in blood samples collected from a healthy control group and pediatric oncological patients during treatment and post-treatment. Significantly higher levels of IL-6 were observed in the patients during active oncological treatment compared to both the control group and survivors ($P=0.002$, $P=0.0002$, respectively), as presented in Table 2, Figure 1. IL-6 levels in the post-treatment group were comparable to those in the control group ($P=0.563$). The mean value of IL-6 was 6.34 ± 4.13 pg/mL among patients during active oncological treatment versus 2.75 ± 3.45 pg/mL among healthy controls and 2.32 ± 2.55 pg/mL among survivors.

In other parameters, such dependencies were not observed (Table 2, Fig. 1).

DISCUSSION

Pediatric cancer patients constitute a particular group of patients, mainly due to the low incidence rate of this disease in children. Neoplasms type, both haematological and solid tumours, also differ from those in the adult population. Observations regarding the interleukin impact in children concern mainly IL-2 regarding its modulating effect on the immune system and the anti-tumour response promotion through lymphocyte activation and their differentiation in progressing or metastatic patients (Schwinger *et al.*, 2005). It is well known that chronic inflammation concomitant with oxidative stress boosts tumour development, especially the skin, lung, colorectal or hepatocellular carcinoma (Bruni *et al.*, 2020).

Pro-inflammatory cytokines such as IL-1 β , IL-6 or TNF- α , which were under investigation in the present study, and NF- κ B, are crucial for metabolic homeostasis.

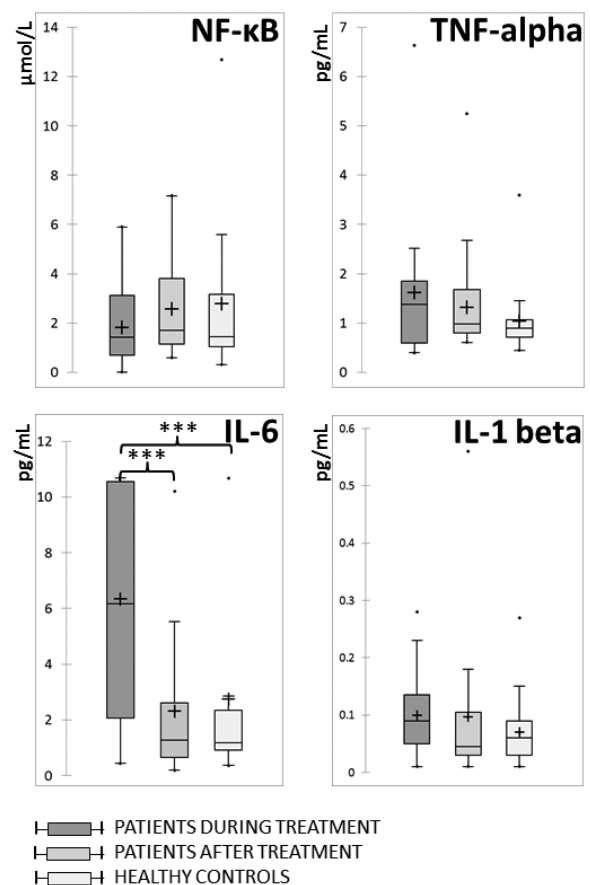


Figure 1. Levels of NF- κ B, TNF- α , IL-6, IL-1 β from patients before or after treatment and healthy controls.

They are secreted by healthy cells, but their overproduction may lead to neoplastic transformation. Also, neoplastic cells derived from fibroblasts and macrophages also release IL-1, IL-6, TNF- α , that serve as source of paracrine factors (Bingle *et al.*, 2002; Kunz-Schughart & Knuechel, 2002).

Among many cytokines present in pediatric oncology patients' sera, the ones determined by the authors seem to have a particular impact on the neoplastic process. The distinctive histology of childhood cancers makes it difficult to predict the behaviour of individual molecules, in contrast to the adult population where the inflammatory component of the neoplastic process has been relatively well studied (Dranoff, 2004; Greten *et al.* 2019; Mantovani *et al.*, 2019).

The tumour microenvironment (TME), which in addition to cancer cells, also contains cancer-associated fibroblasts (CAFs), pericytes, endothelial cells, and immune cells, plays a significant role in tumour proliferation and progression processes. Pro-inflammatory cytokines serve as mediators in these actions (Christofi *et al.*, 2019).

Our pediatric oncological patients showed significant differences in IL-6 levels during active treatment. Importantly, IL-6 values achieved those observed in the control group after the end of treatment. IL-6 is a multitasked substance. Its essential role is associated with the inflammatory response and active participation in the immunological processes. It may also be secreted by TME and cause further tumour development and progression (von Felbert *et al.*, 2005). Interleukin-6 has a pro-oncogenic function as it may activate carcinogenesis. It is one of the mediators of cytokine release syndrome. IL-6 signals to cells through two opposite pathways. The classic pathway is anti-inflammatory and takes part in repair processes. The *trans*-signaling pathway promotes inflammation and may contribute to the progression of many diseases, including cancer (Kumari *et al.*, 2016). The classic pathway is based on transmembrane IL-6R α receptors on a cell surface. The *trans* pathway occurs in the cells capable of expressing the gp130 protein.

IL-6 induces angiogenesis via the vascular endothelial growth factor. The elevated serum level of IL-6 in patients with colon and breast cancer or melanoma patients is a poor prognostic factor (Ma *et al.*, 2017; Kucera *et al.*, 2015). Furthermore, prostate cancer patients showed higher levels of this cytokine compared to a healthy control group. Moreover, it positively correlated with a higher Gleason score (Siemińska *et al.*, 2015). In metastatic prostate cancer patients, the serum level of IL-6 was higher than in patients with localized disease; hence it may serve as a prognostic factor (Michalaki *et al.*, 2004).

Similarly, in breast ductal carcinoma patients, Ma *et al.* (2017) demonstrated that elevated serum IL-6 levels positively correlated with more advanced disease stages and metastases to lymph nodes. Additionally, the authors noticed high levels of IL-6 in ER+ or HER2+ tumours in contrast to those with ER- or HER2 negative. In high-risk neuroblastoma pediatric patients, Egler and others (Egler *et al.*, 2021) showed increased IL-6 levels in their serum and bone marrow. The researchers analyzed the link between the levels of *inter alia*, IL-6 and the genetic polymorphism of this interleukin. Such results may suggest that particular interleukins could serve as potential cancer biomarkers.

Interleukin-1 was initially considered as a pro-inflammatory factor, which plays an essential role in severe systemic infections, but its part in the activation and stimulation of other cytokine secretion or prostaglandin production suggests that it should be considered in a broader aspect (Razavi *et al.*, 2015). It is also known that IL-1 may be partially involved in tumour promotion and could be responsible for metastasis. It develops via different mechanisms, such as matrix metalloproteinases expression, or affects the excretion of VEGF, IL-6,

IL-8 or TNF- α by the surrounding tissues (Konishi *et al.*, 2005; Dinarello, 1996). Anti-inflammatory mechanisms are enhanced by interleukin-1 via the release of e.g., IL-6 (Mantovani *et al.*, 2019). Interleukin-1 β belongs to the IL-1 family and is one of the structural components of IL-1. The other two are IL-1 α and the IL-1 receptor antagonist. More importantly, IL-1 β is initially produced by macrophages as a pro-protein and then converted into IL-1 β with the use of caspase-1 (Teufel *et al.*, 2022). Both alarmins, IL-1 β and IL-1 α , may serve as promoters of carcinogenic mediators: nitric oxide and reactive oxygen species (ROS) (Mantovani *et al.*, 2019). Interleukin-1 β activates macrophages, suppresses NK function, and inhibits CD8+ lymphocytes by inducing neutrophils. The final effect is the production of pro-tumorigenic factors (Zhang *et al.*, 2020). Its role in cancer transformation and progression was observed in colon and prostate cancer patients, whose sera showed elevated levels of this factor (Hai *et al.*, 2016; Saylor *et al.*, 2012). Studies of human cancer cells from ovarian, breast, lung carcinoma, sarcoma and melanoma have shown that they are capable of producing or up-regulating Interleukin-1 β (Elaraj *et al.*, 2006). Barrera and others (Barrera *et al.*, 2018) showed that elevated IL-1 β serum concentrations in lung cancer patients positively correlated with a high percentage of myeloid-derived suppressor cells and were associated with worse prognosis and poor survival. Also, studies carried out on mice demonstrated an increased sera level of IL-1 β and IL-6 following carcinogen administration (Narayan *et al.*, 2012). In our study, we did not observe increased values of IL-1 β in our patients' sera, either during or after treatment, compared to the control group.

Another cytokine, tumour necrosis factor- α (TNF- α), also called cachexin, is of interest to those who study substances involved in developing various cancer types. It is mainly produced by macrophages (also TAMs- tumour associated macrophages) and monocytes, but also lymphocytes T, mast cells, fibroblasts and adipocytes. TNF- α is a part of the TNF superfamily, which also includes ligands and their receptors. When combined, most of them activate the nuclear transcription factor kappa (NF- κ B) (Ware, 2008). Other signalling pathways for this factor are MAPK (mitogen-activated protein kinase) and the apoptosis signalling pathway. It is thought that cachexin may be both an anti-tumour and a pro-tumorigenic agent, depending on the dose (Dobrzycka *et al.*, 2009). There are reports of a direct effect on the stimulation of neoplastic transformation by inducing cell proliferation and transformation (Wang *et al.*, 2008).

Increased TNF- α levels are related to a higher stage of cancer (Zhou *et al.*, 2014; Esquivel-Velazquez *et al.*, 2015). In metastatic prostate cancer patients who started hormonal therapy, elevated serum TNF- α levels are associated with a worse course of the disease and a worse prognosis (Sharma *et al.*, 2014). The researchers are not unanimous. Some authors showed lower serum TNF- α levels in colorectal cancer patients compared to the control group; others did not find it at all (Godos *et al.*, 2017; Abe Vincente *et al.*, 2014). It was found that high levels of this cytokine are associated with stage III and IV colorectal cancer (Obeed *et al.*, 2014). Additional studies focused on the association between TNF- α serum levels and the risk of colon cancer development or polymorphism of the gene encoding TNF- α *versus* cancer development risk. No correlation was found (Joshi *et al.*, 2014; Miao *et al.*, 2018). However, Ma and others (Ma *et al.*, 2017) indicated a correlation between serum concentrations of TNF- α , IL-6 and IL-8 and higher stages

of advancement (III-stage breast ductal carcinoma) and metastases to lymph nodes. We did not find any dependence for TNF- α in pediatric cancer patients compared to the control group, regardless of the treatment period.

Nuclear factor kappa B (NF- κ B) constitutes a family of transcription factors which lead some important signaling pathways that might control cell differentiation, proliferation and angiogenesis during tumorigenesis (Taniguchi, 2018). The dysregulation of NF- κ B is an essential contributor to the development of cancers and their progression or relapse. It is regarded as a potential therapeutic target for patients with neoplastic diseases. An NF- κ B-inducing kinase (NIK), encoded by the gene *MAP3K14* is acclaimed as the central kinase controlling non-canonical NF- κ B activation (Haselager, 2022). This NF- κ B pathway is activated upon stimulation of the BAFF receptor, CD40, receptor activator of NF- κ B or the lymphotoxin β receptor. It accounts for the recruitment of TRAF2/3 to the receptor, resulting in the accumulation of NIK protein levels (Xiao *et al.*, 2001). NIK plays a regulatory role in the process of inflammation. Loss of NIK is associated with severe immune defects, whereas NIK overexpression is observed in inflammatory diseases and malignancies. For this reason, targeting NIK and the non-canonical NF- κ B pathway may display a therapeutic potential in various diseases (Fei *et al.*, 2020; Jang *et al.*, 2020). NF- κ B1 is a subunit of NF- κ B. An aberrant activation of the latter is associated with cancer pathogenesis. The nuclear factor kappa B 1 (NF- κ B1, p105/p50) is a potential target gene of miR-497. It has been reported that NF- κ B1 plays various roles in the development and progression of cancers. On the other hand, NF- κ B1 may act as a tumour suppressor in some gastrointestinal cancers (hepatocellular carcinoma, gastric cancer) (Chen *et al.*, 2022).

CONCLUSIONS

A significant increase in IL-6 in patients during oncological treatment and its absence after successful treatment may be helpful in monitoring the disease and may become an early biomarker of the neoplastic process in combination with other substances. The research carried out, and the results achieved indicate a certain important role of the tested substances in the process of oncogenesis and proliferation in oncohematological diseases in children. Further investigations are needed, including more potential biomarkers and patients with failure to check the course and level changes.

All the procedures performed in the study involving human participants were in accordance with the ethical standards of the institutional and/or national research committee and with the 1964 Helsinki Declaration and its later amendments or comparable ethical standards – the study project of the study was approved by the Ethical Committee of the Medical University of Gdansk, Poland (NKBBN/868/2019).

Informed consent was obtained from the parents and patients over 16 years old.

Declaration

The authors declare that there are no conflicts of interest.

REFERENCES

Abe Vicente M, Donizetti Silva T, Barão K, Vitor Felipe A, Oyama Missae L, Manoukian Forones N (2014) The influence of nutritional

- status and disease on adiponectin and TNF- α ; levels in colorectal cancer patients. *Nutr. Hosp.* **30**: 140–146. <https://doi.org/10.3305/nh.2014.30.1.7132>
- Dobrzycka B, Terlikowski SJ, Garbowicz M, Niklińska W, Bernaczyk PS, Nikliński J, Kinalski M, Chyczewski L (2009) Tumor necrosis factor- α and its receptors in epithelial ovarian cancer. *Folia Histochem. Cytobiol.* **47**: 609–613. <https://doi.org/10.2478/v10042-008-0117-1>
- Barrera L, Montes-Servín E, Hernandez-Martinez JM, Orozco-Morales M, Montes-Servín E, Michel-Tello D, Morales-Flores RA, Flores-Estrada D, Arrieta O (2018) Levels of peripheral blood polymorphonuclear myeloid-derived suppressor cells and selected cytokines are potentially prognostic of disease progression for patients with non-small cell lung cancer. *Cancer Immunol. Immunother.* **67**: 1393–406. <https://doi.org/10.1007/s00262-018-2196-y>
- Bingle L, Brown NJ, Lewis CE (2002) The role of tumour-associated macrophages in tumour progression: implications for new anticancer therapies. *J. Pathol.* **96**: 254–265. <https://doi.org/10.1002/path.1027>
- Borowczak J, Szczerbowski K, Maniewski M, Kowalewski A, Janiczek-Polewska M, Szyłberg A, Marszałek A, Szyłberg Ł (2022) The role of inflammatory cytokines in the pathogenesis of colorectal carcinoma – recent findings and review. *Biomedicines* **10**: 1670. <https://doi.org/10.3390/biomedicines10071670>
- Briukhovetska D, Dörr J, Endres S, Libby P, Dinarello CA, Kobold S (2021) Interleukins in cancer: from biology to therapy. *Nat. Rev. Cancer* **21**: 481–499. <https://doi.org/10.1038/s41568-021-00363-z>
- Brocker C, Thompson D, Matsumoto A, Nebert DW, Vasilou V (2010) Evolutionary divergence and functions of the human interleukin (IL) gene family. *Hum. Genomics* **5**: 30–55. <https://doi.org/10.1186/1479-7364-5-1-30>
- Bruni D, Angell HK, Galon J (2020) The immune contexture and Immunoscope in cancer prognosis and therapeutic efficacy. *Nat. Rev. Cancer* **20**: 662–680. <https://doi.org/10.1038/s41568-020-0285-7>
- Cairns RA, Harris IS, Mak TW (2022) Regulation of cancer cell metabolism. *Nat Rev Cancer* **11**: 85–95. <https://doi.org/10.1038/nrc2981>
- Chen Q, Du X, Ruan P, Ye Y, Zheng J, Hu S (2022) Bioinformatics analysis revealing the correlations between NF- κ B signaling pathway and immune infiltration in gastric cancer. *Comput. Math. Methods Med.* **2022**: 5385456. <https://doi.org/10.1155/2022/5385456>
- Christofi T, Baritaki S, Falzone L, Libra M, Zaravinos A (2019) Current perspectives in cancer immunotherapy. *Cancers (Basel)* **11**(10): 1472. <https://doi.org/10.3390/cancers11101472>
- Dinarello CA (1996) Biologic basis for interleukin-1 in disease. *Blood* **87**: 2095–2147. PMID: 8630372
- Dranoff G (2004) Cytokines in cancer pathogenesis and cancer therapy. *Nat. Rev. Cancer* **4**: 11–22. <https://doi.org/10.1038/nrc1252>
- Egler RA, Burlingame SM, Nuchtern JG, Russell HV (2008) Interleukin-6 and soluble interleukin-6 receptor levels as markers of disease extent and prognosis in neuroblastoma. *Clin. Cancer Res.* **14**: 7028–7034. <https://doi.org/10.1158/1078-0432.CCR-07-5017>
- Elaraj DM, Weinreich DM, Varghese S, Puhlmann M, Hewitt SM, Carroll NM, Feldman ED, Turner EM, Alexander HR (2006) The role of interleukin 1 in growth and metastasis of human cancer xenografts. *Clin. Cancer Res.* **12**: 1088–1096. <https://doi.org/10.1158/1078-0432.CCR-05-1603>
- Esquivel-Velazquez M, Ostoa-Saloma P, Palacios-Arreola MI, Nava Castro KE, Castro JL, Morales-Montor J (2015) The role of cytokines in breast cancer development and progression. *J. Interferon Cytokine Res.* **35**: 1–16. <https://doi.org/10.1089/jir.2014.0026>
- Fei X, Zhang P, Pan Y, Liu Y (2020) MicroRNA-98-5p inhibits tumorigenesis of hepatitis B Virus related hepatocellular carcinoma by targeting NF- κ B-inducing kinase. *Yonsei Med. J.* **61**: 460–470. <https://doi.org/10.3349/ymj.2020.61.4.460>
- Godos J, Biondi A, Galvano F, Basile F, Sciacca S, Giovannucci EL, Grosso G (2017) Markers of systemic inflammation and colorectal adenoma risk: Meta-analysis of observational studies. *World J. Gastroenterol.* **23**: 1909–1919. <https://doi.org/10.3748/wjg.v23.i10.1909>
- Greten FR, Grivennikov SI (2019) Inflammation and cancer: triggers, mechanisms, and consequences. *Immunity* **51**: 27–41. <https://doi.org/10.1016/j.immuni.2019.06.025>
- Hai Ping P, Feng Bo T, Li L, Nan Hui Y, Hong Z (2022) IL-1 β /NF- κ B signaling promotes colorectal cancer cell growth through miR-181a/PTEN axis. *Arch. Biochem. Biophys.* **604**: 20–26. <https://doi.org/10.1016/j.abb.2016.06.001>
- Haselager MV, Eldering E (2022) The therapeutic potential of targeting NIK in B cell malignancies. *Front. Immunol.* **13**: 930986. <https://doi.org/10.3389/fimmu.2022.930986>
- Hou H, Gong L, Zhou L, Qin H, Mei X, Xie Y, Yu C, Hu H (2016) The potential role of microRNA-497 in different cancers. *Int. J. Clin. Exp. Pathol.* **9**: 7813–7818
- Jang H, Park S, Kim J, Kim JH, Kim SY, Cho S, Park SG, Park BC, Kim S, Kim JH (2020) The tumor suppressor, P53, negatively regulates non-canonical NF- κ B signaling through mima-induced silencing of NF- κ B-inducing kinase. *Mol. Cells* **43**: 23–33. <https://doi.org/10.14348/molecules.2019.0239>

- Jansen JE, Aschenbrenner D, Uhlig HH, Coles MC, Gaffney EA (2022) A method for the inference of cytokine interaction networks. *PLoS Comput. Biol.* **18**: e1010112. <https://doi.org/10.1371/journal.pcbi.1010112>
- Joshi RK, Lee S (2014) Obesity related adipokines and colorectal cancer: a review and meta-analysis. *Asian Pacific J. Cancer Prev.* **15**: 397–405. <https://doi.org/10.7314/APJCP.2014.15.1.397>
- Klumper L (2011) Cytokines, inflammation and colon cancer. *Curr. Cancer Drug Targets* **11**: 451–464. <https://doi.org/10.2174/156800911795538066>
- Konishi N, Miki C, Yoshida T, Tanaka K, Toiyama Y, Kusunoki M (2005) Interleukin-1 receptor antagonist inhibits the expression of vascular endothelial growth factor in colorectal carcinoma. *Oncology* **68**: 138–145. <https://doi.org/10.1159/000086768>
- Koppenol WH, Bounds PL, Dang CV (2011) Otto Warburg's contributions to current concepts of cancer metabolism. *Nat. Rev. Cancer* **11**: 325–337. <https://doi.org/10.1038/nrc3038>
- Kucera R, Topolcan O, Treskova I, Kinkorova J, Windrichova J, Fuchsova R, Svobodova S, Treska V, Babuska V, Novak J, Smejkal J (2015) Evaluation of IL-2, IL-6, IL-8 and IL-10 in malignant melanoma diagnostics. *Anticancer Res* **35**: 3537–3541. PMID: 26026122
- Kumari N, Dwarakanath BS, Das A, Bhatt AN (2016) Role of interleukin-6 in cancer progression and therapeutic resistance. *Tumor Biol.* **37**: 11553–11572. <https://doi.org/10.1007/s13277-016-5098-7>
- Kunz-Schughart LA, Knuechel R (2002) Tumor-associated fibroblasts (part I): Active stromal participants in tumor development and progression? *Histol. Histopathol.* **17**: 599–621. <https://doi.org/10.14670/HH-17.599>
- Liu L, Zheng W, Song Y, Du X, Tang Y, Nie J, Han W (2015) Enhances the sensitivity of colorectal cancer cells to neoadjuvant chemotherapeutic drug. *Curr. Protein Pept. Sci.* **16**: 310–315. <https://doi.org/10.2174/138920371604150429154142>
- Ma Y, Ren Y, Dai ZJ, Wu CJ, Ji YH, Xu J (2017) IL-6, IL-8 and TNF- α levels correlate with disease stage in breast cancer patients. *Adv. Clin. Exp. Med.* **26**: 421–426. <https://doi.org/10.17219/acem/62120>
- Mantovani A, Allavena P, Sica A, Balkwill F (2008) Cancer-Related Inflammation. *Nature* **454**: 436–444. <https://doi.org/10.1038/nature07205>
- Mantovani A, Dinarello CA, Molgora M, Garlanda C (2019) Interleukin-1 and related cytokines in the regulation of inflammation and immunity. *Immunity* **50**: 778–795. <https://doi.org/10.1016/j.immuni.2019.03.012>
- Miao Z, Wang K, Wang X, Zhang C, Xu Y (2018) TNF- α -308G/A polymorphism and the risk of colorectal cancer: A systematic review and an updated meta-analysis. *J. BUON.* **23**: 1616–1624. PMID: 30610785
- Michalaki V, Syrigos K, Charles P, Waxman J (2004) Serum levels of IL-6 and TNF- α correlate with clinicopathological features and patient survival in patients with prostate cancer. *Br. J. Cancer.* **90**: 2312–2316. <https://doi.org/10.1038/sj.bjc.6601814>. Erratum in: *Br. J. Cancer.* 2004 **91**: 1227
- Monteleone G, Pallone F, Stolfi C (2012) The dual role of inflammation in colon carcinogenesis. *Int. J. Mol. Sci.* **13**: 11071–11084
- Narayan C, Kumar A (2012) Constitutive over expression of IL-1 β , IL-6, NF- κ B, and Stat3 is a potential cause of lung tumorigenesis in urethane (ethyl carbamate) induced Balb/c mice. *J. Carcinog.* **11**: 9.
- Al Obeid OA, Alkhayal KA, Al Sheikh A, Zubaidi AM, Vaali-Mohammed MA, Boushey R, Mckerrow JH, Abdulla MH (2014) Increased expression of tumor necrosis factor-alpha is associated with advanced colorectal cancer stages. *World J. Gastroenterol.* **20**: 18390–18396. <https://doi.org/10.3748/wjg.v20.i48.18390>
- Owusu-Ansah KG, Song G, Chen R, Edoo MIA, Li J, Chen B, Wu J, Zhou L, Xie H, Jiang D, Zheng S (2019) COL6A1 promotes metastasis and predicts poor prognosis in patients with pancreatic cancer. *Int. J. Oncol.* **55**: 391–404. <https://doi.org/10.3892/ijo.2019.4825>
- Pan X, Wilson M, McConville C, Arvanitis TN, Griffin JL, Kauppinen RA, Peet AC (2013) Increased unsaturation of lipids in cytoplasmic lipid droplets in DAOY cancer cells in response to cisplatin treatment. *J. Metab. Soc.* **9**: 722–729. <https://doi.org/10.1007/s11306-012-0483-8>
- Porta C, Ippolito A, Consonni FM, Carraro L, Celesti G, Correale C, Grizzi F, Pasqualini F, Tartari S, Rinaldi M, Bianchi P, Balzac F, Vetrano S, Turco E, Hirsch E, Laghi L, Sica A (2018) Protumor steering of cancer inflammation by p50 NF-kappa enhances colorectal cancer progression. *Cancer Immunol. Res.* **6**: 578–593. <https://doi.org/10.1158/2326-6066.CIR-17-0036>
- Razavi GSE, Allen T (2015) Emerging role of interleukins in cancer treatment. *Immunome. Res.* **S2**: 006. <https://doi.org/10.4172/1745-7580.S2.006>
- Saylor PJ, Kozak KR, Smith MR, Ancukiewicz MA, Efsthathiou JA, Zietman AL, Jain RK, Duda DG (2012) Changes in biomarkers of inflammation and angiogenesis during androgen deprivation therapy for prostate cancer. *Oncologist.* **17**: 212–219. <https://doi.org/10.1634/theoncologist.2011-0321>
- Schwinger W, Klass V, Benesch M, Lackner H, Dornbusch HJ, Sovinz P, Moser A, Schwantzer G, Urban C (2005) Feasibility of high-dose interleukin-2 in heavily pretreated pediatric cancer patients. *Ann. Oncol.* **16**: 1199–1206. <https://doi.org/10.1093/annonc/mdi226>
- Sharma J, Gray KP, Harshman LC, Evan C, Nakabayashi M, Fichorova R, Rider J, Mucci L, Kantoff PW, Sweeney CJ (2014) Elevated IL-8, TNF- α , and MCP-1 in men with metastatic prostate cancer starting androgen-deprivation therapy (ADT) are associated with shorter time to castration-resistance and overall survival. *Prostate* **74**: 820–828. <https://doi.org/10.1002/pros.22788>
- Siemińska L, Borowski A, Marek B, Nowak M, Kajdaniuk D, Warakowski J, Kos-Kudła B (2015) Serum concentrations of adipokines in men with prostate cancer and benign prostate hyperplasia. *Endokrynol. Pol.* **69**: 120–127. <https://doi.org/10.5603/EP.a2018.0006>
- Tang Z, Xu Z, Zhu X, Zhang J (2021) New insights into molecules and pathways of cancer metabolism and therapeutic implications. *Cancer Commun. (London, England).* **41**: 16–36. <https://doi.org/10.1002/cac2.12112>
- Taniguchi K, Karin M (2018) NF- κ B, inflammation, immunity and cancer: coming of age. *Nat. Rev. Immunol.* **18**: 309–324. <https://doi.org/10.1038/nri.2017.142>
- Teufel LU, Arts RJW, Netea MG, Dinarello CA, Joosten LAB (2022) IL-1 family cytokines as drivers and inhibitors of trained immunity. *Cytokine* **150**: 15577. <https://doi.org/10.1016/j.cyt.2021.155773>
- von Felbert V, Córdoba F, Weissenberger J, Vallan C, Kato M, Nakashima I, Braathen LR, Weis J (2005) Interleukin-6 gene ablation in a transgenic mouse model of malignant skin melanoma. *Am. J. Pathol.* **166**: 831–841. [https://doi.org/10.1016/S0002-9440\(10\)62304-8](https://doi.org/10.1016/S0002-9440(10)62304-8)
- Wang X, Lin Y (2008) Tumor necrosis factor and cancer, buddies or foes? *Acta Pharmacol. Sin.* **29**: 1275–1288. <https://doi.org/10.1111/j.1745-7254.2008.00889.x>
- Ware CF (2008) TNF superfamily 2008. *Cytokine Growth Factor Rev.* **19**: 183–186. <https://doi.org/10.1016/j.cytogfr.2008.05.001>
- Xia Y, Hu C, Lian L, Hui K, Wang L, Qiao Y, Liu L, Liang L, Jiang X (2019) miR-497 suppresses malignant phenotype in non-small lung cancer via targeting KDR. *Oncol Rep.* **42**: 443–452. <https://doi.org/10.3892/or.2019.7163>
- Xiao G, Harhaj EW, Sun SC (2001) NF- κ B – inducing kinase regulates the processing of NF-KappaB P100. *Mol. Cell.* **7**: 401–409. [https://doi.org/10.1016/S1097-2765\(01\)00187-3](https://doi.org/10.1016/S1097-2765(01)00187-3)
- Zhang W, Borcherting N, Kolb R (2020) IL-1 signaling in tumor microenvironment. *Adv. Exp. Med. Biol.* **1240**: 1–23. https://doi.org/10.1007/978-3-030-38315-2_1
- Zhou XL, Fan W, Yang G, Yu MX (2014). The clinical significance of PR, ER, NFkappa B, and TNF-alpha in breast cancer. *Dis. Markers* **2014**: 494581. <https://doi.org/10.1155/2014/494581>

A reverse vaccinology approach to design an mRNA-based vaccine to provoke a robust immune response against HIV-1

Muhammad Naveed¹✉, Urooj Ali¹, Tariq Aziz²✉, Muhammad Junaid Rasool¹, Adil Ijaz¹, Metab Alharbi³, Mousa Essa Alharbi⁴, Abdulrahman Alshammari³ and Abdullah F. Alasmari³

¹Department of Biotechnology, Faculty of Life Sciences, University of Central Punjab, Lahore-54590, Pakistan; ²Department of Agriculture University of Ioannina Arta Greece 47100; ³Department of Pharmacology and Toxicology, College of Pharmacy, King Saud University, P.O. Box 2455, Riyadh 11451, Saudi Arabia; ⁴Ministry of Health Kingdom of Saudi Arabia Riyadh

There have been substantial advances in HIV research over the past three decades, but we are still far from our goal of eliminating HIV-1 infection entirely. Numerous ever-evolving antigens are produced as a result of HIV-1's genetic variability. Developing an effective vaccination is challenging because of the structural properties of the viral envelope glycoprotein that obscure conserved receptor-binding sites and the presence of carbohydrate moieties that prevent antibodies from reaching potential epitopes. To work on an HIV-specific vaccine, this study identified 5 HIV-surface proteins, from the literature, to screen potential epitopes and construct an mRNA vaccine. A wide range of immunological-informatics techniques were utilized to develop a construct that efficiently stimulated cellular and humoral immune responses. The vaccine was produced with 31 epitopes, a TLR4 agonist termed RpfE that acts as an adjuvant, secretion boosters, subcellular trafficking structures, and linkers. It was determined that this suggested vaccine would cover 98.9 percent of the population, making it widely available. We, furthermore, carried out an immunological simulation of the vaccine illustrating the active and stable responses from innate and adaptive immune cells, the memory cells remained active for up to 350 days after vaccine injection, whereas the antigen was excreted from the body within 24 hours. Docking performed with TLR-4 and TLR-3 showed significant interaction with -11.9 kcal/mol and -18.2 kcal/mol⁻¹ respectively. Molecular dynamics simulations further validated the vaccine's stability, with a dissociation constant of $1.7E-11$ for the TLR3-vaccine complex and $5.8E-11$ for the TLR4-vaccine complex. Lastly, codon optimization was carried out to guarantee that the designed mRNA construct would be translated into the host successfully. This vaccine adaptation, if tested *in-vitro*, would be efficacious and potent as predicted.

Keywords: HIV-1, clinical trials, mutagenesis, membrane proteins, immune stimulation.

Received: 28 February, 2023; **revised:** 17 March, 2023; **accepted:** 05 May, 2023; **available on-line:** 17 June, 2023

✉ e-mail: dr.naveed@ucp.edu.pk (MN); iwockd@gmail.com (TA)

Abbreviations: ACC, Auto cross covariance; AUC, Area under the ROC curve; GRAVY, Grand average of hydropathy; iMODS, Internal Coordinates Normal Mode Analysis Server; RMSD, Root Mean square density; RpfE, Resuscitation-promoting factor SARS-Cov-2, severe acute respiratory syndrome coronavirus 2; Theoretical pI, Theoretical Isoelectric Point

INTRODUCTION

AIDS or acquired immunodeficiency syndrome is caused by a very notorious virus called HIV or human

immunodeficiency virus. It directly attacks and affects the immune system of the host and makes it vulnerable and susceptible to many diseases (Del Amo *et al.*, 2020). The HIV consists of two strains namely HIV-1 and HIV-2 both having two RNA strands, 15 different viral proteins and could also contain a few proteins from the last host from which it is transferred (Jewell *et al.*, 2020). All these components are encapsulated by a lipid bilayer membrane. It can be transferred via blood or saliva but not by mere contact. In general, it is transferred through sexual contact, sharing needles or blood transfusion. It can also be transferred to the baby from the mother through breastfeeding (Cooper *et al.*, 2020). HIV-1 is transferred into the host more rapidly and is found all over the world. This infectious virus was first reported on June 5, 1981 in Los Angeles (Finlayson *et al.*, 2019). By the second month of 1983, the Centers for Disease Control in the United States reported that approximately 1000 people were HIV positive (Kanny *et al.*, 2019; Sullivan *et al.*, 2021). Although it was first reported in the United States, it had a greater impact in Africa. Nine countries in Africa had one-third of the world's HIV infection (Lancet HIV, 2020; Ssentongo *et al.*, 2021).

For a long time now, Antiretroviral therapy or ART has been considered the best possible measure for controlling HIV (Jiang *et al.*, 2020). It basically consists of a combination of drugs which are prescribed to infected patients to be taken on daily. This therapy does not cure the viral infection but helps the infected persons to live a comparatively longer and healthier life (Chen, 2019). The virus basically destroys the CD4⁺ T cells which are responsible for fighting off different infections and diseases. The medication basically works by reducing the amount of HIV in the body (Suryawanshi *et al.*, 2018). The virus is not completely eliminated by them but the reduced number gives the body a chance to regrow CD4⁺ T cells and fight off the infections and keep the body healthy (Nami *et al.*, 2019). Another approach to cure HIV is to produce a suitable vaccine. To date, many vaccines have been developed by different research institutions but none of them have been successful enough to be prescribed for mass treatment (Yoshida *et al.*, 2021). All of them had notable demerits due to which they failed the early trial stages. Also, the new approaches to HIV vaccine production were recently leveraged by SARS-Cov 2 response so, the dire need for successful vaccine production remains (Karim *et al.*, 2021).

The sequence variability of HIV is one of the primary underlying reasons why an HIV vaccine is not yet commercially available on a worldwide basis (Vasavi *et al.*, 2019; Fenwick *et al.*, 2019). There are up to 20% differ-

ences between the strains of HIV in terms of proteins that are largely conserved, and there are up to 35% differences between the strains in terms of the outer envelope. Additionally, there is a wide variety of ways in which the virus might spread (Akbari *et al.*, 2021). Due to the fact that it can be introduced into the body by sexual contact or the intravenous route, the virus can spread fast throughout the body; nevertheless, it typically takes between one and two weeks for the virus to colonize healthy cell populations (Ng'uni *et al.*, 2020). The first form of vaccination, also known as the conventional method, involves the use of complete organisms, which might provoke allergic reactions due to the presence of big antigens in the body (Abdulla *et al.*, 2019). Any new epidemic could emerge at any time in the future, just like SARS COV-2 did. The development of an mRNA vaccination that incorporates epitopes from a variety of conserved and membrane proteins is one strategy that can be implemented to reduce the severity of allergic reactions (Andrabi *et al.*, 2018; Naveed *et al.*, 2023a; Naveed *et al.*, 2023b).

The fundamental objective of this study was to design an in-silico technique for the construction of an mRNA-based peptide-based immunization that was based on antigenic proteins derived from HIV-1 (Liang *et al.*, 2023). This was illustrated in Figure 1. (A). (Larijani *et al.*, 2018; Muttaqin *et al.*, 2021). Using a number of approaches, it was possible to make predictions about autoimmune disease as well as B cell, CTL, and HTL epitopes and then confirm these predictions. The construct of the vaccine was made by combining each epitope with several linkers and various adjuvants. RpfE was used as an adjuvant, and other aspects of the vaccine, including its population coverage, antigenicity, allergenicity, and toxicity, were investigated. Both the secondary and tertiary structures of the vaccine had been predicted. In addition, the TLR-3 and TLR-4 molecular docking systems were included in the vaccine construct. Simulations using molecular dynamics confirmed that the vaccine does not lose its effectiveness over time.

MATERIALS AND METHODS

The pipeline of the methodology is described in Fig. 1A.

Viral Proteins Sequence Retrieval

The complete Genome of the Human Immunodeficiency Virus (HIV) was obtained from National Centre for Biotechnology Information Database (NCBI) under Accession number: MN692147.1. The proteins of HIV that were selected based on the previously reported data from UniProt with accession numbers: K0J9R5, Q01804, Q9QBZ6, P04585, 0.5886.

Evaluation and Analysis of Proteins

In order to determine the antigenicity of viral proteins, we utilized the Vaxijen 2.0 internet server. The threshold value was set at 0.4 so that it would be more specific. We utilized a technique called AllerTop to determine whether or not proteins were allergenic (<https://www.ddgpharm.net/Vaxijen/Vaxijen/Vaxijen.html>) and AllerTop v2 is used for determining allergenicity (<https://www.ddgpharm.net/AllerTOP/method.html>).

Physiochemical Analysis

Using the ExPASy Protpram tool (<https://www.expasy.org/resources/protpram>), the physiochemical properties of a chosen protein, including its theoretical PI, amino acids composition, instability index, *in-vitro* and *in-vivo* half-life, aliphatic index, molecular weight, and most important grand average of hydropathicity (GRAVY), were investigated.

B-Cell Epitope Prediction

For the prediction of B-cell epitopes, the IEDB Linear Epitope Prediction Tool version 2.0 was utilized, and its default settings were left alone. It makes use of complicated algorithms that are based on the architecture of antigen-antibody proteins. It was put to use in an accessibility examination of the surface.

CTL and HTL Epitope Prediction

IEDB was utilized in order to make a prediction regarding the T-cell epitopes. When a sequence is supplied in FASTA format, various build-in IEDB tools are used to create MHC-I and MHC-II epitopes. It was decided that humans would serve as the host species. All alleles with length 9 were chosen for further study. As the output format, an XHTML table was utilized, and all of the other parameters and choices were left in their default states. (<http://tools.iedb.org/mhcii/>).

Evaluation of Epitopes

The antigenicity, allergenicity, and toxicity of each single epitope were assessed. We used the Vaxijen antigen server (<http://www.ddg-pharmfac.net/Vaxijen/Vaxijen/Vaxijen.html>) to assess antigenicity. In an alignment-free

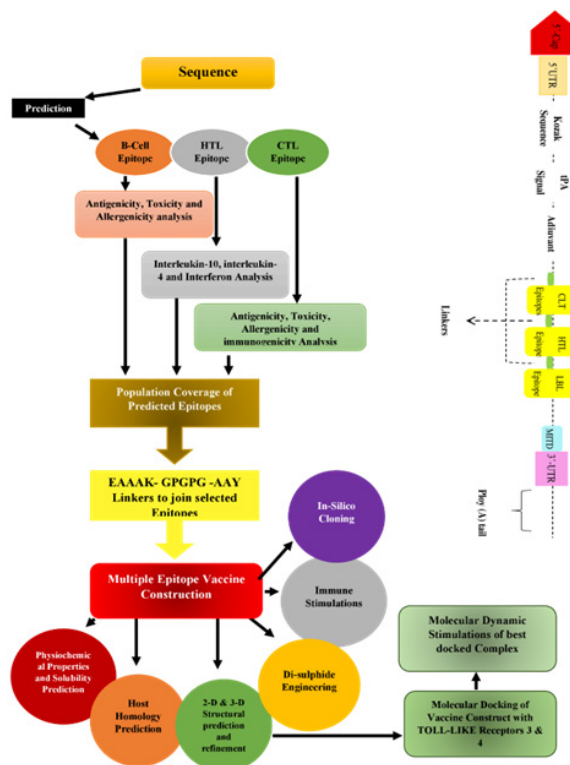


Figure 1. (A) Flow Chart of Diagram of Vaccine Design, (B) Flow Diagram of Vaccine Construct from N-terminal to C-terminal.

method, the physicochemical characteristics of epitopes form the basis for the prediction. For this experiment, bacteria with a cutoff of 0.5 were used. AllerTop V.2.0 (<http://www.ddg-pharmfac.net/AllerTOP>) was used for epitope analysis due to its user-friendly interface and comprehensive database. The parameters were left in their default states (Naveed *et al.*, 2022b). Finally, epitope toxicity was quantified using the ToxinPred (<https://webs.iitd.edu.in/raghava/txnpred/multisubmit.php>) site for toxicity analysis. For further study, only antigenic, non-toxic, and allergy-free epitopes have been selected.

Resemblance with Human Proteins

Using the BLASTp program (<https://blast.ncbi.nlm.nih.gov/Blast.cgi?PAGE=Proteins>), all of the predicted peptides were analyzed in relation to the protein database for Homo sapiens (Taxid:9606). If the E-value is more than 0.05, then all of the peptides in the vaccine are evaluated as potential non-homologous peptides.

Population Coverage Calculation

Population Coverage for vaccine design aimed at targeting T-lymphocyte epitopes and associated MHC I and MHC II alleles can be calculated using the IEDB database (<http://tools.iedb.org/population/>). This number is based on how many different MHC alleles the construct's epitopes are able to identify. This is because there is a wide range in MHC allele distribution across different regions and peoples.

Construct of the proposed vaccine

The construct of the vaccine is shown in Fig. 1B. Each anticipated epitope was joined together using one of three linkers: AAY, KK, or GPGPG. These linkers are necessary for separating and isolating different functional domains. They are tough, bendable, and easy to cut. Resuscitation-promoting factor (RpF) was utilized as an adjuvant in order to boost the adaptive immune response. The mRNA vaccine needs to have a Kozak sequence, which consists of an ORF start codon and a stop codon. In addition, two structures were added to the construct: first, the tissue plasminogen activator (tPA) secretory signal sequence (UniProt ID: P00750) in the 5' region of the construct. Once translated, epitopes can be secreted from cells with the help of this signal sequence. Second, the mRNA vaccine's 3' locus end contains an MHC I-targeting domain (MITD; UniProt ID: Q8WV92).

Evaluation of Vaccine Protein

Antigenicity was analyzed by the Vaxigen v2.0 and for allergenicity we used AllerTop. ToxinPred was used for toxicity analysis. Solubility analysis with the help of SolPro was done to determine the purity of a substance. ExPASy-ProtParam Tool was used for physicochemical properties analysis.

Peptide Secondary and Tertiary Structure Prediction

Secondary and tertiary structures were analyzed by the PsiPred and TsrRosetta respectively to explore multi-epitope vaccine. The tertiary structure was assessed using TrRosetta (<https://yanglab.nankaledu.cn/trRosetta/>).

mRNA Vaccine Secondary Structure Prediction

Predicting the secondary structure of the mRNA vaccine with the help of the RNAfold tool (<http://rna.tbi.univie.ac.at/cgi-bin/RNAWebSuite/RNAfold.cgi>). It

makes use of McCaskill's technique to determine the secondary structure with the lowest free energy (MFE). This method was used to determine the minimum free energy (MFE) of a structure, as well as the MFE of a centroid secondary structure.

Refinement and Validation of tertiary structure

The vaccine's structure was refined using the GalaxyRefine server. This involved, first, the rebuilding and re-packing of sidechains, and second, the relaxation of the structure using molecular dynamics simulation processes. (<http://galaxy.seoklab.org/>). Multiple servers were used to verify the accuracy of the 3D structure based on references. To begin, RAMPAGE (Ramachandran Plot Assessment) was utilized. After that, PROCHECK was utilized to verify the building's integrity. (<https://bip.weizmann.ac.il/toolbox/structure/validation.htm>).

Analysis of Conformation B-Cells Epitope Prediction

New conformational B-cell epitopes can be stimulated by the protein's tertiary structure. Estimates of discontinuous B-cell epitopes in the protein structure were generated using ElliPro, a web-based service (<http://tools.iedb.org/ellipro/>). Ellipro benefits from the 3D model's geometric properties. When compared to other known strategies for predicting discontinuous B-cell epitopes, ElliPro has the greatest AUC value of 0.732 for the protein model.

Docking Analysis

Peptide vaccines with either toll-like receptor 4 (TLR-4) (PDB ID: 3FXI) or TLR-3 (PDB ID: 3FXI) (PDB ID: 1ZIW) To dock 3D structures on the ClusPro server, we employed the PIPER docking method. Both TLR4 and TLR3 were blocked by a RpF adjuvant. It is possible that this server will produce numerous models using various scoring mechanisms. Free binding energy (G), dissociation constant (Kd), and percentages of charged and polar amino acids on the non-interacting surface were calculated by receptor-ligand 3D interaction using the PRODIGY tool on the HADDOCK website (<https://haddock.science.uu.nl/>).

Evaluation of Binding Energies

T cells and MHC alleles underwent a molecular docking simulation to determine their binding affinities. RCSB's PDB database was queried for the tertiary structure of MHC alleles. PyMol was used to visualize the structures, and the Swiss-PDB viewer was employed to reduce power consumption. Epitopes were folded into 3D structures using the PEP-FOLD 3.5 server, and energy was conserved by viewing the structures in the Swiss-PDB viewer. The docking and binding affinity computations were performed on the Cluspro 2.0 server. Additional visualization and analysis were performed using PyMol and Discovery Studio.

Molecular Dynamics Simulations

iMods online was used for molecular dynamics simulations. It studies the molecule and interaction on the basis of torsion angles. It was utilized for the analysis of RMSD values, co-variance among residues, eigenvalue of interacting residues and distortion of structure. It was utilized to discover the stability of the complex.

Table 1. List of Proteins selected Previous Literature

No.	Protein	Uniprot ID	Antigenicity	Function	Location
1	Envelope glycoprotein gp160	K0J9R5	0.5767	Host-Virus Interaction	Surface Protein
2	OTU domain-containing protein 4	Q01804	0.5	Pathogenesis and Innate Immune Response	Cytoplasmic Protein
3	Gag polyprotein	Q9QBZ6	0.58	Virion Assembly	Cell Membrane
4	Gag-Pol polyprotein	P04585	0.6778	Virion Assembly and Lipid Anchor to Host	cell membrane
5	Tat- Protein	Q76PP9	0.5886	Receptor Binding to Host	Cytoplasmic Protein

Codon Optimization and Expression Analysis of Proposed Vaccine

The codon of the vaccine was optimized to ensure that the peptide vaccine construct was produced efficiently in human cells. This was achieved with the help of the GenSmart Codon Optimization software (<http://www.genscript.com/>). In order to determine whether or not a product is of high quality, GenScript uses Rare Codon Analysis (<http://www.genscript.com/>) (GS). How well mRNA is expressed and translated is quantified by the Codon Adaptation Index (CAI). The sequence was back-translated using the backtranseq software EMBOSS 6.0.1 so that the mRNA protein could be expressed in the expression vector. after then, the Java Codon Adaptation Tool was used for codon optimization (JCAT). As an expression vector, we employed the pub18 gene from *E. coli*. SnapGene used in-silico PCR for construct amplification.

Immune Simulation

C-ImmSim was used to verify the immune response. It uses an immune epitope and interaction with the help of a position-specific scoring matrix (PSSM). All the procedure was done at default parameters. (<https://kraken.iac.rm.cnr.it/C-IMMSIM>)

RESULTS

Protein sequence Retrieval

The FASTA format of amino acids of Human immunodeficiency virus 1 proteins that are present on the surface or on transmembrane having accession number CCA61241.1, QEE91975.1, Q9QBZ6.2, NP_057849.4, UED13371.1 respectively, were obtained from the NCBI database. The function and cellular localization of the shortlisted proteins are given in [Table 1](#).

B-cell Epitope Predictions

IEDB Linear Epitope Prediction v2.0 was used to predict the B cell epitopes. At first, 25 epitopes were predicted which were then filtered out on the basis of the antigenicity and allergenicity. At the end, only 8 epitopes were selected for the vaccine construct as shown in [Table 2](#).

CTL or HTL Epitopes and their Evaluation

T-cell Epitopes are of two types: MHC-I and MHC-II. These epitopes are predicted or selected on the basis of the value of IC50. Those epitopes with values lower than 200 are selected. The lower the ic50, the high the binding affinity of the epitope is. For this whole dataset of the HLA alleles are selected. A total of 40,419 MHC Class I Epitopes were predicted and out of them, only 8 were selected on the basis of their antigenicity and their allergenicity. A total of 18,279 MHC Class II Epitopes were predicted and out of them, only 15 were selected on the basis of their antigenicity and their allergenicity. The shortlisted MHC I and II epitopes are shown in [Table 2](#).

Interaction between Epitopes and MHC-alleles

In total, there are 23 T-lymphocyte epitopes and 120 MHC-alleles. As can be seen in [Table 4](#), whereas some epitopes only recognize a single MHC allele, others can detect as many as seventeen different alleles. We selected 5 epitopes that matched up with certain MHC alleles for further molecular docking study. The ClusPro 2.0 server docking results are shown in [Table 4](#) as energy affinities. With an MHC allele (HLA-A*32:01) and its associated epitope, the YALFYKLDIV region displays the highest binding affinity (−9.2 kcal/mol). As can be seen in [Figs 2A and 2B](#), as a result, epitopes bind competently to the MHC-allele binding fork. As can be seen in [Fig. 3](#), we also assessed every potential interaction between the targeted epitope and allele residues.

Proposal for a Vaccine Construct

The proposed design of the vaccine construct is like the following:

5' m7GCap- 5' UTR-Kozak sequence-EAAAKM-KNARTITLIAAAIAGTLVTTSPAGIANADD AGLDP-NAAAGPDAVGFDPNLPPAPDAAPVDTPPAPED-AGFDPNLPPPLAPDFLSPPAEEAPPVPVAYSVN-WDAIAQCESGGNWSINTGNGYYGGRLRFTAGT-WRANGSGSAAANASREEQIRVAENVLRSQGI-RAWPVCGRRG (adjuvant) -YVPPIRGEIGPGPGYAL-FYKLDIVGPG PGWSNKSYYDDIWGPGPGVGRK-KRAAVGPGPGRAAVGLGAVGPGPGGLGAVLL-GFLGPGPGAIAVANWTD RGP GPGGLIGLRIVF-AGPGPGAARAVELLGRSSLKGGKKAAGVGLGAV-LLGFLSTKKALAWDDLRSSKKALFYKLDIVKKA-PAGFAILKCRDKEFKKARAVELLGRSSLKGLK-KAVGLGAVLLGFLSTAKKCAPAGFAILKKCA-PAGFAILKCRDKEKKFYKLDIVPIDDNGKNKKG-

Table 2. List of epitopes candidates to design the vaccine

Cell Type	Sequence of Epitope	Antigenicity
MHC I Cells	YVPPIRGEI	0.6365
	YALFYKLDIV	0.7604
	WSNKSYYDDIW	0.8368
	VGRKKRAAV	1.5567
	RAAVGLGAV	1.1827
	GLGAVLLGFL	0.8696
	AIAVANWTDR	1.2624
	GLIGLRIVFA	1.8903
	AARAVELLGRSSLKG	0.9438
	AAVGLGAVLLGFLST	1.1029
MHC II	ALAWDDLRS	0.8966
	ALFYKLDIV	0.8914
	APAGFAILKCRDKEF	1.3346
	ARAVELLGRSSLKGL	0.926
	AVGLGAVLLGFLSTA	1.083
	CAPAGFAIL	1.1739
	CAPAGFAILKCRDKE	1.3168
	FYKLDIVPIDDNGKN	0.8964
	GDLEITTHSFNCRGE	1.1009
	YDDIWNNTWVWEWER	0.858
B Lymphocytes	YKLDIVPIDDNGKNS	1.0139
	YSPLSFQTL	1.4447
	YSPLSFQTLTHHQRE	1.1407
	NVNSTKNATTPTVTPTPTSLMKDTGEL	0.769
	IRDKKKQEYALF	1.3047
	TIKQACPKMSFDPIP	1.0224
	CRDKEFNGT	0.7076
	ITFNSSAGGDL	0.5866
	NSSSLASNNSEN	0.5
	GKNNTNETFRPAGGDMRDNRWSELYKY	0.6997
	KVVKIKPLGIAPTARRRVVGRKKR	
	QEKNEQDLLALDKWASL	0.752

DLEITTHSFNCRGEKKYDDIWNNTWVWEWERK-KYKLDIVPIDDNGKNSKKYSPLSFQTLKKYSPLSFQTLTHHQREKKNVNSTKNATTPTVTPTPTSLMKDTGELAAAYIRDKKKQEYALFAAYTIKQACPKMSFDPIPAAYCRDKEFNGTAAAYITFNSSAGGDLAAYNSSSLASNNSENAAAYGKNNTNETFRPAGGDMRDNRWSELYKYAAYKVVKIKPLGIAPTARRRVVGRKKRAAYQEKNEQDLLALDKWASLAAY

The antigenicity score of the constructed vaccine is 0.7056 at a threshold of 0.5. The overall allergenicity of

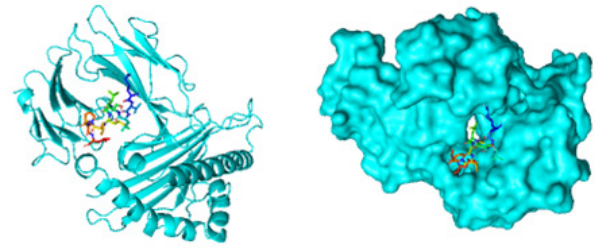


Figure 2. Docking visualization between the epitope AG-FRQYRAASIQVGN and its corresponding MHC allele (HLA-DRB1*01:01) using the PyMol software: (A) Surface View (B) Cartoon View.

the vaccine is predicted as non-allergen. This shows that the construct is a good vaccine candidate.

Physiochemical Properties of Vaccine

To determine the antigenicity, allergenicity, toxicity, and soluble nature of a construct, scientists can use programs like VaxiJen, ANTIGENpro, AllerTOP, ToxinPred, and SolPro. The results showed that the vaccine *met all* of the criteria for an effective vaccine: it was antigenic, non-allergenic, non-toxic, and water-soluble. Table 5 displays the results of using the ExPasy ProtParam service to establish the physiochemical profile of the construct. Based on the vaccine's known physiochemical properties, it was projected that the construct would be thermally stable. Due to the GRAVY value being -0.357, it may be concluded that the vaccine is hydrophilic. These results indicate that the mRNA vaccine design is a promising potential vaccination candidate.

Prediction of Population Coverage

Combining all 120 alleles of the matching 23 epitopes on MHC-I and MHC-II, the IEDB population coverage technique was able to estimate that the human population would be protected against all known pathogens. Eventually, global vaccination rates would reach about 98.9 percent.

Immune Simulation of Vaccine

We used three vaccinations to kick off the immune response (see Fig. 4). Both the second and third options performed better than the first. After antigen suppression, immunoglobulin levels were high, and it was discovered that more IgM than IgG was being produced. This increase may be indicative of the formation of immunological memory following antigen exposure. B-cell isotype persistence across time reveals the existence of memory cells within the B-cell population. It's also true that more CTL and HTL cells were produced as a direct consequence of memory formation. Furthermore, macrophage activity rose while dendritic cell activity remained unchanged. IFN- and IL-2 levels also went up. There is a rise in both innate immunity and the number of epithelial cells, which play a role in innate immunity.

mRNA Vaccine Prediction for secondary structure

The mRNA vaccine's structure was inferred using the RNAfold website. The free energy of the structures was also computed using this site. As a starting point, we took the codons that were optimized for usage in the vaccine. As shown in Fig. 5F, the mRNA vaccine had a minimum free energy of -930.20 kcal/mol during pro-

Table 3. T-Lymphocytes and their corresponding alleles

MHC I Epitopes	MHC I Binding Alleles	MHC II Epitopes	MHC II Binding Alleles
YVPPIRGEI	HLA-B*40:01, HLA-B*44:03, HLA-B*44:02, HLA-A*02:06, HLA-B*08:01, HLA-A*32:01, HLA-B*51:01	AARAVELLGRSSLKKG	HLA-DRB1*12:01, HLA-DRB1*01:01, HLA-DQA1*01:02/DQB1*06:02, HLA-DQA1*05:01/DQB1*03:01
YALFYKLDIV	HLA-B*40:01, HLA-B*44:03, HLA-B*44:02, HLA-A*02:06, HLA-B*08:01, HLA-A*32:01, HLA-B*51:01	AAVGLGAVLLGFLST	HLA-DQA1*05:01/DQB1*03:01
WSNKSYYDDIW	HLA-B*57:01, HLA-B*58:01, HLA-B*53:01, HLA-A*32:01	ALAWDDLRS	HLA-DQA1*05:01/DQB1*03:01
VGRKKRAAV	HLA-A*68:01, HLA-A*31:01, HLA-A*33:01, HLA-A*11:01, HLA-A*03:01, HLA-A*30:01, HLA-A*26:01	ALFYKLDIV	HLA-DRB1*12:01, HLA-DRB1*04:01, HLA-DQA1*05:01/DQB1*03:01, HLA-DRB1*15:01
RAAVGLGAV	HLA-A*02:06, HLA-B*39:01, HLA-B*15:01, HLA-B*35:01, HLA-C*12:03, HLA-B*15:02, HLA-C*14:02	APAGFAILKCRDKEF	HLA-DRB3*02:02, HLA-DRB1*04:01, HLA-DRB1*09:01, HLA-DRB1*01:01, HLA-DRB1*07:01, HLA-DRB1*04:05, HLA-DRB5*01:01
GLGAVLLGFL	HLA-A*68:01	ARAVELLGRSSLKGL	HLA-DRB1*15:01, HLA-DRB1*04:05, HLA-DRB1*07:01, HLA-DQA1*05:01/DQB1*03:01, HLA-DRB1*09:01, HLA-DQA1*01:02/DQB1*06:02, HLA-DRB3*02:02, HLA-DRB1*04:01, HLA-DRB1*08:02, HLA-DPA1*02:01/DPB1*14:01, HLA-DRB1*01:01, HLA-DRB3*01:01, HLA-DQA1*01:01/DQB1*05:01
AIAVANWTDTR	HLA-C*12:03, HLA-A*68:02, HLA-A*02:06, HLA-A*68:01, HLA-C*03:03	AVGLGAVLLGFLSTA	HLA-DRB1*09:01, HLA-DRB1*01:01, HLA-DRB1*07:01, HLA-DRB5*01:01, HLA-DRB1*04:05, HLA-DRB3*01:01
GLIGLRIVFA	HLA-A*68:02, HLA-A*30:01, HLA-A*30:02, HLA-A*26:01, HLA-A*01:01, HLA-A*68:01, HLA-B*58:01	CAPAGFAIL	HLA-DRB1*04:03, HLA-DRB1*04:05, HLA-DRB1*04:01, HLA-DRB1*04:04
	HLA-A*02:01, HLA-A*02:03, HLA-A*02:06, HLA-A*68:02, HLA-B*51:01	CAPAGFAILKCRDKE	HLA-DRB1*04:01, HLA-DRB3*03:01, HLA-DRB1*13:02, HLA-DRB1*04:04, HLA-DRB1*04:05
	HLA-A*68:02, HLA-A*30:01, HLA-A*30:02, HLA-A*26:01, HLA-A*01:01, HLA-A*68:01, HLA-B*58:01	FYKLDIVPIDDNGKN	HLA-DRB1*04:01, HLA-DRB4*01:01, HLA-DPA1*01:03/DPB1*02:01, HLA-DRB1*13:02, HLA-DRB3*02:02
		GDLEITTHSFNCRGE	HLA-DRB5*01:01, HLA-DQA1*05:01/DQB1*03:01, HLA-DRB3*02:02, HLA-DRB1*09:01, HLA-DRB1*04:01
		YDDIWNNTWVE-WER	HLA-DRB3*02:02, HLA-DRB5*01:01, HLA-DRB1*04:01, HLA-DRB1*07:01, HLA-DRB1*01:01, HLA-DRB1*09:01
		YKLDIVPIDDNGKNS	HLA-DRB3*02:02, HLA-DRB3*01:01, HLA-DRB1*09:01, HLA-DRB1*13:02, HLA-DRB5*01:01, HLA-DRB1*15:01
		YSPLSFQTL	HLA-DRB1*01:01, HLA-DRB1*15:01, HLA-DRB1*04:05
		YSPLSFQTLTHHQRE	HLA-DRB5*01:01, HLA-DRB1*04:01, HLA-DRB1*07:01

duction, and the energy of its secondary centroid structure was -700.67 kcal/mol. The results indicate that the mRNA structure will be stable.

Secondary and tertiary structures of the mRNA vaccine

We used the PSIPRED server to try and guess the secondary structure of the vaccine. Figure 5A depicts the structure, which is composed mostly of alpha helices.

To learn about the vaccine's tertiary structure, we used the Tr Rosetta server (see Fig. 5B). The PROCHECK service was then used to confirm the structure's stereochemical accuracy. Figure 5C's Ramachandran plot shows that 98.3% of residues were located in the recommended zones, 1.6% in the additional allowance zone, and 0.2% in the prohibited allowance zone. The vaccine has an overall quality factor of 92.64211, which is

Table 4. Molecular Docking of T-Lymphocytes epitopes with corresponding MHC alleles and their Binding affinity

Type of Epitope	Epitope	MHC Allele	PDB ID	Binding Affinity
MHC I	YALFYKLDIV	HLA-A*32:01	4PR5	-9.2
	VGRKKRAAV	HLA-A*03:01	3RL1	-6.0
	RAAVGLGAV	HLA-B*15:01	1XR8	-4.9
MHC II	APAGFAILKCRDKEF	HLA-DRB1*01:01	2FSE	-5.1
	ARAVELLGRSSLKGL	HLA-DRB1*15:01	1BX2	-5.3

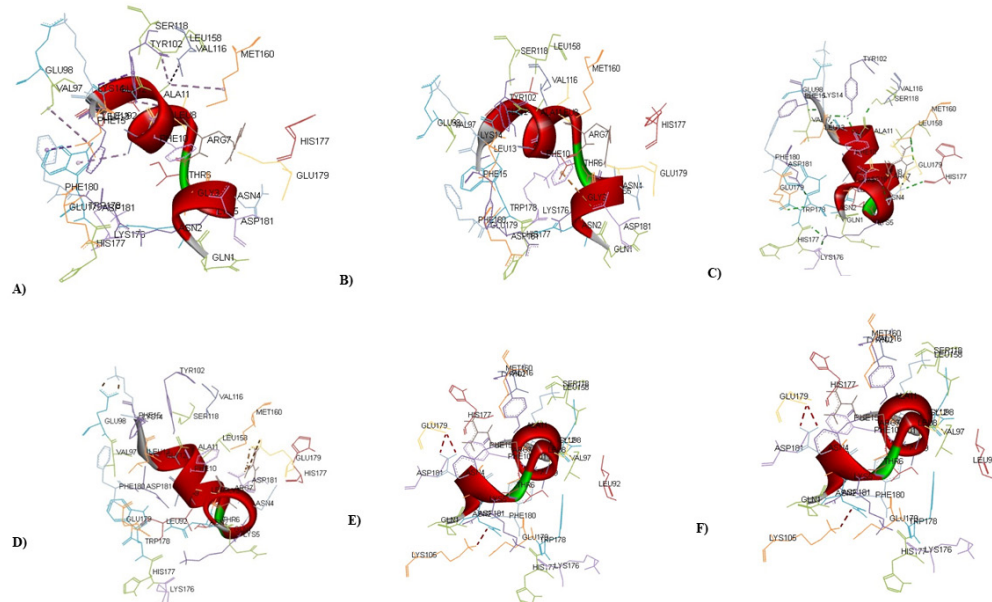


Figure 3. Different Interactions between the epitope and its corresponding MHC allele visualized using the discovery studio. (A) Conventional Hydrogen Bonds (B) Salt Bridge, attractive Charge interactions (C) Hydrophobic Interactions (D) Cation- π interactions (E) Donor-Donor Clash (F) π Donor Hydrogen Bond

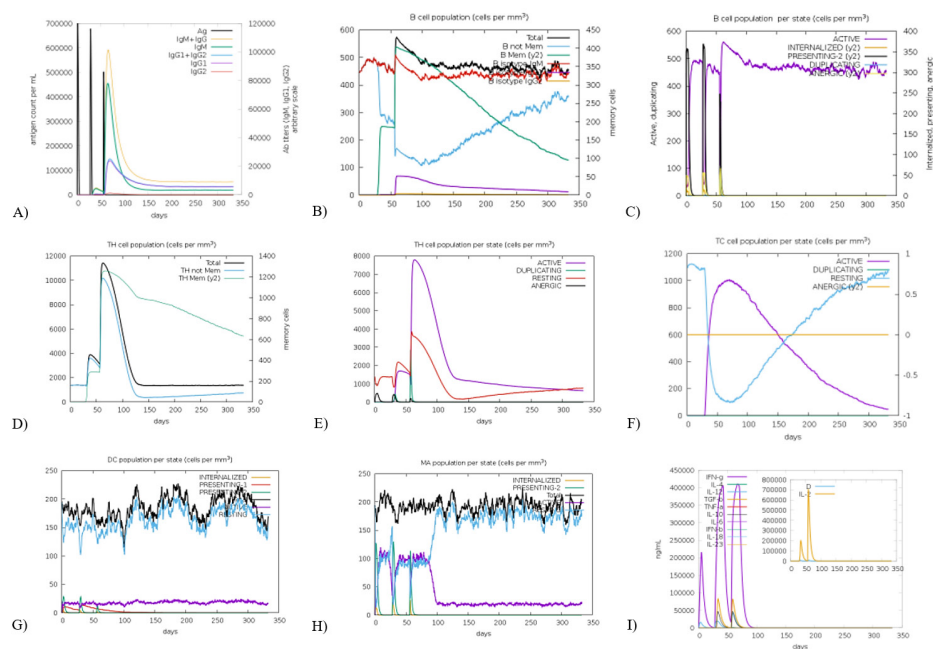


Figure 4. Immune simulation response against Vaccine construct from C-ImmSim server. (A) The immunoglobulin production after antigen injection. (B) The B cell population after three injections. (C) The B Cell Population per state (D) The Helper T Cell Population (E) The Helper T Cell Population per state (F) The Cytotoxic T Cell Population per state (G) Macrophage Population per state (H) Dendritic Cell Population per state (I) Cytokines and Interleukins Production with Simpson Index of the immune response.

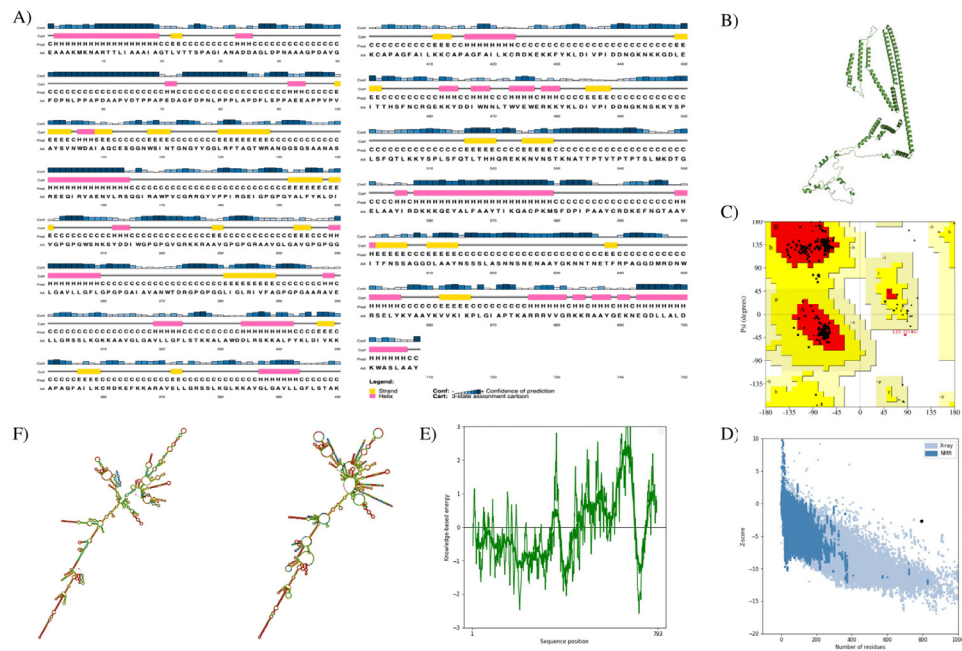


Figure 5. Structure prediction and validation of Vaccine Construct: (A) PSIPRED server results of secondary structure of vaccine (B) The Robetta server used to predict the Tertiary structure of vaccine (C) The PROCHECK server used to analyze the Ramachandran Plot (D) Z-score analysed by the Pro-SA webserver (E) Local Quality Factor (F) mRNA secondary structure

quite high. The tertiary protein model is very consistent, as predicted by the ProSA-web server, which yielded a negative Z-score of -6.01.

Conformational B-cell epitopes Prediction

For the purpose of locating B-cell conformational epitopes, a server named ElliPro was used to execute vaccination model folding. Eleven discontinuous conformational B-cell epitopes were forecast using this method. Figure 6 reveals that the anticipated score for the 285

residues for secondary and tertiary models of conformational cell Epitopes ranges from 0.512 to 0.883.

Molecular Docking

The probable connections between the construction and TLR-4 and TLR-3 receptors were verified using ClusPro software for molecular docking. Additionally, we used the PRODIGY website to analyze the binding affinities and dissociation constants at 37°C for the more

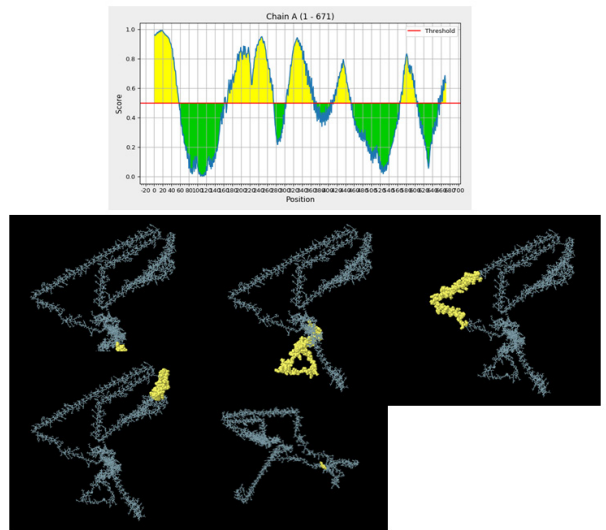


Figure 6. The ElliPro server of IEBD database for the prediction of eleven conformational B-cell epitopes: (I) Position of Conformational B-cell epitopes 2D illustration. (II) 3D models of B-cells epitopes where yellow spheres present the conformational B-cell epitopes.

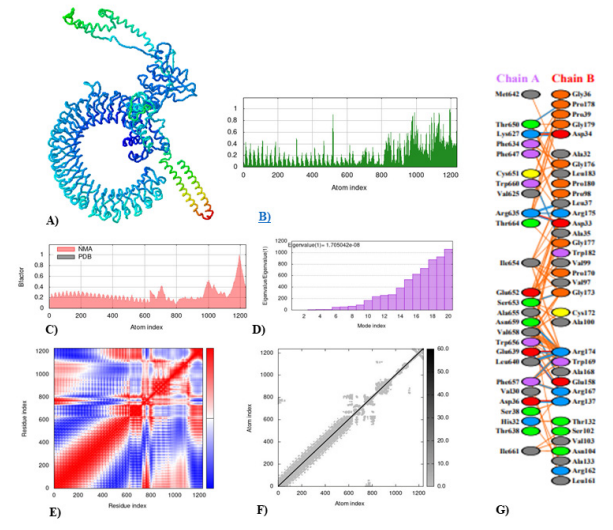


Figure 7. Molecular dynamics simulation, Normal Mode Analysis, and receptor-ligand interactions: (A) Vaccine-TLR4 docked complex using the Cluspro server (B) Deformability graph (C) Eigenvalue of vaccine-TLR4 complex (D) B-factor graph (E) Covariance matrix (F) Elastic network model using the iMODS server (G) Receptor-ligand interaction using the PDBsum webserver.

Table 5. Physiochemical Properties, Antigenicity and Allergenicity of the Vaccine

Property	Measurement	Indication
Total Number of Amino Acid	708	Appropriate
Molecular Weight	75209.01 KDa	Appropriate
Formula	$C_{3380}H_{5329}N_{943}O_{976}S_{13}$	-
Theoretical pI	9.64	Basic
Total number of positively charged residues (Arg + Lys)	64	-
Total number of negatively charged residues (Asp + Glu)	100	-
Total Number of Atoms	10641	-
Instability index (II)	31.84	Stable
Aliphatic Index	76.51	Thermostable
Grand Average of Hydropathicity (GRAVY)	-0.357	Hydrophilic
Antigenicity VaxiJen	0.7596	Antigenic
Antigenicity AntigenPro	0.821798	Antigenic
Allergenicity	Non-allergenic	Non-allergenic
Toxicity	Non-toxic	Non-toxic

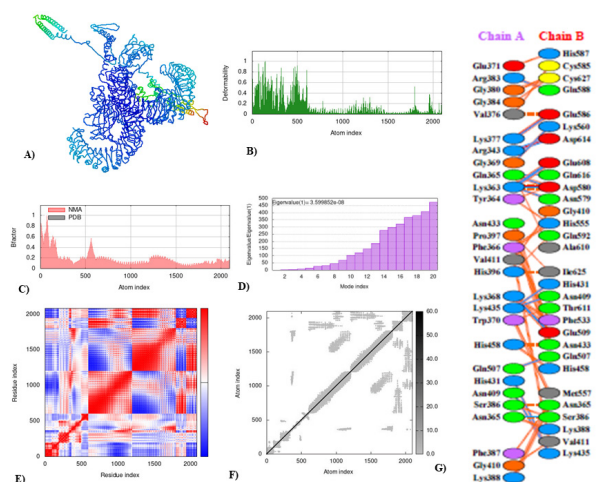


Figure 8. Molecular dynamics simulation, Normal Mode Analysis, and receptor-ligand interactions:

(A) Vaccine-TLR4 docked complex using the Cluspro server (B) Deformability graph (C) Eigenvalue of vaccine-TLR4 complex (D) B-factor graph (E) Covariance matrix (F) Elastic network model using the iMODS server (G) Receptor-ligand interaction using the PDBsum webserver.

clustered component of each complex. As a benchmark, we relied on the adjuvant docked complex.

There was a difference in binding affinity of $-18.2 \text{ kcal/mol}^{-1}$ between the TLR3-Vaccine complex and the control. At 25 degrees Celsius, the complex dissociation constant for Vaccine-TLR3 was $1.7\text{E-}11$, while the value for the control was $1.1\text{E-}06$. The binding affinity for the TLR4-Vaccine complex was $-11.9 \text{ kcal/mol}^{-1}$, while it was only $-9.0 \text{ kcal/mol}^{-1}$ for the control. Vaccine-TLR4 had a complex dissociation constant at 25°C of $5.8\text{E-}11$, significantly higher than the control's value

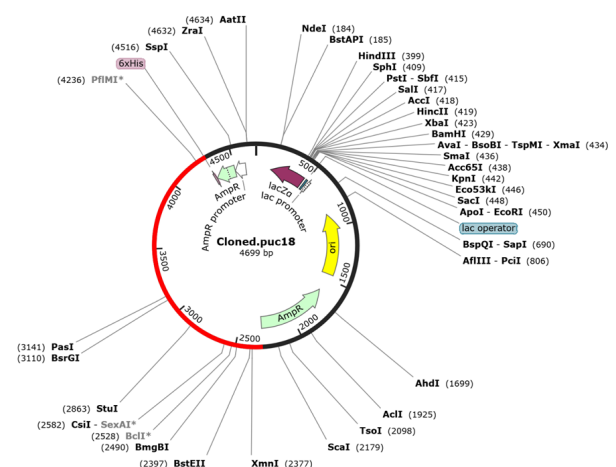


Figure 9. Optimized Vaccine Cloned in PUC18 Vector

of $2.5\text{E-}07$. PDBsum was used to analyze the vaccine's enhanced interaction with TLR-3 and TLR-4 receptors.

Molecular Simulation of Vaccine

When exposing the Vaccine-TLR3 and Vaccine-TLR4 complexes to the iMOD server, molecular dynamic simulation analysis was performed. Vaccine deformable loci and amino acids with coiled forms are both shown by peaks in the deformability graph. NMA (normal mode analysis) is a computational tool for studying protein adaptability. As can be seen in Figs 7C and 8B, the B-factor graph represents the complex's connection to the Normal Mode Analysis and PDB areas. The eigenvalues of the docked complexes are displayed in Figures 7D and 7E, respectively. Figures 7E and 8E demonstrate the

interactions between amino acid duplets in the dynamical area as a covariance matrix, where the red part denotes correlated residues, the white part for anti-correlated residues, and the blue part for non-correlated residues.

Codon Adaptation and In-silico Cloning

JCat which is a codon adaptation tool was used to optimize the vaccine construct codon to get maximum protein expression. The optimized codon (Fig. 9) sequence has 70% GC Content. The optimized codon sequence was inserted into PUC18 Vector to make a recombinant plasmid which is then amplified through In-silico PCR using SnapGene software.

DISCUSSION

Vaccination against a particular disease not only protects individuals from contracting the illness but also results in an overall improvement in the health of the population, cuts down on the spread of the disease, and is very cost-efficient. However, the process of immunization calls for a significant investment of time and money while it is still in the developmental stage. In this context, the contribution of specialists is absolutely essential. Because of advances in technology and the accessibility of various bioinformatics tools, it is now possible to save costs while simultaneously reducing the amount of time spent. Analyses of the pathogen on the genomic and proteomic levels are being carried out in order to create vaccinations (Pandey *et al.*, 2018). The goal of this research is to decrease the amount of viral material that is bound to virus particles and transferred to human cells by focusing on the outer-membrane and transmembrane proteins. The investigation of the secondary and tertiary structure has been demonstrated to offer a highly antigenic potential for the development of vaccines. Based on the allergenicity and antigenicity report of the vaccine, this study demonstrates, in general, the potential of this in silico produced vaccine targeting the gp160 in membrane and trans-membrane.

As a result of advancements in the clinical research field, we are now able to choose and target histocompatibility complex (MHC) T-cells that have the most interaction with human leukocyte antigen (HLA) scheme using computational biology. Alternatively, we can choose to use B-cells as the source of vaccine design. This option is available to us. In the beginning, it is necessary for us to get all of the databases and software that are available for all of the nucleocapsid and trans-membrane epitopes that are feasible on the protein. The IEDB database was selected for the epitope prediction of B-cells because it can predict antigenicity in two different methods. The cut-off score for antigenicity has been set to 5.0. On the other hand, we identified T-cell epitopes by screening them first to find those with an IC50 value of less than 200, which ensures that they are highly active against the targeted protein. After that, the epitopes are combined with MHC Class-I and MHC Class-II Class, and then the two classes are separated for screening (Naveed *et al.* 2023c).

Vaxijen v2.0 may be used to calculate the antigenic characteristics of B and T cells, as well as the ACC of peptides based on their physiochemical parameters. Those with levels more than the limit are considered antigens in nature. This antigenic epitope should be safe in its natural condition, so that it does not cause

problems when employed as an immune response (Cong *et al.*, 2023). We also assess vaccine allergenicity since vaccine allergenicity is the greatest impediment to advancement in the field of vaccine development. Both classes' MHC have shown a high degree of conservation over the world, resulting in an increase in the proportion of the HIV patient population protected by peptide vaccines (Meron-Sudai *et al.*, 2023).

Following the acquisition of all necessary criteria, the process of vaccine manufacturing will involve the selection of 8 epitopes from MHC Class-I T-cells, 8 epitopes from B-cells, and 15 epitopes from MHC Class-I T-cells as the subunits (Naveed *et al.*, 2022c). The vaccine demonstrates a growing response of the vaccination in the identification of pathogens and activation of the immune system, immune-reactivity is one of the features that adjuvants like 50S ribosomal protein L7/L12 are used to boost. In the first stages of the production of multiple epitope vaccines, linkers are utilized for the purpose of fusing B-cell and T-cell epitopes together. Linkers such as EAAAK, CPGPG, KK and AAY were incorporated between the critical predicted epitopes in order to produce a viable vaccine with the highest antigenicity possible.

The generated protein sequence has been subjected to bioinformatic analysis as well as immunologic testing, both of which have concluded that it does not include any allergenic or poisonous components. GalaxyRefine was utilized in order to refine the 3D structure of the chimeric vaccine, which resulted in the acquisition of the desired features (Al Tbeishat, 2022). RAMPAGE, also known as the Ramachandran Plot, demonstrates that a possible vaccination candidate possesses suitable characteristics. According to the findings, the majority of the residues are located in favorable areas, while just a few residues were found in regions that were considered to be outliers (Naveed *et al.*, 2022e).

This demonstrates that the quality of the desired model can be considered acceptable. Clustpro2.0 is utilized in the Docking process, which displays the most promising models of the vaccine-receptor complex by bringing them into close proximity to the reference structure. A simulation using molecular dynamics was carried out, with the goal of emulating the natural behavior of our dynamic system (Naveed *et al.*, 2022d). The docked complex of the vaccine construct of viral gp160 protein and CD4 receptor of the host should that the computational vaccination model of human immunodeficiency virus has the potential to combat Autoimmune Deficiency Syndrome.

The primary emphasis of this research was on the development of an in-silico strategy for the design of an mRNA peptide-based vaccination based on HIV-1 antigenic proteins (Shabani *et al.*, 2022). Using immunoinformatic methods, the advised mRNA vaccine was tested for stability, thermostability, antigenicity, lack of allergenicity, and hydrophilicity. The ability of the vaccine to establish memory cells upon exposure, as well as to produce chemokines that increase B-cell response and humoral response, was verified using molecular simulation after three doses were administered (Naveed *et al.*, 2022a). Macrophages, dendritic cells, and the Simson index were markers for the development of memory cells. Finally, it was determined that the manufactured vaccine shows promise as a potential candidate for use in the prevention of Human Immunodeficiency syndrome infections.

CONCLUSION

Humanity has faced significant scientific, medical, and moral challenges due to HIV/AIDS since its discovery in 1983. The results of this investigation indicate that the vaccine design has both desirable physicochemical properties and immune responses against HIV-1. Using a variety of immune-informatics techniques or methodologies, it was discovered that this immunization will activate an immunological response against HIV-1 in the host. Our results were supported by the immunological response that the vaccine elicited, as measured by Immune Stimulation. Accordingly, this construct is suggested for use as a potential subject for in vitro and in vivo studies against *S. marcescens*, employing a wide variety of serological assays to elicit a reaction. By developing a reliable vaccine, this study aids the global effort to wipe out HIV.

Declarations

Funding. This research work received no external funding.

Acknowledgments. The authors greatly acknowledge and express their gratitude to the Researchers Supporting Project number (RSP2023R462), King Saud University, Riyadh, Saudi Arabia.

Conflicts of Interest. The authors declare no conflict of interest.

REFERENCES

- Abdulla F, Adhikari UK, Uddin MK (2019) Exploring T & B-cell epitopes and designing multi-epitope subunit vaccine targeting integration step of HIV-1 lifecycle using immunoinformatics approach. *Microb Pathog* **137**: 103791. <https://doi.org/10.1016/j.micpath.2019.103791>
- Akbari E, Kardani K, Namvar A, Ajdari S, Ardakani EM, Khalaj V, and Bolhassani AJ (2021) *In silico* design and *in vitro* expression of novel multi-epitope DNA constructs based on HIV-1 proteins and Hsp70 T-cell epitopes. *Biotechnol Lett* **43**: 1513–1550. <https://doi.org/10.1007/s10529-021-03143-9>
- Al Tbeishat H (2022) Novel *In Silico* mRNA vaccine design exploiting proteins of *M. tuberculosis* that modulates host immune responses by inducing epigenetic modifications. *Sci Rep* **12**: 4645. <https://doi.org/10.1038/s41598-022-08506-4>
- Andrabi R, Bhiman JN, Burton DRJ (2018) Strategies for a multi-stage neutralizing antibody-based HIV vaccine. *Curr Opin Immunol* **53**: 143–151. <https://doi.org/10.1016/j.coi.2018.04.025>
- Chen B (2019) Molecular mechanism of HIV-1 entry. *Trends Microbiol* **27**: 878–891. <https://doi.org/10.1016/j.tim.2019.06.002>
- Cong J, Feng X, Kang H, Fu W, Wang L, Wang C, Li X, Chen Y, Rao Z (2023) Structure of the Newcastle Disease Virus L protein in complex with tetrameric phosphoprotein. *Nat Comm* **14**: 1324. <https://doi.org/10.1038/s41467-023-37012-y>
- Cooper TJ, Woodward B, Alom S, Harky AJ (2020) Coronavirus disease 2019 (COVID-19) outcomes in HIV/AIDS patients: a systematic review. *HIV Med* **21**: 567–577. <https://doi.org/10.1111/hiv.12911>
- Del Amo J, Polo R, Moreno S, Díaz A, Martínez E, Arribas JR, Jarrín I, Hernán MA (2020) Incidence and severity of COVID-19 in HIV-positive persons receiving antiretroviral therapy: a cohort study. *Ann Intern Med* **173**: 536–541. <https://doi.org/10.7326/m20-3689>
- Fenwick C, Joo V, Jacquier P, Noto A, Banga R, Perreau M, Pantaleo G (2019) T-cell exhaustion in HIV infection. *Immunol Rev* **292**: 149–163. <https://doi.org/10.1111/imr.12823>
- Finlayson T, Cha S, Xia M, Trujillo L, Denson D, Prejean J, Kanny D, Wejnert C, Abrego M, Al-Tayyib AJM, Report MW (2019) Changes in HIV preexposure prophylaxis awareness and use among men who have sex with men – 20 urban areas, 2014 and 2017. *Morb Mortal Wkly Rep* **68**: 597. <http://dx.doi.org/10.15585/mmwr.mm6827a1>
- Jewell BL, Mudimu E, Stover J, Ten Brink D, Phillips AN, Smith JA, Martin-Hughes R, Teng Y, Glaubius R, Mahiane S (2020) Potential effects of disruption to HIV programmes in sub-Saharan Africa caused by COVID-19: results from multiple mathematical models. *Lancet* **7**: e629–e640. [https://doi.org/10.1016/S2352-3018\(20\)30211-3](https://doi.org/10.1016/S2352-3018(20)30211-3)
- Jiang H, Zhou Y, and Tang W (2020) Maintaining HIV care during the COVID-19 pandemic. *Lancet* **7**: e308–e309. [https://doi.org/10.1016/S2352-3018\(20\)30105-3](https://doi.org/10.1016/S2352-3018(20)30105-3)
- Kanny D, Jeffries IV WL, Chapin-Bardales J, Denning P, Cha S, Finlayson T, Wejnert C, Abrego M, Al-Tayyib A, Anderson BJM (2017) Racial/ethnic disparities in HIV preexposure prophylaxis among men who have sex with men – 23 urban areas. *Morb Mortal Wkly Rep* **68**: 801. <https://doi.org/10.15585/mmwr.mm6837a2>
- Karim F, Moosa MY, Gosnell B, Cele S, Giandhari J, Pillay S, Tegally H, Wilkinson E, San J, Msomi N (2021) Persistent SARS-CoV-2 infection and intra-host evolution in association with advanced HIV infection. *MedRxiv*. <https://doi.org/10.1101/2021.06.03.21258228>
- Lancet HIV (2020). Lockdown fears for key populations. *Lancet* **7**: e373. [https://doi.org/10.1016/S2352-3018\(20\)30143-0](https://doi.org/10.1016/S2352-3018(20)30143-0)
- Larjani, MS, Sadat SM, Bolhassani A, Pouriyaveali MH, Bahramali G, Ramezani A (2018) *In silico* design and immunologic evaluation of HIV-1 p24-Nef fusion protein to approach a therapeutic vaccine candidate. *Curr HIV Res* **16**: 322–337. <https://doi.org/10.2174/1570162x17666190102151717>
- Liang W, Xiao H, Chen JY, Chang YF, Cao SJ, Wen YP, Wu R, Du SY, Yan QG, Huang XB, Zhao Q (2023) Immunogenicity and protective efficacy of a multi-epitope recombinant toxin antigen of *Pasteurella multocida* against virulent challenge in mice. *Vaccine* **S0264-410X(23)00224-4**. Advance online publication. <https://doi.org/10.1016/j.vaccine.2023.02.070>
- Meron-Sudai S, Asato V, Adler A, Bialik A, Goren S, Ariel-Cohen O, Reizis A, Mulard L, Phalipon A, Cohen D (2023) A Shigella flexneri 2a synthetic glycan-based vaccine induces a long-lasting immune response in adults. *NPJ Vaccines* **8**: 35. <https://doi.org/10.1038/s41541-023-00624-y>
- Muttaqin I, Stephanie F, Saragih M, Tambunan USF (2021) Epitope-based vaccine design for tuberculosis HIV Infection through in silico approach. *Pak J Biol Sci* **24**: 765–772. <https://doi.org/10.3923/pjbs.2021.765.772>
- Nami S, Mohammadi R, Vakili M, Khezripour K, Mirzaei H, Morovati HJB (2019) Fungal vaccines, mechanism of actions and immunology: a comprehensive review. *Biomed Pharmacother* **109**: 333–344. <https://doi.org/10.1016/j.biopha.2018.10.075>
- Naveed M, Ali U, Karobari MI, Ahmed N, Mohamed RN, Abul-lais SS, Kader MA, Marya A, Messina P, Scardina GA. (2022a). A Vaccine construction against COVID-19-associated mucormycosis contrived with immunoinformatics-based scavenging of potential mucoralean epitopes. *Vaccines* **10**: 664. <https://doi.org/10.3390/vaccines10050664>
- Naveed M, Jabeen K, Naz R, Mughal MS, Rabaan AA, Bakhrebah MA, Alhoshani FM, Aljeldah M, Shammari BRA, Alissa M, Sabour AA, Alaeq RA, Alshiekheid MA, Garout M, Almogbel MS, Halwani MA, Turkistani SA, Ahmed N (2022b) Regulation of host immune response against *Enterobacter cloacae* proteins via computational mRNA vaccine design through transcriptional modification. *Microorganisms* **10**: 1621. <https://doi.org/10.3390/microorganisms10081621>
- Naveed M, Makhdoom SI, Ali U, Jabeen K, Aziz T, Khan AA, Jamil S, Shahzad M, Alharbi M, Alshammari A (2022e) Immunoinformatics approach to design multi-epitope-based vaccine against machupo virus taking viral nucleocapsid as a potential candidate. *Vaccines* **10**: 1732. <https://doi.org/10.3390/vaccines10101732>
- Naveed M, Mughal MS, Jabeen K, Aziz T, Naz S, Nazir N, Muhammad S, Alharbi M, Alshammari A, Sadhu SS (2022c) Evaluation of the whole proteome to design a novel mRNA-based vaccine against multidrug-resistant *Serratia marcescens*. *Front Microbiol* **15**. <https://doi.org/10.3389/fmicb.2022.960285>
- Naveed M, Sheraz M, Amin A, Waseem M, Aziz T, Khan AA, Ghani M, Shahzad M, Alruways MW, Dablol AS, Elazazy AM, Almalki AA, Alamri AS, Alhomrani M (2022d) Designing a novel peptide-based multi-epitope vaccine to evoke a robust immune response against pathogenic multidrug-resistant *Providencia heimbachae*. *Vaccines* **10**: 1300. <https://doi.org/10.3390/vaccines10081300>
- Naveed M, Waseem M, Aziz T, Hassan JU, Makhdoom SI, Ali U, Alharbi M, Alshammari A (2023a) Identification of bacterial strains and development of an mRNA-based vaccine to combat antibiotic resistance in staphylococcus aureus via *in vitro* and *in silico* approaches. *Biomedicine* **11**: 1039. <https://doi.org/10.3390/biomedicine11041039>
- Naveed M, Shabbir MA, Ain N, Javed K, Mahmood S, Aziz T, Khan AA, Nabi G, Shahzad M, Alharbi ME, Alharbi M, Alshammari A (2023c) Chain-engineering-based de novo drug design against MPX-Vgp169 virulent protein of monkeypox virus: a molecular modification approach. *Bioengineering* **10**: 11. <https://doi.org/10.3390/bioengineering1001011>
- Naveed, Ain NU, Aziz T, Javed K, Shabbir MA, Alharbi M, Alshammari A, Alasmari AF (2023b) Artificial intelligence assisted pharmacophore design for Philadelphia chromosome-positive leukemia with gamma-tocotrienol: a toxicity comparison approach with acsiminib. *Biomedicine* **11**: 1041. <https://doi.org/10.3390/biomedicine11041041>
- Ng'uni T, Chasara C, Ndhlovu Z (2020) Major scientific hurdles in HIV vaccine development: historical perspective and future di-

- reactions. *Front Immunol* **11**: 590780. <https://doi.org/10.3389/fimmu.2020.590780>
- Pandey RK, Ojha R, Aathmanathan VS, Krishnan M, Prajapati V (2018) Immunoinformatics approaches to design a novel multi-epitope subunit vaccine against HIV infection. *Vaccines* **36**: 2262–2272. <https://doi.org/10.1016/j.vaccine.2018.03.042>
- Shabani SH, Kardani K, Milani A, Bolhassani A (2022) In silico and in vivo analysis of HIV-1 rev regulatory protein for evaluation of a multi-epitope-based vaccine candidate. *Immunol Invest* **51**: 1–28. <https://doi.org/10.1080/08820139.2020.1867163>
- Ssentongo P, Heilbrunn ES, Ssentongo AE, Advani S, Chinchilli VS, Nunez JJ, Du PJ (2021) Epidemiology and outcomes of COVID-19 in HIV-infected individuals: a systematic review and meta-analysis. *Sci Rep* **11**: 1–12. <https://doi.org/10.1038/s41598-021-85359-3>
- Sullivan PS, Johnson AS, Pembleton ES, Stephenson R, Justice AC, Althoff KN, Bradley H, Castel AD, Oster AM, Rosenberg ES (2021) Epidemiology of HIV in the USA: epidemic burden, inequities, contexts, and responses. *Lancet* **397**: 1095–1106. [https://doi.org/10.1016/s0140-6736\(21\)00395-0](https://doi.org/10.1016/s0140-6736(21)00395-0)
- Suryawanshi PS, Godbole J, Pawar M, Thakar M, Shete A (2018). Higher expression of human telomerase reverse transcriptase in productively-infected CD4 cells possibly indicates a mechanism for persistence of the virus in HIV infection. *Microbiol Immunol* **62**: 317–326. <https://doi.org/10.1111/1348-0421.12585>
- Vasavi CS, Tamizhselvi R, Munusami P (2019) Exploring the drug resistance mechanism of active site, non-active site mutations and their cooperative effects in CRF01_AE HIV-1 protease: molecular dynamics simulations and free energy calculations. *J Biomol Struct Dyn* **37**: 2608–2626. <https://doi.org/10.1080/07391102.2018.1492459>
- Yoshida Y, Honma M, Kimura Y, Abe HJC (2021) Structure, synthesis and inhibition mechanism of nucleoside analogues as HIV-1 reverse transcriptase inhibitors (NRTIs). *Chem Med Chem* **16**: 743–766. <https://doi.org/10.1002/cmdc.202000695>



OPEN ACCESS

EDITED BY
Grzegorz Węgrzyn,
University of Gdansk, Poland

REVIEWED BY
Nivedita Jaiswal,
Zydzus Cadila, India
Beata Hukowska-Szematowicz,
University of Szczecin, Poland

*CORRESPONDENCE
Ewelina Hallmann,
✉ ehallmann@pzh.gov.pl

RECEIVED 24 October 2023
ACCEPTED 23 January 2024
PUBLISHED 19 February 2024

CITATION
Kondratiuk K, Hallmann E, Szymański K,
Łuniewska K, Poznańska A and
Brydak LB (2024), Prevalence of
circulating antibodies against
hemagglutinin of influenza viruses in
epidemic season 2021/2022 in Poland.
Acta Biochim. Pol. 71:12289.
doi: 10.3389/abp.2024.12289

COPYRIGHT
© 2024 Kondratiuk, Hallmann,
Szymański, Łuniewska, Poznańska and
Brydak. This is an open-access article
distributed under the terms of the
Creative Commons Attribution License
(CC BY). The use, distribution or
reproduction in other forums is
permitted, provided the original
author(s) and the copyright owner(s) are
credited and that the original
publication in this journal is cited, in
accordance with accepted academic
practice. No use, distribution or
reproduction is permitted which does
not comply with these terms.

Prevalence of circulating antibodies against hemagglutinin of influenza viruses in epidemic season 2021/2022 in Poland

Katarzyna Kondratiuk¹, Ewelina Hallmann^{1*}, Karol Szymański¹,
Katarzyna Łuniewska¹, Anna Poznańska² and Lidia B. Brydak¹

¹Laboratory of Influenza Viruses and Respiratory Viruses, Department of Virology, National Institute of Public Health NIH—National Research Institute, Warsaw, Poland, ²Department of Population Health Monitoring and Analysis, National Institute of Public Health NIH—National Research Institute, Warsaw, Poland

The aim of the study was to determine the level of anti-hemagglutinin antibodies in the serum of patients during the 2021/2022 epidemic season in Poland. A total of 700 sera samples were tested, divided according to the age of the patients into 7 age groups: 0–4 years of age, 5–9 years of age, 10–14 years of age, 15–25 years of age, 26–44 years of age, 45–64 years of age and ≥65 years of age, 100 samples were collected from each age group. Anti-hemagglutinin antibody levels were determined using the haemagglutination inhibition assay (OZHA). The results obtained confirm the presence of anti-hemagglutinin antibodies for the antigens A/Victoria/2570/2019 (H1N1) pdm09, A/Cambodia/e0826360/2020 (H3N2), B/Washington/02/2019 and B/Phuket/3073/2013 recommended by World Health Organization (WHO) for the 2021/2022 epidemic season. The analysis of the results shows differences in the levels of individual anti-hemagglutinin antibodies in the considered age groups. In view of very low percentage of the vaccinated population in Poland, which was 6.90% in the 2021/2022 epidemic season, the results obtained in the study would have to be interpreted as the immune system response in patients after a previous influenza virus infection.

KEYWORDS

influenza, hemagglutinin antibodies, protection rate, GMT, serum financial support

Introduction

Influenza is a significant public health threat both in Poland and around the world. It is an acute infectious respiratory viral disease caused by influenza viruses classified into four types: A, B, C, and D. Influenza A virus infects not only humans, but also horses, pigs, aquatic mammals (such as seals, whales), and birds. The influenza B virus only infects humans, while the influenza C virus infects humans and pigs. In contrast, the influenza D virus has so far been detected in pigs and cattle (Ducatez et al., 2015; Gliński and Żmuda, 2022). Human infection with influenza D has not been observed (Wu and Wilson, 2020). This classification is based on antigenic differences between the main proteins of the

virion, i.e., the M protein and the NP nucleoprotein. These types differ epidemiologically (Brydak, 2008). Influenza epidemics are caused by both influenza A (A/H3N2/and A/H1N1/pdm09) and influenza B (B/Yamagata and B/Victoria) lineages, but only influenza A viruses can cause a pandemic and dramatically increase hospitalizations and deaths from post-flu complications (Frey et al., 2023). In most cases, the influenza C virus causes only mild symptoms after infection.

Seasonal influenza mainly occurs during the colder months in regions with temperate climates. Human-to-human transmission of the influenza virus occurs through inhalation of infectious respiratory particles when an infected person coughs or sneezes. There is also evidence that the influenza virus can be transmitted by talking or breathing, that is by transmitting small respiratory particles. The incubation period of the influenza virus is usually 24–48 h. An infected patient is contagious even one to 2 days before the onset of influenza symptoms and for five to 7 days after the onset of symptoms. Infected children and persons taking immunosuppressive drugs may show prolonged secretion of the influenza virus (Gaitonde et al., 2019).

The influenza A virus particle, which deceptively resembles a chestnut with protruding spikes, has a lipid envelope originating from the plasma membrane of the host cell. Two surface proteins are anchored in it: hemagglutinin (HA) and neuraminidase (NA). Hemagglutinin is responsible for the adsorption of the influenza virus into the cell, while neuraminidase is responsible for the release of viruses from the host cells. It is estimated that there are approximately 400 HA spikes and 100 NA spikes per influenza A and B virus particle. The structure of the influenza virus genome is segmented. Influenza A and B viruses are characterized by having 8 viral RNA segments, while the influenza C virus has only 7 viral RNA segments. Influenza C viruses have only one type of spike in the lipid envelope, which serves as hemagglutinin and neuraminidase. The organization of the influenza A virus genome in the form of segments allows for reassortment, which is an important mechanism for the formation of diverse strains (Gliński and Żmuda, 2022). Thus, the influenza A virus is characterized by high antigenic variability, and based on differences in surface antigens, 11 subtypes conditioned by neuraminidase–NA (N1–N11) and 18 subtypes conditioned by hemagglutinin–HA (H1–H18) are distinguished (Brydak, 2008; Wierzbicka-Woś et al., 2015). Pandemic influenza strains arise as a result of antigenic shift and may include avian-derived hemagglutinin (HA) subtypes (such as H5, H7, and H9) or porcine hemagglutinin variants (H1, H2, and H3) which, by acquiring further adaptive mutations, become capable of human-to-human transmission of infection (Bouvier and Palese, 2008; Taubenberger and Kash, 2010; Khalenkov et al., 2023). Vaccination against influenza is the most effective preventive measure. Influenza vaccines reduce the risk of being affected by influenza and prevent the development of serious complications. They also play an important role in

pandemic preparedness plans around the world (Frey et al., 2023).

However, in order to be effective, it requires constant and thorough worldwide supervision and timely updates of the formulation of the influenza vaccine (Khalenkov et al., 2023). Influenza virus infections, like many other infections, induce an immune response in the infected body, reducing or even cessating virus replication and formation of so-called immunological memory in the patient, protecting against subsequent infection. However, this optimistic scenario is hampered by the fact that the influenza A virus is characterized by high antigenic variability and constant mutations. This significantly impedes the formation of memory and immune response, while facilitating the transmission of infections between sick and healthy population (Wierzbicka-Woś et al., 2015). Antigenic drift (antigenic shift) is a consequence of point mutation of genes in the replication of influenza viruses, leading to changes in amino acid sequences that alter antigenic sites in epitopes. New variants and annual influenza epidemics are the result of antigenic changes in the H and N glycoproteins of the virus. This results in the inability to develop a universal formulation of the vaccine and the need to change the composition of influenza vaccines every season (Shao et al., 2017; Gliński and Żmuda, 2022). Anti-hemagglutinin antibodies are characterized by a relatively short persistence in blood serum (Allwinn et al., 2013). Due to all these reasons, seasonal influenza vaccinations are extremely important, contributing to an increase in resistance to influenza infections of the general population, and thus reducing the risk of post-influenza complications and death.

The aim of this study was to determine the level of anti-hemagglutinin antibodies in the sera of persons in different age groups during the 2021/2022 epidemic season in Poland.

Materials and methods

The study material consisted of 700 sera collected by employees of 16 Provincial Sanitary and Epidemiological Stations in Poland, in accordance with the World Health Organization (WHO) recommendations. Samples were collected at voivodeship sanitary and epidemiological stations (VSES) in Poland, between 1st October 2021 and 31st September of 2022. The serum samples were divided into 7 groups according to the age of the patients: 0–4 years of age, 5–9 years of age, 10–14 years of age, 15–25 years of age, 26–44 years of age, 45–64 years old and ≥65 years of age, 100 samples collected from each age group (the number of samples from each voivodeship was not the same). Prior to testing, serum samples were stored at –80°C. Prior the testing sera were selected and checked for haemolysis in sample. If noticed, sample was discarded.

TABLE 1 Influenza virus strains used for the hemagglutination inhibition assay (HAI) in the 2021/2022 epidemic season.

Epidemic season 2021/2022		
Influenza virus strains	A/H1N1/pdm09	A/Victoria/2570/2019 (H1N1)pdm09-like virus
	A/H3N2/	A/Cambodia/e0826360/2020 (H3N2)-like virus
	B Victoria lineage	B/Washington/02/2019 (B/Victoria lineage)-like virus
	B Yamagata lineage	B/Phuket/3073/2013 (B/Yamagata lineage)-like virus

All viruses were obtained from World Influenza Centre at Francis Crick Institute, London, and then propagated in the amniotic cavity on 11- days old chicken embryos in Influenza Virus Research Department, National Influenza Center at the National Institute of Public Health NIH-National Research Institute (NIPH NIH-NRI), in accordance with WHO recommendations (WHO, 2011). The eggs were incubated as follows: for H3N2 and H1N1 viruses (2 days at 37°C); and for influenza B viruses (3 days at 35°C). Then titer of each virus was determined. Labelled vials containing viruses were stored at –80°C upon using in research (WHO, 2011).

The study used antigens for the 2021/2022 epidemic season recommended by WHO (Table 1).

The level of anti-hemagglutinin antibodies was determined by hemagglutination inhibition assay (HAI). The haemagglutination inhibition assay (OZHA) was performed using 8 hemagglutination units of the virus. The sera were inactivated prior to testing according to adopted standards (Tyrell and Horsfall et al., 1952; WHO, 2011). Necessary viruses with high titer were selected to be used in this test. Solution of titer 1:8 from each of the virus was prepared. For example, for virus titer 1:64, suspension of the virus was diluted 8 times. For 1:16—two Times. After preparing all necessary solution, they were stored in 4°C upon adding them on the plates.

PBS and Alsever's solution needed for the OZHA test are prepared in-house. In this study V-bottom, clear, microtitration plates were used.

For OZHA test are used chicken red blood cells. Blood cells delivered to the laboratory were suspended in Alsever's solution. By centrifugation at a speed of 1200 RPM for 10 min, a concentrate of packed blood cells was obtained and used in further research.

Each of the sera was treated with Receptor Destroying Enzyme (RDE) (Thermo Fisher Scientific) for 16 h at 37°C prior to the hemagglutination inhibition test. After this step, to inactivate the enzyme, the mixture was incubated at 56°C for 30 min.

In OZHA test, a serial dilution of each of the sera was made in PBS. Then, the prepared solution of the virus, which has titer of 1: 8 was added to each well on the plate. After virus addition, the plate was incubated for 15 min at room temperature. After incubation, 50 µL of blood cell solution was added. Readings were taken after 30 min of incubation at room temperature, then the results were read.

The analysis of the test results of the study was based on the following parameters: geometric mean titer (GMT) of the anti-hemagglutinin antibody in the tested sera and the protection rate (percentage of people with anti-hemagglutinin antibodies at a level $\geq 1:40$ that appeared after the administration of an influenza vaccine or during the previous infection by the influenza virus) (Brydak, 2008; WHO, 2011; Krammer, 2019). This is the value of anti-hemagglutinin antibody titers, which is considered a protective value (Brydak, 2008).

Statistical analysis

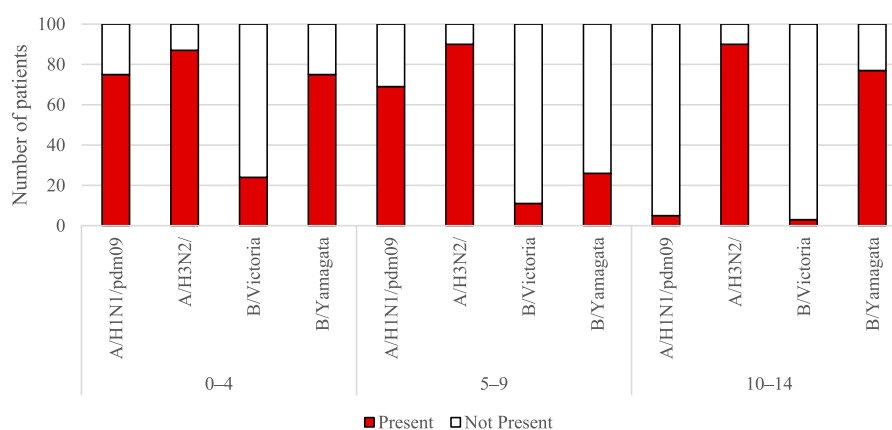
The test chi-square was used to compare age groups regarding the categorical variables (prevalence of anti-hemagglutinin antibodies and reaching their protective titer). The Kruskal-Wallis test was applied to compare the titer distribution between seven age groups, and the Mann-Whitney *U* test was used for two. The significance level for all the tests was assumed to amount to 0.05. The calculations were executed with the SPSS 12.0 PL.

Results

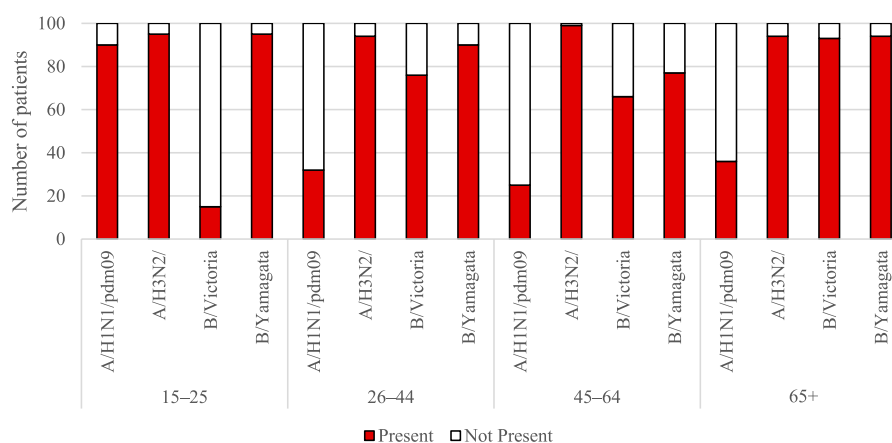
The analysis of the obtained results shows that antibodies against A/Victoria/2570/2019 (H1N1) pdm09 were present in 332 people (47.4% of the studied patients). The largest number of tested patients—649 persons (92.7% of all subjects)—had antibodies against A/Cambodia/e0826360/2020 (H3N2). The smallest number of tested patients had antibodies against B/Washington/02/2019 (B/Victoria lineage), it was 288 patients (41.1% of subjects). Antibodies against B/Phuket/3073/2013 (B/Yamagata lineage) were present in the sera of 534 patients (76.3% of all tested sera).

Figures 1, 2 show the percentage of patients in individual age groups that had antibodies against a particular influenza virus.

Using the chi-square test, it was found that statistically significant differences in the number (and therefore percentage) of those with antibodies between the tested sera of patients from all seven age groups apply to all four types of antibodies for the following types and subtypes of influenza viruses:

**FIGURE 1**

The presence of antibodies in the serum of patients aged 0–4 years, 5–9 years of age and 10–14 years of age in the 2021/2022 epidemic season.

**FIGURE 2**

The presence of antibodies in the serum of patients aged 15–25, 26–44, 45–64, and 65+ years of age in the 2021/2022 epidemic season.

- For the H1 subtype: $p < 0.001$, the percentage of those with antibodies ranged from 5% in the 10–14-year-old group to 90% in the 15–25-year-old group;
- For the H3 subtype: $p = 0.024$, the percentage of those with antibodies ranged from 87% in the 0–4 years old group to 99% in the 45–64 years old group;
- For the B/Victoria line (B/Washington): $p < 0.001$, the percentage of those with antibodies ranged from 3% in the group of 10–14 years old to 93% in the group of 65 years and over;
- For the B/Yamagata line (B/Phuket): $p < 0.001$, the percentage of those with antibodies ranged from 26% in the 5–9 years old group to 95% in the 15–25 years old group.

In Figure 3 shows the geometric mean titers of anti-hemagglutinin antibodies in the sera of patients according to age groups in the 2021/2022 epidemic season in Poland (Figure 1).

Based on the obtained test results, the highest GMT values for hemagglutinin A/H1 were found in patients in the youngest patients' age group 0–4 years old (GMT = 54.3). Lower GMT values for hemagglutinin A/H1 were obtained in the 5–9 age group (GMT = 46.5). In the remaining age groups, GMT values for hemagglutinin A/H1 were comparable, with the lowest value in the age group of 26–44 years (GMT = 20.0).

The highest GMT values for hemagglutinin A/H3 was recorded in the age groups 10–14 years (GMT = 181.0) and 26–44 years (GMT = 180.0). Lower values were found in the age

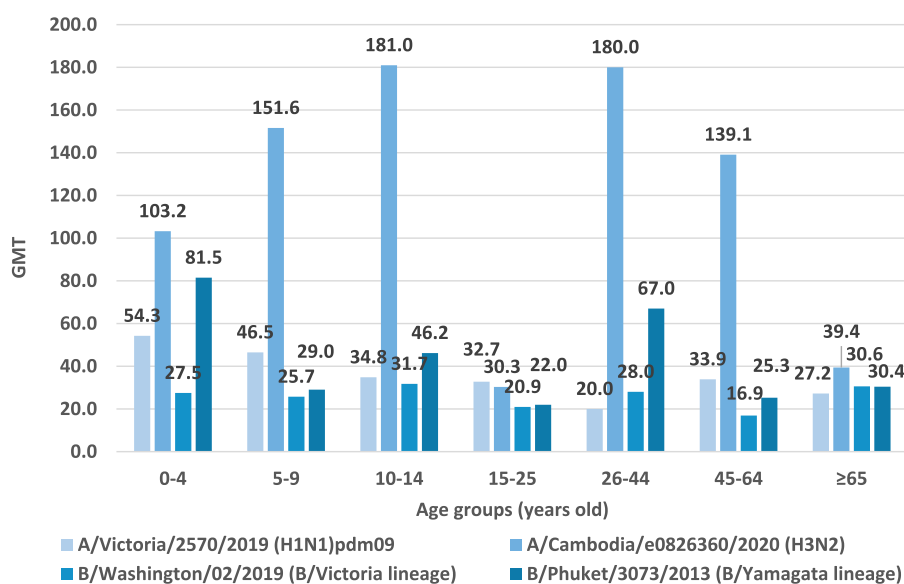


FIGURE 3

Geometric mean titers of anti-haemagglutinin antibodies (GMT) in the epidemic season 2021/2022 in age groups in Poland.

group of the youngest children aged 5–9 (GMT = 151.6), in patients aged 45–64 years (GMT = 139.1) and in the youngest patients' age group 0–4 years old (GMT = 103.2). In the remaining patients, the GMT values for hemagglutinin A/H3 remained at a similar level: in the oldest patients over 65 years of age was 39.4 and in patients aged 15–25 was 30.3.

In the case of type B/Washington/02/2019, the highest GMT value was reported in the 10–14 age group (GMT = 31.7). In the remaining age groups, GMT values were as follows: ≥65 years old (GMT = 30.6), 26–44 years old (GMT = 28.0), 0–4 years old (GMT = 27.5), 5–9 years old (GMT = 25.7), 15–25 years old (GMT = 20.9), 45–64 years old (GMT = 16.9).

According to the analyzed data for type B/Phuket/3073/2013, the highest geometric mean antibody titers was reported for the youngest patients aged 0–4 years (GMT = 81.5). The age group 26–44 had a similar GMT value (GMT = 67.0). For the remaining age groups, the GMT values were: 10–14 years old (GMT = 46.2), ≥65 years old (GMT = 30.4), 5–9 years old (GMT = 29.0), 45–64 years old (GMT = 25.3), 15–25 years old (GMT = 22.0).

In neither age group the geometric mean titer of all of anti-hemagglutinin antibodies (H1, H3, B/Washington/02/2019 and B/Phuket/3073/2013) was not ≥ 40. In two age groups 15–25 and 65+, the average level of none of the antibodies reached 40. Only in the case of the youngest patients aged 0–4 years, the geometric mean titer of three anti-hemagglutinin antibodies (H1, H3 and B/Phuket/3073/2013) was ≥ 40. GMT values were respectively: for H3 GMT = 103.2, for B/Phuket/3073/2013 GMT = 81.5, for H1 GMT = 54.3, respectively.

Statistical analysis performed using the Kruskal-Wallis test showed that for all types of antibodies, the difference in their titer between all seven age groups was statistically significant ($p < 0.001$ in all cases).

- For the H1 subtype: antibodies found in 332 persons, the mean GMT = 37.0, the lowest antibody level in the group of 26–44 years old (GMT = 20.0), the highest in the group of 0–4 years old–GMT = 54.3 ($p < 0.001$);
- For the H3 subtype: antibodies found in 649 persons, the mean GMT = 97.1, the lowest antibody level in the group of 15–25 years old (GMT = 30.3), the highest in the group of 10–14 years old–GMT = 181.0 ($p < 0.001$);
- For the B/Victoria line (B/Washington): antibodies found in 288 persons, the mean GMT = 25.2, the lowest antibody level in the group of 45–64 years (GMT = 16.9), the highest in the group of 10–14 years–GMT = 31.8 ($p < 0.001$);
- For the B/Yamagata (B/Phuket) line: antibodies found in 534 persons, the mean GMT = 38.9, the lowest antibody level in the 15–25 years old group (GMT = 22.0), the highest in the 0–4 years old group–GMT = 81.5 ($p < 0.001$).

Figure 4 shows the percentage of cases with a protective anti-hemagglutinin antibody titer (%), i.e., ≥ 40, in the 2021–2022 epidemic season, in different age groups.

Studies on the effectiveness of influenza vaccination show that the protective coefficient should reach different values depending on the age of the patient in order to achieve the desired effect of vaccination effectiveness. According to the

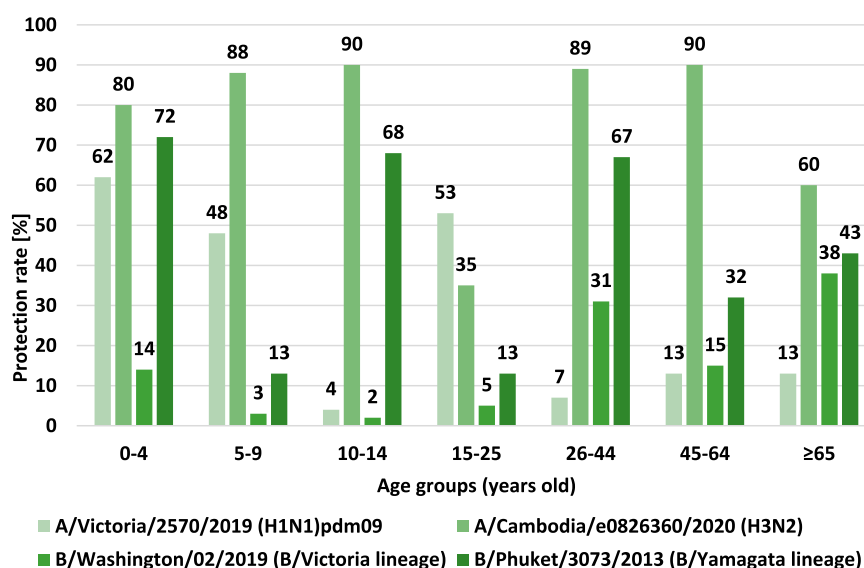


FIGURE 4

Percentage of cases with a protective titer of anti-haemagglutinin antibodies (%) in the 2021/2022 epidemic season in different age groups.

criteria of the CPMP (Committee for Proprietary Medicinal Products) of the European Agency for the Evaluation of Medicinal Products (EMA) and the Commission of the European Communities regarding the harmonization of requirements for influenza vaccination, parameters such as the mean increase in anti-HA antibody titers (MFI), the protective factor and the response rate, measured approximately 3 weeks after vaccination should be taken into account when assessing the serological response to this vaccination. Depending on the age of the patient these values vary (Commission of the European Communities, 1991; Committee for Proprietary Medicinal Products, 1997).

Comparing the results of the protective coefficient results for all hemagglutinins, the highest protective coefficient values were obtained for hemagglutinin H3 and B/Yamagata (B/Phuket) line. The conducted analyzes of the value of the protective coefficient indicate that in the age group of 0–4, 5–9, 10–14, 26–44 and 45–64 years values above 70% and 60% for the 65+ age group have been recorded. These values were obtained only for the above mentioned subtypes. In other cases, the protection rate did not reach the recommended protection level. The highest value of protective coefficient was recorded for hemagglutinin H3. These data correspond to the low level of vaccination of the population in Poland in the 2021/2022 epidemic season (according to data from the Influenza Research Institute, National Influenza Centre).

For all antibody types, there is a statistically significant difference in protective coefficients between all seven age groups, as was demonstrated with the use of the chi-square test.

- For the H1 subtype: 200 subjects had antibodies with titers of ≥ 40 , the protective coefficient was 29%, the statistical significance of differences between age groups was $p < 0.001$, the protective coefficients in age groups ranged from 4% in the group of 10–14 years old to 62% in the group of 0–4 years old;
- For the H3 subtype: 532 subjects had antibodies with titers ≥ 40 , the protective coefficient was 76%, the statistical significance of differences between age groups was $p < 0.001$, the protective coefficients in age groups ranged from 35% in the group of 15–25 years old to 90% in groups of 10–14 years old and 45–64 years old;
- For the B/Victoria line (B/Washington): 108 subjects had antibodies with titers ≥ 40 , the protective coefficient was 15%, statistical significance of differences between age groups was $p < 0.001$, protective coefficients in age groups from 2% in the group 10–14 years old to 38% in the group 65 years old and over;
- For the B/Yamagata (B/Phuket) line: 308 subjects had antibodies with titers ≥ 40 , the protective coefficient was 44%, statistical significance of differences between age groups was $p < 0.001$, protective coefficients in age groups from 13% in groups of 5–9 years old and 15–25 years old to 72% in the 0–4 years old group.

Distributions of antibody levels among the tested sera of children (300 subjects aged 0–14) and adults (400 subjects aged over 14) show clear differences:

- For the H1 subtype: in adults, antibody titer values ranged from 0 to 640, quartiles (Q1/Q2—median/Q3): 0/0 (median)/20; in children values ranged from 0 to 160, quartile: 0/0 (median)/40; the difference in distributions is statistically significant ($p = 0.002$), as determined using the Mann-Whitney U test; the percentages of adults and children with antibodies are similar—45% vs. 50%, the difference is not statistically significant, as determined by the chi-square test; the mean level of antibodies in subjects who have them is significantly higher among children (49.8 vs. 29.1, $p < 0.001$), as shown by the Mann-Whitney U test; as expected (in both compared groups a similar percentage of subjects have antibodies, and their titers are clearly higher in younger ones), children reach the protective level significantly more often (38% vs. 22%; $p < 0.001$);
- For the H3 subtype: in both age groups, antibody titer values ranged from 0 to 640; quartile among adults: 20/80 (median)/160, higher among children 80/160 (median)/320; the difference in distributions is statistically significant ($p < 0.001$)—Mann-Whitney U test; presence of antibodies against H3 is common, 96% in adults and 89% in children, however the difference is statistically significant ($p = 0.001$, chi-square test); the mean level of antibodies (in people who have them) is significantly higher in children (142.0 vs 74.4; $p < 0.001$ —Mann-Whitney U test); children are also a group that achieves the protective level significantly more often (86% vs. 69%; $p < 0.001$);
- For the B/Victoria line (B/Washington): in adults, antibody titer values ranged from 0 to 640, quartile: 0/10 (median)/20; in children, antibody titer values ranged from 0 to 160, quartile 0/0 (median)/0; the difference is statistically significant ($p < 0.001$)—Mann-Whitney U test; 63% of adults and only 13% of children had antibodies against B/Washington, the difference is statistically significant ($p < 0.001$, chi-square test); unlike other antibodies, there is no difference in their mean level in children (27.3) and adults (24.9)—as before, we only count subjects with antibodies; as expected (antibodies in adults are present much more often, and their average titer in both groups is similar), adults reach the protective level significantly more often (22% vs. 6%; $p < 0.001$);
- For the B/Yamagata (B/Phuket) line: in both age groups, antibody titer values ranged from 0 to 640; quartile in adults: 10/20 (median)/40, and in children 0/40/80; difference in distributions bordering on statistical significance ($p = 0.053$)—Mann-Whitney U test; 89% of adults and 59% of children had antibodies against B/Phuket, the difference is statistically significant ($p < 0.001$, chi-square test); the mean level of antibodies (in subjects with antibodies) is significantly higher in children (54.8 vs 32.7; $p < 0.001$ —Mann-Whitney U test). The frequency of reaching the protective level is higher

among children under 14 years of age (51% vs. 39%, $p = 0.001$).

Discussion

The analysis of the study results indicates that antibodies against all four influenza viruses included in the influenza vaccine in the 2021/2022 influenza season were detected in the tested sera of patients from all age groups. Due to the very low vaccination rate of general population in Poland, which in the 2021/2022 epidemic season, despite recommendations and solid, multi-threaded educational campaigns, was estimated at only 6.90% (Grohskopf et al., 2021; NIPH NIH-NRI, 2023) the results obtained in the study should be interpreted as a response of the immune system in patients after a previous infection caused by the influenza virus. The detection of anti-hemagglutinin antibodies in the patient's blood serum may indicate a past infection with influenza viruses or the fact that the patient has been vaccinated against influenza. Immunity after vaccination against influenza usually appears approximately 10–14 days after receiving the vaccine and lasts for approximately 6–12 months, i.e., during one epidemic season, which usually covers period from October to March. For this reason, and because the influenza virus is subject to rapid antigenic changes, seasonal influenza vaccination is extremely important. Vaccination is the most effective preventive measure against influenza infection, mitigating the course of the disease and preventing post-influenza complications, which may be very serious, including complications with death threat. This may not only apply to people in high-risk groups.

Comparing the antigenic composition of the influenza vaccine in effect in the Northern Hemisphere in the 2021/2022 epidemic season and in the 2020/2021 epidemic season, it can be noted that in both epidemic seasons the same antigens for type B influenza viruses were present: B/Washington/02/2019 (B/Victoria lineage)-like virus and B/Phuket/3073/2013 (B/Yamagata lineage)-like virus. In these two epidemic seasons, only the antigens for influenza A viruses mutated, both for the influenza virus of the A/H1N1/pdm09 subtype and for the A/H3N2/virus. The influenza B/Phuket/3073/2013 (B/Yamagata lineage)-like virus antigen has been included in the influenza vaccine recommended for the Northern Hemisphere for several consecutive epidemic seasons. Despite this, this virus reached a protective level only in one age group among the analyzed samples—among the youngest children under 4 years of age (72%).

It is considered necessary to vaccinate 70%–80% of the population to achieve community immunity. It is assumed that the titer of anti-hemagglutinin antibodies in blood sera at a level of $\geq 1:40$ protects against influenza virus infection. The effectiveness of vaccinations in older people is lower than in young people. After vaccination, most young people achieve this

titer, while in the group of older people only $\frac{1}{4}$ do (Carrat and Valleron, 1994; Glathe and Langer, 1995; Brydak, 2008).

Emerging infectious diseases pose a serious threat to global health security, as exemplified by the recent COVID-19 pandemic. Seasonal influenza virus infections, millions of cases registered every epidemic season and thousands of deaths due to post-influenza complications around the world, as well as the threat of another influenza pandemic and cases of human infection with avian influenza viruses in the past make the fight against influenza one of the public health priorities. Effective control of the threats posed by this disease depends, among others, on effective supervision. A worrying but unfortunately common phenomenon among the society is the disregard of the early symptoms of the disease in particular, when influenza is often confused with the common cold. In many cases, this significantly hinders or completely prevents effective antiviral therapy. Referring to the diagnosis of the influenza virus, the serious consequences resulting from the incorrect diagnosis of symptoms and the implementation of unjustified antibiotic therapy are also worth mentioning. The arising problem is antibiotic resistance, i.e., the lack of sensitivity of bacteria to antibiotics. Due to frequent complications, antibiotic therapy is implemented as part of medical prophylaxis, despite the fact that it is widely known that antibiotics are not used in the prevention of viral infections. The trend of increasing drug resistance of microorganisms, which has been observed in recent years, may lead to a very difficult situation, which is the exhaustion of therapeutic options against infections. The use of antibiotics should therefore be justified by appropriate tests.

Fast and effective diagnosis of patients suspected of having influenza may allow for the earliest possible implementation of treatment and bring about both health-related and economic benefits.

Conclusion

Based on the assessment of the level of anti-hemagglutinin antibodies in sera collected from patients in seven age groups during the 2021/2022 epidemic season in Poland, the following conclusions can be drawn:

- The study results confirmed the circulation in the population of four antigens of influenza virus strains included in the influenza vaccine for the 2021/2022 epidemic season: A/Victoria/2570/2019 (H1N1) pdm09-like virus, A/Cambodia/e0826360/2020 (H3N2)-like virus, B/Washington/02/2019 (B/Victoria lineage)-like virus and B/Phuket/3073/2013 (B/Yamagata lineage)-like virus.
- Adult patients (of over 14 years of age) had antibodies against hemagglutinin of influenza viruses more often than children (of under 14 years of age) (with the exception of antibodies against A/Victoria/2570/2019 (H1N1) pdm09—here, the level of antibodies in patients from the two above groups was at a similar level).
- Among the tested subjects with antibodies, their titer is on average higher in children under 14 years of age (the exception being antibodies against B/Washington/02/2019 (B/Victoria lineage)—here the level of antibodies in both adult patients over 14 years of age and in children was at a similar level).
- Tested children aged 0–14 years more often achieved a protective level (anti-hemagglutinin antibody titer ≥ 40) in case of antibodies against A/Victoria/2570/2019 (H1N1) pdm09, A/Cambodia/e0826360/2020 (H3N2) and B/Phuket/3073/2013 (B/Yamagata lineage); the protective level against B/Washington/02/2019 (B/Victoria lineage) was more often achieved by adults over 14 years of age (while as many as 87% of children under 14 years of age did not have anti-hemagglutinin antibodies at all).
- The low percentage of vaccinated persons in particular age groups may indicate that the level of protection obtained may have been the result of a past infection caused by influenza viruses.

Data availability statement

The original contributions presented in the study are included in the article/supplementary material, further inquiries can be directed to the corresponding author.

Ethics statement

Ethical review and approval were waived for this study due to the National Influenza Centre (NIC) cooperating with Voivodship Sanitary Epidemiological Stations (VSES), within the WHO's Global Influenza Surveillance And Response System (GISRS). VSES collected samples from patients during the epidemic season. The studies were conducted in accordance with the local legislation and institutional requirements. The human samples used in this study were provided by VSES. Written informed consent to participate in this study was not required from the participants or the participants' legal guardians/next of kin in accordance with the national legislation and the institutional requirements. Written informed consent was not obtained from the individual(s), nor the minor(s)' legal guardian/next of kin, for the publication of any potentially identifiable images or data included in this article because samples were collected by VSES. All documents regarding patients and their consent, belongs to VSES.

Author contributions

KK—Study Design, Data Collection, Data interpretation, Manuscript Preparation, and Literature Search. EK—Data Collection, Data interpretation, and Literature Search. KS—Data Collection, Data interpretation, and Literature Search. KŁ—Data Collection, Data interpretation, and Literature Search. AP—Statistical Analysis and Manuscript Preparation. LB—Study Design, Data interpretation, Manuscript Preparation, Literature Search, and Funds Collection. All authors contributed to the article and approved the submitted version.

Funding

The study is conducted with the funds of the National Health Program for 2021–2025, financed by the Minister of Health.

References

- Allwinn, R., Bickel, M., Lassmann, C., Wicker, S., and Friedrichs, I. (2013). Trivalent influenza vaccination of healthy adults 3 years after the onset of swine-origin H1N1 pandemic: Restricted immunogenicity of the new A/H1N1v constituent? *Med. Microbiol. Immunol.* 202 (2), 125–130. Epub 2012 Sep 19. PMID: 22986732. doi:10.1007/s00430-012-0259-9
- Bouvier, N. M., and Palese, P. (2008). The biology of influenza viruses. *Vaccine* 26 (4), D49–D53. PMID: 19230160. doi:10.1016/j.vaccine.2008.07.039
- Brydak, L. B. (2008). *Influenza, pandemic flu, myth or real threat?* Warsaw: Rythm, 1–492.
- Carrat, F., and Valleron, A. J. (1994). Anti-influenza vaccine. Bibliographic review. *Rev. Mal. Respir.* 11, 239–255.
- Commission of the European Communities (1991). *Ad hoc working party on Biotechnology/Pharmacy. Harmonization of requirements for influenza vaccines. Document 111/3188/91-EN.* Brussels.
- Committee for Proprietary Medicinal Products (1997). *Note for guidance on harmonisation of requirements for influenza vaccines (CPMP/BWP/214/96)*, 20–21.
- Ducatez, M. F., Pelletier, C., and Meyer, G. (2015). Influenza D virus in cattle, France, 2011–2014. *Emerg. Infect. Dis.* 21, 368–371. doi:10.3201/eid2102.141449
- Frey, S. S., Versage, E., Van Twuijver, E., and Hohenboken, M. (2023). Antibody responses against heterologous H5N1 strains for an MF59-adjuvanted cell culture-derived H5N1 (aH5N1c) influenza vaccine in adults and older adults. *Hum. vaccines Immunother.* 19 (1), 2193119. Epub 2023 Apr 14. PMID: 37057755; PMCID: PMC10114991. doi:10.1080/21645515.2023.2193119
- Gaitonde, D. Y., Moore, F. C., and Morgan, M. K. (2019). Influenza: diagnosis and treatment. *Am. Fam. Physician* 100 (12), 751–758. PMID: 31845781.
- Glathe, H., and Lange, W. (1995). Influenza vaccination in older patients. Immunogenicity, epidemiology and available agents. *Drugs Aging* 6 (5), 368–387. doi:10.2165/00002512-199506050-00004
- Gliński, Z., and Zmuda, A. (2022). Zmienność wirusów – przyczyny i skutki. *Życie Weter.* 97 (2), 75–80.
- Grohskopf, L. A., Alyanak, E., Ferdinands, J. M., Broder, K. R., Blanton, L. H., Talbot, H. K., et al. (2021). Prevention and control of seasonal influenza with vaccines: recommendations of the advisory committee on immunization practices, United States, 2021–22 influenza season. *MMWR Recomm. Rep.* 70 (5), 1–28. PMID: 34448800; PMCID: PMC8407757. doi:10.15585/mmwr.rr7005a1
- Khalkov, A. M., Norton, M. G., and Scott, D. E. (2023). Method for screening influenza neutralizing antibodies in crude human plasma and its derivatives using SPR. *Heliyon* 9 (5), e15651. PMID: 37144181; PMCID: PMC10151358. doi:10.1016/j.heliyon.2023.e15651
- Krammer, F. (2019). The human antibody response to influenza A virus infection and vaccination. *Nat. Rev. Immunol.* 19 (6), 383–397. PMID: 30837674. doi:10.1038/s41577-019-0143-6
- NIPH NIH-NRI (2023). *Szczepienia ochronne w polsce.* [Vaccinations in Poland.]. Available from: http://www.wold.pzh.gov.pl/oldpage/epimeld/index_p.html (Accessed May 20, 2023).
- Shao, W., Li, X., Goraya, M. U., Wang, S., and Chen, J. L. (2017). Evolution of influenza A virus by mutation and re-assortment. *Int. J. Mol. Sci.* 18, 1650. doi:10.3390/ijms18081650
- Taubenberger, J. K., and Kash, J. C. (2010). Influenza virus evolution, host adaptation, and pandemic formation. *Cell Host Microbe* 7, 440–451. PMID: 20542248. doi:10.1016/j.chom.2010.05.009
- Tyrrell, D. A. J., and Horsfall, F. L. (1952). A procedure which eliminates nonspecific inhibitor from human serum but does not affect specific antibodies against influenza viruses. *J. Immunol.* 69, 563–574. doi:10.4049/jimmunol.69.5.563
- WHO (2011). *Manual for the laboratory diagnosis and virological surveillance of influenza.* Geneva: WHO Press – Global Influenza Surveillance Network, 1–153.
- Wierzbicka-Woś, A., Tokarz-Deptuła, B., and Deptuła, W. (2015). Immune system and influenza virus. *Postępy Hig. i Med. Doświadczalnej* 69, 214–220. doi:10.5604/17322693.1140337
- Wu, N. C., and Wilson, I. A. (2020). Influenza hemagglutinin structures and antibody recognition. *Cold Spring Harb. Perspect. Med.* 10 (8), a038778. PMID: 31871236; PMCID: PMC7397844. doi:10.1101/cshperspect.a038778

Conflict of interest

The authors declare that the research was conducted in the absence of any commercial or financial relationships that could be construed as a potential conflict of interest.

Acknowledgments

The authors would like to acknowledge Lidia Malec, PhD and Prof. Henryk Malec, PhD from “Malec” Company for providing hatching eggs. The authors extend special acknowledgements to the STASIN Poultry Plant: Krzysztof Borkowski, President of the Board; Paweł Okrzeja, Director; Grzegorz Borkowski, Director; and Members of the Board: Urszula Lipińska-Witkowska and Ewelina Paprota for providing turkey blood. We would like to thank the employees of the Provincial Sanitary and Epidemiological Stations for collecting, describing and transferring the sera to the NIPH NIH NRI.

**OPEN ACCESS**

EDITED BY
Zbigniew Heleniak,
Medical University of Gdansk, Poland

REVIEWED BY
Iwona Boniecka,
Medical University of Warsaw, Poland
Eliza Wasilewska,
Medical University of Gdansk, Poland

*CORRESPONDENCE
Sylvia Małgorzewicz,
✉ sylvia.malgorzewicz@gumed.edu.pl

RECEIVED 16 July 2024

ACCEPTED 05 November 2024

PUBLISHED 14 November 2024

CITATION

Gofron K, Berezowski A, Gofron M,
Borówka M, Dziedzic M,
Kazimierzczak W, Kwiatkowski M,
Gofron M, Nowaczyk Z and
Małgorzewicz S (2024) *Akkermansia
muciniphila* - impact on the
cardiovascular risk, the intestine
inflammation and obesity.
Acta Biochim. Pol 71:13550.
doi: 10.3389/abp.2024.13550

COPYRIGHT

© 2024 Gofron, Berezowski, Gofron,
Borówka, Dziedzic, Kazimierzczak,
Kwiatkowski, Gofron, Nowaczyk and
Małgorzewicz. This is an open-access
article distributed under the terms of the
[Creative Commons Attribution License](#)
(CC BY). The use, distribution or
reproduction in other forums is
permitted, provided the original
author(s) and the copyright owner(s) are
credited and that the original
publication in this journal is cited, in
accordance with accepted academic
practice. No use, distribution or
reproduction is permitted which does
not comply with these terms.

Akkermansia muciniphila - impact on the cardiovascular risk, the intestine inflammation and obesity

Krzysztof Gofron¹, Adam Berezowski², Maksymilian Gofron³,
Małgorzata Borówka⁴, Michał Dziedzic¹,
Wojciech Kazimierzczak¹, Maciej Kwiatkowski⁵, Maria Gofron¹,
Zuzanna Nowaczyk¹ and Sylvia Małgorzewicz^{6*}

¹Students' Circle of Clinical Nutrition, Medical University of Gdańsk, Gdańsk, Poland, ²Department of Urology and Kidney Transplantation, Nikolay Pirogov Provincial Specialist Hospital, Łódź, Poland, ³Urology Department, Municipal Teaching Hospital in Częstochowa, Częstochowa, Poland, ⁴Department of Otolaryngology, Laryngological Oncology, Audiology and Phoniatrics, Medical University of Łódź, Łódź, Poland, ⁵Department of Orthopedics and Traumatology, Medical University of Warsaw, Warszawa, Poland, ⁶Department of Clinical Nutrition, Medical University of Gdańsk, Gdańsk, Poland

Contemporary scientific discussions are increasingly focusing on *Akkermansia muciniphila* due to its complex influence on intestinal physiology. This article provides a comprehensive analysis of the various effects *Akkermansia muciniphila* has on intestinal inflammation, while also exploring its potential associations with obesity and cardiovascular diseases. A systematic literature search was conducted using PubMed, Google Scholar, and ResearchGate with the following keywords: *Akkermansia muciniphila*, obesity, cardiovascular risk, and inflammatory bowel diseases. The aim of our mini-review was to examine the impact of *Akkermansia* bacteria on the intestines, cardiovascular system, and its relationship with obesity. Through a detailed review of current literature, the article seeks to elucidate the complex interactions of *Akkermansia muciniphila* within the human body, highlighting its potential contributions to health improvement and medical interventions. Research indicates that *Akkermansia muciniphila* positively correlates with maintaining intestinal health, modulating the cardiovascular system, and aiding in weight management. However, the number of studies available is small, and the effects of *Akkermansia muciniphila* on human health require further research.

KEYWORDS

Akkermansia muciniphila, cardiovascular diseases, inflammation, obesity, microbiota

Introduction

In recent years, the microbiome has emerged as a key player in influencing various aspects of human health. Among the myriad of microorganisms inhabiting the human gut, *Akkermansia muciniphila*, isolated from feces and named in 2004 by a group of Dutch scientists, led by professor Willem M. de Vos and PhD. Muriel Derrien has gained considerable attention for its potential role in shaping our overall wellbeing. This microscopic bacterium is particularly intriguing due to its distinctive ability to thrive on mucin, a key component of the protective mucus layer lining the intestines. As research continues to unveil the intricate relationship between *Akkermansia muciniphila* and human health, its profound impact on inflammation within the gastrointestinal tract and the broader implications for cardiovascular health have become subjects of intense scientific exploration (Derrien et al., 2010). This article delves into the multifaceted influence of *Akkermansia muciniphila* on the inflammatory processes within the intestines and its consequential effects on the obesity and cardiovascular system (Figure 1).

Due to the frequent occurrence of diseases such as obesity and cardiovascular diseases, it is important to prevent them through various options, as well as to support available treatments. Modulation of the gut microbiome may be one of the potential possibilities. Therefore, the aim of our mini review was to examine the impact of *Akkermansia* bacteria on the effects on the intestines, cardiovascular system and the relationship with the obesity.

Methods

A systematic literature search was conducted using the PubMed, Google Scholar and ResearchGate with the following keywords: *Akkermansia muciniphila*, obesity, cardiovascular risk, inflammatory bowel diseases. We found 24 trials included studies on humans and animals in 2007–2023 years regarding *A. muciniphila*'s impact on the intestines, cardiovascular risk and obesity. 11 of them were rejected because they did not meet the criteria for an observational or interventional study.

Characteristics of *Akkermansia muciniphila*

A. muciniphila is an anaerobic, gram-negative rod, representing the sole bacterium from the Verrucomicrobiales family in the human body (Derrien et al., 2010). It colonizes the mucosal layer of the crypts in the colon and rectum. Devoid of spore-forming capabilities and independent motility, this bacterium specializes in the degradation of mucins - glycoprotein conjugates produced by epithelial cells to ensure their proper functioning. Elevated production of these proteins, integral to mucosal integrity, correlates with an increased likelihood of colorectal cancer, particularly involving the MUC-1 protein (Nath and Mukherjee, 2014).

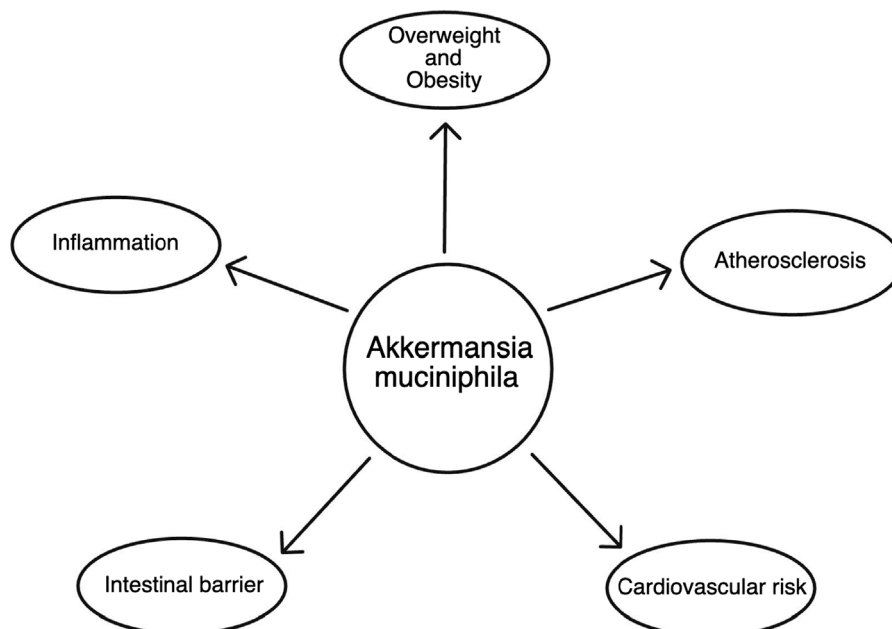


FIGURE 1
The scheme of *Akkermansia muciniphila* impact on health.

A. muciniphila makes its presence in the human gut as early as the first year of life, acquired from maternal milk, constituting approximately 1%–3% of the bacterial population (Collado et al., 2007). Its levels are diminished in individuals with overweight or obesity, and they exhibit an inverse correlation with age (Collado et al., 2007; Dao et al., 2016; Dao et al., 2019). Preliminary studies conducted on a group of nine individuals during Ramadan, simulating intermittent fasting conditions, unequivocally indicate a significant rise in the quantity of *A. muciniphila* in the gut during intermittent fasting (Dao et al., 2016; Dao et al., 2019; Mousavi et al., 2022). Crucially, research on a cohort of patients who underwent bariatric surgery did not confirm a similar increase in *A. muciniphila* levels despite the requisite dietary changes, suggesting that the surge in *A. muciniphila* is specific to intermittent fasting rather than a dietary shift (Dao et al., 2016; Dao et al., 2019). However, further studies on a larger sample size are essential for validation. Although there is no evidence supporting the influence of diet on *A. muciniphila* levels, other factors come into play such as metformin, a first-line medication for type 2 diabetes, which has been found to statistically positively correlate with *A. muciniphila* levels in the gut (Shin et al., 2014).

A. muciniphila is categorized into four phenotypic groups, AmI to AmIV (Becken et al., 2021). The most extensively studied strain and widely available as a probiotic is the pasteurized MucT strain, belonging to the AmI group. Despite initial assumptions of being strictly anaerobic, *A. muciniphila* has demonstrated adaptability to aerobic environments. Even low oxygen concentrations can promote its growth, as evidenced by studies on various strains of the bacterium. Strains belonging to AmII exhibit relatively good tolerance to aerobic conditions, with a survival rate of 60% after 24 h, whereas AmIV strains display very low survival at 0.01% under the same conditions after only 12 h (Becken et al., 2021). *A. muciniphila* also participates in the transformation of cobalamin precursors (Cbi) into cobalamin (vitamin B12), although it cannot synthesize it *de novo* (Mok et al., 2020). To date, there is no evidence supporting the possibility of human infection by *A. muciniphila* with research indicating the absence of negative effects associated with the administration of this bacteria (Depommier et al., 2019).

Cardiovascular impact of *Akkermansia muciniphila*

Akkermansia muciniphila significantly reduces local inflammation of the vascular endothelium, leading to atherosclerosis. An approximately 2.4-fold increase in the quantity of *A. muciniphila* results in a 72.59% decrease in C-reactive protein (CRP) levels, measured by a highly sensitive method (Shin et al., 2014). Studies on mice in 2016 demonstrated that in mice fed a high-fat diet,

administering live cultures of this bacterium reduces the adhesion of macrophages, crucial in atherosclerotic plaque formation to the endothelium by inhibiting the expression of tumor necrosis factor- α (TNF- α), MCP-1, and ICAM-1 (Li et al., 2016; Qu et al., 2021). Additionally, *A. muciniphila* significantly lowers soluble TNF receptor II (sTNFR II), reducing the severity of atherosclerosis. Importantly, the mechanism influencing atherosclerosis does not involve lowering lipid and sugar levels in circulating blood, nor does it affect the concentration of adiponectin, an anti-inflammatory substance (Li et al., 2016; Zhong et al., 2022). *A. muciniphila* plays a crucial role in weight control by reducing the absorption of lipids, achieved through maintaining the proper thickness of the intestinal mucosal layer, made possible by this bacterium's ability to adhere to the mucous membrane (Reunanen et al., 2015). These findings were observed exclusively in mice fed a high-fat diet, with studies on mice fed a normal diet showing no significant impact on these processes (Li et al., 2016).

Another significant cardioprotective action of *A. muciniphila* is counteracting arterial calcification, a component of atherosclerotic disease. This process involves the deposition of calcium salts in atherosclerotic plaques, leading to increased stiffness and, among other things, arterial hypertension. Short-chain fatty acids, propionate, and butyrate produced by human gut bacteria largely contribute to arterial calcification. Propionate reduces arterial calcification, while butyrate increases the intensity of this process (Zhong et al., 2022). Administering live *A. muciniphila* induces the production of, among other things, propionate, which has a protective effect on arterial calcification. No positive effects on the production of short-chain fatty acids were observed when pasteurized bacteria were administered (Yan et al., 2022).

Atrial fibrillation is the most common arrhythmic pathology in society, characterized by asynchronous atrial contractions often exceeding 150 beats per minute. This leads to blood stasis in these areas of the heart, which can result in clot formation and, ultimately, cause embolisms, with the most dangerous being those reaching the brain, often leading to a stroke. Atrial fibrillation is induced by factors such as cardiomyopathies, thyroid disorders, lung diseases, organ obesity, and less obvious factors, including a decrease in ambient temperature (Fustinoni et al., 2013). The latter also has a significant impact on the gut microbiota, including *A. muciniphila*, whose quantity is reduced at lower temperatures. It is *A. muciniphila* that exerts a significant influence on the frequency and duration of atrial fibrillation occurrences (Luo et al., 2022). Administering *A. muciniphila* cultures reduces the synthesis of trimethylamine (TMA), which is transformed into Trimethylamine N-oxide (TMAO). TMAO is responsible for recruiting M1 macrophages, which, by increasing inflammation associated with cytokine production, induce pyroptosis of cardiomyocytes in the heart atria (Luo et al., 2022). This relationship did not occur after administering pasteurized bacteria.

TABLE 1 Main studies dealing with the effects of *Akkermansia muciniphila* in cardiovascular diseases.

Study	Description	Design	Size	Patients	Length	Outcomes
Li et al. (2016)	Healthy	Animal study	—	Apoe ^{-/-} mice	8 weeks	<i>A. muciniphila</i> prevented inflammation induced by a Western diet both in the circulation and in local atherosclerotic plaques
Yan et al. (2022)	Healthy	Observational cohort study	92	Adults	—	<i>A. muciniphila</i> abundance negatively correlates with vascular calcification
Luo et al. (2022)	Healthy	Animal study	7	Rats	3 weeks	Oral supplementation of <i>A. muciniphila</i> mitigated pro-atrial fibrillation properties induced by cold exposure
Warmbrunn et al. (2024)	Healthy	Prospective cohort study	3,860	Adults	—	<i>A. Muciniphila</i> abundance is protective against ischemia heart disease

A. muciniphila demonstrates significant therapeutic value on a potentially large scale in the treatment of cardiovascular diseases. However, all existing studies clearly indicate that administering live bacteria is necessary to achieve a therapeutic effect. The impact on the aforementioned processes suggests the greatest potential application in Western diets, which largely rely on low-nutrient value products with high-saturated fat levels. The Western diet often leads to weight gain, resulting in overweight or even obesity and is the cause of systemic inflammation (Malesza et al., 2021; Warmbrunn et al., 2024). Both obesity and overweight contribute to the development of up to 50 different diseases, with a particular focus on the cardiovascular system. The application of live cultures of *A. muciniphila* reduces pyroptosis of cardiomyocytes, counteracting the development of atrial fibrillation, thereby reducing the risk of strokes (Christ et al., 2019). Moreover, *A. muciniphila* reduces the risk of ischemia heart disease in the African-Surinamese group playing a crucial role in cardiovascular diseases (Christ et al., 2019). Additionally, an increased abundance of this bacterium reduces endothelial inflammation, preventing the formation of atherosclerotic plaques and decreasing calcifications in already existing plaques. The reduction in both the quantity and hardness of atherosclerotic plaques contributes to a lower risk of unstable angina. Weight reduction, facilitated by *A. muciniphila*, also lowers average blood pressure, ultimately relieving the workload on the cardiac muscle counteracting the hypertrophy of the left ventricle and the development of aortic aneurysms. Further research involving a larger sample size is essential for the application of potential therapy. Main studies dealing with the effects of *A. muciniphila* in cardiovascular diseases are presented in Table 1.

Impact of *Akkermansia muciniphila* on the intestine

The main mechanism of action of *A. muciniphila* in the body is its involvement in the formation of the intestinal mucosal layer,

where it resides. A healthy mucosal layer is responsible, among other things, for the efficient absorption of nutrients from food and the human immune response. A deficiency of *A. muciniphila* in the gut microbiota can lead to severe pathological conditions, such as inflammatory bowel diseases, a compromised host immune response, invasive microorganisms, or increased susceptibility to the detrimental effects of toxins on the body.

Inflammatory bowel disease is a term used to describe a group of chronic intestinal inflammations. The two main types are Crohn’s disease (CD) and ulcerative colitis (UC). Despite many similarities, these diseases differ in several aspects. CD can affect any part of the digestive system, while UC primarily affects the large intestine. Another difference lies in the appearance of intestinal inflammation; CD creates skip lesions, whereas UC inflammation spreads continuously. It has been demonstrated that *A. muciniphila* supplementation significantly reduces symptoms of dextran sulfate-induced acute colitis and that its quantity is reduced in inflammatory bowel disease (Qu et al., 2021). It is crucial to minimize intestinal inflammation as much as possible, as inflammatory bowel diseases significantly increase the likelihood of developing colorectal cancer (Yao et al., 2019), (see Table 2).

The first mechanism through which chronic inflammatory bowel symptoms are alleviated (reducing the severity of intestinal inflammation, i.e., depth and extent at the histological level, as well as mitigating weight loss associated with reduced nutrient absorption) is the activation of NLRP3, which exhibits anti-inflammatory and immune actions (Qu et al., 2021; Guo et al., 2020). NLRP3 influences the production of IL-18, which plays a crucial role in creating the protective barrier of the intestine (Guo et al., 2020; Chiang et al., 2022). IL-18 regulates the gut microbiota, reducing the development of invasive colonies. Studies on mice showed significantly reduced mucin production from goblet cells in mice with decreased IL-18 levels compared to mice with normal levels (Chiang et al., 2022), demonstrating a positive correlation between IL-18 and mucin levels, whose breakdown fulfills the carbon and nitrogen needs of *A. muciniphila* (Derrien et al., 2010; Collado et al., 2007). Notably, there is an increase in the levels of Muc-2 and Muc-3 proteins.

TABLE 2 The impact of the *Akkermansia muciniphila* on intestines.

Study	Disease	Design	Size	Patients	Length	Outcomes
Qu et al. (2021)	Healthy	Animal study	10	Dextran Sulfate Sodium - fed mice	18 days	Oral administration of <i>A. muciniphila</i> significantly ameliorated the symptoms in dextran sulfate sodium (DSS)-induced acute colitis
Collado et al. (2007)	Healthy	Observatory study	249	Infants and Adults	—	<i>A. muciniphila</i> is correlated with normal mucosa development
Liu et al. (2022)	Healthy	Animal study	30	Dextran Sulfate Sodium - fed mice	2 weeks	<i>A. muciniphila</i> -based mechanisms play a fundamental role in driving the divergent induction of suppressive ROR γ t ⁺ Treg cells in the gut-specific microenvironment

Another mechanism influenced by *A. muciniphila* is the activation of TLR4 receptors, whose levels are increased in patients with both Crohn's disease and ulcerative colitis (Liu et al., 2022; Hayashi and Nakase, 2022). The positive function of TLR4 in the body is the recognition of PAMPs and DAMPs, responsible for the human immune response in practice, while negatively influencing an increased likelihood of developing inflammatory bowel diseases (Liu et al., 2022; Moresco et al., 2011). The TLR-4-dependent anti-inflammatory response mainly depends on ROR γ t⁺ regulatory T lymphocytes, whose levels are reduced in the intestine during inflammatory bowel diseases (Liu et al., 2022). *A. muciniphila* can also activate TLR-2, but about a tenfold increase in the number of bacteria is required for this, and the activation of this receptor does not significantly impact the immune response stimulated by TLR receptors (Becken et al., 2021). TLR-2 and TLR-4 receptors are much more activated by phenotypic groups AmII and AmIV than by the AmI group, to which the MucT strain belongs.

An additional protective effect of *A. muciniphila* on the intestine is the inhibition of the expression of TNF-alpha, MCP-1, and ICAM-1, which, similar to the vascular endothelium, acts anti-inflammatory and inhibits the action of macrophages.

The association with obesity

Obesity and overweight are among the primary lifestyle diseases, affecting nearly one-third of the global population every day. Both disorders lead to various pathological conditions, predisposing individuals to diseases in almost every system, including the cardiovascular, musculoskeletal, respiratory, hormonal, and others. Cardiovascular diseases, responsible for approximately half of global deaths, prove to be particularly deadly. Although metabolic diseases result from various factors, such as genetic predispositions, gut microbiome, hormonal system, diet, upbringing during childhood, and the culture in which a person was raised, the most significant impact on these disorders still comes from a person's diet. The hope for treatment lies in many

therapies, both non-pharmacological and pharmacological, but the key to success is their simultaneous application (Cao et al., 2023).

Therapy typically begins with non-pharmacological treatment focusing on diet modification and increased physical activity. This is the healthiest way to reduce body weight but is often ineffective due to individuals' habits and accompanying health conditions that limit their ability to move.

When non-pharmacological treatment proves ineffective, the next steps involve introducing medications to assist in weight loss. These medications are usually chosen with attention to coexisting diseases. Examples include glucagon-like peptide-1 (GLP-1) analogs used in type II diabetes patients or thyroxine (T4) analogs in the case of hypothyroidism both proving to reduce weight while treating the underlying cause.

Let's focus on pharmacological treatment by influencing the gut microbiome. A promising and therapeutically valuable approach is the therapy using *A. muciniphila* bacteria. A widely available probiotic containing pasteurized *A. muciniphila* bacteria, specifically the MucT strain of the AmI group, has emerged worldwide. Oral therapy with *A. muciniphila* significantly reduces serum glucose and triglyceride levels, as well as tissue insulin resistance (Dao et al., 2016; Depommier et al., 2019). The reduction in serum glucose and triglyceride levels is likely associated with improved liver function, as indicated by decreases in aspartate aminotransferase (AST) and gamma-glutamyl transferase (GGT) levels, used as markers of liver dysfunction (Dao et al., 2016; Xu et al., 2023). An increase in *A. muciniphila* levels in patients is linked to a decrease in the average volume of adipocytes, making these individuals metabolically healthier (Dao et al., 2016). The adoption of a healthy diet by patients promotes and facilitates weight loss in individuals with higher levels of *A. muciniphila* (Dao et al., 2016; Cao et al., 2023). Results indicating no loss of muscle mass in patients who lost weight and had a higher quantity of *A. muciniphila* compared to those with a lower quantity of this bacterium prove to be very valuable. The studies also demonstrated the absence of the rebound effect in patients (Cao et al., 2023). The reduction in insulin resistance due to *A. muciniphila* lowers the risk of developing type 2 diabetes and

TABLE 3 Main studies dealing with the effects of *Akkermansia muciniphila* in bodyweight management.

Study	Disease	Design	Size	Patients	Length	Outcomes
Dao et al. (2019)	Obesity	Non-randomised prospective study	65	Adults	12 months	<i>A. muciniphila</i> abundance does not affect glucose tolerance and insulin sensitivity in patients after gastric bypass surgery
Shin NR (2014)	Healthy	Animal study	24	HFD-fed mice	6 weeks	<i>A. muciniphila</i> administration reduce adipose tissue inflammation
Depommier et al. (2019)	Overweight and obesity	Randomised double blind study	32	Adults	3 months	Increased <i>A. muciniphila</i> abundance negatively correlates with insulin resistance, inflammation markers and liver disfunction markers
Dao (2016)	Overweight and obesity	Randomised control study	49	Adults	3 months	Increased <i>A. muciniphila</i> abundance positively correlates with insulin sensitivity
Cao et al. (2023)	Obesity	Randomised double blind study	37	Adults	4 months	Increased <i>A. muciniphila</i> abundance positively correlates with weight loss

reduces drowsiness and fatigue. Additionally, it reduces hunger attacks leading to weight gain. It also decreases the activity of dipeptidyl peptidase-IV (DPP-IV) (Depommier et al., 2019), which is responsible for the breakdown of glucagon-like peptide 1 (GLP-1), responsible for inhibiting hunger and intensifying the feeling of fullness. Due to this many positive effects it leads to the assumption that therapies based on *A. Muciniphila* may become world spread. The studied focused on association between *A. muciniphila* and obesity are presented in Table 3.

Discussion and conclusion

The continuous rise in diseases related to overweight and obesity, including cardiovascular diseases, highlights the need for an effective and safe method to address this issue. Diseases associated with excess body weight are closely linked to a systemic inflammatory state triggered by adipocytes and by an imbalance in gut microbiota. It should be noted that while inflammatory bowel diseases (IBD) and metabolic diseases may seem etiologically distinct, treatment for IBD may increase the risk of metabolic conditions, including obesity. Furthermore, inflammation is a common factor in both, heightening the risk of further complications. *Akkermansia muciniphila* meets the criteria for potential treatment, as there is no evidence of human infection by this bacterium, and its use has shown promising results in promoting safe and sustainable weight loss, alongside a reduction in systemic inflammation. There are several reasons to believe that *A. muciniphila* therapy could have a positive impact on cardiovascular diseases, particularly atherosclerosis, which is linked to endothelial inflammation. Additionally, increasing the levels of *A. muciniphila* in the gut appears to alleviate the negative symptoms of chronic inflammatory bowel diseases, such as ulcerative colitis (UC) and Crohn’s disease (CD).

Akkermansia muciniphila has demonstrated potential for comprehensive treatment of these diseases. Given the rising global prevalence of both inflammatory bowel diseases and metabolic disorders, this is a particularly important issue. Moreover, treatment with *Akkermansia muciniphila* is relatively affordable. However, the number of studies exploring the association between *A. muciniphila* and obesity, cardiovascular risk, and intestinal health is limited, and further research is needed to fully understand its effects on human health.

Future direction

The fundamental issue that needs to be addressed is the assessment of the safety of consuming live cultures of *Akkermansia muciniphila*. So far, research suggests a much broader potential for *A. muciniphila* in this form to achieve positive cardiovascular effects. It is essential to direct further research towards the circulatory system because, despite many indications of its positive impact, there is still a lack of large-scale studies involving a greater number of individuals to justify the implementation of such therapy.

Author contributions

Conceptualization: KG, SM, and AB. Methodology: AB and MkG. Software: WK and MK. Check: SM, MB, and MrG. Formal analysis: KG, SM, and ZN. Investigation: MB and WK. Resources: MkG and MrG. Data curation: AB, WK, and MK. Writing - rough preparation: KG and MD. Writing - review and editing: KG and MrG. Visualization: SM, MB, and MD. Supervision: KG, MkG, MK, and ZN. Project administration: KG, MD, and ZN. All authors contributed to the article and approved the submitted version.

Funding

The author(s) declare that financial support was received for the research, authorship, and/or publication of this article. This research was funded by Medical University of Gdansk.

References

- Becken, B., Davey, L., Middleton, D. R., Mueller, K. D., Sharma, A., Holmes, Z. C., et al. (2021). Genotypic and phenotypic diversity among human isolates of *Akkermansia muciniphila*. *mBio* 12 (3), 00478–21. doi:10.1128/mBio.00478-21
- Cao, M.-Z., Wei, C. H., Wen, M. C., Song, Y., Srivastava, K., Yang, N., et al. (2023). Clinical efficacy of weight loss herbal intervention therapy and lifestyle modifications on obesity and its association with distinct gut microbiome: a randomized double-blind phase 2 study. *Front. Endocrinol.* 14, 1054674. doi:10.3389/fendo.2023.1054674
- Chiang, H.-Y., Lu, H. H., Sudhakar, J. N., Chen, Y. W., Shih, N. S., Weng, Y. T., et al. (2022). IL-22 initiates an IL-18-dependent epithelial response circuit to enforce intestinal host defence. *Nat. Commun.* 13 (1), 874. doi:10.1038/s41467-022-28478-3
- Christ, A., Lauterbach, M., and Latz, E. (2019). 'Western diet and the immune system: An inflammatory connection. *Immun.* 51 (5), 794–811. doi:10.1016/j.immuni.2019.09.020
- Collado, M. C., Derrien, M., Isolauri, E., de Vos, W. M., and Salminen, S. (2007). 'Intestinal integrity and *Akkermansia muciniphila*, a mucin-degrading member of the intestinal microbiota present in infants, adults, and the elderly. *Appl. Environ. Microbiol.* 73 (23), 7767–7770. doi:10.1128/aem.01477-07
- Dao, M. C., Belda, E., Prifti, E., Everard, A., Kayser, B. D., Bouillot, J. L., et al. (2019). *Akkermansia muciniphila* abundance is lower in severe obesity, but its increased level after bariatric surgery is not associated with metabolic health improvement. *Am. J. Physiology-Endocrinology Metabolism* 317 (3), E446–E459. doi:10.1152/ajpendo.00140.2019
- Dao, M. C., Everard, A., Aron-Wisniewsky, J., Sokolowska, N., Prifti, E., Verger, E. O., et al. (2016). *Akkermansia muciniphila* and improved metabolic health during a dietary intervention in obesity: Relationship with gut microbiome richness and ecology. *Gut* 65 (3), 426–436. doi:10.1136/gutjnl-2014-308778
- Depommier, C., Everard, A., Druart, C., Plovier, H., Van Hul, M., Vieira-Silva, S., et al. (2019). 'Supplementation with *Akkermansia muciniphila* in overweight and obese human volunteers: a proof-of-concept exploratory study. *Nat. Med.* 25 (7), 1096–1103. doi:10.1038/s41591-019-0495-2
- Derrien, M., van Passel, M. W., van de Bovenkamp, J. H., Schipper, R., de Vos, W., and Dekker, J. (2010). 'Mucin-bacterial interactions in the human oral cavity and digestive tract. *Gut Microbes* 1 (4), 254–268. doi:10.4161/gmic.1.4.12778
- Fustinoni, O., Saposnik, G., Esnaola y Rojas, M. M., Lakkis, S. G., and Sposato, L. A. (2013). Higher frequency of atrial fibrillation linked to colder seasons and air temperature on the day of ischemic stroke onset. *J. Stroke Cerebrovasc. Dis.* 22 (4), 476–481. doi:10.1016/j.jstrokecerebrovasdis.2013.03.009
- Guo, H., Gibson, S. A., and Ting, J. P. (2020). Gut microbiota, NLR proteins, and intestinal homeostasis. *J. Exp. Med.* 217 (10), e20181832. doi:10.1084/jem.20181832
- Hayashi, Y., and Nakase, H. (2022). The molecular mechanisms of intestinal inflammation and fibrosis in Crohn's Disease. *Front. Physiology* 13, 845078. doi:10.3389/fphys.2022.845078
- Li, J., Lin, S., Vanhoutte, P. M., Woo, C. W., and Xu, A. (2016). *Akkermansia muciniphila* protects against atherosclerosis by preventing metabolic Endotoxemia-Induced inflammation in APOE^{-/-} mice. *Circ.* 133 (24), 2434–2446. doi:10.1161/circulationaha.115.019645
- Liu, Y., Yang, M., Tang, L., Wang, F., Huang, S., Liu, S., et al. (2022). TLR4 regulates RORγt+ regulatory T-cell responses and susceptibility to colon inflammation through interaction with *Akkermansia muciniphila*. *Microbiome* 10 (1), 98. doi:10.1186/s40168-022-01296-x

Conflict of interest

The authors declare that the research was conducted in the absence of any commercial or financial relationships that could be construed as a potential conflict of interest.

- Luo, Y., Zhang, Y., Han, X., Yuan, Y., Zhou, Y., Gao, Y., et al. (2022). *Akkermansia muciniphila* prevents cold-related atrial fibrillation in rats by modulation of TMAO induced cardiac pyroptosis. *EBioMedicine* 82, 104087. doi:10.1016/j.ebiom.2022.104087
- Malesza, I. J., Malesza, M., Walkowiak, J., Mussin, N., Walkowiak, D., Aringazina, R., et al. (2021). High-Fat, western-style diet, systemic inflammation, and gut microbiota: a narrative review. *Cells* 10 (11), 3164. doi:10.3390/cells10113164
- Mok, K. C., Sokolovskaya, O. M., Nicolas, A. M., Hallberg, Z. F., Deutschbauer, A., Carlson, H. K., et al. (2020). Identification of a novel cobamide remodeling enzyme in the beneficial human gut bacterium *Akkermansia muciniphila*. *mBio* 11 (6), e02507–e02520. doi:10.1128/mbio.02507-20
- Moresco, E. M. Y., LaVine, D., and Beutler, B. (2011). 'Toll-like receptors. *Curr. Biol.* 21 (13), R488–R493. doi:10.1016/j.cub.2011.05.039
- Mousavi, S. N., Rayyani, E., Heshmati, J., Tavasolian, R., and Rahimlou, M. (2022). Effects of Ramadan and non-Ramadan Intermittent fasting on gut microbiome. *Front. Nutr.* 9, 860575. doi:10.3389/fnut.2022.860575
- Nath, S., and Mukherjee, P. (2014). MUC1: a multifaceted oncoprotein with a key role in cancer progression. *Trends Mol. Med.* 20 (6), 332–342. doi:10.1016/j.molmed.2014.02.007
- Qu, S., Fan, L., Qi, Y., Xu, C., Hu, Y., Chen, S., et al. (2021). *Akkermansia muciniphila* alleviates dextran sulfate sodium (DSS)-induced acute colitis by NLRP3 activation. *Microbiol. Spectr.* 9 (2), e0073021. doi:10.1128/spectrum.00730-21
- Reunanen, J., Kainulainen, V., Huuskonen, L., Ottman, N., Belzer, C., Huhtinen, H., et al. (2015). *Akkermansia muciniphila* adheres to enterocytes and strengthens the integrity of the epithelial cell layer. *Appl. Environ. Microbiol.* 81 (11), 3655–3662. doi:10.1128/aem.04050-14
- Shin, N.-R., Lee, J. C., Lee, H. Y., Kim, M. S., Whon, T. W., Lee, M. S., et al. (2014). An increase in the *Akkermansia* spp. population induced by metformin treatment improves glucose homeostasis in diet-induced obese mice. *Gut* 63 (5), 727–735. doi:10.1136/gutjnl-2012-303839
- Warmbrunn, M. V., Boulund, U., Aron-Wisniewsky, J., de Goffau, M. C., Abeka, R. E., Davids, M., et al. (2024). Networks of gut bacteria relate to cardiovascular disease in a multi-ethnic population: the HELIUS study. *Cardiovasc. Res.* 120, 372–384. doi:10.1093/cvr/cvae018
- Xu, Y., Duan, J., Wang, D., Liu, J., Chen, X., Qin, X. Y., et al. (2023). *Akkermansia muciniphila* alleviates persistent inflammation, immunosuppression, and catabolism syndrome in mice. *Metab.* 13 (2), 194. doi:10.3390/metabo13020194
- Yan, J., Pan, Y., Shao, W., Wang, C., Wang, R., He, Y., et al. (2022). Beneficial effect of the short-chain fatty acid propionate on vascular calcification through intestinal microbiota remodelling. *Microbiome* 10 (1), 195. doi:10.1186/s40168-022-01390-0
- Yao, D., Dong, M., Dai, C., and Wu, S. (2019). Inflammation and inflammatory cytokine contribute to the initiation and development of ulcerative colitis and its associated cancer. *Inflamm. Bowel Dis.* 25 (10), 1595–1602. doi:10.1093/ibd/izz149
- Zhong, H., Yu, H., Chen, J., Mok, S. W. F., Tan, X., Zhao, B., et al. (2022). 'The short-chain fatty acid butyrate accelerates vascular calcification via regulation of histone deacetylases and NF-κB signaling. *Vasc. Pharmacol.* 146, 107096. doi:10.1016/j.vph.2022.107096

Relationship between chemical industrial environment and allergic skin diseases

Shaohua Fu¹, Minli Gong¹ and Guisheng Xing²✉

¹Clinical Laboratory, Ningbo Zhenhai People's Hospital (Ningbo No.7 Hospital), Ningbo, Zhejiang Province, China; ²Department of Medical, Ningbo Zhenhai People's Hospital (Ningbo No.7 Hospital), Ningbo, Zhejiang Province, China

Objective: This study is an exploration of the relationship between chemical industrial environment and allergic skin diseases. **Methods:** In this retrospective analysis, 200 patients with allergic skin diseases who worked or lived in a chemical industrial zone and were admitted in our hospital between January 2018 and January 2020 were enrolled as Group A. Besides, 500 patients with allergic skin disease who lived in Zhenhai New District, five kilometers away from the chemical radiation zone, were selected as Group B. The specific immunoglobulin E (IgE) levels were determined by Western blotting. The allergen positivity, as well as allergen positivity between different age, sex and body mass index (BMI) were compared between the two groups. The positive food-specific allergen IgE antibody (slgE) and positive inhalational slgE were compared between the two groups. **Results:** The positive rate of total IgE and inhalational slgE in Group A was higher than that in Group B ($P < 0.05$), while there was no significant difference in positive rate in food slgE between the two groups ($P > 0.05$). In Group A, the differences in positive rates of total IgE, food-induced slgE and inhalational slgE were not significant between patients with different ages, sexes and BMI ($P > 0.05$). There was no significant difference between the two groups in slgE positive rates of wheat, mango, soybean/peanut/cashew nut combination, limb/beef combination, crab/shrimp/fish combination, milk and egg white ($P > 0.05$). The positive rates of inhalational slgE in tree combination and dust mites/household dust mites combination in Group A were higher than those in Group B ($P < 0.05$), but had no significant difference between the two groups in the positive rates of inhalational slgE in *Humulus japonicus*, mold combination 1, cockroach, cat/dog hair combination, and ragweed/artemisia combination ($P > 0.05$). **Conclusion:** Chemical industrial environment is closely associated with allergic dermatosis, and the positive rate of total IgE and inhalational slgE increases significantly in patients living there.

Keywords: Chemical industrial environment, slgE, skin disease, allergic dermatosis, relevancy

Received: 10 May, 2023; **revised:** 07 October, 2023; **accepted:** 22 October, 2023; **available on-line:** 03 December, 2023

✉ e-mail: xingguisheng012@163.com

Acknowledgements of Financial Support: This study was supported by Zhenhai District Science and Technology Bureau Medical Science and Technology Plan Project (2017S101).

Abbreviations: IgE, specific immunoglobulin E; SPT, skin prick test

INTRODUCTION

Allergic diseases are frequent diseases, which are mediated by the production of specific immunoglobulin E (IgE) antibody. They seriously impair health and have become a major public health issue (Tramper-Stranders *et al.*, 2021). Allergic diseases can occur at all ages and are primarily caused by the combined effects of environmental factors and genetic factors (Golebski *et al.*, 2020). In recent years, with the change of human dietary structure, the increase of antigenic substances, the aggravation of environmental pollution and the improvement of industrialization, the incidence of allergic diseases has continued to increase (Zhang *et al.*, 2021). With the continuous deterioration of environmental pollution, Zhenhai, as one of the chemical industrial zones, has particularly serious air pollution, and the occurrence of allergic diseases has also increased in this area (Lau *et al.*, 2021). It has been reported that air pollution in residential environment is significantly correlated with the high incidence of allergic diseases (Larson *et al.*, 2020).

At present, serum-specific allergen IgE assay (sIg) and skin prick test (SPT) are commonly used for detecting allergens (Du Toit *et al.*, 2018). However, there are rarely reports on chemical industrial environment and allergic skin diseases, and most of which analyzed the allergens in patients with allergic skin diseases (Eljaszewicz *et al.*, 2021). But the differences in allergic skin diseases between people in chemical and non-chemical areas have not been reported yet. This study explored the relationship between chemical industry environment and allergic skin diseases, aiming to provide reference for the prevention of allergic skin diseases.

MATERIALS AND METHODS

General Information

This is a retrospective analysis. A total of 200 patients with allergic skin diseases, who worked or lived in the chemical industry zone and were admitted to the hospital from January 2018 to January 2020, were selected as Group A. Besides, 500 patients with allergic skin diseases, who lived in Zhenhai New District, five kilometers away from the chemical radiation zone, were selected as Group B. This study was approved by the ethic committee of Ningbo Zhenhai People's Hospital.

Inclusion criteria (Eljaszewicz *et al.*, 2021): (1) Patients were diagnosed by examinations based on the criteria of Clinical Dermatology. Allergies occurred on the skin of the body, most of which were located on the head and face. The patient's skin lesions turned white and ap-

Table 1. Comparison of clinical data of two groups

Clinical data	Group A (n=200)	Group B (n=500)	t/χ_2	r
Sex				
Male	124	287		
Female	76	213	.	.
Age (years, $\bar{x}\pm s$)	45.62 \pm 9.83	46.51 \pm 8.78	1.170	0.242
Body mass index (kg/m ² , $\bar{x}\pm s$)	23.24 \pm 1.97	22.95 \pm 1.89	1.812	0.071
Season of onset				
Spring & summer	135	342		
Autumn & winter	65	158	.	.
Disease type				
Urticaria	112	269		
Atopic dermatitis	88	231	.	.

peared as typical white spots, most of which were the size of nails and coins. The lesion shapes were round, oval or irregular, and expanded or merged into a large area with different shapes. Another typical leukoplakia was a strip or cord of discoloration along the nerve, with knife-cut edges. The histopathological features: the epidermis obviously lacked melanocytes and melanin granules, and the basal layer lacked dopa-positive melanocytes. (2) Patients had complete clinical data. (3) Patients received blood sampling after admission.

Exclusion criteria: (1) Patients accompanied by other allergic diseases that might affect the research. (2) Patients had recently taken medications such as glucocorticoids or immunosuppressants. (3) Patients were affected by serious abnormalities of heart, lung, liver or kidney.

Methods

Collection of serum specimens

Peripheral venous blood (5 mL) was collected from all patients, stood for 30 min and was centrifuged for 12 min (centrifugation radius 10.5 cm, 3000 r/min). The collected serum was stored at -70°C until testing.

Measurement of IgE

The reagent strips were put in an incubator box, added with diluted washing solution thickly and put on a mixer to fully wet for 5 min. After the reagent strips were dried, 1 ml of serum specimens were added and incubated in the mixer for 45 min. The above procedures were repeated 5 times. Thereafter, anti-human IgE antibody (Hangzhou Aibo Biotechnology Co., LTD.) was added, incubated for 45 min, and then rinsed repeatedly 5 times. The enzyme conjugate (Hangzhou Aibo Biotechnology Co., LTD.) was incubated in the mixer for 20 min, and then rinsed 5 times. The substrate was added and incubated in the mixer for 20 min. The strips were rinsed under running water, dried and scanned by an allergen scanner (Mediwiss Medical Diagnostics GMBH).

Detection of allergens

The detected allergens included total IgE and allergen-specific IgE antibodies (sIgE). The sIgE included food allergens and inhalational allergens. Food allergens contained wheat, mango, soy/peanut/cashew combination, limb/beef combination, crab/shrimp/fish combination, milk and egg white. Inhalational allergens included tree combination (Willosa/Ulmus/Quercus/Parasitae/Popu-

Table 2. Comparison of allergen positive cases between two groups (%)

Group	Number of cases	Total IgE immunoglobulin E	Food-induced	Inhalational
Group A	200	161 (80.50)	42 (21.00)	113 (56.50)
Group B	500	307 (61.40)	87 (17.40)	204 (40.80)
χ_2		23.520	1.232	14.212
P		<0.001	0.267	<0.001

Table 3. Comparison of allergen positive rates between patients at different ages in Group A (%)

Age	Number of cases	Total IgE	Food-induced immunoglobulin	Inhalational immunoglobulin
			E	E
>45 Years old	106	87 (82.07)	24 (22.64)	62 (58.49)
≤45 Years old	94	74 (78.72)	18 (19.15)	51 (54.26)
χ_2		0.357	0.366	0.364
<i>P</i>		0.550	0.545	0.547

Table 4. Comparison of allergen positive rates between males and females in Group A (%)

Gender	Number of cases	Total IgE	Food-induced immunoglobulin	Inhalational immunoglobulin
			E	E
Male	124	97 (78.23)	28 (22.58)	72 (58.06)
Female	76	64 (84.21)	14 (18.42)	41 (53.95)
χ_2		1.075	0.491	0.325
<i>P</i>		0.300	0.483	0.569

lus deltooides), *Humulus scandens*, mold combination 1 (*Penicillium persicillium*/*Aspergillus fumigatus*/*Mycospora alternaria*), cockroach, cat/dog hair combination, ragweed/*Artemisia*, and dust mite/house dust mite combination.

Observation of Indicators

(1) Allergen positive cases in the two groups were observed. (2) In Group A, allergen positive cases with different ages, different sexes and different body mass index (BMI) were observed. (3) The positive cases of food-induced sIgE and inhalational sIgE were observed in the two groups.

Statistical Processing

SPSS 26.0 software was applied for data processing. Measurement data were represented by (mean \pm standard deviation), and the analysis method was independent samples *t*-test. Enumeration data were represented by *n* (rate), and the analysis method was χ_2 test. Two-tailed *P*<0.05 was considered as statistically significant.

RESULTS

Clinical data

There was no statistical significance between the two groups in sex, age, BMI, seasons of onset and disease types (*P*>0.05); see Table 1.

Comparison of allergen positive cases between two groups

The positive rates of total IgE and inhalational sIgE in Group A were higher than those in Group B (*P*<0.05).

While there was no significant difference in the positive rate of food sIgE between the two groups (*P*>0.05); see Table 2.

Comparison of allergen positive rates between patients at different ages in Group A

There was no significant difference in the positive rates of total IgE, food-induced sIgE and inhalational sIgE between patients of different ages in Group A (*P*>0.05); see Table 3.

Comparison of allergen positive rates between males and females in Group A

There were no significant differences in the positive rates of total IgE, food-induced sIgE and inhalational sIgE between males and females in Group A (*P*>0.05); see Table 4.

Comparison of allergen positive rates between patients with different BMI in Group A

There was no significant difference in the positive rates of total IgE, food-induced sIgE and inhalational sIgE between patients with different BMI in Group A (*P*>0.05); see Table 5.

Comparison of food-induced sIgE positive cases between the two groups

There was no significant difference between the two groups in sIgE positive rates of wheat, mango, soybean/peanut/cashew nut combination, lamb/beef combination, crab/shrimp/fish combination, milk and egg white (*P*>0.05); see Table 6.

Table 5. Comparison of allergen positive rates between patients with BMI in Group A (%)

BMI	Number of cases	Total IgE	Food-induced	Inhalational immunoglobulin
			slgE	E
>24 kg/m ²	81	67 (82.72)	19 (23.46)	47 (58.02)
≤24 kg/m ²	119	94 (78.99)	23 (19.32)	66 (55.46)
χ ₂		0.426	0.495	0.129
P		0.514	0.482	0.720

BMI, body mass index.

Table 6. Comparison of food-induced slgE positivity between the two groups (%)

Group	Number of cases	Wheat	Mango	Soybean/peanut/cashew nut	Sheep/beef	Crab/shrimp/fish	Milk	Egg white
Group A	200	4 (2.00)	5 (2.50)	12 (6.00)	8 (4.00)	7 (3.50)	2 (1.00)	4 (2.00)
Group B	500	9 (1.8)	12 (2.40)	23 (4.60)	19 (3.20)	12 (2.40)	6 (1.20)	6 (1.20)
χ ₂		0.018	0.038	0.590	0.015	0.655	0.029	0.205
P		0.895	0.846	0.443	0.901	0.419	0.866	0.650

Table 7 Comparison of positive inhalational- slgE between two groups (%)

Group	Number of cases	Tree combination	Humulus scandens	Mold combination 1	Cockroach	Cat/dog dander combination	Ragweed/Artemisia combination	Ragweed/Artemisia combination
Group A	200	10 (5.00)	1 (0.50)	2 (1.00)	1 (0.50)	1 (0.50)	3 (1.50)	95 (47.50)
Group B	500	6 (1.20)	8 (1.60)	15 (3.00)	10 (2.00)	9 (1.80)	19 (3.80)	137 (27.40)
χ ₂		7.613	0.633	1.641	1.222	0.916	2.483	26.047
P		0.006	0.426	0.200	0.269	0.339	0.115	<0.001

Comparison of inhalational-slgE positive cases between the two groups

The positive rates of inhalational-sIgE in tree combination and dust mites/household dust mites' combination in Group A were higher than those in Group B ($P<0.05$). There was no significant difference between the two groups in sIgE positive rates of *Humulus japonicus*, mold combination 1, cockroach, cat/dog hair combination, and ragweed/artemisia combination ($P>0.05$); see Table 7.

DISCUSSION

Allergic dermatosis is one of the most common and complex skin diseases with a large number of pathogenic causes and types. Allergens can enter the human body through multiple ways. The inhalational or ingested allergens can combine with antibodies to produce sensitization, form an immune complex to stimulate mast

cells to degranulate and release transmitters such as leukotriene and histamine, thus inducing rapid allergic reactions (Venter *et al.*, 2022; Orengo *et al.*, 2018; Hereford *et al.*, 2021). Common allergic skin diseases include atopic dermatitis, eczema, urticaria and Henoch-Schönlein purpura. Atopic dermatitis refers to skin conditions such as peeling, wind, itching and redness caused by exposure to certain allergens. The most common causes of atopic dermatitis include fungal allergies, chemical fiber materials, rubber shoes, detergents, fertilizers, pesticides, air pollution, dust, pollen, insects, mites, animal fur, food, etc. Atopic dermatitis is usually caused by an allergy to a substance and can gradually disappear when the allergen is removed (Güngör *et al.*, 2019). Eczema is a common allergic skin disease that can occur in any part of the body. The specific cause of eczema has not been completely clarified. It is considered that allergic constitution may be the main cause of the disease (Holl *et al.*, 2020). Clinical surveys have shown that the increasing incidence of eczema may be related to continuous mental stress,

accelerated pace of life, poor management of wastes, environmental pollution and the abuse of chemical products (Yang *et al.*, 2020). Urticaria is a common skin disease with acute and chronic types. The causes of urticaria are various and complex, including parasites, bacteria, sunlight, drugs, nettle, mushrooms, pollen, animal feathers, crab, shrimp, fish, etc. (Fang *et al.*, 2021; Xiang *et al.*, 2021). Due to the extensive food intake and contact with objects in daily life, it is often difficult to identify the fundamental cause of allergies, which leads to recurrent urticaria (Hoof *et al.*, 2020). Henoch-Schönlein purpura is usually considered to be caused by antigenic substances entering the body, reacting with antibodies in the body of the patient, and depositing in the blood vessel wall and causing vascular damage. It is mainly a skin and mucosal lesion caused by allergic inflammation of blood vessels, with petechia or bruise as the main clinical manifestations (Ünal, 2020). The etiology of allergic purpura remains unspecified, and it is considered to be related to immune factors. At the same time, it can be induced by insect bites, drug pollen allergy, viral and bacterial infections, and exotic protein foods such as crab, shrimp and fish (Hanif *et al.*, 2019; Beaulieu *et al.*, 2022).

As a coastal chemical industrial area, Zhenhai provides local people with a lot of seafood. Therefore, total IgE, inhalational allergens and food-induced allergens were selected for detection in this study. We intended to understand the influence of the chemical industrial environment on allergic skin diseases through detecting allergenic factors. At present, the detection of allergens is usually by serum specific allergen IgE and skin prick. Skin prick test is to drop a small amount of highly purified allergen liquid on the forearm of the patient, and then to gently puncture the skin surface.

Allergic response is showing as red and swollen masses similar to mosquito bites and itching reaction at the spot within 15 minutes, and the skin color may also change. However, the skin prick test is an invasive test, which may cause severe systemic reactions, and accidents may occur in patients with severe allergies in acute phase. Serum specific allergen IgE detection, as an *in vitro* test, is safe, painless and non-irritating. Serum specific allergen IgE detection can simultaneously conduct quantitative detection of more than a dozen specific IgE to identify allergens (Rauber *et al.*, 2020).

Chemical industrial pollution mainly exists in the chemical industrial zone, and the pollution sources include air pollution, water pollution, etc. Research reports in Zhenhai District have shown that the harmful substance in its chemical zone is mainly sulfur dioxide in the air. Such polluting substances, especially the inevitable large amount of dust, toxic gas and waste, may lead to the variation of the protein structure on the surface of pollens in the air, so that pollens that originally are not allergenic become highly allergenic (Guttman-Yassky *et al.*, 2019). In order to study the impact of the chemical industrial environment on allergic diseases, this article explored the connected factors of allergic skin diseases in patients who lived in Zhenhai chemical industrial district and Zhenhai New District, aiming to clarify that the identification of allergens is the primary method for prevention, clinical diagnosis and treatment of allergic diseases. The detection results of allergens, serum total IgE degree, and allergen-specific IgE may be different for people of different regions, races and ages. The detection of allergen-specific IgE can clarify the substances that cause allergic reactions in the region and help determine appropriate immunotherapy (Ryu *et al.*, 2020). Therefore, the application of serum allergen-specific IgE

can help find allergens and provides a valuable basis for the prevention and treatment of allergic diseases. With regard to the selection of research population, it was reported that air pollution was significantly reduced in areas 5 kilometers away from the chemical radiation zone (Sadreameli *et al.*, 2021). Therefore, patients with allergic skin diseases living in Zhenhai New District, which was 5 km away from the chemical industry zone, were selected as the control group in this study. This study showed that the positive rates of total IgE and inhalational sIgE of patients in Group A were higher than those in Group B, indicating that the positive rates of total IgE and inhalational sIgE in patients living or working in chemical industrial district were greatly increased. In terms of inhalational sIgE, allergies in tree combination and dust mites/household dust mites were significantly increased in patients living or working in chemical area. Our results are consistent with the previous results (Drislane *et al.*, 2020), which reported states that people living in chemical industrial areas showed more inhalational sIgE. We believe that it may be due to the presence of polluting substances in the air, which change the protein structure of pollen surface, thus triggering an increase in inhalation allergens.

In addition, in order to understand whether individual factors have an influence on allergic skin diseases, we analyzed sex, age and BMI (with 24.0 kg/m² as cut-off value) of patients in the chemical zone. It was found that patient's sex, age or BMI had no effect on the allergens detection results.

However, this is only a preliminary exploration in patients from different regions. We did not conduct in-depth investigations on the main pollutants and their concentrations in the chemical industrial area and did not analyze the mechanism of allergic reactions triggered by pollutants. Therefore, there are certain limitations in the current research. In follow-up studies, we will monitor pollutants and their concentrations in the chemical industrial area to determine whether the concentration of pollutants is related to the incidence of allergic skin diseases, and analyze the influence of chemical pollutants on the immune function of the body and the induction mechanism of allergic reactions *via* animal experiments.

In summary, the chemical industrial environment is significantly involved with allergic dermatosis, and patients who live there have significantly increased total positive IgE and positive aspirational sIgE.

Declarations

Data Availability. The data used to support this study is available from the corresponding author upon request.

Conflicts of Interest. Authors declare that they have no conflicts of interest.

REFERENCES

- Beaulieu V, Auger I, Dessureault J, Houle MC (2022) Systemic allergic dermatitis to dapsone diagnosed with scratch patch tests. *Contact Dermatitis* 87: 195–196. <https://doi.org/10.1111/cod.14121>
- Du Toit G, Sayre PH, Roberts G, Lawson K, Sever ML, Bahnson HT, Fisher HR, Feeney M, Radulovic S, Basting M, Plaut M, Lack G, Immune Tolerance Network Learning Early About Peanut Allergy study team (2018) Allergen specificity of early peanut consumption and effect on development of allergic disease in the Learning Early About Peanut Allergy study cohort. *J Allergy Clin Immunol* 141: 1343–1353. <https://doi.org/10.1016/j.jaci.2017.09.034>
- Drislane C, Irvine AD (2020) The role of filaggrin in atopic dermatitis and allergic disease. *Ann Allergy Asthma Immunol* 124: 36–43. <https://doi.org/10.1016/j.anai.2019.10.008>

- Eljaszewicz A, Ruchti F, Radzikowska U, Globinska A, Boonpiyathad T, Gschwend A, Morita H, Helbling A, Arasi S, Kahlert H, Berrek N, Nandy A, Akdis M, Willers C, Moniuszko M, Akdis CA, Sokolowska M (2021) Trained immunity and tolerance in innate lymphoid cells monocytes and dendritic cells during allergen-specific immunotherapy. *J Allergy Clin Immunol* **147**: 1865–1877. <https://doi.org/10.1016/j.jaci.2020.08.042>
- Fang Z, Li L, Zhang H, Zhao J, Lu W, Chen W (2021) Gut microbiota probiotics and their interactions in prevention and treatment of atopic dermatitis: a review. *Front Immunol* **12**: 720393. <https://doi.org/10.3389/fimmu.2021.720393>
- Guttman-Yassky E, Bissonnette R, Ungar B, Suárez-Fariñas M, Ardeleanu M, Esaki H, Suprun M, Estrada Y, Xu H, Peng X, Silverberg JI, Menter A, Krueger JG, Zhang R, Chaudhry U, Swanson B, Graham NMH, Pirozzi G, Yancopoulos GD, Hamilton JD (2019) Dupilumab progressively improves systemic and cutaneous abnormalities in patients with atopic dermatitis. *J Allergy Clin Immunol* **143**: 155–172. <https://doi.org/10.1016/j.jaci.2018.08.022>
- Golebski K, Layhadi JA, Sahiner U, Steveling-Klein EH, Lenormand MM, Li RCY, Bal SM, Heesters BA, Vilà-Nadal G, Hunewald O, Montamat G, He FQ, Ollert M, Fedina O, Lao-Araya M, Vijverberg SJH, Maitland-van der Zee AH, van Drunen CM, Fokkens WJ, Durham SR, Spits H, Shamji MH (2021) Induction of IL-10-producing type 2 innate lymphoid cells by allergen immunotherapy is associated with clinical response. *Immunity* **54**: 291–307.e7. <https://doi.org/10.1016/j.immuni.2020.12.013>
- Güngör D, Nadaud P, LaPergola CC, Dreibeis C, Wong YP, Terry N, Abrams SA, Beker L, Jacobovits T, Järvinen KM, Nommsen-Rivers LA, O'Brien KO, Oken E, Pérez-Escamilla R, Ziegler EE, Spahn JM (2019) Infant milk-feeding practices and food allergies allergic rhinitis atopic dermatitis and asthma throughout the life span: a systematic review. *Am J Clin Nutr* **109** (Suppl 7): 772S–799S. <https://doi.org/10.1093/ajcn/nqy283>
- Hoof I, Schulten V, Layhadi JA, Stranzl T, Christensen LH, Herrera de la Mata S, Seumois G, Vijayanand P, Lundegaard C, Niss K, Lund A, Ahrenfeldt J, Holm J, Steveling E, Sharif H, Durham SR, Peters B, Shamji MH, Andersen PS (2020) Allergen-specific IgG+ memory B cells are temporally linked to IgE memory responses. *J Allergy Clin Immunol* **146**: 180–191. <https://doi.org/10.1016/j.jaci.2019.11.046>
- Hereford B, Maczuga S, Flamm A (2021) Allergic contact dermatitis and concomitant dermatologic diseases: a retrospective study. *Dermatitis: contact atopic occupational drug* **32**: 251–255. <https://doi.org/10.1097/DER.0000000000000676>
- Holl JL, Bilaver LA, Finn DJ, Savio K (2020) A randomized trial of the acceptability of a daily multi-allergen food supplement for infants. *Pediatric Allergy Immunol* **31**: 418–420. <https://doi.org/10.1111/pai.13223>
- Hanif T, Dhaygude K, Kankainen M, Renkonen J, Mattila P, Ojala T, Joenväärä S, Mäkelä M, Pelkonen A, Kauppi P, Haahtela T, Renkonen R, Toppila-Salmi S (2019) Birch pollen allergen immunotherapy reprograms nasal epithelial transcriptome and recovers microbial diversity. *J Allergy Clin Immunol* **143**: 2293–2296.e11. <https://doi.org/10.1016/j.jaci.2019.02.002>
- Lau HX, El-Heis S, Yap QV, Chan YH, Tan CPT, Karnani N, Tan KML, Tham EH, Goh AEN, Teoh OH, Tan KH, Eriksson JG, Chong YS, Chong MF, Van Bever H, Lee BW, Shek LP, Godfrey KM, Loo EXL (2021) Role of maternal tryptophan metabolism in allergic diseases in the offspring. *Clin Exp Allergy* **51**: 1346–1360. <https://doi.org/10.1111/cea.13953>
- Larson D, Patel P, Salapatek AM, Couroux P, Whitehouse D, Pina A, Johnson JL, Sever ML, Sanda S, Poyser J, Allio T, Scadding GW, Qin T, Shamji MH, Kwok WW, James EA, French D, Lelic A, Larché M, Altman MC, Togias A, Durham SR (2020) Nasal allergen challenge and environmental exposure chamber challenge: A randomized trial comparing clinical and biological responses to cat allergen. *J Allergy Clin Immunol* **145**: 1585–1597. <https://doi.org/10.1016/j.jaci.2020.02.024>
- Orengo JM, Radin AR, Kamat V, Badithe A, Ben LH, Bennett BL, Zhong S, Birchard D, Limnander A, Rafique A, Bautista J, Kostic A, Newell D, Duan X, Franklin MC, Olson W, Huang T, Gandhi NA, Lipsich L, Stahl N, Papadopoulos NJ, Murphy AJ, Yancopoulos GD (2018) Treating cat allergy with monoclonal IgG antibodies that bind allergen and prevent IgE engagement. *Nat Commun* **9**: 1421. <https://doi.org/10.1038/s41467-018-03636-8>
- Rauber MM, Möbs C, Campana R, Henning R, Schulze-Dasbeck M, Greene B, Focke-Tejkl M, Weber M, Valenta R, Pfützner W (2020) Allergen immunotherapy with the hypoallergenic B-cell epitope-based vaccine BM32 modifies IL-10- and IL-5-secreting T cells. *Allergy* **75**: 450–453. <https://doi.org/10.1111/all.13996>
- Ryu MH, Lau KS, Wooding DJ, Fan S, Sin DD, Carlsten C (2020) Particle depletion of diesel exhaust restores allergen-induced lung-protective surfactant protein D in human lungs. *Thorax* **75**: 640–647. <https://doi.org/10.1136/thoraxjnl-2020-214561>
- Sadreameli SC, Ahmed A, Curtin-Brosnan J, Perzanowski MS, Phipatanakul W, Balcer-Whaley S, Divjan A, Peng RD, Newman M, Cunningham A, Bollinger ME, Wise RA, Miller RL, Matsui EC (2021) Indoor environmental factors may modify the response to mouse allergen reduction among mouse-sensitized and exposed children with persistent asthma. *J Allergy Clin Immunol Pract* **9**: 4402–4409.e2. <https://doi.org/10.1016/j.jaip.2021.08.031>
- Tramper-Stranders G, Ambrożej D, Arcolaci A, Atanaskovic-Markovic M, Boccabella C, Bonini M, Karavelia A, Mingomataj E, O'Mahony L, Sokolowska M, Untersmayr E, Feleszko W, EAACI Task Force on Conscious and Rational use of Antibiotics in Allergic Diseases (2021) Dangerous liaisons: Bacteria antimicrobial therapies and allergic diseases. *Allergy* **76**: 3276–3291. <https://doi.org/10.1111/all.15046>
- Ünal D (2020) Effects of perennial allergen immunotherapy in allergic rhinitis in patients with/without asthma: a-randomized controlled real-life study. *Int Archives Allergy Immunol* **181**: 141–148. <https://doi.org/10.1159/000504916>
- Venter C, Palumbo MP, Glueck DH, Sauder KA, O'Mahony L, Fleischer DM, Ben-Abdallah M, Ringham BM, Dabelea D (2022) The maternal diet index in pregnancy is associated with offspring allergic diseases: the Healthy Start study. *Allergy* **77**: 162–172. <https://doi.org/10.1111/all.14949>
- Xiang L, Liu F, Zhi L, Jiang W, Liu C, Xie H, Zhou X, Sun Y, Zheng Y, Zhu R, Tao Z, Xia W, Lai H, Wei Q, Cheng L, Tang Y, Xu R, Huang H, Zhou Q, Chang P (2021) Safety of semi-depot house dust mite allergen extract in children and adolescents with allergic rhinitis and asthma. *Immunotherapy* **13**: 227–239. <https://doi.org/10.2217/imt-2020-0232>
- Yang G, Seok JK, Kang HC, Cho YY, Lee HS, Lee JY (2020) Skin barrier abnormalities and immune dysfunction in atopic dermatitis. *Int J Mol Sci* **21**: 2867. <https://doi.org/10.3390/ijms21082867>
- Zhang MZ, Chu SS, Xia YK, Wang DD, Wang X (2021) Environmental exposure during pregnancy and the risk of childhood allergic diseases. *World J Pediatrics* **17**: 467–475. <https://doi.org/10.1007/s12519-021-00448-7>

Decrease of prothrombin level during thrombolysis in acute myocardium infarction

Daria S. Korolova¹, Alexander M. Parkhomenko², Volodymyr O. Chernyshenko¹✉, Tamara M. Chernyshenko¹, Nadiya M. Druzhyna¹, Olha V. Hornytska¹ and Tetyana M. Platonova¹

¹Palladin Institute of Biochemistry, National Academy of Science of Ukraine; ²State Institutional Scientific Center The M.D. Strazhesko Institute of Cardiology, Clinical and Regenerative Medicine of The National Academy of Medical Sciences of Ukraine

Previously, the direct interactions of B β 26-42 fibrin residues with prothrombin were demonstrated. It was also shown that forming prothrombin complexes with E- or DDE-fragments causes non-enzymatic prothrombin activation. The direct measuring of the prothrombin level in the blood plasma of patients with acute myocardial infarction (AMI) allowed us to find a situation where such an activation can occur *in vivo*. Blood coagulation parameters in the blood plasma of patients with AMI were measured at 2 hours, three days, and seven days after the thrombolysis by streptokinase accompanied with intravenous administration of anticoagulants: unfractionated high molecular weight heparin (HMWH) and low-molecular-weight heparin (LMWH). The prothrombin level in the blood plasma of patients with AMI was normal before thrombolytic therapy and substantially decreased after streptokinase administration. This effect was prominent in the case of concomitant anticoagulant therapy with LMWH and was not observed when HMWH was applied. It can be explained by the fact that LMWH preferentially inhibits factor Xa, while the HMWH is an effective inhibitor of both factor Xa and thrombin. This observation suggested that the prothrombin level decrease was caused by the thrombin-like activity and possible autolysis of prothrombin by thrombin. Also, thrombolytic therapy with streptokinase caused the accumulation of fibrin degradation products (FDPs), some of which were able to bind prothrombin. The dramatic decrease of prothrombin level in the blood plasma of patients with AMI during thrombolysis allowed us to conclude the non-enzymatic prothrombin activation with the following autolysis of prothrombin that contributes to the pathology.

Keywords: Prothrombin, non-enzymatic activation, acute myocardial infarction, thrombosis, soluble fibrin

Received: 28 August, 2023; **revised:** 09 October, 2023; **accepted:** 07 November, 2023; **available on-line:** 27 November, 2023

✉e-mail: bio.cherv@biochem.kiev.ua

Acknowledgements of Financial Support: NAS of Ukraine # 0119U002512.

Abbreviations: AMI, acute myocardial infarction; APTT, activated partial thromboplastin time; ATIII, antithrombin III; FX, factor X; FDPs, fibrin degradation products; HMWH, high molecular weight heparin; LMWH, low-molecular-weight heparin; PC, protein C; pNa, p-nitroaniline; PT, prothrombin time; RVV, Russell's viper venom; SFMCs, soluble fibrin monomeric complexes; SK, streptokinase

INTRODUCTION

Thrombotic complications are the main reason for the development of cardiovascular diseases, particularly acute myocardial infarction (AMI), which causes acute or persistent ischemic anoxia of the coronary artery. Such anoxia and the occlusion of the coronary artery are caused by intravascular thrombus formation that terminates the proper blood flow in coronary vessels (Grover *et al.*, 2018; Karbach *et al.*, 2019; Hudeca *et al.*, 2020; Wiczór *et al.*, 2020).

Activation of the blood coagulation system leads to the appearance in the bloodstream of a considerable amount of thrombin due to the activation of prothrombin. Thrombin leads to the activation of platelets and conversion of fibrinogen to fibrin monomer, which, upon polymerization, forms a fibrin clot – the core of a thrombus (Pasupathy *et al.*, 2018; Toshiaki *et al.*, 2016; Wood *et al.*, 2011).

Thrombin and prothrombin (its inactive precursor) are crucial factors in physiological and pathophysiological coagulation. A general assessment of thrombin activity and prothrombin content is necessary for proper patient management (Korolova *et al.*, 2021). However, determining the prothrombin time, which characterizes the state of the coagulation factors of the external blood clotting pathway, does not allow for determining the contribution of prothrombin in the test result. Increases in thrombin generation are being detected by the determination of prothrombin fragment 1+2, thrombin-antithrombin complex, prethrombin-1, or soluble fibrin as products of thrombin-catalyzed reactions. The total level of prothrombin in the blood plasma of patients needs to be measured (Negrier *et al.*, 2019; Wexels *et al.*, 2016; Zhao *et al.*, 2023; Elged *et al.*, 2016).

The purpose of our work was to apply the direct measuring of the level of prothrombin in the blood plasma of patients with acute myocardial infarction (AMI). To achieve this goal, we studied blood coagulation parameters in the blood plasma of patients with AMI at 2 hours, three days and seven days after the thrombolysis by streptokinase accompanied with intravenous administration of anticoagulants: unfractionated heparin and low-molecular-weight heparin (LMWH).

MATERIALS AND METHODS

Materials

Chromogenic substrates S2238 (H-D-Phe-Pip-Arg-pNA), S2765 (Z-D-Arg-Gly-Arg-pNA), and S2236 (p-Glu-Pro-Arg-pNA) were purchased from BIOPHEN (Neuville-sur-Oise, France). Factor X activator from *Rus-sel vipera* venom (RVV), thrombin from human blood plasma, sodium citrate, phosphate-buffered saline (PBS) tablets (pH 7.2, sodium chloride, 0.15 M) were purchased from Sigma-Aldrich (St. Louis, USA). APTT-reagent, control donors' blood plasma, and test systems for determining Protein C and antithrombin III levels were purchased from Siemens-Biomed (Marburg, Germany). The thrombin-like enzyme was purified from the venom of *Agkistrodon halys halys* according to the method described in (Solovjov *et al.*, 1998). The activator of prothrombin (ecamulin) was purified from *Echis multisquamatis* venom according to the method of Solovjov and others (Solovjov *et al.*, 1996). Monomeric fibrin desAB was purified according to the method described (Pozdnjakova *et al.*, 1979).

Patients

The study included patients with large-focal and transmural AIM under 70 without signs of cardiogenic shock ($n=57$). The patients were treated at the State Institutional Scientific Center The M.D. Strazhesko Institute of Cardiology, Clinical and Regenerative Medicine of The National Academy of Medical Sciences of Ukraine, Kyiv.

On average, patients were taken to the division of reanimation and intensive therapy in the first 6 hours after the heart attack in 3.1 ± 0.2 h. Patients were 57.4 years old on average. Some of them had arterial hypertension (45.5%), diabetes (7%), and 64% were smokers. The average BMI was 28.4 kg/m^2 .

Inclusion criteria were clinical signs of acute coronary syndrome, registration of the elevation of the ST segment of the electrocardiogram by 2 mm or more in two measurements, age from 30 to 70 years.

Exclusion criteria were cardiogenic shock, severe forms of diabetes, bronchial asthma, kidney or liver failure, documented disorders in the blood coagulation system, bleedings during the last six months, level of hemoglobin below 100 g/l, violation of cerebral blood flow, and body weight above 110 kg or below 60 kg.

Systemic thrombolytic therapy was performed with streptokinase (SK) (Kabikinase from 'Pharmacia&Upjohn', USA) at 1500 000 IU and was carried out for 30–40 minutes. All patients received basic anti-platelet therapy, therapy by beta blockers, statins, ADP inhibitors, and nitrates.

Anticoagulant prophylaxis was performed with fraxiparin or heparin 4–6 hours after the start of thrombolytic therapy. Standard unfractionated heparin was administered by an intravenous infusion lasting 48 hours (activated partial thromboplastin time (APTT) was controlled), in an average dose of 1000 IU per hour, then subcutaneously four times a day for 5–7 days.

Fraxiparine ('Sanofi-Synthelabo,' France) was administered by bolus administration (0.6 ml) and then three hours later under the skin at the same dose for 3 days. Administration of Fraxiparine was then continued at half the dose until the 6–7th day of myocardial infarction.

Platelet-poor blood plasma was prepared from citrated blood by centrifugation at $1200 \times g$ for 30 min. Sodium citrate (3.8%) added immediately after collection to the

whole blood at a 1:9 ratio was used as an anticoagulant. All work was conducted under the Declaration of Helsinki. Studies were conducted per the Ethical Committee Approval N 3 form 04.04.2019 (Palladin Institute of Biochemistry of NAS of Ukraine).

Methods

Fibrinogen concentration

Fibrinogen concentration in the blood plasma was determined by the modified spectrophotometric method. Blood plasma (0.2 ml) and PBS (1.7 ml) were mixed in a glass tube. Coagulation was initiated by adding 0.1 ml of the thrombin-like enzyme from the venom of *Agkistrodon halys halys* (1 NIH/ml), which allowed to avoid fibrin cross-linking. The mixture was incubated for 30 min at 37°C . The fibrin clot was removed and re-solved in 5 ml of 1.5% acetic acid. The concentration of protein was measured using a spectrophotometer POP (Optizen, Korea) at 280 nm ($\epsilon=1.5$) (Sokolovska *et al.*, 2002).

Activated partial thromboplastin time

Activated partial thromboplastin time (APTT) was performed following the procedure: 0.1 ml of studied blood plasma was mixed with an equal volume of APTT-reagent and incubated for 3 minutes at 37°C . Then, the coagulation was initiated by adding 0.1 ml of 0.025 M solution of CaCl_2 , and clotting time was monitored. The clotting time was evaluated using a coagulometer CT2410 (Solar, Belarus).

Prothrombin time

Prothrombin time (PT) was measured as follows: clotting was initiated by mixing 0.1 ml of blood plasma with 0.1 ml of 0.025 M CaCl_2 and 0.1 ml of thromboplastin reagent, time of clotting was monitored. Thromboplastin acts through the tissue factor pathway of coagulation and activates only carboxylated and uncleaved forms of prothrombin. The clotting time was evaluated using a coagulometer CT2410 (Solar, Belarus).

Prothrombin level

Total prothrombin level was measured using ecamulin (the prothrombin activator from *Echis multisquamatis* snake venom) and chromogenic thrombin-specific substrate S2238 (H-D-Phe-Pip-Arg-pNA). Ecamulin activates prothrombin and all of its inactive forms to determine total prothrombin level (Korolova *et al.*, 2023).

In a well of a 96-well plate, 0.02 ml of studied blood plasma sample, 0.03 ml of S2238 solution (0.25 mM), and 0.03 ml of ecamulin solution (0.06 mg/ml) were admixed in the PBS with 0.001 M CaCl_2 at final volume of 0.25 ml. The generation of colorful p-nitroaniline (pNa) was monitored at 405 nm using a ThermoMultiscan multi-plate reader (ThermoFisher, USA). Results were presented as % from control values.

Soluble fibrin monomeric complexes (SFMCs)

For the SFMCs measurement in the glass tube, the 0.25 ml of studied blood plasma sample was mixed with an equal volume of 0.1 M KH_2PO_4 buffer pH 7.5. Then 0.4 ml of 1 M KH_2PO_4 buffer pH 7.5 was added to the whole volume after gentle mixing. Samples were incubated for 30 min at ambient temperature. After incubation, the accumulation of saturated SFMCs was estimated semi-quantitatively in the range of concentrations 7–140 $\mu\text{g/ml}$ by following gradation: clear solution without turbidity – negative result;

Table 1. Hemostasis system parameters of the patients with AMI at the time of admission to the clinic. The median value, minimum, and maximum are given.

Parameter	Healthy donors (n=30)	Patients with AMI (n=57)
Fibrinogen level, g/l	2.5 (2.3–3.0)	3.2* (2.2–5.5)
APTT, sec	45 (41–49)	41.0* (23–71)
Prothrombin level, %	100 (85–105)	105* (64–127)
SFMCs, µg/ml	0.0 (0.0–3.0)	40.0* (17–140)
Protein C level, %	100 (90–115)	63* (40–110)
AT III level, %	100 (90–110)	100 (62–120)
Clotting factor X level, %	100 (90–100)	92 (60–120)

* $p < 0.05$, compared to donors

several dots in the solution – up to 7 µg/ml; visible turbidity – up to 35 µg/ml; formation of flakes – up to 70 µg/ml; formation of fibers – up to 90 µg/ml; gel-like sedimentation – up to 140 µg/ml. For the calibration, we used blood plasma samples with monomeric fibrin desAB added at final concentrations from 7–140 µg/ml prepared according to the method (Pozdnjakova *et al.*, 1979).

Protein C level

Protein C (PC) level was determined using the activator of PC (Berichrom, Germany). The generation of activated PC was measured by chromogenic substrate assay using specific chromogenic substrate S2236 (p-Glu-Pro-Arg-pNa). The analysis was performed in 0.05 M Tris-HCl buffer pH 7.4, at 37°C. The chromogenic substrate concentration was 30 mM. The generation of para-nitroaniline was measured at 405 nm on a microtiter plate reader Multiscan EX (Thermo Fisher Scientific, Waltham, USA). Here and below for Multiscan EX: Linearity 0–2 Abs, $\pm 2.0\%$ at 405 nm; accuracy $\pm 2.0\%$ or ± 0.007 Abs at 405 nm. Results were presented as the ratio of PC level in the blood plasma of the studied sample to PC level in the blood plasma of the healthy donor.

Antithrombin level

Antithrombin III (ATIII) activity is determined based on its ability to neutralize thrombin in the presence of heparin. The overabundance of thrombin was inhibited by the ATIII-heparin complex proportionally to the ATIII in blood plasma.

The analysis was performed according to the recommendations of the manufacturer. The remaining activity of thrombin was measured using chromogenic thrombin-specific substrate S2238 (H-D-Phe-Pip-Arg-pNa). Colorful p-nitroaniline (pNa) generation was monitored at 405 nm using ThermoMultiscan (ThermoFisher, USA). The amount of ATIII was determined using the calibration curve.

Factor X level

The total factor X level was determined using RVV (Russell's viper venom reagent that specifically activates factor X) and factor Xa-specific chromogenic substrate S22765 (Z-D-Arg-Gly-Arg-pNa). In a well of 96-well plate, 0.02 ml of studied blood plasma sample, 0.03 ml of S2765 solution (0.25 mM), and 0.01 ml of RVV solution (Sigma, USA) were admixed in the PBS with 0.001 M CaCl_2 at a final volume of 0.25 ml. Colorful p-nitroaniline (pNa) generation was monitored at 405 nm using ThermoMultiscan (ThermoFisher, USA). Results were presented as % of control values (Budzynski *et al.*, 2001).

Statistics

Statistical data analysis was performed using the Wilcoxon-Mann-Whitney (WMW) test using an online calculator provided by Social Science Statistics (<https://www.socscistatistics.com/>). Statistical analysis was performed using Microsoft Excel (Microsoft Corporation, Redmond, WA, USA). Results are presented as the group's median, maximum, and minimum values. All assays were performed in a series of at least three replicates. Data were considered significant when $p < 0.05$.

RESULTS

Blood coagulation system parameters

An analysis of the parameters of the haemostasis system was carried out in 57 patients with great magistral transmural host myocardial infarction (AMI) at admission to the clinic (Table 1).

A significant reduction in the blood plasma clotting time in the APTT test was revealed in 49% of patients, an increase in fibrinogen content in 31% of patients, and an accumulation of SFMC (17–140 µg/ml), which indicates the activation of the blood clotting system, was determined in all studied samples. Simultaneously with the activation of the components of the coagulation system, the potential of the anticoagulant link of the system (PC and ATIII) decreases, which, together with the increased content of fibrinogen, can contribute to the increase of further thrombotic complications and re-occlusions.

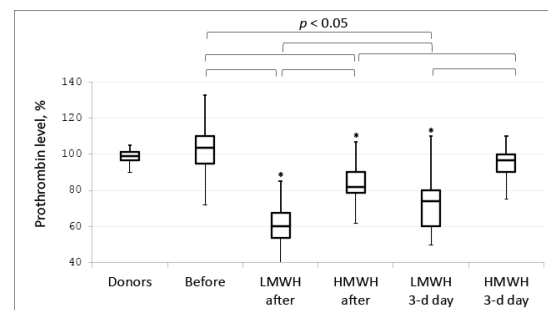


Figure 1. Level of prothrombin in the blood plasma of patients with acute myocardial infarction before thrombolysis (before) and after thrombolysis accompanied by concomitant anticoagulant therapy with low molecular weight heparin (LMWH after, n=28) or high molecular weight heparin (HMWH after, n=29). Samples were collected before, after 2 hours, and on the third day after thrombolysis. Donors – healthy donors' group (n=30). * $p \leq 0.05$ in comparison to donors.

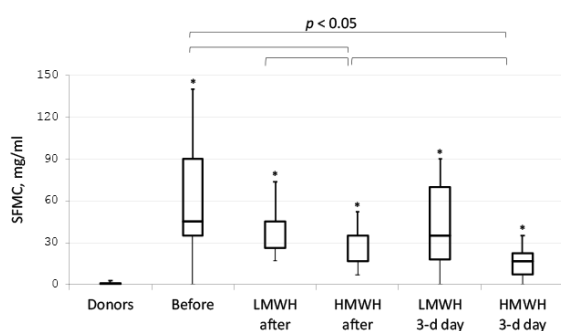


Figure 2. Level of soluble fibrin monomeric complexes (SFMC) in the blood plasma of patients with acute myocardial infarction before thrombolysis (Before) and after thrombolysis accompanied by concomitant anticoagulant therapy with LMWH (LMWH after, $n=28$) or HMWH (HMWH after, $n=29$). Samples were collected before, after 2 hours, and on the third day after thrombolysis. Donors – healthy donors' group ($n=30$). $*p \leq 0.05$ in comparison to donors.

Prothrombin level after thrombolysis

The prothrombin level in the blood plasma of patients with AMI was determined before thrombolytic therapy (at the time of admission to the clinic) and after thrombolytic therapy (on the first, third, and seventh days). The prothrombin total level in the blood plasma of patients with myocardium infarction was normal ($95 \pm 11\%$). During thrombolysis and concomitant therapy with LMWH, there was a decrease in the plasma levels of prothrombin (median 55%; min 40%, max 80%, $p < 0.001$). Whereas less obvious change was observed in the case of HMWH (median 84%; min 56, max 110%, $p < 0.001$) (Fig. 1). Statistic analysis in “Statistica 7” was used to calculate the correlations of total prothrombin level.

The low level of prothrombin in the case of concomitant therapy with LMWH was also found on the third day after thrombolysis. The normalization of prothrombin level was detected only on the seventh day after thrombolysis in this group of patients (median 87%; min 70, max 110%).

Correlation of prothrombin level and SFMC after thrombolysis

A decrease in the level of prothrombin in the blood plasma of patients who were injected with low molecular weight heparin (LMWH) is accompanied by a significant accumulation of SFMC (Fig. 2). In the group of patients who were injected with high molecular weight heparin (HMWH), the level of SFMC after thrombolysis was lower than in the case of LMWH injection. These data correlate to the decrease of prothrombin content at the same time points presented in Fig. 1.

DISCUSSION

A study of the blood coagulation system of patients with AIM revealed a violation of the balance between pro- and anticoagulants, which is a consequence of activating the coagulation link of the hemostasis system. The activation of the blood coagulation system is evidenced by the increased level of fibrinogen, the accumulation of SFMC, and the significant consumption of the main inhibitors – ATIII and protein C (Hudeca *et al.*, 2020; Hoshino *et al.*, 2018; Refaai *et al.*, 2018).

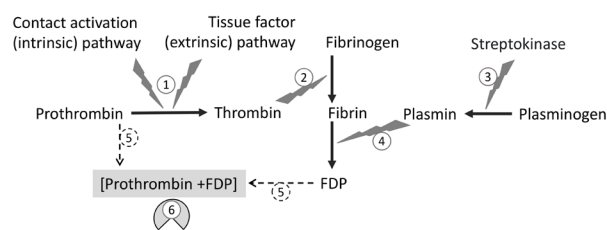


Figure 3. Scheme of prothrombin activation by fibrin degradation products during thrombolysis.

1 – canonical prothrombin activation, 2 – thrombin cleaves fibrinogen with fibrin formation, 3 – streptokinase activates plasminogen with plasmin formation, 4 – plasmin cleaves fibrin with fibrin degradation products (FDP) formation, 5 – prothrombin and FDP form complexes, 6 – prothrombin in (prothrombin-FDP) complex forms thrombin-like active site.

The accumulation of SFMC is the result of the work of the central enzyme of the blood coagulation system – thrombin (Dizhou *et al.*, 2023). The content of SFMC corresponds to the activity of thrombin and characterizes the degree of activation of the hemostasis system. There is no doubt that SFMC, as a marker of activation of the blood coagulation system, has a high prognostic value (Masahiro *et al.*, 2009).

The prothrombin level in the blood plasma of patients with AMI was normal before thrombolytic therapy and substantially decreased after streptokinase administration. This effect was prominent in the case of concomitant anticoagulant therapy with LMWH and was not observed when HMWH was applied. It can be explained by the fact that LMWH preferentially inhibits factor Xa, while the HMWH is an effective inhibitor of both factor Xa and thrombin. This observation suggested that the prothrombin level decrease was caused by the thrombin activity and possible autolysis of prothrombin by thrombin (Croles *et al.*, 2019; Makarem *et al.*, 2023; Spencer *et al.*, 2000).

Another important issue is fibrin degradation products (FDPs) accumulation due to thrombolytic therapy with streptokinase. Some of the FDPs (including DDE-complex and fibrin E-fragment) still have sites of interactions with thrombin and prothrombin (Capitanescu *et al.*, 2016) (Fig. 3).

Previously, we demonstrated the direct interactions of high molecular weight E-fragment of fibrin (E_1 -fragment) and DDE-complex with prothrombin. We confirmed that prothrombin can bind to B β 26-42 fibrin residues, and the formation of such a complex causes a non-enzymatic prothrombin activation (Chernyshenko *et al.*, 2015).

A similar complexation with the formation of a thrombin-like active site was shown for staphylocoagulase. Staphyloprothrombin, similar to prothrombin in a complex with E_1 -fragment, is enzymatically active (Ashoka *et al.*, 2020; Crosby *et al.*, 2016).

As shown *in vitro*, non-enzymatic activation of prothrombin in a complex with E_1 -fragment and DDE-complex was assumed as the additional mechanism of autolysis of prothrombin (Platonova *et al.*, 2002; Savchuk *et al.*, 2006). A study of the state of a hemostatic system at thrombolysis in AMI allowed us to find a pathology in which the proposed mechanism can occur *in vivo*. This suggestion was confirmed by the dramatic decrease of prothrombin level that occurs alongside the accumulation of FDPs and the inability to inhibit thrombin activity by low molecular weight heparin (LMWH).

CONCLUSIONS

The drop in total prothrombin level in the blood plasma of patients with acute myocardial infarction during thrombolysis was observed. It was strongly dependent on the type of anticoagulant therapy and was not obvious in the case of concomitant therapy with HMWH. It can be explained by the non-enzymatic activation of prothrombin by FDPs that contain B β 26-42 residues (DDE, E₁ fragments). Such a novel type of non-enzymatic prothrombin activation was previously shown *in vitro*. Current findings allowed us to conclude the possibility of the activation *in vivo* when a huge amount of FDPs are forming. This newly discovered effect should be taken into consideration during patient management.

Declarations

Ethical Committee Approval. Palladin Institute of Biochemistry of NAS of Ukraine (#3, 04.04.2019).

Conflicts of Interest. The authors declare no conflict of interest.

REFERENCES

- Budzynski AZ (2001) Chromogenic substrates in coagulation and fibrinolytic assays. *Lab Med* **32**: 365–368. <https://doi.org/10.1309/KVYM-1C8E-Y6M4-MJJDY>
- Capitanescu C, Macovei Oprea AM, Ionita D, Dinca GV, Turcule C, Manole G, Macovei RA (2016) Molecular processes in the streptokinase thrombolytic therapy. *J Enzyme Inhib Med Chem* **31**: 1411–1414. <https://doi.org/10.3109/14756366.2016.1142985>
- Chernyshenko VO, Chernyshenko TM, Korolova DS, Volynets GP, Kolesnikova IN, Platonova TM, Lugovskoy EV (2015) Non-enzymatic activation of prothrombin induced by interaction with fibrin β 26-42 region. *Acta Biochim Pol* **62**: 517–522. https://doi.org/10.18388/abp.2014_896
- Crosby HA, Kwiecinski J, Horswill AR (2016) *Staphylococcus aureus* aggregation and coagulation mechanisms, and their function in host-pathogen interactions. *Adv Appl Microbiol* **96**: 1–41. <https://doi.org/10.1016/bs.aambs.2016.07.018>
- Croles FN, Lukens MV, Mulder R, de Maat MPM, Mulder AB, Meijer K (2019) Monitoring of heparins in antithrombin-deficient patients. *Thrombosis Res* **175**: 8–12. <https://doi.org/10.1016/j.thromres.2019.01.007>
- Elged AA, El-Gamal RA, Bastawy SA, Moselhy MS (2016) Soluble fibrin monomer complex assay enhances early and accurate diagnosis of acute myocardial infarction. *Int J Clin Exp Pathol* **9**: 5801–5809
- Grover SP, Mackman N (2018) Tissue factor: an essential mediator of hemostasis and trigger of thrombosis. *Arterioscl Thromb Vasc Biol* **38**: 709–725. <https://doi.org/10.1161/ATVBAHA.117.309846>
- Hoshino K, Muranishi K, Kawano Y, Hatamoto H, Yamasaki S, Nakamura Y, Ishikura H (2018) Soluble fibrin is a useful marker for predicting extracorporeal membrane oxygenation circuit exchange because of circuit clots. *J Artificial Organs* **21**: 196–200. <https://doi.org/10.1007/s10047-018-1021-x>
- Hudec S, Hutyra M, Precek J, Latal J, Nykl R, Spacek M, Sluka M, Sanak D, Tudos Z, Navratil K, Pavlu L, Taborsky M (2020) Acute myocardial infarction, intraventricular thrombus and risk of systemic embolism. *Biomed Papers Med Faculty of the University Palacky, Olomouc, Czechoslovakia* **164**: 34–42. <https://doi.org/10.5507/bp.2020.001>
- Iba T, Ito T, Maruyama I, Jilma B, Brenner T, Müller MC, Juffermans NP, Thachil J (2016) Potential diagnostic markers for disseminated intravascular coagulation of sepsis. *Blood Rev* **30**: 149–155. <https://doi.org/10.1016/j.blre.2015.10.002>
- Ieko M, Naito S, Yoshida M, Kanazawa K, Mizukami K, Sato H, Yui T, Nakabayashi T, Hirabayashi T, Oguma Y (2009) Plasma soluble fibrin monomer complex as a marker of coronary thrombotic events in patients with acute myocardial infarction. *Toboku J Exp Med* **219**: 25–31. <https://doi.org/10.1620/tjem.219.25>
- Karbach S, Lagrange J, Wenzel P (2019) Thromboinflammation and vascular dysfunction. *Hamostaseologie* **39**: 180–187. <https://doi.org/10.1055/s-0038-1676130>
- Korolova D (2021) Regulation and dysregulation of thrombin activity. *Southeastern Eur Med J* **5**: 47–64. <https://doi.org/10.26332/seemedj.v5i1.194>
- Korolova D, Gryshchenko V, Chernyshenko T, Platonov O, Hornytska O, Chernyshenko V, Klymenko P, Reshetnik Y, Platonova T (2023) Blood coagulation factors and platelet response to drug-induced hepatitis and hepatosis in rats. *Anim Models Exp Med* **6**: 66–73. <https://doi.org/10.1002/ame2.12301>
- Maddur AA, Kroh HK, Aschenbrenner ME, Gibson BHY, Panizzi P, Sheehan JH, Meiler J, Bock PE, Verhamme IM (2020) Specificity and affinity of the N-terminal residues in staphylocoagulase in binding to prothrombin. *J Biol Chem* **295**: 5614–5625. <https://doi.org/10.1074/jbc.RA120.012588>
- Makarem A, Zareef R, Abourjeili J, Nassar JE, Bitar F, Arabi M (2023) Low molecular weight heparin in COVID-19: benefits and concerns. *Frontiers Pharmacol* **14**: 1159363. <https://doi.org/10.3389/fphar.2023.1159363>
- Negrier C, Shima M, Hoffman M (2019) The central role of thrombin in bleeding disorders. *Blood Rev* **38**: 100582. <https://doi.org/10.1016/j.blre.2019.05.006>
- Pasupathy S, Rodgers S, Tavella R, McRae S, Beltrame JF (2018) Risk of thrombosis in patients presenting with myocardial infarction with nonobstructive coronary arteries (MINOCA). *TH Open: Comp J Thrombosis Haemos* **2**: e167–e172. <https://doi.org/10.1055/s-0038-1645875>
- Platonova TM, Slominskiy OI, Chernyshenko TM, Makohonenko EM (2002) Activation of key proenzymes of the blood coagulation system by the fibrin E fragment. *Ukrain Biochem J* **74**: 25–29
- Pozdnjakova TM, Musjalkovskaja AA, Ugarova TP, Protvin DD, Kotsjuruba VN (1979) On the properties of fibrin monomer prepared from fibrin clot with acetic acid. *Thrombosis Res* **16**: 283–288. [https://doi.org/10.1016/0049-3848\(79\)90292-5](https://doi.org/10.1016/0049-3848(79)90292-5)
- Refaai MA, Riley P, Mardovina T, Bell PD (2018) The clinical significance of fibrin monomers. *Thrombosis Haemostasis* **118**: 1856–1866. <https://doi.org/10.1055/s-0038-1673684>
- Solovjov DA, Ugarova TP (1993) Purification and characterization of α -specific thrombin-like enzymes from the venoms of middle asian pit viper snakes *Agkistrodon halys halys* and *Agkistrodon halys blomhoffii*. *Biochemistry (Moscow)* **58**: 1221–1233
- Solovjov DA, Platonova TN, Ugarova TP (1996) Purification and characterization of ecamulin – A new prothrombin activator from the *Echis multisquamatus* snake venom. *Biochemistry (Moscow)* **61**: 785–793
- Sokolovska AS, Chernyshenko TM, Ivanenko TI (2002) Comparative characteristic of fibrinogen level determination methods in blood plasma. *Exper Clin Phibchem* **3**: 82–86
- Spencer FA, Ball SP, Zhang Q, Liu L, Benoit S, Becker RC (2000) Enoxaparin, a low molecular weight heparin, inhibits platelet-dependent prothrombinase assembly and activity by factor-Xa neutralization. *J Thrombosis Thrombolysis* **9**: 223–228. <https://doi.org/10.1023/a:1018710526772>
- Savchuk OM, Krasnobryzha IM, Horchev VF, Chernyshenko TM, Havryliuk, SP, Platonova TM (2006) Prothrombin and E-fragment complexation process. *Ukrainian Biochem J* **78**: 99–105 (in Ukrainian)
- Wexels F, Seljeflot I, Pripp AH, Dahl OE (2016) D-Dimer and prothrombin fragment 1+2 in urine and plasma in patients with clinically suspected venous thromboembolism. *Blood Coagul Fibrinol: Int J Haemostasis Thrombosis* **27**: 396–400. <https://doi.org/10.1097/MBC.0000000000000461>
- Wieżór R, Kulwas A, Roś D (2020) Implications of hemostasis disorders in patients with critical limb ischemia—an in-depth comparison of selected factors. *J Clin Med* **9**: 659. <https://doi.org/10.3390/jcm9030659>
- Wood JP, Silveira JR, Maille NM, Haynes LM, Tracy PB (2011) Prothrombin activation on the activated platelet surface optimizes expression of procoagulant activity. *Blood* **117**: 1710–1718. <https://doi.org/10.1182/blood-2010-09-311035>
- Wu D, Prem A, Xiao J, Salisbury FR (2023) Thrombin - A Molecular Dynamics Perspective. *Mini Rev Med Chem. Advance online publication*. <https://doi.org/10.2174/1389557523666230821102655>
- Zhao X, Yang S, Lei R, Duan Q, Li J, Meng J, Sun L (2023) Clinical study on the feasibility of new thrombus markers in predicting massive cerebral infarction. *Front Neurol* **13**: 942887. <https://doi.org/10.3389/fneur.2022.942887>

Relationship of gut microbiota and immunological response in obesity-related non-alcoholic fatty liver disease in children

Paweł Czarnowski¹, Aldona Wierzbicka-Rucińska¹✉ and Piotr Socha²

¹Department of Biochemistry, Radioimmunology and Experimental Medicine, The Children's Memorial Health Institute, Warsaw, Poland; ²Department of Gastroenterology, Hepatology and Nutrition Disorders, The Children's Memorial Health Institute, Warsaw, Poland

In the development of NAFLD plays an important role the intestinal microflora. Our aim was to characterize role microbiota in children. Distinctive gut microbiota composition was observed in children, characterized and short-chain fatty acid producing bacteria. For the treatment of NAFLD it is possible by therapeutic manipulations with prebiotics and probiotics to modulate the gut microbiota and maintain the integrity of the intestinal barrier are potential agents.

Keywords: pediatric NAFLD, dysbiosis, short-chain fatty acids (SCFAs), gut microbiome (GM), Butyrate

Received: 05 December, 2022; **revised:** 31 August, 2023; **accepted:** 01 September, 2023; **available on-line:** 06 September, 2023

✉e-mail: a.wierzbicka-rucinska@ipczd.pl

Acknowledgements of Financial Support: Support from the National Science Center grants UMO-2018/31/B/NZ5/02735

Abbreviations: ALT, alanine aminotransferase; AMPK, AMP-activated protein kinase; AST, aspartate aminotransferase; GLP-2, glucagon-like peptide-2; HFD, high-fat diet; IL-1, interleukin 1; IL-6, interleukin 6; Js, tight junctions; LPS, lipopolysaccharides; NAFLD, non-alcoholic fatty liver disease; NASH, nonalcoholic steatohepatitis; NF-κB, Nuclear factor-κB; PAI-1, plasminogen activator inhibitor-1; SCFAs, short-chain fatty acids; TLR, Toll-like receptor; ZO-1, zonula occludens-1

INTRODUCTION

Non-alcoholic fatty liver disease (NAFLD) is now recognized as one of the most common disorders in the proper functioning of the liver, both in the pediatric and adult population. It is estimated that it affects up to 10% of the entire pediatric population, including 26–41% children with obesity (Anderson *et al.*, 2015; Schwimmer *et al.*, 2006). In the adult population, this percentage ranges from 25 to 40% (Estes *et al.*, 2018). Younossi and others (Younossi *et al.*, 2016) in a systematic review estimated that the global prevalence of NAFLD reached 25%, which resulted in a significant increase in the interest of scientists, who are trying to find out the causes leading to its development. The global increase in NAFLD prevalence among children constitutes a poor prognosis for the future (Obesity Collaborators The GBD 2015). NAFLD by itself is defined as a metabolic dysfunction-associated liver disease caused by excessive accumulation of fat in hepatocytes, where it is possible to rule out secondary factors leading to accumulation of fat in liver cells, such as alcohol consumption, hereditary disorders, and drug intake (Chalasani *et al.*, 2012). Within this disease, we can distinguish a number of liver conditions that vary in severity degree, from steatosis to non-alcoholic steatohepatitis (NASH) with or without fibrosis, to cirrhosis (Buzzetti *et al.*, 2015). In the long term, NASH might progress to hepatocellular carcinoma

(HCC), a condition that increases liver-related morbidity and mortality. NAFLD is also related to metabolic syndrome (MS), including insulin resistance, dyslipidemia and visceral obesity (Boyras *et al.*, 2013). The pathological mechanism leading to the onset and development of NAFLD is not fully known. According to the multiple-hit hypothesis we do know, that there are many factors leading to NAFLD. Among them, we can set apart genetic and epigenetic factors, lipotoxicity, insulin resistance, dietary determinants proinflammatory factors, and gut microbiome, which might be crucial due to the production of large amounts of molecular mediators that affect liver cells (Clemente *et al.*, 2012).

GUT MICROBIOME AND IMMUNOLOGICAL RESPONSE

The gut microbiota affects host physiology at least in part, through the release of metabolites and complex bacterial structural components such as lipopolysaccharides (LPS), peptidoglycans and flagellins. Metabolites derived from the gut microbiota include short-chain fatty acids (SCFAs) and branched-chain fatty acids (BCFAs), aromatic acid metabolites, vitamins, amino acids and other metabolites. Recent studies have shown that gut microbiome (GM) has a significant impact on the development of NAFLD. The gut microbiota includes microorganisms belonging to different kingdoms, such as bacteria, viruses, archaea and fungi. As a whole, they form a complex ecosystem that lives in symbiosis with its host. Human GM is dominated by four bacteria phyla: Actinobacteria, Bacteroidetes, Firmicutes and Proteobacteria, where Firmicutes and Bacteroidetes are most common (Tremaroli *et al.*, 2012). Bacteria are involved in many metabolic processes in the gut. They participate in energy harvest, regulation level of bile-acid, fermentation of polysaccharides, and lastly choline metabolism (Dumas *et al.*, 2006). Intestinal bacteria can also produce substantial amounts of endogenous ethanol, which is transported via the portal vein to the liver, where it might trigger inflammation. Disturbances in the composition of the intestinal microbiota are associated with chronic metabolic syndromes such as obesity, NAFLD and type 2 diabetes mellitus (T2DM) (Turnbaugh *et al.*, 2009; Loomba *et al.*, 2013; Donaldson *et al.*, 2016). Diet is one of the main factors that modulate the composition of gut microbiota – it has an influence on species richness. When the number of species decreases, then it comes to a condition known as dysbiosis, which has been associated with the pathogenesis of inflammatory diseases (Jennison *et al.*, 2021). Gut microbiota is responsible for maintaining of the intestinal epithelial barrier, thus preventing the entry of bacteria and their metabolites into the blood (Fig. 1). It is also known that bacterial metabolites play

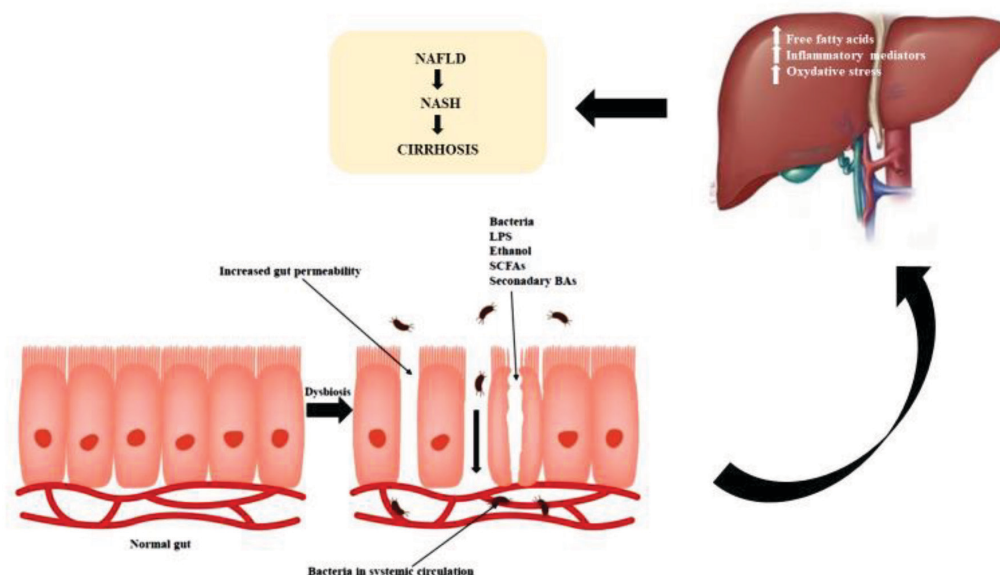


Figure 1. Gut microbiota imbalance contributes to the development of NAFLD, may lead to the nutrition imbalance and change the gut microbiota composition and its metabolites, such as SCFAs, and bile acids.

Microbiota disorders promote the intestinal endocrine L cells to secrete GLP-1 to act on the vagus nerve to activate the gut-brain liver nerve pathway and regulate insulin sensitivity, glucose production, and fatty acid oxidation.

an important role in regulating immune system activity and metabolic functions of the human body, for example, they produce intestinal hormones such as glucagon-like peptide-1 (Svegliati-Baroni *et al.*, 2011). Symbiotic organisms are also responsible for the digestion of polysaccharides, the production of vitamins and the absorption of nutrients. Bäckhed and others (Bäckhed *et al.*, 2004) in his research found out that gut microbiota is involved in adipose tissue growth, due to modulation of energy absorption and stimulation of increased triglycerides synthesis in the liver. Bacteria overgrowth may cause intestinal permeability to increase the amount of endotoxins in the systematic circulation and that will allow for the development of endotoxemia with inflammation in the liver. Some other commensal metabolites may also influence the metabolism of the host and that impact can lead to the development and progression of NAFLD (Aron-Wisniewsky *et al.*, 2020). The human intestine contains at minimum 100 trillion microbes, which belong to at least 1000 different species with 150 times more genes than the human genome has (MetaHIT Consortium *et al.*, 2010; Chassaing *et al.*, 2014). The most common phyla in the human gut are Firmicutes and Bacteroidetes, which are followed by frequently identified Actinobacteria, Proteobacteria, Verrucomicrobia and Fusobacteria (Kamada *et al.*, 2014). There are many factors that influence the composition of GM such as gender, age, diet, hormonal changes, drug intake, travel and pregnancy (Rodríguez *et al.*, 2015; Uchiyama *et al.*, 2019). It is important to keep in mind internal factors that affect the composition of the intestinal microbiota, such as the state of the intestinal mucosa, which affects the permeability of the intestinal barrier and the state of the host immune system (Adams *et al.*, 2008). These factors can lead to unfavorable conditions for some bacteria, leading to lower microbial diversity – dysbiosis. Maintaining homeostasis of GM is crucial for keeping the human body (especially the liver) in good condition. It is linked with beneficial metabolites produced by commensal bacteria. Dysbiosis may occur due to an imbalance in the gut, which will manifest itself through excessive proliferation and overproduction of

harmful substances that affect the liver, due to the fact that the portal vein transports about 70% of the total amount of blood to the liver. This is the main reason why it is exposed to endotoxins or peptidoglycans first – they are transported with blood to the liver, where they will be neutralized. The continuous influx of microbial-derived products may cause disturbances in liver functioning and that might end up with inflammation in liver cells. That generates a response from receptors located on certain types of liver cells such as Kupffer cells, sinusoidal cells, biliary epithelial cells and hepatocytes (Chen *et al.*, 2019). Gut microbiota produce many metabolites and part of them have a negative impact on the liver causing inflammation. Among them, we can highlight bile acids, short-chain fatty acids (SCFAs), choline and ethanol (Chiang *et al.*, 2020). All of them are involved in the development of NAFLD. In this study, not all microbiome metabolites were included due to the character and purpose of this study.

SHORT-CHAIN FATTY ACIDS (SCFAs) ON NAFLD

Another important group of bacterial metabolites are short-chain fatty acids (SCFAs). SCFAs are mainly produced as a result of dietary fiber fermentation in the colon. Then they might be absorbed in the intestine (Liu *et al.*, 2021; Rau *et al.*, 2018). The most common SCFAs are acetate, propionate and butyrate, which are absorbed *via* the portal vein during lipid digestion. SCFAs are binding to G-protein coupled receptor (GPCR), which occurs in many organs, such as the liver, skeletal muscles, adipose tissue, and enteroendocrine L cells, exerting influence on their metabolic and immunological functions (Li *et al.*, 2022). The short-chain fatty acids, mostly acetate and propionate can stimulate gluconeogenesis and lipogenesis, leading to fat accumulation in liver cells (Bastos *et al.*, 2022). Butyrate is responsible for the suppression of insulin resistance and obesity while high fatty diet (HFD) intake in mice model (Gao *et al.*, 2009). Butyrate also has anti-inflammatory potential – it can reduce inflammation in the intestines and reduce inflammatory response due

to activation of regulatory T cells, which will inhibit T cells and Th17 cells (Arpaia *et al.*, 2013). Moreover, it reduces levels of proinflammatory cytokines, such as tumor necrosis factor- α (TNF α) or monocyte chemoattractant protein-1, while increasing levels of prostaglandin E2, which has an anti-inflammatory effect (Smith *et al.*, 2013; Usami *et al.*, 2008; Mouzaki *et al.*, 2019). Butyrate is the most potent anti-inflammatory mediator and can reduce local inflammation in the gut and prevent the progression of inflammatory responses into the systemic circulation. Butyrate can also promote tight junction function and intestinal integrity. Another beneficial effect of butyrate is to provide colonocytes with an energy source to maintain intestinal health. Dysbiosis leads to a decrease in butyrate levels which may cause increased gut permeability, and translocation of bacteria or lipopolysaccharides (LPS) into the systemic circulation, which can lead to the development of NALFD (butyrate promotes the regeneration of enterocytes). T-cells are responsible for releasing Glucagon-like peptides, that stimulate fatty acids β -oxidation in hepatocytes. They also increase insulin sensitivity in liver cells, thus they are important to NALFD development (Svegliati-Baroni *et al.*, 2011). The gut microbiota regulates bile acid homeostasis through biotransformations such as deconjugation, dehydroxylation, oxidation and desulfation. In terms of deconjugation, *Bacteroides*, *Lactobacillus*, *Bifidobacterium*, *Clostridium* and *Listeria* produce bile salt hydrolases (BSH) that deconjugate the taurine and glycine groups in the primary bile acids produced in the liver (Ticho *et al.*, 2019). In experimental animals with dysbiosis or treated with antibiotics, taurine deconjugation by intestinal bacteria was blocked, shifting the balance toward almost exclusively taurine-conjugated bile acids, resulting in increased taurine-conjugated bile acids in the liver, heart and kidneys (Arab *et al.*, 2017). For dehydroxylation, *Clostridium* and *Eubacterium* of the Firmicutes tribe produce 7 α -dehydroxylase of bile acid, which converts primary bile acids (cholic acid and chenodeoxycholic acid) into secondary bile acids (deoxycholic acid, lithocholic acid and ursodeoxycholic acid) (Lund *et al.*, 2018). 7 α -dehydroxylation occurs after deconjugation and is the most physiologically relevant conversion of bile acids in humans. Regarding oxidation, bacteria from genera such as *Bacteroides*, *Clostridium*, *Eubacterium*, *Escherichia*, *Eggerthella*, *Peptostreptococcus* and *Ruminococcus* produce hydroxysteroid bile acid dehydrogenases (HSDH), which convert toxic bile acids into ursodeoxycholic acid, which is less toxic to human cells and more water-soluble (Ni *et al.*, 2022). Finally, several gut bacteria, such as *Clostridium* sp. Strain S2, produce sulfatases that are able to enhance the desulfation of bile acids (Jackson *et al.*, 2022). Desulfation of bile acids by intestinal bacteria facilitates the reabsorption of bile acids (Song *et al.*, 2019) and is essential for the homeostasis of the bile acid pool (Moszak *et al.*, 2021). In the liver are synthesized bile acids by the rate-limiting enzyme cytochrome P450 7A1 (CYP7A1) and secreted into the intestine. Intestinal epithelial cells (IECs) are reabsorbed bile acids by the distal ileum via apical sodium-dependent bile acid transporter (ASBT) where they activate farnesoid X receptor (FXR), inducing the expression and secretion of fibroblast growth factor 15/19 (FGF15/19) to inhibit hepatic bile acid synthesis. Luminal and basolateral bile acids activate Takega G protein-coupled receptor 5 (TGR5) in enteroendocrine L-cells, resulting in the release of the incretin glucagon-like peptide-1 (GLP-1), promoting glucose tolerance (Chiang *et al.*, 2020; Zhou *et al.*, 2014). Overproduction of bile acids can promote di-

arrhea by several distinct mechanisms. In the colon, bile acids disrupt barrier integrity allowing bile acids to reach the basolateral membrane of epithelial cells and induce chloride secretion, though the receptors underlying this phenomenon are unknown. Colonic FXR and TGR5 activation inhibits the secretion of chloride and other electrolytes, which may be a compensatory mechanism. Colonic bile acids activate TGR5 on enterochromaffin cells (ECs), promoting 5-hydroxytryptamine (5-HT) release and motility. Bile acids activate neuronal TGR5, which either stimulates or inhibits motility, depending on the type of neuron and region of the GI tract. Overproduction of bile acids induces colonic secretion and enhances motility, producing a diarrheal phenotype (Wang *et al.*, 2021; Krishnan *et al.*, 2018).

MICROBIAL SYNTHESIS OF ETHANOL

Some bacteria have the ability to produce ethanol in the intestine as a result of polysaccharide fermentation. Normally, the amount of produced ethanol is small, but if dysbiosis occurs its amount may be significantly bigger than that in healthy controls (de Medeiros *et al.*, 2015). The health effect of a high concentration of ethanol is an increase in the permeability of the intestinal barrier, which may result in the development of NALFD and liver steatosis (Chen *et al.*, 2020). Recent studies have shown that increased ethanol levels in the human body are associated with a high abundance of genera *Escherichia*, *Bacteroides*, *Bifidobacterium*, *Clostridium* and *Klebsiella pneumoniae* (Engstler *et al.*, 2016; Mir *et al.*, 2016). Zhu *et al.*, in their study have observed that obese NASH patients have higher levels of endogenous ethanol than non-obese NASH patients or healthy controls. In turn, Yuan and others (Yuan J *et al.*, 2019) proved that the presence of *Klebsiella pneumoniae* K14 was common for patients with NALFD – after transfer, isolates of bacteria cause NALFD-like changes in mice. Also in children with NALFD who were on the same diet as healthy children noticed that ethanol levels were significantly higher. Gut microbiota have enzymes which are involved in the metabolism of ethanol, e.g. aldehyde dehydrogenase. That enzyme converts ethanol into acetaldehyde and acetate. Acetaldehyde takes part in the translocation of microbiota metabolites due to the weakening tight junctions of the intestinal barrier (Schwimme *et al.*, 2020).

OBESITY AND NON-ALCOHOLIC FATTY LIVER DISEASE

Obesity is associated with impaired intestinal barrier function and dysbiosis, resulting in metabolites and other bacterial products such as LPS and other molecular patterns associated with the microbiota, gaining access to the lamina propria in higher concentrations. Diet-induced increases in blood LPS concentrations are known as metabolic endotoxemia. Changes in the intestinal microbiota suggest that changes in diet and intestinal barrier function underlie elevated blood LPS concentrations. Alteration of intestinal TJ proteins, mainly zonula occludens-1 (ZO-1) and occludin, is a major molecular mechanism contributing to increased intestinal permeability (Lin *et al.*, 2022). High-fat diets can lead to intestinal inflammation which in turn can result in TJ changes and increased intestinal permeability. Glucagon-like peptide 2 (GLP2), has been identified as a regulator of TJ protein expression and localization in obese mice. Although the expression pattern of metabolite receptors on

specific tissue-resident leukocytes, such as those in the lamina propria of the gastrointestinal tract, is still poorly understood, manipulation of immune cell metabolism by the gut microbiota may be a powerful approach. Gut-derived metabolites may be a powerful approach to direct the immune response. As is well known, obesity is a risk factor for the development of NAFLD, as well as metabolic syndrome (Rau *et al.*, 2018). The prevalence of overweight and obesity has increased in children and adolescents worldwide over the past 30 years. Gut bacteria produce metabolites by modifying host metabolites, including secondary bile acids. In addition to the classic role of metabolites in bioenergetics and biosynthesis, metabolites can function as signaling molecules, much like hormones and neurotransmitters. Signaling metabolites generated from nutrients or by the intestinal microbiota primarily target the enteroendocrine, neuronal and immune cells in the lamina propria of the intestinal mucosa and liver, and through these tissues to the rest of the body. Metabolites from intermediary metabolism act as metabolic stressors in adipose tissue, liver and pancreas, being effective regulators of pro- and anti-inflammatory regulators of key immune cells, which function as important drivers of low-level inflammation associated with obesity. A large number of metabolite receptors are expressed on immune cells of both the innate and adaptive immune systems, and many different types of immune cells are found in the intestinal mucosa. In lean individuals, the immune cells of the lamina propria are dominated by anti-inflammatory subtypes of innate immune cells, including tolerogenic macrophages and dendritic cells, eosinophils, IL-22-producing innate lymphoid cells and resident regulatory T cells (Tregs) (Miura *et al.*, 2014). Lean but not obese fat is enriched with a unique population of regulatory T cells that influence metabolic parameters. Diet and a sedentary lifestyle are determinants of obesity in children, but obesity in infants is influenced by the gut microbiota profile. As indicated by recently published studies *Bacteroides* and *Lacto Bacillus* spp. are the most common microbes involved in overweight in infants. However, to date, there are no certain species or genera identified as causing childhood obesity *per se* (Clemente *et al.*, 2016). Early gut microbiota in infants can shape weight gain in childhood and controlling factors affecting early infant gut microbiota may prevent later overweight and obesity in children. Exposure to antibiotics changes the diversity of the gut microbiota. Infant exposure to antibiotics is strongly associated with childhood obesity. In children under <6 months of age, repeated antibiotic exposure puts boys at higher risk than girls of developing obesity.

CONCLUSION

In conclusion, bacterial metabolites mediate the communication between the commensal microbiota and the immune system, affecting the balance between pro- and anti-inflammatory mechanisms. Gut dysbiosis has been associated with NAFLD because the effects of an altered gut microbiota in abundance and diversity are mediated by many bacterial metabolites including bile acids, butyrate, choline, amino acids and ethanol. Modulation of the intestinal microbiota and supplementation of some bacterial metabolites may have a therapeutic benefit. The heterogeneous clinical features of NAFLD can be explained by consumption of various dietary factors, interpersonal gut microbiome variability and genetics. In summary, the interplay of dietary factors, gut microbiota

and intestinal barrier integrity plays an important role in the development of obesity and obesity-related NAFLD. Alteration of the gut microbiota is a result of diet, which can promote metabolic endotoxemia and inflammation contributing to the development of obesity and NAFLD. Understanding the role of the gut microbiome, and the mechanism of dietary factor influence gut microbiota, with the identification of components of the microbiome's metabolic activity which significantly affect host metabolism and possibly contribute to obesity and obesity-related NAFLD, might also be an important consideration for NAFLD treatment. Altogether, opportunities and challenges provided by microbiome research lead to future studies, which will hopefully elucidate the more specific role of gut microbiome in NAFLD and establish microbiota-targeted treatment approaches.

Highlights/Perceived strengths

- Intestinal microbiota plays an important role in the development of NAFLD.
- Impaired intestinal barrier integrity, metabolic endotoxemia and inflammation are closely associated with obesity and NAFLD.
- The gut microbiota and intestinal barrier function, promoting metabolic endotoxemia and inflammation can alter the absorption and metabolism of energy-rich foods and their ingredients (e.g., fat and fructose)
- Therapeutic manipulations with prebiotics and probiotics to modulate gut microbiota and maintain integrity of the intestinal barrier are potential efficient agents that should be further tested in NAFLD

Declarations

Author Contributions. AWR, PC and PS drafted the manuscript. AWR and PS contributed to writing the manuscript and critical revision. All authors have read and approved the final manuscript.

Conflicts of Interest. All other authors report no conflict of interest.

REFERENCES

- Adams DH, Eksteen B, Curbishley SM (2008) Immunology of the gut and liver: a love/hate relationship. *Gut* **57**: 838–848. <https://doi.org/10.1136/gut.2007.122168>
- Anderson EL, Howe LD, Jones HE, Higgins JPT, Lawlor DA, Fraser A (2015) The Prevalence of non-alcoholic fatty liver disease in children and adolescents: a systematic review and meta-analysis. *PLoS One* **10**: e0140908. <https://doi.org/10.1371/journal.pone.0140908>
- Arab JP, Karpen SJ, Dawson PA, Arrese M, Trauner M (2017) Bile acids and nonalcoholic fatty liver disease: molecular insights and therapeutic perspectives. *Hepatology* **65**: 350–362. <https://doi.org/10.1002/hep.28709>
- Arpaia N, Campbell C, Fan X, Dikiy S, van der Veeken J, deRoos P, Liu H, Cross JR, Pfeffer K, Coffey PJ, Rudensky AY (2013) Metabolites produced by commensal bacteria promote peripheral regulatory T-cell generation. *Nature* **504**: 451–455. <https://doi.org/10.1038/nature12726>
- Backhed F, Ding H, Wang T, Hooper LV, Koh GJ, Nagy A, Semenkovich CF, Gordon JI (2004) The gut microbiota as an environmental factor that regulates fat storage. *Proc Natl Acad Sci U S A* **101**: 15718–15723. <https://doi.org/10.1073/pnas.0407076101>
- Bastos RMC, Rangel EB (2022) Gut microbiota-derived metabolites are novel targets for improving insulin resistance. *World J Diabetes* **13**: 65–69. <https://doi.org/10.4239/wjcd.v13.i1.65>
- Boyras M, Hatipoğlu N, San E, Akçay A, Taşkın N, Ulucan K, Akçay T (2014) Non-alcoholic fatty liver disease in obese children and the relationship between metabolic syndrome criteria. *Obes Res Clin Pract* **8**: e356–e363. <https://doi.org/10.1016/j.orcp.2013.08.003>
- Buzzetti E, Pinzani M, Tsochatzis EA (2016) The multiple-hit pathogenesis of non-alcoholic fatty liver disease (NAFLD). *Metabolism* **65**: 1038–1048. <https://doi.org/10.1016/j.metabol.2015.12.012>
- Chalasani N, Younossi Z, Lavine JE, Diehl AM, Brunt EM, Cusi K, Charlton M, Sanyal AJ (2012) The diagnosis and management of non-alcoholic fatty liver disease: Practice Guideline by the American Association for the Study of Liver Diseases, American College of

- Gastroenterology, and the American Gastroenterological Association. *Hepatology* 55: 2005–2023. <https://doi.org/10.1002/hep.25762>
- Chassaing B, Etienne-Mesmin L, Gewirtz AT (2014) Microbiota-liver axis in hepatic disease. *Hepatology* 59: 328–339. <https://doi.org/10.1002/hep.26494>
- Chen J, Thomsen M, Vittel L (2019) Interaction of gut microbiota with dysregulation of bile acids in the pathogenesis of nonalcoholic fatty liver disease and potential therapeutic implications of probiotics. *J Cell Biochem* 120: 2713–2720. <https://doi.org/10.1002/jcb.27635>
- Chen X, Zhang Z, Li H, Zhao J, Wei X, Lin W, Zhao X, Jiang A, Yuan J (2020) Endogenous ethanol produced by intestinal bacteria induces mitochondrial dysfunction in non-alcoholic fatty liver disease. *J Gastroenterol Hepatol* 35: 2009–2019. <https://doi.org/10.1111/jgh.15027>
- Chiang JYL, Ferrell JM (2020) Bile acid receptors FXR and TGR5 signaling in fatty liver diseases and therapy. *Am J Physiol-Gastrointest Liver Physiol* 318: G554–G573. <https://doi.org/10.1152/ajpgi.00223.2019>
- Chiang JYL, Pathak P, Liu H, Donepudi A, Ferrell J, Boehme S (2017) Intestinal farnesoid X receptor and Takeda G protein couple receptor 5 signaling in metabolic regulation. *Dig Dis* 35: 241–245. <https://doi.org/10.1159/000450981>
- Clemente JC, Ursell LK, Parfrey LW, Knight R (2012) The impact of the gut microbiota on human health: an integrative view. *Cell* 148: 1258–1270. <https://doi.org/10.1016/j.cell.2012.01.035>
- Clemente MG, Mandato C, Poeta M, Vajro P (2016) Pediatric non-alcoholic fatty liver disease: Recent solutions, unresolved issues, and future research directions. *World J Gastroenterol* 22: 8078–8093. <https://doi.org/10.3748/wjg.v22.i36.8078>
- de Medeiros IC, de Lima JG (2015) Is nonalcoholic fatty liver disease an endogenous alcoholic fatty liver disease? – A mechanistic hypothesis. *Med Hypotheses* 85: 148–152. <https://doi.org/10.1016/j.mehy.2015.04.021>
- Donaldson GP, Lee SM, Mazmanian SK (2016) Gut biogeography of the bacterial microbiota. *Nat Rev Microbiol* 14: 20–32. <https://doi.org/10.1038/nrmicro3552>
- Dumas ME, Barton RH, Toye A, Cloarec O, Blancher C, Rothwell A, Fearnside J, Tatoud R, Blanc V, Lindon JC, Mitchell SC, Holmes E, McCarthy MI, Scott J, Gauguier D, Nicholson JK (2006) Metabolic profiling reveals a contribution of gut microbiota to fatty liver phenotype in insulin-resistant mice. *Proc Natl Acad Sci U S A* 103: 12511–12516. <https://doi.org/10.1073/pnas.0601056103>
- Engstler AJ, Aumiller T, Degen C, Dürr M, Weiss E, Maier IB, Schattenberg JM, Jin CJ, Sellmann C, Bergheim I (2016) Insulin resistance alters hepatic ethanol metabolism: studies in mice and children with non-alcoholic fatty liver disease. *Gut* 65: 1564–1571. <https://doi.org/10.1136/gutjnl-2014-308379>
- Estes C, Razavi H, Loomba R, Younossi Z, Sanyal AJ (2018) Modeling the epidemic of nonalcoholic fatty liver disease demonstrates an exponential increase in burden of disease. *Hepatology* 67: 123–133. <https://doi.org/10.1002/hep.29466>
- Gao Z, Yin J, Zhang J, Ward RE, Martin RJ, Lefevre M, Cefalu WT, Ye J (2009) Butyrate improves insulin sensitivity and increases energy expenditure in mice. *Diabetes* 58: 1509–1517. <https://doi.org/10.2337/db08-1637>
- Jackson KG, Way GW, Zhou H (2022) Bile acids and sphingolipids in non-alcoholic fatty liver disease. *Chin Med J* 135: 1163–1171. <https://doi.org/10.1097/CM9.0000000000002156>
- Jennison E, Byrne CD (2021) The role of the gut microbiome and diet in the pathogenesis of nonalcoholic fatty liver disease. *Clin Mol Hepatol* 27: 22–43. <https://doi.org/10.3350/cmh.2020.0129>
- Kamada N, Núñez G (2014) Regulation of the immune system by the resident intestinal bacteria. *Gastroenterology* 146: 1477–1488. <https://doi.org/10.1053/j.gastro.2014.01.060>
- Krishnan S, Ding Y, Saedi N, Choi M, Sridharan GV, Sherr DH, Yarmush ML, Alaniz RC, Jayaraman A, Lee K (2018) Gut microbiota-derived tryptophan metabolites modulate inflammatory response in hepatocytes and macrophages. *Cell Rep* 23: 1099–1111. <https://doi.org/10.1016/j.celrep.2018.03.109>
- Li D, Li Y, Yang S, Lu J, Jin X, Wu M (2022) Diet-gut microbiota-epigenetics in metabolic diseases: From mechanisms to therapeutics. *Biomed Pharmacother* 153: 113290. <https://doi.org/10.1016/j.biopha.2022.113290>
- Lin YC, Lin HF, Wu CC, Chen CL, Ni YH (2022) Pathogenic effects of *Desulfovibrio* in the gut on fatty liver in diet-induced obese mice and children with obesity. *J Gastroenterol* 57: 913–925. <https://doi.org/10.1007/s00535-022-01909-0>
- Liu P, Wang Y, Yang G, Zhang Q, Meng L, Xin Y, Jiang X (2021) The role of short-chain fatty acids in intestinal barrier function, inflammation, oxidative stress, and colonic carcinogenesis. *Pharmacol Res* 165: 105420. <https://doi.org/10.1016/j.phrs.2021.105420>
- Loomba R, Sanyal AJ (2013) The global NAFLD epidemic. *Nat Rev Gastroenterol Hepatol* 10: 686–690. <https://doi.org/10.1038/nrgastro.2013.171>
- Lund ML, Egerod KL, Engelstoft MS, Dmytryeva O, Theodorsson E, Patel BA, Schwartz TW (2018) Enterochromaffin 5-HT cells – A major target for GLP-1 and gut microbial metabolites. *Mol Metab* 11: 70–83. <https://doi.org/10.1016/j.molmet.2018.03.004>
- MetaHIT Consortium (2010) A human gut microbial gene catalogue established by metagenomic sequencing. *Nature* 464: 59–65. <https://doi.org/10.1038/nature08821>
- Mir H, Meena AS, Chaudhry KK, Shukla PK, Gangwar R, Manda B, Padala MK, Shen L, Turner JR, Dietrich P, Dragatsis I, Rao R (2016) Occludin deficiency promotes ethanol-induced disruption of colonic epithelial junctions, gut barrier dysfunction and liver damage in mice. *Biochim Biophys Acta BBA – Gen Subj* 1860: 765–774. <https://doi.org/10.1016/j.bbagen.2015.12.013>
- Miura K, Ohnishi H (2014) Role of gut microbiota and Toll-like receptors in nonalcoholic fatty liver disease. *World J Gastroenterol* 20: 7381–7391. <https://doi.org/10.3748/wjg.v20.i23.7381>
- Moszak M, Szulinska M, Walczak-Galewska M, Bogdański P (2021) Nutritional approach targeting gut microbiota in NAFLD – to date. *Int J Environ Res Public Health* 18: 1616. <https://doi.org/10.3390/ijerph18041616>
- Mouzaki M, Loomba R (2019) Insights into the evolving role of the gut microbiome in nonalcoholic fatty liver disease: rationale and prospects for therapeutic intervention. *Ther Adv Gastroenterol* 12: 175628481985847. <https://doi.org/10.1177/1756284819858470>
- Ni Y, Lu M, Xu, Y Wang Q, Gu X, Li Y, Zhuang T, Xia C, Zhang T, Gou X, Zhou M (2022) The role of gut microbiota – bile acids axis in the progression of non-alcoholic fatty liver disease. *Front Microbiol* 13: 908011. <https://doi.org/10.3389/fmicb.2022.908011>
- Rau M, Rehman A, Ditttrich M, Groen AK, Hermanns HM, Seyfried F, Beyersdorf N, Dandekar T, Rosenstiel P, Geier A (2018) Fecal SCFAs and SCFA-producing bacteria in gut microbiome of human NAFLD as a putative link to systemic T-cell activation and advanced disease. *United Eur Gastroenterol J* 6: 1496–1507. <https://doi.org/10.1177/2050640618804444>
- Rinninella E, Raoul P, Cintoni M, Franceschi F, Miggiano GAD, Gasbarrini A, Mele MC (2019) What is the healthy gut microbiota composition? A changing ecosystem across age, environment, diet, and diseases. *Microorganisms* 7: 14. <https://doi.org/10.3390/microorganisms7010014>
- Rodríguez JM Murphy K, Stanton C, Ross RP, Kober OI, Juge N, Avershina E, Rudi K, Narbad A, Jenmalm MC, Marchesi JR, Collado MC (2015) The composition of the gut microbiota throughout life, with an emphasis on early life. *Microb Ecol Health Dis* 26. <https://doi.org/10.3402/mehd.v26.26050>
- Schwimmer JB, Johnson JS, Angeles JE, Behling C, Belt PH, Borecki I, Bross C, Durelle J, Goyal NP, Hamilton G, Holtz ML, Lavine JE, Mitreva M, Newton KP, Pan A, Simpson PM, Sirlin CL, Sodergren E, Tyagi R, Yates KP, Weinstock GM, Salzman NH (2019) Microbiome signatures associated with steatohepatitis and moderate to severe fibrosis in children with nonalcoholic fatty liver disease. *Gastroenterology* 157: 1109–1122. <https://doi.org/10.1053/j.gastro.2019.06.028>
- Schwimmer JB, Deutsch R, Kahen T, Lavine JE, Stanley C, Behling C (2006) Prevalence of fatty liver in children and adolescents. *Pediatrics* 118: 1388–1393. <https://doi.org/10.1542/peds.2006.1212>
- Smith PM, Howitt MR, Panikov N, Michaud M, Gallini CA, Bohlooly-Y M, Glickman JN, Garrett WS (2013) The microbial metabolites, short-chain fatty acids, regulate colonic T reg cell homeostasis. *Science* 341: 569–573. <https://doi.org/10.1126/science.1241165>
- Song Z, Cai Y, Lao X, Wang X, Lin X, Cui Y, Kalavagunta PK, Liao J, Jin L, Shang J, Li J (2019) Taxonomic profiling and population patterns of bacterial bile salt hydrolase (BSH) genes based on worldwide human gut microbiome. *Microbiome* 7: 9. <https://doi.org/10.1186/s40168-019-0628-3>
- Svegliati-Baroni G, Saccomanno S, Rychlicki C, Agostinelli L, De Minicis S, Candelaresi C, Faraci G, Pacetti D, Vivarelli M, Nicolini D, Garelli P, Casini A, Manco M, Mingrone G, Risaliti A, Frega GN, Benedetti A, Gastaldelli A (2011) Glucagon-like peptide-1 receptor activation stimulates hepatic lipid oxidation and restores hepatic signalling alteration induced by a high-fat diet in nonalcoholic steatohepatitis: Effect of exenatide on the liver. *Liver Int* 31: 1285–1297. <https://doi.org/10.1111/j.1478-3231.2011.0246>
- The GBD 2015 Obesity Collaborators (2017) Health effects of overweight and obesity in 195 countries over 25 years. *N Engl J Med* 377: 13–27. <https://doi.org/10.1056/NEJMoa1614362>
- Ticho AL, P Malhotra, PK. Dudeja, RK. Gill, WA (2019) Alrfai bile acid receptors and gastrointestinal functions. *Liver Res* 3: 31–39. <https://doi.org/10.1016/j.livres.2019.01.001>
- Tokuura D (2021) Role of the gut microbiota in regulating non-alcoholic fatty liver disease in children and adolescents. *Front Nutr* 8: 700058. <https://doi.org/10.3389/fnut.2021.700058>
- Tremaroli V, Bäckhed F (2012) Functional interactions between the gut microbiota and host metabolism. *Nature* 489: 242–249. <https://doi.org/10.1038/nature11552>
- Turnbaugh PJ, Hamady M, Yatsunenko T, Cantarel BL, Duncan A, Ley RE, Sogin ML, Jones WJ, Roe BA, Affourtit JP, Egholm M, Henrissat B, Heath AC, Knight R, Gordon JI (2009) A core gut

- microbiome in obese and lean twins. *Nature* **457**: 480–484. <https://doi.org/10.1038/nature07540>
- Uchiyama K, Naito Y, Takagi T (2019) Intestinal microbiome as a novel therapeutic target for local and systemic inflammation. *Pharmacol Ther* **199**: 164–172. <https://doi.org/10.1016/j.pharmthera.2019.03.006>
- Usami M, Kishimoto K, Ohata A, Miyoshi M, Aoyama M, Fueda Y, Kotani J (2008) Butyrate and trichostatin A attenuate nuclear factor κ B activation and tumor necrosis factor α secretion and increase prostaglandin E2 secretion in human peripheral blood mononuclear cells. *Nutr Res* **28**: 321–328. <https://doi.org/10.1016/j.nutres.2008.02.012>
- Wang R, Tang R, Li B, Ma X, Schnabl B, Tilg H (2021) Gut microbiome, liver immunology, and liver diseases. *Cell Mol Immunol* **18**: 4–17. <https://doi.org/10.1038/s41423-02-00592-6>
- Wisniewsky JA, Vigliotti C, Witjes J, Le P, Holleboom AG, Verheij J, Nieuwdorp M, Clément K (2020) Gut microbiota and human NAFLD: disentangling microbial signatures from metabolic disorders. *Nat Rev Gastroenterol Hepatol* **17**: 279–297. <https://doi.org/10.1038/s41575-020-0269-9>
- Younossi ZM, Koenig AB, Abdelatif D, Fazel Y, Henry L, Wymer M (2016) Global epidemiology of nonalcoholic fatty liver disease-Meta-analytic assessment of prevalence, incidence, and outcomes. *Hepatology* **64**: 73–84. <https://doi.org/10.1002/hep.28431>
- Yuan J, Chen C, Cui J, Lu J, Yan C, Wei X, Zhao X, Li N, Li S, Xue G, Cheng W, Li B, Li H, Lin W, Tian C, Zhao J, Han J, An D, Zhang Q, Wei H, Zheng M, Ma X, Li W, Chen X, Zhang Z, Zeng H, Ying S, Wu J, Yang R, Liu D (2019) Fatty liver disease caused by high alcohol-producing *Klebsiella pneumoniae*. *Cell Metab* **30**: 675–688. <https://doi.org/10.1016/j.cmet.2019.08.018>
- Zhou X, Cao L, Jiang C, Xie Y, Cheng X, Krausz KW, Oi Y, Sun L, Shah YM, Gonzalez FJ, Wang G, Hao H (2014) PPAR α -UGT axis activation represses intestinal FXR-FGF15 feedback signalling and exacerbates experimental colitis. *Nat Commun* **5**: 4573. <https://doi.org/10.1038/ncomms5573>
- Zhu L, Baker SS, Gill C, Liu W, Alkhourri R, Baker RD, Gill SR (2013) Characterization of gut microbiomes in nonalcoholic steatohepatitis (NASH) patients: A connection between endogenous alcohol and NASH. *Hepatology* **57**: 601–609. <https://doi.org/10.1002/hep.26093>

Age-related effects of fenofibrate on the hepatic expression of sirtuin 1, sirtuin 3, and lipid metabolism-related genes

Adrian Zubrzycki*, Agata Wrońska*✉, Piotr M. Wierzbicki and Zbigniew Kmiec

Department of Histology, Faculty of Medicine, Medical University of Gdańsk, Gdańsk, Poland

Background: Sirtuin 1 (Sirt1) and sirtuin 3 (Sirt3) participate in the regulation of lipid metabolism. Our aim was to investigate the effects of the hypolipemic drug fenofibrate (FN) on hepatic Sirt1 and Sirt3 expression, in relation to the expression of lipid metabolism-related genes and in the context of aging. **Methods and Results:** Young and old male Wistar rats were fed standard chow or supplemented with 0.1% or 0.5% FN for 30 days ($n=7-10$ in each group). In young rats, 0.1% FN did not affect Sirt1 expression, however, 0.5% FN decreased Sirt1 and both doses reduced Sirt3 protein levels. In old rats, 0.5% FN decreased hepatic Sirt1 mRNA and both doses reduced Sirt1 protein levels, but not Sirt3 expression. Although hepatic Ppara protein levels did not change, FN treatment of young rats induced *Cpt1b* expression, whereas *Lcad*, *Acox1*, *Pmp70*, and *Hmgcs2* expression increased only after 0.1% FN, and *Fas2* expression decreased after 0.5% FN. In the liver of old rats, both doses increased *Cpt1b* and *Lcad* expression. Only 0.1% FN increased *Pmp70* and *Hmgcs2* expression, and only 0.5% FN increased *Acox1* and *Fas2* mRNA levels. **Conclusions:** Treatment with fenofibrate at low or high doses may downregulate the expression of Sirt1 and Sirt3 proteins in the rat liver. The dosage of FN affects molecular changes, and aging alters the response to 0.5% FN.

Key words: aging; liver; fenofibrate; sirtuin; lipid metabolism

Received: 01 November, 2022; **revised:** 16 February, 2023; **accepted:** 28 February, 2023; **available on-line:** 06 April, 2023

✉e-mail: agata.wronska@gumed.edu.pl

*Both authors equally contributed to the paper

Acknowledgments of Financial Support: The research was financed by the Polish Ministry of Science and Higher Education in the form of a statutory grant for the Department of Histology, Medical University of Gdańsk, Poland (02-0012) to ZK.

Abbreviations: Acox1, acyl-coenzyme A oxidase; Acl, ATP-citrate lyase; Cpt1b, carnitine palmitoyltransferase 1b; Fas2, fatty acid synthase 2; FGF21, fibroblast growth factor 21; FN, fenofibrate; HFD, high-fat diet; Hmgcs2, 3-hydroxy-3-methylglutaryl-coenzyme A synthase 2; Lcad, long-chain fatty acid dehydrogenase; PGC1 α , peroxisome proliferator-activated receptor gamma coactivator 1 alpha; Pmp70, peroxisomal membrane protein 70; PPAR α , peroxisome proliferator-activated receptor alpha; Sirt1, sirtuin 1; Sirt3, sirtuin 3; SREBP, sterol regulatory element-binding protein

INTRODUCTION

Aging decreases the ability to respond to stress and leads to the accumulation of molecular damage (Pyo *et al.*, 2020). Aging-associated changes in energy metabolism and nutrient sensing pathways may lead to disorders in lipid homeostasis, which manifest as elevated concentrations of triglycerides, total cholesterol, and LDL cholesterol in blood plasma (Liu & Li, 2015). The hypolipemic

drug fenofibrate (FN) is used to counteract disturbances in lipid metabolism. FN decreases serum triglyceride and VLDL- and LDL-cholesterol levels, while it increases serum HDL-cholesterol (Sahebkar *et al.*, 2017). In the liver, FN stimulates fatty acid oxidation in mitochondria and peroxisomes through the induction of peroxisome proliferator-activated receptor alpha (PPAR α) (Gebel *et al.*, 1992). FN exerts additional beneficial effects through PPAR α -dependent and independent mechanisms, e.g. in cardiac, renal, and vascular disorders (Balakumar *et al.*, 2019). FN may thus offer new treatment venues for conditions besides hyperlipidaemia. However, it has not been well investigated whether FN affects the expression of sirtuins in the liver.

Sirtuins (SIRT1-SIRT7) are a family of NAD⁺-dependent deacetylases, which target histones and non-histone proteins (Zhao *et al.*, 2020). Sirtuins can protect cells against metabolic and oxidative stresses, and may therefore safeguard against some aging-associated alterations, as evidenced by genetic studies in mice (Rodgers & Puigserver, 2007; Pfluger *et al.*, 2008; Zhao *et al.*, 2020). The relationships between the activity of sirtuins and energy metabolism make them a potential therapeutic target for the treatment of metabolic diseases. Two members of the sirtuin family are particularly important for lipid metabolism. SIRT1, the best-studied member of the sirtuin family, decreases blood plasma cholesterol and triglyceride concentrations by inhibitory deacetylation of sterol regulatory element-binding proteins (SREBP) in the liver (Walker *et al.*, 2010). The SREBP belong to transcription factors that control lipid homeostasis by promoting the expression of lipogenic (e.g. fatty acid synthase, FAS) and cholesterologenic genes in the fed state (Walker *et al.*, 2010). Moreover, SIRT1 deacetylates peroxisome proliferator-activated receptor gamma coactivator 1-alpha (PGC1 α) in the liver (Rodgers *et al.*, 2005; Rodgers & Puigserver, 2007), skeletal muscle and adipose tissue (Feige *et al.*, 2008). This post-translational regulation of PGC-1 α leads to the induction of gluconeogenic genes and glucose output in the liver (Rodgers *et al.*, 2005) and enhances oxidative metabolism in muscles and brown adipose tissue (Feige *et al.*, 2008). SIRT1 also interacts with the transcription factor PPAR α at the PPAR response element (PPRE) sequence of target genes (e.g. fibroblast growth factor type 21, FGF21). Upon this interaction with SIRT1, PPAR α mediates the adaptive response to fasting and starvation by transcriptional activation of genes involved in fatty acid oxidation (Purushotham *et al.*, 2009).

The mitochondrial sirtuin SIRT3 regulates multiple mitochondrial enzymes both at the transcriptional level and through their reversible deacetylation in mitochondria. SIRT3 is induced during fasting, and

through deacetylation increases the activity of long-chain acyl-coenzyme A dehydrogenase (LCAD), a key enzyme of mitochondrial fatty acid β -oxidation (Hirschey *et al.*, 2010). Similarly, SIRT3 deacetylates and activates 3-hydroxy-3-methylglutaryl-CoA synthase 2 (HMGCS2) (Shimazu *et al.*, 2010), the rate-limiting enzyme in the ketone body β -hydroxybutyrate synthesis. In addition, SIRT3 activates enzymes of the tricarboxylic acid (TCA) cycle and the urea cycle, and regulates reactive oxygen species levels (reviewed by Zhao *et al.*, 2020). Thus, SIRT3 activity is involved in the regulation of multiple metabolic pathways in mitochondria.

Importantly, both SIRT1 and SIRT3 may mitigate metabolic dysfunctions which are often associated with aging. Transgenic models have shown that increased SIRT1 activity protects against insulin resistance, type 2 diabetes (T2D) and diabetic complications, high-fat diet-induced hepatic steatosis, and adipose tissue inflammation (Rodgers & Puigserver, 2007; Pfluger *et al.*, 2008; Guo *et al.*, 2015). Mice with whole-body SIRT3 knock-out showed peripheral insulin resistance due to increased fatty acid oxidation and reduced glucose uptake in skeletal muscle (Lantier *et al.*, 2015). When SIRT3 KO mice were fed a high-fat diet (HFD) they developed hyperlipidemia, impaired glucose tolerance, insulin resistance, and steatohepatitis (Hirschey *et al.*, 2011).

Despite the well-established roles of SIRT1 and SIRT3 in the control of fuel metabolism and suppression of some mechanisms of aging, there is limited data on the expression of these sirtuins in response to pharmacological challenge with fenofibrate, and in the context of ageing. It was reported that Sirt1 protein levels were upregulated by FN in TNF α -treated adipocytes (Wang *et al.*, 2013), the kidney (Kim *et al.*, 2016), endothelial cells (Wang *et al.*, 2014), and cardiac muscle (Liu *et al.*, 2016) in animal models, and Sirt3 protein abundance decreased in the mouse liver after bezafibrate (100 mg/kg/day for 4 weeks) (Barger *et al.*, 2017). However, it is not clear whether FN affects Sirt1 or Sirt3 levels in the liver. We, therefore, undertook to examine: (1) the effect of aging on hepatic expression of Sirt1 and Sirt3 in the rat; (2) whether FN affects the hepatic expression of Sirt1 and Sirt3 in non-obese, normolipemic rats; and (3) whether this effect of FN is modulated by physiological aging. In our previous work, we have demonstrated that FN had a significant hypolipemic effect in normally-bred old rats (Zubrzycki *et al.*, 2020). Therefore, in the present study, we decided to investigate the molecular changes brought about by FN treatment in rat liver in old as compared to young rats bred in standard, non-obesogenic conditions. We examined the gene expression of factors that play key roles in the regulation of lipid metabolism (Murray *et al.*, 2012): the transcriptional regulators *Ppara*, *Pgc1a*, and *Fgf21*; the mitochondrial enzymes carnitine palmitoyltransferase 1b (*Cpt1b*), long-chain fatty acid dehydrogenase (*Lcad*), as well as the rate-limiting ketogenic enzyme *Hmgcs2*. We also determined the expression of genes encoding the peroxisomal acyl-CoA oxidase (*Acox1*) and the organelle's marker, peroxisomal membrane protein 70 (*Pmp70*). Moreover, we investigated the expression of genes encoding the lipogenic enzymes ATP-citrate lyase (*Acl*) and fatty acid synthase 2 (*Fas2*). In this paper, we demonstrate that depending on the dose, fenofibrate differently affects the expression of genes involved in lipid metabolism and that aging affects the response to high-dose fenofibrate treatment.

MATERIALS AND METHODS

Animals, treatment, and material sampling

Young (4-month-old) and old (24-month-old) male Wistar-Han rats were bred in the Academic Animal Experimental Center in Gdańsk, Poland, and housed one *per* cage in standard breeding conditions (22 \pm 2°C, humidity 55 \pm 10%, 12 h/12 h light/dark cycle). For 30 days, the animals were given 0.5% FN (Glentham Life Sciences, Corsham, UK) mixed into standard rodent chow (high dose; $n=10$ young and 9 old animals). Control animals ($n=10$ young and 7 old) were fed the same chow without supplementation (Labofeed H, Wytownia Pasz Morawski, Kcynia, Poland). The dose was expected to provide approximately 100 mg/day FF according to the measured baseline food intake (20.7 \pm 2.43 g, mean \pm S.D., for the young and 23.4 \pm 4.97 g for the old rats). With respect to the mean body weight at the onset of the treatment (395 g for the young and 552 g for the old rats), the 0.5% FN dose was equivalent to 260 and 210 mg/kg body weight in young and old rats, respectively. Because the treatment with 0.5% FN had some negative effects on the histology of the liver in both young and old rats (Zubrzycki *et al.*, 2020), in a separate experiment we treated rats with 0.1% FN for 30 days (low dose; $n=9$ –10 animals in each group) in the same breeding conditions as for 0.5% FN. At the end of the experiments, the animals were sacrificed under full isoflurane anesthesia through exsanguination from heart puncture. Liver samples were collected and immediately frozen in liquid nitrogen for molecular analyses. The experimental procedures were approved by the Local Ethics Committee in Bydgoszcz, Poland (protocols No. 41/2017, 58/2017, 40/2018, and 5/2019), and carried out accordingly.

Quantitative polymerase chain reaction (qPCR)

The mRNA levels of *Acox1*, *Acl*, *Cpt1b*, *Fas2*, *Fgf21*, *Hmgcs2*, *Lcad*, *Pgc1a*, *Pmp70*, *Ppara*, *Sirt1*, and *Sirt3* were assessed in liver samples by qPCR method (StepOne Plus apparatus, Life Technologies-Applied Biosystems, Grand Island, NY, USA). Total RNA Mini kit (A&A Biotechnology, Gdynia, Poland) was used for RNA extraction according to the manufacturer's protocol, and the obtained RNA was stored at -80°C . 1 μg RNA was reverse-transcribed (RT) with M-MuLV RT enzyme (Thermo Fisher Scientific, Fitchburg, WI, USA) and oligo(dT)₁₈ primers (Sigma-Aldrich, Munich, Germany). 5 \times diluted cDNA was used in qPCR reactions with SensiFastSybr™ No-Rox reagent (Bioline, London, UK) and primers at 200 nM final concentration. mRNA levels were quantified relative to the expression of the geometric mean of acidic ribosomal phosphoprotein P0 (*36B4*) and cyclophilin A (*CycloA*) levels, and analysed using the $\Delta\Delta\text{Ct}$ method. The primers were designed using Primer3Plus software based on BLAST, Ensembl, and AceView databases (Table 1).

Western blotting (WB)

The semi-quantification of Sirt1, Sirt3, and Ppara proteins in liver samples (6 animals per group) was performed using the WB method. Whole-cell lysates were prepared with Mammalian Cell Extraction Kit (BioVision, Milpitas, CA, USA). Protein samples were separated by 10% SDS-PAGE, transferred to PVDF membranes (Bio-Rad, Warsaw, Poland), and blocked with

Table 1. Primers used in qPCR.

Gene name and symbol	Primer sequence [5'→3']
<i>Acidic ribosomal phosphoprotein P0 (36B4)</i>	F: CTCAGTGCCTCACTCCATCA R: GGGGCTTAGTCGAAGAGACC
<i>Acyl-CoA oxidase 1 (Acox1)</i>	F: GTCTCTTGATTCTCTCTATGG R: GTAAGATTCATGGACCTCTG
<i>ATP-citrate lyase (Acl)</i>	F: ATGGCAACACCCTCGTAGAC R: CTCACACGGAAGCTCATCAA
<i>Carnitine palmitoyltransferase 1b (Cpt1b)</i>	F: ATGTTTGACCCAAAGCAGTACCC R: TCGCTGCGATCATGTAGGAAAC
<i>Cyclophilin A (CycloA)</i>	F: TGTCTCTTTTCGCCGCTTGCTG R: CACCACCCTGGCACATGAATCC
<i>Fatty acid synthase 2 (Fas2)</i>	F: TACGGTCTGCAGTGCACCCA R: GGTCAGCTTGCCCGTAGC
<i>Fibroblast growth factor type 21 (Fgf21)</i>	F: AGTTTGGGGGTCAAGTCCGA R: AGGAGACTTCTGCGACTGCCGG
<i>Hydroxy-methylglutaryl-CoA synthase 2 (Hmgcs2)</i>	F: ACCACAAGGTGAACCTTCTCTC R: TTTGGGTAACGGCTCTGCTC
<i>Long-chain fatty acid dehydrogenase (Lcad)</i>	F: TCGAGCAGTTTATCCCCCAG R: TGAACACCTTGCTTCCATTGAG
<i>PPAR gamma coactivator-1 alpha (Pgc1a)</i>	F: CACGTTCAAGGTACCCCTACAGC R: TAAATCACACGGCGCTCTTCAAT
<i>70 kDa peroxisomal membrane protein (Pmp70)</i>	F: TGTCTGCCTGTCCACAAG R: CACCACAGCTCGCTCTTCT
<i>Peroxisome proliferator-activated receptor alpha (Ppara)</i>	F: CTATAATTTGCTGTGGAGATCG R: CTACCATCTCAGGAAAAATAG
<i>Sirtuin 1 (Sirt1)</i>	F: CAGAACCAACAAAGCGGAAAAA R: GAAACCCCACTCCAGTCAGAA
<i>Sirtuin 3 (Sirt3)</i>	F: AAGCTGGTTGAAGCTCATGGGTC R: TCCAGGGAGGTCCAAGAATGAG

F, forward primer; R, reverse primer

7% non-fat milk in TBS with 0.1% Tween20 (TBST) for 1 h. The membranes were incubated with the following primary antibodies at 4°C overnight: anti-Sirt1 (Bioss, bs-0921R; Woburn, MA, USA), anti-Sirt3 (Bioss, bs-6105R), or anti-Ppar α (Bioss, bs-3614R) rabbit polyclonal antibodies, diluted 1:1000 in 3% non-fat milk in TBST. After that, the membranes were washed and next incubated with HRP-conjugated anti-rabbit secondary antibodies (1:10000 in 3% non-fat milk in TBS) (Merck Millipore, A9169; Darmstadt, Germany) for 2 h at room temperature. Bands were visualized using Clarity Western ECL Substrate (Bio-Rad, Hercules, CA, USA) and developed using ImageQuant LAS 500 Chemiluminescence CCD Camera (GE Healthcare Life Sciences, Pittsburgh, PA, USA). Sirt1, Sirt3, and Ppar α protein levels were analyzed relative to glyceraldehyde 3-phosphate dehydrogenase (Gapdh) levels (1:50000 in 3% non-fat milk in TBST, 1 h at room temperature) (Merck Millipore, AB2302) using QuantityOne Software (Bio-Rad).

Statistical analysis

Statistical analysis was performed using GraphPad Prism (v. 6.0; San Diego, CA, USA). Data were analyzed for outliers using the Grubbs' test. Because not all sets of data followed a normal distribution (Shapiro-Wilk test), statistical analysis was performed using the nonparametric Kruskal-Wallis ANOVA with Dunn's multiple comparisons test. Data are presented as mean \pm S.D. and normalized to young control animals (expression level=1). Data obtained for control rats on normal diet in the two separately conducted experiments testing 0.1% and 0.5% FF were combined after checking that

there were no significant differences between the control groups. Statistical significance was set at $p < 0.05$.

RESULTS

Sirt1 and Sirt3 expression at the mRNA and protein level

Young and old control rats did not differ with respect to the hepatic mRNA and protein expression levels of Sirt1 and Sirt3 (Fig. 1).

In young rats, FN treatment at either dose did not affect *Sirt1* and *Sirt3* mRNA levels in the liver (Fig. 1A). Even though *Sirt1* expression was notably upregulated in a subset of rats treated with 0.1% FN, no statistical significance was found. In old rats, 0.1% FN did not cause any changes in *Sirt1* expression, but 0.5% FN decreased *Sirt1* expression 6.25-fold ($p < 0.01$; Fig. 1B). FN did not cause any changes in *Sirt3* expression in the liver of old rats (Fig. 1B).

In the liver of young rats, 0.1% FN did not affect Sirt1 protein expression; however, 0.5% FN treatment decreased hepatic Sirt1 protein level by 3.33-fold ($p < 0.05$; Fig. 1C). Moreover, 0.1% and 0.5% FN decreased Sirt3 protein levels 3.86-fold and 3.33-fold, respectively ($p < 0.05$ and $p < 0.001$, respectively; Fig. 1C).

In old rats, 0.1% and 0.5% FN decreased hepatic Sirt1 protein level 3.03-fold and 2.86-fold, respectively ($p < 0.05$ for both; Fig. 1D). However, neither dose of FN affected Sirt3 protein level in the liver of old rats (Fig. 1D).

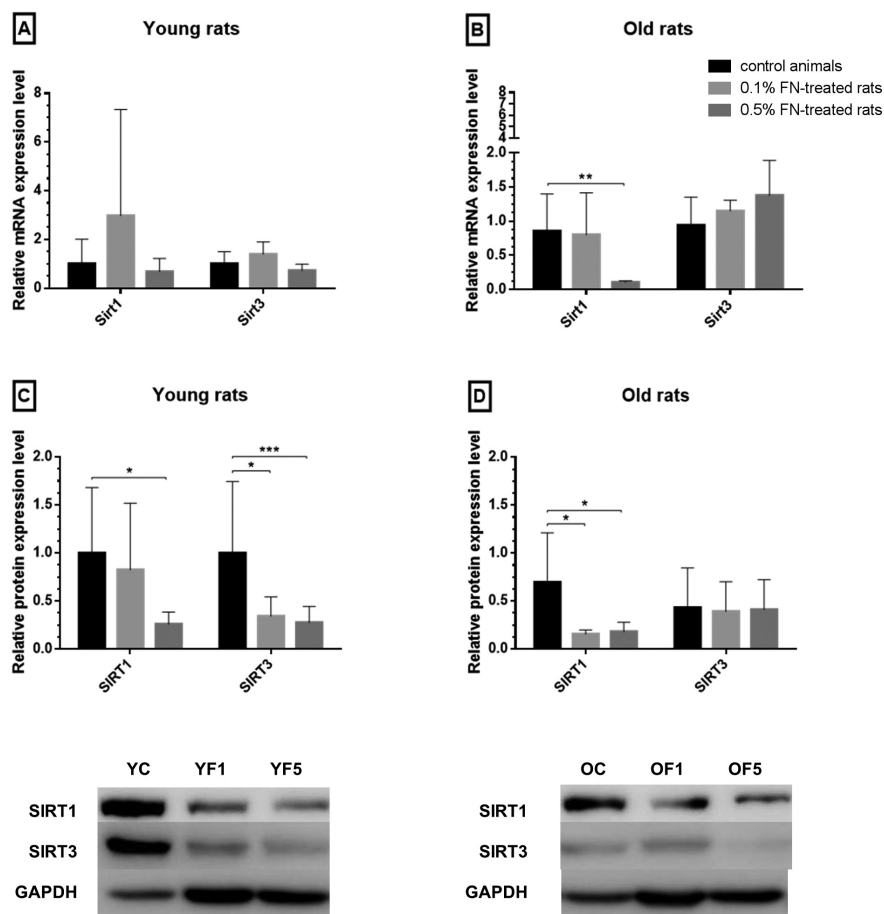


Figure 1. Relative mRNA (A & B) and protein (C & D) expression of Sirt1 and Sirt3 in the liver of control and fenofibrate (FN)-treated young and old rats.

The mRNA and protein expression levels were determined by qPCR and Western blotting, respectively, with representative blots shown. Data are mean \pm S.D., presented relative to the level in young control rats (set as 1), $n=6-10$ animals per group. For clarity, data from young and old rats are separated into two graphs, with the scale maintained. * $p<0.05$, ** $p<0.01$, *** $p<0.001$ (Kruskal-Wallis ANOVA). Abbreviations: YC young (4-month-old) control rats; YF1 young rats treated with 0.1% FN; YF5 young rats treated with 0.5% FN; OC old (24-month-old) control rats; OF1 old rats treated with 0.1% FN; OF5 old rats treated with 0.5% FN.

Ppara expression

In old as compared to young rats, hepatic *Ppara* gene expression was 4-fold higher ($p<0.001$), while *Ppara* protein levels were comparable in the two groups (Fig. 2).

In the liver of young rats, 0.1% FN increased *Ppara* expression by 3-fold ($p<0.05$), while 0.5% FN was without effect (Fig. 2A). In the liver of old rats, 0.1% FN did not affect *Ppara* expression, whereas 0.5% FN treatment decreased *Ppara* expression by 5-fold ($p<0.01$; Fig. 2A).

In both young and old rats, neither dose of FN changed the *Ppara* protein level in the liver (Fig. 2B).

The effects of fenofibrate on the expression of lipid metabolism-related genes in the liver of young and old rats

In our study, aging was not associated with any changes in the hepatic mRNA levels of *Cpt1b*, *Lcad*, *Pgc1a*, *Hmgcs2*, *Acox1*, *Pmp70*, *Acl*, *Fas2*, and *Fgf21* (Fig. 3).

In young rats, FN treatment increased the hepatic expression of genes encoding enzymes involved in mitochondrial β -oxidation of fatty acids. 0.1% and 0.5% FN increased *Cpt1b* expression levels by 100-fold and 90-fold, respectively ($p<0.001$ for both; Fig. 3A) and 0.1% FN increased *Lcad* expression by 1.5-fold ($p<0.01$).

However, neither dose of FN affected *Pgc1a* expression (Fig. 3A).

The expression of the key ketogenic gene, *Hmgcs2*, in the liver of young rats increased 3.5-fold ($p<0.001$; Fig. 3C) upon treatment with 0.1% FN; however, 0.5% FN was without effect. With regard to peroxisomal β -oxidation, the hepatic expression of *Acox1* increased 22-fold ($p<0.01$; Fig. 3C) in rats treated with 0.1% FN, with no effect of 0.5% FN. Similarly, only 0.1% FN highly increased *Pmp70* expression ($p<0.05$; Fig. 3C).

In young rats, the hepatic expression of the lipogenic gene *Acl* was not affected by FN treatment, while the expression of the key lipogenic gene *Fas2* decreased 4-fold ($p<0.05$) after treatment with 0.5% FN, with no effect of 0.1% FN (Fig. 3E).

In the liver of old rats, 0.1% and 0.5% FN increased *Cpt1b* expression 15-fold and 50-fold, respectively ($p<0.01$ for both) and increased *Lcad* expression 6-fold and 2.5-fold ($p<0.001$ and $p<0.05$, respectively; Fig. 3B). Similarly as in the liver of young rats, the mRNA levels of *Pgc1a* were not affected by FN treatment (Fig. 3B).

The expression of the ketogenic gene *Hmgcs2* in the liver of old rats increased 3.2-fold ($p<0.01$; Fig. 3D) upon treatment with 0.1% FN (but not 0.5% FN). In old rats, 0.1% FN did not affect *Acox1* mRNA level, while 0.5% FN increased its expression 17-fold ($p<0.001$;

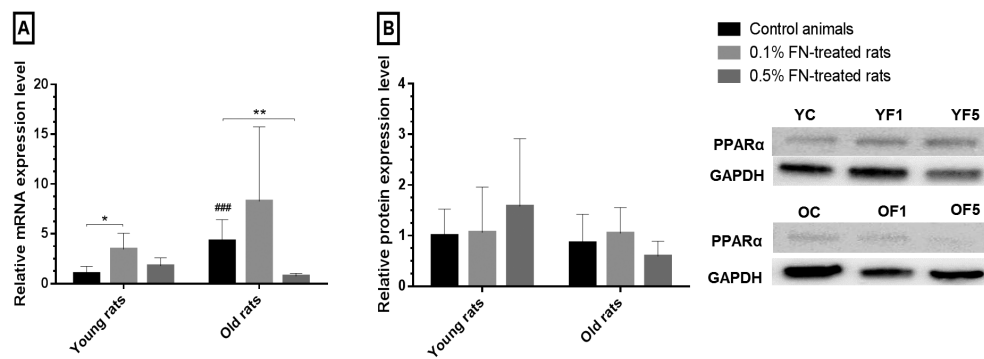


Figure 2. Relative mRNA (A) and protein (B) expression of Ppara in the liver of control and fenofibrate-treated young and old rats. The mRNA and protein expression levels were determined by qPCR and Western blotting, respectively. Representative blots are shown in (B). Data are mean \pm S.D., presented relative to the level in young control rats (set as 1), $n=6-10$ animals per group. * $p<0.05$; ** $p<0.01$; *** $p<0.001$ (Kruskal-Wallis ANOVA). Abbreviations as in the description of Fig. 1.

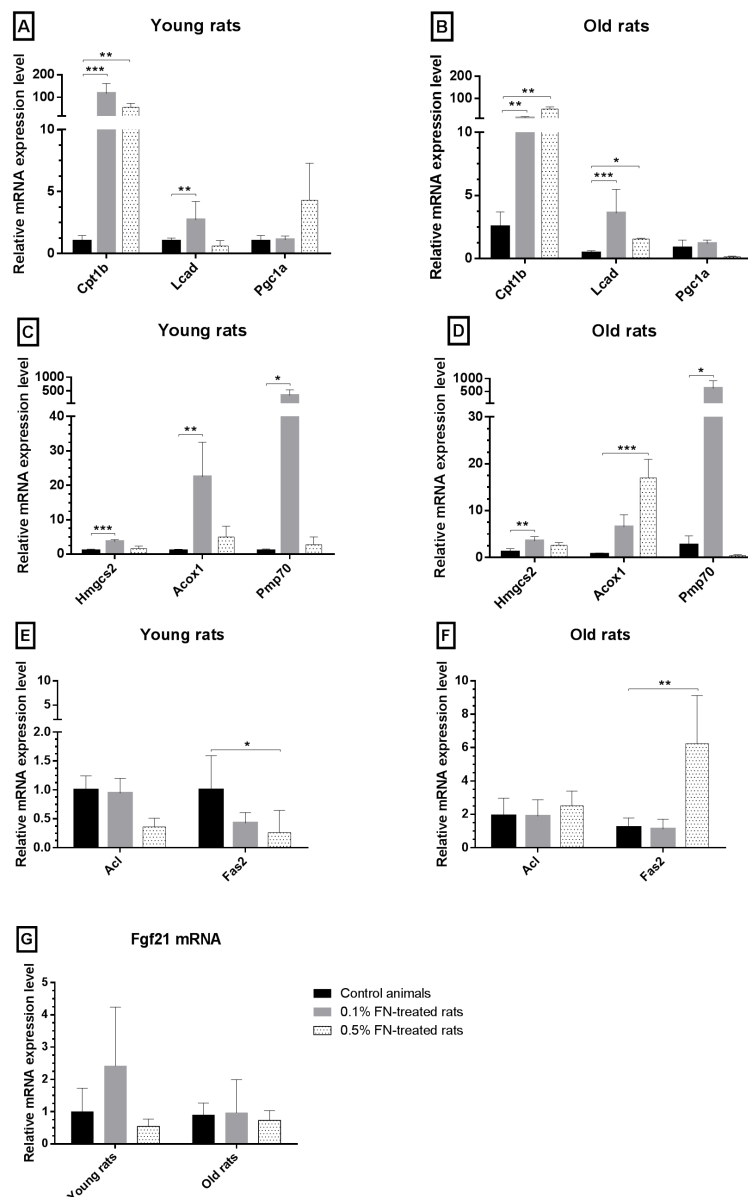


Figure 3. Relative mRNA expression of genes involved in lipid metabolism and Fgf21 in the liver of control and fenofibrate-treated young and old rats. A & B: *Cpt1b*, *Lcad*, and *Pgc1a*. C & D: *Hmgcs2*, *Acox1*, and *Pmp70*. E & F: *Acl* and *Fas2*. G: *Fgf21*. For clarity, data from young and old rats are separated into two graphs (except for G), with the scale maintained. The mRNA expression levels were determined by qPCR and presented as mean \pm S.D. relative to young control rats (set as 1), $n=7-10$ animals per group. * $p<0.05$, ** $p<0.01$, *** $p<0.001$ (Kruskal-Wallis ANOVA)

Fig. 3D). Only 0.1% FN highly increased *Pmp70* expression ($p < 0.05$; Fig. 3D) in the liver of old rats.

The treatment of old rats with 0.5% FN did not alter hepatic *Acl* expression. However, in contrast to young animals, in old rats treated with 0.5% FN the hepatic expression of *Fas2* increased 6-fold ($p < 0.01$; Fig. 3F).

The expression of *Fgf21* was not affected by FN treatment in either young or old rats (Fig. 3G).

DISCUSSION

We present a comprehensive analysis of Sirt1 and Sirt3 expression in the liver, the key organ of lipid metabolism, upon 30-day treatment of young and old rats with two doses of FN, i.e. 0.1% (low dose) and 0.5% (high dose). We demonstrate that these two doses of FN differently affected the expression of genes involved in lipid metabolism, with aging affecting the response to 0.5% FN.

Sirt1 and Sirt3 have both been associated with protection against age-related diseases, including metabolic derangements (reviewed by Zhao *et al.*, 2020). Therefore, we first examined whether aging affects the hepatic expression of these sirtuins. We found no age-related differences in either mRNA or protein levels of Sirt1 and Sirt3. Similarly, no effect of aging on Sirt1 protein level was observed in the liver of 19–26 month-old C57BL/6 mice compared to young, 2–4 month-old animals, even though there were reductions in other tissues (Xu *et al.*, 2020). In contrast, Jin and others (Jin *et al.*, 2011) reported that in the liver of old mice Sirt1 mRNA and protein expression decreased due to repression of the gene promoter by CCAAT/Enhancer Binding Protein/histone deacetylase 1 (C/EBPb-HDAC1) complex. Sirt3 protein level was downregulated in the liver of 20-month-old mice (Kwon *et al.*, 2017) and this reduction was attributed to the decreased level of Sirt1, which deacetylates and stabilizes Sirt3 (Kwon *et al.*, 2017). It is plausible that differences in chow composition and time of probing, together with different genetic backgrounds of rat and mouse strains may account for the discrepancies. Moreover, it is important to consider that aging-related changes differ between organs and tissues. For example, in the same rat strain bred under similar conditions, we have found that the old compared to young rats showed lower *Sirt3* expression in skeletal muscle, but maintained high expression in cardiac muscle (Ławniczak *et al.*, 2022).

Considering the involvement of Sirt1 and Sirt3 in the control of lipid homeostasis, we examined whether the hypolipemic drug FN affects their hepatic expression. Since dyslipidemia is increasingly common with advancing age (Liu & Li, 2015), we chose normal breeding conditions to determine the effect of FN during physiological aging. We found that depending on the dose and the rat's age FN decreased the protein abundance of Sirt1 and Sirt3 in the liver, with little effect on the mRNA levels. It is generally accepted that the protein levels rather than mRNA are more important for the activity of a particular bioactive molecule. Sirt1 activity can be regulated by several mechanisms, including activation through autocatalytic deacetylation (Fang *et al.*, 2017) or cAMP-dependent activating phosphorylation (Gerhart-Hines *et al.*, 2011). With regard to Sirt3, the decrease in protein levels observed in our study upon FN treatment of young rats may be related to the reduction in Sirt1 level, since Sirt1 was shown to deacetylate and stabilize Sirt3 (Kwon *et al.*, 2017).

To our best knowledge, this is the first study examining the expression of Sirt1 and Sirt3 in the liver of young and old FN-treated rats under normal breeding conditions. The FN-induced reduction of Sirt1 abundance is consistent with some other studies conducted in different experimental settings. In young Wistar rats with HFD-induced hyperlipidaemia, the highly elevated hepatic Sirt1 protein and mRNA expression was reduced after treatment with FN for 21 days, although to a level significantly higher than in control animals (Le *et al.*, 2014). In contrast, no effect on hepatic Sirt1 protein level was observed in young mice treated with approx. 400 mg/kg FN for 5 days (Li & Wu, 2018). Reports on hepatic Sirt3 expression upon FN treatment showed either no impact of the drug (approx. 400 mg/kg/day, 5 days) (Li & Wu, 2018) or prevention of iron overload-induced downregulation of Sirt3 (100 mg/kg, i.p., 6 weeks) (Mandala *et al.*, 2021).

We next analyzed the hepatic expression of genes encoding enzymes and transcriptional regulators involved in lipid metabolism, the activity of which is directly or indirectly regulated by SIRT1 and SIRT3. We have previously reported that in our cohort of rats FN exerted a hypolipemic effect, which was more prominent in old than in young animals (Zubrzycki *et al.*, 2020). The major molecular target activated by FN (Gebel *et al.*, 1992), the nuclear receptor PPAR α , is regulated by ligand binding (Balanarasimha *et al.*, 2014) and post-translationally by phosphorylation (Nakamura *et al.*, 2019). Similarly to our results, various studies demonstrated FN action without altering PPAR α level (e.g. Zhao *et al.*, 2015; Liu *et al.*, 2016). We analyzed several transcriptional targets of PPAR α (Rakhshandehroo *et al.*, 2010): *Cpt1b*, an enzyme responsible for the transport of fatty acids across the mitochondrial outer membrane, *Lead*, involved in mitochondrial β -oxidation of fatty acids, and *Acox1*, the rate-limiting enzyme of peroxisomal β -oxidation. Among the *Cpt1* isoforms, the *Cpt1b* gene is expressed in the liver at lower levels than the *Cpt1a* isoform, which is known to be upregulated by FN (e.g. de la Rosa Rodriguez *et al.*, 2018). The *Cpt1b* expression in our study was strongly upregulated by both doses of FN in either age group. *Lead* expression was induced by 0.1% FN and to a smaller degree and only in old rats by 0.5% FN. Stimulation of mitochondrial fatty acid oxidation-related genes by FN confirms the results of most other studies (Karahashi *et al.*, 2013; Zhao *et al.*, 2017). While *Acox1* expression was induced by both FN doses in young rats, its induction by only the higher FN dose in old animals may reflect the general rule that in aging higher doses of activators are needed for the induction of many target genes (e.g. Kobilo *et al.*, 2014; Zubrzycki *et al.*, 2020). The expression of *Pmp70*, which has been described as a specific marker for PPAR α activation and peroxisome proliferation (Colton *et al.*, 2004), was highly induced by 0.1% FN in both age groups.

SIRT1 has been reported to interact with PPAR α at the PPAR response element sequence of target genes (Purushotham *et al.*, 2009). Sirt1 levels in young rats did not change upon 0.1% FN treatment but decreased after 0.5% FN. This may explain the induction of PPAR α -regulated target genes for mitochondrial and peroxisomal enzymes primarily after 0.1% FN in young animals. However, old rats showed downregulation of Sirt1 protein levels after both doses, indicating Sirt1-independent modulation of genes for fatty acid oxidation. Indeed, Bonzo and others (Bonzo *et al.*, 2014) showed that hepatic SIRT1 is dispensable for FN-induced PPAR α function *in vivo*. In young mice treated with 0.1% FN for

5 days following the HFD, hepatocyte-specific *Sirt1* knockout did not affect the induction of PPAR α target genes (Bonzo *et al.*, 2014).

PPAR α also controls the expression of *Fgf21*, a hepatokine that promotes lipid oxidation, lipolysis, and ketogenesis in the liver during ketotic states (Badman *et al.*, 2007) and upon treatment with sodium butyrate (Li *et al.*, 2012). We did not observe any significant changes in *Fgf21* mRNA expression upon treatment with FN, in contrast to the induction of both mRNA and protein levels of FGF21 reported in hepatocytes treated *in vitro* with 500 μ mol/L FN (Li *et al.*, 2012). On the other hand, FGF21 has been recently demonstrated to be dispensable for FN action on lipogenesis- or autophagy-related proteins in the murine liver (Jo *et al.*, 2017). Furthermore, the ketogenesis-related gene *Hmgcs2*, whose transcription is regulated by both PPAR α (Meertens *et al.*, 1998; Vilà-Brau *et al.*, 2011) and reciprocally by FGF21 (Meertens *et al.*, 1998; Badman *et al.*, 2007; Vilà-Brau *et al.*, 2011), was induced in our study after treatment with 0.1% FN in both young and old rats. In line with our results, a principal transcriptomics analysis of the livers of the FN-treated hepatocyte humanized mice revealed that among many established PPAR α targets FN induced *Hmgcs2* (de la Rosa Rodriguez *et al.*, 2018). Likewise, dietary obese mice after a single injection of bezafibrate (100 mg/kg) showed elevated hepatic expression and serum concentration of FGF21, elevated expression of *Hmgcs2*, but no change in the serum concentration of the ketone body β -hydroxybutyrate (Li *et al.*, 2012). In our experimental setting, it is unlikely that the modestly increased *Hmgcs2* expression led to any significant change in ketone body production.

SIRT1 activates PGC1 α by deacetylation (Rodgers *et al.*, 2005), whereas PGC1 α stimulates the expression of SIRT3 (Kong *et al.*, 2010). PGC-1 α and PPAR α cooperate to control the transcription of genes encoding mitochondrial fatty acid oxidation enzymes (Vega *et al.*, 2000), whereas SIRT3 modulates the activity of these enzymes by deacetylation (e.g. Hirschey *et al.*, 2010; Shimazu *et al.*, 2010). Even though we noted no significant changes in *Pgc1a* mRNA expression, it should be stressed that this transcriptional coactivator is regulated primarily post-transcriptionally through phosphorylation, acetylation, monomethylation, and O-linked β -N-acetylglucosaminylation (Housley *et al.*, 2009). Similarly to *Pgc1a*, FN did not affect the mRNA expression of *Sirt3* in either age group. However, FN caused downregulation of the Sirt3 protein, which suggests decreased stability or increased degradation of Sirt3 upon treatment. Regrettably, in our study, it was not possible to assess Sirt3 function, e.g. by examining the acetylation status of Sirt3 target proteins. In contrast to our results, a study in *Ppara* knockout mice treated with 100 mg/kg FN for 6 weeks showed downregulation of hepatic Sirt3 expression, indicating the dependence of Sirt3 expression on PPAR α in mouse liver (Mandala *et al.*, 2021). Moreover, the FN treatment prevented iron-induced downregulation of hepatic Sirt3 in wild-type iron-overloaded mice (Mandala *et al.*, 2021). Modulation of SIRT3 expression by FN appears to be variable under different experimental conditions.

We observed contrasting, dose-dependent effects of FN on the hepatic expression of the rate-limiting lipogenic *Fas2* gene in young and old rats, with *Adl* expression not significantly affected. In young rats, the decrease in *Fas2* expression upon 0.5% FN treatment (though not 0.1% FN) falls in line with similar results reported in adult rats fed a high-fructose diet and treated

subsequently with 100 mg/kg FN for 4 weeks (Abd El-Haleim *et al.*, 2016). Because FAS activity is mainly regulated at the transcriptional level by nutrients and hormones, this decreased expression could contribute to reduced accumulation of lipid droplets, which we observed under a transmission electron microscope in hepatocytes of young 0.1% FN-treated rats (Zubrzycki *et al.*, 2021). In contrast to young rats, in the old ones 0.5% FN increased *Fas2* expression. Similarly, a 2-week treatment with 0.2% FN strongly induced hepatic *de novo* lipogenesis and the expression of *Fas2* in mice (age not specified) (Oosterveer *et al.*, 2009). Likewise, an increase in FAS protein expression, concurrently with increased mSREBP-1c level was observed in the liver of 10–12-week-old mice fed 50 mg/kg/day FN for 3 weeks (Jo *et al.*, 2017). Further studies are needed to explain the reason for the apparent FN dose- and age-dependent differences with regard to the modulation of lipogenic genes' expression. Nevertheless, it should be noted that the impact on hepatic lipogenesis does not preclude the FN hypolipemic effect through mechanisms including the stimulation of fatty acid β -oxidation and increased lipoprotein lipase activity.

Available evidence suggests that PPAR α acts not only as a regulator of fatty acid catabolism but plays a broader role in hepatic lipid metabolism. By using stable isotope techniques, Oosterveer *et al.* demonstrated that the treatment of mice for 2 weeks with 0.2% FN induced hepatic *de novo* lipogenesis and fatty acid elongation *in vivo* in parallel with an increased expression of lipogenic genes (Oosterveer *et al.*, 2009). This lipogenic induction was dependent on SREBP-1c which is a target for inhibitory deacetylation by SIRT1 (Walker *et al.*, 2010). Thus, in terms of our experiment, FN-associated reduction of Sirt1 expression in the liver of old rats may contribute to the increased *Fas2* expression. However, the striking contrast between young and old rats with respect to the effect of FN on lipogenic gene expression warrants further studies. One factor contributing to this outcome could be food intake. We previously reported that 0.5% FN was associated with markedly reduced food intake during the first few days, followed by increased consumption, more rapid in young than old rats (Zubrzycki *et al.*, 2020). A re-feeding effect could contribute to the elevation of lipogenesis in old rats.

Our study provides yet another piece of evidence that at least two concentrations of the studied compound should be applied under both *in vivo* and *in vitro* experimental conditions. We found clear discrepancies in the effects of low dose, i.e. 0.1% FN (equivalent to ca. 52 and 42 mg/kg/day in young and old rats, respectively) versus high dose, i.e. 0.5% FN (equivalent to ca. 260 and 210 mg/kg/day) in regard to the expression of Sirt1, *Ppara*, *Lcad*, *Hmgcs2*, *Acox1*, *Pmp70*, and *Fas2*. It should be noted that during long-term treatment in humans, FN is administered once daily typically at a dose of 50–150 mg (preceded by higher doses), whereas the dosage applied to studies in rodents varies widely, from 50 mg/kg/day (Jo *et al.*, 2017) to 400 mg/kg/day (Li & Wu, 2018). Comparison between FN dosage in humans and rodents is difficult because of species differences in the metabolism and elimination patterns of the drug (Caldwell, 1989).

Our study is not without limitations. Firstly, the results of a study examining PPAR α agonist effects in rats cannot be directly transferred to human conditions. Upon administration of peroxisome proliferator chemicals, rodents respond with peroxisomes proliferation, hepatomegaly, and increased hepatocyte proliferation, whereas

such a response is typically absent in humans (Klaunig *et al.*, 2003; Peters *et al.*, 2005). Secondly, we measured the mRNA and protein levels of Sirt1 and Sirt3. Considering that activation of sirtuins may be achieved by increasing NAD⁺ availability (Zhao *et al.*, 2020), analysis of the hepatic NAD⁺/NADH ratio would give more insight into Sirt1 and Sirt3 activity upon treatment with FN. Nevertheless, NAD⁺-independent mechanisms of sirtuins' activation also exist, including phosphorylation of SIRT1 at Ser434 *via* the cAMP/PKA pathway (Gerhart-Hines *et al.*, 2011). Thirdly, we measured only the mRNA expression of some genes involved in fuel metabolism, selected as representative for particular metabolic processes and/or under PPAR α transcriptional control. Certainly, activity assays, as well as analyses of protein levels and their acetylation status would be more informative with regard to the changes induced by FN. However, these methods were beyond the scope of this project. Lastly, additional studies are needed to examine the mechanisms responsible for the dose-dependent and age-dependent differences in fenofibrate's action in the liver.

CONCLUSIONS

Treatment with fenofibrate at low or high dose affects the hepatic expression of Sirt1 and Sirt3 proteins. The dosage of fenofibrate significantly affects the treatment-induced changes in the expression of lipid metabolism-related genes in the rat liver. Aging influences the response to high-dose fenofibrate. The results of our study emphasize the importance of considering the patient's age before adjusting the fenofibrate dose.

Declarations

Ethical approval: All animal experimental procedures had been authorized by the Local Ethics Committee in Bydgoszcz, Poland (protocols No. 41/2017, 58/2017, 40/2018, and 5/2019), and carried out in compliance with the EU Directive 2010/63/EU for animal experiments.

Conflict of interest: The authors have no relevant financial or non-financial interests to disclose.

Author contributions: Adrian Zubrzycki: Methodology; Investigation; Statistical analysis; Writing – original draft; Preparation of Figures. Agata Wrońska: Conceptualization; Methodology; Investigation; Statistical analysis; Resources; Writing – final draft, review & editing. Piotr M. Wierzbicki: Methodology; Statistical analysis; Writing – review. Zbigniew Kmiec: Conceptualization; Writing – review & editing; Supervision, Funding acquisition.

REFERENCES

- Abd El-Haleim EA, Bahgat AK, Saleh S (2016) Resveratrol and fenofibrate ameliorate fructose-induced nonalcoholic steatohepatitis by modulation of genes expression. *World J Gastroenterol* **22**: 2931–2948. <https://doi.org/10.3748/wjg.v22.i10.2931>
- Badman MK, Pissios P, Kennedy AR, Koukos G, Flier JS, Maratos-Flier E (2007) Hepatic Fibroblast Growth Factor 21 is regulated by PPAR α and is a key mediator of hepatic lipid metabolism in ketotic states. *Cell Metab* **5**: 426–437. <https://doi.org/10.1016/j.cmet.2007.05.002>
- Balakumar P, Sambathkumar R, Mahadevan N, Muhsinah AB, Alsayari A, Venkateswaramurthy N, Dhanaraj SA (2019) Molecular targets of fenofibrate in the cardiovascular-renal axis: A unifying perspective of its pleiotropic benefits. *Pharmacol Res* **144**: 132–141. <https://doi.org/10.1016/j.phrs.2019.03.025>
- Balanarasimha M, Davis AM, Soman FL, Rider SD Jr, Hostetler HA (2014) Ligand-regulated heterodimerization of peroxisome proliferator-activated receptor α with liver X receptor α . *Biochemistry* **53**: 2632–2643. <https://doi.org/10.1021/bi401679y>
- Barger JL, Vann JM, Cray NL, Pugh TD, Mastaloudis A, Hester SN, Wood SM, Newton MA, Weindrich R, Prolla TA (2017) Identification of tissue-specific transcriptional markers of caloric restriction in the mouse and their use to evaluate caloric restriction mimetics. *Aging Cell* **16**: 750–760. <https://doi.org/10.1111/acel.12608>
- Bonzo JA, Brocker C, Jiang C, Wang RH, Deng CX, Gonzalez FJ (2014) Hepatic sirtuin 1 is dispensable for fibrate-induced peroxisome proliferator-activated receptor- α function *in vivo*. *Am J Physiol Endocrinol Metab* **306**: 824–837. <https://doi.org/10.1152/ajpendo.00175.2013>
- Caldwell J (1989) The biochemical pharmacology of fenofibrate. *Cardiology* **76** (Suppl 1): 33–41. <https://doi.org/10.1159/000174545>
- Colton HM, Falls JG, Ni H, Kwanyuen P, Creech D, McNeil E, Casey WM, Hamilton G, Cariello NF (2004) Visualization and quantitation of peroxisomes using fluorescent nanocrystals: treatment of rats and monkeys with fibrates and detection in the liver. *Toxicol Sci* **80**: 183–192. <https://doi.org/10.1093/toxsci/kfh144>
- de la Rosa Rodríguez MA, Sugahara G, Hooiveld GJEJ, Ishida Y, Tateno C, Kersten S (2018) The whole transcriptome effects of the PPAR α agonist fenofibrate on livers of hepatocyte humanized mice. *BMC Genomics* **19**: 443. <https://doi.org/10.1186/s12864-018-4834-3>
- Fang J, Ianni A, Smolka C, Vakhrusheva O, Nolte H, Krüger M, Wietelmann A, Simonet NG, Adrian-Segarra JM, Vaquero A, Braun T, Bober E (2017) Sirt7 promotes adipogenesis in the mouse by inhibiting autocatalytic activation of Sirt1. *Proc Natl Acad Sci U S A* **114**: 8352–8361. <https://doi.org/10.1073/pnas.1706945114>
- Feige JN, Lagouge M, Canto C, Strehle A, Houten SM, Milne JC, Lambert PD, Matakis C, Elliott PJ, Auwerx J (2008) Specific SIRT1 activation mimics low energy levels and protects against diet-induced metabolic disorders by enhancing fat oxidation. *Cell Metab* **8**: 347–358. <https://doi.org/10.1016/j.cmet.2008.08.017>
- Gebel T, Arand M, Oesch F (1992) Induction of the peroxisome proliferator activated receptor by fenofibrate in rat liver. *FEBS Lett* **309**: 37–40. [https://doi.org/10.1016/0014-5793\(92\)80734-x](https://doi.org/10.1016/0014-5793(92)80734-x)
- Gerhart-Hines Z, Dominy JE Jr, Blättler SM, Jedrychowski MP, Banks AS, Lim JH, Chim H, Gygi SP, Puigserver P (2011) The cAMP/PKA pathway rapidly activates SIRT1 to promote fatty acid oxidation independently of changes in NAD⁺. *Mol Cell* **44**: 851–863. <https://doi.org/10.1016/j.molcel.2011.12.005>
- Guo R, Liu W, Liu B, Zhang B, Li W, Xu Y (2015) SIRT1 suppresses cardiomyocyte apoptosis in diabetic cardiomyopathy: An insight into endoplasmic reticulum stress response mechanism. *Int J Cardiol* **191**: 36–45. <https://doi.org/10.1016/j.ijcard.2015.04.245>
- Hirschey MD, Shimazu T, Goetzman E, Jing E, Schwer B, Lombard DB, Grueter CA, Harris C, Biddinger S, Ilkayeva OR, Stevens RD, Li Y, Saha AK, Ruderman NB, Bain JR, Newgard CB, Farese RV Jr, Alt FW, Kahn CR, Verdin E (2010) SIRT3 regulates mitochondrial fatty-acid oxidation by reversible enzyme deacetylation. *Nature* **464**: 121–125. <https://doi.org/10.1038/nature08778>
- Hirschey MD, Shimazu T, Jing E, Grueter CA, Collins AM, Aouizerat B, Stančáková A, Goetzman E, Lam MM, Schwer B, Stevens RD, Muehlbauer MJ, Kakar S, Bass NM, Kuusisto J, Laakso M, Alt FW, Newgard CB, Farese RV Jr, Kahn CR, Verdin E (2011) SIRT3 deficiency and mitochondrial protein hyperacetylation accelerate the development of the metabolic syndrome. *Mol Cell* **44**: 177–90. <https://doi.org/10.1016/j.molcel.2011.07.019>
- Housley MP, Udeshi ND, Rodgers JT, Shabanowitz J, Puigserver P, Hunt DF, Hart GW (2009) A PGC-1 α -O-GlcNAc transferase complex regulates FoxO transcription factor activity in response to glucose. *J Biol Chem* **284**: 5148–57. <https://doi.org/10.1074/jbc.M808890200>
- Jin J, Iakova P, Jiang Y, Medrano EE, Timchenko NA (2011) The reduction of SIRT1 in livers of old mice leads to impaired body homeostasis and to inhibition of liver proliferation. *Hepatology* **54**: 989–998. <https://doi.org/10.1002/hep.24471>
- Jo E, Li S, Liang Q, Zhang X, Wang H, Herbert TP, Jenkins TA, Xu A, Ye JM (2017) Chronic activation of PPAR α with fenofibrate reduces autophagic proteins in the liver of mice independent of FGF21. *PLoS One* **12**: e0173676. <https://doi.org/10.1371/journal.pone.0173676>
- Karahashi M, Hoshina M, Yamazaki T, Sakamoto T, Mitsumoto A, Kawashima Y, Kudo N (2013) Fibrates reduce triacylglycerol content by upregulating adipose triglyceride lipase in the liver of rats. *J Pharmacol Sci* **123**: 356–70. <https://doi.org/10.1254/jphs.13149fp>
- Kim EN, Lim JH, Kim MY, Kim HW, Park CW, Chang YS, Choi BS (2016) PPAR α agonist, fenofibrate, ameliorates age-related renal injury. *Exp Gerontol* **81**: 42–50. <https://doi.org/10.1016/j.exger.2016.04.021>
- Klaunig JE, Babich MA, Baetcke KP, Cook JC, Corton JC, David RM, DeLuca JG, Lai DY, McKee RH, Peters JM, Roberts RA, Fennel-Crisp PA (2003) PPAR α agonist-induced rodent tumors: Modes of action and human relevance. *Crit Rev Toxicol* **33**: 655–780. <https://doi.org/10.1080/713608372>
- Kobilo T, Guerrieri D, Zhang Y, Collica SC, Becker KG, van Praag H (2014) AMPK agonist AICAR improves cognition and motor coord-

- dination in young and aged mice. *Learn Mem* **21**: 119–26. <https://doi.org/10.1101/lm.033332.113>
- Kong X, Wang R, Xue Y, Liu X, Zhang H, Chen Y, Fang F, Chang Y (2010) Sirtuin 3, a new target of PGC-1 α , plays an important role in the suppression of ROS and mitochondrial biogenesis. *PLoS One* **5**: e11707. <https://doi.org/10.1371/journal.pone.0011707>
- Kwon S, Seok S, Yau P, Li X, Kemper B, Kemper JK (2017) Obesity and aging diminish sirtuin 1 (SIRT1)-mediated deacetylation of SIRT3, leading to hyperacetylation and decreased activity and stability of SIRT3. *J Biol Chem* **292**: 17312–17323. <https://doi.org/10.1074/jbc.M117.778720>
- Lantier L, Williams AS, Williams IM, Yang KK, Bracy DP, Goelzer M, James FD, Gius D, Wasserman DH (2015) SIRT3 is crucial for maintaining skeletal muscle insulin action and protects against severe insulin resistance in high-fat-fed mice. *Diabetes* **64**: 3081–92. <https://doi.org/10.2337/db14-1810>
- Le TT, Urasaki Y, Pizzorno G (2014) Uridine prevents fenofibrate-induced fatty liver. *PLoS One* **9**: e87179. <https://doi.org/10.1371/journal.pone.0087179>
- Li H, Gao Z, Zhang J, Ye X, Xu A, Ye J, Jia W (2012) Sodium butyrate stimulates expression of fibroblast growth factor 21 in liver by inhibition of histone deacetylase 3. *Diabetes* **61**: 797–806. <https://doi.org/10.2337/db11-0846>
- Li Y, Wu S (2018) Epigallocatechin gallate suppresses hepatic cholesterol synthesis by targeting SREBP-2 through SIRT1/FOXO1 signaling pathway. *Mol Cell Biochem* **448**: 175–185. <https://doi.org/10.1007/s11010-018-3324-x>
- Liu GZ, Hou TT, Yuan Y, Hang PZ, Zhao JJ, Sun L, Zhao GQ, Zhao J, Dong JM, Wang XB, Shi H, Liu YW, Zhou JH, Dong ZX, Liu Y, Zhan CC, Li Y, Li WM (2016) Fenofibrate inhibits atrial metabolic remodelling in atrial fibrillation through PPAR- α /sirtuin 1/PGC-1 α pathway. *Br J Pharmacol* **173**: 1095–1109. <https://doi.org/10.1111/bph.13438>
- Liu HH, Li JJ (2015) Aging and dyslipidemia: a review of potential mechanisms. *Ageing Res Rev* **19**: 43–52. <https://doi.org/10.1016/j.arr.2014.12.001>
- Ławniczak A, Wrońska A, Wierzbicki PM, Kmiec Z (2022) Aging and short-term calorie restriction differently affect the cardiac and skeletal muscle expression of genes regulating energy substrate utilization in male rats. *Biogerontol* **23**: 325–340. <https://doi.org/10.1007/s10522-022-09965-y>
- Mandala A, Chen WJ, Armstrong A, Malhotra MR, Chavalmane S, McCommis KS, Chen A, Carpenter D, Biswas P, Gnana-Prakasam JP (2021) PPAR α agonist fenofibrate attenuates iron-induced liver injury in mice by modulating the Sirt3 and β -catenin signaling. *Am J Physiol Gastrointest Liver Physiol* **321**: 262–269. <https://doi.org/10.1152/ajpgi.00129.2021>
- Meertens LM, Miyata KS, Cecchetto JD, Rachubinski RA, Capone JP (1998) A mitochondrial ketogenic enzyme regulates its gene expression by association with the nuclear hormone receptor PPAR α . *EMBO J* **17**: 6972–6978. <https://doi.org/10.1007/s00109-005-0678-9>
- Murray RK, Bender DA, Botham KM, Kennelly PJ, Rodwell VW (2012) Harper's Illustrated Biochemistry (Harper's Biochemistry), 29th edn, McGraw-Hill Education, New York
- Nakamura M, Liu T, Husain S, Zhai P, Warren JS, Hsu CP, et al. (2019) Glycogen synthase kinase-3 α promotes fatty acid uptake and lipotoxic cardiomyopathy. *Cell Metab* **29**: 1119–1134.e12. <https://doi.org/10.1016/j.cmet.2019.01.005>
- Oosterveer MH, Grefhorst A, van Dijk TH, Havinga R, Stals B, Kuipers F, Groen AK, Reijngoud DJ (2009) Fenofibrate simultaneously induces hepatic fatty acid oxidation, synthesis, and elongation in mice. *J Biol Chem* **284**: 34036–34044. <https://doi.org/10.1074/jbc.M109.051052>
- Peters JM, Cheung C, Gonzalez FJ (2005) Peroxisome proliferator-activated receptor- α and liver cancer: Where do we stand? *J Mol Med (Berl)* **83**: 774–785. <https://doi.org/10.1007/s00109-005-0678-9>
- Pfluger PT, Herranz D, Velasco-Miguel S, Serrano M, Tschöp MH (2008) Sirt1 protects against high-fat diet-induced metabolic damage. *Proc Natl Acad Sci U S A* **105**: 9793–9798. <https://doi.org/10.1073/pnas.0802917105>
- Purushotham A, Schug TT, Xu Q, Surapureddi S, Guo X, Li X (2009) Hepatocyte-specific deletion of SIRT1 alters fatty acid metabolism and results in hepatic steatosis and inflammation. *Cell Metab* **9**: 327–338. <https://doi.org/10.1016/j.cmet.2009.02.006>
- Pyo IS, Yun S, Yoon YE, Choi JW, Lee SJ (2020) Mechanisms of aging and the preventive effects of resveratrol on age-related diseases. *Molecules* **25**: 4649. <https://doi.org/10.3390/molecules25204649>
- Rakhshandehroo M, Knoch B, Müller M, Kersten S (2010) Peroxisome proliferator-activated receptor α target genes. *PPAR Res* **2010**: 612089. <https://doi.org/10.1155/2010/612089>
- Rodgers JT, Lerin C, Haas W, Gygi SP, Spiegelman BM, Puigserver P (2005) Nutrient control of glucose homeostasis through a complex of PGC-1 α and SIRT1. *Nature* **434**: 113–8. <https://doi.org/10.1038/nature03354>
- Rodgers JT, Puigserver P (2007) Fasting-dependent glucose and lipid metabolic response through hepatic sirtuin 1. *Proc Natl Acad Sci U S A* **104**: 12861–12866. <https://doi.org/10.1073/pnas.0702509104>
- Sahebkar A, Simental-Mendía LE, Watts GF, Serban MC, Banach M (2017) Lipid and blood pressure meta-analysis collaboration (LBP-MC) Group. Comparison of the effects of fibrates versus statins on plasma lipoprotein(A) concentrations: a systematic review and meta-analysis of head-to-head randomized controlled trials. *BMC Med* **15**: 22. <https://doi.org/10.1186/s12916-017-0787-7>
- Shimazu T, Hirschey MD, Hua L, Dittenhafer-Reed KE, Schwer B, Lombard DB, Li Y, Bunkenborg J, Alt FW, Denu JM, Jacobson MP, Verdin E (2010) SIRT3 deacetylates mitochondrial 3-hydroxy-3-methylglutaryl CoA synthase 2 and regulates ketone body production. *Cell Metab* **12**: 654–661. <https://doi.org/10.1016/j.cmet.2010.11.003>
- Vega RB, Huss JM, Kelly DP (2000) The coactivator PGC-1 cooperates with peroxisome proliferator-activated receptor α in transcriptional control of nuclear genes encoding mitochondrial fatty acid oxidation enzymes. *Mol Cell Biol* **20**: 1868–76. <https://doi.org/10.1128/MCB.20.5.1868-1876.2000>
- Vilá-Brau A, De Sousa-Coelho AL, Mayordomo C, Haro D, Marrero PF (2011) Human HMGCS2 regulates mitochondrial fatty acid oxidation and FGF21 expression in HepG2 cell line. *J Biol Chem* **286**: 20423–20430. <https://doi.org/10.1074/jbc.M111.235044>
- Walker AK, Yang F, Jiang K, Ji JY, Watts JL, Purushotham A (2010) Conserved role of SIRT1 orthologs in fasting-dependent inhibition of the lipid/cholesterol regulator SREBP. *Genes Dev* **24**: 1403–1417. <https://doi.org/10.1101/gad.190120>
- Wang W, Bai L, Qiao H, Lu Y, Yang L, Zhang J, Lin R, Ren F, Zhang J, Ji M (2014) The protective effect of fenofibrate against TNF- α -induced CD40 expression through SIRT1-mediated deacetylation of NF- κ B in endothelial cells. *Inflammation* **37**: 177–85. <https://doi.org/10.1007/s10753-013-9728-6>
- Wang W, Lin Q, Lin R, Zhang J, Ren F, Zhang J, Ji M, Li Y (2013) PPAR α agonist fenofibrate attenuates TNF- α -induced CD40 expression in 3T3-L1 adipocytes via the SIRT1-dependent signaling pathway. *Exp Cell Res* **319**: 1523–33. <https://doi.org/10.1016/j.yexcr.2013.04.007>
- Xu C, Wang L, Fozouni P, Evjen G, Chandra V, Jiang J, Lu C, Nicastri M, Bretz C, Winkler JD, Amaravadi R, Garcia BA, Adams PD, Ott M, Tong W, Johansen T, Dou Z, Berger SL (2020) SIRT1 is downregulated by autophagy in senescence and ageing. *Nat Cell Biol* **22**: 1170–1179. <https://doi.org/10.1038/s41556-020-00579-5>
- Zhao L, Cao J, Hu K, He X, Yun D, Tong T, Han L (2020) Sirtuins and their biological relevance in aging and age-related diseases. *Ageing Dis* **11**: 927–945. <https://doi.org/10.14336/AD.2019.0820>
- Zhao Q, Yang R, Wang J, Hu DD, Li F (2017) PPAR α activation protects against cholestatic liver injury. *Sci Rep* **7**: 9967. <https://doi.org/10.1038/s41598-017-10524-6>
- Zhao S, Li J, Wang N, Zheng B, Li T, Gu Q, Xu X, Zheng Z (2015) Fenofibrate suppresses cellular metabolic memory of high glucose in diabetic retinopathy via a sirtuin 1-dependent signalling pathway. *Mol Med Rep* **12**: 6112–8. <https://doi.org/10.3892/mmr.2015.4164>
- Zubrzycki A, Wrońska A, Kotulak-Chrzęszcz A, Wierzbicki PM, Kmiec Z (2020) Fenofibrate impairs liver function and structure more pronounced in old than young rats. *Arch Gerontol Geriatr* **91**: 104244. <https://doi.org/10.1016/j.archger.2020.104244>
- Zubrzycki A, Wronska A, Zauszkiewicz-Pawlak A, Kmiec Z (2021) Short-term fenofibrate treatment improves ultrastructure of hepatocytes of old rats. *Folia Histochem Cytobiol* **59**: 167–177. <https://doi.org/10.5603/FHC.a2021.0018>



OPEN ACCESS

EDITED BY

Grzegorz Wegrzyn,
University of Gdansk, Poland

REVIEWED BY

Michał A. Zmijewski,
Medical University of Gdansk, Poland
Marta Karażniewicz-Łada,
Poznan University of Medical Sciences,
Poland

*CORRESPONDENCE

Joško Osredkar,
✉ josko.osredkar@kclj.si

[†]These authors have contributed equally
to this work

RECEIVED 08 April 2024

ACCEPTED 29 July 2024

PUBLISHED 11 September 2024

CITATION

Osredkar J, Vičič V, Hribar M, Benedik E,
Siuka D, Jerin A, Čegovnik Primožič U,
Fabjan T, Kumer K, Pravst I and Žmitek K
(2024), Seasonal variation of total and
bioavailable 25-hydroxyvitamin D
[25(OH)D] in the healthy adult
Slovenian population.
Acta Biochim. Pol 71:13108.
doi: 10.3389/abp.2024.13108

COPYRIGHT

© 2024 Osredkar, Vičič, Hribar, Benedik,
Siuka, Jerin, Čegovnik Primožič, Fabjan,
Kumer, Pravst and Žmitek. This is an
open-access article distributed under
the terms of the Creative Commons
Attribution License (CC BY). The use,
distribution or reproduction in other
forums is permitted, provided the
original author(s) and the copyright
owner(s) are credited and that the
original publication in this journal is
cited, in accordance with accepted
academic practice. No use, distribution
or reproduction is permitted which does
not comply with these terms.

Seasonal variation of total and bioavailable 25-hydroxyvitamin D [25(OH)D] in the healthy adult Slovenian population

Joško Osredkar^{1,2*†}, Vid Vičič^{3†}, Maša Hribar⁴, Evgen Benedik^{5,6},
Darko Siuka⁷, Aleš Jerin^{1,2}, Urška Čegovnik Primožič¹,
Teja Fabjan¹, Kristina Kumer¹, Igor Pravst⁴ and Katja Žmitek^{4,8}

¹Clinical Institute of Clinical Chemistry and Biochemistry, University Medical Centre Ljubljana, Ljubljana, Slovenia, ²Faculty of Pharmacy, University of Ljubljana, Ljubljana, Slovenia, ³Faculty of Health Sciences, Biomedicine in Healthcare, University of Ljubljana, Ljubljana, Slovenia, ⁴Nutrition Institute, Ljubljana, Slovenia, ⁵Biotechnical Faculty, Department of Food Science and Technology, Group for Nutrition, Ljubljana, Slovenia, ⁶Division of Paediatrics, University Medical Centre Ljubljana, Ljubljana, Slovenia, ⁷Division of Internal Medicine, Department of Gastroenterology, University Medical Centre Ljubljana, Ljubljana, Slovenia, ⁸Faculty of Applied Sciences (VIST), Ljubljana, Slovenia

Objective: The aim of our study was to compare the total 25(OH)D fraction, the bioavailable vitamin fraction, and the free vitamin D fraction in spring and fall in a group of healthy individuals.

Methods: In our study, we collected blood samples from healthy participants at the end of both summer and winter, and measured serum levels of albumin, DBP, and 25(OH)D. Utilizing these data, we calculated the percentage of free and bioavailable vitamin D. Our cohort comprised 87 participants, with a male-to-female ratio of 14:73, aged 35.95 ± 12.55 years, ranging from 19 to 70 years. We employed the chemiluminescence method to determine the vitamin 25(OH)D levels, the ELISA method was utilized to determine DBP levels, the albumin BCP Assay was performed using the ADVIA biochemical analyzer (Siemens) and an online calculator was used to determine the free and bioavailable 25(OH)D levels.

Results: Our findings indicate significantly lower 25(OH)D levels in winter (44.13 ± 17.82 nmol/L) compared to summer (74.97 ± 22.75 nmol/L; $p < 0.001$). For vitamin D binding protein there was no significant difference from summer (236.2 ± 164.39 mg/L) to winter (239.86 ± 141.9 mg/L; $p = 0.77$), albumin levels were significantly higher in summer (49.37 ± 4.15 g/L vs. 47.97 ± 3.91 g/L, $p = 0.01$), but the magnitude of the change may not be large enough to be solely responsible for the stability of vitamin D levels throughout the year. In the winter season a significantly lower calculated bioavailable 25(OH)D vitamin (7.45 ± 5.66 nmol/L against 13.11 ± 8.27 nmol/L; $p < 0.001$) was observed, and the free fraction also showed a significant decrease ($17.3 \pm$

Abbreviations: BMI, body mass index; UV, ultraviolet; D3, cholecalciferol; D2, ergocalciferol; Total 25(OH)D, 25-hydroxycholecalciferol, calcifediol, calcidiol, 25-hydroxyvitamin D3; 1,25-(OH)D, 1,25-dihydroxyvitamin D; DBP, vitamin D binding protein; OR, Odds ratio.

12.9 pmol/L versus 29.7 ± 19.1 pmol/L; $p < 0.0001$). We observed a moderately positive correlation between 25(OH)D and bioavailable percentage in winter ($r = 0.680$; $p < 0.001$), in contrast with a lower positive association in summer ($r = 0.343$; $p < 0.001$).

Conclusion: Our data suggest a positive correlation between total and bioavailable 25(OH)D levels. In addition to the statistically significant variation in 25(OH)D between the two observation periods, there was an additional variation in the free vitamin D percentage. The summertime synthesis of vitamin D in the skin could contribute directly to the free fraction of vitamin D. Standardizing the measurement of free 25(OH)D and clinical studies is necessary to establish reference values before these methods can be implemented in clinical practice.

KEYWORDS

vitamin 25(OH)D, free fraction of vitamin D, bioavailable fraction of vitamin D, seasonal variation, calculated fractions

Introduction

Physiological functions

Vitamin D is a pro-hormone that plays a crucial role in phosphorus-calcium metabolism and is therefore essential for the maintenance of healthy bones and teeth (Holick, 2008a).

Vitamin D is also involved in several other important physiological functions, including: 1) maintaining immune function by stimulating white blood cell production, 2) regulating cell growth and differentiation, which is important for maintaining healthy tissues and organs, 3) reducing the risk of depression and improving cognitive function, and 4) regulating gene expression through vitamin D's involvement in the regulation of several genes important for maintaining health and preventing disease (Holick, 2008a; Haussler et al., 2008; Wacker and Holick, 2013; Bouillon and Carmeliet, 2018; Carlberg and Haq, 2018). In recent years, the status of vitamin D has received much attention in the context of COVID-19, which has also contributed to a significant increase in vitamin D supplementation compared to pre-pandemic levels (Žmitek et al., 2021; Vičič and Pandel Mikuš, 2023).

Vitamin D insufficiency and deficiency

Vitamin D deficiency is associated with bone diseases such as rickets and osteoporosis. Low vitamin D levels are also associated with an increased risk of other chronic diseases such as cardiovascular disease, cancer and autoimmune diseases (Calvo et al., 2004; Holick, 2008b; Heaney et al., 2017).

Based on the data that are now available and clinical considerations, various associations and organizations employ

slightly different criteria for vitamin D insufficiency, deficiency, and sufficiency.

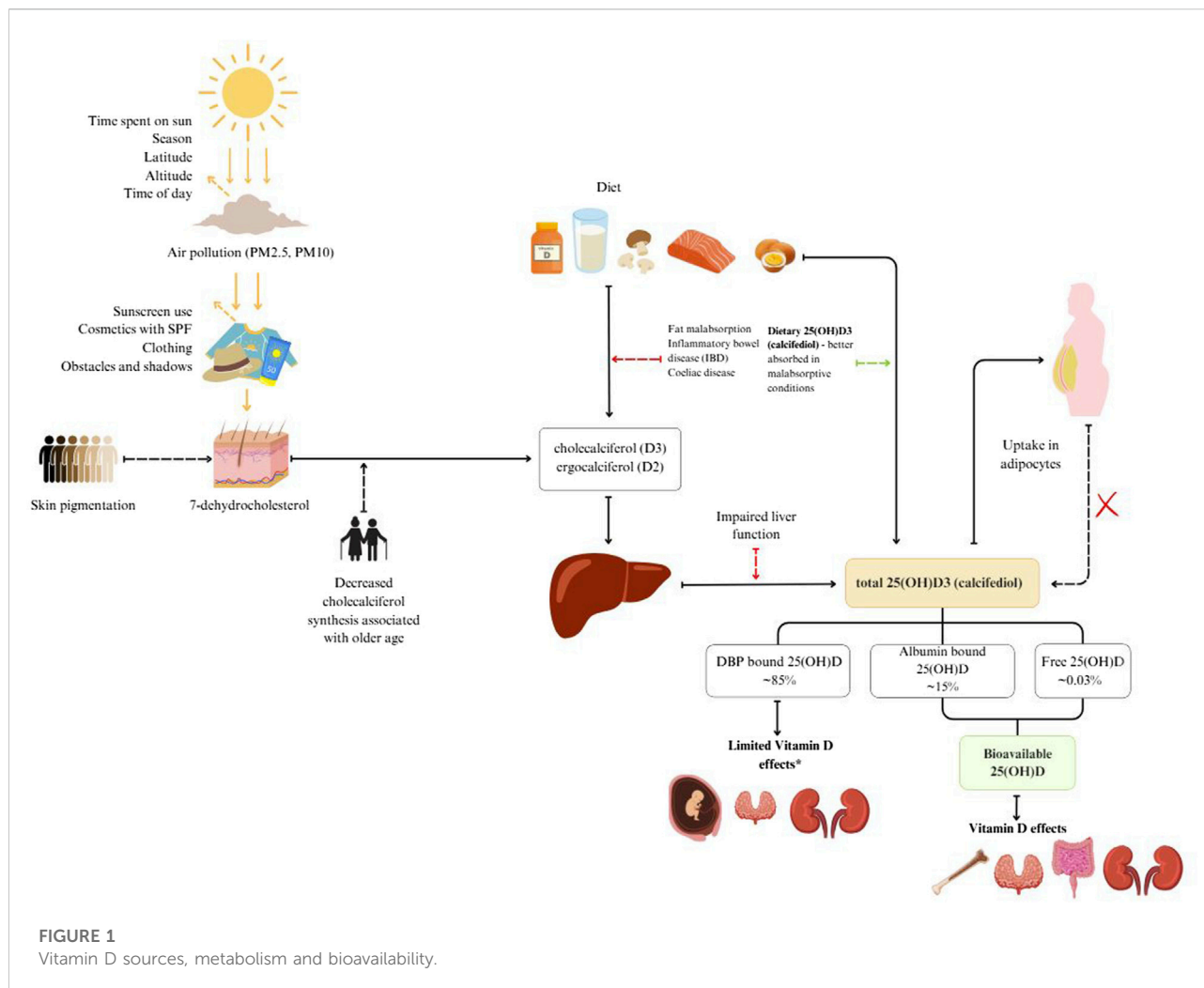
The Endocrine Society recommends that vitamin D status be assessed in patients who are at risk for vitamin D deficiency by measuring the circulating serum 25(OH)D level using an accurate test. A 25(OH)D level of less than 20 ng/mL (50 nmol/L) is considered to be vitamin D insufficiency, whereas a 25(OH)D of 21–29 ng/mL (52.5–72.5 nmol/L) is considered to be vitamin D sufficiency (Holick et al., 2011).

A multidisciplinary Polish panel developed concerns regarding the guidelines for treating and preventing vitamin D insufficiency in both the general population and in high-risk patient groups. The ranges of total blood 25-hydroxyvitamin D concentration indicating suboptimal status (>20 ng/mL, <50 nmol/L), ideal concentration (>30–50 ng/mL, <75 nmol/L), and vitamin D insufficiency (<20 ng/mL, <50 nmol/L) were confirmed on the basis of network discussions (Płudowski et al., 2023).

Vitamin D metabolism and fractions

Vitamin D sources, metabolism and bioavailability are schematically presented in Figure 1. Vitamin D is mainly obtained through diet and skin synthesis when exposed to UVB rays. Sun exposure is the primary source for most people, but without enough UVB exposure, dietary vitamin D becomes essential (Calvo et al., 2004; Spiro and Buttriss, 2014).

Vitamin D₃ is produced from 7-dehydrocholesterol (7-DHC) in the skin through UVB radiation. It is converted to previtamin D₃, which reaches peak concentration within hours (Holick, 2008a). This previtamin D₃ is then transported to the liver via extracellular fluid and dermal capillaries, bound to vitamin D binding protein (DBP) (Holick et al., 2011).



Dietary sources of vitamin D include vitamin D2 (ergocalciferol), D3 (cholecalciferol), and 25-hydroxycholecalciferol [25(OH)D] (Taylor et al., 2014). These forms are transported to the liver in chylomicrons via lymph and blood plasma.

In the blood, two main fractions of vitamin D are measured. Total 25-hydroxyvitamin D (25(OH)D) is the primary circulating form and is often used as a marker for vitamin D status. It binds to DBP and is taken up by the kidneys through receptor-mediated endocytosis involving megalin and cubilin (Nykjaer et al., 2001). The active form, 1,25-dihydroxyvitamin D [1,25(OH)2D], is produced in the kidneys from 25(OH)D under the influence of parathyroid hormone (Lips, 2006; Holick, 2008b). This active form binds to vitamin D receptors, influencing calcium and phosphorus metabolism (Holick, 2008a; Bikle, 2014).

Vitamin D status typically refers to serum 25(OH)D concentration, which does not include vitamin D stored in fat or other tissues (Prentice et al., 2008; Bolland et al., 2018). This

status is influenced by factors like body fat, muscle mass, and genetic variation (Cashman and Kiely, 2011; Ross et al., 2011).

Free 25(OH)D is the fraction that is not bound to DBP and can enter cells directly (Powe et al., 2013a). Bioavailable 25(OH)D includes free and albumin-bound 25(OH)D, making it more readily available for tissue uptake (Bikle and Schwartz, 2019).

DBP transports and stores vitamin D, increasing its stability and protecting it from degradation (Bikle, 2014; Speeckaert et al., 2006). Higher DBP concentrations increase vitamin D binding capacity, forming a larger reservoir of bound vitamin D (Smith and Goodman, 1971).

Measuring free and bioavailable vitamin D is complex and costly, making these measurements uncommon in clinical practice (Chun and Nielson, 2018). These can be calculated using total 25(OH)D, DBP, and albumin levels, although accuracy varies (Vičič et al., 2022).

Vitamin D status fluctuates with the seasons, especially at latitudes above 40°N where UVB exposure is insufficient during

autumn and winter (Spiro and Buttriss, 2014; O'Neill et al., 2016).

Seasonal variation

Sunlight-induced vitamin D synthesis in lighter-skinned populations begins at the end of March, with serum total 25(OH)D levels peaking after the summer months and then declining from October onwards. Therefore, a significant proportion of the European population relies on vitamin D from food and endogenous stores to maintain an adequate vitamin D status, especially during the winter season. A rather high prevalence of vitamin D deficiency has been reported in several countries (Spiro and Buttriss, 2014; O'Neill et al., 2016; Zittermann et al., 2016), and was also found in our previous studies (Hribar et al., 2020; Hribar et al., 2023). In addition to geographic location and season, there are other important factors that influence vitamin D status, such as age, sex, body mass index, constitutional skin color and various lifestyle factors (Webb et al., 2018; 1988; Hribar et al., 2020; Žmitek et al., 2020; Hribar et al., 2023).

The amount of solar radiation reaching an area is affected by the amount of time spent in the sun and factors that affect the angle of the sun: season, latitude, altitude and time of the day. Before sun rays reach the skin they can be blocked by particles in the air (PM_{2.5}, PM₁₀) and later by sunscreen use, cosmetics with SPF, clothing and obstacles such as buildings (Neville et al., 2021). When sun rays reach the skin they are partially blocked by melanin, which is dependent on skin pigmentation (Webb et al., 2018; Neville et al., 2021). In our previous study we showed that constitutive skin color, as well as tanning, hours spent in the sun and protective behaviors against the sun affect individual vitamin D levels (Hribar et al., 2023). Older age is associated with decreased cholecalciferol synthesis in the skin (MacLaughlin and Holick, 1985).

In some cases, taking vitamin D supplements may be recommended to maintain adequate levels of this important nutrient, especially during the winter months or in people who are at higher risk of deficiency (Lips, 2001; Kimball et al., 2007).

Studies have shown that levels of both bioavailable vitamin D and free vitamin D vary seasonally, with higher levels generally observed in the summer months and lower levels observed in the winter months (Zerwekh, 2008; Lehmann et al., 2013).

Aims

The aim of the study was to determine and evaluate the relationship between the total 25(OH)D concentration, the amount of free and bioavailable vitamin D and the level of vitamin D binding protein (DBP) in Slovenian adults at the end of winter and at the end of summer.

Materials and methods

Study participants

Our study included 87 healthy volunteers aged 35.95 ± 12.55 years in the range (19–70 years), and the male-to-female ratio was 14:73. General information is presented in Table 1. The participants were part of the Nutri-D study: “Challenges in achieving adequate Vitamin D status in the adult population.” For this study a sub-sample of the Nutri-D study participants recruited in 2020 (the second year of the study) was used. The study was conducted with two observation periods, one in winter (January–February 2020) and one after the end of summer (September 2020). The invitation to participate in the study was posted on social media and the website of the Nutrition Institute (Slovenia).

Caucasian race (Fitzpatrick skin types I–IV), age over 18 years, desire to abstain from artificial UVB sources, and willingness to adhere to all study protocols were the inclusion criteria. Pregnancy or breastfeeding, severe sun avoidance (e.g., sun allergy), use of sunbeds, use of supplements or medications containing vitamin D, fish oil, or omega-3 fatty acids in the three months prior to study enrolment, regular (daily) consumption of foods enriched with vitamin D (e.g., fortified margarine or plant-based milk alternatives), adherence to a diet prescribed by a dietitian or medical staff, adherence to special diets (e.g., vegetarianism, low-carbohydrate, high-fat, and calorie restriction); current diseases of the kidneys, thyroid, digestive tract, osteoporosis and other bone diseases, skin diseases and other conditions that interfere with the absorption and synthesis of vitamin D, were the exclusion criteria for the study.

The study protocol was carried out in compliance with institutional and local regulations and was approved by the Ethics Committee of the Faculty of Applied Sciences (VIST), SI-1000 Ljubljana, Slovenia (Approval No. 2018/4-ET-SK). It was also registered at [ClinicalTrials.gov](https://clinicaltrials.gov) (ID: NCT03818594). To take part, each subject had to complete an informed consent form.

Methods of determination

In winter (January–February 2020) and after the end of summer (September 2020) a biochemical blood tube (4 mL) was collected. Albumin and total 25(OH)D were analyzed from fresh serum after blood collection, while the aliquot for DBP was stored at minus 80°C until analysis and all samples were analyzed simultaneously. Special care was taken to ensure that samples were taken from the same subject in the same batch on the same plate.

Measurements were performed at the Clinical Institute of Clinical Chemistry and Biochemistry (University Medical Centre, Ljubljana). Serum 25(OH)D, albumin and DBP, were

TABLE 1 Population characteristics, vitamin D status of healthy Slovenian adults aged 19–70 years. The study was conducted in winter (January–February 2020) and after the end of summer (September 2020).

Variable	Category/Unit			
Age at study entry	years	35.95 ± 12.55		
Sex	♀ ♂	♀ 73 (83.9%) ♂ 14 (16.1%)		
Variable	Category/Unit	Winter n = 87	Summer n = 87	p-value
Total 25(OH)D	nmol/L	44.13 ± 17.82	74.97 ± 22.75	<0.001
	Range	10–84	28–166	
	<30	25.3%	2.3%	
	30–50	37.9%	4.6%	
	50–75	31.0%	54.0%	
	>75	5.7%	39.1%	
DBP	mg/L	239.86 ± 141.9	236.2 ± 164.39	0.768
	Range	38.7–853.1	31.6–967.2	
Albumin	g/L	47.97 ± 3.91	49.37 ± 4.15	0.003
	Range	38–60	41–64	
Bioavailable 25(OH)D (Vermulen)	nmol/L	7.45 ± 5.66	13.11 ± 8.27	<0.001
	Range	0.9–35.1	2.14–60.95	
Percentage of bioavailable 25(OH)D	(%)	16.9 ± 12.8	17.49 ± 11.03	
Free 25(OH)D	pmol/L	17.3 ± 12.9	29.7 ± 19.1	<0.0001

DBP, vitamin D binding protein. All values are presented as Mean ± SD or %. Values are presented as mean ± SD, $p < 0.05$ was considered statistically significant (p values of significant variables are in bold print).

measured in all participants using the following methods: vitamin 25(OH)D concentration was measured using a competitive luminescence immunoassay with a limit of quantification of 6 nmol/L (Architect analyzer, Abbott Diagnostics, Lake Forest, United States), Human Vitamin D Binding Protein was measured with ELISA (MyBioSource, Inc., San Diego, CA, United States); the limit of quantification was 31 mg/L. The concentration of albumin was measured with an automated Albumin Assay (ADVIA analyzer, Siemens, New York, United States). The assay is based on the reaction of albumin with bromocresol green followed by spectrophotometric detection; the limit of quantification was 10 g/L.

Specific formulas that use the amounts of total 25-hydroxyvitamin D [25(OH)D], vitamin D-binding protein (DBP), and albumin are used to calculate the bioavailable and free fractions of vitamin D. Predictive equations derived from equilibrium dialysis or ultrafiltration procedures may also be used to approximate these formulas.

Calculation of free vitamin D

Free vitamin D can be calculated using the following formula:

$$[\text{Free } 25(\text{OH})\text{D}] = [\text{Total } 25(\text{OH})\text{D}] / \times \{1 + (K_{DBP} \times [\text{DBP}]) + (K_{Alb} \times [\text{Alb}])\}$$

Where:

- [Total 25(OH)D] is the total concentration of 25-hydroxyvitamin D.
- [DBP] is the concentration of vitamin D binding protein.
- [Alb] is the concentration of albumin.
- K_{DBP} is the affinity constant of 25(OH)D for DBP (approximately $5.98 \times 10^8 \text{ M}^{-1}$).
- K_{Alb} is the affinity constant of 25(OH)D for albumin (approximately $6 \times 10^5 \text{ M}^{-1}$).

Calculation of bioavailable vitamin D

Bioavailable vitamin D includes both the free and albumin-bound fractions. It can be calculated as follows:

$$[\text{Bioavailable } 25(\text{OH})\text{D}] = [\text{Free } 25(\text{OH})\text{D}] + \{[\text{Total } 25(\text{OH})\text{D}] / \times (1 + K_{DBP} \times [\text{DBP}]) + (K_{Alb} \times [\text{Alb}]) \times (K_{Alb} \times [\text{Alb}])\}$$

Simplified, the bioavailable vitamin D formula can be written as:

$$[\text{Bioavailable } 25(\text{OH})\text{D}] = [\text{Total } 25(\text{OH})\text{D}] / \\ \times (1 + (K_{\text{DBP}} \times [\text{DBP}]) + (K_{\text{Alb}} \times [\text{Alb}])) \\ \times (1 + (K_{\text{Alb}} \times [\text{Alb}]))$$

Free and bioavailable 25(OH)D were calculated using an online calculator (Vičić et al., 2022) based on a modified Vermeulen equation (Vermeulen et al., 1999; Powe et al., 2013a; Bikle et al., 2017).

Statistical methods

The observed variables in the statistical analysis were total 25(OH)D, DBP, albumin, calculated bioavailable 25(OH)D and calculated free 25(OH)D. The explanatory variables were season (winter/summer), sex, and age.

The Endocrine Society cut-off values were used to assess total serum 25(OH)D levels target concentration for the optimal vitamin D effect: 75–125 nmol/L, insufficiency: 50–75 nmol/L and deficiency: <50 nmol/L (Holick et al., 2011; Holick et al., 2012; Vieth and Holick, 2018).

A paired sample *t*-test was performed to analyze differences between groups.

Values are expressed as mean \pm SD or percentage (%) in the case of categorical variables. Statistical analysis was performed using SPSS, version 27 and MS Excel 2019.

A Pearson correlation coefficient was calculated to assess the linear relationship (Mukaka, 2012).

Odds ratios (OR) were calculated using binary logistic regression. For OR, 95% confidence intervals were calculated. The significance level was set at $p < 0.05$.

Results and discussion

Our results show that vitamin D levels are lower in the winter months than in the summer months, that serum albumin concentrations are stable, and that DBP remains almost unchanged. Free vitamin D and bioavailable vitamin D levels are higher in the summer compared to the winter.

Total vitamin D levels are significantly lower in winter 44.13 ± 17.82 nmol/L compared to summer 74.97 ± 22.75 nmol/L ($p < 0.001$) (This is likely due to reduced sun exposure and lower cutaneous vitamin D synthesis during the winter, as supported by previous studies (Hribar et al., 2020; Hribar et al., 2023)).

Although there is a small but significant increase in serum albumin concentration from winter 47.97 ± 3.91 g/L to summer 49.37 ± 4.15 g/L ($p < 0.01$), this change is not large enough to explain the year-round stability of vitamin D levels.

There was no significant difference in DBP levels from winter 239.86 ± 141.9 mg/L to summer 236.2 ± 164.39 mg/L ($p = 0.77$).

This suggests that DBP is not a major factor in the seasonal variation of vitamin D levels.

There is a noticeable and significant increase in the free fraction of vitamin D from winter 17.3 ± 12.9 pmol/L to summer 29.7 ± 19.1 pmol/L ($p < 0.0001$), indicating higher availability of unbound vitamin D during the summer months.

The calculated bioavailable 25(OH)D is significantly lower in winter 7.45 ± 5.66 nmol/L compared to summer 13.11 ± 8.27 nmol/L ($p < 0.001$). This highlights the reduced availability of vitamin D for physiological use during the winter months.

The proportion of bioavailable 25(OH)D as a percentage of the total does not show a statistically significant difference between winter $16.9\% \pm 12.8\%$ and summer $17.5\% \pm 11.0\%$. This suggests that while the absolute levels of bioavailable vitamin D vary seasonally, the relative proportion of bioavailable vitamin D to total vitamin D remains stable throughout the year.

These findings underscore the significant seasonal variation in vitamin D status, which is primarily driven by changes in sun exposure and subsequent synthesis of vitamin D. The stability of the proportion of bioavailable vitamin D relative to total vitamin D suggests that the body's mechanisms for maintaining vitamin D homeostasis are robust, even though absolute levels fluctuate with the seasons.

A box plot of the winter and summer total 25(OH)D data and the estimated values of the bioavailable percentage are displayed in Figure 2.

Correlation analysis

As part of our study, we also calculated the correlation between summer and winter total 25(OH)D and bioavailable vitamin results. The results are shown in Table 2.

Wintertime Correlation of Total and Bioavailable 25(OH)D ($p = 0.680$): The robust association suggests that the total 25(OH)D levels are a reliable indicator of the bioavailable 25(OH)D levels during the winter. This suggests that in the absence of considerable sunlight the body's regulatory systems may be at work to maintain a stable percentage of bioavailable vitamin D from the total amount available.

Winter total 25(OH)D and summer bioavailable 25(OH)D are correlated ($p = 0.370$): The fact that the association is smaller suggests that winter total 25(OH)D levels do not predict summer bioavailable 25(OH)D levels as well. Prediction based solely on winter levels is reduced because of seasonal variations and greater sun exposure in the summer, which probably result in additional factors influencing vitamin D bioavailability.

Summertime Correlation of Total and Bioavailable 25(OH)D ($p = 0.343$): Summertime correlations are similar to those observed in winter in that they are weak, meaning that although total 25(OH)D levels do affect bioavailable 25(OH)D

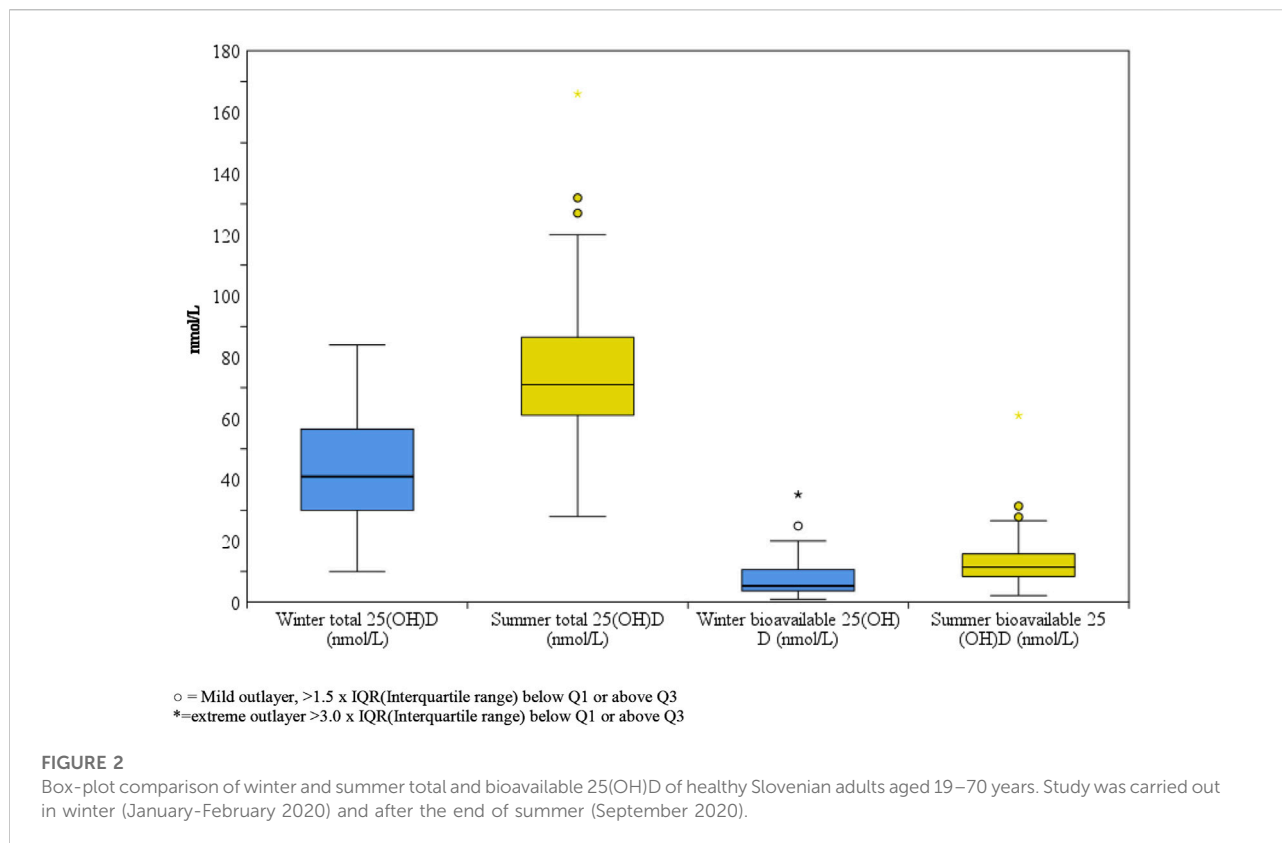


TABLE 2 Pearson correlation coefficients (*r*) of blood biomarkers of healthy Slovenian adults aged 19–70 years. The study was conducted in winter (January–February 2020) and after the end of summer (September 2020).

		Bioavailable 25(OH)D		Total 25(OH)D	
		Winter	Summer	Winter	Summer
Total 25(OH)D	Winter	0.680*	0.370*	1	0.568*
	Summer	0.307*	0.343*	0.568*	1
Bioavailable 25(OH)D	Winter	1	0.509*	0.680*	0.307*
	Summer	0.509*	1	0.370*	0.343*

*Correlation is significant at the 0.01 level (2-tailed).

levels, the effect is not as great. This decreased correlation may be caused by both increased sun exposure and perhaps greater diversity in the sun exposure habits of each subject.

Summer total 25(OH)D and winter bioavailable 25(OH)D are correlated ($p = 0.307$): Summer total 25(OH)D levels appear to be a poor predictor of winter bioavailable 25(OH)D levels, based on this weak association. This is to be expected given the stark variations in sun exposure, which cause the amounts of total and bioavailable vitamin D to change dramatically.

In addition, we looked at how the concentrations of total 25(OH)D and bioavailable vitamin D varied with the seasons. The results are shown in Figure 3.

From winter to summer, there is a noticeable and constant increase in total and bioavailable 25(OH)D levels in all individuals. This seasonal change makes sense given the well-documented consequences of increased sun exposure in the summer. There is observable individual diversity in the absolute levels of total and bioavailable 25(OH)D as well as the degree of growth, despite the general trend. This diversity can be explained by variations in the amount of time that each person spends in the sun, skin type, food consumption, and even hereditary variables that affect the metabolism of vitamin D. Across all the individuals, the proportionate increase in bioavailable 25(OH)D relative to total 25(OH)

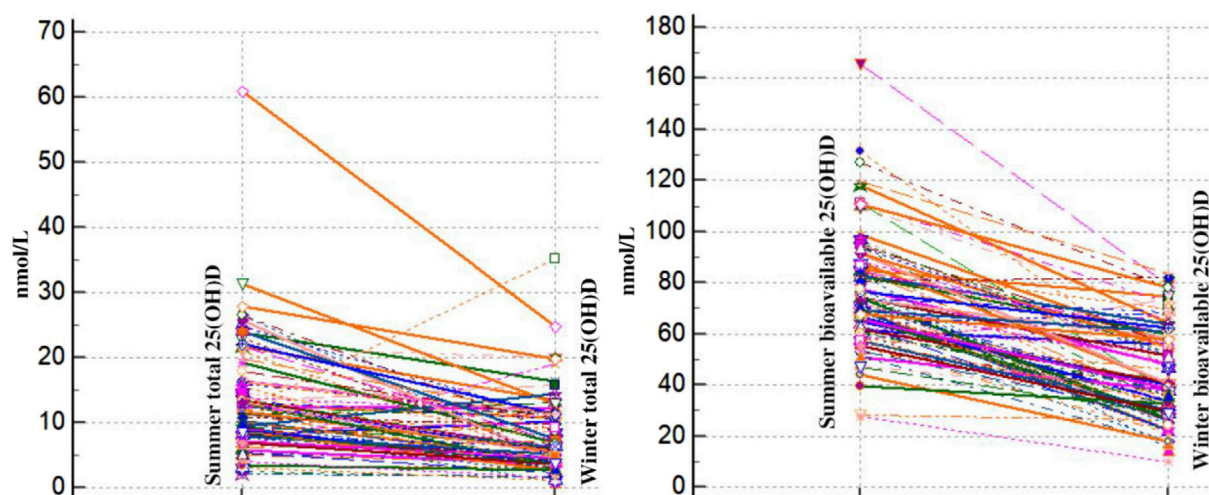


FIGURE 3

Spaghetti plot comparison of winter and summer total and bioavailable 25(OH)D of healthy Slovenian adults aged 19–70 years. Study was carried out in winter (January–February 2020) and after the end of summer (September 2020).

D appears to remain fairly constant. This implies that the mechanisms controlling the conversion and availability of bioavailable vitamin D are operating consistently in response to the elevated total vitamin D levels from summer sun exposure.

Seasonal variation of total 25(OH)D levels

According to our research, the concentration of vitamin 25(OH)D is considerably lower in the winter than it is in the summer (Hribar et al., 2023). This significant seasonal variation is in line with earlier studies showing that seasonal variations in sunlight exposure have an impact on vitamin D levels. Several studies (Hine and Roberts, 1994; Kull et al., 2009; Hribar et al., 2023) have shown comparable trends and linked lower winter levels to decreased ultraviolet B (UVB) radiation. UVB light is necessary for the production of vitamin D in the skin.

Serum albumin concentrations

Serum albumin concentrations varied significantly between the winter and summer ($p = 0.003$), but the magnitude of the variation was small. Higher summer levels of free and accessible vitamin D may be due in part to albumin, a key protein that binds to vitamin D. The small magnitude of variation, however, suggests that albumin alone has a limited effect on the seasonal variations in vitamin D levels.

Vitamin D binding protein (DBP) levels

According to our research, summertime vitamin D binding protein levels are slightly lower than wintertime levels, but the difference is not statistically significant ($p = 0.77$). This is consistent with other research, including the findings of Powe et al. (2013b) that DBP levels do not significantly fluctuate with the seasons. The stability of DBP levels indicates that variations in total 25(OH)D levels are more likely to be the cause of changes in free and bioavailable vitamin D than fluctuations in DBP.

Free fraction of vitamin D

There was a noticeable increase in the percentage of free vitamin D from winter to summer ($p < 0.0001$). There may be more unbound vitamin D available throughout the summer due to this significant seasonal increase in free vitamin D. This result is in line with recent studies showing that summertime increases in free vitamin D levels are caused by increased cutaneous production and decreased binding to albumin and DBP.

Bioavailable 25(OH)D levels

With a p -value < 0.001 , bioavailable 25(OH)D was considerably lower in the winter than in the summer. This notable seasonal variation highlights the influence of a lack of UVB exposure on vitamin D bioavailability. The decrease in bioavailable vitamin D during the winter months may have effects on the immune system and bone health. Bioavailable

vitamin D is essential for physiological processes and includes both free and albumin-bound fractions. These findings support research by several researchers (Bikle et al., 1986; Bouillon and Van Assche, 1995; O'Mahony et al., 2011; Charoenngam and Holick, 2020), highlighting the importance of bioavailable vitamin D in maintaining health.

Proportion of bioavailable 25(OH)D as a percentage of total

Research such as that of Chun et al. (2010), which addresses the homeostatic control of vitamin D bioavailability, supports the relatively stable proportion of bioavailable 25(OH)D as a percentage of total vitamin D (\pm standard deviation), with $16.9\% \pm 12.8\%$ in winter and $17.5\% \pm 11.0\%$ in summer, which is not a statistically significant difference. This stability suggests that while absolute levels of bioavailable vitamin D vary seasonally, the body's regulatory mechanisms maintain a consistent proportion of bioavailable to total vitamin D.

Correlation between total 25-hydroxyvitamin D and bioavailable 25-hydroxyvitamin D levels in winter and summer

Because there are fewer daylight hours and less direct sunlight during the winter, there is less exposure to UVB irradiation of sufficient intensity to induce endogenous vitamin D synthesis. As a result, in order to maintain their vitamin D levels, humans rely primarily on food sources and stored vitamin D (from summer sun exposure). Both newly synthesized and stored vitamin D from food sources are included in total 25(OH)D. Conversely, vitamin D that is attached to albumin and the free fraction of vitamin D are known as bioavailable vitamin D, and these are readily absorbed by cells. Consequently, it is expected that a higher level of bioavailable 25(OH)D would correlate with a higher level of total 25(OH)D. This may be because, in the absence of substantial vitamin D deficiency, part of the stored vitamin D becomes accessible.

Summertime is when humans in our latitudes can produce extra vitamin D in their skin due to increased sun exposure and a higher intensity of UVB irradiation. When more freshly generated vitamin D from sunlight is available in the summer, the weak correlation seen in the winter may become a slightly positive correlation. The amount of stored vitamin D that contributes to total 25(OH)D levels decreases as more vitamin D is produced in the skin during the summer. The association with bioavailable vitamin D may be reduced as a result.

The higher correlation in winter indicates that the body is more dependent on its stored vitamin D at times when vitamin D

availability is reduced. On the other hand, the reduced summer correlation may be a result of higher synthesis rates and distinct binding dynamics during periods of increased vitamin D availability.

A study of healthy adults in Switzerland, for example, found that both total and free vitamin D levels were significantly lower in winter than in summer, while there were no seasonal differences in bioavailable vitamin D levels (Merlo et al., 2015). In contrast, a study of older adults in the United Kingdom found that while total vitamin D levels were lower in winter, there was no significant difference in free or bioavailable vitamin D between summer and winter months (Cashman et al., 2012; Hilger et al., 2014). Vitamin D supplementation may increase total vitamin D levels, including the bioavailable fraction. However, the extent to which supplementation affects the bioavailable fraction may depend on several factors, including the form and dose of vitamin D, individual differences in vitamin D metabolism and absorption, and the presence of underlying medical conditions.

A study conducted on postmenopausal women with low vitamin D levels found that supplementation with vitamin D₃ significantly increased both total and bioavailable vitamin D levels (Hassanein et al., 2023). Another study of overweight and obese adults with vitamin D deficiency showed that daily supplementation with high-dose vitamin D₃ for 16 weeks increased bioavailable vitamin D levels (Entezari et al., 2018).

However, some studies have also reported that vitamin D supplementation does not increase bioavailable levels equally in all individuals. For example, one study of healthy adults found that 12 weeks of vitamin D₃ supplementation did not significantly alter bioavailable vitamin D levels (Jorde and Grimnes, 2011; Chandler et al., 2015; Flueck et al., 2016).

Food fortification with vitamin D can be an effective strategy for increasing vitamin D intake in populations with low sun exposure or inadequate dietary intake.

Possibilities for food fortification with vitamin D are numerous. Examples include but are not limited to: milk, fat spreads (Jääskeläinen et al., 2017), milk alternatives such as soy beverages (Vatanparast et al., 2020), orange juice (Tangpricha et al., 2003), flour and cereals (Allen et al., 2015), UV irradiated mushrooms (Cardwell et al., 2018), UV-irradiated yeast for the preparation of bread (EFSA Panel on Dietetic Products Nutrition and Allergies NDA, 2014), and biofortification of chicken eggs (Browning and Cowieson, 2014; Vičič et al., 2023). The media for fortification should be consumed regularly by the majority of the population and should minimally increase production costs and prices for consumers (Pilz et al., 2018).

Reliable total 25(OH)D, DBP, and albumin levels are necessary for calculation accuracy. Laboratory procedures and assays can differ, which can impact the outcomes.

Genetic variants and individual variations in DBP isoforms can affect binding affinities and concentrations, which in turn

can affect the estimated levels of free and bioavailable 25(OH)D (Fernando et al., 2020).

Although helpful, the formulas for determining the free and available fractions of vitamin D have some drawbacks. These include assumptions regarding individual biological differences, measurement variability in proteins, and binding constants.

Immunoassays made specifically to measure free 25-hydroxyvitamin D [25(OH)D], equilibrium dialysis, and ultrafiltration are direct methods for determining levels of free and bioavailable vitamin D. These techniques directly measure the unbound and albumin-bound fractions of vitamin D, with the goal of giving a more realistic picture of the physiologically active forms of the vitamin but their complexity and resource needs prevent frequent use, and are useful in research contexts and for detailed clinical assessments.

Study limitations and future research

The use of bioavailable 25(OH)D or free 25(OH)D may be useful in physiological and pathological conditions that affect DBP, such as pregnancy, genetic polymorphisms, liver disease, and kidney disease (Tsuprykov et al., 2018a), when comparing vitamin D status in premenopausal and postmenopausal women (Vičič et al., 2022) and in ethnically diverse populations (Aloia et al., 2015; Tsuprykov et al., 2018a; Abidin and Mitra, 2020). There is also a discrepancy between calculated free 25(OH)D and directly measured free 25(OH)D. This is more pronounced in African Americans and has been attributed to differences in DBP binding capacity between ethnic groups (Schwartz et al., 2014). Currently there are no generally accepted reference values for calculated or directly measured free and bioavailable 25(OH)D. Zeng et al. (2021) established reference values for free 25(OH)D through linear regression models but emphasized the need for clinical studies to validate their recommendations. Tsuprykov et al. (2018b) established different reference values in pregnant women for both calculated and measured free 25(OH)D. They concluded that both methods may be appropriate.

We did not evaluate bone health or markers of other significant diseases to determine whether bioavailable/free 25(OH)D is a better predictor of low bone mass density and other conditions. We are currently focusing on this assessment in patients with liver disease.

Conclusion

Calculating vitamin D fractions using formulas is a cost-effective and convenient alternative when direct measurement of individual fractions is not available or feasible. However, it is important to consider the assumptions, accuracy and variability associated with the formulas used and recognize that direct

measurement methods may provide more accurate and reliable results.

Our study provides important insights into seasonal variations in vitamin D status and bioavailability. We found that vitamin 25(OH)D concentrations are significantly lower in winter compared to summer, with a slight, non-significant difference in vitamin D binding protein from summer to winter, and significantly higher albumin concentrations in summer. Both bioavailable and free vitamin D levels are significantly lower in winter.

The primary cause of the winter decrease in total 25(OH)D levels is reduced sunlight exposure, which limits vitamin D synthesis. This also leads to reduced bioavailable and free vitamin D, indicating that not only is less vitamin D produced, but the amount available for use by the body is also reduced. The stable DBP levels suggest that DBP is not the main factor in the seasonal variation of free and bioavailable vitamin D. The seasonal increase in albumin concentration during summer may contribute to a greater amount of bioavailable vitamin D. Albumin's weaker binding affinity for vitamin D compared to DBP allows for easier dissociation of vitamin D, shifting the balance toward more free and albumin-bound vitamin D available for cellular uptake.

There is a moderately positive correlation between total and bioavailable 25(OH)D in winter and a lower positive correlation in summer. This stronger winter correlation suggests that during low vitamin D availability, the body relies more on existing stores, while the weaker summer correlation indicates that with higher vitamin D synthesis, bioavailability dynamics are less dependent on total vitamin D levels.

Data availability statement

The raw data supporting the conclusions of this article will be made available by the authors, without undue reservation.

Ethics statement

The study protocol was approved by the Ethics Committee of the Faculty of Applied Sciences (Approval No. 2018/4-ET-SK). The studies were conducted in accordance with the local legislation and institutional requirements. All participants signed an informed consent form to participate. Study was registered at ClinicalTrials.gov (ID: NCT03818594).

Author contributions

Conceptualization, JO; formal analysis, JO, DS, KK, and MH; investigation, AJ, UČ, and TF; writing—original draft, JO and VV; writing—review and editing, JO, VV, EB, IP, and KŽ. All

authors contributed to the article and approved the submitted version.

Funding

The authors declare financial support was received for the research, authorship, and/or publication of this article. We acknowledge that the study was conducted within the national research project Nutri-D: “Challenges in achieving adequate vitamin D status in the adult population” (L7-1849), co-funded by the Slovenian Research and Innovation Agency and the Ministry of Health of the Republic of Slovenia. We also acknowledge the support of the national research programs “Nutrition and Public Health” (P3-0395), and “Metabolic and hereditary factors of reproductive health-Labour III” (P3-0124), funded by the Slovenian Research and Innovation

Agency, as well as internal research funding of the University Medical Centre Ljubljana, Slovenia (Record IDs 20220017).

Acknowledgments

We would like to thank all the participants who participated in this study. The authors would like to thank Vera Troha Poljančič for her help in processing the serum samples.

Conflict of interest

The authors declare that the research was conducted in the absence of any commercial or financial relationships that could be construed as a potential conflict of interest.

References

- Abidin, N. Z., and Mitra, S. R. (2020). Total vs. bioavailable: determining a better 25(OH)D index in association with bone density and muscle mass in postmenopausal women. *Metabolites* 11, 23. doi:10.3390/metabo11010023
- Allen, R. E., Dangour, A. D., Tedstone, A. E., and Chalabi, Z. (2015). Does fortification of staple foods improve vitamin D intakes and status of groups at risk of deficiency? A United Kingdom modeling study. *Am. J. Clin. Nutr.* 102, 338–344. doi:10.3945/ajcn.115.107409
- Aloia, J., Mikhail, M., Dhaliwal, R., Shieh, A., Usera, G., Stolberg, A., et al. (2015). Free 25(OH)D and the vitamin D paradox in african Americans. *J. Clin. Endocrinol. Metab.* 100, 3356–3363. doi:10.1210/JC.2015-2066
- Bikle, D. D. (2014). Vitamin D metabolism, mechanism of action, and clinical applications. *Chem. Biol.* 21, 319–329. doi:10.1016/j.chembiol.2013.12.016
- Bikle, D. D., Gee, E., Halloran, B., Kowalski, M. A., Ryzen, E., and Haddad, J. G. (1986). Assessment of the free fraction of 25-hydroxyvitamin D in serum and its regulation by albumin and the vitamin D-binding protein. *J. Clin. Endocrinol. Metab.* 63, 954–959. doi:10.1210/jcem-63-4-954
- Bikle, D. D., Malmstroem, S., and Schwartz, J. (2017). Current controversies: are free vitamin metabolite levels a more accurate assessment of vitamin D status than total levels? *Endocrinol. Metab. Clin. N. Am.* 46, 901–918. doi:10.1016/j.ecl.2017.07.013
- Bikle, D. D., and Schwartz, J. (2019). Vitamin D binding protein, total and free vitamin D levels in different physiological and pathophysiological conditions. *Front. Endocrinol. (Lausanne)* 10, 317. doi:10.3389/fendo.2019.00317
- Bolland, M. J., Grey, A., and Avenell, A. (2018). Effects of vitamin D supplementation on musculoskeletal health: a systematic review, meta-analysis, and trial sequential analysis. *Lancet Diabetes Endocrinol.* 6, 847–858. doi:10.1016/S2213-8587(18)30265-1
- Bouillon, R., and Carmeliet, G. (2018). Vitamin D insufficiency: definition, diagnosis and management. *Best Pract. Res. Clin. Endocrinol. Metab.* 32, 669–684. doi:10.1016/j.beem.2018.09.014
- Bouillon, R., and Van Assche, F. A. (1995). The free fraction of 25-hydroxyvitamin D. *Clin. Chem.* 41, 1279–1280. doi:10.1210/edrv-16-2-200
- Browning, L. C., and Cowieson, A. J. (2014). Vitamin D fortification of eggs for human health. *J. Sci. Food Agric.* 94, 1389–1396. doi:10.1002/jsfa.6425
- Calvo, M. S., Whiting, S. J., and Barton, C. N. (2004). Vitamin D fortification in the United States and Canada: current status and data needs. *Am. J. Clin. Nutr.* 80, 1710s–6s. doi:10.1093/ajcn/80.6.1710S
- Cardwell, G., Bornman, J. F., James, A. P., and Black, L. J. (2018). A review of mushrooms as a potential source of dietary vitamin D. *Nutrients* 10, 1498. doi:10.3390/NU10101498
- Carlberg, C., and Haq, A. (2018). The concept of the personal vitamin D response index. *J. Steroid Biochem. Mol. Biol.* 175, 12–17. doi:10.1016/j.jsbmb.2016.12.011
- Cashman, K. D., and Kiely, M. (2011). Towards prevention of vitamin D deficiency and beyond: knowledge gaps and research needs in vitamin D nutrition and public health. *Br. J. Nutr.* 106, 1617–1627. doi:10.1017/S0007114511004995
- Cashman, K. D., Seamans, K. M., Lucey, A. J., Stöcklin, E., Weber, P., Kiely, M., et al. (2012). Relative effectiveness of oral 25-hydroxyvitamin D3 and vitamin D3 in raising wintertime serum 25-hydroxyvitamin D in older adults. *Am. J. Clin. Nutr.* 95, 1350–1356. doi:10.3945/ajcn.111.031427
- Chandler, P. D., Scott, J. B., Drake, B. F., Ng, K., Chan, A. T., Hollis, B. W., et al. (2015). Impact of vitamin D supplementation on adiposity in African-Americans. *Nutr. Diabetes* 5, e147. doi:10.1038/nutd.2014.44
- Charoenngam, N., and Holick, M. F. (2020). Immunologic effects of vitamin D on human health and disease. *Nutrients* 12, 2097. doi:10.3390/nu12072097
- Chun, R. F., Lauridsen, A. L., Suon, L., Zella, L. A., Pike, J. W., Modlin, R. L., et al. (2010). Vitamin D-binding protein directs monocyte responses to 25-hydroxy- and 1,25-dihydroxyvitamin D. *J. Clin. Endocrinol. Metab.* 95, 3368–3376. doi:10.1210/jc.2010-0195
- Chun, R. F., and Nielson, C. M. (2018). Chapter 51—free Vitamin D: concepts, assays, outcomes, and prospects, in *Feldman DBT-VD*. Fourth E ed. Academic Press), 925–937.
- EFSA Panel on Animal Health and Welfare AHAW (2014). Scientific Opinion on porcine epidemic diarrhoea and emerging porcine deltacoronavirus. *J. Eur. Food Saf. Auth.* 12, 3877. doi:10.2903/j.efsa.2014.3877
- Entezari, M., Khosravi, Z., Kafeshani, M., Tavasoli, P., and Zadeh, A. (2018). Effect of vitamin D supplementation on weight loss, glycemic indices, and lipid profile in obese and overweight women: a clinical trial study. *Int. J. Prev. Med.* 9, 63. doi:10.4103/ijpvm.IJPVM_329_15
- Fernando, M., Ellery, S. J., Marquina, C., Lim, S., Naderpoor, N., and Mousa, A. (2020). Vitamin D-binding protein in pregnancy and reproductive health. *Nutrients* 12, 1489. doi:10.3390/nu12051489
- Flueck, J. L., Schlaepfer, M. W., and Perret, C. (2016). Effect of 12-week vitamin D supplementation on 25[OH]D status and performance in athletes with a spinal cord injury. *Nutrients* 8, 586. doi:10.3390/nu8100586
- Hassanein, M. M., Huri, H. Z., Baig, K., and Abduelkarem, A. R. (2023). Determinants and effects of vitamin D supplementation in postmenopausal women: a systematic review. *Nutrients* 15, 685. doi:10.3390/nu15030685
- Haussler, M. R., Haussler, C. A., Bartik, L., Whitfield, G. K., Hsieh, J.-C., Slater, S., et al. (2008). Vitamin D receptor: molecular signaling and actions of nutritional ligands in disease prevention. *Nutr. Rev.* 66, S98–S112. doi:10.1111/j.1753-4887.2008.00093.x

- Heaney, R. P., Holick, M. F., and Rafferty, K. (2017). The vitamin D nutrient reference value: back to the future? *J. Bone Min. Res.* 32, 1317–1319. doi:10.1016/j.jsbmb.2016.12.021
- Hilger, J., Friedel, A., Herr, R., Rausch, T., Roos, F., Wahl, D. A., et al. (2014). A systematic review of vitamin D status in populations worldwide. *Br. J. Nutr.* 111, 23–45. doi:10.1017/S0007114513001840
- Hine, T. J., and Roberts, N. B. (1994). Seasonal variation in serum 25-hydroxy vitamin D3 does not affect 1,25-dihydroxy vitamin D. *Ann. Clin. Biochem.* 31 (Pt 1), 31–34. doi:10.1177/000456329403100105
- Holick, M. F. (2008a). The vitamin D deficiency pandemic and consequences for non-skeletal health: mechanisms of action. *Mol. Aspects Med.* 29, 361–368. doi:10.1016/j.mam.2008.08.008
- Holick, M. F. (2008b). Vitamin D: a D-lightful health perspective. *Nutr. Rev.* 66, S182–S194. doi:10.1111/j.1753-4887.2008.00104.x
- Holick, M. F., Binkley, N. C., Bischoff-Ferrari, H. A., Gordon, C. M., Hanley, D. A., Heaney, R. P., et al. (2011). Evaluation, treatment, and prevention of vitamin D deficiency: an endocrine society clinical practice guideline. *J. Clin. Endocrinol. Metabol.* 96, 1911–1930. doi:10.1210/jc.2011-0385
- Holick, M. F., Binkley, N. C., Bischoff-Ferrari, H. A., Gordon, C. M., Hanley, D. A., Heaney, R. P., et al. (2012). Guidelines for preventing and treating vitamin D deficiency and insufficiency revisited. *J. Clin. Endocrinol. and Metabolism* 97, 1153–1158. doi:10.1210/jc.2011-2601
- Hribar, M., Hristov, H., Gregorič, M., Blaznik, U., Zaletel, K., Oblak, A., et al. (2020). Nutrihealth study: seasonal variation in vitamin D status among the slovenian adult and elderly population. *Nutrients* 12, 1–18. doi:10.3390/NU12061838
- Hribar, M., Pravst, I., Pogačnik, T., and Žmitek, K. (2023). Results of longitudinal nutri-D study: factors influencing winter and summer vitamin D status in a caucasian population. *Front. Nutr.* 10, 1253341. doi:10.3389/fnut.2023.1253341
- Jääskeläinen, T., Itkonen, S. T., Lundqvist, A., Erkkola, M., Koskela, T., Lakkala, K., et al. (2017). The positive impact of general Vitamin D food fortification policy on Vitamin D status in a representative adult Finnish population: evidence from an 11-y follow-up based on standardized 25-hydroxyVitamin D data. *Am. J. Clin. Nutr.* 105, 1512–1520. doi:10.3945/ajcn.116.151415
- Jorde, R., and Grimnes, G. (2011). Vitamin D and metabolic health with special reference to the effect of vitamin D on serum lipids. *Prog. Lipid Res.* 50, 303–312. doi:10.1016/j.plipres.2011.05.001
- Kimball, S. M., Ursell, M. R., O'Connor, P., and Vieth, R. (2007). Safety of vitamin D3 in adults with multiple sclerosis. *Am. J. Clin. Nutr.* 86, 645–651. doi:10.1093/ajcn/86.3.645
- Kull, M. J., Kallikorm, R., Tamm, A., and Lember, M. (2009). Seasonal variance of 25-(OH) vitamin D in the general population of Estonia, a Northern European country. *BMC Public Health* 9, 22. doi:10.1186/1471-2458-9-22
- Lehmann, U., Hirche, F., Stangl, G. I., Hinz, K., Westphal, S., and Dierkes, J. (2013). Bioavailability of vitamin D(2) and D(3) in healthy volunteers, a randomized placebo-controlled trial. *J. Clin. Endocrinol. Metabol.* 98, 4339–4345. doi:10.1210/jc.2012-4287
- Lips, P. (2001). Vitamin D deficiency and secondary hyperparathyroidism in the elderly: consequences for bone loss and fractures and therapeutic implications. *Endocr. Rev.* 22, 477–501. doi:10.1210/er.22.4.477
- Lips, P. (2006). Vitamin D physiology. *Prog. Biophys. Mol. Biol.* 92, 4–8. doi:10.1016/j.pbiomolbio.2006.02.016
- MacLaughlin, J., and Holick, M. F. (1985). Aging decreases the capacity of human skin to produce vitamin D3. *J. Clin. Invest.* 76, 1536–1538. doi:10.1172/JCI112134
- Merlo, C., Trummel, M., Essig, S., and Zeller, A. (2015). Vitamin D deficiency in unselected patients from Swiss primary care: a cross-sectional study in two seasons. *PLoS One* 10, e0138613. doi:10.1371/journal.pone.0138613
- Mukaka, M. M. (2012). Statistics corner: a guide to appropriate use of correlation coefficient in medical research. *Malawi Med. J.* 24, 69–71.
- Neville, J. J., Palmieri, T., and Young, A. R. (2021). Physical determinants of vitamin D photosynthesis: a review. *JBM plus* 5, e10460. doi:10.1002/jbm4.10460
- Nykjaer, A., Fyfe, J. C., Kozyraki, R., Leheste, J. R., Jacobsen, C., Nielsen, M. S., et al. (2001). Cubilin dysfunction causes abnormal metabolism of the steroid hormone 25(OH) vitamin D(3). *Proc. Natl. Acad. Sci. U. S. A.* 98, 13895–13900. doi:10.1073/pnas.241516998
- O'Mahony, L., Stepien, M., Gibney, M. J., Nugent, A. P., and Brennan, L. (2011). The potential role of vitamin D enhanced foods in improving vitamin D status. *Nutrients* 3, 1023–1041. doi:10.3390/nu3121023
- O'Neill, C. M., Kazantzidis, A., Ryan, M. J., Barber, N., Sempos, C. T., Durazo-Arvizu, R. A., et al. (2016). Seasonal changes in vitamin D-effective UVB availability in europe and associations with population serum 25-hydroxyvitamin D. *Nutrients* 8, 533. doi:10.3390/nu8090533
- Pilz, S., März, W., Cashman, K. D., Kiely, M. E., Whiting, S. J., Holick, M. F., et al. (2018). Rationale and plan for vitamin D food fortification: a review and guidance paper. *Front. Endocrinol. (Lausanne)* 9, 373. doi:10.3389/fendo.2018.00373
- Pludowski, P., Kos-Kudła, B., Walczak, M., Fal, A., Zozulińska-Ziolkiewicz, D., Sieroszewski, P., et al. (2023). Guidelines for preventing and treating vitamin D deficiency: a 2023 update in Poland. *Nutrients* 15, 695. doi:10.3390/nu15030695
- Powe, C. E., Evans, M. K., Wenger, J., and Tr, Z. (2013b). Seasonal variations in plasma 25-hydroxyvitamin D and vitamin D-binding protein in African American and white women. *Am. J. Clin. Nutr.* 97, 470–476. doi:10.1056/NEJMoa1306357
- Powe, C. E., Evans, M. K., Wenger, J., Zonderman, A. B., Berg, A. H., Nalls, M., et al. (2013a). Vitamin D-binding protein and vitamin D status of black Americans and white Americans. *N. Engl. J. Med.* 369, 1991–2000. doi:10.1056/NEJMoa1306357
- Prentice, A., Goldberg, G. R., and Schoenmakers, I. (2008). Vitamin D across the lifecycle: physiology and biomarkers. *Am. J. Clin. Nutr.* 88, 500S–506S. doi:10.1093/ajcn/88.2.500S
- Ross, A. C., Manson, J. E., Abrams, S. A., Aloia, J. F., Brannon, P. M., Clinton, S. K., et al. (2011). The 2011 report on dietary reference intakes for calcium and vitamin D from the Institute of Medicine: what clinicians need to know. *J. Clin. Endocrinol. Metab.* 96, 53–58. doi:10.1210/jc.2010-2704
- Schwartz, J. B., Lai, J., Lizaola, B., Kane, L., Markova, S., Weyland, P., et al. (2014). A comparison of measured and calculated free 25(OH) vitamin D levels in clinical populations. *J. Clin. Endocrinol. Metabol.* 99, 1631–1637. doi:10.1210/jc.2013-3874
- Speeckaert, M., Huang, G., Delanghe, J. R., and Taes, Y. E. C. (2006). Biological and clinical aspects of the vitamin D binding protein (Gc-globulin) and its polymorphism. *Clin. Chim. Acta.* 372, 33–42. doi:10.1016/j.cca.2006.03.011
- Spiro, A., and Buttriss, J. L. (2014). Vitamin D: an overview of vitamin D status and intake in Europe. *Nutr. Bull.* 39, 322–350. doi:10.1111/mbu.12108
- Smith, J. E., and Goodman, D. S. (1971). The turnover and transport of vitamin D and of a polar metabolite with the properties of 25-hydroxycholecalciferol in human plasma. *J. Clin. Invest.* 50, 2159–2167. doi:10.1172/JCI106710
- Tangpricha, V., Koutkia, P., Rieke, S. M., Chen, T. C., Perez, A. A., and Holick, M. F. (2003). Fortification of orange juice with vitamin D: a novel approach for enhancing vitamin D nutritional health. *Am. J. Clin. Nutr.* 77, 1478–1483. doi:10.1093/ajcn/77.6.1478
- Taylor, C. L., Patterson, K. Y., Roseland, J. M., Wise, S. A., Merkel, J. M., Pehrsson, P. R., et al. (2014). Including food 25-hydroxyvitamin D in intake estimates may reduce the discrepancy between dietary and serum measures of vitamin D status. *J. Nutr.* 144, 654–659. doi:10.3945/jn.113.189811
- Tsuprykov, O., Buse, C., Skoblo, R., Haq, A., and Hoche, B. (2018b). Reference intervals for measured and calculated free 25-hydroxyvitamin D in normal pregnancy. *J. Steroid Biochem. Mol. Biol.* 181, 80–87. doi:10.1016/j.jsbmb.2018.03.005
- Tsuprykov, O., Chen, X., Hoche, C.-F., Skoblo, R., Yin, L., and Hoche, B. (2018a). Why should we measure free 25(OH) vitamin D? *J. Steroid Biochem. Mol. Biol.* 180, 87–104. doi:10.1016/j.jsbmb.2017.11.014
- Vatanparast, H., Patil, R. P., Islam, N., Shafiee, M., and Whiting, S. J. (2020). Vitamin D intake from supplemental sources but not from food sources has increased in the Canadian population over time. *J. Nutr.* 150, 526–535. doi:10.1093/jn/nxz291
- Vermeulen, A., Verdonck, L., and Kaufman, J. M. (1999). A critical evaluation of simple methods for the estimation of free testosterone in serum. *J. Clin. Endocrinol. and Metabolism* 84, 3666–3672. doi:10.1210/jcem.84.10.6079
- Vičič, V., Kukec, A., Kugler, S., Geršak, K., Osredkar, J., and Pandel Mikuš, R. (2022). Assessment of vitamin D status in Slovenian premenopausal and postmenopausal women, using total, free, and bioavailable 25-hydroxyvitamin D (25(OH)D). *Nutrients* 14, 1–3. doi:10.3390/nu14245349
- Vičič, V., Mikuš, R. P., Kugler, S., Geršak, K., Osredkar, J., and Kukec, A. (2023). Vitamin D fortification of eggs alone and in combination with milk in women aged 44–65 years: fortification model and economic evaluation. *Slovenian J. Public Health* 62, 30–38. doi:10.2478/sjph-2023-0005
- Vičič, V., and Pandel Mikuš, R. (2023). Vitamin D supplementation during COVID-19 lockdown and after 20 months: follow-up study on Slovenian women aged between 44 and 66. *Slovenian J. Public Health* 62, 182–189. doi:10.2478/sjph-2023-0026
- Vieth, R., and Holick, M. F. (2018). “The IOM—endocrine society controversy on recommended vitamin D targets: In support of the endocrine society position,” in *Vitamin D*. Editor D. Feldman 4th ed. (Academic Press), 1091–1107. doi:10.1016/B978-0-12-809965-0.00059-8

Wacker, M., and Holick, M. F. (2013). Vitamin D - effects on skeletal and extraskeletal health and the need for supplementation. *Nutrients* 5, 111–148. doi:10.3390/nu5010111

Webb, A. R., Kazantzidis, A., Kift, R. C., Farrar, M. D., Wilkinson, J., and Rhodes, L. E. (2018). Colour counts: sunlight and skin type as drivers of vitamin D deficiency at UK latitudes. *Nutrients* 10, 457. doi:10.3390/nu10040457

Webb, A. R., Kline, L., and Holick, M. F. (1988). Influence of season and latitude on the cutaneous synthesis of vitamin D₃: exposure to winter sunlight in Boston and edmonton will not promote vitamin D₃ synthesis in human skin. *J. Clin. Endocrinol. and Metabolism* 67, 373–378. doi:10.1210/jcem-67-2-373

Zeng, S., Chu, C., Doebis, C., von Baehr, V., and Hoher, B. (2021). Reference values for free 25-hydroxy-vitamin D based on established total 25-hydroxy-vitamin D reference values. *J. Steroid Biochem. Mol. Biol.* 210, 105877. doi:10.1016/j.jsbmb.2021.105877

Zerwekh, J. E. (2008). Blood biomarkers of vitamin D status. *Am. J. Clin. Nutr.* 87, 1087S–91S. doi:10.1093/ajcn/87.4.1087S

Zittermann, A., Pilz, S., Hoffmann, H., and März, W. (2016). Vitamin D and airway infections: a European perspective. *Eur. J. Med. Res.* 21, 14. doi:10.1186/s40001-016-0208-y

Žmitek, K., Hribar, M., Hristov, H., and Pravst, I. (2020). Efficiency of vitamin D supplementation in healthy adults is associated with body mass index and baseline serum 25-hydroxyvitamin D level. *Nutrients* 12, 1268. doi:10.3390/nu12051268

Žmitek, K., Hribar, M., Lavriša, Ž., Hristov, H., Kušar, A., and Pravst, I. (2021). Socio-demographic and knowledge-related determinants of vitamin D supplementation in the context of the COVID-19 pandemic: assessment of an educational intervention. *Front. Nutr.* 8, 648450. doi:10.3389/fnut.2021.648450



OPEN ACCESS

EDITED BY

Przemysław Mieszko Płonka,
Jagiellonian University, Poland

REVIEWED BY

Beata Hukowska-Szematowicz,
University of Szczecin, Poland
Agnieszka Jaźwa-Kusior,
Jagiellonian University, Poland

*CORRESPONDENCE

Min Peng,

✉ pmfistgo@outlook.com

TingTing Jiang,

✉ jiangtt1203@hotmail.com

[†]These authors have contributed equally
to this work

RECEIVED 08 September 2023

ACCEPTED 19 February 2024

PUBLISHED 20 March 2024

CITATION

Xie F, Zhang H, Peng M and Jiang T
(2024), Clinical study on the difference
in intestinal microecology between
patients with preeclampsia and
pregnant women at different stages
of pregnancy.

Acta Biochim. Pol 71:12020.

doi: 10.3389/abp.2024.12020

COPYRIGHT

© 2024 Xie, Zhang, Peng and Jiang. This
is an open-access article distributed
under the terms of the Creative
Commons Attribution License (CC BY).
The use, distribution or reproduction in
other forums is permitted, provided the
original author(s) and the copyright
owner(s) are credited and that the
original publication in this journal is
cited, in accordance with accepted
academic practice. No use, distribution
or reproduction is permitted which does
not comply with these terms.

Clinical study on the difference in intestinal microecology between patients with preeclampsia and pregnant women at different stages of pregnancy

Fan Xie[†], Huan Zhang[†], Min Peng* and TingTing Jiang*

Department of Obstetrics and Gynecology, Maternal and Child Health Hospital of Hubei Province,
Tongji Medical College, Huazhong University of Science and Technology, Wuhan, Hubei, China

Objective: To explore the difference in intestinal microecology between patients with preeclampsia and pregnant women at different stages of pregnancy.

Methods: From January 2020 to January 2022, clinical data, including blood routine, lipid profile, and renal function indicators, were gathered from a cohort consisting of 5 cases of preeclampsia and 34 cases of non-preeclampsia. The non-preeclampsia group was further categorized into 6 cases in the First trimester, 13 cases in the Second trimester, and 15 cases in the Third trimester. The data collection took place at the Obstetrics Department of the Maternal and Child Health Hospital of Hubei Province. Additionally, fecal samples were obtained from each subject for 16S rDNA gene sequencing and subsequent analysis. The clinical data and composition characteristics of the gut microbiota in each group were analyzed, and the correlation between gut microbiota and clinical data was analyzed by the Spearman correlation analysis method.

Results: In comparison to pregnant women without preeclampsia, preeclampsia patients exhibited a statistically significant elevation in blood routine parameters (WBC, N, L, and PLT count), a rise in lipid-related indicators (TC, TG, and LDL-C levels), a reduction in HDL-C levels, and an increase in renal function-related indicators (Cr, BUN, UA and Pro levels). Compared with non-preeclampsia pregnant women, preeclampsia women exhibited an augmented diversity of gut microbiota. Differences in gut microbiota composition between the two groups were observed at the gate and genus levels. Moreover, there are significant differences in the composition of gut microbiota between the preeclampsia group and the third-trimester group in terms of genus and species, and this difference is mainly caused by *Prevotella* and *s_ Bacteroides_ Uniformis* and *Ruminococcus_ bromii*. In addition, actinobacteria, bifidobacterium at the genus level, and *Ruminococcus_bromii* at the species level are positively correlated with clinically relevant indicators (excluding HDL-C).

Conclusion: There are significant differences in gut microbiota between preeclampsia pregnant women and late pregnancy pregnant without preeclampsia, including *Prevotella* and *Bacteroides*_ *Uniformis*, and *Ruminococcus*_ *bromii*. In addition, these differential bacteria are correlated with most clinical indicators. However, additional comprehensive analysis is required to ascertain the functional correlation between these bacteria and clinical indicators.

KEYWORDS

preeclampsia, lipid metabolism, renal function, intestinal flora, blood cell parameters

Introduction

Preeclampsia is a kind of hypertensive disorder complicating pregnancy (HDP) (Dimitriadis et al., 2023). The incidence of preeclampsia in pregnant women is 3%–5%, which is one of the main reasons for the increased mortality of pregnant women and perinatal infants (Arechvo et al., 2023; Hallum et al., 2023). Preeclampsia has adverse effects on the short-term and long-term health of pregnant women, including stroke, hypertension, and metabolic syndrome (Alanazi et al., 2022). Its offspring are prone to premature delivery, fetal distress, fetal growth restriction (FGR), neonatal hypoglycemia, and even death (Govender et al., 2023). The etiology of preeclampsia is multifactorial, including maternal factors such as family history of preeclampsia, multiple pregnancies, chronic kidney disease, and obesity, and placental factors such as uteroplacental insufficiency and increased placental volume/mass ratio (Syngelaki et al., 2022). However, the pathogenesis of preeclampsia has not been fully clarified. In addition to actively exploring effective treatment methods for preeclampsia and optimizing the prognosis, screening high-risk pregnant women with preeclampsia before pregnancy and taking targeted intervention measures may reduce the incidence of preeclampsia and fundamentally reduce the risk of pregnancy (Zheng et al., 2023).

In recent years, with the in-depth study of intestinal flora, it has been gradually found that changes in intestinal flora may be related to the onset of preeclampsia and affect the intestinal flora of offspring (Chen et al., 2020; Huang et al., 2022). The intestinal microbiota is a complex and huge microbial community living in the digestive tract, which can produce a variety of compounds that regulate the activities of remote organs and play an important role in host metabolism, immunity, and nutrition absorption (Ahmadian et al., 2020). Intestinal microorganisms promote the occurrence of insulin resistance by inducing the chronic inflammatory reaction of the host and causing the accumulation of fat by regulating the energy metabolism gene. Metabolic changes usually occur before clinical symptoms, so metabolic changes can be used as a marker to predict the occurrence and development of preeclampsia. Intestinal microorganisms and the human body form a “superorganism,” and the change and management of intestinal microbial structure are of great significance.

This study focuses on investigating the role of intestinal microflora in preeclampsia by comparing pregnant women with preeclampsia as the research group and healthy pregnant women as the control group. The study utilizes macro genome sequencing of stool samples to analyze the structure, species, functional composition, and metabolic pathways of the intestinal microflora. Furthermore, the study examines the potential significance of key species and gene functions in the development of preeclampsia, aiming to gain insights into its pathogenesis. Additionally, the study aims to provide theoretical support for the application of prevention and control strategies by predicting the macrogenome of intestinal microflora in preeclampsia.

Materials and methods

General information

This study collected 39 pregnant women recruited by the Maternal and Child Health Hospital of Hubei Province from January 2020 to January 2022. Inclusion criteria: 1) Filing for prenatal examination at 12⁺6 weeks of pregnancy; 2) Intrauterine singleton; 3) Age: 20–45 years old; 4) Regular prenatal examination, complete clinical data, and acceptable follow-up. Exclusion criteria: 1) hypertension and/or renal dysfunction were diagnosed before or during pregnancy; 2) Large gastrointestinal surgery before pregnancy; 3) History of antibiotics in the first 3 months of pregnancy; 4) Combined with acute and chronic gastrointestinal diseases and severe autoimmune diseases; 5) Complications included gestational diabetes, gestational heart disease, intrahepatic cholestasis and other serious complications of pregnancy. According to the guidelines for the diagnosis and treatment of hypertensive disorders during pregnancy, pregnant women who were diagnosed with preeclampsia after 20 weeks of pregnancy were regarded as the preeclampsia group ($n = 5$). Pregnant women without preeclampsia were divided into First-trimester (1–12 weeks of pregnancy, $n = 6$), Second-trimester (13–25 weeks of pregnancy, $n = 13$), and Third-trimester (26–40 weeks of pregnancy, $n = 15$). Age, pre-pregnancy body mass, and height were recorded, and pre-pregnancy body mass

index (BMI) was calculated. The participants remained in a state of rest for 5 min, subsequently assuming a seated position, attentively relaxing their limbs, and selecting the cuff. The blood pressure of the right upper limb was measured, the cuff was at the same level as the heart, and the systolic blood pressure (SBP) and diastolic blood pressure (DBP) were recorded. The informed consent of all the subjects was signed by themselves or their families, and the ethics committee of the Maternal and Child Health Hospital of Hubei Province reviewed and approved the research (approval number: 20190911).

Clinical data collection

Determination of blood cell index

Peripheral blood (30 μ L) was collected from the subjects' fingers and mixed with EDTA anticoagulant. The red blood cell (RBC) count, white blood cell (WBC) count, neutrophil count (N), lymphocyte count (L), platelet (PLT) count, and hematocrit (HCT) were measured by SYSMEX 5 classification automatic blood cell analyzer. The sample shall be tested after the quality control is qualified.

Collection and detection of serum samples

In the morning, 5 mL of elbow vein blood was collected from subjects on an empty stomach and centrifuged at 3,000 r/min for 10 min. The supernatant serum was collected, and total cholesterol (TC), triglyceride (TG), low-density lipoprotein cholesterol (LDL-C), high-density lipoprotein cholesterol (HDL-C), creatinine (Cr), urea nitrogen (BUN), and uric acid were measured by Beckman Coulter AU 5800 automatic biochemical analyzer.

Urine sample collection and detection

A sample of 24-h urine was collected, and the first urine was discarded at 6 a.m. All urine after 24 h was collected the day before, including urine at 6 a.m. the next day, and the 24-h total urine output was recorded. Using a Hitachi 7180 biochemical analyzer, the pyrogallol red method was used to measure the quantity of urine protein per milliliter of urine. 24 h urine protein quantity = urine protein quantity per milliliter of urine \times 24 h urine volume.

Collection of stool samples and DNA extraction

Fresh fecal samples were collected from the subjects in sterile containers and immediately stored in liquid nitrogen. Following

the standard protocol, 200 mg of each frozen fecal sample was obtained, and the genome was extracted using the QIAamp DNA Fecal Genomic DNA Extraction Kit (QIAGEN, Germany). The concentration of the extracted DNA was determined using the NanoDrop 2000 spectrophotometer (Thermo Scientific, United States). The 16S rDNA V3 and V4 variable regions of all samples were amplified using the forward primer 338F (5'-ACCTACGGGCGAG-3') and the reverse primer (5'-GACTACHVGGGTWTCTAAT-3').

16S ribosomal RNA (16S rRNA) amplicon pyrosequencing and microbial analysis

The products obtained from polymerase chain reaction (PCR) were quantified using a QuantiFluor ST fluorometer (Promega, United States). The mixture of PCR products was purified using a gel extraction kit provided by QIAGEN (Hilden, Germany). Illumina MiSeq instrument (Illumina, San Diego, California, United States) was utilized to establish a database, and data were assessed using fastqc (version 0.11.8) and multiqc (version 1.10). The metagenomic data underwent automatic low-quality data pruning and filtering using trim_galore (version 0.6.7). Bowtie (version 2.4.5) was used to compare RNA sequences with internal reference genes. Microbiome analysis was performed with Metaplan (version 3.0).

Usearch was used to cluster Tags with a similarity threshold of 97%. The α diversity (Shannon index) was determined using mother (version 1.39.1). Bray Curtis distance algorithm was used for principal component analysis (PCA). By dividing the number of sequences for phyla, genus, and species by the total number of sequences, the relative abundance was determined by applying normalization. The Linear Discriminant Analysis (LDA) method was used to evaluate the difference in species abundance among different samples. The threshold of LDA was 2. To facilitate a more comprehensive comparison of microbial communities, a phylogenetic tree was constructed using FastTree (ver2.1.9).

Statistical analysis

All statistical analyses were performed using SPSS 21.0 software (SPSS Inc., Chicago, Illinois, United States) and the results were presented as mean \pm standard deviation. The statistical significance of differences between two or three groups (or more) was determined using unpaired two-tailed t-tests or one-way ANOVA. The correlation analysis was conducted using Spearman correlation and the results were expressed as Spearman coefficient. The p -value of the Spearman correlation was adjusted using the FDR method. $p < 0.05$ was considered statistically significant. GraphPad Prism 8.0 software (GraphPad Software, Inc., La Jolla, CA, United States) was utilized for data visualization.

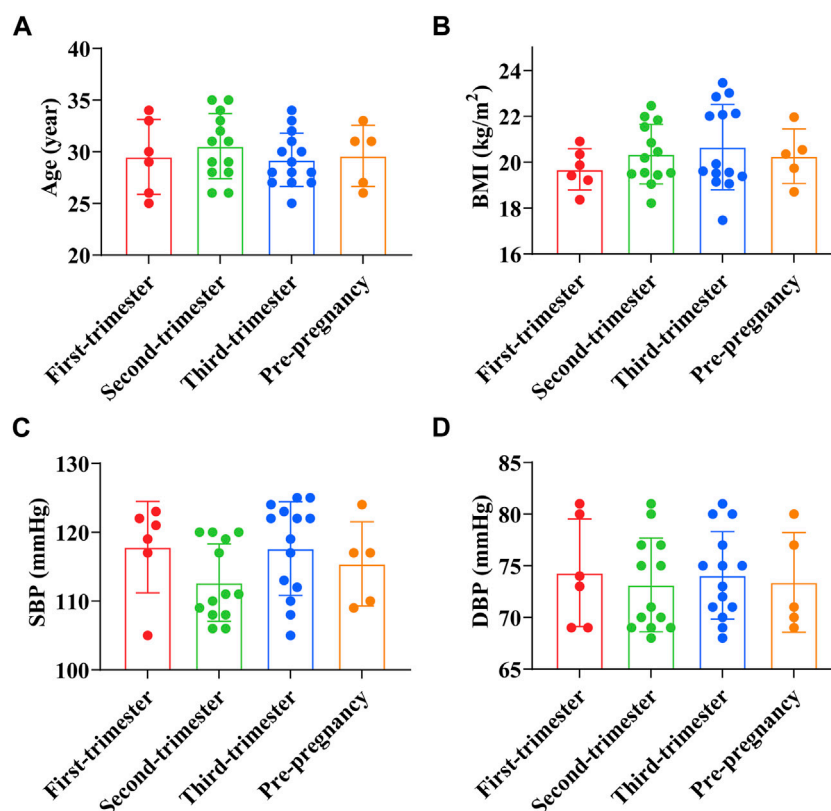


FIGURE 1

Comparison of general data of preeclampsia and pregnant women at different stages of pregnancy. (A) Age; (B) Pre-pregnancy body mass index; (C) Systolic blood pressure; (D) Diastolic blood pressure.

Results

General data comparison

The age of pregnant women in the first trimester was (29.50 ± 3.62) years old, BMI before pregnancy was (19.69 ± 0.90) kg/m², SBP was (117.83 ± 6.65) mmHg, and DBP was (74.33 ± 5.20) mmHg. The age of pregnant women in the second trimester was (30.50 ± 3.15) years old, BMI before pregnancy was (20.35 ± 1.30) kg/m², SBP was (112.69 ± 5.62) mmHg, and DBP was (73.15 ± 4.54) mmHg. The age of pregnant women in the third trimester was (29.21 ± 2.58) years old, BMI before pregnancy was (20.66 ± 1.86) kg/m², SBP was (117.64 ± 6.80) mmHg, and DBP was (74.07 ± 4.23) mmHg. The age of preeclampsia pregnant women was (29.6 ± 2.65) years old, BMI before pregnancy was (20.2 ± 1.06) kg/m², SBP was (115.40 ± 5.46) mmHg, and DBP was (73.40 ± 4.31) mmHg. The results showed that age, BMI before pregnancy, and blood pressure of preeclampsia pregnant women were not significantly different from those of pregnant women at different stages of pregnancy ($p > 0.05$) (Figures 1A–D).

Comparison of blood cell parameters

RBC count of pregnant women in early pregnancy was $(4.05 \pm 0.22) \times 10^{12}/L$, WBC count was $(8.86 \pm 0.72) \times 10^9/L$, PLT count was $(303.50 \pm 25.99) \times 10^9/L$, N count was $(6.98 \pm 0.49) \times 10^9/L$, L count was $(1.64 \pm 0.15) \times 10^9/L$, and HCT was $(36.24 \pm 1.24)\%$. RBC count of pregnant women in the second trimester was $(4.05 \pm 0.25) \times 10^{12}/L$, WBC count was $(8.92 \pm 0.68) \times 10^9/L$, PLT count was $(310.00 \pm 23.32) \times 10^9/L$, N count was $(7.07 \pm 0.37) \times 10^9/L$, L count was $(1.67 \pm 0.13) \times 10^9/L$, and HCT was $(36.04 \pm 2.06)\%$. RBC count of pregnant women in the third trimester was $(4.06 \pm 0.19) \times 10^{12}/L$, WBC count was $(8.90 \pm 0.87) \times 10^9/L$, PLT count was $(307.07 \pm 23.47) \times 10^9/L$, N count was $(7.10 \pm 0.32) \times 10^9/L$, L count was $(1.69 \pm 0.12) \times 10^9/L$, and HCT was $(36.06 \pm 2.47)\%$. RBC count of preeclampsia pregnant women was $(4.09 \pm 0.14) \times 10^{12}/L$, WBC count was $(10.93 \pm 1.23) \times 10^9/L$, PLT count was $(344.00 \pm 23.90) \times 10^9/L$, N count was $(8.17 \pm 0.58) \times 10^9/L$, L count was $(1.92 \pm 0.09) \times 10^9/L$, and HCT was $(36.10 \pm 2.62)\%$. The results showed that the WBC count, N count, L count, and PLT count of preeclampsia pregnant women were significantly higher than those of

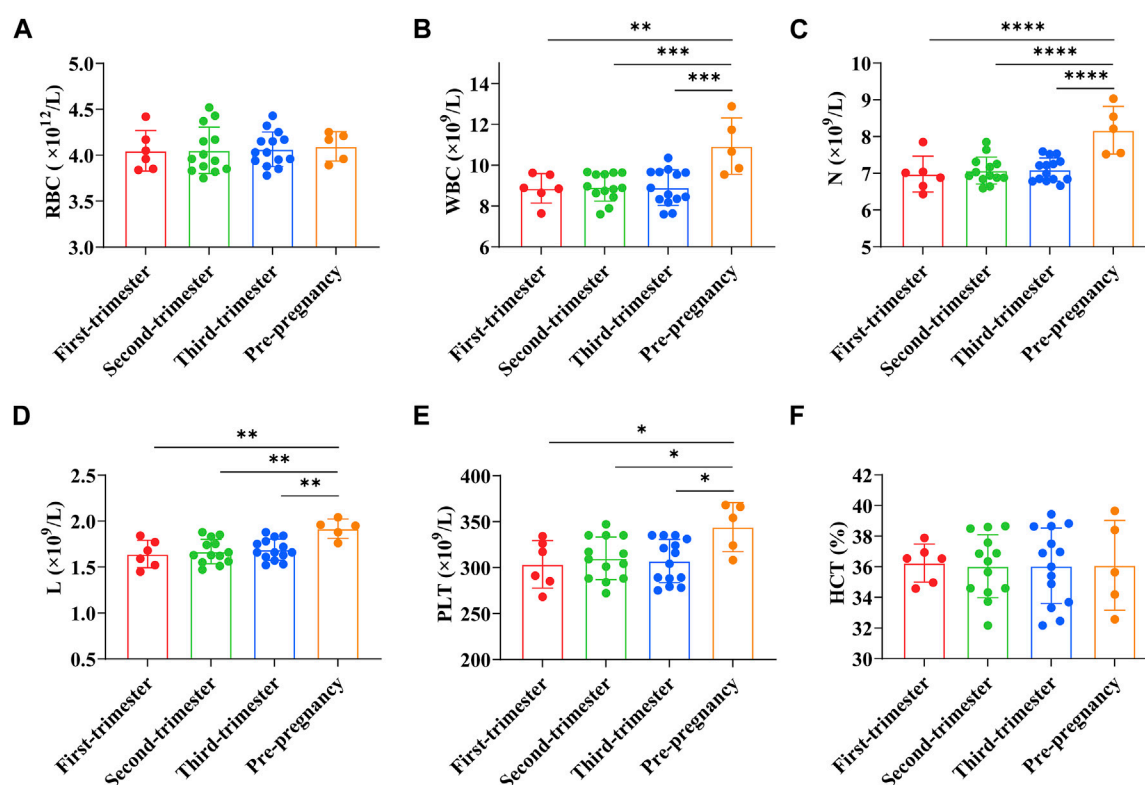


FIGURE 2

Comparison of blood cell parameters between preeclampsia and pregnant women at different stages of pregnancy. (A) Red blood cell count; (B) White blood cell count; (C) Neutrophil count; (D) Lymphocyte count; (E) Platelet count; (F) Hematocrit. * $p < 0.05$, ** $p < 0.01$, *** $p < 0.001$, **** $p < 0.0001$.

pregnant women at different stages of pregnancy ($p < 0.01$, $p < 0.001$, $p < 0.0001$, $p < 0.05$) (Figures 2A–F).

Comparison of serum lipid indexes

TC, TG, LDL-C, and HDL-C were (4.32 ± 0.39) mmol/L, (1.24 ± 0.11) mmol/L, (2.32 ± 0.11) mmol/L, and (1.60 ± 0.15) mmol/L, respectively in early pregnancy. TC, TG, LDL-C, and HDL-C were (4.32 ± 0.32) mmol/L, (1.26 ± 0.13) mmol/L, (2.37 ± 0.14) mmol/L, and (1.53 ± 0.19) mmol/L, respectively in the second trimester of pregnancy. TC, TG, LDL-C, and HDL-C were (4.40 ± 0.22) mmol/L, (1.35 ± 0.11) mmol/L, (2.38 ± 0.14) mmol/L, and (1.52 ± 0.19) mmol/L, respectively in the third trimester of pregnancy. In preeclampsia pregnant women, TC was (4.98 ± 0.40) mmol/L, TG was (1.58 ± 0.11) mmol/L, LDL-C was (2.60 ± 0.10) mmol/L, and HDL-C was (1.27 ± 0.11) mmol/L. The results showed that the levels of TC, TG, and LDL-C in preeclampsia women were significantly higher than those in different stages of pregnancy ($p < 0.01$, $p < 0.001$, $p < 0.0001$, $p < 0.05$), while the levels of HDL-C were significantly lower ($p < 0.05$) (Figures 3A–D).

Comparison of renal function indicators

Cr of pregnant women in early pregnancy was (37.43 ± 1.74) $\mu\text{mol/L}$, BUN was (2.70 ± 0.13) mmol/L, UA was (296.13 ± 11.27) $\mu\text{mol/L}$, and Pro was (0.11 ± 0.02) g/24h. Cr of pregnant women in the second trimester was (37.05 ± 0.02) $\mu\text{mol/L}$, BUN was (2.73 ± 0.21) mmol/L, UA was (308.50 ± 13.82) $\mu\text{mol/L}$, and Pro was (0.11 ± 0.02) g/24h. Cr of pregnant women in the third trimester was (37.85 ± 2.46) $\mu\text{mol/L}$, BUN was (2.72 ± 0.15) mmol/L, UA was (308.86 ± 13.03) $\mu\text{mol/L}$, and Pro was (0.11 ± 0.03) g/24h. Cr of preeclampsia pregnant women was (57.10 ± 1.97) $\mu\text{mol/L}$, BUN was (3.34 ± 0.23) mmol/L, UA was (359.14 ± 22.64) $\mu\text{mol/L}$, and Pro was (0.20 ± 0.03) g/24h. The results showed that the levels of Cr, BUN, UA, and Pro in preeclampsia women were significantly higher than those in different stages of pregnancy ($p < 0.0001$) (Figures 4A–D).

Analysis of flora results

By observing the data quality of the original data, it was found that the sequencing data of 39 fecal samples were normal, and

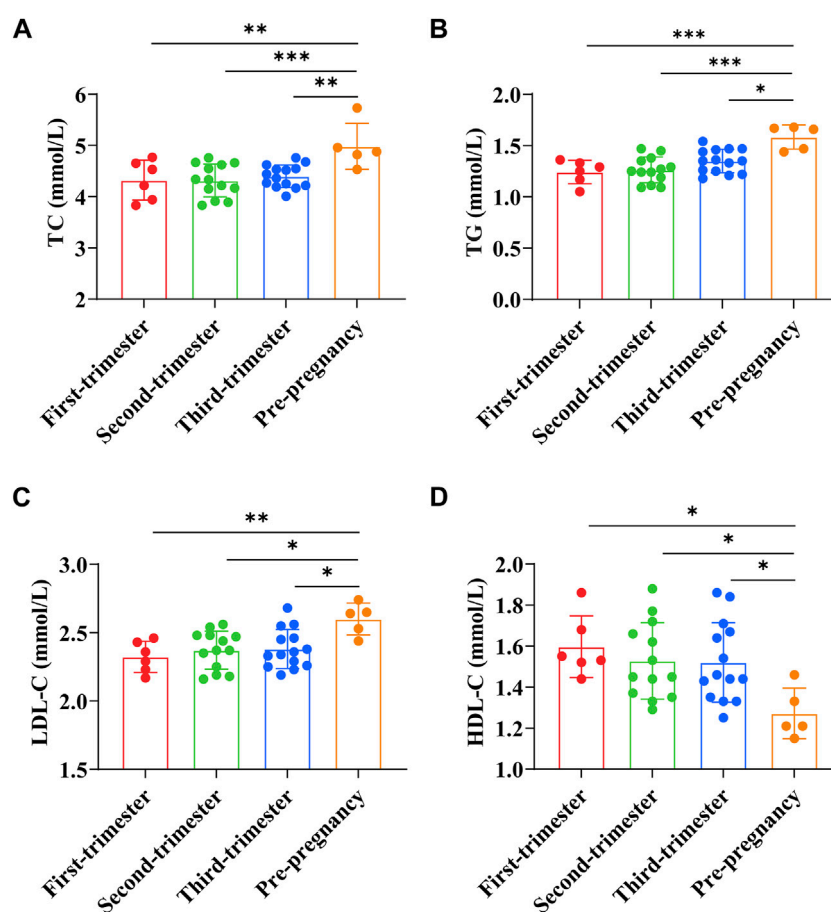


FIGURE 3

Comparison of serum lipid indexes between preeclampsia and pregnant women at different stages of pregnancy. (A) Total cholesterol; (B) Triglyceride; (C) Low-density lipoprotein cholesterol; (D) High-density lipoprotein cholesterol. * $p < 0.05$, ** $p < 0.01$, *** $p < 0.001$, **** $p < 0.0001$.

most of the sequencing readings were above q30, so there was no need to filter the samples. Shannon index can reflect the species diversity of the community. As shown in Figures 5A, B, the preeclampsia group and the First-trimester group had a higher diversity of intestinal flora. In addition, the gradual progression of the pregnancy cycle appears to be associated with a gradual decline in the diversity of the gut microbiota of pregnant women (Figures 5A, B).

At the gate level, the bar chart and the box chart were drawn with the relatively abundant phylum. The results showed that there were significant differences in the levels of *Bacteroides* and *Actinobacteria* between preeclampsia and other gestational periods, and the differences were more obvious between preeclampsia and other pregnancy periods (Figures 6A–C).

At the genus level, the bar chart and box chart were drawn with the relatively abundant bacteria. The results showed that the level of *Bacteroides* and *Bifidobacterium* in preeclampsia and other pregnancy periods was significantly different (Figures 7A, B). In addition, compared with other pregnancy periods,

Lachnospiraceae increased in preeclampsia (Figures 7A, B). The PCA diagram at the generic level also showed that the difference between preeclampsia and late pregnancy was the most obvious in the overall difference comparison of each group, and the difference was mainly caused by *Prevotella* (Figure 7C). According to LDA, there were significant differences in abundance between different groups. At the genus level, the microbial community structure of the First-trimester group was mainly represented by *lachnospira* and *lachnochlostritium* under the phylum Firmicutes. The microbial community structure of the Second-trimester group was mainly represented by unclassified *Proteobacteria* under the phylum *Proteobacteria*; The microbial community structure of the preeclampsia group was mainly represented by *Actinobacteria* and *Bifidobacterium* under Phylum *Actinobacteria* (Figure 7D).

At the species level, the bar chart and box chart were also drawn with the top 10 species of relative abundance. The results showed that the abundance of *Bacteroides_uniformis* was relatively low in preeclampsia, while the abundance of

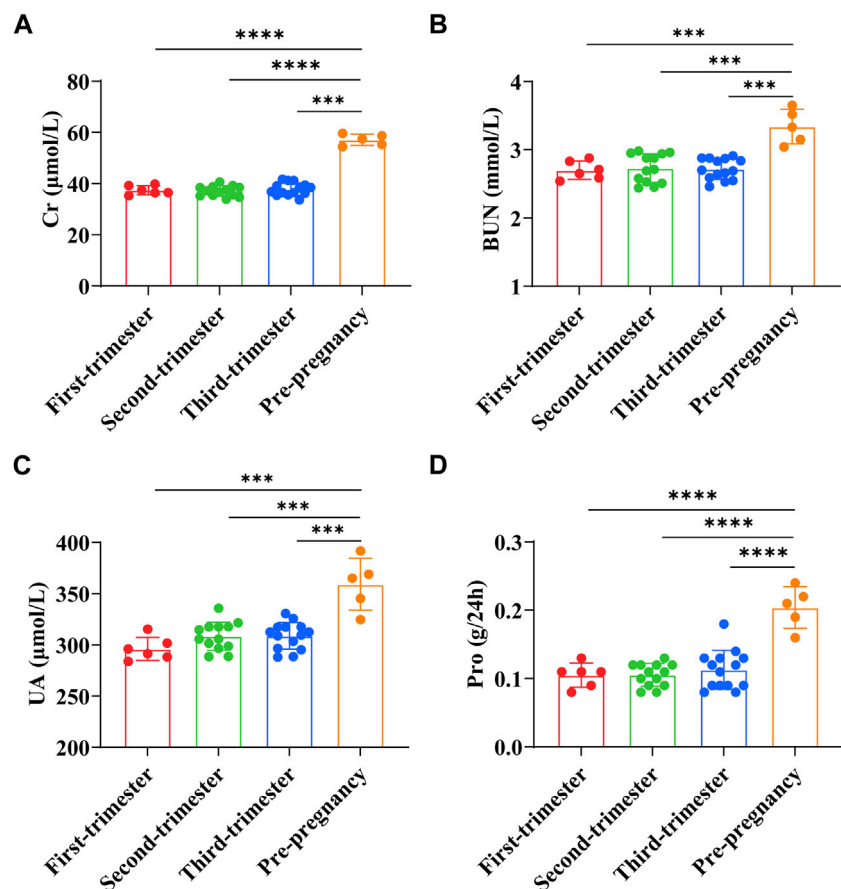
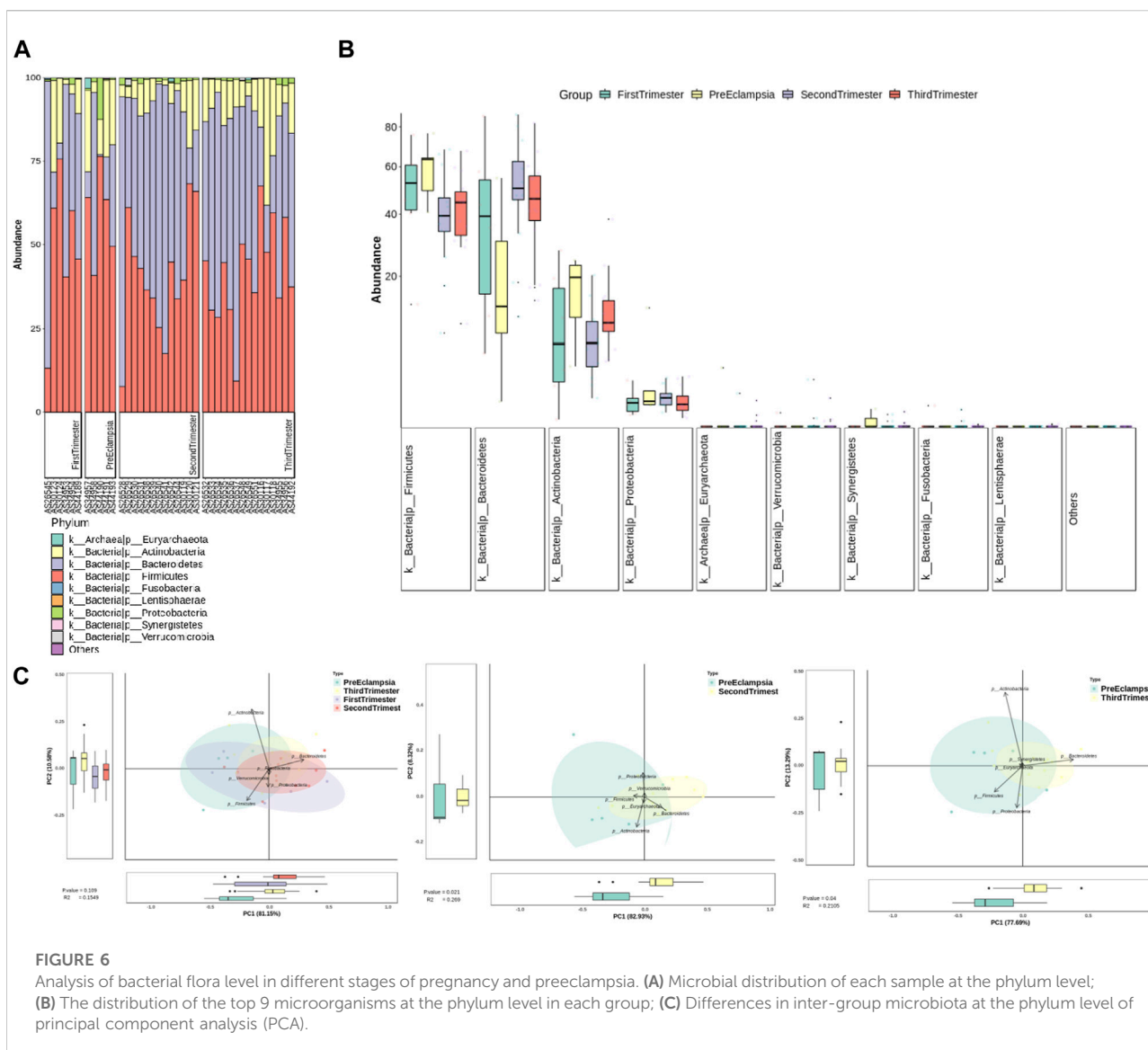


FIGURE 4 Comparison of renal function indexes between preeclampsia and pregnant women at different stages of pregnancy. (A) Creatinine; (B) Urea nitrogen; (C) Uric acid; (D) Urine protein. **** $p < 0.0001$.



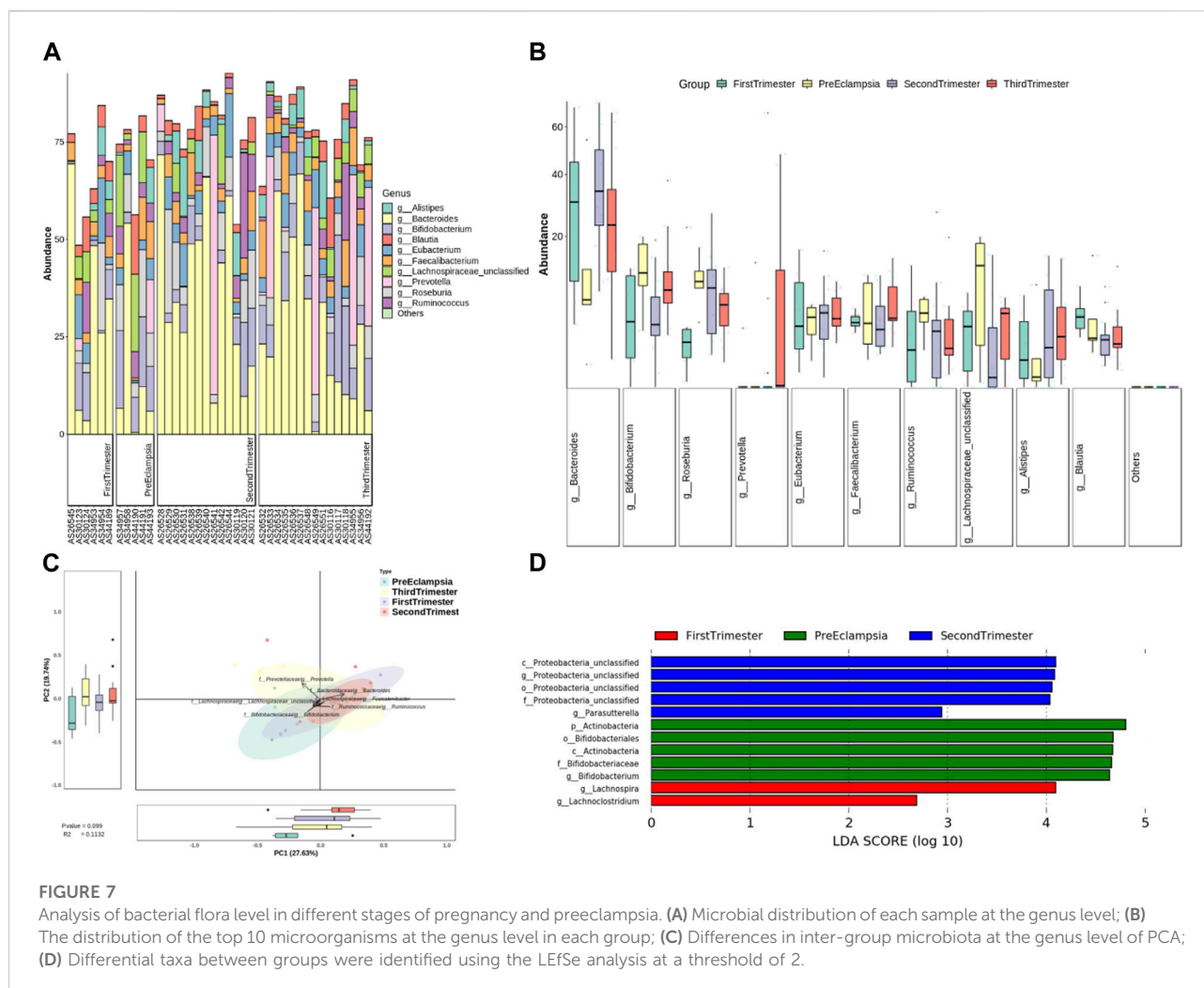
FIGURE 5 Alpha diversity analysis of microbial communities in different stages of pregnancy and preeclampsia. (A) Shannon index analysis of each sample; (B) Compare the Shannon index analysis of samples between groups. The Shannon index reflects the microbial composition. A higher Shannon index signifies a greater level of community diversity.



Eubacterium Rectale was relatively high (Figures 8A, B). The PCA diagram at different levels also showed that in the comparison of the overall differences among the groups, the differences between preeclampsia and late pregnancy were obvious, and the main causes of the differences were *Bacteroides_uniformis* and *Ruminococcus_bromii* (Figures 8C, D). Based on the LDA, at the species level, the microbial community structure in the First-trimester group was predominantly characterized by the presence of *Lachnospira_pentinoschiza*, *Bacteroides_salyersiae* and *Bacteroides_cellulosilyticus*. In the Second-trimester group, the bacterial genus structure was represented by *Proteobacteria_bacterium_CAG_139*, *Parasutterella_excrementihominis*, *Clostridium_citroniae*, and *Clostridium_asparagiforme*. Conversely, the species structure of the preeclampsia microbiota was predominantly represented by *Ruminococcus_gnavus*, *Blautia_sp_CAG_257*, and *Streptococcus_infantis* (Figure 8E).

Correlation analysis

The correlation between different grades of bacteria and clinical data was analyzed. The results showed that *Bacteroides* at the gate level (except HDL-C) and *Bacteroides* at the genus level were negatively correlated with all clinically relevant indicators ($p < 0.05$, $p < 0.01$, $p < 0.001$), while *Bacteroides* at the gate level was positively correlated with HDL-C level ($p < 0.05$) (Figure 9). *Bacteroides_uniformis* at different levels were negatively correlated with WBC, TC, TG, Cr, UA, and Pro (Figure 9). In addition, Actinomycetes at the phylum level, *Bifidobacteria* at the genus level, and *Ruminococcus_bromii* at the species level were positively correlated with almost all clinically relevant indicators (except HDL-C) ($p < 0.05$, $p < 0.01$, $p < 0.001$), and negatively correlated with HDL-C level ($p < 0.01$) (Figure 9).



Discussion

Preeclampsia is a metabolic syndrome related to pregnancy (Udenze, 2016; Hodgman et al., 2022). Hypertension and proteinuria occur after 20 weeks of pregnancy, which is the main cause of morbidity and mortality of pregnant women and perinatal infants. Its pathogenesis and its relationship with obstetric complications is a matter of concern today (Litwinska et al., 2021). At present, there is no reliable, effective, and economic screening method to predict preeclampsia (Khan et al., 2020). Studies have shown that some hematological changes occur during pregnancy, such as preeclampsia. The pathogenesis of preeclampsia is divided into two consecutive stages. Among them, the first stage occurs at the maternal-fetal junction. Due to the insufficient infiltration of trophoblast cells in the uterine wall and spiral artery, the blood flow of the uteroplacental artery is reduced, and the placental perfusion is insufficient, resulting in oxidative stress and placental dysfunction. This hypoxia state can induce

inflammation by releasing chemokines, promoting cytokines, anti-angiogenesis factors, and neutrophils. The second stage begins with the infiltration of activated neutrophils into the maternal vascular tissue and is related to maternal systemic vascular inflammation, which can lead to vasoconstriction, hypertension, endothelial dysfunction, and end-organ ischemia. The above conditions will lead to the increase of white blood cells and neutrophils in the peripheral blood of preeclampsia pregnant women (Gogoi et al., 2019; Lu and Hu, 2019). A blood routine is a simple and practical test item, in which RBC, WBC, PLT, N, and L are common peripheral blood parameters in blood routine. The results of this study showed that the WBC count, N count, L count, and PLT count of preeclampsia pregnant women were significantly higher than those of pregnant women at different stages of pregnancy. The main reason for the increase of WBC during pregnancy is the increase of granulocytes caused by bone marrow proliferation and the left shift of the nucleus, that is, more immature WBC appears in the blood circulation (Awor et al., 2023). Although the

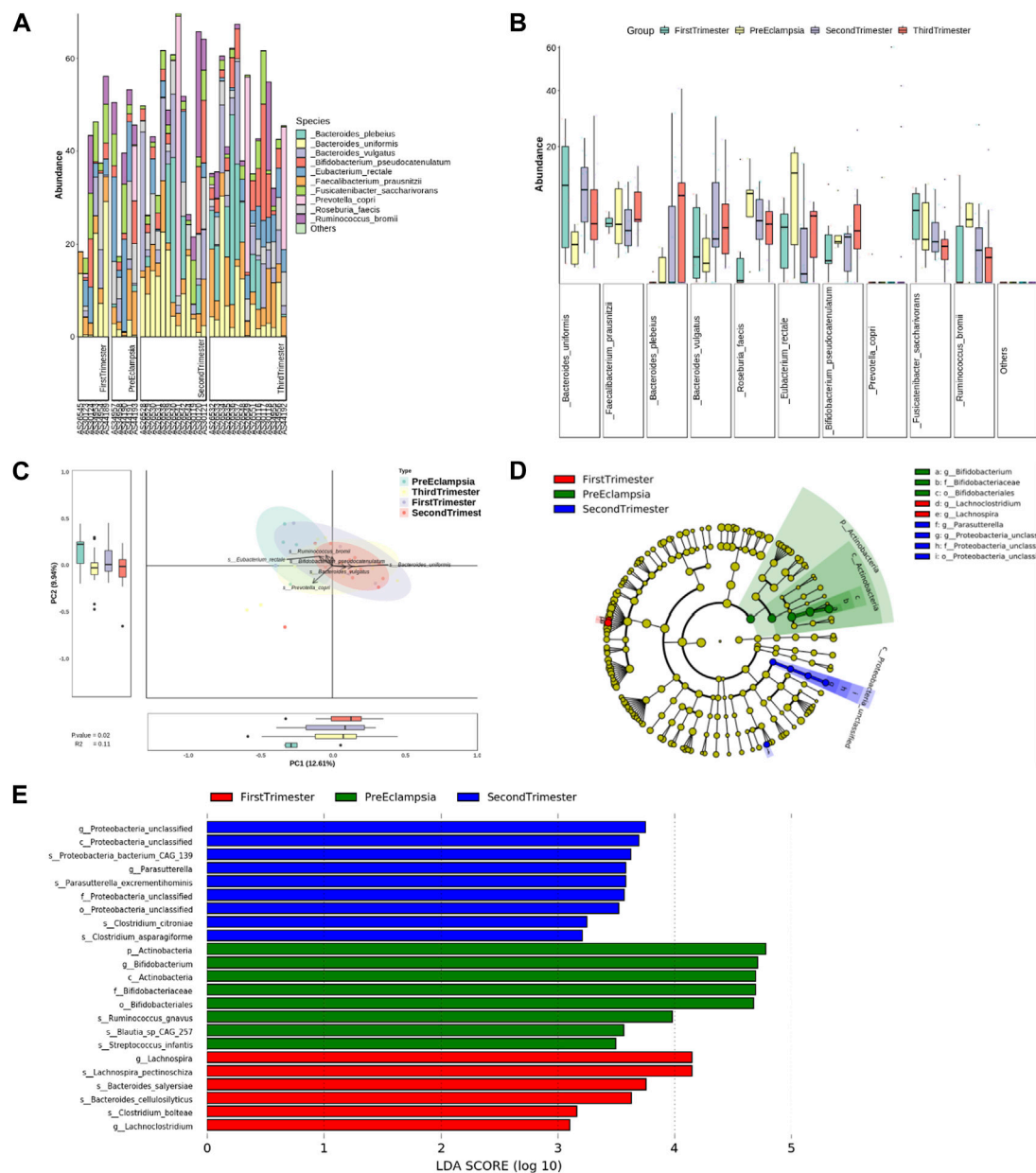
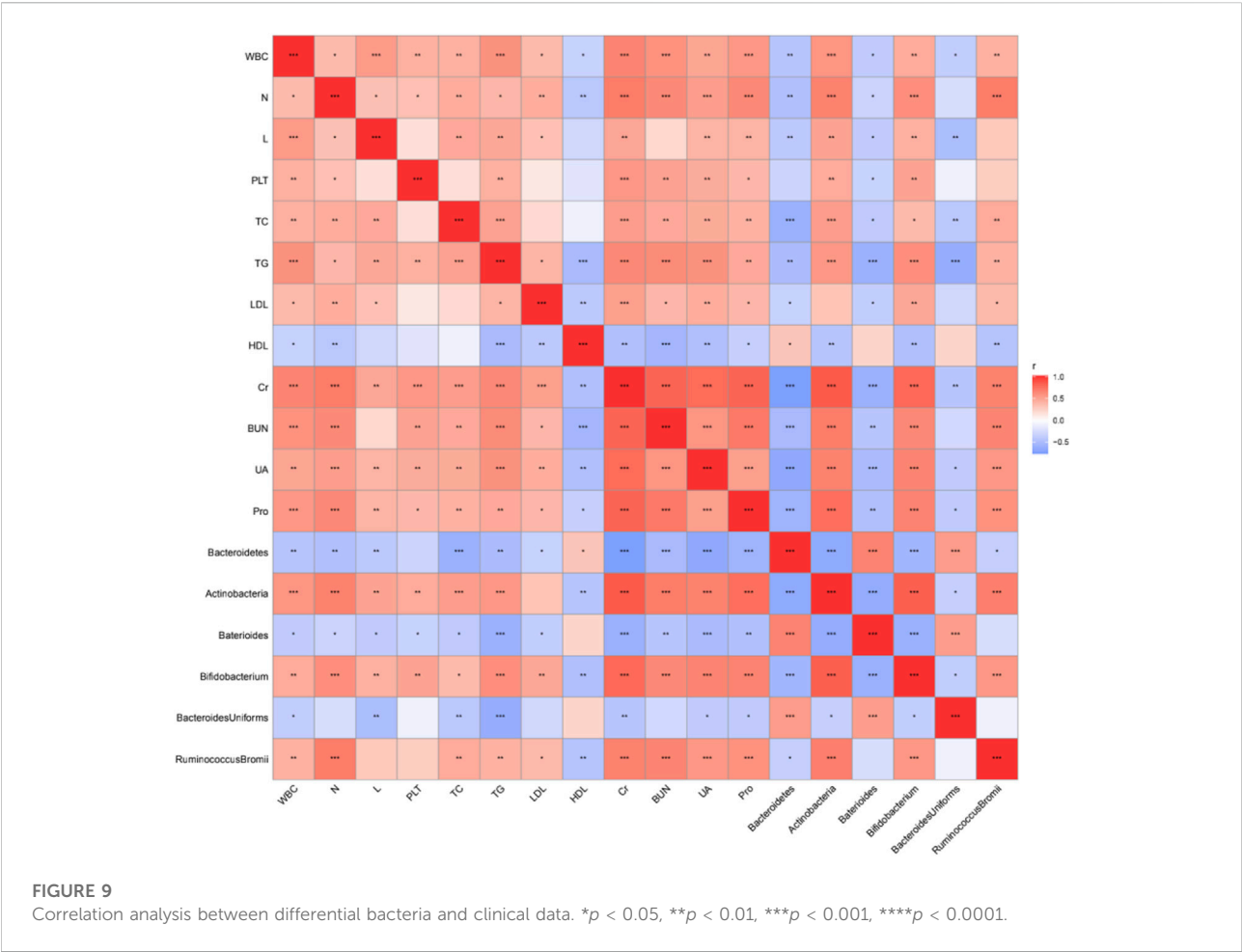


FIGURE 8

Analysis of bacterial flora level in different stages of pregnancy and preeclampsia. (A) Microbial distribution of each sample at the species level; (B) The distribution of the top 10 microorganisms at the species level in each group; (C) Differences in inter-group microbiota at the species level of PCA; (D) Phylogenetic tree analysis; (E) at the species level, differential taxa between groups were identified using the LEfSe analysis at a threshold of 2.

number of WBCs increased, the chemotaxis and adhesion function of WBCs decreased from the second trimester of pregnancy. The inhibition of WBC function during pregnancy was related to the inhibition of humoral-cellular immune regulation function. Due to the poor ability of N denaturation, WBC is detained in the capillary in the low perfusion area of the thrombosis site, which releases

lysosomes, histamines, leukotrienes, and other substances that are harmful to blood flow, resulting in microcirculation blood flow disorder (Moodley et al., 2020; Abdelzahr et al., 2022). The etiology theory of hypertensive disorder complicating pregnancy also believes that the abnormal immune regulation function and the toxic effect of oxidative stress reaction ultimately lead to N inflammatory infiltration.



The process of lipid metabolism *in vivo* is complex, and its parameters are risk factors for the occurrence and development of coronary heart disease, atherosclerosis like artery Congee, hypertension, and other diseases (Negre-Salvayre et al., 2022; Salma, 2022). Research shows that with the growth of pregnancy, the blood lipid level of normal pregnant women will increase (Vaught et al., 2023). The change in blood lipids in pregnant women is considered an adaptive change to support fetal development, but abnormal blood lipids will lead to adverse pregnancy outcomes including preeclampsia (Yang et al., 2022). The results of this study show that the serum lipid level of preeclampsia pregnant women were higher than that of other pregnancy periods, suggesting that the changes in serum lipid in early pregnancy have certain predictive value for preeclampsia. The lipid peroxidation of pregnant women is significantly enhanced, which can further promote the production and secretion of inflammatory factors, cause vascular endothelial damage, and promote the occurrence and development of preeclampsia (Phoswa and Khaliq, 2021).

Creatinine is mainly filtered by glomerulus and not reabsorbed by renal tubules (Tesfa et al., 2022; Wind et al.,

2022). It is a good indicator of glomerular filtration function. Serum uric acid is the product of purine metabolism in the body, and the physiological concentration of uric acid has a positive effect on the body (Atigan et al., 2022). For pregnant and lying-in women, uric acid concentration is affected by continuous physiological changes during the whole pregnancy. In early pregnancy, due to the increase in blood volume and glomerular filtration rate, serum uric acid decreases by about 25%–35%. In the second trimester of pregnancy, the serum uric acid concentration begins to rise and is close to or even higher than the uric acid value of non-pregnant women at term. Research shows that the sudden increase in serum uric acid concentration may be related to the development of potential hypertension, and the adverse outcome of preeclampsia patients is more related to high uric acid concentration (Yu et al., 2023). In addition, a large amount of proteinuria can lead to hypoproteinemia, which can promote the formation of pleural effusion and ascites in severe cases, and affect respiration function in pregnant women. At the same time, hypoproteinemia can also stimulate the mother to increase the synthesis of lipids and lipoproteins (Malz, 1946). Hyperlipidemia

can cause placental atherosclerosis. In addition, the spasm of placental arterioles can increase the blood flow resistance, and the placental blood flow perfusion is insufficient, putting the fetus in a chronic hypoxia state for a long time. It can also cause fetal intrauterine malnutrition, fetal growth restriction, fetal distress, and neonatal asphyxia. Therefore, the continuous occurrence of urinary protein will lead to further aggravation of preeclampsia, which can form a vicious circle. The results of this study showed that the levels of Cr, BUN, UA, and Pro in preeclampsia pregnant women were significantly higher than those in pregnant women at different stages of pregnancy, suggesting that abnormal renal function may be the influencing factor for the occurrence and development of preeclampsia.

In order to adapt to the physiological state during pregnancy and provide a good growth and development environment for the fetus, some metabolic changes will occur in the mother, and the abundance and diversity of intestinal flora will also change significantly during pregnancy, including preeclampsia. Intestinal flora can secrete inflammatory factors and anti-inflammatory factors, which are in a stable balance. Once the flora is out of balance, the balance will be destroyed, and inflammatory factors will increase, which will damage vascular endothelial cells, and then affect the stability of the blood system. *Bacteroides*, *Bifidobacterium*, and *Lachnospiraceae* have been proven to be related to the inflammatory-immune response mediated by intestinal flora (Miao et al., 2021; Huang et al., 2022; Lv et al., 2022). In addition, dyslipidemia and renal dysfunction are also important factors affecting the occurrence and development of preeclampsia. *Bifidobacterium* and *Lachnospiraceae* have been proven to be related to dyslipidemia and renal dysfunction (Sun et al., 2020). This is consistent with the results of this study. In our study, we observed a decrease in the abundance of *Bifidobacteria* and an increase in the abundance of *Lachnospiraceae* within the preeclampsia group. Furthermore, these patients exhibited abnormal blood lipid profiles and renal dysfunction.

To sum up, compared with pregnant women at different stages of pregnancy, the blood routine-related indicators (WBC count, N count, L count, and PLT count) of preeclampsia pregnant women were significantly increased, the blood lipid-related indicators (TC, TG, and LDL-C levels) were significantly increased, while the HDL-C level was significantly decreased, the renal function-related indicators (Cr, BUN, UA, and Pro levels) were significantly increased, the alpha diversity was relatively high, and the flora was relatively rich, which was the largest difference from late pregnancy. Among them, *Bacteroides* and actinomycetes have great differences at the phylum level, *Bacteroides* and *Bifidobacteria* have great differences at the genus level, *Bacteroides uniformis* and *Ruminococcus Bromii* have great differences at the species level, and the difference bacteria have a correlation with the relevant indicators of

pregnancy. However, a more extensive sample size is necessary to conduct further investigation into these findings, particularly in relation to the outcomes of gut microbiota.

Data availability statement

The datasets presented in this study can be found in online repositories. The names of the repository/repositories and accession number(s) can be found in the article/supplementary material.

Ethics statement

The studies involving humans were approved by the Ethics Committee of Maternal and Child Health Hospital of Hubei Province and written informed consent was provided by all patients prior to the study start. All procedures were performed in accordance with the ethical standards of the Institutional Review Board and The Declaration of Helsinki, and its later amendments or comparable ethical standards. The studies were conducted in accordance with the local legislation and institutional requirements. The participants provided their written informed consent to participate in this study. Written informed consent was obtained from the individual(s) for the publication of any potentially identifiable images or data included in this article.

Author contributions

FX and HZ designed the research study. MP and TJ performed the research. FX and HZ provided help and advice on the experiments. MP and TJ analyzed the data. FX and HZ wrote the manuscript. MP and TJ reviewed and edited the manuscript. All authors contributed to the article and approved the submitted version.

Funding

Supported by the Hubei Provincial Health Commission Joint Research Project Fund, WJ2019H302.

Conflict of interest

The authors declare that the research was conducted in the absence of any commercial or financial relationships that could be construed as a potential conflict of interest.

References

- Abdelzaher, W. Y., Mostafa-Hedeab, G., Bahaa, H. A., Mahran, A., Atef Fawzy, M., Abdel Hafez, S. M. N., et al. (2022). Leukotriene receptor antagonist, montelukast ameliorates L-NAME-induced preeclampsia in rats through suppressing the IL-6/jak2/STAT3 signaling pathway. *Pharm. (Basel)* 15 (8), 914. doi:10.3390/ph15080914
- Ahmadian, E., Rahbar Saadat, Y., Hosseiniyan Khatibi, S. M., Nariman-Saleh-Fam, Z., Bastami, M., Zununi Vahed, F., et al. (2020). Preeclampsia: microbiota possibly playing a role. *Pharmacol. Res.* 155, 104692. doi:10.1016/j.phrs.2020.104692
- Alanazi, A. S., Victor, F., Rehman, K., Khan, Y. H., Yunusa, I., Alzarea, A. I., et al. (2022). Pre-existing diabetes mellitus, hypertension and KidneyDisease as risk factors of preeclampsia: a disease of theories and its association with genetic polymorphism. *Int. J. Environ. Res. Public Health* 19 (24), 16690. doi:10.3390/ijerph192416690
- Arechvo, A., Wright, A., Syngelaki, A., von Dadelszen, P., Magee, L. A., Akolekar, R., et al. (2023). Incidence of preeclampsia: effect of deprivation. *Ultrasound Obstetrics Gynecol.* 61 (1), 26–32. doi:10.1002/uog.26084
- Atigan, A., Tan, S., Cetin, H., Guler, O. T., Ozdamar, S., and Karakaya, Y. A. (2022). CD97 expression level and its effect on cell adhesion in Preeclampsia. *BMC Pregnancy Childbirth* 22 (1), 967. doi:10.1186/s12884-022-05280-z
- Awor, S., Abola, B., Byanyima, R., Orach, C. G., Kiondo, P., Kaye, D. K., et al. (2023). Prediction of preeclampsia at St. Mary's hospital lacor, a low-resource setting in northern Uganda, a prospective cohort study. *BMC Pregnancy Childbirth* 23 (1), 101. doi:10.1186/s12884-023-05420-z
- Chen, X., Li, P., Liu, M., Zheng, H., He, Y., Chen, M. X., et al. (2020). Gut dysbiosis induces the development of preeclampsia through bacterial translocation. *Gut* 69 (3), 513–522. doi:10.1136/gutjnl-2019-319101
- Dimitriadis, E., Rolnik, D. L., Zhou, W., Estrada-Gutierrez, G., Koga, K., Francisco, R. P. V., et al. (2023). preeclampsia. *Nat. Rev. Dis. Prim.* 9 (1), 8. doi:10.1038/s41572-023-00417-6
- Gogoi, P., Sinha, P., Gupta, B., Fimal, P., and Rajaram, S. (2019). Neutrophil-to-lymphocyte ratio and platelet indices in preeclampsia. *Int. J. Gynecol. Obstetrics* 144 (1), 16–20. doi:10.1002/ijgo.12701
- Govender, V., Naidoo, T. D., and Foolchand, S. (2023). The preeclampsia, growth restriction, and ductus venosus Doppler (GRADED) study: an observational study of early-onset fetal growth restriction and preeclampsia. *Int. J. Gynecol. Obstetrics* 161 (1), 106–113. doi:10.1002/ijgo.14495
- Hallum, S., Basit, S., Kamper-Jørgensen, M., Sehested, T. S. G., and Boyd, H. A. (2023). Risk and trajectory of premature ischaemic cardiovascular disease in women with a history of preeclampsia: a nationwide register-based study. *Eur. J. Prev. Cardiol.* 30, 506–516. doi:10.1093/eurjpc/zwad003
- Hodgman, C., Khan, G. H., and Atiomo, W. (2022). Coenzyme A restriction as a factor underlying preeclampsia with polycystic ovary syndrome as a risk factor. *Int. J. Mol. Sci.* 23 (5), 2785. doi:10.3390/ijms23052785
- Huang, L., Liu, Z., Wu, P., Yue, X., Lian, Z., He, P., et al. (2022). Puerariae lobatae radix alleviates preeclampsia by remodeling gut microbiota and protecting the gut and placental barriers. *Nutrients* 14 (23), 5025. doi:10.3390/nu14235025
- Khan, N., Andrade, W., De Castro, H., Wright, A., Wright, D., and Nicolaidis, K. H. (2020). Impact of new definitions of preeclampsia on incidence and performance of first-trimester screening. *Ultrasound Obstetrics Gynecol.* 55 (1), 50–57. doi:10.1002/uog.21867
- Litwinska, M., Litwinska, E., Bouariu, A., Syngelaki, A., Wright, A., and Nicolaides, K. H. (2021). Contingent screening in stratification of pregnancy care based on risk of preeclampsia at 19–24 weeks' gestation. *Ultrasound Obstetrics Gynecol.* 58 (4), 553–560. doi:10.1002/uog.23742
- Lu, H. Q., and Hu, R. (2019). The role of immunity in the pathogenesis and development of preeclampsia. *Scand. J. Immunol.* 90 (5), e12756. doi:10.1111/sji.12756
- Lv, L. J., Li, S. H., Wen, J. Y., Wang, G. Y., Li, H., He, T. W., et al. (2022). Deep metagenomic characterization of gut microbial community and function in preeclampsia. *Front. Cell Infect. Microbiol.* 12, 933523. doi:10.3389/fcimb.2022.933523
- Malz, S. S. (1946). Subacute hypoproteinemia in pregnancy. *Harefuah* 31 (9), 154–158.
- Miao, T., Yu, Y., Sun, J., Ma, A., Yu, J., Cui, M., et al. (2021). Decrease in abundance of bacteria of the genus Bifidobacterium in gut microbiota may be related to preeclampsia progression in women from East China. *Food & Nutr. Res.* 65. doi:10.29219/fnr.v65.5781
- Moodley, M., Moodley, J., and Naicker, T. (2020). The role of neutrophils and their extracellular traps in the synergy of preeclampsia and HIV infection. *Curr. Hypertens. Rep.* 22 (6), 41. doi:10.1007/s11906-020-01047-z
- Negre-Salvayre, A., Swiader, A., Salvayre, R., and Guerby, P. (2022). Oxidative stress, lipid peroxidation and premature placental senescence in preeclampsia. *Archives Biochem. Biophysics* 730, 109416. doi:10.1016/j.abb.2022.109416
- Phoswa, W. N., and Khaliq, O. P. (2021). The role of oxidative stress in hypertensive disorders of pregnancy (preeclampsia, gestational hypertension) and metabolic disorder of pregnancy (gestational diabetes mellitus). *Oxidative Med. Cell. Longev.* 2021, 1–10. doi:10.1155/2021/5581570
- Salma, U. (2022). Relationship of serum lipid profiles in preeclampsia and normal pregnancy, Bangladesh. *Afr. Health Sci.* 22 (2), 475–479. doi:10.4314/ahs.v22i2.55
- Sun, B. M., Meng, L., Liu, H., and Bao, D. (2020). Changes in intestinal flora in preeclampsia rats and effects of probiotics on their inflammation and blood pressure. *Eur. Rev. Med. Pharmacol. Sci.* 24 (19), 10155–10161. doi:10.26355/eurrev_202010_23235
- Syngelaki, A., Magee, L. A., von Dadelszen, P., Akolekar, R., Wright, A., Wright, D., et al. (2022). Competing-risks model for preeclampsia and adverse pregnancy outcomes. *Ultrasound Obstetrics Gynecol.* 60 (3), 367–372. doi:10.1002/uog.26036
- Tesfa, E., Munshea, A., Nibret, E., Mekonnen, D., Sinishaw, M. A., and Gizaw, S. T. (2022). Maternal serum uric acid, creatinine and blood urea levels in the prediction of preeclampsia among pregnant women attending anc and delivery services at bahir dar city public hospitals, northwest Ethiopia: a case-control study. *Heliyon* 8 (10), e11098. doi:10.1016/j.heliyon.2022.e11098
- Udenze, I. C. (2016). Association of preeclampsia with metabolic syndrome and increased risk of cardiovascular disease in women: a systemic review. *Niger. J. Clin. Pract.* 19 (4), 431–435. doi:10.4103/1119-3077.180055
- Vaught, A. J., Boyer, T., Ziogos, E., Amat-Codina, N., Minhas, A., Darwin, K., et al. (2023). The role of proprotein convertase subtilisin/kexin type 9 in placental salvage and lipid metabolism in women with preeclampsia. *Placenta* 132, 1–6. doi:10.1016/j.placenta.2022.12.008
- Wind, M., van den Akker-van Marle, M. E., Ballieux, B., Cobbaert, C. M., Rabelink, T. J., van Lith, J. M. M., et al. (2022). Clinical value and cost analysis of the sFlt-1/PlGF ratio in addition to the spot urine protein/creatinine ratio in women with suspected preeclampsia: PREPARE cohort study. *BMC Pregnancy Childbirth* 22 (1), 910. doi:10.1186/s12884-022-05254-1
- Yang, X., Jiang, R., Yin, X., and Wang, G. (2022). Pre-BMI and lipid profiles in association with the metabolic syndrome in pregnancy with advanced maternal age. *Contrast Media & Mol. Imaging* 2022, 1–5. doi:10.1155/2022/4332006
- Yu, Z., Liu, Y., Zhang, Y., Cui, J., Dong, Y., Zhang, L., et al. (2023). Ulinastatin ameliorates preeclampsia induced by N(gamma)-nitro-L-arginine methyl ester in a rat model via inhibition of the systemic and placental inflammatory response. *J. Hypertens.* 41 (1), 150–158. doi:10.1097/hjh.0000000000003316
- Zheng, H., Mai, F., Zhang, S., Lan, Z., Wang, Z., Lan, S., et al. (2023). In silico method to maximise the biological potential of understudied metabolomic biomarkers: a study in preeclampsia. *Gut* 73, 383–385. doi:10.1136/gutjnl-2022-329312

Modified Hongyu Decoction promotes wound healing by activating the VEGF/PI3K/Akt signaling pathway

Xiang Xu^{1#}, Wei-hua Yang^{1#}, Zhi-wei Miao², Chun-yu Zhang², Yi-jia Cheng¹, Yang Chen¹, Jin-gen Lu³ and Ning He¹✉

¹Department of Anal-rectal Surgery, Zhangjiagang TCM Hospital Affiliated to Nanjing University of Chinese Medicine, Zhangjiagang, China;

²Department of Gastroenterology, Zhangjiagang TCM Hospital Affiliated to Nanjing University of Chinese Medicine, Zhangjiagang, China; ³Department of Anal-rectal Surgery, Longhua Hospital, Shanghai University of Traditional Chinese Medicine, Shanghai, China

Wound healing is a considerable problem for clinicians. Ever greater attention has been paid to the role of Chinese herbal monomers and compounds on wound healing. This study aims to elucidate the wound healing mechanism of Modified Hongyu Decoction (MHD) *in vivo* and *in vitro*. MHD wound healing activity *in vivo* was evaluated using an excision rat model. H and E staining, Masson's staining and immunofluorescence of wound tissue on days 7 and 14 were performed to evaluate the efficacy of MHD on wound healing. Subsequently, human umbilical vein endothelial cells (HUVECs) were used to evaluate wound healing characteristics *in vitro*. Cell Counting Kit-8 (CCK-8) and scratch assays were conducted to assess the effects of MHD on the proliferation and migration of HUVECs. The involvement of the VEGF/PI3K/Akt signaling pathway was assessed by western blotting. The rats in the MHD group displayed more neovascularization and collagen fibers. Western blotting of wound tissue showed that VEGF, PI3K, p-Akt and p-eNOS expression were significantly increased ($p < 0.05$) in the MHD group. Cell Counting Kit-8 and scratch assays demonstrated that MHD promoted HUVECs proliferation and migration. MHD treatment significantly increased VEGF, PI3K, p-Akt and p-eNOS expression in HUVECs ($p < 0.05$), which was inhibited by LY294002. Both *in vivo* and *in vitro* data indicated that MHD promotes wound healing by regulating the VEGF/PI3K/Akt signaling pathway.

Keywords: Modified Hongyu Decoction, wound healing, angiogenesis, VEGF/PI3K/Akt signaling pathway

Received: 16 February, 2023; revised: 07 July, 2023; accepted: 11 November, 2023; available on-line: 05 December, 2023

✉ e-mail: huadongdaxiang@126.com

Acknowledgements of Financial Support: This work was supported by the Jiangsu Science and Technology Development Project of Traditional Chinese Medicine (QN202117), Natural Science Foundation of Nanjing University of Traditional Chinese Medicine (XZR2021056), Zhangjiagang Science and Technology Project (No. ZJGQNKJ202131), Science and Technology Project of youth Natural Science Foundation of Zhangjiagang TCM Hospital Affiliated to Nanjing University of Chinese Medicine (No. ZYYQ2008)

#Xiang Xu and Wei-hua Yang contributed equally to this work as Co-first authors.

Abbreviations: eNOS, endothelial Nitric Oxide Synthases; HPLC-Q-TOF/MS, high performance liquid chromatography coupled with quadrupole time-of-flight tandem mass spectrometry; HUVECs, human umbilical vein endothelial cells; MHD, Modified Hongyu Decoction; PI3K, PI3 kinase; rb-bFGF, recombinant bovine basic fibroblast growth factor; VEGF, vascular endothelial growth factor; VEGFR2, vascular endothelial growth factor receptor 2; α -SMA, alpha-smooth muscle actin

INTRODUCTION

Chronic and refractory wounds have become not only a major problem in the medical field, but also a challenge for doctors. Many factors, including chronic inflammation, diabetes mellitus and malignant tumors, can lead to delayed wound healing and even failure to heal. Indeed, millions globally suffer from chronic wounds. For example, a study from Germany in 2012 found that the prevalence of chronic nonhealing wounds was 1% to 2% in the general population (Heyer *et al.*, 2016). This not only affects their normal activities and reduces their quality of life, but also results in major social and economic problems. Care for such conditions has been reported to account for 2% to 3% of the healthcare budgets in developed countries (Frykberg & Banks, 2015; 2013; Richmond *et al.*, 2013). Many biological agents and dressings, containing a variety of growth factors, have been used to accelerate wound healing. However, there are also some complications, including the need for precise dosing to avoid the potential for excess scar formation and bioavailability (Zielins *et al.*, 2015). Additionally, these external treatments may cause adverse stimulation to the local wound, and changing wound dressings may cause unbearable pain for patients.

Wound healing is a dynamic and complex biological process, normally involving four phases: hemostasis, inflammation, proliferation and remodeling (Landen *et al.*, 2016). In the proliferative stage, neovascularization is an essential component of tissue repair, and also a key step of wound healing (Eming *et al.*, 2014; Shiojima & Walsh, 2002). Protein kinase B (Akt), a serine/threonine kinase, is a vital signal center for a wide range of cellular functions. PI3 kinase-dependent activation of Akt further affects the activity of several downstream pathways involved in cell proliferation, angiogenesis, senescence, apoptosis and cellular survival (Hoke *et al.*, 2016; Li & Wang, 2014). As upstream proteins of extracellular signaling, growth factors, including pro-angiogenic growth factors, activate many signaling pathways, including PI3K/Akt, which modulate several cellular activities involved in acute wound healing and maintenance of tissue homeostasis (Squarize *et al.*, 2010). Additionally, the bioactivities of pro-angiogenic growth factors are closely related to endothelial cell chemotaxis at the proliferative phase of angiogenesis and subsequently normal angiogenesis (Eming *et al.*, 2014; Zielins *et al.*, 2015). Among many pro-angiogenic growth factors, vascular endothelial growth factor (VEGF) is the most specific pro-angiogenic growth factor of the vascular endothelium (D'Alessio *et al.*, 2015). It activates the PI3K/Akt signaling pathway

after binding with VEGF receptor 2 (VEGFR2) on the cell membrane of endothelial cells, thereby participating in cell proliferation and angiogenesis (Olsson *et al.*, 2006).

Modified Hongyu Decoction (MHD) is composed of *Pulsatilla chinensis*, *Pseudostellariae radix*, *Sargentodoxa cuneata*, *Patrinia scabiosaeifolia*, *Astragali radix* and *Cornus officinalis*. According to the theory of traditional Chinese medicine, it has the effect of clearing heat and toxic materials, benefiting qi for activating blood circulation. In clinical trials, MHD has been shown to have an outstanding effect on promoting wound healing. However, the underlying mechanisms have not been elucidated. Some active ingredients of MHD have been proved to protect wounds. Previous studies have reported that *A. radix* and its active ingredients, such as Astragaloside IV and Astragalus polysaccharide, promoted wound re-epithelization and angiogenesis and regulated extracellular matrix remodeling by enhancing VEGF expression and activating the PI3K/Akt signaling pathway (Zhang *et al.*, 2009; Chen *et al.*, 2012; Zhao *et al.*, 2017). Other active ingredients, for example, 5-hydroxymethylfurfural derived from processed *C. officinalis*, protected human umbilical vein endothelial cells (HUVECs) injured by high glucose and increased p-Akt protein expression (Cao *et al.*, 2013). Additionally, an aqueous extract of *Patrinia villosa* induced Akt phosphorylation and enhanced HUVECs proliferation and migration, consequently promoting angiogenesis (Jeon *et al.*, 2010). The above research indicated that the Akt signaling pathway may be the vital pathway for MHD to promote wound healing. Therefore, we investigated the therapeutic effect and the mechanism of MHD on wound healing *in vivo* and *in vitro* models.

MATERIALS AND METHODS

MHD preparation

The raw herbs for MHD were purchased from Beijing Tongrentang Co. Ltd (Beijing, China) (origin place of the raw herbs shown in Table S1 at <https://ojs.ptbi-och.edu.pl/index.php/abp/>). *P. chinensis* 15 g (20180620), *P. radix* 15 g (200107), *S. cuneata* 30 g (20191204), *P. villosa* 30 g (200110), *A. radix* 30 g (20200214) and *C. officinalis* 15 g (20191218) were combined and submerged in distilled water (1000 mL) for 30 min. Subsequently, the mixture was extracted twice (1000 mL first followed by 500 mL) over 1 h. After two rounds of extraction, the resulting mixture was filtered. The filtrate was concentrated until the established drug content was 1.35 g/mL. To prepare the MHD extract used for cell experiments, 7.5 mL MHD (1.35 g/mL) was lyophilized using a LAB-1A-50E freeze dryer (Biocool, Beijing, China), yielding 2.02 g powder that was used in the *in vitro* study.

High-performance liquid chromatography of quadrupole time-of-flight mass spectrometry (HPLC-Q-TOF/MS) analysis of the main chemicals in MHD

For the qualitative analysis of the main ingredients in MHD, 0.2 mL MHD was extracted by adding 1 mL ethanol to a 1.5 mL tube. After 10 minutes of vortex, the mixture was centrifuged at 21 000×g for 5 min. The supernatant was collected and injected into a HPLC-Q-TOF/MS system which contained a Shimadzu UFLC 20ADXR system (Kyoto, Japan) and TripleTOF 5600 mass spectrometer (AB SCIEX, USA).

For the column separation, a Waters ACQUITY™ BEH C18 column (1.7 µm, 2.1×50; 1.7 µm) was used, and the column temperature was set at 35°C. Separation was achieved using a mobile phase of 0.02% formic acid-water as solvent A and acetonitrile as solvent B. The flow rate was 0.3 mL/min and the gradient elution program was as follows: 0–2 min, 10% solvent B; 2–30 min, 10–90% solvent B; 30–32 min, 90% solvent B; 32–33 min, 90–10% solvent B; 33–35 min, 10% solvent B. An aliquot of 2 µL supernatant was injected into this system. For the MS analysis, the elution was by ionization using the ESI source both in the positive and negative modes, which could acquire more MS data. In this study, the m/z scan for MS1 was set at a range of 50–1200, and for information-dependent acquisition, the MS2 range was 50–1000. The other parameters used in this study were as follows: ion source gases 1 and 2 were both 50 psi, DP was set at 55 eV, EP was set at 15 eV and the collision energy was 15 eV.

Experimental animals

Twenty-four healthy male Sprague-Dawley (SD) rats (175–195 g) purchased from the Medical Center of Suzhou University (Suzhou, China) (certificate no. SCXK (Su) 2017-0001) were used in this study. Before the experiments, all rats were adaptively fed for one week in polyethylene boxes with free access to autoclaved water and diet under controlled temperature (25°C) and a 12-h light/12-h dark cycle. All experiments were performed in adherence to the guidelines of the Institutional Animal Care and Use Committee of China and were approved by the Ethical Committee of Zhangjiagang TCM Hospital Affiliated to Nanjing University of Chinese Medicine (2021-08-89).

Incisional wound rat model and treatment

The rats were randomly assigned to the following four groups (n=6 rats/group): control group, recombinant bovine basic fibroblast growth factor (rb-bFGF) group (as the positive group), low-dose MHD (L-MHD) group, high-dose MHD (H-MHD) group. All rats were weighed and subsequently anesthetized by intraperitoneal administration of 2% pentobarbital sodium (30 mg/kg). The dorsal hair was shaved, the shaved area was disinfected with 75% alcohol and 2 cm-diameter full-thickness skin wounds were produced on the dorsum in the midline of the backs. The skin wound lost the epidermis, most of the dermis, the fat, and the panniculus carnosus-exposing the fascia layer (Amin *et al.*, 2015).

After surgery, surgical dressing was applied to the rats and the animals were maintained in individual cages. The L-MHD group was given 6.975 g/kg MHD, while the H-MHD group received 13.95 g/kg MHD by intragastric administration once daily. In the rb-bFGF group, each skin wound was topically given rb-bFGF (150 AU/cm², Zhuhai Essex Bio-Pharmaceutical Co., Ltd, Guangdong, China) three times daily. On days 7 and 14, three rats in each group were euthanized by overdose anesthesia (Li *et al.*, 2015), and the wound granulation tissue, liver and kidney were excised from each rat. A portion of the harvested tissue was immediately stored in liquid nitrogen, and the remaining tissue, liver and kidney were maintained in 10% buffered formalin for the following tests.

Wound contraction assay

On days 0, 3, 7, 10 and 14 after injury, an image of each wound area was obtained and measured. The percentage of wound contraction was calculated by the following equation (Amin *et al.*, 2015): wound contraction = (initial wound area – present wound area)/(initial wound area) × 100%.

Histological analysis

The wound tissues, liver and kidney tissues collected at different time points, and livers and kidneys collected after rats sacrificed in each group were fixed with 10% formalin, dehydrated, embedded in paraffin and cut into 5 µm sections. Hematoxylin and Eosin (H&E) staining and Masson trichrome staining were performed using staining kits (Solarbio Technology Co., Ltd, Beijing, China) according to the manufacturer's instructions. Wound healing characteristics, including new epithelium, granulation tissue and collagen deposition, were observed under an inverted microscope (Olympus CX43). Organ sections were stained with H&E for toxicity evaluation.

Immunofluorescence staining

Paraffin sections of wound tissue from days 7 and 14 were dehydrated with xylene and gradient ethanol and subsequently repaired with sodium citrate. Following three washes with 0.3% Triton in PBS to rupture the cell membranes, sections were blocked with immunofluorescence blocking solution for 1 hour at room temperature and incubated with CD31 (ab28364, 1:50, Abcam), α-SMA (#19245, 1:50, CST), VEGFR2 (#9698, 1:800, CST), CD34 (ab81289, 1:100, Abcam) antibodies overnight at 4°C. Subsequently, the sections were incubated with secondary antibodies, including Alexa Fluor 488 donkey anti-rabbit IgG antibody (Invitrogen, Carlsbad, USA) and Alexa Fluor 555 donkey anti-mouse IgG antibody (Invitrogen, Carlsbad, USA), for 1 hour at room temperature at a dilution of 1:800. Finally, slides were counterstained with DAPI for 10 min and were observed with a laser confocal microscope (Olympus, CKX53), with images obtained using LAS X software (Qimaging, USA).

Cell culture and treatment

Human umbilical vein endothelial cells (HUVECs) were purchased from FUHENG Biotechnology Co., Ltd (Shanghai, China) and identified by the American Type Culture Collection (ATCC; Manassas, VA, USA). The cells were cultured in Endothelial Cell Medium (ECM; FUHENG Biotechnology Co., Ltd, Shanghai, China) supplemented with penicillin (100 U/mL), streptomycin (100 µg/mL) and 15% (v/v) fetal bovine serum (FBS; Beijing Biological Industries Co., Ltd, China) and maintained at 37°C under 5% CO₂. After 3 passages, the cells were used for the experiments.

HUVECs were incubated with different MHD concentrations for 24 h. For blocking assay, HUVECs were treated with different concentrations of general PI3K/Akt inhibitor LY294002 (Sigma).

Cell proliferation assay

Cell proliferation was determined using the cell counting kit-8 (CCK-8) kit (MedChemExpress LLC, NJ, USA) according to the manufacturer's instructions. HUVECs (2 × 10⁴ cells, 100 µL per well) with ECM containing 15% FBS were seeded in 96-well plates and incubated

for 24 hours at 37°C under 5% CO₂. The culture medium was replaced by ECM with 15% FBS and different MHD concentrations. For the control group, cells were continued incubation with ECM containing 15% FBS. The MHD concentrations were as follows: 0.1 µg/mL, 1 µg/mL, 5 µg/mL, 10 µg/mL, 50 µg/mL, 75 µg/mL, 100 µg/mL, 200 µg/mL, and 500 µg/mL. Following incubation at 37°C under 5% CO₂. After incubation of 24 hours, the CCK-8 solution was added to each well and incubated at 37°C in humidified 95% air and 5% CO₂ for a further 1 hour. The absorbance was determined at 450 nm for each well using a Microplate Reader (Bio-Rad, Hercules, CA, USA).

Scratch assay

The effect of MHD on HUVECs migration was assessed by the scratch assay (Liang *et al.*, 2007). HUVECs in ECM with 15% FBS were seeded into six-well plates (2 × 10⁵ cells/well) and incubated at 37°C under 5% CO₂. When the cells reached approximately 80% confluence, three vertical scratch lines were made in each well using a 200 µL pipette tip, and cell debris was immediately washed out with phosphate-buffered saline (PBS). Subsequently, serum-free ECM (control) and serum-free ECM with MHD (5 µg/mL, 10 µg/mL, 25 µg/mL or 50 µg/mL) were added to the corresponding wells for 24 h of incubation at 37°C and 5% CO₂. Images of the scratches from the same areas in each well were obtained at 0 and 24 hours, respectively, using an inverted microphotograph (Olympus CX43, Tokyo, Japan) at a magnification of 40×. The scratch area was measured using the Image-J software (NIH, USA).

Western blot

Wound tissues or HUVECs were lysed using lysis buffer with RIPA Lysis Buffer, Phenylmethanesulfonyl fluoride (PMSF), Ethylene Diamine Tetraacetic Acid (EDTA) and protease and phosphatase inhibitor. Total protein concentrations were then quantified using the BCA protein assay kit (Thermo Fisher Scientific, Waltham, USA). Subsequently, equal amounts of proteins were separated by 10% sodium dodecyl sulfate-polyacrylamide gel electrophoresis (SDS-PAGE) and transferred to polyvinylidene difluoride membranes (Millipore, Burlington, MA, USA) using a transfer system (Bio-Rad). After blocking in blocking solution for 1 hour at room temperature, the membranes were incubated overnight at 4°C with primary antibodies diluted in primary antibody dilution buffer, followed by incubation with the horseradish peroxidase-conjugated secondary antibodies for 1 hour at 37°C. The antibodies included anti-phosphorylated Akt (p-Akt, #4060, 1:1000, CST), anti-Akt (#4685, 1:1000, CST), PI3K (#4249, 1:1000, CST), VEGFR2 (#9698, 1:1000, CST), anti-phospho-eNOS (p-eNOS, ab215717, 1:1000, Abcam), anti-β-actin (ab8227, 1:5000, Abcam), horseradish peroxidase-conjugated anti-rabbit IgG (1:5000) and anti-mouse IgG (1:5000). Immunosignals were detected using a chemiluminescence detection kit (Millipore, Burlington, MA, USA) and a gel imaging system (Tanon Science&Technology Co., Ltd., Shanghai, China). β-actin was used as an internal reference. The signal intensity was quantified using Image-J software.

Statistical analysis

For statistical analysis, all data values were analyzed and calculated using GraphPad Prism 8.0 (GraphPad Software Inc., San Diego, CA, USA) and expressed as

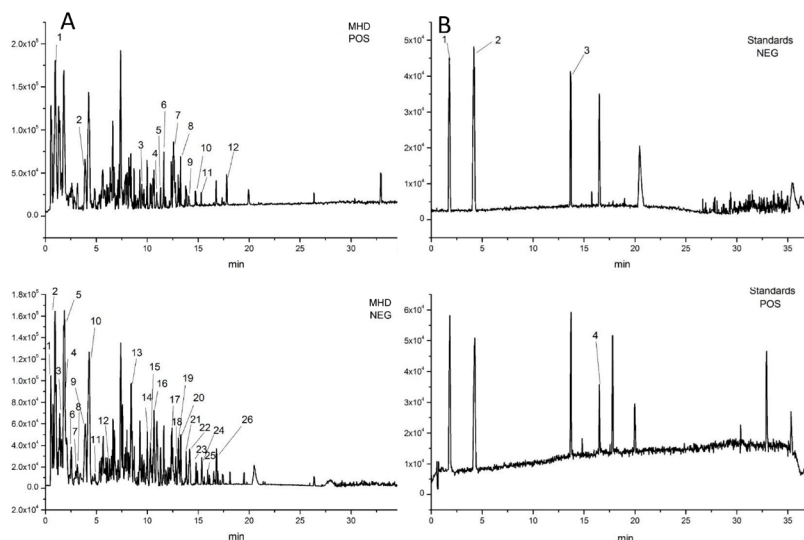


Figure 1. Total ion chromatography of the standards and the Modified Hongyu Decoction (MHD) in negative/positive mode by HPLC-Q-TOF/MS.

mean \pm standard error of the mean (SEM) of three determinations. The data analysis was performed by one-way analysis of variance (ANOVA) followed by Dunnett's test, and $p < 0.05$ was considered statistically significant.

RESULTS

HPLC-Q-TOF/MS analysis of MHD

MHD consists of six herbs that are commonly used in China. For the qualitative analysis of the MHD, we constructed an in-house component library of the MHD, then we compared the MS1 and MS2 data with the literature or the standard solutions. **Figure 1** shows the total ion chromatography of the standards and the MHD. The main chemical components in MHD detected by HPLC-Q-TOF/MS are shown in Table S2 at <https://ojs.ptbioch.edu.pl/index.php/abp/>.

Changes in body weight and hepatorenal toxicity in rats after MHD administration

During the entire experiment, the body weight of all the rats increased gradually. There was no significant difference in body weight among the four groups, which

demonstrated that MHD did not affect body weight (**Fig. 2A**). H&E staining of rats' liver and kidneys showed that, compared with the control group, there were no significant pathological changes in the MHD treatment groups, which indicated that MHD has no hepatorenal toxicity (**Fig. 2B**).

MHD promoted wound healing *in vivo*

The wound areas of rats were observed, and images were obtained on days 0, 3, 7, 10 and 14. The representative images were combined and are presented in **Fig. 3A**. It was clear that the wound area in the four groups gradually decreased with time, indicating that the wounds were gradually healing. On day 7, the wound areas in the H-MHD and rb-bFGF groups were smaller than those in the control and L-MHD groups. On day 14, the wound areas in the H-MHD and rb-bFGF groups were almost healed, while the wound areas in the control and L-MHD groups were still apparent (**Fig. 3A**). Then, the wound areas were measured, and wound contraction of the designated days was plotted against post wounding days, as shown in **Fig. 3B**. From days 3 to 14, the percentages of wound contraction in the control group were respectively: 9.75%, 50.83%, 63.83% and 82.25%; and in the L-MHD group were respectively: 11.84%, 46.66%, 58.07% and 87.96%; H-MHD group were respectively: 11.84%, 77.94%, 93.18% and 99.52%; and the rb-bFGF group were respectively: 20.89%, 77.93%, 87.26% and 99.11%. On days 7, 10 and 14, the percentages of wound contraction in the H-MHD and rb-bFGF groups were significantly increased compared with the control and L-MHD groups. There was no significant difference in the percentages of wound contraction between the H-MHD and rb-bFGF groups (**Fig. 3B**). In general, MHD treatment promoted wound healing in rats.

MHD improved wound granulation tissue *in vivo*

H&E staining showed less inflammatory infiltration in the rb-bFGF and H-MHD groups compared with the control and L-MHD groups on day 7 (**Fig. 4A**). On day 14, epithelial layer regeneration in the H-MHD group

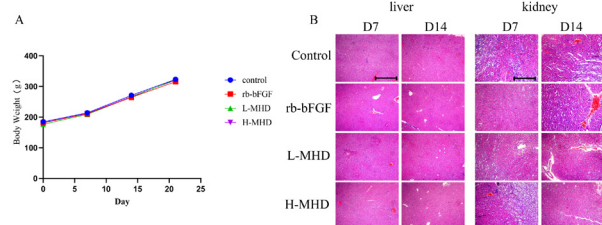


Figure 2. Changes in body weight and hepatorenal toxicity in rats after Modified Hongyu Decoction (MHD) administration. **(A)** The body weight of each group was increased with time. **(B)** Representative images of H&E staining in the liver and kidney of each group were observed on days 7 and 14 (40 \times magnification, scale bar=100 μ m).

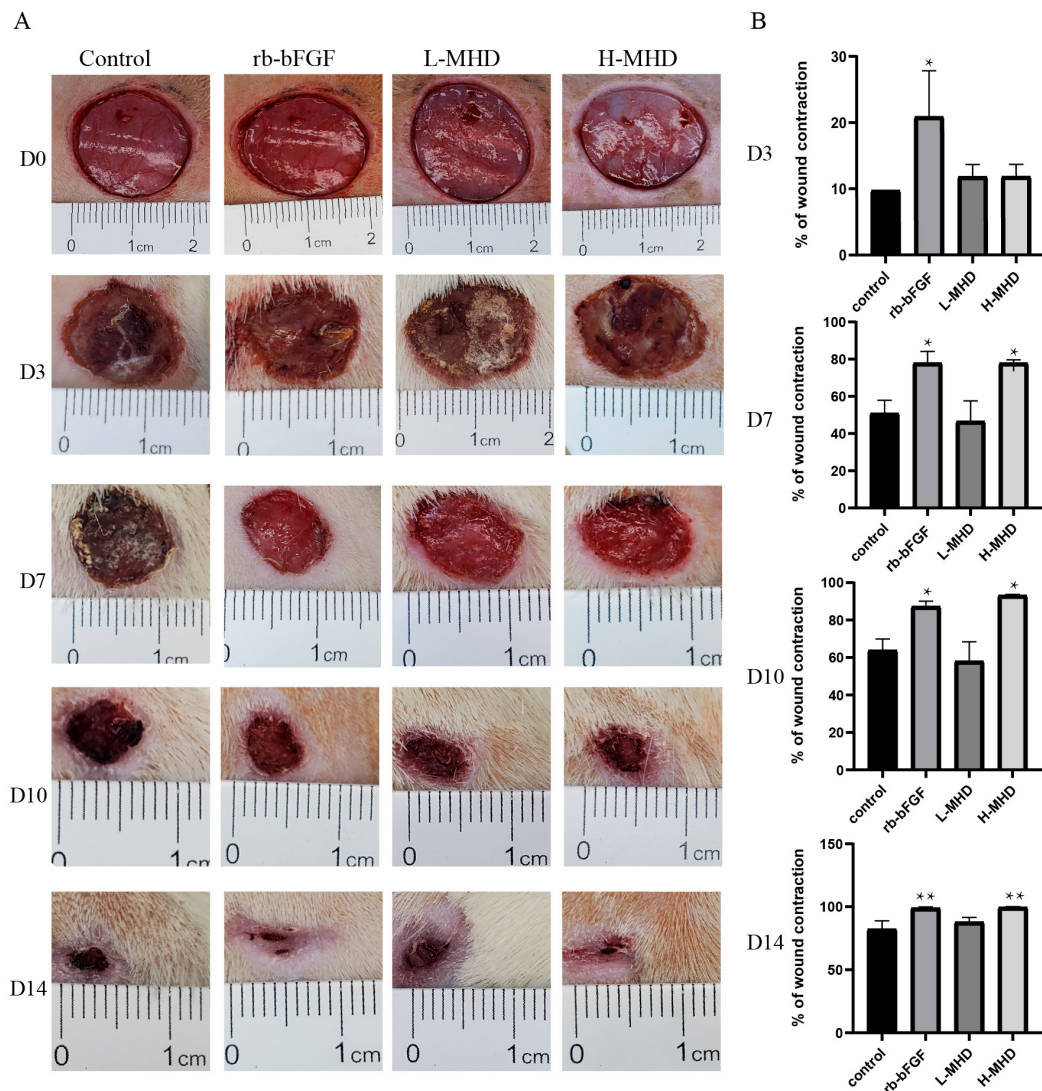


Figure 3. Modified Hongyu Decoction (MHD) promoted wound healing *in vivo*.

(A) Representative images of wound areas in each group on days 0, 3, 7, 10 and 14. (B) Percentage of wound contraction of the different groups on days 0, 3, 7, 10 and 14; $n=3$, * $p<0.05$, ** $p<0.01$, compared with the control group.

was thicker and more complete than in the other groups (Fig. 4A). Masson's staining revealed more collagen fibers in the wounds treated with rb-bFGF or H-MHD than the control and L-MHD groups on both days 7 and 14 (Fig. 4B). These data indicated that H-MHD was almost comparable with rb-bFGF in promoting wound closure, particularly during the later wound healing stage. In conclusion, MHD significantly increased wound closure in rats in a dose-dependent manner.

MHD enhanced angiogenesis in the wound areas of rats

The quantification of new blood vessel density was defined as the ratio of the number of VEGFR2-, CD31-, CD34- and α -SMA-positive staining to DAPI per field. As shown in Fig. 5, both on days 7 and 14, the number of VEGFR2-, CD31-, CD34- and α -SMA-positive staining were rarely observed in the control and L-MHD groups, whereas significantly more positive staining was seen in the rb-bFGF and H-MHD groups (Fig. 5A–B). The quantification showed that both rb-bFGF and H-MHD augmented the production of VEGFR2, CD31, CD34 and α -SMA in the wound areas in rats, and there

was no significant difference between these two groups (Fig. 5C–D). The results demonstrated that MHD could enhance angiogenesis in the wound areas of rats.

MHD activated the VEGF/PI3K/Akt signaling pathway *in vivo*

To investigate molecular mechanisms underlying the therapeutic efficacy of MHD on dorsal full-thickness excisional wounds in rats, we evaluated the expression of proteins related to the VEGF/PI3K/Akt signaling pathway by western blotting. Both on days 7 and 14, the protein expression levels of VEGFR2, PI3K, p-Akt and p-eNOS in the H-MHD and rb-bFGF groups were significantly ($p<0.05$) higher than those in the control and L-MHD groups, whereas no significant differences were observed between the H-MHD and rb-bFGF groups (Fig. 6A–B). These results demonstrated that H-MHD activated the VEGF/PI3K/Akt signaling pathway *in vivo*.

MHD promoted HUVECs proliferation and migration

To determine the effect of MHD on the proliferation and migration of HUVECs, the CCK-8 assay, and

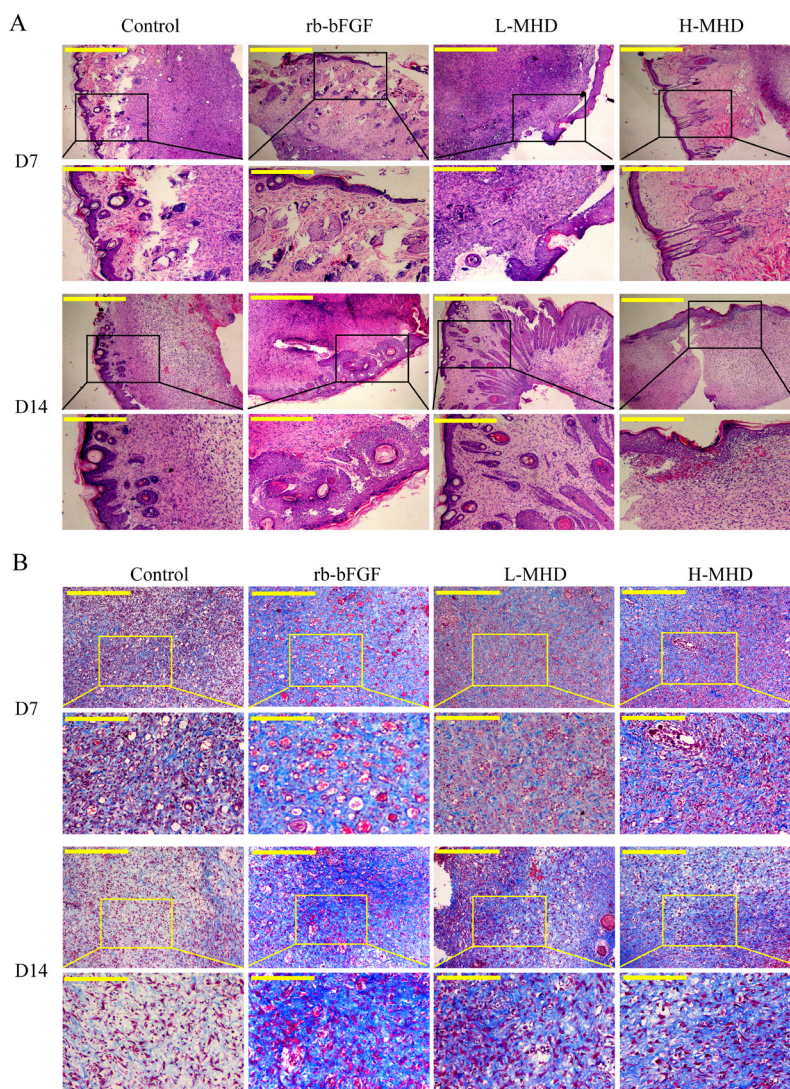


Figure 4. MHD improved wound granulation tissue *in vivo*.

(A) H&E staining was used to observe the wound tissues of each group on days 7 and 14 (upper: 40× magnification, scale bar=100 μm; lower: 200× magnification, scale bar=20 μm) $n=3$. (B) Masson's trichrome staining was used to analyze the changes in wound tissues of each groups on days 7 and 14 (upper: 40× magnification, scale bar=100 μm; lower: 200× magnification, scale bar=20 μm) $n=3$.

scratch assay were performed. The results showed that MHD promoted HUVECs proliferation in a concentration-dependent manner, and that the most potent stimulation was at 50 μg/mL ($p<0.001$) (Fig. 7A). As shown in Fig. 7B–C, the migration areas at 24 h at lower MHD concentrations (5 and 10 μg/mL) were respectively 18.30% and 20.03%, which was similar to that of the control group (11.42%) (Fig. 7B). Treatment with 25 μg/mL MHD clearly ($p<0.05$) reduced the wound width (31.62%), while treatment with 50 μg/mL MHD extensively ($p<0.001$) diminished the wound area (68.83%) at 24 h (Fig. 7B). 25 and 50 μg/mL MHD groups increased the migration rate of HUVECs compared with 5 and 10 μg/mL MHD groups (Fig. 7B). These data indicated that MHD accelerated the proliferation and migration of HUVECs in a concentration-dependent manner.

MHD activated the VEGF/PI3K/Akt signaling pathway in HUVECs

HUVECs were incubated with different MHD concentrations for 24 h, and the protein expressions related

to the VEGF/PI3K/Akt signaling pathway were detected by western blot. MHD treatment increased the protein expression of VEGFR2, PI3K, p-Akt and p-eNOS of HUVECs in a concentration-dependent manner. The protein expressions of VEGFR2, PI3K, p-Akt and eNOS in the 50 μg/mL MHD treatment group were the highest among all concentrations of MHD groups (Fig. 8A).

Then, we observed the effects of different treatment times on the protein expression. The expression of VEGFR2, PI3K, p-Akt and p-eNOS protein at 5–30 min was increased in a time-dependent manner, while the expressions of protein were decreased at 60–120 min. The expressions of VEGFR2, PI3K, p-Akt and p-eNOS protein at 30 min of the treatment group were highest among all groups (Fig. 8B). Overall, these results indicated that MHD activated the VEGF/PI3K/Akt signaling pathway in HUVECs.

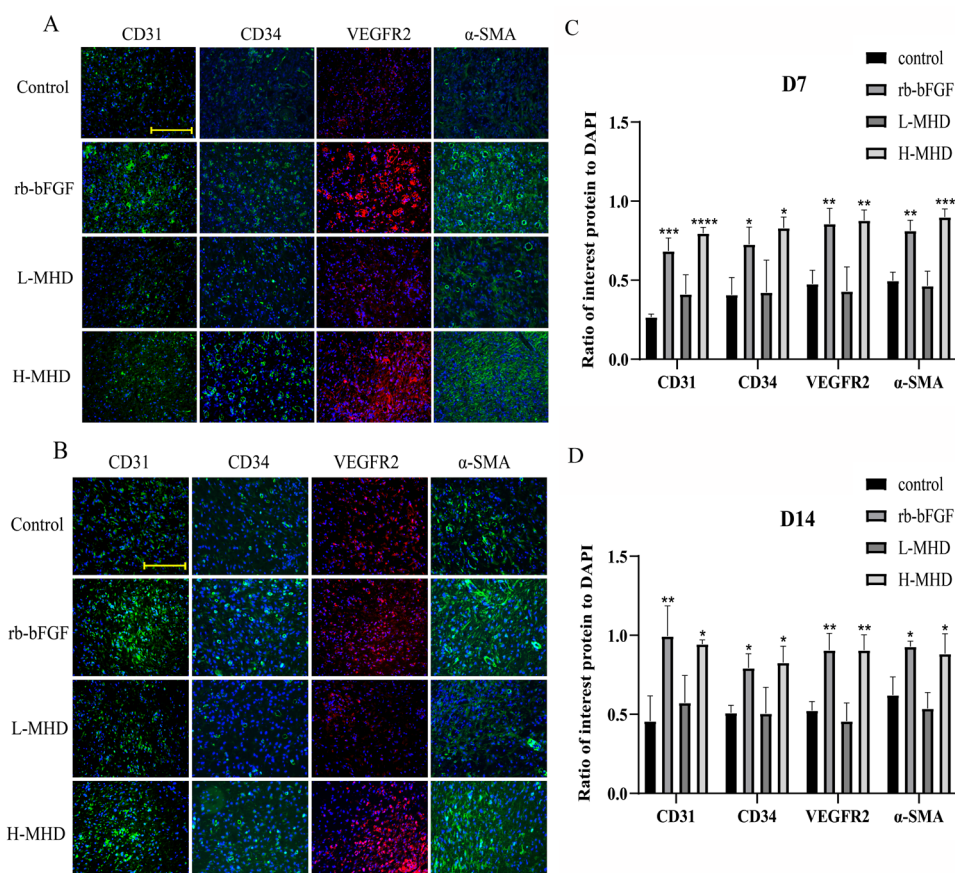


Figure 5. Modified Hongyu Decoction (MHD) enhanced angiogenesis in the wound areas of rats.

(A–B) CD31, VEGF, CD34 and α -SMA immunofluorescence staining of wound sections on days 7 and 14 (200 \times magnification, scale bar =100 μ m) (C–D) Quantitative analysis of fluorescence intensity in CD31, VEGF, CD34 and α -SMA; n=3, * p <0.05, ** p <0.01, *** p <0.001, **** p <0.0001, compared with the control group.

LY294002 reversed the effect of MHD on VEGF/PI3K/Akt signaling pathway in HUVECs

To further determine whether the angiogenic activity of MHD occurred through the Akt signaling pathway,

LY294002 (a PI3K inhibitor) was used. After different concentrations of LY294002 treatment, the expression of PI3K, p-Akt, and p-eNOS were inhibited in a concentration-dependent manner, and the protein expression was significantly decreased after 20 μ M and 50 μ M

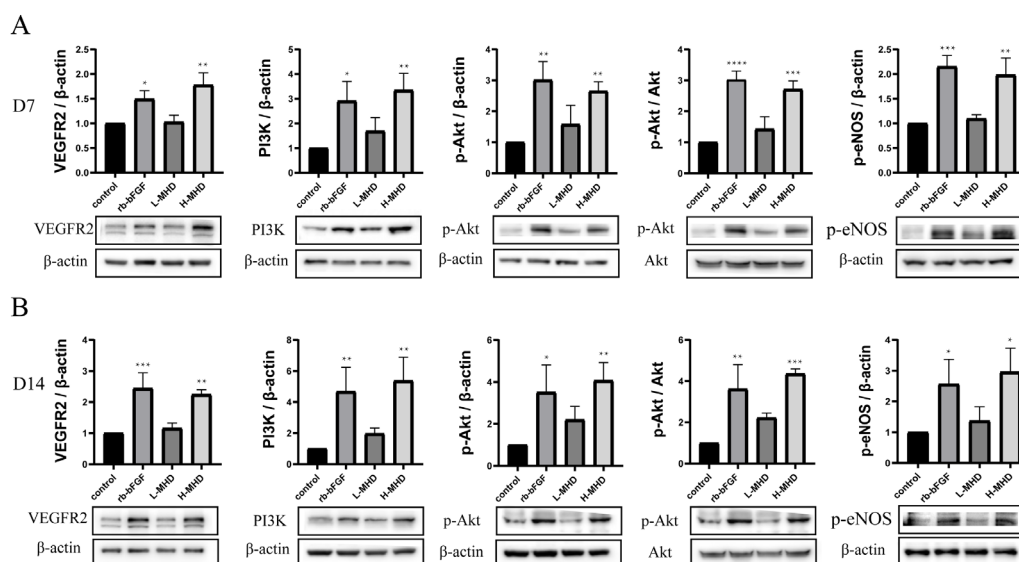


Figure 6. Modified Hongyu Decoction (MHD) activated the VEGF/PI3K/Akt signaling pathway *in vivo*.

(A–B) VEGFR2, PI3K and phosphorylation Akt (p-Akt) and eNOS *in vivo* on day 7 (A) and day 14 (B) were measured by western blot. Data shown in the graphs are representative of the mean \pm SEM; n=3, * p <0.05, ** p <0.01, *** p <0.001, compared with the control group.

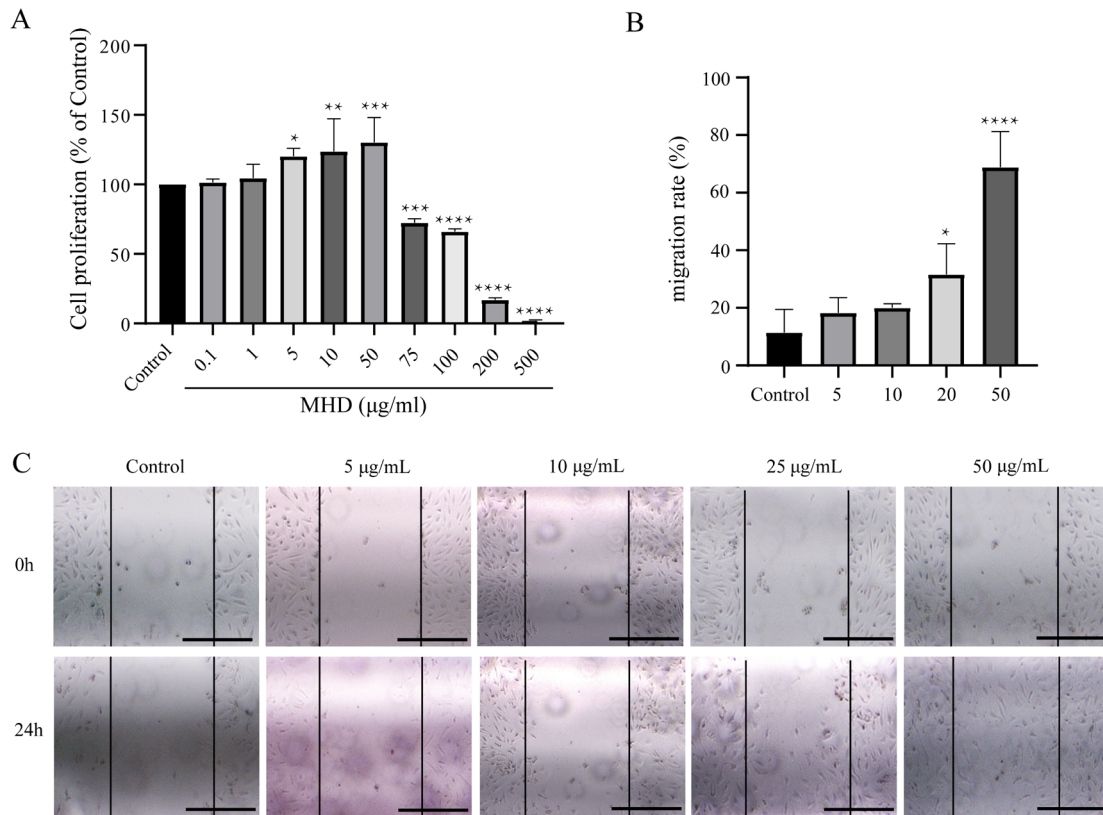


Figure 7. MHD promoted HUVECs proliferation and migration. (A) HUVECs were incubated with different Modified Hongyu Decoction (MHD) concentrations (0.1–500 µg/mL) for 24 h. The concentration-dependent effect of MHD on cell proliferation was determined by the CCK-8 assay; $n=3$, $^*p<0.05$, $^{**}p<0.01$, $^{***}p<0.001$, $^{****}p<0.0001$, compared with the control group. (B–C) The wounds of HUVECs were created and then treated with MHD at 5–50 µg/mL for 24 h. The images were obtained at the same positions at time 0 h and after 24 h treatment with MHD (40 \times magnification, Scale bar = 100 µm), and cell migration rate was assessed by measuring the distance between the wound edges; $n=3$, $^*p<0.05$, $^{****}p<0.0001$, compared with the control group.

LY294002 treatment compared with 0 µM LY294002 (Fig. 9A). Then, 20 µM LY294002 was added to MHD treated HUVECs. MHD treatment increased the PI3K, p-Akt and p-eNOS protein expression and the p-Akt/

Akt ratio in HUVECs. While LY294002 reversed the increasing of PI3K, p-Akt and p-eNOS protein expression and the p-Akt/Akt ratio induced by MHD (Fig. 9B). The results indicated that angiogenic activity of Modi-

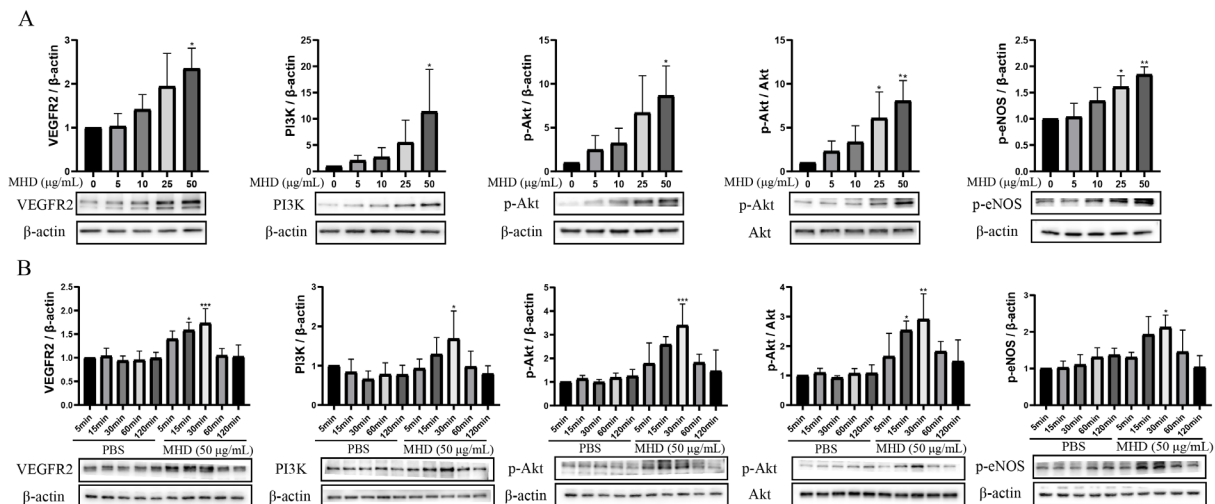


Figure 8. Modified Hongyu Decoction (MHD) activated the VEGF/PI3K/Akt signaling pathway in HUVECs. (A–B) The effects of varying concentration (A, 5–50 µg/mL MHD for 30 min) and time (B, 50 µg/mL MHD for 5–120 min) of MHD on protein expression of VEGFR2, PI3K and p-Akt, Akt and p-eNOS in HUVECs were determined via western blot assay. Values shown are expressed as means \pm SEM, $n=3$. For A, $^*p<0.05$, $^{**}p<0.01$ compared with the 0 µg/mL; For B, $^*p<0.05$, $^{**}p<0.01$, $^{***}p<0.001$, compared with the PBS group.

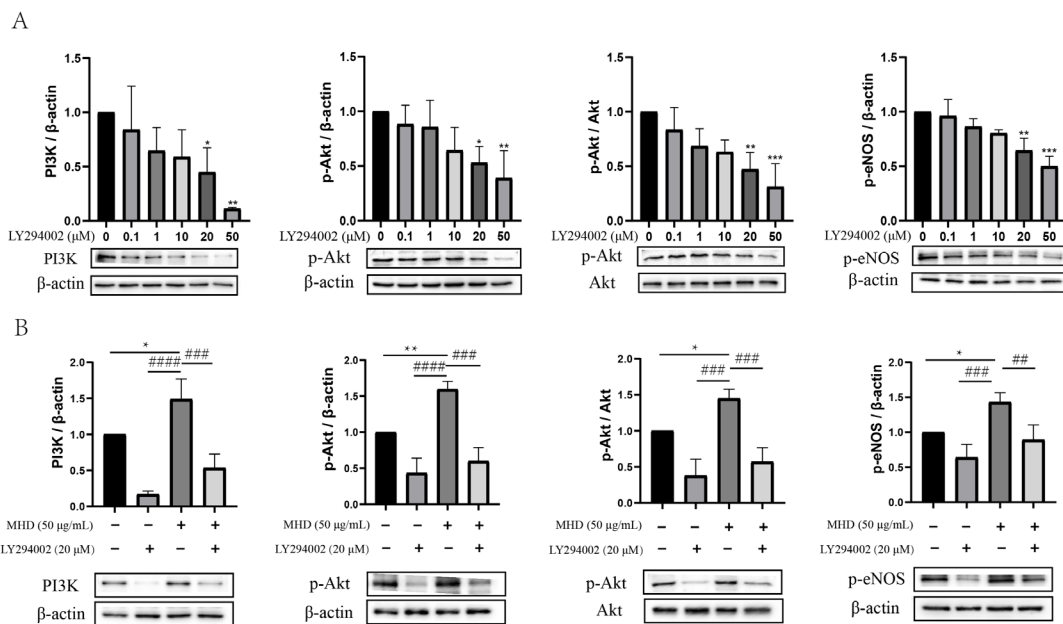


Figure 9. LY294002 reversed the effect of MHD on the VEGF/PI3K/Akt signaling pathway in HUVECs.

(A) HUVECs were incubated with different concentrations of LY294002 (0.1–50 μM) for 24 hours, and the protein expression of PI3K, p-Akt, Akt and p-eNOS was detected by western blot assay. $n=3$, * $p<0.05$, ** $p<0.01$, compared with the 0 μM group. (B) HUVECs were incubated with LY294002 (20 μM) before the exposure to MHD (50 μg/mL). After 24 hours of incubation, the protein expression of PI3K, p-Akt, Akt and p-eNOS was detected by western blot assay. $n=3$, * $p<0.05$, ** $p<0.01$, compared with the untreated cells; ### $p<0.001$, #### $p<0.0001$, compared with MHD-treated cells.

fied Hongyu Decoction (MHD) was responsible for the VEGF/PI3K/Akt signaling pathway.

DISCUSSION

When a wound occurs, granulation tissue composed of new ECM, newly formed blood vessels and fibroblasts will fill the wound bed (Gurtner *et al.*, 2008). Neovascularization can provide oxygen and nutrition for the cells in the wound to maintain fibroblast proliferation, collagen synthesis and reepithelization (Zhang *et al.*, 2016a; Eming *et al.*, 2014), which is essential in wound healing. VEGF is a powerful stimulator of angiogenesis, which directly induces the proliferation and migration of endothelial cells (Simons *et al.*, 2016; Breen, 2007). It is considered to be the key signal molecule of angiogenesis during wound healing (Barrientos *et al.*, 2008). VEGF exerts biological effects by binding and activating VEGFR2 on the cell membrane (Terman *et al.*, 1992; Eremina & Quaggin, 2004), after which several downstream signaling pathways, including the PI3K/Akt, IP3/Ca²⁺/eNOS/NO, FAK, p38 mitogen-activated protein kinase and RAS/RAF-MEK/ERK pathways, can be activated (Olsson *et al.*, 2006). Therefore, the PI3K/Akt pathway is defined to be a VEGF-related signaling pathway (Xu *et al.*, 2014; Peng *et al.*, 2016b; Ewald *et al.*, 2014; Peng *et al.*, 2016a), and it is the central pathway to control the angiogenesis process of endothelial cells (Somanath *et al.*, 2006). Previous studies have shown that the PI3K/Akt signaling pathway is essential for the epithelial-mesenchymal transition and keratinocyte migration, and when dysfunctional, leads to compromised wound healing (Lee *et al.*, 2012). Our study confirmed that MHD promotes wound healing by activating the VEGF/PI3K/Akt pathway *in vitro* and *in vivo*.

In the *in vivo* experiments, we observed that a high MHD dose promoted wound contraction, and the effect was equivalent to the rb-bFGF group. Histological

analysis of wound tissues by H&E and Masson's staining confirmed that both the high MHD dose and rb-bFGF could decrease the number of inflammatory cells, facilitate granulation tissue formation and stimulate new blood vessels and collagen fiber formation. Moreover, H&E staining of the liver and kidney showed that MHD displayed no hepatorenal toxicity. We also labeled the markers of neovascular endothelial cells, such as VEGF, CD31, CD34 and α-SMA, using immunofluorescence. VEGF is an angiogenic factor which has high-efficiency and specific targeting characteristics for endothelial cells, and is closely associated with angiogenesis (Breen, 2007). It plays a key role in the initiation of angiogenesis and participates in the proliferation, migration, adhesion and permeability of vascular endothelial cells and other vascular wall components. VEGF promotes angiogenesis not only in physiological processes but also in inflammation, tumor, trauma and other conditions. CD31 is used to label endothelial cells and is expressed in normal blood vessels (Lertkiatmongkol *et al.*, 2016). CD34 is a type I transmembrane glycoprotein, which is also widely used to label vascular endothelial cells (Lanza *et al.*, 2001). α-SMA is mainly expressed in vascular smooth muscle cells and constitutes the contractile system of the vascular wall (Shinde *et al.*, 2017). The results showed that VEGF, CD31, CD34 and α-SMA in the high MHD dose and rb-bFGF were greater than in the control group. These results confirmed that MHD promotes wound healing by stimulating angiogenesis.

Previous studies suggested that traditional Chinese medicine and extracts, including *Panax ginseng*, *Angelica sinensis*, *A. radix*, *Cinnamomum cassia* and *Salvia miltiorrhiza* among others, could be used as therapeutic agents for wound repair by stimulating angiogenesis and collagen synthesis (Majewska & Gendaszewska-Darmach, 2011). These effects were achieved by activating the VEGF/PI3K/Akt signaling pathway. A number of their monomer components have been shown to be involved in

promoting wound healing by regulating the PI3K/Akt signaling pathway. For example, cinnamaldehyde was reported to promote angiogenesis and wound healing by upregulating the PI3K signaling pathway (Yuan *et al.*, 2018). One of the active ingredients of MHD, astragaloside IV, has also been reported to significantly stimulate angiogenesis through the PI3K/Akt signaling pathway (Zhang *et al.*, 2011). Using western blotting, we also found that a high MHD dose increased VEGF secretion, activated PI3K and induced the phosphorylation of Akt and its downstream target eNOS, thus promoting new blood vessel formation. There are also some reports in the literature about the effect of compounds on wound healing. For example, *Danggui Buxue* extract-loaded liposomes in thermosensitive gel enhanced *in vivo* dermal wound healing via activation of the VEGF/PI3K/Akt and TGF- β /Smads signaling pathways (Cui *et al.*, 2017). These studies were similar to our results and demonstrated that MHD has the potential to promote angiogenesis through the VEGF/PI3K/Akt signaling pathway and is beneficial for wound healing.

HUVECs are frequently used as an *in vitro* model of angiogenesis, as angiogenesis requires endothelial cell migration and morphogenesis (Li *et al.*, 2017). In this study, we also investigated the effect of MHD on HUVECs. In the CCK-8 and scratch assays, MHD promoted HUVECs proliferation and migration. Previous studies have also shown that some of the components of MHD, including *P. villosa* (Cao *et al.*, 2013), *C. officinalis* (Jeon *et al.*, 2010) and *Astragalus* (Lai *et al.*, 2014), stimulate HUVEC proliferation and migration and increase HUVECs viability, with which our results were consistent. By western blotting, we demonstrated that MHD promoted VEGF secretion and activated the PI3K/Akt signaling pathway in both a concentration-dependent and time-dependent manner. One of the active ingredients of MHD, *Astragalus polysaccharides*, has been reported to promote vascular endothelial cell proliferation and repair by activating the PI3K/Akt signaling pathway (Zhang *et al.*, 2016b). Additionally, astragaloside IV was also observed to display an angiogenic effect on endothelial cells, which was reversed by LY294002 (Zhang *et al.*, 2011). Similarly, we also used LY294002 to inhibit the PI3K/Akt signaling pathway and found that PI3K, p-Akt, and p-eNOS were significantly reduced in the MHD+LY294002 group compared with alone MHD group. This indicated that the MHD promotion of HUVECs proliferation depends on the activation of the PI3K/Akt signaling pathway.

While MHD is effective in clinical application, it is, however, a compound composed of a variety of natural medicinal plants. Therefore, the VEGF/PI3K/Akt signaling pathway may not be the only mechanism of its effect on promoting wound healing. Further potential molecular mechanisms need to be investigated. Besides, the limited number of rats used is also a shortage in our study. More animals should be considered in the following research.

CONCLUSIONS

This study showed that MHD significantly promotes wound healing by activating the VEGF/PI3K/Akt signaling pathway. Our study not only helps to explain the mechanism of MHD, but it also provides ideas for the development of new methods to improve wound healing.

Declarations

Availability of data and materials. All data generated or analysed during this study are included in this published article and its supplementary information files.

Acknowledgements. We thank all lab staff for their contributions to this article and the animals sacrificed in this experiment.

Author Contributions. Xiang Xu and Yang Chen performed the cell experiments and wrote the manuscript; Wei-hua Yang and Chun-yu Zhang performed the animal experiments; Yijia Cheng and Jin-gen Lu analyzed the data; Zhi-wei Miao and Ning He designed the research; and all authors proofread and approved the final manuscript.

Competing interests. The authors declare that they have no competing interests.

REFERENCES

- Amin ZA, Ali HM, Alshawsh MA, Darvish PH, Abdulla MA (2015) Application of *Antrpedia campborata* promotes rat's wound healing *in vivo* and facilitates fibroblast cell proliferation *in vitro*. *Evid Based Complement Alternat Med* **2015**: 317693. <https://doi.org/10.1155/2015/317693>
- Barrientos S, Stojadinovic O, Golinko MS, Brem H, Tomic-Canic M (2008) Growth factors and cytokines in wound healing. *Wound Repair Regen* **16**: 585–601. <https://doi.org/10.1111/j.1524-475X.2008.00410.x>
- Breen EC (2007) VEGF in biological control. *J Cell Biochem* **102**: 1358–1367. <https://doi.org/10.1002/jcb.21579>
- Cao G, Cai H, Cai B, Tu S (2013) Effect of 5-hydroxymethylfurfural derived from processed *Cornus officinalis* on the prevention of high glucose-induced oxidative stress in human umbilical vein endothelial cells and its mechanism. *Food Chem* **140**: 273–279. <https://doi.org/10.1016/j.foodchem.2012.11.143>
- Chen X, Peng LH, Li N, Li QM, Li P, Fung KP, Leung PC, Gao JQ (2012) The healing and anti-scar effects of astragaloside IV on the wound repair *in vitro* and *in vivo*. *J Ethnopharmacol* **139**: 721–727. <https://doi.org/10.1016/j.jep.2011.11.035>
- Cui MD, Pan ZH, Pan LQ (2017) Danggui buxue extract-loaded liposomes in thermosensitive gel enhance *in vivo* dermal wound healing via activation of the VEGF/PI3K/Akt and TGF- β /Smads signaling pathway. *Evid Based Complement Alternat Med* **2017**: 8407249. <https://doi.org/10.1155/2017/8407249>
- D'Alessio A, Moccia F, Li JH, Micera A, Kyriakides TR (2015) Angiogenesis and vasculogenesis in health and disease. *Biomed Res Int* **2015**: 126582. <https://doi.org/10.1155/2015/126582>
- Eming SA, Martin P, Tomic-Canic M (2014) Wound repair and regeneration: mechanisms, signaling, and translation. *Sci Transl Med* **6**: 265sr266. <https://doi.org/10.1126/scitranslmed.3009337>
- Eremina V, Quaggin SE (2004) The role of VEGF-A in glomerular development and function. *Curr Opin Nephrol Hypertens* **13**: 9–15. <https://doi.org/10.1097/00041552-200401000-00002>
- Ewald F, Norz D, Grottke A, Hofmann BT, Nashan B, Jucker M (2014) Dual Inhibition of PI3K-AKT-mTOR- and RAF-MEK-ERK-signaling is synergistic in cholangiocarcinoma and reverses acquired resistance to MEK-inhibitors. *Invest New Drugs* **32**: 1144–1154. <https://doi.org/10.1007/s10637-014-0149-7>
- Frykberg RG, Banks J (2015) Challenges in the treatment of chronic wounds. *Adv Wound Care (New Rochelle)* **4**: 560–582. <https://doi.org/10.1089/wound.2015.0635>
- Gurtner GC, Werner S, Barrandon Y, Longaker MT (2008) Wound repair and regeneration. *Nature* **453**: 314–321. <https://doi.org/10.1038/nature07039>
- Heyer K, Herberger K, Protz K, Glaeske G, Augustin M (2016) Epidemiology of chronic wounds in Germany: Analysis of statutory health insurance data. *Wound Repair Regen* **24**: 434–442. <https://doi.org/10.1111/wrr.12387>
- Hoke GD, Ramos C, Hoke NN, Crossland MC, Shawler LG, Boykin JV (2016) Atypical diabetic foot ulcer keratinocyte protein signaling correlates with impaired wound healing. *J Diabetes Res* **2016**: 1586927. <https://doi.org/10.1155/2016/1586927>
- Jeon J, Lee J, Kim C, An Y, Choi C (2010) Aqueous extract of the medicinal plant *Patrinia villosa* Juss. induces angiogenesis via activation of focal adhesion kinase. *Micronas Res* **80**: 303–309. <https://doi.org/10.1016/j.mvr.2010.05.009>
- Lai PK, Chan JY, Kwok HF, Cheng L, Yu H, Lau CP, Leung PC, Fung KP, Lau CB (2014) Induction of angiogenesis in zebrafish embryos and proliferation of endothelial cells by an active fraction isolated from the root of *Astragalus membranaceus* using bioassay-

- guided fractionation. *J Tradit Complement Med* 4: 239–245. <https://doi.org/10.4103/2225-4110.139109>
- Landen NX, Li D, Stahle M (2016) Transition from inflammation to proliferation: a critical step during wound healing. *Cell Mol Life Sci* 73: 3861–3885. <https://doi.org/10.1007/s00018-016-2268-0>
- Lanza F, Healy L, Sutherland DR (2001) Structural and functional features of the CD34 antigen: an update. *J Biol Regul Homeost Agents* 15: 1–13
- Lee SH, Zahoor M, Hwang JK, Min do S, Choi KY (2012) Valproic acid induces cutaneous wound healing *in vitro* and enhances keratinocyte motility. *PLoS One* 7: e48791. <https://doi.org/10.1371/journal.pone.0048791>
- Lertkiatmongkol P, Liao D, Mei H, Hu Y, Newman PJ (2016) Endothelial functions of platelet/endothelial cell adhesion molecule-1 (CD31). *Curr Opin Hematol* 23: 253–259. <https://doi.org/10.1097/MOH.0000000000000239>
- Li T, Wang G (2014) Computer-aided targeting of the PI3K/Akt/mTOR pathway: toxicity reduction and therapeutic opportunities. *Int J Mol Sci* 15: 18856–18891. <https://doi.org/10.3390/ijms151018856>
- Li Y, Wang S, Huang R, Huang Z, Hu B, Zheng W, Yang G, Jiang X (2015) Evaluation of the effect of the structure of bacterial cellulose on full thickness skin wound repair on a microfluidic chip. *Biomacromolecules* 16: 780–789. <https://doi.org/10.1021/bm501680s>
- Li Y, Zhu H, Wei X, Li H, Yu Z, Zhang H, Liu W (2017) LPS induces HUVEC angiogenesis *in vitro* through miR-146a-mediated TGF- β 1 inhibition. *Am J Transl Res* 9: 591–600
- Liang CC, Park AY, Guan JL (2007) *In vitro* scratch assay: a convenient and inexpensive method for analysis of cell migration *in vitro*. *Nat Protoc* 2: 329–333. <https://doi.org/10.1038/nprot.2007.30>
- Majewska I, Gendaszewska-Darmach E (2011) Proangiogenic activity of plant extracts in accelerating wound healing – a new face of old phytochemicals. *Acta Biochim Pol* 58: 449–460
- Olsson AK, Dimberg A, Kreuger J, Claesson-Welsh L (2006) VEGF receptor signalling – in control of vascular function. *Nat Rev Mol Cell Biol* 7: 359–371. <https://doi.org/10.1038/nrm1911>
- Optimal Care of Chronic, Non-Healing, Lower Extremity Wounds: A Review of Clinical Evidence and Guidelines [Internet] (20113) Ottawa (ON): Canadian Agency for Drugs and Technologies in Health
- Peng H, Zhang Q, Li J, Zhang N, Hua Y, Xu L, Deng Y, Lai J, Peng Z, Peng B, Chen M, Peng S, Kuang M (2016a) Apatinib inhibits VEGF signaling and promotes apoptosis in intrahepatic cholangiocarcinoma. *Oncotarget* 7: 17220–17229. <https://doi.org/10.18632/oncotarget.7948>
- Peng S, Zhang Y, Peng H, Ke Z, Xu L, Su T, Tsung A, Tohme S, Huang H, Zhang Q, Lencioni R, Zeng Z, Peng B, Chen M, Kuang M (2016b) Intracellular autocrine VEGF signaling promotes EBDC cell proliferation, which can be inhibited by Apatinib. *Cancer Lett* 373: 193–202. <https://doi.org/10.1016/j.canlet.2016.01.015>
- Richmond NA, Maderal AD, Vivas AC (2013) Evidence-based management of common chronic lower extremity ulcers. *Dermatol Ther* 26: 187–196. <https://doi.org/10.1111/dth.12051>
- Shinde AV, Humeres C, Frangogiannis NG (2017) The role of alpha-smooth muscle actin in fibroblast-mediated matrix contraction and remodeling. *Biochim Biophys Acta Mol Basis Dis* 1863: 298–309. <https://doi.org/10.1016/j.bbadis.2016.11.006>
- Shiojima I, Walsh K (2002) Role of Akt signaling in vascular homeostasis and angiogenesis. *Circ Res* 90: 1243–1250. <https://doi.org/10.1161/01.res.0000022200.71892.9f>
- Simons M, Gordon E, Claesson-Welsh L (2016) Mechanisms and regulation of endothelial VEGF receptor signalling. *Nat Rev Mol Cell Biol* 17: 611–625. <https://doi.org/10.1038/nrm.2016.87>
- Somanath PR, Razorenova OV, Chen J, Byzova TV (2006) Akt1 in endothelial cell and angiogenesis. *Cell Cycle* 5: 512–518. <https://doi.org/10.4161/cc.5.5.2538>
- Squarize CH, Castilho RM, Bugge TH, Gutkind JS (2010) Accelerated wound healing by mTOR activation in genetically defined mouse models. *PLoS One* 5: e10643. <https://doi.org/10.1371/journal.pone.0010643>
- Terman BI, Dougher-Vermazen M, Carrion ME, Dimitrov D, Armellino DC, Gospodarowicz D, Bohlen P (1992) Identification of the KDR tyrosine kinase as a receptor for vascular endothelial cell growth factor. *Biochem Biophys Res Commun* 187: 1579–1586. [https://doi.org/10.1016/0006-291x\(92\)90483-2](https://doi.org/10.1016/0006-291x(92)90483-2)
- Xu D, Ma Y, Zhao B, Li S, Zhang Y, Pan S, Wu Y, Wang J, Wang D, Pan H, Liu L, Jiang H (2014) Thymoquinone induces G2/M arrest, inactivates PI3K/Akt and nuclear factor-kappaB pathways in human cholangiocarcinomas both *in vitro* and *in vivo*. *Oncol Rep* 31: 2063–2070. <https://doi.org/10.3892/or.2014.3059>
- Yuan X, Han L, Fu P, Zeng H, Lv C, Chang W, Runyon RS, Ishii M, Han L, Liu K, Fan T, Zhang W, Liu R (2018) Cinnamaldehyde accelerates wound healing by promoting angiogenesis *via* up-regulation of PI3K and MAPK signaling pathways. *Lab Invest* 98: 783–798. <https://doi.org/10.1038/s41374-018-0025-8>
- Zhang J, Chen C, Hu B, Niu X, Liu X, Zhang G, Zhang C, Li Q, Wang Y (2016a) Exosomes derived from human endothelial progenitor cells accelerate cutaneous wound healing by promoting angiogenesis through Erk1/2 signaling. *Int J Biol Sci* 12: 1472–1487. <https://doi.org/10.7150/ijbs.15514>
- Zhang L, Liu Q, Lu L, Zhao X, Gao X, Wang Y (2011) Astragaloside IV stimulates angiogenesis and increases hypoxia-inducible factor-1 α accumulation *via* phosphatidylinositol 3-kinase/Akt pathway. *J Pharmacol Exp Ther* 338: 485–491. <https://doi.org/10.1124/jpet.111.180992>
- Zhang X, Yao K, Ren L, Chen T, Yao D (2016b) Protective effect of *Astragalus* polysaccharide on endothelial progenitor cells injured by thrombin. *Int J Biol Macromol* 82: 711–718. <https://doi.org/10.1016/j.ijbiomac.2015.09.051>
- Zhang Y, Hu G, Lin HC, Hong SJ, Deng YH, Tang JY, Seto SW, Kwan YW, Waye MM, Wang YT, Lee SM (2009) Radix *Astragal* extract promotes angiogenesis involving vascular endothelial growth factor receptor-related phosphatidylinositol 3-kinase/Akt-dependent pathway in human endothelial cells. *Phytother Res* 23: 1205–1213. <https://doi.org/10.1002/ptr.2479>
- Zhao B, Zhang X, Han W, Cheng J, Qin Y (2017) Wound healing effect of an *Astragalus membranaceus* polysaccharide and its mechanism. *Mol Med Rep* 15: 4077–4083. <https://doi.org/10.3892/mmr.2017.6488>
- Zielins ER, Brett EA, Luan A, Hu MS, Walmsley GG, Paik K, Senarath-Yapa K, Atashroo DA, Wearda T, Lorenz HP, Wan DC, Longaker MT (2015) Emerging drugs for the treatment of wound healing. *Expert Opin Emerg Drugs* 20: 235–246. <https://doi.org/10.1517/14728214.2015.1018176>

Chrysophanol ameliorates oxidative stress and pyroptosis in mice with diabetic nephropathy through the Kelch-like ECH-associated protein 1/nuclear factor erythroid 2-related factor 2 signaling pathway

Xinzhu Yuan^{1#}, Wenwu Tang^{1#}, Changwei Lin¹, Hongni He² and Lingqin Li³✉

¹Department of Nephrology, The Second Clinical Medical Institution of North Sichuan Medical College (Nanchong Central Hospital) and Nanchong Key Laboratory of Basic Science and Clinical Research on Chronic Kidney Disease, Nanchong, China; ²Department of Gynaecology, The Second Clinical Medical Institution of North Sichuan Medical College (Nanchong Central Hospital), Nanchong, China; ³Department of Rheumatology and Immunology, Affiliated Hospital of North Sichuan Medical College, Nanchong, China

Diabetic nephropathy (DN), a microvascular complication of diabetes, increases the risk of all-cause diabetes and cardiovascular mortalities. Moreover, oxidative stress and pyroptosis play important roles in the pathogenesis of DN. Rhubarb is widely used in traditional medicine, and chrysophanol (Chr), a free anthraquinone compound abundant in rhubarb, exhibits potent antioxidant properties and ameliorates renal fibrosis. Therefore, this study aimed to investigate the effects of Chr on renal injury, oxidative stress, and pyroptosis in mice with DN. A DN model was established by feeding the mice a high-sugar and fat diet and injecting them with 50 mg/kg streptozotocin as a positive control. The DN mice had significantly impaired renal function, thickened glomerular thylakoids and basement membranes, increased fibrous tissue, and inflammatory cell infiltration. Superoxide dismutase (SOD) levels were reduced, malondialdehyde (MDA) levels were increased, interleukin (IL)-1 β and IL-18 increased, and cleaved caspase-1, caspase-1, and gasdermin D (GSDMD) involved in the process of pyroptosis were upregulated in DN. Kelch-like ECH-associated protein 1 (Keap1) expression was upregulated, and nuclear factor erythroid 2-related factor 2 (Nrf2) expression was downregulated. Compared to those in the DN group, the Chr-treated mice with DN had improved renal dysfunction, weakened glomerular thylakoid and basement membrane thickening, and reduced fibrous tissue proliferation and inflammatory cell infiltration. Additionally, Chr increased SOD levels, decreased MDA, IL-1 β , and IL-18, down-regulated caspase-1, cleaved caspase-1, GSDMD, and Keap1 expression, and upregulated Nrf2 expression, which reversed the DN. Therefore, Chr reduced oxidative stress and pyroptosis in DN mice by activating the Keap1/Nrf2 pathway.

Keywords: Diabetic nephropathy, Chrysophanol, Keap1/Nrf2 pathway, Oxidative stress, Pyroptosis

Received: 03 April, 2023; **revised:** 23 September, 2023; **accepted:** 29 September, 2023; **available on-line:** 29 November, 2023

✉e-mail: lilingqinnsmc@126.com

Acknowledgments of Financial Support: This study was supported by the Nanchong Technology Strategic Project (22JCYJT0011), and the North Sichuan Medical College Scientific Research Project (CBY21-QA06, CBY21-QA10).

[#]Equal contribution

Abbreviations: Chr, chrysophanol; DN, Diabetic nephropathy; GSDMD, gasdermin D; Keap1, Kelch-like ECH-associated protein 1; MDA, malondialdehyde; Nrf2, nuclear factor erythroid 2-related factor 2; SOD, Superoxide dismutase

INTRODUCTION

Diabetic nephropathy (DN) is the most common and serious microvascular complication of diabetes. More than 15–40% of patients with diabetes mellitus develop DN during their lifetime. Moreover, DN affects patients' quality of life and increases the risk of all-cause diabetes and cardiovascular mortality (Afkarian *et al.*, 2013). Furthermore, DN is characterized by progressive renal impairment with the onset of glomerular basement membrane thickening and widening of the thylakoid matrix (Tervaert *et al.*, 2010). This is followed by trace urine protein, hypertension, edema, renal insufficiency, and even renal failure, leading to end-stage renal disease (ESRD) (Hirawa *et al.*, 2001; Sagoo & Gnudi, 2020).

The glomerular filtration barrier comprises podocytes, which are highly differentiated glomerular epithelial cells, and kidney diseases linked to diabetes may result from damage to podocytes (Lin *et al.*, 2020). Cell death, including apoptosis, necrosis, autophagy, pyroptosis, and ferroptosis, has been observed in the process of DN (Sifuentes-Franco *et al.*, 2018; Al Mamun *et al.*, 2021; Chen *et al.*, 2021). Pyroptosis is a newly discovered form of programmed cell death that has recently attracted increasing attention. In contrast to apoptosis, pyroptosis is a lysis and inflammatory death dependent on inflammatory vesicles and cystatinases and is characterized by plasma membrane rupture, cell swelling, and dissolution, which is mediated by the gasdermin D (GSDMD) protein family (Shi *et al.*, 2017). Evidence suggests that oxidative stress and inflammation play key roles in the development of DN. Chronic hyperglycemia in patients with diabetes is thought to trigger a downstream cascade response. Excessive production of reactive oxygen species (ROS) in podocytes under high-glucose conditions can activate nucleotide-binding domain, leucine-rich-containing family, pyrin domain-containing-3 (NLRP3) to induce podocyte scorching, whereas mitochondrial autophagy can regulate cellular homeostasis and modulate ROS production (Lin *et al.*, 2019; Qiu *et al.*, 2019; Xiaodong & Xuejun, 2022). Podocytes have a huge energy requirement to maintain adequate mitochondrial numbers and normal function; thus, they are more vulnerable to mitochondrial damage (Gujarati *et al.*, 2020; Su *et al.*, 2020a).

Rhubarb is a common traditional Chinese medicine widely used in treating many diseases related to the circulatory, digestive, endocrine, respiratory, and skel-

etal systems, as well as infectious diseases (Rokaya *et al.*, 2012). Chrysophanol (Chr) is a natural anthraquinone component isolated from Rhubarb spp and is also known as chrysophanic acid and 1,8-dihydroxy-3-methyl-anthraquinone. Recent reports have demonstrated that Chr has many beneficial effects, such as anti-inflammatory, anticancer, antidepressant, and neuroprotective (Su *et al.*, 2020b). Renal fibrosis is effectively improved by Chr as the NKG2/NF- κ B pathway is inhibited (Gu *et al.*, 2022). Additionally, Chr alleviates cisplatin-induced nephrotoxicity by simultaneously inhibiting oxidative stress, apoptosis, and inflammation (Ma *et al.*, 2021). Ovarian cancer cell death is induced by Chr which also inhibits cancer invasiveness via mitochondrial calcium overload (Lim *et al.*, 2018). Significant evidence suggests that Chr has strong antioxidant and ameliorating effects on renal fibrosis. However, the Chr function in DN progression remains unknown.

Nuclear factor erythroid 2-related factor 2 (Nrf2) and the endogenous inhibitor, Kelch-like ECH-associated protein 1 (Keap1), are ubiquitous and evolutionarily conserved intracellular defense mechanisms that regulate the redox imbalance caused by oxidative stress (Yang *et al.*, 2013; Bellezza *et al.*, 2018). However, Nrf2 can form an inactive complex with Keap1, which controls the subcellular localization and steady-state level under normal physiological conditions. Activation of the Nrf2 signaling pathway downregulates high glucose-induced ROS levels and podocyte apoptosis. When Nrf2 expression is downregulated, podocytes exposed to high glucose levels exhibit severe mitochondrial dysfunction (Zhang *et al.*, 2018).

Benazepril is considered an effective drug for treating DN because the medication reduces kidney volume and alleviates DN-associated pathological changes (Xue *et al.*, 2017). In the present study, we evaluated the renal pathology of mice with DN, and blood samples were tested for blood glucose, oxidative stress, and pyrogenic levels to assess the effect of Chr, which provides a further understanding of the protective mechanisms of Chr in DN.

MATERIALS AND METHODS

Animal protocols

C57BL/6 mice (6 weeks old, males) were obtained from the Chengdu Dossy Experimental Animals Company, China. The mice were randomized into six groups (seven mice per group): control, DN, DN + 2.5 mg Chr, DN + 5 mg Chr, DN + 10 mg Chr, and DN + benazepril. The control and DN groups were administered 0.9% saline, and the DN + 2.5 mg Chr, DN + 5 mg Chr, and DN + 10 mg Chr groups were administered with Chr at a dose of 2.5, 5, and 10 mg/kg/d, respectively. The benazepril group was administered benazepril at 1 mg/kg/d (Zhao *et al.*, 2016; Dou *et al.*, 2020; Ma *et al.*, 2021). All the mice were placed in an animal room without specific pathogens and under controlled temperature (24°C \pm 1°C) and humidity (50–70%). The mice were adapted to a 12-h light and 12-h dark cycle. The control group was fed standard pellet feed, and the remaining mice were fed high-sugar and high-fat diets for six weeks. They were then injected with 50 mg/kg streptozotocin (STZ) to establish a DN model. Fasting blood glucose levels >7.0 mmol/L were considered to indicate an incidence of diabetes. When the model was successfully established, Chr gavage was ad-

ministered for eight weeks. Benazepril was used as the positive control. All experiments were performed by the guidelines for the care and use of laboratory animals. The kidneys of the mice were weighed, and kidney-to-body weight ratios (KBWR) were calculated based on the weight of the mice. All experimental procedures and protocols were approved by the Medical Ethical Committee of West China Hospital of Sichuan University (20230829001).

Renal function evaluation

After eight weeks of drug treatment, the mice were fasted overnight. All the mice were intraperitoneally injected with 1% sodium pentobarbital. Whole blood was centrifuged (12000 rpm, 4°C, 15 min) to obtain serum. A fully automatic biochemical analyzer, Hitachi 7600-110, was used to measure serum creatinine (Scr), blood urea nitrogen (BUN), and 24-hour urine protein levels.

Hematoxylin and eosin (H&E) and MASSON trichrome staining

Masson trichrome and H&E staining were performed as described previously (Wang *et al.*, 2022). After execution of the mice, kidney samples were isolated and fixed in paraformaldehyde for 24 h, subsequently embedded in paraffin, and sectioned (4–5 μ m). Tissue sections were stained with H&E and Masson trichrome stains.

Enzyme-linked immunosorbent assay (ELISA)

After eight weeks of drug treatment, the samples of kidney cortex from each group of mice were collected, homogenized in 0.05% phosphate-buffered saline (PBS), and centrifuged at 2500 rpm for 20 min. Anti-interleukin (IL)-1 β and anti-IL-18 were purchased from R&D (Minneapolis, MN, USA). The supernatant was collected, and the levels of IL-1 β and IL-18 were detected using corresponding ELISA kits according to the manufacturer's instructions.

Determination of superoxide dismutase (SOD) and malondialdehyde (MDA) activity

After treatment, the kidney cortex was collected from each group of mice, homogenized in 0.05% PBS, and centrifuged at 2500 rpm for 20 min. SOD and MDA kits (NJJCBIO) were used. Optical density was measured using a miniature multifunction panel reader (Biotek Instruments, Inc.). SOD and MDA activities in each group were calculated, according to the manufacturer's instructions.

Western blot (WB) analyses

The cortex tissue samples of the kidneys from each group were homogenized with protease inhibitors, lysis buffer, and a 1 mM mixture of phenylmethylsulfonyl fluoride. Total protein concentration was assayed using a bicinchoninic acid protein assay kit. Equal amounts of total protein extracts were separated by sodium dodecyl sulfate-polyacrylamide gel electrophoresis at 20 μ g per well and transferred to a polyvinylidene difluoride (PVDF) membrane. The PVDF membrane was immersed in tris-buffered saline Tween-20 with 3% bovine serum albumin for 1.5 h. The membrane was then incubated with the following specific primary antibodies (1:1000) overnight at 4°C: anti-Keap1, anti-Nrf2, anti-Pro-Caspase-1, anti-cleaved Caspase-1, and anti-GSDMD. The membranes were then incubated with

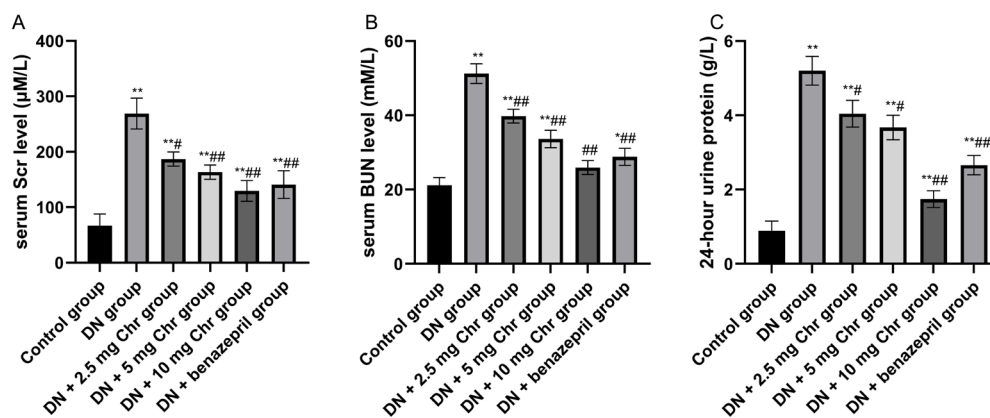


Figure 1. Effects of chrysophanol (Chr) on serum creatinine (Scr, A), blood urea nitrogen (BUN, B) and 24 h urine protein (C) in mice with diabetic nephropathy (DN) analyzed by sarcosine oxidase method, Uricase-GIDH method, and enzyme colorimetry, respectively. Data are presented as mean \pm S.D. Data were compared by one-way ANOVA and Tukey's multiple comparison test. * P <0.05, ** P <0.01 as compared with control group; ## P <0.05, ## P <0.01 as compared with DN group. n =7.

peroxidase-coupled anti-rabbit or anti-mouse antibodies for 2 h at room temperature. Super-enhanced chemiluminescence reagent (Appligen Technologies Inc, Beijing, China) was added to the membrane to visualize the target band. The band intensity was calculated using ImageJ software, and the relative protein intensities were calculated. Anti-Keap1, Nrf2, and caspase-1 were purchased from Servicebio (Wuhan, China), cleaved caspase-1 antibody was purchased from Santa Cruz (1:200, Dallas, TX, USA), and GSDMD and actin antibodies were obtained from Abcam (Cambridge, MA, USA).

Statistical analyses

Data were analyzed using SPSS software (version 20.0; GraphPad Software, La Jolla, CA, USA), and GraphPad Prism 8.0 software was used for drawings. All data are expressed as mean \pm standard deviation. Statistical anal-

yses were performed using a one-way analysis of variance and Tukey's multiple comparison tests for multiple group comparisons. Statistical significance was considered at P <0.05.

RESULTS

Chrysophanol improves Renal Dysfunction in C57BL/6 mice

As displayed in Fig. 1, after eight weeks of treatment, the levels of Scr, BUN, and 24-hour urine protein in the DN group were significantly higher than those in the control group. Moreover, Chr demonstrated varying levels of reduced renal dysfunction in the mice, indicating that Chr was effective in inhibiting a decrease in renal

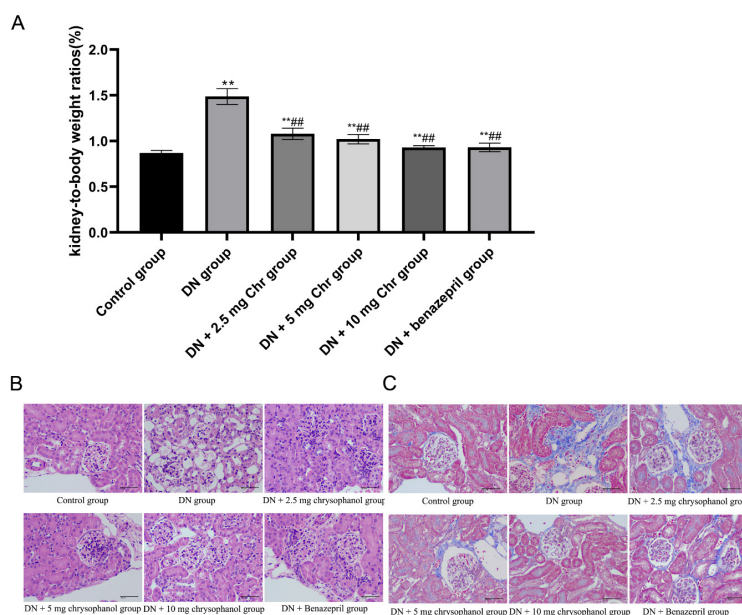


Figure 2. Effects of chrysophanol (Chr) on kidney-to-body weight ratios (A) and pathological features (B and C) in mice with diabetic nephropathy (DN) analyzed by weighing, hematoxylin-eosin staining and Masson staining, respectively. Data are presented as mean \pm S.D. Data were compared by one-way ANOVA and Tukey's multiple comparison test. ** P <0.01 as compared with control group; ## P <0.01 as compared with DN group. n =7. Magnification: \times 40. Scale bar: 50 μ m.

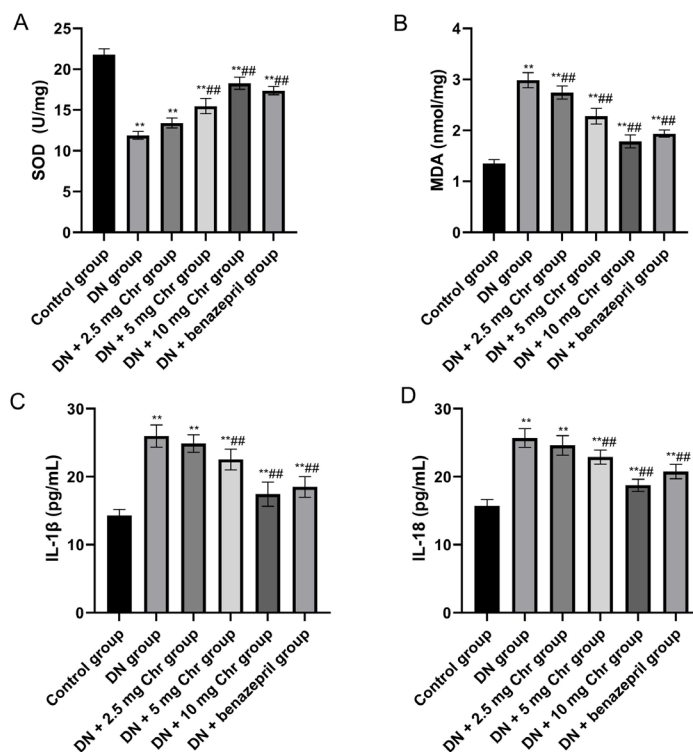


Figure 3. Effects of chrysophanol (Chr) on superoxide dismutase (SOD, A), malondialdehyde (MDA, B), interleukin-1β (IL-1β, C), and interleukin-18 (IL-18, D) in kidneys of mice with diabetic nephropathy (DN) analyzed by Enzyme-Linked Immunosorbent Assay (ELISA).

Data are presented as mean \pm S.D. Data were compared by one-way ANOVA and Tukey's multiple comparison test. ** $P < 0.01$ as compared with control group; *** $P < 0.01$ as compared with DN group. $n = 7$.

function in the DN mice. Additionally, 10 mg of Chr was more effective than benazepril.

Chrysophanol ameliorates morphological and pathological changes in C57BL/6 mice

The kidneys of each mouse group were evaluated. First, we evaluated the KBWR. The KBWR increased significantly in DN mice, but decreased significantly in Chr-treated mice (Fig. 2A). Figures 2B and 2C illustrate kidney slices stained with H&E and Masson's trichrome stains. Thicker glomerular thylakoid and basement membranes, capillary occlusion, epithelial cell swelling, small amounts of interstitial fibrous tissue hyperplasia, and lymphocytic infiltration were observed in the DN group. Compared to those in the DN group, the Chr-treated DN mice exhibited varying degrees of glomerular thylakoid and basement membrane thickening. Additionally, slight epithelial cell degeneration, fibrous tissue hyperplasia, and lymphocyte infiltration were observed in the 2.5 mg Chr group. In the 5 mg Chr group, swelling of epithelial cells with minimal fibrous tissue hyperplasia was observed. No significant fibrous tissue proliferation or inflammatory cell infiltration was observed in the 10 mg Chr group.

Chrysophanol reduces oxidative damage and pyroptosis of the renal cortex in C57BL/6 mice by regulating the Keap1/Nrf2 pathway

To evaluate kidney oxidative stress injury in the C57BL/6 mice, SOD, MDA, IL-1β, and IL-18 were measured and analyzed in the kidney cortex tissue. In the DN group, SOD significantly decreased, and MDA

significantly increased (Fig. 3A and Fig. 3B). However, Chr upregulated SOD and decreased MDA levels in the kidney cortex tissue. Additionally, Chr significantly decreased the levels of IL-1β and IL-18 (Fig. 3C and Fig. 3D), which indicated that Chr could alleviate oxidative stress inflammatory damage in the C57BL/6 mice.

The WB results (Fig. 4A–4G) revealed that the expression of cleaved caspase-1, caspase-1, GSDMD, and Keap1 was upregulated, whereas, the expression of Nrf2 was downregulated in the DN group. Additionally, Chr treatment downregulated the expression of cleaved caspase-1, caspase-1, and GSDMD, which are involved in pyroptosis, downregulated Keap1 protein, and upregulated the expression of Nrf2. These results suggest that Chr inhibits oxidative stress and pyroptosis by regulating the Keap1/Nrf2 signaling pathway.

DISCUSSION

DN is a chronic kidney disease that is a major cause of ESRD and is associated with significant healthcare costs. Although treatment options for DN have progressed, including the use of angiotensin II receptor blockers, angiotensin-converting enzyme inhibitors, sodium-glucose co-transporter protein 2 inhibitors, and salt corticosteroid receptor antagonists, the outcomes remain very limited (Fried *et al.*, 2013; Barrera-Chimal *et al.*, 2019; Tesar, 2022). Thus, an urgent need to develop more valid DN regimens is present. Chr a unique anthraquinone, is a primary component of many plant extensions of traditional Chinese medicine. Moreover, Chr has a broad-spectrum curative potential and eco-relevance (Yusuf *et al.*, 2019), and the drug has been validated to

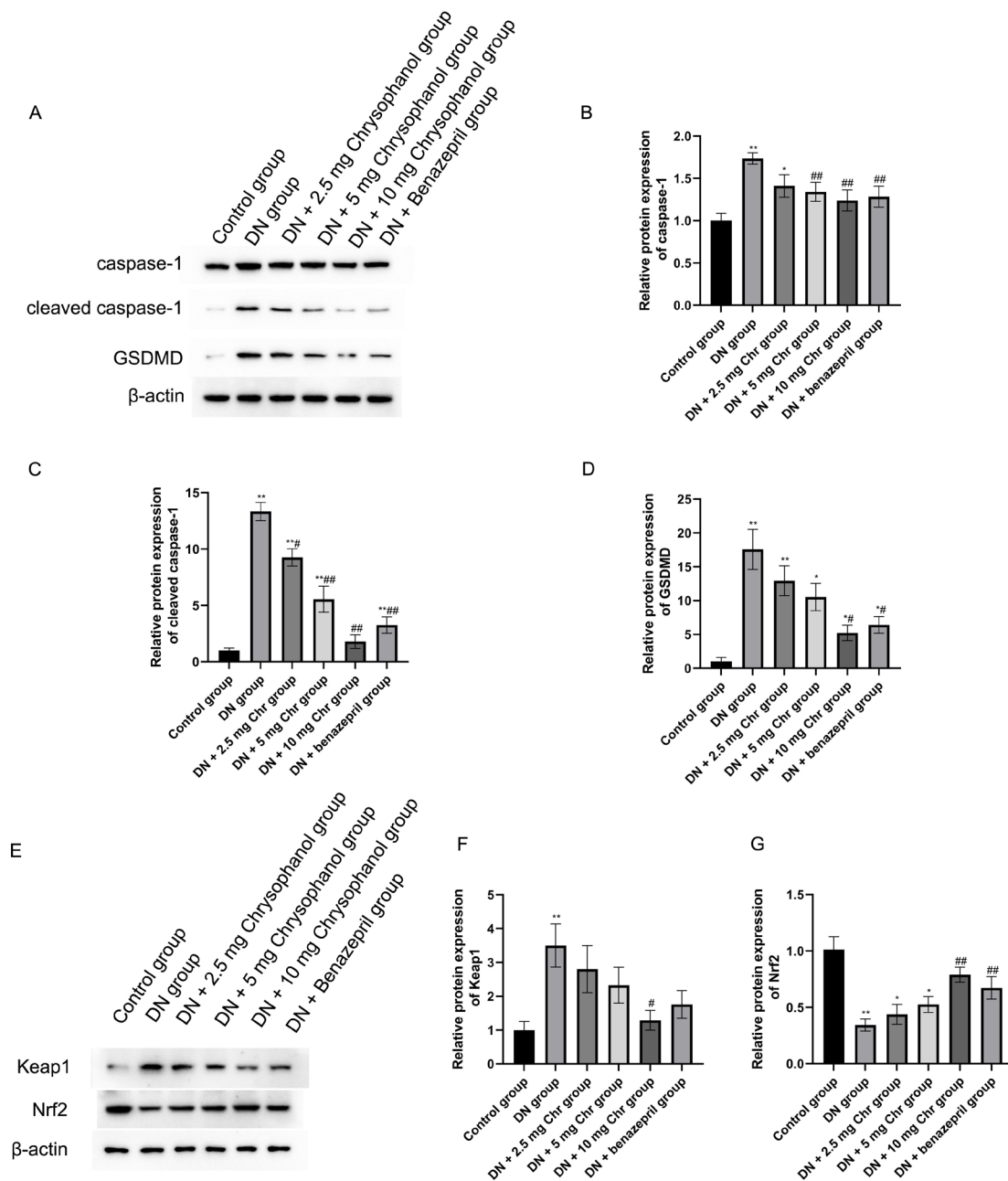


Figure 4. Effects of chrysophanol (Chr) on caspase-1 (A and B), cleaved caspase-1 (A and C), gasdermin D (GSDMD, A and D), kelch-like ECH-associated protein 1 (Keap1, E and F) and nuclear factor erythroid 2-related factor 2 (Nrf2, E and G) in kidneys of mice with diabetic nephropathy (DN) analyzed by western blots (WB).

Data are presented as mean \pm S.D. Data were compared by one-way ANOVA and Tukey's multiple comparison test. * P <0.05, ** P <0.01 as compared with control group; # P <0.05, ## P <0.01 as compared with DN group. n =7.

be effective in the prevention and management of diabetes and its complications (Guo *et al.*, 2020). Benazepril is an angiotensin-converting enzyme inhibitor (ACEI) drug commonly used in treating hypertension and heart failure (Yan *et al.*, 2013). Numerous studies have demonstrated that benazepril improves DN and reduces proteinuria in rats (Jin *et al.*, 2014). In this study, we investigated the underlying effects and potential mechanisms of action of Chr on DN using benazepril as a positive control. Our results suggest that Chr can prevent DN by activating

the Keap1/Nrf2 pathway to attenuate oxidative stress and cellular scorching and reduce inflammation.

The molecular mechanisms underlying DN include inflammation, fibrosis, metabolism, and hemodynamics. Oxidative stress is considered a critical pathway in diabetic kidney injury in the presence of metabolic and hemodynamic abnormalities. Under normal conditions, ROS levels are too low to maintain cellular homeostasis. However, in high conditions, ROS generation in podocytes increases significantly (Bhatti & Usman, 2015). Exposure of podocytes to ROS leads to α -dystroglycan

deglycosylation, thereby decreasing the number of podocytes. Mitochondrial damage-induced podocyte apoptosis is considered to be the most devastating factor in DN progression (Feng *et al.*, 2019). In this study, we identified that Chr could repair high-fat, high-sugar, and STZ-induced mitochondrial damage, enhance antioxidative capacity, and inhibit the generation of oxidation products, thereby preventing apoptosis of podocytes and alleviating DN.

In addition to oxidative stress, inflammation is a key factor in DN development. Several studies have demonstrated that activating inflammatory signaling and infiltrating inflammatory cells are essential for DN progression (Rayego-Mateos *et al.*, 2020). The inflammasome is a multi-protein signaling platform that controls response to inflammation and coordinates antimicrobial host defense (Broz & Dixit, 2016). The NOD-like receptors (NLR), which contain the pyridine structural domain family 3, assemble an intracellular protein complex called the NLRP3 inflammasome when certain pathogen products or sterile danger signals are sensed (Wang *et al.*, 2021). Additionally, NLRP3 is present in natural immune and non-immune cells in the kidney, such as podocytes. NLRP3 recognizes a variety of pathogen- or injury-associated molecular patterns and is involved in intrinsic immune and inflammatory responses (Bai *et al.*, 2017). The NLRP3 inflammasomes mediate pyroptosis and play an important role (Wang *et al.*, 2017; Li *et al.*, 2021). When cells are stimulated externally, they activate the inflammatory complex and Caspase-1, which acts as a direct agonist to cleave IL-1 β and IL-18 precursors, thereby recruiting other inflammatory cells and exacerbating inflammatory response by releasing them extracellularly. Simultaneously, they shear the GSDMD, release the active N-terminal (GSDMD-N) to bind to phospholipids in the inner layer of the plasma membrane, and accelerate nuclear pore formation, which releases mature forms of inflammatory factors to induce pyroptosis (Ystgaard *et al.*, 2015; Rathinam & Fitzgerald, 2016; Sborgi *et al.*, 2016; Sun & Scott, 2016). This inflammatory reaction further promotes the activation of NLRP3 inflammatory corpuscles, forming a vicious circle and aggravating the disease. In the present study, we demonstrated that Chr reduced caspase-1 levels and downregulated GSDMD expression in mice with DN to suppress inflammatory responses, thereby preventing pyroptosis and alleviating DN.

Proteinuria is an important indicator of DN progression (KDOQI Clinical Practice Guidelines and Clinical Practice Recommendations for Diabetes and Chronic Kidney Disease, 2007). However, assessing the severity or prognosis of DN solely based on the degree of proteinuria is accurate (Radcliffe *et al.*, 2017), and pathological changes are a beneficial addition to this assessment. In this study, renal tissue sections from mice in the DN group displayed severe morphological damage and fibrosis. Treatment with Chr restores renal histopathological damage to varying degrees and reduces renal fibrosis in C57BL/6 mice. This implies that Chr may have a protective effect on podocytes in DN. This protective mechanism might be related to the anti-inflammatory and antioxidant properties of Chr.

The present study confirmed that oxidative stress and inflammatory responses are closely associated with DN, and our results suggest that Chr is a potentially effective therapy for DN. Furthermore, because of the common upstream pathogenesis of many diseases, published evidence suggests that Chr may ameliorate various diseases associated with abnormal angiogenesis, including diabetes and cancer, by inhibiting oxidative stress and the Keap1/

Nrf2 pathway (Guo & Mo, 2020). We suggest that this profile could also be deduced from other products of natural origin with antioxidant and anti-inflammatory properties for treating diabetic complications. Furthermore, the findings provide conclusive evidence that the Keap1/Nrf2 signaling pathway is a potential target in DN.

Our study has some limitations. Although the current study suggests that Chr can treat DN by attenuating oxidative stress and inflammation, we did not directly elucidate the origin of oxidative stress-induced damage in the mouse models. The pathogenesis of DN is complex and involves various distinct cell types, such as podocytes, glomerular endothelial cells, thylakoid cells, and renal tubular epithelial cells. Numerous studies have established that oxidative stress and inflammation can affect the aforementioned cells, collectively leading to DN progression. Therefore, we hope that more extensive and targeted investigations will be conducted in the future.

CONCLUSION

In summary, our study provides evidence for the primary role and potential mechanisms of action of Chr in DN. The results display that Chr has a considerable impact on upstream events in the pathogenesis of DN rather than just focusing on late inflammatory infiltration and fiber formation. Chr can manage DN by mitigating both oxidative stress and inflammation and the primary mechanism is related to the inhibition of the Keap1/Nrf2 pathway.

Declarations

Conflict of interest. The authors declare no conflict of interest.

REFERENCES

- Afkarian M, Sachs MC, Kestenbaum B, Hirsch IB, Tuttle KR, Himmelfarb J, De Boer IH (2013) Kidney disease and increased mortality risk in type 2 diabetes. *J Am Soc Nephrol* **24**: 302–308. <https://doi.org/10.1681/asn.2012070718>
- Al Mamun A, Ara Mimi A, Wu Y, Zaeem M, Abdul Aziz M, Aktar Suchi S, Alyafei E, Munir F, Xiao J (2021) Pyroptosis in diabetic nephropathy. *Clin Chim Acta* **523**: 131–143. <https://doi.org/10.1016/j.cca.2021.09.003>
- Bai M, Chen Y, Zhao M, Zhang Y, He J C, Huang S, Jia Z, Zhang A (2017) NLRP3 inflammasome activation contributes to aldosterone-induced podocyte injury. *Am J Physiol Renal Physiol* **312**: F556–F564. <https://doi.org/10.1152/ajprenal.00332.2016>
- Barrera-Chimal J, Girerd S, Jaissier F (2019) Mineralocorticoid receptor antagonists and kidney diseases: pathophysiological basis. *Kidney Int* **96**: 302–319. <https://doi.org/10.1016/j.kint.2019.02.030>
- Bellezza I, Giambanco I, Minelli A, Donato R (2018) Nrf2-Keap1 signaling in oxidative and reductive stress. *Biochim Biophys Acta Mol Cell Res* **1865**: 721–733. <https://doi.org/10.1016/j.bbamcr.2018.02.010>
- Bhatti AB, Usman M (2015) Drug targets for oxidative podocyte injury in diabetic nephropathy. *Cureus* **7**: e393. <https://doi.org/10.7759/cureus.393>
- Broz P, Dixit VM (2016) Inflammasomes: mechanism of assembly, regulation and signalling. *Nat Rev Immunol* **16**: 407–420. <https://doi.org/10.1038/nri.2016.58>
- Chen XC, Li ZH, Yang C, Tang JX, Lan HY, Liu HF (2021) Lysosome depletion-triggered autophagy impairment in progressive kidney injury. *Kidney Dis (Basel)* **7**: 254–267. <https://doi.org/10.1159/000515035>
- Dou F, Ding Y, Wang C, Duan J, Wang W, Xu H, Zhao X, Wang J, Wen A (2020) Chrysophanol ameliorates renal interstitial fibrosis by inhibiting the TGF- β /Smad signaling pathway. *Biochem Pharmacol* **180**: 114079. <https://doi.org/10.1016/j.bcp.2020.114079>
- Feng J, Ma Y, Chen Z, Hu J, Yang Q, Ding G (2019) Mitochondrial pyruvate carrier 2 mediates mitochondrial dysfunction and apoptosis in high glucose-treated podocytes. *Life Sci* **237**: 116941. <https://doi.org/10.1016/j.lfs.2019.116941>

- Fried LF, Emanuele N, Zhang JH, Brophy M, Conner TA, Duckworth W, Leehey DJ, McCullough PA, O'Connor T, Palevsky PM, Reilly RF, Seliger SL, Warren SR, Watnick S, Peduzzi P, Guarino P (2013) Combined angiotensin inhibition for the treatment of diabetic nephropathy. *N Engl J Med* **369**: 1892–903. <https://doi.org/10.1056/NEJMoa1303154>
- Gu M, Zhou Y, Liao N, Wei Q, Bai Z, Bao N, Zhu Y, Zhang H, Gao L, Cheng X (2022) Chrysophanol, a main anthraquinone from Rheum palmatum L. (rhubarb), protects against renal fibrosis by suppressing NKG2D/NF- κ B pathway. *Phytomedicine* **105**: 154381. <https://doi.org/10.1016/j.phymed.2022.154381>
- Gujarati NA, Vasquez JM, Bogenhagen DF, Mallipattu SK (2020) The complicated role of mitochondria in the podocyte. *Am J Physiol Renal Physiol* **319**: F955–F965. <https://doi.org/10.1152/ajprenal.00393.2020>
- Guo C, Wang Y, Piao Y, Rao X, Yin D (2020) Chrysophanol inhibits the progression of diabetic nephropathy via inactivation of TGF- β pathway. *Drug Des Devel Ther* **14**: 4951–4962. <https://doi.org/10.2147/dddt.S274191>
- Guo Z, Mo Z (2020) Keap1-Nrf2 signaling pathway in angiogenesis and vascular diseases. *J Tissue Eng Regen Med* **14**: 869–883. <https://doi.org/10.1002/term.3053>
- Hirawa N, Uehara Y, Ikeda T, Gomi T, Hamano K, Totsuka Y, Yamakado M, Takagi M, Eguchi N, Oda H, Seiki K, Nakajima H, Urade Y (2001) Urinary prostaglandin D synthase (beta-trace) excretion increases in the early stage of diabetes mellitus. *Nephron* **87**: 321–327. <https://doi.org/10.1159/000045937>
- Jin H, Piao SG, Jin JZ, Jin YS, Cui ZH, Jin HF, Zheng HL, Li J, Ji-ang YJ, Yang CW, Li C (2014) Synergistic effects of leflunomide and benazepril in streptozotocin-induced diabetic nephropathy. *Nephron Exp Nephrol* **126**: 148–156. <https://doi.org/10.1159/000362556>
- KDOQI Clinical Practice Guidelines and Clinical Practice Recommendations for Diabetes and Chronic Kidney Disease (2007) *Am J Kidney Dis* **49**: S12–S154. <https://doi.org/10.1053/j.ajkd.2006.12.005>
- Li S, Sun Y, Song M, Song Y, Fang Y, Zhang Q, Li X, Song N, Ding J, Lu M, Hu G (2021) NLRP3/caspase-1/GSDMD-mediated pyroptosis exerts a crucial role in astrocyte pathological injury in mouse model of depression. *JCI Insight* **6**. <https://doi.org/10.1172/jci.insight.146852>
- Lim W, An Y, Yang C, Bazer F W, Song G (2018) Chrysophanol induces cell death and inhibits invasiveness via mitochondrial calcium overload in ovarian cancer cells. *J Cell Biochem* **119**: 10216–10227. <https://doi.org/10.1002/jcb.27363>
- Lin Q, Li S, Jiang N, Shao X, Zhang M, Jin H, Zhang Z, Shen J, Zhou Y, Zhou W, Gu L, Lu R, Ni Z (2019) PINK1-parkin pathway of mitophagy protects against contrast-induced acute kidney injury via decreasing mitochondrial ROS and NLRP3 inflammasome activation. *Redox Biol* **26**: 101254. <https://doi.org/10.1016/j.redox.2019.101254>
- Lin Q, Ma Y, Chen Z, Hu J, Chen C, Fan Y, Liang W, Ding G (2020) Sestrin-2 regulates podocyte mitochondrial dysfunction and apoptosis under high-glucose conditions via AMPK. *Int J Mol Med* **45**: 1361–1372. <https://doi.org/10.3892/ijmm.2020.4508>
- Ma S, Xu H, Huang W, Gao Y, Zhou H, Li X, Zhang W (2021) Chrysophanol relieves cisplatin-induced nephrotoxicity via concomitant inhibition of oxidative stress, apoptosis, and inflammation. *Front Physiol* **12**: 706359. <https://doi.org/10.3389/fphys.2021.706359>
- Qiu Z, He Y, Ming H, Lei S, Leng Y, Xia ZY (2019) Lipopolysaccharide (LPS) aggravates high glucose- and hypoxia/reoxygenation-induced injury through activating ROS-dependent NLRP3 inflammasome-mediated pyroptosis in H9C2 cardiomyocytes. *J Diabetes Res* **2019**: 8151836. <https://doi.org/10.1155/2019/8151836>
- Radcliffe NJ, Seah JM, Clarke M, Macisaac RJ, Jerums G, Ekinci EI (2017) Clinical predictive factors in diabetic kidney disease progression. *J Diabetes Investig* **8**: 6–18. <https://doi.org/10.1111/jdi.12533>
- Rathinam VA, Fitzgerald KA (2016) Inflammasome complexes: emerging mechanisms and effector functions. *Cell* **165**: 792–800. <https://doi.org/10.1016/j.cell.2016.03.046>
- Rayego-Mateos S, Morgado-Pascual J L, Opazo-Ríos L, Guerrero-Hue M, García-Caballero C, Vázquez-Carballo C, Mas S, Sanz AB, Herencia C, Mezzano S, Gómez-Guerrero C, Moreno JA, Egido J (2020) Pathogenic pathways and therapeutic approaches targeting inflammation in diabetic nephropathy. *Int J Mol Sci* **21**: <https://doi.org/10.3390/ijms21113798>
- Rokaya MB, Münzbergová Z, Timsina B, Bhattarai KR (2012) Rheum australe D. Don: a review of its botany, ethnobotany, phytochemistry and pharmacology. *J Ethnopharmacol* **141**: 761–774. <https://doi.org/10.1016/j.jep.2012.03.048>
- Sagoo MK, Gnudi L (2020) Diabetic nephropathy: An overview. *Methods Mol Biol* **2067**: 3–7. https://doi.org/10.1007/978-1-4939-9841-8_1
- Sborgi L, Rühl S, Mulvihill E, Pipercevic J, Heilig R, Stahlberg H, Farady CJ, Müller DJ, Broz P, Hiller S (2016) GSDMD membrane pore formation constitutes the mechanism of pyroptotic cell death. *EMBO J* **35**: 1766–1778. <https://doi.org/10.15252/embj.201694696>
- Shi J, Gao W, Shao F (2017) Pyroptosis: gasdermin-mediated programmed necrotic cell death. *Trends Biochem Sci* **42**: 245–254. <https://doi.org/10.1016/j.tibs.2016.10.004>
- Sifuentes-Franco S, Padilla-Tejeda DE, Carrillo-Ibarra S, Miranda-Díaz AG (2018) Oxidative stress, apoptosis, and mitochondrial function in diabetic nephropathy. *Int J Endocrinol* **2018**: 1875870. <https://doi.org/10.1155/2018/1875870>
- Su J, Ye D, Gao C, Huang Q, Gui D (2020a) Mechanism of progression of diabetic kidney disease mediated by podocyte mitochondrial injury. *Mol Biol Rep* **47**: 8023–8035. <https://doi.org/10.1007/s11033-020-05749-0>
- Su S, Wu J, Gao Y, Luo Y, Yang D, Wang P (2020b) The pharmacological properties of chrysophanol, the recent advances. *Biomed Pharmacother* **125**: 110002. <https://doi.org/10.1016/j.biopha.2020.110002>
- Sun Q, Scott MJ (2016) Caspase-1 as a multifunctional inflammatory mediator: noncytokine maturation roles. *J Leukoc Biol* **100**: 961–967. <https://doi.org/10.1189/jlb.3MR0516-224R>
- Tervaert TW, Mooyaart AL, Amann K, Cohen AH, Cook HT, Drachenberg CB, Ferrario F, Fogo AB, Haas M, De Heer E, Joh K, Noël LH, Radhakrishnan J, Seshan SV, Bajema IM, Bruijn JA (2010) Pathologic classification of diabetic nephropathy. *J Am Soc Nephrol* **21**: 556–563. <https://doi.org/10.1681/asn.2010010010>
- Tesar V (2022) SGLT2 inhibitors in non-diabetic kidney disease. *Adv Clin Exp Med* **31**: 105–107. <https://doi.org/10.17219/acem/145734>
- Wang C, Yang T, Xiao J, Xu C, Alippe Y, Sun K, Kanneganti TD, Monahan JB, Abu-Amer Y, Lieberman J, Mbalaviele G (2021) NLRP3 inflammasome activation triggers gasdermin D-independent inflammation. *Sci Immunol* **6**: eabj3859. <https://doi.org/10.1126/sciimmunol.abj3859>
- Wang Y, Feng F, He W, Sun L, He Q, Jin J (2022) miR-188-3p abolishes geracron-mediated podocyte protection in a mouse model of diabetic nephropathy in type I diabetes through triggering mitochondrial injury. *Bioengineering* **13**: 774–788. <https://doi.org/10.1080/21655979.2021.2012919>
- Wang Y, Gao W, Shi X, Ding J, Liu W, He H, Wang K, Shao F (2017) Chemotherapy drugs induce pyroptosis through caspase-3 cleavage of a gasdermin. *Nature* **547**: 99–103. <https://doi.org/10.1038/nature22393>
- Xiaodong L, Xuejun X (2022) GSDMD-mediated pyroptosis in retinal vascular inflammatory diseases: a review. *Int Ophthalmol* **43**: 1405–1411. <https://doi.org/10.1007/s10792-022-02506-z>
- Xue L, Feng X, Wang C, Zhang X, Sun W, Yu K (2017) Benazepril hydrochloride improves diabetic nephropathy and decreases proteinuria by decreasing ANGPTL-4 expression. *BMC Nephrol* **18**: 307. <https://doi.org/10.1186/s12882-017-0724-1>
- Yan SH, Zhao NW, Zhu XX, Wang Q, Wang HD, Fu R, Sun Y, Li QY (2013) Benazepril inhibited the NF- κ B and TGF- β networking on LV hypertrophy in rats. *Immunol Lett* **152**: 126–134. <https://doi.org/10.1016/j.imlet.2013.05.005>
- Yang G, Zhao K, Ju Y, Mani S, Cao Q, Puukila S, Khaper N, Wu L, Wang R (2013) Hydrogen sulfide protects against cellular senescence via S-sulphydration of Keap1 and activation of Nrf2. *Antioxid Redox Signal* **18**: 1906–1919. <https://doi.org/10.1089/ars.2012.4645>
- Ystgaard MB, Sejersted Y, Løberg EM, Lien E, Yndestad A, Saugstad OD (2015) Early upregulation of NLRP3 in the brain of neonatal mice exposed to hypoxia-ischemia: no early neuroprotective effects of NLRP3 deficiency. *Neonatology* **108**: 211–219. <https://doi.org/10.1159/000437247>
- Yusuf MA, Singh BN, Sudheer S, Kharwar RN, Siddiqui S, Abdel-Azeem AM, Fernandes Fraceto L, Dashora K, Gupta VK (2019) Chrysophanol: a natural anthraquinone with multifaceted biotherapeutic potential. *Biomolecules* **9**: <https://doi.org/10.3390/biom9020068>
- Zhang Q, Deng Q, Zhang J, Ke J, Zhu Y, Wen RW, Ye Z, Peng H, Su ZZ, Wang C, Lou T (2018) Activation of the Nrf2-ARE pathway ameliorates hyperglycemia-mediated mitochondrial dysfunction in podocytes partly through Sirt1. *Cell Physiol Biochem* **48**: 1–15. <https://doi.org/10.1159/000491658>
- Zhao Y, Fang Y, Li J, Duan Y, Zhao H, Gao L, Luo Y (2016) Neuroprotective effects of Chrysophanol against inflammation in middle cerebral artery occlusion mice. *Neurosci Lett* **630**: 16–22. <https://doi.org/10.1016/j.neulet.2016.07.036>

CRISPR-Cas9 guided RNA based model for the treatment of Amyotrophic Lateral Sclerosis: A progressive neurodegenerative disorder

Muhammad Naveed¹✉, Muhammad Aqib Shabbir¹, Tariq Aziz²✉, Hafiz Muhammad Hurraira¹, Sayyeda Fatima Zaidi¹, Ramsha Athar¹, Hassan Anwer Chattha¹, Metab Alharbi³, Abdulrahman Alsahammari³ and Abdullah F. Alasmari³

¹Department of Biotechnology, Faculty of Science and Technology, University of Central Punjab, Lahore Pakistan; ²Department of Agriculture University of Ioannina Arta 47100 Greece; ³Department of Pharmacology and Toxicology, College of Pharmacy, King Saud University, P.O. Box 2455, Riyadh 11451, Saudi Arabia

Amyotrophic lateral sclerosis (ALS) is a progressive neurodegenerative disorder that leads to the degeneration of motor neurons and the weakening of muscles. Despite extensive research efforts, there is currently no cure for ALS and existing treatments only address its symptoms. To address this unmet medical need, genome editing technologies, such as CRISPR-Cas9, have emerged as a promising solution for the development of new treatments for ALS. Studies have shown that CRISPR-Cas9-guided RNAs have the potential to provide accurate and effective silencing in the genetic disease of ALS. Results have demonstrated a 67% on-target score and a 98% off-target score with GC content within the range of 40–60%. This is further validated by the correlation between the gRNA's structural accuracy and the minimum free energy. The use of CRISPR-Cas9 provides a unique opportunity to target this disease at the molecular level, offering hope for the development of a more effective treatment. In silico and computational therapeutic approaches for ALS suggest that the CRISPR-Cas9 protein holds promise as a future treatment candidate. The CRISPR mechanism and the specificity of gRNA provide a novel therapeutic approach for this genetic disease, offering new hope to those affected by ALS. This study highlights the potential of CRISPR-Cas9 as a promising solution for the development of new treatments for ALS. Further research is required to validate these findings in preclinical and clinical trials and to establish the safety and efficacy of this approach in the treatment of ALS.

Keywords: CRISPR-Cas9, RNA-based model, ALS, neurodegenerative disorder, progressive disease, pre-clinical trials

Received: 09 April, 2023; **revised:** 21 May, 2023; **accepted:** 28 May, 2023; **available on-line:** 06 September, 2023

✉e-mail: naveed.quaidian@gmail.com (MN) iwockd@gmail.com (TA)

Acknowledgments of Financial Support: The authors greatly acknowledge and express their gratitude to the Researchers Supporting Project number (RSP2023R335), King Saud University, Riyadh, Saudi Arabia.

Abbreviations: ALS, Amyotrophic lateral sclerosis; SOD1, Superoxide dismutase-1; EMA, European Medicine Agency

INTRODUCTION

Amyotrophic Lateral Sclerosis (ALS), commonly referred to as Lou Gehrig's disease, is a degenerative neurological condition that predominantly impacts the motor

neurons that regulate voluntary muscle movement. The ailment was initially documented by the French neurologist Jean-Martin Charcot in 1869 and has subsequently been acknowledged as among the most catastrophic motor neuron disorders (Longinetti & Feng, 2019). ALS is a condition that impacts individuals of diverse ethnicities and age groups across the globe, with a marginal preponderance in males. The Etiology of ALS remains largely elusive, albeit a small proportion of cases, ranging from 5% to 10%, are deemed familial, stemming from heritable genetic mutations (Hardiman *et al.*, 2017). The vast majority of ALS cases are sporadic, lacking a discernible familial background. The prevalence of ALS exhibits heterogeneity among diverse populations, with an annual occurrence rate of 1 to 3 cases per 100 000 persons. ALS has an estimated prevalence of approximately 4-8 cases per 100 000 individuals, although certain regions have reported higher rates (Longinetti & Fang, 2019). Symptoms of ALS may first appear in the muscles that govern speech and swallowing, as well as in the hands, arms, legs, and feet. ALS has two types, depending upon the gene due to which it is caused. *SOD1* and *C9ORF72* are the genes that are responsible for this fatal disease. These genes play a crucial role in many processes including the control of motor neurons (Masrori & Vane Damme, 2020; Longinetti & Feng, 2019).

Regrettably, at present, there exists no remedy for ALS but the modern artificial intelligence-based technologies can be proved as enhanced treatment strategies with revolutionized drug design approaches (Naveed *et al.*, 2023a; Naveed *et al.*, 2023b). The mainstay of treatment approaches is centred on symptom management, provision of supportive care, and enhancement of the patient's quality of life. The implementation of a multidisciplinary approach entails the collaboration of a diverse group of healthcare professionals, such as neurologists, physical therapists, occupational therapists, speech-language pathologists, nutritionists, and palliative care specialists (Morimoto *et al.*, 2019). The primary objectives of therapy entail the deceleration of the disease advancement, effective symptom management, and the consideration of the emotional and psychological dimensions of the ailment. ALS is a disease that leads to paralysis and causes premature death of patients. A drug named Riluzole is a glutamate antagonist that increases the survival of patients by a few months. Another drug named Enderavone was recently approved by FDA in 2017 (Saitoh & Takahashi, 2020; Yoshino, 2019). However, the European Medicine Agency (EMA)

has not approved this drug. There is no viable treatment for ALS patients despite decades of constant efforts to understand and to develop drugs for this illness. Clinical therapy, including early gastrostomy tube installation for nutritional intervention or non-invasive positive pressure ventilation for respiratory intervention, can help patients to feel better and live longer (Shoesmith *et al.*, 2020). Nevertheless, the condition cannot be cured by these treatments. The complexity of the condition, late diagnosis, and difficulties in developing a treatment that can effectively reach the central nervous system are all factors that can be connected to the failure of conventional pharmacological and interventional therapies (Varghese *et al.*, 2020; Norris *et al.*, 2020).

This research aims to design a proper gene therapy (Insilco) that aids the treatment of ALS. As we know that currently, there is no therapy for ALS other than the anti-glutamatergic compound riluzole, which is less effective in improving symptoms and only increases the survival period of a patient by a few months. The implementation of Insilco approaches for the assessment of current and future treatment strategies in ALS could shorten trial durations and reduce costs and burden on patients, thereby providing hope that effective therapies can be rapidly translated into the ALS clinic.

MATERIALS AND METHODS

Sequence Retrieval

The reference sequence of the Superoxide dismutase-1 (*SOD1*) gene was retrieved from NCBI (Nation Centre for Biotechnology Information) (<https://www.ncbi.nlm.nih.gov>) from the specifically allocated accession ID NM_000454. The sequence was retrieved in the FASTA format and saved in a text document for further utilization (Schoch *et al.*, 2020).

Local alignment of the sequence

To identify the mutations, present in the *SOD1* gene sequence, the sequence was analysed for local alignment by NCBI BLASTx (<https://blast.ncbi.nlm.nih.gov/Blast.cgi>). The BLASTx is a tool of NCBI that performs the local alignment of the query sequences with already available sequences in the database and gives results in the form of amino acids to identify the SNPs that might be responsible for the disease. The disease-causing SNPs were validated by the comparison with the NCBI dbSNP database (<https://www.ncbi.nlm.nih.gov/snp>).

Cas9 Endonuclease Protein

For genome engineering, the particular enzyme Cas9 Endonuclease protein was utilized. This enzyme should be used because it is simple and has all the basic capabilities to split DNA molecules into single strands. The Cas9 genome editing protein includes blunt ends and cuts sites, RNA-guided endonucleases, PAM site (NGG), crRNA, and tracrRNA. It can cut specific regions of the genomic DNA. Cas9 protein caused a double-strand break in the genomic DNA of *SOD1* (Koonin *et al.*, 2023).

Formation of gRNA

The gRNA (guide RNA) is a small synthetic sequence of RNA that functions as a guide for DNA targeting enzymes. These enzymes are used for various purposes like deletion, insertion, or targeting of RNA (Collins *et al.*,

2021). The design of gRNA can be automated through the use of various tools available online. Among these tools we prefer CHOPCHOP (<https://chopchop.cbu.uib.no>), an online tool that offers a wide range of inputs and alignments to minimize search times. This tool is the most authentic and reliable for designing gRNA (Labun *et al.*, 2021).

Steps for generating gRNA

The CHOPCHOP tool provides a user-friendly interface for designing gRNA sequences for the CRISPR-Cas9 system. To start, the user simply enters the gene name on the home page and selects the desired genome version or species. Next, the user selects the specific version of the Cas9 protein to be used. The user then specifies the desired outcome of the experiment, whether it be gene knockout, inhibition, or repression. The general settings of CHOPCHOP can then be left unchanged. Upon clicking the "Find Target" button, the tool provides a list of all gRNA sequences present in the selected gene. The user can then select the desired gRNA sequence for their experiment (Labun *et al.*, 2021).

Verification of gRNA

To verify the effectiveness of gRNA, it is important to assess its on-target and off-target binding capacity. Several online tools are available for this purpose, in this study IDT (Integrated DNA Technology) (<https://www.idtdna.com/site/order/designtool/index/>) was chosen. IDT is a database that facilitates molecular-level analysis of DNA and RNA, where gRNA sequence was submitted for the checking off-target and on-target. The more suitable the gRNA was, the higher its on-target and off-target binding capacity became.

Indicating the off-Target and on-Target Scores

It was found that GC, which includes three hydrogen bonds and is more stable, had a stronger connection between guanine and cytosine. As a result, GC content of up to 50% destabilized off-target hybridization while stabilizing the DNA-RNA duplex. The choice of the number range was made because it fell within the *SOD1* coding zone. This numerical range represented the off-target and on-target ratings for gRNA, with numbers running from 0 to 100 and 100 being considered the best score in each situation. The genomic area of the targeted gene had to be carefully chosen. In the study, the *SOD1* gene was used to obtain accurate off-target scores by IDT (Integrated DNA Technology).

Assembling of gRNA Expression Vector

Assembling of gRNA was done after the selection of the desired gRNA. Since it is being genetically modified for this purpose, a specific expression vector that optimized lentiCRISPR v2 (52963) was selected. It has two expression cassettes, the chimeric guide RNA and hSpCas9. The vectors provided on this list were given by Feng Zhang's laboratory (<https://zlab.bio>) at MIT. All the enlisted plasmids were different, some expressed nuclease-deficient Cas9 that are used for gene activation and repression while others are optimized for genome editing by using CRISPR. For this validation, a new plasmid lentiCRISPR v2 was selected because it includes Cas9 within the same vector that was optimized for the Human Genome (*SOD1* gene).

Calculation Thermodynamic ensemble prediction

The RNAfold program was a reliable tool for estimating hybridization energy and analyzing the thermodynamic interaction between the target gene and the expected sgRNA. Additionally, the Vienna RNA program was also used for this purpose. Both programs showed how RNA sequences base-paired. The calculated communication energies and equilibrium duplex structure concentrations were determined using the RNAfold program.

Secondary Structure Prediction

The Mfold Web server (<http://rna.tbi.univie.ac.at/cgi-bin/RNAWebSuite/RNAfold.cgi>), which included the UNAFold program, was used in the study and considered one of the most reliable and frequently referenced tools for predicting secondary structures. The UNAFold program was used to predict the secondary structure of the sgRNA strand by minimizing free energy, and it was able to predict sgRNA architectures containing pseudoknots.

RESULTS

Sequence Retrieval and Analysis

In this study, the *SOD1* (Superoxide dismutase 1) gene sequence was retrieved from the NCBI (National Center for Biotechnology Information) database (<https://www.ncbi.nlm.nih.gov>) using the accession number NM_000454.4. The selection of the sequence was based on a comprehensive literature review. The chosen sequence was the start codon of the *SOD1* receptor gene located on chromosome X at position 31659693-31668931.

ps://www.ncbi.nlm.nih.gov) using the accession number NM_000454.4. The selection of the sequence was based on a comprehensive literature review. The chosen sequence was the start codon of the *SOD1* receptor gene located on chromosome X at position 31659693-31668931.

Open reading frame (ORF) screening

The screening of the coding region of the *SOD1* gene was performed using the open reading frame finder (<https://www.ncbi.nlm.nih.gov/orffinder>). The ORF finder is a widely used tool for predicting and analysing open reading frames. In the case of the *SOD1* gene, 56 ORFs were identified and were calculated from the genomic coordinates 31659693-31668931. Figure 1 below represents the ORFs of *SOD1* gene.

Analysis of the designed guide RNA

The gRNA design was based on the objective of identifying or cutting the target gene. The CHOPCHOP tool, a web-based platform, was utilized to design the gRNA sequence. The *SOD1* gene was inserted into the software as the targeted gene, with the exon region represented by a blue box and the introns indicated by red lines. The structural representation of *SOD1* gene is given below in the Fig. 2 and the Table 1 below depicts the target sequences with their genomic locations inside the gene.

Table 1. Target sequences and genomic locations of the target sites in *SOD1* gene

Rank	Target sequence	Genomic location	Strand	GC content (%)	Self-complementarity	MM0	MM1	MM2	MM3	Efficiency
1	CTAGCGAGTTATGGCGACGAAGG	chr21:31659760	+	55	2	0	0	0	0	67.55
2	TAACTCGCTAGGCCACGCCGAGG	chr21:31659748	-	65	4	0	0	0	1	69.6
3	CTTCGTCGCCATAACTCGCTAGG	chr21:31659759	-	55	2	0	0	0	1	55.63

Open Reading Frame Viewer

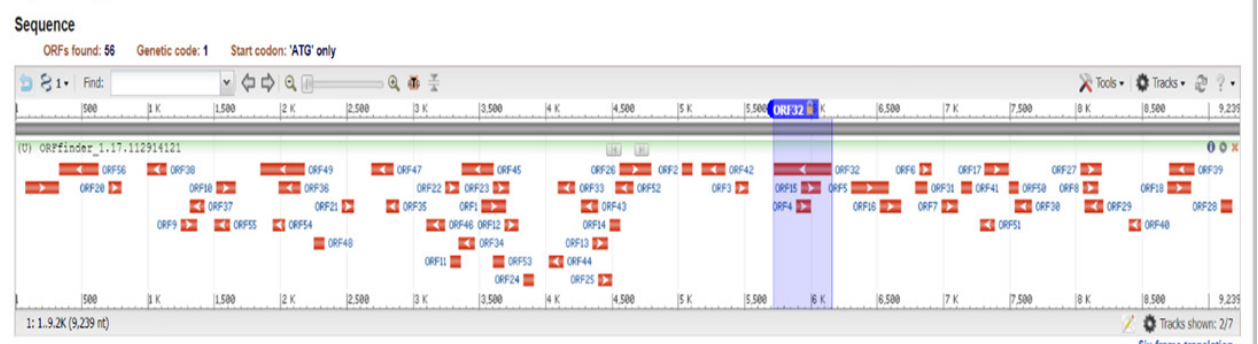


Figure 1. Graphical representation of the open reading frame (ORF) of the *SOD1* gene

SOD1

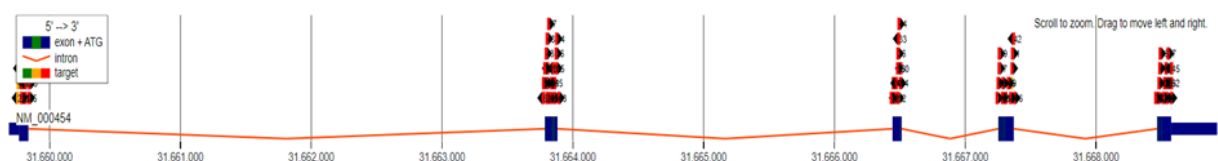


Figure 2. Structural representation of *SOD1* gene

Table 2. The primer specifications and their off-targets for the designed primers of gRNA for rank 1

Pair	Left primers co-ordinates	Left primer	Left primer Tm	Right primer coordinates	Right primer	Right primer Tm	Pair off-target	Product size
1	Chr21:31659647-31659669	CGGAGGTCTG-GCCTATAAAGTA	59.6	Chr21:31659820-31659842	CTTCTGCTCGA-AATTGATGATG	59.8	0	195
2	Chr21:31659657-31659679	GCCTATAAAG-TAGTCGCGGAGA	59.9	Chr21:31659820-31659842	CTTCTGCTCGA-AATTGATGATG	59.8	0	185
3	Chr21:31659660-31659682	TATAAAG-TAGTCGCGGA-GACGG	60.6	Chr21:31659820-31659842	CTTCTGCTCGA-AATTGATGATG	59.8	0	182
4	Chr21:31659657-31659679	GCCTATAAAG-TAGTCGCGGAGA	59.9	Chr21:31659821-31659843	CCTTCTGCTC-GAAATTGATGAT	60.6	0	186
5	Chr21:31659647-31459647	CGGAGGTCTG-GCCTATAAAG-TA	59.6	Chr21:31659821-31659843	CCTTCTGCTC-GAAATTGATGTGAT	60.6	0	196

off-Targets	
Location	No. of Mismatches Sequence
No of Targets	
Shen <i>et al.</i> , 2018 Predictions of Repair Profile – Statistics of GRNA1	
Reference Sequence	GGGGTTTCCGTTGCAGTCCTCGGAACCAGGACCTCGGCCTGGCCTAGCGAGTTATGGCGA < > CGAAGGCCGTGTGCGTGCTGAAGGGCGACGGCCAGTGCAGGGCATCATCAATTCGAGC
Frameshift Frequency	34.94
Precision Score	0.59
Frame+0 Frequency	65.06
Frame+1 Frequency	65.06
Frame+2 Frequency	18.52
1-Bp Ins Frequency	7.46
Highest Del Frequency	44.27
Highest Ins. Frequency	4.16
Highest Outcome Frequency	44.27
Microhomology Deletion Frequency	82.80
Microhomology-Less Deletion Frequency	9.74

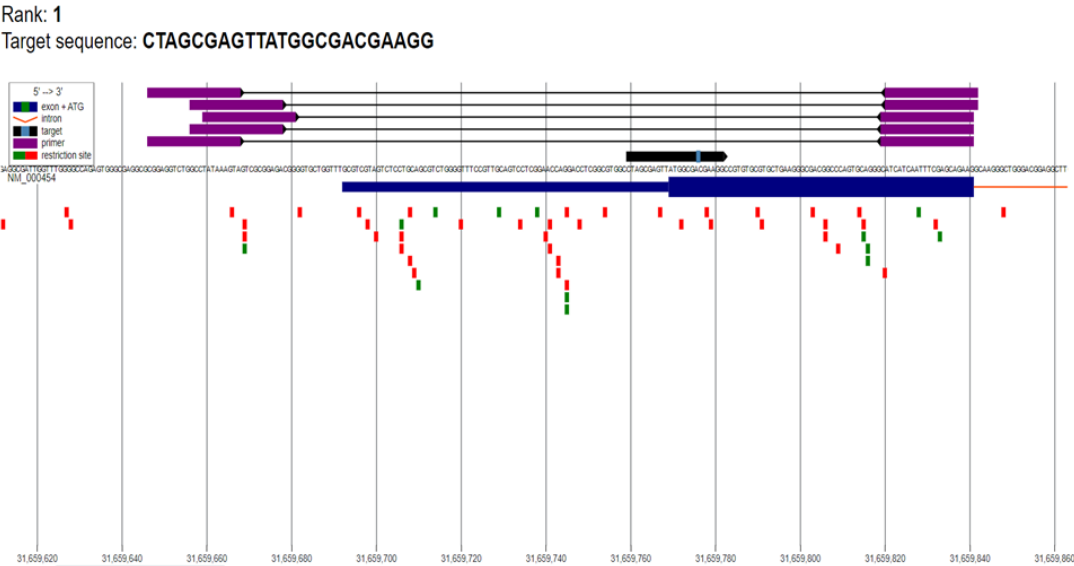


Figure 3. Graphical representation of gRNA along with its primers and off-Targets for rank 1

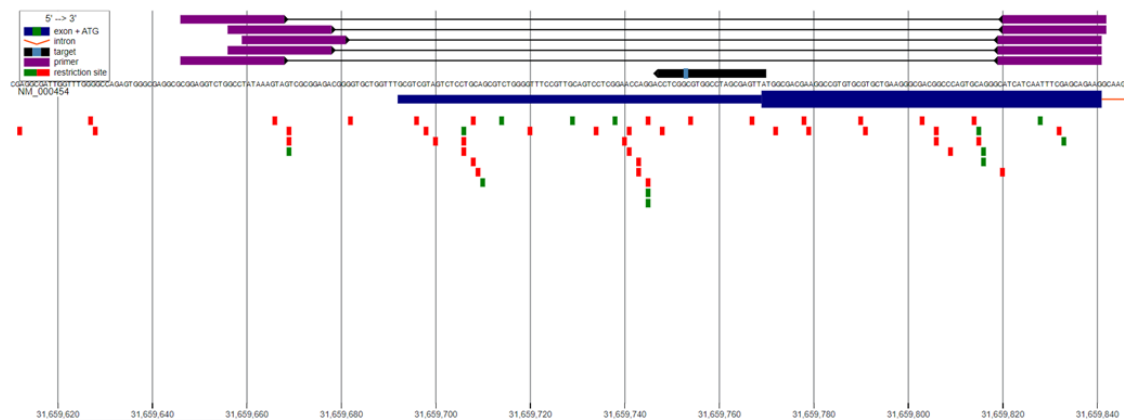
Target: **SOD1**Rank: **2**Target sequence: **TAACTCGCTAGGCCACGCCGAGG**

Figure 4. Graphical representation of gRNA along with its primers and off-Targets for rank 2

Table 3. The primer specifications and their off-targets for the designed primers of gRNA for rank 2

Pair	Left primers coordinates	Left primer	Left primer Tm	Right primer coordinates	Right primer	Right primer Tm	Pair off-target	Product size
1	Chr21:31659647-31659669	CGGAGGTCTGGC-CTATAAAGTA	59.6	Chr21:31659820-31659842	CTTCTGCTC-GAAATTGAT-GATG	59.8	0	195
2	Chr21:31659657-31659679	GCCTATAAAG-TAGTCGCGGAGA	59.9	Chr21:31659820-31659842	CTTCTGCTC-GAAATTGAT-GATG	59.8	0	185
3	Chr21:31659660-31659682	TATAAAG-TAGTCGCGGA-GACGG	60.6	Chr21:31659820-31659842	CTTCTGCTC-GAAATTGAT-GATG	59.8	0	182
4	Chr21:31659657-31659679	GCCTATAAAG-TAGTCGCGGAGA	59.9	Chr21:31659821-31659843	CCTTCTGCTC-GAAATTGAT-GAT	60.6	0	186
5	Chr21:31659647-31459647	CGGAGGTCTGGC-CTATAAAAGTA	59.6	Chr21:31659821-31659843	CCTTCTGCTC-GAAATT-GATGTGAT	60.6	0	196
Highest Outcome Frequency					24.03			
Microhomology Deletion Frequency					77.97			
Microhomology-Less Deletion Frequency					17.49			
off-Targets								
Location		No. of Mismatches		Sequence				
chr1:157046129		3		CCTCGGCGcGGCCTAGCGgGTTc				
Shen <i>et al.</i> , 2018 Predictions of Repair Profile – Statistics of GRNA1								
Reference Sequence		ACTGGGGCCGTCGCCCTTCAGCACGCACACGGCCTTCGTGCGCCATAACTCGCTAGGCCACG<>CCGAGGTCTGGTTCGAGGACTGCAACGGAAACCCAGACGCTGCAGGAGACTACGACG						
Frameshift Frequency		60.99						
Precision Score		0.49						
Frame+0 Frequency		39.01						
Frame+1 Frequency		44.70						
Frame+2 Frequency		16.29						
1-Bp Ins Frequency		4.54						
Highest Del Frequency		24.03						
Hiqhest Ins. Frequency		2.37						

Target: **SOD1**
Rank: **3**
Target sequence: **CTTCGTCGCCATAACTCGCTAGG**

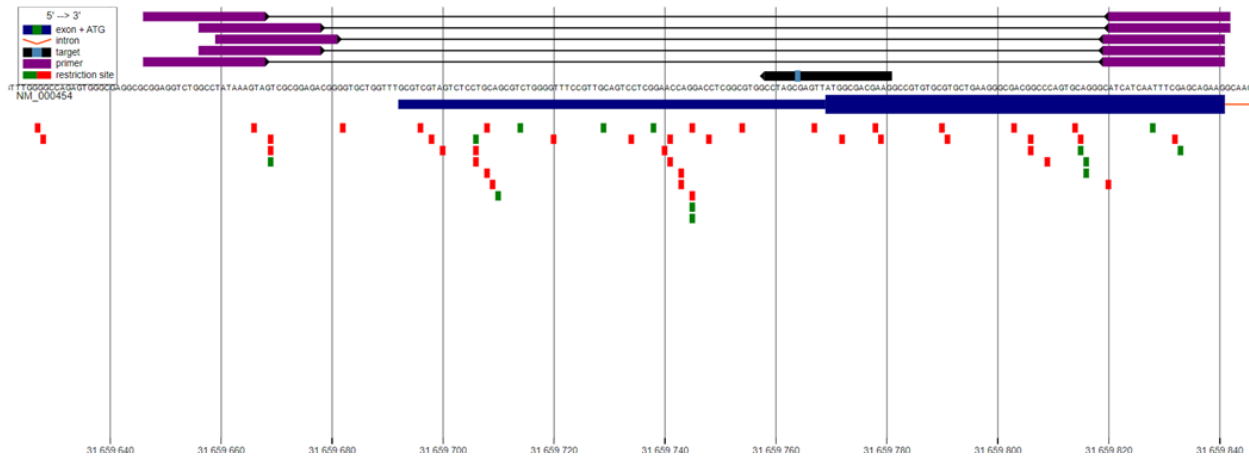


Figure 5. Graphical representation of gRNA along with its primers and off-Targets for rank 3

Table 4. The primer specifications and their off-targets for the designed primers of gRNA for rank 3

Pair	Left primers coordinates	Left primer	Left primer Tm	Right primer coordinates	Right primer	Right primer Tm	Pair off-target	Product size
1	Chr21:31659647-31659669	CGGAGGTCTG-GCCTATAAAG-TA	59.6	Chr21:31659820-31659842	CTTCTGCTCGA-AATTGATGATG	59.8	0	195
2	Chr21:31659657-31659679	GCCTATAAAG-TAGTCGCG-GAGA	59.9	Chr21:31659820-31659842	CTTCTGCTCGA-AATTGATGATG	59.8	0	185
3	Chr21:31659660-31659682	TATAAAG-TAGTCGCGGA-GACGG	60.6	Chr21:31659820-31659842	CTTCTGCTCGA-AATTGATGATG	59.8	0	182
4	Chr21:31659657-31659679	GCCTATAAAG-TAGTCGCG-GAGA	59.9	Chr21:31659821-31659843	CCTTCTGCTCGA-AATTGATGAT	60.6	0	186
5	Chr21:31659647-31459647	CGGAGGTCTG-GCCTATA-AAAGTA	59.6	Chr21:31659821-31659843	CCTTCTGCTCGA-AATTGATGTGAT	60.6	0	196

off-targets		
Location	No. of Mismatches	Sequence
chr16:49703781	3	CtagGTCGCCcTAACTCGCTGGG
Shen <i>et al.</i> , 2018 Predictions of Repair Profile – Statistics of GRNA1		
Reference Sequence	TGATGCCCTGCACTGGGCCGTCGCCCTTCAGCACGCACACGGCCTTCGTGCGCCATAACTC<>GC TAGGCCACGCCGAGGTCTGGTTCCGAGGACTGCAACGGAAACCCAGACGCTGCAGG	
Frameshift Frequency	75.30	
Precision Score	0.46	
Frame+0 Frequency	24.70	
Frame+1 Frequency	35.83	
Frame+2 Frequency	39.47	
1-Bp Ins Frequency	10.15	
Highest Del Frequency	16.98	
Highest Ins. Frequency	7.20	
Highest Outcome Frequency	16.98	
Microhomology Deletion Frequency	68.14	
Microhomology-Less Deletion Frequency	21.70	

Table 5. The target sequences, chromosomal position, and target sources of the *SOD1* target

sgRNAs	Target sequence (5'-3')	Position of <i>SOD1</i> gene	off-target sources	on-target sources	GC% Content
sg(<i>SOD1</i>)1	CTAGCGAGTTATGGCGACGA	Ch21:31659760	98	67	55
sg(<i>SOD1</i>)2	CTTCGTCGCCATAACTCGCT	Ch21:31659759	96	57.6	55
sg(<i>SOD1</i>)3	GTCGCCCTTCAGCACGCACA	Ch21:31659783	82	53	65

Table 6. Validation of the designed primers

Chr21:31659647-31659669 Assembly 1 FWD 5' CGGAGGTCTGGCCTATAAAGTA3' Position +/ T _m 60°C Length 22 GC Content 50% Melting Temp. T _m 59.6°C	Chr21: 31659820-31659842 Assembly 1 REV 5' CTTCTGCTCGAAATTGATGATG 3' Position -/ T _m 60°C Length 22 GC Content 40.9% Melting Temp. T _m 59.8°C
Chr21:31659657-31659679 Assembly 2 FWD 5' GCCTATAAAGTAGTCGCGGAGA3' Position +/ T _m 60°C Length 22 GC Content 50% Melting Temp. T _m 59.9°C	Chr21:31659821-31659843 Assembly 2 REV 5' CCTTCTGCTCGAAATTGATGATG3' Position -/ T _m 60°C Length 22 GC Content 40.9% Melting Temp. T _m 60.6°C
Chr21:31659657-3659679 Assembly 2 FWD 5 GCCTATAAAGTAGTCGCGGAGA 3' Position +/ T _m 60°C Length 22 GC Content 50% Melting Temp. T _m 59.9°C	Chr21:31659902-31659920 Assembly 2 REV 5'CCCGCTCCTAGCAAAGGT3' Position -/ T _m 60°C Length 18 GC Content 61.1% Melting Temp. T _m 60.4°C

The CHOPCHOP tool was utilized to generate multiple gRNA sequences for the target gene [3]. CHOPCHOP displayed the sequence with the minimum number of mismatches at the top, as it was crucial for the number of mismatches to be zero. If the number of mismatches were greater than one, both the targeted and non-targeted regions of the gene would have been cut. The top three target sequences were carefully selected from the CHOPCHOP results, taking into consideration both efficiency and 100% matching with the target. Figure 3 depicts the graphical representation of gRNA along with its primers and off-targets below. The specifications of the designed primers and their off-targets are given below in the Table 2.

The first rank was selected based on the target sequence CTAGCGAGTTATGGCGACGA and its genomic location on chromosome 21 at position 31659760. The target had a GC content of 55% and 2 instances of self-complementarity. The first pair of primers for the left coordinates on chromosome 21, located between positions 31659647 and 31659669, had a sequence of CGGAGGTCTGGCCTATAAAGTA with a melting temperature (T_m) of 59.6°C. The right primer coordinates, located between positions 31659820 and 31659842, had a primer sequence of CTTCTGCTCGAAATTGATGATG and had zero off-targets with a product size of 195. The location of the first gRNA was in the first exon, but in the case of general, mutations

near the C terminus of a protein are less likely to result in loss of function for that protein [4]. The graphical representation of the gRNA and primers for rank 2 are given below in the Fig. 4 and the primer specifications and off-targets are given below in the Table 3.

As represented in Fig. 4, the selection was made for rank 3 with a target sequence of CTTCGTCGCCATAACTCGCT and a genomic location located at chr21:31659759, exhibiting a GC content of 59.6% and 2 instances of self-complementarity. The primer pair for the left primers was situated at chr21:31659647-31659669, with a primer sequence of CGGAGGTCTGGCCTATAAAGTA and a melting temperature (T_m) of 59.6°C. The right primer was positioned at chr21:31659820-31659842, possessing a primer sequence of CTTCTGCTCGAAATTGATGATG, with zero off-target pairs and a product size of 195. It was generally observed that mutations close to the C-terminus of a protein had a reduced probability of causing a loss-of-function mutation in the protein [5]. The graphical representation of the gRNA and primers for rank 3 are given below in the Fig. 5 and the primer specifications and off-targets are given below in the Table 4.

Above figure represents the selection of rank 6, with a target sequence of GTCGCCCTTCAGCACGCACA located on chr21:31659783 and a GC content of 65%, with zero self-complementarity. The first primer

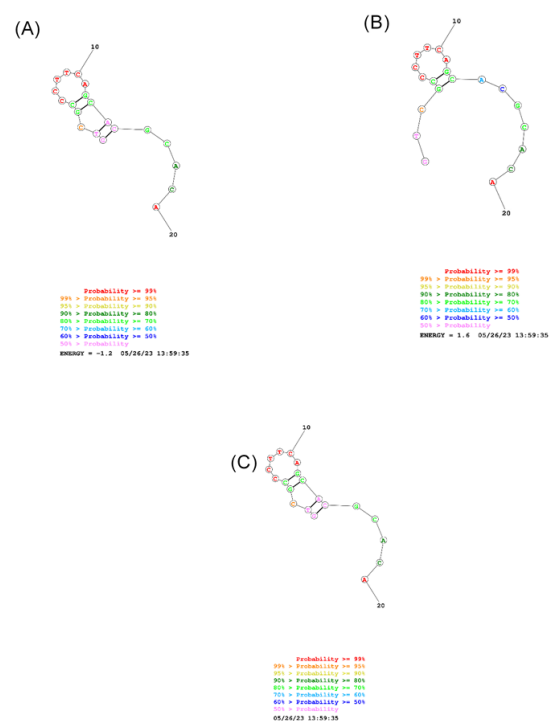


Figure 10. (A) Secondary structure of target gRNA1 fold (B) Secondary structure of target gRNA1 MaxExpect (C) Secondary structure of target gRNA1 Partition.

The approximate prediction of the secondary structure free energy model was represented in **Table 7**. The frequency of the minimum free energy and ensemble diversity were analyzed against the target gRNA sequences. The RNAfold web server (<http://rna.tbi.univie.ac.at/cgi-bin/RNAWebSuite/RNAfold.cgi>) was used to predict the thermodynamic ensemble prediction, as shown in **Figs 9, 10, and 11** (Graphical Representation of Thermodynamic Ensemble Energy).

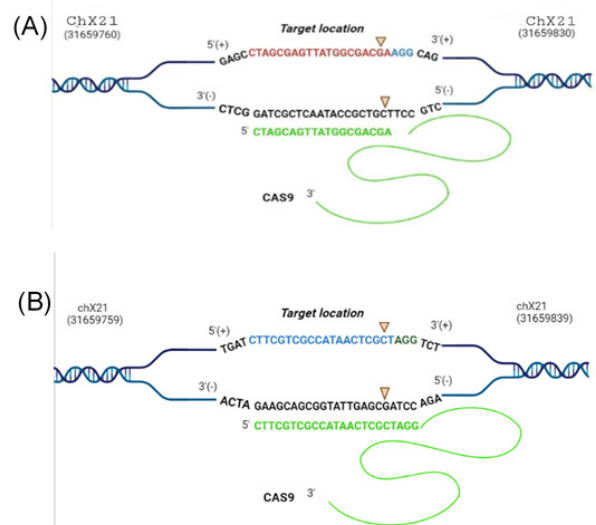


Figure 11. The specificity of the complex was encoded in the first 20 nucleotides of the qRNA

Calculation of the GC Content

In the study, the “RNA /DNA GC Content Calculator” (<http://www.endmemo.com/bio/gc.php>) was used to predict the GC content. The gene to be knocked down needed to have a standard percentage of GC content as a requirement for use as a sgRNA CRISPR-Cas9. The Mfold server was used to predict the free energy of folding and secondary structure for the sgRNA. By using this server, it was found that the gRNA had 52%, 48%, and 43% GC content, respectively. The percentage GC content is given above in Fig. 8 (D).

Prediction of the secondary structure

The secondary structure of gRNA was predicted using an online tool from Mathew's lab (<https://rna.urmc.rochester.edu/RNAstructure.html>). The RNA sequence of interest was first input into the software, which then performed calculations including energy minimization and partition function analysis to predict the most likely secondary structure of the RNA molecule. The tool predicted the structure in a graphical format, such as a dot plot or a secondary structure diagram and outputted the structure in various formats for further analysis.

The Mathew Lab RNA Structure tool was widely used in the RNA research community, and it was capable of predicting the secondary structure of RNAs with high accuracy. However, it is important to note that these predictions were based on thermodynamics, which may not always reflect the true structure of an RNA molecule, particularly in the presence of specific proteins or other molecules that could impact its structure.

Designed gRNA evaluation

In this step, two sgRNAs (sgRNA1 and sgRNA2) were designed to target a specific sequence in the *SOD1* gene. The specificity of the complex was encoded in the first 20 nucleotides of the gRNA, which were represented in Fig. 11 (A) and (B) respectively, represented in green. The alteration of these 20 nucleotides resulted in changes to the DNA sequence.

The analysis of the gRNAs was performed. The Cas-9RNP was joined with the (-) sense strand of the gene and produced the double-strand break at the locations 31659693 and 31659843.

It was crucial to ensure that the gRNA was attached to the complementary sequence. The results confirmed the strong incorporation of the guided strand. The ability of the sgRNA to bind with the complementary sequence of the target region demonstrated its capability as a gRNA.

DISCUSSION

Amyotrophic lateral sclerosis (ALS) is a progressive neurodegenerative disease that affects nerve cells in the brain and spinal cord. It is also known as Lou Gehrig's disease, after the famous baseball player who was diagnosed with the disease in the 1930s. The disease causes the degeneration and death of motor neurons, which are the nerve cells that control muscle movement. As the motor neurons die, the muscles they control weaken and eventually stop working, leading to symptoms such as difficulty in speaking, swallowing, and breathing. The progression of the disease varies widely, with some people experiencing a rapid decline in their health, while others may live for many years with the disease (Krishnan *et al.*, 2020).

The current study demonstrates the proof-of-concept utilizing the cellular disorder model whereby genetic defect ALS could be corrected using CRISPR-Cas9 with results indicating that they are more similar to 99%. It demonstrates the on-target and off-target scores that hold GC content within 40-60%, observed by RNA /DNA GC Content Calculator (Meijboom *et al.*, 2022). This prediction is considered significant for the implementation of sgRNAs action. The CRISPR-Cas9 mechanism on the mutant *SOD1* gene is shown in Figure 6. Three target sites of the *SOD1* gene were selected for designing target sgRNAs based on their location in the exonic region. Notably, the designed sgRNA1 and sgRNA2 targeted a sequence in the *SOD1* gene. The specificity of this complex is encoded in the first 20nt of the gRNA as shown in Figure 5 (A) and (B). The binding ability of sgRNA with the complementary sequence of the target region proves their aptitude for working as gRNA (Raikwar *et al.*, 2019).

The target region in the mutant human *SOD1* gene is near the start codon. Scissors indicate the double-strand break location; black color highlights the CAG repeats in the *SOD1* gene, and orange or yellow indicates sgRNA cassettes. Further validations are the minimum free energy that is considered a benchmark of sgRNAs structural accuracy. It measures the stability of the guide strand. The Mfold web server was used to calculate the minimum free energy (Tyagi *et al.*, 2020).. RNA structure webserver was used to predict the secondary structure of an oligonucleotide by folding minimum free energy. This server predicts the most stable structures of an oligonucleotide with max-expected accuracy as shown in the graphical representation in Graphs 1, 2, and 3. These graphs represent the MFE structure, the thermodynamic ensemble of RNA structures, and the centroid structure. The folded structures of oligonucleotides were predicted at a specific temperature of 39°C. These results indicate that CRISPR-Cas9 can provide one of the best therapeutic approaches to ALS.

Imbued by the CRISPR mechanism and suitability of gRNA, pharmaceuticals and researchers are working to utilize this strategy as a therapeutic approach for the next generation. By using CRISPR technology researchers can easily modify the gene function and alter the DNA sequence. The emergence of CRISPR technology opens a new avenue to correct genetic disorders (Duan *et al.*, 2020; Tyagi *et al.*, 2020). Recently, it has been used as an efficient tool for site-specific genome editing in single cells and entire organisms in a specific manner. This study presents a specific possible future candidate in the treatment of SBMA that holds a tremendous potential therapeutic approach for a genetic disorder (Muhammad *et al.*, 2023a; Muhammad *et al.*, 2023b, Muhammad *et al.*, 2023c; Naveed *et al.*, 2022).

Although these methodologies offer significant perspectives, they are unable to comprehensively depict the intricate biological mechanism within a living organism. Additional investigation utilizing animal models and clinical trials involving humans is imperative to authenticate the effectiveness and safety of CRISPR-Cas9 as a treatment for ALS (Kim *et al.*, 2020).

CONCLUSION

Using bioinformatics techniques, we predicted three sgRNAs against the *SOD1* gene on the X chromosome. The fast development of genome editing technologies and applications has been greatly aided by computational

and experimental work. Advanced alignment techniques are being used simultaneously to enhance gRNA design and forecast off-target regions, which might hasten the development of better and more precise editing tools. It is extremely advantageous to create multiple sgRNAs with the aid of CRISPR technology for the silencing of important genes in different biological systems. CRISPR technology may be an emerging key to a novel therapy against *SOD1*. Compared to other gene-editing methods including TALENs and ZFNs, the CRISPR-Cas9 method is being widely used for gene editing and gene correction treatment strategy for several genetic disorders. All this is because of its cost-effectiveness and ability to edit multiple genes at the same time. This research may open a milestone corridor in the therapy of ALS. Research revealed that CRISPR technology is an effective gene silencing method to cure genetic disorders in the future with much higher efficiency.

RECOMMENDATIONS

Since ALS is a disease caused by the production of toxin proteins, in this research we attempted to block the disease-causing expression of the gene by using CRISPR. The designed gRNA will bind to the target site allowing the enzyme to perform cleavage and this will result in the removal of those extra CAG repeats. This will cause the restoration of regular protein production similar to the use of CRISPR in other diseases, which are caused by abnormal numbers of CAG repeats in the gene, e.g., Huntington's disease. The bioinformatics-based approach has shown accurate results, which need to be backed by in vitro and in vivo results for the clinical manifestation of this method. We encourage further research on this particular and seemingly possible way of curing this disease as CRISPR-based gene editing has a tremendous potential for doing miracles in medical science.

Declarations

Funding: No External funding was received.

Conflicts of Interest: The authors declare no conflict of interest.

REFERENCES

- Collins SP, Rostain W, Liao C, Beisel CL (2021) Sequence-independent RNA sensing and DNA targeting by a split domain CRISPR-Cas12a gRNA switch. *Nucleic Acids Res* **49**: 2985–2999. <https://doi.org/10.1093/nar/gkab100>
- Duan W, Guo M, Yi L, Liu Y, Li Z, Ma Y, Zhang G, Liu Y, Bu H, Song X, Li C (2020) The deletion of mutant *SOD1* via CRISPR/Cas9/sgRNA prolongs survival in an amyotrophic lateral sclerosis mouse model. *Gene Ther* **27**: 157–169. <https://doi.org/10.1038/s41434-019-0116-1>
- Hardiman O, Al-Chalabi A, Chio A, Corr EM, Logroscino G, Robberecht W, Shaw PJ, Simmons Z, van den Berg LH (2017) Erratum: Amyotrophic lateral sclerosis (Nature reviews. Disease primers (2017) 3 (17071)). *Nat Rev Dis Primers* **3**: 17085. <https://doi.org/10.1038/NRDP.2017.85>
- Kim BW, Jeong YE, Wong M, Martin LJ (2020) DNA damage accumulates and responses are engaged in human ALS brain and spinal motor neurons and DNA repair is activatable in iPSC-derived motor neurons with *SOD1* mutations. *Acta Neuropathol Commun* **8**: 7. <https://doi.org/10.1186/s40478-019-0874-4>
- Koonin EV, Gootenberg JS, Abudayyeh OO (2023) Discovery of diverse CRISPR-Cas systems and expansion of the genome engineering toolbox. *Biochemistry* <https://doi.org/10.1021/acs.biochem.3c00159>
- Krishnan G, Zhang Y, Gu Y, Kankel MW, Gao F-B, Almeida S (2020) CRISPR deletion of the C9orf72 promoter in ALS/FTD patient motor neurons abolishes production of dipeptide repeat proteins and rescues neurodegeneration. *Acta Neuropathol* **140**: 81–84. <https://doi.org/10.1007/s00401-020-02154-6>
- Labun K, Krause M, Torres Cleuren Y, Valen E (2021) CRISPR Genome editing made easy through the CHOPCHOP website. *Curr Protoc* **1**: <https://doi.org/10.1002/cpz1.46>
- Longinetti E, Fang F (2019). Epidemiology of amyotrophic lateral sclerosis: an update of recent literature. <https://doi.org/10.1097/WCO.0000000000000730>
- Masrori P, Van Damme P (2020) Amyotrophic lateral sclerosis: a clinical review. *Eur J Neurol* **27**: 1918–1929. <https://doi.org/10.1111/ENE.14393>
- Meijboom KE, Abdallah A, Fordham NP, Nagase H, Rodriguez T, Kraus C, Gendron TF, Krishnan G, Esanov R, Andrade NS, Rybin MJ, Ramic M, Stephens ZD, Edraki A, Blackwood MT, Kahriman A, Henninger N, Kocher J-PA, Benatar M, Brodsky MH et al. (2022) CRISPR/Cas9-mediated excision of ALS/FTD-causing hexanucleotide repeat expansion in C9orf72 rescues major disease mechanisms in vivo and in vitro. *Nat Commun* **13**: 6286. <https://doi.org/10.1038/s41467-022-33332-7>
- Morimoto S, Takahashi S, Fukushima K, Saya H, Suzuki N, Aoki M, Okano H, Nakahara J (2019) Ropinrole hydrochloride remedy for amyotrophic lateral sclerosis – Protocol for a randomized, double-blind, placebo-controlled, single-center, and open-label continuation phase I/IIa clinical trial (ROPALS trial). *Regen Ther* **11**: 143–166. <https://doi.org/10.1016/j.reth.2019.07.002>
- Muhammad N, Waseem M, Aziz T, Hassan JU, Makhdoom SI, Ali U, Alharbi M, Alsahammari A (2023) Identification of bacterial strains and development of anmRNA-based vaccine to combat antibiotic resistance in *Staphylococcus aureus* via in vitro and in silico approaches. *Biomedicine* **11**: 1039. <https://doi.org/10.3390/biomedicine11041039>
- Muhammad N, Ain Nu, Aziz T, Javed K, Shabbir MA, Alharbi M, Alsahammari A, Alasmari AF (2023) Artificial intelligence assisted pharmacophore design for Philadelphia chromosome-positive leukemia with gamma-tocotrienol: a toxicity comparison approach with Asciminib. *Biomedicine* **11**: 1041. <https://doi.org/10.3390/biomedicine11041041>
- Muhammad N, Ain Nu, Aziz T, Shabbir MA, Ayesha S, Zafar A, Ghulam N, Alharbi M, Alsahammari A, Alasmari AF (2023). Side chain inset of neurogenerative amino acids to metalloproteins: a therapeutic signature for huntingtin protein in Huntington's disease. *Eur Rev Med Pharmacol Sci* **27**: 6831–6842. https://doi.org/10.26355/eur-rev_202307_33154
- Naveed M, Noor-ul-Ain, Shabbir MA (2023a) Computational drug shifting towards drug-drug conjugates and monoclonal antibody conjugates in the contradictory excursion of asthma. *Lett Drug Des Discov* **20**: 1219–1229. <https://doi.org/10.2174/1570180819666220422114450>
- Naveed M, Ain N, Aziz T, Javed K, Shabbir M, Alharbi M, Alsahammari A, Alasmari A (2023b) Artificial intelligence assisted pharmacophore design for Philadelphia chromosome-positive leukemia with gamma-tocotrienol: a toxicity comparison approach with Asciminib. *Biomedicine* **11**: 1041. <https://doi.org/10.3390/biomedicine11041041>
- Naveed M, Sheraz M, Amin A, Waseem M, Aziz T, Khan AA, Ghani M, Shahzad M, Alruways MW, Dabool AS, Elazzazy AM, Almalki AA, Alamri AS, Alhomrani M (2022) Designing a novel peptide-based multi-epitope vaccine to evoke a robust immune response against pathogenic multidrug-resistant *Providencia heimbachae*. *Vaccines* **10**: 1300. <https://doi.org/10.3390/vaccines10081300>
- Norris SP, Likhanje M-FN, Andrews JA (2020) Amyotrophic lateral sclerosis: update on clinical management. *Curr Opin Neurol* **33**: 641–648. <https://doi.org/10.1097/WCO.0000000000000864>
- Raikwar SP, Kikkeri NS, Sakuru R, Saeed D, Zahoor H, Premkumar K, Mentor S, Thangavel R, Dubova I, Ahmed ME, Selvakumar GP, Kempuraj D, Zaheer S, Iyer SS, Zaheer A (2019) Next generation precision medicine: CRISPR-mediated genome editing for the treatment of neurodegenerative disorders. *J Neuroimmune Pharmacol* **14**: 608–641. <https://doi.org/10.1007/s11481-019-09849-y>
- Saitoh Y, Takahashi Y (2020) Riluzole for the treatment of amyotrophic lateral sclerosis. *Neurodegener Dis Manag* **10**: 343–355. <https://doi.org/10.2217/nmt-2020-0033>
- Schoch CL, Ciuffo S, Domrachev M, Hotton CL, Kannan S, Khovan-skaya R, Leipe D, McVeigh R, O'Neill K, Robbertse B, Sharma S, Sousoff V, Sullivan JP, Sun L, Turner S, Karsch-Mizrachi I (2020) NCBI Taxonomy: a comprehensive update on curation, resources and tools. *Database* **2020**: <https://doi.org/10.1093/database/baaa062>
- Shoosmith C, Abrahao A, Benstead T, Chum M, Dupre N, Izenberg A, Johnston W, Kalra S, Leddin D, O'Connell C, Schellenberg K, Tandon A, Zinman L (2020) Canadian best practice recommendations for the management of amyotrophic lateral sclerosis. *Can Med Assoc J* **192**: E1453–E1468. <https://doi.org/10.1503/cmaj.191721>
- Tyagi S, Kumar R, Das A, Won SY, Shukla P (2020) CRISPR-Cas9 system: A genome-editing tool with endless possibilities. *J Biotechnol* **319**: 36–53. <https://doi.org/10.1016/j.jbiotec.2020.05.008>
- Varghese GM, John R, Manesh A, Karthik R, Abraham OC (2020) Clinical management of COVID-19. *Indian J Med Res* **151**: 401
- Yoshino H (2019) Edaravone for the treatment of amyotrophic lateral sclerosis. *Expert Rev Neurother* **19**: 185–193. <https://doi.org/10.1080/14737175.2019.1581610>

Association of vitamin D with deoxyribonucleic acid (DNA) damage: A systematic review of animal and human studies

Mayang Indah Lestari^{1,2}, Krisna Murti³✉, Iche Andriyani Liberty⁴, Zen Hafy¹, Violantina Linardi⁵, Muhammad Khoirudin⁵ and Tungki Pratama Umar⁵

¹Doctoral Study Program in Biomedical Science, Faculty of Medicine, Sriwijaya University, Palembang, Indonesia; ²Department of Anesthesiology and Intensive Therapy, Faculty of Medicine, Sriwijaya University-Dr. Mohammad Hoesin General Hospital – Siti Fatimah General Hospital, Palembang, Indonesia; ³Department of Anatomical Pathology, Faculty of Medicine, Sriwijaya University-Dr. Mohammad Hoesin General Hospital, Palembang, Indonesia; ⁴Department of Public Health, Faculty of Medicine, Sriwijaya University, Palembang, Indonesia; ⁵Research Assistant, Department of Anesthesiology and Intensive Therapy, Faculty of Medicine, Sriwijaya University, Palembang, Indonesia

Vitamin D has anti-proliferative, anti-inflammatory, and apoptotic abilities. Vitamin D deficiency can induce deoxyribonucleic acid (DNA) damage. The aim of the study was to create a systematic review to analyze the relationship between vitamin D and DNA damage in various populations. PubMed, Scopus, EbscoHost, Google Scholar, and Epistemonikos were used to identify literature regarding the relationship between vitamin D and DNA damage. Assessment of study quality was carried out by three independent reviewers individually. A total of 25 studies were assessed as eligible and included in our study. Twelve studies were conducted in humans consisting of two studies with experimental design and ten studies with observational pattern. Meanwhile, thirteen studies were conducted in animals (*in vivo*). It is found that the majority of studies demonstrated that vitamin D prevents DNA damage and minimizes the impact of DNA damage that has occurred ($p < 0.05$). However, two studies (8%) did not find such an association and one research only found a specific association in the cord blood, not in maternal blood. Vitamin D has a protective effect against DNA damage. A diet rich in vitamin D and vitamin D supplementation is recommended to prevent DNA damage.

Keywords: vitamin D, DNA damage, observational studies, *in vivo* studies, systematic review

Received: 31 January, 2023; **revised:** 15 May, 2023; **accepted:** 16 May, 2023; **available on-line:** 17 June, 2023

✉e-mail: krisna.arinafril@unsri.ac.id

Abbreviations: γ H2AX, phosphorylated histone H2AX; 1,25(OH)₂D, 1,25-dihydroxyvitamin D; 8-OH-dG, 8-hydroxy-2'-deoxyguanosine; 25(OH)D, 25 hydroxy vitamin D; NF- κ B, Nuclear factor kappa-light-chain-enhancer of activated B cells; ROS, Reactive oxygen species; T2DM, Type 2 diabetes mellitus; UV, Ultraviolet; VDR, Vitamin D receptor

INTRODUCTION

Vitamin D and its receptors play an essential role in cancer development due to its anti-proliferative, anti-inflammatory, and apoptotic properties (Nair-Shalliker *et al.*, 2012a; Deuster *et al.*, 2017; Elhusseini *et al.*, 2018). Endogenous synthesis of vitamin D begins with cholesterol oxidation, producing pro-vitamin D₃. In the skin, Ultraviolet B (UVB) from sunlight converts pro-vitamin D₃ to pre-vitamin D₃. Then, isomerization of pre-vitamin D₃ is done, with vitamin D₃ (cholecalciferol) as its main end product (Osmancevic *et al.*, 2015). Two hydroxylations by the enzymes vitamin D 25-hydroxy-

lase (CYP27A1) and renal mitochondrial 1-hydroxylase (CYP27B1) are required to convert vitamin D₃ to active 1,25(OH)₂D₃ (calcitriol). Calcitriol binds to vitamin D receptors (VDRs) belonging to the nuclear receptor family and forms a complex with RXR to regulate gene expression (Deuster *et al.*, 2017). VDRs are nuclear receptor superfamily members expressed in tumours to regulate cell cycle-related proliferation and angiogenesis (Khrisnan *et al.*, 2012; Christakos *et al.*, 2015). In addition, vitamin D has been shown in several studies to be effective in stimulating Deoxyribonucleic acid (DNA) synthesis in mature alveolar cells, modulating epithelial cell proliferation, and repairing injury (Usman *et al.*, 2021).

Furthermore, adequate vitamin D levels help to maintain DNA integrity. Vitamin D's role can be divided into two categories: primary functions that prevent DNA damage and secondary processes that regulate cell growth rate (Nair-Shalliker *et al.*, 2012a; Wenclewska *et al.*, 2019). Vitamin D is really crucial since its deficiency is associated with an increased frequency of chromosomal aberrations, sister chromatid exchanges, micronuclei formations, and alteration of comet assays (related to oxidative stress, hypoxic, and apoptotic process), some important indicators of DNA damage (Peng *et al.*, 2010; Nair-Shalliker *et al.*, 2012a; O'Callaghan-Gordo *et al.*, 2017; Liu *et al.*, 2019). The potential of vitamin D in reducing oxidative DNA damage in humans refers to clinical trials in which vitamin D supplementation reduced levels of 8-hydroxy-2'-deoxyguanosine (8-OH-dG), an oxidative damage biomarker found in colorectal epithelial crypt cells (Nair-Shalliker *et al.*, 2012a). Vitamin D administration has also been shown to reduce oxidative stress-induced damage and chromosomal aberration, prevent telomere shortening, and inhibit telomerase activity in animal models and cell lines (Siebert *et al.*, 2018). Vitamin D's secondary functions in preventing DNA damage include regulating poly-adenosine diphosphate/ADP-ribose polymerase activity on the DNA damage response pathway during the DNA lesion detection process. Vitamin D can also inhibit the replication of damaged DNA and regulate apoptosis, which promotes cell death (Nair-Shalliker *et al.*, 2012a).

Although vitamin D has long been discussed as one of the essential DNA protectors, a systematic review of the relationship between vitamin D and DNA damage has yet to be found. As a result, the purpose of this study is to use a systematic review approach to examine the association between vitamin D and DNA damage in

different populations of human studies and animal models.

METHODS

The manuscript was arranged using the Preferred Reporting Items for Systematic Reviews and Meta-Analysis (PRISMA) 2020 guidelines (Page *et al.*, 2021). All members approved the review panel's study procedure before conducting the literature search. The protocol has been registered in the International prospective register of systematic reviews (PROSPERO) with the registration number: CRD42023393054.

Literature retrieval

A comprehensive literature search was conducted across five databases to identify manuscripts on the relationship between vitamin D levels and DNA damage in human and animal subjects. The articles were discovered using Scopus, PubMed, EBSCOHost, Google Scholar, and Epistemonikos. Hand-searching was also conducted based on the included study bibliography to identify relevant publications that were not indexed in the previously reported databases (Umar *et al.*, 2022). There will be no restrictions on geographical region or gender. However, we restricted our search to studies published between January 2012 and January 2023. The investigation was completed by January 19th, 2023. To ensure its validity, the study must be published in English. The search terms for this study are available as Supplementary Table 1 at <https://ojs.ptbioch.edu.pl/index.php/abp/>.

Study selection

We sought animal and human studies investigating the link between vitamin D levels and DNA damage. Studies must demonstrate the influence of a single vitamin D substance administration on DNA damage (rather than a formulation containing multiple compounds) to be considered. The study was deemed ineligible if its design consisted of a literature review (e.g., systematic review, narrative review, scoping review), opinion, book chapter, and editorial. Meanwhile, included studies must have ac-

cess to the full text. As a result, we excluded conference abstracts, posters, and unretrieved complete records. Duplicates were removed from the literature retrieval. Three independent reviewers (VL, MK, and ZH) assessed titles and abstracts (primary screening) using a semi-automated process aided by Rayyan QCR software (Ouzzani *et al.*, 2016; Umar & Siburian, 2022). Following the completion of the first screening stage, the full text was assessed by two reviewers (IAL and TPU) to determine its eligibility for inclusion in the review. Any disagreements were discussed and resolved by a senior author (MIL) at any stage of manuscript evaluation.

Data extraction

The following information was extracted from the data: authorship, country of study, research participant data in the form of age, sex, and comorbidities (human), as well as experimental research data on animal type and age (animal studies), DNA damage parameters (comet tail length, tail DNA, and tail moment; phosphorylated Histone H2AX (γ H2AX), 8-hydroxy-2'-deoxyguanosine (8-OHdG), chromosomal aberration, DNA damage score, micronuclei formation, telomere length, urinary cyclobutane thymine (T-T) dimer, and DNA repair indicator), and main findings. The information was recorded on the extraction sheet using Microsoft Office Excel 2019. Because of the vast diversity among included studies, the findings were presented as a qualitative synthesis rather than a meta-analysis.

Risk of bias analysis

The risk of bias (RoB) analysis was conducted for the animal studies using The Systematic Review Center for Laboratory Animal Experimentation's risk of bias (SYRCLE's RoB) tool. The RoB tool from SYRCLE contains ten items related to selection bias, performance bias, detection bias, reporting bias, and other biases (Hooijmans *et al.*, 2014). Meanwhile, we used three different scales for human studies: the Newcastle-Ottawa Scale (for observational studies), the Risk Of Bias In Non-randomized Studies – of Interventions (ROBINS-I), and Version 2 of the Cochrane risk-of-bias tool for randomized trials (ROB-2). The Newcastle Ottawa Scale is divided

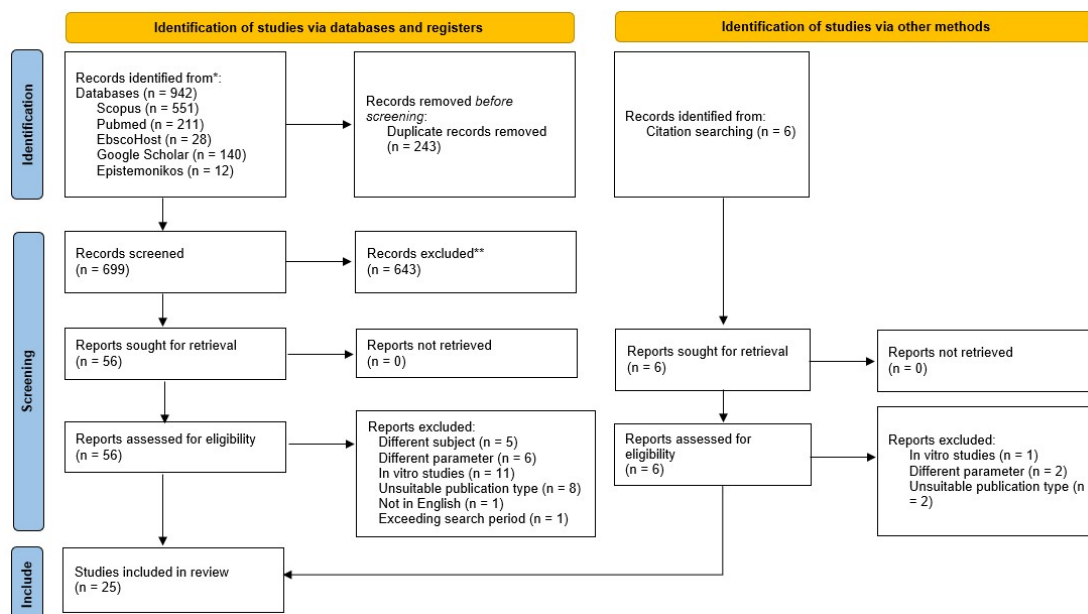


Figure 1. Study selection flow

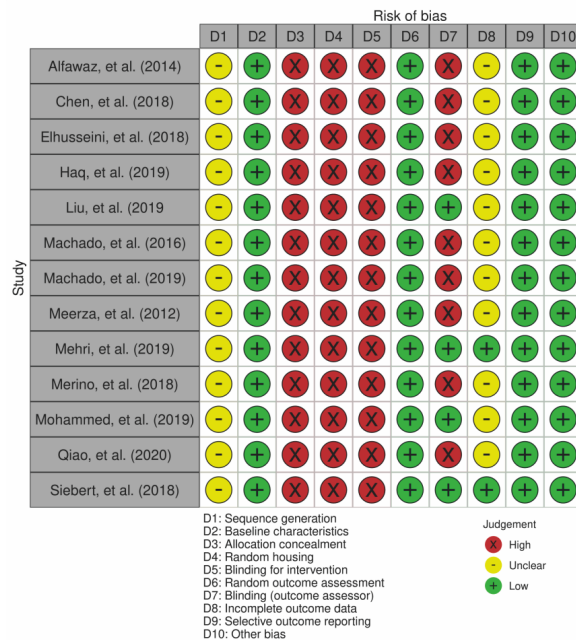


Figure 2. Risk of Bias for Animal Studies

into three major domains (selection, comparability, and outcome) (Liana *et al.*, 2022). In contrast, the ROBINS-I (Sterne *et al.*, 2016) and ROB-2 (Sterne *et al.*, 2019) are divided into several parts within the pre-intervention, intervention, and post-intervention stages. The evaluation was carried out independently by two authors (IAL and TPU). In the event of a disagreement, the decision is made by a senior author (KM).

RESULTS

The search strategy identified a total of 942 studies. The search query found 551 studies on SCOPUS, 140 on Google Scholar, 211 on PubMed, 28 on EbscoHost, and 12 on Epistemionikos. Following duplicate detection, 243 studies were excluded. Then, 699 studies entered title and abstract screening, where 56 studies were deemed eligible for full-text screening, which resulted in 24 studies being included in the final analysis. Meanwhile, six studies were identified from the citation search, and only one was finally contained. This process resulted in 25 selected studies (13 animal studies/*in vivo* and 12 human studies (two experimental studies and ten observational research)) considered in the final process of manuscript evaluation (Fig. 1).

Study characteristics

All of the included studies evaluated the association of vitamin D with DNA damage. Animal studies (Table 1) were done on the vitamin D-deficient diet (Chen *et al.*, 2018; Elhusseini *et al.*, 2018; Merino *et al.*, 2018), hypertension (Machado *et al.*, 2016, 2019), oxidative stress (Haq *et al.*, 2019; Liu *et al.*, 2019), and neurological disorder (Alfawaz *et al.*, 2014; Mehri *et al.*, 2020). Meanwhile, all of the following parameters were assessed only in one study: diabetes mellitus (Meerza *et al.*, 2012), high-fat diet (Merino *et al.*, 2018), kidney disease (Mohammed *et al.*, 2019), aging (Qiao *et al.*, 2020), and ovariectomy (Siebert *et al.*, 2018) model. There are four main DNA damage detection methods, including immunohistochemistry

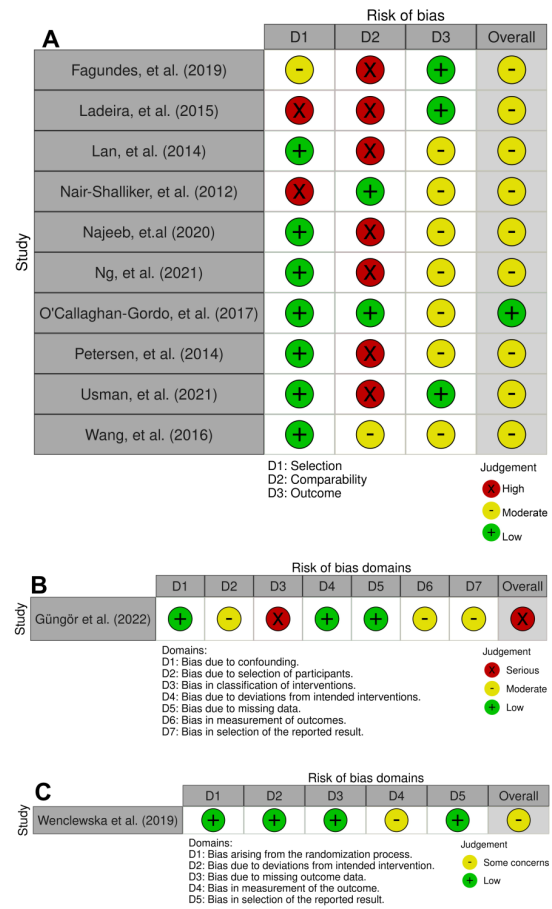


Figure 3. Risk of Bias for Human Studies.

A, Newcastle-Ottawa Scale; **B**, Risk of Bias in Non-randomised Studies - of Interventions (ROBINS-I); **C**, Version 2 of the Cochrane risk-of-bias tool for randomized trials (ROB-2)

(Chen *et al.*, 2018; Elhusseini *et al.*, 2018; Mohammed *et al.*, 2019), comet assay (alkaline comet assay) (Alfawaz *et al.*, 2014; Liu *et al.*, 2019; Machado *et al.*, 2016, 2019; Siebert *et al.*, 2018), Enzyme-linked immunosorbent assay (ELISA) (Haq *et al.*, 2019; Mehri *et al.*, 2020), and micro-nuclei detection (Liu *et al.*, 2019; Machado *et al.*, 2016). Meanwhile, other detection methods are flow cytometry (Merino *et al.*, 2018), gel electrophoresis (Haq *et al.*, 2019), Western blot (Qiao *et al.*, 2020) and reverse transcription polymerase chain reaction (RT-PCR) (Siebert *et al.*, 2018). Rodents, both mice and rats, were used as

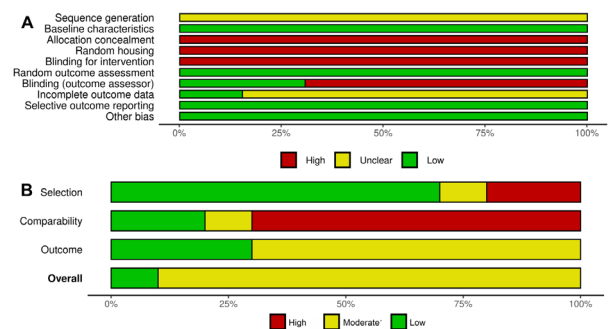


Figure 4. Risk of Bias Summary.

A, Animal studies; **B**, Human studies (limited to observational studies since experimental research only consisted of one study)

Table 1. Data extraction for animal studies

Author (year)	Country	Experimental animal	Disease model and inducer	Parameter	Method	Major findings
(Alfawaz <i>et al.</i> , 2014)	Saudi Arabia	Western Albino rats (± 21 days, $n=28$)	Neurotoxicity by PPA	Tail length Tail Moment (%) Tail Moment (Unit)	Comet DNA assay	There is a potential impact of vitamin D in protecting and treating PPA neurotoxicity, while ameliorating the DNA-damaging effects of PPA. Prevention impact of vitamin D against PPA-induced DNA damage is more profound than its treatment effect
(Chen <i>et al.</i> , 2018)	China	1 α (OH)ase ⁻ and wild-type mice (120 pairs divided into four groups)	Vitamin D-deficient model	γ H2AX 8-OHdG	Immunohistochemistry	There is an increase of DNA damage in 1,25(OH)2D3-deficient mice as measured by γ H2AX and 8-OHdG on tumor cells according to immunohistochemistry
(Elhousseini <i>et al.</i> , 2018)	United States	Female C57BL/6 mice, (4–6 weeks old), control ($n=10$), vitamin D-deficient diet group ($n=10$)	Vitamin D-deficient model	γ H2AX DNA repair (RAD50 and RAD51)	Immunohistochemistry	Vitamin D-deficient mice showed increased γ H2AX in myometrial tissue compared to healthy controls ($P<0.05$) Vitamin D deficiency caused a significant reduction in the expression of DNA repair genes such as RAD50 ($P<0.005$) and RAD51 ($P<0.005$) compared to healthy controls.
(Haq <i>et al.</i> , 2019)	Saudi Arabia	Wistar Albino rats (1 week, $n=4$)	Hydrogen peroxide (H_2O_2)	Chromosomal aberration (DNA fragmentation) 8-OHdG	Gel electrophoresis ELISA	Vitamin D ₃ which was given for 24 hours prior to the induced oxidative stress by H_2O_2 significantly ($p<0.001$) reversed the deleterious and damaging effect of H_2O_2 alone as presented by DNA fragmentation percentage Significantly lower value of 8-OHdG following the administration of vitamin D+ H_2O_2 than H_2O_2 alone ($p<0.05$)
(Liu <i>et al.</i> , 2019)	China	Male mice (7–8 weeks)	CP	DNA damage score, total DNA in the tail (%), tail length, tail moment Micronuclei formation	Alkaline comet assay Buccal Micronuclei Cyto-me assay	Vitamin D ₃ suppressed CP-induced micronucleus formation in mice Buccal cells, with an alleviation range of 36.73–44.46% ($p<0.05$) Vitamin D ₃ injection for a dose of 5,000 IU significantly reduced CP-induced DNA damage, with a 46.6% decrease in tail DNA percentage ($p<0.05$), a 24.2% decrease in tail length ($p<0.05$), and 37.3% decrease in olive tail moment ($P<0.05$). However, it is not significant at the 1,000 or 10,000 IU dose
(Machado <i>et al.</i> , 2016)	Brazil	Male Spontaneously hypertensive rats (SHR) and WKY (20 weeks) divided into six groups	Hypertension model	DNA damage score, total DNA in the tail (%), tail length, tail moment Micronuclei formation	Alkaline comet assay Micronucleus test	Vitamin D ₃ deficient diet was able to increase the percentage of DNA damage in both SHR (49%) and WKY rats (54%) SHR rats with a vitamin D ₃ deficient diet showed a significant increase in the incidence of micronuclei formation in the bone marrow and peripheral blood ($p<0.05$)
(Machado <i>et al.</i> , 2019)	Brazil	Male Spontaneously hypertensive rats (SHR) and WKY (20 weeks) divided into six groups	Hypertension model	Total DNA in the tail (%)	Alkaline comet assay	There was no significant difference in the percentage of DNA in comet tails ($p>0.05$) in the vitamin D deficiency group when compared to the control group. Vitamin D ₃ supplementation or deficiency did not significantly affect cardiac genotoxicity.
(Meezra <i>et al.</i> , 2012)	India	Female albino mice	Diabetes model by alloxan (200 mg/kgBW)	DNA tail length	Comet assay	Vitamin D-supplemented group showed a significant decrease in liver ($21.80 \pm 2.40 \mu m$) and pancreatic ($19.25 \pm 1.90 \mu m$) DNA tail length in diabetic mice
(Mehri <i>et al.</i> , 2020)	Iran	Wistar rats (200–240g, $n=48$)	Alzheimer's Disease by 5 μl of A β -containing solution	8-OHdG	ELISA	The level of DNA damage in Vitamin D and A β + Vitamin D groups in hippocampus and Vitamin D group of serum samples was significantly lower than that of the A β group ($p<0.0001$)
(Merino <i>et al.</i> , 2018)	Chile	Male Sprague-Dawley rats (4 months, $n=20$ divided into four groups)	High-fat diet and vitamin-D deficient-diet	DNA Fragmentation	Flow cytometry	Vitamin D supplementation results in lower DNA fragmentation, either in the control or experimental group ($p<0.05$) The interaction between vitamin D deficiency and diet-induced obesity was significant in DNA fragmentation ($p=0.0359$)

(Mohammed <i>et al.</i> , 2019)	Egypt	Male albino rats (8-10 weeks, n=24 divided into four groups)	Acute renal damage by gentamycin 100 mg/kgBW	8-OHdG	Immunohistochemistry	Vitamin D administration significantly reduces 8-OHdG immunohistochemical expression when compared to the control group (p < 0.01)
(Qiao <i>et al.</i> , 2020)	China	Cyp27b1 ^{+/+} and wild-type mice (9 months)	Aging model	γ-H2AX	Western blot	1,25(OH)2D ₃ insufficiency increases γ-H2AX expression significantly (p < 0.001) compared with the wild type mice
(Siebert <i>et al.</i> , 2018)	Brazil	Wistar Albino rats (90 days or 180 days, divided into four groups)	OVX	DNA damage index Telomere length	Alkaline comet assay RT-PCR	OVX significantly increases DNA damage (p < 0.001) when compared to control. Vitamin D alone decreased the DNA damage index (p < 0.05 and p < 0.001), but when associated with OVX (OVX + VIT D), partially reversed DNA damage induced by OVX (p < 0.001). Vitamin D did not change telomere length (p > 0.05), and when associated with OVX (OVX + VIT D), Vitamin D supplementation was able to reverse the observed telomere shortening (p < 0.005).

Abbreviation: γ-H2AX, γ phosphorylated form of the histone H2AX, 1,25(OH)2D₃, 1,25-dihydroxyvitamin D₃, 1α(OH)ase, 1αph-Hydroxylase, 8-OHdG, 8-Hydroxyguanosine, Aβ, Amyloid beta, C57BL/6, C57 black 6, CP, Cyclophosphamide, Cyp27b1, Cytochrome p450 27B1, DNA, Deoxyribonucleic acid, ELISA, Enzyme-linked immunosorbent assay, H₂O₂, Hydrogen peroxide, IU, International unit, mg/kgBW, milligrams/kilograms body weight, OVX, Ovariectomy, PPA, Propionic acid, RAD50, DNA repair protein RAD50, RAD51, DNA repair protein RAD51, RT-PCR, Reverse transcription polymerase chain reaction, WKY, Wistar Kyoto rat

animal models in all studies. It was found that all DNA damage parameters are associated with vitamin D levels, except in one study which did not find significant difference in the percentage of DNA in comet tails in the vitamin D deficiency group when compared to the control group (Machado *et al.*, 2019). Another study also showed that the preventive impact of vitamin D supplementation is better than its treatment effect to ameliorate DNA damage (Alfawaz *et al.*, 2014).

Human research (Table 2) were conducted in experimental (randomized and non-randomized clinical trial) (Wenclewska *et al.*, 2019; Gungor *et al.*, 2022) and observational (cross-sectional and cohort) (Ladeira *et al.*, 2015; Lan *et al.*, 2014; Nair-Shalliker *et al.*, 2012b; Najeeb *et al.*, 2020; Ng *et al.*, 2021; O'Callaghan-Gordo *et al.*, 2017; Petersen *et al.*, 2014; Usman *et al.*, 2021; Wang *et al.*, 2016; Fagundes *et al.*, 2019) design. In human studies, the most commonly employed parameter is comet assay (comet tail length, DNA damage score, and percentage of DNA in comet tail) (Fagundes *et al.*, 2019; Lan *et al.*, 2014; Najeeb *et al.*, 2020; Ng *et al.*, 2021; Wang *et al.*, 2016; Wenclewska *et al.*, 2019) and micronuclei formation (buccal or lymphocyte) (Fagundes *et al.*, 2019; Ladeira *et al.*, 2015; Nair-Shalliker *et al.*, 2012b; O'Callaghan-Gordo *et al.*, 2017; Usman *et al.*, 2021). Other parameters are aniline blue staining (sperm DNA damage) (Gungor *et al.*, 2022), thymine dimer (Petersen *et al.*, 2014), and ELISA (urinary 8-OHdG) (Usman *et al.*, 2021). Several conditions were observed in the included studies, such as diabetes mellitus, cancer, obesity, vitamin D-deficient state, and infertility. A similar finding was also observed in animal studies when the majority of the investigations revealed a significant association between vitamin D and DNA damage status. However, a study on workers occupationally exposed to formaldehyde (Ladeira *et al.*, 2015) and on the general population (Nair-Shalliker *et al.*, 2012b) did not show a significant association between vitamin D level and micronuclei formation, while another study only found the association in cord blood but not in maternal blood (O'Callaghan-Gordo *et al.*, 2017). Another research also did not present any association between vitamin D level and comet assay result as the DNA damage marker in the general population (Wang *et al.*, 2016).

Risk of Bias

All of the animal studies included in the analysis followed a similar pattern (Figs 2 and 4), with a low risk of bias on baseline characteristics, random outcome assessment, selective outcome reporting, and other biases. However, it is noteworthy that allocation concealment, random housing, and intervention blinding were not met by all studies, resulting in a high risk of bias. Meanwhile, only four studies (Liu *et al.*, 2019; Mehri *et al.*, 2020; Mohammed *et al.*, 2019; Siebert *et al.*, 2018) have a low risk of bias for outcome assessor blinding, and only two studies (Mehri *et al.*, 2020; Siebert *et al.*, 2018) have a low risk of bias for incomplete outcome data analysis.

We assessed the risk of bias in human studies (Fig. 3) using three scales: NOS, ROBINS-I, and ROB-2. Most studies (10/12; 83.33%) have moderate/some concerns about bias. A non-randomized study, on the other hand, runs the risk of bias due to insufficient intervention classification. Meanwhile, there is only one study (O'Callaghan-Gordo *et al.*, 2017) that has a low overall risk of bias. According to the summary graph (Fig. 4) on observational studies, 70% have a high risk of bias on comparability due to a lack of explanation on confound-

Table 2. Data extraction for human studies

Author (year)	Location	Design	Age	% Male	Population	Method	Outcome
(Fagundes <i>et al.</i> , 2019)	Brazil	Prospective cohort	62.11 ± 9.64 ^{ad}	37	75 patients with type 2 diabetes mellitus who were given supplementation of vitamin D3 4000 IU/day for 8 weeks	Comet assay Buccal micronucleus cytome assay	Decreased DNA damage index (comet assay) (p<0.05) and micronuclei formation (p<0.05) following supplementation with vitamin D3 and a wash-out period There is a negative correlation between DNA damage index and vitamin D levels (r=-0.2569; p<0.0001) but not in micronuclei.
(Gungor <i>et al.</i> , 2022)	Turkey	Non-RCT	34.67±4.01 ^{ac}	100	58 men with unexplained infertility (+50 controls)	Aniline blue staining (sperm DNA damage)	There was a negative and significant correlation between vitamin D levels and sperm DNA damage (r = -0.605; p<0.001)
(Ladeira <i>et al.</i> , 2015)	Portugal	Cross-sectional	39.64 ± 11.5 ^{ac}	65.45	55 workers occupationally exposed to Formaldehyde (+80 controls)	CBMN assay (buccal and lymphocyte)	Vitamin D has no association with the frequency of micronuclei (lymphocytes or buccal cells) in workers exposed to formaldehyde
(Lan <i>et al.</i> , 2014)	China	Cross-sectional	50 ± 10 ^{ac}	50	16 patients with severe asthma and vitamin D <30ng/ml (+16 controls and 16 patients with vitamin D >30ng/ml)	Comet assay (DNA damage score)	The total DNA damage score for a subject with Vitamin D deficiency was significantly increased compared to the scores in Vitamin D sufficiency (p = 0.002).
(Nair-Shalliker <i>et al.</i> , 2012b)	Australia	Cross-sectional	46.0 (27.1–61.4) ^{ba}	NA	207 participants	CBMN assay	There is no association between log serum 25(OH)D concentration and log-transformed frequency of any CBMN-cyt assay biomarker (p=0.3)
(Najeeb <i>et al.</i> , 2020)	Iraq	Cross-sectional	61.87 ± 12.77 ^{bc}	48.89	45 cancer patients (+ 35 controls)	Comet assay	Correlation between Tail DNA% and plasma vitamin D is significant in cancer patients (r=-0.3707; p<0.0001) and control (r=-0.2824; p<0.001) with higher damage at lower vitamin D level
(Ng <i>et al.</i> , 2021)	Malaysia	Cross-sectional	29.96 ± 0.63 ^{ac}	0	134 participants (47 obese, 87 non-obese)	Alkaline comet assay	Multivariate analysis revealed that individuals with serum 25(OH)D level of ≥ 31 nmol/L had a significantly lower tail moment (1.06 ± 0.22 nmol/L vs. 2.37 ± 0.60 nmol/L; p = 0.029) and tail olive moment (2.36 ± 0.24 nmol/L versus 3.41 ± 0.46 nmol/L; p = 0.031) compared to those with lower serum 25(OH)D level, in the obese group
(O'Callaghan-Gordo <i>et al.</i> , 2017)	Spain	Cross-sectional	NA	NA	344 participants (173 mothers and 171 newborns)	CBMN assay	In cord blood, 25(OH)D insufficient values (<50 nmol/L) were associated with increased lymphocyte micronuclei frequency (adjusted IRR = 1.32 (1.00, 1.72)), but not in maternal blood
(Petersen <i>et al.</i> , 2014)	Denmark	Cross-sectional	39.74 ± 7.22 ^{ad}	46.48	71 participants	Urinary cyclobutane thymine (T-T) dimers	The association between cyclobutane thymine dimers (T-T dimers) and vitamin D is significant (r = 0.76; p<0.0001), strongly indicating that the harmful DNA effects of ultraviolet radiation are unavoidable
(Usman <i>et al.</i> , 2021)	United Kingdom	Cross-sectional	14.60 ± 2.05 ^{ac}	45.28	132 adolescents (63 obese, control: 59 non-obese)	Buccal micronucleus cytome assay (buccal epithelial cells) ELISA (measures 8-OHdG from urine)	Vitamin D has significant correlation with 8-OHdG (r=-0.245; p<0.01) and buccal micronuclei (r=-0.305; p<0.01)
(Wang <i>et al.</i> , 2016)	China	Cross-sectional	20.69 ± 1.50 ^{ad}	36.36	121 participants (44 males, 77 females)	Comet Assay IV Lite scoring system	No significant correlation was observed between 25(OH)D level and DNA damage (r = -0.0824; P > 0.05).
(Wondolowska <i>et al.</i> , 2019)	Poland	RCT	63.43 ± 1.57 ^{ac}	29.17	92 people with vitamin D deficiency (intervention: 48 people, control: 44 people (14 with T2DM, 30 healthy))	Comet assay (peripheral lymphocyte)	The percentage of DNA in the tail decreased in the intervention group when compared to the control group, either with or without T2DM (p<0.05) DNA oxidative parameters (Fpg) decreased in the intervention group (113.63 ± 4.26 vs. 104.19 ± 3.06; p<0.05), especially in the T2DM group when compared to the control group (p<0.01).

Abbreviation: 25(OH)D, 25 hydroxy vitamin D, 8-OHdG, 8-Hydroxyguanosine, T-T dimers, cyclobutane thymine dimers, CBMN, cytokinesis-block micronuclei, Cyp27b1, Cytochrome p450 27B1, DNA, Deoxyribonucleic acid, ELISA, Enzyme-linked immunosorbent assay, H₂O₂, Hydrogen peroxide, IU, International unit, IRR, Incidence rate ratio, RCT, Randomized controlled trial, T2DM, Type 2 diabetes mellitus. Data was presented as: (a) mean ± SD or (b) median (min-max), (c) exposed mean, (d) overall mean

ing control. However, regarding selection, 70% of the studies have a low risk of bias, and 20% of the included research has a high risk of bias. Most studies have a moderate risk of bias in outcome assessment, primarily due to non-blinding outcome assessment.

DISCUSSION

DNA damage can be divided into two types, endogenous and exogenous. Endogenous DNA damage stems from chemically active DNA involved in hydrolytic and oxidative reactions with air and reactive oxygen species (ROS), which are naturally present in cells. On the contrary, exogenous DNA damage occurs due to the involvement of environmental, physical, and chemical substances such as UV and ionizing radiation, alkylating agents, and cross-linking agents (Chatterjee & Walker, 2018). Vitamin D is regarded as an essential factor in the status of DNA damage (Najeeb *et al.*, 2020). Vitamin D deficiency (plasma 25(OH)D <50 nmol/l) and severe deficiency (<30 nmol/l) have been associated with elevated oxidative stress, DNA damage promotion, and overall mortality (Wang *et al.*, 2016). The impact of vitamin D on DNA damage is prominent in several disorders, including hyperglycemia and cancer (Gabryanczyk *et al.*, 2021).

Hyperglycemia increases the production of free radicals and also induces DNA damage (Giacco & Brownlee, 2010). Studies conducted in patients with type 2 diabetes mellitus (T2DM) showed that vitamin D significantly prevented DNA damage and oxidative stress in patients with T2DM ($p < 0.05$). A vitamin D-responsive element has been identified in the promotion region of the insulin receptor gene in human (Gikas *et al.*, 2009). Pancreatic cells express the nuclear receptor for 1,25-dihydroxyvitamin D₃ (1,25(OH)₂D₃), which modulates insulin action (Bland *et al.*, 2004). Furthermore, vitamin D minimizes insulin resistance by its effect on calcium and phosphorus metabolism along with the upregulation of the insulin receptor gene, as well as suppression of the synthesis of proinflammatory cytokines that contribute to insulin resistance, including interleukins and TNF- α due to its antioxidative properties (Wenclewska *et al.*, 2019; Maestro *et al.*, 2002; Talaci *et al.*, 2013).

In malignancy, vitamin D had positive functions as anti-proliferative, proapoptotic, anti-inflammatory, anti-angiogenesis, anti-metastatic, and anti-invasion as well as estrogen signaling inhibitor (Vuolo *et al.*, 2012; Deuster *et al.*, 2017; Wacker & Holiack, 2013). Calcitriol (the active form of vitamin D) inhibits the proliferation of many malignant cells by inducing cell cycle arrest and cell accumulation in the G₀/G₁ phase of the cell cycle. In cells, calcitriol causes G₁/G₀ arrest in a p53-dependent manner by increasing the expression of the cyclin-dependent kinase inhibitors p21Waf/Cip1 and p27Kip1, decreasing the activity of cyclin-dependent kinase 2 (CDK2), and causing hypo-phosphorylation. Calcitriol also increases the expression of p73, a homolog of p53, which is associated with the induction of apoptosis in several human and murine tumor systems. Suppression of p73 abrogates calcitriol-induced apoptosis and reduces the ability of calcitriol to enhance the cytotoxic effect of agents such as gemcitabine and cisplatin in a squamous cell carcinoma (SCC) model (Krishnan & Feldman, 2010; Khrisnan *et al.*, 2012). In the previous study, it was found that vitamin D deficiency is a risk factor for malignancy (cancer) and accelerates the invasion process (Najeeb *et al.*, 2020; Migliaccio *et al.*, 2022). The

population of the 25 studies in this systematic review is diverse. Twelve studies conducted in humans analyzed DNA damage in patients with comorbid diseases such as T2DM, obesity, infertility, cancer patients, and the general population. Meanwhile, thirteen *in vivo* studies analyzed DNA damage using animal models with hypertension, ovariectomy, nephrotoxicity, vitamin D deficiency, and oxidative stress.

Several studies on vitamin D indicated that the vitamin has a beneficial impact on all organ systems of the human body. Both 25(OH)D and its hormonally active form, 1,25(OH)₂D are vital for physiological functions, especially to reduce inflammation and excessive cellular oxidative stress. The 1,25(OH)₂D hormone or calcitriol modulates cell proliferation through direct and indirect pathways, such as by the inhibition of the transcription factor, Nuclear factor kappa-light-chain-enhancer of activated B cells (NF- κ B) which is associated with an elevation of oxidative stress and cellular response to inflammation and injury (Tilstra *et al.*, 2012). Due to suppression of NF- κ B activation, calcitriol helps to reduce chronic inflammation (Myszka & Klinger, 2014). However, more research into the relationship between DNA damage, oxidative stress, and vitamin D is required.

Vitamin D receptor (VDR) is found in testicular tissue, prostate, and spermatozoa. In addition, the intense metabolism of vitamin D in the male reproductive system and increased expression of VDR in the neck of the sperm cause males to require vitamin D for functionally active sperm (Jensen *et al.*, 2011). Incubation of semen samples with vitamin D for 30 minutes led to a significant increase in sperm velocity parameters. This progressive increase in motility is due to vitamin D-dependent calcium release and subsequent cyclic AMP/protein kinase A (cAMP/PKA) activation and Adenosine triphosphate (ATP) production (Gunter *et al.*, 2004). There was a significant negative correlation ($p < 0.05$) between vitamin D and sperm DNA damage in this systematic review. After binding to the VDR receptor, vitamin D initiates slow genomic effects by stimulating the release of ligand-activated transcription factors in the nucleus. In unexplained infertile patients with vitamin D deficiency, sperm DNA damage may occur due to delayed genomic effects (Jurutka *et al.*, 2001).

Studies in various animal models showed that vitamin D exerts a protective effect on DNA. Vitamin D can reduce the DNA damage index (percentage of DNA in comet tails assessed from comet tests). In addition, in genomic instability animal models induced by cyclophosphamide, vitamin D can reduce the frequency of micronuclei formation (a marker of DNA damage). Besides the percentage of DNA in comet tails and the frequency of micronuclei, DNA damage can also be assessed by the levels of 8-OHdG, a marker of oxidative DNA damage (Smith *et al.*, 2005). Elevated levels of 8-OHdG in rat animal models are also associated with a complete loss of VDR expression. Because the expression of VDR depends on the availability of 1,25(OH)₂D, the loss of VDR suggests that there may be a role for 1,25(OH)₂D in protecting cells against hyperproliferation and oxidative DNA damage (Kállay *et al.*, 2002; Nair-Shalliker *et al.*, 2012a). Decreased levels of 8-OHdG after vitamin D supplementation was proven in the animal model studies (Haque *et al.*, 2019; Mohammed *et al.*, 2019). The results of studies in animal models (*in vivo*) are in line with those of studies in cells (*in vitro*) (Chen *et al.*, 2018; Liu *et al.*, 2019). These outcomes can confirm that vitamin D has a protective effect on DNA.

Various parameters of oxidative stress are also presented in this systematic review. In human studies, vitamin D supplementation led to a significant decrease in NO and total thiols and an increase in the concentration of reduced glutathione (GSH) leading to a decrease in oxidative processes in cells (Fagundes *et al.*, 2019). In a study of animal models with hypertension, vitamin D was not significantly associated with DNA damage. However, vitamin D3 deficiency alters the level of Thio-barbituric Acid Reactive Substance (TBARS) in a mouse model of spontaneous hypertension, which is an indicator of Reactive Oxygen Species (ROS)-initiated peroxidation of unsaturated fatty acids in membrane lipids and alters the permeability, fluidity, and integrity of the plasma membrane (Potter *et al.*, 2011). Lipid peroxidation predisposes patients to conditions such as hypertension and thromboembolic (Yavuzer *et al.*, 2016). Vitamin D can reduce oxidative stress that occurs in cells thereby reducing DNA damage.

This systematic review proved that vitamin D protects against DNA damage. However, there are some limitations to this systematic review. First, the study populations are largely heterogeneous with different diseases and DNA damage parameters; thus, the results can be biased. In addition, human studies are still sparse (only one randomized controlled trial/RCT) and mainly with a moderate RoB. Consequently, the application of the results to humans still needs to be considered. Further studies with randomized controlled trial designs are expected in the future to increase the strength of evidence.

CONCLUSION

There is a significant association between vitamin D and DNA damage. However, although the majority of studies have found that vitamin D has a protective effect against DNA damage, other research found contradictory findings. Thus, the need of further investigations with stricter criteria must be commenced. Nevertheless, it is safe to conclude that a diet with sufficient vitamin D content and supplementation (more than 1000 IU/day, preferably about 2000–5000 IU/day) is recommended to prevent DNA damage and oxidative stress in cells.

REFERENCES

- Alfawaz HA, Bhat RS, Al-Ayadhi L, El-Ansary AK (2014) Protective and restorative potency of vitamin D on persistent biochemical autistic features induced in propionic acid-intoxicated rat pups. *BMC Complement. Altern. Med.* **14**: 416. <https://doi.org/10.1186/1472-6882-14-416>
- Bland R, Markovic D, Hills CE, Hughes S V., Chan SL, Squires PE, Hewison M (2004) Expression of 25-hydroxyvitamin D3-1 α -hydroxylase in pancreatic islets. *J. Steroid Biochem.* 121–125. <https://doi.org/10.1016/j.jsbmb.2004.03.115>
- Chatterjee N, Walker GC (2018) Mechanisms of DNA damage, repair, and mutagenesis. *Environ. Mol. Mutagen.* **58**: 235–263. <https://doi.org/10.1002/em.22087.Mechanisms>
- Chen L, Yang R, Qiao W, Yuan X, Wang S, Goltzman D, Miao D (2018) 1,25-Dihydroxy vitamin D prevents tumorigenesis by inhibiting oxidative stress and inducing tumor cellular senescence in mice. *Int. J. Cancer* **143**: 368–382. <https://doi.org/10.1002/ijc.31317>
- Christakos S, Dhawan P, Verstuyf A, Verlinden L, Carmeliet G (2015) Vitamin D: Metabolism, molecular mechanism of action, and pleiotropic effects. *Physiol. Rev.* **96**: 365–408. <https://doi.org/10.1152/physrev.00014.2015>
- Deuster E, Jeschke U, Ye Y, Mahner S, Czogalla B (2017) Vitamin D and VDR in gynecological cancers-A systematic review. *Int. J. Mol. Sci.* **18**: 2328. <https://doi.org/10.3390/ijms18112328>
- Elhousseini H, Elkafas H, Abdelaziz M, Halder S, Atabekov I, Eziba N, Ismail N, El Andaloussi A, Al-Hendy A (2018) Diet-induced vitamin D deficiency triggers inflammation and DNA damage profile in murine myometrium. *Int. J. Womens. Health* **10**: 503–514. <https://doi.org/10.2147/IJWH.S163961>
- Fagundes G, Macan T, Rohr P, Damiani A, Rocha F Da, Pereira M, Longaretti L, Vilela T, Ceretta L, Mendes C, Silveira P, Teixeira J, Andrade V de (2019) Vitamin D3 as adjuvant in the treatment of type 2 diabetes mellitus: modulation of genomic and biochemical instability. *Mutagenesis* **34**: 135–145. <https://doi.org/10.1093/mutage/gez001>
- Gabryanczyk A, Klimczak S, Szymczak-Pajor I, Śliwińska A (2021) Is vitamin D deficiency related to increased cancer risk in patients with type 2 diabetes mellitus? *Int. J. Mol. Sci.* **22**: 6444. <https://doi.org/10.3390/ijms22126444>
- Giacco F, Brownlee M (2010) Oxidative stress and diabetic complications. *Circ. Res.* 1058–1070. <https://doi.org/10.1161/CIRCRESA-HA.110.223545>
- Gikas A, Sotiropoulos A, Pastromas V, Papazafropoulou A, Apostolou O, Pappas S (2009) Seasonal variation in fasting glucose and HbA1c in patients with type 2 diabetes. *Prim. Care Diabetes* 111–114. <https://doi.org/10.1016/j.pcd.2009.05.004>
- Gungor K, Gungor ND, Basar MM, Cengiz F, Ersahin SS, Cil K (2022) Relationship between serum vitamin D levels semen parameters and sperm DNA damage in men with unexplained infertility. *Eur. Rev. Med. Pharmacol. Sci.* **26**: 499–505. https://doi.org/10.26355/eurrev_202201_27875
- Gunter T, Yule D, Gunter K, Elisee R, Salter J (2004) Calcium and mitochondria. *FEBS Lett.* **567**: 96–102. <https://doi.org/10.1016/j.febslet.2004.03.071>
- Haq SH, AlAfaeq NO, Johari R Al (2019) Vitamin D treatment reverses the induced oxidative stress damage to DNA. *Pak. J. Biol. Sci.* **22**: 8–14. <https://doi.org/10.3923/pjbs.2019.8.14>
- Hooijmans CR, Rovers MM, de Vries RBM, Leenaars M, Ritskes-Hoitinga M, Langendam MW (2014) SYRCL's risk of bias tool for animal studies. *BMC Med. Res. Methodol.* **14**: 43. <https://doi.org/10.1186/1471-2288-14-43>
- Jensen M, Bjerrum P, Jessen T, Nielsen J, Joensen U, Olesen I, Petersen J, Juul A, Dissing S, Jorgensen N (2011) Vitamin D is positively associated with sperm motility and increases intracellular calcium in human spermatozoa. *Hum. Reprod.* **26**: 1307–1317. <https://doi.org/10.1093/humrep/der059>
- Jurutka P, Whitfield G, Hsieh J, Thompson P, Haussler C, Haussler M (2001) Molecular nature of the vitamin D receptor and its role in regulation of gene expression. *Rev. Endocr. Metab. Disord.* **2**: 203–216. <https://doi.org/10.1023/a:1010062929140>
- Kállay E, Bareis P, Bajna E, Kriwanek S, Bonner E, Toyokuni S, Cross HS (2002) Vitamin D receptor activity and prevention of colonic hyperproliferation and oxidative stress. *Food Chem. Toxicol.* **40**: 1191–1196. [https://doi.org/10.1016/s0278-6915\(02\)00030-3](https://doi.org/10.1016/s0278-6915(02)00030-3)
- Khrisan A, Trump D, Johnson C (2012) The role of vitamin D in cancer prevention and treatment. *Rheum. Dis. Clin. North Am.* **38**: 161–78. <https://doi.org/10.1016/j.rdc.2012.03.014>
- Krishnan A V., Feldman D (2010) Molecular pathways mediating the anti-inflammatory effects of calcitriol: Implications for prostate cancer chemoprevention and treatment. *Endocr. Relat. Cancer* **17**: 19–38. <https://doi.org/10.1677/ERC-09-0139>
- Ladeira C, Pádua M, Veiga L, Viegas S, Carolino E, Gomes MC, Brito M (2015) Influence of serum levels of vitamins A, D, and E as well as vitamin D receptor polymorphisms on micronucleus frequencies and other biomarkers of genotoxicity in workers exposed to formaldehyde. *Lifestyle Genomics* **8**: 205–214. <https://doi.org/10.1159/000444486>
- Lan N, Luo G, Yang X, Cheng Y, Zhang Y, Wang X, Wang X, Xie T, Li G, Liu Z (2014) 25-Hydroxyvitamin D3-deficiency enhances oxidative stress and corticosteroid resistance in severe asthma exacerbation. *PLoS One* **9**: e111599. <https://doi.org/10.1371/journal.pone.0111599>
- Liana P, Liberty IA, Murti K, Hafy Z, Salim EM, Zulkarnain M, Umar TP (2022) A systematic review on neutrophil extracellular traps and its prognostication role in COVID-19 patients. *Immunol. Res.* **70**: 449–460. <https://doi.org/10.1007/s12026-022-09293-w>
- Liu H, Feng X, Wu S, Zong T, Li B, Zhang, Zengli (2019) Vitamin D resists cyclophosphamide-induced genomic and DNA damage in CHL cells *in vitro* and in mice *in vivo*. *Nutr. Cancer* **71**: 1030–1039. <https://doi.org/10.1080/01635581.2019.1595050>
- Machado C da S, Venancio VP, Aissa AF, Hernandez LC, de Mello MB, Del Lama JEC, Marzocchi-Machado CM, Bianchi MLP, Antunes LMG (2016) Vitamin D3 deficiency increases DNA damage and the oxidative burst of neutrophils in a hypertensive rat model. *Mutat. Res. Toxicol. Environ. Mutagen.* **798**: 19–26. <https://doi.org/10.1016/j.mrgentox.2016.01.005>
- Machado CDS, Aissa AF, Ribeiro DL, Antune L, Gregg M (2019) Vitamin D supplementation alters the expression of genes associated with hypertension and did not induce DNA damage in rats. *J. Toxicol. Environ. Health* **82**: 299–313. <https://doi.org/10.1080/15287394.2019.1592044>
- Maestro B, Molero S, Bajo S, Dávila N, Calle C (2002) Transcriptional activation of the human insulin receptor gene by 1,25-dihydroxyvi-

- tamin D3. *Cell Biochem. Funct.* **20**: 227–232. <https://doi.org/10.1002/cbf.951>
- Meerza D, Naseem I, Ahmed J (2012) Effect of 1, 25(OH)₂ vitamin D₃ on glucose homeostasis and DNA damage in type 2 diabetic mice. *J. Diabetes Complications* **26**: 363–368. <https://doi.org/10.1016/j.jdiacomp.2012.05.013>
- Mehri N, Haddadi R, Ganji M, Shahidi S, Soleimani Asl S, Taheri Azandariani M, Ranjbar A (2020) Effects of vitamin D in an animal model of Alzheimer's disease: Behavioral assessment with biochemical investigation of hippocampus and serum. *Metab. Brain Dis.* **35**: 263–274. <https://doi.org/10.1007/s11011-019-00529-7>
- Merino O, Sánchez R, Gregorio B, Sampaio F, Risopatrón J (2018) Effects of diet-induced obesity and deficient in vitamin D on spermatogenesis function and DNA integrity in Sprague-Dawley rats. *Biomed Res Int.* **2018**: 5479057. <https://doi.org/10.1155/2018/5479057>
- Migliaccio S, Di Nisio A, Magno S, Romano F, Barrea L, Colao AM, Muscogiuri G, Savastano S (2022) Vitamin D deficiency: a potential risk factor for cancer in obesity? *Int. J. Obes. (Lond.)* **46**: 707–717. <https://doi.org/10.1038/s41366-021-01045-4>
- Mohammed M, Aboulhoda B, Mahmoud R (2019) Vitamin D attenuates gentamicin-induced acute renal damage via prevention of oxidative stress and DNA damage. *Hum. Exp. Toxicol.* **38**: 321–335. <https://doi.org/10.1177/0960327118812166>
- Myszka M, Klinger M (2014) The immunomodulatory role of Vitamin D. *Postępy Hig. Med. Dosw. (Online)* **68**: 865–878. <https://doi.org/10.5604/17322693.1110168>
- Nair-Shalliker V, Armstrong BK, Fenech M (2012a) Does vitamin D protect against DNA damage? *Mutat. Res. – Fundam. Mol. Mech. Mutagen.* **733**: 50–57. <https://doi.org/10.1016/j.mrfmmm.2012.02.005>
- Nair-Shalliker V, Fenech M, Forde PM, Clements MS, Armstrong BK (2012b) Sunlight and vitamin D affect DNA damage, cell division and cell death in human lymphocytes: a cross-sectional study in South Australia. *Mutagenesis* **27**: 609–614. <https://doi.org/10.1093/mutage/ges026>
- Najeeb HA, Othman R, Salih SF, Mohammed AA, Ismael Q Al (2020) Vitamin D level and endogenous DNA damage in patients with cancers in Duhok city, KRG-Iraq. *Ann. Med. Surg.* **10**: 462–467. <https://doi.org/10.1016/j.amsu.2020.10.065>
- Ng CY, Amini F, Ahmad Bustami N, Tan ESS, Tan PY, Mitra SR (2021) Association of DNA damage with vitamin D and hair heavy metals of obese women. *Mol. Cell. Toxicol.* **17**: 429–438. <https://doi.org/10.1007/s13273-021-00149-2>
- O'Callaghan-Gordo C, Kogevinas M, Fthenou E, Pedersen M, Espinosa A, Chalkiadaki G, Daraki V, Dermizaki E, Decordier I, Georgiou V, Merlo DF, Roumeliotaki T, Vande Loo K, Kleinjans J, Kirsch-Volders M, Chatzi L (2017) Vitamin D insufficient levels during pregnancy and micronuclei frequency in peripheral blood T lymphocytes mothers and newborns (*Rhea cohort*, Crete). *Clin. Nutr.* **36**: 1029–1035. <https://doi.org/10.1016/j.clnu.2016.06.016>
- Osmancevic A, Sandström K, Gillstedt M, Landin-Wilhelmsen K, Larkö O, Wennberg Larkö A-M, F. Holick M, Krogstad A-L (2015) Vitamin D production after UVB exposure – A comparison of exposed skin regions. *J. Photochem. Photobiol. B Biol.* **143**: 38–43. <https://doi.org/10.1016/j.jphotobiol.2014.12.026>
- Ouzzani M, Hammady H, Fedorowicz Z, Elmagarmid A (2016) Rayyan – a web and mobile app for systematic reviews. *Syst. Rev.* **5**: 210. <https://doi.org/10.1186/s13643-016-0384-4>
- Page MJ, McKenzie JE, Bossuyt PM, Boutron I, Hoffmann TC, Mulrow CD, Shamseer L, Tetzlaff JM, Akl EA, Brennan SE (2021) The PRISMA 2020 statement: an updated guideline for reporting systematic reviews. *BMJ* **372**: n71. <https://doi.org/10.1136/bmj.n71>
- Peng X, Vaishnav A, Murillo G, Alimirah F, Torres KEO, Mehta RG (2010) Protection against cellular stress by 25-hydroxyvitamin D₃ in breast epithelial cells. *J. Cell. Biochem.* **110**: 1324–1333. <https://doi.org/10.1002/jcb.22646>
- Petersen B, Wulf HC, Triguero-Mas M, Philipsen PA, Thieden E, Olsen P, Heydenreich J, Dadvand P, Basagaña X, Liljendahl TS, Harrison GI, Segerbäck D, Schmalwieser AW, Young AR, Nieuwenhuijsen MJ (2014) Sun and ski holidays improve vitamin D status, but are associated with high levels of DNA damage. *J. Invest. Dermatol.* **134**: 2806–2813. <https://doi.org/10.1038/jid.2014.223>
- Potter TM, Neun BW, Stern ST (2011) Assay to detect lipid peroxidation upon exposure to nanoparticles. *Mol. Biol.* **697**: 181–89
- Qiao W, Yu S, Sun H, Chen L, Wang R, Wu X, Goltzman D, Miao D (2020) 1,25-Dihydroxyvitamin D insufficiency accelerates age-related bone loss by increasing oxidative stress and cell senescence. *Am. J. Transl. Res.* **12**: 507–518. PMID: 32194899
- Siebert C, Santos T Dos, Bertó C, Parisi M, Coelho R, Manfredini V, Barbé-Tuana F, Wyse A (2018) Vitamin D supplementation reverses DNA damage and telomeres shortening caused by ovariectomy in hippocampus of wistar rats. *Neurotox. Res.* **34**: 538–546. <https://doi.org/10.1007/s12640-018-9909-z>
- Smith SM, Zwart SR, Block G, Rice BL, Davis-Street JE (2005) The nutritional status of astronauts is altered after long-term space flight aboard the International Space Station. *J. Nutr.* **135**: 437–443. <https://doi.org/10.1093/jn/135.3.437>
- Sterne JA, Hernán MA, Reeves BC, Savović J, Berkman ND, Viswanathan M, Henry D, Altman DG, Ansari MT, Boutron I, Carpenter JR, Chan AW, Churchill R, Deeks JJ, Hróbjartsson A, Kirkham J, Jüni P, Loke YK, Pigott TD, Ramsay CR, Regidor D, Rothstein HR, Sandhu L, Santaguida PL, Schünemann HJ, Shea B, Shrier I, Tugwell P, Turner L, Valentine JC, Waddington H, Waters E, Wells GA, Whiting PF, Higgins JP (2016) ROBINS-I: a tool for assessing risk of bias in non-randomised studies of interventions. *BMJ* **355**: i4919. <https://doi.org/10.1136/bmj.i4919>
- Sterne JAC, Savović J, Page MJ, Elbers RG, Blencowe NS, Boutron I, Cates CJ, Cheng HY, Corbett MS, Eldridge SM, Emberson JR, Hernán MA, Hopewell S, Hróbjartsson A, Junqueira DR, Jüni P, Kirkham JJ, Lasserson T, Li T, McAleenan A, Reeves BC, Shepperd S, Shrier I, Stewart LA, Tilling K, White IR, Whiting PF, Higgins JPT (2019) RoB 2: a revised tool for assessing risk of bias in randomised trials. *BMJ* **366**: l4898. <https://doi.org/10.1136/bmj.l4898>
- Talaei A, Mohamadi M, Adgi Z (2013) The effect of vitamin D on insulin resistance in patients with type 2 diabetes. *Diabetol. Metab. Syndr.* **5**: 8. <https://doi.org/10.1186/1758-5996-5-8>
- Tilstra JS, Robinson AR, Wang J, Gregg SQ, Clauson CL, Reay DP, Nasto LA, St Croix CM, Usas A, Vo N, Huard J, Clemens PR, Stolz DB, Guttridge DC, Watkins SC, Garinis GA, Wang Y, Niederhoffer LJ, Robbins PD (2012) NF- κ B inhibition delays DNA damage-induced senescence and aging in mice. *J. Clin. Invest.* **122**: 2601–2612. <https://doi.org/10.1172/JCI45785>
- Umar TP, Samudra MG, Nashor KMN, Agustini D, Syakurah RA (2022) Health professional student's volunteering activities during the COVID-19 pandemic: A systematic literature review. *Front. Med.* **9**: 797153. <https://doi.org/10.3389/fmed.2022.797153>
- Umar TP, Siburian R (2022) Routine laboratory testing role for Covid-19 identification: A systematic review. *Med. Sci. J. Adv. Res.* **3**: 99–106. <https://doi.org/10.46966/msjar.v3i3.49>
- Usman M, Woloshynowych M, Britto JC, Bilkevic I, Glassar B, Chapman S, Ford-Adams ME, Desai A, Bain M, Tewfik I, Volpi E V. (2021) Obesity, oxidative DNA damage and vitamin D as predictors of genomic instability in children and adolescents. *Int. J. Obes.* **45**: 2095–2107. <https://doi.org/10.1038/s41366-021-00879-2>
- Vuolo L, Di Somma C, Faggiano A, Colao A (2012) Vitamin D and cancer. *Front. Endocrinol. (Lausanne)* **3**: 1–13. <https://doi.org/10.3389/fendo.2012.00058>
- Wacker M, Holick MF (2013) Vitamin D-effects on skeletal and extra-skeletal health and the need for supplementation. *Nutrients* **5**: 111–148. <https://doi.org/10.3390/nu5010111>
- Wang EW, Collins AR, Pang MYC, Siu PPM, Lai CKY, Woo J, Benzie IFF (2016) Vitamin D and oxidation-induced DNA damage: is there a connection? *Mutagenesis* **31**: 655–659. <https://doi.org/10.1093/mutage/gew033>
- Wenclewska S, Szymczak-Pajor I, Drzewoski J, Bunk M, A Sliwińska (2019) Vitamin D supplementation reduces both oxidative DNA damage and insulin resistance in the Elderly with metabolic disorders. *Int J Mol Sci* **20**: 2891. <https://doi.org/10.3390/ijms20122891>
- Yavuzer H, Yavuzer S, Cengiz M, Erman H, Doventas A, Balci H, Erdinciler DS, Uzun H (2016) Biomarkers of lipid peroxidation related to hypertension in aging. *Hypertens. Res.* **39**: 342–348. <https://doi.org/10.1038/hr.2015.156>

LncRNA AC093850.2 predicts poor outcomes in patients with triple-negative breast cancer and motivates tumor progression by sponging miR-4299

Zhangbo Xu¹, Yongxue Gu², Ying Lei² and Lili Teng³✉

¹Department of Breast and Thyroid Surgery, The Third People's Hospital of Chengdu, Chengdu, China; ²Department of Breast Surgery, Weifang People's Hospital, Weifang, China; ³Department of Infectious Diseases, Weifang People's Hospital, Weifang, China

Background: Accumulating evidence displays that non-coding RNAs (ncRNAs) are involved in the progression of triple-negative breast cancer (TNBC). This study aimed to investigate the role of lncRNA AC093850.2 in TNBC. **Methods:** The AC093850.2 levels were compared using RT-qPCR in TNBC tissues and corresponding normal tissues. The Kaplan-Meier curve method was conducted to assess the clinical significance of AC093850.2 in TNBC. Bioinformatic analysis was used to predict potential miRNA. Cell proliferation and invasion assays were carried out to explore the function of AC093850.2/miR-4299 in TNBC. **Results:** lncRNA AC093850.2 expression is raised in TNBC tissues and cell lines, which is related to the shorter overall survival of patients. AC093850.2 is directly bound to miR-4299 in TNBC cells. Downregulation of AC093850.2 reduces tumor cell proliferation, migration, and invasion abilities, while miR-4299 silence attenuated AC093850.2 silencing induced inhibition of cellular activities in TNBC cells. **Conclusion:** In general, the findings suggest that lncRNA AC093850.2 was closely related to the prognosis and progression of TNBC by sponging miR-4299, which might be a prognosis predictor and potential target for treating TNBC patients.

Keywords: AC093850.2, triple-negative breast cancer, miR-4299, prognosis, progression

Received: 25 February, 2022; **revised:** 01 September, 2022; **accepted:** 26 October, 2022; **available on-line:** 22 February, 2023

✉e-mail: tengliliwf@163.com

Abbreviations: GEPIA, Gene Expression Profiling Interactive Analysis; lncRNA, long non-coding RNA; miRNA, microRNA; ncRNAs, non-coding RNAs; ST6GALNAC4, alphaN-acetyl-neuraminyl-2,3-beta-galactosyl-1,3)-N-acetylgalactosaminide alpha-2,6-sialyltransferase 4; TNBC, triple-negative breast cancer

INTRODUCTION

The incidence and mortality of breast cancer have obvious regional variations around the world (Azamjah *et al.*, 2019). In recent years, the incidence of breast cancer in China has been increasing year by year, and women tend to be younger (Li *et al.*, 2016). The etiology of breast cancer is complex and closely related to a variety of genetic and non-genetic factors (Cappetta *et al.*, 2021). Studies have manifested that being unmarried, childless, on high-fat diet, obese, having multiple x-rays and obvious benign breast diseases are all risk factors for the occurrence of breast cancer (Rojas & Stuckey, 2016; Sun *et al.*, 2017). Currently, surgical resection and chemotherapy are the main treatments for breast cancer. However, breast cancer has the characteristics of being highly metastatic and spreads easily through

lymphatic metastases (Kim, 2021). Breast cancer patients are prone to recurrence after surgical treatment, and the quality of life is also low, which seriously affects the clinical effect of breast cancer prevention and treatment. Among the subtypes of breast cancer, triple-negative breast cancer (TNBC) has a higher risk of recurrence and metastasis (Yin *et al.*, 2020). Due to the obvious heterogeneity of TNBC and the lack of expression of ER, PR, and HER-2, the clinical treatment is more difficult, so the survival rate of TNBC patients is not significantly improved (Yin *et al.*, 2020). Therefore, it is of great significance to explore effective methods and strategies for improving the prevention and treatment of breast cancer.

The functions of non-coding RNA (ncRNA) genes have attracted more attention in normal physiological functions and pathological processes (Panni *et al.*, 2020). ncRNAs are a general term for RNA that are not participating in protein-coding, such as long non-coding RNA (lncRNA) and microRNA (miRNA) (Yang *et al.*, 2020; Zhao *et al.*, 2020). With the continuous in-depth study of ncRNA, it was unexpectedly discovered that the mutation or differential expression of ncRNA is related to the occurrence and progression of many diseases (Anastasiadou *et al.*, 2017). Currently, the role of lncRNA in the process of cell proliferation, differentiation, and disease occurrence has received more and more attention (Mori *et al.*, 2018; Romano *et al.*, 2017). lncRNAs are relatively non-conservative in evolution and can regulate cellular activities at multiple levels, including chromatin modification, transcriptional level, and post-transcriptional level regulation (Barreca *et al.*, 2021). The abnormal lncRNA expression can not only affect tumor growth and metastasis but also serve as indicators for clinical detection and treatment (Schmitt & Chang, 2016; Wang *et al.*, 2017). Several lncRNAs are reported to be involved in the progression of breast cancer, such as NR2F1-AS1 (Zhang *et al.*, 2020), H19, and NEAT1 (Müller *et al.*, 2019). lncRNA AC093850.2 expression was increased in lung adenocarcinoma (Qiu *et al.*, 2015) and gastrointestinal esophageal cancer (Su *et al.*, 2022). A previous study reported that AC093850.2 has prognostic significance for breast cancer based on Gene Expression Profiling Interactive Analysis (GEPIA) (Zhang *et al.*, 2019), while its involvement in TNBC is elusive.

Herein, we investigated the role of AC093850.2 in the progression of TNBC. The expression of AC093850.2 was increased in TNBC tissues. miR-4299 functions as a suppressive miRNA in some types of cancer, such as lung cancer (Yang *et al.*, 2018). We observed that AC093850.2 functioned as the sponge of miR-4299 to regulate the progression of TNBC. Thus, the increased expression of

AC093850.2 may serve as a prognostic marker for TNBC patients and be a novel potential therapeutic target.

MATERIALS AND METHODS

Specimen source

A total of 135 cases of TNBC tissues and corresponding paracentral tissue specimens were collected from Weifang People's Hospital from January 2014 to December 2016 and stored in liquid nitrogen until use. All patients signed the informed consent. This study was approved by the Ethics Committee of Weifang People's Hospital. The inclusion criteria: 1) patients were first onset and initial operation; 2) patients were pathologically diagnosed as TNBC; 3) patients have a complete medical history and five-year follow-up information. The median age of patients was 50.5 years, ranging from 29 to 82 years.

Cell lines and transfection

TNBC cell lines (BT549, MDA-MB-231, and HCC1937), other subtypes of breast cancer cell lines (SKBR3, MCF7, BT474), and normal breast epithelial cell line MCF-10A were acquired from ATCC and were stored in our laboratory. Cells were cultured in a DMEM medium (Gibco) containing 10% FBS (Hyclone) in a 5% CO₂ incubator at 37°C, and the medium was changed every 48–72 h. The cells in good conditions were cultured in 6-well plates until the logarithmic growth period.

MDA-MB-231 and HCC1937 cells were used for cell transfection. The AC093850.2 siRNA (si-AC093850.2), siRNA NC, miR-4299 mimic, mimic negative control (mimic NC), miR-4299 inhibitor (inhi-miR-4299), inhibitor NC were obtained from GenePharma (Shanghai, China). These vectors were transfected or co-transfected into TNBC cells using Lipofectamine 2000 reagent.

RNA isolation and RT-qPCR

Total RNA was prepared from tissue specimens and cell lines using a pre-cooled Trizol isolation kit (Invitrogen) and cDNA synthesis was performed using a Transcriptor First Strand cDNA Synthesis Kit (Roche, Mannheim, Germany) for lncRNA and a miRvana miRNA isolation kit (Applied Biosystems) for miRNA. Then cDNA was amplified by RT-qPCR using a SYBR Green PCR Kit (TaKaRa) for lncRNA or miRCURY LNA miRNA SYBR Green PCR kit (Qiagen) for miRNA. GAPDH and U6 were used as normalization controls. The relative levels of lncRNA and miRNAs were calculated by the comparative Ct method.

MTS assay for cell proliferation

Cell proliferation rate was evaluated using an MTS assay. The cells (3000 cells/well) were incubated in 96-well plates at 37°C. After 24, 48, and 72 h of incubation, the MTS reagent (Promega) was added to the well in a dark environment and incubated in the incubator for 2 h. After incubation, the absorbance value (OD value) of each well was detected at 490 nm by the microplate reader (BioRad).

Transwell assays

For migration and invasion assays, a 24-well Transwell chamber (8 µm core; Corning, NY) was adopted to carry out the experiments. The membrane in the upper chamber of the transwell was precoated with Matrigel (BD), which was used for the evaluation of the invasion abilities of tu-

mor cells. The migration assay does not need to be pre-coated with Matrigel. The serum-free medium was used to incubate the cells (1×10⁵ cells) in the top chamber, and a 600 µl culture medium with 10% FBS was included in the lower chamber. The invading and migrating cells were fixed, stained, and counted with a microscope (Olympus).

Dual-luciferase reporter assay

The 3'UTR of AC093850.2 fragment with miR-4299 binding sites was inserted into the pmirGLO dual-luciferase vector (Promega) and named as AC093850.2 3'UTR WT. The mutant 3'UTR of AC093850.2 was subcloned into pmirGLO and named as AC093850.2 3'UTR MUT. The WT or MUT fragment was co-transfected with miR-4299 mimic, or mimic NC into TNBC cells for 48 h. The luciferase activities were detected using a Dual-luciferase reporter assay kit (KeyGen, China).

Statistical analysis

Results were acquired from at least three independent experiments and were presented as mean ± S.D. The significance was assessed by the SPSS and GraphPad Prism software using the χ^2 test, Student's *t*-test, or one-way ANOVA. The survival rates and clinical prognostic value were evaluated by the Kaplan-Meier method and multivariate Cox regression analysis. The difference was considered statistically significant when *P* < 0.05 for all statistical analyses.

RESULTS

High AC093850.2 expression was related to clinicopathological parameters and shorter overall survival

The expression of AC093850.2 was monitored using RT-qPCR in 135 pairs of tissue specimens. AC093850.2

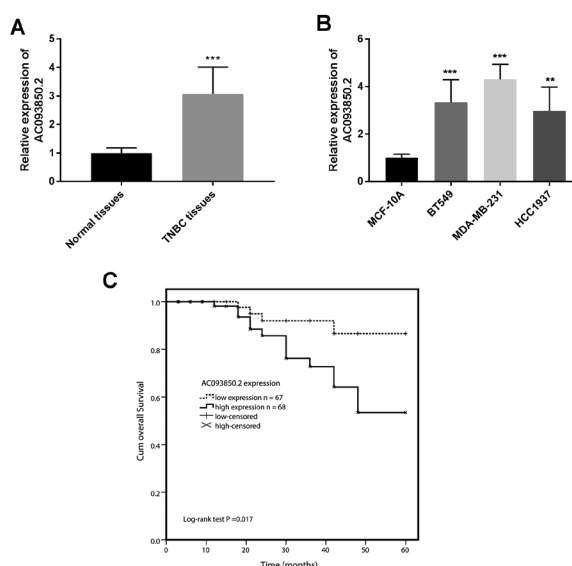


Figure 1. Increased expression of AC093850.2 was related to the shorter overall survival of TNBC patients.

(A) The expression level of AC093850.2 in paired tumor tissues and normal tissues was analyzed by RT-qPCR. ****P* < 0.001. (B) The expression level of AC093850.2 in TNBC cell lines was measured by RT-qPCR. ***P* < 0.01, ****P* < 0.001. (C) The Kaplan-Meier curve was conducted to assess the survival outcome of AC093850.2 in TNBC (log-rank test, *P* = 0.017).

Table 1. Association of LncRNA AC093850.2 expression and clinicopathological parameters of TNBC patients

Variable	Cases (n=135)	AC093850.2 expression		P-value
		Low (n=67)	High (n=68)	
Age (years)				0.436
≤ 50	70	37	33	
> 50	65	30	35	
Tumor size (cm)				0.048
≤ 2	61	36	25	
> 2	74	31	43	
Pathological stage				0.098
I-II	75	42	33	
III	60	25	35	
Lymph node metastasis				0.007
Negative	75	45	30	
Positive	60	22	38	
TNM stage				0.001
I-II	77	48	29	
III	58	19	39	
Ki67				0.024
≤ 14%	86	49	37	
> 14%	49	18	31	

expression was upregulated in TNBC tissues ($P<0.001$, Fig. 1A). Further, the higher AC093850.2 expression was observed in TNBC cell lines (BT549, MDA-MB-231, and HCC1937) as shown in Fig. 1B ($P<0.01$). The expression of AC093850.2 in other subtypes of breast cancer cells was measured. The expression of AC093850.2 was also increased in other subtypes of breast cancer (SKBR3, MCF7, BT474) ($P<0.01$, Supplementary Fig. 1 at <https://ojs.ptbioch.edu.pl/index.php/abp/>), but not as high as that in TNBC cells except for SKBR3 cell.

The χ^2 test was used to evaluate whether the expression of AC093850.2 was associated with the clinical characteristics of TNBC patients. The results in Table 1 indicated that high expression of AC093850.2 was related to the aggressive characteristics of TNBC, including positive lymph node metastasis ($P=0.007$), advanced TNM stage ($P=0.001$), larger tumor size ($P=0.048$), and high Ki67 level ($P=0.024$). The data suggest that AC093850.2 was potentially associated with a higher risk of disease, which may be correlated with patients' survival. The clinical analysis verified high AC093850.2 expression in correlation with poor survival data of pa-

tients with TNBC (log-rank $P=0.017$, Fig. 1C). These results revealed that AC093850.2 upregulation may participate in the progression of TNBC and be potentially a valuable prognostic predictor for this disease. Moreover, multivariate Cox regression analysis included clinical characteristics and AC093850.2 expression in the evaluation of prognostic-related risk factors in TNBC. The results in Table 2 revealed that age and pathological stage were not independent risk factors for prognosis of patients, while AC093850.2 expression, tumor size, lymph node metastasis, TNM stage, and Ki67 were independent risk factors for the shorter prognosis of TNBC patients.

LncRNA AC093850.2 targeted miR-4299 and regulated its expression

Bioinformatics prediction (LncBase Predicted v.2) showed that AC093850.2 could potentially bind to several miRNAs, including miR-4299. Among these miRNAs, miR-4299 expression was found to be increased in AC093850.2-knockdown TNBC cells, as shown in Fig. 2A ($P<0.001$). The targeting relationship between AC093850.2 and miR-4299 was displayed in Fig. 2B.

Table 2. Multivariate Cox analysis of factors for survival of TNBC patients

Variables	Multivariate Cox analysis		
	HR	95%CI	P value
AC093850.2 expression (low vs high)	0.226	0.060–0.846	0.027
Age (≤50 vs >50 years)	0.447	0.160–1.246	0.124
Tumor size (≤2 vs >2 cm)	0.202	0.044–0.920	0.039
Pathological stage (I–II vs III)	0.449	0.149–1.349	0.154
Lymph node metastasis (Negative vs Positive)	0.177	0.036–0.865	0.032
TNM stage (I–II vs III)	0.269	0.083–0.870	0.028
Ki67 (≤14% vs >14%)	0.305	0.099–0.939	0.039

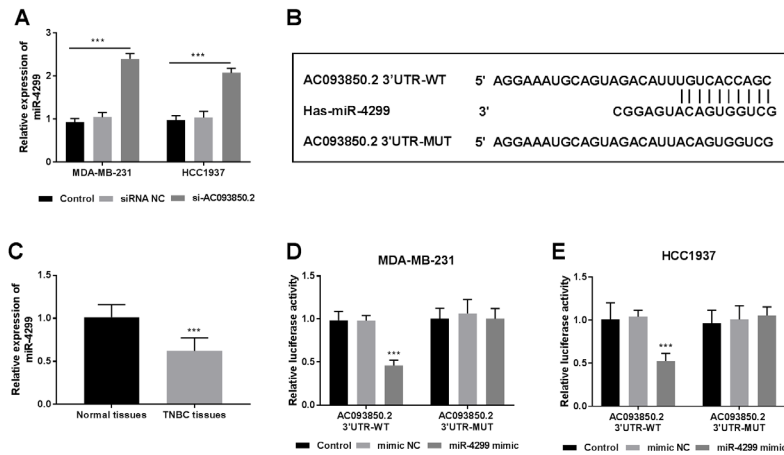


Figure 2. AC093850.2 directly binds to miR-4299 in TNBC cells.

(A) miR-4299 was increased in AC093850.2 silenced cells. *** $P < 0.001$. (B) Sequencing alignment showed putative binding sites between AC093850.2 and miR-4299. (C) The expression of miR-4299 was detected using RT-qPCR in TNBC tissues. *** $P < 0.001$. (D) Overexpression of miR-4299 decreased relative luciferase activity of AC093850.2-WT but not AC093850.2-MUT in MDA-MB-231 cells. *** $P < 0.001$. (E) Increased expression of miR-4299 reduced relative luciferase activity of AC093850.2-WT but not AC093850.2-MUT in HCC1937 cells. *** $P < 0.001$.

Whereafter, the downregulation of miR-4299 expression in TNBC tissues was observed compared with that in normal tissues ($P < 0.001$, Fig. 2C). The dual-luciferase reporter assay validated the binding relationship between AC093850.2 and miR-4299 and the results demonstrated that the luciferase activity of cells co-transfected with AC093850.2-WT and miR-4299 mimic was decreased ($P < 0.001$), while no significant changes were observed in cells co-transfected with AC093850.2-MUT and miR-4299 mimic (Fig. 2D and 2E). The above results revealed that AC093850.2 targeted and regulated the expression of miR-4299.

Silence of AC093850.2 weakened cell proliferation possibly by regulating miR-4299

After transfection, downregulation of AC093850.2 by si-AC093850.2 reached more than 200% in cells of

both TNBC cell lines ($P < 0.001$, Fig. 3A). Silence of AC093850.2 led to the increased expression of miR-4299 in both cell lines, while downregulation of miR-4299 restrained the increased levels of miR-4299 by si-AC093850.2 ($P < 0.001$, Fig. 3A).

Results of cell proliferation experiments indicated that silencing AC093850.2 inhibited proliferation abilities, while knockdown of miR-4299 reversed the inhibitory effect of si-AC093850.2 on the proliferation of cancer cells ($P < 0.05$, Fig. 3B).

Influence of knockdown of AC093850.2 on cellular migration and invasion activities by regulating miR-4299

Following the above cellular experiments, Transwell assays were performed to evaluate the influence of si-AC093850.2 on cell migration and invasion capacities. Silencing of AC093850.2 expression effectively inhibited the migration of cells ($P < 0.001$), whereas the im-

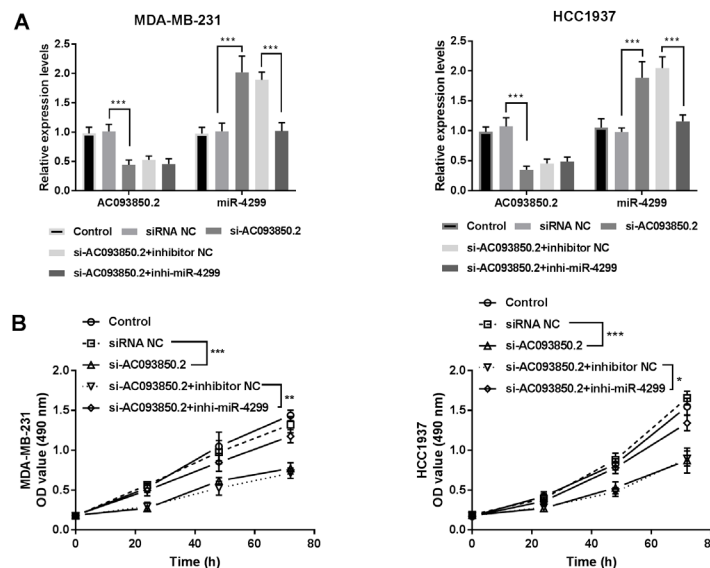


Figure 3. AC093850.2 acts as a ceRNA that regulate cell proliferation by sponging miR-4299.

(A) RT-qPCR analysis of AC093850.2 or miR-4299 expression in MDA-MB-231 and HCC1937 cells after transfection. *** $P < 0.001$. (B) The proliferation abilities were inhibited by the knockdown of AC093850.2 while reversed by the silence of miR-4299. *** $P < 0.001$.

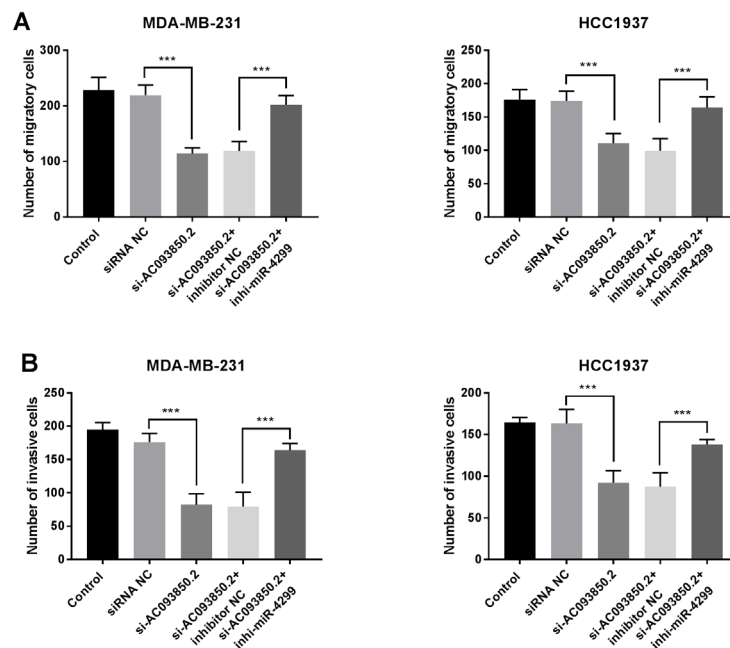


Figure 4. Downregulation of miR-4299 reverses the inhibition of migration and invasion potential in TNBC cells induced AC093850.2 silencing.

(A) A Transwell migration assay was conducted to determine the effects of AC093850.2/miR-4299 knockdown on cell migration. *** $P < 0.001$. (B) Transwell invasion assay was performed to measure the effects of AC093850.2/miR-4299 silencing on cell invasion capacities. *** $P < 0.001$.

pact of knockdown of AC093850.2 was reversed by a miR-4299 inhibitor ($P < 0.001$, Fig. 4A). Similar results were observed in invasion assays ($P < 0.001$, Fig. 4B). These data suggest that AC093850.2 interference is a towards strategy to prevent TNBC progression by targeting miR-4299.

DISCUSSION

TNBC is difficult to cure, easy to relapse, and has a high metastasis rate, which has become a major problem in the treatment of breast cancer. Hence, exploring novel prognostic and therapeutic targets is extremely important for improving clinical strategies and outcomes for TNBC patients. Growing studies suggest that lncRNAs involved in tumor prognosis and progression have been identified (Huang *et al.*, 2021; Volovat *et al.*, 2020). For instance, lncRNA HAGLR (Jin *et al.*, 2021), CARMN (Sheng *et al.*, 2021), and Uc003xsl.1 (Xu *et al.*, 2022) were involved in the tumor progression of TNBC and were associated with patients' prognosis. In this study, we clarified the expression levels of AC093850.2 that were remarkably increased in TNBC tissues compared with corresponding paracancerous normal tissues. Similarly, the expression pattern of AC093850.2 was observed in TNBC cell lines. These results speculated that AC093850.2 may be involved in the regulation of the malignant evolution of TNBC. Interestingly, a high expression of AC093850.2 was observed in an HER-positive breast cancer cell line (SKBR3 cell), which imply that AC093850.2 may not have an actual impact only on TNBC. In this study, we mainly investigated the role of AC093850.2 in TNBC.

To further investigate the association between AC093850.2 and the clinical properties of TNBC, the clinicopathological characteristics of patients were gathered and statistically analyzed. The expression of

AC093850.2 affected the tumor size, lymph node metastasis, TNM stage, and Ki67 of TNBC patients. However, TNBC is regulated by a variety of lncRNAs or other genes, and the expression levels of different lncRNAs in TNBC are not the same, and the relationship with the clinical characteristics of TNBC is not the same. For instance, serum lncRNA SUMO1P3 levels were related to positive lymphovascular invasion, lymph node metastasis, or high grade, but not related to tumor size (Na-Er *et al.*, 2021). Herein, further survival analysis revealed that TNBC patients with high AC093850.2 expression had a poor survival outcome. Multivariate Cox regression analysis revealed that AC093850.2 expression is a risk factor for the overall survival of TNBC patients. The clinical prognostic significance of AC093850.2 was reported in esophageal squamous cell carcinoma (Huang *et al.*, 2018). A previous differently identifying RNA expression profiles study indicated that AC093850.2 has a prognostic value for breast cancer (Zhang *et al.*, 2019). Similarly, results in this study validated the prognostic value of AC093850.2 in TNBC using a bunch of TNBC patients. Therefore, AC093850.2 may be an independent prognostic factor for TNBC.

lncRNAs could act as a competitive endogenous RNA to regulate miRNA function. For instance, lncRNA XLOC-006390 as a ceRNA facilitates cervical cancer tumorigenesis by inhibiting miR-331-3p and miR-338-3p (Luan & Wang, 2018). The expression of lncRNA PCED1B-AS1 expression is increased in colorectal adenocarcinoma tissues and knockdown of PCED1B-AS1 suppresses tumor progression by sponging miR-633 (Liu *et al.*, 2022). In this study, we used an online database to identify miRNAs with AC093850.2 binding sites, which showed a binding relationship between miR-4299 and AC093850.2. The expression of miR-4299 was increased in AC093850.2-silenced tumor cells. We also observed that AC093850.2 functions as a sponge for miR-4299 in

TNBC. We also observed that miR-4299 expression was downregulated in TNBC tumor tissues. These data revealed that lncRNA AC093850.2 may act as a ceRNA to regulate tumor progression of TNBC by inhibiting miR-4299 expression.

The role of lncRNAs in tumorigenesis and progression has been widely investigated. Further cellular experiments were conducted to explore the influence of AC093850.2/miR-4299 on the cellular activities of TNBC cells. miR-4299 was downregulated in non-small cell lung cancer tissues and restrained tumor cell proliferation, migration, and invasion by modulating the activation of the PTEN/AKT/PI3K signaling pathway (Yang *et al.*, 2018). The expression of miR-4299 was also decreased in follicular thyroid carcinoma cells and could mediate the invasive properties by targeting ST6 (alpha-N-acetyl-neuraminyl-2,3-beta-galactosyl-1,3)-N-acetyl-galactosaminide alpha-2,6-sialyltransferase 4 (ST6GALNAC4) (Miao *et al.*, 2016). The current results revealed that knockdown of AC093850.2 restrained cell viability and migration of TNBC cells, whereas the impact of AC093850.2 knockdown was recovered by miR-4299 inhibitor, indicating that AC093850.2 interference is a towards strategy to impede TNBC progression by targeting miR-4299.

There are some limitations of this study. This study mainly investigated the role of AC093850.2 in TNBC, but its impact on other subtypes of breast cancer remains to be explored. In future studies, other subtypes of breast cancer patients will be enrolled to explore the clinical role of AC093850.2 in other subtypes of breast cancer. On the other hand, the detailed mechanism of AC093850.2 in TNBC needs to be investigated in the future.

In general, lncRNA AC093850.2 was elevated in TNBC tissues and related to patients' prognosis. AC093850.2/miR-4299 suggests crosstalk between lncRNA and miRNA that might drive TNBC progression. This crosstalk between AC093850.2 and miR-4299 may reveal the mechanism of AC093850.2 in TNBC, which may be a potential target for TNBC treatment and prognosis prediction.

REFERENCES

- Anastasiadou E, Jacob LS, Slack FJ (2018) Non-coding RNA networks in cancer. *Nat Rev Cancer* **18**: 5–18. <https://doi.org/10.1038/nrc.2017.99>
- Azamjah N, Soltan-Zadeh Y, Zayeri F (2019) Global trend of breast cancer mortality rate: A 25-year study. *Asian Pac J Cancer Prev* **20**: 2015–2020. <https://doi.org/10.31557/apjcp.2019.20.7.2015>
- Barreca M M, Zichittella C, Alessandro R (2021) Hypoxia-induced non-coding RNAs controlling cell viability in cancer. *Int J Mol Sci* **22**: 1857. <https://doi.org/10.3390/ijms22041857>
- Cappetta M, Fernandez L, Brignoni L, Artagaveytia N, Bonilla C, López M, Esteller M, Bertoni B, Berdasco M (2021) Discovery of novel DNA methylation biomarkers for non-invasive sporadic breast cancer detection in the Latino population. *Mol Oncol* **15**: 473–486. <https://doi.org/10.1002/1878-0261.12842>
- Huang GW, Xue YJ, Wu ZY, Xu XE, Wu JY, Cao HH, Zhu Y, He JZ, Li CQ, Li EM, Xu LY (2018) A three-lncRNA signature predicts overall survival and disease-free survival in patients with esophageal squamous cell carcinoma. *BMC Cancer* **18**: 147. <https://doi.org/10.1186/s12885-018-4058-6>
- Huang Y, Wang X, Zheng Y, Chen W, Zheng Y, Li G, Lou W, Wang X (2021) Construction of an mRNA-miRNA-lncRNA network prognostic for triple-negative breast cancer. *Aging (Albany NY)* **13**: 1153–1175. <https://doi.org/10.18632/aging.202254>
- Jin L, Luo C, Wu X, Li M, Wu S, Feng Y (2021) LncRNA-HAGLR motivates triple negative breast cancer progression by regulation of WNT2 via sponging miR-335-3p. *Aging (Albany NY)* **13**: 19306–19316. <https://doi.org/10.18632/aging.203272>
- Kim MY (2021) Breast cancer metastasis. *Adv Exp Med Biol* **1187**: 183–204. https://doi.org/10.1007/978-981-32-9620-6_9
- Li T, Mello-Thoms C, Brennan PC (2016) Descriptive epidemiology of breast cancer in China: incidence, mortality, survival and prevalence. *Breast Cancer Res Treat* **159**: 395–406. <https://doi.org/10.1007/s10549-016-3947-0>
- Liu J, Qian J, Mo Q, Tang L, Xu Q (2022) Long non-coding RNA PCED1B-AS1 promotes the proliferation of colorectal adenocarcinoma through regulating the miR-633/HOXA9 axis. *Bioengineered* **13**: 5407–5420. <https://doi.org/10.1080/21655979.2022.2037225>
- Luan X, Wang Y (2018) LncRNA XLOC_006390 facilitates cervical cancer tumorigenesis and metastasis as a ceRNA against miR-331-3p and miR-338-3p. *J Gynecol Oncol* **29**: e95. <https://doi.org/10.3802/jgo.2018.29.e95>
- Matsui M, Corey DR (2017) Non-coding RNAs as drug targets. *Nat Rev Drug Discov* **16**: 167–179. <https://doi.org/10.1038/nrd.2016.117>
- Miao X, Jia L, Zhou H, Song X, Zhou M, Xu J, Zhao L, Feng X, Zhao Y (2016) miR-4299 mediates the invasive properties and tumorigenicity of human follicular thyroid carcinoma by targeting ST6GALNAC4. *IUBMB Life* **68**: 136–144. <https://doi.org/10.1002/iub.1467>
- Mori T, Ngouy H, Hayashida M, Akutsu T, Nacher JC (2018) ncRNA-disease association prediction based on sequence information and tripartite network. *BMC Syst Biol* **12**: 37. <https://doi.org/10.1186/s12918-018-0527-4>
- Müller V, Oliveira-Ferrer L, Steinbach B, Pantel K, Schwarzenbach H (2019) Interplay of lncRNA H19/miR-675 and lncRNA NEAT1/miR-204 in breast cancer. *Mol Oncol* **13**: 1137–1149. <https://doi.org/10.1002/1878-0261.12472>
- Na-Er A, Xu YY, Liu YH, Gan YJ (2021) Upregulation of serum exosomal SUMO1P3 predicts unfavorable prognosis in triple negative breast cancer. *Eur Rev Med Pharmacol Sci* **25**: 154–160. <https://doi.org/10.26355/eurrev.202101.24379>
- Panni S, Lovering RC, Porras P, Orchard S (2020) Non-coding RNA regulatory networks. *Biochim Biophys Acta Gene Regul Mech* **1863**: 194417. <https://doi.org/10.1016/j.bbaggm.2019.194417>
- Qiu M, Xu Y, Wang J, Zhang E, Sun M, Zheng Y, Li M, Xia W, Feng D, Yin R, Xu L (2015) A novel lncRNA, LUADT1, promotes lung adenocarcinoma proliferation via the epigenetic suppression of p27. *Cell Death Dis* **6**: e1858. <https://doi.org/10.1038/cddis.2015.203>
- Rojas K, Stuckey A (2016) Breast cancer epidemiology and risk factors. *Clin Obstet Gynecol* **59**: 651–672. <https://doi.org/10.1097/grf.0000000000000239>
- Romano G, Veneziano D, Acunzo M, Croce CM (2017) Small non-coding RNA and cancer. *Carcinogenesis* **38**: 485–491. <https://doi.org/10.1093/carcin/bgx026>
- Schmitt AM, Chang HY (2016) Long noncoding RNAs in cancer pathways. *Cancer Cell* **29**: 452–463. <https://doi.org/10.1016/j.ccell.2016.03.010>
- Sheng X, Dai H, Du Y, Peng J, Sha R, Yang F, Zhou L, Lin Y, Xu S, Wu Y, Yin W, Lu J (2021) LncRNA CARMN overexpression promotes prognosis and chemosensitivity of triple negative breast cancer via acting as miR143-3p host gene and inhibiting DNA replication. *J Exp Clin Cancer Res* **40**: 205. <https://doi.org/10.1186/s13046-021-02015-4>
- Su T, Wang T, Zhang N, Shen Y, Li W, Xing H, Yang M (2022) Long non-coding RNAs in gastrointestinal cancers: Implications for protein phosphorylation. *Biochem Pharmacol* **197**: 114907. <https://doi.org/10.1016/j.bcp.2022.114907>
- Sun YS, Zhao Z, Yang ZN, Xu F, Lu HJ, Zhu ZY, Shi W, Jiang J, Yao PP, Zhu HP (2017) Risk Factors and Preventions of Breast Cancer. *Int J Biol Sci* **13**: 1387–1397. <https://doi.org/10.7150/ijbs.21635>
- Volovat SR, Volovat C, Hordila I, Hordila DA, Mirestean CC, Miron OT, Lungulescu C, Scripcariu DV, Stolniceanu CR, Konsoulova-Kirova AA, Grigorescu C, Stefanescu C, Volovat CC, Augustin I (2020) MiRNA and LncRNA as potential biomarkers in triple-negative breast cancer: a review. *Front Oncol* **10**: 526850. <https://doi.org/10.3389/fonc.2020.526850>
- Wang H, Huo X, Yang XR, He J, Cheng L, Wang N, Deng X, Jin H, Wang N, Wang C, Zhao F, Fang J, Yao M, Fan J, Qin W (2017) STAT3-mediated upregulation of lncRNA HOXD-AS1 as a ceRNA facilitates liver cancer metastasis by regulating SOX4. *Mol Cancer* **16**: 136. <https://doi.org/10.1186/s12943-017-0680-1>
- Xu Y, Ren W, Li Q, Duan C, Lin X, Bi Z, You K, Hu Q, Xie N, Yu Y, Xu X, Hu H, Yao H (2022) LncRNA Uc003xsl.1-mediated activation of the NFκB/IL8 axis promotes progression of triple-negative breast cancer. *Cancer Res* **82**: 556–570. <https://doi.org/10.1158/0008-5472.can-21-1446>
- Yang WB, Zhang WP, Shi JL, Wang JW (2018) MiR-4299 suppresses non-small cell lung cancer cell proliferation, migration and invasion through modulating PTEN/AKT/PI3K pathway. *Eur Rev Med Pharmacol Sci* **22**: 3408–3414. <https://doi.org/10.26355/eurrev.201806.15163>
- Yang Y, Yujiao W, Fang W, Linhui Y, Ziqi G, Zhichen W, Zirui W, Shengwang W (2020) The roles of miRNA, lncRNA and circRNA in the development of osteoporosis. *Biol Res* **53**: 40. <https://doi.org/10.1186/s40659-020-00309-z>

- Yin L, Duan JJ, Bian XW, Yu SC (2020) Triple-negative breast cancer molecular subtyping and treatment progress. *Breast Cancer Res* **22**: 61. <https://doi.org/10.1186/s13058-020-01296-5>
- Zhang Q, Li T, Wang Z, Kuang X, Shao N, Lin Y (2020) lncRNA NR2F1-AS1 promotes breast cancer angiogenesis through activating IGF-1/IGF-1R/ERK pathway. *J Cell Mol Med* **24**: 8236–8247. <https://doi.org/10.1111/jcmm.15499>
- Zhang X, Zhuang J, Liu L, He Z, Liu C, Ma X, Li J, Ding X, Sun C (2019) Integrative transcriptome data mining for identification of core lncRNAs in breast cancer. *PeerJ* **7**: e7821. <https://doi.org/10.7717/peerj.7821>
- Zhao Z, Sun W, Guo Z, Zhang J, Yu H, Liu B (2020) Mechanisms of lncRNA/microRNA interactions in angiogenesis. *Life Sci* **254**: 116900. <https://doi.org/10.1016/j.lfs.2019.116900>

Ellagic acid inhibits cell proliferation, migration, and invasion of anaplastic thyroid cancer cells *via* the Wnt/ β -catenin and PI3K/Akt pathways

Xianglong Meng^{1#}, Zhihua Cui^{2#}, Hui Shi^{2#}, Xiaoru Ma³, Wanru Li³, Xianjun Liu^{3✉} and Yang Jiang^{4✉}

¹Department of Burns Surgery, the First Hospital of Jilin University, Changchun 130000, China; ²Department of Ophthalmology, the First Hospital of Jilin University, Changchun 130000, China; ³College of Food Engineering, Jilin Engineering Normal University, Changchun 130000, China; ⁴Department of Gastrointestinal Colorectal and Anal Surgery, the China-Japan Union Hospital of Jilin University, Changchun 130000, China

Anaplastic thyroid cancer (ATC) is a rare but lethal human malignant cancer with no known cure. Ellagic acid (EA), a natural plant extract, has shown antitumor activity against multiple cancers; however, its effects on the malignant phenotypes of ATC cells remain unknown. This study aimed to evaluate the effects of EA on proliferation, migration, and invasion of ATC cells and further explore the associated signaling mechanisms. The normal human thyroid cell line Nthy-ori3-1 and ATC cell line BHT-101 were used. Cytotoxicity assay was performed using the Cell Counting kit-8 (CCK-8) assay. Cell proliferation, migration, and invasion assays were performed using the CCK-8 and colony formation, wound healing, and Transwell invasion assays, respectively. Western blotting was used to detect the levels of related proteins. β -catenin nuclear protein levels were measured to evaluate the Wnt/ β -catenin pathway. The phosphorylation level of the Akt protein was measured and calculated to evaluate the PI3K/Akt pathway. LiCl and IGF-1 were used as pathway agonists to determine the involvement of the corresponding pathway. The results showed that EA inhibited the proliferation, migration, and invasion of ATC cells. Furthermore, both the Wnt/ β -catenin and PI3K/Akt pathways were suppressed by EA treatment, and activation of these two pathways reversed the EA-induced inhibition of the pathological phenotypes of ATC cells. These findings demonstrate that EA inhibits proliferation, migration, and invasion of ATC cells by suppressing the Wnt/ β -catenin and PI3K/Akt pathways, suggesting that EA is a potential drug candidate for treating ATC and provides a theoretical basis for further *in vivo* experiments and clinical applications.

Key words: ellagic acid, anaplastic thyroid cancer, cell behaviors, Wnt/ β -catenin pathway, PI3K/Akt pathway

Received: 10 April, 2022; **revised:** 15 October, 2022; **accepted:** 19 October, 2022; **available on-line:** 11 February, 2023

✉ e-mail: jiangyang@jlu.edu.cn (YJ); liuxianjun@jleu.edu.cn (XL)

#Xianglong Meng, Zhihua Cui, and Hui Shi contributed equally to this work

Acknowledgments of Financial Support: This study was supported by Jilin Provincial Science and Technology Department (no. 20200201509JC, no. 20200201430JC and no. 20220202076NC), Jilin Provincial Development and Reform Commission (no. 2021C043-9), Jilin Provincial Education Department (no. JJKH20220194KJ), the Bethune Plan Research Project of Jilin University (no. 2018B26), and the PhD Research Project of Jilin Engineering Normal University (no. BSKJ201923).

Abbreviations: ATC, Anaplastic thyroid cancer; CCK-8, Cell Counting kit-8; EA, Ellagic acid

INTRODUCTION

Thyroid cancer is the most common malignant endocrine tumor with an increasing incidence worldwide every year (Hsu *et al.*, 2014; Haymart, 2021). Anaplastic thyroid cancer (ATC), also known as undifferentiated thyroid cancer, is a rare subtype of thyroid cancer. Although this subtype accounts for 1–2% of all thyroid cancers, it is the most lethal subtype (Molinaro *et al.*, 2017). Unfortunately, there is currently no effective treatment for ATC. Previous studies have shown that traditional cancer treatments, including surgery, chemotherapy and radiotherapy, do not significantly improve the prognosis of ATC patients (Tuttle *et al.*, 2017; Tiedje *et al.*, 2018). Therefore, it is important to explore novel ATC treatment strategies. Attenuation of proliferation, migration, and invasion of ATC cells is considered an effective strategy for suppressing the development of ATC.

Ellagic acid (EA) (molecular formula $C_{14}H_6O_8$; Fig. 1A) is a natural polyphenolic compound and dimeric gallic acid derivative that is widely distributed in various fruits and nuts. EA possesses a wide range of biological activities, including antioxidant, antiviral, and antitumor activities (Shakeri *et al.*, 2018). In the field of antitumor therapy, EA has been reported to exert inhibitory effects on various cancers, such as colorectal, breast, and prostate cancers (Ceci *et al.*, 2018). Additionally, in our previous study, we demonstrated that EA inhibited the proliferation and migration of hypertrophic scar fibroblasts (Liu *et al.*, 2021). However, the role of EA in ATC remains unclear.

The canonical Wnt/ β -catenin and PI3K/Akt pathways play key roles in tumor development. Unphosphorylated β -catenin enters the nucleus and initiates the transcription of downstream target genes; the nuclear β -catenin level represents the activation level of the Wnt/ β -catenin pathway (Rao & Kühl, 2010). Akt is a key molecule involved in the PI3K/Akt pathway, and its phosphorylation level represents the activation level of this pathway (Jiang *et al.*, 2020). Aberrant activation of the Wnt/ β -catenin and PI3K/Akt pathways is associated with ATC progression (Saji & Ringel, 2010; Sastre-Perona & Santesteban, 2012; Jiang *et al.*, 2022; Zhang *et al.*, 2022).

In this study, we evaluated the effects of EA on proliferation, migration, and invasion of ATC cells. Furthermore, we investigated whether Wnt/ β -catenin and PI3K/Akt signaling pathways are involved in EA-induced regulation.

MATERIALS AND METHODS

Cells culture

The normal human thyroid cell line Nthy-ori3-1 (cat. no. CTCC-003-0031) was obtained from Meisen Cell (Zhejiang, China), and ATC cell line BHT-101 (cat. no. BNCC359868) was obtained from the BeNa Culture Collection (Beijing, China). Both cell lines were cultured in Roswell Park Memorial Institute (RPMI) 1640 medium containing 10% fetal bovine serum (FBS) and 1% penicillin/streptomycin at 37°C with 5% CO₂. All cell culture reagents were purchased from Gibco (Thermo Fisher Scientific, MA, USA).

Antibodies and drugs

The primary antibodies used for western blotting were as follows: anti- β -catenin (1:5000, cat. no. ab32572; Abcam, Cambridge, UK), anti-Histone H3 (1:2000, cat. no. ab1791; Abcam), anti-phospho-pan-Akt (1:500; cat. no. AF0016; Affinity, OH, USA), anti-pan-Akt (1:500; cat. no. AF6261; Affinity), and anti- β -actin (1:2000; 60008-1-Ig; Proteintech, IL, USA). The secondary antibodies (1:5000; goat anti-mouse cat. no. SA00001-1, goat anti-rabbit cat. no. SA00001-2; Proteintech) were used for western blotting analysis. EA (cat. no. B21073; Yanyang Biotech, Shanghai, China) was dissolved in 1 M NaOH. The final concentration of NaOH was $\leq 0.1\%$ (v/v), which did not induce toxicity (Duan *et al.*, 2019). Lithium chloride (LiCl) (cat. no. L9650; Sigma-Aldrich, MO, USA), an agonist of the Wnt/ β -catenin pathway, was dissolved in sterile double-distilled water and used at a concentration of 25 mM. Recombinant human insulin-like growth factor-1 (IGF-1) protein (cat. no. 291-G1; R&D Systems, MN, USA), an agonist of the PI3K/Akt pathway, was dissolved in RPMI 1640 and used at a concentration of 100 ng/mL.

Cytotoxicity assay

The Cell Counting kit (CCK-8) assay was used to perform the cytotoxicity assay. The assay was performed as previously described (Liu *et al.*, 2021). Briefly, cells were seeded at a density of 5×10^4 cells per well in a 96-well plate ($n=3$). After cell attachment, the cells were treated with varied concentrations of EA (0–160 μ M). After treatment for 24 hours, 10 μ L of CCK-8 (cat. no. 40203ES60; Yeasen, Shanghai, China) reagent was added to each well. After incubation for 2 hours at 37°C, the absorbance was measured at 450 nm wavelength using a microplate reader (Thermo Fisher Scientific, MA, USA). The results were expressed as cell survival rates. Cell survival rate (%) = (OD value of treated group – OD value of blank)/(OD value of control group – OD value of blank) $\times 100$.

Proliferation assay

A CCK-8 assay was used to assess cell proliferation. BHT-101 cells were seeded at 5×10^3 cells per well in a 96-well plate ($n=3$), and the OD values were measured at 24, 48, and 72 h after treatment according to the experimental requirements. In addition, the OD value detection method was the same as that of the cytotoxicity assay. The results are expressed as OD values.

A plate colony formation assay was performed to assess cell proliferation. BHT-101 cells were seeded in 12-well plates ($n=3$) at a density of 200 cells/well. After incubation for 12 days at 37°C, colonies were fixed with

4% paraformaldehyde (cat. no. P1110; Solarbio, Beijing, China) for 20 min at room temperature and stained with 0.5% crystal violet stain solution (cat. no. 60506ES60; Yeasen) for 10 min at room temperature, and the number of colonies was counted using ImageJ software (version 1.51w).

Migration assay

A wound healing assay was used to assess cell migration. This assay was performed as previously described (Liu *et al.*, 2021). Briefly, BHT-101 cells were cultured in a 12-well plate ($n=3$) with RPMI 1640 containing 10% FBS until the cell confluence reached 100%. A scratch wound was made in the middle of each well using a 200- μ L pipette tip. The culture medium was then replaced with serum-free RPMI 1640 medium. At 0 and 24 h after scratching, images were captured in five random fields of view using an inverted light microscope (magnification 100 \times ; Olympus Corporation, Tokyo, Japan). The wound area was measured using ImageJ software. The results were expressed as migration rates. Migration rate (%) = (initial wound area – wound area at 24 h)/initial wound area $\times 100$.

Transwell invasion assay

Transwell invasion assay was used to assess cell invasion. Transwell plates (24-well, 8 μ m; Labgic, Beijing, China) were pre-coated with Matrigel (BD Biosciences, CA, USA) for 30 min at 37°C. BHT-101 cells were seeded in the upper chambers of Transwell plates ($n=3$) at a density of 5×10^4 cells/well and incubated in serum-free RPMI 1640 medium. The lower chambers were supplied with a culture medium containing 10% FBS. After 48 h, non-invading cells on the upper face of the membrane were removed with a cotton swab, and the invaded cells were fixed with 4% paraformaldehyde for 20 min at room temperature and stained with 0.5% crystal violet stain solution for 10 min. Images were captured in five random fields of view using an inverted light microscope (magnification 200 \times). The number of cells was counted using ImageJ software.

Western blotting

Western blotting was used to assess protein expression levels. The harvested cells were processed using a nuclear and cytoplasmic protein extraction kit (cat. no. P0028; Beyotime, Shanghai, China) to extract nucleoproteins and RIPA lysis buffer (cat. no. 9806S; CST, MA, USA) to extract the total protein. Western blotting was performed to detect the levels of β -catenin and Histone H3 (loading control) in nucleoprotein, and total Akt (t-Akt), phosphorylated Akt (p-Akt), and β -actin (loading control) in total protein, as described previously (Liu *et al.*, 2021). Samples were separated using 10% SDS-PAGE gels, and subsequently electro-transferred to PVDF membranes (Millipore, MA, USA) for immunoblotting analysis. After incubation with primary antibodies, the membranes were incubated with the corresponding secondary antibodies. Protein chemiluminescence was detected using the Super ECL Detection Reagent (cat. no. 36208ES60; Yeasen) using a KETA GL Imaging System (Wealtec, NV, USA), and the gray values of the bands were quantified using ImageJ software.

Statistical analysis

The quantified data are presented as mean \pm standard deviation (S.D.). The data were assessed for normality

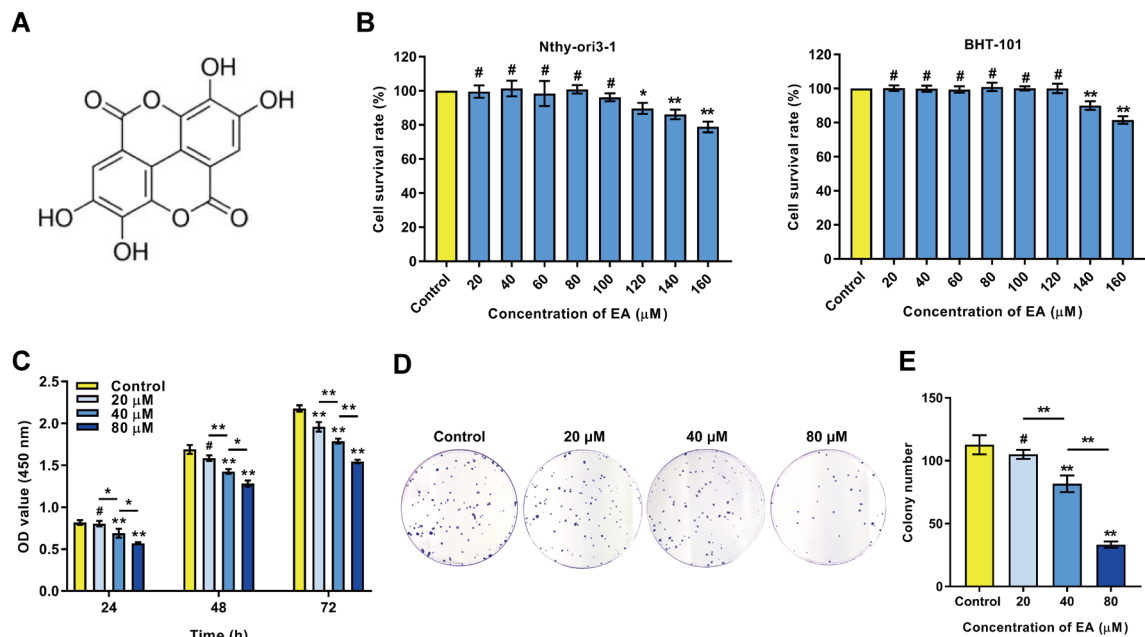


Figure 1. Effect of EA on the proliferation of ATC cells.

(A) The structural formula of EA. (B) Cytotoxicity assay of EA in Nthy-ori3-1 and BHT-101 cells was performed using the CCK-8 assay. The effect of EA on the proliferation of ATC cells was detected by the CCK-8 assay at the indicated time points and colony formation assay. (C) CCK-8 assay results. (D) Colony formation assay. (E) Histogram of the colony number in each group. Untreated cells (0 μM) were used as control. Data are expressed as mean ± S.D.; #*P* > 0.05, **P* < 0.05 and ***P* < 0.01.

using the Shapiro-Wilk test and were analyzed by one-way ANOVA followed by post hoc Dunnett's or Sidak test using the GraphPad Prism (version 7.03) statistical package. A *P*-value of <0.05 indicated a statistically significant difference.

RESULTS

Effect of EA on the proliferation of ATC cells

To determine the appropriate concentration of EA for use in ATC cells, we performed a cytotoxicity assay for EA on Nthy-ori3-1 cells, a normal human thyroid cell line, using the CCK-8 assay. The results showed that EA did not cause significant cytotoxicity in normal cells at a concentration ≤100 μM, which suggested the concentration range used in the following experiments (Fig. 1B). We also examined the cytotoxicity of EA in BHT-101 cells, an ATC cell line, and found that ATC cells were more tolerogenic (Fig. 1B). Next, we evaluated the ef-

fect of EA on ATC cell proliferation using CCK-8 and colony formation assays. As shown in Fig. 1C, ATC cell viability was significantly reduced in the EA-treated group (40 or 80 μM) at all time points. Notably, as the concentration of EA increased, cell viability significantly decreased. Additionally, the results of the colony formation assay showed that the colony number of ATC cells in the EA-treated group (40 or 80 μM) was significantly lower than that in the control group (0 μM), and a higher EA concentration resulted in lower colony number (Fig. 1D and 1E), which exhibited a similar trend to the CCK-8 assay. These data indicated that EA inhibited the proliferation of ATC cells in a dose-dependent manner.

Effect of EA on the migration of ATC cells

To evaluate the effect of EA on ATC cell migration, we performed a wound healing assay. As shown in Fig. 2A and 2B, the migration rate of ATC cells from the treated group (40 or 80 μM) was significantly lower than that of the control group (0 μM). As the concentra-

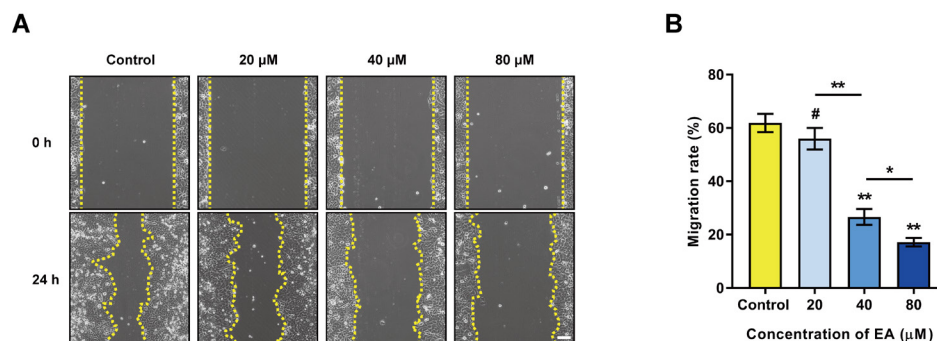


Figure 2. Effect of EA on the migration of ATC cells.

(A) The effect of EA on the migration of ATC cells was detected by the wound healing assay (yellow dashed lines denote the wound edge; scale bar = 100 μm). (B) Histogram of the migration rate of ATC cells in each group. Untreated cells (0 μM) were used as control. Data are expressed as mean ± S.D.; #*P* > 0.05, **P* < 0.05 and ***P* < 0.01.

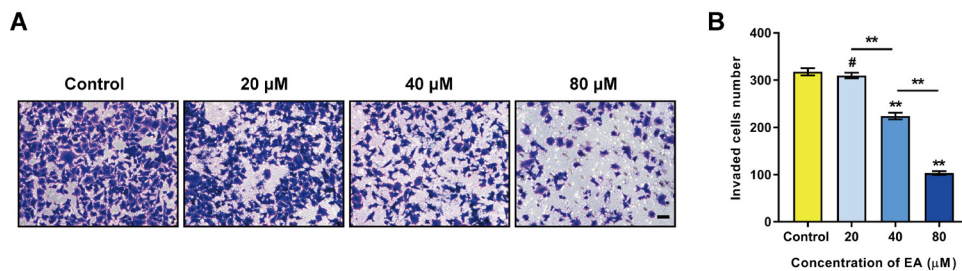


Figure 3. Effect of EA on the invasion of ATC cells.

(A) The effect of EA on the invasion of ATC cells was detected by the Transwell invasion assay (scale bar = 50 μm). (B) Histogram of the number of invaded ATC cells in each group. Untreated cells (0 μM) were used as control. Data are expressed as mean ± S.D.; * $P > 0.05$ and ** $P < 0.01$.

tion of EA increased, the migration rate of ATC cells decreased. These data indicated that EA inhibited the migration of ATC cells in a dose-dependent manner.

Effect of EA on the invasion of ATC cells

To evaluate the effect of EA on the invasion of ATC cells, we performed the Transwell invasion assay to assess cell invasion ability. As shown in Fig. 3A and 3B, the number of invaded ATC cells in the treated group (40 or 80 μM) was significantly lower than that in the control group (0 μM). With an increase in EA concentration, the invasion of ATC cells decreased. These data indicated that EA inhibited the invasion of ATC cells in a dose-dependent manner.

Role of Wnt/β-catenin pathway in EA-induced regulation of ATC cells

We further investigated the role of the Wnt/β-catenin pathway in EA-induced inhibition of ATC cells. First, we evaluated the effect of EA (80 μM) on this signaling pathway in ATC cells. The nucleoprotein level of β-catenin, a marker of the Wnt/β-catenin signaling pathway, was examined by western blotting. As shown in Fig. 4A, EA treatment significantly reduced the level of β-catenin, suggesting that EA inhibited the Wnt/β-catenin pathway in ATC cells. Next, we used LiCl (25 mM), an agonist of the Wnt/β-catenin pathway, to verify whether this signaling pathway was involved in EA-induced inhibition of ATC cells. The results of western blotting showed that LiCl significantly up-regulated the level of β-catenin (LiCl treated group vs. untreated group), and it significantly reversed EA-induced β-catenin down-regulation (EA+LiCl group vs. EA treated group), confirming the validity of LiCl and demonstrating that LiCl could reverse EA-induced inhibition of the Wnt/β-catenin pathway (Fig. 4A). We then measured the effects of activating the Wnt/β-catenin pathway on the EA-induced inhibition of proliferation, migration, and invasion of ATC cells. The results of the CCK-8 and colony formation assays showed that activation of the Wnt/β-catenin pathway significantly reversed the EA-induced inhibition of ATC cell (Fig. 4B and 4C). The results of the wound healing assay showed that activation of the Wnt/β-catenin pathway significantly reversed the EA-induced inhibition of ATC cell (Fig. 4D). The results of the Transwell invasion assay showed that activation of the Wnt/β-catenin pathway significantly reversed the inhibition of ATC cell invasion by EA (Fig. 4E). These data demonstrated that EA attenuated the proliferation, migration, and invasion of ATC cells by inhibiting the Wnt/β-catenin pathway.

Role of the PI3K/Akt pathway in EA-induced regulation of ATC cells

In addition to the Wnt/β-catenin pathway, we evaluated the role of the PI3K/Akt pathway, another ATC-associated signaling pathway, in the EA-induced antitumor effects. First, we assessed the effect of EA (80 μM) on the PI3K/Akt pathway by evaluating the phosphorylation level of the Akt protein, which was determined by the p-Akt/t-Akt ratio. As shown in Fig. 5A, EA treatment significantly decreased Akt phosphorylation levels, indicating that EA inhibited the PI3K/Akt pathway in ATC cells. Next, we used IGF-1 (100 ng/mL), an agonist of the PI3K/Akt pathway, to investigate whether this pathway was involved in the EA-induced regulation of ATC cells. The results of western blotting showed IGF-1 significantly increased Akt phosphorylation levels (IGF-1 treated group vs. untreated group), and it significantly reversed EA-induced inhibition of Akt phosphorylation level (EA+IGF-1 group vs. EA treated group), which proved the validity of IGF-1 as an agonist of the PI3K/Akt pathway (Fig. 5A). We then evaluated the effects of activating the PI3K/Akt pathway on the EA-induced suppression of cell proliferation, migration, and invasion of ATC cells. The results showed that activation of the PI3K/Akt pathway significantly reversed the EA-induced inhibition of cell proliferation (Fig. 5B and 5C), migration (Fig. 5D), and invasion (Fig. 5E). These data demonstrated that EA attenuated the proliferation, migration, and invasion of ATC cells by inhibiting the PI3K/Akt pathway.

DISCUSSION

In recent years, an increasing number of natural plant extracts have attracted the attention of researchers owing to their low toxicity and few side effects. Some natural extracts have been reported to possess anti-ATC activities. Yu and others found that chrysin (Yu *et al.*, 2013b), a natural flavonoid, and resveratrol (Jaskula-Sztul *et al.*, 2013a), a natural polyphenol phytoalexin, suppressed the growth and Notch1 signaling pathway in multiple ATC cell lines. Patel and others found that hesperetin, a natural flavonoid, exerted antitumor effects on ATC cells by inducing cell apoptosis and cellular differentiation (Patel *et al.*, 2014). Lepore *et al.* found that cynaropicrin, a natural sesquiterpene lactone, inhibited the proliferation of ATC cells by reducing NF-κB expression and STAT3 phosphorylation (Lepore *et al.*, 2019). Our study, for the first time, demonstrated that EA inhibited the tumor phenotypes of ATC cells and identified associated downstream signaling pathways, which expands our knowledge in the field.

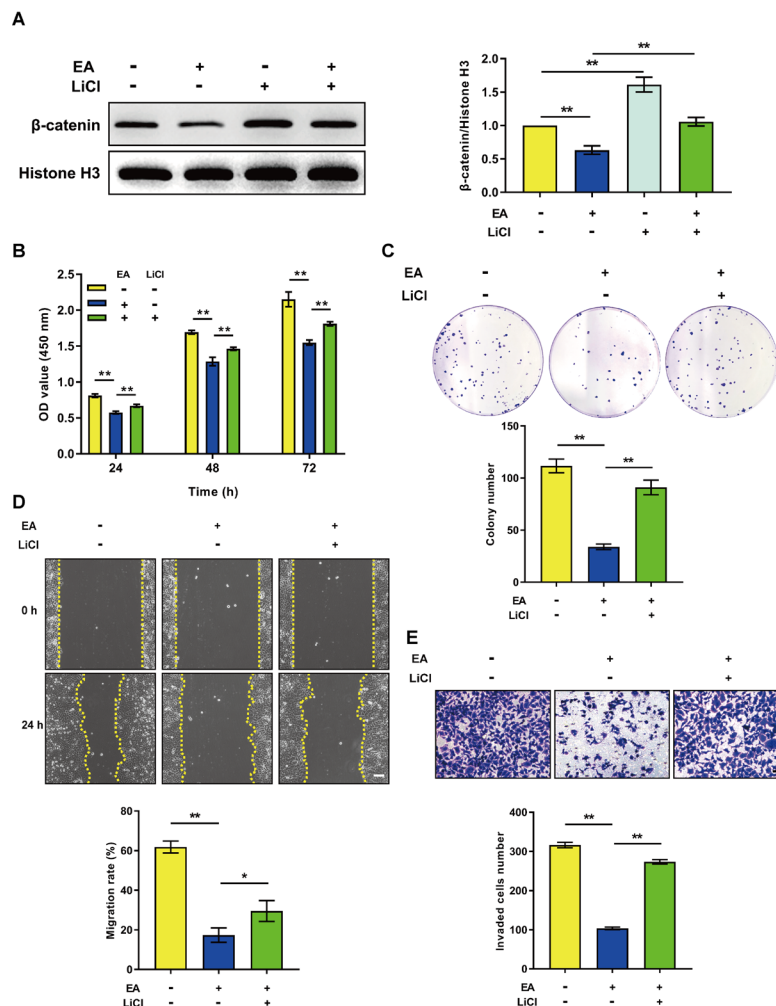


Figure 4. Role of the Wnt/β-catenin pathway in EA-induced regulation of ATC cells.

(A) The level of the Wnt/β-catenin pathway was assessed by detecting the protein level of β-catenin using western blotting. Cell proliferation assay was performed using the (B) CCK-8 and (C) colony formation assays. (D) Cell migration assay was performed using the wound healing assay (yellow dashed lines denote the wound edge; scale bar = 100 μm). (E) Cell invasion assay was performed using the Transwell invasion assay (scale bar = 50 μm). EA was used at 80 μM; LiCl was used at 25 mM as a pathway agonist. Data are expressed as mean ± S.D.; * $P < 0.05$ and ** $P < 0.01$.

Uncontrollable proliferation is an important characteristic of tumor cells. EA has been reported to inhibit the proliferation of multiple cancers. Malik and others reported that EA treatment inhibited the proliferation of prostate cancer cells (Malik *et al.*, 2011). In ovarian carcinoma, EA was found to inhibit the growth of ES-2 and PA-1 cells (Chung *et al.*, 2013). Wang and others suggested that EA exerts an inhibitory effect on the proliferation of glioblastoma cells (Wang *et al.*, 2016). Similar to the above results, our study demonstrated that EA treatment effectively suppressed the proliferation of ATC cells (Fig. 1). Cell migration and invasion play key roles in the metastasis of malignant tumor. It has also been shown to inhibit cell migration and invasion in some cancers. Xu and others reported that EA inhibits the migration and invasion of osteosarcoma cells by down-regulating c-Jun expression (Xu *et al.*, 2018). In melanoma, EA was found to be able to inhibit cell migration and invasion of WM115 and A375 cells via the epidermal growth factor receptor pathway (Wang *et al.*, 2020). Our results were consistent with these studies, and we found that EA attenuated the migration and invasion of ATC cells (Fig. 2 and 3). In addition, the antiproliferative activity of EA was verified in these two

studies. These findings may reveal the broad suppressive effects of EA on cancer cell proliferation, migration, and invasion. However, this has yet to be experimentally confirmed in other cancers.

Previous studies on EA against cancers have revealed that regulation of signaling pathway is involved. Anitha and others found that EA treatment suppressed the Wnt/β-catenin pathway in an animal model of oral oncogenesis (Anitha *et al.*, 2013). In another *in vitro* study, EA inhibited the Wnt/β-catenin pathway in colon cancer cells (Fang *et al.*, 2015). Similar to these two studies, our work showed the inhibitory effect of EA on the Wnt/β-catenin pathway, and further demonstrated that this pathway was involved in EA-induced suppression of the pathological phenotypes of ATC cells (Fig. 4). As for the PI3K/Akt pathway, another ATC-associated signaling pathway, Liu *et al.* reported that EA exerted an inhibitory effect on this pathway in A549 lung cancer cells (Liu *et al.*, 2018). Our study also showed that EA treatment inhibited the PI3K/Akt pathway, by which EA attenuated the proliferation, migration, and invasion of ATC cells (Fig. 5). These results enrich the mechanistic research on the antitumor activity of EA. Our study elaborated on specific signaling mechanisms for

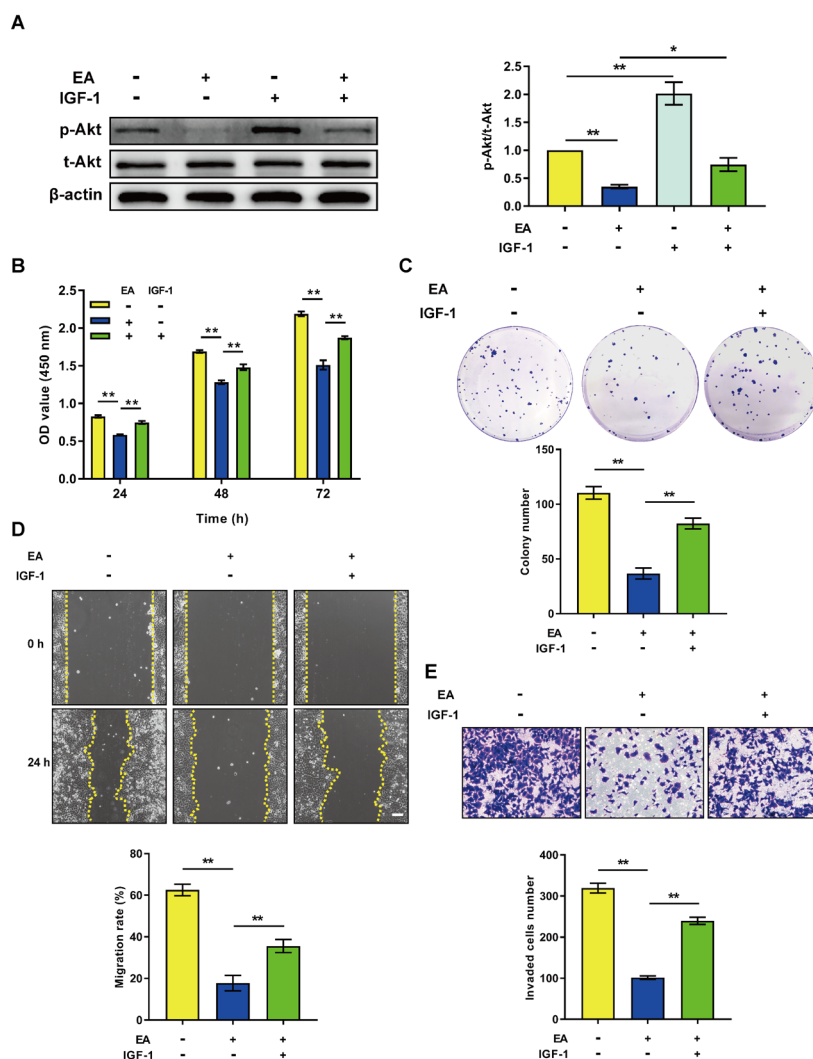


Figure 5. Role of the PI3K/Akt pathway in EA-induced regulation of ATC cells.

(A) The level of the PI3K/Akt pathway was assessed by detecting the phosphorylation level of Akt using western blotting. Cell proliferation assay was performed using the (B) CCK-8 assay and (C) colony formation assay. (D) Cell migration assay was performed using the wound healing assay (yellow dashed lines denote the wound edge; scale bar = 100 μm). (E) Cell invasion assay was performed using the Transwell invasion assay (scale bar = 50 μm). EA was used at 80 μM; IGF-1 was used at 100 ng/mL as a pathway agonist. Data are expressed as mean ± S.D.; * $P < 0.05$ and ** $P < 0.01$.

the EA-induced inhibition of ATC cells (Fig. 6, created with BioRender.com). The mechanisms underlying the EA-induced regulation of ATC remain to be elucidated.

The present study has several limitations; the effects of EA on other phenotypes of ATC cells, such as drug resistance, remain to be investigated. Further *in vivo* animal

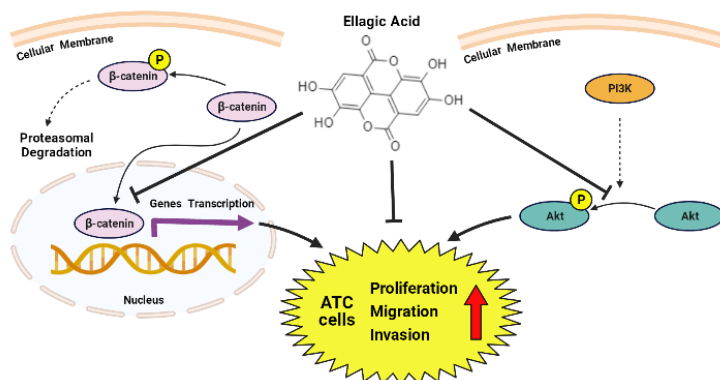


Figure 6. Schematic illustration of this study.

EA inhibits cell proliferation, migration, and invasion of ATC cells via the Wnt/β-catenin and PI3K/Akt pathways.

experiments are required to validate the antitumor effect of EA on ATC. These issues will be explored in future research.

In conclusion, this study demonstrated that EA inhibits the proliferation, migration, and invasion of ATC cells by inhibiting the Wnt/ β -catenin and PI3K/Akt signaling pathways. These findings support EA as a candidate drug for ATC treatment and provide a theoretical basis for further *in vivo* experiments and clinical applications.

Declarations

We thank Editage team for language editing.

REFERENCES

- Anitha P, Priyadarsini RV, Kavitha K, Thiyagarajan P, Nagini S (2013) Ellagic acid coordinately attenuates Wnt/ β -catenin and NF- κ B signaling pathways to induce intrinsic apoptosis in an animal model of oral oncogenesis. *Eur J Nutr* **52**: 75–84. <https://doi.org/10.1007/s00394-011-0288-y>
- Ceci C, Lacal PM, Tentori L, De Martino MG, Miano R, Graziani G (2018) Experimental evidence of the antitumor, antimetastatic and antiangiogenic activity of ellagic acid. *Nutrients* **10**: 11. <https://doi.org/10.3390/nu10111756>
- Chung YC, Lu LC, Tsai MH, Chen YJ, Chen YY, Yao SP, Hsu CP (2013) The inhibitory effect of ellagic acid on cell growth of ovarian carcinoma cells. *eCAM* **2013**: 306705. <https://doi.org/10.1155/2013/306705>
- Duan J, Zhan JC, Wang GZ, Zhao XC, Huang WD, Zhou GB (2019) The red wine component ellagic acid induces autophagy and exhibits anti-lung cancer activity *in vitro* and *in vivo*. *J Cell Mol Med* **23**: 143–154. <https://doi.org/10.1111/jcmm.13899>
- Fang Yang, Zhou Hong, Xia Jian-Fu, Lin Jie-Jun, Li Ri-Zeng, Yang Da-Qing, Xu Mai-Yu, Li Xiao-Yang (2015) Ellagic acid regulates Wnt/ β -catenin signaling pathway and CDK8 in HCT 116 and HT 29 colon cancer cells. *Bangladesh J Pharmacol* **10**. <https://doi.org/10.3329/bjp.v10i1.21068>
- Haymart MR (2021) Progress and challenges in thyroid cancer management. *Endocr Pract* **27**: 1260–1263. <https://doi.org/10.1016/j.eprac.2021.09.006>
- Hsu KT, Yu XM, Audhya AW, Jaime JC, Lloyd RV, Miyamoto S, Prolla TA, Chen H (2014) Novel approaches in anaplastic thyroid cancer therapy. *Oncologist* **19**: 1148–1155. <https://doi.org/10.1634/theoncologist.2014-0182>
- Jiang L, Zhang S, An N, Chai G, Ye C (2022) β ASPM promotes the progression of anaplastic thyroid carcinomas by regulating the Wnt/ β -catenin signaling pathway. *Int J Endocrinol* **2022**: 5316102. <https://doi.org/10.1155/2022/5316102>
- Jiang N, Dai Q, Su X, Fu J, Feng X, Peng J (2020) Role of PI3K/AKT pathway in cancer: the framework of malignant behavior. *Mol Biol Rep* **47**: 4587–4629. <https://doi.org/10.1007/s11033-020-05435-1>
- Lepore SM, Maggisano V, Lombardo GE, Maiuolo J, Mollace V, Bulotta S, Russo D, Celano M (2019) Antiproliferative effects of cyanopiricin on anaplastic thyroid cancer cells. *Endocr Metab Immune Disord Drug Targets* **19**: 59–66. <https://doi.org/10.2174/1871530318666180928153241>
- Liu Q, Liang X, Niu C, Wang X (2018) Ellagic acid promotes A549 cell apoptosis via regulating the phosphoinositide 3-kinase/protein kinase B pathway. *Exp Therap Med* **16**: 347–352. <https://doi.org/10.3892/etm.2018.6193>
- Liu Xianjun, Gao Xinxin, Li Hao, Li Zhandong, Wang Xiaoe, Zhang Li, Wang Bo, Chen Xinxin, Meng Xianglong, Yu Jiao (2021) Ellagic acid exerts anti-fibrotic effects on hypertrophic scar fibroblasts via inhibition of TGF- β 1/Smad2/3 pathway. *Appl Biol Chem* **64**: 67. <https://doi.org/10.1186/s13765-021-00641-2>
- Malik A, Afaq S, Shahid M, Akhtar K, Assiri A (2011) Influence of ellagic acid on prostate cancer cell proliferation: a caspase-dependent pathway. *Asian Pacific J Tropical Med* **4**: 550–555. [https://doi.org/10.1016/s1995-7645\(11\)60144-2](https://doi.org/10.1016/s1995-7645(11)60144-2)
- Molinaro E, Romei C, Biagini A, Sabini E, Agate L, Mazzeo S, Materazzi G, Sellari-Franceschini S, Ribecchini A, Torregrossa L, Basolo F, Vitti P, Elisei R (2017) Anaplastic thyroid carcinoma: from clinicopathology to genetics and advanced therapies. *Nat Rev Endocrinol* **13**: 644–660. <https://doi.org/10.1038/nrendo.2017.76>
- Patel PN, Yu XM, Jaskula-Sztul R, Chen H (2014) Hesperetin activates the Notch1 signaling cascade, causes apoptosis, and induces cellular differentiation in anaplastic thyroid cancer. *Ann Surg Oncol* **S497–S504**. <https://doi.org/10.1245/s10434-013-3459-7>
- Rao TP, Kühl M (2010) An updated overview on Wnt signaling pathways: a prelude for more. *Circ Res* **106**: 1798–1806. <https://doi.org/10.1161/circresaha.110.219840>
- Saji M, Ringel MD (2010) The PI3K-Akt-mTOR pathway in initiation and progression of thyroid tumors. *Mol Cell Endocrinol* **321**: 20–28. <https://doi.org/10.1016/j.mce.2009.10.016>
- Sastre-Perona A, Santisteban P (2012) Role of the wnt pathway in thyroid cancer. *Frontiers Endocrinol* **3**: 31. <https://doi.org/10.3389/fendo.2012.00031>
- Shakeri A, Zirak MR, Sahebkar A (2018) Ellagic acid: a logical lead for drug development? *Curr Pharm Design* **24**: 106–122. <https://doi.org/10.2174/1381612823666171115094557>
- Tiedje V, Stuschke M, Weber F, Dralle H, Moss L, Führer D (2018) Anaplastic thyroid carcinoma: review of treatment protocols. *Endocr Relat Cancer* **25**: R153–R161. <https://doi.org/10.1530/erc-17-0435>
- Tuttle RM, Haugen B, Perrier ND (2017) Updated american joint committee on cancer/tumor-node-metastasis staging system for differentiated and anaplastic thyroid cancer (eighth edition): what changed and why? *Thyroid* **27**: 751–756. <https://doi.org/10.1089/thy.2017.0102>
- Wang D, Chen Q, Liu B, Li Y, Tan Y, Yang B (2016) Ellagic acid inhibits proliferation and induces apoptosis in human glioblastoma cells. *Acta Chirurg Bras* **31**: 143–149. <https://doi.org/10.1590/s0102-865020160020000010>
- Wang F, Chen J, Xiang D, Lian X, Wu C, Quan J (2020) Ellagic acid inhibits cell proliferation, migration, and invasion in melanoma via EGFR pathway. *Am J Transl Res* **12**: 2295–2304
- Xu W, Xu J, Wang T, Liu W, Wei H, Yang X, Yan W, Zhou W, Xiao J (2018) Ellagic acid and Sennoside B inhibit osteosarcoma cell migration, invasion and growth by repressing the expression of c-Jun. *Oncol Lett* **16**: 898–904. <https://doi.org/10.3892/ol.2018.8712>
- Yu XM, Jaskula-Sztul R, Ahmed K, Harrison AD, Kunnimalaiyaan M, Chen H (2013a) Resveratrol induces differentiation markers expression in anaplastic thyroid carcinoma via activation of Notch1 signaling and suppresses cell growth. *Mol Cancer Therap* **12**: 1276–1287. <https://doi.org/10.1158/1535-7163.mct-12-0841>
- Yu XM, Phan T, Patel PN, Jaskula-Sztul R, Chen H (2013b) Chrysin activates Notch1 signaling and suppresses tumor growth of anaplastic thyroid carcinoma *in vitro* and *in vivo*. *Cancer* **119**: 774–781. <https://doi.org/10.1002/cncr.27742>
- Zhang Y, Xing Z, Liu T, Tang M, Mi L, Zhu J, Wu W, Wei T (2022) Targeted therapy and drug resistance in thyroid cancer. *Eur J Med Chem* **238**: 114500. <https://doi.org/10.1016/j.ejmech.2022.114500>

JNK promotes the progression of castration-resistant prostate cancer

Yigeng Feng[#], Hongwen Cao[#], Dan Wang[#], Lei Chen[✉], Renjie Gao[✉] and Peng Sun[✉]

Surgical Department I (Urology Department), LONGHUA Hospital Shanghai University of Traditional Chinese Medicine, Xuhui District, Shanghai 200032, China

Background: Prostate cancer is one of the most common cancers in men worldwide. This study aims to elucidate the roles of c-Jun N-terminal kinase (JNK) in the progression of castration-resistant prostate cancer (CRPC). **Methods:** JNK overexpressing and knockdown cell lines were established on the PC-3 prostate cell line. qPCR and Western blotting were performed to determine the mRNA and protein levels of target genes in prostate tissues and cell lines. MTT and Matrigel invasion assays were conducted to evaluate the cell viability and invasive ability, respectively. The Kaplan-Meier estimator was performed to estimate the overall survival rate and second progression-free survival rate. Pearson's correlation coefficient was used to evaluate the relationship between JNK and prostate-specific antigen (PSA). **Results:** Relative JNK expression was correlated with Gleason score and PSA value in patients with CRPC. Kaplan-Meier analysis revealed that patients with low JNK expression exhibited high overall survival and second progression-free survival rate. *In vitro* assays demonstrated that JNK overexpression promoted cell viability and invasion as well as the protein expressions of extracellular signal-regulated kinase (ERK) and matrix metalloproteinase 1 (MMP1) in PC-3 cell lines. **Conclusions:** JNK overexpression promotes the development of CRPC via the regulation of ERK and MMP1.

Keywords: Prostate cancer, PC3, prostate-specific antigen, castration, JNK

Received: 11 January, 2023; revised: 29 September, 2023; accepted: 08 November, 2023; available on-line: 15 December, 2023

✉ e-mail: chenlei2114@shutcm.edu.cn (LC); gaorenjie02254@shutcm.edu.cn (RG); unpenglhy@126.com (PS)

[#]These authors contributed equally to this work

Acknowledgements of Financial Support: The study was supported by the General Program of National Natural Science Foundation of China (#82174199 and 82274281); Shanghai University of Traditional Chinese Medicine Industry Development Center Medical and Nursing Integrated Science and Technology Innovation Project (#602069D).

Abbreviations: AR, androgen receptor; CRPC, castration-resistant prostate cancer; ECOG, Eastern Cooperative Oncology Group; ERK, extracellular signal-regulated kinase; JNK, c-Jun N-terminal kinase; MMP1, matrix metalloproteinase 1; MTT, 3-(4,5-Dimethylthiazol-2-yl)-2,5-diphenyltetrazolium bromide; PI3K, phosphoinositide 3-kinase; PSA, prostate-specific antigen; SD, standard deviation

INTRODUCTION

Prostate cancer is ranked as the second most common cancer among men and the fourth most common cancer among all types of cancers worldwide (Siegel *et al.*, 2021; Sung *et al.*, 2022). The incidence of prostate cancer is gradually increasing over the past decades (Schatten,

2018; Siegel *et al.*, 2022). For instance, the incidence rates of prostate cancer in the advanced stage have increased by 4%~6% annually from 2014 to 2018 (Schatten, 2018). In 2020, there are an estimated 1.4 million people who are diagnosed with prostate cancer in the world (Sung *et al.*, 2021). Depending on the stage of prostate cancer and its metastasis status, therapeutic options for prostate cancer include surgery, chemotherapy, radiation, androgen deprivation therapy (ADT), and combination therapy (Keyes *et al.*, 2013; Sowery *et al.*, 2007). Androgens are known as a key factor for stimulating prostate cancer cell growth, by lowering or stopping androgens are able to suppress proliferation and invasion of cancer cells (Harris *et al.*, 2009; Sharifi *et al.*, 2005). As one of the standard therapy options for prostate cancer, ADT is commonly used for patients with advanced prostate cancer and is shown to effectively control tumor growth. However, one of the major challenges is castration resistance, as supported by ADT therapy became less effective towards inhibit prostate cancer growth, and most of the patients who had ADT therapy developed castration-resistant prostate cancer (CRPC) (Chandrasekar *et al.*, 2015; Harris *et al.*, 2009; Sharifi *et al.*, 2005). Hence, developing new strategies that can overcome castration resistance is urgently required.

Several molecular pathways, such as the androgen receptor (AR) signaling pathway, c-Jun-N2-terminal kinase (JNK) signaling pathway, phosphoinositide 3-kinase (PI3K) signaling pathway, etc., are known to be involved in the prostate cancer (Mazaris & Tsiotras, 2013; Shtivelman *et al.*, 2014). The major underlying molecular mechanisms inducing CRPC are closely linked with the dysregulation of those signaling pathways (Dutt & Gao, 2009). For instance, the activation of PI3K leads to the phosphorylation of Akt and downstream cellular events, which is known as one of the major drivers of CRPC (Bitting & Armstrong, 2013). The aberrant modifications of AR increase the post-transcriptions of AR-related genes, leading to castration resistance (Yuan *et al.*, 2014). Interestingly, *in vitro* and *in vivo* data supported that targeting PI3K and AR signaling pathways by a combination of AR inhibitor (BEZ235) and mTOR inhibitor (EPI-002) effectively inhibited tumor growth as well as reduced prostate cancer resistance to ADT (Kato *et al.*, 2016). In addition, JNK is known to play a crucial role in the invasive prostate cancer (Xu & Hu, 2020). In 2020, Li and colleagues reported that a combination of JNK inhibitor (AS602801) and AR inhibitor (Enzalutamide) effectively suppressed proliferation and invasion of androgen-resistant prostate cancer cells *in vitro* and reduced tumor growth *in vivo* (Li *et al.*, 2020). These results suggest that targeting JNK might be an effective strategy for ameliorating prostate cancer resistance to ADT.

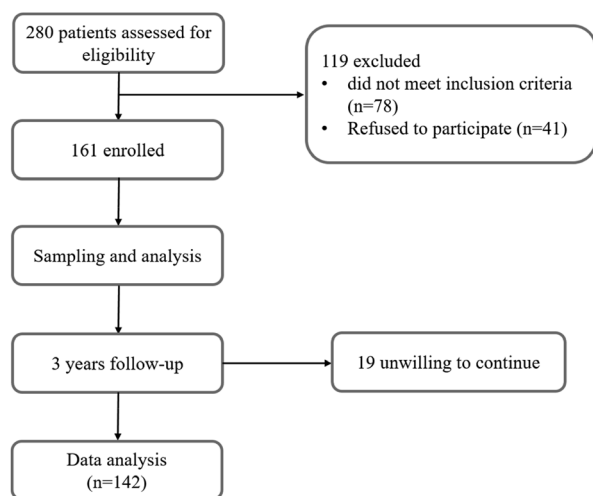


Figure 1. Schematic diagram of study profile.

MATERIAL AND METHODS

Enrollment of participants

As demonstrated in Fig. 1, a total of 280 patients were enrolled to assess eligibility. All patients have read and signed the informed consent. The patients that were aged less than 18 years old were excluded. Eastern Co-operative Oncology Group (ECOG) performance was assessed for all patients. Patients with ECOG performance status scored at 0 or/and 1 were included. In addition, only CRPC patients CRPC without any metastatic diseases were included. Finally, 161 patients who meet eligibility criteria participated in this study. The study was approved by the ethics committee of LONGHUA Hospital Shanghai University of Traditional Chinese Medicine, and the patients signed written consent.

Construction of cell lines

The PC3 cell line was obtained from ATCC (Manassas, VA) and cultured in the complete RPMI medium containing 10% fetal bovine serum and Penicillin-Streptomycin antibiotics. The construction of JNK overexpressing PC3 cell line (JNK OE) and JNK knockdown cell line (sh-JNK) were performed as previously reported. The cells were seeded into the 6-well microplates and incubated overnight to reach 70~80 % confluency. After that, the cells were transfected with plasmid containing JNK sequence or the plasmid containing JNK sequence plus shJNK by using Lipofectamine Transfection Reagent (ThermoFisher Scientific, Waltham, MA).

Cell viability and cell invasion assays

To evaluate the cell viability and cell invasion, 3-(4,5-Dimethylthiazol-2-yl)-2,5-diphenyltetrazolium bromide (MTT) assay and Matrigel invasion assay were determined, respectively. For the MTT assay, cells including PC3 cells, JNK overexpressing PC3 cells, and PC3 cells that were transfected with shJNK were seeded into the 96-well microplates at 1000 cells per well. Abiraterone at concentrations of 5, 10, and 20 μ M was added and incubated for another 3 days. Next, MTT working solution (5 mg/mL) was added to each well and incubated for 4 hours in the dark. Dimethyl sulfoxide solution was then added to dissolve the purple crystals. The plate

was read by using a microplate reader at wavelengths of 590 nm and 690 nm (reference wavelength).

For the Matrigel invasion assay, the invasion chambers were coated with Matrigel (0.5 mg/mL). Next, the cells were seeded into the upper chamber with serum-free medium and the lower chamber was filled with complete RPMI medium. Next, the cells were incubated for 48 hours and the non-invasive cells in the upper chamber were removed, and invasive cells were then fixed and stained with crystal violet staining solution. The cells were observed under a microscope and the number of invasive cells was counted.

qPCR

The prostate cancer tissue samples were collected from the participants. Total RNAs were isolated from the prostate cancer tissues by using the RNA extraction reagent (Invitrogen, Waltham, MA). The cDNA library was then constructed by using a reverse transcription kit (Invitrogen). The primers of JNK and internal control *GADPH* were synthesized by Descript. After that, the PCR reaction was performed and the mRNA levels of JNK were normalized to *GADPH*. The Melt curves were applied to ensure the accuracy of the PCR reaction.

Western blotting

Protein was isolated from the prostate cancer tissues as previously reported (Yang *et al.*, 2017). In brief, a cold radio-immunoprecipitation assay reagent (Bio-Rad, Hercules, CA) was added to the shredded tumor tissues. A homogenizer was used to create the uniformed protein mixture buffer and centrifuge was used to remove the tissue debris. Next, the bicinchoninic acid assay reagent was used to qualify the protein concentration. Protein was loaded into the gel followed by the incubation with the primary antibody solution including anti-JNK (1:2000, Abcam, Cambridge, MA), anti-extracellular signal-regulated kinase (ERK, 1:2000, Abcam), anti-matrix metalloproteinase 1 (MMP1, 1:2500, Abcam), or *GADPH* (1:3000, Sigma, St. Louis). Next, the membrane was blocked with blocking buffer (5% bovine serum albumin) followed by the incubation of the secondary antibody solution. Chemiluminescence blot imaging was used to detect the proteins. The protein expression was normalized to *GADPH*.

Statistical analysis

The Kaplan–Meier estimator was performed to estimate the overall survival percentage and second progression-free survival in patients with low JNK and high JNK. Pearson's correlation coefficient was used to analyze the correlation between JNK expression and PSA levels in patients with CRPC. Prism Software was used for data analysis. Data were expressed as the means \pm standard deviation (S.D.). One-way ANOVA with Tukey's multiple-comparisons test was applied for multiple groups. Any *p*-values that were less than 0.05 were considered as statistical difference.

RESULTS

Trial patients and their clinical characteristics

As displayed in Fig. 1, initially 280 patients were assessed for eligibility, and we finally recruited 161 eligible patients for this study. After sampling and analysis,

Table 1. Patient Characteristics.

	Low JNK level (n=71)	High JNK level (n=71)	p-value
Age (years)	63.2 (7.0)	62.8 (6.7)	0.729
ECOG performance status			
0	58 (81.7)	55 (77.5)	0.678
1	13 (18.3)	16 (22.5)	
PSA (ng/ml)	7.2 (2.7)	8.8 (3.2)	0.002
Gleason score			
≤7	48 (67.6)	30 (42.3)	0.004
>7	23 (32.4)	41 (57.7)	
Metastasis during follow-up			
Bone metastases	21 (29.6)	29 (40.8)	0.219
Lymph node metastases	24 (33.8)	38 (53.5)	0.028
Visceral metastases	13 (18.3)	17 (23.9)	0.538
Therapies			
Abiraterone	63 (88.7)	61 (85.9)	0.802
Docetaxel	52 (73.2)	55 (77.5)	0.697
Cabazitaxel	12 (16.9)	14 (19.7)	0.829

Data are n (%) or mean (S.D.). ECOG, Eastern Cooperative Oncology Group. PSA, prostate-specific antigen.

we conducted a 3-year follow-up study. After excluding the participants who were unwilling to continue, we analyzed the data from the 142 patients. Two cohorts including patients with low JNK levels and patients with high JNK levels were included (Table 1). We noticed that the levels of PSA in patients with low JNK levels were significantly decreased as compared to patients with high JNK levels ($p=0.002$). In addition, we observed less lymph node metastases in patients with low JNK levels as compared to patients with high JNK levels (24 *vs* 38). These results demonstrated that the levels of JNK were associated with the levels of PSA and lymph node metastases in patients with CRPC.

Relative JNK expression was correlated with Gleason score and PSA value in patients with CRPC

Next, we determined the relative JNK expression in CRPC patients with different Gleason scores. Interestingly, we found that the relative JNK expression in CRPC patients with low Gleason score (Gleason score ≤7) was significantly decreased as compared to the CRPC pa-

tients with high Gleason score (Gleason score >7), indicating the correlation between JNK and Gleason score (Fig. 2a). Besides, we also observed a positive correlation of JNK and PSA in patients with CRPC (Fig. 2b).

Patients with low JNK expression exhibited high overall survival and second progression-free survival rate

To explore the relationship between JNK expression and survival rate, we conducted a 3-year follow-up study. We found that patients with low JNK expression showed a higher overall survival rate as compared with those patients with high JNK expression ($p=0.033$, Fig. 3a). Consistently, we observed that patients with low JNK expression showed high second progression-free survival rate as compared with those patients with a high JNK expression ($p=0.005$, Fig. 3b). These results supported that patient with low JNK expression exhibited higher overall survival and second progression-free survival rate as compared to patients with high expression.

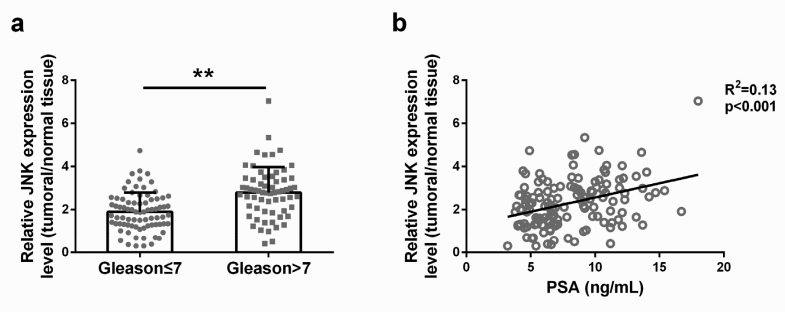


Figure 2. Relative JNK expression was correlated with Gleason score and PSA value in patients with castration-resistant prostate cancer (CRPC).

(a) The relative JNK expression in patients with different Gleason scores. (b) Pearson correlation showed the correlation of relative JNK expression with PSA levels in patients with CRPC. Data were expressed as the means \pm S.D. ** $p<0.01$.

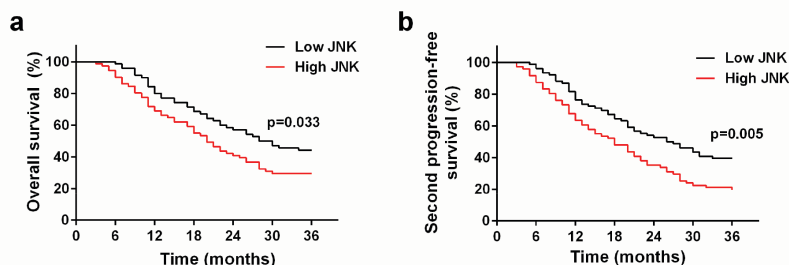


Figure 3. Kaplan-Meier analysis estimated the overall survival percentage (a) and second progression-free survival (b) in patients with low JNK and high JNK.

JNK overexpressing promoted cell viability and invasion of PC3 cells

To confirm the roles of JNK expression in the CRPC, we tested cell viability and invasion in the abiraterone-treated prostate cancer cell line. We found that the cell survival rate of PC3 cells was significantly decreased in the treatment of abiraterone. However, cells with JNK overexpression displayed a higher survival rate as compared with those cells transfected with shJNK (Fig. 4a). Consistently, cell invasion assay also showed that JNK overexpressing cell lines have a higher number of invasive cells, whereas cells that were transfected with shJNK have a smaller number of invasive cells (Fig. 4b). Taken together, these results suggested that JNK overexpression promoted cell viability and invasion of prostate cancer cells.

JNK overexpression enhanced the protein levels of ERK and MMP1 in PC3 cells

Finally, we explored the changes of other cytoplasm proteins in the presence of JNK overexpression in PC3 cells. Cytoplasm proteins including ERK and MMP1 were determined by using Western blotting. The protein expressions of JNK were significantly increased in the JNK overexpressing cells, indicating that the JNK over-

expressing cells were successfully constructed (Fig. 5a and 5b). In addition to JNK, we found that protein expressions of ERK and MMP1 were also increased in the JNK overexpressing cells as compared to the PC3 cells and JNK overexpressing cells that were transfected with shJNK (Fig. 5a, 5c, and 5d). These results suggested that JNK overexpression enhanced the protein levels of ERK and MMP1 in PC3 cells.

DISCUSSION

In this study, we found that JNK expression was positively correlated to Gleason score and PSA value in patients with CRPC. Interestingly, high JNK expression in prostate tumor tissues is associated with low overall survival and second progression-free survival rate as compared with those patients with low JNK expression. In vitro data suggested that JNK overexpression promotes cell proliferation, invasion, and sensitivity to abiraterone treatment, whereas inhibiting JNK reversed these cellular events, suggesting the relationship between JNK and CRPC. Moreover, targeting JNK also resulted in the changes in ERK and MMP1, indicating the roles of JNK on prostate cancer associated with those cytoplasm proteins.

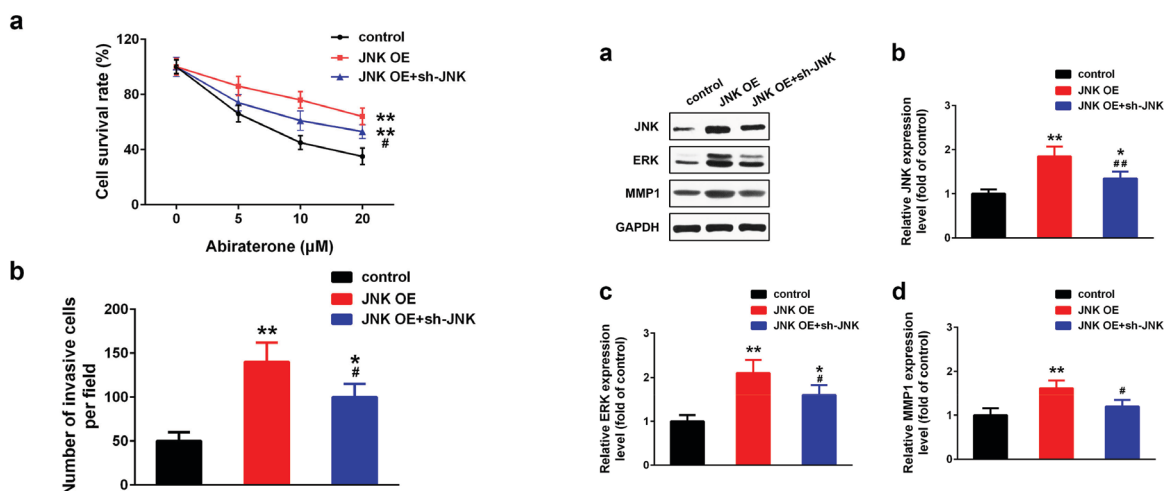


Figure 4. Effects of JNK on cell viability and invasion of PC3 cells. PC3 cells with JNK overexpressing or knockdown were constructed.

(a) JNK overexpressing enhanced abiraterone resistance, whereas the presence of sh-JNK decreased cell viability in PC3 cells. Besides, (b) Cell invasion of PC3 cells was evaluated by using the Transwell assay. Data were expressed as the means \pm S.D. * p <0.05, ** p <0.01 as compared with the control group. # p <0.05 as compared with the JNK OE group.

Figure 5. Effect of JNK on the protein levels of ERK and MMP1 in PC3 cells.

(a) Protein expressions of JNK (b), ERK (c), and MMP1 (d) were determined by using Western blotting. The relative expressions of those biomarkers were expressed as the fold of control. Data were expressed as the means \pm S.D. * p <0.05, ** p <0.01 as compared with the control group. # p <0.05, ## p <0.01 as compared with the JNK OE group.

ADT is commonly recommended for patients with advanced prostate cancer. However, CRPC is still one of the major challenges (Gunner *et al.*, 2016). Previous studies have demonstrated that JNK exerts a variety of functions in the regulation of cell differentiation, proliferation, invasion, and apoptosis in prostate cancer cells (Bode & Dong, 2007; Xu & Hu, 2020). Clinical studies revealed that JNK is highly expressed by the prostate cancer tissues (Bode & Dong, 2007). Interestingly, our study revealed less lymph node metastases in patients with low JNK levels as compared to those with high JNK levels. Consistently, JNK is also positively correlated to the levels of PSA and Gleason score, indicating that high JNK was more frequently observed in patients with advanced prostate cancer. In 2017, Zhang and colleagues reported the positive expression rate of the JNK in prostate patients with survival >5 years (60%) and survival ≤5 years (45%) in a cohort of forty samples (Zhang *et al.*, 2017). Interestingly, they found that the phosphorylation of JNK was higher in patients with survival >5 years than with survival ≤5 years (Zhang *et al.*, 2017). Our study revealed that patients with low JNK expression in their prostate cancer tissues showed a higher overall survival rate and second progression-free survival rate as compared with those patients with high JNK expression.

The link between JNK and AR signaling pathway has been well established by a series of studies (Li *et al.*, 2020; Xu & Hu, 2020). For instance, interactions between AR and JNK substrates regulate the therapeutic effects of the chemotherapy agent, taxane, against CRPC (Tinzl *et al.*, 2013). A reduction in the phosphorylation of JNK is associated with the repression of AR in prostate cancer cells (Shah & Bradbury, 2015). In this study, to confirm the roles of JNK in the CRPC, we established a series of cell lines including JNK overexpressing cells and JNK overexpressing cells that were transfected with shJNK. Interestingly, we observed that JNK overexpression promoted cell viability and invasion of PC3 cells that were treated with abiraterone. However, the presence of shJNK suppressed cell viability and invasion of PC3 cells. These results indicated that the levels of JNK are critical in the CRPC.

Targeting JNK exhibited broad effects in the treatment of prostate cancer (Xu & Hu, 2020). For instance, Kim and colleagues found that targeting ERK/JNK/AKT pathway with Oleanolic acid inhibits tumor growth in the DU145 animal model (Kim *et al.*, 2018). Another study initiated by Ma and colleagues reported that Corosolic acid regulates cell apoptosis in CRPC in part by the regulation of Inositol-requiring enzyme 1 and the JNK signaling pathway (Ma *et al.*, 2018). In our study, we found that targeting JNK regulated cell proliferation and invasion in the abiraterone-treated PC3 cells. However, when the JNK was overexpressed, the PC3 cells became less sensitive to the abiraterone treatment. These results confirmed that targeting JNK might be an effective strategy for regulating castration resistance of prostate cancer cells.

The Extracellular signal-regulated kinase (ERK) is another important kinase in CRPC, which is also known as a therapeutic target for prostate cancer (Gan *et al.*, 2010). The phosphorylation of ERK is a feature of CRPC and is associated with the incidence of prostate cancer recurrence (Nickols *et al.*, 2019). The activation of ERK leads to the overexpression of matrix metalloproteinase-1 (MMP-1) in the tumor tissues, which promotes tumor growth and metastasis (Nickols *et al.*, 2019; Quintero-Fabian *et al.*, 2019; Yang *et al.*, 2015). In this study, we fur-

ther explored the underlying mechanism of JNK on the regulation of CRPC. Interestingly, we observed a positive correlation of JNK with ERK and MMP1, as supported by the protein expressions of ERK and MMP1 were increased in the JNK overexpressing cells. However, the presence of shJNK inhibited the protein levels of ERK and MMP1 in PC3 cells. These results suggested that the effects of JNK on the regulation of cell viability and invasion in prostate cancer cells were associated with ERK and MMP1.

CONCLUSION

JNK expression is positively correlated with Gleason score and PSA value in patients with CRPC. Low JNK expression is also associated with high overall survival and second progression-free survival rate. Interestingly, JNK overexpression promotes cell viability and invasion, which is in part by the regulation of ERK and MMP1. These results suggest that JNK may be considered as an effective target for the CRPC therapy.

Declarations

Statement of Ethics. The study was approved by the ethics committee of LONGHUA Hospital Shanghai University of Traditional Chinese Medicine, and the patients signed written consent. This study followed the Declaration of Helsinki, Ethical Principles for Medical Research Involving Human Subjects.

Consent for publication. Current study is available from the corresponding author on reasonable request.

Author contribution. Concept or design: Yigeng Feng, Hongwen Cao, Dan Wang, Lei Chen, Renjie Gao, Peng Sun. Acquisition of data: Yigeng Feng, Renjie Gao, Peng Sun. Analysis or interpretation of data: Yigeng Feng, Lei Chen, Renjie Gao, Peng Sun. Drafting of the manuscript: Yigeng Feng, Hongwen Cao, Dan Wang, Lei Chen, Renjie Gao and Peng Sun. Critical revision of the manuscript for important intellectual content: All authors. All authors had full access to the data, contributed to the study, approved the final version for publication, and take responsibility for its accuracy and integrity.

Conflict of Interest Statement. None declared.

Data Availability Statement. The data that support the findings of this study are available from the corresponding author, Lei Chen, upon reasonable request.

REFERENCE

- Bitting RL, Armstrong AJ (2013) Targeting the PI3K/Akt/mTOR pathway in castration-resistant prostate cancer. *Endocr Relat Cancer* 20: R83–R99. <https://doi.org/10.1530/ERC-12-0394>
- Bode AM, Dong Z (2007) The functional contrariety of JNK. *Mol Carcinog* 46: 591–598. <https://doi.org/10.1002/mc.20348>
- Chandrasekar T, Yang JC, Gao AC, Evans CP (2015) Mechanisms of resistance in castration-resistant prostate cancer (CRPC). *Transl Androl Urol* 4: 365. <https://doi.org/10.3978/j.issn.2223-4683.2015.05.02>
- Dutt SS, Gao AC (2009) Molecular mechanisms of castration-resistant prostate cancer progression. *Future Oncol* 5: 1403–1413. <https://doi.org/10.2217/fon.09.11>
- Gan Y, Shi C, Inge L, Hibner M, Balducci J, Huang Y (2010) Differential roles of ERK and Akt pathways in regulation of EGFR-mediated signaling and motility in prostate cancer cells. *Oncogene* 29: 4947–4958. <https://doi.org/10.1038/onc.2010.240>
- Gunner C, Gulamhusein A, Rosario DJ (2016) The modern role of androgen deprivation therapy in the management of localised and locally advanced prostate cancer. *J Clin Urol* 9 (Suppl 2): 24–29. <https://doi.org/10.1177/2051415816654048>
- Harris WP, Mostaghel EA, Nelson PS, Montgomery B (2009) Androgen deprivation therapy: progress in understanding mechanisms of resistance and optimizing androgen depletion. *Nat Clin Pract Urol* 6: 76–85. <https://doi.org/10.1038/ncpuro1296>

- Kato M, Banuelos CA, Imamura Y, Leung JK, Caley DP, Wang J, Mawji NR, Sadar MD (2016) Cotargeting androgen receptor splice variants and mTOR signaling pathway for the treatment of castration-resistant prostate cancer. *Clin Cancer Res* **22**: 2744–2754. <https://doi.org/10.1158/1078-0432.CCR-15-2119>
- Keyes M, Crook J, Morton G, Vigneault E, Usmani N, Morris WJ (2013) Treatment options for localized prostate cancer. *Can Fam Physician* **59**: 1269–1274. PMID: 24336537
- Kim G-J, Jo H-J, Lee K-J, Choi JW, An JH (2018) Oleanolic acid induces p53-dependent apoptosis via the ERK/JNK/AKT pathway in cancer cell lines in prostatic cancer xenografts in mice. *Oncotarget* **9**: 26370. <https://doi.org/10.18632/oncotarget.25316>
- Li Z, Sun C, Tao S, Osunkoya AO, Arnold RS, Petros JA, Zu X, Moreno CS (2020) The JNK inhibitor AS602801 synergizes with enzalutamide to kill prostate cancer cells *in vitro* and *in vivo* and inhibit androgen receptor expression. *Transl Oncol* **13**: 100751. <https://doi.org/10.1016/j.tranon.2020.100751>
- Ma B, Zhang H, Wang Y, Zhao A, Zhu Z, Bao X, Sun Y, Li L, Zhang Q (2018) Corosolic acid, a natural triterpenoid, induces ER stress-dependent apoptosis in human castration resistant prostate cancer cells via activation of IRE-1/JNK, PERK/CHOP and TRIB3. *J Exp Clin Cancer Res* **37**: 1–16. <https://doi.org/10.1186/s13046-018-0889-x>
- Mazaris E, Tsiotras A (2013) Molecular pathways in prostate cancer. *Nephrourol Mon* **5**: 792. <https://doi.org/10.5812/numonthly.9430>
- Nickols NG, Nazarian R, Zhao SG, Tan V, Uzunangelov V, Xia Z, Baertsch R, Neeman E, Gao AC, Thomas GV, Howard L, De Hoedt AM, Stuart J, Goldstein T, Chi K, Gleave ME, Graff JN, Beer TM, Drake JM, Evans CP, Aggarwal R, Foye A, Feng FY, Small EJ, Aronson WJ, Freedland SJ, Witte ON, Huang J, Alumkal JJ, Reiter RE, Rettig MB (2019) MEK-ERK signaling is a therapeutic target in metastatic castration resistant prostate cancer. *Prostate Cancer Prostatic Dis* **22**: 531–538. <https://doi.org/10.1038/s41391-019-0134-5>
- Quintero-Fabián S, Arreola R, Becerril-Villanueva E, Torres-Romero JC, Arana-Argáez V, Lara-Riegos J, Ramírez-Camacho MA, Alvarez-Sánchez ME (2019) Role of matrix metalloproteinases in angiogenesis and cancer. *Front Oncol* **9**: 1370. <https://doi.org/10.3389/fonc.2019.01370>
- Schatten H (2018) Brief overview of prostate cancer statistics, grading, diagnosis and treatment strategies. *Adv Exp Med Biol* **1095**: 1–14. https://doi.org/10.1007/978-3-319-95693-0_1
- Shah K, Bradbury NA (2015) Kinase modulation of androgen receptor signaling: implications for prostate cancer. *Cancer Cell Microenviron* **2**: e123. <https://doi.org/10.14800/ccm.1023>
- Sharifi N, Gulley JL, Dahut WL (2005) Androgen deprivation therapy for prostate cancer. *JAMA* **294**: 238–244. <https://doi.org/10.1001/jama.294.2.238>
- Shtivelman E, Beer TM, Evans CP (2014) Molecular pathways and targets in prostate cancer. *Oncotarget* **5**: 7217. 10.18632/oncotarget.2406
- Siegel RL, Miller KD, Fuchs HE, Jemal A (2022) Cancer statistics, 2022. *CA Cancer J Clin* **72**: 7–33. <https://doi.org/10.3322/caac.21708>
- Sowery RD, So AI, Gleave ME (2007) Therapeutic options in advanced prostate cancer: present and future. *Curr Urol Rep* **8**: 53–59. <https://doi.org/10.1007/s11934-007-0021-9>
- Sung H, Ferlay J, Siegel RL, Laversanne M, Soerjomataram I, Jemal A, Bray F (2021) Global cancer statistics 2020: GLOBOCAN estimates of incidence and mortality worldwide for 36 cancers in 185 countries. *CA Cancer J Clin* **71**: 209–249. <https://doi.org/10.3322/caac.21660>
- Tinzl M, Chen B, Chen S-Y, Semenas J, Abrahamsson P-A, Dizdelyi N (2013) Interaction between c-jun and androgen receptor determines the outcome of taxane therapy in castration resistant prostate cancer. *PLoS One* **8**: e79573. <https://doi.org/10.1371/journal.pone.0079573>
- Xu R, Hu J (2020) The role of JNK in prostate cancer progression and therapeutic strategies. *Biomed Pharmacother* **121**: 109679. <https://doi.org/10.1016/j.biopha.2019.109679>
- Yang H, Liu C, Zhang Y-q, Ge L-t, Chen J, Jia X-q, Gu R-X, Sun Y, Sun W-D (2015) Ilexgenin A induces B16-F10 melanoma cell G1/S arrest *in vitro* and reduces tumor growth *in vivo*. *Int Immunopharmacol* **24**: 423–431. <https://doi.org/10.1016/j.intimp.2014.12.040>
- Yang H, Wang J, Fan J-H, Zhang Y-Q, Zhao J-X, Dai X-J, Liu Q, Shen Y-J, Liu C, Sun W-D (2017) Ilexgenin A exerts anti-inflammation and anti-angiogenesis effects through inhibition of STAT3 and PI3K pathways and exhibits synergistic effects with Sorafenib on hepatoma growth. *Toxicol Appl Pharmacol* **315**: 90–101. <https://doi.org/10.1016/j.taap.2016.12.008>
- Yuan X, Cai C, Chen S, Yu Z, Balk S (2014) Androgen receptor functions in castration-resistant prostate cancer and mechanisms of resistance to new agents targeting the androgen axis. *Oncogene* **33**: 2815–2825. <https://doi.org/10.1038/onc.2013.235>
- Zhang P, Han J, Zheng L, Wang K-N, Fan L-M, Xie H-D, Wang S-R, Jiang T (2017) Expressions of JNK and p-JNK in advanced prostate cancer and their clinical implications. *Zhonghua Nan Ke Xue (Nat J Androl)* **23**: 309–314 (in Chinese). PMID: 29714414

Value evaluation of serum (sdLDLc*HCYc)/HDLc ratio in the stability of intracranial arterial plaques in patients with acute cerebral infarction

Hongyu Hao^{1,2}, Xing Xing¹, Yajing Li³, Hongshan Chu¹, Lei Zhao¹, Siqi Cheng¹, Yang Liu⁴,
Tiankui Wang⁵, Nan Meng¹ and Ruisheng Duan¹✉

¹Department of Neurology, Hebei General Hospital, Shijiazhuang, China; ²Hebei Provincial Key Laboratory of Cerebral Networks and Cognitive Disorders, Shijiazhuang, China; ³Department of Pharmacy, Hebei General Hospital, Shijiazhuang, China; ⁴Department of Pathology, Hebei General Hospital, Shijiazhuang, China; ⁵Department of Medical Service, Hebei General Hospital, Shijiazhuang, China

Background: We aimed to analyze the value of serum (sdLDLc*HCYc)/HDLc ratio in the stability of intracranial arterial plaques among patients with acute cerebral infarction. **Methods:** A retrospective analysis was conducted on 140 patients with acute cerebral infarction admitted to the neurology department and 101 healthy individuals for regular examinations in our hospital from 2013 to 2019, who were respectively allocated into the study group and the control group. Participants in both groups were measured for serum sdLDLc, HDLc, and HCYc using peroxidase method, enzyme-linked immunosorbent assay, and enzyme method, respectively. The laboratory indexes of the two groups were compared. The multivariate logistic regression analysis was done to analyze the influencing factors of the stability of intracranial artery plaque in patients with acute cerebral infarction. The value of high-density lipoprotein cholesterol (HDL-C), homocysteine, sdLDLc, (sdLDLc*HCYc)/HDLc in diagnosing the stability of intracranial artery plaque was also evaluated in patients with acute cerebral infarction. **Results:** There was no distinct difference in height, hypertension, diabetes, coronary heart disease, smoking history and drinking history between the two groups ($P>0.05$). The study group showed statistically significant differences in age, gender, weight, and BMI ($P<0.05$). The current study demonstrated no statistical difference in the levels of TG, low-density lipoprotein cholesterol (LDL-C), α -lipoprotein, and HCYc between the two groups ($P>0.05$). However, the levels of TC, HDL-C, sdLDLc, (sdLDLc*HCYc)/HDLc in the study group were significantly different when comparing with the control group ($P<0.05$). No statistically significant difference was found in the levels of TG, triglycerides, LDL-C, α -lipoprotein, and HCYc among patients with different degrees of stenosis in the study group ($P>0.05$). The level of HDL-C was significantly lower in cases of severe stenosis compared to no stenosis, mild stenosis and moderate stenosis, with severe stenosis showing the lowest levels; mild stenosis had lower levels than no stenosis, while moderate stenosis had lower levels than both no stenosis and mild stenosis ($P<0.05$). The levels of sdLDLc, (sdLDLc*HCYc)/HDLc exhibited a significant increase in cases of severe stenosis as compared to no stenosis, mild stenosis, and moderate stenosis. Furthermore, the levels of sdLDLc, (sdLDLc*HCYc)/HDLc were found to be higher in moderate stenosis as compared to no stenosis and mild stenosis. Similarly, the levels of sdLDLc, (sdLDLc*HCYc)/HDLc were observed to be higher in mild stenosis than no stenosis ($P<0.05$). The independent

variables were set as the indicators with difference in single factor comparison, including age, gender, BMI, TC, LDL-C, HDL-C, HCYc, sdLDLc, (sdLDLc*HCYc)/HDLc. The dependent variable was the stability of intracranial artery plaque in patients with acute cerebral infarction. After variable selection, the results showed that the factors influencing the stability of intracranial artery plaque in patients with acute cerebral infarction were age, BMI, (sdLDLc*HCYc)/HDLc. The degree of plaque enhancement was used as a criterion to reflect the stability of plaque. ROC curve analysis showed that (sdLDLc*HCYc)/HDLc had a higher evaluation value for the stability of intracranial artery plaque than HDL-C, homocysteine, and sdLDLc in patients with acute cerebral infarction. **Conclusion:** The serum (sdLDLc*HCYc)/HDLc ratio was found to have potential in evaluating the stability of intracranial arterial plaques in patients with acute cerebral infarction.

Keywords: sdLDLc, HDLc, HCYc, acute cerebral infarction, stability of intracranial arterial plaques

Received: 25 April, 2023; revised: 29 July, 2023; accepted: 16 October, 2023; available on-line: 07 December, 2023

✉e-mail: 13832140261@126.com

Acknowledgements of Financial Support: This study was funded by Government-funded clinical excellence program (NO. ZF2023186).

Abbreviations: HDL-C, high-density lipoprotein cholesterol; LDL-C, low-density lipoprotein cholesterol; sdLDLc, (sdLDLc*HCYc)/HDLc

INTRODUCTION

Currently, acute ischemic cerebral infarction stands as the most prevalent type of stroke, comprising over 75% of all stroke cases. This condition exhibits alarmingly high incidence and disability rates, and is prone to causing neurological function loss, thereby impinging not only upon daily quality of life of patients, but also their life safety (Edwards & Hughes, 2021; Shao *et al.*, 2022). A recent study has revealed that more than 25% of acute cerebral infarction cases arise from the rupture of unstable plaque caused by atherosclerosis, leading to thrombus formation (Kim *et al.*, 2013). The stability of intracranial atherosclerotic plaque is inextricably linked to factors such as plaque surface smoothness, ulcer formation, regularity, and presence of bleeding (Lu *et al.*, 2021; Tao *et al.*, 2021). Therefore, early detection of the nature and structure of intracranial atherosclerotic plaque

holds immense significance in predicting the occurrence of acute cerebral infarction.

The serum low density lipoprotein (LDL) level is acknowledged as the most important risk factor for atherosclerosis. But the determination of LDL level by conventional blood lipid detection methods fails to completely predict the risk of carotid atherosclerosis; some patients at a high risk of cardiovascular disease may have normal LDL level (Hartley *et al.*, 2019). Based on previous research (QiaoZhen *et al.*, 2019), LDL can be subdivided into several subtypes, from LDL1 to LDL7 using the Lipoprint lipoprotein classification detection system. The LDL1-2 lipoprotein is typically regarded as physiologically normal, as it fulfills the role of transporting cholesterol. Conversely, the LDL3-7 lipoproteins are deemed to be abnormal, as they manifest as small dense low-density lipoproteins (sdLDL) that exhibit heightened susceptibility to oxidative stress, possess diminished affinity for LDL receptors, demonstrate a protracted plasma half-life, and exhibit a greater inclination to penetrate the vascular wall, ultimately depositing plaque beneath the endothelium. The cumulative effect of these factors contributes to the development of cardiovascular and cerebrovascular diseases (QiaoZhen *et al.*, 2019). Currently, copious studies are available to show that even if patients have normal LDL levels, an increase in the ratio of sdLDL in total LDL can still result in an increased risk of cardiovascular disease by more than three times (QiaoZhen *et al.*, 2019). Therefore, sdLDL is considered an effective predictor of atherosclerosis. The clinical auxiliary diagnostic value of single biomarkers such as small dense low-density lipoprotein cholesterol (sdLDLc), homocysteine concentration (HCYc) and HDLc concentration (HDLc) for cerebral infarction has been confirmed by many studies (Ishii *et al.*, 2022; QiaoZhen *et al.*, 2019; Santos *et al.*, 2020), while the predictive value of (sdLDLc*HCYc)/HDLc in primary cerebral infarction is higher than that of a single biomarker, including sdLDLc, HCYc, and HDLc (Luo *et al.*, 2022). Based on this, our study aimed to evaluate the value of serum (sdLDLc*HCYc)/HDLc ratio in the stability of intracranial arterial plaques in patients with acute cerebral infarction.

MATERIALS AND METHODS

Clinical data

A retrospective analysis was conducted on 140 patients with acute cerebral infarction admitted to the neurology department and 101 healthy individuals for regular examinations in our hospital from 2013 to 2019, who were allocated into the study group and the control group, respectively. In our hospital, about 100 cases of stroke patients are enrolled every year. Inclusion criteria: All patients met the diagnostic criteria for acute cerebral infarction established at the Fourth National Conference on Cerebrovascular Disease (Wang, 1996) in 1995, and were determined by intracranial high-definition magnetic resonance angiography; no oral or intravenous antibiotics, antiviral, non steroidal, or glucocorticoid drugs were administered within 14 days before the onset of the disease. Exclusion criteria were patients with serious infectious diseases; autoimmune diseases; malignant tumor diseases; diabetes; primary organ disorders, including heart, lung and other systemic diseases; new neurological deficits; other nervous system disease that may lead to neurological dysfunction, such as hereditary degenerative

diseases of the central nervous system, tumors, encephalitis, demyelinating diseases, brain trauma, epilepsy, etc.

The study protocol was approved by the Ethics Committee of Hebei General Hospital. Informed consent was obtained from all the study subjects before enrollment. All methods were designed in accordance with the Declaration of Helsinki.

METHODS

Clinical data

Clinical data of all participants, including age, gender, height, weight, BMI, hypertension, diabetes, coronary heart disease, smoking history, drinking history were collected.

Laboratory examination

After a 12-hour fast, 5 ml of venous blood of the study group was collected the following morning, and venous blood of the control group was also collected in the morning for physical examination. The serum was centrifuged for 10 min with a 3000 r/min high-speed centrifuge, and the supernatant was stored at -80°C for inspection. The experimental indicators were total cholesterol (TC), triglycerides (TG), high-density lipoprotein cholesterol (HDL-C), low-density lipoprotein cholesterol (LDL-C) and other experimental indicators using AU680 automatic biochemical analysis system by Beckman Kurt. Serum sdLDLc was detected using enzyme-linked immunosorbent assay (ELISA) with a kit from Shanghai Enzyme-linked Biotechnology Co., Ltd. The reagent instructions for operation were strictly followed for quality control.

Intracranial high-definition magnetic resonance angiography

Using the HDX platform 3.0T MRI system (GE Healthcare, the US), multi-sequence MRI examinations were performed with application of an 8-channel standard coil. The HRMR scanning matrix was 320×256 . The bright-blood technology was the first choice to perform three-dimensional time-of-flight magnetic resonance angiography, to clarify the location of the affected blood vessels after vascular reconstruction, and then use the black blood technology for multi-sequence scanning of intracranial diseased blood vessels. The scanning parameters were as follows: fast spin-echo T1-weighted imaging, fast spin-echo T2-weighted enhanced imaging, T1-weighted enhanced imaging, with repetition times of 567, 2883, and 567 ms, echo times of 15.8, 49, and 15.8 ms, and imaging field of view of $100 \text{ mm} \times 100 \text{ mm}$, with a layer thickness of 2mm and a spacing of 2.5 mm. The T1-weighted variable flip angle 3D fast spin-echo sequence has a repetition time of 900 ms, an echo time of 5.6 ms, and a layer thickness of 0.5 mm. The enhanced examination was performed using MeglumineZapenate as the contrast agent. The participants were intravenously injected with contrast agent 5 minutes before scanning. The scanning parameters were the same as T1-weighted variable flip angle 3D fast spin-echo sequence. The completion time of the above sequence scanning was 30 to 40 minutes. IV contrast was used during MRI scanning.

The assessment of intracranial responsible vessels included the degree of arterial stenosis and the characteristics of responsible plaques. Responsible blood vessels referred to the blood vessels that supplied responsible

Table 1. Comparison of clinical data

Indicator	Study group (n=139)	Control group (n=101)	χ^2/t	P
Age (year)	59.41±12.02	64 15±11.81	-3.044	0.003
Gender (male/female)	38/102	46/55	18.469	<0.001
Height (cm)	168.11±15.38	166.72±15.02	1.657	0.098
Weight (kg)	74.11±11.99	68.20±11.39	-4.045	<0.001
BMI (kg/cm ²)	26.14±3.23	24.52±3.71	-3.591	<0.001
Hypertension (n)	89	53	2.985	0.084
Diabetes (n)	40	19	3.023	0.082
Coronary heart disease	18	19	1.601	0.206
Smoking history	47	39	0.048	0.827
Drinking history	30	21	0.022	0.882
Degree of vascular stenosis (n)			-	-
Grade 0: no stenosis	23 (16.43)			
Grade 1: mild stenosis	26 (18.57)			
Grade 2: moderate stenosis	29 (20.71)			
Grade 3: severe stenosis	62 (44.29)			

lesions. If there was only one lesion in the blood vessel, the plaque at that lesion was considered the responsible plaque; if there were multiple diseased blood vessels, the plaque with the most severe vascular stenosis was the responsible plaque. According to the warfarin-aspirin symptomatic intracranial disease (WASID) method, the degree of stenosis of the responsible vessel was measured on the maximum intensity projection image of MRA. The degree of stenosis is divided into 5 levels: no obvious stenosis (0%), mild stenosis (1–49%), moderate stenosis (50–69%), severe stenosis (70–99%), and occlusion (100%).

Observation indicators

The laboratory indexes of the two groups were compared. The multivariate logistic regression analysis was done to analyze the influencing factors of the stability of intracranial artery plaque in patients with acute cerebral infarction. The value of HDL-C, homocysteine, sdLDLc, (sdLDLc*HCYc)/HDLc in diagnosing the stability of intracranial artery plaque were also evaluated in patients with acute cerebral infarction.

Statistical analysis

We used SPSS 21.0 software to analyze the data and Excel to establish the database. The measurement data

conforming to the normal distribution was expressed in $\bar{x} \pm s$. Using one-way ANOVA, the overall comparison of the data of each group was performed. And the pairwise comparison of the data between groups and within groups was conducted by LSD method. Moreover, the counting data was expressed in percentage (%) and compared using chi-square χ^2 test. Multiple logistic regression analysis was used to analyze the influencing factors, with $P < 0.05$ as the significant difference.

RESULTS

Comparison of clinical data

There was no distinct difference in height, hypertension, diabetes, coronary heart disease, smoking history and drinking history between the two groups ($P > 0.05$). The study group showed statistically significant differences in age, gender, weight, and BMI ($P < 0.05$) (Table 1).

Comparison of laboratory indicators

The current study demonstrated no statistical difference in the levels of TG, LDL-C, α -lipoprotein, and HCYc between the two groups ($P > 0.05$). However, the levels of TC, HDL-C, sdLDLc, (sdLDLc*HCYc)/HDLc

Table 2. Comparison of laboratory indicators ($\bar{x} \pm s$)

Indicator	Study group (n=139)	Control group (n=101)	t	P
TC (mmol/L)	4.36±1.16	4.65±1.14	2.202	0.029
TG (mmol/L)	1.71±1.87	1.71±0.96	1.281	0.200
HDL-C (mmol/L)	1.03±0.22	1.16±0.30	3.261	0.001
LDL-C (mmol/L)	2.80±0.86	3.00±0.82	-1.762	0.079
α -lipoprotein (mmol/L)	269.81±242.74	266.35±257.75	-0.411	0.681
HCYc(umol/L)	19.43±17.15	15.57±9.06	-1.795	0.073
sdLDLc(ng/dL)	8.13±6.62	5.59±3.63	-2.713	0.007
(sdLDLc*HCYc)/HDLc (%)	167.71±215.81	80.49±78.75	-3.477	0.001

Table 3. Comparison of laboratory indicators for different degrees of stenosis in the study group ($\bar{x} \pm s$)

Indicator	No stenosis (n=23)	Mild stenosis (n=26)	Moderate stenosis (n=29)	Severe stenosis (n=61)	t	P
TC (mmol/L)	4.39±0.16	4.36±0.13	4.34±0.18	4.35±0.15	0.508	0.677
TG (mmol/L)	1.71±0.27	1.72±0.21	1.68±0.25	1.69±0.23	0.171	0.916
HDL-C (mmol/L)	1.07±0.05	1.04±0.09*	1.01±0.07**	0.96±0.11**★	10.159	<0.001
LDL-C (mmol/L)	2.85±0.27	2.82±0.29	2.73±0.25	2.76±0.29	1.076	0.362
α-lipoprotein (mmol/L)	268.76±36.37	269.76±35.17	270.98±36.18	272.81±36.81	0.089	0.966
HCYc(umol/L)	21.51±1.93	21.56±1.87	21.65±1.76	21.87±2.01	0.286	0.835
sdLDLc(ng/dL)	8.01±0.21	8.71±0.71*	9.23±0.67**	9.87±0.87**★	41.639	<0.001
(sdLDLc*HCYc)/HDLc(%)	163.01±12.16	167.28±11.08*	172.18±12.01**	178.82±12.98**★	11.466	<0.001

Note: Compared with no stenosis (* $P<0.05$); compared with mild stenosis (** $P<0.05$); compared with moderate stenosis (★ $P<0.05$).

in the study group were significantly different when comparing with the control group ($P<0.05$) (Table 2).

Comparison of laboratory indicators for different degrees of stenosis in the study group

No statistically significant difference was found in the levels of TG, triglycerides, LDL-C, α-lipoprotein, and HCYc among patients with different degrees of stenosis in the study group ($P>0.05$). The level of HDL-C was significantly lower in cases of severe stenosis compared to no stenosis, mild stenosis and moderate stenosis, with severe stenosis showing the lowest levels; mild stenosis had lower levels than no stenosis, while moderate stenosis had lower levels than both no stenosis and mild stenosis ($P<0.05$). The levels of sdLDLc, (sdLDLc*HCYc)/HDLc exhibited a significant increase in cases of severe stenosis as compared to no stenosis, mild stenosis, and moderate stenosis. Furthermore, the levels of sdLDLc, (sdLDLc*HCYc)/HDLc were found to be higher in moderate stenosis as compared to no stenosis and mild stenosis. Similarly, the levels of sdLDLc, (sdLDLc*HCYc)/HDLc were observed to be higher in mild stenosis than no stenosis ($P<0.05$) (Table 3).

Multivariate logistic regression analysis of factors affecting the stability of intracranial arterial plaques in patients with acute cerebral infarction

The independent variables were set as the indicators with difference in single factor comparison, including age, gender, BMI, TC, LDL-C, HDL-C, HCYc, sdLDLc,

(sdLDLc*HCYc)/HDLc. The dependent variable was the stability of intracranial artery plaque in patients with acute cerebral infarction. After variable selection, the results showed that the factors influencing the stability of intracranial artery plaque in patients with acute cerebral infarction were age, BMI, and (sdLDLc*HCYc)/HDLc. (Table 4).

The value of HDL-C, homocysteine, sdLDLc, (sdLDLc*HCYc)/HDLc in diagnosing the stability of intracranial artery plaque in patients with acute cerebral infarction

The degree of plaque enhancement was used as a criterion to reflect the stability of plaque. ROC curve analysis showed that (sdLDLc*HCYc)/HDLc had a higher evaluation value for the stability of intracranial artery plaque than HDL-C, homocysteine, and sdLDLc in patients with acute cerebral infarction, as shown in Table 5 and Fig. 1.

DISCUSSION

Acute cerebral infarction is a life-threatening ischemic cerebrovascular disease that poses a significant threat to human health worldwide. The incidence of the condition has increased from 1.89% in 2012 to 2.19% in 2016, with a climbing disability rate with the passage of time. Acute cerebral infarction is deemed to be the leading cause of death and disability in adults in China (Zhang & Qin, 2022). Intracranial atherosclerosis accounts for

Table 4. Multivariate logistic regression analysis of influencing factors on the stability of intracranial arterial plaques in patients with acute cerebral infarction

Variable	β	SE	Waldx ²	OR (95%CI)	P value
Age	-0.033	0.014	5.787	0.971(0.945-0.998)	0.032
Gender	0.420	0.157	7.204	2.318(1.255-4.282)	0.226
BMI	0.108	0.045	5.718	1.114(1.020-1.218)	0.017
TC	0.004	0.442	0.000	1.004(0.422-2.389)	0.993
HDL-C	-0.499	0.843	0.350	0.607(0.1163-1.67)	0.554
LDL-C	-400	0.594	0.453	0.670(0.209-2.148)	0.501
Homocysteine	0.010	0.012	0.747	1.010(0.987-1.034)	0.387
sd-LDL	0.112	0.033	11.48	1.119(1.049-1.194)	0.411
Hypertension	-279	0.154	3.275	0.572(0.313-1.047)	-152
Diabetes	-304	0.175	3.018	0.544(0.274-1.081)	-145
(sdLDLc*HCYc)/HDLc	0.004	0.002	6.725	1.004(1.001-1.007)	0.010

Table 5. The value of HDL-C, homocysteine, sdLDLc, (sdLDLc*HCYc)/HDLc in diagnosing the stability of intracranial artery plaque in patients with acute cerebral infarction

ROC model	Area	Standard error	95% wald	Cut-off value	Sensitivity	Specificity
HDL-C	0.6232	0.0377	0.5493	$\leq 1.03\text{mmol/L}$	0.751	0.701
Homocysteine	0.5678	0.0371	0.4950	$\geq 19.43\mu\text{mol/L}$	0.763	0.722
sdLDLc	0.6022	0.0360	0.5316	$\geq 8.13\text{ng/dL}$	0.789	0.746
(sdLDLc*HCYc)/HDLc	0.6313	0.0357	0.5613	$\geq 167.71\%$	0.853	0.817

about 46.6% of cerebral infarction patients in China (Chu & Liu, 2021). The stability of intracranial artery plaque is highly associated with acute cerebral infarction. Earlier research indicated that high resolution magnetic resonance (HRMR) intracranial artery wall imaging was able to effectively assess the size, shape and stability of intracranial atherosclerotic plaque. The degree of plaque enhancement and intra plaque hemorrhage are greatly related to intra-plaque hemorrhage and plaque stability, but serum markers fail to effectively reflect the stability of intracranial atherosclerotic plaque (Xie *et al.*, 2022).

The changes in the composition of LDL-C are particularly pivotal in the progression of acute cerebral infarction. However, LDL-C is heterogeneous. The diameter of LDL-C main peak particles obtained by non-denaturing gradient gel scanning can be subdivided into LDL-C A with high cholesterol content, high density and large volume (diameter peak $\geq 25.8\text{nm}$) and LDL-C B with low cholesterol content, high density and small volume (diameter peak $< 25.8\text{nm}$), that is, small dense low-density lipoprotein cholesterol (sdLDLc) (Kanonidou, 2021). The latest research (Huang & Gu, 2021) asserted that, sdLDLc had a stronger atherogenic ability than LDL-C, and has been included in the newly discovered important risk factors for cardiovascular and cerebrovascular disease recommended by the adult treatment group of the National Cholesterol Education Program. sdLDLc is correlated with the number of atherosclerotic plaques and carotid stenosis caused by atherosclerotic plaques (Ikezaki *et al.*, 2020). Ikezaki and others (Ikezaki *et al.*, 2020) depicted that sdLDLc had a significant impact on

the composition of carotid artery plaque cells. HCYc is an intermediate product of the methionine cycle. High levels of HCYc can promote the proliferation of smooth muscle cells, damage vascular endothelial cells, and affect the oxidation of LDL. It can activate platelets to increase platelet adhesion, promote thrombosis, cause arterial congee, and also reduce the bioavailability of nitric oxide, inhibit fibrin degradation, platelet aggregation, and promote atherosclerosis (Wang *et al.*, 2021). Based on Yang and others (Yang *et al.*, 2019) the severity of carotid atherosclerotic plaque in type 2 diabetes patients complicated with cerebral infarction was higher than that in simple diabetes patients, and the level of serum HCYc was positively correlated with the degree of carotid atherosclerosis, which may be involved in its occurrence and development. α -lipoprotein level is determined by genes and is an LDL-like protein composed of apolipoprotein (apo) A covalently continuous apoB-100. Lp(α) is believed to be involved in the occurrence of atherosclerosis, which is greatly related to thrombosis and fibrinolysis damage (Dai *et al.*, 2019). However, limited clinical research exists on the value evaluation of serum (sdLDLc*HCYc)/HDLc ratio in the stability of intracranial arterial plaques in patients with acute cerebral infarction. Our study showed that the age, gender, weight, and BMI of the study group differed from the control group ($P < 0.05$), indicating that patients diagnosed with acute cerebral infarction exhibited a higher prevalence among the female population, alongside elevated weight and BMI, while their age was comparatively younger. But the small sample size may contribute to the biased results. In our study, the levels of TC, HDL-C, sdLDLc, (sdLDLc*HCYc)/HDLc in the study group were significantly different as compared to the control group ($P < 0.05$), suggesting that the levels of TC, HDL-C in patients with acute cerebral infarction decreased, and the levels of sdLDLc, (sdLDLc*HCYc)/HDLc increased. Gu and others (Gu *et al.*, 2017) showed that HDL-C levels and TC/HDL-C ratios may effectively predict the severity of intracranial vascular stenosis. Similarly, another study (Zhang *et al.*, 2020) depicted that sdLDLc could effectively evaluate the severity of acute cerebral infarction in elderly patients. According to our study, the level of HDL-C was significantly lower in cases of severe stenosis compared to no stenosis, mild stenosis and moderate stenosis, with severe stenosis showing the lowest levels; mild stenosis had lower levels than no stenosis, while moderate stenosis had lower levels than both no stenosis and mild stenosis ($P < 0.05$). The levels of sdLDLc, (sdLDLc*HCYc)/HDLc exhibited a significant increase in cases of severe stenosis as compared to no stenosis, mild stenosis, and moderate stenosis. Furthermore, the levels of sdLDLc, (sdLDLc*HCYc)/HDLc were found to be higher in moderate stenosis as compared to no stenosis and mild stenosis. Similarly, the levels of sdLDLc, (sdLDLc*HCYc)/HDLc were observed to be higher in mild stenosis than no stenosis ($P < 0.05$). It was suggested that the levels of HDL-C, sdLDLc, (sdLDLc*HCYc)/

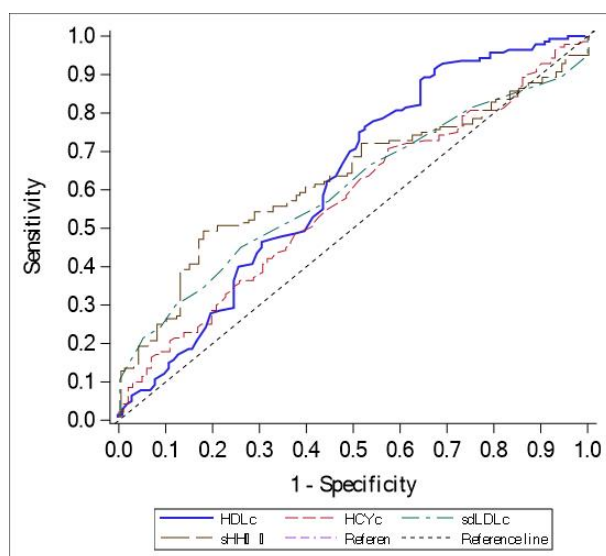


Figure 1. ROC curve of HDL-C, homocysteine, sdLDLc, (sdLDLc*HCYc)/HDLc in diagnosing the stability of intracranial artery plaque in patients with acute cerebral infarction.

HDLc varied in patients with acute cerebral infarction of different stenosis degrees. The more severe the stenosis degree, the lower the level of high-density lipoprotein cholesterol, and the higher the levels of sdLDLc, (sdLDLc*HCYc)/HDLc.

The stability of carotid atherosclerotic plaque in elderly patients with acute cerebral infarction was linked to factors such as age, HCYc (Bai & Wang, 2021). Another study suggested that elevated levels of LDL-C and HCYc were risk factors that affected the stability of carotid plaques in patients with acute cerebral infarction (Hansha *et al.*, 2022). Detecting and controlling the above-mentioned indicators in clinical practice may help stabilize the carotid plaques in patients with acute cerebral infarction, thereby improving their prognosis. Our study showed that the influencing factors for the stability of intracranial arterial plaques in patients with acute cerebral infarction included age, BMI, (sdLDLc*HCYc)/HDLc, which was consistent with the above results. We further analyzed the value of HDL-C, homocysteine, sdLDLc, (sdLDLc*HCYc)/HDLc in diagnosing the stability of intracranial artery plaque in patients with acute cerebral infarction. The results revealed that (sdLDLc*HCYc)/HDLc exhibited a higher value in evaluating the stability of intracranial artery plaque in patients with acute cerebral infarction than HDL-C, homocysteine, and sdLDLc. (sdLDLc*HCYc)/HDLc consists of three components, encompassing their respective effects. The precise reasons are described as follows: (1) The formation of sdLDLc is related to the metabolism of VLDL rich in triacylglycerol. Cholesterol ester transporter protein (CETP) and hepatic lipase (HL) exert important roles in the formation of sdLDLc. When VLDL increases, especially when triglycerides in the core exchange with cholesterol esters in the LDL core, the proportion of cholesterol esters in the LDL decreases, and the proportion of triglycerides gradually increases. When triglycerides in the LDL reach a certain concentration and pass through the liver, they are hydrolyzed by hepatic lipase to remove triacylglycerol. The entire exchange process continuously reduces the diameter of LDL particles, increases density, forms sdLDLc, and the level of triacylglycerol increases. The active exchange process positively generates sdLDLc. During the development of atherosclerosis, sdLDLc is deposited in a certain part of the artery wall through the vascular endothelial gap, which is then taken up by monocyte macrophages, where lipids gradually accumulate and transform into foam cells. The above changes are mainly due to the presence of chondroitin sulfate proteoglycan (CSPG) in the extracellular matrix of tunica intima cells, which can combine with lipoproteins to form complexes, thus prolonging the residence time (Choi & Lee, 2022). In addition, some studies demonstrated that the structure of ApoB in sdLDLc may change, and sdLDLc was difficult to clear in the circulation, so there were more opportunities for sdLDLc to enter tunica intima (Zhou *et al.*, 2020). The above-mentioned results highlight the fact that sdLDLc is closely related to atherosclerosis. (2) HCYc is one of the initiating factors of atherosclerosis. Under the environment of high concentration of HCY, vascular oxidative stress reaction generates free radicals, which reduces the function of endothelial cells. Endothelial cells enter the death process ahead of time. The process can also inhibit the regeneration of endothelial cells, reduce the number of endothelial cells, with lipid deposition and fibrosis in the excess space. Moreover, HCYc has an impact on a variety of cytokines, cyclins and cellular active substances, thus damaging the vascular wall, causing the protection

and proliferation of vascular smooth muscle cells. Finally, the development of ischemia and hypoxia contributes to the vascular fibrosis, hardening and thickening the blood vessel. The impairment of the vascular wall leads to the aggregation of fibrin and platelets in the damaged vascular wall, ultimately contributing to the development of arterial atherosclerosis. HCYc can cause abnormalities in lipid metabolism, increase LDL-C levels, and produce oxidative reactions, resulting in cholesterol accumulation in the blood vessel wall. It also reduces the anti-atherosclerotic function of HDL-C in the blood vessels, where the role of endothelial cells in clearing cholesterol slows down, and then deposits under the vascular endothelium. The accumulated cholesterol gradually increases, ultimately forming arteriosclerosis (Lv *et al.*, 2022). In addition, HCYc is able to cause abnormal platelet function and alter the activity of coagulation factors V and X, leading to platelet aggregation and abnormal coagulation function, and ultimately inducing cerebrovascular disease (Liu *et al.*, 2019). (3) HDLc, as a receptor for cholesterol, mediates the flow of cholesterol from the intima of the arterial wall and transports it to the liver for metabolism through its interaction with the receptor, thereby reducing cholesterol levels in the plasma and preventing the occurrence of arteriosclerosis. HDLc has demonstrated the ability to prevent atherosclerosis *via* inhibiting the oxidation of LDL, which also participates in the reverse transport of oxidized LDL, reducing the damage caused by oxidized LDL. Additionally, HDLc inhibits monocyte cell adhesion and infiltration into the tunica intima and stimulates endothelial cell repair and proliferation. It can also inhibit the proliferation of vascular smooth muscle cells induced by growth factors and other mechanisms. Lastly, it exhibits property of anti-platelet aggregation, safeguarding against thrombosis (Woo *et al.*, 2020; Yin *et al.*, 2021).

CONCLUSION

The patients with acute cerebral infarction showed reduced levels of TC and HDL-C, and elevated levels of sdLDLc, (sdLDLc*HCYc)/HDLc. Age, BMI, (sdLDLc*HCYc)/HDLc were the influencing factors for the stability of intracranial arterial plaque in patients with acute cerebral infarction, of which (sdLDLc*HCYc)/HDLc exhibited superior value in diagnosing the stability of intracranial arterial plaque in such patients. However, there are a few shortcomings in this study. We noted that the participants in control group were not selected based on the age and gender of patients with acute cerebral infarction, resulting in a certain bias in the general data. Further multi-center studies are needed to determine the risk factors for intracranial arteriosclerosis in patients with acute cerebral infarction based on their age.

Declarations

Ethics approval and consent to participate. The study protocol was approved by the Ethics Committee of Hebei General Hospital. Informed consent was obtained from all the study subjects before enrollment.

Consent for publication. Not applicable.

Availability of data and material. The datasets generated and analyzed during the current study are available from the corresponding author on reasonable request.

Competing interests. The authors declare that they have no competing interests.

Authors' contributions. HY H and RS D contributed to the conception and design of the study; XX, YJ

L, HS C, LZ, SQ C, YL, TK W and NM performed the experiments, collected and analyzed data; HY H and RS D wrote the manuscript; HY H and RS D revised the manuscript. All authors reviewed and approved the final version of the manuscript.

Acknowledgements. None.

REFERENCES

- Bai XS, Wang HL (2021) Stability and influencing factors of carotid atherosclerotic plaque in elderly patients with acute cerebral infarction. *Chinese J Gerontol* **41**: 2481–2484. <https://doi.org/10.3969/j.issn.1005-9202.2021.12.006>.
- Choi R, Lee SG (2022) Utilization of small dense low-density lipoprotein cholesterol testing in Korean patients visiting local clinics and hospitals. **14**. <https://doi.org/10.3390/nu14153246>
- Chu HJ, Liu C (2021) Lymphocyte ratio The predictive value of lymphocyte in the severity of intracranial atherosclerotic stenosis in patients with acute cerebral infarction. *Shanxi Med J* **50**: 1683–1686. <https://doi.org/10.3969/j.issn.0253-9926.2021.10.037>
- Dai W, Li D, Cai Y, Qiu E, Xu J, Li J, Wang Y, Guo Y, Li Y, Jiang B, Zhang Y, Ge J, Yao C, Zhang R, Liu G, Yao G, Cai J, Zhao X. (2019) Association between homocysteine and multivascular atherosclerosis in stroke-related vascular beds determined by three-dimensional magnetic resonance vessel wall imaging. *J Clin Neurosci* **70**: 72–78. <https://doi.org/10.1016/j.jocn.2019.08.076>
- Edwards MD, Hughes TAT (2021) Managing blood pressure in acute cerebral infarction. *J Neurol* **268**: 2294–2296. <https://doi.org/10.1007/s00415-021-10622-6>
- Gu LL, Tian YW, He D (2017) Study on blood lipid ratio, TOAST classification and intracranial vascular stenosis degree. *J Hebei Med Univ* **38**: 1122–1126. <https://doi.org/10.3969/j.issn.1007-3205.2017.10.002>
- Hansha RL, Yang ZP, Yuan R, Zhao YQ (2022) Analysis of risk factors affecting the stability of carotid plaque in patients with acute cerebral infarction. *J Baotou Med College* **38**: 7–11
- Hartley A, Haskard D, Khamis R (2019) Oxidized LDL and anti-oxidized LDL antibodies in atherosclerosis – Novel insights and future directions in diagnosis and therapy. *Trends Cardiovasc Med* **29**: 22–26. <https://doi.org/10.1016/j.tcm.2018.05.010>
- Huang J, Gu JX (2021) Elevated serum small dense low-density lipoprotein cholesterol may increase the risk and severity of coronary heart disease and predict cardiovascular events in patients with type 2 diabetes mellitus. **2021**: 5597028. <https://doi.org/10.1155/2021/5597028>
- Ikezaki H, Furusyo N, Yokota Y, Ai M, Asztalos BF, Murata M, Hayashi J, Schaefer EJ (2020) Small dense low-density lipoprotein cholesterol and carotid intimal medial thickness progression. *J Atheroscler Thromb* **27**: 1108–1122. <https://doi.org/10.5551/jat.54130>
- Ishii J, Kashiwabara K, Ozaki Y, Takahashi H, Kitagawa F, Nishimura H, Ishii H, Iimuro S, Kawai H, Muramatsu T, Naruse H, Iwata H, Tanizawa-Motoyama S, Ito H, Watanabe E, Matsuyama Y, Fukumoto Y, Sakuma I, Nakagawa Y, Hibi K, Hiro T, Hokimoto S, Miyauchi K, Ohtsu H, Izawa H, Ogawa H, Daida H, Shimokawa H, Saito Y, Kimura T, Matsuzaki M, Nagai R (2022) Small dense low-density lipoprotein cholesterol and cardiovascular risk in statin-treated patients with coronary artery disease. *J Atheroscler Thromb* **29**: 1458–1474. <https://doi.org/10.5551/jat.63229>
- Kanonidou C (2021) Small dense low-density lipoprotein: Analytical review. *Clin Chim Acta* **520**: 172–178. <https://doi.org/10.1016/j.cca.2021.06.012>
- Kim J, Song TJ, Song D, Lee HS, Nam CM, Nam HS, Kim YD, Heo JH (2013) Nonrelevant cerebral atherosclerosis is a strong prognostic factor in acute cerebral infarction. *Stroke* **44**: 2013–2015. <https://doi.org/10.1161/strokeaha.113.001111>
- Liu Y, Song JH, Hou XH, Ma YH, Shen XN, Xu W, Sun FR, Dong Q, Yu JT, Tan L, Chi S (2019) Elevated homocysteine as an independent risk for intracranial atherosclerotic stenosis. *Aging (Albany NY)* **11**: 3824–3831. <https://doi.org/10.18632/aging.102019>
- Lu Y, Ye MF, Zhao JJ, Diao SS, Li T, Ding DX, Zhang JL, Yao FR, Kong Y, Xu Z (2021) Gadolinium enhancement of atherosclerotic plaque in the intracranial artery. *Neural Res* **43**: 1040–1049. <https://doi.org/10.1080/01616412.2021.1949682>
- Luo C, Luo Y, Ma Q, Chen C, Xian S, Gong F, Zhao W, Zeng J, Luo J (2022) Evaluation of (sdLDLc*HCYc)/HDLc ratio in clinical auxiliary diagnosis of primary cerebral infarction. *BMC Cardiovasc Disord* **22**: 523. <https://doi.org/10.1186/s12872-022-02969-z>
- Lv FH, Yang YY, Liu X, Zhang ZL, Zhang N (2022) Diagnostic value of Lp-PLA 2 and Hcy in vulnerable carotid plaque in patients with acute cerebral infarction. *Clin Misdiagnosis Mistreatment* **35**: 105–107
- QiaoZhen X, AiGuo M, Tong W, Jingjing L, HaiYing L (2019) Correlation between of small dense low-density lipoprotein cholesterol with acute cerebral infarction and carotid atherosclerotic plaque stability. *J Clin Lab Anal* **33**: e22891. <https://doi.org/10.1002/jcla.22891>
- Santos HO, Earnest CP, Tinsley GM, Izidoro LFM, Macedo RCO (2020) Small dense low-density lipoprotein-cholesterol (sdLDL-C): Analysis, effects on cardiovascular endpoints and dietary strategies. *Prog Cardiovasc Dis* **63**: 503–509. <https://doi.org/10.1016/j.pcad.2020.04.009>
- Shao Y, Zhang Y, Wu R, Dou L, Cao F, Yan Y, Tang Y, Huang C, Zhao Y, Zhang J (2022) Network pharmacology approach to investigate the multitarget mechanisms of Zhishi Rhubarb Soup on acute cerebral infarction. *Pharm Biol* **60**: 1394–1406. <https://doi.org/10.1016/j.sbsbs.2022.2103718>
- Tao L, Li XQ, Hou XW, Yang BQ, Xia C, Ntaios G, Chen HS (2021) Intracranial atherosclerotic plaque as a potential cause of embolic stroke of undetermined source. *J Am Coll Cardiol* **77**: 680–691. <https://doi.org/10.1016/j.jacc.2020.12.015>
- Wang X, Yin H, Ji X, Sang S, Shao S, Wang G, Lv M, Xue F, Du Y, Sun Q (2021) Association between homocysteine and white matter hyperintensities in rural-dwelling Chinese people with asymptomatic intracranial arterial stenosis: A population-based study. *Brain Behav* **11**: e02205. <https://doi.org/10.1002/brb3.2205>
- Wang XD (1996) Key points of diagnosis of various cerebrovascular diseases. *Chinese J Neurol* **029**: 379–380
- Woo NE, Na HK, Heo JH, Nam HS, Choi JK, Ahn SS, Choi HS, Lee SK, Lee HS, Cha J, Kim YD (2020) Factors for enhancement of intracranial atherosclerosis in high resolution vessel wall MRI in ischemic stroke patients. *Front Neurol* **11**: 580. <https://doi.org/10.3389/fneur.2020.00580>
- Xie JX, Wang R, Dai Y, Hu XY, Fang K (2022) Association of cytomegalovirus and Mycoplasma pneumoniae infection and apolipoprotein E gene polymorphism with carotid atherosclerosis in patients with cerebral infarction. *Chinese J Nosocomiol* **32**: 1673–1677. <https://doi.org/10.3969/j.issn.0253-3685.2007.12.030>
- Yang P, Liao P, Wu WJ (2019) Relationship between serum homocysteine, C-reactive protein and carotid atherosclerosis in patients with type 2 diabetes mellitus and cerebral infarction. *China Medical Guide* **16**: 126–129; 141. <https://doi.org/CNKI:SUN:YYCY.0.2019-05-031>
- Yin K, Liang S, Tang X, Li M, Yuan J, Wu M, Li H, Chen Z (2021) The relationship between intracranial arterial dolichoectasia and intracranial atherosclerosis. *Clin Neurol Neurosurg* **200**: 106408. <https://doi.org/10.1016/j.clineuro.2020.106408>
- Zhang H, Qin Y (2022) Correlation analysis of Trial of Org 10172 in acute stroke treatment classification and National Institutes of Health Stroke Scale score in acute cerebral infarction with risk factors. **68**: 44–49. <https://doi.org/10.1590/1806-9282.20210413>
- Zhang SS, Ji YF, Zhang Y, Qu ZL (2020) Relationship between sonic hedgehog, small and dense low-density lipoprotein cholesterol, 25-hydroxyvitamin D, transferrin levels and severity and prognosis in elderly patients with acute cerebral infarction. *J Prac Hospital Clin* **17**: 33–36. <https://doi.org/CNKI:SUN:YYLC.0.2020-01-010>
- Zhou P, Liu J, Wang L, Feng W, Cao Z, Wang P, Liu G, Sun C, Shen Y, Wang L, Xu J, Meng P, Li Z, Xu WY, Lan X (2020) Association of small dense low-density lipoprotein cholesterol with stroke risk, severity and prognosis. *J Atheroscler Thromb* **27**: 1310–1324. <https://doi.org/10.5551/jat.53132>

β-catenin promotes resistance to trastuzumab in breast cancer cells through enhancing interaction between HER2 and SRC

Xiaoyan Hao¹, Jialu Zheng², Xiaoqin Yu³, Zhixin Li¹ and Guanghui Ren⁴✉

¹Department of Thyroid, Breast Surgery, Shenzhen Traditional Chinese Medicine Hospital, Shenzhen, China; ²Department of Thyroid, Breast Surgery, Longgang District Central Hospital, Shenzhen, China; ³Department of Ultrasound, Longgang District Central Hospital, Shenzhen, China; ⁴Department of General Surgery, Shenzhen Hospital, Southern Medical University, Baoan District, Shenzhen, Guangdong, China

More than 1 million women worldwide are diagnosed with breast cancer (BC) each year. This study aims to explore the molecular mechanisms of β-catenin affecting the trastuzumab tolerance in HER2-positive BC. β-catenin in BC and non-BC tissue samples were assessed by immunohistochemistry. β-catenin and HER2 were over-expressed and knockdown to evaluate their role in tumorigenicity and trastuzumab resistance in cell and animal models using soft-agar and xenograft assays. Confocal laser immunofluorescence assay and co-immunoprecipitation were used to assess protein-protein binding. Expression of genes was detected using Western blot analysis. β-catenin was highly expressed in primary and metastatic BC, overexpression of β-catenin increased the colony formation of MCF7 cells when it was co-expressed with HER2 and synergically increased the tumor size in immunodeficient mice. Overexpression of β-catenin also increased the phosphorylation of HER2 and HER3 and increased the size of tumor derived from HER2-elevated cells. Confocal laser immunofluorescence assay showed that β-catenin and HER2 were co-localized on the membrane of MDA-MB-231 cells, suggesting that β-catenin binds HER2 to activate the HER2 signaling pathway. Immunoprecipitation of β-catenin and HER2 also confirmed this binding. On the other hand, knockdown of β-catenin in MDA-MB-231 cell lines decreased the activity of SRC and decreased phosphorylation of HER2 at Y877 and Y1248. The interaction between HER2 and SRC was enhanced when β-catenin was overexpressed, and β-catenin increased the resistance of tumor derived from HER2 elevated BT474 cells to trastuzumab. Further analysis showed that trastuzumab inhibited the activation of HER3, but SRC was still highly expressed in cells overexpressing β-catenin. Our work demonstrates that β-catenin is highly expressed in BC and it synergically promotes formation and progress of BC with HER2. β-catenin binds with HER2 leading to enhanced interaction with SRC and resistance to trastuzumab.

polyvinylidene difluoride; SD, standard derivation; SDS-PAGE, sodium dodecyl sulfate-polyacrylamide gel electrophoresis; SRC, tyrosine kinase; VEGF, vascular endothelial growth factor

INTRODUCTION

Over one million women are diagnosed with breast cancer (BC) every year worldwide. Although the overall survival rate of BC has been greatly improved in the last decade, more than 450,000 people still die of BC each year (Anastasiadi *et al.*, 2017; Kolak *et al.*, 2017; Peairs *et al.*, 2017). Therefore, better understanding of the occurrence and development of BC is essential for clinical development for effective interventions (Fahad Ullah, 2019; Ganz & Goodwin, 2015). In the 1980s, the human epidermal growth factor receptor 2 (HER2) signaling pathway was found to be responsible for the abnormal proliferation of HER2 positive (HER2+) BC (Escrivade-Romani *et al.*, 2018; Rajarajan *et al.*, 2020). HER2 is highly expressed in more than 20% of metastatic BCs and is associated with cancer metastasis and poor patient prognosis (Lewis Phillips *et al.*, 2008; Smith *et al.*, 2007).

HER2 is a member of the epidermal growth factor receptor family (ErbB family) and is activated by homo- or heterodimerization to promote phosphorylation of monomers and recruitment of receptor complexes, phosphoinositide 3-kinase (PI3K), SHC, and growth factor receptor-bound protein 2 (GRB2) (Dankort *et al.*, 2001; Ellis & Ma, 2019; Xie & Hung, 1996). Phosphorylated HER2 can activate the PI3K/AKT and MAPK/ERK signaling pathways to promote cell proliferation, survival and differentiation (Lee *et al.*, 2013; Ruiz-Saenz *et al.*, 2018). HER2+ BC is clinically very aggressive and a series of HER2-targeting drugs, such as trastuzumab, lapatinib, pertuzumab and T-DM1 have been developed for clinical treatment of BC with good clinical efficacy and significantly improved outcomes (Cameron *et al.*, 2017a; Derakhshani *et al.*, 2020; Hunter *et al.*, 2020; Rinnerthaler *et al.*, 2019; Saura *et al.*, 2020). However, metastatic HER2+ BC remains an incurable disease and new treatment options are required for better treatment (Bredin *et al.*, 2020; Harbeck *et al.*, 2019). Furthermore, drug resistance, especially trastuzumab resistance, in BC, particularly in HER2+ BC, has eventually emerged in the great majority of treated patients (Nahta *et al.*, 2006). A better understanding of mechanisms underlying the drug resistance in HER2+ BC is therefore critical to develop new treatment strategies and drugs.

Trastuzumab is a Food and Drug Administration (FDA)-approved humanized antibody targeting HER2. It is used in combination with chemotherapy drugs to treat HER2+ BC and has a good response in early-stage

Keywords: β-catenin; HER2-positive BC; trastuzumab; drug resistance

Received: 10 May, 2022; revised: 06 August, 2022; accepted: 11 January, 2023; available on-line: 17 April, 2023

✉e-mail: guanghuirendr@yeah.net

Abbreviations: Akt, protein kinase B; ANOVA, analysis of variance; BC, breast cancer; DAB, diaminobenzidine; DMEM, Dulbecco's modified Eagle medium; ECL, enhanced chemiluminescence; ECOG PS, Eastern Cooperative Oncology Group Performance Status; EMEM, Eagle's minimum essential medium; ERK, extracellular signal-regulated kinase; FDA, Food and Drug Administration; GRB2, growth factor receptor-bound protein 2; HER2, human epidermal growth factor receptor 2; MAPK, mitogen-activated protein kinase; MOI, multiplicity of infection; PI3K, phosphoinositide 3-kinase; PVDF,

BC (Cameron *et al.*, 2017b; Tolaney *et al.*, 2021). Paclitaxel, trastuzumab, and pertuzumab are recommended as first-line therapy for patients with HER2⁺ BC who have not received trastuzumab or who have metastasized after 6 months of adjuvant trastuzumab therapy (Santa-Maria *et al.*, 2016). However, if metastases occur while receiving trastuzumab, T-DM1, may be the best option (Ramagopalan *et al.*, 2021; Uijen *et al.*, 2022). For example, in the CLEOPATRA clinical trial, patients received T-DM1 as a second-line therapy after receiving a first-line chemotherapy regimen (Larionov, 2018). In addition to T-DM1, lapatinib in combination with chemotherapy and trastuzumab is also a standard chemotherapy regimen, although the sequence of these agents has not been fully defined. Due to the development of drug tolerance in patients receiving trastuzumab, numerous studies and clinical trials have attempted to explore new ways to target the HER2 receptor where the Wnt/ β -catenin signaling pathway plays an important role (Schade *et al.*, 2013). Therefore, identifying regulators targeting this pathway may provide new directions and strategies for BC treatment.

Wnt/ β -catenin signaling pathway is involved in the development of early embryos and the occurrence of diseases. It plays an important role in thermogenesis and can promote the abnormal proliferation of tumor cells (Wu *et al.*, 2012; Wu *et al.*, 2017). More than 20 target genes have been identified in the pathway and most of them are related to cell proliferation and occurrence of tumors, such as axin-2 (Doumpas *et al.*, 2019), c-myc, cyclin D1 and VEGF (Liu *et al.*, 2016; Zhang *et al.*, 2012). Studies have shown that Wnt/ β -catenin signaling pathway is abnormally activated in human cancers, including BC (Brennan & Brown, 2004; Song *et al.*, 2016). Alteration of β -catenin expression may result from mutation and amplification, both of them lead to the occurrence and progression of BC (Sefidbakht *et al.*, 2021; Zhang *et al.*, 2021). Because β -catenin plays an important role in the formation and metastasis of tumor formation, small molecule inhibitors that target β -catenin are being developed to suppress tumor progression (Wang *et al.*, 2021). Studies have found that in BC cells with high expression of HER2 and trastuzumab resistance, the Wnt/ β -catenin signaling pathway is highly activated, suggesting that β -catenin plays an important role in HER2 signaling pathway (Hsieh *et al.*, 2016; Mir *et al.*, 2020; Shen *et al.*, 2020). However, how β -catenin promotes resistance to trastuzumab in BC is largely unclear.

This study aimed to explore the molecular mechanism of β -catenin affecting the trastuzumab tolerance in HER2-positive BC. The findings would provide new directions and potential targets for clinical treatment of HER2⁺ BC.

MATERIALS AND METHODS

Patients and tissue samples

Tissue samples were collected from patients undergoing surgical treatments at our hospital between April 2013 and September 2017. Patients were female, aged between 32 and 55 years with primary BC that was histologically or cytologically proven. Patients were included if they were HER-2 positive based on assessments from certified laboratories, with ≤ 1 Eastern Cooperative Oncology Group Performance Status (ECOG PS) and ≥ 3 month predicted survival and at least one measurable lesion based on RECIST1.1. Patients were excluded if

they were male, had incomplete clinical and pathological data (including immunohistochemical), HER2 status was not verified with FISH, had recurrent BC, or died of non-tumor cause during follow-up.

This study was approved by the ethics committee of the Shenzhen Hospital Affiliated with Southern Medical University and carried out in accordance with the declaration of Helsinki (revised in Tokyo in 2004). Written informed consent was obtained from every patient.

Reagents and equipment

Herceptin (trastuzumab) was purchased from Roche, USA. 0.25% trypsin solution (cat no. 25200072), BCA protein assay kit (cat no. 23225), SDS-PAGE sample prep kit (cat no. 89888), RIPA buffer (cat no. J63306.AP), LipofectamineTM 3000 Transfection Reagent (cat no. 13778150), ViraPower Lentiviral Packaging Mix (cat no. K497500), Protease Inhibitor Cocktail I (cat no. J64401.1.Q), Pierce Direct Magnetic IP/Co-IP Kit (cat no. 88828), protein-G Dynabeads (cat no. 10003D), NP-40 lysis buffer (cat no. J60766.AP) were purchased from Thermal Scientific; OPTI-MEM reduced serum medium (cat no. 31985-062) was from Gibco, USA;

Antibodies against β -catenin (cat no. ab223075, 1:1000 dilution), HER2 (cat no. ab134182, 1:1000 dilution), HER2 (phospho Y1248) (cat no. ab201013, 1:1200 dilution), HER3 (cat no. ab32121, 1:1000 dilution), HER3 (phospho Y1289) (cat no. ab76469, 1:1000 dilution), SRC (cat no. ab133283 1:1000 dilution), SRC (phospho Y416) (cat no. ab278693, 1:1000 dilution), horseradish peroxidase (HRP)-conjugated secondary antibody (cat no. ab6728, 1:1500), goat anti-mouse IgG H&L (Alexa Fluor[®] 488) (cat no. ab150113, 1:1500), goat anti-mouse IgG H&L (Alexa Fluor[®] 488) (cat no. ab150113, 1:1500), goat anti-mouse IgG H&L (Alexa Fluor[®] 555) (cat no. ab150114, 1:1500) ECL kit (cat no. ab133406) were purchased from Abcam, Waltham, MA, USA. FLAG antibody (cat no. F1804, 1:1500), type VII agarose (cat no. 39346-81-1) was purchased from Sigma-Aldrich. Colony counter (PhenoBooth+) was purchased from Singer Instruments, UK. Trans-Blot Turbo Transfer System was a product of Bio-Rad laboratories, USA.

Immunohistochemistry

The 5 μ m transverse tissue sections were deparaffinized and rehydrated by going through an ethanol gradient. After washing in water, the slides were autoclaved for 4 min in sodium citrate buffer for antigen retrieval. Endogenous peroxidase activity was suppressed by treating with hydrogen peroxidase for 5 min at room temperature. The tissue sections were rinsed with tris buffered saline 1X (TBS), reacted to primary antibody against β -catenin for 1 h and subsequently washed with TBS for three times, and incubated with horse radish peroxidase-conjugated anti-goat IgG (H+L) for 30 min. Diaminobenzidine (DAB) and haematoxylin chromogen (Dako, Glostrup, Denmark) method was used to visualize the immunoreactivity. The slides were examined under a light microscope to score β -catenin-positive cells. For each sample, 10 randomly selected fields were evaluated.

Cell lines and culture conditions

Human cells MCF7 (cat no. HTB-22), BT474 (cat no. HTB-20), SKBr3 (cat no. HTB-30), and MDA-MB-231 (cat no. HTB-26) were purchased from American Type Collection Center, Manassas, VA, USA and were cultured in Eagle's minimum essential medium (EMEM)

(ATCC cat no. 20-2003) with 10% fetal bovine serum (FBS, (ATCC cat no. 30-2020)), and 50 U/ml penicillin, and 50 μ g/ml streptomycin sulfate (Fisher Scientific MT30001CI). All cell lines were cultured in 5% CO₂ at 37°C in a humidified incubator as instructed by the manufacturer. HEK293T cells were grown to produce virus for transfection experiment as previously described (Cipriano *et al.*, 2010) in DMEM medium (cat no. 12491, Thermo Scientific, Wilmington, Delaware, USA) supplemented with 5% FBS. Cultured cells were routinely tested for mycoplasma contamination using MycoSEQ Mycoplasma Detection Kit (cat no. 4460626, Thermo Scientific) to ensure they were mycoplasma-free.

Vectors and cell transfection

To generate the cell lines overexpressing β -catenin and HER2, Lentiviral vectors pLV-Puro-CMV containing β -catenin and HER2 were constructed (Cyagen Biosciences, USA). BT474 and SKBr3 cells were seeded into the wells of 12-well plates at a density of 1×10^5 cells/well, grown to a confluency of 70–80%. The cells were transfected with vectors at multiplicity of infection (MOI) 50 based on the results of a pilot study. Mock transfection with LV-EGFP was employed as a negative control. Cell morphology was examined after transfection and the culture medium was refreshed 12 h after the transfection. Stably transfected clones were selected using puromycin at 1.5 μ g/ml. The expression of genes was assessed using Western blot analysis.

Plasmids encoding shRNAs targeting SRC were designed using tools provided by the Genetic Perturbation Platform (<https://portals.broadinstitute.org/gpp/public/>) and inserted into pLKO.1. Lentiviral vectors were transfected into HEK293T cells using Lipofectamine 2000 together with ViraPower Lentiviral Packaging Mix according to the manufacturer's instructions. Supernatants containing viruses were collected and used to infect cells for 16 hours. Cells at 90% confluency were harvested, re-suspended in FBS-free DMEM medium, transfected with the shRNA vectors (5 μ g/well) and 250 μ l Opti-MEM and Lipofectamine 3000 according to the manufacturer's instructions. After incubation for 20 min, the transfection mixtures were added to the wells of 24-well plates to culture for 4 h.

Immunoblot and immunoprecipitation

Cells were harvested by centrifugation at $500 \times g$ at room temperature, lysed using RIPA buffer containing protease inhibitor cocktail. The protein content was determined using BCA protein assay kit according to the manufacturer's instructions. About 50 μ g protein per lane was loaded for 10% sodium dodecyl sulfate polyacrylamide gel electrophoresis (SDS-PAGE) or used for an immunoprecipitation reaction. For immunoprecipitation, 5 μ g FLAG antibody was mixed with 50 μ l PBS-washed protein-G Dynabeads in 500 μ l RIPA lysis buffer containing protease and phosphatase inhibitors by rotating for 2 hours at 4°C. The complex beads were washed twice with PBS and added with protein lysates. The antibody-bead conjugates were rotated at 4°C for 2 hours, washed eight times with NP40 lysis buffer (150 mM NaCl, 1% NP-40, 50 mM Tris-Cl pH 8.0) and resuspended in 25 μ l of 2X SDS BME loading dye for immunoblot analysis. After separation by SDS-PAGE, the proteins were transferred electrically to polyvinylidene difluoride (PVDF) membranes ((Millipore)) using Trans-Blot Turbo Transfer System. The membranes were blocked

with 5% non-fat dry milk in 1X TBS buffer containing 0.1% Tween 20 for 6 h at 25°C and incubated with proper primary antibodies at 4°C overnight. After being rinsed three times with the same buffer, the blots were reacted with HRP-conjugated secondary antibodies at 25°C for 2 h and then visualized using the ECL kit as instructed by the supplier. Densitometric determination was conducted using Quantity One software (version v4.6.1; Bio-Rad Laboratories, Inc.) using β -actin as the internal control.

Xenograft assays

Eight-week-old specific-pathogen free (SPF) BALB/c-nu nude mice (female, weight 25–30 g) purchased from Saiye Biotech, Shanghai, were used. The mice were housed in hygienic and pathogen-free conditions at 25–26°C with good ventilation. They had free access to filtered water and diet under a 12/12 hours day/night cycle. Mice were randomly divided (n=36) and MCF7 cells expressing β -catenin and HER2 (100 μ l, 5×10^6) were orthotopically injected into the mammary glands for BC development. Animals bearing tumors were then randomized into cohorts to receive administration of trastuzumab, which was administered intraperitoneally for two weeks (6 times) with a total dose of 10 mg/kg. (n=6 in each group). The control group received PBS only. Mouse sizes were recorded every five days till 35 days after injection. Gross necropsies were performed, and tissues were collected and snap frozen in liquid nitrogen for downstream analysis. At different times after the implanting, mice were sacrificed by euthanization with carbon dioxide applied at a flow rate of 20% of the cage volume per minute (5 L/min) and tumors were isolated for size measurement using Vernier caliper.

The animal experimental protocols were approved by Animal Research Ethics Committee of the Shenzhen Hospital Affiliated with Southern Medical University.

Soft agar assay

Soft agar assays were performed to assess the colony formation ability as previously described (Horibata *et al.*, 2015). Briefly, MCF7 cells (1×10^5 cells/ml) were suspended gently in 0.6% type VII agarose (maintained at 42°C) prepared in RPMI 1640 medium supplemented with 10% FBS and 1% penicillin/streptomycin. The cells were plated in triplicate onto a bottom layer of 1.2% agar in 60-mm dishes. After being solidified at room temperature for 30 min, the plates were covered and were placed into a 37°C humidified incubator to culture. Three weeks later, the cells were stained with 200 μ l of 0.1% crystal violet per well overnight at 37°C. The stained colonies were analyzed using PhenoBooth+colony counter.

Confocal laser immunofluorescence assay

Human breast adenocarcinoma MDA-MB-231 cells were air dried on siliconized glass slides (Dako, Kyoto, Japan) at room temperature, fixed in pre-chilled methanol for 2 min and washed three times with PBS. The cells on the slides were incubated with 100 μ l of each antibody against β -catenin and HER2 overnight at 4°C in a humid box. After being washed with PBS, the slides were incubated with 100 μ l of goat anti-mouse IgG H&L (Alexa Fluor® 488) or goat anti-mouse IgG H&L (Alexa Fluor® 555) for 30 min. The slides were washed three times with PBS and counterstained with DAPI and mounted with buffered glycerol. The cells were visualized and photographed using a Leica confocal laser scan-

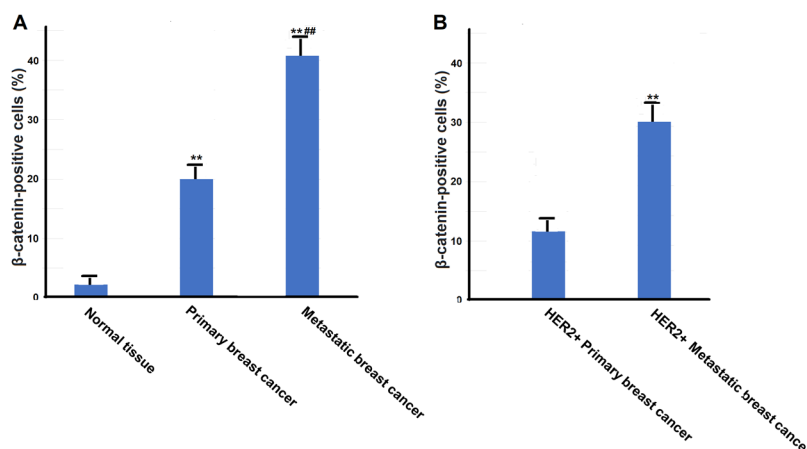


Figure 1. Percentage of β-catenin-positive cells in BC and HER2+BC. (A) in normal (n=55), primary BC (n=45) and metastatic BC (n=39). ** and ## denote $P < 0.01$ vs normal and primary BC tissues, respectively. (B) in HER2⁺ primary BC and HER2 metastatic BC. ** denotes $P < 0.01$ vs primary BC tissues, respectively.

ning microscope equipped with an OG 515 filter (Leica AG, Heerbrugg, Switzerland).

Co-immunoprecipitation

Co-immunoprecipitation of β-catenin and HER2 was performed using Direct Magnetic IP/Co-IP Kit according to supplier's protocols. Briefly, confluent MDA-MB-231 cells expressing β-catenin and HER2 were added with ice-cold IP lysis buffer and the lysates were centrifuged at $\sim 13\,00\times g$ for 10 minutes to pellet the cell debris. The supernatant was added to anti-HER2 antibody coupled beads and gently mixed and incubated on a rotating platform for 30–60 minutes at room temperature. After being washed with a washing buffer, the beads were collected with a magnetic stand and the proteins were eluted and analyzed using Western blot analysis.

Statistical analysis

Statistical analyses were performed with SPSS (version 19.0; SPSS, Inc., Chicago, IL, USA). Data are expressed as the means \pm S.D. Differences between multiple sample means were analyzed using one-way ANOVA and the LSD-t method was used for comparison between the two groups. Statistical significance was defined as a two-tailed $P < 0.05$.

RESULTS

β-catenin is highly expressed in primary and metastatic BC

The Wnt/β-catenin signaling pathway is well known to be involved in various human cancers. To demonstrate the role of β-catenin in human BC, we first analyzed the expression of β-catenin in normal tissues and BC tissues in the clinical samples using immunohistochemistry methods. It was found that β-catenin was expressed in 40.8% cells in the metastatic BC tissues, 20.1% cells in primary BC tissues and cells, and 2.2% in non-cancer tissues (Fig. 1A). Furthermore, among HER2⁺ BC cells, β-catenin was overexpressed in 12% of primary BC cells and 30% of metastatic BC cells (Fig. 1B).

β-catenin and HER2 synergically promote tumor development

To assess the synergy of β-catenin and HER2 in driving tumorigenesis, we established MCF7 cells that stably expressed β-catenin and HER2. Western blot analysis showed that non-transfected MCF7 cells (control) had very low background β-catenin and HER2 expression, and in the transformed cells β-catenin and HER2 expressions were significantly upregulated ($P < 0.01$, Fig. 2A). Notably, only cells expressing both β-catenin and HER2 exhibited an unusual and invasive phenotype when cultured in monolayers, while single expression of either β-catenin or HER2 did not change cellular morphology dramatically (Fig. 2B). To assess the malignancy of transformed cells, soft-agar experiments were performed. Cells expressing β-catenin and HER2 alone formed more colonies than control and had similar number of colonies. However, the number of colonies formed by cells expressing both β-catenin and HER2 was more than doubled as compared with cells expressing single genes ($P < 0.01$, Fig. 2C). To further confirm these findings, MCF7 cells expressing β-catenin and HER2 were used to inoculate immunodeficient mice for tumor development. The animal experiments demonstrated that overexpression of both HER2 and β-catenin significantly promoted tumor formation and progression, resulting in significantly large tumors, although β-catenin and HER2 alone induced tumor formation ($P < 0.01$, Fig. 2D), suggesting that β-catenin might synergize with HER2 to promote the formation and development of tumor cells.

β-catenin promotes the phosphorylation of HER and tumorigenesis

To explore the effect of β-catenin on HER phosphorylation, we overexpressed β-catenin in two HER2-elevated BC cell lines BT474 and SKBr3. We used retrovirus containing GFP-β-catenin or GFP (control) to overexpress β-catenin in these two cell lines. The results showed that compared with the control, β-catenin was remarkably up-regulated. Meanwhile, phosphorylation of HER2 at Y1248 and HER3 at Y1289 was significantly increased ($P < 0.01$, Fig. 3A). Notably, the phosphorylation levels of HER2 and HER3 were also significantly increased when cells were serum-starved (Fig. 3A).

To further examine the effect of β-catenin overexpression on the progression of HER2⁺ BC, we orthotopi-

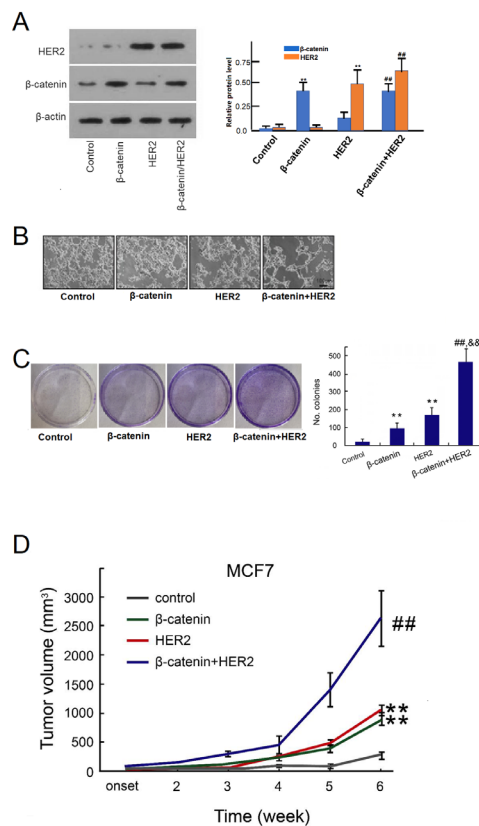


Figure 2. β -catenin and HER2 expression (A), morphology change (B), colony formation (C) and tumor development (D) by stably transformed MCF7 cells.

(A) left panel: Western blots, right panel: relative protein level, ** and # denote $P < 0.01$ vs control and HER2, respectively. (B) invasive morphology. (C) left panel: colony formation by soft agar assay, right panel: colony number, **, # and && denote $P < 0.01$ vs control, β -catenin and HER2, respectively. (D) tumor development in nut mice ($n=6$). ** and # denote $P < 0.01$ vs control, β -catenin and HER2, respectively.

cally injected BT474 cells expressing β -catenin into the mouse mammary glands in immunodeficient mice, and measured tumor growth. The results showed that compared with the control group, at 25 days post-injection, the tumors formed with β -catenin overexpressing cells were significantly greater than control ($P < 0.01$, Fig. 3B).

β -catenin binds to HER2

Since β -catenin can promote the phosphorylation of HER2, we set to investigate if β -catenin and HER2 are physically in contact with each other. Using confocal immunofluorescence assay, we found that β -catenin and HER2 were co-localized on the cell membrane in MDA-MB-231 cell line (Fig. 4A), suggesting that they might be in direct contact with each other. We further performed co-immunoprecipitation of the proteins with extracts from SKBr3 and BT474 cell lines. It was found that β -catenin and HER2 were co-precipitated in both cell lines (Fig. 4B).

β -catenin enhances HER2 interaction with SRC

Elevated SRC has been shown to stabilize HER2 to enhance cellular migration and survival (Mayer & Krop, 2010). Therefore, we investigated the impact of β -catenin on SRC and its phosphorylation. When β -catenin was knocked down in MDA-MB-361 cells, SRC and its phosphorylation, and HER2 phosphorylation at Y877 and

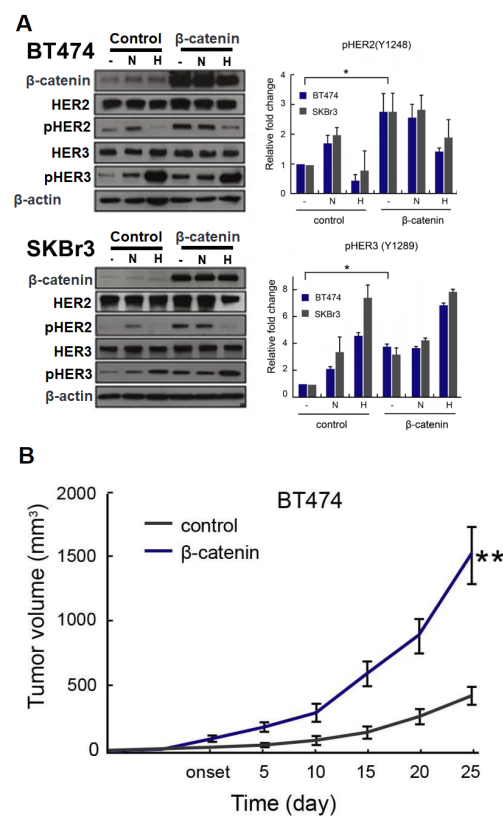


Figure 3. Phosphorylation of HER2 and HER3 expression by β -catenin in HER2-elevated BC cells BT474 and SKBr3c and tumor formation by BT474 overexpressing β -catenin in immunodeficient mice ($n=6$).

(A) Left panel: representative Western blots, right panel: relative protein level. (B) tumor size in nut mice. ** denote $P < 0.01$ vs control.

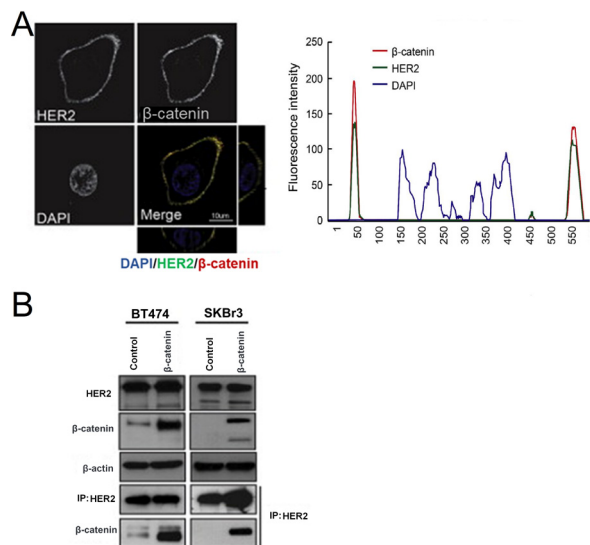


Figure 4. Cellular localization and immunoprecipitation of β -catenin and HER2.

(A) left panel: confocal immunofluorescence microscopy, (B) fluorescence intensity. (B) immunoprecipitation assays of β -catenin and HER2 using SKBr3 and BT474 cell extracts.

Y1248 were significantly reduced (Fig. 4A). To explore whether the inactivation of SRC would affect the activation of HER by β -catenin, SRC was downregulated using two SRC shRNAs in SKBr3 cells expressing β -catenin.

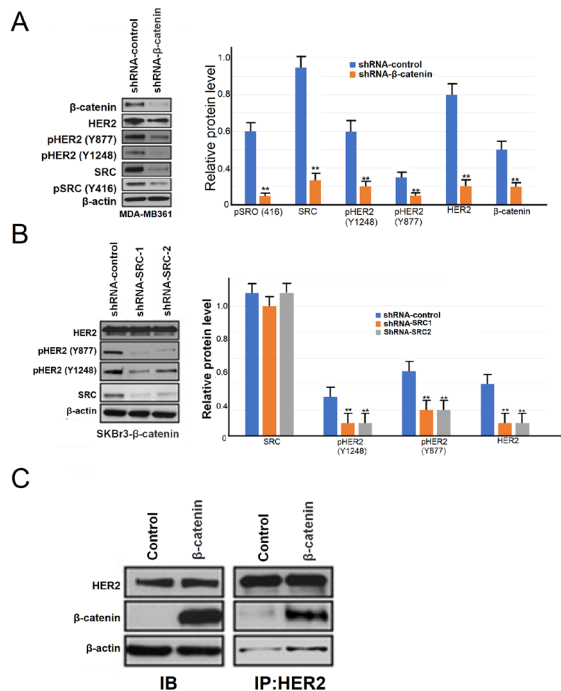


Figure 5. Phosphorylation of SRC and HER2 after knockdown of β -catenin (A) and SRC (B) and interaction between SRC and HER2 after overexpressing β -catenin (C). Left panel: representative Western blots, right panel: relative protein level. ** denote $P < 0.01$ vs control.

As a result, we found that HER2 phosphorylation at Y877 and Y1248 were decreased in the SRC-knockdown cells (Fig. 5B). These results suggest that SRC might regulate β -catenin-mediated HER2 phosphorylation to impact tumor development. On the other hand, when β -catenin was overexpressed, the interaction between HER2 and SRC was enhanced (Fig. 5C).

To further elucidate the functional relevance among β -catenin, HER2, and SRC, we examined the effect of β -catenin overexpression on drug sensitivity of the tumor cells. Recent studies have shown that abnormal activation of SRC can lead to resistance of tumor cells to trastuzumab. We found that in HER2⁺ BC, overexpres-

sion of β -catenin increased the resistance to trastuzumab (Fig. 6A). Further analysis found that trastuzumab inhibited the phosphorylation of HER2, but the SRC remained highly active in cells overexpressing β -catenin as compared to control cells (Fig. 6B).

DISCUSSION

A large number of *in vitro* and *in vivo* studies have shown that HER2 overexpression is related to the occurrence of BC (Loibl & Gianni, 2017). However, there is not enough evidence to confirm that HER2 can drive the transformation from benign to malignant and metastatic BC (Exman & Tolancy, 2021). It is also not clear whether other genomic variations can synergically promote BC with HER2. In this study, we found that β -catenin appears to be an important regulatory protein of HER2 that drives BC development and resistance to trastuzumab. β -catenin is highly expressed in BC, particularly in metastatic BC, and synergically promotes the development of BC in xenograft mouse models probably by increasing the phosphorylation of HER2. We also found that β -catenin binds with HER2 and enhances the interaction between HER2 and SRC, resulting in increased trastuzumab resistance. The findings from this study provide new insights and clues for the development of new therapeutic strategies and targets for BC.

Better understanding the molecular mechanisms underlying the metastatic dissemination of HER2+BC would be helpful to the development of effective clinical interventions. Wnt/ β -catenin signaling pathway is well known to play important roles in human cancers (Zhang & Wang, 2020). Assessment of β -catenin expression in tumor tissues has shown that it is upregulated in BC, particularly in metastatic cancer. As a multifunctional protein with a central role in physiological homeostasis, β -catenin is often upregulated in various diseases, including cancer, as the result of mutations of canonical Wnt signaling pathway genes (Cui *et al.*, 2018; White *et al.*, 2012). In canonical Wnt pathway, Dsh, β -catenin, glycogen synthase kinase 3 beta (GSK3 β), adenomatous polyposis coli (APC), AXIN, and T-cell factor (TCF)/lymphoid enhancement factor (LEF) are the major signal transducers with β -catenin as core protein (Behrens *et al.*, 1996; Yost *et al.*, 1996). Our study further demonstrated that β -catenin is highly upregulated in HER2 BC, suggesting that there might be interactions between the two genes, particularly in metastatic BC. HER2 has been shown to interact with oncogenic/stemness signaling pathways including Wnt/ β -catenin, and HER2 overexpression promotes EMT and the emergence of cancer stem cell properties in BC (Nami & Wang, 2017). Using MCF7 cells, we found that although β -catenin and HER2 alone increase the colony formation ability, co-expression of the two genes results in increased invasive transformation of the cells and higher tumorigenicity in immunodeficient mice as compared to single β -catenin or HER2 protein. These studies further demonstrate that β -catenin and HER2 have synergy in promoting BC. In gastric cancer cells, overexpression of HER2 was shown to increase the stemness and invasiveness, which is regulated by Wnt/ β -catenin signaling (Jung *et al.*, 2019). Previously the aberrant expression of β -catenin was associated with more aggressive behaviors of BC although it was not statistically correlated to HER2 (Sefidbakht *et al.*, 2021). However, in epithelial ovarian cancer (EOC), high expression of β -catenin was found in HER2-positive EOC tissue samples and was correlated with a poor

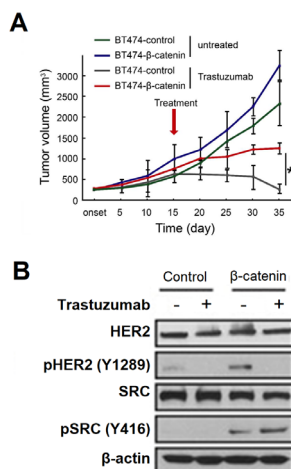


Figure 6. Development of tumors after trastuzumab treatment (A) and phosphorylation of SRC (B) in mice (n=6) xenografted with β -expressing BT474 cells. *denotes $P < 0.01$ vs control.

patient prognosis. Therefore, Wnt3a/ β -catenin/TCF7L2 signaling axis is considered to play an important role in EOC resistance to trastuzumab and HER2-targeted drugs may have the potential for EOC treatment (Shen *et al.*, 2020).

To elucidate the interaction between β -catenin and HER2, we investigated the effect of β -catenin on the HER activity by overexpressing β -catenin in BC cell lines BT474 and SKBr3 with elevated HER2 level. It was found that in these cells, there was increased phosphorylation of HER2 and HER3. Previously, HER2 phosphorylation was found to be due to the activation of other HER receptors, such as reactivation of HER3 and ADAM17-mediated ligand release (Gijzen *et al.*, 2010). In addition, the levels of phosphorylated HER2 increased significantly in cells treated with arenite and exogenous EGF, TGF α , NRG1, and HSP90 through the dimerization of HER2 with other members of HER family, such as HER3 (Jin *et al.*, 2018). Other proteins reported to phosphorylate HER2 include PTPN18 that regulates HER2-mediated cellular functions through defining both its phosphorylation and ubiquitination barcodes (Wang *et al.*, 2014). The activation (phosphorylation) of HER family gene by β -catenin is likely partially responsible for the enhanced tumorigenesis. Study with β -catenin knockdown may further define the relationship between β -catenin and HER2 activation.

To further investigate the model of action of β -catenin and HER2, we studied the co-location of these two proteins using confocal immunofluorescence assay. β -catenin and HER2 were found to be co-localized on the cell membrane, indicating that they might have direct physical contact with each other, and the results from immunoprecipitation in the two cell lines tested support this speculation. To further refine the interaction between β -catenin and HER2, protein variants might be used to better understand the structure-binding relationship.

SRC is one of the non-receptor tyrosine kinases that participates in cell proliferation, differentiation, survival, and invasion through the PI3K, MAPK, STAT3, FAK signaling pathways (Roskoski Jr., 2015). Studies have shown that increased SRC activation can stabilize HER2 to enhance cellular migration and survival and confers resistance of HER2⁺ BC cells to trastuzumab (Peiro *et al.*, 2014). Our analysis showed that the activation (phosphorylation) of both SRC and HER2 is reduced once β -catenin is knockdown, implying that β -catenin might be involved in regulating both SRC and HER2 signaling. On the other hand, knockdown of SRC in SKBr3 cells expressing β -catenin results in decreased HER2 phosphorylation, suggesting that SRC might regulate β -catenin-mediated HER2 phosphorylation to impact tumor development, and this SRC interaction with HER2 is enhanced by β -catenin. Since increased trastuzumab resistance and SRC activation were observed in tumors derived from cells expressing β -catenin, it is likely that SRC might also play a role in the drug resistance. Trastuzumab is a monoclonal antibody that binds HER2 extracellular subdomain IV to treat BC, although its mechanism of action is still not fully understood (Shawver *et al.*, 2002). It was demonstrated to reduce HER2 phosphorylation (Nami *et al.*, 2019). This is consistent with our results that following trastuzumab treatment, phosphorylation of HER2 is reduced. On the other hand, the activation-associated phosphorylation of SRC at tyrosine 416 remained significantly higher in tumors derived from cells expressing β -catenin than control, irrespective of trastuzumab treatment, suggesting that SRC activation is involved in trastuzumab re-

sistance. Previously, the SRC/STAT3 signaling pathway was found to be activated by chromosome condensin 1 complex subunit G (NCAPG), leading to trastuzumab resistance in HER2⁺BC and SRC phosphorylation may enhance nuclear localization and activation of STAT3 (Jiang *et al.*, 2020), leading to trastuzumab resistance (Zhang *et al.*, 2011). Since SRC phosphorylation occurs in tumors derived from cells overexpression β -catenin, further study is needed to explore β -catenin as a therapeutic target to overcome trastuzumab resistance.

CONCLUSION

β -catenin is highly expressed in BC tissues as compared to non-cancer tissue. It synergistically promotes formation and development of BC with HER2. β -catenin interacts with HER2 leading to SRC activation and trastuzumab resistance. Due to these important roles, β -catenin may be further explored as a therapeutic target to overcome trastuzumab resistance in BC.

Declarations

Ethics approval and consent to participate: The Ethics Committee of the Shenzhen Hospital Affiliated with Southern Medical University and written informed consent was obtained from every participant.

Availability of data and material: The datasets used and/or analysed during the current study are available from the corresponding author on reasonable request.

Competing interests: None.

Funding: None.

Acknowledge: Not applicable.

REFERENCES

- Anastasiadi Z, Lianos GD, Ignatiadou E, Harissis HV, Mitsis M (2017) Breast cancer in young women: an overview. *Updates Surg* 69: 313–317. <https://doi.org/10.1007/s13304-017-0424-1>
- Behrens J, von Kries JP, Kuhl M, Bruhn L, Wedlich D, Grosschedl R, Birchmeier W (1996) Functional interaction of beta-catenin with the transcription factor LEF-1. *Nature* 382: 638–642. <https://doi.org/10.1038/382638a0>
- Bredin P, Walshe JM, Denduluri N (2020) Systemic therapy for metastatic HER2-positive breast cancer. *Semin Oncol* 47: 259–269. <https://doi.org/10.1053/j.seminoncol.2020.07.008>
- Brennan KR, Brown AM (2004) Wnt proteins in mammary development and cancer. *J Mammary Gland Biol Neoplasia* 9: 119–131. <https://doi.org/10.1023/B:JOMG.0000037157.94207.33>
- Cameron D, Piccart-Gebhart MJ, Gelber RD, Procter M, Goldhirsch A, de Azambuja E, Castro Jr. G, Untch M, Smith I, Gianni L, Baselga J, Al-Sakaff N, Lauer S, McFadden E, Leyland-Jones B, Bell R, Dowsett M, Jackisch C, Herceptin Adjuvant Trial Study T (2017a) 11 years' follow-up of trastuzumab after adjuvant chemotherapy in HER2-positive early breast cancer: final analysis of the HERceptin Adjuvant (HERA) trial. *Lancet* 389: 1195–1205. [https://doi.org/10.1016/S0140-6736\(16\)32616-2](https://doi.org/10.1016/S0140-6736(16)32616-2)
- Cameron D, Piccart-Gebhart MJ, Gelber RD, Procter M, Goldhirsch A, de Azambuja E, Castro Jr. G, Untch M, Smith I, Gianni L, Baselga J, Al-Sakaff N, Lauer S, McFadden E, Leyland-Jones B, Bell R, Dowsett M, Jackisch C, Herceptin Adjuvant Trial Study T (2017b) 11 years' follow-up of trastuzumab after adjuvant chemotherapy in HER2-positive early breast cancer: final analysis of the HERceptin Adjuvant (HERA) trial. *Lancet* 389: 1195–1205. [https://doi.org/10.1016/S0140-6736\(16\)32616-2](https://doi.org/10.1016/S0140-6736(16)32616-2)
- Cipriano R, Patton JT, Mayo LD, Jackson MW (2010) Inactivation of p53 signaling by p73 or PTEN ablation results in a transformed phenotype that remains susceptible to Nutlin-3 mediated apoptosis. *Cell Cycle* 9: 1373–1379. <https://doi.org/10.4161/cc.9.7.11193>
- Cui C, Zhou X, Zhang W, Qu Y, Ke X (2018) Is beta-Catenin a Drugable Target for Cancer Therapy? *Trends Biochem Sci* 43: 623–634. <https://doi.org/10.1016/j.tibs.2018.06.003>
- Dankort D, Maslikowski B, Warner N, Kanno N, Kim H, Wang Z, Moran MF, Oshima RG, Cardiff RD, Muller WJ (2001) Grb2 and Shc adapter proteins play distinct roles in Neu (ErbB-2)-induced mammary tumorigenesis: implications for human breast cancer. *Mol*

- Cell Biol* **21**: 1540–1551. <https://doi.org/10.1128/MCB.21.5.1540-1551.2001>
- Derakhshani A, Rezaei Z, Safarpour H, Sabri M, Mir A, Sanati MA, Vahidian F, Gholamiyan Moghadam A, Aghadokht A, Hajiasgharzadeh K, Baradaran B (2020) Overcoming trastuzumab resistance in HER2-positive breast cancer using combination therapy. *J Cell Physiol* **235**: 3142–3156. <https://doi.org/10.1002/jcp.29216>
- Doumpas N, Lampart F, Robinson MD, Lentini A, Nestor CE, Cantu C, Basler K (2019) TCF/LEF dependent and independent transcriptional regulation of Wnt/beta-catenin target genes. *EMBO J* **38**: <https://doi.org/10.15252/embj.201798873>
- Ellis H, Ma CX (2019) PI3K Inhibitors in Breast Cancer Therapy. *Curr Oncol Rep* **21**: 110. <https://doi.org/10.1007/s11912-019-0846-7>
- Escriva-de-Romani S, Arumi M, Bellet M, Saura C (2018) HER2-positive breast cancer: Current and new therapeutic strategies. *Breast* **39**: 80–88. <https://doi.org/10.1016/j.breast.2018.03.006>
- Exman P, Tolane SM (2021) HER2-positive metastatic breast cancer: a comprehensive review. *Clin Adv Hematol Oncol* **19**: 40–50.
- Fahad Ullah M (2019) Breast Cancer: Current Perspectives on the Disease Status. *Adv Exp Med Biol* **1152**: 51–64. https://doi.org/10.1007/978-3-030-20301-6_4
- Ganz PA, Goodwin PJ (2015) Breast Cancer Survivorship: Where Are We Today? *Adv Exp Med Biol* **862**: 1–8. https://doi.org/10.1007/978-3-319-16366-6_1
- Gijzen M, King P, Perera T, Parker PJ, Harris AL, Larijani B, Kong A (2010) HER2 phosphorylation is maintained by a PKB negative feedback loop in response to anti-HER2 herceptin in breast cancer. *PLoS Biol* **8**: e1000563. <https://doi.org/10.1371/journal.pbio.1000563>
- Harbeck N, Penault-Llorca F, Cortes J, Gnani M, Houssami N, Poortmans P, Ruddy K, Tsang J, Cardoso F (2019) Breast cancer. *Nat Rev Dis Primers* **5**: 66. <https://doi.org/10.1038/s41572-019-0111-2>
- Horibata S, Vo T V, Subramanian V, Thompson PR, Conrod SA (2015) Utilization of the soft agar colony formation assay to identify inhibitors of tumorigenicity in breast cancer cells. *J Vis Exp* e52727. <https://doi.org/10.3791/52727>
- Hsieh TH, Hsu CY, Tsai CF, Chiu CC, Liang SS, Wang TN, Kuo PL, Long CY, Tsai EM (2016) A novel cell-penetrating peptide suppresses breast tumorigenesis by inhibiting beta-catenin/LEF-1 signaling. *Sci Rep* **6**: 19156. <https://doi.org/10.1038/srep19156>
- Hunter FW, Barker HR, Lipert B, Rothe F, Gebhart G, Piccart-Gebhart MJ, Sotiriou C, Jameson SMF (2020) Mechanisms of resistance to trastuzumab emtansine (T-DM1) in HER2-positive breast cancer. *Br J Cancer* **122**: 603–612. <https://doi.org/10.1038/s41416-019-0635-y>
- Jiang L, Ren L, Chen H, Pan J, Zhang Z, Kuang X, Chen X, Bao W, Lin C, Zhou Z, Huang D, Yang J, Huang H, Wang L, Hou N, Song L (2020) NCAPG confers trastuzumab resistance via activating SRC/STAT3 signaling pathway in HER2-positive breast cancer. *Cell Death Dis* **11**: 547. <https://doi.org/10.1038/s41419-020-02753-x>
- Jin P, Liu J, Wang X, Yang L, Zhou Q, Lin X, Xi S (2018) HER2 Activation factors in arsenite-exposed bladder epithelial cells. *Toxicol Sci* **166**: 354–369. <https://doi.org/10.1093/toxsci/kfy020>
- Jung DH, Bae YJ, Kim JH, Shin YK, Jeung HC (2019) HER2 Regulates cancer stem cell activities via the Wnt signaling pathway in gastric cancer cells. *Oncology* **97**: 311–318. <https://doi.org/10.1159/000502845>
- Kolak A, Kaminska M, Sygk K, Budny A, Surdyka D, Kukiela-Budny B, Burdan F (2017) Primary and secondary prevention of breast cancer. *Ann Agric Environ Med* **24**: 549–553. <https://doi.org/10.26444/aem/75943>
- Larionov AA (2018) Current therapies for human epidermal growth factor receptor 2-positive metastatic breast cancer patients. *Front Oncol* **8**: 89. <https://doi.org/10.3389/fonc.2018.00089>
- Lee YY, Kim HP, Kang MJ, Cho BK, Han SW, Kim TY, Yi EC (2013) Phosphoproteomic analysis identifies activated MET-axis PI3K/AKT and MAPK/ERK in lapatinib-resistant cancer cell line. *Exp Mol Med* **45**: e64. <https://doi.org/10.1038/emmm.2013.115>
- Lewis Phillips GD, Li G, Dugger DL, Crocker LM, Parsons KL, Mai E, Blattler WA, Lambert JM, Chari R v, Lutz RJ, Wong WL, Jacobson FS, Koeppen H, Schwall RH, Kenkare-Mitra SR, Spencer SD, Sliwkowski MX (2008) Targeting HER2-positive breast cancer with trastuzumab-DM1, an antibody-cytotoxic drug conjugate. *Cancer Res* **68**: 9280–9290. <https://doi.org/10.1158/0008-5472.CAN-08-1776>
- Liu H, Mastriani E, Yan ZQ, Yin SY, Zeng Z, Wang H, Li QH, Liu HY, Wang X, Bao HX, Zhou YJ, Kou JJ, Li D, Li T, Liu J, Liu Y, Yin L, Qiu L, Gong L, Liu SL (2016) SOX7 co-regulates Wnt/beta-catenin signaling with Axin-2: both expressed at low levels in breast cancer. *Sci Rep* **6**: 26136. <https://doi.org/10.1038/srep26136>
- Loibl S, Gianni L (2017) HER2-positive breast cancer. *Lancet* **389**: 2415–2429. [https://doi.org/10.1016/S0140-6736\(16\)32417-5](https://doi.org/10.1016/S0140-6736(16)32417-5)
- Mayer EL, Krop IE (2010) Advances in targeting SRC in the treatment of breast cancer and other solid malignancies. *Clin Cancer Res* **16**: 3526–3532. <https://doi.org/10.1158/1078-0432.CCR-09-1834>
- Mir MA, Qayoom H, Mehraj U, Nisar S, Bhat B, Wani NA (2020) Targeting different pathways using novel combination therapy in triple negative breast cancer. *Curr Cancer Drug Targets* **20**: 586–602. <https://doi.org/10.2174/1570163817666200518081955>
- Nahta R, Yu D, Hung MC, Hortobagyi GN, Esteva FJ (2006) Mechanisms of disease: understanding resistance to HER2-targeted therapy in human breast cancer. *Nat Clin Pract Oncol* **3**: 269–280. <https://doi.org/10.1038/ncponc0509>
- Nami B, Wang Z (2017) HER2 in Breast cancer stemness: a negative feedback loop towards trastuzumab resistance. *Cancers (Basel)* **9**: <https://doi.org/10.3390/cancers9050040>
- Nami B, Maadi H, Wang Z (2019) The effects of pertuzumab and its combination with Trastuzumab on HER2 homodimerization and phosphorylation. *Cancers (Basel)* **11**: <https://doi.org/10.3390/cancers11030375>
- Peairs KS, Choi Y, Stewart RW, Sateia HF (2017) Screening for breast cancer. *Semin Oncol* **44**: 60–72. <https://doi.org/10.1053/j.seminoncol.2017.02.004>
- Peiro G, Ortiz-Martinez F, Gallardo A, Perez-Balaguer A, Sanchez-Paya J, Ponce JJ, Tibau A, Lopez-Vilaro L, Escuin D, Adrover E, Barnadas A, Lerma E (2014) Src, a potential target for overcoming trastuzumab resistance in HER2-positive breast carcinoma. *Br J Cancer* **111**: 689–695. <https://doi.org/10.1038/bjc.2014.327>
- Rajajaran N, Mariotti V, Basu A, Kodumudi K, Han H, Czerniecki B, Hoover S (2020) Strategies to Combat Human Epidermal Growth Factor Receptor 2 (HER2) Resistance in HER2-positive breast cancer. *Crit Rev Oncog* **25**: 209–231. <https://doi.org/10.1615/CritRevOncog.2020036417>
- Ramagopalan S v, Pisoni R, Zenin A, Rathore LS, Ray J, Sammon C (2021) Comparative effectiveness of trastuzumab emtansine versus lapatinib plus chemotherapy for HER2+ metastatic breast cancer. *J Comp Eff Res* **10**: 595–602. <https://doi.org/10.2217/ce-2020-0201>
- Rinnerthaler G, Gampenrieder SP, Greil R (2019) HER2 directed antibody-drug-conjugates beyond T-DM1 in breast cancer. *Int J Mol Sci* **20**: <https://doi.org/10.3390/ijms20051115>
- Roskoski Jr. R (2015) Src protein-tyrosine kinase structure, mechanism, and small molecule inhibitors. *Pharmacol Res* **94**: 9–25. <https://doi.org/10.1016/j.phrs.2015.01.003>
- Ruiz-Saenz A, Dreyer C, Campbell MR, Steri V, Gulizia N, Moasser MM (2018) HER2 Amplification in tumors activates PI3K/Akt signaling independent of HER3. *Cancer Res* **78**: 3645–3658. <https://doi.org/10.1158/0008-5472.CAN-18-0430>
- Santa-Maria CA, Nye L, Mutonga MB, Jain S, Gradishar WJ (2016) Management of metastatic HER2-positive breast cancer: where are we and where do we go from here? *Oncology (Williston Park)* **30**: 148–155
- Saura C, Oliveira M, Feng YH, Dai MS, Chen SW, Hurvitz SA, Kim SB, Moy B, Delaloge S, Gradishar W, Masuda N, Palacova M, Trudeau ME, Mattson J, Yap YS, Hou MF, De Laurentiis M, Yeh YM, Chang HT, Yau T, Wildiers H, Haley B, Fagnani D, Lu YS, Crown J, Lin J, Takahashi M, Takano T, Yamaguchi M, Fujii T, Yao B, Bechuk J, Keyvanjah K, Bryce R, Brufsky A (2020) Neratinib plus capecitabine versus Lapatinib plus capecitabine in HER2-positive metastatic breast cancer previously treated with >= 2 her2-directed regimens: phase III NALA trial. *J Clin Oncol* **38**: 3138–3149. <https://doi.org/10.1200/JCO.20.00147>
- Schade B, Lesurf R, Sanguin-Gendreau V, Bui T, Deblois G, O'Toole SA, Millar EK, Zardawi SJ, Lopez-Knowles E, Sutherland RL, Giguere V, Kahn M, Hallett M, Muller WJ (2013) beta-Catenin signaling is a critical event in ErbB2-mediated mammary tumor progression. *Cancer Res* **73**: 4474–4487. <https://doi.org/10.1158/0008-5472.CAN-12-3925>
- Sefidbakht S, Saeedipour H, Saffar H, Mirzaian E (2021) Determination of beta-catenin expression in breast cancer and its relationship with clinicopathologic parameters. *Asian Pac J Cancer Prev* **22**: 3493–3498. <https://doi.org/10.31557/APJCP.2021.22.11.3493>
- Shawver LK, Slamon D, Ullrich A (2002) Smart drugs: tyrosine kinase inhibitors in cancer therapy. *Cancer Cell* **1**: 117–123. [https://doi.org/10.1016/S1535-6108\(02\)00039-9](https://doi.org/10.1016/S1535-6108(02)00039-9)
- Shen G, Gao Q, Liu F, Zhang Y, Dai M, Zhao T, Cheng M, Xu T, Jin P, Yin W, Huang D, Weng H, Chen W, Ren H, Mu X, Wu X, Hu S (2020) The Wnt3a/beta-catenin/TCF7L2 signaling axis reduces the sensitivity of HER2-positive epithelial ovarian cancer to trastuzumab. *Biochem Biophys Res Commun* **526**: 685–691. <https://doi.org/10.1016/j.bbrc.2020.03.154>
- Smith I, Procter M, Gelber RD, Guillaume S, Feyereislova A, Dowsett M, Goldhirsch A, Untch M, Mariani G, Baselga J, Kaufmann M, Cameron D, Bell R, Bergh J, Coleman R, Wardley A, Harbeck N, Lopez RI, Mallmann P, Gelmon K, Wilken M, Wist E, Sánchez Rovira P, Piccart-Gebhart MJ (2007) 2-year follow-up of trastuzumab after adjuvant chemotherapy in HER2-positive breast cancer: a randomised controlled trial. *Lancet* **369**: 29–36. [https://doi.org/10.1016/S0140-6736\(07\)60028-2](https://doi.org/10.1016/S0140-6736(07)60028-2)
- Song L, Liu D, He J, Wang X, Dai Z, Zhao Y, Kang H, Wang B (2016) SOX1 inhibits breast cancer cell growth and invasion through suppressing the Wnt/beta-catenin signaling pathway. *APMIS* **124**: 547–555. <https://doi.org/10.1111/apm.12543>

- Tolaney SM, Tayob N, Dang C, Yardley DA, Isakoff SJ, Valero V, Faggen M, Mulvey T, Bose R, Hu J, Weckstein D, Wolff AC, Reed-Hayes K, Rugo HS, Ramaswamy B, Zuckerman D, Hart L, Gadi VK, Constantine M, Cheng K, Briccetti F, Schneider B, Garrett AM, Marcom K, Albain K, DeFusco P, Tung N, Ardan B, Nanda R, Jankowitz RC, Rimawi M, Abramson V, Pohlmann PR, Van Poznak C, Forero-Torres A, Liu M, Ruddy K, Zheng Y, Rosenberg SM, Gelber RD, Trippa L, Barry W, DeMeo M, Burstein H, Partridge A, Winer EP, Krop I (2021) Adjuvant trastuzumab emtansine versus paclitaxel in combination with trastuzumab for stage I HER2-positive breast cancer (ATEMPT): a randomized clinical trial. *J Clin Oncol* **39**: 2375–2385. <https://doi.org/10.1200/JCO.20.03398>
- Uijen MJM, Lassche G, van Engen-van Grunsven ACH, Driessen CML, van Herpen CML (2022) Case series of docetaxel, trastuzumab, and pertuzumab (DTP) as first line anti-HER2 therapy and ado-trastuzumab emtansine (T-DM1) as second line for recurrent or metastatic HER2-positive salivary duct carcinoma. *Oral Oncol* **125**: 105703. <https://doi.org/10.1016/j.oraloncology.2021.105703>
- Wang HM, Xu YF, Ning SL, Yang DX, Li Y, Du YJ, Yang F, Zhang Y, Liang N, Yao W, Zhang LL, Gu LC, Gao CJ, Pang Q, Chen YX, Xiao KH, Ma R, Yu X, Sun JP (2014) The catalytic region and PEST domain of PTPN18 distinctly regulate the HER2 phosphorylation and ubiquitination barcodes. *Cell Res* **24**: 1067–1090. <https://doi.org/10.1038/cr.2014.99>
- Wang Z, Li Z, Ji H (2021) Direct targeting of beta-catenin in the Wnt signaling pathway: Current progress and perspectives. *Med Res Rev* **41**: 2109–2129. <https://doi.org/10.1002/med.21787>
- White BD, Chien AJ, Dawson DW (2012) Dysregulation of Wnt/beta-catenin signaling in gastrointestinal cancers. *Gastroenterology* **142**: 219–232. <https://doi.org/10.1053/j.gastro.2011.12.001>
- Wu Y, Ginther C, Kim J, Mosher N, Chung S, Slamon D, Vadgama JV (2012) Expression of Wnt3 activates Wnt/beta-catenin pathway and promotes EMT-like phenotype in trastuzumab-resistant HER2-overexpressing breast cancer cells. *Mol Cancer Res* **10**: 1597–1606. <https://doi.org/10.1158/1541-7786.MCR-12-0155-T>
- Wu Y, Tran T, Dwabe S, Sarkissyan M, Kim J, Nava M, Clayton S, Pietras R, Farias-Eisner R, Vadgama J v (2017) A83-01 inhibits TGF-beta-induced upregulation of Wnt3 and epithelial to mesenchymal transition in HER2-overexpressing breast cancer cells. *Breast Cancer Res Treat* **163**: 449–460. <https://doi.org/10.1007/s10549-017-4211-y>
- Xie Y, Hung MC (1996) p66Shc isoform down-regulated and not required for HER-2/neu signaling pathway in human breast cancer cell lines with HER-2/neu overexpression. *Biochem Biophys Res Commun* **221**: 140–145. <https://doi.org/10.1006/bbrc.1996.0559>
- Yost C, Torres M, Miller JR, Huang E, Kimelman D, Moon RT (1996) The axis-inducing activity, stability, and subcellular distribution of beta-catenin is regulated in *Xenopus* embryos by glycogen synthase kinase 3. *Genes Dev* **10**: 1443–1454. <https://doi.org/10.1101/gad.10.12.1443>
- Zhang J, Gill AJ, Issacs JD, Atmore B, Johns A, Delbridge LW, Lai R, McMullen TP (2012) The Wnt/beta-catenin pathway drives increased cyclin D1 levels in lymph node metastasis in papillary thyroid cancer. *Hum Pathol* **43**: 1044–1050. <https://doi.org/10.1016/j.humpath.2011.08.013>
- Zhang J, Zhang S, Li X, Zhang F, Zhao L (2021) HOXB5 promotes the progression of breast cancer through wnt/beta-catenin pathway. *Patol Res Pract* **224**: 153117. <https://doi.org/10.1016/j.prp.2020.153117>
- Zhang S, Huang WC, Li P, Guo H, Poh SB, Brady SW, Xiong Y, Tseng LM, Li SH, Ding Z, Sahin AA, Esteva FJ, Hortobagyi GN, Yu D (2011) Combating trastuzumab resistance by targeting SRC, a common node downstream of multiple resistance pathways. *Nat Med* **17**: 461–469. <https://doi.org/10.1038/nm.2309>
- Zhang Y, Wang X (2020) Targeting the Wnt/beta-catenin signaling pathway in cancer. *J Hematol Oncol* **13**: 165. <https://doi.org/10.1186/s13045-020-00990-3>

Impact of diet modification on body mass and kidney function in patients with diabetic nephropathy: a pilot study

Małgorzata Kaczkan¹, Sylwia Czaja-Stolc¹✉, Małgorzata Sikorska-Wiśniewska², Michał Chmielewski², Alicja Dębska-Słizień² and Sylwia Małgorzewicz¹

¹Department of Clinical Nutrition, Medical University of Gdansk, Gdańsk, Poland; ²Department of Nephrology, Transplantology and Internal Medicine, Medical University of Gdansk, Gdańsk, Poland

Objectives: The increasing trend in chronic kidney disease (CKD) has occurred in parallel with the increased prevalence of obesity and diabetes type 2. The relationship between a reduction in body mass and protein intake in diabetic nephropathy (DN) has not been adequately understood. This study aimed to determine whether dietary intervention in an adult with DN is associated with decreasing proteinuria or changes in kidney function over six months. **Methods:** The study included 120 patients with DN, consecutively admitted to a dietitian from a Kidney Disease Clinic. Patients were classified into two groups: a reduction diet or a normal calorie diet, both with 0.8 g of protein/kg of ideal body weight/day. Anthropometric and laboratory assessments were done before and after observation. **Results:** After six months, in the study group of patients on a reducing diet, a decrease in body mass, body mass index (BMI) and stabilization of estimated glomerular filtration rate (eGFR) were observed. There was also a significant correlation between the time of diabetes diagnosis and eGFR and creatinine (R Spearman=−0.24 and 0.3, respectively; $p=0.05$). There were no other significant associations between body mass, BMI, albuminuria, eGFR, or creatinine. **Conclusions:** The study shows that obesity is a common comorbid disease in patients with DN and that dietary intervention is associated with a significant reduction in body mass and stabilization of eGFR in these patients.

Keywords: diet; obesity; diabetes; diabetic nephropathy; estimated glomerular filtration rate

Received: 13 June, 2023; **revised:** 16 June, 2023; **accepted:** 05 July, 2023; **available on-line:** 17 September, 2023

✉e-mail: sylwia.czaja-stolc@gumed.edu.pl

Abbreviations: BMI, body mass index; BMR, basal metabolic rate; CC, creatinine clearance; CKD, chronic kidney disease; DN, diabetic nephropathy; eGFR, estimated glomerular filtration rate; ESKD, end-stage kidney disease; HbA1c, glycated hemoglobin/hemoglobin A1c; TDEE, total daily energy expenditure; UACR, urine albumin-to-creatinine ratio

INTRODUCTION

Diabetic nephropathy (DN), also known as diabetic kidney disease is one of the most common complications of diabetes and is the leading cause of end-stage kidney disease (ESKD) in the general population (Khan *et al.*, 2018). DN is characterized by the development of progressive albuminuria and the loss of the glomerular filtration rate (GFR) (Tuttle *et al.*, 2014). Published studies have shown that among patients who started renal replacement therapy, the percentage of patients with diabe-

tes (only DN) ranged from 24% to 51% (all causes were counted) and is still increasing (Buyadaa *et al.*, 2020).

According to the World Health Organization (WHO), the number of patients requiring renal replacement therapy is expected to double by 2030 (Luyckx *et al.*, 2018). Therefore, conservative treatment of chronic kidney disease (CKD) is becoming increasingly important from the point of view of preventing an epidemic of this disease. Experts point to the importance of proper dietary management and education in this area as one of the key points in the development of nephroprotective effects, which may have a measurable, positive impact on the quality of life of patients and inhibit the increase in the number of patients at the end-stage of the disease (Tuttle *et al.*, 2014).

The main cause of excess body weight and its complications are lifestyle changes, limitation of physical activity, improper eating habits, and above all, the excessive consumption of high-energy products (Swinburn *et al.*, 2004). Changing incorrect eating habits is most effective in the early stages of diseases such as obesity, diabetes type 2, or CKD, but at every stage it is worth recommending that patients correct any eating mistakes. However, the relationship between overweight or obesity in patients with CKD and the mortality risk is not clear. Dietary intervention is particularly important in patients with CKD, as well as in other disease states and metabolic phenotypes such as obesity and diabetes, which affect the risk of developing and exacerbating the progression of CKD (Díaz-López *et al.*, 2021).

Treatment of DN includes intensive control of glycaemia – glycated hemoglobin/hemoglobin A1c (HbA1c) <7%, proteinuria, hypertension through pharmacotherapy, as well as lifestyle modifications. The American Diabetes Association (ADA) recommendations for people with DKD do not promote a change in the amount of protein in the diet below 0.8 g/kg/day but rather suggest replacing the animal protein source with soybean to reduce cardiovascular risk (American Diabetes Association, 2014). Moreover, the latest recommendations of NKF KDOQI Clinical Practice Guideline On Nutrition In CKD: 2020 Update (Ikizler *et al.*, 2020) indicate the possibility of limiting protein consumption in the range of 0.6–0.8 g/kg/day in the group of adults with diabetes and with estimated glomerular filtration rate (eGFR) <60 mL/min/1.73 m². The study aimed to determine whether dietary intervention in an adult with DN is associated with proteinuria or changes in kidney function during a six-month observation period.

MATERIAL AND METHODS

Study design

The current study was a 6-month interventional study to determine the effects of dietary intervention on renal function and proteinuria in adults with DKD. The nephrologist enrolled DKD patients in the study and referred them to a clinical dietitian. The dietitian then wrote down the rules of the diet and, based on the body mass index (BMI), divided patients into two groups. Dietitian visits were scheduled every 4–6 weeks, and nephrological control visits every 12 weeks.

DKD was diagnosed in patients with diabetes according to recommendations: if indicators of kidney damage persist ≥ 3 months:

- macroalbuminuria – urine albumin-to-creatinine ratio (UACR) >300 mg/g
- microalbuminuria – 30–300 mg/g in the presence of diabetic retinopathy; in diabetes type 1 (additionally), when the duration of the disease is at least ten years (KDOQI, 2007).

Inclusion criteria for the study were: age >18 years old, DKD stages 2–5, good nutritional status, and signed consent to participate in the study.

All subjects gave informed consent to the inclusion before participating in the study. The study was approved by the Bioethical Committee.

Initially, 120 patients were enrolled in the study, but 50 (42%) were excluded because they did not follow the diet and did not attend follow-up visits. The scheme of the study is presented in Fig. 1.

Study population

Ultimately, the study population consisted of 70 clinically stable patients with DKD, at an average age of 65.1 ± 11.8 years, admitted to the dietitian from the ambulatory Department of Nephrology, Transplantology and Internal Medicine at the University Clinical Center in Gdansk (Poland) in the years 2018–2020.

The results were collected over six months of follow-up, with visits every 1–3 months. At each visit, body

weight, laboratory parameters and compliance with dietitian rules were assessed.

Dietary intervention

All patients who consented to participate in the study had a personal appointment with a dietitian with extensive experience in the management of CKD diet. Diet planning methodology included the determination of energy demand by measuring basal metabolic rate (BMR) based on bioimpedance mass indications. The patient's total daily energy expenditure (TDEE) was then calculated using the appropriate level of physical activity (PAL):

- 1.4 – for people with low physical activity,
- 1.6 – for people with medium physical activity,
- 2.0 – for people with high physical activity.

Protein intake was established at 0.8 g/kg of ideal body weight/day, phosphorus 800–1200 mg/day and potassium 2000–2500 mg/day. The ideal body weight is calculated based on Broc's formula.

Patients with BMI ≥ 30 were qualified for the reduction diet – the amount of body weight loss per unit time was set at 0.5–1.0 kilograms per week – to unify the deficit of 500 kcal/day. Patients with BMI <30 were enrolled in a normal calorie diet.

The following nutrient requirements were determined in both groups: protein – 0.8 g/kg of ideal body weight/day, carbohydrates – 45–55% and fats – 30–35% of daily energy requirement. The mineral demand was determined based on the dietary standards of the Polish population. The patients' daily diet is defined as 4–5 meals. During the observation, patients met with a dietitian to obtain nutritional advice. At each control meeting, a 24-hour diet recall was conducted, and patients were asked to record their diet for three days before the visit. Patients were re-educated on the correct application of the diet. Each time during the meeting, patients were subjected to bioimpedance measurements, based on which BMR and TDEE were determined as the starting point for determining energy reduction in the diet, in accordance with the recommendations of the Polish Society of Dietetics and NKF KDOQI (KDOQI, 2007; Gajewska *et al.*, 2015). All patients were instructed to maintain a minimum level of 150 min. per week of physical activity throughout the study period.

BMI

Measurement of body mass with the scale (Tanita BC 420) was performed at each visit by a dietitian. The BMI was calculated using the following formula: $\text{BMI} = \text{body weight} / \text{height}^2$ (kg/m^2). The BMI classification was adopted: <18.5 – underweight; 18.5–24.9 – normal body weight; 25.0–29.9 – overweight; ≥ 30.0 – obesity. The ideal body weight was calculated according to Broc's formula ($\text{height in cm} - 100$); height was measured in a stadiometer.

Laboratory Measurements

Albumin, triglycerides, total cholesterol, phosphorus, potassium, creatinine, fasting glucose, HbA1c, and blood counts were measured for all participants (baseline and at six months) using routine laboratory tests. UACR was calculated from urine albumin and creatinine. eGFR was calculated according to The Modification of Diet in Renal Disease (MDRD) equation and creatinine clearance (CC) was obtained from The Cockcroft-Gault equation. After three months of observation, serum creatinine

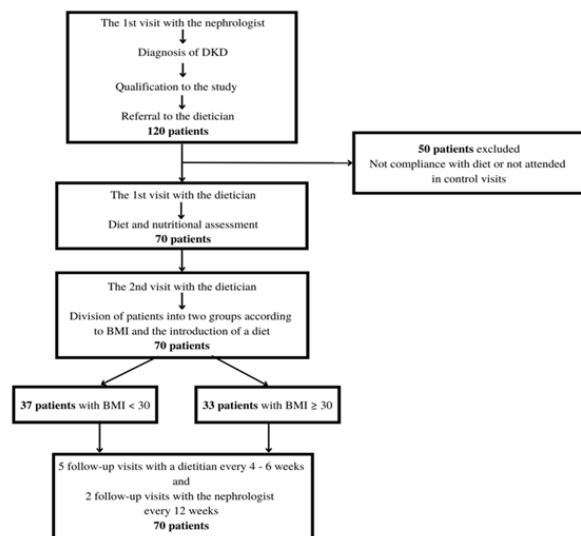


Figure 1. Scheme of the study.

Table 1. Basic characteristics of the studied patients.

Parameters	All patients with DN n=70
Age (years)	65.1±11.8 (40–87)
M/F	40/30
BMI (kg/m ²)	30.4±7.3 (18.4–53.1)
eGFR (ml/min/1.73 m ²) acc. MDRD	41.3±20.5 (8.0–123)
CC (ml/min.) acc. Cockcroft -Gault	60.2±50.5 (8.6–260.0)
Creatinine (mg/dl)	2.0±1.1 (0.6–6.6)
Time since diagnosis of diabetes (years)	9.8±4.8 (4–18)
HbA1c (%)	6.6±1.1 (6.3–7.5)
Stage of CKD	
G2 (%)	11.5
G3 (%)	62.8
G4 (%)	17.1
G5 (%)	8.6

Data are presented as mean ± S.D. and range. Abbreviations: M, men; F, female; BMI, body mass index; eGFR, estimated glomerular filtration rate; MDRD, Modification of Diet in Renal Disease; CC, creatinine clearance; HbA1c, glycated hemoglobin/hemoglobin A1c; CKD, chronic kidney disease

and UACR were measured. All patients performed self-monitoring of blood glucose and blood pressure during follow-up.

Statistical Analysis

Results are expressed as percentages (for categorical variables), mean, and standard deviation. The assumption of normality was verified by the Kolmogorov-Smirnov test. A *p*-value <0.05 was considered statistically significant. The Spearman correlation coefficient (*R*) was used to assess the correlation between the assessed variables. Comparisons between the two groups were assessed using the Student's *t*-test or the U-Mann-Whitney test, respectively. The change in value between the first visit and the last visit (value for the last visit minus the value for the first visit) was compared between the groups. The comparison was made using the Wilcoxon test. Statistical processing of the results was performed with the use of the statistical software STATISTICA PL v 13.0 (Statsoft, Kraków, Poland).

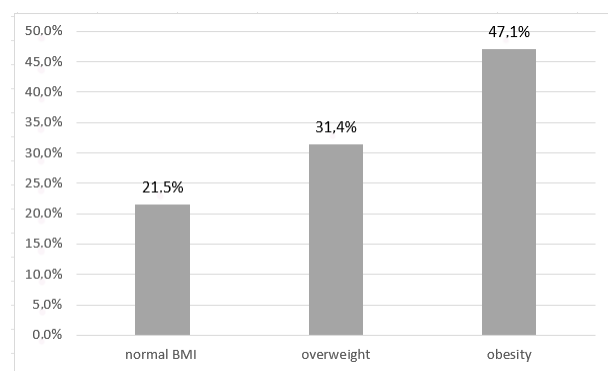


Figure 2. The percentage of patients with excess body mass at baseline.

RESULTS

Characteristics of patients with DN

The results of 70 patients who completed the study were analyzed. The baseline patient characteristics are shown in Table 1. Diabetes type 1 was diagnosed among 11 patients (15%), and diabetes type 2 among 59 (85%). The mean duration of diabetes was 9.84 ± 4.8 years (range 4–18).

There were five obese patients in the G2 stage, G3 had 22 patients, G4 had four patients, and G5 had two patients. Most of the patients were treated with insulin, and 43% received oral antidiabetic drugs from various groups. Antihypertensive treatment with renin-angiotensin system blockers was received by 97% of patients.

Baseline results

A total of 33 patients (47.1%) were obese; 22 (31.4%) were overweight, and 15 (21.5%) presented normal BMI at baseline (Fig. 2).

The mean serum albumin level was 38.2 ± 2.9 mg/L and indicated good nutritional status in patients. Serum levels of potassium and phosphorus were in reference ranges (4.6 ± 0.6 mmol/L; 3.9 ± 0.9 mg/dL, respectively). The mean fasting glucose level was 149.06 ± 54.0 mg/dL and HbA1c – 6.6%. The mean eGFR was 41.3 ± 20.5 mL/min/1.73 m² and the mean CC, according to the Cockcroft-Gault formula, was 60.2 ± 50.5 mL/min. The correlation between eGFR MDRD and CC was high ($R=0.88$; $p<0.05$). The UACR was in the range of 1120 ± 152 mg/g.

In addition, a statistically significant correlation between the time of diabetes diagnosis and eGFR and creatinine (R Spearman = –0.24 and 0.3, respectively; $p=0.05$) was noted. There was no significant relationship between body mass, BMI, albuminuria, eGFR, CC and serum creatinine.

Follow-up results

As presented in Table 2, in the study group, after six months of dietary intervention, a decrease in body mass and BMI was noted in comparison to the baseline parameters. Serum creatinine, eGFR, UACR, albumin, phosphorus, and potassium were changed insignificantly. Changes in eGFR are presented in Fig. 3.

In the obese group, the mean body weight loss over six months was 7.0 ± 2.2 kg, and in the non-obese group,

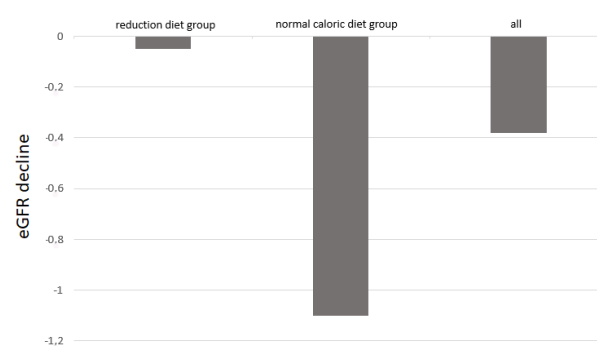


Figure 3. Changes in eGFR according to used diet.

Table 2. The anthropometric and biochemical parameters in patients before and after 6 months of dietary intervention.

Parameters	All n=70 before	All n=70 after	Obese group n=33 before	Obese group n=33 after	Non-obese group n=37 before	Non-obese group n=37 after
Body Mass (kg)	93.8±26.5	89.6±28.7	110.3±20.8	102.4±29.5	71.2±13.5	70.8±13.5
BMI (kg/m ²)	30.4±7.3	29.0±8.2	36.0±6.3	34.0±6.2	25.3±3.4	24.6±5.3
Albumin (g/L)	38.2±2.9	37.1±3.1	37.0±2.7	35.0±1.6	38.7±3.0	37.1±2.1
Phosphorus (mg/dL)	3.9±0.9	3.5±7.4	3.8±0.7	3.5±0.6	4.7±1.7	4.6±2.6
Potassium (mg/dL)	4.6±0.6	4.8±0.9	4.47±0.7	4.5±0.56	4.8±1.9	4.9±2.0
eGFR (mL/min/1.73 m ²) acc. MDRD	41.3±20.5	36.9±2.5	42.8±22.2	42.7±19.7	40.0±19.0	39.4±17.8
Creatinine (mg/dL)	2.0±1.1	2.2±1.3	1.88±9.1	2.06±1.1	2.17±1.5	2.2±2.1
CC (mL/min) acc. Cockcroft-Gault	60.2±50.2	50.1±41.1	80.2±61.7	60.2±43.8	42.7±29.2	40.8±30.1
Hemoglobin (g/dL)	12.9±1.6	12.7±1.9	11.9±1.7	11.8±1.9	12.9±2.2	13.4±2.4
Total cholesterol (mg/dL)	214.4±50.5	198.2±37.8	231±47	221±57	231±45	235±67
HDL (mg/dL)	48.2±14.0	48.9±12.6	43.5±11.4	46.1±13.6	37.8±7.9	38.9±11.1
HbA1C (%)	6.8±1.1	6.7±0.8	6.8±1.2	6.9±1.3	6.8±2.4	6.6±2.1
Glucose fasting (mg%)	148±48	132±54	156±68	143±59	145±87	156±50
UACR (mg/g creatinine)	1120±152	1525.5±120.8	2290±187	2131±213	1241±256	1820±252

Data are presented as mean ±S.D. Aberrations: BMI, body mass index; eGFR, estimated glomerular filtration rate; MDRD, Modification of Diet in Renal Disease; CC, creatinine clearance; HDL, high-density lipoprotein; HbA1c, glycated hemoglobin/hemoglobin A1c; UACR, urine albumin-to-creatinine ratio

it was 0.4±0.4 kg. The urinary protein excretion in both groups did not change significantly.

DISCUSSION

The occurrence of excess body mass in DN patients and the effectiveness of six months of dietitian intervention were observed in the study. The prevalence of obesity was 47%, and about 31% of the patients were overweight. After six months of the reduction diet, 63.6% of patients decreased their body mass and BMI. Excess weight is often associated with type 2 diabetes. Moreover, the accumulation of adipose tissue in the trunk area in patients with type 2 diabetes may be associated with potential consequences, for instance, albuminuria, proteinuria, and a decrease in GFR (Gnacińska *et al.*, 2009). Mild renal failure is associated with high cardiovascular risk in the general population: any decrease in eGFR below the norm of 5 mL/min increases cardiovascular risk by 26% (Schram *et al.*, 2004; Ronald *et al.*, 2002). Serum creatine concentrations >1.6 mg/dL are associated with a 20% increased risk of mortality for all causes, cardiovascular and ischemic cardiovascular conditions (Wanamethee *et al.*, 1997).

The presented results confirm that obesity is a major public health problem among diabetic patients, including those with DN. The prevalence of excess body mass reached 80%, which indicates that a significant number of patients in nephrology outpatients required appropriate nutritional treatment (Bijelic *et al.*, 2020). It is also worth emphasizing that a significant number of patients (50/120, 42%) did not agree with the proposed diet, which is a significant problem in clinical practice. However, in the obese group, about 36% of patients did not lose significant body weight, possibly due to non-compliance with the diet. The resignation from dietitian intervention was more frequent in the beginning – perhaps

more accurate education is needed among patients with diabetes. Despite recommendations for lifestyle modification at every stage of diabetes, patients were not cooperative.

In the current study, a diet of 0.8 g protein/kg ideal body weight/day was followed as recommended. Additionally, in obese patients, a caloric deficit of 500 kcal/day was established. The primary goal of the diet was adequate glycemic control, as measured by self-measured fasting glucose and HbA1c. In the current study, the average level of HbA1c was 6.8% and did not change throughout the observation. The second goal was to reduce body weight in obese patients and to establish an association between weight loss and eGFR, CC, and proteinuria. It is well known that a properly balanced diet allows for a sustained reduction in body weight by an average of 0.5–1 kg per week (Bray *et al.*, 2003; Sacks *et al.*, 2009; Hruby *et al.*, 2015).

In the current study, the mean weight loss in obese patients (BMI>30) was approximately 7 kg/6 months. Despite a weight loss of about 1 kg per month, no statistically significant changes were found in eGFR, CC or albuminuria. The average decrease in eGFR in the study was 0.37 mL/min/1.73 m² and satisfactory and stable results were obtained. The observed decrease in CC from 80.2–60.2 mL/min in the obese group is favorable because it indicates a decrease in hyperfiltration and also indicates that eGFR, according to MDRD, is a less accurate parameter, especially in obese people. Navaneethan S.D. and others showed in a meta-analysis that weight loss as a result of dietary or bariatric intervention is associated with a reduction in proteinuria, blood pressure and, in the case of severe obesity, with normalization of eGFR (Navaneethan *et al.*, 2009). Moreover, Diaz-Lopez *et al.*, in the PREDIMED-Plus trial, concluded that the lifestyle intervention approach may preserve renal function and delay CKD progression in adults with excess body mass (Diaz-Lopez *et al.*, 2021). The RIGOR-TMU

study also indicated that weight loss after bariatric surgery was associated with eGFR preservation in patients with CKD (Becerra-Tomás *et al.*, 2019).

The ADA published a nutrition care model that provided evidence-based, standardized, high-quality care for non-dialyzed patients with CKD. The document reported that: “nutrition care provided by a registered dietitian up to twice monthly over one year can have a valuable role in the medical care of patients with CKD by providing nutrition assessment and interventions to delay kidney disease progression in addition to co-morbid conditions, such as diabetes, cardiovascular disease (CVD), dyslipidemia, gout, and nephrolithiasis” (American Diabetes Association. Choose Your Foods, 2014). In the current study, follow-up visits were established every 4–6 weeks, while in everyday practice, meetings with dietitians are less frequent. The effectiveness of diet modification might be better if the ADA recommendations were applied in both research and practice.

The primary goal of diabetes treatment is to maintain optimal glycemic control and to prevent complications, including renal and cardiovascular complications. The NKF KDOQI recommendations from 2020 focus on dietary protein intake as a factor in the progression of kidney damage and suggest 0.6–0.8 g of protein/kg/day in adult patients with diabetes and CKD stages 3–5. The NKF KDOQI recommendations are based on expert opinion and must be used with caution, i.e., only in patients in good clinical condition, in good nutritional status, and cooperating well, otherwise, there is a risk of malnutrition (Ikizler *et al.*, 2020). In the current study, despite 0.8 g of protein/kg of ideal body weight/per day, there was a tendency to lower the level of albumin.

The Kidney Disease: Improving Global Outcomes (KDIGO) guidelines suggest a more liberal diet when protein intake is 0.8 g/kg body weight per day and does not exceed >1.3 g of protein/kg body weight (Avesani *et al.*, 2005). KDIGO guidelines underline that reducing protein intake is associated with slowing the progression of CKD, improving urea and phosphate levels, and reducing acidosis (Cupisti *et al.*; 2020). However, some studies have shown that low-protein diets reduce hyperfiltration (Kontessis *et al.*, 1990; De Nicola *et al.*, 2020).

In the second studied group (on a normal calorie diet with 0.8 g of protein/kg/day), changes were not noted in any body mass, eGFR, or UACR during the observation period, and the dietitian's assessment indicated good adherence to the recommendations in this group. In the study, a diet based on animal and plant products was used, but there are reports that plant protein is more beneficial in CKD. Some authors (McGraw *et al.*, 2016; Moorthi *et al.*, 2017) have suggested that plant-based diets are more beneficial for DKD patients, especially those with high cardiovascular risk.

In everyday practice, it is very important to correct a patient's diet. It should be noted that not only the supply of protein is important, but also the content of calories, fat, and carbohydrates as well as vitamins and minerals (Skrypnik *et al.*, 2019). The ADA recommends lifestyle modifications based on increased physical activity and the assumptions of the Mediterranean or DASH diet, reducing the consumption of saturated fatty acids and trans isomers and increasing fiber and unsaturated fatty acids (American Diabetes Association. Choose Your Foods, 2014).

The authors would like to emphasize the need to educate patients and medical staff in the field of primary and secondary prevention. Proper modification of the diet is recommended by nephrological societies in delayed kid-

ney dysfunction and is also recommended as prophylaxis of cardiovascular events (Skrypnik *et al.*, 2019; Skrypnik *et al.*, 2020). The current results suggest the advantages of including simultaneous pharmacological and dietary intervention in the overall prevention of ESKD and cardiovascular risk in patients with excess body weight and diabetic nephropathy. To draw more precise conclusions, more research is needed on the effects of weight loss and modification of protein intake on the progression of CKD in obese patients with DN.

LIMITATIONS OF THE STUDY

The current study has several limitations. The first limitation is the small group of patients. Other limitations include the lack of detailed diet analysis and strict control of diet compliance, e.g., by the excretion of urea nitrogen in the urine. The observation time was short, and long-term studies are needed to analyze the renal outcomes, such as the development of renal dysfunction.

The strengths of the study include the demonstration of the role of a dietitian in the treatment of patients with diabetes and kidney diseases and the need to educate patients on non-pharmacological methods of treatment.

CONCLUSION

The study shows that obesity is a common symptom in patients with DN, and dietary intervention is associated with a significant reduction in body weight and stabilization of eGFR in these patients. As the majority of DN patients are at risk of obesity-related mortality, the advice of a dietitian should become part of both routine clinical evaluation and intervention.

PRACTICAL APPLICATION

The study shows the effect of dietary interventions on the progression of DN. The study also emphasizes that it is necessary to educate patients on the impact of diet on the progression of the underlying disease and the risk of complications, especially cardiovascular-related ones.

Declarations

Funding: This research received no external funding.

Author Contributions: Conceptualization, A.D.-Ś., S.M.; methodology, M.K., and S.M.; validation, M.K.; formal analysis, S.C.-S., S.M.; investigation, M.K., M.S.-W.; resources, M.K.; S.C.-S.; data curation, M.K., M.S.-W.; writing – original draft preparation, M.K., S.M.; writing – review and editing, S.C.-S., M.K., S.M.; supervision, M.C., A.D.-Ś., and S.M. All authors have read and agreed to the published version of the manuscript.

Institutional Review Board Statement: The study was conducted in accordance with the Declaration of Helsinki and approved by the Independent Bioethical Committee of the Medical University of Gdańsk (NKBBN/343/2018).

Informed Consent Statement: Informed consent was obtained from all subjects involved in the study.

Data Availability Statement: Not applicable.

Acknowledgments: Not applicable.

Conflicts of Interest: The authors declare no conflict of interest.

REFERENCES

- American Diabetes Association (2014) Choose Your Foods: Food Lists for Weight Management. 1st edn. Chicago, IL: Academy of Nutrition and Dietetics
- American Diabetes Association (2014) Standards of medical care in diabetes 2014. *Diabetes Care* **37** (Suppl 1): S14–S80. <https://doi.org/10.2337/dc14-S014>
- Avesani CM, Kamimura MA, Draibe SA, Cuppari L (2005) Is energy intake underestimated in non-dialyzed chronic kidney disease patients? *J Ren Nutr* **15**: 159–165. <https://doi.org/10.1053/j.jrn.2004.09.010>
- Becerra-Tomás N, Ruiz V, Toledo E, Babio N, Corella D, Fitó M (2019) Effect of weight loss on the estimated glomerular filtration rates of obese patients at risk of chronic kidney disease: the RIGOR-TMU study. *J Cachexia Sarcopenia Muscle* **10**: 756–766. <https://doi.org/10.1002/jcsm.12423>
- Bijelic R, Balaban J, Milicevic S, Sipka SU (2020) The association of obesity and microvascular complications with glycemic control in patients with type 2 diabetes mellitus. *Med Arch* **74**: 14–18. <https://doi.org/10.5455/medarch.2020.74.14-18>
- Bray G, Bouchard C (2003) Handbook of obesity: etiology and pathophysiology, 3rd edn: 19–37. CRC Press
- Buyadaa O, Magliano DJ, Salim A, Koye DN, Shaw JE (2020) Risk of rapid kidney function decline, all-cause mortality, and major cardiovascular events in nonalbuminuric chronic kidney disease in type 2 diabetes. *Diabetes Care* **43**: 122–129. <https://doi.org/10.2337/dc19-1438>
- Cupisti A, Giannese D, Moriconi D, D'Alessandro C, Torreggiani M, Piccoli GB (2020) Nephroprotection by SGLT2i in CKD Patients: may it be modulated by low-protein plant-based diets? *Front Med (Lausanne)* **7**: 622593. <https://doi.org/10.3389/fmed.2020.622593>
- De Nicola L, Gabbai FB, Garofalo C, Conte G, Minutolo R (2020) Nephroprotection by SGLT2 inhibition: back to the future? *J Clin Med* **9**: E2243. <https://doi.org/10.3390/jcm9072243>
- Díaz-López A, Becerra-Tomás N, Ruiz V, Toledo E, Babio N, Corella D, Fitó M, Romaguera D, Vioque J, Alonso-Gómez ÁM, Wärnberg J, Martínez JA, Serra-Majem L, Estruch R, Tinahones FJ, Lapeira J, Pintó X, Tur JA, López-Miranda J, Cano Ibañez N, Delgado-Rodríguez M, Matía-Martín P, Daimiel L, de Paz JA, Vidal J, Vázquez C, Ruiz-Canela M, Bulló M, Sorlí JV, Goday A, Fiol M, García-de-la-Hera M, Tojal Sierra L, Pérez-Farínós N, Zulet MA, Sánchez-Villegas A, Sacanella E, Fernández-García JC, Santos-Lozano JM, Gimenez-Gracia M, Del Mar Bibiloni M, Diez-Espino J, Ortega-Azorin C, Castañer O, Morey M, Torres-Collado L, Sorto Sanchez C, Muñoz MA, Ros E, Martínez-González MA, Salas-Salvado J; PREDIMED-Plus Investigators (2021) Effect of an intensive weight-loss lifestyle intervention on kidney function: a randomized controlled trial. *Am J Nephrol* **8**: 1–14. <https://doi.org/10.1159/000513664>
- Díaz-López A (2021) Effect of an intensive weight-loss lifestyle intervention on kidney function: a randomized controlled trial. *Am J Nephrol* **8**: 1–14. <https://doi.org/10.1159/000513664>
- Gajewska D, Myszkowska-Rydzak J, Lange E, Gudej S, Pawlowska-Goździk E, Bronkowska M, Piekło B, Łuszczki E, Kret M, Bialek-Dratwa A, Pachocka L, Sobczak-Czysn A (2015) Standards of dietary treatment of simple obesity in adults. Position of the Polish Dietetics Association. *J Dietetics* **8**: 13–18 (in Polish)
- Gnanińska M, Małgorzewicz S, Stojek M, Łysiak-Szydłowska W, Sworczak K (2009) Role of adipokines in complications related to obesity: a review. *Adv Med Sci* **54**: 150–157. <https://doi.org/10.2478/v10039-009-00352>
- Hruby A, Hu FB (2015) Epidemiology of obesity: a big picture. *Pharmacoeconomics* **33**: 673–689. <https://doi.org/10.1007/s40273-014-0243-x>
- Ikizler TA, Burrows JD, Byham-Gray LD, Campbell KL, Carrero JJ, Chan W, Fouque D, Friedman AN, Ghaddar S, Goldstein-Fuchs DJ, Kaysen GA, Kopple JD, Teta D, Yee-Moon Wang A, Cuppari L (2020) KDOQI Nutrition in CKD Guideline Work Group. KDOQI clinical practice guideline for nutrition in CKD: 2020 update. *Am J Kidney Dis* **76** (Suppl 1): S1–S107. <https://doi.org/10.1053/j.ajkd.2020.05.006>
- KDOQI Clinical Practice Guidelines and Clinical Practice Recommendations for Diabetes and Chronic Kidney Disease (2007) *Am J Kidney Dis* **49** (Suppl 2): S1–S245. <https://doi.org/10.1053/j.ajkd.2006.12.005>
- Khan A, Uddin S, Srinivasan U (2018) Comorbidity network for chronic disease: A novel approach to understand type 2 diabetes progression. *Int J Med Inform* **115**: 1–9. <https://doi.org/10.1016/j.ijmedinf.2018.04.001>
- Kontessis P, Jones S, Dodds R, Trevisan R, Nosadini R, Fioretto P, Borsato M, Sacerdoti D, Viberti G (1990) Renal, metabolic and hormonal responses to ingestion of animal and vegetable proteins. *Kidney Int* **38**: 136–44. <https://doi.org/10.1038/ki.1990.178>
- Luyckx VA, Tonelli M, Stanifer JW (2018) The global burden of kidney disease and the sustainable development goals. *Bull World Health Org* **96**: 414–422C
- McGraw NJ, Krul ES, Grunz-Borgmann E, Parrish AR (2016) Soy-based renoprotection. *World J Nephrol* **5**: 233–257. <https://doi.org/10.5527/wjn.v5.i3.233>
- Moorthi RN, Vorland CJ, Hill Gallant KM (2017) Diet and diabetic kidney disease: plant versus animal protein. *Curr Diab Rep* **17**: 15. <https://doi.org/10.1007/s11892-017-0843-x>
- Navaneethan SD, Yehner H, Moustarah F, Schreiber MJ, Schauer PR, Beddhu S (2009) Weight loss interventions in chronic kidney disease: a systematic review and meta-analysis. *Clin J Am Soc Nephrol* **4**: 1565–1574. <https://doi.org/10.2215/CJN.02250409>
- Henry RM, Kostense PJ, Bos G, Dekker JM, Nijpels G, Heine RJ, Bouter LM, Stehouwer CD (2002) Mild renal insufficiency is associated with increased cardiovascular mortality: The Hoorn Study. *Kidney Int* **62**: 1402–1407. <https://doi.org/10.1111/j.1523-1755.2002.kid571.x>
- Sacks FM, Bray GA, Carey VJ, Smith SR, Ryan DH, Anton SD, McManus K, Champagne CM, Bishop LM, Laranjo N, Leboff MS, Rood JC, de Jonge L, Greenway FL, Loria CM, Obarzanek E, Williamson DA (2009) Comparison of weight-loss diets with different compositions of fat, protein, and carbohydrates. *N Engl J Med* **360**: 859–887. <https://doi.org/10.1056/NEJMoa0804748>
- Schram MT, Henry RM, van Dijk RA, Kostense PJ, Dekker JM, Nijpels G, Heine RJ, Bouter LM, Westerhof N, Stehouwer CD (2004) Increased central artery stiffness in impaired glucose metabolism and type 2 diabetes: the Hoorn Study. *Hypertension* **43**: 176–181. <https://doi.org/10.1161/01.HYP.0000111829.46090.92>
- Skrypnik D, Bogdański P, Skrypnik K, Mały E, Karolkiewicz J, Szulinska M, Suliburska J, Walkowiak J (2019) Influence of endurance and endurance-strength training on mineral status in women with abdominal obesity: a randomized trial. *Medicine (Baltimore)* **98**: e14909. <https://doi.org/10.1097/MD.00000000000014909>
- Skrypnik D, Mostowska A, Jagodziński PP, Bogdański P (2020) Association of rs699947 (-2578 C/A) and rs2010963 (-634 G/C) Single nucleotide polymorphisms of the VEGF Gene, VEGF-A and leptin serum level, and cardiovascular risk in patients with excess body mass: a case-control study. *J Clin Med* **9**: 469. <https://doi.org/10.3390/jcm9020469>
- Swinburn B, Caterson I, Seidell J, James W (2004) Diet, nutrition and the prevention of excess weight gain and obesity. *Public Health Nutr* **7**: 123–146. <https://doi.org/10.1079/phn2003585>
- Tuttle KR, Bakris GL, Bilous RW, Chiang JL, de Boer IH, Goldstein-Fuchs J, Hirsch IB, Kalantar-Zadeh K, Narva AS, Navaneethan SD, Neumiller JJ, Patel UD, Ratner RE, Whaley-Connell AT, Molitch ME (2014) Diabetic kidney disease: a report from an ADA Consensus Conference. *Am J Kidney Dis* **64**: 510–533. <https://doi.org/10.2337/dc14-1296>
- Wannamethee SG, Shaper AG, Perry IJ (1997) Serum creatinine concentration and risk of cardiovascular disease: a possible marker for increased risk of stroke. *Stroke* **28**: 557–563. <https://doi.org/10.1161/01.STR.28.3.557>

Metformin promotes the normalization of abnormal blood vessels after radiofrequency ablation deficiency in hepatocellular carcinoma by microRNA-302b-3p targeting thioredoxin-interacting protein

HaiGang Niu^{1,2}, ShuYing Dong¹, GuoMing Li³, ShiLun Wu¹ and WenBing Sun¹✉

¹Department of Hepatobiliary Surgery, Beijing Chaoyang Hospital Affiliated to Capital Medical University, Beijing, 100043, China; ²Department of Clinical Medicine, Fenyang College of Shanxi Medical University, Fenyang, Shanxi Province, 032200, China; ³The Second Department of General Surgery, Chaoyang Central Hospital, Chaoyang, Liaoning Province, 122000, China

Metformin has shown great promise in the treatment of HCC. Radiofrequency ablation (RFA) deficiency results in recurrence and metastasis of remaining HCC tumors. Here, we aimed to investigate the role and mechanism of metformin in HCC after RFA deficiency. HCC cell line Hep-G2 was selected to simulate RFA deficiency and named HepG2-H cells. After treating cells with different concentrations of metformin (2.5, 5, 10 μ M) or transfecting related plasmids, cell proliferation, migration, invasion, apoptosis and angiogenesis were detected, *in vitro* permeability test was performed, and an angiogenesis-related protein VEGFA was analyzed. The residual HCC model after RFA deficiency was established in mice. Metformin was administered by gavage to detect changes in tumor volume and weight, and CD31 staining was used to observe microvessels. The targeting relationship between miR-302b-3p and *TXNIP* was demonstrated by the bioinformatics website, dual-luciferase reporter assay, and RNA pull-down assay. The results found that metformin inhibited RFA deficiency-induced growth and angiogenesis of HCC cells *in vitro*. miR-302b-3p counteracted the therapeutic effect of metformin on RFA deficiency. miR-302b-3p targeted regulation of *TXNIP*. The up-regulation of *TXNIP* reversed the effects of over-expression of miR-302b-3p on RFA-deficient HCC cells. Metformin inhibited RFA-deficiency-induced HCC growth and tumor vascular abnormalities *in vivo*. Overall, metformin promotes the normalization of abnormal blood vessels after RFA deficiency in HCC by miR-302b-3p targeting *TXNIP*, which can be used to prevent the progression of HCC after RFA.

Keywords: Metformin; radiofrequency ablation deficiency; MicroRNA-302b-3p; Thioredoxin-interacting protein

Received: 29 March, 2022; revised: 22 August, 2022; accepted: 04 February, 2023; available on-line: 22 December, 2023

✉ e-mail: sunwb_swb440@outlook.com

Abbreviations: HCC, Hepatocellular carcinoma; miRNAs, microRNAs; RFA, Radiofrequency ablation; UTR, 3'-untranslated region

INTRODUCTION

Hepatocellular carcinoma (HCC) is an extremely familiar primary liver malignancy and the main reason for cancer-linked deaths worldwide (Harati *et al.*, 2021). Over the past 10 years, the incidence of HCC has been increasing, causing a huge socioeconomic burden (Schulte *et al.*, 2019). Because the early symptoms of HCC are

ambiguous, most patients are already at an advanced stage when being diagnosed, and are accompanied by distant tumor metastasis, leading to an extremely unpleasant overall survival rate and prognosis (El Shorbagy *et al.*, 2021). Currently, the clinical approaches for HCC mainly cover surgical resection, chemotherapy, drug therapy, and surgical resection. However, not all patients can undergo surgical resection, and there are few effective options for patients at an advanced stage. Radiofrequency ablation (RFA) has been successfully applied to treat diversified primary tumors, covering HCC (Lassandro *et al.*, 2020). However, the malignant progression of residual HCC cells after RFA limits the treatment outcome of patients (Jia *et al.*, 2020).

Metformin is anti-tumor (Shankaraiah *et al.*, 2019) and it can restrain the malignant progression of HCC through multiple signaling pathways. For example, metformin refrains liver cancer cell proliferation by reducing the glycolytic flux of the hypoxia inducible factor (HIF)-1 α /6-phosphofructo-2-kinase/fructose-2,6-bisphosphatase 3/phosphofructokinase-1 pathway (Hu *et al.*, 2019). Metformin represses HCC progression by activating the Hippo pathway (Zhao *et al.*, 2021). Meanwhile, metformin synergizes with other drugs to refrain the progression and the drug resistance of HCC. For example, metformin combined with curcumin refrains HCC growth, metastasis, and angiogenesis *in vitro* and *in vivo* (Zhang *et al.*, 2018). Metformin can enhance the sensitivity of orthotopic HCC mice to sorafenib, thereby decreasing postoperative recurrence and metastasis of HCC (You *et al.*, 2016). However, the role of metformin in HCC after RFA is uncertain.

MicroRNAs (miRNAs) are a class of short endogenous single-stranded non-coding RNAs that reduce mRNA stability and translation by combining with the 3'-untranslated region (UTR) of target mRNAs (Alberti *et al.*, 2018). Plentiful studies have manifested that abnormal expression of miRNAs is linked with the occurrence of cancers covering HCC (Yerukala *et al.*, 2020). For example, miR-15a-3p represses HCC metastasis by interacting with heme oxygenase 1 (Jiang *et al.*, 2020) and miR-448 depresses cell growth by targeting B cell lymphoma 2 in HCC (Liao *et al.*, 2019). MiR-302b-3p is a pluripotency-linked miRNA, which has been discovered to participate in the physiological and pathological processes of cancers, such as pancreatic cancer (Xu *et al.*, 2021), gastric cancer (Wang *et al.*, 2021), and colorectal cancer (Hu *et al.*, 2021). However, no study has indicated its expression and function in HCC.

This study aimed to investigate the function and latent mechanisms of metformin in HCC after RFA deficiency. *In vivo* and *in vitro* experiments were conducted to determine the function of metformin in the growth and angiogenesis of residual HCC cells after RFA deficiency, and further analyze the interaction between metformin and miR-302b-3p. It is hypothesized that metformin promotes the normalization of abnormal blood vessels after HCC by miR-302b-3p targeting the thioredoxin-interacting protein, offering new insights into HCC treatment.

MATERIALS AND METHODS

Tissue sample

Human HCC tissue and para-tumor samples were collected from 45 HCC patients who underwent surgical resection, while 18 of them were residual tumors from RFA-undertreated HCC patients. All tissue samples were kept in liquid nitrogen at -80°C , and informed consent was obtained and approved by the Ethics Committee of our hospital.

Cell culture

HCC cell line Hep-G2 (Type Culture Bank of the Chinese Academy of Sciences, Shanghai, China) and normal human liver cell line L02 (Shanghai Academy of Sciences, Shanghai) were cultured with 10% fetal bovine serum, 100 U/mL penicillin, and 100 mg/mL streptomycin in Roswell Park Memorial Institute-1640 medium (Gibco) (Ni *et al.*, 2021). All the media were provided by Gibco.

In vitro RFA deficiency

RFA deficiency was modeled *in vitro* as previously described (Zhang *et al.*, 2017). Briefly, Hep-G2 cells were seeded in 6-well plates (5×10^4 cells/well) and immersed in water at 47°C after 24 h. Afterward, cells were allowed to recover, and when the surviving cells reached 80% confluence, cells were propagated into 6-well plates and treated for 10 min as described above. This process was repeated ten times for 15, 20, and 25 min in sequence. Cells that survived were named HepG2-H cells.

Cell transfection

The pcDNA3.1 (+) vector for *TXNIP* overexpression and its corresponding control, miR-302b-3p mimic, miR-302b-3p inhibitor, and their negative controls were all synthesized by GenePharma (Shanghai, China). Cells were seeded in 6-well plates at a density of 5×10^5 cells/well and transfected after 24 h of incubation. *In vitro* transfection was performed using LipofectamineTM 3000 reagent (Thermo Fisher Scientific).

Cell viability

A total of 5×10^3 cells were seeded and incubated in 96-well plates. Then, 10 μL CCK-8 solution (CCK-8, Dojindo, Tokyo, Japan) was added to each well. Finally, the absorbance was read at 450 nm (Zhang *et al.*, 2021).

Colony formation assay

Cells were plated in 6-well plates at 500 cells/well. The colonies formed on the plate were fixed with 4% paraformaldehyde (Solabio), stained with 0.5% crystal violet, and counted (Zhu *et al.*, 2019).

2Transwell assay

Cells were made into cell suspension at $1 \times 10^6/\text{mL}$. In the invasion assay, 50 mg/L Matrigel was diluted at a ratio of 1: 8 and spread on the bottom of the chamber. Matrigel was not applied in the migration assay. Then, 600 μL complete medium was added to the lower chamber and 200 μL cell suspension was placed in the bottom chamber. After 24 h, the chamber was washed with phosphate-buffered saline (PBS), and the cells were fixed with paraformaldehyde (40 g/L) and stained with crystal violet (1 g/L). Finally, cells were counted under an inverted microscope in 6 fields of view (Xu *et al.*, 2021).

Apoptosis detection

Apoptosis assays were performed with Alexa Fluor 488-Annexin V/propidium iodide (PI) (Invitrogen, CA, USA). A BD LSR II flow cytometer (BD Biosciences, San Jose, CA, USA) was utilized to acquire the data and FlowJo analysis software (Tree Star, Inc., Ashland, OR, USA) was used to evaluate the results. Annexin V positive cells were regarded as apoptotic cells.

Tube formation experiment

A conditioned medium of tumor cells was collected. Afterward, 2×10^4 human umbilical vein endothelial cells (HUVECs) were incubated with 100 μL conditioned medium and observed with an inverted microscope (CKX40, Olympus). The branch point numbers were counted in 5 random fields.

In vitro permeability assay

HUVECs were plated on transwell membranes (0.4 μm in diameter; Corning-Costar, New York, USA). Subsequently, rhodamine-dextran (average MW $\sim 70,000$; 20 mg/ml) was added to the upper chamber. The absorption of 40 μL the lower cavity medium was measured at 544 nm excitation wavelength and 590 nm emission wavelength.

Quantitative real-time polymerase chain reaction (PCR)

Extraction of total RNA was done using Trizol (15596-018, Invitrogen). cDNA was synthesized from 1 μg RNA by cDNA Synthesis Kit (K1631, Thermo Fisher Scientific). In a PCR detection system (CFX96, Bio-Rad, Hercules, CA, USA), PCR reactions were performed with the One-step PrimeScript RT-PCR kit (RR064B, Takara, Shiga, Japan). The thermal protocol was set as pre-denaturation at 95°C for 5 min, denaturation at 95°C for 15 s, annealing at 58°C for 30 s, extension at 72°C for 30 s, for a total of 40 cycles, and extension at 72°C for 10 min. Glyceraldehyde-3-phosphate dehydrogenase (GAPDH) and $\beta\text{-actin}$ were internal controls. The primer sequences were manifested in Table 1. Relative expression was analyzed by the $2^{-\Delta\Delta\text{CT}}$ method (Teng *et al.*, 2020).

Western blot

Cells were lysed by a mixture of protease inhibitor and radio-immunoprecipitation assay lysis buffer. Protein samples were separated by 10% sodium dodecyl sulfate-polyacrylamide gel electrophoresis and then electro-blotted onto polyvinylidene fluoride (PVDF) membranes (Bio-Rad). After blocking with 5% skim milk powder, the PVDF membranes were incubated with anti-human *TXNIP* (ab188865, 1: 1000, Abcam), vascular endothelial growth factor A (ab46154, VEGFA; 1: 1000, Abcam),

Table 1 Primer sequence

Genes		Primer sequence (5'-3')
miR-302b-3p	Human	ACACTCCAGCTGGGTAAGTGCTTCCATGTTT
		TGGTGTCTGGAGTCG
	mouse	ACACTCCAGCTGGGTAAGTGCTTCCATGTTT
		TGGTGTCTGGAGTCG
TXNIP	Human	GGTCTTTAACGACCCTGAAAAGG
		ACACGAGTAACCTCACACACCT
	mouse	GGCCGGACGGGAATAGTG
		AGCGCAAGTAGTCCAAAGTCT
U6	Human	CTCGCTTCGGCAGCACA
		AACGCTTCACGAATTGCGT
	mouse	CTCGCTTCGGCAGCACA
		AACGCTTCACGAATTGCGT
GAPDH	Human	GGAGCGAGATCCCTCCAAAAT
		GGCTGTTGTCATACTTCTCATGG
	mouse	ATCACTGCCACCCAGAAG
		ATCACTGCCACCCAGAAG

Genes		Primer sequence (5'-3')
MiR-302b-3p		F: 5'-GCGTAAGTGCTTCCATGTT-3'
		R: 5'-TCCAGGGACCGAGGA-3'
TXNIP		F: 5'-CGCCTCCTGCTTGAACTA-AC-3'
		R: 5'-AATATACGCCGCTGGTTACACT-3'
U6		F: 5'-CTCGCTTCGGCAGCACA-3'
		R: 5'-AACGCTTCACGAATTGCGT-3'
GAPDH		F: 5'-CGCTCTCTGCTCCTCTGTT-3'
		R: 5'-ATCCGTTGACTCCGACCTTCAC-3'

Note: F, forward; R, reverse.

and GAPDH (2118, 1: 1000, Cell Signaling Technology). Proteins were developed by a chemiluminescence detection system (Millipore, MA, USA) and imaged by a FluroChem E imager (Protein Simple, Santa Clara, CA, USA) (Sun *et al.*, 2021). Densitometry and quantification were performed using Image Lab™ software (version 3.0) (Bio-Rad Laboratories).

The luciferase activity assay

The target genes of miR-302b-3p were predicted by Starbase 3.0. The wild-type (Wt) or mutant (Mut) sequence of *TXNIP* was cloned into the dual-luciferase reporter vector pGL3. The reporter was then co-transfected with miR-302b-3p mimic or NC into HepG2-H cells using Lipofectamine 2000 (Invitrogen). The relative luciferase activity was determined in the light of the instructions of the dual luciferase reporter kit (Promega) (Yuan *et al.*, 2020).

RNA pull-down analysis

HepG2-H cells were transfected with biotinylated miR-302b-3p (Bio-miR-302b-3p) and biotinylated NC (Bio-NC) (RiboBio). Then, cells were lysed and incu-

bated with streptavidin beads (Thermo Fisher Scientific). Afterwards, the bound RNA was eluted and purified using the RNeasy Mini Kit (Qiagen) and analyzed by PCR to measure *TXNIP* expression.

Tumors in nude mice

Twelve male BALB/c nude mice (nu/nu) (6 weeks old; body weight of 16–20 g) were purchased from the Model Animal Research Center of Nanjing University. The mice were raised in cages (n=6/cage) and placed in a sterile room with 12-h light/dark cycle with free access to food and water. All animal studies complied with the regulations of the Institutional Animal Care and Use Committee and were approved by the Medical Ethics Committee of Beijing ChaoYang Hospital, Capital Medical University. HepG2-H cells (5×10^6) were suspended in 200 μ l serum-free Dulbecco's Modified Eagle Medium and Matrigel (1:1) and injected subcutaneously in the upper right flank. After 1 week, mice were orally administered metformin (200 mg/kg/d) or PBS as a control for 24 d. The size of the xenograft tumor was measured with a vernier caliper every 6 d, and the tumor volume was calculated according to the formula of

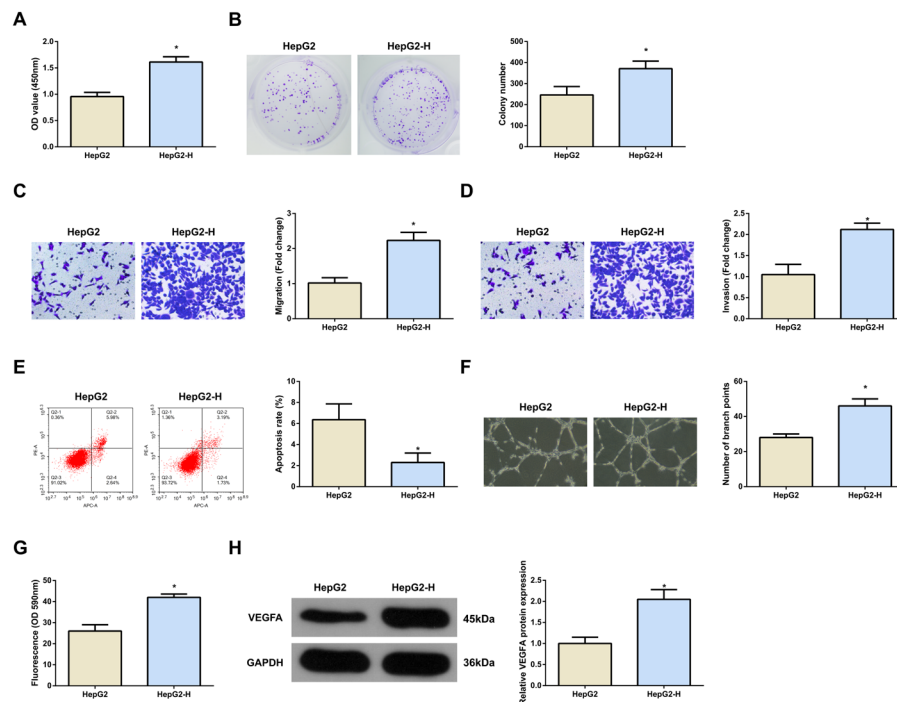


Figure 1. RFA promotes HCC cell growth and tumor angiogenesis

After RFA treatment, (A) CCK-8 detection of cell viability; (B) Plate clone detection of cell proliferation; (C/D) Transwell detection of cell migration and invasion; (E) Flow cytometry detection of cell apoptosis; (F) Detection of angiogenesis; (G) Permeability assay *in vitro*. (H) Western blot detection of angiogenesis-linked protein VEGFA. N=3. The measurement data were presented as mean ± S.D. *vs. the HepG2, $P < 0.05$.

0.5×length×width². After 24 d, the mice were euthanized by cervical dislocation, and tumor tissues were collected for pathological and molecular expression analysis.

CD31 immunohistochemistry

Tumor tissue was fixed and embedded in paraffin. The tumor sections (5 μm) were incubated with a rabbit monoclonal antibody CD31 (550274, eBioscience, Inc., San Diego, CA, USA) or the universal NC antibody control. After incubation with the appropriate biotinylated secondary antibody, the sections were incubated with horseradish peroxidase-conjugated streptavidin (KeyGen Biotech.), followed by the addition of 3,3'-diaminobenzidine working solution (Sigma) and counterstaining with hematoxylin. Quantification of intratumoral microvessel density (IMVD) was performed by counting CD31-positive (brown) cells in the nine most vascularized areas.

Statistical analysis

Data were analyzed with SPSS (IBM, Armonk, NY, USA) and manifested as mean ± standard deviation (S.D.). Differences were analyzed by Student's *t*-test or one-way analysis of variance (ANOVA) and Tukey's post-hoc test. Correlation analysis was done with Pearson analysis. $P < 0.05$ emphasized statistical meaning.

RESULTS

This study explored the potential role and mechanism of metformin in RFA deficiency of HCC. *In vivo* and *in vitro* experiments were performed to determine the function of metformin in the cell growth and angiogenesis of HCC after RFA deficiency, and the interaction between

metformin and miR-302b-3p was further analyzed. It is concluded that metformin promotes the normalization of abnormal blood vessels after RFA deficiency in HCC by miR-302b-3p targeting *TXNIP*, which can be used to prevent the progression of HCC after RFA.

RFA promotes the growth of HCC cells and accelerates tumor angiogenesis

To study the impact of metformin on RFA-deficient HCC cells, RFA deficiency *in vitro* was simulated to construct a cell model named HepG2-H. As measured, the proliferation, invasion, and migration were promoted and apoptosis was reduced in HepG2-H cells after RFA (Fig. 1A–E). Angiogenesis, the process by which original blood vessels grow out of new blood vessels, has been implicated in the growth and progression of solid tumors (Ramjiawan *et al.*, 2017). This study found that the relative lumen number of cells was increased after RFA (Fig. 1F). Vascular permeability experiments found severe vascular leakage of HUVECs after HepG2-H incubation (Fig. 1G). In addition, the angiogenesis-related protein VEGFA was also detected and the finding indicated that VEGFA expression was elevated in HepG2-H cells after RFA (Fig. 1H). The above experiments manifested that RFA accelerated the growth of HCC cells and tumor angiogenesis.

Metformin restrains the growth and angiogenesis of HCC cells induced by RFA deficiency *in vitro*

To figure out whether metformin could mediate RFA deficiency-induced impacts on HCC cells, HCC cells were treated with metformin. Our data found that metformin inhibited the viability of HepG2 and HepG2-H cells and reduced colony numbers in a dose-dependent

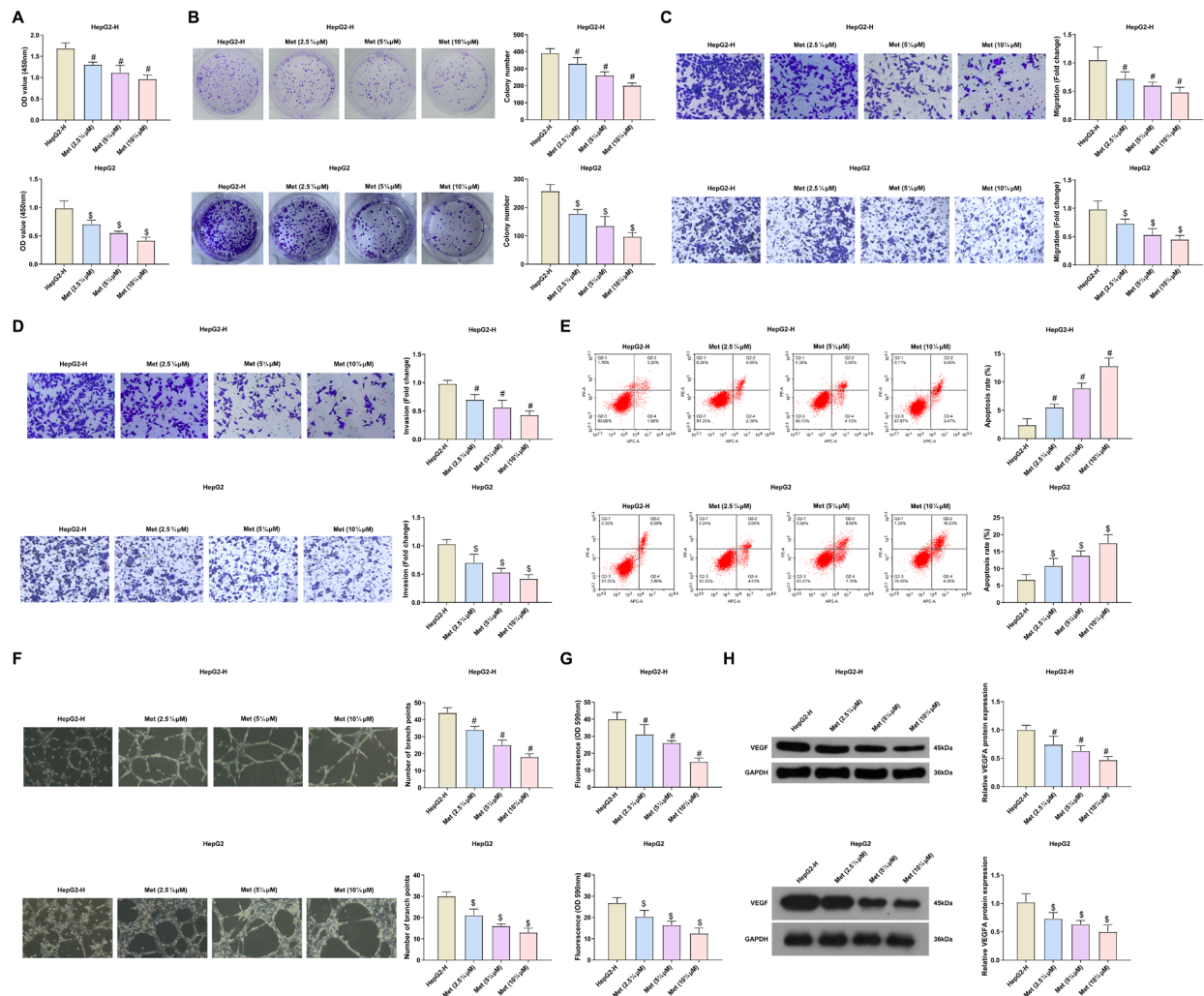


Figure 2. Metformin refrains the growth and angiogenesis of HCC cells induced by RFA deficiency *in vitro*

After metformin treatment, (A) CCK-8 detection of cell viability; (B) Plate clone detection of cell proliferation; (C/D) Transwell detection of cell migration and invasion; (E) Flow cytometry detection of cell apoptosis; (F) Detection of angiogenesis; (G) Permeability assay *in vitro*. (H) Western blot detection of angiogenesis-linked protein VEGFA. N=3. The measurement data were presented as mean \pm S.D. #vs. the HepG2-H, $P < 0.05$; vs. the HepG2, $P < 0.05$.

manner (Fig. 2A, B). RFA-induced quantitative increases in cell migration and invasion were also inhibited by metformin (Fig. 2C, D). Meanwhile, metformin also increased the apoptosis rate of HepG2 and HepG2-H cells in a dose-dependent manner (Fig. 2E) and inhibited tumor angiogenesis and permeability *in vitro* (Fig. 2F-H). All in all, metformin could refrain the growth and angiogenesis of HCC cells induced by RFA deficiency *in vitro*. The treatment effect of 10 μ M metformin was most pronounced and was therefore selected for further experiments.

MiR-302b-3p counteracts the therapeutic effect of metformin on RFA deficiency

Notably, miR-302b-3p levels were elevated in RFA-induced HepG2-H cells (Fig. 3A) which was dose-dependently counteracted by metformin (Fig. 3B). In addition, a decrease in miR-302b-3p expression was also detected in metformin-treated HepG2 cells (Fig. 3B). To further figure out miR-302b-3p's impacts on RFA deficiency, miR-302b-3p mimic and inhibitor were transfected in metformin-treated HepG2-H and HepG2 cells, and the

transfection efficiency was verified (Fig. 3C). Subsequent experiments manifested that miR-302b-3p mimic counteracted the therapeutic effects of metformin on HepG2-H and HepG2 cells, leading to promoted cell growth, angiogenesis, and vascular leakage, whereas miR-302b-3p inhibitor had the opposite effects (Fig. 3E-K).

MiR-302b-3p targets *TXNIP*

It was also found that *TXNIP* expression was reduced in RFA-induced HepG2-H cells (Fig. 4A, B), while metformin dose-dependently elevated *TXNIP* expression (Fig. 4C,D). TargetScan 7.2 predicted the binding site sequences of *TXNIP* and miR-302b-3p (Fig. 4E). The interaction between the two was further confirmed, clarifying that after co-transfection of the miR-302b-3p mimic with the psiCHECK-2 *TXNIP* 3'UTR Wt plasmid, the luciferase activity was reduced by 50% (Fig. 4F). It was further confirmed that miR-302b-3p could combine with *TXNIP* in RNA pull-down assay (Fig. 4G). In addition, the expression of miR-302b-3p and *TXNIP* in normal human liver cell line L02 and HepG2 cells was detected by PCR, and it was found that compared with L02, the

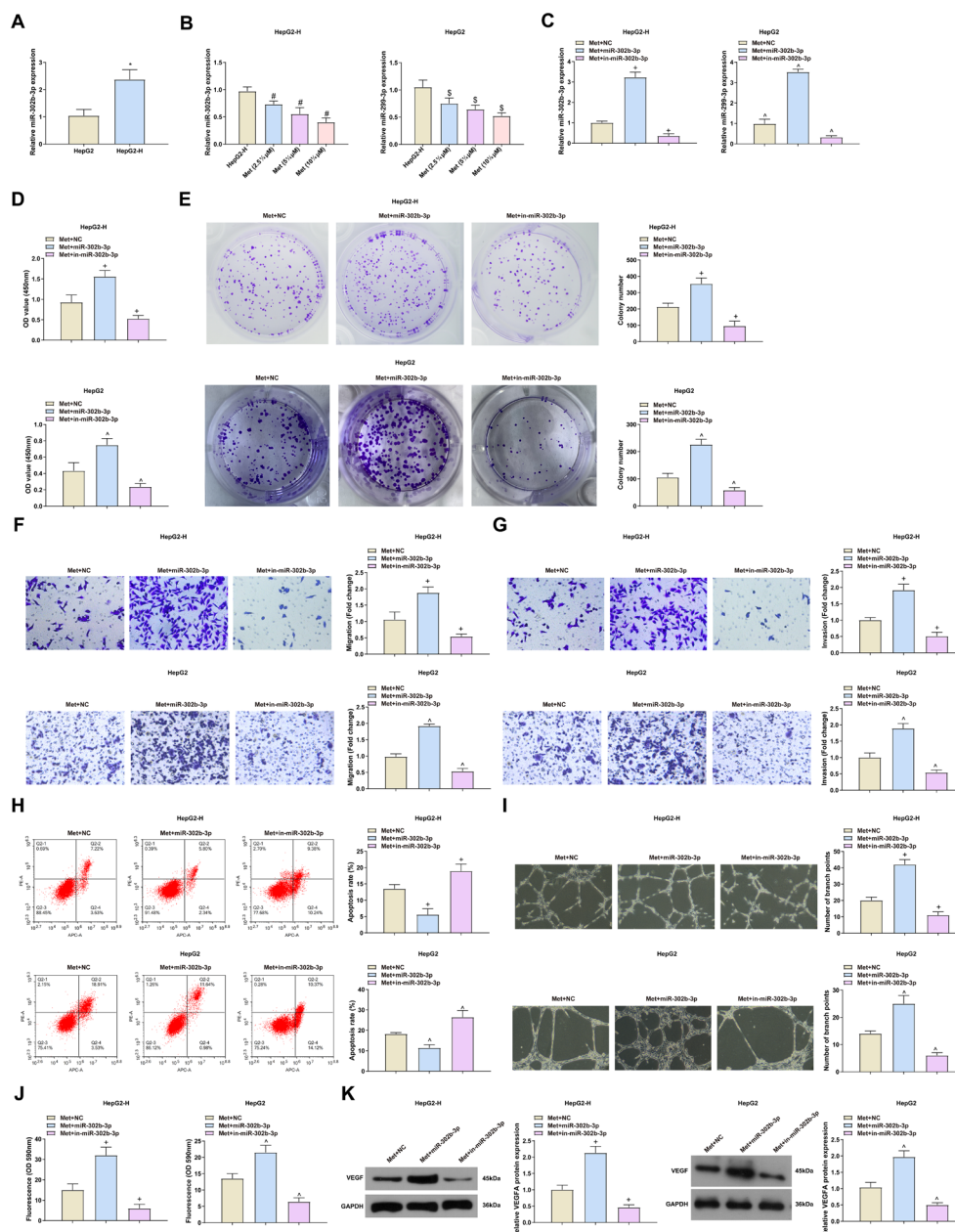


Figure 3. MIR-302b-3p counteracts the therapeutic effect of metformin on RFA deficiency

(A–C) PCR detection of miR-302b-3p; (D) CCK-8 detection of cell viability; (E) Plate clone detection of cell proliferation; (F/G) Transwell detection of cell migration and invasion; (H) Flow cytometry detection of cell apoptosis; (I) Detection of angiogenesis after metformin treatment; (J) Permeability assay *in vitro*. (K) Western blot detection of angiogenesis-linked protein VEGFA. N=3. The measurement data were presented as mean \pm S.D. *vs. the HepG2, $P<0.05$; #vs. the HepG2-H, $P<0.05$; + or ^vs. the Met+NC, $P<0.05$.

expression of miR-302b-3p was increased, and the expression of *TXNIP* was decreased in HepG2 cells (Supplementary Fig. 1A,B). Next, *TXNIP* expression was measured in cells transfected with miR-302b-3p mimic or inhibitor, showing that miR-302b-3p mimic reduced *TXNIP*, while miR-302b-3p inhibitor elevated *TXNIP* expression (Supplementary Fig. 1C, Fig. 4HI at <https://ojs.ptbioch.edu.pl/i>). Taken together, miR-302b-3p could directly target *TXNIP*.

***TXNIP* turns around the effect of elevated miR-302b-3p on RFA-deficient HCC cells**

To further figure out the mechanism between *TXNIP* and miR-302b-3p, HepG2-H+Met cells or HepG2+Met

cells transfected with miR-302b-3p mimics were transfected with *TXNIP* overexpression vector (Fig. 5A). It was found that *TXNIP* reversed the effect of overexpression of miR-302b-3p on RFA-deficient HCC cells, reduced cell proliferation, migration, and invasion levels, increased apoptosis, and inhibited angiogenesis and permeability *in vitro* (Fig. 5B–I). In short, *TXNIP* turned around the effect of elevated miR-302b-3p on RFA-deficient HCC cells.

Metformin refrains RFA deficiency-induced HCC tumor growth and tumor vascular abnormalities *in vivo*

To figure out the application potential of metformin in the treatment of RFA deficiency *in vivo*, a residual can-

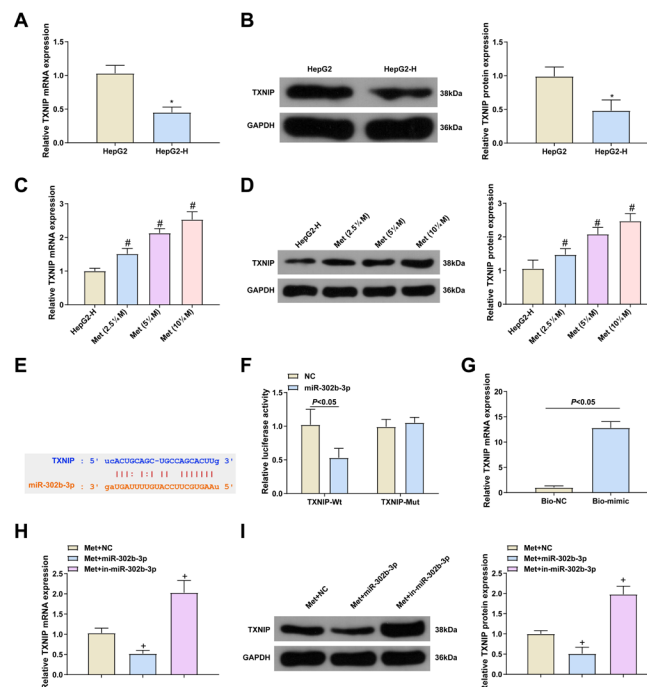


Figure 4. MiR-302b-3p targets TXNIP

(A–D) PCR and Western blot detection of TXNIP in cells; (E) TargetScan manifested the predicted TXNIP binding sequence of miR-302b-3p; (F) The luciferase activity assay in HepG2-H cells after co-transfection. (G) Enrichment of miR-302b-3p and TXNIP by RNA pull-down analysis; (H/I) PCR and Western blot detection of TXNIP in cells. N=3. The measurement data were presented as mean \pm S.D. *vs. the HepG2, $P < 0.05$; #vs. the HepG2-H, $P < 0.05$; +vs. the Met, $P < 0.05$.

cer model of HCC after incomplete RFA was established in mice, and metformin was administered by gavage. It was discovered that tumor weight and volume were reduced in the HepG2-H+Met group (Fig. 6A–C). MiR-302b-3p and TXNIP expression in mouse tumor tissue was detected, manifesting that miR-302b-3p expression was reduced, but TXNIP expression was elevated in the HepG2-H+Met group (Fig. 6D, E). Moreover, microvessels were observed by CD31 staining and it was found that metformin reduced IMVD (Fig. 6F). Taken together, metformin repressed RFA-deficiency-induced HCC cell growth and tumor vascular abnormalities *in vivo*.

Up-regulation of miR-302b-3p enhances the malignancy of residual HCC cells after RFA

Finally, the correlation of miR-302b-3p with HCC development was analyzed. As shown in Fig. 7A, miR-302b-3p was elevated in HCC tissues compared with para-tumor tissues. More interestingly, miR-302b-3p was further enhanced in residual HCC tissues collected from RFA-deficient patients (Fig. 7B). These results suggest that miR-302b-3p may play an accelerating role in the development of residual HCC after RFA.

DISCUSSION

Angiogenesis has been reported to take on a critical role in the development, progression, and metastasis of HCC (Lin *et al.*, 2018). Many studies have testified that RFA is a safe and efficient approach for liver metastases, while residual tumors can grow aggressively after RFA, driven in part by the upregulation of VEGF (Agarwal *et al.*, 2014). Meanwhile, RFA deficiency promotes angiogenesis of residual HCC cells through HIF-1 α /VEGFA

axis (Kong *et al.*, 2012). These studies suggest that angiogenesis after RFA is a momentous physiological process in residual HCC. In the present study, it was found that RFA treatment accelerated HCC cell growth *in vitro*, increased cell relative lumen number, vascular permeability, and VEGFA expression. Metformin treatment could repress the facilitating effect of RFA on HCC. The *in vivo* results also confirmed that metformin could repress the growth and angiogenesis of HCC cells after RFA treatment.

It is well known that metformin is an anti-diabetic biguanide drug with safety and pleiotropic effects. In recent years, it has been proved to have anti-tumor effects in diversified cancers, such as cervical (Xia *et al.*, 2020), breast (Teufelsbauer *et al.*, 2020), and gastric cancers (Cunha Júnior *et al.*, 2021). Although some of the functions of metformin in HCC have been elucidated, many of its specific underlying mechanisms in HCC have not been identified, especially in HCC treated with RFA. In the study, RFA deficiency was simulated *in vitro* to construct a cell model, and it was found that RFA treatment facilitated HCC cell growth and angiogenesis, while metformin treatment restrained HCC cell growth, tumor angiogenesis, permeability, and VEGFA expression. Next, an RFA-deficient HCC *in vivo* model was established and administered metformin by gavage. It was discovered that metformin refrained RFA-deficiency-induced HCC cell growth and tumor vascular abnormalities *in vivo*, suggesting that metformin partially counteracts RFA deficiency-induced vascular abnormalities in HCC tumors. Some former studies have manifested that metformin represses tumorigenesis by modulating miRNAs. For example, metformin induces G1 cell cycle arrest by up-regulating tumor suppressors miR-let-7a, miR-let-7b, and miR-let-7e, thereby restraining HCC cell proliferation (Miyoshi *et al.*, 2014). Metformin stimulates pyroptosis

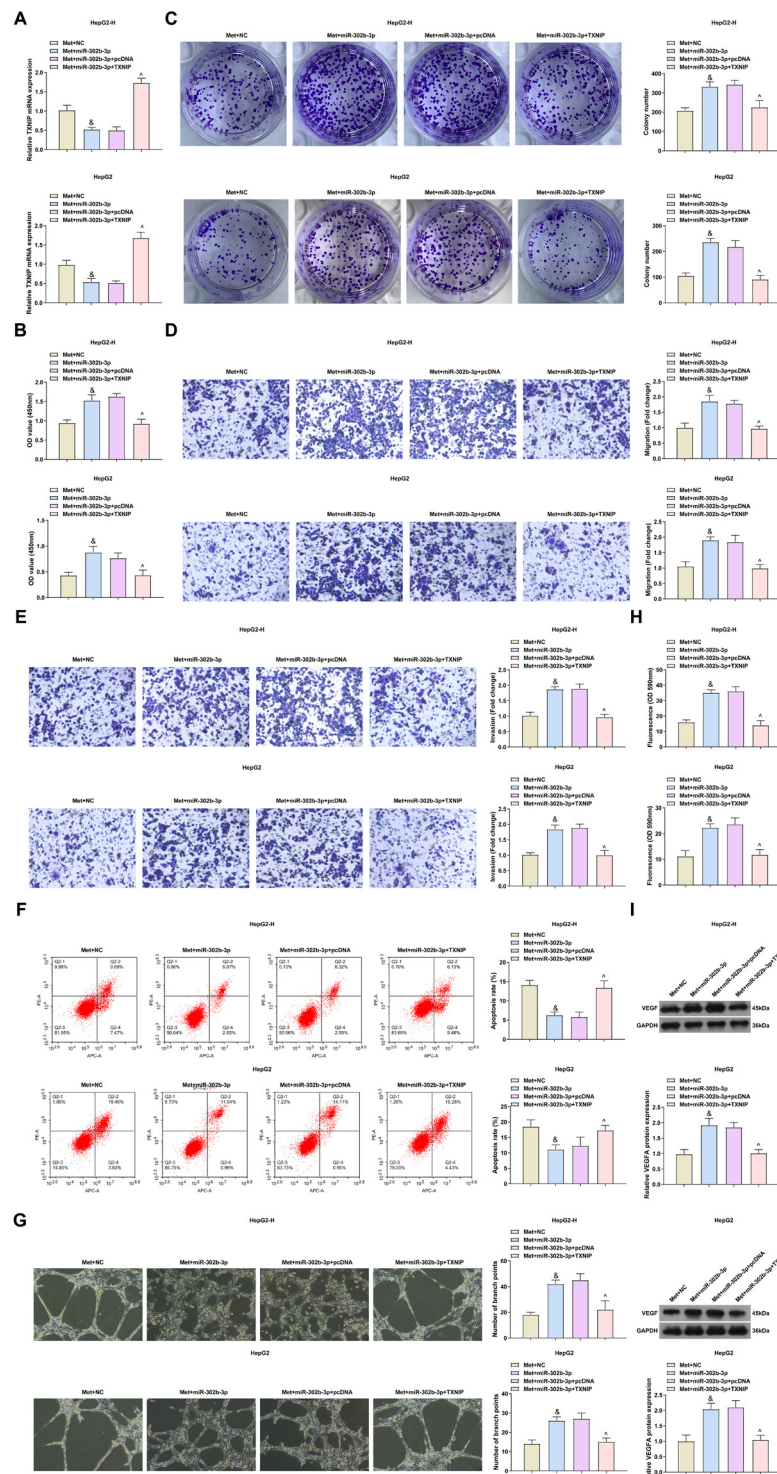


Figure 5. TXNIP turns around the effect of elevated miR-302b-3p on RFA-deficient HCC cells

(A) PCR detection of *TXNIP* in cells; (B) CCK-8 detection of cell viability; (C) Plate clone detection of cell proliferation; (D/E) Transwell detection of cell migration and invasion; (F) Flow cytometry detection of cell apoptosis; (G) Detection of angiogenesis after metformin treatment; (H) Permeability assay *in vitro*. (I) Western blot detection of angiogenesis-linked protein VEGFA. N=3. The measurement data were presented as mean \pm S.D. In HepG2-H cells, $^{\&}$ vs. the Met+NC, $^{\wedge}$ vs. the Met+miR-302b-3p+pcDNA, $P<0.05$.

in human esophageal cancer cells by regulating miR-497 (Wang *et al.*, 2019). Here, it was discovered that metformin treatment downregulated miR-302b-3p in HCC.

Former studies have manifested that miR-302b-3p is abnormally expressed in diversified cancers (Liang *et al.*, 2019) and that it is also associated with nerve cell inflammation (He *et al.*, 2020) and neuronal damage (Li

et al., 2021). In this study, it was originally found that miR-302b-3p was elevated in RFA-induced HCC cells, and up-regulation of miR-302b-3p counteracted the therapeutic effect of metformin on HCC cells, while down-regulation of miR-302b-3p further enhanced the therapeutic effect of metformin on HCC. This result suggests miR-302b-3p was a downstream target of metformin in

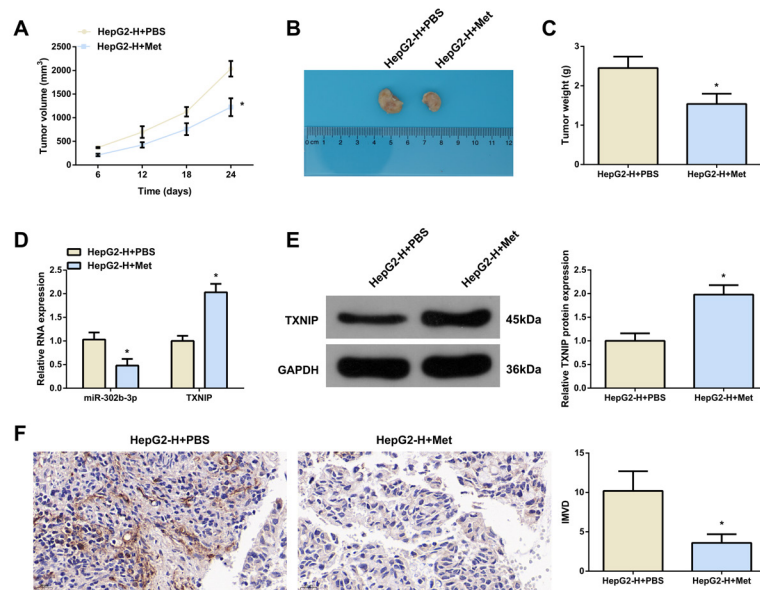
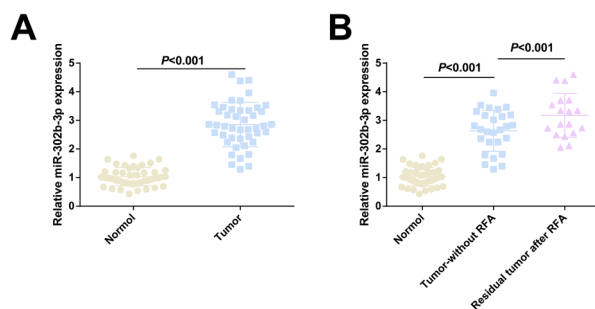


Figure 6. Metformin depresses RFA deficiency-induced HCC cell growth and tumor vascular abnormalities *in vivo* (A–C) Detection of the changes of tumor weight and volume in 30 d; (D/E) qPCR and Western Blot detection of miR-302b-3p and TXNIP in mouse tumor tissue; (F) CD31 staining to observe micro-vessels. $n=8$. The measurement data were presented as mean \pm S.D. *vs. the HepG2-H+PBS, $P<0.05$.



HCC. Many studies have manifested that miRNAs function in various diseases by targeting mRNAs. For example, miR-302b-3p targeting insulin-like growth factor 1 receptor represses gastric cancer cell proliferation (Guo *et al.*, 2017). Next, it was found that miR-302b-3p targeted TXNIP in RFA-induced HCC cells. TargetScan 7.2 forecasted the existence of binding sites for miR-302b-3p and TXNIP.

TXNIP is an α -arrest family protein that modulates intracellular reactive oxygen species (ROS) (Sheth *et al.*, 2006). TXNIP takes on an irreplaceable role in the development of HCC, and TXNIP deficiency is sufficient to induce HCC and TXNIP is a new tumor suppressor gene for HCC (Sheth *et al.*, 2006). In the present study, it was found that TXNIP was down-regulated in RFA-induced HCC cells, and elevation of TXNIP turned around the effect of elevated miR-302b-3p on RFA-deficient HCC and refrained HCC cell growth, angiogenesis, and permeability *in vitro*. These results suggested that metformin repressed HCC cell growth and angiogenesis *in vitro* and *in vivo* by targeting the miR-302b-3p/TXNIP axis.

However, the research still has some limitations. First, the sample size was insufficient due to limited laboratory conditions. Meanwhile, it has been documented that ROS production is elevated after RFA (Richter *et*

al., 2012), while the effect of RFA deficiency on ROS production and whether ROS in turn affects HCC cell growth and angiogenesis remains to be further verified. It is hoped that these issues can be further addressed.

CONCLUSION

Overall, the study manifests that RFA deficiency can accelerate cell growth and angiogenesis in HCC, while metformin can alleviate the negative impact of RFA deficiency on HCC. The results suggest that metformin represses HCC cell growth and angiogenesis *in vitro* and *in vivo* by miR-302b-3p to upregulate TXNIP. The results offer brand-new insights into overcoming RFA deficiency to promote the malignant progression of residual HCC cells.

Declarations

Acknowledgments. Not applicable.

Ethics Statement. All procedures and animal care were approved by Beijing Chaoyang Hospital Affiliated to Capital Medical University of Science and Technology Animal Care Committee and performed according to NIH guidelines. Ethics approval number: BJ2018TSJ2203.

Funding. Not applicable

Declaration of Conflicting Interests. Authors declared no conflict of interest.

REFERENCES

- Agarwal A, Daly KP, Butler-Bowen H, Saif MW (2014) Safety and efficacy of radiofrequency ablation with aflibercept and FOLFIRI in a patient with metastatic colorectal cancer. *Anticancer Res* **34**: 6775–6778
- Alberti C, Manzenreither RA, Sowemimo I, Burkard TR, Wang J, Mahofsky K, Ameres SL, Cochella L (2018) Cell-type specific sequencing of microRNAs from complex animal tissues. *Nat Methods* **15**: 283–289. <https://doi.org/10.1038/nmeth.4610>

- Cunha Júnior AD, Bragagnoli AC, Costa FO, Carvalheira JBC (2021) Repurposing metformin for the treatment of gastrointestinal cancer. *World J Gastroenterol* **27**: 1883–1904. <https://doi.org/10.3748/wjg.v27.i17.1883>
- El Shorbagy S, abuTaleb F, Labib HA, Ebiam H, Harb OA, Mohammed MS, Rashied HA, Elbana KA, Haggag R (2021) Prognostic significance of VEGF and HIF-1 α in hepatocellular carcinoma patients receiving sorafenib versus metformin sorafenib combination. *J Gastrointest Cancer* **52**: 269–279. <https://doi.org/10.1007/s12029-020-00389-w>
- Guo B, Zhao Z, Wang Z, Li Q, Wang X, Wang W, Song T, Huang C (2017) MicroRNA-302b-3p suppresses cell proliferation through AKT pathway by targeting IGF-1R in human gastric cancer. *Cell Physiol Biochem* **42**: 1701–1711. <https://doi.org/10.1159/000479419>
- Harati R, Vandamme M, Blanchet B, Bardin C, Praz F, Hamoudi RA, Desbois-Mouthon C (2021) Drug-drug interaction between metformin and sorafenib alters antitumor effect in hepatocellular carcinoma cells. *Mol Pharmacol* **100**: 32–45. <https://doi.org/10.1124/molpharm.120.000223>
- He Q, Li Y, Zhang W, Chen J, Deng W, Liu Q, Liu Y, Liu D (2021) Role and mechanism of TXNIP in ageing-related renal fibrosis. *Mech Ageing Dev* **196**: 111475. <https://doi.org/10.1016/j.mad.2021.111475>
- He R, Tang GL, Niu L, Ge C, Zhang XQ, Ji XF, Fang H, Luo ZL, Chen M, Shang XF (2020) Quietness Circ 0000962 promoted nerve cell inflammation through PIK3CA/Akt/NF- κ B signaling by miR-302b-3p in spinal cord injury. *Ann Palliat Med* **9**: 190–198. <https://doi.org/10.21037/apm.2020.02.13>
- Hu F, Li M, Mo L, Xiao Y, Wang X, Xie B (2021) SOX-17 is involved in invasion and apoptosis of colorectal cancer cells through regulating miR-302b-3p expression. *Cell Biol Int* **45**: 1296–1305. <https://doi.org/10.1002/cbin.11594>
- Hu L, Zeng Z, Xia Q, Liu Z, Feng X, Chen J, Huang M, Chen L, Fang Z, Liu Q, Zeng H, Zhou X, Liu J (2019) Metformin attenuates hepatoma cell proliferation by decreasing glycolytic flux through the HIF-1 α /PFKFB3/PFK1 pathway. *Life Sci* **239**: 116966. <https://doi.org/10.1016/j.lfs.2019.116966>
- Jia G, Li F, Tong R, Liu Y, Zuo M, Ma L, Ji X (2020) c-Met/MAPK pathway promotes the malignant progression of residual hepatocellular carcinoma cells after insufficient radiofrequency ablation. *Med Oncol* **37**: 117. <https://doi.org/10.1007/s12032-020-01444-z>
- Jiang C, He ZL, Hu XH, Ma PY (2020) MiRNA-15a-3p inhibits the metastasis of hepatocellular carcinoma by interacting with HMOX1. *Eur Rev Med Pharmacol Sci* **24**: 12694–12700. https://doi.org/10.26355/eurrev_202012_24167
- Kong J, Kong J, Pan B, Ke S, Dong S, Li X, Zhou A, Zheng L, Sun WB (2012) Insufficient radiofrequency ablation promotes angiogenesis of residual hepatocellular carcinoma via HIF-1 α /VEGFA. *PLoS One* **7**: e37266. <https://doi.org/10.1371/journal.pone.0037266>
- Lassandro G, Picchi SG, Bianco A, Di Costanzo G, Coppola A, Ierardi AM, Lassandro F (2020) Effectiveness and safety in radiofrequency ablation of pulmonary metastases from HCC: a five years study. *Med Oncol* **37**: 25. <https://doi.org/10.1007/s12032-020-01352-2>
- Li L, Lu S, Fan X (2021) Silencing of miR-302b-3p alleviates isoflurane-induced neuronal injury by regulating PTEN expression and AKT pathway. *Brain Res Bull* **168**: 89–99. <https://doi.org/10.1016/j.brainresbull.2020.12.016>
- Liao ZB, Tan XL, Dong KS, Zhang HW, Chen XP, Chu L, Zhang BX (2019, May) miRNA-448 inhibits cell growth by targeting BCL-2 in hepatocellular carcinoma. *Dig Liver Dis* **51**: 703–711. <https://doi.org/10.1016/j.dld.2018.09.021>
- Lin J, Cao S, Wang Y, Hu Y, Liu H, Li J, Chen J, Li P, Liu J, Wang Q, Zheng L (2018) Long non-coding RNA UBE2CP3 enhances HCC cell secretion of VEGFA and promotes angiogenesis by activating ERK1/2/HIF-1 α /VEGFA signalling in hepatocellular carcinoma. *J Exp Clin Cancer Res* **37**: 113. <https://doi.org/10.1186/s13046-018-0727-1>
- Miyoshi H, Kato K, Iwama H, Maeda E, Masaki T (2014) Effect of the anti-diabetic drug metformin in hepatocellular carcinoma *in vitro* and *in vivo*. *Int J Oncol* **45**: 322–332. <https://doi.org/10.3892/ijo.2014.2419>
- Ni C, Yang S, Ji Y, Duan Y, Yang W, Yang X, Li M, Xie J, Zhang C, Lu Y, Lu H (2021) Hsa_circ_0011385 knockdown represses cell proliferation in hepatocellular carcinoma. *Cell Death Discov* **7**: 270. <https://doi.org/10.1038/s41420-021-00664-0>
- Ramjiawan RR, Griffioen AW, Duda DG (2017) Anti-angiogenesis for cancer revisited: Is there a role for combinations with immunotherapy? *Angiogenesis* **20**: 185–204. <https://doi.org/10.1007/s10456-017-9552-y>
- Richter B, Gwechenberger M, Socas A, Zorn G, Albinni S, Marx M, Bergler-Klein J, Binder T, Wojta J, Gössinger HD (2012) Markers of oxidative stress after ablation of atrial fibrillation are associated with inflammation, delivered radiofrequency energy and early recurrence of atrial fibrillation. *Clin Res Cardiol* **101**: 217–225. <https://doi.org/10.1007/s00392-011-0383-3>
- Schulte L, Scheiner B, Voigtländer T, Koch S, Schweitzer N, Marhenke S, Ivanyi P, Manns MP, Rodt T, Hinrichs JB, Weinmann A, Pinter M, Vogel A, Kirstein MM (2019) Treatment with metformin is associated with a prolonged survival in patients with hepatocellular carcinoma. *Liver Int* **39**: 714–726. <https://doi.org/10.1111/liv.14048>
- Shankaraiah RC, Callegari E, Guerriero P, Rimessi A, Pinton P, Gramantieri L, Silini EM, Sabbioni S, Negrini M (2019) Metformin prevents liver tumorigenesis by attenuating fibrosis in a transgenic mouse model of hepatocellular carcinoma. *Oncogene* **38**: 7035–7045. <https://doi.org/10.1038/s41388-019-0942-z>
- Sheth SS, Bodnar JS, Ghazalpour A, Thippavong CK, Tsutsumi S, Tward AD, Demant P, Kodama T, Aburatani H, Lusis AJ (2006) Hepatocellular carcinoma in Txnip-deficient mice. *Oncogene* **25**: 3528–3536. <https://doi.org/10.1038/sj.onc.1209394>
- Sun Y, Liu L, Xing W, Sun H (2021) microRNA-148a-3p enhances the effects of sevoflurane on hepatocellular carcinoma cell progression via ROCK1 repression. *Cell Signal* **83**: 109982. <https://doi.org/10.1016/j.cellsig.2021.109982>
- Teng F, Zhang JX, Chang QM, Wu XB, Tang WG, Wang JF, Feng JF, Zhang ZP, Hu ZQ (2020) LncRNA MYLK-AS1 facilitates tumor progression and angiogenesis by targeting miR-424-5p/E2F7 axis and activating VEGFR-2 signaling pathway in hepatocellular carcinoma. *J Exp Clin Cancer Res* **39**: 235. <https://doi.org/10.1186/s13046-020-01739-z>
- Teufelsbauer M, Rath B, Plangger A, Staud C, Nanobashvili J, Huk I, Neumayer C, Hamilton G, Radtke C (2020) Effects of metformin on adipose-derived stromal cell (ADSC) – Breast cancer cell lines interaction. *Life Sci* **261**: 118371. <https://doi.org/10.1016/j.lfs.2020.118371>
- Wang D, Jiang X, Liu Y, Cao G, Zhang X, Kuang Y (2021) Circular RNA circ_HN1 facilitates gastric cancer progression through modulation of the miR-302b-3p/ROCK2 axis. *Mol Cell Biochem* **476**: 199–212. <https://doi.org/10.1007/s11010-020-03897-2>
- Wang L, Li K, Lin X, Yao Z, Wang S, Xiong X, Ning Z, Wang J, Xu X, Jiang Y, Liu D, Chen Y, Zhang D, Zhang H (2019) Metformin induces human esophageal carcinoma cell pyroptosis by targeting the miR-497/PELP1 axis. *Cancer Lett* **450**: 22–31. <https://doi.org/10.1016/j.canlet.2019.02.014>
- Xia C, Liu C, He Z, Cai Y, Chen J (2020) Metformin inhibits cervical cancer cell proliferation by modulating PI3K/Akt-induced major histocompatibility complex class I-related chain A gene expression. *J Exp Clin Cancer Res* **39**: 127. <https://doi.org/10.1186/s13046-020-01627-6>
- Xu G, Zhang P, Liang H, Xu Y, Shen J, Wang W, Li M, Huang J, Ni C, Zhang X, Zhu X (2021) Circular RNA hsa_circ_0003288 induces EMT and invasion by regulating hsa_circ_0003288/miR-145/PD-L1 axis in hepatocellular carcinoma. *Cancer Cell Int* **21**: 212. <https://doi.org/10.1186/s12935-021-01902-2>
- Xu H, Miao X, Li X, Chen H, Zhang B, Zhou W (2021) LncRNA SNHG16 contributes to tumor progression via the miR-302b-3p/SLC24A4 axis in pancreatic adenocarcinoma. *Cancer Cell Int* **21**: 51. <https://doi.org/10.1186/s12935-020-01715-9>
- Yerukala Sathipati S, Ho SY (2020) Novel miRNA signature for predicting the stage of hepatocellular carcinoma. *Sai Rep* **10**: 14452. <https://doi.org/10.1038/s41598-020-71324-z>
- You A, Cao M, Guo Z, Zuo B, Gao J, Zhou H, Li H, Cui Y, Fang F, Zhang W, Song T, Li Q, Zhu X, Yin H, Sun H, Zhang T (2016) Metformin sensitizes sorafenib to inhibit postoperative recurrence and metastasis of hepatocellular carcinoma in orthotopic mouse models. *J Hematol Oncol* **9**: 20. <https://doi.org/10.1186/s13045-016-0253-6>
- Yuan Z, Ye M, Qie J, Ye T (2020) FOXA1 Promotes cell proliferation and suppresses apoptosis in HCC by directly regulating miR-212-3p/FOXA1/AGR2 signaling pathway. *Oncotargets Ther* **13**: 5231–5240. <https://doi.org/10.2147/ott.s252890>
- Zhang HH, Zhang Y, Cheng YN, Gong FL, Cao ZQ, Yu LG, Guo XL (2018) Metformin in combination with curcumin inhibits the growth, metastasis, and angiogenesis of hepatocellular carcinoma *in vitro* and *in vivo*. *Mol Carcinog* **57**: 44–56. <https://doi.org/10.1002/mc.22718>
- Zhang Q, Kong J, Dong S, Xu W, Sun W (2017) Metformin exhibits the anti-proliferation and anti-invasion effects in hepatocellular carcinoma cells after insufficient radiofrequency ablation. *Cancer Cell Int* **17**: 48. <https://doi.org/10.1186/s12935-017-0418-6>
- Zhang Y, Zhang H, Wu S (2021) LncRNA-CCDC144NL-AS1 Promotes the development of hepatocellular carcinoma by inducing WDR5 expression via sponging miR-940. *J Hepatocell Carcinoma* **8**: 333–348. <https://doi.org/10.2147/jhc.s306484>
- Zhao D, Xia L, Geng W, Xu D, Zhong C, Zhang J, Xia Q (2021) Metformin suppresses interleukin-22 induced hepatocellular carcinoma by upregulating Hippo signaling pathway. *J Gastroenterol Hepatol* **36**: 3469–3476. <https://doi.org/10.1111/jgh.15674>
- Zhu L, Yang N, Li C, Liu G, Pan W, Li X (2019) Long noncoding RNA NEAT1 promotes cell proliferation, migration, and invasion in hepatocellular carcinoma through interacting with miR-384. *J Cell Biochem* **120**: 1997–2006. <https://doi.org/10.1002/jcb.27499>

An mRNA-based reverse-vaccinology strategy to stimulate the immune response against *Nipah virus* in humans using fusion glycoproteins

Muhammad Naveed¹✉, Sarmad Mahmood¹, Tariq Aziz²✉, Muhammad Hammad Arif¹, Urooj Ali^{1,3}, Faisal Nouroz⁴, Christos Zacharis², Metab Alharbi⁵, Abdulrahman Alshammari⁵ and Abdullah F. Alasmari⁵

¹Department of Biotechnology, Faculty of Science and Technology, University of Central Punjab, Lahore, 54590 Pakistan; ²Department of Agriculture, University of Ioannina Arta, 47132 Greece; ³Department of Biotechnology, Quaid-I-Azam University Islamabad, 45320 Pakistan; ⁴Department of Bioinformatics, Hazara University Mansehra, 21300 Pakistan; ⁵Department of Pharmacology and Toxicology, College of Pharmacy, King Saud University, 11451 Riyadh, Saudi Arabia

The zoonotic pathogen, Nipah virus, is considered a potential healthcare threat due to its high mortality rates and detrimental symptoms like encephalitis. Ribavirin, an antiviral drug helps in overcoming the number of casualties and reducing the mortality rate, but no long-lasting solution has been proposed yet putting global health security in jeopardy. Given the cognizance of mRNA-based vaccines as safe and efficacious preventative strategies against pathogens, the current study has utilized the reverse-vaccinology approach coupled with immunoinformatics to propose an mRNA-based vaccine candidate against the Nipah virus. To ensure the effectiveness of the vaccine candidate against all strains of Nipah and associated viruses, three fusion glycoproteins from Nipah and Hendra viruses were selected. A total of 30 potential epitopes, 10 B-cell-, 10 MHC-I-, and 10 MHC-II-specific, were screened for the construct. The finalized epitopes were highly antigenic with scores ranging from 0.75 to 1.7615 at a threshold of 0.4 for viruses and non-homologous to *Homo sapiens* eradicating any chance of immune tolerance. The construct, with a World population coverage of 97.2%, was structurally stable, thermostable, and hydrophilic with indices of 32.91, 93.62, and -0.002, respectively. The vaccine candidate's tertiary structure was predicted with a TM score of 0.131 and the refined model displayed superlative RAMA improvement (98.2) and MolProbity score (0.975). A quality factor of 93.5421% further validated the structural quality and stability. A prompt and stable immune response was also simulated, and the vaccine candidate was shown to eliminate from the body within the first five days of injection. Immune complexes count of 7000 mg/mL was predicted against the antigen with a small but non-significant danger signal, countered by the cytokines. Lastly, strong molecular interactions of the vaccine candidate with TLR-3 (331.09 kcal/mol) and TLR-4 (-333.31 kcal/mol) and molecular dynamics simulation analysis authenticated the immunogenic potential of the vaccine candidate. This vaccine candidate can serve as a foundation for future *in-vitro* and *in-vivo* trials to minimize or eradicate the diseases associated with the Nipah virus or the Henipaviral family.

Keywords: nipah virus, hendra virus, fusion glycoproteins, immunoinformatics, reverse-vaccinology

Received: 06 March, 2023; **revised:** 17 April, 2023; **accepted:** 15 July, 2023; **available on-line:** 17 September, 2023

✉e-mail: dr.naveed@ucp.edu.pk (MN); iwockd@gmail.com (TA)

Acknowledgements of Financial Support: The authors greatly acknowledge and express their gratitude to the Researchers Supporting Project number (RSP2023R 462), King Saud University, Riyadh, Saudi Arabia.

Abbreviations: CDC, Centers for Disease Control; NHV, Nipah and Hendra viruses; SARS-Cov-2, Severe Acute Respiratory Syndrome Coronavirus 2

INTRODUCTION

Nipah Viral Disease is a zoonotic disease that has a high mortality rate of 91% (Pillai *et al.*, 2020). The disease first emerged in 1998 in Malaysia and spread to neighboring countries including South-East Asia, like Bangladesh, Singapore, and India (Aditi & Shariff, 2019). It was isolated and identified at the University of Malaysia, Faculty of Medicine in 1999. As this virus was first spread in the Malaysian village Sungai Nipah, in pig farms and people associated with them, so scientists named this virus as Nipah virus (Pillai *et al.*, 2020). This virus belongs to the Paramyxoviridae family and genus Henipa viruses. This virus is classified into two strains, the first one was isolated from Malaysia and Cambodia, and the other one was isolated from India and Bangladesh (Mourya *et al.*, 2018). This virus leads to the development of rapid progressive illness in the human respiratory tract and causes encephalitis in the brain. Initially, because of the encephalitis-related symptoms, scientists thought of this disease as Japanese encephalitis, but it was confirmed later that the Nipah virus causes a different disease (Singh *et al.*, 2019). The main host reservoirs for Henipa viruses are fruit bat *Pteropus*. These bats manipulate different fruits like date palms by secreting saliva and urine that is further consumed by animals. The most recent outbreak ruptured in Kerala, India with a loss of 17 human lives (Weingartl *et al.*, 2009). The Nipah virus causes severe breathing issues, destroying the human lung structures and the membrane of the cerebrum. In this condition, the brain enlarges, causing memory loss and severe pain (Rockx *et al.*, 2010). Its symptoms include brain encephalitis, headache, muscular pain, and respiratory disorders. Nausea, giddiness, and fever are also clinically significant (Reddy, 2018). According to the Centers for Disease Control (CDC), the Nipah virus has the potential to create a global emergency and, hence, deserves the immediate attention of the scientific community (Fischer *et al.*, 2018). Ribavirin, an antiviral drug helps in overcoming the number of casualties and reducing the mortality rate,

but no long-lasting solution has been proposed yet (Deb *et al.*, 2019). Vaccines are an efficacious solution to fight this deadly viral agent. mRNA-based vaccines are among the most effective candidates utilized to develop protective immunity against the pathogen. The vaccine shots activate the immune system, and the B-cells and T-cells develop immunologic memory for when a real pathogen attacks the host the immune system recognizes and destroys it. The mRNA vaccines are further appreciated for being cost-effective and timesaving (Kumar *et al.*, 2015). With computational approaches, the labor intensity and process complexity are minimized (Naveed *et al.*, 2022; Naveed *et al.*, 2023a; Naveed *et al.*, 2023b), making mRNA vaccines worthy solutions against viruses like the Nipah virus.

The current work is based on the proposition of an mRNA vaccine utilizing *in-silico* and immunoinformatics tools. The computational approach is considered to safely predict the immune response against the proposed vaccines. Three transmembrane proteins of the Nipah virus were selected for their significant role in the early interactions with the hosts. The selection of the transmembrane proteins was based on their antigenicity, allergenicity, non-toxicity, and non-resemblance with human proteins. Potential epitopes following the criteria of Naveed and others (Naveed *et al.*, 2022a; Naveed *et al.*, 2022b) are shortlisted and the construct is evaluated based on its population coverage, immune response simulations, molecular docking with respective toll-like receptor(s), and physicochemical properties.

MATERIALS AND METHODS

Selection of Target Proteins

The Nipah and Hendra Henipavirus genomes were retrieved from the NCBI database and downloaded in FastA format. CELLO2GO, an online server available at (<http://cello.life.nctu.edu.tw/cello2go/>), was utilized to study the gene ontology and localization of all the proteins present in the genomes. The conservation and homology evaluation was performed using blastp available at (<https://blast.ncbi.nlm.nih.gov/Blast.cgi?PAGE=Proteins>). It ensured that the selected proteins based on protein localization are non-homologous to the human host and are conserved across Henipaviruses. Lastly, the online servers Vaxijen2.0, available at (<http://www.ddg-pharmfac.net/vaxijen/Vaxijen/VaxiJen.html>), and AllerTop, 2.0 accessed at (<https://www.ddg-pharmfac.net/AllerTOP/method.html>), were utilized to predict the antigenicity and allergenicity of the shortlisted proteins, respectively.

Protein Selection & Sequence Retrieval

The online server UniProt (www.uniprot.org) was used to retrieve the Nipah virus virulent protein sequences. Based on different factors like higher antigenic capacity, non-allergenicity, non-toxicity, and non-resemblance with *Homo sapiens*, three trans-membrane fusion glycoproteins (one belonging to Hendra virus and two belonging to the identified strains of Nipah virus) were selected for a potential vaccine candidate.

Prediction of B-cell Epitopes

ABCpred webserver (https://webs.iitd.edu.in/raghava/abcpred/ABC_submission.html) was used for the prediction of B cell epitopes from each protein. We only

selected the epitopes having non-allergenic, highly antigenic, and non-toxic analyses. We used the online server (<https://www.ddg-pharmfac.net/AllerTOP/>), Vaxijen 2.0 (<http://www.ddg-pharmfac.net/vaxijen>), and ToxinPred (<http://crdd.osdd.net/raghava/toxinpred/>), respectively. Moreover, we screened the predicted epitopes to see if they have homologs among humans and excluded the epitopes which might induce autoimmunity.

Prediction of the MHC-I Epitopes

MHC-I binding prediction tool of IEDB (<http://tools.iedb.org/mhci/>) was used to predict the conserved epitopes with the NetMHCpan BA 4.0 version (Reynisson *et al.*, 2020). MHC source specie was selected as human and epitopes were screened based on higher antigenicity value, non-allergenicity, and a specified range of IC₅₀ values lower than 100.

Prediction of MHC-II Epitopes

MHC-II binding prediction tool (<http://tools.iedb.org/mhcii/>) was used to predict the conserved epitopes. NetMHCIIpan 4.0 BA version (Reynisson *et al.*, 2020) was utilized to predict the conserved epitopes. Epitopes were screened based on higher antigenicity value, non-allergenicity, and a specified range of IC₅₀ values lower than 100.

Population Coverage

The evaluation of population coverage of the selected MHC-I and MHC-II epitopes was carried out with the IEDB population coverage tool (<http://tools.iedb.org/population/>). All the selected epitopes with their corresponding alleles were included in the input file. On the input page, the number of epitopes was changed accordingly. A combined MHC-I and MHC-II epitopes input file was provided, and the World was selected as the target population.

Vaccine Construct

The finalized epitopes of B- and T-cells were reverse-translated and fused together with the help of linkers, adjuvants, a MITD sequence, polyA-tail, 5' and 3' UTRs, and methyl-guanosine cap at the start of the construct to enable it for in-host expression.

Analysis of Physicochemical Properties

The physicochemical properties of the vaccine construct were predicted by the ProtParam tool of the ExPasy web server (<https://web.expasy.org/protparam/>). Toxicity prediction was done using Toxinpred. The Vaxijen tool was run to predict the antigenicity of the vaccine construct and to check the vaccine construct's allergenicity.

Prediction of Secondary Structure of the Proposed mRNA Vaccine

PSIPRED (<http://bioinf.cs.ucl.ac.uk/psipred/>) was used for the prediction of the secondary structure. The mRNA vaccine candidate sequence was first translated to its primary protein sequence using EXPASY translate, and this primary sequence was used as an input sequence on PSIPRED. Out of a variety of analyses available on the server, the cartoon structure along with the basic prediction was interpreted.

Prediction and Refinement of the Tertiary Structure

The tertiary structure of the mRNA was predicted using the online server trRosetta <https://yanglab.nankai.edu.cn/trRosetta/>. This online server for protein docking has been continuously extended and refactored. Its advantages include interoperability between modeling capabilities and performance (Leman *et al.*, 2020). Refinement of the tertiary structure of our proposed mRNA vaccine was done by Galaxy WEB's Galaxy REFINE <https://galaxy.seoklab.org/>.

Validation of Tertiary Structure of the Proposed mRNA Vaccine

After refinement of the tertiary structure, we validated our proposed mRNA tertiary structure by Ramachandran plot analysis using the PROCHECK server (<http://save.mbi.ucla.edu/>), whereas the structure quality was validated using ERRAT quality score on the PROCHECK server.

Immune Simulations

To validate whether the mRNA-based vaccine construct has the potential to elicit a stable immune response, C-IMMSIM analyses were performed through the webserver available at <https://kraken.iac.rm.cnr.it/C-IMMSIM/index.php?page=1>. An immunogenic response of single-dose injection was calculated.

Molecular Docking and Simulation Analysis

Molecular docking predicted the immune response stimulation capacity and molecular interaction between the proposed mRNA vaccine protein and toll-like receptors. HDock webserver (<https://www.nature.com/articles/s41596-020-0312-x>) was used. For this purpose, TLR-3 (PDB ID: 3ULV) and TLR-4 (PDB ID: 4R7N) were retrieved from RCSB PDB (<https://www.rcsb.org/>). For simulation analysis of the docked complexes, iMODS (<https://imods.iqfr.csic.es/>) was utilized.

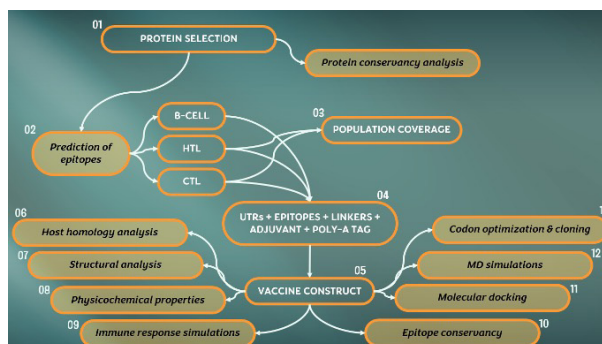


Figure 1. Process overview of the mRNA-based vaccine construct

Cloning of the Construct

The mRNA-based construct was converted into the DNA sequence after codon optimization using JCAT (<http://www.jcat.de/Result.jsp>). The optimized construct was cloned in the pBluescribe vector at the BsoB1 site with the removal of overhangs using Snapgene <https://www.snapgene.com/>. The methodology is schematically represented in Fig. 1.

RESULTS

Target Proteins' Selection

Analyzing 2335 proteins present in the genomes of Nipah and Hendra Henipavirus on the CELLO2GO tool, we selected several pathogenic transmembrane proteins. Out of 108 transmembrane proteins, 3 transmembrane proteins were selected for vaccine design.

Selection and Sequence Retrieval of Transmembrane Proteins

Based on different factors like higher antigenic capacity, non-allergenicity, non-toxicity and non-resemblance with a human protein, three transmembrane fusion glycoproteins

Table 1. List of selected transmembrane proteins for vaccine design against the Nipah virus

Accession ID	Protein name	Antigenicity	Allergenicity	Toxicity
Q9IH63 (Nipah virus)	Fusion glycoprotein F0	0.5012	Non-Allergen	Non-toxic
O89342 (Hendra virus)	Fusion glycoprotein F0	0.5534	Non-Allergen	Non-toxic
A0A1L7B8D7 (Nipah)	Fusion glycoprotein F0	0.5056	Non-Allergen	Non-toxic

Table 2. List of Predicted B-cell Epitopes for vaccine design

Protein	Epitope	Antigenicity	Allergenicity
1	LGSVNYNSEGIAIGPP	1.1587	Non-Allergen
	GVAIGIATAAQITAGV	0.9828	Non-Allergen
	SRLEDRRVRPTSSGDL	1.0553	Non-Allergen
2	YVQELLPVSFNNDNSE	0.6083	Non-Allergen
	GITRKYKIKSNPLTKD	0.6437	Non-Allergen
	VGDVVKLAGVVMAGIAI	0.8857	Non-Allergen
	KRGNYSRLDDRQVRPV	1.2056	Non-Allergen
3	EGIAIGPPVFTDKVDI	0.7407	Non-Allergen
	LSMIILYVLSIASLCI	0.8365	Non-Allergen
	KKRNTYSRLEDRRVRP	0.7484	Non-Allergen

Table 3. List of predicted MHC-I-restricted epitopes for vaccine design

Protein	Epitope	Antigenicity	Alleles
1	SLCIGLITFI	1.0498	HLA-A*02:03, HLA-A*02:01, HLA-A*02:06, HLA-A*68:02
	FISFIIVEKK	1.7539	HLA-A*68:01, HLA-A*11:01, HLA-A*03:01,
	TELSLDLAL	1.1768	HLA-B*40:01, HLA-B*44:03, HLA-B*44:02,
2	FISFVIVEK	1.4849	HLA-A*68:01, HLA-A*11:01, HLA-A*03:01,
	KSRLTGILS	0.7552	HLA-A*30:01, HLA-A*30:02
	IGLITISFV	1.1281	HLA-A*02:03, HLA-A*02:01, HLA-A*02:06, HLA-A*68:02,
	RLKCLLCGI	1.5082	HLA-A*02:03, HLA-A*30:01, HLA-A*02:06, HLA-A*02:01, HLA-A*32:01, HLA-B*15:01
3	FISFIIVEK	1.1861	HLA-A*68:01, HLA-A*11:01, HLA-A*03:01, HLA-A*33:01, HLA-A*31:01
	KIKSNPLTK	0.725	HLA-A*30:01, HLA-A*03:01, HLA-A*11:01, HLA-A*31:01,
	SLCIGLITFI	1.0498	HLA-A*02:03, HLA-A*02:01, HLA-A*02:06, HLA-A*68:02, HLA-A*32:01, HLA-B*15:01

were selected for vaccine design. UniProt protein database was used for the sequence retrieval of fusion glycoproteins under specific allocated UniProt IDs given in Table 1.

Prediction of B cells Epitopes

After protein selection and their sequence retrieval, we screened the predicted B-epitopes according to their higher antigenic capacity, non-allergenicity, non-homology, and non-toxicity. Ten B-cells epitopes, shown in Table 2, extracted from three selected fusion glycoproteins were included in the vaccine construct. All the short-listed epitopes were non-allergenic and antigenic with a score between 0.7 and 1.21, having a threshold of 0.4.

Prediction of MHC-1 Epitopes

For the prediction of MHC-I-restricted epitopes, all alleles of the HLA dataset were selected, and the peptide length was taken as 9 and 10. The epitopes were sorted based on predicted IC50 values. All other parameters were kept as default. The shortlisted epitopes were screened based on higher antigenicity value, allergenicity

and an IC50 value <100 giving a total of 10 epitopes, provided in Table 3.

Prediction of MHC-II epitopes

The length of the predicted MCH-2 cell epitopes was set at 15 and all other parameters were kept as default. The predicted epitopes were saved as an XHTML output table and peptides are sorted according to their adjusted rank. Further screening relied upon antigenicity values and non-allergenicity. The finalized epitopes, shown in Table 4, having a higher antigenicity value, non-allergenicity and IC50 values <100 were selected for the vaccine construct. The restricting alleles for both the MHC-I-restricted and MHC-II-restricted epitopes were recorded for population coverage analysis.

Vaccine Construct

The screened epitopes with a cumulative World population coverage of 97.2%, shown in Fig. 6A, were converted to the mRNA sequence, and fused together using universal linkers (EAAAK, GPGPG, KK, AAY). The 5'

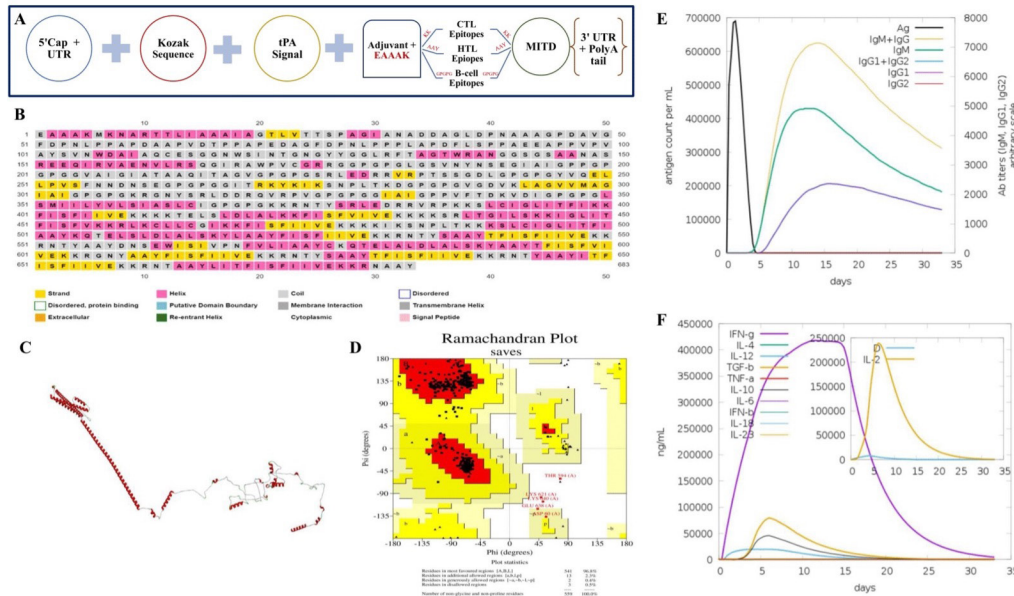


Figure 2. (A) The final vaccine construct; (B) The predicted secondary structure of the construct; (C) The predicted tertiary structure refined by GalaxyREFINE; (D) Ramachandran plot validating the refined tertiary structure; (E) Antigen and Immune complex counts plotted over a month period; (F) Danger signal produced by the body in response to the injection and the cytokines production plotted over a month.

Table 4. List of predicted MHC-II cell epitopes for vaccine design

Protein	Epitope	Antigenicity	Alleles
1	KQTELSL-DLALSKYL	0.8424	HLA-DRB1*03:01, HLA-DRB3*01:01, HLA-DRB1*07:01, HLA-DRB1*04:01, HLA-DRB5*01:01, HLA-DRB4*01:01, HLA-DRB1*13:02, HLA-DPA1*03:01/DPB1*04:02, HLA-DRB1*09:01, HLA-DRB1*15:01, HLA-DRB1*01:01, HLA-DRB1*04:05
	FISFIIVEK-KRNTYS	1.4463	HLA-DRB1*11:01, HLA-DRB1*08:02, HLA-DPA1*02:01/DPB1*05:01, HLA-DRB5*01:01, HLA-DRB4*01:01, HLA-DRB1*03:01, HLA-DPA1*03:01/DPB1*04:02, HLA-DRB1*12:01, HLA-DPA1*02:01/DPB1*01:01, HLA-DRB1*15:01, HLA-DRB1*13:02, HLA-DRB1*04:05, HLA-DRB1*04:01, HLA-DRB1*07:01, HLA-DRB1*01:01
	TFISFIIVEK-KRNTY	1.4822	HLA-DRB1*11:01, HLA-DPA1*02:01/DPB1*05:01, HLA-DRB1*08:02, HLA-DRB5*01:01, HLA-DRB4*01:01, HLA-DPA1*03:01/DPB1*04:02, HLA-DPA1*02:01/DPB1*01:01, HLA-DRB1*03:01, HLA-DPA1*01:03/DPB1*02:01, HLA-DRB1*12:01, HLA-DPA1*01:03/DPB1*04:01, HLA-DRB1*04:05, HLA-DRB1*15:01, HLA-DRB1*04:01, HLA-DRB1*13:02, HLA-DRB1*07:01, HLA-DRB1*01:01, HLA-DRB1*09:01
	DNSEWISI-VPNFVLI	0.789	HLA-DRB1*15:01, HLA-DRB1*07:01, HLA-DRB1*12:01, HLA-DRB1*04:05, HLA-DRB1*13:02, HLA-DRB1*01:01, HLA-DRB1*09:01, HLA-DQA1*05:01/DQB1*02:01, HLA-DRB1*04:01, HLA-DPA1*01:03/DPB1*04:01, HLA-DPA1*03:01/DPB1*04:02, HLA-DPA1*02:01/DPB1*01:01, HLA-DPA1*01:03/DPB1*02:01, HLA-DRB1*08:02, HLA-DRB4*01:01
	CKQTELAL-DLALSKY	0.8828	HLA-DRB1*03:01, HLA-DRB3*01:01, HLA-DRB1*04:01, HLA-DPA1*03:01/DPB1*04:02, HLA-DPA1*02:01/DPB1*01:01, HLA-DRB5*01:01, HLA-DRB4*01:01, HLA-DRB1*13:02
2	TFISFVIVEK-KRGNY	1.7615	HLA-DRB1*11:01, HLA-DRB1*08:02, HLA-DPA1*02:01/DPB1*05:01, HLA-DRB5*01:01, HLA-DPA1*03:01/DPB1*04:02, HLA-DPA1*02:01/DPB1*01:01, HLA-DRB4*01:01, HLA-DPA1*01:03/DPB1*02:01, HLA-DRB1*04:05, HLA-DRB1*04:01, HLA-DRB1*15:01, HLA-DRB1*07:01
	FISFIIVEK-KRNTYS	1.4463	HLA-DRB1*11:01, HLA-DRB1*08:02, HLA-DPA1*02:01/DPB1*05:01, HLA-DRB5*01:01, HLA-DRB4*01:01, HLA-DRB1*03:01, HLA-DPA1*03:01/DPB1*04:02, HLA-DRB1*12:01, HLA-DPA1*02:01/DPB1*01:01, HLA-DRB1*15:01, HLA-DRB1*13:02, HLA-DRB1*04:05, HLA-DRB1*04:01, HLA-DRB1*07:01, HLA-DRB1*01:01
	TFISFIIVEK-KRNTY	1.4822	HLA-DRB1*11:01, HLA-DPA1*02:01/DPB1*05:01, HLA-DRB1*08:02, HLA-DRB5*01:01, HLA-DRB4*01:01, HLA-DPA1*03:01/DPB1*04:02, HLA-DPA1*02:01/DPB1*01:01, HLA-DRB1*03:01, HLA-DPA1*01:03/DPB1*02:01, HLA-DRB1*12:01, HLA-DPA1*01:03/DPB1*04:01, HLA-DRB1*04:05, HLA-DRB1*15:01, HLA-DRB1*04:01, HLA-DRB1*13:02, HLA-DRB1*07:01, HLA-DRB1*01:01, HLA-DRB1*09:01
	ITFISFIIVEK-KRNT	1.7597	HLA-DPA1*02:01/DPB1*05:01, HLA-DRB1*11:01, HLA-DRB5*01:01, HLA-DRB1*08:02, HLA-DPA1*03:01/DPB1*04:02, HLA-DPA1*02:01/DPB1*01:01, HLA-DRB4*01:01, HLA-DPA1*01:03/DPB1*04:01, HLA-DPA1*01:03/DPB1*02:01, HLA-DRB1*04:05, HLA-DRB1*12:01, HLA-DRB1*03:01, HLA-DRB1*15:01, HLA-DRB1*04:01, HLA-DRB1*07:01, HLA-DRB1*13:02, HLA-DRB1*01:01, HLA-DRB1*09:01
	LITFISFIIVEK-KRN	1.5214	HLA-DPA1*02:01/DPB1*05:01, HLA-DRB1*11:01, HLA-DRB5*01:01, HLA-DRB1*08:02, HLA-DPA1*03:01/DPB1*04:02, HLA-DPA1*02:01/DPB1*01:01, HLA-DPA1*01:03/DPB1*04:01, HLA-DPA1*01:03/DPB1*02:01, HLA-DRB4*01:01, HLA-DRB1*04:05, HLA-DRB1*12:01, HLA-DRB1*15:01, HLA-DRB1*04:01, HLA-DRB1*07:01, HLA-DRB1*01:01, HLA-DRB1*13:02, HLA-DRB1*09:01
3	ITFISFIIVEK-KRNT	1.7597	HLA-DPA1*02:01/DPB1*05:01, HLA-DRB1*11:01, HLA-DRB5*01:01, HLA-DRB1*08:02, HLA-DPA1*03:01/DPB1*04:02, HLA-DPA1*02:01/DPB1*01:01, HLA-DRB4*01:01, HLA-DPA1*01:03/DPB1*04:01, HLA-DPA1*01:03/DPB1*02:01, HLA-DRB1*04:05, HLA-DRB1*12:01, HLA-DRB1*03:01, HLA-DRB1*15:01, HLA-DRB1*04:01, HLA-DRB1*07:01, HLA-DRB1*13:02, HLA-DRB1*01:01, HLA-DRB1*09:01
	LITFISFIIVEK-KRN	1.5214	HLA-DPA1*02:01/DPB1*05:01, HLA-DRB1*11:01, HLA-DRB5*01:01, HLA-DRB1*08:02, HLA-DPA1*03:01/DPB1*04:02, HLA-DPA1*02:01/DPB1*01:01, HLA-DPA1*01:03/DPB1*04:01, HLA-DPA1*01:03/DPB1*02:01, HLA-DRB4*01:01, HLA-DRB1*04:05, HLA-DRB1*12:01, HLA-DRB1*15:01, HLA-DRB1*04:01, HLA-DRB1*07:01, HLA-DRB1*01:01, HLA-DRB1*13:02, HLA-DRB1*09:01
	ITFISFIIVEK-KRNT	1.7597	HLA-DPA1*02:01/DPB1*05:01, HLA-DRB1*11:01, HLA-DRB5*01:01, HLA-DRB1*08:02, HLA-DPA1*03:01/DPB1*04:02, HLA-DPA1*02:01/DPB1*01:01, HLA-DRB4*01:01, HLA-DPA1*01:03/DPB1*04:01, HLA-DPA1*01:03/DPB1*02:01, HLA-DRB1*04:05, HLA-DRB1*12:01, HLA-DRB1*03:01, HLA-DRB1*15:01, HLA-DRB1*04:01, HLA-DRB1*07:01, HLA-DRB1*13:02, HLA-DRB1*01:01, HLA-DRB1*09:01
	LITFISFIIVEK-KRN	1.5214	HLA-DPA1*02:01/DPB1*05:01, HLA-DRB1*11:01, HLA-DRB5*01:01, HLA-DRB1*08:02, HLA-DPA1*03:01/DPB1*04:02, HLA-DPA1*02:01/DPB1*01:01, HLA-DPA1*01:03/DPB1*04:01, HLA-DPA1*01:03/DPB1*02:01, HLA-DRB4*01:01, HLA-DRB1*04:05, HLA-DRB1*12:01, HLA-DRB1*15:01, HLA-DRB1*04:01, HLA-DRB1*07:01, HLA-DRB1*01:01, HLA-DRB1*13:02, HLA-DRB1*09:01
	LITFISFIIVEK-KRN	1.5214	HLA-DPA1*02:01/DPB1*05:01, HLA-DRB1*11:01, HLA-DRB5*01:01, HLA-DRB1*08:02, HLA-DPA1*03:01/DPB1*04:02, HLA-DPA1*02:01/DPB1*01:01, HLA-DPA1*01:03/DPB1*04:01, HLA-DPA1*01:03/DPB1*02:01, HLA-DRB4*01:01, HLA-DRB1*04:05, HLA-DRB1*12:01, HLA-DRB1*15:01, HLA-DRB1*04:01, HLA-DRB1*07:01, HLA-DRB1*01:01, HLA-DRB1*13:02, HLA-DRB1*09:01

and 3' components along with the RpfE adjuvant and the Kozak sequence were added to the construct, shown in Fig. 1A, for stability, improved immunogenicity, and ease of entry into the host cells.

Physicochemical Properties Prediction

The physicochemical properties computed for the vaccine candidate by translating the construct into its peptide sequence indicated that it was antigenic (0.8746), non-allergenic, stable (32.91), thermostable (93.62), hydrophilic (-0.002), non-toxic, and had 683 amino acids. Table 5 discusses the analysis and indication of the physicochemical properties of peptides.

Prediction of Secondary Structure

The secondary structure predicted by PSIPRED, shown in Fig. 2B, depicts the alpha-helices, beta-turns, and coils of the vaccine candidate. Most of the amino acid residues were predicted as coils indicating the vaccine candidate's transmembrane localization.

Prediction and Refinement of Tertiary Structure

trRosetta predicted the tertiary model of the vaccine candidate with a TM-score of 0.131. Since, this was

below the ideal TM score, the model was refined and GalaxyREFINE predicted 5 models, out of which the first one was selected (depicted in Fig. 2C) based on the most improved RAMA scores (98.2) indicating the torsion angle distribution of the vaccine candidate. Other metrics like MolProbity (0.975) that evaluates the model quality at both protein and nucleic-acid levels and least RMSD (0.356) calculating the difference in protein backbone conformation in the initial and final structures were also considered for model selection.

Validation of Tertiary Structure

ERRAT calculated the overall quality factor score of 93.5421 and the Ramachandran plot (Fig. 2D) indicated that most of the residues lie in the most favored region. 541 residues constituted 96.8% of the total protein, residues in the additional allowed region were 2.3%, in the generally allowed region were 0.4% and in the disallowed region were 0.5%.

Immune Simulation Response

C-IMMSIM predicted a potent and stable immune response against the injected antigen. The graph in Fig. 2E illustrates that the server predicted the antigen to be eliminated from the host system within the first 5 days

Table 5. The Physiochemical Properties of the proposed mRNA vaccine

Property	Measurement	Indication
Antigenicity	0.8746	Antigenic
Allergenicity	Non-Allergen	Non-Allergen
No. of Amino Acids	683	Appropriate
Formula	$C_{3337}H_{5316}N_{880}O_{933}S_{11}$	Appropriate
Total number of -ve charged residues (Asp + Glu)	52	–
Total number of +ve charged residues (Arg + Lys)	90	–
Theoretical pI	9.74	Basic
Estimated Half Life (mammalian reticulocytes)	1 hour	Easily eliminated
Instability Index	32.91	Stable
Aliphatic Index	93.62	Thermostable
Grand average of hydropathicity (GRAVY)	–0.002	Hydrophilic
Toxicity of Vaccine Construct	Non-toxic	Non-toxic

after escalating to 700 000 antigen count per mL on the first day. The immune complexes (IgG+IgM) were generated when the antigen count was almost 0 and escalated up to 7000 for the first 15 days of injection. The complex count decreased afterward but became steady at 3600 after a month indicating stability and longevity of the immune response. The graph in Fig. 2F illustrates the cytokine production and danger-signal produced by the body in response to the antigen. A small danger signal was produced lasting for up to 25 days but was not significant. The interleukin-2 count escalated up to 250 000 mg/mL on the 5th day and steadily decreased afterward. It was clear from the graph that the increase in IL-2 count was a direct response to the signal validating the potent response. IFN-gamma was also readily produced by the immune system.

Molecular Docking Analysis

HDOCK webserver predicted 10 models of the docking poses of mRNA vaccine construct with TLR-3 (PDB ID: 3ULV) and 10 models with TLR-4 (PDB ID: 4R7N). With TLR-3 docking, the first model was selected having a docking score of –331.09 kcal/mol and a confidence score of 0.9740, shown in Fig. 3A. With TLR-4 docking, the first model (Fig. 3B) was selected for having a dock-

ing score of –333.31 kcal/mol and a confidence score of 0.975.

Molecular Dynamics Simulations

With an eigenvalue of 2.95646e-06 and 4.0524e-06, illustrated in Figs. 4d and 5d respectively, the docked complex (Figs. 4a, 5a) was predicted to be stiff with little dynamic residues. The B-factor (shown in Figs. 4b and 5b) also showed minimal flexibility, except for the last few residues. The deformability plot shown in Figs. 4c and 5c was found consistent with the eigenvalue and the B-factor plot indicating that only a few residues towards the end of the docked complex were flexible/deformable. The variance and co-variance map (Figs. 4e, 5e and Figs. 4f and 5f, respectively) show stable amino acid-pair interactions validating strong molecular interactions. Lastly, the elastic network map showed that the atoms in the docked complex are closely linked to each other, demonstrated in Figs. 4g and 5g, reflecting on the covariance findings.

Expression Analysis

The CAI score of 0.95518 and GC content of 67.057% reflected the maximum codon optimization of the construct sequence, illustrated in Fig. 6B. pBluescribe plasmid was utilized for the *in-silico* cloning experiment. The plasmid was cut by the AHD-I enzyme producing sticky ends, enabling unidirectional cloning of the construct into the vector. Figure 6C shows the cloning process, whereas Fig. 6D represents the cloned vector.

DISCUSSION

Nipah virus first emerged in the late nineties, with fruit bat as its mediatory host. First, it was observed in the pig but was soon observed in the human population (Aditi & Shariff, 2019). Due to a high fatality rate in developing countries, this virus is thought to evoke a potential zoonotic pandemic like coronavirus (Kulkarni *et al.*, 2013). Ribavirin, a drug initially used against hepatitis and liver-virus infection, has been utilized to minimize viral load in Nipah viral disease patients (Deb *et al.*, 2019). However, the mortality rates are still high (Naveed *et al.*, 2021). Owing to the absence of preventative strate-

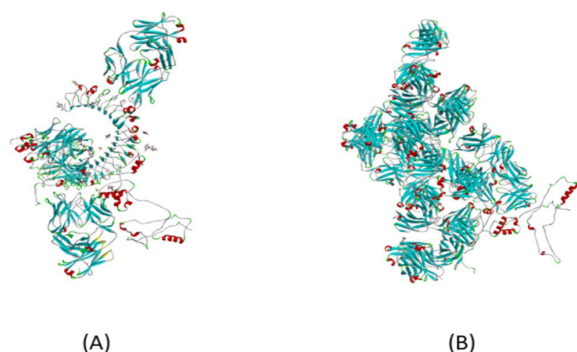


Figure 3. (A) Docking complex with TLR-3 (PDB ID: 3ULV); (B) docking complex with TLR-4 (PDB ID: 4R7N)

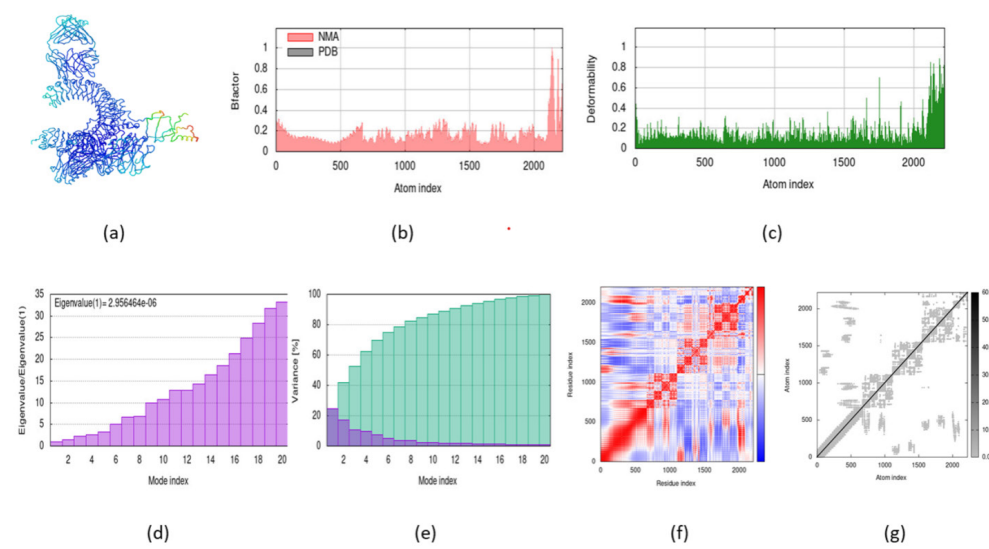


Figure 4. The results of the iMDS simulation study of the proposed mRNA vaccine and TLR-3 docked complex. (a) MNA mobility, (b) deformability, (c) B factor, (d) Eigen values, (e) variance (green color indicated cumulative variances and purple color indicates the individual variance), (f) co-variance map (uncorrelated as white, correlated as red, and anti-correlated as blue motions) and (g) elastic network (darker grey regions indicate stiffer regions).

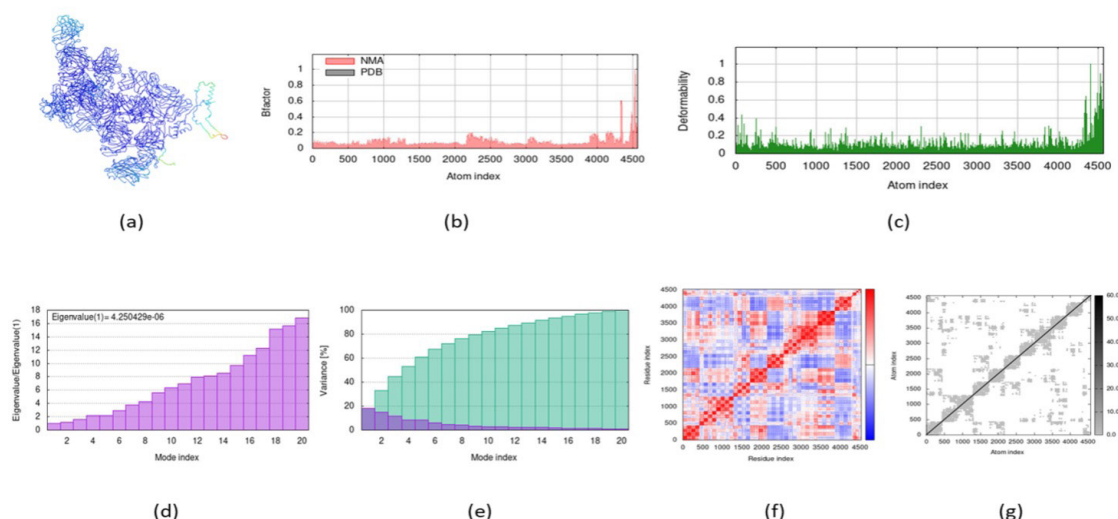


Figure 5. The results of the iMDS simulation study of the proposed mRNA vaccine and TLR-4 docked complex. (a) MNA mobility, (b) deformability, (c) B factor, (d) Eigen values, (e) variance (green color indicated cumulative variances and purple color indicates the individual variance), (f) co-variance map (uncorrelated as white, correlated as red, and anti-correlated as blue motions) and (g) elastic network (darker grey regions indicate stiffer regions).

gies being present, this study proposed a mRNA-based vaccine design to develop protective immunity against the pathogen. This effort was in line with the previous studies proposing protective immunity against diseases (Al Tbeishat *et al.*, 2022) like mucormycosis (Maruggi *et al.*, 2017) and HPIV-1 (Naveed *et al.*, 2022). Recently, COVID-19 RNA-based vaccines like Pfizer-BioNtech's 'Comirnaty' have worked wonders by developing prior immunity in the human body against the SARS-Cov-2 attack (Rotshild *et al.*, 2021). It has been observed that vaccines have some epigenetic impact on immune system genes, which train the immune system (Kumar *et al.*, 2015). Likewise, the focus of this study was to develop a long-lasting memory in the form of activated B cells and T cells. The HTL induces IL-10, IL-4, and IFN- γ , antigen-presenting cells express epitopes of HTL, and the lymphocyte can secrete chemokines, all play crucial roles

against the virus (Al Tbeishat *et al.*, 2022). We observed the production of all these immune system components in response to the antigen. Except for the memory cells, all the immune cells died and were eliminated with the destroyed antigen. B cells with membrane-bound immunoglobulin receptors identified the antigen epitopes and internalized them to become presenting cells for memory-making units of the immune system. Furthermore, we noticed a hike in plasma-secreted antibodies (up to 40000 counts) that are utilized to neutralize the antigen (vaccine candidate injection) and produce memory cells. Our results were consistent with previous mRNA-based vaccine findings (Naveed *et al.*, 2022; Maruggi *et al.*, 2017), predicting an efficacious vaccine construct with the ability to elicit long-lasting protective immunity.

The tools utilized in this study have revolutionized biotechnological research. The reverse-vaccinology ap-

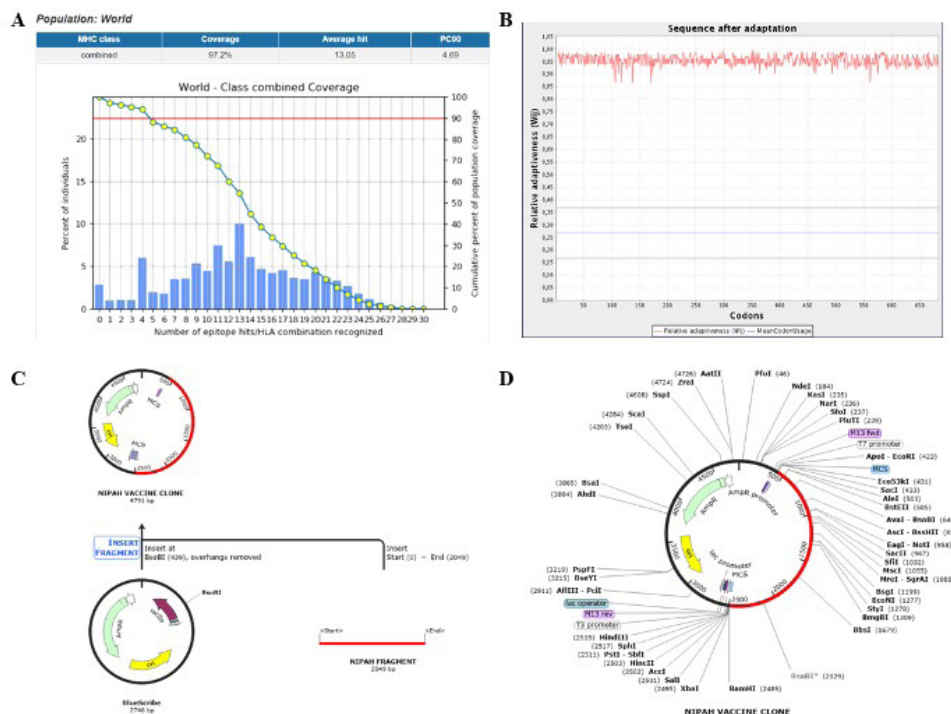


Figure 6. (A) Population coverage of the T-cell-specific epitopes; (B) Codon optimization chart of the proposed mRNA vaccine construct; (C) The history map of cloning, the black vector shows pBluescribe plasmid, 2040 bps long, the red line shows vaccine construct and the final construct after insertion in which red color shows gene of interest (4791 bps long); (D) The cloned Bluescribe vector with the gene of interest shown in red color

proach has saved time, preliminary clinical trials, and labor costs (Kumar *et al.*, 2015). We followed this approach because of its proclaimed merits in prediction (Naveed *et al.*, 2022a; Naveed *et al.*, 2022b) as well as clinical studies (Hall *et al.*, 2021; Pormohammad *et al.*, 2021). The *in-silico* prediction of antigenicity, allergenicity, and toxicity significantly helped us in characterizing the potential epitopes. These tools have the potential to save lives at pre-clinical trials (Xinhui *et al.*, 2021) as researchers may have already predicted the immunogenic, allergenic, or toxic outcome of a proposed vaccine before it is administered to the public (Naveed *et al.*, 2023a; Naveed *et al.*, 2023b). Lastly, the wide population coverage of the proposed candidate validates that it can be efficacious worldwide irrespective of race, ethnicity, or area.

Declarations

Ethics approval and consent to participate: Not applicable.

Competing interests: The authors declare no conflict of interest.

Funding: No external funding was received.

Authors' contributions: Conceptualization, M.N. and S.M.; methodology, M.H.A.; software, U.A.; validation, F.N., and T.A.; formal analysis, M.N.; investigation, U.A. and S.M.; resources, M.N.; data curation, M.S. and M.E.A.; writing – original draft preparation, M.A. and C.Z.; writing – review and editing, T.A.; visualization, M.A. A.F.A., and A.A.S.; supervision, T.A.; project administration, M.N.; funding acquisition, T.A.

Availability of data and material: All the data used in this research work has been included in this manuscript.

REFERENCES

- Aditi, Shariff M (2019) Nipah virus infection: A review. *Epidemiol. Infect.* **147**. <https://doi.org/10.1017/S0950268819000086>
- Al Tbeishat H (2022) Novel *in silico* mRNA vaccine design exploiting proteins of *M. tuberculosis* that modulates host immune responses by inducing epigenetic modifications. *Sci. Rep.* **12**. <https://doi.org/10.1038/s41598-022-08506-4>
- Deb S, Vyas DB, Pendharkar AV, Rezaii PG, Schoen MK, Desai K, Gephart MH, Desai A (2019) Socioeconomic predictors of pituitary surgery. *Cureus* **11**: e3957. <https://doi.org/10.7759/cureus.3957>
- Fischer K, Diederich S, Smith G, Reiche S, Pinho dos Reis V, Stroh E, Groschup MH, Weingartl HM, Balkema-Buschmann A (2018) Indirect ELISA based on Hendra and Nipah virus proteins for the detection of henipavirus specific antibodies in pigs. *PLoS One* **13**: e0194385. <https://doi.org/10.1371/journal.pone.0194385>
- Hall VG, Ferreira VH, Ku T, Ierullo M, Majchrzak-Kita B, Chaparro C, Selzner N, Schiff J, McDonald M, Tomlinson G, Kulasingam V, Kumar D, Humar A (2021) Randomized trial of a third dose of mRNA-1273 vaccine in transplant recipients. *N. Engl. J. Med.* **385**: 1244–1246. <https://doi.org/10.1056/NEJMc2111462>
- Kulkarni DD, Tosh C, Venkatesh G, Senthil Kumar D (2013) Nipah virus infection: current scenario. *Virusdisease* **24**: 398–408. <https://doi.org/10.1007/s13337-013-0171-y>
- Kumar G, Menanteau-Ledouble S, Saleh M, El-Matbouli M (2015) *Yersinia truckeri*, The causative agent of enteric redmouth disease in fish. *Vet. Res.* **46**. <https://doi.org/10.1186/s13567-015-0238-4>
- Leman JK, Weitzner BD, Lewis SM, Adolf-Bryfogle J, Alam N, Alford RF, Abrahamian M, Baker D, Barlow KA, Barth P, Basanta B, Bender BJ, Blacklock K, Bonet J, Boyken SE, Bradley P, Bystroff C, Conway P, Cooper S, Correia BE (2020) Macromolecular modeling and design in Rosetta: recent methods and frameworks. *Nat. Methods* **17**: 665–680. <https://doi.org/10.1038/s41592-020-0848-2>
- Maruggi G, Chiarot E, Giovani C, Buccato S, Bonacci S, Frigimelica E, Margarit I, Geall A, Bensi G, Maione D (2017) Immunogenicity and protective efficacy induced by self-amplifying mRNA vaccines encoding bacterial antigens. *Vaccines* **35**: 361–368. <https://doi.org/10.1016/j.vaccine.2016.11.040>
- Mourya DT, Yadav P, Sudeep AB, Gokhale, MD, Gupta, N, Gangakhedkar RR, Bhargava B (2018) Spatial association between a nipah virus outbreak in India and nipah virus infection in pteropus bats. *Clin. Infect. Dis.* **69**: 378–379. <https://doi.org/10.1093/cid/ciy1093>

- Naveed M, Mughal MS, Jabeen K, Aziz T, Naz S, Nazir N, Shahzad M, Alharbi M, Alshammari A, Sadhu SS (2022) Evaluation of the whole proteome to design a novel mRNA-based vaccine against multidrug-resistant *Serratia marcescens*. *Front. Microbiol.* **13**: 960285. <https://doi.org/10.3389/fmicb.2022.960285>
- Naveed M, Tehreem S, Arshad S, Bukhari SA, Shabbir MA, Essa R, Ali N, Zaib S, Khan A, Al-Harrasi A, Khan I (2021) Design of a novel multiple epitope-based vaccine: An immunoinformatics approach to combat SARS-CoV-2 strains. *J. Infect. Public Health* **14**: 938–946. <https://doi.org/10.1016/j.jiph.2021.04.010>
- Naveed M, Ain N, Aziz T, Ali I, Aqib Shabbir M, Javed K, Alharbi M, Alshammari A, Alasmari AF (2023) Revolutionizing treatment for toxic shock syndrome with engineered super chromones to combat antibiotic-resistant *Staphylococcus aureus*. *Eur. Rev. Med. Pharmacol. Sci.* **27**: 5301–5309. https://doi.org/10.26355/eurrev_202306_32649
- Naveed M, Ain N, Aziz T, Javed K, Ishfaq H, Khalil S, Alharbi M, Alshammari A, Alasmari AF (2023) Pharmacophore screening approach of homeopathic phenols for a renovated design of fragment-optimized Bauhiniastatin-1 as a drug against acromegaly. *Eur. Rev. Med. Pharmacol. Sci.* **27**: 5530–5541. https://doi.org/10.26355/eurrev_202306_32790
- Naveed M, Ali U, Karobari MI, Ahmed N, Mohamed RN, Abullais SS, Kader MA, Marya A, Messina P, Scardina GA (2022) A vaccine construction against COVID-19-associated mucormycosis contrived with immunoinformatics-based scavenging of potential mucoralean epitopes. *Vaccines* **10**: 664. <https://doi.org/10.3390/vaccines10050664>
- Naveed M, Jabeen K, Naz R, Mughal MS, Rabaa AA, Bakhrebah MA, Alhoshani FM, Aljeldah M, Shammari BRA, Alissa M, Sabour AA, Alaeq RA, Alshiekheid MA, Garout M, Almogbel MS, Halwani MA, Turkistani SA, Ahmed N (2022) Regulation of host immune response against enterobacter cloacae proteins via computational mRNA vaccine design through transcriptional modification. *Microorganisms* **10**: 1621. <https://doi.org/10.3390/microorganisms10081621>
- Naveed M, Sheraz M, Amin A, Waseem M, Aziz T, Khan AA, Ghani M, Shahzad M, Alruways MW, Dablood AS, Elazzazy AM, Almalki AA, Alamri AS, Alhomrani M (2022) Designing a novel peptide-based multi-epitope vaccine to evoke a robust immune response against pathogenic multidrug-resistant *Providencia heimbachae*. *Vaccines* **10**: 1300. <https://doi.org/10.3390/vaccines10081300>
- Naveed M, Shabbir MA, Ain N-u, Javed K, Mahmood S, Aziz T, Khan AA, Nabi G, Shahzad M, Alharbi ME, Alharbi M, Alshammari A (2022) Chain-engineering-based *de novo* drug design against MPXV-gp169 virulent protein of monkeypox virus: a molecular modification approach. *Bioengineering* **10**: 11. <https://doi.org/10.3390/bioengineering10010011>
- Naveed M, Ain Nu, Aziz T, Javed K, Shabbir MA, Alharbi M, Alshammari A, Alasmari AF (2023) Artificial intelligence assisted pharmacophore design for philadelphia chromosome-positive leukemia with gamma-tocotrienol: a toxicity comparison approach with asciminib. *Biomedicines* **11**: 1041. <https://doi.org/10.3390/biomedicines11041041>
- Naveed M, Waseem M, Aziz T, Hassan Ju, Makhdoom SI, Ali U, Alharbi M, Alshammari A (2023) Identification of bacterial strains and development of anmrna-based vaccine to combat antibiotic resistance in *Staphylococcus aureus* via *in vitro* and *in silico* approaches. *Biomedicines* **11**: 1039. <https://doi.org/10.3390/biomedicines11041039>
- Pillai VS, Krishna G, Valiya Veetil, M (2020) Nipah virus: past outbreaks and future containment. *Viruses* **12**: 465. <https://doi.org/10.3390/v12040465>
- Pormohammad A, Zarei M, Ghorbani S, Mohammadi M, Razizadeh MH, Turner DL, Turner RJ (2021) Efficacy and safety of COVID-19 vaccines: a systematic review and meta-analysis of randomized clinical trials. *Vaccines* **9**: 467. <https://doi.org/10.3390/vaccines9050467>
- Reddy K (2018) Nipah Virus (NiV) Infection: an emerging zoonosis of public health concern. *J. Gandaki Med. Coll. Nepal*. **11**. <https://doi.org/10.3126/jgmcn.v11i02.22897>
- Reynisson B, Alvarez B, Paul S, Peters B, Nielsen M (2020) NetMHCpan-4.1 and NetMHCIIpan-4.0: improved predictions of MHC antigen presentation by concurrent motif deconvolution and integration of MS MHC eluted ligand data. *Nucl. Acids. Res.* **48**: W449–W454. <https://doi.org/10.1093/nar/gkaa379>
- Rockx B, Bossart KN, Feldmann F, Geisbert JB, Hickey AC, Brining D, Callison J, Safronetz D, Marzi A, Kercher L, Long D, Broder CC, Feldmann H, Geisbert TW (2010) A novel model of lethal Hendra virus infection in African Green monkeys and the effectiveness of Ribavirin treatment. *J. Virol.* **84**: 9831–9839. <https://doi.org/10.1128/JVI.01163-10>
- Sharma V, Kaushik S, Kumar R, Yadav JP, Kaushik S (2018) Emerging trends of Nipah virus: A review. *Rev. Med. Virol.* **29**: e2010. <https://doi.org/10.1002/rmv.2010>
- Singh RK, Dhama K, Chakraborty S, Tiwari R, Natesan S, Khandia R, Munjal A, Vora KS, Latheef SK, Karthik K, Singh Malik, Singh R, Chaicumpa W, Mourya DT (2019) Nipah virus: epidemiology, pathology, immunobiology and advances in diagnosis, vaccine designing and control strategies – a comprehensive review. *Vet. Q.* **39**: 26–55. <https://doi.org/10.1080/01652176.2019.1580827>
- Weingartl HM, Berhane Y, Czub M (2009) Animal models of henipavirus infection: A review. *Vet. J.* **181**: 211–220. <https://doi.org/10.1016/j.tvjl.2008.10.016>
- Xinhui Cai, Jiao Jiao Li, Tao Liu, Oliver Brian, Jinyan Li (2021) Infectious disease mRNA vaccines and a review on epitope prediction for vaccine design. *Brief. Funct. Genom.* **20**: 289–303. <https://doi.org/10.1093/bfpg/elab027>
- Zhang C, Maruggi G, Shan H, Li J (2019) Advances in mRNA vaccines for infectious diseases. *Front. Immunol.* **10**. <https://doi.org/10.3389/fimmu.2019.00594>

Design and development of new inhibitors against breast cancer, Monkeypox and Marburg virus by modification of natural Fisetin *via in silico* and SAR studies

Shopnil Akash¹, Md. Mominur Rahman¹, Clara Mariana Gonçalves Lima², Talha Bin Emran³, Sharifa Sultana¹, Sumaira Naz⁴, Tariq Aziz⁵✉, Metab Alharbi⁶, Abdulrahman Alshammari⁶ and Abdullah F. Alasmari⁶

¹Department of Pharmacy, Faculty of Allied Health Sciences, Daffodil International University, Dhaka 1207, Bangladesh; ²Federal University of Lavras, Brazil; ³Department of Pharmacy, BGC Trust University Bangladesh, Chittagong 4381, Bangladesh; ⁴Department of Biochemistry University of Malakand, Chakdara 18800 Pakistan; ⁵Department of Agriculture, University of Ioannina, 47100 Arta, Greece; ⁶Department of Pharmacology and Toxicology, College of Pharmacy, King Saud University, P.O. Box 2455, Riyadh 11451, Saudi Arabia

The natural Fisetin and its derivatives have been shown to have effective bioactivity and strong pharmacological profile, which is continuously drawing the interest of therapeutic applications to the development of new biomolecules against Breast cancer and Monkeypox, and Marburg viral infection, while computational approaches and the study of their structure-activity relationship (SAR) are the most eloquent and reliable platform for performing their hypothetical profile renovation. So, the main perspective of this investigation is to evaluate dual function of Fisetin and its derivatives against both virus and cancerous target. First and foremost, the prediction of activity spectra for materials (PASS) valuation has provided preliminary data on the antiviral, antibacterial, antiparasitic, and anticancer possibilities of the mentioned compounds. According to the evidence, PASS predicted scores were shown to perform better in antineoplastic and antiviral than antibacterial, and antiparasitic efficiency; as evidenced by their higher PASS scores in antineoplastic and antiviral drug tests. Breast cancer, Monkeypox, and Marburg virus have been selected as targeted pathogens, and different *in silico* studies were conducted to determine the dual function of mention derivatives. The "Lipinski five rules," on the other hand, has been subjected to extensive testing for drug-like characteristics. Molecular docking against Breast cancer, Monkeypox, and Marburg virus have been accomplished after confirmation of their bioactivity. The molecular docking evaluation against targeted disease displayed re-markable binding affinity and non-bonding engagement, with most of the results indicating that derivatives are more effective than the FDA approved standard antiviral, and antineoplastic drugs. Finally, the ADMET characteristics have been computed, and they indicate that the substance is suitable to use and did not have any chance to produce adverse effects on aquatic or non-aquatic environment, as well as having a highly soluble capacity in water medium, high G.I absorption rate, with outstanding bioavailability index. Therefore, these mentioned Fisetin derivatives could be suggested as potential medication against Breast cancer and newly reported Monkeypox, and Marburg virus, and may further proceed for laboratory experiment, synthesis, and clinical trials to evaluate their practical value.

Keywords: ADMET, molecular docking, Lipinski rule and pharmacokinetics, pass prediction

Received: 13 February, 2023; **revised:** 14 March, 2023; **accepted:** 17 March, 2023; **available on-line:** 07 September, 2023

✉e-mail: iwocdk@gmail.com

Acknowledgments of Financial Support: The authors greatly acknowledge and express their gratitude to the Researchers Supporting Project number (RSP2023R335), King Saud University, Riyadh, Saudi Arabia.

Abbreviations: CADD, computer-aided drug design; PASS, prediction of activity spectra for materials; SAR, structure-activity relationship

INTRODUCTION

Breast cancer is the most frequent cancer in women globally, where it is accompanied with a devastating impact on life among females (Bhattacharyya *et al.*, 2020). Every year, many patients have been identified by Breast cancer globally. Among them, many patients cannot survive due to limitation of proper treatment. Currently, finding on literature review, chemotherapeutics drugs, radiation therapy, surgery, hormone therapy, targeted therapy, and immune therapy seem to be the treatment options for Breast cancer that applies, which is very expensive with numerous side effects like killing healthy cells (Eniu *et al.*, 2008; Pilla *et al.*, 2018; Schirrmaker, 2003). Recently, it has been seen that several cancer-fighting medications (chemotherapeutic agent) are becoming increasingly ineffective or cancerous cells gain resistance against them. As a result, alternative options for Breast cancer treatment should be found for the future generation (Naveed *et al.*, 2022a; Naveed *et al.*, 2023b; Afshari *et al.*, 2022; Farkona *et al.*, 2016; Poojan *et al.*, 2020).

One the other side, human Monkeypox seems to be a *zoonotic orthopoxvirus* and composed of double stranded DNA, transmitted by Monkey to human, which is particularly reported in tropical Western and Central African areas. It was first reported in 1958 when during the out-breaks of a pox-like infection (Naveed *et al.*, 2023c; Mileto *et al.*, 2022; Pal *et al.*, 2017). Previously, tropical Western and Central African areas were a major region of Monkeypox virus (MPXV), but recently the MPXV resurfacing and expanding throughout the world is causing a major threat to human life and it especially affected most of the European countries, as well as North and South America (Hatmal *et al.*, 2022; Majie *et al.*, 2023). About 4900 infected of human Monkeypox were reported in more than 50 countries at the end of June 2022, and one infected person has died (Mucker *et al.*, 2022). So, it is a reminder that another pandemic might happen around the globe, which make concern to the global policymaker, and healthcare system. For more

Table 1. Data of PASS prediction data

S/N	Antiviral (Herpes)		Antibacterial		Antiparasitic		Antineoplastic	
	Pa	Pi	Pa	Pi	Pa	Pi	Pa	Pi
01	0.471	0.014	0.388	0.033	0.404	0.031	0.783	0.014
02	0.447	0.019	0.420	0.026	0.309	0.053	0.818	0.010
03	0.427	0.025	0.376	0.036	0.240	0.078	0.849	0.007
04	0.428	0.025	0.298	0.061	0.358	0.040	0.556	0.055
05	0.419	0.028	0.279	0.068	0.340	0.045	0.508	0.069
06	0.442	0.020	0.336	0.047	0.410	0.019	0.735	0.020
07	0.421	0.027	0.299	0.060	0.401	0.031	0.727	0.022
08	0.405	0.033	0.364	0.039	0.342	0.044	0.775	0.015
09	0.392	0.039	0.327	0.050	0.301	0.056	0.754	0.018

than couple of decades, scientists have worked to enhance Smallpox vaccinations and find medicines to assure immunity against Smallpox or Smallpox-like illnesses. But investigation reported that there is no authorized medication against MPXV till now (Gong *et al.*, 2022). Besides, following corona virus epidemic, another pandemic is knocking at the door, which might be caused by Marburg virus (MARV). The Marburg virus (MARV) has been considered as the deadly hemorrhagic infection that may produce a fatal condition. MARV is suspected to be a zoonotic infection spread by animals (Albaqami *et al.*, 2023; Reuben & Abunike, 2023). The virus may spread from bats to people by extended exposure to 'bat colonies' tunnels and caves, and by interaction with bat saliva, excrement, and infected fruits (Asad *et al.*, 2020; Mortlock, 2013). Recently, it was in the headlines in mid-July 2022 due to an epidemic in Ghana, an African country, where two affected people have died. MARV is an enclosed single-stranded RNA virus of the *Filovirus* genus, which composed to the *Filoviridae* family, like the Ebola virus. Although, the MARV is happening consciously and infects the patients, Scientists did not find any suitable treatment for the inhibition of MARV (Chakraborty *et al.*, 2022; Sah *et al.*, 2022). The natural bioactive compounds of Fisetin should be an alternative approach for the treatment of Breast cancer, and Monkeypox, and Marburg virus. So, in this research, the natural compounds of Fisetin have been counted as

primary compounds and we modified its structure by different functional groups to develop a potential medication, which might have better efficacy, lower toxicity, and capability to inhibit Breast cancer, Monkeypox, and Marburg virus.

In these circumstances, computational drug design tool is used, which is the most efficient approach of finding potential therapeutic candidates and implementing them into the therapy regimen in short period of time (Aziz *et al.*, 2023; Moingeon *et al.*, 2022; Patel *et al.*, 2022; Aziz *et al.*, 2022). In comparison to traditional drug discovery procedures, computational drug design offers many benefits, including substantially lower costs, faster drug development durations, and possibility to eliminate phase 1 clinical trial. Thus, this approach of computer-aided drug design (CADD) could be a helpful method.

RESULTS AND DISCUSSION

PASS prediction analysis

It seems that a substantial proportion of investigations should not go to the end of the process due to significant harmful side effects and toxicity that are unclear. These undesirable effects are discovered or manifest much too late in the development. In today's high-tech, possibility to fail or reject any compounds has been min-

Table 2. Data of Lipinski rule, and pharmacokinetics.

Ligand No	Hydrogen bond acceptor	Hydrogen bond donor	Topological polar surface area Å ²	Lipinski rule		Molecular weight	Bioavailability Score	G.I. absorption
				Result	Violation			
01	06	04	111.13	Yes	00	286.24	0.55	High
02	08	05	132.39	Yes	00	331.28	0.55	High
03	10	06	153.65	Yes	01	376.32	0.55	Low
04	07	03	109.37	Yes	00	316.26	0.55	High
05	08	02	107.59	Yes	00	346.29	0.55	High
06	06	03	100.13	Yes	00	362.33	0.55	High
07	06	02	89.13	Yes	00	438.43	0.55	Low
08	08	04	137.43	Yes	00	330.25	0.56	High
09	10	04	163.73	Yes	00	374.26	0.11	Low

Table 3. Binding affinity against Breast cancer protein

Drug molecules No	Breast cancer protein (PDB: 3HB5)	Breast cancer protein (PDB: 7KCD)	Breast cancer protein (PDB 6NLV)
	Binding affinity (kcal/mol)	Binding affinity (kcal/mol)	Binding affinity (kcal/mol)
01	-8.7	-7.0	-7.6
02	-9.7	-8.5	-7.5
03	-9.3	-7.4	-7.3
04	-8.8	-7.2	-7.3
05	-8.0	-8.1	-7.2
06	-9.6	-9.3	-8.0
07	-11.0	-9.6	-9.1
08	-9.3	-8.8	-7.8
09	-9.0	-7.2	-7.5
Epirubicin hydrochloride	-9.1	-7.0	-8.0

imized since the probability to be active and probability to be inactive for any molecules could be identified as early stages (Filimonov *et al.*, 2014). In Table 1 below, probability to be active (Pa) and probability to be inactive (Pi) has been listed and it has been shown that the mentioned bioactive molecules are most potent against antineoplastic and antiviral effects compared to antibacterial and antiparasitic effects. In antiviral, the range of Pa is reported from 0.392–0.471 while the Pa score against antineoplastic is found between 0.508–0.849. So, based on the score, the Breast cancer and Monkeypox, and Marburg virus has been chosen and completed the investigation.

Lipinski rule, and pharmacokinetics

Lipinski rule is a potential assessment of any pharmacological or bioactive molecules which makes them to be a potential oral medication based on different parameters. So, in view of Lipinski rule, number of hydrogen bond acceptor 06–10, hydrogen bond donor 02–06, topological polar surface area 89.13 Å² to 163.73 Å², which has shown that all the medications are fully accepted and followed Lipinski rule by all Fisetin derivatives (Santos *et al.*, 2016; Walters, 2012). For any oral medication, bioavailability is the most essential parameter, and it is noticed that almost all the drugs are highly effective and

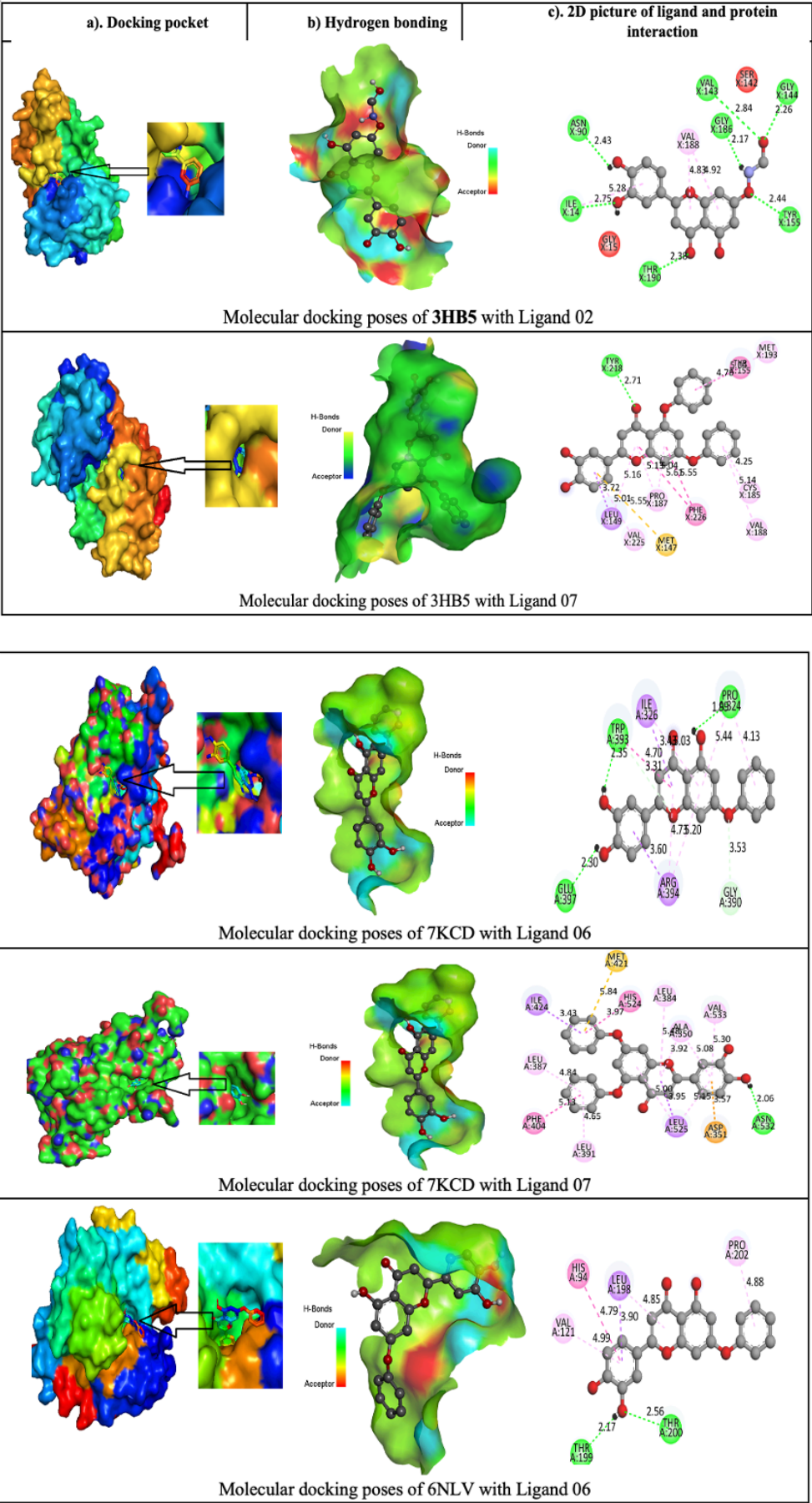
have a similar score and that only Ligand 09 has poor bioavailability. On the other portion, six ligands out of nine molecules have higher G.I absorption rate, which is another important parameter to make them as oral medication. Finally, it is said that these mentioned molecules could be effective against the Breast cancer, Monkeypox, and Marburg virus. Data of Lipinski rule, and pharmacokinetics are displayed in Table 2.

Molecular docking against Breast cancer

Molecular docking is an established and effective method for explaining how two molecules interact and make the optimal ligand arrangement to produce a complex. Any molecules could be active and produce biological response if their minimum binding energy is -6.0 kcal/mol and considered as a potential drug (Nath *et al.*, 2021). In view of these studies, all the bioactive Fisetin derivatives have been documented that they have much better binding affinity than the standard and FDA approved Epirubicin hydrochloride. The maximum docking energy has been obtained in ligand 07 (-11.00 kcal/mol) against PDB: 3HB5, in protein PDB: 7KCD, the maximal score is found to be -9.6 kcal/mol, and the last one PDB: 6NLV has obtained -9.1 kcal/mol maximum in the same ligand (Table 3). In the overall analysis, it is clear that all the ligands have crossed the binding affini-

Table 4. Binding affinity for bacteria against Monkeypox and Marburg virus

Drug molecules No	Monkeypox virus (PDB ID 4QWO)	Marburg virus (PDB 4OR8)
	Binding affinity (kcal/mol)	Binding affinity (kcal/mol)
01	-7.8	-7.2
02	-8.2	-7.0
03	-7.9	-7.3
04	-7.7	-7.0
05	-7.6	-6.5
06	-9.0	-8.5
07	-9.4	-10.1
08	-8.2	-7.4
09	-8.0	-7.1
Standard (acyclovir)	-6.3	-5.8



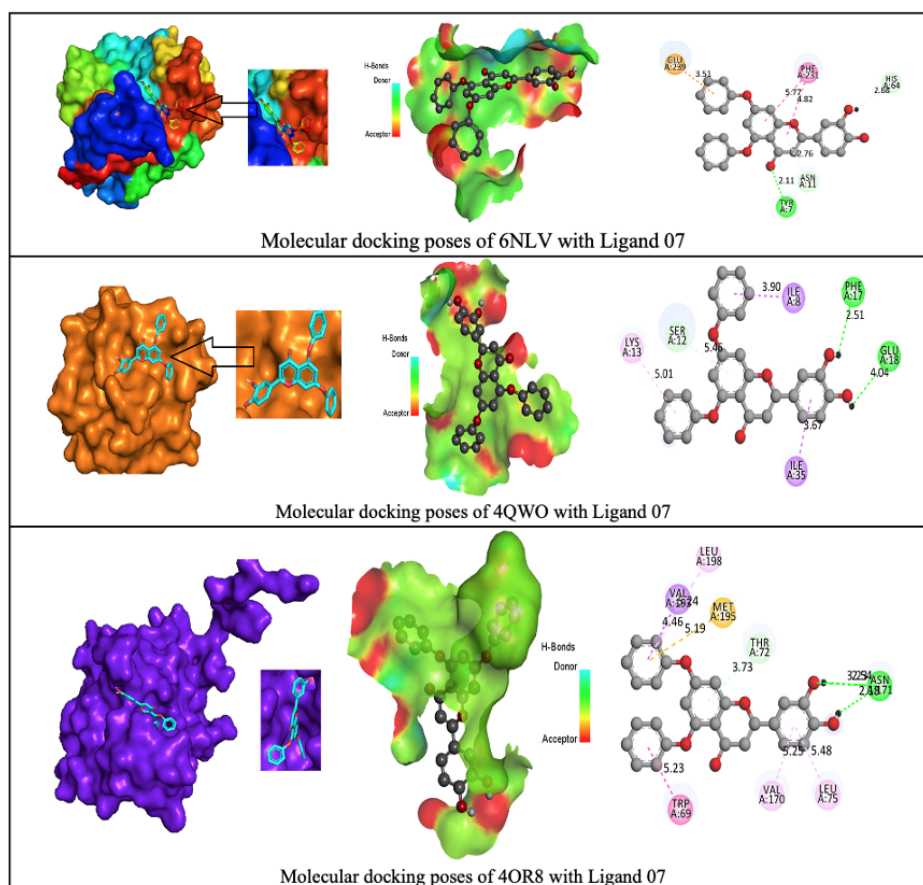


Figure 1. Molecular docking poses breast cancer, Monkeypox, and Marburg virus.

ties and compared much better to standard drugs, which turn into them as oral medication against breast cancer protein.

Binding affinities against pathogenic Monkeypox and Marburg virus

According to the result of pass prediction value, it was shown that these mentioned ligands could be effective against viral pathogens, followed by antibacterial and antiparasitic, since the antiviral score is higher than the antibacterial and antiparasitic. So, the Monkeypox and Marburg virus are also included in this investigation, and it is found that the reported ligand may also act as a potential inhibitor against Monkeypox and Marburg virus. In given Table 4, it is notable that the maximum affinities for Monkeypox virus (PDB ID 4QWO) is -9.0 kcal/mol, -9.4 kcal/mol, where -10.1 kcal/mol has been obtained against Marburg virus (PDB 4OR8), and it has also significantly better binding affinities. As, there is no documented or authorized medication against Monkeypox and Marburg virus, a common antiviral medication (acyclovir) is also compared with our development drug, where the standard acyclovir has provided -6.3 kcal/mol and -5.8 kcal/mol, which is much lower than the reported ligands. So, it is understood that all these may be possible therapeutic approaches as inhibitors against Monkeypox and Marburg virus.

Ligand-protein interaction and molecular docking poses

The interactions between the inhibitor and the targeted protein active side, docking pocket drug-protein are graphically represented in Figs 1a, 1b and 1c. In the 2D

configuration, the active side of amino acid residue with bond angle has been seen and in most cases the number of hydrophobic bond residue is higher than the other bonds, such as hydrogen, electrostatic, Van der Waals interactions and Halogen bond. This result has been obtained by importing protein ligand complex file into the Discovery Studio Visualizer (Balasubramaniam & Reis, 2020; Wang *et al.*, 2015). This figure has been configured based on maximum binding energy. The first illustration (Fig. 1a) determined drug-protein pocket, or how a drug attached to protein during the formation of the complex. It has been designed after molecular docking, by using Pymol application. Then, (Fig. 1b) represented hydrogen bonding donor or acceptor region, where the sky blue indicates donor region, and red hue indicates acceptor region. Finally; (c). 2D picture of ligand and protein interaction, where X: TYR-218, X: LEU-149, X: MET-147, X: TYR-155, X: PHE-226, X: PHE-226, X:PRO-187, X: LEU-149, X:PRO-187, X: VAL-225, X: MET-193, X: CYS-185, X: VAL-1-88, against breast cancer, A: GLU-18, A: GLU-18, A: PHE-17, A: SER-12, A: SER-12, A: ILE-8, A: ILE-35, A: LYS-13, against Monkeypox virus, and A: ASN-171, A: THR-72, A: VAL-193, A: MET-195, A: TRP-69, A: LEU-75, A:VA-L170, A: LEU-198, against Marburg virus are seen in most of the cases.

Absorption, Distribution, Metabolism and Excretion. (ADME) studies

It was possible to forecast the ADMET features of drugs or chemical compounds by utilizing the free PkC-SM online web tool, which was developed by machine

Table 5. ADME Properties summary

S/N	Absorption		Distribution		Metabolism		Excretion	
	Water solubility Log S	Caco-2 permeability (10 ⁻⁶ cm/s)	VDss (human)	BBB permeability	CYP450 1A2 Inhibitor	CYP450 2C9 Inhibitor	Total Clearance (ml/min/kg)	Renal OCT2 substrate
01	-3.207	0.86	-0.103	No	Yes	No	0.662	No
02	-3.665	-0.293	-0.041	No	Yes	No	0.802	No
03	-3.767	0.40	-0.12	No	Yes	No	0.912	No
04	-4.157	0.928	-1.364	No	Yes	No	0.732	No
05	-4.196	0.893	-0.539	No	No	Yes	0.791	No
06	-4.083	0.928	-0.756	No	Yes	Yes	0.450	No
07	-3.442	1.076	-1.169	No	No	Yes	0.513	No
08	-4.036	-0.061	-0.484	No	Yes	No	0.653	No
09	-3.317	-0.621	-0.788	No	Yes	No	0.621	No

Table 6. Aquatic and non-aquatic toxicity

Aquatic and non-aquatic Toxicity different parameter							
S/N	AMES toxicity	Max. tolerated dose (human) mg/kg/day	Oral Rat Acute Toxicity (LD50) (mol/kg)	Oral Rat Chronic Toxicity (mg/kg/day)	Hepato-toxicity	Skin Sensitization	T. Pyriformis toxicity (log ug/L)
01	No	0.982	2.178	2.259	No	No	0.352
02	No	1.046	2.162	1.947	No	No	0.305
03	No	1.211	2.291	1.785	No	No	0.292
04	No	0.913	2.24	2.221	No	No	0.294
05	No	0.731	2.507	2.768	No	No	0.86
06	No	0.329	2.675	1.56	Yes	No	0.288
07	No	0.432	3.163	0.698	Yes	No	0.285
08	No	0.983	2.13	2.21	No	No	0.289
09	No	0.963	2.471	2.50	No	No	0.285

learning (Pires *et al.*, 2015). ADME is the key factor of any drug molecules to establish them as safe and usable medication. In listed data, it is observed that the drugs are moderately soluble in water and the Caco-2 permeability range is -0.621 to 1.076. VDss (human) level is -0.041 to -1.364 and no drugs can penetrate the BBB (Table 5). All the drugs can inhibit the CYP450 1A2 inhibitor except 05 and 07 and only ligands 05, 06, and 07 can inhibit the CYP450 2C9 inhibitor. Finally, almost all the ligands have better Total clearance rate, and no drugs can substrate through Renal OCT2 substrate. Above all discussion, the Table 5 data for ADME parameters might suggest them as a suitable medication.

Aquatic and non-aquatic toxicity

Aquatic and non-aquatic toxicity studies are performed to analyze the drug safety of animals and the environment, because during the production of drugs they might be mixed with environment, which may have an impact on surrounding animals (Kar & Roy, 2012). Our findings on the aquatic and non-aquatic toxicity of the examined substances have shown that all of the medications investigated are non-carcinogenic and non-AMES poisonous and only 06 and 07 may be responsible for hepatotoxicity. So, patients with liver disease may use these two medications with caution. Secondly, the max. tolerated daily dose could be between 0.329 mg/kg/day

to 1.211 mg/kg/day. The Oral Rat Acute Toxicity and Oral rat chronic toxicity level is also lower compared to standard drugs and no drugs can produce skin sensitization. These findings give insight into these new modified Fisetin derivatives that are safer to use (Table 6).

Experimental methodology

Preparation of Ligand and Structural Activity relationship (SAR) studies

Firstly, we have collected the chemical structure of Fisetin from the PubChem database. After that, we have observed how it is antineoplastic and antiviral properties change if the side chain is substituted by adding different functional group. So, all the derivatives of Fisetin have been generated using ChemBioDraw 12.0 and in each case, two -OH functional groups have been substituted by four functional groups such as Benzene ring, NH-CH₂-OH, OCH₃, and -COOH (Milne, 2010). Finally, geometry optimization has been conducted by using density functional theory (DFT) in material studio at the DFT/B3LYP/6-31G and after optimization has been done, all the atoms of molecule have been reached at the most stable state with the optimum ground state energy and saved as PBD format for molecular docking, ADMET, and other computational experiment (Eno *et al.*, 2022; Oyeneyin *et al.*, 2022). The optimization technique is utilized in the

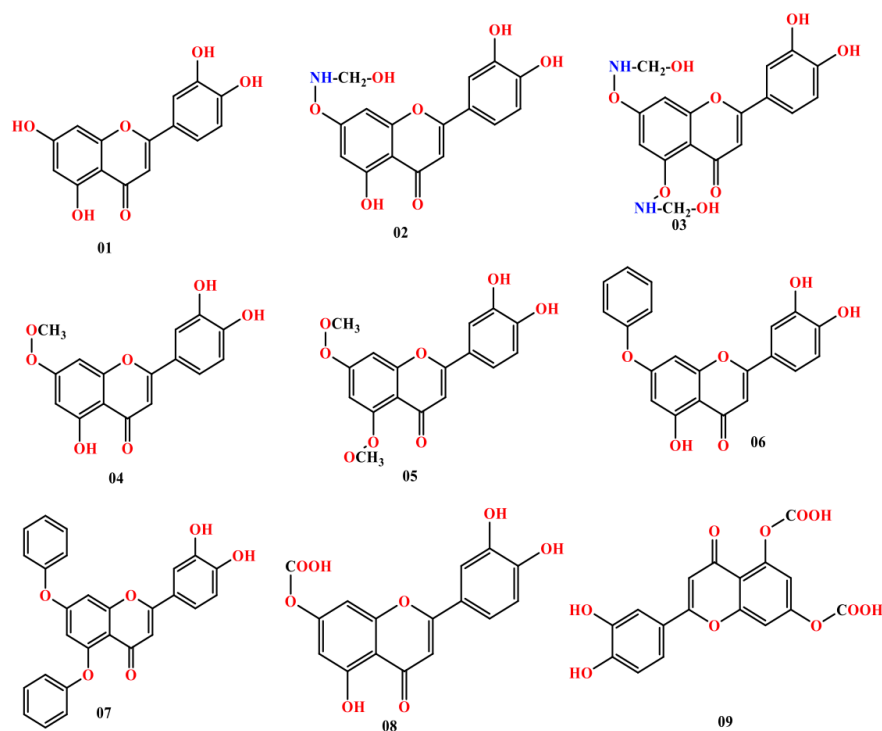


Figure 2. Chemical structure of Genistein and its derivatives

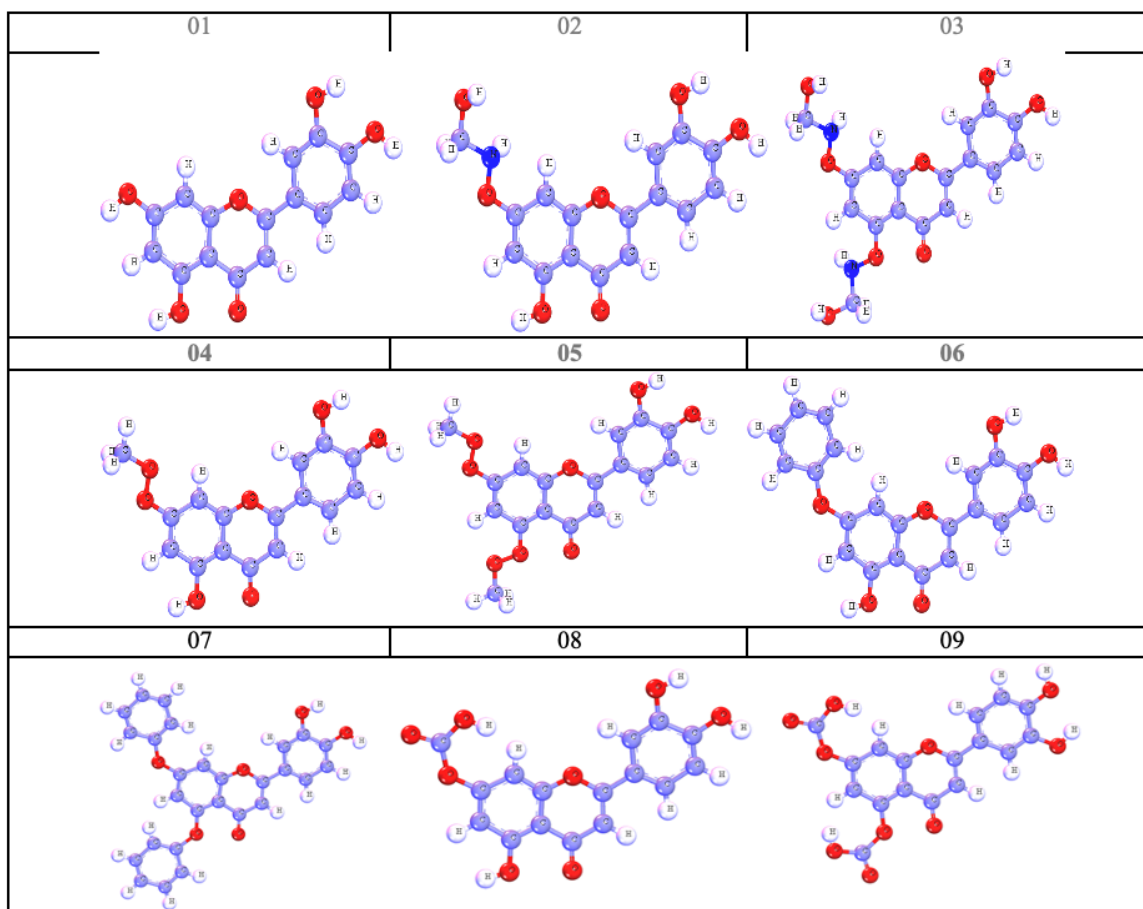


Figure 3. Optimized molecular structure of Fisetin derivatives.


Breast cancer protein PDB: 3HB5	Breast cancer protein PDB: 5KCD	Breast cancer protein PDB: 6NLV
Organism: Homo sapiens	Organism: Homo sapiens	Organism: Homo sapiens
Resolution: 2.00 Å	Resolution: 1.80 Å	Resolution: 1.79 Å
		
Ref. (Mazumdar et al., 2009)	Ref. (Srinivasan et al., 2017)	Ref. (Mboge et al., 2021)

Figure 4. Three-dimensional protein structure of Breast cancer

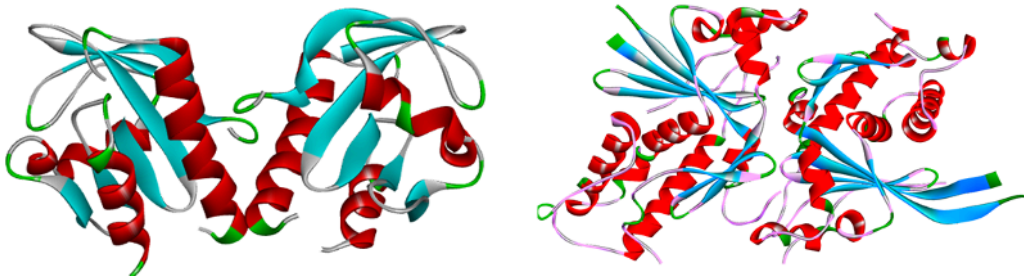
Monkeypox Virus (PDB ID 4QWO)	Marburg virus (PDB 4OR8)
Organism: Monkeypox virus Zaire-96-I-16	Organism: Marburg virus - Musoke, Kenya, 1980
Method: X-ray diffraction	Method: X-ray diffraction
Resolution: 1.52 Å	Resolution: Resolution 2.65 Å
	
Ref. (Minasov, Inniss, Shuvalova, Anderson, & Satchell, 2022)	Ref.(Oda et al., 2016)

Figure 5. Three-dimensional protein structure of Monkeypox, and Marburg virus

context of protein-ligand docking investigation to determine the optimal binding posture of a ligand against a bioreceptor. Optimization is the fundamental and important parameter for an accurate design of the ligands (Kobir *et al.*, 2022). The modified structures, and the optimized figures are given in Fig. 2 and Fig. 3.

Pass prediction

The pass prediction is an important feature for computer-based drug design, which is described by Pa and Pi ratio, where Pa means probability to be active and Pi means probability to be inactive. It is possible to separate most active molecules by screening pass prediction values which reduce the time and cost for developing new drugs (Pa>Pi value) (Filimonov *et al.*, 2014; Poroikov & Filimonov, 2005). The pass prediction data has been collected from the PASS online website "<http://way2drug.com/PassOnline/predict.php>". First enter the PASS online then the Pa>Pi value has been collected for the selected molecule and all the values are shown in Table 1.

Determination of ADMET, Lipinski rule and pharmacokinetics

With the help of pkCSM (<http://biosig.unimelb.edu.au/pkcsml/prediction>), and SwissADME, (<http://www.swissadme.ch/index.php>) we investigated the overall pharmacokinetic parameter of Fisetin and its derivatives. This section mostly investigated human intestinal absorption, distribution, metabolism, excretion, water solubility, bioavailability, toxicity, carcinogenicity, and drug likeness (Azzam, 2023). The Lipinski Rule and drug likeness are important features for oral medication development (Tian *et al.*, 2015). Once the drugs have satisfied the Lipinski Rule, they should be considered as oral drug candidates.

Protein preparation and Molecular docking study and visualization

The crystal structure of Monkeypox virus (PDB ID 4QWO), Marburg virus (PDB ID 4OR8), and Breast Cancer (PDB: 3HB5, PDB: 5KCD and 6NLV) (Figs. 4

and 5) have been collected from the databank of RCSB protein (<http://www.rcsb.org>). Inadequate bonds, omitted hydrogens and side chain defects, access water have then been investigated and rectified, as necessary. Once all these issues have been resolved, they were saved as pdbqt file format. Then, the structure file has been loaded into PyRx AutoDock Tools, followed by usual processes to obtain binding affinities (Dallakyan & Olson, 2015). Finally, BIOVIA Discovery Studio Visualizer was used to investigate the interaction between the ligands and the protein (Zothanthuanga, 2021).

CONCLUSIONS

This investigation has been designed to identify the dual mode of function of the ligands against virus and cancerous proteins. Our computational investigation has found that all the evaluated natural Fisetin derivatives demonstrated adequate reactivity with excellent binding affinity to be a viable therapeutic target for Breast cancer, Monkeypox, and Marburg virus. The biological characteristics of reported compounds such as toxicity, carcinogenicity, and Lipinski rule are good enough for human usage of the selected drug. We ran their various parameters *in silico* to verify their durability as a highly potential drug candidate, and these results assessed their acceptability as a potential new drug candidate. Following the investigation of protein-ligand (drug) interactions, several outstanding binding affinities were discovered, which will effectively assist in the discovery of the ideal natural medication or a novel drug. The highest value of docking energy has been found in Ligand 07 (−11.00 kcal/mol) against PDB: 3HB5 for breast cancer and the highest docking energy for Monkeypox virus (PDB ID 4QWO) is −9.0 kcal/mol, −9.4 kcal/mol, where −10.1 kcal/mol has been obtained against Marburg virus (PDB 4OR8). Besides, the results of pharmacokinetics, drug likeness and aquatic toxicity meet the requirements of the newly developed molecules. All the parameters are recorded as significant and better than standard. Concluding, the reported drug can be a candidate for further use.

Declarations

Author Contributions. Conceptualization, S.A, M.R, SS, C.M.L and T.B.E; methodology, T.A., A.S, and G.N; software, M.A; validation, A.A.S; formal analysis, T.A.; investigation, S.A, M.R, SS, C.M.L and T.B.E; resources, M.A and A.A.S.; data curation, A.S.; writing – original draft preparation, T.A and S.N.; writing – review and editing, A.S and S.N.; visualization, A.F.A, A.S; supervision, T.A and S.N.; project administration, A.A.S and M.A ; funding acquisition, T.A

Data Availability statement. The datasets used and/or analyzed during the current study available from the corresponding author on reasonable request.

Conflicts of Interest. The authors declare no conflict of interest.

REFERENCES

Afshari AR, Sanati M, Mollazadeh H, Kesharwani P, Johnston TP, Sahhebkar A (2022) Nanoparticle-based drug delivery systems in cancer: A focus on inflammatory pathways. *Sem Cancer Biol* **86**: 860–872. <https://doi.org/10.1016/j.semcancer.2022.01.008>

Albaqami FF, Altharawi A, Altharwi HN, Alharthy KM, Qasim M, Muhseen ZT, Tahir ul Qamar M (2023) Computational modeling and evaluation of potential mRNA and peptide-based vaccine against Marburg Virus (MARV) to provide immune protection

against hemorrhagic fever. *BioMed Res Int* **2023**: 1–18. <https://doi.org/10.1155/2023/5560605>

Asad A, Aamir A, Qureshi NE, Bhimani S, Jatoti NN, Batra S, Diwan MN (2020) Past and current advances in Marburg virus disease: a review. *Infect Med* **28**: 332–345

Azzam KA (2023) SwissADME and pkCSM Webservers predictors: an integrated online platform for accurate and comprehensive predictions for *in silico* ADME/T properties of artemisinin and its derivatives. *Kompleksnoe Ispol'zovanie Mineralnogo Syra* **325**: 14–21. <https://doi.org/10.31643/2023/6445.13>

Aziz T, Naveed M, Makhdoom SI, Ali U, Mughal MS, Sarwar A, Khan AA, Zhennai Y, Sameeh MY, Dabool AS, Alharbi AA, Shahzad M, Alamri AS, Alhomrani M (2023) Genome investigation and functional annotation of *Lactiplantibacillus plantarum* YW11 revealing streptin and ruminococcin – A as potent nutritive bacteriocins against gut symbiotic pathogens. *Molecules* **28**: 491. <https://doi.org/10.3390/molecules28020491>

Aziz T, Naveed M, Sarwar A, Makhdoom SI, Mughal MS, Ali U, Yang Z, Shahzad M, Sameeh MY, Alruways, MW, Dabool AS, Almalki AA, Alamri AS, Alhomrani M (2022) Functional annotation of *Lactiplantibacillus plantarum* 13-3 as a potential starter probiotic involved in the food safety of fermented products. *Molecules* **27**: 5399. <https://doi.org/10.3390/molecules27175399>

Balasubramaniam M, Reis RJS (2020) Computational target-based drug repurposing of elbasvir, an antiviral drug predicted to bind multiple SARS-CoV-2 proteins. *Chem Rxiv* **22**: 1476. <https://doi.org/10.26434/chemrxiv.12084822>

Bhattacharyya GS, Doval DC, Desai CJ, Chaturvedi H, Sharma S, Somashekhar S (2020) Overview of breast cancer and implications of overtreatment of early-stage breast cancer: an Indian perspective. *JCO Global Oncol* **6**: 789–798. <https://doi.org/10.1200/GO.20.00033>

Chakraborty S, Chandran D, Mohapatra RK, Rabaan AA, Alhumaid S, Al Mutairi A, Dhama K (2022) Sexual transmission of recently re-emerged deadly Marburg virus (MARV) needs explorative studies and due attention for its prevention and feasible spread–Correspondence. *Int J Surgery* **106**: 106884. <https://doi.org/10.1016/j.ijssu.2022.106884>

Dallakyan S, Olson AJ (2015) Small-molecule library screening by docking with PyRx. *Chem Biol Methods Prot* **1263**: 243–250. https://doi.org/10.1007/978-1-4939-2269-7_19

Eniu A, Carlson RW, El Saghir NS, Bines J, Bese NS, Vorobiof D, Panel BHGIT (2008) Guideline implementation for breast health-care in low- and middle-income countries: Treatment resource allocation. *Cancer* **113**: 2269–2281. <https://doi.org/10.1002/cncr.23843>

Eno EA, Mbonu JI, Louis H, Patrick Inezi FS, Gber TE, Unimuke TO, Offiong OE (2022) Antimicrobial activities of 1-phenyl-3-methyl-4-trichloroacetyl-pyrazolone: Experimental, DFT studies, and molecular docking investigation. *J Indian Chem Soc* **99**: 100524. <https://doi.org/10.1016/j.jics.2022.100524>

Parkona S, Diamandis EP, Blasutig IM (2016) Cancer immunotherapy: the beginning of the end of cancer? *BMC Med* **14**: 1–18. <https://bmcmecine.biomedcentral.com/articles/10.1186/s12916-016-0623-5>

Filimonov D, Lagunin A, Glorizova T, Rudik A, Druzhilovskii D, Pogodin P, Poroikov V (2014) Prediction of the biological activity spectra of organic compounds using the PASS online web resource. *Chem Heterocyclic Comp* **50**: 444–457. https://journals.scholarportal.info/details/00093122/v50i0003/444_potbasutpowr.xml

Gong Q, Wang C, Chuai X, Chiu S (2022) Monkeypox virus: a re-emergent threat to humans. *Virolo Sin* **37**: 477–448. <https://doi.org/10.1016/j.virs.2022.07.006>

Hatmal MM, Al Hatamleh MA, Olaimat AN, Ahmad S, Hasan H, Ahmad Suhaimi NA, Mohamud R (2022) Comprehensive literature review of monkeypox. *Emerging Microbes Infect* **11**: 2600–2631. <https://doi.org/10.1080/22221751.2022.2132882>

Kar S, Roy K (2012) Risk assessment for ecotoxicity of pharmaceuticals—an emerging issue. *Exp Opin Drug Safety* **11**: 235–274. <https://doi.org/10.1517/14740338.2012.644272>

Kobir ME, Ahmed A, Roni MAH, Chakma U, Amin MR, Chandro A, Kumer A (2022) Anti-lung cancer drug discovery approaches by polysaccharides: an *in silico* study, quantum calculation and molecular dynamics study. *J Biomol Struct Dyn* **13**: 1–17. <https://doi.org/10.1080/07391102.2022.2110156>

Majie A, Saha R, Sarkar B (2023) The outbreak of the monkeypox virus in the shadow of the pandemic. *Environ Sci Pollut Res Int* **30**: 48686–48702

Mazumdar M, Fournier D, Zhu DW, Cadot C, Poirier D, Lin SX (2009) Binary and ternary crystal structure analyses of a novel inhibitor with 17β-HSD type 1: a lead compound for breast cancer therapy. *Biochem J* **424**: 357–366. <https://doi.org/10.1042/BJ20091020>

Mboge MY, Combs J, Singh S, Andring J, Wolff A, Tu C, Frost SC (2021) Inhibition of carbonic anhydrase using SLC-149: support for a noncatalytic function of CAIX in breast cancer. *J Med Chem* **64**: 1713–1724. <https://pubs.acs.org/doi/abs/10.1021/acs.jmedchem.0c02077>

- Mileto D, Riva A, Cutrera M, Moschese D, Mancon A, Meroni L, Gismondo MR (2022) New challenges in human monkeypox outside Africa: A review and case report from Italy. *Travel Med Infect Dis* **49**: 102386. <https://doi.org/10.1016/j.tmaid.2022.102386>
- Milne GW (2010) Software review of ChemBioDraw 12.0: ACS Publications. <https://pubs.acs.org/doi/full/10.1021/ci100385n>
- Minasov G, Inniss NL, Shuvalova L, Anderson WF, Satchell KJ (2022) Structure of the Monkeypox virus profilin-like protein A42R reveals potential functional differences from cellular profilins. *Acta Crystall Section F: Struct Biol Commun* **78**: 371–377. <https://doi.org/10.1107/S2053230X22009128>
- Moingeon P, Kuenemann M, Guedj M (2022) Artificial intelligence-enhanced drug design and development: Toward a computational precision medicine. *Drug Discovery Today* **27**: 215–222. <https://doi.org/10.1016/j.drudis.2021.09.006>
- Mortlock M (2013) Detection and characterization of genetically diverse paramyxoviruses from African bats. University of Pretoria. <http://hdl.handle.net/2263/79784>
- Mucker EM, Shamblyn JD, Raymond JL, Twenhafel NA, Garry RF, Hensley LE (2022) Effect of Monkeypox Virus preparation on the lethality of the intravenous cynomolgus Macaque model. *Viruses* **14**: 1741. <https://doi.org/10.3390/v14081741>
- Nath A, Kumer A, Zaben F, Khan M (2021) Investigating the binding affinity, molecular dynamics, and ADMET properties of 2, 3-dihydrobenzofuran derivatives as an inhibitor of fungi, bacteria, and virus protein. *Beni-Suef Univ J Basic Appl Sci* **10**: 1–13. <https://bjbas.springeropen.com/articles/10.1186/s43088-021-00117-8>
- Naveed M, Waseem M, Aziz T, Hassan Ju, Makhdoom SI, Ali U, Alharbi M, Alshammari A (2023) Identification of bacterial strains and development of an mRNA-based vaccine to combat antibiotic resistance in *Staphylococcus aureus* via *in vitro* and *in silico* approaches. *Biomedicine* **11**: 1039. <https://doi.org/10.3390/biomedicine11041039>
- Naveed M, Shabbir MA, Ain NU, Javed K, Mahmood S, Aziz T, Khan AA, Nabi G, Shahzad M, Alharbi ME, Alharb M, Alshammari A (2023) Chain-engineering-based *de novo* drug design against MPX-Vgp169 virulent protein of monkeypox virus: a molecular modification approach. *Bioengineering* **10**: 11. <https://doi.org/10.3390/bioengineering10010011>
- Naveed M, Shabbir MA, Ain NU, Javed K, Shabbir MA, Alharb M, Alshammari A, Alasmari AF (2023) Artificial intelligence assisted pharmacophore design for Philadelphia chromosome-positive leukemia with gamma-tocotrienol: a toxicity comparison approach with asciminib. *Biomedicine* **11**: 1041. <https://doi.org/10.3390/biomedicine11041041>
- Naveed M, Makhdoom SI, Ali U, Jabeen K, Aziz T, Khan AA, Jamil S, Shahzad M, Alharbi M, Alshammari A (2022) Immunoinformatics approach to design multi-epitope-based vaccine against Machupo virus taking viral nucleocapsid as a potential candidate. *Vaccines* **10**: 1732. <https://doi.org/10.3390/vaccines10101732>
- Naveed M, Sheraz M, Amin A, Waseem M, Aziz T, Khan AA, Ghani M, Shahzad M, Alruways MW, Dabool AS, Elazazy AM, Almalki AA, Alamri AS, Alhomrani M (2022) Designing a novel peptide-based multi-epitope vaccine to evoke a robust immune response against pathogenic multidrug-resistant *Providencia heimbachae*. *Vaccines* **10**: 1300. <https://doi.org/10.3390/vaccines10081300>
- Oda SI, Noda T, Wijesinghe KJ, Halfmann P, Bornholdt ZA, Abelson DM, Saphire EO (2016) Crystal structure of Marburg virus VP40 reveals a broad, basic patch for matrix assembly and a requirement of the N-terminal domain for immunosuppression. *J Virol* **90**: 1839–1848. <https://doi.org/10.1128/JVI.01597-15>
- Oyeneyin OE, Ojo ND, Ipinloju N, James AC, Agbaffa EB (2022) Investigation of corrosion inhibition potentials of some aminopyridine schiff bases using density functional theory and Monte Carlo simulation. *Chem Africa* **5**: 319–332. <https://link.springer.com/article/10.1007/s42250-021-00304-1>
- Pal M, Mengstie F, Kandi V (2017) Epidemiology, diagnosis, and control of monkeypox disease: a comprehensive review. *Am J Infect Dis Microbiol* **5**: 94–99. <http://pubs.sciepub.com/ajidm/5/2/4/index.html>
- Patel JR, Joshi HV, Shah UA, Patel JK (2022) A Review on computational software tools for drug design and discovery. *Indo Global J Pharm Sci* **12**: 53–81. <https://doi.org/10.35652/IGJPS.2022.12006>
- Pilla L, Ferrone S, Maccalli C (2018) Methods for improving the immunogenicity and efficacy of cancer vaccines. *Exp Opin Biol Therap* **1**: 765–784. <https://doi.org/10.1080/14712598.2018.1485649>
- Pires DE, Blundell TL, Ascher DB (2015) pkCSM: predicting small-molecule pharmacokinetic and toxicity properties using graph-based signatures. *J Med Chem* **58**: 4066–4072. <https://pubs.acs.org/doi/full/10.1021/acs.jmedchem.5b00104>
- Poojan S, Bae SH, Min JW, Lee EY, Song Y, Kim HY, Lee HO (2020) Cancer cells undergoing epigenetic transition show short-term resistance and are transformed into cells with medium-term resistance by drug treatment. *Exp Mol Med* **52**: 1102–1115. <https://www.nature.com/articles/s12276-020-0464-3>
- Poroikov V, Filimonov D (2005) PASS: prediction of biological activity spectra for substances *Predictive Toxicol* (471–490): CRC Press. <https://pubmed.ncbi.nlm.nih.gov/12570709/>
- Reuben RC, Abunike SA (2023) Marburg virus disease: the paradox of Nigeria's preparedness and priority effects in co-epidemics. *Bull Natl Res Centre* **47**: 10. <https://link.springer.com/article/10.1186/s42269-023-00987-1>
- Sah R, Mohanty A, Reda A, Siddiq A, Mohapatra RK, Dhama K (2022) Marburg virus re-emerged in 2022: recently detected in Ghana, another zoonotic pathogen coming up amid rising cases of Monkeypox and ongoing COVID-19 pandemic-global health concerns and counteracting measures. *Vet Quart* **42**: 167–171. <https://doi.org/10.1080/01652176.2022.2116501>
- Santos GB, Ganesan A, Emery FS (2016) Oral administration of peptide-based drugs: beyond Lipinski's Rule. *Chem Med Chem* **11**: 2245–2251. <https://doi.org/10.1002/cmdc.201600288>
- Schirmaker V (2003) Improvements of survival in nine phase II clinical studies with different types of cancer upon anti-tumor vaccination with an autologous tumor cell vaccine modified by virus infection to introduce danger signals. Paper presented at the New Trends in Cancer for the 21 st Century: Proceedings of the International Symposium on Cancer: New Trends in Cancer for the 21 st Century, held November 10–13, 2002, in Valencia, Spain. https://link.springer.com/chapter/10.1007/978-1-4615-0081-0_14
- Srinivasan S, Nwachukwu JC, Bruno NE, Dharmarajan V, Goswami D, Kastrati I, Zhou HB (2017) Full antagonism of the estrogen receptor without a prototypical ligand side chain. *Nature Chem Biol* **13**: 111–118. <https://www.nature.com/articles/nchembio.2236>
- Tian S, Wang J, Li Y, Li D, Xu L, Hou T (2015) The application of *in silico* drug-likeness predictions in pharmaceutical research. *Adv Drug Deliv Rev* **86**: 2–10. <https://doi.org/10.1016/j.addr.2015.01.009>
- Walters WP (2012) Going further than Lipinski's rule in drug design. *Exp Opin Drug Discov* **7**: 99–107. <https://doi.org/10.1517/1746044.41.2012.648612>
- Wang Q, He J, Wu D, Wang J, Yan, Li, H (2015) Interaction of α -cyperone with human serum albumin: Determination of the binding site by using Discovery Studio and *via* spectroscopic methods. *J Luminescence* **164**: 81–85. <https://doi.org/10.1016/j.jlumin.2015.03.025>
- Zothantluanga JH (2021) Molecular docking simulation studies, toxicity study, bioactivity prediction, and structure-activity relationship reveals rutin as a potential inhibitor of SARS-CoV-2 3CL pro. *J Sci Res* **65**: 96–104. <https://doi.org/10.37398/JSR.2021.650511>

Long noncoding RNA TPTEP1 suppresses diabetic retinopathy by reducing oxidative stress and targeting the miR-489-3p/NRF2 axis

Xinfa Wang¹, Xianbo Zhou¹, Fang Wang², Nan Zhang¹, Yan Zhang³, Zhen Ao⁴✉ and Fang He⁴✉

¹Department of Ophthalmology, The First People's Hospital of Lin'an District, Hangzhou City, Zhejiang Province 311300, China; ²Department of Nephrology, General Hospital of Central Theater Command of PLA, Wuhan City, Hubei Province 430010, China; ³Department of Ophthalmology, The Seventh Medical Center of the PLA General Hospital, Haidian District, Beijing 100700, China; ⁴Department of Ophthalmology, The Eighth Medical Center of the PLA General Hospital, Haidian District, Beijing 100091, China

Background: Diabetic retinopathy (DR) is a diabetic complication with complex etiology and severe visual impairment. Dysregulated long noncoding RNAs (lncRNAs) are closely associated with DR. This article focused on the impact of lncRNA transmembrane phosphatase with tensin homology pseudogene 1 (TPTEP1) in DR. **Methods:** First, sera were collected from DR patients and healthy control. Human retinal vascular endothelial cells (HRVECs) were exposed to high glucose (HG) to construct a DR model *in vitro*. A real-time quantitative polymerase chain reaction (RT-qPCR) was carried out to detect TPTEP1. Targeting relationships were predicted using StarBase and TargetScan, and confirmed by the Dual-Luciferase Reporter Assay. Cell Counting Kit 8 (CCK-8) and EdU staining were applied to measure cell viability and proliferation, respectively. Protein expression was determined by a western blotting assay. **Results:** lncRNA TPTEP1 expression was significantly decreased in the serum of DR patients and HG-stimulated HRVECs. Overexpression of TPTEP1 reduced cell viability and proliferation induced by HG and oxidative stress. In addition, overexpression of miR-489-3p impaired the effects of TPTEP1. Nrf2, which was targeted by miR-489-3p, was down-regulated in HG-treatment HRVECs. Knock-down of Nrf2 enhanced the influence of miR-489-3p and antagonized the effects of TPTEP1. **Conclusion:** This study demonstrated that a TPTEP1/miR-489-3p/NRF2 axis affects the development of DR by regulating oxidative stress.

Keywords: diabetic retinopathy, TPTEP1, oxidative stress, NRF2

Received: 18 November, 2021; **revised:** 17 February, 2022; **accepted:** 08 March, 2022; **available on-line:** 16 February, 2023

✉e-mail: superwceg@163.com (FH); jinru8811@163.com (ZA)

Abbreviations: ceRNA, competitive endogenous RNA; DR, Diabetic retinopathy; HRVECs, Human retinal vascular endothelial cells; lncRNAs, Long non-coding RNAs; MAPK, mitogen-activated protein kinase; MRE, miRNA response element; OS, Oxidative stress; TPTEP1, tensin homology pseudogene 1

INTRODUCTION

DR is a common ocular complication in diabetic patients. Recent years have witnessed an increased annual incidence of DR (Yumnamcha *et al.*, 2020). Moreover, DR patients are inductive to blindness (Crawford *et al.*, 2009). Recent studies evidence that abnormal angiogenesis, metabolic abnormalities, inflammation and oxidative stress caused by hyperglycemia are important factors for DR. Nowadays, the prevailing strategy for DR is anti-vas-

cular endothelial growth factor (VEGF) therapy, which is only effective for patients with advanced DR (Singer *et al.*, 2016). Therefore, it is urgent to develop a new therapy for the prevention and treatment of DR.

Oxidative stress (OS) is caused by the imbalance of the oxidation system and antioxidant system, which frequently induces tissue damage. Hyperglycemia is an important reason for inducing OS response, the accumulation of which contributes to multiple complications in patients with diabetes (Brownlee, 2005). Studies have shown that OS in the retina can lead to DR by regulating the pathways involved in polyol metabolism, hexosamine metabolism (Eshaq *et al.*, 2014). NRF2 can up-regulate the expression of antioxidant proteins (Yu & Kensler, 2005). However, the roles of Nrf2 in DR are still unclear.

Long non-coding RNAs (lncRNAs) are a number of RNA with a length greater than 200 nt but without the function of protein-coding properties. As an important regulator of gene expression, lncRNAs play an important role in chromatin remodeling, transcription, post-transcriptional regulation and protein metabolism (Shi *et al.*, 2013). lncRNAs regulate gene expression in the form of competitive endogenous RNA (ceRNA) through the miRNA response element (MRE) (Thomson & Dinger, 2016; Yan *et al.*, 2014). Recently, the roles of lncRNAs in DR attract increasing attention. The abnormal expression of lncRNAs in DR patients regulates the chemokine signaling pathway, mitogen-activated protein kinase (MAPK) signaling pathway, and pyruvate metabolism (Yan *et al.*, 2014). Therefore, lncRNAs may be a potential regulatory factor of the pathogenic mechanism of DR. Aberrant expressed lncRNA TPTE pseudogene 1 (TPTEP1) is closely associated with the pathogenesis of DR (Sun *et al.*, 2021). However, the roles of TPTEP1 in DR have not been fully elucidated.

In our research, the roles of TPTEP1 in DR were investigated. A luciferase assay was performed to verify the binding sites between miR-489-3p and TPTEP1 or NRF2. Cellular functions were detected using CCK-8 and EdU assays. TPTEP1/miR-489-3p/NRF2 axis may be a potential target for DR.

MATERIALS AND METHODS

Patient samples

Clinical blood samples were gathered from DR patients (n=50) and healthy volunteers (n=50) at The

Table 1. Clinical and pathological parameters in all subjects

Variables	Control (n=50)	DR (n= 0)
Male/Female	21/29	32/18
Age (years)	52.8±5.5	53.5±4.3
Diabetes duration (years)	/	12.2±2.9
BMI (kg/m ²)	23.4±1.8	33.5± 3.3 ^a
FPG (mmol/L)	4.55± 0.96	8.21± 0.16 ^a

Note: a Mean values within a row with unlike superscript letters were significantly different ($P<0.05$). Control: healthy volunteers; DR, diabetic retinopathy patients; BMI, body mass index; FPG, fasting plasma glucose.

Eighth Medical Center of the PLA General Hospital. The study was approved by The Eighth Medical Center of the PLA General Hospital. Signed informed consents were obtained from each individual. The blood samples of the patients were collected with the fasting abdomen in the morning and stored at -80°C for further experiments. The clinical and pathological parameters in all subjects was shown in Table 1.

The inclusion criteria: patients who met the 1999 WHO diabetes diagnosis (fasting blood glucose $\geq 7.0\text{ mmol/l}$ or postprandial blood glucose $\geq 11.10\text{ mmol/l}$); Fundus examination conforms to DR diagnostic criteria. The exclusion criteria: suffering from heart, liver, kidney and other organic diseases; with multiple eye diseases; combined with malignant tumor; suffering from infectious diseases; combined with other types of diabetes mellitus; abnormal endocrine function; mental illness and consciousness disorder.

Cell culture and cell transfection

HRVECs were purchased from the Type Culture Collection of the Chinese Academy of Sciences (Shanghai, China). DMEM with 10% foetal bovine serum, 100 mg/mL of penicillin and 100 U/mL of streptomycin (all from Gibco, Waltham, MA, USA) was applied to culture cells. Cells were grown in the condition with 5% CO_2 at 37°C . HRVECs were planted in 6-well cell culture plates at a density of 1.5×10^6 cells/well in the HG treatment experiments, and then incubated in 5.5 mM for 24 h. Then HG (33 mmol/L) or mannitol isotonic control (33 mmol/L) were used to treat cells for 24 h.

TPTEP1 overexpression plasmids, miR-489-3p mimic/inhibitor, NRF2 small interference RNA (si-NRF2) and their negative controls (Abiotech Biotech Co., Ltd.), were transfected into the cells with Lipofectamine[®] 2000 reagent (Invitrogen) at 37°C according to manufacturer's protocols. After 48 h transfection, cells were used in the following experiments.

Real-time quantitative polymerase chain reaction (RT-qPCR)

Total RNA was extracted using the TRIzol[®] reagent (Invitrogen; Thermo Fisher Scientific, Inc.). The concentration and purity of the total RNA were assessed from OD 260/280 readings (ratio > 1.8) using a spectrophotometer (NanoDrop Technologies, Wilmington, DE, USA). Reverse transcription and qPCR were carried out by BlazeTaq One-Step SYBR Green RT-qPCR Kit (with ROX) (QP071; GeneCopoeia Inc.) on SEDI Thermo Cycler controlled by the Control Bus Net software package (Wealtec Bioscience Co., Ltd). All primers were de-

signed and synthesized by Nanjing Genscript Biotech Co., Ltd., the GAPDH and U6 were used as an internal reference. Fold changes of the indicated genes were calculated with the $2^{-\Delta\Delta\text{Ct}}$ method. The sequences of the primers used were as followed:

TPTEP1:

F: 5'-CTGGGAGAAGTGCCCTTGC-3',

R: 5'-CACCTCATCAGTCATTTGCTCA-3';

miR-489-3p:

F: 5'-GCGCGGTGACATCACATATAC -3',

R: 5'-AGTGCAGGGTCCGAGGTATT -3';

NRF2:

F: 5'-GAGACAGGTGAATTTCTCCCAAT-3',

R: 5'-TTTGGGAATGTGGGCAAC-3';

GAPDH:

F: 5'-ACTCTTCCACCTTCGATGC-3',

R: 5'-CCGTATTCATTGTCATACCAGG-3';

U6:

F: 5'-CGACAAGACGATCCGGGTAAA-3',

R: 5'-GGTTGAGGAGTGGGTCAAG-3'.

The PCR products were detected by agarose gel electrophoresis. And the thermal profiles and of TPTEP1, miR-489-3p and NRF2 were shown in Supplementary materials.

Cell viability assay

After resuspended to 1×10^5 cells/ml, 100 μl HRVECs were seeded in 96-well plates. Each well was added with 10 μl CCK8 reagent (AMJ-KT0001; AmyJet Technology Co., Ltd.) and cultured for 4 h at 37°C . The absorbance values were evaluated with a microplate reader (HBS-1096C; Nanjing DeTie Experimental Equipment Co., Ltd.) at the wavelength of 450 nm.

5-Ethynyl-2'-deoxyuridine assay

HRVECs were fixed with 4% paraformaldehyde and treated with EdU. Then 1X Apollo reaction cocktail was used to stain cells for 0.5 hours before incubating with Hoechst 33342. Afterwards, cells were captured with a fluorescence microscope (Leica, Germany).

Assessment of reactive oxygen species (ROS), malondialdehyde (MDA), and Glutathione (GSH) activity

The level of ROS was detected with a fluorescence probe dichloro-dihydro-fluorescein diacetate (Jiancheng Biotech, Nanjing, China). MDA Assay Kit and GSH Assay Kit (Beyotime, Jiangsu, China) to examine MDA and GSH, respectively.

Western blot analysis

After rinsing cells with pre-chilled PBS solution, pre-chilled RIPA lysis buffer was applied for the extraction of total protein for 30 min. The protein concentration was quantified by a BCA Protein Assay Kit (Beyotime, Jiangsu, China). Next, running electrophoresis was performed to separate the protein with 10% SDS-PAGE at 120v until the bromophenol blue reach the separation adhesive base. Then the separated protein was transferred onto the PVDF membranes (Millipore) in an ice box at 100v for 1.5 h. The membranes were blocked with a blocking buffer at 4°C for 1 h. After being washed with TBST solution, primary antibodies including anti-NRF2, anti-HO-1, anti-NQO1 (1:1,000; Abcam) and anti-GAPDH (1:3000, Leading Biology) were used to incubate the membranes on a

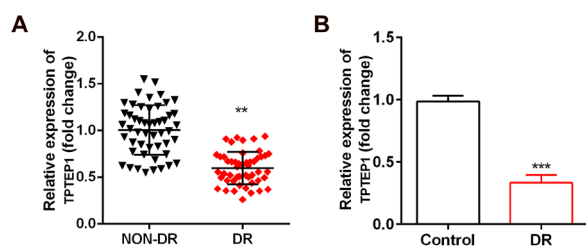


Figure 1. TPTEP1 is downregulated in DR.

(A) The expression level of TPTEP1 in DR patients. $^{**}P<0.01$ versus normal. (B) The expression level of TPTEP1 HG stimulated cells. $^{***}P<0.001$ versus control. DR, diabetic retinopathy; HG, high glucose.

shaking table at 4°C overnight and with anti-IgG antibody (1:2000, MultiSciences, Shanghai, China) for 2 h at room temperature. At last, the protein bands were captured by the ECL system (Thermo Fisher Scientific, Inc.).

Dual luciferase reporter assay

The wild (WT) and mutant (MUT) type 3'-UTR region of TPTEP1 and NRF2 luciferase reporter vectors were designed and synthesized by Guangzhou Ribobio Co., Ltd. After 24 h, cells were co-transfected with luciferase reporter vectors as well as miR-489-3p mimic/control for 48 h. Luciferase activities were detected by a Luciferase Reporter Assay Kit (K801-200; BioVision Tech Co., Ltd.). The luciferase activity normalized the luciferase activity to Renilla luciferase activity.

Statistical Analysis

Each experiment was performed at least three times. GraphPad Prism (version 7, GraphPad Software Inc.) was used to analyze all data. Data were presented as mean \pm S.D. The Student's *t*-test was used to compare the differences between two groups, and the compari-

son among multiple groups used the analysis of variance (ANOVA) followed by Duncan's post-hoc test. $P<0.05$ suggested a significant difference.

RESULTS

TPTEP1 was downregulated in DR.

The expression level of TPTEP1 in serum of patients with DR was significantly reduced compared with normal controls (Fig. 1A). Besides, the expression of TPTEP1 in HRVECs stimulated with HG was also significantly decreased compared with a control group (Fig. 1B).

TPTEP1 promoted cell proliferation and ameliorated oxidative stress stimulated by HG.

Figure 2A showed that the expression of TPTEP1 was significantly increased, indicating that cell transfection was successful. Overexpression of TPTEP1 significantly suppressed the increase in cell viability induced by HG (Fig. 2B). Moreover, TPTEP1 overexpression remarkably inhibited the proliferation of HRVECs (Fig. 2C). Additionally, overexpression of TPTEP1 alleviated the increase of ROS and MDA and the decrease of GSH induced by HG (Fig. 2D-2F). For further exploration of the effect of TPTEP1 on oxidative stress, NRF2, NQO1 and HO-1 proteins' expressions were also measured. The results showed that overexpression of TPTEP1 could increase the expression of antioxidant-related proteins (Fig. 2G).

TPTEP1 directly bound to miR-489-3p.

TPTEP1 might function as ceRNA and regulate biological processes via sponging miRNAs. So, we used the online database Starbase 3.0 (<http://starbase.sysu.edu.cn/>) to predict the potential target miRNAs of TPTEP1. Figure 3A showed the binding region of miR-489-3p and TPTEP1, which was further verified via dual luciferase reporter assay

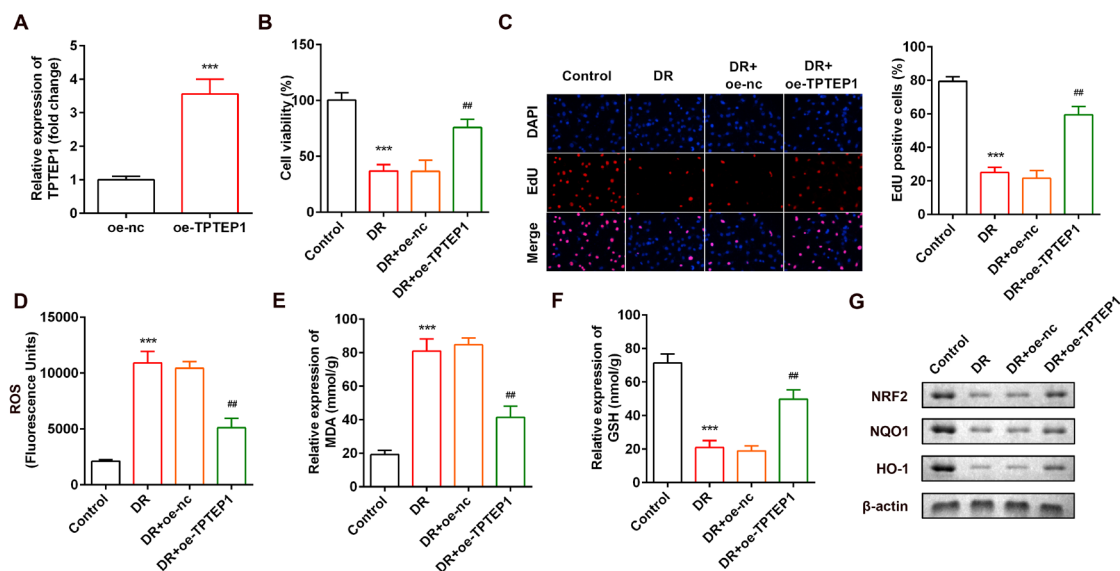


Figure 2. Overexpression of TPTEP1 inhibits cell viability and proliferation and reduces oxidative stress.

(A) Overexpression of TPTEP1 in HRVECs. $^{***}P<0.001$ versus empty vectors (B) Cell viability of HRVECs. $^{***}P<0.001$, $^{##}P<0.01$ versus control. (C) Cell proliferation of HRVECs. $^{***}P<0.001$, $^{##}P<0.01$ versus control. (D) ROS level in HRVECs. $^{***}P<0.001$, $^{##}P<0.01$ versus control. (E, F) The expression of MDA and GSH in HRVECs. $^{***}P<0.001$, $^{##}P<0.01$ versus control. (G) The protein expression of NRF2, NQO1 and HO-1 in HRVECs. HG, high glucose; HG+oe-nc, high glucose plus empty vectors; HG+oe-TPTEP1, high glucose plus overexpression of TPTEP1.

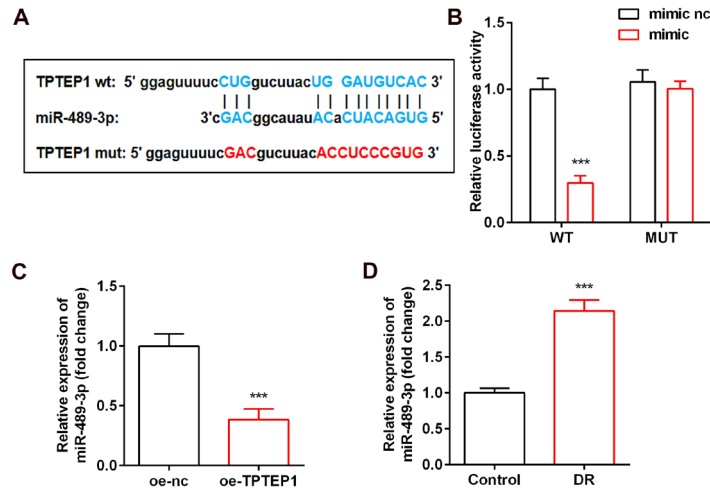


Figure 3. TPTEP1 sponges miR-489-3p.

(A) The binding sites between miR-489-3p and TPTEP1. (B) The luciferase activity of HRVECs. *** $P < 0.001$ versus empty vectors (C) Expression of miR-489-3p. *** $P < 0.001$ versus empty vectors. (D) Expression of miR-489-3p in HG cells. *** $P < 0.001$ versus control.

(Fig. 3B). Furthermore, miR-489-3p expression was significantly declined by TPTEP1 (Fig. 3C). However, miR-489-3p expression was significantly increased by HG (Fig. 3D).

Overexpression of miR-489-3p reversed the effects of TPTEP1 on cell proliferation and oxidative stress

As shown in Fig. 4A, the expression of miR-489-3p in the mimic group was significantly increased compared with the empty vector group, but the expression was significantly declined in the inhibitor group, indicating that the transfection was successful. Overexpressed miR-489-3p significantly weakened the inhibitory effect of TPTEP1 on cell viability (Fig. 4B), and promoted cell proliferation of HRVECs (Fig. 4C). In addition, overexpressed miR-489-3p alleviated the

effects of TPTEP1 on the release of ROS, MDA and GSH (Fig. 4D–4F). Moreover, overexpressing the miR-489-3p inhibited the protein expression of anti-oxidant genes, such as NRF2, NQO1 and HO-1 (Fig. 4G).

3.5 miR-489-3p targeted NRF2

In order to find specific regulatory pathways containing TPTEP1 and miR-489-3p, TargetScan (http://www.targetscan.org/mamm_31/) was applied to predict the target gene of miR-489-3p. We found dramatically that the OS-related NRF2 mentioned above was its target gene (Fig. 5A). Dual luciferase reporter assay further confirmed the targeting relationship between NRF2 and miR-489-3p (Fig. 5B). In addition, the expression of NRF2 in miR-

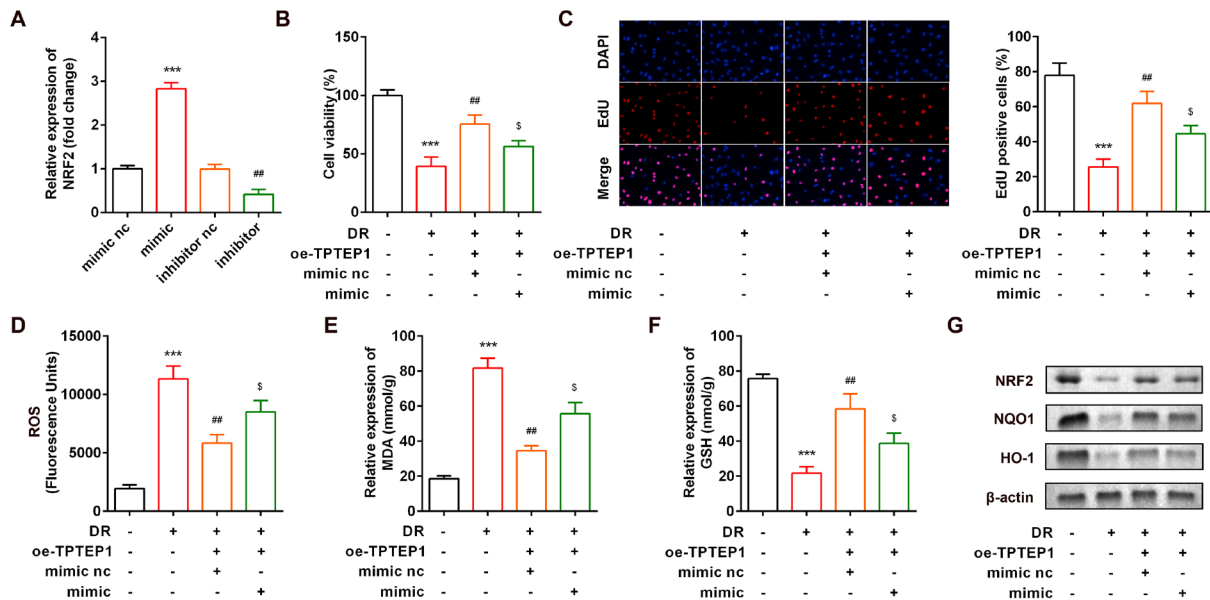


Figure 4. Overexpression of miR-489-3p promotes cell viability and proliferation and reduces oxidative stress.

(A) Overexpression and knockdown of miR-489-3p in HRVECs. *** $P < 0.001$, ** $P < 0.01$, $P < 0.05$ versus empty vectors. (B) Cell viability of HRVECs. *** $P < 0.001$, ** $P < 0.01$, $P < 0.05$ versus control. (C) Cell proliferation of HRVECs. *** $P < 0.001$, ** $P < 0.01$, $P < 0.05$ versus control. (D) ROS level in HRVECs. *** $P < 0.001$, ** $P < 0.01$, $P < 0.05$ versus control. (E, F) The release of MDA and GSH in HRVECs. *** $P < 0.001$, ** $P < 0.01$, $P < 0.05$ versus control. (G) The protein expression of NRF2, NQO1 and HO-1 in HRVECs. HG, high glucose; oe-TPTEP1, overexpression of TPTEP1; mimic nc, empty vectors; mimic, overexpression of miR-489-3p.

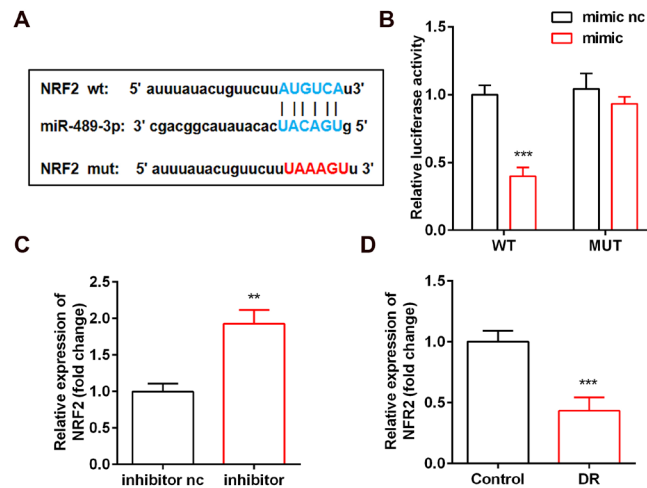


Figure 5. NRF2 is a target of miR-489-3p.

(A) The binding sites between miR-489-3p and NRF2. (B) The luciferase activity of HRVECs. *** $P < 0.001$ versus empty vectors (C) Expression of NRF2 in cells with inhibition of miR-489-3p. ** $P < 0.01$ versus empty vectors. (D) Expression of NRF2 in HG cells. *** $P < 0.001$ versus control.

489-3p inhibitor group was significantly increased (Fig. 5C). Additionally, the expression of NRF2 was significantly declined in cells exposed to HG (Fig. 5D).

Knockdown of NRF2 reversed the regulation of miR-489-3p on cell proliferation and oxidative stress

As shown in Fig. 6A, NRF2's expression was significantly declined in both si-NRF2 groups, indicating successful transfection. si-NRF2 2# was more potent, which, therefore, was used in all subsequent experiments. Fig. 6B and Fig. 6C showed that NRF2 knockdown alleviated the regulation of miR-489-3p inhibitor and promoted the proliferation of HRVECs. In addition, knockdown of NRF2

increased the release of ROS, MDA and decreased GSH as well as suppressed the expression of NRF2, NQO1 and HO-1 (Fig. 6D–G).

DISCUSSION

Diabetic retinopathy is a common eye complication in diabetic patients and an important cause of blindness (Bourne *et al.*, 2013). Oxidative stress response in eye tissue and cells induced by a long-term high glucose environment is considered to be positively correlated with the severity of DR (Arden & Sivaprasad, 2011). The activation of the anti-oxidant NRF2 signaling pathway inhibits

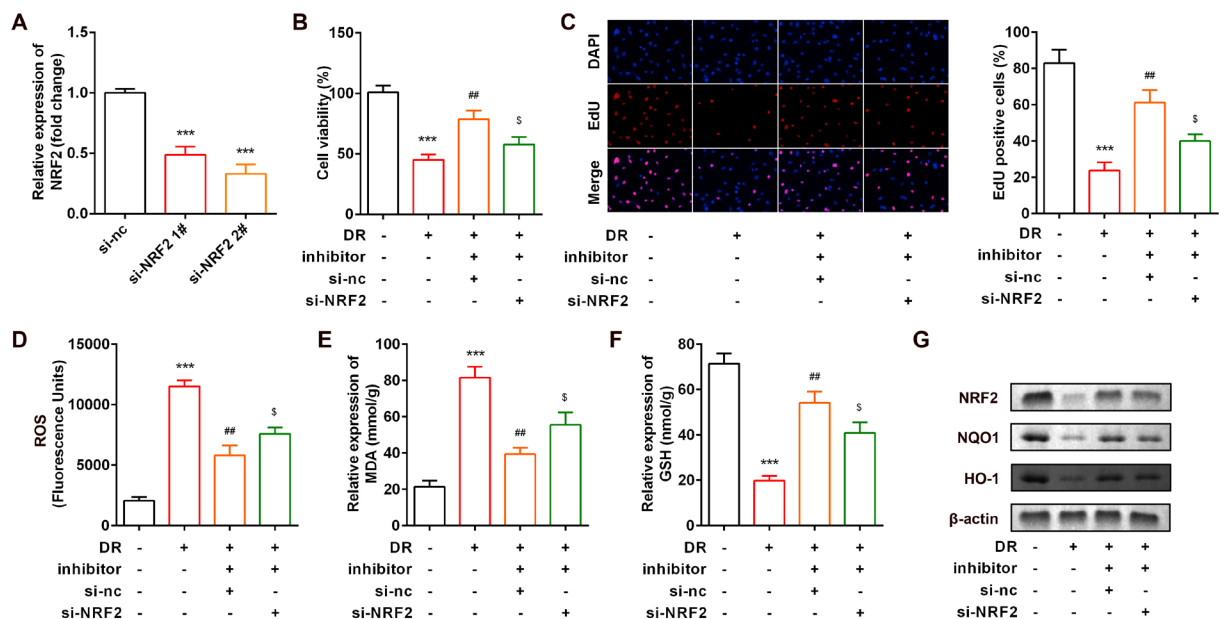


Figure 6. Knockdown of NRF2 inhibits cell viability and proliferation and reduces oxidative stress.

Knockdown of NRF2 in HRVECs. *** $P < 0.001$ versus empty vectors. (B) Cell viability of HRVECs. *** $P < 0.001$, ** $P < 0.01$, $^sP < 0.05$ versus control. (C) Cell proliferation of HRVECs. *** $P < 0.001$, ** $P < 0.01$, $^sP < 0.05$ versus control. (D) ROS level in HRVECs. *** $P < 0.001$, ** $P < 0.01$, $^sP < 0.05$ versus control. (E, F) The release of MDA and GSH in HRVECs. *** $P < 0.001$, ** $P < 0.01$, $^sP < 0.05$ versus control. (G) The protein expression of NRF2, NQO1 and HO-1 in HRVECs. HG, high glucose; inhibitor, inhibition of miR-489-3p; si-nc, empty vectors; si-NRF2, knockdown of NRF2.

the occurrence and development of DR (Tan *et al.*, 2014). Dysregulated lncRNA TPTEP1 is associated with a variety of diseases, including DR (Yan *et al.*, 2014). Dysregulated TPTEP1 interacts with STAT3 and induces the progression of DR (Sun *et al.*, 2021). Therefore, our study explored the regulatory role of TPTEP1 in DR and the potential molecular mechanism. In this study, TPTEP1 was significantly reduced in DR patients and HRVECs stimulated by HG. Overexpression of TPTEP1 sponged miR-489-3p to activate the NRF2 signaling pathway, which suppressed oxidative stress and proliferation of HRVECs.

lncRNAs are usually used as a competitive RNA binding miRNA to regulate the target genes' expression. At present, the lncRNA-miRNA axis has been proved to be related to the pathogenesis of DR (Zhang *et al.*, 2017; Kovacs *et al.*, 2011). For example, lncRNA BANCER inhibits the proliferation and migration of HRVECs in DR (Zhang *et al.*, 2019). HOTAIR prevents oxidative stress response in DR (Biswas *et al.*, 2021). In this study, the expression of TPTEP1 was decreased in DR, which was consistent with a previous study (Sun *et al.*, 2021). Overexpression of TPTEP1 inhibited the viability and proliferation of HRVECs, and suppressed oxidative stress, suggesting that TPTEP1 could be a potential target for DR. Additionally, further study showed that TPTEP1 could directly target miR-489-3p. MiR-489-3p is related to the regulation of gastric cancer (Mao *et al.*, 2021) and inflammatory response (Wang *et al.*, 2021; Ye *et al.*, 2021). However, miR-489-3p is rarely studied in the development of DR/The reports on the roles of miR-489-3p in DR are limited. In this study, the expression level of miR-489-3p in DR patients was overexpressed. However, overexpressed miR-489-3p relieved the effects of TPTEP1 on the proliferation of HRVECs and oxidative stress.

NRF2 belongs to the Cap-n-Collar (CNC) regulatory protein family, which is a transcription factor with a highly conserved basic leucine zipper (bZip) structure. NRF2 signaling possesses antioxidant properties in various diseases, including diabetic complications. NRF2 effectively combats OS and inhibits the occurrence and development of DR (Liu *et al.*, 2014). Moreover, NRF2 reduces the toxicity of hydrogen peroxide and protects retinal vascular endothelial cells by regulating heme oxygenase-1 (HO-1) (Castilho *et al.*, 2012). In this study, NRF2 was the target gene of miR-489-3p. NRF2 knockdown promoted oxidative stress and proliferation of HRVECs, suggesting its beneficial roles in DR.

In summary, the expression of TPTEP1 was reduced in DR. Overexpression of TPTEP1 resisted oxidative stress and proliferation of HRVECs through miR-489-3p/NRF2 axis, thereby inhibiting the development of DR. These findings may provide a therapeutic target for DR.

Declarations

Authors' contributions. All authors participated in the design, interpretation of the studies and analysis of the data and review of the manuscript; X W drafted the work and revised it critically for important intellectual content; X Z, F W, N Z, Y Z and Z A were responsible for the acquisition, analysis, or interpretation of data for the work; F H made substantial contributions to the conception or design of the work.

Declaration of Competing Interest. No conflict of interest exists in the submission of this manuscript, and the manuscript is approved by all authors for publication.

Acknowledgments. Not applicable.

Funding. Not applicable.

Data Availability Statement. The datasets used and analyzed during the current study are available from the corresponding author on reasonable request.

REFERENCES

- Arden GB, Sivaprasad S (2011) Hypoxia and oxidative stress in the causation of diabetic retinopathy. *Curr Diabetes Rev* 7: 291–304. <https://doi.org/10.2174/157339911797415620>
- Biswas S, Feng B, Chen S, Liu J, Aref-Eshghi E, Gonder J, Ngo V, Sadikovic B, Chakrabarti S (2021) The long non-coding RNA HOTAIR is a critical epigenetic mediator of angiogenesis in diabetic retinopathy. *Invest Ophthalmol Vis Sci* 62: 20. <https://doi.org/10.1167/iovs.62.3.20>
- Bourne RR, Stevens GA, White RA, Smith JL, Flaxman SR, Price H, Jonas JB, Keeffe J, Leasher J, Naidoo K, Pesudovs K, Resnikoff S, Taylor HR; Vision Loss Expert Group (2013) Causes of vision loss worldwide, 1990–2010: a systematic analysis. *Lancet Glob Health* 1: e339–e349. [https://doi.org/10.1016/S2214-109X\(13\)70113-X](https://doi.org/10.1016/S2214-109X(13)70113-X)
- Brownlee M (2005) The pathobiology of diabetic complications: a unifying mechanism. *Diabetes* 54: 1615–1625. <https://doi.org/10.2337/diabetes.54.6.1615>
- Castilho A, Avelaira CA, Leal EC, Simões NF, Fernandes CR, Meirinhos RI, Baptista FI, Ambrósio AF (2012) Heme oxygenase-1 protects retinal endothelial cells against high glucose- and oxidative/nitrosative stress-induced toxicity. *PLoS One* 7: e42428. <https://doi.org/10.1371/journal.pone.0042428>
- Crawford TN, Alfaro DV 3rd, Kerrison JB, Jablon EP (2009) Diabetic retinopathy and angiogenesis. *Curr Diabetes Rev* 5: 8–13. <https://doi.org/10.2174/157339909787314149>
- Eshaq RS, Wright WS, Harris NR (2014) Oxygen delivery, consumption, and conversion to reactive oxygen species in experimental models of diabetic retinopathy. *Redox Biol* 2: 661–666. <https://doi.org/10.1016/j.redox.2014.04.006>
- Kovacs B, Lumayag S, Cowan C, Xu S (2011) MicroRNAs in early diabetic retinopathy in streptozotocin-induced diabetic rats. *Invest Ophthalmol Vis Sci* 52: 4402–4409. <https://doi.org/10.1167/iovs.10-6879>
- Liu R, Liu H, Ha Y, Tilton RG, Zhang W (2014) Oxidative stress induces endothelial cell senescence via downregulation of Sirt6. *Biomed Res Int* 2014: 902842. <https://doi.org/10.1155/2014/902842>
- Mao SH, Zhu CH, Nie Y, Yu J, Wang L (2021) Levobupivacaine induces ferroptosis by miR-489-3p/SLC7A11 signaling in gastric cancer. *Front Pharmacol* 12: 681338. <https://doi.org/10.3389/fphar.2021.681338>
- Shi X, Sun M, Liu H, Yao Y, Song Y (2013) Long non-coding RNAs: a new frontier in the study of human diseases. *Cancer Lett* 339: 159–166. <https://doi.org/10.1016/j.canlet.2013.06.013>
- Singer MA, Kermany DS, Waters J, Jansen ME, Tyler L (2016) Diabetic macular edema: it is more than just VEGF. *F1000Res* 5: F1000 Faculty Rev-1019. <https://doi.org/10.12688/f1000research.8265.1>
- Sun X, Lu Y, Lei T (2021) TPTEP1 suppresses high glucose-induced dysfunction in retinal vascular endothelial cells by interacting with STAT3 and targeting VEGFA. *Acta Diabetol* 58: 759–769. <https://doi.org/10.1007/s00592-020-01663-w>
- Tan SM, de Haan JB (2014) Combating oxidative stress in diabetic complications with Nrf2 activators: how much is too much?. *Redox Rep* 19: 107–117. <https://doi.org/10.1179/1351000214Y.00000000087>
- Thomson DW, Dinger ME (2016) Endogenous microRNA sponges: evidence and controversy. *Nat Rev Genet* 17: 272–283. <https://doi.org/10.1038/nrg.2016.20>
- Wang J, Chen Z, Feng X, Yin L (2021) Shikonin ameliorates injury and inflammatory response of LPS-stimulated WI-38 cells via modulating the miR-489-3p/MAP2K1 axis. *Environ Toxicol* 36: 1775–1784. <https://doi.org/10.1002/tox.23298>
- Yan B, Tao ZF, Li XM, Zhang H, Yao J, Jiang Q (2014) Aberrant expression of long noncoding RNAs in early diabetic retinopathy. *Invest Ophthalmol Vis Sci* 55: 941–951. <https://doi.org/10.1167/iovs.13-13221>
- Yan B, Wang ZH, Liu JY, Tao ZF, Li XM, Qin J (2014) Long non-coding RNAs: versatile players in biological processes and human disorders. *Epigenomics* 6: 375–379. <https://doi.org/10.2217/epi.14.29>
- Ye Y, Wang P, Zhou F (2021) miR-489-3p inhibits TLR4/NF- κ B signaling to prevent inflammation in psoriasis. *Exp Ther Med* 22: 744. <https://doi.org/10.3892/etm.2021.10176>
- Yu X, Kensler T (2005) Nrf2 as a target for cancer chemoprevention. *Mutat Res* 591: 93–102. <https://doi.org/10.1016/j.mrfmm.2005.04.017>
- Yumnamcha T, Guerra M, Singh LP, Ibrahim AS (2020) Metabolic dysregulation and neurovascular dysfunction in diabetic retinopathy. *Antioxidants (Basel)* 9: 1244. <https://doi.org/10.3390/antiox9121244>
- Zhang X, Zou X, Li Y, Wang Y (2019) Downregulation of lncRNA BANCER participates in the development of retinopathy among diabetic patients. *Exp Ther Med* 17: 4132–4138. <https://doi.org/10.3892/etm.2019.7444>
- Zhang Y, Sun X, Icli B, Feinberg MW (2017) Emerging roles for MicroRNAs in diabetic microvascular disease: novel targets for therapy. *Endocr Rev* 38: 145–168. <https://doi.org/10.1210/er.2016-1122>

Overexpression of miR-483-5p predicts venous thromboembolism onset in patients with lung cancer especially in high BMI cases

Miao Zhang¹, Juanjuan Li², Guigang Tai³, Chao Li⁴ and Hongcai Wu⁵✉

¹Department of Respiratory Medicine, Qingdao Jiaozhou Central Hospital, Jiaozhou 266300, Shandong, China; ²Endocrinology and Blood Department, Qingdao Jiaozhou Central Hospital, Jiaozhou 266300, Shandong, China; ³Emergency Department, Qingdao Jiaozhou Central Hospital, Jiaozhou 266300, Shandong, China; ⁴Internal Medicine Department, Jiaozhou Jiaodong Sub-district Office Central Health Center, Jiaozhou 266317, Shandong, China; ⁵Cardiothoracic Surgery Department, Jiaozhou Hospital, East Hospital Affiliated to Tongji University, Jiaozhou 266300, Shandong, China

Background: Venous thromboembolism (VTE) is a common complication in patients with lung cancer. The important roles of microRNAs (miRNAs) in VTE have emerged, however, studies about the roles of miRNAs in VTE remain scarce. This study aimed to measure the expression of miR-483-5p in lung cancer patients with VTE, evaluate whether miR-483-5p could predict VTE onset in patients, and further evaluate its predictive value in patients with different BMI values. **Methods:** A total of 170 patients with lung cancer were recruited in this study, including 70 patients with VTE, and 110 patients with non-VTE. The expression of miR-483-5p was detected by quantitative real time PCR. Receiver operating characteristic analysis was used to screen VTE patients from non-VTE patients. Whether miR-483-5p was independently associated with VTE onset in lung cancer patients was evaluated by univariate and multivariate logistic regression analyses. **Results:** miR-483-5p was higher in VTE patients than that in non-VTE patients. miR-483-5p was correlated with body mass index (BMI), hypertension, C-reactive protein (CRP), and platelet count in VTE patients. In addition, miR-483-5p had high diagnostic value to differentiate between VTE patients and non-VTE patients and served as an independent biomarker in predicting the VTE onset in lung cancer patients. Moreover, miR-483-5p had the highest diagnostic accuracy to screen VTE patients from non-VTE patients in patients with high BMI values. **Conclusion:** miR-483-5p, increased in VTE patients, can independently predict VTE onset in lung cancer patients especially in patients with high BMI values.

Keywords: miR-483-5p; Predict; Venous thromboembolism; Lung cancer; BMI

Received: 15 February, 2022; revised: 11 May, 2022; accepted: 07 July, 2022; available on-line: 16 May, 2023

✉e-mail: wuhongcai_lung@163.com

Abbreviations: AUC, area under the curve; BMI, body mass index; CDFI, color Doppler ultrasound imaging; CRP, C-reactive protein; CTPA, CT pulmonary angiography; miRNAs, microRNAs; PCSK9, proprotein convertase subtilisin/kexin type 9; qRT-PCR, Quantitative real time PCR; RBM5, RNA binding motif protein 5; ROC, receiver operating characteristic; 3'-UTR, 3'-untranslated region; VET, Venous thromboembolism

INTRODUCTION

Venous thromboembolism (VTE) is a common vascular disease in which blood clots occur within a vessel.

The pathogenesis of VTE formation is endothelial injury, hypercoagulability or vessel walls injury, and blood stasis, known as Virchow's triad (Kruger *et al.*, 2019). It is known that cancer was one of the most common risk factors for VTE (Falanga & Zacharski, 2005), and the risk of VTE occurrence among cancer patients was estimated to be 4 to 7 times that of the general population (Heit *et al.*, 2000; Walker *et al.*, 2013; Blom *et al.*, 2005). In cancer patients, VTE is not only associated with a worse prognosis, but also with increased medical costs and worse quality of life (Lopez-Nunez *et al.*, 2018). The prevalence of VTE in patients with lung cancer is one of the highest among all cancer patients (Corrales-Rodriguez & Blais, 2012). The risk factors for VTE in lung cancer patients are diverse, such as obesity and high body mass index (BMI), trauma, leukocyte, complications and platelet elevation (Du & Chen, 2018). Notably, obesity has been found to function as an independent and moderate risk factor for VTE (Hotoleanu, 2020). A previous study has found that the survival rate in lung cancer patients with VTE is lower than that in lung cancer patients without VTE (Chen *et al.*, 2015). Thus, early and accurate assessment to identify the patients who at high risk for VTE is clinically necessary for the right treatment option. However, to date, reliable VTE risk assessment tools for lung cancer patients treated with anticancer therapies remain an unmet medical need. Therefore, exploring the key molecules involved in the VTE development may provide targets for treating VTE in lung cancer patients.

The microRNAs (miRNAs) are a group of endogenous, small (about 22 nucleotides) non-coding RNAs that can regulate gene expression by binding to the 3'-untranslated region (3'-UTR) of their target mRNAs (Li *et al.*, 2016). Many studies have demonstrated that miRNAs are associated with VTE development and can be used as markers for the prediction of VTE. For example, miR-134 may be a novel biomarker for predicting VTE (Xiang *et al.*, 2019). miR-374b-5p promotes the formation of VTE and may be used as a promising diagnostic marker for VTE (Zhang, Miao, *et al.*, 2020). However, there are only a few studies on the relationship between miRNAs and VTE disease. miR-483-5p has been found to be significantly associated with obesity and BMI (Gallo *et al.*, 2018), and serves as an angiogenesis-regulating factor (Qiao *et al.*, 2011). In addition, a study has shown that miR-483-5p can regulate the function of pulmonary microvascular endothelial cells (Leng *et al.*,

2020). Thus, we speculated that miR-483-5p may be associated with VTE development.

Therefore, the purpose of this study was to measure the expression of miR-483-5p in VTE and non-VTE patients, and to explore its clinical value for predicting VTE occurrence in patients and in patient groups with different BMI values. This study will provide new biomarker and insight for early predicting VTE occurrence in lung cancer patients.

MATERIALS AND METHODS

Patient recruitment

This study was approved by the Ethics Committee of Qingdao Jiaozhou Central Hospital and all patients had signed the informed consent before this study. A total of 170 patients with lung cancer who received therapy in Qingdao Jiaozhou Central Hospital from 2017 to 2020 were enrolled in the case-control study. Sixty of the lung cancer patients developed VTE after surgery (VTE group), and 110 patients with lung cancer did not develop VTE after surgery (non-VTE group). The inclusion criteria were as follows: (a) age ≥ 18 years, (b) patients received surgical therapy, (c) patients were diagnosed with lung cancer pathologically, and (d) VTE was diagnosed by CT pulmonary angiography (CTPA) and/or vascular color Doppler

ultrasound imaging (CDFI). Patients were excluded if they: (a) had other malignant tumors, (b) had other hematologic diseases, (c) had combined VTE before surgery or had previous history of VTE, (d) got anticoagulant therapy preoperatively and postoperatively because of other diseases, (e) were in TNM stage IV, and (f) were in gestation and lactation.

Collection of serum samples

Venous blood samples were collected from all the lung cancer patients on admission. Then, serum was obtained by centrifuging blood samples at $1500 \times g$ for 10 min at 4°C and stored at -80°C for further use.

RNA isolation

Total RNA was isolated from the serum using TRIzol Reagent (Invitrogen; Thermo Fisher Scientific, Inc.). To prevent contamination of genomic DNA, samples were treated with RNase free DNase I (Fermentas, Thermo Fisher Scientific). Then, the optical density (OD) at 260 nm and 280 nm (OD 260/OD 280) was measured using a NanoDrop 2000 (Thermo Fisher Scientific, Waltham, MA, USA) to evaluate the purity of total RNA, and the concentration of total RNA was evaluated by the OD at 260 nm. All the protocols were performed following the instructions of manufacturers.

Table 1. Baseline characteristics of all the patients

Characteristics	VTE patients (n=60)	Non-VTE patients (n=110)	P value
Age (years)	63.39 \pm 12.46	61.93 \pm 8.96	0.380
Gender			
Female	27	42	0.387
Male	33	68	
BMI (kg/m ²)	22.36 \pm 3.17	20.67 \pm 3.05	0.001
Histological type			
SCLC	23	38	0.623
NSCLC	37	72	
TNM stage			
I-II	24	35	0.284
III	36	75	
Hypertension			
Yes	41	57	0.037
No	19	53	
Diabetes			
Yes	26	41	0.440
No	34	69	
Coronary heart disease			
Yes	31	50	0.438
No	29	60	
CRP (mg/L)	17.07 \pm 8.84	14.55 \pm 5.35	0.022
Hemoglobin (g/L)	130.45 \pm 14.10	135.40 \pm 19.14	0.080
Platelet count (10 ⁹ /L)	244.16 \pm 33.25	234.70 \pm 20.54	0.023
Leukocyte count (10 ⁹ /L)	9.19 \pm 2.28	8.49 \pm 2.02	0.041

Abbreviations: VTE, venous thromboembolism; BMI, body mass index; SCLC, small cell lung cancer; NSCLC, non-small cell lung cancer; CRP, C-reactive protein

Quantitative real time PCR (qRT-PCR)

At first, a reverse transcription step was performed to synthesize the cDNA of miRNA with the PrimeScript RT reagent kit (Takara Bio Inc.). The SYBR Green PCR Master Mix kit (Invitrogen; Thermo Fisher Scientific, Inc.) was used for the qRT-PCR analysis of miR-483-5p expression in a 7300 Real-Time PCR System (Applied Biosystems; Thermo Fisher Scientific, Inc.). All procedures were performed according to the manufacturer's instructions. The thermocycling conditions were as follows: an initial denaturation step at 95°C for 10 min, followed by 40 cycles at 95°C for 30 s, 60°C for 30 s and 72°C for 10 s. Primer sequences were as follows (5'-3'): miR-483-5p, forward: GCCGAGAAGACGGGAGGAAA and reverse: CTCAACTGGTGTCTGTGGA; U6, forward: CTCGCTTCGGCAGCACA and reverse: AACGCTTCACGAATTTGCGT. The data of the relative miR-483-5p expression levels were calculated using the $2^{-\Delta\Delta C_t}$ method (Livak & Schmittgen, 2001). U6 was used as an internal control for miR-483-5p expression.

Statistical analysis

SPSS 21.0 software (SPSS, Inc., Chicago, USA) and GraphPad Prism 7.0 software (GraphPad Software, Inc.) were used to perform all statistical analyses in this study. All data were shown as mean \pm standard deviation (S.D.). Differences between two groups of continuous variables and categorical variables were compared using Student's *t*-test and Chi-square test, respectively. Pearson correlation analysis was used to analyze the correlation of miR-483-5p with continuous variables, and Chi-square test was used to analyze the association between miR-483-5p and categorical variables. The ability of miR-483-5p to differentiate between VTE patients and non-VTE patients in all the patients and in patient groups with different BMI values was evaluated by receiver operating characteristic (ROC) analysis. Univariate and multivariate logistic regression analyses were used to evaluate the ability of miR-483-5p to predict VTE onset in lung cancer patients. $P < 0.05$ was considered as statistically significant.

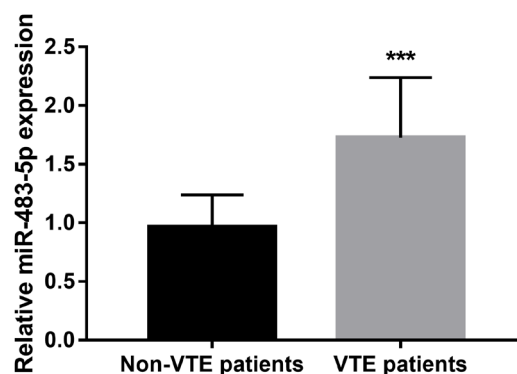


Figure 1. The expression level of miR-483-5p in VTE patients and non-VTE patients.

*** $P < 0.001$ vs. Non-VTE patients. VTE, venous thromboembolism.

RESULTS

Baseline characteristics of lung cancer patients

The baseline characteristics of all patients with lung cancer were presented in Table 1. There were no significant differences in age, gender, histological type, TNM stage, diabetes, coronary heart disease, and hemoglobin between VTE patients and non-VTE patients (all $P > 0.05$). Additionally, compared to non-VTE patients, VTE patients had significantly higher BMI ($P = 0.001$), C-reactive protein (CRP, $P = 0.022$), platelet count ($P = 0.023$), leukocyte count ($P = 0.041$), and a higher proportion of population with hypertension ($P = 0.037$).

High miR-483-5p expression in VTE patients

The expression level of miR-483-5p was presented in Fig. 1. miR-483-5p expression was significantly upregulated in VTE patients compared with that in non-VTE patients ($P < 0.001$).

Correlation between miR-483-5p expression and VTE patients' clinicopathological characteristics

As shown in Table 2, miR-483-5p expression was found to be correlated with BMI ($r = 0.416$, $P = 0.001$), hy-

Table 2. Correlation between miR-483-5p expression and the clinicopathological characteristics of VTE patients

Characteristics	Mean \pm S.D./Number (n=60)	miR-483-5p	
		χ^2/r value	P value
Age (years)	63.39 \pm 12.46	0.104	0.429
Male	33	1.684	0.194
BMI (kg/m ²)	22.36 \pm 3.17	0.416	0.001
Histological type (NSCLC)	37	0.071	0.791
TNM stage (III)	36	2.500	0.114
Hypertension	41	6.239	0.012
Diabetes	26	2.443	0.118
Coronary heart disease	31	1.669	0.196
CRP (mg/L)	17.07 \pm 8.84	0.301	0.020
Hemoglobin (g/L)	130.45 \pm 14.10	-0.116	0.379
Platelet count (10 ⁹ /L)	244.16 \pm 33.25	0.291	0.024
Leukocyte count (10 ⁹ /L)	9.19 \pm 2.28	0.276	0.038

VTE, venous thromboembolism; BMI, body mass index; NSCLC, non-small cell lung cancer; CRP, C-reactive protein; S.D., standard deviation

Table 3. Logistic analysis of factors influencing the risk of VTE in lung cancer patients

Characteristics	Univariate analysis		Multivariate analysis	
	OR (95% CI)	P	OR (95% CI)	P
Age	1.190 (0.616–2.300)	0.605		
Gender	1.325 (0.700–2.506)	0.387		
BMI	2.939 (1.338–6.456)	0.007	3.587 (1.411–9.119)	0.009
Histological type	1.178 (0.614–2.261)	0.623		
TNM stage	1.429 (0.743–2.748)	0.285		
Hypertension	2.006 (1.037–3.883)	0.039	1.901 (0.874–4.134)	0.112
Diabetes	1.287 (0.678–2.442)	0.440		
Coronary heart disease	1.283 (0.683–2.409)	0.439		
CRP	1.937 (1.022–3.672)	0.043	1.401 (0.612–3.207)	0.389
Hemoglobin	1.414 (0.752–2.660)	0.283		
Platelet count	2.231 (1.169–4.258)	0.015	2.023 (0.921–4.443)	0.081
Leukocyte count	1.323 (1.049–1.668)	0.048	1.304 (0.899–1.891)	0.093
miR-483-5p	7.747 (3.720–16.135)	<0.001	8.075 (3.723–17.514)	<0.001

VTE, venous thromboembolism; BMI, body mass index; CRP, C-reactive protein; OR odds ratio; CI, confidence interval

pertension ($P=0.012$), CRP ($r=0.301$, $P=0.020$), platelet count ($r=0.291$, $P=0.024$), and leukocyte count ($r=0.276$, $P=0.024$) in VTE patients. In addition, no correlation was found between miR-483-5p expression and age, male, histological type, TNM stage, diabetes, coronary heart disease and hemoglobin (all $P>0.05$).

The significance of miR-483-5p for predicting VTE onset in lung cancer patients

The clinical characteristics that might predict the onset of VTE in lung cancer patients were included in the logistic regression analysis, and the analysis results were shown in Table 3. The results after multivariate correction demonstrated that BMI [odds ratio (OR)=3.731; 95% confidence interval (CI)=1.414–9.848; $P=0.008$] and miR-483-5p (OR=8.441; 95% CI=3.732–19.094; $P<0.001$) were independently associated with VTE onset in lung cancer patients. In addition, by ROC analysis (Fig. 2), miR-483-5p was demonstrated to have high ability to screen VTE patients from non-VTE patients with an area under the ROC curve (AUC) of 0.907. At the cutoff value of 1.32, the sensitivity and specificity were 71.67% and 92.73%, respectively.

Comparison of the predictive value of miR-483-5p in patients with different BMI values

As shown in Fig. 3, the percentage referred to the ratio of the number of VTE patients in different BMI groups to the total VTE patients, and the ratio of the number of non-VTE patients in different BMI groups to the total non-VTE patients. Patients with BMI<18.5, $18.5\leq\text{BMI}<24$, and $\text{BMI}\geq 24$ were defined as underweight, normal BMI, and overweight groups, respectively. The percentage of VTE patients and non-VTE patients was the highest in the normal BMI group. The percentage of VTE patients was higher and the percentage of non-VTE patients was lower in the overweight group than that in the underweight group. In addition, in the underweight group, the percentage of non-VTE patients was higher than the percentage of VTE patients. In the overweight group, the percentage of VTE patients was higher than the percentage of non-VTE patients. miR-483-5p had a

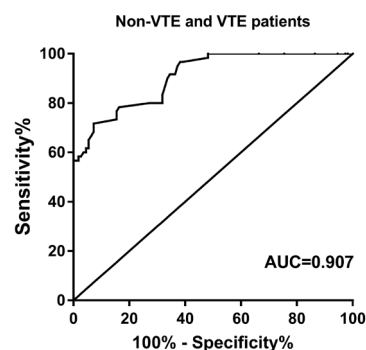


Figure 2. ROC analysis results showed that miR-483-5p had high diagnostic value in screening VTE patients from non-VTE patients (AUC=0.907). AUC, area under the ROC curve; ROC, receiver operating characteristic. VTE, venous thromboembolism.

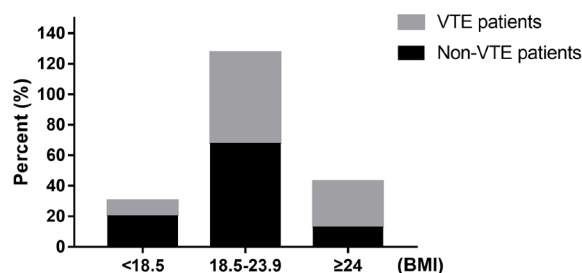


Figure 3. The percent of VTE patients and non-VTE patients in patients with different BMI values. VTE, venous thromboembolism.

certain role in differentiating between VTE patients ($n=6$) and non-VTE patients ($n=22$) in the underweight group (AUC=0.780, Fig. 4A). Figure 4B revealed that miR-483-5p had the ability to discriminate between VTE patients ($n=36$) and non-VTE patients ($n=74$) in the normal BMI group with an AUC of 0.906 (sensitivity of 80.56%, specificity of 85.14% and cutoff value of 1.21). Figure 4C showed the high ability of miR-483-5p in screening VTE

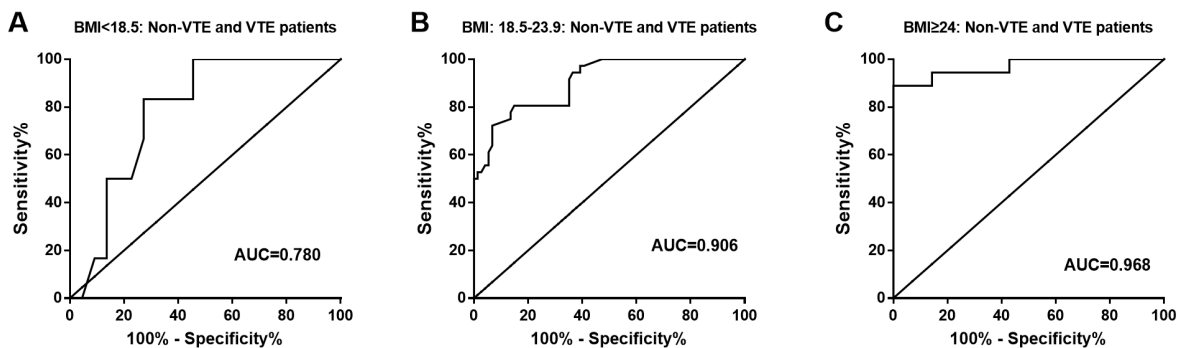


Figure 4. ROC analysis for miR-483-5p for screening VTE patients in different BMI level group.

The ability of miR-483-5p in differentiating between VTE patients and non-VTE patients in BMI<18.5 group (Fig. 4A, AUC=0.780), in normal BMI group (Fig. 4B, AUC=0.906), and in BMI≥24 group (Fig. 4C, AUC=0.968). AUC, area under the ROC curve; ROC, receiver operating characteristic. VTE, venous thromboembolism.

patients (n=18) from non-VTE patients (n=14) in the overweight group (AUC=0.968, sensitivity=88.89%, specificity=100% and cutoff value=1.705).

DISCUSSION

Increasing evidence has indicated the correlation of miRNAs with VTE. For example, Wang and others have shown the role of miR-195-5p and miR-205-5p as potential biomarkers in cervical cancer patients treated for VTE (Wang *et al.*, 2020). Zhang and others have reported that miR-338-5p is downregulated in VTE and that it suppresses VTE (Zhang *et al.*, 2020). In addition, miR-483-5p has been found to play an inhibitory effect on angiogenesis (Qiao *et al.*, 2011). A study has shown that miR-483-5p can regulate the function of pulmonary microvascular endothelial cells (Leng *et al.*, 2020). Therefore, we concluded that miR-483-5p may also be correlated with the progression of VTE. This study revealed a higher miR-483-5p expression in VTE patients than that in non-VTE patients. In addition, the correlation of miR-483-5p with BMI, hypertension, CRP, and platelet count in VTE patients was found. Thus, miR-483-5p may be correlated with VTE progression in lung cancer patients.

miRNAs may be ideal biomarkers with the advantages of low detection limits and strong stability. Many studies have shown the prognostic value of miRNAs for various diseases. For instance, miR-892a may act as a prognostic marker for patients with gastric cancer (Lv *et al.*, 2020). Serum miR-22 may be used as a new prognostic biomarker for acute myeloid leukemia (Qu *et al.*, 2020). miR-211-5p can serve as an independent prognostic factor for the poor prognosis of atherosclerosis (Zhang *et al.*, 2021). In addition, many studies have found the potential of miRNAs in predicting the VTE occurrence, such as miR-296-5p (Pan *et al.*, 2021), miR-195-5p (Jin *et al.*, 2019), and miR-374b-5p (Zhang *et al.*, 2020). In this study, Cox analysis results indicated that BMI and miR-483-5p were independently correlated with the occurrence of VTE in lung cancer patients. Additionally, ROC analysis results indicated that miR-483-5p has a high ability to differentiate between VTE patients and non-VTE patients. Thus, our study results demonstrated that miR-483-5p can be used as an independent predictor of VTE in lung cancer patients. Notably, aberrant miR-483-5p has been reported to be a biomarker for other diseases, such as adrenocortical cancer (Oreglia *et al.*, 2020), coronary plaque rupture (Li *et al.*, 2017), and esophageal squamous cell carcinoma (Xue *et al.*, 2017).

Thus, serum miR-483-5p may function as an independent biomarker to predict the occurrence of VTE in lung cancer patients.

Considering that miR-483-5p and BMI were two independent risk factors for VTE occurrence and that they were significantly correlated, we analyzed the predictive value of miR-483-5p for VTE occurrence in three groups of patients with different BMI values. Notably, it has been found that BMI is an independent risk factor for VTE (Hotoleanu, 2020), and a study has demonstrated that miR-483-5p is significantly correlated with obesity and BMI (Gallo *et al.*, 2018). The results of this study indicated that miR-483-5p had the highest ability in differentiating between VTE patients and non-VTE patients in the overweight group. Thus, in the group with high BMI values, referencing miR-483-5p levels would enable a more accurate screening of patients at high risk of VTE. Therefore, it can be speculated that miR-483-5p may be related to obesity and BMI, thereby participating in the occurrence and development of BMI-related diseases. In clinical practice, patients with higher BMI should pay more attention to their miR-483-5p levels, because patients with significantly increased miR-483-5p levels have a higher risk of developing VTE.

Further validation analyses are important, so we estimate the statistical power of the study due to the time limitation. A total of 170 lung cancer patients treated at our hospital were enrolled in this study, including 60 VTE patients and 110 non-VTE patients. Where an included sample has been identified, the statistical power has a high probability value of meeting the statistical data variation of VTE patients being different from non-VTE patients, suggesting that the included VTE patients indeed differ from non-VTE patients in a statistical sense and that the findings were reliable. However, there were some limitations. First, of the 170 lung cancer patients recruited who met the inclusion criteria, there were only 32 (18.82%) overweight lung cancer patients, including 18 (30.00%) overweight lung cancer patients who developed VTE after surgery, and 14 (12.73%) overweight lung cancer patients did not develop VTE after surgery. Whether it concerns the overall included lung cancer patients or the overweight lung cancer patients, the sample size of this study is small and further research is needed on a larger scale. Second, this study has not elucidated how miR-483-5p functions in VTE, and the mechanism is urgently needed to be explored by further experimental analysis. Previous studies have shown that miR-483-5p targeted RNA binding motif protein 5 (RBM5) (Wang *et al.*, 2018) and proprotein convertase subtilisin/kexin type 9 (PCSK9) (Dong *et al.*, 2020) and was involved in the disease progression. The results

of the present study revealed that miR-483-5p was increased in VTE patients and could independently predict VTE onset in lung cancer patients, eliciting a potential indirect link of VTE to RBM5 and PCSK9 via miR-483-5p. Therefore, we speculated that the mechanism might be that miR-483-5p was associated with VTE by targeting RBM5 or PCSK9. However, this speculation needs to be verified by further experimental analysis, which is also our next research direction.

In conclusion, the findings of this study indicate that miR-483-5p is higher in VTE patients than that in non-VTE patients, is associated with BMI in VTE patients, and can serve as an independent predictor of VTE in lung cancer patients. Additionally, miR-483-5p had the highest value in differentiating patients with and without VTE in patients with high BMI. Thus, miR-483-5p overexpression can independently predict VTE onset in patients with lung cancer, especially in patients with high BMI. This study may provide new targets and ideas for screening patients with high VTE risk among lung cancer patients.

Declaration

Ethics approval and consent to participate. The experimental procedures were all in accordance with the guideline of the Ethics Committee of Qingdao Jiaozhou Central Hospital and has approved by the Ethics Committee of Qingdao Jiaozhou Central Hospital. This study complies with the Declaration of Helsinki.

A signed written informed consent was obtained from each patient.

Consent for publication. Not applicable.

Availability of data and materials. The data used and analyzed can be obtained from the corresponding author under a reasonable request.

Competing interests. The authors declare that they have no competing interests.

Funding. None.

Acknowledgements. Not applicable.

Authors' contributions. MZ carried out the research design and conception; JL and CL analyzed and interpreted the data regarding; GT performed the examination of sample; JL and GT contributed essential reagents or tools. MZ and HW authors wrote and revised the manuscript. All authors read and approved the final manuscript.

REFERENCES

- Blom JW, Doggen CJ, Osanto S, Rosendaal FR (2005) Malignancies, prothrombotic mutations, and the risk of venous thrombosis. *JAMA* **293**: 715–722. <https://doi.org/10.1001/jama.293.6.715>
- Chen W, Zhang Y, Yang Y, Zhai Z, Wang C (2015) Prognostic significance of arterial and venous thrombosis in resected specimens for non-small cell lung cancer. *Thromb Res* **136**: 451–455. <https://doi.org/10.1016/j.thromres.2015.06.014>
- Corrales-Rodriguez L, Blais N (2012) Lung cancer associated venous thromboembolic disease: a comprehensive review. *Lung Cancer* **75**: 1–8. <https://doi.org/10.1016/j.lungcan.2011.07.004>
- Dong J, He M, Li J, Pessentheiner A, Wang C, Zhang J, Sun Y, Wang WT, Zhang Y, Liu J, Wang SC, Huang PH, Gordts PL, Yuan ZY, Tsimikas S, Shyy JY (2020) microRNA-483 ameliorates hypercholesterolemia by inhibiting PCSK9 production. *JCI Insight* **5**. <https://doi.org/10.1172/jci.insight.143812>
- Du H, Chen J (2018) Occurrence of venous thromboembolism in patients with lung cancer and its anticoagulant therapy. *Zhongguo Fei Ai Za Zhi* **21**: 784–789 (in Chinese). <https://doi.org/10.3779/j.issn.1009-3419.2018.10.09>
- Falanga A, Zacharski L (2005) Deep vein thrombosis in cancer: the scale of the problem and approaches to management. *Ann Oncol* **16**: 696–701. <https://doi.org/10.1093/annonc/mdl165>
- Gallo W, Esguerra JLS, Eliasson L, Melander O (2018) miR-483-5p associates with obesity and insulin resistance and independently associates with new onset diabetes mellitus and cardiovascular disease. *PLoS One* **13**: e0206974. <https://doi.org/10.1371/journal.pone.0206974>
- Heit JA, Silverstein MD, Mohr DN, Petterson TM, O'Fallon WM, Melton LJ, 3rd (2000) Risk factors for deep vein thrombosis and pulmonary embolism: a population-based case-control study. *Arch Intern Med* **160**: 809–815. <https://doi.org/10.1001/archinte.160.6.809>
- Hotoleanu C (2020) Association between obesity and venous thromboembolism. *Med Pharm Rep* **93**: 162–168. <https://doi.org/10.15386/MPR-1372>
- Jin J, Wang C, Ouyang Y, Zhang D (2019) Elevated miR-195-5p expression in deep vein thrombosis and mechanism of action in the regulation of vascular endothelial cell physiology. *Exp Ther Med* **18**: 4617–4624. <https://doi.org/10.3892/etm.2019.8166>
- Kruger PC, Eikelboom JW, Douketis JD, Hankey GJ (2019) Deep vein thrombosis: update on diagnosis and management. *Med J Aust* **210**: 516–524. <https://doi.org/10.5694/mja2.50201>
- Leng C, Sun J, Xin K, Ge J, Liu P, Feng X (2020) High expression of miR-483-5p aggravates sepsis-induced acute lung injury. *J Toxicol Sci* **45**: 77–86. <https://doi.org/10.2131/jts.45.77>
- Li S, Lee C, Song J, Lu C, Liu J, Cui Y, Liang H, Cao C, Zhang F, Chen H (2017) Circulating microRNAs as potential biomarkers for coronary plaque rupture. *Oncotarget* **8**: 48145–48156. <https://doi.org/10.18632/oncotarget.18308>
- Li T, Pan H, Li R (2016) The dual regulatory role of miR-204 in cancer. *Tumour Biol* **37**: 11667–11677. <https://doi.org/10.1007/s13277-016-5144-5>
- Livak KJ, Schmittgen TD (2001) Analysis of relative gene expression data using real-time quantitative PCR and the 2⁻(Delta Delta C(T)) method. *Methods* **25**: 402–408. <https://doi.org/10.1006/meth.2001.1262>
- Lopez-Nunez JJ, Trujillo-Santos J, Monreal M (2018) Management of venous thromboembolism in patients with cancer. *J Thromb Haemost* **16**: 2391–2396. <https://doi.org/10.1111/jth.14305>
- Lv J, Zhang H, Gao Z, Zhang X, Huang X, Jia X (2020) Prognostic value of miR-892a in gastric cancer and its regulatory effect on tumor progression. *Cancer Biomark* **28**: 247–254. <https://doi.org/10.3233/CBM-191323>
- Oreglia M, Sberia S, Fassnacht M, Guyon L, Denis J, Cristante J, Chabre O, Cherradi N (2020) Early postoperative circulating miR-483-5p is a prognosis marker for adrenocortical cancer. *Cancers (Basel)* **12**. <https://doi.org/10.3390/cancers12030724>
- Pan Z, Zhang Y, Li C, Yin Y, Liu R, Zheng G, Fan W, Zhang Q, Song Z, Guo Z, Rong J, Shen Y (2021) MiR-296-5p ameliorates deep venous thrombosis by inactivating S100A4. *Exp Biol Med (Maywood)* **153**: 702211023034. <https://doi.org/10.1177/15353702211023034>
- Qiao Y, Ma N, Wang X, Hui Y, Li F, Xiang Y, Zhou J, Zou C, Jin J, Lv G, Jin H, Gao X (2011) MiR-483-5p controls angiogenesis in vitro and targets serum response factor. *FEBS Lett* **585**: 3095–3100. <https://doi.org/10.1016/j.febslet.2011.08.039>
- Qu H, Zheng G, Cheng S, Xie W, Liu X, Tao Y, Xie B (2020) Serum miR-22 is a novel prognostic marker for acute myeloid leukemia. *J Clin Lab Anal* **34**: e23370. <https://doi.org/10.1002/jcla.23370>
- Walker AJ, Card TR, West J, Crooks C, Grainge MJ (2013) Incidence of venous thromboembolism in patients with cancer – a cohort study using linked United Kingdom databases. *Eur J Cancer* **49**: 1404–1413. <https://doi.org/10.1016/j.ejca.2012.10.021>
- Wang F, Zhang X, Zhong X, Zhang M, Guo M, Yang L, Li Y, Zhao J, Yu S (2018) Effect of miR-483-5p on apoptosis of lung cancer cells through targeting of RBM5. *Int J Clin Exp Pathol* **11**: 3147–3156
- Wang Y, Zhang Z, Tao P, Reyila M, Qi X, Yang J (2020) The Abnormal expression of miR-205-5p, miR-195-5p, and VEGF-A in human cervical cancer is related to the treatment of venous thromboembolism. *Biomed Res Int* **2020**: 3929435. <https://doi.org/10.1155/2020/3929435>
- Xiang Q, Zhang HX, Wang Z, Liu ZY, Xie QF, Hu K, Zhang Z, Mu GY, Ma LY, Jiang J, Cui YM (2019) The predictive value of circulating microRNAs for venous thromboembolism diagnosis: A systematic review and diagnostic meta-analysis. *Thromb Res* **181**: 127–134. <https://doi.org/10.1016/j.thromres.2019.07.024>
- Xue L, Nan J, Dong L, Zhang C, Li H, Na R, He H, Wang Y (2017) Upregulated miR-483-5p expression as a prognostic biomarker for esophageal squamous cell carcinoma. *Cancer Biomark* **19**: 193–197. <https://doi.org/10.3233/CBM-160506>
- Zhang Y, Miao X, Zhang Z, Wei R, Sun S, Liang G, Li H, Chu C, Zhao L, Zhu X, Guo Q, Wang B, Li X (2020) miR-374b-5p is increased in deep vein thrombosis and negatively targets IL-10. *J Mol Cell Cardiol* **144**: 97–108. <https://doi.org/10.1016/j.yjmcc.2020.05.011>
- Zhang Y, Wang H, Xia Y (2021) The expression of miR-211-5p in atherosclerosis and its influence on diagnosis and prognosis. *BMC Cardiovasc Disord* **21**: 371. <https://doi.org/10.1186/s12872-021-02187-z>
- Zhang Y, Zhang Z, Wei R, Miao X, Sun S, Liang G, Chu C, Zhao L, Zhu X, Guo Q, Wang B, Li X (2020) IL (Interleukin)-6 contributes to deep vein thrombosis and is negatively regulated by miR-338-5p. *Arterioscler Thromb Vasc Biol* **40**: 323–334. <https://doi.org/10.1161/ATVBAHA.119.313137>

A novel ferroptosis-related gene signature associated with cuproptosis for predicting overall survival in breast cancer patients

Xiaoyu Zhang¹ and Qunchen Zhang²✉

¹Department of Thoracic Surgery, The First Affiliated Hospital of Shantou University Medical College, Shantou City, Guangdong Province, P.R. China; ²Department of Breast, Jiangmen Central Hospital, Jiangmen City, Guangdong Province, P.R. China

Purpose Ferroptosis and cuproptosis are both metal-dependent regulated cell death that play an important role in cancer. However, the expression patterns and the prognostic values of ferroptosis-related genes (FRGs) associated with cuproptosis in breast cancer (BC) are largely unknown. This study aims to explore the prognostic value of cuproptosis-related FRGs and their relationship with tumor microenvironments in BC. **Methods** The clinical and RNA sequencing data of BC patients from TCGA, METABRIC and GEO databases were analyzed. The least absolute shrinkage and selection operator regression analysis was used to establish prognostic signatures based on cuproptosis-related FRGs. The overall survival between risk subgroups was assessed by Kaplan-Meier analysis. The changes in risk score during neoadjuvant chemotherapy, and differences in immune cells, immune checkpoints, and drug sensitivity between risk subgroups were also analyzed in this study. **Results** A successful development of a prognostic signature based on cuproptosis-related FRGs in the TCGA cohort was achieved and it was validated in the METABRIC cohort. Gene set enrichment analysis results revealed the enrichment of steroid biosynthesis and ABC transporters in the high-risk group. Moreover, the signature was also found to be associated with immune cells and immune checkpoints. Lower risk score in patients after neoadjuvant chemotherapy and higher sensitivity of the high-risk group to AKT inhibitor VIII and cisplatin was also observed. **Conclusion** Cuproptosis-related FRGs can be used as a novel prognostic signature for predicting the overall survival of BC patients. This can provide meaningful insights into the selection of immunotherapy and antitumor drugs for BC.

Keywords: breast cancer, ferroptosis, cuproptosis, immune microenvironment, prognosis

Received: 06 March, 2023; **revised:** 15 August, 2023; **accepted:** 25 August, 2023; **available on-line:** 06 November, 2023

✉ e-mail: qc Zhang2014@163.com

Abbreviations: BC, breast cancer; ER, estrogen receptor; FRGs, ferroptosis-related genes; HER-2, human epidermal growth factor receptor; GEO, gene expression omnibus; GO, gene ontology; GSEA, gene set enrichment analysis; IC50, half-maximal inhibitory concentration; KEGG, kyoto encyclopedia of genes and genomes; LASSO, least absolute shrinkage and selection operator; METABRIC, molecular taxonomy of breast cancer international consortium; OS, overall survival; PPI, protein-protein interaction; PR, progesterone receptor; ROC, receiver operating characteristic; TCGA, the cancer genome atlas.

INTRODUCTION

Breast cancer (BC) is one of the most frequently diagnosed cancer in women worldwide, with an extremely high rate of mortality (Azamjah *et al.*, 2019). Its incidence and death rates have increased over recent years making it the second most common cause of mortality in women (DeSantis *et al.*, 2019). Its progressive impact on younger individuals is a cause of concern. Although the etiology and mechanism of BC are not completely understood, biological features including cell infiltration and genetic abnormalities are thought to be the major causes associated with the progression and metastasis of the disease (Feng *et al.*, 2018; Loibl *et al.*, 2021). Although there have been advancements in diagnosis, chemotherapy, endocrine and targeted therapies, the median survival in the case of advanced BC is only 31.8 months (Caswell-Jin *et al.*, 2018; Sung *et al.*, 2021). Early diagnosis and intervention are of paramount importance. Therefore, research on novel prognostic markers and therapeutic targets will provide improved opportunities for individualized treatment of BC.

Metals are essential components of metabolic processes. A significant portion of the proteases requires binding to metals, such as calcium, magnesium, iron, and copper for proper functioning (Waldron *et al.*, 2009). However, dysregulation of metal metabolism can lead to cell death. Ferroptosis, unlike apoptosis and autophagy, is an iron-dependent process of regulated cell death that is characterized by intracellular buildup of reactive oxygen species (ROS) and products of lipid peroxidation (Huang *et al.*, 2020). The primary mechanism of ferroptosis is the catalysis of the highly expressed unsaturated fatty acids on the cell membrane to produce liposome peroxidation, resulting in cell death, under the influence of divalent iron or ester oxygenase (Dixon *et al.*, 2012). Ferroptosis-related genes (FRGs) play an important role in the development of various cancers, including lung cancer, melanoma, renal cell carcinoma, BC, etc. (Friedmann Angeli *et al.*, 2019; Wang *et al.*, 2020; Zhao *et al.*, 2022). Activation of ferroptosis has been shown to prevent the growth and proliferation of tumors (Hassannia *et al.*, 2019). Therefore, ferroptosis can be a potential target for cancer therapy, especially in patients who have grown resistant to conventional forms of therapy (Hassannia *et al.*, 2019; Zhang *et al.*, 2022). For example, the sensitivity of triple-negative BC cells to gefitinib was enhanced by the inhibition of *GPX4* activation of Ferroptosis (Song *et al.*, 2020). Cuproptosis is a method of copper-induced regulated cell death. The direct interaction between copper ions and lipidated protein compo-

nents in the tricarboxylic acid cycle interferes with the iron-sulfur cluster proteins in the respiratory chain complex which ultimately leads to proteotoxic stress and cell death (Kahlson & Dixon, 2022). This could be another regulatory mechanism for the development of cancer (Jiang *et al.*, 2022). Iron-sulfur cluster proteins are able to maintain iron homeostasis in mitochondria (Pain & Dancis, 2016). Several mitochondrial proteins (including NFS1, ISCU, CISD1, and CISD2) require iron for iron-sulfur cluster biogenesis reactions for the negative regulation of ferroptosis (Yuan *et al.*, 2016; Alvarez *et al.*, 2017; Kim *et al.*, 2018; Du *et al.*, 2019). Moreover, elesclomol stimulates copper retention and the subsequent buildup of ROS via the degradation of ATP7A, which promotes ferroptosis in colorectal cancer cells (Gao *et al.*, 2021). Cuprizone, which is a copper chelator, regulates demyelination by the stimulation of ferroptosis and eventually leads to the loss of oligodendrocytes (Jhelum *et al.*, 2020). Therefore, an association between iron and copper metabolism has been well-established in scientific literature. These findings highlight the role of ferroptosis and cuproptosis as potential targets for the treatment of cancer.

In this study, a predictive model based on cuproptosis-related FRGs was built successfully to evaluate the prognosis of patients with BC and the predictive performance of the model was further validated. The findings of this study may enhance the effectiveness of individualized treatment and prognostic evaluations in patients with BC.

MATERIALS AND METHODS

Patient and gene set data collection

Clinical and RNA-sequencing data of 1097 BC patients were obtained from the cancer genome atlas (TCGA) database and 1053 patients containing complete clinical data including overall survival, age, gender, T stage, N stage, M stage, and TNM stage, were obtained after screening, while 44 patients who lacked complete clinical data were excluded. The intrinsic subtype was defined by PAM 50 (Parker *et al.*, 2009). Moreover, 1904 cases of RNA-sequencing and corresponding clinical data were obtained from the molecular taxonomy of breast cancer international consortium (METABRIC) database as the validation set for prognosis, and datasets GSE18728 and GSE87455 from gene expression omnibus (GEO) database were used to compare changes in risk score before and after neoadjuvant chemotherapy. Furthermore, 13 cuproptosis-related genes were obtained from the cuproptosis-related study (Tsvetkov *et al.*, 2022), and 259 FRGs were downloaded from the FerrDb website (Zhou & Bao, 2020).

Identification and prognosis of cuproptosis-related FRGs

The correlation between the expression of cuproptosis-related genes and FRGs was determined using the Pearson correlation coefficients. The criteria used to identify cuproptosis-related FRGs was of P value <0.001 and the absolute value of the Pearson correlation coefficient >0.3 ($|R|>0.3$). The univariate Cox regression analysis was used to screen the prognosis-related genes.

Building and validation of a prognostic model

Based on the outcome of univariate Cox regression analysis, the least absolute shrinkage and selection opera-

tor (LASSO) regression method was used for the identification of the best survival-related genes via glmnet R package (Tibshirani, 1997; Wang & Liu, 2020). The prognostic risk score formula was created using the coefficients obtained from LASSO regression and the expression levels of genes. The formula can be mathematically represented as: Risk Score = \sum corresponding regression coefficient * expression of the gene. The risk scores of the patients with BC were determined and the patients were grouped into two groups: the high-risk group and the low-risk group using the median risk score as the cutoff. The Kaplan-Meier survival analysis was used to demonstrate the presence of survival differences between the two groups. A receiver operator characteristic (ROC) curve via survivalROC R package was constructed to evaluate the effectiveness of the prognostic model and the METABRIC cohort was used for further validation.

Establishment of a nomogram based on risk score and clinical characteristics

Univariate and multivariate COX regression analyses were used for the evaluation of risk scores and clinical characteristics as independent prognostic factors. A nomogram based on risk score and clinical characteristics was established to predict the probability of 3-, 5- and 10-year overall survival (OS) for patients with BC, and the performance of the nomogram was assessed by calibration curves.

Functional enrichment analysis, protein-protein interaction (PPI), and gene set enrichment analysis (GSEA)

The Gene Ontology (GO) analysis was carried out for the identification of biological activities, molecular mechanisms, and cellular components via clusterprofiler R package. Additionally, the signaling pathways were observed using the Kyoto Encyclopedia of Genes and Genomes (KEGG) analysis. Cuproptosis-related FRGs were submitted to the STRING database (<http://www.string-db.org/>) for obtaining insights into PPI. The Cytoscape program was used to build and render PPI networks. Using the MCODE plug-in, the most important modules were selected based on MCODE score >5 . GSEA was carried out to investigate potential enrichment pathways in the high- and low-risk groups. P value <0.05 was considered statistically significant.

Immune cell analysis

Different algorithms including CIBERSORT (Newman *et al.*, 2015), CIBERSORT-ABS, EPIC (Racle *et al.*, 2017), MCP-counter (Becht *et al.*, 2016), QUANTISEQ (Finotello *et al.*, 2019), TIMER (Li *et al.*, 2017), and XCELL (Aran *et al.*, 2017) were compared to assess the level of immune cell infiltration between the high- and low-risk groups. The correlation between immune cells and cuproptosis-related FRGs was identified by using the TIMER database. Potential immune checkpoints were obtained from scientific literature and differences in expression in immune checkpoints among high- and low-risk groups were explored using the ggpubr and limma packages.

Drug sensitivity analysis

To compare the difference in drug sensitivity between the two groups, the half-maximal inhibitory concentration (IC50) of drugs was assessed by the pRRophetic

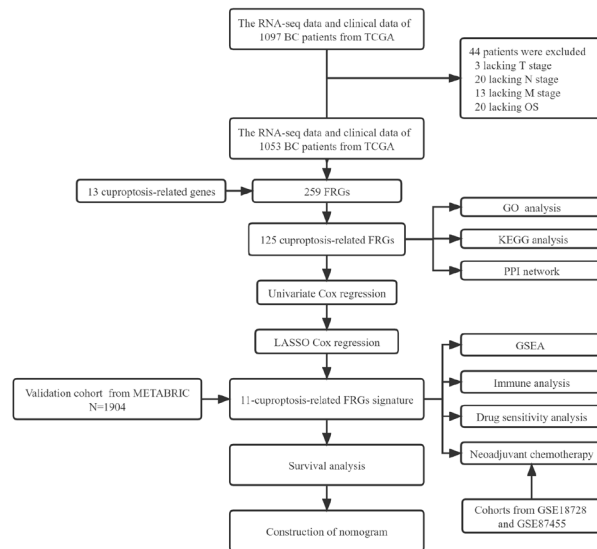


Figure 1 Flow chart of this study.

package. P value <0.05 was considered statistically significant.

Statistics analysis

Statistical analysis was performed using R version 4.2.1. The Wilcoxon test was used to compare expression differences between the two groups. P value <0.05 was considered to be a statistically significant difference.

RESULTS

Identification of cuproptosis-related FRGs and their prognostic value in the TCGA cohort

The design of the study has been depicted using the flowchart (Fig. 1). A total of 125 FRGs were confirmed to be correlated with cuproptosis-related genes in the TCGA dataset (Supplementary Fig. S1 at <https://ojs.ptbioch.edu.pl/index.php/abp/>). Univariate Cox regression analysis was used to explore the prognostic value of these cuproptosis-related FRGs, and the results revealed that 15 genes had prognostic value (Fig. 2).

Establishment and validation of cuproptosis-related FRG signature

Based on the 15 cuproptosis-related FRGs of prognostic value described above, LASSO Cox regression analysis was performed at the minimum λ value to create a risk model consisting of 11 genes (Supplementary Fig. S2 at <https://ojs.ptbioch.edu.pl/index.php/abp/>). The risk score for each patient was calculated using the following formula:

$$\text{Risk Score} = 0.187 * ANO6 + 0.099 * CHAC1 + (-0.075) * CHMP6 + 0.115 * CS + 0.305 * EMC2 + 0.195 * G6PD + (-0.024) * GPX4 + 0.178 * PANX1 + 0.055 * PIK3CA + 0.048 * SLC7A5 + (-0.197) * SOCS1.$$

Patients with BC were divided into the high-risk group ($n=526$) and the low-risk group ($n=527$) based on the median risk score. Overall survival was significantly shorter in the high-risk group than in the low-risk group ($P<0.001$), suggesting a negative correlation between risk

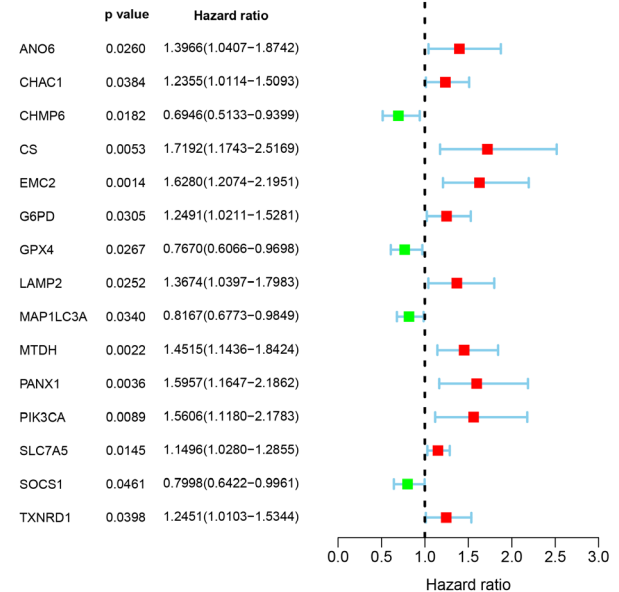


Figure 2. Identification of prognostic cuproptosis-related FRGs. FRGs, ferroptosis-related genes.

score and prognosis (Fig. 3A). Time-dependent ROC curve analysis verified the accuracy of the prognostic signature of patients with BC, with AUCs reaching 0.669 for 3 years, 0.643 for 5 years, and 0.711 for 10 years (Fig. 3B).

To verify the stability of the cuproptosis-related FRG signature, risk scores were calculated for patients in the METABRIC cohort by using the risk score formula ob-

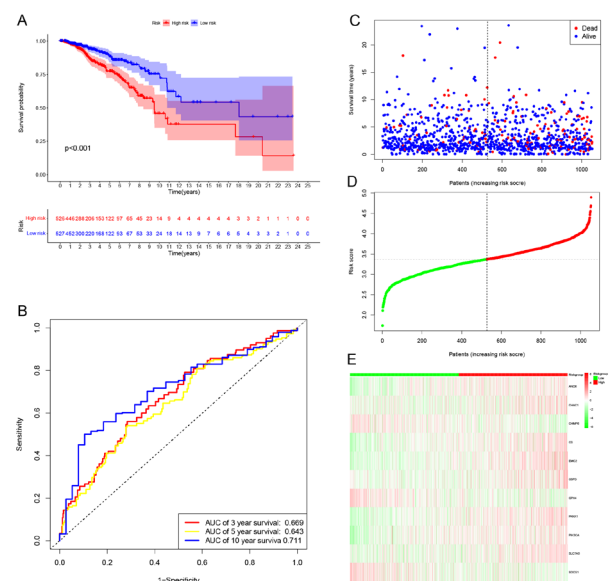


Figure 3. Construction of the prognostic signature based on cuproptosis-related FRGs in TCGA cohort.

(A) Kaplan-Meier curves for OS of BC patients between high-risk and low-risk groups. (B) Time-dependent ROC curves for OS. (C) Distribution of survival status based on the risk score. (D) The high-risk and low-risk groups were divided based on the median risk score. (E) Heatmap showed the difference in expression of 11 cuproptosis-related FRGs in high- and low-risk patients. BC, breast cancer; FRGs, ferroptosis-related genes; OS, overall survival; ROC, receiver operating characteristic; TCGA, the cancer genome atlas.

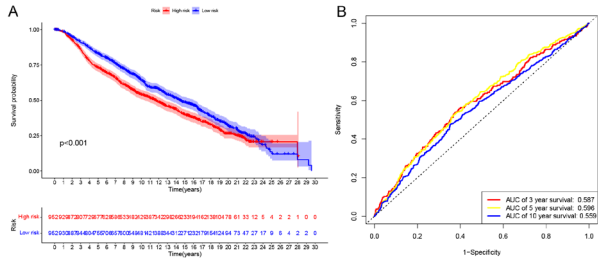


Figure 4. Construction of the prognostic signature based on cuproptosis-related FRGs in METABRIC cohort. (A) Kaplan-Meier curves for OS of BC patients between high-risk and low-risk groups. (B) Time-dependent ROC curves for OS. BC, breast cancer; FRGs, ferroptosis-related genes; METABRIC, molecular taxonomy of breast cancer international consortium; OS, overall survival; ROC, receiver operating characteristic.

tained from the TCGA cohort. K-M survival analysis revealed a poor prognosis in the high-risk group (Fig. 4A, $P<0.001$). The result obtained was consistent with the TCGA dataset. The time-dependent ROC curves showed AUCs of 0.587 at 3 years, 0.596 at 5 years, and 0.559 at 10 years (Fig. 4B).

The signature based on cuproptosis-related FRGs was an independent indicator of BC prognosis

For further assessment of the independent prognostic value of cuproptosis-related FRG signature, univariate and multivariate Cox regression analyses of clinical characteristics, including age, gender, and TNM stage were performed. Univariate analysis revealed that higher risk scores, T stage, N stage, and M stage were significantly associated with adverse OS in patients with BC (Fig. 5A), and negative estrogen receptor (ER) and progesterone receptor (PR) were suggestive of poor prognosis. The risk score, age, N stage, and M stage were shown to be independent risk factors for OS in the multivariate Cox analysis (Fig. 5B). Therefore, the cuproptosis-related FRG signature was an independent prognostic indicator for patients with BC.

Association between the risk score and clinical characteristics

For the assessment of the impact of cuproptosis-related FRG signature in the development and progression of BC, the association between risk score and clinical characteristics was explored. Chi-square test analysis revealed significant differences between risk groups in T stage, N stage, TNM stage, PR, ER, human epidermal growth factor receptor (HER-2), and intrinsic subtype (Fig. 6). In addition, HER-2-enriched, ER-negative, PR-negative, HER-2-positive, higher N stage, and TNM stage indicated a higher risk score (Fig. 7). Stratified analysis was carried out for the identification of the prognostic value of the cuproptosis-related FRG signature in subgroups. The results revealed that this signature had significant prognostic efficacy in age ≤ 65 ($P=0.001$), age >65 ($P=0.009$), female ($P<0.001$), T1 stage ($P=0.011$), T2-T4 stage ($P=0.001$), N0 stage ($P<0.001$), N1-N3 stage ($P=0.018$), M0 stage ($P<0.001$), stage I ($P=0.047$) and II-IV ($P<0.001$). However, no significant prognostic value was observed in the male patients and the M1 stages ($P>0.05$) (Fig. 8).

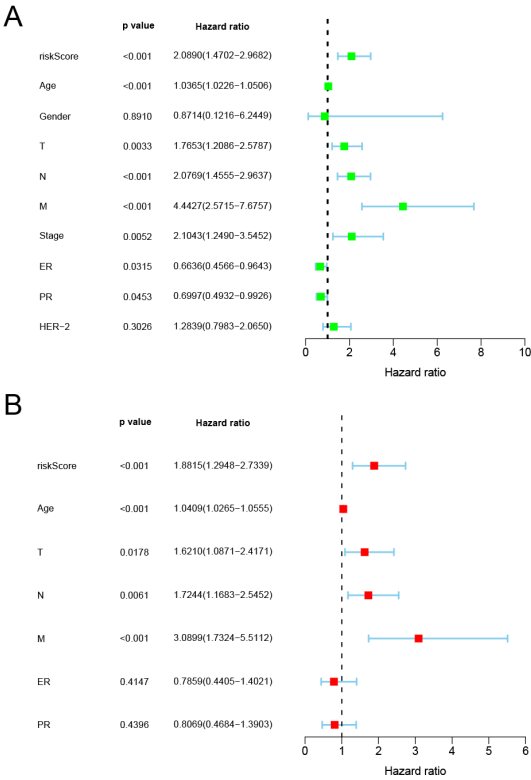


Figure 5. Cuproptosis-related FRG signature was shown to be an independent risk factor for OS in TCGA. (A) Univariate Cox regression analysis between OS and various prognostic parameters. (B) Multivariate Cox regression analysis between OS and various prognostic parameters. FRG, ferroptosis-related gene; OS, overall survival; TCGA, the cancer genome atlas.

Establishment of nomogram

A nomogram was constructed using risk score and clinical characteristics, including age, T stage, N stage, and M stage (Fig. 9A). The nomogram predicted the survival of BC patients at 3, 5, and 10 years. The calibration curves further validated the consistency of the actual OS of the patients with the predictions of the nomogram (Fig. 9B).



Figure 6. Relationship between signature and clinical characteristics. * for $P<0.05$; *** for $P<0.001$.

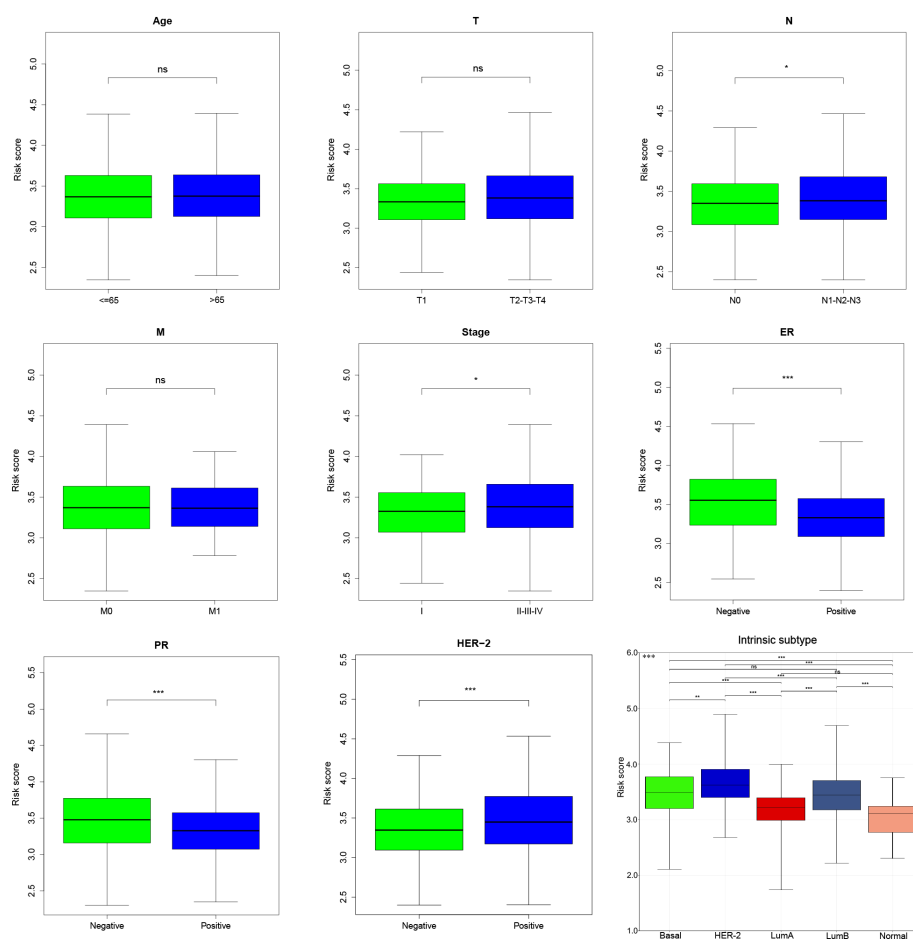


Figure 7. Relationship between signature and clinical characteristics.
ns for $P > 0.05$; * for $P < 0.05$; ** for $P < 0.01$; *** for $P < 0.001$.

Functional enrichment and PPI of cuproptosis-related FRGs

The potential biological functions involved in 125 cuproptosis-related FRGs were analyzed using the GO and KEGG databases. GO analysis revealed the association of FRGs with biological processes like response to oxidative stress, cellular response to chemical stress, and response to nutrient levels (Supplementary Fig. S3A at <https://ojs.ptbioch.edu.pl/index.php/abp/>). In addition, in the KEGG pathway, the results revealed the involvement of FRGs in lipid and atherosclerosis, autophagy, FoxO signaling pathway, central carbon metabolism in cancer, and ferroptosis (Supplementary Fig. S3B at <https://ojs.ptbioch.edu.pl/index.php/abp/>). STRING database revealed that the PPI network of cuproptosis-related FRGs consisted of 125 nodes and 276 edges (Supplementary Fig. S3C at <https://ojs.ptbioch.edu.pl/index.php/abp/>). The most significant module consisted of 11 cuproptosis-related FRGs, including 11 nodes and 66 edges.

GSEA

GSEA was used to further explore the potential mechanisms of cuproptosis-related FRG signature. The results revealed the enrichment of steroid biosynthesis, ABC transporters, base excision repair, glycosaminoglycan biosynthesis, other glycan degradation, and protein export in the high-risk group (Supplementary Fig. S3D at <https://ojs.ptbioch.edu.pl/index.php/abp/>). In con-

trast, ascorbate and aldarate metabolism, olfactory transduction, pentose and glucuronate interconversions, and systemic lupus erythematosus were mainly enriched in the low-risk group (Supplementary Fig. S3E at <https://ojs.ptbioch.edu.pl/index.php/abp/>).

Immune infiltration level of cuproptosis-related FRG signature

The heatmap depicted the relationship between the cuproptosis-related FRG signature and immune cell subgroups according to the analysis of CIBERSORT, CIBERSORT-ABS, EPIC, MCP-counter, QUANTISEQ, TIMER, and XCELL algorithms (Fig. 10). The CIBERSORT result showed a higher proportion of CD4+ memory T cells, resting NK cells, M0 macrophages, M1 macrophages, M2 macrophages, eosinophils, and neutrophils in the high-risk group, whereas the low-risk group had higher proportions of memory B cells, CD8+ T cells, T follicular helper cells, Tregs, activated NK cells, monocytes, myeloid dendritic cells, activated mast cells, and resting mast cells (Supplementary Fig. S4 at <https://ojs.ptbioch.edu.pl/index.php/abp/>). In addition, the TIMER database was used to analyze the correlation between each FRG and immune cells. *ANO6*, *CS*, *EMC2*, *PANX1*, and *PIK3CA* were found to be positively correlated with multiple immune cells such as CD8+ T cells, macrophages, neutrophils, and dendritic cells. *CHAC1*, *SLC7A5*, and *SOC31* were positively correlated with B cells, neutrophils, and dendritic cells. *CHMP6* was nega-

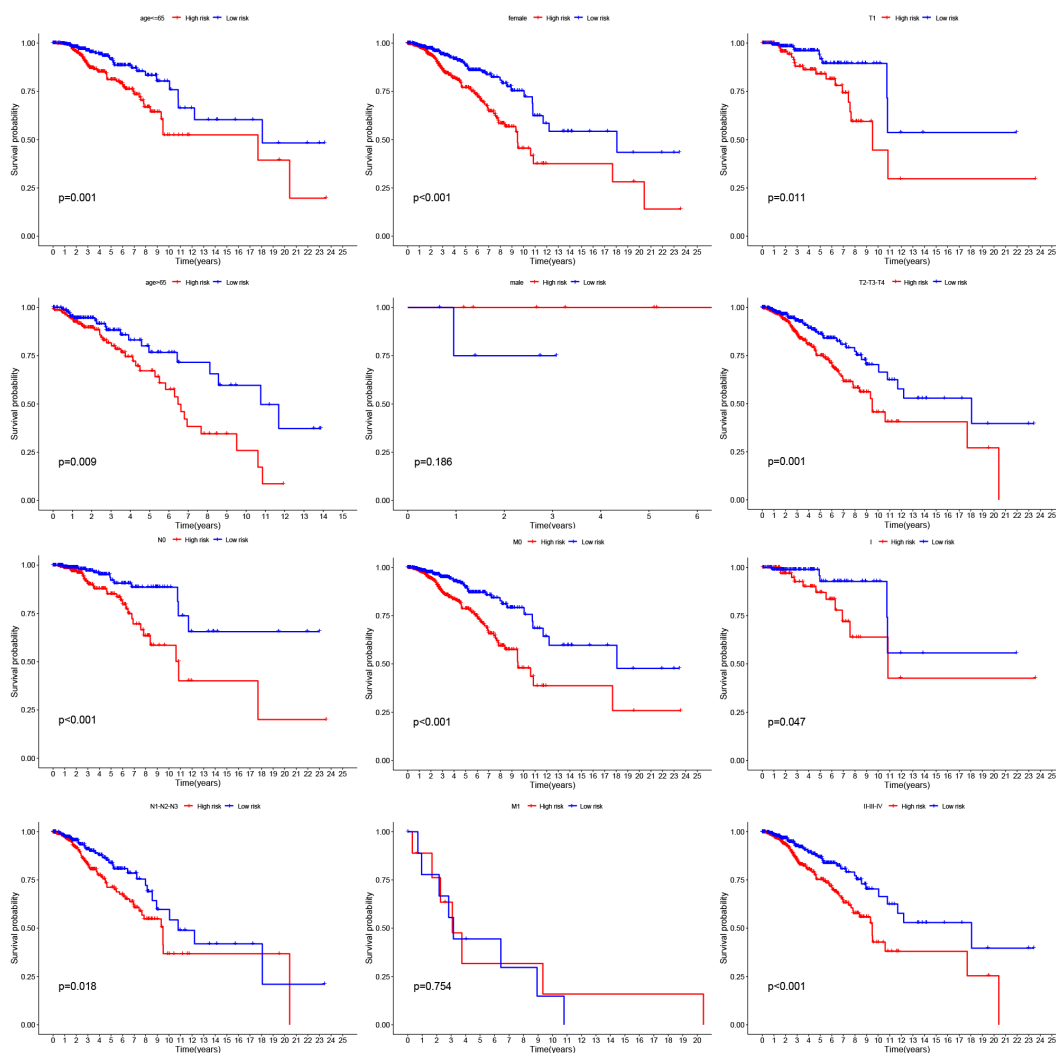


Figure 8. Kaplan-Meier curves of OS differences between high- and low-risk groups stratified by age, gender, T stage, N stage, M stage or TNM stage. OS, overall survival.

tively correlated with CD8⁺ T cells while positively correlated with CD4⁺ T cells. *GPX4* was negatively correlated with B cells, CD8⁺ T cells, macrophage, neutrophil, and dendritic cells. *G6PD* was positively correlated with B cells (Supplementary Fig. S5-6 at <https://ojs.ptbioch.edu.pl/index.php/abp/>).

Due to the importance of immunotherapy, the differences in immune checkpoints between risk score subgroups were analyzed. The results indicated higher expression of most immune checkpoints including *PDCD1*, *LAG3*, etc. in the low-risk group, suggesting a greater benefit of immune checkpoint suppression therapy in low-risk patients. The high expression of *CD80*, *PD-L2*, and *TNFSF4* in the high-risk group can aid in guiding the study for the optimization of immune checkpoint inhibitors (Fig. 11).

Neoadjuvant chemotherapy and drug sensitivity analysis

To investigate whether the risk score of tumors changes during neoadjuvant chemotherapy. We used two chemotherapy BC cohorts. A significant reduction in risk score was observed in patients treated with docetaxel and capecitabine by comparing paired patients from GSE18728 (Fig. 12A). In the GSE87455 cohort treated

with epirubicin and docetaxel, 69 paired patients who received two cycles of treatment had significantly lower risk score than before treatment (Fig. 12B). Meanwhile, 57 paired patients who received six cycles of treatment had significantly lower risk score than before treatment (Fig. 12C). To further optimize chemotherapy in patients with BC, potential antitumor drugs were screened to compare the differences in drug sensitivity between the high- and low-risk groups. The results of sensitivity analysis showed that the IC₅₀ values of drugs including AUY922, docetaxel, etoposide, imatinib, mitomycin C, paclitaxel, and SL 0101-1 were significantly reduced in the low-risk group, suggesting a higher sensitivity of the patients in the low-risk group to these drugs (Fig. 13A-G). Patients in the high-risk group were found to be more sensitive to AKT inhibitor VIII and cisplatin (Fig. 13H-I).

DISCUSSION

With the development of molecular diagnostic studies, medical professionals are increasingly resorting to the clinical practice of molecular diagnostics in BC, such as Oncotype dX and MammaPrint (Li *et al.*, 2017; Barzaman *et al.*, 2020). BC is a systemic disease and has

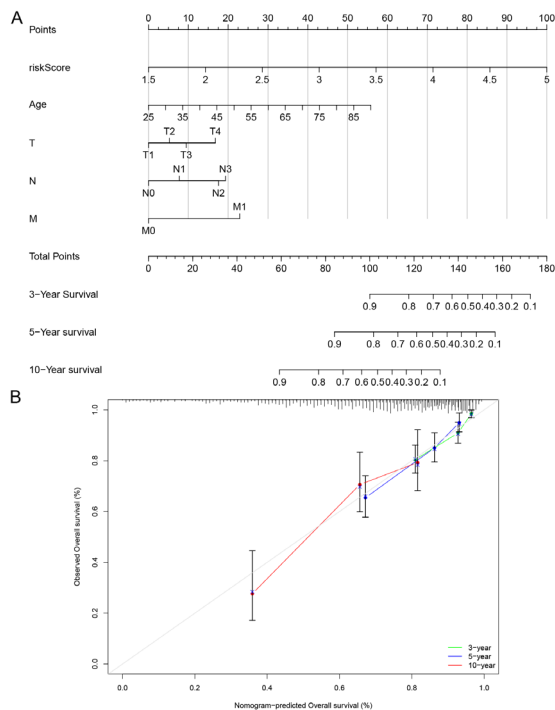


Figure 9. Construction of a prognostic nomogram. (A) Nomogram of OS prediction with age, T stage, N stage, M stage and signature as parameters. (B) The calibration curves of the nomogram for 3-, 5-, and 10-year OS prediction. OS, overall survival.

evolved from the conventional surgical treatment to the current combination therapy including radiotherapy, chemotherapy, hormonal therapy, and biological therapy (Ben-Dror *et al.*, 2022). Patients with BC may have to choose among different options for postoperative systemic therapy. Therefore, it is imperative to find more effective biomarkers to adapt adjuvant therapies to individualize treatment for patients.

To the best of our knowledge, this is the first study to explore the correlation between FRGs and cuproptosis-related genes in patients with BC. Unlike other regulatory cell death processes, cuproptosis is primarily associated with adiposity of the tricarboxylic acid cycle and in-

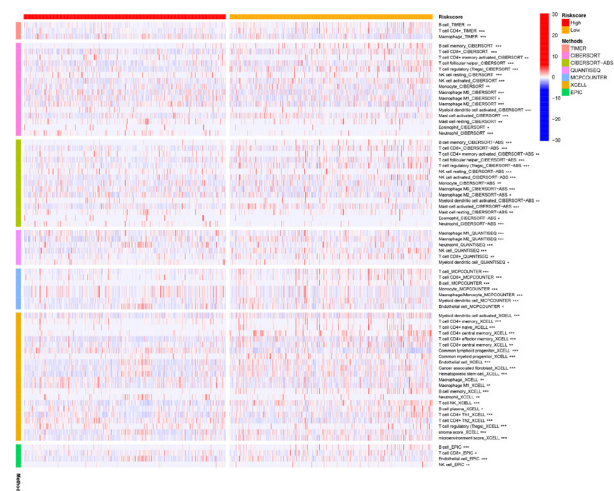


Figure 10. Analysis of immune cells between high- and low-risk groups.
* for $P<0.05$; ** for $P<0.01$; *** for $P<0.001$.

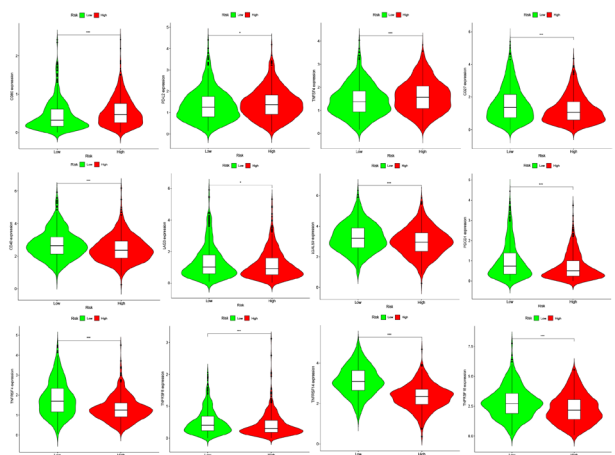


Figure 11. Differences in immune checkpoints between the high- and low-risk groups.
* for $P<0.05$; *** for $P<0.001$.

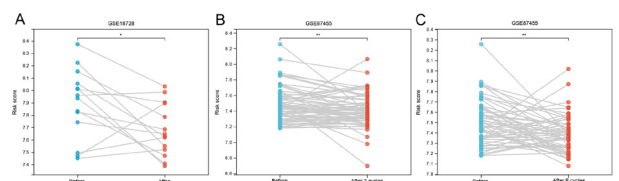


Figure 12. Pairwise comparison of risk score in GSE18728, GSE87455 by pre-chemotherapy and post-chemotherapy.
* for $P<0.05$; ** for $P<0.01$.

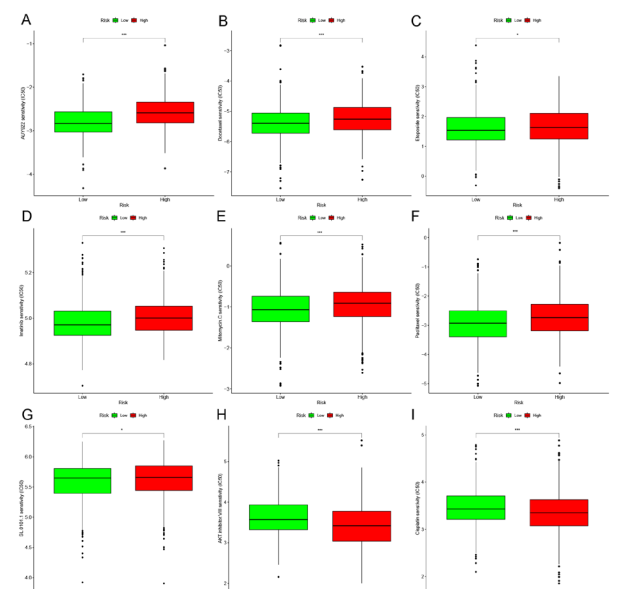


Figure 13. Sensitivity analysis of antitumor drugs between high-risk and low-risk groups. (A) AUY922; (B) docetaxel; (C) etoposide; (D) imatinib; (E) mitomycin C; (F) paclitaxel; (G) SL 0101-1; (H) AKT inhibitor VIII; (I) cisplatin. * for $P<0.05$; *** for $P<0.001$.

volves the loss of iron-sulfur cluster proteins and induction of ROS (Li *et al.*, 2022; Tsvetkov *et al.*, 2022). Gao and others (Gao *et al.*, 2021) reported the accumulation of ROS due to copper retention, which inhibited the *SLC7A11* levels, thereby enhancing oxidative stress and ferroptotic cell death in colorectal cancer. Thus, FRGs

may cause regulated cell death through the cuproptosis-related mechanism.

In this study, the relationship between 259 FRGs and 13 cuproptosis-related genes in BC was comprehensively evaluated and screened for cuproptosis-related FRGs. The relationship between cuproptosis-related FRGs and OS in BC was analyzed and a novel prognostic model containing 11 cuproptosis-related FRGs was constructed. The accuracy of the model was verified by the METABRIC cohort. Survival and ROC analyses revealed a good predictive ability of the model. Univariate and multivariate Cox analysis established the risk score of cuproptosis-related FRG signature to be an independent prognostic indicator for BC. The risk score was further found to be correlated with immune infiltrating cells and the expression of immune checkpoints between risk subgroups was analyzed. Finally, two neoadjuvant chemotherapy cohorts were used to show that the risk score was significantly reduced over the course of treatment, and nine antitumor drugs were screened for the treatment of patients with BC in different risk subgroups.

A significant difference between cuproptosis-related FRG signature and the clinical stage was observed, suggesting that higher risk scores were concentrated in more advanced tumor stages, ER-negative, PR-negative, and HER-2-positive, which further validates the poorer prognosis in the high-risk group. Meanwhile, the prognosis of cuproptosis-related FRG signature was confirmed in different subgroups with different clinical characteristics, except for male patients and patients with distant metastases, which could be because of the small sample size in these two subgroups. Therefore, the proposed model has demonstrated generalizability in different strata of patients with BC.

The cuproptosis-related FRG signature included *ANO6*, *CHAC1*, *CHMP6*, *CS*, *EMC2*, *G6PD*, *GPX4*, *PANX1*, *PIK3CA*, *SLC7A5*, and *SOCs1*. These genes included ferroptosis driver genes (*ANO6*, *CHAC1*, *CS*, *EMC2*, *G6PD*, *PANX1*, and *PIK3CA*) and ferroptosis suppressor genes (*CHMP6*, *PGX4*, and *SOCs1*). Currently, *SLC7A5* is an unclassified regulator whose role in ferroptosis is unclear. There is growing evidence of the involvement of *ANO6* in multiple forms of cell death, including necroptosis, pyroptosis, and ferroptosis (Ousingsawat *et al.*, 2017; Ousingsawat *et al.*, 2018; Simões *et al.*, 2018). As a non-selective Ca^{2+} -activated ion channel, lipid scramblase *ANO6* plays a critical role in the induction of ferroptotic cell death by disrupting the stability of membrane phospholipids (Ousingsawat *et al.*, 2019). Chen *et al.* reported that *CHAC1* contributes to cystine starvation and thereby induces ferroptotic cell death in triple-negative BC cells via the GCN2-eIF2 α -ATF4 pathway (Chen *et al.*, 2017). Overexpression of *CHAC1* has been linked to the enhanced sensitivity of prostate cancer cells to docetaxel, but the effect was reversed after co-treatment with ferroptosis inhibitors, suggesting that *CHAC1* functions as a potential therapeutic target for castration-resistant prostate cancer by inducing ferroptotic cell death (He *et al.*, 2021). Ferroptosis activators such as erastin and RSL3 increased *CHMP6* accumulation by triggering calcium influx. Silencing of *CHMP6* expression sensitized cancer cells to lipid peroxidation-mediated ferroptosis but did not affect iron accumulation (Dai *et al.*, 2020). *CS* increased the accumulation of citrate in hypoxic triple-negative BC cells, which promoted the migration and invasion of cancer cells (Peng *et al.*, 2019). The overexpression of *G6PD* suggests a poor prognosis in hepatocellular carcinoma and inhibits ferroptotic cell death of the tumor by targeting cytochrome

oxidoreductase (Cao *et al.*, 2021). Luo *et al.* reported the resistance of *G6PD* for doxorubicin-induced apoptosis in triple-negative BC cells by the maintenance of high glutathione levels (Luo *et al.*, 2022). Genetic models were used for the identification of *GPX4* as a key regulator of ferroptosis and that inhibition of *GPX4*-induced ferroptosis enhanced the sensitivity of triple-negative BC cells to gefitinib (Seibt *et al.*, 2019; Song *et al.*, 2020). A recent study reported that high expression of *PANX1* induced local immunosuppression in tumor microenvironment of basal-like BC, as evidenced by high infiltration levels of neutrophils and adenosine production (Chen *et al.*, 2022). *SLC7A5* supported the proliferation and growth of tumor cells by increasing mTORC1 activity through the upregulation of regulatory transcription factors under hypoxic conditions (Nachev *et al.*, 2021). In addition, *SLC7A5* inhibitors were used to treat patients with advanced biliary tract cancer such that no disease progression occurred for two years (Hayes *et al.*, 2015). *SOCs1* sensitizes cells to ferroptosis by the activation of p53 target gene expression and glutathione level reduction (Saint-Germain *et al.*, 2017).

The results of GO analysis and KEGG pathway analysis revealed the relation of 125 cuproptosis-related FRGs to certain biological functions or pathways, such as response to oxidative stress, cellular response to chemical stress, autophagy, FoxO signaling pathway, and central carbon metabolism in cancer. Therefore, lipid peroxidation, a key to the induction of ferroptosis, is mediated by oxidative and antioxidant systems, along with autophagy (Chen *et al.*, 2021).

Tumor-associated macrophages have been shown to promote tumor invasion in BC by promoting angiogenesis and remodeling the tumor extracellular matrix while evading the host immune response and suppressing the antitumor effects of cytotoxic T cells (Choi *et al.*, 2018; Mehta *et al.*, 2021). The results of this study revealed higher levels of macrophage infiltration in the high-risk group, accrediting the poor prognosis in the high-risk group to the immunosuppression of the tumor microenvironment. It was also found that patients in the low-risk group had a higher likelihood of benefitting from immunotherapy, while patients in the high-risk group may be more sensitive to immunosuppressive agents targeting *CD80*, *PD-L2*, and *TNFSF4*. Risk score was found to become lower after treatment through the neoadjuvant cohort, which may suggest a remission of the tumor. Finally, the sensitivity of high- and low-risk groups to different antitumor drugs was explored and results revealed that patients in the high-risk group were more sensitive to AKT inhibitor VIII and cisplatin. The results obtained from this study combined with the data available in the literature will aid the facilitation of the optimization of chemotherapy regimens for patients with BC.

However, the objects of this study were from public databases, and clinical data is essential for further validation. Although 125 cuproptosis-related FRGs have been identified, the correlation between FRGs and cuproptosis-related genes was not established. Finally, subgroup-related pathways, immune infiltration, and drug sensitivity require further experimental validation.

Declarations

Acknowledgements. We thank Bullet Edits Limited for the linguistic editing and proofreading of the manuscript.

Author contributions. QZ and XZ contributed to this study's design, data analysis, and manuscript prep-

aration. The authors have read and approved the final manuscript.

Availability of data. The raw data of this study are derived from the TCGA database (<https://portal.gdc.cancer.gov/>), GEO database (<https://www.ncbi.nlm.nih.gov/geo/>) and METABRIC database (http://www.cbioportal.org/study/summary?id=brca_metabric), which are publicly available databases.

Code availability. The code used in this study are available from the corresponding author on reasonable request.

Conflict of interests. The authors declare that there is no conflict of interest regarding the publication of this paper.

REFERENCES

- Alvarez SW, Svendsen VO, Terzi EM, Papagiannakopoulos T, Moreira AL, Adams S, Sabatini DM, Birsoy K, Possemato R (2017) NFS1 undergoes positive selection in lung tumours and protects cells from ferroptosis. *Nature* **551**: 639–643. <https://doi.org/10.1038/nature24637>
- Aran D, Hu Z, Butte AJ (2017) xCell: digitally portraying the tissue cellular heterogeneity landscape. *Genome Biol* **18**: 220. <https://doi.org/10.1186/s13059-017-1349-1>
- Azamjah N, Soltan-Zadeh Y, Zayeri F (2019) Global trend of breast cancer mortality rate: a 25-year study. *Asian Pac J Cancer Prev* **20**: 2015–2020. <https://doi.org/10.31557/APJCP.2019.20.7.2015>
- Barzaman K, Karami J, Zarei Z, Hosseinzadeh A, Kazemi MH, Moradi-Kalbolandi S, Safari E, Farahmand L (2020) Breast cancer: Biology, biomarkers, and treatments. *Int Immunopharmacol* **84**: 106535. <https://doi.org/10.1016/j.intimp.2020.106535>
- Becht E, Giraldo NA, Lacroix L, Buttard B, Elarouci N, Petitprez F, Selves J, Laurent-Puig P, Sautès-Fridman C, Fridman WH, de Reyniès A (2016) Estimating the population abundance of tissue-infiltrating immune and stromal cell populations using gene expression. *Genome Biol* **17**: 218. <https://doi.org/10.1186/s13059-016-1070-5>
- Ben-Dror J, Shalamov M, Sonnenblick A (2022) The History of Early Breast Cancer Treatment. *Genes (Basel)* **13**. <https://doi.org/10.3390/genes13060960>
- Cao F, Luo A, Yang C (2021) G6PD inhibits ferroptosis in hepatocellular carcinoma by targeting cytochrome P450 oxidoreductase. *Cell Signal* **87**: 110098. <https://doi.org/10.1016/j.cellsig.2021.110098>
- Caswell-Jin JL, Plevritis SK, Tian L, Cadham CJ, Xu C, Stout NK, Sledge GW, Mandelblatt JS, Kurian AW (2018) Change in survival in metastatic breast cancer with treatment advances: meta-analysis and systematic review. *JNCI Cancer Spectr* **2**: pky062. <https://doi.org/10.1093/jncics/pky062>
- Chen MS, Wang SF, Hsu CY, Yin PH, Yeh TS, Lee HC, Tseng LM (2017) CHAC1 degradation of glutathione enhances cystine-starvation-induced necroptosis and ferroptosis in human triple negative breast cancer cells via the GCN2-eIF2 α -ATF4 pathway. *Oncotarget* **8**: 114588–114602. <https://doi.org/10.18632/oncotarget.23055>
- Chen W, Li B, Jia F, Li J, Huang H, Ni C, Xia W (2022) High PAX1 expression leads to neutrophil recruitment and the formation of a high adenosine immunosuppressive tumor microenvironment in basal-like breast cancer. *Cancers (Basel)* **14**. <https://doi.org/10.3390/cancers14143369>
- Chen X, Kang R, Kroemer G, Tang D (2021) Broadening horizons: the role of ferroptosis in cancer. *Nat Rev Clin Oncol* **18**: 280–296. <https://doi.org/10.1038/s41571-020-00462-0>
- Choi J, Gyamfi J, Jang H, Koo JS (2018) The role of tumor-associated macrophage in breast cancer biology. *Histol Histopathol* **33**: 133–145. <https://doi.org/10.14670/HH-11-916>
- Dai E, Meng L, Kang R, Wang X, Tang D (2020) ESCRT-III-dependent membrane repair blocks ferroptosis. *Biochem Biophys Res Commun* **522**: 415–421. <https://doi.org/10.1016/j.bbrc.2019.11.110>
- DeSantis CE, Ma J, Gaudet MM, Newman LA, Miller KD, Goding Sauer A, Jemal A, Siegel RL (2019) Breast cancer statistics, 2019. *CA Cancer J Clin* **69**: 438–451. <https://doi.org/10.3322/caac.21583>
- Dixon SJ, Lemberg KM, Lamprecht MR, Skouta R, Zaitsev EM, Gleason CE, Patel DN, Bauer AJ, Cantley AM, Yang WS, Morrison B 3rd, Stockwell BR (2012) Ferroptosis: an iron-dependent form of nonapoptotic cell death. *Cell* **149**: 1060–1072. <https://doi.org/10.1016/j.cell.2012.03.042>
- Du J, Wang T, Li Y, Zhou Y, Wang X, Yu X, Ren X, An Y, Wu Y, Sun W, Fan W, Zhu Q, Wang Y, Tong X (2019) DHA inhibits proliferation and induces ferroptosis of leukemia cells through autophagy dependent degradation of ferritin. *Free Radic Biol Med* **131**: 356–369. <https://doi.org/10.1016/j.freeradbiomed.2018.12.011>
- Feng Y, Spezia M, Huang S, Yuan C, Zeng Z, Zhang L, Ji X, Liu W, Huang B, Luo W, Liu B, Lei Y, Du S, Vuppallapati A, Luu HH, Haydon RC, He TC, Ren G (2018) Breast cancer development and progression: Risk factors, cancer stem cells, signaling pathways, genomics, and molecular pathogenesis. *Genes Dis* **5**: 77–106. <https://doi.org/10.1016/j.gendis.2018.05.001>
- Finotello F, Mayer C, Plattner C, Laschober G, Rieder D, Hackl H, Krogsdam A, Loncova Z, Posch W, Wilflingseder D, Sopfer S, Jsselssteijn M, Brouwer TP, Johnson D, Xu Y, Wang Y, Sanders ME, Estrada MV, Ericsson-Gonzalez P, Charoentong P, Balko J, de Miranda NFDCC, Trajanoski Z (2019) Molecular and pharmacological modulators of the tumor immune contexture revealed by deconvolution of RNA-seq data. *Genome Med* **11**: 34. <https://doi.org/10.1186/s13073-019-0638-6>
- Friedmann Angeli JP, Krysko DV, Conrad M (2019) Ferroptosis at the crossroads of cancer-acquired drug resistance and immune evasion. *Nat Rev Cancer* **19**: 405–414. <https://doi.org/10.1038/s41568-019-0149-1>
- Gao W, Huang Z, Duan J, Nice EC, Lin J, Huang C (2021) Elesclomol induces copper-dependent ferroptosis in colorectal cancer cells via degradation of ATP7A. *Mol Oncol* **15**: 3527–3544. <https://doi.org/10.1002/1878-0261.13079>
- Hassannia B, Vandenabeele P, Vanden Berghe T (2019) Targeting ferroptosis to iron out cancer. *Cancer Cell* **35**: 830–849. <https://doi.org/10.1016/j.ccell.2019.04.002>
- Hayes GM, Chinn L, Cantor JM, Cairns B, Levashova Z, Tran H, Vellila T, Dwey D, Lippincott J, Zachwieja J, Ginsberg MH, H van der Horst E (2015) Antitumor activity of an anti-CD98 antibody. *Int J Cancer* **137**: 710–720. <https://doi.org/10.1002/ijc.29415>
- He S, Zhang M, Ye Y, Zhuang J, Ma X, Song Y, Xia W (2021) ChAC glutathione specific γ -glutamylcystyltransferase 1 inhibits cell viability and increases the sensitivity of prostate cancer cells to docetaxel by inducing endoplasmic reticulum stress and ferroptosis. *Exp Ther Med* **22**: 997. <https://doi.org/10.3892/etm.2021.10429>
- Huang L, McClatchy DB, Maher P, Liang Z, Diedrich JK, Soriano-Castell D, Goldberg J, Shokhirev M, Yates JR 3rd, Schubert D, Currais A (2020) Intracellular amyloid toxicity induces oxytosis/ferroptosis regulated cell death. *Cell Death Dis* **11**: 828. <https://doi.org/10.1038/s41419-020-03020-9>
- Jhelum P, Santos-Nogueira E, Teo W, Haumont A, Lenoël I, Stys PK, David S (2020) Ferroptosis mediates cuprizone-induced loss of oligodendrocytes and demyelination. *J Neurosci* **40**: 9327–9341. <https://doi.org/10.1523/JNEUROSCI.1749-20.2020>
- Jiang Y, Huo Z, Qi X, Zuo T, Wu Z (2022) Copper-induced tumor cell death mechanisms and antitumor therapeutic applications of copper complexes. *Nanomedicine (Lond)* **17**: 303–324. <https://doi.org/10.2217/nmm-2021-0374>
- Kahlson MA, Dixon SJ (2022) Copper-induced cell death. *Science* **375**: 1231–1232. <https://doi.org/10.1126/science.abc3959>
- Kim EH, Shin D, Lee J, Jung AR, Roh JL (2018) CSD2 inhibition overcomes resistance to sulfasalazine-induced ferroptotic cell death in head and neck cancer. *Cancer Lett* **432**: 180–190. <https://doi.org/10.1016/j.canlet.2018.06.018>
- Li G, Hu J, Hu G (2017) Biomarker studies in early detection and prognosis of breast cancer. *Adv Exp Med Biol* **1026**: 27–39. https://doi.org/10.1007/978-981-10-6020-5_2
- Li SR, Bu LL, Cai L (2022) Cuproptosis: lipoylated TCA cycle proteins-mediated novel cell death pathway. *Signal Transduct Target Ther* **7**: 158. <https://doi.org/10.1038/s41392-022-01014-x>
- Li T, Fan J, Wang B, Traugh N, Chen Q, Liu JS, Li B, Liu XS (2017) TIMER: A web server for comprehensive analysis of tumor-infiltrating immune cells. *Cancer Res* **77**: e108–e110. <https://doi.org/10.1158/0008-5472.CAN-17-0307>
- Loibl S, Poortmans P, Morrow M, Denkert C, Curigiano G (2021) Breast cancer. *Lancet* **397**: 1750–1769. [https://doi.org/10.1016/S0140-6736\(20\)32381-3](https://doi.org/10.1016/S0140-6736(20)32381-3)
- Luo M, Fu A, Wu R, Wei N, Song K, Lim S, Luo KQ (2022) High expression of G6PD increases doxorubicin resistance in triple negative breast cancer cells by maintaining GSH level. *Int J Biol Sci* **18**: 1120–1133. <https://doi.org/10.7150/ijbs.65555>
- Mehta AK, Kadel S, Townsend MG, Oliwa M, Guerriero JL (2021) Macrophage biology and mechanisms of immune suppression in breast cancer. *Front Immunol* **12**: 643771. <https://doi.org/10.3389/fimmu.2021.643771>
- Nachev M, Ali AK, Almutairi SM, Lee SH (2021) Targeting SLC1A5 and SLC3A2/SLC7A5 as a potential strategy to strengthen anti-tumor immunity in the tumor microenvironment. *Front Immunol* **12**: 624324. <https://doi.org/10.3389/fimmu.2021.624324>
- Newman AM, Liu CL, Green MR, Gentles AJ, Feng W, Xu Y, Hoang CD, Diehn M, Alizadeh AA (2015) Robust enumeration of cell subsets from tissue expression profiles. *Nat Methods* **12**: 453–457. <https://doi.org/10.1038/nmeth.3337>
- Ousingsawat J, Cabrita I, Wanitchakool P, Sirianant L, Krautwald S, Linkermann A, Schreiber R, Kunzelmann K (2017) Ca²⁺ signals, cell membrane disintegration, and activation of TMEM16F during

- necroptosis. *Cell Mol Life Sci* **74**: 173–181. <https://doi.org/10.1007/s00018-016-2338-3>
- Ousingsawat J, Schreiber R, Kunzelmann K (2019) TMEM16F/Anoctamin 6 in Ferroptotic Cell Death. *Cancers (Basel)* **11**. <https://doi.org/10.3390/cancers11050625>
- Ousingsawat J, Wanitchakool P, Schreiber R, Kunzelmann K (2018) Contribution of TMEM16F to pyroptotic cell death. *Cell Death Dis* **9**: 300. <https://doi.org/10.1038/s41419-018-0373-8>
- Pain D, Dancis A (2016) Roles of Fe-S proteins: from cofactor synthesis to iron homeostasis to protein synthesis. *Curr Opin Genet Dev* **38**: 45–51. <https://doi.org/10.1016/j.gde.2016.03.006>
- Parker JS, Mullins M, Cheang MC, Leung S, Voduc D, Vickery T, Davies S, Fauron C, He X, Hu Z, Quackenbush JF, Stijleman IJ, Palazzo J, Marron JS, Nobel AB, Mardis E, Nielsen TO, Ellis MJ, Perou CM, Bernard PS (2009) Supervised risk predictor of breast cancer based on intrinsic subtypes. *J Clin Oncol* **27**: 1160–1167. <https://doi.org/10.1200/JCO.2008.18.1370>
- Peng M, Yang D, Hou Y, Liu S, Zhao M, Qin Y, Chen R, Teng Y, Liu M (2019) Intracellular citrate accumulation by oxidized ATM-mediated metabolism reprogramming via PFKF and CS enhances hypoxic breast cancer cell invasion and metastasis. *Cell Death Dis* **10**: 228. <https://doi.org/10.1038/s41419-019-1475-7>
- Racle J, de Jonge K, Baumgaertner P, Speiser DE, Gfeller D (2017) Simultaneous enumeration of cancer and immune cell types from bulk tumor gene expression data. *Elife* **6**. <https://doi.org/10.7554/eLife.26476>
- Saint-Germain E, Mignacca L, Vernier M, Bobbala D, Ilangumaran S, Ferbeyre G (2017) SOCS1 regulates senescence and ferroptosis by modulating the expression of p53 target genes. *Aging (Albany NY)* **9**: 2137–2162. <https://doi.org/10.18632/aging.101306>
- Seibt TM, Proneth B, Conrad M (2019) Role of GPX4 in ferroptosis and its pharmacological implication. *Free Radic Biol Med* **133**: 144–152. <https://doi.org/10.1016/j.freeradbiomed.2018.09.014>
- Simões F, Ousingsawat J, Wanitchakool P, Fonseca A, Cabrita I, Benedetto R, Schreiber R, Kunzelmann K (2018) CFTR supports cell death through ROS-dependent activation of TMEM16F (anoctamin 6). *Pflugers Arch* **470**: 305–314. <https://doi.org/10.1007/s00424-017-2065-0>
- Song X, Wang X, Liu Z, Yu Z (2020) Role of GPX4-mediated ferroptosis in the sensitivity of triple negative breast cancer cells to gefitinib. *Front Oncol* **10**: 597434. <https://doi.org/10.3389/fonc.2020.597434>
- Sung H, Ferlay J, Siegel RL, Laversanne M, Soerjomataram I, Jemal A, Bray F (2021) Global Cancer Statistics 2020: GLOBOCAN Estimates of Incidence and Mortality Worldwide for 36 Cancers in 185 Countries. *CA Cancer J Clin* **71**: 209–249. <https://doi.org/10.3322/caac.21660>
- Tibshirani R (1997) The lasso method for variable selection in the Cox model. *Stat Med* **16**: 385–395. [https://doi.org/10.1002/\(sici\)1097-0258\(19970228\)16:4<aid-sim380>3.0.co;2-3](https://doi.org/10.1002/(sici)1097-0258(19970228)16:4<aid-sim380>3.0.co;2-3)
- Tsvetkov P, Coy S, Petrova B, Dreishpoon M, Verma A, Abdusamad M, Rossen J, Joesch-Cohen L, Humeidi R, Spangler RD, Eaton JK, et al. (2022) Copper induces cell death by targeting lipoylated TCA cycle proteins. *Science* **375**: 1254–1261. <https://doi.org/10.1126/science.abf0529>
- Waldron KJ, Rutherford JC, Ford D, Robinson NJ (2009) Metalloproteins and metal sensing. *Nature* **460**: 823–830. <https://doi.org/10.1038/nature08300>
- Wang W, Liu W (2020) Integration of gene interaction information into a reweighted Lasso-Cox model for accurate survival prediction. *Bioinformatics* **36**: 5405–5414. <https://doi.org/10.1093/bioinformatics/btaa1046>
- Wang Y, Wei Z, Pan K, Li J, Chen Q (2020) The function and mechanism of ferroptosis in cancer. *Apoptosis* **25**: 786–798. <https://doi.org/10.1007/s10495-020-01638-w>
- Yuan H, Li X, Zhang X, Kang R, Tang D (2016) C1SD1 inhibits ferroptosis by protection against mitochondrial lipid peroxidation. *Biochem Biophys Res Commun* **478**: 838–844. <https://doi.org/10.1016/j.bbrc.2016.08.034>
- Zhang C, Liu X, Jin S, Chen Y, Guo R (2022) Ferroptosis in cancer therapy: a novel approach to reversing drug resistance. *Mol Cancer* **21**: 47. <https://doi.org/10.1186/s12943-022-01530-y>
- Zhao L, Zhou X, Xie F, Zhang L, Yan H, Huang J, Zhang C, Zhou F, Chen J, Zhang L (2022) Ferroptosis in cancer and cancer immunotherapy. *Cancer Commun (Lond)* **42**: 88–116. <https://doi.org/10.1002/cac2.12250>
- Zhou N, Bao J (2020) FerrDb: a manually curated resource for regulators and markers of ferroptosis and ferroptosis-disease associations. *Database (Oxford)* **2020**. <https://doi.org/10.1093/database/baaa021>

Circ-PGPEP1 augments renal cell carcinoma proliferation, Warburg effect, and distant metastasis

PeiRui Wang^{1#}, Jin Chen^{2#}, Xin Ye³, RuYi Wang⁴, Lin Chen⁴ and HanChao Zhang^{4✉}

¹Department of Urology, Affiliated Hospital of Zunyi Medical University, Zunyi City, Guizhou Province, 563000, China; ²Department of Pediatric Surgery, Affiliated Hospital of Zunyi Medical University, Zunyi City, Guizhou Province, 563000, China; ³Department of Urology, Institute of Urology, West China Hospital of Sichuan University, Chengdu City, Sichuan Province, 610000, China; ⁴Department of Urology, Affiliated Hospital and Clinical Medical College of Chengdu University, Chengdu City, Sichuan Province, 610081, China

Circular RNAs (circRNAs) contribute to the malignant phenotype and progression of several types of human cancers, including renal cell carcinoma (RCC). This study probed the molecular mechanism of circPGPEP1 regulating RCC proliferation, Warburg effect, and distant metastasis by targeting the miR-378a-3p/JPT1 axis. Here identified higher circPGPEP1 expression in RCC tissues and cells by RT-qPCR, and high levels of circPGPEP1 were positively correlated with high histological grade and distant metastasis in RCC patients. Furthermore, patients with high levels of circPGPEP1 had a worse survival prognosis. Functional assays presented that knockdown of circPGPEP1 inhibited RCC proliferation, invasion, migration, EMT, and Warburg effect. Dual-luciferase reporter assay, RNA immunoprecipitation, nucleoplasmic RNA isolation, and functional rescue experiments confirmed that circPGPEP1 induced JPT1 expression by sponging miR-378a-3p, thereby promoting RCC malignant phenotype. Xenograft assays and metastasis models further demonstrated that down-regulation of circPGPEP1 effectively inhibited tumor growth and distant metastasis of RCC. Taken together, circPGPEP1, a prognostic circRNA in RCC, acts through the miR-378a-3p/JPT1 axis to regulate RCC progression.

Keywords: circSEC61A1, miR-378a-3p, JPT1, renal cell carcinoma, Warburg effect, distant metastasis

Received: 07 October, 2022; **revised:** 13 May, 2023; **accepted:** 24 May, 2023; **available on-line:** 18 September, 2023

✉e-mail: zhcandjay@163.com

[#]PeiRui Wang and Jin Chen contributed equally to this work.

Acknowledgements of Financial Support: Science Foundation of Affiliated Hospital and Clinical Medical College of Chengdu University (No. Y202207).

Abbreviations: circRNAs, Circular RNAs; miRNAs, microRNAs; RCC, Renal cell carcinoma

INTRODUCTION

Renal cell carcinoma (RCC) is the second leading cause of death in patients with urinary system tumors, accounting for about 3% of all adult malignant tumors (Scelo & Larose, 2018). Although partial and radical nephrectomy is the most effective treatment for early or localized RCC, approximately one-third of RCC patients are primarily diagnosed with advanced disease, and despite aggressive treatment, RCC at this stage has a low overall survival rate (Li *et al.*, 2020). In addition, recurrence and metastasis occur in approximately 30% of RCC patients (Choueiri & Motzer, 2017; Lara & Evans, 2019). RCC proliferation is a complex network involving

multiple carcinogens and diverse genetic backgrounds, resulting in alterations in tumor suppressors or oncogenes (Moch *et al.*, 2014). There is a need to identify molecular mechanisms of RCC progression.

Circular RNAs (circRNAs) can be formed through back splicing events, in which upstream splice acceptor sites join with downstream splice donor sites, resulting in exon circularization (Yu *et al.*, 2020; Zhang *et al.*, 2014). Due to the stability and abundance of circRNAs, an increasing number of circRNAs have been identified to be aberrantly expressed in RCC (Zhou *et al.*, 2022). Mechanistically, these circRNAs act as sponges for microRNAs (miRNAs), thereby protecting downstream mRNAs from miRNAs-mediated degradation (Han *et al.*, 2018). For example, circ_0005875 knockdown suppresses RCC progression by regulating the miR-502-5p/ETS1 axis (Luo *et al.*, 2022). circNUP98, a potential biomarker, acts as an oncogene in RCC through the miR-567/PRDX3 axis (Yu *et al.*, 2020). circ_PGPEP1 is a sponge for miR-1297 and is involved in gastric carcinogenesis (Wang *et al.*, 2021). However, the role and mechanism of circPGPEP1 in RCC development remain to be explored.

Most malignancies are characterized by the Warburg effect (aerobic glycolysis), a unique mode of cellular metabolism in cancer cells that exhibits increased rates of glucose uptake and lactic acid fermentation in an aerobic environment (Cao *et al.*, 2020). Warburg effect has been intensively studied in the cellular progression of cancer cells over the past decade (Liberti & Locasale, 2016). circRNAs have been identified that can modulate the Warburg effect in human cancers (Li *et al.*, 2021), such as circRNA-FOXP1 (Fang *et al.*, 2021) and circ_0091579 (Chen *et al.*, 2021).

This study focused on the biological role of circPGPEP1 in RCC progression, and the Warburg effect, in combination with the regulatory network of circPGPEP1/miR-378a-3p/JPT1 involved in RCC. Taken together, these findings may provide new insights into the treatment of RCC.

MATERIALS AND METHODS

Clinical samples

Specimens were RCC tissue and adjacent normal renal tissue (>5 cm from cancer tissue) collected by radical or partial nephrectomy from 48 cases of RCC patients (no radiation or chemotherapy or other tumors) between 2013 and 2015 at Affiliated Hospital and Clinical Medical College of Chengdu University. Histological features of the specimens were confirmed by 2 pathologists. Dis-

tant metastases of tumor cells were evaluated by examining the lungs, liver, bone, intestine, and pancreas of patients with RCC. Samples were rapidly frozen at -80°C after enucleation for subsequent studies. This work was approved by the Ethics Committee of Affiliated Hospital and Clinical Medical College of Chengdu University and all patients gave written informed consent.

RT-qPCR

Total RNA acquisition was done with TRIzol® Reagent (Invitrogen, Thermo Fisher Scientific). RNA reverse transcription was performed at 37°C for 60 min using M-MLV buffers, dNTP and random primers, and Moloney Mouse leukemia virus RT kits (all from Promega, USA). Next, on a Bio-Rad CFX96 system (BioRad), PCR was done with SYBR Green Real-time PCR Master Mix (Solarbio, Beijing, China). Relative gene expression was determined using the $2^{-\Delta\Delta Ct}$ method. The primer sequences are listed in Table 1. GAPDH and U6 were used as endogenous controls for genes.

Table 1. Primers in PCR

	Primer sequence (5'-3')
GAPDH	Forward: 5'-GGAGCGAGATCCCTCCAAAAT-3'
	Reverse: 5'-GGCTGTTGTCATACTTCTCATGG-3'
U6	Forward: 5'-CTCGCTTCGGCAGCAC-3'
	Reverse: 5'-AACGCTTCACGAATTTGCGT-3'
CircPEP1	Forward: 5'-GTCTCGAAGTCTGACCTCA -3'
	Reverse: 5'-CACGGTGTGTTCCCAAAAG-3'
miR-378a-3p	Forward: 5'-CGCGACTGGACTTGAGTC-3'
	Reverse: 5'-AGTGCAGGGTCCGAGGTATT-3'
JPT1	Forward: 5'-AAGAACAGGTTTCTCTGTCTCT-3'
	Reverse: 5'-AGCTTTCCTCCAATCTACTACT-3'

Cell culture

Human renal tubular epithelial cell line (HK-2) and human RCC cell lines (786-O, ACHN, Caki1, Caki2, and 769-P) were obtained from ATCC and maintained in RPMI 1640 medium containing 10% FBS (Gibco), penicillin (100 U/ml) and streptomycin (100 µg/ml).

RNase R and Actinomycin D treatment

Extracted RNA (2 µg) from ACHN cells was treated with 3 U/µg RNase R (Epicenter Technologies). For the RNA stability assay, RNA extracted from ACHN cells was incubated with actinomycin D (Sigma-Aldrich) at 5 µg/ml for the indicated times. circPGPEP1 RNA expression levels were detected by RT-qPCR.

Cell transfection

To overexpress circPGPEP1 and JPT1, the overexpression plasmids of circPGPEP1 and JPT1 were constructed using the pcDNA 3.1 vector (Green Seed Biotech). siRNAs targeting circPGPEP1 and JPT1 were synthesized by Genescript, while mimic/inhibitor (oligonucleotides) of miRNA and negative control were by RiboBio. The transfection reagent was Lipofectamine 2000 (Invitrogen).

Colony formation assay

Cells were maintained in DMEM containing 10% FBS for 2 weeks and those fixed in methanol were dyed with 1% crystal violet and counted under a microscope (Olympus).

Proliferation assay

A certain amount of 5-ethynyl-2'-deoxyuridine (EdU) solution (RiboBio) was added to each well containing 1×10^4 cells and incubated for 2 h. After being fixed with 4% paraformaldehyde, cells were reacted with glycine, 0.5% Triton X-100, and Apollo reaction solution until Hoechst 33342 staining and imaging under a fluorescence microscope.

Glucose uptake and lactate production

Cellular glucose uptake was quantified by Glucose Uptake Colorimetric Assay Kit (BioVision) (Qin *et al.*, 2021), while lactate concentration was by Lactate Assay Kit (K627, BioVision).

Extracellular acidification rate (ECAR)

ECAR (mpH/min) was determined by Seahorse Extracellular Flux Analyzer XF96 (Seahorse Bioscience) to reflect glycolytic activity in cells. 2×10^4 cells were grown overnight in 96-well plates and treated accordingly. Data were analyzed using Seahorse XF-96 Wave software.

Transwell

Cell migration and invasion were detected by transwell chambers with or without Matrigel (Corning Life Sciences, USA) (Zhu *et al.*, 2021). First, cells were added to 100 µl serum-free medium and seeded into the upper chamber, then 500 µl of DMEM with 10% serum were seeded into the lower chamber. Cells attached to the lower surface were then fixed with 4% paraformaldehyde after 24 h of incubation. After crystal violet staining, the samples were observed under a microscope and analyzed statistically.

Western blot

RIPA Lysis Buffer was utilized for the lysis of cells or tissues. Total protein was extracted and analyzed by the bicinchoninic acid assay (BCA) method to determine the protein quantity. The samples separated by 10% SDS-polyacrylamide gel electrophoresis were loaded onto a polyvinylidene fluoride membrane which was then supplementary to primary antibodies and the secondary antibody. Followed by visualization using ECL reagents (Millipore), the bands were evaluated by Image-Pro Plus 6.0 software. JPT1 (ab126705, Abcam), E-cadherin (3195, Cell Signaling Technology), N-cadherin (ab18203, Abcam), Snail (ab53519, Abcam), Ki-67 (ab15580, Abcam), HK2 (ab209847, Abcam), PKM2 (4053, Cell Signaling Technology), GAPDH (ab8245, Abcam) were used in the assay.

Nucleoplasmic RNA isolation

A nucleoplasmic RNA purification kit (Norgen Biotek Corp) was adopted to locate circPGPEP1 in cells. Afterward, concentrations of nuclear and cytoplasmic circPGPEP1 RNA were determined by RT-qPCR.

Table 2. Relationship between circPGPEP1 and clinicopathological features of RCC patients

Characteristic	Cases	circPGPEP1 expression		P
	n = 48	Low (n = 24)	High (n = 24)	
Age (year)				
≤ 60	14	5	9	0.2042
> 60	34	19	15	
Tumor size				
< 3 cm	19	7	12	0.14
≥ 3 cm	29	17	12	
FIGOa stage				
I-II	28	21	7	<0.0001*
II-IV	20	3	17	
Lymph node metastasis				
Positive	25	14	11	0.3861
Negative	23	10	13	
Distant metastasis				
Positive	10	2	8	0.0330*
Negative	38	22	16	

pression of circPGPEP1 is related to the malignant progression of RCC.

Knockdown of circPGPEP1 inhibits RCC cell proliferation, invasion, migration, EMT, and Warburg effect

Next, the biological function of circPGPEP1 in RCC cells was explored. CircPGPEP1-targeting siRNA was transfected into ACHN cells to knock down circPGPEP1 (Fig. 2A). The proliferation ability of cells was

first evaluated by colony formation assay and EdU assay. The clonogenic ability of cells decreased and the ratio of EdU-positive cells decreased after the down-regulation of circPGPEP1 (Fig. 2B, C). The invasive and migratory abilities were subsequently assessed by Transwell, and it was found that knocking down circPGPEP1 reduced the number of cells invaded and migrated (Fig. 2D). Since EMT is a key process in the distant metastasis of cancer

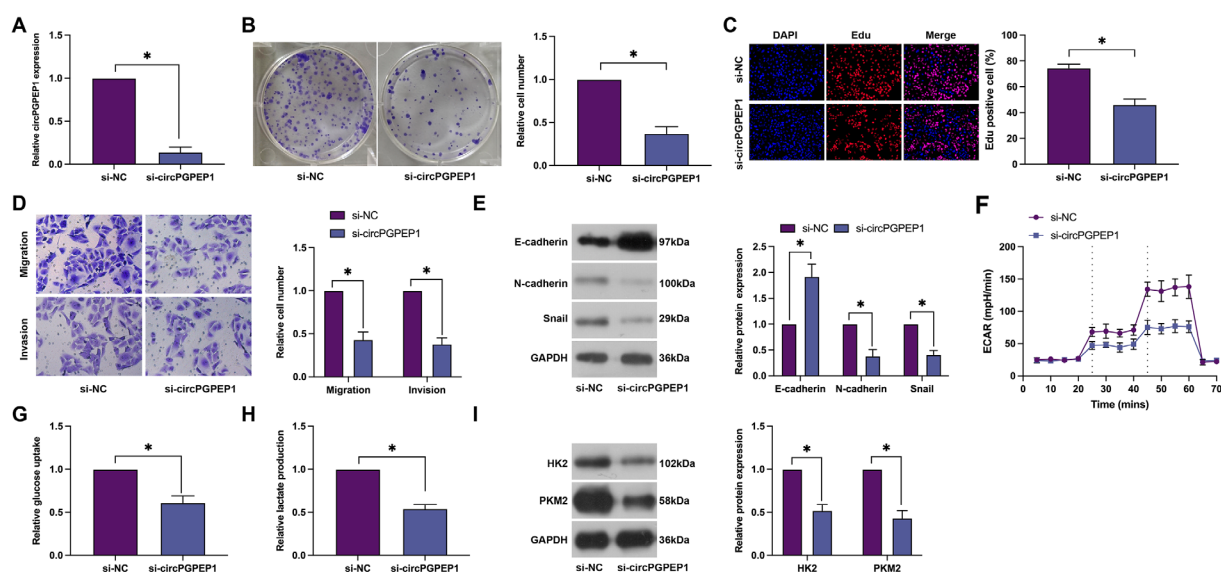


Figure 2. Silencing circPGPEP1 inhibits RCC cell proliferation, invasion, migration, EMT, and Warburg effect

CircPGPEP1-targeting siRNA was transfected into ACHN cells. (A) RT-qPCR analyzed the knockdown efficiency of si-circPGPEP1; (B–C) Colony formation assay and EdU assay tested analyzed proliferation ability; (D) Transwell assay tested invasion and migration ability; (E) Immunoblot assayed protein expression of EMT-related proteins (E-cadherin, N-cadherin, and Snail); (F) cellular ECAR; (G) glucose uptake; (H) lactate production capacity; (I) Immunoblot assayed protein expression of aerobic glycolysis-related proteins (HK2 and PKM2); data representation = mean ± S.D. (N=3); $P < 0.05$.

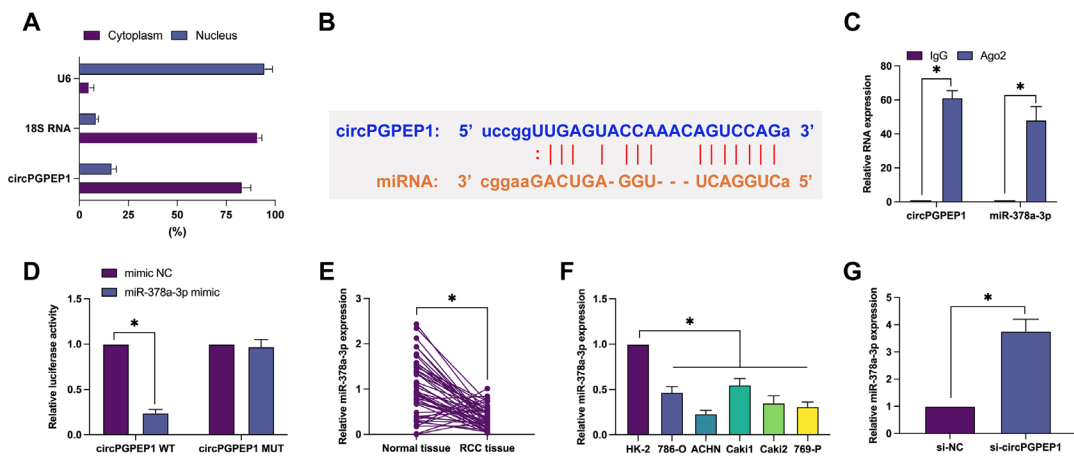


Figure 3. Competitive adsorption of miR-378a-3p by circPGPEP1

(A) Nucleoplasmic RNA isolation assay analyzed the subcellular localization of circPGPEP1 in ACHN cells; (B) Potential binding sites of circPGPEP1 and miR-378a-3p; (C) RIP experiment checked the binding relationship between circPGPEP1 and miR-378a-3p; (D) Dual luciferase reporter assay tested the targeting relationship between circPGPEP1 and miR-378a-3p; (E) RT-qPCR tested miR-378a-3p expression in RCC tissues and normal tissues; (F) RT-qPCR tested miR-378a-3p expression in RCC cell lines and HK-2 cells; (G) RT-qPCR tested miR-378a-3p expression in ACHN cells after knockdown of circPGPEP1; data representation = mean \pm S.D. (N=3); $P < 0.05$.

cells, EMT-related proteins were evaluated by immunoblot. It was presented that knockdown of circPGPEP1 suppressed N-cadherin and Snail and promoted E-cadherin expression (Fig. 2E). Warburg effect is an important way for cancer cells to acquire capacity through aerobic glycolysis (Vaupel & Multhoff, 2021). Therefore, changes in the Warburg effect were observed in RCC cells after interfered with circPGPEP1. As reported in Fig. 2F–H, ECAR, glucose uptake, and lactate production were reduced after the knockdown of circPGPEP1

(Fig. 2F–H). The expression of proteins associated with aerobic glycolysis was then evaluated. Knockdown of circPGPEP1 inhibited the expression of HK2 and PKM2 proteins (Fig. 2I).

Competitive adsorption of miR-378a-3p by circPGPEP1

Our research focus was shifted to the downstream molecules of circPGPEP1. The subcellular localization of circPGPEP1 was first assessed, finding that circPG-

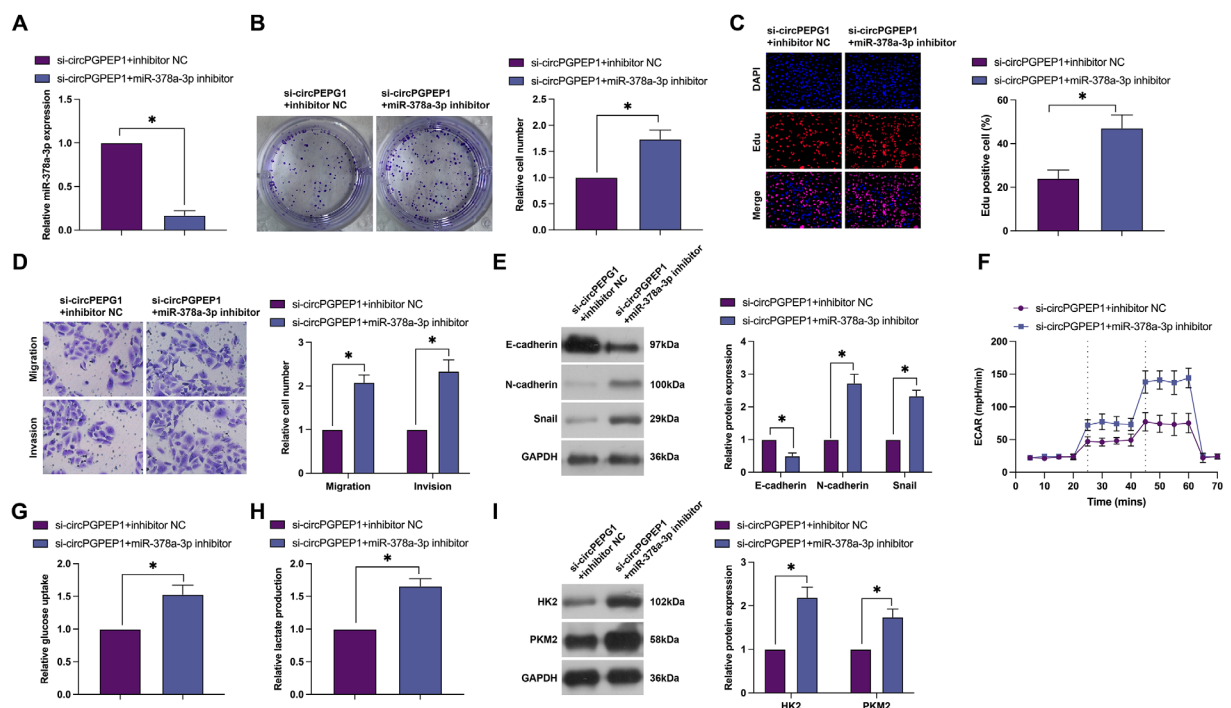


Figure 4. miR-378a-3p contributes to a reversal of effects of si-circPGPEP1 on RCC

si-circPGPEP1 and miR-378a-3p inhibitor were co-transfected into ACHN cells for functional rescue experiments. (A) RT-qPCR tested miR-378a-3p expression; (B–C) Colony formation assay and EdU assay tested analyzed proliferation ability; (D) Transwell assay tested invasion and migration ability; (E) Immunoblot assayed protein expression of EMT-related proteins (E-cadherin, N-cadherin, and Snail); (F) cellular ECAR; (G) glucose uptake; (H) lactate production capacity; I: Immunoblot assayed protein expression of aerobic glycolysis-related proteins (HK2 and PKM2); data representation = mean \pm S.D. (N=3); $P < 0.05$.

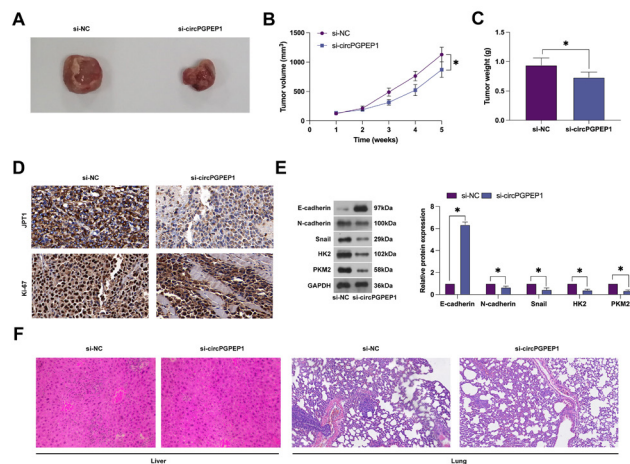


Figure 7. circPGPEP1 promotes RCC tumor growth and distant metastasis in vivo

ACHN cells with stable knockdown of circPGPEP1 were injected subcutaneously or intravenously into nude mice to evaluate tumor growth and distant metastasis. (A) representative image of tumor; (B–C) tumor volume and weight; (D) IHC staining evaluated tumor JPT1 and Ki-67 expression; (E) Immunoblot assayed E-cadherin, N-cadherin, Snail, HK2, and PKM2 proteins level in tumors; (F) HE staining assessed the ability of the tumor to metastasize to lung and liver; data representation = mean \pm S.D. (n=5); $P < 0.05$.

PEP1 was mainly localized in the cytoplasm of ACHN cells (Fig. 3A), which suggested that circPGPEP1 mediates gene expression mainly by targeting and adsorbing miRNAs. The bioinformatics website <https://starbase.sysu.edu.cn> predicted 10 miRNAs with potential binding sites for circPGPEP1, which were screened by RIP experiments to find that miR-378a-3p and circPGPEP1 were enriched in the Ago2 precipitation complex (Fig. 3B, C). Their targeting relationship was further examined by dual-luciferase, showing that when miR-378a-3p was overexpressed, the luciferase activity decreased in circPGPEP1 WT (Fig. 3D). Subsequently, the expression of miR-378a-3p in RCC was evaluated. Both RCC tissues and RCC cell lines expressed miR-378a-3p at a low level (Fig. 3E, F). Interestingly, miR-378a-3p expression was effectively restored in ACHN cells after knockdown of circPGPEP1 (Fig. 3G). These data suggest that circPGPEP1 binds to miR-378a-3p in RCC and regulates miR-378a-3p expression.

miR-378a-3p contributes to a reversal of the effects of si-circPGPEP1 on RCC

miR-378a-3p inhibitor was simultaneously transfected in ACHN cells transfected with si-circPGPEP1 to determine whether circPGPEP1 affects RCC development by regulating miR-378a-3p. The promoting effect of si-circPGPEP1 on miR-378a-3p expression was restrained by miR-378a-3p inhibitor (Fig. 4A). Furthermore, functional experiments observed that the preventive effects of si-circPGPEP1 on ACHN cell proliferation, invasion and migration, EMT, and aerobic glycolysis were all blocked after co-transfection of miR-378a-3p inhibitor (Fig. 4B–I). These data suggest that circPGPEP1 affects the biological behavior of RCC by regulating the expression of miR-378a-3p.

miR-378a-3p targets JPT1 expression

Next, the downstream target genes of miR-378a-3p were explored. The bioinformatics website <https://starbase.sysu.edu.cn> found 10 mRNAs with potential binding sites for miR-378a-3p. Among them, JPT1 was found to be significantly enriched with miR-378a-3p in the Ago2 precipitation complex in ACHN cells (Fig. 5A, B). Dual

luciferase reporter experiments showed that co-transfection of JPT1 WT with miR-378a-3p mimic mediated a decrease in the luciferase activity (Fig. 5C). Subsequently, the expression of JPT1 in RCC was explored by immunoblot. JPT1 protein expression was higher in RCC tissues and cells than in normal tissues or cells (Fig. 5D, E). In addition, decreased or increased expression of JPT1 was detected in ACHN cells overexpressing or knocking down miR-378a-3p, respectively (Fig. 5F). These data suggest that targeting miR-378a-3p regulates JPT1 expression.

circPGPEP1 affects RCC progression via miR-378a-3p/JPT1 axis

To test the conjecture that circPGPEP1 affects RCC progression by miR-378a-3p/JPT1 axis, si-JPT1 was introduced in ACHN cells overexpressing circPGPEP1. Overexpressing circPGPEP1 promoted circPGPEP1 and JPT1 levels and inhibited miR-378a-3p expression. si-JPT1 decreased JPT1, but did not affect circPGPEP1 and miR-378a-3p levels (Fig. 6A, B). Furthermore, circPGPEP1 overexpression increased cell colony-forming ability and EdU-positive cell rate but knocking down JPT1 prevents these changes (Fig. 6C, D). Transwell assay and immunoblot showed that circPGPEP1 overexpression increased the number of invasive and migratory cells and N-cadherin and Snail protein expression, but JPT1 knockdown reversed these phenomena (Fig. 6E, F). Furthermore, the stimulative effect of circPGPEP1 overexpression on aerobic glycolysis was impeded by knocking down JPT1 (Fig. 6G–J). These data suggest that circPGPEP1 promotes RCC proliferation, invasion, migration, EMT, and Warburg effect by regulating the miR-378a-3p/JPT1 axis.

circPGPEP1 promotes RCC tumor growth and distant metastasis in vivo

In vivo experiments were included to further support the above *in vitro* results. Tumor growth and distant metastasis were assessed by subcutaneous inoculation or tail vein injection of ACHN cells stably knocking down circPGPEP1 into nude mice. Depleting circPGPEP1 suppressed tumor volume and weight (Fig. 7A–C).

IHC staining showed that knockdown of circPGPEP1 inhibited JPT1 and Ki-67 positive cell ratio in tumors (Fig. 7D). Immunoblot found that depleting circPGPEP1 reduced N-cadherin, Snail, HK2, and PKM2 protein levels, and elevated E-cadherin protein levels (Fig. 7E). HE staining exhibited that silencing circPGPEP1 reduced the number of lung and liver metastatic nodules (Fig. 7F). These data suggest that down-regulating circPGPEP1 effectively inhibits tumor growth and distal metastasis of RCC.

DISCUSSION

RCC is a malignancy in the urinary system that has a poor prognosis despite improved treatments (15). The plight of RCC treatment makes it necessary to further explore its mechanism and find effective RCC therapeutic targets. Recently, circRNAs have been intensively studied as a promising direction for gene-targeted therapy (Wang *et al.*, 2020). In line with this, the circPGPEP1-oriented mechanism in RCC was probed through miR-378a-3p/JPT1.

CircPGPEP1 was stably and highly expressed in human RCC tissues and cells, and high levels of circPGPEP1 were associated with poor clinicopathological features and prognosis in RCC patients. Recently, a large number of studies have proposed that circRNAs are involved in the malignant progression in RCC, such as circNUP98 (Yu *et al.*, 2020), Circ_0005875 (Luo *et al.*, 2022), Circ-EGLN3 (Zhang *et al.*, 2021), etc., which are highly expressed in RCC cells and are closely related to the growth and metastasis of RCC. Wang *et al.*, disclosed that circPGPEP1 silencing hampers pro-apoptosis, migration, and invasion of cancer cells, and reduces tumor growth *in vivo* (Wang *et al.*, 2021). In the present study, circPGPEP1 silencing led to a reduction of cell proliferation, invasion, and migration in RCC cells. Influences of circPGPEP1 on EMT-related proteins were studied since EMT is a key process in the distant metastasis of cancer cells (Piva *et al.*, 2016), which showed that circPGPEP1 silencing inhibited EMT progression. Tumor cells obtain energy through the Warburg effect to maintain tumor development (Liberti and Locasale 2016) and circRNAs enable themselves to mediate the Warburg effect in RCC (Li *et al.*, 2021). Here, our study confirmed that down-regulated circPGPEP1 inhibited the Warburg effect in RCC cells. Additionally, inhibiting circPGPEP1 could effectively inhibit the tumor growth and distant metastasis of RCC, further reflecting the tumor-promoting action of circPGPEP1 in RCC. Recently, it has been gradually discovered that circRNAs in exosomes act in intercellular communication, tumor immune response, tumor cell migration, and invasion (Liu *et al.*, 2021). Therefore, RCC cell exosomes can be a study target in subsequent studies.

CircRNAs have been widely demonstrated to act as ceRNAs to counteract the effects of miRNAs (Jorgensen and Ro 2022). Accumulated miRNAs have conferred regulatory influences on RCC metastasis, implicated in a variety of cellular processes, including proliferation, migration, invasion, EMT, and Warburg effect (Abozed *et al.*, 2017). It is known that miR-378a-3p expresses differentially in cancers, including hepatocellular carcinoma (Li *et al.*, 2022), prostate cancer (Cannistraci *et al.*, 2022), breast cancer (Niu *et al.*, 2021), etc. Notably, miR-378a-5p is considered a tumor suppressor in RCC and correlates with a good prognosis for patients (Pan *et al.*, 2019). The present study focused on miR-378a-3p and

revealed that miR-378a-3p was down-regulated in RCC. miR-378a-3p could be targeted and regulated by circRNA and then involved in cancer progression (Mao *et al.*, 2020). More importantly, the present study confirmed that circPGPEP1 mainly mediates gene expression by absorbing miRNAs, and circPGPEP1 affects RCC development by regulating miR-378a-3p. In detail, the preventive influences of silencing circPGPEP1 on RCC cells were all hampered when miR-378a-3p was inhibited.

miRNAs are widely involved in cancer promotion and repression by regulating cancer-related genes (Abozed *et al.*, 2017). JPT1 is a ~16 kDa protein (Q9UK76, uniprot.org) that was originally identified as an abundant transcript in mouse hematopoietic and brain cells (Bateman *et al.*, 2020; Tang *et al.*, 1997). Notably, JPT1 is abnormally high expressed in cancers. For example, JPT1 expression is 3 times higher in ovarian cancer cells than in normal ovarian epithelial cells (Lu *et al.*, 2004). In glioma, lowering JPT1 reduces tumor growth (Laughlin *et al.*, 2009). In addition, JPT1 can interact with STMN1 to promote the growth and metastasis of thyroid anaplastic carcinoma (Pan *et al.*, 2021). Likewise, the present study noted that JPT1 was upregulated in RCC and JPT1 acted as an oncogene in RCC. Knockdown of JPT1 reversed the promotion effect of circPGPEP1 overexpression on proliferation, invasion, migration, EMT, and glycolysis of RCC cells. This suggests that circPGPEP1 plays a role in promoting cancer by up-regulating JPT1 expression.

Although the circPGPEP1/miR-378a-3p/JPT1 axis-related mechanism in RCC progression has been partially elucidated, further investigation is still required. For example, it is necessary to further determine circPGPEP1 pattern in the serum of RCC patients and to determine the potential of circEHD2 as a diagnostic biomarker for RCC. Furthermore, the downstream pathways of JPT1 in RCC cell progression need to be further elucidated.

CONCLUSION

Our findings suggest that circPGPEP1 is an “oncogene” in RCC. Highly circPGPEP1 promotes cell proliferation and metastasis through miR-378a-3p-mediated JPT1. Our findings not only explain the mechanism of circPGPEP1 in regulating RCC cell progression but also provide potential therapeutic targets for RCC.

Declarations

Acknowledgments. Not applicable.

Competing interests. The authors have no conflicts of interest to declare.

Data available. Data is available from the corresponding author on request.

REFERENCES

- Abozed M, Alsulaiti G, Almannaci F, Raza A, El Beltagi A, Ayyad A (2017) Anterior clinoid mucocoele causing optic neuropathy: A case report and review of literature. *eNeurologicalSci* 7: 57–59. <https://doi.org/10.1016/j.ensci.2017.05.005>
- Bateman NW, Teng PN, Hope E, Hood BL, Oliver J, Ao W, Zhou M, Wang G, Tommarello D, Wilson K, Litzy T, Conrads KA, Hamilton CA, Darcy KM, Casablanca Y, Maxwell GL, Bae-Jump V, Conrads TP (2020) Jupiter microtubule-associated homolog 1 (JPT1): A predictive and pharmacodynamic biomarker of metformin response in endometrial cancers. *Cancer Med* 9: 1092–1103. <https://doi.org/10.1002/cam4.2729>
- Cannistraci A, Hascoet P, Ali A, Mundra P, Clarke NW, Pavet V, Marais R (2022) MiR-378a inhibits glucose metabolism by suppressing GLUT1 in prostate cancer. *Oncogene* 41: 1445–1455. <https://doi.org/10.1038/s41388-022-02178-0>

- Cao L, Wang M, Dong Y, Xu B, Chen J, Ding Y, Qiu S, Li L, Karamfilova Zaharieva E, Zhou X, Xu Y (2020) Circular RNA circRNF20 promotes breast cancer tumorigenesis and Warburg effect through miR-487a/HIF-1 α /HK2. *Cell Death Dis* 11: 145. <https://doi.org/10.1038/s41419-020-2336-0>
- Chen Y, Song S, Zhang L, Zhang Y (2021) Circular RNA hsa_circ_0091579 facilitates the Warburg effect and malignancy of hepatocellular carcinoma cells via the miR-624/H3F3B axis. *Clin Transl Oncol* 23: 2280–2292. <https://doi.org/10.1007/s12094-021-02627-4>
- Choueiri TK, Motzer RJ (2017) Systemic therapy for metastatic renal-cell carcinoma. *N Engl J Med* 376: 354–366. <https://doi.org/10.1056/NEJMra1601333>
- Fang L, Ye T, An Y (2021) Circular RNA FOXP1 induced by ZNF263 upregulates U2AF2 expression to accelerate renal cell carcinoma tumorigenesis and Warburg effect through sponging miR-423-5p. *J Immunol Res* 2021: 8050993. <https://doi.org/10.1155/2021/8050993>
- Han B, Chao J, Yao H (2018) Circular RNA and its mechanisms in disease: From the bench to the clinic. *Pharmacol Ther* 187: 31–44. <https://doi.org/10.1016/j.pharmthera.2018.01.010>
- Jorgensen BG, Ro S (2022) MicroRNAs and 'Sponging' competitive endogenous RNAs dysregulated in colorectal cancer: potential as noninvasive biomarkers and therapeutic targets. *Int J Mol Sci* 23. <https://doi.org/10.3390/ijms23042166>
- Lara PN, Jr, Evans CP (2019) Cytoreductive nephrectomy in metastatic renal cell cancer: not all that it's cut out to be. *JAMA Oncol* 5: 171–172. <https://doi.org/10.1001/jamaoncol.2018.5503>
- Laughlin KM, Luo D, Liu C, Shaw G, Warrington KH, Jr, Qiu J, Yachnis AT, Harrison JK (2009) Hematopoietic- and neurologic-expressed sequence 1 expression in the murine GL261 and high-grade human gliomas. *Pathol Oncol Res* 15: 437–444. <https://doi.org/10.1007/s12253-008-9147-4>
- Li J, Huang C, Zou Y, Yu J, Gui Y (2020) Circular RNA MYLK promotes tumour growth and metastasis via modulating miR-513a-5p/VEGFC signalling in renal cell carcinoma. *J Cell Mol Med* 24: 6609–6621. <https://doi.org/10.1111/jcmm.15308>
- Li T, Xian HC, Dai L, Tang YL, Liang XH (2021) Tip of the Iceberg: roles of CircRNAs in cancer glycolysis. *Oncotargets Ther* 14: 2379–2395. <https://doi.org/10.2147/ott.S297140>
- Li Y, Zhou T, Cheng X, Li D, Zhao M, Zheng WV (2022) microRNA-378a-3p regulates the progression of hepatocellular carcinoma by regulating PD-L1 and STAT3. *Bioengineered* 13: 4730–4743. <https://doi.org/10.1080/21655979.2022.2031408>
- Liberti MV, Locasale JW (2016) The Warburg effect: how does it benefit cancer cells? *Trends Biochem Sci* 41: 211–218. <https://doi.org/10.1016/j.tibs.2015.12.001>
- Liu J, Ren L, Li S, Li W, Zheng X, Yang Y, Fu W, Yi J, Wang J, Du G (2021) The biology, function, and applications of exosomes in cancer. *Acta Pharm Sin B* 11: 2783–2797. <https://doi.org/10.1016/j.apsb.2021.01.001>
- Liu S, Wu M, Peng M (2020) Circ_0000260 Regulates the development and deterioration of gastric adenocarcinoma with cisplatin resistance by upregulating MMP11 via targeting MiR-129-5p. *Cancer Manag Res* 12: 10505–10519. <https://doi.org/10.2147/cmar.S272324>
- Lu KH, Patterson AP, Wang L, Marquez RT, Atkinson EN, Baggerly KA, Ramoth LR, Rosen DG, Liu J, Hellstrom I, Smith D, Hartmann L, Fishman D, Berchuck A, Schmandt R, Whitaker R, Gershenson DM, Mills GB, Bast RC, Jr (2004) Selection of potential markers for epithelial ovarian cancer with gene expression arrays and recursive descent partition analysis. *Clin Cancer Res* 10: 3291–3300. <https://doi.org/10.1158/1078-0432.Ccr-03-0409>
- Luo S, Deng F, Yao N, Zheng F (2022) Circ_0005875 sponges miR-502-5p to promote renal cell carcinoma progression through up-regulating E2f6 transformation specific-1. *Anticancer Drugs* 33: e286–e298. <https://doi.org/10.1097/cad.0000000000001205>
- Mao Y, Li W, Hua B, Gu X, Pan W, Chen Q, Xu B, Lu C, Wang Z (2020) Circular RNA PDHX promotes the proliferation and invasion of prostate cancer by sponging MiR-378a-3p. *Front Cell Dev Biol* 8: 602707. <https://doi.org/10.3389/fcell.2020.602707>
- Moch H, Srigley J, Delahunt B, Montironi R, Egevad L, Tan PH (2014) Biomarkers in renal cancer. *Virchows Arch* 464: 359–365. <https://doi.org/10.1007/s00428-014-1546-1>
- Niu M, Shan M, Liu Y, Song Y, Han JG, Sun S, Liang XS, Zhang GQ (2021) DCTPP1, an oncogene regulated by miR-378a-3p, promotes proliferation of breast cancer via DNA repair signaling pathway. *Front Oncol* 11: 641931. <https://doi.org/10.3389/fonc.2021.641931>
- Pan X, Zhao L, Quan J, Liu K, Lai Y, Li Z, Zhang Z, Xu J, Xu W, Guan X, Li H, Yang S, Gui Y, Chen Y, Lai Y (2019) MiR-378a-5p acts as a tumor suppressor in renal cell carcinoma and is associated with the good prognosis of patients. *Am J Transl Res* 11: 2207–2218
- Pan Z, Fang Q, Li L, Zhang Y, Xu T, Liu Y, Zheng X, Tan Z, Huang P, Ge M (2021) HN1 promotes tumor growth and metastasis of anaplastic thyroid carcinoma by interacting with STMN1. *Cancer Lett* 501: 31–42. <https://doi.org/10.1016/j.canlet.2020.12.026>
- Piva F, Giulietti M, Santoni M, Occhipinti G, Scarpelli M, Lopez-Beltran A, Cheng L, Principato G, Montironi R (2016) Epithelial to mesenchymal transition in renal cell carcinoma: implications for cancer therapy. *Mol Diagn Ther* 20: 111–117. <https://doi.org/10.1007/s40291-016-0192-5>
- Qin C, Lu R, Yuan M, Zhao R, Zhou H, Fan X, Yin B, Yu H, Bian T (2021) Circular RNA 0006349 augments glycolysis and malignance of non-small cell lung cancer cells through the microRNA-98/MKP1 axis. *Front Cell Dev Biol* 9: 690307. <https://doi.org/10.3389/fcell.2021.690307>
- Scelo G, Larose TL (2018) Epidemiology and risk factors for kidney cancer. *J Clin Oncol* 36: Jco2018791905. <https://doi.org/10.1200/jco.2018.79.1905>
- Tang W, Lai YH, Han XD, Wong PM, Peters LL, Chui DH (1997) Murine Hn1 on chromosome 11 is expressed in hemopoietic and brain tissues. *Mamm Genome* 8: 695–696. <https://doi.org/10.1007/s003359900540>
- Vaupel P, Mülthoff G (2021) Revisiting the Warburg effect: historical dogma versus current understanding. *J Physiol* 599: 1745–1757. <https://doi.org/10.1113/jp278810>
- Wang Y, Liu X, Wang L, Zhang Z, Li Z, Li M (2021) Circ_PGPEP1 serves as a sponge of miR-1297 to promote gastric cancer progression via regulating E2F3. *Dig Dis Sci* 66: 4302–4313. <https://doi.org/10.1007/s10620-020-06783-5>
- Wang Y, Zhang Y, Wang P, Fu X, Lin W (2020) Circular RNAs in renal cell carcinoma: implications for tumorigenesis, diagnosis, and therapy. *Mol Cancer* 19: 149. <https://doi.org/10.1186/s12943-020-01266-7>
- Wang Z, Deng M, Chen L, Wang W, Liu G, Liu D, Han Z, Zhou Y (2020) Circular RNA Circ-03955 promotes epithelial-mesenchymal transition in osteosarcoma by regulating miR-3662/metalloproteinase pathway. *Front Oncol* 10: 545460. <https://doi.org/10.3389/fonc.2020.545460>
- Yu R, Yao J, Ren Y (2020) A novel circRNA, circNUP98, a potential biomarker, acted as an oncogene via the miR-567/PRDX3 axis in renal cell carcinoma. *J Cell Mol Med* 24: 10177–10188. <https://doi.org/10.1111/jcmm.15629>
- Zhang G, Wang J, Tan W, Han X, Han B, Wang H, Xia Y, Sun Y, Li H (2021) Circular RNA EGLN3 silencing represses renal cell carcinoma progression through the miR-1224-3p/HMGXB3 axis. *Acta Histochem* 123: 151752. <https://doi.org/10.1016/j.acthis.2021.151752>
- Zhang XO, Wang HB, Zhang Y, Lu X, Chen LL, Yang L (2014) Complementary sequence-mediated exon circularization. *Cell* 159: 134–147. <https://doi.org/10.1016/j.cell.2014.09.001>
- Zhou Y, Li C, Wang Z, Tan S, Liu Y, Zhang H, Li X (2022) CircRNAs as novel biomarkers and therapeutic targets in renal cell carcinoma. *Front Mol Biosci* 9: 833079. <https://doi.org/10.3389/fmolb.2022.833079>
- Zhu J, Xiang XL, Cai P, Jiang YL, Zhu ZW, Hu FL, Wang J (2021) CircRNA-ACAP2 contributes to the invasion, migration, and apoptosis of neuroblastoma cells through targeting the miRNA-143-3p-hexokinase 2 axis. *Transl Pediatr* 10: 3237–3247. <https://doi.org/10.21037/tp-21-527>

Circular RNA sirtuin-1 restrains the malignant phenotype of non-small cell lung cancer cells *via* the microRNA-510-5p/SMAD family member 7 axis

ZiRan Zhao^{1#}, HongYan Zhang^{2#}, Fan Zhang¹, Ying Ji¹, Yue Peng¹, Fei Wang³ and Liang Zhao^{1✉}

¹Department of Thoracic Surgery, National Cancer Center/National Clinical Research Center for Cancer/Cancer Hospital, Chinese Academy of Medical Sciences and Peking Union Medical College, Beijing, People's Republic of China, Beijing, 100021, China; ²Department of Oncology, The Third Medical Center of PLA General Hospital, Beijing, 100143, China; ³Department of Oncology, The Seventh Medical Center of PLA General Hospital, Beijing, 100010, China

Circular RNA (circRNA) sirtuin-1 (SIRT1) is differentially expressed in non-small cell lung cancer (NSCLC), but its specific mechanism is still uncertain. The study was to figure out the latent molecular mechanism of circSIRT1 in NSCLC. The results clarified that circSIRT1 and SMAD family member 7 (SMAD7) were downregulated, but microRNA (miR)-510-5p was upregulated in NSCLC. Circ-SIRT1 expression was linked with tumor-node-metastasis staging and tumor size in NSCLC patients. Elevating circSIRT1 or suppressing miR-510-5p refrained NSCLC cell activities and glycolysis and inactivated the wnt/ β -catenin pathway, while knockdown of circSIRT1 promoted the malignant behavior of NSCLC cells. Besides, inhibition of malignant behavior in NSCLC cells by elevating circSIRT1 was reversed by knockdown of SMAD7. circ-SIRT1 bound to miR-510-5p to target SMAD7. In short, circSIRT1 represses NSCLC cell malignant development *via* miR-510-5p to target SMAD7, making it a latent target for NSCLC treatment.

Keyword: Circular RNA sirtuin-1, non-small cell lung cancer, SMAD family member 7, MicroRNA-510-5p, proliferation

Received: 16 February, 2023; revised: 20 June, 2023; accepted: 07 August, 2023; available on-line: 18 October, 2023

✉ e-mail: zhaolzl@hotmail.com

#These authors contributed equally to this work.

Acknowledgements of Financial Support: Beijing Hope Marathon Special Fund, Cancer Foundation of China (LC2018A02)

Abbreviations: CC, Colon cancer; circPTK2, Circular RNA protein tyrosine kinase 2; circRNAs, Circular RNAs; EdU, 5-ethynyl-2'-deoxyuridine; FBS, Fetal Bovine Serum; FITC, Fluorescein isothiocyanate; GAPDH, Glyceraldehyde-3-phosphate dehydrogenase; GC, Gastric cancer; GLS, 1Glutaminase; HK-2, Hexokinase 2; KISS1, Kisspeptin-1; LC, Lung cancer; miRNA, MicroRNA; MUT, Mutant type; NC, Negative control; NF- κ B, Nuclear factor-kappaB; NSCLC, Non-small cell lung cancer; RPMI, Roswell Park Memorial Institute; -1640RT-qPCR, Reverse transcription quantitative polymerase chain reaction; SIRT1, Circ-sirtuin-1; SMAD, 7SMAD family member 7; TNM, Tumor-node-metastasis; TRIM2, 9Tripartite motif-containing 29; WT, Wild-type

INTRODUCTION

Lung cancer (LC) takes up 17% of new cancer cases and 23% of cancer deaths (de Sousa *et al.*, 2018). Owing to smoking and environmental pollution, the number of new cases of LC and relevant deaths in China is elevated (Cao *et al.*, 2019). Non-small cell lung cancer (NSCLC) is the major kind of LC, taking up about 85% (Subramaniam *et al.*, 2013). The cure for metastatic liver cancer

has long been a challenge for clinicians and researchers, and the molecular mechanisms are not well understood.

Circular RNAs (circRNAs) are a new class of ubiquitous endogenous RNA. Unlike linear RNA, circRNA forms a continuous ring with no 5' or 3' covalent closure (Meng *et al.*, 2017; Yang *et al.*, 2020). Abnormal expression of circRNAs is associated with the occurrence and development of tumors. For instance, circPTK2 is crucial in the growth and metastasis of colon cancer (CC), making it supposed to be a latent target for CC metastasis treatment, and a biomarker for early diagnosis of metastasis (Su *et al.*, 2019). A study by Su *et al.* clarifies that circRNA Cdr1 promotes LC development (Qin *et al.*, 2016). HSA_circ_0001649 expression is downregulated in LC tissues and is associated with tumor size and tumor embolism in hepatocellular carcinoma. While circ-ABC10 motivates NSCLC cell proliferation, it refrains apoptosis *via* depressing KISS1 (Kong *et al.*, 2019). Circ-sirtuin-1 (SIRT1) controls NF- κ B activation through sequence-specific interactions and enhances SIRT1 expression *via* combining with microRNA (miR)-132/212 in vascular smooth muscle cells (Li *et al.*, 2021). Meanwhile, circSIRT1 is discovered to be a tumor suppressor gene in gastric cancer (GC) (Sun *et al.*, 2020). However, the function and mechanism of circSIRT1 in NSCLC have not been figured out yet.

The purpose of this study was to explore the potential molecular mechanism of circSIRT1 in NSCLC. It was assumed that circSIRT1 was a tumor suppressor gene in NSCLC. The potential downstream factor of circSIRT1 was identified by the dual luciferase reporting assay and bioinformatics website. In addition, in this work, it was confirmed that circSIRT1 blocks the activation of the wnt/ β -catenin pathway in NSCLC cell lines.

MATERIALS AND METHODS

Clinical tissues obtaining

54 NSCLC patients were recruited and have signed the informed consent. No preoperative chemotherapy or radiotherapy was performed on the recruited patients. The study was approved by the Ethics Committee of Chinese Academy of Medical Sciences and Peking Union Medical College (Approval Number C201612M11). All clinicopathological factors of NSCLC patients were shown in Table 1. NSCLC tissues were confirmed by two histopathological experts. Cancer and adjacent nor-

Table 1. CircSIRT1 is implicated in TNM staging and tumor size of NSCLC patients

Features	Group	Cases	Circ SIRT1 expression		P
			Elevation (n=27)	Reduction (n=27)	
Age (years)	<60	18	7	11	0.2482
	≥60	36	20	16	
Gender	Male	38	17	21	0.2332
	Female	16	10	6	
Tumor size (cm)	<3	29	21	8	0.0004
	≥3	25	6	19	
Lymph node metastasis	Yes	31	14	17	0.4090
	No	23	13	10	
Tumor, node, and metastasis stage	I + II	21	16	5	0.0021
	III-IV	33	11	22	
Differentiation degree	Good	15	8	7	0.7613
	Medium/bad	39	19	20	

Note: The relationship between circSIRT1 and clinicopathological features of NSCLC was examined using Spearman correlation analysis.

mal tissues (>5 cm from the tumor) were harvested from 54 cases of NSCLC patients. Afterward, the tissues were immediately frozen in liquid nitrogen and stored in a refrigerator at -80°C .

Cell culture

NSCLC cell lines (A549, H1975, H1650, and HCC827) and non-cancerous bronchial epithelial cell lines (BEAS-2B) (American Type Culture Collection, Manassas, VA, USA) were cultured in Roswell Park Memorial Institute (RPMI)1640 (Thermo Fisher Scientific, Waltham, MA, USA) consisting of 100 U/mL penicillin, 100 U/mL streptomycin (Invitrogen, Carlsbad, CA, USA) and 10% Fetal Bovine Serum (FBS) (Thermo Fisher Scientific).

Actinomycin D and RNase R treatments

To verify the stability of circSIRT1 in A549 cells, actinomycin D and RNase R assays were conducted (Chen *et al.*, 2020). For actinomycin D treatment, A549 cells were cultured in a complete medium supplemented with 2 $\mu\text{g}/\text{mL}$ actinomycin D (Sigma, St Louis, MO, USA) or dimethyl sulfoxide (Sigma). For RNA detachment, total RNA from A549 cells was incubated with 3 U/ μg RNase R (Genesee, Guangzhou, China) or diethyl pyrocarbonate-treated water (Sigma). CircSIRT1 or glyceraldehyde-3-phosphate dehydrogenase (GAPDH) expression was detected by reverse transcription quantitative polymerase chain reaction (RT-qPCR).

Cell transfection

siRNA targeting circSIRT1 and SMAD family member 7 (SMAD7) (si-circSIRT1: AGTTTGCAAAGATAACCTTCT; si-SMAD7: CTCCAGATACCCGATG-GATTTTC) or pcDNA3.1 (pcDNA3.1-circSIRT1), si-negative control (NC) and pcDNA3.1 NC were purchased from GenePharma (Shanghai, China), and miR-510-5p mimic (UCUCUGGGCCUGUGUCUUAGGC)/inhibitor (GCCUAAGACACAGGCCAGAGC) and mimic/inhibitor NC were purchased from Sangon (Shanghai). At 80% confluence, cells were transfected in a 6-well plate using lipofectamine 2000 (Invitrogen). Cells were then collected for subsequent experiments.

Colony formation assay

Transfected NSCLC cells ($5 \times 10^2/\text{well}$) were seeded in a 6-well plate (Thermo Fisher) containing FBS. After incubation at 37°C with 5% CO_2 for 10 days, the colonies were stained with 0.1% crystal violet solution (Sigma). Colonies (over 50 cells) were then counted under a microscope (Nikon Eclipse E600, Nikon Instruments, Melville, NY, USA) (Li *et al.*, 2020).

5-ethynyl-2'-deoxyuridine (EdU) analysis

A549 and H1650 cells (1×10^4) were seeded in a 96-well plate. Each well was added with 10 μM EdU solution (Genecopoeia, USA). After incubation, the cells were fixed with 4% paraformaldehyde, incubated with glycine, and then washed with phosphate-buffered saline consisting of 0.5% TritonX-100. The cells were incubated with Andy FluorTM 555 azide (A004, Genecopoeia, USA) or 4',6-diamidino-2-phenylindole. EdU-positive cells were observed under a fluorescence microscope (XSP-BM13C, Shanghai CSOIF. Co., China). Cell proliferation rate = the number of proliferating cells/total number of cells $\times 100\%$ (Zhu *et al.*, 2021).

Transwell detection of invasion and migration

For invasion detection, Matrigel (BD Biosciences, San Jose, CA, USA) was coated in the Transwell chamber (BD Biosciences). The lower chamber was added with 600 μL RPMI1640 medium consisting of 10% FBS (Thermo Fisher Scientific), and the upper chamber was supplemented with 200 μL serum-free medium consisting of 1×10^5 cells. Cells not passing through the membrane were removed, and the remaining cells were fixed with methanol, stained with crystal violet, and observed under a microscope. Five fields of view were randomly selected to calculate the average number of cells. A Transwell chamber not coated with matrigel was used in the migration assay, and the remaining steps were the same as the invasion (Tang *et al.*, 2021).

Glycolysis test

In line with the manufacturer's instructions, a glucose measurement kit and a lactic acid measurement kit

Table 2. RT-qPCR primer sequence

Genes	Primer sequence (5'-3')
GAPDH	Forward: 5'- ATCTCCAGGAGCGAGATCCC-3'
	Reverse: 5'- TGAGTCCTTCCACGATACCAA-3'
U6	Forward: 5'- CTCGCTTCGGCAGCACA-3'
	Reverse: 5'- AACGCTTCACGAATTTGCGT-3'
CircSIRT1	Forward: 5'- AGAGATTGTGTTTTTGGTGAA-3'
	Reverse: 5'- GAAGGTTATTTGGAATTAGTGC-3'
miR-510-5p	Forward: 5'- GCATAATGGTTCAGCATGTG -3'
	Reverse: 5'- GCATCATGGCAGCATTTACA C-3'
SMAD7	Forward: 5'- TTGCTGTGAATCTTACGGGAAG -3'
	Reverse: 5'- GGTTTGAGAAAATCCATCGGGT -3'

(Biovision, San Francisco, CA, USA) were utilized to evaluate cellular glycolysis. Absorbance was measured using an automated microplate reader (Molecular Devices LLC, Sunnyvale, CA, USA).

Flow cytometry detection of apoptosis

Annexin V-fluorescein isothiocyanat (FITC) apoptosis detection kit (Sigma-Aldrich, St. Louis, MO, USA) was utilized for analysis of cell apoptosis (Huang *et al.*, 2020). NSCLC cells were resuspended in a 1× binding buffer. After staining with Annexin V-FITC and propidium iodide, cells were evaluated to analyze the apoptosis rate on a flow cytometer (BD Biosciences).

RT-qPCR

RNA was extracted from tissues and cells using the RNeasy Mini Kit (Qiagen, Duesseldorf, Germany). RNase-free treatment was used to avoid RNA contamination. RNA was quantified using a NanoDrop ND-1000 device (Thermo Fisher Scientific). RNA was reverse-transcribed into complementary DNA (cDNA) using M-MLV Reverse Transcriptase Kit (Invitrogen). After mixing cDNA with SYBR GreenER qPCR SuperMix Universal (Invitrogen), RT-qPCR was performed in the PCR system (Applied Biosystems PCR Thermal Cyclers, thermo fisher). GAPDH or U6 was the loading control gene for mRNA and miRNA, respectively. The $2^{-\Delta\Delta CT}$ method was applied for data analysis. Primer sequences were manifested in Table 2.

Western blot

Total proteins were extracted from tissues and cells using Radio-Immunoprecipitation assay lysis buffers containing protease inhibitors. Proteins were separated by 10% sodium dodecyl sulfate-polyacrylamide gel electrophoresis, and 30 µg sample was electro-blotted onto a polyvinylidene fluoride membrane (Millipore), blocked with 5% skimmed milk, and incubated with primary antibodies and the secondary antibody. Primary antibodies were SMAD7 (25840-1-AP, Proteintech, 1:1000), HK-2 (22029-1-AP, Proteintech, 1:1000), GLS1 (ab156876, Abcam, 1:1000), β -catenin (ab32572, Abcam, 1:1000), GAPDH (ab8245, Abcam, 1:1000), *c*-myc (M4439, Sigma, 1:1000), with goat anti-rabbit Immunoglobulin G (7076, Cell Signaling Technology) as the secondary antibody. Protein signals were detected by the BeyoECL Star ECL

kit (Beyotime) and analyzed by ImageJ software (National Institutes of Health, Maryland, USA).

Luciferase activity assay

circSIRT1 and SMAD7 wild-type (WT) and mutant (MUT) luciferase reporter vectors (circSIRT1/SMAD7 WT/MUT) consisting of putative binding sites of miR-510-5p were purchased from Promega (Madison, Wisconsin, USA). A549 and H1650 cells were seeded in a 48-well plate (4.5×10^4 /well) and cultured to 70% confluence. Co-transfection of the above vectors was done with miR-510-5p mimic or mimic NC in A549 and H1650 cells using lipofectamine 2000. Luciferase activities were measured in the dual luciferase reporter gene detection system (Promega).

Statistical analysis

Statistical analysis was performed by GraphPad Prism software (La Jolla, CA, USA). Data were shown as mean \pm standard deviation (S.D.). Student's t-test or one-way analysis of variance (ANOVA) followed by Tukey's post-hoc test was utilized to analyze two or more groups. $P < 0.05$ emphasized obvious statistical meaning. The relationship between circSIRT1 and the clinical features of patients was determined using Spearman correlation tests. All experiments were carried out with at least three biological replicates ($N=3$).

RESULTS

CircSIRT1 is reduced in NSCLC and is associated with NSCLC clinicopathological features

In order to clarify the potential characteristics of circSIRT1 in NSCLC, circSIRT1 expression was examined in NSCLC. CircSIRT1 in NSCLC tissues and the four NSCLC cell lines were reduced compared with normal tissues and the bronchial epithelial cell line BEAS-2B (Fig. 1A, B). Subsequently, the circular structure of circSIRT1 in A549 cells was examined by actinomycin D and RNase R assay. As shown in Fig. 1C and 1D, circSIRT1 had a longer half-life period and was not degraded by RNase R compared to linear GAPDH mRNA.

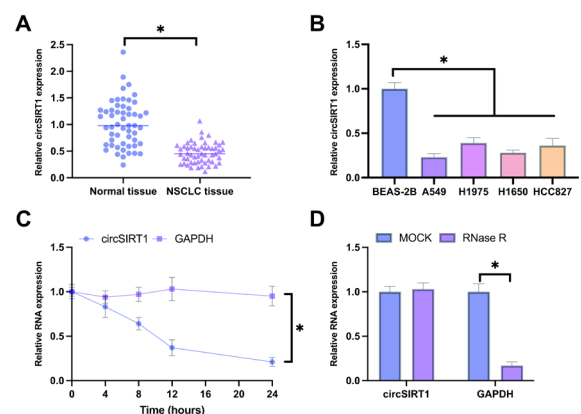


Figure 1. CircSIRT1 expression is reduced in NSCLC

(A, B) RT-qPCR detection of circSIRT1 expression in NSCLC tissue and adjacent normal tissue, NSCLC cell lines A549, H1975, H1650, HCC827 and non-cancerous bronchial epithelial cell line BEAS-2B; (C, D) Actinomycin D and RNase R assay test of circular structure of circSIRT1. The data were manifested as the mean \pm S.D. ($N=3$); $*P < 0.05$.

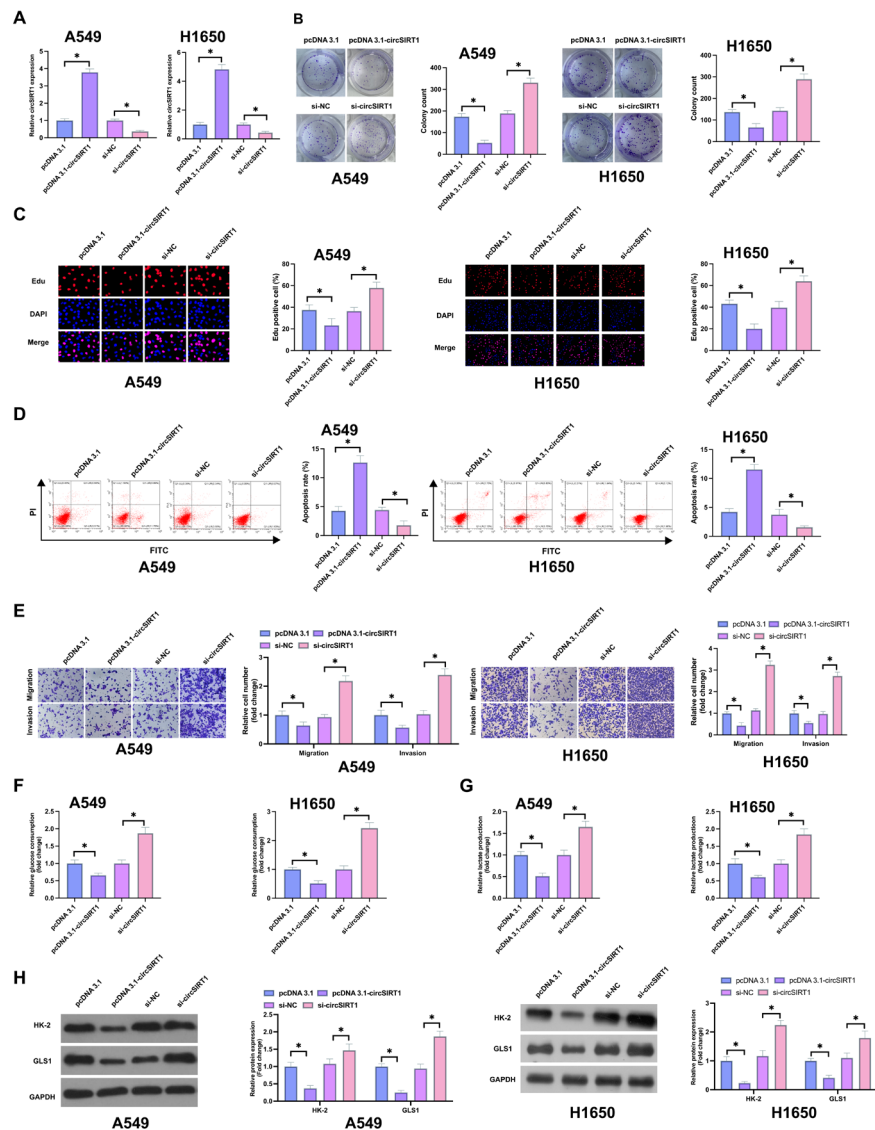


Figure 2. CircSIRT1 performs as a key gene to suppress the malignant phenotype of NSCLC cells

(A) RT-qPCR detection of circSIRT1 expression; (B) Colony formation assay detection of cell proliferation; (C) EdU assay detection of DNA replication; (D) Flow cytometry detection of cell apoptosis; (E) Transwell detection of cell invasion and migration; (F, G) Glycolytic ability of cells; (H) Western blot detection of HK-2 and GLS1; In A549 and H1650 cells after transfection of pcDNA 3.1 and siRNA targeting circSIRT1. The data were manifested as mean \pm S.D. (N=3); * P <0.05.

To determine whether circSIRT1 was associated with clinicopathological features of NSCLC patients, patients were divided into circSIRT1 low expression group and circSIRT1 high expression group according to the median expression of circSIRT1, and Spearman correlation analysis was performed. CircSIRT1 was associated with tumor-node-metastasis (TNM) staging and tumor size of NSCLC patients (Table 1). These results indicated that circSIRT1 expression was reduced in NSCLC and was supposed to be related to NSCLC development.

CircSIRT1 performs as a key gene to suppress the malignant phenotype of NSCLC

As circSIRT1 expression levels were the lowest in A549 and H1650 cells, these two cell lines were selected for subsequent experiments. Subsequently, whether circSIRT1 was associated with the malignant phenotype of NSCLC was explored. circSIRT1 was upregulated and

inhibited in A549 and H1650 cells, respectively, by transfection of circSIRT1-targeted overexpression plasmid and siRNA (Fig. 2A). Functional tests clarified that up-regulating circSIRT1 was available to repress A549 and H1650 cell proliferation, invasion, migration and DNA replication, but elevated the apoptosis rate (Fig. 2B–E). Cancer cells usually require a lot of energy to survive. Next, it was explored whether circSIRT1 controls the glycolysis capacity of NSCLC cells. Up-regulation of circSIRT1 suppressed glucose consumption and lactate production in A549 and H1650 cells (Fig. 2F, G). Meanwhile, upregulating circSIRT1 also repressed glycolytic rate-limiting enzyme HK-2 and glutamine hydrolase GLS1 in A549 and H1650 cells (Fig. 2H). However, after the elimination of circSIRT1, the exact opposite result was shown (Fig. 2B–H). Overall, circSIRT1 performed as a tumor suppressor gene in NSCLC cells.

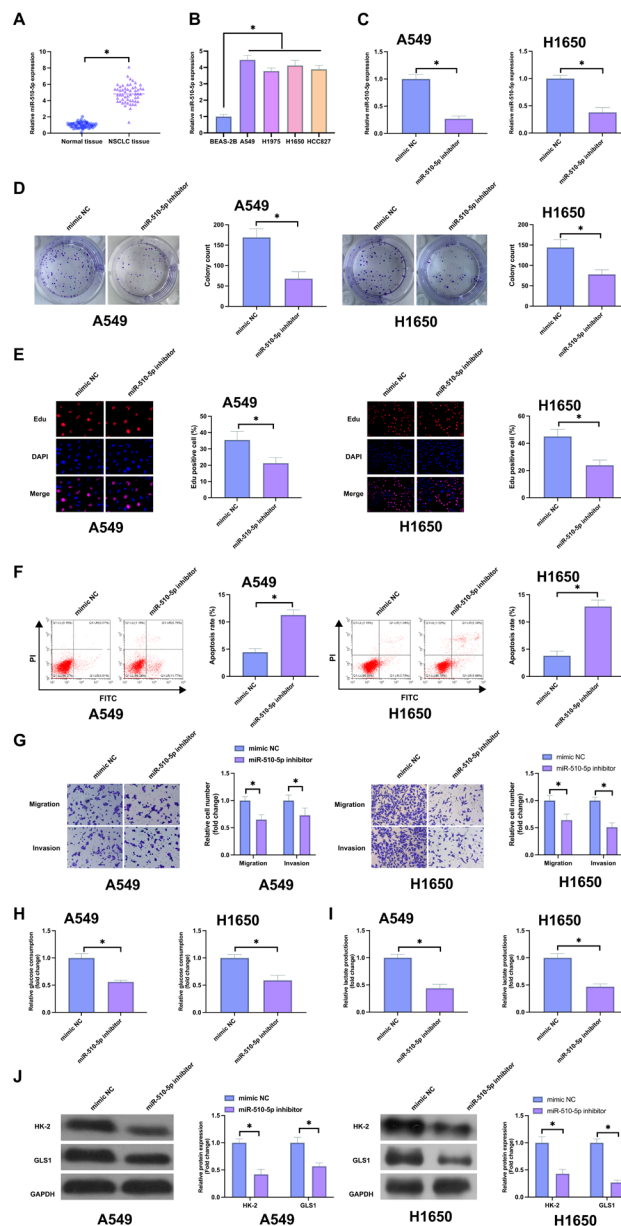


Figure 3. MiR-510-5p accelerates the malignant behavior of NSCLC

(A, B) RT-qPCR detection of miR-510-5p expression in NSCLC tissue and adjacent normal tissue, NSCLC cell lines A549, H1650, H1975, HCC827 and non-cancerous bronchial epithelial cell line BEAS-2B; (C) RT-qPCR detection of miR-510-5p expression; (D) Colony formation assay detection of cell proliferation; (E) EdU assay detection of DNA replication; (F) Flow cytometry detection of apoptosis; (G) Transwell detection of cell invasion and migration; (H, I) Glycolytic ability of cells; (J) Western blot detection of HK-2 and GLS1 expression; C-J, in A549 and H1650 cells after transfection with miR-510-5p inhibitor. The data were manifested as mean \pm S.D. (N=3); * P <0.05.

circSIRT1 binds to miR-510-5p to target SMAD7

CircSIRT1 can perform as a sponge of miRNA to modulate protein expression and impact disease development. Subsequently, downstream miRNAs absorbed by circSIRT1 were analyzed. It was found that circSIRT1 had a potential binding site with miR-510-5p through bioinformatics website query (Fig. 3A). Subsequently, a dual luciferase reporting assay was carried out. The results showed that wild-type circSIRT1 lowered the luciferase activity in the miR-510-5p mimic group, while mutant circSIRT1 had no effect on the luciferase activity in the miR-510-5p mimic group (Fig. 3B). After elevation or knockdown of circSIRT1, miR-510-5p expression in A549 and H1650 cells was enhanced or repressed,

respectively (Fig. 3C). This indicated that miR-510-5p might be a downstream target of circSIRT1.

Potential binding sites between SMAD7 and miR-510-5p were found on the bioinformatics website (Fig. 3D). WT SMAD7 could reduce the luciferase activity of the miR-510-5p mimic group (Fig. 3E). Former studies have noted that SMAD7 is under-expressed in various cancers, including LC. Consistent results were also gained in this study (Fig. 3F, G). Meanwhile, SMAD7 was promoted or inhibited in A549 and H1650 cells with downregulated or upregulated miR-510-5p, respectively (Fig. 3H). Therefore, SMAD7 was supposed to be a target gene of miR-510-5p.

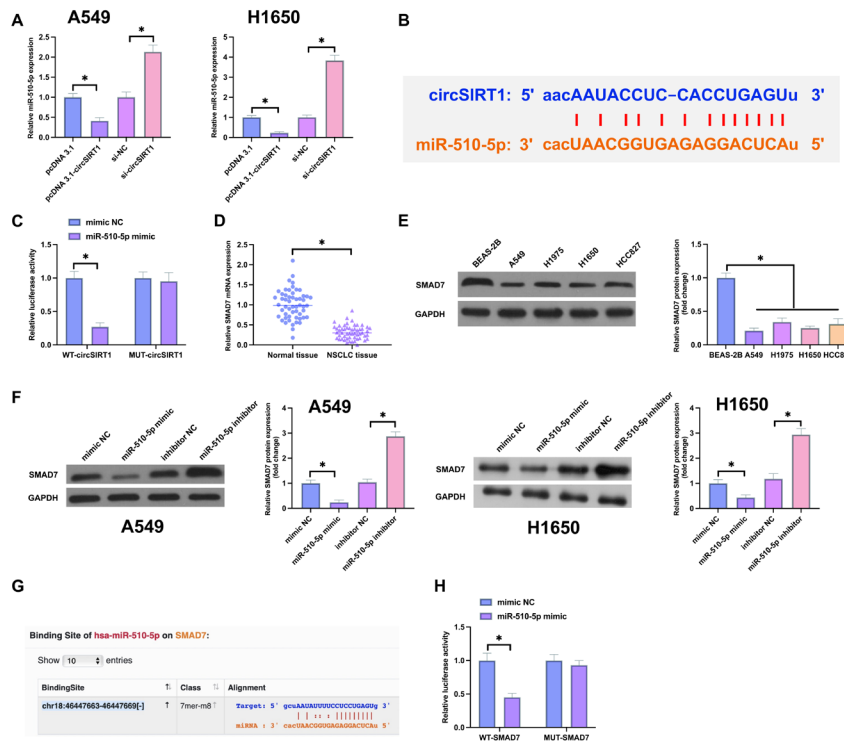


Figure 4. circSIRT1 binds to miR-510-5p to target SMAD7

(A) RT-qPCR detection of miR-510-5p expression in A549 and H1650 cells after transfection of pcDNA 3.1 and siRNA targeting circSIRT1; (B) Bioinformatics website <http://starbase.sysu.edu.cn/> to predict binding sites between circSIRT1 and miR-510-5p; (C) The luciferase activity assay for verification of the targeting relationship between circSIRT1 and miR-510-5p; (D) RT-qPCR detection of SMAD7 mRNA expression in NSCLC tissue and adjacent normal tissue; (E) Western blot detection of SMAD7 protein expression in NSCLC cell lines A549, H1975, H1650, HCC827 and non-cancerous bronchial epithelial cell line BEAS-2B; (F) Western blot detection of SMAD7 protein expression in A549 and H1650 cells introduced with miR-510-5p mimic/inhibitor; (G) Bioinformatics website <http://starbase.sysu.edu.cn/> to predict the binding site of SMAD7 and miR-510-5p; (H) The luciferase activity assay for verification of targeting relationship between SMAD7 and miR-510-5p; The data were manifested as mean \pm S.D. (N=3); * $P < 0.05$.

miR-510-5p motivates the malignant behavior of NSCLC cells

Former studies have confirmed the promoting effect of miR-510-5p on renal cell carcinoma and thyroid cancer development (Liu *et al.*, 2019; Zhan *et al.*, 2020). miR-510-5p expression was evaluated in NSCLC. As manifested in Fig. 4A, B, higher miR-510-5p was presented in NSCLC patients and cell lines. Subsequently, miR-510-5p was knocked down in A549 and H1650 cells after transfecting with miR-510-5p inhibitor (Fig. 4C). Downregulating miR-510-5p repressed A549 and H1650 cell proliferation, DNA replication, migration and invasion, elevated apoptosis rate, and reduced glucose consumption, lactate production, HK-2 and GLS1 protein expression (Fig. 4D–J). Briefly, miR-510-5p motivated the malignant behavior of NSCLC cells.

CircSIRT1 represses the malignant behavior of NSCLC cells by controlling the miR-510-5p/SMAD7 axis

Next, the researchers explored whether circSIRT1 influences the malignant behavior of NSCLC through the miR-510-5p/SMAD7 axis. pcDNA 3.1-circSIRT1 and si-SMAD7 were co-transfected into A549 and H1650 cells. It came out that pcDNA 3.1-circSIRT1 elevated SMAD7 expression, and after co-transfection with si-SMAD7, SMAD7 expression was repressed (Fig. 5A). The suppressive effects of upregulating circSIRT1 on A549 and H1650 cell proliferation, DNA replication, migration, invasion, and glycolysis, as well as the promoting effect

on apoptosis, were turned around after knocking down SMAD7 (Fig. 5B–H). In short, circSIRT1 repressed the malignant behavior of NSCLC cells by controlling the miR-510-5p/SMAD7 axis.

CircSIRT1 refrains the wnt/ β -catenin signal activation via the miR-510-5p/SMAD7 axis

The activation of Wnt/ β -catenin signaling is able to accelerate NSCLC proliferation, migration, invasion, and stem cell maintenance (Chen *et al.*, 2016). Next, it was examined whether circSIRT1 affected the wnt/ β -catenin pathway. Upregulating circSIRT1 or silencing miR-510-5p could reduce β -catenin and c-myc expression, a downstream target gene of the Wnt pathway, in A549 and H1650 cells. The repressive impacts of elevated circSIRT1 on the Wnt/ β -catenin pathway were reversed by upregulating miR-510-5p and knocking down SMAD7 (Fig. 6A, B). The findings clarified that circSIRT1 refrained from the activation of the Wnt/ β -catenin pathway in NSCLC via miR-510-5p/SMAD7 axis.

DISCUSSION

LC is a very familiar tumor in clinical practice, and it is also the malignant tumor with the highest mortality rate in the world. NSCLC is characterized by a high degree of malignancy and a very low 5-year survival rate. This is mainly due to a lack of understanding of the basic biology of NSCLC, which in turn leads to a

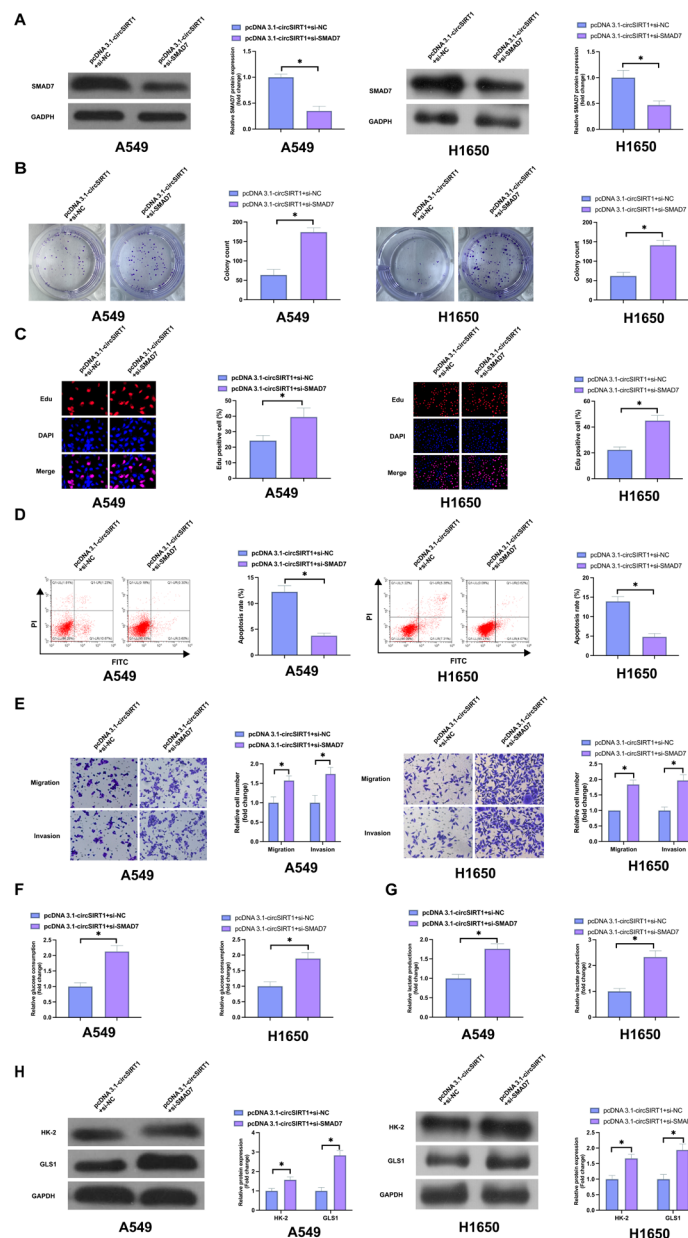


Figure 5. CircSIRT1 restrains the malignant behavior of NSCLC via controlling the miR-510-5p/SMAD7 axis

(A) Western blot detection of SMAD7 expression; (B) Colony formation assay detection of cell proliferation; (C) EdU assay detection of DNA replication; (D) Flow cytometry detection of cell apoptosis; (E) Transwell assay detection of cell invasion and migration; (F, G) Glycolytic ability of cells; (H) Western blot detection of HK-2 and GLS1 expression; In A549 and H1650 cells after co-transfection of pcDNA 3.1-circ-SIRT1 and si-SMAD7. The data were manifested as mean \pm S.D. (N=3); * P <0.05.

lack of reliable biomarker tests and effective therapeutic drugs (Tang *et al.*, 2016). The prognosis of patients with advanced or metastatic LC is quite unpleasing (Gupta *et al.*, 2006). Hence, understanding the pathogenesis of LC is essential for the development of therapeutic targets. The research of circRNA in LC has attracted much attention recently. At present, the key characteristics and latent functions of circRNAs are not well understood (Qu *et al.*, 2015; Hansen *et al.*, 2013). Certain circRNAs are crucial in cancer. For instance, hsa_circRNA_102958 expression in GC tissues is up-regulated and is positively linked with TNM staging (Wei *et al.*, 2020). Hsa_circRNA_102034 motivates LC progression via activating NR2F6 (Wang *et al.*, 2019); In NSCLC, a former study has discovered that hsa_circRNA_012515 expression in

NSCLC tissues is overexpressed and is closely implicated in the lymph node metastasis and TNM staging of NSCLC. In the meantime, NSCLC patients with elevated hsa_circRNA_012515 have a clearly shorter survival time (Fu *et al.*, 2020). In the research, it was discovered that circSIRT1 overexpression was available to repress NSCLC proliferation, invasion, migration and glycolysis, but promotes apoptosis.

Subsequently, we further clarified the function of circSIRT1 from the molecular mechanism. CircRNA frequently serves as a ceRNA for miRNA. A former study has clarified that miR-510-5p induces renal cell carcinoma and thyroid cancer cell proliferation, invasion and migration (Wang *et al.*, 2021; Zhang *et al.*, 2020). In this study, it was discovered that miR-510-5p, as a down-

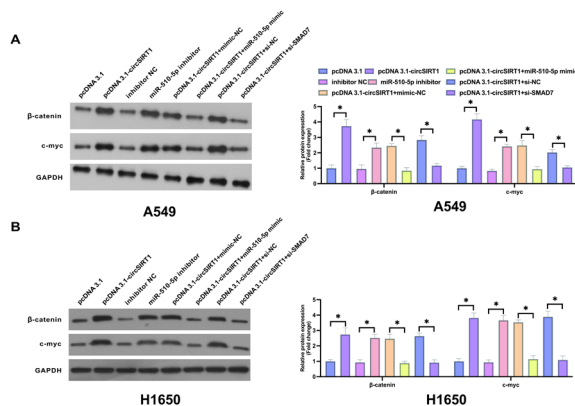


Figure 6. CircSIRT1 restrains wnt/ β -catenin signal activation via miR-510-5p/SMAD7 axis (A, B) Wnt/ β -catenin pathway-linked proteins β -catenin and c-myc expression after transfection of pcDNA3.1-circSIRT1, miR-510-5p inhibitor alone or co-transfection of pcDNA 3.1-circSIRT1 and miR-510-5p mimic or co-transfection of pcDNA 3.1-circSIRT1 and si-SMAD7. The data were manifested as mean \pm S.D. (N=3); * P <0.05.

stream factor of circSIRT1, also had a cancer-promoting impact on NSCLC cells. However, it is worth noting that miR-510-5p has tumor suppressor impact on glioblastoma and esophageal squamous cell carcinoma (Xu *et al.*, 2019). Hence, it is complicated to determine the characteristics of miR-510-5p in cancer, and its function in cancer is supposed to be linked with the target gene combined with it.

Wnt/ β -catenin pathway is a crucial cascade pathway closely implicated in tumor progression, and it is a frequently activated pathway in tumors, including LC. For instance, TRIM29 blocks LC development by repressing the Wnt/ β -catenin pathway (Chen *et al.*, 2019). believe that lncRNA SNHG7 knockdown suppresses the proliferation and migration of bladder cancer cells *via* motivating the Wnt/ β -catenin pathway. discovered that silenced cZNF292 refrains the formation of human glioma tubular structures *via* the Wnt/ β -catenin pathway (Yang *et al.*, 2016). Here, elevating circSIRT1 or repressing miR-510-5p repressed the motivation of the wnt/ β -catenin pathway, thus blocking NSCLC malignant behaviors.

In the research, the impacts of circSIRT1/miR-510-5p/SMAD7 on NSCLC were not explored in an *in vivo* model. Moreover, circSIRT1 can affect the wnt/ β -catenin pathway, but whether it represses NSCLC development *via* the wnt/ β -catenin pathway should be examined further in the wnt/ β -catenin knockdown model. This is the limitation of the research.

CONCLUSION

Overall, circSIRT1 blocks wnt/ β -catenin signal activation and NSCLC malignant behaviors *via* miR-510-5p/SMAD7. These findings offer favorable data support for further understanding of the characteristics of circRNAs in LC and offer a probable therapeutic target for the later treatment of NSCLC.

Declarations

Acknowledgments. Not applicable.

Declaration of Conflicting Interests. Authors declared no conflict of interest.

REFERENCES

- Cao M, Chen W (2019) Epidemiology of lung cancer in China. *Thorac Cancer* 10: 3–7. <https://doi.org/10.1111/1759-7714.12916>
- Chen W, Cen S, Zhou X, Yang T, Wu K, Zou L, Luo J, Li C, Lv D, Mao X (2020) Circular RNA CircNOLC1, upregulated by nf-kappab, promotes the progression of prostate cancer *via* miR-647/PAQR4 axis. *Front Cell Dev Biol* 8: 624764. <https://doi.org/10.3389/fcell.2020.624764>
- Chen W, Zheng R, Baade PD, Zhang S, Zeng H, Bray F, Jemal A, Yu XQ, He J (2016) Cancer statistics in China, 2015. *CA Cancer J Clin* 66: 115–132. <https://doi.org/10.3322/caac.21338>
- Chen Y, Peng Y, Xu Z, Ge B, Xiang X, Zhang T, Gao L, Shi H, Wang C, Huang J (2019) Knockdown of lncRNA SNHG7 inhibited cell proliferation and migration in bladder cancer through activating Wnt/ β -catenin pathway. *Pathol Res Pract* 215: 302–307. <https://doi.org/10.1016/j.prp.2018.11.015>
- de Sousa VML, Carvalho L (2018) Heterogeneity in lung cancer. *Pathobiology* 85: 96–107. <https://doi.org/10.1159/000487440>
- Fu Y, Huang L, Tang H, Huang R (2020) hsa_circRNA_012515 Is highly expressed in nscl patients and affects its prognosis. *Cancer Manag Res* 12: 1877–1886. <https://doi.org/10.2147/cmar.s245525>
- Gupta GP, Massagué J (2006) Cancer metastasis: building a framework. *Cell* 127: 679–695. <https://doi.org/10.1016/j.cell.2006.11.001>
- Hansen TB, Kjems J, Damgaard CK (2013) Circular RNA and miR-7 in cancer. *Cancer Res* 73: 5609–5612. <https://doi.org/10.1158/0008-5472.can-13-1568>
- Huang L, Han J, Yu H, Liu J, Gui L, Wu Z, Zhao X, Su S, Fu G, Li F (2020) CircRNA_000864 upregulates b-cell translocation gene 2 expression and represses migration and invasion in pancreatic cancer cells by binding to miR-361-3p. *Front Oncol* 10: 547942. <https://doi.org/10.3389/fonc.2020.547942>
- Kong P, Yu Y, Wang L, Dou YQ, Zhang XH, Cui Y, Wang HY, Yong YT, Liu YB, Hu HJ, Cui W, Sun SG, Li BH, Zhang F, Han M (2019) circ-Sirt1 controls NF- κ B activation *via* sequence-specific interaction and enhancement of SIRT1 expression by binding to miR-132/212 in vascular smooth muscle cells. *Nucleic Acids Res* 47: 3580–3593. <https://doi.org/10.1093/nar/gkz141>
- Li G, Zhao C, Zhang H, Yu J, Sun Y, Zhang Y (2020) Hsa_circ_0046263 Drives the carcinogenesis and metastasis of non-small cell lung cancer through the promotion of NOVA2 by absorbing Mir-940 as a molecular sponge. *Cancer Manag Res* 12: 12779–12790. <https://doi.org/10.2147/cmar.s272603>
- Li QK, Liu YK, Li JW, Liu YT, Li YF, Li BH (2021) Circ-sirt1 inhibits growth and invasion of gastric cancer by sponging miR-132-3p/miR-212-3p and upregulating sirt1 expression. *Neoplasia* 68: 780–787. https://doi.org/10.4149/neo_2021_210218N222
- Liu Y, Li J, Li M, Li F, Shao Y, Wu L (2019) microRNA-510-5p promotes thyroid cancer cell proliferation, migration, and invasion through suppressing SNHG15. *J Cell Biochem* 120: 11738–11744. <https://doi.org/10.1002/jcb.28454>
- Meng S, Zhou H, Feng Z, Xu Z, Tang Y, Li P, Wu M (2017) CircRNA: functions and properties of a novel potential biomarker for cancer. *Mol Cancer* 16: 94. <https://doi.org/10.1186/s12943-017-0663-2>
- Qin M, Liu G, Huo X, Tao X, Sun X, Ge Z, Yang J, Fan J, Liu L, Qin W (2016) Hsa_circ_0001649: A circular RNA and potential novel biomarker for hepatocellular carcinoma. *Cancer Biomark* 16: 161–169. <https://doi.org/10.3233/cbm-150552>
- Qu S, Yang X, Li X, Wang J, Gao Y, Shang R, Sun W, Dou K, Li H (2015) Circular RNA: A new star of noncoding RNAs. *Cancer Lett* 365: 141–148. <https://doi.org/10.1016/j.canlet.2015.06.003>
- Su Y, Lv X, Yin W, Zhou L, Hu Y, Zhou A, Qi F (2019) CircRNA Cdr1as functions as a competitive endogenous RNA to promote hepatocellular carcinoma progression. *Aging (Albany NY)* 11: 8183–8203. <https://doi.org/10.18632/aging.102312>
- Subramaniam S, Thakur RK, Yadav VK, Nanda R, Chowdhury S, Agrawal A (2013) Lung cancer biomarkers: State of the art. *J Carcinog* 12: 3. <https://doi.org/10.4103/1477-3163.107958>
- Sun J, Pan S, Cui H, Li H (2020) CircRNA SCARB1 Promotes renal cell carcinoma progression *via* Mir- 510-5p/SDC3 axis. *Curr Cancer Drug Targets* 20: 461–470. <https://doi.org/10.2174/1568009620666200409130032>
- Tang W, Han M, Ruan B, Jin W, Lou J, Yuan X, Chen D, Chen Y, Shin VY, Jin H, Wang X (2016) Overexpression of GOLPH3 is associated with poor survival in Non-small-cell lung cancer. *Am J Transl Res* 8: 1756–1762
- Tang X, Wen X, Li Z, Wen D, Lin L, Liu J, Li M (2021) Hsa_circ_0102171 aggravates the progression of cervical cancer through targeting miR-4465/CREBRF axis. *J Cell Physiol* 236: 4973–4984. <https://doi.org/10.1002/jcp.30210>
- Wang B, Tang D, Liu Z, Wang Q, Xue S, Zhao Z, Feng D, Sheng C, Li J, Zhou Z (2021) LINC00958 promotes proliferation, migration, invasion, and epithelial-mesenchymal transition of oesophageal squamous cell carcinoma cells. *PLoS One* 16: e0251797. <https://doi.org/10.1371/journal.pone.0251797>

- Wang L, Long H, Zheng Q, Bo X, Xiao X, Li B (2019) Circular RNA circRHOT1 promotes hepatocellular carcinoma progression by initiation of NR2F6 expression. *Mol Cancer* **18**: 119. <https://doi.org/10.1186/s12943-019-1046-7>
- Wei J, Wei W, Xu H, Wang Z, Gao W, Wang T, Zheng Q, Shu Y, De W (2020) Circular RNA hsa_circRNA_102958 may serve as a diagnostic marker for gastric cancer. *Cancer Biomark* **27**: 139–145. <https://doi.org/10.3233/cbm-182029>
- Xu M, Hu J, Zhou B, Zhong Y, Lin N, Xu R (2019) TRIM29 prevents hepatocellular carcinoma progression by inhibiting Wnt/ β -catenin signaling pathway. *Acta Biochim Biophys Sin (Shanghai)* **51**: 68–77. <https://doi.org/10.1093/abbs/gmy151>
- Yang H, Li X, Meng Q, Sun H, Wu S, Hu W, Liu G, Li X, Yang Y, Chen R (2020) CircPTK2 (hsa_circ_0005273) as a novel therapeutic target for metastatic colorectal cancer. *Mol Cancer* **19**: 13. <https://doi.org/10.1186/s12943-020-1139-3>
- Yang P, Qiu Z, Jiang Y, Dong L, Yang W, Gu C, Li G, Zhu Y (2016) Silencing of cZNF292 circular RNA suppresses human glioma tube formation via the Wnt/ β -catenin signaling pathway. *Oncotarget* **7**: 63449–63455. <https://doi.org/10.18632/oncotarget.11523>
- Zhan W, Li Y, Liu X, Zheng C, Fu Y (2020) ZNF671 Inhibits the Proliferation and Metastasis of NSCLC via the Wnt/ β -Catenin Pathway. *Cancer Manag Res* **12**: 599–610. <https://doi.org/10.2147/cmar.s235933>
- Zhang W, Xu C, Guo J, Guo L, Huo H, Wang H (2020) Circ-ELF2 Acts as a competing endogenous RNA to facilitate glioma cell proliferation and aggressiveness by targeting MiR-510-5p/MUC15 signaling. *Onco Targets Ther* **13**: 10087–10096. <https://doi.org/10.2147/ott.s275218>
- Zhu Z, Wu Q, Zhang M, Tong J, Zhong B, Yuan K (2021) Hsa_circ_0016760 exacerbates the malignant development of non-small cell lung cancer by sponging miR-145-5p/FGF5. *Oncol Rep* **45**: 501–512. <https://doi.org/10.3892/or.2020.7899>

A case-control study in NAT2 gene polymorphism studies in patients diagnosed with acute myeloid leukemia

Abdullah Farasani^{1,2}✉

¹Biomedical Research Unit, Medical Research Center, Jazan University, Saudi Arabia; ²Department of Medical Laboratory Technology, Faculty of Applied Medical Sciences, Jazan University, Saudi Arabia

Introduction: Acute myeloid leukemia (AML) is a clinically defined heterogeneous disease whose pathophysiology is currently unknown. The association of NAT2 acetylation profiles with human cancer risks, particularly with AML, was investigated in molecular epidemiological studies. Additionally, the NAT2 gene was carried out with acute lymphoid leukemia and other cancers. **Aim:** In this case-control study, C481T (rs1799929) and G857A (rs1799931) polymorphism studies were investigated in diagnosed AML patients in the Saudi population. **Methods:** This case-control study included 100 AML patients and 100 control subjects recruited in Saudi Arabia. The C481T and G857A polymorphisms were genotyped using specific primers and restriction enzymes. Statistical analysis was performed on the AML patients and controls using chi-square tests, genotyping, and allele frequencies (odds ratios, 95% of confidence intervals, and *P*-values). **Results:** Hardy Weinberg Equilibrium was determined to be both within and outside of the G857A and C481T polymorphisms. The allele and genotyping frequencies in AML and control subjects were analyzed, and the results corroborated the unfavorable connection with C481T (CC vs CT+TT; OR-1.12; (95% CIs: 0.64–1.96); *P*=0.67 and T vs C; OR-0.89; (95% CIs: 0.59–1.35) and *P*=0.60) and G857A polymorphisms (GG vs GA+AA; OR-1.50; (95% CIs: 0.83–2.71); *P*=0.17 and A vs G; OR-0.71; (95% CIs: 0.43–1.19) and *P*=0.19) in the NAT2 gene. **Conclusion:** The study results revealed a negative correlation as well as a protective factor for AML with the C481T and G857A polymorphisms in the NAT2 gene.

Keywords: Acute myeloid leukemia, C481T, G857A and NAT2 gene

Received: 24 February, 2022; **revised:** 08 August, 2022; **accepted:** 06 August, 2023; **available on-line:** 16 September, 2023

✉e-mail: aofarasani@jazanu.edu.sa

Acknowledgements of Financial Support: The author extends their appreciation to the Deputyship for Research & Innovation, Ministry of Education in Saudi Arabia for funding this Research work through the project number ISPP22-21.

Abbreviations: AML, Acute myeloid leukemia; HWE, Hardy-Weinberg Equilibrium; MDS, myelodysplastic syndromes; NAT2, N-acetyl transferase 2; SNP, Single nucleotide polymorphisms; PCR, polymerase chain reaction

INTRODUCTION

Acute myeloid leukemia (AML) is classified as an aggressive condition in which too many immature, non-lymphoblastic, white blood cells in the bone marrow and blood are identified. AML is also known as acute myelogenous leukemia or acute nonlymphocytic leukemia (Cucchi *et al.*, 2021). Myeloid malignancies are a subset of hematopoietic stem/progenitor cell tumors that include

AML and myelodysplastic syndromes (MDS) (Döhner *et al.*, 2015). An estimated 21450 cases were reported in 2019, representing between 15–20% of leukemias in the United States (Sasaki *et al.*, 2021). The prognosis for AML patients beyond the age of sixty has not changed significantly in decades and remains bleak (Docking *et al.*, 2021). AML is a clonal hematopoiesis condition defined by genetic and epigenetic changes that lead to a block of myeloid progenitor development in the bone marrow and blood and the accumulation of leukemia. Although the overall survival rate of AML patients is poor, around 20% to 30% of them never achieve complete remission, and 50% of them relapse beyond complete remission, often within 2–3 years after diagnosis (Bhatnagar *et al.*, 2021). AML can also be caused by a growing MDS, such as a clonal condition of hematopoietic stem cells (Chamseddine *et al.*, 2016). Despite efforts to enhance the clinical result of AML, current medications fail to eradicate the leading leukemic stem cells (Pegoraro *et al.*, 2020). Based on the French and American classification, AML is classified into eight subtypes, M0–M7, depending on the type of leukemia that develops and the stage of leukemia maturity (Lafuente *et al.*, 1993).

AML is the most frequent acute leukemia in adults, which causes many deaths from malignancy. Fatigue owing to anemia, easier bleeding due to thrombocytopenia, increasing leukopenia and bone soreness are further symptoms of AML. Acute leukemia may be myeloid or lymphoblastic depending on the type of cells impacted. The specific etiology of AML is not fully understood, although risk factors for the development of AML are also present. In the great majority of AML cases, genetic mutations are discovered. Some AML-associated chromosomal translocations include t(15:17) and t(8:21). Risk factors include patients with a hematologic condition underlying AML, people who underwent alkylating or radiation chemotherapy in previous cancer treatments, genetic disorders such as Down's syndrome and increased age (Kaser *et al.*, 2021). New predictors of diseases like cancer and indications of efficacy of chemotherapy response were developed in single nucleotide polymorphisms (SNPs). To date, most SNPs in AML have been identified with oncological therapy responses (Castro *et al.*, 2021). Over the last three decades, genomic aberrations have dominated the pathogenesis of AML, and diagnostic and prognostic indications of cytogenesis have emerged. The Cancer Genome Atlas project has reported a small number of mutations in often disrupted pathways including *NPM1*, *FLT3*, *CEBPA*, *DNMT3A*, *IDH1*, and *IDH2*, as well as genes recently implicated in leukemogenesis like *EZH2*, *U2AF1*, *SMC1A*, and *SMC3*. *NPM1*, *CEBPA*, and *RUNX1* mutations are frequent in AML (Bullinger *et al.*, 2017). Apart from this multi-

Table 1. NAT2 gene SNP details

Gene	NC	Rsnumber	Forward Primers	Reverse Primers	PCR	RE	NB	MB
NAT2	C481T	rs1799929	GGAACAAATTGGACTTGG	TAACGTGAGGGTAGAGAGGAT	920bp	KpnI	486/434bp	920bp
NAT2	G857A	rs1799931	GGAACAAATTGGACTTGG	TAACGTGAGGGTAGAGAGGAT	920bp	BamHI	810/110bp	920bp

Table 2. Anthropometric information on the patients in this study

Anthropometric measurements	AML cases (n=100)	Controls (n=100)	P-Value
Age (Years)	38.9±15.1	39.9±12.06	0.60
Minimum and maximum ages	19–82	18–63	–
Males (Gender)	61 (61%)	54 (54%)	–
Females (Gender)	39 (39%)	46 (46%)	–

ple single nucleotide polymorphisms were documented in the AML. N-acetyl transferase 2 (NAT2) is a phase II metabolizing enzymes that are vital in the acetylation and detoxification of various hazardous metabolites and carcinogenic agents such as aryl or aromatic amines and hydrazines, which are implicated in the development of carcinogenesis (Yarosh *et al.*, 2014). Several molecular epidemiological studies have investigated the link between NAT2 acetylation profiles and the risk of human cancer. In addition, a significant study showed that persons with the NAT2 phenotype are at greater risk of developing AML. Furthermore, SNPs in the NAT2 gene also control human sensitivity to different cancers such as pulmonary cancer, bladder cancer, gastric cancer etc (Zou *et al.*, 2017). Growing evidence revealed that NAT2 polymorphic diseases were combined with higher vulnerability to other diseases, notably acute lymphoblastic leukemia and lung squamous carcinoma. In addition, various studies have shown the relationship of distinct NAT2 polymorphisms with a high risk for acute development of leukaemia, notably AML, with contradictory results (AbdelGhaffar *et al.*, 2019).

Leukemia is the third and sixth most common malignancy in Saudi men and women, respectively. In 2013, 12% of newly reported leukemia cases were AML patients. AML is an age-related disease in Saudi Arabia, with a median age of 70 years. AML is the most common adult leukemia, with an increased frequency with age. In 2013, 684 new cases of adult leukemia were reported in the most recent cancer-incidence report in Saudi Arabia in every 100,000 persons and this represents 5.9% of all new adult malignancies (Gaafar *et al.*, 2018). Presently, limited studies have been carried out in the Saudi population and unfortunately there are no documented studies on the C481T and G857A polymorphism in the NAT gene in patients diagnosed with AML in the Saudi population. Therefore, the present study aimed to investigate the case-control study in C481T and G857A polymorphism with NAT gene in Saudi patients diagnosed with AML.

MATERIALS AND METHODS

The Ministry of Health provided an ethical grant for this study, which was carried out in accordance with the Helsinki Declaration. In this case-control study, 200 Saudi individuals were recruited as 100 patients were diagnosed with AML and 100 were non-AML (healthy subjects). All of the recruited samples were obtained from the Riyadh regional laboratory in Saudi Arabia's capital city. Both cases and controls were chosen based

on the inclusion and exclusion criteria discussed in the earlier publication (Farasani, 2019). The inclusion criteria for AML subjects were recruited based on the diagnosis of the AML with histopathological and cytogenetic confirmation, signed informed consent and Saudi adults. The exclusion criteria for AML cases were patients diagnosed with other cancers, unsigned consent form with non-Saudi subjects. The AML cases were diagnosed with bone-marrow examination, complete blood count and flow cytometry. Additionally, cytogenetics and FISH tests were implemented for reconfirmation. The inclusion criteria for healthy controls did not include any type of cancer or other diseases. The exclusion criteria were non-Saudi subjects.

Sample selection

2 ml of EDTA blood was obtained from each patient (n=200) and utilized for DNA extraction and molecular analysis (Alshammery *et al.*, 2023).

Molecular analysis

Genomic DNA extraction was done with the specific kits used for separation of the DNA and nanodrop was used to measure the DNA quantification (Alshammery *et al.*, 2023). Genotyping was performed with C481T and G857A polymorphism in the NAT2 gene using the precise primers as described in the Table 1. Genotyping was carried out with polymerase chain reaction (PCR) which was performed with a total reaction mix of 50 µl micro-liters consisting of 4 µl genomic DNA and 30 µl PCR mixes, which contain 10X, MgCl₂, dNTPs and 10X Taq DNA polymerases. The Master Mix was complemented by 10pmoles of 2 µL of forward and reverse primers followed by 12 µL of distilled water. For the final amount of 50 µL, the PCR reaction has been standardized (Alshammery & Khan, 2021). Both the C481T and G857A primers from earlier studies have been used. After PCR 35 cycles were performed starting with initial denaturation running 5 min at 95°C, 30 s at 95°C for denaturation, various annealing temperatures for both the polymorphisms at 65/60°C – 30 s, extension at 72°C – 45 s and final extension at 72°C – 5 min. The 910bp of PCR products were digested with *KpnI* and *BamHI* enzymes at 37°C for 18 hours and further samples were loaded on 3% agarose gel stained with ethidium bromide. Further details were shown in the Table 1.

Statistical analysis

SPSS software (version 20) was used to examine the clinical data. Hardy-Weinberg Equilibrium (HWE) was

Table 3. The studies distribution genotype frequencies of C481T and G857A polymorphisms

NAT2 (rs1799929)	Cases (n=100)	Controls (n=100)	OR (95%CI)	P-Value
CC	51 (51%)	48 (48%)	Position	Position
CT	30 (30%)	31 (31%)	0.91 (0.48–1.72)	0.77
TT	19 (19%)	21 (21%)	0.85 (0.40–1.77)	0.66
CC vs CT+TT	51 (51%)	48 (48%)	1.12 (0.64–1.96)	0.67
C	132 (0.66)	127 (0.635)	Position	Position
T	68 (0.34)	73 (0.365)	0.89 (0.59–1.35)	0.60
NAT2 (rs1799931)	Cases (n=100)	Controls (n=100)	OR (95%CI)	P-Value
GG	71 (71%)	62 (62%)	Position	Position
GA	26 (26%)	34 (34%)	0.66 (0.36–1.23)	0.19
AA	03 (03%)	04 (04%)	0.65 (0.14–3.04)	0.58
GG vs GA+AA	71 (71%)	62 (62%)	1.50 (0.83–2.71)	0.17
G	168 (0.84)	158 (0.79)	Position	Position
A	32 (0.16)	42 (0.21)	0.71 (0.43–1.19)	0.19

used for comparing the observed and anticipated genotype frequencies using control subjects. The odds ratios, upper, and lower ranges of 95% confidence intervals (95% CI) for C481T and G857A polymorphisms in the NAT2 gene were used in the genotype differences between AML cases and healthy control subjects. The $P < 0.05$ were considered statistically significant (Khan *et al.*, 2019).

RESULTS

Clinical details for AML cases and controls

Table 2 documents the clinical characteristics between AML and non-AML (controls) involved in this study. In this case-control study, 100 AML cases and 100 healthy controls were selected within the Saudi population. 38.9 ± 15.1 and 39.9 ± 12.06 was the known mean age for AML cases and control subjects documented with non-significant association ($P = 0.60$). Between 19–82 is the minimum and maximum age for AML cases and 18–63 is the minimum-maximum age for the control subjects documented in this study. The male and female patients in the AML cases were 61% and 39%, respectively, whereas the male and female participants in the controls were 54% and 46%.

HWE analysis

HWE analysis was performed in both the C481T and G857A polymorphisms and HWE was not in accordance with the control subjects for C481T; $VAF = 0.37$; $\chi^2 = 10.98$ and $P = 0.0009$ and for G857A is in accordance with the control subjects $VAF = 0.21$; $\chi^2 = 0.60$ and $P = 0.80$.

Genotype analysis for C481T and G857A polymorphisms

The genotype frequencies between CC, CT and TT were found to be 51%, 30% and 19% in the AML cases, whereas in the control subjects 48%, 31% and 21% were documented as CC, CT and TT genotypes. 66% of the C allele and 34% of the T alleles have been documented in AML cases and in the control subjects, 0.365% of the T allele and 0.635% of the C allele were confirmed. The genotype [CT *vs* CC; OR-0.91; (95% CIs: 0.48–1.72) and

$P = 0.77$ and TT *vs* CC; OR-0.85; (95% CIs: 0.40–1.77) and $P = 0.66$] and dominant model also showed the non-significant association (CC *vs* CT+TT; OR-1.12; (95% CIs: 0.64–1.96); $P = 0.67$ allele frequencies [T *vs* C; OR-0.89; (95% CIs: 0.59–1.35) and $P = 0.60$] was also confirmed and non-significantly associated. Table 3 confirms the genotype distribution as well as allele frequencies in AML cases and control subjects. The GG, GA, and AA genotype frequencies of G857A polymorphism were 71%, 26%, and 3% in AML cases, respectively, and 62%, 34%, and 4% in control genotypes. The allelic discrimination between G and A alleles in AML cases was found to be 84% and 16%, respectively, whereas in control subjects it was 79% and 21%. The genotype [GA *vs* GG; OR-0.66; (95% CIs: 0.36–1.23) and $P = 0.19$ and AA *vs* GG; OR-0.65; (95% CIs: 0.14–3.04) and $P = 0.58$] and dominant model also showed the non-significant association (GG *vs* GA+AA; OR-1.50; (95% CIs: 0.83–2.71); $P = 0.17$ allele frequencies [A *vs* G; OR-0.71; (95% CIs: 0.43–1.19) and $P = 0.19$] was also confirmed and non-significantly associated.

DISCUSSION

In this case-control study, C481T and G857A polymorphisms in the NAT2 gene were studied in the Saudi patients diagnosed with AML and the study results confirmed the negative association with any of the allele or genotype frequencies. AML is one of a particular type of cancer that modifies the drug-metabolization enzymes and mainly because of genetic heterogeneity of the various human populations in the fields of drug metabolism and disease sensitivity, NAT2 is a key subject in pharmacogenetic study. Seven SNPs of the NAT2 gene were studied in human diseases at 191, 282, 590, 857, 481, 803 and 314 positions, and many more SNPs have been reported in worldwide studies (Adole *et al.*, 2016). The NAT2 isoform is encoded by the NAT2 gene, which is situated on chromosome 8 (8p22), and this gene is positioned combined with the NAT1 gene and the pseudogene NATP. the observed variety of the described alleles derives from the combination of single-base mutations selected from among the several bases. Enzyme activity, affinity for substrate, and stability of resultant protein can all be affected by existing SNPs in

the coding region of the gene. The C481T (rs1799929), G590A (rs1799930), G857A (rs1799931), and G191A (rs1801279) have been useful in the context of NAT2 as an acetylator phenotype to detect them (Santos *et al.*, 2016). C481T polymorphism is a synonymous SNP frequently associated with T341C, which occurs in clusters NAT2*5, as A, B, F, G, H, I, L, and M in the variant alleles 6E, 11A&B, 12 and 14 C. C481T (NAT2*11A) is exceedingly rare, and has not been found in over 2600 individuals of European descent (Garcia-Martin, 2008). G857A substitution results in a change in the amino acid glutamate in the protein (G286E). This mutation alters the active site of the enzyme, lowering its selectivity and capacity to operate as a catalyst. The polymorphism in the NAT2 gene identified in the G857A variant reduces aromatic and heterocyclic amines. Only 11 NAT2 alleles have the mutation G857A, and two of these are the result of a slow acetylator phenotype, while the others have not yet been identified (Rajasekaran *et al.*, 2011). In this study, only C481T and G857A polymorphisms have been studied in the Saudi patients confirmed with the AML disease. The current study results with G857A polymorphism were associated with a previous study documented in the Jordanian population (Jarrar *et al.*, 2010).

A function for NAT2 gene polymorphism in several cancer types has been proposed, and AML has been documented in multiple studies in the global population (Gra *et al.*, 2008; Majumdar *et al.*, 2008; Zanrosso *et al.*, 2012; Zou *et al.*, 2017). Limited studies have been recorded in the Saudi population with the NAT2 gene in different diseases. C481T and G857A polymorphisms have been linked to T2DM in the Saudi Arabian population, and the study results validated the favorable connection with G857A polymorphism. However, none of the SNPs was shown to be positively associated in this study, which may be due to the function of the specific disease (Al-Shaqha *et al.*, 2015). A previous study in the Arab control population in Saudi Arabia with both the C481T and G857A polymorphisms in the NAT2 gene was performed (Bu *et al.*, 2004). A similar study on the NAT2 gene was conducted in the Saudi Arabian population in Al-Ahsa, where it was discovered that persons with the NAT2 gene had an elevated risk of slow acetylators, potentially impacting the efficacy and vulnerability to numerous diseases (Zahra *et al.*, 2020). A similar pattern of this study was replicated in the Jordanian population (Jarrar *et al.*, 2018). The frequency of NAT2 gene polymorphism in Saudi Arabia, Oman, and Emirati populations varies (Al-Ahmad *et al.*, 2017; Tanira *et al.*, 2003; Zahra *et al.*, 2020). The NAT2 gene was screened in the Egyptian population in children diagnosed with lymphoblastic leukemia, and the study results indicated that the NAT2 gene is slowly related with the acetylator phenotype with ALL risk in pediatric children (Kamel *et al.*, 2015). In the NCBI dbSNP NAT2 C481T and G857A database, the worldwide Minor Allele Frequency was T=0.27 and A=0.08. G857A is a rather infrequent polymorphism, according to these frequencies (Fayez *et al.*, 2018). The proportion of mutant alleles was validated in this study as 0.34 in T-allele and 0.16 in A-allele of both described polymorphisms in the NAT2 gene.

A meta-analysis of NAT2 gene variants in isoniazid-induced hepatotoxicity (IIH) found that these genetic variants had a substantial impact on IIH. The NAT2 genotyping test can help with a better knowledge of drug-enzyme metabolism as well as an earlier prediction of IIH (Khan *et al.*, 2019). A documented meta-analysis found rs1799931 to be a protective factor against cancer development (Tian *et al.*, 2014), which was consistent

with the current report's results as well as those of others (Zou *et al.*, 2017). A meta-analysis study on acute leukemia with the NAT2 gene was conducted (Zhu *et al.*, 2019). This study has added strengths and limitations and one of the strengths of this study was opting for a minimum of 100 Saudi patients diagnosed with AML cases and 100 healthy Saudi controls involved in this study. Opting for only 2 SNPs involved in this study is one of the major limitations of this study. Missing of anthropometrical and clinical data was another limitation of this study.

CONCLUSION

In conclusion, the current study findings revealed a negative correlation as well as a protective factor for AML with the C481T and G857A polymorphisms in the NAT2 gene. The current study findings verified the comparable correlation found in Chinese studies.

Declarations

Conflict of Interest: I don't have any conflict of Interest towards this manuscript.

REFERENCE

- AbdelGhaffar MT, Allam AA, Darwish S, Al-Ashrawy GM, Eshra KA, Ibrahim RR (2019) Study of N-acetyl transferase 2 single-gene polymorphism (rs1799931) in patients with acute myeloid leukemia. *Egyptian J Haematol* 44: 157. https://doi.org/10.4103/ejh.ejh_35_22
- Adole PS, Kharbada PS, Sharma S (2016) N-acetyltransferase 2 (NAT2) gene polymorphism as a predisposing factor for phenytoin intoxication in tuberculous meningitis or tuberculoma patients having seizures-A pilot study. *Indian J Med Res* 143: 581. <https://doi.org/10.4103/0971-5916.187106>
- Al-Shaqha WM, Alkharfy KM, Al-Daghri NM, Mohammed AK (2015) N-acetyltransferase 1 and 2 polymorphisms and risk of diabetes mellitus type 2 in a Saudi population. *Ann Saudi Med* 35: 214-221. <https://doi.org/10.5144/0256-4947.2015.214>
- Al-Ahmad MM, Amir N, Dhanasekaran S, John A, Abdulrazzaq YM, Ali BR, Bastaki S (2017) Studies on N-Acetyltransferase (NAT2) genotype relationships in Emiratis: confirmation of the existence of phenotype variation among slow acetylators. *Ann Hum Genet* 81: 190-196. <https://doi.org/10.1111/ahg.12198>
- Alshammary AF, Al-Hakeem MM, Ali Khan I (2023) Saudi community-based screening study on genetic variants in β -cell dysfunction and its role in women with gestational diabetes mellitus. *Genes* 14: 924. <https://doi.org/10.3390/genes14040924>
- Alshammary AF, Ansar S, Farzan R, Alsobaie SF, Alageel AA, Al-Hakeem MM, Ali Khan I (2023) Dissecting the molecular role of ADIPOQ SNPs in Saudi women diagnosed with gestational diabetes mellitus. *Biomedicine* 11: 1289. <https://doi.org/10.3390/biomedicine11051289>
- Alshammary AF, Khan IA (2021). Screening of obese offspring of first-cousin consanguineous subjects for the angiotensin-converting enzyme gene with a 287-bp alu sequence. *J Obesity Metab Syndrome* 30: 63. <https://doi.org/10.7570/jomes20086>
- Bhatnagar B, Kohlschmidt J, Mrózek K, Zhao Q, Fisher JL, Nicolet D, Giacomelli B (2021) Poor survival and differential impact of genetic features of Black patients with acute myeloid leukemia. *Cancer Dis* 11: 626-637. <https://doi.org/10.1158/2159-8290.CD-20-1579>
- Bu R, Gutierrez M, Al-Rasheed M, Belgaumi A, Bhatia K (2004) Variable drug metabolism genes in Arab population. *Pharmacogenom J* 4: 260-266. <https://doi.org/10.1038/sj.tpj.6500251>
- Bullinger L, Döhner K, Döhner H (2017) Genomics of acute myeloid leukemia diagnosis and pathways. *J Clin Oncol* 35: 934-946. <https://doi.org/10.1200/JCO.2016.71.2208>
- Castro I, Sampaio-Marques B, C Arcias A, Sousa H, Fernandes Â, Sanchez-Maldonado JM, Ludovico P (2021) Functional genetic variants in ATG10 are associated with acute myeloid leukemia. *Cancers* 13: 1344. <https://doi.org/10.3390/cancers13061344>
- Chamseddine AN, Jabbour E, Kantarjian HM, Bohannon ZS, Garcia-Manero G (2016) Unraveling myelodysplastic syndromes: current knowledge and future directions. *Curr Oncol Rep* 18: 1-11. <https://doi.org/10.1007/s11912-015-0489-2>
- Cucchi DG, Polak TB, Ossenkuppele GJ, Uyl-De Groot CA, Cloos J, Zweegman S, Janssen JJ (2021) Two decades of targeted thera-

- pies in acute myeloid leukemia. *Leukemia* **35**: 651–660. <https://doi.org/10.1038/s41375-021-01164-x>
- Docking TR, Parker JD, Jädersten M, Duns G, Chang L, Jiang J, Chiu R (2021) A clinical transcriptome approach to patient stratification and therapy selection in acute myeloid leukemia. *Nat Commun* **12**: 1–15. <https://doi.org/10.1038/s41467-021-22625-y>
- Döhner H, Weisdorf DJ, Bloomfield CD (2015) Acute myeloid leukemia. *New Engl J Med* **373**: 1136–1152. <https://doi.org/10.1056/NEJMra1406184>
- Farasani A (2019) Genetic variants of glutathione S-transferase and the risk of acute myeloid leukemia in a Saudi population. *Saudi J Biol Sci* **26**: 1525–1530. <https://doi.org/10.1016/j.sjbs.2018.12.011>
- Fayez D, Saliminejad K, Irani S, Kamali K, Memariani T, Khorshid HRK (2018) Arylamine N-acetyltransferase 2 polymorphisms and the risk of endometriosis. *Avicenna J Med Biotechnol* **10**: 163
- Gaafar A, Sheereen A, Almohareb F, Eldali A, Chaudhri N, Mohamed SY, El Fakih R (2018) Prognostic role of KIR genes and HLA-C after hematopoietic stem cell transplantation in a patient cohort with acute myeloid leukemia from a consanguineous community. *Bone Marrow Transplant* **53**: 1170–1179. <https://doi.org/10.1038/s41409-018-0123-7>
- García-Martin E (2008) Interethnic and intraethnic variability of NAT2 single nucleotide polymorphisms. *Curr Drug Metab* **9**: 487–497. <https://doi.org/10.2174/138920008784892155>
- Gra O, Glotov A, Kozhekbayeva ZM, Makarova O, Nasedkina T (2008). Genetic polymorphism of GST, NAT2, and MTRR and susceptibility to childhood acute leukemia. *Mol Biol* **42**: 187–197. <https://doi.org/10.1134/S0026893308020039>
- Jarrar Y, Ismail S, Irshaid Y (2010) N-Acetyltransferase-2 (NAT2) genotype frequency among Jordanian volunteers. *Int J Clin Pharmacol Therap* **48**: 688
- Jarrar YB, Balasmeh AA, Jarrar W (2018) Sequence analysis of the N-acetyltransferase 2 gene (NAT2) among Jordanian volunteers. *Libyan J Med* **13**. <https://doi.org/10.1080/19932820.2017.1408381>
- Kamel AM, Ebid GT, Moussa HS (2015) N-Acetyltransferase 2 (NAT2) polymorphism as a risk modifier of susceptibility to pediatric acute lymphoblastic leukemia. *Tumor Biol* **36**: 6341–6348. <https://doi.org/10.1007/s13277-015-3320-7>
- Kaser EC, Zhao L, D'mello KP, Zhu Z, Xiao H, Wakefield MR, Fang Y (2021) The role of various interleukins in acute myeloid leukemia. *Med Oncol* **38**: 1–6. <https://doi.org/10.1007/s12032-021-01498-7>
- Khan IA, Jahan P, Hasan Q, Rao P (2019) Genetic confirmation of T2DM meta-analysis variants studied in gestational diabetes mellitus in an Indian population. *Diabetes Metab Syndr* **13**: 688–694. <https://doi.org/10.1016/j.dsx.2018.11.035>
- Khan S, Mandal RK, Elaslali AM, Dar SA, Jawed A, Wahid M, Akhter N (2019) Pharmacogenetic association between NAT2 gene polymorphisms and isoniazid induced hepatotoxicity: trial sequence meta-analysis as evidence. *Biosci Rep* **39**. <https://doi.org/10.1042/BSR20180845>
- Lafuente A, Pujol F, Carretero P, Villa JP, Cuchi A (1993) Human glutathione S-transferase μ (GST μ) deficiency as a marker for the susceptibility to bladder and larynx cancer among smokers. *Cancer Lett* **68**: 49–54. [https://doi.org/10.1016/0304-3835\(93\)90218-X](https://doi.org/10.1016/0304-3835(93)90218-X)
- Majumdar S, Mondal BC, Ghosh M, Dey S, Mukhopadhyay A, handra S, Dasgupta UB (2008) Association of cytochrome P450, glutathione S-transferase and N-acetyl transferase 2 gene polymorphisms with incidence of acute myeloid leukemia. *Eur J Cancer Prev* **17**: 125–132
- Pegoraro A, Orioli E, De Marchi E, Salvestrini V, Milani A, Di Virgilio F, Adinolfi E (2020) Differential sensitivity of acute myeloid leukemia cells to daunorubicin depends on P2X7A versus P2X7B receptor expression. *Cell Death Dis* **11**: 1–12. <https://doi.org/10.1038/s41419-020-03058-9>
- Rajasekaran M, Abirami S, Chen C (2011) Effects of single nucleotide polymorphisms on human N-acetyltransferase 2 structure and dynamics by molecular dynamics simulation. *PLoS One* **6**: e25801. <https://doi.org/10.1371/journal.pone.0025801>
- Santos ECL d, Pinto AC, Klumb EM, Macedo JMB (2016) Polymorphisms in NAT2 (N-acetyltransferase 2) gene in patients with systemic lupus erythematosus. *Revista Brasileira Reumatol* **56**: 521–529. <https://doi.org/10.1016/j.rbre.2016.09.015>
- Sasaki K, Ravandi F, Kadia TM, DiNardo CD, Short NJ, Borthakur G, Kantarjian HM (2021) De novo acute myeloid leukemia: A population-based study of outcome in the United States based on the Surveillance, Epidemiology, and End Results (SEER) database, 1980 to 2017. *Cancer* **127**: 2049–2061. <https://doi.org/10.1002/cncr.33458>
- Tanira, MO, Simsek M, Al Balushi K, Al Lawatia K, Al Barawani H, Bayoumi RA (2003) Distribution of arylamine N-acetyltransferase 2 (NAT2) genotypes among Omanis. *J Sci Res Med Sci/Sultan Qaboos Univ* **5**: 9
- Tian FS, Shen L, Ren YW, Zhang Y, Yin ZH, Zhou BS. (2014) N-acetyltransferase 2 gene polymorphisms are associated with susceptibility to cancer: a meta-analysis. *Asian Pacific J Cancer Prev* **15**: 5621–5626. <https://doi.org/10.7314/APJCP.2014.15.14.5621>
- Yarosh SL, Kokhtenko EV, Churnosov MI, Ataman AV, Solodilova MA, Polonikov AV (2014) Synergism between the N-acetyltransferase 2 gene and oxidant exposure increases the risk of idiopathic male infertility. *Reproductive Biomed Online* **29**: 362–369. <https://doi.org/10.1016/j.rbmo.2014.04.008>
- Zahra MA, Kandeel M, Aldossary SA, Al-Taher A (2020) Study on genotyping polymorphism and sequencing of N-acetyltransferase 2 (NAT2) among Al-Ahsa population. *BioMed Res Int* **2020**: 8765347. <https://doi.org/10.1155/2020/8765347>
- Zanrosso CW, Emerenciano M, Faro A, de Aguiar Gonçalves BA, Mansur MB, Pombo-de-Oliveira MS (2012) Genetic variability in N-acetyltransferase 2 gene determines susceptibility to childhood lymphoid or myeloid leukemia in Brazil. *Leukemia Lymphoma* **53**: 323–327. <https://doi.org/10.3109/10428194.2011.619605>
- Zhu X, Liu Y, Chen G, Guo Q, Zhang Z, Zhao L, Wang B (2019) Association between NAT2 polymorphisms and acute leukemia risk: A meta-analysis. *Medicine* **98**. <https://doi.org/10.1097/MD.00000000000014942>
- Zou Y, Dong S, Xu S, Gong Q, Chen J (2017) Genetic polymorphisms of NAT2 and risk of acute myeloid leukemia: a case-control study. *Medicine* **96**. <https://doi.org/10.1097/MD.00000000000007499>

Discovery of a novel genetic variant in the *N-acetyltransferase2* (*NAT2*) gene that is associated with bladder cancer risk

Lina Elsalem¹✉, Ahmad Al Shatnawi^{1,2}, Mahmoud A Alfaqih^{3,4}, Ayat Alshoh¹, Saddam Al Demour⁵, Ali Al-Daghmin^{6,7}, Omar Halalsheh⁸, Khalid Kheirallah⁹ and Mamoun Ahram¹⁰

¹Jordan University of Science and Technology, Faculty of Medicine, Department of Pharmacology, Irbid, Jordan; ²Royal Medical Services, Department of Clinical Pharmacy, Irbid, Jordan; ³Department of Biochemistry, College of Medicine and Medical Sciences, Arabian Gulf University, Manama, Bahrain; ⁴Department of Physiology and Biochemistry, Faculty of Medicine, Jordan University of Science and Technology, Irbid, Jordan; ⁵The University of Jordan, School of Medicine, Department of Special Surgery, Division of Urology, Amman, Jordan; ⁶King Hussein Cancer Center, Department of Surgery, Amman, Jordan; ⁷Abdali Medical Center, Amman, Jordan; ⁸Jordan University of Science and Technology, Faculty of Medicine, Department of General Surgery and Urology, Irbid, Jordan; ⁹Jordan University of Science and Technology, Faculty of Medicine, Department of Public Health and Community Medicine, Irbid, Jordan; ¹⁰The University of Jordan, School of Medicine, Department of Physiology and Biochemistry, Amman, Jordan

Smoking is a main risk factor for bladder cancer (BC). *NAT2* is a drug-metabolizing enzyme that catalyses the detoxification of many xenobiotics and carcinogens. Single nucleotide polymorphism (SNP) in *NAT2* results in different acetylation phenotypes (fast, intermediate or slow). Certain *NAT2* SNPs were associated with BC and/or modified the association of BC with smoking. However, limited evidence is available among BC patients or smokers from Jordan. This study aimed to discover novel SNPs in *NAT2* and to assess the association with BC. This was a case-control study among 120 BC patients and 120 controls. Amplification of a 446 bp fragment of *NAT2* encoding the N-catalytic domain was conducted using a polymerase chain reaction. Gene sequencing was done using Sanger-based technology. A total of 40 SNPs were detected. Two variants were significantly associated with BC ($p < 0.05$); namely a novel c.87G>A and the reported c.341T>C. Regarding c.87G>A, genotype distribution was significantly associated with BC and subgroup analysis confirmed that this was significant in both smokers ($p = 0.007$) and non-smokers ($p = 0.001$). Regression subgroup analysis suggested GA as a risk factor among smokers (AOR = 2.356). The frequencies of TC and CC genotypes of c.341T>C were significantly higher in BC ($p < 0.05$). This was statistically significant among smokers only ($p = 0.044$), upon subgroup analysis. Multivariate analysis showed that subjects with TC genotype are 6.15 more likely to develop BC and regression subgroup analysis revealed TC as a risk factor among smokers (AOR = 5.47). This is the first study from Jordan to report the association of smoking and two *NAT2* variants with BC. The data supports the use of GA and TC genotypes of the novel c.87G>A and the reported c.341T>C SNPs, respectively as potential biomarkers of BC, particularly among smokers. Future investigations with a larger population are required to support our findings.

Keywords: *NAT2*, single nucleotide polymorphism, smoking, bladder cancer, c.87G>A, c.341T>C

Received: 21 December, 2022; revised: 10 April, 2023; accepted: 12 April, 2023; available on-line: 18 August, 2023

✉e-mail: lmelsalem@just.edu.jo

Acknowledgements of Financial Support: This study was funded by the Deanship of Research of Jordan University of Science and Technology, Grant number 20180049.

Abbreviations: AOR, adjusted odds ratio; BC, Bladder cancer; BMI, body mass index; CI, confidence interval; EDTA,

Ethylene-Diamine-Tetra-Acetic acid; *NAT2*, *N-acetyltransferase 2*; OR, odds ratio; PCR, Polymerase chain reaction; SNPs, single nucleotide polymorphisms

INTRODUCTION

Globally, bladder cancer (BC) ranks as the 10th most common malignancy (Bray *et al.*, 2018) with tobacco smoking being a main risk factor for the disease development (Freedman *et al.*, 2011, Saginala *et al.*, 2020). Studies reported a 4-folds increased risk for BC among smoker individuals in comparison to non-smokers (Colombel *et al.*, 2008). In addition, more invasive phenotypes of BC were described in smoker patients compared with non-smokers (Jiang *et al.*, 2012). It is well known that tobacco contains more than 4000 chemicals, 60 of which are listed as carcinogens (Richter *et al.*, 2008). Examples of carcinogenic chemicals that are found in cigarette smoking are aromatic and heterocyclic amines (Turesky and Le Marchand 2011). These chemicals are detoxified by different drug-metabolizing enzymes including *N-acetyltransferase 2* (*NAT2*) (Sanderson *et al.*, 2007).

Human *NAT2* is a Phase II drug metabolizing enzyme that is involved in the detoxification of many xenobiotics and carcinogens by catalyzing the transfer of an acetyl group from acetyl CoA as a donor to the acceptor compound (Grant *et al.*, 1992). Many studies reported inter-individual variations in the rate of acetylation, with subjects classified as fast, intermediate or slow acetylators (Werely *et al.*, 2007; Garcia-Martin 2008; Sabbagh *et al.*, 2011; Al-Ahmad *et al.*, 2017; Aklilu *et al.*, 2018). Phenotypic differences in acetylation rate explain some of the variation observed in the therapeutic/side effect profile of drugs metabolized by *NAT2* such as isoniazid, sulfonamides and others (Werely *et al.*, 2007; Ladero 2008; Sim *et al.*, 2014; Adole *et al.*, 2016). Moreover, many reports suggested that the above differences may also modify the risk of developing BC (Hein 2006) and/or modify the association of BC with smoking (Tao *et al.*, 2010; Moore *et al.*, 2011; Ribouh-Arras *et al.*, 2019). Tao *et al.*, showed that environmental tobacco smoke increased the risk of BC among slow *NAT2* acetylators (Tao *et al.*, 2010). In addition, a large population-based study from the US revealed that exposure intensity to tobacco smoking was correlated with BC risk in patients with slow acetylation (Moore *et al.*, 2011). A recent study among the Lebanese population has shown that patients

with high BC risk were mainly males, current smokers, alcohol drinkers and those with occupational history of exposure to aromatic amines (Nasr *et al.*, 2017). Further investigations have shown a strong association between NAT2 slow acetylator phenotype and smoking which is attributed to higher BC risk among the Algerian population (Ribouh-Arras *et al.*, 2019).

The NAT2 acetylation phenotype is largely determined by genetic variations in the sequence of the gene encoding the NAT2 enzyme. This gene, also known as *NAT2*, is located on chromosome 2 and has two exons separated by one intron (Blum *et al.*, 1990). Transient heterologous transfection of constructs that contain only the second exon of *NAT2* is sufficient to produce a fully functional enzyme upon its translation (Boukouvala *et al.*, 2003). Not surprisingly, most of the sequence variations in *NAT2* that result in phenotypic differences in acetylation are located within the second exon which is 873 bps in length (Boukouvala *et al.*, 2003; Ribouh-Arras *et al.*, 2019).

Jordan is a Third World Middle Eastern country with one of the highest numbers of cigarette smokers per capita worldwide (Jaghhir *et al.*, 2014). BC is considered the third most cancer in male patients and accounts for almost 5% of all cancer cases diagnosed in Jordan (Directorate-MOH 2014). In addition, BC is a foremost cause of cancer related death in Jordan. Up to our knowledge, no research group in Jordan has ever sequenced the coding region of *NAT2* to search for novel population specific polymorphisms, despite the importance of having such a database from a pharmacogenetic and personalized medicine standpoint. In addition, no studies to date examined the association between genetic variants of *NAT2* and BC risk in Jordan.

The N-catalytic domain of the NAT2 enzyme is found within the second exon of *NAT2*. Several reports found that most of the genetic variation in the *NAT2* gene that leads to changes in acetylation activity is located within the above domain (Boukouvala *et al.*, 2003; Ribouh-Arras *et al.*, 2019). Given the above gaps, we sequenced a stretch of the second exon of the *NAT2* gene from subjects of a BC case-control study to discover novel sequence polymorphisms in *NAT2*, test their association with BC in Jordan, and examine if these polymorphisms modify the link between BC and smoking.

MATERIALS AND METHODS

Ethical approval

This study has the approval of the Deanship of Research and the Institutional Review Board committees of (Jordan University of Science and Technology, King Abdullah University Hospital (KAUH)), (University of Jordan, Jordan University Hospital (JUH)) and (King Hussein Cancer Center (KHCC)), (IRB numbers 25/112/2018, 2018/127 and 30/2018, respectively). Subjects were enrolled in this study after providing an informed consent form.

Study Settings and Subjects Enrolment

This was a case-control study among 120 BC patients from Jordan who attended the Urology clinics of KAUH located in the North of Jordan. Patients were also enrolled from the Urology clinics of JUH and the Oncology clinics of KHCC, both located in the capital city.

Patients were included if they were diagnosed with transitional cell carcinoma (TCC) of BC as their primary cancer and were being treated for BC at the time of enrolment at each respective hospital. On the other hand, patients were excluded if they have BC of other subtypes rather than TCC or if BC was a secondary tumor.

Patients were interviewed by a clinical research coordinator who described the study's objectives and clarified that the study will include the collection of demographic, anthropometric measurements and clinical data as well as a blood sample.

Demographic data included the patient age, gender and smoking status, while anthropometric data included the patient height and weight needed to calculate the Body Mass Index (BMI). Clinical data including the pathological stage of the tumor at the time of its diagnosis was obtained from the electronic medical records.

Regarding the control group, it included 120 subjects who attended Family Medicine clinics of KAUH and JUH without a medical history of bladder disease. Control subjects were matched with cases by gender, BMI and smoking status. Subjects in the control group were excluded if they had a medical history of any urology-related symptoms (difficulty upon urinating, blood and other discharges in the urine, burning upon urination).

Of note, all interviews of both groups were conducted by the same coordinator for the duration of patient recruitment.

Blood sample collection

A single venous blood sample (3 ml) was collected from each subject using ethylenediamine tetraacetic acid (EDTA) tubes (AFCO, Amman, Jordan). Tubes were mixed properly to prevent clotting. Blood samples were stored at 4°C for the subsequent DNA extraction.

DNA extraction, PCR and sequencing

Genomic DNA extraction was carried out using the QIAamp DNA Blood Mini Kit (Qiagen, Hilden, Germany) according to the manufacturer's instructions. Following the final step of the protocol, DNA concentration was measured using an ND-2000 Nanodrop (Thermo Scientific, Waltham, MA, USA). DNA samples were stored at -80°C for further processing (i.e. amplification followed by sequencing).

Using the Ensembl genome browser 98 (<http://www.ensembl.org/index.html>), the location of the N-catalytic domain was mapped on the nucleotide sequence of the second exon. A primer pair that flanks the N-catalytic domain was then designed using Primer 3 software (<http://primer3.ut.ee>). Primers were designed to amplify a 446 bp fragment. The sequence of the forward primer was (5' to 3'): CTTGCTTAGGGGATCATGGA while the sequence of the reverse primer was (5' to 3'): GGCTGATCCTTCCCAGAAAT.

Conventional polymerase chain reaction (PCR) was then used to amplify the aforementioned 446 bp fragment. The details of the PCR reaction mixture were as Alfaqih and others (Alfaqih *et al.*, 2018). The PCR reaction mixture was then incubated in a T100 thermal cycler (Biorad, Berkeley, CA, USA) under the following reaction conditions; (i) initial denaturation step (95°C, 3 minutes), (ii) 35 denaturation cycles (95°C, 3 minutes), (iii) annealing (65°C, 30 seconds) and (iv) extension (72°C, one minute) and (v) a final extension (72°C, 5 minutes).

Prior to sequencing the PCR products, 5 µl of the PCR mixture were loaded into a 2% agarose gel stained with ethidium bromide. The electrophoresis was run at

Table 1. Distribution of study subjects by independent variables and by disease status

Variable	Controls (n=120)	Bladder cancer (n=120)	p-value
Gender (n) (%)			
Males	106 (88.3%)	104 (86.7%)	0.423
Females	14 (11.7%)	16 (13.3%)	
Smoking (n) (%)			
Yes	68 (56.7%)	79 (65.8%)	0.093
No	52 (43.3%)	41 (34.2%)	
Age (years) ^a	60.46 (12.02)	64.80 (12.32)	0.006
BMI (kg/m ²) ^a	28.50 (5.00)	28.60 (7.20)	0.906

^amean \pm standard deviation; BMI, body mass index. The *p*-values were calculated by Pearson Chi-square test for gender, and smoking (%), while the student's *t*-test was used for Age, BMI

140 volts for 40 minutes. Ultraviolet light was used to visualize the products. PCR products of the previous step were sent to (Center Name) for sequencing using Sanger-based technology. Sequencing was performed from both ends of the fragment using the forward and reverse primers of the original PCR reaction.

The Chromas Pro Software (<http://technelysium.com.au/wp/chromas>) was used to visualize sequence chromatograms. The above software was also used for sequence alignment with a reference sequence of the second exon of *NAT2* to identify genetic variants in the sequence. The NCBI (<http://www.ncbi.nlm.nih.gov>) and Ensemble genome browsers were used to indicate if any of the identified genetic variants are new or previously reported.

Of note, the alleles and genotypes were successfully determined for all SNPs among all enrolled subjects. The allele and genotype frequencies of each SNP were calculated using standard methods. Deviations from Hardy Weinberg equilibrium were tested using a chi-square test.

In-silico predictions for the effect of genetic SNPs on NAT2 protein

Four web-based applications; PolyPhen 2.0 (<http://genetics.bwh.harvard.edu/pph2/>), SIFT (<https://sift.bii.a-star.edu.sg/>), PROVEAN (<http://provean.jcvi.org/index.php>) and Mutation Taster (<http://www.mutationtaster.org/>) were used to predict the effect of NAT2 SNPs on protein structure and function.

Statistical analysis

The minimum sample size required to meet the study objective was estimated based on Pourhoseingholi and others (Pourhoseingholi *et al.*, 2013): BC prevalence in Jordan (5%), a margin of error which was set to be $\pm 5\%$ and, a confidence level that was set to be 95%, with 5% alpha level, and power level of 80%. Based on the above information, the minimum sample size required was 73. The number of BC patients who enrolled was 120.

Statistical analysis was carried out using the Statistical Package for Social Studies (SPSS) software (version 23, IBM, NY). Student *t*-test was used to evaluate if significant differences exist between cases and controls in terms of age and BMI, while Pearson Chi-square was used for gender and smoking status. Pearson's Chi-square was also used to evaluate the association of allele or genotype distributions with BC risk. Subgroup analysis was also done according to smoking status. Results were considered significant if $p \leq 0.05$.

Multivariate logistic regression analysis was done to define the association of c.341T>C and c.87G>A SNPs with BC risk in the presence of potential confounders

including age, gender, smoking, and BMI. Results were considered significant if $p \leq 0.05$ with a confidence limit of 95%. Regression subgroup analysis was also conducted according to smoking status.

RESULTS

Subject characteristics

A total of 240 subjects were recruited in this study; 120 BC cases and 120 controls. The characteristics are summarized in Table 1. Among cases, the majority (86.7%) were males and 65.8% were smokers. The majority of the cases were in earlier stages of BC; non-muscle-invasive (Ta=48.33% and T1=36.67%) and muscle-invasive (T2=7.5%, T3=5% and T4=2.5%).

Among controls, 88.3% were males and 56.7% were smokers. While significant differences in case status by gender, smoking status, and BMI were not statistically significant, the mean age of cases (64.80 (12.32)) was significantly higher than that for controls (60.46 (12.02)) ($p=0.006$).

Mutational analyses of a 446 bp fragment of the second exon of the NAT2 gene among study subjects

A total number of 40 variants were detected in our sample. These were a substitution in one single nucleotide (SNPs) and we did not detect any insertions or deletions (Fig. 1 Supplementary at <https://ojs.ptbioch.edu.pl/index.php/abp/>). Out of the 40 SNPs detected in our population, 12 SNPs were previously reported while 28 SNPs were not reported in any of the publicly available databases (GenBank or Ensembl) (Table A Supplementary at <https://ojs.ptbioch.edu.pl/index.php/abp/>). None of the SNPs detected in this study had a minor allele frequency of less than 0.2. All of the SNPs were in agreement with Hardy Weinberg Equilibrium except for the two novel SNPs (c.147G>C) and (c.162T>C) ($P < 0.05$). These two SNPs were thus excluded from further analysis. All of the remaining SNPs were brought forward for further evaluation of their association with the risk of BC.

The association of genotypic and allelic frequencies of NAT2 SNPs with bladder cancer

The relationship between 38 SNPs discovered in the sequenced region of the *NAT2* gene and BC was evaluated. Out of 38 SNPs that fit these criteria, only two SNPs showed a significant relationship with BC case status ($p < 0.05$); the reported SNP (c.341T>C) and the novel SNP (c.87G>A).

Table 2. Genotype frequencies of NAT2 SNPs in study subjects.

SNP ID	Genotype	Control n (%)	Bladder cancer n (%)	p-value
c.341T>C	TT	15 (12.5%)	3 (2.5%)	0.0097
	TC	105 (87.5%)	113 (94.2%)	
	CC	0 (0.0%)	4 (3.3%)	
	Total	120 (100%)	120 (100%)	
c.87G>A	GG	66 (55.0%)	53 (44.2%)	0.001
	GA	54 (45.0%)	51 (42.5%)	
	AA	0 (0.0%)	16 (13.3%)	
	Total	120 (100%)	120 (100%)	

The *p*-values were calculated by the Pearson Chi-square test

Table 3. Allele frequencies of NAT2 SNPs in study subjects.

SNP ID	Allele	Control n (%)	Bladder cancer n (%)	p-value
c.341T>C	T	135 (56.2%)	119 (49.6%)	0.143
	C	105 (43.8%)	121 (50.4%)	
c.87G>A	G	186 (77.5%)	157 (65.4%)	0.003
	A	54 (22.5%)	83 (34.6%)	

The *p*-values were calculated by the Pearson Chi-square test

Genotype distribution of c.341T>C by case status was statistically significant ($p=0.0097$). The frequency of the heterozygous TC and the homozygous CC genotypes was higher among BC cases than their control counterparts (Table 2). Similarly, the genotype distribution of c.87G>A was significantly different by case status ($p=0.001$). The homozygous GG and the heterozygous GA were higher among controls compared to cases, while the homozygous AA genotype was higher in BC cases (Table 2).

Regarding the analysis of alleles association with BC (Table 3), it was found that for c.341T>C, the frequency of the T allele was higher among controls, compared to BC cases, while the frequency of the C allele was higher in cases. For c.87G>A, the frequency of the G allele was significantly higher among controls, while the frequency of the A allele was significantly higher in BC cases ($p=0.003$).

Upon subgroup analysis of genotype frequency among smokers and non-smokers, separately (Table 4), the genotype distribution of c.341T>C showed a significant association with disease status, cases vs. controls, among smokers only ($p=0.044$). Among non-smokers,

the distribution of c.341T>C by disease status, cases vs. controls, was not statistically significant ($p=0.063$) (Table 4). Regarding the genotype distribution of the novel SNP c.87G>A by case status among smokers and non-smokers, statistically significant differences were detected between genotype and case status among both smokers and non-smokers.

Multivariate regression analysis of NAT2 SNPs with bladder cancer

BC patients in this study were significantly older than controls and the percentage of smokers was higher in BC patients than in controls but not statistically significant. Accordingly, a multivariate regression analysis was done to assess if any of the NAT2 SNPs significantly modulates BC risk upon adjustment of potential confounders. Table 5 represents all variables in the model to assess the effect of genotypes on BC after controlling the effects of age, gender, BMI, and smoking.

It was found that smoking and age increased the risk of BC ($p<0.05$). Upon controlling for the effect of gender, age, BMI, and smoking status, the genotype distribution of c.341T>C was significantly involved in BC

Table 4. The Genotyping frequencies and smoking status

Smoking status	SNP ID	Genotype	Control n (%)	Bladder cancer n (%)	p-value
Smokers	c.341T>C	TT	7 (10.3%)	2 (2.5%)	0.044
		TC	61 (89.7%)	74 (93.7%)	
		CC	0 (0.0%)	3 (3.8%)	
		Total	68 (100%)	79 (100%)	
	c.87G>A	GG	44 (64.7%)	35 (44.3%)	0.007
		GA	24 (35.3%)	37 (46.8%)	
		AA	0 (0.0%)	7 (8.9%)	
		Total	68 (100.0%)	79 (100%)	
Non-Smokers	c.341T>C	TT	8 (15.4%)	1 (2.4%)	0.063
		TC	44 (84.6%)	39 (95.1%)	
		CC	0 (0.0%)	1 (2.4%)	
		Total	52 (100.0%)	41 (100.0%)	
	c.87G>A	GG	22 (42.3%)	18 (43.9%)	0.001
		GA	30 (57.7%)	14 (34.1%)	
		AA	0 (0.0%)	9 (22.0%)	
		Total	52 (100%)	41 (100.0%)	

The *p*-values were calculated by the Pearson Chi-square test

Table 5. Adjusted effects of genotypes on Bladder Cancer

	p-value	AOR (95% C.I.)
BMI	0.762	0.992 (0.943-1.044)
Age	0.002	1.042 (1.015-1.068)
Gender Females vs Male	0.319	0.63 (0.254-1.563)
Smoker vs non-smoker	0.037	1.908 (1.038-3.507)
c.341T>C		
TT	0.007	Ref
TC	0.999	6.158 (1.652-22.953)
CC		—*
c.87G>A		
GG	0.261	Ref
GA	0.998	1.394 (0.781-2.49)
AA		—*

AOR, adjusted odds ratio; CI, confidence interval; *Distorted AOR.

development. Subjects with the TC genotype were 6.15 more likely to develop BC compared to TT ($p=0.007$ and 95% C.I.=1.6 to 22.9). Regarding the c.87G>A genotype distribution, the p -value indicated no significant difference ($p>0.05$).

Regression subgroup analysis with smoking status

We further conducted the analysis by smoking status **Table 6**. Regarding the c.341T>C SNP, the TC was a risk factor among smokers (5.47 times), ($p=0.044$ and 95% C.I.=1.044 to 28.679). Regarding c.87G>A, GA was a risk factor only among smoker patients (AOR=2.356, $p=0.019$ and 95% C.I.=1.152 to 4.819).

Prediction of the effect of NAT2 SNPs on protein function and phenotype

All SNPs effects were predicted depending on different in-silico predictions websites which are Mutation Taster, PROVEAN, Polyphen-2 and Sift. **Table 7** represents the prediction of the reported SNP c.341T>C and the novel SNP c.87G>A. For c.341T>C, Isoleucine amino acid was changed to Threonine at position 114 of the amino acids sequence. It was predicted as being polymorphism, deleterious, affecting the protein function and reflecting slow acetylator phenotype. Regarding c.87G>A, no change was detected in the amino acid sequence (Glutamine amino acid), however, it was predicted as a disease-causing, neutral and tolerated.

DISCUSSION

Globally, BC is considered the 10th most common malignancy, and the 13th most fatal cancer, accounting for 2.1% of all cancer fatalities (Halaseh *et al.*, 2022). In Jordan, BC was found to be the fourth most prevalent cancer and accounting for 4.1% of all cancer deaths (Abdo *et al.*, 2021). NAT2 is an important enzyme that metabolizes xenobiotics, via acetylation reactions, hence,

Table 6. Regression subgroup analysis with smoking status

Genotype	p-value	AOR (95% C.I.)
Smokers		
c.341T>C		
TT	Ref	Ref
TC	0.044	5.472 (1.044-28.679)
CC	0.999	—*
c.87G>A		
GG	Ref	2.356 (1.152-4.819)
GA	0.019	—*
AA	0.999	
Non- Smokers		
c.341T>C		
TT	Ref	Ref
TC	0.061	9.106 (0.901-92.043)
CC	1	—*
c.87G>A		
GG	Ref	Ref
GA	0.286	0.559 (0.192-1.626)
AA	0.999	—*

AOR, adjusted odds ratio; CI, confidence interval; *Distorted AOR.

modulating susceptibility to environmental carcinogens and toxins that arise from tobacco products, diet, or other environmental exposures (Mittal *et al.*, 2004).

NAT2 gene is a polymorphic gene that encodes for NAT2 enzyme (Magalon *et al.*, 2008). Genetic variations in this gene result in three different phenotypes; rapid, intermediate, and slow acetylators affecting the drug metabolism, therapeutic effects and adverse effects, as well as the vulnerability of the individual to several carcinogens (Garcia-Martin, 2008; Ladero, 2008; Sabbagh *et al.*, 2011). Genetic polymorphisms of NAT2 have been found to be associated with susceptibility to develop different cancer types with various degrees (Avirmed *et al.*, 2021; Zhu *et al.*, 2021). It has been hypothesized that the increased susceptibility to BC among smokers is caused by genetic polymorphisms in the NAT2 gene that results in slow acetylation of the aromatic molecules that exist in tobacco (Tao *et al.*, 2010; Ribouh-Arras *et al.*, 2019), thus we aimed to test this hypothesis in our study.

To the extent of our knowledge, this study was the first to explore NAT2 polymorphism and its association with BC among the Jordanian population. Moreover, in our study, the effect of single nucleotide polymorphism of the NAT2 gene was stratified by smoking status to identify the effect of genetic variations regardless of smoking status.

Our study revealed – as expected – that the majority of BC patients were males and smokers. BC patients were found to be overweight, which is a previously known risk factor for BC in addition to the male gender and smoking (Kirkali *et al.*, 2005; Nasr *et al.*, 2017; Rezaei *et al.*, 2019).

We have investigated the association of several SNPs in the N-terminal catalytic domain in the NAT2 gene with the risk of BC. The results of our genetic analysis

Table 7. Prediction of novel NAT2 SNPs on NAT2 protein function and phenotype

SNP ID	NP	Mutation taster	PROVEAN	Polyphen-2	Sift
c.341T>C	p.Ile114Thr	Polymorphism	Deleterious	Benign	Affect protein function
c.87G>A	P.Glu29=	Disease causing	Neutral	Benign	Tolerated

showed that the frequency of the A allele and the AA genotype of the novel SNP c.87G>A was significantly higher in BC. Since tobacco smoking is a major risk factor for the development of BC we performed a stratified analysis. Interestingly, the analysis showed that these results were significant in both smokers and non-smokers, Regression subgroup analysis, however, showed that GA genotype was a risk factor for BC among smokers only. This may indicate that smoking modifies the association between BC and GA genotype of this SNP.

Individuals with the TC genotype of c.341T>C SNP are 6 times more likely to have BC compared to those with the TT genotype. This is consistent with findings of previous studies that revealed c.341T>C SNP with its slow acetylation phenotype to increase the risk of BC especially among smokers (El Desoky *et al.*, 2005; García-Closas *et al.*, 2005; Quan *et al.*, 2016; Song *et al.*, 2020). Furthermore, our results found that only smoking individuals carrying the C allele in our population could be at a higher risk of BC in view of their slower acetylation of tobacco smoking confirming the results of others (Marcus *et al.*, 2000), while contrasting other studies that indicate no difference in BC risk between different genotypes (Mittal *et al.*, 2004; Saleh *et al.*, 2019).

The reported SNP c.341T>C was predicted as polymorphism, benign, and affecting protein function with deleterious effects. In addition, this SNP is linked to slow acetylator phenotype. As mentioned earlier, this SNP increased the risk of BC among smokers. This is in accordance with other studies, where SNPs with slow acetylation are associated with a higher risk for different cancer types including BC, and mainly among smokers (Zhu *et al.*, 2015; Marcus *et al.*, 2000; Kabir & Rehman, 2018).

Our sequence analysis was limited to a short stretch (446 bp) of the second exon of the coding region of the *NAT2* gene; an area that only encompassed the N- catalytic functional domain of the enzyme. Sequence analysis of the entire coding region of the gene is required in future studies. This is especially important since previous studies from other populations showed that genetic areas outside the area sequenced in this investigation may contain genetic variants that affect enzyme function and acetylation phenotype (Boukouvala *et al.*, 2003; Ribouh-Arras *et al.*, 2019).

A high degree of polymorphism was discovered in this gene across a short stretch of the coding sequence. Previous studies also reported the *NAT2* gene as being highly polymorphic upon gene sequencing (Sekine *et al.*, 2001; Matimba *et al.*, 2009). Considering that more than half of the genetic variants discovered in this investigation were not previously reported, a more comprehensive evaluation of the *NAT2* gene polymorphism should be conducted on a larger number of individuals representing different geographic areas and ethnic backgrounds present in Jordan.

This report highlights the discovery of a novel SNP in the *NAT2* gene and its association with BC. Studies that examine the effect of the above SNP on enzyme function and/or structure should be conducted using purified enzyme preparations or mammalian cells transfected with vectors carrying the coding region of the enzyme. The above investigations could be coupled with *in vivo* assays which examine the acetylation kinetics of individuals that carry the different genotypes using safe and well tolerated substrates (for example, caffeine).

Considering that *NAT2* polymorphisms may affect the therapeutic dose and safety profile of many of the most commonly prescribed medications and the high

degree of polymorphism discovered in *NAT2* (at least among the Jordanian population), we suggest to build a national database of the most frequent alleles of the *NAT2* gene in Jordan including their effect on the metabolism of various drugs and medications. This database can then be used as a tool to promote *NAT2* pharmacogenetic profiling of patients as part of their treatment protocol.

The major strengths of this study include being the first study in Jordan in which a gene of pharmacogenetic importance was sequenced. This population-based study could represent the first step toward establishing a database of *NAT2* gene variants in Jordan – this gene is known to have wide variations across ethnicities (Yee *et al.*, 2020). Moreover, our study was not limited to investigating the effects of already reported polymorphisms but rather attempted to discover novel – not previously reported – variants. This might set up the stage for future population-based studies in the region. Moreover, stratifying our analyses according to smoking status enabled us to control smoking as a potential confounder. Our sample was retrieved from three major centers, one of them is the only specialized cancer center in Jordan, in which cancer patients are treated from all over the country. This makes our results generalizable to all Jordanians with BC.

Yet, this investigation is subject to several limitations. First, the relatively small sample size limits our ability to attain sufficient statistical power and increases the risk of type II error. Second, we acknowledge that we were not able to quantitatively assess the smoking status of participants in order to assess its dose-response relationship with BC, compared to what was done by Moore and others (Moore *et al.*, 2011). Third, this study did not investigate the acetylation activity of the enzyme nor evaluated the acetylation phenotype (by measuring N-acetylated metabolites after administration of drugs like isoniazid, or caffeine) (Grant *et al.*, 1984) distribution among study participants. Since this information is also lacking in Jordan, future studies investigating *NAT2* phenotype and genotype associated with BC in the Jordanian population are needed. The lack of enzyme modelling studies assessing the effects of newly discovered variants was another limitation. Finally, despite controlling for smoking status as a confounder, causal inferences still cannot be made due to the nature of observational studies, such as case-control studies, where a temporal sequence is lost.

CONCLUSION

This case-control study demonstrated that smoking and genetic variation in the *NAT2* gene are associated with BC risk. Although several investigations across multiple populations explored the association of *NAT2* polymorphism with the risk of BC, this is the first study from Jordan. Furthermore, this is the first report from the region to present genomic sequence data on the N-catalytic domain of the *NAT2* gene. This genomic-based approach allowed us to identify a novel variant c.87G>A that was not reported before and was found here to be associated with BC risk. In addition, we detected the previously reported SNP (c.341T>C) that was related to slow acetylation phenotype and was also found to increase BC risk. Our data supports the use of TC and GA genotypes of c.341T>C and c.87G>A SNPs, respectively as potential biomarkers of BC, particularly among smokers. However, further investigations with a larger

population are needed to validate our findings. Given the high prevalence of tobacco smoking in Jordan, the initiation of awareness campaigns that explain the implications of cigarette smoking on health and disease is strongly recommended.

Declarations

Authors' contributions. Conception: LE and MAA; Funding acquisition: LE; Methodology: LE, MAA, AAS, and AA; Interpretation or analysis of data: AAS, AA, and KK; Writing original draft: LE and MAA; Revision for important intellectual content: OH, SAD, AAD, KK and MA; Supervision: LE, MAA, OH, SAD, AAD, and MA. All authors have critically reviewed and approved the final draft and are responsible for the content.

Conflict of interests. The authors have no conflict of interest to disclose.

Acknowledgements. Many thanks to all bladder cancer patients and control subjects who participated in this study. Special thanks to staff members of the urology and oncology clinics of King Abdullah University Hospital, Jordan University Hospital and King Hussein Cancer Center.

Availability of data and materials. Data is available from the corresponding author upon reasonable request.

REFERENCES

- Abdo N, Alsoukhni M, Batieha A, Arqoub K (2021) Survival of patients with urinary bladder cancer in Jordan, 2005–2014. *East. Mediterr. Health J.* **27**: 648–655. <https://doi.org/10.26719/2021.27.7.648>
- Adole PS, Kharbanda PS, Sharma S (2016) N-acetyltransferase 2 (NAT2) gene polymorphism as a predisposing factor for phenytoin intoxication in tuberculous meningitis or tuberculoma patients having seizures – A pilot study. *Indian J. Med. Res.* **143**: 581–590. <https://doi.org/10.4103/0971-5916.187106>
- Aklilu E, Carrillo JA, Makonnen E, Bertilsson L, Djordjevic N (2018) N-Acetyltransferase-2 (NAT2) phenotype is influenced by genotype-environment interaction in Ethiopians. *Eur. J. Clin. Pharmacol.* **74**: 903–911. <https://doi.org/10.1007/s00228-018-2448-y>
- Al-Ahmad MM, Amir N, Dhanasekaran S, John A, Abdulrazzaq YM, Ali BR, Bastaki S (2017) Studies on N-acetyltransferase (NAT2) genotype relationships in emiratis: confirmation of the existence of phenotype variation among slow acetylators. *Ann. Hum. Genet.* **81**: 190–196. <https://doi.org/10.1111/ahg.12198>
- Alfaqih MA, Al-Mughales F, Al-Shboul O, Al Qudah M, Khader YS, Al-Jarrah M (2018) Association of Adiponectin and rs1501299 of the ADIPOQ Gene with Prediabetes in Jordan. *Biomolecules* **8**. <https://doi.org/10.3390/biom8040117>
- Avirmed S, Khuanbai Y, Sanjaajamts A, Selenge B, Dagvadorj BU, Ohashi M (2021) Modifying effect of smoking on GSTM1 and NAT2 in relation to the risk of bladder cancer in Mongolian population: A case-control study. *Asian Pac. J. Cancer Prev.* **22**: 2479–2485. <https://doi.org/10.31557/apjcp.2021.22.8.2479>
- Blum M, Grant DM, McBride W, Heim M, Meyer UA (1990) Human arylamine N-acetyltransferase genes: isolation, chromosomal localization, and functional expression. *DNA Cell Biol.* **9**: 193–203. <https://doi.org/10.1089/dna.1990.9.193>
- Boukouvla S, Price N, Plant KE, Sim E (2003) Structure and transcriptional regulation of the Nat2 gene encoding for the drug-metabolizing enzyme arylamine N-acetyltransferase type 2 in mice. *Biochem. J.* **375**: 593–602. <https://doi.org/10.1042/bj20030812>
- Bray F, Ferlay J, Soerjomataram I, Siegel RL, Torre LA, Jemal A (2018) Global cancer statistics 2018: GLOBOCAN estimates of incidence and mortality worldwide for 36 cancers in 185 countries. *CA Cancer J. Clin.* **68**: 394–424. <https://doi.org/10.3322/caac.21492>
- Colombel M, Soloway M, Akaza H, Böhle A, Palou J, Buckley R, Lamm D, Brausi M, Witjes JA, Persad R (2008) Epidemiology, staging, grading, and risk stratification of bladder cancer. *Eur. Urol. Suppl.* **7**: 618–626. <https://doi.org/10.1016/j.eursup.2008.08.002>
- Directorate-MOH, N-CD (2014) Cancer Incidence in Jordan – 2014. *Statistic Summary Jordan Cancer Registry*
- El Desoky ES, AbdelSalam YM, Salama RH, El Akkad MA, Atanasova S, von Ahsen N, Armstrong VW, Oellerich M (2005) NAT2*5/*5 genotype (341T>C) is a potential risk factor for schistosomiasis-associated bladder cancer in Egyptians. *Ther. Drug Monit.* **27**: 297–304. <https://doi.org/10.1097/01.fid.0000164197.95494.aa>
- Freedman ND, Silverman DT, Hollenbeck AR, Schatzkin A, Abnet CC (2011) Association between smoking and risk of bladder cancer among men and women. *JAMA* **306**: 737–745. <https://doi.org/10.1001/jama.2011.1142>
- García-Closas M, Malats N, Silverman D, Dosemeci M, Kogevinas M, Hein DW, Tardón A, Serra C, Carrato A, García-Closas R, Lloreta J, Castaño-Vinyals G, Yeager M, Welch R, Chanock S, Chatterjee N, Wacholder S, Samanic C, Torà M, Fernández F, Real FX, Rothman N (2005) NAT2 slow acetylation, GSTM1 null genotype, and risk of bladder cancer: results from the Spanish Bladder Cancer Study and meta-analyses. *Lancet (London, England)* **366**: 649–659. [https://doi.org/10.1016/s0140-6736\(05\)67137-1](https://doi.org/10.1016/s0140-6736(05)67137-1)
- García-Martin E (2008) Interethnic and intraethnic variability of NAT2 single nucleotide polymorphisms. *Curr. Drug Metab.* **9**: 487–497. <https://doi.org/10.2174/138920008784892155>
- Grant DM, Tang BK, Kalow W (1984) A simple test for acetylator phenotype using caffeine. *Br. J. Clin. Pharmacol.* **17**: 459–464. <https://doi.org/10.1111/j.1365-2125.1984.tb02372.x>
- Grant DM, Blum M, Meyer UA (1992) Polymorphisms of N-acetyltransferase genes. *Xenobiotica* **22**: 1073–1081. <https://doi.org/10.3109/00498259209051861>
- Halaseh SA, Halaseh S, Alali Y, Ashour ME, Alharayzah MJ (2022) A review of the etiology and epidemiology of bladder cancer: all you need to know. *Cureus* **14**: e27330. <https://doi.org/10.7759/cureus.27330>
- Hein DW (2006) N-acetyltransferase 2 genetic polymorphism: effects of carcinogen and haplotype on urinary bladder cancer risk. *Oncogene* **25**: 1649–1658. <https://doi.org/10.1038/sj.onc.1209374>
- Jaghbir M, Shreif S, Ahram M (2014) Pattern of cigarette and waterpipe smoking in the adult population of Jordan. *East. Mediterr. Health J.* **20**: 529–537. <https://doi.org/10.26719/2014.20.9.529>
- Jiang X, Castela JE, Yuan J-M, Stern MC, Conti DV, Cortessis VK, Pike MC, Gago-Dominguez M (2012) Cigarette smoking and subtypes of bladder cancer. *Int. J. Cancer* **130**: 896–901. <https://doi.org/10.1002/ijc.26068>
- Kabir S, Rehman A (2018) Carcinogenic potential of arylamine N-acetyltransferase in Asian populations. *J. Cancer Res. Pract.* **5**: 131–135. <https://doi.org/10.1016/j.jcrpr.2018.07.001>
- Kirkali Z, Chan T, Manoharan M, Algaba F, Busch C, Cheng L, Kiemeny L, Kriegmair M, Montironi R, Murphy WM, Sesterhenn IA, Tachibana M, Weider J (2005) Bladder cancer: epidemiology, staging and grading, and diagnosis. *Urology* **66**: 4–34. <https://doi.org/10.1016/j.urolgy.2005.07.062>
- Ladero JM (2008) Influence of polymorphic N-acetyltransferases on non-malignant spontaneous disorders and on response to drugs. *Curr. Drug Metab.* **9**: 532–537. <https://doi.org/10.2174/138920008784892038>
- Magalon H, Patin E, Austerlitz F, Hegay T, Aldashev A, Quintana-Murci L, Heyer E (2008) Population genetic diversity of the NAT2 gene supports a role of acetylation in human adaptation to farming in Central Asia. *Eur. J. Hum. Genet.* **16**: 243–251. <https://doi.org/10.1038/sj.ejhg.5201963>
- Marcus PM, Vincis P, Rothman N (2000) NAT2 slow acetylation and bladder cancer risk: a meta-analysis of 22 case-control studies conducted in the general population. *Pharmacogenetics* **10**: 115–122. <https://doi.org/10.1097/00008571-200003000-00003>
- Matimba A, Del-Favero J, Van Broeckhoven C, Masimirembwa C (2009) Novel variants of major drug-metabolising enzyme genes in diverse African populations and their predicted functional effects. *Hum. Genomics* **3**: 169. <https://doi.org/10.1186/1479-7364-3-2-169>
- Mittal RD, Srivastava DSL, Mandhani A (2004) NAT2 gene polymorphism in bladder cancer: a study from North India. *Int. Braz. J. Urol.* **30**: 279–285. <https://doi.org/10.1590/s1677-55382004000400003>
- Moore LE, Baris DR, Figueroa JD, García-Closas M, Karagas MR, Schwenn MR, Johnson AT, Lubin JH, Hein DW, Dagnall CL, Colt JS, Kida M, Jones MA, Schned AR, Cherala SS, Chanock SJ, Cantor KP, Silverman DT, Rothman N (2011) GSTM1 null and NAT2 slow acetylation genotypes, smoking intensity and bladder cancer risk: results from the New England bladder cancer study and NAT2 meta-analysis. *Carcinogenesis* **32**: 182–189. <https://doi.org/10.1093/carcin/bgq223>
- Nasr R, Temraz S, Mukherji D, Shamseddine A, Akika R, Abbasi S, Khauli R, Bulbul M, Tamim H, Zgheib NK (2017) Distribution and role of N-acetyltransferase 2 genetic polymorphisms in bladder cancer risk in a lebanese population. *Asian Pac. J. Cancer* **18**: 2561–2568. <https://doi.org/10.22034/apjcp.2017.18.9.2561>
- Pourhoseingholi MA, Vahedi M, Rahimzadeh M (2013) Sample size calculation in medical studies. *Gastroenterol. Hepatol. Bed. Bench.* **6**: 14–17
- Quan L, Chattopadhyay K, Nelson HH, Chan KK, Xiang YB, Zhang W, Wang R, Gao YT, Yuan JM (2016) Differential association for N-acetyltransferase 2 genotype and phenotype with bladder cancer risk in Chinese population. *Oncotarget* **7**: 40012–40024. <https://doi.org/10.18632/oncotarget.9475>
- Rezaei F, Tabatabaee HR, Rahmani V, Mirahmadian A, Hassanipour S (2019) The correlation between bladder cancer and obesity,

- overweight, physical inactivity, and tobacco use: an ecological study in Asian countries. *Ann. Glob. Health* **85**. <https://doi.org/10.5334/aogh.2545>
- Ribouh-Arras A, Chaoui-Kherouatou N, Hireche A, Abadi N, Satta D (2019) Joint effect of N-acetyltransferase 2 gene and smoking status on bladder carcinogenesis in Algerian population. *BioTechnologia* **100**: 155–168. <https://doi.org/10.5114/bta.2019.85846>
- Richter P, Pechacek T, Swahn M, Wagman V (2008) Reducing levels of toxic chemicals in cigarette smoke: a new Healthy People 2010 objective. *Public Health Rep.* **123**: 30–38. <https://doi.org/10.1177/003335490812300105>
- Sabbagh A, Darlu P, Crouau-Roy B, Poloni ES (2011) Arylamine N-acetyltransferase 2 (NAT2) genetic diversity and traditional subsistence: a worldwide population survey. *PLOS One* **6**: e18507. <https://doi.org/10.1371/journal.pone.0018507>
- Saginala K, Barsouk A, Aluru JS, Rawla P, Padala SA, Barsouk A (2020) Epidemiology of bladder cancer. *Med. Sci.* **8**: 15. <https://doi.org/10.3390/medsci8010015>
- Saleh SAER, Zaghlal HMA, Bawady SAH, Kotb M, Hammad WI (2019) Assessment of N-acetyltransferase 2 (NAT2) gene polymorphisms in bladder cancer patients. *J. Nephropharmacol.* **8**: e30–e30. <https://doi.org/10.15171/npj.2019.30>
- Sanderson S, Salanti G, Higgins J (2007) Joint effects of the N-acetyltransferase 1 and 2 (NAT1 and NAT2) genes and smoking on bladder carcinogenesis: a literature-based systematic HuGE review and evidence synthesis. *Am. J. Epidemiol.* **166**: 741–751. <https://doi.org/10.1093/aje/kwm167>
- Sekine A, Saito S, Iida A, Mitsunobu Y, Higuchi S, Harigae S, Nakamura Y (2001) Identification of single-nucleotide polymorphisms (SNPs) of human N-acetyltransferase genes NAT1, NAT2, AANAT, ARD1 and L1CAM in the Japanese population. *J. Hum. Genet.* **46**: 314–319. <https://doi.org/10.1007/s100380170065>
- Sim E, Abuhammad A, Ryan A (2014) Arylamine N-acetyltransferases: from drug metabolism and pharmacogenetics to drug discovery. *Br. J. Pharmacol.* **171**: 2705–2725. <https://doi.org/10.1111/bph.12598>
- Song Y, Qi X, Liu X (2020) N-acetyltransferase 2 polymorphism is associated with bladder cancer risk: An updated meta-analysis based on 54 case-control studies. *Gene* **757**: 144924. <https://doi.org/10.1016/j.gene.2020.144924>
- Tao L, Xiang Y-B, Wang R, Nelson HH, Gao Y-T, Chan KK, Yu MC, Yuan J-M (2010) Environmental tobacco smoke in relation to bladder cancer risk – the Shanghai bladder cancer study (corrected). *Cancer Epidemiol. Biomarkers Prev.* **19**: 3087–3095. <https://doi.org/10.1158/1055-9965.EPI-10-0823>
- Turesky RJ, Le Marchand L (2011) Metabolism and biomarkers of heterocyclic aromatic amines in molecular epidemiology studies: lessons learned from aromatic amines. *Chem. Res. Toxicol.* **24**: 1169–1214. <https://doi.org/10.1021/tx200135s>
- Werely CJ, Donald PR, Helden PDv (2007) NAT2 polymorphisms and their influence on the pharmacology and toxicity of isoniazid in TB patients. *Per. Med.* **4**: 123–131. <https://doi.org/10.2217/17410541.4.2.123>
- Yee J, Kim SM, Han JM, Lee N, Yoon HY, Gwak HS (2020) The association between NAT2 acetylator status and adverse drug reactions of sulfasalazine: a systematic review and meta-analysis. *Sci. Rep.* **10**: 3658. <https://doi.org/10.1038/s41598-020-60467-8>
- Zhu K, Xu A, Xia W, Li P, Zhang B, Jiang H, Zhou S, Wang R (2021) Association between NAT2 polymorphism and lung cancer risk: a systematic review and meta-analysis. *Front. Oncol.* **11**: 567762. <https://doi.org/10.3389/fonc.2021.567762>
- Zhu Z, Zhang J, Jiang W, Zhang X, Li Y, Xu X (2015) Risks on N-acetyltransferase 2 and bladder cancer: a meta-analysis. *Oncotargets Ther.* **8**: 3715–3720. <https://doi.org/10.2147/ott.s82927>

Alpha-Mangostin ameliorates acute kidney injury via modifying levels of circulating TNF- α and IL-6 in glycerol-induced rhabdomyolysis animal model

Heba M. Eltahir¹✉, Hossein M. Elbadawy², Ali Alalawi², Ahmed J. Aldhafiri², Sabrin R.M. Ibrahim^{3,4}, Gamal A. Mohamed^{5,6}, Abdel-Gawad S. Shalkami^{7,8}, Mohannad A. Almikhlaifi², Muayad Albadrani⁹, Yaser Alahmadi¹⁰, Mekky M. Abouzied^{1,11} and Maiiada H. Nazmy¹¹

¹Department of Pharmacology and Toxicology, Division of Biochemistry, Taibah University, Medina, Kingdom of Saudi Arabia; ²Department of Pharmacology and Toxicology, Taibah University, Medina, Kingdom of Saudi Arabia; ³Preparatory Year Program, Batterjee Medical College, Jeddah 21442, Saudi Arabia; ⁴Department of Pharmacognosy, Faculty of Pharmacy, Assiut University, Assiut 71526, Egypt; ⁵Department of Natural Products and Alternative Medicine, Faculty of Pharmacy, King Abdulaziz University, Jeddah, Saudi Arabia; ⁶Department of Pharmacognosy, Faculty of Pharmacy, Al-Azhar University, Assiut Branch, Assiut, Egypt; ⁷Department of Pharmacology and Toxicology, Faculty of Pharmacy, Al-Azhar University, Assiut, Egypt; ⁸Clinical Pharmacy Program, Faculty of Health Science and Nursing, Al-Rayan Colleges, Medina, Kingdom of Saudi Arabia; ⁹Department of Family and Community Medicine, College of Medicine, Taibah University, Medina, Kingdom of Saudi Arabia; ¹⁰Department of Clinical and Hospital pharmacy, Taibah University, Medina, Kingdom of Saudi Arabia; ¹¹Department of Biochemistry, Faculty of Pharmacy, Minia University, Minia, Egypt

Alpha mangostin (AM), isolated from *G. mangostana*, showed beneficial effects in several disorders due to its antioxidant and anti-inflammatory properties. Acute kidney injury (AKI) due to different etiologies can develop into severe complications, resulting in high mortality rates. In this work, AM is tested for its ability to alleviate AKI in glycerol-induced AKI rat model, where 30 Male Sprague-Dawley rats were assigned to a healthy group, glycerol-treated group and AM-treated group. Glycerol- and AM groups received a single dose of glycerol (per IM, 50% glycerol in saline, 8 ml/kg), whereas control group was injected with saline. AM treatment (a single daily dose, per IP, 175mg/kg) was accomplished for three days. Animals were executed to collect blood samples and kidney tissue for biochemical and histological examination. It was found that glycerol induced increase in serum creatinine, blood urea nitrogen (BUN), lipid peroxidation, serum magnesium, TNF- α and IL-6. It also induced renal edema and hypocalcemia along with histopathological renal damage. AM treatment improved renal histological features and alleviated increase in serum creatinine, BUN, serum magnesium, TNF- α and IL-6 levels, as well as renal edema and lipid peroxidation but did not affect serum calcium levels. This suggests AM as a potential therapeutic agent for treating AKI mainly via its antioxidant and anti-inflammatory properties.

Keywords: AKI, alpha mangostin, rhabdomyolysis, antioxidant, TNF- α , IL-6, anti-inflammatory

Received: 04 October, 2022; **revised:** 29 January, 2023; **accepted:** 19 February, 2023; **available on-line:** 17 April, 2023

✉e-mail: Heba_m.eltahir@yahoo.com

Abbreviations: AKI, Acute kidney injury; AM, alpha mangostin; IL-6, interleukin-6; NF- α , tumor necrosis factor- α ; BUN, blood urea nitrogen; MDA, malodialdehyde; TBARS, thiobarbituric acid reactive substances; Ca²⁺, calcium ion; Mg²⁺, magnesium ion; iNOS, inducible nitric oxide synthase; SOD, superoxide dismutase; NFkB, Nuclear factor kB; ROS, reactive oxygen species; TGF- β , transforming growth factor- β ; KW/BW, kidney weight to body weight ratio

INTRODUCTION

Fruits are highly consumed and largely appreciated throughout the world. They represent a wealthy pool of diverse bioactive compounds, which have shown variable health benefits in reducing the incidence of various diseases such as hyperlipidemia, cancer, oxidative stress, inflammation and heart disease in addition to their effects as anti-diabetic, antimicrobial, neuroprotective, immune-stimulant and anticonvulsant (Karasawa & Mohan, 2018). *Garcinia mangostana* together with nearly 400 other species belongs to *Garcinia* genus; the biggest genus of the *Clusiaceae* family (Magadula, 2010). *G. mangostana*'s round, reddish- to dark purple fruits have a sweet, slightly acidic flavor and have been used to treat a wide variety of medical conditions (Ovalle-Magallanes *et al.*, 2017). *G. mangostana* fruit is reported to be rich in xanthones; tricyclic oxygenated compounds (Fig. 1) that exhibit nu-

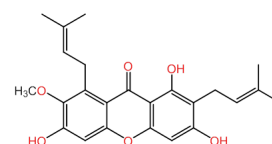


Figure 1. Structure of α -mangostin (AM).

merous bioactivities such as α -amylase inhibitory, anti-HIV, antimicrobial, antioxidant, anti-inflammatory, anti-malarial, and antihypertensive effects in addition to its cytotoxic effect on various tumor cell lines (Mohamed *et al.*, 2017; Ibrahim *et al.*, 2019a; Ibrahim *et al.*, 2019b; Gutierrez-Orozco & Failla, 2013). α -Mangostin (AM, Fig. 1) is one of the major xanthones isolated from *G. mangostana* that has antioxidant properties and possesses diverse bio-activities, such as anti-tumor, anti-inflammatory, cardio-protective, anti-diabetic, larvicidal, antifungal, α -amylase inhibitory, anti-parasitic, anti-obesity, and antioxidant (Chen *et al.*, 2008; Devi Sampath & Vijayaraghavan, 2007; Watanabe *et al.*, 2018; Larson *et al.*, 2010; Perez-Rojas *et al.*, 2016; Chen *et al.*, 2018).

Despite the number of reports suggesting a beneficial effect for AM in alleviating nephropathy (Perez-Rojas *et al.*, 2009; Sanchez-Perez *et al.*, 2010), no reports investigating its role in the management of acute kidney injury (AKI) are yet available. AKI is a high mortality rate clinical condition characterized by a sudden renal impairment; with multiple complicated underlying causes including hemorrhagic shock, infection, rhabdomyolysis, and urethral obstruction (Chawla *et al.*, 2014; Bosch *et al.*, 2009). Epidemiological screening showed that the incidence rate in ICU for AKI-patients was 30–50% and the mortality rate among those patients was 63% (Glodowski & Wagener, 2015). Surviving patients need 6–12 months to completely recover their kidney functions (Li *et al.*, 2020a), whereas 19–31% of AKI patients reach end-stage renal failure (Goldberg & Dennen, 2008; Venkatachalam *et al.*, 2015). Therefore, early intervention to improve kidney functions and treat AKI plays a key role to ameliorate the progression to chronic nephropathy (Homsy *et al.*, 2010).

Intramuscular Glycerol injection is one of the most common protocols used in rats to induce rhabdomyolysis (RM) that ends by AKI, one of the most severe complications of RM (Al Asmari *et al.*, 2017; Sun *et al.*, 2018). RM is a condition caused by extensive skeletal muscle breakdown due to ischemia, toxins, physical effects and infections, resulting in leakage of overwhelming amounts of intracellular contents including myoglobin accessing the blood circulation. Myoglobin exerts toxic effect on the kidneys, where it induces oxidative stress due to production of ROS and inflammation ending by apoptosis. When myoglobin becomes filtered through the kidneys, it is engulfed into the tubular cells via endocytosis, where the ferrous-myoglobin is converted to ferric-myoglobin releasing highly reactive hydroxyl radicals. These radicals induce lipid peroxidation and affect membrane integrity, resulting in AKI (Panizo *et al.*, 2015). ROS-induced inflammation results in infiltration of immune cells to the site of inflammation, where these cells start producing proinflammatory mediators, such as TNF- α and different interleukins that further aggravate the inflammatory response. Both TNF- α and IL-6 have been linked to disease severity in case of AKI and are used as markers for predicting the clinical outcome and mortality (Shimazui *et al.*, 2019; Ramesh & Reeves, 2004).

In the current work, we aimed at evaluating the therapeutic potential of AM against glycerol-induced AKI via assessing its anti-inflammatory, antioxidant and tissue protective effects.

METHODS

Materials

All materials utilized in the current study were of analytical grade and were purchased from local suppliers unless otherwise stated. AM was isolated and purified from fruit bulb and purity was estimated to be 98% (see supplementary data).

Animals and Treatment

Thirty Male Sprague-Dawley rats, 8 weeks-old (180–200 g), were housed in controlled temperature under 12hrs light/dark cycle with free access to food and water and were allowed to accommodate for one week before initiating the experimental procedure. Animals were assigned randomly into three groups with 10 animals in each; a healthy control group, a positive control group (AKI-group) and AKI-AM treated group.

To induce the AKI model in the second and third groups, rats in these groups were deprived of water for 24 hrs before being injected with a calculated dose of 50%, v/v glycerol/saline divided equally on both hind limbs (IM, 8 ml/kg body weight). Healthy control animals were treated similarly to AKI animals but received an equivalent volume of sterile saline instead of glycerol. One hour before inducing the AKI model, animals of AKI-AM group received AM (175 mg/kg in DMSO, IP injection), and the AKI group animals received a corresponding amount of DMSO, and the treatment was repeated once a day for three consecutive days.

Twenty four hours after the last dose of AM, animals were weighed then sacrificed under anesthesia. Blood was collected by cardiac puncture and kidneys were promptly collected, rinsed in ice-cold saline and weighed individually and the recorded weight was used for calculating KW/BW ratio. The right kidney from each animal was stored in 10% neutral formalin solution for further histological examination, whereas the left one was homogenized in Tris-buffer and frozen for further biochemical evaluation.

All animal handling protocols were approved by the local Institutional Animal Care and Use Committee, faculty of pharmacy, Minia university (project code number: ES10/2022), and were in compliance with the International Guidelines for the Care and Use of Laboratory Animals.

Kidney weight-to-body weight ratio

The average weight of the freshly isolated kidneys was divided by the corresponding animal body weight and the value was multiplied by 100 to represent it as a percentage.

Biochemical analysis

Renal parameters. Collected blood samples were allowed to clot at room temperature for 15–20 minutes before being centrifuged at 3000 rpm at 4°C for 10 min to separate the serum. Assessment of blood urea nitrogen (BUN), creatinine, calcium (Ca²⁺), and magnesium (Mg²⁺) levels were performed spectrophotometrically using the commercially available kits according to the manufacturer's instructions (Randox®, UK).

Lipid peroxidation. Kidney homogenates were centrifuged at 5000 rpm for 15 minutes and the supernatants were collected for the quantification of thiobarbituric acid reactive substances (TBARS) in an attempt to assess lipid peroxidation based on the earlier established protocol (Ohkawa *et al.*, 1979) and according to the manufacturer's instructions (Lipid peroxidation (MDA) assay kit, Sigma Aldrich, USA). Kidney lipid peroxidation in tissue was calculated as $\mu\text{mole MDA/g}$ of tissue.

Assessment of TNF- α and ILs using enzyme-linked immunosorbent assay (ELISA). Levels of circulating proinflammatory markers TNF- α and interleukin-6 (IL-6) were evaluated in serum using commercially available ELISA kits according to the manufacturer's instructions (Sigma Aldrich, USA).

Assessment of relative gene expression using qRT-PCR

In brief, primers specific to the genes of interest: glutathione peroxidase (GPx), glutathione reductase (GRs) and superoxide dismutase (SOD) along with that of ribosomal protein S-18 (RPS-18) as a house keeping gene were utilized (as shown in primers list, Table 1) to perform, quantitative RT-PCR analyses. Freshly isolated kidney tissues were homogenized, and RNA was isolated using

Table 1. sequence of the primers used for quantitative evaluation of GPx, GRS, TSOD expression

Gene	Sense	Anti-sense
GPx	GTCCACCGTGTATGCCTTCT	TCTGCAGATCGTTCATCTCG
GRs	CAATTGGCATGTCATCAAGG	CCATCTCGAAATGTTGCGTA
TSOD	TGGTGAACCAGTTGTGGTGT	AAAATGAGGTCCTGCAGTGG
RPS-18	AGTTGGTGGAGCGATTTGTC	GAACGCCACTTGTCCTCTA

miRNeasy Mini (Qiagen, Germany), followed by reverse transcription to create the cDNA using ImProm-II™ reverse transcription system according to the manufacturer's instructions (Promega, USA). Expression level of target genes mRNA was evaluated based on the cDNA, then the relative target gene expression was calculated by comparative Ct ($2^{-\Delta Ct}$) method using RPS-18 as a house keeping gene. Data were presented as mean \pm standard error of means for three independent experiments.

Histopathological examination

After being excised, kidneys were rinsed in saline then fixed in 10% neutral formalin solution for 24 hrs followed by dehydration in a series of increasing alcohol concentrations. Finally, they were embedded in paraffin, and 5-microns sections were cut on a microtome and mounted on glass slides for histological investigation. After being deparaffinized, the sections were rehydrated and stained with Hematoxylin & Eosin to evaluate and quantify the extent of tubular injury, dilatation, vacuolation and necrosis in kidney tissues as previously described (Wu *et al.*, 2017).

Data and Statistical Analysis

All data are expressed as means \pm S.E.M. (n=10) for all the experiments. Multiple comparisons of data were analyzed by one-way analysis of variance, as appropriate, and group means were compared using Tukey Kramer post hoc test. *p*-values less than 0.05 were considered as statistically significant.

RESULTS

Effect of glycerol and AM on serum biochemical parameters and lipid peroxidation

Injection of glycerol into the animals resulted in signs of renal injury that was characterized by a significant three-fold elevation of serum creatinine when comparing these animals to healthy control group (*p*<0.05). Glycerol

administration also resulted in significant increase in blood urea nitrogen (BUN) compared to healthy control animals (*p*<0.05) (Fig. 2A and B).

Acute renal injury induced by glycerol also resulted in a significant increase in lipid peroxidation (*p*<0.05) in comparison to healthy control animals. Interestingly, administration of AM in glycerol-induced AKI animals effectively ameliorated the signs of renal injury. It significantly decreased serum creatinine as well as BUN levels to values that are comparable to normal healthy group (1.2 ± 0.01 mg/dL and 43.66 ± 25.66 mg/dL respectively, *p*<0.05) (Fig. 2A and B).

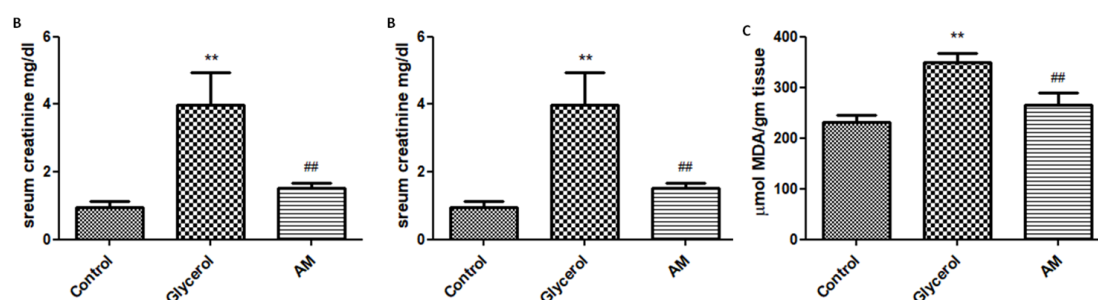
In addition, AM was significantly capable of ameliorating glycerol-induced lipid peroxidation when compared to animals receiving glycerol alone (*p*<0.05) as shown in Fig. 2C.

Effect of glycerol and AM on serum calcium and magnesium levels

Analysis of electrolytes in the sera of test animals revealed a significant elevation in serum magnesium (Mg^{2+}) in AKI group compared to the healthy control group (4.1 ± 0.02 mg/dl *vs.* 2.48 ± 0.14 mg/dl, *p*<0.05). In contrast, a significant reduction in serum calcium (Ca^{2+}) was observed in this group compared to the healthy control (2.39 ± 0.01 mg/dl *vs.* 8.56 ± 0.31 mg/dl, *p*<0.05) as seen in Fig. 3A and B. It is worth to note that the treatment with AM significantly ameliorated the increase in serum Mg^{2+} levels induced by glycerol compared to glycerol-treated animals which didn't receive AM (*p*<0.05). In the same time, serum Mg^{2+} levels were significantly indistinguishable when comparing AM-treated animals with the healthy control ones (*p*>0.05). On the other hand, depleted (Ca^{2+}) levels in response to glycerol treatment were not replenished upon AM treatment (*p*>0.05) and remained significantly less than the healthy control (*p*<0.05, Fig. 3).

Effect of glycerol and AM on endogenous antioxidants

The relative expression of GPx, GRs and SOD was assessed to investigate the effect of the different treatments. Glycerol injection resulted in a significant reduction in the relative gene expression of all three enzymes compared to control animals (*p*<0.05; Figs 4A, B and C). Interestingly, treating AKI animals with AM significantly ameliorated the glycerol-induced reduction in GPx, GRs and SOD compared to animals that received glycerol only (*p*<0.05; Figs 4A, B and C). It is to be mentioned that relative gene expression of GPx and GRs was indistinguishable from that of healthy control animals upon AM treatment (*p*>0.2), whereas the relative expression of

**Figure 2. effect of glycerol and AM on biochemical parameters.**

Glycerol administration induced a significant increase in serum urea (A), creatinine (B) and lipid peroxidation compared to healthy control (***p*<0.05). Animals treated with AM show significant reduction in all three parameters compared to glycerol treated animals (#*p*<0.05). Values are expressed as mean \pm S.E.M., n=10, **/#*p*<0.001, */#*p*<0.01.

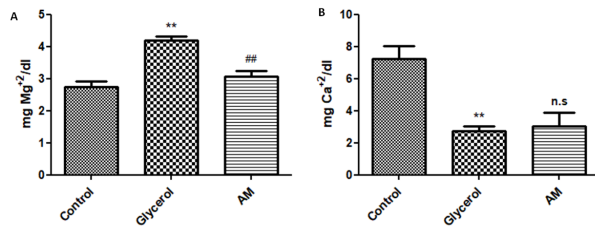


Figure 3. effect of glycerol and AM treatments on serum calcium and magnesium.

Glycerol administration induced a significant increase in serum Mg²⁺ (A, $p < 0.05$) and reduction in serum Ca²⁺ (B, $p < 0.001$) compared to healthy control. Animals treated with AM showed a significant reduction in magnesium levels compared to the glycerol treated group ($p < 0.05$) but no significant changes in serum calcium levels ($p > 0.05$) was achieved compared to the glycerol treated group. In AM treated animals, Mg²⁺ levels are comparable to control but Ca²⁺ levels are significantly lower than control ($p > 0.26$ and $p < 0.001$ respectively). Values are expressed as mean \pm S.E.M., $n = 10$, **/## $p < 0.001$, */# $p < 0.05$

SOD was still significantly less than that of control after AM treatment ($p < 0.05$).

Effect of glycerol and AM on circulating inflammatory markers level

Animals exposed to glycerol treatment revealed a significant increase in levels of circulating TNF- α and IL-6 when compared to healthy control animals (Fig. 5A and B, $p < 0.05$). Interestingly, treating animals with AM resulted in significant amelioration in serum levels of both proinflammatory cytokines ($p < 0.05$).

Effect of glycerol and AM on kidney index

As expected, glycerol-treated animals suffered from renal edema as observed by a significant increase in kidney index (KW/BW ratio) when compared to the healthy group (0.57% vs. 0.31% respectively, $p < 0.05$). Interestingly, treating the animals with AM was capable of reducing KW/BW ratio in the corresponding animals compared to the AKI group animals; however, this reduction was not statistically significant (0.42% vs. 0.57%, $p > 0.05$) (Fig. 6).

Histopathological findings

Administration of glycerol effectively induced AKI as observed in the form of severe degenerative changes in renal corpuscles accompanied with accumulation of protein casts in the mesangial tissue when compared to control group animals (Fig. 7C and D, arrow head). In addition,

marked degeneration of the renal tubules could be detected (arrow) where the lumen of such tubules was obliterated by protein casts. These changes were accompanied by severe congestion of the renal blood vessels (Fig. 7C and D).

Interestingly, treating AKI animals with AM resulted in marked alleviation of the degenerative changes induced by glycerol. Figures 6E and F show normal renal corpuscles (C) and glomerular capillaries. Despite the mild degree of hydropic degeneration that can be detected in some renal tubules (arrow), the majority of the tubules showed normal morphological features (I). It is to be noted that some protein materials can be detected in few tubules but less than that observed in the glycerol-treated animals. A comparison among the test groups regarding these morphological changes is presented in Table 2.

DISCUSSION

AKI is a renal dysfunction that is characterized by prompt loss of renal filtration rate and accumulation of protein debris within the renal tissues, where rhabdomyolysis (RM) is a main cause of AKI (Parekh *et al.*, 2012). Glycerol-induced rhabdomyolysis is an established model that mimics AKI in human as it induces a myoglobinuric condition and a significant reduction in filtration rate that result mainly from oxidative stress, which induces inflammation and consequently apoptosis (Zager, 1996).

In the current study, glycerol injection induced a significant increase in serum creatinine and BUN, indicating renal dysfunction that was associated with renal edema in response to the toxic levels of myoglobin reaching the kidneys as observed by the increased KW/BW ratio. These pathological changes were confirmed by the histological examination that showed signs of tubular necrosis, congestion and protein casts accumulation within the tubules and mesangial tissue. The observed effects of glycerol were reported earlier by several research groups (Al Asmari *et al.*, 2017; Ustundag *et al.*, 2009; Korrapati *et al.*, 2012).

Despite the possibility of recovering the renal functions affected by RM within few months, some reports have shown that structural changes, including fibrosis, possibly take place as a result of excessive extracellular matrix deposition and the released pro-inflammatory and pro-fibrotic factors (Wen *et al.*, 2011). This causes RM-induced AKI to be a serious condition that needs rapid intervention to improve the prognosis and to prevent long term complications.

RM can result from muscle damage caused by direct traumatic insults or excessive muscular effort that dam-

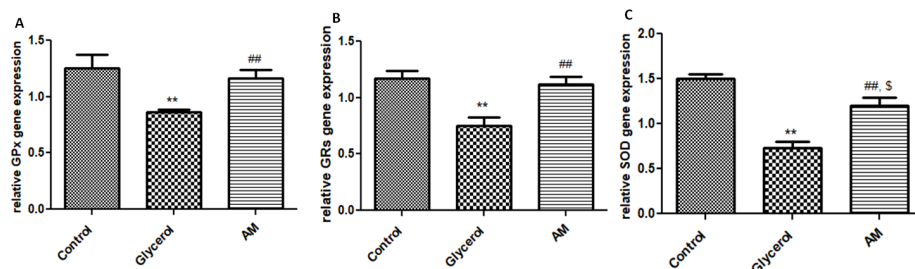


Figure 4. effect of glycerol and AM treatments on endogenous antioxidant enzyme gene expression.

Administration of glycerol significantly reduced the relative expression of GPx (A, $p < 0.01$), GRs (B, $p < 0.01$) and SOD (C, $p < 0.001$) compared to healthy control animals. Treating animals with AM significantly increased gene expression of GPx (A, $p < 0.05$), GRs (B, $p < 0.05$) and SOD (C, $p < 0.05$) compared to glycerol treated animals. No significant difference in relative gene expression of GPx and GRs could be detected between AM treated animals and control ones. Values are expressed as mean \pm S.E.M., $n = 10$, **/##/\$ $p < 0.001$, */#/\$ $p < 0.05$.

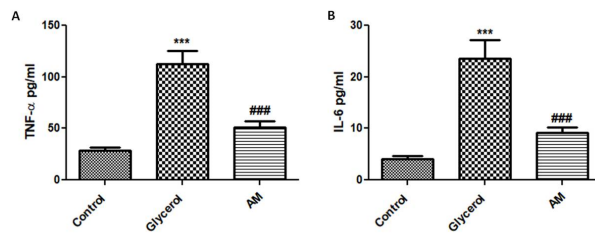


Figure 5. effect of glycerol and AM treatments on circulating proinflammatory cytokines.

Glycerol treatment induced a significant increase in both TNF- α (A, $p < 0.001$), and IL-6 (B, $p < 0.001$) compared to healthy control. AM treatment significantly ameliorated the increase in serum levels of both TNF- α (A, $p < 0.001$) and IL-6 (B, $p < 0.001$) compared to glycerol treated group. Values are expressed as mean \pm S.E.M., $n = 10$, **/### $p < 0.001$, */# $p < 0.05$

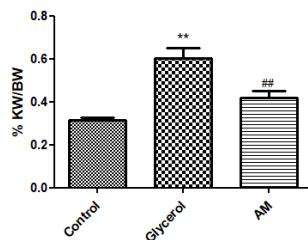


Figure 6. kidney index of the different test groups.

Glycerol administration induced a significant increase in kidney-to-body weight ratio compared to healthy control group ($p < 0.01$). AM treatment resulted in reduction in kidney index compared to glycerol treated group ($p < 0.05$). Values are expressed as mean \pm S.E.M., $n = 10$, **/## $p < 0.001$, */# $p < 0.01$

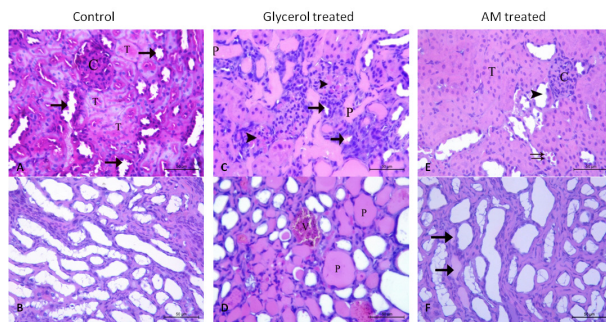


Figure 7. Photomicrographs of kidney sections from the different test groups.

A&B: sections from healthy control showing normal renal corpuscles with normal glomerular capillaries (C) and normal renal tubules (T) as well as normal collecting tubules (arrow, H&E stain, $\times 400$). **B:** renal medulla showing normal collecting tubules with cuboidal lining epithelium and normal loop of Henle's (H&E stain, $\times 400$). **C&D:** sections from glycerol treated group showing degenerative changes in renal corpuscles (C) with accumulation of protein materials in the mesangial tissue and renal tubules (arrowheads) with protein casts (arrow) and protein casts in the renal tubules' lumen (P). **D:** renal medulla showing severe congestion of the renal blood vessels (V) and protein casts (P). **E&F:** sections from AM-treated group with normal renal corpuscles (C), almost normal renal tubules (T) and collecting tubules (arrowhead) with few ones showing mild degree of hydropic degeneration (arrow). Scanty amounts of protein are present in few tubules (double arrow). **F:** renal medulla showing normal renal tubules. Protein casts present in few tubules (arrow). (H&E stain, $\times 400$)

ages muscle cells, some metabolic disorders, bacterial and viral infections, alcohol intake and exposure to various types of drugs like statins, heroine and cocaine as well as prolonged immobilization (Holt & Moore, 2001).

Table 2. Effect of glycerol and AM on the kidney morphological features

	Control group	AKI group	AKI-AM group
Degenerated corpuscles	–	+++	–
Congestion	–	++	–
Protein casts	–	+++	+
Necrosis	–	+++	–
Hydropic degeneration	–	+++	+

Key: – no pathological change, +mild degree pathological change, ++moderate pathological change, +++severe pathological change

As these factors induce RM, damaged muscle cells start to release unexpectedly large amounts of myoglobin which becomes filtered through the renal tubules, but instead of being excreted, myoglobin is mostly endocytosed inside the renal tubules' cells. These endocytosed myoglobin molecules undergo several oxidation reactions releasing hydroxyl free radicals among other ROS, initiating a cascade of oxidation and peroxidation reactions to generate a condition of oxidative stress (Boutaud & Roberts, 2011). As observed in the current study, glycerol treatment significantly induced peroxidation as one of oxidative stress outcomes that can be evaluated by MDA tissue content, in agreement with several studies reporting lipid peroxidation in AKI models (Al Asmari *et al.*, 2017).

In rodents, it is believed that glycerol-induced AKI is a result of myoglobinuric nephrotoxicity and renal ischemia (Parekh *et al.*, 2012; Zager, 1996), where the molecular events observed in this model are similar to those observed clinically, which causes the glycerol-induced RM a very common model to study AKI (Stein *et al.*, 1978). In other words, pathophysiology of RM-induced AKI includes oxidative stress, cast formation in renal tubules, vasoconstriction and inflammation of renal tissues (Shanu *et al.*, 2013).

In response to oxidative stress, pro-inflammatory cytokines are released activating macrophages and T-lymphocytes at the site of inflammation, which in turn produces various cytokines e.g. TGF- β and TNF- α to propagate the inflammation condition. Released pro-inflammatory TNF- α interacts with various cell types and induces NF- κ B activation and nuclear translocation. This activates the transcription of NF- κ B downstream pro-inflammatory target genes, resulting in the release of increased amounts of proinflammatory cytokines e.g. IL-6 (Moreno *et al.*, 2012).

Several reports have shown that antioxidants are capable of protecting against myoglobin-induced oxidative stress via scavenging the released ROS, improving the endogenous antioxidant defense mechanisms, preventing lipid peroxidation or ameliorating the inflammatory response, and hence protecting against the renal damage. These molecules included ascorbic acid, vitamin E, polyphenols, suramin, curcumin and quinacrine among others (Al Asmari *et al.*, 2017; Korrapati *et al.*, 2012; Usundag *et al.*, 2009).

AM, a xanthone isolated from *G. mangostana* fruit, has been implicated in a lot of studies for its wide range of therapeutic effects as previously mentioned (Sanchez-Perez *et al.*, 2010; Devi Sampath and Vijayaraghavan, 2007; Jung *et al.*, 2006). It has been shown to exert its action via its positive effects on the endogenous antioxidant defense mechanisms, as it was previously reported to improve the superoxide dismutase and glu-

tathione peroxidase activity, in addition to replenishing glutathione tissue content (Fang *et al.*, 2016). In addition, AM was shown to combat inflammation and suppress the production of various inflammatory mediators and fibrogenic mediators via scavenging different free radicals like superoxide and peroxynitrite according to *in vivo* and *in vitro* studies investigating its potential effects in nephrotoxicity models (Perez-Rojas *et al.*, 2009; Li *et al.*, 2020b; Muhamad Adyab *et al.*, 2019; Sanchez-Perez *et al.*, 2010). Some reports related the anti-inflammatory effect of AM to its ability to activate SIRT-1, a nuclear histone deacetylase, which inhibits NF- κ B signaling and consequently its downstream pro-inflammatory effectors (Franceschelli *et al.*, 2016), whereas others reported the ability of AM to inhibit leukocyte migration as well as the production and secretion of inflammatory mediators e.g. IL-2, IL-6 and TNF- α from different cell types (Kim *et al.*, 2021; John *et al.*, 2022). Despite these positive effects of AM, its effect on RM-induced AKI in glycerol model is not yet investigated.

In the current research, we found that AM administration to glycerol-induced AKI rats could efficiently alleviate signs of AKI as it normalized BUN and creatinine levels and alleviated renal edema. It also alleviated the oxidative stress induced by glycerol administration as observed in ameliorating MDA tissue content. It significantly reduced serum magnesium levels, however, serum calcium levels were not improved upon treatment. AM treatment also normalized the relative gene expression of the antioxidant enzymes SOD, GPx and GRs, and ameliorated the expected increase in circulating TNF- α and IL-6, which were upregulated upon AKI induction. On the cellular level, AM could reverse most of the histopathological changes induced by glycerol injection, regaining normal corpuscles and renal tubules with minimal protein deposition indicating good signs of recovery from tissue damage.

These effects can be explained by the previously reported ROS scavenging activity of AM and its ability to replenish the endogenous antioxidant mechanism (Fang *et al.*, 2016; Martinez *et al.*, 2011). In this context, AM was reported to achieve its antioxidant effect via increasing the activity of various antioxidant enzymes including SOD and GPx, and retrieving the gene expression of endogenous antioxidant enzymes as well (Perez-Rojas *et al.*, 2009). In addition, its previously reported mitochondrial-stabilizing, antiapoptotic effect prevents cell death and protects against tissue damage, enabling the recovery of renal functions upon its use (Perez-Rojas *et al.*, 2009; Sanchez-Perez *et al.*, 2010). AM has been also reported previously for its anti-inflammatory effect and its ability to reduce/ameliorate TNF- α and other inflammatory cytokines e.g. IL-6, IL-1 β and IL-8 in several models including kidney disease models via its inhibitory effect on NF- κ B and TLR-4 signaling in addition to other signaling pathways linked to inflammation in renal tissues (Tewtrakul *et al.*, 2009; Xu *et al.*, 2017; Zou *et al.*, 2019).

Hypocalcemia is expected in the early stage of AKI where calcium becomes deposited within the cells as a result of Ca²⁺-ATPase pumps dysfunction and the damaged sarcoplasmic reticulum, leading to a significant decrease in serum calcium levels. In a later response, proteases and phospholipases attack the cell membranes resulting in leakage of cellular contents, which consequently destroy cells in the near proximity. It is to be noted that renal injury-induced hypocalcemia is observed only in the early oliguric phase of AKI (Graziani *et al.*, 2011; Edelstein *et al.*, 1997).

In contrast, the increase in serum magnesium level in AKI could be attributed to the expected hypovolemic condition that may affect magnesium concentrations, and the impaired tubular filtration mechanisms following AKI that could affect its excretion. It is well established that the decline in renal functions is commonly associated with increased serum magnesium levels (Swaminathan, 2003; Quamme, 1989). The observed effect of AM on serum magnesium levels could be attributed to its ability to retrieve the renal functions and hence improved filtration rate leading to decreasing magnesium levels.

TNF- α is a proinflammatory cytokine that is produced by infiltrating immune cells in addition to various cell types within the renal tissue i.e. mesangial cells, podocytes, and endothelial cells of the proximal tubules, collecting ducts and thick ascending limbs (Ramseyer & Garvin, 2013). It is produced in response to different stimuli such as oxidative stress, infections, complement reaction and exposure to lipopolysaccharides. It has been reported earlier that normalizing the oxidative stress levels using superoxide dismutase (SOD) mimics ameliorated TNF- α production and renal pathological changes in a diabetic nephropathy animal model (Ebenezer *et al.*, 2009). TNF- α aggravates the inflammatory process via its effect on activating nuclear translocation of the transcriptional factor NF- κ B with the subsequent activation of the transcribing its downstream proinflammatory target genes (e.g. TNF- α , IL-6, inducible nitric oxide synthase (iNOS) and adhesion molecules). A large body of evidence has confirmed the role of TNF- α in inducing renal damage (Shahid *et al.*, 2008; Sun & Kanwar, 2015; Mehaffey & Majid, 2017). It has been reported that TNF- α can enhance the expression of the pro-fibrotic factor TGF- β via activating ERK signaling. This cross talking between both cytokines causes both to be crucial players in the process of tissue remodeling and fibrosis as reported earlier (Sullivan *et al.*, 2005; Liu *et al.*, 2021). IL-6 is a proinflammatory cytokine that is produced by immune- as well as renal cells in response to inflammation. Previous reports have correlated its serum levels with the severity of organ failure and dysfunction in ICU-admitted systemic inflammatory conditions (Shimazui *et al.*, 2019). The previously reported ability of AM to reduce the gene expression level of TNF- α , TGF- β and IL-6 allows it to break the vicious circle of oxidative stress- inflammation-tissue damage-remodeling and fibrosis (Yiemwattana & Kaomongkolgit, 2015), resulting in a significant improvement in the renal functions and histology and preventing fibrosis, which is a main complication of AKI as observed in the current study.

In conclusion, this work represents AM as a safe natural product that can be potentially used to ameliorate the devastating renal effects of RM on kidneys directly via its antioxidant and anti-inflammatory effects and indirectly by preventing fibrosis. It can modulate the inflammatory process through its effect on the proinflammatory cytokines, TNF- α and IL-6, bringing the inflammation to a halt and achieve better recovery in the renal tissue. This may provide a medicinal tool to combat the transition of these acute effects into chronic, long lasting damages and hence decrease AKI-related mortality rates.

LIMITATIONS

Despite the interesting findings, there are some limitations to this study. Serum creatinine and blood urea nitrogen were used as biochemical markers to evaluate re-

nal function, and these data were confirmed by the histopathological examination of renal tissue sections. Urine analysis based studies including urine volume, urine creatinine and creatinine clearance tests could have supported the findings that AM attenuates glycerol-induced renal impairment. In addition, further studies are required to understand the molecular mechanism by which AM exerts its nephroprotective effect and to confirm the efficacy of AM to improve kidney functions in AKI.

Declarations

Funding. The authors declare no specific funding for this work.

Competing interests. The authors declare there are no competing interests.

Author contribution statement. Conceptualization: Heba M Eltahir, Mekky M Abouzied; Formal analysis: Ahmed J. Aldhafiri, Maiada H Nazmy, Muayad Albadrani; Investigation: Hussein Elbadawy, Abdel-Gawad S. Shalkami, Mohannad A Almikhlaft; Methodology: Heba Eltahir, Mekky Abouzied, Muayad Albadrani, Hussein Elbadawy, Sabrin Ibrahim, Gamal Mohamed; Project administration: Mekky M Abouzied, Ahmed J. Aldhafiri; Supervision: Heba Eltahir, Mekky Abouzied, Gamal Mohamed; Visualization: Ali Alalawi, Abdel-Gawad S. Shalkami, Hussein Elbadawy; Writing original draft: Heba Eltahir, Ali Alalawi, Sabrin Ibrahim; Writing review and editing: Mohannad A Almikhlaft, Maiada H Nazmy, Hussein Elbadawy, Yaser Alahmadi

REFERENCES

- Al Asmari AK, Al Sadoon KT, Obaid AA, Yesunayagam D, Tariq M (2017) Protective effect of quinacrine against glycerol-induced acute kidney injury in rats. *BMC Nephrol* **18**: 41. <https://doi.org/10.1186/s12882-017-0450-8>
- Bosch X, Poch E, Grau JM (2009) Rhabdomyolysis and acute kidney injury. *N Engl J Med* **361**: 62–72. <https://doi.org/10.1056/NEJMra0801327>
- Boutaud O, Roberts LJ 2nd (2011) Mechanism-based therapeutic approaches to rhabdomyolysis-induced renal failure. *Free Radic Biol Med* **51**: 1062–1067. <https://doi.org/10.1016/j.freeradbiomed.2010.10.704>
- Chawla LS, Eggers PW, Star RA, Kimmel PL (2014) Acute kidney injury and chronic kidney disease as interconnected syndromes. *N Engl J Med* **371**: 58–66. <https://doi.org/10.1056/NEJMr1214243>
- Chen G, Li Y, Wang W, Deng L (2018) Bioactivity and pharmacological properties of alpha-mangostin from the mangosteen fruit: a review. *Expert Opin Ther Pat* **28**: 415–427. <https://doi.org/10.1080/13543776.2018.1455829>
- Chen LG, Yang LL, Wang CC (2008) Anti-inflammatory activity of mangostins from *Garcinia mangostana*. *Food Chem Toxicol* **46**: 688–693. <https://doi.org/10.1016/j.fct.2007.09.096>
- Devi Sampath P, Vijayaraghavan K (2007) Cardioprotective effect of alpha-mangostin, a xanthone derivative from mangosteen on tissue defense system against isoproterenol-induced myocardial infarction in rats. *J Biochem Mol Toxicol* **21**: 336–339. <https://doi.org/10.1002/jbt.20199>
- Ebenezer PJ, Mariappan N, Elks CM, Haque M, Francis J (2009) Diet-induced renal changes in Zucker rats are ameliorated by the superoxide dismutase mimetic TEMPOL. *Obesity (Silver Spring)* **17**: 1994–2002. <https://doi.org/10.1038/oby.2009.137>
- Edelstein CL, Alkhunaizi AA, Schrier RW (1997) The role of calcium in the pathogenesis of acute renal failure. *Ren Fail* **19**: 199–207. <https://doi.org/10.3109/08860229709026276>
- Fang Y, Su T, Qiu X, Mao P, Xu Y, Hu Z, Zhang Y, Zheng X, Xie P, Liu Q (2016) Protective effect of alpha-mangostin against oxidative stress induced-retinal cell death. *Sci Rep* **6**: 21018. <https://doi.org/10.1038/srep21018>
- Franceschelli S, Pesce M, Ferrone A, Patruno A, Pasqualone L, Carlucci G, Ferrone V, Carlucci M, de Lutiis MA, Grilli A, Felaco M, Speranza L (2016) A novel biological role of alpha-mangostin in modulating inflammatory response through the activation of SIRT-1 signaling pathway. *J Cell Physiol* **231**: 2439–2451. <https://doi.org/10.1002/jcp.25348>
- Glodowski SD, Wagener G (2015) New insights into the mechanisms of acute kidney injury in the intensive care unit. *J Clin Anesth* **27**: 175–180. <https://doi.org/10.1016/j.jclinane.2014.09.011>
- Goldberg R, Dennen P (2008) Long-term outcomes of acute kidney injury. *Adv Chronic Kidney Dis* **15**: 297–307. <https://doi.org/10.1053/j.ackd.2008.04.009>
- Graziani G, Calvetta A, Cucchiari D, Valaperta S, Montanelli A (2011) Life-threatening hypercalcemia in patients with rhabdomyolysis-induced oliguric acute renal failure. *J Nephrol* **24**: 128–131. <https://doi.org/10.5301/jn.2010.5794>
- Gutierrez-Orozco F, Failla ML (2013) Biological activities and bioavailability of mangosteen xanthones: a critical review of the current evidence. *Nutrients* **5**: 3163–3183. <https://doi.org/10.3390/nu5083163>
- Holt SG, Moore KP (2001) Pathogenesis and treatment of renal dysfunction in rhabdomyolysis. *Intensive Care Med* **27**: 803–811. <https://doi.org/10.1007/s001340100878>
- Homs E, de Brito SM, Janino P (2010) Silymarin exacerbates p53-mediated tubular apoptosis in glycerol-induced acute kidney injury in rats. *Ren Fail* **32**: 623–632. <https://doi.org/10.3109/08860221003778064>
- Ibrahim SRM, Abdallah HM, El-Halawany AM, Nafady AM, Mohamed GA (2019a) Mangostanxanthone VIII, a new xanthone from *Garcinia mangostana* and its cytotoxic activity. *Nat Prod Res* **33**: 258–265. <https://doi.org/10.1080/14786419.2018.1446012>
- Ibrahim SRM, Mohamed GA, Elfaky MA, Al Haidari RA, Zayed MF, El-Kholy AA, Khedr AIM (2019b) Garcixanthone A, a new cytotoxic xanthone from the pericarps of *Garcinia mangostana*. *J Asian Nat Prod Res* **21**: 291–297. <https://doi.org/10.1080/10286020.2017.1423058>
- John OD, Mushunje AT, Surugau N, Quad RM (2022) The metabolic and molecular mechanisms of alpha-mangostin in cardiometabolic disorders (Review). *Int J Mol Med* **50**. <https://doi.org/10.3892/ijmm.2022.5176>
- Jung HA, Su BN, Keller WJ, Mehta RG, Kinghorn AD (2006) Antioxidant xanthones from the pericarp of *Garcinia mangostana* (Mangosteen). *J Agric Food Chem* **54**: 2077–2082. <https://doi.org/10.1021/jf052649z>
- Karasawa MMG, Mohan C (2018) Fruits as prospective reserves of bioactive compounds: a review. *Nat Prod Bioprospect* **8**: 335–346. <https://doi.org/10.1007/s13659-018-0186-6>
- Kim HJ, Park S, Shin HY, Nam YR, Lam Hong PT, Chin YW, Nam JH, Kim WK (2021) Inhibitory effects of alpha-mangostin on T cell cytokine secretion via ORAI1 calcium channel and K(+) channels inhibition. *PeerJ* **9**: e10973. <https://doi.org/10.7717/peerj.10973>
- Korrapati MC, Shaner BE, Schnellmann RG (2012) Recovery from glycerol-induced acute kidney injury is accelerated by suramin. *J Pharmacol Exp Ther* **341**: 126–136. <https://doi.org/10.1124/jpet.111.190249>
- Larson RT, Lorch JM, Pridgeon JW, Becnel JJ, Clark GG, Lan Q (2010) The biological activity of alpha-mangostin, a larvicidal botanical mosquito sterol carrier protein-2 inhibitor. *J Med Entomol* **47**: 249–257. <https://doi.org/10.1603/me09160>
- Li K, Chen Y, Zhang J, Guan Y, Sun C, Li X, Xie X, Zhang D, Yu X, Liu T, Zhang X, Kong F, Zhao S (2020a) Microenvironment derived from metanephros transplantation inhibits the progression of acute kidney injury in glycerol-induced rat models. *Ren Fail* **42**: 89–97. <https://doi.org/10.1080/0886022X.2019.1708393>
- Li Q, Yan XT, Zhao LC, Ren S, He YF, Liu WC, Wang Z, Li XD, Jiang S, Li W (2020b) alpha-Mangostin, a dietary xanthone, exerts protective effects on cisplatin-induced renal injury via PI3K/Akt and JNK signaling pathways in HEK293 cells. *ACS Omega* **5**: 19960–19967. <https://doi.org/10.1021/acsomega.0c01121>
- Liu ZW, Zhang YM, Zhang LY, Zhou T, Li YY, Zhou GC, Miao ZM, Shang M, He JP, Ding N, Liu YQ (2021) Duality of interactions between TGF-beta and TNF-alpha during tumor formation. *Front Immunol* **12**: 810286. <https://doi.org/10.3389/fimmu.2021.810286>
- Magadula JJ (2010) A bioactive isoprenylated xanthone and other constituents of *Garcinia edulis*. *Fitoterapia* **81**: 420–423. <https://doi.org/10.1016/j.fitote.2009.12.002>
- Martinez A, Galano A, Vargas R (2011) Free radical scavenger properties of alpha-mangostin: thermodynamics and kinetics of HAT and RAF mechanisms. *J Phys Chem B* **115**: 12591–12598. <https://doi.org/10.1021/jp205496u>
- Mehaffey E, Majid DSA (2017) Tumor necrosis factor-alpha, kidney function, and hypertension. *Am J Physiol Renal Physiol* **313**: F1005–F1008. <https://doi.org/10.1152/ajprenal.00535.2016>
- Mohamed GA, Al-Abd AM, El-Halawany AM, Abdallah HM, Ibrahim SRM (2017) New xanthones and cytotoxic constituents from *Garcinia mangostana* fruit hulls against human hepatocellular, breast, and colorectal cancer cell lines. *J Ethnopharmacol* **198**: 302–312. <https://doi.org/10.1016/j.jep.2017.01.030>
- Moreno JA, Martin-Cleary C, Gutierrez E, Toldos O, Blanco-Colio LM, Praga M, Ortiz A, Egido J (2012) AKI associated with macroscopic glomerular hematuria: clinical and pathophysiologic consequences. *Clin J Am Soc Nephrol* **7**: 175–184. <https://doi.org/10.2215/CJN.01970211>

- Muhamad Adyab NS, Rahmat A, Abdul Kadir NAA, Jaafar H, Shukri R, Ramli NS (2019) Mangosteen (*Garcinia mangostana*) flesh supplementation attenuates biochemical and morphological changes in the liver and kidney of high fat diet-induced obese rats. *BMC Complement Altern Med* **19**: 344. <https://doi.org/10.1186/s12906-019-2764-5>
- Ohkawa H, Ohishi N, Yagi K (1979) Assay for lipid peroxides in animal tissues by thiobarbituric acid reaction. *Anal Biochem* **95**: 351–358. [https://doi.org/10.1016/0003-2697\(79\)90738-3](https://doi.org/10.1016/0003-2697(79)90738-3)
- Ovalle-Magallanes B, Eugenio-Perez D, Pedraza-Chaverri J (2017) Medicinal properties of mangosteen (*Garcinia mangostana* L.): A comprehensive update. *Food Chem Toxicol* **109**: 102–122. <https://doi.org/10.1016/j.fct.2017.08.021>
- Panizo N, Rubio-Navarro A, Amaro-Villalobos JM, Egido J, Moreno JA (2015) Molecular mechanisms and novel therapeutic approaches to rhabdomyolysis-induced acute kidney injury. *Kidney Blood Press Res* **40**: 520–532. <https://doi.org/10.1159/000368528>
- Parekh R, Care DA, Tainter CR (2012) Rhabdomyolysis: advances in diagnosis and treatment. *Emerg Med Pract* **14**: 1–15; quiz 15
- Perez-Rojas JM, Cruz C, Garcia-Lopez P, Sanchez-Gonzalez DJ, Martinez-Martinez CM, Ceballos G, Espinosa M, Melendez-Zajigla J, Pedraza-Chaverri J (2009) Renoprotection by alpha-Mangostin is related to the attenuation in renal oxidative/nitrosative stress induced by cisplatin nephrotoxicity. *Free Radic Res* **43**: 1122–1132. <https://doi.org/10.1080/10715760903214447>
- Perez-Rojas JM, Gonzalez-Macias R, Gonzalez-Cortes J, Jurado R, Pedraza-Chaverri J, Garcia-Lopez P (2016) Synergic effect of alpha-mangostin on the cytotoxicity of cisplatin in a cervical cancer model. *Oxid Med Cell Longev* **2016**: 7981397. <https://doi.org/10.1155/2016/7981397>
- Quamme GA (1989) Control of magnesium transport in the thick ascending limb. *Am J Physiol* **256**: F197–F210. <https://doi.org/10.1152/ajprenal.1989.256.2.F197>
- Ramesh G, Reeves WB (2004) Inflammatory cytokines in acute renal failure. *Kidney Int Suppl* **S56**–S61. <https://doi.org/10.1111/j.1523-1755.2004.09109.x>
- Ramseyer VD, Garvin JL (2013) Tumor necrosis factor-alpha: regulation of renal function and blood pressure. *Am J Physiol Renal Physiol* **304**: F1231–F1242. <https://doi.org/10.1152/ajprenal.00557.2012>
- Sanchez-Perez Y, Morales-Barcenas R, Garcia-Cuellar CM, Lopez-Marure R, Calderon-Oliver M, Pedraza-Chaverri J, Chirino YI (2010) The alpha-mangostin prevention on cisplatin-induced apoptotic death in LLC-PK1 cells is associated to an inhibition of ROS production and p53 induction. *Chem Biol Interact* **188**: 144–150. <https://doi.org/10.1016/j.cbi.2010.06.014>
- Shahid M, Francis J, Majid DS (2008) Tumor necrosis factor-alpha induces renal vasoconstriction as well as natriuresis in mice. *Am J Physiol Renal Physiol* **295**: F1836–F1844. <https://doi.org/10.1152/ajprenal.90297.2008>
- Shanu A, Groebler L, Kim HB, Wood S, Weekley CM, Aitken JB, Harris HH, Witting PK (2013) Selenium inhibits renal oxidation and inflammation but not acute kidney injury in an animal model of rhabdomyolysis. *Antioxid Redox Signal* **18**: 756–769. <https://doi.org/10.1089/ars.2012.4591>
- Shimazui T, Nakada TA, Tateishi Y, Oshima T, Aizimu T, Oda S (2019) Association between serum levels of interleukin-6 on ICU admission and subsequent outcomes in critically ill patients with acute kidney injury. *BMC Nephrol* **20**: 74. <https://doi.org/10.1186/s12882-019-1265-6>
- Stein JH, Lifschitz MD, Barnes LD (1978) Current concepts on the pathophysiology of acute renal failure. *Am J Physiol* **234**: F171–F181. <https://doi.org/10.1152/ajprenal.1978.234.3.F171>
- Sullivan DE, Ferris M, Pociask D, Brody AR (2005) Tumor necrosis factor-alpha induces transforming growth factor-beta1 expression in lung fibroblasts through the extracellular signal-regulated kinase pathway. *Am J Respir Cell Mol Biol* **32**: 342–349. <https://doi.org/10.1165/rcmb.2004-0288OC>
- Sun L, Kanwar YS (2015) Relevance of TNF-alpha in the context of other inflammatory cytokines in the progression of diabetic nephropathy. *Kidney Int* **88**: 662–665. <https://doi.org/10.1038/ki.2015.250>
- Sun X, Luan Q, Qiu S (2018) Valsartan prevents glycerol-induced acute kidney injury in male albino rats by downregulating TLR4 and NF-kappaB expression. *Int J Biol Macromol* **119**: 565–571. <https://doi.org/10.1016/j.ijbiomac.2018.07.149>
- Swaminathan R (2003) Magnesium metabolism and its disorders. *Clin Biochem Rev* **24**: 47–66
- Tewtrakul S, Wattanapiromsakul C, Mahabusarakam W (2009) Effects of compounds from *Garcinia mangostana* on inflammatory mediators in RAW264.7 macrophage cells. *J Ethnopharmacol* **121**: 379–382. <https://doi.org/10.1016/j.jep.2008.11.007>
- Ustundag S, Sen S, Yalcin O, Ciftci S, Demirkan B, Ture M (2009) L-Carnitine ameliorates glycerol-induced myoglobinuric acute renal failure in rats. *Ren Fail* **31**: 124–133. <https://doi.org/10.1080/08860220802599130>
- Venkatachalam MA, Weinberg JM, Kriz W, Bidani AK (2015) Failed tubule recovery, AKI-CKD transition, and kidney disease progression. *J Am Soc Nephrol* **26**: 1765–1776. <https://doi.org/10.1681/ASN.2015010006>
- Watanabe M, Gangitano E, Francomano D, Addessi E, Toscano R, Costantini D, Tuccinardi D, Mariani S, Basciani S, Spera G, Gnassi L, Lubrano C (2018) Mangosteen extract shows a potent insulin sensitizing effect in obese female patients: a prospective randomized controlled pilot study. *Nutrients* **10**. <https://doi.org/10.3390/nu10050586>
- Wen X, Peng Z, Kellum JA (2011) Pathogenesis of acute kidney injury: effects of remote tissue damage on the kidney. *Contrib Nephrol* **174**: 129–137. <https://doi.org/10.1159/000329382>
- Wu J, Pan X, Fu H, Zheng Y, Dai Y, Yin Y, Chen Q, Hao Q, Bao D, Hou D (2017) Effect of curcumin on glycerol-induced acute kidney injury in rats. *Sci Rep* **7**: 10114. <https://doi.org/10.1038/s41598-017-10693-4>
- Xu Y, Zhou H, Cai L (2017) Alpha-mangostin attenuates oxidative stress and inflammation in adjuvant-induced arthritic rats. *Trop J Pharm Res* **16**: 2611–2616
- Yiemwattana I, Kaomongkolgit R (2015) Alpha-mangostin suppresses IL-6 and IL-8 expression in *P. gingivalis* LPS-stimulated human gingival fibroblasts. *Odontology* **103**: 348–355. <https://doi.org/10.1007/s10266-014-0160-7>
- Zager RA (1996) Rhabdomyolysis and myohemoglobinuric acute renal failure. *Kidney Int* **49**: 314–326. <https://doi.org/10.1038/ki.1996.48>
- Zou W, Yin P, Shi Y, Jin N, Gao Q, Li J, Liu F (2019) A novel biological role of alpha-mangostin via TAK1-NF-kappaB pathway against inflammatory. *Inflammation* **42**: 103–112. <https://doi.org/10.1007/s10753-018-0876-6>

MiR-375 attenuates sorafenib resistance of hepatocellular carcinoma cells by inhibiting cell autophagy

Dan Wang¹ and Jingbo Yang^{2✉}

¹Department of Neurology, the First Hospital of Changsha, Changsha, Hunan 410011, P.R. China; ²Department of Gastroenterology, the First Affiliated Hospital of Shenzhen University, Shenzhen Second People's Hospital, Shenzhen, Guangdong 518028, P.R. China

Objective: Sorafenib is the first-line treatment for hepatocellular carcinoma (HCC), but its efficacy is limited by the drug resistance of HCC cells. MiR-375 has been shown to be an inhibitor of autophagy that contributes to sorafenib resistance of HCC cells. In this context, this study probed into the unaddressed molecular target of miR-375 in inhibiting the autophagy of HCC cells under sorafenib treatment. **Methods:** Western blotting and qRT-PCR (quantitative reverse transcription-polymerase chain reaction) have been applied to measure the expressions of miR-375 and SIRT5 in parental HCC cells (HepG2 and Huh7) and sorafenib-resistant HCC cells (HepG2/so and Huh7/so). HepG2/so cells were accordingly transfected with miR-375 mimic, miR-375 inhibitor, sh-SIRT5, pcDNA3.1-SIRT5 or negative control. Expressions of p62, LC3I and LC3II in HCC cells have been measured by Western blotting. Viability and apoptosis of HCC cells have been assessed by CCK-8 (cell counting kit 8) and flow cytometry respectively. Bioinformatics techniques and dual-luciferase reporter assay have been used to predict and verify the targeting relationship between miR-375 and SIRT5. **Results:** MiR-375 was under-expressed and SIRT5 was over-expressed in HCC cells. An autophagy inhibitor impaired the survival of HepG2/so cells transfected with miR-375 inhibitor. An autophagy activator enhanced the drug resistance of HepG2/so cells transfected with miR-375 mimic. MiR-375 suppressed the drug resistance of HepG2/so cells by inhibiting autophagy. SIRT5 enhanced the drug resistance of HepG2/so cells by promoting autophagy and it could be targeted by miR-375. **Conclusion:** MiR-375 suppresses autophagy to attenuate the sorafenib resistance of HCC cells by regulating SIRT5. The findings of this study may provide new therapeutic targets for treating HCC.

Keywords: MiR-375, SIRT5, autophagy, drug resistance, Sorafenib, hepatocellular carcinoma cell

Received: 14 April, 2021; revised: 18 October, 2021; accepted: 01 February, 2023; available on-line: 17 April, 2023

✉e-mail: jingboyang.ssp@foxmail.com

Acknowledgements of Financial Support: This research was funded by the grant from the National Natural Science Foundation of China (Grant No. 81602601).

Abbreviations: ATG2A, autophagy-related gene 2A; BCA, bicinchoninic acid; CCK-8, cell counting kit 8; DMEM, Dulbecco's modified Eagle medium; FITC, fluorescein isothiocyanate; HCC, hepatocellular carcinoma; PVDF, polyvinylidene fluoride; PI, propidium iodide; PBS, phosphate-buffered saline; PBST, PBS Tween 20; qRT-PCR, quantitative reverse transcription-polymerase chain reaction; RAP, rapamycin; 3-MA, 3-Methyladenine

INTRODUCTION

Liver cancer belongs to the commonest deadly cancers worldwide. The death rate of liver cancer rose from 2012 to 2016 and the incidence rate continues to increase (Siegel *et al.*, 2019). Hepatocellular carcinoma (HCC) accounts for the vast majority of primary liver cancers, which can be caused by cirrhosis, infection of hepatitis B or C virus, alcohol abuse and other risk factors (Villanueva, 2019). Sorafenib is a multikinase inhibitor that has been considered the first treatment option and standard therapy for advanced-stage HCC for over a decade (Marisi *et al.*, 2018). Sorafenib targets multiple tyrosine kinases and therefore impairs proliferation, migration and angiogenesis and activates apoptosis in HCC (Brunetti *et al.*, 2019). However, a considerable portion of patients with HCC are insensitive to sorafenib, resulting in an unsatisfactory overall efficacy of this widely used drug (Cheng *et al.*, 2020). HCC cells developing sorafenib resistance exhibit significant mesenchymal phenotypes and stemness features (Xia *et al.*, 2020). Therefore, exploration of the mechanisms of sorafenib resistance is important for prolonging the survival of patients with HCC.

Autophagy is a metabolic process that is unavoidably altered in cancers and it can be well manipulated to improve the clinical outcomes of cancer patients (Levy *et al.*, 2017). Autophagy prevents cell damage and improves survival in response to energy or nutrient shortage and various cytotoxic insults (Dikic & Elazar, 2018). An autophagy inhibitor, chloroquine, overcame the resistance of liver cancer cells to drugs targeting hepatocyte growth factor-activated MET kinase which stimulated liver carcinogenesis and tumor metastasis (Huang *et al.*, 2019). Autophagy is also suggested to be an important participant in mediating sorafenib resistance of HCC. For instance, depletion of METTL3, a primary m⁶A methyltransferase, enhanced the sorafenib resistance of HCC cells by activating autophagy-associated pathways through destabilization of FOXO3 mRNA (Lin *et al.*, 2020). CD24 activated autophagy by regulating PP2A/AKT/mTOR signaling pathway and therefore decreased the sorafenib sensitivity of HCC cells (Lu *et al.*, 2018). MicroRNA (miR)-541 inhibited autophagy-dependent sorafenib resistance of HCC cells by directly targeting autophagy-related gene (ATG) 2A and Ras-related protein Rab-1B (Xu *et al.*, 2020).

In recent years, microRNAs (miRNAs) have shown great promise as therapeutic targets for cancer treatment. MiRNAs regulate gene function in diverse cellular activities including autophagy. MiR-375 is known to be an autophagy inhibitor in many disease conditions. As an example, miR-375 promoted inflammation and apoptosis

of acinar cells in severe acute pancreatitis by inhibiting ATG7-mediated autophagy (Zhao *et al.*, 2020). MiR-375 also inhibited autophagy to facilitate the sorafenib therapy for HCC (Zhao *et al.*, 2018). However, the mechanism of miR-375 in regulating autophagy-dependent sorafenib resistance in HCC remains largely unknown.

SIRT5 is a sirtuin family member that resides primarily in mitochondrial matrix and regulates cellular homeostasis (Kumar & Lombard, 2018). Overexpression of SIRT5 is associated with tumorigenesis in breast cancer, colorectal cancer, HCC and more (Greene *et al.*, 2019; Shi *et al.*, 2019; Zhang *et al.*, 2019). Garva and others found that SIRT5 positively regulated autophagy and proliferation of tumor cells under stress conditions (Garva *et al.*, 2019). However, there is no report on either SIRT5-mediated autophagy in HCC or the interaction between miR-375 and SIRT5. The authors used Jefferson database to predict whether SIRT5 mRNA and miR-375 have binding sites (<https://cm.jefferson.edu/>) and designed this study to verify the involvement of miR-375/SIRT5 axis in autophagy-mediated sorafenib resistance of HCC cells.

MATERIALS AND METHODS

Cell cultivation

A healthy liver cell line (L-02) and human HCC cell lines (HepG2 and Huh7) were purchased from the American Type Culture Collection. L-02, HepG2 and Huh7 cells were cultured in Dulbecco's modified Eagle medium (DMEM), MEM and high-glucose DMEM, respectively. All media were supplemented with 10% fetal bovine serum and 2 mM glutamine. These cells were incubated in a moist environment (37°C, 5% CO₂) and used for experiments until they reached the logarithmic growth phase.

Establishment of sorafenib-resistant HCC cell models

Sorafenib treatment was given to HepG2 and Huh7 cells at the logarithmic growth phase. The initial dose of sorafenib was set at 1 µmol/L. The culture medium was renewed every 24 hours, in which the sorafenib concentration increased by 0.25 µmol/L each time until reaching a total of 12 µmol/L. The half maximal inhibitory concentration (IC₅₀) >10 µM indicated resistance to sorafenib. Sorafenib-resistant HepG2 and Huh7 cells (HepG2/so and Huh7/so) were continuously treated with sorafenib to enhance the drug resistance. The cells were observed and photographed under an inverted microscope.

Cell transfection and treatment

L-02 or HepG2/so cells were transfected with miR-375 mimic, miR-375 inhibitor, sh-SIRT5, pcDNA3.1-SIRT5 or their negative control (mimic NC, inhibitor NC, sh-NC or pcDNA3.1) in 3.5 cm culture dishes (2×10⁶ cells per dish) using Lipofectamine 2000 (Invitrogen, California, USA). The plasmids and RNAs were provided by GenePharma (Shanghai, China). All other experiments were carried out 48 hours after the transfection.

For analyzing the effect of autophagy on sorafenib resistance of HCC cells, HepG2/so cells transfected with miR-375 mimic were treated with an autophagy activator rapamycin (RAP, 0.2 µg/10 µl; Cell Signaling Technology, MA, USA) for 24 hours and HepG2/so cells transfected with miR-375 inhibitor were treated with an au-

tophagy inhibitor 3-Methyladenine (3-MA, 50 µM; Selleck, USA) for 24 hours. The use of RAP and 3-MA was based on existing literature (Ding *et al.*, 2021; Lendvai *et al.*, 2021).

CKK-8 assay

The assay was applied to measure the IC₅₀ of parental and sorafenib-resistant HCC cells. The survival rates of HCC cells were measured 24 hours after treatment with sorafenib of different concentrations (1, 2, 4, 8, 16, 32 µmol/L). The influence of miR-375 or SIRT5 on the survival of sorafenib-resistant HCC cells was also assessed. Cells of each group were cultured in a 96-well plate where every well contained 1.5×10⁴ cells. Cells in each well were incubated with 10 µl of CCK-8 reagent at 37°C for 3 hours. The absorbance value was measured at 450 nm.

Flow cytometry

Cells in each group were made into suspension for centrifugation at 2000 r/min. The cells were washed twice with phosphate-buffered saline (PBS) and then resuspended in binding buffer. Cell suspension (195 µL, about 1×10⁵ cells) was mixed with 5 µL of Annexin-V-fluorescein isothiocyanate (FITC) and propidium iodide (PI) solution. The cells were incubated in the dark for 10 minutes and their apoptosis rates were measured by a flow cytometer (BD Biosciences, Suzhou, China).

qRT-PCR

Total RNA was obtained from 4 ~ 5×10⁴ cells per well using a TRIzol kit. cDNA reverse transcribed from the RNA was used as the template for qRT-PCR. The reaction was performed according to the instruction of SYBR Prime Script RT-PCR kit. The total reactants consisted of 0.8 µl of cDNA, 5.0 µl of SYBR Primix Ex Taq, 1.0 µl of primers and 3.2 µl of RNase H₂O. The thermal cycling was set as follows: 5 minutes at 95°C; 30 cycles of 15 seconds at 95°C, 30 seconds at 95°C and 40 seconds at 72°C. GAPDH served as a reference gene. Each sample had three duplicates. The results were analyzed using the 2^{-ΔΔCt} method: ΔΔCt = (Ct_{target gene} - Ct_{reference gene})_{experimental group} - (Ct_{target gene} - Ct_{reference gene})_{control group}. Sequences of the primers used in the PCR are presented in Table 1.

Table 1. Primer sequences

miR-375-F	CACAAAATTTGTCGTTCCGGCT
miR-375-R	GTGCAGGGTCCGAGGT
SIRT5-F	ACAATGGCTCGTCCAAGTTC
SIRT5-R	CCAGTAACCTCCTGCTCCTCT
GAPDH-F	GACAGTCAGCCGCATCTTCT
GAPDH-R	GCGCCCAATACGACCAAATC

Note: F, forward; R, reverse.

Western blotting

Cells were cultured for 48 h before Western blotting analysis in which 1 ~ 2×10⁶ cells per well were used. After two PBS washes, the cells were lysed in lysis buffer on ice for 45 minutes and shaken at 15-minute intervals. After quantification by a bicinchoninic acid (BCA) kit, proteins extracted from the cells were mixed with loading buffer and transferred onto a polyvinylidene fluoride

(PVDF) membrane after SDS-PAGE electrophoresis. Non-specific binding was blocked in 5% skim milk for 2 hours (room temperature). After that, the membrane was incubated with primary antibodies of SIRT5 (#8779, 1:1000), LC3II/I (#12741, 1:1000), p62 (#88588, 1:1000), acetylated-lysine (#9814, 1:500) (Cell Signaling Technology, Beverly, MA, USA) or LDHB (ab53292, Abcam, Cambridge, MA, USA) at 4°C overnight and washed with PBS Tween 20 (PBST) for 3×15 minutes. The proteins were then incubated with the secondary antibody (ab6728, 1:2000, Abcam, Cambridge, MA, USA) for 1 hour. Protein expressions were reflected by chemiluminescence. GAPDH (Cell Signaling, #5174, 1:1000) acted as a reference protein.

Dual-luciferase reporter assay

MiR-375 was found to have a binding site on the 3'UTR of SIRT5 mRNA based on the analysis of jeferson (<https://cm.jefferson.edu/>). Wild and mutant SIRT5-3'UTR (WT-SIRT5 and MUT-SIRT5) were synthesized and cloned to luciferase reporter vectors and then co-transfected with miR-375 mimic or mimic NC into HEK-293T cells. Luciferase activities in the cells were assessed 48 hours after transfection using a fluorescent luminescence detector based on the instruction of the dual-luciferase reporter assay kit (Beyotime, Shang-

hai, China). Relative luciferase activity = Firefly luciferase activity/Renilla luciferase activity.

Statistical analysis

SPSS 18.0 (IBM Corp., Armonk, NY, USA) and GraphPad Prism 7.0 (GraphPad Software Inc.) were applied for statistical analysis. Data were finally presented as mean ± standard deviation (S.D.). T-test and one-way analysis of variance were used to analyze the differences of two groups and multi-groups, respectively. Differences were deemed statistically significant when $P < 0.05$.

RESULTS

MiR-375 is under-expressed in sorafenib-resistant HCC cells

The parental strains of HCC cells (HepG2 and Huh7) were continuously cultured in sorafenib of increasing concentrations to obtain sorafenib-resistant HCC cells (HepG2/so and Huh7/so). The morphology of HepG2 and Huh7 cells under the inverted microscope were changed from a plump, pebble-like shape (epithelial phenotype) into a spindle shape (mesenchymal phenotype) (Fig. 1A). CCK-8 assay detected that the IC₅₀ of sorafenib in HepG2/so and

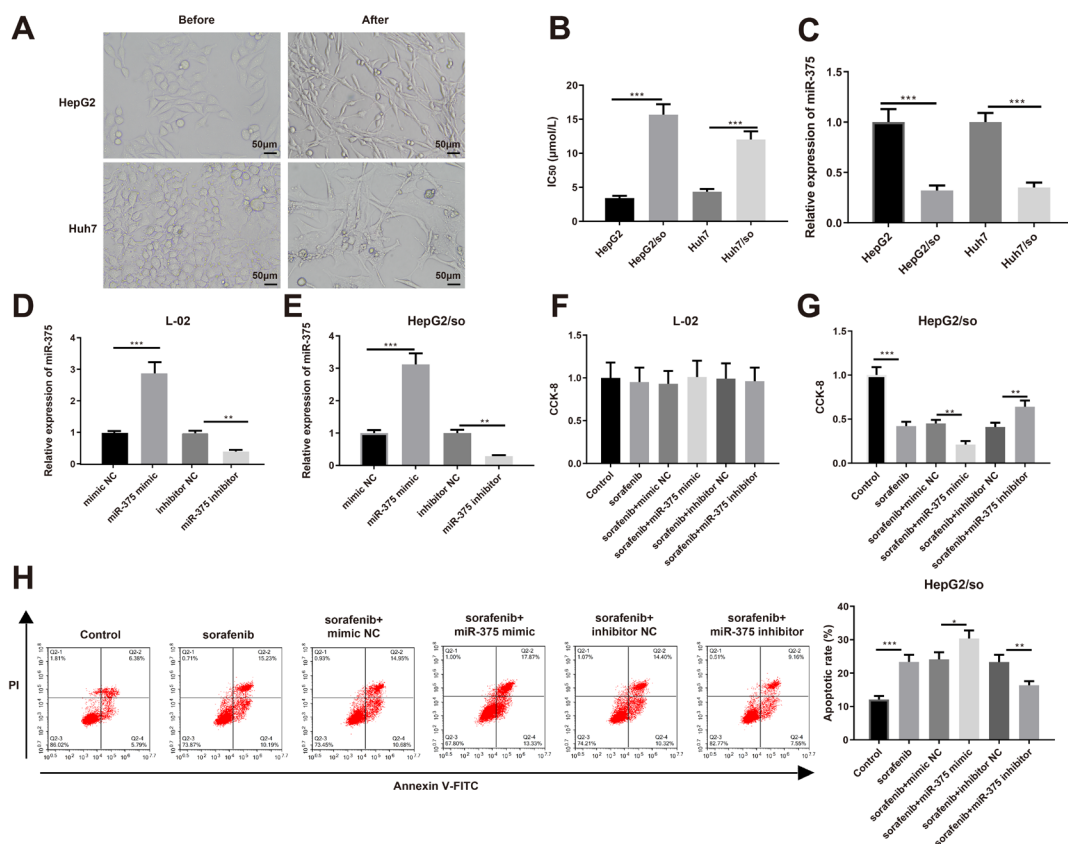


Figure 1. MiR-375 is under-expressed in sorafenib-resistant HCC cells

(A) The morphology of HepG2 and Huh7 cells under an inverted microscope. (B) CCK-8 assay measured the sorafenib IC₅₀ of HepG2, Huh7, HepG2/so and Huh7/so cells. (C) The expression of miR-375 in HepG2, Huh7, HepG2/so and Huh7/so cells. (D–E) qRT-PCR detected the expression of miR-375 in HepG2/so (D) or L-02 (E) cells transfected with miR-375 mimic or miR-375 inhibitor. (F) CCK-8 assay assessed the survival of the transfected L-02 cells. CCK-8 assay (G) and flow cytometry (H) assessed the survival and apoptosis of the transfected HepG2/so cells after sorafenib treatment. N=3; * $P < 0.05$, ** $P < 0.01$, *** $P < 0.001$; data were presented as mean ± S.D.; T-test was for comparison between two groups; one-way analysis of variance was for multi-group comparison; the Tukey test was for *post hoc* multiple comparisons after ANOVA; HCC, hepatocellular carcinoma; cell counting kit 8; qRT-PCR, quantitative reverse transcription-polymerase chain reaction.

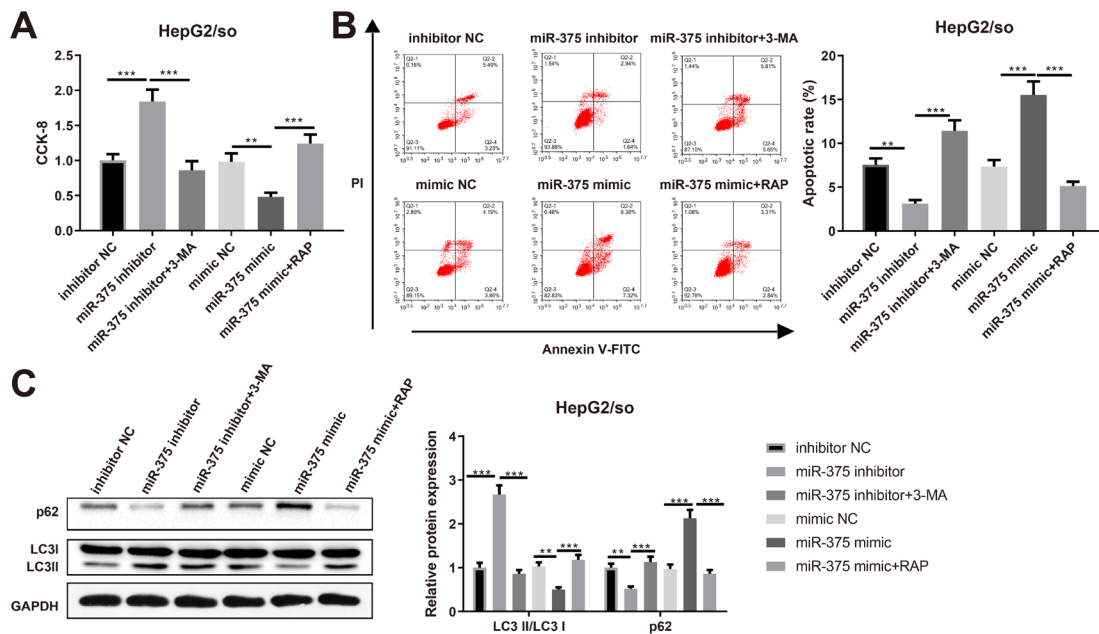


Figure 2. Autophagy acts on miR-375-mediated drug resistance of HCC cells

(A) CCK-8 assay assessed the survivability of HepG2/so cells; (B) Annexin-V-FITC/PI staining and flow cytometry assessed the apoptosis of HepG2/so cells; (C) Western blotting measured the expressions of p62, LC3I and LC3II in HepG2/so cells. N=3; * $P<0.05$, ** $P<0.01$, *** $P<0.001$; data were presented as mean \pm S.D; T-test was for comparison between two groups; one-way analysis of variance was for multi-group comparison; the Tukey test was for *post hoc* multiple comparisons after ANOVA; HCC, hepatocellular carcinoma; CCK-8, cell counting kit 8; FITC, fluorescein isothiocyanate; PI, propidium iodide; RAP, rapamycin; 3-MA, 3-Methyladenine.

Huh7/so cells was higher than in HepG2 and Huh7 cells (Fig. 1B, $P<0.05$), suggesting stronger tolerance of HepG2/so and Huh7/so cells to sorafenib.

MiR-375 was under-expressed in HepG2/so and Huh7/so cells compared to HepG2 and Huh7 cells (Fig. 1C, $P<0.05$). To investigate the potential effect of miR-375 expression on sorafenib resistance and on healthy liver cells, HepG2/so and L-02 cells were transfected with miR-375 mimic or miR-375 inhibitor. MiR-375 was up-regulated in the miR-375 mimic group and down-regulated in the miR-375 inhibitor group (Fig. 1D–E, $P<0.05$, *vs* the mimic NC or inhibitor NC group), suggesting successful cell transfection. The results of CCK-8 assay showed that transfection of miR-375 mimic/inhibitor had no significant impact on the survival of healthy liver cells (Fig. 1F). After the transfection, HepG2/so cells were exposed to sorafenib for 24 hours. Sorafenib treatment impeded the survival of HepG2/so cells (Fig. 1G, $P<0.05$). The survival of HepG2/so cells was further damaged by miR-375 mimic while improved by miR-375 inhibitor (Fig. 1G, $P<0.05$). The results of flow cytometry showed that miR-375 mimic promoted sorafenib-induced apoptosis of HepG2/so cells while miR-375 inhibitor attenuated the apoptosis (Fig. 1H, $P<0.05$).

Autophagy acts on miR-375-mediated drug resistance of HCC cells

The autophagy level in transfected HepG2/so cells was inhibited by 3-MA or activated by RAP. CCK-8 assay detected that 3-MA treatment impaired the viability of HepG2/so cells transfected with miR-375 inhibitor, while RAP treatment enhanced the viability of HepG2/so cells overexpressing miR-375 (Fig. 2A, $P<0.05$, *vs* the miR-375 inhibitor group or miR-375 mimic group). The apoptosis of HepG2/so cells was reduced in the miR-375 inhibitor group, while enhanced in the miR-375 inhibitor + 3-MA group (Fig. 2B, $P<0.05$, *vs* the inhibitor

NC group and miR-375 inhibitor group, respectively). The apoptosis of HepG2/so cells was promoted in the miR-375 mimic group, while inhibited in the miR-375 mimic + RAP group (Fig. 2B, $P<0.05$).

Meanwhile, according to the Western blotting measurement of the expressions of p62, LC3I and LC3II, the autophagy of HepG2/so cells was inhibited in the miR-375 inhibitor + 3-MA group, while enhanced in the miR-375 mimic + RAP group (Fig. 2C, $P<0.05$, *vs* the miR-375 inhibitor group and miR-375 mimic group, respectively).

MiR-375 attenuates sorafenib resistance by mediating autophagy in HCC cells

According to the CCK-8 analysis of cell viability, HepG2/so cells were less susceptible to sorafenib than HepG2 cells ($P<0.05$). The drug resistance of HepG2/so cells was enhanced by miR-375 inhibitor and reduced by miR-375 mimic (Fig. 3A, $P<0.05$). The apoptosis rate of HepG2/so cells was significantly reduced compared to that of HepG2 cells ($P<0.05$). The number of apoptotic HepG2/so cells was decreased after transfection of miR-375 inhibitor, while increased after transfection of miR-375 mimic (Fig. 3B, $P<0.05$).

Furthermore, the LC3II/LC3I ratio was increased and p62 was decreased in HepG2/so cells compared to HepG2 cells ($P<0.05$). The above mentioned expression trends of p62, LC3I and LC3II in HepG2/so cells were promoted by miR-375 inhibitor, while perturbed by miR-375 mimic (Fig. 3C, $P<0.05$).

SIRT5 is targeted and down-regulated by miR-375

SIRT5 was detected to be a downstream target of miR-375 based on the bioinformatics analysis of jeferson (Fig. 4A). Dual-luciferase reporter assay was designed to confirm the potential regulation between miR-375 and SIRT5. miR-375 mimic attenuated the relative

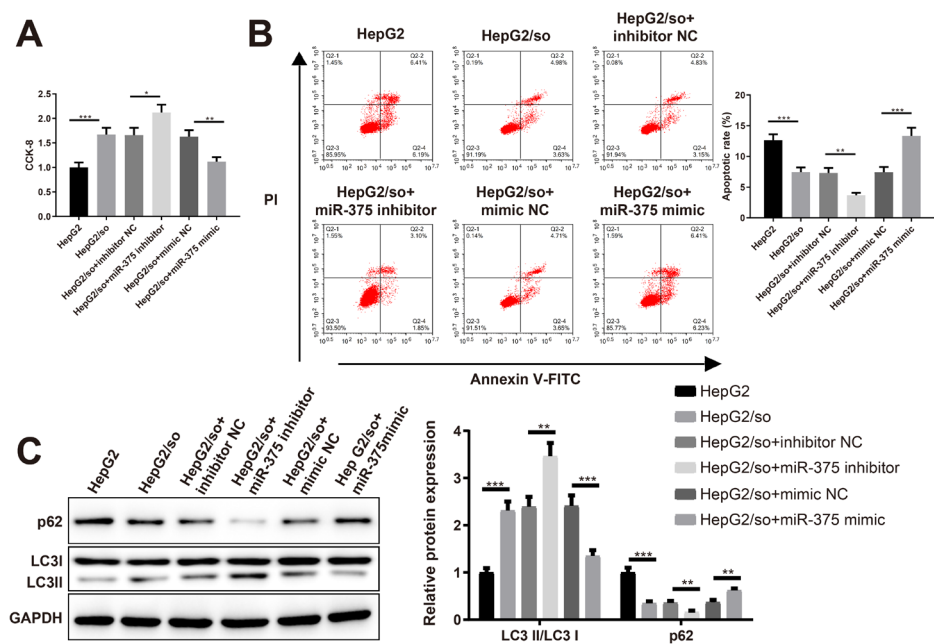


Figure 3. MiR-375 attenuates sorafenib resistance by mediating autophagy in HCC cells (A) The survival rates of HepG2 and HepG2/so cells; (B) the apoptosis rates of HepG2 and HepG2/so cells; (C) the levels of p62, LC3I and LC3II in HepG2 and HepG2/so cells. N=3; * $P<0.05$, ** $P<0.01$, *** $P<0.001$; data were presented as mean \pm S.D.; T-test was for comparison between two groups; one-way analysis of variance was for multi-group comparison; the Tukey test was for *post hoc* multiple comparisons after ANOVA; HCC, hepatocellular carcinoma.

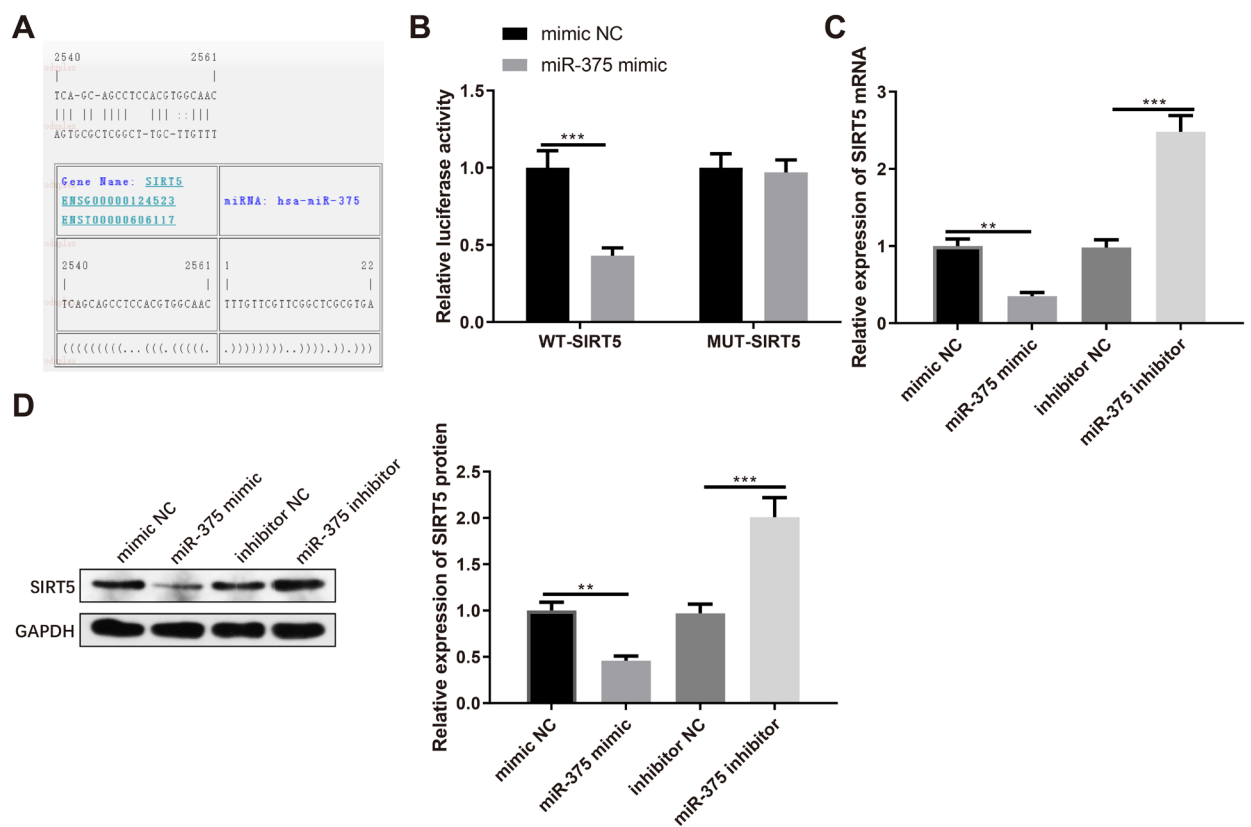


Figure 4. SIRT5 is targeted and down-regulated by miR-375 (A) The binding sites between miR-375 and SIRT5 were predicted by Jefferson; (B) dual-luciferase reporter assay verified the binding between miR-375 and SIRT5; (C–D) the expression of SIRT5 in cells transfected with miR-375 mimic or miR-375 inhibitor. N=3; * $P<0.05$, ** $P<0.01$, *** $P<0.001$; data were presented as mean \pm S.D.; one-way analysis of variance was for multi-group comparison; the Tukey test was for *post hoc* multiple comparisons after ANOVA.

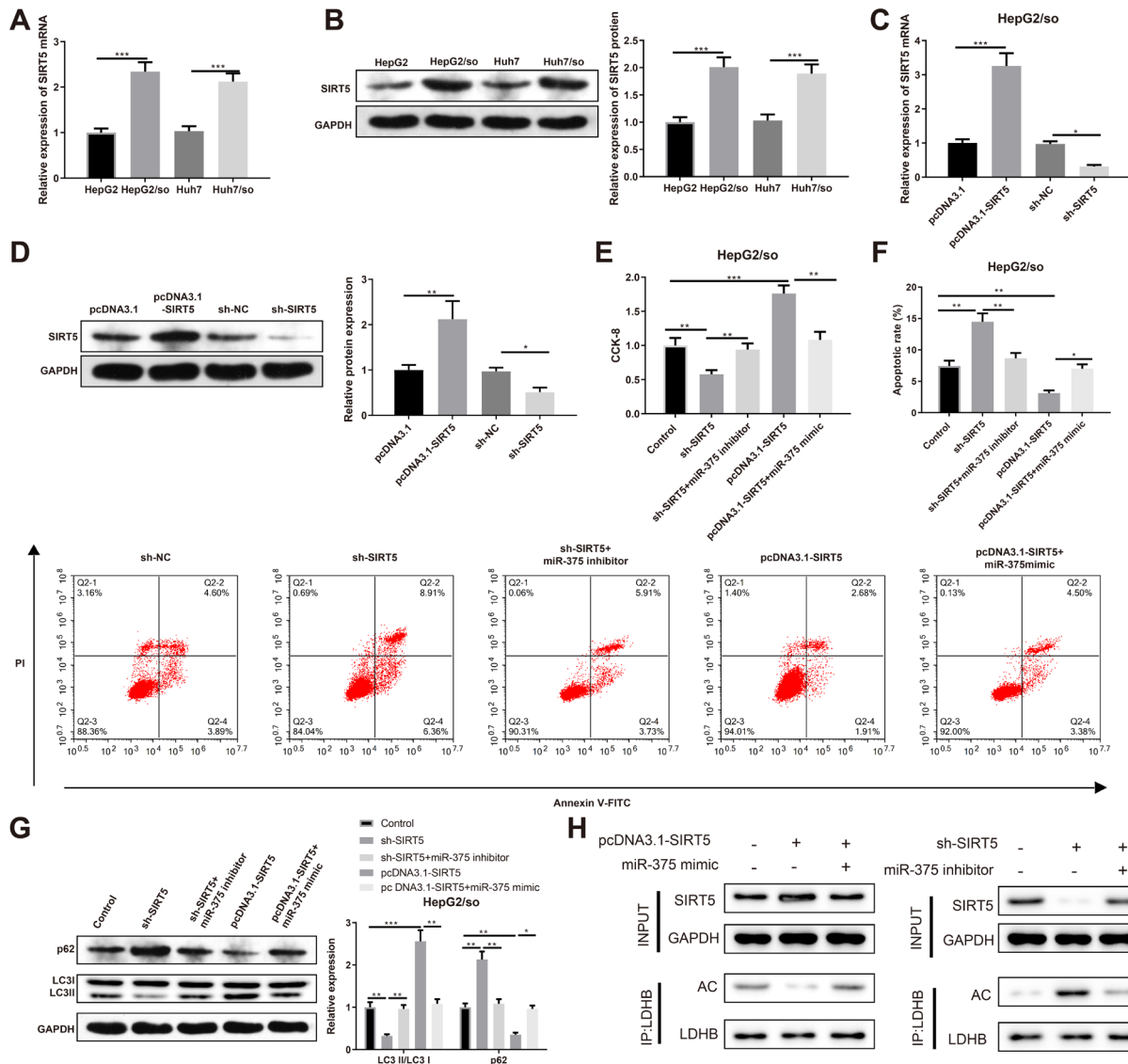


Figure 5. SIRT5 is over-expressed in sorafenib-resistant HCC cells and reverses the suppressive effect of miR-375 on sorafenib resistance

(A–B) The expression of SIRT5 in HepG2, Huh7, HepG2/so and Huh7/so cells. After HepG2/so cells were transfected with pcDNA3.1-SIRT5 or sh-SIRT5, qRT-PCR (C) and Western blotting (D) measured the expression of SIRT5 in HepG2/so cells; (E) CCK-8 assessed the survival rate of HepG2/so cells; (F) Annexin-V-FITC/PI staining and flow cytometry assessed the apoptosis of HepG2/so cells; Western blotting measured the expressions of p62, LC3I and LC3II (G) and the acetylation level of LDHB (H) in HepG2/so cells. N=3; * $P<0.05$, ** $P<0.01$, *** $P<0.001$; data were presented as mean \pm S.D.; T-test was for comparison between two groups; one-way analysis of variance was for multi-group comparison; the Tukey test was for *post hoc* multiple comparisons after ANOVA; HCC, hepatocellular carcinoma.

luciferase activity of WT-SIRT5 (Fig. 4B, $P<0.01$), but did not affect that of MUT-SIRT5. In cells, the expression of SIRT5 was negatively regulated by miR-375 (Fig. 4C–D, $P<0.01$).

SIRT5 is over-expressed in sorafenib-resistant HCC cells and reverses the suppressive effect of miR-375 on sorafenib resistance

According to the results of qRT-PCR and Western blotting, HepG2/so and Huh7/so cells had higher expressions of SIRT5 than HepG2 and Huh7 cells (Fig. 5A–B, $P<0.05$). To investigate the effect of SIRT5 on sorafenib resistance, SIRT5 was either knocked down or over-expressed in HepG2/so cells *via* transfection of sh-SIRT5 or pcDNA3.1-SIRT5 (Fig. 5C–D, $P<0.05$). SIRT5 inhibition aggravated the damage to the survival of HepG2/so cells whereas SIRT5 overexpression im-

proved the survival (Fig. 5E, $P<0.05$). The suppressive or promotive effect of SIRT5 inhibition or overexpression on sorafenib resistance of HepG2/so cells was reversed by miR-375 inhibitor or miR-375 mimic (Fig. 5E, $P<0.05$). SIRT5 inhibition exacerbated sorafenib-induced apoptosis of HepG2/so cells, which was later attenuated by miR-375 inhibitor (Fig. 5F, $P<0.05$). SIRT5 overexpression ameliorated the deaths of sorafenib-treated HepG2/so cells, while the apoptosis rate was increased in the pcDNA3.1-SIRT5 + miR-375 mimic group (Fig. 5F, $P<0.05$).

SIRT5 promotes autophagy by catalyzing the deacetylation of LDHB (Shi *et al.*, 2019). The ratio of LC3II/LC3I was reduced, the expression of p62 was up-regulated and the acetylation level of LDHB was increased in the sh-SIRT5 group (*vs* the sh-NC group) and pcDNA3.1-SIRT5 + miR-375 mimic group (*vs* the

pcDNA3.1-SIRT5 + mimic NC group); different expression patterns of LC3II, LC3I and p62 and a decreased acetylation level of LDHB were found in the pcDNA3.1-SIRT5 group (*vs* the pcDNA3.1 group) and sh-SIRT5 + miR-375 inhibitor group (*vs* sh-SIRT5 + inhibitor NC group) (Fig. 5G–H, $P < 0.05$).

The above experiment data exhibited that SIRT5 knockdown inhibited autophagy to augment the susceptibility of HCC cells to sorafenib, and miR-375 down-regulation abolished the assistance of SIRT5 knockdown to sorafenib treatment. In addition, SIRT5 overexpression enhanced the resistance to sorafenib via autophagy activation in HCC cells, while miR-375 up-regulation improved the sensitivity of SIRT5 overexpressing HCC cells to sorafenib. Taken together, miR-375 mediated the tolerance of HCC cells to sorafenib by regulating SIRT5.

DISCUSSION

HCC is the predominant primary liver cancer caused by both intrinsic and extrinsic risk factors (Ghouri *et al.*, 2017). As the first-line treatment option for HCC, sorafenib significantly improves the overall survival of HCC patients but the drug efficacy has been greatly limited by high its resistance rate (Niu *et al.*, 2017). Some biological processes in tumor microenvironment, including angiogenesis, inflammation, fibrosis, autophagy and viral reactivation, are associated with sorafenib resistance (Chen *et al.*, 2015). To further explore the molecular mechanisms underlying sorafenib resistance-related biological processes would help amplify the benefits of sorafenib. The present paper elucidates the regulatory mechanism of miR-375 in autophagy-mediated sorafenib resistance of HCC cells.

First of all, sorafenib-resistant HCC cells (HepG2/so and Huh7/so) were established. HepG2/so and Huh7/so cells obtained increased cell viability and decreased apoptosis compared to HepG2 and Huh7 cells. MiR-375 was found to be down-regulated in HepG2/so and Huh7/so cells compared with parental HepG2 and Huh7 cells. Sorafenib impaired the survival of HepG2/so cells and miR-375 overexpression further enhanced sorafenib-induced cell death. To confirm the potential regulation of endogenous miR-375 in HCC cells under sorafenib treatment, the expression of miR-375 was either up-regulated or down-regulated in HepG2/so cells. According to the measurement of cell viability and apoptosis, miR-375 inhibition made HepG2/so cells more resistant to sorafenib, while miR-375 overexpression increased the drug sensitivity. The assistance of miR-375 in anti-tumor therapy has already been uncovered. MiR-375 augmented the susceptibility of HCC cells to sorafenib by targeting the autophagy-related gene, ATG14 (Yang *et al.*, 2020). MiR-375 also inhibited the survival of fulvestrant-resistant breast cancer cells by restraining autophagy (Liu *et al.*, 2018).

Numerous existing scientific reports have authenticated that autophagy inhibition results in suppression on sorafenib resistance of HCC cells. For instance, SNHG16 promoted sorafenib resistance by enhancing autophagy via the miR-23b-3p/EGR1 axis in HCC (Jing *et al.*, 2020). LncRNA HANR enhanced autophagy-dependent sorafenib resistance of HCC cells by competing with ATG9A for miR-29b (Shi *et al.*, 2020). The LC3II/LC3I ratio was increased and p62 was decreased in HepG2/so cells in comparison with HepG2 cells, suggesting activated autophagy in sorafenib-resistant HCC cells. After transfection of miR-375 inhibitor or miR-375

mimic, the autophagy level was promoted or inhibited in HepG2/so cells. Autophagy activated or inhibited in HepG2/so cells by miR-375 inhibitor or miR-375 mimic was thereafter inhibited by 3-MA or promoted by RAP. The results of viability and apoptosis tests showed that autophagy manipulation counteracted with the effect of miR-375 on sorafenib resistance. Therefore, miR-375 inhibited sorafenib resistance by regulating autophagy in HCC cells.

Based on the bioinformatics analysis and dual-luciferase reporter assay, SIRT5 was found to be targeted and down-regulated by miR-375. SIRT5 was up-regulated in HepG2/so and Huh7/so cells compared with parental cells. SIRT5 is a vital metabolic regulator and promotes the progression of HCC in some cases (Chang *et al.*, 2018; Dang *et al.*, 2018; Tang & Yang, 2020). In the present study, SIRT5 inhibition suppressed autophagy and increased apoptosis of HepG2/so cells, while SIRT5 overexpression had the opposite effects. Down-regulation of miR-375 reversed the effects of SIRT5 inhibition, promoting sorafenib resistance of HepG2/so cells. On the other hand, up-regulation of miR-375 inhibited autophagy activated by SIRT5 overexpression and suppressed sorafenib resistance of HepG2/so cells.

Collectively, miR-375 mediates autophagy to enhance the sorafenib resistance of HCC cells partially by directly down-regulating SIRT5. MTDH, also known as AEG-1, is another target of miR-375 in mediating multidrug resistance of HCC cells (Xue *et al.*, 2017; Provisiero *et al.*, 2019; Li *et al.*, 2021). Therefore, downregulation of MTDH may also contribute to miR-375-induced sorafenib sensitivity of HCC cells. Moreover, sorafenib can directly inhibit SLC7A11 (also called System Xc-) and consequently impede glutathione biosynthesis to induce ferroptosis in HCC cells (Li *et al.*, 2021). MiR-375 may also sensitize HCC cells to sorafenib-induced ferroptosis. Sorafenib resistance exists in most cases of HCC treatment. Despite this unsatisfactory outcome, sorafenib is still a potent drug for advanced HCC. The miR-375/SIRT5 axis discovered in the present study may serve as a new target for increasing sorafenib sensitivity and therefore improve the outcomes of HCC treatment.

Declarations

Acknowledgements. Not applicable.

Conflict of interests. The authors report no relationships that could be construed as a conflict of interest.

REFERENCES

- Brunetti O, Gnoni A, Licchetta A, Longo V, Calabrese A, Argentiero A, Delcuratolo S, Solimando AG, Casadei-Gardini A, Silvestris N (2019) Predictive and prognostic factors in HCC patients treated with Sorafenib. *Medicina (Kaunas)* **55**. <https://doi.org/10.3390/medicina55100707>
- Chang L, Xi L, Liu Y, Liu R, Wu Z, Jian Z (2018) SIRT5 promotes cell proliferation and invasion in hepatocellular carcinoma by targeting E2F1. *Mol Med Rep* **17**: 342–349. <https://doi.org/10.3892/mmr.2017.7875>
- Chen J, Jin R, Zhao J, Liu J, Ying H, Yan H, Zhou S, Liang Y, Huang D, Liang X, Yu H, Lin H, Cai X (2015) Potential molecular, cellular and microenvironmental mechanism of sorafenib resistance in hepatocellular carcinoma. *Cancer Lett* **367**: 1–11. <https://doi.org/10.1016/j.canlet.2015.06.019>
- Cheng Z, Wei-Qi J, Jin D (2020) New insights on sorafenib resistance in liver cancer with correlation of individualized therapy. *Biochim Biophys Acta Rev Cancer* **1874**: 188382. <https://doi.org/10.1016/j.bbcan.2020.188382>
- Dang S, Zhou J, Wang Z, Wang K, Dai S, He S (2018) MiR-299-3p functions as a tumor suppressor via targeting Sirtuin 5 in hepatocellular carcinoma. *Biomed Pharmacother* **106**: 966–975. <https://doi.org/10.1016/j.biopha.2018.06.042>

- Dikic I, Elazar Z (2018) Mechanism and medical implications of mammalian autophagy. *Nat Rev Mol Cell Biol* **19**: 349–364. <https://doi.org/10.1038/s41580-018-0003-4>.
- Ding B, Bao C, Jin L, Xu L, Fan W, Lou W (2021) CASK Silence overcomes sorafenib resistance of hepatocellular carcinoma through activating apoptosis and autophagic cell death. *Front Oncol* **11**: 681683. <https://doi.org/10.3389/fonc.2021.681683>
- Garva R, Thepmalee C, Yasamut U, Sudsaward S, Guazzelli A, Rajendran R, Tongmuang N, Khunchai S, Meysami P, Limjindaporn T, Yenchitsomanus PT, Mutti L, Krstic-Demonacos M, Demonacos C (2019) Sirtuin family members selectively regulate autophagy in osteosarcoma and mesothelioma cells in response to cellular stress. *Front Oncol* **9**: 949. <https://doi.org/10.3389/fonc.2019.00949>
- Ghouri YA, Mian I, Rowe JH (2017) Review of hepatocellular carcinoma: Epidemiology, etiology, and carcinogenesis. *J Carcinog* **16**: 1. https://doi.org/10.4103/jcar.JCar_9_16
- Greene KS, Lukey MJ, Wang X, Blank B, Druso JE, Lin MJ, Stal-neckner CA, Zhang C, Negron Abrial Y, Erickson JW, Wilson KF, Lin H, Weiss RS, Cerione RA (2019) SIRT5 stabilizes mitochondrial glutaminase and supports breast cancer tumorigenesis. *Proc Natl Acad Sci U S A* **116**: 26625–26632. <https://doi.org/10.1073/pnas.1911954116>
- Huang X, Gan G, Wang X, Xu T, Xie W (2019) The HGF-MET axis coordinates liver cancer metabolism and autophagy for chemotherapeutic resistance. *Autophagy* **15**: 1258–1279. <https://doi.org/10.1080/15548627.2019.1580105>
- Jing Z, Ye X, Ma X, Hu X, Yang W, Shi J, Chen G, Gong L (2020) SNGH16 regulates cell autophagy to promote Sorafenib resistance through suppressing miR-23b-3p via sponging EGR1 in hepatocellular carcinoma. *Cancer Med* **9**: 4324–4338. <https://doi.org/10.1002/cam4.3020>
- Kumar S, Lombard DB (2018) Functions of the sirtuin deacylase SIRT5 in normal physiology and pathobiology. *Crit Rev Biochem Mol Biol* **53**: 311–334. <https://doi.org/10.1080/10409238.2018.1458071>
- Lendvai G, Szekerczes T, Illyes I, Csengeri M, Schlachter K, Szabo E, Lotz G, Kiss A, Borka K, Schaff Z (2021) Autophagy activity in cholangiocarcinoma is associated with anatomical localization of the tumor. *PLoS One* **16**: e0253065. <https://doi.org/10.1371/journal.pone.0253065>
- Levy JMM, Towers CG, Thorburn A (2017) Targeting autophagy in cancer. *Nat Rev Cancer* **17**: 528–542. <https://doi.org/10.1038/nrc.2017.53>
- Li D, Wang T, Sun FF, Feng JQ, Peng JJ, Li H, Wang C, Wang D, Liu Y, Bai YD, Shi ML, Zhang T (2021) MicroRNA-375 represses tumor angiogenesis and reverses resistance to sorafenib in hepatocellular carcinoma. *Cancer Gene Ther* **28**: 126–140. <https://doi.org/10.1038/s41417-020-0191-x>
- Li ZJ, Dai HQ, Huang XW, Feng J, Deng JH, Wang ZX, Yang XM, Liu YJ, Wu Y, Chen PH, Shi H, Wang JG, Zhou J, Lu GD (2021) Artesunate synergizes with sorafenib to induce ferroptosis in hepatocellular carcinoma. *Acta Pharmacol Sin* **42**: 301–310. <https://doi.org/10.1038/s41401-020-0478-3>
- Lin Z, Niu Y, Wan A, Chen D, Liang H, Chen X, Sun L, Zhan S, Chen L, Cheng C, Zhang X, Bu X, He W, Wan G (2020) RNA m(6) A methylation regulates sorafenib resistance in liver cancer through FOXO3-mediated autophagy. *EMBO J* **39**: e103181. <https://doi.org/10.15252/embj.2019103181>
- Liu L, Shen W, Zhu Z, Lin J, Fang Q, Ruan Y, Zhao H (2018) Combined inhibition of EGFR and c-ABL suppresses the growth of fulvestrant-resistant breast cancer cells through miR-375-autophagy axis. *Biochem Biophys Res Commun* **498**: 559–565. <https://doi.org/10.1016/j.bbrc.2018.03.019>
- Lu S, Yao Y, Xu G, Zhou C, Zhang Y, Sun J, Jiang R, Shao Q, Chen Y (2018) CD24 regulates sorafenib resistance via activating autophagy in hepatocellular carcinoma. *Cell Death Dis* **9**: 646. <https://doi.org/10.1038/s41419-018-0681-z>
- Marisi G, Cucchetti A, Ulivi P, Canale M, Cabibbo G, Solaini L, Foschi FG, De Matteis S, Ercolani G, Valgiusti M, Frassinetti GL, Scartozzi M, Casadei Gardini A (2018) Ten years of sorafenib in hepatocellular carcinoma: Are there any predictive and/or prognostic markers? *World J Gastroenterol* **24**: 4152–4163. <https://doi.org/10.3748/wjg.v24.i36.4152>
- Niu L, Liu L, Yang S, Ren J, Lai PBS, Chen GG (2017) New insights into sorafenib resistance in hepatocellular carcinoma: Responsible mechanisms and promising strategies. *Biochim Biophys Acta Rev Cancer* **1868**: 564–570. <https://doi.org/10.1016/j.bbcan.2017.10.002>
- Provisiero DP, Negri M, De Angelis C, Di Gennaro G, Patalano R, Simeoli C, Papa F, Ferrigno R, Auremma RS, De Martino MC, Colao A, Pivonello R, Pivonello C (2019) Vitamin D reverts resistance to the mTOR inhibitor everolimus in hepatocellular carcinoma through the activation of a miR-375/oncogenes circuit. *Sci Rep* **9**: 11695. <https://doi.org/10.1038/s41598-019-48081-9>
- Shi L, Yan H, An S, Shen M, Jia W, Zhang R, Zhao L, Huang G, Liu J (2019) SIRT5-mediated deacetylation of LDHB promotes autophagy and tumorigenesis in colorectal cancer. *Mol Oncol* **13**: 358–375. <https://doi.org/10.1002/1878-0261.12408>
- Shi Y, Yang X, Xue X, Sun D, Cai P, Song Q, Zhang B, Qin L (2020) HANR enhances autophagy-associated sorafenib resistance through miR-29b/ATG9A axis in hepatocellular carcinoma. *Oncotargets Ther* **13**: 2127–2137. <https://doi.org/10.2147/OTT.S229913>
- Siegel RL, Miller KD, Jemal A (2019) Cancer statistics, 2019. *CA Cancer J Clin* **69**: 7–34. <https://doi.org/10.3322/caac.21551>
- Tang SJ, Yang JB (2020) LncRNA SNHG14 aggravates invasion and migration as ceRNA via regulating miR-656-3p/SIRT5 pathway in hepatocellular carcinoma. *Mol Cell Biochem* **473**: 143–153. <https://doi.org/10.1007/s11010-020-03815-6>
- Villanueva A (2019) Hepatocellular Carcinoma. *N Engl J Med* **380**: 1450–1462. <https://doi.org/10.1056/NEJMr1713263>
- Xia S, Pan Y, Liang Y, Xu J, Cai X (2020) The microenvironmental and metabolic aspects of sorafenib resistance in hepatocellular carcinoma. *EBioMedicine* **51**: 102610. <https://doi.org/10.1016/j.ebiom.2019.102610>
- Xu WP, Liu JP, Feng JF, Zhu CP, Yang Y, Zhou WP, Ding J, Huang CK, Cui YL, Ding CH, Zhang X, Lu B, Xie WF (2020) miR-541 potentiates the response of human hepatocellular carcinoma to sorafenib treatment by inhibiting autophagy. *Gut* **69**: 1309–1321. <https://doi.org/10.1136/gutjnl-2019-318830>
- Xue H, Yu Z, Liu Y, Yuan W, Yang T, You J, He X, Lee RJ, Li L, Xu C (2017) Delivery of miR-375 and doxorubicin hydrochloride by lipid-coated hollow mesoporous silica nanoparticles to overcome multiple drug resistance in hepatocellular carcinoma. *Int J Nanomedicine* **12**: 5271–5287. <https://doi.org/10.2147/IJN.S135306>
- Yang S, Wang M, Yang L, Li Y, Ma Y, Peng X, Li X, Li B, Jin H, Li H (2020) MicroRNA-375 targets ATG14 to inhibit autophagy and sensitize hepatocellular carcinoma cells to Sorafenib. *Oncotargets Ther* **13**: 3557–3570. <https://doi.org/10.2147/OTT.S247655>
- Zhang R, Wang C, Tian Y, Yao Y, Mao J, Wang H, Li Z, Xu Y, Ye M, Wang L (2019) SIRT5 promotes hepatocellular carcinoma progression by regulating mitochondrial apoptosis. *J Cancer* **10**: 3871–3882. <https://doi.org/10.7150/jca.31266>
- Zhao P, Li M, Wang Y, Chen Y, He C, Zhang X, Yang T, Lu Y, You J, Lee RJ, Xiang G (2018) Enhancing anti-tumor efficiency in hepatocellular carcinoma through the autophagy inhibition by miR-375/sorafenib in lipid-coated calcium carbonate nanoparticles. *Acta Biomater* **72**: 248–255. <https://doi.org/10.1016/j.actbio.2018.03.022>
- Zhao SP, Yu C, Xiang KM, Yang MS, Liu ZL, Yang BC (2020) miR-375 Inhibits autophagy and further promotes inflammation and apoptosis of acinar cells by targeting ATG7. *Pancreas* **49**: 543–551. <https://doi.org/10.1097/MPA.0000000000001536>

Long noncoding RNA LGALS8-AS1 promotes angiogenesis and brain metastases in non-small cell lung cancer

Jian Zhong^{1,2} and Bo Wang^{1,2}✉

¹Department of Thoracic Surgery, Affiliated Brain Hospital of Nanjing Medical University, Nanjing City, Jiangsu Province, 210000, China; ²Department of Thoracic surgery, Affiliated Nanjing Brain Hospital, Nanjing Medical University, Nanjing 210029, China

Brain metastases (BM) are associated with poor prognosis in patients with non-small cell lung cancer (NSCLC). Considering that, LGALS8-AS1-mediated progression of BM was probed in NSCLC. The clinical characteristics of 60 NSCLC patients (30 without BM and 30 with BM) were analyzed. NSCLC patients with BM had higher levels of LGALS8-AS1 than NSCLC patients without BM. Depleting LGALS8-AS1 prevented NSCLC cell proliferation, migration, invasion, and angiogenesis *in vitro*, and NSCLC tumorigenesis and BM *in vivo*. LGALS8-AS1 targeted miR-885-3p to mediate Fascin actin-bundling protein 1 (FSCN1) expression. Restoring miR-885-3p inhibited NSCLC growth, angiogenesis, and BM, and FSCN1 induction rescued the performance of LGALS8-AS1 depletion on NSCLC cells. Our results provide new insights into LGALS8-AS1-mediated NSCLC metastasis and suggest that LGALS8-AS1 may be a useful biomarker for identifying NSCLC with metastatic potential.

Keywords: LGALS8-AS1, miR-885-3p, Fascin actin-bundling protein 1, non-small cell lung cancer, angiogenesis, brain metastases

Received: 26 September, 2022; **revised:** 21 February, 2023; **accepted:** 17 March, 2023; **available on-line:** 16 September, 2023

✉e-mail: wang_bo4132@hotmail.com

Abbreviations: BM, Brain metastases; CCK-8, Cell counting kit; FSCN1, Fascin actin-bundling protein 1; GAPDH, Glyceraldehyde-3-phosphate dehydrogenase; HUVECs, Human umbilical vein endothelial cells; lncRNAs, Long non-coding RNAs; miRNAs, MicroRNAs; MUT, Mutant type; NC, Negative control; NSCLC, Non-small cell lung cancer; RPMI, Roswell Park Memorial Institute; RT-qPCR, Real-time reverse transcriptase-polymerase chain reaction; 3'-UTR, 3' untranslated region; WT, Wild type

INTRODUCTION

Non-small cell lung cancer (NSCLC) is one of the deadliest malignancies, accounting for more than 80% of lung cancer cases worldwide, with a current 5-year survival rate of only 15% (Salehi *et al.*, 2020). Patients with advanced NSCLC generally die within 18 months of diagnosis mainly due to metastatic spread (Wood *et al.*, 2014). Brain metastases (BM) are a common complication of advanced NSCLC (Chen *et al.*, 2012), for which the management always involves systemic therapy (Fang *et al.*, 2021). Since angiogenesis is associated with aggressiveness in NSCLC (Schettino *et al.*, 2012), targeting inhibition of angiogenesis is promising in the treatment of NSCLC and many clinical trials have evaluated the addition of anti-angiogenic therapy to standard therapy in patients with NSCLC (Alshangiti *et al.*, 2018). Therefore, exploring the regulatory mechanism of angiogenesis is helpful for understanding the pathogenesis of NSCLC and developing new therapeutic drugs.

Long non-coding RNAs (lncRNAs) are of significance in the physiological and pathological processes of diseases (Xie *et al.*, 2018; Zhang *et al.*, 2019). The occurrence of human malignant tumors is often accompanied by the deregulation of lncRNA (Kondo *et al.*, 2017). More and more studies have shown that lncRNAs play a key role in tumorigenesis and metastasis (Hanniford *et al.*, 2020; Yang *et al.*, 2018; Gupta *et al.*, 2010). lncRNAs usually regulate their downstream target genes by competing endogenous RNAs with microRNAs (miRNAs), which can affect the proliferation and metastasis of various cancer types (Zheng *et al.*, 2019; Wang *et al.*, 2018; Hao *et al.*, 2019). For example, lncRNA GAN1 inhibits tumor progression in NSCLC *via* decoying miR-26a-5p; lncRNA LINC00473 promotes proliferation, migration, invasion, and inhibition of apoptosis of NSCLC cells by acting as a sponge of miR-497-5p (Xu *et al.*, 2021). LGALS8-AS1 has been confirmed to be highly expressed in breast cancer and promotes breast cancer metastasis by targeting miR-125b-5p (Zhai *et al.*, 2021). However, the expression and role of LGALS8-AS1 in NSCLC remain unclear.

MiRNAs are a group of short endogenous non-coding RNAs with a length of about 18-22 nucleotides, which can regulate post-transcriptional gene expression by binding to the 3'-UTR of target gene mRNA to inhibit mRNA translation and reduce mRNA stability (Ahn *et al.*, 2020). MiRNAs are involved in almost all biological processes, including tumor angiogenesis (Mao *et al.*, 2015). For example, miR-543 promotes tumorigenesis and angiogenesis in NSCLC (Wang *et al.*, 2020) whereas miR-20a-5p inhibits tumor angiogenesis (Han *et al.*, 2021). It is studied that miR-885-3p can architect cell autophagy and apoptosis in squamous cell carcinoma cells (Huang *et al.*, 2011). However, the biological function of miR-885-3p in NSCLC has not been fully elucidated.

Therefore, this study aims to explore the role of LGALS8-AS1 in NSCLC metastasis and angiogenesis through regulating miR-885-3p expression and its potential mechanism. The study identified a lncRNA, LGALS8-AS1, which is associated with NSCLC metastasis and angiogenesis and elucidated the molecular regulatory mechanism of LGALS8-AS1 in NSCLC and provides a new reference for the treatment of NSCLC patients.

METHODS

Tissue sampling

This study was approved by the ethics committee of Affiliated Brain Hospital of Nanjing Medical University. Written informed consent was obtained from all sub-

jects, 60 patients who were histologically confirmed with NSCLC. BM are confirmed by whole-brain CT scan or MRI. Tumor tissues and adjacent normal tissues were collected during surgery.

Cell culture

Human lung cancer cells (A549) and human umbilical vein endothelial cells (HUVECs) were purchased from the Institute of Biochemistry and Cell Biology, Chinese Academy of Sciences. Under humidified air conditions of 37°C and 5% CO₂, cells were cultured in Roswell Park Memorial Institute (RPMI)-1640 (Gibco, USA) medium supplemented with 10% fetal bovine serum, 100 U/ml penicillin, and 100 mg/ml streptomycin (Invitrogen, USA).

Cell transfection

Both miR-885-3p mimic and mimic negative control (NC) were purchased from RiboBio (Guangzhou, China). The shRNA sequence targeting LGALS8-AS1 was purchased from Genescript (Shanghai, China). Fascin actin-bundling protein 1 (FSCN1) was cloned into the pcDNA3.1 vector (Invitrogen). Cells were transiently transfected with RNAiMax and Lipofectamine 3000 with Plus reagent (Thermo Fisher Scientific).

Cell counting kit (CCK)-8

Cells growing on the 96-well plates were tested by a CCK-8 kit (Liji, Shanghai, China) to determine proliferative activity. Quantitative results were obtained on a microplate reader (SAFAS Xenius XL, Ruixuan, Shanghai, China) at 450 nm.

Flow cytometry

Cells were stained with annexin V-fluorescein isothiocyanate and propidium iodide according to the manufacturer's instructions (Bioscience, Shanghai, China). Then the apoptosis rate was detected by flow cytometry (Beckman, USA). The percentage of cells in the Q3 quadrant represents early apoptosis, and the percentage of cells in the Q2 quadrant represents late apoptosis (Wang *et al.*, 2020).

Transwell assay

Transwell chambers (8-μm pore size; Corning Costar, Cambridge, MA, USA) measure cell migration and invasion capacity. For cell invasion, cells suspended in serum-free RPMI-1640 medium were seeded into the upper chamber pre-coated with Matrigel. The lower chamber was PMI-1640 medium with 20% serum as a chemotactic agent. After 24 h culture, the cells were fixed with 90% formaldehyde and stained with 0.1% crystal violet. The cells were photographed under a microscope and counted. In the cell migration experiment, there was no matrigel coating, and the other operations were the same as the invasion experiment (Yang *et al.*, 2018).

Tube formation

Matrigel (0.5mmol/L) was coated with pre-cooled 96-well plates. HUVECs were starved without serum for 1 h and then re-suspended in Dulbecco's modified Eagle medium to make a cell suspension. Next, cell suspensions (1×10⁵ cells/mL) were inoculated into a matrigel coating containing cell conditioned culture-medium with 3 repeat wells per treatment. The plates were then incubated at 37°C for 6 to 8 h. The tube formation was

observed under a microscope (Olympus). The number of tubes in a branch (a branch point is a skeleton part where three or more tubes meet) and the number of rings (a ring is a background area surrounded by [or almost] tubular structures) were counted.

Real-time reverse transcriptase-polymerase chain reaction (RT-qPCR)

Total RNA was extracted using a Trizol reagent according to the manufacturer's instructions (Invitrogen, Carlsbad, CA, USA). RNA purity was determined using a NanoDrop spectrophotometer (Thermo Fisher Scientific, Waltham, MA, USA). cDNA reverse transcription kit (Promega, Madison, WI, USA) was used to reverse transcribed 1 μg total RNA into the first strand cDNA. Power SYBR Green PCR Master Mix (Promega) quantitative PCR was used to detect RNA levels. LncRNA and protein-coding gene were normalized to glyceraldehyde-3-phosphate dehydrogenase (GAPDH) mRNA, and miRNA was normalized to U6. The primer sequences used are presented in Table 1.

Western blot

Total protein lysates were subjected to 10% or 12% sodium dodecyl sulfate-polyacrylamide gel electrophoresis, loading on a polyvinylidene fluoride membrane (Millipore, USA), and blocking the membrane with 5% non-fat milk. After that, primary antibodies FSCN1 (1:1000, sc-21743, Santa Cruz Biotechnology) and GAPDH (1:1000, ab8245, Abcam) were supplemented, and Immunoreactive bands were visualized after incubation with secondary antibody (Invitrogen) by enhanced chemiluminescent detection system (Thermo Fischer Scientific).

Luciferase reporter gene assay

pGL3 luciferase reporters for LGALS8-AS1 and FSCN1 were designed by Genomeditech (Shanghai, China), named LGALS8-AS1-wild type (WT), LGALS8-AS1-mutant type (MUT), FSCN1-WT, and FSCN1-MUT. These reporters and miR-885-3p mimic or mimic NC were co-transfected into A549 cells, thus measuring luciferase activity with a luciferase assay kit (Promega) (Wu *et al.*, 2021).

Table 1. Primer sequences

Genes	Primer sequences (5'– 3')
LGALS8-AS1	F: ACATCCGAATGCCATCCTCC
	R: AGGACTGACTCCTGTGCGCTT
miR-885-3p	F: AGGCAGCGGGGTGTAGTGGATAG
	R: CCACTGTCAGGGTCCGAGGTATTC
FSCN1	F: ACAGCAGGGGACTCAG
	R: CCCACCGTCCAGTATTT
U6	F: CTCGCTTCGGCAGCAC
	R: AACGCTTCACGAATTTGCGT
GAPDH	F: CACCACTCCTCCACCTTTG
	R: CCACCACTCTGTTGCTGTAG

Note: LGALS8-AS1, long noncoding RNA LGALS8-AS1; miR-885-3p, microRNA-885-3p; FSCN1, Fascin actin-bundling protein 1; GAPDH, glyceraldehyde 3-phosphate dehydrogenase

Table 2. Analysis of clinical characteristics of NSCLC patients with and without BM

Characteristics	NSCLC with BM (n=30)	NSCLC without BM (n=30)
Age (years), median (range)	56 (50-63)	59 (55-66)
Gender		
Male	12 (40.0%)	23 (76.7%)
Female	18 (60.0%)	7 (23.3%)
Tumor histology		
Adenocarcinoma	26 (86.7%)	18 (60.0%)
Squamous cell carcinoma	4 (13.3%)	6 (20.0%)
Carcinosarcoma	–	2 (6.7%)
Large cell carcinoma	–	1 (3.3%)
Neuroendocrine carcinoma	–	3 (10.0%)
Disease stage at diagnose		
I	–	3 (10.0%)
II	–	6 (20.0%)
III	–	7 (23.3%)
IV	30 (100.0%)	14 (46.7%)
Smoking history		
Smoker	8 (26.7%)	5 (16.7%)
Former smoker	4 (13.3%)	10 (33.3%)
Never	18 (60.0%)	15 (50.0%)
Lymph node metastatic status		
N0	2 (6.7%)	4 (13.3%)
N1	4 (13.3%)	3 (10.0%)
N2	9 (30.0%)	9 (30.0%)
N3	15 (50.0%)	14 (46.7%)

Xenograft models in nude mice

For xenograft models, 4-week-old BALB/c nude mice (Cyagen Biosciences) bred under pathogen-free conditions were subcutaneously injected with A549 cells stably transfected with sh-LGALS8-AS1 and sh-NC (5×10^6 , $n=6/\text{group}$). A549 cells were pre-diluted in 200 μL phosphate-buffered saline (PBS) + 200 μL Matrigel (BD Biosciences). During 28-h housing, mice were measured for longitudinal diameter and lateral diameter at an interval of 7 days to calculate tumor volume as $0.5 \times L \times D^2$. On day 28, xenograft tumors were dissected from mice and weighed.

A lung cancer BM model was established according to previous studies (Li *et al.*, 2017; Nguyen *et al.*, 2009). A549 cells after transfection were resuspended in 100 μL of PBS and injected into the right ventricle of mice (1×10^6 , $n=6/\text{group}$). Finally, brain tissues were collected and prepared for HE staining and observations of metastatic nodules.

Statistical analysis

The selected way to perform statistical analysis was SPSS 19.0, and that to construct graphs was GraphPad Prism 6. Two-tailed paired Student's *t*-test and one-way analysis of variance were of utility for data comparison of two groups and more than two groups, respectively. Tukey's post hoc test validated pairwise comparisons.

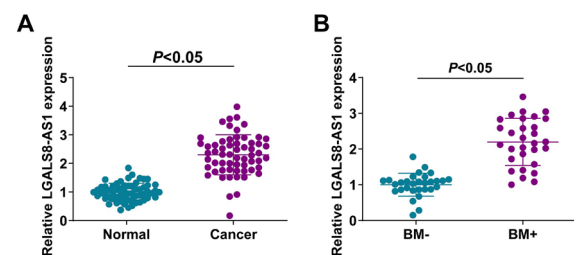


Figure 1. LGALS8-AS1 is more expressed in NSCLC patients with BM

LGALS8-AS1 expression in clinical samples (A–B); the values were expressed as mean \pm standard deviation ($n=60$).

Pearson correlation analysis assessed gene correlation. $P < 0.05$ was considered to indicate a statistically significant difference.

RESULTS

LGALS8-AS1 is more expressed in NSCLC patients with BM

A total of 60 patients with NSCLC were included in the study, of which 30 had BM and the remaining 30 did not. The clinical characteristics are shown in Table 2. Examinations of LGALS8-AS1 found that LGALS8-AS1

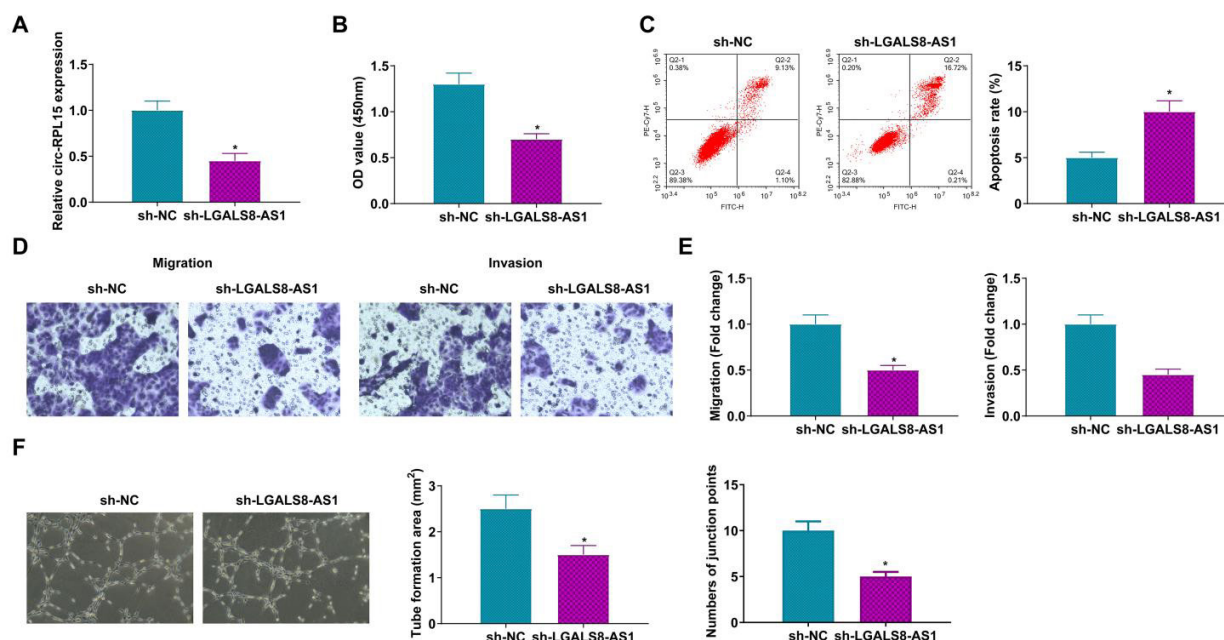


Figure 2. Targeting suppression of LGALS8-AS1 blocks NSCLC development

Based on sh-LGALS8-AS1-induced knockdown of LGALS8-AS1 (A), assays were to determine proliferation (B), apoptosis (C), migration (D), invasion (E), and angiogenesis (F); values are presented as mean \pm standard deviation (N=3) * P <0.05 vs. sh-NC.

was increased in tumor tissues, and it was higher in tumor tissues of NSCLC patients with BM (Fig. 1A, B).

Targeting suppression of LGALS8-AS1 blocks NSCLC development

Firstly, the effect of LGALS8-AS1 on the progression of NSCLC cells was investigated. A549 cells were transfected with sh-LGALS8-AS1 to silence the expression of LGALS8-AS1, and the transfection was verified by RT-qPCR (Fig. 2A). Cell proliferation was then detected by CCK-8, and it was found that A549 cell proliferation decreased after down-regulating LGALS8-AS1 (Fig. 2B). Apoptosis was detected by flow cytometry, and the results showed that apoptosis of A549 cells increased after downregulation of LGALS8-AS1 (Fig. 2C). Transwell was used to detect cell migration and invasion,

and it was found that A549 cell migration and invasion decreased after downregulating LGALS8-AS1 (Fig. 2D, E). Angiogenesis was also examined by tube formation assays, which showed that angiogenesis was attenuated after down-regulating LGALS8-AS1 (Fig. 2F). These results indicate that down-regulation of LGALS8-AS1 inhibits proliferation, migration, invasion, and angiogenesis of NSCLC cells, and promotes cell apoptosis.

LGALS8-AS1 deficiency suppresses tumor growth and BM *in vivo*

Based on our findings that LGALS8-AS1 is involved in NSCLC cell progression, the study further explored its role in tumor growth and brain metastasis *in vivo*. Tumor growth was studied by subcutaneous injection of A549 cells stably transfected with sh-LGALS8-AS1 into

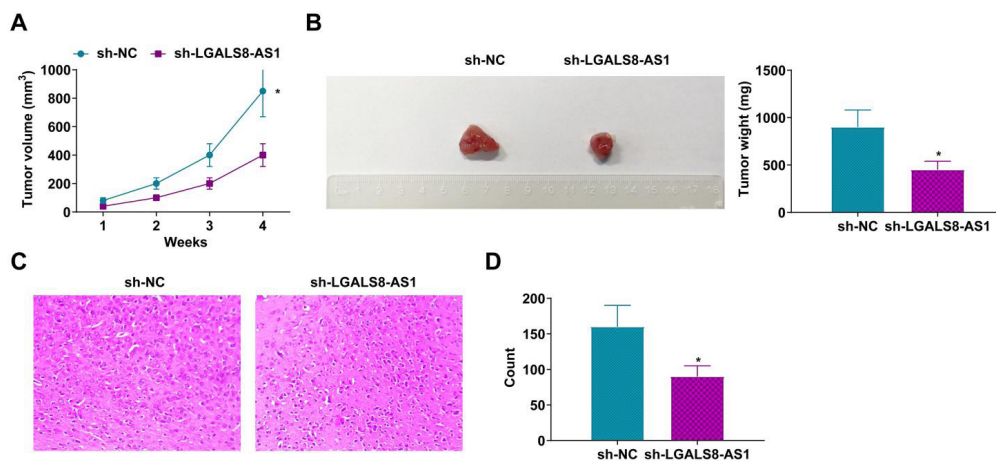


Figure 3. LGALS8-AS1 deficiency suppresses tumor growth and BM *in vivo*

In nude mice injected with sh-LGALS8-AS1, tumor volume and weight were measured (A–B) and BM was evaluated (C–D); values are presented as mean \pm standard deviation (n=6) * P <0.05 vs. sh-NC.

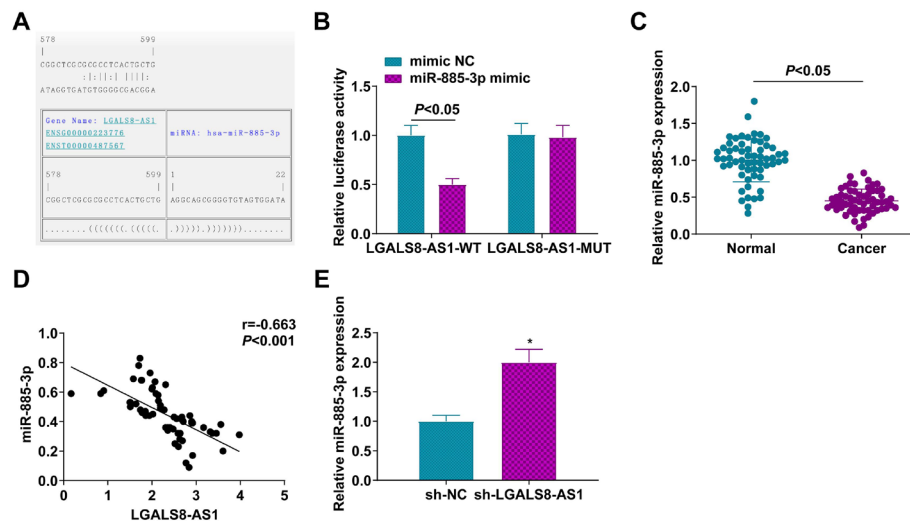


Figure 4. miR-885-3p expression is controlled by LGALS8-AS1

A potential binding relationship between LGALS8-AS1 and miR-885-3p was predicted (A) and confirmed by detecting luciferase activity (B) miR-885-3p expression in clinical samples (C) and its correlation with LGALS8-AS1 expression (D) miR-885-3p expression was altered by sh-LGALS8-AS1 in A549 cells (E); values are presented as mean \pm standard deviation (N=3) * P <0.05 vs. sh-NC.

nude mice. As measured, LGALS8-AS1 down-regulation reduced tumor volume and weight (Fig. 3A, B). BM were explored by injecting A549 cells stably transfected with sh-LGALS8-AS1 into the right ventricle of nude mice. As presented in HE staining results, the number of brain metastatic nodules was reduced in sh-LGALS8-AS1-treated mice (Fig. 3C, D).

miR-885-3p expression is controlled by LGALS8-AS1

Next, LGALS8-AS1 was predicted to have binding sites with miR-885-3p through the RNA22 database (Fig. 4A). Subsequently, dual luciferase assay was performed to verify their targeting relationship, and the results showed that the luciferase activity of A549 cells could be significantly reduced by co-transfection of LGALS8-AS1-WT with miR-885-3p mimic (Fig. 4B). In addition, the expression of miR-885-3p in clinical samples was detected, and it was found that miR-885-3p in lung cancer tissues was down-regulated (Fig. 4C) and negatively correlated with LGALS8-AS1 expression (Fig. 4D). Moreover, after downregulating LGALS8-AS1, it was found that miR-885-3p expression was increased in A549 cells (Fig. 4E). The results showed that LGALS8-AS1 inhibited miR-885-3p expression by targeting miR-885-3p.

miR-885-3p represses NSCLC development *in vitro*

In order to investigate the effect of miR-885-3p on NSCLC cells, miR-885-3p mimic or mimic NC was transfected into A549 cells, and successful transfection was verified by RT-qPCR (Fig. 5A). In A549 cells over-expressing miR-885-3p, it could be recognized that proliferative, invasive, migratory, and an-apoptotic activities were all in a weakened status, and the same was true for angiogenic capacity (Fig. 5B–F). These results suggest that up-regulation of miR-885-3p inhibits proliferation, migration, invasion, and angiogenesis of NSCLC cells, and promotes cell apoptosis.

miR-885-3p targets FSCN1

Subsequently, the RNA22 database predicted that miR-885-3p and FSCN1 had binding sites (Fig. 6A).

Then, dual luciferase assay was performed to verify the targeting relationship between them. The results showed that the luciferase activity of A549 cells could be significantly reduced by co-transfection of FSCN1-WT with miR-885-3p mimic (Fig. 6B). RT-qPCR detected FSCN1 mRNA expression in lung cancer tissues, and the results showed that FSCN1 mRNA expression was up-regulated (Fig. 6C) and was negatively correlated with the expression of miR-885-3p (Fig. 6D). Moreover, mRNA and protein expression of FSCN1 in A549 cells decreased after up-regulation of miR-885-3p (Fig. 6E). These results suggest that targeting miR-885-3p regulates FSCN1 expression.

LGALS8-AS1-mediated impairments of A549 cell activities can be rescued by FSCN1

To verify the regulatory role of LGALS8-AS1/miR-885-3p/FSCN1 axis in lung cancer cells, sh-LGALS8-AS1 + pcDNA3.1-FSCN1 and sh-LGALS8-AS1 + pcDNA3.1-NC were transfected into A549 cells. RT-qPCR and Western blot results showed that pcDNA3.1-FSCN1 reversed the inhibition effect of sh-LGALS8-AS1 on FSCN1 expression (Fig. 7A). The results of CCK-8, flow cytometry, Transwell and tube formation experiments showed that up-regulation of FSCN1 mitigated the impact of down-regulation of LGALS8-AS1 on proliferation, apoptosis, migration, invasion, and angiogenesis of A549 cells (Fig. 7B–F). In conclusion, LGALS8-AS1 promotes NSCLC cell progression by regulating the miR-885-3p/FSCN1 axis.

DISCUSSION

As studies indicate, 90% of lung cancer deaths are caused by distant metastasis, and BM is a common site of distant metastasis in NSCLC (Rybarczyk-Kasiuchnicz *et al.*, 2021). LncRNA dysregulation is fundamental for tumorigenesis and distant metastasis of NSCLC and serves as a biomarker for NSCLC (Pan *et al.*, 2020). In the present study, LGALS8-AS1 was up-regulated in NSCLC patients' tumor tissues and was more expressed in NSCLC patients with BM. Silencing LGALS8-AS1

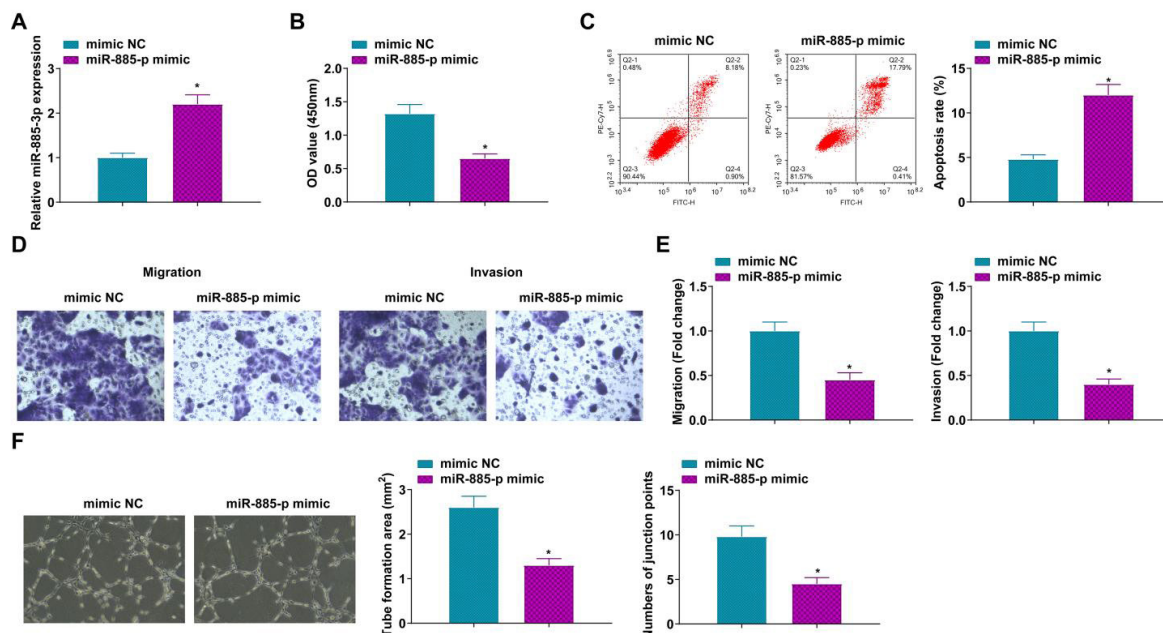


Figure 5. miR-885-3p represses NSCLC development *in vitro*.

Based on miR-885-3p mimic-induced elevation of miR-885-3p expression (A), assays were to determine proliferation (B), apoptosis (C), migration (D), invasion (E), and angiogenesis (F); values are presented as mean \pm standard deviation (N=3) * P <0.05 vs. mimic NC.

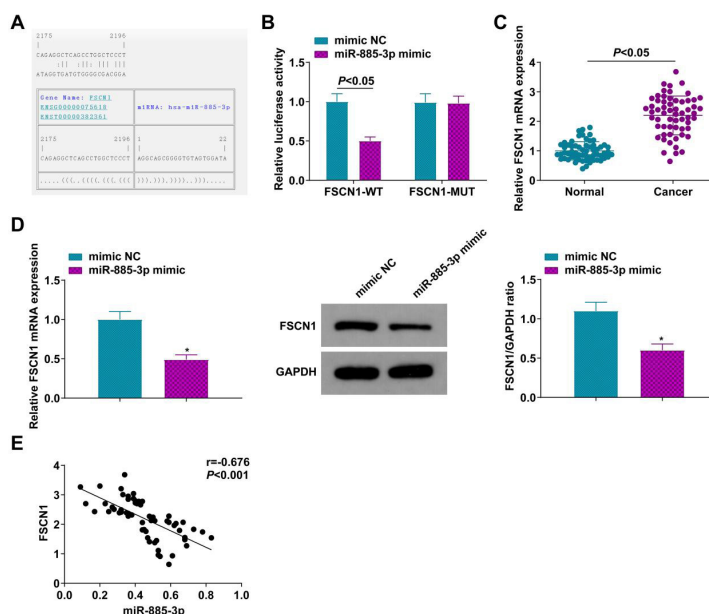


Figure 6. miR-885-3p targets FSCN1.

A potential binding relationship between FSCN1 mRNA and miR-885-3p was predicted (A) and confirmed by detecting luciferase activity (B); FSCN1 mRNA expression in clinical samples (C) and its correlation with miR-885-3p expression (D) FSCN1 mRNA and protein expression was altered by miR-885-3p mimic in A549 cells (E); values are presented as mean \pm standard deviation (N=3) * P <0.05 vs. mimic NC.

blocked the malignant phenotype and angiogenesis in NSCLC cells, as well as inhibiting tumor growth and BM *in vivo*. Overall, LGALS8-AS1 plays a critical role in NSCLC metastasis and serves as a potential therapeutic target for NSCLC metastasis.

Abnormally expressed lncRNAs are involved in regulating NSCLC development by acting as miRNA sponges. For example, lncRNA plasmacytoma variant translocation 1 promotes angiogenesis in NSCLC by competitive absorption of miR-29c (Wang *et al.*, 2018). lncRNA

DNAH17 antisense RNA 1 induces the occurrence and metastasis of NSCLC by binding to miR-877-5p (Du *et al.*, 2020). LGALS8-AS1 has only been reported in breast cancer considered an oncogenic gene regarding its potential to induce malignant phenotype and metastasis. Here, the study observed high LGALS8-AS1 expression in NSCLC, and LGALS8-AS1 expression was able to discriminate whether NSCLC patients developed BM. Cell and animal experiments consistently confirmed that LGALS8-AS1 knockdown played a negative role in

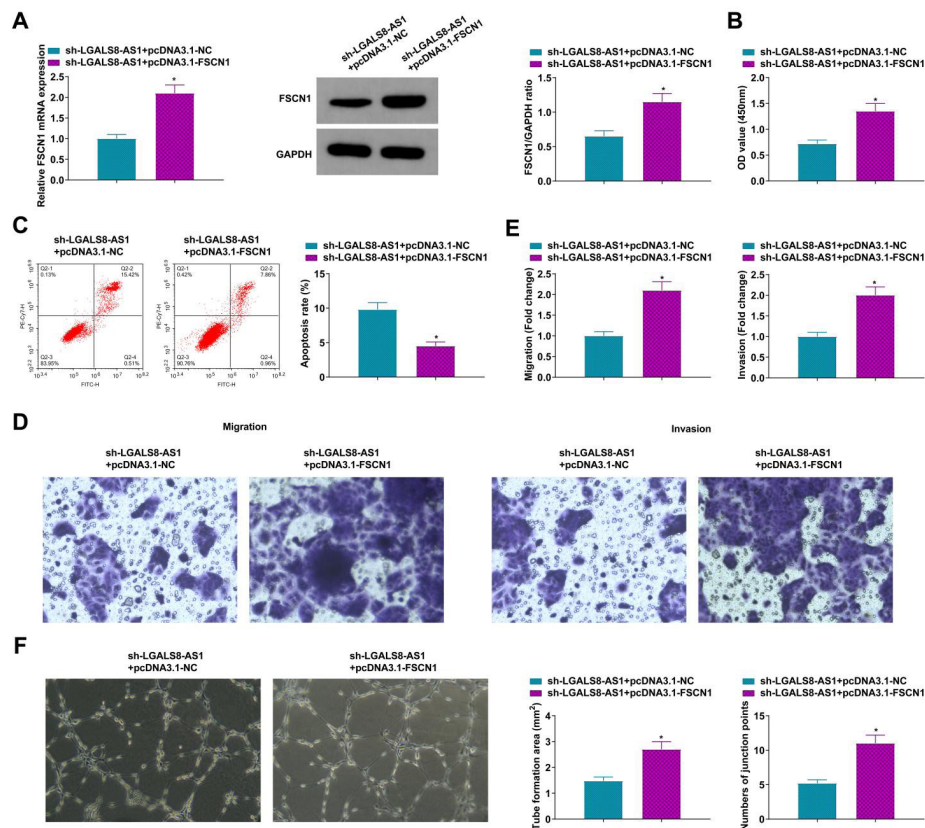


Figure 7. LGALS8-AS1-mediated impairments of A549 cell activities can be rescued by FSCN1.

Based on pcDNA3.1-FSCN1-induced elevation of FSCN1 expression in sh-LGALS8-AS1-treated A549 cells (A), assays were to determine proliferation (B), apoptosis (C), migration (D), invasion (E), and angiogenesis (F); values are presented as mean \pm standard deviation (N=3) *P<0.05 vs. sh-LGALS8-AS1 + pcDNA3.1-NC.

NSCLC for cell growth, angiogenesis, and tumor growth and metastasis. In addition, the RNA22 database predicted that LGALS8-AS1 had a binding site with miR-885-3p.

miR-885-3p was mediated by LGALS8-AS1 in this study. miR-885-3p has received academic attention in the field of cancer. miR-885-3p expression decline has previously been found in lung adenocarcinoma to be associated with pathological stage and poor survival in patients (Yang *et al.*, 2021). Functionally discussed, miR-885-3p impairs gastric cancer cell activities and oxidative stress (He *et al.*, 2021), and tumor angiogenesis in colon cancer (Xiao *et al.*, 2015). This study confirmed the reduction in miR-885-3p expression in NSCLC, and the suppressive effects of miR-885-3p on NSCLC cell growth and angiogenesis.

miRNAs usually function by binding to target gene mRNAs (Datta *et al.*, 2019). Here, FSCN1 was selected to be a target of miR-885-3p. FSCN1 is a structurally unique and highly conserved actin cross-linking protein that mediates cellular interaction (Liu *et al.*, 2019). It has been described that dysregulation of FSCN1 aggrandizes tumor motility and invasiveness by altering the structure of cell protrusions and focal extracellular matrix adhesions (Gao *et al.*, 2019). Therefore, FSCN1 is considered an oncogene in cancers, including adrenocortical carcinoma (Liang *et al.*, 2019), ovarian cancer (Li *et al.*, 2018), laryngeal squamous cell carcinoma (Gao *et al.*, 2018), and NSCLC (Xiao *et al.*, 2016). Here, FSCN1 was overexpressed in NSCLC and can mitigate the effects of LGALS8-AS1 knockdown, promoting NSCLC cell growth and angiogenesis.

This study did not address a possible direct relationship between LGALS8-AS1 expression and clinical factors, including tumor node metastasis staging and survival analysis, due to insufficient clinical sample size and lack of a long-term follow-up of all included patients. Also, this study did not further explore the effects of overexpression of LGALS8-AS1 and downregulation of miR-885-3p alone on NSCLC cells. In addition, FSCN1 has been confirmed to mediate NSCLC cell migration and invasion by altering the Mitogen-activated protein kinase pathway (Zhao *et al.*, 2018). Whether the MAPK pathway or other signaling pathways are involved in the regulation of LGALS8-AS1 in NSCLC still needs to be further explored to determine detailed and comprehensive mechanics.

CONCLUSION

Our study provides new insights into the mechanism by which lncRNAs regulate NSCLC progression. Our findings suggest that the LGALS8-AS1/miR-885-3p/FSCN1 axis is an essential signaling pathway for NSCLC cell growth, angiogenesis, and BM.

Declarations

Acknowledgments. Not applicable.

Funding Statements. Not applicable.

Declaration of Conflicting Interests. Authors declared no conflict of interest.

Ethical statement. All procedures performed in this study involving human participants were in accordance

with the ethical standards of the Affiliated Brain Hospital of Nanjing Medical University research committee and with the 1964 Helsinki Declaration and its later amendments or comparable ethical standards. All subjects were approved by the Affiliated Brain Hospital of Nanjing Medical University.

REFERENCES

- Ahn YH, Ko YH (2020) Diagnostic and therapeutic implications of microRNAs in non-small cell lung cancer. *Int J Mol Sci* **21**. <https://doi.org/10.3390/ijms21228782>
- Alshangiti A, Chandhoke G, Ellis PM (2018) Antiangiogenic therapies in non-small-cell lung cancer. *Curr Oncol* **25** (Suppl 1): S45–S58. <https://doi.org/10.3747/co.25.3747>
- Chen LT, Xu SD, Xu H, Zhang JF, Ning JF, Wang SF (2012) MicroRNA-378 is associated with non-small cell lung cancer brain metastasis by promoting cell migration, invasion and tumor angiogenesis. *Med Oncol* **29**: 1673–1680. <https://doi.org/10.1007/s12032-011-0083-x>
- Datta A, Das P, Dey S, Ghuwalewala S, Ghatak D, Alam SK, Chatterjee R, Roychoudhury S (2019) Genome-wide small RNA sequencing identifies microRNAs deregulated in non-small cell lung carcinoma harboring gain-of-function mutant p53. *Genes (Basel)* **10**. <https://doi.org/10.3390/genes10110852>
- Du LJ, Mao LJ, Jing RJ (2020) Long noncoding RNA DNAH17-AS1 promotes tumorigenesis and metastasis of non-small cell lung cancer via regulating miR-877-5p/CCNA2 pathway. *Biochem Biophys Res Commun* **533**: 565–572. <https://doi.org/10.1016/j.bbrc.2020.09.047>
- Fang L, Zhao W, Ye B, Chen D (2021) Combination of immune checkpoint inhibitors and anti-angiogenic agents in brain metastases from non-small cell lung cancer. *Front Oncol* **11**: 670313. <https://doi.org/10.3389/fonc.2021.670313>
- Gao W, An C, Xue X, Zheng X, Niu M, Zhang Y, Liu H, Zhang C, Lu Y, Cui J, Zhao Q, Wen S, Thorne RF, Zhang X, Wu Y, Wang B (2019) Mass spectrometric analysis identifies AIMP1 and LTA4H as FSCN1-binding proteins in laryngeal squamous cell carcinoma. *Proteomics* **19**: e1900059. <https://doi.org/10.1002/pmic.201900059>
- Gao W, Zhang C, Li W, Li H, Sang J, Zhao Q, Bo Y, Luo H, Zheng X, Lu Y, Shi Y, Yang D, Zhang R, Li Z, Cui J, Zhang Y, Niu M, Li J, Wu Z, Guo H, Xiang C, Wang J, Hou J, Zhang L, Thorne RF, Cui Y, Wu Y, Wen S, Wang B (2019) Promoter methylation-regulated miR-145-5p inhibits laryngeal squamous cell carcinoma progression by targeting FSCN1. *Mol Ther* **27**: 365–379. <https://doi.org/10.1016/j.ymthe.2018.09.018>
- Gupta RA, Shah N, Wang KC, Kim J, Horlings HM, Wong DJ, Tsai MC, Hung T, Argani P, Rinn JL, Wang Y, Brzoska P, Kong B, Li R, West RB, van de Vijver MJ, Sukumar S, Chang HY (2010) Long non-coding RNA HOTAIR reprograms chromatin state to promote cancer metastasis. *Nature* **464**: 1071–1076. <https://doi.org/10.1038/nature08975>
- Han J, Hu J, Sun F, Bian H, Tang B, Fang X (2021) MicroRNA-20a-5p suppresses tumor angiogenesis of non-small cell lung cancer through RRM2-mediated PI3K/Akt signaling pathway. *Mol Cell Biochem* **476**: 689–698. <https://doi.org/10.1007/s11010-020-03936-y>
- Hanniford D, Ulloa-Morales A, Karz A, Berzoti-Coelho MG, Mobarak RS, Sánchez-Sendra B, Kloetgen A, Davalos V, Imig J, Wu P, Vasudevaraja V, Argibay D, Lilja K, Tabaglio T, Montegudo C, Guccione E, Tsirigos A, Osman I, Aifantis I, Hernandez E (2020) Epigenetic silencing of CDR1as Drives IGF2BP3-mediated melanoma invasion and metastasis. *Cancer Cell* **37**: 55–70.e15. <https://doi.org/10.1016/j.ccell.2019.12.007>
- Hao XZ, Yang K (2019) LncRNA MAGI2-AS3 suppresses the proliferation and invasion of non-small cell lung carcinoma through miRNA-23a-3p/PTEN axis. *Eur Rev Med Pharmacol Sci* **23**: 7399–7407. https://doi.org/10.26355/eurrev_201909_18848
- He Y, Zhang Z, Wang Z, Jiao Y, Kang Q, Li J (2022) Downregulation of circ-SFMBT2 blocks the development of gastric cancer by targeting the miR-885-3p/CHD7 pathway. *Anticancer Drugs* **33**: e247–e259. <https://doi.org/10.1097/cad.0000000000001195>
- Huang Y, Chuang AY, Ratovitski EA (2011) Phospho-ΔNp63α/miR-885-3p axis in tumor cell life and cell death upon cisplatin exposure. *Cell Cycle* **10**: 3938–3947. <https://doi.org/10.4161/cc.10.22.18107>
- Kondo Y, Shinjo K, Katsushima K (2017) Long non-coding RNAs as an epigenetic regulator in human cancers. *Cancer Sci* **108**: 1927–1933. <https://doi.org/10.1111/cas.13342>
- Li J, Zhang S, Pei M, Wu L, Liu Y, Li H, Lu J, Li X (2018) FSCN1 Promotes epithelial-mesenchymal transition through increasing Snail in ovarian cancer cells. *Cell Physiol Biochem* **49**: 1766–1777. <https://doi.org/10.1159/000493622>
- Li QX, Zhou X, Huang TT, Tang Y, Liu B, Peng P, Sun L, Wang YH, Yuan XL (2017) The Thr300Ala variant of ATG16L1 is associated with decreased risk of brain metastasis in patients with non-small cell lung cancer. *Autophagy* **13**: 1053–1063. <https://doi.org/10.1080/15548627.2017.1308997>
- Liang J, Liu Z, Wei X, Zhou L, Tang Y, Zhou C, Wu K, Zhang F, Zhang F, Lu Y, Zhu Y (2019) Expression of FSCN1 and FOXM1 are associated with poor prognosis of adrenocortical carcinoma patients. *BMC Cancer* **19**: 1165. <https://doi.org/10.1186/s12885-019-6389-3>
- Liu H, Cui J, Zhang Y, Niu M, Xue X, Yin H, Tang Y, Dai L, Dai F, Guo Y, Wu Y, Gao W (2019) Mass spectrometry-based proteomic analysis of FSCN1-interacting proteins in laryngeal squamous cell carcinoma cells. *IUBMB Life* **71**: 1771–1784. <https://doi.org/10.1002/iub.2121>
- Mao G, Liu Y, Fang X, Liu Y, Fang L, Lin L, Liu X, Wang N (2015) Tumor-derived microRNA-494 promotes angiogenesis in non-small cell lung cancer. *Angiogenesis* **18**: 373–382. <https://doi.org/10.1007/s10456-015-9474-5>
- Nguyen DX, Chiang AC, Zhang XH, Kim JY, Kris MG, Ladanyi M, Gerald WL, Massagué J (2009) WNT/TCF signaling through LEF1 and HOXB9 mediates lung adenocarcinoma metastasis. *Cell* **138**: 51–62. <https://doi.org/10.1016/j.cell.2009.04.030>
- Pan J, Bian Y, Cao Z, Lei L, Pan J, Huang J, Cai X, Lan X, Zheng H (2020) Long noncoding RNA MALAT1 as a candidate serological biomarker for the diagnosis of non-small cell lung cancer: A meta-analysis. *Thorac Cancer* **11**: 329–335. <https://doi.org/10.1111/1759-7714.13265>
- Rybaczek-Kasiuchnicz A, Ramlau R, Stencl K (2021) Treatment of brain metastases of non-small cell lung carcinoma. *Int J Mol Sci* **22**. <https://doi.org/10.3390/ijms22020593>
- Salehi M, Movahedpour A, Tavarani A, Shabaninejad Z, Pourhanifeh MH, Mortezaei E, Nickdasti A, Mottaghi R, Davoodabadi A, Khan H, Savardastaki A, Mirzaei H (2020) Therapeutic potentials of curcumin in the treatment of non-small-cell lung carcinoma. *Phytother Res* **34**: 2557–2576. <https://doi.org/10.1002/ptr.6704>
- Schettino C, Bareschino MA, Rossi A, Maione P, Sacco PC, Colantuoni G, Rossi E, Gridelli C (2012) Targeting angiogenesis for treatment of NSCLC brain metastases. *Curr Cancer Drug Targets* **12**: 289–299. <https://doi.org/10.2174/156800912799277476>
- Wang D, Cai L, Tian X, Li W (2020) MiR-543 promotes tumorigenesis and angiogenesis in non-small cell lung cancer via modulating metastasis associated protein 1. *Mol Med* **26**: 44. <https://doi.org/10.1186/s10020-020-00175-1>
- Wang PS, Chou CH, Lin CH, Yao YC, Cheng HC, Li HY, Chuang YC, Yang CN, Ger LP, Chen YC, Lin FC, Shen TL, Hsiao M, Lu PJ (2018) A novel long non-coding RNA linc-ZNF469-3 promotes lung metastasis through miR-574-5p-ZEB1 axis in triple negative breast cancer. *Oncogene* **37**: 4662–4678. <https://doi.org/10.1038/s41388-018-0293-1>
- Wang Y, Han D, Pan L, Sun J (2018) The positive feedback between lncRNA TNK2-AS1 and STAT3 enhances angiogenesis in non-small cell lung cancer. *Biochem Biophys Res Commun* **507**: 185–192. <https://doi.org/10.1016/j.bbrc.2018.11.004>
- Wang Z, Li TE, Chen M, Pan JJ, Shen KW (2020) miR-106b-5p contributes to the lung metastasis of breast cancer via targeting CNN1 and regulating Rho/ROCK1 pathway. *Aging (Albany NY)* **12**: 1867–1887. <https://doi.org/10.18632/aging.102719>
- Wood SL, Pernemalm M, Crosbie PA, Whetton AD (2014) The role of the tumor-microenvironment in lung cancer-metastasis and its relationship to potential therapeutic targets. *Cancer Treat Rev* **40**: 558–566. <https://doi.org/10.1016/j.ctrv.2013.10.001>
- Wu D, Deng S, Li L, Liu T, Zhang T, Li J, Yu Y, Xu Y (2021) TGF-β1-mediated exosomal lnc-MMP2-2 increases blood-brain barrier permeability via the miRNA-1207-5p/EPB41L5 axis to promote non-small cell lung cancer brain metastasis. *Cell Death Dis* **12**: 721. <https://doi.org/10.1038/s41419-021-04004-z>
- Xiao F, Qiu H, Cui H, Ni X, Li J, Liao W, Lu L, Ding K. (2015) MicroRNA-885-3p inhibits the growth of HT-29 colon cancer cell xenografts by disrupting angiogenesis via targeting BMPR1A and blocking BMP/Smad/Id1 signaling. *Oncogene* **34**: 1968–1978. <https://doi.org/10.1038/onc.2014.134>
- Xie Y, Zhang Y, Du L, Jiang X, Yan S, Duan W, Li J, Zhan Y, Wang L, Zhang S, Li S, Wang L, Xu S, Wang C (2018) Circulating long noncoding RNA act as potential novel biomarkers for diagnosis and prognosis of non-small cell lung cancer. *Mol Oncol* **12**: 648–658. <https://doi.org/10.1002/1878-0261.12188>
- Xu SH, Bo YH, Ma HC, Zhang HN, Shao MJ (2021) lncRNA LINC00473 promotes proliferation, migration, invasion and inhibition of apoptosis of non-small cell lung cancer cells by acting as a sponge of miR-497-5p. *Oncol Lett* **21**: 429. <https://doi.org/10.3892/ol.2021.12690>
- Yang XZ, Cheng TT, He QJ, Lei ZY, Chi J, Tang Z, Liao QX, Zhang H, Zeng LS, Cui SZ (2018) LINC01133 as ceRNA inhibits gastric cancer progression by sponging miR-106a-3p to regulate APC expression and the Wnt/β-catenin pathway. *Mol Cancer* **17**: 126. <https://doi.org/10.1186/s12943-018-0874-1>
- Yang XZ, Cheng TT, He QJ, Lei ZY, Chi J, Tang Z, Liao QX, Zhang H, Zeng LS, Cui SZ (2021) CircTUBGCP3 facilitates the tumo-

- rigeneration of lung adenocarcinoma by sponging miR-885-3p. *Cancer Cell Int* **21**: 651. <https://doi.org/10.1186/s12935-021-02356-2>
- Yang YX, Wei L, Zhang YJ, Hayano T, Piñeiro Pereda MDP, Nakao H, Li Q, Barragán Mallofret I, Lu YZ, Tamagnone L, Inoue I, Li X, Luo JY, Zheng K, You H (2018) Long non-coding RNA p10247, high expressed in breast cancer (lncRNA-BCHE), is correlated with metastasis. *Clin Exp Metastasis* **35**: 109–121. <https://doi.org/10.1007/s10585-018-9901-2>
- Zhai D, Li T, Ye R, Bi J, Kuang X, Shi Y, Shao N, Lin Y (2021) LncRNA LGALS8-AS1 promotes breast cancer metastasis through miR-125b-5p/SOX12 feedback regulatory network. *Front Oncol* **11**: 711684. <https://doi.org/10.3389/fonc.2021.711684>
- Zhang G, Lan Y, Xie A, Shi J, Zhao H, Xu L, Zhu S, Luo T, Zhao T, Xiao Y, Li X (2019) Comprehensive analysis of long noncoding RNA (lncRNA)-chromatin interactions reveals lncRNA functions dependent on binding diverse regulatory elements. *J Biol Chem* **294**: 15613–15622. <https://doi.org/10.1074/jbc.RA119.008732>
- Zhao D, Zhang T, Hou XM, Ling XL (2018) Knockdown of fascin-1 expression suppresses cell migration and invasion of non-small cell lung cancer by regulating the MAPK pathway. *Biochem Biophys Res Commun* **497**: 694–699. <https://doi.org/10.1016/j.bbrc.2018.02.134>
- Zheng ZQ, Li ZX, Zhou GQ, Lin L, Zhang LL, Lv JW, Huang XD, Liu RQ, Chen F, He XJ, Kou J, Zhang J, Wen X, Li YQ, Ma J, Liu N, Sun Y (2019) Long noncoding RNA FAM225A promotes nasopharyngeal carcinoma tumorigenesis, metastasis by acting as ceRNA to sponge miR-590-3p/miR-1275 and upregulate ITGB3. *Cancer Res* **79**: 4612–4626. <https://doi.org/10.1158/0008-5472.can-19-0799>



OPEN ACCESS

EDITED BY
Grzegorz Węgrzyn,
University of Gdansk, Poland

REVIEWED BY
Pundrik Jaiswal,
National Institutes of Health (NIH),
United States
Weidong An,
University of Texas Southwestern
Medical Center, United States

*CORRESPONDENCE
Dan Wang,
✉ danwangcn@outlook.com

RECEIVED 23 November 2023

ACCEPTED 15 March 2024

PUBLISHED 02 April 2024

CITATION

Yang Z, Zhao H, Shan L and Wang D
(2024), Clinical features and risk factors
for primary Sjögren's syndrome
combined with interstitial lung disease:
a retrospective study.
Acta Biochim. Pol. 71:12461.
doi: 10.3389/abp.2024.12461

COPYRIGHT

© 2024 Yang, Zhao, Shan and Wang.
This is an open-access article
distributed under the terms of the
Creative Commons Attribution License
(CC BY). The use, distribution or
reproduction in other forums is
permitted, provided the original
author(s) and the copyright owner(s) are
credited and that the original
publication in this journal is cited, in
accordance with accepted academic
practice. No use, distribution or
reproduction is permitted which does
not comply with these terms.

Clinical features and risk factors for primary Sjögren's syndrome combined with interstitial lung disease: a retrospective study

Zhixia Yang¹, Hao Zhao², Lei Shan¹ and Dan Wang^{1*}

¹Department of Rheumatology, Yueyang Hospital of Integrated Traditional Chinese and Western Medicine, Shanghai University of Traditional Chinese Medicine, Shanghai, China, ²Department of Emergency, Shanghai Traditional Chinese Medicine—Integrated Hospital, Shanghai University of Traditional Chinese Medicine, Shanghai, China

Objective: To analyze the clinical characteristics of primary Sjögren's syndrome (pSS) combined with interstitial lung disease (ILD), so as to provide a theoretical basis for the early diagnosis, treatment and prevention of PSS-ILD.

Methods: From October 2017 to January 2022, patients with pSS who were admitted to the Department of Rheumatology at Yueyang Hospital of Integrated Traditional Chinese and Western Medicine, Shanghai University of Traditional Chinese Medicine were included in this retrospective study. Patients were divided into the pSS-ILD (102 cases) and pSS-non-ILD groups (154 cases) based on the presence or absence of ILD on high-resolution computed tomography (HRCT). Demographics information, clinical symptoms, laboratory indicators and HRCT features were compared, and the logistic regression analysis was utilized to identify the risk factors.

Results: A total of 256 patients were included. Patients with pSS-ILD were more often female, and their age and disease duration were significantly higher than those in the pSS-non-ILD group ($p < 0.05$). The HRCT imaging classification included ground glass-like shadow (78.4%) and patchy solid shadow (17.6%), and Non-specific interstitial pneumonitis (NSIP) (72.5%) was the predominant typology. Regarding the laboratory indexes, the positive rates of erythrocyte sedimentation rate, C-reactive protein, white blood cell count, neutrophil/lymphocyte ratio, triglycerides, total cholesterol, and anti-SS-A52 antibodies were significantly higher in the pSS-ILD patients than in the pSS-non-ILD group, while the positive rates of anti-synaptic antibodies were lower than in the pSS-non-ILD group, and the differences between two groups were statistically significant ($p < 0.05$). Logistic regression showed that age >60 years, longer duration of disease, higher triglycerides, and cholesterol were risk factors for pSS-ILD patients.

Conclusion: The clinical features of pSS-ILD patients were xerophthalmia, cough and shortness of breath, and HRCT can help to diagnose the disease at an early stage. Age over 60 years, chronic course of disease, and elevated lipid levels are risk factors for ILD in pSS patients, and the relationship between autoimmune antibody levels and the occurrence of ILD needs to be further

confirmed in follow-up studies with large sample sizes. These findings have the potential to provide useful information for early diagnosis, treatment, and prevention of the development of pSS-ILD.

KEYWORDS

primary Sjögren's syndrome, interstitial lung disease, clinical characteristics, risk factors, diagnosis

Introduction

Primary Sjögren's syndrome (pSS) is a common chronic autoimmune disease with a prevalence of 0.33%–0.77%, which is characterized by exocrine lymphocyte infiltration, mainly involving salivary glands and lacrimal glands (Zhang et al., 1993; Mariette and Criswell, 2018). Due to the presence of multiple autoantibodies in the patient's serum, pSS is a complex heterogeneous autoimmune disease with a diverse clinical face, with almost three-quarters of patients developing extracardiac lesions, including the lungs, kidneys, liver, and nervous system (Martin-Nares and Hernandez-Molina, 2019; Yayla et al., 2020; Manfre et al., 2022). Pulmonary lesions are one of the most common extraglandular manifestations of pSS, with an incidence of 9%–75% (Palm et al., 2013; Reina et al., 2016; Manfredi et al., 2017; Roca et al., 2017; Lee et al., 2021), of which the incidence of Interstitial Lung Disease (ILD) can reach 30.1% (Zhao et al., 2020). Moreover, pulmonary involvement is closely related to the prognosis of pSS patients. Compared to pSS patients without lung involvement, patients with lung involvement have a significantly lower quality of life (Dogru et al., 2017). It is reported that patients with pSS-ILD have a mortality rate of up to 39% and a 4-fold increase in mortality after 10 years (Parambil et al., 2006; Palm et al., 2013). Therefore, early screening of patients with high risk for the development of ILD is of great significance for prompt intervention in order to improve prognosis.

Prior studies have found that male gender, older age, and elevated levels of C-reactive protein (CRP) are risk factors associated with the development of interstitial lung disease in patients with primary Sjögren's syndrome (He et al., 2020). However, there is still limited reporting on the comprehensive assessment of ILD in pSS patients, which combines the patients' immune antibody levels and high-resolution computed tomography (HRCT) manifestations. Thus, this study aimed to analyze the clinical characteristics of pSS-ILD and identified the risk factors related to the development of interstitial lung lesions in pSS patients.

Materials and methods

Study design and participants

This retrospective study started with identification of pSS patients by searching the electronic medical records. We enrolled

patients with pSS who were admitted to the Department of Rheumatology at Yueyang Hospital of Integrated Traditional Chinese and Western Medicine, Shanghai University of Traditional Chinese Medicine between October 2017 and January 2022.

Inclusion criteria for participants were as follows: 1) age over 18 years old; 2) meeting the 2012 American College of Rheumatology (ACR) recommended SS classification criteria (Shiboski et al., 2012); 3) presence of respiratory symptoms or lung abnormalities on HRCT; 4) at least one HRCT examination within 1 year.

The exclusion criteria were as follows: 1) secondary dry syndrome or combined with other rheumatic diseases; 2) combined pulmonary infections, chronic obstructive pulmonary disease, pneumoconiosis and lung diseases such as tumors, tuberculosis, and pulmonary nodules; 3) patients with severe primary diseases of the heart, lungs, liver, kidneys and other organs; 4) patients with incomplete clinical information. Then all patients were divided into pSS-ILD group and pSS-non-ILD group based on whether their HRCT features showed ILD or not. pSS patients whose imaging features supporting ILD in HRCT (e.g., ground-glass opacity, reticulation, consolidation, nodules, traction bronchiectasis, honeycombing) were diagnosed as pSS-ILD (Lohrmann et al., 2004). Altogether 256 pSS patients were screened in this study and divided into the pSS-ILD (102 cases) and pSS-non-ILD groups (154 cases). This study was approved by the Ethics Committee of Shanghai University of Traditional Chinese Medicine (No. 2018-014) and was registered at Chinese Clinical Trial Registry (No. ChiCTR2000037057).

Data collection

Demographic and clinical data were collected from patients' medical records, including age, sex, disease duration. Clinical features associated with pSS and pSS-ILD were fully recorded as well, such as xerostomia, xerophthalmia, cough, shortness of breath. Moreover, the blood biochemical data were also collected, including complete blood cell count, erythrocyte sedimentation rate (ESR), C-reactive protein (CRP), blood lipids, rheumatoid factor (RF), immunoglobulin, complement 3 (C3), complement 4 (C4), antinuclear antibody (ANA) spectrum, cytokine.

Blood biochemical data testing methods: Complete blood cell count: The BC-6800 automatic hematology analyzer (mindray,

China) was used for testing. The mindray series analyzer's auto hematology analyzer reagent (mindray, China) was used.

Erythrocyte sedimentation rate (ESR): The TEST 1 Automatic Rapid Blood Sedimentation Analyzer (Alifax, Italy) was used for determination. EDTA anticoagulant was used for blood collection.

C-reactive protein (CRP): The high-sensitivity human C-reactive protein detection kit (mindray, China) was used for the determination of C-reactive protein in human whole blood samples by latex-enhanced immunoscattering turbidimetric assay.

Blood lipids: Enzyme method was used for testing, including total cholesterol (TC), triglycerides (TG), high-density lipoprotein (HDL), and low-density lipoprotein (LDL) testing. Reagent brands: glucose oxidase-cholesterol dehydrogenase method TG kit, glucose oxidase-peroxidase method TC kit, Direct HDL-cholesterol (HDL-c) assays Kit and Direct LDL-c kit (Beckman, United States).

Rheumatoid factor (RF): The N Latex RF Kit (Siemens healthineers, Germany) was used for testing.

Immunoglobulin (Ig), complement 3 (C3), complement 4 (C4): The Scattering turbidimetric method was used for testing. The reagent kit brand was N Antiserum to Immunoglobulin A (IgA), immunoglobulin M (IgM), immunoglobulin G (IgG), complement C3 and complement C4 reagent kit (Siemens healthineers, Germany).

Antinuclear antibody (ANA) spectrum: The EUROLINE ANA profile 3 (Euroimmun Medizinische Labordiagnostika, Germany) was used for testing.

Cytokines: Luminex[®] xMAP (Luminex Corporation, United States) technology was used for quantitative detection of tumor necrosis factor- α (TNF- α), Interleukin 2 receptor (IL-2R), IL-6 and IL-8. The reagent kit brand was 12 Human Cytokine assay kit (RAISECARE, China).

In addition, all patients underwent HRCT examination. Approach to Radiological Analysis: The Philips iCT 256 spiral computed tomography (CT) scanner was used for image analysis. The tracheal level was selected as the starting position, and the scan was conducted downwards until the bottom of the lungs (excluding the lung apex). The scan parameters were as follows: pitch 1, reconstruction slice thickness of 1.0 mm, interlayer spacing of 1.0 mm, tube current of 40–120 mA, voltage of 120 KV, and reconstruction with a wide window level setting of 2000 HU/-600 HU. All imaging data were reviewed by two experienced radiologists in batches. For high-resolution CT images, a qualitative analysis method and reproducible calculated measurement parameters, including the morphology, extent, and severity of interstitial lung disease (such as linear, nodular, reticular, honeycombing, traction bronchiectasis lesions) were used for classification, counting, and scoring. The maximum diameter and area of all lesions were measured, and the CT density value (CT value) was calculated to evaluate the degree and type of lesion. During

the analysis process, independent assessments were performed first, followed by a consensus reached through discussion.

For HRCT abnormalities, different HRCT features of pSS-ILD patients were image-typed according to the American Thoracic Society/European Respiratory Society (2013) International Multidisciplinary Classification of idiopathic interstitial pneumonia (Travis et al., 2013), including Non-specific interstitial pneumonitis (NSIP), Unusual interstitial pneumonia (UIP), Lymphocytic interstitial pneumonitis (LIP), Organizing pneumonia (OP). Additionally, we refer to the literature to stage the severity of fibrosis by chest HRCT in pSS-ILD patients into stages 1, 2, and 3 (Qiu et al., 2008). Stage 1 is defined as early or active lesion with ground glass shadow, increased interlobular stroma and thickened interlobular septa; stage 2 is defined as progressive or chronic prolonged lesion with stage 1 manifestations and interface signs, subpleural arcuate shadow, intrapulmonary lamellar solidity and small nodular shadow; stage 3 is defined as advanced lesion with stage 1, stage 2 and reticular shadow, fibrous streak shadow, honeycomb shadow, multiple large alveoli, distended bronchial dilatation and diffuse fibrosis. Determination of HRCT results were determined by both radiologists and rheumatologist.

Statistics

All data were statistically analyzed using SPSS 24.0 statistical software. Continuous variables were presented as mean \pm standard deviation (SD) for normally distributed data; if the variance had chi-square, two independent samples t-test was used, and if the variance was not chi-square, approximate t-test was used. Median (interquartile spacing) was used for non-normally distributed data and non-parametric test was used for statistical analysis. Categorical variables were presented as the percentages and were compared using chi-square test or Fisher's exact test. Logistic regression analysis was used to identify the factors associated with the development of ILD in patients with pSS. All reported *p*-values were two sided and *p* < 0.05 was considered to be statistically significant.

Results

Demographic and clinical features in patients with pSS-interstitial lung disease (ILD)

This study included a total of 256 patients with pSS. Of these, there were 102 patients in the pSS-ILD group, with a mean age of 63.36 ± 9.22 years, of whom 66 (64.71%) were over 60 years old. The pSS-non-ILD group consisted of 154 patients, with a mean age of 57.16 ± 12.72 years, of whom 73 (47.40%) were over

TABLE 1 Demographics and clinical characteristics of the primary Sjögren's syndrome (pSS)- interstitial lung disease (ILD) and pSS-non-ILD.

	pSS-ILD (<i>n</i> = 102)	pSS-non-ILD (<i>n</i> = 154)	<i>p</i> -value
Demographics			
Sex (male, %)	4 (3.92%)	12 (7.79%)	0.210
Age (years)	63.36 ± 9.22	57.16 ± 12.72	0.000*
Disease duration (months)	90 (24, 156)	48 (24, 120)	0.006*
Clinical symptoms			
Xerostomia (<i>n</i> , %)	90 (88.24%)	137 (88.96%)	0.858
Xerophthalmia (<i>n</i> , %)	87 (85.29%)	115 (74.68%)	0.041*
Arthralgia (<i>n</i> , %)	44 (43.14%)	62 (40.26%)	0.647
Fever (<i>n</i> , %)	18 (17.65%)	23 (14.94%)	0.562
Fatigue (<i>n</i> , %)	18 (17.65%)	23 (14.94%)	0.359
Raynaud's phenomenon (<i>n</i> , %)	18 (17.65%)	23 (14.94%)	0.606
Cough (<i>n</i> , %)	7 (6.86%)	9 (5.84%)	0.742
Cough and sputum (<i>n</i> , %)	7 (6.86%)	9 (5.84%)	0.000*
Chest tightness (<i>n</i> , %)	7 (6.86%)	9 (5.84%)	0.050
Shortness of breath (<i>n</i> , %)	23 (22.55%)	4 (2.60%)	0.000*
Skin rash (<i>n</i> , %)	23 (22.55%)	4 (2.60%)	0.553
Myalgia (<i>n</i> , %)	4 (3.92%)	8 (5.19%)	0.768*
Laboratory metrics			
ESR (mm/h)	24.5 (13.75, 49.25)	20 (11, 75)	0.044*
CRP elevation (<i>n</i> , %)	23 (22.55%)	20 (12.99%)	0.045*
WBC (×10 ⁹ /L)	5.40 (4.10, 7.03)	5.10 (3.68, 6.30)	0.027*
PLT (×10 ⁹ /L)	183.00 (153.00, 226.00)	182.50 (137.00, 233.25)	0.888
Hb (g/L)	123.08 ± 13.42	120.14 ± 13.69	0.091
NLR	2.49 (1.65, 4.13)	2.13 (1.50, 3.17)	0.044*
TG (mmol/L)	1.28 (0.96, 1.84)	1.12 (0.84, 1.51)	0.004*
TC (mmol/L)	4.80 (3.90, 5.49)	4.50 (3.70, 5.10)	0.046*
HDL (mmol/L)	1.22 (0.99, 1.48)	1.22 (1.02, 1.44)	0.828
LDL (mmol/L)	2.93 (2.36, 3.40)	2.75 (2.32, 3.26)	0.099
RF ⁺ (<i>n</i> , %)	32 (31.37%)	36 (23.38%)	0.193
ANA ⁺ (<i>n</i> , %)	87 (85.29%)	133 (86.36%)	0.810
Anti-Ro52 ⁺ (<i>n</i> , %)	65 (63.73%)	77 (50.00%)	0.040*
Anti-Ro60 ⁺ (<i>n</i> , %)	65 (63.73%)	102 (66.23%)	0.690
Anti-SSB ⁺ (<i>n</i> , %)	39 (38.24%)	42 (27.27%)	0.075
Anti-centromere ⁺ (<i>n</i> , %)	9 (8.82%)	32 (20.78%)	0.014*
C3 (g/L)	0.89 (0.78, 1.00)	0.89 (0.77, 1.02)	0.896
C4 (g/L)	0.195 (0.15, 0.24)	0.20 (0.15, 0.24)	0.528

(Continued on following page)

TABLE 1 (Continued) Demographics and clinical characteristics of the primary Sjögren's syndrome (pSS)- interstitial lung disease (ILD) and pSS-non-ILD.

	pSS-ILD (<i>n</i> = 102)	pSS-non-ILD (<i>n</i> = 154)	<i>p</i> -value
IgG (g/L)	13.95 (11.28, 18.20)	14.25 (11.55, 17.30)	0.948
IgM (g/L)	0.80 (0.60, 1.16)	0.88 (0.63, 1.22)	0.386
IgA (g/L)	2.65 (1.92, 3.75)	2.46 (1.72, 3.42)	0.163
IL-2R (u/mL)	507.00 (375.50, 645.30)	452.50 (355.50, 591.00)	0.175
IL-6 (pg/mL)	3.32 (2.00, 6.23)	2.39 (2.00, 4.16)	0.030*
IL-8 (pg/mL)	28.80 (17.80, 57.30)	28.60 (16.80, 59.80)	0.717
TNF-α (pg/mL)	10.00 (7.70, 12.70)	9.50 (7.40, 11.70)	0.271

ESR, erythrocyte sedimentation rate; CRP, C-reactive protein; WBC, white blood cell count; PLT, platelets; NLR, neutrophil/lymphocyte ratio; Hb, hemoglobin; TG, triglycerides; TC, total cholesterol; HDL, high-density lipoprotein; LDL, low-density lipoprotein; RF, rheumatoid factor; ANA, antinuclear antibody; C3, complement 3; C4, complement 4; IgG, immunoglobulin G; IgM, immunoglobulin M; IgA, immunoglobulin A; IL-2R, interleukin-2 receptor; IL-6, interleukin-6; IL-8, interleukin-8; TNF-α, tumor necrosis factor-α. *, The difference between the groups was statistically significant. *, denotes calculation using Fisher's exact probability method.

The meaning of the bold values indicates statistically significant differences.

60 years old. Generally, there were significant differences between the pSS-ILD and total pSS-non-ILD groups related to age ($p < 0.01$) and disease duration ($p < 0.001$) characteristics studied (Table 1).

Next, clinical symptoms of the two groups were analyzed. Among 256 patients with pSS, the most common clinical manifestations were xerostomia, xerophthalmia, and arthralgias. Fever, fatigue, Raynaud's phenomenon, cough and sputum, chest tightness and shortness of breath, skin rash, muscle aches and pains have been observed in a few patients. Patients with pSS-ILD have a significantly higher proportion of clinical manifestations of xerophthalmia (85.2%), cough (25.4%), and shortness of breath (22.5%) compared with patients without ILD ($p < 0.05$) (Table 1).

Laboratory metrics

As shown in Table 1, ESR, CRP, white blood cell count (WBC), neutrophil/lymphocyte ratio (NLR), TC, and TG were significantly higher in the pSS-ILD group than in the pSS-non-ILD group ($p < 0.05$). As for the immunologic index, the positivity for different autoantibodies in pSS-ILD groups was as follows: 87 cases (85.29%) for ANA, 65 cases (63.73%) for Ro52, 65 cases (63.73%) for Ro60, 39 cases (38.24%) for SSB, and 9 cases (8.82%) for anti-centromere antibodies. By chi-square test, patients in the pSS-ILD group had a higher rate of anti-Ro52⁺ and a lower rate of anti-centromere⁺ than those in the pSS-non-ILD group, and the differences between the two groups were statistically significant ($p < 0.05$) (Table 1).

In addition, among all pSS patients, cytokines were measured and analyzed in 222 patients showed that IL-6 was significantly higher in the pSS-ILD group than in the pSS-non-ILD group ($p < 0.05$), while no statistically significant differences between the remaining cytokines in the two groups ($p > 0.05$) (Table 1).

HRCT features

HRCT provides superior evaluation of the lung compared with conventional radiographs. If HRCT findings are characteristic, lung biopsy is not necessary to confirm ILD in humans. In our study, all 256 patients underwent HRCT and 102 of them showed interstitial lung lesions on HRCT. For HRCT abnormalities, the percentages of different patterns were showed in Table 2. Of note, ground glass-like shadow described as a hazy increased opacity of the lungs was the most common, followed by patchy solid shadow. The percentages of different stages were as follows: 38 patients (34.3%) were in stage 1 (early stage), 35 patients (34.3%) were in stage 2 (chronic prolongation), and 29 patients (28.4%) were in stage 3 (late stage). And then HRCT imaging classification of pSS-ILD patients were showed as follows: 74 cases (72.5%) with NSIP, 10 cases (9.8%) with UIP, 6 cases (5.9%) with LIP, and 2 cases (2.0%) with OP. However, due to atypical HRCT imaging manifestations that could not be clearly defined to which imaging type they belonged, or the presence of two or more types of imaging manifestations at the same time, they were categorized as other in our study results (10 cases, 9.8%) (Table 2).

Additionally, we investigated the features for ILD detected by HRCT in pSS patients with or without respiratory symptoms. It is noteworthy that 50 percentage of patients without obvious pulmonary symptoms exhibited abnormalities, consistent with ILD symptoms, in HRCT-scan. We further observed the characteristics of HRCT in these patients without respiratory symptoms (imaging performance, staging and classification). Obviously, HRCT features in pSS-ILD patients without obvious pulmonary symptoms are predominantly early compared to patients with obvious pulmonary symptoms (Figure 1). This suggests that regular HRCT should also be performed in patients with pSS without respiratory symptoms.

TABLE 2 Clinical characteristics of patients with primary Sjögren's syndrome (pSS)-interstitial lung disease (ILD).

	Number of patients (%)
Subjects	102 (39.84)
Gender, male	4 (3.92)
respiratory symptoms	51 (50.00)
HRCT features	
Ground-glass opacity	80 (78.43)
Reticulation	18 (17.65)
consolidation	18 (17.65)
Honeycombing	3 (2.94)
NSIP	74 (72.55)
UIP	10 (9.80)
LIP	6 (5.88)
OP	2 (1.96)
Stage 1	38 (37.3)
Stage 2	35 (34.3)
Stage 3	29 (28.4)

NSIP, non-specific interstitial pneumonia; UIP, usual interstitial pneumonia; LIP, lymphocytic interstitial pneumonia; OP, organizing pneumonia.

Risk factors for the development of ILD and predictive model

Furthermore, we also performed logistic regression analysis to investigate the independent risk factors of interstitial lung lesions in patients with pSS. In the univariate logistic regression analysis comparing the pSS-ILD cohort with the control cohort, several variables showed statistically significant odds ratios. The pSS-ILD cohort had an odds ratio (OR) of 2.034 (95% CI 1.216–3.414, $p = 0.007$) for age > 60 years, 1.006 (95% CI 1.003–1.010, $p < 0.001$) for disease duration, 0.103 (95% CI 0.024–0.446, $p = 0.002$) for shortness of breath. Among the laboratory metrics, the following ORs were observed: ESR (OR = 1.010, 95% CI 1.000–1.020, $p = 0.046$); CRP (OR = 1.951, 95% CI 1.008–3.776, $p = 0.047$); WBC (OR = 1.150, 95% CI 1.032–1.281, $p = 0.011$); NLR (OR = 1.179, 95% CI 1.043–1.333, $p = 0.008$); TG (OR = 1.793, 95% CI 1.191–2.700, $p = 0.005$); TC (OR = 1.329, 95% CI 1.038–1.702, $p = 0.024$); Anti-Ro52⁺ (OR = 1.949, 95% CI 1.167–3.255, $p = 0.011$); Anti-centromere⁺ (OR = 0.369, 95% CI 0.168–0.811, $p = 0.013$).

Based on the results and clinical relevance, 11 variables were a step forward included in the multivariate logistic regression analysis. The finally results showed that older than 60 years (OR = 2.381, 95% IC 1.302–4.355, $p < 0.05$), longer duration of disease (OR = 1.007, 95% IC 1.003–1.012, $p < 0.001$), higher TG (OR = 1.652, 95% CI 1.014–2.691, $p < 0.05$), higher TC (OR =

1.424, 95% CI 1.059–1.915, $p < 0.05$) and anti-Ro52⁺ (OR = 1.949, 95% CI 1.167–3.255, $p = 0.011$) were risk factors for ILD in pSS patients. Interestingly, we also found a protective factor for ILD in pSS patients was anti-centromere⁺ (OR = 0.402, 95% CI 0.17–0.935, $p < 0.05$) (Table 3).

Discussion

The pathogenesis of pSS-ILD is not fully elucidated. An early study revealed that the combined involvement of genetic, environmental and infection susceptibility factors result in recruitment of inflammatory cells into the interstitial and alveolar spaces of the lung, releasing inflammatory factors and causing alveolar epithelial damage. Consequently, fibroblasts and myofibroblasts in the interstitial spaces of the lung become activated and produce extracellular matrix proteins, leading to lung fibrosis (Wells and Denton, 2014; Panagopoulos et al., 2021). In our study, patients in the pSS-ILD group had significantly higher WBC counts than patients in the pSS-non-ILD group. WBC, as an inflammatory cell, can activate inflammatory responses in certain pathological conditions, so is it possible that patients in the pSS-ILD group had higher inflammatory indicators? We then further analyzed the inflammatory indexes in both groups and found that CRP, ESR, NLR, and IL-6 were significantly higher in the pSS-ILD group than that in the patients without ILD. NLR, as a new inflammatory index that can reflect the systemic inflammatory status, is commonly used in the diagnosis and assessment of prognosis of infectious diseases. It includes lymphocyte and neutrophil counts, which has the advantages of being simple, easy to operate, inexpensive and reproducible. And it is more clinically meaningful than single lymphocyte and neutrophil counts, and can be widely used in clinical practice to assess the inflammatory status of diseases in combination with CRP, ESR and other indexes. IL-6 is a multifunctional cytokine with multiple immunomodulatory effects, and its elevation is positively correlated with inflammation. Previous study (Boumba et al., 1995; Mavragani, 2017) reported that IL-6, IL-8, IL-10, and TNF- α may be involved in the occurrence and development of ILD in patients with pSS, suggesting that the occurrence of pSS-ILD is closely related to the inflammatory response and needs clinical attention.

In addition, pSS also can attack blood lipids and promote the development of atherosclerosis (Vaudo et al., 2005). Previous study reported that pSS patients had a strong trend to present dyslipidemia when compared to healthy individuals (Cruz et al., 2010). Consistently, our study showed that TG and TC were significantly higher in the pSS-ILD group than in the pSS-non-ILD group. As for the reasons, the elevation of TG and TC may be related to the older age of patients. On the other hand, it also suggested that pSS-ILD patients were more likely to have abnormal TG and TC than patients without ILD. In clinical

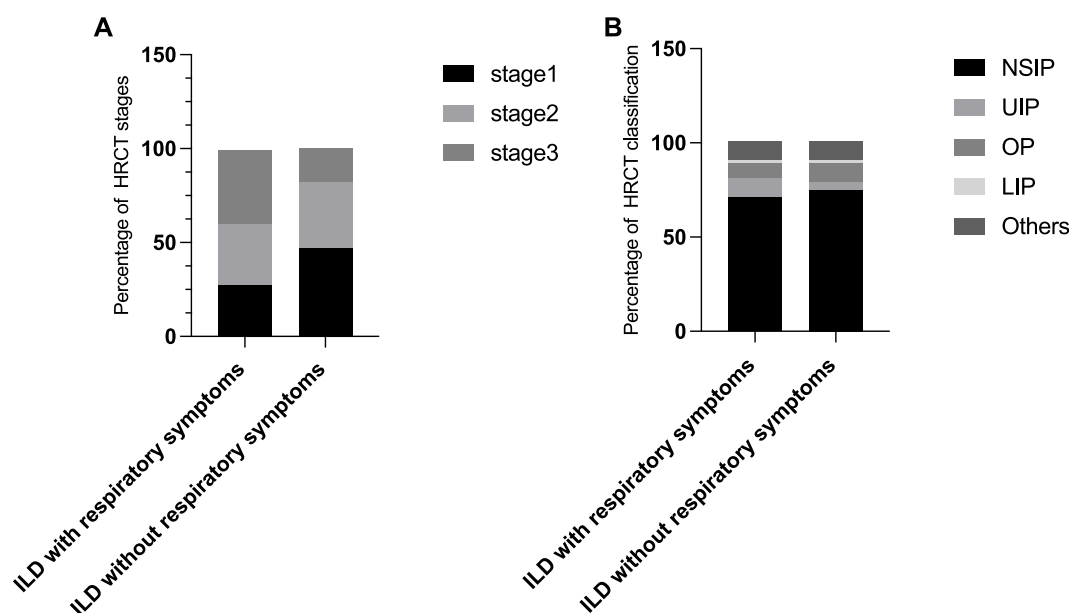


FIGURE 1

Characteristics of HRCT in pSS-ILD patients with or without respiratory symptoms. (A,B) Percentage of different HRCT staging (A) and classification (B) in ILD patients with and without respiratory symptoms.

treatment, we need to pay more attention to and monitor the lipid profile of patients in order to reduce the risk of cardiovascular and cerebrovascular adverse events in patients. Certainly, glucocorticoid can also cause dyslipidemia in patients, which could be a potential confounding factor.

Moreover, immunological factors also play an important role in the pathogenesis of pSS-ILD, and multiple immune cells are jointly involved in the pathogenesis (Ytterberg et al., 2015). We further analyzed the immunological indicators between the two groups, and the results showed that the anti-RO52⁺ rate in pSS-ILD group was significantly higher than that in non-ILD group, while the positive rates of immunoglobulin and complement were not significantly different, indicating that anti-Ro52⁺ pSS patients were more prone to ILD. Davidson et al. (2000) have reported that lung involvement occurs primarily in pSS patients who are positive for anti-RO antibodies and can occur early in the disease. This suggests that early screening should be conducted for such patients in clinical practice.

pSS-ILD is asymptomatic and easy to be missed, and some patients have no obvious clinical symptoms in the early stage. HRCT can detect abnormal changes in the lungs of pSS patients at an early stage with a specificity of 90%, which is the same as the pathological findings of lung biopsy. In this study, 256 patients underwent HRCT of the lung, and 102 of them showed interstitial lung lesions, which mainly consisted of ground glass-like shadow, patchy solid shadow, fibrous streak shadow, lattice shadow and honeycomb shadow, among which ground

glass-like shadow was the most common, followed by patchy solid shadow. HRCT staging of patients based on imaging presentation revealed that NSIP was the most common type of ILD in patients with pSS. Abrasive glassy shadow is an early manifestation of interstitial lung changes, mostly reversible, while lattice-like and honeycomb-like changes are indicative of intermediate and advanced stages of irreversible fibrosis. In addition, it is noteworthy that 50% patients without obvious pulmonary symptoms exhibited abnormalities, consistent with ILD features in HRCT-scan, although these were relatively early. Therefore, HRCT can help to diagnose the disease at an early stage so that we can better grasp the timing of treatment. In addition, respiratory symptoms appeared later than pulmonary imaging findings in some patients, which requires clinicians to judge whether there is pulmonary involvement in pSS patients, not only based on respiratory symptoms, but also regular imaging examinations to achieve the purpose of early diagnosis.

Pulmonary involvement increases the 10-year mortality of pSS patients by 4 times (Palm et al., 2013). Early diagnosis and treatment can prevent pulmonary lesions from progressing from reversible inflammatory stage to irreversible pulmonary fibrosis stage, and significantly improve the prognosis of patients. After single factor screening, eleven clinical variables were found to be significantly different between two groups. These factors were age, course of disease, CRP, ESR, WBC, NLR, TG, TC, anti-Ro52⁺, anti-centromere⁺, and IL-6. The multivariate analysis showed that age ≥ 60 years, chronic disease, high TG and high

TABLE 3 Possible relevant risk factors of developing interstitial lung disease among primary Sjögren’s syndrome (pSS) patients.

Characteristics	Univariate			Multivariate		
	Odds ratio	95% CI	<i>p</i> -value	Odds ratio	95% CI	<i>p</i> -value
Gender, male	0.483	0.151–1.541	0.219			
Age>60 (years)	2.034	1.216–3.414	0.007**	2.035	1.140–3.634	0.016*
Disease duration (months)	1.006	1.003–1.010	0.000***	1.006	1.002–1.010	0.002**
Xerostomia	1.304	0.580–2.934	0.520			
Xerophthalmia	0.866	0.471–1.592	0.642			
Shortness of breath	0.103	0.024–0.446	0.002**			
Chest tightness	0.657	0.341–1.256	0.209			
ESR (mm/h)	1.010	1.000–1.020	0.046*	1.003	0.988–1.107	0.711
CRP elevation	1.951	1.008–3.776	0.047*	1.902	0.662–5.461	0.232
WBC (×10 ⁹ /L)	1.150	1.032–1.281	0.011**	1.045	0.908–1.203	0.538
NLR	1.179	1.043–1.333	0.008**	1.038	1.002–1.010	0.660
TG (mmol/L)	1.793	1.191–2.700	0.005**	1.664	1.020–2.714	0.041*
TC (mmol/L)	1.329	1.038–1.702	0.024*	1.349	1.004–1.812	0.047*
HDL (mmol/L)	0.905	0.426–1.923	0.795			
LDL (mmol/L)	1.413	0.998–1.999	0.051			
Anti-Ro52 ⁺	1.949	1.167–3.255	0.011*	1.812	1.002–3.287	0.049*
Anti-Ro60 ⁺	0.896	0.530–1.512	0.680			
Anti-SSB ⁺	1.651	0.968–2.816	0.066			
Anti-adnexin ⁺	0.369	0.168–0.811	0.013*	0.405	0.174–0.945	0.037*
RF ⁺	1.498	0.855–2.625	0.157			
ANA ⁺	1.076	0.613–1.890	0.799			

NLR, neutrophil–lymphocyte ratio; LDL, low-density lipoprotein; TC, total cholesterol; TG, triglyceride; RF, rheumatoid factor; ANA, antinuclear antibodies. **p* < 0.05; ***p* < 0.01; ****p* < 0.001.
The meaning of the bold values indicates statistically significant differences.

TC were the high risk factors for ILD in pSS patients, which was consistent with previous studies (Gao et al., 2018). Analysis of the reason may be induced in older adults with the body immune function change matter more, thus easier to cause the change of immune, eventually lead to the occurrence of ILD. Surprisingly, our study also found that anti-centromere⁺ is a protective factor for ILD, which is similar to what has been reported in previous studies, the antibodies against the centromere has protective effect to the organs in the diffuse systemic sclerosis (dsSSc) (Caetano et al., 2018). However, in our literature review, we found no reports of anti-Ro52⁺ and ILD in pSS patients. The correlation between the level of autoimmune antibodies in pSS patients and the incidence of ILD is worthy of further investigation.

In addition, there were some limitations in our study. First of all, this study was a retrospective, single-center, and small-scale study, which may affect the universality and practical clinical

significance of the results. Second, there was a correlation between some of the indicators, such as high age and elevated lipid levels, which may have led to potential confusion. Third, some results with statistical differences lacked appropriate clinical interpretation, which affected the authenticity of the results. In the next step, we will conduct a multi-center study with a large sample size and collect more comprehensive patient clinical data to reduce controllable interference factors and provide advantages for early diagnosis, treatment and prognosis of pSS-ILD.

Conclusion

The clinical features of pSS-ILD patients were xerophthalmia, cough and shortness of breath, and HRCT can help to diagnose the disease at an early stage. Age over 60 years,

chronic course of disease, and elevated lipid levels are risk factors for ILD in pSS patients, and the relationship between autoimmune antibody levels and the occurrence of ILD needs to be further confirmed in follow-up studies with large sample sizes.

Data availability statement

The raw data supporting the conclusion of this article will be made available by the authors, without undue reservation.

Ethics statement

The studies involving humans were approved by the Ethics Committee of Shanghai University of Traditional Chinese Medicine (No. 2018-014) and was registered at Chinese Clinical Trial Registry (No. ChiCTR2000037057). Informed consent was obtained from all the study subjects before enrollment. The studies were conducted in accordance with the local legislation and institutional requirements. The participants provided their written informed consent to participate in this study.

References

- Boumba, D., Skopouli, F. N., and Moutsopoulos, H. M. (1995). Cytokine mRNA expression in the labial salivary gland tissues from patients with primary Sjogren's syndrome. *Rheumatology* 34, 326–333. doi:10.1093/rheumatology/34.4.326
- Caetano, J., Nihtyanova, S. I., Harvey, J., Denton, C. P., and Ong, V. H. (2018). Distinctive clinical phenotype of anti-centromere antibody-positive diffuse systemic sclerosis. *Rheumatology Adv. Pract.* 2, rky002. doi:10.1093/rap/rky002
- Cruz, W., Fialho, S., Morato, E., Castro, G., Zimmermann, A., Ribeiro, G., et al. (2010). Is there a link between inflammation and abnormal lipoprotein profile in Sjogren's syndrome? *Jt. Bone Spine* 77, 229–231. doi:10.1016/j.jbspin.2010.02.011
- Davidson, B. K., Kelly, C. A., and Griffiths, I. D. (2000). Ten year follow up of pulmonary function in patients with primary Sjogren's syndrome. *Ann. Rheumatic Dis.* 59, 709–712. doi:10.1136/ard.59.9.709
- Dogru, G., Balkarli, A., and Dogru, A. (2017). Chronic non-productive cough in patients with primary Sjogren's syndrome. *Arch. Rheumatol.* 32, 303–308. doi:10.5606/archrheumatol.2017.6160
- Gao, H., Zhang, X. W., He, J., Zhang, J., An, Y., Sun, Y., et al. (2018). Prevalence, risk factors, and prognosis of interstitial lung disease in a large cohort of Chinese primary sjogren syndrome patients: a case-control study. *Med. Baltim.* 97, e11003. doi:10.1097/md.00000000000011003
- He, C., Chen, Z., Liu, S., Chen, H., and Zhang, F. (2020). Prevalence and risk factors of interstitial lung disease in patients with primary Sjögren's syndrome: a systematic review and meta-analysis. *Int. J. Rheumatic Dis.* 23, 1009–1018. doi:10.1111/1756-185x.13881
- Lee, A. S., Scofield, R. H., Hammit, K. M., Gupta, N., Thomas, D. E., Moua, T., et al. (2021). Consensus guidelines for evaluation and management of pulmonary disease in Sjogren's. *Chest* 159, 683–698. doi:10.1016/j.chest.2020.10.011
- Lohrmann, C., Uhl, M., Warnatz, K., Ghanem, N., Kotter, E., Schaefer, O., et al. (2004). High-resolution CT imaging of the lung for patients with primary Sjogren's syndrome. *Eur. J. Radiology* 52, 137–143. doi:10.1016/j.ejrad.2004.01.006
- Manfredi, A., Sebastiani, M., Cerri, S., Cassone, G., Bellini, P., Della Casa, G., et al. (2017). Erratum to: prevalence and characterization of non-sicca onset primary Sjogren syndrome with interstitial lung involvement. *Clin. Rheumatol.* 36, 1931. doi:10.1007/s10067-017-3635-4
- Manfre, V., Chatzis, L. G., Cafaro, G., Fonze, S., Calvacchi, S., Fulvio, G., et al. (2022). Sjogren's syndrome: One year in review 2022. *Clin. Exp. Rheumatology* 40, 2211–2224. doi:10.55563/clinexprheumatol/43z8gu
- Mariette, X., and Criswell, L. A. (2018). Primary Sjogren's syndrome. *N. Engl. J. Med.* 378, 931–939. doi:10.1056/nejmcp1702514
- Martin-Nares, E., and Hernandez-Molina, G. (2019). Novel autoantibodies in Sjogren's syndrome: a comprehensive review. *Autoimmun. Rev.* 18, 192–198. doi:10.1016/j.autrev.2018.09.003
- Mavragani, C. P. (2017). Mechanisms and new strategies for primary Sjogren's syndrome. *Annu. Rev. Med.* 68, 331–343. doi:10.1146/annurev-med-043015-123313
- Palm, O., Garen, T., Berge Enger, T., Jensen, J. L., Lund, M. B., Aalokken, T. M., et al. (2013). Clinical pulmonary involvement in primary Sjogren's syndrome: prevalence, quality of life and mortality—a retrospective study based on registry data. *Rheumatol. Oxf.* 52, 173–179. doi:10.1093/rheumatology/kes311
- Panagopoulos, P., Goules, A., Hoffmann-Vold, A. M., Matteson, E. L., and Tzioufas, A. (2021). Natural history and screening of interstitial lung disease in systemic autoimmune rheumatic disorders. *Ther. Adv. Musculoskelet. Dis.* 13, 1759720X2110375. doi:10.1177/1759720x211037519
- Parambil, J. G., Myers, J. L., Lindell, R. M., Matteson, E. L., and Ryu, J. H. (2006). Interstitial lung disease in primary Sjogren syndrome. *Chest* 130, 1489–1495. doi:10.1378/chest.130.5.1489
- Qiu, J., Pan, X., Yu, S., Xing, W., and Nie, J. (2008). Clinical value of high resolution CT staging of lung interstitial disease in connective tissue disease. *J. Pract. Radiology* 231, 1188–1190+1193. doi:10.3969/j.issn.1002-1671.2008.09.010
- Reina, D., Roig Vilaseca, D., Torrente-Segarra, V., Cerda, D., Castelli, I., Diaz Torne, C., et al. (2016). Sjogren's syndrome-associated interstitial lung disease: a multicenter study. *Reumatol. Clínica* 12, 201–205. doi:10.1016/j.reuma.2015.09.003
- Roca, F., Dominique, S., Schmidt, J., Smail, A., Duhaut, P., Levesque, H., et al. (2017). Interstitial lung disease in primary Sjogren's syndrome. *Autoimmun. Rev.* 16, 48–54. doi:10.1016/j.autrev.2016.09.017
- Shiboski, S. C., Shiboski, C. H., Criswell, L., Baer, A., Challacombe, S., Lanfranchi, H., et al. (2012). American College of Rheumatology classification criteria for Sjogren's syndrome: a data-driven, expert consensus approach in the Sjogren's

Author contributions

ZY and DW contributed to the conception and design of the study; HZ, LS, and ZY performed the experiments, collected and analyzed data; ZY wrote the manuscript; All authors contributed to the article and approved the submitted version.

Funding

This study was supported by Funding of Yueyang Hospital of Integrated Traditional Chinese and Western Medicine, Shanghai University of Traditional Chinese Medicine (No. 2019YYZ06), The Second Round of “Guo Yi Qiang You” Three Year Action Plan in Hongkou District, Shanghai (HKGYQYXM-2022-02), and National Nature Science Foundation of China (No. 82374342).

Conflict of interest

The authors declare that the research was conducted in the absence of any commercial or financial relationships that could be construed as a potential conflict of interest.

international collaborative clinical alliance cohort. *Arthritis Care & Res.* 64, 475–487. doi:10.1002/acr.21591

Travis, W. D., Costabel, U., Hansell, D. M., King, T. E., JR., Lynch, D. A., Nicholson, A. G., et al. (2013). An official American Thoracic Society/European Respiratory Society statement: update of the international multidisciplinary classification of the idiopathic interstitial pneumonias. *Am. J. Respir. Crit. Care Med.* 188, 733–748. doi:10.1164/rccm.201308-1483st

Vaudo, G., Bocci, E. B., Shoenfeld, Y., Schillaci, G., Wu, R., Del Papa, N., et al. (2005). Precocious intima-media thickening in patients with primary Sjogren's syndrome. *Arthritis & Rheumatism* 52, 3890–3897. doi:10.1002/art.21475

Wells, A. U., and Denton, C. P. (2014). Interstitial lung disease in connective tissue disease--mechanisms and management. *Nat. Rev. Rheumatol.* 10, 728–739. doi:10.1038/nrrheum.2014.149

Yayla, M. E., Karaman, Z., Torgutalp, M., Kelesoglu Dincer, A. B., Aydemir Guloksuz, E. G., Sezer, S., et al. (2020). Early onset primary Sjogren syndrome, clinical and laboratory characteristics. *Clin. Rheumatol.* 39, 2689–2696. doi:10.1007/s10067-020-05017-3

Ytterberg, A. J., Joshua, V., Reynisdottir, G., Tarasova, N. K., Rutishauser, D., Ossipova, E., et al. (2015). Shared immunological targets in the lungs and joints of patients with rheumatoid arthritis: Identification and validation. *Ann. Rheum. Dis.* 74, 1772–1777. doi:10.1136/annrheumdis-2013-204912

Zhang, N. Z., Shi, Q. S., and Yao, Q. P. (1993). Epidemiological studies on primary Sjogren's syndrome. *Zhonghua Nei Ke Za Zhi* 32, 522–524.

Zhao, R., Wang, Y., Zhou, W., Guo, J., He, M., Li, P., et al. (2020). Associated factors with interstitial lung disease and health-related quality of life in Chinese patients with primary Sjogren's syndrome. *Clin. Rheumatol.* 39, 483–489. doi:10.1007/s10067-019-04753-5



OPEN ACCESS

EDITED BY

Grzegorz Węgrzyn,
University of Gdansk, Poland

REVIEWED BY

Dharmendra Kumar Pipal,
All India Institute of Medical Sciences
Gorakhpur, India
Zhibo Qu,
Guangdong Medical University, China

*CORRESPONDENCE

Yiting Cai,
✉ yitingcai@protonmail.com

RECEIVED 05 November 2023

ACCEPTED 31 January 2024

PUBLISHED 19 March 2024

CITATION

Gao M, Chen M, Dai G, Zhu D and Cai Y
(2024), Clinical study: the impact of
goal-directed fluid therapy on volume
management during enhanced
recovery after surgery in
gastrointestinal procedures.
Acta Biochim. Pol. 71:12377.
doi: 10.3389/abp.2024.12377

COPYRIGHT

© 2024 Gao, Chen, Dai, Zhu and Cai.
This is an open-access article
distributed under the terms of the
Creative Commons Attribution License
(CC BY). The use, distribution or
reproduction in other forums is
permitted, provided the original
author(s) and the copyright owner(s) are
credited and that the original
publication in this journal is cited, in
accordance with accepted academic
practice. No use, distribution or
reproduction is permitted which does
not comply with these terms.

Clinical study: the impact of goal-directed fluid therapy on volume management during enhanced recovery after surgery in gastrointestinal procedures

Ming Gao, Minggan Chen, Gang Dai, Dengfeng Zhu and
Yiting Cai*

Department of Gastrointestinal Surgery, Chongming Hospital Affiliated to Shanghai University of
Medicine and Health Sciences, Shanghai, China

Background: Goal-directed fluid therapy, as a crucial component of accelerated rehabilitation after surgery, plays a significant role in expediting postoperative recovery and enhancing the prognosis of major surgical procedures.

Methods: In line with this, the present study aimed to investigate the impact of target-oriented fluid therapy on volume management during ERAS protocols specifically for gastrointestinal surgery. Patients undergoing gastrointestinal surgery at our hospital between October 2019 and May 2021 were selected as the sample population for this research.

Results: 41 cases of gastrointestinal surgery patients were collected from our hospital over 3 recent years. Compared with T1, MAP levels were significantly increased from T2 to T5; cardiac output (CO) was significantly decreased from T2 to T3, and significantly increased from T4 to T5; and SV level was significantly increased from T3 to T5. Compared with T2, HR and cardiac index (CI) were significantly elevated at T1 and at T3–T5. Compared with T3, SVV was significantly decreased at T1, T2, T4, and T5; CO and stroke volume (SV) levels were increased significantly at T4 and T5. In this study, pressor drugs were taken for 23 days, PACU residence time was 40.22 ± 12.79 min, time to get out of bed was 12.41 ± 3.97 h, exhaust and defecation time was 18.11 ± 7.52 h, and length of postoperative hospital stay was 4.47 ± 1.98 days. The average HAMA score was 9.11 ± 2.37 , CRP levels were 10.54 ± 3.38 mg/L, adrenaline levels were 132.87 ± 8.97 ng/L, and cortisol levels were 119.72 ± 4.08 ng/L. Prealbumin levels were 141.98 ± 10.99 mg/L at 3 d after surgery, and 164.17 ± 15.84 mg/L on the day of discharge. Lymphocyte count was 1.22 ± 0.18 (10^9 /L)

Abbreviations: ERAS, enhanced recovery after surgery; TAP, transabdominal plane; GDFT, goal-directed fluid therapy; CO, cardiac output; CI, cardiac index; SV, stroke volume; SVV, stroke volume variation; MAP, mean arterial pressure; HR, heart rate.

at 3 d after surgery, and 1.47 ± 0.17 (10^9 /L) on the day of discharge. Serum albumin levels were 30.51 ± 2.28 (g/L) at 3 d after surgery, and 33.52 ± 2.07 (g/L) on the day of discharge.

Conclusion: Goal-directed fluid therapy (GDFT) under the concept of Enhanced Recovery After Surgery (ERAS) is helpful in volume management during radical resection of colorectal tumors, with good postoperative recovery. Attention should be paid to the influence of pneumoperitoneum and intraoperative posture on GDFT parameters.

KEYWORDS

accelerated rehabilitation surgery, goal-directed fluid therapy, volume variation, cardiac index, pneumoperitoneum, fluid supplement volume, vasoactive drug

Introduction

During gastrointestinal surgery, patients are influenced by various factors, such as their psychological state, anesthesia, surgical procedures, and pain. As a result, they may experience different levels of illness-related effects. These effects manifest in the form of a robust surgical stress response, leading to the production of significant amounts of stress hormones in patients' bodies. Consequently, symptoms such as elevated blood pressure, inadequate oxygen supply, and accelerated heart rate may arise, ultimately impacting the surgical outcomes (Pu et al., 2020; Daca-Alvarez et al., 2022; Ding et al., 2022; Erdem et al., 2022). Therefore, it is particularly important to implement effective perioperative management for patients undergoing gastrointestinal surgery (Ayala et al., 2022).

Fluid therapy plays a crucial role in ensuring the safety of patients during surgery and facilitating postoperative recovery within the context of Enhanced Recovery After Surgery (ERAS) protocols (Ashok et al., 2020). Consequently, this factor has garnered significant attention not only from surgeons but also from anesthesiologists (Feldheiser et al., 2016). In recent years, with the widespread adoption of the ERAS concept, there has been a surge in the number of medium-to high-risk patients requiring surgical interventions, as well as an increase in the complexity and volume of surgeries performed. This trend has led to a growing interest among scholars in exploring and researching various aspects of fluid therapy (Gustafsson et al., 2019). Building upon traditional fluid replacement and restrictive fluid therapy approaches, the concept of goal-directed fluid therapy (GDFT), which offers more precise and accurate administration, has gained widespread recognition (Arena et al., 2021).

GDFT, or goal-directed fluid therapy, refers to an individualized rehydration approach that relies on monitoring hemodynamic indicators to assess the body's fluid requirements (Di et al., 2020). The effectiveness of GDFT within the ERAS framework often hinges on various common risk factors associated with both the surgery and the patient (Giusto et al.,

2021). Previous research has demonstrated that personalized GDFT during surgical procedures can yield significant benefits for patients categorized as medium-to-high risk (Bisgaard et al., 2020; Jiang et al., 2021). Consequently, recent studies have primarily focused on investigating the application of GDFT in ERAS protocols for major surgery involving middle- and high-risk patients (Aaen et al., 2021). This present study aimed to examine the impact of goal-directed fluid therapy on volume management during ERAS in gastrointestinal surgery.

Materials and methods

General information

This study was approved by the Medical Ethics Committee of our hospital (NO: 2020051617), and all patients signed an informed consent form. Adult patients who were scheduled to undergo surgery in Gastrointestinal Procedures under general anesthesia from October 2019 to May 2021 were selected, regardless of gender and ASA score (class I or II).

Exclusion criteria

Severe uncontrolled cardiovascular, endocrine, or respiratory disease; severe digestive tract obstruction; significant liver and kidney dysfunction; abnormal blood coagulation function; contraindications for artery puncture and central vein catheterization prior to surgery; severe nervous system disease; abnormal mental states; inability to communicate normally.

Exit criteria

Active request by the patient to withdraw during the study; failure to effectively cooperate with the treatment plan, leading to the failure of normal research protocols; serious accidents during

treatment; transfer to an intensive care unit (ICU) for monitoring and treatment after operation.

Before the withdrawal of any subject, the reason for withdrawal was recorded accurately, and a new subject was not included instead.

Procedures under the research program

Before the surgery, the doctor informed the patient about possible anesthesia methods, possible complications and solutions during anesthesia, and postoperative analgesia strategy. One day before surgery, the patient took laxatives orally to clean the intestines, without undergoing mechanical enema. Solid food was fasted from 6 h before the operation; 2 hours before anesthesia induction, patients took 4 mL/kg of multidimensional carbohydrate drink orally (surgical energy).

After entering the room, patients were monitored for non-invasive blood pressure, electrocardiogram, SpO₂, respiratory rate, and body temperature; depth of anesthesia was monitored using a Narcotrend monitor. A FloTrac/Vigileo sensor was connected after radial artery catheterization under local anesthesia to monitor cardiac output (CO), cardiac index (CI), stroke volume (SV), and stroke volume variation (SVV). Before anesthesia induction, midazolam 0.05 mg/kg, pentoxifylline hydrochloride 0.4–0.6 mg, and lansoprazole 30 mg were injected intravenously. Anesthesia induction consisted of etomidate 0.3 mg/kg, sufentanil 0.4–0.6 μ g/kg, cisatracurium 0.15 mg/kg, and mask-assisted respiration, nitrogen removal, and oxygen delivery; the anesthesia machine was connected after endotracheal intubation, with respiratory parameters FiO₂ 30%–50%, tidal volume 6–8 mL/kg, respiratory rate 12–15 times/min, and I:E = 1:2. Subsequently, the right subclavian vein was punctured and catheterized. Ultrasound-guided transabdominal plane (TAP) block was given at the head end of the bilateral iliac crest, with 0.375% ropivacaine 20 mL on each side. Propofol rate was 3–6 mg/(kg/h), remifentanyl was 0.05–0.2 μ g/(kg/min), and 1%–1.5% sevoflurane was inhaled. During the operation, the concentration of sevoflurane was adjusted according to the Narcotrend value, and the Narcotrend value was maintained at 37–45. Muscle relaxants were added according to the needs of the operation. Ulinastatin 5 000 U/kg was injected into the crystal solution during the operation.

Fluid management plan

(1) (Daca-Alvarez et al., 2022) Compensatory dilatation (5 mL/kg) was supplemented 30 min before anesthesia induction. Crystalloid solution (Ringer Lactate) was used as the background infusion. Before laparotomy, crystalloid solution (2 mL/kg/h) was input. At the laparotomy stage, 5 mL/(kg/h) was used as the background infusion until the

end of the operation (Ding et al., 2022). SVV \leq 13% was taken as the reference range of volume reactivity. If SVV > 13% at a measured time point, this was defined as a low-volume time point, and volume-loading treatment was carried out: that is, 150 mL of hydroxyethyl starch 130/0.4 sodium chloride injection was given intravenously for 10 min, and SVV was re-evaluated until SVV \leq 13%. If SVV \leq 13% at a measured time point, CI was further evaluated. (Erdem et al., 2022). If CI < 2.5 L/(min/m²), dobutamine 2.5–10 μ g/(kg/min) was used. When the heart rate (HR) was higher than 100 beats/min, dobutamine was reduced or stopped. (Pu et al., 2020). Central venous oxygen saturation (ScvO₂) was evaluated. When ScvO₂ < 73% and Hb < 10 g/dL, concentrated red blood cells were infused to bring Hb \geq 10 g/dL. If it was still the case that ScvO₂ < 73%, dobutamine 2.5–20 μ g/(kg • min) was used until ScvO₂ \geq 73%.

Intraoperative management and analgesia plan

When MAP < 65 mmHg, intravenous infusion of norepinephrine 40 μ g was administered; arterial blood samples were taken every 60 min for blood gas analysis. During the operation, blood glucose was maintained between 5.6 and 10 mmol/L. During the operation, central temperature (nasopharynx temperature) was maintained no lower than 36°C by means of air heater and liquid heating; this was maintained until the patient was transferred back to the ward. Before the end of the operation, 5 mg of dizosine, 6 mg of tropisetron, 5 mg of dexamethasone, 1.5 mg of droperidol, and 0.375% ropivacaine were given for local infiltration anesthesia.

The PCIA formula for postoperative analgesia consisted of deszocin 0.4–0.5 mg/kg, flurbiprofen lipid 5 mg/kg, tropisetron 12–18 mg, background dose 2 mL/h, pressing dose 0.5 mL, locking time 15 min. After the operation, the patient was decannulated and transferred to the PACU. Once the patient was awake, respiration and circulation were stable, and VAS was less than 3 points, he was transferred back to the ward.

Observed indicators

Mean arterial pressure (MAP), HR, CO, CI, SV, and SVV were recorded after endotracheal intubation (T1), after skin incision (T2), 60 min after pneumoperitoneum (T3), 5 min after laparotomy (T4), at the end of surgery (T5). For this study, the intraoperative fluid infusion volume (crystalloid/colloid), intraoperative blood loss, surgical duration, and amount of vasoactive drugs used during the procedure were recorded. The patient's time of awakening, status of gas/bowel movements, and postoperative hospital stay were also documented.

TABLE 1 General information of gastrointestinal surgery.

Group	
Number	41
Age	61.56 ± 10.74
Sex	23 (Man)/18 (Woman)
BMI	23.52 ± 3.52
Cancer category	
Colon cancer	28
Rectal cancer	13
ASA	
ASA-I	17
ASA-II	24

Statistical methods

SPSS 21.0 statistical software was used for statistical analysis. Measurement variables that followed a normal distribution are expressed in the form of $\bar{x} \pm s$, and repeated-measures ANOVA was used to compare different time points. Differences were regarded as statistically significant if $p < 0.05$.

Results

Comparison of patient characteristics

A total of 41 patients who underwent gastrointestinal surgery at our hospital were included in this study, covering a span of 3 years. Table 1 presents demographic data for the patients, including gender, age, and disease type. Statistical analysis revealed no significant differences in these variables among the patient groups ($p > 0.05$).

Hemodynamic changes during surgery

In comparison to the baseline measurement (T1), there was a significant increase in mean arterial pressure (MAP) from T2 to T5 ($p < 0.05$, Table 2). Cardiac output (CO) was significantly decreased from T2 to T3, but notably increased from T4 to T5 ($p < 0.05$, Table 2). Stroke volume (SV) levels exhibited a significant increase from T3 to T5 ($p < 0.05$, Table 2). Heart rate (HR) and cardiac index (CI) were significantly higher at T1 and T3–T5 than at T2 ($p < 0.05$, Table 1). Moreover, systolic volume variation (SVV) was significantly decreased at T1, T2, T4, and T5 in comparison to T3 ($p < 0.05$, Table 2). At T4 and T5, both CO and SV demonstrated a significant increase ($p < 0.05$, Table 2). These data indicate that GDFT-significant hemodynamic changes were observed during the surgical procedure. GDFT can significantly improve postoperative cardiac function and has potential cardiac protective effects.

Postoperative follow-up

The duration of pressor drug administration was recorded as 23 days in this study. The average time spent in the post-anesthesia care unit (PACU) was 40.22 ± 12.79 min, while the time taken for patients to mobilize and get out of bed was 12.41 ± 3.97 h. The interval prior to bowel movement/defecation was observed to be 18.11 ± 7.52 h. The average length of the postoperative hospital stay was determined to be 4.47 ± 1.98 days (Table 3). GDFT can significantly improve the duration of PACU stay, time to mobilize and get out of bed, and length of hospital stay.

Surgical stress indices

Assessment of surgical stress indices revealed an average HAMA score of 9.11 ± 2.37 . Additionally, C-reactive protein (CRP) levels were measured at 10.54 ± 3.38 mg/L, adrenaline levels at 132.87 ± 8.97 ng/L, and cortisol levels at $119.72 \pm$

TABLE 2 Hemodynamic changes during operation.

Group	T1	T2	T3	T4	T5
MAP (mmHg)	80.55 ± 8.31	82.61 ± 7.22*	85.22 ± 10.11*	84.97 ± 7.25*	87.91 ± 6.21*
HR (time/min)	62.32 ± 8.95#	57.74 ± 6.95	60.04 ± 6.68#	66.85 ± 10.05#	61.96 ± 8.52#
CO (L/min)	3.85 ± 0.61	3.22 ± 0.52*	3.84 ± 0.69*	4.33 ± 0.56* ^s	4.07 ± 0.53* ^s
CI [L/(min/m ²)]	2.77 ± 0.71#	2.33 ± 0.84	3.03 ± 0.74#	2.71 ± 0.42#	2.75 ± 0.66#
SV (mL)	58.97 ± 9.11	56.19 ± 8.87	62.53 ± 9.01*	66.05 ± 7.74* ^s	64.18 ± 9.28* ^s
SVV (%)	11.35 ± 2.98 ^s	12.98 ± 3.31 ^s	13.53 ± 3.37	10.35 ± 2.57 ^s	9.42 ± 2.99 ^s

*Compared with T1, $p < 0.05$; # compared with T2, $p < 0.05$; ^scompared with T3, $p < 0.05$.

TABLE 3 Postoperative follow-up.

Group	
Pressor drug	23
PACU residence time (min)	40.22 ± 12.79
Time for getting out of bed (h)	12.41 ± 3.97
Exhaust and defecation time (h)	18.11 ± 7.52
Postoperative hospital stay (day)	4.47 ± 1.98

TABLE 4 Surgical stress indexes.

Group	
HAMA (Score)	9.11 ± 2.37
CRP (mg/L)	10.54 ± 3.38
Adrenaline (ng/L)	132.87 ± 8.97
Cortisol (ng/L)	119.72 ± 4.08

4.08 ng/L (Table 4). GDFT can significantly improve surgical stress index measurements.

Nutritional status

Regarding patients' nutritional status, prealbumin levels were found to be 141.98 ± 10.99 mg/L at 3 days after surgery; levels increased to 164.17 ± 15.84 mg/L on the day of discharge from the hospital (Table 5). Lymphocyte counts at 3 days after surgery were reported as 1.22 ± 0.18 (10⁹/L), rising to 1.47 ± 0.17 (10⁹/L) on the day of discharge (Table 5). Serum albumin levels at 3 days after surgery were recorded as 30.51 ± 2.28 g/L, increasing to 33.52 ± 2.07 g/L on the day of discharge. GDFT can significantly improve postoperative nutritional status.

Discussion

Gastrointestinal surgery is characterized by significant trauma, a high risk of blood loss, and a high proportion of elderly patients or those with multiple comorbidities (Harada et al., 2022). The application of Enhanced Recovery After Surgery (ERAS) principles in gastrointestinal surgery has received extensive scholarly attention, and this framework has been implemented extensively in clinical practice, gradually reaching a mature stage (Jabłońska et al., 2022). However, fluid management during gastrointestinal surgery is critical, as both fluid overload and inadequate circulating blood volume can have adverse effects on patient outcomes. Specifically, fluid

TABLE 5 Nutritional status.

Group	
Prealbumin (mg/L)	
3 d after surgery	141.98 ± 10.99
The day of leave hospital	164.17 ± 15.84
Lymphocyte count (×10⁹ L)	
3 d after surgery	1.22 ± 0.18
The day of leave hospital	1.47 ± 0.17
Serum albumin (g/L)	
3 d after surgery	30.51 ± 2.28
The day of leave hospital	33.52 ± 2.07

overload can lead to an increased incidence of postoperative complications such as anastomotic leakage and delayed recovery of gastrointestinal function (Pu et al., 2021; Lata et al., 2022). Conversely, insufficient effective circulating blood volume can result in inadequate tissue perfusion, hypoxia, and an elevated risk of postoperative complications and mortality (Mao et al., 2022). In gastrointestinal surgery, devices such as Esophageal Doppler (ED) and FloTrac/Vigileo, among others, are commonly used for real-time monitoring of stroke volume (SV), systolic volume variation (SVV), and pulse pressure variation (PPV) to assess dynamic changes in fluid status and optimize fluid management (Ross et al., 2022). In this study, we collected data from 41 patients who underwent gastrointestinal surgery at our hospital over the past 3 years. Table 1 presents the general characteristics of these patients, including gender, age, and disease type. Makaryus et al. showed that optimization of perioperative fluid management is crucial for Enhanced Recovery Pathways (ERPs), as this helps improve lung function, tissue oxygenation, gastrointestinal motility, and wound healing (Makaryus et al., 2018). Therefore, in this study, data were collected from 41 patients who underwent gastrointestinal surgery to examine the impact of goal-directed fluid therapy on volume management during ERAS in gastrointestinal surgery.

While there has been limited research on the application of goal-directed fluid therapy (GDFT) in gastrointestinal surgery under the ERAS framework, it is worth noting that existing studies have small sample sizes and provide only weak evidence (Scott et al., 2015; Pędziwiatr et al., 2018; Low et al., 2019). Intraoperative GDFT plays a crucial role in perioperative fluid therapy within the ERAS management approach (Sica et al., 2020). Most studies related to ERAS include intraoperative GDFT as a component (Wobith and Weimann, 2021). Therefore, this article aimed to review and discuss the current application and research progress of GDFT in gastrointestinal

surgery within the context of ERAS, drawing on high-quality studies. In this study, we observed a significant increase in mean arterial pressure (MAP) from T2 to T5, while cardiac output (CO) was decreased from T2 to T3 but increased from T4 to T5. Grass et al. showed that among these 5,155 patients, 2,320 patients (45.1%) received more than 3 L of intravenous fluids on postoperative day 0 (Grass et al., 2020). Thus, these data also show the encouraging efforts of GDFT, as it has been found to be associated with better outcomes and indicates potential for customization in specific patient populations.

Goal-directed fluid therapy (GDFT) utilizes various observational indicators, including traditional static measurements such as SvO₂, central venous pressure, pulmonary capillary wedge pressure, and lactic acid, as well as functional hemodynamic indicators such as stroke volume (SV), SV variation (Δ SV), systolic volume variation (SVV), and pulse pressure variation (PPV) (Wobith and Weimann, 2021). Recently, there has been a growing interest in studying SV, Δ SV, SVV, and PPV, and similar parameters measured by equipment such as the FloTrac/Vigileo and LiDCO, as they provide new insights into the cardiac preload of the body (Joosten et al., 2021). It is important to note that SVV or PPV should be evaluated when patients are mechanically ventilated and free from complications such as thoracotomy, arrhythmia, or myocardial disease. In contrast, SV and Δ SV are not influenced by tidal volume or rhythm and can be evaluated in awake patients or those with arrhythmias (Liu et al., 2021). In our study, we observed a significant increase in SV from T3 to T5, while HR and cardiac index (CI) values were notably elevated at T1 and T3–T5. Moreover, CO and SV demonstrated a significant increase at T4 and T5. Makaryus et al. showed that GDFT improves blood flow intraoperatively, and ultimately reduce LOS and complications (Makaryus et al., 2018). Therefore, this treatment method improves pulmonary function, tissue oxygenation, gastrointestinal motility, and wound healing. The clinical demand for evidence-based Enhanced Recovery After Surgery (ERAS) programs is increasing with the rise in the number of patients undergoing major surgeries with medium to high risk levels (McLain et al., 2021). Early research on ERAS has shown that optimizing intraoperative fluid management can significantly benefit patients (Mizunoya et al., 2019). The debate surrounding intraoperative fluid management schemes has evolved from traditional rehydration approaches to restrictive rehydration and ultimately to individualized goal-directed fluid therapy (GDFT) supported by evidence-based medicine (Mohammed El-Hadi Shoukat Mohammed et al., 2021). Numerous high-quality studies have demonstrated the significant advantages of GDFT for medium-to high-risk patients undergoing major surgery, including a reduction in the incidence and mortality of postoperative complications, shorter hospital stays, lower medical costs, faster postoperative recovery, and improved quality of life, aligning with the principles of ERAS (Rollins et al., 2020). It is worth noting

that perioperative fluid management under the ERAS model should encompass the entire diagnostic and treatment process, including the stages before, during, and after surgery, as fluid management at each stage can significantly impact patient prognosis (Turi et al., 2021). In this study, the duration of pressor drug administration was recorded as 23 days, while the average time spent in the post-anesthesia care unit (PACU) was 40.22 ± 12.79 min. Patients took an average of 12.41 ± 3.97 h to mobilize and get out of bed, and 18.11 ± 7.52 h for bowel movements/defecation; the average length of the postoperative hospital stay was 4.47 ± 1.98 days. Additionally, the average HAMA score was determined to be 9.11 ± 2.37 ; CRP levels were measured at 10.54 ± 3.38 mg/L, adrenaline levels at 132.87 ± 8.97 ng/L, and cortisol levels at 119.72 ± 4.08 ng/L. Lee et al. reported that goal-directed fluid therapy is associated with earlier progression to a postoperative soft diet, reduced acute postoperative pain intensity, and less rescue analgesics (Lee et al., 2021). Thus, these data also illustrate the fact that goal-directed fluid therapy leads to better postoperative recovery and a better renal protective effect.

However, it is important to acknowledge that inappropriate treatment at any stage of the diagnostic and treatment process can undermine the entire ERAS pathway and affect the final outcome (Turi et al., 2022). This article has primarily focused on intraoperative fluid management within the ERAS framework, without delving into preoperative and postoperative fluid management schemes (Virág et al., 2022). Due to the current medical model and the roles assigned in implementing the overall ERAS program, anesthesiologists are primarily responsible for controlling and accurately managing the intraoperative stages of fluid management, while preoperative and postoperative fluid management is often carried out by surgeons (Xie et al., 2021). This approach contradicts the concept of continuous and unified fluid management advocated by anesthesiologists during the perioperative period (Weinberg et al., 2019; Zorrilla-Vaca et al., 2021). Regarding nutritional status, in this study, prealbumin levels were found to be 141.98 ± 10.99 mg/L at 3 days after surgery, increasing to 164.17 ± 15.84 mg/L upon discharge from the hospital. Lymphocyte counts at 3 days after surgery were reported to be 1.22 ± 0.18 (10⁹/L), increasing to 1.47 ± 0.17 (10⁹/L) on the day of discharge. Serum albumin levels at 3 days after surgery were recorded as 30.51 ± 2.28 g/L, increasing to 33.52 ± 2.07 g/L on the day of discharge. These data indicate that goal-directed fluid therapy has a better effect at discharge.

While the concept of perioperative fluid management has been established for some time, its implementation in clinical practice lacks uniformity within the current medical development model. However, with the emergence of perioperative medicine as a specialized discipline, it is expected that a standardized approach to managing the perioperative process will be developed in the future. This may enable anesthesiologists to implement continuous and

consistent fluid management for patients undergoing elective surgery.

It is worth mentioning that this article has specifically focused on the application of GDFT in gastrointestinal surgeries under the ERAS model, without covering its utilization in other areas. Additionally, this article has not delved extensively into preoperative and postoperative fluid management schemes and their impact on patients. Finally, due to the limited sample size of 41 cases from the author's institution, further validation through larger-scale studies is required to confirm the findings of this study.

Data availability statement

The raw data supporting the conclusion of this article will be made available by the authors, without undue reservation.

Ethics statement

The studies involving humans were approved by the Ethics Committee of the Chongming Hospital Affiliated to Shanghai University of Medicine and Health Sciences. The studies were conducted in accordance with the local legislation and

institutional requirements. Written informed consent for participation in this study was provided by the participants' legal guardians/next of kin.

Author contributions

MG designed the experiments. MC and GD performed the experiments. DZ and YC collected and analyzed the data. MC and YC drafted manuscript. All authors contributed to the article and approved the submitted version.

Funding

This study was supported by the Project of Shanghai Chongming District Science and Technology Commission (No. CKY2022-01).

Conflict of interest

The authors declare that the research was conducted in the absence of any commercial or financial relationships that could be construed as a potential conflict of interest.

References

- Aaen, A. A., Voldby, A. W., Storm, N., Kildsig, J., Hansen, E. G., Zimmermann-Nielsen, E., et al. (2021). Goal-directed fluid therapy in emergency abdominal surgery: A randomised multicentre trial. *Br. J. Anaesth.* 127, 521–531. doi:10.1016/j.bja.2021.06.031
- Arena, S., Di Fabrizio, D., Impellizzeri, P., Gandullia, P., Mattioli, G., and Romeo, C. (2021). Enhanced recovery after gastrointestinal surgery (ERAS) in pediatric patients: A systematic review and meta-analysis. *J. Gastrointest. Surg.* 25, 2976–2988. doi:10.1007/s11605-021-05053-7
- Ashok, A., Niyogi, D., Ranganathan, P., Tandon, S., Bhaskar, M., Karimundackal, G., et al. (2020). The enhanced recovery after surgery (ERAS) protocol to promote recovery following esophageal cancer resection. *Surg. Today* 50, 323–334. doi:10.1007/s00595-020-01956-1
- Ayala, D., González T, J., Pedroza, F., Rey Chaves, C. E., Conde, D., and Sabogal Olarte, J. C. (2022). Hemosuccus pancreaticus as an unusual cause of upper gastrointestinal bleeding: case report and literature review. *Int. J. Surg. Case Rep.* 99, 107624. doi:10.1016/j.ijscr.2022.107624
- Bisgaard, J., Madsen, R., Dybdal, L. L., Lauridsen, J. T., Mortensen, M. B., and Jensen, A. G. (2020). Goal-directed therapy with bolus albumin 5% is not superior to bolus ringer acetate in maintaining systemic and mesenteric oxygen delivery in major upper abdominal surgery: a randomised controlled trial. *Eur. J. Anaesthesiol.* 37, 491–502. doi:10.1097/eja.0000000000001151
- Daca-Alvarez, M., Martí, M., Spinelli, A., de Miranda, NFFC, Palles, C., Vivas, A., et al. (2022). Familial component of early-onset colorectal cancer: opportunity for prevention. *Br. J. Surg.* 109, 1319–1325. doi:10.1093/bjs/znac322
- Di, L. L., Wang, Y. X., Ma, S. X., Wu, W., Sun, N., Wang, Z., et al. (2020). The effect of goal-directed fluid therapy combines closed-loop anesthesia management on postoperative rehabilitation of patients undergoing laparoscopic pancreaticoduodenectomy. *J. Clin. Anesth.* 60, 115–117. doi:10.1016/j.jclinane.2019.09.005
- Ding, P., Guo, H., Sun, C., Chen, S., Yang, P., Tian, Y., et al. (2022). Serum creatinine/cystatin C ratio is a systemic marker of sarcopenia in patients with gastrointestinal stromal tumours. *Front. Nutr.* 9, 963265. doi:10.3389/fnut.2022.963265
- Erdem, H., Gencturk, M., Emir, S., Sisik, A., and Sozen, S. (2022). Incidental detection of gastrointestinal stromal tumors during laparoscopic sleeve gastrectomy. What to do? *Ann. Ital. Chir.* 11.
- Feldheiser, A., Aziz, O., Baldini, G., Cox, B. P. B. W., Fearon, K. C. H., Feldman, L. S., et al. (2016). Enhanced recovery after surgery (ERAS) for gastrointestinal surgery, part 2: consensus statement for anaesthesia practice. *Acta Anaesthesiol. Scand.* 60, 289–334. doi:10.1111/aas.12651
- Giusto, G., Vercelli, C., and Gandini, M. (2021). Comparison of liberal and goal-directed fluid therapy after small intestinal surgery for strangulating lesions in horses. *Veterinary Rec.* 188, e5. doi:10.1002/vetr.5
- Grass, F., Hübner, M., Mathis, K. L., Hahnloser, D., Dozois, E. J., Kelley, S. R., et al. (2020). Challenges to accomplish stringent fluid management standards 7 years after enhanced recovery after surgery implementation-The surgeon's perspective. *Surgery* 168, 313–319. doi:10.1016/j.surg.2020.01.019
- Gustafsson, U. O., Scott, M. J., Hubner, M., Nygren, J., Demartines, N., Francis, N., et al. (2019). Guidelines for perioperative care in elective colorectal surgery: enhanced recovery after surgery (ERAS[®]) society recommendations: 2018. *World J. Surg.* 43, 659–695. doi:10.1007/s00268-018-4844-y
- Harada, H., Ohashi, M., Hiki, N., Fujisaki, J., Hirasawa, T., Yamamoto, Y., et al. (2022). Excellent oncological outcomes besides short-term safety of laparoscopic and endoscopic cooperative surgery for gastric gastrointestinal stromal tumor. *Endosc. Int. Open* 10, E1254–E1260. doi:10.1055/a-1895-9507
- Jabłońska, B., Szmigiel, P., Wosiewicz, P., Baron, J., Szczesny-Karczewska, W., and Mrowiec, S. (2022). A jejunal gastrointestinal stromal tumor with massive gastrointestinal hemorrhage treated by emergency surgery: a case report. *Med. Baltim.* 101, e30098. doi:10.1097/md.00000000000030098
- Jiang, Z., Chen, J., Gao, C., Tan, M., Zhang, W., and Xie, Y. (2021). Effects of PICCO in the guidance of goal-directed fluid therapy for gastrointestinal function after cytoreductive surgery for ovarian cancer. *Am. J. Transl. Res.* 13, 4852–4859.
- Joosten, A., Van der Linden, P., Vincent, J. L., and Duranteau, J. (2021). Goal-directed fluid therapy for oesophagectomy surgery. *Br. J. Anaesth.* 126, e54–e55. doi:10.1016/j.bja.2020.10.025

- Lata, T., Peacock, T., Limmer, A., Tan, J. E., Wu, S., and Yeh, D. (2022). Impact of inter-hospital transfer on success of angioembolization for lower gastrointestinal bleeding. *ANZ J. Surg.* 92, 3242–3246. doi:10.1111/ans.18054
- Lee, K. Y., Yoo, Y. C., Cho, J. S., Lee, W., Kim, J. Y., and Kim, M. H. (2021). The effect of intraoperative fluid management according to stroke volume variation on postoperative bowel function recovery in colorectal cancer surgery. *J. Clin. Med.* 10, 1857. doi:10.3390/jcm10091857
- Liu, X., Zhang, P., Liu, M. X., Ma, J. L., Wei, X. C., and Fan, D. (2021). Preoperative carbohydrate loading and intraoperative goal-directed fluid therapy for elderly patients undergoing open gastrointestinal surgery: A prospective randomized controlled trial. *BMC Anesthesiol.* 157. doi:10.1186/s12871-021-01377-8
- Low, D. E., Allum, W., De Manzoni, G., Ferri, L., Immanuel, A., Kuppusamy, M., et al. (2019). Guidelines for perioperative care in esophagectomy: enhanced recovery after surgery (ERAS[®]) society recommendations. *World J. Surg.* 43, 299–330. doi:10.1007/s00268-018-4786-4
- Makaryus, R., Miller, T. E., and Gan, T. J. (2018). Current concepts of fluid management in enhanced recovery pathways. *Br. J. Anaesth.* 120, 376–383. doi:10.1016/j.bja.2017.10.011
- Mao, L., Zhou, S., Liao, J., Zhou, X., and Wang, J. (2022). Effect of wound protectors in reducing the incidence of surgical site wound infection in lower gastrointestinal surgery: a meta-analysis. *Int. Wound J.* 20, 813–821. doi:10.1111/iwj.13928
- McLain, N., Parks, S., and Collins, M. J. (2021). Perioperative goal-directed fluid therapy: a prime component of enhanced recovery after surgery. *AANA J.* 89, 351–357.
- Mizunoya, K., Fujii, T., Yamamoto, M., Tanaka, N., and Morimoto, Y. (2019). Two-stage goal-directed therapy protocol for non-donor open hepatectomy: an interventional before-after study. *J. Anesth.* 33, 656–664. doi:10.1007/s00540-019-02688-4
- Mohammed El-Hadi Shoukat Mohammed, H., Mohamed Hamed El Halafaway, Y., Saad, A., and Mahran, E. (2021). Hypertonic saline for goal-directed therapy guided by capstesia in gastrointestinal surgery: A randomized controlled study. *Anesthesiol. Intensive Ther.* 53, 296–303. doi:10.5114/ait.2021.105771
- Pędzwiatr, M., Mavrikis, J., Witowski, J., Adamos, A., Major, P., Nowakowski, M., et al. (2018). Current status of enhanced recovery after surgery (ERAS) protocol in gastrointestinal surgery. *Med. Oncol.* 35, 95. doi:10.1007/s12032-018-1153-0
- Pu, Z., Xu, M., Yuan, X., Xie, H., and Zhao, J. (2020). Circular RNA circCUL3 accelerates the warburg effect progression of gastric cancer through regulating the STAT3/HK2 Axis. *Mol. Ther. - Nucleic Acids* 22, 310–318. doi:10.1016/j.omtn.2020.08.023
- Pu, Z., Zhang, W., Wang, M., Xu, M., Xie, H., and Zhao, J. (2021). Schisandrin B attenuates colitis-associated colorectal cancer through SIRT1 linked SMURF2 signaling. *Am. J. Chin. Med.* 49, 1773–1789. doi:10.1142/s0192415x21500841
- Rollins, K. E., Mathias, N. C., and Lobo, D. N. (2020). Authors' reply: meta-analysis of goal-directed fluid therapy using transoesophageal Doppler in patients undergoing elective colorectal surgery. *BJS Open* 4, 165. doi:10.1002/bjs.5.02228
- Ross, R. C., Akinde, Y. M., Schauer, P. R., le Roux, C. W., Brennan, D., Jernigan, A. M., et al. (2022). The role of bariatric and metabolic surgery in the development, diagnosis, and treatment of endometrial cancer. *Front. Surg.* 9, 943544. doi:10.3389/fsurg.2022.943544
- Scott, M. J., Baldini, G., Fearon, K. C., Feldheiser, A., Feldman, L. S., Gan, T. J., et al. (2015). Enhanced recovery after surgery (ERAS) for gastrointestinal surgery, part 1: pathophysiological considerations. *Acta Anaesthesiol. Scand.* 59, 1212–1231. doi:10.1111/aas.12601
- Sica, G. S., Campanelli, M., Bellato, V., and Monteleone, G. (2020). Gastrointestinal cancer surgery and enhanced recovery after surgery (ERAS) during COVID-19 outbreak. *Langenbecks Arch. Surg.* 405, 357–358. doi:10.1007/s00423-020-01885-0
- Turi, S., Marmiere, M., and Beretta, L. (2021). Impact of intraoperative goal-directed fluid therapy in patients undergoing transthoracic oesophagectomy. Comment on Br J anaesth 2020; 125: 953-61. *Br. J. Anaesth.* 126, e94–e95. doi:10.1016/j.bja.2020.11.024
- Turi, S., Marmiere, M., and Beretta, L. (2022). Dry or wet? Fluid therapy in upper gastrointestinal surgery patients. *Updat. Surg.* 75, 325–328. doi:10.1007/s13304-022-01352-z
- Virág, M., Rottler, M., Gede, N., Ocskay, K., Leiner, T., Tuba, M., et al. (2022). Goal-directed fluid therapy enhances gastrointestinal recovery after laparoscopic surgery: a systematic review and meta-analysis. *J. Personalized Med.* 12, 734. doi:10.3390/jpm12050734
- Weinberg, L., Mackley, L., Ho, A., McGuigan, S., Ianno, D., Yui, M., et al. (2019). Impact of a goal directed fluid therapy algorithm on postoperative morbidity in patients undergoing open right hepatectomy: A single centre retrospective observational study. *BMC Anesthesiol.* 19, 135. doi:10.1186/s12871-019-0803-x
- Wobith, M., and Weimann, A. (2021). Oral nutritional supplements and enteral nutrition in patients with gastrointestinal surgery. *Nutrients* 13, 2655. doi:10.3390/nut13082655
- Xie, T., Jiang, Z., Wen, C., Shen, D., Bian, J., Liu, S., et al. (2021). Blood metabolomic profiling predicts postoperative gastrointestinal function of colorectal surgical patients under the guidance of goal-directed fluid therapy. *Aging (Albany NY)* 13, 8929–8943. doi:10.18632/aging.202711
- Zorrilla-Vaca, A., Mena, G. E., Ripolles-Melchor, J., Abad-Motos, A., Aldecoa, C., Lorente, J. V., et al. (2021). Goal-directed fluid therapy and postoperative outcomes in an enhanced recovery program for colorectal surgery: a propensity score-matched multicenter study. *Am. Surg.* 87, 1189–1195. doi:10.1177/0003134820973365

Protective effect of tretinoin derivative and TXNRD1 protein on streptozotocin induced gestational diabetes *via* an age-rage signaling-pathway

Wensheng Wang  and Lin Wang

Department of Nursing, Hebi Polytechnic, Changjiang Street QibinHebi, Henan 458030, China

Background: In the present study effect of tretinoin derivative was investigated on the pathogenesis of gestational diabetes mellitus (GDM) in mice model *in vivo*. **Materials and Methods:** Diabetes was induced in mice by injecting Streptozotocin (STZ) for 5 consecutive days at a dose of 65 mg/kg body weight through the intraperitoneal route. Tretinoin derivative was given to the mice at 0.12 and 0.25 mg/kg doses through gavage in normal saline alternately for one week after STZ injection. **Results:** The results demonstrated that tretinoin derivative administration to the diabetic mice significantly ($P<0.05$) alleviated the blood FBG and FINS levels. Administration of tretinoin derivative to the diabetic mice significantly ($P<0.05$) promoted the blood HDL level and alleviated TC and TG levels. The administration of tretinoin derivative to the diabetic mice significantly ($P<0.05$) alleviated the CRP, IL-6 and TNF- α production in pancreatic tissues. Tretinoin derivative administration to the diabetic mice significantly ($P<0.05$) elevated the SOD activity, and CAT level and lowered the MDA level in pancreatic tissues. The TXNRD1 expression in diabetic mice was comparable to that in the normal group after administration of tretinoin derivative at the dose of 0.25 mg/kg dose. *In silico* data demonstrated that tretinoin derivative interacts with TXNRD1 protein with the binding affinity ranging from -10 to 9.4 kcal/mol. **Conclusion:** In conclusion, tretinoin derivative administration effectively regulated streptozotocin-induced changes in fasting blood glucose, insulin level, high-density lipid level and triglyceride level in diabetic mice *in vivo*. The streptozotocin-induced excessive production of C-reactive protein and inflammatory cytokines was also down-regulated in diabetic mice on administration of tretinoin derivative. Therefore, tretinoin derivative can be investigated further as a therapeutic agent for the treatment of gestational diabetes mellitus.

Keywords: Streptozotocin, Cytokines, Gestational diabetes, Triazoles, Antioxidant

Received: 26 July, 2023; revised: 21 October, 2023; accepted: 27 October, 2023; available on-line: 07 December, 2023

 e-mail: hlxy126@126.com

Acknowledgements of Financial Support: The research and practice of "Dual-element" cooperative loose-leaf teaching material development in schools and enterprises—taking "Applied Anatomy of Nursing" as an example; The 2022 Henan Province vocational education reform research and practice project (Grant No. Henan Education [2023]03053). Henan Engineering and Technology Research Center of home care products for the mentally incapacitated elderly; 2022 Henan Engineering and Technology Research Center. Document number: Laboratory and Platform Base Construction Office of Henan Science and Technology Agency [2023] No. 1.

Abbreviations: GDM, Gestational diabetes mellitus; STZ, Streptozotocin; FBS, Fasting plasma glucose; FBI, Fasting blood insulin; CRP, C-reactive protein; IL, Interleukin; TNF- α , Tumor necrosis factor- α

INTRODUCTION

Gestational diabetes mellitus (GDM) is a leading medical complication in pregnant females characterized by high glucose level (Metzger *et al.*, 1998). It has been observed that the bodies of pregnant females react differently to elevated sugar levels. In most cases high blood glucose level during pregnancy leads to miscarriage or premature birth (Metzger *et al.*, 1998). Despite being the leading life threat to pregnant females and their babies the pathogenesis of GDM is yet to be fully known (Johns *et al.*, 2018). Studies have revealed that one of the major factors involved in the development and pathogenesis of GDM is insulin resistance (IR) (Hajifaraji *et al.*, 2018; Sha *et al.*, 2019). Furthermore, the pathogenesis of GDM is complicated by the excessive release of inflammatory factors and induction of oxidative stress pathways during pregnancy (Hajifaraji *et al.*, 2018; Sha *et al.*, 2019). During type-2 diabetes, the expression of the antioxidant gene, thioredoxin reductase-1 cytoplasmic (TXNRD1) is markedly elevated which complicates the disorder (Baig *et al.*, 2020; Nazem *et al.*, 2019). The activity of superoxide dismutase (SOD) is also found to be higher in patients suffering from type-2 diabetes (Baig *et al.*, 2020; Nazem *et al.*, 2019). It is reported that elevated levels of inflammatory factors persistently in pregnant females play a prominent role in the pathogenesis of GDM (Sudharshana *et al.*, 2018).

The TrxR1, a member of the thioredoxin system which is encoded by TXNRD1 plays a vital role in regulating the redox system. It also constitutes an important part of the antioxidant defense system and inhibits Trx expression to maintain the reduced state of intracellular proteins (Cebula *et al.*, 2015). Up-regulation of TXNRD1 plays a crucial role in increasing the resistance of cells to oxidative stress by neutralizing hydrogen peroxide and inactivation of apoptotic pathway. Thus, increasing the expression of TXNRD1 is believed to be of therapeutic significance for the treatment of diabetes (Kabuyama *et al.*, 2008; Chang *et al.*, 2018). The TrxR/Trx system has been demonstrated to be associated with inhibition of oxidative stress, inactivation of apoptosis, DNA synthesis and regulation of NF- κ B pathway (Park *et al.*, 2015; Raninga *et al.*, 2016; Matsui *et al.*, 1996). It is also reported that inflammatory response in cells is regulated by TXNRD1 expression (Shi *et al.*, 2020).

Triazoles are known for various pharmaceutical activities, such as anti-cancer, antioxidant, anti-inflammatory, anti-HIV, anti-diabetic, and anti-protozoal properties. Structural-activity relationship investigations have revealed that the 1,2,3-triazole part is the most active pharmacophoric group in numerous bioactive compounds.

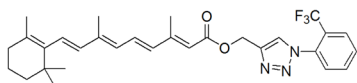


Figure 1. Chemical structure of tretinoin derivative.

The pharmacological activity of 1,2,3-triazoles is mainly attributed to various types of interactions such as hydrogen bonds, van der Waals forces, and dipole–dipole bonds with proteins, enzymes and different receptors in living organisms (Bonandi *et al.*, 2017; Bozorov *et al.*, 2019). The compounds containing 1,2,3-triazole scaffold have been found to exhibit various pharmaceutical activities like antibacterial (Zhang, 2019; Chu *et al.*, 2020), antimalarial (Chu *et al.*, 2019; Feng *et al.*, 2020), anti-tubercular (Yan *et al.*, 2020), anti-viral (Feng *et al.*, 2021), and anti-cancer (Slavova *et al.*, 2020) properties. The present study was designed to investigate the therapeutic effect of a tretinoin derivative on gestational diabetes mellitus and understand the underlying mechanism.

MATERIALS AND METHODS

Mice model of gestational diabetes

Male C57BL/6 mice eighty in number (body weight 18–30 g and around 10 weeks old) were supplied by the Experimental Animal Center belonging to the Hospital in Shanghai, China [Registration number 09/2020]. The mice were kept in cages in the animal center at a regulated temperature of $24 \pm 1^\circ\text{C}$, humidity of 65%, and exposed to 12/12-hour light/dark cycles. Mice in the normal group were fed a normal diet and those in the model GDM groups were given fat rich and sucrose diet. The animal experimental procedures were conducted in compliance with the guidelines of the institutional laboratory and Guide of the National Institute of Health for Care and Use of Laboratory Animals [Ethical clearance certificate number 102/2020].

The female mice were caged overnight with male mice at the proestrus stage and microscopy was performed to confirm the pregnancy on the following day. Diabetes was induced in mice by injecting STZ (Sigma-Aldrich, St. Louis, MO, USA) for 5 consecutive days at a dose of 65 mg/kg body weight through intraperitoneal route. Induction of diabetes in mice was confirmed by measuring the glucose blood for 8 weeks after STZ injection. The mice having elevated level of blood glucose (16.7 mmol/L) and suffering from polyuria, polyphagia and weight loss were considered to be diabetic (John *et al.*, 2012). The mice were divided into four groups of 10 each; normal, model diabetes and two tretinoin derivative treatment (administered with 0.12 and 0.25 mg/kg body weight) groups. Tretinoin derivative was given to the mice by gavage at doses of 0.12 and 0.25 mg/kg in normal saline alternately for one week after STZ injection.

Mice were fasted for 10 hours and then injected with 1% pentobarbital sodium (50 mg/kg) anesthesia after completion of the treatment. The blood samples were collected from the abdominal aorta of the mice for biochemical analysis of the various parameters. The collected blood samples were stored overnight in a refrigerator and then centrifuged at 4°C for 25 minutes at $12000 \times g$ to collect the serum. Tissue samples were extracted from the pancreatic islets and placental for investigation of pathological changes.

Assay for FBG, FINS, IR, HDL and TG determination

The blood samples collected from the mice abdominal aorta were analyzed for FBG level using the commercially available glucose test strips (Nova Biomedical Corporation) according to the supplier's instructions. The enzyme-linked immunosorbent assay kits (Shanghai Hu-zhen Biological Technology Co., Ltd.) were used for the measurement of FINS in the mice blood samples as per manufacturer's guidelines. BK-400 automatic biochemical analyzer (BioBase) was used for the measurement of TG and HDL levels in the mice blood samples. The HOMA-IR was calculated using the reported formula $[\text{FBG (mmol/L)} \times \text{FINS (mU/L)}] / 22.5$.

Measurement of oxidative stress factors in mice pancreatic tissues

The tissue sections from the pancreas of the mice were extracted, sliced into thin sections and then homogenized. The lysate obtained was subjected to centrifugation at $2000 \times g$ for 15 min at 4°C to separate the supernatant for measurement of various oxidative factors. The commercially available UV-visible spectrophotometer assay kits (Beyotime Institute of Biotechnology) were used for the measurement of CAT, MDA levels, and activity of SOD in mice pancreatic tissues.

Western blot analysis

The pancreatic tissue samples of the mice were lysed on treatment with RIPA lysis buffer (Sigma-Aldrich; Merck KGaA) to obtain the tissue lysate. The protein content in the tissue lysates was estimated using the Bradford method. Protein samples (30 μg) in equal quantities were separated on 10% SDS-PAGE gel and then transferred onto the PVDF membranes. Incubation of the membranes was performed with 5% skimmed milk powder for 2 hours at 4°C to block the non-specific sites. Membranes were incubated overnight with anti-CRP (cat. no. ab207756), anti-TNF- α (cat. no. ab205587), anti-IL-6 (cat. no. ab208113), anti-TXNRD1 (cat. no. ab124954) and anti-GAPDH (cat. no. ab9485; all purchased from Abcam) primary antibodies at 4°C . After washing with PBS the membranes were incubated again at room temperature for 1 hour with HRP-conjugated secondary antibodies (cat. no. ab7090; 1:10,000; Abcam). Expression of protein bands was visualized using the Chemiluminescence enhancement reagent (Thermo Fisher Scientific, Inc.) and analyzed by the ImageJ software (version 1.46r; National Institutes of Health).

Statistical analysis

The presented data are the mean \pm S.D. of the three independently conducted experiments. Analysis of the data was performed using the Graph-Pad Prism software (version 8; Graph-Pad Software, Inc.). The difference between the groups was determined using the Student's test and ANOVA followed by Tukey's post hoc test. The values at $P < 0.05$ were considered to represent the statistically significant differences.

RESULTS

Tretinoin derivative administration alleviates FBG and FINS levels in diabetic mice

In diabetic mice, the FBG as well as FINS levels were significantly ($P < 0.05$) elevated in blood compared to the

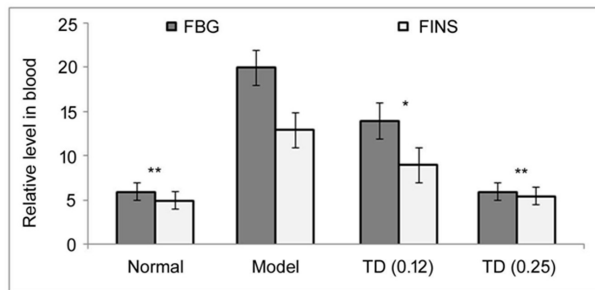


Figure 2. Effect of tretinoin derivative on blood FBG and FINS levels in diabetic mice.

Diabetic mice were administered Tretinoin derivative at 0.12 and 0.25 mg/kg doses or physiological saline (normal and model groups). Commercially available glucose test strips and enzyme-linked immunosorbent assay kits were used for the determination of blood FBG and FINS levels, respectively in mice. * $P<0.05$, ** $P<0.01$ vs model group.

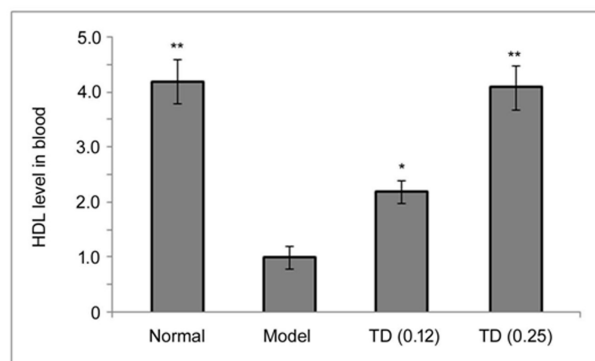


Figure 3. Effect of tretinoin derivative on blood HDL level in diabetic mice.

Diabetic mice were administered tretinoin derivative at 0.12 and 0.25 mg/kg doses or physiological saline (normal and model groups). A commercially available BK-400 automatic biochemical analyzer was used for the determination of blood HDL in mice. * $P<0.05$, ** $P<0.01$ vs model group.

normal group (Fig. 2). Tretinoin derivative administration to the diabetic mice significantly ($P<0.05$) alleviated the blood FBG as well as FINS levels in a dose-dependent manner. The FBG and FINS levels in diabetic mice were reduced more closely to those in the normal group after treatment with 0.25 mg/kg tretinoin derivative compared with the 0.12 mg/kg group.

Tretinoin derivative administration promoted HDL level in diabetic mice

The HDL level showed a significant ($P<0.05$) decrease in blood samples of diabetic mice compared to the normal group (Fig. 3). Administration of tretinoin derivative to the diabetic mice significantly ($P<0.05$) promoted the blood HDL level in a dose-dependent manner. The HDL level in diabetic mice was promoted more comparable to those in the normal group after treatment with tretinoin derivative at a dose of 0.25 mg/kg compared to the group receiving 0.12 mg/kg.

Tretinoin derivative administration alleviates TC and TG levels in diabetic mice

In diabetic mice, the TC and TG levels were significantly ($P<0.05$) elevated in blood compared to the normal group (Fig. 4). Administration of tretinoin derivative to the diabetic mice significantly ($P<0.05$) alleviated the

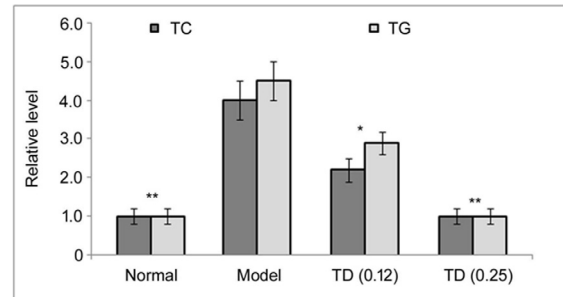


Figure 4. Effect of tretinoin derivative on blood TC and TG levels in diabetic mice.

Diabetic mice were administered tretinoin derivative at 0.12 and 0.25 mg/kg doses or physiological saline (normal and model groups). The BK-400 automatic biochemical analyzer was used for the determination of blood TC and TG levels, respectively in mice. * $P<0.05$, ** $P<0.01$ vs model group.

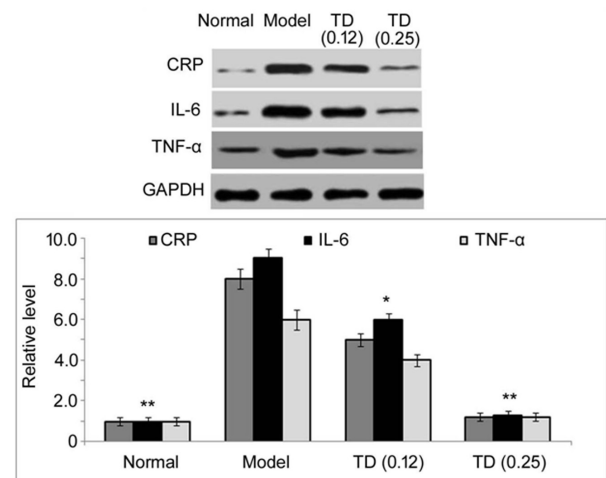


Figure 5. Effect of tretinoin derivative on CRP, IL-6 and TNF-α production in pancreatic tissues of diabetic mice.

Diabetic mice were administered tretinoin derivative at 0.12 and 0.25 mg/kg doses or physiological saline (normal and model groups). Western blotting assay was performed to assess the production of CRP, IL-6 and TNF-α in mice pancreatic tissues. * $P<0.05$, ** $P<0.01$ vs model group.

blood TC and TG levels in a dose-dependent manner. The TC and TG levels in diabetic mice were reduced more comparable to the normal group on treatment with 0.25 mg/kg dose tretinoin derivative compared to the 0.12 mg/kg group.

Tretinoin derivative administration alleviates inflammation of pancreatic islets in diabetic mice

In diabetic mice, the CRP and IL-6 production showed a significant ($P<0.05$) increase in pancreatic tissues compared to the normal group (Fig. 5). Additionally, the TNF-α level in diabetic mice pancreatic tissues was also significantly ($P<0.05$) increased compared to the normal group. However, the administration of tretinoin derivative to the diabetic mice significantly ($P<0.05$) alleviated the CRP and IL-6 production in pancreatic tissues in a dose-dependent manner. The tretinoin derivative administration also suppressed the TNF-α level in diabetic mice pancreatic tissues comparable to the normal group.

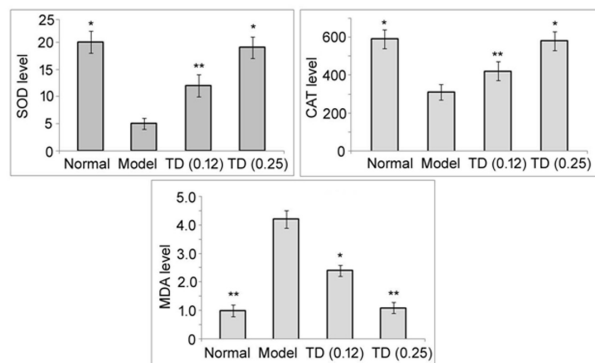


Figure 6. Effect of tretinoin derivative on SOD activity and CAT and MDA levels in pancreatic tissues of diabetic mice.

Diabetic mice were administered tretinoin derivative at 0.12 and 0.25 mg/kg doses or physiological saline (normal and model groups). The UV-visible spectrophotometer was used for the determination of SOD activity and CAT and MDA levels in mice pancreatic tissues. * $P < 0.05$, ** $P < 0.01$ vs model group.

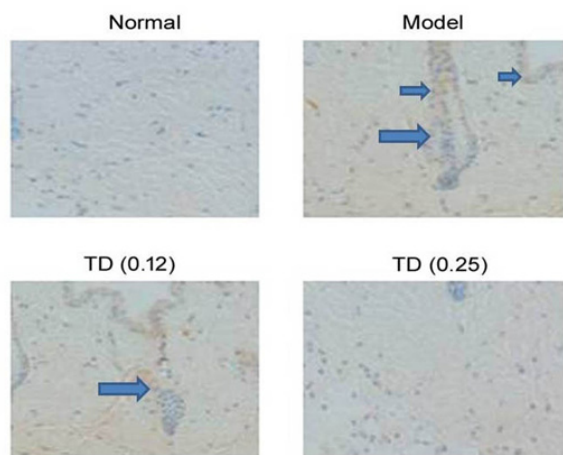


Figure 7. Effect of tretinoin derivative on the expression of AGEs in dermal tissues of diabetic mice.

Diabetic mice were administered tretinoin derivative at 0.12 and 0.25 mg/kg doses or physiological saline (normal and model groups). Immunohistochemical staining was used for the determination of the expression of AGEs in mice.

Tretinoin derivative administration alleviates inflammatory response in diabetic mice

The SOD activity and CAT level showed a significant ($P < 0.05$) decrease in pancreatic tissues of diabetic mice compared to the normal group (Fig. 6). Moreover, the level of MDA showed a significant ($P < 0.05$) increase in diabetic mice pancreatic tissues in comparison to the normal group. Administration of tretinoin derivative to the diabetic mice significantly ($P < 0.05$) elevated the SOD activity and CAT level in pancreatic tissues in a dose-dependent manner. The SOD activity and CAT level in diabetic mice were elevated comparable to the normal group on the administration of 0.25 mg/kg dose of tretinoin derivative. The tretinoin derivative administration lowered the MDA level in diabetic mice pancreatic tissues close to the normal group. The MDA level in diabetic mice pancreatic tissues was lowered to the level of the normal group on administration of tretinoin derivative at 0.25 mg/kg dose.

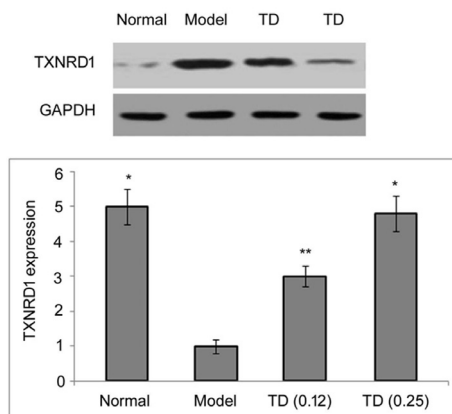


Figure 8. Effect of tretinoin derivative on TXNRD1 expression in serum samples of diabetic mice.

Diabetic mice were administered tretinoin derivative at 0.12 and 0.25 mg/kg doses or physiological saline (normal and model groups). The western blotting assay was used for the determination of TXNRD1 protein in mice serum samples. * $P < 0.05$, ** $P < 0.01$ vs model group.

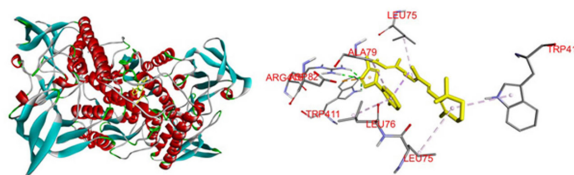


Figure 9. The *in silico* interaction between tretinoin derivative and TXNRD1 protein.

The binding of tretinoin derivative with TXNRD1 protein was investigated using the AutoDock Vina and Discovery Studio software.

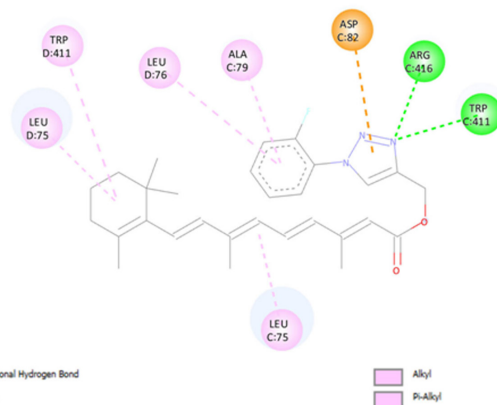


Figure 10. Demonstration of binding between tretinoin derivative and TXNRD1 protein through two-dimensional diagram.

AutoDock Vina and Discovery Studio software were used for understanding the binding of tretinoin derivative with TXNRD1 protein.

Tretinoin derivative targets AGEs in diabetic mice

The expression of AGEs was prominently higher in the dermal tissues of diabetic mice compared to the normal group (Fig. 7). However, the administration of tretinoin derivative effectively alleviated the expression of AGEs in dermal tissues of diabetic mice in a dose-dependent manner. The expression of AGEs in diabetic mice was reduced comparable to the normal group on

administration of 0.25 mg/kg dose tretinoin derivative compared to the 0.12 mg/kg group.

Tretinoin derivative administration elevates TXNRD1 expression in diabetic mice

The TXNRD1 expression showed a remarkable decrease in diabetes mice serum samples compared to the normal group (Fig. 8). However, administration of tretinoin derivative to the diabetic mice led to a prominent increase in TXNRD1 expression in serum samples in a dose-dependent manner. The TXNRD1 expression in diabetic mice was promoted comparable to the normal group on administration of 0.25 mg/kg dose of tretinoin derivative compared to the 0.12 mg/kg group.

Tretinoin derivative interacts with TXNRD1 protein

It was observed from *in silico* data that tretinoin interacts with TXNRD1 protein (3EAN) with the binding affinity ranging from -10 to 9.4 kcal/mol (Fig. 9). The binding of tretinoin derivative with TXNRD1 protein involves arginine (ARG C:416) and tryptophan (TRP C:411) amino acid residues of TXNRD1 *via* conventional hydrogen bonds (Fig. 10). Moreover, the protein interacts with tretinoin derivative *via* pi-alkyl and alkyl interactions involving leucine (LEU D:75), tryptophan (TRP D:411), leucine (LEU D:76) and alanine (ALA C:79) amino residues.

DISCUSSION

Expecting mothers have a serious life threat to themselves as well as to their children because of gestational diabetes mellitus (Johns *et al.*, 2018). Unfortunately, the incidence of the disorder has been increasing every year over the past decade in Chinese women (Johns *et al.*, 2018). High blood glucose levels during pregnancy have been found to be responsible for premature deliveries and increased abortion rate (Poston *et al.*, 2016). The present study was designed to understand the effect of tretinoin derivative on gestational diabetes in mice model *in vivo*. Initially, it was observed that streptozotocin administration in the mice caused a significant increase in FBG and FINS levels compared to the normal group. Other specific features of diabetes such as polyuria, polydipsia, polyphagia and weight loss were also observed in the mice administered with streptozotocin. Thus, these features confirmed the induction of diabetes in mice model. However, the administration of tretinoin derivative to the diabetic mice significantly ($P < 0.05$) alleviated the blood FBG and FINS levels in a dose-dependent manner. Further, it was observed that FBG and FINS levels in diabetic mice were alleviated comparable to the normal group on treatment with 0.25 mg/kg dose of tretinoin derivative. In diabetic mice, the HDL level showed a significant ($P < 0.05$) decrease in blood samples compared to the normal group. On the other hand, tretinoin derivative administration effectively promoted the blood HDL level in diabetic mice in a dose-dependent manner. The TC and TG levels were also elevated significantly in blood samples of the diabetic mice compared to the normal group. However, the administration of tretinoin derivative to the diabetic mice significantly ($P < 0.05$) reversed the streptozotocin-induced increase in TC and TG levels in blood samples in a dose-dependent manner. Thus, initial data clearly showed that tretinoin derivative reverses streptozotocin-induced changes in FBG, FINS, lipoprotein and triglyceride levels in the

mice and therefore needs to be investigated further for possible role in the treatment of diabetes.

The increased expression of C-reactive protein (CRP) in diabetic patients is an indicator of inflammatory reactions and it is also associated with insulin resistance (Bateman *et al.*, 2016). It is reported that CRP promotes activation of various substrates of insulin receptors and inhibits tyrosine kinase activity (Kaushik *et al.*, 2009). Thus, insulin synthesis and its secretion are inhibited by CRP thereby leading to the development of resistance to the insulin action. Additionally, excessive secretion of TNF- α has been found to down-regulate the expression of glucose transporter-T4 and consequently increase insulin resistance. Studies have also demonstrated that elevated IL-6 production is associated with a decrease in insulin sensitivity and an increase in secretion of glucocorticoids and growth hormones. Thus, excessive IL-6 level in diabetic patients promotes insulin resistance and increase the level of blood glucose (Skórzyńska-Dziduszko *et al.*, 2016; Roca-Rodríguez *et al.*, 2017; Khal-iq *et al.*, 2018; Bhat *et al.*, 2018; Dar *et al.*, 2016; Ansari *et al.*, 2018). In the present study, the CRP and IL-6 production was elevated in diabetic mice pancreatic tissues compared to the normal group. The TNF- α level in diabetic mice pancreatic tissues was also increased remarkably compared to the normal group. On the other hand, tretinoin derivative administration in diabetic mice effectively alleviated the CRP and IL-6 production in pancreatic tissues in a dose-dependent manner. Further, tretinoin derivative administration also led to a prominent reduction in TNF- α level in diabetic mice pancreatic tissues. In diabetic mice, SOD activity and CAT level showed a prominent decrease in pancreatic tissues than those of the normal group. The level of MDA also showed a remarkable increase in diabetic mice pancreatic tissues in comparison to the normal group. Fortunately, administration of tretinoin derivative to diabetic mice effectively elevated the SOD activity and CAT level in pancreatic tissues. It was found that tretinoin derivative administration lowered the MDA level in diabetic mice pancreatic tissues. Administration of tretinoin derivative to the diabetic mice also reversed the streptozotocin-induced increase in TXNRD1 protein expression effectively.

CONCLUSION

In conclusion, tretinoin derivative administration effectively regulated streptozotocin-induced changes in fasting blood glucose, insulin level, high-density lipid level and triglyceride level in diabetic mice *in vivo*. The streptozotocin-induced excessive production of C-reactive protein and inflammatory cytokines was also down-regulated in diabetic mice on administration of tretinoin derivative. Furthermore, the activity of SOD and the level of CAT in diabetic mice were elevated by tretinoin administration. Tretinoin derivative administration suppressed TXNRD1 protein expression and *in silico* data revealed that it binds to arginine (ARG C:416) and tryptophan (TRP C:411) amino acid residues of the protein *via* conventional hydrogen bonds. Therefore, tretinoin derivative can be investigated further as a therapeutic agent for the treatment of gestational diabetes mellitus.

REFERENCES

- Ansari K, Lone AM, Shah WA, Singh J, Siddiqui IR (2018) Site selective [bmIm]OH catalyzed CC bond functionalization under green

- conditions. *Tetrahedron Lett* **59**: 654–657. <https://doi.org/10.1016/j.tetlet.2018.01.010>
- Baig S, Rizzi EP, Shabeer M, Agrawal M (2020) Heredity of type 2 diabetes confers increased susceptibility to oxidative stress and inflammation. *BMJ Open Diabetes Res Care* **8**: e000945. <https://doi.org/10.1136/bmjdr-2019-000945>
- Bateman RM, Sharpe MD, Jagger JE, Ellis CG, Sole-Violan J, Lopez-Rodriguez M, Herrera-Ramos E, Ruiz-Hernandez J, Borderías L, Horcajada J, et al. (2016) 36th International Symposium on Intensive Care and Emergency Medicine: Brussels, Belgium. 15–18 March 2016. *Crit Care* **20** (Suppl 2): 94. <https://doi.org/10.1186/s13054-016-1208-6>. Erratum in: *Crit Care* 2016; **20**: 347. PMID: 27885969; PMCID: PMC5493079
- Bhat MA, Malik RA, Prakash P, Lone AM (2018) Preparation and evaluation of antibacterial potential of *Pithecellobium dulce* root extract against Gram positive and Gram negative bacteria. *Microb Pathog* **116**: 49–53. <https://doi.org/10.1016/j.micpath.2018.01.013>
- Bozorov K, Zhao J, Aisa HA (2019) 1,2,3-Triazole-containing hybrids as leads in medicinal chemistry: a recent overview. *Bioorg Med Chem* **27**: 3511–3531. <https://doi.org/10.1016/j.bmc.2019.07.005>
- Bonandi E, Christodoulou MS, Fumagalli G, Perdicchia D, Rastelli G, Passarella D (2017) The 1,2,3-triazole ring as a bioisostere in medicinal chemistry. *Drug Discov Today* **22**: 1572–1581. <https://doi.org/10.1016/j.drudis.2017.05.014>
- Cebula M, Schmidt EE, Arner ES (2015) TrxR1 as a potent regulator of the Nrf2-Keap1 response system. *Antioxid Redox Signal* **23**: 823–853. <https://doi.org/10.1089/ars.2015.6378>
- Chang E, Kim D-H, Yang H, Lee DH, Bae SH, Park C-Y (2018) CB1 receptor blockade ameliorates hepatic fat infiltration and inflammation and increases Nrf2-AMPK pathway in a rat model of severely uncontrolled diabetes. *PLoS ONE* **13**: e0206152. <https://doi.org/10.1371/journal.pone.0206152>
- Chu XM, Wang C, Wang WL, Liang LL, Liu W, Gong KK, Sun KL (2019) Triazole Derivatives and Their Antiplasmodial and Antimalarial Activities. *Eur J Med Chem* **166**: 206–223. <https://doi.org/10.1016/j.ejmech.2019.01.047>
- Dar BA, Lone AM, Shah WA, Qurishi MA (2016) Synthesis and screening of ursolic acid-benzylidene derivatives as potential anticancer agents. *Eur Med Chem* **111**: 26–32. <https://doi.org/10.1016/j.ejmech.2016.01.026>
- Feng LS, Zheng MJ, Zhao F, Liu D (2021) 1,2,3-Triazole hybrids with anti-HIV-1 activity. *Arab Pharm* **354**: e2000163. <https://doi.org/10.1002/ardp.202000163>
- Feng LS, Xu Z, Chang L, Li C, Yan XF, Gao C, Ding C, Zhao F, Shi F, Wu X (2020) Hybrid molecules with potential *in vitro* antiplasmodial and *in vivo* antimalarial activity against drug-resistant *Plasmodium falciparum*. *Med Res Rev* **40**: 931–971. <https://doi.org/10.1002/med.21643>
- Hajifaraji M, Jahanjou F, Abbasalizadeh F, Aghamohammadzadeh N, Abbasi MM, Dolatkhan N (2018) Effect of probiotic supplements in women with gestational diabetes mellitus on inflammation and oxidative stress biomarkers: a randomized clinical trial. *Asia Pac J Clin Nutr* **27**: 581–591. <https://doi.org/10.6133/apjcn.082017.03>
- Johns EC, Denison FC, Norman JE, Reynolds RM (2018) Gestational diabetes mellitus: mechanisms, treatment, and complications. *Trends Endocrinol Metab* **29**: 743–754. <https://doi.org/10.1016/j.tem.2018.09.004>
- John CM, Ramasamy R, Al Naeqee G, Al-Nuaimi AH, Adam A (2012) Nicotinamide supplementation protects gestational diabetic rats by reducing oxidative stress and enhancing immune responses. *Curr Med Chem* **19**: 5181–5186. <https://doi.org/10.2174/092986712803530449>
- Kabuyama Y, Kitamura T, Yamaki J, Homma MK, Kikuchi SI, Homma Y (2008) Involvement of thioredoxin reductase 1 in the regulation of redox balance and viability of rheumatoid synovial cells. *Biochem Biophys Res Commun* **367**: 491–496. <https://doi.org/10.1016/j.bbrc.2007.12.178>
- Kaushik SV, Plaisance EP, Kim T, Huang EY, Mahurin AJ, Grandjean PW, Mathews ST (2009) Extended-release niacin decreases serum fetuin-A concentrations in individuals with metabolic syndrome. *Diabetes Metab Res Rev* **25**: 427–434. <https://doi.org/10.1002/dmrr.967>
- Khalik T, Waseem MA, Lone AM, Hassan QP (2018) *Oscimum sanctum* extract inhibits growth of Gram positive and Gram negative bacterial strains. *Microb Pathog* **118**: 211–213. <https://doi.org/10.1016/j.micpath.2018.03.040>
- Matsui M, Oshima M, Oshima H, Takaku K, Maruyama T, Yodoi J, Taketo MM (1996) Early embryonic lethality caused by targeted disruption of the mouse thioredoxin gene. *Dev Biol* **178**: 179–185. <https://doi.org/10.1006/dbio.1996.0208>
- Metzger BE, Coustan DR (1998) Summary and recommendations of the Fourth International Workshop-Conference on Gestational Diabetes Mellitus. *Organizing Committee Diabetes Care* **21** (Suppl 2): B161–7. PMID: 9704245
- Nazem MR, Asadi M, Jabbari N, Allameh A (2019) Effects of zinc supplementation on superoxide dismutase activity and gene expression, and metabolic parameters in overweight type 2 diabetes patients: a randomized, double-blind, controlled trial. *Clin Biochem* **69**: 15–20
- Park HR, Lee SE, Yang H, Son GW, Jin YH, Park YS (2015) Induction of thioredoxin reductase 1 by Korean Red Ginseng water extract regulates cytoprotective effects on human endothelial cells. *Evid Based Complement Alternat Med* **2015**: 972040
- Poston L, Caleyachetty R, Cnattingius S, Corvalán C, Uauy R, Herring S, Gillman MW (2016) Preconceptional and maternal obesity: epidemiology and health consequences. *Lancet Diabetes Endocrinol* **4**: 1025–1036. [https://doi.org/10.1016/S2213-8587\(16\)30217-0](https://doi.org/10.1016/S2213-8587(16)30217-0)
- Raniga PV, Di Trapani G, Vuckovic S, Tonissen KF (2016) TrxR1 inhibition overcomes both hypoxia-induced and acquired bortezomib resistance in multiple myeloma through NF- κ B inhibition. *Cell Cycle* **15**: 559–572. <https://doi.org/10.1080/15384101.2015.1136038>
- Roca-Rodríguez MDM, López-Tinoco C, Fernández-Deudero Á, Murri M, García-Palacios MV, García-Valero MDA, Tinahones FJ, Aguilar-Diosdado M (2017) Unfavorable cytokine and adhesion molecule profiles during and after pregnancy, in women with gestational diabetes mellitus. *Endocrinol Diabetes Nutr* **64**: 18–25. <https://doi.org/10.1016/j.endinu.2016.10.003>
- Sha H, Zeng H, Zhao J, Jin H (2019) Mangiferin ameliorates gestational diabetes mellitus-induced placental oxidative stress, inflammation and endoplasmic reticulum stress and improves fetal outcomes in mice. *Eur J Pharmacol* **859**: 172522. <https://doi.org/10.1016/j.ejphar.2019.172522>
- Sudharshana Murthy KA, Bhandiwada A, Chandan SL, Gowda SL, Sindhusree G (2018) Evaluation of oxidative stress and proinflammatory cytokines in gestational diabetes mellitus and their correlation with pregnancy outcome. *Indian J Endocrinol Metab* **22**: 79–84. https://doi.org/10.4103/ijem.IJEM_232_16
- Shi X, Wang W, Zheng S, Zhang Q, Xu S (2020) Selenomethionine relieves inflammation in the chicken trachea caused by LPS through inhibiting the NF- κ B pathway. *Biol Trace Elem Res* **194**: 525–535. <https://doi.org/10.1007/s12011-019-01789-1>
- Skórzyńska-Dziduszko KE, Kimber-Trojnar Ż, Patro-Malysza J, Olszewska A, Zaborowski T, Malecka-Massalska T (2016) An Interplay between obesity and inflammation in gestational diabetes mellitus. *Curr Pharm Biotechnol* **17**: 603–613. <https://doi.org/10.2174/1389201017666160127105926>
- Slavova KI, Todorov LT, Belskaya NP, Palafox MA, Kostova IP (2020) Developments in the application of 1,2,3-triazoles in cancer treatment. *Recent Pat Anticancer Drug Discov* **15**: 92–112. <https://doi.org/10.2174/1574892815666200717164457>
- Xu Z (2020) 1,2,3-Triazole-containing hybrids with potential antibacterial activity against methicillin-resistant *Staphylococcus aureus* (MRSA). *Eur J Med Chem* **206**. <https://doi.org/10.1016/j.ejmech.2020.112686>
- Yan M, Xu L, Wang Y, Wan J, Liu T, Liu W, Wan Y, Zhang B, Wang R, Li Q (2020) Opportunities and challenges of using five-membered ring compounds as promising antitubercular agents. *Drug Dev Res* **81**: 402–418. <https://doi.org/10.1002/ddr.21638>
- Zhang B (2019) Comprehensive review on the anti-bacterial activity of 1,2,3-triazole hybrids. *Eur J Med Chem* **168**: 357–372. <https://doi.org/10.1016/j.ejmech.2019.02.055>

Identification of AHNAK expression associated with the pathogenesis of chronic obstructive pulmonary disease by bioinformatic analysis

Chunhui Zhang and Yu Liu✉

Department of Respiratory and Critical Care Medicine, Fujian Geriatric Hospital, Fuzhou 350003, China

Background: Chronic obstructive pulmonary disease (COPD) was a risk factor for lung cancer tumorigenesis. This study aimed to discover novel diagnostic biomarkers for COPD patients and determine their underlying pathogenetic mechanisms. **Materials and methods:** Differentially expressed genes (DEGs) in COPD samples and normal controls were analyzed and utilized to construct a network associated with a high risk for COPD occurrence. Enrichment analysis was applied on the strength of Gene Ontology (GO) annotations and Kyoto Encyclopedia of Genes and Genomes (KEGG) pathway analysis. The RT-qPCR analysis was performed to determine 10 hub genes in COPD. ELISA assay was utilized to measure IL-1 β , IL-6, and IL-10 levels. Spearman's correlation analysis was conducted to detect the correlation between inflammatory cytokines and AHNAK expression. Cell proliferation and apoptosis were evaluated by CCK-8 and flow cytometry assays. **Results:** AHNAK was significantly increased in COPD serum samples compared with non-COPD smokers and strongly correlated with inflammation. AHNAK level could also discriminate COPD from non-COPD with high accuracy. **Conclusion:** AHNAK may be a feasible biomarker playing crucial functions in the diagnosis and progression of COPD.

Keywords: AHNAK, chronic obstructive pulmonary disease, differentially expressed genes, enrichment analysis, PPI network

Received: 23 November, 2021; **revised:** 21 February, 2022; **accepted:** 12 December, 2022; **available on-line:** December, 2023

✉ e-mail: liuyu2020@hotmail.com

Abbreviations: COPD, Chronic obstructive pulmonary disease; DEGs, Differentially expressed genes; GO, Gene Ontology; KEGG, Kyoto Encyclopedia of Genes and Genomes; PPI, protein-protein interaction

INTRODUCTION

Chronic obstructive pulmonary disease (COPD) was a classic chronic respiratory disease with a global average prevalence of 13.1% (Blanco *et al.*, 2019). In 2015, about 3.2 million people died of COPD (Jolliffe *et al.*, 2019); by 2030, COPD is expected to be the fourth most common cause of death and the fifth most common cause of disability worldwide (Barnes, 2007). Its main features included persistent airflow limitation and recurrent airway inflammation, including emphysema, parenchymal emphysema destruction, and mucus overproduction due to capillary bronchitis (Hogg *et al.*, 2009). However, the molecular pathogenesis of COPD remains unclear, and effective prevention and treatment methods were lacking. Therefore,

further research on the molecular mechanisms of COPD was needed to identify new drug targets.

Patients with COPD frequently presented with abnormal lung inflammation characterized by increased numbers of inflammatory cells (neutrophils, macrophages, and T-lymphocytes) and the release of multiple inflammatory mediators (lipids, chemokines, cytokines, and growth factors) (Guiedem *et al.*, 2018; Barnes, 2016). The main cause of COPD is exposure to noxious gases or particles, with smoking being one of the major risk factors (Salvi, 2014). The increase in inflammatory response cells and subsequent release of mediators further amplified the normal inflammatory response to smoking in COPD disease (Barnes, 2017). Up to now, nearly 1 billion people worldwide were smokers (Propper, 2020). However, only a minority of smokers eventually developed COPD, and the exact molecular and cellular pathogenesis of this complex process was not fully understood.

In this study, we used differential analysis from the NCBI Gene Expression Omnibus (GEO) database to screen for AHNAK, a critical gene that was highly expressed in COPD. Furthermore, bioinformatics analysis was utilized to explore its potential pathogenesis. Collectively, these results suggested that AHNAK may be a useful biomarker for COPD.

MATERIALS AND METHODS

Subject enrollment

68 healthy non-COPD smokers who underwent physical examination, 79 stable-COPD patients, and 83 acute exacerbation COPD (AECOPD) patients admitted to Fujian Geriatric Hospital between August 2017 and May 2020 were enrolled in our study. There was no significant difference in gender and age between the two groups ($P > 0.05$). COPD was diagnosed according to the standard of the Global Initiative for Chronic Obstructive Lung Disease (GOLD). The specific manifestations were: pulmonary function first-second force exhalation volume (FEV1) to force spirometry (FVC) ratio less than 0.7 after an inhaled bronchodilator (salbutamol 200 μ g), combined with clinical symptoms and signs, excluding irreversible obstructive pulmonary ventilation dysfunction caused by other factors. Exclusion criteria: (1) cases with bronchial asthma, bronchiectasis, interstitial pneumonia, lung cancer, and other definite severe lung diseases were excluded from this study; (2) cardiovascular diseases, metabolic diseases, rheumatic immune diseases, and acute and chronic inflammatory diseases in

Table 1. Clinical information on COPD patients and healthy controls

	Control (n=68)	Stable COPD (n=79)	acute exacerbation COPD (n=83)	P value
Age (years)	65.11±7.83	64.84±6.98	65.25±7.92	0.9412
Gender (Male/Female)	38/30	46/33	51/32	0.7835
BMI (kg/m ²)	21.62±3.51	21.75±2.99	21.06±2.37	0.2914
FEV1/FVC (%)	83.59±9.22	60.33±6.41	53.47±7.25	<0.0001
CRP (mg/L)	5.19±1.67	25.71±13.36	51.28±27.49	<0.0001
Smoking history(Yes/No)	45/23	75/4	80/3	<0.0001

other parts of the body were excluded; (3) those who had been treated with antibiotics, systemic corticosteroid therapy, or immunosuppressive drugs within 3 months.

All included subjects were drawn 10 ml of venous blood after 8 h fasting, and all samples were sent to the laboratory department for centrifugation. The upper serum layer was taken, and the samples were stored at -80°C until use. All the subjects' information was shown in Table 1. This study was approved by the Ethics Committee of Fujian Geriatric Hospital and followed the Declaration of Helsinki. All participants were informed of the study plan and signed a written informed consent form.

Data download and differentially expressed genes (DEGs) analysis

We used the 'chronic obstructive pulmonary disease' search term as the keyword and limited the search scope to 'expression profile by array' to search the GEO database. In our study, our dataset included 10 samples from COPD patients and 10 control samples. All the data were downloaded and analyzed by R and GEOquery. After analysis, 122 up-regulated DEGs were found in COPD, which was used for subsequent analysis.

Gene Ontology (GO) annotations and Kyoto Encyclopedia of Genes and Genomes (KEGG) analysis

GO annotations and the Database conducted KEGG analysis of the integrated DEGs in COPD for Annotation, Visualization, and Integrated Discovery (DAVID; v 6.7).

Identification of protein-protein interaction (PPI) network

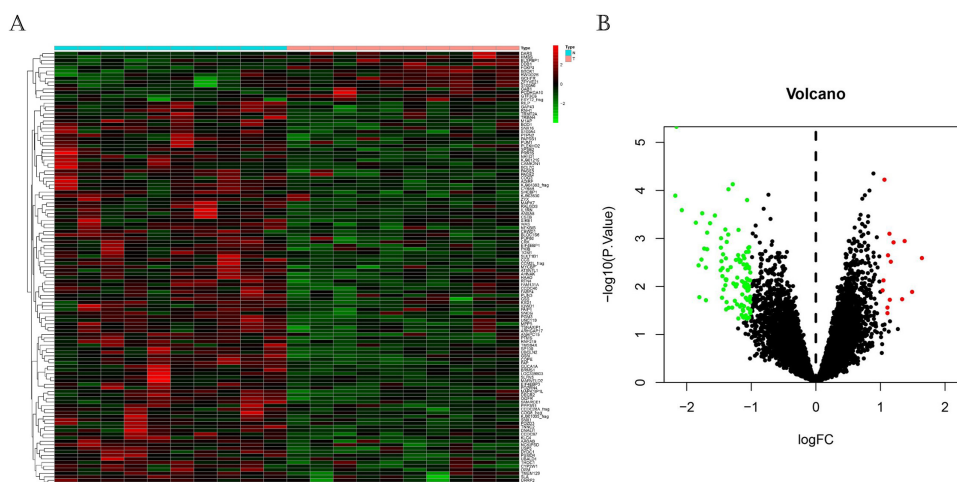
A hub gene was considered a gene with an absolute value of clinical trait relatio0.8ip of more than 0.2 and an absolute value of Spearman's correlation value of more than 0.8. The interaction of the hub gene and the DEGs were deemed to be key genes.

Real-time quantitative polymerase chain reaction analysis

Total RNAs were extracted from serum samples and cells using TRIzol reagent (Invitrogen, Carlsbad, CA). Then, reverse transcription was conducted to synthesize cDNA from RNA using a PrimeScript RT reagent kit (Takara, Japan). Finally, RT-qPCR was performed on a 7500 Real-time PCR System (Applied Biosystems, Beijing, China) using SYBR Premix EX Taq reagent (Takara, Japan) following the protocol. U6 functioned as an internal control, and data were analyzed relative to GAPDH based on the $2^{-\Delta\Delta CT}$ equation. The primers sequences were as follows: AHNAK forward, 5'-AGCGTCTGTAGCTTCCTTGT-3', and reverse 5'-GGCAGCCTCAGTCGTGTATT-3'; GAPDH forward, 5'-TGGCACCCTCAAGGCTGAGA-3', and reverse, 5'-TGGTGAAGACGCCAGTGGACTC-3'.

ELISA assay

IL-1 β and IL-6 levels in serum samples were determined by corresponding ELISA kits obtained from Solarbio Life Sciences (Beijing, China). The detailed infor-

**Figure 1. DEGs in COPD.**

(A) Heatmap results of DEGs in COPD samples and healthy controls. (B) Volcano result of DEGs in COPD. COPD, chronic obstructive pulmonary disease; DEG, differentially expressed genes.

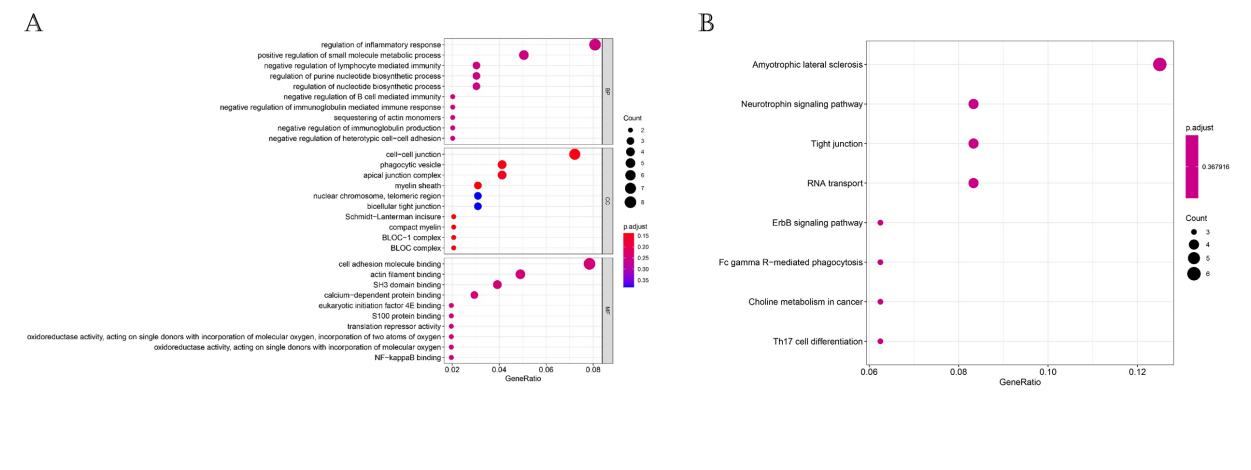


Figure 2. The GO of BP, CC and MF, and KEGG pathways after GEOs analysis. (A) GO results. (B) KEGG results. GO, gene ontology; BP, biological process; CC, cellular component; MF, molecular function; KEGG, Kyoto encyclopedia of genes and genomes; DEG, differentially expressed genes.

mation of all ELISA kits was as follows: IL-1 β (SEKH-0002), IL-6 (SEKH-0013).

Statistical analysis

GraphPad Prism 6.0 and R version 3.5.3 were applied to analyze the data. All the data were presented as mean \pm standard deviation (S.D.). Differences between the two groups were compared and analyzed using Student's *t*-test followed by Tukey's posthoc test. A *P*-value of less than 0.05 was considered to be statistically significant.

RESULTS

DEGs of COPD

122 up-regulated genes were identified in our study and presented as a Volcano map (Fig. 1A). Figure 1B displayed the heatmaps of the 122 DEGs in our dataset.

GO functional analysis and pathway-enrichment KEGG analysis of DEGs

Three functional groups of GO analysis consisted of biological processes (BP), cell composition (CC), and molecular function (MF). As shown in Fig. 2A, with the BP results, the up-regulated DEGs were enriched in the categories of regulation of inflammatory response, positive regulation of the small molecular, metabolic process, negative regulation of lymphocyte-mediated immunity, regulation of purine nucleotide biosynthetic process, and regulation of nucleotide biosynthetic process. As for the CC functional groups, the up-regulated DEGs were concentrated at the cell-cell junction, phagocytic vesicle, apical junction complex, myelin sheath, nuclear chromosome, telomeric region, and bicellular tight junction. Finally, with the MF groups, the up-regulated DEGs were enriched at cell adhesion molecule binding, actin filament binding, SH3 domain binding, and calcium-dependent protein binding.

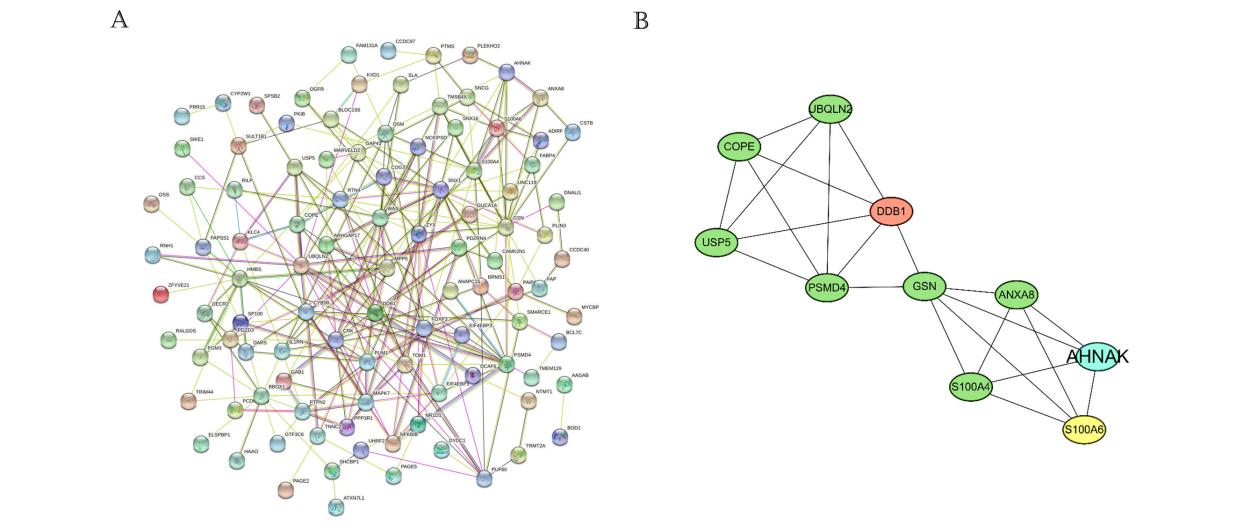


Figure 3. PPI network of DEGs. (A) PPI network results of DEGs. (B) The 10 top hub genes in the PPI network. PPI, protein-protein interaction; DEG, differentially expressed genes.

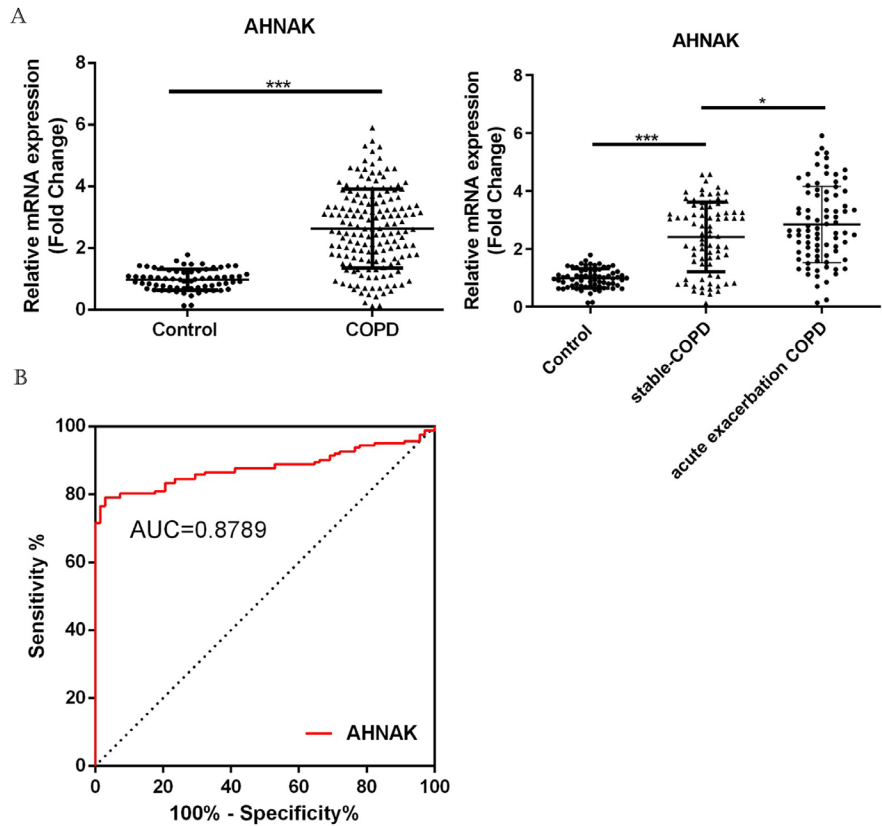


Figure 4. The AHNAK expression in COPD. (A) Expression of AHNAK in COPD serum samples. (B) ROC analysis of AHNAK in COPD. COPD, chronic obstructive pulmonary disease

In addition, as shown in Fig. 2B, the KEGG pathways analysis of the DEGs in COPD unveiled that they were mostly concentrated in the categories of amyotrophic lateral sclerosis, neurotrophin signaling pathway, tight junction, and RNA transport.

PPI results of DEGs

The PPI network for integrated DEGs was shown in Fig. 3A and Fig. 3B. The 10 hub genes that extensively interacted with other genes in COPD were AHNAK, S100A6, S100A4, ANXA8, GSN, DDB1, PSMD4, USP5, COPE, and UBQLN2.

Up-regulation in COPD patients

Furthermore, patients were divided into stable COPD and acute exacerbation COPD groups, and the clinical information of the patients and healthy controls were shown in Table 1. Next, after collecting COPD and non-COPD serum samples, we found that AHNAK expression was significantly increased in COPD patients (Fig. 4A, $P < 0.001$); moreover, compared with stable-COPD patients, AHNAK was up-regulated in serum samples of acute exacerbation COPD patients ($P < 0.05$). the area under the curve (AUC) of AHNAK concerning discriminating COPD from non-COPD smokers was 0.8789 (Fig. 4B, cut-off value > 1.454 , sensitivity 75.95, specificity 92.65).

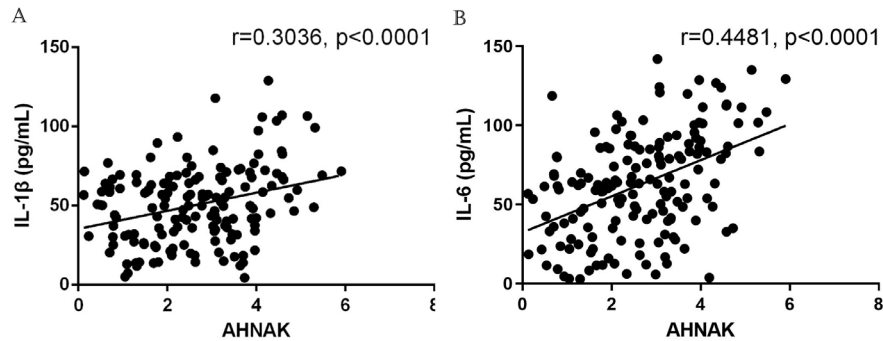


Figure 5. Correlation between AHNANK expression and inflammatory cytokines. Correlation with AHNANK expression and IL-1 β (A) and IL-6 (B) levels in COPD.

Association between AHNAK and inflammation in COPD

To determine the correlation between AHNAK and inflammation in COPD, we measured inflammatory cytokines levels and performed Spearman's correlation analysis accordingly. As shown in Figs 5A and B, AHNAK was strongly correlated with IL-1 β and IL-6 levels in COPD.

DISCUSSION

High-throughput sequencing made rapid progress in the past decade, and advances in bioinformatics deepened our understanding of disease mechanisms and facilitated drug target development, including COPD (Scherer *et al.*, 2017; Dorn *et al.*, 2014; Regan *et al.*, 2019; Mattsson *et al.*, 2016). Several studies have identified hundreds of DEGs based on mRNA gene expression profiles in COPD (Huang *et al.*, 2019; Zhu *et al.*, 2020; Morrow *et al.*, 2017). A hub gene was a gene playing a critical role in biological processes, and the regulation of other genes in a related pathway was often influenced by this gene. Therefore, the hub gene was often an important target and a hot spot for research. In this study, we screened 122 up-regulated DEGs and analyzed the expression profiles using WGCNA. Among them, we identified 10 hub genes, of which AHNAK was the shared central gene and DEG. These results suggested that AHNAK may play an important role in the progression of COPD.

AHNAK was a large structural scaffold protein with 700 kDa, which was implicated in blood-brain barrier formation, cardiac calcium channel regulation, and tumor metastasis (Alvarez *et al.*, 2010; Gentil *et al.*, 2005; Haase *et al.*, 2005; Sohn *et al.*, 2018). What we all know is that AHNAK has been proved to be implicated in various diseases, functioning as a potential biomarker for disease detection or predicting the prognosis. For instance, Zhao and others (Zhao *et al.*, 2017) reported that AHNAK was down-regulated in glioma cell lines, inhibiting glioma tumor growth and associated with poor prognosis. Lee and others (Lee *et al.*, 2018) revealed that AHNAK was a crucial candidate for bladder urothelial carcinoma diagnosis based on in-depth proteomics. Dumitru and others (Dumitru *et al.*, 2013) discovered that AHNAK was dysregulated in laryngeal carcinoma and significantly correlated with poor clinical outcomes in laryngeal carcinoma patients. Sudo and others (Sudo *et al.*, 2014) proposed that AHNAK was highly expressed in several mesothelioma cell lines, playing a key role in regulating mesothelioma cell migration and invasion. Zhang and others (Zhang *et al.*, 2019) suggested that high AHNAK expression was strongly correlated with short disease-free survival and poor prognosis, exerting as an oncogene in pancreatic ductal adenocarcinoma. More importantly, Nedeljkovic and others (Nedeljkovic *et al.*, 2018) implied that AHNAK abnormal expression could be novel candidate variants in COPD. The data we obtained from clinical samples also confirmed the specific high expression of AHNAK in COPD patients, which was consistent with the comprehensive bioinformatic analysis. Therefore, this study provided new insights into the complex pathogenesis of COPD.

In order to explore the mechanisms involved in disease progression, we performed a PPI dynamic analysis. Based on KEGG and GO's enrichment results, we identified 38 pathways enriched in the dynamic PPI network. The top 12 processes were inflammation response, small molecular, metabolic process, cell-cell junction, phagocytic vesicle, apical junction complex, cell adhesion

molecular binding, actin filament binding, SH3 domain binding, amyotrophic lateral sclerosis, neurotrophin, tight junction, and RNA transport. Thus, we verified the relationship between AHNAK and inflammatory factors in COPD, and the outcome demonstrated that AHNAK was closely associated with IL-1 β and IL-6 levels in COPD patients. These results support that AHNAK represents a sensitive biomarker for the diagnosis of COPD.

Nevertheless, this study maintains some limitations. First, the specific mechanism of action of AHNAK in COPD requires further in vivo studies. In addition, the sample size in this study was relatively small, and the DEGs between the different stages of COPD could not be determined due to the sample size. In future studies, we will use a larger sample size consisting of samples from patients with different stages of COPD to avoid accidental errors. Finally, long-term follow-up investigations of COPD patients are recommended to determine the impact of abnormal AHNAK expression on COPD prognosis.

CONCLUSION

AHNAK was significantly elevated in COPD, functioning as a potential biomarker for COPD detection and treatment.

Declarations

Acknowledgment. This study protocol was approved by the Ethics Committee of Fujian Geriatric Hospital. Written informed consent was provided before the study. No data were used to support this study. The authors declare that they have no competing interests.

Ethics approval. The study was performed according to the international, national and institutional rules considering animal experiments, clinical studies and biodiversity rights. The study protocol was approved by the Ethics Committee of Fujian Geriatric Hospital.

REFERENCES

- Alvarez JL, Petzhold D, Pankonien I, Behlke J, Kouno M, Vassort G, Morano I, Haase H (2010) Ahnak1 modulates L-type Ca (2+) channel inactivation of rodent cardiomyocytes. *Pflügers Arch* **460**: 719–730. <https://doi.org/10.1007/s00424-010-0853-x>
- Barnes PJ (2007) Chronic obstructive pulmonary disease: a growing but neglected global epidemic. *PLoS Med* **4**: e112. <https://doi.org/10.1371/journal.pmed.0040112>
- Barnes PJ (2016) Inflammatory mechanisms in patients with chronic obstructive pulmonary disease. *J Allergy Clin Immunol* **138**: 16–27. <https://doi.org/10.1016/j.jaci.2016.05.011>
- Barnes PJ (2017) Cellular and molecular mechanisms of asthma and COPD. *Clin Sci (Lond)* **131**: 1541–1558. <https://doi.org/10.1042/CS20160487>
- Blanco I, Diego I, Bueno P, Casas-Maldonado F, Miravittles M (2019) Geographic distribution of COPD prevalence in the world displayed by Geographic Information System maps. *Eur Respir J* **54**: 1900610. <https://doi.org/10.1183/13993003.00610-2019>
- Dorn C, Grunert M, Sperling SR (2014) Application of high-throughput sequencing for studying genomic variations in congenital heart disease. *Brief Funct Genomics* **13**: 51–65. <https://doi.org/10.1093/bfpg/elt040>
- Dumitru CA, Bankfalvi A, Gu X, Zeidler R, Brandau S, Lang S (2013) AHNAK and inflammatory markers predict poor survival in laryngeal carcinoma. *PLoS One* **8**: e56420. <https://doi.org/10.1371/journal.pone.0056420>
- Gentil BJ, Benaud C, Delphin C, Remy C, Berezowski V, Cecchetti R, Feraud O, Vittet D, Baudier J (2005) Specific AHNAK expression in brain endothelial cells with barrier properties. *J Cell Physiol* **203**: 362–371. <https://doi.org/10.1002/jcp.20232>
- Guiedem E, Ikomey GM, Nkenfou C, Walter PE, Mesembe M, Chegou NN, Jacobs GB, Okomo Assoumou MC (2018) Chronic obstructive pulmonary disease (COPD): neutrophils, macrophages

- and lymphocytes in patients with anterior tuberculosis compared to tobacco-related COPD. *BMC Res Notes* **11**: 192. <https://doi.org/10.1186/s13104-018-3309-6>
- Haase H, Alvarez J, Petzhold D, Doller A, Behlke J, Erdmann J, Hetzer R, Regitz-Zagrosek V, Vassort G, Morano I (2005) Ahnak is critical for cardiac Ca (V)1.2 calcium channel function and its beta-adrenergic regulation. *FASEB J* **19**: 1969–1977. <https://doi.org/10.1096/fj.05-3997com>
- Hogg JC, Timens W (2009) The pathology of chronic obstructive pulmonary disease. *Annu Rev Pathol* **4**: 435–459. <https://doi.org/10.1146/annurev.pathol.4.110807.092145>
- Huang XW, Li YW, Guo XR, Zhu Z, Kong X, Yu F, Wang Q (2019) Identification of differentially expressed genes and signaling pathways in chronic obstructive pulmonary disease via bioinformatic analysis. *FEBS Open Bio* **9**: 1880–1899. <https://doi.org/10.1002/2211-5463.12719>
- Jolliffe DA, Greenberg L, Hooper RL, Mathysen C, Rafiq R, de Jongh RT, Camargo CA, Griffiths CJ, Janssens W, Martineau AR (2019) Vitamin D to prevent exacerbations of COPD: systematic review and meta-analysis of individual participant data from randomised controlled trials. *Thorax* **74**: 337–345. <https://doi.org/10.1136/thoraxjnl-2018-212092>
- Lee H, Kim K, Woo J, Park J, Kim H, Lee KE, Kim H, Kim Y, Moon KC, Kim JY, Park IA, Shim BB, Moon JH, Han D, Ryu HS (2018) Quantitative proteomic analysis identifies AHNAK (neuroblast differentiation-associated protein AHNAK) as a novel candidate biomarker for bladder urothelial carcinoma diagnosis by liquid-based cytology. *Mol Cell Proteomics* **17**: 1788–1802. <https://doi.org/10.1074/mcp.RA118.000562>
- Matsson H, Söderhäll C, Einarsson E, Lamontagne M, Gudmundsson S, Backman H, Lindberg A, Rönmark E, Kere J, Sin D, Postma DS, Boss, BosLundbäck B, Klar J (2016) Targeted high-throughput sequencing of candidate genes for chronic obstructive pulmonary disease. *BMC Pulm Med* **16**: 146. <https://doi.org/10.1186/s12890-016-0309-y>
- Morrow JD, Zhou XB, Lao TT, Jiang Z, DeMeo DL, Cho MH, Qiu W, Cloonan S, Pinto-Plata V, Celli B, Marchetti N, Criner GJ, Bueno R, Washko GR, Glass K, Quackenbush J, Choi AM, Silverman EK, Hersh CP (2017) Functional interactors of three genome-wide association study genes are differentially expressed in severe chronic obstructive pulmonary disease lung tissue. *Sci Rep* **7**: 44232. <https://doi.org/10.1038/srep44232>
- Nedeljkovic I, Terzikhan N, Vonk JM, van der Plaat DA, Lahousse L, van Diemen CC, Hobbs BD, Qiao D, Cho MH, Brusselle GG, Postma DS, Boezen HM, van Duijn CM, Amin N (2018) A Genome-wide linkage study for chronic obstructive pulmonary disease in a Dutch genetic isolate identifies novel rare candidate variants. *Front Genet* **9**: 133. <https://doi.org/10.3389/fgene.2018.00133>
- Propper RE (2020) Does cigarette smoking protect against SARS-CoV-2 infection? *Nicotine Tob Res* **22**: 1666. <https://doi.org/10.1093/ntr/ntaa073>
- Regan EA, Hersh CP, Castaldi PJ, DeMeo DL, Silverman EK, Crapo JD, Bowler RP (2019) Omics and the search for blood biomarkers in chronic obstructive pulmonary disease. Insights from COPD Gene. *Am J Respir Cell Mol Biol* **61**: 143–149. <https://doi.org/10.1165/rcmb.2018-0245PS>
- Salvi S (2014) Tobacco smoking and environmental risk factors for chronic obstructive pulmonary disease. *Clin Chest Med* **35**: 17–27. <https://doi.org/10.1016/j.ccm.2013.09.011>
- Scherer F, Kurtz DM, Diehn M, Alizadeh AA (2017) High-throughput sequencing for noninvasive disease detection in hematologic malignancies. *Blood* **130**: 440–452. <https://doi.org/10.1182/blood-2017-03-735639>
- Sohn M, Shin S, Yoo JY, Goh Y, Lee IH, Bae YS (2018) Ahnak promotes tumor metastasis through transforming growth factor- β -mediated epithelial-mesenchymal transition. *Sci Rep* **8**: 14379. <https://doi.org/10.1038/s41598-018-32796-2>
- Sudo H, Tsuji AB, Sugyo A, Abe M, Hino O, Saga T (2014) AHNAK is highly expressed and plays a key role in cell migration and invasion in mesothelioma. *Int J Oncol* **44**: 530–538. <https://doi.org/10.3892/ijo.2013.2183>
- Zhang ZW, Liu XD, Huang R, Liu XG, Liang ZY, Liu TH (2019) Up-regulation of nucleoprotein AHNAK is associated with poor outcome of pancreatic ductal adenocarcinoma prognosis via mediating epithelial-mesenchymal transition. *J Cancer* **10**: 3860–3870. <https://doi.org/10.7150/jca.31291>
- Zhao ZJ, Xiao SH, Yuan XR, Yuan J, Zhang C, Li H, Su J, Wang X, Liu Q (2017) AHNAK as a prognosis factor suppresses the tumor progression in glioma. *J Cancer* **8**: 2924–2932. <https://doi.org/10.7150/jca.20277>
- Zhu YZ, Zhou AY, Li QY (2020) Whole transcriptome analysis of human lung tissue to identify COPD-associated genes. *Genomics* **112**: 3135–3141. <https://doi.org/10.1016/j.ygeno.2020.05.025>

***LINC00707* promotes multidrug resistance of ovarian cancer cells by targeting the miR-382-5p/*LRRK2* axis**

Min-Wen Zhao^{1#}, Chang-Jie Lin^{2#} and Jian-Ping Qiu¹✉

¹Department of Obstetrics and Gynecology, The Affiliated Suzhou Hospital of Nanjing Medical University, Suzhou Municipal Hospital, Gusu School, Nanjing Medical University, Suzhou, Jiangsu 215000, China; ²Department of General Surgery, The Second Affiliated Hospital of Soochow University, Suzhou, Jiangsu 215000, China

Multidrug resistance severely limits the efficacy of ovarian cancer (OC) treatment. Recent studies have revealed the carcinogenic role of *LINC00707* RNA. However, the role of *LINC00707* in the development of multidrug resistance in OC has not been clarified. Therefore, the aim of this study was to investigate the relationship between *LINC00707* and multidrug resistance in OC, which can facilitate the development of new therapeutic agents for effectively addressing this issue. The RNA expression of *LINC00707*, *miR-382-5p* and leucine-rich repeat kinase 2 (*LRRK2*) in SKOV3 (a human OC cell line) cells was detected by qRT-PCR. The effects of *LINC00707* on the proliferation and viability of SKOV3 cells were determined by MTT assay and colony formation assay. The interaction of *LINC00707*, *miR-382-5p*, and *LRRK2* was bioinformatically predicted and verified with dual-luciferase reporter assay. In addition, the effect of *LINC00707* on drug resistance in SKOV3 cells through targeting the *miR-382-5p*/*LRRK2* axis was explored. The expression of *LINC00707* and *LRRK2* was significantly increased in SKOV3 cells, while *miR-382-5p* expression was significantly decreased. The results of bioinformatic prediction and colony formation assay demonstrated that *LINC00707* could regulate *LRRK2* expression in SKOV3 cells by targeting *miR-382-5p*. Additionally, knockdown of *LINC00707* markedly increased expression of *miR-382-5p* and decreased that of *LRRK2*, increased cell proliferation and viability, as well as sensitivity to chemotherapeutic agents in SKOV3 cells. Notably, these manifestations were more obvious with simultaneous knockdown of *LINC00707* and *miR-382-5p* compared with knockdown of *LINC00707* alone. *LINC00707* is overexpressed in SKOV3 cells and promotes SKOV3 cell proliferation and resistance to chemotherapeutic drugs via targeting the *miR-382-5p*/*LRRK2* axis.

Keywords: ovarian cancer; *LINC00707*; *miR-382-5p*; *LRRK2*; multidrug resistance

Received: 27 September, 2022; **revised:** 17 February, 2023; **accepted:** 07 June, 2023; **available on-line:** 03 October, 2023

✉ e-mail: doc_qiu@163.com

[#]Min-Wen Zhao and Chang-Jie Lin contributed equally to this work as a first co-author

Abbreviations: ATCC, American Type Culture Collection; FBS, fetal bovine serum; IgG, immunoglobulin G; *LRRK2*, leucine-rich repeat kinase 2; miRNAs, MicroRNAs; OC, ovarian cancer; PVDF, polyvinylidene fluoride; qRT-PCR, Quantitative real-time PCR; S.D., standard deviation

INTRODUCTION

Ovarian cancer (OC) is one of the deadliest malignancies in women. Global cancer statistics in 2020 re-

ported more than 310,000 new cases and nearly 210,000 deaths of OC, with increasing morbidity and mortality rates each year (Kuroki & Guntupalli, 2020; Sung *et al.*, 2021). Although more than a third of OC patients can be diagnosed at an early stage (Sadeghi *et al.*, 2011), distant metastases usually occur in about 60% of these patients, which results in a five-year survival rate of only 30% (Siegel *et al.*, 2020). In addition, surgical resection of the tumor and cisplatin-based chemotherapy are the two major standard treatments for newly diagnosed OC patients in clinical settings. Unfortunately, clinical data have shown that with prolonged treatment, OC loses sensitivity to cisplatin and can even completely acquire resistance to it, resulting in treatment failure (Luo *et al.*, 2020). Consequently, resistance, particularly multidrug resistance, continues to be the primary challenge when employing chemotherapeutic drugs for OC. Therefore, it is important to explore the mechanism of drug resistance in OC cells.

To date, multiple studies have shown that the acquisition of drug resistance in OC is affected by multiple factors, of which genetic and epigenetic factors are the most significant (Bast *et al.*, 2009). Particularly, long non-coding RNAs (lncRNAs), a class of RNA transcripts with more than 200 nucleotides but no capacity for protein coding, play a key role in the development of multidrug resistance. By interacting with chromatin, RNA, and proteins, lncRNAs affect numerous processes in a cancer cell such as cell proliferation, anti-apoptosis, and migration (Raveh *et al.*, 2015). Moreover, lncRNAs have also been reported to be associated with acquired resistance in cancer cells. When paclitaxel-resistant cells were subjected to lncRNA sequencing, Xu and others speculated that five upregulated lncRNAs and 21 downregulated lncRNAs were linked to multidrug resistance (Xu *et al.*, 2018). Wang *et al.* suggested that lncRNA *EPIC1* could promote AKT-mTORC1 signaling and resistance to rapamycin in breast cancer and OC by binding to the transcription factor Myc (Wang *et al.*, 2020). Shi *et al.* discovered a significant increase in the expression of *LINC01118* in paclitaxel-resistant OC tissues, which promoted cell migration and invasion while inhibiting apoptosis (Shi & Wang, 2018). All these data indicate the significance of lncRNAs in the multidrug resistance of OC. Notably, *LINC00707* has been shown to behave as a cancer-promoting factor in both colorectal and cervical malignancies (Guo *et al.*, 2021). A recent study on cisplatin-resistant non-small cell lung cancer (NSCLC) cells showed that knocking down *LINC00707* expression significantly restored the sensitivity of the resistant cells to cisplatin (Zhang *et al.*, 2019). In summary, *LINC00707* not only promotes cancer development, but

also increases the susceptibility of cancer cells to medication resistance.

MicroRNAs (miRNAs), small non-coding RNAs of about 20 nucleotides in size, regulate the expression level of genes by binding to the 3' UTR region of target genes, thereby affecting the regular activities of cells (Sun *et al.*, 2019). MiRNAs may play a direct or indirect role in the progression of cancer and the emergence of drug resistance to chemotherapeutics. A study showed that downregulated *miR-130a* was associated with multidrug resistance in various cancers, and *miR-130a* targeted *MET* and enhanced TRAIL sensitivity in NSCLC cells (Acunzo *et al.*, 2012). According to the results of previous studies, *miR-382-5p* may be a tumor suppressor gene, and reduction of its expression can promote cancer progression (Xie & Pan, 2021). Furthermore, increased *miR-382-5p* expression levels led to significant reduction in iron levels in OC cells (Sun *et al.*, 2021). However, no studies have yet been conducted on the role of *miR-382-5p* in acquisition of multidrug resistance in OC cells. Interestingly, an interaction between *LINC00707* and *miR-382-5p* has been revealed, which is shown to affect cancer progression (Guo *et al.*, 2021), but the role of this relationship in OC remains unclear. We proposed the multidrug resistance mechanism of OC as follows: *LINC00707* acted as a molecular sponge for *miR-382-5p* and increased OC progression and resistance to chemotherapeutic agents by targeting *miR-382-5p*. This hypothesis was further supported by *in vitro* cell experiments.

MATERIALS AND METHODS

Cell culture and treatment

Human normal ovarian surface epithelial cell line (IOSE80) and human OC cell line (SKOV3) were obtained from the American Type Culture Collection (ATCC, VA, USA). The cells were cultured in DMEM/F12 medium supplemented with 100 U/mL penicillin, 0.1 mg/mL streptomycin sulfate, and 10% fetal bovine serum (FBS), then the medium was incubated at 37°C and 5% CO₂.

According to the manufacturer's instructions, the following plasmids or fragments were transfected into the cells using Lipofectamine™ 2000 transfection reagent: control shRNA, *LINC00707* shRNA, control pcDNA3.1 vector, pcDNA3.1-*LINC00707*, control mimics, *miR-382-5p* mimics, control inhibitor, and *miR-382-5p* inhibitor. Next, *LINC00707* shRNA and *miR-382-5p* inhibitor were transfected into SKOV3 cells together, upon which the following groups were obtained: sh-NC, sh-*LINC00707*, control vector, *LINC00707*, *miR-NC*, *miR-382-5p*, Anti-NC, Anti-*miR-382-5p*, and sh-*LINC00707* + Anti-*miR-382-5p*. The medium was replaced with fresh medium six hours after transfection for two days of culture. Finally, the transfection efficiency was verified using qRT-PCR.

Quantitative real-time PCR (qRT-PCR)

The TRIzol™ Plus RNA Purification Kit was used to extract total RNA from SKOV3 cells following the manufacturer's instructions. The concentration and purity of RNA were subsequently measured by NanoDrop One ultramicrospectrophotometer. With the help of PrimeScript RT Master Mix, cDNA was obtained by reverse transcription. qRT-PCR was performed to detect the expression levels of *LINC00707*, *miR-382-5p*, and leucine-

Table 1. Primer Sequences for qRT-PCR

RNA	Sequences (5' to 3')
LINC00707	F: 5'- CCAACAGGGTATCAGAATTCTC
	R: 5'- TGCTGACAATAGCCATTAGG
miR-382-5p	F: 5'- CTCGCTTCGGCAGCAC
	R: 5'- TATGGTTGTAGAGGACTCCTTGAC
LRRK2	F: 5'- AGCAAGGGACAGGCTGAAGTTG
	R: 5'- GCAGGCTTTGCGTTGCTTCTCA
U6	F: 5'- AACGCTTCACGAATTGCGT
	R: 5'- CTCGCTTCGGCAGCAC
GAPDH	F: 5'- GCACCGTCAAGGCTGAGAAC
	R: 5'- ACCACCCTGTTGCTGTAGCCAA

rich repeat kinase 2 (*LRRK2*) according to the instructions of the SYBR Premix Ex Taq II kit. *GAPDH* or *U6* served as an internal control, and six replicates were set up for the experiment. The experimental data obtained by qRT-PCR were used to calculate the relative expression of the target gene with the help of the 2^{-ΔΔCt} method. The primer sequences used are shown in Table 1.

MTT assay

The transfected SKOV3 cells were seeded in a 96-well plate at a density of 5×10³ cells/well, and to each well, 20 μL MTT solution (5 mg/mL) was added. After 4 h of incubation at 37°C, the supernatant was aspirated and 200 μL DMSO was then added into each well. Later, the absorbance values at a wavelength of 490 nm were measured by a microplate reader, and the cell viability was evaluated. In order to observe the drug resistance of cells, the transfected SKOV3 cells were incubated with different concentrations of paclitaxel (PTX, 2, 4, 8, 16, 32 μmol/L), doxorubicin (Dox, 0.5, 1, 2, 4, 8 μmol/L), methotrexate (MTX, 2, 4, 8, 16, 32 μmol/L), and cisplatin (DDP, 0.25, 0.5, 1, 2, 4 μmol/L) for 48 h. Subsequent to the addition of 20 μL MTT solution to each well, the supernatant was aspirated after 4 h of incubation at 37°C. Again, 200 μL DMSO was added to each well, and the absorbance at 590 nm was detected by a microplate reader. Half-maximal inhibitory concentration (IC₅₀) was calculated with the use of GraphPad Prism 7 software.

Colony formation assay

The transfected SKOV3 cells were inoculated into 6-well culture plates at 1×10⁶ cells/well and cultured in DMEM/F12 medium containing 10% FBS for two weeks, with the medium replaced every three days. Afterwards, SKOV3 cells were fixed with 4% paraformaldehyde and stained with 0.1% crystal violet.

Dual-luciferase reporter assay

In order to verify the interaction among *LINC00707*, *miR-382-5p*, and *LRRK2*, wild type *LINC00707* and *LRRK2*, or *LINC00707* and *LRRK2* fragments with

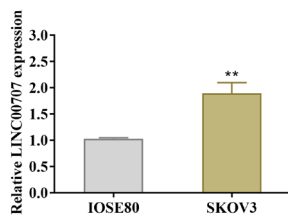


Figure 1. *LINC00707* is upregulated in ovarian cancer (OC) cells. The expression levels of *LINC00707* RNA in human normal ovarian surface epithelial cells (IOSE80) and human OC cells (SKOV3) detected by qRT-PCR. ** $p < 0.01$, vs IOSE80 group.

mutated nucleic acid sequences were constructed and then inserted into the luciferase reporter gene of pMIR-REPORT (pGL3) plasmid (H306, Obio Technology, Shanghai, China) based on the predicted binding sites of *LINC00707* and *LRRK2* with *miR-382-5p*. The cells were accordingly divided into four groups: wild type pGL3-*LINC00707* (*LINC00707*-WT) and pGL3-*LRRK2* (*LRRK2*-WT) or mutant pGL3-*LINC00707* (*LINC00707*-MUT) and pGL3-*LRRK2* (*LRRK2*-MUT) vectors. Next, *miR-382-5p* mimics and pGL3 plasmids were transfected together into SKOV3 cells using Lipofectamine™ 2000. Subsequently, luciferase activity was assessed using the Dual-Luciferase Reporter System Kit (E1910, Promega, USA).

Western blot

The cells were lysed in lysis buffer (RIPA) supplemented with a protease inhibitor (PMSF). Equal amounts of protein (20 μ g) were separated by sodium dodecyl sulfate-polyacrylamide gel electrophoresis (SDS-PAGE) and transferred to polyvinylidene fluoride (PVDF) membranes. After that, the membranes were blocked with 5% milk in Tris-buffered saline containing 0.1% Tween-20 for 1 h at ambient temperature. The membranes were subsequently incubated overnight at 4°C with primary *LRRK2* antibody (1:1000, ab133474, Abcam, Cambridge, UK), followed by 1 h of incubation at 37°C with peroxidase conjugated goat anti-rabbit immunoglobulin G (IgG) antibody (1:3000; ab97051). Next, immunoreac-

tive bands were visualized using enhanced chemiluminescence reagents (Thermo Fisher Scientific, Waltham, USA) and imaged using a Luminescent Image Analyzer ChemiDoc XRS Plus (Bio-Rad). Optical densitometric quantification of band intensities from four independent experiments was performed using Image-Pro Plus 6.0 software, and relative expression levels of target proteins were normalized to band intensities of GAPDH.

Data analysis

Measurement data were presented as mean \pm standard deviation (S.D.). The *t*-test was adopted when comparing only two groups, and one-way analysis of variance with Tukey' test was employed when comparing more than two groups. Pearson correlation was applied to analyze the expression correlation. All statistical analyses were performed using SPSS 26.0 software (IBM, Armonk, NY, USA), with two-tailed $p < 0.05$ as the level of statistical significance. All experiments were performed in triplicate, with at least three independent experiments.

RESULTS

LINC00707 is upregulated in SKOV3 cells

QRT-PCR was used to determine *LINC00707* expression in OC cells in this study. We found that *LINC00707* was expressed at significantly higher levels in SKOV3 than in IOSE80 cells (Fig. 1), which suggests that *LINC00707* may be involved in OC development.

Knockdown of *LINC00707* suppresses the proliferation of SKOV3 cells

In order to investigate the effect of *LINC00707* on OC, *LINC00707* was knocked down or overexpressed using plasmids, and the transfection efficiency was detected by qRT-PCR. The qRT-PCR results demonstrated that the expression level of *LINC00707* was significantly decreased in cells in the sh-*LINC00707* group compared with that in the sh-NC group and was notably increased

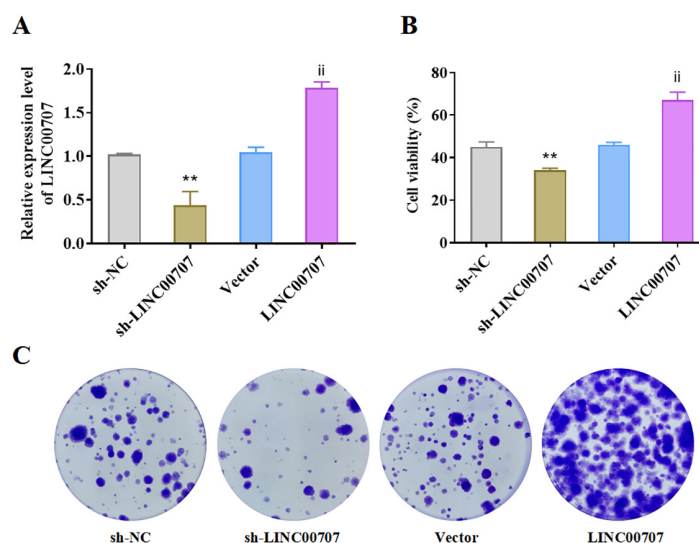


Figure 2. Knockdown of *LINC00707* suppresses the proliferation of ovarian cancer (OC) cells.

(A) Expression level of *LINC00707* in SKOV3 cells after transfection measured with qRT-PCR. (B) The effect of *LINC00707* knockdown or overexpression on SKOV3 cell viability assessed with MTT assay (C) Cell colony formation assay results of the effect of *LINC00707* knockdown or overexpression on SKOV3 cell proliferation. ** $p < 0.01$, vs sh-NC; ⁱⁱ $p < 0.01$, vs Vector. sh, short hairpin; NC, negative control.

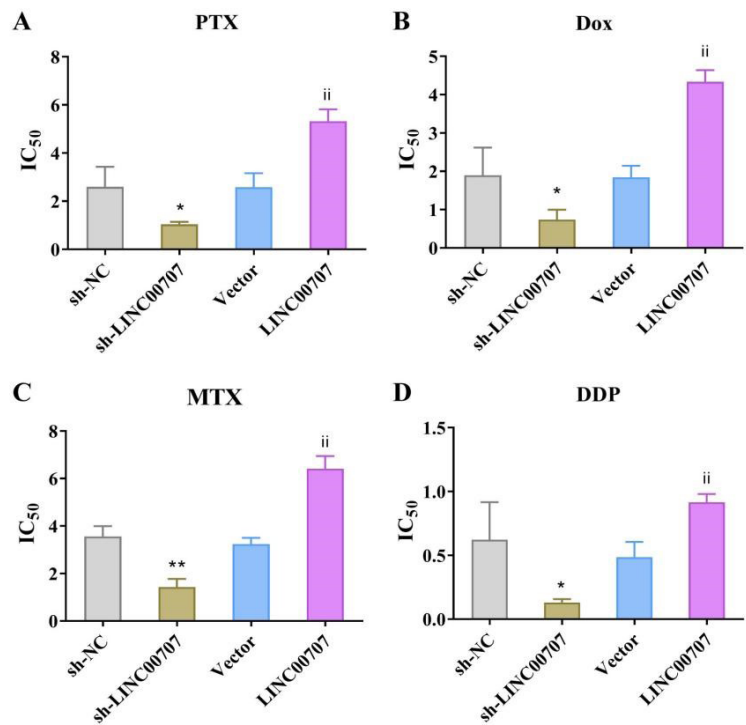


Figure 3. Knockdown of *LINC00707* decreases multidrug resistance in ovarian cancer (OC) cells. (A–D) MTT assay results of the effect of PTX (A), Dox (B), MTX (C) and DDP (D) on drug resistance in SKOV3 cells with knocked down or overexpressed *LINC00707*. ** $p < 0.01$, vs sh-NC; ⁱⁱ $p < 0.01$, vs Vector. sh, short hairpin; NC, negative control; PTX, paclitaxel; Dox, doxorubicin; MTX, methotrexate; DDP, cisplatin.

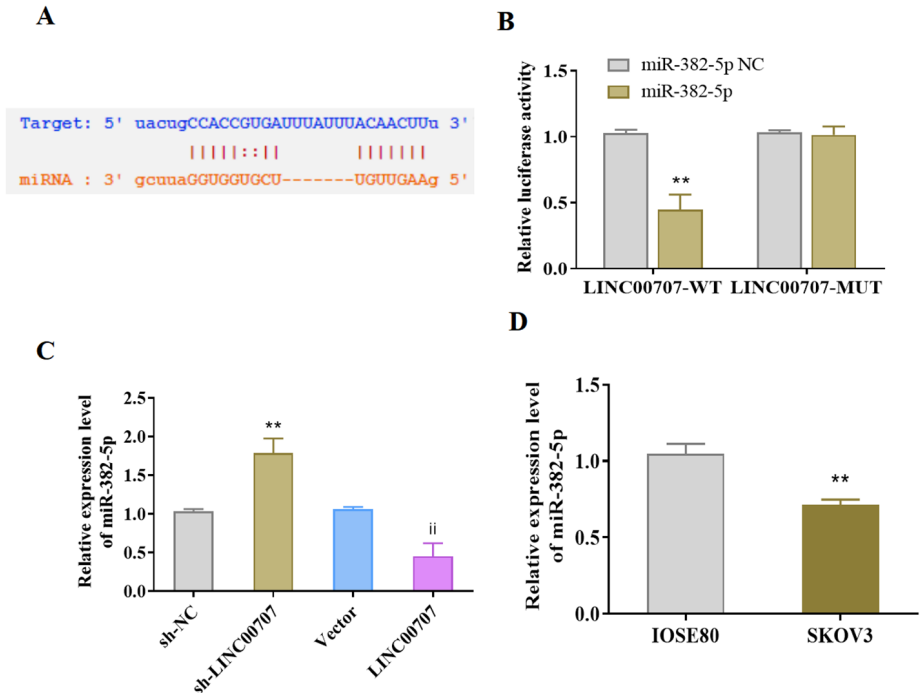


Figure 4. *LINC00707* targets *miR-382-5p* and negatively interacts with *miR-382-5p* in ovarian cancer (OC) cells. (A) The binding sites between *LINC00707* and *miR-382-5p* predicted by IncBASE software. (B) Dual-luciferase reporter assay results of relative luciferase activity in SKOV3 cells transfected with LINC00707 WT + *miR-382-5p* mimics and LINC00707 MUT + *miR-382-5p* mimics. (C) qRT-PCR results of the expression level of *miR-382-5p* in SKOV3 cells transfected with LINC00707. (D) qRT-PCR results of the expression levels of *miR-382-5p* in IOSE80 cells and SKOV3 cells. ** $p < 0.01$, vs sh-NC (or *miR-382-5p* NC); ⁱⁱ $p < 0.01$, vs Vector. WT, wild type; MUT, mutant; sh, short hairpin; NC, negative control.

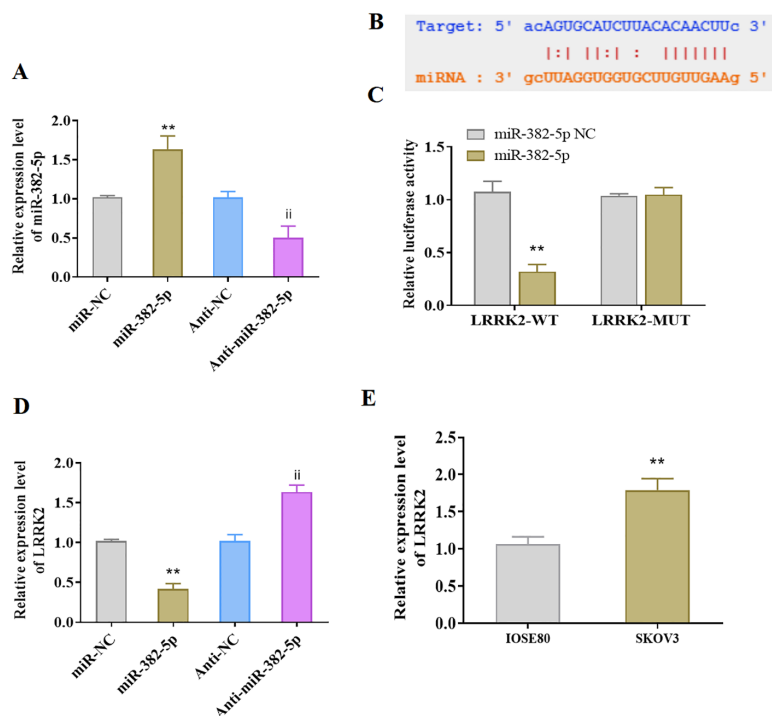


Figure 5. MiR-382-5p targets *LRRK2* mRNA and negatively interacts with *LRRK2* expression in ovarian cancer (OC).

(A) qRT-PCR results of the expression of *miR-382-5p* in SKOV3 cells after transfection. (B) The targeting relationship of *miR-382-5p* to *LRRK2* mRNA predicted by starbase2.0 (<https://starbase.sysu.edu.cn/starbase2/index.php>), and the predicted *miR-382-5p* binding site in *LRRK2* mRNA. (C) Dual-luciferase reporter assay results validating the association between *miR-382-5p* and *LRRK2*. (D) qRT-PCR results of the expression level of *LRRK2* mRNA in SKOV3 cells transfected with *miR-382-5p*. (E) qRT-PCR results of the expression level of *LRRK2* mRNA in IOSE80 cells and SKOV3 cells. ** $p < 0.01$ vs sh-NC (or *miR-382-5p* NC); WT, wild type; MUT, mutant.

in the LINC00707-oe group compared with the control vector group (Fig. 2A). Later, we examined cell proliferation and viability through MTT and colony formation assays. Combining the results of both assays, we observed that the proliferation and viability of cells in the sh-LINC00707 group were much lower than those in the sh-NC group, and the proliferation and viability of cells in the LINC00707-oe group were much higher than those in the control vector group (Fig. 2B, 2C). Thus, knockdown of *LINC00707* can significantly inhibit SKOV3 cell proliferation.

Knockdown of LINC00707 decreases multidrug resistance in SKOV3 cells

Subsequently, in order to observe the effect of *LINC00707* on chemoresistance of SKOV3 cells, the resistance of LINC00707-knock-down and LINC00707 overexpressing SKOV3 cells to PTX, Dox, MTX, and DDP was studied using MTT assay. The MTT results showed that the IC50 of SKOV3 cells treated with PTX, Dox, MTX, and DDP was markedly decreased in the sh-LINC00707 group compared with the sh-NC group, while being considerably increased in the LINC00707-oe group relative to the control vector group (Fig. 3A–D). In brief, knockdown of *LINC00707* can reduce the resistance of SKOV3 cells to chemotherapeutic agents.

LINC00707 targets *miR-382-5p*

LINC00707 was predicted to target *miR-382-5p* using lncBASE software (Fig. 4A). According to the findings of dual-luciferase reporter assay, co-transfection of WT-LINC00707 3'-UTR with *miR-382-5p* mimics in the *miR-382-5p* group greatly reduced the luciferase activity

compared with the *miR-NC* group (Fig. 4B). qRT-PCR results indicated that SKOV3 cells in which *LINC00707* was knocked down showed significant increase in the *miR-382-5p* expression compared with the cells in the sh-NC group, and those with *LINC00707* overexpression showed significant downregulation of *miR-382-5p* expression compared with those in the control vector group (Fig. 4C). In addition, the expression level of *miR-382-5p* was much lower in SKOV3 cells than in IOSE80 cells (Fig. 4D). Overall, *LINC00707* targets *miR-382-5p* and sh-LINC00707 can significantly upregulate the *miR-382-5p* expression in OC.

LRRK2 is a target gene of *miR-382-5p*

Firstly, we generated SKOV3 cells with *miR-382-5p* knock down or overexpression to determine the relationship between *miR-382-5p* and *LRRK2*. The expression level of *miR-382-5p* in SKOV3 cells was significantly elevated in the *miR-382-5p* group compared with the *miR-NC* group and the expression level of *miR-382-5p* was markedly lowered in the Anti-*miR-382-5p* group relative to the Anti-NC group (Fig. 5A). Subsequently, with the help of starbase2.0 (<https://starbase.sysu.edu.cn/starbase2/index.php>), *miR-382-5p* was predicted to target *LRRK2* mRNA (Fig. 5B). The dual-luciferase reporter assay results showed that the *miR-382-5p* group presented a significant decrease in luciferase activity after co-transfection of the WT-LRRK2 3'-UTR with *miR-382-5p* mimics (Fig. 5C). qRT-PCR results indicated that *miR-382-5p* overexpression could considerably reduce *LRRK2* expression compared with the *miR-NC* group in SKOV3 cells, while *miR-382-5p* knockdown significantly upregulated *LRRK2* expression compared with the Anti-

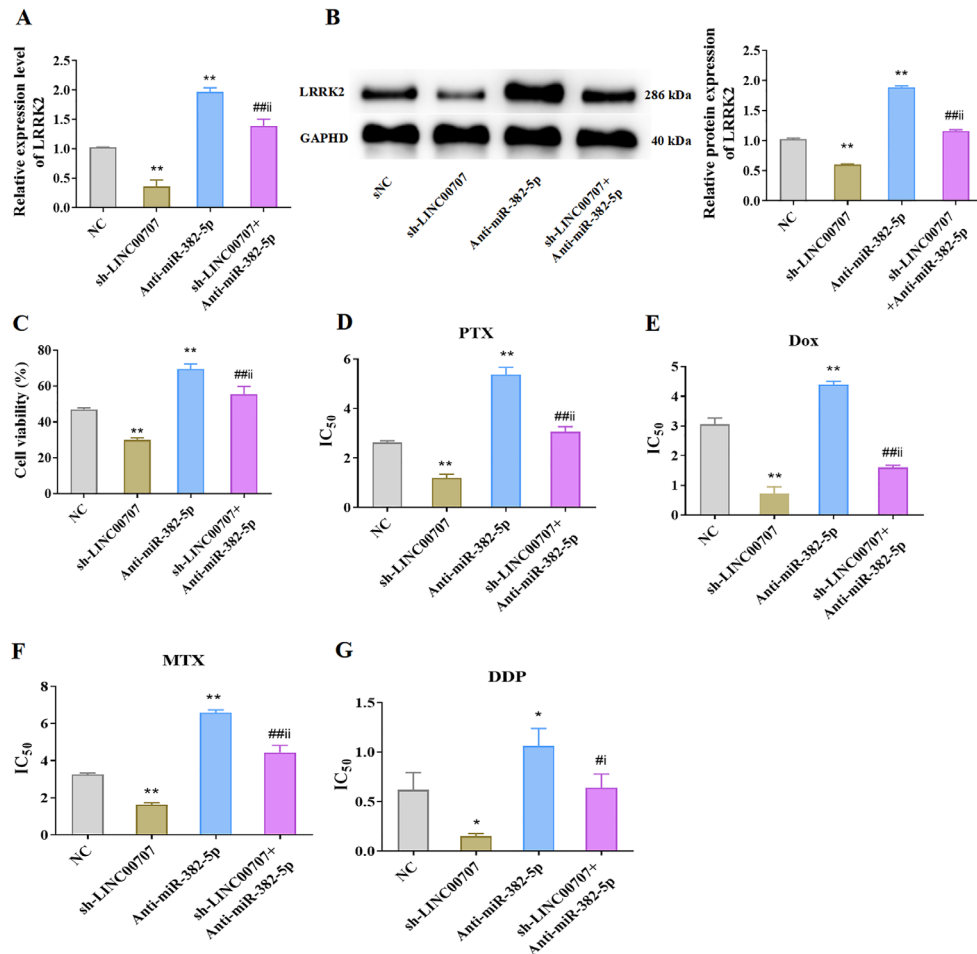


Figure 6. *LINC00707* promotes proliferation and resistance of ovarian cancer (OC) cells to chemotherapeutic agents by targeting the *miR-382-5p/LRRK2* axis.

(A) QRT-PCR results of the expression level of *LRRK2* in SKOV3 cells after simultaneous transfection of *LINC00707* shRNA and *miR-382-5p* inhibitor. (B) Western blot results of *LRRK2* protein levels in SKOV3 cells after transfection. (C) MTT results of the viability of SKOV3 cells after transfection. (D–G) MTT results of the tolerance of SKOV3 cells to PTX (D), Dox (E), MTX (F), and DDP (G) after simultaneous transfection of *LINC00707* shRNA and *miR-382-5p* inhibitor. ** $p < 0.01$, vs. NC; * $p < 0.05$, vs. sh-*LINC00707*; # $p < 0.05$, vs. Anti-*miR-382-5p*. sh, short hairpin; NC, negative control.

NC group (Fig. 5D). Additionally, *LRRK2* was expressed at quite higher levels in SKOV3 cells than in IOSE80 cells (Fig. 5E). Collectively, we found that *miR-382-5p* expression and *LRRK2* expression are upregulated in OC, *miR-382-5p* directly targets *LRRK2*, and knockdown of *miR-382-5p* significantly promotes *LRRK2* expression.

***LINC00707* promotes proliferation and multidrug resistance of SKOV3 cells by targeting the *miR-382-5p/LRRK2* axis**

In order to further investigate the effect of *LINC00707* on OC cell viability and drug resistance, the expression level of *LRRK2* was detected by qRT-PCR and Western blot by targeting the *miR-382-5p/LRRK2* axis, after simultaneous knockdown of *LINC00707* and *miR-382-5p* in SKOV3 cells. The results showed that the sh-*LINC00707* + Anti-*miR-382-5p* group displayed a much higher expression level of *LRRK2* than the sh-*LINC00707* group; and the expression level of *LRRK2* was significantly decreased in the sh-*LINC00707* + Anti-*miR-382-5p* group compared with the Anti-*miR-382-5p* group (Fig. 6A, 6B). The MTT assay outcomes indicated that cell viability was considerably increased in the sh-

LINC00707 + Anti-*miR-382-5p* group compared with the sh-*LINC00707* group, but significantly reduced in the sh-*LINC00707* + Anti-*miR-382-5p* group compared with the Anti-*miR-382-5p* group (Fig. 5C). Next, the resistance of SKOV3 cells to chemotherapeutic agents (PTX, Dox, MTX, and DDP) was detected using MTT assay. We discovered that the sh-*LINC00707* + Anti-*miR-382-5p* group had a much higher IC₅₀ than the sh-*LINC00707* group, and the sh-*LINC00707* + Anti-*miR-382-5p* group presented a lower IC₅₀ than the Anti-*miR-382-5p* group (Fig. 6D–G). These results suggest that *LINC00707* promotes proliferation and resistance of SKOV3 cells to chemotherapeutic agents by targeting the *miR-382-5p/LRRK2* axis.

DISCUSSION

OC, one of the gynecological malignancies with the highest mortality rates, poses a severe threat to female health worldwide. Research suggests that chemoresistance of OC cells significantly contributes to the high mortality (Barriga-Rivera *et al.*, 2016). Currently, the combination of Dox and PTX is typically effective at first, but the

condition relapses in the majority of patients, and is then usually incurable, with just an 18-month-survival rate (Yang *et al.*, 2017). Therefore, a thorough understanding of the molecular mechanism of multidrug resistance in OC is crucial for improving the prognosis. Our study's findings showed that *LINC00707*, which was expressed at a considerably higher level in OC, could boost cellular resistance to chemotherapeutic drugs by targeting the *miR-382-5p/LRRK2* axis.

lncRNAs, described in recent studies, hold promise as potential biomarkers for cancer diagnosis, prognosis, and treatment. Notably, many lncRNAs are dysregulated in OC, which may play crucial roles in the incidence and progression of tumors (Wang *et al.*, 2018). Among them, lncRNA *HOXD-AS1* is an OC-associated lncRNA that is overexpressed in both OC tissues and cells and can indicate poor prognosis in patients (Zhang *et al.*, 2017). Recently, Zahra and coworkers performed high-throughput sequencing and found that *LINC00707* was highly upregulated in OC tissues and has potential as a diagnostic marker (Zahra *et al.*, 2021). Although earlier research indicated that *LINC00707* is a proto-oncogene (Guo *et al.*, 2021), it is not clear how *LINC00707* and OC are related. Therefore, the aim of our study was to investigate the effect of *LINC00707* in OC and its molecular mechanism. In this study, *LINC00707* was overexpressed in SKOV3 cells, and *LINC00707* overexpression markedly increased the proliferation and viability of SKOV3 cells, while *LINC00707* knockdown inhibited the proliferation and viability of cells. Furthermore, studies on several malignancies have shown that lncRNAs have a role in controlling chemosensitivity (Xu *et al.*, 2018). Our findings clearly showed that *LINC00707* overexpression increased resistance to PTX, Dox, MTX, and DDP in SKOV3 cells. These findings are in line with the results of *LINC00707* overexpression in cancer cells in the bladder (Gao & Ji, 2021) and breast (Yuan *et al.*, 2020). Thus, it is clear that *LINC00707* overexpression induces OC resistance to chemotherapeutic agents.

Recent evidence has suggested that the interaction between lncRNAs and microRNAs may have an impact on a number of pathological mechanisms, including the development of cancer and the acquisition of drug resistance. By functioning as a competitive endogenous RNA sponge for *miR-17* and altering *STAT3* expression, lncRNA *H19* was discovered by Huang *et al.* to accelerate the development of NSCLC (Huang *et al.*, 2018). Li *et al.* discovered that lncRNA *SNHG1* promoted the resistance of hepatocellular carcinoma cells to sorafenib by increasing *miR-21* expression to activate the Akt pathway (Li *et al.*, 2019). Through bioinformatic predictions and several experiments in our study, we demonstrated that there was a binding site in *LINC00707* for *miR-382-5p*, and *LINC00707* acted as the molecular sponge of *miR-382-5p*. Interestingly, Guo *et al.* also proved the interaction between *LINC00707* and *miR-382-5p* (Wang *et al.*, 2020). However, our study is the first to find that *miR-382-5p* expression is significantly downregulated in OC cells and inversely correlated with *LINC00707* expression. Although *miR-382-5p* has only been the subject of a few studies, they have shown that this microRNA suppresses the genes involved in tumor development. For instance, the expression level of *miR-382-5p* is significantly downregulated in colorectal cancer tissues (Xie & Pan, 2021). Likewise, few studies were conducted on the downstream target genes of *miR-382-5p*. In this regard, our study discovered that *miR-382-5p* targeted the *LRRK2*mRNA 3'-UTR region and regulated the expression level of *LRRK2*. Mutations in *LRRK2* were first

thought to be critical for inducing familial Parkinson's disease (Deniston *et al.*, 2020). Interestingly, the expression level of *LRRK2* was found to be significantly downregulated in NSCLC tissues (Ma *et al.*, 2019). However, the role of *LRRK2* in cancer has rarely been reported. In our study, the expression level of *LRRK2* was discovered to be significantly upregulated in SKOV3 cells and was clearly inversely regulated by *miR-382-5p*; *LRRK2* expression level in SKOV3 cells was significantly higher when *LINC00707* and *miR-382-5p* were simultaneously knocked down than that when either of them was knocked down alone. Moreover, SKOV3 cells in the sh-*LINC00707* + Anti-*miR-382-5p* group were significantly more resistant to chemotherapeutic agents than those in the Anti-*miR-382-5p* group, but significantly less resistant than those in the sh-*LINC00707* group. Therefore, *LINC00707* induced multidrug resistance of SKOV3 cells by targeting the *miR-382-5p/LRRK2* axis.

CONCLUSION

In summary, *LINC00707* is highly expressed in SKOV3 cells. *LINC00707* regulates the expression of *LRRK2* by targeting *miR-382-5p*, thereby enhancing the proliferation and viability of SKOV3 cells and inducing multidrug resistance in them. Therefore, knocking down *LINC00707* expression is key for addressing multidrug resistance in OC cells. However, the role of *LINC00707* is multifaceted, and more research is required to fully elucidate its function.

Declarations

Conflict of Interest. All authors declare no conflict of interest.

Consent for Publication. Not applicable.

Authors' Contributions. Min-Wen Zhao conceived and designed the experiments; Chang-Jie Lin analyzed and interpreted the results of the experiments; YZM performed the experiments; and Jian-Ping Qiu revised the manuscript.

REFERENCES

- Acunzo M, Visone R, Romano G, Veronese A, Lovat F, Palmieri D, Bottoni A, Garofalo M, Gasparini P, Condorelli G, Chiariello M, Croce CM (2012) *miR-130a* targets MET and induces TRAIL-sensitivity in NSCLC by downregulating *miR-221* and *222*. *Oncogene* **31**: 634–642. <https://doi.org/10.1038/onc.2011.260>
- Barriga-Rivera A, Morley JW, Lovell NH, Suanning GJ (2016) Cortical responses following simultaneous and sequential retinal neurostimulation with different return configurations. *Annu Int Conf IEEE Eng Med Biol Soc* **2016**: 5435–5438. <https://doi.org/10.1109/EMBC.2016.7591956>
- Bast RC, Jr., Hennessey B, Mills GB (2009) The biology of ovarian cancer: new opportunities for translation. *Nat Rev Cancer* **9**: 415–428. <https://doi.org/10.1038/nrc2644>
- Deniston CK, Salogiannis J, Mathea S, Snead DM, Lahiri I, Matyszewska M, Donosa O, Watanabe R, Bohning J, Shiao AK, Knapp S, Villa E, Reck-Peterson SL, Leschziner AE (2020) Structure of *LRRK2* in Parkinson's disease and model for microtubule interaction. *Nature* **588**: 344–349. <https://doi.org/10.1038/s41586-020-2673-2>
- Gao T, Ji Y (2021) Long Noncoding RNA *LINC00707* Accelerates tumorigenesis and progression of bladder cancer via targeting *miR-145/CDCA3* Regulatory Loop. *Urol Int* **105**: 891–905. <https://doi.org/10.1159/000514388>
- Guo H, Li J, Fan F, Zhou P (2021) *LINC00707* regulates *miR-382-5p/VEGFA* pathway to enhance cervical cancer progression. *J Immunol Res* **2021**: 5524632. <https://doi.org/10.1155/2021/5524632>
- Huang Z, Lei W, Hu HB, Zhang H, Zhu Y (2018) *H19* promotes non-small-cell lung cancer (NSCLC) development through *STAT3* signaling via sponging *miR-17*. *J Cell Physiol* **233**: 6768–6776. <https://doi.org/10.1002/jcp.26530>
- Kuroki L, Guntupalli SR (2020) Treatment of epithelial ovarian cancer. *BMJ* **371**: m3773. <https://doi.org/10.1136/bmj.m3773>

- Li W, Dong X, He C, Tan G, Li Z, Zhai B, Feng J, Jiang X, Liu C, Jiang H, Sun X (2019) LncRNA SNHG1 contributes to sorafenib resistance by activating the Akt pathway and is positively regulated by miR-21 in hepatocellular carcinoma cells. *J Exp Clin Cancer Res* **38**: 183. <https://doi.org/10.1186/s13046-019-1177-0>
- Luo S, Zhang Y, Yang Y, Zhu S, Liu W, Zhu J, Liang X, Jiang Z, Sun S, Hou X, Xiao Y, Li X (2020) Clonal tumor mutations in homologous recombination genes predict favorable clinical outcome in ovarian cancer treated with platinum-based chemotherapy. *Gynecol Oncol* **158**: 66–76. <https://doi.org/10.1016/j.ygyno.2020.04.695>
- Ma Q, Xu Y, Liao H, Cai Y, Xu L, Xiao D, Liu C, Pu W, Zhong X, Guo X (2019) Identification and validation of key genes associated with non-small-cell lung cancer. *J Cell Physiol* **234**: 22742–22752. <https://doi.org/10.1002/jcp.28839>
- Raveh E, Matouk IJ, Gilon M, Hochberg A (2015) The H19 Long non-coding RNA in cancer initiation, progression and metastasis – a proposed unifying theory. *Mol Cancer* **14**: 184. <https://doi.org/10.1186/s12943-015-0458-2>
- Sadeghi R, Tabasi KT, Bazaz SM, Kakhki VR, Massoom AF, Gholami H, Zakavi SR (2011) Sentinel node mapping in the prostate cancer. Meta-analysis. *Nuklearmedizin* **50**: 107–115. <https://doi.org/10.3413/nukmed-0339-10-07>
- Shi C, Wang M (2018) LINC01118 modulates paclitaxel resistance of epithelial ovarian cancer by regulating miR-134/ABCC1. *Med Sci Monit* **24**: 8831–8839. <https://doi.org/10.12659/MSM.910932>
- Siegel RL, Miller KD, Jemal A (2020) Cancer statistics, 2020. *CA Cancer J Clin* **70**: 7–30. <https://doi.org/10.3322/caac.21590>
- Sun D, Li YC, Zhang XY (2021) Lidocaine promoted ferroptosis by targeting miR-382-5p /SLC7A11 axis in ovarian and breast cancer. *Front Pharmacol* **12**: 681223. <https://doi.org/10.3389/fphar.2021.681223>
- Sun LP, Xu K, Cui J, Yuan DY, Zou B, Li J, Liu JL, Li KY, Meng Z, Zhang B (2019) Cancer-associated fibroblast-derived exosomal miR3825p promotes the migration and invasion of oral squamous cell carcinoma. *Oncol Rep* **42**: 1319–1328. <https://doi.org/10.3892/or.2019.7255>
- Sung H, Ferlay J, Siegel RL, Laversanne M, Soerjomataram I, Jemal A, Bray F (2021) Global cancer statistics 2020: GLOBOCAN estimates of incidence and mortality worldwide for 36 cancers in 185 countries. *CA Cancer J Clin* **71**: 209–249. <https://doi.org/10.3322/caac.21660>
- Wang Y, Zhang M, Wang Z, Guo W, Yang D (2020) MYC-binding lncRNA EPIC1 promotes AKT-mTORC1 signaling and rapamycin resistance in breast and ovarian cancer. *Mol Carcinog* **59**: 1188–1198. <https://doi.org/10.1002/mc.23248>
- Wang Y, Zhang W, Wang Y, Wang S (2018) HOXD-AS1 promotes cell proliferation, migration and invasion through miR-608/FZD4 axis in ovarian cancer. *Am J Cancer Res* **8**: 170–182
- Xie L, Pan Z (2021) Circular RNA circ_0000467 regulates colorectal cancer development via miR-382-5p/EN2 axis. *Bioengineered* **12**: 886–897. <https://doi.org/10.1080/21655979.2021.1889130>
- Xu J, Wu J, Fu C, Teng F, Liu S, Dai C, Shen R, Jia X (2018) Multidrug resistant lncRNA profile in chemotherapeutic sensitive and resistant ovarian cancer cells. *J Cell Physiol* **233**: 5034–5043. <https://doi.org/10.1002/jcp.26369>
- Yang K, Hou Y, Li A, Li Z, Wang W, Xie H, Rong Z, Lou G, Li K (2017) Identification of a six-lncRNA signature associated with recurrence of ovarian cancer. *Sci Rep* **7**: 752. <https://doi.org/10.1038/s41598-017-00763-y>
- Yuan RX, Bao D, Zhang Y (2020) Linc00707 promotes cell proliferation, invasion, and migration via the miR-30c/CTHRC1 regulatory loop in breast cancer. *Eur Rev Med Pharmacol Sci* **24**: 4863–4872. <https://doi.org/10.26355/eurev.202005.21175>
- Zahra A, Dong Q, Hall M, Jeyaneethi J, Silva E, Karteris E, Sisu C (2021) Identification of Potential Bisphenol A (BPA) Exposure biomarkers in ovarian cancer. *J Clin Med* **10**. <https://doi.org/10.3390/jcm10091979>
- Zhang H, Luo Y, Xu W, Li K, Liao C (2019) Silencing long intergenic non-coding RNA 00707 enhances cisplatin sensitivity in cisplatin-resistant non-small-cell lung cancer cells by sponging miR-145. *Oncol Lett* **18**: 6261–6268. <https://doi.org/10.3892/ol.2019.10959>
- Zhang Y, Dun Y, Zhou S, Huang XH (2017) LncRNA HOXD-AS1 promotes epithelial ovarian cancer cells proliferation and invasion by targeting miR-133a-3p and activating Wnt/beta-catenin signaling pathway. *Biomed Pharmacother* **96**: 1216–1221. <https://doi.org/10.1016/j.biopha.2017.11.096>

Genetic association between vitamin D receptor gene and Saudi patients confirmed with Familial Hypercholesterolemia

May Salem Al-Nbaheen ✉

College of Health Sciences, Saudi Electronic University, Riyadh, Saudi Arabia

Introduction: Familial Hypercholesterolemia (FH) is a common condition caused by inherited genetic abnormalities. Inadequate clearance of the circulating low-density lipoproteins (LDL) is the primary cause of the excessive concentrations of LDL seen in FH patients. The relation with vitamin D deficiency and vitamin D receptor (VDR) gene is well documented in the Saudi Arabia. **Aim:** The aim of this study was to investigate the role of molecular analysis studied between FH patients and four polymorphisms associated with VDR gene in Saudi Population. **Methods:** In this case-control study, 120 patients were selected, and 50 patients were confirmed as FH and 70 subjects were confirmed as healthy controls. Genotyping was performed with polymerase chain reaction followed by restriction fragment length polymorphism analysis using Apal, BsmI, TaqI and FokI polymorphisms in the VDR gene. **Results:** The current study results confirmed no association between clinical characteristics studied between FH cases and controls ($p > 0.05$). Hardy Weinberg Equilibrium analysis was present in Apal and FokI polymorphisms ($p < 0.05$). Only Apal (C vs A: OR-15.1 (95% CI:5.78-39.41); $p < 0.001$; AC+CC vs AA: OR-6.59 (95% CI:2.42-17.95); $p = 0.0006$) and BsmI (G vs A: OR-2.88 (95% CI:1.54-5.38); $p = 0.0006$ and AG+GG vs AA: OR-3.79 (95% CI:1.72-8.35); $p = 0.0007$) polymorphisms showed both allele and genotype association between FH patients and controls. ANOVA analysis confirmed that TG levels were associated ($p = 0.02$) with combination of heterozygous and homozygous genotypes present in all four polymorphisms studied in this population. **Conclusion:** Apal and BsmI polymorphisms in the VDR gene showed association with FH patients in the Saudi Population.

Keywords: Familial Hypercholesterolemia, low-density lipoproteins, vitamin D

Received: 28 January, 2023; revised: 15 July, 2023; accepted: 09 August, 2023; available on-line: 28 November, 2023

✉ e-mail: malnbaheen@seu.edu.sa

Abbreviations: BMI, Body Mass Index; DLCN, Dutch lipid clinical network; FH, Familial Hypercholesterolemia; HoFH, Homozygous Familial Hypercholesterolemia; HWE, Hardy-Weinberg equilibrium; LDL, low-density lipoproteins; PCR, Polymerase Chain Reaction; TC, total cholesterol; TG, Triglycerides; VDR, vitamin D receptor

INTRODUCTION

Familial Hypercholesterolemia (FH) is defined as a common disorder caused due to inherited genetic defects which is responsible for elevated LDLc levels due to inadequate clearance of the circulating LDL (Hori *et al.*, 2023). The definition of FH is described as elevated levels of LDLc which describes in time the development

of atherosclerosis process in the arteries with subsequent high risk of cardiovascular diseases (Maşaleru *et al.*, 2022). Extremely high levels of LDL-c are the result of homozygous familial hypercholesterolemia (HoFH), a severe and rare form of FH. If ignored, HoFH can cause atherosclerotic cardiovascular disease in the early decades of life. An estimated 1 in 300 000–360 000 people in the United States have HoFH. Isolated groups and those experiencing the founder effect also have a higher incidence (Kayikcioglu & Tokgozoglu, 2023). Clinical scoring systems for the diagnosis of FH are widely used and approved, and numerous sets of criteria have been created, encompassing clinical, biochemical, and genetic factors. The most commonly used criteria are Simon Broome, MedPed and Dutch lipid clinical network (DLCN), the last one being used predominantly in the European countries (Huangfu *et al.*, 2023; Todorovova *et al.*, 2023). Some patients have unusual alleles in the minor genes *APOA5*, *ABCG5*, *ABCG8*, *LIPA*, and *STAP1*, whereas the vast majority have mutations in the classically related FH genes *LDLR*, *APOB*, or *PCSK9*. Interestingly, many FH cases either demonstrate a mixture and accumulation of numerous common variations or have no known genetic etiology. In addition, inflammation, vascular tone, cellular proliferation, and other unknown processes account for 80% of common DNA variations that predispose an individual to coronary artery disease (Ruiz-Pesini *et al.*, 2023). Previous meta-analysis estimates the worldwide frequency of heterozygous FH to be 1:313 (Beheshti *et al.*, 2020). However, the estimated heterozygous FH prevalence in the Arabian Gulf region is 1:112, which is around three times the predicted incidence worldwide (Alhabib *et al.*, 2021). Based on the incidence of 1:200–500, the estimated number of HeFH patients in Saudi Arabia ranges from 63 485 to 158 712. The lack of genetic screening programs and governmental data makes it difficult to determine the true FH incidence in Saudi Arabia and the Middle East (Alzahrani *et al.*, 2020). In Saudi Arabia, information on the genetics of FH is extremely scarce. The literature revealed that 21 variations were linked to *LDLR*, *APOB* and *PCSK9* genes and 80% of these variants were predicted to influence the *LDLR* gene, and c.1332dup (p.D445*) and c.2026delG (p. G676Afs*33) mutations were confirmed to be novel variants in the *LDLR* gene (Al-Allaf *et al.*, 2014).

In Saudi Arabia, the main causes of vitamin D deficiency are cultural practices, climate, genetic disposition, and skin color. Furthermore, high temperatures are predisposed to this deficiency (Al-Ålyani *et al.*, 2018). It was well-established that Vitamin D will be converting into 25-hydroxyvitamin D in liver and kidney will be converting into 1,25-dihydroxyvitamin D₃, which has a biological purpose (Bikle, 2014). Expression of *VDR* in mel-

anocytes allows it to control melanin production. Vitamin D is effective at treating a variety of skin conditions in humans (Tang *et al.*, 2018). The vitamin D receptor (VDR) is a nuclear steroid receptor that functions as a DNA-binding transcription factor. Vitamin D activity and metabolic concentrations are both affected by polymorphisms in the *VDR* gene (Guo *et al.*, 2023). The *VDR* gene is present on chromosome 12p13, which has variants in exons 2 and 3 for the enzymes *Apal*, *BsmI*, and *TaqI*, and in exon 2 for the enzyme *FokI*. The restriction enzymes for *VDR* gene polymorphisms can be used to analyze the gene's many polymorphic sites in its untranslated region; which influences the functional stability of the transcript. Alleles with and without certain restriction sites are designated A-a, B-b, T-t, and F-f, respectively (Ghada Bin Saif & Imran Ali Khan, 2022). Numerous studies on the *VDR* gene in various human diseases have been conducted in Saudi Arabia, but no studies on the *VDR* gene and FH have been documented. The aim of this study was to investigate the role of *VDR* gene polymorphism studies in FH patients in the Saudi Arabia.

MATERIALS AND METHODS

FH subjects

A case-control study was conducted from King Khalid University Hospital in Riyadh city. The FH cases were confirmed based on Dutch group protocol (Alharbi *et al.*, 2015) which is an inclusion criteria. The FH subjects without Dutch group criteria is considered to be excluded. The Dutch group criteria is defined as the diagnosis of FH based on clinical, genetic and family history. However, in our study, clinicians have confirmed the FH cases based on the previous study (Alharbi *et al.*, 2015).

Healthy controls were selected based on normal levels of lipid profile. In this study, 70 FH cases and 50 healthy controls were recruited based on signing of patient informed consent form. This study was performed based on Declaration of Helsinki and ethical grant was approved within the hospital premises (E-19-1176). All patients (n=120) have signed the informed consent form to enroll in this study.

BMI details

Body Mass Index (BMI) was calculated based on Alshammary *et al.* studies using body weight and height (Alshammary & Khan, 2021).

Sample collection

In this study, 5ml of blood was collected from 120 participants. Peripheral blood was separated into 3ml serum sample and 2ml in EDTA tube. Serum blood was used to measure the lipid profile parameters such as LDLc, HDLc, total cholesterol (TC) and triglycerides

(TG). Lipid profile was performed based on the previous study (Batais *et al.*, 2019).

Molecular analysis

EDTA sample was used for extraction of genomic DNA using DNA isolation kit. Extracted genomic DNA was used to quantify the DNA quality using NanoDrop spectrophotometer. *VDR* gene primers were adapted from the recently published article (Ghada Bin Saif & Imran Ali Khan, 2022) and all 4 single nucleotide polymorphisms were selected. The primer sequence of four polymorphisms were shown below:

(*Apal*/*TaqI*) F: AGAGCATGGACAGGGAGCAAG and R: GCAACTCCTCATG GCTGAGGTCTCA; (*BsmI*) F: CAACCAAGACTACAACCGCGTCAGTGA and R: AACCAGCGGAAGAGGTCAAGGG; (*FokI*) F: AACCAGCGGAAGAGGTCAAGGG and R: ATG-GAAACACCTTGCTTCTTCTCCCTC

Next, Polymerase Chain Reaction (PCR) was amplified with 4 polymorphisms present in the *VDR* gene. The initial denaturation took place for 10 mins at 95°C, denaturation at 95°C–30s, annealing took place at different temperatures for 4 polymorphisms, extension took place at 72°C–45s and final extension at 72°C–10 mins. The conditions of thermal cycle were followed for 35 cycles. After completion of amplification, PCR products were run on 2% of agarose gel stained with ethidium bromide and then restriction fragment length polymorphism analysis was performed using specific restriction enzymes as discussed in Table 1. Digestion was performed based on previous study (Alharbi *et al.*, 2017) for 24 hours. All types of PCR products were run on 2% agarose gel.

Statistical analysis

The visible data is regularly distributed and reported as mean \pm S.D.; this study was conducted as a frequency-based analysis. Chi-square analysis was used to identify statistically significant differences between the case and control groups. Goodness-of-fit analysis was used to establish Hardy-Weinberg equilibrium (HWE). The frequencies of each genotype and allele were computed. Genotype and allelic frequencies comparisons were made between healthy controls and vitiligo patients, and other genetic models. This study was determined as the odds ratio and its 95% CI. In this study, a one-way Anova analysis (Khan *et al.*, 2019) was used in Table 4. However, *p*-values below 0.05 were regarded as statistically significant (*p*<0.05).

RESULTS

In this research, a total of 70 FH cases and 50 healthy control subjects were enrolled. The FH patients were clinically diagnosed based on Dutch group criteria and equally 50% of males and females were selected in both FH cases and controls. The mean age for both study groups were in between 51.98 \pm 10.61 in controls

Table 1. List of *VDR* gene polymorphism and restriction enzymes used in this study

Rs number	PCR products	Annealing temperature	Restriction enzymes	Restriction time	Temperature for digestion	Digested products
rs79785232	746bp	66°C	Apal	18 hours	37°C	746/529/217bp
rs1544410	872bp	66°C	BsmI	18 hours	37°C	872/701/171bp
rs731236	746bp	66°C	TaqI	18 hours	37°C	427/293/252/201/169/92bp
rs2228570	267bp	66°C	FokI	18 hours	37°C	267/193/70bp

Table 2. Anthropometric measurements between FH cases and control subjects

S. No	Patients' measurements/Values	FH (n=70)	Controls (n=50)	T-tests
1	Age (years)	52.47±10.51	51.98±10.61	0.80
2	Gender (Female: Male)	35:35	25:25	0.99
3	Weight (kgs)	73.75±9.15	73.15±9.21	0.35
4	Height (cms)	165.56±7.47	165.35±7.58	0.15
5	BMI (kg/m ²)	26.84±2.49	26.81±2.53	0.06
6	TG (mmol/L)	2.02±1.34	1.67±0.87	0.11
7	TC (mmol/L)	5.29±0.94	5.01±0.98	0.11
8	HDLc (mmol/L)	0.68±0.21	0.63±0.24	0.22
9	LDLc (mmol/L)	3.76±0.83	3.80±0.92	0.80

Table 3. HWE analysis was studied in POLYMORPHISMS s in the VDR gene

Polymorphisms	Minor allele	VAF	χ^2	HW <i>p</i> -value
rs79785232	C	0.05	0.13	0.70
rs1544410	G	0.17	6.55	0.01
rs731236	C	0.27	6.83	0.008
rs2228570	T	0.13	1.11	0.29

P-value indicates one degree of freedom (if *p*<0.05 indicates non-consistent with HWE; VAR – Variable Allele Frequencies)

Table 4. Genotype and allele frequencies between FH cases and controls in the VDR gene

VDR-Genotypes	Controls (n=50)	FH cases (n=70)	ORs (95%CI); <i>p</i> -values
AA (ApaI)	45 (90%)	39 (55.7%)	Reference
AC	05 (10%)	31 (44.3%)	OR-7.15 (95% CI: 2.53-20.18); <i>p</i> =0.0005
CC*	00 (0%)	00 (0%)	OR-1.15 (95% CI: 0.02-59.39); <i>p</i> =0.94*
AC+CC vs AA*	05 (10%)	31 (44.3%)	OR-6.59 (95% CI: 2.42-17.95); <i>p</i> =0.0006
A	95 (0.95)	78 (0.56)	Reference
C	05 (0.05)	62 (0.44)	OR-15.1 (95% CI: 5.78-39.41); <i>p</i> <0.001
AA (BsmI)	37 (74%)	30 (42.9%)	Reference
AG	09 (18%)	28 (40%)	OR-3.83 (95% CI: 1.57-9.36); <i>p</i> =0.002
GG	04 (08%)	12 (17.1%)	OR-3.7 (95% CI: 1.08-12.65); <i>p</i> =0.02
AG+GG vs AA	13 (26%)	40 (57.1%)	OR-3.79 (95% CI: 1.72-8.35); <i>p</i> =0.0007
A	83 (0.83)	88 (0.63)	Reference
G	17 (0.17)	52 (0.37)	OR-2.88 (95% CI: 1.54-5.38); <i>p</i> =0.0006
TT (TaqI)	23 (46%)	46 (65.7%)	Reference
TC	27 (54%)	24 (34.3%)	OR-0.44 (95% CI: 0.21-0.93); <i>p</i> =0.03
CC*	00 (0%)	00 (0%)	OR-0.51 (95% CI: 0.009-26.27); <i>p</i> =0.73
TC+CC vs TT*	27 (54%)	24 (34.3%)	OR-0.45 (95% CI: 0.21-0.94); <i>p</i> =0.03
T	73 (0.73)	116 (0.83)	Reference
C	27 (0.27)	24 (0.17)	OR-0.55 (95% CI: 0.31-1.05); <i>p</i> =0.06
CC (FokI)	37 (74%)	53 (75.7%)	Reference
CT	13 (26%)	17 (24.3%)	OR-0.91 (95% CI: 0.39-2.11); <i>p</i> =0.83
TT*	00 (0%)	00 (0%)	OR-0.71 (95% CI: 0.01-36.11); <i>p</i> =0.85
CT+TT vs CC*	13 (26%)	17 (24.3%)	OR-0.90 (95% CI: 0.39-2.07); <i>p</i> =0.81
C	87 (0.87)	123 (0.88)	Reference
T	13 (0.13)	17 (0.12)	OR-0.92 (95% CI: 0.42-2.01); <i>p</i> =0.84

Table 5. Anova Analysis Performed between Heterozygous and Variant genotypes in FH cases with BMI and lipid profile

	rs79785232 (AC=31)	rs1544410 (AG+GG=40)	rs731236 (TC=24)	rs2228570 (CT=17)	p-value
BMI (kg/m ²)	27.32±2.29	27.08±2.61	26.54±2.69	27.76±1.56	0.12
TG (mmol/L)	2.32±1.63	2.01±1.18	1.91±1.16	2.31±1.96	0.02
TC (mmol/L)	5.34±0.84	5.41±0.91	5.62±0.90	5.42±1.16	0.48
HDLc (mmol/L)	0.67±0.18	0.68±0.20	0.69±0.19	0.65±0.25	0.46
LDLc (mmol/L)	3.74±0.90	3.83±0.82	3.72±0.88	3.90±0.81	0.93

and 52.74±10.51 in FH cases ($p=0.80$). Both cases, FH (26.84±2.49) and controls (26.81±2.53), were found to be overweight ($p=0.06$) and mean levels of weight was found to be an average of 73kg in both groups ($p=0.35$). None of the parameters of lipid profile (TG/TC=0.11; HDLc=0.22 and LDLc=0.80) were associated when compared between FH group and control. Table 2 defines the general characteristics used for FH group and control group.

The polymorphic site studied in VDR gene was in Hardy Weinberg Equilibrium in the whole sample. In this study, p -value was measured with one degree of freedom in which $p<0.05$ is considered as non-consistent. In this study, ApaI ($p=0.70$ and $X^2=0.13$) and FokI ($p=0.008$ and $X^2=6.83$) were associated whereas in other polymorphisms such as BsmI ($p=0.01$ and $X^2=6.55$) and TaqI were non-significant. Table 3 consists of HWE analysis details.

Table 4 presents the group of polymorphisms present in the VDR gene in FH cases and controls. The ApaI polymorphism was strongly associated with allele (OR-15.1 (95% CI: 5.78-39.41); $p<0.001$), genotypes (AC vs AA: OR-7.15 (95% CI: 2.53-20.18); $p=0.0005$) and dominant model (OR-6.59 (95% CI: 2.42-17.95); $p=0.0006$). A similar association was found in BsmI polymorphism (G vs A: OR-2.88 (95% CI: 1.54-5.38); $p=0.0006$; AG vs AA: OR-3.83 (95% CI: 1.57-9.36); $p=0.002$ and AG+GG vs AA: OR-3.79 (95% CI: 1.72-8.35); $p=0.0007$). A negative impact was confirmed in both TaqI (C vs T: OR-3.79 (95% CI: 1.72-8.35); $p=0.0007$; TC vs TT: OR-0.44 (95% CI: 0.21-0.93); $p=0.03$ and TC+CC vs TT: OR-0.45 (95% CI: 0.21-0.94); $p=0.03$) and FokI (T vs C: OR-0.92 (95% CI: 0.42-2.01); $p=0.84$; CT vs CC: OR-0.91 (95% CI: 0.39-2.11); $p=0.83$ and CT+TT vs CC: OR-0.90 (95% CI: 0.39-2.07); $p=0.81$). Yates correction couldn't document the association in any of genotypes or allele in FH groups.

Anova analysis was confirmed in TG group ($p=0.02$) in the lipid profile and BMI parameters. TC ($p=0.48$), HDLc ($p=0.46$), LDLc ($p=0.93$) and BMI ($p=0.12$) were not associated when compared with heterozygous and homozygous mutants in ApaI, BsmI, TaqI and FokI polymorphisms in VDR gene. Table 5 shows the ANOVA analysis within FH heterozygous and homozygous mutants in the VDR gene.

DISCUSSION

The hypercholesterolemia that runs in families is called familial hypercholesterolemia, and it's inherited in an autosomal dominant pattern. Patients are typically heterozygous, meaning they carry only one copy of the genetic mutation. Homozygosity occurs exceedingly infrequently when a patient gets an erroneous gene from both parents; having homozygous FH results in extraordinarily high blood cholesterol levels. LDLR gene mutations are frequently responsible. Gain-of-function mu-

tations in *ApoB* and *PCSK9* genes, among others, have been reported (Pejic & Lee, 2006). Patients with FH have elevated LDL-c blood levels, which increases the risk of coronary artery disease and heart attack in the future (Alharbi *et al.*, 2015). The relationship between cholesterol and vitamin D is that human skin cells require cholesterol in order to produce vitamin D when exposed to sunlight. The initial phase requires cholesterol, but vitamin D is converted further in the liver and kidneys. Increased risk of cardiovascular disease (CVD) has been associated with low serum 25-hydroxyvitamin D [25(OH)D] levels, which plays an important part in the onset of osteoporosis, but it has also been connected to other health problems. Diabetes (type 1 and 2), multiple sclerosis, autoimmune, and viral diseases have all been linked to vitamin D deficiency. The relation between Vitamin D and cholesterol is connected with 7DHC, making the influence of vitamin D status on blood lipids particularly intriguing, despite conflicting findings from earlier studies (Gumus *et al.*, 2023; Hong, 2022). Documented studies in vitamin D deficiency have been discovered as a potential risk factor for CVD, either independently or in conjunction with other cardiovascular risk factors such as diabetes, hypertension, or obesity (Burgess & Gill, 2022; Norman & Powell, 2014; Pilz *et al.*, 2016). The main cause of vitamin D deficiency include a lack of sun exposure, a sedentary lifestyle, being overweight, having type 2 diabetes, lower HDLc level, being over age, having dark skin, living far from the equator, experiencing winter, being a smoker, being exposed to secondhand smoke, having impaired absorption due to renal and liver disease, and taking certain medications (Mozos & Marginean, 2015).

The aim of this study was to investigate the role of VDR gene polymorphism in diagnosed FH patients in the Saudi population. The present study results confirmed that ApaI and FokI polymorphisms were found to be in HWE analysis. Only ApaI and BsmI polymorphisms showed both allele and genotype association between FH patients and controls ($p<0.05$). In our study, ApaI (AC vs AA: $p=0.0005$, AC+CC vs AA: $p=0.0006$ and C vs A: $p<0.001$) and BsmI (AG vs AA: $p=0.002$, GG vs AA: $p=0.02$, AG+GG vs AA: $p=0.0007$ and G vs A: $p=0.0006$) polymorphism was associated when compared between FH cases and controls. ANOVA analysis confirmed that TG levels were associated with combination of heterozygous and homozygous genotypes present in all four polymorphisms studied in this population. The first step was measuring the cholesterol and vitamin D levels of healthy women. As a result of Gemfibrozil and Atorvastatin's ability to inhibit HMG-CoA reductase production, blood cholesterol levels have dropped dramatically in the second phase. Within this population, vitamin D levels also went down. Women who took medication for vitamin D, on the other hand, had a low vitamin D level (Han *et al.*, 2021). Other similar studies have been documented between vitamin D and

cholesterol related diseases. One of the Spanish studies measured vitamin D (25(OH)D) levels in hypercholesterolemia patients and found a significant correlation (Cutillas-Marco *et al.*, 2013). Rady and others confirmed that the FF genotype in the VDR gene is associated with a threefold risk of juvenile idiopathic arthritis (Rady *et al.*, 2022). The study by Han and others shows compelling evidence that vitamin D insufficiency is linked to atherogenic dyslipidemia, and in particular, elevated small dense LDL-C levels in middle-aged adults without CVD (Han *et al.*, 2021). Previous studies have linked dyslipidemia (Jorde & Grimnes, 2011) and lipid profile (Ponda *et al.*, 2012) to vitamin D deficiency. Lipid levels in adulthood are also correlated with vitamin D levels, which are in turn linked to the gene's steady association with vitamin D levels in the blood (Jorde & Grimnes, 2011; Nissen *et al.*, 2014; Thongthai *et al.*, 2015).

Vital biological functions like cell proliferation, regulation, and differentiation, bone formation, and immune response modulation are all influenced by the endocrine vitamin D system. VDR is a member of the steroid hormone family of nuclear receptors and is responsible for the transcriptional control of a number of hormone-responsive genes by its binding to the active metabolite calcitriol. Due to the presence of VDRs in all major cardiovascular cell types, including vascular smooth muscle cells, endothelial cells, cardiomyocytes, platelets, and most immune cells, it is possible that VDR gene polymorphisms influence CVD. In addition, the VDR plays a crucial role in modulating the expression of several proteins that play a role in controlling the cardiovascular system. These include renin, endothelial nitric oxide synthase, and NADPH oxidase (Abouzid *et al.*, 2021). The role of vitamin D and the VDR gene in Saudi Arabia is critical, as one meta-analysis study conducted in Saudi Arabia revealed that 60% of the healthy population in Saudi Arabia has a vitamin deficiency (Al-Alyani *et al.*, 2018). The normal value of vitamin D deficiency in Saudi Arabia has been confirmed as 24.96 nmol/L which is below the limit (Albaik *et al.*, 2016). The VDR gene polymorphism studies were carried out in the Saudi population with different human diseases and confirmed all forms of association (Ali *et al.*, 2018; Alkhayal *et al.*, 2016; Alzaim *et al.*, 2022; Ansari *et al.*, 2021; Mansy *et al.*, 2019; Nemenqani *et al.*, 2015; G. B. Saif & I. A. Khan, 2022; Taha *et al.*, 2019; Zeidan *et al.*, 2022). Additionally, there are limited documented studies of Saudi Arabian patients with confirmed FH. The lack of cholesterol data was one of the study limitations.

CONCLUSION

Both ApaI and BsmI polymorphisms was associated to FH via allele and genotype frequencies in the Saudi population. The Saudi Arabia VDR gene polymorphism link was built with FH patients.

Declarations

Conflict of interest: Not applicable for this study.

REFERENCES

- Abouzid M, Kruszyna M, Burchardt P, Kruszyna L, Głowska FK, Karañiewicz-Lada M (2021) Vitamin D receptor gene polymorphism and vitamin d status in population of patients with cardiovascular disease – a preliminary study. *Nutrients* 13: 3117. <https://doi.org/10.3390/nu13093117>
- Al-Allaf FA, Athar M, Abduljaleel Z, Bouazzaoui A, Taher MM, Own R, Al-Allaf AF, AbuMansour I, Azhar Z, Ba-Hammam FA (2014) Identification of a novel nonsense variant c. 1332dup p.(D445*) in the LDLR gene that causes familial hypercholesterolemia. *Human Genome Variation* 1: 1–3. <https://doi.org/10.1038/hgv.2014.21>
- Al-Alyani H, Al-Turki H. A., Al-Essa O. N., Alani F. M., Sadat-Ali M (2018) Vitamin D deficiency in Saudi Arabians: a reality or simply hype: a meta-analysis (2008–2015) *J Family Commun Med* 25: 1. https://doi.org/10.4103/jfcm.JFCM_73_17
- Albaik M, Khan J, Iyer A (2016) Vitamin D status in Saudi population: a mini review. *Indian J Endocrinol Metab* 6: 629–632
- Alhabib KF, Al-Rasadi K, Almighal TH, Batais MA, Al-Zakwani I, Al-Allaf FA, Al-Waili K, Zadjali F, Alghamdi M, Alnouri F (2021) Familial hypercholesterolemia in the Arabian Gulf region: Clinical results of the gulf fh registry. *PLoS One* 16: e0251560. <https://doi.org/10.1371/journal.pone.0251560>
- Alharbi KK, Alnabaheen MS, Alharbi FK, Hasanato RM, Khan IA (2017) Q192R polymorphism in the PON1 gene and familial hypercholesterolemia in a Saudi population. *Ann Saudi Med* 37: 425–432. <https://doi.org/10.5144/0256-4947.2017.425>
- Alharbi KK, Kashour TS, Al-Hussaini W, Nabaheen MS, Hasanato RM, Mohamed S, Tamimi W, Khan IA (2015) Screening for genetic mutations in LDLR gene with familial hypercholesterolemia patients in the Saudi population. *Acta Biochim Pol* 62: 559–562. https://doi.org/10.18388/abp.2015_1015
- Ali R, Fawzy I, Mohsen I, Settin A (2018) Evaluation of vitamin D receptor gene polymorphisms (Fok-I and Bsm-I) in T1DM Saudi children. *J Clin Lab Anal* 32: e22397. <https://doi.org/10.1002/jcla.22397>
- Alkhayal KA, Awadalia ZH, Vaali-Mohammed MA, Al Obeed OA, Al Wesaimer A, Halwani R, Zubaidi A. M, Khan Z, Abdulla MH (2016) Association of vitamin D receptor gene polymorphisms with colorectal cancer in a Saudi Arabian population. *PLoS One* 11: e0155236. <https://doi.org/10.1371/journal.pone.0155236>
- Alshammery AF, Khan IA (2021) Screening of obese offspring of first-cousin consanguineous subjects for the angiotensin-converting enzyme gene with a 287-bp Alu sequence. *J Obesity Metabolic Syndrome* 30: 63–71. <https://doi.org/10.7570/jomes20086>
- Alzahrani SH, Bima A, Algethami MR, Awan Z (2020) Assessment of medical intern's knowledge awareness and practice of familial hypercholesterolemia at academic institutes in Jeddah Saudi Arabia. *Lipids Health Dis* 19: 1–11. <https://doi.org/10.1186/s12944-020-01266-y>
- Alzaim M, Al-Daghri NM, Sabico S, Fouda MA, Al-Musharaf S, Khatat MNK, Mohammed AK, Al-Ajlan A, Binjawhar DN, Wood R (2022) The association between foki vitamin d receptor polymorphisms with metabolic syndrome among pregnant Arab women. *Front Endocrinol (Lausanne)* 13: 844472. <https://doi.org/10.3389/fendo.2022.844472>
- Ansari MGA, Mohammed AK, Wani KA, Hussain SD, Alnaami AM, Abdi S, Aljohani NJ, Al-Daghri NM (2021) Vitamin D receptor gene variants susceptible to osteoporosis in Arab post-menopausal women. *Curr Issues Mol Biol* 43: 1325–1334. <https://doi.org/10.3390/cimb43030094>
- Batais MA, Almighal TH, Shaik NA, Alharbi FK, Alharbi KK, Khan IA (2019) Screening of common genetic variants in the APOB gene related to familial hypercholesterolemia in a Saudi population: a case – control study. *Medicine* 98: e14247. <https://doi.org/10.1097/MD.00000000000014247>
- Beheshti SO, Madsen CM, Varbo A, Nordestgaard BG (2020) Worldwide prevalence of familial hypercholesterolemia: meta-analyses of 11 million subjects. *J Am College Cardiol* 75: 2553–2566. <https://doi.org/10.1016/j.jacc.2020.03.057>
- Bikle DD (2014) Vitamin D metabolism mechanism of action and clinical applications. *Chem Biol* 21: 319–329. <https://doi.org/10.1016/j.chembiol.2013.12.016>
- Burgess S, Gill D (2022) Genetic evidence for vitamin D and cardiovascular disease: choice of variants is critical. *Eur Heart J* 43: 2659. <https://doi.org/10.1093/eurheartj/ehac070>
- Cutillas-Marco E, Prosper AF, Grant WB, Morales-Suárez-Varela MM (2013) Vitamin D status and hypercholesterolemia in Spanish general population. *Dermato-Endocrinol* 5: 358–362. <https://doi.org/10.4161/derm.27497>
- Gumus R, Capik O, Gundogdu B, Tatar A, Altinkaynak K, Ozdemir Tozlu O, Karatas OF (2023) Low vitamin D and high cholesterol facilitate oral carcinogenesis in 4NQO-induced rat models via regulating glycolysis. *Oral Diseases* 29: 978–989. <https://doi.org/10.1111/odi.14117>
- Guo Y, Zhang Y, Tang X, Liu X, Xu H (2023) Association between Vitamin D receptor (VDR) gene polymorphisms and hypertensive disorders of pregnancy: a systematic review and meta-analysis. *Peer J* 11: e15181. <https://doi.org/10.7717/peerj.15181>
- Han Y-Y, Hsu SH-J, Su T-C (2021) Association between vitamin D deficiency and high serum levels of small dense LDL in middle-aged adults. *Biomedicine* 9: 464. <https://doi.org/10.3390/biomedicine9050464>
- Hong J (2022) A new perspective on cholesterol in pediatric health: association of vitamin D metabolism respiratory diseases and

- mental health problems. *Clin Exp Pediatr* **65**: 65–72. <https://doi.org/10.3345/cep.2020.00934>
- Hori M, Takahashi A, Hosoda K, Ogura M, Harada-Shiba M (2023) A low-frequency APOB p.(Pro955Ser) variant contributes to the severity of/variability in familial hypercholesterolemia. *J Clin Endocrinol Metabol* **108**: 422–432. <https://doi.org/10.1210/clinem/dgac572>
- Huangfu G, Jaltotage B, Pang J, Lan NS, Abraham A, Otto J, Ildayhid AR, Rankin JM, Chow BJ, Watts GF (2023) Hepatic fat as a novel marker for high-risk coronary atherosclerotic plaque features in familial hypercholesterolaemia. *Metabolism* **139**: 155370. <https://doi.org/10.1016/j.metabol.2022.155370>
- Jorde R, Grimnes G (2011) Vitamin D and metabolic health with special reference to the effect of vitamin D on serum lipids. *Progress Lipid Res* **50**: 303–312. <https://doi.org/10.1016/j.plipres.2011.05.001>
- Kayikcioglu M, Tokgozoglu L (2023) Current treatment options in homozygous familial hypercholesterolemia. *Pharmaceuticals* **16**: 64. <https://doi.org/10.3390/ph16010064>
- Khan IA, Jahan P, Hasan Q, Rao P (2019) Genetic confirmation of T2DM meta-analysis variants studied in gestational diabetes mellitus in an Indian population. *Diabetes Metabol Syndrome: Clin Res Rev* **13**: 688–694. <https://doi.org/10.1016/j.dsx.2018.11.035>
- Mansy W, Ibrahim NH, Al-Gawhary S, Alsubaie SS, Abouelkheir MM, Fatani A, Abd Al Reheem F, El Awady H, Zakaria EA (2019) Vitamin D status and vitamin D receptor gene polymorphism in Saudi children with acute lower respiratory tract infection. *Mol Biol Rep* **46**: 1955–1962. <https://doi.org/10.1007/s11033-019-04645-6>
- Maštaleru A, Cojocariu SA, Oancea A, Constantin MML, Roca M, Zota IM, Abdulan I, Rusu C, Popescu R, Antoci LM (2022) Genetic polymorphisms in a familial hypercholesterolemia population from North-Eastern Europe. *J Personalized Med* **12**: 429. <https://doi.org/10.3390/jpm12030429>
- Mozos I, Marginean O (2015) Links between vitamin D deficiency and cardiovascular diseases. *BioMed Res Int* **2015**: 109275. <https://doi.org/10.1155/2015/109275>
- Nemenqani DM, Karam RA, Amer MG, Abd El Rahman TM (2015) Vitamin D receptor gene polymorphisms and steroid receptor status among Saudi women with breast cancer. *Gene* **558**: 215–219. <https://doi.org/10.1016/j.gene.2014.12.065>
- Nissen J, Rasmussen LB, Ravn-Haren G, Andersen EW, Hansen B, Andersen R, Mejbom H, Madsen KH, Vogel U (2014) Common variants in CYP2R1 and GC genes predict vitamin D concentrations in healthy Danish children and adults. *PLoS One* **9**: e89907. <https://doi.org/10.1371/journal.pone.0089907>
- Norman P, Powell J (2014) Vitamin D and cardiovascular disease. *Circulation Research* **114**: 379–393. <https://doi.org/10.1161/CIRCRES-SAHA.113.301241>
- Pejic RN, Lee DT (2006) Hypertriglyceridemia. *J Am Board Family Med* **19**: 310–316. <https://doi.org/10.3122/jabfm.19.3.310>
- Pilz S, Verheyen N, Grubler MR, Tomaschitz A, März W (2016) Vitamin D and cardiovascular disease prevention. *Nat Rev Cardiol* **13**: 404–417. <https://doi.org/10.1038/nrcardio.2016.73>
- Ponda MP, Huang X, Odeh M, A, Breslow JL, Kaufman HW (2012) Vitamin D may not improve lipid levels: a serial clinical laboratory data study. *Circulation* **126**: 270–277. <https://doi.org/10.1161/CIRCULATIONAHA.111.077875>
- Rady SA, Doudar NA, Boutros OE, Hana MT, Meabed MH (2022) Effect of vitamin D receptor gene polymorphism on lipid profile in Egyptian children with juvenile idiopathic arthritis. *Egyptian Rheumatol* **44**: 251–255. <https://doi.org/10.1016/j.ejr.2022.01.004>
- Ruiz-Pesini E, Bayona-Bafaluy MP, Sanclemente T, Puzo J, Montoya J, Pacheu-Grau D (2023) Mitochondrial genetic background may impact statins side effects and atherosclerosis development in familial hypercholesterolemia. *Int J Mol Sci* **24**: 471. <https://doi.org/10.3390/ijms24010471>
- Saif GB, Khan IA (2022) Association of genetic variants of the vitamin D receptor gene with vitiligo in a tertiary care center in a Saudi population: a case-control study. *Ann Saudi Med* **42**: 96–106. <https://doi.org/10.5144/0256-4947.2022.96>
- Taha IM, Allah AMA, El Tarhoumy S (2019) Association of vitamin D gene polymorphisms and bone mineral density in healthy young Saudi females. *Curr Mol Med* **19**: 196–205. <https://doi.org/10.2174/1566524019666190409122155>
- Tang L, Fang W, Lin J, Li J, Wu W, Xu J (2018) Vitamin D protects human melanocytes against oxidative damage by activation of Wnt/ β -catenin signaling. *Lab Invest* **98**: 1527–1537. <https://doi.org/10.1038/s41374-018-0126-4>
- Thongthai P, Chailurkit L-o, Chanprasertyothin S, Nimitphong H, Sritara P, Aekplakorn W, Ongphiphadhanakul B (2015) Vitamin D binding protein gene polymorphism as a risk factor for vitamin D deficiency in Thais. *Endoc Pract* **21**: 221–225. <https://doi.org/10.4158/EP14266.OR>
- Todorovova V, Altschmiedova T, Vrablik M, Ceska R (2023) Familial hypercholesterolemia: real-world data of 1236 patients attending a Czech lipid clinic. *Genetics Familial Hypercholesterol: New Insight*, Vol II, 16648714
- Zeidan NMS, Lateef HMAE, Selim DM, Razek SA, Abd-Elrehim GAB, Nashat M, ElGyar N, Waked NM, Soliman AA, Elhewala AA, Shehab MMM, Ibraheem AAA, Shehata H, Yousif YM, Akeel NE, Hashem MIA, Ahmed AA, Emam AA, Abdelmohsen MM, Ahmed MF, Saleh ASE, Eltrawy HH, Shahin GH, Nabil RM, Hosny TA, Abdelhamed MR, Afify MR, Alharbi MT, Nagshabandi MK, Tarabulsi MK, Osman SF, Abd-Elrazek ASM, Rashad MM, El-Gaaly SAA, Gad SAB, Mohamed MY, Abdelkhalek K, Yousef AA (2022) Vitamin D deficiency and vitamin D receptor FokI polymorphism as risk factors for COVID-19. *Pediatr Res* **93**: 1383–1390. <https://doi.org/10.1038/s41390-022-02275-6>

Formononetin enhances the chemosensitivity of triple negative breast cancer *via* BTB domain and CNC homolog 1-mediated mitophagy pathways

Shan Li[✉], Linlian Zhu[#], Yufeng He and Ting Sun

Oncology Department, Dongtai People's Hospital, Dongtai City, Jiangsu Province 224200, China

This study aimed to investigate the effects of formononetin on triple negative breast cancer (TNBC). Clinical samples were collected from patients with TNBC. Overall survival rates were evaluated using the Kaplan-Meier method. Gene expression was determined using immunohistochemistry, immunofluorescence and western blot. Cellular functions were determined using CCK-8, colony formation and propidium iodide (PI) staining. Xenograft assay was performed to further verify the effects of formononetin (FM) on TNBC. We found that FM combined therapy suppressed the metastasis of TNBC and increased the overall survival rates of TNBC patients. Moreover, FM suppressed the proliferation and induced mitochondrial damage and apoptosis of TNBC cells. FM increased the expression of the BTB domain and CNC homolog 1 (BACH1) in TNBC tissues as well as cells. However, BACH1 knockdown antagonized the effects of FM and promoted the survival of TNBC cells. FM suppressed the tumor growth of TNBC. Taken together, FM suppressed the aggressiveness of TNBC *via* BACH1/p53 signaling. Therefore, FM may be an alternative strategy for TNBC.

Keywords: triple negative breast cancer, formononetin, chemosensitivity, BACH1, mitophagy

Received: 18 August, 2022; revised: 02 March, 2023; accepted: 16 April, 2023; available on-line: 06 September, 2023

✉e-mail: lishan_dtp@163.com

[#]Shan Li and Linlian Zhu contributed equally in this study.

Abbreviations: BACH1, BTB domain and CNC homolog 1; FM, formononetin; PI, propidium iodide; TNBC, triple negative breast cancer

INTRODUCTION

Breast cancer is the most common tumor among women worldwide (Braden *et al.*, 2014; Burstein *et al.*, 2019). Recent decades witness an increase in the incidence and mortality of breast cancer in China (Ding *et al.*, 2020; Fan *et al.*, 2014). Triple negative breast cancer (TNBC) is characterized by a high proliferative index, histological grade, and metastatic states (Garrido-Castro *et al.*, 2019). Although great advances have been made in chemotherapy, radiotherapy, and surgery for TNBC (Bianchini *et al.*, 2016). However, the overall survival rates of TNBC are still unsatisfactory (Newman and Kaljee 2017). The high recurrence and metastatic properties of TNBC neutralize the clinical outcomes (Xu *et al.*, 2020). Therefore, a new strategy for TNBC is urgently needed.

Traditional Chinese medicine (TCM), with high efficiency and few side effects, is widely applied in the treatment of breast cancer (Chan *et al.*, 2021; Yang *et*

al., 2021). Formononetin (FM), extracted from *astragalus membranaceus* and *spatolobus suberectus* and with anti-inflammatory and anti-carcinogenic properties, is used as adjuvant therapy for breast cancer (Ma *et al.*, 2020; Xin *et al.*, 2019; Yu *et al.*, 2020). Previous studies reveal that formononetin exerts its anti-cancer function *via* modulating several signaling. For instance, formononetin suppresses the chemoresistance of TNBC *via* inactivating autophagy (Li *et al.*, 2021). Formononetin induces prostate cancer cell mitochondrial and apoptosis *via* regulating IGF-1/IGF-1R pathways (Huang *et al.*, 2013). Additionally, formononetin inhibits the immune suppressiveness of cervical cancer through inactivating MYC/STAT3/PD-L1 signaling (Wang *et al.*, 2022). This study explored the effects of NP (vinorelbine and cisplatin) combined with formononetin on TNBC.

MATERIALS AND METHODS

Patients

Clinical samples were collected from patients with refractory TNBC undergoing chemotherapy (vinorelbine and cisplatin, NP) with or without FM. at People's Hospital of Dongtai City from April 1, 2019 to March 31, 2021. The samples were immediately stored in liquid nitrogen at -80°C . This study was approved by the Ethical Committee of People's Hospital of Dongtai City. All patients signed confirmed consent. The inclusion criteria are: (1) the patients diagnosed with mTNBC; (2) women under the age of 70; (3) no serious complications occurred after the operation; (4) general condition score: ECOG 0-2; (5) patients in the combined group insisted on taking formononetin for at least 8 months. The exclusion criteria are: the mTNBC patients with an estimated ≤ 3 months of survival time; (2) patients accompanied by severe impairment or insufficiency of heart, liver and kidney functions; (3) patients with poor compliance and unable to adhere to treatment.

Immunohistochemistry

Sections were deparaffinized. Then the slides were blocked with 0.1% Triton X-100. After washing with 10 PBS, the section was incubated in 3% H_2O_2 . The sections were incubated with primary antibody against BTB domain and CNC homolog 1 (BACH1) (ab128486, 1:150, Abcam, USA) at 4°C overnight in shade. The next day, the section was incubated with a secondary antibody at 37°C for 1.5 h in the shade. The slices were counterstained using hematoxylin for 10 min. Finally, the sections were visualized using a microscope (Nikon, Japan).

Cell culture and transfection

Breast cancer cell line MCF7 was purchased from ATCC. Cells were incubated with DMEM containing 10% FBS at 37°C in 5% CO₂.

Cells were treated with 1.5 µM of vinorelbine, 2 µM of cisplatin, 80 µmol/L of FM or 10 mM of N-acetylcysteine (NAC).

Cells were transfected with shBACH1 (sh1, F: 5'-CCGGCCAGCAAGAATGCCCAAGAACTC-3' and R: 5'-AATTCAAAAACCAGCAAGAATGCCCAAGA-3'; sh2, F: 5'-CCGGGCCCATATGCTTGTGT-CATTACTCGA-3' and R: 5'-AATTCAAAAAGCCCAT-ATGCTTGTGTCAAT-3', sh-p53 (5'-GACUCCAGUG-GUAAUCUAC-3') and the negative control (NC, F: 5'-CCGGCAACAAGATGAAGAGCACCAACTC-GAGTTGGTGCTCTTCATCTTGTGTTTTTG-3' and R: 5'-AATTCAAAAACAACAAGATGAAGAGCACCAA CTCGAGTTGGTGCTCTTCATCTTGTG-3') by using Lipofectamine® 3000 for 48 h.

Western blot

Protein was collected from TNBC tissues and cells. Protein concentrated with BCA kit (Beyontine, Shanghai). The protein was isolated using 12% SDS-PAGE. The separated protein was moved onto the PVDF membrane, which was then blocked using 5% skimmed milk. Afterwards, the membranes were incubated with primary antibodies, such as anti-cyto C (ab133504, 1:2000, Abcam, USA), anti-caspase3 (ab32351, 1:5000, Abcam, USA), anti-Bcl-2 (ab32124, 1:1000, Abcam, USA), anti-Bax (ab32503, 1:1000, Abcam, USA), anti-BACH1 (ab300130, 1:1000, Abcam, USA), anti-p53 (ab32389, 1:10000, Abcam, USA), anti-PARK2 (ab73015, 1:1000, Abcam, USA), anti-PINK1 (ab300623, 1:1000, Abcam, USA) and anti-GAPDH (ab9485, 1: 2000, Abcam, USA), and then with secondary antibodies (ab6721, 1:5000, Abcam, USA). Finally, the bands were captured using an ECL kit and analyzed using ImageJ software.

MDA and SOD determination

The release of MDA and SOD was determined using specific commercial kits (Beyotime, Shanghai).

Immunofluorescence

Cells were fixed with 4% paraformaldehyde and permeabilized with 0.2% Triton X-100. Afterwards, cells were sealed with 5% bovine serum. Then cells were incubated with primary antibodies against Hsp60 (ab190828, 1:200, Abcam, USA), BACH1 (ab300130, 1:100, Abcam, USA), cyto-C (ab133504, 1:100, Abcam, USA) and then with secondary antibody. Then cells were counterstained with DAPI. The results were visualized using an immunofluorescence microscope (Zeiss, Germany).

CCK-8 assay

After 48-hour transfection, cells were collected. Then cells were plated into 24-well plates and cultured for 0, 12, 24, and 48 h. After being supplemented with CCK-8 regents and cultured for another 2 h, cells were detected by a microplate reader at the wavelength of 450 nm.

Colony formation assay

After transfection, cells were plated into a 24-well plate. After 2 weeks of culture, cells were fixed and stained with 0.1% crystal violet. Subsequently, the colonies were visualized using a microscope.

Table 1. Baseline demographics and disease

Characteristics	N=88
Female, n (%)	88 (100)
Age, years, median(range)	52 (23-84)
Postmenopausal, n (%)	53 (60.23)
ECOG performance status, n (%)	
0	56 (63.64)
1	32 (36.36)
LDH concentration, n (%)	
<1 xULN	45 (51.14)
≥1 x ULN to <2.5 x ULN	38 (43.18)
≥2.5xULN	2 (2.27)
Unknown	3 (3.41)
Target lesion size, mm, median (range)	48.5 (9-194)
No. of metastatic organ sites, n (%)	
1	26 (29.55)
2	48 (54.55)
≥3	14 (15.90)
Visceral± nonvisceral disease, n (%)	55 (62.50)
Prior NP therapy, n (%)	56 (63.64)
Disease-free interval	
<12 months	39 (44.32)
≥12 months	49 (55.68)
Previous FM therapy, n (%)	32 (36.36)
No. of previous lines of therapy for re-current/metastatic disease, n(%)	
0	85 (96.59)
1	3 (3.41)

Propidium iodide (PI) staining

After transfection, cells were plated into a 24-well plate. Then cells were treated with PI solution (2 µg/mL). Finally, PI positive cells were captured by a fluorescence microscope (Leica, Germany).

Xenograft assay.

18 BALB/c nude mice (6–8 weeks, 18–22 g) were purchased from the Animal Center of Nanjing Medical University. Mice were randomly divided into three groups: control group, NP+FM group, and NP+FM+CDDO-ME (CDDO-ME) group. Each mouse was inoculated subcutaneously with 3×10⁴ cells. The tumor was measured every three days. Tumor size was calculated as followed: $V=lw^2/2$. At 21 days, mice were euthanized, and tumor were collected. This study was authorized by the Animal Care Broad of People's Hospital of Dongtai City.

Statistical analysis

All data were analyzed using SPSS 20.0. The difference was analyzed using the Student t-test and ANOVA assay. The survival rates of patients were analyzed using Kaplan Meier and log-rank test. $P<0.05$ was deemed as a significant difference.

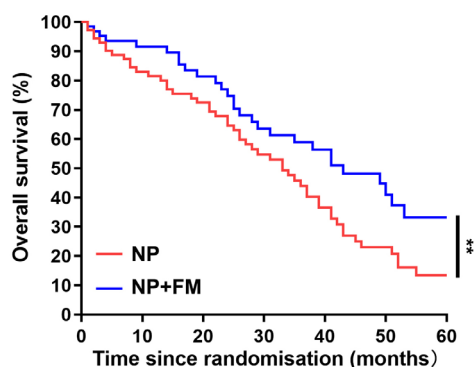


Figure 1. The survival rates of TNBC patients.
The overall survival rates of TNBC patients. ** $P < 0.01$.

RESULTS

The characteristics of TNBC patients

As shown in Table 1, the participants were all female. 68% of the TNBC patients had increased LDH levels. 45% showed visceral metastasis and 33% with recurrence. Additionally, combined therapy significantly improved the overall survival rate of TNBC patients (Fig. 1).

FM promotes oxidative stress and mitochondrial damage in TNBC

Previous studies reveal that FM suppresses the progression of multiple myeloma *via* inducing oxidative stress. Then we determined the release of oxidative stress in TNBC. FM enhanced the effects of NP on the release of MDA and GSH (Figs 2A and B). FM enhanced mitochondrial aggregation induced by NP (Fig.

2C). Moreover, FM+NP markedly increased cyto C protein expression compared with the NP group (Fig. 2D).

FM suppresses the aggressiveness of TNBC cells.

To further verify the effects of FM on TNBC, we determined the MCF7 cellular functions. Compared to the control group, FM treatment significantly suppressed the cell viability of MCF7 cells (Fig. 3A). This was consistent with the results from the colony formation assay. FM markedly inhibited the proliferation of MCF7 cells (Fig. 3B). Additionally, FM significantly enhanced the apoptosis of MCF7 cells (Fig. 3C). FM remarkably increased the protein expression of BAX and Caspase3 and decreased Bcl2 (Fig. 3D).

FM increases BACH1 expression

BACH1 is evidenced to play a vital role in mitochondrial function. We then determined the potentials of BACH1 in TNBC. The online database showed that BACH1 expression was decreased in invasive breast cancer tumors (Fig. 4A). To further verify this, we determined BACH1 expression in TNBC patients. As shown in Fig. 4B, BACH1 expression in patients administrated with NP+FM. Moreover, the protein expression of BACH1 was markedly increased in cells treated with NP+FM (Figs. 4C and D).

BACH1 transmits ROS signaling to mitochondria

BACH1 suppresses the aggressiveness of cancer cells *via* increasing the release of mitochondrial ROS (Hao *et al.*, 2021). We, therefore investigated the potentials of BACH1 mitochondrial ROS. Figure 5A showed the transcription efficiency of sh-BACH1. BACH1 knockdown antagonized the effects of FM and increased the cell ability of MCF7 cells (Fig. 5B). Moreover, BACH1 knockdown suppressed the protein expression of cyto C, and cleaved caspase3 and -9 (Fig. 5C). Additionally, BACH1 knockdown suppressed mitochondrial aggrega-

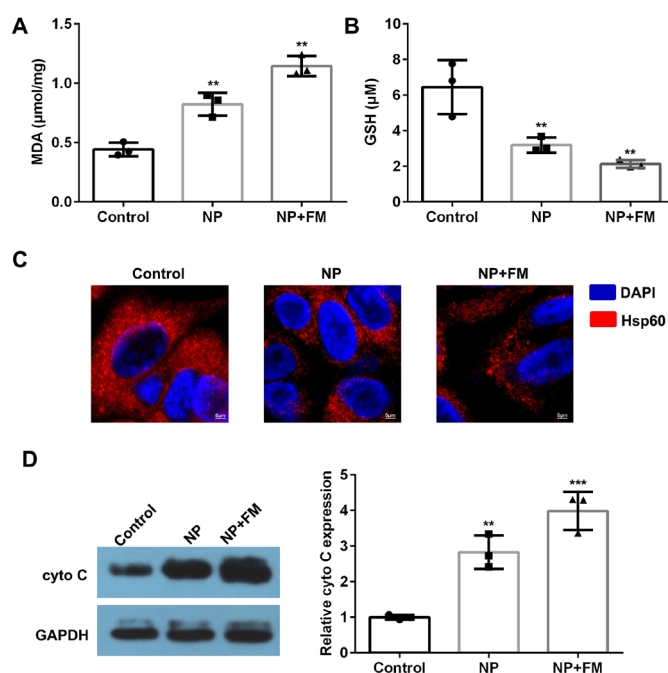


Figure 2. FM increases oxidative stress and mitochondrial damage in TNBC.

The release of MDA (A) and GSH (B) in MCF7 cells. (C) Mitochondrial aggregation determined by immunofluorescence. (D) The protein expression of cyto C in MCF7 cells determined using western blot. ** $P < 0.01$, *** $P < 0.001$.

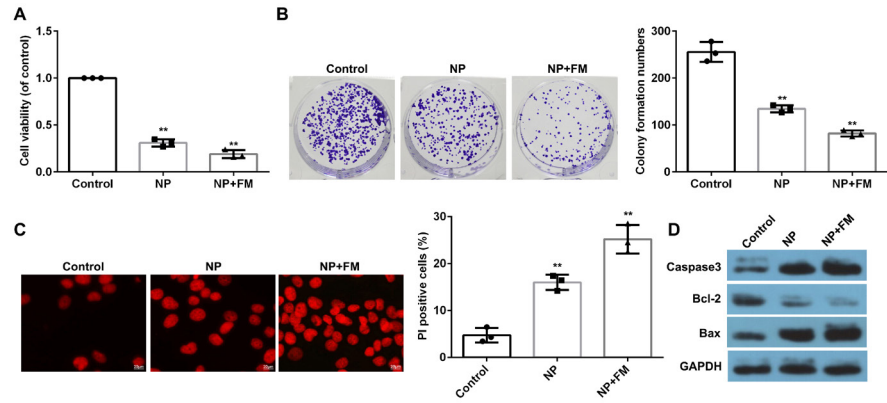


Figure 3. FM suppresses the aggressiveness of MCF7 cells. (A) MCF7 cell viability determined using CCK-8 assay. (B) The proliferation of MCF7 cells detected using a colony formation assay. (C) The apoptosis of MCF7 cells detected using PI staining. (D) The protein expression determined using western blot. ** $P < 0.01$.

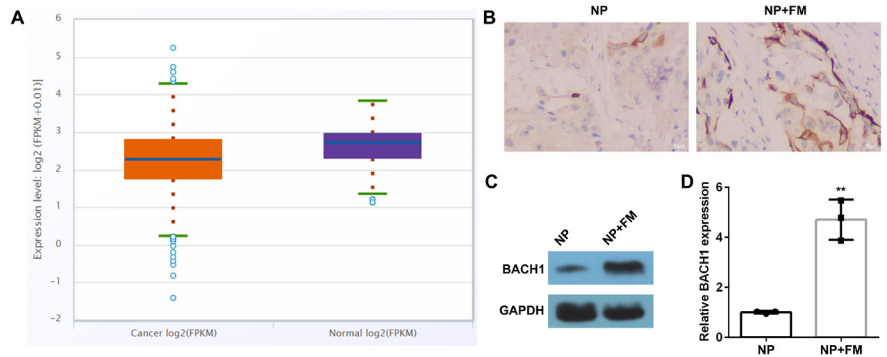


Figure 4. FM increases BACH1 expression. (A) The expression of BACH1. (B) The expression of BACH1 in TNBC patients determined using immunohistochemistry. (C and D) BACH1 protein expression detected using western blot. ** $P < 0.01$.

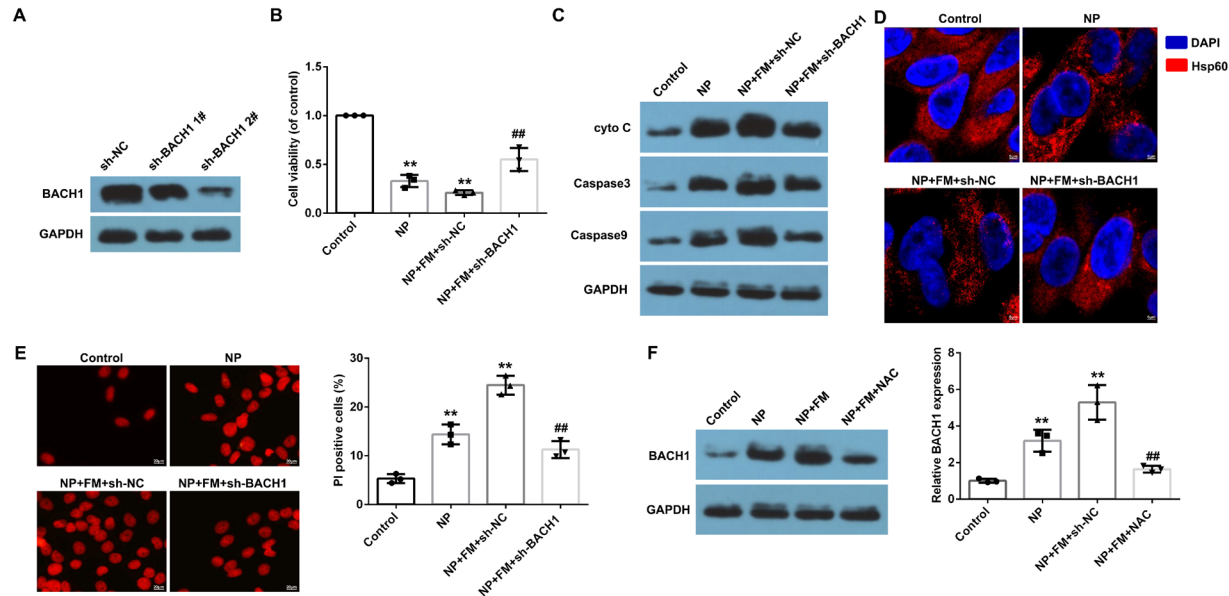


Figure 5. BACH1 transmits ROS signaling to mitochondria. (A) BACH1 protein expression detected using western blot. (B) MCF7 cell viability determined using CCK-8 assay. (C) Caspase3 and -9 protein expression detected using western blot. (D) Mitochondrial aggregation determined by immunofluorescence. (E) The apoptosis of MCF7 cells detected using PI staining. (F) BACH1 protein expression detected using western blot. ** $P < 0.01$, ## $P < 0.01$.

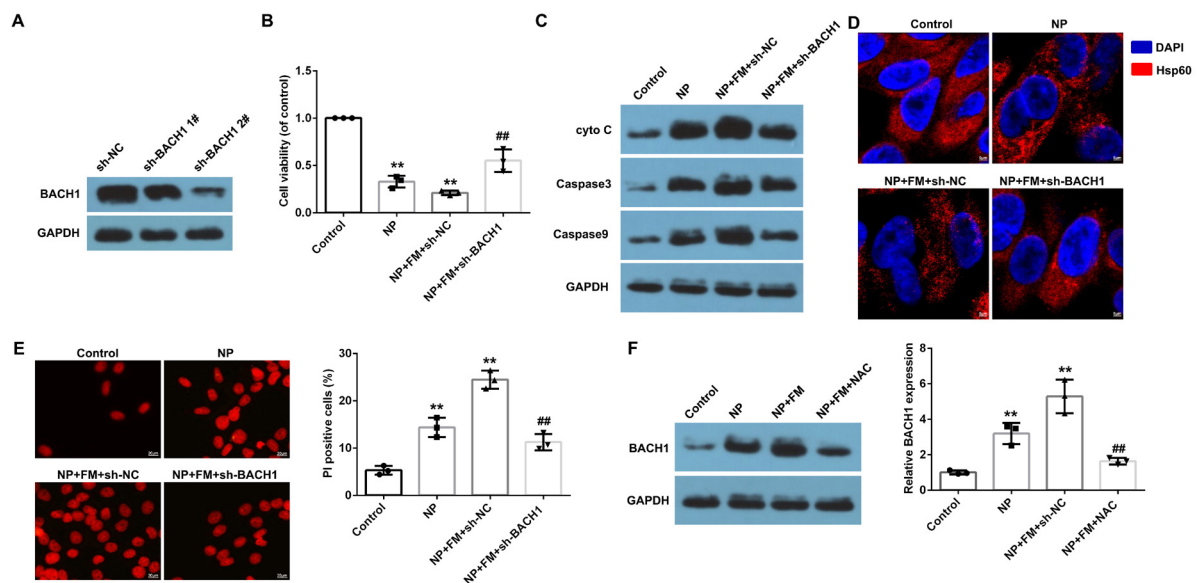


Figure 6. FM suppresses mitophagy via inducing BACH1-mediated activation of p53.

(A) The interaction between BACH1 and p53 predicted using STING. (B) p53 expression determined using immunofluorescence. (C) p53 protein expression determined using western blot. (D) Mitochondrial aggregation determined by immunofluorescence. (E) cyto-C and caspase-9 protein expression determined using western blot. (F) PINK1 and PARK2 protein expression determined using western blot. (G) Cell viability determined using CCK-8 assay. (H) The apoptosis of MCF7 cells detected using PI staining. ** $P < 0.01$, ## $P < 0.01$.

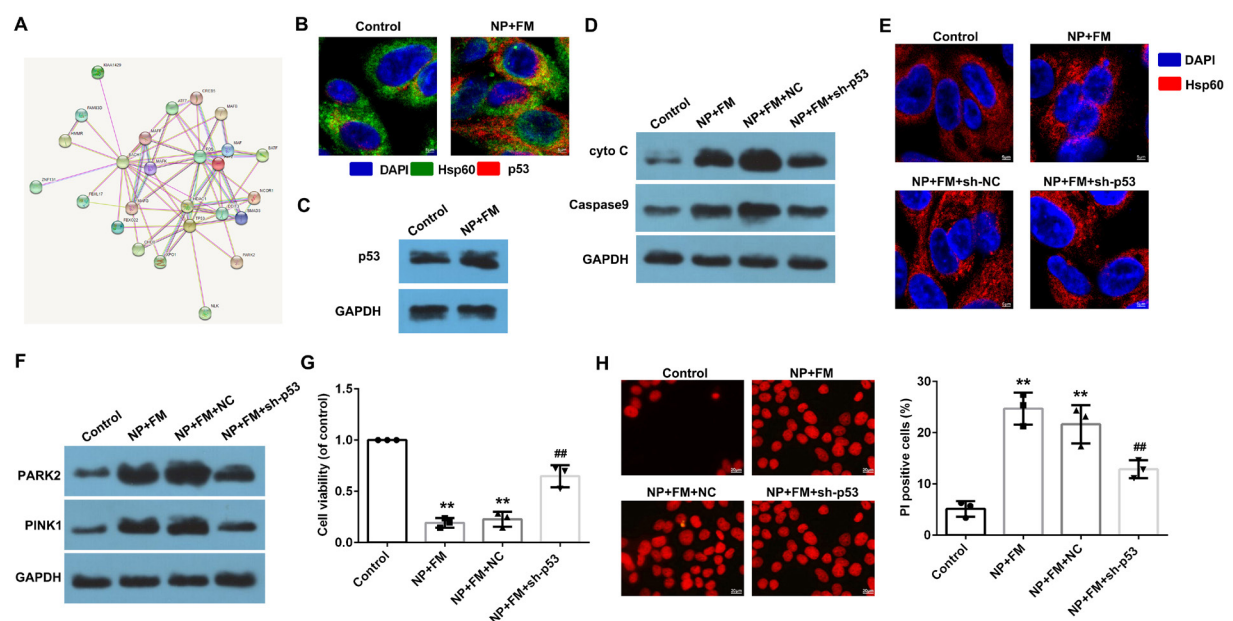


Figure 7. FM suppresses the tumor growth of TNBC via regulating BACH1.

The tumor size (A), volume (B), and weight (C) of TNBC in vivo. ** $P < 0.01$, *** $P < 0.001$, ## $P < 0.01$.

tion (Fig. 5D). The apoptosis rates were significantly decreased in the sh-BACH1 group (Fig. 5E). To further confirm the roles of BACH1 in mitochondrial ROS. Cells were exposed to NAC (an ROS inhibitor). As shown in Fig. 5F, NAC antagonized the effects of FM and decreased the protein expression of BACH1.

FM regulates mitophagy via inducing BACH1-mediated activation of p53

We further investigated the potential underlying mechanisms. The online database STING predicted the po-

tential genes interacting with BACH1 (Fig. 6A). Then we found that BACH1 may regulate the expression of p53. To further verify this, cells were treated with FM and/or sh-p53. As shown in Figs 6B and C, FM promoted p53 translocation from cytoplasm to mitochondria. p53 deficiency suppressed protein expression of cyto C and Caspase9 mitochondrial aggregation (Fig. 6D) as well as mitochondrial aggregation (Fig. 6E). Moreover, p53 knockdown decreased the protein expression of PINK1, PARK2 (Fig. 6F). p53 knockdown promoted the cell

viability and inhibited the apoptosis of MCF7 cells (Figs 6G and H).

FM suppresses the tumor growth of TNBC via regulating BACH1

To further verify the effects of FM on TNBC, *in vivo* assay was performed. As shown in Fig. 7A–C, FM suppressed the tumor size, volume and weight, which was abated by BACH1 deficiency.

DISCUSSION

In this study, FM suppressed improved the clinical outcome of TNBC patients. FM induced oxidative stress and apoptosis of MCF7 cells suppressed tumor growth. Additionally, FM suppressed mitophagy *via* inactivating BACH1/p53 signaling pathways.

Formononetin (FM) possesses anti-tumor properties in various cancers (Tay *et al.*, 2019). For instance, FM suppressed the proliferation and metastasis of ovarian cancer cells (Zhang *et al.*, 2018). FM suppresses the growth and migration of gastric cancer (Yao *et al.*, 2019). In breast cancer, FM induced breast cancer cell cycle rest (Chen *et al.*, 2011). FM inhibits Taxol-chemoresistance of breast cancer cells *via* suppressing autophagy signaling (Wu *et al.*, 2021). However, seldom study focuses on the mitochondrial functions in breast cancer cells. In this study, FM transmitted ROS to mitochondria to release cyto C and induced the cascades of caspase-3 and caspase-9, the activation of which induced the apoptosis of MCF7 cells. These findings suggest that FM may exert its anti-tumor functions *via* impeding the mitochondrial function in breast cancer cells.

BACH1, a member of the cap'n'collar (CNC) b-Zip family, plays a key role in regulating oxidative stress (Wiel *et al.*, 2019). BACH1 is a key regulator of mitochondrial metabolisms in cancer (Lignitto *et al.*, 2019). For instance, BACH1 knockdown induces mitochondrial respiration and increases the chemosensitivity of papillary thyroid cancer cells to metformin (Yu *et al.*, 2022). Moreover, BACH1 is overexpressed in TNBC patients and High levels of BACH1 predict poor overall survival and disease-free survival rates (Ou *et al.*, 2019). Overexpressed BACH1 inhibits glycolysis as well as suppresses lactate catabolism in the tricarboxylic acid (TCA) cycle, and promotes breast cancer bone metastasis (Lee *et al.*, 2019; Padilla *et al.*, 2022). These studies dictate that BACH1 may function as an oncogene in breast cancer. In this study, BACH1 was overexpressed in TNBC patients and MCF7 cells. Moreover, overexpressed BACH1 suppressed the release of oxidative stress and cancer cell apoptosis. Moreover, BACH1 alleviated FM-induced mitochondrial damage.

Mitochondrial metabolism plays a vital role in mitochondrial function, requiring intensive integration of mitochondrial morphology and dynamics (Chan, 2020). Mitophagy, erasing damaged mitochondria *via* autophagy, is a key process to maintaining mitochondrial quality (Srinivasan *et al.*, 2017). However, dysfunction of mitophagy may induce the pathogenesis of cancer, such as hepatocellular carcinoma, colon as well as breast cancer (Chen *et al.*, 2019; Deng *et al.*, 2021; Yin *et al.*, 2021). Therefore, unraveling the underlying mechanisms may provide a novel target for cancer therapy. In this study, FM treatment induced the overexpression of p53. As a tumor suppressor, p53 suppresses tumorigenesis *via* inducing apoptosis, pyroptosis, ferroptosis as well as autophagy. In this study, FM stimulated p53/PINK1/PARK2 signaling

pathways *via* inactivating BACH1, which promoted the release of cyto C and caspases as well as mitophagy-mediated mitochondrial dysfunction.

However, there are several limitations to this study. A large number of patients could make the results more convincing. Therefore, future studies will recruit more metastatic TNBC patients. Additionally, mitochondrial damage and mitophagy may induce other forms of death, such as ferroptosis and pyroptosis. Whether FM induced ferroptosis or pyroptosis. This needs further study.

In conclusion, FM improved the clinical outcomes of TNBC patients. Additionally, FM suppressed the aggressiveness of TNBC *via* regulating BACH1 signaling. Therefore, FM may be an alternative strategy for TNBC.

Declarations

Conflict of interest. None.

Funding. None.

REFERENCES

- Braden AV, Stankowski RV, Engel JM, Onitilo AA (2014) Breast cancer biomarkers: risk assessment, diagnosis, prognosis, prediction of treatment efficacy and toxicity, and recurrence. *Curr Pharm Des* 20: 4879–4898. <https://doi.org/10.2174/1381612819666131125145517>
- Bianchini G, Ballo JM, Mayer IA, Sanders ME, Gianni L (2016) Triple-negative breast cancer: challenges and opportunities of a heterogeneous disease. *Nat Rev Clin Oncol* 13: 674–690. <https://doi.org/10.1038/nrclinonc.2016.66>
- Burstein HJ, Curigliano G, Loibl S, Dubsy P, Gnant M, Poortmans P, Colleoni M, Denkert C, Piccart-Gebhart M, Regan M, Senn HJ, Winer EP, Thürlimann B; Members of the St. Gallen International Consensus Panel on the Primary Therapy of Early Breast Cancer (2019) Estimating the benefits of therapy for early-stage breast cancer: the St. Gallen International Consensus Guidelines for the primary therapy of early breast cancer 2019. *Ann Oncol* 30: 1541–1557. <https://doi.org/10.1093/annonc/mdz235>
- Chan DC (2020) Mitochondrial dynamics and its involvement in disease. *Annu Rev Pathol* 15: 235–259. <https://doi.org/10.1146/annurev-pathmechdis-012419-032711>
- Chan PW, Chiu JH, Huang N, *et al.* (2021) Influence of traditional Chinese medicine on medical adherence and outcome in estrogen receptor (+) breast cancer patients in Taiwan: a real-world population-based cohort study. *Phytotherapy* 80: 153365. <https://doi.org/10.1016/j.phymed.2020.153365>
- Chen J, Zeng J, Xin M, Huang W, Chen X (2011) Formononetin induces cell cycle arrest of human breast cancer cells *via* IGF1/PI3K/Akt pathways *in vitro* and *in vivo*. *Horm Metab Res* 43: 681–686. <https://doi.org/10.1055/s-0031-1286306>
- Chen Y, Chen HN, Wang K, Zhang L, Huang Z, Liu J, Zhang Z, Luo M, Lei Y, Peng Y, Zhou ZG, Wei Y, Huang C (2019) Ketocarbazole exacerbates mitophagy to induce apoptosis by downregulating cyclooxygenase-2 in hepatocellular carcinoma. *J Hepatol* 70: 66–77. <https://doi.org/10.1016/j.jhep.2018.09.022>
- Deng R, Zhang HL, Huang JH, Cai RZ, Wang Y, Chen YH, Hu BX, Ye ZP, Li ZL, Mai J, Huang Y, Li X, Peng XD, Feng GK, Li JD, Tang J, Zhu XF (2021) MAPK1/3 kinase-dependent ULK1 degradation attenuates mitophagy and promotes breast cancer bone metastasis. *Autophagy* 17: 3011–3029. <https://doi.org/10.1080/15548627.2020.1850609>
- Ding Y, Chen X, Zhang Q, Liu Q (2020) Historical trends in breast Cancer among women in China from age-period-cohort modeling of the 1990–2015 breast Cancer mortality data. *BMC Public Health* 20: 1280. <https://doi.org/10.1186/s12889-020-09375-0>
- Fan L, Strasser-Weippl K, Li JJ, St Louis J, Finkelstein DM, Yu KD, Chen WQ, Shao ZM, Goss PE (2014) Breast cancer in China. *Lancet Oncol* 15: e279–e89. [https://doi.org/10.1016/S1470-2045\(13\)70567-9](https://doi.org/10.1016/S1470-2045(13)70567-9)
- Garrido-Castro AC, Lin NU, Polyak K (2019) Insights into molecular classifications of triple-negative breast cancer: improving patient selection for treatment. *Cancer Discov* 9: 176–198. <https://doi.org/10.1158/2159-8290.CD-18-1177>
- Hao S, Zhu X, Liu Z, Wu X, Li S, Jiang P, Jiang L (2021) Chronic intermittent hypoxia promoted lung cancer stem cell-like properties *via* enhancing Bach1 expression. *Respir Res* 22: 58. <https://doi.org/10.1186/s12931-021-01655-6>
- Huang WJ, Bi LY, Li ZZ, Zhang X, Ye Y (2013) Formononetin induces the mitochondrial apoptosis pathway in prostate cancer cells *via* downregulation of the IGF-1/IGF-1R signaling pathway. *Pharm Biol.* Epub ahead of print. <https://doi.org/10.3109/13880209.2013.842600>

- Lee J, Yesilkalan AE, Wynne JP, Frankenberger C, Liu J, Yan J, El-baz M, Rabe DC, Rustandy FD, Tiwari P, Grossman EA, Hart PC, Kang C, Sanderson SM, Andrade J, Nomura DK, Bonini MG, Locasale JW, Rosner MR (2019) Effective breast cancer combination therapy targeting BACH1 and mitochondrial metabolism. *Nature* **568**: 254–258. <https://doi.org/10.1038/s41586-019-1005-x>
- Li T, Zhang S, Chen F, Hu J, Yuan S, Li C, Wang X, Zhang W, Tang R (2021) Formononetin ameliorates the drug resistance of Taxol resistant triple negative breast cancer by inhibiting autophagy. *Am J Transl Res* **13**: 497–514. PMID: 33594306
- Lignitto L, LeBoeuf SE, Homer H, Jiang S, Askenazi M, Karakousi TR, Pass HI, Bhutkar AJ, Tsigos A, Ueberheide B, Sayin VI, Pappiannakopoulos T, Pagano M (2019) Nrf2 Activation promotes lung cancer metastasis by inhibiting the degradation of Bach1. *Cell* **178**: 316–329 e18. <https://doi.org/10.1016/j.cell.2019.06.003>
- Ma C, Xia R, Yang S, Liu L, Zhang J, Feng K, Shang Y, Qu J, Li L, Chen N, Xu S, Zhang W, Mao J, Han J, Chen Y, Yang X, Duan Y, Fan G (2020) Formononetin attenuates atherosclerosis via regulating interaction between KLF4 and SRA in apoE(-/-) mice. *Theranostics* **10**: 1090–1106. <https://doi.org/10.7150/thno.38115>
- Newman LA, Kaljee LM (2017) Health disparities and triple-negative breast cancer in african american women: a review. *JAMA Surg* **152**: 485–493. <https://doi.org/10.1001/jamasurg.2017.0005>
- Ou X, Gao G, Bazhabayi M, Zhang K, Liu F, Xiao X (2019) MALAT1 and BACH1 are prognostic biomarkers for triple-negative breast cancer. *J Cancer Res Ther* **15**: 1597–1602. https://doi.org/10.4103/jcrt.JCRT_282_19
- Padilla J, Lee BS, Zhai K, Rentz B, Bobo T, Dowling NM, Lee J (2022) A Heme-binding transcription factor BACH1 regulates lactate catabolism suggesting a combined therapy for triple-negative breast cancer. *Cells* **11**. <https://doi.org/10.3390/cells11071177>
- Srinivasan S, Guha M, Kashina A, Avadhani NG (2017) Mitochondrial dysfunction and mitochondrial dynamics – The cancer connection. *Biochim Biophys Acta Bioenerg* **1858**: 602–614. <https://doi.org/10.1016/j.bbmbio.2017.01.004>
- Tay KC, Tan LT, Chan CK, Hong SL, Chan KG, Yap WH, Pusparajah P, Lee LH, Goh BH (2019) Formononetin: a review of its anticancer potentials and mechanisms. *Front Pharmacol* **10**: 820. <https://doi.org/10.3389/fphar.2019.00820>
- Wang JY, Jiang MW, Li MY, Zhang ZH, Xing Y, Ri M, Jin CH, Xu GH, Piao LX, Jin HL, Ma J, Jin Y, Zuo HX, Jin X (2022) Formononetin represses cervical tumorigenesis by interfering with the activation of PD-L1 through MYC and STAT3 downregulation. *J Nutr Biochem* **100**: 108899. <https://doi.org/10.1016/j.jnutbio.2021.108899>
- Wiel C, Le Gal K, Ibrahim MX, Jahangir CA, Kashif M, Yao H, Ziegler DV, Xu X, Ghosh T, Mondal T, Kanduri C, Lindahl P, Sayin VI, Bergo MO (2019) BACH1 Stabilization by antioxidants stimulates lung cancer metastasis. *Cell* **178**: 330–345 e22. <https://doi.org/10.1016/j.cell.2019.06.005>
- Wu J, Xu W, Ma L, Sheng J, Ye M, Chen H, Zhang Y, Wang B, Liao M, Meng T, Zhou Y, Chen H (2021) Formononetin relieves the facilitating effect of lncRNA AFAP1-AS1-miR-195/miR-545 axis on progression and chemo-resistance of triple-negative breast cancer. *Aging (Albany NY)* **13**: 18191–18222. <https://doi.org/10.18632/aging.203156>
- Xin M, Wang Y, Ren Q, Guo Y (2019) Formononetin and metformin act synergistically to inhibit growth of MCF-7 breast cancer cells *in vitro*. *Biomed Pharmacother* **109**: 2084–2089. <https://doi.org/10.1016/j.biopha.2018.09.033>
- Xu M, Yuan Y, Yan P, Jiang J, Ma P, Niu X, Ma S, Cai H, Yang K (2020) Prognostic significance of androgen receptor expression in triple negative breast cancer: a systematic review and meta-analysis. *Clin Breast Cancer* **20**: e385–e396. <https://doi.org/10.1016/j.clbc.2020.01.002>
- Yang Z, Zhang Q, Yu L, Zhu J, Cao Y, Gao X (2021) The signaling pathways and targets of traditional Chinese medicine and natural medicine in triple-negative breast cancer. *J Ethnopharmacol* **264**: 113249. <https://doi.org/10.1016/j.jep.2020.113249>
- Yao JN, Zhang XX, Zhang YZ, Li JH, Zhao DY, Gao B, Zhou HN, Gao SL, Zhang LF (2019) Discovery and anticancer evaluation of a formononetin derivative against gastric cancer SGC7901 cells. *Invest New Drugs* **37**: 1300–1308. <https://doi.org/10.1007/s10637-019-00767-7>
- Yin K, Lee J, Liu Z, Kim H, Martin DR, Wu D, Liu M, Xue X (2021) Mitophagy protein PINK1 suppresses colon tumor growth by metabolic reprogramming via p53 activation and reducing acetyl-CoA production. *Cell Death Differ* **28**: 2421–2435. <https://doi.org/10.1038/s41418-021-00760-9>
- Yu X, Gao F, Li W, Zhou L, Liu W, Li M (2020) Formononetin inhibits tumor growth by suppression of EGFR-Akt-Mcl-1 axis in non-small cell lung cancer. *J Exp Clin Cancer Res* **39**: 62. <https://doi.org/10.1186/s13046-020-01566-2>
- Yu Y, Feng C, Kuang J, Guo L, Guan H (2022) Metformin exerts an antitumoral effect on papillary thyroid cancer cells through altered cell energy metabolism and sensitized by BACH1 depletion. *Endocrine* **76**: 116–131. <https://doi.org/10.1007/s12020-021-02977-7>
- Zhang J, Liu L, Wang J, Ren B, Zhang L, Li W (2018) Formononetin, an isoflavone from *Astragalus membranaceus* inhibits proliferation and metastasis of ovarian cancer cells. *J Ethnopharmacol* **221**: 91–99. <https://doi.org/10.1016/j.jep.2018.04.014>



OPEN ACCESS

EDITED BY

Teresa Stachowicz-Stencel,
University Medical Centre Gdansk,
Poland

REVIEWED BY

Anna Synakiewicz,
Medical University of Gdansk, Poland
Joanna Stefanowicz,
Medical University of Gdansk, Poland

*CORRESPONDENCE

Anna Milaniuk,
✉ milaniuk.ania@gmail.com
Katarzyna Drabko,
✉ katarzyna.drabko@umlub.pl

RECEIVED 24 August 2024

ACCEPTED 01 November 2024

PUBLISHED 15 November 2024



CITATION

Milaniuk A, Drabko K and Choęta A
(2024) Role of albumin and prealbumin
in assessing nutritional status and
predicting increased risk of infectious
complications during childhood
cancer treatment.
Acta Biochim. Pol 71:13693.
doi: 10.3389/abp.2024.13693

COPYRIGHT

© 2024 Milaniuk, Drabko and Choęta.
This is an open-access article
distributed under the terms of the
[Creative Commons Attribution License](#)
(CC BY). The use, distribution or
reproduction in other forums is
permitted, provided the original
author(s) and the copyright owner(s) are
credited and that the original
publication in this journal is cited, in
accordance with accepted academic
practice. No use, distribution or
reproduction is permitted which does
not comply with these terms.

Role of albumin and prealbumin in assessing nutritional status and predicting increased risk of infectious complications during childhood cancer treatment

Anna Milaniuk^{1*}, Katarzyna Drabko ^{1*} and
Agnieszka Choęta ²

¹Department of Hematology, Oncology and Transplantology, Medical University of Lublin, Lublin, Poland, ²Department of Pediatric Laboratory Diagnostic, Medical University of Lublin, Lublin, Poland

Introduction: Proper nutrition in patients with cancer is important for preventing treatment complications and achieving remission. Malnutrition in these patients leads to reduced production of essential structural proteins.

Purpose: The aim of the study was to assess the role of albumin and prealbumin in assessing the nutritional status of cancer patients and in predicting an increased risk of infectious complications during treatment.

Patients and Methods: The study included 40 pediatric patients with newly diagnosed cancer and 30 healthy children serving as controls. Prealbumin, albumin, and C-reactive protein (CRP) levels and the upper arm muscle area (UAMA) were measured before and after treatment in children with cancer and compared with the control group to evaluate nutritional status. Additionally, we assessed associations between these parameters and the incidence of infectious complications during cancer treatment in patients with anthropometric malnutrition, as well as associations with an increased risk of malnutrition related to inflammation before treatment.

Results: At baseline, patients with cancer had lower prealbumin and albumin levels ($p < 0.001$), higher CRP levels ($p < 0.001$), and lower UAMA percentiles ($p = 0.0245$) compared with controls. Cancer treatment resulted in an increase in prealbumin and albumin levels ($p < 0.001$) and a reduction in CRP levels ($p < 0.001$), with no change in UAMA ($p = 1.000$). Prealbumin deficiency was more common than albumin deficiency before and after cancer treatment. Median prealbumin and albumin levels tended to increase with an increasing UAMA percentile range, but these differences were not significant ($p > 0.05$). The incidence of infectious complications during treatment in patients with risk factors for inflammation-related malnutrition was similar to that in patients with pre-existing anthropometric malnutrition without inflammation ($p = 1.000$). In a univariable logistic regression model including prealbumin and albumin deficiency, as well as low UAMA percentile, albumin deficiency before treatment was shown to be a significant predictor of 3 or more infectious episodes during treatment ($p = 0.02$).

Conclusion: Albumin and prealbumin deficiency may predict the risk of malnutrition associated with inflammation in patients with cancer. Hypoalbuminemia may predict an unfavorable course of treatment complicated by frequent infections in these patients.

KEYWORDS

albumin, prealbumin, children, cancer, malnutrition

Introduction

Thanks to advances in pediatric cancer treatment, the number of childhood cancer survivors is growing. In recent years, a reduction in childhood cancer mortality has been observed in Europe, with Poland being one of the countries with the lowest leukemia mortality rates (Bertuccio et al., 2020). On the other hand, the long duration of cancer treatment, the use of cytostatic and biologic drugs, as well as radiotherapy and surgery, may lead to treatment-related complications. The most common complications are infections, which can be life-threatening in immunosuppressed patients, and thus reduce cancer survival (Esbenshade et al., 2023; Zawitkowska et al., 2019). As a result, cancer remains the third leading cause of death (after accidents and injuries) in the pediatric population (Cunningham et al., 2018).

Supportive care in cancer patients is important to prevent serious complications or to mitigate their effects (Esbenshade et al., 2023). One component of supportive care is to improve the nutritional status of patients. Malnutrition at diagnosis increases the risk of mortality during and after treatment (Barr and Stevens, 2020). Proper nutritional status in cancer patients promotes remission and improves patient comfort (Rogers and Barr, 2020). Therefore, it is important to identify patients at risk for malnutrition.

The assessment of nutritional status in children with cancer should include common anthropometric measures such as body weight and body mass index, as well as baseline body composition evaluated by mid-upper arm circumference and triceps skinfold thickness, or by more advanced tests such as bioelectrical impedance analysis and dual-energy X-ray absorptiometry (Ladas et al., 2016). Anthropometric nutritional status can also be determined by the upper arm muscle area (UAMA) index, which represents lean body mass and is calculated using the Frisancho formula (Frisancho, 1990).

Increased catabolism and energy expenditure in cancer patients results in reduced production of structural proteins (Bauer et al., 2011; Co-Reyes et al., 2012; Laviano et al., 2005; Sala et al., 2004; Soeters et al., 2021; Romano et al., 2022). These metabolic processes manifest clinically as muscle wasting and poor muscle function both in adult and pediatric patients (Joffe et al., 2019; Shachar et al., 2016; Cederholm et al., 2017). Malnutrition in cancer is a type of

disease-related malnutrition with inflammation, where the degree of disease-induced metabolic response determines the rate of catabolism and the onset of clinically significant malnutrition (Cederholm et al., 2017; Viani et al., 2020). Patients with precachexia are at risk for malnutrition due to the inflammatory response induced by the underlying disease (Sala et al., 2004).

Given that low serum protein levels may predict inflammatory malnutrition, we aimed to assess the protein status of children with newly diagnosed cancer and the effect of pretreatment albumin and prealbumin deficiency on the incidence of infectious complications during treatment (Cehreli et al., 2019; Luo et al., 2019).

Patients and methods

Study design

This observational, prospective, single-center study was conducted in pediatric patients with newly diagnosed cancer who were hospitalized between October 2019 and January 2022 in the Pediatric Department of Hematology, Oncology and Transplantology at University Hospital in Lublin, Poland. In total, 40 children with cancer were included. The results of the study group were compared with the results of the control group, which was recruited from volunteers. The control group included children who were not receiving specialized care for chronic diseases, were not taking any chronic medications, and had no evidence of active infection on enrollment.

Median age at the time of cancer diagnosis was 11.29 years (IQR, 5.25–13.27), and the median age of the control group was 6.5 years (IQR, 4.65–9.96). Most patients were male (67.5%), had a diagnosis of hematological malignancy (75%), and received low-intensity or intermediate-intensity treatment (55%). The median follow-up was 39.93 weeks (IQR, 26.57–48.64), and the median time between the end of cancer treatment and study measurements was 6.07 weeks (IQR, 3.21–11.89). The baseline characteristics of the study are summarized in Table 1.

In all patients, the levels of visceral serum proteins (prealbumin and albumin) and C-reactive protein (CRP) were assessed, and anthropometric measurements were performed before and after cancer treatment to evaluate nutritional status

TABLE 1 Characteristics of 40 children with cancer.

Characteristics of 40 children with cancer	
Sex	n (%)
Female	13 (32.5)
Male	27 (67.5)
Age, years	Median (Q1-Q3) 11.29 (5.25–13.27) Range 2.08–17.67
Primary diagnosis	n (%)
Hematological malignancies	30 (75.0)
Acute lymphoblastic leukemia	15
Acute myeloid leukemia	2
Non-Hodgkin's lymphoma	5
Hodgkin's lymphoma	8
Solid tumors	10 (25.0)
Central nervous system tumors	2
Wilms tumor	2
Soft tissue sarcoma	3
Ewing sarcoma	2
Germ cell tumors	1
Intensity of treatment*	n (%)
Low/intermediate	22 (55.0)
High	18 (45.0)

*Treatment intensity was defined according to risk group classification or disease stage as follows: SR, standard risk; IR, intermediate risk, stage I, II (low/intermediate intensity of treatment), HR, high risk, stage III, and IV (high intensity of treatment).

as well as associations between these parameters and the incidence of infectious complications during cancer treatment. As malnutrition is a risk factor for infectious complications, we assessed the incidence of complications in patients with anthropometric malnutrition and those with an increased risk of malnutrition related to inflammation before treatment. Patients with anthropometric malnutrition met the following criteria: low UAMA percentile range and low albumin and/or low prealbumin and normal CRP levels, whereas patients with normal/high UAMA and low albumin and/or low prealbumin and elevated CRP levels were suspected of malnutrition with inflammation.

The clinical and demographic data of patients were obtained from hospital medical records. In all patients, cancer was diagnosed based on the International Classification of Childhood Cancer ver. 3 (Steliarova-Foucher et al., 2005). Patients received standard treatment according to the type and stage of cancer.

Detailed clinical, demographic, and social characteristics of study participants were reported previously (Milaniuk and Drabko, 2024).

Informed consent was obtained from parents or legal guardians of each participant included in the study.

Ethics approval

This study was conducted in accordance with the principles of the Declaration of Helsinki. Approval was granted by the Ethics Committee of the Medical University of Lublin (26 Sep 2019/No KE-0254/278/2019).

Biochemical assessment of serum protein levels

Blood samples were collected from patients after an overnight fast during routine sampling for laboratory measurements. Serum prealbumin levels were determined by enzyme-linked immunosorbent assay (IDK® prealbumin ELISA, Immunodiagnostik AG, Germany) in samples previously stored at -20°C . Albumin and CRP levels were determined immediately after sample collection. Albumin deficiency was defined as a level of 3.5 g/dL or lower and prealbumin deficiency as a level of 0.2 g/L or lower. Prealbumin levels of less than 0.1 g/L indicated severe deficiency. CRP levels greater than 0.5 mg/L indicated the risk of inflammation.

Assessment of anthropometric protein-energy undernutrition

In this study, UAMA was used to anthropometrically assess protein-energy undernutrition (PEU) in cancer patients. It was calculated using the Frisancho formula: $\text{UAMA (cm}^2\text{)} = [\text{MUAC} - (\text{TSFT} \times \pi)]^2 / (4 \times \pi)$, where MUAC is the mid-upper arm circumference and TSFT is the triceps skinfold thickness.

UAMA percentiles were classified into the following categories: low muscle (<5th percentile), below average (5th to <15th percentile), average (15th to <85th percentile), above average (85th to <95th percentile), and high muscle (≥ 95 percentile) according to age- and sex-adjusted growth charts (Frisancho, 1990).

Assessment of infectious complications

The medical records of participants were reviewed for the history of the following infectious complications during treatment: respiratory infections, gastrointestinal inflammation, stomatitis, soft tissue inflammation, fever of unknown origin (FUO), and sepsis. Standardized International Classification of Diseases, Tenth Revision (ICD-10) diagnostic codes were used in the analysis.

Statistical analysis

Patient characteristics were evaluated using descriptive statistics, categorical variables were described as numbers and percentages, and numerical variables were described as mean, standard deviation, median, quartiles, and range. Differences between groups were assessed using Fisher, χ^2 , Mann-Whitney, Wilcoxon, Kruskal-Wallis. A single-variable logistic regression analysis was used to assess prealbumin and albumin deficiency and low percentile ranges of the UAMA as predictors

TABLE 2 Protein concentrations in patients before and after cancer treatment and in controls.

	Proteins					p-value
	Prealbumin g/L	p-value	Albumin g/dL	p-value	CRP mg/L	
Study group n = 40 before treatment	0.08 (0.07–0.15) 0.02–0.34	<0.001 ^a	4.11 (3.87–4.44) 3.06–5.07	<0.001 ^a	0.68 (0.07–3.31) 0.01–23.13	<0.001 ^a
Study group n = 40 after treatment	0.18 (0.15–0.25) 0.1–0.38		4.58 (4.42–4.73) 3.92–5.11		0.09 (0.03–0.26) 0.01–2.09	
Controls group n = 30	0.17 (0.15–0.22) 0.12–0.47	<0.001 ^b	0.17 (0.15–0.22) 0.12–0.47	<0.001 ^b	0.03 (0.03–0.03) 0.03–0.27	0.001 ^b

Data are presented as median (Q1–Q3) and range, and the differences in parameters were calculated using the Wilcoxon test.

^aPatients before vs. after cancer treatment.

^bPatients before cancer treatment vs. control group.

Abbreviations: CRP, C-reactive protein.

of infectious complications during treatment. For each explanatory variable OR was calculated. A p-value of <0.05 was considered significant. All statistical analyses were performed using R version 4.1.1.

Results

Protein levels and UAMA percentile ranges in cancer patients and controls

Albumin and prealbumin levels were significantly lower in cancer patients than in controls. In the cancer group, albumin and prealbumin levels were higher after vs. before treatment (Table 2). In contrast, CRP levels were significantly higher in cancer patients than in controls. Cancer treatment led to a significant reduction in CRP levels (Table 2).

Regarding UAMA, there was a significantly higher number of patients with low percentiles in the cancer group compared with the control group. There were no differences in the distribution of UAMA percentiles before vs. after treatment in cancer patients (Table 3).

Protein levels and UAMA values in patients with hematological malignancies and solid tumors

There were no significant differences in protein levels and UAMA values between group of patients with hematological malignancies and those with solid tumors (neither before nor after cancer treatment ($p > 0.05$)). However, the comparison within groups demonstrated that in patients with hematological malignancies prealbumin and albumin concentrations were significantly higher after treatment than before. Similar observation was made in patients with solid tumors, but it regard only to albumin concentrations (Table 4).

Assessment of prealbumin and albumin deficiency

In patients with cancer, prealbumin deficiency was more common before vs. after treatment ($p < 0.001$). Before treatment, it was noted in 35 patients (87.5%), of whom 23 (57.5%) had severe prealbumin deficiency. After treatment, prealbumin deficiency was reported in 25 patients (67.5%). None of the cancer patients had severe prealbumin deficiency after treatment. Albumin deficiency was found in 5 patients (12.5%) before treatment, while it was not observed in any of the patients after treatment ($p = 0.0547$). Before treatment, 21 patients (52.5%) had elevated CRP levels, as compared with 8 patients (20%) after treatment ($p = 0.0053$).

The median prealbumin level across all UAMA percentile ranges was less than 0.2 g/L. However, patients with UAMA below the 85th percentile had the median prealbumin level below 0.1 g/L, what indicated a severe deficiency. The median albumin level for all UAMA percentile ranges was greater than 3.5 g/dL. In addition, median albumin and prealbumin levels tended to increase with an increasing UAMA percentile, but the difference was not significant ($p > 0.05$). There was no association between CRP levels and UAMA percentile range (Table 5).

Associations between nutritional status at diagnosis and infectious complications

The most common infectious complications during the course of treatment affected respiratory system ($n = 17$) with almost half of them being pulmonary mycosis ($n = 8$), and oral cavity ($n = 15$) with stomatitis reaching grade III and IV of severity ($n = 5$). The third most common infectious complication were gastrointestinal tract infections ($n = 9$). Sepsis was diagnosed in 8 patients and FUO occurred in 5. The

TABLE 3 Distribution of UAMA percentiles in patients before and after cancer treatment and in controls.

	UAMA percentile			p-value ^a	p-value ^b
	<5–15th	15–85th	>85th		
Study group n=40 before treatment	11 (27.5)	22 (55.0)	7 (17.5)	0.0245 ^c	1.0000 ^d
Study group n=40 after treatment	11 (27.5)	22 (55.0)	7 (17.5)		
Controls group n=30	1 (3.3)	22 (73.3)	7 (23.3)		

Data are presented as number and percentage (%). The differences in parameters were calculated using the Fisher test^c and χ^2 test^d.

^aPatients before cancer treatment vs. control group.

^bPatients before vs. after cancer treatment.

UAMA, upper arm muscle area.

TABLE 4 Protein concentrations and UAMA values in patients before and after cancer treatment according to cancer type.

Type of cancer	Prealbumin g/L	p-value	Albumin g/dL	p-value	UAMA (cm ²)	p-value
Hematological malignancies, n = 30 before treatment	0.08 (0.06–0.1) 0.02–0.2	<0.001	4.11 (3.86–4.49) 3.06–5.07	0.0012	24.14 (16.59–36.02) 10.26–65.4	0.0803
Hematological malignancies, n = 30 after treatment	0.18 (0.16–0.25) 0.1–0.38		4.57 (4.38–4.8) 3.92–5.11		25.12 (19.2–35.42) 12.15–62.82	
Solid tumors n = 10 before treatment	0.14 (0.09–0.19) 0.03–0.34	0.4922	4.19 (3.91–4.42) 3.68–4.64	0.0098	21 (19.51–26.3) 16.1–53.48	0.8127
Solid tumors n = 10 after treatment	0.15 (0.13–0.18) 0.1–0.26		4.6 (4.48–4.64) 4.38–4.74		21.63 (20.09–28.48) 15.56–55.81	

Data are presented as median (Q1–Q3) and range. Differences in parameters were calculated the Wilcoxon test.

Abbreviations: UAMA, upper arm muscle area.

TABLE 5 Pretreatment prealbumin, albumin, and CRP levels depending on the UAMA percentile range.

UAMA percentile range	Prealbumin g/L	p-value	Albumin g/dL	p-value	CRP (mg/L)	p-value
<5–15th n = 11	0.08 (0.06–0.14) 0.02–0.2	0.1013	4.08 (3.74–4.35) 3.32–4.61	0.4759	0.13 (0.03–0.3) 0.03–1.34	0.2002
15–85th n = 22	0.08 (0.06–0.1) 0.03–0.21		4.05 (3.88–4.48) 3.06–5.07		0.03 (0.03–0.15) 0.01–2.09	
>85th n = 7	0.14 (0.11–0.18) 0.07–0.34		4.42 (4.07–4.58) 3.36–4.67		0.1 (0.1–0.7) 0.03–1.43	

Data are presented as median (Q1–Q3) and range. Differences in parameters were calculated using the Kurskal-Wallis test.

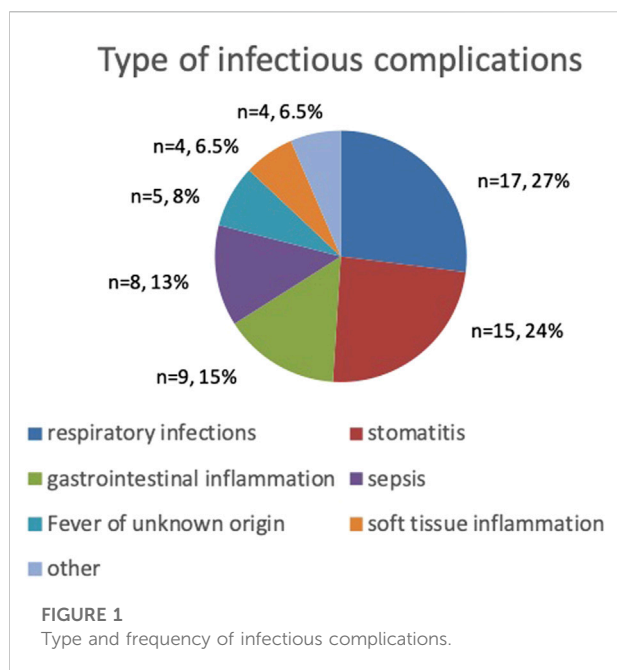
Abbreviations: CRP, C-reactive protein; UAMA, upper arm muscle area.

remaining infections regard to soft tissue infections, asymptomatic COVID-19 and varicella (Figure 1). Severe mucosal inflammation (typhlitis, stomatitis) required total parenteral nutrition in 2 patients. In the remaining cases, oral nutritional interventions were used.

Infectious complications occurred in 23 patients with cancer (57.5%), with 3 or more infectious episodes reported in 11 patients (27.5%). The incidence of complications was influenced by tumor type, with 3 or more episodes occurring

significantly more often in patients with hematological malignancies than in those with solid tumors (63.2% vs. 40%; $p = 0.0381$). Factors such as sex, intensity of treatment, and patient age had no effect on the incidence of infectious complications ($p > 0.05$).

Pretreatment prealbumin and albumin levels were slightly lower in patients with infectious complications during cancer treatment compared with patients without complications (Table 6). However, these differences were not significant,



except borderline significance for prealbumin. Patients with hypoalbuminemia were significantly more likely to have 3 or more infectious episodes (Table 7).

Infectious complications in patients with anthropometric malnutrition and risk of malnutrition with inflammation

The incidence of infectious complications during cancer treatment was compared between patients with anthropometric malnutrition without inflammation and those at risk of malnutrition due to inflammation. Only 4 patients (10%) met the diagnostic criteria for malnutrition without inflammation, while 15 patients (37.5%) were at risk for malnutrition due to inflammation. The remaining 21 patients with cancer (52.6%) did not meet any of the criteria to be included in either subgroup. We found no differences in the incidence of infectious complications between subgroups, and over 50% of patients in both subgroups had 3 or more infectious episodes (Table 8).

Effect of protein deficiency and low UAMA on the incidence of complications during cancer treatment

In a univariable logistic regression model including prealbumin and albumin deficiency, as well as low UAMA percentile, pretreatment albumin deficiency was shown to be a significant predictor of 3 or more infectious episodes during cancer treatment ($p = 0.02$) (Table 9).

Discussion

This study highlights the importance of identifying malnutrition in children with cancer. We present an analysis of the protein and anthropometric status of protein malnutrition in cancer, which indicates the risk of infectious complications in malnourished patients and those at risk of malnutrition.

Previous studies confirmed that cancer patients have lower blood protein levels than healthy individuals and in addition that protein deficiency affects the treatment course and survival of these patients (Cehreli et al., 2019; Luo et al., 2019; McLean et al., 2020; Sanches et al., 2015; Kuvibidila et al., 2000). In our study, prealbumin and albumin levels were also significantly lower in children at the time of cancer diagnosis compared with healthy control. Moreover, blood protein levels increased after cancer treatment, which may indicate a metabolic switch to anabolic processes in cancer remission.

Protein in the diet is very important for cancer patients, whose metabolic rate is particularly high. Therefore, supportive cancer care should include nutritional management of malnourished patients. For this reason, the Polish Society for Pediatric Clinical Nutrition and the Polish Society for Pediatric Oncology and Hematology have developed guidelines for assessing the clinical risk of malnutrition in children with cancer and the indications for implementing nutritional interventions before and during treatment in patients at risk of malnutrition and malnourished patients (Budka-Chrząszcz et al., 2024). The enrichment of meals with foods that are high in protein and calories is a basic principle in the choice of diet for children with cancer. However, during cancer treatment, children's taste and smell preferences often change, and treatment with cytostatic drugs is associated with vomiting

TABLE 6 Pretreatment prealbumin and albumin levels according to the occurrence of infectious complications.

Infectious complications	Prealbumin g/L	p-value	Albumin g/dL	p-value
Yes n = 23	0.08 (0.05–0.1) 0.02–0.2	0.0504	0.12 (0.08–0.19) 0.03–0.34	0.073
No n = 17	0.12 (0.08–0.19) 0.03–0.34		4.38 (4.08–4.52) 3.06–5.07	

Data are presented as median (Q1–Q3) and range. Differences in parameters were calculated using the U Mann-Whitney test.

TABLE 7 Distribution of prealbumin and albumin deficiency according to the number of infectious episodes.

	Infectious complications		p-value
	0–2 episodes n = 29	3–5 episodes n = 11	
Prealbumin deficiency			
Yes n = 35	24 (68.6)	11 (31.4)	0.2975
No n = 5	5 (100.0)	0 (0.0)	
Albumin deficiency			
Yes n = 5	1 (20.0)	4 (80.0)	0.0152
No n = 35	28 (80.0)	7 (20.0)	

Data are presented as number (percentage) of patients. Differences in parameters were calculated using the Fisher test.

TABLE 8 Incidence of infectious complications in patients with anthropometric malnutrition and patients at risk for malnutrition with inflammation.

Infectious complications	Patients with anthropometric malnutrition n = 4	Patients at risk for malnutrition with inflammation n = 15	p-value
Yes	3 (75.0)	9 (60.0)	1.000
No	1 (25.0)	6 (40.0)	
Infectious complications			
	0–2 episodes	3–5 episodes	1.000
Patients with anthropometric malnutrition n = 4	1 (25.0)	3 (75.0)	
Patients at risk for malnutrition with inflammation n = 15	6 (40.0)	9 (60.0)	

Data are presented as number (percentage). Differences in parameters were calculated using the Fisher test.

TABLE 9 Univariable logistic regression analysis of prealbumin and albumin deficiency, as well as low UAMA percentile, as predictors of infectious complications during treatment.

Variable	Estimate	OR	LCI	UCI	p-value
Prealbumin deficiency	16.786	19,499,705.588	0.000	NA	0.992
Albumin deficiency	2.773	16.000	1.994	341.07	0.02
Low UAMA percentile	1.161	3.194	0.713	14.71	0.126

Odds ratio (OR), and lower (LCI) and upper (UCI) 95% confidence intervals for main risk factors.

Abbreviations: NA, not available; UAMA, upper arm muscle area.

and nausea, making it difficult to follow dietary recommendations. Patients at risk of permanent malnutrition during treatment should therefore be treated with nutritionally complete and energy-rich enteral formulas, this form of management provides uninterrupted nutritional support. In some cases, patients who have developed gastrointestinal mucosal complications may have difficulty with oral intake, and special situations such as acute pancreatitis and bowel obstruction may require temporary parenteral nutrition. The indications for nutritional interventions developed by the above

Polish societies are supported by literature data (Bauer, et al., 2011; Ladas et al., 2016).

In our study group, up to 87% of children were found to be protein deficient before treatment. The results of our study did not confirm significant differences in protein status and the incidence of PEU when comparing the group of patients with solid tumours and hematological malignancies both before and after treatment. In contrast, the results of the analysis showed that there was an increase in protein levels after treatment in both tumour groups, with significantly higher levels of prealbumin

and albumin in the hematological malignancies and significantly higher levels of albumin in the solid tumour group.

In our study, prealbumin deficiency was more common than albumin deficiency before treatment and was present in most patients. Prealbumin (transthyretin) is a transport protein for thyroid hormones. Serum prealbumin levels below 0.1 g/L are considered to indicate a significant risk of malnutrition (Keller, 2019; Beck and Rosenthal et al., 2002; Bharadwaj et al., 2016). In our study, 67.5% of patients had prealbumin deficiency after treatment, but the deficiency was not severe. We also observed that achieving higher prealbumin concentrations after treatment occurred in patients with hematological malignancies, who are at lower risk of malnutrition due to their tumour type. Additionally, most patients with hematological malignancies received low and intermediate intensity treatment due to their low risk group classification (standard risk or intermediate risk), while most patients with solid tumours received high intensity treatment due to their high stage of disease. Compared with albumin, prealbumin has a short half-life of only 2 days. Due to its favorable amino acid composition, prealbumin can be used to assess changes in the patient's diet, such as insufficient caloric intake or dietary improvement (Keller, 2019; Beck and Rosenthal et al., 2002; Bharadwaj et al., 2016). In our study, a lower percentage of patients with prealbumin deficiency after treatment may indicate an improvement in the nutrition of cancer patients in remission and thus predict an improvement in the nutritional status of patients. However, this hypothesis cannot be confirmed due to the limited duration of the study and the lack of monitoring of nutritional status and prealbumin levels in cancer survivors.

Literature data report a different prevalence of hypoalbuminemia at diagnosis in children with cancer, ranging from 7.4% to 45.8% (McLean et al., 2020; Leraas et al., 2023; Tandon et al., 2015; Yaprak et al., 2021). In our study, albumin deficiency was found in only 12.5% of children before treatment and in no children after treatment. Therefore, albumin was shown to be less useful than prealbumin in predicting malnutrition due to inflammation.

Our study highlights the measurement of UAMA as a simple but important tool for assessing lean body mass, particularly muscle mass, which is a key component of metabolic and immune health. The prevalence of anthropometric malnutrition according to UAMA in our patients did not change during the observation period. A low UAMA percentile was reported in 27.5% of cancer patients at diagnosis, and this rate remained stable until the end of treatment. Iniesta et al. (Revuelta Iniesta et al., 2019) reported a lower prevalence of PEU in their study group including 64 children with cancer. The highest prevalence of 14% was found at baseline and decreased to 10% at 3 months and to 12.5% at 24 months of follow-up. None of the patients had PEU at 30 and 36 months after diagnosis (Revuelta Iniesta et al., 2019). In our study, we did not confirm a significant relationship between PEU and the levels of selected proteins. However, we found that patients with normal and high UAMA percentiles had higher serum prealbumin and albumin levels

than patients with low UAMA. In contrast, Yaprak et al. (2021) reported an association between anthropometric malnutrition in children with cancer and prealbumin deficiency. The rates of low serum prealbumin levels on admission and at follow-up were 54.3% and 39.4%, respectively. Low prealbumin levels were reported in 73% of patients with malnutrition vs. 42% of those without ($p = 0.007$). In contrast, Gürlek Gökçebay et al. (2015) highlighted significant changes in prealbumin levels following dietary intervention in patients diagnosed with anthropometric malnutrition. At 3 months of follow-up, there was a significant decrease in prealbumin levels in patients with vs. those without malnutrition ($p = 0.04$), while no significant reduction in the proportion of patients with malnutrition was reported. At 6 months, the proportion of patients with malnutrition was significantly lower than at baseline ($p = 0.006$) (Gürlek Gökçebay et al., 2015). These results indicate that it is possible to modify the UAMA parameter in those patients who have improved their diet, but that its improvement and increase from deficient values to normal values can be achieved over a longer period of time after completion of oncological treatment. However, this hypothesis also cannot be confirmed due to the limited duration of the study and the lack of monitoring of nutritional status and prealbumin levels in cancer survivors.

Malnutrition can make a person more susceptible to infection, which in turn increases the body's need for energy and also contributes to the onset or worsening of malnutrition (Katona and Katona-Apte, 2008). In the inflammatory condition, protein synthesis processes in the liver correlate inversely with increases in CRP, so visceral protein deficiencies are often found in disease states where acute phase proteins are elevated (Evans et al., 2020). Proteins play an important role in supporting the immune system, and their deficiency can adversely affect immune function. They are essential for the proper functioning of immune cells, including T and B lymphocytes, and influence the production of cytokines that regulate immune responses. An adequate supply of protein is also necessary for the proper functioning of the complement system. In addition, proteins play a role in wound healing and a deficiency can interfere with tissue repair (Morales et al., 2023).

The incidence of infectious complications in cancer is influenced by disease- and treatment-related factors, such as bone marrow suppression, as well as by patient-related factors, such as inadequate nutritional status (Pedretti et al., 2023). Consequently, every patient with cancer is at risk for developing infectious complications during cancer treatment, which leads to a delayed completion of cancer treatment, increased risk of infection-related mortality, and cancer treatment failure. Among the infectious complications analysed in our patient group, some were serious and life-threatening (sepsis, FUO, fungal infections, stomatitis in stages III and IV, typhlitis). However, due to small sample size we did not analyze patients grouped according to infections severity, but we assessed the impact of prealbumin and albumin deficiency and PEU on the incidence of infectious

complications during cancer treatment. We found a significantly higher number of infectious complications in patients diagnosed with hematological malignancies compared with those with solid tumors. Our findings are in line with the study by Zajac-Spychala et al. (2021). In our study, the incidence of infectious complications during treatment in patients with risk factors for inflammatory malnutrition was similar to that in patients with pre-existing anthropometric malnutrition without inflammation. We also found that patients at risk for malnutrition with inflammation were more than 3 times more likely to have known anthropometric malnutrition without inflammation. Although the diagnosis of malnutrition based on protein assessment is not recommended (Evans et al., 2021), our findings confirm that they can be used to identify inflammation leading to malnutrition that increases the risk of infectious complications during cancer treatment to the same extent as the presence of malnutrition itself.

We found lower pretreatment prealbumin and albumin levels in patients with infectious complications, with borderline statistical significance shown for prealbumin. In addition, pretreatment prealbumin deficiency was present in all patients who had more than 3 infectious episodes during treatment. This finding may support the role of proteins, particularly prealbumin, in assessing changes in nutritional status in children with cancer and in recognizing the need to implement supportive nutritional measures during cancer treatment. Liang et al. (2018) reported a significant increase in total protein, albumin, and prealbumin levels after nutritional intervention in children with acute lymphoblastic leukemia during induction treatment. They also showed a lower incidence of infection during induction treatment in patients who received nutritional therapy (Liang et al., 2018). Although most of our patients had prealbumin deficiency and hypoalbuminemia was less common, albumin deficiency was shown to be a significant predictor of 3 or more episodes of infectious complications during treatment in our patients. The role of hypoalbuminemia as a negative prognostic factor for treatment outcome was demonstrated by other authors (McLean et al., 2020; Leraas et al., 2023; Tandon et al., 2015; Sonowal and Gupta, 2012).

The study has its strengths and limitations. The strengths include prospective design which enables to collect data in unified way and interdisciplinary approach of the study that combines clinical, nutritional and, in some cases, immunological perspectives relevant to supportive care during oncological treatment of childhood cancer. One of its limitations is the small sample size, which may have affected the statistical significance of the results. However, the number of patients included reflects the capacity of the department where the study was conducted at the time of the study. We are also aware that the study group was heterogeneous regarding diagnosis but subjecting to analysis only patients with one type of cancer would make the study group even more smaller. The treatment approach is also different, as patients

with hematological malignancies received steroid therapy. However, this is a standard treatment for this type of cancer, so we could not avoid its possible influence on the study results. We did not analyse the effect of nutritional interventions on the biochemical results obtained in this study, but we believe that the questions raised will encourage further research.

Conclusions

The presence of protein-energy malnutrition in children with cancer at the time of diagnosis increases the risk of infectious complications during treatment. In our study, albumin and prealbumin deficiencies were shown to indicate the risk of malnutrition related to inflammation in patients with childhood cancer. Hypoalbuminemia may be useful for identifying cancer patients who are at risk for an adverse treatment course, complicated by frequent infections. Implementing nutritional interventions will be beneficial in patients with PEU and in those with suspected malnutrition with inflammation. Proper nutrition in cancer improves nutritional status and reduces the risk of infectious complications during treatment.

Data availability statement

The original contributions presented in the study are included in the article/supplementary material, further inquiries can be directed to the corresponding author.

Ethics statement

The studies involving humans were approved by the Ethics Committee of the Medical University of Lublin (26 Sep 2019/ No KE-0254/278/2019). The studies were conducted in accordance with the local legislation and institutional requirements. Written informed consent for participation in this study was provided by the participants' legal guardians/next of kin.

Author contributions

AM and KD are responsible for the conception and design of the study. AC conducted laboratory work. Material preparation, data collection and analysis were performed by AM. The first draft of the manuscript was written by AM and all authors commented on previous versions of the manuscript. KD supervised the study. All authors read and approved the final. All authors contributed to the article and approved the submitted version.

Funding

The author(s) declare that no financial support was received for the research, authorship, and/or publication of this article.

References

- Barr, R. D., and Stevens, M. C. G. (2020). The influence of nutrition on clinical outcomes in children with cancer. *Pediatr. Blood and Cancer* 67 (S3), 281177–e28211. doi:10.1002/pbc.28117
- Bauer, J., Jürgens, H., and Frühwald, M. C. (2011). Important aspects of nutrition in children with cancer. *Adv. Nutr.* 2 (2), 67–77. doi:10.3945/an.110.000141
- Beck, F. K., and Rosenthal, T. C. (2002). Prealbumin: a marker for nutritional evaluation. *Am. Fam. Physician* 65 (8), 1575–1578.
- Bertuccio, P., Alicandro, G., Malvezzi, M., Carioli, G., Boffetta, P., Levi, F., et al. (2020). Childhood cancer mortality trends in Europe, 1990–2017, with focus on geographic differences. *Cancer Epidemiol.* 67, 101768. doi:10.1016/j.canep.2020.101768
- Bharadwaj, S., Ginoya, S., Tandon, P., Gohel, T. D., Guirguis, J., Vallabh, H., et al. (2016). Malnutrition: laboratory markers vs nutritional assessment. *Gastroenterol. Rep.* 4 (4), 272–280. doi:10.1093/gastro/gow013
- Budka-Chrząszcz, A., Szlagatyś-Sidorkiewicz, A., Bień, E., Irga-Jaworska, N., Borkowska, A., Krawczyk, M. A., et al. (2024). Managing undernutrition in pediatric oncology: a consensus statement developed using the delphi method by the polish society for clinical nutrition of children and the polish society of pediatric oncology and Hematology. *Nutrients* 16 (9), 1327. doi:10.3390/nu16091327
- Cederholm, T., Barazzoni, R., Austin, P., Ballmer, P., Biolo, G., Bischoff, S., et al. (2017). ESPEN guidelines on definitions and terminology of clinical nutrition. *Clin. Nutr.* 36 (1), 49–64. doi:10.1016/j.clnu.2016.09.004
- Cehreli, R., Yavuzsen, T., Ates, H., Akman, T., Ellidokuz, H., and Oztup, I. (2019). Can inflammatory and nutritional serum markers predict chemotherapy outcomes and survival in advanced stage nonsmall cell lung cancer patients? *BioMed Res. Int.* 2019, 1–8. doi:10.1155/2019/1648072
- Co-Reyes, E., Li, R., Huh, W., and Chandra, J. (2012). Malnutrition and obesity in pediatric oncology patients: causes, consequences, and interventions. *Pediatr. Blood and Cancer* 59 (7), 1160–1167. doi:10.1002/pbc.24272
- Cunningham, R. M., Walton, M. A., and Carter, P. M. (2018). The major causes of death in children and adolescents in the United States. *N. Engl. J. Med.* 379 (25), 2468–2475. doi:10.1056/nejmsr1804754
- Esbenshade, A. J., Sung, L., Brackett, J., Dupuis, L. L., Fisher, B. T., Grimes, A., et al. (2023). Children's Oncology Group's 2023 blueprint for research: cancer control and supportive care. *Pediatr. Blood and Cancer* 70 (S6), 305688–e30577. doi:10.1002/pbc.30568
- Evans, D. C., Corkins, M. R., Malone, A., Miller, S., Mogensen, K. M., Guenter, P., et al. (2021). The use of visceral proteins as nutrition markers: an ASPEN position paper. *Nutr. Clin. Pract.* 36 (1), 22–28. doi:10.1002/ncp.10588
- Frisancho, A. R. (1990). *Anthropometric standards for the assessment of growth and nutritional status*. Ann Arbor (MI): University of Michigan Press. doi:10.1002/ajpa.1330840116
- Gürlek Gökçeyab, D., Emir, S., Bayhan, T., Demir, H. A., Gunduz, M., and Tunc, B. (2015). Assessment of nutritional status in children with cancer and effectiveness of oral nutritional supplements. *Pediatr. Hematol. Oncol.* 32 (6), 423–432. doi:10.3109/08880018.2015.1065303
- Joffe, L., Schadler, K. L., Shen, W., and Ladas, E. J. (2019). Body composition in pediatric solid tumors: state of the science and future directions. *JNCI Monogr.* 2019 (54), 144–148. doi:10.1093/jncimonographs/lgz018
- Katona, P., and Katona-Apte, J. (2008). The interaction between nutrition and infection. *Clin. Infect. Dis.* 46 (10), 1582–1588. doi:10.1086/587658
- Keller, U. (2019). Nutritional laboratory markers in malnutrition. *J. Clin. Med.* 8 (6), 775. doi:10.3390/jcm8060775
- Kuvibidila, S., Yu, L., Gardner, R., Velez, M., Ode, D., and Warriar, R. P. (2000). Association between increased levels of TNF- α , decreased levels of prealbumin and retinol-binding protein, and disease outcome. *J. Natl. Med. Assoc.* 92 (10), 485–491.
- Ladas, E. J., Brijesh, A., Scott, C. H., Paul, R. C., Terezia, T. M., and Barr, R. D. (2016). A framework for adapted nutritinal therapy for children with cancer in low-

Conflict of interest

The authors declare that the research was conducted in the absence of any commercial or financial relationships that could be construed as a potential conflict of interest.

and middle-income countries: a report from the SIOF podc nutrition working group. *Pediatr. Blood Cancer* 63 (8), 1339–1348. doi:10.1002/pbc.26016

Laviano, A., Meguid, M. M., Inui, A., Muscaritoli, M., and Rossi-Fanelli, F. (2005). Therapy insight: cancer anorexia-cachexia syndrome - when all you can eat is yourself. *Nat. Clin. Pract. Oncol.* 2 (3), 158–165. doi:10.1038/ncponc0112

Leraas, H. J., Schaps, D., Thornton, S. W., Moya-Mendez, M., Donohue, V., Hoover, A., et al. (2023). Risk of surgical intervention in children with diagnoses of cancer and preoperative malnutrition: a national analysis. *J. Pediatr. Surg.* 58 (6), 1191–1194. doi:10.1016/j.jpedsurg.2023.02.019

Liang, R., Chen, G. Y., Fu, S. X., Zhong, J., and Ma, Y. (2018). Benefit of oral nutritional supplements for children with acute lymphoblastic leukaemia during remission induction chemotherapy: a quasi-experimental study. *Asia Pac J. Clin. Nutr.* 27 (1), 144–147. doi:10.6133/apjcn.032017.04

Luo, H., Huang, J., Zhu, Z., and Zhu, P. (2019). Prognostic value of pretreatment serum transthyretin level in patients with gastrointestinal cancers. *Dis. Markers* 2019, 1–8. doi:10.1155/2019/7142065

McLean, T. W., Stewart, R. M., Curley, T. P., Dewsnup, M. Y., Thomas, S. G., Russell, T. B., et al. (2020). Hypoalbuminemia in children with cancer treated with chemotherapy. *Pediatr. Blood and Cancer* 67 (2), e28065–e28066. doi:10.1002/pbc.28065

Milaniuk, A., and Drabko, K. (2024). Changes in the nutritional status of children with cancer depending on clinical, demographic and social factors. *Acta Haematol. Pol.* 5 (5), 260–272. doi:10.5603/ahp.101236

Morales, F., Montserrat-de la Paz, S., Leon, M. J., and Rivero-Pino, F. (2023). Effects of malnutrition on the immune system and infection and the role of nutritional strategies regarding improvements in children's health status: a literature review. *Nutrients* 16 (1), 1. doi:10.3390/nu16010001

Pedretti, L., Massa, S., Leardini, D., Muratore, E., Rahman, S., Pession, A., et al. (2023). Role of nutrition in pediatric patients with cancer. *Nutrients* 15 (3), 710–722. doi:10.3390/nu15030710

Revuelta Iniesta, R., Paciarotti, I., Davidson, I., McKenzie, J. M., Brougham, M. F. H., and Wilson, D. C. (2019). Nutritional status of children and adolescents with cancer in scotland: a prospective cohort study. *Clin. Nutr. ESPEN* 32, 96–106. doi:10.1016/j.clnesp.2019.04.006

Rogers, P. C., and Barr, R. D. (2020). The relevance of nutrition to pediatric oncology: a cancer control perspective. *Pediatr. Blood and Cancer* 67 Suppl 3 (S3), e28213–e28218. doi:10.1002/pbc.28213

Romano, A., Triarico, S., Rinninella, E., Natale, L., Brizi, M. G., Cintoni, M., et al. (2022). Clinical impact of nutritional status and sarcopenia in pediatric patients with bone and soft tissue sarcomas: a pilot retrospective study (SarcoPed). *Nutrients* 14 (2), 383. doi:10.3390/nu14020383

Sala, A., Pencharz, P., and Barr, R. D. (2004). Children, cancer, and nutrition - a dynamic triangle in review. *Cancer* 100 (4), 677–687. doi:10.1002/cncr.11833

Sanches, F. L. F. Z., Nitsch, T. M., Vilela, M. M. S., and Sgarbieri, V. C. (2015). Comparison of biochemical and immunological profile of pediatric patients with acute myeloid leukemia in relation to healthy individuals. *J. Pediatr. Versão em Port.* 91 (5), 478–484. doi:10.1016/j.jpeds.2014.12.004

Shachar, S. S., Williams, G. R., Muss, H. B., and Nishijima, T. F. (2016). Prognostic value of sarcopenia in adults with solid tumours: a meta-analysis and systematic review. *Eur. J. Cancer* 57, 58–67. doi:10.1016/j.ejca.2015.12.030

Soeters, P. B., Shenkin, A., Sobotka, L., Soeters, M. R., de Leeuw, P. W., and Wolfe, R. R. (2021). The anabolic role of the Warburg, Cori-cycle and Crabtree effects in health and disease. *Clin. Nutr.* 40 (5), 2988–2998. doi:10.1016/j.clnu.2021.02.012

Sonowal, R., and Gupta, V. (2021). Nutritional status in children with acute lymphoblastic leukemia, and its correlation with severe infection. *Indian J. Cancer.* 58 (2), 190–194. doi:10.4103/ijc.IJC_110_19

Steliarova-Foucher, E., Stiller, C., Lacour, B., and Kaatsch, P. (2005). International classification of childhood cancer, third edition. *Cancer* 103, 1457–1467. doi:10.1002/cncr.20910

Tandon, S., Moulik, N. R., Kumar, A., Mahdi, A. A., and Kumar, A. (2015). Effect of pre-treatment nutritional status, folate and vitamin B12 levels on induction chemotherapy in children with acute lymphoblastic leukemia. *Indian Pediatr.* 52 (5), 385–389. doi:10.1007/s13312-015-0642-x

Viani, K., Trehan, A., Manzoli, B., and Schoeman, J. (2020). Assessment of nutritional status in children with cancer: a narrative review. *Pediatr. Blood and Cancer* 67 Suppl 3 (S3), e28211. doi:10.1002/pbc.28211

Yaprak, D. S., Yalçın, B., Pınar, A. A., and Büyükpamukçu, M. (2021). Assessment of nutritional status in children with cancer: significance of arm anthropometry and

serum visceral proteins. *Pediatr. Blood and Cancer* 68 (1), e28752–e28758. doi:10.1002/pbc.28752

Zajac-Spychala, O., Wachowiak, J., Gryniewicz-Kwiatkowska, O., Gietka, A., Dembowska-Baginska, B., Semczuk, K., et al. (2021). Prevalence, epidemiology, etiology, and sensitivity of invasive bacterial infections in pediatric patients undergoing oncological treatment: a multicenter nationwide study. *Microb. Drug Resist.* 27 (1), 53–63. doi:10.1089/mdr.2019.0393

Zawitkowska, J., Drabko, K., Szmydki-Baran, A., Zaucha-Prazmo, A., Lejman, M., Czyżewski, K., et al. (2019). Infectious profile in children with ALL during chemotherapy: a report of study group for infections. *J. Infect. Chemother.* 25 (10), 774–779. doi:10.1016/j.jiac.2019.04.005



OPEN ACCESS

EDITED BY

Witold Norbert Nowak,
Jagiellonian University, Poland

REVIEWED BY

Walentyna Balwierz,
University Children's Hospital in Krakow,
Poland
Artur Palasz,
Medical University of Silesia, Poland
Hevidar Taha,
University of Duhok, Iraq

*CORRESPONDENCE

Paulina Skowera,
✉ paulina.skowera@umlub.pl
Magdalena Stelmach,
✉ magdalena.stelmach@umlub.pl

[†]These authors have contributed equally
to this work

RECEIVED 08 February 2024

ACCEPTED 12 June 2024

PUBLISHED 10 July 2024

CITATION

Winnicka D, Skowera P, Stelmach M,
Styka B and Lejman M (2024),
Application of the FISH method and
high-density SNP arrays to assess
genetic changes in
neuroblastoma—research by
one institute.
Acta Biochim. Pol 71:12821.
doi: 10.3389/abp.2024.12821

COPYRIGHT

© 2024 Winnicka, Skowera, Stelmach,
Styka and Lejman. This is an open-
access article distributed under the
terms of the [Creative Commons
Attribution License \(CC BY\)](#). The use,
distribution or reproduction in other
forums is permitted, provided the
original author(s) and the copyright
owner(s) are credited and that the
original publication in this journal is
cited, in accordance with accepted
academic practice. No use, distribution
or reproduction is permitted which does
not comply with these terms.

Application of the FISH method and high-density SNP arrays to assess genetic changes in neuroblastoma—research by one institute

Dorota Winnicka[†], Paulina Skowera^{*†}, Magdalena Stelmach^{*},
Borys Styka and Monika Lejman

Independent Laboratory of Genetic Diagnostics, Medical University of Lublin, Lublin, Poland

Neuroblastoma is the most common extracranial solid tumor in children. Amplification of the MYCN gene has been observed in approximately 20%–30% of tumors. It is strongly correlated with advanced-stage disease, rapid tumor progression, resistance to chemotherapy and poor outcomes independent of patient age and stage of advanced disease. MYCN amplification identifies high-risk patients. To assess neuroblastoma tumors with MYCN amplification we used paraffin-embedded tissue sections in 57 patients and intraoperative tumor imprints in 10 patients by fluorescence *in situ* hybridization (FISH). Positive results for MYCN amplification have been observed in twelve patients' paraffin-embedded tissue sections and in three patients' intraoperative tumor imprints, which represents 22.4% of all patients tested in the analysis. Fluorescence *in situ* hybridization is a highly sensitive and useful technique for detecting MYCN amplification on paraffin-embedded tissue sections of neuroblastoma tumors and intraoperative tumor imprints thus facilitating therapeutic decisions based on the presence or absence of this important biologic marker. The presence of structural changes, regardless of MYCN gene amplification status, influences the clinical behavior of neuroblastoma. High-Density SNP Arrays have emerged as the perfect tools for detecting these changes due to their exceptional accuracy, sensitivity and ability to analyze copy number and allele information. Consequently, they are proven to be highly valuable in the genomic diagnosis of immature neuroectodermal tumors.

KEYWORDS

neuroblastoma, childhood tumours, MYCN amplification, high-density SNP arrays, FISH

Introduction

Neuroblastoma is a malignant tumor in children aged 0–15 years. It accounts for 8%–10% of all childhood tumors, with 80% affecting children under the age of 5 years and approximately 15% representing all cancer deaths in children (Aygün, 2018; Swift et al., 2018). Approximately 60–70 of the new incidences of neuroblastoma are diagnosed each year in Poland (Whittle et al., 2017).

Neuroblastoma derives from primitive cells of the sympathetic nervous system. It occurs in the retroperitoneum, posterior mediastinum, neck, or pelvis. The clinical symptoms in neuroblastoma depend on the tumor mass, the extent of metastasis and catecholamine and vasoactive intestinal peptide secretion by the tumor cells. The diagnosis of neuroblastoma is based on histopathological results and the presence of tumor cells in the bone marrow accompanied by elevated levels of urinary catecholamines. In addition to clinical, histopathological and laboratory data, genetic test results are crucial in determining prognosis (Adamkiewicz-Drożyńska, 2006; Schulte et al., 2018).

The most common cytogenetic changes include deletions of chromosome 1p, amplification of the oncogene *MYCN*, ploidy changes, gains of chromosome arm 17q and deletion of 11q in tumor cells. Genetic abnormalities are very powerful predictors of response to therapy and outcome and provide important information to guide optimal patient management (Bhat and McGregor, 2017; Lim et al., 2020).

The *MYCN* gene is a cellular protooncogene of the *MYC* family. *MYCN* maps to the 2p24 chromosome. Structural alterations leading to amplification can manifest in the form of double minute chromosomes (dmns) or homogeneous staining regions (HSRs). Dmns represent extra chromosomal material, while HSRs denote duplicate material within chromosomes. Dmns are commonly observed in tumor-derived cells, whereas HSRs are more prevalent in cell lines. However, without traditional karyotype analysis, we are unable to precisely determine what type of changes we are dealing with (Van Noesel and Versteeg, 2004; Jeison et al., 2010).

MYCN is an oncogenic transcription factor involved in the regulation of proliferation, transformation, differentiation and apoptosis (Swift et al., 2018).

MYCN amplification is detected in 20%–30% of neuroblastoma patients (Yue et al., 2017; Otte et al., 2020). It is strongly correlated with advanced disease stage, rapid tumor progression, resistance to chemotherapy and poor outcomes. The *MYCN* amplification test result is included in medical protocols around the world, it is an independent indicator in the assessment of the patient outcome and it is one of the qualifying factors for a group requiring the most aggressive treatment (Brodeur et al., 1985; Huang and Weiss, 2013; Ahmed et al., 2017; Kaczówka et al., 2018; Croteau et al., 2021). *MYCN* amplification is present in 38% of patients with

stages 3 and 4 (Ahmed et al., 2017) but only in 5%–10% of patients with stages 1, 2, and 4 s (Morandi, 2022). The level of *MYCN* gene amplification is necessary to avoid either under- or over-treating patients (Lee et al., 2018). The gold standard in the assessment of *MYCN* amplification is fluorescence *in situ* hybridization on paraffin-embedded tissue sections and intraoperative tumor imprints.

The independent factors that predict the outcome of treatment are: tumor histology, level of *MYCN* amplification and chromosomal copy number changes (Chicard et al., 2016; Lerone et al., 2021). In addition to these two main genetic markers, a number of segmental aberrations involving different chromosomes have also been described that, in addition to *MYCN* amplification, have a strong effect on the development of neuroblastoma, making it more aggressive and resistant to treatment (Lerone et al., 2021). Currently, the diagnosis of neuroblastoma also relies on molecular methods, such as microarrays, but it is not always possible to isolate good-quality DNA from paraffin-embedded tissue sections. An alternative method to obtain good-quality DNA is the intraoperative collection of tumor scrap from which DNA isolation is performed directly.

SNP array analysis provides comprehensive detection of the presence of deletions and duplications involving chromosomal fragments and allows for simultaneous assessment of DNA copy number.

SNP array analysis can also detect loss of heterozygosity (LOH). Studies of neuroblastoma cells have identified LOH in several chromosomal regions, of which LOH 1p and 4p correlate with poor patient outcomes.

In addition to these relatively large genomic aberrations, deletion aberrations of single genes, parts of genes or point mutations e.g., *TERT*, *ALK*, *ATRX*, and *ARID1A*, have recently been described as having unfavorable clinical outcomes and implications for clinical management (Brunner et al., 2016).

The aim of this study was to demonstrate the effectiveness of the FISH method for the evaluation of *MYCN* amplification on paraffin-embedded tissue sections and intraoperative tumor imprints together with HD SNP array analysis in neuroblastoma patients.

Materials and methods

The study materials consisted of 57 paraffin-embedded tissue sections with freshly removed tumors and 10 intraoperative tumor imprints, along with archival sections from 67 patients with an established clinical diagnosis of neuroblastoma (31 little girls and 36 little boys; median age: 3 years 2 months). All of the children were admitted to the Department of Pediatric Hematology, Oncology and Transplantology, Children's University Hospital, Lublin, Poland between 1994 and 2023.

TABLE 1 Patient characteristics.

	Criterion	Number
Age at diagnosis	<18 m	31
	>18 m	36
Diagnosis	NB	52
	GNB	11
	GN	1
	ND	3
INSS risk group	1	7
	2	3
	3	24
	4s	3
	4	30
Primary site	Abdomen	22
	Adrenal glands	25
	Mediastinum	11
	Pelvis	7
	Cervical	2
MYCN amplification	Yes	15
	No	52

The collected clinical data included the patient’s age at diagnosis, stage according to the INSS (International Neuroblastoma Staging System) criteria (Park et al., 2017), tumor location, histopathological diagnosis of the examined tissues and MYCN amplification [Table 1]. Detailed patient data can be found in the Supplementary Material. All studies were performed between 1994–2023.

FISH method

We used the Pretreatment Kit (Vysis) and the LSI N-MYC (2p24) SpectrumGreen/CEP 2 SpectrumOrange Probe (Vysis) to estimate MYCN amplification.

Paraffin-embedded tissue blocks were cut into 4-micron thick sections on silanized slides and they were baked at 56°C overnight. Slides were soaked twice in xylene for 10 min and dehydrated in ethanol at 100%, 96%, 80%, and 70% for 2–5 min in each solution. Slides were then immersed in 0.2 N hydrochloric acid for 20 min and rinsed in water and wash buffer for 3 min in each of them. The slides were immersed in Pretreatment Solution at 80°C for 30 min and they were washed twice in 2xSSC for 5 min.

In the next step, the tissue sections were digested in protease solution at 37°C for 30 min and then the slides were immersed in 2xSSC cooled to 5°C.

The slides were then fixed in 10% formalin for 10 min. Fixed tissue, washed twice in 2xSSC and dried on a hot plate at 45°C–50°C.

Slides with intraoperative tumor imprints were immersed in a fixative prepared by mixing 3 parts methanol and 1 part acetic

acid for 30 min. The slides were then dried at room temperature for 24 h.

To detect the presence of MYCN gene amplification, on paraffin-embedded tissue sections and intraoperative imprints of neuroblastoma tumors, we used fluorescence *in situ* hybridization (FISH) on interphase nuclei. Molecular cytogenetics uses the FISH method to identify specific DNA sequences on chromosomes using DNA probes that are directly labeled by the fluorophore. The labeled probe and the target DNA are denatured in the first step of this method. Hybridization is the second step of the FISH method. Combining the denatured probe and target DNA allows for the annealing of complementary DNA sequences.

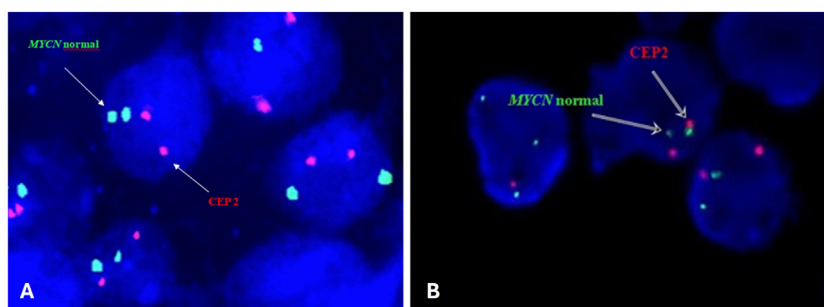
We used 1 µL of direct fluorochrome-labeled, dual color DNA Probe for the MYCN gene locus (2p24) and α-satellite DNA identifying the centromeric region of chromosome 2 (Vysis LSI N-MYC (2p24) SpectrumGreen/CEP 2 SpectrumOrange Probe) combined with the 7 µL Hybridization Buffer and 2 µL water. The probe was placed on a slide, then covered with a coverslip and secured with rubber cement. The slides were incubated at 72°C for 5 min to denature the DNA. Hybridization was performed for 14–18 h at 37°C.

The slides were subsequently immersed in post-hybridization wash buffer at room temperature for 15–20 min until the coverslip fell off. Then they were immersed in post-hybridization wash buffer warmed to 72°C for 5 min. The cells were counterstained with DAPI. The signals were evaluated by eye or captured with Applied Spectral Imaging- ASI- Israel at ×100 magnification on the Nikon epifluorescence microscope equipped with a 100-W mercury arc lamp and an appropriate set of filters (single filters for FITC and TexasRed fluorochromes and a triple bandpass filter for FITC/TR/DAPI). A minimum of 200 nuclei was evaluated for each of the MYCN and CEP2 loci. Nuclei with two visible red and two green signals were scored as negative for MYCN amplification (Figure 1). According to the guidelines, the cutoff point for MYCN amplification was set at 10 signals (amplification ≥10; gain <10) only in the presence of disomy of chromosome 2. In the presence of polysomy of chromosome 2 in tumor cells, confirmation of MYCN gene amplification was based on the guideline that the number of tested signals must exceed that of control signals by at least four times (Ambros et al., 2009; Winnicka et al., 2020).

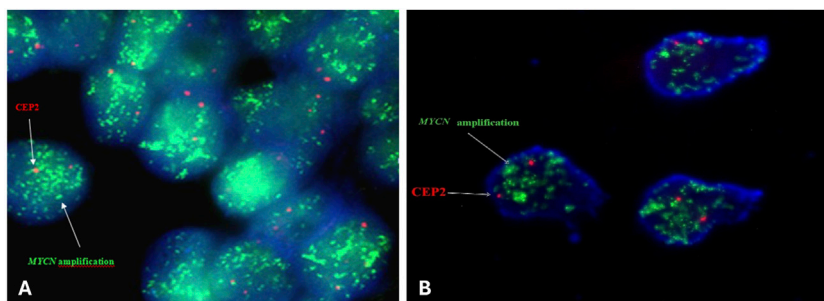
The study was approved by the Ethics Committee of the Medical University of Lublin (KE-0254/229/2012).

HD SNP array method

In eight patients, we isolated DNA from tumor tissue and performed microarray testing using the CytoScan HD array to

**FIGURE 1**

Representative FISH image on paraffin-embedded tissue section (A) and intraoperative tumor imprints (B) using the Vysis LSI N-MYC (2p24) SpectrumGreen/CEP 2 SpectrumOrange Probe from a neuroblastoma tumor showing normal interphase nuclei captured with Applied Spectral Imaging- ASI-Israel at x100 magnification on the Nikon epifluorescence microscope.

**FIGURE 2**

Representative FISH image on paraffin-embedded tissue section (A) and intraoperative tumor imprints (B) using Vysis LSI N-MYC (2p24) SpectrumGreen/CEP 2 SpectrumOrange Probe from a neuroblastoma tumor showing amplification MYCN captured with Applied Spectral Imaging- ASI- Israel at x100 magnification on the Nikon epifluorescence microscope.

evaluate additional cytogenetic abnormalities. In one case, the quality of the DNA did not allow for the array procedure.

Genomic DNA was isolated with the QIAamp DNA Blood Mini Kit (Qiagen, Hilden, Germany) according to the manufacturer's protocols. DNA samples were stored at -20°C until the next step. The concentration and quality of DNA were determined using a spectrophotometric method (NanoDrop 8000; Thermo Fisher Scientific, Waltham, MA, United States). In total, 250 ng of genomic DNA was used in accordance with the manufacturer's protocols. Microarray testing was performed with the use of a CytoScan HD array [2,670,000 markers, including 750,000 SNP and 1,900,000 non-polymorphic copy number variant (CNV) markers] (Applied Biosystems, part of Thermo Fisher Scientific). All subsequent steps and data analysis were performed as described previously by Lejman et al. (2020). The scanned data file was analyzed with Chromosome Analysis Suite v 3.3 (ChAS; Thermo Fisher Scientific) using the CRCh37 (hg19) reference genome.

Results

Results of *MYCN* amplification by fluorescence *in situ* hybridization (FISH)

Sixty-seven patients participated in this study. Thirty-four (50.7%) of patients had localized neuroblastoma (1–3 stages), 4.5% stage 4S, and 44.8% stage 4 disease. Forty-seven (70.1%) of patients had an abdominal/adrenal mass at diagnosis. Thirty-one (46.3%) patients were <18 months of age, and thirty-six (53.7%) patients were >18 months of age. Of 67 patient samples, including 52 neuroblastomas, 11 ganglioneuroblastomas, and 1 ganglioneuroma, 3 samples had no definitive diagnosis.

Positive results for *MYCN* amplification were observed in twelve patients' paraffin-embedded tissue sections and in three patients' intraoperative tumor imprints which represents 22.4% of all tested patients in the analysis (Figure 2).

There were 9 (60%) little boys and 6 (40%) little girls included in the study. Of the 15 patients, 1 (6.7%) had stage 3 disease, 1

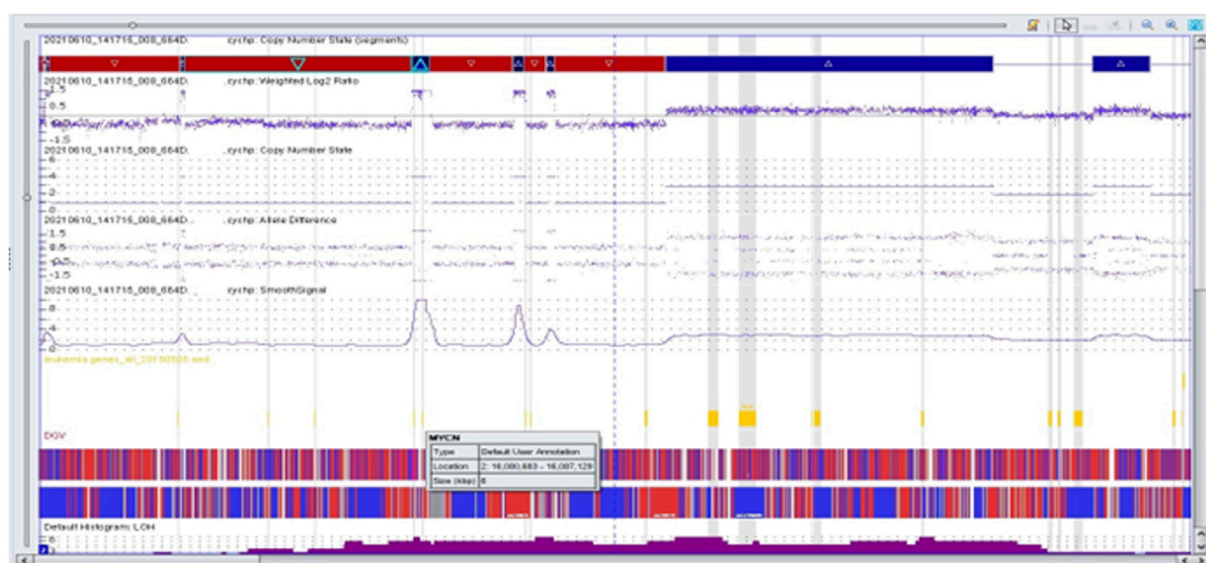


FIGURE 3

Complex copy number gains and losses in the region 2p25.3p21 of chromosome 2 in patient 63. With Neuroblastoma by single-nucleotide polymorphism (SNP) array. Colored segmental regions (top line: red color—deletions; blue color—gains), copy number status, allelic difference, and smooth signal aberrations by SNP array.

(6.7%) had stage 4 s disease, and 13 (86.6%) had stage 4 disease. Of these 15 patients with MYCN amplifications 5 (33.3%) were <18 months of age, and 10 (66.7%) were >18 months of age. Five (33.3%) of the patients with MYCN amplification had a tumor mass in the abdomen and ten (66.7%) had a tumor mass in the adrenal gland.

Molecular karyotype results

To evaluate additional molecular abnormalities we performed microarray testing on 6 patients with different stages of disease, tumor localization and ages at diagnosis.

We performed microarray testing on a patient with stage 4 disease and tumor localization in the adrenal gland. The patient was a girl who was over 18 months of age at the time of diagnosis. Through fluorescence *in situ* hybridization we observed positive results for MYCN amplification. Microarray analysis revealed a deletion within the short arm of chromosome 1 (arr [GRCh37] 1p36.33p36.22 (849466_9304205)x1), and a duplication involving a fragment of the short arm of chromosome 1, and the long arm of chromosome 1 (arr [GRCh37] 1p13.3q44 (110062169_249224684)x3). In region 2p25.3p21 we observed chromothripsis (arr [GRCh37] 2p25.3p21 (12770_46642249) cth) (Figure 3). The MYCN gene (2p24.3) was amplified in this region (10 copies). In addition, the ALK gene (2p23.2-p23.1) was also duplicated. Monosomy of chromosome 3 and trisomy of chromosome 18 were identified (Figure 4).

The second patient was a boy over 18 months of age at diagnosis, with stage 4 disease and tumor localization in the adrenal gland. Through fluorescence *in situ* hybridization we did not observe any amplification of the MYCN gene. Microarray analysis identified 3 cell lines with various genetic changes (Figure 5). We present the results in the table below (Table 2).

The third patient was a girl who was over 18 months of age at diagnosis, with stage 3 disease and tumor localization in the abdomen. Through fluorescence *in situ* hybridization we did not observe any amplification of the MYCN gene. Microarray analysis revealed mosaic monosomy of chromosome X and duplication of region 22q11.21 (arr [GRCh37] 22q11.21 (18979347_21800471)x3). The Whole Genome View (WGV) showed a decrease in the log2ratio value, which may indicate the presence of monosomy on chromosomes 3, 4, 9, 10, 14, 15, 19, and 21, and an increase in the log2ratio value, which may indicate the presence of trisomy on chromosome 13. An ambiguous assessment of chromosome copy number may be the result of incorrect material collection. The fourth patient was a boy who was over 18 months of age at diagnosis, with stage 3 disease and tumor localization in the abdomen. MYCN amplification was negative. With microarray analysis we identified a duplication involving a fragment of the short arm of chromosome 1 (arr [GRCh37] 1p36.33p36.32 (849467_3627839)x3 [0.3]) and deletions in the following regions: arr [GRCh37] 12q24.23q24.31 (118233114_125556278)x1 [0.2], 19p13.3p11 (260912_24505049)x1 [0.2]. As with the previous patient the Whole Genome View (WGV) showed a decrease in the log2ratio

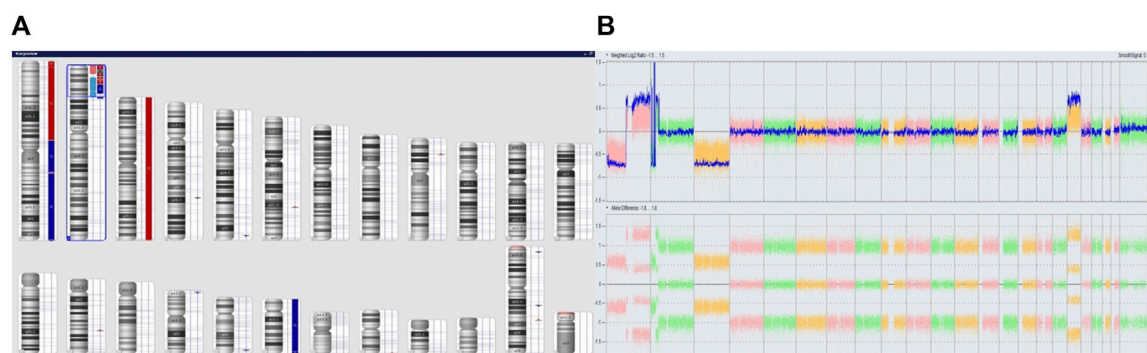


FIGURE 4
Complex copy number gains and losses in the whole genome of patient 63. With Neuroblastoma. Colored segmental regions (top line: red color—deletions; blue color—gains) (A) and Whole Genome View (B).

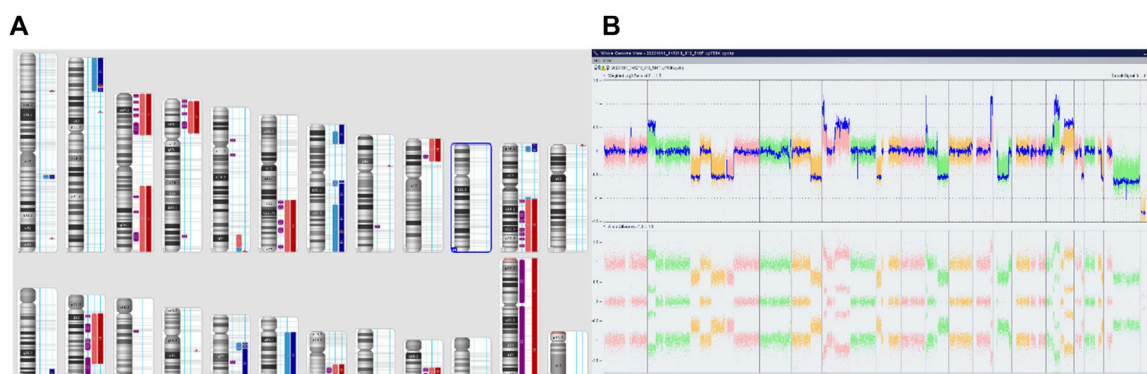


FIGURE 5
Complex copy number gains and losses in the whole genome of patient 64 with Neuroblastoma. Colored segmental regions (top line: red color—deletions; blue color—gains) (A) and Whole Genome View (B).

value, which may indicate the presence of monosomy on chromosomes 3, 4, 9, 10, 14, and 15 and an increase in the \log_2 ratio value, which may indicate the presence of trisomy on chromosome 13. The microarray results for the two patients were normal and did not reveal any additional changes in the molecular karyotype.

Discussion

In recent years, significant progress has been made in understanding the genetic basis of neuroblastoma. Numerous studies have been published on somatic mutations and chromosomal abnormalities associated with the development of neuroblastoma. However, their role in treatment response, prognosis, and the development of metastasis has not been fully elucidated. Based on our

research, we have divided patients into two groups: those with *MYCN* amplification and those without it.

High-risk patients are identified by the presence of *MYCN* amplification. *MYCN* amplification is a powerful prognostic factor for advanced stages and rapid tumor progression (Lau et al., 2015). Interphase FISH analysis provides a direct and rapid method. Only a small number of tumor cells are required, compared with primary tumor biopsies, and FISH is more sensitive by counting the *MYCN* copy number in each single cell (Tibiletti, 2007; Campbell et al., 2017).

The fluorescence *in situ* hybridization (FISH) method is faster to prepare than molecular biology techniques or traditional cytogenetic analysis. FISH can be used on interphase nuclei, in contrast to karyotype analysis, and it can be performed on formalin-fixed nuclei, in cases where a fresh or frozen tumor is not available (e.g., small biopsies or retrospective studies). However, molecular methods, such as microarrays, have

TABLE 2 Molecular changes identified in the microarray analysis of patient 64.

	Molecular karyotype	
	Different aberrations	Common aberrations
First cell line	arr [GRCh37] 1q21.3q23.1 (153001296_157812399)x3 [0.7], 2p25.3p21 (12771_42229545)x3 [0.7], 3p26.3p21.2 (61892_51747702)x1 [0.7], 3q13.31q29 (115403680_197851444)x1 [0.7], 4p16.3p13 (2744163_43086625)x1 [0.7], 6q21q27 (106487938_170914297)x1 [0.7], 7p21.3p15.3 (8582953_24331799)x3 [0.7], 7q11.22q36.3 (70144228_159119707)x3 [0.7], 9p24.3p21.1 (208455_28198623)x1 [0.7], 11p15.4 (3189610_10187920)x3 [0.7] 11q13.3q25 (69472473_134937416)x1 [0.7] 14q11.2q31.3 (24238818_89633472)x1 [0.7], 17q12q21.32 (36152227_46070727)x3 [0.7], 18q11.2q23 (19414307_78013728)x3 [0.7], 19q13.2q13.43 (42791601_58956816)x1 [0.7], 21q22.11q22.3 (35184499_48093361)x1 [0.7]	arr [GRCh37] (Y)x0, 7p22.3p21.3 (43377_8573211)x3~4, 11p15.5p15.4 (230681_3021529)x3~4, 13q33.1q34 (103826264_115107733)x3~4 14q31.1q32.33 (81449690_107279475)x2hms 17q21.32q25.3 (46073099_81041823)x3~4
Second cell line	arr [GRCh37]11q13.2q13.3 (66814096_69464793)x3 [0.4]	
Third cell line	arr [GRCh37]5q33.3q35.2 (159230740_174855411)x1 [0.25], 5q35.2q35.3 (174856439_180715096)x3 [0.25]	

strong limitations when analyzing *MYCN* amplification and other genetic changes in neuroblastoma because molecular methods are based on DNA from a mixture of cells and therefore only provide an average result for a particular tumor. When a tumor is highly amplified, this is not a problem for diagnosis. However, with low levels of *MYCN* amplification, it can be difficult to interpret the results. The first possibility is that there is a heterogeneous population of tumor cells in which a small number of cells are highly amplified or have other anomalies. Or it may be a highly amplified tumor mixed with normal tissue. Finally, it may be a low level of amplification occurring in tumor cells (e.g., a triploid population) (Shapiro et al., 1993; Squire et al., 1996; Thorner et al., 2006).

In the Polish population, tumor imprints are routinely used to assess *MYCN* amplification. However, this is not always possible and then the only material for *MYCN* amplification is a paraffin tissue section. It can be done on both fresh and archived tissues from many years ago.

For this study we used intraoperative tumor imprints and fresh paraffin-embedded tissue sections in addition to archival materials. Fresh material was obtained from a tumor removed from a patient 2 weeks before the study and archival paraffin sections were removed from a patient operated on 8 years and 2 months before the study. In our opinion both fresh tissue and tissue from years before preserved in a paraffin block were adequate materials for the test. The quality of the specimens was similar and the evaluation of both archival and fresh specimens was consistent with previous studies. Intraoperative tumor imprints were taken immediately after their removal. The

quality of these specimens is much better compared to the paraffin-embedded tissue sections, as only the tumor cells are on the slide, with no surrounding tissue. The assessment of *MYCN* amplification on intraoperative tumor imprints does not cause any diagnostic problems.

Microarray testing of neuroblastoma samples provides additional information on other chromosomal changes observed in patients with and without *MYCN* amplification, which has a strong impact on prognosis. In a sample from a patient with *MYCN* amplification we found a deletion within the short arm of chromosome 1 (1p36.33p36.22), and a duplication involving a fragment of the short arm of chromosome 1 and the long arm of chromosome 1 (1p13.3q44). In the literature, deletion or loss of heterozygosity (LOH) of the 1p36 chromosomal band is correlated with high-risk neuroblastoma features, including older age at diagnosis, metastatic disease, *MYCN* amplification and poor prognosis. Unfavorable abnormalities also include segmental copy number alterations, such as loss of 3p, deletion or LOH 11q23, 14q23qter and gain of 17q (Marrano et al., 2017). Amplification of the *MYCN* gene was observed only at a level of 10 copies. Unfortunately, this can be considered a limitation of the molecular method because the FISH analysis showed the amplification of the *MYCN* gene at a level of approximately 30 copies. In our opinion, the gold standard for the assessment of *MYCN* amplification is fluorescence *in situ* hybridization on intraoperative tumor imprints. Furthermore, microarray analysis showed a duplication of the 2p23.2p23.1 region, including the *ALK* gene. Anaplastic lymphoma kinase (*ALK*) is an important regulator of stem cell functions,

including STAT3 dependent self-renewal, and as a transcriptional target of *MYCN*, high expression indicates an unfavorable prognosis (Rosswog et al., 2023). According to studies carried out on genetically engineered mouse models of NB, the *MYCN* and *ALK* genes cooperate to promote oncogenesis (Vivancos Stalin et al., 2019). Additionally, CytoScan HD analysis revealed a monosomy of chromosome 3 and a trisomy of chromosome 18.

In 3 out of 5 patients without changes in *MYCN* amplifications, we observed complex alterations in the microarray pattern. In two samples, discrete changes indicating the presence of monosomy of chromosomes 3, 4, 9, 10, 14, and 15. According to scientific research chromosome 10 is the most frequent loss. On the long arm of chromosome 10, there are tumor suppressor genes such as *PTEN*, *DBMT*, and *LGII*, while the short arm contains *ID1*, *AKRIC3*, *DDH1*, *NET1A*, *PRKCQ*, and *GATA-binding protein 3*. Among these, *PTEN* is the second most commonly deleted/mutated gene in human tumors, with a mutation rate of 50%. The GDNF family receptor alpha 2 (*GFRA2*) promotes the proliferation of NB cells (Li et al., 2019). According to the literature, patients with neuroblastoma and an abnormal chromosome 10 had a significantly lower 3-year OS compared to the group of patients with a normal copy number of chromosome 10 (Jiang et al., 2021). In the same samples we noted an extra copy of chromosome 13, which, according to other researchers (Bilke et al., 2008; Ambros et al., 2014) is a common chromosome in the trisomy of neuroblastoma. Interestingly, some authors show that there are no structural changes on chromosome 13 in neuroblastoma (Bogen et al., 2016). While its prognostic significance in neuroblastoma has not been precisely determined, in other cancers, including ALL, AML, and MDS, trisomy 13 is closely associated with an unfavorable prognosis for the patient. The presence of trisomy 13 in acute leukemia cells indicates a poor response to chemotherapy (Spirito et al., 2003; Herold et al., 2014). Monosomy of chromosome X and duplication of region 22q11.21 have not been described in the literature in patients with neuroblastoma so far. However, our results unequivocally demonstrate that such alterations may also be present in this type of cancer.

According to the Polish “Standards for the genetic diagnostics of solid tumors in children” structural changes involving chromosomal regions 1p, 1q, 2p, 3p, 4p, 6p, 6q, 11q, and 17q are most commonly observed in advanced stages of the disease in older children and represent unfavorable prognostic factors, increasing the risk of disease recurrence, regardless of the specific chromosomal pairs affected (Trubicka et al., 2023). In one of our patients with stage 4 disease, the FISH study found no amplification of the *MYCN* gene, while the microarray analysis identified 3 cell lines in which some of the above-mentioned structural changes were noted (including: 1p, 2p, 3p, 4p, 6q, 11q, and 17q) stratifying the patient into a group with an unfavorable prognosis.

In the literature, high-risk patients had long-term survival rates of only 10%–20% with combination chemotherapy, surgery, and local radiation therapy (Tolbert and Matthay, 2018). However, treatment approaches that used a combination of induction therapy, myeloablative consolidation therapy with stem cell support, and biological therapy had improved 5-year survival rates from less than 15%–40% (Nakagawara et al., 2018).

Despite many biochemical, molecular and genetic indicators as markers of poor prognosis, *MYCN* amplification is still used to stratify patients into risk groups and is a marker of poor prognosis. These patients respond poorly to conventional therapy. The ability to determine this biological marker is necessary for appropriate clinical management. Unfortunately, treatment failure has been reported in all patient groups, even without *MYCN* amplification, suggesting that additional prognostic markers must be discovered to improve treatment protocols (Feng et al., 2023).

In conclusion, both the FISH technique and microarray testing have their advantages and disadvantages. In addition to *MYCN* gene amplification, cytogenetic abnormalities are also a marker of an unfavorable prognosis in patients diagnosed with neuroblastoma. Therefore, it is very important that the result be based on both, fluorescence *in situ* hybridization and molecular karyotype.

Data availability statement

The original contributions presented in the study are included in the article/Supplementary Material, further inquiries can be directed to the corresponding authors.

Ethics statement

The study was conducted according to the guidelines of the Declaration of Helsinki and approved by the Ethics Committee of the Medical University of Lublin (KE-0254/229/2012). The studies were conducted in accordance with the local legislation and institutional requirements. Written informed consent for participation in this study was provided by the participants' legal guardians/next of kin.

Author contributions

DW and ML are responsible for the conception and design of the study. DW and BS conducted laboratory work. BS and PS were responsible for the acquisition of literatures for manuscript. DW and BS were responsible for interpretation of data. DW, PS, MS, and ML prepared final manuscript for publication. All authors contributed to the article and approved the submitted version.

Funding

The author(s) declare that no financial support was received for the research, authorship, and/or publication of this article.

Acknowledgments

Preprint: “Winnicka et al., 2020” is part of this article, which has been enriched with additional research and updated.

References

- Adamkiewicz – Drożyńska, E. (2006). Ocena znaczenia wybranych wskaźników proliferacji i angiogenezy w guzach z grupy nerwiaka zarodkowego współczulnego dla prognozowania klinicznego. *Ann. Acad. Med. Gedanensis* 5, 1–208.
- Ahmed, A. A., Zhang, L., Reddivalla, N., and Hetherington, M. (2017). Neuroblastoma in children: update on clinicopathologic and genetic prognostic factors. *Pediatr. Hematol. Oncol.* 34 (3), 165–185. doi:10.1080/08880018.2017.1330375
- Ambros, I. M., Brunner, C., Abbasi, R., Frech, C., and Ambros, P. F. (2014). Ultra-high density SNParray in neuroblastoma molecular diagnostics. *Front. Oncol.* 4, 202. doi:10.3389/fonc.2014.00202
- Ambros, P. F., Ambros, I. M., Brodeur, G. M., Haber, M., Khan, J., Nakagawara, A., et al. (2009). International consensus for neuroblastoma molecular diagnostics: report from the international neuroblastoma risk group (INRG) biology committee. *Br. J. Cancer* 100 (9), 1471–1482. doi:10.1038/sj.bjc.6605014
- Aygun, N. (2018). Biological and genetic features of neuroblastoma and their clinical importance. *Curr. Pediatr. Rev.* 14 (2), 73–90. doi:10.2174/1573396314666180129101627
- Bhat, N., and McGregor, L. (2017). Neuroblastoma: the clinical aspects. *Neuroblastoma—current state and recent updates*. InTech. doi:10.5772/intechopen.70486
- Bilke, S., Chen, Q. R., Wei, J. S., and Khan, J. (2008). Whole chromosome alterations predict survival in high-risk neuroblastoma without MYCN amplification. *Clin. Cancer Res.* 14 (17), 5540–5547. doi:10.1158/1078-0432.CCR-07-4461
- Bogen, D., Brunner, C., Walder, D., Ziegler, A., Abbasi, R., Ladenstein, R. L., et al. (2016). The genetic tumor background is an important determinant for heterogeneous MYCN-amplified neuroblastoma. *Int. J. Cancer* 139 (1), 153–163. doi:10.1002/ijc.30050
- Brodeur, G. M., Seeger, R. C., Schwab, M., Varmus, H. E., and Bishop, J. M. (1985). Amplification of N-myc sequences in primary human neuroblastomas: Correlation with advanced disease stage. *Prog. Clin. Biol. Res.* 175, 105–113.
- Brunner, C., Brunner-Herglotz, B., Ziegler, A., Frech, C., Amann, G., Ladenstein, R., et al. (2016). Tumor touch imprints as source for whole genome analysis of neuroblastoma tumors. *PLoS one* 11 (8), e0161369. doi:10.1371/journal.pone.0161369
- Campbell, K., Gastier-Foster, J. M., Mann, M., Naranjo, A. H., Van Ryn, C., Bagatell, R., et al. (2017). Association of MYCN copy number with clinical features, tumor biology, and outcomes in neuroblastoma: a report from the children's Oncology group. *Cancer* 123 (21), 4224–4235. doi:10.1002/cncr.30873
- Chicard, M., Boyault, S., Colmet Daage, L., Richer, W., Gentien, D., Pierron, G., et al. (2016). Genomic copy number profiling using circulating free tumor DNA highlights heterogeneity in neuroblastoma. *Clin. Cancer Res.* 22 (22), 5564–5573. doi:10.1158/1078-0432.CCR-16-0500
- Croteau, N., Nuchtern, J., and LaQuaglia, M. P. (2021). Management of neuroblastoma in pediatric patients. *Surg. Oncol. Clin. N. Am.* 30 (2), 291–304. doi:10.1016/j.soc.2020.11.010
- Feng, L., Li, S., Wang, C., and Yang, J. (2023). Current status and future perspective on molecular imaging and treatment of neuroblastoma. *Seminars Nucl. Med.* 53 (4), 517–529. doi:10.1053/j.semnuclmed.2022.12.004
- Herold, T., Metzler, K. H., Vosberg, S., Hartmann, L., Röhl, C., Stölzel, F., et al. (2014). Isolated trisomy 13 defines a homogeneous AML subgroup with high

Conflict of interest

The authors declare that the research was conducted in the absence of any commercial or financial relationships that could be construed as a potential conflict of interest.

Supplementary material

The Supplementary Material for this article can be found online at: <https://www.frontierspartnerships.org/articles/10.3389/abp.2024.12821/full#supplementary-material>

- frequency of mutations in spliceosome genes and poor prognosis. *Blood* 124 (8), 1304–1311. doi:10.1182/blood-2013-12-540716
- Huang, M., and Weiss, W. A. (2013). Neuroblastoma and MYCN. *Cold Spring Harb. Perspect. Med.* 3 (10), a014415. doi:10.1101/cshperspect.a014415
- Jeison, M., Ash, S., Halevy-Berko, G., Mardoukh, J., Luria, D., Avigad, S., et al. (2010). 2p24 gain region harboring MYCN gene compared with MYCN amplified and nonamplified neuroblastoma: biological and clinical characteristics. *Am. J. Pathology* 176 (6), 2616–2625. doi:10.2353/ajpath.2010.090624
- Jiang, Cy., Xu, X., Jian, Bl., Zhang, X., Yue, Z. X., Guo, W., et al. (2021). Chromosome 10 abnormality predicts prognosis of neuroblastoma patients with bone marrow metastasis. *Italian J. Pediatr.* 47 (1), 134. doi:10.1186/s13052-021-01085-6
- Kaczówka, P., Wieczorek, A., Czogała, M., Książek, T., Szewczyk, K., and Balwier, W. (2018). The role of N-Myc gene amplification in neuroblastoma childhood tumour - single-centre experience. *Współczesna Onkol.* 22 (4), 223–228. doi:10.5114/wo.2018.81402
- Lau, D. T., Flemming, C. L., Gherardi, S., Perini, G., Oberthuer, A., Fischer, M., et al. (2015). MYCN amplification confers enhanced folate dependence and methotrexate sensitivity in neuroblastoma. *Oncotarget* 6 (17), 15510–15523. doi:10.18632/oncotarget.3732
- Lee, J. W., Son, M. H., Cho, H. W., Ma, Y. E., Yoo, K. H., Sung, K. W., et al. (2018). Clinical significance of MYCN amplification in patients with high-risk neuroblastoma. *Pediatr. blood cancer* 65 (10), e27257. doi:10.1002/pbc.27257
- Lejman, M., Włodarczyk, M., Styka, B., Pastorczak, A., Zawitkowska, J., Taha, J., et al. (2020). Advantages and limitations of SNP array in the molecular characterization of pediatric T-cell acute lymphoblastic leukemia. *Front. Oncol.* 10, 1184. doi:10.3389/fonc.2020.01184
- Lerone, M., Ognibene, M., Pezzolo, A., Martucciello, G., Zara, F., Morini, M., et al. (2021). Molecular genetics in neuroblastoma prognosis. *Child. (Basel, Switz.)* 8 (6), 456. doi:10.3390/children8060456
- Li, Z., Xie, J., Fei, Y., Gao, P., Xie, Q., Gao, W., et al. (2019). GDNF family receptor alpha 2 promotes neuroblastoma cell proliferation by interacting with PTEN. *Biochem. Biophys. Res. Commun.* 510 (3), 339–344. doi:10.1016/j.bbrc.2018.12.169
- Lim, H., Son, M. H., Hyun, J. K., Cho, H. W., Ju, H. Y., Lee, J. W., et al. (2020). Clinical significance of segmental chromosomal aberrations in patients with neuroblastoma: first report in Korean population. *J. Korean Med. Sci.* 35 (14), e82. doi:10.3346/jkms.2020.35.e82
- Marrano, P., Irwin, M. S., and Thorner, P. S. (2017). Heterogeneity of MYCN amplification in neuroblastoma at diagnosis, treatment, relapse, and metastasis. *Genes, chromosomes cancer* 56 (1), 28–41. doi:10.1002/gcc.22398
- Morandi, F. (2022). Molecular determinants of neuroblastoma. *Int. J. Mol. Sci.* 23 (7), 3751. doi:10.3390/ijms23073751
- Nakagawara, A., Li, Y., Izumi, H., Muramori, K., Inada, H., and Nishi, M. (2018). Neuroblastoma. *Jpn. J. Clin. Oncol.* 48 (3), 214–241. doi:10.1093/jjco/hyx176
- Otte, J., Dyberg, C., Pepich, A., and Johnsen, J. I. (2020). MYCN function in neuroblastoma development. *Front. Oncol.* 10, 624079. doi:10.3389/fonc.2020.624079
- Park, J. R., Bagatell, R., Cohn, S. L., Pearson, A. D., Villablanca, J. G., Berthold, F., et al. (2017). Revisions to the international neuroblastoma response criteria: a

consensus statement from the national cancer Institute clinical trials planning meeting. *J. Clin. Oncol.* 35 (22), 2580–2587. doi:10.1200/JCO.2016.72.0177

Rosswog, C., Fassunke, J., Ernst, A., Schömig-Markieffka, B., Merkelbach-Bruse, S., Bartenhagen, C., et al. (2023). Genomic ALK alterations in primary and relapsed neuroblastoma. *Br. J. cancer* 128 (8), 1559–1571. doi:10.1038/s41416-023-02208-y

Schulte, M., Köster, J., Rahmann, S., and Schramm, A. (2018). Cancer evolution, mutations, and clonal selection in relapse neuroblastoma. *Cell Tissue Res.* 372, 263–268. doi:10.1007/s00441-018-2810-5

Shapiro, D. N., Valentine, M. B., Rowe, S. T., Sinclair, A. E., Sublett, J. E., Roberts, W. M., et al. (1993). Detection of N-myc gene amplification by fluorescence *in situ* hybridization. Diagnostic utility for neuroblastoma. *Am. J. pathology* 142 (5), 1339–1346.

Spirito, F. R., Mancini, M., Derme, V., Cimino, G., Testi, A. M., Tafuri, A., et al. (2003). Trisomy 13 in a patient with common acute lymphoblastic leukemia: Description of a case and review of the literature. *Cancer Genet. Cytogenet.* 144 (1), 69–72. doi:10.1016/s0165-4608(02)00924-x

Squire, J. A., Thorner, P., Marrano, P., Parkinson, D., Ng, Y. K., Gerrie, B., et al. (1996). Identification of MYCN copy number heterogeneity by direct FISH analysis of neuroblastoma preparations. *Mol. Diagn.* 1 (4), 281–289. doi:10.1016/s1084-8592(96)70010-3

Swift, C. C., Eklund, M. J., Kravka, J. M., and Alazraki, A. L. (2018). Updates in diagnosis, management, and treatment of neuroblastoma. *RadioGraphics* 38 (2), 566–580. doi:10.1148/rg.2018170132

Thorner, P. S., Ho, M., Chilton-MacNeill, S., and Zielenska, M. (2006). Use of chromogenic *in situ* hybridization to identify MYCN gene copy number in neuroblastoma using routine tissue sections. *Am. J. Surg. Pathology* 30 (5), 635–642. doi:10.1097/01.pas.0000202163.82525.5c

Tibiletti, M. G. (2007). Interphase FISH as a new tool in tumor pathology. *Cytogenet. genome Res.* 118 (2-4), 229–236. doi:10.1159/000108305

Tolbert, V. P., and Matthay, K. K. (2018). Neuroblastoma: Clinical and biological approach to risk stratification and treatment. *Cell tissue Res.* 372 (2), 195–209. doi:10.1007/s00441-018-2821-2

Trubicka, J., Mlynarski, W., Lejman, M., Balwierz, W., Małdyk, J., Pastorczak, A., et al. (2023). Standards for the genetic diagnostics of solid tumors in children. *Pediatr. Rev.* 52 (3), 6–27.

Van Noesel, M. M., and Versteeg, R. (2004). Pediatric neuroblastomas: genetic and epigenetic “danse macabre”. *Gene* 325 (1-2), 1–15. doi:10.1016/j.gene.2003.09.042

Vivancos Stalin, L., Gualandi, M., Schulte, J. H., Renella, R., Shakhova, O., and Mühlethaler-Mottet, A. (2019). Expression of the neuroblastoma-associated ALK-F1174L activating mutation during embryogenesis impairs the differentiation of neural crest progenitors in sympathetic ganglia. *Front. Oncol.* 9, 275. doi:10.3389/fonc.2019.00275

Whittle, S. B., Smith, V., Doherty, E., Zhao, S., McCarty, S., and Zage, P. E. (2017). Overview and recent advances in the treatment of neuroblastoma. *Expert Rev. anticancer Ther.* 17 (4), 369–386. doi:10.1080/14737140.2017.1285230

Winnicka, D., Babicz, M., Styka, B., Skowera, P., Zawitkowska, J., and Lejman, M. (2020). Application of fluorescence *in situ* hybridization to detect MYCN amplification on paraffin-embedded tissue sections of neuroblastoma - single Institute study. *Research Square [Preprint]*. Version 1. doi:10.21203/rs.3.rs-95672/v1 (accessed October 26, 2020).

Yue, Z. X., Huang, C., Gao, C., Xing, T. Y., Liu, S. G., Li, X. J., et al. (2017). MYCN amplification predicts poor prognosis based on interphase fluorescence *in situ* hybridization analysis of bone marrow cells in bone marrow metastases of neuroblastoma. *Cancer Cell Int.* 17, 43. doi:10.1186/s12935-017-0412-z

Prevalence of poor nutrition status in multiple sclerosis patients assessed by different diagnostic tools

Natalia Mogiłko¹ and Sylwia Małgorzewicz^{2✉}

¹Department of Neurology and Clinical Neuroimmunology of the Specialist Hospital in Grudziądz, Grudziądz, Poland; ²Department of Clinical Nutrition, Medical University of Gdańsk, Gdańsk, Poland

Patients with multiple sclerosis (MS) present a spectrum of nutritional disorders from obesity to malnutrition. The purpose of this study was an assessment of the nutritional status of MS patients by NRS-2002 and GLIM criteria. Methods: 147 patients were included in the study. The nutritional status was assessed by NRS 2002, GLIM, and body composition analysis. The routine biochemical parameters were measured. **Results:** Deterioration of the nutritional status was observed in 87.8% of patients. GLIM criteria indicated that 20% of patients were malnourished and 80% were at risk. The percentage of patients with excess body mass was 46.8%, and of underweight patients was 6.6%. The risk of malnutrition was positively associated with low content of adipose tissue ($R=-0.24$; $p=0.00$), low BMI ($R=-0.22$; $p=0.00$), and higher weight loss in the last 6 months ($R=0.47$; $p=0.00$). Additionally, a significant ($p<0.05$) correlation between malnutrition state and s-albumin ($R=-0.2$) and CRP ($R=0.23$) was observed. **Conclusion:** Overweight and obesity concerned a large proportion of the studied group of MS patients, but this does not exclude the risk of malnutrition. Dietary care and regular outpatient nutritional status assessment should be provided throughout the disease.

Keywords: multiple sclerosis, nutritional status, body composition, s-albumin

Received: 11 December, 2022; revised: 13 March, 2023; accepted: 30 April, 2023; available on-line: 31 May, 2023

✉e-mail: sylwiam@gumed.edu.pl

Abbreviations: BMI, Body Mass Index; CRP, C reactive protein; ESPEN, European Society for Clinical Nutrition and Metabolism; GLIM, Global Leadership Initiative on Malnutrition; MS, Multiple Sclerosis; NRS-2002, Nutritional Risk Screening 2002; UBWL, Unintentional body weight loss

INTRODUCTION

Multiple sclerosis is a chronic neurological disease that leads to disability (Oh *et al.*, 2018). At the beginning of the disease, patients often present excess body weight, while in advanced stages, signs of malnutrition appear, and the need to introduce enteral nutrition. It seems that the spectrum of disorders from obesity to malnutrition may be of clinical significance. The symptomatology of MS is very diverse, patients suffer from movement disorders (limb paresis, ataxia), sensory disorders (persistent paraesthesia, hypoesthesia, hyperesthesia), cranial nerves lesion (oculomotor paralysis, visual disturbances, trigeminal neuralgia), as well as vegetative and mental disorders (cognitive and mood disorders) (Łabuz-Roszak *et al.*, 2013). Depression, mood disorders, mobility limita-

tions, and dysphagia directly affect the nutritional status of people suffering from multiple sclerosis.

At the beginning of the disease, mood disorders, lack of proper diet, and the desire to comfort with food result in the consumption of processed foods rich in sugar and saturated fats – which is associated with body composition disturbances, including an increased amount of adipose tissue (Pilutti *et al.*, 2016; Mokry *et al.*, 2016). Additionally, steroid therapy and a sedentary lifestyle due to progressive disability increase the risk of obesity and its characteristic complications. In the later stages, gastrointestinal problems, such as gastroesophageal reflux, delayed gastric emptying, constipation, and dysphagia can be diagnosed. Dysphagia is the cause of dehydration and malnutrition (D’Amico *et al.*, 2018; Ansari *et al.*, 2020).

The dietitian should adjust the composition of the diet and the amount, volume, and consistency of meals and recommend thickeners depending on the patient’s current situation. Next, oral nutritional supplementation or enteral or parenteral nutrition may be necessary (Affi *et al.*, 2021; Burgos *et al.*, 2008). There is a need for the early identification of patients at risk of malnutrition because the therapeutic possibilities are much greater in this stage than in advanced cachexia.

Therefore, our study was aimed at exploring the nutritional status by NRS 2002 and GLIM criteria of patients treated for multiple sclerosis in a stable clinical condition.

MATERIALS AND METHODS

The population of the study consisted of 147 MS patients ($M=38$), with an average age of 40.4 ± 11.6 years, consecutively admitted to the neurology ward of a Specialist Hospital during a six-month period. All subjects gave their informed consent for inclusion before they participated in the study. The study received the approval of the Ethics Committee of the Medical University of Gdańsk. The 57.8% of patients presented the following comorbidities: 18% hypothyroidism, 16% hypertension, 16% hyperlipidemia, 12% depression, 6% Hashimoto’s disease, 5% diabetes, 5% allergy or asthma, 3% hyperthyroidism, 3% epilepsy, 2% anemia, and 1% psoriasis. The mean time since MS diagnosis was 6.5 ± 4.9 ; there is no dysphagia recognized in the study group.

Nutritional status and body composition were evaluated at admission by the NRS 2002 (the Nutritional Risk Screening) and the GLIM (the Global Leadership Initiative on Malnutrition) criteria which were applied by a trained clinical examiner. In addition, each patient underwent an analysis of his/her medical records to obtain information regarding concomitant diseases and anthro-

pometric parameters, such as body mass by electronic weight and body mass index calculation (BMI), and bio-impedance analysis with the use of the InBody 120 analyzer.

The following biochemical parameters were measured by routine laboratory methods: C-reactive protein (CRP), s-albumin level, lipid profile, and whole blood morphology.

Statistical analysis

Results are expressed as mean and standard deviation or percentages (for categorical variables). The Shapiro-Wilk W test was used to evaluate the normal distribution of the tested parameters. On the other hand, the Leven (Brown-Forsythe) test was used to test the hypothesis of equal variances. Pearson and/or Spearman correlation coefficients were used to calculate the correlation between the variables. A p -value <0.05 was considered to be statistically significant. Statistical processing of the results was performed with the use of the statistical software STATISTICA PL v 13.0 (Statsoft, Krakow, Poland).

RESULTS

In the study group, the mean body weight was 72.6 ± 16.9 (range 45.0–130.0 kg) and the mean BMI was 25.1 kg/m^2 (range 16.1–43.4). 6.6% of patients presented as underweight with a body mass index $<18.5 \text{ kg/m}^2$ (14.4% with BMI <20), and normal body weight was observed in 74 subjects (50.3%). High BMI (BMI >25) was presented in 42.1% of pts. The mean content of % body fat was 30.7 (range 9.9–52.0) – for females – 33.1% and for men 23.7%.

Independently of the BMI, according to the GLIM criteria, the majority of patients (85.5%) were at risk of malnutrition and 15.5% exhibited malnutrition. Based on the NRS 2002, a slight deterioration of the nutritional status was observed in 87.8% of patients, moderate in 9.5% and severe in 2.7%. Analysis showed a strong correlation between both methods ($R=0.8$; $p<0.05$).

Unintentional body weight loss (UBWL) in the last 6 months was observed in 28% of patients in mean level 1.4 kg (range 0–20 kg). 58% of patients did not change their body weight within the last 6 months. 9% of patients reduced their body weight intentionally by using various diets, including those generally available on the Internet, individual diets from dietitians, or by restricting selected groups of food products. There was also a group of patients who gained weight (5%).

The malnourished patients in comparison to patients “at risk” were older (57.4 ± 12.8 vs 43.3 ± 13.3 , $p<0.05$) and presented significantly lower body fat (25.8 ± 7.0 vs 31.3 ± 8.8 , $p<0.05$), FFMI (14.8 ± 1.1 vs 17.9 ± 2.6 , $p<0.00$), s-albumin (26.0 ± 4.1 vs 39.4 ± 4.0 , $p<0.05$) and higher CRP serum level (12.1 ± 3.2 vs 4.4 ± 13.4 , $p<0.05$) (see Table 1).

The risk of malnutrition was positively associated with low content of adipose tissue ($R=-0.24$; $p=0.00$), low BMI ($R=-0.22$; $p=0.00$), and higher weight loss in the last 6 months ($R=0.47$; $p=0.00$). However, a statistically significant correlation was observed between the malnutrition diagnosis and s-albumin ($R=-0.2$; $p<0.05$) and CRP ($R=0.23$; $p<0.05$).

DISCUSSION

The aim of the study was to estimate the prevalence of risk for malnutrition and malnutrition among MS patients treated on neurology wards assessed with the NRS 2002, routine screening method in hospital patients (Burgos *et al.*, 2008). It was evaluated in comparison to the GLIM criteria, the newest and recommended by the ESPEN tool for nutritional status assessment, as well as in comparison to BMI (Håkonsen *et al.*, 2015; Cederholm *et al.*, 2020). To our knowledge, there are no other studies that used GLIM criteria in a group of patients with multiple sclerosis.

Our data show that the risk of malnutrition is a significant problem among MS patients. The prevalence of deterioration of nutritional status reached 85.5%, indicating that a considerable number of patients were in need of appropriate nutritional advice.

It is worth emphasizing that regardless of the BMI, there may be observed unfavorable changes in body composition and nutritional status such as UBWL or decreased albumin level in this group of patients. A high BMI should not delay nutritional interventions because, in the early stages, the interventions are much more effective (Atuk Kahraman *et al.*, 2021; Synnot *et al.*, 2016).

In our study, malnutrition was associated with elevated CRP. Some authors (Palavra *et al.*, 2016; Taheri *et al.*, 2017) reported an increase in inflammatory markers in MS patients. For example, interleukin (IL-6) plays a significant role in the development of malnutrition through the catabolism of muscle proteins and the anorectic effect of cytokines (increased leptin production and lipolysis). An increased level of cytokines is characteristic of hypoalbuminemic patients and is associated with shorter survival

Table 1. Selected parameters in study MS groups. Data are presented as mean \pm S.D. or %.

Parameters	All MS patients n =147	MS patients at risk n=123	MS patients malnourished n=23	References values
Age (yr)	40.4 \pm 11.6	43.3 \pm 13.3	57.4 12.8*/**	–
BMI	25.1 \pm 5.5	25.4 \pm 5.6	22.4 \pm 3.3	18.5–24.99
Comorbidities (%)	57.8%	51.7%	54.6%	–
FFMI	17.2 \pm 2.7	17.9 \pm 2.6	14.8 \pm 1.1*	>16
Body fat (%)	30.7 \pm 8.8	31.3 \pm 8.8*	25.8 \pm 7.0*	26.4 \pm 6.7
Albumin (g/l)	43.7 \pm 5.0	39.4 \pm 4.0*	26.0 \pm 4.1*	43.5 \pm 2.4
CRP (mg/l)	2.7 \pm 4.5	4.4 \pm 13.4	12.1 \pm 3.2*	1.8 \pm 1.5

*malnourished vs at risk; $p<0.05$; FFMI, fat free mass index; CRP, C-reactive protein

in a different group of chronically ill patients (Yalachkov *et al.*, 2021).

Many authors and ESPEN guidelines postulated that the analysis of body composition should be an essential part of the assessment of nutritional status (Burgos *et al.*, 2018; Hedström *et al.*, 2012). In patients with multiple sclerosis, an analysis of body composition may indicate loss / low muscle mass regardless of excess body weight, suggesting an initial stage of malnutrition. Risk factors for sarcopenia or sarcopenic obesity are metabolic disorders due to chronic diseases, treatment with glucocorticosteroids, and reduced physical activity (Kvistad *et al.*, 2015). The research shows that people diagnosed with multiple sclerosis lead a sedentary lifestyle and usually do not engage in physical activity (Cavanaugh *et al.*, 2011; Goldman *et al.*, 2008). Other authors point to poor dietary habits (Bromley *et al.*, 2019).

Additionally, many patients with MS already seek complementary and alternative treatments or diets for their condition. Unfortunately, the Internet remains the central source of information for most patients, frequently leading to choices and behaviors lacking any scientific support. A scientific analysis of different dietary patterns or other gut-oriented interventions is necessary (Synnot *et al.*, 2016; Bromley *et al.*, 2019).

Therefore, in patients with MS diagnosis, the weight loss process in the case of obesity should be controlled by an experienced dietitian in order to maintain muscle mass.

The limitation of our study is the relatively low number of patients. Further studies in patients with MS (e.g., multicenter) are needed to confirm our results.

CONCLUSIONS AND CLINICAL IMPLICATION

Overweight and obesity concerned a large proportion of the studied group of patients with multiple sclerosis, not excluding the risk of malnutrition confirmed by methods such as NRS 2002 and GLIM. This risk may increase or may develop malnutrition as the disease progresses. Therefore, regular nutritional assessment and dietary consultation should be part of the care. In addition to screening methods, an assessment of nutritional status should include body composition and diet estimation to prevent nutritional problems.

Declarations

The authors have no potential conflicts of interest to disclosure.

REFERENCES

- Afifi ZE, Shehata RI, el Sayed AF, Hammad ESM, Salem MR (2021) Nutritional status of multiple sclerosis (MS) patients attending Kasr Alainy MS unit: an exploratory cross-sectional study. *J. Egypt. Pub. Health Assoc.* **96**: 20. <https://doi.org/10.1186/s42506-021-00080-3>
- Ansari N, Tarameshlu M, Ghelichi L (2020) Dysphagia in multiple sclerosis patients: diagnostic and evaluation strategies. *Degener. Neurol. Neuromuscul. Dis.* **10**: 15–28. <https://doi.org/10.2147/DNND.S198659>
- Atuk Kahraman T, Yılmaz M, Yetkin MF, Mirza M (2022) The nutritional status of relapsing-remitting multiple sclerosis (RRMS) patients compared to that of healthy people: a Turkish hospital-based. *Nutr. Neurosci.* **25**: 2279–2287. <https://doi.org/10.1080/1028415X.2021.1956253>
- Bromley L, Horvath PJ, Bennett SE, Weinstock-Guttman B, Ray AD (2019) Impact of nutritional intake on function in people with mild-to-moderate multiple sclerosis. *Int. J. MS Care* **21**: 1–9. <https://doi.org/10.7224/1537-2073.2017-039>
- Burgos R, Bretón I (2018) ESPEN guideline clinical nutrition in neurology. *Clin. Nutr.* **37**: 354–396. <https://doi.org/10.1016/j.clnu.2017.09.003>
- Cavanaugh JT, Gappmaier VO, Dibble LE, Gappmaier E (2011) Ambulatory activity in individuals with multiple sclerosis. *J. Neurol. Phys. Ther.* **35**: 26–33. <https://doi.org/10.1097/NPT.0b013e3182097190>
- Cederholm T, Krznaric Z, Pirlich M (2020) Diagnosis of malnutrition in patients with gastrointestinal diseases: recent observations from a Global Leadership Initiative on Malnutrition perspective. *Curr. Opin. Clin. Nutr. Metab. Care* **23**: 361–366. <https://doi.org/10.1097/MCO.0000000000000678>
- D'Amico E, Zanghì A, Serra A, Murabito P, Zappia M, Patti F, Cocuzza S (2019) Management of dysphagia in multiple sclerosis: current best practice. *Expert Rev. Gastroenterol. Hepatol.* **13**: 47–54. <https://doi.org/10.1080/1747412420191544890>
- Goldman MD, Marrie RA, Cohen JA (2008) Evaluation of the six-minute walk in multiple sclerosis subjects and healthy controls. *Mult. Scler.* **14**: 383–390. <https://doi.org/10.1177/1352458507082607>
- Häkonsen SJ, Pedersen PU, Ilich, Bath-Hextall F, Kirkpatrick P (2015) Diagnostic test accuracy of nutritional tools used to identify undernutrition in patients with colorectal cancer: a systematic review. *JBI Database System Rev. Implement. Rep.* **13**: 141–187. <https://doi.org/10.1112/jbisir-2015-1673>
- Hedström AK, Olsson T, Alfredsson L (2012) High body mass index before age 20 is associated with increased risk for multiple sclerosis in both men and women. *Mult. Scler.* **18**: 1334–1336. <https://doi.org/10.1177/1352458512436596>
- Kvistad SS, Myhr KM, Holmøy T, Šaltytė Benth J, Wergeland S, Beiske AG, Bjerre KS, Hovdal H, Lilleås F, Midgard R, Pedersen T, Bakke SJ, Michelsen AE, Aukrust P, Ueland T, Sagen JV, Torkildsen Ø (2015) Body mass index influence interferon-beta treatment response in multiple sclerosis. *J. Neuroimmunol.* **288**: 92–97. <https://doi.org/10.1016/j.jneuroim.2015.09.008>
- Łabuz-Roszak B, Kubicka-Bączek K, Pierzchała K, Horynieccki M, Machowska-Majchrzak A, Augustyńska-Mutryn D, Kosalka K, Michalski K, Pyszał D, Wach J (2013) Quality of life in multiple sclerosis – association with clinical features, fatigue and depressive syndrome. *Psychiatr. Pol.* **47**: 433–442. (in Polish) PMID: 23885537
- Mokry NJ, Ross S, Timpon NJ, Sawcer S, Davey Smith G, Richards JB (2016) Obesity and multiple sclerosis: a mendelian randomization study. *PLoS Med.* **28**: e1002053. <https://doi.org/10.1371/journal.pmed.1002053>
- Oh J, Vidal-Jordana A, Montalban X (2018) Multiple sclerosis: clinical aspects. *Curr. Opin. Neurol.* **31**: 752–759. <https://doi.org/10.1097/WCO.0000000000000622>
- Palavra F, Almeida L, Ambrósio AF, Reis F (2016) Obesity and brain inflammation: a focus on multiple sclerosis. *Obes. Rev.* **17**: 211–224. <https://doi.org/10.1111/obr.12363>
- Pilutti LA, Motl RW (2016) Body mass index underestimates adiposity in persons with multiple sclerosis. *Arch. Phys. Med. Rehabil.* **97**: 405–412. <https://doi.org/10.1016/j.apmr.2015.09.014>
- Synnot AJ, Hill SJ, Garner KA, Summers MP, Filippini G, Osborne RH, Shapland SD, Colombo C, Mosconi P (2016) Online health information seeking: how people with multiple sclerosis find, assess and integrate treatment information to manage their health. *Health Expect.* **19**: 727–737. <https://doi.org/10.1111/hex.12253>
- Taheri S, Baradaran A, Aliakbarian M, Mortazavi M (2017) Level of inflammatory factors in chronic hemodialysis patients with and without cardiovascular disease. *J. Res. Med. Sci.* **22**: 47. https://doi.org/10.4103/jrms.JRMS_282_15
- Yalachkov Y, Anschuetz V, Jakob J, Schaller-Paule MA, Schaefer JH, Reilaender A, Friedauer L, Behrens M, Foerch C (2021) C-Reactive protein levels and gadolinium-enhancing lesions are associated with the degree of depressive symptoms in newly diagnosed multiple sclerosis. *Front. Neurol.* **12**: 719088. <https://doi.org/10.3389/fneur.2021.719088>

Mutational analysis of *FOLR1* and *FOLR2* genes in children with Myelomeningocele

Nageen Hussain¹, Saira Malik¹, Tayyaba Faiz¹, Fiza Shafqat¹, Ayaz Ali Khan², Taqweem Ul Haq², Waqar Ali², Tariq Aziz³, Metab Alharbi⁴, Abdulrahman Alsahammari⁴ and Abdullah F. Alasmari⁴

¹Institute of Microbiology and Molecular Genetics, New Campus, University of the Punjab, Lahore, Pakistan; ²Department of Biotechnology University of Malakand 18800 Pakistan; ³Department of Agriculture, University of Ioannina, 47100 Arta, Greece; ⁴Department of Pharmacology and Toxicology, College of Pharmacy, King Saud University, P.O. Box 2455, Riyadh 11451, Saudi Arabia

Myelomeningocele (MMC) is a congenital disease. For a long time, molecular mechanism of MMC, the role of folate receptor and transporter proteins remain unclear. Folate from maternal lumen to developing embryo is carried out with the help of folate transporters (SLC46A1, SLC19A1, FOLH1 and SLC25A32) and folate receptor (FOLR1, FOLR2 and FOLR3). Due to the loss of function of these important genes, complications can facilitate the risk of MMC. This study focused on the mutational analysis of *FOLR1* and *FOLR2* genes in children suffering from MMC. Myelomeningocele is a rare disorder so twenty blood samples from the children were collected. Primers of selected exons for *FOLR1* and *FOLR2* genes were designed with the help of PrimerFox software. Extracted DNA was amplified, and PCR based mutational analysis was done to check any type of mutation/SNPs in these genes. Sanger sequencing method was performed to confirm mutation in *FOLR1* and *FOLR2* genes. The results showed that certain environmental factors (smoking, low socio-economic status of mother bearing MMC fetus) were found to be significantly ($P < 0.05$) associated with MMC but no mutation in the selected exons of *FOLR1* and *FOLR2* genes was detected. Thus, genetic variations in the folate transporter gene may have no role in the progression of MMC in the studied population.

Keywords: FOLR1, FOLR2, Congenital, Myelomeningocele, phenotype, mutation

Received: 10 March, 2023; **revised:** 08 August, 2023; **accepted:** 25 August, 2023; **available on-line:** 26 October, 2023

✉ e-mail: iwockd@gmail.com

Acknowledgments of Financial Support: The authors greatly acknowledge and express their gratitude to the Researchers Supporting Project number (RSP2023R335), King Saud University, Riyadh, Saudi Arabia

Abbreviations: CSF, Cerebrospinal fluid; FOLR1, Folate Receptor Alpha; FOLR2, Folate Receptor Beta; MMC, Myelomeningocele

INTRODUCTION

One of the most important and congenital forms of spina bifida is Myelomeningocele (MMC). In this disease, two sides of backbone become unable to fuse with one another and forms a gap between them (Hassan *et al.*, 2022). This usually happens after about 2–4 weeks of gestation. Due to the failure of fusion of both backbone side nerves, spinal cord and meninges remain uncovered. This can lead to the partial or complete paralysis of the body. Partial paralysis happens in the lower portion of

the body from the point of opening (Moldenhauer & Adzick, 2017). The evidence of this disease in first-degree relatives and second-degree relatives is about 3–4% and 1–2%, respectively (Farmer *et al.*, 2018). Genomic and environmental factors are responsible for this situation. Folic acid plays a vital role in the organ development of fetus in placenta (O’Byrne *et al.*, 2010). Genes involved in folate transport play an important contribution in the development of MMC. Other environmental factors such as deficiency of vitamins, certain medications, tobacco usage, drug addiction, maternal infections, maternal hyperthermia and exposure to some metals play vital role in tube defects in developing fetus (Naveed *et al.*, 2023; Muhammad *et al.*, 2023; Naveed *et al.*, 2022; Tauheed *et al.*, 2017).

Studies on animal models illustrate involvement of about 200 genes in tube defects (Cavalheiro *et al.*, 2021). It is proposed that certain genes and their variants make an interaction with each other and, being affected by environmental factors, cause MMC (Mazumdar *et al.*, 2015). Certain studies highlighted certain mutations and/or SNPs i.e. rs223622 and rs180113 in the MTHFR gene, MTHFDM1 gene, rs13908 in FOLR2 and rs792687, rs792554 and rs792698 in FOLR3 gene (Ntimani *et al.*, 2020). These mutations have been reported in different ethnic groups, such as Dutch, Italian, and British population. The role of folate transporter genes has already been documented worldwide (Wolujewicz *et al.*, 2021). Unfortunately, little work has been done on this among the Pakistani population so far. The main objective of this study is to check the role of environmental factors and to perform the mutational analysis of *FOLR1* and *FOLR2* genes with reference to Myelomeningocele.

METHODOLOGY

All the patients in this study had less than 2 years of age. Before the procedure, informed consent of the parents was taken. The skin of the patients was sterilized with alcohol swabs. About 2 to 3cc blood of MMC patients was collected with the help of sterilized syringes and stored in refrigerator at 4°C in an EDTA vacutainer. The sample of mothers of MMC patients was also collected when it was possible. DNA extraction was done by using the standard method (Albertsen *et al.*, 2015). Forward and reverse primers were prepared for exons 3–4 and 5 for *FOLR1* gene, and exons 3–4, 5 of *FOLR2* gene. Primers were designed by using PrimerFox Software (Table 1).

Table 1. Forward and reverse primers for exons 3–4 and 5 of *FOLR1* and *FOLR2* genes

Primers	Sequence (5'-3')	Tm (°C)	Length (nt)
FOLR2 exon 5 forward	TCCTGGATGCCCTTATG	57	19
FOLR2 exon 5 reverse	GCAACAGATGGGTGACAGA	59	20
FOLR2 exon 3–4 forward	ACCATCACTGGGAACCTGA	58	20
FOLR2 exon 3–4 reverse	CAGCTGGCACTTGTTAACTC	61	20
FOLR1 Exon 5 forward	ATTGGAGTGTAGGGCTG	55.2	19
FOLR1 Exon 5 reverse	TTCTCAAGACACATGTGCG	56.7	
FOLR1 Exon 3–4 forward	GCTGGGAATCAAGGACTA	59	
FOLR1 Exon 3–4 reverse	GCCCGGAACATCTTGAGGT	59	

Table 2. Association of Environmental factors with MMC

Characteristics	MMC (n=20)	Controls (n=20)	OR (95%CI)	P-value
Smoking				
Exposed	14.0 (70)	7.0 (35)	4.33 (1.115–16.32)	0.0302
Not exposed	6.0 (30)	13.0 (65)		
Supplements (Folic acid) intake				
Yes	10.0 (50%)	8.0 (40%)	1.5 (0.42–5.24)	0.52
No	10.0 (50%)	12.0 (60%)		
Weight of Mother				
Under	16.0 (80%)	12.0 (60%)	2.66 (0.64–10.9)	0.17
Over	4.0 (20%)	8.0 (40%)		
History of Abortions/Premature birth				
Yes	7.0 (35%)	5.0 (25%)	1.615 (0.41–6.33)	0.491
No	13.0 (65%)	15.0 (75%)		
Age of Mother (Years)				
Under 30	14.0 (70%)	17.0 (85%)	0.411 (0.086–1.95)	0.263
Above 30	6.0 (30%)	3.0 (15%)		
Family income				
Poor	12.0 (60%)	4.0 (20%)	6 (1.45–24.6)	0.013
Middle + affluent	8.0 (40%)	16.0 (80%)		

The standard PCR procedure was followed for the amplification of *FOLR1* and *FOLR2* genes (Lorenz, 2012). The denaturation temperature was 95°C for both *FOLR1* and *FOLR2* genes and it was done for 4 minutes. The annealing temperature for *FOLR1* gene was 58°C for 45 seconds and 51–59°C for *FOLR2* gene and it was done for about 45 seconds. Elongation temperature was 72°C and it was done for one minute and finally for 4 minutes. To get the appropriate amount of PCR product, 35 cycles of PCR were run. Holding temperature of the PCR vials was 4°C. Afterward, the PCR product was loaded on agarose gel and visualized with the help of UV light. To rule out mutation sequencing of the amplified products Sanger Sequencing method was done. Statistical analysis was done with the use of GraphPad Prism software v13.

RESULTS

Current study includes 20 MMC patients. Most of the patients lie within the age group of (1–2 years). Patients usually belong to Northern and Southern Punjab and

most of the mothers were malnutritional due to poverty as shown in Fig. 1. The statistical analysis was done to check the association of different environmental factors (Smoking, weight/age of the mother, Folic acid intake, history of abortion and family socio-economic status) with MMC. Smoking and poor socio-economic status of

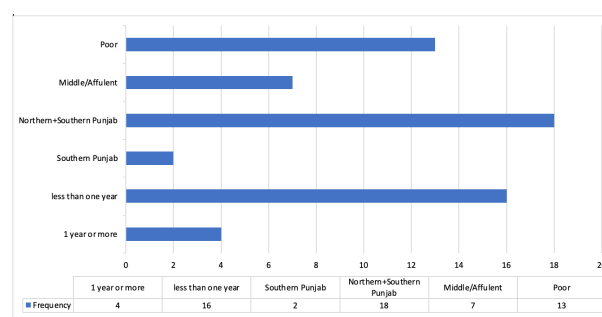
**Figure 1. Age groups, geographical location and economic background of subjects**

Table 3. Location of MMC and hydrocephalus common in the patients (n=20)

		Frequency
Location		
Valid	Lumber	12 (60%)
	Cervical	7 (35%)
	Both	1 (5%)
	Total	20 (100%)
Hydrocephalus		
Valid	No	14 (70%)
	Yes	6 (30%)
	Total	20 (100%)

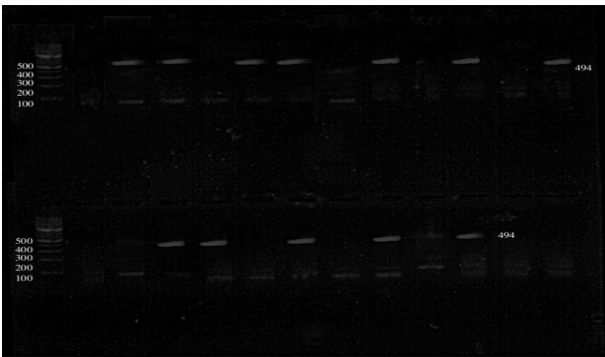


Figure 2. Amplified DNA band of Exon 5 *FOLR1* gene in patients



Figure 3. Chromatogram of Exon 5 *FOLR1* gene in MMC patients

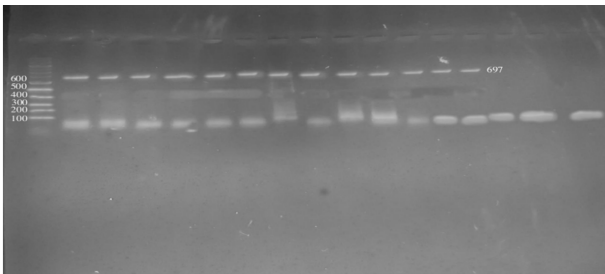


Figure 4. Amplified DNA Band of exon 3–4 of *FOLR1* gene in patients.

the mother was found to be significantly associated with MMC as the *P*-value is less than 0.05 (Table 2). If we look at the clinical symptoms, 70% (n=14) of the patients were hydrocephalus. The position of Myelomeningocele varies among patients, 35% (n=7) had in cervical region, 60% (n=12) covered lumbar region while 5% (n=1) showed in both cervical and lumbar regions (Table 3). Primer was designed for exon 5 of *FOLR1* gene. After performing PCR, PCR product was visualized on 1.5% agarose gel. There was a clear bright band on 494bp location which indicates no mutation in it (Fig. 2). Fur-

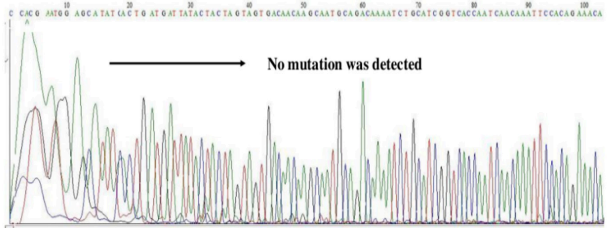


Figure 5. Chromatogram of Exon 3–4 *FOLR1* in patients

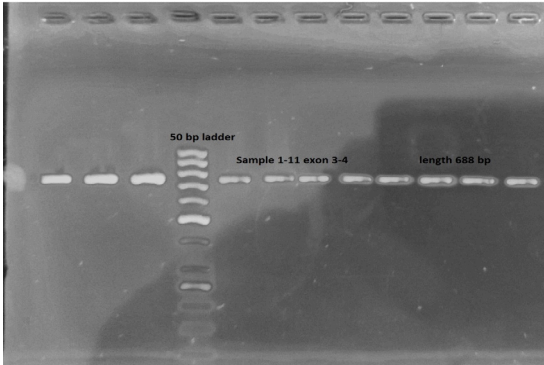


Figure 6. Amplified DNA Band of exon 3–4 of *FOLR2* gene in patients

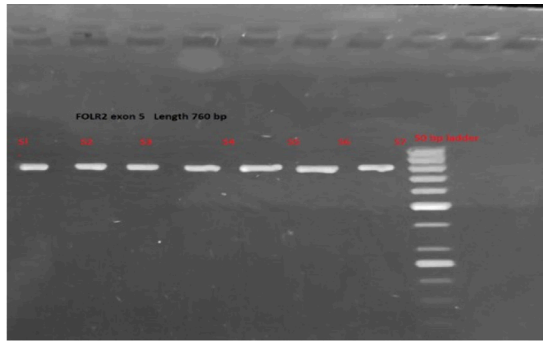


Figure 7. Amplified DNA Band of exon 5 of *FOLR2* gene in patients

ther, sequencing was done, and the chromatogram also showed no mutations (Fig. 3). Exons 3-4 of *FOLR1* gene primers were also designed and the band of interest was of 679bp. This clearly indicates no mutation in these exons as well (Fig. 4). This was also confirmed by the chromatogram of these exons in *FOLR1* gene (Fig. 5).

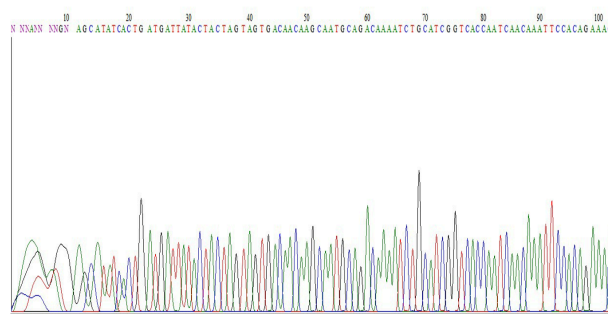


Figure 8. Chromatogram showing exons 3–4 sequences of *FOLR2* gene.

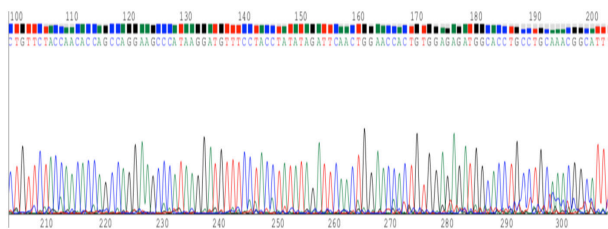


Figure 9. Chromatogram showing exon 5 sequences of *FOLR2* gene.

FOLR2 is another important gene involved in MMC. So, primers were designed for exons 3–4, 5 and PCR was performed. The PCR product for exons 3–4 showed a clear band of 686bp (Fig. 6) and exon 5 of 760 bp (Fig. 7) which indicates that there is no mutation in these exons as well and it was confirmed by sequencing (Figs 8 and 9).

DISCUSSION

Myelomeningocele is an important congenital disorder. It usually occurs after the 2–4 weeks of pregnancy. Folic acid deficiency can lead towards the exaggeration of MMC disease. Folate is needed for fetal organ development (Mazumdar *et al.*, 2015). Its demand increases significantly during pregnancy and is found to be significantly associated with MMC. Due to pediatric neurodegeneration resulting from neural folate deficiency, the role of FR can significantly inhibit folate uptake in the CSF (Canfield *et al.*, 2009). In the present study, various environmental factors like folic acid intake, body weight and age of mother, and history of abortion were found to be insignificantly associated with MMC ($P > 0.05$). However smoking habit in mother in the form of hukkah, cigarettes, sheesha and burning of fossil fuels was found to be significantly associated with MMC. Similarly, a poor family socio-economic status was found to be significantly associated with MMC ($P < 0.05$). (Nageen *et al.*, 2023; Hussain *et al.*, 2023).

Defects in folic acid receptor or transport protein can lead towards the MMC disorder. Many studies have been done for the mutational analysis of *FOLR1* and *FOLR2* genes but only a few studies have reported some mutations in these genes. Studies done in 2014 and 2020 indicated some novel mutations in these genes. (Tenpenny *et al.*, 2014; Steele *et al.*, 2020). In 2017, a study was done in the United States of America and it showed the down regulation of *FOLR1* gene in MMC patients (Findley *et al.*, 2017). In 2020, a study confirmed twelve new mutations in Folate receptor genes (Hillman *et al.*, 2020). This

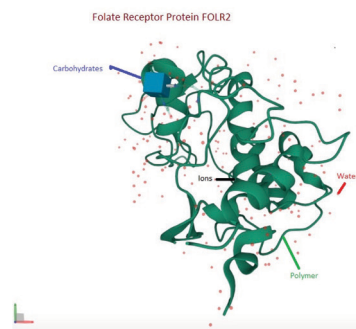


Figure 10. FOLR2 protein structure in MMC patients (n=20)

proved the direct link of *FOLR1* protein in the disease. Just like Boyles *et al.*, the present study also showed no mutation in *FOLR1* and *FOLR2* genes (Boyles *et al.*, 2006).

In 2022, another study showed the low level of *FOLR1* protein (known as glycosyl-phosphatidylinositol-anchored plasma membrane protein) in MMC patients as compared to healthy people. *FOLR2* gene is present on chromosome 11 and belongs to the folate receptor family, producing folate receptor beta protein. FR β , is a member of this family of reduced folate (Han *et al.*, 2022). In the present study, MMC patients showed no alteration in the cluster of Folate receptor protein *FOLR2* (Fig. 10).

CONCLUSION

This study showed no mutation in *FOLR1* gene exons 3–4 and 5, and *FOLR2* gene exons 3–4 and 5. This study emphasises the significance of maternal health and dietary consumption in determining the trajectory of these receptor genes, especially *FOLR1* and *FOLR2*, given the critical role of folate in satisfying the developmental demands of a growing fetus. The results of this study indicate that genetic variations in the folate receptor genes may not significantly contribute to the development of MMC (Myelomeningocele), but environmental factors are more important in this situation. The limitation of this study includes small sample size, as it is a rare disease. Furthermore, this study lacks ultrasound report of the infants or toddlers, maternal folic acid levels and other blood profile data during and before conceiving.

Declarations

Author Contributions. Conceptualization, N.H, S.M, T.F, F.S and T.A.; methodology, N.H, S.M, T.F, F.S; software, T.A; validation, A.A.S; formal analysis, T.A.; investigation, N.H, S.M, T.F, F.S; resources, M.A and A.A.S.; data curation, T.A.; writing – original draft preparation, T.A and E.A; writing – review and editing, A.A. K, T.Q, W.A and A.F.A; visualization, A.A.S; supervision, T.A and B.I.; project administration, A.A.S and M.A; funding acquisition, T.A.

Funding. This research work received no external funding.

Conflict of interest. The authors have declared no conflict of interest.

REFERENCES

Albertsen M, Karst SM, Ziegler AS, Kirkegaard RH, Nielsen PH (2015) Back to basics – The influence of DNA extraction and

- primer choice on phylogenetic analysis of activated sludge communities. *PLoS One* 10: e0132783. <https://doi.org/10.1371/journal.pone.0132783>
- Boyles AL, Billups AV, Deak KL, Siegel DG, Mehlretter L, Slifer SH, Bassuk AG, Kessler JA, Reed MC, Nijhout HF, George TM, Enterline DS, Gilbert JR, Speer MC NTD Collaborative Group (2006) Neural tube defects and folate pathway genes: family-based association tests of gene–gene and gene–environment interactions. *Environ Health Perspect* 114: 1547–1552. <https://doi.org/10.1289/ehp.9166>
- Canfield MA, Marengo L, Ramadhani TA, Suarez L, Brender JD, Scheuerle A (2009) The prevalence and predictors of anencephaly and spina bifida in Texas. *Paediatr Perinat Epidemiol* 23: 41–50. <https://doi.org/10.1111/j.1365-3016.2008.00975.x>
- Cavalheiro S, Costa MDS, Barbosa MM, Patricia AD, Jardel NM, Daniela C, Antonio FM (2021) Hydrocephalus in myelomeningocele. *Childs Nerv Syst* 37: 3407–3415. <https://doi.org/10.1007/s00381-021-05333-2>
- Farmer DL, Thom EA, Brock JW 3rd, Burrows PK, Johnson MP, Howell LJ, Farrell JA, Gupta N, Adzick NS (2018) Management of Myelomeningocele Study Investigators. The Management of Myelomeningocele Study: full cohort 30-month pediatric outcomes. *Am J Obstet Gynecol* 218: 256.e1–256.e13. <https://doi.org/10.1016/j.ajog.2017.12.001>
- Findley TO, Tenpenny JC, O'Byrne MR, Morrison AC, Hixson JE, Northrup H, Au KS (2017) Mutations in folate transporter genes and risk for human myelomeningocele. *Am J Med Genet A* 173: 2973–2984. <https://doi.org/10.1002/ajmg.a.38472>
- Han X, Cao X, Aguiar-Pulido V, Yang W, Karki M, Ramirez PAP, Cabrera RM, Lin YL, Włodarczyk BJ, Shaw GM, Ross ME, Zhang C, Finnell RH, Lei Y (2022) CIC missense variants contribute to susceptibility for spina bifida. *Hum Mutat* 43: 2021–2032. <https://doi.org/10.1002/humu.24460>
- Hassan AS, Du YL, Lee SY, Wang A, Farmer DL (2022) Spina bifida: a review of the genetics, pathophysiology and emerging cellular therapies. *J Dev Biol* 10: 22. <https://doi.org/10.3390/jdb10020022>
- Hillman P, Baker C, Hebert L, Brown M, Hixson J, Ashley-Koch A, Morrison AC, Northrup H, Au KS (2020) Identification of novel candidate risk genes for myelomeningocele within the glucose homeostasis/oxidative stress and folate/one-carbon metabolism networks. *Mol Genet Genomic Med* 8: e1495. <https://doi.org/10.1002/mgg3.1495>
- Hussain N, Mumtaz M, Adil M, Ali Nadeem A, Sarwar A, Aziz T, Alharbi M, Alshammari A, Alasmari AF, Alharbi ME (2023) Investigation of VEGF (rs 699947) polymorphism in the progression of Rheumatoid Arthritis (RA) and *in-silico* nanoparticle drug delivery of potential phytochemicals to cure RA. *Acta Biochim Pol* 70: 591–598. https://doi.org/10.18388/abp.2020_6654
- Lorenz TC (2012) Polymerase chain reaction: basic protocol plus troubleshooting and optimization strategies. *J Vis Exp* 22: e3998. <https://doi.org/10.3791/3998>
- Mazumdar M, Ibne Hasan MO, Hamid R, Valeri L, Paul L, Selhub J, Rodrigues EG, Silva F, Mia S, Mostofa MG, Quamruzzaman Q, Rahman M, Christiani DC (2015) Arsenic is associated with reduced effect of folic acid in myelomeningocele prevention: a case control study in Bangladesh. *Environ Health* 14: 34. <https://doi.org/10.1186/s12940-015-0020-0>
- Mazumdar M, Valeri L, Rodrigues EG, Ibne Hasan MO, Hamid R, Paul L, Selhub J, Silva F, Mostofa MG, Quamruzzaman Q, Rahman M, Christiani DC (2015) Polymorphisms in maternal folate pathway genes interact with arsenic in drinking water to influence risk of myelomeningocele. *Birth Defects Res A Clin Mol Teratol* 103: 754–762. <https://doi.org/10.1002/bdra.23399>
- Moldenhauer JS, Adzick NS (2017) Fetal surgery for myelomeningocele: After the Management of Myelomeningocele Study (MOMS) *Semin Fetal Neonatal Med* 22: 360–366. <https://doi.org/10.1016/j.siny.2017.08.004>
- Muhammad N, Ain, T Aziz, I Ali, M Aqib Shabbir, K Javed, M Alharbi, A Alshammari, AF Alasmari (2023) Revolutionizing treatment for toxic shock syndrome with engineered super chromosomes to combat antibiotic-resistant *Staphylococcus aureus*. *Eur Rev Med Pharmacol Sci* 27: 5301–5309. https://doi.org/10.26355/eurrev_202306_32649
- Nageen H, Alkhateeb MA, Bashir A, Iqbal R, Hussain T, Aziz T, AlAbbas NS, Shaer NA, Alamri AS, Alhomrani M, Shakoori A, Labban S (2023) Deletions of SMN1 gene exon 7 and NAIP gene exon 5 in spinal muscular atrophy patients in selected population. *Eur Rev Med Pharmacol Sci* 27: 7935–7945. https://doi.org/10.26355/eurrev_202309_33552
- Naveed M, Ali U, Aziz T, Rasool MJ, Ijaz A, Alharbi M, Alharbi ME, Alshammari A, Alasmari AF (2023) A reverse vaccinology approach to design an mRNA-based vaccine to provoke a robust immune response against HIV-1. *Acta Biochim Pol* 70: 407–418. https://doi.org/10.18388/abp.2020_6696
- Naveed M, Sheraz M, Amin A, Waseem M, Aziz T, Khan AA, Ghani M, Shahzad M, Alruways MW, Dabool AS, Ahmad ME, Abdulhakeem AA, Abdulhakeem SA, Majid A (2022) Designing a novel peptide-based multi-epitope vaccine to evoke a robust immune response against pathogenic multidrug-resistant *providencia heimbachae*. *Vaccines* 10: 1300. <https://doi.org/10.3390/vaccines10081300>
- Ntimbari J, Kelly A, Lekgwara P (2020) Myelomeningocele-A literature review. *Interdiscip Neurosurg* 19: 100502. <https://doi.org/10.1016/j.inat.2019.100502>
- O'Byrne MR, Au KS, Morrison AC, Lin JI, Fletcher JM, Ostermaier KK, Tyerman GH, Doebel S, Northrup H (2010) Association of folate receptor (FOLR1, FOLR2, FOLR3) and reduced folate carrier (SLC19A1) genes with meningomyelocele. *Birth Defects Res A Clin Mol Teratol* 88: 689–694. <https://doi.org/10.1002/bdra.20706>
- Steele JW, Kim SE, Finnell RH (2020) One-carbon metabolism and folate transporter genes: Do they factor prominently in the genetic etiology of neural tube defects? *Biochimie* 173: 27–32. <https://doi.org/10.1016/j.biochi.2020.02.005>
- Tauheed J, Sanchez-Guerra M, Lee JJ, Paul L, Ibne Hasan MOS, Quamruzzaman Q, Selhub J, Wright RO, Christiani DC, Coull BA, Baccarelli AA, Mazumdar M (2017) Associations between post translational histone modifications, myelomeningocele risk, environmental arsenic exposure, and folate deficiency among participants in a case control study in Bangladesh. *Epigenetics* 12: 484–491. <https://doi.org/10.1080/15592294.2017.1312238>
- Wolujewicz P, Steele JW, Kaltschmidt JA, Finnell RH, Ross ME (2021) Unraveling the complex genetics of neural tube defects: From biological models to human genomics and back. *Genesis* 59: e23459. <https://doi.org/10.1002/dvg.23459>



OPEN ACCESS

EDITED BY

Przemysław Mieszko Płonka,
Jagiellonian University, Poland

REVIEWED BY

Martyna Elas,
Jagiellonian University, Poland
Agata Niewczas,
Medical University of Lublin, Poland

*CORRESPONDENCE

Sophio Kalmakhelidze,
✉ s.kalmakhelidze@tsmu.edu

RECEIVED 16 November 2023

ACCEPTED 23 January 2024

PUBLISHED 05 February 2024

CITATION

Bayandurov E, Orjonikidze Z,
Kraveishvili S, Orjonikidze R,
Ormotsadze G, Kalmakhelidze S and
Sanikidze T (2024), Selected
osteointegration markers in different
timeframes after dental implantation:
findings and prognostic value.
Acta Biochim. Pol 71:12433.
doi: 10.3389/abp.2024.12433

COPYRIGHT

© 2024 Bayandurov, Orjonikidze,
Kraveishvili, Orjonikidze, Ormotsadze,
Kalmakhelidze and Sanikidze. This is an
open-access article distributed under
the terms of the [Creative Commons
Attribution License \(CC BY\)](https://creativecommons.org/licenses/by/4.0/). The use,
distribution or reproduction in other
forums is permitted, provided the
original author(s) and the copyright
owner(s) are credited and that the
original publication in this journal is
cited, in accordance with accepted
academic practice. No use, distribution
or reproduction is permitted which does
not comply with these terms.

Selected osteointegration markers in different timeframes after dental implantation: findings and prognostic value

Emir Bayandurov¹, Zurab Orjonikidze¹, Sophio Kraveishvili¹,
Ramaz Orjonikidze¹, George Ormotsadze²,
Sophio Kalmakhelidze^{2*} and Tamar Sanikidze²

¹Department of Oral Surgery and Implantology, Tbilisi State Medical University, Tbilisi, Georgia,

²Department of Physics, Biophysics, Biomechanics and Informational Technologies, Tbilisi State
Medical University, Tbilisi, Georgia

The study aimed to determine the osteointegration markers after dental implantation and evaluate their predictive value. The study was performed on 60 practically healthy persons who needed teeth rehabilitation using dental implants. The conical-shaped implants (CI) and hexagonal implants (HI) were used. The content of Osteopontin (OPN), Osteocalcin (OC), Alkaline Phosphatase (ALP), Osteoprotegerin (OPG), and nitric oxide (NO) was determined in patients' gingival crevicular fluid (GCF) and peri-implant sulcular fluid (PISF), collected 1, 3, and 6 months after implantation. During the 3–6 months of observation level of OPN increased in patients with CIs (<50 years > 50 years) and HIs (<50 years) (CI: <50 years $F = 36.457$, $p < 0.001$; >50 years $F = 30.104$, $p < 0.001$; HI < 50 years $F = 2.246$, $p < 0.001$), ALP increased in patients with CIs (<50 years: $F = 19.58$, $p < 0.001$; >50 years: $F = 12.01$; $p = 0.001$) and HIs (<50 years) ($F = 18.51$, $p < 0.001$), OC increased in patients <50 years (CI: $F = 33.72$, $p < 0.001$; HI: $F = 55.57$, $p < 0.001$), but in patients >50 years - on the 3 days month (CI: $F = 18.82$, $p < 0.001$; HI: $F = 26.26$, $p < 0.001$), but sharply decreased at the end of sixth month. OPG increased during 1–3 months of the observation in patients <50 years (CI: $F = 4.63$, $p = 0.037$; HI: $F = 2.8927$, $p = 0.046$), but at the end of the sixth month returned to the initial level; NO content in PISF increased in patients with CI (>50 years) during 1–6 months of the observation ($F = 27.657$, $p < 0.001$). During the post-implantation period, age-related differences in osteointegration were observed. Patients <50 years old had relatively high levels of OPN, ALP, OC, and OPG in PISF, resulting in less alveolar bone destruction around dental implants and more intensive osteointegration. These indicators may be used as biological markers for monitoring implant healing. The process of osseointegration was more intense in CIs due to their comparatively high mechanical loading.

KEYWORDS

osteopontin, osteocalcin, bone alkaline phosphatase, osteoprotegerin, nitric oxide

Introduction

Aesthetic and functional rehabilitation using dental implants offers highly predictable and esthetical results; hence it has become one of the alternatives to be included in the therapeutic options for the treatment of totally or partially edentulous patients. Despite this, the risk of failure remains high but difficult to predict (Scarano et al., 2023).

The implant's stability significantly depends on the osteointegration process between the bone and the implant. Osteointegration is a continuous process of osteoclast and osteoblast activation, necessary for bone repair, formation, and functional recovery (Martin and Sims, 2005).

Bone remodeling is critical to maintaining long-term stable osseointegration. The mechanisms of wound healing around dental implants are characterized by several features. The cellular and molecular mechanisms of the osseointegration process have not yet been fully established and require further research in this direction (Matsuura and Yamashita, 2018).

Early monitoring of sensitive clinical-laboratory indicators of patients with dental implants, correlated with pathological disorders in the osteointegration process in the early stages of the implantation, can be used to identify predictive markers of possible complications and their severity at its later stages. This can be useful for providing guides to treatment strategies and preventing complications, maintaining long-term stable osseointegration.

Since the array of clinical indices of periodontal origin, such as indices recording gingival inflammation, plaque accumulation, and bleeding and probing depths (clinical index) most frequently gives the possibility only determining the soft tissue inflammatory response, rather than detecting its early predictors (Greenstein, 1996), for the determination of peri-implant clinical status, various oral fluids are used, the molecules of which are associated with the inflammatory response, bone metabolism, and proteinases.

The gingival crevicular fluid is the osmotically mediated physiological exudate originating from serum and tissue fluid that seeps through the crevicular and junctional epithelium. Gingival crevicular fluid plays a special part in maintaining the structure of junctional epithelium and the antimicrobial defense of periodontium, reflects the cellular response in the periodontium by the constituents from the gingival crevice, and is an important determinant of the status of periodontal tissues (Akman et al., 2018). The peri-implant sulcus is, anatomically, functionally, and environmentally quite similar to periodontal crevices (Berglundh et al., 1991; Piattelli et al., 1996; Buser et al., 1997); this fluid was termed the peri-implant sulcular fluid. Peri-implant sulcular fluid like gingival crevicular fluid is composed of serum and locally generated materials such as tissue breakdown products, inflammatory mediators (cytokines, prostaglandins), tissue degradation components, mineralized tissue components, bone turnover markers, and antibodies directed against dental

plaque bacteria (Akman et al., 2018; Subbarao et al., 2019). Peri-implant sulcular fluid analysis can potentially reflect the actual status of peri-implant soft and hard tissues (Lang and Berglundh, 2011). GCF and PISF could be useful markers of early inflammation in gingival and peri-implant tissues (Shama et al., 2016).

The study aimed to determine the osteointegration markers in different timeframes after dental implantation and their prognostic value.

Materials and methods

The study was performed on 60 persons (aged from 18 to 65 years) who performed teeth rehabilitation using dental implants based on Dental Clinic and Training-Research Center UniDent and Dental Clinic A1 during 2020–2022 years.

Patient inclusion criteria in the study

Practically healthy male persons (without comorbidities) (60 patients) who needed rehabilitation using dental implants in the chewing teeth in the mandible, with good hygiene of the oral cavity (Board index <20%) (Ainamo and Bay, 1975) were included in the study.

Patients excluding criteria in the study

Females were excluded from the study to avoid the possible influence of pre-menopause/menopause-related hormonal imbalances on the process of osseointegration. Patients with various accompanying diseases (allergy, cancer, hepatitis, diabetes, endocrine system disorders, stomach ulcer, chronic gastritis, colitis, respiratory diseases, and pregnant women), also were patients who, during the last 6 months before implantation, used medications that can change the osseointegration (including anti-inflammatory drugs) were excluded from the study.

The research plan was approved by the Ethics Committee of Tbilisi State Medical University. All subjects signed informed consent.

The conical-shaped implants (CIs) (<50 years—10 patients, >50 years—20 patients) and hexagonal implants (HIs) (<50 years—15 patients, >50 years—15 patients) from the AlphaBio were used.

The selected age range (18–65 years) lowered chronic comorbidity risk. The age limit of 50 years was chosen to equally distribute patients between groups while considering the mean number of patients of different ages. This distribution of the patients will give the possibility to assess the dynamic intensity of osteointegration processes with aging.

The GSF and PSF were collected from patients 1, 3, and 6 months after implantation, and the content of Osteopontin (OPN), Osteocalcin (OC), bone Alkaline Phosphatase (ALP), Osteoprotegerin (OPG), and nitric oxide (NO) was determined.

Collection of gingival crevicular fluid (GCF) and peri-implant sulcular fluid (PISF)

PISF and GCF were obtained by the method considering minimal mechanical irritation (Rudin et al., 1970). The area to be sampled was treated with sterile cotton swabs to remove dental plaque and then air-dried to prevent plaque and saliva contamination. To obtain a sample PISF strips of standardized paper (Periopaper, no. 593525) were placed at the entrance of the grooves of the implant and healthy teeth and inserted to a standardized depth of 1 mm at each site regardless of probing depth to avoid further mechanical irritation. To obtain a sample GCF strips of standardized paper (Periopaper, no. 593525) were placed at the entrance of the grooves between the healthy teeth and inserted to a standardized depth of 1 mm at each site regardless of probing depth to avoid further mechanical irritation. The sampling time is standardized and equal to 30 s. Samples contaminated with blood were not used.

For safe storage of PISF and GCF samples, the paper strips will be placed in sterile Eppendorf and stored at -80°C until laboratory analysis.

Analysis

After the paper strips in Eppendorf tubes were kept at room temperature for at least 30 min, 100 μL assay buffer included in the kit was added to each Eppendorf tube and put into the shaker device for 45 min. Then the tubes were centrifuged at 11,200 rpm for 15 min. After the GCF/PISF in the paper strips were transferred to the assay buffer, the assay buffer in the Eppendorf was taken using a clean polypropylene pipette, and the levels of OPN, OC, bone ALP, and OPG were measured according to the manufacturer's instructions.

The bone markers in PISF and GCF samples were determined by immuno-enzymatic method (ELISA) using HumaReader SETPROD immune-enzymatic counter. OPG was determined by use of EH0247 Human OPG ELISA Kit OC—EH3468 Human OC/BGP ELISA Kit, OPN—EH0248 Human OPN ELISA Kit, bone ALP—BIOLABO Kit.

For the determination of NO content in PISF and GCF, distilled water (130 μL per sample) was added to the Eppendorfs containing PISF and GCF, and the Eppendorfs were shaken vigorously to dissolve the nitrite in the water. To the 100 μL of the obtained extract, 0.5 mL of freshly prepared Greiss reagent was added; after a 10-minute incubation at room temperature, the

TABLE 1 Statistical significance of OC, OPG, OPN, ALP, and NO in the gingival crevicular fluid alterations after the 6 months after implantation (analysis of variance (ANOVA) F, between-group variability/within-group variability; *p*, level of significance of Null Hypothesis).

VAR	AGE <50		Age \geq 50	
	<i>F</i>	<i>p</i>	<i>F</i>	<i>p</i>
OC	0.059	0.942	0.366	0.698
OPG	0.022	0.977	0.027	0.972
OPN	0.154	0.858	0.036	0.964
ALP	0.010	0.989	0.130	0.878
NO	0.884	0.438	0.134	0.875

absorbance intensity of each sample placed on the microplate was measured at a wavelength of 540 nm (Grisham et al., 1996). A standard curve was prepared using sodium nitrite to calculate the nitrite (NO_x) concentration in the GSF and PISF.

Statistical analysis

Statistical significance was tested using analysis of variance ANOVA and a two-sample *t*-test. Relationships yielding *p*-values less than 0.05 were considered significant. All values were expressed as the mean \pm SE.

Results

As follows from the data presented in Table 1 the content of OPN, OC, bone ALP, OPG, and NO in the gingival crevicular fluid did not change statistically significantly during the entire observation period.

Figures 1–5 show alterations of OPN, OC, bone ALP, and OPG, and NO content in the patients' GSF and PISF after 1, 3, and 6 months after implantation.

Figure 1 shows that after the implantation the level of OPN in patients' peri-implant sulcular fluid (PISF) increased in comparison to its level in gingival crevicular fluid (GSF). In the case of the CIs in both age groups the content of OPN in PISF increased during the entire observation period (1–6 months) and reached a maximum by the end of 6 months of observation (<50 years— $F = 36.457$; $p < 0.001$; >50 years— $F = 30.104$; $p < 0.001$), but in case of HIs, an increase in the OPN content was recorded during the observation period only in patients of the age group <50 years ($F = 22.246$; $p < 0.001$); in age group >50 years, an increase in the level of OPN in PISF was not statistically significant.

Figure 2 shows that during the first month after implantation, the content of ALP in peri-implant sulcular fluid (PISF) did not

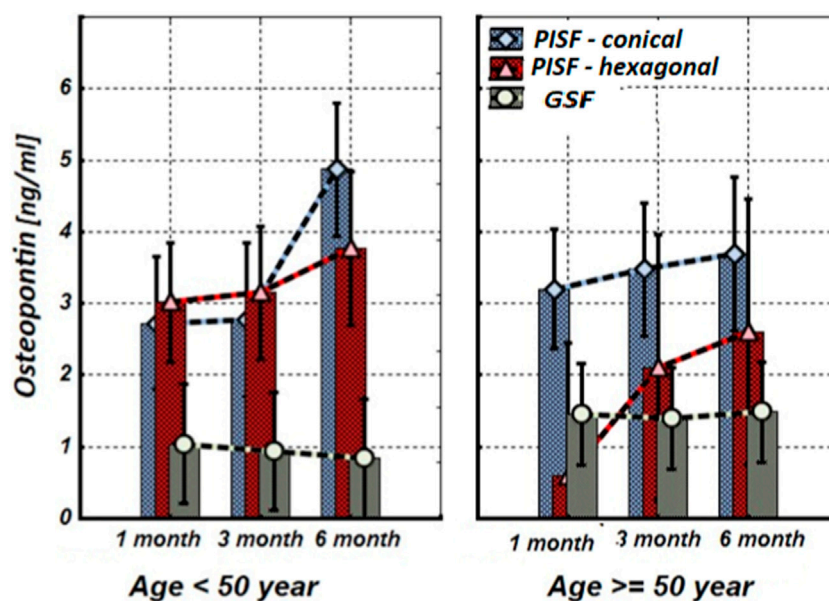


FIGURE 1

The levels of OPN in the gingival crevicular fluid (GCF) and peri-implant sulcular fluid (PISF) of patients of different age groups during the post-implantation period (after 1, 3, and 6 months), in cases of conical-shaped implants (CIs) and hexagonal implants (HIs).

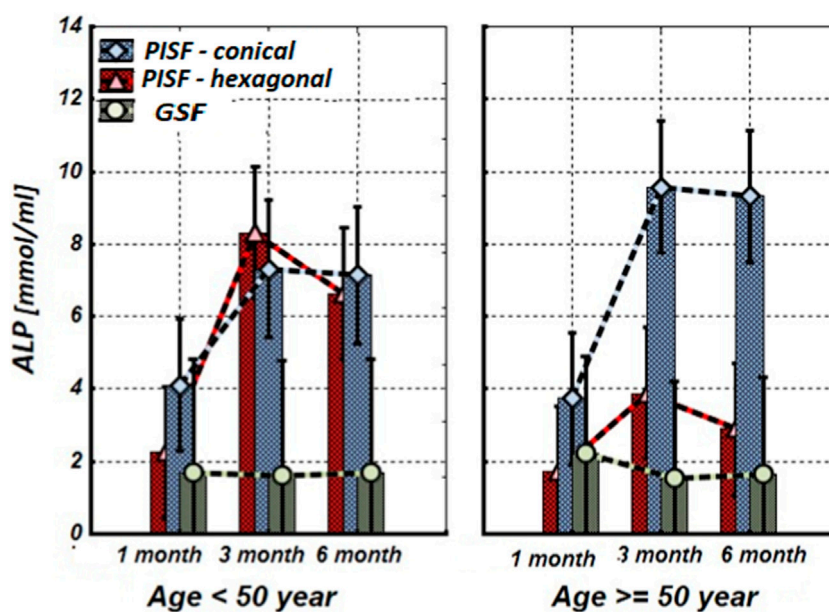


FIGURE 2

The levels of ALP in the gingival crevicular fluid (GCF) and peri-implant sulcular fluid (PISF) of patients of different age groups during the post-implantation period (after 1, 3, and 6 months), in cases of conical-shaped implants (CIs) and hexagonal implants (HIs).

change significantly in comparison to its level in gingival crevicular fluid (GSF) (CI: <50 years— $F = 1.15$; $p = 0.297$; >50 years— $F = 1.35$; $p = 0.258$; HI: <50 years— $F = 2.43$; $p =$

0.135; >50 years— $F = 2.99$; $p = 0.099$) and increased in both age groups at 3 months after the implantation. In patients with CIs, this tendency continued for 3–6 months and was statistically

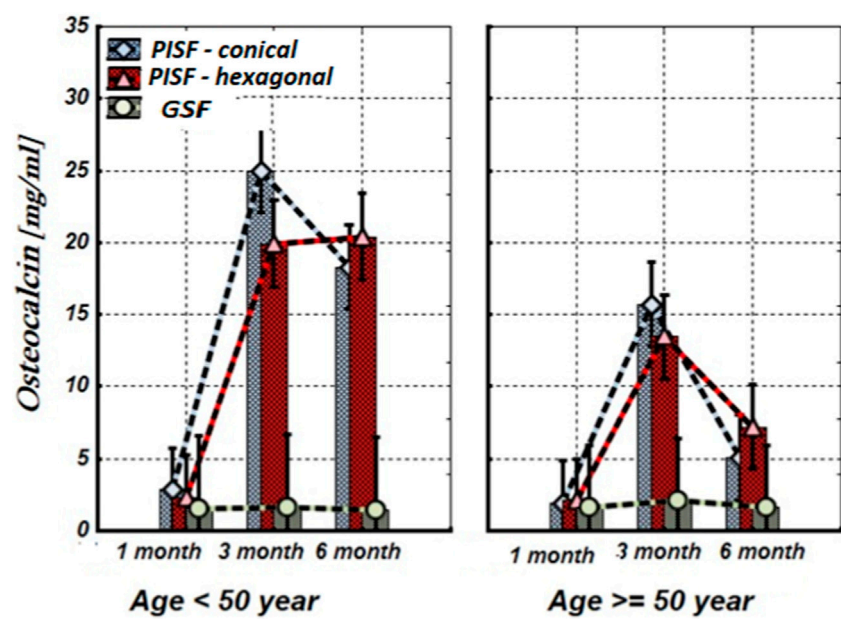


FIGURE 3
The levels of OC in the gingival crevicular fluid (GCF) and peri-implant sulcular fluid (PISF) of patients of different age groups during the post-implantation period (after 1, 3, and 6 months), in cases of conical-shaped implants (CIs) and hexagonal implants (HIs).

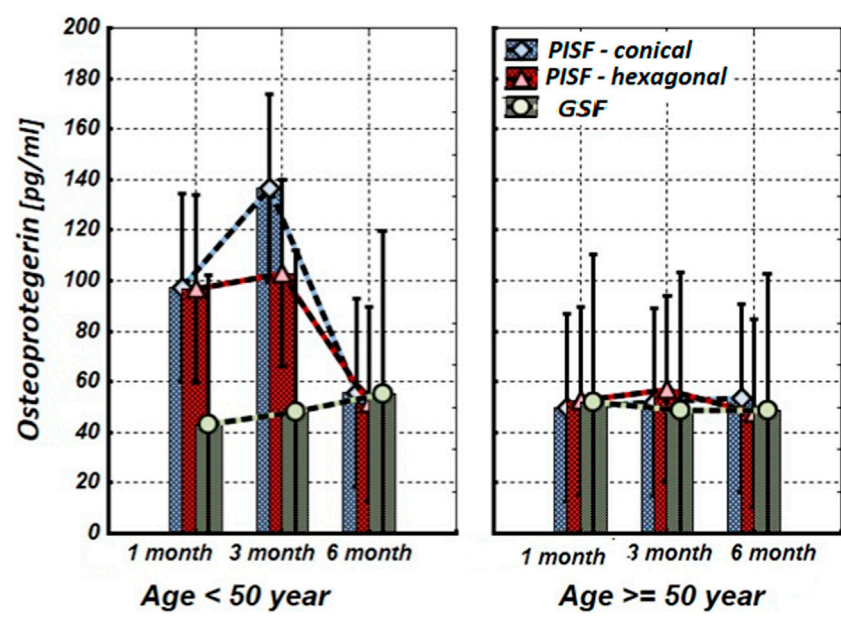


FIGURE 4
The levels of OPG in the gingival crevicular fluid (GCF) and peri-implant sulcular fluid (PISF) of patients of different age groups during the post-implantation period (after 1, 3, and 6 months), in cases of conical-shaped implants (CIs) and hexagonal implants (HIs).

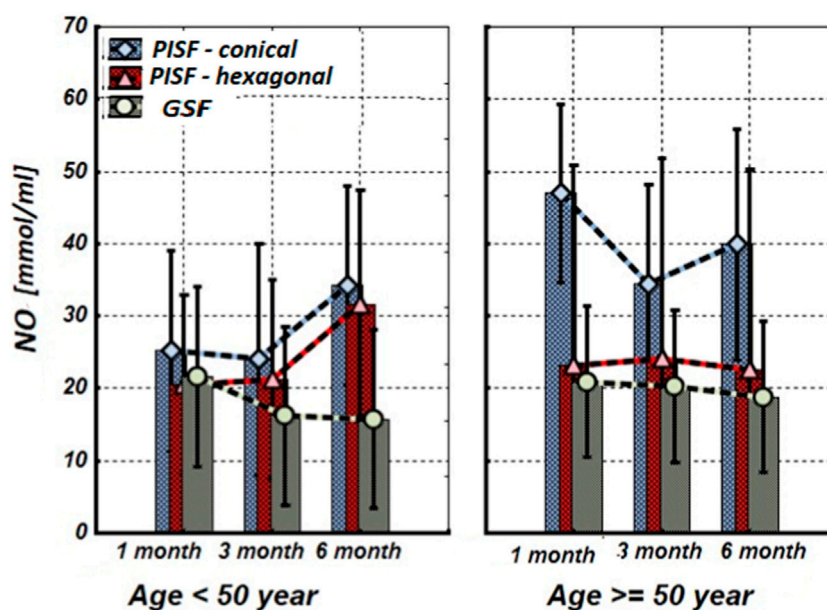


FIGURE 5

The levels of nitrite (NO_x) concentration in the gingival crevicular fluid (GCF) and peri-implant sulcular fluid (PISF) of patients of different age groups during the post-implantation period (after 1, 3, and 6 months), in cases of conical-shaped implants (CIs) and hexagonal implants (HIs).

significant in both age groups (<50 years— $F = 19.58$; $p < 0.001$; >50 years— $F = 12.01$; $p = 0.001$). In patients with HIs during the 3–6-month period in the age group <50 years the ALP content in PISF increased significantly ($F = 18.51$; $p < 0.001$), but in patients older than 50 years the statistical significance of the difference was not high ($F = 1.30$; $p = 0.233$).

As follows from Figure 3, 1 month after implantation OC levels in peri-implant sulcular fluid (PISF) did not differ from the corresponding values in gingival crevicular fluid (GCF) (conical: $F = 2.065$; $p = 0.164$; hexagonal: $F = 1.107$; $p = 0.304$); its content began to increase only 3–6 months after the implantation. In patients under the age of 50 years the level of OC in PISF was high during the 3–6 months of the observation period (CI: $F = 33.72$; $p < 0.001$; HI: $F = 55.57$; $p < 0.001$), whereas in patients of the age group after 50 years, the level of OC in PISF increased up to the 3 months of observation (conical: $F = 18.82$; $p < 0.001$; hexagonal: $F = 26.26$; $p < 0.001$), and sharply decreased by the end of 6 months (CI: $F = 1.10$; $p = 0.261$; HI: $F = 1.71$; $p = 0.204$).

As follows from Figure 4, during the first 3 months of observation (1–3 months) OPG in peri-implant sulcular fluid (PISF) in patients of the age group <50 years increased (CI: $F = 4.63$; $p = 0.037$; HI: $F = 2.8927$; $p = 0.046$) compared to its level in gingival crevicular fluid (GCF), but by the end of the sixth month it was returned to the initial level (CI: $F = 1.03$; $p = 0.29$; HI: $F = 1.07$; $p = 0.31$). In patients of the age group >50, the level of OPG in PISF did not change statistically significantly compared to its

level in GCF during the entire follow-up period (CI: $F = 1.23$; $p = 0.246$; HI: $F = 1.03$; $p = 0.301$).

As follows from Figure 5, in patients of the age group <50 years, the mean values of the nitrite (NO_x) concentration in peri-implant sulcular fluid (PISF) did not change during whole observation period compared with the corresponding values in gingival crevicular fluid (GCF) only at the end (6-th months) after implantation (CI: $F = 1.615$; $p = 0.2443$; HI: $F = 1.524$; $p = 0.263$). In patients of the age group >50 years with a CIs, the NO_x concentration in PISF increased statistically significantly compared to the corresponding values in GCF during the whole period (1–6 months) of the observation ($F = 27.657$; $p < 0.001$), while in the case of a HIs, did not statistically significantly change compared to the corresponding values in GCF ($F = 0.596$; $p = 0.448$).

Discussion

The success of the osteogenic process requires careful chronological coordination of molecular signals to drive the proliferation, migration, and differentiation of mesenchymal precursor cells in osteoblasts (Zaidi, 2007). In the last decades, periodontal research has focused on the analysis of potential host markers that can be used to diagnose the healing intensity of implants and determine prognosis (Arikan et al., 2008).

Bone is in a constant state of remodeling, which is important for the maintenance of its normal structure and function. Many types of cells and factors are involved in the process of bone remodeling.

Osteoblasts, responsible for new bone formation, and osteoclasts responsible for bone resorption, are the two main cell types participating in those processes (Matsuoka et al., 2014; Chen et al., 2018). These processes are stable and balanced under physiological conditions; However, bone architecture or function will be disturbed when the balance is disordered.

The process of osseointegration begins after the placement of the dental implant in the jaw bone; the implant integrates with the living bone by healing the bone wound. OPN and OC are major non-collagenous proteins involved in bone matrix organization and deposition. They are produced during bone formation, later in the mineralization process, and involved in organizing the extracellular matrix and coordinating cell-matrix, mineral-matrix interactions, which play key roles in the biological and mechanical functions of bone, regulate whole-bone structure and morphology (Bailey et al., 2017).

At first, OPN is secreted on the hard surface of the bone. This extracellular matrix protein is a major factor affecting osteoclast attachment, wound healing, and angiogenesis, plays an important role in bone mineralization, cell adhesion, differentiation, and foreign body response, since it has several binding sites with implant hydroxyapatite crystals, collagen, and various integrins, through the calcium ions and Arg-Gly-Asp motif (Makishi et al., 2022).

Secretion of OPN at the resorption site during bone remodeling regulates migration, adhesion, differentiation, and activation of osteoclasts to form a bone matrix, also, migration, adhesion, and differentiation of osteoblasts. OPN positively affects osteoblasts in direct osteogenesis after implantation (Dodds et al., 1995; McKee and Nanci, 1995).

As follows from the results of our study level of OPN in patients' PISF increased in comparison to its level in GSF from the early stages after the implantation. In the case of CIs, the content of OPN in PISF was higher compared to the corresponding values in GCF during the entire observation period (1–6 months) and reached a maximum by the end of sixth month at both age groups, but in the case of HIs, an increase in the OPN content in PISF from the beginning to the end of the observation (sixth month), was recorded only in patients of the age group <50 years, in age group >50 years, an increase in the level of OPN in PISF was not statistically significant.

During bone mineralization, osteoblasts secrete a specific membrane-bound glycoprotein, ALP, that catalyzes the hydrolysis of phosphate monoesters and supports a high concentration of phosphate on the surface of osteoblasts (Sharma et al., 2014). Elevated levels of ALP in sulcular fluid are observed as a compensatory mechanism in response to destructive disease processes and indicate active bone formation (Malik et al., 2015).

According to our study results, OC and ALP content increase in PISF began 3 months after implantation. In patients with CIs, ALP remains this statistically significant tendency for 3–6 months in both age groups, however, in patients with HIs in patients older than 50 years the statistical significance of this growth was not high. Regarding OC, under the age of 50 years in patients with conical-shaped and hexagonal implants, the level of OC in PISF was high during 3–6 months after implantation, whereas in patients of the age group after 50 years, the level of OC in PISF increased on to the 3 months of observation, and sharply decreased at the end of 6 months. In literature, age-related decline of OC has been established (Vanderschueren et al., 1990). A weak correlation between the bone markers ALP and OC levels, and the dental implant stability quotient (ISQ) over the healing period was revealed, which is in harmony with the intensification of a gene expression of bone markers in PICF (Tirachaimongkol et al., 2016) and indicates that these biological markers may be used for monitoring of implant healing.

These data indicate that when using CIs, the process of osseointegration proceeds intensively in both age groups, while when using HIs, the intensity of this process in elderly patients decreases. This is due to the comparatively higher mechanical loading produced by the CIs (Bayandurov et al., 2023), as well as age-related characteristics of osteogenesis—in young (<50 years) patients content of the OPG, ALP, and OC in PISF was especially high.

Osteointegration success is determined by the incorporation of the woven bone and the bone mass adaptation to bearing a load (Parithimarkalaignan and Padmanabhan, 2013). Disruption of the balance of factors regulating host response can induce impairment osteointegration process and bone remodeling, stimulation of osteoclasts activity with consequent alveolar bone resorption, and implant loss (Giannopoulou et al., 2012).

Osteoclastogenesis is coordinated by the interaction of three members of the tumor necrosis factor (TNF) superfamily: receptor activator of nuclear factor- κ B (NF- κ B) ligand (RANKL), RANK, and OPG. The RANK, RANKL, and OPG, known together as the RANK-RANKL-OPG system, effectively control the balance between osteoblasts and osteoclasts activity. RANKL is expressed by osteoblasts, stromal cells, fibroblasts, B cells, and T cells when stimulated by cytokines and bacterial lipopolysaccharides. The binding of RANK and RANKL on the surface of preosteoclast/osteoblast cells, activates the formation, maturation, and activation of osteoclasts, resulting in bone destruction. Conversely, OPG, produced by periodontal ligament cells, gingival fibroblasts, and epithelial cells, is a soluble circulating decoy receptor of RANK, blocks the activation of RANK by preferentially binding itself to RANKL, and thus protects bone against destruction. Therefore, RANKL and OPG regulate bone resorption by positive or negative stimulation of RANK on osteoclast cells (Giannopoulou et al., 2012). OPG is involved in the regulation of alveolar bone

destruction around dental implants through the regulation of osteoclast differentiation.

As follows from the results of our study, in patients of the age group <50 years OPG in PISF during the first 3 months of observation (1–3 months) increased compared to its level in GCF, but by the end of the sixth month returned to the initial level. In patients of the age group >50, the level of OPG in PISF did not statistically significantly change compared to its level in GCF during the entire follow-up period. Consequently, in the early stages of osteointegration in young patients, OPG protects alveolar bone destruction around dental implants and promotes osteointegration, while in older patients the effectiveness of this mechanism decreases.

In the regulation of inflammation in soft tissues around the implant, immunomodulation, antimicrobial defense, as well as anabolic reactions, and bone resorption process important role plays NO, a small-sized, highly reactive molecule, that is a secondary messenger in a living organism. During implantation, it is possible an increase in NO production as a result of the intensification of iNOS activity induced by proinflammatory cytokines, or a decrease in NO content related to its conversion into peroxynitrite in inflammation-induced oxidative stress conditions (Allaker et al., 2001). Mechanical stimulus, one of the factors involved in the bone remodeling process around implants, mediates osteoclast activity and also stimulates NO production (Baloul, 2016; Gokmenoglu et al., 2018). Therefore, NO metabolism is associated with the clinical state of peri-implant tissues, NO seems to have a biphasic effect on osteoblastic activity. *In vitro*, studies have shown that a small amount of NO constitutively produced by osteoblasts, or slowly released by donors, can act as a stimulator of osteoblast growth and differentiation, while high NO concentration has a potent inhibitory effect on osteoblastic growth and differentiation, and/or stimulates bone resorption, that may be partly due to its pro-apoptotic effect. In inflamed peri-implant tissues, the NO level was found to be higher than in healthy sites (Nascimento et al., 2020).

Our study results show that in patients with CIs and HIs of the age group <50 years, the mean values of NO_x concentration in PISF statistically insignificantly increased compared with the corresponding values in GCF on the sixth month of the implantation. In patients of the age group >50 years CIs induced a statistically significant increase of NO_x concentration in PISF, while in the case of HIs, it did not change statistically significantly compared to the corresponding values in GCF during the entire observation period.

It can be assumed that in patients <50 years there is a slight increase in NO_x concentration in PISF stimulates osteoblast growth and differentiation, and therefore, the osteointegration process, whereas the statistically significant increase of NO_x

concentration in PISF in >50 years old patients in the case of a CIs, may be related with the inflammatory reaction (which needs correction) or other factors (oxidative stress, mechanical stimulus, etc.) (Orjonikidze et al., 2020).

Conclusion

During the post-implantation period, the process of osteointegration is affected by age-related factors. Patients <50 years have higher levels of OPN, ALP, OC, and OPG, which result in lesser alveolar bone destruction around dental implants and a more intensive osteointegration process. Biological markers such as OPN, OC, ALP, PNG, and NO content in PISF can be used to monitor implant healing. The use of CIs leads to a more intensive process of osseointegration due to the higher mechanical loading produced by them.

Data availability statement

The raw data supporting the conclusion of this article will be made available by the authors, without undue reservation.

Ethics statement

The studies involving humans were approved by Tbilisi State medical University Ethics committee. The studies were conducted in accordance with the local legislation and institutional requirements. The participants provided their written informed consent to participate in this study.

Author contributions

EB—Study design, taking responsibility in execution of the experiments. ZO—Reviewing the article. SKr—collecting data. RO—Taking responsibility in execution of the experiments. GO—Data analysis. SKa—Planning methodology to reach the conclusion. TS—Taking responsibility in the construction of the whole or body of the manuscript. All authors contributed to the article and approved the submitted version.

Conflict of interest

The authors declare that the research was conducted in the absence of any commercial or financial relationships that could be construed as a potential conflict of interest.

References

- Ainamo, J., and Bay, I. (1975). Problems and proposals for recording gingivitis and plaque. *Int. Dent. J.* 25, 229–235.
- Akman, A. C., Buyukozdemir Askin, S., Guncu, G. N., and Nohutcu, R. M. (2018). Evaluation of gingival crevicular fluid and peri-implant sulcus fluid levels of periostin: a preliminary report. *J. Periodontology* 89 (2), 195–202. doi:10.1902/jop.2017.170315
- Allaker, R. P., Silva Mendez, L. S., Hardie, J. M., and Benjamin, N. (2001). Antimicrobial effect of acidified nitrite on periodontal bacteria. *Oral Microbiol. Immunol.* 16 (4), 253–256. doi:10.1034/j.1399-302x.2001.160410.x
- Arikan, F., Buduneli, N., and Kütükçüler, N. (2008). Osteoprotegerin levels in peri-implant crevicular fluid. *Clin. Oral Implants Res.* 19 (3), 283–288. doi:10.1111/j.1600-0501.2007.01463.x
- Bailey, S., Karsenty, G., Gundberg, C., and Vashishth, D. (2017). Osteocalcin and osteopontin influence bone morphology and mechanical properties. *Ann. N. Y. Acad. Sci.* 1409 (1), 79–84. doi:10.1111/nyas.13470
- Baloul, S. S. (2016). Osteoclastogenesis and osteogenesis during tooth movement. *Front. Oral Biol.* 18, 75–79. doi:10.1159/000351901
- Bayandurov, E., Orjonikidze, Z., Sanikidze, T., Mantskava, M., and Tortladze, M. (2023). Characteristics of human saliva and rheological parameters as markers of the implantation success. *Ser. Biomechanics* 37 (2), 103–111. doi:10.7546/sb.11.02.2023
- Berglundh, T., Lindhe, J., Ericsson, I., Marinello, C. P., Liljenberg, B., and Thomsen, P. (1991). The soft tissue Barrier at implants and teeth. *Clin. Oral Implants Res.* 2, 81–90. doi:10.1034/j.1600-0501.1991.020206.x
- Buser, D., Mericske-Stern, R., Pierre Bernard, J. P., Behneke, A., Behneke, N., Hirt, H. P., et al. (1997). Long-term evaluation of non-submerged ITI implants. Part 1: 8-year life table analysis of a prospective multi-center study with 2359 implants. *Clin. Oral Implants Res.* 8 (3), 161–172. doi:10.1034/j.1600-0501.1997.080302.x
- Chen, X., Wang, Z., Duan, N., Zhu, G., Schwarz, E. M., and Xie, C. (2018). Osteoblast-osteoclast interactions. *Connect. Tissue Res.* 59 (2), 99–107. doi:10.1080/03008207.2017.1290085
- Dodds, R. A., Connor, J. R., James, I. E., Lee Rykaczewski, E., Appelbaum, E., Dul, E., et al. (1995). Human osteoclasts, not osteoblasts, deposit osteopontin onto resorption surfaces: an *in vitro* and *ex vivo* study of remodeling bone. *J. Bone Mineral Res.* 10, 1666–1680. doi:10.1002/jbmr.5650101109
- Giannopoulou, C., Martinelli-Klay, C. P., and Lombardi, T. (2012). Immunohistochemical expression of RANKL, RANK and OPG in gingival tissue of patients with periodontitis. *Acta Odontol. Scand.* 70, 629–634. doi:10.3109/00016357.2011.645064
- Gokmenoglu, C., Ozmeric, N., Sungur, C., Sahin Bildik, R., Erguder, I., and Elgun, S. (2018). Nitric oxide and arginase levels in peri-implant tissues after delayed loading. *Archives Oral Biol.* 85, 207–211. doi:10.1016/j.archoralbio.2017.10.019
- Greenstein, G. (1997). Contemporary interpretation of probing depth assessments: diagnostic and therapeutic implications. A literature review. *J. Periodontology* 68, 1194–1205. doi:10.1902/jop.1997.68.12.1194
- Grisham, M. B., Johnson, G. G., and Lancaster, J. R. (1996). Quantitation of nitrate and nitrite in extracellular fluids. *Methods Enzymol.* 268, 237–246. doi:10.1016/s0076-6879(96)68026-4
- H M Nascimento, M., T Pelegrino, M., C Pieretti, J., and B. Seabra, A. (2020). How can nitric oxide help osteogenesis? *AIMS Mol. Sci.* 7 (1), 29–48. doi:10.3934/molsci.2020003
- Lang, N. P., and Berglundh, T. (2011). Working group 4 of seventh european workshop on periodontology. Peri-Implant diseases: where are we now? The consensus of the seventh European workshop on periodontology. *J. Clin. Periodontology* 38 (Suppl. 11), 178–181. doi:10.1111/j.1600-051x.2010.01674.x
- Makishi, S., Yamazaki, T., and Ohshima, H. (2022). Osteopontin on the dental implant surface promotes direct osteogenesis in osseointegration. *Int. J. Mol. Sci.* 23 (3), 1039. doi:10.3390/ijms23031039
- Malik, N., Naik, D., and Uppoor, A. (2015). Levels of myeloperoxidase and alkaline phosphatase in periimplant sulcus fluid in health and disease and after nonsurgical therapy. *Implant Dent.* 24 (4), 434–440. doi:10.1097/id.0000000000000277
- Martin, T. J., and Sims, N. A. (2005). Osteoclast-derived activity in the coupling of bone formation to resorption. *Trends Mol. Med.* 11, 76–81. doi:10.1016/j.molmed.2004.12.004
- Matsuoka, K., Park, K. A., Ito, M., Ikeda, K., and Takeshita, S. (2014). Osteoclast-derived complement component 3a stimulates osteoblast differentiation. *J. Bone Mineral Res.* 29, 1522–1530. doi:10.1002/jbmr.2187
- Matsuura, T., and Yamashita, J. (2018). *Dental implants and osseous healing in the oral cavity*. Treasure Island (FL): StatPearls Publishing, 940–956.
- McKee, M. D., and Nanci, A. (1995). Osteopontin and the bone remodeling sequence: colloidal-gold immunocytochemistry of an interfacial extracellular matrix protein^a. *Ann. N. Y. Acad. Sci.* 760, 177–189. doi:10.1111/j.1749-6632.1995.tb44629.x
- Orjonikidze, A., Mgebrishvili, S., Orjonikidze, M., Barbakadze, I., Kipiani, N. V., and Sanikidze, T. (2020). New approaches to the treatment of periimplantitis (review). *Georgian Med. News* (302), 28–33. PMID: 32672685.
- Parithimarkalaignan, S., and Padmanabhan, T. V. (2013). Osseointegration: an update. *J. Indian Prosthodont. Soc.* 13, 2–6. doi:10.1007/s13191-013-0252-z
- Piattelli, A., Scarano, A., Corigliano, M., and Piattelli, M. (1996). Effects of alkaline phosphatase on bone healing around plasma-sprayed titanium implants: A pilot study in rabbits. *Biomaterials* 17 (14), 1443–1449. doi:10.1016/0142-9612(96)87288-7
- Rudin, H. J., Overdiek, H. F., and Rateitschak, K. H. (1970). Correlation between sulcus fluid rate and clinical and histological inflammation of the marginal gingiva. *Helv. Odontol. Acta* 14, 21–26.
- Scarano, A., Khater, A. G. A., Gehrke, S. A., Serra, P., Francesco, I., Di Carmine, M., et al. (2023). Current status of peri-implant diseases: a clinical review for evidence-based decision making. *J. Funct. Biomaterials* 14 (4), 210. doi:10.3390/jfb14040210
- Shama, M. M., Aboukhadr, M., Madi, M., and Abdelhady, S. (2016). Comparison between level of interleukin 10 in the gingival crevicular fluid and peri-implant sulcular fluid around healthy dental implants (split mouth study). *Alexandria Dent. J.* 41 (26), 30.
- Sharma, U., Pal, D., and Prasad, R. (2014). Alkaline phosphatase: an overview. *Indian J. Clin. Biochem.* 29, 269–278. doi:10.1007/s12291-013-0408-y
- Subbarao, K. C., Nattuthurai, G. S., Sundararajan, S. K., Sujith, I., Joseph, J., and Syedshah, Y. P. (2019). Gingival crevicular fluid: an overview. *J. Pharm. Bioallied Sci.* 11 (Suppl. 2), S135–S139. doi:10.4103/jpbs.jpbs_56_19
- Tirachaimongkol, C., Pothacharoen, P., Reichart, P. A., and Khongkhunthian, P. (2016). Relation between the stability of dental implants and two biological markers during the healing period: A prospective clinical study. *Int. J. Implant Dent.* 2, 27. doi:10.1186/s40729-016-0058-y
- Vanderschueren, D., Gevers, G., Raymaekers, G., Devos, P., and Dequeker, J. (1990). Sex- and age-related changes in bone and serum osteocalcin. *Calcif. Tissue Int.* 46 (3), 179–182. doi:10.1007/bf02555041
- Zaidi, M. (2007). Skeletal remodeling in health and disease. *Nat. Med.* 13, 791–801. doi:10.1038/nrm1593

Simvastatin attenuates diabetes mellitus erectile dysfunction in rats by miR-9-5p-regulated PDCD4

YiMing Weng^{1#}, YuanShen Mao^{3#}, YanQiu Wang¹, YuFan Jiao¹, Jun Xiang^{2✉} and Wei Le^{2✉}

¹Department of Reproductive Center, Tongji Hospital, Tongji University School of Medicine, Shanghai, 200065, China; ²Department of Urology, Tongji Hospital, Tongji University School of Medicine, Shanghai, 200092, China; ³Department of Urology, Shanghai Ninth People's Hospital, Shanghai Jiao Tong University School of Medicine, Shanghai, 201999, China

DMED is a common complication of diabetes, for which new treatment methods are urgently required. Focused on DMED, the pharmacological mechanism of simvastatin (Sim) was probed. A model of DMED was made in rats with streptozotocin and orally medicated with Sim. Lentiviral vectors that interfere with miR-9-5p or PDCD4 were injected, and the erectile function, histopathology of cavernous tissue, and α -SMA expression were evaluated. Cavernous smooth muscle cells (CMSCs) obtained from DMED rats were treated with Sim and transfected with the plasmid vector that interferes with miR-9-5p or PDCD4 to observe cell viability and apoptosis. The binding relationship between miR-9-5p and PDCD4 was checked. After 8-week treatment with Sim, erectile function was improved and the corpus cavernosum injury was alleviated. Upregulating miR-9-5p or downregulating PDCD4 further improved erectile function and cavernous injury in rats. miR-9-5p targeted regulation of PDCD4. *In vitro* cell experiment results showed that Sim induced proliferation and reduced apoptosis of CMSCs by enhancing miR-9-5p-targeted regulating PDCD4 *in vitro*. Sim attenuates DMED in rats via miR-9-5p/PDCD4.

Keywords: Simvastatin, miR-9-5p, PDCD4, Diabetes, Erectile dysfunction

Received: 08 August, 2023; **revised:** 20 May, 2023; **accepted:** 25 June, 2023; **available on-line:** 06 November, 2023

✉ e-mail: catottisina@hotmail.com (JX); wallyxiang@126.com (WL)

#These authors contributed equally to this work

Acknowledgements of Financial Support: This work was funded by the Shanghai Municipal Health Commission's Research Project (Grant Number 202040078). The present study was sponsored by National Natural Science Foundation of China (82001610).

Abbreviations: CMSCs, Cavernous smooth muscle cells; DMED, diabetes mellitus erectile dysfunction; ED, erectile dysfunction; Sim, simvastatin

INTRODUCTION

Erectile dysfunction (ED) is defined as erection failure during sexual intercourse and is a common complication of diabetes (Che *et al.*, 2020). With lifestyle changes and population ages, the incidence rate of ED is increasing (He *et al.*, 2019). The incidence rate of ED in the normal population is 0.1–18%, while that in diabetic patients is nearly 3 times higher (Seftel, 2005). ED can affect physical, emotional, social, sexual, and interpersonal relationships, for which drug therapy is the main treatment, including PDE5 inhibitors, androgen therapy, and vasoactive drugs (Lau *et al.*, 2007). Compared with other treatments, such as intracavernous injection or intraurethral injection of alprostadil, drug treatment is less invasive (Talib *et al.*, 2021). However, the effect of oral medica-

tion on ED is significantly lower (Martínez-Salamanca *et al.*, 2014). Therefore, there is an urgent need to develop new drugs for the treatment of diabetes mellitus erectile dysfunction (DMED).

Statins are 3-hydroxy-3-methylglutaryl CoA reductase inhibitors, which are widely used to reduce cholesterol levels in patients with lipid metabolism disorders. Simvastatin (Sim) is one of the most widely used lipophilic statins (Aschenbrenner *et al.*, 2021) that has therapeutic value in human diseases, such as fracture healing (Hajjalzade *et al.*, 2020), tumorigenesis (Kopacz *et al.*, 2020), hydrocephalus (Chen *et al.*, 2017), Parkinson's disease (Carroll *et al.*, 2017). Sim can alleviate DMED by enhancing autophagy (Ding *et al.*, 2020), but other potential mechanisms of Sim action have not been fully studied.

MicroRNA (miRNA) involves in a variety of disease-related signaling pathways after transcription (Rupaimoole *et al.*, 2017). miR-126-engineered MDSCs can reconstruct blood vessels and repair rat cavernous injury, to reduce ED caused by rat cavernous injury (Zou *et al.*, 2021) and miR-205 is involved in the pathogenesis of DMED (Wen *et al.*, 2019). miR-9-5p has been widely studied in tumors, such as liver cancer (Wang *et al.*, 2020), prostate cancer (Wang *et al.*, 2021), and gastric cancer (Ba *et al.*, 2021). However, the role of miR-9-5p in DMED is not yet clear.

Our research aims to explore the potential mechanism of DMED by targeting miR-9-5p/PDCD4 and provide a new treatment for DMED.

MATERIALS AND METHODS

DMED rat model

The animal treatment complied with the “Experimental Animal Care and Guide” and was approved by the Experimental Animal Ethics Committee of Tongji Hospital, Tongji University School of Medicine, Shanghai (NO.T20116A301). Healthy male SD rats, aged 8 weeks old, were standard fed in a non-pathogenic environment, and blood glucose was tested a week later. After 24 h of fasting, 64 rats were injected with streptozotocin (STZ)-citrate buffer at 60 mg/kg, and the other 6 rats were with citric acid buffer. After that, rats were given normal feeding. At 24 h, 72 h, and 1-week post-injection, blood glucose was assessed and >16.67 mmol/L indicated the induction of diabetes. After 8 w of normal feeding, rats were subcutaneously injected with Apomorphine (APO) at 100 μ g/kg in the neck and placed in the dark for 30 min during which the number of penis erections was re-

corded. A total of 54 DMED rats (rats without erection) were established, and the success rate was 84.4%.

Animal treatment

After modeling, rats were given oral medication with Sim (dissolved in DMSO and physiological saline, 2 mg/kg) or saline, once a day, for 8 days. Meanwhile, 48 DMED rats were intravenously injected with 7.6×10^7 IFU lentivirus (10 mg/kg), carrying miR-9-5p agomir, agomir NC, miR-9-5p antagomir, antagomir NC, si-PDCD4, si-NC, miR-9-5p agomir + oe-PDCD4, and miR-9-5p agomir + oe-NC, respectively. After the last injection, rats were fed ad libitum for 3 days, and body weight and blood glucose were measured. The rats were euthanized to harvest corpus cavernosum which was preserved in liquid nitrogen.

Construction and injection of lentivirus

Plasmid DNA (12.5 µg) and liposomes (9 µL) were diluted in 250 µL of serum-free RPMI1640 medium (R8758, Gibco, CA, USA), respectively, and mixed to form a plasmid-liposome complex which was then added into 293T cells (ATCC, VA, USA). After that, cells were incubated for 6–8 hours, and the whole culture medium was centrifuged at 716 g for 20 min to obtain lentivirus-enriched supernatant. Next, the supernatant was filtered through a 0.45 µm filter, stored at -80°C , and injected into the tail vein of DMED rats.

Evaluation of erectile function in vivo

Rats were anesthetized by intraperitoneal injection of 2% pentobarbital sodium (3 mg/kg). After the separation of the corpus cavernosum, the prostate was exposed and then the left common carotid artery was separated. Intracavernous pressure (ICP) and mean arterial pressure (MAP) to 50-s electrical stimulation were monitored (20 Hz, 5 V, 0.2 ms). The electrode stimulation interval lasted 15 min.

H&E staining

Penile tissue was routinely made into paraffin slices (about 4 µm) for staining with hematoxylin for 5 min and with eosin for 2 min. Afterward, the slices were dehydrated with ethanol, cleared with xylene, and sealed with neutral glue for microscopic observation.

Immunofluorescence

Sections were dewaxed, dehydrated in gradient ethanol, treated overnight with sodium citrate buffer solution (pH 6.0), permeabilized with 0.5% Triton X-100 and incubated at 5% bovine serum albumin. The slices were then treated with primary antibody α -SMA (1:200, millipore sigma) and the secondary antibody combined with Alexa fluor 488 or Alexa fluor 555 (1:200). Next, counter-staining with 4,6-diamidino-2-phenylindole was performed to capture the images under a fluorescence microscope (Olympus, ix83-fv3000, Tokyo, Japan) followed by quantification using ImageJ (v1.8.0, NIH, MD, USA).

TUNEL staining

Apoptosis in the paraffin section was detected by Apop Tag Plus In situ apoptosis Detection kit (Oncor Inc, Gaithersburg) and analyzed under an optical microscope (Nikon, Japan) (Hirfanoglu *et al.*, 2019).

Cell culture

The euthanized DMED rats were sterilized in 75% alcohol, the penis was dissected along the inferior edge of the pubis, and the glans of the penis were collected. The albuginea vessels and urethra were stripped, and the corpus cavernosum was cut into 0.5–1 mm³ pieces and cultured for 5–7 days in a medium containing 20% fetal bovine serum. After 2–3 passages, cavernous smooth muscle cells (CMSCs) were treated with Sim (2 µM) for 24 h.

Cell transfection

CMSCs were transfected with miR-9-5p mimic, mimic NC, miR-9-5p inhibitor, inhibitor NC, sh-NC, sh-PDCD4, miR-9-5p mimic + pcDNA-PDCD4 and miR-9-5p mimic + pcDNA-NC using Lipofectamine 2000 (11668019, Invitrogen). The above plasmid was constructed by Sangon (Shanghai, China) with pEGFP-4.1N (Invitrogen) as the vector.

Cell viability assay

CMSCs proliferation was assessed at 24, 48, and 72 h using cell counting kit-8 (CK04, Dojindo, Kumamoto, Japan) by evaluating the optical density (OD) at 450 nm on a microplate reader.

Flow cytometry

CMSCs apoptosis was measured by annexin V-FITC apoptosis Kit (Abcam, Cambridge, UK) and detected on a flow cytometer (br168323; Luminex, Austin, TX, USA). Data were analyzed by Kaluza C analysis software (Beckman Coulter, CA, USA).

RNA extraction and analysis

Total RNA was extracted with RNeasy Mini Kit (Qiagen, CA, USA), and cDNA was generated with PrimeScript RT reagent Kit (RR047A, Takara, Japan) or miRNA first-strand cDNA synthesis Kit (Sangon). qPCR was performed using SYBR Premix Ex TaqTM II (Perfect Real Time) kit (DRR081, Takara, Japan) and ABI7500 Real-Time PCR system (ABI, Foster City, USA). Glycer-

Table 1. Primer sequences

Genes	Sequences (5'– 3')
miR-9-5p	F: GTGCAGGGTCCGAGGT
	R: GCGCTCTTTGGTTATCTAGC
PDCD4	F: ATGTGGAGGAGGTGGATGTG
	R: TGGTGTTAAAGTCTTCTCAAATGC
PCNA	F: GCCATATTGGAGATGCTGT
	R: TGAGTGTCCACGGTTGAAGA
Bax	F: GATCGAGCAGGGCGAATG
	R: CATCTCAGCTGCCACTCG
U6	F: CTCGCTTCGGCAGCACA
	R: AACGCTTCACGAATTTGCGT
GAPDH	F: CGGAGTCAACGGATTGGTCGTAT
	R: AGCCTTCTCCATGGTGGTGAAGAC

Note: miR-9-5p, microRNA-9-5p; PDCD4, Programmed cell death 4; PCNA, Proliferating cell nuclear antigen; Bax, Bcl-2-associated X; GAPDH, glyceraldehyde 3-phosphate dehydrogenase

aldehyde-3-phosphate dehydrogenase (GAPDH) and U6 were considered internal controls. The primer sequences are shown in Table 1, miRNA negative primers and U6 upstream primers were provided by miRNA first-strand cDNA synthesis (Tailing Reaction) kit. Relative expression levels were calculated using the $2^{-\Delta\Delta Ct}$ method.

Western Blot

Proteins were extracted using RIPA lysis buffer (P0013C, Beyotime, China) and analyzed BCA protein detection kit (20201ES76, Yeasen, Shanghai, China). Proteins were separated by sodium dodecyl sulfate-polyacrylamide gel electrophoresis and then transferred to polyvinylidene fluoride membranes. After blocking with 5% skim milk, membranes were incubated with primary antibodies PDCD4 (1:1000, 9535, Cell Signaling Technology) and GAPDH (1:1000, ab8245, Abcam) and with goat anti-rabbit IgG (ab205718, Abcam) to analyze gray values using ImageJ 1.48u (NIH).

Dual-Luciferase Reporter Experiment

The 3'UTR fragment of PDCD4 and its mutation containing potential miR-9-5p binding site were inserted into the PGLO vector, namely PGLO-PDCD4 wild type (WT) and PGLO-PDCD4 mutant (MUT). The vectors were co-transfected with miR-9-5p mimic and mimic NC into 293T cells, respectively, thereby analyzing luciferase activity using a dual luciferase reporter gene detection system (e1910, Promega, WI, USA).

Data analysis

All data were statistically analyzed by SPSS 21.0 statistical software. Reported as mean \pm standard deviation, the measurement data were compared by independent sample *t*-test if following normal distribution, otherwise by one-way ANOVA and Tukey's multiple comparison post hoc analysis. With $P < 0.05$, the difference was considered to be statistically significant.

RESULTS

Sim can improve ED in DMED rats

Before intraperitoneal injection of STZ, rats showed no significant difference in body weight, blood glucose, or erectile function. Except for 8 rats that died due to STZ, the other 64 diabetic rats and 6 normal rats were subjected to the APO test. Among them, 1-3 erections happened in 10 diabetic rats in 30 min, and no erection in the other 54 diabetic rats. To verify the improvement effect of Sim on DMED rats, DMED rats took Sim orally. Diabetic rats had reduced body weight and increased blood glucose, which could be ameliorated by Sim (Fig. 1A, B). The ICP/MAP values were decreased in diabetic rats and could be restored by Sim (Fig. 1C). Then, we observed the pathological condition of the cavernous by HE staining, which showed that the capillaries of the cavernous sinus contained erythrocytes, which were intertwined in a network. A large number of capillaries were seen in the corpus cavernosum tissue of sham-operated rats while less in diabetic rats; after Sim treatment, the corpus cavernosum injury was relieved (Fig. 1D). Immunofluorescence analysis in the penile cavernous demonstrated that α -SMA expression was decreased in DMED rats; Sim increased α -SMA expression (Fig. 1E, F). In addition, RNA and protein expression analysis revealed that miR-9-5p expression was decreased and PDCD4 expression was increased in DMED rats; after Sim treatment, their expression trends were recovered (Fig. 1G).

miR-9-5p alleviates corpus cavernosum damage in DMED rats

For defining the impacts of miR-9-5p in DMED rats, Sim-treated DMED rats were injected with the lentiviral vector into the tail vein to interfere with miR-9-5p expression (Fig. 2A). Due to miR-9-5p overexpression,

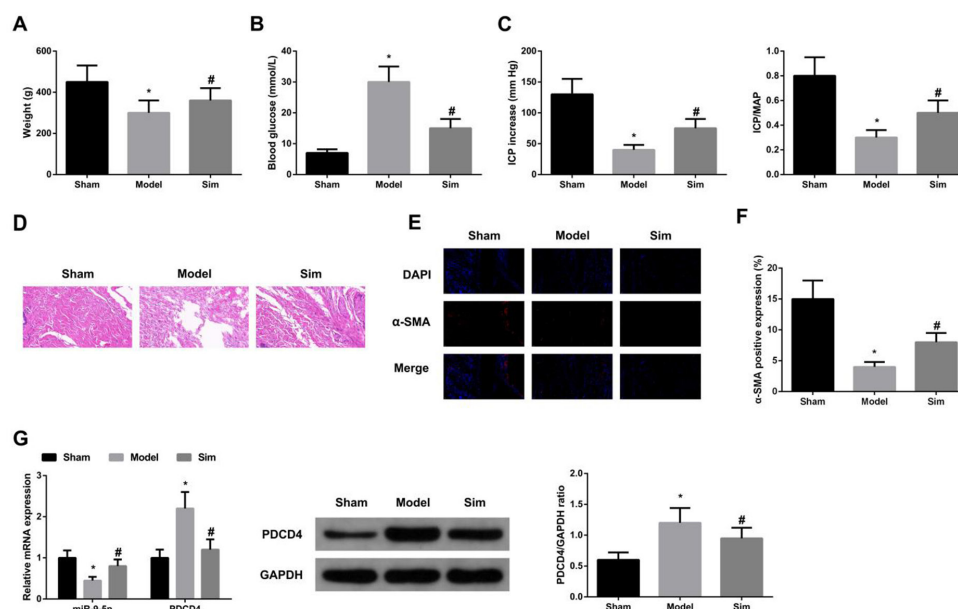


Figure 1. Sim can improve ED in DMED rats

(A–B) Changes in body weight and blood glucose of rats; (C) Erectile function assessment *in vivo*; (D) HE staining; (E–F) immunohistochemical staining for α -SMA; (G) miR-9-5p and PDCD4 expression; values are expressed as mean \pm standard deviation; * $P < 0.05$ vs. Sham group; # $P < 0.05$ vs. Model group.

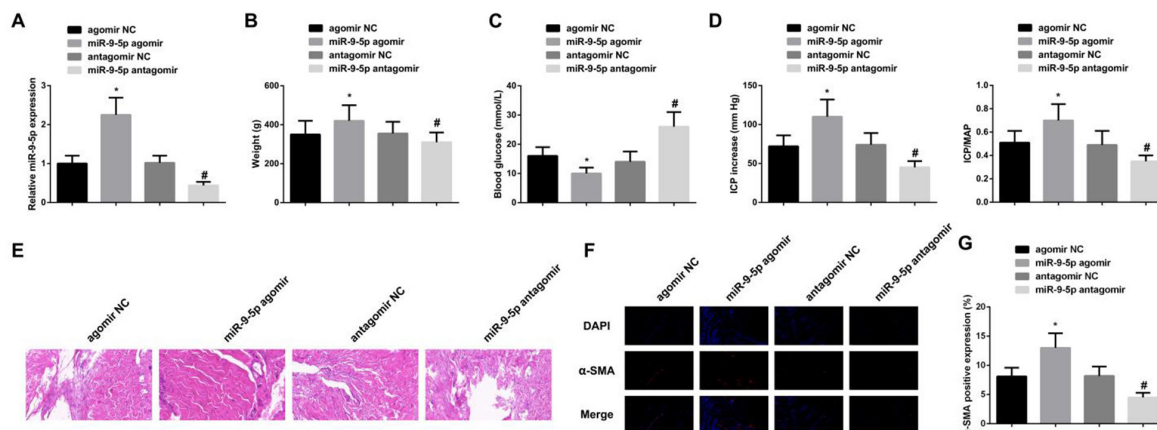


Figure 2. miR-9-5p reduces corpus cavernosum damage in DMED rats.

(A) miR-9-5p expression; (B–C) Changes in body weight and blood glucose of rats; (D) Erectile function assessment *in vivo*; (E) HE staining; (F–G) immunohistochemical staining for α-SMA; values are expressed as mean ± standard deviation; **P* < 0.05 vs. agomir NC group; #*P* < 0.05 vs. antagomir NC group.

rats gained weight, blood glucose decreased, and ICP/MAP values elevated (Fig. 2B–D), the corpus cavernosum damage was alleviated (Fig. 2E), and α-SMA expression was raised (Fig. 2F, G). While miR-9-5p inhibition counter-acted the ameliorating effect of Sim (Fig. 2B–G).

miR-9-5p targets PDCD4

The specific binding site between PDCD4 and miR-9-5p was identified through the bioinformatic website RNA22 (Fig. 3A). The binding of miR-9-5p to PDCD4 was verified by dual-luciferase reporter gene assay based on the experimental result that miR-9-5p mimic induced the impairment of PGLO-PDCD4-WT luciferase activity (Fig. 3B). Analysis of PDCD4 expression indicated that with the change in miR-9-5p expression, PDCD4 expression was altered in an opposite way (Fig. 3C).

Depleting PDCD4 attenuates ED in DMED rats

In Sim-treated DMED rats, a lentiviral vector carrying si-PDCD4 or miR-9-5p agomir + oe-PDCD4 was injected into the tail vein (Fig. 4A). It was verified that si-PDCD4

had the ameliorating effects as miR-9-5p agomir, however, oe-PDCD4 mitigated the protective role of miR-9-5p agomir in Sim-treated DMED rats (Fig. 4B–G).

Sim protects CSMCs *in vitro* by enhancing miR-9-5p and suppressing PDCD4 expression

The regulatory role of Sim through the miR-9-5p/PDCD4 axis was tested using CSMCs. CSMCs were treated with Sim and then transfected. Quantitative PCR detection (Fig. 5A) manifested that Sim treatment elevated miR-9-5p and restrained PDCD4 expression in CSMCs; miR-9-5p mimic and miR-9-5p inhibitor transfection could strengthen and impair Sim-mediated effects; sh-PDCD4 transfection promoted the inhibitory effect of Sim on PDCD4 expression; pcDNA-PDCD4 enhanced the level of PDCD4 that had been suppressed by miR-9-5p mimic. The regulatory effect of Sim on the biological characteristics of CSMCs was investigated, showing that Sim-mediated induction of proliferation and reduction of apoptosis could be further bolstered by overexpressing miR-9-5p or suppressing PDCD4 while impaired by inhibiting miR-9-5p; PDCD4 expression in-

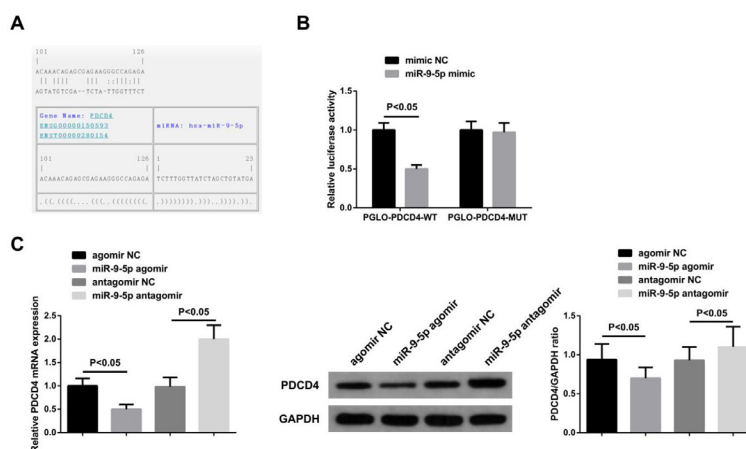


Figure 3. miR-9-5p targets PDCD4

(A) binding site of miR-9-5p and PDCD4; (B) the targeting relationship between miR-9-5p and PDCD4; (C) PDCD4 expression; values are expressed as mean ± standard deviation.

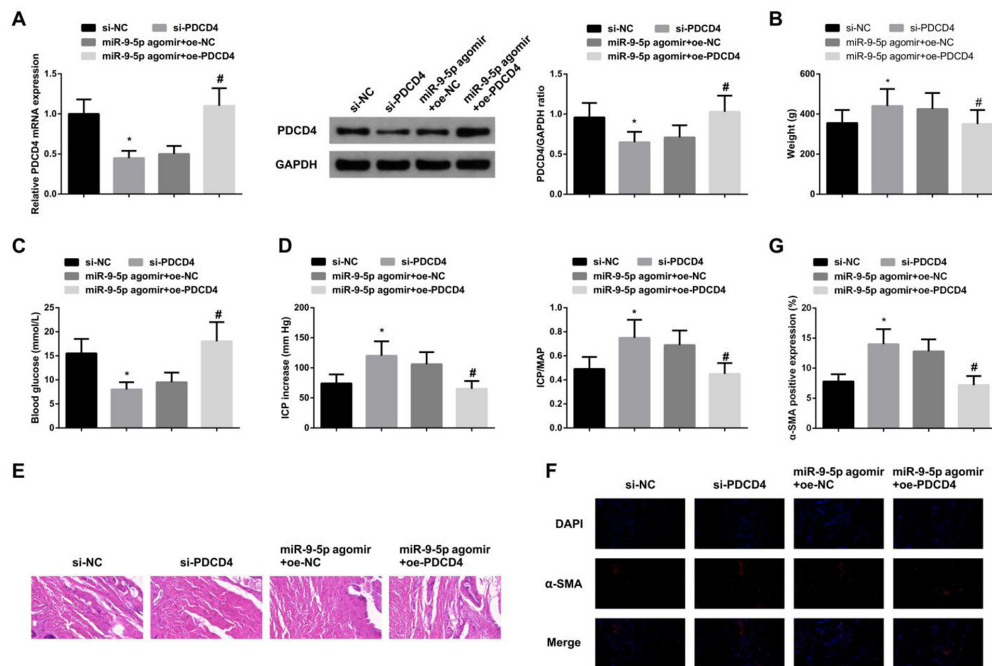


Figure 4. Depleting PDCD4 ameliorates ED in DMED rats

(A) PDCD4 expression; (B–C) Changes in body weight and blood glucose of rats; (D) Erectile function assessment *in vivo*; (E) HE staining; (F–G) immunohistochemical staining for α-SMA; values are expressed as mean ± standard deviation; * $P < 0.05$ vs. si-NC group; # $P < 0.05$ vs. miR-9-5p agomir + oe-NC group.

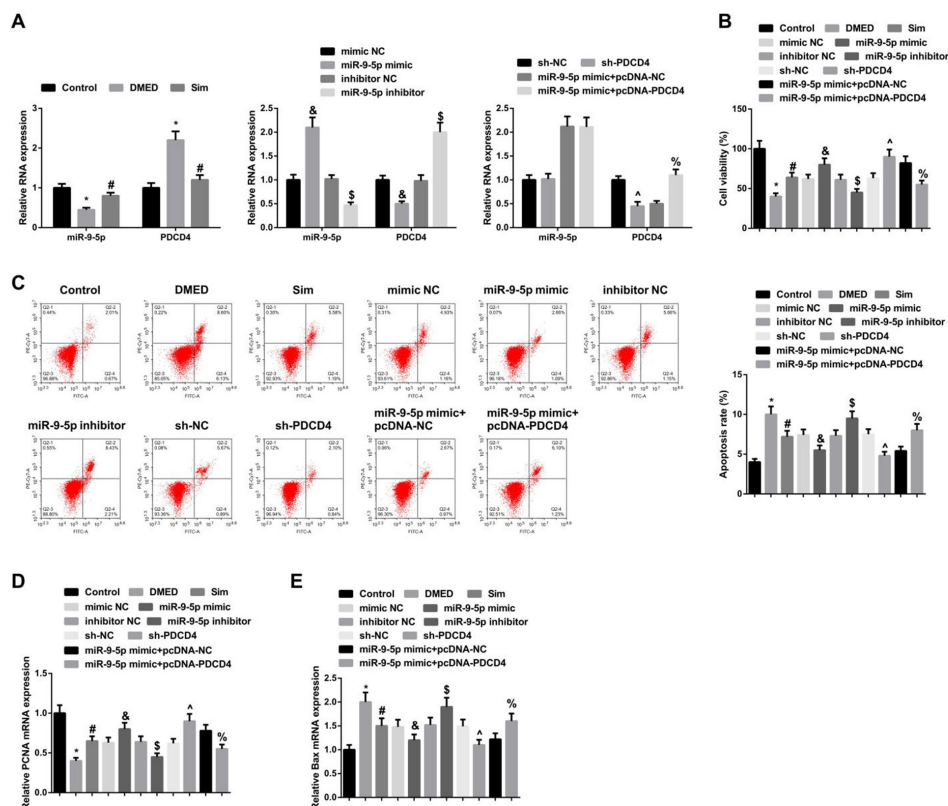


Figure 5. Sim protects CSMCs *in vitro* by enhancing miR-9-5p and suppressing PDCD4 expression

(A) miR-9-5p and PDCD4 expression; (B) cell viability; (C) cell apoptosis; (D–E) PCNA and Bax mRNA expression; values are expressed as mean ± standard deviation; * $P < 0.05$ vs. Control group; # $P < 0.05$ vs. DMED group; % $P < 0.05$ vs. mimic NC group; ^ $P < 0.05$ vs. sh-NC group; & $P < 0.05$ vs. miR-9-5p mimic + pcDNA-NC group.

duction served a blocker for miR-9-5p-mediated protection against anti-proliferation and apoptosis (Fig. 5B, C). As expected, mRNA expression of PCNA and Bax also confirmed the above results (Fig. 5D, E).

DISCUSSION

The number of diabetic patients is increasing every year and DMED affects more than half of men with diabetes (Huo *et al.*, 2020). The pathogenesis of DMED involves a contraction-relaxation imbalance of CSMCs. It has been reported that CSMCs can change their phenotype from a contractile state to a diastolic state under hyperglycemic conditions (Wei *et al.*, 2012). At present, oral drugs are often used in the clinical treatment of ED. Sim, a commonly used cholesterol-lowering drug, has been found to improve ED in patients over the age of 40 (Trivedi *et al.*, 2014). Particularly, our study suggested the therapeutic action of Sim in DMED by miR-9-5p/PDCD4 axis and further provided evidence to verify the therapeutic potential of Sim for DMED.

Bilateral cavernous nerve injury is a cause of ED, leading to profound changes in the penis and damage to CSMCs (Hannan *et al.*, 2014). It has been reported that a sufficient amount of relaxed smooth muscle is required for penile erection, and the lack of smooth muscle can lead to venous occlusive dysfunction that exacerbates the symptoms of ED (Rogers *et al.*, 2003). α -SMA, an important marker of smooth muscle, is downregulated during ED (Cho *et al.*, 2015). It is well known that Sim treatment upregulates α -SMA and enhances erectile function. Erectile function is generally assessed by measuring ICP/MAP and low ICP/MAP is detectable in ED rats (Wang *et al.*, 2019). We constructed an STZ-induced DMED rat model and evaluated it by APO. As the results presented, STZ treatment reduced body weight, ICP/MAP value, and α -SMA expression, increased blood glucose and corpus cavernosum damage, while Sim treatment attenuated the damage of STZ to DMED rats. Furthermore, we determined that Sim exerted its effects by targeting the regulation of the miR-9-5p/PDCD4 axis. To our knowledge, this is the first report that indicates that Sim regulates DMED by regulating miRNA expression.

Some miRNAs are abnormally expressed in the corpus cavernosum of ED rats, including miR-1, miR-200a, miR-203, and miR-206 (Pan *et al.*, 2014). In addition, miR-101a, miR-138, miR-338, and miR-142 are dysregulated in a rat model of bilateral cavernous nerve crush (Liu *et al.*, 2018). The abnormal expression of miR-9-5p is obvious in diabetes and controlling miR-9-5p confers a protection against pyroptosis in the illness (Roshanravan *et al.*, 2020). In addition, miR-9-5p has also been surveyed to affect the biological behavior of smooth muscle cells (Wang *et al.*, 2021). Our paper described for the first time that miR-9-5p was downregulated in DMED rats, and upregulating miR-9-5p could further enhance the ameliorating role of Sim in ED rats and CSMCs while downregulating miR-9-5p resulted in the opposite consequences.

PDCD4 was selected as a downstream target gene of miR-9-5p. PDCD4 is a pro-apoptotic gene that regulates many important cellular processes (Shuvalova *et al.*, 2021) and involves in the progression of ED (Huo *et al.*, 2020). Our research presented that PDCD4 expression was upregulated in DMED rats, and silencing PDCD4 protected DMED rats and CSMCs, but over-expressing PDCD4 mitigated the protection induced by miR-9-5p.

However, the study had limitations. First of all, the sample size of the study was small, and we hope to verify our research results with a larger sample size in the future. Secondly, we only explored the regulatory axis of Sim/miR-9-5p/PDCD4, and other possible regulatory mechanisms of Sim in DMED were not explored. For example, studies have shown that Sim can improve the endothelial function of retinal capillary endothelial cells under high glucose conditions by increasing the expression level of eNOS mRNA and NO production (Tun *et al.*, 2017). NOS is a kind of NO-generating enzyme with three isoforms: nNOS, iNOS, and eNOS (Suksawat *et al.*, 2018). Recently, an increasing number of studies have demonstrated that NO is a critical neurotransmitter in the corpus cavernosum for the mediation of penile erection (Coletto *et al.*, 2018; Li *et al.*, 2017). Evidence from previous studies indicates that OS-induced NO-mediated endothelial dysfunction is a key process in DMED (Castela *et al.*, 2016). Therefore, we hope to further explore NOS-related pathways in future studies and improve the molecular mechanism of simvastatin alleviating DMED.

CONCLUSION

Our study demonstrated that DMED was associated with apoptosis and Sim attenuated DMED by enhancing miR-9-5p-targeted regulation of PDCD4 expression to ameliorate cavernosal injury and apoptosis in CSMCs. Our results provide a reference for Sim as a therapeutic drug for DMED.

Declarations

Acknowledgments. Not applicable.

Competing interests. The authors have no conflicts of interest to declare.

REFERENCES

- Aschenbrenner B, Negro G, Savic D, Sorokin M, Buzdin A, Ganswindt U, Cemazar M, Sersa G, Skvortsov S, Skvortsova I (2021) Simvastatin is effective in killing the radioresistant breast carcinoma cells. *Radiol Oncol* **55**: 305–316. <https://doi.org/10.2478/raon-2021-0020>
- Ba MC, Ba Z, Gong YF, Lin KP, Wu YB, Tu YN (2021) Knock-down of lncRNA ZNRD1-AS1 suppresses gastric cancer cell proliferation and metastasis by targeting the miR-9-5p/HSP90AA1 axis. *Aging (Albany NY)* **13**: 17285–17301. <https://doi.org/10.18632/aging.203209>
- Carroll CB, Wyse RKH (2017) Simvastatin as a potential disease-modifying therapy for patients with Parkinson's disease: rationale for clinical trial, and current progress. *J Parkinsons Dis* **7**: 545–568. <https://doi.org/10.3233/jpd-171203>
- Castela A, Costa C (2016) Molecular mechanisms associated with diabetic endothelial-erectile dysfunction. *Nat Rev Urol* **13**: 266–274. <https://doi.org/10.1038/nrurol.2016.23>
- Che D, Fang Z, Yan L, Du J, Li F, Xie J, Feng J, Yin P, Qi W, Yang Z, Ma J, Yang X, Gao G, Zhou T (2020) Elevated pigment epithelium-derived factor induces diabetic erectile dysfunction via interruption of the Akt/Hsp90 β /eNOS complex. *Diabetologia* **63**: 1857–1871. <https://doi.org/10.1007/s00125-020-05147-y>
- Chen Q, Shi X, Tan Q, Feng Z, Wang Y, Yuan Q, Tao Y, Zhang J, Tan L, Zhu G, Feng H, Chen Z (2017) Simvastatin promotes hematoma absorption and reduces hydrocephalus following intraventricular hemorrhage in part by upregulating CD36. *Transl Stroke Res* **8**: 362–373. <https://doi.org/10.1007/s12975-017-0521-y>
- Cho MC, Park K, Kim SW, Paick JS (2015) Restoration of erectile function by suppression of corporal apoptosis, fibrosis and corporal veno-occlusive dysfunction with rho-kinase inhibitors in a rat model of cavernous nerve injury. *J Urol* **193**: 1716–1723. <https://doi.org/10.1016/j.juro.2014.10.099>
- Coletto E, Dolan JS, Pritchard S, Gant A, Hikima A, Jackson MJ, Benham CD, Chaudhuri KR, Rose S, Jenner P, Iravani MM (2019) Contractile dysfunction and nitregic dysregulation in small intestine

- of a primate model of Parkinson's disease. *NPJ Parkinsons Dis* 5: 10. <https://doi.org/10.1038/s41531-019-0081-9>
- Ding F, Shan C, Li H, Zhang Y, Guo C, Zhou Z, Zheng J, Shen W, Dai Q, Ouyang Q, Wu X (2020) Simvastatin alleviated diabetes mellitus-induced erectile dysfunction in rats by enhancing AMPK pathway-induced autophagy. *Andrology* 8: 780–792. <https://doi.org/10.1111/andr.12758>
- Hajjalizade M, Moghtadaci M, Mirzaei A, Abdollahi Kordkandi S, Babaeidarian P, Pazoki-Toroudi H, Yeganeh A (2020) Significant effect of simvastatin and/or ezetimibe-loaded nanofibers on the healing of femoral defect: An experimental study. *Mater Sci Eng C Mater Biol Appl* 111: 110861. <https://doi.org/10.1016/j.msec.2020.110861>
- Hannan JL, Kutlu O, Stopak BL, Liu X, Castiglione F, Hedlund P, Burnett AL, Bivalacqua TJ (2014) Valproic acid prevents penile fibrosis and erectile dysfunction in cavernous nerve-injured rats. *J Sex Med* 11: 1442–1451. <https://doi.org/10.1111/jsm.12522>
- He J, Li X, Dai HH, Wang JS, Li HS, Zhang XJ, Wang P, Zhang D, Zuo LY, Xie N, Li Y (2019) The safety and efficacy of PDE5-inhibitors-wardenafil on treating diabetes mellitus erectile dysfunction: A protocol for systematic review and meta analysis. *Medicine (Baltimore)* 98: e18361. <https://doi.org/10.1097/md.00000000000018361>
- Hirfanoglu I, Turkylmaz C, Turkylmaz Z, Onal E, Soylemezoglu F, Karabulut R, Atalay Y (2019) Neuroprotective effect of L-arginine in a neonatal rat model of hypoxic-ischemia. *Int J Neurosci* 129: 1139–1144. <https://doi.org/10.1080/00207454.2019.1636794>
- Huo W, Li H, Zhang Y, Li H (2020) Epigenetic silencing of microRNA-874-3p implicates in erectile dysfunction in diabetic rats by activating the Nupr1/Chop-mediated pathway. *Faseb J* 34: 1695–1709. <https://doi.org/10.1096/fj.201902086R>
- Huo W, Li Y, Zhang Y, Li H (2020) Mesenchymal stem cells-derived exosomal microRNA-21-5p downregulates PDCD4 and ameliorates erectile dysfunction in a rat model of diabetes mellitus. *Faseb J* 34: 13345–13360. <https://doi.org/10.1096/fj.202000102RR>
- Kopacz A, Werner E, Grochot-Pręcerek A, Klóska D, Hajduk K, Neumayer C, Józkwicz A, Piechota-Polanczyk A (2020) Simvastatin attenuates abdominal aortic aneurysm formation favoured by lack of Nrf2 transcriptional activity. *Oxid Med Cell Longev* 2020: 6340190. <https://doi.org/10.1155/2020/6340190>
- Kopacz A, Werner E, Grochot-Pręcerek A, Klóska D, Hajduk K, Neumayer C, Józkwicz A, Piechota-Polanczyk A (2007) Gene therapy and erectile dysfunction: the current status. *Asian J Androl* 9: 8–15. <https://doi.org/10.1111/j.1745-7262.2007.00224.x>
- Li R, Cui K, Liu K, Li H, Zhang Y, Liu X, Chen R, Li M, Wang T, Wang S, Liu J, Rao K (2017) Metabolic syndrome in rats is associated with erectile dysfunction by impairing PI3K/Akt/eNOS activity. *Sci Rep* 7: 13464. <https://doi.org/10.1038/s41598-017-12907-1>
- Liu C, Cao Y, Ko TC, Chen M, Zhou X, Wang R (2018) The changes of MicroRNA expression in the corpus cavernosum of a rat model with cavernous nerve injury. *J Sex Med* 15: 958–965. <https://doi.org/10.1016/j.jsxm.2018.05.006>
- Martínez-Salamanca JL, La Fuente JM, Cardoso J, Fernández A, Cuevas P, Wright HM, Angulo J (2014) Nebivolol potentiates the efficacy of PDE5 inhibitors to relax corpus cavernosum and penile arteries from diabetic patients by enhancing the NO/cGMP pathway. *J Sex Med* 11: 1182–1192. <https://doi.org/10.1111/jsm.12477>
- Pan F, Xu J, Zhang Q, Qiu X, Yu W, Xia J, Chen T, Pan L, Chen Y, Dai Y (2014) Identification and characterization of the MicroRNA profile in aging rats with erectile dysfunction. *J Sex Med* 11: 1646–1656. <https://doi.org/10.1111/jsm.12500>
- Rogers RS, Graziottin TM, Lin CS, Kan YW, Lue TF (2003) Intracavernosal vascular endothelial growth factor (VEGF) injection and adeno-associated virus-mediated VEGF gene therapy prevent and reverse venogenic erectile dysfunction in rats. *Int J Impot Res* 15: 26–37. <https://doi.org/10.1038/sj.ijir.3900943>
- Roshanravan N, Alamdari NM, Jafarabadi MA, Mohammadi A, Shabestari BR, Nasirzadeh N, Asghari S, Mansoori B, Akbarzadeh M, Ghavami A, Ghaffari S, Ostadrahimi A (2020) Effects of oral butyrate and inulin supplementation on inflammation-induced pyroptosis pathway in type 2 diabetes: A randomized, double-blind, placebo-controlled trial. *Cytokine* 131: 155101. <https://doi.org/10.1016/j.cyto.2020.155101>
- Rupaimoole R, Slack FJ (2017) MicroRNA therapeutics: towards a new era for the management of cancer and other diseases. *Nat Rev Drug Discov* 16: 203–222. <https://doi.org/10.1038/nrd.2016.246>
- Seftel AD (2005) Erectile dysfunction is strongly linked with decreased libido in diabetic men. *J Urol* 174: 657–658
- Shuvalova E, Egorova T, Ivanov A, Shuvalov A, Biziaev N, Mukba S, Pustogarov N, Terenin I, Alkalaeva E (2021) Discovery of a novel role of tumor suppressor PDCD4 in stimulation of translation termination. *J Biol Chem* 297: 101269. <https://doi.org/10.1016/j.jbc.2021.101269>
- Suksawat M, Techasen A, Namwat N, Boonsong T, Titapun A, Ungarreevittaya P, Yongvanit P, Loilome W (2018) Inhibition of endothelial nitric oxide synthase in cholangiocarcinoma cell lines – a new strategy for therapy. *FEBS Open Bio* 8: 513–522. <https://doi.org/10.1002/2211-5463.12388>
- Talib R, Alnadhari I, Canguen O, Yassin A, Shamsodini A, Alrumaihi K, Al-Ansari A (2021) HbA1c over 8.5% is not predictive of increased infection rate following penile prosthesis implant surgery in diabetic patients with erectile dysfunction. *Andrologia* 53: e14132. <https://doi.org/10.1111/and.14132>
- Trivedi D, Wellsted DM, Collard JB, Kirby M (2014) Simvastatin improves the sexual health-related quality of life in men aged 40 years and over with erectile dysfunction: additional data from the erectile dysfunction and statin trial. *BMC Urol* 14: 24. <https://doi.org/10.1186/1471-2490-14-24>
- Tun T, Kang YS (2017) Effects of simvastatin on CAT-1-mediated arginine transport and NO level under high glucose conditions in conditionally immortalized rat inner blood-retinal barrier cell lines (TR-iBRB). *Micronase Res* 111: 60–66. <https://doi.org/10.1016/j.mvr.2017.01.002>
- Wang HS, Ruan Y, Banie L, Cui K, Kang N, Peng D, Liu T, Wang T, Wang B, Wang G, Shindel AW, Lin G, Lue TF (2019) Delayed low-intensity extracorporeal shock wave therapy ameliorates impaired penile hemodynamics in rats subjected to pelvic neurovascular injury. *J Sex Med* 16: 17–26. <https://doi.org/10.1016/j.jsxm.2018.11.003>
- Wang J, Tan Q, Wang W, Yu J (2020) Mechanism of the regulatory effect of overexpression of circMT01 on proliferation and apoptosis of hepatoma cells via miR-9-5p/NOX4 axis. *Cancer Manag Res* 12: 3915–3925. <https://doi.org/10.2147/cmar.s240719>
- Wang X, Cai J, Zhao L, Zhang D, Xu G, Hu J, Zhang T, Jin M (2021) NUMB suppression by miR-9-5P enhances CD44(+) prostate cancer stem cell growth and metastasis. *Sci Rep* 11: 11210. <https://doi.org/10.1038/s41598-021-90700-x>
- Wang X, Xu R, Chi D, Dai C, Sheng M (2021) Role of NEAT1/MiR-9-5p/SLC26A2 pathway on human airway smooth muscle cell. *Yonsei Med J* 62: 858–867. <https://doi.org/10.3349/ymj.2021.62.9.858>
- Wei AY, He SH, Zhao JF, Liu Y, Liu Y, Hu YW, Zhang T, Wu ZY (2012) Characterization of corpus cavernosum smooth muscle cell phenotype in diabetic rats with erectile dysfunction. *Int J Impot Res* 24: 196–201. <https://doi.org/10.1038/ijir.2012.16>
- Wen Y, Liu G, Zhang Y, Li H (2019) MicroRNA-205 is associated with diabetes mellitus-induced erectile dysfunction via down-regulating the androgen receptor. *J Cell Mol Med* 23: 3257–3270. <https://doi.org/10.1111/jcmm.14212>
- Zou Z, Chai M, Guo F, Fu X, Lan Y, Cao S, Liu J, Tian L, An G (2021) MicroRNA-126 engineered muscle-derived stem cells attenuates cavernosa injury-induced erectile dysfunction in rats. *Aging (Albany NY)* 13: 14399–14415. <https://doi.org/10.18632/aging.203057>

Effect of artemisinin combined with allicin on improving cardiac function, fibrosis and NF- κ B signaling pathway in rats with diabetic cardiomyopathy

Lingjuan Kong✉, Xiaoqing Ji, Yan Liu and YingJie Du

Chengde Medical College, College of Traditional Chinese Medicine, Shuangqiao District, Chengde, Hebei, 067050 China

Myocardial fibrosis and inflammation cause cardiac hypertrophy, arrhythmias, and heart failure in diabetics, a leading cause of mortality. Since it's complicated, no drug treats diabetic cardiomyopathy. This research examined the effects of artemisinin and allicin on heart function, myocardial fibrosis, and the nuclear factor kappa-light-chain-enhancer of activated B cells (NF- κ B) signaling pathway in diabetic cardiomyopathy rats. A total of 50 rats were separated into 5 groups, 10 of which were the control group. 40 rats received 65 μ g/g streptozotocin intraperitoneally. 37 of 40 animals fit the investigation. The artemisinin, allicin, and artemisinin/allicin groups each included nine animals. The artemisinin group received 75 mg/kg of artemisinin, the allicin group received 40 mg/kg of allicin, and the combination group received equal dosages of artemisinin and allicin gavage for four weeks. After the intervention, in each group cardiac functions, myocardial fibrosis, and NF- κ B signaling pathway protein expression were assessed. All of the examined groups had greater levels of LVEDD, LVESD, LVEF, FS, E/A, and the NF- κ B pathway proteins: NF- κ B p65 and p-NF- κ B p65 than the normal group, except for the combination group. Artemisinin and allicin did not vary statistically. Compared to the model group, the artemisinin, allicin, and combined groups showed various degrees of improvement from the pathological pattern, with more intact muscle fibers, neater arrangement, more normal cell morphology, artemisinin and allicin alleviated cardiac dysfunction and decreased myocardium fibrosis in diabetic cardiomyopathy rats by inactivating the NF- κ B signaling cascade.

Keywords: artemisinin, allicin, diabetic cardiomyopathy, cardiac function, myocardial fibrosis, nuclear factor- κ B

Received: 25 February, 2023; **revised:** 06 March, 2023; **accepted:** 09 March, 2023; **available on-line:** 12 June, 2023

✉e-mail: konglingjuan09@163.com

Abbreviations: DC, Diabetic cardiomyopathy; DM, Diabetes mellitus; FAC, Fractional area change; FS, Fractional shortening; H&E, Hematoxylin and Eosin; iNOS, Inducible nitric oxide synthase; IkB- α , Inhibitory protein kappa B alpha; LVEDD, Left ventricular end-diastolic internal diameter; LVEF, Left ventricular ejection fraction; LVESD, Left ventricular end-systolic internal diameter; MOG, Myelin oligodendrocyte glycoprotein; NF- κ B, Nuclear factor kappa-light-chain-enhancer of activated B cells

INTRODUCTION

Diabetic cardiomyopathy (DC) is a primary cause of mortality in people with diabetes mellitus (DM) and is characterized by myocardial fibrosis and myocardial inflammation, with cardiac hypertrophy, arrhythmias, and

heart failure as the main manifestations (Dillmann, 2019). DC is complex and involves several factors, so there is no specific drug to treat this disease. Allicin, the active component of garlic (*Allium sativum*), has been clinically shown to have an anti-cardiac fibrosis effect, and it has been reported that allicin is effective in diabetic cardiomyopathy, but a single drug may not completely inhibit the progression of diabetic cardiomyopathy (Liu *et al.*, 2021). Artemisinin belongs to the extract of the Chinese herb *Artemisia annua*, which was found to attenuate myocardial fibrosis and ventricular remodeling *via* inhibition of the cascade of nuclear factor kappa-light-chain-enhancer of activated B cells (NF- κ B) (Gu *et al.*, 2012).

Artemisinin has recently been found to decrease inducible nitric oxide synthase (iNOS) generation and NF- κ B stimulation in human astrocytoma T67 cells. SM933, an artemisinin derivative, has been reported to suppress NF- κ B activity by blocking its breakdown through overexpression of its inhibitory protein kappa B alpha (IkB- α) and MOG-reactive splenocytes (Zhang *et al.*, 2020). Combined, these findings suggest that artemisinin may have a role in immunological modulation and inflammation reduction. The effects of the anti-inflammatory properties of artemisinin on microglial activation are not clear (Kim *et al.*, 2019). The current study was carried out to assess the maximum extent of inhibition of diabetic cardiomyopathy development and the reduction of fibrosis and regulation of the NF- κ B cascade by a combination of allicin and artemisinin.

MATERIALS AND METHODS

Study area

The present study was carried out at the Chengde Medical College, College of Traditional Chinese Medicine from January to April 2022.

Main reagents

Streptozotocin (Beijing Ita Biotechnology Co., Ltd.), artemisinin (Nanjing Guangrun Biological Products Co., Ltd.), allicin (Zhengda Tianqing Group Co., Ltd.), NF- κ B p65, p-NF- κ B p65 antibody (primary) (Abcam, USA).

Animals study

In this study, 50 SPF pure standard Wistar male rats (6–8 weeks old, 220 \pm 20 g) were received from Hangzhou Qizhen Research Animal Technology Co., China. In this study, 7 days of acclimatization under constant temperature (22 \pm 2°C), humidity (55 \pm 5%), and artificial

12 hrs light and dark cycle. All were free to move, drink, and take food. Chengde Medical College, College of Traditional Chinese Medicine ethics committee gave its approval to carry out this investigation (approval number: FEH83456).

Modeling and intervention

In total, 50 animals ($n=50$, 16-week-old) were used in this study, of which 10 were chosen as the normal group. The remaining 40 animals were given a single injection of 65 g/kg streptozotocin intraperitoneally, and their blood glucose levels were evaluated one week later. If the blood glucose value was ≥ 16.7 mmol/L and there were polyuria, polydipsia, and polyphagia, then the modelling of diabetes was successful (Togashi *et al.*, 2016). Streptozotocin was administered to 40 animals, and these animals were successfully established as a model of diabetes. They were fed by standard fodder until 16 weeks, and 3 animals were detected by ultrasound as not having developed cardiomyopathy, and the remaining animals ($n=37$) were successfully established as diabetic cardiomyopathy models.

Experimental design

- Normal group: without treatment ($n=10$);
- Model group: saline treatment (10 μ L) ($n=10$);
- Artemisinin group: 75 mg/kg of artemisinin ($n=9$);
- Allicin group: 40 mg/kg of allicin ($n=9$);
- Artemisinin and allicin groups: 75 mg/kg of artemisinin+ 40 mg/kg of allicin ($n=9$).

All of these groups were treated continuously for 4 weeks, and the changes in experimental indexes in each group were observed after 20 weeks.

Measurement of cardiac function

After the last pharmacological intervention, echocardiographic parameters were taken by using a 7.5-MHz transducer (Toshiba Co., Japan) in each group to determine changes in cardiac function, and left ventricular end-diastolic internal diameter (LVEDD), left ventricular end-systolic internal diameter (LVESD), left ventricular ejection fraction (LVEF), and short-axis shortening (FS) measurements were utilized to examine alteration in cardiac function, maximum mitral valve velocity in early dilatation (E), and maximum atrial systolic velocity (A) ratio. Echocardiographic measures were collected from grayscale M-mode images captured in the parasternal short-axis perspective at the mid-papillary level, as well as from B-mode images recorded in the parasternal long- and short-axis views. End-diastolic diameter (LVEDD), end-systolic diameter, anterior and posterior wall thicknesses, FS, wall thickening, fractional area change (FAC), end-systolic and end-diastolic volumes, EF, and LV mass were all traditional LV measures.

Table 1. Comparison of cardiac function in each group ($\bar{x} \pm s$)

Group	LVEDD (mm)	LVESD (mm)	LVEF (%)	FS (%)	E/A
Normal group ($n=10$)	5.70 \pm 0.11	2.20 \pm 0.08	78.75 \pm 2.31	57.54 \pm 2.10	2.23 \pm 0.12
Model group ($n=10$)	7.00 \pm 0.23*	4.65 \pm 0.10*	63.32 \pm 2.45*	36.55 \pm 1.04*	1.30 \pm 0.09*
Artemisinin group ($n=9$)	6.51 \pm 0.11*#	4.00 \pm 0.14*#	66.75 \pm 2.11*#	40.62 \pm 1.33*#	1.55 \pm 0.10*#
Allicin group ($n=9$)	6.48 \pm 0.11*#	4.03 \pm 0.16*#	66.98 \pm 2.09*#	40.55 \pm 1.54*#	1.58 \pm 0.11*#
Combined group ($n=9$)	6.00 \pm 0.10*#&Δ	2.98 \pm 0.09*#&Δ	73.42 \pm 2.76*#&Δ	53.39 \pm 2.13*#&Δ	2.07 \pm 0.13*#&Δ

Note: "*" indicates significant comparison with the normal group; "#" indicates significant comparison with the model group; "&" indicates significant comparison with the artemisinin group; "Δ" indicates meaningful comparison with the allicin group.

Observation of myocardial fibrosis

After the completion of cardiac function measurement, rapid sacrifice of rats, preparation of myocardial tissue, tissue sectioning and then Hematoxylin and Eosin (H&E) staining, Masson staining, and microscopic observation of myocardial fibrotic lesions were performed in each group. After soaking in 4% neutral formalin solution for 24 h, all tissues were promptly cut and stained with Masson's trichrome kit (Sigma-Aldrich, USA). On each slide, three sections were examined, and each region was divided into 100 squares. Collagen points (blue stains) were scored as 1 (existent) or 0 (absence). The findings are presented as a proportion of the total region covered by fibrosis.

NF-κB signaling cascade protein expression measurement

The expression of the NF-κB signaling pathway proteins NF-κB p65 and p-NF-κB p65 was determined using the Western blot technique. Myocardial tissue was obtained, 80 μ L of lysis buffer was added, tissue protein was extracted, and 50 mg of the resulting protein were mixed with 2 \times SDS loading buffer. Following electrophoresis, 15% denaturing gels were prepared according to the method of Summer and others (Summer *et al.*, 2009). In this study, membrane transfer, and antisera binding, NF-κB p65 and p-NF-κB p65 primary antibodies diluted at a 1:1000 ratio in TBST buffer were used, and the cells were maintained at 4°C. After 1 day, the TBST buffer was washed, an HRP-labeled secondary antibody was applied, and the membrane was rinsed. The diaminobenzidine technique was utilised for colour development, and GAPDH was employed as an internal reference to get the protein expression of NF-κB p65 and p-NF-κB p65.

Statistical analysis

The SPSS 22.0 statistical tool (V13.0; SPSS, Inc., USA) was employed to evaluate the data, and one-way ANOVA was utilised to examine variance between groups. For two-by-two comparisons among groups, the LSD-t test was utilized. After natural logarithm transformation and non-parametric test, the data did not adhere to normally distributed and were expressed as M (Qn) for data comparison. The threshold of significance was fixed at $p<0.05$.

RESULTS

Assessment of cardiac function in each group

The model group, artemisinin group, allicin group, and combined group had greater LVEDD, LVESD,

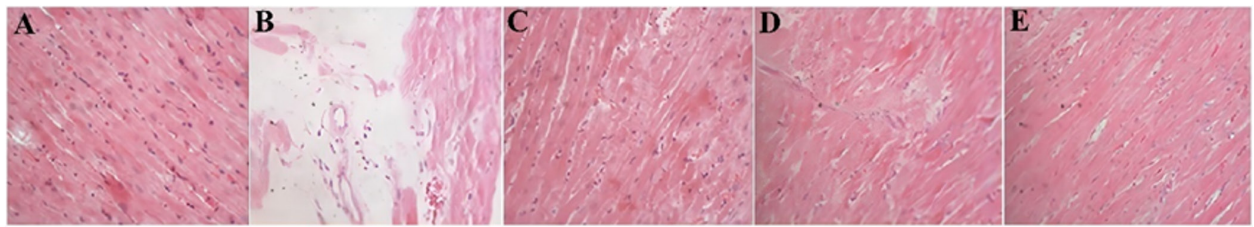


Figure 1. HE staining observation of myocardial tissue ($\times 200$)

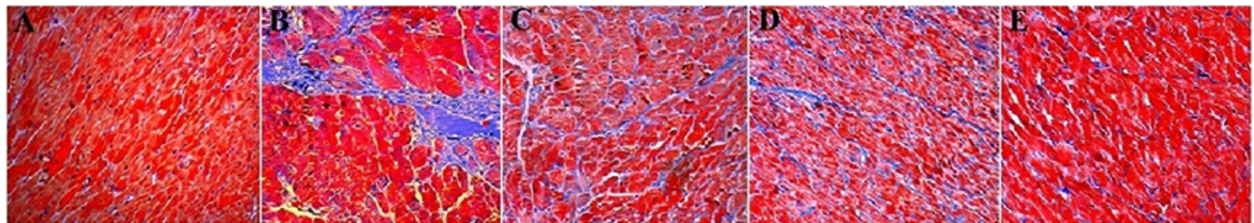


Figure 2. Myocardial tissue Masson staining observation map ($\times 200$)

Note: A, Normal group; B, Model group; C, Artemisinin group; D, Allicin group; E, Combination group

LVEF, FS, E/A, etc. and cardiac function indexes than the normal control, and the variation was statistically relevant ($p < 0.05$). The cardiac function indicators LVEDD, LVESD, LVEF, FS, and E/A were decreased in the artemisinin group, allicin group, and combined group compared to the model group, and the change was statistically significant ($p < 0.05$). The cardiac performance parameters LVEDD, LVESD, LVEF, FS, and E/A were lower in the combination group compared to artemisinin and allicin groups, with significant variations ($p < 0.05$). There was no discernible difference between the groups treated with artemisinin and allicin in terms of LVEDD, LVESD, LVEF, FS, E/A, and the cardiac function indices ($p > 0.05$). For further details, see Table 1.

Myocardial fibrosis observation

Microscopic analysis of animal cardiac tissues revealed that myocardium cells in the normal group were in a healthy condition, but a minor quantity of collagen fibres and no pathological alterations were observed. The collagen fibres multiplied and structured themselves into a network in the model group, which led to many fibrous scar formations, cardiomyocyte enlargement, uneven staining, nucleus consolidation, fragmentation, and even disappearance. Myocardial fibrosis was dramatically reduced in each treatment group as compared to the model group, cell morphology was gradually recovered and staining was more uniform, and myofibers tended to be intact, in comparison to the artemisinin and allicin groups, pathological alterations were more clearly restored in the combination group (Figs 1 and 2).

Comparison of NF- κ B signaling pathway protein expression among groups

The model group, artemisinin group, allicin group, and combined group had increased expression of NF- κ B p65 and p-NF- κ B p65, the NF- κ B signaling pathway proteins, then the normal group, in which the variation was statistically relevant ($p < 0.05$). The proteins of the NF- κ B signaling pathway, NF- κ B p65 and p-NF- κ B p65, were expressed at lower levels in the artemisinin, allicin, and combination groups than in the model group, and the difference was statistically significant ($p < 0.05$). The combined group had lower levels of

NF- κ B p65 and p-NF- κ B p65, the NF- κ B signaling pathway proteins, than the artemisinin and allicin groups, and

Table 2. Protein expression of the NF- κ B signaling pathway in different groups

Group	NF- κ B p65	p-NF- κ B p65
Normal group (n=10)	0.35 \pm 0.04	0.56 \pm 0.07
Model group (n=10)	1.89 \pm 0.22*	1.93 \pm 0.24*
Artemisinin group (n=9)	1.03 \pm 0.15 [#]	1.12 \pm 0.15 [#]
Allicin group (n=9)	1.06 \pm 0.12 [#]	1.14 \pm 0.13 [#]
Combination group (n=9)	0.70 \pm 0.08 ^{##Δ}	0.88 \pm 0.09 ^{##Δ}

Note: "*" indicates significant comparison with the normal group; "[#]" indicates significant comparison with the model group; "^g" indicates significant comparison with the artemisinin group; "^Δ" indicates significant comparison with the allicin group.

the variation was statistically significant ($p < 0.05$). There were no substantial changes in the expression of NF- κ B, p65 and p-NF- κ B, p65, the NF- κ B signaling pathway proteins, between the artemisinin and allicin groups ($p > 0.05$). More data was shown in Table 2.

DISCUSSION

Allicin causes cell death and limits cell growth in mammalian cell lines, including cancer cells, by reacting redox with thiol groups in glutathione and proteins, inhibiting bacterial and fungal proliferation or killing them completely in a dose-dependent manner. Allicin has a number of health-promoting qualities, including effects on cholesterol and blood pressure that are beneficial to the cardiovascular system. According to Kuo and others (Kuo *et al.*, 2013), allicin seems to prevent high-glucose-induced cardiomyocyte apoptosis *via* reducing NADPH oxidase-related ROS and its subsequent NF- κ B signaling, and may have therapeutic potential for diabetic cardiomyopathy.

Artemisinin belongs to the sesquiterpene lactones with peroxy bridges, which were first used in the treatment of malaria and have anticancer, antiviral, antiparasitic *in vitro* and *in vivo* anti-inflammatory properties, in addition

to their antimalarial effects (Ma *et al.*, 2020; Talman *et al.*, 2019). With extensive clinical studies on artemisinin, it has been found that it can alter fibrosis *via* several pathways, such as TGF β , MAPK, Wnt/catenin, PI3K/AKT/mTOR, FRX and Notch, NF- κ B signaling pathways, as well as BMP-7 and cellular autophagy, which contribute to the anti-fibrotic process, as does its anti-inflammatory effect (Li *et al.*, 2019; Dolivo *et al.*, 2021).

The results of this paper showed that compared with artemisinin and allicin alone, the cardiac function of rats with the combined administration of both interventions improved more significantly. In HE and Masson staining, it was found that the myocardium of rats with diabetic cardiomyopathy showed obvious fibrosis, as well as the severity of cardiac fibrosis was relieved after the intervention of artemisinin and allicin, the myocardial fibers were more intact and neatly arranged, the cell morphology tended to be normal, and the staining was more homogeneous, but the improvement was more obvious with artemisinin combined with allicin, indicating that the myocardial damage was more serious in the occurrence of diabetic cardiomyopathy, and the cardiac function of rats with artemisinin and allicin administration improved significantly and the myocardial fibrosis was relieved.

The myocardial structure is altered when the animal cells are under prolonged hyperglycemia, and the NF- κ B signaling cascade is initiated during this process. NF- κ B is secreted by vascular endothelium, vascular smooth muscle cells, etc.; this is a nuclear transcription factor that degrades IB with the help of inflammatory mediators, turns on and activates NF- κ B, and when NF- κ B is activated it can increase the binding to nuclear DNA to some extent, which in turn acts on cardiomyocyte behavior and leads to apoptosis (Youssef *et al.*, 2021; Yao *et al.*, 2021; Tang *et al.*, 2018). In addition, NF- κ B activates inflammatory cytokines including interleukins and tumor necrosis factor and further circulates to activate NF- κ B itself, amplifying the local cascade response in this circulatory pattern and promoting the progression of myocardial injury (Yang *et al.*, 2018; Jin *et al.*, 2020; Ni *et al.*, 2020). The effects on the NF- κ B signaling pathway in diabetic cardiomyopathy rats were examined in this work. Transartemisinin combined with allicin reduced NF- κ B p65 expression and NF- κ B p65 phosphate activation level in diabetic cardiomyopathy rats, which inhibited over-activation of the NF- κ B signaling pathway, enhanced cardiac function, and reduced the degree of myocardial fibrosis, according to the findings. In summary, the present study found a rat model of diabetic cardiomyopathy and confirmed that artemisinin combined with allicin intervention improved cardiac function, myocardial fibrosis and NF- κ B signaling pathway in diabetic cardiomyopathy rats, implying that artemisinin conjunction with allicin intervention may perform a role in improving cardiac functions and inhibiting myocardial fibrosis via the NF- κ B signaling pathway, which has positive implications. However, this study also has its limitation in that the development of diabetic cardiomyopathy is associated with multiple factors and involves several mechanisms and further studies are needed regarding whether both act *via* other pathways.

CONCLUSION

Myocardial fibrosis and inflammation cause cardiac hypertrophy, arrhythmias, and heart failure in diabetics, a leading cause of mortality. Since it is complicated, no

drug treats diabetic cardiomyopathy. Therefore, there is a need to find a solution to this problem. This study was carried out to determine the effectiveness of artemisinin and allicin on heart function, myocardial fibrosis, and the nuclear factor kappa-light-chain-enhancer of activated B cells signaling pathway in diabetic cardiomyopathy rats. According to the findings of the study, artemisinin combined with allicin improved cardiac dysfunction and reduced myocardial fibrosis in rats with diabetic cardiomyopathy, and both may act *via* promoting the inactivation of NF- κ B signaling cascade.

Declarations

Acknowledgements. The authors acknowledge the facilities offered by the department higher authorities.

Data availability. The information used to justify this investigation is provided upon request.

Conflicts of interest. The authors state that they do not have any conflicts of interest.

Funding. This investigation did not obtain any funding.

REFERENCES

- Dillmann WH (2019) Diabetic Cardiomyopathy. *Circ Res* **124**: 1160–1162. <https://doi.org/10.1161/CIRCRESAHA.118.314665>
- Dolivo D, Weathers P, Dominko T (2021) Artemisinin and artemisinin derivatives as anti-fibrotic therapeutics. *Acta Pharm Sin B* **11**: 322–339. <https://doi.org/doi:10.1016/j.apsb.2020.09.001>
- Gu Y, Wang X, Wang X, Yuan M, Wu G, Hu J, Tang Y, Huang C (2012) Artemisinin attenuates post-infarct myocardial remodeling by down-regulating the NF- κ B Pathway. *Toboku J Exp Med* **227**: 161–170. <https://doi.org/10.1620/tjem.227.161>
- Jin W, Zhang Y, Xue Y, Han X, Zhang X, Ma Z, Sun S, Chu X, Cheng J, Guan S, Li Z, Chu L (2020) Crocin attenuates isoprenaline-induced myocardial fibrosis by targeting TLR4/NF- κ B signaling: connecting oxidative stress, inflammation, and apoptosis. *Naunyn-Schmiedeberg's Arch Pharmacol* **393**: 13–23. <https://doi.org/10.1007/s00210-019-01704-4>
- Kim SH, Zhang Z, Moon YJ, Park IW, Cho YG, Jeon R, Park BH (2019) SPA0355 prevents ovariectomy-induced bone loss in mice. *Korean J Physiol Pharmacol* **23**: 47–54. <https://doi.org/10.4196/kjpp.2019.23.1.47>
- Kuo WW, Wang WJ, Tsai CY, Way CL, Hsu HH, Chen LM (2013) Diallyl trisulfide (DATS) suppresses high glucose-induced cardiomyocyte apoptosis by inhibiting JNK/NF- κ B signaling *via* attenuating ROS generation. *Int J Cardiol* **168**: 270–280. <https://doi.org/10.1016/j.ijcard.2012.09.080>
- Li L, Luo W, Qian Y, Zhu W, Qian J, Li J, Jin Y, Xu X, Liang G (2012) Luteolin protects against diabetic cardiomyopathy by inhibiting NF- κ B-mediated inflammation and activating the Nrf2-mediated antioxidant responses. *Phytomedicine* **59**: 152774. <https://doi.org/10.1016/j.phymed.2018.11.034>
- Liu M, Yang P, Fu D, Gao T, Deng X, Shao M, Liao J, Jiang H, Li X (2021) Allicin protects against myocardial I/R by accelerating angiogenesis via the miR-19a-3p/PI3K/AKT axis. *Aging (Albany NY)* **13**: 22843–22855. <https://doi.org/10.18632/aging.203578>
- Ma N, Zhang Z, Liao F, Jiang T, Tu Y (2020) The birth of artemisinin. *Pharmacol Ther* **216**: 107658. <https://doi.org/10.1016/j.pharmthera.2020.107658>
- Ni SY, Zhong XL, Li ZH, Huang DJ, Xu WT, Zhou Y, Ou CW, Chen MS (2020) Puerarin alleviates lipopolysaccharide-induced myocardial fibrosis by inhibiting PARP-1 to prevent HMGB1-mediated TLR4/NF- κ B signaling pathway. *Cardiovasc Toxicol* **20**: 482–491. <https://doi.org/10.1007/s12012-020-09571-9>
- Talman AM, Clain J, Duval R, Ménard R, Arieu F (2019) Artemisinin bioactivity and resistance in malaria parasites. *Trends Parasitol* **35**: 953–963. <https://doi.org/10.1016/j.pt.2019.09.005>
- Tang SG, Liu XY, Ye JM, Hu TT, Yang YY, Han T, Tan W (2018) Isosteviol ameliorates diabetic cardiomyopathy in rats by inhibiting ERK and NF- κ B signaling pathways. *J Endocrinol* **238**: 47–60. <https://doi.org/10.1530/JOE-17-0681>
- Togashi Y, Shirakawa J, Okuyama T, Yamazaki S, Kyohara M, Miyazawa A, Suzuki T, Hamada M, Terauchi Y (2016) Evaluation of the appropriateness of using glucometers for measuring the blood glucose levels in mice. *Sci Rep* **6**: 25465. <https://doi.org/10.1038/srep25465>
- Yang L, Peng C, Xia J, Zhang W, Tian L, Tian Y, Yang X, Cao Y (2018) Effects of icarisiside II ameliorates diabetic cardiomyopathy in

- streptozotocin-induced diabetic rats by activating Akt/NOS/NF- κ B signaling. *Mol Med Rep* **17**: 4099–4105. <https://doi.org/10.3892/mmr.2017.8342>
- Yao J, Li Y, Jin Y, Chen Y, Tian L, He W (2021) Synergistic cardioprotection by tilianin and syringin in diabetic cardiomyopathy involves interaction of TLR4/NF- κ B/NLRP3 and PGC1 α /SIRT3 pathways. *Int Immunopharmacol* **96**: 107728. <https://doi.org/10.1016/j.intimp.2021.107728>
- Youssef ME, Abdelrazek HM, Moustafa YM (2021) Cardioprotective role of GTS-21 by attenuating the TLR4/NF- κ B pathway in streptozotocin-induced diabetic cardiomyopathy in rats. *Naunyn-Schmiedeberg's Arch Pharmacol* **394**: 11–31. <https://doi.org/10.1007/s00210-020-01957-4>
- Zhang C, Fortin PY, Barnoin G, Qin X, Wang X, Fernandez Alvarez A, Bijani C, Maddelein ML, Hemmert C, Cuvillier O, Gornitzka H (2020) An artemisinin-derivative-(NHC) Gold(I) hybrid with enhanced cytotoxicity through inhibition of NRF2 transcriptional activity. *Angew Chem Int Ed* **59**: 12062–12068. <https://doi.org/10.1002/anie.202002992>

Overexpression of long non-coding RNA GASL1 induces apoptosis and G₀/G₁ cell cycle arrest in human oral cancer cells

Rui Zhang¹, Wanjun Tao² and Lei Yu¹✉

¹Department of Pharmacy, West China Hospital, Sichuan University, Chengdu, 610041 China; ²Department of Pharmacy, Chengdu Women's and Children's Central Hospital, School of Medicine, University of Electronic Science and Technology of China, Chengdu 611731, China

Oral cancer is one of the commonly reported malignancies of the human oral cavity and pharynx. It accounts for a significant level of cancer-based mortality across the globe. Long non-coding RNAs (lncRNAs) are emerging as important study targets in cancer therapy. The present study aimed to characterize the role of lncRNA GASL1 in regulating the growth, migration, and invasion of human oral cancer cells. The qRT-PCR showed significant ($P<0.05$) upregulation of GASL1 in oral cancer cells. Overexpression of GASL1 led to the loss of viability of HN6 oral cancer cells by inducing apoptosis which was associated with upregulation of Bax and downregulation of Bcl-2. The apoptotic cell percentage increased from 2.81% in control to 25.89% upon GASL1 overexpression. Cell cycle analysis showed that overexpression of GASL1 increased the G₁ cells from 35.19% in control to 84.52% upon GASL1 overexpression indicative of G₀/G₁ cell cycle arrest. Cell cycle arrest was also accompanied by inhibition of cyclin D1 and CDK4 protein expression. Wound healing and transwell assays showed that overexpression of GASL1 significantly ($P<0.05$) inhibited the migration and invasion of HN6 oral cancer cells. The invasion of the HN6 oral cancer cells was found to be decreased by more than 70%. Finally, the results of *in vivo* study revealed that GASL1 overexpression inhibits the xenografted tumor growth *in vivo*. Thus, the results are thus suggestive of the tumor-suppressive molecular role of GASL1 in oral cancer cells.

Keywords: oral cancer, long non-coding RNA, GASL1, apoptosis, metastasis, prognosis

Received: 15 January, 2023; revised: 02 March, 2023; accepted: 17 April, 2023; available on-line: 12 June, 2023

✉e-mail: leiyou0092@gmail.com

Acknowledgements of Financial Support: This study was supported by West China Hospital, Sichuan University, Chengdu, China (under project No: SU/2021/33).

Abbreviations: CDK4, Cyclin-dependent kinase-4; cDNA, Complementary DNA; DAPI, 4',6-diamidino-2-phenylindole; DMEM, Dulbecco's modified Eagle's medium; EdU, 5-ethynyl-2'-deoxyuridine; FBS, Fetal bovine serum; lncRNAs, Long non-coding RNAs; ncRNAs, Non-coding RNAs; OSCC, Oral squamous cell carcinoma; PVDF, Polyvinylidene difluoride membranes; qRT-PCR, Quantitative real time polymerase chain reaction

the most dominant type of oral cancer which is often detected at advanced stages and exhibits poor prognosis (Meng *et al.*, 2021; Panarese *et al.*, 2019). In addition, this neoplastic disorder is linked with lymph node metastasis (Panarese *et al.*, 2019). OSCC is highly lethal owing to the invasion of cancer to distant body parts (Peng *et al.*, 2020). The currently applied chemotherapy is often reported to exhibit less soothing clinical results. Moreover, it is linked with a number of side effects negatively affecting overall human health. Pertinent to this backdrop, there is vast scope for the development of efficient and reliable prognostic and therapeutic targets against oral cancer.

The non-coding RNAs (ncRNAs) have attained considerable research attention over the past years. Several studies have put forward that ncRNAs exhibit frequent involvement in tumorigenesis of different types of human cancers including oral cancer (Yi *et al.*, 2019; Irimie *et al.*, 2017). Long non-coding RNAs (lncRNAs), a subclass of single-stranded ncRNAs with an average size of more than 200 nucleotides, are known to regulate the key hallmarks of human cancer (Vafadar *et al.*, 2019). There is growing support that lncRNAs play diverse roles in the human body by regulating the expression of several target genes at transcriptional, post-transcriptional/translational or epigenetic levels (Statello *et al.*, 2021). The molecular dysregulations of lncRNAs have been shown to be associated with tumor development and progression (Sun *et al.*, 2018). lncRNAs regulate the crucial aspects of cancer cells including proliferation, apoptosis, migration, and invasion (de Oliveira *et al.*, 2019). They have been shown to be involved in the remodeling of the micro-environment and metastasis of human tumors (Lin *et al.*, 2018). Furthermore, the lncRNAs are involved in maintaining the stemness of different types of human cancers (Ma *et al.*, 2019). Considering the pivotal role of this group of regulatory RNAs, there is mounting evidence that lncRNA-based cancer therapeutics might soon change from a mere concept to reality, soon.

Consistently, the present study was designed to investigate the role of lncRNA GASL1 in regulating the growth and metastasis of human oral cancer cells.

MATERIALS AND METHODS

Cell lines

The oral cancer cell lines (SCC9, HN4, HN6 and Cal127) as well as the normal human epithelial ovarian cells (NCE) were bought from the ATCC, USA. The cell lines were cultured in Dulbecco's modified Eagle's medium (DMEM, Gibco, Gaithersburg, USA) supplemented

INTRODUCTION

Oral cancer is ranked among the most prevalent cancers of the human oral cavity and pharynx (Chaturvedi *et al.*, 2022). This malignancy is responsible for a significant level of mortality and morbidity throughout the world (Dhanuthai *et al.*, 2018). Among the different histological sub-types, oral squamous cell carcinoma (OSCC) is

with 10% FBS and streptomycin-penicillin (100 U/ml). The cells were maintained using humidified incubated CO₂ incubator at 37°C with 5% CO₂.

Transfection

LncRNA GASL1 was amplified using cDNA prepared from the HN6 cell line and cloned into the pcDNA3.1 over-expression vector. Cell transfection was carried out in serum-free medium using Lipofectamine 2000 (Invitrogen, Carlsbad, CA, USA) following the manufacturer's protocol. 6 h post-transfection, fresh complete medium was used to incubate cells. About 48 h later, the cells were collected for detection. The pcNAD3.1 vector alone transfected cells were used to serve as the negative control cells.

qRT-PCR expression analysis

Trizol reagent and Revert Aid First Strand cDNA synthesis kit (both from Thermo Fisher Scientific) was used for total RNA isolation and reverse transcription of RNA, respectively as per the manufacturer guidelines. SYBR PCR master mix (Takara, Japan) was used to perform the qRT-PCR on QuantStudio 3.0 PCR system (Applied Biosystems). The cycling conditions were 95°C for 5 min, followed by 40 cycles of 95°C for 15 s, and 60°C for 60 s. GAPDH genes were used as an internal control in the expression study. The 2^{-ΔΔC_t} method was used to calculate the relative expression levels of GASL1. The qRT-PCR primers used were: GASL1, 5'-CTGAG-GCCAAAGTTTCCAAC-3' (forward) and 5'-CAGC-CTGACTTTCCCTCTTCT-3' (reverse); GAPDH, 5'-GTCTCCTCTGACTTCAACAGCG-3' (forward) and 5'-ACCACCCTGTTGCTGTAGCCAA-3' (reverse).

CCK-8 assay

Cell viability was determined with the help of a Cell Counting Kit-8 (Beyotime). In brief, 1×10⁵ HN6 cells transfected with pcDNA-GASL1 or control vector (pcDNA3.1) were added per well of a 96-well plate and cultured for 24 h at 37°C. At this, the CCK-8 solution was added to each well and 37°C incubation was extended for 1 h. Next, the absorbance at 570 nm (OD₅₇₀) was determined for each well with the help of a microplate reader to analyze the cell viability.

EdU assay

The proliferation of HN6 cancer cells over-expressing GASL1 was studied with reference to negative control cells with the help of an EdU Apollo *in vitro* flow cytometry kit (RiboBio, Guangzhou, China) in accordance with the manufacturer's recommendations. Approximately, 1.5×10⁶ transfected cells /well were cultured in 12 well plates for 24 h at 37°C. Afterwards, the cells were added with EdU solution at a concentration of 50 μmol/L and incubated for 2 h. The cells were then PBS washed, fixed with 4% paraformaldehyde, and stained using Apollo staining solution (San Francisco, CA) for 25 min. The cells were also counterstained with DAPI. The cells were visualized under a fluorescence microscope (Olympus, Japan) for nuclear fluorescence.

Annexin V/PI staining assay

To analyze the effect of GASL1 over-expression on HN6 cancer cell apoptosis, pcDNA-GASL1 transfected cells (1.5×10⁶/well) as well as the negative control cells were initially cultured in DMEM for 24 h in a 12-well

plate at 37°C. Next, the cells were harvested and washed three times with PBS. Annexin V-FITC/PI double staining was performed using an Annexin V-FITC Apoptosis Detection Kit (BD Biosciences, San Jose, CA) as per the manufacturer's instructions. The cells were examined using a BD FACSCantoII flow cytometer (BD Biosciences) and analyzed by FlowJo 6.0 software to determine the relative percentage of apoptotic cells.

Cell cycle analysis

Approximately, 1.5×10⁶ HN6 cells/well transfected with NC and pcDNA-GASL1 were harvested 48 h after culture. Subsequently, the cells were PBS washed and fixed in 500 μl of 75% cold ethanol at 4°C overnight. The cells were then washed again with PBS, and stained by 100 μl propidium iodide (prepared in 3.8 mM sodium citrate, pH 7.0) containing RNase A (10 mg/ml) for 35 min in the dark at 37°C. The percentage of cells in different phases of the cell cycle was determined by flow cytometry (Beckman Coulter, Inc., Brea, CA, USA), and analyzed using ModiFit software.

Wound healing assay

For studying the migration of GASL1 over-expressing HN6 cancer cells with respect to the negative control cells, the wound-healing assay was performed. For the wound-healing assay, 5×10⁵ transfected HN6 cells were placed into each well of a six-well plate. The cells were allowed to grow for 24 h. At this, the growth medium was removed, and the cell surface was scratched with a pipette tip to carve a uniform linear scratch which was photographed under a light microscope (Olympus). The plate was incubated at 37°C for 24 h and then the wound was again analyzed and photographed under a microscope.

Transwell assay

The transwell assay was performed to investigate the invasion of the transfected HN6 cancer cells. Here, the transwell chamber (8 μM, Corning Incorporated, Corning, NY) plated with Matrigel was used for invasion assay. 2.5 ×10⁴ cells suspended in 200 μl of serum-free medium were placed in the upper chamber while the lower chamber was added with serum-free medium alone. After 24 h of incubation at 37°C, the cells invading the lower chamber were fixed with 70% ethanol, stained with 0.2% crystal violet solution, and analyzed under a light microscope.

Western blotting

The RIPA lysis and extraction buffer (Thermo Fisher Scientific) was used to extract total proteins from the transfected HN6 cancer cells. Bradford's assay was performed to examine the concentration of proteins isolated. Exactly, 35 μg of protein samples were isolated using the sodium dodecyl sulfate polyacrylamide gel electrophoresis (SDS-PAGE). Resolved proteins were transferred onto the activated polyvinylidene difluoride membranes (PVDF; Millipore, Billerica, MA, USA). 5% skimmed milk powder was used to block the membranes for 1 h. Next, the PVDF membranes were incubated overnight 4°C with the primary antibodies like anti-Bax (Abcam, cat no. ab216494, 1:1000), anti-Bcl-2 (Abcam, cat no. A95253, 1:800), anti-Cyclin D1 (Abcam, cat no. ab226977, 1:600) anti-CDK4 (Bio-Rad, cat no. AHP2454, 1:1000) and β-actin (Santa Cruz, cat no. sc-47778, 1:1000). This was followed by the incubation of the membranes with peroxidase-conjugated anti-rabbit secondary antibody (Cell signaling technology,

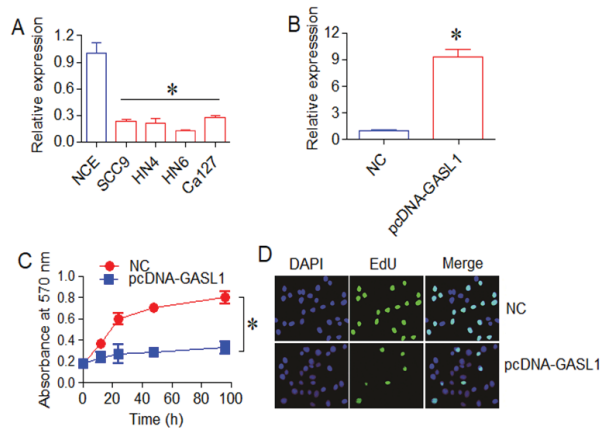


Figure 1. GASL1 restrained the growth of oral cancer cells.

(A) Relative expression of GASL1 in oral cancer cell lines (SCC9, HN4, HN6 and Cal127) with respect to NCE normal oral epithelial cells (B) relative expression of GASL1 in pcDNA-GASL1 transfected HN6 cancer cells with respect to pcDNA3.1 vector transfected HN6 cells (C) CCK-8 assay of viability analysis of transfected HN6 cells (D) EdU incorporation assay of transfected HN6 cells. Three replicates were used for performing the experiments (* $P < 0.05$)

cat no. 7074, 1:3000) for 1 h at room temperature. Finally, the protein bands were detected through chemiluminescence and analyzed with Image J software. β -actin served as the endogenous control.

In vivo study

Around 7-8 weeks old female SCID/NOD mice were maintained in well ventilated rooms under standard conditions on a 12-h light-dark cycle and given access to sterilized food and water. The study was approved by the animal research ethics committee of Sichuan University, Chengdu, China (SU/223/2021-23). HN6 cells at the density of 4×10^6 to induce tumor development. As the tumors reached 0.15–0.20 cm³, the mice were randomly divided into 2 groups NC group and pcDNA-GASL1 group ($n=10$ for each group). Thereafter the mice were administered with intra-tumor injections (five in total, each after 3 days) carrying NC (empty vector) or pcDNA-GASL1 constructs. At the end of 3 weeks, the mice were sacrificed, and tumor weight (g) and volume (cm³) were determined. The volume of tumors was calculated following this formula: $0.5 \times \text{length} \times \text{width}^2$ (mm³).

Statistical analysis

The experiments were performed in triplicates and final values were given as the mean \pm standard deviation. Student's *t*-test was performed using GraphPad Prism v6.0 (GraphPad Software, Inc.) to analyze the statistical difference between the two groups. The *p*-values less than 0.05 were considered to be representative of a statistically significant difference.

RESULTS

GASL1 is downregulated in oral cancer cells

In order to examine the expression levels of lncRNA GASL1 in different oral cancer cell lines (SCC9, HN4, HN6 and Cal127) with reference to normal oral epithelial

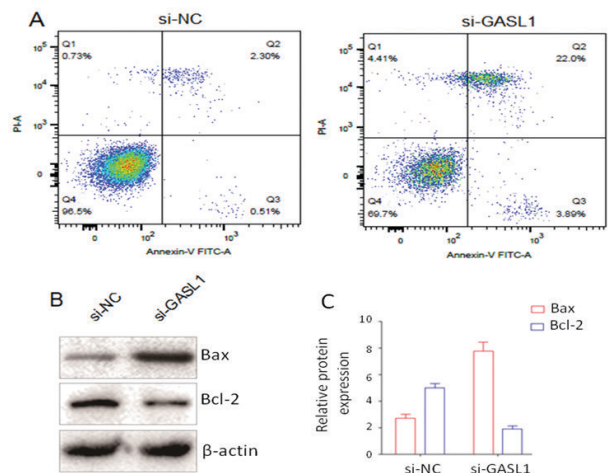


Figure 2. GASL1 induced apoptosis in oral cancer cells.

(A) Flow cytometric analysis for percentage cell apoptosis analysis of transfected HN6 cancer cells double stained with Annexin V-FITC/PI (B) western blot analysis of Bax and Bcl-2 proteins from transfected HN6 cells. (C) Densitometry analysis of western blot. Three replicates were used for performing the experiments.

cells (NCE), qRT-PCR was performed. The results showed that GASL1 expression is significantly down-regulated ($P < 0.05$) in all the oral cancer cells (Fig. 1A). HN6 cancer cells were shown to express the least transcript levels of GASL1 and were thus chosen for further experimentation.

GASL1 inhibits proliferation and colony formation of oral cancer cells

GASL1 was over-expressed in HN6 oral cancer cells, and its upregulation was confirmed by qRT-PCR (Fig. 1B). Whether GASL1 has any bearing on the viability of oral cancer cells, a CCK-8 assay was performed to examine the effect of GASL1 over-expression on HN6 host cell proliferation. It was found that HN6 cancer cells over-expressing GASL1 showed a significant decline in their proliferation with reference to the corresponding negative control cells (Fig. 1C). In addition, over-expression of GASL1 was found to markedly decline the incorporation of EdU into HN6 cancer cells indicative of the loss of cell viability (Fig. 1D).

GASL1 induces apoptosis in oral cancer cells

To look for the possible mechanism mediating the anti-proliferative effects of GASL1 against oral cancer cells, the study of cell apoptosis was performed using Annexin V-FITC/PI staining method. It was shown that GASL1 over-expression in HN6 oral cancer cells significantly enhanced ($P < 0.05$) the percentage of both early and late apoptotic host cells with reference to the negative control cancer cells (Fig. 2A). The apoptotic HN6 cell percentage increased from 2.81% in control to 25.89% upon GASL1 overexpression. The western blotting study also showed that HN6 cancer cells up-regulating GASL1 exhibited significantly higher ($P < 0.05$) expression of Bax protein while expression of Bcl-2 protein was markedly repressed with respect to the negative control cells (Fig. 2B).

GASL1 induces G0/G1 cell cycle arrest in oral cancer cells

To determine whether GASL1 overexpression affects cell cycle progression, cell cycle distribution was

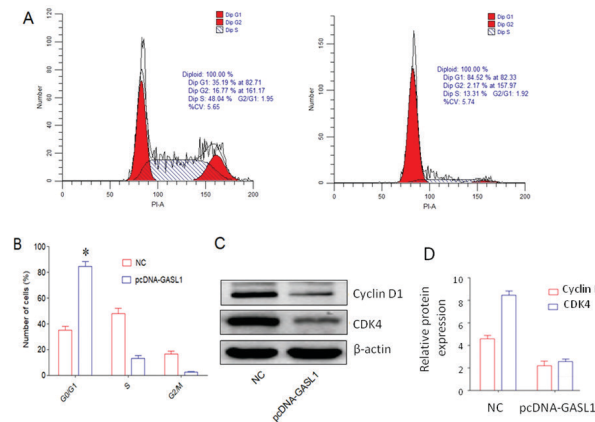


Figure 3. Cell cycle analysis:

(A, B) Flow cytometry analysis showed that G0/G1 cells increased significantly ($P<0.05$) in HN6 cells upon GASL1 overexpression. (C) Western blots analysis for cyclin D1 and CDK4 expression. (D) Densitometry analysis of western blot. Three replicates were used for performing the experiments.

investigated by flow cytometry. The results showed that the proportions of G0/G1 cells increased significantly ($P<0.05$) in HN6 cells upon GASL1 overexpression indicative of G0/G1 arrest (Fig. 3A and 3B). To further evaluate the effect of GASL1 overexpression on cell cycle progression, cycle-related protein expression was determined by western blot analysis. It was found that GASL1 inhibited the expression of cyclin D and CDK4, consistent with a G0/G1 cell cycle arrest (Fig. 3C).

GASL1 inhibits the migration and invasion of oral cancer cells

The effect of GASL1 was also studied on the migration and invasion of oral cancer cells *in vitro*. Wound-healing assay showed that migration of HN6 cancer cells significantly decreased ($P<0.05$) by GASL1 overexpression (Fig. 4A). The percentage of cell migration has been

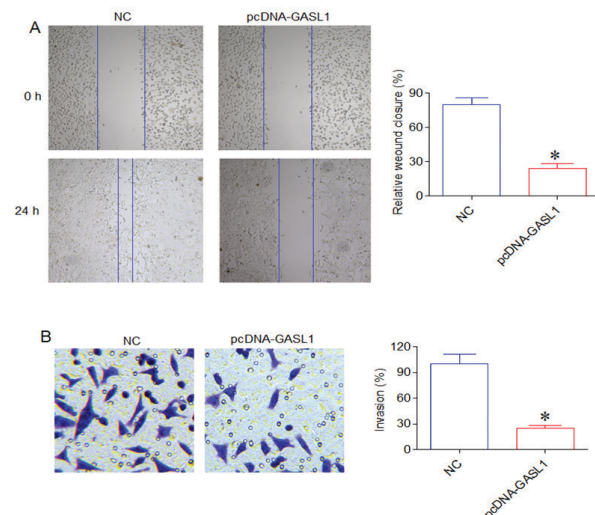


Figure 4. (A) Wound-healing migration assay of HN6 cells transfected with pcDNA-GASL1 or pcDNA3.1 control vector (B) Transwell chamber invasion assay of HN6 cells transfected with pcDNA-GASL1 or pcDNA3.1 control vector. Three replicates were used for performing the experiment ($*P<0.05$). Three replicates were used for performing the experiment ($*P<0.05$).

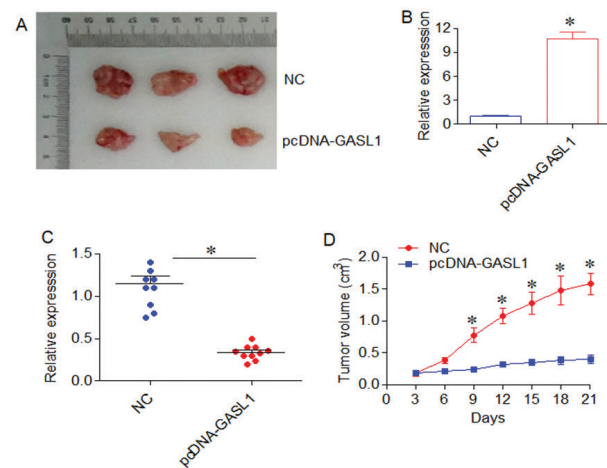


Figure 5. Overexpression of GASL1 inhibits xenografted tumor growth *in vivo*.

(A) Effects of GASL1 on xenografted tumor growth *in vivo*. (B, C) Showed significant upregulation of GASL1 in pcDNA-GASL1 tumors. (D) Showed that the volume and tumor weight of pcDNA-GASL1 tumors was significantly lower than the NC tumors.

shown to be decreased by more than 70% in HN6 cells over-expressing GASL1 with respect to negative control cells. Similarly, the invasion of HN6 cancer cells was significantly reduced under GASL1 up-regulation (Fig. 4B). The HN6 oral cancer cells over-expressing GASL1 showed only one-fourth of the rate of invasion of the negative control cells.

GASL1 inhibits tumor growth *in vivo*

The effects of GASL1 were also investigated on xenografted tumor growth *in vivo* (Fig. 5A). To confirm the overexpression of GASL1 in xenografted tumors, expression analysis was carried out which showed significant upregulation of GASL1 in pcDNA-GASL1 tumors (Fig. 5B). Moreover, tumor volume and tumor weight of pcDNA-GASL1 tumors were significantly lower than the NC tumors (Fig. 5C). These findings indicate that overexpression of GASL1 inhibits xenografted tumor growth *in vivo*.

DISCUSSION

There is growing support that long non-coding RNAs (lncRNAs) affect the key biological, cellular, and physiological aspects of the human body (Statello *et al.*, 2021; Li & Chang, 2014). This group of RNAs is seen to lack the protein-coding capability however is crucial for homeostasis at molecular level (Ji *et al.*, 2020; Zhang *et al.*, 2019). The dysregulation of lncRNAs reportedly surfaces the development and progression of different human pathological conditions including cancer (Forrest and Khalil, 2017; Tan *et al.*, 2021). Several studies have implicated that lncRNAs play a key role in regulating the malignant behavior of human cancer cells (Suzuki *et al.*, 2016; Huo *et al.*, 2017; Acha-Sagredo *et al.*, 2020). They have also been shown to be involved in shaping the tumor microenvironment and affect the cellular dynamics related to cancer cell invasion and metastasis (Yuan *et al.*, 2014; Liu *et al.*, 2021; Wu *et al.*, 2015). In the present study, lncRNA GASL1 was studied for its possible involvement in the regulation of growth and metastasis of human oral cancer. As per recent studies, GASL1

exhibits significant down-regulation in human cancers like gastric cancer and esophageal cancer and acts as a tumor-suppressor to regulate cancer cell growth and proliferation (Liu *et al.*, 2020; Ren *et al.*, 2021). The results of the current study were reflective of GASL1 repression in oral cancer cells. The decline in cell viability by GASL1 overexpression signifies its anti-proliferative regulatory role in oral cancer. GASL1 inhibited oral cancer cell growth by inducing apoptosis and modulating the Bax/Bcl-2 protein ratio. Bax protein was upregulated while Bcl-2 was repressed in GASL1 up-regulating oral cancer cells. This sort of expressional modulation of Bax and Bcl-2 is known to favor the onset of cell apoptosis (Nazeri *et al.*, 2020; Wang *et al.*, 2016).

Metastasis is the process that promotes the development of secondary tumorigenesis at sites distant from the original tumor development (Fares *et al.*, 2020; Chang & Pauklin, 2021). The former is considered the major cause responsible for cancer-based mortality and failure of treatment procedures (Esposito *et al.*, 2021; Riggio *et al.*, 2021). Moreover, the process of cancer metastasis is poorly understood. It thus becomes interesting to study this important hallmark of human cancer and to identify the various regulators of cancer metastasis. Cancer cell migration and invasion to distant tissues are vital to the process of metastasis (Novikov *et al.*, 2021; Winkler *et al.*, 2020). The results of the current study indicated that oral cancer cells over-expressing GASL1 showed significantly lower rates of migration and invasion *in vitro*. This is in confirmation with a recent study wherein GASL1 has been shown to be involved in the regulation of esophageal squamous cell carcinoma (Ren *et al.*, 2021; Weidle & Birzele, 2022). The finding thus insights into the therapeutic utility of GASL1 against oral cancer. In sum, the study established the role of GASL1 in regulating growth and metastasis of human oral cancer cells however the same needs to be confirmed *in vivo* also.

Our findings imply that lncRNA GASL1 may serve as a new biomarker for the detection and management of oral cancer. Hence, a thorough understanding of the lncRNA GASL1 functioning mechanism will be beneficial for the detection and management of oral cancer. As master controllers of gene expression, lncRNAs are interesting candidates for targeted epigenetic pharmacological therapy. There are now tractable pharmacological methods that can either destroy excessive lncRNAs or competitively decrease their activity. For the first time, medicines that target particular lncRNAs may now be created, allowing for the epigenetic modulation of particular metabolic pathways. If this is the case, lncRNA medicines will significantly improve upon the relatively low specificity of currently available medications that serve as epigenetic regulators.

CONCLUSION

Taken together, oral cancer cells exhibit significant downregulation of lncRNA GASL1. GASL1 overexpression inhibited the cancer cell proliferation by inducing apoptosis. Interestingly, the oral cancer cell migration and invasion was significantly declined by GASL1 upregulation. The study thus confirmed the tumor-suppressive action of GASL1 in oral cancer however the findings need to be verified further.

Declarations

Conflict of interest. None.

Acknowledgements. Declared none.

Author Contributions. RZ: Perform experiments, WT: Data collection and analysis, Manuscript writing, LY: Study design, analysis, and interpretation of the results. All authors approved the final manuscript.

REFERENCES

- Acha-Sagredo A, Uko B, Pantazi P, Bediaga NG, Moschandrea C, Rainbow L, Marcus MW, Davies MPA, Field JK, Liloglou T (2020) Long non-coding RNA dysregulation is a frequent event in non-small cell lung carcinoma pathogenesis. *Br J Cancer* **122**: 1050–1058. <https://doi.org/10.1038/s41416-020-0742-9>
- Chang CH, Pauklin S (2021) ROS and TGFbeta: from pancreatic tumour growth to metastasis. *J Exp Clin Cancer Res* **40**: 152. <https://doi.org/10.1186/s13046-021-01960-4>
- Chaturvedi AK, Freedman ND, Abnet CC (2022) The evolving epidemiology of oral cavity and oropharyngeal cancers. *Cancer Res* **82**: 2821–2823. <https://doi.org/10.1158/0008-5472.CAN-22-2124>
- de Oliveira JC, Oliveira LC, Mathias C, Pedrosa GA, Lemos-DS, Salviano-Silva A, Jucoski TS, Lobo-Alves SC, Zambalde EP, Cipolla GA, Gradia DF (2019) Long non-coding RNAs in cancer: Another layer of complexity. *J Gene Med* **21**: e3065. <https://doi.org/10.1002/jgm.3065>
- Dhanuthai K, Rojanawatsirivej S, Thosaporn W, Kintarak S, Subarnhesaj A, Darling M, Kryshalskyj E, Chiang CP, Shin HI, Choi SY, *et al* (2018) Oral cancer: A multicenter study. *Med Oral Patol Oral Cir Bucal* **23**: e23–e29. <https://doi.org/10.4317/medoral.21999>
- Esposito M, Ganesan S, Kang Y (2021) Emerging strategies for treating metastasis. *Nat Cancer* **2**: 258–270. <https://doi.org/10.1038/s43018-021-00181-0>
- Fares J, Fares MY, Khachfe HH, Salhab HA, Fares Y (2020) Molecular principles of metastasis: a hallmark of cancer revisited. *Signal Transduct Target Ther* **5**: 28. <https://doi.org/10.1038/s41392-020-0134-x>
- Forrest ME, Khalil AM (2017) Review: Regulation of the cancer epigenome by long non-coding RNAs. *Cancer Lett* **407**: 106–112. <https://doi.org/10.1016/j.canlet.2017.03.040>
- Huo X, Han S, Wu G, Latchoumanin O, Zhou G, Hebbard L, George J, Qiao L (2017) Dysregulated long noncoding RNAs (lncRNAs) in hepatocellular carcinoma: implications for tumorigenesis, disease progression, and liver cancer stem cells. *Mol Cancer* **16**: 165. <https://doi.org/10.1186/s12943-017-0734-4>
- Irimie AI, Braicu C, Sonea L, Zimta AA, Cojocneanu-Petric R, Tonchev K, Mehterov N, Diudea D, Buduru S, Berindan-Neagoe I (2017) A looking-glass of non-coding RNAs in oral cancer. *Int J Mol Sci* **18**: 2620. <https://doi.org/10.3390/ijms18122620>
- Ji E, Kim C, Kim W, Lee EK (2020) Role of long non-coding RNAs in metabolic control. *Biochim Biophys Acta Gene Regul Mech* **1863**: 194348. <https://doi.org/10.1016/j.bbagr.2018.12.006>
- Li L, Chang HY (2014) Physiological roles of long noncoding RNAs: insight from knockout mice. *Trends Cell Biol* **24**: 594–602. <https://doi.org/10.1016/j.tcb.2014.06.003>
- Lin YH, Wu MH, Yeh CT, Lin KH (2018) Long non-coding RNAs as mediators of tumor microenvironment and liver cancer cell communication. *Int J Mol Sci* **19**: 3742. <https://doi.org/10.3390/ijms19123742>
- Liu D, Xiao P, Feng C, Meng H, Bi E (2020) Long non-coding RNA GASL1 restrains gastric carcinoma cell proliferation and metastasis by sponging microRNA-106a. *Cell Cycle* **19**: 2611–2621. <https://doi.org/10.1080/15384101.2020.1812918>
- Liu SJ, Dang HX, Lim DA, Feng FY, Maher CA (2021) Long noncoding RNAs in cancer metastasis. *Nat Rev Cancer* **21**: 446–460. <https://doi.org/10.1038/s41568-021-00353-1>
- Ma Z, Wang YY, Xin HW, Wang L, Arfuso F, Dharmarajan A, Kumar AP, Wang H, Tang FR, Warriar S, Tergaonkar V, Sethi G (2019) The expanding roles of long non-coding RNAs in the regulation of cancer stem cells. *Int J Biochem Cell Biol* **108**: 17–20. <https://doi.org/10.1016/j.biocel.2019.01.003>
- Meng X, Lou QY, Yang WY, Wang YR, Chen R, Wang L, Xu T, Zhang L (2021) The role of non-coding RNAs in drug resistance of oral squamous cell carcinoma and therapeutic potential. *Cancer Commun (Lond)* **41**: 981–1006. <https://doi.org/10.1002/cac2.12194>
- Nazeri M, Mirzaie-Asl A, Saidijam M, Moradi M (2020) Methanolic extract of Artemisia absinthium prompts apoptosis, enhancing expression of Bax/Bcl-2 ratio, cell cycle arrest, caspase-3 activation and mitochondrial membrane potential destruction in human colorectal cancer HCT-116 cells. *Mol Biol Rep* **47**: 8831–8840. <https://doi.org/10.1007/s11033-020-05933-2>
- Novikov NM, Zolotaryova SY, Gautreau AM, Denisov EV (2021) Mutational drivers of cancer cell migration and invasion. *Br J Cancer* **124**: 102–114. <https://doi.org/10.1038/s41416-020-01149-0>
- Panarese I, Aquino G, Ronchi A, Longo F, Montella M, Cozzolino I, Rocuzzo G, Colella G, Caraglia M, Franco R (2019) Oral and Oropharyngeal squamous cell carcinoma: prognostic and predictive

- parameters in the etiopathogenetic route. *Expert Rev Anticancer Ther* **19**: 105–119. <https://doi.org/10.1080/14737140.2019.1561288>
- Peng QS, Cheng YN, Zhang WB, Fan H, Mao QH, Xu P (2020) circRNA_0000140 suppresses oral squamous cell carcinoma growth and metastasis by targeting miR-31 to inhibit Hippo signaling pathway. *Cell Death Dis* **11**: 112. <https://doi.org/10.1038/s41419-020-2273-y>
- Ren Y, Guo T, Xu J, Liu Y, Huang J (2021) The novel target of esophageal squamous cell carcinoma: lncRNA GASL1 regulates cell migration, invasion and cell cycle stagnation by inactivating the Wnt3a/beta-catenin signaling. *Pathol Res Pract* **217**: 153289. <https://doi.org/10.1016/j.prp.2020.153289>
- Riggio AI, Varley KE, Welm AL (2021) The lingering mysteries of metastatic recurrence in breast cancer. *Br J Cancer* **124**: 13–26. <https://doi.org/10.1038/s41416-020-01161-4>
- Statello L, Guo CJ, Chen LL, Huarte M (2021) Gene regulation by long non-coding RNAs and its biological functions. *Nat Rev Mol Cell Biol* **22**: 96–118. <https://doi.org/10.1038/s41580-020-00315-9>
- Sun H, Huang Z, Sheng W, Xu MD (2018) Emerging roles of long non-coding RNAs in tumor metabolism. *J Hematol Oncol* **11**: 106. <https://doi.org/10.1186/s13045-018-0648-7>
- Suzuki H, Maruyama R, Yamamoto E, Niinuma T, Kai M (2016) Relationship between noncoding RNA dysregulation and epigenetic mechanisms in cancer. *Adv Exp Med Biol* **927**: 109–135. https://doi.org/10.1007/978-981-10-1498-7_4
- Tan X, Liu Y, Zhang T, Cong S (2021) Dysregulation of long non-coding RNAs and their mechanisms in Huntington's disease. *J Neurosci Res* **99**: 2074–2090. <https://doi.org/10.1002/jnr.24825>
- Vafadar A, Shabaninejad Z, Movahedpour A, Mohammadi S, Fathollahzadeh S, Mirzaei HR, Namdar A, Savardashtaki A, Mirzaei H (2019) Long non-coding RNAs as epigenetic regulators in cancer. *Curr Pharm Des* **25**: 3563–3577. <https://doi.org/10.2174/1381612825666190830161528>
- Wang Q, Zhang L, Yuan X, Ou Y, Zhu X, Cheng Z, Zhang P, Wu X, Meng Y (2016) The relationship between the Bcl-2/Bax proteins and the mitochondria-mediated apoptosis pathway in the differentiation of adipose-derived stromal cells into neurons. *PLoS One* **11**: e0163327. <https://doi.org/10.1371/journal.pone.0163327>
- Weidle UH, Birzele F (2022) Long non-coding RNAs with *in vitro* and *in vivo* efficacy in preclinical models of esophageal squamous cell carcinoma which act by a non-microRNA sponging mechanism. *Cancer Genomics Proteomics* **19**: 372–389. <https://doi.org/10.21873/cgp.20327>
- Winkler J, Abisoye-Ogunniyan A, Metcalf KJ, Werb Z (2020) Concepts of extracellular matrix remodelling in tumour progression and metastasis. *Nat Commun* **11**: 5120. <https://doi.org/10.1038/s41467-020-18794-x>
- Wu Y, Zhang L, Zhang L, Wang Y, Li H, Ren X, Wei F, Yu W, Liu T, Wang X, Zhou X, Yu J, Hao X (2015) Long non-coding RNA HOTAIR promotes tumor cell invasion and metastasis by recruiting EZH2 and repressing E-cadherin in oral squamous cell carcinoma. *Int J Oncol* **46**: 2586–2594. <https://doi.org/10.3892/ijo.2015.2976>
- Yi J, Li S, Wang C, Cao N, Qu H, Cheng C, Wang Z, Wang L, Zhou L (2019) Potential applications of polyphenols on main ncRNAs regulations as novel therapeutic strategy for cancer. *Biomed Pharmacother* **113**: 108703. <https://doi.org/10.1016/j.biopha.2019.108703>
- Yuan JH, Yang F, Wang F, Ma JZ, Guo YJ, Tao QF, Liu F, Pan W, Wang TT, Zhou CC, Wang SB, Wang YZ, Yang Y, Yang N, Zhou WP, Yang GS, Sun SH (2014) A long noncoding RNA activated by TGF-beta promotes the invasion-metastasis cascade in hepatocellular carcinoma. *Cancer Cell* **25**: 666–681. <https://doi.org/10.1016/j.ccr.2014.03.010>
- Zhang L, Meng X, Zhu XW, Yang DC, Chen R, Jiang Y, Xu T (2019) Long non-coding RNAs in Oral squamous cell carcinoma: biologic function, mechanisms and clinical implications. *Mol Cancer* **18**: 102. <https://doi.org/10.1186/s12943-019-1021-3>

Vitamin D supplementation improves the therapeutic effect of mometasone on allergic rhinitis

Minfei Guo✉

Respiratory Department, Huichang People's Hospital, Ganzhou, China

This study aimed to investigate the efficacy and safety of vitamin D supplementation in the treatment of allergic rhinitis (AR) using mometasone. A total of 140 patients with moderate and severe AR treated at our hospital between January 2017 and August 2020 were recruited as subjects for this study. The patients were randomly divided into control and experimental groups, with 70 patients in each group. Mometasone nasal spray was used in both groups, and vitamin D was administered to the experimental group for four weeks. The total nasal symptom scores (TNSS) and rhinoconjunctivitis quality of life questionnaire (RQLQ) were used to assess the efficacy of treatment. T lymphocyte subsets (CD3⁺, CD4⁺ and CD8⁺) and serum anti-inflammatory and proinflammatory cytokines such as interleukin-10 (IL-10), tumor necrosis factor- α (TNF- α), and interferon- γ (IFN- γ) were analyzed. The incidence of adverse reactions was recorded. Serum vitamin D levels were lower in patients with AR. After 4 weeks of treatment, total TNSS scores, T lymphocyte subsets (CD3⁺, CD4⁺), CD4⁺/CD8⁺ ratio, TNF- α , and total RQLQ scores were significantly reduced compared to the initial testing ($P < 0.05$) in the two groups; CD8⁺, IFN- γ , and IL-10 levels as well as serum vitamin D were significantly increased compared to the initial test ($P < 0.05$). The improvement in these parameters in the experimental group was significantly greater than that in the control group ($P < 0.05$), except for sneezing and eye symptoms in the TNSS and RQLQ scores. It was concluded that vitamin D supplementation improves the therapeutic effect of mometasone nasal spray on AR and is thus recommended as an adjuvant therapy for moderate and severe AR.

Keywords: vitamin D, mometasone, allergic rhinitis, immunomodulation

Received: 24 January, 2023; **revised:** 14 March, 2023; **accepted:** 17 August, 2023; **available on-line:** 16 September, 2023

✉e-mail: minfeigu@yeah.net

Abbreviations: AR, allergic rhinitis; ELISA, enzyme-linked immunosorbent assay; IL, interleukin; TNF, tumor necrosis factor- α ; IFN, interferon; RQLQ, rhino conjunctivitis quality of life questionnaire; S.D., standard deviation; TNSS, Total nasal symptom score

INTRODUCTION

Allergic rhinitis (AR), although a non-life-threatening disease, is a common disorder that frequently occurs in children and adolescents after exposure to allergens in a highly prevalent environment (Meng *et al.*, 2019). It is often associated with other allergic diseases such as asthma and has adverse effects on sleep, school performance, quality of life, and important short-term and long-term health consequences (Foresi, 2000; Schuler & Montejo, 2019). AR patients develop specific immunoglobulin E (IgE) antibody responses to allergens, resulting in repeat-

ed sneezing, rhinorrhea, nasal congestion, itching, ocular redness, tearing, and itching (Bernstein *et al.*, 2016). Epidemiological studies have shown that the prevalence of this disease among adults and children has increased in recent years (Kakli & Riley, 2016; Khan, 2014). The etiology of AR is complex and is affected by many factors, including heredity, environment, and immune function (Eifan & Durham, 2016; Khan, 2014). Several pharmacotherapy guidelines have been developed to treat the disease, and routine therapy options consist of the use of antihistamines, intranasal corticosteroids, and decongestant drugs such as cetirizine, montelukast, mometasone, and desloratadine (Bousquet *et al.*, 2020; Okubo *et al.*, 2020). Although these drugs have demonstrated efficacy in AR, they require a long treatment time and have poor patient compliance (Khare & Martin, 1995). Furthermore, despite recent epidemiologic data showing that the incidence of AR is increasing worldwide, less than 12% of AR patients seek medical recommendations, resulting in the disease being frequently under-recognized, misdiagnosed, and ineffectively treated (Berger, 2003; Dennis *et al.*, 2012).

Vitamin D is an important human nutrient and functions as an immunomodulatory hormone. In recent years, studies have shown that vitamin D has an immune regulatory effect and can be used as a supplement to treat asthma and other immune-related diseases, including AR, with satisfactory results (Charoenngam & Holick, 2020; Forno *et al.*, 2020; Yepes-Nunez *et al.*, 2018). Vitamin D plays an important role in regulating the immune system and has been demonstrated to have therapeutic benefits in the treatment of various diseases, such as melanoma, inflammatory bowel diseases, rheumatoid arthritis, tuberculosis, sepsis, and respiratory infection (Battistini *et al.*, 2020; Charoenngam & Holick, 2020; Sun *et al.*, 2021). It may alleviate AR symptoms by reducing IgE, cytokines, interleukin (IL)-4, IL-5, and interferon (IFN) to suppress inflammation (Cho *et al.*, 2019; Yu *et al.*, 2017). However, the therapeutic effect of vitamin D on AR remains controversial (Bhardwaj & Singh, 2021; Liu *et al.*, 2020; Luo *et al.*, 2022) and the effect of vitamin D on AR treated with corticosteroids has not been fully explored. In the present study, the impact of vitamin D supplementation was assessed in patients with moderate-to-severe seasonal pollen AR.

MATERIALS AND METHODS

Trial design and study population

We conducted a randomized, assessor/statistician-blinded, single-center trial with two parallel groups to investigate the effects of vitamin D on AR. Patients

treated at our hospital between January 2017 and January 2022 were enrolled in this study. Patients were included if they met the diagnostic criteria of the Guidelines for Diagnosis and Treatment of Allergic Rhinitis (Subspecialty Group of Rhinology *et al.*, 2016), confirmed by allergen tests, had moderate-to-severe AR (symptoms (nasal congestion, runny nose, itchy nose, or sneezing) occurring ≥ 4 days per week for consecutive 4 weeks and were severe enough to affect quality of life) according to the disease severity classification based on the above guidelines, did not receive any AR-related treatment within two weeks of diagnosis, were aged between 16 and 60 years, and had good drug compliance. Patients were excluded if they had non-allergic rhinitis, severe organ dysfunction, malignant tumor, other respiratory diseases, and nasal cavity abnormalities such as sinusitis and nasal polyps. Pregnant and lactating women were excluded from the study. The sample size was determined using the formula $N(\text{each group}) = (t+1)(Z\alpha/2 + Z1-\beta)^2 \sigma^2 / rd^2$ (Suresh & Chandrashekar, 2012). In a pilot study, the minimal detectable difference means (d) of the two groups was 0.62 scores on the total nasal symptom scale (TNSS) and 1.21 the standard deviation (σ), respectively. Therefore, the minimum sample size for each group required to detect the mean difference between the two means was 37 persons/group. Considering a dropout rate of 10%, 45 patients were required for each treatment group. This study was approved by the Ethics Committee of the Huichang People's Hospital, Ganzhou, China. Informed consent was obtained from all the patients.

Randomization and blinding

After baseline evaluations and routine laboratory tests, the patients were randomly allocated 1:1 to the control and experimental groups. The assignment was made according to a computer-generated randomization table created by a biostatistician. The treatments were labelled A and B to ensure blinding of the biostatistician. A physician from another department was tasked with using a randomization list to allocate patients. All assessors were blinded to group allocation, treatment details, and patient information.

Treatment

Patients in both groups were administered 200 μg mometasone nasal spray (Xianju Pharmaceutical, Zhejiang, China) 2 puffs BD for four weeks. In addition, two oral vitamin D capsules (400 IU vitamin D per capsule, Shuangjing Pharmaceuticals, Qingdao, China) were given BD in the experimental group for 4 weeks.

Biochemical assessments

Peripheral venous blood samples were collected before and one month after treatment. Lymphocytes and T lymphocyte subsets (CD3^+ , CD4^+ , and CD8^+) were measured on a flow cytometer (Accuri C6 plus cell analyzer, BD, US) using monoclonal four-color antibody CD3/CD4/CD8/CD45 (cat. no. 561707), monoclonal antibodies to CD3 (cat. no. 30062), CD4 (cat. no. 100538), and CD8 (cat. no. 561644) (produced by BD, USA). The contents of interleukin-10 (IL-10, IL-10 Human ProcartaPlex™ Simplex Kit, cat. no. EPX01A-10215-90), tumor necrosis factor ($\text{TNF-}\alpha$, TNF alpha Human ProQuantum Immunoassay Kit, cat. no. A35601), and interferon- γ (IFN- γ , IFN gamma Human ProQuantum Immunoassay Kit, cat. no. A35576) were assessed by enzyme-linked immunosorbent assay (ELISA) using kits purchased from Thermo Fisher Scientific, USA, according to the manufacturer's instructions. Vitamin D levels were assessed using ELISA kit (cat. no. EY-01H1295) was obtained from Yiyang Biotech (Shanghai, China). All assays were performed in triplicate.

Clinical efficacy evaluation

The TNSS and rhinoconjunctivitis quality of life questionnaire (RQLQ) were used to assess the efficacy. The TNSS is a subjective evaluation tool used to measure the severity of the main symptoms of patients with AR (Downie *et al.*, 2004). Four symptoms, runny nose, itchy nose, nasal congestion, and sneezing, were assessed in all patients using a score of 4 (0 = no symptoms and 3 = severe symptoms), with lower scores indicating less severe symptoms.

Patients were also assessed for improvement in their quality of life after treatment using the RQLQ. The

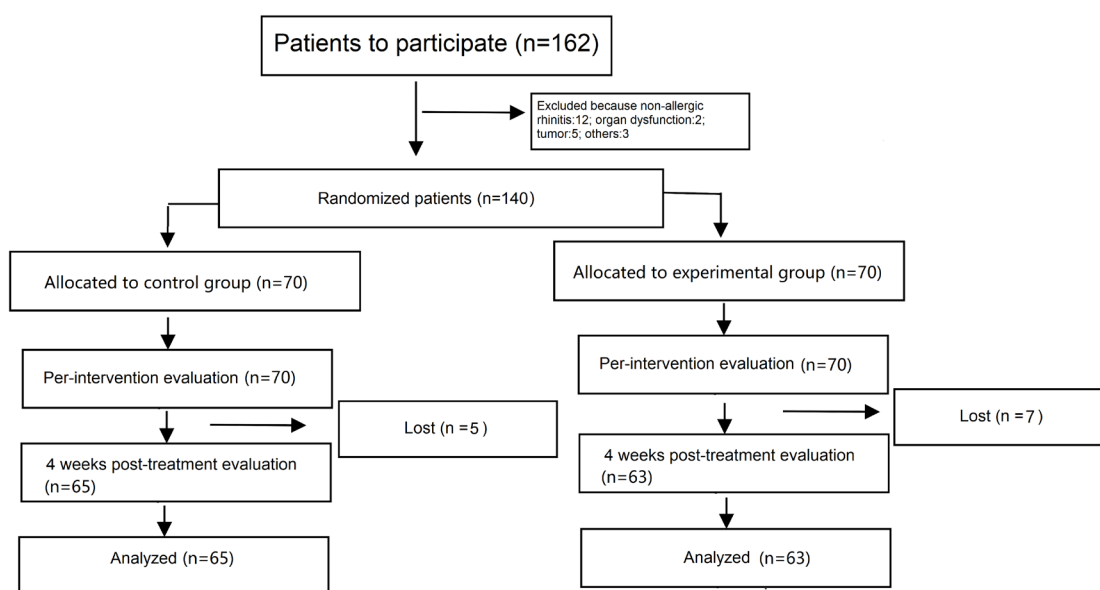


Figure 1. Diagram of patient selection, treatment and analysis

Table 1. Baseline characteristics of patients

Variable	Control group (n=65)	Experimental group (n=63)	P-value*
Female, n (%)	19 (29.2)	20 (31.7)	0.725 ^c
Age; yrs., mean (S.D.)	32.1 (11.1)	32.8 (10.2)	0.159 ^a
Severity of disease			
Moderate, n (%)	45 (69.2)	42 (66.7)	0.237 ^c
Severe, n (%)	20 (30.8)	21 (33.3)	0.531 ^c
Mean course of disease; yrs., mean (S.D.)	4.3 (1.6)	4.1 (1.2)	0.164 ^a

Statistical analysis: a. independent two-sample Student's *t*-test, b. Mann Whitney U Test and c. chi-square test

Table 2. The scores of total nasal symptoms scores in the two groups

Items assessed	Assessment date (weeks)	Treatment		<i>t</i> -value	<i>P</i> -value
		Control	Experimental		
Total TNSS score	0	14.60±2.25	14.63±2.26	0.224	0.327
	4	4.40±0.29*	1.62±0.27*	4.201	<0.01
Runny nose	0	3.11±0.76	3.42±0.87	0.529	0.782
	4	1.14±0.27*	0.31±0.11*	2.115	<0.01
Itchy nose	0	4.73±1.02	4.21±0.89	0.162	0.744
	4	1.53±0.16*	0.30±0.17*	8.665	<0.01
Nasal congestion	0	4.21±0.11	4.42±0.11	0.313	0.541
	4	0.92±0.11*	0.25±0.07*	3.771	<0.01
Sneezing	0	2.55±0.67	2.58±0.62	0.326	0.667
	4	0.81±0.11*	0.76±0.12*	0.310	0.451

Statistical analysis: repeated measured ANOVA, *denotes significant difference from before treatment within group ($P<0.05$), *t* value of independent two-sample Student's *t*-test.

RQLQ has 28 questions in 7 sections (activity limitation, sleep disturbances, nose symptoms, eye symptoms, non-nose/eye symptoms, practical problems, and emotional function). Patients responded to the questions on a 7-point scale (0 = not impaired at all, 6 = severely impaired), with higher scores indicating worse quality-of-life (Juniper & Guyatt, 1991).

Safety evaluation

Adverse reactions, including nausea, diarrhea, nasal dryness and bleeding, and throat irritation in the two groups were recorded to assess the safety of the treatment.

Statistical analysis

All statistical analyses were performed using the SPSS19.0 statistical software. Quantitative data were described as mean ± standard deviation (S.D.), and the independent *t*-test or Mann Whitney U test was used to compare the mean values between the two groups. Qualitative data are described as [n (%)], and compared using the χ^2 test or Fisher's exact test. A *P*-value of <0.05 was considered to indicate statistical significance.

RESULTS

Baseline characteristics

A total of 140 patients were enrolled and randomized to two groups, and 128 patients completed the study

after 5 and 7 patients were lost during the treatments. There were 46 males and 19 females with an average age of 31.4 ± 12.7 years in the control group and 43 males and 20 females with an average age of 30.9 ± 10.7 years in the experimental group (Fig. 1). The numbers of patients with moderate and severe AR were 45 and 20 in the control group and 42 and 21 in the experimental group, respectively. The mean courses of disease were 4.2 and 4.0 years, respectively, in the two groups. Statistical analysis showed that there was no difference in sex, age, disease severity, or course of disease between the two groups (Table 1; $P>0.05$).

Vitamin D improves AR symptoms and quality-of-life

After 4-week treatment, the TNSS scores in both groups were assessed and compared (Table 2). The results showed that the total TNSS scores were significantly reduced compared with those before treatment in both groups for all four main symptoms assessed: itching, runny nose, nasal congestion, and sneezing ($P<0.05$). The improvements with vitamin D supplementation were significantly greater than those of the control group in the symptoms assessed, except for sneezing (Table 2, $P<0.05$).

At the end of the 4-week treatment, we assessed the quality-of-life of the participating AR patients using the RQLQ. The results showed that the scores in both groups were significantly lower after the therapy than before the therapy in all aspects ($P<0.05$), and the improvements with vitamin D supplementation were significantly greater than those in the control group, except for eye symptoms, which were improved, but the differ-

Table 3. The scores of quality of life of AR patients the two groups

Items assessed	Assessment date (weeks)	Treatment		t-value	P-value
		Control	Experimental		
Total RQLQ score	0	17.4±2.01	16.98±2.14	0.112	0.327
	4	7.29 ±1.11*	3.68±0.86*	5.661	<0.01
Activity limitation	0	3.25±0.56	3.29±0.77	0.439	0.862
	4	1.11±0.67*	0.52±0.10*	2.825	0.002
Sleep problems	0	3.44±0.84	3.47±0.91	0.223	0.708
	4	1.44±0.11*	0.55±0.10*	5.675	<0.01
Non-nose/eye symptoms	0	2.71±0.14	2.77±0.10	0.323	0.241
	4	0.92±0.12*	0.41±0.06*	2.751	0.014
Practical problems	0	2.55±0.62	2.64±0.60	0.316	0.510
	4	0.88±0.10*	0.42±0.13*	1.380	0.034
Nose symptoms	0	3.58±0.45	3.49±0.52	0.376	0.310
	4	1.07±0.12*	0.42±0.13*	2.931	0.023
Eye symptoms	0	2.44±0.24	2.47±0.36	0.336	0.455
	4	0.88±0.11*	0.79±0.10*	1.251	0.087
Emotion	0	2.18±0.34	2.22±0.23	0.397	0.450
	4	0.99±0.15*	0.53±0.12*	3.651	0.018

Statistical analysis: T-test for paired samples. *denotes significant difference from before treatment within group ($P<0.05$), t value of independent two-sample Student's t-test.

Table 4. Compositions of T lymphocyte subsets between the two groups

Assessment date (weeks)	CD3+ (%)		CD4+ (%)		CD8+ (%)		CD4+/ CD8+ ratio	
	0	4	0	4	0	4	0	4
Control	64.72±5.14	63.72±4.16	41.2±3.14	35.11 ±3.27*	22.40±2.58	29.15±3.46*	1.82±0.12	1.20±0.11*
Experimental	63.74±5.21	62.65±4.08	42.52±3.37	30.81 ±2.44*	22.34±2.67	36.17±4.19*	1.90±0.12	0.92±0.08*
T value	0.029	1.199	0.165	3.718	0.342	7.229	0.260	6.855
P-value	0.435	0.315	0.826	<0.01	0.562	<0.01	0.775	<0.01

Statistical analysis: T-test for paired samples. *denotes significant difference from before treatment within group ($P<0.05$), t value of independent two-sample Student's t-test.

ence was not statistically significant as compared to the control ($P<0.05$, Table 3).

Vitamin D alters T lymphocyte subsets

We also compared the levels of T lymphocyte subsets before and after the therapy. The results showed that while the percentage of CD3+ in the lymphocytes remained unchanged, the percentages of CD4+ and CD4+/CD8+ ratios were reduced, and the percentages of CD8+ were increased in the two groups after the therapy compared to before the therapy ($P<0.05$). Furthermore, compared to the control group, vitamin D supplementation resulted in greater changes in the subsets (Table 4).

Vitamin D changes serum levels of pro-inflammatory anti-inflammatory cytokines

To further assess the impact of vitamin D on AR-associated inflammation, we profiled the serum levels of pro-inflammatory and anti-inflammatory cytokines before and after therapy. The data showed that TNF- α levels

were significantly decreased, and IFN- γ and IL-10 levels were significantly increased in the two groups after the therapy compared to before the therapy ($P<0.05$, Table 5). These changes were significantly greater in the experimental group than in the control group ($P<0.01$, Table 5).

Vitamin D is reduced in patients with AR and increased after treatment

To elucidate the role of vitamin D in AR, we analyzed serum vitamin D levels in patients with AR before and after treatment. The results showed that compared to healthy participants, patients with AR had significantly lower serum vitamin D levels, which were significantly increased after vitamin D supplementation (Table 6).

Adverse reactions

No serious adverse reactions were observed in either of the groups. In the experimental group, one patient

Table 5. Comparison of serum pro-inflammatory anti-inflammatory cytokine levels between the two groups

Group	IL-10 (pg/mL)		TNF-α (pg/mL)		IFN-γ (pg/mL)	
	Before	After	Before	After	Before	After
Control (n=45)	5.93±0.82	7.79±1.21*	6.24±0.71	5.06±0.42*	4.68±0.57	6.62±1.02*
Experimental (n=45)	5.96±0.71	9.52±1.69*	6.19±0.72	4.56±0.44*	4.79±0.48	7.64±1.19*
t	0.439	4.622	0.435	4.331	0.114	3.603
P	0.673	<0.01	0.541	<0.01	0.763	0.01

Statistical analysis: T-test for paired samples. *denotes significant difference from before treatment within group ($P<0.05$), t value of independent two-sample Student's t-test.

Table 6. Serum vitamin D contents in healthy and AR patients before and after treatment.

Group	n	Vitamin D (nmol/L)
Healthy participants	25	42.12±4.07
Patients not supplemented with vitamin D	45	
Before treatment		36.40±3.01 ^a
After treatment		36.11±3.01 ^a
Patients not supplemented with vitamin D	51	
Before treatment		36.61±3.58 ^a
After treatment		39.41±3.21 ^b

^a $P<0.05$ compared with healthy participants; ^b $P<0.05$ compared with patients not supplemented with vitamin D

reported a mild dry nasal membrane that was relieved without medical treatment.

DISCUSSION

In this study, we investigated the effect of vitamin D as a supplementary therapeutic to mometasone in moderate-to-severe AR. Our results showed that vitamin D effectively improved the therapeutic efficacy of mometasone. It moderates T lymphocyte subsets and pro-inflammatory and anti-inflammatory cytokine levels, leading to significantly better quality-of-life with AR.

As a common disease that seriously affects the physical and mental health and quality of life of patients. Currently, there is no cure for RA, but active treatment can effectively control the pathological symptoms of patients to reduce pain and stop or slow further damage (Bullock *et al.*, 2018). Therefore, it is important to develop better treatment plans with fewer complications, better patient compliance, and lower costs. Nasal glucocorticoids and antihistamines are the first-line clinical drugs for AR with excellent efficacy for persistent moderate-to-severe AR, and the combination of intranasal antihistamines and corticosteroids is conducive to the rapid control of symptoms and reduction of TNSS (Wheatley & Togias, 2015), there are various adverse effects, including osteoporosis, dyslipidemia, body fat redistribution, insulin resistance, glucose intolerance, and even diabetes associated with glucocorticoid drugs (Sundahl *et al.*, 2015). Recent studies have shown that vitamin D deficiency is common in AR patients whose serum contains less vitamin D than in healthy individuals (Chen *et al.*, 2016). Vitamin D, as an important human nutrient, does not cause any adverse reactions if taken at the dose recommended by the physician. Vitamin D has been demon-

strated to have various immunomodulatory effects and to protect against a number of autoimmune diseases, including multiple sclerosis and inflammatory bowel disease (Christakos *et al.*, 2016; Holick, 2007). However, the benefits of vitamin D in AR treatment with corticosteroids have not yet been fully explored.

The corticosteroid drug mometasone has been demonstrated to be effective and safe for treating inflammatory diseases of the nose and paranasal sinuses including AR (Yarom *et al.*, 1982). As expected, treatment with nasal spray for one month, resulted in significant control of all AR-related symptoms as well as better quality of life in our cohort with moderate-to-severe AR, as assessed using the TNSS and RQLQ, both of which are well-recognized tools that assess the primary outcome in clinical trials on AR. Furthermore, the assessments showed that Vitamin D supplementation further improved the control of AR and quality-of-life of AR patients in all assessed items except sneezing and eye symptoms. These data demonstrate that vitamin D supplementation improves the overall therapeutic effect of corticosteroid drugs, to a certain extent.

In the present study, the vitamin D dose prescribed were 1600 IU per day based on the manufacture's recommendation to minimize potential adverse effect. Previously, various doses have been used from 100 IU per day for patients with refractory allergic rhinitis (Chen *et al.*, 2016), 2000 IU over 2 months in children (Tiazhka & Selska, 2020) to 42000 IU per day via nasal dropping (Liu *et al.*, 2018) and 50000 IU/week of vitamin D for 8 weeks along with antihistamines (Bakhshaei *et al.*, 2019). It is likely that the optimal dose is depending on the formulations (chew pill, soft gel and capsule) and patient populations and need to be defined further.

To better understand the mechanisms underlying the improved therapeutic effect of vitamin D supplementation, we compared the changes in T lymphocyte subsets following the therapies. The results showed that the levels of CD4⁺, CD8⁺, and CD4⁺/CD8⁺ in the experimental groups were changed compared to those in the control group, suggesting that vitamin D might modulate cellular immune function by lowering the levels of CD4⁺ and increasing the level of CD8⁺. Vitamin D receptor (VDR) is produced in respiratory epithelial cells, where Vitamin D binds to vitamin D receptor (VDR) to enhance both innate and acquired immunity *via* various immune cells, including dendritic cells, monocytes, megaphagocytes, T lymphocytes, and B lymphocytes (Bakdash *et al.*, 2014; Mailhot & White, 2020). It inhibits the proliferation of T lymphocytes and promotes the differentiation of Foxp3⁺ regulatory T cells (Barragan *et al.*, 2015; Hewison, 2011). Therefore, at least part of the enhanced therapeutic effect of vitamin D is likely due to the modulation of immune function in patients with AP.

Vitamin D also exerts regulatory effects on many cytokines involved in inflammation. For example, it down-regulates the production of IL-12, TNF- α , and IL-2 and upregulates the synthesis of IL-4 and IL-10 (Barragan *et al.*, 2015; Hewison, 2011), which are secreted by immune cells to regulate their proliferation and differentiation of immune cells. Our data showed that pro-inflammatory cytokine TNF- α levels were significantly reduced and anti-inflammatory cytokine IFN- γ and IL-10 levels were significantly increased after vitamin D supplementation, suggesting that vitamin D may improve the therapeutic effect by modulating cytokine production to inhibit inflammation. IL-10 and IFN- γ can not only inhibit the T cell response but also inhibit the production of immunoglobulin E, which plays a negative role in regulating AR pathological symptoms. TNF- α mediates various inflammatory reactions, and a reduction in TNF- α levels may lead to the inhibition of AR-related inflammation.

In addition, vitamin D supplementation may attenuate vitamin D deficiency in patients with AR and modulate immune function to strengthen its anti-inflammatory effect. In this study, the serum level of vitamin D was found to be lower in AR patients, and this vitamin D deficiency was partially alleviated after vitamin D supplementation. These results are consistent with those of previous studies on children and women (Aryan *et al.*, 2017; Srimani *et al.*, 2017).

This study had several limitations. Although this trial was blinded to the assessors, the patients were aware of their treatment because of the absence of placebo indistinguishable from patients, resulting in potential bias in treatment outcomes. In addition, physiologic measures, including peak nasal inspiratory flow and nasal airflow, were not used to measure the outcomes, yielding potential bias in the results. A single dose of vitamin D was applied in the therapy; patients were not classified based on the AR etiologies, such as seasonal allergic rhinitis or perennial allergic rhinitis, for better treatment and explanation of the therapeutic outcome. For example, patients with seasonal allergic rhinitis pass the onset season and recover spontaneously. Since this was a single-center, short-term, and small-scale study, more extensive multi-center work is needed to address the limitations and to validate our conclusion.

CONCLUSIONS

Vitamin D supplementation of mometasone nasal spray is effective and safe for improving AR symptoms and quality of life. These improvements were partially due to the modulation of cellular immunity and inhibition of inflammation. Therefore, vitamin D adjuvant therapy is highly recommended for patients with moderate or severe seasonal AR.

Declarations

Ethics approval and consent to participate: The Ethics Committee of Huichang People's Hospital, Ganzhou, China, obtained written informed consent from all participants.

Consent for publication: N/A.

Availability of data and material: The datasets used and/or analyzed during the current study are available from the corresponding author upon reasonable request.

Competing interests: None.

Funding: None.

Acknowledge: Not applicable.

Authors' contributions: MG designed the study, performed the research, analyzed the data, wrote the manuscript, confirmed the authenticity of all raw data, and read and approved the final manuscript.

REFERENCES

- Aryan Z, Rezaei N, Camargo CA, Jr (2017) Vitamin D status, aeroallergen sensitization, and allergic rhinitis: A systematic review and meta-analysis. *Int Rev Immunol* **36**: 41–53. <https://doi.org/10.1080/08830185.2016.1272600>
- Bakdash G, van Capel TM, Mason LM, Kapsenberg ML, de Jong EC (2014) Vitamin D3 metabolite calcidiol primes human dendritic cells to promote the development of immunomodulatory IL-10-producing T cells. *Vaccine* **32**: 6294–6302. <https://doi.org/10.1016/j.vaccine.2014.08.075>
- Bakhshaei M, Sharifian M, Esmatinia F, Rasoulouian B, Mohebbi M (2019) Therapeutic effect of vitamin D supplementation on allergic rhinitis. *Eur Arch Otorhinolaryngol* **276**: 2797–2801. <https://doi.org/10.1007/s00405-019-05546-x>
- Barragan M, Good M, Kolls JK (2015) Regulation of dendritic cell function by vitamin D. *Nutrients* **7**: 8127–8151. <https://doi.org/10.3390/nu7095383>
- Battistini C, Ballan R, Herkenhoff ME, Saad SMI, Sun J (2020) Vitamin D modulates intestinal microbiota in inflammatory bowel diseases. *Int J Mol Sci* **22**. <https://doi.org/10.3390/ijms22010362>
- Berger WE (2003) Overview of allergic rhinitis. *Ann Allergy Asthma Immunol* **90**: 7–12. <https://doi.org/10.1016/j.annall.2006.10.616>
- Bernstein DI, Schwartz G, Bernstein JA (2016) Allergic rhinitis: mechanisms and treatment. *Immunol Allergy Clin North Am* **36**: 261–278. <https://doi.org/10.1016/j.iac.2015.12.004>
- Bhardwaj B, Singh J (2021) Efficacy of vitamin D supplementation in allergic rhinitis. *Indian J Otolaryngol Head Neck Surg* **73**: 152–159. <https://doi.org/10.1007/s12070-020-01907-9>
- Bousquet J, Schunemann HJ, Togias A, Bachert C, Erhola M, Hellings PW, Klimek L, Pfaar O, Wallace D, Ansotegui I, Agache I, Bedbrook A, Bergmann KC, Bewick M, Bonniat P, Bosnic-Anticevich S, Bosse I, Bouchard J, Boulet LP, Brozek J, Brusselle G, Calderon MA, Canonica WG, Caraballo L, Cardona V, Casale T, Cecchi L, Chu DK, Costa EM, Cruz AA, Czarlewski J, Jutel M, Kaidashev I, Khaitov M, Kalayci O, Kleine Tebbe J, Kowalski ML, Kuna P, Kvedariene V, La Grutta S, Larenas-Linnemann D, Lau S, Laune D, Le L, Lieberman P, Lodrup Carlsen KC, Lourenco O, Marien G, Carreiro-Martins P, Melen E, Menditto E, Neffen H, Mercier G, Mosques R, Mullol J, Muraro A, Namazova L, Novellino E, O'Hehir R, Okamoto Y, Ohta K, Park HS, Panzner P, Passalacqua G, Pham-Thi N, Price D, Roberts G, Roche N, Rolland C, Rosario N, Ryan D, Samolinski B, Sanchez-Borges M, Scadding GK, Shamji MH, Sheikh A, Bom AT, Toppila-Salmi S, Tsiligianni I, Valentin-Rostan M, Valiulis A, Valovirta E, Ventura MT, Walker S, Wasserman S, Yorgancioglu A, Zuberbier T, Allergic R, Its Impact on Asthma Working G (2020) Next-generation Allergic Rhinitis and Its Impact on Asthma (ARIA) guidelines for allergic rhinitis based on Grading of Recommendations Assessment, Development and Evaluation (GRADE) and real-world evidence. *J Allergy Clin Immunol* **145**: 70–80 e73. <https://doi.org/10.1016/j.jaci.2019.06.049>
- Bullock J, Rizvi SAA, Saleh AM, Ahmed SS, Do DP, Ansari RA, Ahmed J (2018) Rheumatoid arthritis: a brief overview of the treatment. *Med Princ Pract* **27**: 501–507. <https://doi.org/10.1159/000493390>
- Charoenngam N, Holick MF (2020) Immunologic Effects of Vitamin D on Human Health and Disease. *Nutrients* **12**. <https://doi.org/10.3390/nu12072097>
- Chen B, Liu Y, Li X, Ma Y, Wu J, Li Y, Zhang L, Yang Q, Yao C (2016) Refractory allergic rhinitis serum levels of vitamin D and vitamin D Calcium chewable tablet therapeutic value. *J Clin Otolaryngol Head Neck Surg (China)* **30**: 1397–1400
- Chen P, Liu Y, Lee S, Mao Y, Wu Q, Li Y, Zhang L, Yang Q, Yao Z (2016) Refractory allergic rhinitis serum levels of vitamin D and vitamin D calcium chewable tablet therapeutic value. *J Clin Otolaryngol Head Neck Surg (China)* **30**: 1397–1400
- Cho SW, Zhang YL, Ko YK, Shin JM, Lee JH, Rhee CS, Kim DY (2019) Intranasal treatment with 1, 25-dihydroxyvitamin D3 alleviates allergic rhinitis symptoms in a mouse model. *Allergy Asthma Immunol Res* **11**: 267–279. <https://doi.org/10.4168/aaar.2019.11.2.267>
- Christakos S, Dhawan P, Verstuyf A, Verlinden L, Carmeliet G (2016) Vitamin D: metabolism, molecular mechanism of action, and pleiotropic effects. *Physiol Rev* **96**: 365–408. <https://doi.org/10.1152/physrev.00014.2015>
- Dennis RJ, Caraballo L, Garcia E, Rojas MX, Rondon MA, Perez A, Aristizabal G, Penaranda A, Barragan AM, Ahumada V, Jimenez S

- (2012) Prevalence of asthma and other allergic conditions in Colombia 2009-2010: a cross-sectional study. *BMC Pulm Med* **12**: 17. <https://doi.org/10.1186/1471-2466-12-17>
- Downie SR, Andersson M, Rimmer J, Leuppi JD, Xuan W, Akerlund A, Peat JK, Salome CM (2004) Symptoms of persistent allergic rhinitis during a full calendar year in house dust mite-sensitive subjects. *Allergy* **59**: 406–414. <https://doi.org/10.1111/j.1398-9995.2003.00420.x>
- Eifan AO, Durham SR (2016) Pathogenesis of rhinitis. *Clin Exp Allergy* **46**: 1139–1151. <https://doi.org/10.1111/cea.12780>
- Foresi A (2000) A comparison of the clinical efficacy and safety of intranasal fluticasone propionate and antihistamines in the treatment of rhinitis. *Allergy* **55** (Suppl 62): 12–14. <https://doi.org/10.1034/j.1398-9995.2000.055suppl62012.x>
- Forno E, Bacharier LB, Phipatanakul W, Guilbert TW, Cabana MD, Ross K, Covar R, Gern JE, Rosser FJ, Blatter J, Durran S, Han YY, Wisniewski SR, Celedon JC (2020) Effect of vitamin D3 supplementation on severe asthma exacerbations in children with asthma and low vitamin D levels: The VDKA randomized clinical trial. *JAMA* **324**: 752–760. <https://doi.org/10.1001/jama.2020.12384>
- Hewison M (2011) Vitamin D and innate and adaptive immunity. *Vitam Horm* **86**: 23–62. <https://doi.org/10.1016/B978-0-12-386960-9.00002-2>
- Holick MF (2007) Vitamin D deficiency. *N Engl J Med* **357**: 266–281. <https://doi.org/10.1056/NEJMr070553>
- Juniper EF, Guyatt GH (1991) Development and testing of a new measure of health status for clinical trials in rhinoconjunctivitis. *Clin Exp Allergy* **21**: 77–83. <https://doi.org/10.1111/j.1365-2222.1991.tb00807.x>
- Kakli HA, Riley TD (2016) Allergic rhinitis. *Prim Care* **43**: 465–475. <https://doi.org/10.1016/j.pop.2016.04.009>
- Khan DA (2014) Allergic rhinitis and asthma: epidemiology and common pathophysiology. *Allergy Asthma Proc* **35**: 357–361. <https://doi.org/10.2500/aap.2014.35.3794>
- Khare VK, Martin DC (1995) Anecdotal association of endosalpinxitis with chlamydia trachomatis IgG titers and Fitz-Hugh-Curtis adhesions. *J Am Assoc Gynecol Laparosc* **2**: 143–145. [https://doi.org/10.1016/s1074-3804\(05\)80008-8](https://doi.org/10.1016/s1074-3804(05)80008-8)
- Liu S, Liu S, Shen S, Yang H (2018) Effects of vitamin D3 adjuvant therapy for clinical efficacy, peripheral blood eosinophils and serum IL-4 levels in patients with allergic rhinitis. *Chin Arch Otolaryngol Head Neck Surg* **25**: 143–146
- Liu X, Liu X, Ren Y, Yang H, Sun X, Huang H (2020) Clinical efficacy of vitamin D3 adjuvant therapy in allergic rhinitis: a randomized controlled trial. *Iran J Immunol* **17**: 283–291. <https://doi.org/10.22034/iji.2020.84336.1652>
- Luo C, Sun Y, Zeng Z, Liu Y, Peng S (2022) Vitamin D supplementation in pregnant women or infants for preventing allergic diseases: a systematic review and meta-analysis of randomized controlled trials. *Chin Med J (Engl)* **135**: 276–284. <https://doi.org/10.1097/CM9.0000000000001951>
- Mailhot G, White JH (2020) Vitamin D and immunity in infants and children. *Nutrients* **12**. <https://doi.org/10.3390/nu12051233>
- Meng Y, Wang C, Zhang L (2019) Recent developments and highlights in allergic rhinitis. *Allergy* **74**: 2320–2328. <https://doi.org/10.1111/all.14067>
- Okubo K, Kurono Y, Ichimura K, Enomoto T, Okamoto Y, Kawauchi H, Suzuki H, Fujieda S, Masuyama K, Japanese Society of A (2020) Japanese guidelines for allergic rhinitis 2020. *Allergol Int* **69**: 331–345. <https://doi.org/10.1016/j.alit.2020.04.001>
- Schuler IV CF, Montejó JM (2019) Allergic rhinitis in children and adolescents. *Pediatr Clin North Am* **66**: 981–993. <https://doi.org/10.1016/j.pcl.2019.06.004>
- Srimani S, Saha I, Chaudhuri D (2017) Prevalence and association of metabolic syndrome and vitamin D deficiency among postmenopausal women in a rural block of West Bengal, India. *PLoS One* **12**: e0188331. <https://doi.org/10.1371/journal.pone.0188331>
- Subspecialty Group of Rhinology EBoCJoOH, Neck S, Subspecialty Group of Rhinology SoOH, Neck Surgery CMA (2016) (Chinese guidelines for diagnosis and treatment of allergic rhinitis). *Zhonghua Er Bi Yan Hou Tou Jing Wai Ke Za Zhi* **51**: 6–24. <https://doi.org/10.3760/cma.j.issn.1673-0860.2016.01.004>
- Sun L, Arbesman J, Piliang M (2021) Vitamin D, autoimmunity and immune-related adverse events of immune checkpoint inhibitors. *Arch Dermatol Res* **313**: 1–10. <https://doi.org/10.1007/s00403-020-02094-x>
- Sundahl N, Bridelance J, Libert C, De Bosscher K, Beck IM (2015) Selective glucocorticoid receptor modulation: New directions with non-steroidal scaffolds. *Pharmacol Ther* **152**: 28–41. <https://doi.org/10.1016/j.pharmthera.2015.05.001>
- Suresh K, Chandrashekar S (2012) Sample size estimation and power analysis for clinical research studies. *J Hum Reprod Sci* **5**: 7–13. <https://doi.org/10.4103/0974-1208.97779>
- Tiazhka OV, Selska ZV (2020) Application of vitamin D in different dosage to treat children with allergic diseases. *Wiad Lek* **73**: 1377–1383
- Wheatley LM, Togias A (2015) Clinical practice. Allergic rhinitis. *N Engl J Med* **372**: 456–463. <https://doi.org/10.1056/NEJMc1412282>
- Yarom R, Meyer S, More R (1982) Negative surface charge on platelets of patients with idiopathic scoliosis. *Haemostasis* **12**: 289–292. <https://doi.org/10.1159/000214685>
- Yepes-Nunez JJ, Brozek JL, Fiocchi A, Pawankar R, Cuello-Garcia C, Zhang Y, Morgano GP, Agarwal A, Gandhi S, Terracciano L, Schunemann HJ (2018) Vitamin D supplementation in primary allergy prevention: Systematic review of randomized and non-randomized studies. *Allergy* **73**: 37–49. <https://doi.org/10.1111/all.13241>
- Yu ZJ, Zeng L, Luo XQ, Geng XR, Xu R, Chen K, Yang G, Luo X, Liu ZQ, Liu ZG, Liu DB, Yang PC, Li HB (2017) Vitamin D3 inhibits micro RNA-17-92 to promote specific immunotherapy in allergic rhinitis. *Sci Rep* **7**: 546. <https://doi.org/10.1038/s41598-017-00431-1>

Silencing circCAMSAP1 suppresses malignant behavior of endometrial cancer by targeting microRNA-370-3p/MAPK1

Hai Feng Zhang¹, Cheng Cheng Cao¹, Cui Cui Nie² and Ting Zhang²✉

¹Department of Gynecology, Affiliated Hospital of Weifang Medical College, Weifang City, Shandong Province, 261000, China; ²Department of Gynecology and Obstetrics, Sunshine Union Hospital, Weifang City, Shandong Province, 250131, China

The study was conducted to figure out the function and mechanism of circular RNA circCAMSAP1 in repressing malignant behavior of endometrial carcinoma (EC) by targeting microRNA (miR)-370-3p /MAPK1. Tumor tissues and normal adjacent tissues of EC patients were harvested, and circCAMSAP1 and MAPK1 were elevated but miR-370-3p was reduced in tissues and cells of EC patients. Functional test results clarified transfection of si-circCAMSAP1 or miR-370-3p-mimic refrained cancer cell proliferation, migration and invasion, but motivated cancer cell apoptosis. Meanwhile, the amount of E-cadherin elevated and the amount of N-cadherin elevated or reduced. After co-transfection with si-circCAMSAP1 and miR-370-3p-inhibitor, miR-370-3p-inhibitor blocked si-circCAMSAP1's therapeutic impact. Furthermore, after co-transfection of pcDNA-circCAMSAP1 and si-MAPK1, si-MAPK1 turned around the malignant effect of pcDNA-circCAMSAP1. It was testified that miR-370-3p was circCAMSAP1's target, and inversely controlled via circCAMSAP1. Meanwhile, enhancing miR-370-3p led to repressive MAPK1, which was recognized as miR-370-3p's downstream target. All in all, the results of this study convey silencing circCAMSAP1 refrains the malignant behavior of EC by controlling miR-370-3p /MAPK1 axis.

Key words: Circular RNA CAMSAP1, MicroRNA-370-3p, MAPK1, Target binding, Endometrial carcinoma

Received: 31 March, 2022; **revised:** 15 July, 2022; **accepted:** 11 October, 2022; **available on-line:** 01 March, 2023

✉e-mail: ztodoctormi@outlook.com

Abbreviations: circRNA, Circular RNA; EC, Endometrial cancer; hEEC, endometrial endothelial cells

INTRODUCTION

Endometrial cancer (EC) is an extremely familiar cancer in women, with over 380 000 new pathologies diagnosed globally every year. Recently, EC's presence has been increasing, especially in developed countries. EC ranks second among female genital cancers in China, with a mortality rate of 2.7 per 100 000 (Wilczynski *et al.*, 2020). ECs' recently new molecular classification is on grounds of the research of the Cancer Genome Atlas Research Network and assignation of them into 4 molecular subgroups is conducted. Among them, endometrioid ECs are present in all subgroups (Cancer Genome Atlas Research *et al.*, 2013), and their molecular diversity may cause more aggressive tumors in many women with type I EC. The treatment options for EC largely rely on the stage of the disease, and surgery is still the major method of early treatment, covering but not limited to pelvic lymph node cesarean section, bilateral salpingo-

ophorectomy, etc. (Sonoda, 2012). Several molecular targeted therapies for EC are currently under study, like epidermal growth factor inhibitors, phosphatidylinositol 3-kinase (PI3K)/AKT inhibitors, etc. (Leslie *et al.*, 2012; Oza *et al.*, 2015). Targeted molecular identification has facilitated the diagnosis and cure of EC.

Circular RNA (circRNA) is a kind of covalent body, which is dorsally linked to the precursor mRNA and is in the form of a closed single strand (Ebbesen *et al.*, 2017). CircRNAs are not easily degraded by RNase R due to their absence of 5'-3' ends and polyadenylated tails, so they are more stable vs. linear RNAs (Suzuki *et al.*, 2014). CircCAMSAP1, a circular RNA, also known as circ_0004338, is linked with the regulation of the occurrence and development of diversified cancers (Chen *et al.*, 2021). For instance, circCAMSAP1 can motivate the biological function of hepatocellular carcinoma *in vitro* and *in vivo* via the miR-1294/GRAMD1A molecular axis (Luo *et al.*, 2021); CircCAMSAP1 can be employed as a latent therapeutic target and a biomarker for diagnosis and prognosis of colon cancer (Zhou *et al.*, 2020). However, circCAMSAP1's role and regulatory mechanism in EC remains uncertain.

By targeting and combining with mRNA in the 3' untranslated region, microRNA (miRNA) can control gene expression, cause messenger RNA (mRNA) cleavage, or lead to translational repression of target genes. Therefore, miRNA takes a momentous function in cell growth, apoptosis, migration, etc. (Bueno *et al.*, 2008). Numerous studies have clarified miRNAs can control the specificity of diversified cancers, for example, miR-411-5p can restrain the growth and metastasis of bladder cancer, and target the transport of ZnT1 protein (Finnson *et al.*, 2012); MiR-153-3p can target CFL2 to control the carcinogenesis process of breast cancer cells (Zhang *et al.*, 2021) and so on. Some researchers find miR-370-3p can down-regulate EDN1 in endometrial stromal cells, thereby depressing endometriosis' development (Zhou *et al.*, 2021); MiR-370-3p represses the cell proliferation of endometrium by regulating steroid synthesis factors (Hu *et al.*, 2019). However, the regulatory mechanism of miR-370-3p on EC is unknown.

In this paper, circCAMSAP1 was chosen as the research object to deeply figure out and study the regulatory mechanism and impacts of the circCAMSAP1/miR-370-3p/MAPK1 molecular axis on EC, offering new therapeutic targets and ideas for EC.

MATERIAL AND METHODS

Experimental subjects

Fifty EC tissue specimens and adjacent normal tissues (≥ 4 cm) were harvested from patients with primary EC

confirmed by surgery and pathology in Affiliated Hospital of Weifang Medical College from July 2014 to July 2018. The mean age of the patients was 45.1 ± 7.2 years. In the light of the surgical and pathological staging of endometrial cancer, 8 cases of stage I, 12 cases of stage II, 15 cases of stage III, and 15 cases of stage IV were presented. Tissues were stored in liquid nitrogen and transferring to -80°C until total RNA or protein extraction. All patients signed signature of the informed letter, and this study was reviewed and approved by the Ethics Committee of Affiliated Hospital of Weifang Medical College (No: 201302WF353L).

Cell culture and transfection

EC cell lines (HEC-1A, HEC-1B, KLE) and endometrial endothelial cells (hEEC) (Thermo Scientific, USA) were cultured in high glucose [Dulbecco's phosphate buffer modified Eagle culture medium (Hyclone, USA) and replenishment of 10% FBS (Gibco, USA), 110 U/mL penicillin and 110 mg/mL streptomycin (Hyclone, USA)] at 37°C with 5% CO_2 , selection for were conducted. Cells were sub-cultured before transfection and cells in logarithmic growth phase was selected for cell transfection. Si-circCAMSAP1, si-NC, pcDNA-circCAMSAP1, pcDNA3.1, si-MAPK1, miR-370-3p-inhibitor, miR-370-3p-mimic, and mimic/inhibitor-NC were produced and validated by GeneStar (Shanghai, China). The above plasmids or oligonucleotides were transfected into HEC-1A cells using Lipofectamine 2000 (ThermoFisher, USA) according to the manufacturer's instructions. The transfection efficiency was verified by RT-QPCR, and the cells were obtained for subsequent experiments.

Cell counting kit (CKK)-8 and EdU assay

The proliferation ability of EC cells was detected via CKK-8 kit and EdU kit (Enzyme-Linked Bio, Shanghai, China) in the light of the manufacturer's instructions. In the CKK-8 experiment, transfected HEC-1A cells (2×10^4 cells/well) was seeded in 96-well plates. Adding 10 μL CKK-8 solution at 24, 48, 72 and 96 h while incubation was conducted. The absorbance at 450 nm was measured with a microplate reader and the curve was drawn. In the EdU experiment, transfected HEC-1A cells (2×10^4 cells/well) was added to EdU medium, and fluorescence staining solution was added after incubation. The DNA replication activity of the fluorescently labeled mixture at 350 nm was tested applying a fluorescence microscope (Troth & Kyle, 2021).

Transwell assay

Transfected HEC-1A cells (2×10^4 cells/well) were seeded on transwell plates. The upper chamber covered serum-free DMEM (Gibco, USA), and the lower chamber covered 600 μL DMEM and 10% FBS. The upper cavity was incubated, fixed with 95% ethanol and stained. The number of cells in 5 fields was calculated randomly to analyze the migration ability of cells. Matrigel was flattened on each transwell plate and placed. After the basement membrane gel was solidified, hydration of the basement membrane was with serum-free DMEM to analyze the cell invasion ability (Huang & Li, 2021).

Flow cytometry detection

Cells were stained with fluorescein isothiocyanate (FITC) kit (ThermoFisher, USA) according to the manufacturer's instructions. The adherent cells were harvested

by trypsin; The supernatant was taken by centrifugation for the second time and mixed with the binding solution, V-FITC and propidium iodide in the kit for incubation. Part of the sample solution was added into the buffer to take effect, and then flow cytometry was performed (Zong *et al.*, 2020).

Reverse transcription quantitative polymerase chain reaction (RT-qPCR)

Total RNA from BMSC cells was extracted via Trizol reagent (Invitrogen, Carlsbad, CA, USA). Assessment of the quantity and quality of RNA was via adopting a NanoDrop spectrophotometer (Thermo, USA). Then, reverse transcription of the RNA was into cDNA employing PrimeScript RT Master Mix (Takara, Dalian, China). Glyceraldehyde-3-phosphate dehydrogenase (GAPDH) and U6 were applied as the loading controls for mRNA and miRNA separately. Primer sequences were manifested in Table 1. PCR detection was performed in the light of the instructions of Hieff® qPCR SYBR® Green Master Mix (Yisheng Bio, Shanghai, China), and the $2^{-\Delta\Delta\text{Ct}}$ method was put into effect to calculate circCAMSAP1, miR-370-3p and MAPK1 in EC cells (Huang *et al.*, 2020).

Western blot detection

Cells were lysed by Radio-Immunoprecipitation assay-covering lysis buffer (Beyotime, Shanghai, China), and the supernatant was harvested after high-speed centrifugation (12000 rpm/min, 15 min) at 4°C . The protein concentration's detection was by bicinchoninic acid kit (Enzyme-Linked Biology, China). Isolation of proteins was by Sodium dodecyl sulfate-polyacrylamide gel electrophoresis (120 V, 1.5 h) and electrically transferring to polyvinylidene fluoride membrane was conducted (300 mA, 1.5 h). Incubation of membranes was with primary antibody MAPK1, anti-E-Cadherin antibody, anti-N-Cadherin antibody and anti-GAPDH antibody (all 1:1000) overnight at 4°C , add horseradish peroxidase-labeled goat anti-rabbit secondary antibody (1:5000) for 1 h. Antibodies were bought from Abbott (Shanghai, China). After incubation, electrogenerated chemiluminescence luminescent solution (Yisheng Bio, Shanghai, China) was used to obtain bands and calculation of protein expression were conducted (Yang *et al.*, 2021).

Table 1. Primer sequence

Genes	Primer sequence	
MiR-370-3p	F	GCCGAGGCCTGCTGGGGTGG
	R	GCAGGGTCCGAGGTATTC
U6	F	GCTTCGGCAGCACATATACTAAAAT
	R	CGCTTCACGAATTGCGTGTCTAT
CircCAMSAP1	F	GTGTCAAGCGCTTCTCAACG
	R	GCTGGACAGGAGAAGCTTGA
MAPK1	F	TGGATTCCTGTTCTCTCTAAAG
	R	GGGTCTGTTTCCGAGGATGA
GAPDH	F	CGCTCTGCTCCTCTCTGTTT
	R	ATCCGTTGACTCCGACCTTCAC

The luciferase activity assay

HEC-1A cells were seeded in 24-well plates to reach 65% confluence. circCAMSAP1 or MAPK1 3'UTR WT and MUT (Zima Pharmaceuticals, Shanghai, China) were cloned into empty plasmids (Miaoling Bio, Wuhan, China). Lipofectamine 2000 (ThermoFisher, USA) was employed for co-transfecting luciferase reporter plasmids into cells with miR-370-3p-mimic and miR-370-3p-NC. Then measurement of the luciferase activity of the samples was conducted applying a dual luciferase reporter gene analysis system (Promega, Shanghai, China).

RNA immunoprecipitation (RIP) assay

EZ-Magna RIP kit (Millipore, USA) was applied for RIP determination. Cells were lysed in RIP lysis buffers and then incubated in RIP buffers covered with magnetic beads coupled with negative controls (normal mouse IgG) or human anti-Argonaute 2 (Ago2, Millipore). Then, conducting Isolation, purification, and final detection by RT-qPCR of the co-precipitated RNA (Wang & Yang, 2021).

Statistical analysis

Data were analyzed employing PSS 24.0 software and presented as mean \pm standard deviation (S.D.). A *t*-test was used for the comparison between the two groups with normal distributions, a nonparametric test was used for the comparison between the two groups with abnormal distributions. Repeating all functional tests in the research was for three times. GraphPad Prism 7.0 software was applied to draw the result pictures, and evaluation of the correlation between the expression levels and cells was by the linear correlation coefficient *r*. *P* < 0.05 clarified statistical significance.

RESULTS

CircCAMSAP1 is elevated in EC cell lines and tissues

In contrast with adjacent normal tissues, circCAMSAP1 was clearly enhanced in EC tissues (*P* < 0.05) (Fig. 1A). Compared with hEEC, circCAMSAP1 was also elevated in HEC-1A, HEC-1B and KLE cells (*P* < 0.05). Among them, HEC-1A cells had the highest expression (*P* < 0.01), followed by the lowest expression of KLE, and HEC-1B (Fig. 1B). Since circCAMSAP1 had the highest expression in HEC-1A cells, HEC-1A cells were chosen for subsequent experiments. These data suggested circCAMSAP1 might participate in the EC disease process.

The effect of knockdown circCAMSAP1 on the biological function of EC cells

After transfection of si-circCAMSAP1, circCAMSAP1 in cells was clearly reduced (*P* < 0.05) (Fig. 2A). Cell progression results showed knocking down circCAMSAP1 reduced cell proliferation (*P* < 0.05) (Fig. 2B), and EdU positive cells declined (*P* < 0.05) (Fig. 2C). Meanwhile, the amount of N-cadherin declined in HEC-1A cells (both *P* < 0.05) (Fig. 2D–E); Cell migration and invasion ability were descended (both *P* < 0.05) (Fig. 2F–G). Moreover, the apoptosis rate was enhanced after knockdown circCAMSAP1 (*P* < 0.05) (Fig. 2H). These data conveyed silencing circCAMSAP1 could refrain EC cells' advancement.

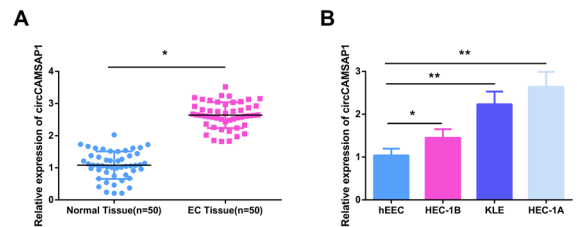


Figure 1. CircCAMSAP1 is elevated in EC cell lines and tissues (A, B) CircCAMSAP1 in EC tissues and cell lines; Measurement data were clarified as mean \pm S.D.; **P* < 0.05, ***P* < 0.01.

CircCAMSAP1 targets miR-370-3p

Plentiful studies have clarified circRNA takes on a role in controlling diseases via competitive adsorption of downstream miRNAs (Tu *et al.*, 2021). The target genes of circCAMSAP1 were forecast employing the bioinformatics database, and miR-370-3p was found to be a candidate target gene of circCAMSAP1 (Fig. 3A). The results of luciferase activity assay illustrated the luciferase activity of HEC-1A cells were declined after co-transfection of miR-370-3p-mimic and circCAMSAP1 WT, while the co-transfection of miR-370-3p-mimic and circCAMSAP1 MUT had no clear impact on luciferase activity (*P* < 0.05) (Fig. 3B). After transfection of si-circCAMSAP1, miR-370-3p in HEC-1A cells was clearly enhanced (*P* < 0.05) (Fig. 3C). Meanwhile, it was also confirmed that circCAMSAP1 and miR-370-3p were abundant in the anti-Ago group (both *P* < 0.05) (Fig. 3D). Moreover, miR-370-3p in EC tissues and cell lines was clearly reduced vs. adjacent normal tissues and hEEC cells (both *P* < 0.05) (Fig. 3E–F); MiR-370-3p was opposite to that of circCAMSAP1 (*r* = -0.7929, *P* < 0.0001) (Fig. 3G). The above results proved miR-370-3p was circCAMSAP1's target gene, and the expression patterns of the two were inversely associated.

Elevation of miR-370-3p can depress EC cell evil behavior

MiR-370-3p's biological role in EC was examined by functional acquisition experiments. After introduction of miR-370-3p-inhibitor, miR-370-3p-mimic and mimic/inhibitor-NC into HEC-1A cells, miR-370-3p was measured. It turned out transfection of miR-370-3p-mimic/inhibitor elevated but reduced miR-370-3p respectively (*P* < 0.05) (Fig. 4A). The results of functional experiments clarified miR-370-3p-mimic refrained the proliferation ability of HEC-1A cells, and fewer EdU positive cells exhibited (both *P* < 0.05) (Fig. 4B–C). Meanwhile, the amount of E-cadherin was elevated but the amount of N-cadherin was declined (both *P* < 0.05) (Fig. 4D–E), cell migration and invasion abilities were descended, but apoptosis rate was enhanced (both *P* < 0.05) (Fig. 4F–H). The opposite results were gained after transfection of miR-370-3p-inhibitor. These experimental results exhibited elevation of miR-370-3p could refrain EC cell biological function.

Depressive miR-370-3p blocks the therapeutic effect of silencing circCAMSAP1

Transfection or co-transfection of si-circCAMSAP1 and miR-370-3p-inhibitor was to study their effects and regulation on the malignant behavior of EC cells. After transfection with si-circCAMSAP1, miR-370-3p in HEC-1A cells were elevated, while after co-transfection with

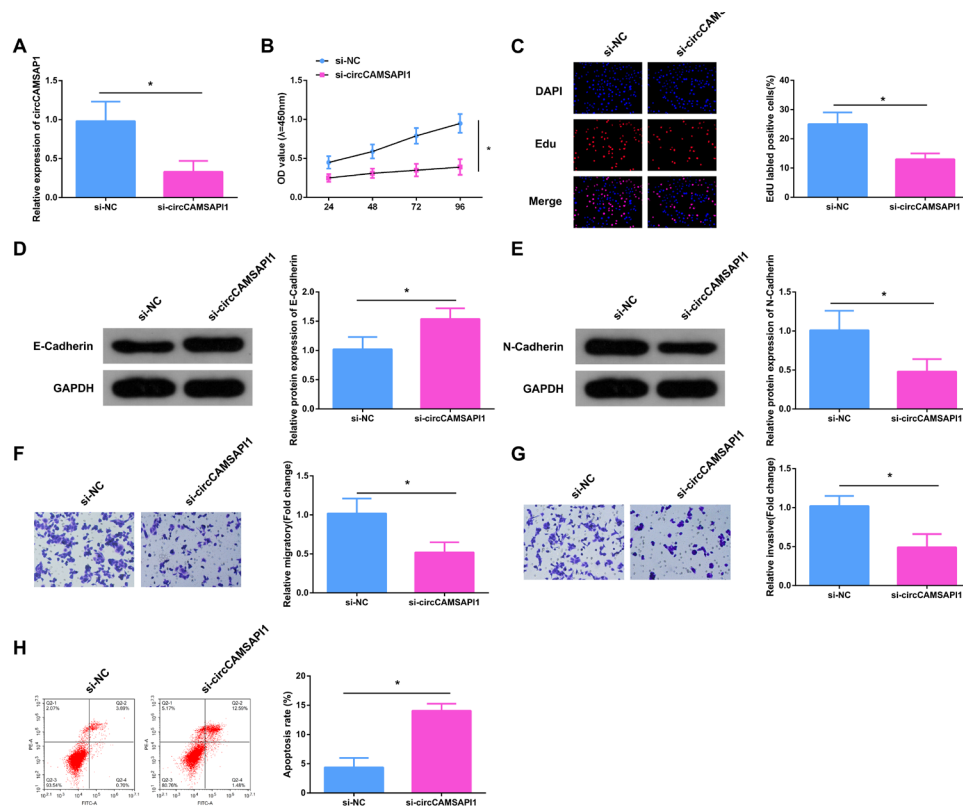


Figure 2. The effect of knockdown circCAMSAP1 on the biological function of EC cells

(A) RT-qPCR to test circCAMSAP1; (B–C) CCK-8 and EdU experiments to evaluate the effect of circCAMSAP1 down-regulation on EC cell proliferation; (D–E) Western blot to examine the amount of E-cadherin and N-cadherin after repressing circCAMSAP1; (F–G) Transwell assay to evaluate the effect of circCAMSAP1 down-regulation on EC cell migration and invasion; (H) EC cell apoptosis rate after circCAMSAP1 down-regulation was detected by flow cytometry; * $P < 0.05$.

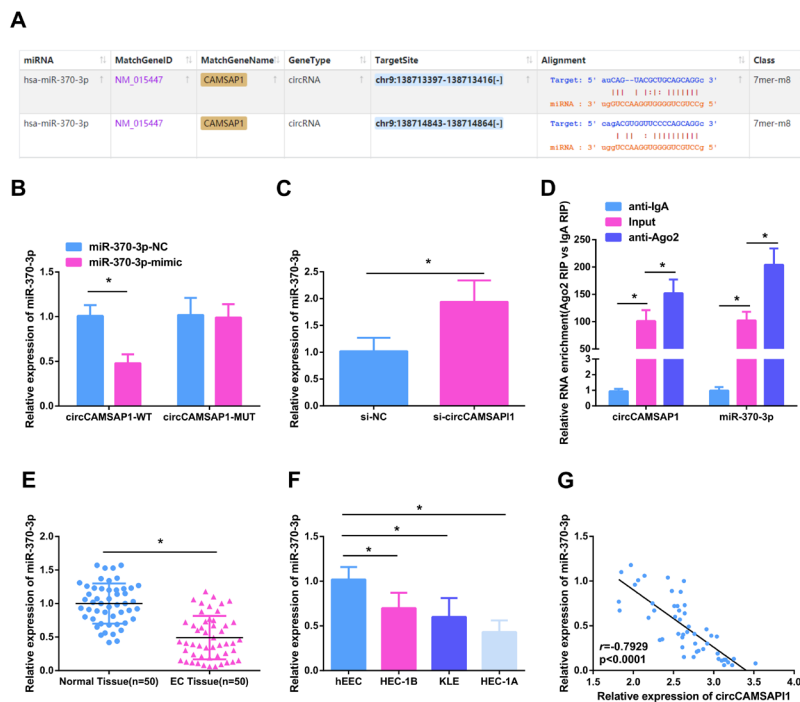


Figure 3. CircCAMSAP1 targets miR-370-3p

(A) Binding region of miR-370-3p and circCAMSAP1; (B) The luciferase activity assay to detect circCAMSAP1 and miR-370-3p's targeting; (C) MiR-370-3p after silencing circCAMSAP1; (D) CircCAMSAP1 and miR-370-3p were enriched in anti-Ago2 group; (E–F) MiR-370-3p in EC tissues and cells; (G) Correlation between circCAMSAP1 and miR-370-3p expression pattern; * $P < 0.05$.

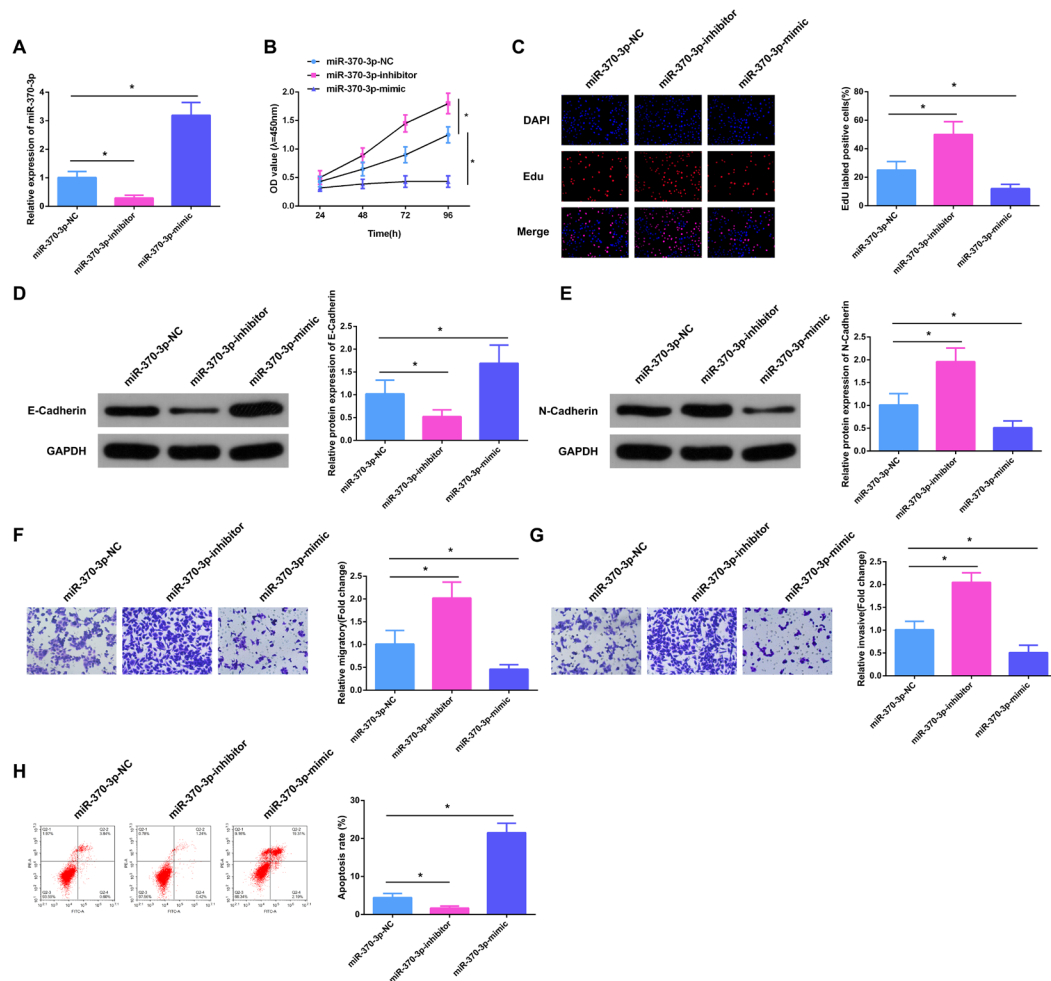


Figure 4. Elevation of miR-370-3p can depress EC cells' biological behaviors

MiR-370-3p in EC cells was regulated by transfection of miR-370-3p-mimic /inhibitor. (A) RT-qPCR to test miR-370-3p; (B–C) CCK-8 and EdU experiments to examine cell proliferation; (D–E) Western blot to examine the amount of E-cadherin and N-cadherin; (F–G) Transwell assay to check cell migration and invasion; (H) EC cell apoptosis was detected by flow cytometry; * $P < 0.05$.

si-circCAMSAP1 and miR-370-3p-inhibitor, miR-370-3p in HEC-1A cells were declined (both $P < 0.05$) (Fig. 5A). After circCAMSAP1 was silenced, the proliferation ability of HEC-1A cells (both $P < 0.05$) (Fig. 5B), and the number of EDU-positive cells were declined (Fig. 5C), the amount of E-cadherin was elevated but the amount of N-cadherin was declined (both $P < 0.05$) (Fig. 5D–E); The migration and invasion abilities were repressed (both $P < 0.05$) (Fig. 5F–G), but the apoptosis rate was enhanced ($P < 0.05$) (Fig. 5H). These effects were blocked by transfection of miR-370-3p-inhibitor. These data suggested silencing circCAMSAP1 downregulated EC and blocked the malignant behavior of miR-370-3p-inhibitor in EC cells.

MiR-370-3p targeted MAPK1

MiRNAs frequently combines with the 3 untranslated regions of mRNA and are transcribed to control miRNA expression (Jiang *et al.*, 2021). Therefore, it was predicted the target mRNA of miR-370-3p by StarBase and discovered a latent binding site between MAPK1 and miR-370-3p (Fig. 6A). It came out MAPK1 was elevated in EC tissues and cells (both $P < 0.05$) (Fig. 6B–C). In the light of the validation results of the bidirectional luciferase activity assay, transfection of miR-370-3p-mimic clearly

restrained the reporter activity of MAPK1-WT, while miR-370-3p-inhibitor elevated the reporter activity of MAPK1-WT. The reporter activity of MAPK1-MUT was almost unchanged ($P < 0.05$) (Fig. 6D). Meanwhile, it came out miR-370-3p and MAPK1 were also abundant in the anti-Ago2 group (both $P < 0.05$) (Fig. 6E). Furthermore, miR-370-3p-mimic downregulated MAPK1, whereas miR-370-3p-inhibitor did the opposite (both $P < 0.05$) (Fig. 6 F–G). These results clarified miR-370-3p inversely controlled MAPK1 in EC cells. Linear analysis exhibited MAPK1 was negatively linked with miR-370-3p ($r = -0.7086$, $P < 0.0001$) (Fig. 6H). The above experimental results conveyed circCAMSAP1 could target MAPK1 through miR-370-3p.

Si-MAPK1 turns around the malignant effect of pcDNA-circCAMSAP1

Functional rescue experiments were conducted to figure out the mechanism by which circCAMSAP1 controls EC development through the miR-370-3p/MAPK1 molecular axis. The experimental results manifested after transfection of pcDNA-circCAMSAP1, miR-370-3p in HEC-1A cells was reduced but MAPK1 was elevated. After co-transfection of pcDNA-circCAMSAP1 and si-MAPK1, miR-370-3p was enhanced but MAPK1 was

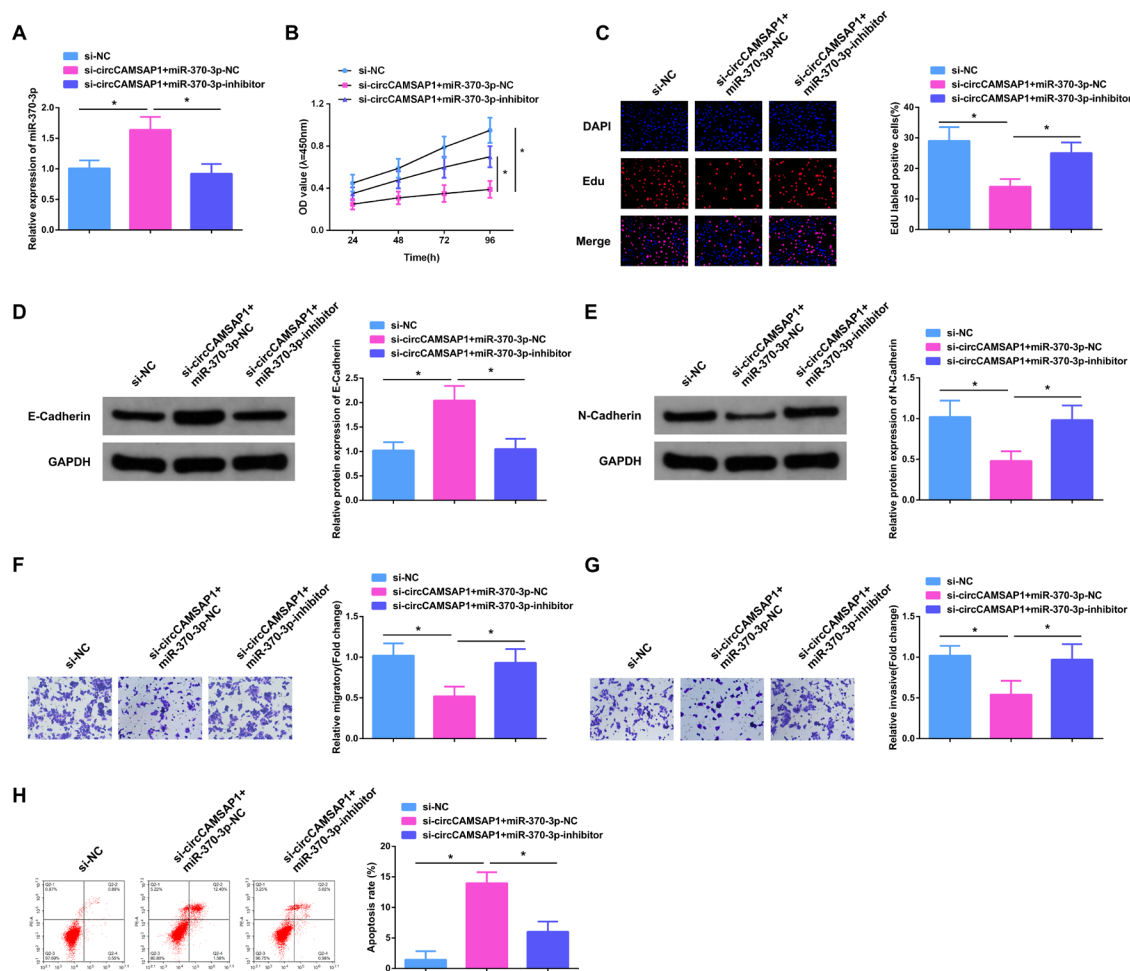


Figure 5. Depressive miR-370-3p blocks the therapeutic effect of silencing circCAMSAP1

Si-circCAMSAP1 was blocked by transfection with miR-370-3p-inhibitor. (A) RT-qPCR to test miR-372-3p; (B–C) CCK-8 and EdU experiments to examine cell proliferation; (D–E) Western blot to examine the amount of E-cadherin and N-cadherin; (F–G) Transwell assay to check cell migration and invasion; (H) EC cell apoptosis was detected by flow cytometry; * $P < 0.05$.

decreased in HEC-1A cells (both $P < 0.05$) (Fig. 7A). Results of functional experiments confirmed the proliferation ability of HEC-1A cells was enhanced after elevation of circCAMSAP1 ($P < 0.05$) (Fig. 7B), and the number of EDU-positive cells was elevated ($P < 0.05$) (Fig. 7C). Meanwhile, the amount of E-cadherin was reduced but the amount of N-cadherin was elevated (Fig. 7D–E), cell migration and invasion ability were strengthened (both $P < 0.05$) (Fig. 7F–G), but apoptosis rate was declined ($P < 0.05$) (Fig. 7H). These effects were blocked by transfection of si-MAPK1. The experimental results showed elevation of circCAMSAP1 up-regulated MAPK1 by depressing miR-370-3p.

DISCUSSION

Targeted therapy can impact tumor cell growth, apoptosis, signaling, receptor activation, etc., and is considered as a breakthrough in human cancer therapy (Padma *et al.*, 2015). Noncoding RNAs are increasingly momentous in this field as they are implicated in clinical and functional cancer development (Wang *et al.*, 2019). Although patients with early-stage EC have a relevant high survival rate, patients with advanced or recurrent disease still have poor prognosis and limited treatment options

(Mitamura *et al.*, 2019). This study contrasted circCAMSAP1 in EC tissue samples and cells with normal paracancerous tissues and cells for the first time, and found that circCAMSAP1 was elevated in EC tissues and cells, suggesting that circCAMSAP1 might have adverse effects on EC development.

CircRNAs, highly conserved and stable non-coding RNAs, have received extensive attention owing to their great potential in cancer therapy (Barrett & Salzman, 2016). They have diversified miRNAs binding sites, which can mediate the activity of targeted miRNAs and competitively combine them, thereby depressing the transcription of downstream target genes (Mitra *et al.*, 2018). For instance, circ_0001073 targeting miR-626 can depress the occurrence and development of lung cancer (Liu *et al.*, 2021a); Circ_0004507 targeting miR-873 can upregulate drug resistance proteins, thereby motivating the development of laryngeal cancer (Yi *et al.*, 2021). In former studies, it is found that CAMSAP1 is a gene encoding mammalian astroglial cytoskeleton and neuron-associated cytoskeleton-linked proteins (Yamamoto *et al.*, 2009). Meanwhile, CAMSAP1 is expressed on mature astrocytes in the adult brain and is also considered a novel marker of cells of the astrocyte lineage (Yoshioka *et al.*, 2012). Circ_0001900 derived from exons 2 to 3 of the CAMSAP1 gene, also known as circCAMSAP1,

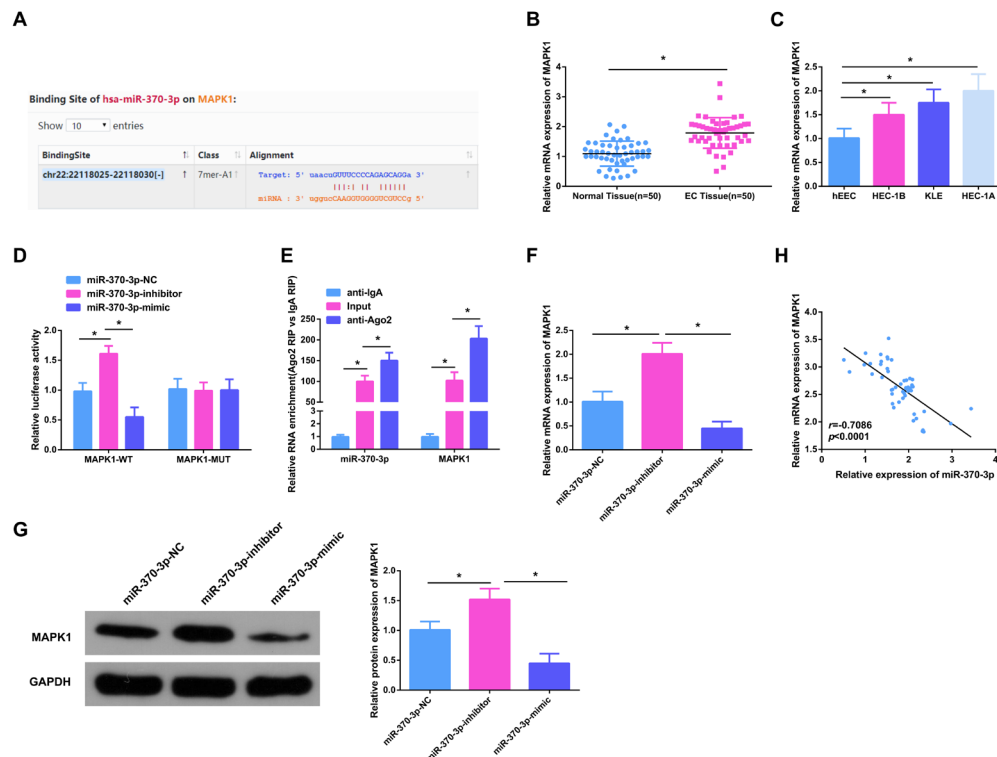


Figure 6. MiR-370-3p targeted MAPK1

(A) Binding region of miR-370-3p and MAPK1; (B, C) MAPK1 in EC tissues and cells; (D) The luciferase activity assay to detect miR-370-3p and MAPK1's targeting; (E) MiR-370-3p and MAPK1 were abundant in anti-Ago2 group; (F–G) RT-qPCR and western blot examination of miR-370-3p and MAPK1's targeting; (H) Correlation between MAPK1 and miR-370-3p; * $P < 0.05$.

which has been clarified to have a momentous role in colorectal cancer. Circ_0004338 (circCAMSAP1 in the research) is derived from exons 1 to 7 of the CAMSAP1 gene and is spliced to form a single-stranded continuous loop structure network by connecting the 3' and 5' ends. These features convey circCAMSAP1 is formed by “direct splicing” and is stably expressed in different cell lines and tissues (Jeck *et al.*, 2014). Although circCAMSAP1 has been well studied in plentiful cancers, it has been less studied in EC. This study is the first to propose and demonstrate that circCAMSAP1 was elevated in EC, and its expression is significant. In the light of the experimental results, knockout of circCAMSAP1 can reduce the proliferation, migration, and invasion of EC cells, but motivate cancer cell apoptosis.

Recently, studies have found circRNAs can combine with miRNAs, thereby exerting tumor-promoting or tumor-suppressing effects (Han *et al.*, 2017). Using Starbase database, circCAMSAP1 and miR-370-3p were found to have binding sites. Subsequent analysis showed circCAMSAP1 refrained miR-370-3p in EC cells. The role of miR-370 as a tumor-promoting or tumor-suppressor gene in different human tumors is controversial. For instance, miR-370 is a latent oncogene in melanoma (Wei *et al.*, 2017); up-regulation of miR-370 suppresses the tumor suppressor FOXO1 in prostate and gastric cancers and motivates cancer cell proliferation (Fan *et al.*, 2013). In contrast, miR-370 has been testified to perform as a tumor suppressor in colon and liver cancer by depressing cell proliferation and accelerating apoptosis (Shen *et al.*, 2018; Sun *et al.*, 2016). In this study, the correlation of miR-370-3p with EC was figured out for the first time, and it was found to be reduced in EC cells. Meanwhile, the results of luciferase activity assay confirmed miR-

370-3p had a binding site with circCAMSAP1, and circCAMSAP1 could target miR-370-3p. The experimental results clarified elevation of miR-370-3p could depress the proliferation, migration and invasion of EC cells but accelerate apoptosis, and restraining miR-370-3p blocked the therapeutic effect of silencing circCAMSAP1. These data demonstrated miR-370-3p could downregulate EC and accelerate cancer cell apoptosis.

The MAPK signaling cascade is an intracellular series of serine/threonine protein kinases that take on key roles in diversified cellular functions (Xiong *et al.*, 2021). Studies have shown the p38-MAPK signaling pathway participates in signal transduction, and is initiated by extracellular signals to initiate cascade transduction. Phospho-p38-MAPK forms double phosphorylation through threonine and tyrosine binding sites, and is transferred to the nucleus. Depending on the corresponding target, this can motivate hepatic stellate cell activation (Yang *et al.*, 2021). Meanwhile, MAPK can also control various cellular activities, such as proliferation, differentiation, apoptosis, etc. (Yi *et al.*, 2021). Some studies have suggested MAPK signaling is a promising target for cancer therapeutic intervention (Zhang *et al.*, 2021). As a member of the MAPK family, MAPK1 is a extensively used oncogene that can be activated or expressed, and is elevated in various types of human cancers (Zhao *et al.*, 2021). At present, MAPK1 has been confirmed to combine with diversified miRNAs to regulate downstream signals to achieve cell biological functions (Liu *et al.*, 2021b). This study originally demonstrated miR-370-3p could bind MAPK1 to regulate EC. In the light of the target gene prediction and the results of the bidirectional luciferase activity assay, this study confirmed MAPK1 was miR-370-3p's target gene, and miR-370-3p could

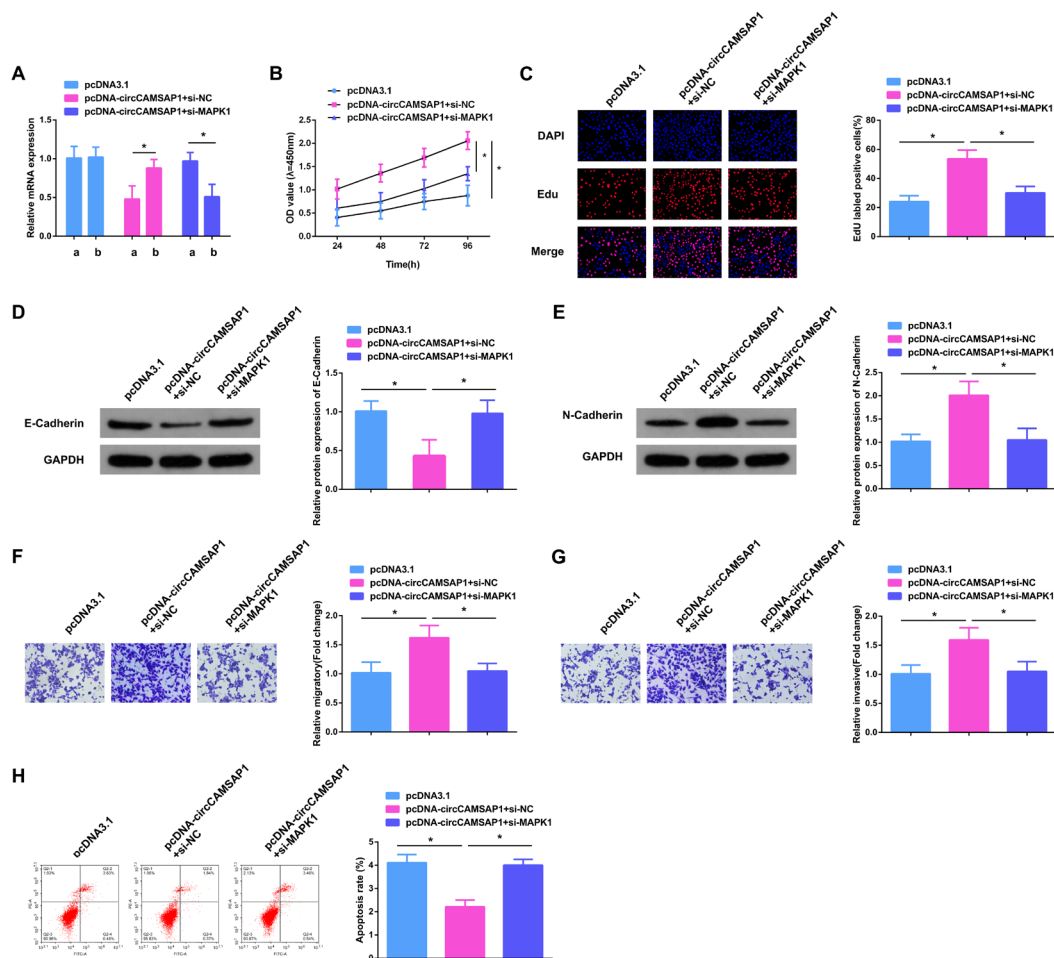


Figure 7. Si-MAPK1 turns around the malignant effect of pcDNA-circCAMSAP1

PcDNA 3.1-circCAMSAP1 was reversed by transfection of si-MAPK1. (A) RT-qPCR to test miR-370-3p (a) and MAPK1 (b); (B–C) CCK-8 and EdU experiments to examine cell proliferation; (D–E) Western blot to examine the amount of E-cadherin and N-cadherin; (F–G) Transwell assay to check cell migration and invasion; (H) EC cell apoptosis was detected by flow cytometry; * $P < 0.05$.

negatively regulate MAPK1. MAPK1 was elevated. The present study also found silencing MAPK1 could reverse the malignant effects of overexpressing circCAMSAP1 on cells. These experimental results suggested MAPK1 could regulate EC and upregulate disease.

CONCLUSION

In summary, silencing circCAMSAP1 can restrain EC cells' biological functions by targeting the miR-370-3p/MAPK1 molecular axis. The circCAMSAP1/miR-370-3p/MAPK1 axis can become a new marker for EC diagnosis and treatment, and offer a theoretical basis for more research later. However, the research still takes on several limitations. In the research, it was only figured out the circCAMSAP1/miR-370-3p/MAPK1 signaling pathway, more mechanistic signaling pathways, and the possibility of targeting miR-370-3p or MAPK1 to treat EC require to be explored, and further investigation and research are needed.

Declarations

Conflict of interest statement. There are no conflicts to declare.

Acknowledgements. Not applicable.

Funding. Not applicable.

REFERENCE

- Barrett SP, Salzman J (2016) Circular RNAs: analysis, expression and potential functions. *Development* **143**: 1838–1847. <https://doi.org/10.1242/dev.128074>
- Bueno MJ, Pérez de Castro I, Malumbres M (2008) Control of cell proliferation pathways by microRNAs. *Cell Cycle* **7**: 3143–3148. <https://doi.org/10.4161/cc.7.20.6833>
- Chen Z, Xu W, Zhang D, Chu J, Shen S, Ma Y, Wang Q, Liu G, Yao T, Huang Y, Ye H, Wang J, Ma J, Fan S (2021) circCAMSAP1 Promotes osteosarcoma progression and metastasis by sponging miR-145-5p and regulating FLI1 expression. *Mol Ther Nucleic Acids* **23**: 1120–1135. <https://doi.org/10.1016/j.omtn.2020.12.013>
- Ebbesen KK, Hansen TB, Kjems J (2017) Insights into circular RNA biology. *RNA Biol* **14**: 1035–1045. <https://doi.org/10.1080/15476286.2016.1271524>
- Fan C, Liu S, Zhao Y, Han Y, Yang L, Tao G, Li Q, Zhang L (2013) Upregulation of miR-370 contributes to the progression of gastric carcinoma via suppression of FOXO1. *Biomed Pharmacother* **67**: 521–526. <https://doi.org/10.1016/j.biopha.2013.04.014>
- Finnsen KW, Chi Y, Bou-Gharios G, Leask A, Philip A (2012) TGF- β signaling in cartilage homeostasis and osteoarthritis. *Front Biosci (Schol Ed)* **4**: 251–268. <https://doi.org/10.2741/s266>
- Han D, Li J, Wang H, Su X, Hou J, Gu Y, Qian C, Lin Y, Liu X, Huang M, Li N, Zhou W, Yu Y, Cao X (2017) Circular RNA circ-MTO1 acts as the sponge of microRNA-9 to suppress hepatocel-

- lular carcinoma progression. *Hepatology* **66**: 1151–1164. <https://doi.org/10.1002/hep.29270>
- Hu Z, Mamillapalli R, Taylor HS (2019) Increased circulating miR-370-3p regulates steroidogenic factor 1 in endometriosis. *Am J Physiol Endocrinol Metab* **316**: E373–E382. <https://doi.org/10.1152/ajpendo.00244.2018>
- Huang D, Li C (2021) circ-ACACA promotes proliferation, invasion, migration and glycolysis of cervical cancer cells by targeting the miR-582-5p/ERO1A signaling axis. *Oncol Lett* **22**: 795. <https://doi.org/10.3892/ol.2021.13056>
- Huang W, Lu Y, Wang F, Huang X, Yu Z (2020) Circular RNA circ-cRNA_103809 accelerates bladder cancer progression and enhances chemo-resistance by activation of miR-516a-5p/FBXL18 axis. *Cancer Manag Res* **12**: 7561–7568. <https://doi.org/10.2147/cmar.s263083>
- Jeck WR, Sharpless NE (2014) Detecting and characterizing circular RNAs. *Nat Biotechnol* **32**: 453–461. <https://doi.org/10.1038/nbt.2890>
- Jiang C, Xu M, Zhu J, Yang D, Xue B (2022) CircTHBS1 facilitates the progression of interstitial cystitis depending on the regulation of miR-139-5p/MFN2 axis. *Drug Dev Res* **83**: 351–361. <https://doi.org/10.1002/ddr.21864>
- Cancer Genome Atlas Research Network; Kandoth C, Schultz N, Cherniack AD, Akbani R, Liu Y, Shen H, Robertson AG, Pashtan I, Shen R, Benz CC, Yau C, Laird PW, Ding L, Zhang W, Mills GB, Kucherlapati R, Mardis ER, Levine DA (2013) Integrated genomic characterization of endometrial carcinoma. *Nature* **497**: 67–73. <https://doi.org/10.1038/nature12113>
- Leslie KK, Sill MW, Lankes HA, Fischer EG, Godwin AK, Gray H, Schilder RJ, Walker JL, Tewari K, Hanjani P, Abulafia O, Rose PG (2012) Lapatinib and potential prognostic value of EGFR mutations in a Gynecologic Oncology Group phase II trial of persistent or recurrent endometrial cancer. *Gynecol Oncol* **127**: 345–350. <https://doi.org/10.1016/j.ygyno.2012.07.127>
- Liu Q, Cao G, Wan Y, Xu C, He Y, Li G (2021) Hsa_circ_0001073 targets miR-626/LIFR axis to inhibit lung cancer progression. *Environ Toxicol* **36**: 1052–1060. <https://doi.org/10.1002/tox.23104>
- Liu Y, Wu Y, Zhu Z, Gong J, Dou W (2021) Knockdown of lncRNA PVT1 inhibits the proliferation and accelerates the apoptosis of colorectal cancer cells via the miR-761/MAPK1 axis. *Mol Med Rep* **24**. <https://doi.org/10.3892/mmr.2021.12434>
- Luo Z, Lu L, Tang Q, Wei W, Chen P, Chen Y, Pu J, Wang J (2021) CircCAMSAP1 promotes hepatocellular carcinoma progression through miR-1294/GRAMD1A pathway. *J Cell Mol Med* **25**: 3793–3802. <https://doi.org/10.1111/jcmm.16254>
- Mitamura T, Dong P, Ihira K, Kudo M, Watari H (2019) Molecular-targeted therapies and precision medicine for endometrial cancer. *Jpn J Clin Oncol* **49**: 108–120. <https://doi.org/10.1093/jcco/hyy159>
- Mitra A, Pfeifer K, Park KS (2018) Circular RNAs and competing endogenous RNA (ceRNA) networks. *Transl Cancer Res* **7**: S624–S628. <https://doi.org/10.21037/tcr.2018.05.12>
- Oza AM, Pignata S, Poveda A, McCormack M, Clamp A, Schwartz B, Cheng J, Li X, Campbell K, Dodion P, Haluska FG (2015) Randomized phase II trial of *Ridaforolimus* in advanced endometrial carcinoma. *J Clin Oncol* **33**: 3576–3582. <https://doi.org/10.1200/jco.2014.58.8871>
- Padma VV (2015) An overview of targeted cancer therapy. *Biomedicine (Taipei)* **5**: 19. <https://doi.org/10.7603/s40681-015-0019-4>
- Shen X, Zuo X, Zhang W, Bai Y, Qin X, Hou N (2018) MiR-370 promotes apoptosis in colon cancer by directly targeting MDM4. *Oncol Lett* **15**: 1673–1679. <https://doi.org/10.3892/ol.2017.7524>
- Sonoda Y (2014) Surgical treatment for apparent early stage endometrial cancer. *Obstet Gynecol Sci* **57**: 1–10. <https://doi.org/10.5468/ogs.2014.57.1.1>
- Sun G, Hou YB, Jia HY, Bi XH, Yu L, Chen DJ (2016) MiR-370 promotes cell death of liver cancer cells by Akt/FoxO3a signaling pathway. *Eur Rev Med Pharmacol Sci* **20**: 2011–2019. PMID: 27249599
- Suzuki H, Tsukahara T (2014) A view of pre-mRNA splicing from RNase R resistant RNAs. *Int J Mol Sci* **15**: 9331–9342. <https://doi.org/10.3390/ijms15069331>
- Troth EV, Kyle DE (2021) EdU incorporation to assess cell proliferation and drug susceptibility in *Naegleria fowleri*. *Antimicrob Agents Chemother* **65**: e0001721. <https://doi.org/10.1128/aac.00017-21>
- Tu Q, You X, He J, Hu X, Xie C, Xu G (2021) Circular RNA Circ-0003006 promotes hepatocellular carcinoma proliferation and metastasis through sponging miR-542-3p and regulating HIF-1A. *Cancer Manag Res* **13**: 7859–7870. <https://doi.org/10.2147/cmar.s315894>
- Wang G, Yang H (2021) CircRNA DUSP16 knockdown suppresses colorectal cancer progression by regulating the miR-432-5p/E2F6 Axis. *Cancer Manag Res* **13**: 6599–6609. <https://doi.org/10.2147/cmar.s323437>
- Wang WT, Han C, Sun YM, Chen TQ, Chen YQ (2019) Noncoding RNAs in cancer therapy resistance and targeted drug development. *J Hematol Oncol* **12**: 55. <https://doi.org/10.1186/s13045-019-0748-z>
- Wei S, W (2017) MiR-370 functions as oncogene in melanoma by direct targeting pyruvate dehydrogenase B. *Biomed Pharmacother* **90**: 278–286. <https://doi.org/10.1016/j.bioph.2017.03.068>
- Wilczynski M, Senderowska D, Krawczyk T, Szymanska B, Malinowski A (2020) MiRNAs in endometrioid endometrial cancer metastatic loci derived from positive lymph nodes. *Acta Obstet Gynecol Scand* **99**: 1085–1091. <https://doi.org/10.1111/aogs.13833>
- Xiong H, Yu H, Jia G, Yu J, Su Y, Zhang J, Zhou J (2021) circZFR regulates thyroid cancer progression by the miR-16/MAPK1 axis. *Environ Toxicol* **36**: 2236–2244. <https://doi.org/10.1002/tox.23337>
- Yamamoto M, Yoshimura K, Kitada M, Nakahara J, Seiwa C, Ueki T, Shimoda Y, Ishige A, Watanabe K, Asou H (2009) A new monoclonal antibody, A3B10, specific for astrocyte-lineage cells recognizes calmodulin-regulated spectrin-associated protein 1 (Camsap1). *J Neurosci Res* **87**: 503–513. <https://doi.org/10.1002/jnr.21853>
- Yang L, Zhou YN, Zeng MM, Zhou N, Wang BS, Li B, Zhu XL, Guan QL, Chai C (2021) Circular RNA Circ-0002570 accelerates cancer progression by regulating VCAN via MiR-587 in gastric cancer. *Front Oncol* **11**: 733745. <https://doi.org/10.3389/fonc.2021.733745>
- Yi X, Chen W, Li C, Chen X, Lin Q, Lin S, Wang D (2021) Circular RNA circ_0004507 contributes to laryngeal cancer progression and cisplatin resistance by sponging miR-873 to upregulate multidrug resistance 1 and multidrug resistance protein 1. *Head Neck* **43**: 928–941. <https://doi.org/10.1002/hed.26549>
- Yoshioka N, Asou H, Hisanaga S, Kawano H (2012) The astrocytic lineage marker calmodulin-regulated spectrin-associated protein 1 (Camsap1): phenotypic heterogeneity of newly born Camsap1-expressing cells in injured mouse brain. *J Comp Neurol* **520**: 1301–1317. <https://doi.org/10.1002/cne.22788>
- Zhang L, Zhang W, Zuo Z, Tang J, Song Y, Cao F, Yu X, Liu S, Cai X (2022) Circ_0008673 regulates breast cancer malignancy by miR-153-3p/CFL2 axis. *Arch Gynecol Obstet* **305**: 223–232. <https://doi.org/10.1007/s00404-021-06149-w>
- Zhao L, Zhou R, Wang Q, Cheng Y, Gao M, Huang C (2021) MicroRNA-320c inhibits articular chondrocytes proliferation and induces apoptosis by targeting mitogen-activated protein kinase 1 (MAPK1). *Int J Rheum Dis* **24**: 402–410. <https://doi.org/10.1111/1756-185x.14053>
- Zhou C, Liu HS, Wang FW, Hu T, Liang ZX, Lan N, He XW, Zheng XB, Wu XJ, Xie D, Wu XR, Lan P (2020) circCAMSAP1 Promotes tumor growth in colorectal cancer via the miR-328-5p/E2F1 axis. *Mol Ther* **28**: 914–928. <https://doi.org/10.1016/j.ymthe.2019.12.008>
- Zhou S, Huang C, Wang W, Liu J (2021) MiR-370-3p inhibits the development of human endometriosis by downregulating EDN1 expression in endometrial stromal cells. *Cell Biol Int* **45**: 1183–1190. <https://doi.org/10.1002/cbin.11552>
- Zong ZH, Liu Y, Chen S, Zhao Y (2020) Circ_PUM1 promotes the development of endometrial cancer by targeting the miR-136/NOTCH3 pathway. *J Cell Mol Med* **24**: 4127–4135. <https://doi.org/10.1111/jcmm.15069>

MiR-92a regulates PTEN/Akt signaling axis to promote paclitaxel resistance in ovarian cancer cells

Xiujuan Deng^{1#}, Haigen Wu^{1#}, Liping Xiong², Mouxi Wu¹, Jinfu Cao¹, Jing Liu³ and Wenyang Xie¹✉

¹Department of Gynaecology, Jiujiang Maternal and Child Health Hospital. Jiujiang, Jiangxi 332000, China; ²Department of Obstetrics and Gynecology, De'an County People's Hospital. Jiujiang, Jiangxi 330499, China; ³Department of Obstetrics and Gynecology, Jiujiang Maternal and Child Health Hospital. Jiujiang, Jiangxi 332000, China

To investigate the function and possible mechanism of miR-92a in malignant behaviors such as paclitaxel resistance in ovarian cancer (OC) cells. The miR-92a and PTEN expression were detected by real-time PCR (RT-PCR). The cell viability and apoptosis were detected by MTT, colony formation and flow cytometry assay, respectively. Dual-luciferase reporter assay was adopted to verify the targeting relationship between miR-92a and PTEN. Besides, we measured the relative protein levels of PTEN and p-AKT/AKT by Western blot. MiR-92a was significantly highly expressed in OC cells, and its high expression could notably enhance paclitaxel resistance, cell proliferation and colony formation, as well as inhibit apoptosis in SKOV3-Tax cells. Further luciferase reporter assay and expression detection showed that miR-92a could target and regulate PTEN and that there was a targeted relationship between them. In addition, further exploration of the mechanism revealed that miR-92a regulated PTEN/Akt signaling pathway. MiR-92a not only promotes the proliferation, colony formation and paclitaxel resistance of SKOV3-Tax cells in OC, but also inhibits apoptosis, and it may be related to the regulation of the PTEN/Akt signaling pathway. MiR-92a serves as a potential biomarker for the malignant biological behavior of OC cells.

Keywords: MiR-92a, PTEN/Akt signaling axis, Ovarian cancer (OC), Paclitaxel resistance, Biomarkers

Received: 04 July, 2022; **revised:** 15 November, 2022; **accepted:** 09 January, 2023; **available on-line:** 03 February, 2023

✉e-mail: 516603686@qq.com

[#]Xiujuan Deng and Haigen Wu contributed equally to this work as Co-first authors

Acknowledgements of Financial Support: Science and Technology Plan of Jiangxi Provincial Health Commission, China No.: SKJP220218084

Abbreviations: miRNAs, microRNAs; OC, ovarian cancer; PI, propidium iodide; Tax, paclitaxel

INTRODUCTION

Ovarian cancer (OC), a common gynecological malignancy in the world, is the fifth leading cause of cancer death (Kossai *et al.*, 2018; Funston *et al.*, 2020). Due to inconspicuous early symptoms, most patients with OC are diagnosed at an advanced stage, and thus their 5-year survival rate is approximately 30% (Sehouli Grabowski, 2019; Rooth, 2013). Chemotherapy and immunotherapy are currently the first-line clinical treatments for OC patients. However, most patients develop resistance after a period of treatment (Narod, 2016; Kurnit *et al.*, 2021; Shang *et al.*, 2019). The main treatment for OC is surgi-

cal resection of the visible tumor followed by chemotherapy adjuvant with drugs such as paclitaxel (Mueller *et al.*, 2016). Most patients with OC develop resistance to paclitaxel leading to recurrence. Nevertheless, the molecular mechanisms of paclitaxel resistance are not yet fully understood. Therefore, exploring effective clinical therapeutic targets and clarifying their mechanism will be conducive to the treatment of OC.

MicroRNAs (miRNAs) are small non-coding RNAs of approximately 18–25 nucleotides in length. As important epigenetic regulators, miRNAs are widespread in the biological community and considered highly conservative (Filipowicz *et al.*, 2008). Much research has demonstrated that miRNAs are involved in the evolution of tumors and play a vital role. For example, miRNAs not only participate in the development of tumors by acting as tumor suppressor genes (Gai *et al.*, 2018) or proto-oncogenes (Huang *et al.*, 2019) but also regulate the proliferation, migration and invasion of tumor cells *via* serving as significant biological molecules. In addition, increasing evidence manifested that aberrantly expressed miRNAs exerted an essential effect on drug resistance or drug sensitivity in chemotherapy (Du Pertsemidis, 2012; De Cecco *et al.*, 2017). As a known carcinogenic miRNA, miR-92a in most cases enhances the development of tumors such as lung cancer (Zhou *et al.*, 2015), cervical cancer (Lin *et al.*, 2013), and pancreatic cancer (Ohayagi-Hara *et al.*, 2013) by regulating the expression of tumor-related genes. In recent years, the biological characteristics and function of miR-92a have been preliminarily understood, but its effect and mechanism in the proliferation, apoptosis and paclitaxel resistance of OC are still unclear. Therefore, we probed into the role of miR-92a in OC by knocking down and overexpressing miR-92a in SKOV3-Tax cells, and its possible molecular regulatory mechanism by bioinformatics prediction and molecular biology experiments. And we believed that with the continuous deepening of the study of miR-92a-related downstream target genes, there would be a scientific basis and clues provided for the diagnosis, treatment and prognosis analysis of OC.

MATERIALS AND METHODS

Cell culture and transfection

Human normal ovarian epithelial cells IOSE80 and OC cell line SKOV3 were purchased from the National Collection of Authenticated Cell Cultures. All cells were cultured in RPMI-1640 medium (Gibco, USA) contain-

ing 10% FBS (Gibco, USA) and 1% penicillin-streptomycin (Gibco, USA) in an incubator at 37°C with 5% CO₂ and 95% humidity. Paclitaxel (Tax)-resistant model cells of SKOV3 (SKOV3-Tax) were constructed using induction of concentration gradient.

NC mimics and miR-92a mimics, NC inhibitor and miR-92a inhibitor were purchased from GenePharma Co., Ltd. (China). SKOV3-Tax cells in the logarithmic growth phase were collected and seeded in a 6-well plate. Transfection was performed when the cells were cultured to about 80% confluence. Subsequently, the above plasmids were transferred into SKOV3-Tax cells according to the instructions of Lipofectamine 2000, and were named NC mimics group, miR-92a mimics group, NC inhibitor group and miR-92a inhibitor group, respectively. The plate was placed in the cell incubator for 48-h culture and then the cells were collected.

Real-time PCR (qRT-PCR)

Total cellular RNA was extracted with Trizol reagent (Invitrogen), and the quality and concentration of extracted RNA were determined by Nanodrop. The cDNA was synthesized by reverse transcription according to the instructions of the reverse transcription-PCR kit (Takara, Japan). The PTEN expression level and miR-92a were tested based on the instructions of the SYBR Green PCR Master Mix kit, with GAPDH and U6 as their internal control genes, respectively. The primer sequences were seen in Table 1. And the data analysis was performed by the 2^{-ΔΔC_t} method (Zhu *et al.*, 2019).

Table 1. Primer Sequences

Genes	Primer Sequences (5' to 3')
PTEN	F ATCAACAGCCAACAAATACC
	R TTCTTATCACCGTCACCCT
miR-92a	F GCTGAGTATTGCACTTGTCCTG
	R GTGTCGTGGAGTCGGCAA
U6	F CTCGCTTCGGCAGCACA
	R AACGCTTCACGAATTGCGT
GAPDH	F GGAGCGAGATCCCTCCAAAAT
	R GGCTGTTGTCATTCTCATTCATGGGG

MTT

The transfected SKOV3-Tax cells were collected and seeded in a 96-well plate at 5×10³ cells/well, and then cultured in a cell incubator until the cell adhesion was presented. Next, the cell proliferation was determined at 0 h- and 24 h- adherence as referring to the instructions of MTT kit (Beyotime, China). And then 20 μl MTT solution (5 mg/ml) was added to each well for 4-h culture. After removal of the supernatant, 150 μl DMSO was added to each well, and they were mixed well at ambient temperature for 5 min to dissolve the formazan crystals. The absorbance value at 490 nm was determined by a

microplate reader. Finally, different concentrations (0, 1, 2, 3, 4, and 5 logs [Tax] nM) of paclitaxel (Tax) were added for 24-h co-culture after cell adhesion presented in the paclitaxel resistance assay, and then cell survival rate was tested by MTT.

Cell colony formation assay

The transfected SKOV3-Tax cells were collected and seeded in a 6-well plate at 800 cells/well, and then cultured in a cell incubator for 10–14 days. After they formed macroscopic clones, the culture medium was discarded. Afterwards, the cultured cells were fixed with 4% paraformaldehyde (Beyotime, China) for 15 min, and later stained with a crystal violet staining solution (Beyotime, China). The excess staining solution was washed off with PBS and eventually the cells were dried and photographed.

Flow cytometry

Annexin V-FITC/propidium iodide (PI) apoptosis detection kit (BD Pharmingen, USA) was applied to detect SKOV3-Tax in apoptosis. The cells were collected and washed twice with cold PBS buffer, and 500 μl of 1× Binding Buffer was adopted to prepare 1×10⁶ cells/ml cell suspension. With the addition of 5 μl of Annexin V-FITC solution, the treated cells were incubated in the dark for 15 min, followed by 10 μl of PI solution at ambient temperature (20–25°C) for another incubation in the dark for 5 min. Lastly, the early and late apoptosis rates of the cells were measured by a flow cytometry system (Becton Coulter, USA) within 1 h.

Dual-luciferase reporter assay

When reaching 80~90% confluence, 293T cells were co-transfected with constructed wild-type (PTEN WT) or mutant-type (PTEN MUT) dual-luciferase reporter vectors of PTEN and miR-92a mimics or NC mimics. Subsequently, the transfected cells were incubated for 48 h and then collected to be lysed at ambient temperature for 20 min. After that, the cell centrifugation was performed, and then the supernatant was collected and stored at -20°C. Subsequently, luciferase substrate was directly added to the supernatant and the luciferase activity was measured by luminescence. The relative firefly luciferase activity was calculated with Renilla luciferase activity as an internal control (Zou *et al.*, 2019).

Western blot

RIPA lysate was added to the cells in each group and cells were lysed on ice for 20 min and centrifugated at 10000 rpm, 4°C for 20 min to obtain the protein supernatant. Afterwards, the protein concentration was detected by the BCA kit (Solarbio, China). There was 20 μl of total protein separated using SDS PAGE (sodium dodecyl sulfate-polyacrylamide gel electrophoresis). Next, the protein was transferred to PVDF membranes, blocked with 3% BSA blocking solution for 1 h at ambient temperature, and then incubated overnight at 4°C in diluted primary antibodies (anti-PTEN, ab32199, Abcam; anti-p-Akt, #9271, CST; anti-Akt, #9272, CST; anti-GAPDH, ab8245, Abcam; USA). Later, the membranes were washed twice with TBST, and then a diluted secondary antibody (ZSGB-Bio Co., Ltd., China) was added for 1-h incubation at ambient temperature. After that, the membranes were washed three times with TBST, and then ECL luminescence solution was added to the membranes. And then, the membranes were exposed to

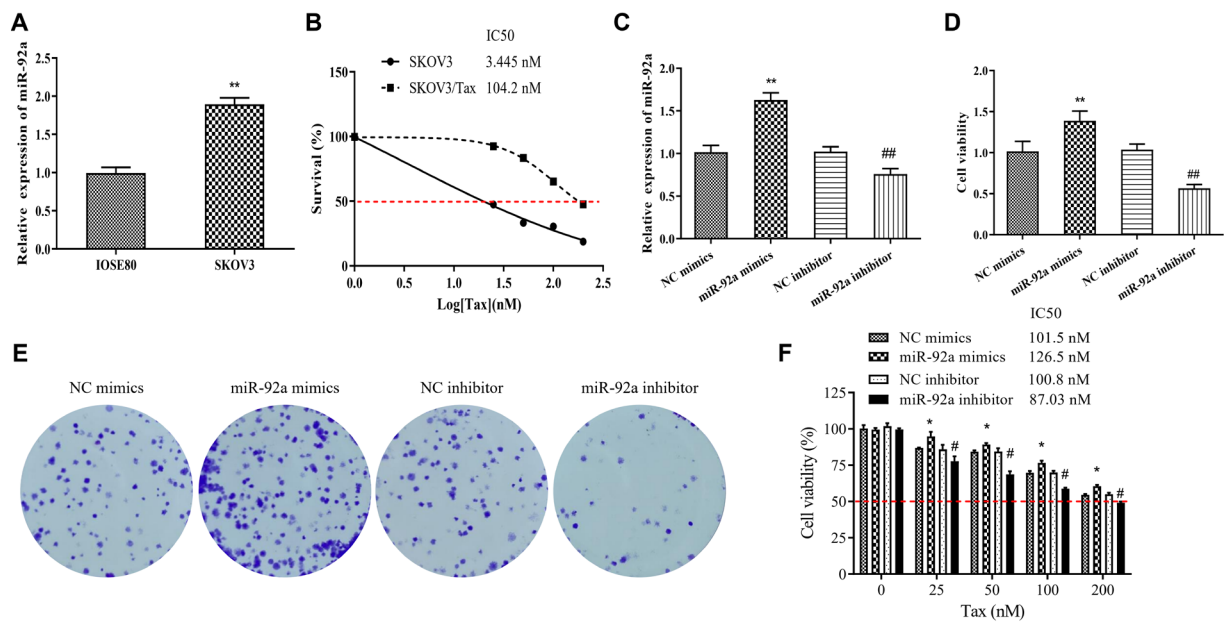


Figure 1. MiR-92a promotes SKOV3 cell proliferation, colony formation and improves paclitaxel resistance of the cells. (A) qRT-PCR to detect the miR-92a expression level in normal ovarian epithelial cells IOSE80 and ovarian cancer (OC) cells SKOV3, ** $P < 0.01$ vs., IOSE80; (B) MTT to test the effect of paclitaxel (Tax) on the activity of SKOV3 and SKOV3-Tax; (C) qRT-PCR to determine the miR-92a expression level in SKOV3-Tax cells of each group; (D/E) MTT and colony formation assay to assess the activity (D) and colony formation ability (E) of SKOV3-Tax cells in each group, respectively; (F) MTT to detect the effect of different concentrations of Tax on the cell activity of SKOV3-Tax cells in each group, * $P < 0.05$ and ** $P < 0.01$ vs., NC mimics, # $P < 0.05$ and ## $P < 0.01$ vs., NC inhibitor.

the gel imaging system for photography. Finally, the gray values of the protein bands were analyzed by Image pro plus software, and then the relative expression level of the proteins was analyzed with GAPDH as an internal control.

Statistical analysis

All results were expressed as mean \pm standard deviation (S.D.) and GraphPad Prism 9.0 was utilized to plot. Statistical analysis was performed with GraphPad Prism 9.0 and SPSS 24.0 software. *T*-test was adopted to compare the two groups, and a one-way analysis of variance was employed for comparison among multiple groups.

$P < 0.05$ was considered a statistically significant difference.

RESULTS

MiR-92a promotes SKOV3-Tax cell proliferation, colony formation and improves paclitaxel resistance of cells

Examination of miR-92a expression in normal ovarian epithelial cells IOSE80 and OC cells SKOV3 revealed that miR-92a expression was notably higher in SKOV3 than in IOSE80 ($P < 0.01$, Fig. 1A). To clarify the role

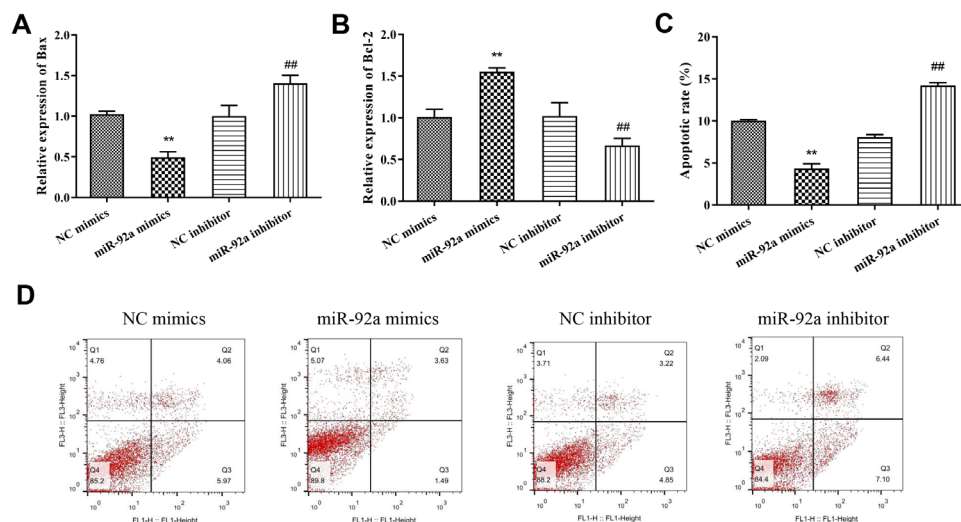


Figure 2. MiR-92a inhibits apoptosis of SKOV3-Tax cells. (A/B) qRT-PCR to detect the expression level of pro-apoptotic gene Bax and anti-apoptotic gene Bcl-2 in SKOV3-Tax cells of each group; (C/D) flow cytometry to test the apoptosis rate of SKOV3-Tax cells in each transfection group. ** $P < 0.01$ vs., NC mimics, ## $P < 0.01$ vs., NC inhibitor.

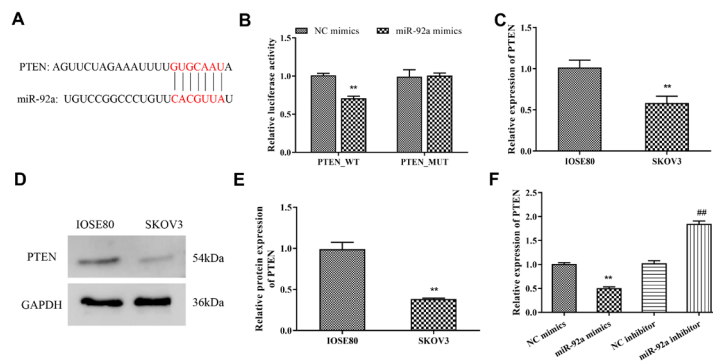


Figure 3. MiR-92a targets PTEN.

(A) TargetScan to predict the targeting sequences between miR-92a and PTEN; (B) dual-luciferase reporter assay to validate the targeting relationship between miR-92a and PTEN; C, qRT-PCR to detect the PTEN expression level in IOSE80 and SKOV3 cells, $**P<0.01$ vs., IOSE80; (D/E) Western blot to detect PTEN protein expression level in IOSE80 and SKOV3 cells, $**P<0.01$ vs., IOSE80; F, qRT-PCR to detect PTEN expression level in SKOV3-inhibitor cells after knockdown or overexpression of miR-92a, $**P<0.01$ vs., NC mimics, $**P<0.01$ vs., NC inhibitor.

of miR-92a in OC, we induced SKOV3-Tax, a cell line with apparent resistance to paclitaxel, by concentration gradient (Fig. 1B). Then miR-92a was knocked down and overexpressed respectively in SKOV3-Tax cells by transfection, and the efficiencies of knockdown and overexpression were shown in Fig. 1C. Compared with NC mimics, miR-92a mimics remarkably increased miR-92a expression in SKOV3-Tax cells; compared with NC inhibitor, miR-92a inhibitor markedly inhibited miR-92a expression in SKOV3-Tax cells ($P<0.01$). Meanwhile, the results of MTT and colony formation assays revealed a noticeable climb in proliferation, colony formation and cell activity under different concentrations of Tax treatment of SKOV3-Tax cells in the miR-92a mimics group, compared with the NC mimics group; while in the miR-92a inhibitor group, the above items exhibited an evident reduction compared with the NC inhibitor group (Fig. 1D/E). These results suggested that miR-92a promoted SKOV3-Tax cell proliferation, colony formation as well as resistance to Tax.

MiR-92a inhibits apoptosis of SKOV3-Tax cells

Subsequently, the effect of miR-92a on the apoptosis of SKOV3-Tax cells was further explored. As results shown, compared with the NC mimics group, the apoptosis rate of SKOV3-Tax cells in the miR-92a mimics group was greatly reduced, and the expression level of pro-apoptotic gene Bax in the cells was considerably lowered, while the level of anti-apoptotic gene Bcl-2 was evidently increased ($P<0.01$). By contrast, the opposite results were shown after inhibiting miR-92a in SKOV3-Tax cells by miR-92a inhibitor: The apoptosis level of the cells and the Bax expression level were significantly increased, whereas the Bcl-2 expression was markedly decreased ($P<0.01$) (Fig. 2A–D), indicating that overexpression of miR-92a inhibited apoptosis of SKOV3-Tax cells, while knockdown of miR-92a enhanced apoptosis of SKOV3-Tax cells.

MiR-92a targets PTEN

MicroRNAs mediate the expression of target genes mainly by directly targeting the 3'-untranslated region (3'-UTR) of mRNAs, thereby regulating the behavior of a variety of malignancies (Shi *et al.*, 2021). And we predicted the downstream target gene of miR-92a on the online website TargetScan (https://www.targetscan.org/vert_72/). The outcomes reported that miR-92a was

able to target and regulate PTEN and their targeting sequences were displayed in Fig. 3A. The results of subsequent dual-luciferase reporter assay also manifested that co-transfection of miR-92a mimics notably suppressed the luciferase activity of cells in the PTEN-WT group, but the luciferase activity of the PTEN-MUT group was not obviously changed (Fig. 3B). And the above confirmed that there was a targeting relationship between PTEN and miR-92a. The mRNA and protein expression level of PTEN in SKOV3 cells was significantly lower than those in IOSE80 cells ($P<0.01$, Fig. 3C–E). In addition, the PTEN expression in the cells was remarkably declined after the overexpression of miR-92a in SKOV3-Tax cells, while the opposite was true after the knockdown of miR-92a (Fig. 3F). From the above, it was suggested that miR-92a could target and regulate PTEN expression.

MiR-92a regulates PTEN/Akt signaling pathway in SKOV3-Tax cells

Several studies have demonstrated that through the PTEN/Akt signaling pathway, miR-92a promotes the malignant behavior of tumors such as prostate cancer, nasopharyngeal carcinoma as well as osteosarcoma (Yan-shen *et al.*, 2021; Zhang *et al.*, 2016; Xiao *et al.*, 2017). To clarify miR-92a function in OC to promote proliferation, inhibit apoptosis and improve chemoresistance to Tax whether, through the PTEN/Akt signaling pathway, we analyzed the expression of PTEN/Akt signaling pathway by Western blot. And a noticeable decrease was revealed by the results in the PTEN expression level ($P<0.01$), while a marked climb in both the phosphorylation level of Akt and the ratio of p-Akt/Akt ($P<0.01$) in SKOV3-Tax cells in the miR-92a mimics group when compared with the NC mimics group. Besides, in SKOV3-Tax cells in the miR-92a inhibitor group, the PTEN expression level remarkably rose ($P<0.01$), while the phosphorylation level of Akt and the ratio of p-Akt/Akt notably reduced ($P<0.01$) compared with the NC inhibitor group ($P<0.01$) (Fig. 4A/B). All these indicated that miR-92a was able to regulate the PTEN/Akt signaling pathway in SKOV3-Tax cells.

DISCUSSION

Despite the progress at the social medical level, the incidence of malignant tumors is still growing year by year,

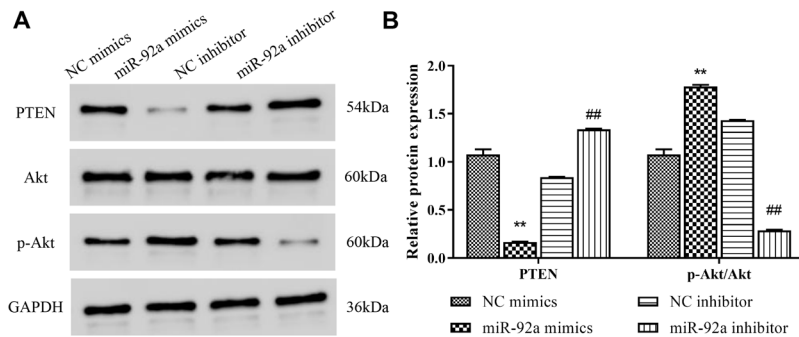


Figure 4. MiR-92a regulates PTEN/Akt signaling pathway in SKOV3-Tax cells.

(A/B) Western blot to detect the protein level of PTEN, p-Akt and Akt in SKOV3-Tax cells of each group and grayscale analysis was performed for the relative expression level of PTEN and p-Akt/Akt, ** $P < 0.01$ vs., NC mimics, ## $P < 0.01$ vs., NC inhibitor.

and the age of onset of malignant tumors is increasingly younger. Therefore, how to improve the overall health of mankind is a concern and attention in the world today (Vasan *et al.*, 2019). As an important component of cell signaling pathways, miRNAs have been suggested by increasing evidence that are major regulators of many life activities, such as cell proliferation, differentiation, apoptosis, stress response, and angiogenesis. These activities function by binding the 3'UTR region of multiple target genes (Ji *et al.*, 2017). It has been revealed that miRNAs can act as suppressor genes and oncogenes to regulate the development of tumors (Schwarzenbach *et al.*, 2014). In addition, several researchers have reported that miRNAs also play a crucial role in the migration, differentiation, apoptosis, and other processes of OC (Li *et al.*, 2019; Ye *et al.*, 2019). MiR-92a, a novel miRNA discovered in recent years, is highly expressed and exerts a cancer-promoting effect in a variety of tumors (Zhou *et al.*, 2015; Lin *et al.*, 2013; Ohyagi-Hara *et al.*, 2013). In this study, miR-92a was remarkably highly expressed in OC cells *via* a series of in vitro cell experiments. Furthermore, high miR-92a expression promoted OC cell proliferation, colony formation, and paclitaxel resistance, while inhibiting apoptosis.

Peptidyl-prolyl cis/trans isomerase (NIMA-interacting 1, PTEN) is a tumor suppressor gene with bispecific phosphohydrolase function and a high mutation rate in various human cancers (Li *et al.*, 1997). The PTEN gene is located on the short arm of chromosome 10 (10q23.3), with a complex encoded protein structure and a variety of physiological functions. PTEN gene can act not only on the nucleus to regulate the cell cycle, but also on the cell membrane to participate in cell-cell interaction and adhesion functions (Leslie den Hertog, 2014). Studies have manifested that PTEN presents low expression in some human tumors (Yeh Means, 2007). For example, PTEN was down-regulated in various tumors such as lung cancer (Malaney *et al.*, 2018), liver cancer (Liu *et al.*, 2018) and breast cancer (Ngeow *et al.*, 2017). Loss of PTEN function has been demonstrated to stimulate cell growth and survival by excessively activating the PI3K/AKT signaling pathway (Salmena *et al.*, 2008; Hollander *et al.*, 2011; Xie *et al.*, 2021). In this study, PTEN was found to be a downstream target gene of miR-92a through a miRNA-mRNA interaction database. Additionally, luciferase reporter assay and expression analysis revealed that miR-92a could target and regulate the PTEN expression, and down-regulation of miR-92a expression greatly promoted the PTEN expression. More importantly, we discovered that overexpression of miR-

92a notably increased the p-Akt level and the ratio of p-Akt/Akt in OC cells; however, inhibition of miR-92a expression considerably lowered the p-Akt level and the ratio of p-Akt/Akt in OC cells. The above is consistent with the results of previous studies that miR-92a promotes the malignant behavior of tumors such as prostate cancer, nasopharyngeal carcinoma and osteosarcoma through the PTEN/Akt signaling pathway (Zhang *et al.*, 2016; Xiao *et al.*, 2017; Yanshen *et al.*, 2021).

The present study experimentally demonstrated that miR-92a promoted the proliferation, colony formation and paclitaxel resistance of OC cells, and inhibited apoptosis. However, only one OC cell line was tested in this study without mutual confirmation of multiple cell lines. Moreover, this study was an experimental exploration only in cells and did not validate whether miR-92a exerts the same function *in vivo*. Besides, only PTEN/Akt signaling pathway has been investigated in mechanism exploration, and it is not certain whether miR-92a also acts through other pathways. The above issues need to be further experimentally validated and explored.

CONCLUSIONS

In summary, miR-92a was up-regulated in OC cell line SKOV3, and high miR-92a expression not only promoted the proliferation, colony formation and resistance to paclitaxel chemotherapy of SKOV3-Tax cells, but also inhibited apoptosis. Additionally, miR-92a may play a cancer-promoting role by regulating the PTEN/Akt signaling pathway. And miR-92a/PTEN/Akt signaling is possibly a potential therapeutic target for OC patients in the future.

Declarations

Disclosure. No author has any potential conflict of interest.

Data availability statement. The data that support the findings of this study are available from the authors upon reasonable request.

REFERENCES

- De Cecco L, Giannoccaro M, Marchesi E, Bossi P, Favales F, Locati LD, Licitra L, Pilotti S, Canevari S (2017) Integrative miRNA-gene expression analysis enables refinement of associated biology and prediction of response to cetuximab in head and neck squamous cell cancer. *Genes (Basel)* 8: 35. <https://doi.org/10.3390/genes8010035>

- Du L, Pertsemlidis A (2012) microRNA regulation of cell viability and drug sensitivity in lung cancer. *Expert Opin Biol Ther* **12**: 1221–1239. <https://doi.org/10.1517/14712598.2012.697149>
- Filipowicz W, Bhattacharyya SN, Sonenberg N (2008) Mechanisms of post-transcriptional regulation by microRNAs: are the answers in sight? *Nat Rev Genet* **9**: 102–114. <https://doi.org/10.1038/nrg2290>
- Funston G, Hardy V, Abel G, Crosbie EJ, Emery J, Hamilton W, Walter FM (2020) Identifying ovarian cancer in symptomatic women: a systematic review of clinical tools. *Cancers (Basel)* **12**: 3686. <https://doi.org/10.3390/cancers12123686>
- Gai C, Camussi F, Broccoletti R, Gambino A, Cabras M, Molinaro L, Carossa S, Camussi G, Arduino PG (2018) Salivary extracellular vesicle-associated miRNAs as potential biomarkers in oral squamous cell carcinoma. *BMC Cancer* **18**: 439. <https://doi.org/10.1186/s12885-018-4364-z>
- Hollander MC, Blumenthal GM, Dennis PA (2011) PTEN loss in the continuum of common cancers, rare syndromes and mouse models. *Nat Rev Cancer* **11**: 289–301. <https://doi.org/10.1038/nrc3037>
- Huang J, Wang X, Wen G, Ren Y (2019) miRNA2055p functions as a tumor suppressor by negatively regulating VEGFA and PI3K/Akt/mTOR signaling in renal carcinoma cells. *Oncol Rep* **42**: 1677–1688. <https://doi.org/10.3892/or.2019.7307>
- Ji W, Sun B, Su C (2017) Targeting MicroRNAs in cancer gene therapy. *Genes (Basel)* **8**: 21. <https://doi.org/10.3390/genes8010021>
- Kossai M, Leary A, Scoazec JY, Genestie C (2018) Ovarian cancer: a heterogeneous disease. *Pathobiology* **85**: 41–49. <https://doi.org/10.1159/000479006>
- Kurnit KC, Fleming GF, Lengyel E (2021) Updates and new options in advanced epithelial ovarian cancer treatment. *Obstet Gynecol* **137**: 108–121. <https://doi.org/10.1097/AOG.0000000000004173>
- Leslie NR, den Hertog J (2014) Mutant PTEN in cancer: worse than nothing. *Cell* **157**: 527–529. <https://doi.org/10.1016/j.cell.2014.04.008>
- Li J, Yen C, Liaw D, Podsypanina K, Bose S, Wang SI, Puc J, Miliareis C, Rodgers L, McCombie R, Bigner SH, Giovanella BC, Ittmann M, Tycko B, Hibshoosh H, Wigler MH, Parsons R (1997) PTEN, a putative protein tyrosine phosphatase gene mutated in human brain, breast, and prostate cancer. *Science* **275**: 1943–1947. <https://doi.org/10.1126/science.275.5308.1943>
- Li X, Chen W, Jin Y, Xue R, Su J, Mu Z, Li J, Jiang S (2019) miR-142-5p enhances cisplatin-induced apoptosis in ovarian cancer cells by targeting multiple anti-apoptotic genes. *Biochem Pharmacol* **161**: 98–112. <https://doi.org/10.1016/j.bcp.2019.01.009>
- Lin HY, Chiang CH, Hung WC (2013) STAT3 upregulates miR-92a to inhibit RECK expression and to promote invasiveness of lung cancer cells. *Br J Cancer* **109**: 731–738. <https://doi.org/10.1038/bjc.2013.349>
- Liu H, Cheng L, Cao D, Zhang H (2018) Suppression of miR-21 expression inhibits cell proliferation and migration of liver cancer cells by targeting phosphatase and tensin homolog (PTEN). *Med Sci Monit* **24**: 3571–3577. <https://doi.org/10.12659/MSM.907038>
- Malaney P, Palumbo E, Semidey-Hurtado J, Hardee J, Stanford K, Kathiriyi JJ, Patel D, Tian Z, Allen-Gipson D, Dave V (2018) PTEN Physically interacts with and regulates E2F1-mediated transcription in lung cancer. *Cell Cycle* **17**: 947–962. <https://doi.org/10.1080/15384101.2017.1388970>
- Mueller JJ, Zhou QC, Iasonos A, O'Cearbhaill RE, Alvi FA, El Haraki A, Eriksson AG, Gardner GJ, Sonoda Y, Levine DA, Aghajanian C, Chi DS, Abu-Rustum NR, Zivanovic O (2016) Neoadjuvant chemotherapy and primary debulking surgery utilization for advanced-stage ovarian cancer at a comprehensive cancer center. *Gynecol Oncol* **140**: 436–442. <https://doi.org/10.1016/j.ygyno.2016.01.008>
- Narod S (2016) Can advanced-stage ovarian cancer be cured? *Nat Rev Clin Oncol* **13**: 255–261. <https://doi.org/10.1038/nrclinonc.2015.224>
- Ngeow J, Sesock K, Eng C (2017) Breast cancer risk and clinical implications for germline PTEN mutation carriers. *Breast Cancer Res Treat* **165**: 1–8. <https://doi.org/10.1007/s10549-015-3665-z>
- Ohyagi-Hara C, Sawada K, Kamiura S, Tomita Y, Isobe A, Hashimoto K, Kinose Y, Mabuchi S, Hisamatsu T, Takahashi T, Kumasawa K, Nagata S, Morishige K, Lengyel E, Kurachi H, Kimura T (2013) miR-92a inhibits peritoneal dissemination of ovarian cancer cells by inhibiting integrin alpha5 expression. *Am J Pathol* **182**: 1876–1889. <https://doi.org/10.1016/j.ajpath.2013.01.039>
- Rooth C (2013) Ovarian cancer: risk factors, treatment and management. *Br J Nurs* **22**: S23–S30. <https://doi.org/10.12968/bjon.2013.22.Sup17.S23>
- Salmena L, Carracedo A, Pandolfi PP (2008) Tenets of PTEN tumor suppression. *Cell* **133**: 403–414. <https://doi.org/10.1016/j.cell.2008.04.013>
- Schwarzenbach H, Nishida N, Calin GA, Pantel K (2014) Clinical relevance of circulating cell-free microRNAs in cancer. *Nat Rev Clin Oncol* **11**: 145–156. <https://doi.org/10.1038/nrclinonc.2014.5>
- Sehoul J, Grabowski JP (2019) Surgery in recurrent ovarian cancer. *Cancer* **125** (Suppl 24): 4598–4601. <https://doi.org/10.1002/cncr.32511>
- Shang A, Wang W, Gu C, Chen C, Zeng B, Yang Y, Ji P, Sun J, Wu J, Lu W, Sun Z, Li D (2019) Long non-coding RNA HOITIP enhances IL-6 expression to potentiate immune escape of ovarian cancer cells by upregulating the expression of PD-L1 in neutrophils. *J Exp Clin Cancer Res* **38**: 411. <https://doi.org/10.1186/s13046-019-1394-6>
- Shi Y, Liu Z, Lin Q, Luo Q, Cen Y, Li J, Fang X, Gong C (2021) MiRNAs and Cancer: Key Link in Diagnosis and Therapy. *Genes (Basel)* **12**: 1289. <https://doi.org/10.3390/genes12081289>
- Vasan K, Satgunaseelan L, Anand S, Asher R, Selinger C, Low TH, Palme CE, Clark JR, Gupta R (2019) Tumour mismatch repair protein loss is associated with advanced stage in oral cavity squamous cell carcinoma. *Pathology* **51**: 688–695. <https://doi.org/10.1016/j.pathol.2019.08.005>
- Xiao J, Yu W, Hu K, Li M, Chen J, Li Z (2017) miR-92a promotes tumor growth of osteosarcoma by targeting PTEN/AKT signaling pathway. *Oncol Rep* **37**: 2513–2521. <https://doi.org/10.3892/or.2017.5484>
- Xie P, Peng Z, Chen Y, Li H, Du M, Tan Y, Zhang X, Lu Z, Cui CP, Liu CH, He F, Zhang L (2021) Neddylatation of PTEN regulates its nuclear import and promotes tumor development. *Cell Res* **31**: 291–311. <https://doi.org/10.1038/s41422-020-00443-z>
- Yanshen Z, Lifan Y, Xilian W, Zhong D, Huihong M (2021) miR-92a promotes proliferation and inhibits apoptosis of prostate cancer cells through the PTEN/Akt signaling pathway. *Libyan J Med* **16**: 1971837. <https://doi.org/10.1080/19932820.2021.1971837>
- Ye W, Zhou Y, Xu B, Zhu D, Rui X, Xu M, Shi L, Zhang D, Jiang J (2019) CD247 expression is associated with differentiation and classification in ovarian cancer. *Medicine (Baltimore)* **98**: e18407. <https://doi.org/10.1097/MD.00000000000018407>
- Yeh ES, Means AR (2007) PIN1, the cell cycle and cancer. *Nat Rev Cancer* **7**: 381–388. <https://doi.org/10.1038/nrc2107>
- Zhang H, Cao H, Xu D, Zhu K (2016) MicroRNA-92a promotes metastasis of nasopharyngeal carcinoma by targeting the PTEN/AKT pathway. *Oncol Targets Ther* **9**: 3579–3588. <https://doi.org/10.2147/OTT.S105470>
- Zhou C, Shen L, Mao L, Wang B, Li Y, Yu H (2015) miR-92a is up-regulated in cervical cancer and promotes cell proliferation and invasion by targeting FBXW7. *Biochem Biophys Res Commun* **458**: 63–69. <https://doi.org/10.1016/j.bbrc.2015.01.066>
- Zhu J, Liu B, Wang Z, Wang D, Ni H, Zhang L, Wang Y (2019) Exosomes from nicotine-stimulated macrophages accelerate atherosclerosis through miR-21-3p/PTEN-mediated VSMC migration and proliferation. *Theranostics* **9**: 6901–6919. <https://doi.org/10.7150/thno.37357>
- Zou P, Zhu M, Lian C, Wang J, Chen Z, Zhang X, Yang Y, Chen X, Cui X, Liu J, Wang H, Wen Q, Yi J (2019) miR-192-5p suppresses the progression of lung cancer bone metastasis by targeting TRIM44. *Sci Rep* **9**: 19619. <https://doi.org/10.1038/s41598-019-56018-5>

Promoting action of long non-coding RNA small nucleolar RNA host gene 4 in ovarian cancer

Chao Liu¹, Shu Zhao², Zhi Xiang Lv³ and Xiao Juan Zhao²✉

¹Department of Obstetrics and Gynecology, Maternal and Child Health Hospital of Ningyang County, Tai'an City, Shandong Province, 271499, China; ²Department of Obstetrics, Qingdao Central Hospital, Qingdao City, Shandong Province, 266042, China; ³Department of Vascular Surgery, Qingdao Central Hospital, Qingdao City, Shandong Province, 266042, China

Objective: Long non-coding RNA (LncRNA) small nucleolar RNA host gene 4 (SNHG4) has been shown to be aberrantly expressed in a variety of cancers and involved in cancer development, but its role in ovarian cancer (OC) is unclear. The purpose of this study was to explore the biological function of SNHG4 in OC and reveal its potential downstream molecular targets. **Methods:** OC tumor tissue and normal tissue were collected; normal human ovarian epithelial cell line (IOSE80) and human ovarian cancer cell line (A2780, SKOV-3, OV-90 and CAOV3) were selected. RT-qPCR was used to detect SNHG4, miR-98-5p, and TMED5, while western blot was used to detect the protein expression levels of TMED5, Ki67, MMP-9, Bcl-2, Bax, Gsk3 β , Wnt3a, and β -catenin. The subcellular localization of SNHG4 was assessed by nucleocytoplasmic separation assay. CCK-8, colony formation assay, flow cytometry, and Transwell were used to assess the biological behavior of OC cells. The targeting relationship between SNHG4, miR-98-5p and TMED5 was verified by dual luciferase reporter assay and RIP assay. **Results:** In OC, SNHG4 and TMED5 were highly expressed, and miR-98-5p was underexpressed. Knockdown of SNHG4 inhibited OC cell proliferation, migration and invasion, promoted apoptosis, and prevented Wnt/ β -catenin pathway activation. The effect of knockdown of SNHG4 was reversed by knockdown of miR-98-5p or overexpression of TMED5. Mechanistically, SNHG4 competitively adsorbed miR-98-5p to mediate TMED5 expression, thereby activating the Wnt/ β -catenin pathway. **Conclusion:** SNHG4 accelerates OC development *via* mediating the miR-98-5p/TMED5 axis and activating the Wnt/ β -Catenin pathway. SNHG4 gene silencing might be a novel option for OC treatment.

Keywords: ovarian cancer, Long non-coding RNA small nucleolar RNA host gene 4, MicroRNA-98-5p, Transmembrane emp24 protein transport domain containing 5, Wnt/ β -Catenin signaling pathway

Received: 10 January, 2022; revised: 11 July, 2022; accepted: 11 October, 2022; available on-line: 19 January, 2023

✉e-mail: z_xiaojuan185@outlook.com

Abbreviations: CC, cervical cancer; ceRNA, competitive endogenous RNA; LC, liver cancer; LncRNAs, Long non-coding RNA; OC, ovarian cancer; SNHG4, small nucleolar RNA host gene 4

INTRODUCTION

Ovarian cancer (OC) is an extremely lethal gynecological tumor in women, taking up about 14,000 deaths per annum, which severely threatens women's health and safety around the world (Elsayed *et al.*, 2021). OC's cause remains elusive, and presently, genetic and endocrine factors are regarded as the crucial reason (Gao *et al.*,

2021). Presently, surgery, chemotherapy and radiotherapy are the crucial cure strategies for treating OC (Redondo *et al.*, 2021). These methods have achieved a tremendous breakthroughs, the 5-year survival rate of OC patients is still inferior owing to the lack of elevated specificity of long-term imperative treatment and easy recurrence after recovery (Zhu *et al.*, 2021; Oplawski *et al.*, 2021). Consequently, to improve OC patients' quality of life has been a hot topic to explore the molecular mechanism of OC occurrence and development and hunt for brand-new therapeutic targets.

Long non-coding RNA (LncRNAs), a group of ncRNA composed of more than 200 nucleotides transcribed *via* RNA polymerase II, have been testified in multiple cancer occurrence and development (Zhang *et al.*, 2021). Accumulated evidence has illuminated that LncRNAs exert the regulatory role in OC biological functions *via* modulating genes, genomic stability, a competitive endogenous RNA (ceRNA) mechanism and epigenetics after transcription (Xu *et al.*, 2021; Xie *et al.*, 2021). For instance, it has been reported that LINC02323 boosts OC cell growth *via* targeting miR-1343-3p to stimulate TGF- β receptor 1 (Li *et al.*, 2021). Yu and others (Yu *et al.*, 2018) also maintain that LncRNA LUCAT1 accelerates OC malignant tumors *via* modulating the miR-612/HOXA13 pathway. LncRNA small nucleolar RNA host gene 4 (SNHG4) has been identified as a novel target for multiple cancers covering osteosarcoma (OS) (Xu *et al.*, 2018), non-small cell lung cancer (NSCLC) (Li *et al.*, 2021), liver cancer (LC) (Jiao *et al.*, 2020), and cervical cancer (CC) (Ji *et al.*, 2019) and a novel target in human diseases (Chu *et al.*, 2021). Nevertheless, the role of SNHG4 in ovarian cancer is unclear.

In terms of mechanism, LncRNA-mediated ceRNA network is frequently explored (Xu *et al.*, 2021). LncRNA prevents mRNA degradation *via* interacting with microRNA (miRNA) (Braga *et al.*, 2020). Consequently, SNHG4-associated miRNA (miR-98-5p) and miRNA (TMED5) were studied. Studies have manifested that miR-98-5p is implicated in OC (Dong *et al.*, 2020). Additionally, reports have clarified that miR-G-1 boosts CC cell nuclear autophagy and malignant behaviors by targeting LMNB1 and TMED5 in CC (Yang *et al.*, 2019).

This research hypothesized that SNHG4 might be involved in the occurrence and development of OC. Through loss-of-function and gain-of-function experiments, the role of SNHG4 was identified as a tumor-promoting factor in OC. Through functional rescue experiments, it was confirmed that SNHG4 affects the biological behavior of OC by regulating the miR-98-5p/TMED5 axis.

MATERIALS AND METHODS

Clinical specimens

A total of 40 pairs of ovarian tumor tissues and adjacent normal tissues were collected from patients undergoing oophorectomy at Maternal and Child Health Hospital of Ningyang County from January 2017 to December 2018. Tissue specimens were histopathologically and clinically diagnosed by a pathologist and stored at -80°C . This study was approved by the Ethics Committee of Maternal and Child Health Hospital of Ningyang County (approval number: 20160811ER), and written informed consent was obtained from all participants. Clinical studies were conducted following the guidelines of the Declaration of Helsinki, and subjects were anonymized during data analysis.

Cell culture and transfection

Normal human ovarian epithelial cell line (IOSE80) and human OC cell line (A2780, SKOV-3, OV-90 and CAOV3) were purchased from the Cell Bank of the Chinese Academy of Sciences (Shanghai, China) and identified by STR. Cell culture was done using Roswell Park Memorial Institute-1640 medium (Gibco) covering 10% fetal bovine serum, 2% sodium pyruvate and 1% streptomycin penicillin (Gibco) (Qiao *et al.*, 2021).

Cells were harvested when SKOV-3 cells were subcultured for 3–4 passages and were 70–80% confluent. SKOV-3 cells were divided into 6 groups: si-negative control (NC), si-SNHG4, si-SNHG4 + in-NC, si-SNHG4 + in-miR-98-5p, si-SNHG4 + pcDNA3.1, si-SNHG4 + pcDNA-TMED5. Human TMED5 (Accession: NM_001167830.2) coding sequence (lack of 3' untranslated region (UTR)) was combined with BamH I and EcoR V sites. The recombinant control sequences were synthesized by BGI (Shenzhen, China) and inserted into the pcDNA3.1 vector (Invitrogen). TMED5 overexpression plasmid (pcDNA-TMED5) and negative control (pcDNA) were generated with the BamH I and EcoR V sites opened (Zou, Chen, Liu, & Gan, 2021). SNHG4 small interfering RNA (siRNA) and control siRNA were generated (Invitrogen). miR-98-5p mimic (miR-98-5p), miR-98-5p inhibitor (in-miR-98-5p), NC mimic (miR-NC), and NC inhibitor (in-NC) were obtained (RIBOBIO, Guangzhou, China). Then transfection or co-transfection was implemented using Lipofectamine 2000 transfection reagent (Invitrogen). Wnt/ β -catenin signal inhibitor X-AV939 was purchased (Selleck Chemicals, Shanghai, China) (L. N. Gao *et al.*, 2021). The transfection efficiency was verified by reverse transcription quantitative polymerase chain reaction (RT-qPCR) after 48 h.

Subcellular localization analysis

Cytoplasmic RNA and nuclear RNA of SKOV-3 cells were isolated using PARIS Kit (Ambion, Austin, TX, United States). SNHG4 expression was tested by RT-qPCR, taking U6 and glyceraldehyde-3-phosphate dehydrogenase (GAPDH) as nuclear and cytoplasmic control, respectively.

RT-qPCR

Extraction of total RNA was done using Trizol reagent (Invitrogen). Reverse transcription for lncRNA/mRNA and miRNA was implemented *via* InRcute lncRNA cDNA kit and Rcute Plus miRNA cDNA kit (TIANGEN, China), respectively. RT-qPCR was done

Table 1. Primer sequences

Genes	Primer sequences (5'–3')
SNHG4	F: 5'-GGCTAGAGTACAGTGGCTCG-3'
	R: 5'-GCAATCGCAAGGTCAGG-3'
MiR-98-5p	F: 5'-GCGCGTGAGGTAGTAAGTTGT-3'
	R: 5'-GCAGGGTCCGAGGTATTC-3'
TMED5	F: 5'-CCCTCGATAGCGACTTCACC-3'
	R: 5'-TGTGATGGATTCCAGGATGTCT-3'
U6	F: 5'-CTCGCTTCGGCAGCAC-3'
	R: 5'-AACGCTTCACGAATTTGCGT-3'
GAPDH	F: 5'-CACCCACTCTCCACCTTTG-3'
	R: 5'-CCACCACCCTGTTGCTGTAG-3'

Note: F, forward; R, reverse.

using SYBR Green kit (Thermo Fisher Scientific) and Mx3005P QPCR system (Agilent Technologies, Santa Clara, CA, USA). U6 and GAPDH were loading controls for miRNA and mRNA/lncRNA, respectively. The primer sequence was manifested in Table 1. All primers were designed and validated through the primer-BLAST website.

Western blot

Total protein extraction was done with 500 μL Radio-Immunoprecipitation assay lysis buffer (Beyotime, China). Protein (20 μg) was loaded onto 8% sulfate polyacrylamide gel electrophoresis gel (Solarbio), electroblotted onto a polyvinylidene fluoride membrane (Invitrogen), and blocked with 5% skim milk. Then incubation with primary antibodies and horseradish peroxidase conjugating with goat anti-rabbit secondary antibody Immunoglobulin G (IgG) (1:1000, ab181236, Abcam) was conducted. The signals were visualized using an enhanced chemiluminescence kit (34080, Thermo Fisher Scientific, Waltham, Massachusetts, USA). Density analysis was done with ImageJ software. Primary antibodies were TMED5, Ki67, MMP-9, Bcl-2, Bax, Gsk3 β , Wnt3a, and β -catenin (TMED5 and Gsk3 β were from Millipore-Sigma; Others were from Cell Signaling Technology, Beverly, MA, USA, and the dilution was 1:1000) (T. Liu *et al.*, 2021).

Cell Counting Kit-8 (CCK-8) detection

SKOV-3 cells (1×10^3 cells/well) were seeded on 96-well plates and added with 10 μL CCK-8 reagent (Dojindo, Kumamoto, Japan) at the designated time points (0, 24, 48 and 72 h). Ultimately, the absorbance was determined with a SPECTROstar nano spectrophotometer (Germany) at a wavelength of 450 nm.

Colony formation assay

SKOV-3 cells (1×10^3 cells/well) were seeded in a 6-well plate for 1 week. After, the cells were fixed with 4% formaldehyde and GIMSA staining was performed. Ultimately, colonies ($\geq 100 \mu\text{m}$) were counted with a microscope (Olympus, Tokyo, Japan).

Flow Cytometry

After transfection, SKOV-3 cells were detached with 0.25% trypsin, and mixed with 100 μL binding buffer to

prepare 1×10^6 cells/mL suspension. Then 5 μ L Annexin V-fluorescein isothiocyanate and propidium iodide were added in sequence, and cells were loaded on a CytoFLEX flow cytometer for data analysis (Xu *et al.*, 2021).

Transwell analysis

SKOV-3 cell invasion and migration were assessed by Transwell chamber (8 μ m well, Corning Inc. Corning, NY, USA). The upper chamber was covered with 6×10^3 cells in 0.1 mL serum-free medium, and the lower chamber with a medium covering 20% fetal calf serum. Matrigel (356234, Millipore, Burlington, MA, USA) was coated only for invasion. After 12 h, 1% crystal violet staining (Sigma-Aldrich, St. Louis, MO, USA) was performed on the cells in the lower chamber, followed by cell counting under a light microscope (Yu *et al.*, 2021).

The luciferase activity assay

SNHG4 and TMED5 wild-type sequences (SNHG4/TMED5-WT) and corresponding mutant sequences (SNHG4/TMED5-MUT) containing the miR-98-5p binding site were synthesized by RiboBio. These sequences were inserted into the psiCHECK2 reporter vector (Promega, WI, USA). The SNHG4-WT/MUT reporter vector was co-transfected with in-miR-98-5p or in-NC into

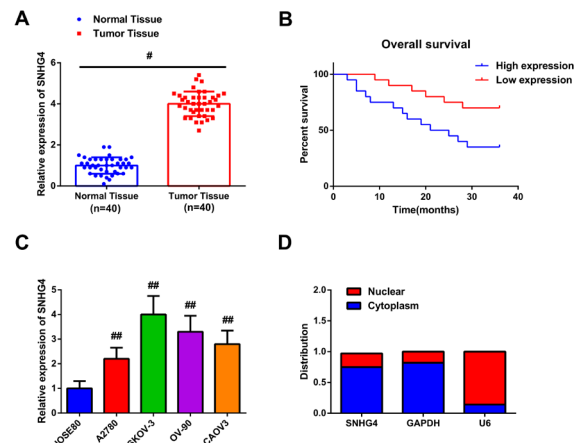


Figure 1. SNHG4 is elevated in OC and is linked with unpleasing clinical features

(A) RT-qPCR detection of SNHG4 in normal and tumor tissues; (B) Kaplan-Meier analysis of OC patients' survival prognosis; (C) RT-qPCR test of SNHG4 in OC cells; (D) SNHG4 localization in SKOV-3 cells; Measurement data were in the form of mean \pm S.D.; *vs. the Normal Tissue, n=40, $P < 0.05$; **vs. the IOSE80, N=3, $P < 0.05$.

Table 2. Association of SNHG4 with clinicopathological characteristics in OC patients

Characteristic	Cases	SNHG4		P
	n = 40	Reduction (n = 20)	Elevation (n = 20)	
Age (year)				
60 or less	19	10	9	0.915
More than 60	21	10	11	
Tumor size				
Less than 3 cm	21	16	5	0.005*
3 cm or more	19	4	15	
FIGO ^a stage				
I/II	15	11	4	0.003*
II/IV	25	9	16	
Pathologic type				
Serous	31	18	13	0.268
Mucous and others ^b	9	2	7	
Lymph node metastasis				
Positive	29	11	18	0.001*
Negative	11	9	2	
Distant metastasis				
Positive	14	9	5	0.158
Negative	26	11	15	

FIGO^a: Federation Internationale de Gynecologie and Obstetrique. Others^b: Endometrioid carcinoma, clear cell carcinoma and undifferentiated OC.

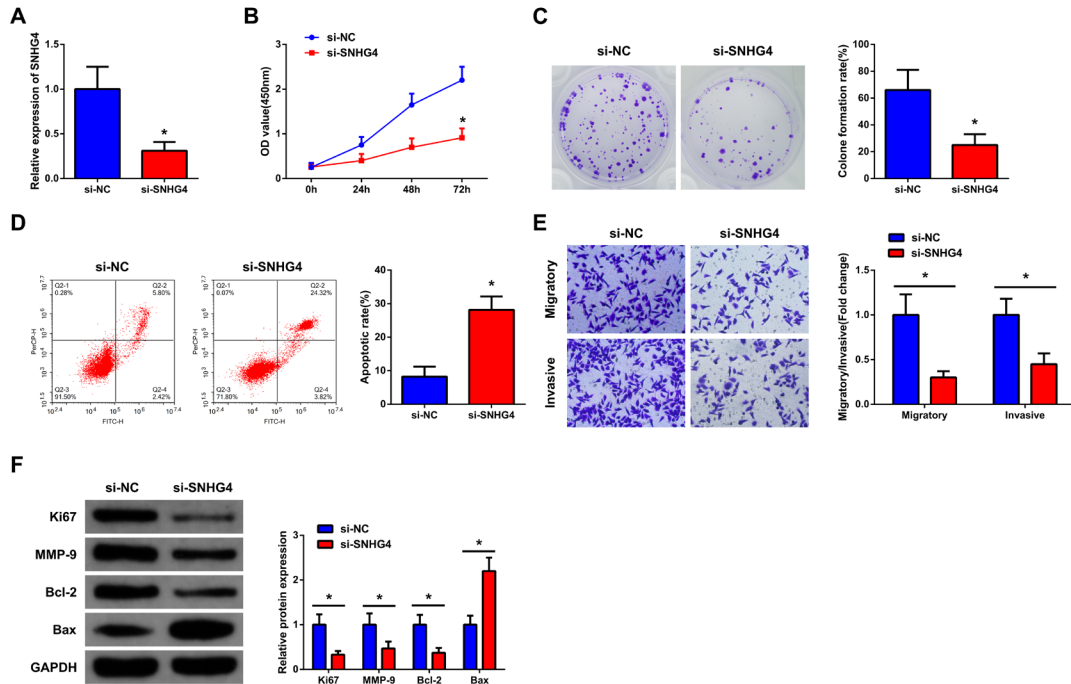


Figure 2. Silenced SNHG4 gene is available to constrain OC's deterioration

(A) RT-qPCR test of transfection efficiency in SKOV-3 cells; (B–C) CCK-8 method and plate cloning experiment examination of cell proliferation ability; (D) Flow cytometry detection of cell apoptosis rate; (E) Transwell test of cell migration and invasion; (F) Western blot examination of Ki67 (proliferation marker), MMP-9 (invasion marker), Bcl-2 (anti-apoptotic molecule) and Bax (pro-apoptotic molecule). Measurement data were in the form of mean \pm S.D.*vs. the si-NC, N=3, $P<0.05$.

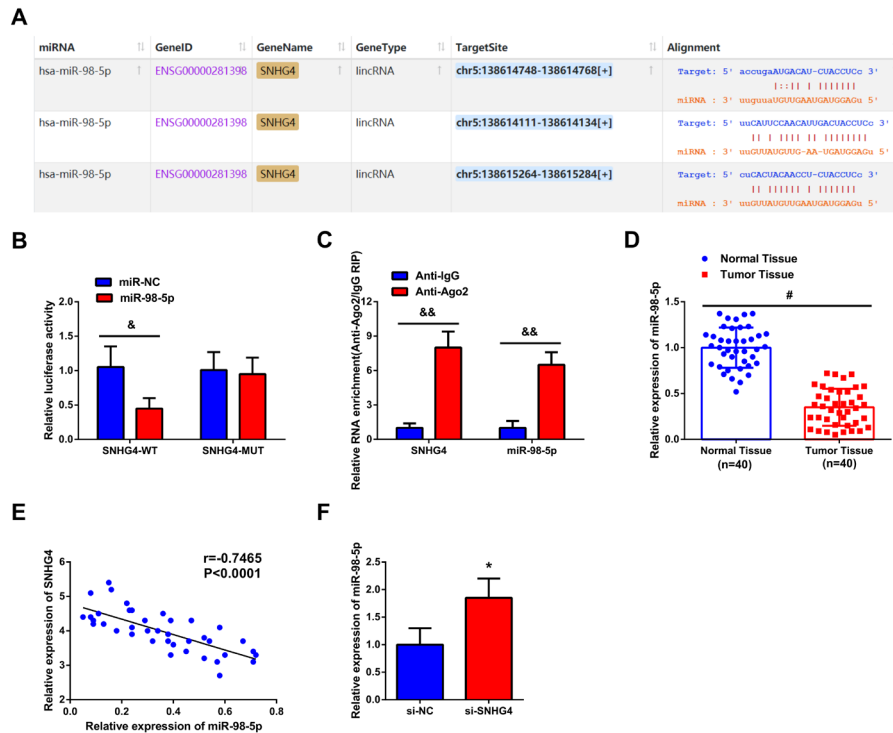


Figure 3. SNHG4 performs like a sponge for miR-98-5p

(A) The bioinformatics website prediction of the binding site of SNHG4 with miR-98-5p; (B–C) The luciferase activity assay and RIP experiment evaluation of the interaction of SNHG4 with miR-98-5p; (D) RT-qPCR detection of miR-98-5p in each tissue; (E) Pearson association analysis assessment of the relevance of miR-98-5p with SNHG4; (F) RT-qPCR test of miR-98-5p in SKOV-3 cells. Measurement data were in the form of mean \pm S.D.; #vs. the Normal Tissue, n=40, $P<0.05$; &vs. the miR-NC, &&vs. the Anti-IgG, *vs. the si-NC, N=3, $P<0.05$.

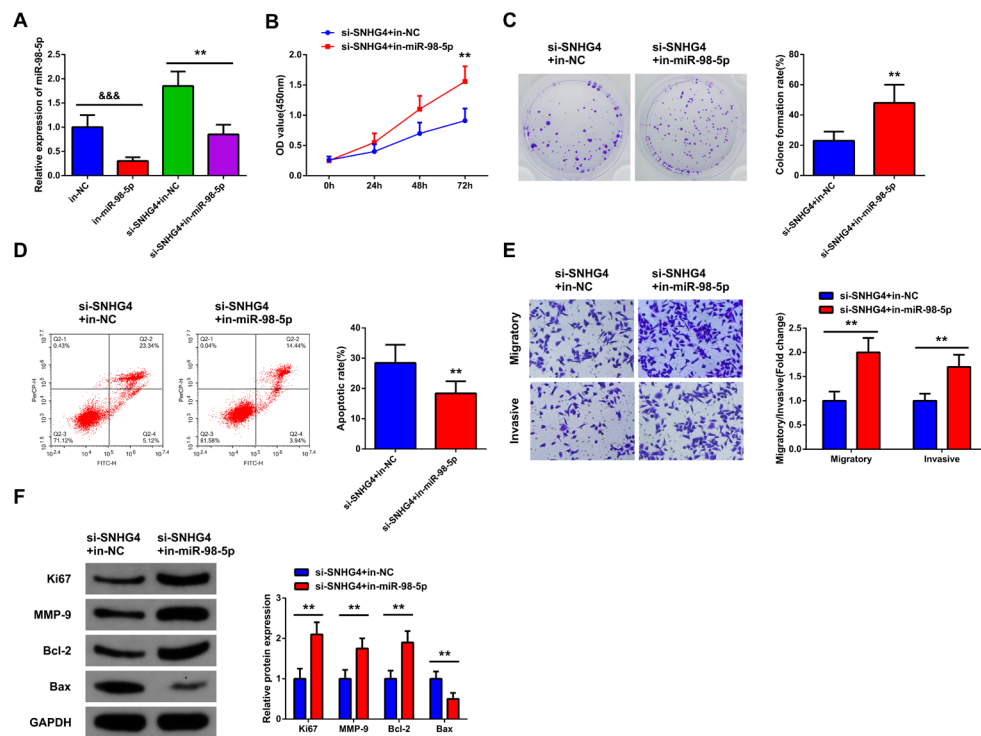


Figure 4. SNHG4 impacts OC cell progression via targeting miR-98-5p

(A) RT-qPCR examination of different transfections' efficiency in SKOV-3 cells; (B–C) CCK-8 and plate cloning experiments tested cell proliferation ability; (D) Flow cytometry detection of cell apoptosis rate; (E) Transwell examination of cell migration and invasion; (F) Western blot test of Ki67 (proliferation marker), MMP-9 (invasion marker), Bcl-2 (anti-apoptotic molecule) and Bax (pro-apoptotic molecule). The measurement data were in the form of mean \pm S.D. &&&vs. the in-NC, **vs. the si-SNHG4 + in-NC, N=3, $P<0.05$.

SKOV-3 cells. After transfection of 48 h, an assessment of the luciferase activity was done using the luciferase reporter test kit (Promega) (Xing, An, & Chen, 2021).

RNA immunoprecipitation (RIP) detection

RIP was implemented using Magna RIP kit (Millipore). The cells were lysed with complete RIP lysis buffer and combined with magnetic beads. Subsequently, the magnetic beads were combined with human anti-ago2 or normal mouse immunoglobulin G (Millipore). After digestion with proteinase K, immunoprecipitated RNA was analyzed by RT-qPCR (Liu *et al.*, 2021).

Statistical analysis

The data were analyzed by SPSS 21.0 (SPSS, Inc, Chicago, IL, USA) statistical software. After Kolmogorov-Smirnov test, the data were normally distributed, and the results were manifested in the form of mean \pm standard deviation (S.D.). Two-group comparison was done using *t*-test and multiple-group comparison was performed with one-way analysis of variance (ANOVA) and Fisher's least significant difference *t*-test. *P* was a two-sided test, and $P<0.05$ was accepted as indicative of distinct differences.

RESULTS

SNHG4 is elevated in OC and associated with adverse clinical characteristics

SNHG4 has been shown to be highly expressed in various cancers. The expression of SNHG4 was assessed

in OC. As presented in Fig. 1A, SNHG4 expression in OC tissues was higher than that in normal tissues. Clinical analysis indicated that SNHG4 expression was linked with tumor size, lymph node metastasis and tumor node metastasis (TNM) staging, but had no link with age, distant metastasis and pathological type (Table 2). Additionally, survival analysis (Kaplan-Meier) elaborated that OC patients with high expression of SNHG4 had poor overall survival (OS) rates (Fig. 1B). SNHG4 expression in all human OC cell lines (A2780, SKOV-3, OV-90 and CAOV3) was higher in the normal human ovarian epithelial cell line (IOSE80) (Fig. 1C). Nucleocytoplasmic separation experiments also confirmed that SNHG4 was mainly expressed in the cytoplasm of SKOV-3 cells (Fig. 1D).

To sum up, SNHG4 was elevated in OC and might be implicated in OC progression.

Silenced SNHG4 gene is available to restrain OC's deterioration

Since SNHG4 has the highest expression level in SKOV-3 cells, the SKOV-3 cell line was selected for subsequent functional experiments. To explore the function of SNHG4 in ovarian cancer, an SNHG4 knockdown cell model was constructed. The transfection efficiency was affirmed by RT-qPCR, as manifested in Fig. 2A, si-SNHG4 restrained SNHG4 expression in SKOV-3 cells. Silenced SNHG4 constrained the SKOV-3 cell proliferation (Fig. 2B–C). After restraining SNHG4, SKOV-3 cell apoptosis was promoted and migration and invasion were suppressed (Fig. 2D, E). Meanwhile, knockdown of SNHG4 suppressed the expression of Ki67, MMP-9, Bcl-2 proteins and increased

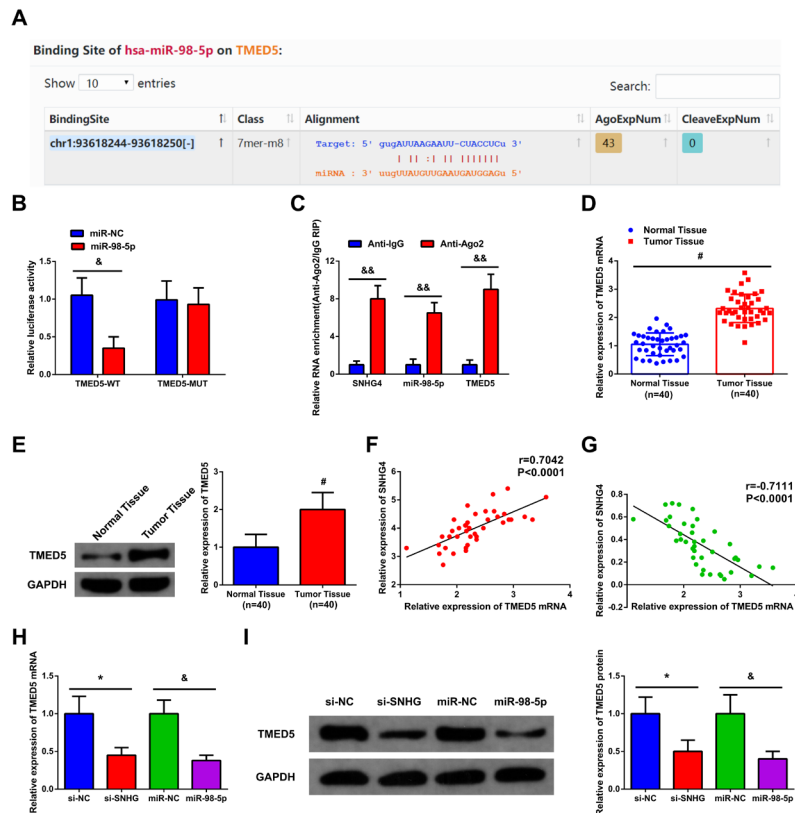


Figure 5. MiR-98-5p immediately targets TMED5

(A) The bioinformatics website predicted the binding site of TMED5 with miR-98-5p; (B–C) The luciferase activity assay and RIP experiment evaluation of the interaction of TMED5 with miR-98-5p; (D–E) RT-qPCR and Western blot test of TMED5 in OC tumor tissues; (F–G) Pearson association analysis of TMED5 with miR-98-5p and SNHG4; (H–I) RT-qPCR and Western blot detection of TMED5 in SKOV-3. Measurement data were in the form of mean \pm S.D.; #vs. the Normal Tissue, $n=40$, $P<0.05$; &vs. the miR-NC, &&vs. the Anti-IgG, *vs. the si-NC, $N=3$, $P<0.05$.

the expression of Bax protein (Fig. 2F). These data suggest that knockdown of SNHG4 suppresses the biological behaviors of OC.

SNHG4 performs like a sponge for miR-98-5p

To investigate the novel mechanism by which SNHG4 regulates OC progression, the bioinformatics website <https://starbase.sysu.edu.cn> was utilized to predict potential miRNAs of SNHG4. miR-98-5p was found to have a potential binding site for SNHG4 (Fig. 3A). The interaction between miR-98-5p and SNHG4 was verified by dual-luciferase reporter gene assay. As shown in Fig. 3B, overexpression of miR-98-5p significantly inhibited the luciferase activity of SNHG4-WT, but not SNHG4-MUT. RIP assay also further confirmed that both SNHG4 and miR-98-5p were enriched in Ago2 magnetic beads (Fig. 3C). Additionally, miR-98-5p expression was downregulated in OC tumor tissues (Fig. 3D) and was negatively linked with SNHG4 expression (Fig. 3E). RT-qPCR data showed that inhibition of SNHG4 promoted the expression of miR-98-5p in SKOV-3 cells (JIP 3F). In short, SNHG4 targeted miR-98-5p.

SNHG4 impacts OC cell progression via targeting miR-98-5p

To explore whether miR-98-5p is involved in the regulation of SNHG4 in OC, a functional rescue experiment was performed. si-SNHG4 and miR-98-5p

inhibitor were co-transfected into SKOV-3 cells. RT-qPCR showed that knockdown of SNHG4 promoted the expression of miR-98-5p, which was reversed by miR-98-5p inhibitor (Fig. 4A). Functional experiments showed that knockdown of SNHG4 inhibited cell proliferation, invasion and migration, and promoted apoptosis, but these effects were reversed by knockdown of miR-98-5p (Fig. 4B–F). In brief, SNHG4 impacts OC cell progression *via* targeting miR-98-5p.

MiR-98-5p immediately targets TMED5

Subsequently, potential downstream mRNAs of miR-98-5p were explored. First, miR-98-5p was found to have potential binding sites with TMED5 by starBase prediction (Fig. 5A). Meanwhile, dual-luciferase reporter assays revealed that miR-98-5p overexpression could attenuate the luciferase activity of TMED5-WT, while the luciferase activity of TMED5-MUT was not significantly changed (Fig. 5B). Additionally, SNHG4, miR-98-5p and TMED5 are all enriched in RNA-induced silencing complexes immunoprecipitated by Ago2 antibody (Fig. 5C). TMED5 expression in OC tumor tissues was higher than in normal tissues (Fig. 5D–E) and positively associated with SNHG4 while negatively linked with miR-98-5p (Fig. 5F–G). Additionally, in SKOV-3 cells depleted of SNHG4 or restored of miR-98-5p, TMED5 expression was suppressed (Fig. 5H–I). In general, TMED5 was a downstream gene of miR-98-5p.

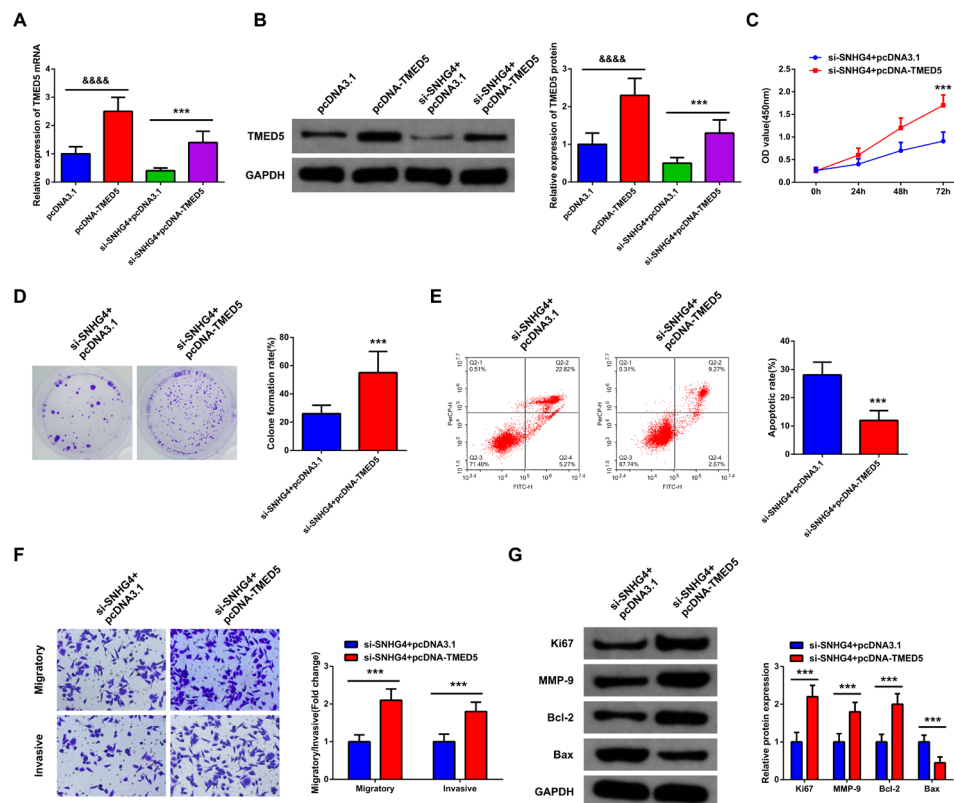


Figure 6. SNHG4 modulates OC's advancement via targeting miR-98-5p/TMED5 axis

(A–B) RT-qPCR and western blot test of transfection efficiency in SKOV-3 cells; (C–D) CCK-8 and plate cloning experiments detection of cell proliferation ability; (E) Flow cytometry examination of cell apoptosis; (F) Transwell detection of cell migration and invasion; (G) Western blot examination of Ki67 (proliferation marker), MMP-9 (invasion marker), Bcl-2 (anti-apoptotic molecule) and Bax (pro-apoptotic molecule). Measurement data were in the form of mean \pm S.D.; &&&vs. the pcDNA3.1, ***vs. the si-SNHG4 + pcDNA-3.1, N=3, $P<0.05$.

SNHG4 modulates OC progression via targeting the miR-98-5p/TMED5 axis

To assess whether SNHG4 is involved in ovarian cancer progression through miR-98-5p-regulated TMED5, a functional rescue assay was performed. In SKOV-3 cells, transfection of pcDNA-TMED5 elevated TMED5 expression, while TMED5 expression was partially up-regulated after pcDNA-TMED5 blocked si-SNHG4 (Fig. 6A–B). As manifested in Fig. 6C–E, upregulation of TMED5 reversed the proliferation-inhibiting and apoptosis-promoting effects of SNHG4 silencing on SKOV-3 cells. At the same time, transfection with overexpressing TMED5 plasmid also reversed the inhibitory effect of si-SNHG4-induced migration and invasion of SKOV-3 cells (Fig. 6F). Additionally, Ki67, MMP-9 and Bcl-2 protein expression were augmented, while Bax protein expression was inhibited after pcDNA-TMED5 blocked si-SNHG4 (Fig. 6G). In brief, SNHG4 modulates OC progression via targeting the miR-98-5p/TMED5 axis.

Wnt/ β -Catenin pathway participates in SNHG4/miR-98-5p/TMED5 axis-mediated OC cell growth

Wnt/ β -Catenin pathway may lead to uncontrolled cell growth. Therefore, we further investigated whether SNHG4 regulates the downstream target of miR-98-5p, TMED5, to alter the Wnt/ β -catenin signaling pathway in OC cells. Western blot results showed that the expression of Gsk3 β was decreased, while the expressions of

Wnt3a and β -catenin were upregulated in SKOV-3 cells transfected with pcDNA-TMED5 (Fig. 7A).

To determine whether the Wnt/ β -catenin signaling pathway is involved in SNHG4-induced OC progression, the Wnt/ β -catenin-specific inhibitor XAV939 (10 μ M) was added to pcDNA-TMED5-treated SKOV-3 cells. XAV939 treatment increased Gsk3 β expression in pcDNA-TMED5-treated SKOV-3 cells, while Wnt3a and β -catenin protein expression decreased (Fig. 7B). In addition, XAV939 also inhibited the effect of pcDNA-TMED5 on the promotion of proliferation and inhibition of apoptosis in SKOV-3 cells (Fig. 7C/D/E). Similarly, XAV939 inhibited the promoting effect of pcDNA-TMED5 on SKOV-3 cell migration and invasion (Fig. 7F). More importantly, Western blot results showed that the expression of Ki67, MMP-9, and Bcl-2 proteins decreased, while the expression of Bax protein increased (Fig. 7G). In short, SNHG4 activated the Wnt/ β -Catenin pathway by targeting the miR-98-5p/TMED5 axis.

DISCUSSION

Some factors like late diagnosis, chemotherapy resistance and easy recurrence lead to unpleasing prognosis and high mortality rate in OC patients (Wu *et al.*, 2021). Novel evidence has illuminated that targeting aberrantly-expressed lncRNAs in OC may be latent biomarkers and curative targets for OC (Guo *et al.*, 2021). Additionally, the lncRNA-microRNA-mRNA regulatory

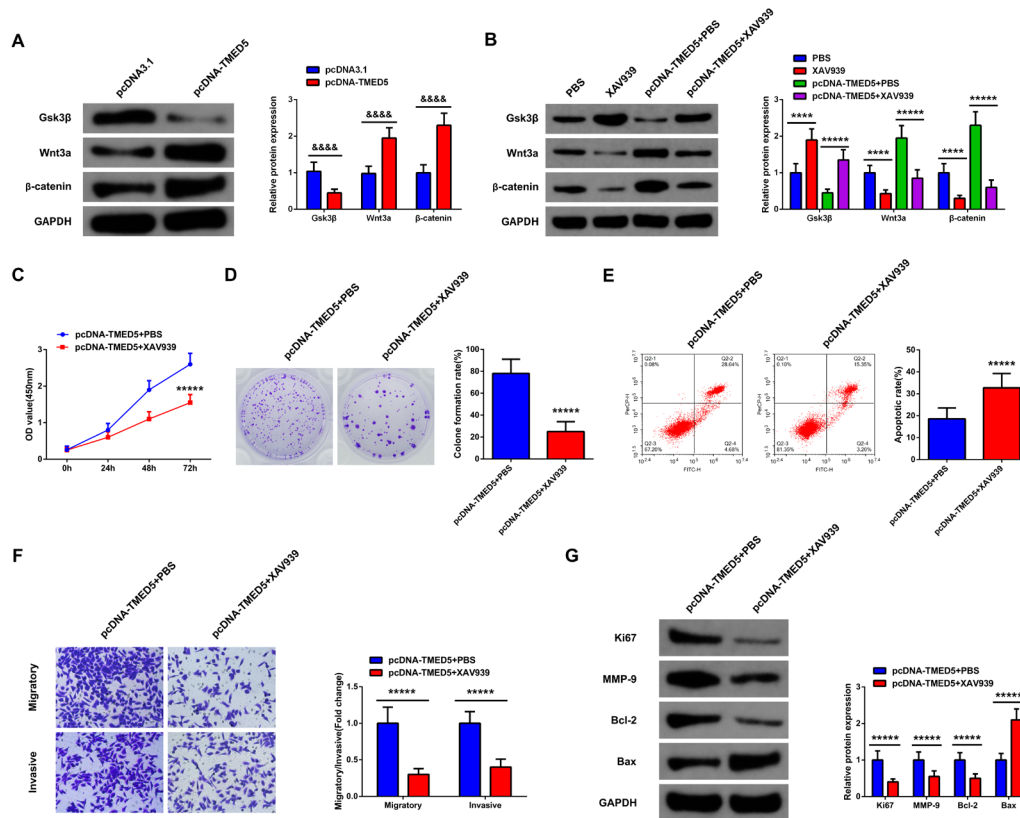


Figure 7. Wnt/ β -Catenin pathway implicates in the SNHG4/miR-98-5p/TMED5 axis-mediated OC cells' deterioration

(A–B) Western blot test of Gsk3 β , Wnt3a and β -catenin; (C–D) CCK-8 and plate cloning experiments examination of cell proliferation ability; (E) Flow cytometry test of cell apoptosis; (F) Transwell examination of cell migration and invasion; (G) Western blot test of Ki67 (proliferation marker), MMP-9 (invasion marker), Bcl-2 (anti-apoptotic molecule) and Bax (pro-apoptotic molecule). Measurement data were in the form of mean \pm S.D.; &&&& vs. the pcDNA3.1, **** vs. the PBS, ***** vs. the pcDNA-TMED5 + PBS, N=3, P<0.05.

network offers novel perspective for brand-new therapy strategies for OC (Lin *et al.*, 2021).

As reported, SNHG4 is elevated in OS (Xu *et al.*, 2018), NSCLC (Li *et al.*, 2021), LC (Jiao *et al.*, 2020), CC (Ji *et al.*, 2019). SNHG4 has been considered a biomarker for cancer prognosis or diagnosis. Likewise, our work found the upregulated SNHG4 in OC tissues was associated with patients' pathological characteristics and prognosis. Accumulated evidence has elaborated that SNHG4 exerts a regulatory role in cancer cells with multiple biological functions like chemotherapy resistance (Chu *et al.*, 2021). For instance, in colorectal cancer (CRC), suppression of SNHG4 constrains CRC cell growth with immune escape (Zhou *et al.*, 2021). In CC, silenced SNHG4 distinctly restrains CC cell progression (Li *et al.*, 2019). As expected, in this study, suppressing SNHG4 was available to constrain OC cell development (HeLa), clarifying that SNHG4 performed as an oncogene in OC.

In terms of mechanism, lncRNAs, as ceRNAs, elevate mRNA expression *via* interacting with miRNAs (Xu *et al.*, 2021; Xie *et al.*, 2021). It is speculated that SNHG4 may act as a ceRNA to regulate genes, thereby promoting the malignant phenotype of OC cells. In this research, miR-98-5p was confirmed as SNHG4's downstream miRNA in OC. As reported, miR-98-5p is negatively mediated by SNHG4 in LC (Tang *et al.*, 2019). Additionally, a report has illuminated that miR-98-5p expression is reduced in OC, and its silencing is available to alleviate OC cell development with cisplatin resistance (Guo *et al.*, 2021).

Likewise, in this research, miR-98-5p was downregulated in OC tissues, and SNHG4 combined with miR-98-5p in OC cells. Besides, silencing miR-98-5p rescued the effects of silenced SNHG4 on OC cells.

In this research, miR-98-5p immediately targeted TMED5's 3'UTR in OC, leading to degradation of TMED5 and repression of its transcription. TMED5, pertaining to the TMED protein family, is implicated in vesicular transport of proteins. As reported, TMED5 expression is elevated in CC and boosts CC cell malignant behaviors (Zou *et al.*, 2021). In this research, TMED5 was augmented in OC tissues, while SNHG4 was available to positively modulate TMED5 *via* miR-98-5p. Additionally, elevated TMED5 rescued silenced SNHG4-mediated repression on OC cell development.

Wnt/ β -Catenin, the crucial oncogenic pathway, exerts in multiple cancer progression covering OC and OS (Gao *et al.*, 2021; Guo *et al.*, 2021). Numerous studies have clarified that the Wnt/ β -Catenin pathway is linked with OC development with chemotherapy resistance (Vallée *et al.*, 2021). For instance, it has been reported that miR-217 constrains the Wnt/ β -Catenin pathway activation, thereby suppressing OC cell progression with drug resistance (Liu & Zhao, 2021). LncRNA HCP5 stimulates OC cell development with epithelial-mesenchymal transition (EMT) *via* the miR-525-5p/PRC1/Wnt/ β -Catenin axis (Wang *et al.*, 2020). TMED5 is available to activate the Wnt/ β -Catenin pathway in CC (Yang *et al.*, 2019). As expected, in this study, TMED5 declined Gsk3 β expression, while enhanced Wnt3a and β -catenin

expression, illuminating that TMED5 activated the Wnt/ β -Catenin pathway in OC. Additionally, SNHG4 activated the Wnt/ β -Catenin pathway *via* targeting the miR-98-5p/TMED5 axis, thereby boosting OC cell development. We speculate that SNHG4/miR-98-5p/TMED5 may also be involved in the chemoresistance of OC, which may affect the drug resistance of OC by regulating the Wnt/ β -catenin pathway. Notably, although we demonstrated *in vitro* that SNHG4 can regulate the biological behavior of the SKOV-3 cell line, more cell lines are needed to validate the role of SNHG4 in OC. In addition, it is unclear whether SNHG4 has similar effects in animal models of OC, which needs to be explored in follow-up studies. SNHG4 may target a variety of molecules in OC, including miRNA and mRNA, and it is necessary to further refine the regulatory network of SNHG4 in the future.

In conclusion, this work demonstrates for the first time that SNHG4 is highly expressed in OC and reveals the role of SNHG4 as a tumor-promoting factor in OC by regulating the miR-98-5p/TMED5 axis. The SNHG4/miR-98-5p/TMED5 axis may serve as a potential therapeutic target for OC in the future.

REFERENCES

- Braga EA, Fridman MV, Moscovtsev AA, Filippova EA, Dmitriev AA, Kushlinskii NE (2020) LncRNAs in ovarian cancer progression, metastasis, and main pathways: ceRNA and alternative mechanisms. *Int J Mol Sci* **21**: 8855. <https://doi.org/10.3390/ijms21228855>
- Chu Q, Gu X, Zheng Q, Guo Z, Shan D, Wang J, Zhu H (2021) Long noncoding RNA SNHG4: a novel target in human diseases. *Cancer Cell Int* **21**: 583. <https://doi.org/10.1186/s12935-021-02292-1>
- Dong L, Cao X, Luo Y, Zhang G, Zhang D (2020) A Positive feedback loop of lncRNA DSCR8/miR-98-5p/STAT3/HIF-1 α plays a role in the progression of ovarian cancer. *Front Oncol* **10**: 1713. <https://doi.org/10.3389/fonc.2020.01713>
- Elsayed AM, Bayraktar E, Amero P, Salama SA, Abdelaziz AH, Ismail RS, Zhang X, Ivan C, Sood AK, Lopez-Berestein G, Rodriguez-Aguayo C (2021) PRKAR1B-AS2 long noncoding RNA promotes tumorigenesis, survival, and chemoresistance *via* the PI3K/AKT/mTOR pathway. *Int J Mol Sci* **22**: 1882. <https://doi.org/10.3390/ijms22041882>
- Gao J, Liu F, Zhao X, Zhang P (2021) Long non-coding RNA FOXD2-AS1 promotes proliferation, migration and invasion of ovarian cancer cells *via* regulating the expression of miR-4492. *Exp Ther Med* **21**: 307. <https://doi.org/10.3892/etm.2021.9738>
- Gao LN, Hao M, Liu XH, Zhang L, Dong Y, Zhang YF, He XC (2021) CXCL14 facilitates the growth and metastasis of ovarian carcinoma cells *via* activation of the Wnt/ β -catenin signaling pathway. *J Ovarian Res* **14**: 159. <https://doi.org/10.1186/s13048-021-00913-x>
- Guo F, Du J, Liu L, Gou Y, Zhang M, Sun W, Yu H, Fu X (2021) lncRNA OR3A4 promotes the proliferation and metastasis of ovarian cancer through KLF6 pathway. *Front Pharmacol* **12**: 727876. <https://doi.org/10.3389/fphar.2021.727876>
- Guo H, Ha C, Dong H, Yang Z, Ma Y, Ding Y (2019) Cancer-associated fibroblast-derived exosomal microRNA-98-5p promotes cisplatin resistance in ovarian cancer by targeting CDKN1A. *Cancer Cell Int* **19**: 347. <https://doi.org/10.1186/s12935-019-1051-3>
- Guo H, Peng J, Hu J, Chang S, Liu H, Luo H, Chen X, Tang H, Chen Y (2021) BAIAP2L2 promotes the proliferation, migration and invasion of osteosarcoma associated with the Wnt/ β -catenin pathway. *J Bone Oncol* **31**: 100393. <https://doi.org/10.1016/j.jbo.2021.100393>
- Ji N, Wang Y, Bao G, Yan J, Ji S (2019) LncRNA SNHG14 promotes the progression of cervical cancer by regulating miR-206/YWHAZ. *Pathol Res Pract* **215**: 668–675. <https://doi.org/10.1016/j.prp.2018.12.026>
- Jiao Y, Li Y, Jia B, Chen Q, Pan G, Hua F, Liu Y (2020) The prognostic value of lncRNA SNHG4 and its potential mechanism in liver cancer. *Biosci Rep* **40**: BSR20190729. <https://doi.org/10.1042/bsr20190729>
- Li H, Hong J, Wijayakulathilaka WSMA (2019) Long non-coding RNA SNHG4 promotes cervical cancer progression through regulating c-Met *via* targeting miR-148a-3p. *Cell Cycle* **18**: 3313–3324. <https://doi.org/10.1080/15384101.2019.1674071>
- Li Y, Zhao Z, Sun D, Li Y (2021) Novel long noncoding RNA LINC02323 promotes cell growth and migration of ovarian cancer *via* TGF- β receptor 1 by miR-1343-3p. *J Clin Lab Anal* **35**: e23651. <https://doi.org/10.1002/jcla.23651>
- Li Z, Zhuo Y, Li J, Zhang M, Wang R, Lin L (2021) Long non-coding RNA SNHG4 is a potential diagnostic and prognostic indicator in non-small cell lung cancer. *Ann Clin Lab Sci* **51**: 654–662. PMID: 34686507
- Lin N, Lin JZ, Tanaka Y, Sun P, Zhou X (2021) Identification and validation of a five-lncRNA signature for predicting survival with targeted drug candidates in ovarian cancer. *Bioengineered* **12**: 3263–3274. <https://doi.org/10.1080/21655979.2021.1946632>
- Liu HR, Zhao J (2021) Effect and mechanism of miR-217 on drug resistance, invasion and metastasis of ovarian cancer cells through a regulatory axis of CUL4B gene silencing/inhibited Wnt/ β -catenin signaling pathway activation. *Eur Rev Med Pharmacol Sci* **25**: 94–107. https://doi.org/10.26355/eurrev_202101_24353
- (2021) Circular RNA hsa_circ_0006117 facilitates pancreatic cancer progression by regulating the miR-96-5p/KRAS/MAPK signaling pathway. *J Oncol* **2021**: 9213205. <https://doi.org/10.1155/2021/9213205>
- Liu X, Liu C, Zhang A, Wang Q, Ge J, Li Q, Xiao J (2021) Long non-coding RNA SDCBP2-AS1 delays the progression of ovarian cancer *via* microRNA-100-5p-targeted EPDR1. *World J Surg Oncol* **19**: 199. <https://doi.org/10.1186/s12957-021-02295-2>
- Oplawski M, Nowakowski R, Średnicka A, Ochnik D, Grabarek BO, Boroń D (2021) Molecular landscape of the epithelial-mesenchymal transition in endometrioid endometrial cancer. *J Clin Med* **10**: 1520. <https://doi.org/10.3390/jcm10071520>
- Qiao ZW, Jiang Y, Wang L, Wang L, Jiang J, Zhang JR, Mu P (2021) LINC00852 promotes the proliferation and invasion of ovarian cancer cells by competitively binding with miR-140-3p to regulate AGTR1 expression. *BMC Cancer* **21**: 1004. <https://doi.org/10.1186/s12885-021-08730-7>
- Redondo A, Guerra E, Manso L, Martin-Lorente C, Martinez-Garcia J, Perez-Fidalgo JA, Varela MQ, Rubio MJ, Barretina-Ginesta MP, Gonzalez-Martin A (2021) SEOM clinical guideline in ovarian cancer (2020). *Clin Transl Oncol* **23**: 961–968. <https://doi.org/10.1007/s12094-020-02545-x>
- Tang Y, Wu L, Zhao M, Zhao G, Mao S, Wang L, Liu S, Wang X (2019) LncRNA SNHG4 promotes the proliferation, migration, invasiveness, and epithelial-mesenchymal transition of lung cancer cells by regulating miR-98-5p. *Biochem Cell Biol* **97**: 767–776. <https://doi.org/10.1139/bcb-2019-0065>
- Vallée A, Lecarpentier Y, Vallée JN (2021) The key role of the WNT/ β -catenin pathway in metabolic reprogramming in cancers under normoxic conditions. *Cancers (Basel)* **13**: 5557. <https://doi.org/10.3390/cancers13215557>
- Wang L, He M, Fu L, Jin Y (2020) Role of lncRNAHCP5/microRNA-525-5p/PRC1 crosstalk in the malignant behaviors of ovarian cancer cells. *Exp Cell Res* **394**: 112129. <https://doi.org/10.1016/j.yexcr.2020.112129>
- Wu Y, Gu W, Han X, Jin Z (2021) LncRNA PVT1 promotes the progression of ovarian cancer by activating TGF- β pathway *via* miR-148a-3p/AGO1 axis. *J Cell Mol Med* **25**: 8229–8243. <https://doi.org/10.1111/jcmm.16700>
- Xie W, Sun H, Li X, Lin F, Wang Z, Wang X (2021) Ovarian cancer: epigenetics, drug resistance, and progression. *Cancer Cell Int* **21**: 434. <https://doi.org/10.1186/s12935-021-02136-y>
- Xing X, An M, Chen T (2021) LncRNA SNHG20 promotes cell proliferation and invasion by suppressing miR-217 in ovarian cancer. *Genes Genomics* **43**: 1095–1104. <https://doi.org/10.1007/s13258-021-01138-4>
- Xu H, Ding Y, Yang X (2021) Overexpression of long noncoding RNA H19 downregulates miR-140-5p and activates PI3K/AKT signaling pathway to promote invasion, migration and epithelial-mesenchymal transition of ovarian cancer cells. *Biomed Res Int* **2021**: 6619730. <https://doi.org/10.1155/2021/6619730>
- Xu R, Feng F, Yu X, Liu Z, Lao L (2018) LncRNA SNHG4 promotes tumour growth by sponging miR-224-3p and predicts poor survival and recurrence in human osteosarcoma. *Cell Prolif* **51**: e12515. <https://doi.org/10.1111/cpr.12515>
- Xu Z, Jin H, Duan X, Liu H, Zhao X, Fan S, Wang Y, Yao T (2021) LncRNA PSMA3-AS1 promotes cell proliferation, migration, and invasion in ovarian cancer by activating the PI3K/Akt pathway *via* the miR-378a-3p/GALNT3 axis. *Environ Toxicol* **36**: 2562–2577. <https://doi.org/10.1002/tox.23370>
- Yang Z, Sun Q, Guo J, Wang S, Song G, Liu W, Liu M, Tang H (2019) GRSF1-mediated MIR-G-1 promotes malignant behavior and nuclear autophagy by directly upregulating TMED5 and LMNB1 in cervical cancer cells. *Autophagy* **15**: 668–685. <https://doi.org/10.1080/15548627.2018.1539590>
- Yu H, Xu Y, Zhang D, Liu G (2018) Long noncoding RNA LUC-AT1 promotes malignancy of ovarian cancer through regulation of miR-612/HOXA13 pathway. *Biochem Biophys Res Commun* **503**: 2095–2100. <https://doi.org/10.1016/j.bbrc.2018.07.165>
- Yu J, Fan Q, Li L (2021) The MCM3AP-AS1/miR-126/VEGF axis regulates cancer cell invasion and migration in endometrioid carcinoma.

- noma. *World J Surg Oncol* **19**: 213. <https://doi.org/10.1186/s12957-021-02316-0>
- Zhang Q, Zhong C, Duan S (2021) The tumorigenic function of LINC00858 in cancer. *Biomed Pharmacother* **143**: 112235. <https://doi.org/10.1016/j.biopha.2021.112235>
- Zhou N, Chen Y, Yang L, Xu T, Wang F, Chen L, Liu J, Liu G (2021) LncRNA SNHG4 promotes malignant biological behaviors and immune escape of colorectal cancer cells by regulating the miR-144-3p/MET axis. *Am J Transl Res* **13**: 11144–11161. PMID: 34786048
- Zhu D, Shi C, Jiang Y, Zhu K, Wang X, Feng W (2021) Cisplatin inhibits the growth and induces apoptosis of ovarian cancer cells by promoting lincRNA-p21. *Bioengineered* **12**: 1505–1516. <https://doi.org/10.1080/21655979.2021.1916271>
- Zou H, Chen H, Liu S, Gan X (2021) Identification of a novel circ_0018289/miR-183-5p/TMED5 regulatory network in cervical cancer development. *World J Surg Oncol* **19**: 246. <https://doi.org/10.1186/s12957-021-02350-y>



OPEN ACCESS

EDITED BY

Grzegorz Wegrzyn,
University of Gdansk, Poland

REVIEWED BY

Mohamad Taufik Hidayat Baharudin,
National Defence University of Malaysia,
Malaysia
Łukasz Grabowski,
University of Gdansk, Poland

*CORRESPONDENCE

Chengmin Wang,
✉ chengminwang@tom.com

[†]These authors have contributed equally
to this work

RECEIVED 15 December 2023

ACCEPTED 08 March 2024

PUBLISHED 30 April 2024

CITATION

Wang X, Yang C, Zhang X, Ye C, Liu W
and Wang C (2024), Marine natural
products: potential agents for
depression treatment.
Acta Biochim. Pol. 71:12569.
doi: 10.3389/abp.2024.12569

COPYRIGHT

© 2024 Wang, Yang, Zhang, Ye, Liu and
Wang. This is an open-access article
distributed under the terms of the
Creative Commons Attribution License
(CC BY). The use, distribution or
reproduction in other forums is
permitted, provided the original
author(s) and the copyright owner(s) are
credited and that the original
publication in this journal is cited, in
accordance with accepted academic
practice. No use, distribution or
reproduction is permitted which does
not comply with these terms.

Marine natural products: potential agents for depression treatment

Xunqiang Wang[†], Cece Yang[†], Xing Zhang, Caiping Ye,
Wenping Liu and Chengmin Wang*

Department of Psychiatry, Shenzhen Longgang Center for Chronic Disease Control, Shenzhen, China

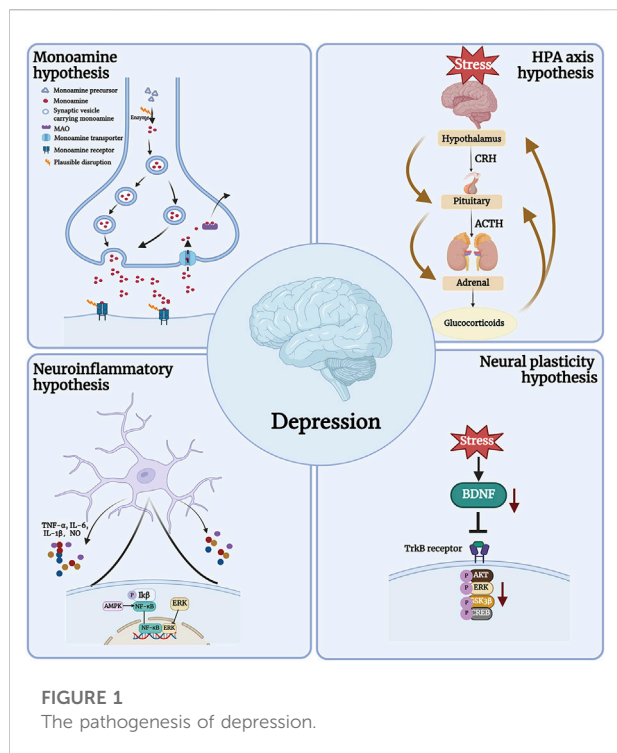
Depression is a common psychiatric disorder. Due to the disadvantages of current clinical drugs, including poor efficacy and unnecessary side effects, research has shifted to novel natural products with minimal or no adverse effects as therapeutic alternatives. The ocean is a vast ecological home, with a wide variety of organisms that can produce a large number of natural products with unique structures, some of which have neuroprotective effects and are a valuable source for the development of new drugs for depression. In this review, we analyzed preclinical and clinical studies of natural products derived from marine organisms with antidepressant potential, including the effects on the pathophysiology of depression, and the underlying mechanisms of these effects. It is expected to provide a reference for the development of new antidepressant drugs.

KEYWORDS

depression, marine natural products, neurotransmitter systems, synaptic plasticity, anti-inflammatory

Introduction

As one of the most common mental illnesses, there are currently at least 50 million patients with depression in China (Huang et al., 2019). The incidence of depression is increasing year by year, and it is expected to become one of the major causes of disease burden in China by 2030 (Huang et al., 2019). Depression imposes a heavy burden on individuals, families and society due to its high incidence, high disability rate and high suicide rate (Cipriani et al., 2018). Selective serotonin reuptake inhibitors (SSRIs), norepinephrine reuptake inhibitors (NRIs), and dopamine reuptake inhibitors (DRIs) are the main first-line antidepressants used in clinical practice today (Harmer et al., 2017; Moragrega and Ríos, 2021). These medications either work on the neurotransmitter systems of serotonin (5-HT), Norepinephrine (NE), and dopamine (DA) or they suppress the action of the enzyme monoamine oxidase (MAO) to produce antidepressant effects (Harmer et al., 2017). However, even after adequate and sufficient antidepressant treatment, about one-third of patients still do not have a significant therapeutic effect. Patients often experience side effects such as gastrointestinal discomfort and loss of libido, in addition to poor treatment compliance. Therefore, it is of great significance to find more effective and safer antidepressant compounds from a wide range of natural



products, and it can also provide new ideas for the development of antidepressant products.

The living environment of marine organisms is complex, resulting in a large number of marine natural products (MNPs). Studies have shown that MNPs have significant pharmacological activities, and the toxicity and side effects are significantly lower than those of synthetic compounds (Corona, 2018). These marine-derived active substances have played an important role in the prevention and treatment of many diseases, and their pharmacodynamic mechanisms are constantly being elucidated. In recent years, with the relentless exploration of researchers, the bioactive substances derived from MNPs have increased. The metabolites isolated from marine organisms have diverse chemical structures, including polyketides, terpenoids, alkaloids, macrolides, cyclic peptides, quinones, polyethers, sterols, polysaccharides, unsaturated fatty acids, and a wide range of pharmacological activities, including antibacterial, antiparasitic, enzyme inhibitor, antioxidant, cytotoxic activity, etc. The majority of marine drug research and development is focused on anti-tumor, anti-cardiovascular disease, and antibacterial agents (Russo et al., 2015; Lima and Medeiros, 2022). Many marine compounds have received clinical approval for use, including the analgesic ziconotide and the anti-cancer drug cytarabine (Jimenez et al., 2020; Yang et al., 2021). MNPs and compounds generated from MNPs are becoming more and more valuable due to their biological activities. Numerous studies have recently revealed that MNPs have antidepressant properties and may slow the course of depression (Subermaniam et al., 2021a). MNPs may be a useful resource for the development of brand-new

antidepressant alternatives. This article examines preclinical and clinical studies on the antidepressant effects of MNPs and research on the neuroscience of depression.

Subsections relevant to the subject

Pathogenesis of depression

The pathogenesis of depression is complex and the biological mechanism is not fully understood (Jesulola et al., 2018). Currently, the widely accepted pathogenic hypotheses include the Monoamine hypothesis, the Neural plasticity hypothesis, the Neuroinflammatory hypothesis, and the Hypothalamic-pituitary-adrenal (HPA) axis (Figure 1) (Subermaniam et al., 2021a; Borbély et al., 2022). It should be mentioned that depression has a complex etiology and may be brought on by a confluence of various pathogenic variables. The search for drugs with multiple targets is thus a crucial area of research for the development of antidepressants.

Monoamine hypothesis

One of the primary causes of depression has been determined to be decreased levels and functional deficiencies of 5-HT, DA, and NE, which are typically present in the brains of depressed patients (Matraszek-Gawron et al., 2019; Wang et al., 2022). The monoamine hypothesis is strongly supported by the fact that 5-HT or NERI can alleviate depression (Locher et al., 2017; Rana et al., 2021). By improving neurotransmission in the central nervous system and increasing the amount of related monoamine neurotransmitters in the synaptic cleft, this class of medications reduces the symptoms of depression (Locher et al., 2017; Yohn et al., 2017).

Neural plasticity hypothesis

The pathogenesis of depression is significantly influenced by neuroplasticity and remodeling failure (Wang et al., 2021a). The neurotrophic family includes brain-derived neurotrophic factor (BDNF), which regulates neuronal plasticity (Castrén and Monteggia, 2021). On the one hand, it might have an impact on the development of synaptic structures, such as axons and dendrites, and their growth and remodeling. On the other hand, it might enhance the long-term synaptic transmission function of the hippocampus through pre- and post-synaptic pathways (Wardle and Poo, 2003). Decreased levels of BDNF have been found in brain samples from depressed patients (Chen et al., 2001; Dwivedi, 2009; Dwivedi et al., 2009; Carlino et al., 2013). In contrast, antidepressant treatment increases the expression of BDNF in the brains of depressed patients (Chen et al., 2001). Therefore, it shows great potential in the treatment of depression as it increases BDNF levels.

TABLE 1 Antidepressant Natural Products of Marine animal Origin.

Natural products	Model establishment	Behavioral outcome	Mechanism	Ref.
Tilapia skin peptides	CP	FST, TST, OFT	Decreased Iba-1, TNF- α , and IL-1 β levels	Zhao et al. (2022a)
			Increased Keap1, SOD, and GSH-Px levels via the Nrf2/HO-1 pathway	
			Increased Bcl-2, Bax, and caspase-3 levels via the BDNF/TrkB/CREB pathway	
Bryostatin-1	CUMS	Open water swimming	N.A.	Alkon et al. (2017)
EPA and DHA	CUMS	SPT, TST, OFT	Decreased IL-1 β , IL-6, TNF- α , and CD11b levels	Peng et al. (2020)
			Increased BDNF, GDNF and NGF levels	
Resolvin D1	myocardial infarction	FST	Anti-inflammation	Gilbert et al. (2014)
Krill oil	CLET	FST	Increased BDNF levels	Wibrand et al. (2013)
5,6-Br-DMT	FST	FST, TST	N.A.	Zhang et al. (2023)
Astaxanthin	LPS	FST, TST	Decreased TNF- α , IL-1 β , IL-6, iNOS, nNOS and COX-2 levels via the NF- κ B pathway	Jiang et al. (2016), Jiang et al. (2017)

EPA, eicosapentaenoic acid; DHA, docosahexaenoic acid; 5,6-Br-DMT, 5,6-dibromo-N, N-dimethyltryptamine; CP, cyclophosphamide; CUMS, chronic unpredictable mild stress; CLET, conditioned light extinction test; LPS, lipopolysaccharides; FST, forced swim test; TST, tail suspension test; OFT, open field test; N.A., not applicable.

Neuroinflammatory hypothesis

Glial cells and cytokines play a role in the immune response known as neuroinflammation that occurs in the central nervous system (Zhou et al., 2022). Depression is an inflammation-related disease that worsens as inflammation increases and progresses (Yirmiya et al., 2015; Wang et al., 2021b). According to research, aberrant glial cell activation in the brains of depressed patients results in the release of pro-inflammatory cytokines such as interleukin-6 (IL-6), interleukin 1 beta (IL-1 β), and tumor necrosis factor-alpha (TNF- α), which can lead to neuroinflammation and neuronal death (Matraszek-Gawron et al., 2019). In addition, glial cells produce nitric oxide synthase (NOS), and cyclooxygenase-2 (COX-2) could also induce neuroinflammation by promoting oxidative stress levels. Neuroinflammation has emerged as a novel target for the treatment of depression (Wang et al., 2021b; Zhou et al., 2022).

Hypothalamic-pituitary-adrenal (HPA) axis

The hypothalamus, pituitary, and adrenal glands work together as part of the HPA axis to govern the body's reaction to physiological or psychological stimuli (Herman et al., 2016; Lew et al., 2020). Patients with depression have been discovered to have HPA dysfunction, resulting in high glucocorticoid (GC) levels, which in turn cause neuronal dysfunction and structural changes in the hippocampus (Dean and Keshavan, 2017). Clinical trials have established the antidepressant properties of

glucocorticoid receptor (GR) antagonists and the viability of targeting HPA regulation in the treatment of depression (Dean and Keshavan, 2017).

MNPs have anti-depressant potential

A significant number of MNPs are produced by the complex living environment of marine animals, and a novel entity structure and enormous diversity are provided by the chemical structure with strong biological activity (Zhao et al., 2022a). Some MNPs have participated in antidepressant preclinical or clinical trials and have proven to be great sources for novel and effective antidepressants (Tables 1, 2). The marine environment is a rich source of novel pharmaceuticals, many of the substances found there can regulate brain activity, reduce anxiety, and have potential therapeutic applications for disorders associated with anxiety and depression (Zhao et al., 2022a). At present, with the interaction between academia and the pharmaceutical sector, a large number of MNPs have been discovered and tested using current analytical methods.

Antidepressant natural products of marine animal origin

Tilapia skin peptides (TSP)

Tilapia skin peptides (TSP), derived from tilapia (*Oreochromis mossambicus*) scraps (Zhao et al., 2022a), have

TABLE 2 Antidepressant compounds derived from marine plants.

Natural products	Model establishment	Behavioral outcome	Mechanism	Ref.
Spirulina	FST	FST	Increased serum BUN and LDH levels	Kim et al. (2008)
Neoechinulin A	LPS	FST	N.A.	Sasaki-Hamada et al. (2016)
Zeaxanthin	diabetic rats	OFT, FST	Decreased IL-6, IL-1 β and TNF- α levels	Peng et al. (2020)
Fucoxanthin	LPS	FST, TST	Decreased TNF- α , IL-1 β , IL-6, iNOS, and COX-2 level via the AMPK/NF- κ B pathway	Gilbert et al. (2014)
Lutein	corticosterone	TST, OFT	Decreased corticosterone levels	Wibrand et al. (2013)
β -Carotene	FST	FST	Decreased TNF- α and IL-6 levels	Kim et al. (2016)
			Increased DNF and p-ERK levels	
Total Sterols and β -sitosterol	FST and TST	FST, TST	Increased NE, 5-HT, and the metabolite 5-HIAA	Zhao et al. (2016)
Fucoidan	LPS and CRS	FST, TST	Inhibited caspase-1 levels	Li et al. (2020)
			Increased BDNF levels	
Fucosterol	FST and TST	FST, TST	Increased NE and 5-HT levels	Zhen et al. (2015)
Alternanthera philoxeroides	ovariectomized	FST, TST	Inhibited MAO-A and MAO-B with IC50 values of 252.9 and 90.69 μ g/mL, respectively	Khamphukdee et al. (2018)
Botryococcus braunii	FST	FST	Increased BDNF, TH, and PC levels	Sasaki et al. (2017)
Padina australis	corticosterone	N.A.	Decreased corticosterone levels	Subermaniam et al. (2020)
Ulva species	FST	FST	N.A.	Violle et al. (2018)
Chlorella vulgaris	patients	N.A.	N.A.	Jiang et al. (2016), Jiang et al. (2017)
				Panahi et al. (2015)

LPS, lipopolysaccharides; CRS, chronic restraint stress; FST, forced swim test; OFT, open field test; TST, tail suspension test; N.A., not applicable.

biological actions that are antioxidant, anti-inflammatory, anti-apoptotic and hypotensive (Ling et al., 2018; Zhao et al., 2022b; Song et al., 2022). Hippocampal neurons in mice that received an intraperitoneal infusion of cyclophosphamide (CP) experienced oxidative stress, neuroinflammation, and neuronal death (Iqbal et al., 2019). TSP [1,000 mg/kg/d, intragastrically (*i.g.*)] could improve CP-induced depressive-like behaviors such as Sucrose Preference Test (SPT), Forced Swim Test (FST), Tail Suspension Test (TST) and Open Field Test (OFT) in mice (Zhao et al., 2022a). Mechanistically, TSP may reduce CP-induced neuroinflammation by decreasing the expression of ionized calcium-binding adaptor molecule 1 (Iba-1), TNF- α , and IL-1 β in the hippocampus of mice. TSP also attenuated CP-induced oxidative stress by increasing the Nrf2/HO-1 signaling pathway and increasing the levels of kelch-like ECH-associated protein 1 (Keap1), superoxide dismutase (SOD), glutathione peroxidase (GSH-Px) and malondialdehyde (MDA). In addition, TSP could also reduce neuronal apoptosis by increasing Bcl-2/Bax/Caspase-3 through the BDNF/TrkB/CREB signaling pathway. In conclusion, the antidepressant effect of the TSP may be

involved in the regulation of synaptic plasticity and anti-inflammatory activity (Zhao et al., 2022a).

Bryostatin-1

Bugula neritina-derived bryostatin-1 can increase the expression of protein kinase C (PKC), induce PKC membrane translocation, and enhance synaptic plasticity (Nelson et al., 2017). PKC activity was reduced in the brains of depressed individuals (Pandey et al., 2021). In the rat model of depression generated by chronic unpredictable mild stress (CUMS), PKC expression was markedly reduced (Han et al., 2015). According to these investigations, PKC levels and the development of depression may be related. Furthermore, PKC has the ability to significantly alter synaptic transmission (Wierda et al., 2007; Shen et al., 2021). Bryostatin-1 [100 nmol/kg, intravenous (*i.v.*)] shortened the immobility time in the FST in rats. This antidepressant effect of Bryostatin-1 is largely abolished by 1-(5-isoquinolylsulfonyl)-2-methylpiperazine (H-7), a PKC inhibitor, which suggests that Bryostatin-1 may have an

antidepressant effect by enhancing synaptic plasticity through activation of PKC action (Alkon et al., 2017).

Eicosapentaenoic acid (EPA) and docosahexaenoic acid (DHA)

Eicosapentaenoic acid (EPA) and docosahexaenoic acid (DHA) are mainly derived from the Omega-3 long-chain polyunsaturated fatty acids (n-3 PUFA) of deep-sea fish and shrimp, which play a key role in brain development (Andraka et al., 2020). Continuous oral administration (*p.o.*) of EPA or DHA for 45 days reduced the weight loss and depressive-like behavior caused by CUMS in SPT/OFT/FST. Mechanistically, EPA and DHA effectively reduced CUMS-induced expression of IL-1 β , IL-6, TNF- α , microglial marker α M Integrin α M (CD11b), and increased expression of astrocyte marker glial fibrillary acidic protein (GFAP) by regulating the NF- κ B/p38 signaling pathway (Peng et al., 2020). Additionally, EPA and DHA modulated the BDNF/TrkB signaling pathway to upregulate the production of BDNF, glial cell-derived neurotrophic factor (GDNF), nerve growth factor (NGF), and Bcl-2 and reduce the expression of Bax, reversing the effects of CUMS-induced neurotrophic factor deficiency and apoptosis (Peng et al., 2020). Moreover, EPA and DHA can also reduce the serum total cholesterol (STC) contents of serum total cholesterol and corticosterone (a glucocorticoid), and induce 5-HT and NE deficiency in the hippocampus, suggesting that EPA and DHA exert antidepressant activity by regulating HPA (Peng et al., 2020). Notably, EPA was more effective than DHA in reducing depressive-like behavior, which was also confirmed in clinical studies. Lipopolysaccharide (LPS) activates BV2 microglia, and docosapentaenoic acid (DPA, a PUFA) balances microglial M1 and M2 polarization, inhibiting NF- κ B and p38 while activating neuronal BDNF/TrkB-PI3K/AKT pathways to protect neurons from neuroinflammatory damage (Liu et al., 2021). By increasing the expression of DA, decreasing the expression of NE and gamma-aminobutyric acid (GABA), and reducing the turnover rate of 5-HT in the mouse hippocampus, PUFAs may also enhance CUMS-induced depressive-like behaviors in the SPT, OFT, and FST (Yang et al., 2019). More importantly, a previous clinical trial has been carried out as a result of the positive safety and antidepressant characteristics of EPA and DHA (Su et al., 2014). Nobody left the study during the 2 weeks due to adverse events and, as determined by the investigators, the incidence of Interferon-alpha (IFN- α)-induced depression in patients with hepatitis C virus infection was significantly lower in those treated with EPA but not in those treated with DHA (Su et al., 2014). In a population-based study to prevent the risk of *postpartum* depression in Brazilian pregnant women, a daily intake of 1.8 g of PUFAs (1.08 g of EPA and 0.72 g of DHA) for 16 weeks starting at 22–24 weeks of gestation had no significant effect on early depressive symptoms during pregnancy or *postpartum* (Vaz et al., 2017). However, the

Edinburgh Postnatal Depression Scale (EPDS) scores of women in the EPA/DHA group with a history of depression showed a greater decrease from the second trimester to the *postpartum* period. Additionally, there were no changes between the EPA/DHA groups and control groups in terms of gestational duration or birth weight (Vaz et al., 2017). According to a recent meta-analysis, both EPA and DHA have antidepressant effects, although EPA's are more potent (Sublette et al., 2011).

Resolvin D1

Resolvin D1, a PUFA metabolite mostly found in deep-sea fish and shrimp, is effective in reducing inflammation by activating Akt and binding to 2 G-protein-coupled receptors (ALX and GPR32) (Serhan and Chiang, 2008; Nelson et al., 2014). Resolvin D1 reduces the depressive-like behavior seen in experimental models of myocardial infarction when administered before ischemia or 5 minutes after reperfusion (Gilbert et al., 2014). In the FST, there was a statistically significant relationship between infarct size, and immobility time (Gilbert et al., 2014). After myocardial infarction, inflammation is indeed well-documented, especially in the first hours of reperfusion (Sharma and Das, 1997; Nah and Rhee, 2009). Therefore, the anti-inflammatory effect may be the reason for its antidepressant-like function.

Krill oil

Antarctic krill (*Euphausia superba*), a zooplankton that resembles shrimp and is rich in EPA, DHA, and astaxanthin, is used to produce krill oil (Wibrand et al., 2013). The conditioned Light Extinction Test (CLET) - induced depressive-like behavior in the FST was reduced in rats after 7 weeks of krill oil administration. Additionally, krill oil reduced depressive-like behaviors by modifying the expression levels of synaptic plasticity-related genes in the prefrontal cortex and hippocampus (Wibrand et al., 2013). Moreover, krill oil supplementation in mice ameliorated chronic unpredictable mild stress (CUMS)-induced depressive-like behaviors by prompting the metabolism of glycerophospholipids and sphingolipids through regulation of differentially expressed genes mainly enriched in the membrane structures and neuroactive ligand-receptor interaction pathway (Zhang et al., 2023). Additionally, Krill oil facilitated fear extinction and reduced depressive-like behaviors by increasing hippocampal calcineurin A levels in mice (Alvarez-Ricartes et al., 2018).

5,6-dibromo-N, N-dimethyltryptamine (5,6-Br-DMT)

5,6-dibromo-N, N-dimethyltryptamine (5,6-Br-DMT) was isolated as a pale light yellow crystal. The precise mechanism underlying how 5,6-Br-DMT [20 mg/kg, intraperitoneally, (*i.p.*)] ameliorated depressive-like behaviors in the FST and TST in mice has not been determined. Indole alkaloids related to 5,6-Br-

DMT have been found to have a strong affinity for 5-HT₂ receptors, indicating that their antidepressant effects may be caused by inhibition of 5-HT reuptake (Hu et al., 2002).

Astaxanthin

The red carotenoid pigment astaxanthin is abundant in microalgae, salmon, trout, and marine invertebrates (Ávila-Román et al., 2021). It has numerous pharmacological properties, such as anti-inflammatory and antioxidant activities (Wu et al., 2015; Ballelli et al., 2016). Trans-astaxanthin (20–80 mg/kg, *p.o.*) for 7 days prevented mice from displaying depressive-like symptoms after being exposed to LPS (Jiang et al., 2016). Neurochemical analysis showed that trans-astaxanthin could also reverse LPS-induced overexpression of IL-1 β , IL-6, and TNF- α , and reduce the expression of inducible nitric oxide synthase (iNOS), neuronal nitric oxide synthase (nNOS), and COX-2 by modulating the NF- κ B pathway (Jiang et al., 2016). In conclusion, trans-astaxanthin may produce antidepressant effects through its potent anti-inflammatory properties (Jiang et al., 2016). Similarly, administration of astaxanthin (20–80 mg/kg, *i.g.*) to mice improved their depressive-like behavior and reduced immobility time during the FST and TST (Jiang et al., 2017). Pretreatment with para-chlorophenylalanine (PCPA) (a 5-HT synthesis inhibitor) abolished the anti-immobility effect of Astaxanthin in FST and TST, suggesting that the mechanism of the antidepressant-like effects of Astaxanthin may involve the 5-HT system (Jiang et al., 2017). More importantly, a clinical trial investigated the effects of Astaxanthin on 28 adults diagnosed with depression and fatigue. The study also recruited healthy, active, and non-depressed adults. Subjects who received 12 mg of Astaxanthin daily for 8 weeks significantly reduced depression and fatigue, compared to the group who received a matching placebo (Talbot et al., 2019).

Natural antidepressants derived from marine plants

Spirulina

Spirulina is a kind of true filamentous spiral cyanobacteria protoplasm that has the biological activities of enhancing immunity, antioxidation, reducing cholesterol levels, and relieving hyperlipidemia (Kim et al., 2008; Subermaniam et al., 2021b). Hydrolyzed Spirulina by malted barley reduces immobility time on FST in mice and increases serum blood urea nitrogen (BUN) and LDH levels (Kim et al., 2008). Moreover, Spirulina improved adolescent stress-induced anxiety and depressive-like symptoms via oxidative stress and alterations in prefrontal cortex BDNF and 5HT-3 receptors in female rats (Moradi-Kor et al., 2020). The specific mechanism needs to be further explored.

Neoechinulin A

Aspergillus amstelodami yielded Neoechinulin A, an isoprenyl indole alkaloid with antioxidant, anti-tumor, and anti-apoptotic properties from *Aspergillus fumigatus* MR2012 from the Red Sea. Neoechinulin A [300 ng/kg, Intracerebroventricularly, (*i.c.v.*)] significantly ameliorated memory decline caused by LPS and restored immobility time in the FST in mice. This effect may be due to modulation of the 5-HT system by direct or indirect action on the 5-HT_{1A} receptor (Sasaki-Hamada et al., 2016).

Zeaxanthin

Zeaxanthin, a yellow-orange xanthophyll, has been extracted from the cyanobacteria *Synechocystis sp.* and *Microcystis aeruginosa* and the microalgae *Nannochloropsis oculata* (Lee et al., 2006; Wojtasiewicz and Stoń-Egiert, 2016). Daily oral zeaxanthin administration from weeks 6–19 could reduce depressive-like behaviors in the OFT and FST of diabetic rats. Zeaxanthin administration could also reduce IL-6, IL-1, and TNF- α overproduction, indicating that it has anti-inflammatory characteristics that help minimize depressive-like behaviors in diabetic rats (Zhou et al., 2018a).

Fucoxanthin

Fucoxanthin, a natural carotenoid, is abundant in edible brown seaweed and has been shown to have excellent antioxidant, anti-inflammatory, and anti-diabetic effects (Mérésse et al., 2020; Bustamam et al., 2021). In the FST and TST of mice, fucoxanthin (200 mg/kg, *i.g.*) significantly reversed LPS-induced depressive-like behaviors (Jiang et al., 2019). Biochemical analysis showed that Fucoxanthin could inhibit LPS-induced overexpression of IL-1 β , IL-6, TNF- α , iNOS, and COX-2 in the hippocampus, frontal cortex, and hypothalamus by regulating the AMPK-NF- κ B signaling pathway (Jiang et al., 2019).

Lutein

Lutein, orange-yellow, is mainly found in microalgae and *Chlorella vulgaris* (Jalali Jivan and Abbasi, 2019; Wang et al., 2020), and has neuroprotective effects (Stringham et al., 2019). In the TST, OFT, and Splash test (ST), lutein (10 mg/kg, *p.o.*) administered once daily for 7 or 21 days significantly reversed corticosterone-induced depressive-like behaviors. This suggests that Lutein may regulate the HPA to exert neuroprotective effects by reducing the level of glucocorticoids (Zeni et al., 2019).

β -Carotene

β -Carotene has been extracted mainly from the microalga *Dunaliella salina* (Han et al., 2019). β -Carotene has also been shown to be a potent inhibitor of oxidative stress and inflammation (Zhou et al., 2018b). Oral administration of β -carotene once daily for 28 days significantly reduced immobility time during the FST in mice (Kim et al., 2016). When compared

to the control group, β -Carotene significantly reduced the levels of TNF- α and IL-6, and increased the levels of BDNF and pERK (Kim et al., 2016).

Total sterols and β -sitosterol

Total Sterols and β -sitosterol have been extracted from *Sargassum horneri*, a brown seaweed found in the Northwestern Pacific Ocean and adjacent seas of Korea, Japan, and China (Zhao et al., 2016). Total sterols and β -sitosterol have been used to treat scrofula, gall, goiter, and edema (Shao et al., 2014; Shao et al., 2015). In both the FST and TST, mice who received total sterols (100–200 mg/kg, *p.o.*) and β -sitosterol (10–30 mg/kg, *i.p.*) had significantly shorter immobility times. Additionally, NE, 5-HT, and the metabolite of 5-Hydroxyindoleacetic acid (5-HIAA) were all considerably elevated by total sterols and β -sitosterol in the mouse brain, suggesting that these neurotransmitters may be involved in mediating the antidepressant-like function (Zhao et al., 2016).

Fucoidan

Fucoidan is a bioactive sulfated polysaccharide abundant in brown seaweed with anti-inflammatory activity (Li et al., 2017). Fucoidan (50–100 mg/kg, *p.o.*) significantly attenuated LPS and chronic restraint stress (CRS) induced depressive-like behaviors in the TST and FST in mice (Li et al., 2020). Fucoidan also reduced the downregulation of BDNF-dependent synaptic plasticity in the mouse hippocampus and decreased caspase-1-mediated inflammation (Li et al., 2020). Furthermore, blocking BDNF abolished the antidepressant-like effects of fucoidan in mice, indicating that fucoidan ameliorates depression by inhibiting inflammation and modulating synaptic plasticity (Li et al., 2020).

Fucosterol

Fucosterol is a bioactive compound belonging to the sterol group that can be isolated from algae, seaweed and diatoms (Meinita et al., 2021). Fucosterol exhibits various biological activities including anticancer, anti-inflammatory, anti-neurological, and antioxidant characteristics (Lee et al., 2003; Jung et al., 2013; Gan et al., 2019). Fucosterol (10–40 mg/kg, *i.p.*) significantly shortened the immobility time in the FST and TST of mice. The expression of NE and 5-HT was strongly upregulated by fucosterol in the mouse brain, suggesting that fucosterol may act via these neurotransmitters (Zhen et al., 2015).

Alternanthera philoxeroides

Alternanthera philoxeroides is a true puree of filamentous, spiral-shaped, blue-green freshwater microalgae (Kim et al., 2008). The crude ethanolic extract of *A. philoxeroides* (250–500 mg/kg, *p.o.* once daily for 8 weeks) significantly ameliorated antidepressant-like behaviors in the FST and TST of ovariectomized mice (Khamphukdee et al., 2018). Additionally, it was discovered that the crude extract

controlled the levels of BDNF in the frontal cortex and hippocampus. In addition, the crude ethanol extract of *A. philoxeroides* was found to inhibit both MAO-A and MAO-B with IC₅₀ values of 252.9 and 90.69 μ g/mL, respectively. These findings suggest that the antidepressant effect of the *A. philoxeroides* extract may be involved in regulating synaptic plasticity and inhibiting MAO activity (Khamphukdee et al., 2018).

Botryococcus braunii

Botryococcus braunii is a pyramid-shaped green colonial microalga that contains triterpenes (Cheng et al., 2019). Daily administration of *B. braunii* ethanol extract (100 mg/kg, for 14 days, *p.o.*) ameliorated depressive-like behaviors with decreased immobility in the FST (Sasaki et al., 2017). The administration of *B. braunii* ethanol extract induced upregulation of gene expression associated with energy metabolism (polyribonucleotide nucleotidyltransferase 1/PNPT1), dopamine production (arginine/serine-rich coiled-coil 1/SRC1), and neurogenesis (short stature homeobox 2/SHOX2, paired-like homeodomain transcription factor 2/PITX2, teashirt zinc finger family member 1/TSHZ1, LIM homeobox 9/LHX9). In addition, the expression of BDNF, tyrosine 3-monooxygenase (TH), and pyruvate carboxylase (PC) was also upregulated (Sasaki et al., 2017). The antidepressant effect of *B. braunii* in animal models of depression is mediated by enhancing energy promotion, neurogenesis, and dopamine synthesis in the brain.

Padina australis

Padina australis is a species of brown macroalgae belonging to the class Phaeophyceae (Subermaniam et al., 2021a). *P. australis* has been reported to possess numerous biological activities including antioxidant, anti-neuroinflammatory, and anti-acetylcholinesterase properties (Gany et al., 2014). pretreatment with *P. australis* (0.25 mg/mL) attenuated high-dose corticosterone-mediated oxidative damage in a PC12 cell model mimicking depression (Subermaniam et al., 2020). *P. australis* reversed the effects of corticosterone, which decreased cell viability, glutathione levels, aconitase activity, and mitochondrial membrane potential while increasing the release of lactate dehydrogenase. This finding indicates that *P. australis* could be developed as a mitochondria-targeted antioxidant to mitigate antidepressant-like effects (Subermaniam et al., 2020).

Ulva species

Ulva species are green macroalgae found in marine, fresh, and brackish waters. *U. species* are widely distributed throughout the world with 18 species identified in Japan (Shimada et al., 2008). Acute and subchronic oral toxicity studies showed that 10–40 mg/kg body weight/day of hydrophilic extract of *U. species* for 14 days significantly reduced the immobility time

in the FST in rats (Violle et al., 2018). *U. species* have the potential to be a useful supplement or replacement for currently prescribed antidepressants. Further studies are necessary to confirm the mechanism of action of MSP and its modulation of brain function (Violle et al., 2018).

Chlorella vulgaris

Chlorella vulgaris is a unicellular green microalgae with many pharmacological properties that include antioxidant, anti-inflammatory, antihypertensive, detoxifying, and anti-atherosclerotic effects (Panahi et al., 2012a; Panahi et al., 2012b). A clinical trial investigated the effects of *C. vulgaris* *Beijerinck* on 92 patients with major depression. 42 patients were assigned to adjuvant therapy with *C. vulgaris*, while 50 patients received standard antidepressant therapy. Participants in the *C. vulgaris* intervention group received six 300 mg tablets per day for 6 weeks, and the intervention group showed improvements in somatic and cognitive symptoms of depression and anxiety (Panahi et al., 2015).

Current regulatory situation and commercialization of MNPs

MNPs are the source of modern marine pharmaceuticals. The study of MNPs, which originated in the 1930 s, can be regarded as the starting point of modern marine drug research. So far, about 33,200 new MNPs have been reported. Based on these new MNPs, the FDA has approved eight marine drugs, i.e., Cefalotin, Alexan, Zikonotide, Omega-3 fatty acid ethyl ester, Ericline mesylate, Brentuximab vedotin, and Trabectedin. Research on MNPs in China began in the 1970 s. In China, the first Marine Pharmaceutical Symposium was held in 1979. In 1982, the journal “Chinese Marine Drugs” was founded. In 1985, the first marine polysaccharide new drug, alginate diester sodium (for cardiovascular disease), was successfully developed and approved for marketing in China in 1990. In view of the unique structure and significant activity of MNPs, the Ministry of Science and Technology launched the Marine “863” Science and Technology Project (“863” Marine Biotechnology Research Program) in 1996. The National Natural Science Foundation of China also separated marine drugs from medicinal chemistry and funded them separately in 2008. These initiatives have greatly promoted the development of marine natural products in China and trained a group of excellent marine drug researchers. So far, about 6,700 new MNPs have been found in China, accounting for approximately 20% of the world’s new MNPs.

Discussion

With the continuous development of modern society, the incidence of depression is increasing, but the existing antidepressant drugs are not effective enough to meet the

clinical needs. Therefore, the need for novel, effective antidepressant treatments is critical. In total, 95% of biodiversity and 71% of the Earth’s surface are in the oceans (Haefner, 2003; Sagar et al., 2010). The physical and chemical conditions of the ocean provide marine organisms with unique active compounds that offer new possibilities for the development of new drugs. The data presented in this review shows the great value of MNPs and their derivatives in the prevention and treatment of depression, demonstrating the potential of MNPs as a promising source of antidepressant drugs. Through a variety of processes, such as the modulation of neurotransmitter systems, synaptic plasticity, anti-inflammatory qualities, and the modulation of HPA function, these MNPs exhibit antidepressant properties. However, most of the current efficacy of MNPs and derivatives in the treatment of depression is based on data from *in vitro* and *in vivo* studies, and a large number of clinical studies are still needed to prove their safety and efficacy, which will help to develop promising new medicines. With the in-depth exploration of marine organisms by mankind, an increasing number of new compounds will be continuously extracted and isolated from marine organisms, which will bring new impetus to the treatment of depression, a disease that plagues the world.

Author contributions

Conceptualization: XW and CW; literature collection and summarization: XZ, CY, and WL; data curation: XW and CY; writing–original draft preparation: XW and CY; writing–review and editing: XW and CW. All authors contributed to the article and approved the submitted version.

Funding

The author(s) declare financial support was received for the research, authorship, and/or publication of this article. This work was supported by the Zhejiang Province Medical and Health Technology Project (2024KY503) and Special Fund for Economic and Technological Development of Longgang District, Shenzhen (LGWJ2021-124).

Conflict of interest

The authors declare that the research was conducted in the absence of any commercial or financial relationships that could be construed as a potential conflict of interest.

Acknowledgments

We thank all authors for their contributions to the article.

References

- Alkon, D. L., Hongpaisan, J., and Sun, M. K. (2017). Effects of chronic bryostatin-1 on treatment-resistant depression in rats. *Eur. J. Pharmacol.* 807, 71–74. doi:10.1016/j.ejphar.2017.05.001
- Alvarez-Ricartes, N., Oliveros-Matus, P., Mendoza, C., Perez-Urrutia, N., Echeverria, F., Iarkov, A., et al. (2018). Intranasal cotinine plus krill oil facilitates fear extinction, decreases depressive-like behavior, and increases hippocampal calcineurin A levels in mice. *Mol. Neurobiol.* 55 (10), 7949–7960. doi:10.1007/s12035-018-0916-0
- Andraka, J. M., Sharma, N., and Marchalant, Y. (2020). Can krill oil be of use for counteracting neuroinflammatory processes induced by high fat diet and aging? *Neurosci. Res.* 157, 1–14. doi:10.1016/j.neures.2019.08.001
- Ávila-Román, J., García-Gil, S., Rodríguez-Luna, A., Motilva, V., and Talero, E. (2021). Anti-inflammatory and anticancer effects of microalgal carotenoids. *Mar. Drugs* 19 (10), 531. doi:10.3390/md19100531
- Baliotti, M., Giannubilo, S. R., Giorgetti, B., Solazzi, M., Turi, A., Casoli, T., et al. (2016). The effect of astaxanthin on the aging rat brain: Gender-related differences in modulating inflammation. *J. Sci. Food Agric.* 96 (2), 4295–4618. doi:10.1002/jsfa.7865
- Borbély, E., Simon, M., Fuchs, E., Wiborg, O., Czéh, B., and Helyes, Z. (2022). Novel drug developmental strategies for treatment-resistant depression. *Br. J. Pharmacol.* 179 (6), 1146–1186. doi:10.1111/bph.15753
- Bustamam, M. S. A., Pantami, H. A., Azizan, A., Shaari, K., Min, C. C., Abas, F., et al. (2021). Complementary analytical platforms of NMR spectroscopy and LCMS analysis in the metabolite profiling of isochrysis galbana. *Mar. Drugs* 19 (3), 139. doi:10.3390/md19030139
- Carlino, D., De Vanna, M., and Tongiorgi, E. (2013). Is altered BDNF biosynthesis a general feature in patients with cognitive dysfunctions? *Neuroscientist* 19 (4), 345–353. doi:10.1177/1073858412469444
- Castrén, E., and Monteggia, L. M. (2021). Brain-derived neurotrophic factor signaling in depression and antidepressant action. *Biol. Psychiatry* 90 (2), 128–136. doi:10.1016/j.biopsych.2021.05.008
- Chen, B., Dowlatabadi, D., MacQueen, G. M., Wang, J. F., and Young, L. (2001). Increased hippocampal BDNF immunoreactivity in subjects treated with antidepressant medication. *Biol. Psychiatry* 50 (4), 260–265. doi:10.1016/s0006-3223(01)01083-6
- Cheng, P., Okada, S., Zhou, C., Chen, P., Huo, S., Li, K., et al. (2019). High-value chemicals from *Botryococcus braunii* and their current applications - a review. *Bioresour. Technol.* 291, 121911. doi:10.1016/j.biortech.2019.121911
- Cipriani, A., Furukawa, T. A., Salanti, G., Chaimani, A., Atkinson, L. Z., Ogawa, Y., et al. (2018). Comparative efficacy and acceptability of 21 antidepressant drugs for the acute treatment of adults with major depressive disorder: a systematic review and network meta-analysis. *Focus Am Psychiatr. Publ.* 16 (4), 420–429. doi:10.1176/appi.focus.16407
- Corona, J. C. (2018). Natural compounds for the management of Parkinson's disease and attention-deficit/hyperactivity disorder. *BioMed Res. Int.* 2018, 1–12. doi:10.1155/2018/4067597
- Dean, J., and Keshavan, M. (2017). The neurobiology of depression: an integrated view. *Asian J. Psychiatry* 27, 101–111. doi:10.1016/j.ajp.2017.01.025
- Dwivedi, Y. (2009). Brain-derived neurotrophic factor: Role in depression and suicide. *Neuropsychiatric Dis. Treat.* 5, 433–449. doi:10.2147/ndt.s5700
- Dwivedi, Y., Rizavi, H. S., Zhang, H., Mondal, A. C., Roberts, R. C., Conley, R. R., et al. (2009). Neurotrophin receptor activation and expression in human postmortem brain: Effect of suicide. *Biol. Psychiatry* 65 (4), 319–328. doi:10.1016/j.biopsych.2008.08.035
- Gan, S. Y., Wong, L. Z., Wong, J. W., and Tan, E. L. (2019). Fucosterol exerts protection against amyloid β -induced neurotoxicity, reduces intracellular levels of amyloid β and enhances the mRNA expression of neuroglobin in amyloid β -induced SH-SY5Y cells. *Int. J. Biol. Macromol.* 121, 207–213. doi:10.1016/j.ijbiomac.2018.10.021
- Gany, S. A., Tan, S. C., and Gan, S. Y. (2014). Antioxidative, anticholinesterase and anti-neuroinflammatory properties of Malaysian Brown and green seaweeds. World academy of science, engineering and Technology. *Int. J. Pharmacol. Pharm. Sci.* 8 (11), 1269.
- Gilbert, K., Bernier, J., Godbout, R., and Rousseau, G. (2014). Resolvin D1, a metabolite of omega-3 polyunsaturated fatty acid, decreases post-myocardial infarct depression. *Mar. drugs* 12 (11), 5396–5407. doi:10.3390/md12115396
- Haefner, B. (2003). Drugs from the deep: Marine natural products as drug candidates. *Drug Discov. Today* 8 (12), 536–544. doi:10.1016/s1359-6446(03)02713-2
- Han, J., Wang, L. U., Bian, H., Zhou, X., and Ruan, C. (2015). Effects of paroxetine on spatial memory function and protein kinase C expression in a rat model of depression. *Exp. Ther. Med.* 10 (4), 1489–1492. doi:10.3892/etm.2015.2663
- Han, S. I., Kim, S., Lee, C., and Choi, Y. E. (2019). Blue-Red LED wavelength shifting strategy for enhancing beta-carotene production from halotolerant microalga, *Dunaliella salina*. *J. Microbiol.* 57 (2), 101–106. doi:10.1007/s12275-019-8420-4
- Harmer, C. J., Duman, R. S., and Cowen, P. J. (2017). How do antidepressants work? New perspectives for refining future treatment approaches. *lancet Psychiatry* 4 (5), 409–418. doi:10.1016/s2215-0366(17)30015-9
- Herman, J. P., McKlveen, J. M., Ghosal, S., Kopp, B., Wulsin, A., Makinson, R., et al. (2016). Regulation of the hypothalamic-pituitary-adrenocortical stress response. *Compr. Physiol.* 6 (2), 603–621. doi:10.1002/cphy.c150015
- Hu, J. F., Schetz, J. A., Kelly, M., Peng, J. N., Ang, K. K. H., Flotow, H., et al. (2002). New anti-infective and human 5-HT₂ receptor binding natural and semisynthetic compounds from the Jamaican sponge *Smenospongia aurea*. *J. Nat. Prod.* 65 (4), 476–480. doi:10.1021/np010471e
- Huang, Y., Wang, Y., Wang, H., Liu, Z., Yu, X., Yan, J., et al. (2019). Prevalence of mental disorders in China: A cross-sectional epidemiological study. *Lancet Psychiatry* 6 (3), 211–224. doi:10.1016/s2215-0366(18)30511-x
- Iqbal, A., Sharma, S., Najmi, A. K., Syed, M. A., Ali, J., Alam, M. M., et al. (2019). Nerolidol ameliorates cyclophosphamide-induced oxidative stress, neuroinflammation and cognitive dysfunction: plausible role of Nrf2 and NF- κ B. *Life Sci.* 236, 116867. doi:10.1016/j.lfs.2019.116867
- Jalali Jivan, M., and Abbasi, S. (2019). Nano based lutein extraction from marigold petals: Optimization using different surfactants and co-surfactants. *Heliyon* 5 (4), e01572. doi:10.1016/j.heliyon.2019.e01572
- Jesulola, E., Micalos, P., and Baguley, I. J. (2018). Understanding the pathophysiology of depression: from monoamines to the neurogenesis hypothesis model - are we there yet? *Behav. Brain Res.* 341, 79–90. doi:10.1016/j.bbr.2017.12.025
- Jiang, X., Chen, L., Shen, L., Chen, Z., Xu, L., Zhang, J., et al. (2016). Trans-astaxanthin attenuates lipopolysaccharide-induced neuroinflammation and depressive-like behavior in mice. *Brain Res.* 1649 (Pt A), 30–37. doi:10.1016/j.brainres.2016.08.029
- Jiang, X., Wang, G., Lin, Q., Tang, Z., Yan, Q., and Yu, X. (2019). Fucoxanthin prevents lipopolysaccharide-induced depressive-like behavior in mice via AMPK-NF- κ B pathway. *Metab. Brain Dis.* 34 (2), 431–442. doi:10.1007/s11011-018-0368-2
- Jiang, X., Zhu, K., Xu, Q., Wang, G., Zhang, J., Cao, R., et al. (2017). The antidepressant-like effect of trans-astaxanthin involves the serotonergic system. *Oncotarget* 8 (15), 25552–25563. doi:10.18632/oncotarget.16069
- Jimenez, P. C., Wilke, D. V., Branco, P. C., Bauermeister, A., Rezende-Teixeira, P., Gaudêncio, S. P., et al. (2020). Enriching cancer pharmacology with drugs of marine origin. *Br. J. Pharmacol.* 177 (1), 3–27. doi:10.1111/bph.14876
- Jung, H. A., Jin, S. E., Ahn, B. R., Lee, C. M., and Choi, J. S. (2013). Anti-inflammatory activity of edible brown alga *Eisenia bicyclis* and its constituents fucosterol and phlorotannins in LPS-stimulated RAW264.7 macrophages. *Food Chem. Toxicol.* 59, 199–206. doi:10.1016/j.fct.2013.05.061
- Khamphukdee, C., Monthakantirat, O., Chulikhit, Y., Buttachon, S., Lee, M., Silva, A., et al. (2018). Chemical constituents and antidepressant-like effects in ovarietomized mice of the ethanol extract of *Alternanthera philoxeroides*. *Molecules* 23 (9), 2202. doi:10.3390/molecules23092202
- Kim, N. H., Jeong, H. J., Lee, J. Y., Go, H., Ko, S. G., Hong, S. H., et al. (2008). The effect of hydrolyzed *Spirulina* by malted barley on forced swimming test in ICR mice. *Int. J. Neurosci.* 118 (11), 1523–1533. doi:10.1080/00207450802325603
- Kim, N. R., Kim, H. Y., Kim, M. H., Kim, H. M., and Jeong, H. J. (2016). Improvement of depressive behavior by Sweetme Sweet Pumpkin™ and its active compound, β -carotene. *Life Sci.* 147, 39–45. doi:10.1016/j.lfs.2016.01.036
- Lee, M. Y., Min, B. S., Chang, C. S., and Jin, E. (2006). Isolation and characterization of a xanthophyll aberrant mutant of the green alga *Nannochloropsis oculata*. *Mar. Biotechnol. (NY)* 8 (3), 238–245. doi:10.1007/s10126-006-5078-9
- Lee, S., Lee, Y. S., Jung, S. H., Kang, S. S., and Shin, K. H. (2003). Anti-oxidant activities of fucosterol from the marine algae *Peltvetia siliculososa*. *Arch. Pharm. Res.* 26 (9), 719–722. doi:10.1007/bf02976680
- Lew, S. Y., Teoh, S. L., Lim, S. H., Lim, L. W., and Wong, K. H. (2020). Discovering the potentials of medicinal mushrooms in combating depression - a review. *Mini-Reviews Med. Chem.* 20 (15), 1518–1531. doi:10.2174/1389557520666200526125534

- Li, J., Zhang, Q., Li, S., Dai, W., Feng, J., Wu, L., et al. (2017). The natural product fucoidan ameliorates hepatic ischemia-reperfusion injury in mice. *Biomed. Pharmacother.* 94, 687–696. doi:10.1016/j.biopha.2017.07.109
- Li, M., Sun, X., Li, Q., Li, Y., Luo, C., Huang, H., et al. (2020). Fucoidan exerts antidepressant-like effects in mice via regulating the stability of surface AMPARs. *Biochem. Biophysical Res. Commun.* 521 (2), 318–325. doi:10.1016/j.bbrc.2019.10.043
- Lima, E., and Medeiros, J. (2022). Marine organisms as alkaloid biosynthesizers of potential anti-alzheimer agents. *Mar. Drugs* 20 (1), 75. doi:10.3390/md20010075
- Ling, Y., Liping, S., and Yongliang, Z. (2018). Preparation and identification of novel inhibitory angiotensin-I-converting enzyme peptides from tilapia skin gelatin hydrolysates: Inhibition kinetics and molecular docking. *Food & Funct.* 9 (10), 5251–5259. doi:10.1039/c8fo00569a
- Liu, B., Zhang, Y., Yang, Z., Liu, M., Zhang, C., Zhao, Y., et al. (2021). ω -3 DPA protected neurons from neuroinflammation by balancing microglia M1/M2 polarizations through inhibiting NF- κ B/MAPK p38 signaling and activating neuron-BDNF-PI3K/AKT pathways. *Mar. Drugs* 19 (11), 587. doi:10.3390/md19110587
- Locher, C., Koechlin, H., Zion, S. R., Werner, C., Pine, D. S., Kirsch, I., et al. (2017). Efficacy and safety of selective serotonin reuptake inhibitors, serotonin-norepinephrine reuptake inhibitors, and placebo for common psychiatric disorders among children and adolescents: a systematic review and meta-analysis. *JAMA psychiatry* 74 (10), 1011–1020. doi:10.1001/jamapsychiatry.2017.2432
- Matraszek-Gawron, R., Chwil, M., Terlecka, P., and Skoczylas, M. M. (2019). Recent studies on anti-depressant bioactive substances in selected species from the genera *hemerocallis* and *gladiolus*: a systematic review. *Pharm. (Basel)* 12 (4), 172. doi:10.3390/ph12040172
- Meinita, M. D. N., Harwanto, D., Tirtawijaya, G., Negara, BFSP, Sohn, J. H., Kim, J. S., et al. (2021). Fucosterol of marine macroalgae: bioactivity, safety and toxicity on organism. *Mar. Drugs* 19 (10), 545. doi:10.3390/md19100545
- Méresse, S., Fodil, M., Fleury, F., and Chénais, B. (2020). Fucoxanthin, a marine-derived carotenoid from Brown seaweeds and microalgae: a promising bioactive compound for cancer therapy. *Int. J. Mol. Sci.* 21 (23), 9273. doi:10.3390/ijms21239273
- Moradi-Kor, N., Dadkhah, M., Ghanbari, A., Rashidipour, H., Bandegi, A. R., Barati, M., et al. (2020). Protective effects of *Spirulina platensis*, voluntary exercise and environmental interventions against adolescent stress-induced anxiety and depressive-like symptoms, oxidative stress and alterations of BDNF and 5HT-3 receptors of the prefrontal cortex in female rats. *Neuropsychiatric Dis. Treat.* 16, 1777–1794. doi:10.2147/ndt.s247599
- Moragrega, I., and Ríos, J. L. (2021). Medicinal plants in the treatment of depression: evidence from preclinical studies. *Planta. Medica* 87 (9), 656–685. doi:10.1055/a-1338-1011
- Nah, D. Y., and Rhee, M. Y. (2009). The inflammatory response and cardiac repair after myocardial infarction. *Korean Circ. J.* 39 (10), 393–398. doi:10.4070/kcj.2009.39.10.393
- Nelson, J. W., Leigh, N. J., Mellas, R. E., McCall, A. D., Aguirre, A., and Baker, O. J. (2014). ALX/FPR2 receptor for RvD1 is expressed and functional in salivary glands. *Am. J. Physiology-Cell Physiology* 306 (2), C178–C185. doi:10.1152/ajpcell.00284.2013
- Nelson, T. J., Sun, M. K., Lim, C., Sen, A., Khan, T., Chirila, F. V., et al. (2017). Bryostatin effects on cognitive function and PKC ϵ in alzheimer's disease phase IIa and expanded access trials. *J. Alzheimer's Dis.* 58 (2), 521–535. doi:10.3233/jad-170161
- Panahi, Y., Badeli, R., Karami, G. R., Badeli, Z., and Sahebkar, A. (2015). A randomized controlled trial of 6-week *Chlorella vulgaris* supplementation in patients with major depressive disorder. *Complementary Ther. Med.* 23 (4), 598–602. doi:10.1016/j.ctim.2015.06.010
- Panahi, Y., Ghamarchehreh, M. E., Beiraghdar, F., Zare, R., Jalalian, H. R., and Sahebkar, A. (2012b). Investigation of the effects of *Chlorella vulgaris* supplementation in patients with non-alcoholic fatty liver disease: A randomized clinical trial. *Hepato-gastroenterology* 59 (119), 2099–2103. doi:10.5754/hge10860
- Panahi, Y., Tavana, S., Sahebkar, A., Masoudi, H., and Madanchi, N. (2012a). Impact of adjunctive therapy with *chlorella vulgaris* extract on antioxidant status, pulmonary function, and clinical symptoms of patients with obstructive pulmonary diseases. *Sci. Pharm.* 80 (3), 719–730. doi:10.3797/scipharm.1202-06
- Pandey, G. N., Sharma, A., Rizavi, H. S., and Ren, X. (2021). Dysregulation of protein kinase C in adult depression and suicide: evidence from postmortem brain studies. *Int. J. Neuropsychopharmacol.* 24 (5), 400–408. doi:10.1093/ijnp/pyab003
- Peng, Z., Zhang, C., Yan, L., Zhang, Y., Yang, Z., Wang, J., et al. (2020). EPA is more effective than DHA to improve depression-like behavior, glia cell dysfunction and hippocampal apoptosis signaling in a chronic stress-induced rat model of depression. *Int. J. Mol. Sci.* 21 (5), 1769. doi:10.3390/ijms21051769
- Rana, T., Behl, T., Sehgal, A., Mehta, V., Singh, S., Sharma, N., et al. (2021). Elucidating the possible role of FoxO in depression. *Neurochem. Res.* 46 (11), 2761–2775. doi:10.1007/s11064-021-03364-4
- Russo, P., Del Bufalo, A., and Fini, M. (2015). Deep sea as a source of novel anticancer drugs: Update on discovery and preclinical/clinical evaluation in a systems medicine perspective. *EXCLI J.* 14, 228–236. doi:10.17179/excli2015-632
- Sagar, S., Kaur, M., and Minneman, K. P. (2010). Antiviral lead compounds from marine sponges. *Mar. Drugs* 8 (10), 2619–2638. doi:10.3390/md8102619
- Sasaki, K., Othman, M. B., Demura, M., Watanabe, M., and Isoda, H. (2017). Modulation of neurogenesis through the promotion of energy production activity is behind the antidepressant-like effect of colonial green alga, *Botryococcus braunii*. *Front. Physiol.* 8, 900. doi:10.3389/fphys.2017.00900
- Sasaki-Hamada, S., Hoshi, M., Niwa, Y., Ueda, Y., Kokaji, A., Kamisuki, S., et al. (2016). Neoechinulin A induced memory improvements and antidepressant-like effects in mice. *Prog. Neuro-Psychopharmacology Biol. Psychiatry* 71, 155–161. doi:10.1016/j.pnpbp.2016.08.002
- Serhan, C. N., and Chiang, N. (2008). Endogenous pro-resolving and anti-inflammatory lipid mediators: A new pharmacologic genus. *Br. J. Pharmacol.* 153 (Suppl. 1), S200–S215. doi:10.1038/sj.bjp.0707489
- Shao, P., Chen, X., and Sun, P. (2014). Chemical characterization, antioxidant and antitumor activity of sulfated polysaccharide from *Sargassum horneri*. *Carbohydr. Polym.* 105, 260–269. doi:10.1016/j.carbpol.2014.01.073
- Shao, P., Liu, J., Chen, X., Fang, Z., and Sun, P. (2015). Structural features and antitumor activity of a purified polysaccharide extracted from *Sargassum horneri*. *Int. J. Biol. Macromol.* 73, 124–130. doi:10.1016/j.ijbiomac.2014.10.056
- Sharma, H. S., and Das, D. K. (1997). Role of cytokines in myocardial ischemia and reperfusion. *Mediat. Inflamm.* 6 (3), 175–183. doi:10.1080/09629359791668
- Shen, C., Cao, K., Cui, S., Cui, Y., Mo, H., Wen, W., et al. (2021). Corrigendum to “SiNiSan ameliorates depression-like behavior in rats by enhancing synaptic plasticity via the CaSR-PKC-ERK signaling pathway” [Biomed. Pharmacother. 124 (2020) 109787]. *Biomed. Pharmacother.* 133, 110892. doi:10.1016/j.biopha.2020.110892
- Shimada, S., Yokoyama, N., Arai, S., and Hiraoka, M. (2008). Phylogeography of the genus *Ulva* (Ulvophyceae, Chlorophyta), with special reference to the Japanese freshwater and brackish taxa. *J. Appl. Phycol.* 20 (5), 979–989. doi:10.1007/s10811-007-9296-y
- Song, X., Li, Z., Li, Y., and Hou, H. (2022). Typical structure, biocompatibility, and cell proliferation bioactivity of collagen from *Tilapia* and Pacific cod. *Colloids Surfaces B Biointerfaces* 210, 112238. doi:10.1016/j.colsurfb.2021.112238
- Stringham, N. T., Holmes, P. V., and Stringham, J. M. (2019). Effects of macular xanthophyll supplementation on brain-derived neurotrophic factor, pro-inflammatory cytokines, and cognitive performance. *Physiology Behav.* 211, 112650. doi:10.1016/j.physbeh.2019.112650
- Su, K. P., Lai, H. C., Yang, H. T., Su, W. P., Peng, C. Y., Chang, J. P. C., et al. (2014). Omega-3 fatty acids in the prevention of interferon-alpha-induced depression: Results from a randomized, controlled trial. *Biol. Psychiatry* 76 (7), 559–566. doi:10.1016/j.biopsych.2014.01.008
- Subermaniam, K., Teoh, S. L., Yow, Y. Y., Tang, Y. Q., Lim, L. W., and Wong, K. H. (2021a). Marine algae as emerging therapeutic alternatives for depression: a review. *Iran. J. basic Med. Sci.* 24 (8), 997–1013. doi:10.22038/ijbms.2021.54800.12291
- Subermaniam, K., Teoh, S. L., Yow, Y. Y., Tang, Y. Q., Lim, L. W., and Wong, K. H. (2021b). Marine algae as emerging therapeutic alternatives for depression: a review. *Iran. J. Basic Med. Sci.* 24 (8), 997–1013. doi:10.22038/ijbms.2021.54800.12291
- Subermaniam, K., Yow, Y. Y., Lim, S. H., Koh, O. H., and Wong, K. H. (2020). Malaysian macroalga *Padina australis* Hauck attenuates high dose corticosterone-mediated oxidative damage in PC12 cells mimicking the effects of depression. *Saudi J. Biol. Sci.* 27 (6), 1435–1445. doi:10.1016/j.sjbs.2020.04.042
- Sublette, M. E., Ellis, S. P., Geant, A. L., and Mann, J. J. (2011). Meta-analysis of the effects of eicosapentaenoic acid (EPA) in clinical trials in depression. *J. Clin. Psychiatry* 72 (12), 1577–1584. doi:10.4088/jcp.10m06634
- Talbot, S. M., Hantla, D., Capelli, B., Ding, L., Li, Y., and Artaria, C. (2019). Effect of astaxanthin supplementation on psychophysiological heart-brain Axis dynamics in healthy subjects. *Funct. Foods Health Dis.* 9 (8), 521–531. doi:10.31989/fthd.v9i8.636
- Vaz, J. D. S., Farias, D. R., Adegboye, A. R. A., Nardi, A. E., and Kac, G. (2017). Omega-3 supplementation from pregnancy to postpartum to prevent depressive symptoms: A randomized placebo-controlled trial. *BMC Pregnancy Childbirth* 17 (1), 180. doi:10.1186/s12884-017-1365-x

- Violle, N., Rozan, P., Demais, H., Nyvall Collen, P., and Bisson, J. F. (2018). Evaluation of the antidepressant- and anxiolytic-like effects of a hydrophilic extract from the green seaweed *Ulva* sp. in rats. *Nutr. Neurosci.* 21 (4), 248–256. doi:10.1080/1028415x.2016.1276704
- Wang, H., He, Y., Sun, Z., Ren, S., Liu, M., Wang, G., et al. (2022). Microglia in depression: An overview of microglia in the pathogenesis and treatment of depression. *J. Neuroinflammation* 19 (1), 132. doi:10.1186/s12974-022-02492-0
- Wang, H., Yang, Y., Yang, S., Ren, S., Feng, J., Liu, Y., et al. (2021b). Ginsenoside Rg1 ameliorates neuroinflammation via suppression of Connexin43 ubiquitination by food waste hydrolysate. *Front. Pharmacol.* 12, 709019. doi:10.3389/fphar.2021.709019
- Wang, X., Zhang, M. M., Sun, Z., Liu, S. F., Qin, Z. H., Mou, J. H., et al. (2020). Sustainable lipid and lutein production from *Chlorella* mixotrophic fermentation by food waste hydrolysate. *J. Hazard. Mater.* 400, 123258. doi:10.1016/j.jhazmat.2020.123258
- Wang, Y. T., Wang, X. L., Feng, S. T., Chen, N. H., Wang, Z. Z., and Zhang, Y. (2021a). Novel rapid-acting glutamatergic modulators: targeting the synaptic plasticity in depression. *Pharmacol. Res.* 171, 105761. doi:10.1016/j.phrs.2021.105761
- Wardle, R. A., and Poo, M. M. (2003). Brain-derived neurotrophic factor modulation of GABAergic synapses by postsynaptic regulation of chloride transport. *J. Neurosci.* 23 (25), 8722–8732. doi:10.1523/jneurosci.23-25-08722.2003
- Wibrand, K., Berge, K., Messaoudi, M., Duffaud, A., Panja, D., Bramham, C. R., et al. (2013). Enhanced cognitive function and antidepressant-like effects after krill oil supplementation in rats. *Lipids health Dis.* 12, 6. doi:10.1186/1476-511x-12-6
- Wierda, K. D., Toonen, R. F., de Wit, H., Brussaard, A. B., and Verhage, M. (2007). Interdependence of PKC-dependent and PKC-independent pathways for presynaptic plasticity. *Neuron* 54 (2), 275–290. doi:10.1016/j.neuron.2007.04.001
- Wojtasiewicz, B., and Stoń-Egiert, J. (2016). Bio-optical characterization of selected cyanobacteria strains present in marine and freshwater ecosystems. *J. Appl. Phycol.* 28, 2299–2314. doi:10.1007/s10811-015-0774-3
- Wu, H., Niu, H., Shao, A., Wu, C., Dixon, B., Zhang, J., et al. (2015). Astaxanthin as a potential neuroprotective agent for neurological diseases. *Mar. Drugs* 13 (9), 5750–5766. doi:10.3390/md13095750
- Yang, M., Xuan, Z., Wang, Q., Yan, S., Zhou, D., Naman, C. B., et al. (2021). Fucoxanthin has potential for therapeutic efficacy in neurodegenerative disorders by acting on multiple targets. *Nutr. Neurosci.* 25, 2167–2180. doi:10.1080/1028415x.2021.1926140
- Yang, R., Zhang, M. Q., Xue, Y., Yang, R., and Tang, M. M. (2019). Dietary of n-3 polyunsaturated fatty acids influence neurotransmitter systems of rats exposed to unpredictable chronic mild stress. *Behav. Brain Res.* 376, 112172. doi:10.1016/j.bbr.2019.112172
- Yirmiya, R., Rimmerman, N., and Reshef, R. (2015). Depression as a microglial disease. *Trends Neurosci.* 38 (10), 637–658. doi:10.1016/j.tins.2015.08.001
- Yohn, C. N., Gergues, M. M., and Samuels, B. A. (2017). The role of 5-HT receptors in depression. *Mol. Brain* 10 (1), 28. doi:10.1186/s13041-017-0306-y
- Zeni, A. L. B., Camargo, A., and Dalmagro, A. P. (2019). Lutein prevents corticosterone-induced depressive-like behavior in mice with the involvement of antioxidant and neuroprotective activities. *Pharmacol. Biochem. Behav.* 179, 63–72. doi:10.1016/j.pbb.2019.02.004
- Zhang, H., Liu, X., Li, B., Zhang, Y., Gao, H., Zhao, X., et al. (2023). Krill oil treatment ameliorates lipid metabolism imbalance in chronic unpredictable mild stress-induced depression-like behavior in mice. *Front. Cell Dev. Biol.* 11, 1180483. doi:10.3389/fcell.2023.1180483
- Zhao, D., Zheng, L., Qi, L., Wang, S., Guan, L., Xia, Y., et al. (2016). Structural features and potent antidepressant effects of total sterols and β -sitosterol extracted from *Sargassum horneri*. *Mar. Drugs* 14 (7), 123. doi:10.3390/md14070123
- Zhao, Y. T., Yin, H., Hu, C., Zeng, J., Shi, X., Chen, S., et al. (2022b). Tilapia skin peptides restore cyclophosphamide-induced premature ovarian failure via inhibiting oxidative stress and apoptosis in mice. *Food & Funct.* 13 (3), 1668–1679. doi:10.1039/d1fo04239d
- Zhao, Y. T., Yin, H., Hu, C., Zeng, J., Zhang, S., Chen, S., et al. (2022a). Tilapia skin peptides ameliorate cyclophosphamide-induced anxiety- and depression-like behavior via improving oxidative stress, neuroinflammation, neuron apoptosis, and neurogenesis in mice. *Front. Nutr.* 9, 882175. doi:10.3389/fnut.2022.882175
- Zhen, X. H., Quan, Y. C., Jiang, H. Y., Wen, Z. S., Qu, Y. L., and Guan, L. P. (2015). Fucosterol, a sterol extracted from *Sargassum fusiforme*, shows antidepressant and anticonvulsant effects. *Eur. J. Pharmacol.* 768, 131–138. doi:10.1016/j.ejphar.2015.10.041
- Zhou, L., Ouyang, L., Lin, S., Chen, S., Liu, Y., Zhou, W., et al. (2018b). Protective role of β -carotene against oxidative stress and neuroinflammation in a rat model of spinal cord injury. *Int. Immunopharmacol.* 61, 92–99. doi:10.1016/j.intimp.2018.05.022
- Zhou, S., Chen, R., She, Y., Liu, X., Zhao, H., Li, C., et al. (2022). A new perspective on depression and neuroinflammation: non-coding RNA. *J. Psychiatric Res.* 148, 293–306. doi:10.1016/j.jpsychires.2022.02.007
- Zhou, X., Gan, T., Fang, G., Wang, S., Mao, Y., and Ying, C. (2018a). Zeaxanthin improved diabetes-induced anxiety and depression through inhibiting inflammation in hippocampus. *Metab. Brain Dis.* 33 (3), 705–711. doi:10.1007/s11011-017-0179-x

Investigation of VEGF (rs 699947) polymorphism in the progression of Rheumatoid Arthritis (RA) and *in-silico* nanoparticle drug delivery of potential phytochemicals to cure RA

Nageen Hussain¹, Mohsin Mumtaz², Muhammad Adil¹, Abad Ali Nadeem³, Abid Sarwar³, Tariq Aziz⁴✉, Metab Alharbi⁵, Abdulrahman Alsahammari⁵, Abdullah F Alasmari⁵ and Mousa Essa Alharbi⁶

¹Institute of Microbiology and Molecular Genetics, University of the Punjab Lahore-54590, Pakistan; ²School of Women's and Children's Health, Faculty of Medicine and Health, the University of New South Wales, Australia; ³Food and Biotechnology Research Center PCSIR Laboratories, Lahore, Pakistan; ⁴Department of Agriculture, University of Ioannina, 47100 Arta, Greece; ⁵Department of Pharmacology and Toxicology, College of Pharmacy, King Saud University, P.O. Box 2455, Riyadh 11451, Saudi Arabia; ⁶Ministry of Health King of Saudi Arabia Riyadh, King of Saudi Arabia

Mutation in the VEGF gene disturbs the production of chondrocytes and angiogenesis which are essential for cartilage health. Cytokines and chemokines produced by auto-activation of B-cells degrade cartilage. Bruton's Tyrosine Kinase (BTK) plays a crucial role in the activation of these B-cells. VEGF has a central part in angiogenesis, in the recruitment of endothelial cells, and is involved in mechanisms that result in tumour formation. The objective of this research is to investigate the potential role of VEGF polymorphism in the development of Rheumatoid Arthritis (RA) and the screening of potential natural, synthetic BTK inhibitor compounds as possible *in-silico* chemotherapeutic agents to control auto-activation of B-cells and cartilage degrading cytokines. In this study, it had been shown that allele A frequency was significantly higher than that of allele C in RA-positive patients as compared to controls. Hence it depicts that allele A of VEGF (rs699947) can increase the risk of RA while allele C has a protective role. The phytochemicals which showed maximum binding affinity at the inhibitory site of BTK include beta boswellic acid, tanshinone, and baicalin. These phytochemicals as BTK inhibitor give insights to use them as anti-arthritis compounds by nanoparticle drug delivery mechanism.

Keywords: angiogenesis, phytochemicals, Bruton's tyrosine kinase, Rheumatoid Arthritis, VEGF gene

Received: 06 February, 2023; revised: 18 April, 2023; accepted: 21 April, 2023; available on-line: 05 September, 2023

✉e-mail: iwockd@gmail.com

Abbreviations: BTK, Bruton's Tyrosine Kinase; RA, Rheumatoid Arthritis

INTRODUCTION

Rheumatoid Arthritis is an inflammatory auto-immune disorder of joints (van Delft & Huizinga, 2020). The inflammatory process enhances as new blood vessels originate and supply different growth factors, oxygen, and cytokines to the cells which leads to the development of irregular fibrous tissues and ultimately cause the destruction of joints (Nakkala *et al.*, 2021). A ratio of 1:3 between male and female susceptibility can be seen in previous studies. The worldwide prevalence of RA is 0.5–1% depending on geographical changes. The stud-

ies conducted in Pakistan and India represent the RA prevalence as 0.5% and 0.2–1% respectively (Bahari *et al.*, 2021). Population diversity is responsible for the higher prevalence of RA in India (Oton & Carmona, 2019). There are some influential factors of RA that play a significant role in the susceptibility of RA like genetic factors and environmental factors. Almost 60% of the susceptibility is caused due to genetic factors. Although further studies are required to explain the role of environmental factors in the onset of RA, however, it is reported that smoking, dietary contents, micro-organisms, and silica exposure have a detrimental effect and they can also exacerbate the condition of RA patients (Ganesan *et al.*, 2020). Dietary contents may also have a role in the severity of the disease. The majority of patients claimed that eating foods like dairy, red meat, green leafy vegetables, etc. made their medical state worse. Red meat contains high amounts of protein and fats which enhance the pro-inflammatory process resulting in increased severity of the disease in patients with RA (Karami *et al.*, 2019).

There are evidence and studies which support that many autoimmune ailments like rheumatoid arthritis along with systemic lupus erythematosus (SLE) and multiple sclerosis are linked with the VEGF gene (Martins & Fonseca, 2019). VEGF gene has eight exons with alternate splicing, and it is present on chromosome 6p 12. During embryonic developmental stages, the multiplication and migration of endothelial cells are induced by VEGF, and have crucial involvement in tumour development, angiogenesis, and wound healing (Jutley *et al.*, 2017). In the synovial fluid of obstructed joints of RA patient, enhanced expression of VEGF is observed. The enhanced expression also results in inflammation, changes in joints, and different pathological conditions in patients along with angiogenesis. The severity of the disorder or disease can be determined by the VEGF level in the serum of patients. An elevated level of VEGF has been recorded in patients suffering from RA as compared to controls (healthy individuals) and osteoarthritis patients (Philippou *et al.*, 2021). SNPs that are known and also illustrate a significant role in the expression of VEGF proteins are VEGF-2578 A/C (rs 699947), +405 G/C, -460 C/T +936 C/T (Aterido *et al.*, 2017). According to a study in Korea, an association is seen between VEGF SNPs and RA (Qindeel *et al.*, 2020).

Although VEGF is very significant to proliferate cartilage and bone cells but in RA auto-activation of B-cells produces chemicals that damage these cells so, this auto-activity of the B-cells must be controlled (Goswami *et al.*, 2022). Their activation is mediated by a regulatory protein Burton's Tyrosine Kinase. This protein stimulates B-cells to produce cytokines and chemokines. In a healthy individual, synoviocytes produce lubrication and nutrition for the surrounding cartilage tissue, and the synovium has a minimal number of cellular infiltrates. In RA, B-cells infiltrate the synovium and release cytokines, chemokines, and enzymes that promote joint deterioration and inflammation (Wang *et al.*, 2021). It causes the synovium to enlarge, causing synoviocyte production and inflammatory cell penetration to form a pannus that eventually invades the nearby bone and cartilage. B-cell receptor-dependent cell proliferation is inhibited by BTK inhibition, which ultimately results in a decrease in inflammatory cytokines. Targeting the BTK's activity may therefore result in the loss of B cell signaling, which in turn may open up a treatment option for RA. The cytoplasmic, non-receptor tyrosine kinase BTK transmits signals via numerous cell surface molecules. All hematopoietic cell types, except for T, NK, and plasma cells, express it (Miao *et al.*, 2020). BTK communicates with chemokine receptors, Fc receptors, Toll-like receptors, B cells receptors, CD40, and B cells receptors. These activated proteins damage tissues, especially joints. A high level of BTK causes autoimmunity while a low level of BTK helps in improving autoimmune diseases like RA (De Vries *et al.*, 2019). The abnormal activity of BTK might be ceased via various inhibitor synthetic as well as natural bioactive compounds. The core aim of this study was to find out VEGF SNP in the Pakistani population and possible chemotherapeutic drugs.

METHODOLOGY

Sampling

Samples of blood from 100 healthy individuals (controls) and 100 RA patients who were positive for Rheumatoid Factor were collected from two major cities of Pakistan. These blood samples were collected from D.H.Q Hospital Toba Tek Singh, Sheikh Zaid Hospital, Lahore, and Fatima Memorial Hospital Lahore. The participant's approval was taken on an informed consent form and their disease history was recorded on a Proforma (covered all aspects related to disease and the risk factors associated with RA). Afterwards the experimental work was carried out at the Institute of Microbiology and Molecular Genetics of the University of the Punjab, Lahore-Pakistan.

IRB approval

The ethical approval for this research study was granted by Departmental Research Ethics and Biosafety Committee under the issuance certificate D/2302/MMG, dated 6-12-2019.

DNA Isolation and Amplification

The fast DNA extraction method makes it simpler to extract DNA from blood and produces a significant volume of non-degraded DNA. The application of triton X-100 prevents DNA degradation (Shahraki *et al.*, 2022). $MgCl_2$ acts as a buffering agent in the red blood cell lysis buffer, whereas EDTA acts as a chelating agent,

stops DNA deterioration, and concentrates DNA. Nuclear lysis buffer and red cell lysis buffer both lysed red blood cells, break the nuclear wall and release the nuclear material inside. SDS was added to the lysis buffer to solubilize proteins and lipids, and chloroform was used to breakdown proteins and purify DNA. Chloroform was used to separate the organic phase from the aqueous phase while maintaining DNA protection in the latter. The precipitation of DNA was accomplished using ethanol. The first procedure involved transferring 500 μ l of blood into an Eppendorf tube and then adding 1000 μ l of RBC lysis buffer. The Eppendorf was centrifuged for 2 minutes at 7000 rpm (revolutions per minute) after being lightly inverted or gently shaken. After that, the supernatant was removed, and the Eppendorf tube containing the pellet received another 1000 μ l addition of RBCs lysis buffer. Once more, the particle was centrifuged at 7000 rpm for 2 minutes, three to four times, until the haemoglobin was eliminated. After RBC lysis buffer was added, the tube was vortexed to break up the pellet and remove the haemoglobin, revealing that the particle exclusively contained WBCs. The tube was then positioned downward on the tissue paper for a brief period of time. The Eppendorf tube was then filled with 600 μ l of chloroform (kept at 4°C), 400 μ l of nucleic lysis buffer, 100 μ l of NaCl, and 400 μ l of lysis buffer (kept at 4°C). After that, centrifugation took place for two minutes at 7000 rpm. The result was two phases, an organic phase and an aqueous phase, separated by a layer. Then, 800 μ l of 100% ethanol (pre-chilled and maintained at -20°C) was added to the Eppendorf tube containing the supernatant after 400 μ l of the supernatant had been emptied into another Eppendorf tube. After the vortex, the DNA manifested itself in the aqueous phase as a white thread-like structure. The tube was centrifuged at 12000 rpm for one minute, the supernatant was removed, and the tube was dried at room temperature (on tissue paper). After adding 100 μ l of T.E. buffer, the tube was vortexed. The DNA-filled Eppendorf tube was then kept at -20°C. The stock solution for the primers was created using a 1:10 ratio.

- Forward inner primer (A allele) "GCCAGCTGTAGGC-CAGACCCTGGT"
- Reverse inner primer (C allele) "TCAGTCTGATTATC-CACCCAGACCG"
- Forward outer primer "GTGCACGAATGATGGAAAGG-GAGG"
- Reverse outer primer "CCCCATCCCATTCTTGCAT-ATAGG"

50 μ l were used to conduct the PCR reaction. Forward and reverse primers, genomic DNA, 10 μ l of nuclease-free water, and 25 μ l of the master mix were all added. The DNA strand was first denaturized at 95°C for 5 minutes, and then it was finally denaturized at 95°C for 30 seconds. For rs699947, the DNA strand was annealed at 67.3°C for 30 seconds, extended at 72°C for 1 minute, and finally extended for 5 minutes at 72°C. The PCR was run for 30 cycles. The PCR products had lengths of 183 bp and 299 bp for rs 699947 and were kept at a temperature of 4°C. On electrophoresis on 1.3% agarose gel, the amplified products were seen. The size of the PCR products was measured using Thermo Scientific's quick ruler low-range DNA ladder (SM1103).

In-Silico Screening of BTK Inhibitor Chemicals

Plants have a variety of bioactive compounds that can block the activity of BTK to control the auto-activation

Table 1. The laboratory parameters and disease activity in association with VEGF

Parameters	AA		CA + CC		P
	N	Median (IQR)	N	Median (IQR)	
Age (Years)	71	47 (20–60)	29	45 (20–60)	0.014*
Duration of Disease (Years)	63	7 (6 months – 15 Years)	24	7 (6 months – 15 Years)	0
CRP (mg/L)	47	12 (6–30)	25	14 (6–34)	0.049*
Number of Tender Joints	56	5 (2–9)	22	7 (2–11)	0.105
Number of Swollen Joints	51	3 (0–5)	18	2 (0–8)	0.126
ESR (mm/h)	23	34 (18–50)	28	23 (16–48)	0.121
	AA		CA + CC		P
	N	n (%)	N	n (%)	
Anti – Cyclic Citrullinated Peptide Antibody (CCP)	54	30 (55%)	25	14 (56%)	0.222
RF Presence	71	71 (100%)	29	27 (93%)	0.269

*P<0.05, Significant; P>0.05, non-Significant

of the B-cell, chemokines, and cytokines. Screening of these phytochemicals has been done by using computational tools and online databases. To avoid a huge number of resources, funding, and wastage of time to sort out a particular chemical as a BTK inhibitor, in-silico screening is the best approach to screen out target bioactive chemicals. The target protein BTK was found in PDB to have a 3D structure (1D-6J6M). Using PyMol (version 2.5.2), water molecules and already-bound ligands were removed (Hari, 2017). Target ligand information was gathered from a variety of sources, and 3D ligand structures were acquired in SDF format from online chemical databases like Zinc 15, PubChem, and ChEMBL database. Then, using Swiss ADME and Lipinski's Rule of Five, the ligands' drug resemblance was evaluated. Online SMILES Translator (nii.gov) was used to convert the SDF format of the ligands to the PDB format, and Auto Dock Vina (version 1.5.7) was used to convert the PDB to the PDBQT format and then docking by using the command prompt (Samdani & Vetrivel, 2018).

RESULTS

Patients were diagnosed according to the criteria defined American College of Rheumatology (ACR) in 2010. Among those 100 patients, males were only 33% while females constitute a major proportion (67%) of

the study. The common symptoms in RA patients, whose blood samples were used, found morning stiffness (82%), tenderness in the joints (78%), fatigue (25%), severe pain in joints (85%), fever (20%), and joint Swelling (63%) (Fig. 1) (Ganesan *et al.*, 2020). The risk factors associated with RA were genetic disorder (9%), smoking (7%), diet (33%), hormonal changes (17%), other infectious diseases (6%), and no response (28%) (Fig. 2).

Single Nucleotide Polymorphism in DNA due to extrinsic or intrinsic factors has both deleterious and beneficial effects depending on its nature. In this study, a base change in the VEGF gene in different populations showed significant results in the progression of rheumatoid arthritis. In Table 1, a possible linkage between VEGF polymorphism with RA disease activity was analyzed based on the demographic and clinical condition of the patients. The alleles of the VEGF gene were correlated with disease duration, rheumatoid factor, age of patients and C-reactive protein level.

The appearance of 183bp DNA bands on agarose gel electrophoresis indicated A allele (Fig. 3) and 299bp DNA bands represented C allele (Fig. 4), and the DNA ladder used was Fermentas SM1103. In VEGF, C allele functions as a major allele and A allele as a minor allele. The frequencies of genotype and allele were considerably different in patients and controls. The percentage of AA genotype in RA patients and in controls was 71% and 39% respectively. However, the percentage of CC

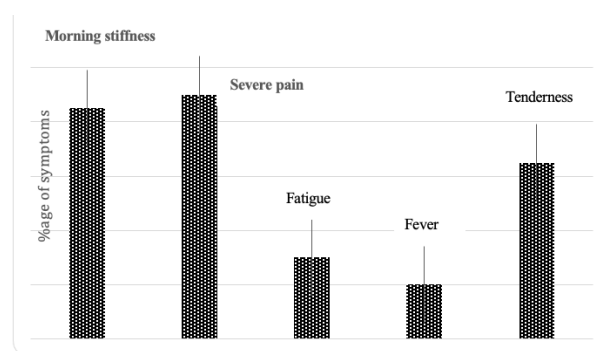


Figure 1. Symptoms reported by Rheumatoid Arthritis

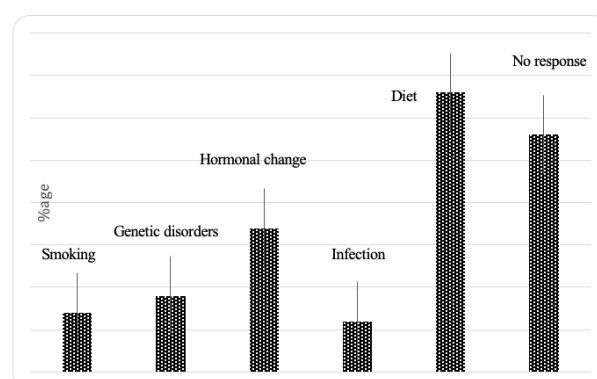


Figure 2. Risk factors involved in progression in RA patients

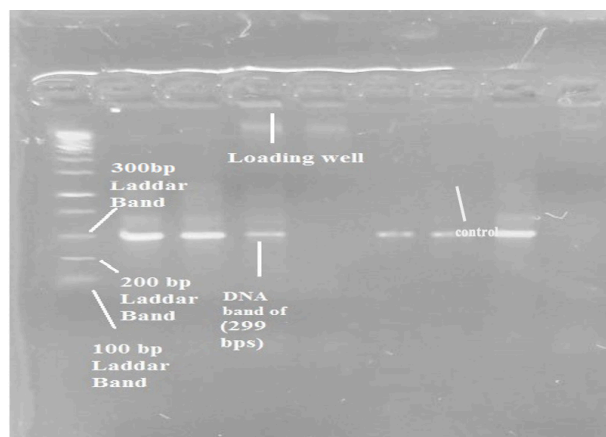


Figure 3. Amplified DNA band of our interest (183bp) shown under the UV Illuminator

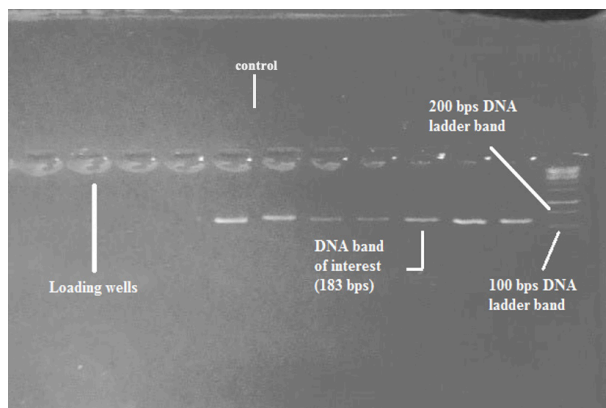


Figure 4. Amplified DNA band of our interest (299bp) shown under the UV Illuminator

genotype in RA patients and control was 23% and 52% respectively.

Moreover, in heterogeneous conditions where both alleles (A and C) were present, the percentage of AC genetic constitution in patients and controls was 06% and 09% respectively. Hence, the above data endorsed that VEGF A/C polymorphism has a role in association with the risk of rheumatoid arthritis. Table 2 and Table 3 revealed different frequencies of genotypes and frequencies of alleles in controls and patients. Our findings suggested that the AA genotype of VEGF was observed considerably higher in RA patients but lower

in healthy individuals that depicted the role of SNPs in the severity of RA.

The chi-square test was done by keeping a degree of freedom (df) value 2, the *p*-value was 0.034 which is less than 0.05, and the regression value was 0.461. All these values showed that the VEGF gene SNP has a significant influence on rheumatoid arthritis progression.

Bioactive Compounds to Inhibit BTK Activity

Plants have a variety of bioactive compounds capable of curing rheumatoid arthritis. These compounds can be screened out in-silico by using different computational tools. The results of docked compounds have been given in Tables 4 and 5 showing binding affinities to block BTK. Protein-ligands docking was done by targeting THR 474, GLU 475, MET 477, and CYS 481 residues of BTK. The results were observed in PyMol (Version: 2.5.2) and noted binding affinities in KJ/mol shown in Fig. 5. The Pleckstrin homology (PH) domain, the Tec homology (TH) domain, the Src homology (SH3) domain, the SH2 domain, and the C-terminal region containing kinase activity are the five sections that make up BTK, according to its structures. BTK inhibitors can be divided into two categories based on how they bind to BTK and how their chemical scaffold structures and mechanisms of action. The amino acid residue CYS 481 in the ATP-binding region of BTK is a covalently bonded target for irreversible BTK inhibitors (Wang *et al.*, 2021). The other class of BTK inhibitors are reversible inhibitors, which bind to an inactive form of the kinase by accessing the particular SH3 pocket of BTK. In order to treat RA, phytochemicals are delivered as drugs via nanoparticles, acting as a BTK inhibitor (Fig. 6).

DISCUSSION

The VEGF gene has a prominent role in the onset of many other autoimmune diseases. There are almost thirteen studies that depict the evidence that VEGF was higher in RA patients in contrast to healthy individuals, and hence are in favour of an association between RA and the VEGF gene. But contrary to that there are also many studies that deny this and report no association among VEGF and the risk of RA like + 936 T/C, VEGF-634 C/G, -1154 A/G and -2578 A/C polymorphisms have no relation with RA. In another study, a significant association was observed between VEGF (rs 699947) SNPs and RA (Paradowska-Gorycka *et al.*, 2016). The studies show a relationship between the VEGF gene and RA in terms of severity along with overlap-

Table 2. Genotypes and Allele frequencies of VEGF C/A polymorphism

Gene mutation	Genotypes	Genotype frequency cases (n=100)	Genotype frequency controls (n=100)	Alleles	Allele frequency cases (n=100)	Allele frequency controls (n=100)
VEGF rs699947	CC	23	52	C	52	113
	AA	71	39	A	148	87
	CA	06	09			

Table 3. Analysis of the VEGF gene SNP rs699947 by Chi-square test

Subjects	Homozygous CC	Heterozygous CA	Homozygous AA	Total	χ^2 df = 2	<i>p</i> -value	Regression
Cases	23	06	71	100	23.32	0.034	0.461 ^a
Controls	52	09	39	100			

Table 4. Potential Phytochemicals Inhibitors of Burton's Kinase (BTK)

Sr. No	Compound name	Binding affinity (KJ/mol)	Configuration
	BETA-BOSWELLIC-ACID	-8.4	ASN 479 (CN-OH,3.1)
	TANSHINONE	-8.3	MET 477 (CO-OH,3.0) ALA 478 (CO-OH,3.4)
	BAICALIN	-8.2	CYS 481 (CN-OH,2.9) ASN 479 (CN-OH,2.3) ASN 484 (CN-OH,3.1)
	BERBERASTINE	-8.1	MET 477 (CN-OH,3.2)
	APIGENIN	-7.8	MET 477 (CN-OH,3.3) ASN 484 (CN-OH,2.9) THR 410 (CN-OH,3.1)
	6-DEOXYJACAREUBIN	-7.8	LYS 430 (CN-OH,3.3) MET 477 (CN-OH,3.2) MET 477 (CO-OH,2.4)
	(-)-ALPHA-BISABOLOL	-6.3	LYS 430 (CN-OH,3.0)
	QUERCETIN	-7.6	MET 477 (CN-OH,3.0) MET 477 (CN-OH,3.2) MET 477 (CN-OH,2.4) THR 474 (CO-OH,2.9) THR 410 (CN-OH,3.1)
	SPEBRUTINIB	-7.5	ASN 484 (CN-CO,3.0) MET 477 (CO-NH,2.5)
	CEPHARANOLINE	-7.4	CYS 481 (CN-OH,3.1) THR 410 (CO-OH,2.1)

Table 5. Synthetic BTK Inhibitors

Sr. No.	Phytochemical	Binding Energy (kJ/mol)	Configurations (PyMol)
1.	RN-486	-7.9	CYS 481 (CN-CO,3.0) LYS 430 (CN-OH,3.1) ASN 479 (CO-OH,3.2)
2.	BARICITINIB	-7.6	MET 477 (CO-NH,3.5) MET 477 (CO-NH,2.5) THR 410 (CO-SO,3.1)
3.	SPEBRUTINIB	-7.5	ASN 484 (CN-CO,3.0) MET 477 (CO-NH,2.5)
4.	FENEBRUTINIB	-7.0	MET 477 (CN-OH,3.1) MET 477 (CO-OH,2.7)
5.	IBRUTINIB	-7.3	MET 477 (CO-NH,3.2) LEU 408 (CO-NH,3.5)
6.	SPEBRUTINIB	-7.5	ASN 484 (CN-CO,3.0) MET 477 (CO-NH,2.5)
7.	TIRABRUTINIB	-6.9	ASN 484 (CN-OH,3.4)
8.	UPADACITINIB	-5.8	ASN 484 (CN-CO,3.3)
9.	ZANUBRUTINIB	-6.5	CYS 481 (CN-CO,3.5) LYS 430 (CN-OH,3.1)
10.	ACALABRUTINIB	-5.0	GLU 488 (CO-CO,2.8) ALA 478 (CO-NH,3.5)

ping of various other disease parameters i.e., activity of disease, functional disability, and joint damage. The main objective behind this work was to access the risk of single nucleotide polymorphism of the *VEGF* gene in RA patients. Two alleles A and C were studied, and their frequency was determined. It had been shown that allele A frequency was significantly higher than that of allele C in RA-positive patients. On the other hand, controls have more frequency of allele C as compared to allele A. Hence it depicts that allele C plays a minor role in the

risk or severity of the RA disease. Recent studies also indicated that allele A of *VEGF* (rs699947) can increase the risk of RA; however, only a protective role is seen in the case of allele C (Saravani *et al.*, 2019). A low level of VEGF is due to allele A and its genotype AA can be its risk factor. While in the case of atherosclerosis, allele C has a protective effect. A relationship has been observed between low serum level and the AA genotype of VEGF in RA patients, as illustrated by a cohort study of 419 patients (Laurindo *et al.*, 2022). Similarly, another

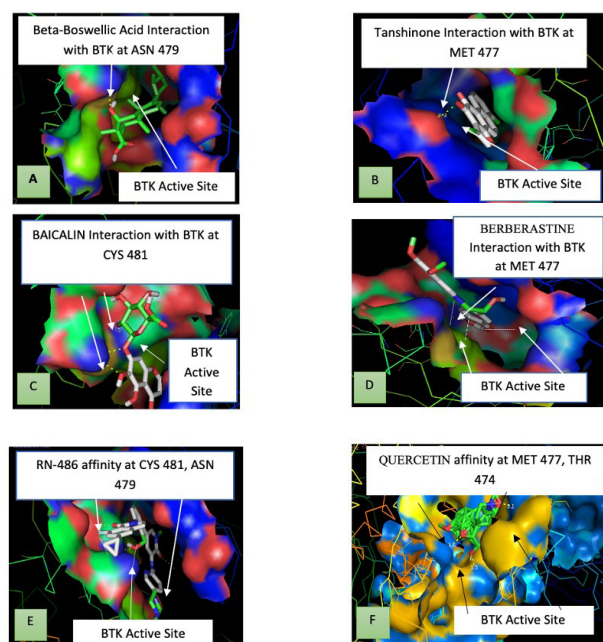


Figure 5. BTK inhibition interactions with different chemicals; (A) BETA-BOSWELIC ACID, (B) TANSHINONE, (C) BAICALIN, (D) BERBERASTINE, (E) RN-486, (F) QUERCETIN

research study elucidates that functional polymorphism of VEGF (A/C) may increase the risk of RA in older and Anti-Citrullinated Peptide Antibody negative patients (Arleevskaya *et al.*, 2021). There are some other factors that may be involved in the progression of RA like auto-activation of BTK protein, age, and CRP (Alam *et al.*, 2017).

Rheumatoid arthritis is a multifactorial joint disorder, and VEGF SNP is one of those factors at a genetic level and abnormally activated BTK protein is another one. Only we found that mutation in this gene causes disturbance in angiogenesis proliferation and cartilage repair which is the major possible effect of a mutated VEGF gene. On the other hand, targeting the BTK protein is a phenotypic therapeutic approach which is involved in the destruction of joint lining. So, it is better to cease the damaging effects of this abnormally activated BTK protein to protect the remaining joints' assets. The effect of SNP on the VEGF product protein is the formation of abnormal heparin-binding protein which does not involve in repairing the cartilage and in the proliferation of new blood vessels (Huang and Wang, 2020).

Tanshinone showed binding affinity -8.3 (kJ/mol) at MET 477 (CO-OH,3.0), and ALA 478 (CO-OH,3.4). This chemical is extracted from red sage or commonly known as behmansurkh which is a root of *Salvia miltiorrhiza* and belongs to the Labiatae family of plant kingdom native to China and Japan (Li *et al.*, 2021). For 2000 years ago in China, it is also being used to treat cardiovascular and cerebrovascular disorders, functions of blood flowing into the heart and liver by removing blood stasis according to Traditional Chinese Medicine (TCM) (Deng *et al.*, 2019).

Baicalin showed binding energy of -8.2 (kJ/mol) at CYS 481 (CN-OH,2.9), ASN 479 (CN-OH,2.3), ASN 484 (CN-OH,3.1) residues. It is a flavonoid phytochemical obtained from the root of *Scutellaria baicalensis* belonging to the mint family of flowering plants. This plant is commonly known as Chinese Skullcap or Huangqin. It has powerful antioxidant properties greater than ascor-

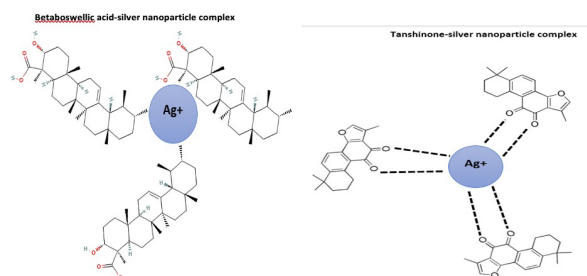


Figure 6. Phytochemicals used via nanoparticle drug delivery as BTK inhibitor to cure RA

bic acid which can scavenge toxic free radicals like superoxide ion, hydroxyl ion, hydroquinone, and polycyclic aromatic compounds (Shakya *et al.*, 2023). It has anti-inflammatory, anti-allergic, anti-bacterial, anti-hypertensive, and food condiment (Ma *et al.*, 2021). Berberastine showed binding energy of -8.1 (KJ/mol) at MET 477 (CN-OH,3.2). It is a phytochemical obtained from the rhizome of *Hydrastis canadensis* belonging to the Ranunculaceae family of angiosperm plants. It is utilized as a yellow dye, astringent, and insect repellent. Goldenseal contains various alkaloids like hydrastine, berberine, canadine, tetrahydroberberastine and berberastine which have great pharmaceutical importance (Brullo *et al.*, 2021).

RN-486 is a synthetic chemical under development which showed binding energy of -7.9 (kJ/mol) at CYS 481 (CN-CO,3.0), LYS 430 (CN-OH,3.1), and ASN 479 (CO-OH,3.2). It binds directly to CYS 481 amino acid to inhibit the enzyme, Bruton's Tyrosine Kinase. RN-486 inhibits inflammation of joints and other systemic inflammation alone or along with methotrexate. It potentially inhibits BTK as small molecule disease-modifying drugs to treat rheumatoid arthritis and other auto-immune disorders (Sakthivel and Habeeb, 2018). It is a potent reversible BTK inhibitor. It also blocks the signals of BCR to inhibit phosphorylation of both BTK and PLC-2 in B-cells. RN-486 shows similar activities in both human and rodent models to prevent type I and type III hypersensitivity responses effectively (Arneson *et al.*, 2021). Ibrutinib is a commercially available synthetic drug, but it has some side effects like diarrhea, upper respiratory tract infection, bleeding, fatigue and cardiac side effects. But RN-486 is a synthetic and under development chemical which has only in-silico trials as compared to phytochemicals which showed more binding affinity than RN-486 to inhibit BTK. Moreover, synthetic drugs take more time and expense, but phytochemicals are ready-made with less or no side effects at the very cheapest cost and can be extracted from plants (Aziz *et al.*, 2023a; Naveed *et al.*, 2023a; Naveed *et al.*, 2023b; Naveed *et al.*, 2023c; Naveed *et al.*, 2022a; Naveed *et al.*, 2022b).

CONCLUSIONS

From this study, it is concluded that AA and CC were the most common genotypes. The allele A of VEGF (rs699947) can increase the risk of RA; however, only a protective role is seen in the case of allele C. There are some possible chemotherapeutic drugs in plants like beta boswellic acid, tanshinone, baicalin etc. that can be used via nanoparticle drug delivery to cure RA by inhibiting BTK, auto-activation of B-cells and cytokines that damage cartilage. There are some limitations of this study in that the genetic variability cannot be accessed entirely by

the polymorphism on a functional basis because RA is an autoimmune and multifactorial disease, and the genome of the Pakistani population is relatively homogeneous because of the cousin marriages.

Declarations

Author Contributions. Conceptualization, N.H., M.A., M.M., A.A.N and A.S.; methodology, N.H., M.A., M.M., A.A.N and A.S. software, T.A.; validation, A.A.S.; formal analysis, T.A.; investigation, N.H., M.A., M.M., A.A.N and A.S.; resources, M.A. and A.A.S.; data curation, T.A.; writing—original draft preparation, T.A. and A.S.; writing—review and editing, M.E.A., A.F.A and A.S.; visualization, N.H.; supervision, T.A.; project administration, A.A.S and M.A.; funding acquisition, T.A.

Funding. This research work received no external funding.

Acknowledgments. The authors greatly acknowledge and express their gratitude to the Researchers Supporting Project number (RSP2023R335) King Saud University, Riyadh, Saudi Arabia.

Conflicts of Interest. The authors declare no conflict of interest.

REFERENCES

- Aziz T, Ihsan F, Ali Khan A, Ur Rahman S, Zamani GY, Alharbi M, Alshammari A, Alasmari AF (2023) Assessing the pharmacological and biochemical effects of *Salvia hispanica* (Chia seed) against oxidized *Helianthus annuus* (sunflower) oil in selected animals. *Acta Biochim Pol* 70: 211–218. <https://doi.org/10.18388/abp.2020.6621>.
- Alam J, Jantan I, Bukhari SNA (2017) Rheumatoid arthritis: recent advances on its etiology, role of cytokines and pharmacotherapy. *Biomed Pharmacother* 92: 615–633. <https://doi.org/10.1016/j.biopha.2017.05.055>
- Arleevskaya M, Takha E, Petrov S, Kazarian G, Novikov A, Larionova R, Renaudineau Y (2021) Causal risk and protective factors in rheumatoid arthritis: A genetic update. *J Transl Autoimmun* 4: 100–119. <https://doi.org/10.1016/j.jtauto.2021.100119>
- Arneson LC, KJ Carroll, EM Ruderman, (2021) Bruton's tyrosine kinase inhibition for the treatment of rheumatoid arthritis. *Immunotargets Therap* 10: 333–342. <https://doi.org/10.2147/itt.s288550>
- Aterido A, Julià A, Carreira P, Blanco R, López-Longo, JJ, Venegas JJP, Marsal S (2017) Genome-wide pathway analysis identifies VEGF pathway association with oral ulceration in systemic lupus erythematosus. *Arthritis Res Therap* 19: 1–11. <https://doi.org/10.1186/s13075-017-1345-6>
- Bahari G, Tabasi F, Hashemi M, Zakeri Z, Taheri M (2021) Association of P2X7 receptor genetic polymorphisms and expression with rheumatoid arthritis susceptibility in a sample of the Iranian population: a case-control study. *Clin Rheumatol* 40: 3115–3126. <https://doi.org/10.1007/s10067-021-05645-3>
- Brullo C, Villa C, Tasso B, Russo E, Spallarossa A (2021) Btk Inhibitors: a medicinal chemistry and drug delivery perspective. *Int J Mol Sci* 22: 7641. <https://doi.org/10.3390/ijms22147641>
- De Vries TJ, El Bakkali I, Kamradt T, Schett G, Jansen ID, D'Amelio P (2019) What are the peripheral blood determinants for increased osteoclast formation in the various inflammatory diseases associated with bone loss? *Front Immunol* 10: 505. <https://doi.org/10.3389/fimmu.2019.00505>
- Deng C, Hao X, Shi M, Fu R, Wang Y, Zhang Y, Kai G (2019) Tanshinone production could be increased by the expression of Sm-WRKY2 in *Salvia miltiorrhiza* hairy roots. *Plant Sci* 284: 1–8. <https://doi.org/10.1016/j.plantsci.2019.03.007>
- Ganesan S, Gaur GS, Negi VS, Sharma VK, Pal GK (2020) Effect of yoga therapy on disease activity, inflammatory markers, and heart rate variability in patients with rheumatoid arthritis. *J Alternat CompMed* 26: 501–507. <https://doi.org/10.1089/acm.2019.0228>
- Goswami AG, Basu S, Huda F, Pant J, Ghosh Kar A, Banerjee T, Shukla VK (2022) An appraisal of vascular endothelial growth factor (VEGF): the dynamic molecule of wound healing and its current clinical applications. *Growth Factors* 40: 73–88. <https://doi.org/10.1080/08977194.2022.2074843>
- Hari S (2019) *In silico* molecular docking and ADME/T analysis of plant compounds against IL17A and IL18 targets in gouty arthritis. *J Appl Pharm Sci* 9: 018–026. <http://dx.doi.org/10.7324/JAPS.2019.90703>
- Huang L, Wang L (2020) Association between VEGF gene polymorphisms (11 sites) and polycystic ovary syndrome risk. *Biosci Rep* 40: BSR20191691. <https://doi.org/10.1042/bsr20191691>
- Jutley GS, Latif ZP, Raza K (2017) Symptoms in individuals at risk of rheumatoid arthritis. *Best Practice Res Clin Rheumatol* 31: 59–70. <https://doi.org/10.1016/j.berh.2017.09.016>
- Karami J, Aslani S, Jamshidi A, Garshasbi M, Mahmoudi M (2019) Genetic implications in the pathogenesis of rheumatoid arthritis; an updated review. *Gene* 702: 8–16. <https://doi.org/10.1016/j.gene.2019.03.033>
- Laurindo LF, de Maio, MC, Barbalho SM, Guiguer EL, Araújo AC, de Alvares Goulart R, Bechara MD (2022) Organokines in rheumatoid arthritis: A critical review. *Int J Mol Sci* 23: 6193. <https://doi.org/10.3390/ijms23116193>
- Li H, Gao C, Liu C, Liu L, Zhuang J, Yang J, Wu, J (2021) A review of the biological activity and pharmacology of cryptotanshinone, an important active constituent in Danshen. *Biomed Pharmacotherap* 137: 111332. <https://doi.org/10.1016/j.biopha.2021.111332>
- Ma XD, Zhang XG, Guo SJ, Ma GY, Liu WJ, Wang N, Su Y (2021) Application of enzyme-assisted extraction of baicalin from *Scutellaria baicalensis* Georgi. *Prep Biochem Biotechnol* 51: 241–251. <https://doi.org/10.1080/10826068.2020.1808791>
- Martins P, Fonseca JE (2019) How to investigate: pre-clinical rheumatoid arthritis. *Best Practice Res Clin Rheumatol* 33: 101438. <https://doi.org/10.1016/j.berh.2019.101438>
- Miao R, Lim VY, Kothapalli N, Ma Y, Fossati J, Zehentmeier S, Pereira JP (2020) Hematopoietic stem cell niches and signals controlling immune cell development and maintenance of immunological memory. *Front Immunol* 11: 600127. <https://doi.org/10.3389/fimmu.2020.600127>
- Nakkala JR, Li Z, Ahmad W, Wang K, Gao, C (2021) Immunomodulatory biomaterials and their application in therapies for chronic inflammation-related diseases. *Acta Biomaterialia* 123: 1–30. <https://doi.org/10.1016/j.actbio.2021.01.025>
- Naveed M, Waseem M, Aziz T, Hassan Ju, Makhdoom SI, Ali U, Alharbi M, Alshammari A (2023) Identification of bacterial strains and development of anmRNA-based vaccine to combat antibiotic resistance in *Staphylococcus aureus* via *in vitro* and *in silico* approaches. *Biomedicine* 11: 1039. <https://doi.org/10.3390/biomedicine11041039>
- Naveed M, Shabbir MA, Ain NU, Javed K, Mahmood S, Aziz T, Khan AA, Nabi G, Shahzad M, Alharbi ME, Alharb, M, Alshammari A (2023) Chain-engineering-based *de novo* drug design against MPX-Vgp169 virulent protein of monkeypox virus: a molecular modification approach. *Bioengineering* 10: 11. <https://doi.org/10.3390/bioengineering10010011>
- Naveed M, Shabbir MA, Ain NU, Javed K, Shabbir MA, Alharb, M, Alshammari A., Alasmari AF (2023) Artificial intelligence assisted pharmacophore design for Philadelphia chromosome-positive leukemia with gamma-tocotrienol: a toxicity comparison approach with Asciminib. *Biomedicine* 11: 1041. <https://doi.org/10.3390/biomedicine11041041>
- Naveed M, Makhdoom SI, Ali U, Jabeen K, Aziz T, Khan AA, Jamil S, Shahzad M, Alharbi M, Alshammari A (2022) Immunoinformatics approach to design multi-epitope-based vaccine against machupo virus taking viral nucleocapsid as a potential candidate. *Vaccines* 10: 1732. <https://doi.org/10.3390/vaccines10101732>
- Naveed M, Sheraz M, Amin A, Waseem M, Aziz T, Khan AA, Ghani M, Shahzad M, Alruways MW, Dabool AS, Elazzazy AM, Almalki AA, Alamri AS, Alhomrani M (2022) Designing a novel peptide-based multi-epitope vaccine to evoke a robust immune response against pathogenic multidrug-resistant *Providencia heimbachae*. *Vaccines* 10: 1300. <https://doi.org/10.3390/vaccines10081300>
- Otón T, Carmona L (2019) The epidemiology of established rheumatoid arthritis. *Best Practice Res Clin Rheumatol* 33: 101477. <https://doi.org/10.1016/j.berh.2019.101477>
- Paradowska Gorycka A, Pawlik A, Romanowska Prochnicka K, Haladyj E, Malinowski D, Stypinska B, Olesinska, M (2016) Relationship between VEGF gene polymorphisms and serum VEGF protein levels in patients with rheumatoid arthritis. *PLoS One* 11: e0160769. <https://doi.org/10.1371/journal.pone.0160769>
- Philippou E, Petersson SD, Rodomar C, Nikiphorou E (2021) Rheumatoid arthritis and dietary interventions: systematic review of clinical trials. *Nutrit Rev* 79: 410–428. <https://doi.org/10.1093/nutrit/nuaa033>
- Qindeel M, Ullah MH, Ahmed N (2020) Recent trends, challenges and future outlook of transdermal drug delivery systems for rheumatoid arthritis therapy. *J Contr Rel* 327: 595–615. <https://doi.org/10.1016/j.jconrel.2020.09.016>
- Sakthivel S, Habeeb S (2018) Combined pharmacophore, virtual screening and molecular dynamics studies to identify Bruton's tyrosine kinase inhibitors. *J Biomol Struct Dynam* 36: 4320–4337. <https://doi.org/10.1080/07391102.2017.1415821>
- Samdani A, Vetrivel U (2018) POAP: A GNU parallel based multi-threaded pipeline of open babel and AutoDock suite for boosted high throughput virtual screening. *Comp Biol Chem* 74: 39–48. <https://doi.org/10.1016/j.compbiolchem.2018.02.012>

- Saravani M, Rokni M, Mehrbani M, Amirkhosravi A, Faramarz S, Fatemi, Nematollahi MH (2019) The evaluation of VEGF and HIF-1 α gene polymorphisms and multiple sclerosis susceptibility. *J Gene Med* **21**: e3132. <https://doi.org/10.1002/jgm.3132>
- Shahraki S, Bideskan AE, Aslzare M, Tavakkoli M, Bahrami AR, Hosseinian S, Rad AK (2022) Decellularization with triton X-100 provides a suitable model for human kidney bioengineering using human mesenchymal stem cells. *Life Sci* **295**: 120167. <https://doi.org/10.1016/j.lfs.2021.120167>
- Shakya AK, Mallick B, Nandakumar KS (2023) A perspective on oral immunotherapeutic tools and strategies for autoimmune disorders. *Vaccines* **11**: 1031. <https://doi.org/10.3390/vaccines11061031>
- van Delft MA, Huizinga TW (2020) An overview of autoantibodies in rheumatoid arthritis. *J Autoimmun* **110**: 102392. <https://doi.org/10.1016/j.jaut.2019.102392>
- Wang Y, Wu H, Deng R (2021) Angiogenesis as a potential treatment strategy for rheumatoid arthritis. *Eur J Pharmacol* **910**: 174500. <https://doi.org/10.1016/j.ejphar.2021.174500>

Circ-POLA2-mediated miR-138-5p/SEMA4C axis affects colon cancer cell activities

YanDong Huang^{1#}, QingYang Bai^{1#}, HongBo Yu², YanRu Li¹, Hao Lu¹, HuiMin Kang¹, XueWei Shi¹ and Kai Feng^{1✉}

¹Department of Oncology, The First Affiliated Hospital of Baotou Medical College, Inner Mongolia University of Science and Technology, Baotou City, Inner Mongolia Autonomous Region, 014017, China; ²Practical Teaching Skills Center, Baotou Medical College, Inner Mongolia University of Science and Technology, Baotou City, Inner Mongolia Autonomous Region, 014017, China

This study aimed to investigate the mechanism of circ-POLA2 in colon cancer (CC). Circ-POLA2, miR-138-5p, and SEMA4C levels in CC tissues and cells were recorded. The influences mediated by circ-POLA2, miR-138-5p or SEMA4C on cell proliferation, migration, invasion, and apoptosis were determined. The feedback loop of circ-POLA2/miR-138-5p/SEMA4C was surveyed. As measured, circ-POLA2 and SEMA4C were highly expressed, while miR-138-5p was poorly expressed. Meanwhile, circ-POLA2 could mediate SEMA4C through miR-138-5p targeting. Circ-POLA2 knockdown caused the blockade for cell activities, but this effect was alleviated by miR-138-5p inhibition or SEMA4C overexpression. Overall, circ-POLA2 is tumorigenic for CC through miR-138-5p/SEMA4C axis, which may provide a promising molecular target for CC therapy.

Keywords: Circ-POLA2, miR-138-5p, SEMA4C, colon cancer, proliferation, migration, invasion, apoptosis

Received: 09 August, 2022; revised: 11 March, 2023; accepted: 21 March, 2023; available on-line: 17 August, 2023

✉e-mail: fengkai8018266@hotmail.com

[#]These authors contributed equally to this work.

Abbreviations: CC, colon cancer; CRC, colorectal cancer

INTRODUCTION

More than 1,090,000 new cases of colon cancer (CC) are diagnosed annually, of which approximately 50% die due to the high rate of metastasis (Siegel *et al.*, 2017; Bray *et al.*, 2018). With changes in people's lifestyle and diet, new cases of CC and young patients are increasing year by year (Zheng *et al.*, 2017). Today, the mainstay of treatment for CC is segmental or total colectomy followed by anastomosis, possibly with the introduction of adjuvant chemotherapy if necessary (Benson *et al.*, 2017; Sun *et al.*, 2020). However, high recurrence/metastasis rates after surgery have not been effectively solved, which is a future direction for CC management.

Circular RNAs (circRNAs) take part in the occurrence, development, metastasis and invasion of CC, and confer diagnostic and prognostic values (Zhao *et al.*, 2019; Han *et al.*, 2021). Indeed, circRNAs are newly discovered in a variety of cells (Wang *et al.*, 2022). Currently, the interaction between circRNAs and miRNAs has been a study focus (Lux & Bullinger, 2018). miRNAs primarily act on target mRNA 3'UTR and are key regulatory roles in CC (Wang *et al.*, 2022; Siciliano *et al.*, 2013; Hollis *et al.*, 2015). Circ-POLA2, a cancer-associated circRNA, has been clarified to express abnormally in

endometrial cancer (Fang *et al.*, 2021), acute myeloid leukemia (Li *et al.*, 2021), cervical squamous cell carcinoma (Cao *et al.*, 2020) and lung cancer (Fan *et al.*, 2020). But its relationship with CC has not been reported. Through multiple bioinformatics tools, miRNA (miR-138-5p) and mRNA (SEMA4C) of circ-POLA2 were predicted. miR-138-5p has been confirmed to have decreased expression in colorectal cancer (CRC) and have anti-tumor effects (Wei *et al.*, 2021) and SEMA4C has been illustrated to promote CC progression (Hung *et al.*, 2022). Based on this, circ-POLA2 is likely to competitively upregulate SEMA4C by sponging miR-138-5p, thereby participating CC. Here, circ-POLA2/miR-138-5p/SEMA4C axis-related function and mechanisms were explored, finding new insights into CC treatment.

METHODS

Clinical samples

Following Declaration of Helsinki, the study procedures proceeded with approval of the Ethics Committee of The First Affiliated Hospital of Baotou Medical College, Inner Mongolia University of Science and Technology. All patients has informed of the study and signed written informed consent. CC tumor tissues and adjacent tissues were operationally collected from 40 patients (19 males and 21 females) and immediately frozen in liquid nitrogen. None of patients received preoperative chemotherapy or radiotherapy. Patients with other intestinal diseases, primary cancers, or organ failure were excluded.

Cell lines and culture

SW480, SW620, HT29, and HCT116 were human CC cell lines purchased from ATCC, and NCM460 was normal human colonic mucosal epithelial cell line provided by INCELL Corporation LLC. In a Dulbecco's modified Eagle's medium made of 10% fetal bovine serum (Thermo Fisher Scientific, USA), 100 IU/mL penicillin (SigmaAldrich, USA), and 100 µg/mL streptomycin (SigmaAldrich), the cell lines were maintained.

Cell transfection

Short hairpin RNA (shRNA) stably against circ-POLA2 (sh-POLA2), circ-POLA2 overexpression (oe-POLA2), miR-138-5p mimic, miR-138-5p inhibitor, pcDNA-SEMA4C, and corresponding controls were obtained from RiboBio (Guangzhou, China). After Lipo-

fetamine 2000 (Invitrogen)-guided transient transfection, cells were amasses after 24 h.

CCK-8

On the 96-well plates, each well was covered with 5×10^3 SW480 cells and added with 10 μ L of CCK-8 solution (Beyotime) after 72 h. The absorbance at 450 nm was recorded on a microplate reader (Tecan Sunrise, Mannedorf, Switzerland) after 4 h.

Clone formation

On the 6-well plates, each well was filled with 1×10^3 SW480 cells for 14 d until staining with 1% crystal violet (Corning). The stained colonies were counted using a microplate reader (Tecan Sunrise).

Transwell

SW480 cells (2×10^5) were seeded into upper chambers (Corning) containing serum-free medium. Matrigel (BD Biosciences, USA) was only coated for testing invasion. Fresh medium containing 10% FBS (Thermo Fisher Scientific) in the lower chamber aimed to attract cell movement. The transmembrane cells during 24 h were conditioned to crystal violet dyeing (0.1%) and microscopical counting.

Flow cytometry

On 1×10^6 SW480 cells, apoptosis was detected by the AnnexinV-fluorescein isothiocyanate/propidium iodide kit (BD Pharmingen, USA) and the apoptosis rate was measured by a BD FACS Aria (BD Biosciences).

RT-qPCR

All tissues and cells were processed for extracting total RNA using Trizol[®] reagent (Thermo Fisher Scientific). After determination of RNA quality and concentration by NanoDrop 2000 (Thermo Fisher Scientific), reverse transcription was done with SuperScript IV VILO kit (Invitrogen) and All-in-One First-Strand cDNA Synthesis kit (GeneCopoeia, Guangzhou, China). With ABI SYBR Green Master Mix (Invitrogen), PCR was carried out to measure gene expression according to the calculation method $2^{-\Delta\Delta CT}$. The primer sequences are shown in Table 1.

Immunoblotting

Sample lysates collected by RIPA lysis buffer (Pierce, USA) were measured by BCA assay kit (Beyotime, China). Proteins were separated by 10-12% sodium dodecyl sulfate polyacrylamide gel electrophoresis (Beyotime), loaded onto a polyvinylidene fluoride membrane (Millipore), after which 5% nonfat dry milk was added, and primary antibodies SEMA4C (1:10000; sc-136445; Santa Cruz Biotechnology) and GAPDH (1:1000; ab8245; Abcam), and horseradish peroxidase-conjugated secondary antibody (1:5000; sc-2054; Santa Cruz Biotechnology) were supplemented. Protein levels were detected by Bio-Rad Gel Imaging System using enhanced chemiluminescence (Thermo Fisher Scientific).

Dual-luciferase reporter gene assay

pmiR-GLO (Promega) was inserted with the amplified wild-type or mutant sequences (POLA2-WT, SEMA4C-WT, POLA2-MUT, SEMA4C-MUT) and co-transfected with miR-138-5p or miR-NC into SW480 cells with Lipofectamine 2000 (Thermo Fisher Scientific), and the

Table 1. Sequences used for PCR

Genes	Sequences (5'-3')
circ-POLA2	Forward; TGAGCTTGTGAGTGAGTGGT
	Reverse; GCAAGGAGAATGGCGAGATG
miR-138-5p	Forward; CGAGCTGGTGTGTGAATC
	Reverse; GCAGGGTCCGAGGTATTC
SEMA4C	Forward; ACCTTGTGCCGCGTAAGACAG
	Reverse; CGTCAGCGTCAGTGTACAGAA
U6	Forward; CTCGCTTCGGCAGCAC
	Reverse; AACGCTTCACGAATTTGCGT
GAPDH	Forward; CACCCACTCCTCCACCTTTG
	Reverse; CCACCACCTGTTGCTGTAG

Note: circ-POLA2, circular RNA POLA2; miR-138-5p, microRNA-138-5p; SEMA4C, Semaphorin 4C; GAPDH, glyceraldehyde-3-phosphate dehydrogenase

luciferase activity was detected using a dual-luciferase reporter gene detection system (Genomeditech, Shanghai, China).

RNA pull-down

Pierce Magnetic RNA-Protein Pull-Down Kit (Thermo Fisher Scientific) was used. SW480 cells (1×10^7) were lysed in RIP lysis buffer (Thermo Fisher Scientific), followed by interaction with circ-POLA2 probe-coated C-1 magnetic beads. The final results were obtained by RT-qPCR.

Statistical analysis

SPSS 21.0 software and GraphPad Primer 6.0 were employed to perform statistical analysis. All data presented as mean \pm standard deviation were analyzed by Student's *t*-test and one-way ANOVA. The Kaplan-Meier method was utilized to assess survival and analyzed by the Log rank test while Pearson analysis was to analyze the gene correlation. $P < 0.05$ was considered statistically significant.

RESULTS

circ-POLA2 is associated with CC progression

High circ-POLA2 was expressed in CC patients' tumor tissues (Fig. 1A), and circ-POLA2 expression was further increased in CC patients' tumor tissues in TNM stage III and with lymph node metastasis (Fig. 1B, C). CC patients were divided into high or low circ-POLA2 expression groups defined by circ-POLA2 median value, and Kaplan-Meier analysis evaluated that patients with high circ-POLA2 expression had lower overall survival (Fig. 1D). These findings suggest that circ-POLA2 is up-regulated in tumor tissues of patients with CC and is associated with poor prognosis.

Circ-POLA2 knockdown inhibits activities of CC cells

Circ-POLA2 in CC cells and normal colon epithelial cells was detected by RT-qPCR. The results showed that circ-POLA2 expression was increased in CC cell lines (SW480, SW620, HT29 and HCT116), and circ-

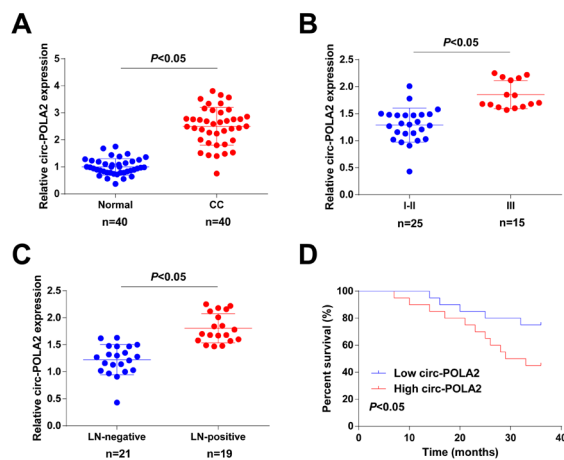


Figure 1. Upregulation of circ-POLA2 is associated with CC progression

(A) circ-POLA2 in tumor tissues of CC patients was detected by RT-qPCR. (B) circ-POLA2 in tumor tissues of CC patients with TNM stage III was detected by RT-qPCR. (C) circ-POLA2 in tumor tissues of CC patients with lymph node metastasis was detected by RT-qPCR. (D) Kaplan-Meier analysis of overall survival of CC patients; values are expressed as mean \pm standard deviation.

POLA2 expression was most significantly increased in SW480 cells (Fig. 2A). Therefore, SW480 cells were analyzed for subsequent experiments. After transfection of sh-POLA2 or oe-POLA2, circ-POLA2 in SW480 cells decreased or increased accordingly (Fig.

2B), indicating that the cells were successfully transfected. CCK-8 assay, colony formation assay, Transwell assay, and flow cytometry were then performed to explore the role of circ-POLA2 in CC cells. CCK-8 results showed that circ-POLA2 knockdown inhibited SW480 cell activity (Fig. 2C). Meanwhile, colony formation experiments determined that circ-POLA2 knockdown inhibited the proliferation of SW480 cells (Fig. 2D, E). Transwell analysis presented that circ-POLA2 knockdown inhibited SW480 cell migration and invasion (Fig. 2F, G). In addition, flow cytometry suggested that circ-POLA2 knockdown promoted apoptosis of SW480 cells (Fig. 2H, I). However, the effect of circ-POLA2 overexpression on CC cells was opposite to that of circ-POLA2 knockdown (Fig. 2C–I). In conclusion, circ-POLA2 plays a carcinogenic role by promoting proliferation, migration, and invasion of CC cells and inhibiting cell apoptosis.

Circ-POLA2 confers mediation of miR-138-5p

miR-138-5p was cross-screened on bioinformatics websites (CircBank, starBase, miRanda, and RNAhybrid) to be the potential miRNA of circ-POLA2 (Fig. 3A). Measurements of luciferase activity demonstrated that miR-138-5p inhibited the luciferase activity of POLA2-WT (Fig. 3B) and RNA pull-down test discovered that circ-POLA2 significantly increased miR-138-5p enrichment (Fig. 3C). Actually, miR-138-5p expression kept lowly in CC patients' tumor tissues (Fig. 3D), which was in an inverse correlation with circ-POLA2 expression (Fig. 3E). Likewise, miR-138-

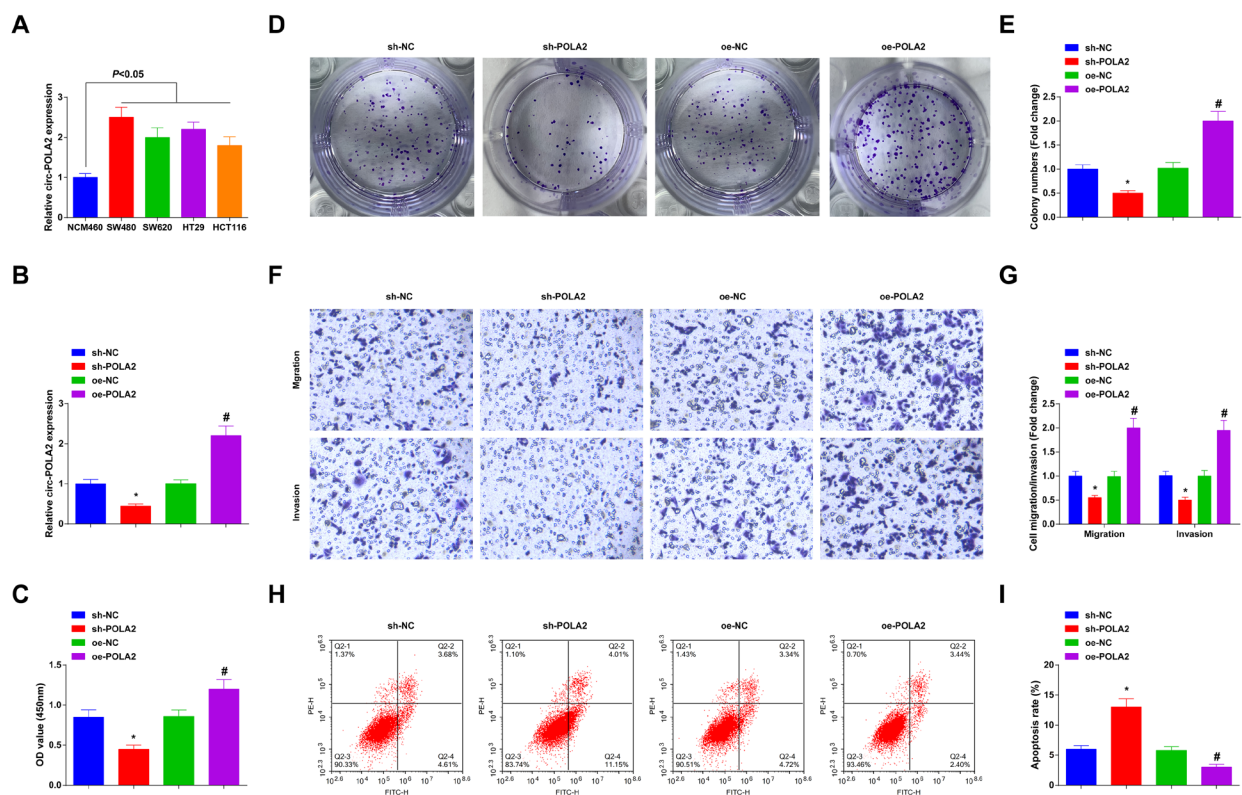


Figure 2. Circ-POLA2 knockdown inhibits activities of CC cells

(A) circ-POLA2 in CC cell lines was detected by RT-qPCR. (B) The transfection efficacy of sh-POLA2, sh-NC, oe-POLA2 or oe-NC was verified by RT-qPCR. (C) Cell viability was detected by CCK-8 after circ-POLA2 expression intervention. (D–E) Cell proliferation was detected by colony formation assay after circ-POLA2 expression intervention. (F–G) Cell migration and invasion were analyzed by Transwell after circ-POLA2 expression intervention. (H–I) Apoptosis was analyzed by flow cytometry after circ-POLA2 expression intervention; values are expressed as mean \pm standard deviation. * $P < 0.05$ vs. sh-NC; # $P < 0.05$ vs. oe-NC.

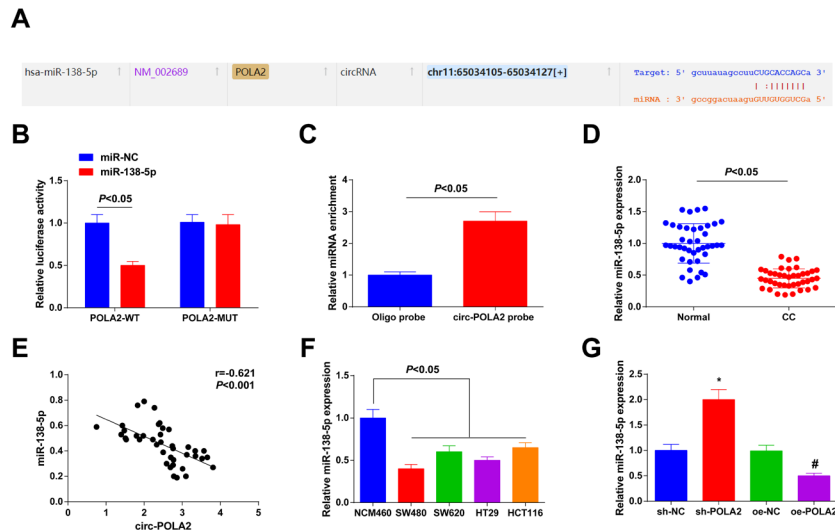


Figure 3. circ-POLA2 confers mediation of miR-138-5p

(A) Bioinformatics sites predicted the binding sites of circ-POLA2 and miR-138-5p. (B–C) The binding relationship between circ-POLA2 and miR-138-5p was verified by dual luciferase reporter assay and RNA Pull-Down assay. (D) miR-138-5p in tumor tissues of CC patients was detected by RT-qPCR. (E) The correlation between circ-POLA2 and miR-138-5p expression in CC tissues was evaluated by Pearson correlation coefficient. (F) miR-138-5p in CC cell lines was detected by RT-qPCR. G: miR-138-5p was detected by RT-qPCR after circ-POLA2 expression intervention; values are expressed as mean \pm standard deviation. * $P < 0.05$ vs. sh-NC group; # $P < 0.05$ vs. oe-NC.

5p expression was downregulated in CC cells lines (SW480, SW620, HT29, and HCT116) (Fig. 3F). While miR-138-5p was up-regulated in SW480 cells intervened with sh-POLA2 and down-regulated in those transfected with oe-POLA2 (Fig. 3G). In conclusion, circ-POLA2 acts as a molecular sponge for miR-138-5p to inhibit miR-138-5p expression.

miR-138-5p prevents the aggressive activities of CC cells

After transfection with miR-138-5p mimic or inhibitor, miR-138-5p in SW480 cells increased or decreased accordingly (Fig. 4A). CCK-8 detection results showed that upregulating miR-138-5p inhibited the activity of SW480 cells (Fig. 4B). Colony formation assay found that upregulating miR-138-5p inhibited the proliferation

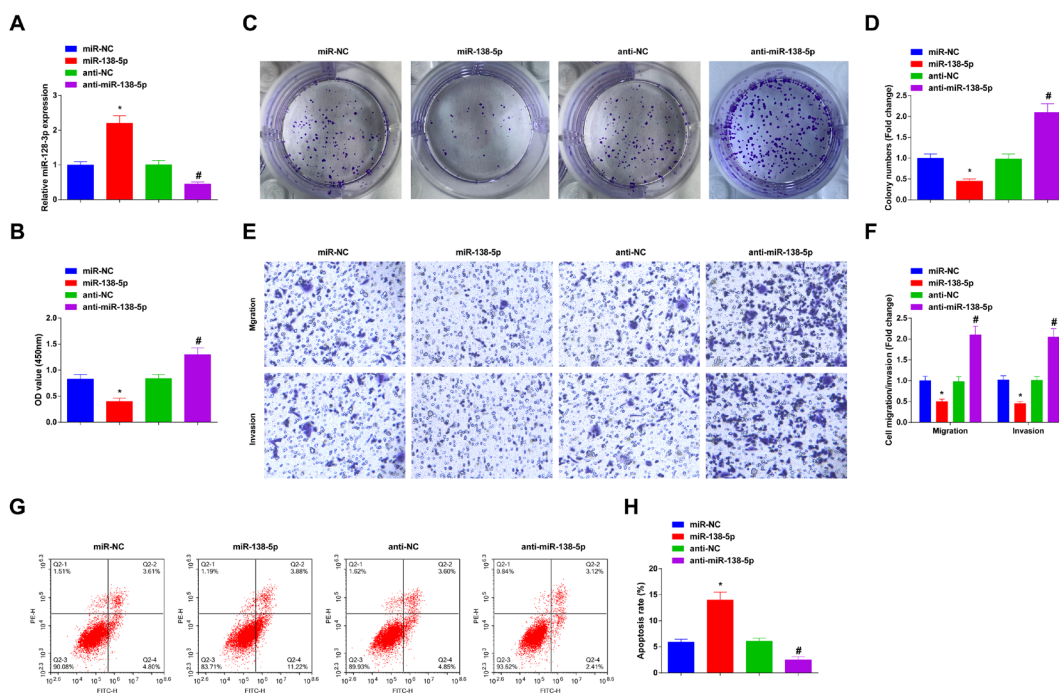


Figure 4. miR-138-5p prevents the malignant activities of CC cells

(A) The transfection efficacy of miR-138-5p, miR-NC, anti-miR-138-5p, or anti-NC was verified by RT-qPCR. (B) Cell viability was detected by CCK-8 after miR-138-5p expression intervention. (C–D) Cell proliferation was detected by colony formation assay after miR-138-5p expression intervention. (E–F) Cell migration and invasion were analyzed by Transwell after miR-138-5p expression intervention. (G–H) Apoptosis was analyzed by flow cytometry after miR-138-5p expression intervention; values are expressed as mean \pm standard deviation. * $P < 0.05$ vs. miR-NC; # $P < 0.05$ vs. anti-NC.

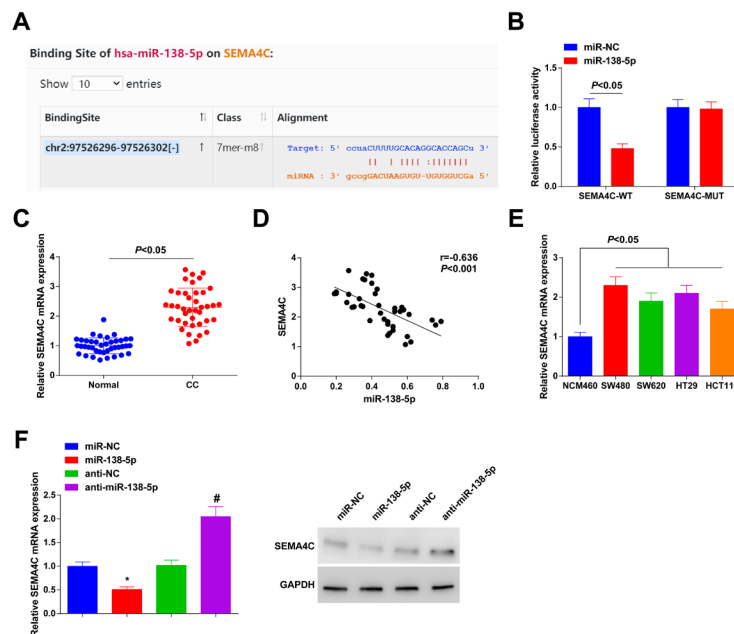


Figure 5. miR-138-5p has a modificatory action on SEMA4C expression

(A) Bioinformatics sites predicted the binding sites of miR-138-5p and SEMA4C. (B) The binding relationship between miR-138-5p and SEMA4C was verified by dual luciferase reporter assay. (C) SEMA4C in tumor tissues of CC patients was detected by RT-qPCR. (D) The correlation between miR-138-5p and SEMA4C expression in CC tissues was evaluated by Pearson correlation coefficient. (E) SEMA4C in CC cell lines was detected by RT-qPCR. (F) SEMA4C was detected by RT-qPCR and Western blot after miR-138-5p expression intervention; values are expressed as mean \pm standard deviation. $*P < 0.05$ vs. sh-NC group; $\#P < 0.05$ vs. oe-NC.

of SW480 cells (Fig. 4C, D). Transwell analysis showed that overexpressing miR-138-5p inhibited the migration and invasion of SW480 cells (Fig. 4E, F). Flow cytometry showed that upregulating miR-138-5p promoted apoptosis of SW480 cells (Fig. 4G, H). Down-regulation of miR-138-5p had opposite effects on CC cells compared with upregulation of miR-138-5p (Fig. 4B–H). These data indicate that miR-138-5p plays an antitumor function by inhibiting cell proliferation, migration, and invasion and promoting cell apoptosis.

miR-138-5p has a modificatory action on SEMA4C expression

On the bioinformatics website starBase, miR-138-5p had a targeted binding site with SEMA4C (Fig. 5A). Further detection results revealed that the luciferase activity of the SEMA4C-WT was inhibited by miR-138-5p transfection (Fig. 5B). High SEMA4C expression was measured in CC patients' tumor tissues (Fig. 5C) in a negative correlation with miR-138-5p expression (Fig. 5D). The upregulation of SEMA4C was also seen in CC cell lines (SW480, SW620, HT29, and HCT116) (Fig. 5E) and cellular SEMA4C levels could be negatively modified by miR-138-5p (Fig. 5F). These results suggest that SEMA4C expression is negatively regulated by miR-138-5p.

miR-138-5p/SEMA4C axis can intervene the influences of circ-POLA2 on CC

miR-138-5p or SEMA4C expression was intervened in sh-POLA2-modified SW480 cells and the successful transfection was verified, as evidenced by miR-138-5p inhibitor-induced decline of miR-138-5p and SEMA4C-induced elevation of SEMA4C expression (Fig. 6A). CCK-8 assay showed that the sh-POLA2-mediated decrease in SW480 cell viability was reversed by anti-miR-138-5p or SEMA4C (Fig. 6B). Meanwhile, colony for-

mation assay showed that anti-miR-138-5p or SEMA4C could attenuate sh-POLA2-induced proliferation inhibition in SW480 cells (Fig. 6C, D). Furthermore, anti-miR-138-5p or SEMA4C mitigated Sh-POLA2-mediated decrease in SW480 cell migration and invasion (Fig. 6E, F). In addition, anti-miR-138-5p or SEMA4C mitigated an increase in sh-POLA2-mediated apoptosis in SW480 cells (Fig. 6G, H). In conclusion, circ-POLA2 can promote proliferation, migration, and invasion of CC cells and inhibit cell apoptosis by regulating miR-138-5p/SEMA4C axis.

DISCUSSION

Accumulating evidence suggests that circRNAs can act as tumor biomarkers and regulate CC progression (Chen and Shen 2020). Ju and others (Ju *et al.*, 2019) analyzed 667 cases of stage II/III CC with R0 resection and found that circRNA could predict postoperative recurrence of stage II/III CC. Abnormal expression of circRNAs is indicative of patients' prognosis in CC (Hsiao *et al.*, 2017; Zhou *et al.*, 2020; Zheng *et al.*, 2019). In CC patients' tumor, circ-POLA2 was upregulated, having an association with TNM stage III, lymph node metastasis, as well as low overall survival rate. Furthermore, our findings suggest that circ-POLA2 exerts oncogenic effects via miR-138-5p/SEMA4C axis.

The up-regulated expression and stability of circ-POLA2 make it a potential biomarker and diagnostic and therapeutic target for human cancer (Fang *et al.*, 2021; Li *et al.*, 2021; Cao *et al.*, 2020; Fan *et al.*, 2020). Furthermore, circ-POLA2 can sponge different miRNAs, including miR-31, miR-34a, miR-326 and miR-34a, to intercede tumor progression. Similarly, this study clarified a competitive binding of circ-POLA2 to miR-138-5p.

miR-138-5p is a cancer-related miRNA in gastric cancer (Zhang *et al.*, 2020), prostate cancer (Huang *et al.*,

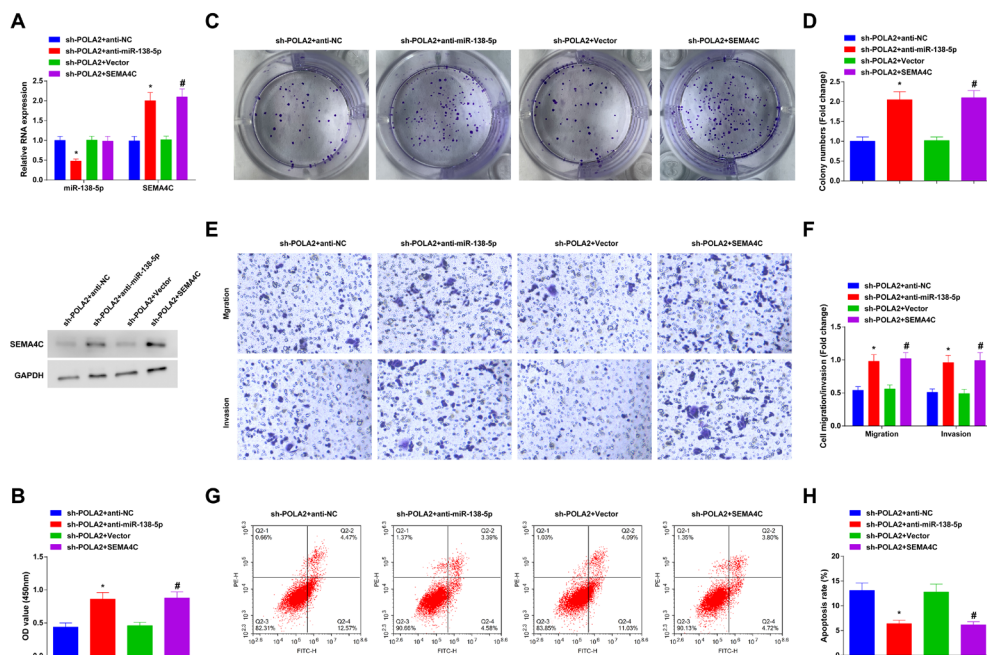


Figure 6. miR-138-5p/SEMA4C axis can intervene the influences of circ-POLA2 on CC

(A) The transfection efficacy of sh-POLA2 + anti-miR-138-5p, sh-POLA2 + anti-NC, sh-POLA2 + SEMA4C, or sh-POLA2 + Vector was verified by RT-qPCR and Western blot. (B) Cell viability was detected by CCK-8. (C–D) Cell proliferation was detected by colony formation assay. (E–F) Cell migration and invasion were analyzed by Transwell. (G–H) Apoptosis was analyzed by flow cytometry; values are expressed as mean \pm standard deviation. * $P < 0.05$ vs. sh-POLA2 + anti-NC; # $P < 0.05$ vs. sh-POLA2 + Vector.

2020), and cervical cancer. Notably, it is known that miR-138-5p is decreased in CRC and that miR-138-5p serves to disrupt the aggressive activities of CRC cells (Wei *et al.*, 2021). Here, miR-138-5p expression was reduced in CC and was anti-tumorigenic achieved by impeding cell malignancy.

SEMA4C, a member of the semaphorin family originally named M-SemaF, can mediate directional growth of axons and the development of myotubes (Yang *et al.*, 2020). As miRNAs target, SEMA4C is associated with various tumors. For example, SEMA4C mediates chemoresistance in cervical cancer (Jing *et al.*, 2019), induces tumor progression in pancreatic cancer (Fei *et al.*, 2020), and is considered an epigenetic regulator involved in CC progression (Hung *et al.*, 2022). Here, SEMA4C was upregulated in CC, and involved in circ-POLA2/miR-138-5p axis-regulated progression of CC. In detail, miR-138-5p downregulation or SEMA4C upregulation could attenuate the reduction of cell activities mediated by circ-POLA2 knockdown.

Although this study found that circ-POLA2/miR-138-5p/SEMA4C axis promotes CC progression *in vitro*, it has not been further validated *in vivo*. Circ-POLA2 expression in serum of CC patients should also be detected in the future to verify whether circ-POLA2 is of feasibility for blood biopsy of CC patients. Furthermore, circRNAs may encode proteins or peptides to participate in tumor progression (Qian *et al.*, 2018; Peng *et al.*, 2021; Wang *et al.*, 2021; Wu *et al.*, 2021). However, this research did not investigate the coding ability of circ-POLA2.

CONCLUSION

Circ-POLA2 has potent oncogenic activity in CC and an association with patients' poor prognosis. Furthermore, circ-POLA2 upregulates SEMA4C expression by

miR-138-5p, thereby promoting cancer development. This study extends the understanding of circRNA function in CC pathogenesis and proposes a novel circRNA as a therapeutic target for CC.

Declarations

Acknowledgments: Not applicable.

Funding Statements: Not applicable.

Conflicts of Interest: The authors declare no conflicts of interest.

Data available: Data is available from the corresponding author on request.

REFERENCES

- Benson AB, 3rd, Venook AP, Cederquist L, Chan E, Chen YJ, Cooper HS, Deming D, Engstrom PF, Enzinger PC, Fichera A, Grem JL, Grothey A, Hochster HS, Hoffs S, Hunt S, Kamel A, Kirilcuk N, Krishnamurthi S, Messersmith WA, Mulcahy MF, Murphy JD, Nurkin S, Saltz L, Sharma S, Shibata D, Skibber JM, Sofocleous CT, Stoffer EM, Stotsky-Himelfarb E, Willett CG, Wu CS, Gregory KM, Freedman-Cass D (2017) Colon Cancer, Version 1.2017, NCCN Clinical Practice Guidelines in Oncology. *J Natl Compr Canc Netw* 15: 370–398. <https://doi.org/10.6004/jnccn.2017.0036>
- Bray F, Ferlay J, Soerjomataram I, Siegel RL, Torre LA, Jemal A (2018) Global cancer statistics 2018: GLOBOCAN estimates of incidence and mortality worldwide for 36 cancers in 185 countries. *CA Cancer J Clin* 68: 394–424. <https://doi.org/10.3322/caac.21492>
- Cao Y, Li J, Jia Y, Zhang R, Shi H (2020) CircRNA circ_POLA2 promotes cervical squamous cell carcinoma progression via regulating miR-326/GNB1. *Front Oncol* 10: 959. <https://doi.org/10.3389/fonc.2020.00959>
- Chen S, Shen X (2020) Long noncoding RNAs: functions and mechanisms in colon cancer. *Mol Cancer* 19: 167. <https://doi.org/10.1186/s12943-020-01287-2>
- Fan Z, Bai Y, Zhang Q, Qian P (2020) CircRNA circ_POLA2 promotes lung cancer cell stemness via regulating the miR-326/GNB1 axis. *Environ Toxicol* 35: 1146–1156. <https://doi.org/10.1002/tox.22980>
- Fang X, Wang J, Chen L, Zhang X (2021) circRNA circ_POLA2 increases microRNA-31 methylation to promote endometrial cancer cell proliferation. *Oncol Lett* 22: 762. <https://doi.org/10.3892/ol.2021.13023>

- Fei X, Jin HY, Gao Y, Kong LM, Tan XD (2020) Hsa-miR-10a-5p promotes pancreatic cancer growth by BDNF/SEMA4C pathway. *J Biol Regul Homeost Agents* **34**: 927–934. <https://doi.org/10.23812/20-61-a-47>
- Han Z, Chen H, Guo Z, Zhu J, Xie X, Li Y, He J (2021) Bioinformatics analysis: the regulatory network of hsa_circ_0007843 and hsa_circ_0007331 in colon cancer. *Biomed Res Int* **2021**: 6662897. <https://doi.org/10.1155/2021/6662897>
- Hollis M, Nair K, Vyas A, Chaturvedi LS, Gambhir S, Vyas D (2015) MicroRNAs potential utility in colon cancer: Early detection, prognosis, and chemosensitivity. *World J Gastroenterol* **21**: 8284–8292. <https://doi.org/10.3748/wjg.v21.i27.8284>
- Hsiao KY, Lin YC, Gupta SK, Chang N, Yen L, Sun HS, Tsai SJ (2017) Noncoding effects of circular RNA CCDC66 promote colon cancer growth and metastasis. *Cancer Res* **77**: 2339–2350. <https://doi.org/10.1158/0008-5472.Can-16-1883>
- Huang H, Xiong Y, Wu Z, He Y, Gao X, Zhou Z, Wang T (2020) MIR-138-5P inhibits the progression of prostate cancer by targeting FOXC1. *Mol Genet Genomic Med* **8**: e1193. <https://doi.org/10.1002/mgg3.1193>
- Hung YH, Lai MD, Hung WC, Chen LT (2022) Semaphorin 4C promotes motility and immunosuppressive activity of cancer cells via CRMP3 and PD-L1. *Am J Cancer Res* **12**: 713–728
- Jing L, Bo W, Yourong F, Tian W, Shixuan W, Mingfu W (2019) Sema4C mediates EMT inducing chemotherapeutic resistance of miR-31-3p in cervical cancer cells. *Sci Rep* **9**: 17727. <https://doi.org/10.1038/s41598-019-54177-z>
- Ju HQ, Zhao Q, Wang F, Lan P, Wang Z, Zuo ZX, Wu QN, Fan XJ, Mo HY, Chen L, Li T, Ren C, Wan XB, Chen G, Li YH, Jia WH, Xu RH (2019) A circRNA signature predicts postoperative recurrence in stage II/III colon cancer. *EMBO Mol Med* **11**: e10168. <https://doi.org/10.15252/emmm.201810168>
- Li H, Bi K, Feng S, Wang Y, Zhu C (2021) CircRNA circ-POLA2 is Upregulated in acute myeloid leukemia (AML) and promotes cell proliferation by suppressing the production of mature miR-34a. *Cancer Manag Res* **13**: 3629–3637. <https://doi.org/10.2147/cmar.S281690>
- Lux S, Bullinger L (2018) Circular RNAs in cancer. *Adv Exp Med Biol* **1087**: 215–230. https://doi.org/10.1007/978-981-13-1426-1_17
- Peng Y, Xu Y, Zhang X, Deng S, Yuan Y, Luo X, Hossain MT, Zhu X, Du K, Hu F, Chen Y, Chang S, Feng X, Fan X, Ashktorab H, Smoot D, Meltzer SJ, Hou G, Wei Y, Li S, Qin Y, Jin Z (2021) A novel protein AXIN1-295aa encoded by circAXIN1 activates the Wnt/ β -catenin signaling pathway to promote gastric cancer progression. *Mol Cancer* **20**: 158. <https://doi.org/10.1186/s12943-021-01457-w>
- Qian L, Yu S, Chen Z, Meng Z, Huang S, Wang P (2018) The emerging role of circRNAs and their clinical significance in human cancers. *Biochim Biophys Acta Rev Cancer* **1870**: 247–260. <https://doi.org/10.1016/j.bbcan.2018.06.002>
- Siciliano V, Garzilli I, Fracassi C, Crisculo S, Ventre S, di Bernardo D (2013) MiRNAs confer phenotypic robustness to gene networks by suppressing biological noise. *Nat Commun* **4**: 2364. <https://doi.org/10.1038/ncomms3364>
- Siegel RL, Miller KD, Fedewa SA, Ahnen DJ, Meester RGS, Barzi A, Jemal A (2017) Colorectal cancer statistics, 2017. *CA Cancer J Clin* **67**: 177–193. <https://doi.org/10.3322/caac.21395>
- Sun Y, Cao B, Zhou J (2020) Roles of DANCR/microRNA-518a-3p/MDMA ceRNA network in the growth and malignant behaviors of colon cancer cells. *BMC Cancer* **20**: 434. <https://doi.org/10.1186/s12885-020-06856-8>
- Wang J, Zhou L, Chen B, Yu Z, Zhang J, Zhang Z, Hu C, Bai Y, Ruan X, Wang S, Ouyang J, Wu A, Zhao X (2022) Circular RNA circCSPP1 promotes the occurrence and development of colon cancer by sponging miR-431 and regulating ROCK1 and ZEB1. *J Transl Med* **20**: 58. <https://doi.org/10.1186/s12967-022-03240-x>
- Wang L, Zhou J, Zhang C, Chen R, Sun Q, Yang P, Peng C, Tan Y, Jin C, Wang T, Ji J, Sun Y (2021) A novel tumour suppressor protein encoded by circMAPK14 inhibits progression and metastasis of colorectal cancer by competitively binding to MKK6. *Clin Transl Med* **11**: e613. <https://doi.org/10.1002/ctm2.613>
- Wei J, Lin Y, Wang Z, Liu Y, Guo W (2021) Circ_0006174 accelerates colorectal cancer progression through regulating miR-138-5p/MACC1 axis. *Cancer Manag Res* **13**: 1673–1686. <https://doi.org/10.2147/cmar.S295833>
- Wu P, Fang X, Liu Y, Tang Y, Wang W, Li X, Fan Y (2021) N6-methyladenosine modification of circCUX1 confers radioresistance of hypopharyngeal squamous cell carcinoma through caspase1 pathway. *Cell Death Dis* **12**: 298. <https://doi.org/10.1038/s41419-021-03558-2>
- Yang L, Yu Y, Xiong Z, Chen H, Tan B, Hu H (2020) Downregulation of SEMA4C inhibit epithelial-mesenchymal transition (EMT) and the invasion and metastasis of cervical cancer cells via inhibiting transforming growth factor-beta 1 (TGF- β 1)-induced hela cells p38 mitogen-activated protein kinase (MAPK) activation. *Med Sci Monit* **26**: e918123. <https://doi.org/10.12659/msm.918123>
- Zhang W, Liao K, Liu D (2020) MiR-138-5p inhibits the proliferation of gastric cancer cells by targeting DEK. *Cancer Manag Res* **12**: 8137–8147. <https://doi.org/10.2147/cmar.S253777>
- Zhao X, Cai Y, Xu J (2019) Circular RNAs: biogenesis, mechanism, and function in human cancers. *Int J Mol Sci* **20**. <https://doi.org/10.3390/ijms20163926>
- Zheng R, Zeng H, Zhang S, Chen W (2017) Estimates of cancer incidence and mortality in China, 2013. *Chin J Cancer* **36**: 66. <https://doi.org/10.1186/s40880-017-0234-3>
- Zheng X, Chen L, Zhou Y, Wang Q, Zheng Z, Xu B, Wu C, Zhou Q, Hu W, Wu C, Jiang J (2019) A novel protein encoded by a circular RNA circPPP1R12A promotes tumor pathogenesis and metastasis of colon cancer via Hippo-YAP signaling. *Mol Cancer* **18**: 47. <https://doi.org/10.1186/s12943-019-1010-6>
- Zhou P, Xie W, Huang HL, Huang RQ, Tian C, Zhu HB, Dai YH, Li ZY (2020) circRNA_100859 functions as an oncogene in colon cancer by sponging the miR-217-HIF-1 α pathway. *Aging (Albany NY)* **12**: 13338–13353. <https://doi.org/10.18632/aging.103438>

Hsa_circ_0023826 protects against glaucoma by regulating miR-188-3p/MDM4 axis

Bin Qu¹, Jing Wang¹, Yan Li¹, XiaoWei Wu¹ and MingYing Zhang²✉

¹Department of Ophthalmology, Muping District Hospital of Traditional Chinese Medicine, Yantai City, Shandong Province, 253400, China; ²Department of Ophthalmology, Ningjin County People's Hospital, Dezhou City, Shandong Province, 253400, China

Objective: Circular RNAs (circRNAs) are characterized as a class of covalently closed circRNA transcripts and are associated with various cellular processes and neurological diseases by sponging microRNAs. The most common feature of glaucoma, a form of retinal neuropathy, is the loss of retinal ganglion cells. Although the pathogenesis of glaucoma is not fully understood, elevated intraocular pressure is undoubtedly the only proven modifiable factor in the classic glaucoma model. This study investigated the role of circ_0023826 in glaucoma-induced retinal neurodegeneration by modifying the miR-188-3p/mouse double minute 4 (MDM4) axis. **Methods:** The expression pattern of circ_0023826 was analyzed during retinal neurodegeneration. The effect of circ_0023826, miR-188-3p, and MDM4 on retinal neurodegeneration *in vivo* was assessed by visual behavioral testing and H&E staining in glaucoma rats, while that on *in vitro* retinal ganglion cells (RGCs) was evaluated by MTT assay, flow cytometry, Western blot, and ELISA. Bioinformatics analysis, RNA pull-down assay, luciferase reporter assay were performed to reveal the regulatory mechanism of circ_0023826-mediated retinal neurodegeneration. **Results:** Circ_0023826 expression was downregulated during retinal neurodegeneration. Upregulating circ_0023826 attenuated the visual impairment in rats and promoted the survival of RGCs *in vitro*. Circ_0023826 acted as a sponge of miR-188-3p sponge, resulting in increased expression of MDM4. MDM4 silencing or miR-188-3p upregulation reversed the protective effect of upregulated circ_0023826 on glaucoma-induced neuroretinal degeneration *in vitro* and *in vivo*. **Conclusion:** Overall, circ_0023826 protects against glaucoma by regulating the miR-188-3p/MDM4 axis, and targeted intervention of circ_0023826 expression is a promising therapeutic strategy for the treatment of retinal neurodegeneration.

Keywords: Circular RNA 0023826; microRNA-188-3p; Mouse Double Minute 4; Neuroretinal degeneration; Retinal ganglion cells

Received: 12 April, 2022; **revised:** 27 June, 2022; **accepted:** 25 July, 2022; **available on-line:** 12 June, 2023

✉e-mail: njzmy668@hotmail.com

INTRODUCTION

Glaucoma, a retinal neurodegenerative disease characterized by progressive and irreversible degeneration of retinal ganglion cells (RGCs) and optic nerve, is the second leading cause of blindness (Quigley *et al.*, 2006). Elevated intraocular pressure (IOP) is a risk factor and RGC apoptosis is the core cause of glaucoma (Geva *et*

al., 2021). At present, the treatment methods of glaucoma mainly include surgery and drugs (Hooshmand *et al.*, 2022). Despite effective medical and surgical treatment to lower IOP, many patients will continue to lose vision due to the death of RGCs and degeneration of the optic nerve. Therefore, further elucidation of the pathogenesis of glaucoma is still required.

CircRNAs are a new class of non-coding RNAs characterized by closed-loop structures (Ebbesen *et al.*, 2017). With bioinformatics analysis and high-throughput sequencing, circRNA may participate in the pathogenesis and progression of various eye diseases, including glaucoma, diabetic retinopathy, and retinoblastoma (Guo *et al.*, 2019). Therefore, an in-depth understanding of circRNAs involved in glaucoma will help to open up new avenues for early diagnosis and clinical treatment.

CircRNAs serve as gene modulators of microRNAs (miRNAs) (Yang *et al.*, 2021), thereby participating in the progression of glaucoma. have found that circ_0023826 is upregulated in glaucoma-related retinal neurodegeneration, and is capable of regulating neurodegeneration by acting as a miR-615 sponge (Wang *et al.*, 2018). In another report, circZNRANB1 directly regulates Müller cell function and RGC function through miR-217 (Wang *et al.*, 2018). TENM4-encoded circ_0023826 has been identified as a diagnostic biomarker for glaucoma (Chen *et al.*, 2020), but rare studies have reported its action in glaucoma.

The present paper hypothesized that circ_0023826 protects against retinal neurodegeneration by regulating the miR-188-3p/MDM4 axis. First, we constructed a glaucoma model by chamber injection of microbeads and isolated RGCs to study the expression patterns of circ_0023826 in glaucoma-induced retinal neurodegeneration. Then, we confirmed the downstream miRNA (miR-188-3p) and target gene (MDM4) to elucidate the regulation of circ_0023826/miR-188-3p/MDM4 in glaucoma, targeting to develop a new theoretical basis for glaucoma therapy.

MATERIALS AND METHODS

Collection of patient tissues

From January 2017 to March 2018, 12 pairs of human fascia tissue and normal human fascia tissue (3 mm from the conjunctival edge) from glaucoma patients were collected at Muping District Hospital of Traditional Chinese Medicine. Tissue samples were frozen in liquid nitrogen and then stored at -80°C. All procedures were performed under the review of the Ethics Committee of

Muping District Hospital of Traditional Chinese Medicine. All patients provided written consent.

Establishment of a glaucoma model

All animal experiments were performed with the approval of the Animal Ethics Committee of Muping District Hospital of Traditional Chinese Medicine. Forty-eight Sprague Dawley (SD) rats (male, 200–250 g) were purchased from Hunan SJA Laboratory Animal Co., Ltd. After one week of adaptive feeding, 42 rats were randomly selected to construct a glaucoma model by intra-chamber injection of microbeads. In short, anesthetized by intraperitoneal injection of a mixture of xylazine (10 mg/kg) and ketamine (75 mg/kg), the rats were injected with sterile microbeads into one eye and dropped with 0.5% moxifloxacin hydrochloride in each eye. IOP was measured after 24 h. At 4 weeks post-injection, the second injection of microbeads was performed. IOP was measured every 4 days using a digital tonometer. An equal volume of phosphate-buffered saline (PBS) served as a sham operation procedure.

Lentiviral intervention

The glaucoma rats were randomly divided into 7 groups: Glaucoma group, sh-NC group, sh-circ_0023826 group, Lenti-NC group, Lenti-circ_0023826 group, Lenti-circ_0023826 + Lenti-miR-188-3p group, Lenti-circ_0023826 + sh-MDM4 group. Except for the Glaucoma group, the other rats were additionally injected with a single injection of shRNA lentiviral vector or lentiviral overexpression vector targeting circ_0023826/miR-188-3p/MDM4. After 3 weeks, the rats were subjected to visual behavioral testing and subsequently euthanized by inhalation of excess CO₂ and the eyeball tissue was collected. The above lentiviral vectors were prepared by GenePharma.

Visual behavior test

An infrared light-illuminated black room (0.3 m×0.5 m×0.5 m) and a larger infrared light-illuminated white room (0.5 m×0.5 m×0.5 m) were used for visual behavior testing. There is a 10 cm×12 cm hole between the two rooms, allowing rats to freely shuttle from one room to another. The activity of the rats was recorded by a camera and the time spent by the rats in the dark room was calculated using Nordx ethovision XT 8.0 software (Li *et al.*, 2018).

Hematoxylin-eosin (H&E) staining

Rats' eyeballs were fixed with 4% paraformaldehyde (Solarbio). The cornea was incised along the sclera, the iris and lens were obtained, and the retinas were frozen in 30% sucrose and sectioned into 5 µm. Frozen tissues were stained with H&E solution (Solarbio) routinely and observed under an optical microscope (BX-51, Olympus, Tokyo, Japan) in 5 fields. The thickness of the ganglion cell layer (GCL) and the inner plexiform layer (IPL) was measured with SE IPS image analyzer. Each group selected 3 slices from 5 rats for measurement (Nie *et al.*, 2018).

Isolation and culture of RGCs

The retinas were isolated from 10 normal rats under a dissecting microscope, digested with 0.125% trypsin, and centrifuged at 179×g. The retinal pellet was centrifuged with 0.25% trypsin inhibitor (Sigma Aldrich), rinsed with Krebs solution containing magnesium and 1% bovine serum albu-

min (BSA), and made into a single-cell suspension. The cell suspension (1×10⁶ cells) was treated with 0.1 mg/ml poly-L-ornithine (Sigma Aldrich) and 1 g/ml laminin (Sigma Aldrich), cultured in basal medium Eagle (BME) medium (Nanjing SenBeiJia Biological Technology) containing 10% FBS, 25 mol/l glutamine and 0.1 mg/ml gentamicin.

Retinal single-cell suspension was incubated with goat anti-mouse IgG antibody (ab-6785; 1:1,000; Abcam) and rat anti-mouse Thy-1.1 antibody (ab-44898; 1:1,000; Abcam). The adherent cells were digested with 0.125% trypsin, centrifuged at 1000 rpm, and cultured with polylysine. Every three days, half of the medium was renewed (Xu *et al.*, 2021). The isolated RGCs were immunocytochemically stained for Thy-1 (Kong *et al.*, 2014). Briefly, antigen retrieval treatments were performed in citrate buffer in the microwave on medium heat for 5 min and then cooled to room temperature. After washing 3 times with PBS buffer, the slides were sealed with goat serum (ZSGB Bio, Beijing, China) for 30 min and incubated with anti-Thy-1 (Abcam, ab92574) overnight at 4°C. After 30 min incubation with HRP-conjugated secondary antibody solution (PV-6001, ZSGB Bio) at room temperature, staining was performed using DAB (ZSGB Bio). RGCs specific markers Brn3a (Abcam, ab245230, 1/1000), Thy-1 (Abcam, ab92574, 1/1500) and NF-L (Abcam, ab223343, 1/1000) were all analyzed by Western blot.

To establish an *in vitro* glaucoma model, RGCs were treated with N-methyl-D-aspartic acid (NMDA, 100 µmol/L) and glycine (10 µmol/L) for one hour. PBS-treated RGCs served as a negative control.

Lentiviral transfection

NMDA- and glycine-treated RGCs were collected. Transfection was performed when cells reached 70–80% confluence. shRNA targeting circ_0023826/MDM4 lentiviral vector (sh-circ_0023826/sh-MDM4), lentiviral vector overexpressing circ_0023826/miR-188-3p (Lenti-circ_0023826/Lenti-miR-188-3p), sh-NC and Lenti-NC were from GenePharma. RGCs were transfected using Lipofectamine 2000 reagent (Invitrogen). The medium was changed 24 h after transfection (Shen *et al.*, 2020).

Subcellular localization analysis

Cytoplasmic and nuclear RNAs of cells were isolated using the PARIS Kit (Invitrogen) and allowed to quantitatively analyze circ_0023826 expression.

Table 1. Primer sequences

Genes	Primer sequences (5'–3')
Hsa_circ_0023826	Forward: 5'-CTCTGACGGGAGCCTCTATG-3'
	Reverse: 5'-CCTGTCAGGGGTCTCTAAGC-3'
miR-188-3p	Forward: 5'-CCATGCACCTGTTTGGCCTA-3'
	Reverse: 5'-ACTCCAGTACTCCAGTAGC-3'
MDM4	Forward: 5'-TCCGATATAATAACAACCT-3'
	Reverse: 5'-GTGCAGGGTCCGAGGT-3'
U6	Forward: 5'-CTCGCTTCGGCAGCACA-3'
	Reverse: 5'-AACGCTTCACGAATTTGCGT-3'
GAPDH	Forward: 5'-TCCCATCACCATCTTCCA-3'
	Reverse: 5'-CATCAGCCACAGTTTCC-3'

Note: miR-188-3p, microRNA-188-3p; MDM4, Mouse Double Minute 4; GAPDH, glyceraldehyde-3-phosphate dehydrogenase

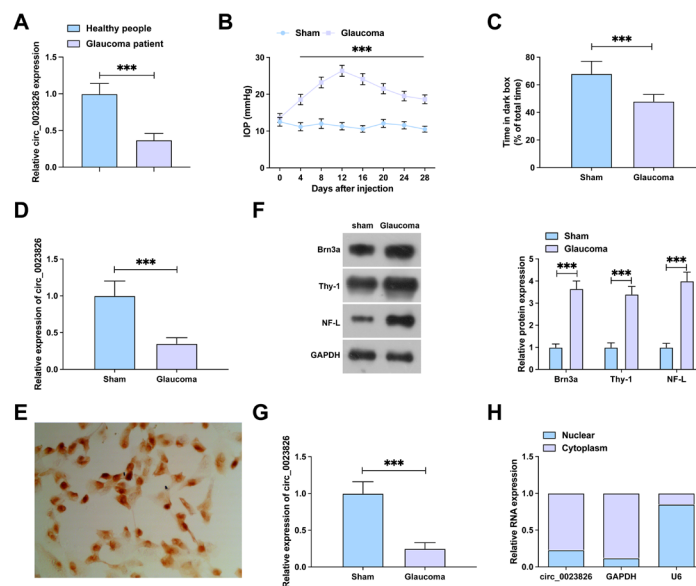


Figure 1. hsa_circ_0023826 is downregulated during glaucoma.

(A) RT-qPCR detected the expression of circ_0023826 in the fascia of normal human and glaucoma patients. (B) IOP levels of glaucoma rats. (C) Time of the rats in the dark room. (D) circ_0023826 expression in rat retina. (E) Immunocytochemical analysis of Thy-1 in isolated RGCs. (F) Immunoblotting for RGCs markers (Brn3a, Thy-1 and NF-L) in RGCs and rat eyeball tissue. (G) circ_0023826 expression in the isolated RGCs. (H) Nucleocytoplasmic separation experiments to analyze the subcellular localization of circ_0023826 in RGCs. Data are presented as mean \pm S.D. (n=3 or 6). * $p < 0.05$, ** $p < 0.01$, *** $p < 0.001$.

RT-qPCR

Based on the Trizol reagent (Invitrogen), total RNA was extracted for reverse transcription of circRNA/mRNA and miRNA using PrimeScript RT reagent kit (Takara, Tokyo, Japan) and miRNA First Strand Synthesis kit (Takara), respectively. SYBR Green kit (Thermo Fisher Scientific, Waltham, MA, USA) in combination with the Mx3005P QPCR system (Agilent Technologies, CA, USA) was employed for PCR. U6 and GAPDH were used as internal controls. The primer sequences are shown in Table 1.

Western blot

Total protein was extracted with RIPA lysis buffer (Beyotime, China), loaded on 8% SDS-PAGE gels (Solarbio), transferred to PVDF membranes (Invitrogen), and blocked with 5% skim milk. It was incubated with primary antibodies MDM4 (ab39470, Abcam), Bax (ab32503, Abcam), Bcl-2 (ab196495, Abcam), cleaved caspase-3 (ab2302, Abcam), GAPDH (ab8245, Abcam) and with the HRP-conjugated goat anti-rabbit IgG secondary antibody (Beyotime, China). Developed by ECL kit (34080, Thermo Fisher Scientific), signals were analyzed using ImageJ software (Li *et al.*, 2022).

Cell viability assay

After 24 h of different treatments, transfected or untransfected RGCs (1×10^5 cells/well) were added with 1 mL of MTT solution (Beyotime) for 2 h, and with 1 mL DMSO for 10 min. Finally, optical density_{570 nm} values were recorded with a microplate reader (PerkinElmer) (Zhang *et al.*, 2021).

Flow cytometry

RGCs were centrifuged at $1000 \times g$, resuspended in 195 μ L Annexin V-FITC binding buffer, and added with 5 μ L Annexin V-FITC and 10 μ L propidium io-

dide. The apoptosis of RGCs was detected by a FACS-Calibur flow cytometer (BD Biosciences).

ELISA

ELISA kits TNF- α (Abcam, ab181421), IL-6 (Abcam, ab178013) and IL-1 β (Sigma-Aldrich, RAB0273) were employed to measure inflammation in the culture supernatants (Gao *et al.*, 2020).

Dual-luciferase reporter assay

Potential binding sites for hsa_circ_0023826 and miR-188-3p were predicted by <https://circinteractome.nia.nih.gov>, while those for miR-188-3p and MDM4 were predicted by <https://cm.jefferson.edu/rna22/>. Based on the above wild-type sequence of hsa_circ_0023826 containing the miR-188-3p binding site, a mutant sequence was designed. RGCs were transfected with PGL4 containing hsa_circ_0023826/MDM4 wild-type sequence (hsa_circ_0023826/MDM4-WT) or hsa_circ_0023826/MDM4 mutant sequence (hsa_circ_0023826/MDM4-mut) together with miR-188-3p mimic or miR-NC. A dual-luciferase reporter assay system (Promega, Madison, WI, USA) was implicated to measure luciferase activity (Sui *et al.*, 2020).

RNA pull-down experiment

A biotin-labeled RNA (Roche, Shanghai, China) was used. After RGCs were lysed using RIPA lysis buffer (Beyotime, China), biotin miR-188-3p-labeled streptavidin magnetic beads were added for 1-h incubation. After elution, the RNA levels were analyzed (Wei *et al.*, 2021).

Statistical analysis

SPSS 21.0 statistical software was used to analyze the data, and the Kolmogorov-Smirnov test showed that the data were normally distributed, and the results were expressed as mean \pm standard deviation (S.D.). One/Two-

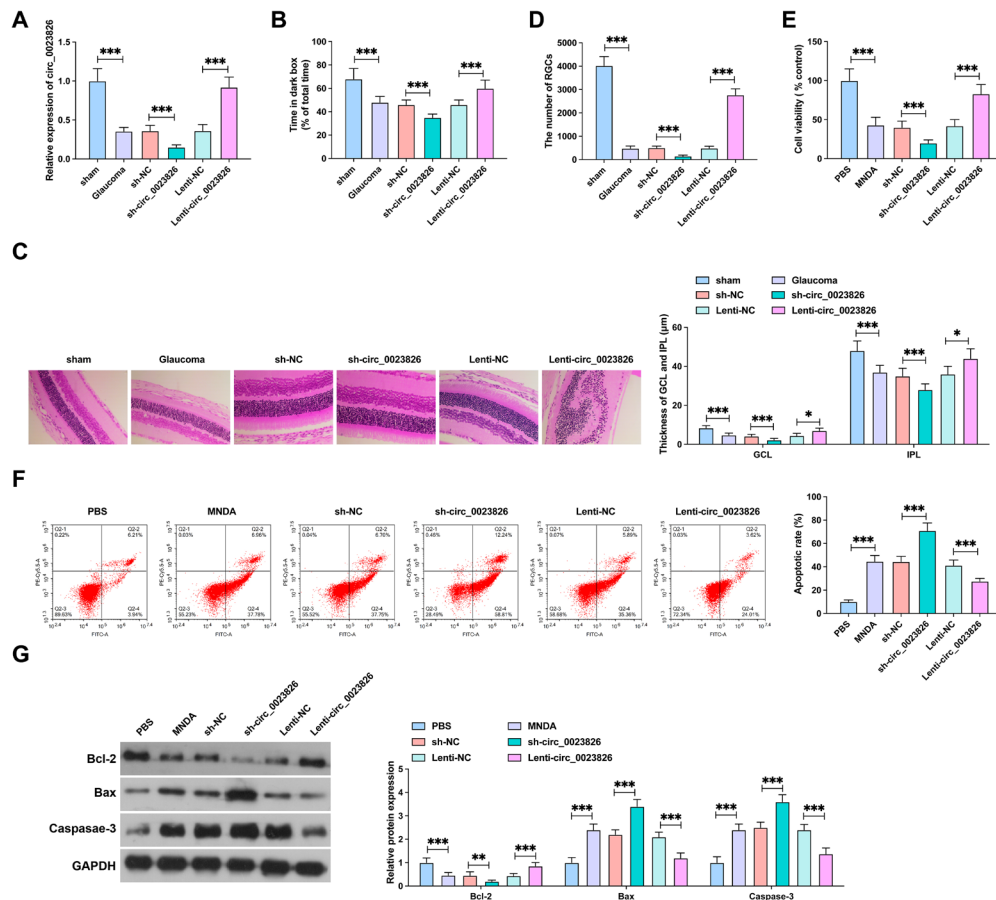


Figure 2. hsa_circ_0023826 improves glaucoma symptoms and survival of RGCs.

(A) RT-qPCR detection of the expression of circ_0023826 in rats; (B) Time of the rats in the dark room. (C) H&E staining (200 ×) of retina tissue of rats. (D) Counting of RGCs in retinal tissue of rats. (E) Proliferation of RGCs. (F) Apoptotic ability of RGCs. (G) Immunoblotting for Bcl-2, Bax and Caspase-3 in RGCs. Data are presented as mean ± S.D. (n=3 or 6). * $p < 0.05$, ** $p < 0.01$, *** $p < 0.001$.

way ANOVA analysis of variance and the least significant difference t test were suitable for comparing data. P was a two-sided test, and $P < 0.05$ was considered statistically significant.

RESULTS

Hsa_circ_0023826 is downregulated during glaucoma

A previous study showed that circ_0023826 was downregulated in chronic glaucoma rats. It was speculated that circ_0023826 may have an important relationship with the development of glaucoma. Circ_0023826 expression was assessed in glaucoma patients. As shown in Fig. 1A, circ_0023826 expression in the eye fascia of glaucoma patients was lower than that of normal human eye fascia. Then, a rat model of glaucoma was constructed and the IOP was tested before and after modeling. The results showed that the IOP of the glaucoma rats began to increase after the microbead injection, and the IOP was higher than that of the rats in the Sham group until the end of the modeling (Fig. 1B). The visual behavior test manifested that the rats treated with microbead surgery stayed longer in the dark room than the rats in the sham-operated group (Fig. 1C), indicating that the increase of IOP caused by the injection of microbeads impairs the visual function of rats. These results indicated that a rat model of glaucoma was successfully constructed.

Circ_0023826 expression pattern in retinal tissue was checked by RT-qPCR, manifesting a decline in glaucoma rats (Fig. 1D). Subsequently, RGCs were isolated from rat eyeball tissues. The isolated cells were confirmed to be positive for Thy-1 expression by IHC staining (Fig. 1E). In addition, the expression of RGCs markers (Brn3a, Thy-1, and NF-L) in the isolated cells was higher than that in the rat eyeball tissue (Fig. 1F). This indicates that the collected cells were high-purity RGCs. Subsequently, an *in vitro* model of glaucoma was established by MNDA induction. As shown in Fig. 1G, the expression of circ_0023826 in the MNDA-treated RGCs was significantly higher than that in the PBS-treated RGCs. Subcellular isolation test further confirmed that circ_0023826 was a cytoplasmic RNA (Fig. 1H). All the above data suggest that circ_0023826 may be involved in the development of glaucoma at the cellular post-transcriptional translational level.

Hsa_circ_0023826 improves glaucoma symptoms and survival of RGCs

To explore the role of circ_0023826 in glaucoma, circ_0023826 was upregulated and downregulated in glaucoma rats (Fig. 2A). Visual behavioral test showed that knockdown of circ_0023826 increased the dark room dwell time of rats, while overexpression of circ_0023826 decreased the dark room dwell time of rats (Fig. 2B). H&E staining observed the morphological changes of the retinas, showing that IPL and GCL

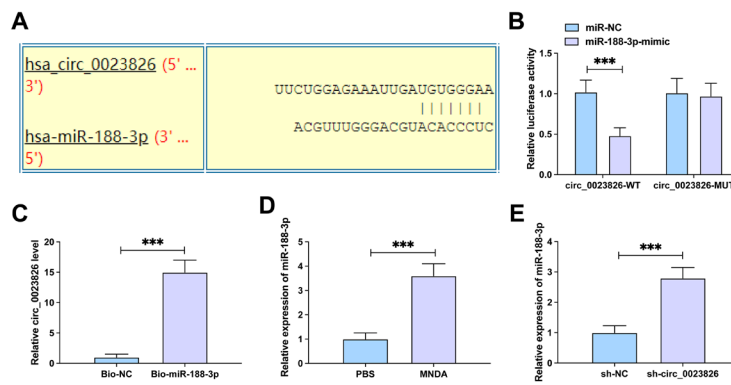


Figure 3. circ_0023826 is a sponge for miR-188-3p.

(A) The binding site (<https://circinteractome.nia.nih.gov/>) between circ_0023826 and miR-188-3p. (B–C) Dual-luciferase reporter assay and RNA pull-down assay to evaluate the interaction between circ_0023826 and miR-188-3p. (D) Changes of miR-188-3p in RGCs after MNDA induction (E) miR-188-3p expression after downregulating circ_0023826 in isolated RGCs. Data are presented as mean \pm S.D. (n=3). ** p <0.01, *** p <0.001.

were reduced in the Glaucoma group, while knockdown of circ_0023826 resulted in further reduction of IPL and GCL, but overexpression of circ_0023826 restored the levels of IPL and GCL (Fig. 2C). In addition, the number of RGCs in glaucoma rats was significantly reduced, knockdown of circ_0023826 further reduced the number of RGCs, while overexpression of circ_0023826 was able to restore the number of RGCs (Fig. 2D). Subsequently, the effect of circ_0023826 on the biological behavior of RGCs was examined. As shown in Fig. 2E, MNDA reduced the viability of RGCs, while knockdown of circ_0023826 resulted in a further decrease in the cell viability of RGCs, but overexpression of circ_0023826 restored the cell viability of RGCs. In addition, MNDA promoted the apoptosis rate of RGCs and increased the expression of apoptosis-related proteins Bax and cleaved caspase-3, which was further enhanced by knockdown

of circ_0023826, but attenuated by overexpression of circ_0023826 (Fig. 2F, G). These data suggest that overexpression of circ_0023826 improves glaucoma by promoting the cell viability of RGCs.

Circ_0023826 is a sponge for miR-188-3p

To reveal the underlying mechanism by which circ_0023826 works, a bioinformatics website was used to predict the downstream miRNAs of circ_0023826. miR-188-3p was found to have a targeted binding site of circ_0023826 (Fig. 3A). Next, their interaction was verified by dual-luciferase reporter assay and the results revealed that the luciferase activity decreased after co-transfection of miR-188-3p-mimic and circ_0023826-WT, but did not change after co-transfection with circ_0023826-MUT (Fig. 3B). Meanwhile, RNA pull-down assay showed that Bio-miR-188-3p was able to

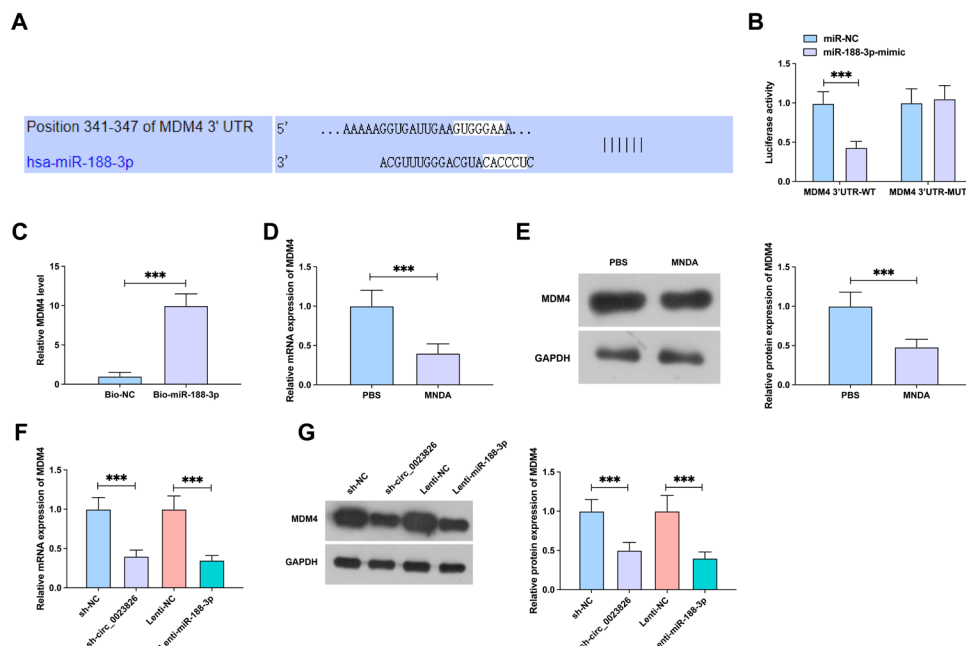


Figure 4. miR-188-3p directly targets MDM4.

(A) The bioinformatics website (<https://cm.jefferson.edu/rna22/>) predicts the binding site between MDM4 and miR-188-3p. (B–C) Dual-luciferase reporter assay and RNA pull-down assay to assess the interaction between MDM4 and miR-188-3p. (D–E) Effects of MNDA treatment on MDM4 expression in RGCs detected by RT-qPCR or western blot. (F–G) Effects of down-regulation of circ_0023826 or up-regulation of miR-188-3p on MDM4 expression detected by RT-qPCR or western blot. Data are presented as mean \pm S.D. (n=3). * p <0.05, ** p <0.01, *** p <0.001.

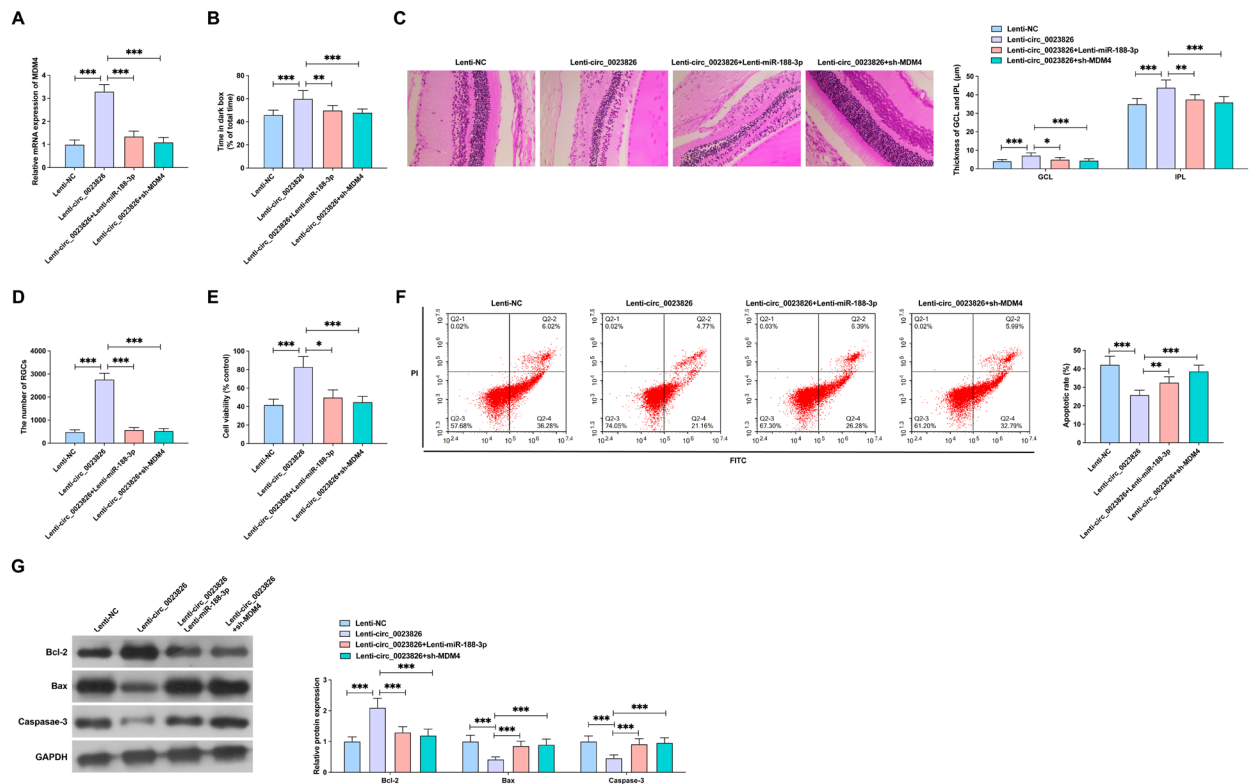


Figure 5. circ_0023826 alleviates glaucoma and the survival of RGCs by miR-188-3p targeting MDM4.

(A) RT-qPCR detection of MDM4 expression in rats. (B) Time of the rats in the dark room. (C) H&E staining (200 ×) of retina tissue of rats. (D) Counting of RGCs in retinal tissue of rats. E. Proliferation of RGCs. (F) Apoptotic ability of RGCs. (G) Immunoblotting for Bcl-2, Bax and Caspase-3 in RGCs. Data are presented as mean ± S.D. (n=3). * $p < 0.05$, ** $p < 0.01$, *** $p < 0.001$.

pull down circ_0023826 (Fig. 3C). Furthermore, MND4 promoted the expression of miR-188-3p in RGCs (Fig. 3D); knockdown of circ_0023826 increased the expression of miR-188-3p (Fig. 3E). The above data indicated that miR-188-3p was the target gene of circ_0023826.

MiR-188-3p directly targets MDM4

There are multiple complementary binding sites in miR-188-3p and MDM4 based on bioinformatics analysis (Fig. 4A). The results of dual-luciferase reporter gene assay confirmed that co-transfection of miR-188-3p-mimic with MDM4-WT reduced luciferase activity, while co-transfection with MDM4-MUT had no effect on luciferase activity (Fig. 4B). Meanwhile, the results of RNA pull-down experiment detected that Bio-miR-188-3p enriched MDM4 (Fig. 4C). Furthermore, MND4 treatment decreased MDM4 expression in RGCs (Fig. 4D, E). Knockdown of circ_0023826 or overexpression of miR-188-3p also inhibited the expression of MDM4 (Fig. 4F, G). The above data indicate that MDM4 is a downstream target gene of miR-188-3p.

Circ_0023826 alleviates glaucoma and the survival of RGCs by miR-188-3p targeting MDM4

To investigate the effect of circ_0023826 on glaucoma via the miR-188-3p/MDM4 axis, Lenti-NC, Lenti-circ_0023826, Lenti-circ_0023826 + Lenti-miR-188-3p, Lenti-circ_0023826 + sh-MDM4 were injected into the eyes of rats, respectively. As shown in Fig. 5A, overexpression of circ_0023826 promoted the expression of MDM4, but this effect was reversed by overexpression of miR-188-3p or knockdown of MDM4 (Fig.

5A). The results of visual behavioral test showed that up-regulation of circ_0023826 could improve visual function in rats, while up-regulation of miR-188-3p or down-regulation of MDM4 could reverse the improvement of visual function in rats by circ_0023826 addition (Fig. 5B). H&E staining found that Lenti-circ_0023826 significantly protected the reduction of GCL and IPL, and significantly increased the number of RGCs. However, Lenti-miR-188-3p or sh-MDM4 could reverse the effects of Lenti-circ_0023826 (Fig. 5C, D). As shown in Fig. 5E–G, Lenti-circ_0023826 can increase the cell viability and inhibit apoptosis of RGCs. However, Lenti-miR-188-3p or sh-MDM4 could reverse the effects of Lenti-circ_0023826. Taken together, circ_0023826 ameliorates glaucoma symptoms and promotes the survival of RGCs by regulating the miR-188-3p/MDM4 axis.

DISCUSSION

Glaucoma is a major cause of irreversible vision loss and is characterized by retinal neurodegeneration (Van *et al.*, 2022). Directly or indirectly promoting the survival of RGCs can delay or prevent the progression of glaucoma. Here, we reported that circ_0023826 was downregulated during glaucoma and demonstrated that circ_0023826 alleviated visual impairment in glaucoma rats and promoted the survival of RGCs. Mechanistically, circ_0023826 worked through sponge-absorbing miR-188-3p, which affected its downstream gene MDM4. Regarding study novelty, we reported for the first time that circ_0023826 was involved in the pathogenesis of glaucoma through the downstream miR-188-3p/MDM4 axis.

CircRNAs are abundant in the eukaryotic transcriptome (Jeck *et al.*, 2013) and significantly enriched in human brain and retinal tissues (Akhter *et al.*, 2018). It has been reported that circRNAs may drive changes that lead to glaucoma progression through one or more of these pathophysiological processes and lead to RGC death (Rong *et al.*, 2021). Studies have revealed the significance of circRNAs in glaucoma, including circZNF609 and circZNRANB1. circ_0023826 suggests a diagnostic value in glaucoma. We first studied circ_0023826's biological function in glaucoma. Apoptosis and inflammation of RGCs are important pathological features of eye diseases such as glaucoma (Ou *et al.*, 2021). We found that circ_0023826 in glaucoma-induced rats could alleviate the visual impairment, increase the number of RGCs, and inhibit the apoptosis of RGCs.

It has been demonstrated that circRNAs can act as miRNA sponges to regulate targeted downstream gene expression. Therefore, we predicted the targeted miRNA (miR-188-3p) of circ_0023826. miRNAs are important regulators of the complex biological progression of various neurodegenerative diseases (Mead *et al.*, 2022). Recently, miRNAs have been widely reported to be involved in the regulation of cell growth, differentiation, metabolism and apoptosis in the biological progression of glaucoma (Greene *et al.*, 2022). MiR-126 promotes retinal ganglion cell apoptosis in glaucoma rats (Wang *et al.*, 2020) and miR-223 induces retinal ganglion cell apoptosis. miR-188-3p has been reported to be associated with various diseases, such as cancer (Luo *et al.*, 2021), cardiovascular disease (Mi *et al.*, 2020), and diabetic nephropathy (Jin *et al.*, 2021). miR-188-3p has been reported to disrupt gemmarone-mediated podocyte protection in a mouse model of type 1 diabetic nephropathy by triggering mitochondrial damage (Wang *et al.*, 2021). Despite accumulating evidence that miR-188-3p exerts anti-apoptotic roles in several cell types, its function in retinal ganglion cell apoptosis and glaucoma progression is unclear. We first found that miR-188-3p was upregulated in RGCs isolated from retinal tissue of glaucoma rats and confirmed that circ_0023826's effect on the survival of RGCs could be reversed by overexpressing miR-188-3p.

Subsequently, we further predicted downstream factors of miR-188-3p and found that MDM4 was downregulated during glaucoma. MDM4 protein, also known as MDMX, was first discovered in 1996 by screening for p53-binding proteins (Shvarts *et al.*, 1996). It has been reported that MDMX is often amplified and highly expressed in human cancers, promoting cancer cell growth, and inhibiting apoptosis (Yu *et al.*, 2020). However, the function of MDMX in retinal ganglion cell apoptosis and glaucoma progression is currently unclear. To further verify the regulatory effect of circ_0023826/miR-188-3p/MDM4 axis on NSCLC, we performed rescue assays and confirmed that downregulating MDM4 or up-regulating miR-188-3p could reverse the therapeutic effect of circ_0023826 on glaucoma progression.

Taken together, our study confirmed our hypothesis that circ_0023826 protected against glaucoma by targeting the miR-188-3p/MDM4 axis. Nonetheless, we focused on retinal ganglion cells, other retinal cell types may also be affected by circ_0023826; because our findings are based on cell culture investigations and experimental animal studies, they cannot be directly generalized to patients. In the future, we will conduct more experiments to further verify the molecular mechanism of circ_0023826 protecting glaucoma *in vitro* and *in vivo*.

CONCLUSION

Our study reports the protective effect of circ_0023826 in glaucoma-induced neuroretinal degeneration. It was confirmed that upregulating circ_0023826 expression in glaucoma-induced rats can alleviate the damage to visual function in rats, increase the number of RGCs, and inhibit the apoptosis of RGCs. Mechanistically, our results suggest that circ_0023826 acts in glaucoma-induced neuroretinal degeneration by regulating the miR-188-3p/MDM4 axis and defines circ_0023826 as a new target for neuroprotective therapy of glaucoma.

REFERENCES

- Akhter R (2018) Circular RNA and Alzheimer's disease. *Adv Exp Med Biol* **1087**: 239–243. https://doi.org/10.1007/978-981-13-1426-1_19
- Chen X, Zhou R, Shan K, Sun Y, Yan B, Sun X, Wang J (2020) Circular RNA expression profiling identifies glaucoma-related circular RNAs in various chronic ocular hypertension rat models. *Front Genet* **11**: 556712. <https://doi.org/10.3389/fgene.2020.556712>
- Ebbesen KK, Hansen TB, Kjems J (2017) Insights into circular RNA biology. *RNA Biol* **14**: 1035–1045. <https://doi.org/10.1080/15476286.2016.1271524>
- Gao Z, Li Q, Zhang Y, Gao X, Li H, Yuan Z (2020) Ripasudil alleviated the inflammation of RPE cells by targeting the miR-136-5p/ROCK/NLRP3 pathway. *BMC Ophthalmol* **20**: 134. <https://doi.org/10.1186/s12886-020-01400-5>
- Geva M, Gershoni-Emek N, Naia L, Ly P, Mota S, Rego AC, Hayden MR, Levin LA (2021) Neuroprotection of retinal ganglion cells by the sigma-1 receptor agonist pridopidine in models of experimental glaucoma. *Sci Rep* **11**: 21975. <https://doi.org/10.1038/s41598-021-01077-w>
- Greene KM, Stamer WD, Liu Y (2022) The role of microRNAs in glaucoma. *Exp Eye Res* **215**: 108909. <https://doi.org/10.1016/j.exer.2021.108909>
- Guo N, Liu XF, Pant OP, Zhou DD, Hao JL, Lu CW (2019) Circular RNAs: Novel promising biomarkers in ocular diseases. *Int J Med Sci* **16**: 513–518. <https://doi.org/10.7150/ijms.29750>
- Hooshmand S, Voss J, Hirabayashi M, McDaniel L, An J (2022) Outcomes of initial and repeat micro-pulse transscleral cyclophotocoagulation in adult glaucoma patients. *Ther Adv Ophthalmol* **14**: 25158414211064433. <https://doi.org/10.1177/25158414211064433>
- Jin J, Wang Y, Zheng D, Liang M and He Q (2022) A novel identified circular RNA, mmu_circRNA_0000309, involves in gemmarone-mediated improvement of diabetic nephropathy through regulating ferroptosis by targeting miR-188-3p/GPX4 signaling axis. *Antioxid Redox Signal* **36**: 740–759. <https://doi.org/10.1089/ars.2021.0063>
- Kong N, Lu X, Li B (2014) Downregulation of microRNA-100 protects apoptosis and promotes neuronal growth in retinal ganglion cells. *BMC Mol Biol* **15**: 25. <https://doi.org/10.1186/s12867-014-0025-1>
- Li B, Lou G, Zhang J, Cao N, Yu X (2022) Repression of lncRNA PART1 attenuates ovarian cancer cell viability, migration and invasion through the miR-503-5p/FOXK1 axis. *BMC Cancer* **22**: 124. <https://doi.org/10.1186/s12885-021-09005-x>
- Li R, Jin Y, Li Q, Sun X, Zhu H, Cui H (2018) MiR-93-5p targeting PTEN regulates the NMDA-induced autophagy of retinal ganglion cells via AKT/mTOR pathway in glaucoma. *Biomed Pharmacother* **100**: 1–7. <https://doi.org/10.1016/j.biopha.2018.01.044>
- Luo Z, Fan Y, Liu X, Liu S, Kong X, Ding Z, Li Y, Wei L (2021) MiR-188-3p and miR-133b Suppress cell proliferation in human hepatocellular carcinoma via post-transcriptional suppression of NDRG1. *Technol Cancer Res Treat* **20**: 15330338211033074. <https://doi.org/10.1177/15330338211033074>
- Mead B, Tomarev S (2022) The role of miRNA in retinal ganglion cell health and disease. *Neural Regen Res* **17**: 516–522. <https://doi.org/10.4103/1673-5374.320974>
- Mi S, Wang P, Lin L (2020) miR-188-3p Inhibits vascular smooth muscle cell proliferation and migration by targeting fibroblast growth factor 1 (FGF1). *Med Sci Monit* **26**: e24394. <https://doi.org/10.12659/msm.924394>
- Nie XG, Fan DS, Huang YX, He YY, Dong BL, Gao F (2018) Downregulation of microRNA-149 in retinal ganglion cells suppresses apoptosis through activation of the PI3K/Akt signaling pathway in mice with glaucoma. *Am J Physiol Cell Physiol* **315**: C839–C849. <https://doi.org/10.1152/ajpcell.00324.2017>
- Okholm TLH, Nielsen MM, Hamilton MP, Christensen LL, Vang S, Hedegaard J, Hansen TB, Kjems J, Dyrskjot L, Pedersen JS (2017) Circular RNA expression is abundant and correlated to aggressive-

- ness in early-stage bladder cancer. *NPJ Genom Med* 2: 36. <https://doi.org/10.1038/s41525-017-0038-z>
- Ou-Yang Y, Liu ZL, Xu CL, Wu JL, Peng J, Peng QH (2020) miR-223 induces retinal ganglion cells apoptosis and inflammation via decreasing HSP-70 *in vitro* and *in vivo*. *J Chem Neuroanat* 104: 101747. <https://doi.org/10.1016/j.jchemneu.2020.101747>
- Quigley HA, Broman AT (2006) The number of people with glaucoma worldwide in 2010 and 2020. *Br J Ophthalmol* 90: 262–267. <https://doi.org/10.1136/bjo.2005.081224>
- Rong R, Wang M, You M, Li H, Xia X, Ji D (2021) Pathogenesis and prospects for therapeutic clinical application of noncoding RNAs in glaucoma: Systematic perspectives. *J Cell Physiol* 236: 7097–7116. <https://doi.org/10.1002/jcp.30347>
- Shen W, Wang C, Huang B (2020) Oxidative stress-induced circH-BEGF promotes extracellular matrix production via regulating miR-646/EGFR in human trabecular meshwork cells. *Oxid Med Cell Longev* 2020: 4692034. <https://doi.org/10.1155/2020/4692034>
- Shvarts A, Steegenga WT, Riteco N, van Laar T, Dekker P, Bazuine M, van Ham RC, van der Houven van Oordt W, Hateboer G, van der Eb AJ, Jochemsen AG (1996) MDMX: a novel p53-binding protein with some functional properties of MDM2. *EMBO J* 15: 5349–5357. PMID: 8895579
- Sui H, Fan S, Liu W, Li Y, Zhang X, Du Y, Bao H (2020) LINC00028 regulates the development of TGFβ1-treated human tenon capsule fibroblasts by targeting miR-204-5p. *Biochem Biophys Res Commun* S0006-291X(20)30165-0. <https://doi.org/10.1016/j.bbrc.2020.01.096>
- Van Hook MJ (2022) Influences of glaucoma on the structure and function of synapses in the visual system. *Antioxid Redox Signal* 37: 842–861. <https://doi.org/10.1089/ars.2021.0253>
- Wang JJ, Liu C, Shan K, Liu BH, Li XM, Zhang SJ, Zhou RM, Dong R, Yan B, Sun XH (2018) Circular RNA-ZNF609 regulates retinal neurodegeneration by acting as miR-615 sponge. *Theranostics* 8: 3408–3415. <https://doi.org/10.7150/thno.25156>
- Wang JJ, Shan K, Liu BH, Liu C, Zhou RM, Li XM, Dong R, Zhang SJ, Zhang SH, Wu JH, Yan B (2018) Targeting circular RNA-ZRANB1 for therapeutic intervention in retinal neurodegeneration. *Cell Death Dis* 9: 540. <https://doi.org/10.1038/s41419-018-0597-7>
- Wang LJ, Wang XZ, Li ZM, Kou D, Zhang D, Xu ZZ (2020) MiR-126 facilitates apoptosis of retinal ganglion cells in glaucoma rats via VEGF-Notch signaling pathway. *Eur Rev Med Pharmacol Sci* 24: 8635–8641. <https://doi.org/10.26355/eurev.202009.22800>
- Wang Y, Feng F, He W, Sun L, He Q, Jin J (2022) miR-188-3p abolishes germacrone-mediated podocyte protection in a mouse model of diabetic nephropathy in type I diabetes through triggering mitochondrial injury. *Bioengineered* 13: 774–788. <https://doi.org/10.1080/21655979.2021.2012919>
- Wei H, Li L, Zhang H, Xu F, Chen L, Che G, Wang Y (2021) Circ-FOXO1 knockdown suppresses non-small cell lung cancer development by regulating the miR-149-5p/ATG5 axis. *Cell Cycle* 20: 166–178. <https://doi.org/10.1080/15384101.2020.1867780>
- Xu K, Li S, Yang Q, Zhou Z, Fu M, Yang X, Hao K, Liu Y, Ji H (2021) MicroRNA-145-5p targeting of TRIM2 mediates the apoptosis of retinal ganglion cells via the PI3K/AKT signaling pathway in glaucoma. *J Gene Med* 23: e3378. <https://doi.org/10.1002/jgm.3378>
- Yang J, Hao R, Zhang Y, Deng H, Teng W, Wang Z (2021) Construction of circRNA-miRNA-mRNA network and identification of novel potential biomarkers for non-small cell lung cancer. *Cancer Cell Int* 21: 611. <https://doi.org/10.1186/s12935-021-02278-z>
- Yu DH, Xu ZY, Mo S, Yuan L, Cheng XD, Qin JJ (2020) Targeting MDMX for cancer therapy: rationale, strategies, and challenges. *Front Oncol* 10: 1389. <https://doi.org/10.3389/fonc.2020.01389>
- Zhang Q, He C, Li R, Ke Y, Sun K, Wang J (2021) miR-708 and miR-335-3p Inhibit the apoptosis of retinal ganglion cells through suppressing autophagy. *J Mol Neurosci* 71: 284–292. <https://doi.org/10.1007/s12031-020-01648-y>

Prognostic value of serum albumin level in patients with diffuse large B cell lymphoma

Liyan Chen¹, Lili Pan² and Tingbo Liu³✉

¹Department of Breast Surgery, Zhuhai Maternity and Child Health Hospital, Zhuhai, China; Fujian Medical University Union Hospital, Fujian, China; ²Pediatric Hematology Department, Fujian Medical University Union Hospital, Fujian, China; ³Hematology Department, Fujian Medical University Union Hospital, Fujian, China

Objective: To investigate the prognostic value of serum albumin (SA) levels before chemotherapy in patients with diffuse large B-cell lymphoma (DLBCL) after receiving chemotherapy. **Methods:** This is a retrospective study, and 127 patients with DLBCL including 71 males (55.9%) and 56 females (44.1%) were included. Patients' gender, age, Ann Arbor staging, eastern cooperative oncology group (ECOG) score, treatment options, international prognostic index, response rate, overall survival (OS), and progression-free survival (PFS) were obtained for statistical analysis. **Results:** Univariate analysis showed that SA≤34 g/L, Ann Arbor III-IV, B symptoms, ECOG≥2, and bone marrow involvement suggest a poor prognosis in patients with DLBCL. Patients with persistent SA>34 g/L had significantly longer OS than patients with persistent SA≤34 g/L ($P=0.020$). Multivariate analysis showed that SA≤34 g/L (HR=0.48, 95% CI=0.26-0.90, $P=0.022$) and R-CHOP-like treatment regimen (HR=0.43, 95% CI=0.24-0.76, $P=0.004$) are independent factors that could affect the prognosis of patients with DLBCL. **Conclusion:** SA can be used as an indicator of prognosis in patients with DLBCL before the first chemotherapy. DLBCL patients with SA≤34 g/L are associated with short OS and poor prognosis, which may potentially provide guidance for the clinician to pay more attention to this population before the first chemotherapy.

Keywords: diffuse large B-cell lymphoma, serum albumin, chemotherapy, prognosis, IPI

Received: 22 January, 2022; revised: 08 April, 2022; accepted: 15 November, 2023; available on-line: 05 December, 2023

✉ e-mail: tb_liu19@sina.com

Abbreviations: aalPI, Age adjusted international Prognostic index; ADM, Adriamycin; CR, Complete remission; CTX, Cyclophosphamide; DLBCL, Diffuse large b cell lymphoma; ECOG, Eastern cooperative oncology group; EFS, Event free survival; EPB, Epirubicin; GCB, Germinal center b cell like; IPI, International prognostic index; LDH, Serum lactate dehydrogenase level; NCCN-IPI, An enhanced international Prognostic index; NHL, Non-hodgkin's lymphoma; Non, GCB, Non-germinal center b cell like; NRR, No remission; ORR, Overall responderate; OS, Overall survival; PD, Progressive disease; PFS, Progression free survival; PR, Partial remission; Pred, Prednisone; R, Rituximab; SA, Serum albumin; SD, Stable disease; VCR, Vincristine; VDS, Vindesine

INTRODUCTION

Diffuse large B-cell lymphoma (DLBCL) is the most common pathological subtype of non-Hodgkin's lymphoma (NHL), and its incidence rate is 6.3% with an estimated more than 25 thousand new cases in the United States in 2016 (Li *et al.*, 2018). The heterogeneities of

DLBCL in clinical manifestations and histomorphology lead to differences in treatment response and prognosis.

The international prognostic index (IPI) is currently the common risk stratification criteria for lymphoma, which includes age, Ann Arbor disease stage, serum lactate dehydrogenase (LDH) level, extranodal involvement and eastern cooperative oncology group (ECOG) score (Ziepert *et al.*, 2010). Afterwards, the age-adjusted international prognostic (aalPI) can be used to assess the long-term prognosis of patients aged ≤60 years (Sehn *et al.*, 2007).

The National Comprehensive Cancer Network International Prognostic Index (NCCN-IPI) followed the five clinical features of IPI, and the LDH and age factors were more subdivided, and their evaluation was better than IPI (1993). The R-CHOP regimen is effective in the treatment of patients with DLBCL, and its overall survival (OS) and event-free survival (EFS) are superior to the CHOP-like regimen (Coiffier *et al.*, 2002; Coiffier *et al.*, 2010; Pfreundschuh *et al.*, 2006).

BCL-2, MYC, and BCL-6 molecular biological indicators have made significant progress in assessing prognosis (Miyaoaka *et al.*, 2018), though the examination is expensive. Serum albumin (SA) results show that patients with low SA have lower OS (Dalia *et al.*, 2014), and SA can predict the prognosis of patients with DLBCL (Eatrdes *et al.*, 2015), but it is excluded from the IPI prognosis approach due to insufficient data (1993). In this study, we aimed to investigate the prognostic value of SA levels before chemotherapy in patients with DLBCL after receiving chemotherapy. After determining the optimal threshold of SA level in DLBCL patients, the patients were divided into high and low cut-off SA groups. The OS and progression-free survival (PFS) were analyzed to assess the effectiveness of NCCN-IPI in DLBCL patients, especially those under 60 years of age. This retrospective analysis of DLBCL patients with different SA levels might provide more clinically relevant guidance for clinicians to assess the prognostic outcomes of patients before the first chemotherapy.

OBJECTIVES AND METHODS

Object selection

This retrospective study was approved by the Ethics Committee of Fujian Medical University Union Hospital (the approval number: 2019KY029) in Fuzhou City, Fujian Province, China in 2019. A total of 127 patients with DLBCL admitted to the Union Hospital of Fujian Medi-

Table 1A. The International Prognostic Index (IPI)

Index	0 Point	1 Point
Age (Year)	≤60	>60
ECOG	0 or 1	≥2
LDH	≤Normal Value	>Normal Value
Extranodal involvement	0 or 1	>1
Ann Arbor staging	I or II	III or IV

Low-risk group, 0–1 point; low-intermediate risk group, 2 points; high-intermediate risk group, 3 points; high-risk group, 4–5 points. ECOG, Eastern Cooperative Oncology Group; LDH, Lactate Dehydrogenase.

Table 1B. The age-adjusted international Prognostic Index (aalPI)

Index	0 Point	1 Point
ECOG	< 2	≥2
LDH	≤Normal Value	>Normal Value
Ann Arbor staging	I or II	III or IV

Low-risk group, 0 points; low-intermediate risk group, 1 point; high-intermediate-risk group, 2 points; high-risk group, 3 points. ECOG, Eastern Cooperative Oncology Group; LDH, Lactate Dehydrogenase.

Table 1C. The National Comprehensive Cancer Network International Prognostic Index (NCCN-IPI)

Index	Grouping	Point
Age	<41 Year	0
	41–60 Year	1
	61–75 Year	2
	>75 Year	3
ECOG	0 or 1	0
	≥2	1
LDH	<1 of Normal Value	0
	1–3 of Normal Value	1
	>3 of Normal Value	2
Extranodal involvement	No	0
	Yes	1
Ann Arbor staging	I or II	0
	III or IV	1

Low-risk group, 0–1 point; low-intermediate risk group, 2–3 points; high-intermediate risk group, 4–5 points; high-risk group, ≥6 points. ECOG, Eastern Cooperative Oncology Group; LDH, Lactate Dehydrogenase.

cal University from January 1, 2010 to December 31, 2014 were consecutively enrolled. Inclusion criteria were as follows: 1) initial treatment and age ≥18 years; 2) initial diagnosis of DLBCL; 3) pathological tissues were diagnosed according to WHO lymphoma typing (Fmedsci & Frs, 2015); 4) no severe heart, lung, liver, and kidney dysfunction; 5) patients were treated with rituximab and CHOP (R-CHOP) like regimen or CHOP-like regimen. Exclusion criteria were as follows: 1) initial treatment and age <18 years; 2) no chemotherapy in our hospital or incomplete data; 3) patients with history of heart, lung, liver, or kidney dysfunction; 4) patients were diagnosed with primary central nervous system diffuse large

B-cell lymphoma, primary diffuse large B-cell lymphoma, primary mediastinal diffuse large B-cell lymphoma, or Epstein-Barr virus (EBV)-positive elderly diffuse large B-cell lymphoma. The clinical data, including gender, age, germinal center B cell-like (GCB) subtypes (by the Hans algorithm (Hans *et al.*, 2004)), Ann Arbor staging (Sehn *et al.*, 2005), B symptoms, ECOG, extranodal involvement, LDH, SA, treatment regimen, and NCCN-IPI, were analyzed in this study. All patient details were de-identified and the identity of patients could not be ascertained from this study. Meanwhile, the reporting of this study conforms to the STROBE statement (von Elm *et al.*, 2007).

Treatment

The patients' consent to treatment was obtained in this study. All patients received an R-CHOP-like regimen (rituximab (R) 375 mg/m² once, cyclophosphamide (CTX) 750 mg/m² once, vincristine (VCR) 1.4 mg/m² or vindesine (VDS) once, doxorubicin (Adriamycin, ADM) 50 mg/m² once and epirubicin (EPI) or prednisone (Pred) 40 mg/m² for 5 continuous days) repeated at 14-day intervals for 1–6 cycles, or CHOP-like regimen (CTX, VCR or VDS, ADM, EPI or Pred) for 1–6 cycles (Lamy *et al.*, 2018).

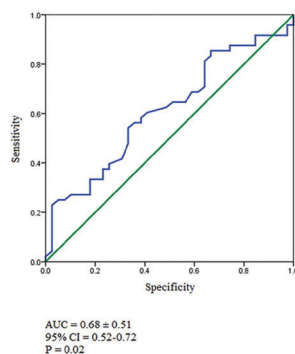


Figure 1. Receiver operating characteristic (ROC) curve of serum albumin.

Table 2. Information of the Patients with DLBCL

Index	Patients No.	Ratio (%)	SA		<i>P</i>
			≤34 g/L (%)	>34 g/L (%)	
Sex					0.512
Male	71	55.9	42 (59.2)	29 (40.8)	
Female	56	44.1	29 (51.8)	27 (48.2)	
Age (Year)					0.257
≤60	82	64.6	46 (56.1)	36 (43.9)	
>60	45	35.4	25 (55.6)	20 (44.4)	
Ann Arbor staging					0.003
I-II	41	32.3	18 (43.9)	23 (56.1)	
III-IV	86	67.7	53 (61.6)	32 (37.2)	
B symptoms					0.007
Yes	45	35.4	35 (77.8)	10 (22.2)	
No	82	64.6	37 (45.1)	45 (54.9)	
ECOG score					0.004
<2	105	82.7	52 (49.5)	54 (51.4)	
≥2	22	17.3	19 (85.4)	3 (13.6)	
Extranodal involvement					0.301
Yes	69	54.3	45 (65.2)	24 (34.8)	
No	58	45.7	27 (46.6)	31 (53.4)	
Bone marrow involvement					0.038
Yes	32	25.2	23 (71.9)	9 (28.1)	
No	95	74.8	47 (49.5)	48 (50.5)	
LDH (U/L)					0.019
>250	67	52.8	48 (71.6)	19 (28.4)	
≤250	60	47.2	23 (38.3)	37 (61.7)	
Pathological type					0.389
GCB	45	35.4	26 (57.8)	19 (42.2)	
Non-GCB	81	63.8	44 (54.3)	37 (45.7)	
Treatment					0.002
CHOP-like	54	42.5	35 (64.8)	19 (35.2)	
R-CHOP like	69	54.3	35 (50.7)	34 (49.3)	
IPI/aalPI					0.003
Low-risk	34	26.8	14 (41.2)	20 (58.8)	
Low-intermediate risk	34	26.8	17 (50)	17 (50)	
High-intermediate risk	30	23.6	20 (66.7)	10 (33.3)	
High-risk	29	22.8	21 (72.4)	8 (27.6)	
NCCN-IPI					0.000
Low-risk	23	18.1	10 (43.5)	13 (56.5)	
Low-intermediate risk	64	50.4	31 (48.4)	33 (51.6)	
High-intermediate risk	32	25.2	24 (75)	8 (25)	
High-risk	8	6.3	8 (100)	0 (0)	

DLBCL, diffuse large B-cell lymphoma; ECOG, eastern cooperative oncology group; LDH, lactate dehydrogenase; GCB, germinal center B cell-like; IPI, international prognostic index; aalPI, age-adjusted international prognostic index; NCCN-IPI, the national comprehensive cancer network international prognostic index.

Prognostic assessment method

Patients were assessed by IPI, aaIPI and NCCN-IPI (Table 1A, B and C). NCCN-IPI assessment includes patients' age, ECOG score, serum lactate dehydrogenase level (LDH), extranodal involvement (involved distinct sites, such as bone marrow, CNS, gastrointestinal tract, liver or lung), and Ann Arbor stage. By using this assessment method, patients were divided into low-risk group (NCCN-IPI=0–1), low-intermediate risk group (NCCN-IPI=2–3), high-intermediate risk group (NCCN-IPI=4–5) and high-risk group (NCCN-IPI ≥ 6) (Table 1C).

SA grouping

The cut-off value of SA was obtained by analyzing the SA level- receiver operating characteristic (ROC) curve. Following this approach, the cut-off value of SA was 34 g/L. Therefore, in this study, the DLBCL patients were divided into low SA ≤ 34 g/L and high SA > 34 g/L groups (Fig. 1).

Efficacy criteria

The short-term efficacy evaluation was based on the Response Criteria for Malignant Lymphoma (Cheson *et al.*, 2007) by using CT or PET-CT imaging techniques after the first chemotherapy. Generally, the short-term efficacy was divided into four groups: complete remission (CR, defined as disappearance of all evidence of disease), partial remission (PR, defined as regression of measurable disease and no new sites), stable disease (SD, defined as failure to attain the CR/PR), Progressive disease (PD, defined as any new lesion or increase by 50% of previously involved sites from nadir). OS and PFS are followed up by inpatient medical records or by telephone. The deadline is the study endpoint December 31, 2017, to obtain 3-year and 3-year of OS and PFS data. OS: The primary endpoint was OS with 3 years (3-year OS), defined as the time from diagnosis to death from any cause, following the IPI criteria. PFS was defined as the time from DLBCL diagnosis until the disease recurrence, death-from-any-cause, or censoring (Cheson *et al.*, 2007).

Data processing method

All data were analyzed using SPSS 20.0. ROC curve analysis was performed to obtain the cut-off SA value. OS and PFS were assessed by using the Kaplan-Meier estimator. Univariate and multivariate analyses were performed using the Cox regression model, and short-term efficacy analysis was performed by using the chi-square test. $P < 0.05$ was statistically significant.

RESULT

General clinical characteristics of patients with DLBCL

A total of 156 cases of DLBCL were diagnosed by pathology in our hospital from January 1, 2010 to December 31, 2014, while 26 cases were not treated with chemotherapy and 3 cases were combined with other tumors. Therefore, 127 patients were finally collected, including 71 males (55.9%) and 56 females (44.1%). Generally, the median age of patients was 56 (18–86) years, while 45 patients (35.4%) were aged > 60 years. The ECOG < 2 points were reported in 105 cases (82.7%), while ECOG ≥ 2 points were reported in 22 cases (17.3%). There were 82 cases (64.6%) who had no

B symptoms, and 45 cases (35.4%) were with B symptoms. The patients with normal LDH levels were found in 60 cases (47.2%), while 67 cases (52.8%) were shown with high LDH. The low SA (≤ 34 g/L) was observed in 70 cases (55.1%) and high SA (> 34 g/L) was in 54 cases (42.5%). The other clinical characteristics of these patients are shown in Table 2.

Pathologically diagnosed with germinal center B cell-like (GCB) was found in 45 cases (35.4%) and non-GCB was in 81 cases (63.8%). Meanwhile, 41 cases (32.3%) were diagnosed with Ann Arbor staging I–II, while 86 cases (67.7%) were Ann Arbor staging III–IV. In addition, 58 cases (45.7%) were not found with extranodal involvement, while 69 cases (54.3%) were shown with extranodal involvement. According to the NCCN-IPI assessment, there were 23 cases (18.1%) in the low-risk group, 64 cases (50.4%) in the low-intermediate risk group, 32 cases (25.2%) in the high-intermediate risk group, and 8 cases (6.3%) in the high-risk group, with 3-year OS of 76.5%, 73.8%, 32.5%, 37.5 %, respectively. Meanwhile, 54 patients (42.5%) received CHOP-like regimens, 69 patients (54.3%) received R-CHOP-like regimens, and the other 4 patients received other chemotherapy (Table 2).

Survival and prognosis analysis

Up to the last follow-up date, the rate of loss to follow-up was 15.7%, while the mortality rate was 35.4%. The median follow-up time was 25 (0–66) months. The OS of 1 year, 3 years and 5 years were 70.3%, 61.0% and 50.5%, respectively. The PFS rates of 1 year, 3 years and 5 years were 56.7%, 41.2% and 32.0%, respectively (Fig. 2A and B).

Cox regression analysis of factors in association with OS of patients with DLBCL

By using univariate Cox analysis, it showed that Ann Arbor staging ($P=0.008$), B symptoms ($P=0.008$), ECOG score ($P=0.004$), bone marrow involvement ($P=0.017$), LDH levels ($P=0.063$), SA levels ($P=0.002$), and treatment regimens ($P=0.003$) were significantly associated with 3-year OS in patients with DLBCL (Table 3). However, when using the multivariate Cox regression model, it showed that Ann Arbor staging, B symptoms, ECOG score, bone marrow involvement, and LDH levels had no significant correlation with the prognostic values of DLBCL patients. On the contrary, SA levels ($P=0.022$) and treatment regimens ($P=0.004$) were an independent prognostic factor for patients with DLBCL (Table 4).

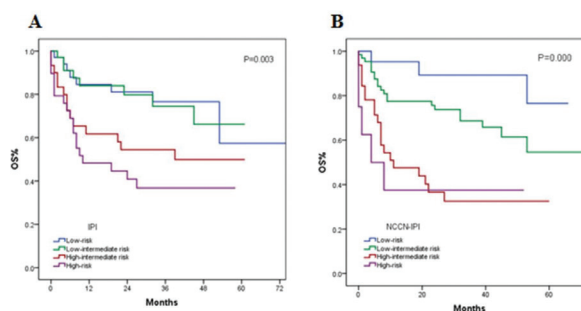


Figure 2. The 3-year overall survival of the low-risk group, the low-intermediate-risk group, the high-intermediate-risk group and the high-risk group of the IPI/aaIPI (A) and the NCCN-IPI (B).

Table 3. Results of univariate Cox regression model

Index	3-year OS		
	HR	95% CI	P
Sex (Male vs Female)	1.045	0.788-1.385	0.762
Age (≤60 years vs >60 years)	0.945	0.528-1.691	0.849
Ann Arbor staging (I-II vs III-IV)	2.689	1.302-5.553	0.008
B symptoms (Yes vs No)	0.469	0.267-0.823	0.008
ECOG Score (<2 vs ≥2)	2.55*	1.348-4.824	0.004
Extranodal involvement (Yes vs No)	0.972	0.732-1.290	0.842
Bone marrow involvement (Yes vs No)	0.701	0.524-0.938	0.017
LDH (Normal vs > Normal)	0.761	0.571-1.015	0.063
Low SA vs High SA	1.629	1.193-2.224	0.002
GCB vs non-GCB	1.151	0.647-2.045	0.633
CHOP- like vs R-CHOP-like	1.571	1.208-2.044	0.003
IPI	1.571	1.208-2.044	0.001
NCCN-IPI	2.131	1.522-2.984	0.000

*Example in this analysis: HR is obtained from the exponential regression coefficient, and gives the effect size of the predictors. In our example, the ECOG variable had an HR =2.55, meaning that the hazard (year OS) in patients with ECOG ≥2 is about 2.55 times higher than in the patients with ECOG <2. ECOG, Eastern Cooperative Oncology Group; LDH, Lactate Dehydrogenase; GCB, germinal center B cell-like; IPI, International Prognostic Index; SA, serum albumin; NCCN-IPI, the National Comprehensive Cancer Network International Prognostic Index; OS, overall survival; HR, hazard ratio; CI, confidence interval.

The association of SA concentration with short-term efficacy

In the SA of ≤34 g/L population (n=70), the overall response rate (ORR) was 58.6%, with 28 complete remission (CR) patients and 13 partial remission (PR) patients, while the non-remission rate (NRR) was 41.4%. In the SA>34 g/L population (n=54), the ORR was 90.7% (n=49), while the NRR was 9.3% (n=5). The short-term efficacy of patients with DLBCL between these two groups was statistically significant (P=0.033), indicating the low SH patient has a low CR rate after receiving chemotherapy (Table 5). In addition, the 3-year OS and PFS in the high SA group were 57.4% and 32.8%, which was significantly better than that in the low SA group (P=0.002 and P=0.022) (Fig. 3 and Table 6).

Prognostic value of SA level in association with other factors of patients with DLBCL

The 3-year OS in patients with a sustained SA of >34 g/L was significantly longer than those with a continuous SA of ≤34 g/L (P=0.02), whereas there was no significant difference in terms of PFS, suggesting that patients with SA>34 g/L before the initial chemotherapy have longer OS than that of patients with SA≤34 g/L, while the level of SA did not affect on PFS of patients with DLBCL (Fig. 4). The 3-year OS of high SA patients with NCCN-IPI stratified low-intermediate risk group was significantly higher than the 3-year OS of low SA (P=0.029), while there was no significant difference in 3-year OS between high and low SA levels in low-risk/high-intermediate group (P>0.05) (Fig. 5). The 3-year OS of patients with high SA with ECOG score of 0-1 was significantly higher than that of pa-

Table 4. Results of multivariate Cox regression model

Index	3-year OS		
	HR	95.0% CI	P
Ann Arbor staging (I-II vs III-IV)	1.67	0.74-3.79	0.219
B symptoms (Yes vs No)	0.73	0.37-1.42	0.350
ECOG score (2 vs ≥2)	1.58*	0.77-3.25	0.212
Bone marrow involvement (Yes vs No)	0.78	0.4-1.48	0.451
LDH (Normal vs > Normal)	1.14	0.60-2.18	0.685
Low SA vs High SA	0.48	0.26-0.90	0.022
CHOP-like vs R-CHOP -like	0.43	0.24-0.76	0.004

*Example in this analysis: HR is obtained from the exponential of regression coefficient, and gives the effect size of the predictors. In our example, the ECOG variable had an HR=1.58, meaning that the hazard (3-year OS) in patients with ECOG ≥2 is about 1.58 times higher than in the patients with ECOG <2. ECOG, Eastern Cooperative Oncology Group; LDH, Lactate Dehydrogenase; OS, overall survival; HR, hazard ratio; CI, confidence interval.

Table 5. Comparison of serum albumin levels and short-term efficacy

Serum albumin (g/L)	CR (%)	NRR (%)	ORR (%)
≤34 g/L (n=70)	28 (40)	29 (41.4)	41 (58.6)*
>34 g/L (n=54)	32 (59.3)	5 (9.3)	49 (90.7)*

*P=0.033; CR: complete remission; NRR, non-remission rate; ORR, overall response rate.

Table 6. Analysis of Serum albumin levels and 3-year OS/PFS by univariate Cox regression model

%	HR	95% CI	P
3-year OS ratio: low SA (43.6%) vs high SA (57.4%)	1.629	1.193-2.224	0.002
3-year PFS ratio: low SA (20%) vs high SA (32.8%)	0.607	0.392-0.938	0.022

OS, overall survival; PFS, progression-free survival; SA, serum albumin; HR, hazard ratio; CI, confidence interval.

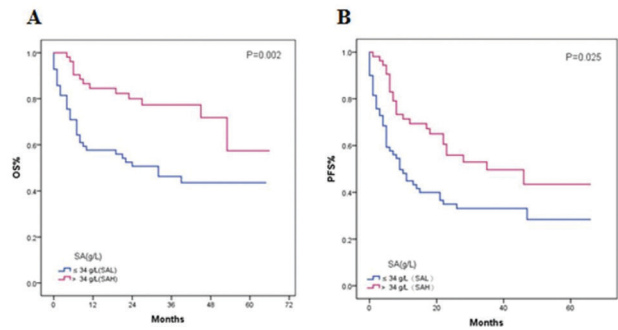


Figure 3. Analysis of 3-year OS (A) and PFS (B) in the low and high SA patients.

tients with low SA with ECOG score of 0-1 (HR=0.439, 95% CI=0.232–0.831, P=0.011) (Table 7). In the non-GCB group, the low SA patients survived for 47.9% in 3 years, and the 3-year survival rate of high SA patients was 78.3 %, which was statistically significant (P=0.004, Table 8). The 3-year OS of low SA patients in group III-IV was 33.2 %, which was significantly lower than 72 % in high SA patients (P=0.018) (Fig. 6 and Table 9).

Analysis of 3-year OS of treatment regime grouped SA group by univariate Cox regression model

The Kaplan–Meier test showed that in the CHOP-like treatment group, the 3-year OS ratio of patients in the high SA group was higher than that in the low SA group (62% *vs* 38%) (P=0.087, Fig. 7A). In the R-CHOP like treatment group, the 3-year OS ratio of patients in the high SA group was higher than that in the low SA group (87% *vs* 61% (P=0.101, Fig. 7B). Univariate Cox regression analysis showed that there were significantly different in the 3-year OS between low and high SA among the CHOP like (P=0.035) and R-CHOP like groups (P=0.04) (Table 10).

DISCUSSION

In this study, we retrospectively analyzed the 127 patients with DLBCL and found that the cut-off SA value of 34 g/L could be used as a prognostic predictor for DLBCL patients in the clinic. Similarly, Wei and others (Wei *et al.*, 2021) reported that the best cutoff value of SA for survival analysis of patients with DLBCL was 39.2 g/L, and also concluded that hypoalbuminemia can act as a simple and effective adverse prognostic factor in

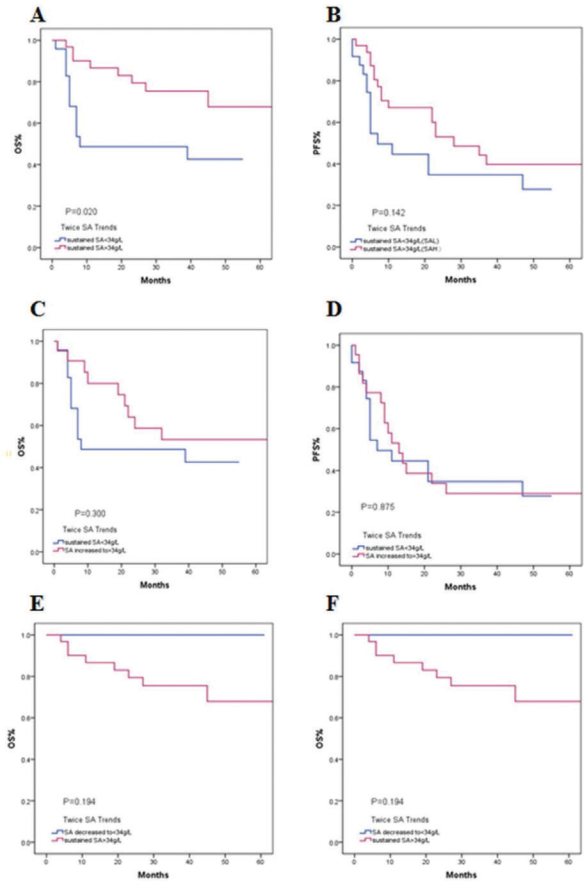


Figure 4. Analysis of 3-year OS and 3-year PFS in low and high SA patients before and after the chemotherapy. 3-years OS (A) and 3-year PFS (B) in patients with two SAs>34 g/L and two SAs ≤ 34 g/L before the first two chemotherapy. 3 years OS (C) and 3-year PFS (D) in patients with two SAs≤34 g/L and initial SA 34 g/L, second SA>34 g/L before the first two chemotherapy. 3-year OS (E) and 3-year PFS (F) in patients with two SAs>34 g/L and initial SA>34 g/L, second SA≤34 g/L before the first two chemotherapy.

these patients. In addition, Eatrdes and others (Eatrdes *et al.*, 2015) showed that SA <37g/L in patients treated with R-CHOP like had a lower OS and PFS. However, in this study, we divided the DLBCL patients into >34 g/L and SA≤34 g/L groups, and compared the prognostic outcomes of these patients in different subgroups, including NCCN-IPI risk grouping, before and after

Table 7. Analysis of 3-year OS of ECOG score stratified serum albumin levels by univariate Cox regression model

ECOG score	SA group	Patients No. (%)	3-year OS		
			HR	95% CI	P
0-1 point	Low SA	51/102 (50)	0.439	0.232-0.831	0.011
	High SA	51/102 (50)			
2-4 points	Low SA	19/22 (86.4)	0.034	0.000-12.697	0.263
	High SA	3/22 (13.6)			

OS, overall survival; ECOG, Eastern Cooperative Oncology Group; SA, serum albumin; HR, hazard ratio; CI, confidence interval.

Table 8. Analysis of 3-year OS of pathological grade-stratified serum albumin group by univariate Cox regression model

Pathological diagnosis	SA group	3-year OS ratio (%)	3-year OS		
			HR	95% CI	P
GCB	Low SA	35.6	0.441	0.176-1.109	0.082
	High SA	74.9			
non-GCB	Low SA	47.9	0.315	0.143-0.693	0.004
	High SA	78.3			

OS, overall survival; GCB, germinal center B cell like; SA, serum albumin; HR, hazard ratio; CI, confidence interval.

Table 9. Analysis of 3-year OS of Ann Arbor staging-stratified serum albumin group by univariate Cox regression model

Ann Arbor staging	SA group	3-year OS ratio (%)	3-year OS		
			HR	95% CI	P
I-II	Low SA	72.8	0.658	0.196-2.206	0.498
	High SA	85.2			
III-IV	Low SA	33.2	0.454	0.236-0.875	0.018
	High SA	72			

OS, overall survival; SA, serum albumin; HR, hazard ratio; CI, confidence interval.

Table 10. Analysis of 3-year OS of treatment regime grouped serum albumin group by univariate Cox regression model

Treatment regime	SA group	3-year OS ratio (%)	3-year OS ratio		
			HR	95% CI	P
CHOP -like	Low SA	29.7	0.427	0.194-0.940	0.035
	High SA	63			
R-CHOP -like	Low SA	83.7	0.375	0.147-0.957	0.04
	High SA	60.6			

OS, overall survival; SA, serum albumin; HR, hazard ratio; CI, confidence interval.

chemotherapy, Ann Arbor staging, ECOG score, treatment options, respectively. By evaluating SA concentration predictive efficacy in these subgroups, it showed that SA may serve as the prognostic predictor in DLBCL patients with specific clinical characteristics.

IPI/aaIPI/NCCN – IPI assessment

IPI/aaIPI has been used as a prognostic indicator for DLBCL. In this study, univariate Cox regression model analysis IPI/aaIPI showed significant differences in OS of different risk stratification, indicating that IPI/aaIPI may effectively assess the prognosis of patients. Ziepert et al reported that rituximab increases OS in patients with DLBCL, and IPI can effectively assess patient prognosis in both CHOP-like and R-CHOP like regimens (Ziepert *et al.*, 2010). In this study, patients with DLBCL who received an R-CHOP regimen had

longer OS than patients with DLBCL who received a CHOP-like regimen, which is consistent with other studies. IPI was able to assess the prognosis of patients with DLBCL treated with the R-CHOP-like regimen but was unable to completely distinguish the four risk stratifications and the effectiveness of IPI in assessing the prognosis of such patients was limited (Salles *et al.*, 2011). Multivariate analysis showed that age ≥ 60 years, elevated LDH levels, low SA and Ann Arbor staging were independent prognostic risk factors (Ngo *et al.*, 2008). Zhou and others (Zhou *et al.*, 2014) studied patient data from seven clinical centers and proposed an NCCN-IPI prognostic assessment model to assess the prognosis of patients with DLBCL treated with the R-CHOP-like regimen.

NCCN-IPI is effective in assessing OS in patients treated with CHOP-like and R-CHOP-like regimens, and

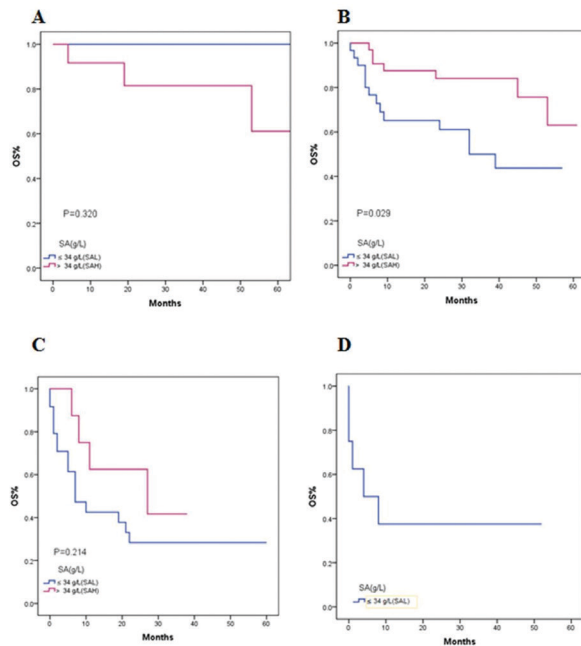


Figure 5. 3-year overall survival of patients with SA \leq 34 g/L and with SA $>$ 34 g/L in NCCN-IPI risk stratification grouping. (A) low-risk group; (B) low-intermediate risk group, (C) high-intermediate risk group; (D) high-risk group.

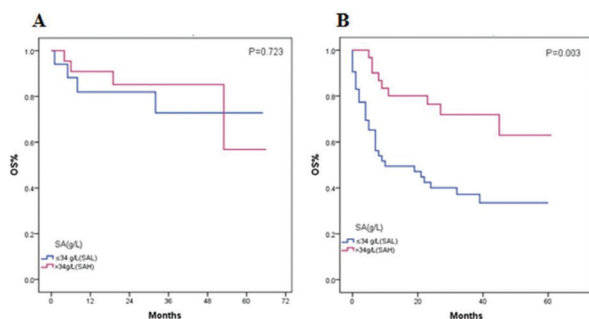


Figure 6. Comparison of OS between SA $>$ 34 g/L and SA \leq 34 g/L patients. (A) Ann Arbor staging I-II group; (B) Ann Arbor staging III-IV group.

is more effective than IPI/aaIPI, in patients treated by R-CHOP-like (Salles *et al.*, 2011; Ngo *et al.*, 2008; Zhou *et al.*, 2014). However, Melchardt and others (Melchardt *et al.*, 2015) believe that the effectiveness of NCCN-IPI in evaluating the prognosis of patients treated with an R-CHOP-like regimen is still insufficient. Our study was stratified by age and the results showed that NCCN-IPI was able to effectively assess risk stratification in patients >60 years old and ≤ 60 years old.

SA levels

As an independent prognostic risk factor, SA has been confirmed in other hematological malignancies, including Hodgkin's lymphoma, myelodysplastic syndrome, acute myeloid leukemia, primary cutaneous T-cell lymphoma, spleen marginal lymphoma, and Primary mediastinal DLBCL (Huang *et al.*, 2015; Chihara *et al.*, 2009; Watanabe *et al.*, 2010; Zhu *et al.*, 2011; Arcaini *et al.*, 2006; Kharfan-Dabaja *et al.*, 2011; Komrokji *et al.*, 2012). The SA detection cycle is short, and the cost is

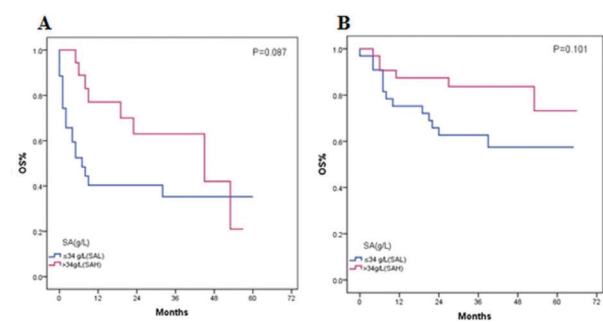


Figure 7. Comparison of 3-year OS between SA $>$ 34 g/L and SA \leq 34 g/L patients. (A) CHOP-like treatment group; (B) R-CHOP like treatment group.

low, which can cover the population in remote areas. At the same time, SA is also a stable biomarker. A previous study showed that the 3-year OS in patients with SA levels >34 g/L before chemotherapy was significantly higher than low SA (Eatrudes *et al.*, 2015), which was consistent with our current finding. SA levels before chemotherapy are an independent prognostic risk factor for DLBCL. After chemotherapy, patients with low SA had shorter OS. CHOP like and R-CHOP-like treated patients with low SA had shorter OS than patients with high SA.

Evaluation of SA concentration predictive efficacy

The chi-square test showed a difference in CR between the two groups of SA that the short-term efficacy of low SA was poor. The long-term efficacy evaluation of COX regression showed that patients with low SA had significantly shorter PFS/OS than high SA patients. Patients with SA sustained >34 g/L before the second chemotherapy had longer OS than patients with SA sustained ≤ 34 g/L. Before the initial chemotherapy, patients with SA >34 g/L had higher OS than patients with SA ≤ 34 g/L and were not affected by SA changes before the second chemotherapy.

Limitations

There were some limitations in this study. Firstly, this is a retrospective clinical analysis and should eliminate mutual interference between effective factors by using multivariate analysis. Secondly, as a limited case number was involved in this study, a comparison of chemotherapy courses was not performed among these patients. Thirdly, the patients with the CHOP regimen had a very high population in this study, while the current chemotherapy is commonly applied with the R-CHOP regimen. Therefore, further investigations among DLBCL patients who received R-CHOP should be required to provide the guidance for the current clinical settings. Last but not least, as this is a single-center retrospective study, further studies with multi-center with larger sample size can help reinforce our current findings.

CONCLUSION

Before the initial chemotherapy, high SA patients had a longer 3-year OS than the low SA group. Pre-chemotherapy SA is an independent prognostic risk

factor for patients with DLBCL. This study indicates that the CR and NRR of SA \leq 34 g/L patients will be significantly lower than that of SA>34 g/L patients. In addition, the R-CHOP-like regimen may help improve low and high SA patients 3-year OS.

Declarations

Funding. None.

Conflict of Interest. The authors declare that they have no competing interests.

Authorship. LC and TL were involved in the guarantor of integrity of the entire study, study design and manuscript review; LC was dedicated to design concepts, definition of intellectual content, literature research, clinical studies, experimental studies, data acquisition, data analysis, statistical analysis, manuscript preparation and manuscript editing, LP performed study design, manuscript editing and manuscript review. All authors have read and approved this article.

REFERENCES

- Arcaini L, Lazzarino M, Colombo N, Burcheri S, Boveri E, Paulli M, Morra E, Gambacorta M, Cortelazzo S, Tucci A, Ungari M, Ambrosetti A, Menestrina F, Orsucci L, Noviero D, Pulsoni A, Frezzato M, Gaidano G, Vallisa D, Minardi V, Tripodo C, Callea V, Baldini L, Merli F, Federico M, Franco V, Iannitto E, Intergroup Italiano Linfomi (2006) Splenic marginal zone lymphoma: a prognostic model for clinical use. *Blood* **107**: 4643–4649. <https://doi.org/10.1182/blood-2005-11-4659>
- Cheson BD, Pfistner B, Juweid ME, Gascoyne RD, Specht L, Horning SJ, Coiffier B, Fisher RI, Hagenbeek A, Zucca E, Rosen ST, Stroobants S, Lister TA, Hoppe RT, Dreyling M, Tobinai K, Vose JM, Connors JM, Federico M, Diehl V, International Harmonization Project on Lymphoma (2007) Revised response criteria for malignant lymphoma. *J Clin Oncol* **25**: 579–586. <https://doi.org/10.1200/JCO.2006.09.2403>
- Chihara D, Oki Y, Ine S, Yamamoto K, Kato H, Taji H, Kagami Y, Yatabe Y, Nakamura S, Morishima Y (2009) Analysis of prognostic factors in peripheral T-cell lymphoma: prognostic value of serum albumin and mediastinal lymphadenopathy. *Leuk Lymphoma* **50**: 1999–2004. <https://doi.org/10.3109/10428190903318311>
- Coiffier B, Lepage E, Briere J, Herbrecht R, Tilly H, Bouabdallah R, Morel P, Van Den Neste E, Salles G, Gaulard P, Reyes F, Lederlin P, Gisselbrecht C (2002) CHOP chemotherapy plus rituximab compared with CHOP alone in elderly patients with diffuse large-B-cell lymphoma. *New Engl J Med* **346**: 235–242. <https://doi.org/10.1056/NEJMoa011795>
- Coiffier B, Thieblemont C, Van Den Neste E, Lepeu G, Plantier I, Castaigne S, Lefort S, Marit G, Macro M, Sebban C, Belhadi K, Bordessoule D, Fermé C, Tilly H (2010) Long-term outcome of patients in the LNH-98.5 trial, the first randomized study comparing rituximab-CHOP to standard CHOP chemotherapy in DLBCL patients: a study by the Groupe d'Etudes des Lymphomes de l'Adulte. *Blood* **116**: 2040–2045. <https://doi.org/10.1182/blood-2010-03-276246>
- Dalia S, Chavez J, Little B, Bello C, Fisher K, Lee JH, Chervenick P, Sokol L, Sotomayor E, Shah B (2014) Serum albumin retains independent prognostic significance in diffuse large B-cell lymphoma in the post-rituximab era. *Ann Hematol* **93**: 1305–1312. <https://doi.org/10.1007/s00277-014-2031-2>
- Eatrides J, Thompson Z, Lee JH, Bello C, Dalia S (2015) Serum albumin as a stable predictor of prognosis during initial treatment in patients with diffuse large B cell lymphoma. *Ann Hematol* **94**: 357–358. <https://doi.org/10.1007/s00277-014-2150-9>
- Fmedsci Avhmdfffd, Frs Drhmf (2015) 51. *WHO Classification: Tumours of the Haematopoietic and Lymphoid Tissues* (2008). John Wiley & Sons, Ltd
- Hans CP, Weisenburger DD, Greiner TC, Gascoyne RD, Delabie J, Ott G, Müller-Hermelink HK, Campo E, Brazier RM, Jaffe ES, Pan Z, Farinha P, Smith LM, Falini B, Banham AH, Rosenwald A, Staudt LM, Connors JM, Armitage JO, Chan WC (2004) Confirmation of the molecular classification of diffuse large B-cell lymphoma by immunohistochemistry using a tissue microarray. *Blood* **103**: 275–282. <https://doi.org/10.1182/blood-2003-05-1545>
- Huang CE, Chen YY, Lu CH, Chen PT, Lee KD, Chen CC (2015) Validation of an enhanced International Prognostic Index (NCCN-IPI) in an Asian cohort of patients with diffuse large B cell lymphoma. *Ann Hematol* **94**: 1063–1065. <https://doi.org/10.1007/s00277-014-2293-8>
- International Non-Hodgkin's Lymphoma Prognostic Factors Project (1993) A predictive model for aggressive non-Hodgkin's lymphoma. *N Engl J Med* **329**: 987–994. <https://doi.org/10.1056/NEJM199309303291402>
- Kharfan-Dabaja MA, Chavez JC, Yu D, Zhu W, Fernandez-Vertiz EI, Perkins J, Shapiro J, Bookout R, Perez L, Fernandez HF, Komrokji RS, Lancet J, Brand L, Field T, Ayala E, Janssen W, List AF, Anasetti C (2011) Severe hypoalbuminemia at day 90 predicts worse nonrelapse mortality and overall survival after allogeneic hematopoietic stem cell transplantation for acute myelogenous leukemia and myelodysplastic syndrome. *Biol Blood Marrow Tr* **17**: 384–393. <https://doi.org/10.1016/j.bbmt.2010.07.011>
- Komrokji RS, Corrales-Yepez M, Kharfan-Dabaja MA, Al Ali NH, Padron E, Rollison DE, Pinilla-Ibarz J, Zhang L, Epling-Burnette PK, Lancet JE, List AF (2012) Hypoalbuminemia is an independent prognostic factor for overall survival in myelodysplastic syndromes. *Am J Hematol* **87**: 1006–1009. <https://doi.org/10.1002/ajh.23303>
- Lamy T, Damaj G, Soubeyran P, Gyan E, Cartron G, Bouabdallah K, Gressin R, Cornillon J, Banos A, Le Du K, Benchalal M, Moles MP, Le Gouill S, Fleury J, Godmer P, Maisonneuve H, Deconinck E, Houot R, Laribi K, Marolleau JP, Tournilhac O, Branger B, Devillers A, Vuillez JP, Fest T, Colombat P, Costes V, Szablewski V, Béné MC, Delwail V, LYSA Group (2018) R-CHOP 14 with or without radiotherapy in nonbulky limited-stage diffuse large B-cell lymphoma. *Blood* **131**: 174–181. <https://doi.org/10.1182/blood-2017-07-793984>
- Li S, Young KH, Medeiros LJ (2018) Diffuse large B-cell lymphoma. *Pathology* **50**: 74–87. <https://doi.org/10.1016/j.pathol.2017.09.006>
- Melchardt T, Troppan K, Weiss L, Hufnagl C, Neureiter D, Tränkschuh W, Hopfinger G, Magnes T, Deutsch A, Neumeister P, Hackl H, Greil R, Pichler M, Egle A (2015) A modified scoring of the NCCN-IPI is more accurate in the elderly and is improved by albumin and beta2-microglobulin. *British J Haematol* **168**: 239–245. <https://doi.org/10.1111/bjh.13116>
- Miyaoka M, Kikuti YY, Carreras J, Ikoma H, Hiraiwa S, Ichiki A, Kojima M, Ando K, Yokose T, Sakai R, Hoshikawa M, Tomita N, Miura I, Takata K, Yoshino T, Takizawa J, Bea S, Campo E, Nakamura N (2018) Clinicopathological and genomic analysis of double-hit follicular lymphoma: comparison with high-grade B-cell lymphoma with MYC and BCL2 and/or BCL6 rearrangements. *Mod Pathol* **31**: 313–326. <https://doi.org/10.1038/modpathol.2017.134>
- Ngo L, Hee SW, Lim LC, Tao M, Quek R, Yap SP, Loong EL, Sng I, Hwan-Cheong TL, Ang MK, Ngeow J, Tham CK, Tan MH, Lim ST (2008) Prognostic factors in patients with diffuse large B cell lymphoma: Before and after the introduction of rituximab. *Leuk Lymphoma* **49**: 462–469. <https://doi.org/10.1080/10428190701809156>
- Pfreundschuh M, Trümper L, Osterborg A, Pettengell R, Trneny M, Imrie K, Ma D, Gill D, Walewski J, Zinzani PL, Stahl R, Kvaloy S, Shpilberg O, Jaeger U, Hansen M, Lehtinen T, López-Guillermo A, Corrado C, Scheliga A, Milpied N, Mendila M, Rashford M, Kuhnt E, Loeffler M, MabThera International Trial Group (2006) CHOP-like chemotherapy plus rituximab versus CHOP-like chemotherapy alone in young patients with good-prognosis diffuse large-B-cell lymphoma: a randomised controlled trial by the MabThera International Trial (MInT) Group. *Lancet Oncol* **7**: 379–391. [https://doi.org/10.1016/S1470-2045\(06\)70664-7](https://doi.org/10.1016/S1470-2045(06)70664-7)
- Salles G, De Jong D, Xie W, Rosenwald A, Chhanabhai M, Gaulard P, Klapper W, Calaminici M, Sander B, Thoms C, Campo E, Molina T, Lee A, Pfreundschuh M, Horning S, Lister A, Sehn LH, Rasmack J, Hagenbeek A, Gascoyne RD, Weller E (2011) Prognostic significance of immunohistochemical biomarkers in diffuse large B-cell lymphoma: a study from the Lunenburg Lymphoma Biomarker Consortium. *Blood* **117**: 7070–7078. <https://doi.org/10.1182/blood-2011-04-345256>
- Sehn LH, Berry B, Chhanabhai M, Fitzgerald C, Gill K, Hoskins P, Klasa R, Savage KJ, Shenker T, Sutherland J, Gascoyne RD, Connors JM (2007) The revised international prognostic index (R-IPI) is a better predictor of outcome than the standard IPI for patients with diffuse large B-cell lymphoma treated with R-CHOP. *Blood* **109**: 1857–1861. <https://doi.org/10.1182/blood-2006-08-038257>
- Sehn LH, Donaldson J, Chhanabhai M, Fitzgerald C, Gill K, Klasa R, MacPherson N, O'Reilly S, Spinelli JJ, Sutherland J, Wilson KS, Gascoyne RD, Connors JM (2005) Introduction of combined CHOP plus rituximab therapy dramatically improved outcome of diffuse large B-cell lymphoma in British Columbia. *J Clin Oncol* **23**: 5027–5033. <https://doi.org/10.1200/JCO.2005.09.137>
- von Elm E, Altman DG, Egger M, Pocock SJ, Göttsche PC, Vandenbroucke JP, STROBE Initiative (2007) The Strengthening the Reporting of Observational Studies in Epidemiology (STROBE) statement: guidelines for reporting observational studies. *Ann Intern Med* **147**: 573–577. <https://doi.org/10.7326/0003-4819-147-8-200710160-00010>
- Watanabe T, Kinoshita T, Itoh K, Yoshimura K, Ogura M, Kagami Y, Yamaguchi M, Kurosawa M, Tsukasaki K, Kasai M, Tobinai K,

- Kaba H, Mukai K, Nakamura S, Ohshima K, Hotta T, Shimoyama M (2010) Pretreatment total serum protein is a significant prognostic factor for the outcome of patients with peripheral T/natural killer-cell lymphomas. *Leuk Lymphoma* **51**: 813–821. <https://doi.org/10.3109/10428191003721359>
- Wei XL, Zheng JX, Zhang ZW, Liu QZ, Zhan ML, Huang WM, Chen JJ, Wei Q, Wei YQ, Feng R. (2021) Consecutive hypoalbuminemia predicts inferior outcome in patients with diffuse large B-cell lymphoma. *Front Oncol* **10**: 3167. <https://doi.org/10.3389/fonc.2020.610681>
- Zhou Z, Sehn LH, Rademaker AW, Gordon LI, Lacasce AS, Crosby-Thompson A, Vanderplas A, Zelenetz AD, Abel GA, Rodriguez MA, Nademane A, Kaminski MS, Czuczman MS, Milenson M, Niland J, Gascoyne RD, Connors JM, Friedberg JW, Winter JN (2014) An enhanced International Prognostic Index (NCCN-IPi) for patients with diffuse large B-cell lymphoma treated in the rituximab era. *Blood* **123**: 837–842. <https://doi.org/10.1182/blood-2013-09-524108>
- Zhu YJ, Huang JJ, Xia Y, Zhao W, Jiang WQ, Lin TY, Huang HQ, Li ZM (2011) Primary mediastinal large B-cell lymphoma (PM-LBCL) in Chinese patients: clinical characteristics and prognostic factors. *Int J Hematol* **94**: 178–184. <https://doi.org/10.1007/s12185-011-0898-4>
- Ziepert M, Hasenclever D, Kuhnt E, Glass B, Schmitz N, Pfreundschuh M, Loeffler M (2010) Standard International prognostic index remains a valid predictor of outcome for patients with aggressive CD20+ B-cell lymphoma in the rituximab era. *J Clin Oncol* **28**: 2373–2380. <https://doi.org/10.1200/JCO.2009.26.2493>

Imiquimod-induced psoriasis model: induction protocols, model characterization and factors adversely affecting the model

Manahel Mahmood Alsabbagh 

College of Medicine and Medical Sciences, Arabian Gulf University, Manama 329, Kingdom of Bahrain

Imiquimod-induced psoriasis is widely-employed to study disease pathogenesis and to screen drugs. While the original protocol was published more than a decade ago and has been rigorously used in research since then, a modified protocol was described recently with several advantages including milder systemic manifestations although the disease morphology is highly conserved. Being a toll-like receptor 7 and 8 agonist, IL-23/IL-17 axis predominates in imiquimod-induced psoriasis. In addition, different immunocytes were described to aggravate or suppress the disease. This article aims to review the currently available protocols of imiquimod-induced psoriasis *in vivo*, to characterize the model as described in literature and to define the five important independent factors adversely influencing the model which researchers should pay attention to.

Keywords: animal model, B-cell, IL-17, IL-23, imiquimod-induced psoriasis, T-cell

Received: 14 July, 2022; **revised:** 15 May, 2023; **accepted:** 18 July, 2023; **available on-line:** 22 November, 2023

 e-mail: mms080138@rcsi.com

Abbreviations: PASI, Psoriasis Area and Severity Index

INTRODUCTION

Animal models of psoriasis are categorized into four categories: the first category represents models resulting from spontaneous mutations, such as homozygous asbeia (*Scd1^{ab}/Scd1^{ab}*) and flaky skin (*Ttc^{fsn}/Ttc^{fsn}*) mice where the latter model shares with human psoriasis acanthosis, parakeratosis, and corneal neutrophils infiltration. The second category represents genetically-engineered models where epidermal proteins like keratins and/or cytokines are modified to produce features resembling psoriasis. The third category includes humanized models or models generated by xenotransplantation where lesional skin biopsy or skin equivalent is transplanted to mice. A recently-described but frequently used model is the directly induced model, where imiquimod is used to produce an immunological reaction resembling the one seen in psoriasis, largely mediated by IL-23/IL-17 axis and TNF- α (Guerrero-Aspizua *et al.*, 2020; Jean & Pouliot, 2010; Jeong & Lee, 2018).

This article aims to review the model of imiquimod-induced psoriasis, highlighting the currently published two induction protocols and characterizing the model in terms of dominant cytokines and cellular infiltrate. It also tackles the five factors that may influence disease modelization.

THE ORIGINAL AND MODIFIED PROTOCOLS OF IMIQUIMOD-INDUCED PSORIASIS

Imiquimod was first described in the mid-1990s as an immunomodulatory agent that augments the innate and adaptive immune systems. It is a toll-like receptor-7 and 8 agonist. It obtained the US Food and Drug Administration approval to treat anogenital warts, facial actinic keratoses and superficial basal cell carcinoma (Hanna *et al.*, 2016). Topical application of imiquimod may induce psoriasis (Wu & Strutton, 2004).

Van der Fits and others (van der Fits *et al.*, 2009) were the first to employ imiquimod to modelize psoriasis *in vivo*. They applied 62.5 mg of imiquimod 5% cream (Aldara) daily, equivalent to 3.125 mg of active ingredient, on the shaved back and right ear of BALB/c and C57BL/6 mice for five or six consecutive days and they assessed the severity of psoriasis using modified Psoriasis Area and Severity Index (PASI). Signs of psoriasis start to appear within the first three days and severity steadily increases till the end of the experiment. Authors reported lack of difference between the two strains of mice. Imiquimod-treated skin shows the cardinal histopathological features of psoriasis such as acanthosis (Singh *et al.*, 2019), parakeratosis and hypogranulosis. Immunohistochemical staining shows infiltration of dendrocytes, neutrophils and CD4⁺ cells. Imiquimod also induces IL-23 and augments IL-17A, IL-17F and IL-22 production (van der Fits *et al.*, 2009).

Horvath and others (Horvath *et al.*, 2019) further modified the original protocol. They applied 25 mg of imiquimod 5% cream in Finn chambers on the back of C57BL/6 mice daily. This protocol results in erythema after the second application and scaling and skin thickening after the third application. The modified protocol was reported to be comparable to the original one. On histological examination, features of psoriasis such as parakeratosis, acanthosis, Munro microabscesses and dilated blood vessels in the dermal papillae were observed among both groups. Consistently, immunohistochemical examination reveals overexpression of Ki-67 in both. However, the modified protocol minimizes systemic manifestations and allows for prolonged imiquimod treatments.

Imiquimod-induced psoriasis model is largely used to study disease pathogenesis and to screen drugs. The model was employed for drug screening in more than 100 publications. In the majority of studies, the experimental drug of interest was administered concurrently on the same day of psoriasis induction. In a limited number of studies, it was started a few days before (1–21 days) or after induction. Regarding the protocol of induction, majority of studies complied with the original duration described as five or six consecutive days; few, however,

er, applied the cream for shorter (three to four days) or longer periods (vast majority for seven days, up to 15 days). Prolonged daily application of imiquimod cream results in tachyphylaxis where Ki-67 expression diminishes in alignment with spontaneous attenuation and disappearance of erythema and scaling at three to four weeks despite continuous application of the cream (Kataoka *et al.*, 2018).

Some studies lack a positive control; but where a positive control was used, it is a topical or systemic preparation that matches the route of administration of the experimental agent. Topical control preparations include betamethasone, calcipotriol, clobetasol, dexamethasone, dithranol, methotrexate and tacrolimus. Systemic control preparations include cyclosporine orally, dexamethasone orally and intraperitoneally, etanercept, methotrexate orally and intraperitoneally and tacrolimus.

CHARACTERIZATION OF IMIQUIMOD-INDUCED PSORIASIS MODEL

Jabeen and others (Jabeen *et al.*, 2020) characterized the model of imiquimod-induced psoriasis where they applied 62.5 mg of imiquimod 5% cream for eight days. Cutaneous concentration of imiquimod approaches 100 µg/g on day 2 and it doubles by six folds on day 8 corresponding with a pronounced worsening of redness, thickness, scaling and total modified PASI. Acanthosis is evident on day 8 compared with day 2, explaining the clinically apparent thickness. Dermal hypervascularity is also marked, explaining the progressive redness. In terms of cytokine profile, elevation of IL-1 β , IL-6 and IL-17A was observed in skin and TNF- α and IL-17A in serum. Disease progression associates with elongation of spleen, enlargement of total area of lymph nodes, and loss of weight independently of food intake (Zhang *et al.*, 2020).

Macrophages and dendrocytes were investigated in the current model of psoriasis. While plasmacytoid dendrocytes are absent in imiquimod-induced lesions, the model shows a biphasic cellular behaviour. During the early phase, neutrophils infiltrate the epidermis and monocytes predominate in the dermis. Whereas in the late phase, Langerhans cells are pronounced in the epidermis and macrophages in the dermis. Depletion of Langerhans cells results in massive neutrophil infiltrate during the late phase, suggesting a potential anti-inflammatory role of Langerhans cells (Terhorst *et al.*, 2015). On the contrary (Xiao *et al.*, 2017) concluded that Langerhans cell depletion attenuates psoriasis and downregulates psoriasis-associated cytokine gene expression. (Lee *et al.*, 2018) found that resident and monocyte-derived Langerhans cells secrete IL-23. Depletion of these cells inhibits IL-22 and IL-17A secretion (Lee *et al.*, 2018), diminishes gamma-delta T-cell infiltration (Lee, 2016) and ultimately, attenuates psoriasis (Lee *et al.*, 2018). Parallely (Yoshiki *et al.*, 2014) found IL-23-secreting Langerhans cells to induce IL-17A-producing gamma-delta T-cells. Depletion of Langerhans cells decreases Th-17-related cytokines and ameliorates psoriasis. In contrast, Kusuba and others (Kusuba *et al.*, 2016) found that depletion of neutrophils early during psoriasis induction inhibits the infiltration of dermal monocytes, whereas depletion of both, neutrophils and monocytes, significantly attenuates psoriasis (Kusuba *et al.*, 2016).

While IL-17 receptor is expressed on different cells, including T-cells and keratinocytes, its importance is cell-specific. For instance, deletion of keratinocyte's IL-17 receptor reduces neutrophil infiltration and abolishes

psoriasis; yet, this is not the case with T-cell-expressed receptor, emphasizing on keratinocytes' role in neutrophil chemoattraction (Moos *et al.*, 2019). Likewise, IL-17 abrogation inhibits imiquimod-induced psoriasis (Ha *et al.*, 2013). On the contrary (El Malki *et al.*, 2013) found that in IL-17A receptor-knockout mice, imiquimod may still induce psoriasis independently of IL-17 pathway. The C-X-C motif chemokine receptor type-2 is involved in neutrophil chemoattraction as well. It promotes neutrophil-produced leukotriene-B₄ and augments neutrophil chemotaxis and infiltration (Sumida *et al.*, 2014). Likewise, kallikrein-related peptidase-8 is elevated in psoriasis. If knocked out, the severity of imiquimod-induced psoriasis is comparable to wildtype, however, lesions lack neutrophil microabscesses (Iinuma *et al.*, 2015).

IL-1 and IL-36 α chemoattract neutrophils. Both molecules mediate human generalized pustular psoriasis which is accompanied by systemic symptoms such as fever and malaise. In the current model of psoriasis, mice also display systemic symptoms such as weight loss and generalized malaise, suggesting the contribution of IL-1 and IL-36 α to model development. Deficiency of IL-1 receptor-1 or IL-36 α variably attenuates psoriasis; however, deficiency of both absolutely abolishes the disease (Alvarez & Jensen, 2016). IL-36 role is further verified in IL-36 receptor-knockout mice where these are resistant to imiquimod (Goldstein *et al.*, 2019).

Imiquimod-treated mice exhibit antihistamine-resistant itching that is largely driven by μ -opioid receptor located in the epidermis, the dorsal root ganglia, and the spinal cord. In alignment, naloxone, a μ -opioid antagonist successfully inhibits itching in imiquimod-treated mice (Takahashi *et al.*, 2017). Itching is also mediated by sphingosine 1-phosphate receptor-3, which if knocked out, scratching behaviour improves (Hill *et al.*, 2020). In addition, Oishi and others (Oishi *et al.*, 2019) found imiquimod treatment to associate with expansion of mastocytes and overexpression of the nerve growth factor, the neurotrophic factor neurotrophin 3 and enkephalin precursor preproenkephalin (Oishi *et al.*, 2019).

REGULATION OF IMIQUIMOD-INDUCED PSORIASIS

Imiquimod-induced psoriasis is negatively regulated by B-cells (Yanaba *et al.*, 2013), regulatory T-cells (Choi *et al.*, 2020; Oka *et al.*, 2017), matrix remodelling associated-7 (Ning *et al.*, 2018), indoleamine 2, 3-dioxygenase 2 (Elizei *et al.*, 2018; Fujii *et al.*, 2020), IFN regulatory factor-2 (Kawaguchi *et al.*, 2018), IFN regulatory factor-5 (Nakao *et al.*, 2020), dermokine β/γ (Tokuriki *et al.*, 2016), IL-10 (Jin *et al.*, 2018), IL-27 (Chen *et al.*, 2017; Shibata *et al.*, 2013), poly(ADP-ribose) polymerase-1 (Kiss *et al.*, 2020), endogenous n-3 polyunsaturated fatty acids (Qin *et al.*, 2014), L-selectin and ICAM-1 (Mitsui *et al.*, 2015).

The regulatory role of B-cells, regulatory T-cells and IL-10 is evident in different studies. In a model of CD19^{-/-} mice, exacerbation of psoriasis is attributed to the loss of IL-10-secreting regulatory B-cell subset (Yanaba *et al.*, 2013). Likewise, depletion of regulatory T-cells disturbs the closely regulated gamma-delta T-cells, augments TNF- α and IL-17A secretion and aggravates the disease (Choi *et al.*, 2020). Neutralization of IL-10 in imiquimod-induced psoriasis promotes epidermal thickening, increases neutrophil infiltration and accentuates IL-23/IL-17 axis (Xu *et al.*, 2018). Likewise, knocking out IL-10 aggravates psoriasis macroscopically and mi-

croscopically, emphasising on its anti-inflammatory role in the disease (Jin *et al.*, 2018).

FACTORS INFLUENCING IMIQUIMOD-INDUCED PSORIASIS

Five factors adversely modify the model of imiquimod-induced psoriasis: the brand of imiquimod 5% cream, mouse strain, mouse sex, stress and obesity.

The brand of the commercially available imiquimod 5% cream may interfere with the model. While (Singh *et al.*, 2019) claimed generic formulations of imiquimod to produce a psoriasiform inflammation that is comparable to Aldara, Luo and others (Luo *et al.*, 2016) found that in comparison with Aldara, Likejé creams mediates a milder form of psoriasis with a modified PASI of 3.25 ± 1.56 (compared with 9.81 ± 0.84 in Aldara), a less pronounced acanthosis with a Backer's score of 2.93 ± 1.07 (compared with 6.47 ± 1.50 in Aldara) and an epidermal thickness of $49.79 \pm 14.16 \mu\text{m}$ (compared with $85.62 \pm 17.55 \mu\text{m}$ in Aldara), concluding that different brands may adversely affect the successful establishment of the model (Luo *et al.*, 2016).

In terms of the employed strain of mice, although van der Fits and others (van der Fits *et al.*, 2009) described their protocol in two different strains, (Swindell *et al.*, 2017) reported variation in modelization across six different strains of mice using a five-day course of 62.5 mg imiquimod 5% cream (Aldara). Microarray showed gene expression of imiquimod-induced psoriasis to largely overlap with that of human psoriasis. C57BL/6 mice, in particular, show the highest consistency, in contrast to MOLF/Eij and 129X1/Sv mice where gene expression is opposite to human psoriasis. In terms of IL-17 gene expression, C57BL/6 mice highly express IL-17A, IL-17B, IL-17C and IL-17F. D'Souza and others (D'Souza *et al.*, 2020) examined the psoriatic changes induced by imiquimod in two different strains: BALB/c and the Swiss mice and concluded that imiquimod induces psoriatic changes macroscopically and microscopically among both strains, although these are more pronounced in the Swiss mice.

In terms of sex differences, and compared with male mice, female mice develop severe psoriasis in response to imiquimod, resulting in a greater weight loss, significant distress and unexpected early death. Inductions in females may also mandate euthanization (Alvarez & Jensen, 2016). In contrast, the influence of patient's sex on the severity of psoriasis is controversial. While female patients were found to significantly display milder psoriasis than male patients in two studies conducted in Swaziland and Sweden (Guillet *et al.*, 2022; Hagg *et al.*, 2017), this was contradicted by a third study (Goldburg *et al.*, 2022).

Wang and others (Wang *et al.*, 2020) investigated the effect of stress on imiquimod-induced psoriasis in a model of mice with emotional stress. In comparison with a control group with psoriasis kept off stress, stress was found to prolong the disease, to upregulate IL-1 β , IL-17 and IL-22 gene expression and to increase IL-1 β , IL-12, IL-17 and IL-22 secretion. This should further explain the role of stress in human psoriasis. For instance, stressful events were found to proceed psoriasis onset and were reported to trigger the disease in 31–88% of patients. Stress was also observed to aggravate psoriasis where daily stressors may expand the disease and worsens pruritus (Rigas *et al.*, 2019; Rousset & Halioua, 2018). This is evident in pediatrics as well, where child-

hood trauma is commoner in patients with psoriasis, and likewise, children with psoriasis score higher in anxiety scores (Wintermann *et al.*, 2022).

Obesity is known to exacerbate psoriasis in humans. This is also evident in imiquimod-induced psoriasis model where obese mice display thicker psoriatic lesions compared with non-obese subjects. Diet restriction partially improves psoriasis and cytokine profile (Hong *et al.*, 2019; Kanemaru *et al.*, 2015) and consistently, leptin deficiency attenuates the disease (Stjernholm *et al.*, 2017). The relationship between human psoriasis and obesity was vigorously studied. A meta-analysis found the odd ratio of obesity in psoriasis is 1.66, and it can approach 2.23 in patients with severe disease (Armstrong *et al.*, 2012). A systematic review did also conclude that seven out of nine studies found a statistically significant association between increased psoriasis severity and increased body mass index (Fleming *et al.*, 2015). Such an association is attributed to a shared mechanism involving inflammatory mediators and adipokines (Jensen & Skov, 2016).

CONCLUSIONS

Imiquimod-induced psoriasis serves as an acceptable model to study IL-23/IL-17 axis and to screen pharmaceutical agents in psoriasis. While the model could be induced using two protocols, the original protocol described by van der Fits and others (van der Fits *et al.*, 2009) is widely employed in different studies. To ensure consistency of results, researchers should take into account that variation in the brand of imiquimod 5% cream, strain of mice, sex of mice, exposure to stress and obesity may adversely modify the course of disease.

Declarations

Interest statement. Author declares no conflict of interest.

REFERENCES

- Alvarez P, Jensen LE (2016) Imiquimod treatment causes systemic disease in mice resembling generalized pustular psoriasis in an IL-1 and IL-36 dependent manner. *Mediators Inflamm* 2016: 6756138. <https://doi.org/10.1155/2016/6756138>
- Armstrong AW, Harskamp CT, Armstrong EJ (2012) The association between psoriasis and obesity: a systematic review and meta-analysis of observational studies. *Nutr Diabetes* 2: e54. <https://doi.org/10.1038/nutd.2012.26>
- Chen W, Gong Y, Zhang X, Tong Y, Wang X, Fei C, Xu H, Yu Q, Wang Y, Shi Y (2017) Decreased expression of IL-27 in moderate-to-severe psoriasis and its anti-inflammation role in imiquimod-induced psoriasis-like mouse model. *J Dermatol Sci* 85: 115–123. <https://doi.org/10.1016/j.jdermsci.2016.11.011>
- Choi CW, Kim BR, Yang S, Kim Y, Kang JS, Youn SW (2020) Regulatory T cells suppress skin inflammation in the imiquimod-induced psoriasis-like mouse model. *J Dermatol Sci* 98: 199–202. <https://doi.org/10.1016/j.jdermsci.2020.04.008>
- D'Souza L, Badanthadka M, Salwa F (2020) Effect of animal strain on model stability to imiquimod-induced psoriasis. *Indian J Physiol Pharmacol* 64: 83–91
- El Malki K, Karbach SH, Huppert J, Zayoud M, Reissig S, Schuler R, Nikolaev A, Karraam K, Munzel T, Kuhlmann CR, Luhmann HJ, von Stebut E, Wortge S, Kurschus FC, Waisman A (2013) An alternative pathway of imiquimod-induced psoriasis-like skin inflammation in the absence of interleukin-17 receptor signaling. *J Invest Dermatol* 133: 441–451. <https://doi.org/10.1038/jid.2012.318>
- Elizei SS, Pakyari M, Ghoreishi M, Kilani R, Mahmoudi S, Ghahary A (2018) IDO-expressing fibroblasts suppress the development of imiquimod-induced psoriasis-like dermatitis. *Cell Transplant* 27: 557–570. <https://doi.org/10.1177/0963689718757482>
- Fleming P, Kraft J, Gulliver WP, Lynde C (2015) The relationship of obesity with the severity of psoriasis: a systematic review. *J Cutan Med Surg* 19: 450–456. <https://doi.org/10.1177/1203475415586332>

- Fujii K, Yamamoto Y, Mizutani Y, Saito K, Seishima M (2020) Indoleamine 2,3-dioxygenase 2 deficiency exacerbates imiquimod-induced psoriasis-like skin inflammation. *Int J Mol Sci* **21**: 5515. <https://doi.org/10.3390/ijms21155515>
- Goldburg S, Chen R, Langholf W, Lafferty KP, Gooderham M, Jong EMd, Strober B (2022) Sex differences in moderate to severe psoriasis: analysis of the psoriasis longitudinal assessment and registry. *J Psoriasis Psoriatic Arthritis* **7**: 132–139. <https://doi.org/10.1177/24755303221099848>
- Goldstein J, Basso E, Palomo J, Rodriguez E, Gabay C (2019) IL-36 signaling in keratinocytes is mandatory in imiquimod-induced psoriasis in mice. *ARD* **78**: A1–A83. <https://doi.org/10.1136/annrheumdis-2018-EWRR2019.82>
- Guerrero-Aspizua S, Carretero M, Conti CJ, Del Rio M (2020) The importance of immunity in the development of reliable animal models for psoriasis and atopic dermatitis. *Immunol Cell Biol* **98**: 626–638. <https://doi.org/10.1111/imcb.12365>
- Guillet C, Seeli C, Nina M, Maul LV, Maul JT (2022) The impact of gender and sex in psoriasis: What to be aware of when treating women with psoriasis. *Int J Womens Dermatol* **8**: e010. <https://doi.org/10.1097/WJ9.0000000000000010>
- Ha H-L, Wang H, Pisitkun P, Kim J-C, Morasso M, Udey M, Siebenlist U (2013) Critical cell-type specific functions of the IL-17 receptor signaling adaptor CIKS/ACT1 in imiquimod-induced psoriasis. *Cytokine* **63**: 268
- Hagg D, Sundstrom A, Eriksson M, Schmitt-Egenolf M (2017) Severity of psoriasis differs between men and women: a study of the clinical outcome measure psoriasis area and severity index (PASI) in 5438 Swedish register patients. *Am J Clin Dermatol* **18**: 583–590. <https://doi.org/10.1007/s40257-017-0274-0>
- Hanna E, Abadi R, Abbas O (2016) Imiquimod in dermatology: an overview. *Int J Dermatol* **55**: 831–844. <https://doi.org/10.1111/ijd.13235>
- Hill RZ, Rifi Z, Vuong C, Bautista DM (2020) Loss of S1PR3 attenuates scratching behaviors in mice in the imiquimod model of psoriasis, but not in the MC903 model of atopic dermatitis. *Itch* **5**: e35
- Hong SM, Kim JU, Cho GJ, Jin WJ, Park SH, Park IH, Seol JE, Jung SY, Wang HY, Kim H (2019) Obesity exacerbates imiquimod-induced psoriasis by enhancing IL-6 production and Th17 cell differentiation in C57BL/6 mice. *프로그래밍(구조·조직)* **71**: 389 (in Korean)
- Horvath S, Komlodi R, Perkecz A, Pinter E, Gyulai R, Kemeny A (2019) Methodological refinement of Aldara-induced psoriasisform dermatitis model in mice. *Sci Rep* **9**: 3685. <https://doi.org/10.1038/s41598-019-39903-x>
- Iinuma S, Kishibe M, Saito N, Igawa S, Honma M, Takahashi H, Bando Y, Yoshida S, Iizuka H, Ishida-Yamamoto A (2015) Klr8 is required for microabscess formation in a mouse imiquimod model of psoriasis. *Exp Dermatol* **24**: 887–889. <https://doi.org/10.1111/exd.12794>
- Jabeen M, Boisgard AS, Danoy A, El Kholti N, Salvi JP, Bouliou R, Fromy B, Verrier B, Lamrayah M (2020) Advanced characterization of imiquimod-induced psoriasis-like mouse model. *Pharmaceutics* **12**. <https://doi.org/10.3390/pharmaceutics12090789>
- Jean J, Pouliot R (2010) *In vivo* and *in vitro* models of psoriasis. In Eberli D ed. *Tissue Engineering*. InTech
- Jensen P, Skov L (2016) Psoriasis and obesity. *Dermatology* **232**: 633–639. <https://doi.org/10.1159/000455840>
- Jeong I, Lee HJ (2018) Psoriasis skin models as promising tools in psoriasis research. *Biomed J Sci Tech Res* **2**. <https://doi.org/10.26717/BJSTR.2018.02.000760>
- Jin SP, Koh SJ, Yu DA, Kim MW, Yun HT, Lee DH, Yoon HS, Cho S, Park HS (2018) Imiquimod-applied Interleukin-10 deficient mice better reflects severe and persistent psoriasis with systemic inflammatory state. *Exp Dermatol* **27**: 43–49. <https://doi.org/10.1111/exd.13403>
- Kanemaru K, Matsuyuki A, Nakamura Y, Fukami K (2015) Obesity exacerbates imiquimod-induced psoriasis-like epidermal hyperplasia and interleukin-17 and interleukin-22 production in mice. *Exp Dermatol* **24**: 436–442
- Kataoka S, Yamamoto M, Ohko K, Nakajima K, Sano S (2018) Distinct kinetics of two pathologies induced in mice by topical treatment with imiquimod cream: Psoriasis-like inflammation and systemic autoimmunity. *J Dermatol Sci* **91**: 225–228. <https://doi.org/10.1016/j.jdermsci.2018.05.001>
- Kawaguchi M, Oka T, Sugaya M, Suga H, Kimura T, Morimura S, Fujita H, Sato S (2018) IRF-2 haploinsufficiency causes enhanced imiquimod-induced psoriasis-like skin inflammation. *J Dermatol Sci* **90**: 35–45. <https://doi.org/10.1016/j.jdermsci.2017.12.014>
- Kiss B, Szanto M, Hegedus C, Antal D, Szodenyi A, Marton J, Mehes G, Virag L, Szegedi A, Bai P (2020) Poly(ADP-ribose) polymerase-1 depletion enhances the severity of inflammation in an imiquimod-induced model of psoriasis. *Exp Dermatol* **29**: 79–85. <https://doi.org/10.1111/exd.14061>
- Lee M (2016) *Functional role of epidermal Langerhans cells in imiquimod-induced psoriasis-like dermatitis model* [Master's thesis]. Yonsei University
- Lee M, Kim SH, Kim TG, Park J, Lee JW, Lee MG (2018) Resident and monocyte-derived Langerhans cells are required for imiquimod-induced psoriasis-like dermatitis model. *J Dermatol Sci* **91**: 52–59. <https://doi.org/10.1016/j.jdermsci.2018.04.003>
- Luo DQ, Wu HH, Zhao YK, Liu JH, Wang F (2016) Original Research: Different imiquimod creams resulting in differential effects for imiquimod-induced psoriatic mouse models. *Exp Biol Med (Maywood)* **241**: 1733–1738. <https://doi.org/10.1177/1535370216647183>
- Mitsui A, Tada Y, Shibata S, Kamata M, Hau C, Asahina A, Sato S (2015) Deficiency of both L-selectin and ICAM-1 exacerbates imiquimod-induced psoriasis-like skin inflammation through increased infiltration of antigen presenting cells. *Clin Immunol* **157**: 43–55. <https://doi.org/10.1016/j.clim.2014.12.011>
- Moos S, Mohebiany AN, Waisman A, Kurschus FC (2019) Imiquimod-induced psoriasis in mice depends on the IL-17 signaling of keratinocytes. *J Invest Dermatol* **139**: 1110–1117. <https://doi.org/10.1016/j.jid.2019.01.006>
- Nakao M, Miyagaki T, Sugaya M, Sato S (2020) Exacerbated imiquimod-induced psoriasis-like skin inflammation in IRF5-deficient mice. *Int J Mol Sci* **21**: 3681. <https://doi.org/10.3390/ijms21103681>
- Ning J, Shen Y, Wang T, Wang M, Liu W, Sun Y, Zhang F, Chen L, Wang Y (2018) Altered expression of matrix remodelling associated 7 (MXRA7) in psoriatic epidermis: Evidence for a protective role in the psoriasis imiquimod mouse model. *Exp Dermatol* **27**: 1038–1042. <https://doi.org/10.1111/exd.13687>
- Kusuba N, Kitoh A, Miyachi Y, Kabashima K (2016) Role of neutrophils in the pathogenesis of imiquimod-induced psoriasis-like skin lesions. *J Dermatol Sci* **84**: e73
- Oishi N, Iwata H, Kambe N, Kobayashi N, Fujimoto K, Sato H, Hissaka A, Ueno K, Yamaura K (2019) Expression of precipitating factors of pruritus found in humans in an imiquimod-induced psoriasis mouse model. *Heliyon* **5**: e01981. <https://doi.org/10.1016/j.heliyon.2019.e01981>
- Oka T, Sugaya M, Takahashi N, Takahashi T, Shibata S, Miyagaki T, Asano Y, Sato S (2017) CXCL17 attenuates imiquimod-induced psoriasis-like skin inflammation by recruiting myeloid-derived suppressor cells and regulatory T cells. *J Immunol* **198**: 3897–3908. <https://doi.org/10.4049/jimmunol.1601607>
- Qin S, Wen J, Bai XC, Chen TY, Zheng RC, Zhou GB, Ma J, Feng JY, Zhong BL, Li YM (2014) Endogenous n-3 polyunsaturated fatty acids protect against imiquimod-induced psoriasis-like inflammation via the IL-17/IL-23 axis. *Mol Med Rep* **9**: 2097–2104. <https://doi.org/10.3892/mmr.2014.2136>
- Rigas HM, Bucur S, Ciurduc DM, Nita IE, Constantin MM (2019) Psychological stress and depression in psoriasis patients – a dermatologist's perspective. *Maedica (Bucur)* **14**: 287–291. <https://doi.org/10.26574/maedica.2019.14.3.287>
- Rousset L, Halioua B (2018) Stress and psoriasis. *Int J Dermatol* **57**: 1165–1172. <https://doi.org/10.1111/ijd.14032>
- Shibata S, Tada Y, Asano Y, Yanaba K, Sugaya M, Kadono T, Kanda N, Watanabe S, Sato S (2013) IL-27 activates Th1-mediated responses in imiquimod-induced psoriasis-like skin lesions. *J Invest Dermatol* **133**: 479–488. <https://doi.org/10.1038/ijd.2012.313>
- Singh TP, Zhang HH, Hwang ST, Farber JM (2019) IL-23- and imiquimod-induced models of experimental psoriasis in mice. *Curr Protoc Immunol* **125**: e71. <https://doi.org/10.1002/cpim.71>
- Sjernerholm T, Ommen P, Langkilde A, Johansen C, Iversen L, Rosada C, Stenderup K (2017) Leptin deficiency in mice counteracts imiquimod (IMQ)-induced psoriasis-like skin inflammation while leptin stimulation induces inflammation in human keratinocytes. *Exp Dermatol* **26**: 338–345. <https://doi.org/10.1111/exd.13149>
- Sumida H, Yanagida K, Kita Y, Abe J, Matsushima K, Nakamura M, Ishii S, Sato S, Shimizu T (2014) Interplay between CXCR2 and BLT1 facilitates neutrophil infiltration and resultant keratinocyte activation in a murine model of imiquimod-induced psoriasis. *J Immunol* **192**: 4361–4369. <https://doi.org/10.4049/jimmunol.1302959>
- Swindell WR, Michaels KA, Sutter AJ, Diaconu D, Fritz Y, Xing X, Sarkar MK, Liang Y, Tsoi A, Gudjonsson JE, Ward NL (2017) Imiquimod has strain-dependent effects in mice and does not uniquely model human psoriasis. *Genome Med* **9**: 24. <https://doi.org/10.1186/s13073-017-0415-3>
- Takahashi N, Tominaga M, Kosaka R, Kamata Y, Umehara Y, Matsuda H, Sakaguchi A, Ogawa H, Takamori K (2017) Involvement of micro-opioid receptors and kappa-opioid receptors in itch-related scratching behaviour of imiquimod-induced psoriasis-like dermatitis in mice. *Acta Derm Venereol* **97**: 928–933. <https://doi.org/10.2340/00015555-2704>
- Terhorst D, Chelbi R, Wohn C, Malosse C, Tamoutounour S, Sorquera A, Bajenoff M, Dalod M, Malissen B, Henri S (2015) Dynamics and transcriptomics of skin dendritic cells and macrophages in an imiquimod-induced, biphasic mouse model of psoriasis. *J Immunol* **195**: 4953–4961. <https://doi.org/10.4049/jimmunol.1500551>
- Tokuriki A, Chino T, Luong V, Oyama N, Higashi K, Saito K, Hasegawa M (2016) Dermokine β/γ deficiency enhances imiquimod-induced psoriasis-like inflammation. *J Dermatol Sci* **84**: e89–e180

- van der Fits L, Mourits S, Voerman JS, Kant M, Boon L, Laman JD, Cornelissen F, Mus AM, Florencia E, Prens EP, Lubberts E (2009) Imiquimod-induced psoriasis-like skin inflammation in mice is mediated via the IL-23/IL-17 axis. *J Immunol* **182**: 5836–5845. <https://doi.org/10.4049/jimmunol.0802999>
- Wang Y, Li P, Zhang L, Fu J, Di T, Li N, Meng Y, Guo J, Zhao J (2020) Stress aggravates and prolongs imiquimod-induced psoriasis-like epidermal hyperplasia and IL-1beta/IL-23p40 production. *J Leukoc Biol* **108**: 267–281. <https://doi.org/10.1002/JLB.3MA0320-363RR>
- Wintermann GB, Bierling AL, Peters EMJ, Abraham S, Beissert S, Weidner K (2022) Childhood trauma and psychosocial stress affect treatment outcome in patients with psoriasis starting a new treatment episode. *Front Psychiatry* **13**: 848708. <https://doi.org/10.3389/fpsyt.2022.848708>
- Wu JK, Siller G, Strutton G (2004) Psoriasis induced by topical imiquimod. *Australas J Dermatol* **45**: 47–50. <https://doi.org/10.1111/j.1440-0960.2004.00030.x>
- Xiao C, Zhu Z, Sun S, Gao J, Fu M, Liu Y, Wang G, Yao X, Li W (2017) Activation of Langerhans cells promotes the inflammation in imiquimod-induced psoriasis-like dermatitis. *J Dermatol Sci* **85**: 170–177. <https://doi.org/10.1016/j.jdermsci.2016.12.003>
- Xu X, Prens E, Florencia E, Boon L, Asmawidjaja P, Otten-Mus A-M, Lubberts E (2018) IL-10 Regulates skin thickness and scaling in imiquimod-induced psoriasis-like skin inflammation in mice. *Ann Rheum Dis* **77**: A1–A77
- Yanaba K, Kamata M, Ishiura N, Shibata S, Asano Y, Tada Y, Sugaya M, Kadono T, Tedder TF, Sato S (2013) Regulatory B cells suppress imiquimod-induced, psoriasis-like skin inflammation. *J Leukoc Biol* **94**: 563–573. <https://doi.org/10.1189/jlb.1112562>
- Yoshiki R, Kabashima K, Honda T, Nakamizo S, Sawada Y, Sugita K, Yoshioka H, Ohmori S, Malissen B, Tokura Y, Nakamura M (2014) IL-23 from Langerhans cells is required for the development of imiquimod-induced psoriasis-like dermatitis by induction of IL-17A-producing gammadelta T cells. *J Invest Dermatol* **134**: 1912–1921. <https://doi.org/10.1038/jid.2014.98>
- Zhang J, Yang X, Hong Qiu, Chen W (2020) Weight loss may be unrelated to dietary intake in the imiquimod-induced plaque psoriasis mice model. *Open Life Sci* **15**: 79–82

MicroRNA-508-3p regulates the proliferation of human lung cancer cells by targeting G1 to S phase transition 1 (GSPT1) protein

Xingyou Chen¹, Chen Feng², Jiliang Zha², Zihao Shen² and Wei Ji³✉

¹School of Medicine, Nantong University, Nantong, Jiangsu, 226007, China; ²Department of Thoracic Surgery, The Affiliated Hospital of Nantong University, Medical School of Nantong University, Nantong, Jiangsu, 226001, China; ³Department of Thoracic Surgery, Rudong People's Hospital, Nantong, Jiangsu, 226499, China

Purpose: Due to its crucial cancer regulatory role, microRNA-508-3p has been reported as a potential therapeutic anticancer molecular target. The present work encompassed the molecular characterization of microRNA-508-3p in lung cancer emphasizing on understanding the possible mechanism of its regulatory action. **Methods:** qRT-PCR was performed to estimate the relative gene expression of microRNA-508-3p in the tissue samples. The proliferation of cancer cells was determined by cell counting kit-8. The colony formation from cancer cells was analyzed by clonogenic assay. Mitotic phase distribution was understood by employing the flow cytometric technique. Edu-Hoechst staining was used for the assessment of cell viability. *In silico* analysis and dual-luciferase assay were used for target identification of microRNA-508-3p in lung cancer. Immunofluorescence and western blotting studies were carried out for relative protein expression. The rat models were used for performing the *in vivo* experimental procedures. **Results:** The study showed the significant down-regulation of microRNA-508-3p in lung cancer. The lower expression levels of microRNA-508-3p were shown to be associated with poor survival of lung cancer patients. The over-expression of microRNA-508-3p was found to decline the proliferation and viability of cancer cells together with the induction of mitotic cell cycle arrest at G1 by targeting G1 to S phase transition 1 (GSPT1) protein. MicroRNA-508-3p up-regulation inhibited the *in vivo* tumor growth in rat models. **Conclusion:** Our study identifies miR-508-3p as a pivotal regulator of lung cancer cell proliferation by targeting the GSPT1 protein. This highlights its potential as a tumor suppressor and a therapeutic target for lung cancer. Our findings offer mechanistic insights into miRNA-mediated cancer progression, prompting further research in this intricate regulatory network.

Keywords: Lung cancer, micro-RNA, proliferation, qRT-PCR, immunofluorescence staining, cell cycle arrest, G1 to S phase transition 1

Received: 11 February, 2023; **revised:** 26 September, 2023; **accepted:** 28 October, 2023; **available on-line:** 22 November, 2023

✉ e-mail: rdryjiwei@163.com

Abbreviations: 3'UTR, 3'-Untranslated region; eRF, 1Eukaryotic release factor 1; GSPT1, G1 to S phase transition 1; miRNA, MicroRNA; mRNA, Messenger RNA; qRT-PCR, Quantitative Real Time PCR; SCC, Esophageal squamous cell carcinoma

INTRODUCTION

Lung cancer is the most commonly diagnosed human cancer worldwide and accounts for the highest mortality

rate among both sexes of the human population at the global level (Thandra *et al.*, 2021; Malhotra *et al.*, 2016). On average, about 1.2 million new lung cancer cases are reported annually, worldwide (Cheng *et al.*, 2016). In 2018, more than 2 million lung cancer cases were diagnosed and the total number of deaths from lung cancer was 1.76 million (Bray *et al.*, 2018). Lung cancer has a very poor prognosis and the 5-year survival rates range between 10–20% making it a very destructive disorder (Hirsch *et al.*, 2017). In recent times, scientists have suggested an in-depth understanding of the molecular mechanics of lung cancer primarily aiming at the exploration of various genetic alterations to develop better prognostic and therapeutic measures against the severity of this dominant malignancy (Rong & Yang, 2018). In this regard, the research investigations apart from focusing on the protein-coding genes have laid considerable stress on the characterization of non-coding RNAs including micro-RNAs (miRNAs) for their cancer regulatory role (Bhan *et al.*, 2017).

The miRNAs include the class of very short, single-stranded and non-coding RNAs which typically regulate the gene expression in eukaryotes at post-transcriptional/translational level through mRNA degradation or by restraining the translation of eukaryotic genes through direct interaction with their 3'-untranslated region (3'-UTR; O'Brien *et al.*, 2018). The miRNAs have been reported to regulate the vital aspects of human physiology and have an important role in disease development. The miRNAs exhibit altered expression in many human cancers suggesting their possible role in cancer growth and proliferation (D'Angelo *et al.*, 2016). Several miRNAs were found to be dysregulated in lung cancer and these were proposed to act as prognostic biomarkers against lung cancer (Wu *et al.*, 2019). MicroRNA-508-3p (miRNA-508-3p) has been shown to regulate the tumor growth and proliferation of many human cancers like gastric and liver cancers (Shang *et al.*, 2016; Wu *et al.*, 2017). miR-508-3p exhibits reduced expression in cancer cells displaying resistance to treatment, which correlates with unfavorable survival outcomes (Zhao *et al.*, 2019). Additionally, diminished levels of miR-508-3p in breast cancer are linked to the occurrence of distant and lymph node metastases. Furthermore, within the same cluster of miRNAs, including miR-508-3p, miR-509-3p, miR-509-3-5p, and miR-514a-3p, there is a frequent downregulation in advanced and recurrent ovarian carcinoma (Bagnoli *et al.*, 2011), implying their coordinated regulation and co-expression. Various studies have also highlighted the prognostic relevance of these miRNAs in diverse cancer types (Hiramoto *et al.*, 2017; Shang *et al.*, 2014), although

exceptions exist. For instance, in esophageal squamous cell carcinoma (SCC), elevated miR-508-3p expression is paradoxically associated with shorter disease-free and overall survival. The growth regulatory role of microRNA-508-3p in lung cancer tumorigenesis has not been worked out.

The G1 to S phase transition 1 (GSPT1) protein is pivotal in orchestrating cell cycle progression, making it a significant player in cancer biology (Dang *et al.*, 2017). Its involvement in cancer pathogenesis has garnered attention across various cancer types, with an emerging focus on its implications within lung cancer. GSPT1's essential role lies in mediating the transition of cells from the growth-arrested G1 phase to the proliferative S phase of the cell cycle (Nishiguchi *et al.*, 2021). By regulating the translation termination process, GSPT1 controls gene expression, impacting fundamental cellular functions such as DNA replication and cell division. Its role extends beyond its involvement in the cell cycle, as GSPT1 has been implicated in cellular stress responses, mRNA quality control, and RNA metabolism.

In the context of cancer, GSPT1's dysregulation contributes to tumorigenesis through various mechanisms. Elevated GSPT1 expression has been associated with increased proliferation rates, reduced apoptosis, and altered gene expression patterns, all hallmark cancer cell features (Long *et al.*, 2021). Additionally, GSPT1's potential involvement in angiogenesis and metastasis underscores its multifaceted contributions to cancer progression (Tian *et al.*, 2018). Specifically, in lung cancer, GSPT1's perturbation has garnered attention due to its potential role in disease pathogenesis. Altered GSPT1 expression has been reported in lung cancer tissues, and its over-expression has been correlated with unfavorable clinical outcomes (Cheng *et al.*, 2021). GSPT1's regulatory influence over cellular processes in lung cancer aligns with its broader roles in other cancer types.

Understanding GSPT1's intricate role in cancer development and progression opens up avenues for therapeutic exploration. Targeting GSPT1 holds promise as a strategy to curtail uncontrolled proliferation and enhance the efficacy of cancer treatments. The intricate interplay of GSPT1 within cellular pathways underscores its potential as a druggable target. The primary objective of this study is to delve into the pivotal role played by miRNA-508-3p in governing the proliferation of human lung cancer cells. This investigation centers on the specific mechanism through which miRNA-508-3p exerts its influence, by targeting the GSPT1.

MATERIALS AND METHODS

Human clinical samples and cell lines

Sixty-five (65) paired specimens of lung cancer and normal adjacent tissues (taken from tumor margins and representing pathologically normal lung tissues) were collected from lung cancer patients after surgery at The Affiliated Hospital of Nantong University from 2014 to 2018. The patients didn't receive chemo or radiotherapy during tissue collection. The patients were informed about the study in advance and tissues were collected only after consent. The tissues were frozen immediately after collection in liquid nitrogen and then stored at -80°C till experimental use. The study was approved by the institutional ethical guidelines committee. The study has been approved by the ethics committee of The Affiliated Hospital of Nantong University (No: AADEx124).

Four lung cancer cell lines (A427, A549, SK-LU-1 and HCC827) and the normal lung cell line (MRC5) were purchased from the American Type Culture Collection and their propagation was performed at 37°C with 5% CO₂. Dulbecco's Modified Eagle's Medium (DMEM, Gibco BRL) containing 10% FBS (v/v, Hyclone) was used as the cell culturing medium.

For transfection purposes, lung cancer cell lines (2×10⁵ per well) were seeded in 6-well plates and allowed to attach for at least 18 h. miR-508 mimics (100 pmol), si-GSPT1 (100 pmol) together with their negative controls (100 pmol; designed and synthesized by Ribo-Bio, Guangzhou, China) were transfected into cells using Lipofectamine 2000 reagent (Thermo Fisher Scientific) according to manufacturer guidelines. Over-expression of GSPT1 was achieved using the over-expression vector pcDNA3.1 (4 µg). The transfections were performed at 37°C for 48 h. Total RNA and protein were collected 48 hours post-transfection.

RNA isolation and qRT-PCR

Total cellular RNA from tissues and cell lines was extracted using the Trizol method (Thermo Fisher Scientific) which was reverse transcribed to cDNA with Reverse Transcription Kit (Takara). The following thermal cycling conditions were applied: 16°C for 30 min, 42°C for 30 min and 85°C for 5 min. The gene expression analysis was performed through qRT-PCR with the help of SYBR Green PCR Master Mix (Thermo Fisher Scientific). The qRT-PCR procedure was executed according to the following temperature protocol: an initial step at 50°C for 2 minutes, followed by denaturation at 95°C for 10 minutes. Subsequently, 40 cycles were performed, involving denaturation at 95°C for 15 seconds, followed by an annealing/extension step at 60°C for 60 seconds. Relative expression levels were estimated by the 2^{-ΔΔCT} method. U6 was used as the internal expression control. The primer sequences used were as follows: miR-508-3p forward, 5'-TTCAAGAGACATGAGTGAC-3' and reverse, 5'-TCTCTTGAACATGAGTGACG-3'; U6 forward, 5'-TGCGGGTGCTCGCTTCGGCAGC-3' and reverse, 5'-CCAGTGCAGGGTCCGAGGT-3.

Proliferation and clonogenic assays

The proliferation of stably transfected lung cancer cells was analyzed through an MTT assay. The transfected cells were incubated in 96-well plates at 37°C for 0 h, 20 h, 40 h, 60 h, 80 h or 100 h prior to the addition of MTT reagent (0.5% final concentration) to wells. The plate for incubated for 4 h again after adding MTT. Then the culture medium was replaced with 250 µl DMSO to dissolve the formazan crystals. Using a microplate reader (ELx808™, Agilent, USA), the optical density (OD) values were recorded at 570 nm for each well. These values were used for analyzing the relative cell proliferation using the formula: Cell viability (%) = (Absorbance of treated samples/Absorbance of control samples) × 100.

After their stable transfection for 48 hours, the cells at a cellular density of 500 cells per well were propagated for 14 days at 37°C. The colonies were then fixed with methanol for 20 min and stained with 1.0% crystal violet. The relative colony number was estimated by manually counting the colonies in 10 random fields under a microscope.

Cell cycle analysis

The stably transfected cancer cells were cultured in the 12-well plates at 37°C for 48 h using an initial cellular concentration of 1.6×10^6 cells/well. The cells were harvested and fixed with 70% ethanol at 4°C overnight. Staining of cells with 50 µg/ml propidium iodide (Thermo Fisher Scientific) followed by flow cytometric analysis was carried out for studying the cancer cell mitosis. The fluorescence-activated cell sorting (FACS) Calibur and Cell Quest software were used for estimating the cell cycle phase distribution of cancer cells.

Edu-Hoechst staining

Approximately 0.5×10^5 transfected cells were seeded per well of the 96-well plate. Each well was added to the EdU-medium for 2.5 h. The cells were then washed with PBS and ethanol fixed. The EdU assay kit (RiboBio) was used for viability assessments. The cells were also incubated with Hoechst solution for whole sample staining.

In vivo experiments

The nude rat xenografts were obtained using five- to six-week-old BALB/c nude male rats. The rats were distributed into 2 groups (10 rats per group). The rats were maintained using the institute's central animal house facility. The animal flanks were subcutaneously injected with 5×10^6 matrigel suspended A549 cancer cells to obtain the xenograft models. After tumor induction, the rats were treated with intra-tumor injections carrying miR-508-3p mimics or its negative control on alternate days. The intra-tumor injections were given for a varied number of days. On the 25th day after tumor induction, the rats were sacrificed and rat tumors were rescued. The size and weight of tumors were determined and used for calculating the tumor volume. The protein levels of PCNA and Cyclin D1 in rat tumors were analyzed through immune-histochemical staining.

Western blotting

Total cellular proteins were extracted by treating the cells with RIPA lysis and extraction buffer (Thermo Fisher Scientific). The protein expression was determined through chemiluminescence after PAGE and protein blotting using specifically designed primary antibodies like anti-GSPT1 (Novus Biologicals, NBP2-16754, 1:1000) and anti-actin (Sigma Aldrich, A2066, 1:1000). After overnight incubation, followed by proper washing, blots were incubated with HRP-linked secondary antibody (Cell Signaling Technology, 7074, 1:2000). Human actin protein served as the internal reference in western blotting study.

Bioinformatics and dual luciferase assay

To predict the molecular targets of miRNA-508, online miRNA target prediction software like Starbase (<http://starbase.sysu.edu.cn>) and TargetScan (<http://www.targetscan.org/>) were used. The latter also predicted the microRNA-508-3p binding site in the 3'-UTR of GSPT1. The prediction was assessed by luciferase assay using a dual luciferase reporter assay system (Promega). The 3'-UTR binding site (in native, WT or mutated, MUT state) bearing stretch of GSPT1 was cloned into the pGL3 vector for generating the reporter construct. The latter was co-transfected with miR-508-3p mimics or miR-NC into A549 cancer cells. The luciferase activ-

ity measurements were performed as per the manufacturer's protocol.

Statistical analysis

The experiments carried three replicates and the final data represented mean \pm S.D. Student's t-test and one-way ANOVA were performed using SPSS software (SPSS 22.0, Chicago, IL, USA) to analyze the statistical difference between the two values performed. The *p*-values < 0.05 were deemed to represent a statistically significant difference between the two values.

RESULTS

Decreased microRNA-508-3p correlates with poor survival of lung cancer patients

The gene expression of microRNA-508-3p was determined from 65 of each lung cancer tissue samples and normal adjacent tissues through qRT-PCR. It was found that microRNA-508-3p has significantly lower expression in lung cancer tissues in comparison to normal lung tissues (Fig. 1A). The analysis of microRNA-508-3p expression from the paired cancerous and normal adjacent samples also revealed a similar inference (Fig. 1B). Interestingly, the 5-year study on the survival period of the patients from the month of detection of lung cancer receiving the similar therapy procedures was analyzed with the expression level of miRNA-508. It was found that the expression of microRNA-508-3p positively correlated with the period of patient's survival (months), i.e., the higher the expression of miRNA-508, the longer the survival period (Fig. 1C). Further, when the expression of miR-508 was determined in four lung cancer cell lines (A427, A549, SK-LU-1 and HCC827) and compared with its expression in a normal lung cell line (MRC5);

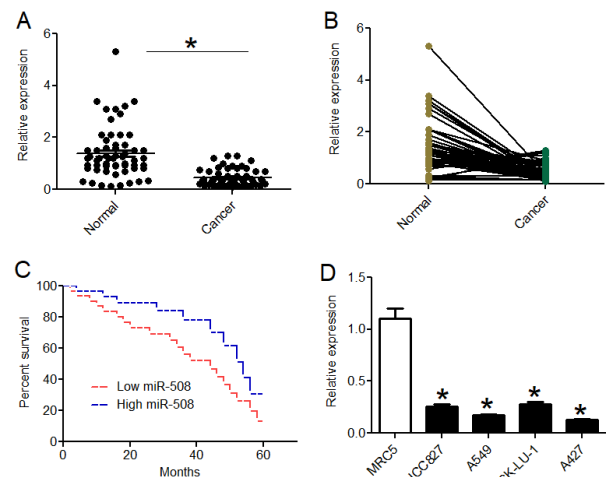


Figure 1. Decreased microRNA-508-3p correlates with poor survival of lung cancer patients.

(A) Lower microRNA-508-3p expression in lung cancer tissues in comparison to the normal lung tissues. (B) microRNA-508-3p expression from the paired cancerous and normal adjacent samples revealed a similar inference. (C) microRNA-508-3p expression positively correlated with the period of patient's survival (months), i.e., the higher the expression of miRNA-508, the higher the survival period. (D) qRT-PCR expression analysis revealing significant down regulation of microRNA-508-3p in lung cancer cell lines (A427, A549, SK-LU-1 and HCC827) in comparison to normal lung cell line (MRC5). Experiments were carried out in three replicates. (*) represents statistical significance at $p < 0.05$ vs normal control.

it was seen that the panel of lung cancer cell lines exhibited significantly lower microRNA-508-3p expression in comparison to the normal lung cell line (Fig. 1D). The cancer cell lines, A427 and A549 were seen to exhibit the least expression among the four cancer cell lines used and were thus used for further characterization of miRNA-508. The results thus reveal significant repression of microRNA-508-3p in lung cancer and its decreased expression negatively correlating with lung cancer patient survival.

MicroRNA-508-3p overexpression declined the cancer cell growth and colony formation

To infer whether the lowered expression level of microRNA-508-3p has any doing with the lung cancer cell growth, microRNA-508-3p was over-expressed in A549 and A427 cancer cell lines and its over-expression was confirmed by RT-PCR (Fig. 2A). Both the cell lines over-expressing microRNA-508-3p showed significantly lower proliferation in comparison to the respective negative control cells (Fig. 2B). Again, the colony formation was markedly reduced by microRNA-508-3p over-expression (Fig. 2C). Both A549 and A427 cancer cell lines exhibited almost 50 % lower colony formation when microRNA-508-3p was over-expressed in them (Fig. 2D). The results suggest that microRNA-508-3p negatively regulates the growth of lung cancer cells and higher proliferation of cancer cells might be achieved through low-

ered microRNA-508-3p down-regulation among other regulatory factors.

The cell cycle was arrested at the G1 phase in cancer cells over-expressing miRNA-508

The flow cytometric analysis of A427 and A549 cancer cells over-expressing microRNA-508-3p was performed to study the mitotic phase distribution which was compared with the negative control cells. A significantly higher percentage of cancer cells was shown to depict the Go/G1 cell cycle phase for the cancer cells over-expressing microRNA-508-3p while the percentage of cells was significantly lower exhibiting S and G2/M when compared with the phase distribution of negative control cells (Fig. 3A). To further validate the finding, the cancer cells over-expressing microRNA-508-3p in comparison with negative control cells were stained with EdU fluorescent stain to detect the relative number of cells which had undergone DNA synthesis. The number of EdU-stained cells was significantly lower under microRNA-508-3p overexpression in comparison to negative control cells (Fig. 3B). The percent number of EdU-positive cells was as low as 10% for both A549 and A427 cancer cell lines over-expressing microRNA-508-3p when compared with the respective negative control cells (Fig. 3C). Together, the results indicated that microRNA-508-3p overexpression induced lung cancer cells with cell cycle arrest at the G1 stage and thus reduced their *in vitro* proliferation.

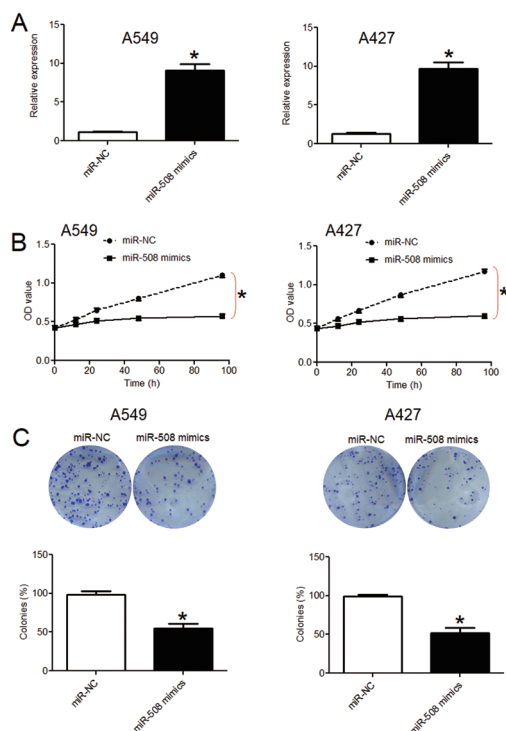


Figure 2. MicroRNA-508-3p overexpression declined the cancer cell growth and colony formation. (A) A549 and A427 cells transfected with microRNA-508-3p mimics showing significant up-regulation of microRNA-508-3p in comparison to respective miR-NC transfected cells. (B) A549 and A427 cells overexpressing microRNA-508-3p exhibit limited growth *in vitro* than the respective miR-NC transfected cells. (C) A549 and A427 cells over expressing microRNA-508-3p exhibit significantly lower colony formation than the respective miR-NC transfected cells (magnification $\times 100$). Experiments were carried out in three replicates. (*) represents statistical significance at $p < 0.05$ vs miR-NC.

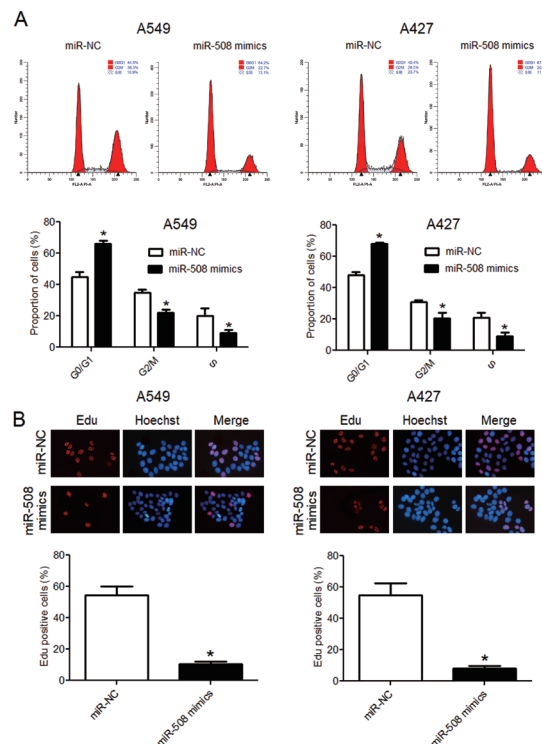


Figure 3. Cell cycle was arrested at the G1 phase in cancer cells overexpressing miRNA-508. (A) Flow cytometry analysis of A549 and A427 cells showed that overexpression of microRNA-508-3p produces a significantly higher percentage of cancer cells in the G0/G1 cell cycle phase while a significantly lower percentage of cancer cells in S and G2/M compared with the phase distribution of negative control cells. (B) A549 and A427 cells overexpressing microRNA-508-3p showed a lower number of EdU stained cells (10%) than the respective miR-NC transfected cells (magnification $\times 200$). Experiments were carried out in three replicates. (*) represents statistical significance at $p < 0.05$ vs miR-NC.

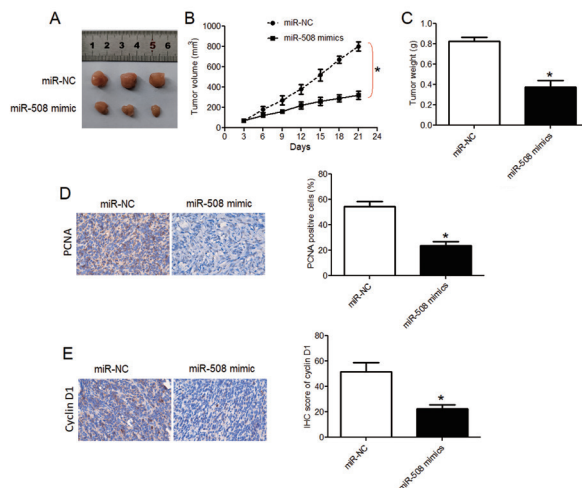


Figure 4. MicroRNA-508-3p up-regulation inhibited *in vivo* rat tumorigenesis.

(A) Morphological comparison of the rat tumors rescued from the animals overexpressing miR-NC and microRNA-508-3p mimic. (B) *In vivo* rat tumor volume was significantly decreased under microRNA-508-3p over-expression than the respective miR-NC. (C) Tumor weight was significantly decreased under microRNA-508-3p over-expression than the respective miR-NC. (D, E) The IHC staining of PCNA revealed that tumors exhibited significantly lower PCNA protein expression under microRNA-508-3p over-expression and a similar observation was made about the expression level of cyclin D1 (magnification $\times 20$). Experiments were carried out in three replicates. (*) represents statistical significance at $p < 0.05$ vs miR-NC.

MicroRNA-508-3p up-regulation inhibited *in vivo* rat tumorigenesis

During the *in vivo* study, the intra-tumor overexpression was achieved in the rat models. The morphological comparison of the rat tumors rescued from the animals after their sacrifice revealed that the rat tumor size was significantly lower under microRNA-508-3p over-expression when compared with that of the negative control rats (Fig. 4A). Similarly, the *in vivo* rat tumor volume was significantly decreased under microRNA-508-3p over-expression (Fig. 4B). Tumor weight also showed a similar trend (Fig. 4C). The immune-histochemical staining of proliferating cell nuclear antigen (PCNA) revealed that rat tumors exhibited significantly lower PCNA protein expression under microRNA-508-3p overexpression and a similar observation was made about the expression level of cyclin D1, both of which are used as the proliferation markers (Fig. 4D and 4E). Hence, the results suggest that up-regulation of microRNA-508-3p inhibited the growth and proliferation of *in vivo* rat tumors indicating its tumor-suppressive role in lung cancer.

MicroRNA-508-3p exercised its effects by targeting GSPT1 in lung cancer

To look for the possible regulatory mechanism of action of microRNA-508-3p in lung cancer, online bio-informatics was performed. MicroRNA-508-3p was predicted to be targeting G1 to S phase transition 1 (GSPT1) protein (Fig. 5A). MicroRNA-508-3p was shown to specifically bind with the 3'-UTR of GSPT1 in sequence-specific fashion (Fig. 5B). The dual luciferase reporter assay was performed to confirm this prediction. The significant reduction in the luciferase activity when the overexpression construct of microRNA-508-3p was co-transfected with the native (WT) reporter construct

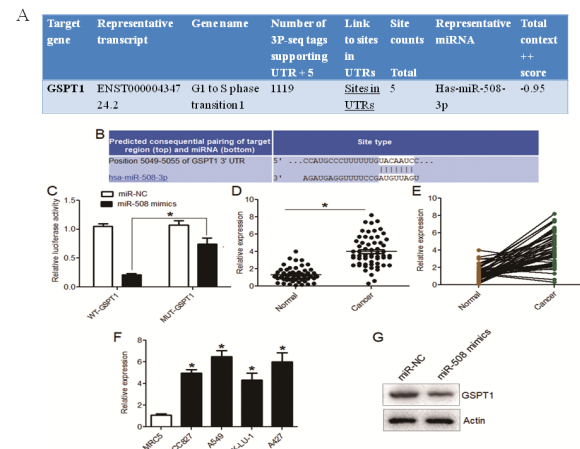


Figure 5. MicroRNA-508-3p exercised its effects by targeting GSPT1 in lung cancer.

(A) TargetScan software predicted that microRNA-508-3p targets the GSPT1 protein. (B) *In silico* analysis predicted a specific microRNA-508-3p binding site in 3'-UTR of GSPT1. (C) The significant reduction in the luciferase activity when the overexpression construct of microRNA-508-3p was co-transfected with the native (WT) reporter construct of GSPT1 in A549 cancer cells showed that microRNA-508-3p interacted with 3'-UTR of GSPT1. (D) Expression of GSPT1 in normal and lung cancer tissues. (E) GSPT1 expression from the paired cancerous and normal adjacent samples revealed a similar inference. (F) Expression analysis of GSPT1 in lung cancer cell lines in comparison to normal liver epithelial cell line. (G) Over-expression of microRNA-508-3p in A549 cancer cells negatively affected the protein level of GSPT1 suggesting post-transcriptional/translational targeting of the latter by microRNA-508-3p in lung cancer. Experiments were carried out in three replicates. (*) represents statistical significance at $p < 0.05$ vs miR-NC.

of GSPT1 in A549 cancer cells showed that microRNA-508-3p interacted with 3'-UTR of GSPT1 (Fig. 5C). Further support was attained from the expression study of the GSPT1 gene from lung cancer tissues and cancer cell lines in comparison to normal tissues and cell line. GSPT1 was found to have significantly higher expression in cancer tissues and cell lines corresponding to lower microRNA-508-3p expression (Fig. 5D, 5E and 5F). Further, the over-expression of microRNA-508-3p in A549 cancer cells negatively affected the protein level of GSPT1 suggesting post-transcriptional/translational targeting of the latter by microRNA-508-3p in lung cancer (Fig. 5G).

MicroRNA-508-3p directly binds to GSPT1 in lung cancer

To explore whether the observed effects of microRNA-508-3p against lung cancer were modulated through GSPT1 targeting, RNA interference-mediated silencing of GSPT1 was performed in A549 cancer cells and repression was confirmed by qRT-PCR (Fig. 6A). The cancer cells exhibited significantly lower proliferation under GSPT1 silencing (Fig. 6B). GSPT1 silencing was seen to induce G0/G1 phase cell cycle arrest (Fig. 6C). Similar to microRNA-508-3p over-expression, the down-regulation of GSPT1 reduced the proliferative viability of lung cancer cells (Fig. 6D). Confirming the execution of microRNA-508-3p role in lung cancer through GSPT1, the over-expression of GSPT1 in A549 cancer cells minimized the antiproliferative effects of microRNA-508-3p up-regulation (Fig. 6E). Summing up, the results are suggestive of direct binding of microRNA-508-3p with GSPT1 to down-regulate the expression of latter translationally in lung cancer and exertion of mi-

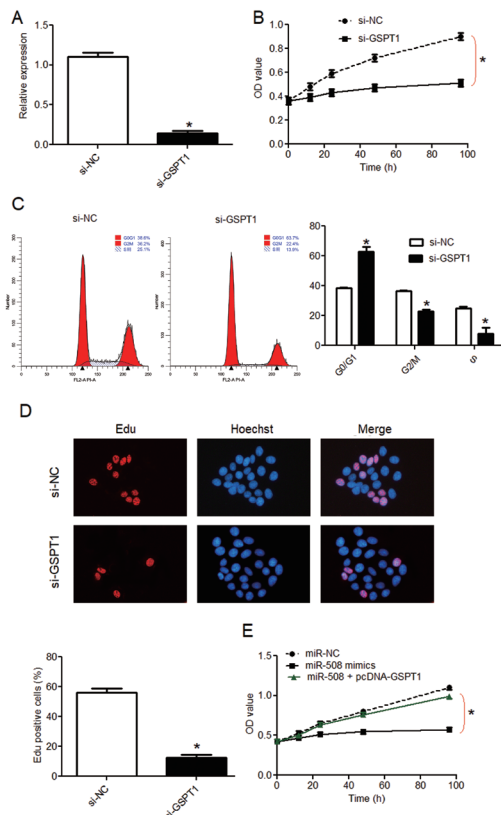


Figure 6. MicroRNA-508-3p directly binds to GSPT1 in lung cancer.

(A) Relative expression of GSPT1 in A549 cancer cells after silencing of GSPT compared to si-NC. (B) A549 cancer cells exhibited significantly lower proliferation under GSPT1 silencing compared to cells transfected with si-NC. (C) A549 cancer cells with GSPT1 silencing were seen to induce G0/G1 phase cell cycle arrest compared to cells transfected with si-NC. (D) A549 cancer cells transfected with si-GSPT1 were found to reduce the proliferative viability of lung cancer cells compared to cells transfected with si-NC. (E) Over-expression of GSPT1 in A549 cancer cells minimized the anti-proliferative effects of microRNA-508-3p up-regulation compared to cells transfected with si-NC. Experiments were carried out in three replicates. (*) represents statistical significance at $p < 0.05$ vs si-NC.

croRNA-508-3p tumorigenesis regulatory role through miRNA-508/GSPT1 molecular axis which further insights into the therapeutic value of miRNA-508/GSPT1 axis against the deadliest cancer, the human lung cancer.

DISCUSSION

Lung cancer is by far the deadliest human cancer with high incidence and mortality rates worldwide (Busch *et al.*, 2016). The disease is reportedly induced through genetic alterations and external environmental factors (Samet, 2013). A thorough understanding of lung cancer progression is essential for formulating effective treatment measures against this lethal menace. At the molecular level, the studies have focused on exploring different regulatory molecules regulating the growth and propagation of lung cancer including the non-coding RNAs (Lin & Yang, 2018). Falling in the category of non-coding RNAs, the micro-RNAs (miRNAs) were shown to profoundly affect the tumorigenesis of many human cancers (Vannini *et al.*, 2018). Many miRNAs have been shown to exercise a key developmental role in human lung cancer (Kabekkodu *et al.*, 2020). Although

microRNA-508-3p has been found to exhibit active involvement in a number of cancer types, but its in-depth role has not been explored in lung cancer. The current study revealed a significant transcriptional down-regulation of microRNA-508-3p in lung cancer. microRNA-508-3p has also been elucidated to exhibit transcriptional repression in human cancers like gastric cancer, and colon cancer (Wang & Jin, 2019). Additionally, the level of microRNA-508-3p down-regulation negatively correlated with the survival of lung cancer patients. This indicated that microRNA-508-3p functions as a tumor suppressor in lung cancer and other human cancers, as reported by earlier studies (Huang *et al.*, 2016). The microRNA-508-3p over-expression declined lung cancer growth both *in vitro* and *in vivo*. The anti-cancer effects of microRNA-508-3p up-regulation were also evidenced as the arrest of lung cancer cell cycle at the G1 sub-phase of mitotic interphase, which suggests that microRNA-508-3p negatively regulates lung cancer cell growth as has been supported by previous studies (Bao *et al.*, 2016). Importantly, the current study showed that G1 to S phase transition 1 (GSPT1) protein is functionally targeted by microRNA-508-3p in lung cancer. The role of microRNA-508-3p was found to be attenuated via GSPT1. The GSPT1 is a protein-coding gene that regulates the translational termination in eukaryotes associated with eukaryotic release factor 1 (eRF1; Zhouravleva *et al.*, 2006). It is involved in cell cycle regulation and cell apoptosis. In the present study, the GSPT1 over-expression resulted from microRNA-508-3p repression and the former was proved to considerably affect the molecular level progression of lung cancer. The up-regulation of GSPT1 was also reported to be linked with the growth and development of gastric and breast cancer (Tian *et al.*, 2018). In another report, the expression of GSPT1 was shown to be significantly higher in non-small lung cancer cells and negatively correlated with miRNA-27b-3p expression (Sun *et al.*, 2019). The miRNA/GSPT1 axes have been suggested to act as potential therapeutic targets against human cancers including lung cancer (Li *et al.*, 2020). Concluding with a similar inference, the miRNA-508/GSPT1 was unravelled as a vital growth regulatory link in lung cancer. The results of the present study support its therapeutic utility against human lung cancer.

The functional analyses conducted in this study provide mechanistic insights into how microRNA-508-3p exerts its tumor-suppressive effects in lung cancer. The inhibition of cancer cell proliferation and viability following microRNA-508-3p overexpression aligns with the notion that this microRNA acts as a negative regulator of tumor growth. The induction of cell cycle arrest at the G1 phase, as evidenced by the down-regulation of the GSPT1 protein, suggests that microRNA-508-3p exerts its antiproliferative effects by interfering with key cell cycle regulatory pathways. These findings offer a clearer picture of the molecular events modulated by microRNA-508-3p that contribute to its tumor-suppressive functions.

The *in vivo* experiments using rat models provide a relevant and translational dimension to the study. The observed inhibition of tumor growth in response to microRNA-508-3p up-regulation underscores the potential therapeutic application of this microRNA in lung cancer treatment. These results add to the growing body of evidence supporting microRNA-based therapies as promising avenues for cancer intervention.

It is worth noting that the findings of this study resonate with the broader understanding of microRNA dysregulation in cancer and reinforce the idea that targeting

specific microRNAs could hold immense therapeutic potential. However, further investigations are warranted to delve deeper into the exact mechanisms through which miRNA-508-3p modulates its target gene(s), potentially involving intricate regulatory networks that influence cancer progression.

The current study significantly contributes to our understanding of the role of microRNA-508-3p in lung cancer. The comprehensive molecular characterization, functional analyses, and in vivo experiments underscore the potential of microRNA-508-3p as a promising therapeutic target for lung cancer treatment. By elucidating its regulatory mechanisms and demonstrating its impact on tumor growth, this research opens up avenues for developing innovative therapeutic strategies to improve patient outcomes in lung cancer management.

CONCLUSIONS

The current study showed that microRNA-508-3p experiences a key regulatory role in the growth and proliferation of lung cancer, and the lowered expression levels of microRNA-508-3p account for poor disease survival. The results were conclusive of the prognostic and therapeutic role of microRNA-508-3p against lung cancer, which might be utilized as a novel and alternative anti-cancer therapy for the treatment of lung cancer.

REFERENCES

- Bagnoli M, De Cecco L, Granata A, Nicoletti R, Marchesi E, Alberti P, Valeri B, Libra M, Barbareschi M, Raspagliesi F, Mezzanzanica D, Canevari S (2011) Identification of a chrXq27.3 microRNA cluster associated with early relapse in advanced stage ovarian cancer patients. *Oncotarget* 2: 1265–1278. <https://doi.org/10.18632/oncotarget.401>
- Bao G, Wang N, Li R, Xu G, Liu P, He, B (2016) MiR-508-5p Inhibits the progression of glioma by targeting glycoprotein non-metastatic melanoma B. *Neurochem Res* 41: 1684–1690. <https://doi.org/10.1007/s11064-016-1884-2>
- Bhan A, Soleimani M, Mandal SS (2017) Long noncoding RNA and cancer: a new paradigm. *Cancer Res* 77: 3965–3981. <https://doi.org/10.1158/0008-5472.CAN-16-2634>
- Bray F, Ferlay J, Soerjomataram I, Siegel RL, Torre LA, Jemal A (2018) Global cancer statistics 2018: GLOBOCAN estimates of incidence and mortality worldwide for 36 cancers in 185 countries. *CA Cancer J Clin* 68: 394–424. <https://doi.org/10.3322/caac.21492>
- Busch SE, Hanke ML, Kargl J, Metz HE, MacPherson D, Houghton AM (2016) Lung cancer subtypes generate unique immune responses. *J Immunol* 197: 4493–4503. <https://doi.org/10.4049/jimmunol.1600576>
- Cheng TY, Cramb SM, Baade PD, Youliden DR, Nwogu C, Reid ME (2016) The international epidemiology of lung cancer: latest trends, disparities, and tumor characteristics. *J Thorac Oncol* 11: 1653–1671. <https://doi.org/10.1016/j.jtho.2016.05.021>
- Cheng Y, Wang S, Mu X (2021) Long non-coding RNA LINC00511 promotes proliferation, invasion, and migration of non-small cell lung cancer cells by targeting miR-625-5p/GSPT1. *Transl Cancer Res* 10: 5159–5173. <https://doi.org/10.21037/tcr-21-1468>
- D'Angelo B, Benedetti E, Cimini A, Giordano A (2016) MicroRNAs: a puzzling tool in cancer diagnostics and therapy. *Anticancer Res* 36: 5571–5575. <https://doi.org/10.21873/anticancer.11142>
- Dang CV, Reddy EP, Shokat KM, Soucek L (2017) Drugging the 'undruggable' cancer targets. *Nat Rev Cancer* 17: 502–508. <https://doi.org/10.1038/nrc.2017.36>
- Hiramoto H, Muramatsu T, Ichikawa D, Tanimoto K, Yasukawa S, Otsuji E, Inazawa J (2017) miR-509-5p and miR-1243 increase the sensitivity to gemcitabine by inhibiting epithelial-mesenchymal transition in pancreatic cancer. *Sci Rep* 7: 4002. <https://doi.org/10.1038/s41598-017-04191-w>
- Hirsch FR, Scagliotti GV, Mulshine JL, Kwon R, Curran WJ, Jr, Wu YL, Paz-Ares L (2017) Lung cancer: current therapies and new targeted treatments. *Lancet* 389: 299–311. [https://doi.org/10.1016/S0140-6736\(16\)30958-8](https://doi.org/10.1016/S0140-6736(16)30958-8)
- Huang T, Kang W, Zhang B, Wu F, Dong Y, Tong JH, Yang W, Zhou Y, Zhang L, Cheng AS, Yu J, To KF (2016) miR-508-3p concordantly silences NFKB1 and RELA to inactivate canonical NF-kappaB signaling in gastric carcinogenesis. *Mol Cancer* 15: 9. <https://doi.org/10.1186/s12943-016-0493-7>
- Kabekkodu SP, Shukla V, Varghese VK, Adiga D, Vethil Jishnu P, Chakrabarty S, Satyamoorthy K (2020) Cluster miRNAs and cancer: Diagnostic, prognostic and therapeutic opportunities. *Wiley Interdiscip Rev RNA* 11: e1563. <https://doi.org/10.1002/wrna.1563>
- Li Z, Xie X, Fan X, Li X (2020) Long non-coding RNA MINCR Regulates miR-876-5p/GSPT1 axis to aggravate glioma progression. *Neurochem Res* 45: 1690–1699. <https://doi.org/10.1007/s11064-020-03029-8>
- Lin C, Yang L (2018) Long noncoding RNA in cancer: wiring signaling circuitry. *Trends Cell Biol* 28: 287–301. <https://doi.org/10.1016/j.tcb.2017.11.008>
- Long X, Zhao L, Li G, Wang Z, Deng Z (2021) Identification of GSPT1 as prognostic biomarker and promoter of malignant colon cancer cell phenotypes via the GSK-3beta/CyclinD1 pathway. *Aging* 13: 10354–10368. <https://doi.org/10.18632/aging.202796>
- Malhotra J, Malvezzi M, Negri E, La Vecchia C, Boffetta P (2016) Risk factors for lung cancer worldwide. *Eur Respir J* 48: 889–902. <https://doi.org/10.1183/13993003.00359-2016>
- Nishiguchi G, Keramatnia F, Min J, Chang Y, Jonchere B, Das S, Actis M, Price J, Chepyala D, Young B, et al (2021) Identification of potent, selective, and orally bioavailable small-molecule GSPT1/2 degraders from a focused library of cereblon modulators. *J Med Chem* 64: 7296–7311. <https://doi.org/10.1021/acs.jmedchem.0c01313>
- O'Brien J, Hayder H, Zayed Y, Peng C (2018) Overview of microRNA biogenesis, mechanisms of actions, and circulation. *Front Endocrinol* 9: 402. <https://doi.org/10.3389/fendo.2018.00402>
- Rong B, Yang S (2018) Molecular mechanism and targeted therapy of Hsp90 involved in lung cancer: New discoveries and developments (Review). *Int J Oncol* 52: 321–336. <https://doi.org/10.3892/ijo.2017.4214>
- Samet JM (2013) Tobacco smoking: the leading cause of preventable disease worldwide. *Thorac Surg Clin* 23: 103–112. <https://doi.org/10.1016/j.thorsurg.2013.01.009>
- Shang Y, Feng B, Zhou L, Ren G, Zhang Z, Fan X, Sun Y, Luo G, Liang J, Wu K, Nie Y, Fan D (2016) The miR27b-CCNG1-P53-miR-508-5p axis regulates multidrug resistance of gastric cancer. *Oncotarget* 7: 538–549. <https://doi.org/10.18632/oncotarget.6374>
- Shang Y, Zhang Z, Liu Z, Feng B, Ren G, Li K, Zhou L, Sun Y, Li M, Zhou J, An Y, Wu K, Nie Y, Fan D (2014) miR-508-5p regulates multidrug resistance of gastric cancer by targeting ABCB1 and ZNRD1. *Oncogene* 33: 3267–3276. <https://doi.org/10.1038/onc.2013.297>
- Sun W, Zhang L, Yan R, Yang Y, Meng X (2019) LncRNA DLX6-AS1 promotes the proliferation, invasion, and migration of non-small cell lung cancer cells by targeting the miR-27b-3p/GSPT1 axis. *Oncotargets Ther* 12: 3945–3954. <https://doi.org/10.2147/OTT.S196865>
- Thandra KC, Barsouk A, Saginala K, Aluru JS (2021) Epidemiology of lung cancer. *Contemp Oncol* 25: 45–52. <https://doi.org/10.5114/wo.2021.103829>
- Tian QG, Tian RC, Liu Y, Niu AY, Zhang J, Gao WF (2018) The role of miR-144/GSPT1 axis in gastric cancer. *Eur Rev Med Pharmacol Sci* 22: 4138–4145. https://doi.org/10.26355/eurrev_201807_15406
- Vannini I, Fanini F, Fabbri M (2018) Emerging roles of microRNAs in cancer. *Curr Opin Genet Dev* 48: 128–133. <https://doi.org/10.1016/j.gde.2018.01.001>
- Wang Z, Jin J (2019) LncRNA SLCO4A1-AS1 promotes colorectal cancer cell proliferation by enhancing autophagy via miR-508-3p/PARD3 axis. *Aging* 11: 4876–4889. <https://doi.org/10.18632/aging.102081>
- Wu KL, Tsai YM, Lien CT, Kuo PL, Hung AJ (2019) The roles of microRNA in lung cancer. *Int J Mol Sci* 20. <https://doi.org/10.3390/ijms20071611>
- Wu SG, Huang YJ, Bao B, Wu LM, Dong J, Liu XH, Li ZH, Wang XY, Wang L, Chen BJ, Chen W (2017) miR-508-5p acts as an anti-oncogene by targeting MESDC1 in hepatocellular carcinoma. *Neoplasma* 64: 40–47. https://doi.org/10.4149/neo_2017_105
- Zhao L, Wang W, Xu L, Yi T, Zhao X, Wei Y, Vermeulen L, Goel A, Zhou S, Wang X (2019) Integrative network biology analysis identifies miR-508-3p as the determinant for the mesenchymal identity and a strong prognostic biomarker of ovarian cancer. *Oncogene* 38: 2305–2319. <https://doi.org/10.1038/s41388-018-0577-5>
- Zhouravleva G, Schepachev V, Petrova A, Tarasov O, Inge-Vechtomov S (2006) Evolution of translation termination factor eRF3: is GSPT2 generated by retrotransposition of GSPT1's mRNA? *JUBMB life* 58: 199–202. <https://doi.org/10.1080/15216540600686862>

Circular RNA METTL15/miR-374a-5p/ESCO2 axis induces colorectal cancer development

Feng Guo, Yang Luo, GuangYao Ye and WeiJun Tang✉

Department of Gastrointestinal Surgery, Renji Hospital, Shanghai Jiaotong University School of Medicine, Shanghai City, 200127, China

This study investigated the biological role and mechanism of circMETTL15 in colorectal cancer (CRC). Cancer tissues and matched adjacent normal tissues were collected. CircMETTL15, miR-374a-5p, and ESCO2 levels were detected by RT-qPCR and Western Blot. LoVo cells were selected for loss- and gain-of-function assays and rescue assays. Cell proliferation was detected by CCK-8 and colony formation tests, cell apoptosis and cell cycle were detected by flow cytometry, cell migration and invasion were detected by Transwell assay, and protein expression of ki-67, E-cadherin, N-cadherin, and cleaved caspase-3 was detected by Western blot. Through bioinformatics analysis and verification assays, the targeting relationship between circMETTL15, miR-374a-5p, and ESCO2 was studied. The results suggest that circMETTL15 was a stable circRNA that was highly expressed in CRC tissues and cells and was associated with tumor size, higher TNM staging, and lymph node metastasis in CRC patients. Functionally, knocking down circMETTL15 inhibited the proliferation, migration, invasion, and EMT of LoVo cells, and induced apoptosis. Overexpression of circMETTL15 showed the opposite effect. The effects of knockdown or overexpression of circMETTL15 on the biological behavior of LoVo cells were reversed by knockdown of miR-374a-5p or knockdown of ESCO2, respectively. Mechanistically, circMETTL15 acts as a ceRNA for miR-374a-5p to regulate ESCO2 expression, thereby promoting the biological behavior of LoVo cells. In conclusion, the results of this study reveal the role of circMETTL15 in CRC and the underlying molecular mechanism, which provides potential data support for the development of future CRC drugs.

Keywords: circular RNA METTL15, colorectal cancer, MicroRNA-374a-5p, the establishment of sister chromatid cohesion N-acetyltransferase 2

Received: 22 August, 2022; revised: 29 November, 2022; accepted: 08 December, 2022; available on-line: 16 September, 2023

✉e-mail: drtangweijun@hotmail.com

Abbreviations: BCA, Bicinchoninic acid; CCK-8, Cell counting kit-8; ceRNA, Competing endogenous RNA; circMETTL15, Methyltransferase-like 15; circRNA, Circular RNA; CRC, Colorectal cancer; DMEM, Dulbecco's modified essential medium; EMT, Epithelial-mesenchymal transition; ESCO2, Establishment of sister chromatid cohesion N-acetyltransferase 2; FITC, Fluorescein isothiocyanate; GAPDH, Glyceraldehyde-3-phosphate dehydrogenase; IHC, Immunohistochemistry; MUT, Mutant type; PI, Propidium iodide; RIP, RNA immunoprecipitation assay; RIPA, Radio-Immunoprecipitation Assay; RT-qPCR, Real-time reverse transcriptase-polymerase chain reaction; TNM, Tumor node metastasis; WT, Wild type

INTRODUCTION

Colorectal cancer (CRC) remains one of the leading causes of cancer deaths worldwide (Ameli-Mojarad *et*

al., 2021). So far, surgery, chemotherapy, and radiotherapy have been the main treatment strategies for CRC (Shao *et al.*, 2021). Most patients are diagnosed in an intermediate or late stage because of the hidden early symptoms (Simon, 2016). In addition, limited efficacy, postoperative recurrence, and long-term metastasis lead to poor prognosis for CRC patients (Díaz-Tasende, 2018). Accumulating studies have shown that changes at the genetic and epigenetic levels of oncogenes and tumor suppressor genes are involved in the development and progression of CRC and act as potential therapeutic targets for CRC (Tsai *et al.*, 2021; Slattery *et al.*, 2017). Therefore, identifying these regulatory genes will offer new insights into the development of molecularly targeted therapies for CRC.

Circular RNA (circRNA) has been widely confirmed to be involved in cancer development (Zhang *et al.*, 2021) and is associated with drug resistance, differentiation, metastasis, angiogenesis, proliferation, migration, and apoptosis (Ameli-Mojarad *et al.*, 2021). For example, circPCLE1 promotes CRC epithelial-mesenchymal transition (EMT), glycolysis, and tumor-associated macrophage polarization (Yi *et al.*, 2022) and N-methyladenosine modification of circALG1 promotes CRC migration, invasion, and metastasis (Lin *et al.*, 2022). It can be seen that the regulation of circRNA has a profound impact on the occurrence and progression of CRC. As a member of circRNA, methyltransferase-like 15 (circMETTL15) is involved in the proliferation, metastasis, immune escape, and apoptosis of lung cancer (Zhang *et al.*, 2022). Based on this, we speculate that circMETTL15 may be involved in the regulation of CRC.

In recent years, the competing endogenous RNA (ceRNA) hypothesis has been widely proposed (Salmena *et al.*, 2011). We predicted circMETTL15-related miRNAs (miR-374a-5p) and miRNA target genes (The establishment of sister chromatid cohesion N-acetyltransferase 2, ESCO2). As a short non-coding RNA, miR-374a-5p negatively regulates gene expression and regulates various biological processes (Lin *et al.*, 2020; Guo *et al.*, 2021). miR-374a-5p abnormal expression has been tested in CRC indicating a correlation with patients' survival rates (Slattery *et al.*, 2015; Slattery *et al.*, 2017). ESCO2 is an evolutionarily conserved cohesion acetyltransferase (Zhu *et al.*, 2021) that can suppress the development of CRC (Guo *et al.*, 2018).

This study aimed to investigate the effect of circMETTL15 on the biological function of CRC cells and to discover the molecular mechanism of circMETTL15 with miR-374a-5p and ESCO2 in CRC.

MATERIALS AND METHODS

Clinical samples

Between 2016 and 2019, 78 cancer tissues and matched adjacent normal tissues (≥ 3 cm from cancer tissue) were surgically resected from CRC patients (excluding those receiving radiotherapy or chemotherapy) at Renji Hospital, Shanghai Jiaotong University School of Medicine. All tissues were kept at -80°C . All clinical and pathological diagnoses were validated by two independent pathologists according to the AJCC and UICC guidelines. This study was approved by the Ethics Committee of Renji Hospital, Shanghai Jiaotong University School of Medicine. Each patient was informed about the content.

Cell culture

LoVo, Caco-2, SW620, SW480, and NCM460 cells were maintained in DMEM, HT-29 and HCT-116 were in DMEM/F12 medium, while DLD-1 was in RPMI-1640 medium. All the media (Gibco, CA, USA) were added with 10% fetal bovine serum, 1% penicillin, and streptomycin, and all cell lines were offered by the Chinese Academy of Sciences Culture Collection (Shanghai, China) and grown in a 5% CO_2 humidified incubator at 37°C .

RNA analysis

With Trizol reagent (Takara, Japan), circRNA, mRNA, and miRNA were extracted from tissues and cells for reverse transcription after detection on Nanodrop 2000 (Thermo Fisher Scientific). In the reverse transcription system, PrimeScript RT master mix (Takara) was utilized for mRNA and circRNA, while for miRNA, Bulge-Loop™ miRNA Quantitative Real-Time Polymerase Reaction Starter Kit (RIBOBIO, China) was applied. cDNA amplification was implemented in the ABI Prism 7500 Sequence Detection System with TB Green Premix Ex Taq II (Takara). The PCR cycling parameters are as follows: 95°C for 30 s followed by 40 cycles at 95°C for 5 s and 60°C for 30 s. mRNA and circRNA were normalized to GAPDH, while miRNA was to U6. The calculation of relative expression was dependent on the $2^{-\Delta\Delta\text{CT}}$ method. Primers are listed in Table 1.

Table 1. Primer sequences

Genes	Primers
circMETTL15	F: 5'-GCCAGCATCGTTGACAGATT-3'
	R: 5'-GCTGTTGGGTCTCTGTCCAA-3'
miR-374a-5p	F: 5'-CGCGCGTTATAATAACAACCTGA-3'
	R: 5'-GCAGGGTCCGAGGTATTC-3'
GAPDH	F: 5'-CACCCACTCTCCACCTTTG-3'
	R: 5'-CCACCACCTGTTGCTGTAG-3'

Note: F, forward; R, reverse; circMETTL15, circular RNA METTL15; miR-374a-5p, microRNA-374a-5p; GAPDH, glyceraldehyde-3-phosphate dehydrogenase

Nucleic acid electrophoresis

Agarose gel electrophoresis (2%) was performed using 45 mmol/L Tris-boric acid and 1 mmol/L EDTA (TBE). DNA was separated by electrophoresis at 120 V

for 30 min, taking marker L (50-500 bp) as the DNA marker (Beyotime, China). UV irradiation was used to examine the bands.

Actinomycin D and RNase R

RNase R (3 U/g, Epicenter) was used to treat RNA (10 μg) from LoVo cells. After incubation at 37°C for 30 min, circRNA and linear mRNA were detected using reverse transcription and RT-qPCR.

Actinomycin D (2 $\mu\text{g}/\text{mL}$, Sigma) was adopted to treat LoVo cells for 4, 8, 12, and 24 h, followed by checking the stability of linear mRNA and circRNA by RT-qPCR.

Cell transfection

siRNA or pcDNA 3.1 overexpression vectors targeting circMETTL15 and ESCO2, and miR-374a-5p mimic/inhibitor were constructed and provided by Genepharma (Shanghai, China). The oligonucleotides and plasmids were transiently transfected into LoVo cells using Lipofectamine 3000 (Invitrogen) and gene expression was analyzed by RT-qPCR and western blot after 48 h.

CCK-8 assay

LoVo cells (2000 cells/well) were plated in 96-well plates and added with 10 μL of CCK-8 reagent (Sangon Biotech, Shanghai, China) at the indicated time points (24, 48, and 72 h). Absorbance at 450 nm was measured using an iMark microplate reader (Bio-Rad) after 2 h.

Colony formation test

LoVo cells were grown at 1000 cells/well in 6-well plates to allow colony formation at 37°C . The colonies were observed every 3 days, and after 2 weeks, the colonies fixed with paraformaldehyde were counted under a microscope (Olympus) after 0.1% crystal violet staining.

Flow cytometry

Cells were fixed overnight at -20°C in 75% alcohol, washed 3 times, and detected by a cell cycle analysis kit (Beyotime). Cells were digested by trypsin, washed in cold PBS, and analyzed by an Annexin V-FITC/PI kit (Vazyme, Nanjing, China) to assess cell apoptosis. Cell cycle distribution and apoptosis rate were determined on the BD FACSCanto II (BD Biosciences).

Transwell assays

LoVo cells were suspended in a fresh medium (100 μL) and added to the upper Transwell chamber (BD Bioscience). Matrigel coating (BD Bioscience) was required for the invasion test but not the migration test. After 24-h induction, cells appearing in the lower chamber were fixed with paraformaldehyde and stained with 0.1% crystal violet for microscopic observations ($\times 100$, Olympus).

Protein analysis

Protein samples collected by RIPA buffer were separated by 12% sodium dodecyl sulfate-polyacrylamide gel electrophoresis after quantification using a BCA kit (Beyotime). Next, the samples were transferred to polyvinylidene fluoride membranes and blocked with 5% non-fat milk for 2 h. After reaction with the primary antibody overnight at 4°C , the membranes were incubated with the secondary antibody (1:5000, CST, MA, USA) for 2

h. The protein blots which were visualized by Omni-ECL chemiluminescent reagent (EpiZyme, China) were then analyzed by Image Lab. Primary antibodies: ESCO2 (ab86003, Abcam), E-cadherin (610181, BD Biosciences), N-cadherin (22018-1-AP, Proteintech), cleaved caspase-3 (ab2302, Abcam), Ki-67 (ab15580, Abcam).

Dual-luciferase reporter assay

Genepharma constructed PGL4 luciferase reporters (Promega) containing circMETTL15 wild-type sequence or mutant sequence (with or without miR-374a-5p binding site), namely circMETTL15-WT and circMETTL15-MUT, respectively. Likewise, ESCO2 3'UTR-WT and ESCO2 3'UTR-MUT were also constructed. The luciferase reporter vector was co-transfected with miR-374a-5p mimic or mimic NC into LoVo cells using Lipofectamine 3000 (Invitrogen) and its luciferase activity was determined in the Dual Luciferase Assay System (Promega) after 48 h.

RIP experiment

Under the guidance of the Magna RIP kit (Millipore), LoVo cells were lysed and mixed with Ago2 antibody-conjugated or IgG antibody-conjugated magnetic beads. RNA complexes on magnetic beads were eluted to isolate total RNA for calculation of RNA expression by RT-qPCR.

Observation of tumor formation

Animal experiments were approved by the Animal Ethics Committee of Renji Hospital, Shanghai Jiaotong University School of Medicine (Approval number:

201511F760). LoVo cells (1×10^6 , 100 μ L) stably transfected with si-circMETTL15 or si-NC were injected subcutaneously into the axilla of 5-week-old male BALB/c nude mice ($n=5$ /group). After 1 week, the tumor volume ($\text{length} \times \text{width}^2/2$) was calculated and recorded once a week. Five weeks later, mice were euthanized to resect tumors for IHC analysis (Zhou *et al.*, 2021).

Data analysis

At least 3 biological replicates were run for each experiment. All statistical analyses were performed using GraphPad Prism 9.0 software (La Jolla, CA, USA). Bilateral comparisons were run by Student's *t*-test, while multiple comparisons were by one-way ANOVA. The correlation between circMETTL15 expression and clinicopathological data was assessed by Chi-square test, while that between circMETTL15 expression and overall survival was by Log-rank (Mantel-Cox) test. $P < 0.05$ was considered as significant difference.

RESULTS

circMETTL15 is abnormally highly expressed in CRC

To investigate whether circMETTL15 participates in CRC, its expression was analyzed in 78 cancer tissues and matched adjacent normal tissues by RT-qPCR. CircMETTL15 was abnormally highly expressed in the tumor samples compared with paired normal tissues (Fig. 1A). Also, circMETTL15 expression was analyzed in CRC cell lines, and elevated circMETTL15 was demonstrated in CRC cell lines than in NCM460 cell line

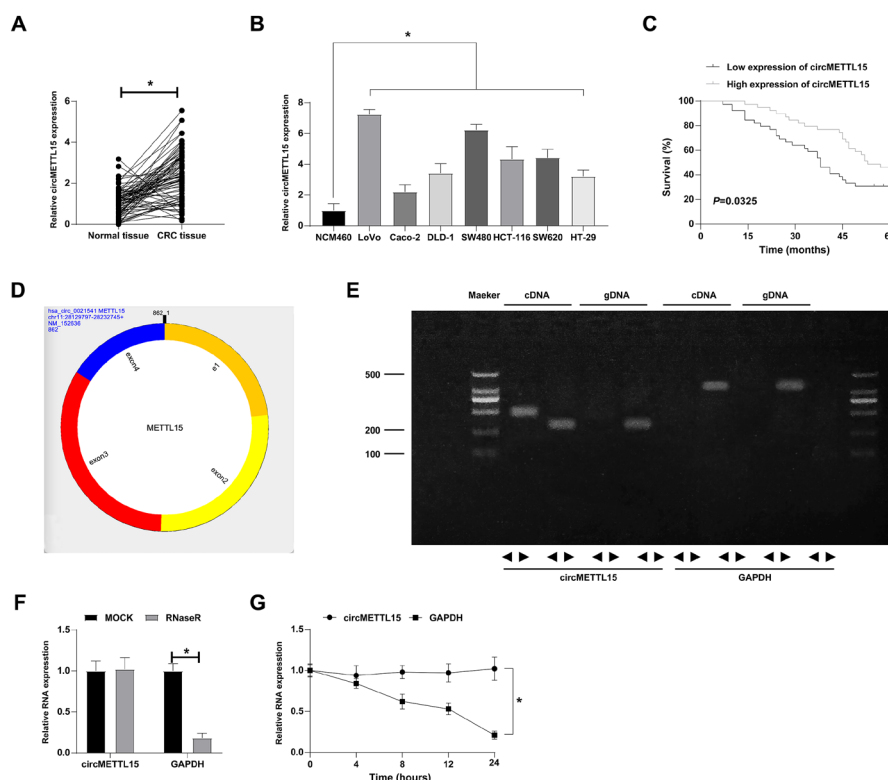


Figure 1. circMETTL15 is abnormally highly expressed in colon cancer

(A) RT-qPCR to detect circMETTL15 in CRC tissues and paired normal tissues. (B) RT-qPCR to detect circMETTL15 in human colorectal cancer cell lines and human colon epithelial mucosa cell line (NCM460). (C) Correlation analysis between circMETTL15 and survival rate of CRC patients. (D) Genetic information of circMETTL15. (E) Agarose gel electrophoresis confirmed the amplification of circMETTL15 by diverging primers in cDNA but not in gDNA. (F) RNase R experiment verified the ring structure of circMETTL15. (G) Actinomycin D experiment verified the ring structure of circMETTL15; data are expressed as mean \pm S.D. (N=3).

Table 2. Relationship between circMETTL15 and clinicopathological features of CRC patients

Characteristic	Cases	The expression of circMETTL15		P
	n=78	Low (n=39)	High (n=39)	
Gender				
Male	48	23	25	0.6416
Female	30	16	14	
Age (year)				
≤ 60	14	5	9	0.2379
> 60	64	34	30	
Tumor size				
< 3 cm	52	33	19	0.0008
≥ 3 cm	26	6	20	
TNM staging				
I/II	19	14	5	0.0176
II/IV	59	25	34	
Lymph node metastasis				
Positive	34	12	22	0.0224
Negative	44	27	17	
Distant metastasis				
Positive	29	13	16	0.4821
Negative	49	26	23	

(Fig. 1B). Next, the relationship between circMETTL15 levels and clinicopathological characteristics of CRC patients was explored, and the data emphasized that the abundance of circMETTL15 was positively associated with tumor size, TNM stage, and lymph node metastasis

(Table 2). “Log-rank (Mantel-Cox) test” survival analysis showed that CRC patients with high circMETTL15 had poorer overall survival (Fig. 1C). Subsequently, the genetic information of circMETTL15 was determined from the bioinformatics website circbase. circMETTL15 was generated from exon 1 to exon 4 of the METTL15 gene with a full length of 862 bp (Fig. 1D). Agarose gel electrophoresis indicated that circMETTL15 was successfully detected by convergent primers for gDNA and cDNA, but it could only be generated from cDNA by different primers in LoVo cells (Fig. 1E). To further verify the stability of circMETTL15, RNase R and actinomycin D were used. CircMETTL15 was resistant to digestion by RNase R and had a longer half-life compared with linear mRNA (Fig. 1F, G).

circMETTL15 inhibition blocks CRC cell proliferation, invasion, migration, and EMT and promotes apoptosis

Subsequently, the effects of circMETTL15 on the biological behavior of CRC cells were investigated by loss of function assay. si-circMETTL15 was transfected into LoVo cells to downregulate circMETTL15 (Fig. 2A). CCK-8 and colony formation assays were utilized to evaluate cell proliferation ability. It was observed that knockdown of circMETTL15 reduced LoVo cell proliferation rate (Fig. 2B) and colony formation capacity (Fig. 2C). Then, cell cycle was detected by flow cytometry. As shown in Fig. 2D, knockdown of circMETTL15 increased the proportion of cells in G0/G1 phase and decreased the proportion of cells in G2/M phase. To investigate the effect of circMETTL15 on apoptosis, Annexin V-FITC/PI kit was used to evaluate apoptosis rates. As shown in Fig. 2E, circMETTL15 knockdown resulted in an increased apoptosis rate. In addition, the invasion and migration ability of LoVo cells was examined by Transwell assay. The results showed that circMETTL15 knockdown reduced the number of cells that invaded and migrated (Fig. 2F). At last, the changes of apoptosis, proliferation, and EMT-related proteins were observed by Western blot. As shown in Fig. 2G, after circMETTL15 downregulation, N-cadherin and Ki-67 expression decreased but cleaved caspase-3 and E-cadherin expression increased in LoVo cells. These data suggest that circMETTL15 knockdown inhibits LoVo cell proliferation, invasion, migration, and EMT, pro-

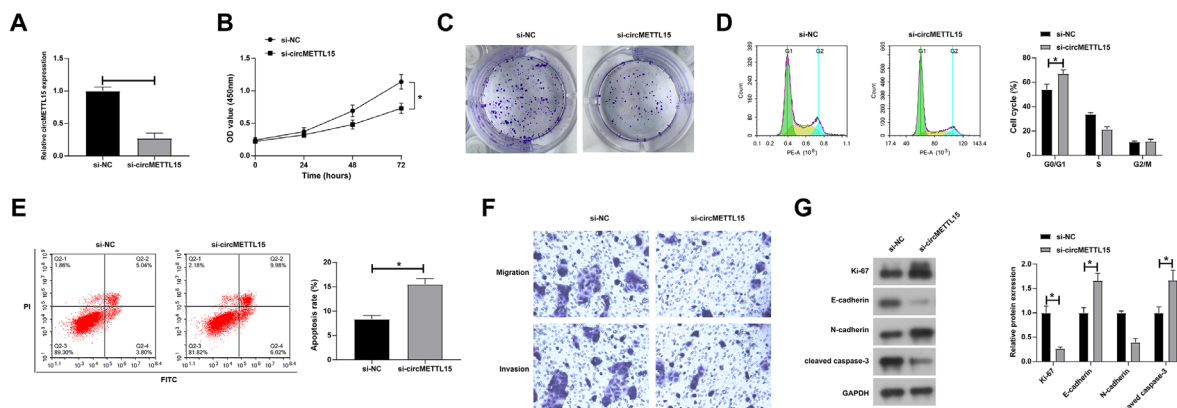


Figure 2. circMETTL15 inhibition blocks CRC cell proliferation, invasion, migration, and EMT and promotes apoptosis circMETTL15 was downregulated by transfection of siRNA targeting circMETTL15 into LoVo cells. (A) RT-qPCR to detect circMETTL15. (B) CCK-8 to detect cell proliferation rate. (C) Colony formation assay to detect cell proliferation. (D) Flow cytometry to detect cell cycle. (E) Flow cytometry to detect apoptosis. (F) Transwell assays to detect cell invasion and migration. (G) Western blot to evaluate Ki-67, E-cadherin, N-cadherin, and cleaved caspase-3 expression; data are expressed as mean \pm S.D. (N=3).

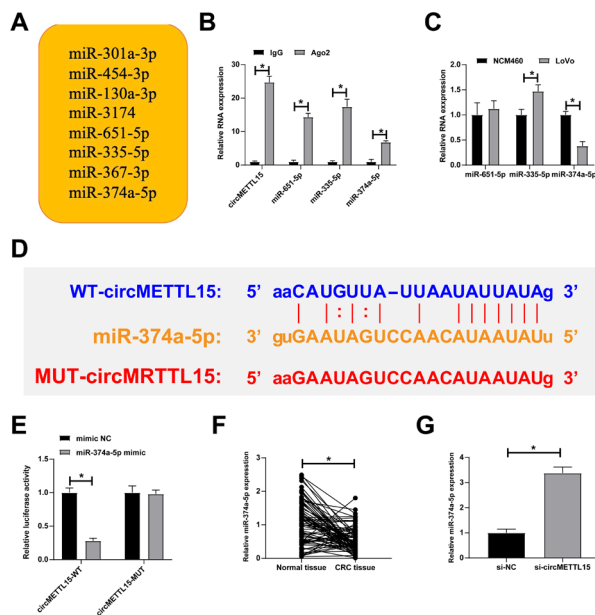


Figure 3. circMETTL15 binds to miR-374a-5p (A) Schematic diagram showing the potential miRNA of circMETTL15 based on circinteractome and StarBase. (B) RIP assay confirmed that three miRNAs and circMETTL15 were enriched in LoVo cells. (C) RT-qPCR to detect miR-374a-5p in LoVo cells. (D) Potential binding sites of circMETTL15 and miR-374a-5p predicted based on starbase. (E) Dual luciferase reporter assay to verify the targeting relationship between circMETTL15 and miR-374a-5p. (F) RT-qPCR to detect miR-374a-5p in CRC tissues and paired normal tissues. (G) RT-qPCR to confirm that circMETTL15 knockdown inhibited miR-374a-5p expression; data are expressed as mean \pm S.D. (N=3).

motes apoptosis, and increases the proportion of G0/G1 phase cells.

circMETTL15 binds to miR-374a-5p

Given that circRNAs primarily act as miRNA sponges in the cytoplasm, online databases (<https://starbase.sysu.edu.cn> and <https://circinteractome.nia.nih.gov>) predicted the possible miRNAs that bind to circMETTL15, and screened 8 kinds of overlapping of miRNAs (Fig. 3A). RIP experiments confirmed that three of the eight miRNAs were enriched with circMETTL15 (Fig. 3B), but only miR-374a-5p was downregulated in LoVo cells (Fig. 3C). Therefore, miR-374a-5p might be a downstream miRNA of circMETTL15. With their predicted potential binding sites (Fig. 3D), circMETTL15-WT and circMETTL15-MUT reporters were constructed, and their luciferase activity was observed by dual luciferase reporter assay. The results were consistent with the prediction, that is, circMETTL15 targets miR-374a-5p (Fig. 3E). RT-qPCR analyzed miR-374a-5p expression in patients' tissues and found its downregulation in CRC tissues (Fig. 3F). CircMETTL15 knockdown effectively increased miR-374a-5p expression in LoVo cells (Fig. 3G).

The effects of circMETTL15 on CRC cell proliferation, invasion, migration, apoptosis, cell cycle, and EMT are reversed by the silencing of miR-374a-5p

To explore whether miR-374a-5p is involved in the process of circMETTL15 regulating the biological behavior of LoVo cells, a functional rescue experiment was performed. Firstly, the expression changes of miR-374a-5p were evaluated by RT-qPCR. As shown in Fig. 4A, miR-374a-5p mimic and si-circMETTL15 both promoted miR-374a-5p expression, but miR-374a-5p inhibitor re-

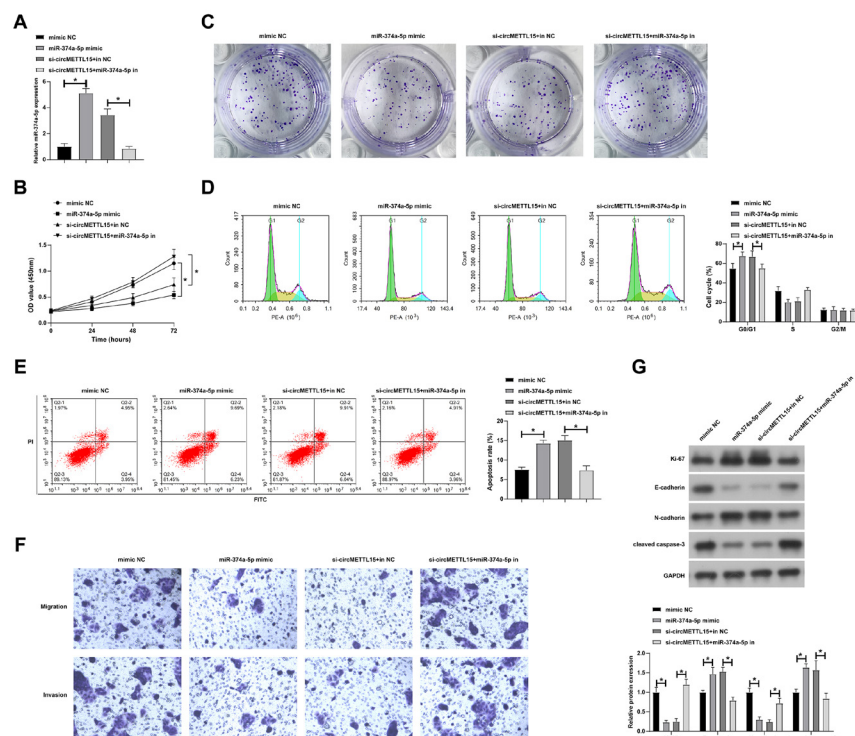


Figure 4. The effects of circMETTL15 on CRC cell proliferation, invasion, migration, apoptosis, cell cycle, and EMT are reversed by the silencing of miR-374a-5p miR-374a-5p mimic/inhibitor and si-circMETTL15 were transfected into LoVo cells. (A) RT-qPCR to detect miR-374a-5p. (B) CCK-8 to detect cell proliferation rate. (C) Colony formation assay to detect cell proliferation. (D) Flow cytometry to detect cell cycle. (E) Flow cytometry to detect apoptosis. (F) Transwell assays to detect cell invasion and migration. (G) Western blot to evaluate Ki-67, E-cadherin, N-cadherin, and cleaved caspase-3 expression; data are expressed as mean \pm S.D. (N=3).

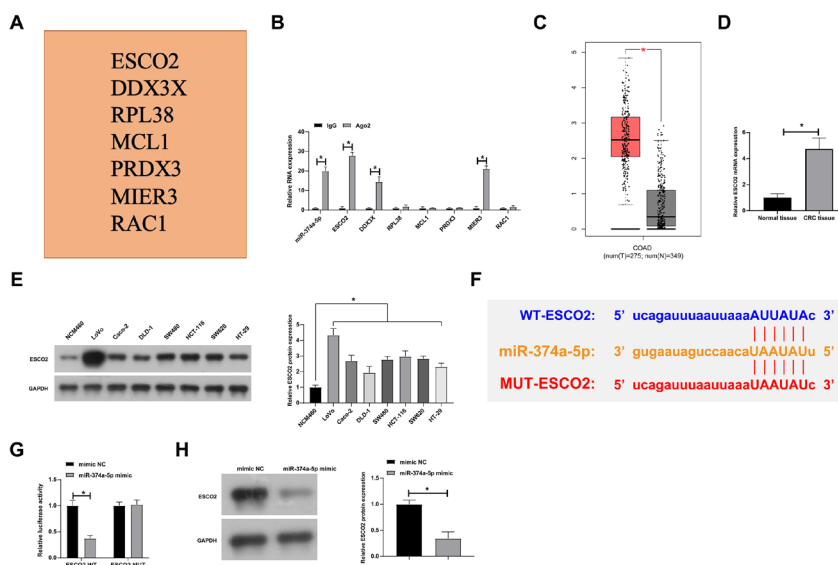


Figure 5. miR-374a-5p serves as a regulator of ESCO2 expression

(A) Potential downstream mRNA of miR-374a-5p predicted based on starbase, TargetScan, and miRDB; (B) RIP assay confirmed that three mRNAs and miR-374a-5p were enriched in LoVo cells. (C) GEPIA database analysis of ESCO2 in CRC. (D) RT-qPCR to detect ESCO2 in CRC tissues. (E) Western blot to detect ESCO2 in CRC cell lines. (F) Potential binding sites of miR-374a-5p and ESCO2 predicted based on starbase. (G) Dual luciferase reporting assay to explore the targeting relationship between miR-374a-5p and ESCO2. (H) Western blot to investigate ESCO2 expression after overexpression of miR-374a-5p; data are expressed as mean \pm S.D. (N=3).

duced miR-374a-5p expression. CCK-8 assay and colony formation assay showed that si-circMETTL15 and miR-374a-5p mimic inhibited cell proliferation rate and the number of colonies, but the effects of si-circMETTL15 were reversed by knockdown of miR-374a-5p (Fig. 4B, C). Flow cytometry showed that si-circMETTL15 and miR-374a-5p mimic increased the proportion of G0/G1 phase cells but reduced the proportion of G0/G1 phase cells after knockdown of miR-374a-5p (Fig. 4D). In addition, si-circMETTL15 and miR-374a-5p mimic promoted apoptosis rates, while the effects of si-circMETTL15 were reversed by silencing miR-374a-5p (Fig. 4E).

Transwell assay showed that si-circMETTL15 and miR-374a-5p mimic reduced the number of cells that invaded and migrated, while silencing miR-374a-5p reversed the effects of si-circMETTL15 (Fig. 4F). Western blot evaluated that si-circMETTL15 and miR-374a-5p mimic inhibited protein expression of N-cadherin and Ki-67 and promoted protein expression of cleaved caspase-3 and E-cadherin. However, knockdown of miR-374a-5p prevented changes in these proteins (Fig. 4G). These findings indicated that overexpression of miR-374a-5p inhibited the proliferation, invasion, and migration of LoVo cells, promoted apoptosis, increased the proportion of

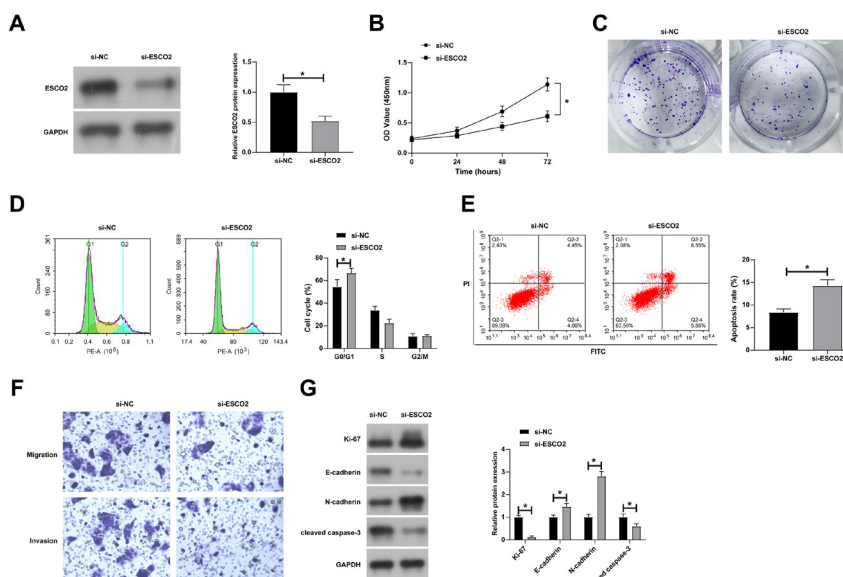


Figure 6. Knockdown of ESCO2 inhibits CRC cell proliferation, invasion, migration, and EMT and promotes apoptosis

siRNA targeting ESCO2 was transfected into LoVo cells. (A) Western blot to detect ESCO2. (B) CCK-8 to detect cell proliferation rate. (C) Colony formation assay to detect cell proliferation. (D) Flow cytometry to detect cell cycle. (E) Flow cytometry to detect apoptosis. (F) Transwell assays to detect cell invasion and migration. (G) Western blot to evaluate Ki-67, E-cadherin, N-cadherin, and cleaved caspase-3 expression; data are expressed as mean \pm S.D. (N=3).

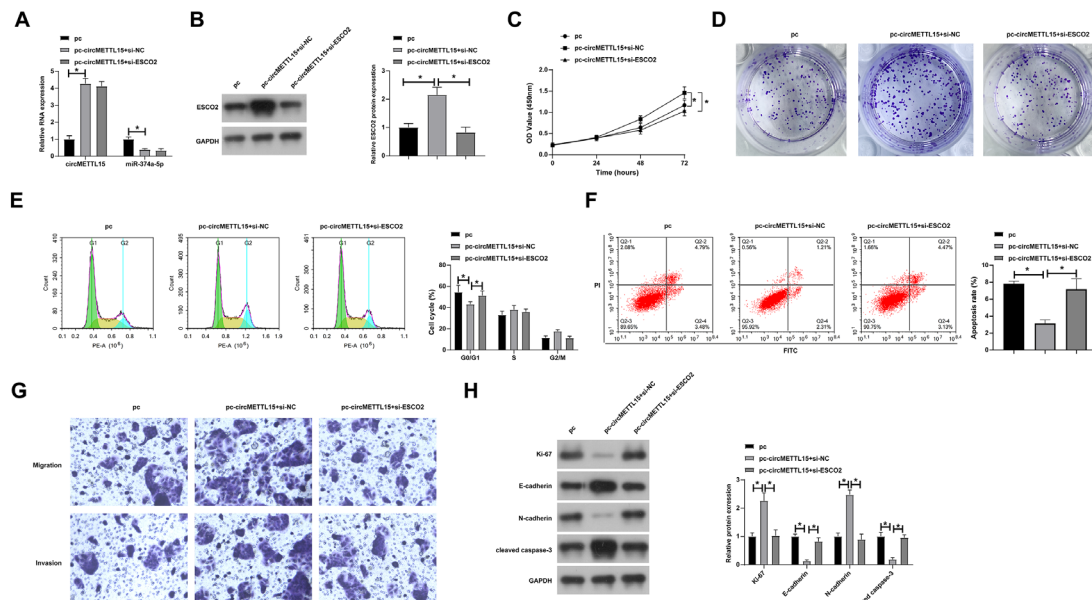


Figure 7. circMETTL15 affects CRC cell proliferation, cell cycle, apoptosis, invasion, migration, and EMT processes by regulating miR-374a-5p/ESCO2 axis

pcDNA 3.1-circMETTL15 and si-ESCO2 were transfected into LoVo cells. (A) RT-qPCR to detect circMETTL15 and miR-374a-5p. (B) Western blot to detect ESCO2. (C) CCK-8 to detect cell proliferation rate. (D) Colony formation assay to detect cell proliferation. (E) Flow cytometry to detect cell cycle. (F) Flow cytometry to detect apoptosis. (G) Transwell assays to detect cell invasion and migration. (H) Western blot to evaluate Ki-67, E-cadherin, N-cadherin, and cleaved caspase-3 expression; data are expressed as mean \pm S.D. (N=3).

G0/G1 phase cells, and circMETTL15 affected the proliferation, apoptosis, cell cycle, invasion, migration, and EMT processes of CRC cells by regulating miR-374a-5p.

miR-374a-5p serves as a regulator of ESCO2 expression

To explore downstream targets regulated by miR-374a-5p, starbase, TargetScan and miRDB predicted seven overlapping candidate downstream genes (Fig. 5A). Three were identified to be enriched with miR-374a-5p by RIP screening (Fig. 5B), among which ESCO2 was found to be upregulated in CRC by TCGA database analysis (Fig. 5C). ESCO2 upregulation was also demonstrated in CRC patients and cell lines (Fig. 5D, E). Sub-

sequently, the targeting relationship between ESCO2 and miR-374a-5p was confirmed by dual luciferase reporter experiments (Fig. 5F, G). Furthermore, ESCO2 expression reduced accordingly when miR-374a-5p was overexpressed (Fig. 5H).

Knockdown of ESCO2 inhibits CRC cell proliferation, invasion, migration, and EMT and promotes apoptosis

Subsequently, the effects of ESCO2 on the biological behavior of LoVo cells were examined. Western blot assay showed that transfection of si-ESCO2 decreased ESCO2 expression in LoVo cells (Fig. 6A). CCK-8 and colony formation experiments showed that knockdown of ESCO2 inhibited cell proliferation rate and colony-forming ability (Fig. 6B, C). Flow cytometry showed that knockdown of ESCO2 resulted in an increased proportion of cells arrested in the G0/G1 phase (Fig. 6D) and resulted in increased apoptosis (Fig. 6E). Transwell assay showed that the invasion and migration abilities of cells were reduced after ESCO2 knockdown (Fig. 6F). Western blot analysis showed that ESCO2 inhibition decreased N-cadherin and Ki-67 expression and increased cleaved caspase-3 and E-cadherin expression (Fig. 6G). The above data indicated that knockdown of ESCO2 effectively inhibited CRC proliferation, invasion, migration, and EMT and promoted apoptosis.

circMETTL15 affects CRC cell proliferation, cell cycle, apoptosis, invasion, migration, and EMT processes by regulating miR-374a-5p/ESCO2 axis

To explore whether the miR-374a-5p/ESCO2 axis is involved in the process of circMETTL15 regulating the biological behavior of CRC cells, LoVo cells were subjected to a co-transfection design with pcDNA 3.1 overexpression vector targeting circMETTL15 and si-ESCO2. pcDNA 3.1 overexpression vector targeting circMETTL15 promoted circMETTL15 and ESCO2 expression

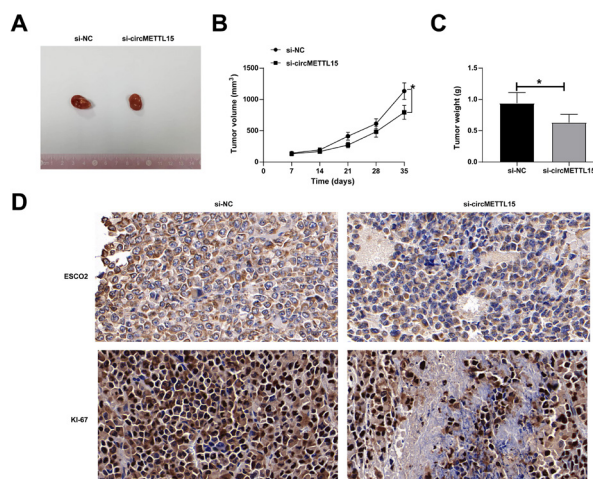


Figure 8. Knockdown of circMETTL15 inhibits CRC tumorigenesis *in vivo*

(A) Representative images of tumors. (B–C) Tumor volume and weight. (D) IHC staining to measure ESCO2 and Ki-67 expression in tumors; data are expressed as mean \pm S.D. (n=5).

and suppressed miR-374a-5p expression, while si-ESCO2 made ESCO2 expression partially recovered (Fig. 7A, B). CCK-8 and colony formation assays showed that overexpression of circMETTL15 promoted cell proliferation rate and cell cloning ability, but knockdown of ESCO2 reversed this phenomenon (Fig. 7C, D). Flow cytometry showed that overexpression of circMETTL15 reduced the proportion of cells arrested in G0/G1 phase, while knockdown of ESCO2 increased the proportion of G0/G1 phase cells (Fig. 7E). Annexin V-FITC/PI apoptosis kit tests showed that the overexpression of circMETTL15 reduced apoptosis rate, while knockdown of ESCO2 reversed this effect (Fig. 7F). Transwell assay showed that overexpression of circMETTL15 enhanced cell invasion and migration, but knockdown of ESCO2 reduced the number of invasion and migration cells (Fig. 7G). In addition, overexpression of circMETTL15 promoted expression of N-cadherin and Ki-67 and inhibited expression of cleaved caspase-3 and E-cadherin, but knockdown of ESCO2 prevented changes in these proteins (Fig. 7H). These data suggest that circMETTL15 promotes LoVo cell proliferation, invasion, migration, and EMT and reduces apoptosis by regulating the miR-374a-5p/ESCO2 axis.

Knockdown of circMETTL15 inhibits CRC tumorigenesis *in vivo*

At last, LoVo cells stably knocking down circMETTL15 were implanted into nude mice to explore the effect of circMETTL15 on the growth of CRC tumors *in vivo*. CircMETTL15 depletion suppressed tumor volume and weight (Fig. 8A–C). IHC staining showed that knockdown of circMETTL15 decreased ESCO2 expression and Ki-67 expression in tumors (Fig. 8D).

DISCUSSION

Late detection is the main reason for annual mortality in CRC (Ameli-Mojarad *et al.*, 2021), therefore, the search for an optimal biomarker for disease diagnosis and prognosis is necessary for identifying and treating CRC cases. Molecular biology and genomics have emphasized the significance of non-coding RNAs in tumor development (Chu *et al.*, 2021). Therefore, we attempted to investigate the effects of circMETTL15 involved in CRC, as well as related molecular mechanisms. Further experiments demonstrated that silence of circMETTL15 by suppressing miR-374a-5p and promoting ESCO2 expression could effectively inhibit the malignant behavior of CRC.

circRNAs are more suitable as new biomarkers for CRC and have potential clinical value in the early diagnosis and prognostic assessments of CRC (C. Lin *et al.*, 2022; Radanova *et al.*, 2021). For example, circ_001659 has a good predictive value and probability ratio for the diagnosis of CRC and confers pro-tumor influence on CRC development (He *et al.*, 2021) and circMYLK is associated with poor prognosis and some unfavorable clinical features of CRC patients (Huang & Dai, 2021). Similarly, our findings suggested that a higher abundance of circMETTL15 was correlated with tumor size, TNM stage, lymph node metastasis, and poor overall survival. The results indicated that circMETTL15 may be a prognostic or diagnostic biomarker in CRC, which needs to be verified by detecting circMETTL15 expression in CRC serum in subsequent studies. In a recent study, circMETTL15 is highly expressed in lung cancer and regulates malignant progression and immune escape

(Zhang *et al.*, 2022). The results of this study further support the role of circMETTL15 as a cancer-promoting factor, which promotes ESCO2 expression by binding miR-374a-5p, thus promoting CRC development. The study speculates that circMETTL15 also has the function of regulating immune checkpoint in CRC, and it may be feasible to employ circMETTL15 as a new target for immunotherapy, but this needs to be explored in subsequent studies.

miRNAs have been widely recognized as key regulators in cancers (Yamamoto & Mori, 2016). According to the ceRNA network, circRNAs can bind to miRNAs, thereby reducing the biological functions of miRNAs (Jorgensen & Ro, 2022). The study predicted and then verified that miR-374a-5p was a downstream miRNA of circMETTL15 in CRC. miR-374a-5p is considered a tumor oncogenic factor in ovarian cancer (Hao, Huang, & Han, 2020), triple-negative breast cancer (Son *et al.*, 2019), gastric cancer (Ji *et al.*, 2019), whereas a tumor suppressor in non-small cell lung cancer (Guo *et al.*, 2021) and esophageal squamous cell carcinoma (Chen *et al.*, 2019). Notably, it is recorded that miR-374a-5p is downregulated in CRC and is related to patients' survival rate (Slattery *et al.*, 2017; Slattery *et al.*, 2015). The study continuously explored miR-374a-5p in CRC and, as expected, miR-374a-5p could suppress the malignant phenotype of CRC cells while miR-374a-5p downregulation rescued the effect of circMETTL15 silencing on the biological behavior of CRC cells.

For this study, the downstream target (ESCO2) of miR-374a-5p was screened, which was upregulated in CRC. ESCO2, a member of the Eco1 family, contributes to sister chromatid cohesion during cell cycle progression (Wang & Liu, 2020). It is well known that different states of cohesin are associated with different phases of the cell cycle (Alomer *et al.*, 2017) and ESCO2 is involved in cohesion-mediated DNA repair (Rahman, Jones, & Jallepalli, 2015). Because of this, ESCO2 has received increasing attention in cancer development. It is noted that ESCO2 promotes lung adenocarcinoma (Zhu *et al.*, 2021) and gastric cancer (Chen *et al.*, 2018). Notably, ESCO2 is recently reported as an epigenetic regulator to suppress tumor metastasis in CRC (Guo *et al.*, 2018). Based on this, a functional rescue experiment was performed to reveal that ESCO2 knockdown rescued the promotion of circMETTL15 overexpression on the malignant progression of CRC cells.

However, how ESCO2 interacts with other epigenetic regulators or pathways to influence the development and progression of CRC has not been thoroughly investigated. In the follow-up experiments, we should further carry out multi-center trials and animal experiments to clarify the therapeutic effect and mechanism of circMETTL15 on CRC. In addition, multicenter trials and animal experiments are needed to elucidate the role of circMETTL15 in CRC.

CONCLUSION

In conclusion, this study suggests that circMETTL15 sponges miR-374a-5p to regulate ESCO2 and promote CRC malignant behavior. These data provide new molecular targets for the development of CRC-targeted drugs and future combination therapies. However, the results of this study have so far only been verified in LoVo cells and animal experiments. Therefore, it is not suitable for clinical trials. More basic experiments (such as validation in more CRC cell lines) are needed in the

future to further explore the influence of the circMETTL15/miR-374a-5p/ESCO2 axis on CRC biological behavior.

Declarations

Acknowledgments. Not applicable.

Funding Statements. Not applicable.

Declaration of Conflicting Interests. Authors declared no conflict of interest.

Ethical approval. All procedures performed in this study involving human participants were in accordance with the ethical standards of the Renji Hospital, Shanghai Jiaotong University School of Medicine research committee and with the 1964 Helsinki Declaration and its later amendments or comparable ethical standards. All subjects were approved by Renji Hospital, Shanghai Jiaotong University School of Medicine.

REFERENCES

- Alomer RM, da Silva EML, Chen J, Piekarczyk KM, McDonald K, Sansam CG, Sansam CL, Rankin S (2017) Esco1 and Esco2 regulate distinct cohesin functions during cell cycle progression. *Proc Natl Acad Sci U S A* **114**: 9906–9911. <https://doi.org/10.1073/pnas.1708291114>
- Ameli-Mojarad M, Ameli-Mojarad M, Hadizadeh M, Young C, Babini H, Nazemalhosseini-Mojarad E, Bonab MA (2021) The effective function of circular RNA in colorectal cancer. *Cancer Cell Int* **21**: 496. <https://doi.org/10.1186/s12935-021-02196-0>
- Chen H, Zhang L, He W, Liu T, Zhao Y, Chen H, Li Y (2018) ESCO2 knockdown inhibits cell proliferation and induces apoptosis in human gastric cancer cells. *Biochem Biophys Res Commun* **496**: 475–481. <https://doi.org/10.1016/j.bbrc.2018.01.048>
- Chen W, Zhang Y, Wang H, Pan T, Zhang Y, Li C (2019) LINC00473/miR-374a-5p regulates esophageal squamous cell carcinoma via targeting SPIN1 to weaken the effect of radiotherapy. *J Cell Biochem* **120**: 14562–14572. <https://doi.org/10.1002/jcb.28717>
- Chu J, Fang X, Sun Z, Gai L, Dai W, Li H, Yan X, Du J, Zhang L, Zhao L, Xu D, Yan S (2021) Non-coding RNAs regulate the resistance to anti-EGFR therapy in colorectal cancer. *Front Oncol* **11**: 801319. <https://doi.org/10.3389/fonc.2021.801319>
- Díaz-Tasende J (2018) Colorectal cancer screening and survival. *Rev Esp Enferm Dig* **110**: 681–683. <https://doi.org/10.17235/reed.2018.5870/2018>
- Guo Q, Wang H, Xu Y, Wang M, Tian Z (2021) miR-374a-5p inhibits non-small cell lung cancer cell proliferation and migration via targeting NCK1. *Exp Ther Med* **22**: 943. <https://doi.org/10.3892/etm.2021.10375>
- Guo XB, Huang B, Pan YH, Su SG, Li Y (2018) ESCO2 inhibits tumor metastasis via transcriptionally repressing MMP2 in colorectal cancer. *Cancer Manag Res* **10**: 6157–6166. <https://doi.org/10.2147/cmar.S181265>
- Hao T, Huang S, Han F (2020) LINC-PINT suppresses tumour cell proliferation, migration and invasion through targeting miR-374a-5p in ovarian cancer. *Cell Biochem Funct* **38**: 1089–1099. <https://doi.org/10.1002/cbf.3565>
- He B, Chao W, Huang Z, Zeng J, Yang J, Luo D, Huang S, Pan H, Hao Y (2021) Hsa_circ_001659 serves as a novel diagnostic and prognostic biomarker for colorectal cancer. *Biochem Biophys Res Commun* **551**: 100–106. <https://doi.org/10.1016/j.bbrc.2021.02.121>
- Huang L, Dai G (2021) CircMYLK promotes cell proliferation, migration, and invasion in colorectal cancer. *Ann Clin Lab Sci* **51**: 339–346
- Ji R, Zhang X, Gu H, Ma J, Wen X, Zhou J, Qian H, Xu W, Qian J, Lin J (2019) miR-374a-5p: A new target for diagnosis and drug resistance therapy in gastric cancer. *Mol Ther Nucleic Acids* **18**: 320–331. <https://doi.org/10.1016/j.omtn.2019.07.025>
- Jorgensen BG, Ro S (2022) MicroRNAs and ‘Sponging’ competitive endogenous RNAs dysregulated in colorectal cancer: potential as noninvasive biomarkers and therapeutic targets. *Int J Mol Sci* **23**. <https://doi.org/10.3390/ijms23042166>
- Lin C, Ma M, Zhang Y, Li L, Long F, Xie C, Xiao H, Liu T, Tian B, Yang K, Guo Y, Chen M, Chou J, Gong N, Li X, Hu G (2022) The N(6)-methyladenosine modification of circALG1 promotes the metastasis of colorectal cancer mediated by the miR-342-5p/PGF signalling pathway. *Mol Cancer* **21**: 80. <https://doi.org/10.1186/s12943-022-01560-6>
- Lin Q, Zhou CR, Bai MJ, Zhu D, Chen JW, Wang HF, Li MA, Wu C, Li ZR, Huang MS (2020) Exosome-mediated miRNA delivery promotes liver cancer EMT and metastasis. *Am J Transl Res* **12**: 1080–1095
- Long C, Xu QB, Ding L, Huang LJ, Ji Y (2022) Circular RNAs as diagnostic and prognostic indicators of colorectal cancer: a pooled analysis of individual studies. *Pathol Oncol Res* **28**: 1610037. <https://doi.org/10.3389/pore.2022.1610037>
- Radanova M, Mihaylova G, Tasinov O, Ivanova DP, Stoyanov GS, Nazifova-Tasinova N, Manev R, Salim A, Nikolova M, Ivanova DG, Conev N, Mihaylova Z, Donev I (2021) New circulating circular RNAs with diagnostic and prognostic potential in advanced colorectal cancer. *Int J Mol Sci* **22**. <https://doi.org/10.3390/ijms222413283>
- Rahman S, Jones MJ, Jallepalli PV (2015) Cohesin recruits the Esco1 acetyltransferase genome wide to repress transcription and promote cohesion in somatic cells. *Proc Natl Acad Sci U S A* **112**: 11270–11275. <https://doi.org/10.1073/pnas.1505323112>
- Salmena L, Poliseno L, Tay Y, Kats L, Pandolfi PP (2011) A ceRNA hypothesis: the Rosetta Stone of a hidden RNA language? *Cell* **146**: 353–358. <https://doi.org/10.1016/j.cell.2011.07.014>
- Shao Q, Wang L, Yuan M, Jin X, Chen Z, Wu C (2021) TIGIT induces (CD3+) T cell dysfunction in colorectal cancer by inhibiting glucose metabolism. *Front Immunol* **12**: 688961. <https://doi.org/10.3389/fimmu.2021.688961>
- Simon K (2016) Colorectal cancer development and advances in screening. *Clin Interv Aging* **11**: 967–976. <https://doi.org/10.2147/cia.S109285>
- Slattery ML, Herrick JS, Mullany LE, Valeri N, Stevens J, Caan BJ, Samowitz W, Wolff RK (2015) An evaluation and replication of miRNAs with disease stage and colorectal cancer-specific mortality. *Int J Cancer* **137**: 428–438. <https://doi.org/10.1002/ijc.29384>
- Slattery ML, Pellatt AJ, Lee FY, Herrick JS, Samowitz WS, Stevens JR, Wolff RK, Mullany LE (2017) Infrequently expressed miRNAs influence survival after diagnosis with colorectal cancer. *Oncotarget* **8**: 83845–83859. <https://doi.org/10.18632/oncotarget.19863>
- Son D, Kim Y, Lim S, Kang HG, Kim DH, Park JW, Cheong W, Kong HK, Han W, Park WY, Chun KH, Park JH (2019) miR-374a-5p promotes tumor progression by targeting ARRB1 in triple negative breast cancer. *Cancer Lett* **454**: 224–233. <https://doi.org/10.1016/j.canlet.2019.04.006>
- Tsai WL, Wang CY, Lee YC, Tang WC, Anuraga G, Ta HDK, Wu YF, Lee KH (2021) A new light on potential therapeutic targets for colorectal cancer treatment. *Biomedicines* **9**. <https://doi.org/10.3390/biomedicines9101438>
- Wang QL, Liu L (2020) Establishment of cohesion 1 homolog 2 facilitates cell aggressive behaviors and induces poor prognosis in renal cell carcinoma. *J Clin Lab Anal* **34**: e23163. <https://doi.org/10.1002/jcla.23163>
- Yamamoto H, Mori M (2016) MicroRNAs as therapeutic targets and colorectal cancer therapeutics. *Adv Exp Med Biol* **937**: 239–247. https://doi.org/10.1007/978-3-319-42059-2_13
- Yi B, Dai K, Yan Z, Yin Z (2022) Circular RNA PLCE1 promotes epithelial mesenchymal transformation, glycolysis in colorectal cancer and M2 polarization of tumor-associated macrophages. *Bioengineered* **13**: 6243–6256. <https://doi.org/10.1080/21655979.2021.2003929>
- Zhang R, Shang L, Nan J, Niu K, Dai J, Jin X, Zhang X (2022) CircMETTL15 contributes to the proliferation, metastasis, immune escape and restrains apoptosis in lung cancer by regulating miR-1299/PDL1 axis. *Autoimmunity* **55**: 8–20. <https://doi.org/10.1080/08916934.2021.2001801>
- Zhang S, Sun J, Gu M, Wang G, Wang X (2021) Circular RNA: A promising new star for the diagnosis and treatment of colorectal cancer. *Cancer Med* **10**: 8725–8740. <https://doi.org/10.1002/cam4.4398>
- Zhou J, Wang L, Sun Q, Chen R, Zhang C, Yang P, Tan Y, Peng C, Wang T, Jin C, Ji J, Jin K, Sun Y (2021) Hsa_circ_0001666 suppresses the progression of colorectal cancer through the miR-576-5p/PCDH10 axis. *Clin Transl Med* **11**: e565. <https://doi.org/10.1002/ctm2.565>
- Zhu HE, Li T, Shi S, Chen DX, Chen W, Chen H (2021) ESCO2 promotes lung adenocarcinoma progression by regulating hnRNPA1 acetylation. *J Exp Clin Cancer Res* **40**: 64. <https://doi.org/10.1186/s13046-021-01858-1>

Recent studies on non-invasive biomarkers useful in biliary atresia – a literature review

Anna Lew-Tusk¹✉, Marta Pęksa² and Teresa Stachowicz-Stencel³

¹Department of Neonatology and Neonatal Intensive Care Unit, St Wojciech Hospital, Gdańsk, Poland; ²Department of Obstetrics, Medical University of Gdansk, Gdańsk, Poland; ³Department of Pediatrics, Hematology and Oncology, Medical University of Gdansk, Gdańsk, Poland

The aim of this review is to specify new potential reliable and non-invasive methods for the diagnosis of biliary atresia (BA) that could shorten the way to diagnose BA, and finally the surgical treatment. Apart from the biomarkers that have been proven helpful and are used nowadays in neonatal wards, there are several new potential biomarkers that researchers have found to be helpful in the diagnosis of biliary atresia. Circulating microRNAs, matrix metalloproteinase-7, stool proteins, interleukin-33, Th17-associated cytokines, urinary metabolomics, anti-smooth muscle antibodies, heat shock proteins 90 and positive biliary epithelial cells CD56 are among those presented in this summary. These markers may play a new significant role in BA diagnosis. The described methods include Nomogram, Circulating microRNAs (miRNAs), Matrix metalloproteinase-7 (MMP-7), Stool proteins, Interleukin-33 (IL-33), Th17-associated cytokines, Alpha-aminoadipic acid and N-acetyl-d-mannosamine in urine, Anti-smooth muscle antibodies (ASMA), Heat shock proteins 90 (HSP90), Positive biliary epithelial cells CD56.

Key words: biliary atresia, neonatal cholestasis, jaundice

Received: 29 May, 2023; revised: 04 September, 2023; accepted: 04 September, 2023; available on-line: 17 September, 2023

✉e-mail: ano.lew@wp.pl

Abbreviations: ALP, alkaline phosphatase; ALT, Alanine transaminase; ASMA, Anti-smooth muscle antibodies; AST, aminotransferase; AUC-ROC, the area under the receiver operating characteristic curve; BA, biliary atresia; DB, direct bilirubin; GC-MS, gas chromatography-mass spectrometry metabolomics; GGT, gamma-glutamyl transpeptidase; HSP90, Heat shock proteins; IHS, infantile hepatitis syndrome; ILF, indirect immunofluorescence; IL-33, Interleukin-33; MIP3a, macrophage inflammatory protein-3alpha; MMP-7, Matrix metalloproteinase-7; MRCP, magnetic resonance cholangiopancreatography; OPLS-DA, orthogonal partial least squares discriminant analysis; TB, total bilirubin

INTRODUCTION

Biliary atresia (BA) (ORPHA:244283; OMIM: 210500) is an uncommon infancy fibroinflammatory obliterative cholangiopathy that affects extrahepatic and intrahepatic biliary ducts. It is associated with obstructive jaundice, pale stools and hepatomegaly, and leads to severe cholestasis and fatal biliary cirrhosis. The etiology of BA remains elusive. If not treated in time with hepatoportocenterostomy which restores bile flow (Kasai procedure KPE – the primary treatment of BA), it leads to liver failure within 2 years (Basset *et al.*, 2008; Chardot, 2006; Sokol *et al.*, 2007; Feldman *et al.*, 2015). BA remains the most common cause of a liver transplant in young children. It affects approximately 1 in 5000 to 25000 live

births. It is more common in the Asia-Pacific region, especially in South China where the prevalence is about 1/5000 (Chen *et al.*, 2019).

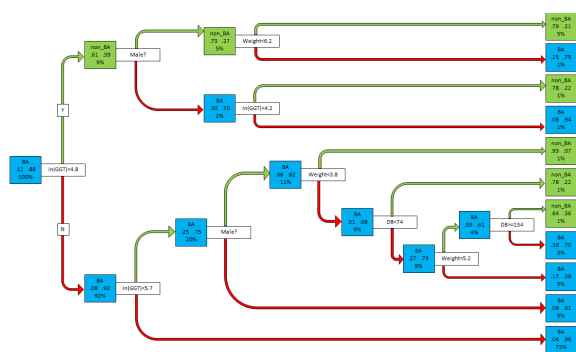
An early diagnosis is highly problematic due to unspecific symptoms which can mimic other cholestatic diseases (non-BA). There are no reliable and specific biomarkers that are recommended for routine clinical use. Currently, the gold standard for BA diagnosis is an intraoperative cholangiogram which is highly invasive. Liver biopsy with 96.6% accuracy is the most reliable method (Chen *et al.*, 2016). The longer it takes to diagnose chronic cholestasis, the higher the risk of liver fibrosis. Because the success of Kasai portoenterostomy depends, among others, on age at the time of surgery, due to delayed diagnosis many infants with BA lose the chance for proper treatment. Also, a late diagnosis worsens the outcomes of other cholestasis-associated diseases like hypopituitarism, galactosaemia and tyrosinaemia.

The investigation of biliary atresia requires taking the following blood tests: gamma-glutamyl transpeptidase (GGT), also combined with total bilirubin, direct bilirubin, alkaline phosphatase, and aminotransferase (AST). The diagnosis is also based on clinical evaluation, hepatomegaly, stool colour, duodenal juice colour, bile acid in duodenal juice, ultrasonography (the gallbladder triad, the triangular cord sign or strip-apparent hyperechoic foci), hepatobiliary scintigraphy, MRCP and liver biopsy (Dong *et al.*, 2018).

NOMOGRAM

In the Dong and others research, bile acid level in duodenal juice and hepatobiliary scintigraphy showed the highest (100%) sensitivity for diagnosing BA (Dong Ch *et al.*, 2018). Ultrasonography (triangular cord sign or presence of strip-apparent hyperechoic foci) showed the highest specificity (99.5%). The colour of the stool is also pathognomic. High levels of bilirubin alter the hue of the stool and turn it into light yellow. The diagnostic accuracy by feces color was 84.3% with a sensitivity of 96.1% and specificity of 74.8% in Dong's and others research (Dong Ch *et al.*, 2018). All of the known differential diagnosis methods are useful. Gamma-glutamyl transpeptidase (GGT) is used in combination with other biomarkers of BA cholestasis (Chen *et al.*, 2016; Liu *et al.*, 1998; Cabrera-Abreu *et al.*, 2002; Rendon-Macias *et al.*, 2008; Tang *et al.*, 2007; Maggiore *et al.*, 1991). Younger infants with BA (age <30 days) proved to have significantly higher GGT levels than older patients (Dong Ch *et al.*, 2018). The researchers demonstrated that in a 2-year treatment, 53.7% of patients survived with their native liver, while the remaining patients needed liver

transplantation. Sira and others reported that the serum activity of GGT had a sensitivity of 76.7% and specificity of 80% for the diagnosis of BA (Sira *et al.*, 2012). Nonetheless, the GGT level was also increased in the serum of infants on the day of birth or varied depending on age (Dong Ch *et al.*, 2018). In the Dong's and others research, carried out in a large Chinese children's hospital on 1728 patients, to confirm BA intraoperative cholangiography and liver biopsy for histological assessment were used (Dong R *et al.*, 2018). 1512 patients were diagnosed with BA and 216 patients were confirmed to have non-BA cholestasis. 80% of non-BA patients were male, however, there was no statistical difference in gender in the BA group (51% male, 49% female). The research also included weight, age and the levels of: total bilirubin (TB), direct bilirubin (DB), alkaline phosphatase (ALP), and gamma-glutamyl transpeptidase (GGT), AST and ALT (Alanine transaminase). There was no significant difference in TB, AST and ALT levels. Patients' age also did not show any notable influence on results. The non-BA group presented higher alkaline phosphatase levels (ALP). Gender, weight, DB, ALP, and GGT showed a good prediction with the AUC-ROC curve (the area under the receiver operating characteristic curve) >0.8 (a value close to 1 is considered perfect discrimination). Rui Dong and others (Dong R *et al.*, 2018) created a nomogram based on those factors (gender, weight, DB, ALP, and GGT) allowing to predict BA.



Nomogram based on various factors (gender, weight, DB, ALP, and GGT) proved helpful in diagnosing BA.

The nomogram demonstrated a good discriminative ability with a sensitivity of 85.7% and specificity of 80.3%. It proved useful in diagnosing BA and, additionally, to have the potential for clinical application (Dong R *et al.*, 2018).

CIRCULATING MICRORNAS (miRNAS)

Zahm and others (Zahm *et al.*, 2011) hypothesized that unique miRNAs may serve as a new class of biomarkers that could help to distinguish BA from other forms of neonatal cholestasis and therefore become a new diagnostic biomarker of BA. Goldschmidt's analysis says that circulating MicroRNA as the miR-21 and miR-29a cluster may be used as markers of liver diseases in children (Goldschmidt *et al.*, 2016). MicroRNAs are short non-coding parts of RNAs which are necessary for organ development (Thai *et al.*, 2007; Lynn *et al.*, 2007; Hand *et al.*, 2009). MiRNAs are dysregulated in many pathologies including BA. Increased levels of circulating miRNAs can suggest specific tissue damage (Morimura *et*

al., 2011; Laterza *et al.*, 2009; Zahm *et al.*, 2011). Zahm *et al.* proved that a cluster of miRNAs (miR-200b/429) is elevated in BA patients' sera compared to cholestatic control samples. The researchers used serum samples obtained from patients with confirmed BA (by cholangiography, operative exploration, and/or histology) and extrahepatic bile duct tissue from mouse liver. 11 miRNAs were selected for further analysis out of which the miR-200b showed significant alterations. To prove the importance of miR-200b, they measured levels of miR-200a and miR-429 (which are co-transcribed with miR-200b from the miR-200b/429 locus (Zahm *et al.*, 2012)). They were both altered in the sera of BA patients. The AUC values 0.8 for the miR-200b/429 cluster with a sensitivity of 71% and specificity of 92%. Adam M. Zahm *et al.* also discovered that cholangiocytes serve as the source of miR-200b/429 cluster in biliary atresia. Detecting elevated levels of miR-200b/429 in serum can be useful not only in distinguishing BA from non-BA patients, but also in predicting survival after KPE. The miR-200b/429 cluster classifies correctly 85% of patients (Zahm *et al.*, 2012). Because not all samples are correctly classified, further research is needed. Nevertheless, elevated circulating miR-200b/429 levels may prove useful in BA diagnostics. Another microRNA analysis done by Zahm and others (Zahm *et al.*, 2011) showed that circulating miR-4429 and miR-4689 can play a certain role in diagnosing BA. The AUC of miR-4429 was 0.789 with a sensitivity of 83.3% and a specificity of 80.0%, and the AUC of miR-4689 was 0.722 with a sensitivity of 66.7% and specificity of 80.0% for the prediction of BA (Zahm *et al.*, 2012).

MATRIX METALLOPROTEINASE-7 (MMP-7)

MMP-7 (also known as matrilysin (Hugh, 2017)) is a zinc-dependent endopeptidase that breaks down the extracellular matrix and its expression can correlate with BA-related liver fibrosis (Yang *et al.*, 2018; Jiang *et al.*, 2019). The researchers have recently discovered that an altered level of MMP-7 in the serum of a cholestatic patient can be associated with biliary atresia (Yang *et al.*, 2018; Jiang *et al.*, 2019). To prove the diagnostic value of MMP-7, Yang and others (Yang *et al.*, 2018) tested 135 infants with cholestasis (75 with BA and 60 non-BA) and a 54 control group at three pediatric centers. The results showed that MMP-7 levels in BA patients sera were significantly higher than in non-BA cases. Serum levels of MMP-7 in a non-cholestatic group had a median of 2.86 ng/mL, the non-BA group was circa 11.47 ng/mL and BA patients had an average with a median of 121.1 ng/mL, that is 10-times higher than in others. Yang and others (Yang *et al.*, 2018) have also compared GGT and MMP-7 levels in the sera of BA- neonates. The AUC of MMP-7 was 0.9900 and the AUC for GGT was 0.7186. For GGT, the sensitivity was 64.00% and the specificity was 71.67%. In comparison, the sensitivity and the specificity of MMP-7 were respectively 98.67% and 95.00%. The negative predictive value of MMP-7 was 98.28% (Yang *et al.*, 2018). The number needed to misdiagnose (NNM) was also calculated and for MMP-7 it was 25 (which means that 1 out of 25 patients was misdiagnosed). For GGT, the NNM was 3 (so 1 out of 3 was misdiagnosed). Combining MMP-7 and GGT with an AUC of 0.9898 does not increase diagnostic accuracy (Hugh, 2017; Yang *et al.*, 2018). Lertudomphonwanit *et al.* investigated samples of 35 BA patients and 35 cases with intrahepatic cholestasis. Serum levels of MMP7 and

GGT were different in these two groups and the researchers estimated that 19.1 infants could be diagnosed with BA with the MMP7 plus GGT as a biomarker (Lertudomphonwanit *et al.*, 2017; Hugh, 2017). Jiang and others (Jiang *et al.*, 2019) diagnosed 288 patients with jaundice. The median of MMP-7 in BA group sera was 38.89 ng/mL and in non-BA: 4.4 ng/mL. The sensitivity, specificity, positive predictive value and negative predictive value were 95.19%, 93.07%, 97.27%, and 91.43%, respectively. The accuracy was improved when MMP-7 was combined with GGTP. Based on this data, alterations in the serum MMP-7 levels may be helpful in the diagnosis of biliary atresia. It also correlates with liver fibrosis, therefore it can be potentially used as a therapeutic target or a prognostic biomarker (Hugh, 2017; Yang *et al.*, 2018; Jiang *et al.*, 2019). Another study by Wu *et al.* was based on a group of 100 neonates including 36 with BA. The serum level of MMP-7 > 1.43 ng/mL for predicting biliary atresia has a median of 10.26 ng/mL for BA (Yang *et al.*, 2018; Harpavat, 2019). They also observed that serum MMP-7 levels may rise with age, as liver damage proceeds, and that MMP-7 is a less useful serum marker in neonates due to its correlation with other liver diseases. There is pressure to include the MMP-7 level in the prognostic algorithm. However, the usefulness of this marker has limitations: the values of the MMP-7 level can vary depending on the type of immunosorbent assay kits used (Yang *et al.*, 2018; Harpavat, 2019). In comparison, the median serum MMP-7 levels were 38.89 ng/mL for the BA group and 4.4 ng/mL for the non-BA group in the Yang *et al.* research. Hence, the role of MMP-7 as a reliable biomarker remains controversial. The confirmation of the diagnostic utility of serum MMP-7 levels may be an objective for therapeutics.

STOOL PROTEINS

There are two kinds of stool tests: Sudan III staining of stool fat and measurement of duodenal bile acid. Steatorrhea in a stool is pathognomic for BA patients as well as acholic feces (Okajima *et al.*, 2016). Detection of steatorrhea in Sudan III straining is an easy-to-obtain and rapid examination. Gu *et al.* have published their research where they claim that the fat content of a stool may be helpful especially when feces are non-acholic (Gu *et al.*, 2015). They have examined 313230 infants, 34 with biliary atresia. The stool colour card screening showed 76.5% sensitivity and 99.9% specificity in this research. Lien *et al.*'s analysis also shows that stool colour card is useful in detecting BA patients. The research includes babies born before 2002 – the beginning of using the stool colour card in Taiwan, and after 2002. The analysis conclusion was that the stool colour card screening program allows to implement earlier Kasai operation (Lien *et al.*, 2010).

Another research concerned an analysis of proteins using data-independent acquisition mass spectrometry (DIA-MS) (Watanabe *et al.*, 2020). The assumption was that because of the obstruction of the normal flow of bile juice, BA patients' stool contains fewer proteins that are produced in the biliary tract. Also, some specific proteins that originate from the biliary tract are possibly absent or reduced compared to the non-BA patients (Watanabe *et al.*, 2020). The researchers examined four patients with BA and three others with non-BA cholestasis. They proved that 49 proteins were higher and 54 proteins lower in the stool of BA patients. The analysis

showed that proteins RBP4, SHMT2, HMGCS1, ADH6, ALDH1A1, ACADS, ADK, KHK, ACAA2, PSAT1, AMACR, and PTGR1 are lower in stool samples of BA-patients (Watanabe *et al.*, 2020). And conversely: the CEACAM1, CEACAM5, and CEACAM8 were significantly higher in patients with BA (Watanabe *et al.*, 2020). CHI3L1 is correlated with worse BA outcome (Watanabe *et al.*, 2020). The measurement of those dominant proteins in the stool of BA patients could be of assistance in the early diagnosis of the disease. Watanabe *et al.* emphasized that the research needs evaluation on a larger cohort.

INTERLEUKIN-33 (IL-33)

A specific cytokine involved in the pathogenesis of liver fibrosis and severe inflammation (Tan *et al.*, 2018). It is released in the course of cell death (Rinella, 2015; Zhang *et al.*, 2015). It is assumed that IL-33 assists as an "alarm signal" released by stressed hepatocytes (Heymann *et al.*, 2016). In the following research, Ola G. Behairy *et al.* observed 60 infants with cholestasis (BA and non-BA) and 30 healthy ones. BA diagnosis was based on surgical cholangiography. Cholestasis was recognized when conjugated bilirubin was 20% of the total bilirubin or when total bilirubin exceeded 17 mg/dL. The level of IL-33 in the serum was measured and the results showed that the IL-33 gene expression in the BA group was markedly upregulated. The median in the BA group was 48.0 pg/mL and in the non-BA group with cholestasis it was 17.3 pg/mL (Behairy *et al.*, 2020), while at the same time, healthy infants presented a 7.3 pg/mL average. There was also a gradual increase in the serum IL-33 level in BA and non-BA group with fibrosis stage (Behairy *et al.*, 2020) with the cut-off level determined at 20.8 pg/mL (specificity of 95% and sensitivity of 96.7%) (Behairy *et al.*, 2020). Still, jaundice, ascites and stool colour were the most visible symptoms in both cholestatic patient groups. Significantly, the aminotransferases and total leucocytic count levels were higher in the non-BA group, and gamma-glutamyl transferase, total protein, alkaline phosphatase and total and direct bilirubin levels were higher in the BA cohort (Behairy *et al.*, 2020). The total protein showed the highest level in the group of healthy infants, whereas the total leucocytic count was the lowest. The role of IL-33 in the diagnostics of biliary atresia is indisputable. Its serum concentration correlates with the levels of aminotransferases, as well as total and direct bilirubin levels (Behairy *et al.*, 2020). Another analysis made by Liu and others (Liu *et al.*, 2019) consists of 36 BA patients and 8 patients as a control group. The expression level of IL-33 was increased in BA patients compared to the control group (3.9 ± 0.5 vs. 1.0 ± 0.3). The result of the analysis was that the IL-33/ST2 receptor signaling axis is activated in BA patients. IL-33 exacerbates inflammatory reactions and drives liver fibrosis (Li *et al.*, 2014). Measuring serum interleukin-33 levels may have a diagnostic value in infants with biliary atresia as a reliable, non-invasive and fast tool.

Th17-ASSOCIATED CYTOKINES

Those cytokines are the ones that play an important role in the immune-mediated injury against intrahepatic bile duct epithelial cells (Chen *et al.*, 2019). Chen and colleagues conducted a study of 31 BA-infants and 45 non-BA infants with cholestasis. They tested 25 Th17-associated cytokines in those groups. They observed a

different gene expression of cytokines: IL-17F, IL-10, macrophage inflammatory protein-3 α (MIP3a), IL-22, IL-13, IL-33, IL-6, IL-17E, IL-27, IL-31, TNF- α and TNF- β in BA patients (Chen *et al.*, 2019). The highest AUC showed MIP3a in comparison to the others (Chen *et al.*, 2019). MIP3a – cysteine motif chemokine ligand 20 (CCL20) used alone or in combination with other biomarkers may become useful in BA diagnosis. MIP3a overexpression is related to inflammatory damage in bile ducts and to the development of BA (Chen *et al.*, 2019). For validation, Chen and others studied another group of 68 cholestatic patients (30 BA and 38 non-BA). BA was diagnosed by intraoperative cholangiography. In both studies, BA samples showed clay stool and higher GGT levels. 12 following cytokines showed a significant difference in concentrations between BA and non-BA infants: IL-17F, IL-10, MIP3a, IL-22, IL-13, IL-33, IL-6, IL-17E, IL-27, IL-31, TNF- α and TNF- β (Chen *et al.*, 2019). MIP3a showed better results in the diagnosis of BA than the other cytokines. Furthermore, the AUCs of MIP3a, IL-13 and TNF α were higher than 0.8. The sensitivity and the specificity of MIP3a were 90.40% and 80.0%. The AUC of GGT was 0.802 and clay stool showed an AUC of 0.792. The researchers went further and investigated if combining the marker with clay stool and GGT would increase the diagnostic value compared to the marker alone. Their research showed that the AUC of clay stool + GGT, clay stool + MIP3a, GGT + MIP3a and clay stool + GGT + MIP3a was 0.824, 0.918, 0.880 and 0.892 respectively (Chen *et al.*, 2019). A combined test would increase the diagnostic specificity. This finding indicates that a single MIP3a plus a single biomarker increases the diagnostic accuracy of BA (Chen *et al.*, 2019).

ALPHA-AMINOADIPIC ACID AND N-ACETYL-D-MANNOSAMINE IN URINE

Metabolomics can aid in understanding the disease mechanisms and identifying biomarkers for the diagnosis and, furthermore, monitoring the disease (Mamas *et al.*, 2011; Vinayavekhin *et al.*, 2010). By analyzing the urine we can observe the underway metabolic processes. Urine is an excellent material for discovering new biomarkers because it can be obtained non-invasively. Li and others (Li *et al.*, 2014) characterized urinary metabolomic profiles in infants with BA and infantile hepatitis syndrome (IHS). The levels of identified metabolites were further measured using the human metabolome database to determine if they were endogenous or exogenous. A urinalysis from an infant is simple because of its restricted diet. The research was based on 25 BA patients, 38 IHS patients, and on 38 healthy ones. The researchers used gas chromatography-mass spectrometry metabolomics (GC-MS) and orthogonal partial least squares discriminant analysis (OPLS-DA) for testing. In the analysis, total bilirubin, GGT and alkaline phosphatase were significantly higher in BA patients compared to IHS. 41 urine metabolites demonstrated a different expression between BA *vs.* NC, IHS *vs.* NC, and BA *vs.* IHS (Li *et al.*, 2018). The most notable differences showed N-acetyl-D-mannosamine and alpha-aminoadipic acid obtained from the urine of children with BA. The alpha-aminoadipic acid level was significantly increased in IHS (Li *et al.*, 2018). Alpha-aminoadipic acid's AUC was 0.95 in distinguishing BA from IHS in the training set, and 0.88 in distinguishing BA from IHS in the test set. N-acetyl-D-mannosamine had an AUC of 0.91 for distinguishing BA from

IHS in the training set, and 0.94 in the test set (Li *et al.*, 2018). After using the permutation test, the researchers presumed that alpha-aminoadipic acid and D-man-nosamine may be useful in BA diagnosis. On the other hand, 19 metabolites showed the same trend in BA *vs.* NC and IHS *vs.* NC (ex. lysine, leucine and tyrosine, tyrosine metabolite-hydroxyphenyllactic acid, ornithine, glutamine and glyco-cyamine), which suggests that those two diseases may have the same metabolic mechanism (Chen *et al.*, 2019). Li *et al.* study showed that the level of adenine was also increased, and the xanthine level was reduced in BA and IHS infants. They also found that Myo-inositol and glucuronic acid were elevated in BA and IHS patients. According to the study, urinary metabolites may be useful as potential biomarkers for a differential diagnosis of BA and IHS, but it still needs to be validated in further studies.

ANTI-SMOOTH MUSCLE ANTIBODIES (ASMA)

The study of Rafeey and others (Rafeey *et al.*, 2021) included 18 BA patients and 12 patients with neonatal hepatitis. The research showed a higher expression of anti-smooth muscle antibodies (ASMA) in the sera of BA patients. ASMA is detected by indirect immunofluorescence (IIF), fibroblasts, or HEp-2 cells. The conclusion was that ASMA levels were higher in neonatal hepatitis samples but not statistically significant in BA (the sensitivity and specificity were respectively 66.7% and 75%) (Rafeey *et al.*, 2021), whereas GGT and ALP levels were significantly increased in the sera of BA patients (for GGT, the sensitivity and specificity were 88.9%, 66.7% and for ALP the sensitivity and specificity were 77.8% and 75%). The study showed that ASMA may be useful for the differentiation of BA from neonatal hepatitis, however, it still needs to be further evaluated.

HEAT SHOCK PROTEINS 90 (HSP90)

HSP 90 are proteins involved in the folding and unfolding of other proteins (Dong R *et al.*, 2013). Their level is higher in response to stress (De Maio, 1999). Another HSP protein – HSP 47 has been linked to fibrosis in BA (Deng *et al.*, 2011). Cholangiocytes or hepatocytes secrete proteins in response to cholestatic diseases such as BA (De Maio, 1999). Cholangiocytes affect the bile composition (Dong R *et al.*, 2013). Following that thought, Dong *et al.* have looked for a protein that plays a crucial role in biliary atresia pathogenesis. They used liver tissue obtained by biopsy of 20 BA patients and 12 non-BA cholestatic infants (Dong R *et al.*, 2013). In the study, two-dimensional electrophoresis was used to reveal 15 proteins highly upregulated in BA. From among that group, nine were elevated and six were downregulated in the liver tissues of BA patients. Among 19 proteins, the HSP90 level was significantly higher. The mean level of HSP90 in BA patients was significantly lower than in non-BA cholestatic patients (Dong R *et al.*, 2013). To confirm those results, mass spectrometric identification and immunoblotting analysis of HSP90 were used. Dong and others (Dong *et al.*, ???) suggest that HSP 90 could play a protective role during cholestasis and may serve as a prognostic marker for NC compared to BA. Yet, further analyses need to be conducted on a larger cohort of patients.

POSITIVE BILIARY EPITHELIAL CELLS CD56

cells that play an important role in morphogenesis, remodeling, and migration in several organs through cell-cell and cell-matrix interactions (Sira *et al.*, 2012). In Sira *et al.* research, 30 infants with BA and 30 infants with non-BA cholestasis were included. CD56-positive cells were found in the epithelium of bile ducts and ductules where their level was significantly higher in the BA group (83.3%) than in the non-BA group (6.7%) (Sira *et al.*, 2012). BA patients with biliary causes compared to the non-BA group had a significantly higher CD56 staining in the biliary epithelium than in the BA group. The results showed that the CD56 cells were highly elevated in the sera of BA patients. Simultaneously, CD56 natural killer cells were significantly elevated in the non-BA group. The research concluded that CD56 immunostaining could be helpful in differentiating patients with BA.

SUMMARY

Biliary atresia is a cause of chronic cholestasis in neonates and if untreated leads to liver failure. BA has to be managed operatively as soon as it is possible. Because of a lack of non-invasive markers, the worth of a reliable and easy-to-obtain biliary atresia marker is invaluable. New discoveries allow us to have a new picture of diagnosing BA. Plenty of studies showed the diagnostic validity of laboratory investigations in the differentiation of BA from other cases of cholestasis. Circulating microRNAs with their 92% specificity (Zahm *et al.*, 2012) have a great value in diagnosing BA. Levels of the miR-200b/429 cluster were elevated in BA patients in comparison to cholestatic controls. Nevertheless, future work on a larger cohort is needed. Matrix metalloproteinase-7 (MMP-7), as noted in several reports, still needs more evaluation because its level depends on the patient's age and the type of laboratory kit used. Stool proteins and alpha-aminoadipic acid, and N-acetyl-D-mannosamine obtained from urine may be the future of BA diagnostics. The sample is easy to obtain and there is no need to keep it sterile. It is especially worth it when it comes to developing countries. The research shows that Interleukin-33 (IL-33) along with gamma-glutamyl transferase, total protein, alkaline phosphatase and total and direct bilirubin can be useful in diagnosing BA (Behairy *et al.*, 2020). In the study diagnostic accuracy of Anti-smooth muscle auto-antibody (ASMA) was evaluated. Compared with the accuracy rates of invasive procedures ASMA may be a useful marker for the differentiation of BA from non-BA patients. Heat shock protein 90 (HSP90) needs tissue from a liver biopsy to evaluate the result which makes it hard to determine. The nomogram presented in Chen Dong and others research (Dong Ch *et al.*, 2018) is a good way to deduce the probability of biliary atresia using gender, weight, GGT, ALP and direct bilirubin levels. Bile acid level in duodenal juice and hepatobiliary scintigraphy showed the highest (100%) sensitivity for diagnosing BA (Dong Ch *et al.*, 2018). On the basis of all the above-mentioned findings, we may conclude that an easier diagnostics of biliary atresia in newborns is within range of our hospital capabilities. Clearly, some medical research will still require more comprehensive verification. Rapid and accurate diagnostics with possible avoidance of liver biopsy is crucial in the case of cholestasis of an unknown nature, therefore every additional parameter achieved in a non-invasive way, straight from a laboratory, would be of life impor-

tance. In the opinion of the authors, in clinical practice, the Stool Proteins method seems to be the most promising and practical thanks to its simplicity and fully non-invasive character.

REFERENCES

- Bassett MD, Murray KF (2008) Biliary atresia: recent progress. *J Clin Gastroenterol* 42: 720–729. <https://doi.org/10.1097/MCG.0b013e3181646730>
- Behairy O, Elsadek A, Behiry E, Elhenawy I, Shalan N, Sayied K (2020) Clinical value of serum interleukin-33 biomarker in infants with neonatal cholestasis. *J Pediatr Gastroenterol Nutr* 70: 344–349. <https://doi.org/10.1097/MPG.0000000000002565>
- Benchimol E, Walsh C, Ling SC (2009) Early diagnosis of neonatal cholestatic jaundice: Test at 2 weeks. *Can Fam Physician* 55: 1184–92
- Cabrera-Abreu JC, Green A (2002) Gamma-glutamyltransferase: value of its measurement in paediatrics. *Ann Clin Biochem* 39: 22–25
- Chardot C (2006) Biliary atresia. *Orphanet J Rare Dis* 1: 28. <https://doi.org/10.1186/1750-1172-1-28>
- Chen P, Zhong Z, Jiang H, Chen H, Lyu J, Zhou L (2019) Th-17 associated cytokines multiplex testing indicates the potential of macrophage inflammatory protein-3 alpha in the diagnosis of biliary atresia. *Cytokine* 116: 21–26
- Chen X, Dong R, Shen Z, Yan W, Zheng S (2016) Value of gamma-glutamyl transpeptidase for diagnosis of biliary atresia by correlation with age. *J Pediatr Gastroenterol Nutr* 63: 370–373. <https://doi.org/10.1097/MPG.0000000000001168>
- Chitsaz E, Schreiber RA, Collet JP, Kaczorowski J (2009) Biliary atresia: The timing needs a changin. *Can J Public Health* 100: 475–477. <https://doi.org/10.1007/BF03404348>
- Chiu CY, Chen PH, Chan CF, Chang MH, Wu TC (2013) Biliary atresia in preterm infants in Taiwan: a nationwide survey. *J Pediatr* 163: 100–103. <https://doi.org/10.1016/j.jpeds.2012.12.085>
- Deng YH, Pu CL, Li YC, Zhu J, Xiang C (2011) Analysis of biliary epithelial-mesenchymal transition in portal tract fibrogenesis in biliary atresia. *Digestive Dis Sci* 56: 731–740. <https://doi.org/10.1007/s10620-010-1347-6>
- De Maio A (1999) Heat shock proteins: facts, thoughts and dreams. *Shock (Augusta, Ga)* 11: 1–12. <https://doi.org/10.1097/00024382-199901000-00001>
- Dong Ch, Hui-yun Z, Yun-chao Ch, Xiao-ping L, Zhi-hua H (2018) Clinical assessment of differential diagnostic methods in infants with cholestasis due to biliary atresia or non-biliary atresia. *Curr Med Sci* 38: 137–143. <https://doi.org/10.1007/s11596-018-1857-6>
- Dong R, Deng P, Huang Y, Shen Ch, Xue P, Zheng S (2013) Identification of HSP90 as Potential biomarker of biliary atresia using two-dimensional electrophoresis and mass spectrometry. *PLoS One* 8: e68602. <https://doi.org/10.1371/journal.pone.0068602>
- Dong R, Jiang J, Zhang S, Shen Z, Chen G, Huang Y, Zheng Y, Zheng S (2018) Development and validation of novel diagnostic models for biliary atresia in a large cohort of Chinese patients. *EBioMedicine* 34: 223–230
- Feldman AG, Mack CL (2015) Biliary atresia: clinical lessons learned. *J Pediatr Gastroenterol Nutr* 61: 167–175. <https://doi.org/10.1097/MPG.0000000000000075>
- Goldschmidt I, Thum T, Baumann U (2016) Circulating miR-21 and miR-29a as markers of disease severity and etiology in cholestatic pediatric liver disease. *J Clin Med* 5: 28. <https://doi.org/10.3390/jcm5030028>
- Gu YH, Yokoyama K, Mizuta K, Tsuchioka T, Kudo T, Sasaki H (2015) Stool color card screening for early detection of biliary atresia and long-term native liver survival: a 19-year cohort study in Japan. *J Pediatr* 166: 897–902. <https://doi.org/10.3390/jcm5030028>
- Hand NJ, Master ZR, Eauclore SF (2009) The microRNA-30 family is required for vertebrate hepatobiliary development. *Gastroenterology* 136: 1081–1090. <https://doi.org/10.1053/j.gastro.2008.12.006>
- Jiang J, Wang J, Shen Z, Lu X, Chen G, Huang Y, Dong R, Zheng S (2019) Serum MMP-7 in the diagnosis of biliary atresia. *Pediatriatrics* 144: e20190902. <https://doi.org/10.1542/peds.2019-0902>
- Harpavat S (2019) MMP-7: The next best serum biomarker for biliary atresia? *J Pediatr* 208: 8–9. <https://doi.org/10.1016/j.jpeds.2019.01.026>
- Hartley JL, Davenport M, Kelly DA (2009) Biliary atresia. *Lancet* 374: 1704–1713. [http://dx.doi.org/10.1016/S0140-6736\(09\)60946-6](http://dx.doi.org/10.1016/S0140-6736(09)60946-6)
- Heymann F, Tacke F (2016) Immunology in the liver—from homeostasis to disease. *Nature reviews. Gastroenterol Hepatol* 13: 88–110
- Hugh T (2017) MMP7 — a diagnostic biomarker for biliary atresia. *Nature reviews. Gastroenterol Hepatol* 15: 68
- Laterza OF, Lim L, Garrett-Engle PW (2009) Plasma MicroRNAs as sensitive and specific biomarkers of tissue injury. *Clin Chem* 55: 1977–1983. <https://doi.org/10.1093/clinchem.2009.131797>
- Lertudomphonwanit C, Mourya R, Fei L, Zhang Y, Gutta S, Yang L, Bove KE, Shivakumar P, Bezerra JA (2017) Large-scale proteom-

- ics identifies MMP-7 as a sentinel of epithelial injury and of biliary atresia. *Sci Transl Med* **9**: eaan8462. <https://doi.org/10.1126/scitranslmed.aan8462>
- Li J, Razumilava N, Gores GJ, Walters S, Mizuochi T, Mourya R, Bessho K, Wang YH, Glasser SS, Shivakumar P, Bazerra JA (2014) Biliary repair and carcinogenesis are mediated by IL-33-dependent cholangiocyte proliferation. *J Clin Invest* **124**: 3241–3251. <https://doi.org/10.1172/JCI73742>
- Li WW, Yang Y, Dai OG, Lin LL, Xie T, He LL, Tao JL, Shan JJ, Wang Sch (2018) Non-invasive urinary metabolomic profiles discriminate biliary atresia from infantile hepatitis syndrome. *Metabolomics* **14**: 90. <https://doi.org/10.1007/s11306-018-1387-z>
- Lien TH, Chand MH, Wu JF, Chen HJ, Lee Hch, Chen Ach, Tiao MM, Wu Tch, Yang YJ, Lin ChCh, Lai MW, Hsu HY, Ni YH (2010) Effects of the infant stool color card screening program on 5-year outcome of biliary atresia in Taiwan. *Hepatology* **53**: 202–208. <https://doi.org/10.1002/hep.24023>
- Liu CS, Chin TW, Wei CF (1998) Value of gamma-glutamyl transpeptidase for early diagnosis of biliary atresia. *Zhonghua Yi Xue Za Zhi (Taipei)* **161**: 716–720 (in Chinese)
- Liu J, Yang YF, Zheng Ch, Chen G, Shen Z, Zheng Sh, Dong R (2019) Correlation of Interleukin-33/ST2 Receptor and liver fibrosis progression in biliary atresia patients. *Front Pediatr* **1**: 403. <https://doi.org/10.3389/fped.2019.00403>
- Lynn FC, Skewes-Cox P, Kosaka Y (2007) MicroRNA expression is required for pancreatic islet cell genesis in the mouse. *Diabetes* **56**: 2938–2945. <https://doi.org/10.2337/db07-0175>
- Mack CL, Feldman AG, Sokol RJ (2012) Clues to the etiology of bile duct injury in biliary atresia. *Seminars Liver Dis* **32**: 307–316. <https://doi.org/10.1055/s-0032-1329899>
- Mack CL (2015) What causes biliary atresia? Unique aspects of the neonatal immune system provide clues to disease pathogenesis. *Cell Mol Gastroenterol Hepatol* **1**: 267–274. <https://doi.org/10.1016/j.jcmgh.2015.04.001>
- Maggiore G, Bernard O, Hadchouel M, Lemonnier A, Alagille D (1991) Diagnostic value of serum gamma-glutamyl transpeptidase activity in liver diseases in children. *J Pediatr Gastroenterol Nutr* **12**: 21–26
- Mamas M, Dunn WB, Neyses L, Goodacre R (2011) The role of metabolites and metabolomics in clinically applicable biomarkers of disease. *Archiv Toxicol* **85**: 5–17. <https://doi.org/10.1007/s00204-010-0609-6>
- Morimura R, Komatsu S, Ichikawa D (2011) Novel diagnostic value of circulating miR-18a in plasma of patients with pancreatic cancer. *Br J Cancer* **105**: 1733–1740
- Nizery L (2016) Biliary atresia: clinical advances and perspectives. *Clin Res Hepatol Gastroenterol* **40**: 281–287. <https://doi.org/10.1016/j.clinre.2015.11.010>
- Okajima K, Nagaya K, Azuma H, Suzuki T (2016) Biliary atresia and stool: Its consistency and fat content, another potentially useful information. *Eur J Gastroenterol Hepatol* **28**: 180. <https://doi.org/10.1097/MEG.0000000000000504>
- Rafeey M, Saboktakin L, Hasani J, Naghash S (2021) Diagnostic value of anti-smooth muscle antibodies and liver enzymes in differentiation of extrahepatic biliary atresia and idiopathic neonatal hepatitis. *African J Paediatr Sur: AJPS* **13**: 63–68
- Rendon-Macias ME, Villasis-Keever MA, Castaneda-Mucino G, Sandoval-Mex AM (2008) Improvement in accuracy of gamma-glutamyl transferase for differential diagnosis of biliary atresia by correlation with age. *Turkish J Pediatr* **50**: 253–259
- Rinella ME (2015) Nonalcoholic fatty liver disease: a systematic review. *JAMA* **313**: 2263–73. <https://doi.org/10.1001/jama.2015.5370>
- Sira MM, El-Guindi MAS, Saber MA, Ehsan NA, Rizk MS (2012) Differential hepatic expression of CD56 can discriminate biliary atresia from other neonatal cholestatic disorders. *Eur J Gastroenterol Hepatol* **24**: 1227–1233. <https://doi.org/10.1097/MEG.0b013e328356aee4>
- Sokol RJ, Shepherd RW, Superina R, Bezerra JA, Robuck P, Hoofnagle JH (2007) Screening and outcomes in biliary atresia: summary of a National Institutes of Health workshop. *Hepatology* **46**: 566–581. <https://doi.org/10.1002/hep.21790>
- Tan Z, Liu Q, Jiang R, Lv L, Shoto SS, Maillet I, Quesniaux V, Tang J, Zhang W, Sun B, Ryffel B (2018) Interleukin-33 drives hepatic fibrosis through activation of hepatic stellate cells. *Cell Mol Immunol* **15**: 388–398. <https://doi.org/10.1038/cmi.2016.63>
- Tang KS, Huang LT, Huang YH (2007) Gamma-glutamyl transferase in the diagnosis of biliary atresia. *Acta Paediatrica Taiwanica* **48**: 196–200
- Thai TH, Calado DP, Casola S (2007) Regulation of the germinal center response by microRNA-155. *Science* **316**: 604–608. <https://doi.org/10.1126/science.1141229>
- Vinayavekhin N, Homan EA, Saghatelian A (2010). Exploring disease through metabolomics. *ACS Chem Biol* **5**: 91–103. <https://doi.org/10.1021/cb900271r>
- Watanabe E, Kawashima Y, Suda W, Kakiyama T, Takazawa S, Nakajima D, Nakamura R, Nishi A, Suzuki K, Ohara O, Fujishiro J (2020) Discovery of candidate stool biomarker proteins for biliary atresia using proteome analysis by data-independent acquisition mass spectrometry. *Proteomes* **8**: 36. <https://doi.org/10.3390/proteomes8040036>
- Yang L, Zhou Y, Xu P, Mourya R, Lei H, Cao G, Xiong X, Xu H, Duan X, Wang N, Fei L, Chang X, Zhang X, Jiang M, Bezerra JA, Tang S (2018) Diagnostic accuracy of serum matrix metalloproteinase-7 for biliary atresia. *Hepatology (Baltimore, MD)* **68**: 2069–2077. <https://doi.org/10.1002/hep.30234>
- Zahm AM, Hand NJ, Boateng LA, Friedman JR (2012) Circulating microRNA is a biomarker of biliary atresia. *J Pediatr Gastroenterol Nutr* **55**: 366–369. <https://doi.org/10.1097/MPG.0b013e318264e648>
- Zahm AM, Thayu M, Hand NJ (2011) Circulating microRNA is a biomarker of pediatric Crohn disease. *J Pediatr Gastroenterol Nutr* **53**: 26–33. <https://doi.org/10.1097/MPG.0b013e31822200cc>
- Zhan J (2017) Incidence of biliary atresia congenital malformations: a retrospective multicenter study in China. *Asian J Surgery* **40**: 429–433. <https://doi.org/10.1016/j.asjsur.2016.04.003>
- Zhang Y, Huang D, Gao W (2015) Lack of IL-17 signaling decreases liver fibrosis in murine schistosomiasis japonica. *Int Immunol* **27**: 317–25. <https://doi.org/10.1093/intimm/dxv017>

Circular RNA LPAR3 targets JPT1 *via* microRNA-513b-5p to facilitate glycolytic activation but repress prostate cancer radiosensitivity

Yuan Yuan Chen¹, Li Ping Luo¹✉ and Ke Chong Deng²✉

¹Department of Oncology, Wuhan Wuchang Hospital Affiliated to Wuhan University of Science and Technology, Wuhan City, Hubei Province, 430063, China; ²Department of Emergency, Wuhan Wuchang Hospital Affiliated to Wuhan University of Science and Technology, Wuhan City, Hubei Province, 430063, China

A great many circular RNAs (circRNAs) are considered key modulators of human malignancies. However, the function of circRNA lysophosphatidic acid receptor 3 (LPAR3) in the radioresistance of prostate cancer (PCa) cells is still uncertain. circLPAR3, microRNA (miR)-329-3p, and JPT1 expression in PCa tissues and cells were detected by real-time quantitative PCR or western blot. Cell proliferation was detected by CCK-8 (cell proliferation assay) and colony formation assay, apoptosis was by flow cytometry, and migration and invasion ability were by Transwell assay. Cell glycolysis was analyzed by glucose uptake, lactate production, and ATP metabolism. Under different doses of radiation, the radiosensitivity of PCa cells was detected by colony formation assay. The relationship between circLPAR3, miR-513b-5p, and JPT1 was confirmed by dual luciferase reporter gene detection and RIP assay. The data presented that circLPAR3 and JPT1 expression was elevated in PCa, while miR-513b-5p expression was reduced. Repression of circLPAR3 depressed cell advancement, and restrained glycolysis, but enhanced the radiosensitivity of PCa cells. CircLPAR3's target miRNA was miR-513b-5p which targeted JPT1. Elevated JPT1 reversed the repressive effects of circLPAR3 knockdown or miR-513b-5p overexpression on PCa advancement, glycolysis, and radiosensitivity. In summary, the knockdown of circLPAR3 reduces glycolysis, but promotes PCa radiosensitivity *via* the miR-513b-5p/JPT1 axis, discovering a novel mechanism in PCa progression.

Keywords: prostate cancer, circular RNA lysophosphatidic acid receptor 3, MicroRNA-513b-5p, Jupiter microtubule associated homolog 1, glycolysis, radiosensitivity

Received: 31 May, 2022; **revised:** 09 October, 2022; **accepted:** 29 January, 2023; **available on-line:** 17 March, 2023

✉e-mail: 1329195378@qq.com (LPL); 65490595@qq.com (KCD)

Abbreviations: circRNA, circular RNA; JPT1, Jupiter microtubule associated homolog 1; LC, lung cancer; LPAR3, lysophosphatidic acid receptor; miRNAs, MicroRNAs; PCa, prostate cancer

INTRODUCTION

Prostate cancer (PCa) is a common cancer among men worldwide, and its mortality rate ranks 2nd among men's cancers (Wu *et al.*, 2019). Recently, the incidence rate of PCa in China has manifested an upward trend (Zhou *et al.*, 2021). In addition to surgical resection, radiotherapy is another treatment approach that can cure PCa (Li *et al.*, 2020). Nevertheless, owing to radioresistance, the ef-

fectiveness of radiotherapy is unsatisfactory. Therefore, it is vital to explore a way to promote radiosensitivity.

Circular RNA (circRNA) is an endogenous non-coding RNA transcribed by RNA polymerase II, and featured by linking the 3' with 5' ends *via* exon or intron cycles (Kong *et al.*, 2017). Studies have clarified that circRNA is crucial in various biological processes like apoptosis, cell vascularization, and cell invasion (Yuan *et al.*, 2019). For instance, circRNA La-related RNA-binding protein 4 (LARP4) represses cell migration and invasion of PCa *via* targeting FOXO3A (Weng *et al.*, 2020). circRNA is differentially manifested in cancers and could serve as a latent modulator of tumorigenesis or cancer advancement. For instance, circ-membrane bound O-acyltransferase domain containing 2 accelerates PCa advancement *via* the miR-1271-5p/mTOR axis (Shi *et al.*, 2020). CircRNA lysophosphatidic acid receptor 3 (LPAR3), a novel circRNA discovered recently, has been testified to be aberrantly manifested in several human cancers, like esophageal cancer (Shi *et al.*, 2020) and ovarian cancer (Xu *et al.*, 2020). However, its expression and function in PCa are not yet distinct.

MicroRNAs (miRNAs) are a set of short endogenous non-coding RNAs that could control approximately 30–50% of human protein-coding genes and molecular signaling pathways in cells (Porzycki *et al.*, 2018). Accumulating evidence clarify that miRNAs are differentially expressed in cancers and impact cell growth, differentiation and apoptosis processes (Ghafouri-Fard *et al.*, 2020). miRNA expression has become a latent biomarker for PCa diagnosis and prognosis (Nayak *et al.*, 2020). For instance, miR-424/572 in recurrent PCa specimens are novel biomarkers for predicting PCa progression (Suer *et al.*, 2019). MiR-215-5p reduces the metastasis of PCa *via* targeting phosphoglycerate kinase 1 (Chen *et al.*, 2020). MiR-513b-5p is dysregulated in multiple human cancers, like lung cancer (LC) (Cai *et al.*, 2020), hepatocellular carcinoma (Jin *et al.*, 2021) and breast cancer (Lin *et al.*, 2020). However, no research is presented to manifest what effects miR-513b-5p has on PCa.

In this study, we discovered the expression of circLPAR3 was more highly expressed in PCa samples than in controls. Therefore, we knock down circLPAR3 expression to identify its potential roles and explore possible mechanisms in carcinogenesis of PCa. Here, we demonstrated that circLPAR3 acted as a miR-513b-5p sponge to up-regulated Jupiter microtubule associated homolog 1 (JPT1). The research suggests that a novel circRNA may serve as a new biomarker for the early diagnosis and treatment of PCa.

MATERIALS AND METHODS

Sample collection

Tumors and normal tissues adjacent to cancer were harvested from 58 patients with PCa in The Affiliated Hospital of Jiaxing University and stored in liquid nitrogen. Approval of this study was obtained from the Ethics Committee of The Affiliated Hospital of Jiaxing University and written informed consent was gained from each patient (Approval number: JX20156211).

Cell culture

PCa cell lines PC-3, LNCaP, VCaP, DU145 and human normal prostate epithelial cell line RWPE-1 were purchased from ATCC (MA, USA). PC3 cells were cultured in FK12 medium (Gibco, CA, USA), LNCaP cells were in RPMI-1640 medium (Gibco), VCaP cells were in 90% Dulbecco's modified Eagle's medium (Gibco), DU145 cells were in Eagle's Minimum Essential Medium; and RWPE-1 cells were in Keratinocyte Serum-Free Medium Kit (Invitrogen, CA, USA). The mediums for PC cell culture were supplemented with 10% fetal bovine serum (Gibco).

Cell transfection

For the inhibition of circLPAR3 and JPT1, shRNA sequences targeting circLPAR3 and JPT1-specific siRNA (si-JPT1) sequences were synthesized by GenePharma. For miRNA overexpression, miR-513b-5p mimic was obtained from GenePharma. Gene overexpression vector (pcDNA-JPT1) and control vector (pcDNA) were purchased from Nanjing Jinrui Biotechnology Co., Ltd. After 24 h of cell culture, plasmids were transfected using Lipofectamine 3000 Transfection Reagent (Invitrogen).

RNase R treatment test

RNase R (6 units, Genesee Biotech) was added to every 2 g RNA. After RNase R treatment, reverse transcription-quantitative polymerase chain reaction (RT-qPCR) was applied to detect circLPAR3 and LPAR3 in LNCaP cells PMID: 34913472.

Actinomycin D test

The actinomycin D test was performed with LNCaP cells incubated with actinomycin D (2 mg/mL; Sigma-Aldrich, Tokyo, Japan) for 0, 4, 8, 12 and 24 h PMID: 34913472.

Cell counting kit (CCK-8) assay

About 3×10^3 cells were seeded in each well of a 96-well plate and detected proliferation at 24, 48 and 72 hours by CCK-8 (Dojindo, Haidian, Beijing, China). The

absorbance at 450 nm was recorded at each time point, and the cell proliferation curve was drawn.

X-ray exposure

X-ray generator (Varian, Palo Alto, CA, USA) was applied to radiation management at a fixed rate of 4 Gy/min.

Colony formation and survival analysis

Approximately 140 transfected cells were incubated in each well of a 6-well plate for 14 to 21 days. Then the staining with 0.5% crystal violet (Yeasten) was observed under an inverted microscope ($\times 40$; Leica, Germany). For survival analysis, 200 cells were seeded on a 6-well plate and irradiated at 0, 2, 4, 6, and 8 Gy X-ray or not. Subsequently, a colony formation test was performed as described above.

Flow cytometry

Cells were treated with double-staining with fluorescein isothiocyanate-labeled annexin V (Invitrogen) and propidium iodide and then detected on a FACS Calibur flow cytometer (Becton Dickinson, San Jose, CA, USA) equipped with Cell Quest software (Becton, Franklin Lakes, NJ, USA) PMID: 31733095.

Migration and invasion test

A 24-well transwell chamber (Millipore, Billerica, MA, USA) with an 8 μ m polycarbonate membrane was used to perform migration tests on LNCaP cells. Briefly, LNCaP cells (5×10^5 cells/well) were added into the upper chamber with 200 μ L of serum-free medium, and the complete medium was added into the lower chamber as a chemoattractant. After 24 h, the migrating submembrane cells were fixed with 95% ethanol for staining with crystal violet (Beyotime, Shanghai, China) and imaging under the microscope (Leica). Image Lab software 5.2 (Bio-Rad, Hercules, CA, USA) was used for data analysis. The 24-well transwell was pre-covered with Matrigel (BD Biosciences) and was needed for invasion detection PMID: 31387394.

Glucose consumption, lactate production and adenosine triphosphate (ATP) levels

A glucose determination kit (Sigma), lactic acid colorimetric/fluorescence determination kit (BioVision) and CellTiter Glo Luminescent Cell survival Assay (Promega) were put to detect glucose consumption, lactate production and ATP levels (Zheng *et al.*, 2020).

qPCR

Total RNA was isolated from PC tissues and cells using TRIzol (Invitrogen). To measure miRNA expres-

Table 1. Fluorescence quantitative PCR primer sequence

Genes	Forward (5'-3')	Reverse (5'-3')
CircLPAR3	GAGTTACCTTGTCTTCTGGACA	TGGAGAAGTGAACATCCTAAG
JPT1	ATAGCTCCCGAGTTTGGCG	TTGGCCCAAGAAGCTTGA
GAPDH	GGGAAGCTCACTGGCATGGCCTTCC	CATGTGGGCCATGAGGTCCACCAC
MIR-513b-5p	GGCCGGGGAGCTGGAGAAGA	TCCATGGAGGGTTGGGGTTCC
U6	CTCGCTTCGGCAGCACATATATT	ACGCTTCACGAATTTGCGTGGC

sion, RNA was reverse transcribed into cDNA using the TaqMan miRNA Reverse Transcription Kit (Applied Biosystems) and then quantified by real-time PCR using TaqMan Universal PCR Master Mix and TaqMan RNA Detection (Applied Biosystems). To measure circRNA expression, RNA was reverse transcribed into cDNA using PrimeScript RT Reagent (Takara) and then quantified by SYBR Premix Ex Taq (Takara). U6 and glyceraldehyde 3-phosphate dehydrogenase (GAPDH) were used as the internal reference. The $2^{-\Delta\Delta C_t}$ method was put into use to calculate the relative miR-513b-5p and the target gene. RT-qPCR primer sequence was manifested in Table 1 PMID: 34515615.

Western blot analysis

Total protein was extracted from cell lysis buffer (Sangon Biotech), separated on 12% sulfate-polyacrylamide gel, and electroblotted onto a polyvinylidene fluoride membrane (Millipore, Billerica, MA, USA). Using primary antibodies JPT1 (ab126705; 1:1000; Abcam) and glyceraldehyde-3-phosphate dehydrogenase (GAPDH) (ab8245; 1:1000; Abcam), the membrane was incubated overnight. Added with the secondary antibody (1:2000, Promega), the membrane was analyzed by Odyssey Infrared Imaging System (LI-COR, Lincoln, NE, USA) PMID: 31624242.

The luciferase activity assay

Co-transfection of circLPAR3/JPT1-wild/mutant types (WT/MUT), miR-513b-5p mimic or miR-NC was conducted in LNCaP cells (Thermo Fisher Scientific) with Lipofectamine 3000. After 48 h, the relative activity of luciferase was detected via the dual Glo luciferase detection system (Promega, Shanghai, China).

RNA binding protein immunoprecipitation (RIP) assay

RNA immunoprecipitation kit (Millipore, Bedford, MA, USA) was carried out for RIP detection. LNCaP cells at a density of 5×10^5 cells/plate were treated with

ice-cold radioimmunoprecipitation (RIPA) lysis buffer (Beyotime, Shanghai, China), incubated with protein A/G beads containing Anti-Argonaute 2 (anti-Ago2) or anti-Immunoglobulin G (anti-IgG). circLPAR3, miR-513b-5p and JPT1 were examined by RT-qPCR. N=3 (Du *et al.*, 2020).

Statistical analysis

SPSS 21.0 (SPSS, Inc, Chicago, IL, USA) statistical software was applied to analyze the data. After the Kolmogorov-Smirnov test, the data were normally distributed and manifested as mean \pm standard deviation (S.D.). The two-group comparison was conducted via *t*-test, while the comparison among multiple groups was via one-way analysis of variance (ANOVA), and Fisher's least significant difference *t*-test (LSD-*t*). Enumeration data reported as rate or percentage were compared by chi-square test. *P* was a two-sided test; *P*<0.05 emphasized obvious statistical meaning.

RESULTS

We aimed to investigate circLPAR3 expression in PCa and its underlying molecular mechanism of regulating PCa progression by targeting JPT1 through miR-513b-5p. By collecting PCa clinical specimens and culturing PCa cells *in vitro*, we determined the relative expression levels of circLPAR3, miR-513b-5p and JPT1, and further verified their targeting relationship and interaction relationship. Our experiments found that circLPAR3 promoted glycolytic activation by targeting JPT1 through miR-513b-5p and inhibited PCa radiosensitivity. Therefore, our data are the first to investigate the function and mechanism of circLPAR3 in PCa, providing new insights into the pathogenesis of PCa.

Elevated circLPAR3 suggests an unpleasing into bad for PCa patients

CircRNAs are considered to be a promising marker for cancer diagnosis and prognosis. It has been report-

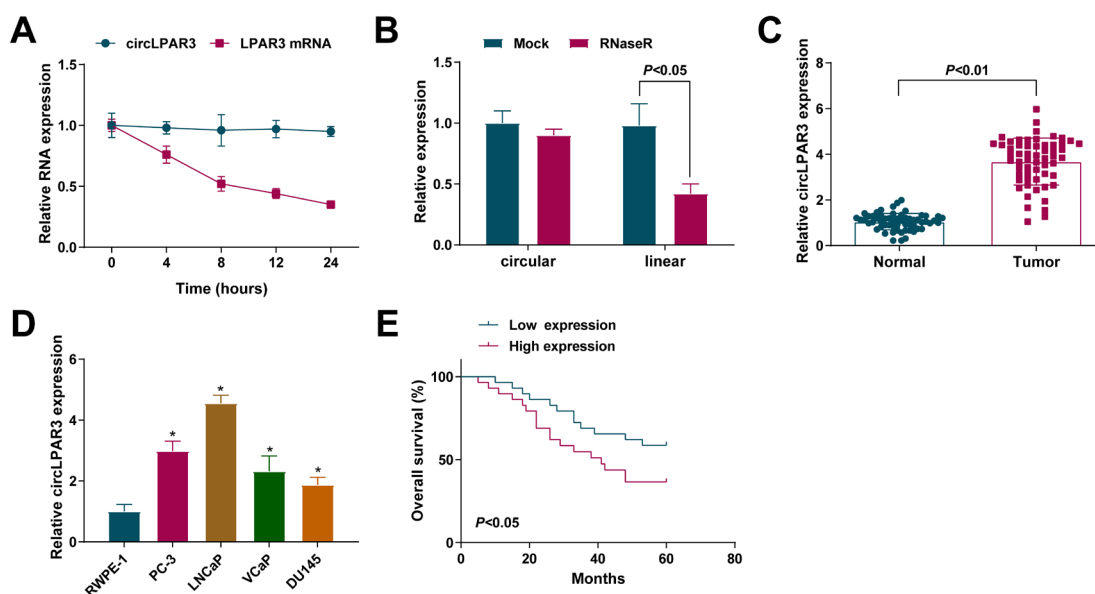


Figure 1. Upregulated circLPAR3 suggests an unpleasing prognosis for PCa patients

(A) Actinomycin D and (B) circLPAR3 expression after RNase R. G treatment; (C) RT-PCR to detect circLPAR3 in PCa specimens vs. normal specimens, n=58. (D) RT-PCR to examine circLPAR3 in human normal prostate epithelial cell lines RWPE-1 and PCa cells (PC-3, LNCaP, VCaP, DU145). (E) The survival analysis calculated by the Kaplan Meier plotter manifested the survival rate of PCa patients with elevated or reduced circLPAR3, n=58. N=3; The data in the figure were all measurement data, the manifestation of which was as mean \pm S.D. *vs. RWPE-1 cells, *P*<0.05.

Table 2. Correlation between circLPAR3 expression and clinicopathologic characteristics of PCa patients in cohort

Characteristics	Patient frequency (%)	circLPAR3 expression level		p-value ^a
		Low	High	
Total cases	58	29	29	
Age				0.424
<65	24	10	14	
≥65	34	19	15	
PSA level (μg/L)				0.585
≤10	21	9	12	
>10	37	20	17	
Gleason score				0.031*
≤7	35	22	13	
>7	23	7	16	
Pathologic stage				0.021*
T1-2	46	27	19	
T3-4	12	2	10	
Lymph-node status				0.279
Negative	39	22	17	
Positive	19	8	12	
Distant metastasis				0.016*
No	34	22	12	
Yes	24	7	17	

Abbreviations: ^aChi-square test, *P<0.05.

ed that circLPAR3 promotes the migration, invasion and metastasis of esophageal cancer PMID: 32495982. However, the role of circLPAR3 in PCa is still unclear. We first explored the properties of circLPAR3: actinomycin D (Fig. 1A) and RNase R experiments (Fig. 1B) manifested that circLPAR3 was much larger than the linear transcript. circLPAR3 expression in PCa patient specimens was clearly elevated (Fig. 1C). In PCa cell lines, it was discovered that circLPAR3 in PCa cells was enhanced (Fig. 1D). Subsequently, we divided circLPAR3 into high expression and low expression according to the median expression level of circLPAR3 in clinical patients, and analyzed the clinicopathological characteristics of PCa patients, and found that circLPAR3 expression was associated with high Gleason score, advanced pathological T stage and distant metastases (Table 2). The survival analysis calculated by Kaplan Meier affirmed that PCa patients with elevated circLPAR3 had a lower survival rate than those with reduced circLPAR3 (Fig. 1E). All in all, the results affirmed that circLPAR3 suggested an unpleasing prognosis for PCa patients.

Silenced circLPAR3 weakens cell advancement and glycolysis, but enhances radiosensitivity

In order to immediately examine the functional role of circLPAR3 in PCa progression, the introduction of sh-circLPAR3 clearly reduced circLPAR3 (Fig. 2A). It was worth noting that knockdown of circLPAR3 repressed cell advancement (Fig. 2B–F). Glycolysis, characterized by enhanced glucose uptake and lactate accumulation, is a common feature of cancer cells PMID: 34237309. In the meantime, it was manifested that repressing circLPAR3 restrained glucose uptake, lactate production and ATP levels (Fig. 2G–I). To

improve the radiotherapy effect of PCa and improve the radiosensitivity, it is a hot research topic to understand the mechanism of cellular radioresistance PMID: 33033519. It was also determined whether circLPAR3 could impact the radiosensitivity of LNCaP cells *in vitro*. Moreover, with the application of sh-circLPAR3, the cell survival rate was clearly decreased after radiation exposure (Fig. 2J), revealing that circLPAR3 silencing enhanced cell radiosensitivity. The above data clarified silenced circLPAR3 weakened cell advancement with glycolysis but enhanced radiosensitivity *in vitro*.

CircLPAR3 absorbs miR-513b-5p in PCa cells

CircRNAs are involved in the regulation of miR sponges in PCa cells PMID: 34515615. Interestingly, the starBase database predicted a latent binding site between circLPAR3 and miR-513b-5p (Fig. 3A). For verifying whether circLPAR3 could adsorb miR-513b-5p, an experiment was implemented. It was discovered that miR-513b-5p mimic was available to reduce the luciferase activity of the circLPAR3-WT reporter plasmid, while had no clear effect on that of the MUT one (Fig. 3B). Then it was clarified that compared to the control IgG, circLPAR3 and miR-513b-5p were rich in microribonucleoprotein consisting of Ago2 (Fig. 3C). Moreover, reduced miR-513b-5p was detected in PCa (Fig. 3D, E) and was negatively linked with circLPAR3 expression in PCa samples ($r=-0.637$, Fig. 3F). In cells silencing circLPAR3, miR-513b-5p was found to be up-regulated (Fig. 3G). In general, circLPAR3 adsorbed miR-513b-5p and negatively modulated its levels in PCa cells.

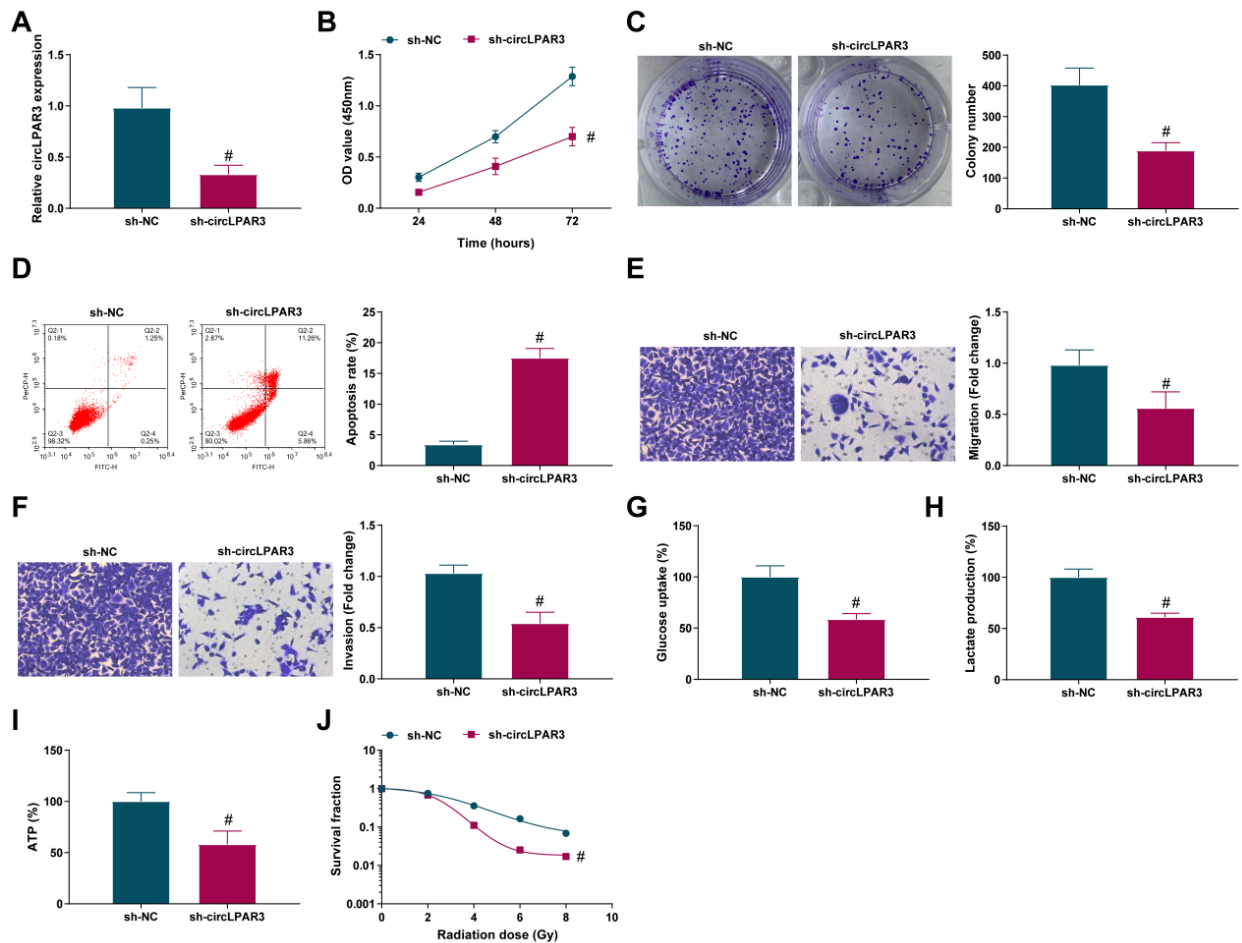


Figure 2. Repressive circLPAR3 weakens cell advancement with glycolysis, but facilitates radiosensitivity *in vitro*

(A) circLPAR3-shRNA lentiviral transfection efficiency; (B) CCK-8 and (C) plate clone to detect cell proliferation ability after repressing circLPAR3; (D) Flow cytometry to detect cell apoptosis after depressing circLPAR3; (E, F) Transwell detection of cell migration and invasion abilities after restrained circLPAR3; (G–I) Glucose uptake, lactate production and ATP metabolism analysis of cell glycolysis; (J) Under radiation (0, 2, 4, 6 and 8 Gy) irradiation, colony formation assay to analyze the survival of the transduced cells. N = 3; The data in the figure were all measurement data, the manifestation of which was as mean \pm S.D. *vs. the sh-NC, $P < 0.05$.

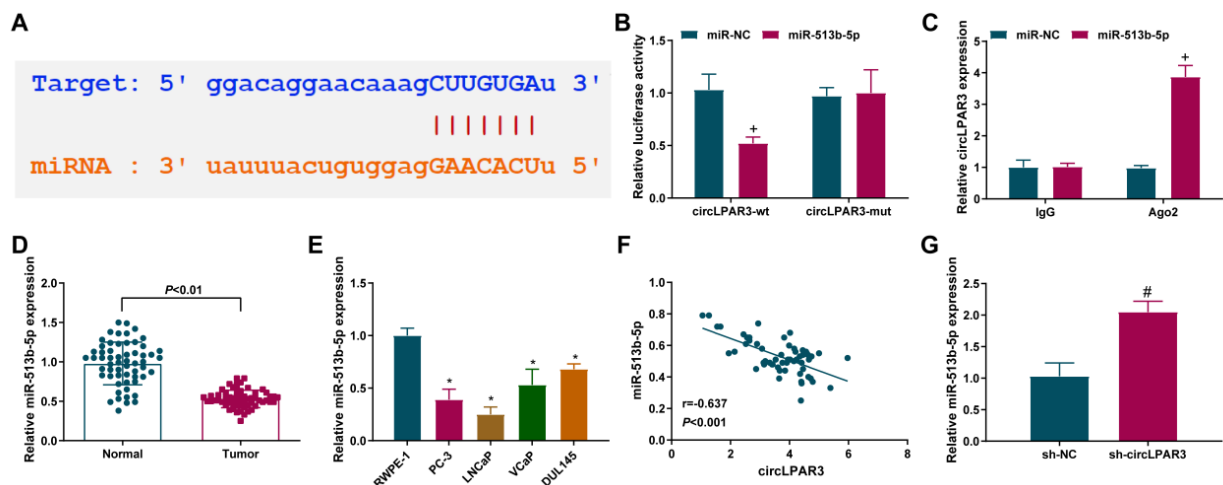


Figure 3. CircLPAR3 absorbs miR-513b-5p in PCA cells

(A) Using bioinformatics to predict the latent binding site of circLPAR3 with miR-513b-5p. (B) Co-transfection of 293 T cells with WT or MUT circLPAR3 luciferase reporter vector and miR-NC or miR-513b-5p mimic to detect the luciferase activity. (C) RIP assay to confirm that circLPAR3 and miR-513b-5p were enriched in microRNA-containing Ago2. (D) qPCR detection of miR-513b-5p in 58 PCA and normal tissues, $n = 58$; (E) qPCR detection of miR-513b-5p in PCA and normal cells; (F) Pearson analysis showed circLPAR3 in PCA tissue was negatively linked with miR-513b-5p, $n = 58$. (G) Clearly elevated miR-513b-5p in cells with repressive circLPAR3. N = 3; The data in the figure were all measurement data, the manifestation of which was as mean \pm S.D. *vs. the miR-NC, $P < 0.05$. *vs. RWPE-1 cells, $P < 0.05$. #vs. the sh-NC, $P < 0.05$.

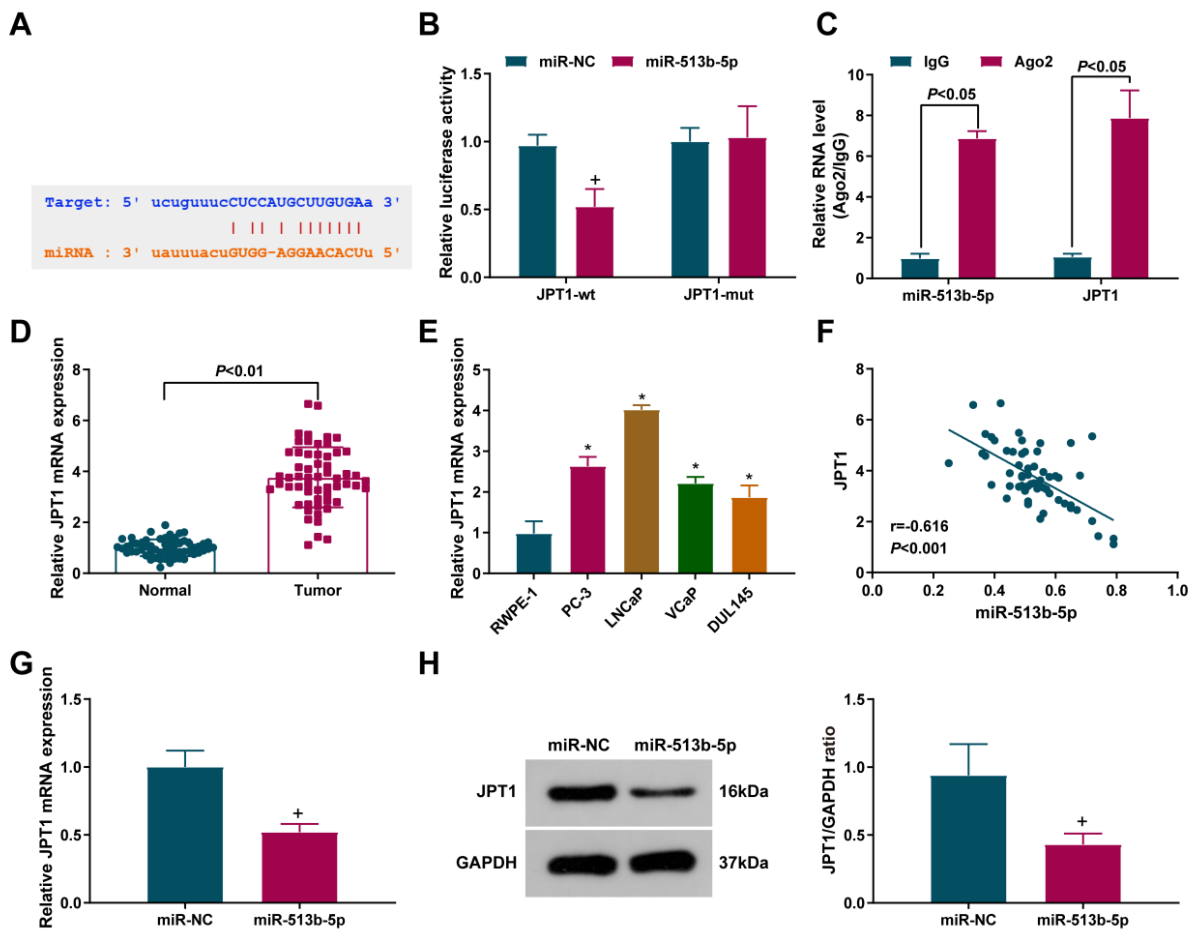


Figure 4. MiR-513b-5p refrains PCa cell growth and glycolysis and promotes cellular radiosensitivity

(A) RT-qPCR to detect miR-513b-5p in cells transfected with miR-513b-5p mimic. (B) CCK-8 method and (C) plate clone to detect PCa cell proliferation after up-regulation of miR-513b-5p. (D) Flow cytometry to detect cell apoptosis after elevated miR-513b-5p; (E, F) Transwell method to detect the migration and invasion of PCa cells after elevated miR-513b-5p. (G–I) Glucose uptake, lactic acid production and ATP metabolism analysis of cellular glycolysis; (J) Under different doses of radiation, the survival rate of PCa cells detected by colony formation experiments. N=3; The data in the figure were all measurement data, the manifestation of which was as mean \pm S.D. +vs. the miR-NC, $P<0.05$.

MiR-513b-5p reduces PCa cell growth and glycolysis and promotes cellular radiosensitivity

Altered miRNA expression has been shown to play an important role in PCa invasion and metastasis PMID:34461437, while the expression of miR-513b-5p in PCa is unclear. It was confirmed that miR-513b-5p expression was elevated after miR-513b-5p mimic transfected into LNCaP cells (Fig. 4A). Subsequently, functional test data manifested that up-regulated miR-513b-5p repressed cell progression with glycolysis, but enhanced radiosensitivity *in vitro* (Fig. 4B–J). The above data confirmed that miR-513b-5p restrained growth and glycolysis, and promoted cellular radiosensitivity of PCa cells.

JPT1 is the immediate target of miR-513b-5p

As manifested in Fig. 5A, JPT1 was predicted to be miR-513b-5p's target on StarBase. The miR-513b-5p-transfected JPT1 3'untranslated region (UTR)-WT group produced reduced luciferase activity. At the same time, for verifying whether the predicted binding site of JPT1 with miR-513b-5p was necessary for the two's binding, mutation of the JPT1 binding site was conducted to construct the JPT1 3'UTR-MUT reporter plasmid. When co-transfection with miR-NC/513b-5p,

the luciferase activity of the JPT1 3'UTR-MUT group was not impacted (Fig. 5B), suggesting that miR-513b-5p immediately interacted with JPT1. The other experiment also manifested miR-513b-5p was available to combine with JPT1 (Fig. 5C). JPT1 mRNA was clearly up-regulated in cancer tissues and PCa cells than normal tissues adjacent to cancer, and RWPE-1 cells (Fig. 5D, E). It was also discovered that JPT1 and miR-513b-5p were negatively linked ($r = -0.616$, Fig. 5F). In the meantime, in cells with up-regulated miR-513b-5p, it was found that JPT1 expression was suppressed (Fig. 5G). In summary, miR-513b-5p directly interacted with JPT1 in PCa cells.

Inhibition of JPT1 inhibits cell growth and glycolysis and promotes radiosensitivity *in vitro*

To further examine the functional role of JPT1 in PCa, we knocked down JPT1 in cells (Fig. 6A). Responded to inhibition of JPT1, cell growth and glycolysis were suppressed and radiosensitivity was induced (Fig. 6B–J). Collectively, inhibition of JPT1 inhibits cell growth and glycolysis, and promotes radiosensitivity *in vitro*.

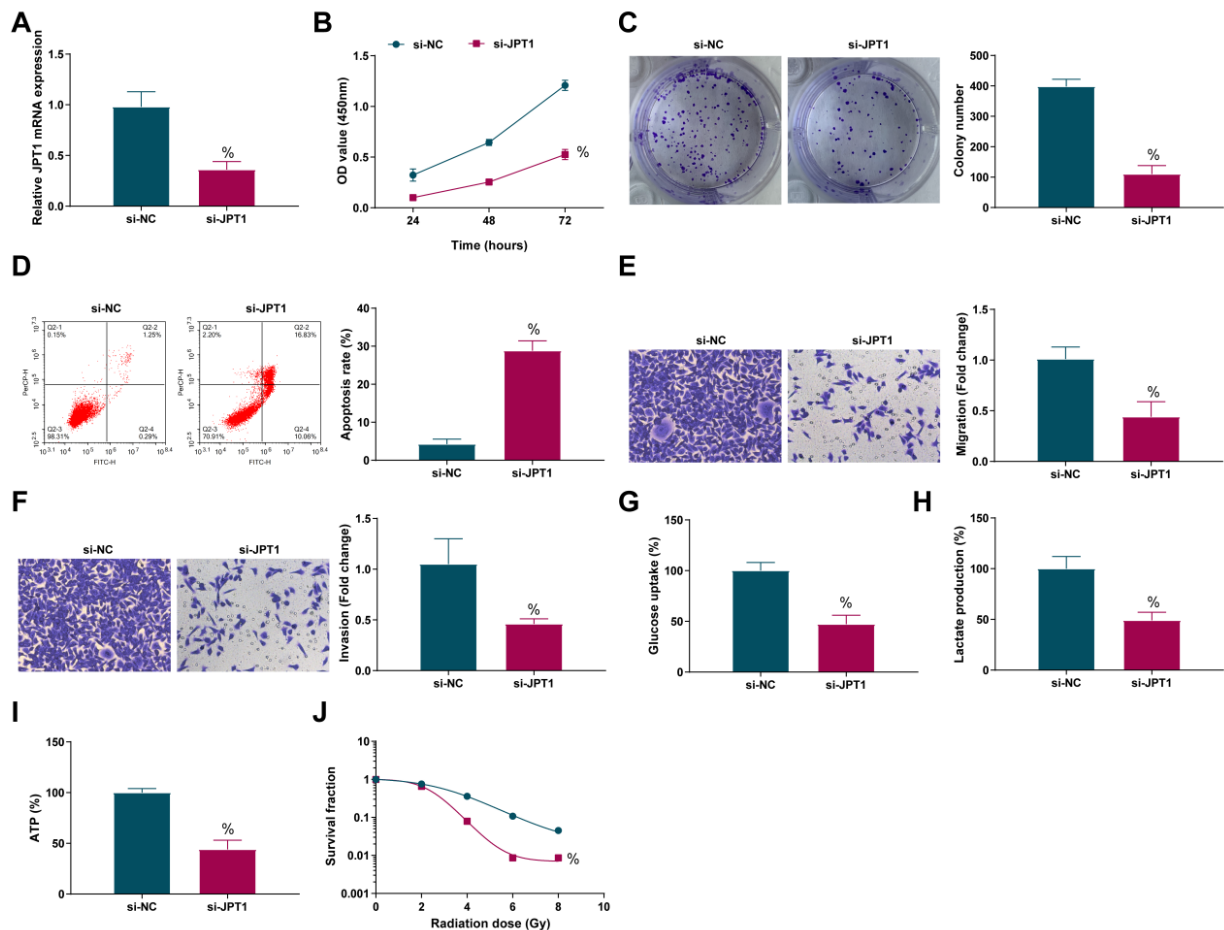


Figure 5. JPT1 is the immediate target of miR-513b-5p

(A) Prediction of the binding area between JPT1 and miR-513b-5p using the StarBase database. (B) The luciferase activity assay to detect the interaction between miR-513b-5p and JPT1 target protein. (C) RIP test to evaluate the binding of miR-513b-5p to JPT1. (D, E) RT-qPCR to detect JPT1 mRNA in PCa tissues and cells, $n=58$. (F) Pearson to analyze the linear relationship between miR-513b-5p and JPT1, $n=58$. (G, H) RT-qPCR and Western blot to detect JPT1 in PCa cells after up-regulated miR-513b-5p. $N=3$; The data in the figure were all measurement data, the manifestation of which was as mean \pm S.D. *vs. RWPE-1 cells, $P<0.05$; +vs. the miR-NC, $P<0.05$

Overexpression of JPT1 reversed the role of downregulated circLPAR3 or upregulated miR-513b-5p on cancer cell growth

For determining the influence of miR-513b-5p on PCa development and the possible mechanism, a rescue experiment was conducted by transfection with sh-circLPAR3 + pcDNA-NC, sh-circLPAR3 + JPT1, miR-513b-5p + pcDNA-NC or miR-513b-5p + JPT1 in LNCaP cells (Fig. 7A). The experiment clarified that elevated JPT1 reversed the repressive effects of silenced circLPAR3 or up-regulated miR-513b-5p on PCa advancement with glycolysis, and radiosensitivity (Fig. 7B–J). All in all, overexpression of JPT1 reversed the inhibition of circLPAR3 or upregulated miR-513b-5p on cancer cell growth.

DISCUSSION

At present, PCa has surpassed LC to become the most prevalent malignant tumor in American men. Although the overall survival rate of PCa patients has been improved owing to crucial advances in early screening and cancer management programs, the pathogenesis of PCa is still ambiguous yet (Wang *et al.*, 2019). CircRNA has been proven to be a critical modulator of human

cancer, and it can perform its functions *via* cooperating with its host gene (Liu *et al.*, 2020). In this study, it was discovered for the first time that circLPAR3 was elevated in PCa patients, and PCa patients with upregulated circLPAR3 had a lower survival rate. This result suggested circLPAR3 could be applied as a latent biomarker for poor prognosis. Hence, exploring the function of circRNA in PCa can be a breakthrough to understand the pathogenesis of PCa.

A study has clarified that the reprogramming of cell metabolism is closely implicated in tumorigenesis and can be applied to cancer treatment (Xia *et al.*, 2020). Because cancer cells have a strong ability to reproduce, hypoxia frequently shows up during tumor growth (Wang *et al.*, 2019). As we all know, normal cells generally produce energy through mitochondrial oxidative phosphorylation, while quick cancer cell proliferation requires more energy. Therefore, the metabolic pathway of hypoxic cancer cells must be different from the normal metabolic pathway. It is reported that hypoxia facilitates the development of tumor cells to produce the inefficient pathways of ATP, making them inclined to gain energy *via* the glucose-dependent glycolysis pathway, which is necessary to maintain the rapid growth of tumors, also known as the Warburg effect (Dyshlovoy *et al.*, 2020). Hence, repressing the activation of

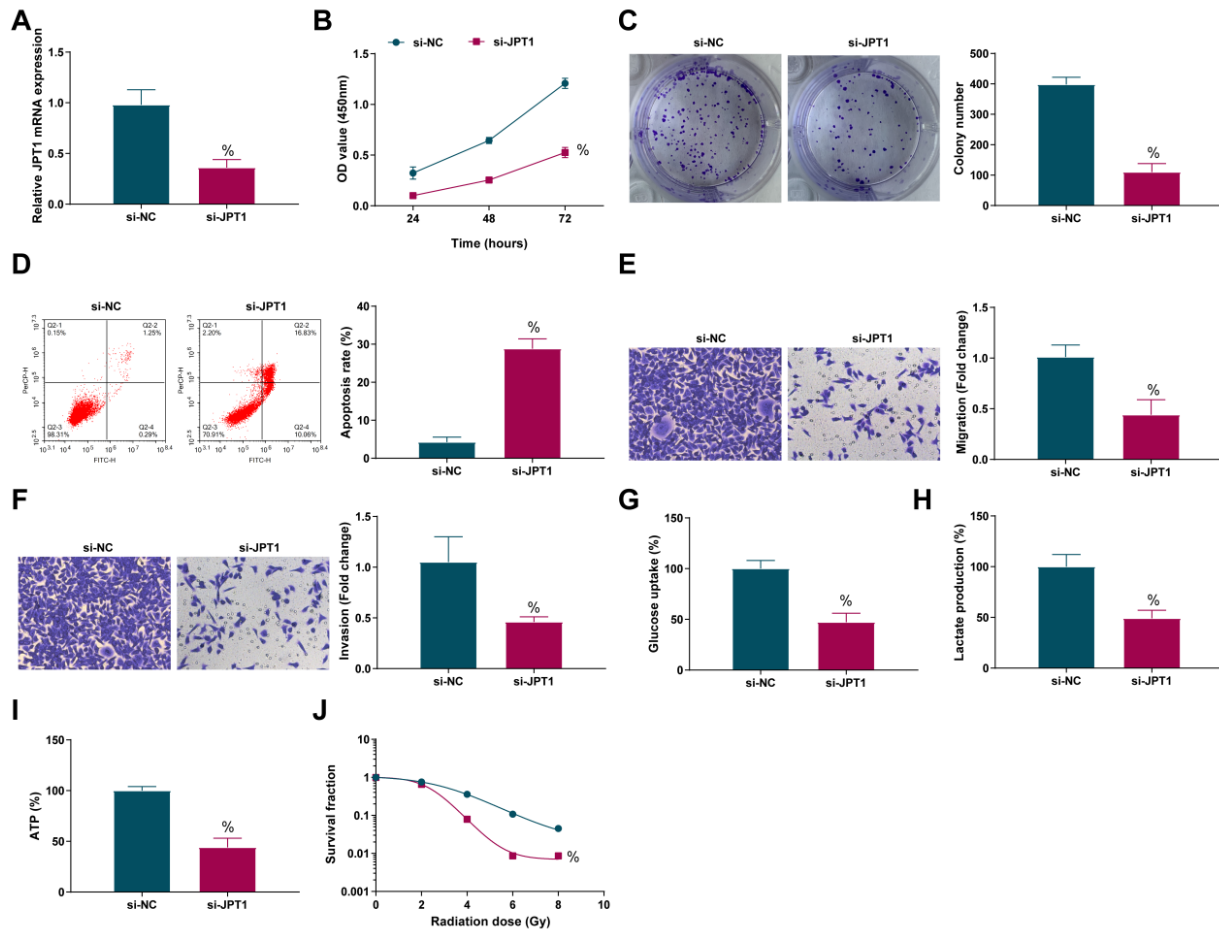


Figure 6. Inhibition of JPT1 inhibits cell growth and glycolysis, and promotes radiosensitivity *in vitro*

(A) circLPAR3-shRNA lentiviral transfection efficiency; (B) CCK-8 and (C) plate clone to detect cell proliferation ability after repressing circLPAR3; (D) Flow cytometry to detect cell apoptosis after depressing circLPAR3; (E, F) Transwell detection of cell migration and invasion abilities after restrained circLPAR3; (G–I) Glucose uptake, lactate production and ATP metabolism analysis of cell glycolysis; (J) Under radiation (0, 2, 4, 6 and 8 Gy) irradiation, colony formation assay to analyze the survival of the transduced cells. N=3; The data in the figure were all measurement data, the manifestation of which was as mean ± S.D. %vs. the si-NC, $P < 0.05$.

glycolysis is an effective treatment to prevent PCa. Numerous studies have clarified that circRNA is available to impact the glycolysis of cancer cells. For instance, circDENND4C accelerates the advancement with glycolysis of colorectal cancer cells *via* the miR-760/GLUT1 axis (Zhang *et al.*, 2020). Circ_0057553/miR-515-5p controls PCa cell advancement with glycolysis *via* targeting YES1 (Zhang *et al.*, 2020). In the meantime, in this study, it was discovered that circLPAR3 expression was also elevated in PCa cells. Knockdown of circLPAR3 clearly repressed cell advancement with glycolysis. Additionally, at the clinical level, radiation therapy is the most familiar and ideal cure way for PCa (Miszczyk *et al.*, 2021). However, because cancer cells have different repair abilities after radiation, radioresistance has always been a challenge for cure (Ihara *et al.*, 2019). It came out that the silencing of circLPAR3 clearly enhanced radiosensitivity.

Former studies have manifested that circRNA is available to be applied as a competitive endogenous RNA (ceRNA) of miRNA to adsorb miRNA to modulate mRNA gene expression (Shu *et al.*, 2019). For instance, circ CCNB2 knockdown depresses autophagy of PCa cells *via* targeting the miR-30b-5p/KIF18A axis and makes PCa sensitive to radiation (Cai *et al.*, 2020). In this study, it was confirmed that miR-513b-5p was a circLPAR3's target. Former stud-

ies have testified that miR-513b-5p is crucial in various human cancers, like embryonic testicular cancer (Wang *et al.*, 2017), breast cancer (Muti *et al.*, 2018) and pancreatic cancer (Li *et al.*, 2021). In the research, it was discovered the reduction of miR-513b-5p in PCa; Up-regulated miR-513b-5p repressed cell progression with glycolysis but enhanced radiosensitivity *in vitro*. As far as we know, this is the first study on miR-513b-5p in PCa.

Next, it was further figured out the downstream target genes of miR-513-5p. JPT1 is a protein-coding gene that impacts cell apoptosis and signal transduction (Bateman *et al.*, 2020). A previous study has clarified that JPT1 is linked with the progression of PCa (Cheng *et al.*, 2021). However, since there is very little research on JPT1, further studies are required to figure out the molecular mechanism of its action. In the research, it was discovered that JPT1 mRNA was clearly up-regulated in PCa. Moreover, elevated JPT1 reversed the effect of knocking down circLPAR3 or up-regulating miR-513b-5p on PCa cells, facilitating the advancement with glycolysis, but repressing radiosensitivity. All in all, JPT1 involves in circLPAR3/miR-513b-5p axis-regulated PCa cell growth and metastasis.

However, this research still has some limitations. First, owing to limited conditions, the sample size an-

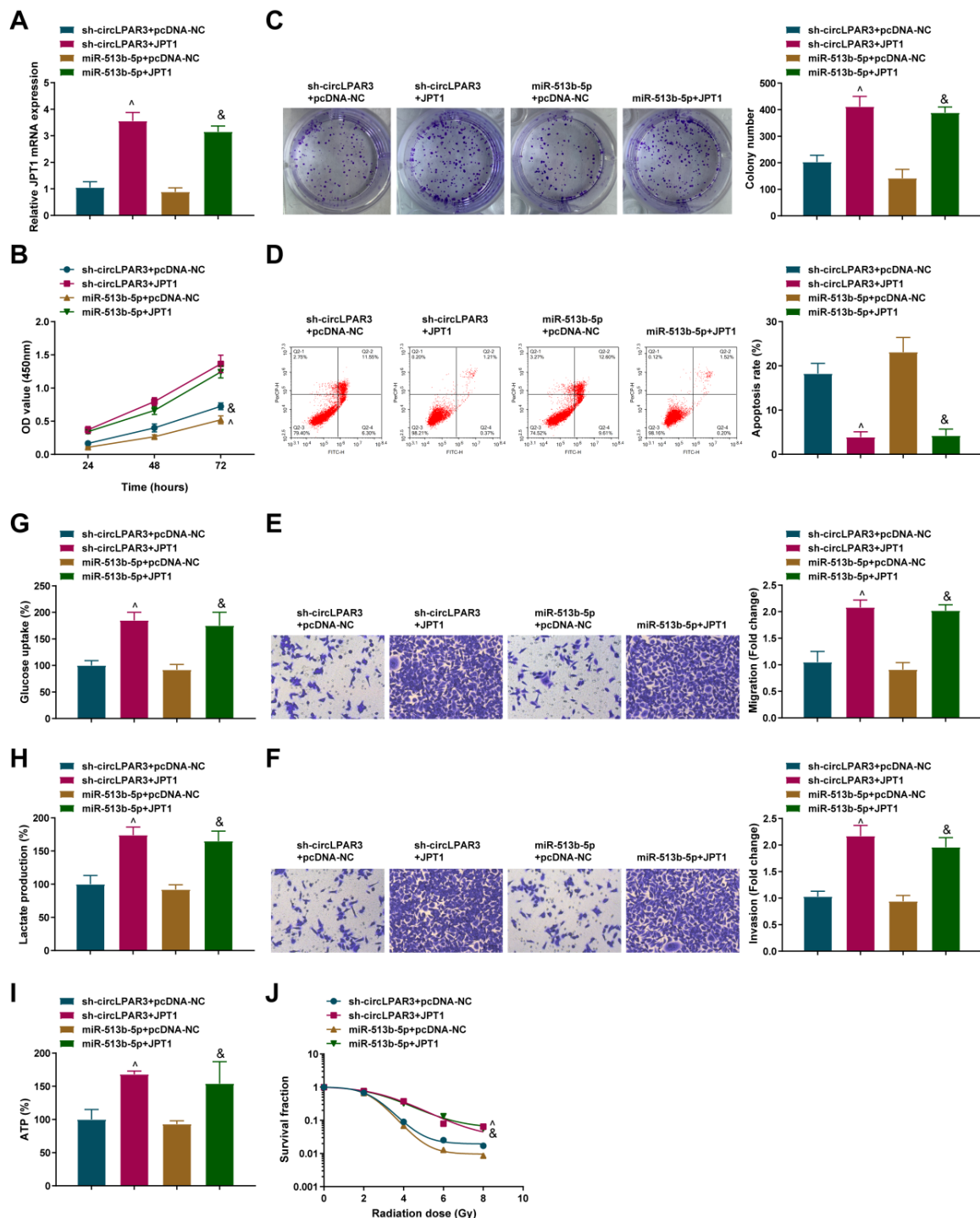


Figure 7. Overexpression of JPT1 reversed the role of downregulated circLPAR3 or upregulated miR-513b-5p on cancer cell growth. (A) qPCR to detect transfection efficiency; (B) CCK-8 method and (C) plate clone to detect cell proliferation. (D) Flow cytometry to detect cell apoptosis; (E) Transwell method to detect cell migration and invasion. (F–I) Glucose uptake, lactic acid production and ATP metabolism analysis of cellular glycolysis; (J) Under different doses of radiation, the survival rate of PCa cells detected by colony formation experiments. N=3; The data in the figure were all measurement data, the manifestation of which was as mean \pm S.D. ^vs. the sh-circLPAR3+pcDNA-NC, $P<0.05$; &vs. the miR-513b-5p+pcDNA-NC, $P<0.05$.

alyzed is limited. Secondly, *in vivo* animal experiments were not further conducted to verify the influence of the circLPAR3/miR-513b-5p/JPT1 axis on PCa *in vivo*. Finally, further exploration of the downstream target genes of JPT1 was not implemented. We hope that these issues can be further figured out in later studies.

CONCLUSION

In conclusion, the research has discovered a new mechanism of action of circRNA in PCa. It is found that circLPAR3 performs as a sponge of miR-513b-5p in PCa to restrain PCa cell glycolysis and accelerate radio-sensitivity, while upregulation of JPT1 reverses this ef-

fect. The results indicate the circLPAR3/miR-513b-5p/JPT1 axis is supposed to be a latent prognostic and therapeutic target to improve the diagnosis and treatment of PCa.

Declarations

Acknowledgments. Not applicable.

Declaration of Conflicting Interests. The author(s) declared no potential conflicts of interest with respect to the research, authorship, and/or publication of this article.

REFERENCES

- Bateman NW, Teng PN, Hope E, Hood BL, Oliver J, Ao W, Zhou M, Wang G, Tommarello D, Wilson K, Litzy T, Conrads KA, Hamilton CA, Darcy KM, Casablanca Y, Maxwell GL, Bae-Jump V, Conrads TP (2020) Jupiter microtubule-associated homolog 1 (JPT1): A predictive and pharmacodynamic biomarker of metformin response in endometrial cancers. *Cancer Med* 9: 1092–1103. <https://doi.org/10.1002/cam4.2729>
- Cai F, Li J, Zhang J, Huang S (2022) Knockdown of Circ_CCNB2 sensitizes prostate cancer to radiation through repressing autophagy by the miR-30b-5p/KIF18A axis. *Cancer Biother Radiopharm* 37: 480–493. <https://doi.org/10.1089/cbr.2019.3538>
- Cai Y, Wu Q, Liu Y, Wang J (2020) AZIN1-AS1, a novel oncogenic lncRNA, promotes the progression of non-small cell lung cancer by regulating miR-513b-5p and DUSP11. *Oncotargets Ther* 13: 9667–9678. <https://doi.org/10.2147/ott.s261497>
- Chen JY, Xu LF, Hu HL, Wen YQ, Chen D, Liu WH (2020) MiRNA-215-5p alleviates the metastasis of prostate cancer by targeting PGK1. *Eur Rev Med Pharmacol Sci* 24: 639–646. <https://doi.org/10.26355/eurev.202001.20040>
- Cheng Y, Xiong HY, Li YM, Zuo HR, Liu Y, Liao GL (2021) LncRNA HOXA11-AS promotes cell growth by sponging miR-24-3p to regulate JPT1 in prostate cancer. *Eur Rev Med Pharmacol Sci* 25: 4668–4677. <https://doi.org/10.26355/eurev.202107.26377>
- Du S, Zhang P, Ren W, Yang F, Du C (2020) Circ-ZNF609 accelerates the radioresistance of prostate cancer cells by promoting the glycolytic metabolism through miR-501-3p/HK2 axis. *Cancer Manag Res* 12: 7487–7499. <https://doi.org/10.2147/cmar.s257441>
- Dyshlovoy SA, Pelageev DN, Hauschild J, Sabutskii YE, Khmelevskaya EA, Krisp C, Kaune M, Venz S, Borisova KL, Busenbender T, Denisenko VA, Schlüter H, Bokemeyer C, Graefen M, Polonik SG, Anufriev VP, Amsberg GV (2020) Inspired by sea urchins: warburg effect mediated selectivity of novel synthetic non-glycoside 1,4-naphthoquinone-6s-glucose conjugates in prostate cancer. *Mar Drugs* 18. <https://doi.org/10.3390/md18050251>
- Ghafari-Fard S, Shoori H, Taheri M (2020) Role of microRNAs in the development, prognosis and therapeutic response of patients with prostate cancer. *Gene* 759: 144995. <https://doi.org/10.1016/j.gene.2020.144995>
- Ihara M, Ashizawa K, Shichijo K, Kudo T (2019) Expression of the DNA-dependent protein kinase catalytic subunit is associated with the radiosensitivity of human thyroid cancer cell lines. *J Radiat Res* 60: 171–177. <https://doi.org/10.1093/jrr/rry097>
- Jin W, Liang Y, Li S, Lin G, Liang H, Zhang Z, Zhang W, Nie R (2021) MiR-513b-5p represses autophagy during the malignant progression of hepatocellular carcinoma by targeting PIK3R3. *Aging (Albany NY)* 13: 16072–16087. <https://doi.org/10.18632/aging.203135>
- Kong Z, Wan X, Zhang Y, Zhang P, Zhang Y, Zhang X, Qi X, Wu H, Huang J, Li Y (2017) Androgen-responsive circular RNA circSMARCA5 is up-regulated and promotes cell proliferation in prostate cancer. *Biochem Biophys Res Commun* 493: 1217–1223. <https://doi.org/10.1016/j.bbrc.2017.07.162>
- Li S, Zhang Q, Liu W, Zhao C (2021) Silencing of FTX suppresses pancreatic cancer cell proliferation and invasion by upregulating miR-513b-5p. *BMC Cancer* 21: 290. <https://doi.org/10.1186/s12885-021-07975-6>
- Li XR, Zhou KQ, Yin Z, Gao YL, Yang X (2020) Knockdown of FBP1 enhances radiosensitivity in prostate cancer cells by activating autophagy. *Neoplasma* 67: 982–991. https://doi.org/10.4149/neo_2020_190807N728
- Lin W, Ye H, You K, Chen L (2020) Up-regulation of circ_LARP4 suppresses cell proliferation and migration in ovarian cancer by regulating miR-513b-5p/LARP4 axis. *Cancer Cell Int* 20: 5. <https://doi.org/10.1186/s12935-019-1071-z>
- Liu T, Ye P, Ye Y, Lu S, Han B (2020) Circular RNA hsa_circRNA_002178 silencing retards breast cancer progression via microRNA-328-3p-mediated inhibition of COL1A1. *J Cell Mol Med* 24: 2189–2201. <https://doi.org/10.1111/jcmm.14875>
- Miszczak J, Przydacz M, Zembrzusi M, Chłosta PL (2021) Investigation of chromosome 1 aberrations in the lymphocytes of prostate cancer and benign prostatic hyperplasia patients by fluorescence in situ hybridization. *Cancer Manag Res* 13: 4291–4298. <https://doi.org/10.2147/cmar.s293249>
- Muti P, Donzelli S, Sacconi A, Hossain A, Ganci F, Frixa T, Sieri S, Krogh V, Berrino F, Biagioni F, Strano S, Beyene J, Yarden Y, Blandino G (2018) MiRNA-513a-5p inhibits progesterone receptor expression and constitutes a risk factor for breast cancer: the hOrnone and Diet in the ETiology of breast cancer prospective study. *Carcinogenesis* 39: 98–108. <https://doi.org/10.1093/carcin/bgx126>
- Nayak B, Khan N, Garg H, Rustagi Y, Singh P, Seth A, Dinda AK, Kaushal S (2020) Role of miRNA-182 and miRNA-187 as potential biomarkers in prostate cancer and its correlation with the staging of prostate cancer. *Int Braz J Urol* 46: 614–623. <https://doi.org/10.1590/s1677-5538.2019.0409>
- Porzycki P, Ciszewicz E, Semik M, Tyrka M (2018) Combination of three miRNA (miR-141, miR-21, and miR-375) as potential diagnostic tool for prostate cancer recognition. *Int Urol Nephrol* 50: 1619–1626. <https://doi.org/10.1007/s12555-018-1938-2>
- Shi J, Liu C, Chen C, Guo K, Tang Z, Luo Y, Chen L, Su Y, Xu K (2020) Circular RNA circMBOAT2 promotes prostate cancer progression via a miR-1271-5p/mTOR axis. *Aging (Albany NY)* 12: 13255–13280. <https://doi.org/10.18632/aging.103432>
- Shi Y, Fang N, Li Y, Guo Z, Jiang W, He Y, Ma Z, Chen Y (2020) Circular RNA LPAR3 sponges microRNA-198 to facilitate esophageal cancer migration, invasion, and metastasis. *Cancer Sci* 111: 2824–2836. <https://doi.org/10.1111/cas.14511>
- Shu X, Cheng L, Dong Z, Shu S (2019) Identification of circular RNA-associated competing endogenous RNA network in the development of cleft palate. *J Cell Biochem* 120: 16062–16074. <https://doi.org/10.1002/jcb.28888>
- Suer I, Guzel E, Karatas OF, Creighton CJ, Ittmann M, Ozen M (2019) MicroRNAs as prognostic markers in prostate cancer. *Prostate* 79: 265–271. <https://doi.org/10.1002/pros.23731>
- Wang C, Tao W, Ni S, Chen Q (2019) SENP1 interacts with HIF1α to regulate glycolysis of prostatic carcinoma cells. *Int J Biol Sci* 15: 395–403. <https://doi.org/10.7150/ijbs.27256>
- Wang J, Li X, Xiao Z, Wang Y, Han Y, Li J, Zhu W, Leng Q, Wen Y, Wen X (2019) MicroRNA-488 inhibits proliferation and glycolysis in human prostate cancer cells by regulating PFKFB3. *FEBS Open Bio* 9: 1798–17807. <https://doi.org/10.1002/2211-5463.12718>
- Wang X, Zhang X, Wang G, Wang L, Lin Y, Sun F (2017) Hsa-miR-513b-5p suppresses cell proliferation and promotes P53 expression by targeting Irf2 in testicular embryonal carcinoma cells. *Gene* 626: 344–353. <https://doi.org/10.1016/j.gene.2017.05.033>
- Weng XD, Yan T, Liu CL (2020) Circular RNA_LARP4 inhibits cell migration and invasion of prostate cancer by targeting FOXO3A. *Eur Rev Med Pharmacol Sci* 24: 5303–5309. <https://doi.org/10.26355/eurev.202005.21312>
- Wu QQ, Zheng B, Weng GB, Yang HM, Ren Y, Weng XJ, Zhang SW, Zhu WZ (2019) Downregulated NOX4 underlies a novel inhibitory role of microRNA-137 in prostate cancer. *J Cell Biochem* 120: 10215–10227. <https://doi.org/10.1002/jcb.28306>
- Xia L, Sun J, Xie S, Chi C, Zhu Y, Pan J, Dong B, Huang Y, Xia W, Sha J, Xue W (2020) PRKAR2B-HIF-1α loop promotes aerobic glycolysis and tumour growth in prostate cancer. *Cell Prolif* 53: e12918. <https://doi.org/10.1111/cpr.12918>
- Xu F, Ni M, Li J, Cheng J, Zhao H, Zhao J, Huang S, Wu X (2020) Circ004390 promotes cell proliferation through sponging miR-198 in ovarian cancer. *Biochem Biophys Res Commun* 526: 14–20. <https://doi.org/10.1016/j.bbrc.2020.03.024>
- Yuan Y, Chen X, Huang E (2019) Upregulation of circular RNA Itchy E3 ubiquitin protein ligase inhibits cell proliferation and promotes cell apoptosis through targeting miR-197 in prostate cancer. *Technol Cancer Res Treat* 18: 1533033819886867. <https://doi.org/10.1177/1533033819886867>
- Zhang Y, Shi Z, Li Z, Wang X, Zheng P, Li H (2020) Circ_0057553/miR-515-5p regulates prostate cancer cell proliferation, apoptosis, migration, invasion and aerobic glycolysis by targeting YES1. *Oncotargets Ther* 13: 11289–11299. <https://doi.org/10.2147/ott.s272294>
- Zhang ZJ, Zhang YH, Qin XJ, Wang YX, Fu J (2020) Circular RNA circDENND4C facilitates proliferation, migration and glycolysis of colorectal cancer cells through miR-760/GLUT1 axis. *Eur Rev Med Pharmacol Sci* 24: 2387–2400. <https://doi.org/10.26355/eurev.202003.20506>
- Zhang ZJ, Zhang YH, Qin XJ, Wang YX, Fu J (2020) Circular RNA circMDM2 accelerates the glycolysis of oral squamous cell carcinoma by targeting miR-532-3p/HK2. *J Cell Mol Med* 24: 7531–7537. <https://doi.org/10.1111/jcmm.15380>
- Zhou K, Wei Y, Li X, Yang X (2021) MiR-223-3p targets FOXO3a to inhibit radiosensitivity in prostate cancer by activating glycolysis. *Life Sci* 282: 119798. <https://doi.org/10.1016/j.lfs.2021.119798>

Bionics investigation of blood 25-hydroxyvitamin D in the interpretable biomechanics diagnosis of childhood anemia

Lechi Zhang^{1#}, Aijie Huang^{2#}, Jingye Cai³, Jiangting Hou³, Hongyan Deng³ and Chenxiao Liu^{2✉}

¹Department of Rehabilitation Medicine, The Affiliated Su-zhou Hospital of Nanjing Medical University, Suzhou Municipal Hospital, Gusu School, Nanjing Medical University, 286 Guangji Road, Jiangsu 215008, People's Republic of China; ²Department of Endocrinology, The Affiliated Suzhou Hospital of Nanjing Medical University, Suzhou Municipal Hospital, Gusu School, Nanjing Medical University, 242 Guangji Road, Jiangsu 215008, People's Republic of China; ³Department of Child Health Care, Zhang Jiagang Maternity and Child Health Care Hospital, Zhang jiagang, People's Republic of China

Vitamin D deficiency (VDD) causes a wide range of health problems, including anemia in infants. If not treated promptly, it may create serious issues for infants with long-term impacts. Therefore, a satisfactory solution to this problem is required. This investigation was to explore the correlation between the blood 25-hydroxyvitamin D (25(OH)D) levels and childhood anemia. In this investigation, a cross-sectional examination was performed on 2,942 babies ranging in age from 2 to 36 months and classified into three cohorts: VDD (Vitamin D deficiency), VDI (Vitamin D insufficiency), and VDS (Vitamin D sufficiency). Multiple-variables and multinomially-related logistic regressions for examining the anemia status-vitamin D (Vit-D) relationship of the baseline as the interpretable visual quality models were examined. The median serum 25(OH)D level in 2,942 infants was 24.72 ± 4.26 ng/l, with 661 cases (22.5%) of VDD and 1710 cases of deficiency (58.1%), and a noticeable seasonal variation ($p < 0.05$). Anemia was present in 28.5% of the VDD group compared with 3.3% in vit-D sufficient infants ($p < 0.0001$). Lower levels of 25(OH)D were found to be associated with an increased risk of anemia in a multiple-variable regression analysis. In healthy children, low 25(OH)D levels were associated with increased risk of anemia. Biologically inspired, primary care physicians should assess Vit-D levels and place a greater emphasis on adequate supplementation for deficiency prevention.

Keywords: Low 25(OH)D; childhood anemia; healthy children; vitamin D

Received: 17 February, 2023; revised: 18 April, 2023; accepted: 17 May, 2023; available on-line: 06 September, 2023

✉e-mail: chenxiaoliu2010@rediffmail.com

[#]Lechi Zhang and Aijie Huang contributed equally to this work.

Acknowledgements of Financial Support: This investigation was sponsored by the Zhang Jiagang Science and Technology Bureau's Science and Technology Support Project (ZKS1633) and the Suzhou City Introduces Clinical Medicine Expert Team Project (SZYJTD201808).

Abbreviations: Hb, hemoglobin; VDD, Vitamin D deficiency; VDI, Vitamin D insufficiency; 25(OH)D, blood 25-hydroxyvitamin D

INTRODUCTION

Anemia is a pervasive issue in pediatrics and is an important part of standard care for all pediatric patients. If not treated in time, it can cause significant problems for children, and the effects can be long lasting (Khan, 2018). The hemoglobin (Hb) level in these patients is too

low to meet cellular oxygen demands (D'Souza, 2020). It is necessary to employ better tactics, like the targeted screening of high-risk children, such as iron insufficiency and VDD. VDD refers to a highly frequent nutrition-related deficiency globally, especially in young children (Laway *et al.*, 2014). The effect of 25(OH)D, a key circulation vitamin D (vit-D) state, on calcium absorption and bone metabolic processes is noteworthy (Uberti *et al.*, 2016; Alyasin *et al.*, 2011). It has been progressively found to that decreased vit-D extents display relationships to diabetes mellitus (Sharma *et al.*, 2015), hypertension, cancer and the maintenance of immune homeostasis (Atkinson *et al.*, 2014). Existing studies show that serum 25(OH)D, which has long been thought to be the greatest indication of overall vit-D status, has a relationship with Hb level (Alyasin *et al.*, 2011), but the studies either used small sample sizes or focused primarily on women, the elderly, or adults in a healthcare setting (Shin & Shim, 2013; Yoo & Cho, 2015). In addition, lower 25 (OH)D extents have displayed an individual associating process to anemia in adults exhibiting chronic diseases (e.g., heart failing state, end-stage renal disease and diabetes) (Ernst *et al.*, 2015; Holick, 2007), even among healthy adults (Yazici *et al.*, 2018). However, this association has not been explored in infants with health conditions. It is generally considered that vit-D impacts proliferating and differentiating processes of stem cells in marrow of bone and may impact red cell proliferating process (Uberti *et al.*, 2016). For this reason, VDD may have an influence on Hb metabolism and induce anemia (Balasubramanian, 2011). Nevertheless, the likely relating characteristic of the VDD and anemia is still unclear. Thus, our intention was to assess the degree of vit-D in Zhang Jiagang's common children. Furthermore, the current investigation revealed the components that might be impacting VDD, the associations between feeding category, Hb extents, anemia status, and VDD, and the connection between the blood 25-hydroxyvitamin D level and childhood anemia.

MATERIALS AND METHODS

This experiment was performed at the Zhang Jiagang Maternity and Child Health Care Hospital in China from 2011 to 2016. This experiment was approved by the ethical committee of the Zhang Jiagang Maternity and Child Health Care Hospital, China. (Reg. No. 38563/2010/VIT-D/11.07.2010), and written informed consent was obtained from each participant. Totally, 2,942 infants

were chosen from the Child Health Care outpatient department at Zhang Jiagang Maternity and Child Health Care in China.

Inclusion criteria

1. Infants age limit from 2 months to 3 years. 2. Experimental duration August 2011 to November 2016.

Exclusion criteria

1. Systemically-related illness, 2. covering celiac disease, 3. liver, kidney disorders, rickets, joint pain, malnutrition, hypothyroidism, 4. hematologically-related disorders (e.g., anemia, G-6PD deficiency and thalassemia) besides iron insufficiency anemia received the exclusion. Feeding figures received the grouping process to 3 types specific to formula, cow's milk, and breast milk applications.

Anemia

Anemia is brought on by disruptions in the Hb production process. Anemia received the definition of Hb less than 110 mg/dL for males and females. Mild anemia = Hb 100 to 109 mg/dL; Moderate anemia = Hb 70 to 99 mg/dL; Severe anemia = Hb <70 mg/dL (Molloy *et al.*, 2017).

Further children were grouped as VDD was classified as serum 25(OH) D extents <20 ng/mL, VDI as 25(OH) D extents between 20 and 30 ng/mL, VDS as >30 ng/mL, VDS intoxication as >150 ng/mL (Balasubramanian, 2011; Holick *et al.*, 2015).

ELISA analysis

Serum 25(OH)D levels were determined by ELISA (Immunodiagnostic Systems Ltd., Beijing Bohui Innovation Technology) according to the manufacturer's instructions. In the first analytical phase, calibrators and specimens of blood are diluted with biotin-labeled 25(OH)D and added to microplate wells coated with monoclonal anti-25(OH)D antibodies. During the incubation, an unknown quantity of 25(OH)D in the blood sample competes with a known amount of biotin-labeled

25(OH)D for antibody binding sites in the microplate wells. Washing removes unbound 25(OH)D. A second incubation with peroxidase-labelled streptavidin is used to identify bound biotin-labelled 25(OH)D. The attached peroxidase induces a colour response in a third incubation with the peroxidase substrate tetramethylbenzidine (TMB). To halt the process, an acidic stopping solution is introduced. The intensity of the colour is related to the concentration of 25(OH)D. The intraassay CVs were 4.9% at a 25(OH)D mean concentration of 27.0 nmol/L, 6.9% at a 25(OH)D mean concentration of 61.5 nmol/L, and 3.2% at a 25(OH)D mean concentration of 160.3 nmol/L.

Haemoglobin (Hb) determination

The Hb was determined using the spectrophotometric cyanmethaemoglobin (HiCN) method by the XK-2 analysing tool. This approach is to convert haemoglobin to cyanmethemoglobin by adding potassium cyanide and ferricyanide, and then measure the absorbance at 540 nm in a photoelectric calorimeter against a reference solution. The test was carried out exactly as described by Bhaskaram and others (Bhaskaram *et al.*, 2003).

Statistical Analysis

Overall, statistically-related processes were carried out by SPSS, 12.0 Ver software. The information had the expression "proportions" or "mean \pm standard deviation". The key features were evaluated within the groups using *t*-testing methods. The chi-square and Fisher's test methods were utilised to effectively assess the categorical data. The Pearson correlation assay was undertaken to assess the connection among 25(OH)D and Hb levels. Multiple logistic regression analysis techniques were employed to assess the baseline anemia conditions of the different vit-D groups. The regulations for the mothers' years of schooling, family income, sex, season, and child age based on the models were mentioned. The multinomial logistic regression studies for measuring the relationship between VDD and various anemia (moderate and mild) in contrast to non-anemia at baseline were

Table 1. Subject population characteristics

Characteristics	6 Mo~	12 Mo~	24 Mo~	36 Mo~
Total no	594 (20.2)	318 (10.8)	1,094 (37.2)	936 (31.8)
Male	300 (50.5)	186 (58.5)	585 (53.5)	470 (50.2)
Female	294 (49.5)	132 (41.5)	509 (46.5)	466 (49.8)
Feeding pattern				
Breast milk only	567 (95.5)	226 (71.1)	477 (43.6)	15 (1.6)
Breast milk and formula	27 (4.5)	65 (20.4)	502 (45.9)	715 (76.4)
Formula only	–	27 (8.5)	115 (10.5)	206 (22.0)
25(OH)D deficiency (levels <20 ng/mL)	164 (27.6)	125 (39.3)	298 (27.2)	74 (7.91)
25(OH)D insufficiency (levels 20–30 ng/mL)	426 (71.7)	187 (58.8)	640 (58.5)	457 (48.8)
25(OH)D sufficiency (levels >30 ng/mL)	4 (0.7)	6 (1.8)	156 (14.3)	405 (43.3)
25(OH)D intoxication (levels >150 ng/mL)	0 (0)	0 (0)	0 (0)	0 (0)
Anemia (Hb <110 mg/dL)	393 (66.2)	210 (66.0)	593 (54.2)	307 (32.8)

Values are presented as-number (%). Month: Mo; 25-hydroxyvitamin D: 25 (OH)D.

Table 2. Comparison of haematological and biochemical profiles according to vitamin D status (in total 2,942 patients)

Parameters	25 (OHD) <20 ng/mL (VDD)	25(OHD) 20~30 ng/mL (VDI)	25(OHD) >30 ng/mL (VDS)	<i>p</i> value
Total no. (%)	661 (22.5)	1,710 (58.1)	571 (19.4)	<0.05*
Mean age (MO)	11.58±7.98	19.40±9.64	27.77±8.55	<0.001*
Male (%)	334 (50.5)	838 (49)	385 (67.4)	0.088
Female (%)	327 (49.5)	872 (51)	186 (32.6)	0.081
Breast feeding (%)	258 (39.0)	373 (21.8)	372 (65.1)	<0.05*
Mean 25(OH)D (ng/mL)	18.68±0.36	25.05±2.84	30.81±0.72	<0.001*
Mean Hb (mg/dL)	112.54±10.67	118.63±8.52	122.77±8.21	<0.001*

Values are presented as Mean ± S.D. or %. MO, month. 25 (OH)D, 25-hydroxyvitamin D. Hb, hemoglobin; VDD, vitamin D deficiency. VDI, vitamin D insufficiency. VDS, vitamin D sufficiency.

also employed. A *p* value of <0.05 exhibited statistics-related significance.

RESULTS

The characteristics of study population characteristics

The features of the investigated participant are demonstrated in Table 1. Among the total 2942 infants enrolled here. Among these, 1541 (52.4%) were men and 1401 (47.6%) were girls. In this, 594 (20.2%) were below 6 months of age, whereas 318 (10.8%), 1094 (37.2%) and 936 (31.8%) from 6–12, 12–24, and 24–36, respectively. In infants <6 month, 95.5% were breastfed, whereas 4.5% received Breast milk and formula. In 6–12 months, 71.1% were breastfed and 20.4% were received Breast milk and formula, 8.5% received only formula. In 12–24 months, 43.6% were breastfed only, 45.9% were received only breast milk and formula and 10.5% received only formula. In 24–36 months, 1.6% were only breastfed and 75.4% were received breast milk and formula, 22% received only formula. The 25(OH)D deficiency levels <20 ng/mL showed 27.6% in the below 6 month. The 25(OH)D deficiency levels of <0 ng/mL were noted 27.6% in the below six months babies, 39.3% in 6–12 months, 27.2% in 12 to 24 months and 7.9% in 24 to 36 months. The 71.7% of below 6 months babies were showed 25(OH)D insufficiency levels of 20–30 ng/mL, 58.8% showed by 6–12 months babies, 58.5% were showed by 12 to 24 months, 48.8% showed in 24 to 36 months. In the study, 71.7%, 58.8%, 58.5%, and 48.8% of babies as follows: below 6 months, 6–12 months, 12–24 months, and 24–36 months showed 25(OH)D insufficiency levels (20–30 ng/mL). In the study, 0.7%, 1.9%, 14.2%, and 43.3% of babies as follows: below 6 months, 6–12 months, 12–24 months, and 24–36 months showed 25(OH)D sufficiency (levels >30 ng/mL). No 25(OH)D intoxication levels >150 ng/mL were reported in this study. In the study, 66.2%, 66%, 54.2%, and 32.8% babies as follows: below 6 months, 6–12 months, 12–24 months, and 24–36 months showed Anemia (Hb <110 mg/dL).

The associating process of VDD presence and breastfeeding exhibited statistics-related significance

In the tested babies, 22.5% showed by VDD, 58.1% expressed by VDI and 19.4% showed by VDS (Table 2). Mean age of the children who in VDD cohort was 11.58±7.98 months, while it in VDI group reached 19.40±9.64 months and in the VDS group

was 27.77±8.55 months. The male (%) in the VDD was 50.5%, 49.0% in VDI and in VDS 67.4%. the female (%) in the VDD was 49.5%, 51.0% in VDI and in VDS 32.6%. The rate of exclusive breast feeding in the three cohorts was 39.0%, 21.8% and 65.1%. For this reason, the associating process of VDD presence and breastfeeding exhibited statistics-related significance (*p*<0.05). The significant diversification between Hb extents is among 3 cohorts. Among children VDD, 28.5% of infants were with Hb <110 mg/dL and mean Hb as 112.54±10.67 mg/dL. However, 8.2% of overall in the VDI cohort exhibiting mean Hb as 118.63±8.52 mg/dL and 3.3% of overall in the VDS cohort exhibiting mean Hb as 122.77±8.21 mg/dL (*p*<0.001). Thus, in vit-D deficient cohort, cases number exhibiting low Hb extents (<110 mg/dL) was higher in comparison with vit-D sufficient cohort (Fig. 1).

Anemia condition of different patients

Table 3 lists the anemia condition for different levels of vit-D. About 95.2% of the recruited infants had Mild anemia, covering 73.4% Moderate anemia and 17.6% sever anemia. When confounders (the mothers' years of schooling, family income, sex, season, and infant age) were controlled for, no connections were noted between vit-D and anaemia condition; however, moderate anaemia had a higher risk in 25(OH)D 30 mg/mL infants than in 25(OH)D 30 mg/mL infants [relative risk (RR), 1.59; 95% confidence interval (CI), 1.09–2.31]. The frequency of mild anaemia showed a weak correlation with vit-D status (RR, 1.04; 95% CI, 0.97–1.29). In Fig. 2, the authors also analyzed case number with 25(OH)D deficiency, insufficiency and sufficiency and the extents of 25(OH)D in line with seasons. The number of cases with vit-D levels of <30 ng/mL in the autumn (September to November) was 536 (76.9%), 625 (74.4%) in the summer

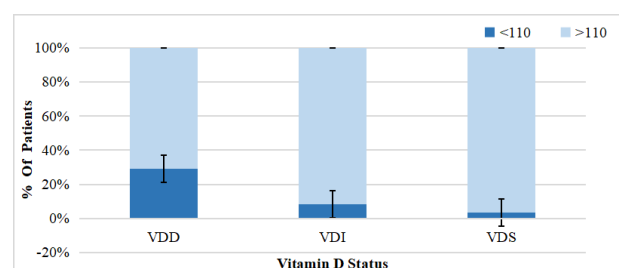


Figure 1. The Ratio of anaemia in VDD was significantly higher than that in VDI and VDS, *p*<0.05*. VDD, vitamin D deficiency. VDI, vitamin D insufficiency. VDS, vitamin D sufficiency.

Table 3. Prevalence of anemia in different levels of 25 (OH)D children

Variable	25(OH)D<30 mg/mL (n=2371)	25(OH)D≥30 mg/mL (n=571)	Unadjusted OR (95% CI)	Adjusted OR (95% CI)*
Mild anemia (Hb<110mg/dL)	1264 (53.3)	239 (41.9)	1.23 (0.45, 1.68)	1.23 (0.12, 1.35)
Subgroup				
Anemia (Hb 70-99 mg/dL)	367 (15.5)	12 (2.1)	1.53 (1.11, 2.09)	1.59 (1.09, 2.31)
Moderate anemia (Hb 100-109 mg/dL)	897 (33.6)	227 (39.8)	1.06 (0.73, 1.55)	1.04 (0.97, 1.29)

*ORs were calculated by using logistic regression and adjusted for age of the child, season, sex, family income and mothers' years of schooling.

**ORs were calculated by using multinomial logistic regression and adjusted age of the child, season, sex, family income and mothers' years of schooling.

Table 4. Factors associated with vitamin D deficiency

Variable	Odds ratio	95 % CI
Male	0.89	0.72-3.36
Female	0.81	0.66-3.27
Age (<12 Mo)	1.88*	0.65-6.06
Breast feeding	0.78	0.45-1.57
Serum mean Hb level	1.51*	1.02-2.84
Vitamin D tested in winter/spring	3.22*	1.13-4.57

*p value <0.001; VDD, vitamin D deficiency.

(June to August), 453 (87.3%) in the winter (December to February), and 757 (85.4%) in the spring (March to May). The average serum 25(OH)D level was significantly lower in spring/winter than in summer/autumn (25.28 ± 4.31 v/s 23.78 ± 4.34 ng/mL, $p < 0.01$). The winter season exhibited the maximum VDD ratio (31.6%), and the spring season achieved the maximum VDI ratio (62.4%). The lone risk element for VDD determined by multiple-variable logistic regression was 25OHD in the winter or spring [odds ratio, 3.22; 95% CI, 1.13 to 4.57]. Several factors related to sex and breastfeeding that were seen in the univariate research had no independent relationship with VDD (Table 4). The risk element in terms

of VDD developing process was evident in babies with anemia ($p < 0.001$) and if 25(OH) D extents received the testing process in winter/spring ($p < 0.001$).

DISCUSSION

The present work suggests that in a large, group-related Zhang Jiagang infants cohort with health condition, lower 25(OH)D extents displayed associations to elevated anemia risk. The identified associating process of vit-D condition and anemia was determined by other elements probably inducing anemia risk such as the mothers' years of schooling, family income, sex, season and age of infants. In the present work 28.5% and 8.2% of the infants achieved Hb <110 mg/dL in the vit-D deficient cohort (VDD and VDI), but merely 3.3% of the infants achieved Hb <110 mg/dL in the vit-D sufficient cohort. vit-D is vital nutrient required by an infant to grow and develop (Harinarayan & Joshi, 2009). The experts recommended that all only breastfeeding-based infants were required to undergo 400 IU per day of vit-D supplementing processes, which should be initiated several days after birth. No diversification received the identification in mean extents of vit-D in sex. However, the vit-D adequacy ratios of boy were slightly higher than in girls, which may be related to boys spending more time outdoors than girls. The authors further identified a noticeable correlating characteristic of <6 months age and VDD. Such correlating characteristic is likely to result from declined vit-D stores in such age cohort, breastfeeding almost exclusively and increased vit-D requirements and/or insufficient sun exposure. Balasubramanian and others (Balasubramanian *et al.*, 2011) suggest that a greater risk of VDD received the identification in infants having undergone exclusive breastfeeding process with no adequate vit-D supplementing process and appropriate exposure to sunlight. Furthermore, only a small number of breastfed infants get vit-D supplements since very few mothers follow their physician's suggestion for vit-D supplement because they think breast milk may provide critical nutrients (Yoon *et al.*, 2012). The majority of them prefer to buy health supplements like fish glycerides and DHA online. They consider that the vit-D presented by the hospital is easy to poison, and only part of the mother will take vit-D supplements during pregnancy.

The relating characteristic between VDD and anemia identified here complies with several recently conducted

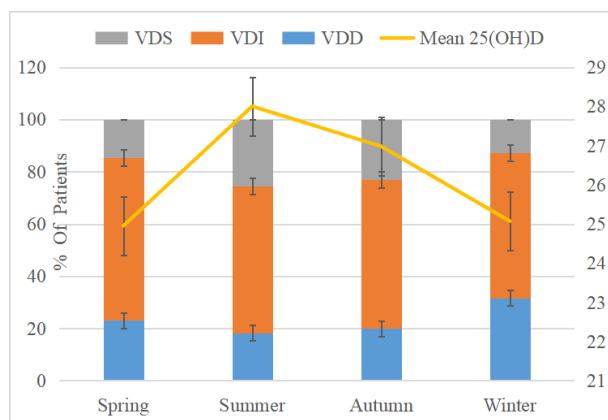


Figure 2. The levels of 25(OH)D status increased from spring to summer and then decreased in autumn and winter. VDD, vitamin D deficiency. VDI, vitamin D insufficiency. VDS, vitamin D sufficiency.

researched on a range of groups (Alyasin *et al.*, 2011; Ernst *et al.*, 2015; Htet *et al.*, 2014). Several potential mechanisms could explain the associating characteristic of VDD and anemia in healthy infants. Major possibility is that VDD in infants is suggested displaying relationship to lifestyle and nutrition-related elements covering reduced milk intake and obesity as aforesaid. Inadequate 25(OH)D levels decrease local calcitriol synthesis in the bone marrow, resulting in decreased erythropoiesis (Sim *et al.*, 2010). Calcitriol could reduce cytokine producing process, thereby reducing inflammation-related milieu and anemia. The abundance of vitamin D receptors and vit-D in bone marrow seem to trigger erythroid precursors. High levels of 25(OH)D in hematopoietic tissues have been linked to erythroid progenitor cell paracrine activation. Moreover, there is considerable evidence that inflammatory cytokines affect erythropoiesis. Immunomodulation-related influences exerted by vit-D are likely to critically impact its role to prevent anemia by the modulating process related to systemically-related cytokine producing process, probably suppressing particular inflammation-related channels facilitating anemia progression. Furthermore, because of anemia people are commonly tired and less probably going externally for obtaining adequate sun exposing to generate vit-D. Anemia may also in turn contribute to VDD.

The season-related varying process acted as a single predicting element for VDD among infants subjected to anemia, abiding by existing works (Jin *et al.*, 2013). Given vit-D is primarily sourced by skin casually exposed to sunlight. 7-dehydrocholesterol (7-DHC) is isomerized to pre-vitamin D3 in the exposing process of the UVB (290 to 315 nm) part pertaining to sun photolyzes. When the relevant forming process is achieved, pre-vitamin D3 will undergo thermally isomerizing process for synthesize vit-D3. Solar UVB radiation amount accessing into the biosphere refers to one function pertaining to wavelength and ozone amount traveled by solar radiating process via the air, one function pertaining to the solar zenith angle, is determined by day time, season as well as latitude. Because the sun largely drives the vit-D synthesizing process in the body, it was reported that VDD was more common; serum 25(OH)D extent was noticeably low in the spring/winter season than in the autumn/summer season. This is most likely due to summer/autumn sun exposure is adequate illumination than winter/spring and children outdoor time is longer. Human skin can be exposed to ultraviolet B radiation to produce more vit-D. Moreover, as suggested from recently conducted researches, genetically-related predisposition is likely to critically impact susceptible characteristic to VDI, and both vit-D uptake via diet and supplementing processes and skin-forming process when solar exposure is achieved may be determined by single genetically-related varying processes (Anastasiou *et al.*, 2017). The present multiple-variables-based logistic study suggested that season-based varying process in 25(OH)D acted as the merely noticeable single risk element in terms of VDD. For this reason, the present work demonstrates the season-based varying process is the primary risk component of VDD in Infants with anemia. Accordingly, the significance of sunshine and the requirement for vit-D supplement, especially throughout the winter and spring, are stressed. More research is required to explore the relationship among blood 25-hydroxyvitamin D levels and childhood anaemia.

CONCLUSION

To be specific, the present work on Zhang Jiagang infants suggested the correlative characteristics between anemia severity and VDD. For presenting the optimal nutritional condition for infants, breastfeeding continues to be worth recommending. However, educational efforts are required publicly and those breastfed in an exclusive manner (even under asymptomatic child) for increasing abundance by vit-D supplementing requirements.

Limitations

The present work showed several limitations. Subjects had varying ages; thus, their dietary intake and habits of feeding were likely to vary, probably causing a memory bias. It is better to compare plasma Hb and ferritin extents in the same patients, complying with the vital elements in Hb synthesis. It will be better to demonstrate the relationship to vit-D condition and categories of anemia and the strength of association differs among types of anemia. Considerable trials under randomization-based controlling should be conducted for determining if enhancing vit-D condition is capable of reducing anemia severity in normal groups.

Declarations

Acknowledgments. The authors like to acknowledge the employees at Suzhou Municipal Hospital and Zhang Jiagang Maternity and Child Health Care Hospital for their assistance with this study. Furthermore, the authors acknowledge and appreciate the interviewers' and respondents' time and effort put into this research.

Data and resources Transparency. The data obtained and compiled for this work are not publicly accessible; however, they may be obtained from the corresponding author if you make a request.

Consent for publication. Not applicable.

Conflict of interest. There are no conflicts of interest.

REFERENCES

- Alyasin S, Momen T, Kashef S, Alipour A, Amin R (2011) The relationship between serum 25 hydroxy vitamin d levels and asthma in children. *Allergy Asthma Immunol Res* 3: 251–255. <https://doi.org/10.4168/aa.2011.3.4.251>
- Anastasiou A, Karras SN, Bais A, Grant WB, Kotsa K, Goulis DG (2017) Ultraviolet radiation and effects on humans: the paradigm of maternal vitamin D production during pregnancy. *Eur J Clin Nutr* 71: 1268–1272. <https://doi.org/10.1038/ejcn.2016.188>
- Atkinson MA, Melamed ML, Kumar J, Roy CN, Miller ER 3rd, Furth SL, Fadowski JJ (2014) Vitamin D, race, and risk for anemia in children. *J Pediatr* 164: 153–158. e151. <https://doi.org/10.1016/j.jpeds.2013.08.060>
- Balasubramanian S (2011) Vitamin D deficiency in breastfed infants & the need for routine vitamin D supplementation. *Indian J Med Res* 33: 250–252
- Bhaskaram P, Balakrishna N, Radhakrishna KV, Krishnaswamy K (2003) Validation of hemoglobin estimation using Hemocue. *Indian J Pediatr* 70: 25–28. <https://doi.org/10.1007/BF02722739>
- D'Souza AM (2020) A general pediatrician's approach to anemia in childhood. *Pediatr Ann* 49: e10–e16. <https://doi.org/10.3928/19382359-20191212-01>
- Ernst JB, Becker T, Kuhn J, Gummert JF, Zittermann A (2015) Independent association of circulating vitamin D metabolites with anemia risk in patients scheduled for cardiac surgery. *PLoS One* 10: e0124751. <https://doi.org/10.1371/journal.pone.0124751>
- Harinarayan CV, Joshi SR (2009) Vitamin D status in India – its implications and remedial measures. *J Assoc Physicians India* 57: 40–48.
- Holick MF (2007) Vitamin D deficiency. *N Engl J Med* 357: 266–281. <https://doi.org/10.1056/NEJMra070553>
- Holick MF, Binkley NC, Bischoff-Ferrari HA, Gordon CM, Hanley DA, Heaney RP, Murad MH, Weaver CM; Endocrine Society (2011) Evaluation, treatment, and prevention of vitamin D deficiency

- cy: an Endocrine Society clinical practice guideline. *J Clin Endocrinol Metab* **96**: 1911–1930. <https://doi.org/10.1210/jc.2011-0385>
- Htet MK, Fahmida U, Dillon D, Akib A, Utomo B, Thurnham DI (2014) The influence of vitamin A status on iron-deficiency anaemia in anaemic adolescent schoolgirls in Myanmar. *Public Health Nutr* **17**: 2325–2332. <https://doi.org/10.1017/S1368980013002723>
- Jin HJ, Lee JH, Kim MK (2013) The prevalence of vitamin D deficiency in iron-deficient and normal children under the age of 24 months. *Blood Res* **48**: 40–45. doi: 10.5045/br.2013.48.1.40.
- Khan L (2018) Anemia in childhood. *Pediatr Ann* **47**: e42–e47. <https://doi.org/10.3928/19382359-20180129-01>
- Laway BA, Kotwal SK, Shah ZA (2014) Pattern of 25 hydroxy vitamin D status in North Indian people with newly detected, type 2 diabetes: A prospective case control study. *Indian J Endocrinol Metab* **18**: 726–730. <https://doi.org/10.4103/2230-8210.139242>
- Molloy J, Koplin JJ, Allen KJ, Tang MLK, Collier F, Carlin JB, Saffery R, Burgner D, Ranganathan S, Dwyer T, Ward AC, Moreno-Betancur M, Clarke M, Ponsonby AL, Vuillermin P; BIS Investigator Group (2017) Vitamin D insufficiency in the first 6 months of infancy and challenge-proven IgE-mediated food allergy at 1 year of age: a case-cohort study. *Allergy* **72**: 1222–1231. <https://doi.org/10.1111/all.13122>
- Sharma S, Jain R, Dabla PK (2015) The role of 25-hydroxy vitamin D deficiency in iron deficient children of north India. *Indian J Clin Biochem* **30**: 313–317. <https://doi.org/10.1007/s12291-014-0449-x>
- Shin JY, Shim JY (2013) Low vitamin D levels increase anemia risk in Korean women. *Clin Chim Acta* **421**: 177–180. <https://doi.org/10.1016/j.cca.2013.02.025>
- Sim JJ, Lac PT, Liu IL, Meguerditchian SO, Kumar VA, Kujubu DA, Rasgon SA (2010) Vitamin D deficiency and anemia: a cross-sectional study. *Ann Hematol* **89**: 447–452. <https://doi.org/10.1007/s00277-009-0850-3>
- Uberti F, Morsanuto V, Lattuada D, Colciaghi B, Cochis A, Bulfoni A, Colombo P, Bolis G, Molinari C (2016) Protective effects of vitamin D3 on fimbrial cells exposed to catalytic iron damage. *J Ovarian Res* **9**: 34. <https://doi.org/10.1186/s13048-016-0243-x>
- Yazici KU, Percinel Yazici I, Ustundag B (2018) Vitamin D levels in children and adolescents with obsessive compulsive disorder. *Nord J Psychiatry* **72**: 173–178. <https://doi.org/10.1080/08039488.2017.1406985>
- Yoo EH, Cho HJ (2015) Prevalence of 25-hydroxyvitamin D deficiency in Korean patients with anemia. *J Clin Lab Anal* **29**: 129–134. <https://doi.org/10.1002/jcla.21740>
- Yoon JW, Kim SW, Yoo EG, Kim MK (2012) Prevalence and risk factors for vitamin D deficiency in children with iron deficiency anemia. *Korean J Pediatr* **55**: 206–211. <https://doi.org/10.3345/kjp.2012.55.6.206>
- Zhou S, Glowacki J (2017) Chronic kidney disease and vitamin D metabolism in human bone marrow-derived MSCs. *Ann N Y Acad Sci* **1402**: 43–55. <https://doi.org/10.1111/nyas.13464>

Hexafluoro-2-propanol represses colorectal cancer proliferation by regulating transaminases

Zhongxin Shao^{1‡}, Lu Sun^{2‡} and Wenxin Lin^{1✉}

¹Department of Anaesthesiology, Zhongshan Hospital of Xiamen University, School of Medicine, Xiamen University, Xiamen, 361004, People's Republic of China; ²Department of Anaesthesiology, First affiliated Hospital of Xiamen University, School of Medicine, Xiamen University, Xiamen, 361026, People's Republic of China

Hexafluoro-2-propanol (HFIP) is a metabolite of sevoflurane used as part of the general anaesthesia technique. This study aims to investigate the effect of HFIP in colorectal cancer (CRC) and the regulation of associated genes. The differentially expressed genes (DEGs) with HFIP treatment were analysed based on GEO dataset GSE56256. Due to the restricted number of studies performing RNA-Seq in CRC with HFIP treatment, we selected a CRC patient cohort (GSE23878) to obtain DEGs that were compared with DEGs from GSE56256. The DEGs with opposite expression patterns in these two GEO datasets indicate that the genes mediate the function of HFIP, thereby repress the progression of CRC. The DEGs from these two GEO datasets were analysed independently. We obtained 10 up-regulated genes in GSE23878 (CRC patient cohort) were also down-regulated in GSE56256 (HFIP cohort), therefore, these 10 genes may function as tumor suppressors in CRC and may be involved in the function of HFIP. STRING analysis demonstrated an interaction in GPT2, PSAT1 and SLC7A11. The high expression of GPT2, PSAT1 and SLC7A11 were confirmed in TCGA-COAD datasets and in CRC cells. HFIP treatment repressed GPT2, PSAT1 and SLC7A11, which resulted in an inhibited proliferation and colony formation ability of DLD-1 and HCT-116 cells. Silencing GPT2, PSAT1 and SLC7A11 showed similar effect compared to HFIP treatment. Overexpression of GPT2, PSAT1 and SLC7A11 abrogated the effect of HFIP. In conclusion, the sevoflurane metabolite HFIP plays a cancer suppression role depending on cell proliferation in colorectal cancer through the down-regulation of GPT2, PSAT1 and SLC7A11 expression.

Key words: hexafluoro-2-propanol, transaminase, colorectal cancer

Received: 18 May, 2022; **revised:** 16 October, 2022; **accepted:** 08 January, 2023; **available on-line:** 23 February, 2023

✉e-mail: wenxin.lin@gmx.net

‡Authors contributed equally

Abbreviations: AKG, α-ketoglutarate; CRC, colorectal cancer; DEG, differentially expressed gene; HFIP, hexafluoro-2-propanol; LPS, lipopolysaccharide

INTRODUCTION

Sevoflurane is a commonly used anaesthetic because of the safety with fewer side effects compared with other inhalation anaesthetics (Kanaya *et al.*, 2014). Studies confirmed that volatile anaesthetics influence cancer cells and show potential regulatory effect on a variety of tumours (Sumi *et al.*, 2019; Zhao *et al.*, 2020). During the metabolism of sevoflurane, water-soluble hexafluoro-2-propanol (HFIP) presents as a primary metabolite of

sevoflurane (Buratti *et al.*, 2002). Previous researches have shown that HFIP attenuates inflammation *in vitro* by repressing related inflammatory mediators (Uerner *et al.*, 2015). However, few studies investigated the effect of HFIP on cancer progression especially on colorectal cancer, therefore, we demonstrated the function of HFIP in colorectal cancer cells and aimed to illustrate the potential molecular mechanisms.

The growth of mammalian cells is supported by nutrient sources including glucose and glutamine, which are involved in energy production and are related to cancer progression (Hosios *et al.*, 2016). Most cancer cells proliferate depending on glutamine. Glutamine starvation results in growth inhibition. GPT2 is a type of glutamic pyruvate transaminase catalysing the reversible transamination between alanine and α-ketoglutarate (AKG) generating pyruvate and glutamate (Welch, 1975). Previous studies have shown that GPT2, PSAT1 and SLC7A11 are involved in the progression of different cancers: GPT2 is highly expressed in cancers, such as breast cancer and pancreatic cancer (Cao *et al.*, 2017). Therefore, GPT2 is a potential biomarker and target in cancer therapy. PSAT1 was identified highly expressed in various cancers including colorectal cancer and non-small cell lung cancer (Qian *et al.*, 2017; Lodovichi *et al.*, 2019). Studies demonstrated that PSAT1 is involved in serine biosynthesis and mediates cell cycle progression, which implies a promising target for anticancer therapy. In the regulation of nutrient dependency of cancer cells, SLC7A11 plays emerging roles which maintain redox homeostasis (Koppula *et al.*, 2018). In colorectal cancer stem cells (CSCs), SLC7A11 has a higher level compared to colorectal cancer cells. Repression of SLC7A11 sensitizes colorectal CSCs to ferroptosis and chemotherapy drugs (Xu *et al.*, 2020). Furthermore, repression of SLC7A11 inhibits metastasis of pancreatic cancer by blocking the PI3K/Akt signaling pathway (Zhang *et al.*, 2021). The pro-death functions of SLC7A11 happen under glucose starvation (Karunakaran *et al.*, 2008). Overexpression of SLC7A11 confers resistance to MEK and BRAF inhibitors in *BRAF*^{V600E} mutant melanoma via increasing intracellular GSH contents (Wang *et al.*, 2018). Cancer cells employ up-regulated SLC7A11 to mediate cystine uptake, which results in better capabilities of cancer cells to survive in oxidative stress conditions (Koppula *et al.*, 2018). SLC7A11 provides a novel and effective therapeutic strategy for cancer treatment.

In our study, the regulation of GPT2, PSAT1 and SLC7A11 by HFIP was investigated in colorectal cancer. This study showed that HFIP repressed colorectal cancer proliferation *via* regulating glutamine metabolism related genes.

MATERIAL AND METHODS

Cell culture and treatment

Human colorectal cancer cell lines DLD-1, HCT-116 and RKO were obtained from ATCC. Human colon epithelium cell HCoEpiC was purchased from National Collection of Authenticated Cell Culture. Cells were cultivated in McCoy's 5A medium containing 10% fetal bovine serum (FBS), penicillin 100 units/ml and streptomycin 100 µg/ml with 5% CO₂ in 37°C. HFIP (105528) was purchased from Sigma Aldrich and dissolved in DMSO to a stock concentration of 100 mM. Working concentration of 50 mM was achieved by diluting HFIP stock solution with HBSS. Before different experiments cells were treated with HFIP for 12 h.

Transfection

GPT2, PSAT1 and SLC7A11 pcDNA3.1 overexpressing vectors were designed and constructed by BGI (Beijing, China). Specific siRNAs of GPT2, PSAT1 and SLC7A11 were purchased from QIAGEN (Germany). For transfection, cells were seeded into 6-well plate at the density of 5×10^5 cells/well and cultivated to at least 70% confluence. Vectors were transfected with Lipofectamine 2000, and siRNAs were transfected with Lipofectamine RNAiMAX (Thermo Fisher, USA) at 1:1 ratio (v/v) according to the protocol provided by the manufacturer. The final concentration of vector and siRNA were 2 µg/ml and 25 nM, respectively.

RNA isolation and quantitative real-time PCR (q-PCR)

Total RNAs were isolated and purified by High Pure RNA Isolation Kit (Roche, Switzerland) based on the instruction of the kit. 100 ng of isolated RNA was used for reverse transcription with verso cDNA synthesis kit (Thermo Fisher, USA). Q-PCR was performed with SYBR® Premix Ex Taq™ (RR420A; Takara) in Roche LightCycler 480 system. The data were normalized to GAPDH and calculated using $2^{-\Delta\Delta Ct}$ value. Primers used in q-PCR were listed in Table 1.

Table 1.. Primers used in q-PCR analysis

Genes	Sequence 5'-3'
GPT2 F	GTGATGGCACTATGCACCTAC
GPT2 R	TTCACGGATGCAGTTGACACC
PSAT1 F	TGCCGCACTCAGTGTGTTAG
PSAT1 R	GCAATCCCGCACAGATTCT
SLC7A11 F	TCTCAAAGGAGGTACCTGC
SLC7A11 R	AGACTCCCCTCAGTAAAGTGAC
GAPDH F	CTGGGCTACACTGAGCACC
GAPDH R	AAGTGGTCGTTGAGGGCAATG

Western blot

Total protein was isolated from colorectal cancer cells after different treatments by applying RIPA lysis buffer. Protein concentrations of each group were quantified with BCA kit based on the instructions. Total 40 µg of protein was loaded onto 10% sodium dodecyl sulfate polyacrylamide gel (SDS-PAGE). Electrophoresis conditions were 120 V for 120 min. It was then transferred to a polyvinylidene difluoride membrane (300 mA, 90 min).

Membranes were blocked by 5% milk in 1×TBST and then incubated with primary antibodies GPT2 (1:1000, Life, USA), PSAT1 (1:1000, Santacruz, USA), SLC7A11 (1:1000, Abcam, USA) and β-actin (1:2000, Abcam, USA) overnight at 4°C.

MTT assay

For cell proliferation rate, after different treatments, cells were seeded in 96-well plates in 100 µl of medium. Three parallel wells were assigned for each time points. MTT solution (5 mg/ml) was added to each well and incubation continued for 4 hours. It was followed by removing medium and washing with PBS twice. Afterwards, 150 µl DMSO was added into each well and then plate was shaken for 10 min. OD values were measured at 490 nm wavelength.

Colony formation assay

After different treatments, cells were seeded into 6-well plate at the density of 500 cells/well and cultivated to 3 weeks until cell colonies could be observed by eye. Cells were fixed with methanol for 15 min and then stained with crystal violet for 30 min. After staining, cells were washed under running water and taken pictures of by camera. Colony numbers were counted by using Image J software.

Bioinformatic analysis

GSE56256 and GSE23878 were obtained from GEO database (<https://www.ncbi.nlm.nih.gov/geo/>), and the download data format was MINIML. GSE56256 includes two groups of lipopolysaccharides (LPS)/HFIP treated endothelial cells and three groups of LPS treated endothelial cells (Urner *et al.*, 2015). The array profiling was performed on the platform of Agilent-028004 SurePrint G3 Human GE 8x60K Microarray. GSE23878 contains 35 colorectal cancer patient samples and 24 normal samples (Uddin *et al.*, 2011). The cDNA microarray was performed on the [HG-U133_Plus_2] Affymetrix Human Genome U133 Plus 2.0 Array. Limma package (version: 3.40.2) of R software was used to study the differential expression of mRNAs. The adjusted *P*-value was analysed to correct for false positive results in GEO datasets. “Adjusted *P*<0.05 and |Log₂[Fold Change]| >1” were defined as the thresholds for the screening of differential expression of mRNAs. To further confirm the underlying function of potential targets, the data were analyzed by functional enrichment. To better understand the carcinogenesis of mRNA, ClusterProfiler package (version: 3.18.0) in R was employed to analyze the GO function of potential targets and enrich the KEGG pathway. The box plot is implemented by the R software package ggplot2; PCA graphs are drawn by R software package ggplot2; the heat map is displayed by the R software package heatmap. All the above analysis methods and R package were implemented by R foundation for statistical computing (2020) version 4.0.3.

Statistics

SPSS 21.0 was used to calculate all the values (means ± standard error of the mean). Statistical analyses were analysed with Student's *t* test in two-groups comparison. One-way analysis of variance (ANOVA) test was used to verify the significance among experimental groups. The statistical significance was *P*<0.05. All experiments were performed in triplicate.

RESULTS

Analysis of differentially expressed genes with HFIP treatment

Since few studies performed next generation analysis of HFIP treatment in colorectal cancer cells or patients, here we selected a GEO dataset GSE56256 which investigated that HFIP as an anti-inflammation reagent in li-

popolysaccharides (LPS) induced inflammatory response in lung cancer. Therefore, we could obtain genes that are regulated by HFIP. We compared the duplicate of LPS-HFIP co-treatment groups to the triplicate of LPS treatment groups. A total of 5583 genes were down-regulated with $\text{Log}_2[\text{Fold Change}] < -1$ while a total of 54 genes were up-regulated with $\text{Log}_2[\text{Fold Change}] > 1$ after HFIP treatment (Fig. 1A and 1B). From the results, DEGs were mainly enriched in down-regulated group. Next, DEGs were put into KEGG signalling pathway

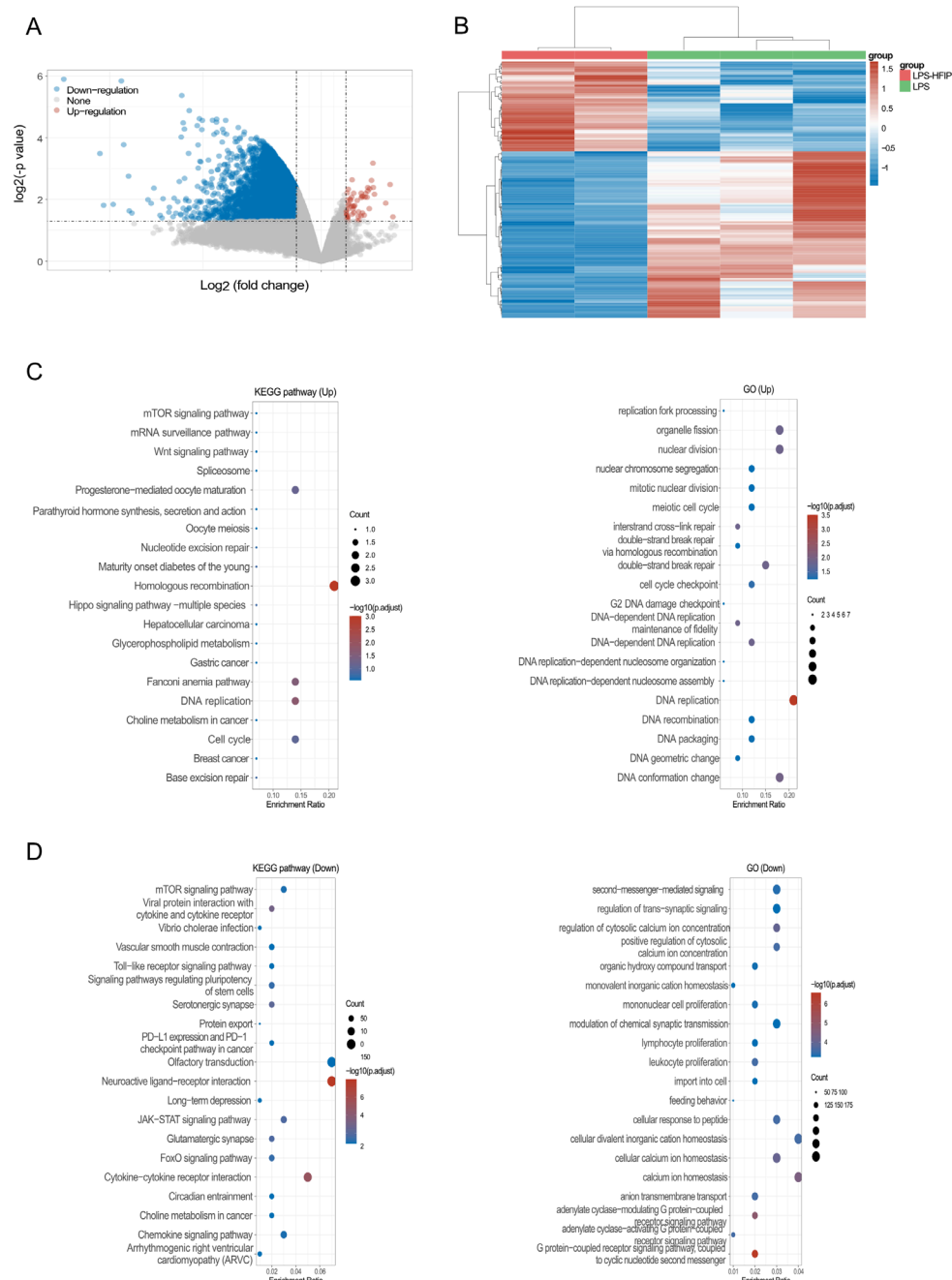


Figure 1. Analysis of differentially expressed genes with HFIP treatment.

(A) Volcano plot of differentially expressed genes with $|\text{Log}_2[\text{Fold Change}]| > 1$ after HFIP treatment compared to LPS treatment only (GSE56256). Down regulated genes were represented by blue dots and up-regulated genes were represented by red dots. (B) Heat map of differentially expressed genes after HFIP treatment compared to LPS treatment only (GSE56256). Down regulated genes were marked with blue bars and up-regulated genes were marked with red bars. (C) Kyoto Encyclopedia of Genes and Genomes (KEGG) and gene ontology (GO) analysis of up-regulated genes after HFIP treatment in GSE56256. (D) KEGG and GO analysis of down-regulated genes after HFIP treatment in GSE56256.

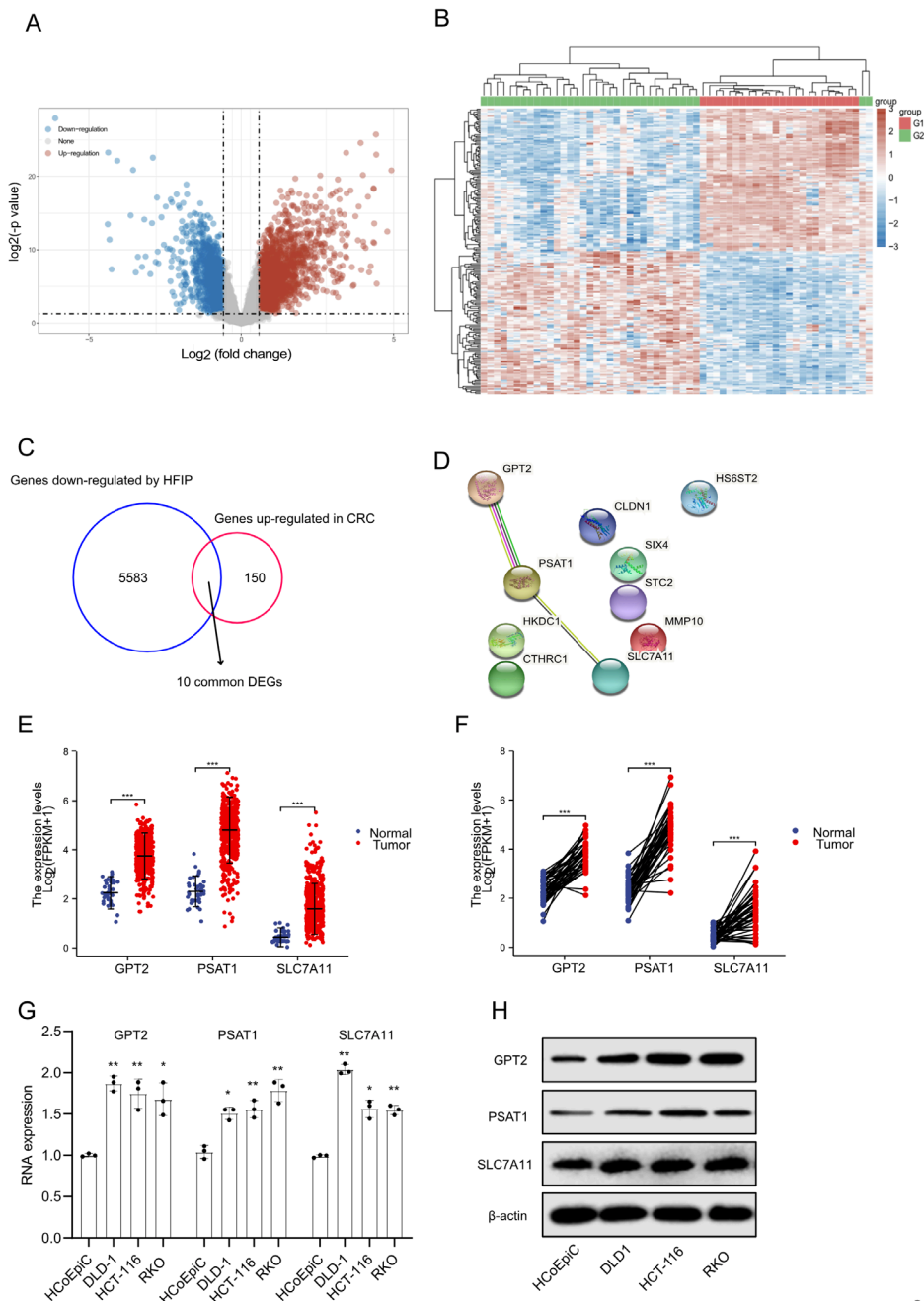


Figure 2. HFIP potentially regulates transaminases in colorectal cancer.

(A) Volcano plot of differentially expressed genes in colorectal cancer patients. Down regulated genes were marked with blue dots and up-regulated genes were marked with red dots. (B) Heat map of differentially expressed genes in colorectal cancer patients (GSE23878). Down regulated genes were marked with blue bars and up-regulated genes were marked with red bars. (C) Venn diagram showed overlapped genes of HFIP down-regulated genes selected from GSE56256 and up-regulated genes in colorectal cancer patients from GSE23878. (D) STRING database analysis of selected 10 common DEGs. (E) and (F) Unpaired and paired analysis of GPT2, PSAT1 and SLC7A11 in TCGA-COAD dataset. (G) q-PCR analysis of GPT2, PSAT1 and SLC7A11 in three indicated CRC cell lines (n=3) compared to HCoEpiC cell, normalized to *GAPDH*. (H) Western blot analysis of GPT2, PSAT1 and SLC7A11 in three indicated CRC cell lines compared to HCoEpiC cell, normalized to β -actin. The quantification of western blot was also presented (n=3). * $P < 0.05$, ** $P < 0.01$, *** $P < 0.001$.

and gene ontology (GO) analysis. Both KEGG analysis and GO analysis results demonstrated that the up-regulated genes were mainly enriched in pathways and biological processes involving cell cycle, DNA replication (Fig. 1C). For down-regulated genes, they were mainly enriched in chemokine signalling and immune cell func-

tions (Fig. 1D). The above analysis indicates that HFIP treatment reduces inflammation response. Since the chronic inflammation is a significant causal factor in the development of colorectal cancer, our results imply that HFIP has a potential protective effect in colorectal cancer treatment.

Table 2. 10 common DEGs up-regulated in GSE23878 and down-regulated in GSE56256

Gene symbol	Description
STC2	stanniocalcin 2
CLDN1	claudin 1
CTHRC1	collagen triple helix repeat containing 1
PSAT1	phosphoserine aminotransferase 1
HS6ST2	heparan sulfate 6-O-sulfotransferase 2
MMP10	matrix metalloproteinase 10
HKDC1	hexokinase domain containing 1
SLC7A11	solute carrier family 7 member 11
SIX4	SIX homeobox 4
GPT2	glutamic-pyruvic transaminase 2

HFIP potentially regulates transaminases in colorectal cancer

Since inflammation is one of the factors of arising colorectal cancer, we would like to know whether the genes regulated by HFIP in endothelial cells of the lung are also involved in the progression of colorectal cancer. Due to the restricted number of studies performing RNA-Seq in colorectal cancer with HFIP treatment, we selected a colorectal cancer patient cohort (GSE23878) to obtain DEGs that were compared with DEGs from GSE56256. The DEGs from these two GEO datasets were analysed independently. The DEGs with opposite expression patterns in these two GEO datasets may indicate the genes that mediate the function of HFIP, thereby repress the progression of colorectal cancer. GSE23878 contains 35 colorectal cancer samples and 24 normal samples. A total of 150 genes were up-reg-

ulated with Log₂[Fold Change] >1 while a total of 610 genes were down-regulated with Log₂[Fold Change] <-1 (Fig. 2A and 2B). Since HFIP is supposed to have a repression effect in cancers, it is intriguing to compare the genes downregulated by HFIP in GSE56256 to the genes up-regulated in colorectal cancer samples in GSE23878. Finally, we obtained 10 genes that overlapped (Fig. 2C) and were listed in Table 2, indicating that these 10 genes may serve as tumor suppressors and mediate the function of HFIP in colorectal cancer. Next, all the 10 genes were analysed *via* STRING database to get the potential protein interaction network. As presented in Fig 2D, only GPT2, PSAT1 and SLC7A11 showed interactions in those 10 genes. GPT2 and PSAT1 are transaminases and SLC7A11 is a cysteine/glutamate transporter (Welch, 1975; Qian *et al.*, 2017; Koppula *et al.*, 2018), which are associated with glutamine metabolism. Furthermore, GPT2, PSAT1 and SLC7A11 contribute to the cancer progression. Interestingly, GPT2, PSAT1 and SLC7A11 were validated to be highly expressed in colorectal cancer from the data of TCGA-COAD dataset (Fig. 2E and 2F). In addition, q-PCR analysis indicated a higher expression level of GPT2, PSAT1 and SLC7A11 in DLD-1, HCT-116 and RKO cells compared to a normal cell line HCoEpiC (Fig. 2G). Western blot also showed similar results (Fig. 2H). Therefore, GPT2, PSAT1 and SLC7A11 serve as oncogenes independent of tissue context. Collectively, HFIP potentially regulates glutamine metabolism in colorectal cancer through mediating GPT2, PSAT1 and SLC7A11.

HFIP represses proliferation of colorectal cancer cells

The effect of HFIP on colorectal cancer cells was investigated in the following studies. The proliferation rate of DLD-1 cells was repressed by HFIP treatment, which was concentration dependent (Fig. 3A). 20 mM HFIP repressed colony formation capability of DLD-

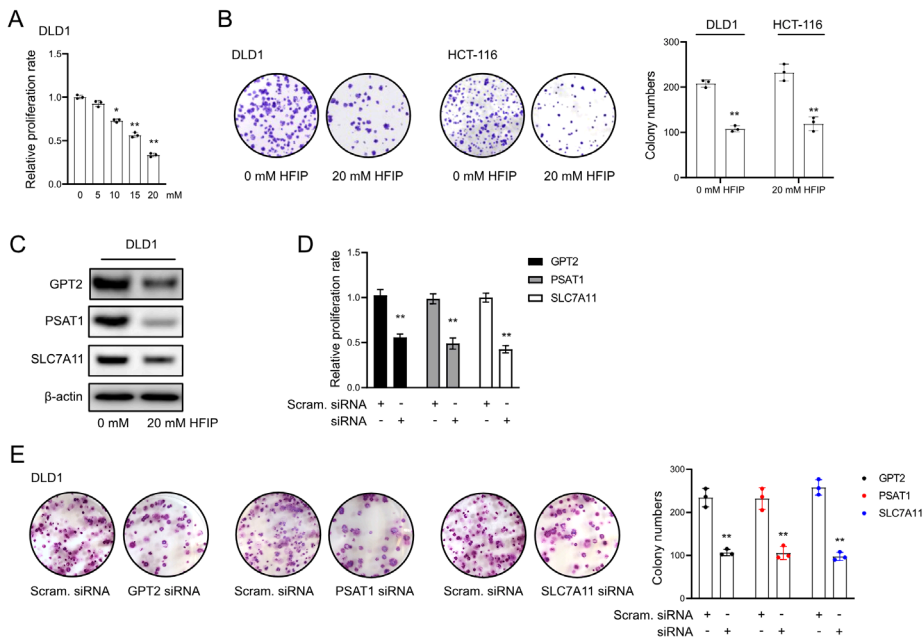


Figure 3. HFIP represses proliferation of colorectal cancer cells. (A) MTT assay showed relative proliferation rate of DLD-1 cells after treated by HFIP with indicated concentration. Proliferation rate was compared to untreated group. (B) Colony formation assay was performed in DLD-1 and HCT-116 cells treated with 20 mM HFIP compared to untreated group. (C) Western blot analysis of GPT2, PSAT1 and SLC7A11 in DLD-1 cell treated with 20 mM HFIP compared to untreated group. (D) MTT assay showed relative proliferation rate of DLD-1 cells after treated by GPT2, PSAT1 or SLC7A11 siRNA. Proliferation rate was compared to scrambled siRNA group. (E) Colony formation assay was performed in DLD-1 cell after treated by GPT2, PSAT1 or SLC7A11 siRNA. Proliferation rate was compared to scrambled siRNA group. **P*<0.05, ***P*<0.01.

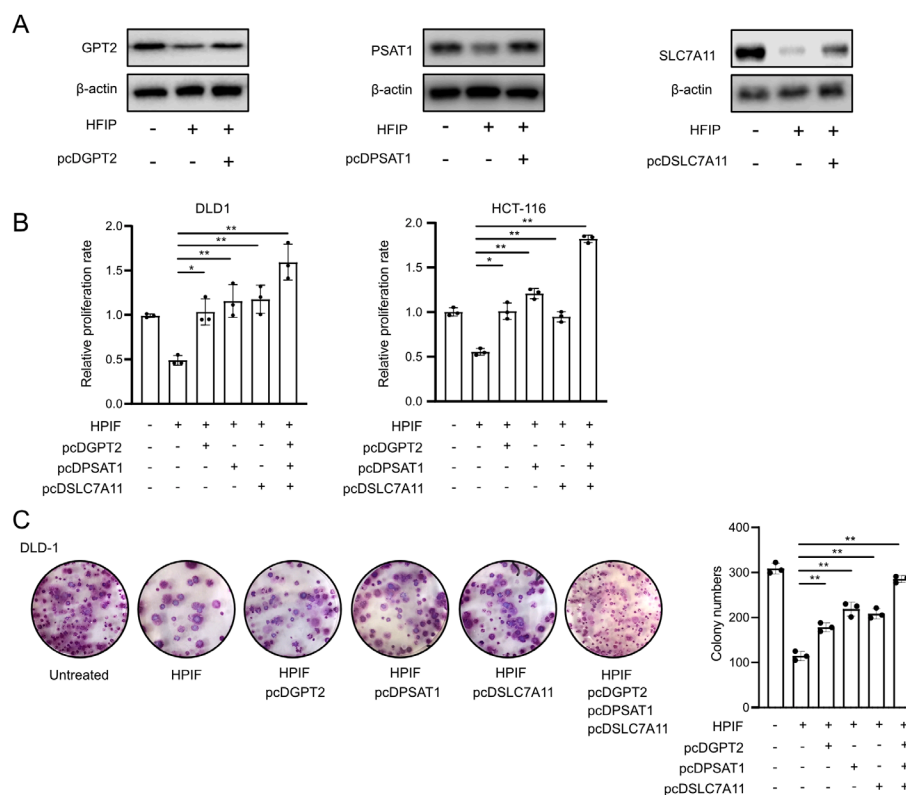


Figure 4. GPT2, PSAT1 and SLC7A11 are required for HFIP effect.

(A) Western blot analysis of GPT2, PSAT1 and SLC7A11 in DLD-1 cell treated with 20 mM HFIP together with overexpression vectors. (B) MTT assay showed relative proliferation rate of DLD-1 and HCT-116 cells treated with 20 mM HFIP together with overexpression vectors. (C) Colony formation assay was performed in DLD-1 cell treated with 20 mM HFIP together with overexpression vectors. * $P < 0.05$, ** $P < 0.01$.

1 and HCT-116 cells (Fig. 3B). Above results demonstrated that HFIP suppressed proliferation of colorectal cancer cells. Since GPT2, PSAT1 and SLC7A11 are supposed to be repressed by HFIP in bioinformatic analysis and the expression of these genes was validated in colorectal cancer cells, next we further validated that HFIP treatment significantly repressed the protein level of GPT2, PSAT1 and SLC7A11 compared to control group in DLD-1 cells (Fig. 3C). In addition, silencing GPT2, PSAT1 and SLC7A11 repressed DLD-1 cell proliferation rate (Fig. 3D) and inhibited DLD-1 cell colony formation ability (Fig. 3E). Taken together, HFIP treatment and GPT2/PSAT1/SLC7A11 silence repressed proliferation of colorectal cancer cells, in which the effect of HFIP is potentially mediated by GPT2/PSAT1/SLC7A11.

GPT2, PSAT1 and SLC7A11 are required for HFIP function

As GPT2, PSAT1 and SLC7A11 were validated to be down-regulated by HFIP, here we investigated whether GPT2, PSAT1 and SLC7A11 are required for HFIP function. DLD-1 cells were treated with HFIP and co-transfected with one of the GPT2, PSAT1 and SLC7A11 overexpression vectors. The protein level of GPT2, PSAT1 and SLC7A11 stayed at a high level by co-transfected with overexpression vector and treated with HFIP (Fig. 4A). In both DLD-1 and HCT-116 cells, ectopic expressing GPT2, PSAT1 or SLC7A11 abrogated the effect of HFIP treatment on cell proliferation rate repression. The strongest abrogation effect was observed in the common overexpressing GPT2, PSAT1 and SLC7A11

(Fig. 4B). Similarly, GPT2, PSAT1 or SLC7A11 overexpression abrogated the effect of HFIP on reducing DLD-1 cell colony formation ability (Fig. 4C). Above results indicated that GPT2, PSAT1 and SLC7A11 mediated the effect of HFIP in colorectal cancer cells.

DISCUSSION

In this study, we investigated the function of sevoflurane metabolite HFIP on repressing colorectal cancer cell proliferation. Two transaminases and one cysteine/glutamate transporter were inhibited by HFIP treatment, which mediates the effect of HFIP. Previous studies identified that HFIP is a water soluble primary metabolite of the volatile anaesthetic sevoflurane (Buratti *et al.*, 2002), which is associated with attenuating inflammation through repressing inflammatory mediators (Uerner *et al.*, 2015). In line with these conclusions, analysis in RNA-seq data from GSE56256 revealed that HFIP treatment represses more 5000 genes in LPS induced inflammatory response cases. Among those HFIP repressing genes, many genes are mainly enriched in signalling pathway and biological process involving cytokine-cytokine receptor interaction and immunocyte proliferation, which provides the evidence that HFIP has an effect on inflammation.

Since inflammation plays a pivotal role in tumorigenesis *via* multiple molecular mechanisms, here we explored the effect of HFIP on colorectal cancer, which is at a high risk for the patients with inflammatory bowel disease (Herszenyi *et al.*, 2015). Since few studies performed Micro-array analysis in colorectal cancer patients

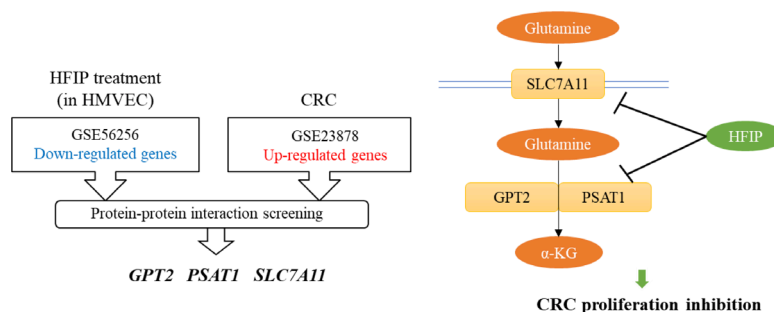


Figure 5. The regulation model of HFIP in colorectal cancer.

GPT2, PSAT1 and SLC7A11 were screened from two independent patient cohorts. HFIP repressed proliferation of colorectal cancer cells through down-regulating GPT2, PSAT1 and SLC7A11 expression, which are involved in glutamine metabolism of colorectal cancer.

with HFIP treatment, we endeavoured an alternative way to find the tumor suppressive genes that are involved in the function of HFIP: We performed differentially expressed gene analysis in a colorectal cancer patient cohort (GSE23878) to obtain DEGs that were compared with DEGs from GSE56256. The DEGs from these two GEO datasets were analysed independently. The DEGs with opposite expression patterns in these two GEO datasets indicate the genes that mediate the function of HFIP, thereby repress the progression of CRC. We obtained 10 up-regulated genes in GSE23878 (CRC patient cohort) that were also down-regulated in GSE56256 (HFIP cohort). Since the two GEO datasets are from different tissues, we exclude the context specificity of the 10 genes. Among those 10 genes, GPT2, PSAT1 and SLC7A11 showed connections with each other, which implies that these three genes play critical roles as a network in HFIP function. Actually, GPT2, PSAT1 and SLC7A11 are involved in glutamine metabolism in cancer progression dependent on proliferation and cell growth (Cao *et al.*, 2017; Qian *et al.*, 2017; Koppula *et al.*, 2018). Indeed, altered cellular energetics is an established hallmark of cancer. Glutamine normally provides carbon and nitrogen for biosynthesis involved in cancer survival and proliferation. SLC7A11 functions as a cysteine/glutamate transporter, while GPT2 and PSAT1 are transaminases that convert glutamine to AKG. Here we confirmed that HFIP treatment repressed proliferation of colorectal cancer cells. Meanwhile, silencing GPT2, PSAT1 and SLC7A11 also inhibited cell proliferation. Therefore, we suppose that the effect of HFIP on cell proliferation repression is mediated by GPT2, PSAT1 and SLC7A11. In addition, glutamine can be transported into cells by the SLC7A11, and it is possible that SLC7A11 takes first place in the response to HFIP treatment.

Furthermore, Overexpression of GPT2, PSAT1 and SLC7A11 abrogated the effect of HFIP on repressing colorectal cancer cells, which demonstrates that GPT2, PSAT1 and SLC7A11 are necessary for HFIP function. Notably, common overexpressing of GPT2/PSAT1/SLC7A11 showed the strongest effect on the abrogation of HFIP function. Therefore, GPT2, PSAT1 and SLC7A11 may have a synergetic effect and mediate HFIP effect together.

In conclusion, HFIP represses proliferation of colorectal cancer cells through down-regulating GPT2, PSAT1 and SLC7A11 expression, which are involved in glutamine metabolism of colorectal cancer, summarized in Fig. 5.

Declarations

Data availability. The authors confirm that the data supporting the findings of this study are available within the article.

Conflicts of Interest. The authors declare that there is no conflict of interest regarding the publication of this article.

Acknowledgement. None.

Funding statement. Do not apply.

Author contributions statement. Z.X.S: conception and design of study, acquisition of data, analysis and/or interpretation of data, drafting the manuscript. This author is co-first author. L.S.: conception and design of study, acquisition of data, analysis and/or interpretation of data, drafting the manuscript. This author is co-first author. W.X.L: conception and design of study, revising the manuscript critically for important intellectual content supervising the study.

REFERENCES

- Buratti M, Valla C, Xaiz D, Brambilla G, Colombi A (2002) Determination of hexafluoroisopropanol, a sevoflurane urinary metabolite, by 9-fluorenylmethyl chloroformate derivatization. *J Chromatogr B Analyt Technol Biomed Life Sci* **776**: 237–243. [https://doi.org/10.1016/S1570-0232\(02\)00310-0](https://doi.org/10.1016/S1570-0232(02)00310-0)
- Cao Y, Lin SH, Wang Y, Chin YE, Kang L, Mi J (2017) Glutamic pyruvate transaminase GPT2 promotes tumorigenesis of breast cancer cells by activating sonic hedgehog signaling. *Theranostics* **7**: 3021–3033. <https://doi.org/10.7150/thno.18992>
- Herszenyi L, Barabas L, Miheller P, Tulassay Z (2015) Colorectal cancer in patients with inflammatory bowel disease: the true impact of the risk. *Dig Dis* **33**: 52–57. <https://doi.org/10.1159/000368447>
- Hosios AM, Hecht VC, Danai LV, Johnson MO, Rathmell JC, Steinhilber ML, Manalis SR, Vander Heiden MG (2016) Amino acids rather than glucose account for the majority of cell mass in proliferating mammalian cells. *Dev Cell* **36**: 540–549. <https://doi.org/10.1016/j.devcel.2016.02.012>
- Kanaya A, Kuratani N, Satoh D, Kurosawa S (2014) Lower incidence of emergence agitation in children after propofol anesthesia compared with sevoflurane: a meta-analysis of randomized controlled trials. *J Anesth* **28**: 4–11. <https://doi.org/10.1007/s00540-013-1656-y>
- Karunakaran S, Umaphathy NS, Thangaraju M, Hatanaka T, Itagaki S, Munn DH, Prasad PD, Ganapathy V (2008) Interaction of tryptophan derivatives with SLC6A14 (ATB0,+) reveals the potential of the transporter as a drug target for cancer chemotherapy. *Biochem J* **414**: 343–355. <https://doi.org/10.1042/BJ20080622>
- Koppula P, Zhang Y, Zhuang L, Gan B (2018) Amino acid transporter SLC7A11/xCT at the crossroads of regulating redox homeostasis and nutrient dependency of cancer. *Cancer Commun (Lond)* **38**: 12. <https://doi.org/10.1186/s40880-018-0288-x>
- Lodovichi S, Mercatanti A, Cervelli T, Galli A (2019) Computational analysis of data from a genome-wide screening identifies new PARP1 functional interactors as potential therapeutic targets. *Oncotarget* **10**: 2722–2737. <https://doi.org/10.18632/oncotarget.26812>
- Qian C, Xia Y, Ren Y, Yin Y, Deng A (2017) Identification and validation of PSAT1 as a potential prognostic factor for predicting clinical outcomes in patients with colorectal carcinoma. *Oncol Lett* **14**: 8014–8020. <https://doi.org/10.3892/ol.2017.7211>

- Sumi C, Matsuo Y, Kusunoki M, Shoji T, Uba T, Iwai T, Bono H, Hirota K (2019) Cancerous phenotypes associated with hypoxia-inducible factors are not influenced by the volatile anesthetic isoflurane in renal cell carcinoma. *PLoS One* **14**: e0215072. <https://doi.org/10.1371/journal.pone.0215072>
- Uddin S, Ahmed M, Hussain A, Abubaker J, Al-Sanea N, AbdulJabbar A, Ashari LH, Alhomoud S, Al-Dayel F, Jehan Z, Bavi P, Siraj AK, Al-Kuraya KS (2011) Genome-wide expression analysis of Middle Eastern colorectal cancer reveals FOXM1 as a novel target for cancer therapy. *Am J Pathol* **178**: 537–547. <https://doi.org/10.1016/j.ajpath.2010.10.020>
- Urner M, Schlapfer M, Herrmann IK, Hasler M, Schimmer RR, Booy C, Roth Z'graggen B, Rehrauer H, Aigner F, Minshall RD, Stark WJ, Beck-Schimmer B (2015) Insight into the beneficial immunomodulatory mechanism of the sevoflurane metabolite hexafluoro-2-propanol in a rat model of endotoxaemia. *Clin Exp Immunol* **181**: 468–479. <https://doi.org/10.1111/cei.12648>
- Wang L, Leite de Oliveira R, Huijberts S, Bosdriesz E, Pencheva N, Brunen D, Bosma A, Song JY, Zevenhoven J, Los-de Vries GT, Horlings H, Nuijen B, Beijnen JH, Schellens JHM, Bernards R (2018) An acquired vulnerability of drug-resistant melanoma with therapeutic potential. *Cell* **173**: 1413–1425 e1414. <https://doi.org/10.1016/j.cell.2018.04.012>
- Welch S (1975) Comparative studies on the human glutamate-pyruvate transaminase phenotypes – GPT 1, GPT 2-1, GPT 2. *Humangenetik* **30**: 237–249. <https://doi.org/10.1007/BF00279189>
- Xu X, Zhang X, Wei C, Zheng D, Lu X, Yang Y, Luo A, Zhang K, Duan X, Wang Y (2020) Targeting SLC7A11 specifically suppresses the progression of colorectal cancer stem cells via inducing ferroptosis. *Eur J Pharm Sci* **152**: 105450. <https://doi.org/10.1016/j.ejps.2020.105450>
- Zhang T, Li M, Lu H, Peng T (2021) Up-regulation of circEIF6 contributes to pancreatic cancer development through targeting miR-557/SLC7A11/PI3K/AKT signaling. *Cancer Manag Res* **13**: 247–258. <https://doi.org/10.2147/CMAR.S280307>
- Zhao H, Xing F, Yuan J, Li Z, Zhang W (2020) Sevoflurane inhibits migration and invasion of glioma cells via regulating miR-34a-5p/MMP-2 axis. *Life Sci* **256**: 117897. <https://doi.org/10.1016/j.lfs.2020.117897>

Circular RNA CSPP1 motivates renal cell carcinoma carcinogenesis and the Warburg effect by targeting RAC1 through microRNA-493-5p

Dong Zhang, XiaoJie Yang, QiDong Luo, DeLai Fu, HongLiang Li, Peng Zhang✉ and Chong Tie

Department of Urology, The Second Affiliated Hospital of Xi'an Jiaotong University, Xi'an City, Shaanxi Province, 710004, China

Circular RNAs (circRNAs) take on regulatory roles in renal cell carcinoma (RCC). The research's goal was to figure out circ-CSPP1's role and molecular mechanism in RCC. The results clarified that circ-CSPP1 expression was enhanced in RCC. Down-regulating circ-CSPP1 refrained the proliferation, migration, invasion, and Warburg effect (aerobic glycolysis), but accelerated apoptosis of RCC cells. The luciferase activity assay exhibited that circ-CSPP1 could perform as an endogenous sponge for miR-493-5p. Elevating miR-493-5p repressed RCC progression. The bioinformatics website starBase confirmed that ras-related C3 botulinum toxin substrate 1 (RAC1) was a target gene of miR-493-5p. Circ-CSPP1 up-regulated RAC1 by sponging miR-493-5p, and elevating RAC1 could turn around the effect of down-regulating circ-CSPP1 on RCC cells. Taken together, circ-CSPP1 is identified as a novel RCC-promoting RNA that could serve as a latent therapeutic target for RCC therapy.

Keywords: Circ-CSPP1, MiR-493-5p, RAC1; renal cell carcinoma, Warburg effect

Received: 31 March, 2022; revised: 23 May, 2023; accepted: 28 June, 2023; available on-line: 18 September, 2023

✉e-mail: zpbill013@hotmail.com

Acknowledgements of Financial Support: The National Natural Science Foundation of China (NSFC No.81101937).

Abbreviations: circRNAs, Circular RNAs; HCC, hepatocellular carcinoma; miRNAs, MicroRNAs; RCC, Renal cell carcinoma; RAC1, Ras-related C3 botulinum toxin substrate 1

INTRODUCTION

Renal cell carcinoma (RCC) is a class of diversified malignant neoplasms of the renal cortex with diverse clinical, morphological, and genetic features (Rysz *et al.*, 2021). Though clinical interventions like chemotherapy, surgery, and radiotherapy have made great progress, RCC patients' prognosis is still unpleasing. Therefore, it is imperative to develop new therapeutic strategies considering the biological characteristics of RCC cells. It is well known that metabolic reprogramming, a recognized hallmark of cancer, achieves tumor cell proliferation and survival by changing bioenergetic and biosynthetic pathways. Tumor cells having glycolysis high rates (Warburg effect) is a phenomenon that has been extensively studied in RCC (Emberley *et al.*, 2021). Therefore, figuring out the regulatory mechanism of the Warburg effect is likely to be beneficial for the development of effective RCC treatments.

Circular RNAs (circRNAs), a class of covalently closed endogenous RNAs without a 5' cap or 3' poly(A) tail, are cell-specific, tissue-specific, and developmental stage-specific (Huang *et al.*, 2020). For a long time, circRNAs have been regarded as waste products of splicing errors. Recent studies have discovered circRNAs can perform as gene regulators in diversified physiological and pathological processes and can regulate tumorigenesis and cancer progression (Li *et al.*, 2020). Meanwhile, circRNAs have also been clarified to exert biological functions by performing as miRNA sponges or protein sponges (van Zonneveld *et al.*, 2021). Therefore, circRNAs have been identified as latent biomarkers for tumor diagnosis (Zhu *et al.*, 2021). Circ-CSPP1 is a newly identified circRNA that has been confirmed to take on a momentous role in tumorigenesis (Xue, 2020; Sun *et al.*, 2020). However, its role in RCC and its latent mechanisms remain uncertain.

MicroRNAs (miRNAs) are a class of single-stranded non-coding RNAs that post-transcriptionally control gene expression (Bushati *et al.*, 2007). miRNA dysregulation is the key to the pathogenesis of diversified diseases, including cancer (Ali Syeda *et al.*, 2020) and can function as latent oncogenes or tumor suppressor genes (Iorio *et al.*, 2012). For instance, miR-133b impacts cell proliferation, chemosensitivity, and invasion of RCC cells by refraining the ERK signaling pathway (Xu *et al.*, 2020). A former study clarified that miR-493-5p expression is reduced in hepatocellular carcinoma (HCC) (Yang *et al.*, 2021). However, miR-493-5p's functions in RCC and its interaction with circ-CSPP1 remain ambiguous.

Ras-related C3 botulinum toxin substrate 1 (RAC1) is also commonly present in mammalian tissues and cells as a multiplex regulator of epithelial differentiation and is involved in apoptosis-related pathways through the production of reactive oxygen species (Lee *et al.*, 2012). RAC1 has been implicated in multiple cellular processes, such as cell proliferation, tumor metastasis, and epithelial-mesenchymal transition (Yoon *et al.*, 2017). The same pathways shared by circRNAs, miRNAs, and RAC1 suggest that they might function coordinately to orchestrate tumorigenesis. RAC1 has been reported to contribute to the tumorigenesis of RCC (Zhang, 2022; Shan *et al.*, 2017). Thus, RAC1 could be the target gene of miRNAs to regulate the tumorigenesis of RCC.

This study was conducted to figure out the biological characteristics and latent mechanisms of circ-CSPP1 in RCC progression and Warburg effect. Circ-CSPP1 motivated RCC progression and the Warburg effect by targeting miR-493-5p to control RAC1, suggesting that circ-CSPP1 may offer a novel biomarker and latent therapeutic target for RCC.

MATERIALS AND METHODS

Clinical sample collection

The research was approved by the Ethics Committee of The Second Affiliated Hospital of Xi'an Jiaotong University (Approval number.201803XAH), and informed consent was obtained from each subject before sample collection. Forty pairs of RCC tumor tissues and adjacent normal tissues were harvested from patients in the urology department at The Second Affiliated Hospital of Xi'an Jiaotong University, and two pathologists independently made a definite pathological diagnosis. Adjacent normal tissue was harvested at least 3 cm from the tumor site. Tissues were kept in liquid nitrogen. Clinical data including clinical stage, age, gender, tumor stage, lymph node metastasis, and distant metastasis were recorded.

Cell culture

RCC cell lines (786-O, ACHN, CAKI-1, and OSRC2) and human normal kidney cell line (HK-2) were bought from the Chinese Academy of Sciences (Shanghai, China). Cells were cultured in Roswell Park Memorial Institute (RPMI) 1640 medium plus 10% fetal bovine serum (Gibco, Carlsbad, CA, USA), 100 units (U)/ml penicillin, and 100 U/ml streptomycin (Gibco).

Cell transfection

Transfection of miRNA mimics, inhibitors, small interfering RNAs (siRNAs), and plasmids was done with Lipofectamine 3000 (Invitrogen, Carlsbad, CA) in the light of the manufacturer's instructions. MiR-493-5p mimic, miR-493-5p inhibitor, circ-CSPP1 siRNA (si-circ-CSPP1), RAC1 siRNA (si-RAC1) and their negative controls (NCs) were bought from GenePharma (Shanghai, China). pcDNA 3.1 circRNA mini vector was utilized to elevate circ-CSPP1 expression in RCC cells.

Cell counting kit (CKK)-8 assay

Transfected cells were seeded in 96-well plates (Gibco BRL, Gaithersburg, MD, USA). Measurement of optical density at 450 nm was done with a microplate reader (Millipore, Billerica, MA, USA) (Chen *et al.*, 2020).

Colony formation assay

Transfected cells were seeded in 6-well plates and cultivated for colony formation assay. The colonies were fixed with 4% formaldehyde (Macklin, Shanghai, China), and then staining with 0.3% crystal violet was implemented. Counting and analyzing visible colonies were done by Image J software 1.8.0 (Wang *et al.*, 2020).

Flow cytometry

Apoptosis was tested by Annexin V- fluorescein isothiocyanate/propidium iodide (PI) apoptosis detection kit (Invitrogen). Briefly, double-staining was done with Annexin V and PI, and then the apoptosis rate was examined via FACSCalibur (Becton Dickinson) and FlowJo 10.0 software (Lin *et al.*, 2020).

Transwell assays

For cell invasion assay, transfected cells were seeded into 24-well transwell chambers with Matrigel. After incubation, non-invasive cells were wiped off, invasive

cells were fixed with paraformaldehyde, and then staining with crystal violet was implemented. Counting and photographing stained cells in each well were conducted under an inverted microscope (Olympus, Japan). As for the migration experiment, cells were seeded into the upper chamber without Matrigel, and other steps were similar to the cell invasion experiments.

Lactate production, glucose uptake, and ATP

Quantification of glucose levels was done using a glucose assay kit (Sigma-Aldrich, St. Louis, MO, USA). Measurement of lactate levels was implemented using a lactate assay kit (BioVision, Mountain View, CA, USA). ATP levels were tested by the CellTiter-Glo fluorescent cell viability assay (Promega, Madison, MI, USA).

Reverse transcription quantitative polymerase chain reaction (RT-qPCR)

Total RNA was extracted from tissues or cells using the RNeasy Mini Kit (QIAGEN, Hilden, Germany) according to the manufacturer's protocol. cDNA was generated using the Promega reverse transcription kit. RT-qPCR was carried out in the ABI7500 system using the SYBR Green method. Relative gene expression was determined by the $2^{-\Delta\Delta Ct}$ method. The primers were clarified in Table 1 (Cao *et al.*, 2020).

Western blot

RIPA lysis buffer (Beyotime) was used to extract total protein. Proteins were separated by 12% Sodium dodecyl sulfate-polyacrylamide gel electrophoresis and electro-blotted onto polyvinylidene fluoride membranes. The membranes were incubated with primary antibodies RAC1 (05-389, 1:1000, MilliporeSigma) and GAPDH (2118, 1:1000, Cell Signaling Technology). Bands were visualized via enhanced chemiluminescence (Millipore) after incubation with the HRP-conjugated secondary antibody. Relative band intensities were quantified by the ChemiDoc XRS imaging system (Liu *et al.*, 2020).

Table 1. RT-qPCR primers

Genes	Primer sequence (5'-3')
Circ-CSPP1	F: CCATCCCATCAGTTCATCCT
	R: TTCACCTCCAAGAGCATCC
miR-493-5p	F: TTGTACATGGTAGGCTTTCATT
	R: AACCATTTATTCTCCCGACC
RAC1	F: AACCAATGCATTTCTGGAG
	R: TGTTTCGGATAGGATAGGG
U6	F: CTCGCTTCGGCAGCACA
	R: AACGCTTCACGAATTTGCGT
GAPDH	F: CACCACTCCTCCACCTTTG
	R: CCACCACCTGTTGCTGTAG

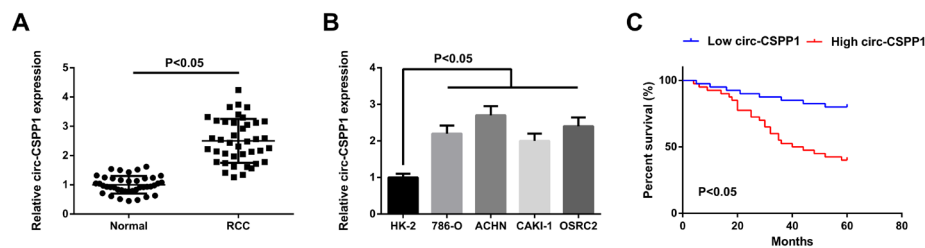


Figure 1. Circ-CSPP1 is elevated in RCC and is linked with poor prognosis

(A, B) RT-qPCR to test circ-CSPP1 in RCC tissues and adjacent tissues (n=40), and RCC cell lines; (C) Kaplan-Meier survival analysis. Measurement data were shown as mean \pm S.D.

Luciferase activity assay

After predicting the binding sites of circ-CSPP1 and RAC1 3'UTR in miR-493-5p, pmirGLO reporter vector (Promega) was utilized to construct circ-CSPP1 and RAC1 3'UTR wild-type (WT) and Mutant (MUT) reporter vectors. A549 cells were incubated with miR-545-5p mimic or mimic NC with the reporter vectors. Then cell luciferase activity was tested by the dual luciferase reporter gene detection kit (Promega) (Yuan *et al.*, 2021).

Statistics

All data were processed by SPSS 21.0 statistical software (SPSS, Inc, Chicago, IL, USA). Measurement data were shown as mean \pm standard deviation (S.D.). For the measurement data obeyed a normal distribution, a t-test was used for comparison between the two groups, and a one-way analysis of variance and the Bonferroni post-hoc test were used for comparison among multiple groups. To evaluate the relationship between circ-CSPP1 and the survival prognosis of RCC patients, the Kaplan-Meier method was used for survival analysis, and a log-rank test was used to determine that the difference between high and low expression curves was statistically

significant. Pearson correlation analysis in clinical samples was conducted. $P<0.05$ emphasized obvious statistical meaning.

RESULTS

Circ-CSPP1 is elevated in RCC and is associated with poor prognosis

Circ-CSPP1 was up-regulated in RCC tissues (Fig. 1A). Endogenous circ-CSPP1 was elevated in RCC cell lines, and highest in ACHN cells (Fig. 1B). Therefore, ACHN cells were chosen for subsequent experiments. The 40 patients were divided into two groups according to circ-CSPP1 expression, and circ-CSPP1 was associated with distant metastasis, clinical stage, and tumor stage (Table 2). Meanwhile, it came out that clinical stage, tumor stage, distant metastasis, and circ-CSPP1 were independent predictors of overall survival (OS) of RCC patients (Table 3). Kaplan-Meier survival analysis exhibited that RCC patients with higher circ-CSPP1 expression had poor OS (Fig. 1C). These results suggested

Table 2. The link between circ-CSPP1 and clinicopathological features of RCC

Characteristics	Number	circ-CSPP1		P
		Low (n = 20)	High (n = 20)	
Age				0.527
<60	21	12	9	
≥ 60	19	8	11	
Gender				1.000
Male	23	11	12	
Female	17	9	8	
Clinical stage				0.022
I-II	24	16	8	
III-IV	16	4	12	
Tumor stage				0.025
T1+T2	22	15	7	
T3+T4	18	5	13	
Distant metastasis				0.001
M0	25	18	7	
M1	15	2	13	

Table 3. Univariate and multivariate analysis of clinicopathological indexes for overall survival within RCC patients

Risk factors	Univariate analysis		Multivariate analysis	
	HR (95%CI)	P	HR (95%CI)	P
Age (years)	1.023 (0.348-2.316)	0.874		
Gender	0.912 (0.556-2.875)	0.456		
Clinical stage	1.686 (1.004-4.731)	0.005	1.712 (1.013-4.178)	0.016
Tumor stage	2.616 (1.063-4.129)	0.006	2.175 (1.238-3.662)	0.018
Distant metastasis	3.174 (1.319-7.627)	0.004	2.747 (1.312-6.533)	0.002
circ-CSPP1 expression	1.389 (1.086-5.643)	0.001	1.266 (1.064-5.242)	0.003

that circ-CSPP1 is elevated in RCC and is associated with poor prognosis.

Circ-CSPP1 motivates RCC progression and glycolysis

For studying the biological function of circ-CSPP1 in RCC, si-circ-CSPP1, pcDNA3.1-circ-CSPP1, and corresponding NCs were introduced into ACHN cells, and the transfection efficiency was verified (Fig. 2A). The results clarified that repression of circ-CSPP1 restrained cell proliferation, invasion, and migration, and induced

apoptosis, but elevation of circ-CSPP1 had the opposite effect (Fig. 2B–F). Meanwhile, Warburg effect correlation analysis clarified that suppressing circ-CSPP1 reduced lactate production, glucose uptake, and ATP, while up-regulation of circ-CSPP1 resulted in the opposite results (Fig. 2G–I). In addition, similar results were found in KAKi-1 cells (Supplementary Fig. 1A–I at <https://ojs.ptbioch.edu.pl/index.php/abp>). These data suggested that circ-CSPP1 motivated RCC progression and glycolysis.

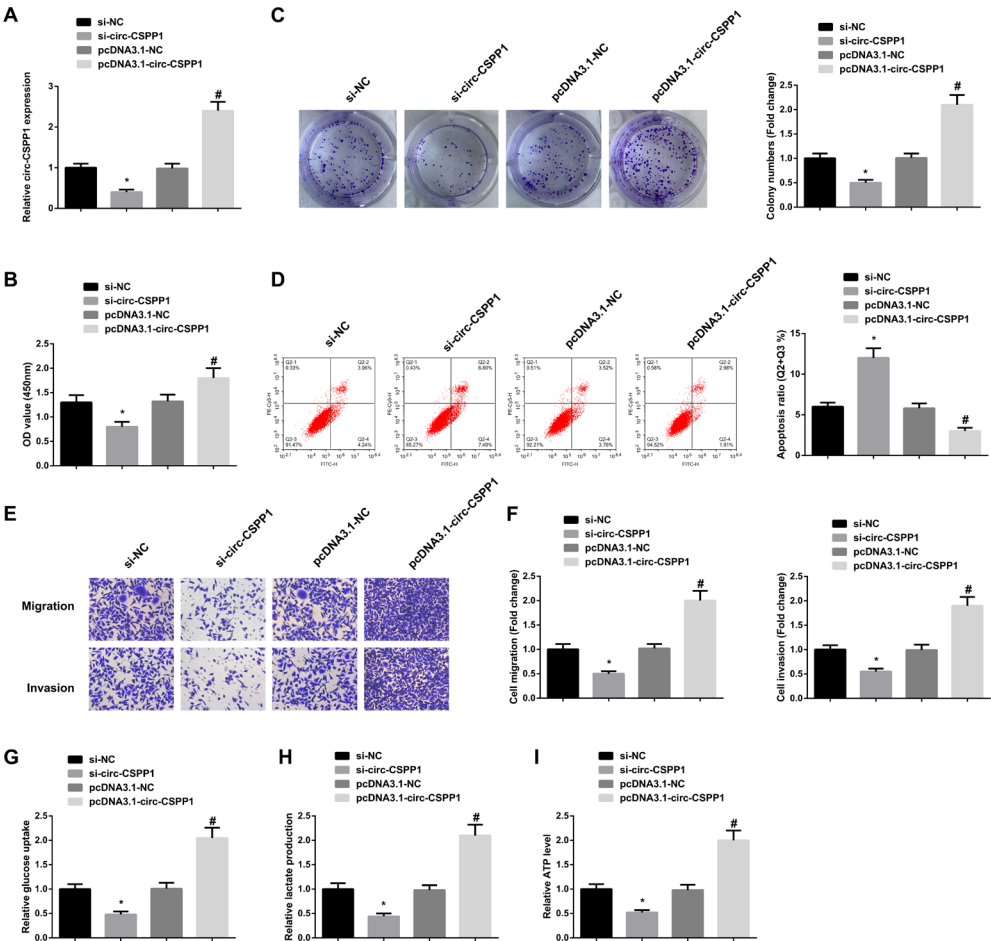


Figure 2. Circ-CSPP1 motivates RCC progression and glycolysis. (A) RT-qPCR to test circ-CSPP1; (B/C) CCK-8 and clone formation assay to examine cell proliferation; (D) Flow cytometry to detect cell apoptosis; (E–F) Transwell to detect cell migration and invasion; (G–I) Glucose uptake, lactate production and ATP. Measurement data were shown as mean \pm S.D. **vs the si-NC, $P < 0.05$; #vs the pcDNA3.1-NC, $P < 0.05$.

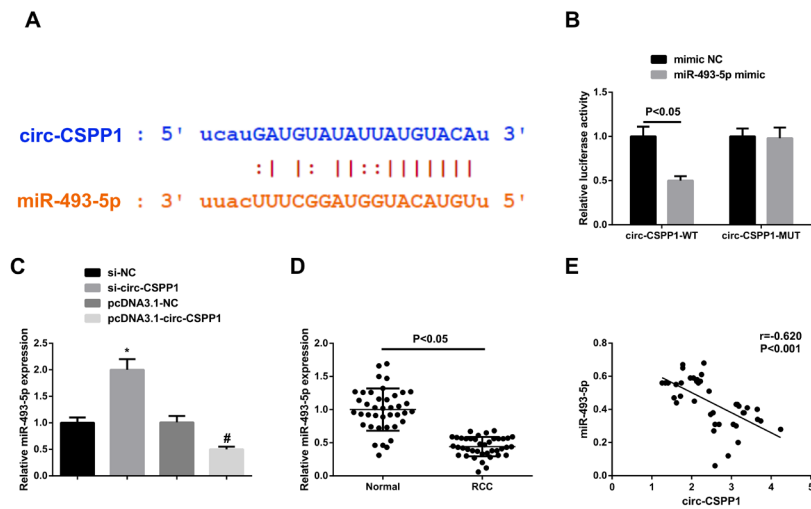


Figure 3. Circ-CSPP1 adsorbs miR-493-5p in RCC.

(A) StarBase to forecast binding sites for circ-CSPP1 and miR-493-5p; (B) The luciferase activity assay to testify the interaction between circ-CSPP1 and miR-493-5p; (C) RT-qPCR detection of miR-493-5p after the intervention of circ-CSPP1; (D) RT-qPCR to test miR-493-5p in RCC tissues; (E) Pearson correlation analysis of circ-CSPP1 and miR-493-5p in clinical samples. Measurement data were shown as mean \pm S.D. **vs the si-NC, $P < 0.05$; #vs the pcDNA3.1-NC, $P < 0.05$.

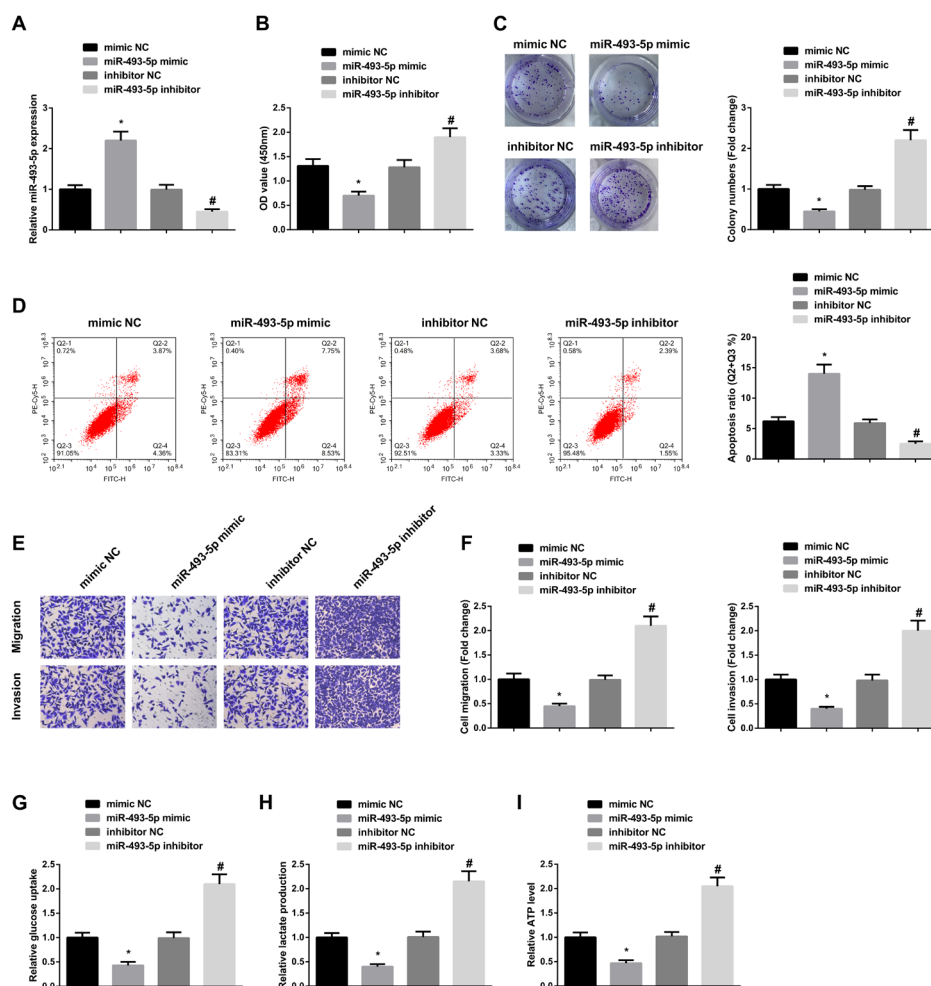


Figure 4. MiR-493-5p represses RCC progression and glycolysis.

(A) RT-qPCR to test miR-493-5p; (B–C) CCK-8 and clone formation assay to examine cell proliferation; (D) Flow cytometry to detect cell apoptosis; E/F: Transwell to detect cell migration and invasion; (G–I) ATP, glucose uptake and lactate production. Measurement data were shown as mean \pm S.D. ** $P < 0.05$, vs the mimic NC; # $P < 0.05$, vs the inhibitor-NC.

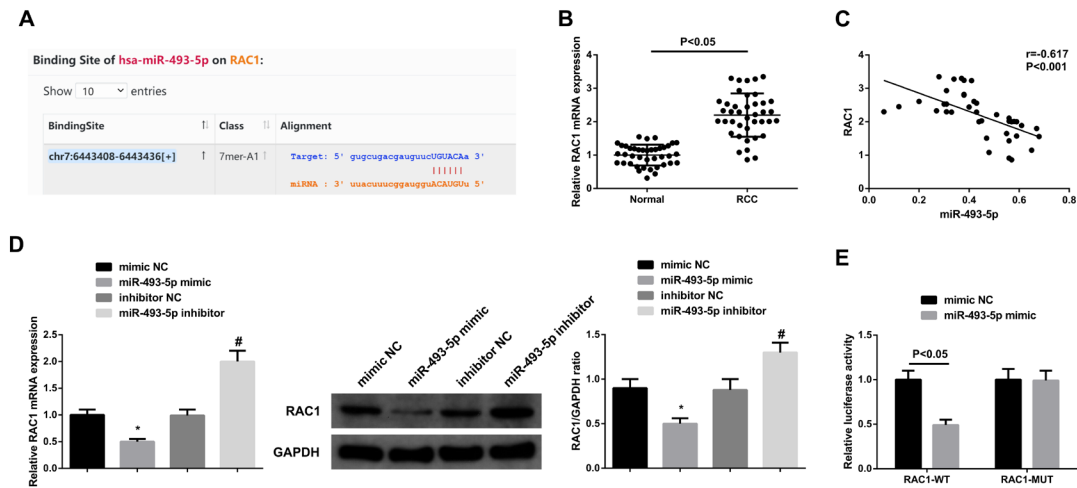


Figure 5. RAC1 is miR-493-5p's downstream target in RCC.

(A) StarBase to predict that miR-493-5p and RAC1 had targeted binding sites; (B) RT-qPCR examination of RAC1 in RCC tissues; (C) Pearson correlation analysis of miR-493-5p and RAC1 in clinical samples; (D) RT-qPCR and Western blot test of RAC1 after intervening miR-493-5p; (E) The luciferase activity detection to testify the targeting relationship between miR-493-5p and RAC1. Measurement data were shown as mean \pm S.D. $^{**}P < 0.05$, vs the mimic NC; $^{\#}P < 0.05$, vs the inhibitor-NC.

Circ-CSPP1 adsorbs miR-493-5p in RCC

The targeting sites for circ-CSPP1 and miR-493-5p were predicted by starBase (Fig. 3A). Luciferase activity assay was performed to testify the binding relationship between circ-CSPP1 and miR-493-5p, and it came out that circ-CSPP1-WT with miR-493-5p mimic reduced luciferase activity, indicating that circ-CSPP1 could combine with miR-493-5p (Fig. 3B). As expected, depression of circ-CSPP1 elevated miR-493-5p expression in ACHN cells, whereas upregulating circ-CSPP1 suppressed miR-493-5p expression (Fig. 3C). Moreover, it was discovered that circ-CSPP1 was inversely correlated with miR-493-5p expression in RCC tissues (Fig. 3D–E). Taken together, these findings suggested that circ-CSPP1 adsorbed miR-493-5p in RCC.

MiR-493-5p represses RCC progression and glycolysis

For studying miR-493-5p's biological function in RCC, miR-493-5p mimic, miR-493-5p inhibitor and corresponding NCs were introduced into ACHN cells, and the transfection efficiency was testified (Fig. 4A). It turned out that elevating miR-493-5p refrained cell progression while repressing miR-493-5p had the opposite effect (Fig. 4B–F). The Warburg effect correlation analysis clarified that elevation of miR-493-5p reduced ATP, glucose uptake and lactate production, while depression of miR-493-5p caused the opposite results (Fig. 4G–I). These results suggested that miR-493-5p depressed RCC progression and glycolysis.

RAC1 is miR-493-5p's downstream target in RCC

starBase was applied for predicting that miR-493-5p had a targeted binding site with RAC1 (Fig. 5A). RAC1 expression was elevated in RCC tissues (Fig. 5B), and miR-493-5p was inversely linked with RAC1 expression in RCC tissues (Fig. 5C). Furthermore, it was found that miR-493-5p mimic could reduce RAC1 expression, whereas miR-493-5p inhibitor could elevate RAC1 expression (Fig. 5D). In the luciferase activity assay, it was found that the luciferase activity was suppressed after introduction of RAC1-WT and miR-493-5p mim-

ic (Fig. 5E). All in all, RAC1 was miR-493-5p's downstream target in RCC.

Circ-CSPP1 accelerates RCC progression and glycolysis through the miR-493-5p/RAC1 axis

After verifying that RAC1 is the target of miR-493-5p, we investigated whether circ-CSPP1 accelerates the development of RCC by controlling the miR-493-5p/RAC1 axis. It was found that upregulation of circ-CSPP1 elevated RAC1 expression, and repression of RAC1 restored RAC1 expression following upregulation of circ-CSPP1 (Fig. 6A). It turned out that repression of RAC1 abolished the motivation of cell proliferation by elevation of circ-CSPP1 (Fig. 6B, C). Likewise, the repressive effect of up-regulated circ-CSPP1 on apoptosis was abolished by down-regulated RAC1 (Fig. 6D). Moreover, RAC1 repression attenuated the promoting effect of circ-CSPP1 upregulation on cell invasion and migration (Fig. 6E, F). Also, repression of RAC1 could turn around the motivation of cellular glycolysis by up-regulation of circ-CSPP1 (Fig. 6G–I). Taken together, these data suggested that circ-CSPP1 motivated RCC progression and glycolysis through the miR-493-5p/RAC1 axis.

DISCUSSION

CircRNAs are extensively studied cancer markers recently (Yan *et al.*, 2021). More studies have shown that circRNA takes on a crucial role in the genesis and progression of diversified tumors. For example, hsa_circ_0065217 is elevated in RCC and motivates RCC growth and metastasis *via* controlling the miR-214-3p-ALPK2 axis (Zhang *et al.*, 2021). Circ_001842 is elevated in RCC and exerts an oncogenic role in RCC *via* a miR-502-5p-dependent SLC39A14 mechanism (Zeng *et al.*, 2020). Our research revealed that circ-CSPP1 was upregulated in RCC tissues, and RCC patients with high circ-CSPP1 expression had a poor prognosis, suggesting that circ-CSPP1 may be a prognostic biomarker for RCC patients. Meanwhile, circ-CSPP1 silencing restrained RCC cell progression *in vitro*, while elevation of circ-CSPP1

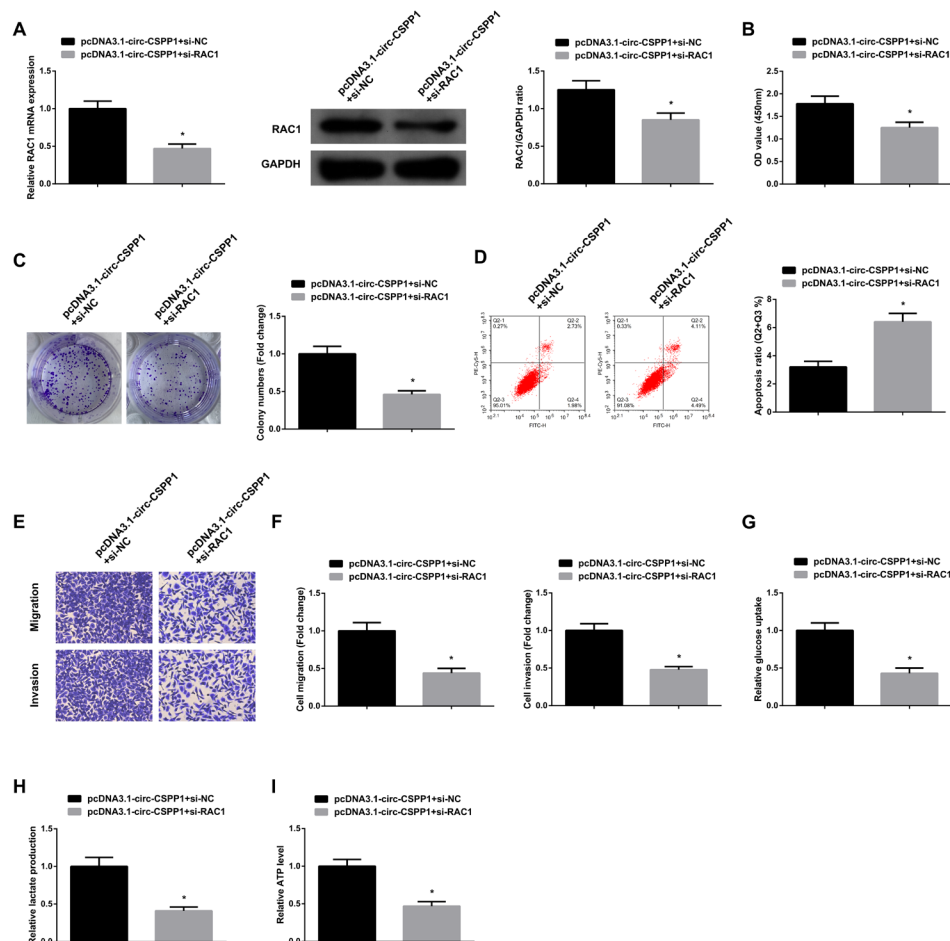


Figure 6. Circ-CSPP1 accelerates RCC progression and glycolysis through the miR-493-5p/RAC1 axis.

(A) RT-qPCR and Western blot to test RAC1; (B–C) CCK-8 and clone formation assay to examine cell proliferation; (D) Flow cytometry to detect cell apoptosis; (E–F) Transwell to detect cell migration and invasion; (G–I) ATP, glucose uptake and lactate production. Measurement data were shown as mean \pm S.D. *vs. the pcDNA3.1-circ-CSPP1+si-NC, $P < 0.05$.

showed opposite results. These data suggested that circ-CSPP1 motivated the progression of RCC.

It is well known that mammalian cells generate energy through oxidative phosphorylation under aerobic conditions, and during tumorigenesis, cancer cells must rewire their metabolism to maintain survival and reproduction (Urbano *et al.*, 2021). Most cancer cells utilize the Warburg effect to support anabolic growth and tumorigenesis, namely aerobic glycolysis, a metabolic mode that is favored even in the presence of oxygen (Lundø *et al.*, 2020). Warburg effect was found to be beneficial for cancer cell progression and was involved in immune responses and drug resistance (Samec, 2020; Icard *et al.*, 2018). Recent studies have shown that circRNAs can modulate tumor phenotypes, such as metastasis and the Warburg effect. For example, circFOXPI motivates RCC progression and Warburg effect by sponging miR-423-5p to upregulate U2AF2 (Fang *et al.*, 2021). This study identified a novel circRNA as a regulator of the Warburg effect. The results clarified that downregulation of circ-CSPP1 suppressed the Warburg effect in RCC cells.

Several studies have shown that circ-CSPP1 performs as an oncogene in diversified human cancers and exerts its biological functions by adsorbing miRNAs. For example, circ-CSPP1 is elevated in cervical cancer (CC), and circ-CSPP1 knockdown suppresses CC tumor

growth and migration via downregulating ITGB1, PI3K and Akt expression by sponging miR-361-5p (Yang *et al.*, 2020). Circ-CSPP1 is upregulated in ovarian cancer (OC), and silencing circ-CSPP1 represses OC cell biological functions via upregulating miR-1236-3p (Li *et al.*, 2019). Here, it was confirmed that circ-CSPP1 was a decoy of miR-493-5p. Furthermore, repressing miR-493-5p turned around the effect of circ-CSPP1 silencing on RCC cell progression and Warburg effect, while elevating miR-493-5p turned around the effect of upregulating circ-CSPP1 on RCC progression and Warburg effect in HCC. These results suggested that circ-CSPP1 controlled RCC progression and the Warburg effect via performing as a sponge for miR-493-5p.

MiRNAs control gene expression by combining with mRNAs' 3'-UTR, thereby regulating diversified aspects of cellular activity (Huang *et al.*, 2011). Here, RAC1 was a target of miR-493-5p. RAC1 is a highly conserved rho family small GTPase that is essential for diversified cellular and developmental processes (Banka *et al.*, 2022). RAC1 is elevated in different types of tumors, including RCC, and motivates tumorigenesis by participating in tumor cell biological behaviors (Liang *et al.*, 2021; Goka *et al.*, 2020). This study also confirmed that RAC1 was elevated in RCC tissues, and its expression was up-regulated by elevation of circ-CSPP1 but refrained by upreg-

ulation of miR-493-5p. Moreover, repression of RAC1 clearly turned around the effect of circ-CSPP1 elevation on RCC cell progression and the Warburg effect. These results suggested that circ-CSPP1 motivated RCC progression and glycolysis through miR-493-5p/RAC1 axis.

However, the research still takes on several limitations. Although the role of circ-CSPP1 in RCC progression has been partially elucidated, the study had a small sample size, and more tissue samples are still needed to further examine circ-CSPP1 expression trend in RCC. Also, further animal experiments are required to validate the effect of the circ-CSPP1/miR-493-5p/RAC1 axis on RCC tumor growth *in vivo*. Moreover, the Crabtree effect (inhibitory effect of high glucose on mitochondrial oxidative phosphorylation) may also exist in cancer cells. In other words, under the condition of high glucose concentration, glycolytic metabolism is dominated in cells while aerobic respiration is inhibited, thus generating lactic acid (Diaz *et al.*, 2011; Redman *et al.*, 2013). The Crabtree effect is similar to the Warburg effect, the only difference being that the Crabtree effect is caused by high concentrations of glucose (Hammad *et al.*, 2016), therefore, in future studies, exogenous glucose concentration will be a parameter that needs to be designed more precisely to exclude the interference of Crabtree effect as much as possible.

CONCLUSION

All in all, circ-CSPP1 motivates RCC progression and the Warburg effect by acting as a miR-493-5p sponge to upregulate RAC1. The study findings suggest that circ-CSPP1 may serve as a hopeful diagnostic and therapeutic target for RCC.

Declarations

Acknowledgments. Not applicable.

Competing interests. The authors have no conflicts of interest to declare.

REFERENCES

- Ali Syeda Z, Langden SSS, Munkhzul C, Lee M, Song SJ (2020) Regulatory mechanism of MicroRNA expression in cancer. *Int J Mol Sci* **21**. <https://doi.org/10.3390/ijms21051723>
- Banka S, Bennington A, Baker MJ, Rijckmans E, Clemente GD, Ansor NM, Sito H, Prasad P, Anyane-Yeboah K, Badalato L, Dimitrov B, Fitzpatrick D, Hurst ACE, Jansen AC, Kelly MA, Krantz I, Rieubland C, Ross M, Rudy NL, Sanz J, Stouffs K, Xu ZL, Malliri A, Kazanietz MG, Millard TH (2022) Activating RAC1 variants in the switch II region cause a developmental syndrome and alter neuronal morphology. *Brain* **145**: 4232–4245. <https://doi.org/10.1093/brain/awac049>
- Bushati N, Cohen SM (2007) microRNA functions. *Annu Rev Cell Dev Biol* **23**: 175–205. <https://doi.org/10.1146/annurev.cell-bio.23.090506.123406>
- Cao L, Wang M, Dong Y, Xu B, Chen J, Ding Y, Qiu S, Li L, Karafilova Zaharieva E, Zhou X, Xu Y (2020) Circular RNA circ-RNF20 promotes breast cancer tumorigenesis and Warburg effect through miR-487a/HIF-1 α /HK2. *Cell Death Dis* **11**: 145. <https://doi.org/10.1038/s41419-020-2336-0>
- Chen L, Wu D, Ding T (2020) Circular RNA circ_0001368 inhibited growth and invasion in renal cell carcinoma by sponging miR-492 and targeting LATS2. *Gene* **753**: 144781. <https://doi.org/10.1016/j.gene.2020.144781>
- Diaz-Ruiz R, Rigoulet M, Devin A (2011) The Warburg and Crabtree effects: On the origin of cancer cell energy metabolism and of yeast glucose repression. *Biochim Biophys Acta* **1807**: 568–576. <https://doi.org/10.1016/j.bbabi.2010.08.010>
- Emberley E, Pan A, Chen J, Dang R, Gross M, Huang T, Li W, MacKinnon A, Singh D, Sotirovska N, Steggerda SM, Wang T, Parlati F (2021) The glutaminase inhibitor telaglenastat enhances the antitumor activity of signal transduction inhibitors everolimus and cabozantinib in models of renal cell carcinoma. *PLoS One* **16**: e0259241. <https://doi.org/10.1371/journal.pone.0259241>
- Fang L, Ye T, An Y (2021) Circular RNA FOXP1 induced by ZNF263 upregulates U2AF2 expression to accelerate renal cell carcinoma tumorigenesis and warburg effect through sponging miR-423-5p. *J Immunol Res* **2021**: 8050993. <https://doi.org/10.1155/2021/8050993>
- Goka ET, Chaturvedi P, Lopez DTM, Lippman ME (2020) Rac Signaling drives clear cell renal carcinoma tumor growth by priming the tumor microenvironment for an angiogenic switch. *Mol Cancer Ther* **19**: 1462–1473. <https://doi.org/10.1158/1535-7163.mct-19-0762>
- Hammad N, Rosas-Lemus M, Uribe-Carvajal S, Rigoulet M, Devin A (2016) The Crabtree and Warburg effects: Do metabolite-induced regulations participate in their induction? *Biochim Biophys Acta* **1857**: 1139–1146. <https://doi.org/10.1016/j.bbabi.2016.03.034>
- Huang A, Zheng H, Wu Z, Chen M, Huang Y (2020) Circular RNA-protein interactions: functions, mechanisms, and identification. *Theranostics* **10**: 3503–3517. <https://doi.org/10.7150/thno.42174>
- Huang Y, Shen XJ, Zou Q, Wang SP, Tang SM, Zhang GZ (2011) Biological functions of microRNAs: a review. *J Physiol Biochem* **67**: 129–139. <https://doi.org/10.1007/s13105-010-0050-6>
- Icard P, Shulman S, Farhat D, Steyaert JM, Alifano M, Lincet H (2018) How the Warburg effect supports aggressiveness and drug resistance of cancer cells? *Drug Resist Updat* **38**: 1–11. <https://doi.org/10.1016/j.drup.2018.03.001>
- Iorio MV, Croce CM (2012) MicroRNA dysregulation in cancer: diagnostics, monitoring and therapeutics. A comprehensive review. *EMBO Mol Med* **4**: 143–159. <https://doi.org/10.1002/emmm.201100209>
- Lee NH, Chang JW, Choi J, Jung HH, Im GJ (2013) Expression of Ras-related C3 botulinum toxin substrate 1 (RAC1) in human cholesteatoma. *Eur Arch Otorhinolaryngol* **270**: 455–459. <https://doi.org/10.1007/s00405-012-1966-y>
- Li QH, Liu Y, Chen S, Zong ZH, Du YP, Sheng XJ, Zhao Y (2019, Jun) circ-CSPP1 promotes proliferation, invasion and migration of ovarian cancer cells by acting as a miR-1236-3p sponge. *Biomed Pharmacother* **114**: 108832. <https://doi.org/10.1016/j.biopha.2019.108832>
- Li R, Luo S, Zhang D (2020) Circular RNA hsa_circ_0054537 sponges miR-130a-3p to promote the progression of renal cell carcinoma through regulating cMet pathway. *Gene* **754**: 144811. <https://doi.org/10.1016/j.gene.2020.144811>
- Liang J, Oyang L, Rao S, Han Y, Luo X, Yi P, Lin J, Xia L, Hu J, Tan S, Tang L, Pan Q, Tang Y, Zhou Y, Liao Q (2021) Rac1, A potential target for tumor therapy. *Front Oncol* **11**: 674426. <https://doi.org/10.3389/fonc.2021.674426>
- Lin L, Cai J (2020, Nov) Circular RNA circ-EGLN3 promotes renal cell carcinoma proliferation and aggressiveness via miR-1299-mediated IRF7 activation. *J Cell Biochem* **121**: 4377–4385. <https://doi.org/10.1002/jcb.29620>
- Liu G, Zhou J, Piao Y, Zhao X, Zuo Y, Ji Z (2020) Hsa_circ_0085576 promotes clear cell renal cell carcinoma tumorigenesis and metastasis through the miR-498/YAP1 axis. *Aging (Albany NY)* **12**: 11530–11549. <https://doi.org/10.18632/aging.103300>
- Lundø K, Traulsen M, Pedersen SF, Schwartz TW (2020) Why Warburg works: lactate controls immune evasion through GPR81. *Cell Metab* **31**: 666–668. <https://doi.org/10.1016/j.cmet.2020.03.001>
- Redman EK, Brookes PS, Karcz MK (2013) Role of p90(RSK) in regulating the Crabtree effect: implications for cancer. *Biochem Soc Trans* **41**: 124–126. <https://doi.org/10.1042/bst20120277>
- Rysz J, Franczyk B, Ławiński J, Gluba-Brzązka A (2021) Characteristics of clear cell papillary renal cell carcinoma (ccpRCC). *Int J Mol Sci* **23**. <https://doi.org/10.3390/ijms23010151>
- Samec M, Liskova A, Koklesova L, Samuel SM, Zhai K, Buhrmann C, Varghese E, Abotaleb M, Qaradakh T, Zulli A, Kello M, Mojzis J, Zubor P, Kwon TK, Shakibaei M, Büßelberg D, Sarria GR, Golubnitschaja O, Kubatka P (2020) Flavonoids against the Warburg phenotype-concepts of predictive, preventive and personalised medicine to cut the Gordian knot of cancer cell metabolism. *EPMA J* **11**: 377–398. <https://doi.org/10.1007/s13167-020-00217-y>
- Shan G, Tang T, Qian H, Xia Y (2017) Expression of Tiam1 and Rac1 proteins in renal cell carcinoma and its clinical-pathological features. *Int J Clin Exp Pathol* **10**: 11114–11121
- Sun Q, Yu R, Wang C, Yao J, Zhang L (2020) Circular RNA circ-CSPP1 regulates CCNE2 to facilitate hepatocellular carcinoma cell growth via sponging miR-577. *Cancer Cell Int* **20**: 202. <https://doi.org/10.1186/s12935-020-01287-8>
- Urbano AM (2021) Otto Warburg: The journey towards the seminal discovery of tumor cell bioenergetic reprogramming. *Biochim Biophys Acta Mol Basis Dis* **1867**: 165965. <https://doi.org/10.1016/j.bbadi.2020.165965>
- van Zonneveld AJ, Kölling M, Bijkerk R, Lorenzen JM (2021) Circular RNAs in kidney disease and cancer. *Nat Rev Nephrol* **17**: 814–826. <https://doi.org/10.1038/s41581-021-00465-9>
- Wang X, Shi J, Niu Z, Wang J, Zhang W (2020) MiR-216a-3p regulates the proliferation, apoptosis, migration, and invasion of lung cancer cells via targeting COPB2. *Biosci Biotechnol Biochem* **84**: 2014–2027. <https://doi.org/10.1080/09168451.2020.1783197>

- Xu Y, Ma Y, Liu XL, Gao SL (2020) miR-133b affects cell proliferation, invasion and chemosensitivity in renal cell carcinoma by inhibiting the ERK signaling pathway. *Mol Med Rep* **22**: 67–76. <https://doi.org/10.3892/mmr.2020.11125>
- Xue YF, Li M, Li W, Lin Q, Yu BX, Zhu QB, Chen HJ (2020) Roles of circ-CSPP1 on the proliferation and metastasis of glioma cancer. *Eur Rev Med Pharmacol Sci* **24**: 5519–5525. https://doi.org/10.26355/eurev_202005_21337
- Yan JS, Chen Q, Li YL, Gao YQ (2021) Hsa_circ_0065217 promotes growth and metastasis of renal cancer through regulating the miR-214-3p-ALPK2 axis. *Cell Cycle* **20**: 2519–2530. <https://doi.org/10.1080/15384101.2021.1991123>
- Yang G, Xu Q, Wan Y, Zhang L, Wang L, Meng F (2021) Circ-CSPP1 knockdown suppresses hepatocellular carcinoma progression through miR-493-5p releasing-mediated HMGB1 downregulation. *Cell Signal* **86**: 110065. <https://doi.org/10.1016/j.cellsig.2021.110065>
- Yang W, Xie T (2020, Jan) Hsa_circ_CSPP1/MiR-361-5p/ITGB1 regulates proliferation and migration of cervical cancer (CC) by modulating the PI3K-Akt signaling pathway. *Reprod Sci* **27**: 132–144. <https://doi.org/10.1007/s43032-019-00008-5>
- Yoon C, Cho SJ, Chang KK, Park DJ, Ryeom SW, Yoon SS (2017) Role of Rac1 pathway in epithelial-to-mesenchymal transition and cancer stem-like cell phenotypes in gastric adenocarcinoma. *Mol Cancer Res* **15**: 1106–1116. <https://doi.org/10.1158/1541-7786.mcr-17-0053>
- Yuan Y, Zhou X, Kang Y, Kuang H, Peng Q, Zhang B, Liu X, Zhang M (2021) Circ-CCS is identified as a cancer-promoting circRNA in lung cancer partly by regulating the miR-383/E2F7 axis. *Life Sci* **267**: 118955. <https://doi.org/10.1016/j.lfs.2020.118955>
- Zeng J, Feng Q, Wang Y, Xie G, Li Y, Yang Y, Feng J (2020) Circular RNA circ_001842 plays an oncogenic role in renal cell carcinoma by disrupting microRNA-502-5p-mediated inhibition of SLC39A14. *J Cell Mol Med* **24**: 9712–9725. <https://doi.org/10.1111/jcmm.15529>
- Zhang Y, Chen M, Liu M, Xu Y, Wu G (2021) Glycolysis-related genes serve as potential prognostic biomarkers in clear cell renal cell carcinoma. *Oxid Med Cell Longev* **2021**: 6699808. <https://doi.org/10.1155/2021/6699808>
- Zhang Y, Zhang H, Han Z, Wang X, Li X, Yuan P, Ji S, Liu Q (2022) A-kinase interacting protein 1 regulates the cell proliferation, invasion, migration and angiogenesis of clear cell renal cell carcinoma cells and affects the ERK/c-Myc signaling pathway by binding to Rac1. *Exp Ther Med* **24**: 558. <https://doi.org/10.3892/etm.2022.11489>
- Zhu G, Chang X, Kang Y, Zhao X, Tang X, Ma C, Fu S (2021) CircRNA: A novel potential strategy to treat thyroid cancer (Review) *Int J Mol Med* **48**. <https://doi.org/10.3892/ijmm.2021.5034>

MiR-96-5p is involved in permethrin-promoted proliferation and migration of breast cancer cells

Yi Yan, Tian Wen Long, Xi Niu, Jia Fu Wang and Sheng Li✉

Key Laboratory of Plant Resource Conservation and Germplasm Innovation in Mountainous Region (Ministry of Education), Collaborative Innovation Center for Mountain Ecology & Agro-Bioengineering, CICMEAB, College of Life Sciences/Institute of Agro-Bioengineering, Guizhou University, Guiyang 550025, Guizhou Province, China

MicroRNAs (miRNAs) are major players in cellular responses to xenobiotic compounds and toxins. However, the role of miRNAs in pyrethroid pesticide-induced cancer progression remains unclear. This study aimed to investigate the function of miR-96-5p in permethrin-induced proliferation and migration in breast cancer cells. In our study, the expression of miR-96-5p was upregulated in permethrin-treated MCF-7 cells. MiR-96-5p promoted MCF-7 cell proliferation and migration, accompanied by changes in the expression of proteins involved in cell proliferation, migration, and apoptosis. Homeobox A5 (HOXA5) was identified as a direct target of miR-96-5p. HOXA5 silencing had the opposite effects with miR-96-5p inhibition. In conclusion, these results suggest that miR-96-5p is involved in permethrin-promoted proliferation and migration of breast cancer cells by targeting HOXA5.

Keywords: miR-96-5p, permethrin, proliferation and migration, MCF-7 cells, HOXA5

Received: 23 October, 2022; **revised:** 16 November, 2022; **accepted:** 22 March, 2023; **available on-line:** 17 August, 2023

✉e-mail: sl1@gzu.edu.cn

Acknowledgments of Financial Support: This study was supported by the National Natural Science Foundation of China (No. 22166010 and No. 31401091).

Abbreviations: miRs, MicroRNAs; HOXA5, homeobox A5; CCK-8, Cell counting kit-8; 3'-UTR, 3'-untranslated regions; WT, Wild-type

INTRODUCTION

Permethrin is a synthetic pyrethroid pesticide widely used in agriculture. Permethrin typically disturbs the nervous system of insects through slackening sensitivity toward voltage on the intramembrane and extramembrane of axons in the nervous system of insects (Park *et al.*, 2021; Wang *et al.*, 2016). Due to the efficient insecticidal properties of permethrin, it is not only applied to control crop diseases and pests but also used in mosquito killing and malaria treatment (Richards *et al.*, 2017; Richards *et al.*, 2018; Thievent *et al.*, 2019). However, the residual toxicity of permethrin has attracted great attention from the public. In vitro studies indicated that permethrin competitively combined with estrogen receptor (ER) against estradiol (E2) (McCarthy *et al.*, 2006) and promoted the proliferation of breast cancer cells, which could be blocked by estrogen antagonists (Kim *et al.*, 2004; Sun *et al.*, 2014). In addition, the wet weight of the uterus of female rats increased after being injected subcutaneously with permethrin, which was similar to the effect caused by E2, and permethrin-induced weight increase in the uterus could be inhibited by antiestrogen-

gens. When male mice were given permethrin *per os*, their luteinizing hormone (LH) significantly increased, while testosterone (T) level and sperm vitality dramatically decreased (Kim *et al.*, 2005). These studies indicate that pyrethroid pesticides such as permethrin have estrogen effects and belong to environmental hormones. According to epidemiological observation, workers exposed to low-dose permethrin for a long time have higher risks of colorectal cancer, breast cancer, lung cancer, and leukemia (Rusiecki *et al.*, 2009). However, the underlying mechanisms remain elusive.

MicroRNA (miRNA) is a kind of non-coding small RNA and regulates protein expression by binding to the 3'-untranslated region (3'-UTR) of target genes (Burnett *et al.*, 2021; Cao *et al.*, 2021). miRNAs play an essential role in regulating the organismic response to toxic effects caused by xenobiotic compounds, including pesticides. For example, miR-22 restrained endothelial cell dysfunction caused by the pesticide endosulfan (Xu *et al.*, 2017). MiR-513 protected renal cells from DDVP-induced apoptosis by targeting BCL-2 (Li *et al.*, 2018). MiR-96-5p was initially identified as a 23-nucleotide miRNA and abundant evidence has shown that miR-96 is related to cell proliferation and apoptosis. For example, overexpression of miR-96-5p was shown to induce gastric adenocarcinoma cell apoptosis through targeting FOXO3 (He & Zou, 2020), and it also inhibited hepatocellular carcinoma cell apoptosis (Iwai *et al.*, 2018). MiR-96-5p inhibited the expression of the target gene *MTSS1* and enhanced the growth of glioma cells (Zhang & Guo, 2019). These findings indicate that miR-96-5p is involved in tumor cell proliferation, migration, and apoptosis. However, the role of miR-96 in the cellular response to exogenous toxicants remains unclear.

HOXA5 is a member of homeobox gene clusters, which is involved in the regulation of cell differentiation. The role of HOXA5 in tumorigenesis is controversial. HOXA5 is generally regarded as a tumor suppressor in many cancers, such as cervical cancer and breast cancer. In these cancers, HOXA5 is normally the target of various miRNAs. On the other hand, HOXA5 is reported to be capable of promoting tumor progression, which needs further investigation.

Notably, the mechanism by which permethrin promotes breast cancer is not fully understood, and the role of miR-96-5p in breast cancer remains elusive. Therefore, in this study, we aimed to determine the regulatory role of miR-96-5p in mediating the estrogen effect of permethrin. Our study confirmed that miR-96-5p targeted HOXA5 to promote breast cancer induced by permethrin.

MATERIALS AND METHODS

Cell line and main reagents

MCF-7 cells were obtained from China Center for Type Culture Collection (CCTCC, China). Cell lines were cultured and maintained in Dulbecco's modified Eagle's medium (DMEM) (Gibco, USA) supplemented with 10% fetal bovine serum (FBS) (Gibco, USA), 1% penicillin and 1% streptomycin (both from Solarbio) under 5% CO₂ at 37°C. Permethrin standard (purity 99.1%) and 17β-estradiol standard (purity 99.2%) were purchased from China Center for Standard Substance; Trypsin was purchased from Sigma (USA); CCK-8 kit, Apoptosis-HOECHST staining kit, RNA Extracting Kit, PBS buffer, enhanced RIPA lysis buffer, BCA protein assay kit, and Lipo8000™ were purchased from Beyotime Technology (China). The primary and secondary antibodies were obtained from Beijing Quailtyard Biotechnology (China); U6 snRNA Real-time PCR Normalization Kit was purchased from Shanghai GenePharma (China).

Cell proliferation assay

MCF-7 cells were seeded into 96-well plates at a density of 3×10^3 cells/well. After overnight incubation, the cells reached about 70% confluency. Different concentrations of permethrin (10^{-4} , 10^{-5} , 10^{-6} , 10^{-7} mol/L) and estradiol (10^{-6} , 10^{-7} , 10^{-8} , 10^{-9} mol/L) were used to treat MCF-7 cells for 48 h or 72 h. Each treatment has five repeats and the medium with different drugs was refreshed daily. Cells untreated with drugs were set as the control group, and wells added only with the medium were set as the blank group. CCK-8 reagent allows the sensitive colorimetric assay to determine the number of viable cells in the cell proliferation assay. Therefore, 20 μL CCK-8 reagent was added to each well after different periods. After 30 min of incubation, the OD values of the solution in each well at 450 nm were measured to calculate cell viability according to the formula:

$$\text{Cell viability (\%)} = \frac{\text{OD}_{\text{treated group}} - \text{OD}_{\text{blank group}}}{\text{OD}_{\text{control group}} - \text{OD}_{\text{blank group}}} \times 100\%$$

Cell transfection

MCF-7 cells were seeded into 6-well plates. After 70% confluency was reached, the cells in the control group were treated with 100 pmol scramble miRNA (marked as miR-NC group), while the cells in the experimental group were treated with 100 pmol miR-96-5p inhibitor or miR-96-5p mimic (marked as miR-96-5p inhibitor group or miR-96-5p mimic group) (GenePharma, China) using Lipofectamine 2000 (Invitrogen, USA). The medium was refreshed after 4 h, followed by 24 h incubation.

Quantitative Real-time PCR

Total RNA was extracted with RNAeasy™ Animal RNA Isolation Kit and was reverse transcribed into cDNA using GenePharma RT Reagent Kit. The expression of miR-96-5p was measured with GenePharma qRT-PCR Kit. U6 snRNA was used as an internal reference for miRNA analysis. QRT-PCR was conducted using the CFX96 system. Primers were listed as follows: miR-96-5p, forward: 5'-CGAAGTTTGGCACTAG-GCACATT-3', reverse: 5'-TATGGTTTGTGACGACT-GTGTGAT-3'; U6, forward: 5'-CAGCACATATAC-

TAAAATTGGAACG-3', reverse: 5'-ACGAATTT-GCGTGTTCATCC-3'.

The relative expression of target genes was quantified using the $2^{-\Delta\Delta C_t}$ method.

Luciferase reporter assay

The targets of miR-96 were predicted by Target Scan Human (<http://www.targetscan.org>), miRDB (<http://mirdb.org>), and miRTarbase (<http://mirtarbase.mbc.nctu.edu.tw/php/index.php>). For the luciferase reporter assay, the wild-type (WT-HOXA5) or mutant 3'-untranslated regions (MUT-HOXA5) of HOXA5 were subcloned into the luciferase reporter gene vector (pMIR-REPORTER Luciferase, cat. # QYV0423, Qualityard, China). MCF-7 cells were cultured in 24-well plates, and co-transfected with miR-96-5p or miR-NC and WT-HOXA5 or MUT-HOXA5 plasmids using Lipofectamine 2000. The luciferase activity was calculated through the ratio of firefly and renilla luciferase activity following the manufacturer's instructions.

In vitro wound healing assay

Cells were cultured in 12-well plates at a density of 3×10^5 cells per well. After transfection with miR-NC, miR-96-5p mimic, and miR-96-5p inhibitor, cells were inoculated until 95% confluency was reached. A sterile 200-μL pipette tip was used to scratch the cell layer manually, and the time point was set as 0 h. Next, the cells were rinsed with PBS 3 times to remove all cellular debris. Fresh complete medium was then added. The subsequent colonization of the denuded surface was quantified with Image J, and the relative migration distance was calculated by subtracting the width at 0 h from the width at each migration time point.

Western blot analysis

Cells were collected after 48 hours of transfection. Radio immuno-precipitation assay (RIPA) lysis buffer was used to extract total proteins and Bicinchoninic acid (BCA) protein assay kit was used to measure the concentrations of total proteins. Proteins of different molecular weights were separated by SDS-PAGE and transferred onto the membranes. After blocking with 5% skim milk for 1 h, proteins were incubated with primary antibodies, rabbit anti-HOXA5, and rabbit anti-β-actin at 4°C overnight. Subsequently, the membranes were washed with TBST solution, incubated with the secondary antibody goat anti-rabbit IgG coupled with HRP at room temperature for 2 h, and washed with TBST solution. The membranes were exposed using an ECL kit and Gel Imaging System. Each experiment was repeated 3 times.

Statistical analysis

Data analysis, graph generation, and statistical analysis were performed with the software GraphPad Prism 8.3 (GraphPad Software Inc., Philadelphia, USA). Data were represented as mean ± standard deviation (S.D.). The comparison between the two groups was analyzed by *t*-test and the comparison of multiple groups such as different concentrations were analyzed by One-way analysis of variance (ANOVA). *P* values less than 0.05 were considered significant.

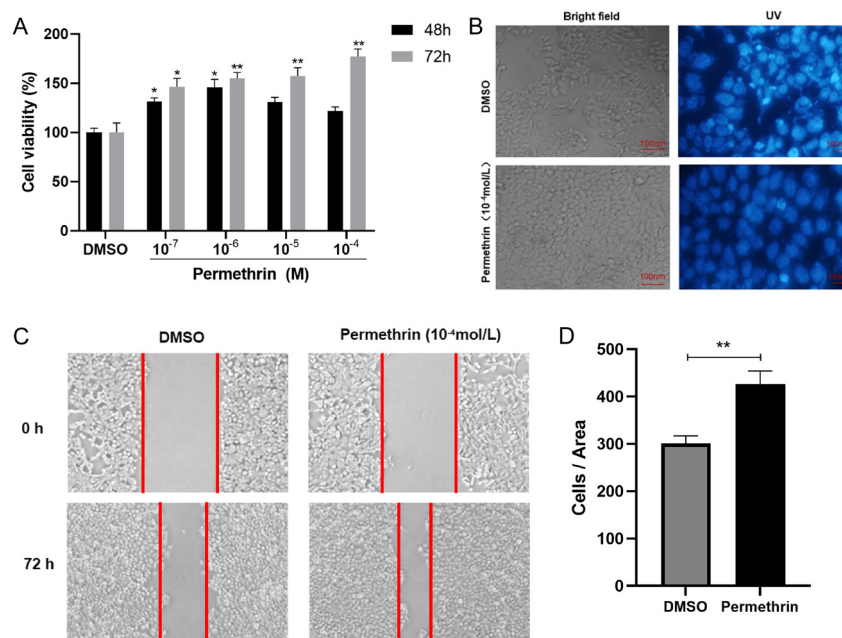


Figure 1. Low-dose permethrin promoted the proliferation and migration of MCF-7 cells.

(A) MCF-7 cells were treated with permethrin at different concentrations (10^{-4} – 10^{-7} M) for 48 h or 72 h, and cell viability was assessed by CCK-8 assay. (B) Fluorescent microscopic images of Hoechst-stained MCF-7 cells after permethrin or control treatment. Bright blue fluorescence indicated apoptosis. (C) Wound of MCF-7 cells immediately after scratching and after 72 h culture in the control group and permethrin-treated group. (D) Statistical analysis of wound healing of MCF-7 cells. Data were mean \pm S.D. (n=3). * P <0.05, ** P <0.01 versus NC groups.

RESULTS

Low-dose permethrin promoted the proliferation of MCF-7 cells

To determine the effect of permethrin on MCF-7 cell viability, the cells were treated with different concentrations of permethrin for 48 h or 72 h. The results showed that permethrin promoted MCF-7 cell proliferation in a dosage range from 10^{-7} M to 10^{-4} M (Fig. 1A). The maximum viability in MCF-7 cells was seen when cells were treated with 10^{-4} M permethrin for 72 h. Hoechst staining showed that cells in treatment groups had higher viability. The nuclei were evenly stained, compared with the control group (Fig. 1B). IWH assay showed that MCF-7 cell migration was significantly promoted after treatment with 10^{-4} M permethrin for 72 h (Fig. 1C). These results indicate that low-dose permethrin promotes MCF-7 cell proliferation and migration.

Permethrin promoted ER- α and STAT3 expression and upregulated miR-96

Next, we investigated whether permethrin regulated the expression of genes involved in cell proliferation, employing estradiol as the positive control. As is shown in Fig. 2A, after treatment with low-dose estradiol and permethrin for 72 h, the expression of estrogen receptor- α (ER- α) and Signal Transducer and Activator of Transcription (STAT3) in MCF-7 cells increased.

We performed a qRT-PCR assay to detect miR-96 expression in MCF-7 cells treated with different concentrations of permethrin. The results showed that miR-96 expression in MCF-7 cells in the permethrin-treated group increased in a dose-dependent manner (Fig. 2B).

HOXA5 was a target of miR-96-5p in MCF-7 cells

HOXA5 gene was predicted to be the target of miR-96-5p by the TargetScan program (Fig. 3A). To verify the prediction, we constructed a luciferase reporter containing either the wild-type HOXA5 3' UTR or a mutated HOXA5 3' UTR and then co-transfected into

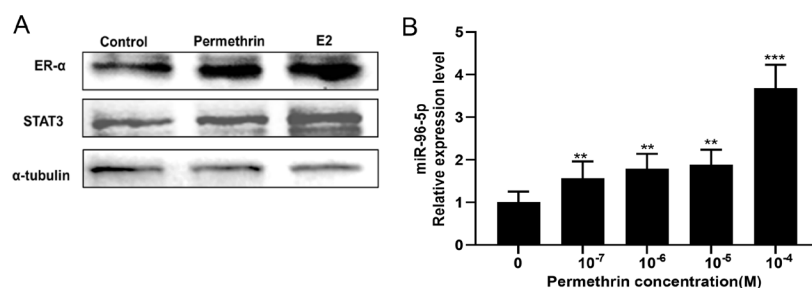


Figure 2. Permethrin promoted ER- α and STAT3 expression and upregulated miR-96.

(A) Western blot analysis of protein levels of ER- α and STAT3 in permethrin-treated MCF-7 cells. (B) PCR analysis of miR-96-5p levels in permethrin-treated MCF-7 cells. Data were mean \pm S.D. (n=3). * P <0.05, ** P <0.01, *** P <0.001 versus NC groups.

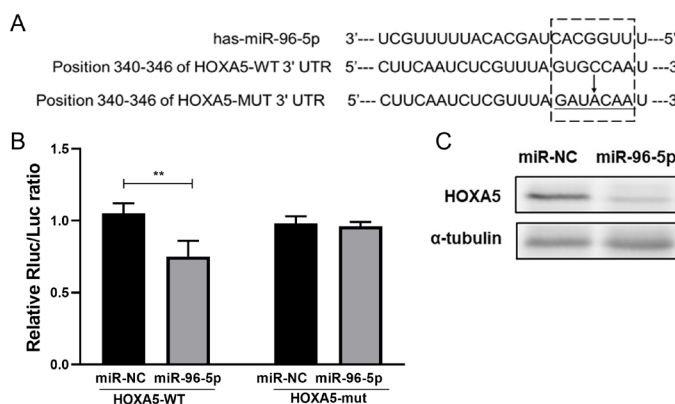


Figure 3. *HOXA5* is a target of miR-96-5p in MCF-7 cells.

(A) The predicted position of the miR-96-5p target site in the 3' UTR of *HOXA5*. The miR-96-5p seed sequence was shown in the box. (B) Luciferase report assay in cells co-transfected with *HOXA5* or *HOXA5* mutation reporter and miR-NC or miR-96-5p. (C) Western blot analysis of protein levels of *HOXA5* in miR-NC or miR-96-5p transfected MCF-7 cells. Data were mean \pm S.D. (n=3). * P <0.05, ** P <0.01 versus NC groups.

MCF-7 cells with miR-96-5p mimic or negative control (NC) miRNAs. A significant decrease of luciferase activity was detected in cells co-transfected with *HOXA5* 3' UTR construct and miR-96-5p mimics, compared with cells co-transfected with miR-NC or mutant *HOXA5* 3' UTR (Fig. 3B). Compared with the miR-NC group, a significant decrease of *HOXA5* expression in miR-96-5p mimic group was observed (Fig. 3C). These results indicate that *HOXA5* is a direct target of miR-96-5p.

miR-96-5p promoted permethrin-induced proliferation and migration of MCF-7 cells by targeting *HOXA5*

To further investigate the mechanism of miR-96-5p in permethrin-induced MCF-7 cell proliferation and migration, the miR-96 inhibitor was transfected into permethrin-treated MCF-7 cells. IWH assay showed that permethrin-induced migration of MCF-7 cells was increased and *HOXA5* expression was upregulated after miR-96

was inhibited, compared with cells treated with permethrin only. In rescue experiments, permethrin-induced proliferation and migration of MCF-7 cells were decreased by silencing *HOXA5* expression (Fig. 4A, B, C). These results suggest that miR-96 regulates the proliferation and migration of MCF-7 cells by targeting *HOXA5*.

DISCUSSION

Estrogens are crucially involved in the development of breast cancer (Yi *et al.*, 2009; Chaudhuri *et al.*, 2021). Estrogen activates the ER dimer in the promoter domain of the target gene to regulate gene expression in cells (Krieg *et al.*, 2001). Estrogen also promotes the phosphorylation of related transcription factors (Sengupta *et al.*, 2019). Human breast cancer cell line MCF-7 is capable of expressing estrogen receptor and is sensitive to estrogen. Therefore, in the present study, we employed

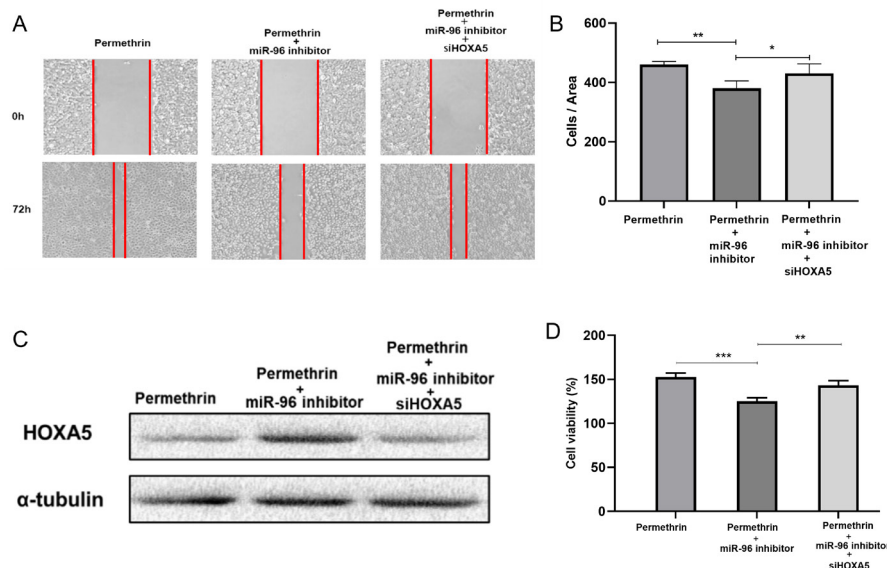


Figure 4. miR-96-5p promoted permethrin-induced proliferation and migration of MCF-7 cells through targeting *HOXA5*.

(A) Wound of permethrin-treated MCF-7 cells immediately after scratching and after 72 h culture in control or miR-96 inhibitor transfected group or miR-96 inhibitor/siHOXA5 co-transfected group. (B) Statistical analysis of wound healing of MCF-7 cells. (C) Western blot analysis of *HOXA5* expression after permethrin exposure in MCF-7 cells of the control group, transfected group, or co-transfected group. (D) Statistical analysis of the viability of MCF-7 cells in different groups. Data were mean \pm S.D. (n=3). * P <0.05, ** P <0.01, *** P <0.001 for the comparison.

the MCF-7 cell line as the experiment model and found that low-dose permethrin promoted the proliferation and migration of estrogen-sensitive MCF-7 cells. Moreover, we found that permethrin increased ER α protein expression as E2 did, indicating that permethrin plays a role in enhancing the metabolism of the estrogen receptor.

As a critical downstream transcription factor of ER, phosphorylated STAT3 passes through the nuclear pore to activate the transcription of target genes (Kettner *et al.*, 2019; Wang *et al.*, 2021). In our study, when MCF-7 cells were treated with low-dose permethrin, the expression of STAT3 and ER- α increased, compared with E2 treatment as the positive control. These results suggest that permethrin has an estrogen effect and promotes cell proliferation by activating the estrogen receptor and STAT-related estrogen pathway.

STAT3 is an important transcription factor of the miR-96-182-183 family (Lei *et al.*, 2021; Xiao *et al.*, 2021). MiR-96 was reported to influence the cell cycle (Xu *et al.*, 2018). miR-96 inhibitor arrested the cell cycle at the G1 phase, while fewer cells entered the S phase, suggesting that inhibition of miR-96 induces cell arrest in the G1 phase. Therefore, we speculated that miR-96 might promote cell proliferation and migration induced by permethrin. Our results showed that the miR-96 inhibitor attenuated permethrin-induced proliferation and migration of MCF-7 cells, which confirmed our speculation.

Next, TargetScan, miRDB, and miRTarbase were employed to predict the target genes of miR-96 (Guo *et al.*, 2021). *HOXA5* is highly correlated with cell proliferation and tumorigenesis. *HOXA5* is a member of the homeobox gene family encoding homologous proteins, and its biological function is to control embryonic development and cell differentiation. *HOXA5* is regulated by AKT/mTORC1/S6K1 signal pathway (Feng *et al.*, 2017), and inhibits cell progression by regulating AKT/p27 pathway (Wang *et al.*, 2019). *HOXA5* expression was closely related to tumor histological grade (Dziobek *et al.*, 2020; Aubin *et al.*, 2002). Inhibition and overexpression of *HOXA5* promoted proliferation and apoptosis of osteosarcoma cells through the p53 and p38 α /MAPK pathways (Chen *et al.*, 2019). Inhibition of *HOXA5* significantly enhanced viability and proliferation in U2OS and MG63 cells, while overexpression of *HOXA5* promoted cell apoptosis and caspase-3 activity. Knockdown of *HOXA5* in HCC cells provoked capillary tube formation, while overexpression of *HOXA5* inhibited cell proliferation and invasion and promoted cell apoptosis. Based on the luciferase assay, we confirmed that *HOXA5* was a target gene of miR-96. When *HOXA5* was overexpressed, proliferation and migration in MCF-7 cells induced by permethrin were inhibited. Therefore, overexpression of *HOXA5* could reverse the effects of miR-96. These results suggest that miR-96 promotes permethrin-induced proliferation and migration in MCF-7 cells via the downregulation of *HOXA5*. A recent study reported the potential of miRNAs as biomarkers of breast cancer (Shaaban *et al.*, 2022). It would be interesting to evaluate the application of miR-96 in the early diagnosis of breast cancer.

This study has certain limitations. First, the downstream mechanism of Permethrin, miR-96-5p, and *HOXA5* in promoting breast cancer is still obscure. In addition, we need to perform *in vivo* experiments to confirm our conclusion in future studies. Beyond these limitations, this is the first study to demonstrate that miR-96-5p targeted *HOXA5* to promote cancer progression.

In conclusion, our results suggest that permethrin, as a pseudo estrogen, upregulates ER- α and STAT3 expres-

sion in MCF-7 cells. STAT3 activates the transcription of miR-96, which specifically inhibits *HOXA5* expression and promotes the proliferation and migration of MCF-7 cells.

Conflict of Interest

The authors declare that there are no conflicts of interest.

REFERENCES

- Aubin J, Dery U, Lemieux M, Chailier P, Jeannotte L (2002) Stomach regional specification requires *HOXA5*-driven mesenchymal-epithelial signaling. *Development* **129**: 4075–4087. <https://doi.org/10.1242/dev.129.17.4075>
- Burnett M, Rodolico V, Shen F, Leng R, Zhang M, Eisenstat D D, Serge C (2021) PathVisio Analysis: An application targeting the miRNA network associated with the p53 signaling pathway in osteosarcoma. *Biocell* **45**: 17–26
- Cao L, Yang DM, Bai B. (2021) Mir-1247 Affects the proliferation, invasion and apoptosis of osteosarcoma cells through SOX9. *Oncologie* **23**: 149–158
- Chaudhuri S, Thomas S, Munster P. (2021) Immunotherapy in breast cancer: A clinician's perspective. *J Natl Cancer Center* **1**: 47
- Chen YQ, Yang TQ, Zhou B, Yang MX, Feng HJ, Wang YL (2019) *HOXA5* overexpression promotes osteosarcoma cell apoptosis through the p53 and p38 α MAPK pathway. *Gene* **689**: 18–23. <https://doi.org/10.1016/j.gene.2018.11.081>
- Dziobek K, Oplawski M, Zmarzly N, Gabarek BO, Kielbasinski R, Kielbasinski K, Kieszkowski P, Talkowski K, Boron D (2020) Assessment of expression of homeobox A5 in endometrial cancer on the mRNA and protein level. *Curr Pharm Biotechnol* **21**: 635–641. <https://doi.org/10.2174/1389201021666191227121627>
- Feng F, Ren Q, Wu S, Saeed M, Sun C (2017) *HOXA5* increases mitochondrial apoptosis by inhibiting Akt/mTORC1/S6K1 pathway in mice white adipocytes. *Oncotarget* **8**: 95332–95345. <https://doi.org/10.18632/oncotarget.20521>
- Guo Q, Yuan Y, Zhang X, Lei X, Yuan Q, Li H (2021) miR-181a-3p inhibits malignant biological behavior of non-small cell lung cancer via down-regulating RAD21 expression. *J Comp Mol Sci Genet* **2**: 12–23
- He X, Zou K (2020) MiRNA-96-5p contributed to the proliferation of gastric cancer cells by targeting FOXO3. *J Biochem* **167**: 101–108. <https://doi.org/10.1093/jb/mvz080>
- Iwai N, Yasui K, Tomie A, Gen Y, Terasaki K, Kitaichi T, Soda T, Yamada N, Dohi O, Seko Y, Umemura A, Nishikawa T, Yamaguchi K, Moriguchi M, Konishi H, Naito Y, Itoh Y (2018) Oncogenic miR-96-5p inhibits apoptosis by targeting the caspase-9 gene in hepatocellular carcinoma. *Int J Oncol* **53**: 237–245. <https://doi.org/10.3892/ijo.2018.4369>
- Kettner NM, Vijayaraghavan S, Durak MG, Bui T, Kohansal M, Ha MJ, Liu B, Rao X, Wang J, Yi M, Carey JPW, Chen X, Eckols TK, Raghavendra AS, Ibrahim NK, Karuturi MS, Watowich SS, Sahin A, Tweardy DJ, Hunt KK, Tripathy D, Keyomarsi K (2019) Combined inhibition of STAT3 and DNA repair in palbociclib-resistant ER-positive breast cancer. *Clin Cancer Res* **25**: 3996–4013. <https://doi.org/10.1158/1078-0432.CCR-18-3274>
- Kim IY, Shin JH, Kim HS, Lee SJ, Kang IH, Kim TS, Moon HJ, Choi KS, Moon A, Han SY (2004) Assessing estrogenic activity of pyrethroid insecticides using *in vitro* combination assays. *J Reprod Dev* **50**: 245–255. <https://doi.org/10.1262/jrd.50.245>
- Kim SS, Lee RD, Lim KJ, Kwack SJ, Rhee GS, Seok JH, Lee GS, An BS, Jeung EB, Park KL (2005) Potential estrogenic and antiandrogenic effects of permethrin in rats. *J Reprod Dev* **51**: 201–210. <https://doi.org/10.1262/jrd.16060>
- Krieg SA, Krieg AJ, Shapiro DJ (2001) A unique downstream estrogen responsive unit mediates estrogen induction of proteinase inhibitor-9, a cellular inhibitor of IL-1 β -converting enzyme (caspase 1). *Mol Endocrinol* **15**: 1971–1982. <https://doi.org/10.1210/mend.15.11.0719>
- Lei H, Shi J, Teng Y, Song C, Zou L, Ye F, Zhang H (2021) Baicalein modulates the radiosensitivity of cervical cancer cells *in vitro* via miR-183 and the JAK2/STAT3 signaling pathway. *Adv Clin Exp Med* **30**: 727–736. <https://doi.org/10.17219/acem/135478>
- Li S, Xu YN, Niu X, Li Z, Wang JF (2018) miR-513a-5p targets Bcl-2 to promote dichlorvos induced apoptosis in HK-2 cells. *Biomed Pharmacother* **108**: 876–882. <https://doi.org/10.1016/j.biopha.2018.09.101>
- McCarthy AR, Thomson BM, Shaw IC, Abell AD (2006) Estrogenicity of pyrethroid insecticide metabolites. *J Environ Monit* **8**: 197–202. <https://doi.org/10.1039/b511209e>
- Park SK, Lee HJ, Song E, Kim Y, Kim DY, Lee JH, Yoo HJ, Oh JE, Kwon JH (2021) Exposure to permethrin used as a home in-

- secticide: A case study comparing model predictions and excretion of metabolites. *Environ Int* **155**: 106581. <https://doi.org/10.1016/j.envint.2021.106581>
- Richards SL, Balanay JAG, Harris JW, Banks VM, Meshnick S (2017) Residual effectiveness of permethrin-treated clothing for prevention of mosquito bites under simulated conditions. *J Environ Health* **79**: 8–15
- Richards SL, Agada N, Balanay JAG, White AV (2018) Permethrin treated clothing to protect outdoor workers: evaluation of different methods for mosquito exposure against populations with differing resistance status. *Pathog Glob Health* **112**: 13–21. <https://doi.org/10.1080/20477724.2018.1437692>
- Rusiecki JA, Patel R, Koutros S, Beane-Freeman L, Landgren O, Bonner MR, Coble J, Lubin J, Blair A, Hoppin JA, Alavanja MC (2009) Cancer incidence among pesticide applicators exposed to permethrin in the Agricultural Health Study. *Environ Health Perspect* **117**: 581–586. <https://doi.org/10.1289/ehp.11318>
- Sengupta S, Sevigny CM, Bhattacharya P, Jordan VC, Clarke R (2019) Estrogen-induced apoptosis in breast cancers is phenocopied by blocking dephosphorylation of eukaryotic initiation factor 2 Alpha (eIF2alpha) protein. *Mol Cancer Res* **17**: 918–928. <https://doi.org/10.1158/1541-7786.MCR-18-0481>
- Shaaban NZ, Ibrahim NK, Saada HN, El-Rashidy FH, Shaaban HM (2022). The Implication of microRNAs as non-invasive biomarkers in 179 Egyptian breast cancer female patients. *Oncol Res* **30**: 269–276
- Sun H, Chen W, Xu X, Ding Z, Chen X, Wang X (2014) Pyrethroid and their metabolite, 3-phenoxybenzoic acid showed similar (anti)estrogenic activity in human and rat estrogen receptor alpha-mediated reporter gene assays. *Environ Toxicol Pharmacol* **37**: 371–377. <https://doi.org/10.1016/j.etap.2013.11.031>
- Thievent K, Hauser G, Elaïan O, Koella JC (2019) The interaction between permethrin exposure and malaria infection affects the host-seeking behaviour of mosquitoes. *Malar J* **18**: 79. <https://doi.org/10.1186/s12936-019-2718-x>
- Wang X, Martinez MA, Dai M, Chen D, Ares I, Romero A, Castellano V, Martinez M, Rodriguez JL, Martinez-Larranaga MR, Anadon A, Yuan Z (2016) Permethrin-induced oxidative stress and toxicity and metabolism. A review. *Environ Res* **149**: 86–104. <https://doi.org/10.1016/j.envres.2016.05.003>
- Wang Y, Duan Y, Chen K, Li H, Quan Y. (2021) Protective effects of docosahexaenoic acid against non-alcoholic hepatic steatosis through activating of JAK2/STAT3 signaling pathway. *Biocell* **45**: 307–316
- Wang Z, Yu C, Wang H (2019) *HOXA5* inhibits the proliferation and induces the apoptosis of cervical cancer cells via regulation of protein kinase B and p27. *Oncol Rep* **41**: 1122–1130. <https://doi.org/10.3892/or.2018.6874>
- Xiao Y, Huang W, Huang H, Wang L, Wang M, Zhang T, Fang X, Xia X (2021) miR-182-5p and miR-96-5p target PIAS1 and mediate the negative feedback regulatory loop between PIAS1 and STAT3 in endometrial cancer. *DNA Cell Biol* **40**: 618–628. <https://doi.org/10.1089/dna.2020.6379>
- Xu D, Guo Y, Liu T, Li S, Sun Y (2017) miR-22 contributes to endosulfan-induced endothelial dysfunction by targeting SRF in HUVECs. *Toxicol Lett* **269**: 33–40. <https://doi.org/10.1016/j.toxiclet.2017.01.014>
- Xu T, Du XW, Hu JB, Zhu YF, Wu HL, Dai GP, Shu YM, Ouyang J (2018) Anticancer effect of miR-96 inhibitor in bladder cancer cell lines. *Oncol Lett* **15**: 3814–3819. <https://doi.org/10.3892/ol.2018.7745>
- Yi JM, Kwon HY, Cho JY, Lee YJ (2009) Estrogen and hypoxia regulate estrogen receptor alpha in a synergistic manner. *Biochem Biophys Res Commun* **378**: 842–846. <https://doi.org/10.1016/j.bbrc.2008.11.142>
- Zhang S, Guo W (2019) Long noncoding RNA MEG3 suppresses the growth of glioma cells by regulating the miR965p/MTSS1 signaling pathway. *Mol Med Rep* **20**: 4215–4225. <https://doi.org/10.3892/mmr.2019.10659>

circ_0013613 Promotes the recovery of spinal cord injury by regulating mir-370-3p/caspase1 to regulate neuronal pyroptosis

Yong Guo^{1,2}, Li Ma^{2,3} and Zhuo Zhang⁴✉

¹Orthopedics department, The People's Hospital of Danyang, Danyang, Jiangsu 212300, China; ²Affiliated Danyang Hospital of Nantong University, Danyang, Jiangsu 212300, China; ³Blood Purification Center, The People's Hospital of Danyang, Danyang, Jiangsu 212300, China; ⁴Department of Spinal and Bone Tumor Surgery, Ningxia Hui Autonomous Region People's Hospital, Jinfeng District, Yinchuan, Ningxia Hui Autonomous Region 750004, China

Spinal cord injury (SCI) is a common disease of the central nervous system. Circular RNAs (circRNAs) play an essential role in neuron disorders. This study aimed to investigate the role and regulatory mechanism of circ_0013613 in promoting functional recovery of spinal cord injury (SCI). The mRNA and miRNA expressions were calculated by RT-QPCR. The characteristics of circ_0013613 in nerve cells was determined by actinomycin D and RNase R assay. Protein expression was detected using Western blot. Lactate dehydrogenase (LDH) activity assay was performed to determine cytotoxicity. ELISA was conducted to detect the release of cytokines. MTT assay and flow cytometry were applied to measure cellular functions. In SCI patients and lipopolysaccharide (LPS)-induced primary spinal cord neurons circ_0013613 was increased. Knockdown of circ_0013613 suppressed LPS-stimulated cytotoxicity, inflammation and inflammation-induced pyroptosis. Additionally, circ_0013613 negatively regulated miR-370-3p, downregulation of which degraded cellular functions of spinal cord neurons. Moreover, miR-370-3p targeted Caspase1 (CASP1), overexpression of which promoted the inflammation and pyroptosis of spinal cord neurons. circ_0013613 can promote the recovery of SCI by regulating miR-370-3p/CASP1 to mediate neuronal pyroptosis.

Key words: nerve injury, pyroptosis, circ_0013613, miR-370-3p, Caspase1

Received: 03 March, 2022; **revised:** 11 May, 2022; **accepted:** 13 October, 2022; **available on-line:** 03 February, 2023

✉e-mail: dr.zhangzhuo@hotmail.com

Acknowledgements of Financial Support: This study was supported by Hospital Training and Revitalizing Research Project (201905)

Abbreviations: CASP1, caspase1; circRNAs, circular RNAs; LDH, lactate dehydrogenase; LPS, lipopolysaccharide; miRNA, microRNA; SCI, spinal cord injury

INTRODUCTION

Spinal cord injury (SCI) is a serious disease of the central nervous system and an important cause of disability and death in patients. Its prevention, treatment and rehabilitation have always been the focus of attention and research by clinicians and related scholars (Lu *et al.*, 2020; Kumar *et al.*, 2019).

Circular RNAs (circ RNAs) are a kind of non-coding RNAs with closed circular structure widely existing in eukaryotic cells. It is formed by reverse splicing and plays an important role in cell proliferation, apoptosis and inflammation through microRNA (miRNA) sponges, RNA-binding proteins, regulatory gene transcription and

peptide translation. Some studies have pointed out that circRNAs with abnormal expression exist in the process of SCI, which may be a potential target for the treatment of SCI (Yao *et al.*, 2020). Some scholars have found that circRNA plays a role in the pathogenesis and treatment of SCI based on circRNA-miRNA-mRNA network. The expression of circ_0003801, circ_0014620, circ_0013613 and circ_0007259 is up-regulated in rats after SCI (Peng *et al.*, 2020). Based on previous studies, we analyzed serum samples and SCI cell models of patients with SCI. Among the four circRNAs, circ_0013613 was the most significantly up-regulated. At the same time, the mechanism of circ_0013613 in SCI recovery is not completely clear.

CASP1 is a member of the Caspase family. It is also the core executor of scorched cell death. It plays an important role in the process of cell death and inflammatory process. (Man *et al.*, 2017; Sun & Scott, 2016). Some studies have pointed out that miR-370-3p is low expressed in SCI cell model *in vitro* and plays an important role in the process of neuronal apoptosis (Li *et al.*, 2021). CASP1 activation mediated sorosis is closely related to SCI (Li *et al.*, 2020). However, it is not clear whether miR-370-3p participates in the occurrence and development of SCI by regulating the CASP1-mediated sorosis pathway. Based on this, this study aims to explore the role of circ_0013613 in promoting SCI function recovery, and to observe whether the mechanism of action is related to the regulation of miR-370-3p/CASP1 pathway mediated neuronal pyroptosis.

MATERIALS AND METHODS

Experimental materials

This study was approved by the Ethics Committee of Ningxia Hui Autonomous Region People's Hospital. A total of 40 SCI Patients and healthy subjects with similar age and gender distribution were enrolled in the spinal surgery department of our hospital from October 2020 to May 2021. The participants' informed consent was obtained from all of the participants. The serum was collected by centrifugation at 3000 r/min for 10 min at 4°C and stored in the refrigerator at -80°C for detection. DMEM medium, fetal bovine serum and horse serum were purchased from Sigma Company in the United States (MA, USA). IL-18 (SP10189), IL-1 β (SP10180), IL-6 (SP10234) and TNF-α (SP10205) ELISA kits are purchased from Wuhan Saipai Biotechnology Co., Ltd (Wuhan, Chi-

an). The LDH test kit was purchased from Nanjing Jiancheng Bioengineering Research Institute (A020-2-2, Nanjing, China). Reverse transcription kits, Lipofectamine 2000 and TRIzol reagents were purchased from Invitrogen Company in the United States (MA, USA). SYBR Green Mix was purchased from TaKaRa Company in Japan (Tokyo, Japan). Biotin-labeled circ_0013613 probe was purchased from Shenggong Bioengineering (Shanghai) Co., Ltd (Shanghai, China). CircCCS WT, circCCS MUT, circCCS siRNA and siRNA control were constructed by Shanghai Albus Biotechnology Co., Ltd (Shanghai, China). miR-370-3p mimic, miR-370-3p inhibitor and their corresponding negative controls were purchased from Guangzhou Ruibo Co., Ltd (Guangzhou, China). miR-370-3p mimic, miR-370-3p inhibitor and their corresponding negative controls were purchased from Guangzhou Ruibo Co., Ltd (Guangzhou, China). GSDMD-N (69469), NLRP3 (13158), ASC (67824) and GAPDH (5174) antibodies are purchased from Cell Signaling Technology Company in the United States (MA, USA). The double luciferase detection kit was purchased from Promega Company in the United States (CA, USA). BCA protein quantitative kit is purchased from Thermo Company in the United States (MA, USA).

Cultivate and identification of primary spinal cord neurons

Spinal cord tissue isolated from pregnant mice was cut into small pieces according to references (Lan W *et al.*, 2021) and digested using 0.125% trypsin for 25 min. The cells density was 6.0×10^5 /mL and inoculated with 10% FBS on the petri dish of DMEM medium with 10% horse serum. After being cultured in a 5% CO₂ incubator at 37°C for 6 h, the medium was replaced with a serum-free medium containing 1% glutamine, 2% B27, 1% N₂ and 96% Neurobasal. After 7-9 days of culture, high purity primary spinal cord neurons were obtained by observing the number of tubulin β -positive cells under a microscope.

Construction of SCI cell model, experimental grouping and cell transfection

SCI cell model was constructed by stimulating primary spinal myeloid neurons with 100 ng/mL LPS according to the literature (Li *et al.*, 2021). The experiment was divided into 1) Control group: no treatment was done; 2) LPS group: treated with 100 ng/mL LPS for 24 h; 3) NC inhibitor group: negative control transfected with miR-370-3p inhibitor; 4) NC mimic group: negative control was transfected with miR-370-3p mimic; 5) Inhibitor group: transfected miR-370-3p inhibitor; 6) Mimic group: transfected miR-370-3p mimic; 7) LPS+ Si-circ_0013613 + NC inhibitor group: 100 ng/mL LPS was added to si-circ_0013613 and miR-370-3p inhibitor negative irradiation after 24 h co-transfection for 24 h; 8) LPS+ Si-circ_0013613 +inhibitor group: After co-transfection of Si-circ_0013613 and miR-370-3p inhibitor negative control group, LPS treatment was added; 9) oe-nc group: transfection of empty plasmid; 10) oe-*CASP1* group: transfection of *CASP1* overexpression vector plasmid; 11) LPS+mimic+oe-nc group: co-transfection of miR-370-3p mimic and empty plasmid was given LPS treatment, 14) LPS+mimic+oe-*CASP1* group: co-transfection of miR-370-3p mimic and *CASP1* overexpression vector plasmid was co-transfected with LPS treatment.

The transfection method was carried out according to the Lipofectamine 2000 instructions for 24 h.

RT-qPCR detection

After collecting the serum or cells to be detected, the total RNA was extracted by Trizol method. The purity of RNA was detected by ultraviolet spectrophotometer. After reverse transcription, cDNA was synthesized, and then PCR reaction was carried out with SYBR Green Premix Ex Taq: The 20 μ L reaction system consisted of 2 μ L cDNA, 10 μ L TB Green Premix Ex Taq, 1 μ L forward and backward primers and 6 μ L ddH₂O. The 40 cyclic reaction conditions are: 94°C 30 s, 94°C 5 s, 60°C 30 s. circ_0013613 was calculated by 2^{- $\Delta\Delta C_t$} method (*GAPDH* as internal parameter). Expression levels of miR-370-3p (with U6 as internal reference) and *CASP1* (with *GAPDH* as internal reference). Primers for circ_0013613, miR-370-3p and *CASP1* were provided by Shanghai Shenggong Biological Co., LTD.

MTT detection

The cells were inoculated 100 μ L (density: 1×10^7 /mL) in each well into 96-well plates. Cells were conventionally cultured in 37°C, 5% CO₂ incubator. 10 μ L MTT was added and incubated at 37°C for 4 h. Next, they were incubated at room temperature for 10 min with 150 μ L dimethyl sulfoxide solution. Determination of optical density of 490 nm was done with the use of an enzyme labeling instrument. The survival rate of control cells was 100%. The ratio of experimental treatment group to its group represents the cell viability of this group.

LDH activity detection

The culture medium of the cells to be detected in each group was collected, and the LDH activity of the cells was detected using LDH detection kit according to the instructions.

ELISA detection

After collecting the cells to be detected in each group, the supernatant was collected by trypsin digestion and centrifugation. The contents of IL-18, IL-1 β , IL-6 and TNF- α were detected with specific ELISA kits according to the instructions.

Western blot detection

After collecting the cells to be detected in each group, cell lysis solution was added and placed on ice for full lysis. Then, protein concentration was quantified by BCA method. The sample size of 50 μ g per well was transferred onto membrane after SDS-PAGE electrophoresis. Next, the PVDF membrane was sealed with 5% skim milk powder for 2 h and incubated with the first antibody (GSDMD-N, 1:1000; NLRP3, 1:600; ASC, 1:800; GAPDH, 1:2500) overnight at 4°C. After being washed by TBST 3 times, the secondary antibody diluent (HRP labeled secondary antibody diluted according to 1/5 000) was incubated at room temperature for 2 h. ECL was used to develop color and Bio-Rad was used to take pictures. GAPDH was set as a reference to observe the grayscale of the target protein.

Flow cytometry detection

The cells were collected, washed twice with PBS solution, and then added to 100 μ L Annexin V Binding Buffer suspension cells. Then, 5 μ L Annexin V-FITC

and 5 μ L PI were added. After being mixed, cells were incubated for 15 min in the dark. After the 400 μ L Annexin V Binding Buffer was added, flow cytometry was performed within 60 min.

Double luciferase reporter gene assay

Circular RNA Interactome (<https://circinteractome.nia.nih.gov/index.html>), TargetScan 7.2 (http://www.targetscan.org/vert_72/) and miRcode data libraries were used to analyze the complementary binding sites between miR-370-3p and circ_0013613/*CASP1*, circ_0013613/*CASP1* containing miR-370-3p binding sites were used to construct wild-type double luciferase reporter gene carrier, labeled WT. The mutated vector constructed by the sequence of circ_0013613 containing miR-370-3p binding site and *CASP1* site-directed mutation was used as MUT. Wt and MUT were co-transfected with miR-370-3p mimics (mimics) and negative control (NC mimics) for 48 h. To detect the luciferase activity of cells, refer to the double luciferase reporter gene detection kit for specific steps.

RNA Pull down experiment

Trizol reagent was added to 100 μ g circ_0013613 or *CASP1* overexpression cells to extract the total RNA. After washing the streptavidin magnetic beads, 200 pmol biotin labeled miR-370-3p mimic was added. After setting for 5 min at room temperature, shake it upside down. Next, it was added to the extracted total RNA and incubated for 30 min at room temperature. After the elution buffer was added, the pulled RNA complex was collected in the magnetic field. The expression of circ_0013613 or *CASP1* was detected by RT-qPCR.

RNase R and actinomycin D test

After the total RNA of circ_0013613 overexpression cells was extracted, 5 mg and 3 U/mg RNase R were incubated at 37°C for 15 min. circ_0013613 expression was detected by RT-qPCR. Nerve cells were treated with 2 g/L actinomycin D for 0, 4, 8, 12, 24 h. The total RNA was extracted and the expression of circular and linear in circ_0013613 was detected by RT-qPCR.

Statistical analysis

SPSS26.0 software was used to analyze the experimental data. Data results were calculated as means \pm standard deviation ($\bar{x} \pm s$). Single factor variance is used to compare multi-group differences. *T*-test corrected by Bonferroni was used for pairwise comparison of data between groups. The difference was accepted as statistically significant at $P < 0.05$.

RESULTS

circ_0013613 expression increased in SCI

RT-qPCR showed that compared with the control group, the expression of circ_0003801, circ_0014620, circ_0013613 and circ_0007259 was significantly up-regulated in LPS-induced neuronal cells, and circ_0013613 had the highest expression ($P < 0.001$, Fig. 1A). Meanwhile, circ_0013613 was also found to be highly expressed in peripheral blood samples of

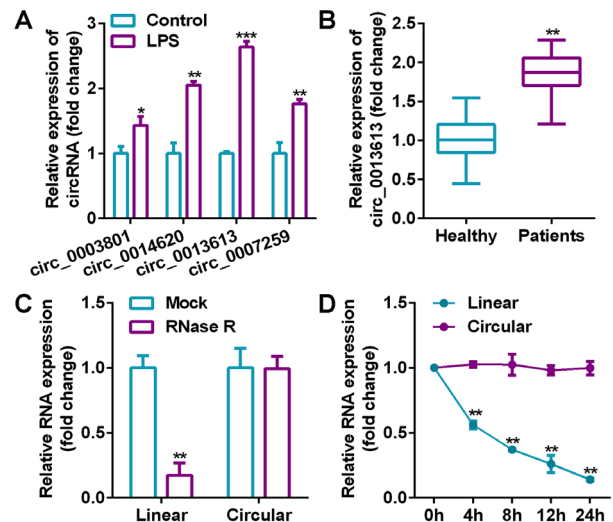


Figure 1. circ_0013613 expression in SCI cell model and patients.

(A) The expression of circ_0013613 was the highest in SCI cell model, compared with Control, $*P < 0.05$, $**P < 0.01$, $***P < 0.001$; (B) The expression of circ_0013613 was the highest in SCI cell model, compared with Control, $*P < 0.05$, $**P < 0.01$, $***P < 0.001$; (C) Line RNase R is processed to confirm the closed-loop structure of circ_0013613, compared with Mock, $**P < 0.01$; (D) Actinomycin D analysis to evaluate the stability of circ_0013613 closed-loop structure, compared with Linear, $**P < 0.01$.

40 patients with spinal cord injury (Fig. 1B). The expression of circ_0013613 was not affected by RNase R digestion. The abundance of linear RNA decreased significantly. The results showed that the closed-loop structure circ_0013613 was not easily degraded by exonuclease (Fig. 1C). In addition, actinomycin D analysis showed that circ_0013613 was more stable than linear transcription in nerve cells (Fig. 1D).

circ_0013613 down-regulation promotes SCI recovery by alleviating pyroptosis of nerve cells

RT-QPCR results showed that compared with Si-NC, the expression of circ_0013613 was down-regulated after transfection with Si-circ_0013613-1 and Si-circ_0013613-2 ($P < 0.05$), and si-circ_0013613-1 has a more significant effect ($P < 0.01$, Fig. 2A). The results of MTT assay showed that the down-regulation of circ_0013613 significantly weakened the inhibitory effect of LPS on the viability of nerve cells (Fig. 3B). Additionally, the LDH activity of nerve cells induced by LPS was significantly higher than that of control ($P < 0.01$). However, the down-regulation of circ_0013613 could attenuate the effect of LPS on the activity of LDH in nerve cells ($P < 0.01$, Fig. 3C). The contents of IL-18, IL-1 β , IL-6 and TNF- α in the supernatant of nerve cells treated with LPS were significantly higher than those of control. However, the above-mentioned effects of LPS on nerve cells were significantly weakened after transfection with Si-circ_0013613 ($P < 0.01$, Fig. 3D–G). The protein expression of pyroptosis biomarkers (such as GSDMD-N, NLRP3, and ASC) was decreased by circ_0013613 knockdown (Fig. 3H). The pyroptosis rates of neuronal cells were significantly decreased after transfection of Si-circ_0013613 ($P < 0.01$, Fig. 3H–I).

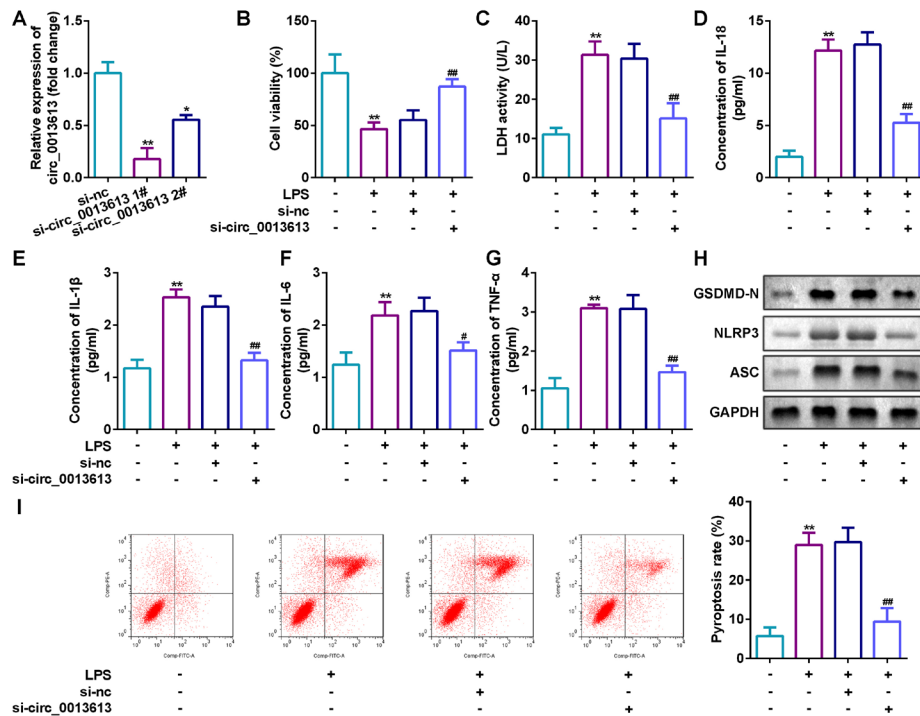


Figure 2. The targeting relationship between circ_0013613 and miR-370-3p and the expression of miR-370-3p in SCI cell model and patients.

(A) binding site of circ_0013613 to miR-370-3p, (B) luciferase activity, compared with NC mimic, $^{**}P<0.01$; (B) RNA pull-down results, compared with biotin-NC, $^{**}P<0.01$; (D) The regulatory effect of circ_0013613 on miR-370-3p, compared with si-NC, $^{**}P<0.01$; (E) miR-370-3p was low expressed in SCI cell model, compared with Control, $^{**}P<0.01$; (F) low expression of miR-370-3p in plasma of SCI patients, compared with Healthy, $^{**}P<0.01$

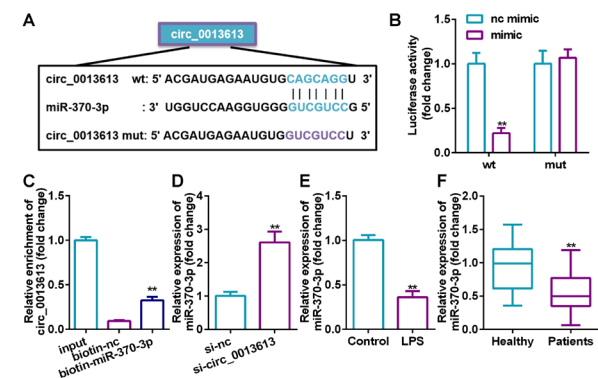


Figure 3. circ_0013613 down-regulation promotes SCI recovery by alleviating pyroptosis and inflammatory injury of nerve cells.

(A) RT-QPCR confirmed the down-regulation effect of circ_0013613: compared with si-NC, $^{*}P<0.05$, $^{**}P<0.01$; (B) MTT assay for cell viability; (C) LDH activity test results; (D–G) ELISA method was used to detect the content of cytokines in cell supernatant; Compared with Control, $^{**}P<0.01$; Compared with LPS+ si-NC, $^{*}P<0.05$, $^{**}P<0.01$; (H) Western blot analysis of GSDMD-N, NLRP3 and ASC protein expression; (I) The results of cytokine detection by flow cytometry were compared with Control, $^{**}P<0.01$; Compared with LPS+ si-NC, $^{**}P<0.01$.

miR-370-3p is the target gene of circ_0013613 and has low expression after SCI

It was predicted by Circular RNA Interactome that there were complementary binding sites between circ_0013613 and miR-370-3p (Fig. 3A). Dual-luciferase reporter gene assay confirmed that miR-370-3p mimics reduced luciferase activity of circ_0013613-WT (Fig. 3B). circ_0013613 was highly enriched in the biotin-miR-370-3p group compared with the Biotin-NC

group ($P<0.01$, Fig. 3C). In addition, transfection of Si-circ_0013613 significantly induced the upregulation of miR-370-3p (Fig. 3D). Meanwhile, miR-370-3p expression was significantly decreased in SCI cell model and patient plasma (Fig. 3E–F).

miR-370-3p low expression can reverse the promoting effect of circ_0013613 downregulation on SCI recovery

Compared with the corresponding control, nc inhibitor and NC mimic, transfection with miR-370-3p inhibitor and mimic successfully induced low expression and overexpression of miR-370-3p in nerve cells (Fig. 4A). We further verified whether circ_0013613 plays a role in promoting SCI recovery by directly regulating miR-370-3p expression. Compared with LPS+ Si-circ_0013613 + NC inhibitor, cell viability of LPS+ Si-circ_0013613 + inhibitor group was decreased. The contents of IL-18, IL-1β, IL-6 and TNF-α in cell supernatant, as well as the gray level of protein expression of GSDMD-N, NLRP3 and ASC, LDH activity and pyroptosis rates were significantly increased ($P<0.01$, Fig. 4B–I).

CASP1 is the target gene of miR-370-3p

It was predicted by TargetScan that there were complementary binding sites between CASP1 and miR-370-3p ($P<0.01$, Fig. 5A). Dual luciferase reporter gene assay, RNA pull-down assay and RT-QPCR detection were found. miR-370-3p mimics can reduce luciferase activity and CASP1 mRNA expression of CASP1-WT, and CASP1 was highly enriched in the biotin-miR-370-3p group ($P<0.01$, Fig. 5B and C). Moreover, miR-370-3p overexpression significantly decreased the expression of CASP1 ($P<0.01$, Fig. 5D). In addition, RT-QPCR detection showed that miR-

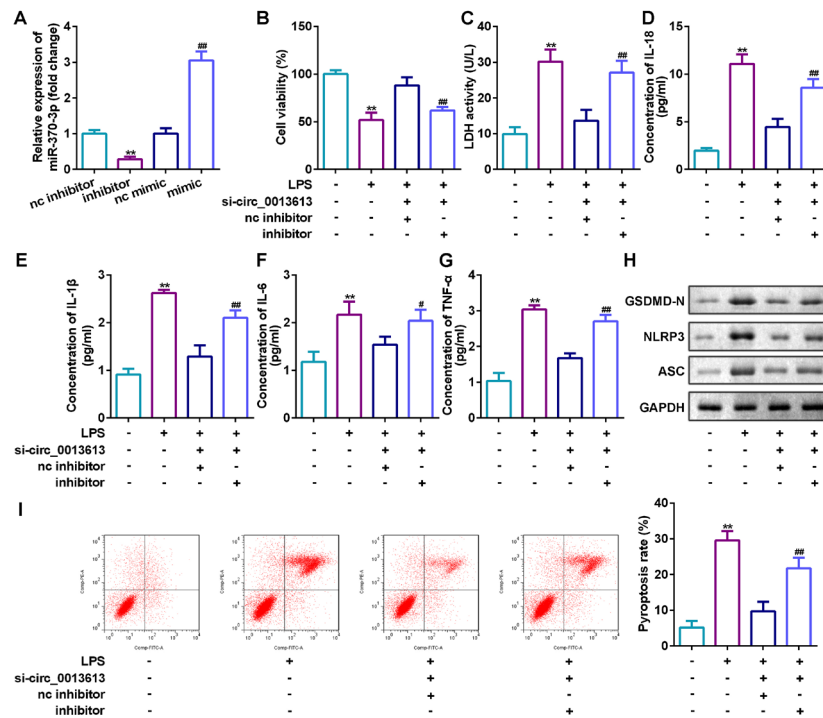


Figure 4. Low expression of miR-370-3p attenuated the promoting effect of circ_0013613 downregulation on SCI recovery.

(A) RT-QPCR confirmed the effect of miR-370-3p low expression and overexpression: compared with NC inhibitor, $^{**}P<0.01$; Compared with NC mimic, $^{##}P<0.01$; (B) MTT assay for cell viability, (C) LDH activity detection results, (D–G) ELISA detection results of cytokine death pathway related genes in cell supernatant: Compared with Control or LPS+ Si-circ_0013613 + NC inhibitor, $^{**}P<0.01$; Compared with LPS+ Si-circ_0013613 + NC inhibitor, $^{*}P<0.05$, $^{##}P<0.01$; (H) Western blot analysis of GSDMD-N, NLRP3 and ASC protein expression; (I) pyroptosis results of cells detected by flow cytometry compared with Control or LPS+ Si-circ_0013613 + NC inhibitor, $^{**}P<0.01$; Compared with LPS+ Si-circ_0013613 + NC inhibitor, $^{##}P<0.01$.

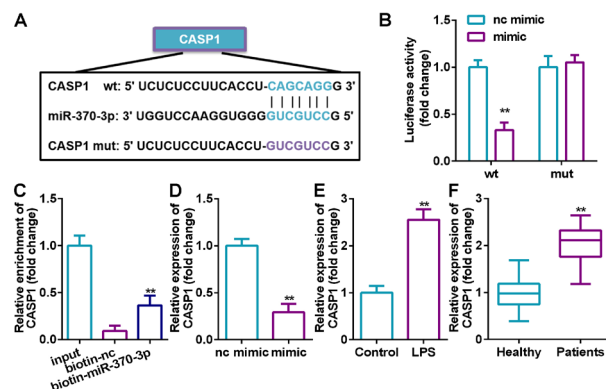


Figure 5. The targeting relationship between miR-370-3p and CASP1 and the expression of CASP1 in SCI cell model and patients.

(A) Binding site of CASP1 to miR-370-3p; (B) Luciferase activity, compared with NC mimic, $^{**}P<0.01$; (C) RNA pull-down results, compared with biotin-NC, $^{**}P<0.01$; (D) miR-370-3p regulation of CASP1, compared with NC mimic, $^{**}P<0.01$; (E) CASP1 was highly expressed in SCI cell model, compared with Control, $^{**}P<0.01$; (F) CASP1 was highly expressed in plasma of SCI patients, compared with Healthy, $^{**}P<0.01$.

370-3p was highly expressed in SCI cell model and SCI patients ($P<0.01$, Fig. 5E–F).

Up-regulation of CASP1 induced the degradation of neuronal cells

As shown in Fig. 6A, the expression of CASP1 was significantly increased in CASP1 OE group ($P<0.01$),

suggesting that cells were successfully transfected. Over-expression of CASP1 suppressed the cell viability of neuronal cells ($P<0.01$, Fig. 6B), and promoted cytotoxicity ($P<0.01$, Fig. 6C), inflammatory response ($P<0.01$, Fig. 6D–G) and pyroptosis ($P<0.01$, Fig. 6H and I).

DISCUSSION

Previous studies have shown that there are abnormal circRNAs in SCI. Restoration of its expression can inhibit secondary injury and promote functional recovery after SCI, which is expected to be a potential molecular marker for the diagnosis and treatment of SCI (Dai *et al.*, 2019). In this study, the expression of circ_0003801, circ_0014620, circ_0013613 and circ_0007259 was up-regulated, especially that of circ_0013613. Therefore, this study focuses on circ_0013613. Scorched cell death is one of the important ways of programmed cell death. Involving the classic CASP1-mediated inflammasome pathway and/or the non-classical caspase-11/4/5 pathway, inhibition of pyroptosis may be a promising treatment for SCI (Chalfouh *et al.*, 2020; Dai *et al.*, 2019). In this study, it was found that circ_0013613 had good stability in the nerve cells. Knocking down the expression of circ_0013613 can improve the activity of nerve cells by inhibiting the expression of IL-18, IL-1β, IL-6, TNF-α and related proteins GSDMD-N, NLRP3, ASC and scorch death to reduce SCI damage and promote SCI recovery. The results showed that circ_0013613 down-regulation may promote SCI recovery by alleviating pyroptosis of nerve cells. The results suggest that circ_0013613 may be a potential therapeutic target for SCI.

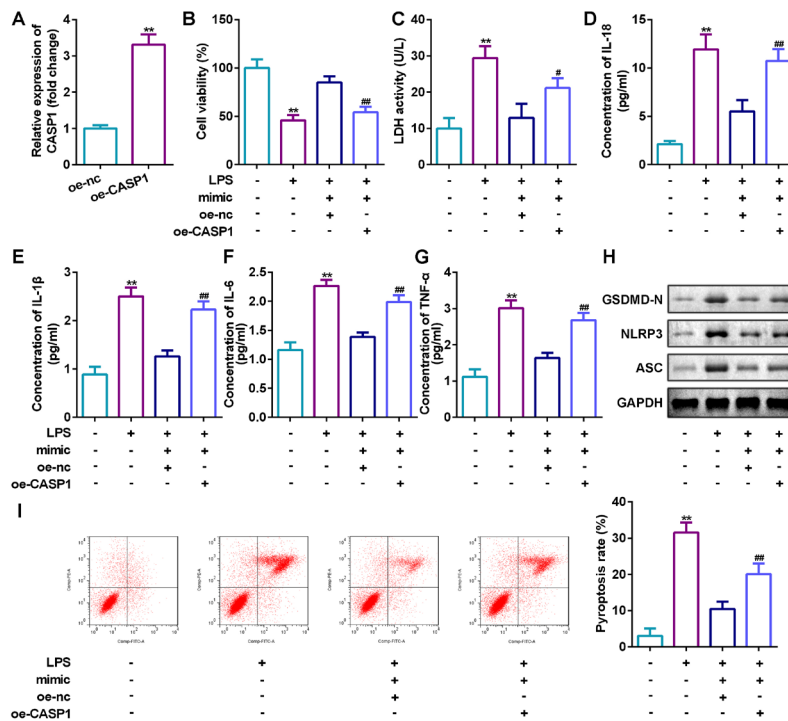


Figure 6. Up-regulation of *CASP1* can reverse the promoting effect of Mir-370-3p overexpression on SCI recovery.

(A) RT-QPCR confirmed the overexpression of *CASP1*: ** $P<0.01$ compared with OE-NC; (B) Cell viability was detected by MTT assay; (C) LDH activity detection results; (D–G) ELISA method was used to detect the content of cytokine death pathway related genes in cell supernatant; Compared with Control or LPS+ MIMIC + OE-NC, ** $P<0.01$; compared with LPS+ MIMIC + OE-NC, * $P<0.05$, ** $P<0.01$; (H) Western blot analysis of GSDMD-N, NLRP3 and ASC protein expression; (I) Results of cell pyroptosis detected by flow cytometry: Compared with Control or LPS+ MIMIC + OE-NC, ** $P<0.01$; compared with LPS+ MIMIC + OE-NC, ** $P<0.01$.

As is known to all, circRNAs are rich in specific binding sites with miRNAs. CircRNA is a new type of regulatory molecule that regulates the function of miRNA. The role of competitive endogenous RNA can be exerted by targeted adsorption of miRNA to relieve its inhibitory effect on target genes (Chen *et al.*, 2021). In this study, we used bioinformatics software to screen the circ_0013613 target gene. Mir-370-3p is a miRNA closely related to neurosystemic diseases and tissue damage. It has been reported that it can inhibit the occurrence and development of glioma by targeting β -catenin to regulate cell proliferation and cycle. It can reduce neuronal damage in rats with depression and play an important role in the protective effect of paclitaxel on acute renal injury induced by LPS (Mamun *et al.*, 2020; Shi *et al.*, 2021). In addition, in LPS-induced acute kidney injury, Mir-370-3p can be targeted by LNC-MALAT1 to play a positive role in the protection of paclitaxel against renal tissue injury (Du & Andrea, 2013). We found that Mir-370-3p is the target gene of circ_0013613, and its low expression can promote the recovery of nerve cell scoria inhibition SCI. This is because there are complementary binding sites between circ_0013613 and Mir-370-3p. Double luciferase reporter gene assay and RNA Pull down assay confirmed that circ_0013613 could competitively bind miR-370-3p. RT-qPCR confirmed that down-regulation of circ_0013613 could increase the expression of miR-370-3p. In addition, low expression of miR-370-3p could reverse the down-regulated effect of circ_0013613 on the recovery of SCI. This suggests that circ_0013613 may regulate cell pyroptosis by regulating Mir-370-3p and thus affect SCI recovery. Our results may provide new insights into the molecular regulation of circ_0013613 on the circRNA/miRNA network, thus regulating the progression of SCI.

In order to further explore the mechanism of Mir-370-3p in regulating SCI injury, we used bioinformatics software to predict its potential target genes. *CASP1* is a cysteine aspartate specific proteolytic enzyme that cleaves the N-terminal and C-terminal domains of the executive protein GSDMD. The activation of N-domain can promote the release of IL-1 β and IL-18, which play an important role in the process of inflammation and cell death (Peng *et al.*, 2016). The decrease in Caspase-1 activity causes a decrease in the amount of IL-1 β because caspase-1 activates pro-IL-1 β to IL-1 β (Malik & Kanne-ganti, 2017). Some studies have pointed out that inhibition of Caspase-1 can reduce the expression of IL-1 β and IL-18 after SCI, reduce the secondary injury after SCI, and may play a positive role in the repair of SCI (Nadaradjane *et al.*, 2018). We found that *CASP1* is the target gene of miR-370-3p. Its overexpression can promote the scorched death of nerve cells and inhibit the recovery of SCI. This is because we found that there are complementary binding sites between *CASP1* and miR-370-3p. At the same time, double luciferase reporter gene assay and RT-qPCR confirmed that miR-370-3p could target the regulation of *CASP1*. In addition, up-regulation of *CASP1* expression could reverse the promoting effect of miR-370-3p overexpression on SCI recovery. The results suggest that miR-370-3p can promote the recovery of SCI through targeted regulation of *CASP1*-mediated neuronal necrotic death.

In conclusion, circ_0013613 expression was increased in SCI. circ_0013613 sponged miR-370-3p promoted degradation of neurons by promoting *CASP1*-mediated inflammatory response and inflammation-induced pyroptosis. Circ_0013613/miR-370-3p/*CASP1* axis may be a therapeutic target for SCI.

REFERENCE

- Al Mamun A, Wu Y, Monalisa I, Jia C, Zhou K, Munir F, Xiao J (2020) Role of pyroptosis in spinal cord injury and its therapeutic implications. *J Adv Res* **28**: 97–109. <https://doi.org/10.1016/j.jare.2020.08.004>
- Chalfouh C, Guillou C, Hardouin J, Delarue Q, Li X, Duclos C, Schapman D, Marie JP, Cosette P, Guérout N (2020) The regenerative effect of trans-spinal magnetic stimulation after spinal cord injury: mechanisms and pathways underlying the effect. *Neurotherapeutics* **17**: 2069–2088. <https://doi.org/10.1007/s13311-020-00915-5>
- Chen J, Fu B, Bao J, Su R, Zhao H, Liu Z (2021) Novel circular RNA 2960 contributes to secondary damage of spinal cord injury by sponging miRNA-124. *J Comp Neurol* **529**: 1456–1464. <https://doi.org/10.1002/cne.25030>
- Dai W, Wang X, Teng H, Li C, Wang B, Wang J (2019) Celastrol inhibits microglial pyroptosis and attenuates inflammatory reaction in acute spinal cord injury rats. *Int Immunopharmacol* **66**: 215–223. <https://doi.org/10.1016/j.intimp.2018.11.029>
- Du Toit A (2013) RNA: Circular RNAs as miRNA sponges. *Nature Rev Mol Cell Biol* **14**: 195. <https://doi.org/10.1038/nrm3557>
- Hou WZ, Chen XL, Wu W, Hang CH (2017) MicroRNA-370-3p inhibits human vascular smooth muscle cell proliferation via targeting KDR/AKT signaling pathway in cerebral aneurysm. *Eur Rev Med Pharmacol Sci* **21**: 1080–1087. PMID: 28338184
- Lan W, Lin J, Liu W, Wang F, Xie Y (2021) Sulfiredoxin-1 protects spinal cord neurons against oxidative stress in the oxygen-glucose deprivation/reoxygenation model through the bax/cytochrome c/caspase 3 apoptosis pathway. *Neurosci Lett* **744**: 135615. <https://doi.org/10.1016/j.neulet.2020.135615>
- Li X, Qian Y, Tang K, Li Y, Tao R, Gong C, Huang L, Zou K, Liu L (2021) Inhibition of lncRNA H19/miR-370-3p pathway mitigates neuronal apoptosis in an in vitro model of spinal cord injury (SCI). *Transl Neurosci* **12**: 103–113. <https://doi.org/10.1515/tnsci-2021-0013>
- Li X, Yu Z, Zong W, Chen P, Li J, Wang M, Ding F, Xie M, Wang W, Luo X (2020) Deficiency of the microglial Hv1 proton channel attenuates neuronal pyroptosis and inhibits inflammatory reaction after spinal cord injury. *J Neuroinflammation* **17**: 263. <https://doi.org/10.1186/s12974-020-01942-x>
- Li Y, Zong J, Zhao C (2020) lncRNA CTBP1-AS2 promotes proliferation and migration of glioma by modulating miR-370-3p-Wnt/7a-mediated epithelial-mesenchymal transition. *Biochem Cell Biol* **98**: 661–668. <https://doi.org/10.1139/bcb-2020-0065>
- Lu Y, Yang J, Wang X, Ma Z, Li S, Liu Z, Fan X (2020) Research progress in use of traditional Chinese medicine for treatment of spinal cord injury. *Biomed Pharmacother* **127**: 110136. <https://doi.org/10.1016/j.biopha.2020.110136>
- Malik A, Kanneganti TD (2017) Inflammasome activation and assembly at a glance. *J Cell Sci* **130**: 3955–3963. <https://doi.org/10.1242/jcs.207365>
- Man SM, Karki R, Briard B, Burton A, Gingras S, Pelletier S, Kanneganti TD (2017) Differential roles of caspase-1 and caspase-11 in infection and inflammation. *Sci Rep* **7**: 45126. <https://doi.org/10.1038/srep45126>
- Nadaradjane A, Briand J, Bougras-Cartron G, Disdero V, Vallette FM, Frenel JS, Cartron PF (2018) miR-370-3p Is a therapeutic tool in anti-glioblastoma therapy but is not an intratumoral or cell-free circulating biomarker. *Mol Ther Nucleic Acids* **13**: 642–650. <https://doi.org/10.1016/j.omtn.2018.09.007>
- Peng P, Zhang B, Huang J, Xing C, Liu W, Sun C, Guo W, Yao S, Ruan W, Ning G, Kong X, Feng S (2020) Identification of a circRNA-miRNA-mRNA network to explore the effects of circRNAs on pathogenesis and treatment of spinal cord injury. *Life Sci* **257**: 118039. <https://doi.org/10.1016/j.lfs.2020.118039>
- Peng Z, Wu T, Li Y, Xu Z, Zhang S, Liu B, Chen Q, Tian D (2016) MicroRNA-370-3p inhibits human glioma cell proliferation and induces cell cycle arrest by directly targeting β -catenin. *Brain Res* **1644**: 53–61. <https://doi.org/10.1016/j.brainres.2016.04.066>
- Shi Z, Yuan S, Shi L, Li J, Ning G, Kong X, Feng S (2021) Programmed cell death in spinal cord injury pathogenesis and therapy. *Cell Prolif* **54**: e12992. <https://doi.org/10.1111/cpr.12992>
- Sun Q, Scott MJ (2016) Caspase-1 as a multifunctional inflammatory mediator: noncytokine maturation roles. *J Leukoc Biol* **100**: 961–967. <https://doi.org/10.1189/jlb.3MR0516-224R>
- Yao Y, Wang J, He T, Li H, Hu J, Zheng M, Ding Y, Chen YY, Shen Y, Wang LL, Zhu Y (2020) Microarray assay of circular RNAs reveals circRNA.7079 as a new anti-apoptotic molecule in spinal cord injury in mice. *Brain Res Bull* **164**: 157–171. <https://doi.org/10.1016/j.brainresbull.2020.08.004>
- Zhao C, Xing Z, Zhang C, Fan Y, Liu H (2021) Nanopharmaceutical-based regenerative medicine: Promising therapeutic strategy for spinal cord injury. *J Mater Chem B* **9**: 2367–2383. <https://doi.org/10.1039/d0tb02740e>

The cadherin protein CDH19 mediates cervical carcinoma progression by regulating AKT/NF- κ B signaling

Jia Yu, Xin Sun, Yani Yu and Xiaorong Cui✉

Department of Gynecology, Zibo Central Hospital, No. 54 Gongqingtuan West Road, Zibo 255036, Shandong, China

The cell adhesion protein cadherin 19 (CDH19) has been reported to be involved in various types of cancer, but its role in cervical carcinoma remains unknown. We collected and analyzed the patients' data using the GEPIA Kaplan-Meier plotter databases. CDH19 was overexpressed in cervical carcinoma cells to assess its effect on cell proliferation and activation of AKT and NF- κ B signaling pathways. A xenograft mouse model was established to study the function of CDH19 *in vivo*. We found that CDH19 expression was significantly downregulated in cervical carcinoma tissues compared to adjacent normal tissues. Patients with high expression of CDH19 had a significantly better overall survival rate than those with low CDH19 expression. CDH19 expression was negatively correlated with the expression of the proliferation marker Ki-67, and overexpression of CDH19 significantly inhibited cervical carcinoma cell proliferation. Furthermore, overexpression of CDH19 suppressed the activation of the AKT and NF- κ B signaling pathways, and CDH19-overexpressing cervical carcinoma tumors exhibited significantly slower growth *in vivo*. CDH19 plays an important role in cervical carcinoma by suppressing both cell proliferation and the activation of AKT and NF- κ B signaling pathways. Therefore, CDH19 may be a potential therapeutic target for cervical carcinoma.

Keywords: CDH19, cervical carcinoma, AKT, NF- κ B, nude mice

Received: 29 June, 2023; **revised:** 16 November, 2023; **accepted:** 17 November, 2023; **available on-line:** 05 December, 2023

✉ e-mail: CuiXiaorong1989@163.com

Abbreviations: AKT, Protein Kinase B; CCK-8, Cell Counting Kit-8; CDH19, Cadherin 19; CIN, Cervical Intraepithelial Neoplasia; GEPIA, Gene Expression Profiling Interactive Analysis; HPV, human papillomavirus; NF- κ B, Nuclear Factor kappa B

INTRODUCTION

Cervical carcinoma is a type of cancer that typically develops in the cervix of women, which is the lower part of the uterus that connects to the vagina. It is caused by the uncontrolled growth of abnormal cells in the cervix. These abnormal cells can spread to other parts of the body and invade nearby tissues and organs. Cervical cancer is one of the most common cancers in women worldwide, with more than 500 000 new cases and over 300 000 deaths reported annually. It is mostly diagnosed in women aged 35 to 44 years, but it can occur in women of any age (Kaur *et al.*, 2003; Lazo, 1999).

The main cause of cervical cancer is the human papillomavirus (HPV), which is sexually transmitted. Cervical cancer often develops slowly over many years, and the early stages of the disease may not cause any noticeable symptoms. However, as cancer progresses, symptoms

may include abnormal vaginal bleeding, unusual vaginal discharge, pain during sex, and pelvic pain. But cervical carcinoma can often be successfully treated if detected early (Petereit *et al.*, 1995). Current treatment options for cervical cancer may include surgery, radiation therapy, chemotherapy, or a combination of these approaches, depending on the stage and extent of cancer. However, these treatments might be physically taxing, so it is worthwhile to explore the mechanisms of cervical cancer development can help find new potential therapeutic targets.

Cadherin 19 (CDH19) is a type II classical cadherin protein, which is a cell adhesion molecule that plays an important role in the formation and maintenance of cell-cell contacts. CDH19 protein is expressed in various tissues throughout the body, including the brain, lungs, heart, and kidneys. It is believed to play a crucial role in the development of the nervous system and in the regulation of cell growth and differentiation (Woods *et al.*, 2021). Mutations or alterations in the CDH19 gene have been associated with several different diseases and conditions (Avila & Southard-Smith, 2022; Niu *et al.*, 2008; Tervasmäki *et al.*, 2014). A genetic variation in CDH19 has been linked to a rare neurodevelopmental disorder known as CDH19-related X-linked intellectual disability syndrome. This syndrome is characterized by intellectual disability, seizures, delayed speech and language development, and other neurological and developmental abnormalities. Additionally, CDH19 has been implicated in the developing and progression of certain types of cancer. For example, several studies have reported that CDH19 expression was decreased in cancers including colorectal cancer, gastric cancer, and ovarian cancer. In these cases, reduced CDH19 expression has been associated with poorer outcomes, such as increased tumor invasiveness and poorer survival rates (Blons *et al.*, 2002; Gao & Yang, 2022; Koski *et al.*, 2009; Niu *et al.*, 2008). On the other hand, other studies have reported that CDH19 expression was increased in cancers such as esophageal squamous cell carcinoma and non-small cell lung cancer (Bailis *et al.*, 2019; H. Wang *et al.*, 2021). Overexpression of CDH19 may contribute to cancer growth and metastasis by promoting cell proliferation, invasion, and migration. In these cases, increased CDH19 expression has been associated with more aggressive tumor behavior and poorer prognosis. Overall, the relationship between CDH19 and cancer appears to be complex and may vary depending on the specific type of cancer and other factors. Further research is needed to fully understand the role of CDH19 in cancer development and progression.

Furthermore, there is limited research on the relationship between CDH19 and cervical carcinoma, but some studies have suggested that the expression of CDH19

may be altered in cervical cancer. One study found that CDH19 expression was significantly decreased in cervical cancer tissues compared to normal cervical tissues. Another study reported that CDH19 was upregulated in a group of cervical cancer patients compared to healthy controls (Gu *et al.*, 2021). However, more research is needed to fully understand the role of CDH19 on cervical carcinoma.

The AKT (Protein Kinase B)/NF- κ B (Nuclear Factor kappa B) signaling pathway is a crucial pathway involved in cell survival, proliferation, and inflammation. Abnormal activation of this pathway has been implicated in various diseases, including cancer. In cervical carcinoma, studies have shown that the AKT/NF- κ B pathway is frequently activated, which leads to the proliferation and survival of cancer cells (Vara *et al.*, 2004). Specifically, activation of the AKT pathway promotes cell survival by inhibiting apoptosis and promoting cell cycle progression, while activation of the NF- κ B pathway promotes inflammation and cell proliferation. Moreover, the HPV, which is the primary cause of cervical carcinoma, has been shown to activate the AKT/NF- κ B pathway (Bossler *et al.*, 2019). HPV-mediated activation of AKT/NF- κ B signaling is thought to contribute to the development and progression of cervical carcinoma by promoting cell survival, proliferation, and inflammation. Overall, the AKT/NF- κ B signaling pathway plays a critical role in the development and progression of cervical carcinoma, and targeting this pathway may offer a promising approach for the treatment of this disease. Therefore, our study aimed to explore CDH19's functions and potential therapeutic applications in cervical cancer through AKT/NF- κ B signaling pathway.

MATERIALS AND METHODS

GEPIA database and analysis

The expression of CDH19 in cervical carcinoma was collected and analyzed using GEPIA (Gene Expression Profiling Interactive Analysis) database (<http://gepia2.cancer-pku.cn>). Correlation analysis of gene expression was performed using the Correlation Analysis tool available in the cancer public database GEPIA (<http://gepia2.cancer-pku.cn/#correlation>).

qPCR

Total RNA was extracted from cells or tissues using a total RNA kit (Invitrogen), followed by the examination of the RNA purity and concentration. The RNA was then reverse transcribed into cDNA using Moloney Murine Leukemia Virus Reverse Transcriptase (BioTeke, China). RT-PCR analysis was performed using the SYBR-Green method. GAPDH was used as an endogenous control for normalization. The relative expression levels of RNAs were calculated using the $2^{-\Delta\Delta CT}$ method. Details of the gene primers used in the study are provided below.

CDH19 F: 5'-CATTGTAGGCGTGGTGT-3';
CDH19 R: 5'-GTGGCTGTAATACTTAGGTTGT-3';
GAPDH F: 5'-GGT ATCGTGGAAGGACTCATGAC-3';
GAPDH R: 5'-GGT ATCGTGGAAGGACTCATGAC-3'.

KM Plotter database analysis

We analyzed the overall survival of cervical carcinoma patients with high and low levels of CDH19 expression using KM (Kaplan-Meier) Plotter database online

(<http://kmplot.com>) as previously described (Nagy *et al.*, 2021).

Cell culture

The CaSki and C-33A cell lines were purchased from ATCC and cultured as previously described (Liu *et al.*, 2021). Briefly, the frozen cells were thawed rapidly in a water bath at 37°C and transferred immediately to a culture hood where the vial contents were quickly transferred to a sterile tube containing pre-warmed growth medium. Using a hemocytometer or an automated cell counter, the cells were counted to determine the density. Plate or flask choice depended on the experimental requirements and growth characteristics. For routine maintenance, a T25 flask or a 6-well plate was suitable. The cells were seeded and placed in a 37°C incubator with 5% CO₂, creating a controlled environment mimicking physiological conditions. The cells were regularly checked under a microscope to monitor growth and passaged when they reached 70–80% confluency. To this end, the cells were detached using trypsin-EDTA, next neutralized with the growth medium, and the desired number of cells was transferred to new plates.

Western blot

Protein was extracted from cells or tissues using RIPA lysis buffer, and protein concentration was determined in the lysate. Western blot was performed as previously described (Liu *et al.*, 2012). Briefly, the same amount of protein from different treatment groups were loaded into SDS-PAGE gels, subjected to electrophoresis, and then transferred into PVDF membrane. Then membranes were blocked using 5% milk, then incubated with primary antibody overnight. The primary antibodies against CDH19, p-AKT, AKT, GAPDH were purchased from Abcam. GAPDH was used as a loading control.

Cell Counting Kit-8 Assay

Cell proliferation was evaluated using the Cell Counting Kit-8 (CCK-8) assay (Boster, China), following the manufacturer's instructions. In brief, 3×10^3 cells in 100 μ L medium were seeded into each well of a 96-well plate, while wells without cells were used as blank controls. Cells in each well were incubated daily with 10 μ L of CCK-8 solution for 2 hours at 37°C for 4 consecutive days. Subsequently, absorbance was measured at a wavelength of 450 nm using a microplate reader. The intensity of absorbance is positively correlated with the number of surviving cells (Hou *et al.*, 2022).

Construction and virus packaging of PLVX-CDH19

The full-length human CDH19 gene was amplified via PCR and then inserted into the pLVX-AcGFP lentiviral vector from Thermo Fisher Scientific. Lentiviral particles were produced using a specific protocol that has been previously described (Wang *et al.*, 2017). Cells were transfected with PLVX-NC (negative control) or PLVX-CDH19 for 48 hours.

Nude mouse xenograft model

After transfecting with PLVX-CDH19 for 48 hours, 2×10^6 tumor cells were suspended in 0.2 ml serum-free DMEM and injected subcutaneously into the left flank of each 4–6-week female BALB/c nude mouse. The same number of PLVX-NC-transfected cells was injected into the right flank of each mouse as control. Tu-

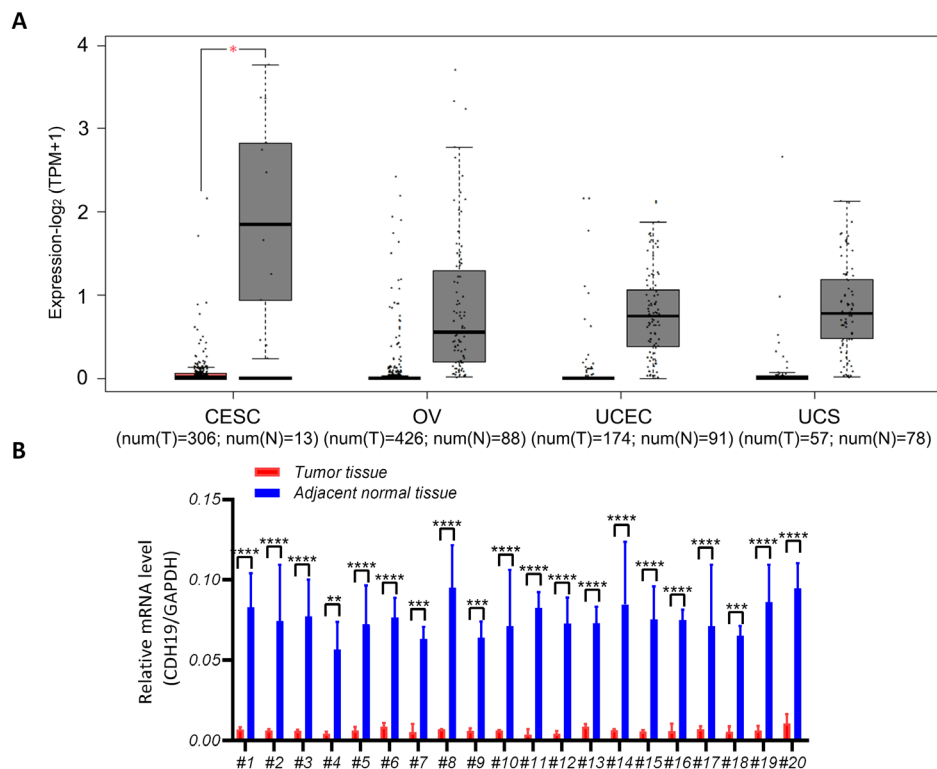


Figure 1. CDH19 is downregulated in cervical carcinoma.

(A) The expression of CDH19 in gynecological cancer was analyzed by GEPIA online tool that matches TCGA and GTEx tumor and control transcriptomic data (<http://gepia2.cancer-pku.cn>). CESC, cervical squamous cell carcinoma and endocervical adenocarcinoma; OV, ovarian serous cystadenocarcinoma; UCEC, uterine corpus endometrial carcinoma; UCS, uterine carcinosarcoma. * $p < 0.01$. (B) Twenty pairs of cervical carcinoma tumor tissues and paracancerous normal tissues were collected for QPCR analysis against CDH19 and GAPDH. ** $p < 0.01$, *** $p < 0.001$, **** $p < 0.0001$.

mor size was recorded every three days. On day 21, the tumors were collected, weighted, and lysed for further analysis as previously described (Liu *et al.*, 2020; S. Wang *et al.*, 2021). The animal-related protocols were approved by the ethics committee of Zibo Central Hospital. This study was performed in strict accordance with the NIH guidelines for the care and use of laboratory animals (NIH Publication No. 85-23 Rev. 1985).

Statistical analysis

The data was presented as means \pm standard deviation, and analyzed with Student's *t*-test, or two-way ANOVA analysis with a post hoc test using GraphPad software. The result was considered statistically significant when the *p*-values were less than 0.05.

RESULTS

CDH19 is downregulated in cervical carcinoma

We used the public cancer database GEPIA to investigate the expression levels of CDH19 in gynecological tumors, including cervical squamous cell carcinoma and endocervical adenocarcinoma (CESC); ovarian serous cystadenocarcinoma (OV); uterine corpus endometrial carcinoma (UCEC) and uterine carcinosarcoma (UCS) and matched normal tissues. The overall expression of CDH19 was low in gynecological tumor tissues, with significant downregulation observed in cervical carcinoma tissues compared to matched normal tissues ($p < 0.01$) (Fig. 1A). To confirm these findings, we collected 20 pairs of cervical carcinoma and adjacent non-cancerous

tissues and examined the expression of CDH19. We observed significant downregulation of CDH19 in all 20 cervical carcinoma tumor tissues (Fig. 1B). These results suggest that CDH19 may play a role in the development or progression of cervical carcinoma and could potentially serve as a diagnostic or therapeutic target for this disease.

CDH19 predicts a positive index for cervical carcinoma

Next, we used the public cancer database Kaplan-Meier plotter to perform an online analysis of the overall survival of cervical carcinoma patients with diverse levels of CDH19 expression. As shown in Fig. 2, patients with high CDH19 expression had significantly higher overall

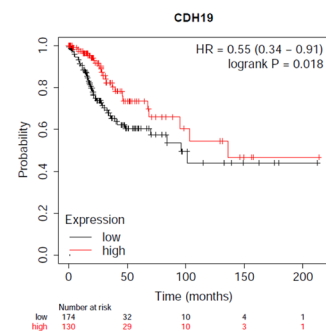


Figure 2. CDH19 predicts a positive index for cervical carcinoma. The overall survival of cervical squamous cell carcinoma with low or high CDH19 was analyzed by Kaplan-Meier Plotter online based on pan-cancer RNA-seq data (<http://kmplot.com/>).

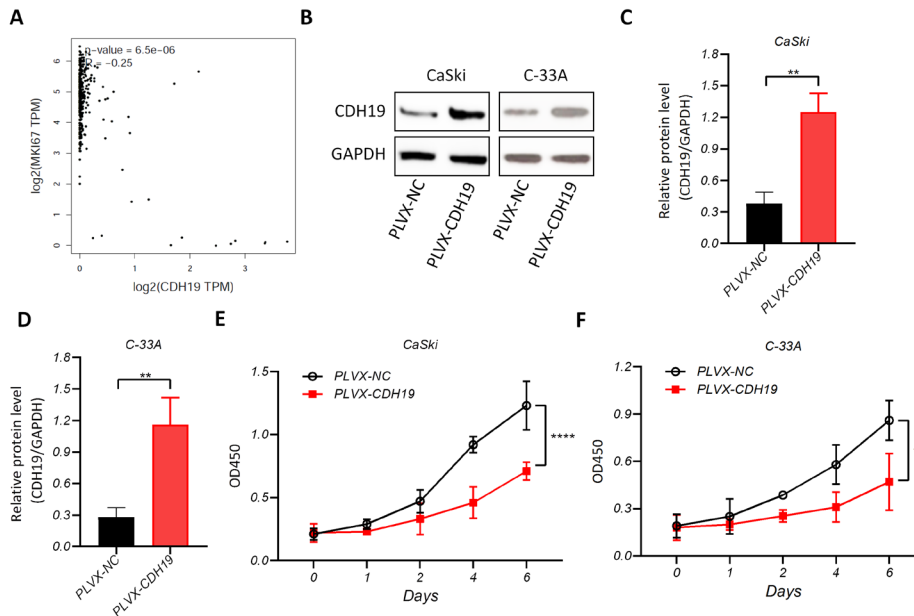


Figure 3. CDH19 overexpression inhibits cervical carcinoma cell proliferation.

(A) The correlation analysis between Ki-67 (MKI67) and CDH19 in cervical carcinoma (<http://gepia2.cancer-pku.cn>). (B–D) CaSki and C-33A cells infected with PLVX-NC or PLVX-CDH19-derived lentivirus were lysed for immunoblotting against CDH19 and GAPDH (B), and the optical density of the blots was analyzed (C & D). E & F. CaSki (E) and C-33A (F) cells infected with PLVX-NC or PLVX-CDH19-derived lentivirus were prepared for CCK-8 assay at indicated time. ** $p < 0.01$, *** $p < 0.001$, **** $p < 0.0001$.

survival rates than those with low CDH19 expression. These findings suggest that CDH19 expression may be a prognostic biomarker for cervical carcinoma and could potentially be used to stratify patients for more personalized treatment strategies.

CDH19 overexpression inhibits cervical carcinoma cell proliferation

To investigate the potential association between CDH19 and cervical carcinoma cell proliferation, we used the public cancer database GEPIA to analyze the correlation between CDH19 and the proliferation marker Ki-67 in cervical carcinoma tissues. We found a significant negative correlation between CDH19 expression

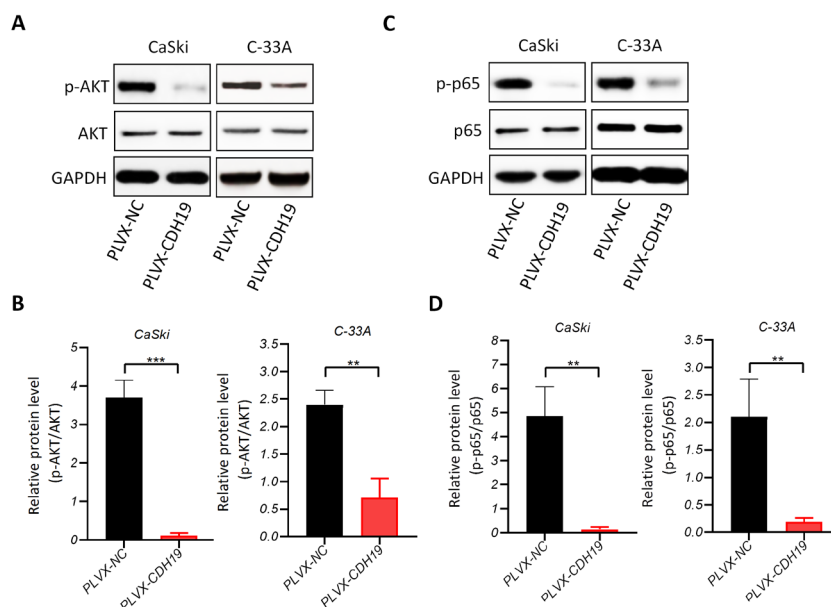


Figure 4. CDH19 overexpression inhibits AKT and NF-κB signaling in cervical carcinoma cells.

(A & B) CaSki and C-33A cells were infected with PLVX-NC or PLVX-CDH19-derived lentivirus for 73 hours and then cells were lysed for immunoblotting against p-AKT and AKT (A). GAPDH was used as a loading control. The optical density for the blots was also analyzed (B). C & D. The above cells were also lysed for immunoblotting against p-p65 and NF-κB p65 (C), and the optical density of the immunoblotting was also analyzed (D). ** $p < 0.01$, *** $p < 0.001$, **** $p < 0.0001$.

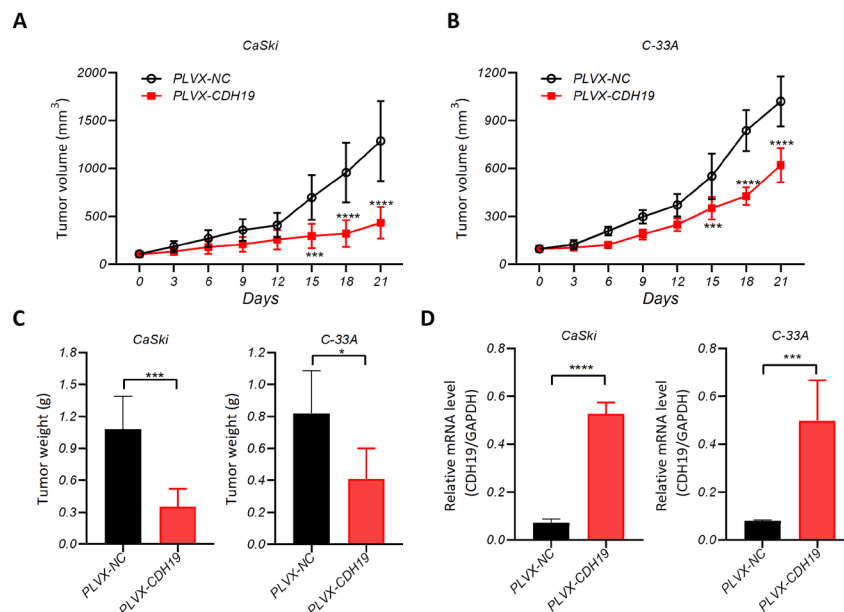


Figure 5. CDH19 overexpression inhibits tumor growth of cervical carcinoma.

(A & B) The tumor growth curves. (C) At the end of the animal study, tumors were excised and weighed. (D) Tumors were lysed for QPCR against CDH19 and GAPDH. * $p < 0.05$, *** $p < 0.001$, **** $p < 0.0001$.

and Ki-67 expression (Fig. 3A). Furthermore, we overexpressed CDH19 in cervical carcinoma cells, which was confirmed by Western blot and PCR (Fig. 3B–D), and observed a significant inhibition of cell proliferation in comparison with negative control (Fig. 3E and F). These findings provide further evidence of a close association between CDH19 and cervical carcinoma cell proliferation, suggesting that CDH19 may play a role in regulating the proliferation of cervical carcinoma cells.

CDH19 overexpression inhibits AKT and NF- κ B signaling in cervical carcinoma cells

We further investigated the activity of signaling pathways closely related to cell proliferation and found that overexpression of CDH19 significantly inhibited the activation of the AKT pathway as reflected by the decreased AKT phosphorylation both in CaSki and C-33A cells (Fig. 4A, B). In addition, overexpression of CDH19 significantly inhibited the activation of the NF- κ B pathway as evidenced with the decreased phosphorylation of NF- κ B p65 subunit (Fig. 4C–D). These findings suggest that CDH19 may be involved in regulating cervical carcinoma cell proliferation through the modulation of AKT and NF- κ B signaling pathways.

CDH19 overexpression inhibits tumor growth of cervical carcinoma

Finally, to further validate the functional role of CDH19 in cervical carcinoma, we constructed a xenograft tumor model in nude mice. We found that cervical carcinoma tumors overexpressing CDH19 had significantly slower growth rates *in vivo*, as evidenced by the significantly smaller tumor volume (Fig. 5A, B) and weight (Fig. 5C). Also, CDH19 mRNA expression was significantly upregulated in both CaSki and C-33A cells after transfection (Fig. 5D). These findings provide strong evidence of the inhibitory effect of CDH19 on cervical carcinoma tumor growth and suggest a potential therapeutic target for cervical carcinoma.

DISCUSSION

Cadherins (CDHs) are a family of calcium-dependent cell adhesion molecules that play important roles in the maintenance of tissue structure, and cell-cell communication. CDHs are involved in several key cellular processes, including cell adhesion, migration, proliferation, differentiation, and apoptosis. There are several types of cadherins, including E-cadherin, N-cadherin, P-cadherin, and VE-cadherin. These proteins are expressed in different tissues and play a significant role in embryonic development, tissue morphogenesis, and maintenance of tissue integrity.

Previous studies have shown that alterations in the expression and function of cadherins are associated with various types of cancer. In particular, the loss of E-cadherin expression is a common event in many types of epithelial cancers, including breast, gastric, colon, and prostate cancers. E-cadherin is a tumor suppressor protein that helps to maintain cell-cell adhesion, and its loss leads to reduced cell adhesion and increased cell motility, which are important events in cancer metastasis (Li *et al.*, 2020). Additionally, mutations in the genes encoding cadherins have been reported in some cancers, including stomach and breast cancer. For example, mutations in the CDH1 gene, which encodes E-cadherin, have been identified in familial gastric cancer and hereditary diffuse gastric cancer syndrome. These mutations can impair E-cadherin function and lead to an increased risk of developing gastric cancer.

Moreover, changes in the expression and function of other cadherin family members have also been associated with cancer. For instance, N-cadherin is upregulated in many types of cancers and plays a role in promoting cancer cell migration and invasion. Similarly, P-cadherin has been found to be upregulated in certain breast cancers and is associated with a more aggressive tumor phenotype. It is believed that upregulation of N-cadherin and P-cadherin, found in some types of cancer, is associated with a more aggressive tumor phenotype.

In summary, alterations in the expression and function of CDH family members are closely related to the development and progression of cancer. The loss of E-cadherin expression, in particular, is a common event in many types of epithelial cancer and is associated with an increased risk of cancer metastasis (Lechner *et al.*, 2013). Understanding the molecular mechanisms underlying these alterations may provide new insights into cancer pathogenesis and may also offer new therapeutic targets for cancer treatment.

CDH19, a member of the cadherin family of cell adhesion molecules, has been implicated in various types of cancers. However, its role in gynecological tumors, especially cervical carcinoma, has not been studied sufficiently (de Mello *et al.*, 2017). In this study, we first analyzed the expression of CDH19 in gynecological tumors (CESC, OV, UCEC, and UCS) using the GEPIA database and found that CDH19 expression was overall downregulated in these tumors, including cervical carcinoma.

To further investigate the role of CDH19 in cervical carcinoma, we analyzed the overall survival of cervical carcinoma patients with high or low CDH19 expression levels using the Kaplan-Meier plotter database. We found that patients with high CDH19 expression had significantly better overall survival than those with low CDH19 expression. This data suggested that CDH19 expression was associated with the overall survival rate of cervical carcinoma patients.

Cervical Intraepithelial Neoplasia (CIN) is a grading system used to classify the severity of abnormal cell growth in the cervix. CIN is divided into three grades based on the degree of abnormal cell growth: CIN1 (mild dysplasia), CIN2 (moderate dysplasia), and CIN3 (severe dysplasia or carcinoma *in situ*). The CIN grading system is widely used in clinical practice to guide management and treatment decisions for patients with abnormal cervical cell growth. In the future, performing the correlation of CDH19 expression with CIN, may better elucidate its role in cervical carcinoma development.

To explore whether CDH19 is associated with cervical carcinoma cell proliferation, we analyzed the correlation between CDH19 and the proliferation marker Ki-67 in cervical carcinoma patient tissues using the GEPIA database. We found that CDH19 expression was negatively correlated with Ki-67 expression. To validate this observation, we overexpressed CDH19 in cervical carcinoma cells and found that CDH19 overexpression significantly inhibited cell proliferation. That means, loss of the CDH19 expression caused abnormal cell growth, and additional CDH19 can significantly inhibit the abnormal growth. These data further give us a hint that CDH19 might be a potential therapeutic target of cervical carcinoma.

We also investigated the activation of signaling pathways that are closely related to cell proliferation and found that CDH19 overexpression significantly inhibited the AKT and NF- κ B signaling pathways. There are several studies supporting potential connection between CDH19 and AKT. For example, in prostate cancer, CDH19 has been found to regulate the AKT/mTOR signaling pathway and promote cancer cell migration and invasion (Qian *et al.*, 2019). In addition, in breast cancer, CDH19 has been shown to interact with the extracellular matrix protein laminin-511, which activates the AKT signaling pathway and promotes tumor growth (Gudlaugsson *et al.*, 2010). These studies suggest that there may be crosstalk between CDH19 and the AKT signaling pathway in various types of cancer. However, so far

there are no studies that directly investigate the relationship between CDH19 and the AKT signaling pathway in cervical carcinoma.

Finally, we constructed a xenograft model in nude mice and found that CDH19 overexpression significantly reduced the growth rate of cervical carcinoma tumors *in vivo*. These results further provide evidence that CDH19 might serve as a therapeutic target of cervical carcinoma.

The findings on CDH19 in cervical carcinoma are quite significant in clinic. It not only provides a prognostic marker of cervical carcinoma, but also proposes a therapeutic target. Understanding that CDH19 suppresses the AKT and NF- κ B signaling pathways provides crucial insights into the underlying mechanisms of cervical carcinoma. This knowledge could help in developing more targeted and effective therapies that focus on these pathways. Moreover, the *in vivo* studies in a xenograft mouse model validate the potential therapeutic relevance of CDH19. The slower growth of tumors in mice with CDH19-overexpressing cervical carcinoma cells indicates the potential for further exploration in preclinical models, which could eventually lead to human clinical trials. Overall, these findings suggest that CDH19 could have multifaceted clinical implications in the diagnosis, prognosis, and treatment of cervical carcinoma. However, further research and validation are crucial to determine if targeting CDH19 could indeed be a viable approach in clinical settings.

The study shows promising results in cell cultures and xenograft models. However, cellular responses *in vitro* may not always replicate the complexities of human physiology accurately. The behaviors observed in a controlled lab setting might not fully represent the actual response in human patients. Furthermore, this study primarily relies on data collected from databases such as GEPIA and the Kaplan-Meier plotter. While these resources provide valuable insights, they may have inherent limitations, including data quality, biases, or potential errors in the data collection or analysis methods used in these databases. The number and diversity of samples used in the study is limited to 300 (GEPIA dataset) and 400 (TCGA dataset). The findings might not be universally applicable across different demographic or genetic backgrounds. For comprehensive and robust conclusions, a larger and more diverse sample pool should be considered. The findings show correlation between CDH19 expression and patient survival as well as direct influence of CDH19 expression on cell proliferation, and activation of signaling pathways. It's crucial to continue mechanistic studies to further test the cause-effect relationship between CDH19, activation of the cell signaling pathways and patient outcomes to validate the role of CDH19 in cervical carcinoma and to determine its potential as a therapeutic target. While the findings presented in our study are promising, they represent a steppingstone for more in-depth research before any clinical implications can be drawn.

CONCLUSIONS

Taken together, our findings suggest that CDH19 plays an important role in cervical carcinoma, potentially through its regulation of the AKT and NF- κ B signaling pathways and inhibition of cell proliferation. Further studies are needed to fully elucidate the underlying mechanisms and potential therapeutic implications of CDH19 in cervical carcinoma.

Declarations

Ethical Approval. The animal-related protocols were approved by the ethics committee of Zibo Central Hospital. This study was performed in strict accordance with the NIH guidelines for the care and use of laboratory animals.

Consent for publication. Current study is available from the corresponding author on reasonable request.

Disclosure of potential conflicts of interest. The authors declare that they have no competing interests.

Funding. None.

Data availability statement. The raw data supporting the conclusions of this article will be made available by the authors, without undue reservation.

Acknowledgment. None.

REFERENCES

- Avila JA, Southard-Smith EM (2022) "Going the extra mile": A Sox10 target, Cdh19, is Required for Sacral NC Migration in ENS Development. *Gastroenterology* **162**: 42–44. <https://doi.org/10.1053/j-gastro.2021.10.001>
- Bailis JM, Lee F, Giffin M, Hughes P, Tsoi J, Robert L, Graeber TG, Ribas A, Coxon A (2019) Melanoma subtypes that emerge during adaptive resistance to therapy are targets for bispecific T cell engager (BiTE®) antibody constructs directed to CDH19 and DLL3. *Cancer Res* **79** (Suppl 13): 553–553. <https://doi.org/10.1158/1538-7445.AM2019-553>
- Blons H, Laccourreye O, Houllier A-M, Carnot F, Brasnu D, Beaune P, Zucman-Rossi J, Laurent-Puig P (2002) Delineation and candidate gene mutation screening of the 18q22 minimal region of deletion in head and neck squamous cell carcinoma. *Oncogene* **21**: 5016–5023. <https://doi.org/10.1038/sj.onc.1205626>
- Bossler F, Hoppe-Seyler K, Hoppe-Seyler F (2019) PI3K/AKT/mTOR signaling regulates the virus/host cell crosstalk in HPV-positive cervical cancer cells. *Int J Mol Sci* **20**: 2188. <https://doi.org/10.3390/ijms20092188>
- de Mello JBH, Cirilo PDR, Michelin OC, Domingues MAC, Rudge MVC, Rogatto SR, Maestá I (2017) Genomic profile in gestational and non-gestational choriocarcinomas. *Placenta* **50**: 8–15. <https://doi.org/10.1016/j.placenta.2016.12.009>
- Gao W, Yang M (2022) Identification by bioinformatics analysis of potential key genes related to the progression and prognosis of gastric cancer. *Front Oncol* **12**: 881015. <https://doi.org/10.3389/fonc.2022.881015>
- Gu M, He T, Yuan Y, Duan S, Li X, Shen C (2021) Single-cell RNA sequencing reveals multiple pathways and the tumor microenvironment could lead to chemotherapy resistance in cervical cancer. *Front Oncol* **11**: 753386. <https://doi.org/10.3389/fonc.2021.753386>
- Gudlaugsson E, Skaland I, Janssen EA, van Diest PJ, Voorhorst FJ, Kjellevold K, zur Hausen A, Baak JP (2010) Prospective multi-center comparison of proliferation and other prognostic factors in lymph node negative lobular invasive breast cancer. *Breast Cancer Res Treat* **121**: 35–40. <https://doi.org/10.1007/s10549-009-0442-x>
- Hou H, Li J, Wang J, Zhou L, Li J, Liang J, Yin G, Li X, Cheng Y, Zhang K (2022) ITGA9 Inhibits proliferation and migration of dermal microvascular endothelial cells in psoriasis. *Clin Cosmet Investig Dermatol* **15**: 2795–2806. <https://doi.org/10.2147/ccid.S394398>
- Kaur H, Silverman PM, Iyer RB, Verschraegen CF, Eifel PJ, Charnsangavej C (2003) Diagnosis, staging, and surveillance of cervical carcinoma. *Am J Roentgenol* **180**: 1621–1631. <https://doi.org/10.2214/ajr.180.6.1801621>
- Koski TA, Lehtonen HJ, Jee KJ, Ninomiya S, Joosse SA, Vahteristo P, Kiuru M, Karhu A, Sammalkorpi H, Vanharanta S (2009) Array comparative genomic hybridization identifies a distinct DNA copy number profile in renal cell cancer associated with hereditary leiomyomatosis and renal cell cancer. *Genes Chromosomes Cancer* **48**: 544–551. <https://doi.org/10.1002/gcc.20663>
- Lazo P (1999) The molecular genetics of cervical carcinoma. *Brit J Cancer* **80**: 2008–2018. <https://doi.org/10.1038/sj.bjc.6690635>
- Lechner M, Fenton T, West J, Wilson G, Feber A, Henderson S, Thirlwell C, Dibra HK, Jay A, Butcher L (2013) Identification and functional validation of HPV-mediated hypermethylation in head and neck squamous cell carcinoma. *Genome Med* **5**: 1–16. <https://doi.org/10.1186/gm419>
- Li C, Ao H, Chen G, Wang F, Li F (2020) The interaction of CDH20 with β -catenin inhibits cervical cancer cell migration and invasion via TGF- β /smad/SNAIL mediated EMT. *Front Oncol* **9**: 1481. <https://doi.org/10.3389/fonc.2019.01481>
- Liu C, Li X, Feng G, Cao M, Liu F, Zhang G, Lu Y (2020) Down-regulation of USP12 inhibits tumor growth via the p38/MAPK pathway in hepatocellular carcinoma. *Mol Med Rep* **22**: 4899–4908. <https://doi.org/10.3892/mmr.2020.11557>
- Liu Z, Iyer MR, Godlewski G, Jourdan T, Liu J, Coffey NJ, Zawatsky CN, Puhl HL, Wess J, Meister J, Liow JS, Innis RB, Hassan SA, Lee YS, Kunos G, Cinar R (2021) Functional selectivity of a biased cannabinoid-1 receptor (CB1R) antagonist. *ACS Pharmacol Transl Sci* **4**: 1175–1187. <https://doi.org/10.1021/acspsci.1c00048>
- Liu Z, Luo H, Zhang L, Huang Y, Liu B, Ma K, Feng J, Xie J, Zheng J, Hu J, Zhan S, Zhu Y, Kong W, Wang X (2012) Hyperhomocysteinemia exaggerates adventitial inflammation and angiotensin II-induced abdominal aortic aneurysm in mice. *Circ Res* **111**: 1261–1273. <https://doi.org/10.1161/circresaha.112.270520>
- Nagy Á, Munkácsy G, Györfi B (2021) Pancancer survival analysis of cancer hallmark genes. *Sci Rep* **11**: 6047. <https://doi.org/10.1038/s41598-021-84787-5>
- Niu J, Azfer A, Zhelyabovska O, Fatma S, Kolattukudy PE (2008) Monocyte chemotactic protein (MCP)-1 promotes angiogenesis via a novel transcription factor, MCP-1-induced protein (MCPIP). *J Biol Chem* **283**: 14542–14551. <https://doi.org/10.1074/jbc.M802139200>
- Petereit DG, Sarkaria JN, Chappell R, Fowler JF, Hartmann TJ, Kinsella TJ, Stitt JA, Thomadsen BR, Buchler DA (1995) The adverse effect of treatment prolongation in cervical carcinoma. *Int J Rad Oncol Biol Phys* **32**: 1301–1307. [https://doi.org/10.1016/0360-3016\(94\)00635-X](https://doi.org/10.1016/0360-3016(94)00635-X)
- Qian Y, Yan Y, Lu H, Zhou T, Lv M, Fang C, Hou J, Li W, Chen X, Sun H, Li Y, Wang Z, Zhao N, Gu Y, Ding Y, Liu Y (2019) Celastrol orbiculatus extracts inhibit the metastasis through attenuating PI3K/Akt/mTOR signaling pathway in human gastric cancer. *Anticancer Agents Med Chem* **19**: 1754–1761. <https://doi.org/10.2174/1871520619666190731162722>
- Tervasmäki A, Winqvist R, Jukkola-Vuorinen A, Pykkäs K (2014) Recurrent CYP2C19 deletion allele is associated with triple-negative breast cancer. *BMC Cancer* **14**: 1–7. <https://doi.org/10.1186/1471-2407-14-902>
- Vara JÁF, Casado E, de Castro J, Cejas P, Belda-Iniesta C, González-Barón M (2004) PI3K/Akt signalling pathway and cancer. *Cancer Treat Rev* **30**: 193–204. <https://doi.org/10.1016/j.ctrv.2003.07.007>
- Wang H, Chen J, Liao X, Liu Y, Tang A, Mei H (2021) Identification of hub genes related to the progression of bladder cancer by an integrated bioinformatics analysis. *Research Square* 2021. <https://doi.org/10.21203/rs.3.rs-819606/v1>
- Wang S, Juan J, Zhang Z, Du Y, Xu Y, Tong J, Cao B, Moran MF, Zeng Y, Mao X (2017) Inhibition of the deubiquitinase USP5 leads to c-Maf protein degradation and myeloma cell apoptosis. *Cell Death Dis* **8**: e3058. <https://doi.org/10.1038/cddis.2017.450>
- Wang S, Liu Z, Ma YM, Guan X, Jiang Z, Sun P, Liu ER, Zhang YK, Wang HY, Wang XS (2021) Upregulated insulin receptor tyrosine kinase substrate promotes the proliferation of colorectal cancer cells via the bFGF/AKT signaling pathway. *Gastroenterol Rep (Oxf)* **9**: 166–175. <https://doi.org/10.1093/gastro/goaa032>
- Woods C, Kapur RP, Bischoff A, Lovell M, Arnold M, Peña A, Flockton A, Sharkey KA, Belkind-Gerson J (2021) Neurons populating the rectal extrinsic nerves in humans express neuronal and Schwann cell markers. *Neurogastroenterol Motility* **33**: e14074. <https://doi.org/10.1111/nmo.14074>

Use of sertraline and agomelatine in hemodialysis patients: A case series report

Alicja Kubanek¹✉, Mateusz Przybylak², Przemysław Paul¹, Anna Sylwia Kowalska³, Michał Błaszczuk⁴, Aleksandra Macul-Sanewska⁴, Marcin Renke¹, Przemysław Rutkowski⁵, Leszek Bidzan² and Jakub Grabowski²

¹Department of Occupational, Metabolic and Internal Diseases, Medical University of Gdansk, 80-210 Gdańsk, Poland; ²Division of Developmental, Psychotic and Geriatric Psychiatry, Department of Psychiatry, Medical University of Gdansk, 80-210 Gdańsk, Poland; ³ISPL Anna Sylwia Kowalska, 80-156 Gdańsk, Poland; ⁴Adult Psychiatry Scientific Circle, Division of Developmental, Psychotic and Geriatric Psychiatry, Department of Psychiatry, Medical University of Gdansk, 80-210 Gdańsk, Poland; ⁵Department of Internal and Paediatric Nursing, Faculty of Health Sciences, Medical University of Gdansk, 80-210 Gdańsk, Poland

Objective: Major depressive disorder (MDD) is one of the most common psychiatric issues in hemodialysis population. However, the research on proper diagnostic tools and its treatment is still insufficient. The study was performed to investigate the safety and effectiveness of sertraline and agomelatine in a group of hemodialysis patients. **Patients and Methods:** 78 adult patients from one dialysis centre in Poland were included into the study. The Beck Depression Inventory II (BDI-II) was used to screen for depressive symptoms and was followed by the clinical interview with the psychiatrist. Nine patients diagnosed with major depressive disorder received antidepressant treatment with sertraline or agomelatine, according to the best clinical practice. The additional treatment with vortioxetine was used if the initial one was not effective. The time of observation was 24 weeks. The psychiatric follow up as well as the laboratory data were obtained during the course of observation. **Results:** All patients receiving sertraline achieved remission of depressive symptoms. In patients receiving agomelatine no remission was observed despite dose augmentation. The side effects of antidepressants were mild and did not result in treatment discontinuation. No abnormalities in liver enzymes levels were observed. In five cases the significant decrease of haemoglobin level was noticed, with no cases of bleeding reported. **Conclusion:** In patients receiving sertraline the antidepressant effect was satisfactory. No remission of depressive symptoms was observed in patients taking agomelatine. The side effects of antidepressants were mild and transient. Further research on depression treatment in hemodialysis patients is needed, including newer medications.

Keywords: hemodialysis, depression, sertraline, agomelatine

Received: 23 July, 2023; **revised:** 24 July, 2023; **accepted:** 04 October, 2023; **available on-line:** 03 December, 2023

✉ e-mail: akubanek@gumed.edu.pl

Abbreviations: BDI-II, Beck Depression Inventory-II; CGI-S, Clinical Global Impression-Severity scale; CKD, chronic kidney disease; DSM-5, Diagnostic and Statistical Manual of Mental Disorders 5; ERBP, European Renal Best Practice; ESRD, end-stage renal disease; MADRS, Montgomery-Asberg Depression Rating Scale; MCI, mild cognitive impairment; MDD, major depressive disorder; MMSE, Mini Mental State Examination; PSP, Personal and Social Performance Scale; QoL, quality of life; SSRIs, serotonin reuptake inhibitors

INTRODUCTION

Chronic kidney disease (CKD) and depression plays a significant role in global health (GBD Chronic Kidney Disease Collaboration, 2020; GBD 2019 Diseases and Injuries Collaborators, 2020). Patients suffering from end-stage renal disease (ESRD), requiring renal replacement therapy, are at a high risk of major depressive disorder (MDD) (Kimmel *et al.*, 2019). According to the studies, around twenty to forty percent of maintenance hemodialysis patients suffer from major depressive disorder, depending on the methodological approach used (Palmer *et al.*, 2019). Individuals with chronic kidney disease have significantly lower quality of life (QoL) (Fletcher *et al.*, 2022) and higher mortality rate (Ozieh *et al.*, 2021). Furthermore, depression is the known independent risk factor of decreased QoL (Belayev *et al.*, 2015) and mortality (Farrokhi *et al.*, 2014), as well as higher nonadherence in hemodialysis population (Gebrie *et al.*, 2019). Patients undergoing hemodialysis are often excluded from clinical trials, due to the safety reasons, as pharmacokinetics of antidepressants in hemodialysis are not fully explored (Constantino *et al.*, 2019). The European Renal Best Practice (ERBP) suggests treatment with serotonin reuptake inhibitors (SSRIs), as the first line in patients who meet depression criteria (Nagler *et al.*, 2012). However, the recognition and treatment of depression in ESRD patients remain insufficient (Lopes *et al.*, 2004; Pena-Polanco, 2017).

Sertraline is known to be safe and does not require additional doses after the dialysis session (Schwenk *et al.*, 1995; Constantino *et al.*, 2019). However, its effects in hemodialysis patients may be heterogeneous (Kubanek *et al.*, 2021). Studies evaluating safety and efficacy of this SSRI in ESRD patients usually had small samples and lacked placebo control (Palmer *et al.*, 2016). In the randomized, controlled trial by Friedli *et al.* there were no significant differences between sertraline and placebo group in improving depression symptoms. (Friedli *et al.*, 2017).

Agomelatine is the atypical antidepressant with melatonin agonism and 5-HT_{2c} antagonism. It was shown to be effective and well tolerated in treating major depressive disorder in general population (Cipriani *et al.*, 2018). It is not contraindicated in patients with severe renal impairment, however the data considering CKD population is scarce (Chen *et al.*, 2018). One of the side effects of agomelatine is liver enzymes elevation and it

requires aminotransferase monitoring in the course of treatment. Vortioxetine is an antidepressant with multimodal activity used in major depression disorders treatment, recognized as having the best efficacy and safety in head-to-head studies (Koesters *et al.*, 2017; Cipriani *et al.*, 2018).

METHODOLOGY

Patients over eighteen years old from one dialysis centre in Gdańsk (Poland), who had been receiving hemodialysis treatment for at least three months, were recruited. The study received approval of the Independent Bioethics Committee for Scientific Research of the Medical University of Gdańsk. All patients gave their written informed consent. Dialysis Center provides public health services for approximately 200 patients. There is no psychiatric or psychological assistance provided in patients' routine. Individuals suffering from major psychiatric disorders other than depression were excluded. The study group received the high-flux hemodialysis or hemodiafiltration three times per week. Cognitive functions were evaluated using Mini Mental State Examination (MMSE) and assessed clinically by the psychiatrist (Folstein *et al.*, 1975). MMSE was completed subsequently at the end of observation. Patients diagnosed with moderate and severe cognitive impairment were excluded from the further depression diagnosis. The clinical and laboratory data of the study group was also obtained.

The depression screening was performed using Beck Depression Inventory II (BDI-II), followed by the psychiatric assessment (Beck *et al.*, 1996). The diagnosis of major depressive disorder was based on the Diagnostic and Statistical Manual of Mental Disorders 5 (DSM-5). Psychiatrists were using Montgomery-Asberg Depression Rating Scale (MADRS), Clinical Global Impression-Severity scale (CGI-S) and Personal and Social Performance Scale (PSP) to evaluate the severity of depression symptoms and psychosocial functioning of patients (Montgomery *et al.*, 1979; Morosini *et al.*, 2000; Busner *et al.*, 2007). MADRS is a standard in monitoring depressive disorders and improvement during treatment. Tests were performed in the middle of the dialysis session, at

least one hour after the initiation and one hour before the termination of the procedure.

Individuals who were diagnosed with major depressive disorder by the psychiatrist and agreed to receive the antidepressant treatment were subjected to further observation. The medications were chosen according to the best clinical practice guidelines. Six patients received treatment with sertraline in the daily dose of 25-100 mg. One patient had been already receiving sertraline (50 mg/day) before the study. Two patients received agomelatine treatment (25–50 mg/day). The time of observation was twenty-four weeks. Psychiatric evaluation, laboratory and dialysis parameters control were performed every six weeks. The additional treatment and dose changes were adjusted during the time of observation. ERBP guidelines suggest that trials with SSRIs in patients, who meet criteria for moderate MDD, should last for eight to twelve weeks, followed by medical evaluation (Nagler *et al.*, 2012). However, the psychiatric clinical practice's assessment for depressive and anxiety patients is usually done after four weeks.

RESULTS

The cognitive functions were rated in 82 patients. According to the MMSE screening and clinical assessment mild cognitive impairment (MCI) and mild dementia were observed in thirty two percent of patients, while moderate dementia in four percent. Patients that agreed to remain in the study and were not diagnosed with moderate or severe dementia were subjected to further evaluation. 78 patients underwent the depression screening and clinical assessment of the psychiatrist. The percentage of individuals with depressive symptoms using BDI-II alone was forty-three. In the clinical interview, performed by the psychiatrist, the criteria of MDD requiring antidepressant treatment were fulfilled in thirteen cases. Two patients did not agree to receive antidepressants. Three patients had been already treated for depression before the study. One person, who had been receiving sertraline, was monitored for possible adverse events. In the group treated with antidepressants there were five women and four men. The age range was between 36

Table 1. Clinical data and test results of patients with depression diagnosis

No.	Sex	Age	CCI	DM	Dialysis time (years)	MMSE	BDI-II	MADRS	CGI-S	PSP	Medication
1.	M	51	3	no	5	28	7	29	5	55	sertraline
2.	F	63	6	yes	7	29	23	14	3	90	agomelatine
3.	M	37	5	yes	2	30	31	31	5	62	sertraline
4.	M	36	7	yes	5	23	24	22	4	41	sertraline
5.	F	64	7	yes	2	28	14	15	3	71	agomelatine
6.	F	66	4	no	2	29	8	30	5	49	sertraline
7.	F	76	8	yes	3	–	14	10	2	25	sertraline
8.	M	60	5	no	2	21	8	30	6	30	sertraline
9.	F	70	8	yes	1	27	25	13	2	35	sertraline -during treatment

M, male; F, female; CCI, Charlson Comorbidity Index; DM, diabetes mellitus; MMSE, Mini-Mental State Examination; BDI-II, Beck Depression Inventory II; MADRS, Montgomery-Asberg Depression Rating Scale; CGI-S, Clinical Global Impression – Severity scale; PSP, Personal and Social Performance Scale

Table 2. Test results during antidepressant treatment.

No.	I MADRS	II MADRS	III MADRS	remission after 24 weeks	I MMSE	II MMSE	I CGI-S	II CGI-S	I PSP	II PSP
1.	29	–	–	–	28	28	5	–	55	–
2.	14	10	11	no	29	30	3	2	90	90
3.	31	3	3	yes	30	30	5	1	62	79
4.	22	5	4	yes	23	25	4	1	41	85
5.	8	15	13	no 6 week observation	28	29	2	3	71	71
6.	30	10	9	yes	29	30	5	2	49	64
7.	10	25	11	yes	–	–	2	2	25	55
8.	30	9	–	yes 6 week observation	21	24	6	2	30	–
9.	13	–	–	–	27	–	2	–	35	–

I, result at the beginning of observation; II, result after 24 weeks of observation; MADRS, Montgomery-Asberg Depression Rating Scale; MMSE, Mini-Mental State Examination; CGI-S, Clinical Global Impression – Severity scale; PSP, Personal and Social Performance Scale

and 76 years and the comorbidity index in most patients was over 4 points. (Table 1).

During the observation two patients resigned from the follow up and one received kidney transplantation. Five patients receiving sertraline achieved remission according to MADRS, CGI-S and clinical evaluation. However, two patients required treatment modification and switching to vortioxetine (10–15 mg). Patients treated with agomelatine had no remission during the observation (one person was observed for 24 weeks and the other for 6 weeks, since the treatment was started during the study). Both required the agomelatine dose augmentation. One

had quetiapine and the other vortioxetine added to the treatment. In the sertraline group the dose of 50 mg was the minimal one to achieve remission, one patient required 100 mg dose. One person receiving agomelatine reported dizziness after 12 weeks of observation, but the treatment was continued. One patient treated with sertraline reported headaches after 6 weeks; the effect was transient and disappeared after splitting the dose into twice a day regimen. In the other individuals we observed no side effects. All patients that agreed to perform dementia screening using MMSE in the end of observation improved or had the equal test result. In the

Table 3. Laboratory parameters over the course of observation in patients receiving antidepressant treatment.

No.	I CaxPi mg/dl <79	II CaxPi mg/dl <79	I Kt/V >1.2	II Kt/V >1.2	I Hb g/dl 11.5–16.5 (F), 13–18 (M)	II Hb g/dl 11.5–16.5 (F), 13–18 (M)	I WBC G/l 4.0–11.0	II WBC G/l 4.0–11.0	I PLT G/l 150–400	II PLT G/l 150–400	I ALT U/l <41	II ALT U/l <41	Albumin g/l 35–52
1	68	70	1.6	1.6	9.7	10	5.8	4.8	167	180	6	8	44
2	54	44	1.2	1.1	11.4	8.7	8.6	6.3	555	656	7	3	43
3.	85	66	1.3	–	11.1	10.8	8.5	7.5	285	292	22	21	40
4.	57	35	3.1	1.7	12.7	9.2	8.9	5.6	135	248	10	10	39
5.	56	49	1.6	1.4	12.1	10.3	11.9	9.1	221	221	15	13	43
6.	37	27	1.4	1.2	11.8	11.6	6.1	5.4	222	221	17	15	40
7.	41	69	1.4	1.5	11.7	10.6	7.8	6.8	139	155	15	11	37
8.	18	39	1.7	1.5	9.3	10.1	4.7	3.9	231	189	20	7	46
9.	50	33	–	–	13.3	9.3	6	5.3	177	181	7	3	44

I, result at the beginning of observation; II, result after 24 weeks of observation; Kt/V (K, dialyzer clearance of urea; t, dialysis time; V, volume of distribution of urea; approximately equal to patient's total body water). Ca x Pi, calcium phosphate index; Hb, haemoglobin; F, female; M, male; WBC, white blood cells; PLT, platelet count; ALT, aminotransferase

patient that refused undertaking the test no clinical features of cognitive decline were observed (Table 2).

The laboratory results were also monitored during observation (Table 3). No abnormalities in liver transaminase levels were observed and the albumin level remained within the normal range in all the patients. In all individuals either no significant changes or the decrease in Kt/V were observed. White blood cells count decreased during the antidepressant treatment but remained within or slightly below the norm. The platelet count stayed within or above the normal range. We noticed the decrease of the haemoglobin level (above 1 g/dl) in five cases- in both patients treated with agomelatine and three patients receiving sertraline in the daily dose of 50 mg. No bleedings were reported in the study group.

DISCUSSION

The prevalence of depressive symptoms and cognitive impairment in the observed group of hemodialysis patients was significant. However, when the gold standard methodological tools in diagnosing major depressive disorder are used and age, coexisting diseases, dementia screening are taken into consideration, it is similar to other elderly populations with high comorbidity rate (Luppa *et al.*, 2012; Wang *et al.*, 2017). It is important while analysing the effectiveness of self-reported questionnaires, which may over-diagnose depressive symptoms. Thus, the psychiatrist examination remains a crucial point in diagnosing depression in a dialysis centre. Increasing its availability for the dialysis patients might have a positive impact on their quality of life and compliance. Moreover, it could upgrade the motivation to proceed in kidney transplantation process.

Taking into consideration the small study group, the number of patients that refused antidepressant treatment or resigned from the follow up was high. The results are consistent with the National Kidney Foundation survey, referring that half of the hemodialysis patients do not adhere to the dialysis regimen (Estrella *et al.*, 2013). Hemodialysis patients suffer from numerous comorbidities and often require polypharmacy, which may be one of the reasons of the incompliance. It might be the group of patients that would agree to psychotherapy or other nonpharmacological approach.

All patients treated with antidepressants that agreed to perform MMSE in the end of observation improved the cognitive functions or achieved the equal test result. It may indicate that some of the observed cognitive disorders in dialysis patients are functional, related to mood disorders. During the treatment, the regular laboratory testing is needed. The decrease of haemoglobin level might be triggered among others by the platelet dysfunction and bleeding caused by the antidepressant agent. The decrease of white blood cells count might be connected with the potential anti-inflammatory effect of antidepressants suggested in previous studies (Taraz *et al.*, 2013). Kt/V is used to evaluate dialysis adequacy; however, its interpretation should be individual due to its limitations as a single parameter (Jones *et al.*, 2018).

The treatment tolerance was good, and the adverse effects of the antidepressants were mild and transient. The antidepressant effect of sertraline in the observed group was satisfactory, however two patients required treatment with vortioxetine. Sertraline is known to be safe to use in the end-stage kidney disease population, but its effectiveness requires further research. Individuals that received treatment with agomelatine did not achieve re-

mission according to psychiatrist evaluation. More studies considering newer antidepressant agents, causing less adverse effects (Cipriani *et al.*, 2018), including agomelatine and vortioxetine, are needed.

CONCLUSIONS

In patients receiving sertraline the antidepressant effect was satisfactory. No remission of depressive symptoms was observed in individuals treated with agomelatine. The side effects of used medications were mild and transient. All patients treated with antidepressants improved or had equal cognitive performance at the end of the follow-up. Further research on depression treatment in hemodialysis patients is needed, including the newer antidepressant agents.

REFERENCES

- Beck AT, Steer RA, Brown GK (1996) *Manual for the Beck depression inventory – II*. San Antonio, TX: Psychological Corporation
- Belayev LY, Mor MK, Sevik MA, Shields AM, Rollman BL, Palevsky PM, Arnold RM, Fine MJ, Weisbord SD. (2015) Longitudinal associations of depressive symptoms and pain with quality of life in patients receiving chronic hemodialysis. *Hemodial Int* 19: 216–224. <https://doi.org/10.1111/hdi.12247>
- Busner J, Targum SD (2007) The clinical global impressions scale: applying a research tool in clinical practice. *Psychiatry* (Edgmont) 4: 28–37
- Chen JW, Xie SQ (2018) Agomelatine versus paroxetine in treating depressive and anxiety symptoms in patients with chronic kidney disease. *Neuropsychiatr Dis Treat* 14: 547–552. <https://doi.org/10.2147/NDT.S159636>
- Cipriani A, Furukawa TA, Salanti G, Chaimani A, Atkinson LZ, Ogawa Y, Leucht S, Ruhe HG, Turner EH, Higgins JPT, Egger M, Takeshima N, Hayasaka Y, Imai H, Shinohara K, Tajika A, Ioannidis JPA, Geddes JR. (2018) Comparative efficacy and acceptability of 21 antidepressant drugs for the acute treatment of adults with major depressive disorder: a systematic review and network meta-analysis. *Lancet* 391: 1357–1366. [https://doi.org/10.1016/S0140-6736\(17\)32802-7](https://doi.org/10.1016/S0140-6736(17)32802-7)
- Constantino JL, Fonseca VA (2019) Pharmacokinetics of antidepressants in patients undergoing hemodialysis: a narrative literature review. *Braz J Psychiatry* 41: 441–446. <https://doi.org/10.1590/1516-4446-2018-0264>
- Estrella MM, Jaar BG, Cavanaugh KL, Fox CH, Perazella MA, Soman SS, Howell E, Rocco MV, Choi MJ (2013) National Kidney Foundation. Perceptions and use of the national kidney foundation KDOQI guidelines: a survey of U.S. renal healthcare providers. *BMC Nephrol* 14: 230. <https://doi.org/10.1186/1471-2369-14-230>
- Farrokhi F, Abedi N, Beyene J, Kurdyak P, Jassal SV (2014) Association between depression and mortality in patients receiving long-term dialysis: a systematic review and meta-analysis. *Am J Kidney Dis* 63: 623–635. <https://doi.org/10.1053/j.ajkd.2013.08.024>
- Fletcher BR, Damery S, Aiyegbusi OL, Anderson N, Calvert M, Cockwell P, Ferguson J, Horton M, Paap MCS, Sidey-Gibbons C, Slade A, Turner N, Kyte D (2022) Symptom burden and health-related quality of life in chronic kidney disease: A global systematic review and meta-analysis. *PLoS Med* 19: e1003954. <https://doi.org/10.1371/journal.pmed.1003954>
- Folstein MF, Folstein SE, McHugh PR (1975) “Mini-mental state”. A practical method for grading the cognitive state of patients for the clinician. *J Psychiatr Res* 12: 189–198. [https://doi.org/10.1016/0022-3956\(75\)90026-6](https://doi.org/10.1016/0022-3956(75)90026-6)
- Friedli K, Guirguis A, Almond M, Day C, Chilcot J, Da Silva-Gane M, Davenport A, Fineberg NA, Spencer B, Wellsted D, Farrington K (2017) Sertraline versus placebo in patients with major depressive disorder undergoing hemodialysis: a randomized, controlled feasibility trial. *Clin J Am Soc Nephrol* 12: 280–286. <https://doi.org/10.2215/CJN.02120216>
- GBD Chronic Kidney Disease Collaboration (2020) Global, regional, and national burden of chronic kidney disease, 1990–2017: a systematic analysis for the Global Burden of Disease Study 2017. *Lancet* 395: 709–733. [https://doi.org/10.1016/S0140-6736\(20\)30045-3](https://doi.org/10.1016/S0140-6736(20)30045-3)
- GBD 2019 Diseases and Injuries Collaborators (2020) Global burden of 369 diseases and injuries in 204 countries and territories, 1990–2019: a systematic analysis for the Global Burden of Disease Study 2019. *Lancet* 396: 1204–1222. Erratum in: *Lancet* 396: 1562. [https://doi.org/10.1016/S0140-6736\(20\)30925-9](https://doi.org/10.1016/S0140-6736(20)30925-9)

- Gebrie MH, Ford J (2019) Depressive symptoms and dietary non-adherence among end stage renal disease patients undergoing hemodialysis therapy: systematic review. *BMC Nephrol* **20**: 429. <https://doi.org/10.1186/s12882-019-1622-5>
- Jones CB, Bargman JM (2018) Should we look beyond Kt/V urea in assessing dialysis adequacy? *Semin Dial* **31**: 420–429. <https://doi.org/10.1111/sdi.12684>
- Kimmel PL, Fwu CW, Abbott KC, Moxey-Mims MM, Mendley S, Norton JM, Eggers PW (2019) Psychiatric illness and mortality in hospitalized ESKD dialysis patients. *Clin J Am Soc Nephrol* **14**: 1363–1371. <https://doi.org/10.2215/CJN.14191218>
- Koesters M, Ostuzzi G, Guaiana G, Breilmann J, Barbui C (2017) Vortioxetine for depression in adults. *Cochrane Database Syst Rev* **7**: CD011520. <https://doi.org/10.1002/14651858.CD011520.pub2>
- Kubanek A, Paul P, Przybylak M, Kancierz K, Rojek JJ, Renke M, Bidzan L, Grabowski J (2021) Use of sertraline in hemodialysis patients. *Medicina* (Kaunas) **57**: 949. <https://doi.org/10.3390/medicina57090949>
- Lopes AA, Albert JM, Young EW, Satayathum S, Pisoni RL, Andreucci VE, Mapes DL, Mason NA, Fukuhara S, Wikström B, Saito A, Port FK (2004) Screening for depression in hemodialysis patients: associations with diagnosis, treatment, and outcomes in the DOPPS. *Kidney Int* **66**: 2047–2053. Erratum in: *Kidney Int.* **66**: 2486. <https://doi.org/10.1111/j.1523-1755.2004.00977.x>
- Luppa M, Sikorski C, Luck T, Ehreke L, Konnopka A, Wiese B, Weyerer S, König HH, Riedel-Heller SG (2012) Age- and gender-specific prevalence of depression in latest-life – systematic review and meta-analysis. *J Affect Disord* **136**: 212–221. <https://doi.org/10.1016/j.jad.2010.11.033>
- Montgomery SA, Asberg M (1979) A new depression scale designed to be sensitive to change. *Br J Psychiatry* **134**: 382–389. <https://doi.org/10.1192/bjp.134.4.382>
- Morosini PL, Magliano L, Brambilla L, Ugolini S, Pioli R (2000) Development, reliability and acceptability of a new version of the DSM-IV Social and Occupational Functioning Assessment Scale (SOFAS) to assess routine social functioning. *Acta Psychiatr Scand* **101**: 323–329
- Nagler EV, Webster AC, Vanholder R, Zoccali C (2012) Antidepressants for depression in stage 3–5 chronic kidney disease: A systematic review of pharmacokinetics, efficacy and safety with recommendations by European Renal Best Practice (ERBP) *Nephrol Dial Transplant* **27**: 3736–3745. <https://doi.org/10.1093/ndt/gfs295>
- Ozieh MN, Garacci E, Walker RJ, Palatnik A, Egede LE (2021) The cumulative impact of social determinants of health factors on mortality in adults with diabetes and chronic kidney disease. *BMC Nephrol* **22**: 76. <https://doi.org/10.1186/s12882-021-02277-2>
- Palmer S, Vecchio M, Craig JC, Tonelli M, Johnson DW, Nicolucci A, Pellegrini F, Saglimbene V, Logroscino G, Fishbane S, Strippoli GF (2013) Prevalence of depression in chronic kidney disease: systematic review and meta-analysis of observational studies. *Kidney Int* **84**: 179–191. <https://doi.org/10.1038/ki.2013.77>
- Palmer SC, Natale P, Ruospo M, Saglimbene VM, Rabindranath KS, Craig JC, Strippoli GF (2016) Antidepressants for treating depression in adults with end-stage kidney disease treated with dialysis. *Cochrane Database Syst Rev* **2016**: CD004541. <https://doi.org/10.1002/14651858.CD004541.pub3>
- Pena-Polanco JE, Mor MK, Tohme FA, Fine MJ, Palevsky PM, Weisbord SD (2017) Acceptance of antidepressant treatment by patients on hemodialysis and their renal providers. *Clin J Am Soc Nephrol* **12**: 298–303. <https://doi.org/10.2215/CJN.07720716>
- Schwenk MH, Verga MA, Wagner JD (1995) Hemodialyzability of sertraline. *Clin Nephrol* **44**: 121–124
- Taraz M, Khatami MR, Dashti-Khavidaki S, Akhonzadeh S, Noorbala AA, Ghaeli P, Taraz S (2013) Sertraline decreases serum level of interleukin-6 (IL-6) in hemodialysis patients with depression: results of a randomized double-blind, placebo-controlled clinical trial. *Int Immunopharmacol* **17**: 917–923. <https://doi.org/10.1016/j.intimp.2013.09.020>
- Wang J, Wu X, Lai W, Long E, Zhang X, Li W, Zhu Y, Chen C, Zhong X, Liu Z, Wang D, Lin H (2017) Prevalence of depression and depressive symptoms among outpatients: a systematic review and meta-analysis. *BMJ Open* **7**: e017173. <https://doi.org/10.1136/bmjopen-2017-017173>

Circ_PWWP2A promotes lung fibroblast proliferation and fibrosis via the miR-27b-3p/GATA3 axis, thereby aggravating idiopathic pulmonary fibrosis

LiQing Su^{1#}, Ying Nian^{1#} and TianJi Zhu^{1✉}

Department of Respiratory and Critical Care Medicine, Affiliated Hospital of Inner Mongolia Medical University, Hohhot City, Inner Mongolia Autonomous Region, 010050, China

Objective: This paper was to investigate the effect of circ_PWWP2A-mediated miR-27b-3p/GATA3 axis on idiopathic pulmonary fibrosis (IPF). **Methods:** circ_PWWP2A expression in lung fibroblasts MLg2908 induced by different concentrations of TGF- β was detected. The relationship between circ_PWWP2A or GATA3 and miR-27b-3p was analyzed by RNA immunoprecipitation and dual-luciferin reporter assay. The proliferation of MLg2908 cells was determined by MTT. GATA3, α -SMA, Collagen-I, and Collagen-III in cells were detected by RT-qPCR and Western blot. The rat model of IPF induced by bleomycin (BLM) was constructed and treated with circ_PWWP2A siRNA injection. HE and Masson staining were of utility to evaluate the pathological conditions of rat lung tissue, and circ_PWWP2A, miR-27b-3p, and GATA3 levels in lung tissues were detected by RT-qPCR. Immunohistochemistry was used to detect the staining of α -SMA, collagen I, and collagen III in the lung tissues of rats. **Results:** circ_PWWP2A in MLg2908 cells induced by TGF- β decreased in a concentration-dependent manner. MLg2908 cells transfected with circ_PWWP2A siRNA were induced by 5 ng/ml TGF- β , decreasing circ_PWWP2A and GATA3 levels, increasing miR-27b-3p expression, and suppressing cell proliferation. The targeting relationship between circ_PWWP2A and miR-27b-3p, as well as miR-27b-3p and GATA3, was confirmed. Depleting miR-27b-3p reduced the inhibitory effect of circ_PWWP2A down-regulation on the proliferation of TGF- β -treated MLg2908 cells, accompanied by increased expression of α -SMA, Collagen 1, and Collagen 3, and increased expression of GATA3. The *in vivo* results showed that BLM-induced fibrosis in rat lung tissue was obvious, accompanied by increased expression of circ_PWWP2A and GATA3, decreased expression of miR-27b-3p, and deepened staining of α -SMA, collagen I, and collagen III, but circ_PWWP2A siRNA could improve these phenomena. **Conclusion:** Silencing circ_PWWP2A can inhibit the proliferation of lung fibroblasts induced by TGF- β through the miR-27b-3p/GATA3 axis, and reduce BLM-induced pulmonary fibrosis in rats, which may be a potential therapeutic target for IPF.

Keywords: Lung fibroblasts, circ_PWWP2A, miR-27b-3p, GATA3, Idiopathic pulmonary fibrosis

Received: 10 August, 2022; **revised:** 25 May, 2023; **accepted:** 29 May, 2023; **available on-line:** 06 September, 2023

✉e-mail: hutianjinmg@hotmail.com

[#]These authors contributed equally to this work

Abbreviations: circRNA, Circular RNA; IPF, Idiopathic pulmonary fibrosis

INTRODUCTION

Idiopathic pulmonary fibrosis (IPF) is a diffuse parenchymal lung disease, which is a group of interstitial lung diseases (Martinez *et al.*, 2017; Xaubet *et al.*, 2017). IPF is a representative interstitial lung disease (Sgalla *et al.*, 2016) that is pathologically featured by diffuse alveolitis, pulmonary fibrosis, and progressive scarring. The clinical manifestations are mainly no obvious cause, and the initial symptoms are exertional dyspnea and chronic cough without sputum (Konigsberg *et al.*, 2021; Wolters *et al.*, 2014).

At present, there are mainly anti-inflammatory drugs (such as prednisone) for inflammation, and immunosuppressants (such as cyclophosphamide) for immune response. However, the application of these two types of drugs can affect the inflammatory response of IPF, but not improve the progress of immune response and immune response much, or increase the survival rate of patients (Hewlett *et al.*, 2018; Somogyi *et al.*, 2019). These include nintedanib (Ofev[®]) and pirfenidone (Esbriet[®]). These medications are called anti-fibrotic agents, Nintedanib inhibits inflammation and fibrosis by blocking a variety of tyrosine kinase receptors, including platelet-derived growth factor, vascular endothelial growth factor, and fibroblast growth factor (Hilberg *et al.*, 2008). The main antifibrotic effect of pirfenidone is to down-regulate transforming growth factor- β (Nakayama *et al.*, 2008). Such as Tananchai *et al.* data confirm that multicenter phase III randomized controlled trial of pirfenidone and nintedanib (ASCEND and INPULSIS Q7) showed a similar reduction in lung function decline compared with placebo (King *et al.*, 2014). The long-term effects of antifibrotic therapy on mortality are unknown. Real-world and registry-based studies have been published describing the long-term use of antifibrotic drugs in clinical practice (Nathan *et al.*, 2017). These studies showed that about 40 percent of patients had drug-related adverse effects, including diarrhea, gastrointestinal distress, and elevated transaminases. However, only 5% of patients receiving antifibrotic therapy permanently discontinued treatment (Ceri *et al.*, 2019). Such studies also add to the growing number of reports on the long-term efficacy of antifibrotic drugs. Therefore, IPF has a poor prognosis and a high mortality rate (Wakwaya & Brown, 2019). IPF generally affects men after the age of 60 years and a median survival time of 2–4 years, even worse than many cancers (Vancheri *et al.*, 2010; Sgalla *et al.*, 2016). It was reported that the survival rate is as low as 2–5 years after diagnosis of the IPF (Richeldi *et*

al., 2017). Therefore, how to prevent and treat IPF more effectively is a difficult problem faced by clinicians.

Circular RNA (circRNA) closed circular RNA molecules formed by covalent bonds (Kristensen *et al.*, 2019). Studies have proved that circRNAs exerts a regulatory role in eukaryotic life activities and disease developments, such as cardiovascular diseases (Altesha *et al.*, 2019), tumors (Lei *et al.*, 2020; Li *et al.*, 2020), kidney-related diseases (Jin *et al.*, 2020), and lung-related diseases (M. *et al.*, 2020), including IPF (Li *et al.*, 2018). For example, *hsa_circ_0058493* knockdown inhibits fibrosis by affecting the epithelial-mesenchymal transition (EMT) process in IPF (Cheng *et al.*, 2022). *Has_circ_PWWP2A*, also known as *hsa_circ_0074837* (Zhang *et al.*, 2018), was found to be associated with promoting liver fibrosis (Liu *et al.*, 2019). A reliable function of circRNAs is to directly or indirectly bind target miRNAs to inhibit miRNA function through a process commonly referred to as miRNA sponge adsorption (Huang *et al.*, 2020). Through ENCORI comprehensive database, we found that *circ_PWWP2A* has a potential binding site with *miR-27b-3p*. *miR-27b-3p* has been discovered to be correlated with renal fibrosis (Conserva *et al.*, 2019). Microarray analysis revealed that downregulation of *miR-27b-3p* is associated with fibrosis (Kim *et al.*, 2017). Furthermore, *miR-27b-3p* expression alters significantly during lung exacerbation in cystic fibrosis patients (Stachowiak *et al.*, 2020).

Therefore, this article targeted to reveal the mechanism related to *circ_PWWP2A* and the regulatory network of *circ_PWWP2A/miR-27b-3p/GATA3* in IPF, with the purpose to develop molecule-based therapy.

MATERIALS AND METHODS

Cell culture and treatment

The murine lung fibroblast cell line MLg2908 (ATCC, CCL-206, USA) was maintained in EMEM (30-2003, ATCC, USA) containing 10% FBS and treated with different concentrations of recombinant human TGF- β (10 ng/ml; PeproTech, USA; 0, 5, 10 ng/ml) for 24 h (Y. J. Li *et al.*, 2006). *circ_PWWP2A* siRNA#1, *circ_PWWP2A* siRNA#2, and NC siRNA were transfected in MLg2908 cells according to Lipofectamine 3000 reagent (L3000001, Thermo Fisher Scientific), and the more effective siRNA was selected for later experiments. MLg2908 were treated with TGF- β at an optimal concentration of 5 ng/ml for 24 h. Before induction, Cells were cultured in 6-well plates with a concentration of 4×10^5 cells/well, the cells were transfected with the following plasmids, including *circ_PWWP2A* siRNA#2 and *miR-27b-3p* inhibitors (#AM17000, Thermo Fisher Scientific). Cells were incubated with 2 ml Opti-MEM medium (GIBCO, USA) containing plasmids (1 μ g) and Lipofectamine 3000 (2.5 μ l). The medium was changed after 6 h, and the RNA extraction was performed at 48 h to verify the transfection efficiency.

RNA immunoprecipitation (RIP)

Protein-A/G-coated magnetic beads were resuspended in 100 μ l NT-2 buffer and let stand with 5 μ g AGO2-labeled antibody (Millipore, Billerica, MA, USA). Cells were centrifuged, and 100 μ l of the supernatant was added to 900 μ l of magnetic beads resuspended in NET-2 buffer. Appropriate antisense probes were designed according to the unique trans-cleavage site of circRNA, and the corresponding sense sequences were used as control negative

probes. Briefly, cells were lysed in RIP lysis buffer, then supernatants were transferred to nuclease-free tubes, magnetic beads conjugated to Ago2 or IgG antibodies were added and incubated for 6 hours at 4°C. The immunoprecipitates bound to the beads were eluted with elution buffer, and the purified RNA fragments were analyzed by RT-qPCR.

MTT experiment

Cells were taken after trypsinization and centrifuged to prepare a cell suspension at 5×10^4 cells/mL. Seeded into 96-well plates to 45 Wells, 200 μ L of cell suspension was cultured for 24 h and centrifuged at 1000 r/min (supernatant was removed). Afterward, 200 μ L of serum-free culture medium and 20 μ L of 5 mg/ml MTT were added to each well for an additional 4 h, centrifuged at 1000 rpm/min (supernatant was removed), and reacted with 200 μ L DMSO to record OD₄₉₀ value on a microplate reader.

Luciferase activity assay

Bioinformatics software predicted the binding sites of *circ_PWWP2A* and *miR-27b-3p*, as well as *miR-27b-3p* and *GATA3*, and a *miR-27b-3p* recombinant firefly luciferase reporter plasmid containing the *circ_PWWP2A/GATA3* binding sequence was designed and synthesized. *circ_PWWP2A* WT/*circ_PWWP2A* MUT/*GATA3* WT/*GATA3* MUT was co-transfected with mimic NC or *miR-27b-3p* mimics into MLg2908, respectively. After 48 h, the luciferase activity of the cells was detected according to the instructions of the Dual-Luciferase reporter system kit (Promega).

Immunoblot analysis

Proteins were extracted by lysing cells with RIPA buffer (Sigma, USA) containing protease inhibitors and subsequently quantified by a BCA protein concentration assay kit (Beyotime Biotechnology, Nanjing, China). Total protein was loaded onto PVDF membrane (ThermoFisher Scientific, USA) after 10% SDS-PAGE gel electrophoresis, then blocked with 5% nonfat milk powder, and with primary antibodies at 4°C overnight, including α -SMA at 1 μ g/ml (ab5694, Abcam), collagen I (1:5000, ab260043, Abcam), collagen III (1:5000, ab7778, Abcam), *GATA3* (1:1000, ab199428, Abcam) and GAPDH (1:2500, ab9548, Abcam). The next day, secondary antibodies were added and incubated for 40 min, the membrane interacted with HRP-conjugated goat anti-rabbit IgG secondary antibody (#31460, Thermo Fisher Scientific). Immunoblots were visualized in IBright FL1500 Intelligent Imaging System (ThermoFisher, USA) and GAPDH was used as an internal control.

Establishment and treatment of IPF rat model

Twenty-four SD male rats, weighing about 200 g, were treated accordingly (6 rats in each group). The rats were anesthetized by intraperitoneal 10% chloral hydrate and fixed in a supine position to expose the trachea. After anesthesia, 1 mg BLM was added to 0.5 ml PBS for intratracheal administration (Otsuka *et al.*, 2017), while the Sham group was only given 0.5 ml PBS. Fourteen days after modeling (day 15), 1 μ l/g siRNA was intravenously injected into rats at 0.75 mg/kg/day, three times every other day. Twenty-four hours after the last injection, rats were euthanized by pentobarbital sodium, and lungs were harvested for HE staining and Masson stain-

Table 1. Primer sequences for PCR

Genes	Sequence (5'-3')	
	Forward	Reverse
circ_PWWP2A	AAGACAGGACTTGAGAAAATGC	GGCATGGCTTCTGGTTTATC
miR-27b-3p	AGTGGCTAAGTTCTGCCTCAAC	CTCAACTGGTGTCTGGAGTC
GATA3	AAGCTCAGTATCCGCTGACG	GTTCCGTAGTAGGACGGGAC
α -SMA	CCCAGACATCAGGGAGTAATGG	TCTATCGGATACTTCAGCGTCA
collagen I	GCTCTCTTAGGGGCCACT	ATTGGGGACCTTAGGCCAT
collagen III	CTGTAACATGGAACTGGGGAAA	CCATAGCTGAACTGAAAACCACC
U6	GATTCGGACGTTGTATCGCTG	CTCGGAGTTGCACCAATCC
GAPDH	TGGATTGGACGCGATTGGTC	TTTGCACTGGTACGTGTGTAT

Note: circ_PWWP2A, circular RNA PWWP2A; miR-27b-3p, microRNA-27b-3p; GATA3, GATA Binding Protein-3; α -SMA, α -smooth muscle actin; GAPDH, glyceraldehyde-3-phosphate dehydrogenase.

ing (Milara *et al.*, 2018; Otsuka *et al.*, 2017). Fibrosis was scored according to the Ashcroft assay.

Immunohistochemistry

Fresh paraffin tissues (4 μ m) were placed in an oven at 65°C for 2 h, deparaffinized to water, and microwave in EDTA buffer. Sections were placed in 3% hydrogen peroxide solution for 10 min, blocked with 5% BSA for 20 min, added about 50 μ l of diluted primary antibody overnight including α -SMA at 1 μ g/ml (ab5694, Abcam), collagen I (1:5000, ab260043, Abcam), collagen III (1:5000, ab7778, Abcam), GATA3 (1:1000, ab199428, Abcam) and GAPDH (1:2500, ab9548, Abcam), and 50-100 μ l secondary antibody for 50 min (membrane interacted with HRP-conjugated goat anti-rabbit IgG secondary antibody (#31460, Thermo Fisher Scientific). After the addition of DAB solution, the sections were counterstained with hematoxylin, differentiated with 1% hydrochloric acid alcohol, immersed in ammonia, dehydrated with gradient alcohol, cleared with xylene, and mounted with neutral gum.

RT-qPCR

Cell and tissue RNA was extracted by the Trizol method, and the concentration and quality of the RNA solution were determined on a DU730 instrument. RNA

was reverse transcribed into cDNA using SuperScript IV Reverse Transcriptase (#18090010, Invitrogen) and treated with qPCR according to the SuperScript III Platinum SYBR Green One-Step qRT-PCR Kit (#11736059, Invitrogen). The primer sequences are shown in Table 1. Transcription level of the target gene was calculated by $2^{-\Delta\Delta C_t}$ method.

Statistical analysis

SPSS 19.0 software was of utility for statistical analysis and Graphpad 6.0 was for drawing graphs. One-way analysis of variance, along with Tukey's HSD test was suitable for assessing data collected from multiple groups. Differences were considered statistically significant at $P < 0.05$.

RESULTS

circ_PWWP2A can affect the proliferation of TGF- β -treated MLg2908

To investigate the function of circ_PWWP2A in MLg2908 cells, we first knocked it down by transforming the cells using two lentiviral vectors encoding independent shRNAs targeting circ_PWWP2A.

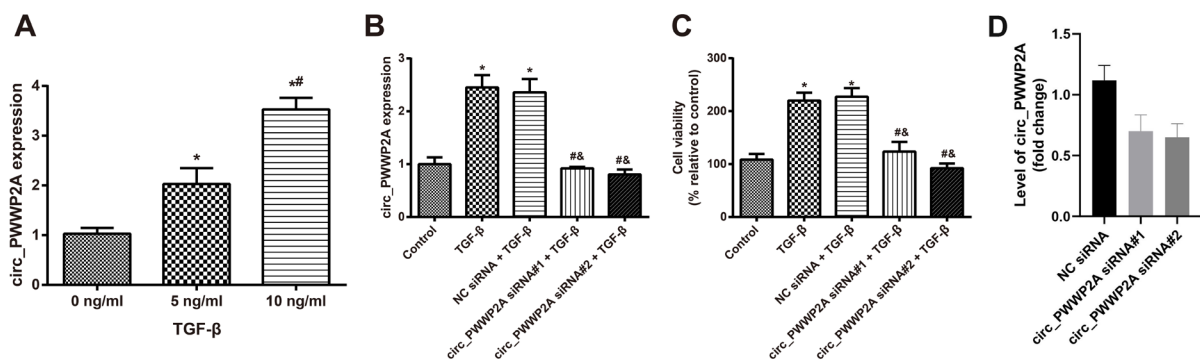


Figure 1. circ_PWWP2A can inhibit the proliferation of mouse lung fibroblasts treated with TGF- β

(A) circ_PWWP2A expression after MLg2908 cells were treated with different concentrations of TGF- β (0, 5, 10 ng/ml), *vs. 0 ng/ml TGF- β , $P < 0.05$; #vs. 5 ng/ml TGF- β , $P < 0.05$; (B) circ_PWWP2A expression in MLg2908 cells co-treated with circ_PWWP2A siRNA and 5 ng/ml TGF- β ; (C) Proliferation of MLg2908 cells after co-treatment with circ_PWWP2A siRNA and 5 ng/ml TGF- β ; *vs. Control group, $P < 0.05$; #vs. TGF- β group and NC siRNA + TGF- β group, $P < 0.05$; (D) qRT-PCR analysis of circ_PWWP2A levels in MLg2908 cells infected with a lentiviral vector encoding circ_PWWP2A siRNA#1 or circ_PWWP2A siRNA#2

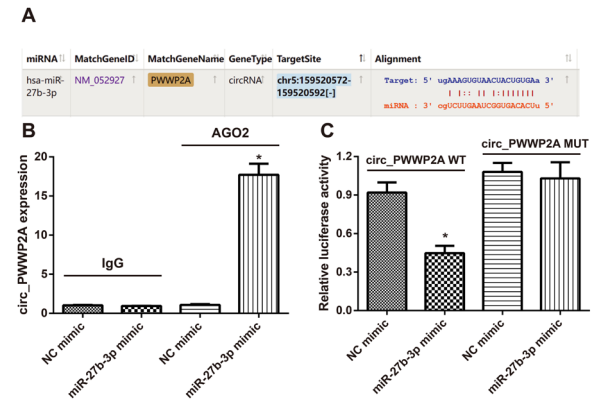


Figure 2. circ_PWWP2A can adsorb miR-27b-3p (A) ENCORI found that circ_PWWP2A and miR-27b-3p have potential binding sites; (B) RIP to further verify the interaction relationship between circ_PWWP2A and miR-27b-3p; (C) dual luciferase reporter experiment to verify the targeting relationship between circ_PWWP2A and miR-27b-3p; *vs. other three groups, $P < 0.05$.

RT-qPCR analysis confirmed that circ_PWWP2A levels were suppressed to a greater degree by expression of circ_PWWP2A (Fig. 1D), which was then utilized in subsequent experiments. In MLg2908 cells treated with different concentrations of TGF- β (0, 5, 10 ng/ml), circ_PWWP2A was increased in a concentration-dependent manner (Fig. 1A), indicating that circ_PWWP2A is promoted during lung fibroblast activation. MLg2908 cells were transfected with circ_PWWP2A siRNA and then induced by 5 ng/ml TGF- β , and it was found that circ_PWWP2A in the cells was decreased (Fig. 1B), After 48 h of TGF- β treatment accompanied by a decrease in proliferation activity (Fig. 1C). It indicated that the low expression of circ_PWWP2A could inhibit the proliferation of lung fibroblasts induced by TGF- β .

circ_PWWP2A can adsorb miR-27b-3p

Bioinformatics analysis ENCORI found that circ_PWWP2A has a potential binding site with miR-27b-3p (Fig. 2A). Next, RIP assays in MLg2908 cells further verified the interaction between circ_PWWP2A and miR-27b-3p. circ_PWWP2A was richly precipitated with anti-AGO2 after overexpressing miR-27b-3p in cells (Fig. 2B). Dual-luciferase reporter gene assay results showed that miR-27b-3p can reduce the luciferase activity of circ_PWWP2A WT (Fig. 2C) but not circ_PWWP2A MUT, indicating that circ_PWWP2A has a direct interaction with miR-27b-3p.

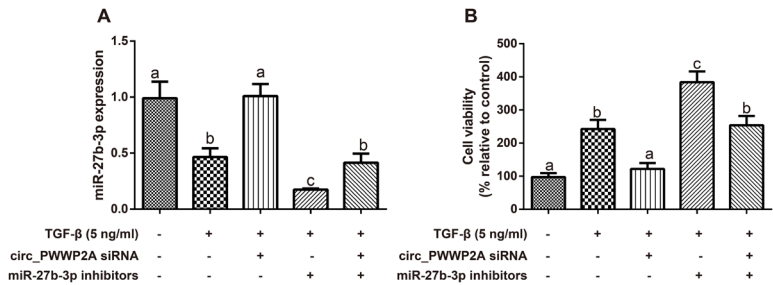


Figure 3. Depleting miR-27b-3p enhances the proliferation of TGF- β -induced MLg2908 cells (A) miR-27b-3p expression in MLg2908 cells; (B) Proliferation of MLg2908 cells; the same letter indicates no statistical significance, $P > 0.05$; different letters indicate statistical differences, $P < 0.05$.

Consuming miR-27b-3p enhances the proliferation of TGF- β -induced MLg2908 cells

Figure 3A showed that 5 ng/ml TGF- β can inhibit miR-27b-3p expression in MLg2908 cells, and after co-treatment with miR-27b-3p inhibitors, miR-27b-3p expression was further reduced, and the accompanying cell proliferation was further activated. circ_PWWP2A siRNA could reduce TGF- β -regulated inhibition of miR-27b-3p, that is, circ_PWWP2A siRNA augmented miR-27b-3p expression in TGF- β -treated MLg2908 cells.

Silencing miR-27b-3p affects fibrosis-related genes in lung fibroblasts

α -SMA, collagen I, and collagen III in cells were determined by RT-qPCR and immunoblot analysis (Fig. 4A, B), demonstrating an increase α -SMA, collagen I, and collagen III increased in MLg2908 after TGF- β induction, which was promoted α -SMA, collagen I, and collagen III express after co-treatment with miR-27b-3p inhibitors, but alleviated α -SMA, collagen I, and collagen express III after circ_PWWP2A siRNA co-treatment. miR-27b-3p inhibitor co-treatment lessened circ_PWWP2A siRNA-regulated suppression of these fibrosis-related genes.

circ_PWWP2A can regulate GATA3 expression through miR-27b-3p

ENCORI database showed that GATA3 was a direct target gene of miR-27b-3p (Fig. 5A). The interaction between the two was further verified by luciferase experiments, as the results showed that miR-27b-3p mimic reduced the luciferase activity of GATA3 WT without affecting that of GATA3 MUT (Fig. 5B). Our test results also found that circ_PWWP2A siRNA could inhibit the increase of GATA3 in MLg2908 cells induced by TGF- β , while miR-27b-3p inhibitors did oppositely. GATA3 was down-regulated in MLg2908 cells co-treated with TGF- β and circ_PWWP2A siRNA, but this phenomenon was reversed by miR-27b-3p inhibitors (Fig. 5C–E).

Therapeutic effect of circ_PWWP2A siRNA on IPF rats

HE staining and Masson staining showed (Fig. 6A): in rats receiving sham operation, lung structure was normal, the alveolar interval was uniform, no obvious exudation was seen in the cavity, and a small number of collagen fibers dyed in light blue can be seen in the alveoli, but without obvious pathological change. However, BLM injection destroyed the alveolar structure, reduced the alveolar cavity, exfoliated alveolar epithelium and protein exudate, and caused obvious collagen deposition and fibrosis areas. circ_PWWP2A siRNA-treated rats consti-

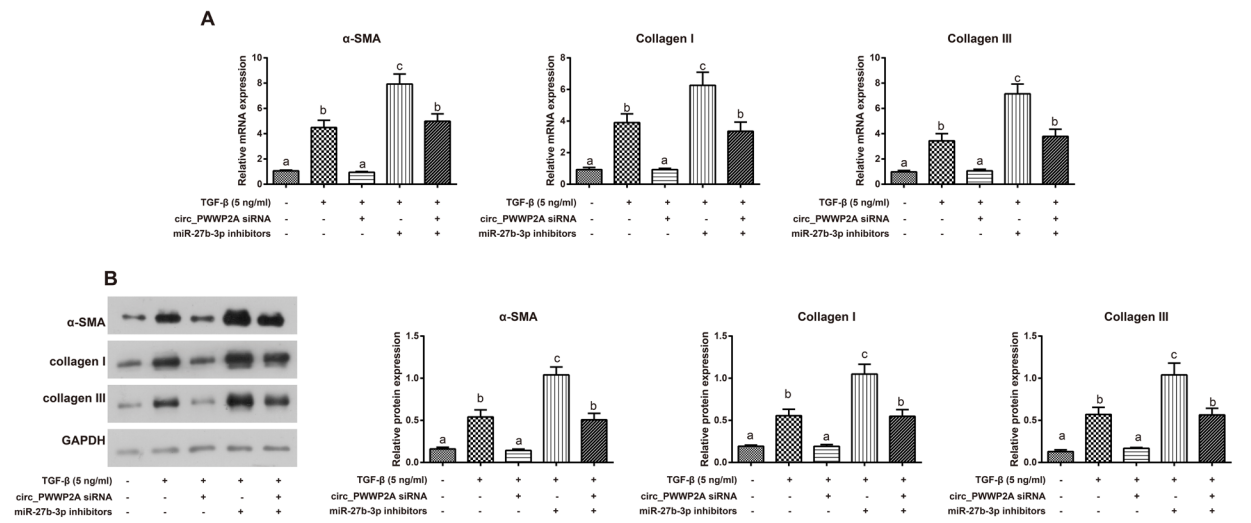


Figure 4. Silencing miR-27b-3p affects fibrosis-related genes in lung fibroblasts (A) qRT-PCR analysis α-SMA, collagen I, and collagen III in MLg2908 cells (Three technical replicates and three biological replicates); the same letter indicates no statistical significance, $P>0.05$; different letters indicate statistical differences, $P<0.05$. (B) WB analysis α-SMA, collagen I, and collagen III in MLg2908 cells (Three technical replicates and three biological replicates); the same letter indicates no statistical significance, $P>0.05$; different letters indicate statistical differences, $P<0.05$.

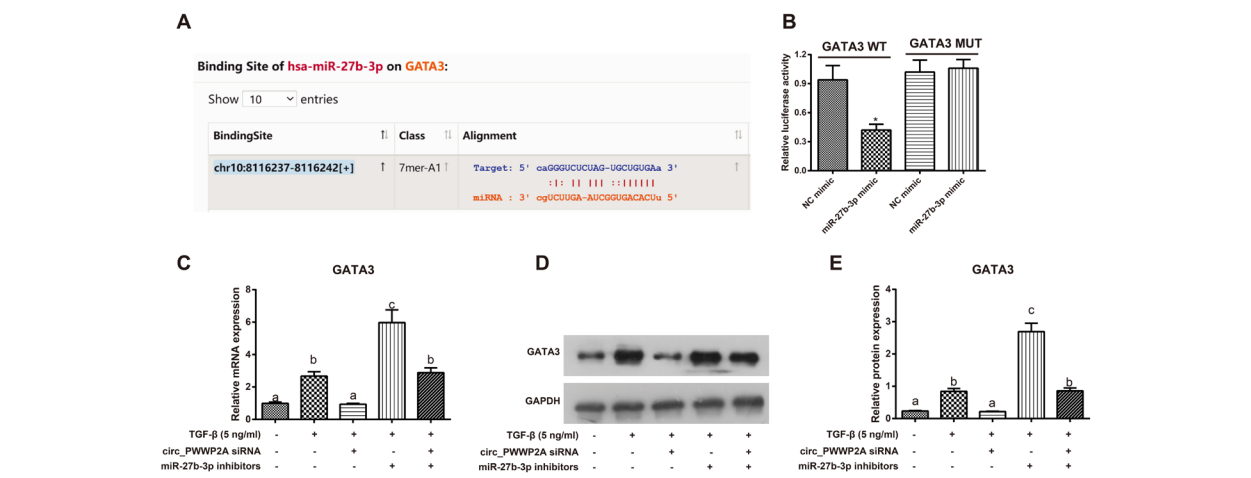


Figure 5. circ_PWWP2A can regulate GATA3 expression through miR-27b-3p (A) ENCORI showed that GATA3 is a direct target gene of miR-27b-3p; (B) Dual luciferase reporter experiment verified the targeting relationship between GATA3 and miR-27b-3p, *vs. other three groups, $P<0.05$; (C-E) GATA3 expression in cells; the same letter indicates no statistical significance, $P>0.05$; different letters indicate statistical differences, $P<0.05$.

tuted mild hyperplasia of fibroblasts, deposition of collagen fibers in the pleura and alveolar septa, and mild to moderate pulmonary fibrosis. Ashcroft scores indicated that BLM-induced rats had higher Ashcroft scores, but circ_PWWP2A siRNA reduced Ashcroft scores in BLM-treated rats (Fig. 6B). BLM-induced increased expression of circ_PWWP2A and GATA3 in rat lung tissue, while decreased expression of miR-27b-3p, was reversed by circ_PWWP2A siRNA treatment (Fig. 6C). BLM rats had enhanced immunohistochemical staining results of α-SMA, collagen I and collagen III in lung tissue, but the staining degree was reduced after circ_PWWP2A siRNA injection (Fig. 6D).

DISCUSSION

In humans, IPF is a progressive disease associated with aging caused by uncontrolled proliferation and dif-

ferentiation of fibroblasts resulting from sustained damage to the alveolar epithelium. These myofibroblasts are responsible for hyperproliferation, EMT, ECM production, and contribute to collagen deposition in the affected organ (King *et al.*, 2011). Transforming growth factor-β1 (TGF-β1) is a key member of the TGF-β superfamily. It was discovered in 1983 for its ability to stimulate the growth of rat fibroblasts cultured in soft AGAR and has been identified as a master cytokine in liver fibrosis (Xu *et al.*, 2016). In fibrosis, increased TGF-β signaling significantly affects the behavior of the fibroblast population, which represents the majority of cells in fibrotic lesions. In addition, low levels of TGF-β promoted fibroblast proliferation (Zhang *et al.*, 2017). These activities may explain the number of fibroblasts in fibrotic lesions. TGF-β-induced mesenchymal characteristics enable epithelial and endothelial cells to contribute to fibroblast popula-

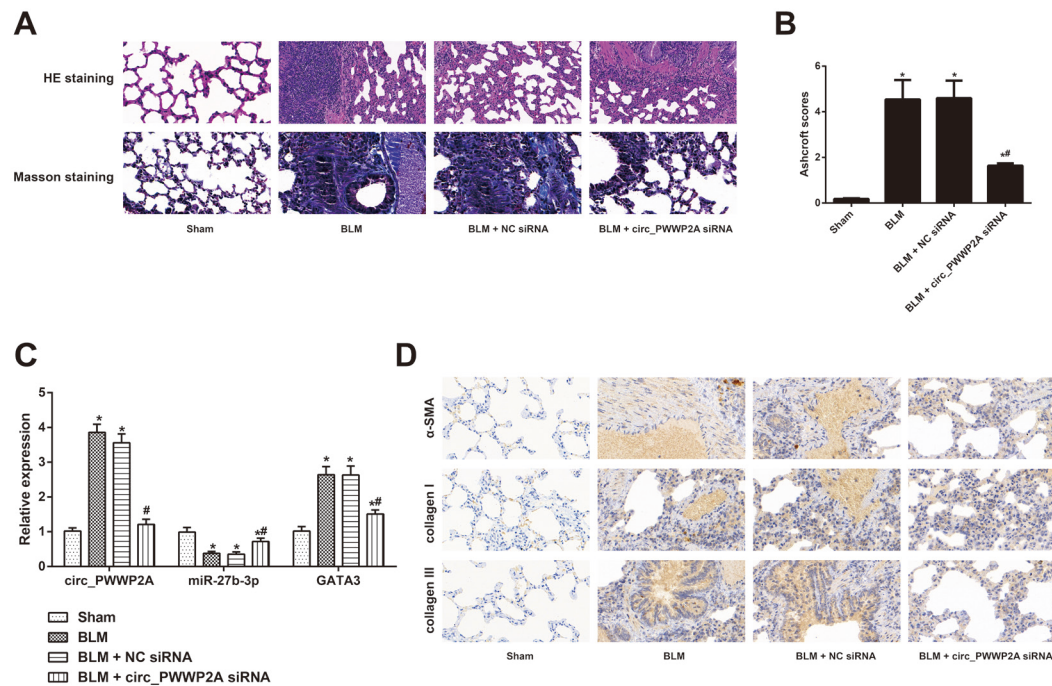


Figure 6. Therapeutic effect of circ_PWWP2A siRNA on IPF rats

(A) HE staining and Masson staining of lung tissue; (B) Ashcroft scores in lung tissue; (C) circ_PWWP2A, miR-27b-3p and GATA3 expression in lung tissue; (D) Immunohistochemical detection of α-SMA, collagen I, and collagen III staining in lung tissue.

tion in fibrotic diseases, which has been revealed in a mouse model of fibrosis (Katsuno *et al.*, 2021).

With the rapid development of deep transcriptome sequencing technology, the research on noncoding RNAs is growing exponentially (Matsui *et al.*, 2017). Although in some cases ncRNAs lack protein-coding capabilities and appear to lack biological functions, increasing evidence confirms that they play a critical role in controlling gene expression through multiple mechanisms, such as targeting transcripts (Liu *et al.*, 2012). Reports have demonstrated that several lncRNAs and miRNAs play critical roles in the progression of IPF. For instance, Li and others (Li *et al.*, 2020) reported that circTADA2A could repress fibroblasts activation and proliferation *via* miR-526b/Cav1 and miR-203/Cav2 pathway, thus alleviating IPF. Another hsa_circ_0044226 was markedly higher in lung tissues from IPF patients than from healthy controls. which RLE-6TN cells and in a bleomycin-induced mouse model of IPA and diminished TGF-β1-induced fibrosis. these findings indicate that downregulation of hsa_circ_0044226 attenuates pulmonary fibrosis *in vitro* and *in vivo* by inhibiting CDC27, which in turn suppresses EMT. This suggests hsa_circ_0044226 may be a useful therapeutic target for the treatment of IPF (Qi *et al.*, 2020). In addition, lncRNA H19 (Lu *et al.*, 2018), MEG3 (Gokey *et al.*, 2018) have been also confirmed to play critical roles in IPF.

At present, previous studies have found that circ_PWWP2A plays a role in various diseases. For example, in OB-6 osteoblasts and primary human osteoblasts, overexpression of circ_PWWP2A can effectively inhibit dexamethasone-induced cell death and apoptosis (Hong *et al.*, 2019). circ_PWWP2A is up-regulated in mouse fibrotic liver tissue and is positively correlated with HSC activation and proliferation (Liu *et al.*, 2019). Similarly, MLg2908 cells were treated with TGF-β (0, 5, 10 ng/ml) and circ_PWWP2A expression was analyzed to be increased in a concentration-dependent manner. Animal

experiments also found that circ_PWWP2A was also up-regulated in BLM-induced rat lung tissue, suggesting that circ_PWWP2A involves the activation of lung fibroblasts and may be a pathogenic factor for IPF. After inhibiting circ_PWWP2A expression in TGF-β-induced MLg2908 cells, cell proliferation ability was reduced, which verified our speculation.

The most important function of circRNA is to play as miRNA “sponge” (Shi *et al.*, 2020). The present study proved that circ_PWWP2A could adsorb miR-27b-3p. In this study, miR-27b-3p expression in MLg2908 cells induced by TGF-β was decreased, which is consistent with previous reports: for example, exosomal miR-27b derived from human umbilical cord mesenchymal stem cells can ameliorate subretinal fibrosis (Li *et al.*, 2021). Also, miR-27b-3p knockout can reduce cardiac hypertrophy, fibrosis, and inflammation induced by a pathological cardiac hypertrophy model (Li *et al.*, 2021). Furthermore, miR-27b-3p overexpression attenuates renal fibrosis by downregulating α-SMA and collagen III (Bai *et al.*, 2021). All of the studies indicate that miR-27b-3p is a fibrosis-related gene, and its overexpression the role can be anti-fibrotic. Our data further described that low expression of miR-27b-3p could reverse the effect of circ_PWWP2A siRNA on TGF-β-induced mouse lung fibroblast proliferation, and circ_PWWP2A siRNA could reduce the expression of miR-27b-3p in lung tissue of IPF rats, indicating that circ_PWWP2A could adsorb miR-27b-3p thus promoting TGF-β-induced proliferation and activating MLg2908 cells. α-SMA, collagen I and collagen III, as fibrosis-related genes are overexpressed in various tissue fibrosis, such as experimental pulmonary fibrosis (Huang *et al.*, 2020), cardiac fibrosis (Zeng *et al.*, 2019), liver fibrosis (Cheng *et al.*, 2019), and kidney fibrosis (Zheng *et al.*, 2019). Here, the expression patterns of α-SMA, collagen I, and collagen III in MLg2908 cells induced by TGF-β were increased, which were similar to the results of previous studies (Cheng *et al.*, 2019; Liu *et*

al., 2017), but circ_PWWP2A siRNA can inhibit its increase. circ_PWWP2A depletion can alleviate mouse liver fibrosis, accompanied by decreased α -SMA and collagen I expression (Liu *et al.*, 2019). *In vivo* experiments from the present study clarified that low expression of circ_PWWP2A can improve BLM-induced pulmonary fibrosis in rats, accompanied by decreased expression of α -SMA, collagen I, and collagen III, indicating that the inhibitory effect of circ_PWWP2A on IPF may be through the reduction of fibrosis-related genes.

miRNAs are endogenous small non-coding RNAs (Chen *et al.*, 2019), which can bind to the 3'UTR of target gene mRNA (Bartel, 2009). miR-27b-3p can target the regulation of GATA3 located at 10p14 (Enciso-Mora *et al.*, 2010). T cells regulate the activation of skin fibroblasts, which is in part achieved by GATA3-mediated unique tissue-restricted transcriptional program (Kalekar *et al.*, 2019). GATA3 is also involved in pulmonary fibrosis development (Iturra *et al.*, 2018).

On the whole, the study only discusses the mechanism from experimental tests, and future clinical experiments are required to verify our results; how GATA3 is involved in circ_PWWP2A-mediated adsorption of miR-27b-3p regulating IPF needs to be done as funds and time allow.

CONCLUSION

circ_PWWP2A expression in MLg2908 cells induced by TGF- β decreases in a concentration-dependent manner. Silencing circ_PWWP2A can inhibit the role of TGF- β in the activation and proliferation of lung fibroblasts through the miR-27b-3p/GATA3 axis, and reduce BLM-induced IPF in rats, potentially renewing therapeutic targets for IPF.

Declarations

Competing interests. The authors declare that they have no competing interests.

Ethical statement. All animal experiments were complied with the ARRIVE guidelines and performed in accordance with the National Institutes of Health Guide for the Care and Use of Laboratory Animals. The experiments were approved by the Affiliated Hospital of Inner Mongolia Medical University.

Acknowledgments. Not applicable.

Funding Statements. Not applicable.

Declaration of Conflicting Interests. Authors declared no conflict of interest.

REFERENCES

Altesha MA, Ni T, Khan A, Liu K, Zheng X (2019) Circular RNA in cardiovascular disease. *J Cell Physiol* **234**: 5588–5600. <https://doi.org/10.1002/jcp.27384>

Bai L, Lin Y, Xie J, Zhang Y, Wang H, Zheng D (2021) MiR-27b-3p inhibits the progression of renal fibrosis via suppressing STAT1. *Hum Cell* **34**: 383–393. <https://doi.org/10.1007/s13577-020-00474-z>

Bartel DP (2009) MicroRNAs: target recognition and regulatory functions. *Cell* **136**: 215–233. <https://doi.org/10.1016/j.cell.2009.01.002>

Chen L, Heikkinen L, Wang C, Yang Y, Sun H, Wong G (2019) Trends in the development of miRNA bioinformatics tools. *Brief Bioinform* **20**: 1836–1852. <https://doi.org/10.1093/bib/bby054>

Cheng Q, Li C, Yang CF, Zhong YJ, Wu D, Shi L, Chen L, Li YW, Li L (2019) Methyl ferulic acid attenuates liver fibrosis and hepatic stellate cell activation through the TGF- β 1/Smad and NOX4/ROS pathways. *Chem Biol Interact* **299**: 131–139. <https://doi.org/10.1016/j.cbi.2018.12.006>

Cheng Z, Zhang Y, Wu S, Zhao R, Yu Y, Zhou Y, Zhou Z, Dong Y, Qiu A, Xu H, Liu Y, Zhang W, Tian T, Wu Q, Gu H, Chu M (2022) Peripheral blood circular RNA hsa_circ_0058493 as a

potential novel biomarker for silicosis and idiopathic pulmonary fibrosis. *Ecotoxicol Environ Saf* **236**: 113451. <https://doi.org/10.1016/j.ecoenv.2022.113451>

Conserva F, Barozzino M, Pesce F, Divella C, Oranger A, Papale M, Sallustio F, Simone S, Laviola L, Giorgino F, Gallone A, Pontrelli P, Gesualdo L (2019) Urinary miRNA-27b-3p and miRNA-1228-3p correlate with the progression of Kidney Fibrosis in Diabetic Nephropathy. *Sci Rep* **9**: 11357. <https://doi.org/10.1038/s41598-019-47778-1>

Enciso-Mora V, Broderick P, Ma Y, Jarrett RF, Hjalgrim H, Hemminki K, van den Berg A, Olver B, Lloyd A, Dobbins SE, Lightfoot T, van Leeuwen FE, Försti A, Diepstra A, Broeks A, Vijayakrishnan J, Shield L, Lake A, Montgomery D, Roman E, Engert A, von Strandmann EP, Reiners KS, Nolte IM, Smedby KE, Adami HO, Russell NS, Glimelius B, Hamilton-Dutoit S, de Bruin M, Ryder LJ, Molin D, Sorensen KM, Chang ET, Taylor M, Cooke R, Hofstra R, Westers H, van Wezel T, van Eijk R, Ashworth A, Rostgaard K, Melbye M, Sverdlow AJ, Houlston RS (2010) A genome-wide association study of Hodgkin's lymphoma identifies new susceptibility loci at 2p16.1 (REL), 8q24.21 and 10p14 (GATA3). *Nat Genet* **42**: 1126–1130. <https://doi.org/10.1038/ng.696>

Hewlett JC, Kropski JA, Blackwell TS (2018) Idiopathic pulmonary fibrosis: Epithelial-mesenchymal interactions and emerging therapeutic targets. *Matrix Biol* **71–72**: 112–127. <https://doi.org/10.1016/j.matbio.2018.03.021>

Hong H, Sun Y, Deng H, Yuan K, Chen J, Liu W, Cui Z (2019) Dysregulation of cPWWP2A-miR-579 axis mediates dexamethasone-induced cytotoxicity in human osteoblasts. *Biochem Biophys Res Commun* **517**: 491–498. <https://doi.org/10.1016/j.bbrc.2019.07.095>

Huang A, Zheng H, Wu Z, Chen M, Huang Y (2020) Circular RNA-protein interactions: functions, mechanisms, and identification. *Theranostics* **10**: 3503–3517. <https://doi.org/10.7150/thno.42174>

Huang H, Wang X, Zhang X, Wang H, Jiang W (2020) Roxadustat attenuates experimental pulmonary fibrosis *in vitro* and *in vivo*. *Toxicol Lett* **331**: 112–121. <https://doi.org/10.1016/j.toxlet.2020.06.009>

Iturra PA, Rojas DA, Pérez FJ, Méndez A, Ponce CA, Bonilla P, Bustamante R, Rodríguez H, Beltrán CJ, Vargas SL (2018) Progression of type 2 helper T cell-type inflammation and airway remodeling in a rodent model of naturally acquired subclinical primary pneumocystis infection. *Am J Pathol* **188**: 417–431. <https://doi.org/10.1016/j.ajpath.2017.10.019>

Jin J, Sun H, Shi C, Yang H, Wu Y, Li W, Dong YH, Cai L, Meng XM (2020) Circular RNA in renal diseases. *J Cell Mol Med* **24**: 6523–6533. <https://doi.org/10.1111/jcmm.15295>

Kalekar LA, Cohen JN, Prevel N, Sandoval PM, Mathur AN, Moreau JM, Lowe MM, Nosbaum A, Wolters PJ, Haemel A, Boin F, Rosenblum MD (2019) Regulatory T cells in skin are uniquely poised to suppress profibrotic immune responses. *Sci Immunol* **4**: <https://doi.org/10.1126/sciimmunol.aaw2910>

Kim MK, Lee SK, Park JH, Lee JH, Yun BH, Park JH, Seo SK, Cho S, Choi YS (2017) Ginsenoside Rg3 decreases fibrotic and invasive nature of endometriosis by modulating miRNA-27b: *in vitro* and *in vivo* studies. *Sci Rep* **7**: 17670. <https://doi.org/10.1038/s41598-017-17956-0>

Konigsberg IR, Borie R, Walts AD, Cardwell J, Rojas M, Metzger F, Hauck SM, Fingerlin TE, Yang IV, Schwartz DA (2021) Molecular signatures of idiopathic pulmonary fibrosis. *Am J Respir Cell Mol Biol* **65**: 430–441. <https://doi.org/10.1165/rcmb.2020-0546OC>

Kristensen LS, Andersen MS, Stagsted LVW, Ebbesen KK, Hansen TB, Kjems J (2019) The biogenesis, biology and characterization of circular RNAs. *Nat Rev Genet* **20**: 675–691. <https://doi.org/10.1038/s41576-019-0158-7>

Lei M, Zheng G, Ning Q, Zheng J, Dong D (2020) Translation and functional roles of circular RNAs in human cancer. *Mol Cancer* **19**: 30. <https://doi.org/10.1186/s12943-020-1135-7>

Li D, Zhang J, Liu Z, Gong Y, Zheng Z (2021) Human umbilical cord mesenchymal stem cell-derived exosomal miR-27b attenuates subretinal fibrosis via suppressing epithelial-mesenchymal transition by targeting HOXC6. *Stem Cell Res Ther* **12**: 24. <https://doi.org/10.1186/s13287-020-02064-0>

Li G, Shao Y, Guo HC, Zhi Y, Qiao B, Ma K, Du J, Lai YQ, Li Y (2022) MicroRNA-27b-3p down-regulates FGF1 and aggravates pathological cardiac remodelling. *Cardiovasc Res* **118**: 2139–2151. <https://doi.org/10.1093/cvr/cvab248>

Li J, Sun D, Pu W, Wang J, Peng Y (2020) Circular RNAs in cancer: biogenesis, function, and clinical significance. *Trends Cancer* **6**: 319–336. <https://doi.org/10.1016/j.trecan.2020.01.012>

Li M, Hua Q, Shao Y, Zeng H, Liu Y, Diao Q, Zhang H, Qiu M, Zhu J, Li X, Ling Y, Zhang R, Jiang Y (2020) Circular RNA circBbs9 promotes PM(2.5)-induced lung inflammation in mice via NLRP3 inflammasome activation. *Environ Int* **143**: 105976. <https://doi.org/10.1016/j.envint.2020.105976>

Li R, Wang Y, Song X, Sun W, Zhang J, Liu Y, Li H, Meng C, Zhang J, Zheng Q, Lv C (2018) Potential regulatory role of circular RNA in idiopathic pulmonary fibrosis. *Int J Mol Med* **42**: 3256–3268. <https://doi.org/10.3892/ijmm.2018.3892>

- Li YJ, Azuma A, Usuki J, Abe S, Matsuda K, Sunazuka T, Shimizu T, Hirata Y, Inagaki H, Kawada T, Takahashi S, Kudoh S, Omura S (2006) EM703 improves bleomycin-induced pulmonary fibrosis in mice by the inhibition of TGF- β signaling in lung fibroblasts. *Respir Res* 7: 16. <https://doi.org/10.1186/1465-9921-7-16>
- Liu JC, Wang F, Xie ML, Cheng ZQ, Qin Q, Chen L, Chen R (2017) Osthole inhibits the expressions of collagen I and III through Smad signaling pathway after treatment with TGF- β 1 in mouse cardiac fibroblasts. *Int J Cardiol* 228: 388–393. <https://doi.org/10.1016/j.ijcard.2016.11.202>
- Liu W, Feng R, Li X, Li D, Zhai W (2019) TGF- β - and lipopolysaccharide-induced upregulation of circular RNA PWWP2A promotes hepatic fibrosis via sponging miR-203 and miR-223. *Aging (Albany NY)* 11: 9569–9580. <https://doi.org/10.18632/aging.102405>
- Martinez FJ, Collard HR, Pardo A, Raghu G, Richeldi L, Selman M, Swigris JJ, Taniguchi H, Wells AU (2017) Idiopathic pulmonary fibrosis. *Nat Rev Dis Primers* 3: 17074. <https://doi.org/10.1038/nrdp.2017.74>
- Milara J, Ballester B, Morell A, Ortiz JL, Escrivá J, Fernández E, Perez-Vizcaino F, Cogolludo A, Pastor E, Artigues E, Morcillo E, Cortijo J (2018) JAK2 mediates lung fibrosis, pulmonary vascular remodelling and hypertension in idiopathic pulmonary fibrosis: an experimental study. *Thorax* 73: 519–529. <https://doi.org/10.1136/thoraxjnl-2017-210728>
- Otsuka M, Shiratori M, Chiba H, Kuronuma K, Sato Y, Niitsu Y, Takahashi H (2017) Treatment of pulmonary fibrosis with siRNA against a collagen-specific chaperone HSP47 in vitamin A-coupled liposomes. *Exp Lung Res* 43: 271–282. <https://doi.org/10.1080/01902148.2017.1354946>
- Qiao Y, Liu L, Yin L, Xu L, Tang Z, Qi Y, Mao Z, Zhao Y, Ma X, Peng J (2019) FABP4 contributes to renal interstitial fibrosis via mediating inflammation and lipid metabolism. *Cell Death Dis* 10: 382. <https://doi.org/10.1038/s41419-019-1610-5>
- Sgalla G, Biffi A, Richeldi L (2016) Idiopathic pulmonary fibrosis: Diagnosis, epidemiology and natural history. *Respirology* 21: 427–437. <https://doi.org/10.1111/resp.12683>
- Shi Y, Jia X, Xu J (2020) The new function of circRNA: translation. *Clin Transl Oncol* 22: 2162–2169. <https://doi.org/10.1007/s12094-020-02371-1>
- Somogyi V, Chaudhuri N, Torrisi SE, Kahn N, Müller V, Kreuter M (2019) The therapy of idiopathic pulmonary fibrosis: what is next? *Eur Respir Rev* 28. <https://doi.org/10.1183/16000617.0021-2019>
- Stachowiak Z, Wojsyk-Banaszak I, Jończyk-Potoczna K, Narożna B, Langwiński W, Kycler Z, Sobkowiak P, Bręborowicz A, Szczepankiewicz A (2020) MiRNA expression profile in the airways is altered during pulmonary exacerbation in children with cystic fibrosis—a preliminary report. *J Clin Med* 9. <https://doi.org/10.3390/jcm9061887>
- Wakwaya Y, Brown KK (2019) Idiopathic pulmonary fibrosis: epidemiology, diagnosis and outcomes. *Am J Med Sci* 357: 359–369. <https://doi.org/10.1016/j.amjms.2019.02.013>
- Wolters PJ, Collard HR, Jones KD (2014) Pathogenesis of idiopathic pulmonary fibrosis. *Annu Rev Pathol* 9: 157–179. <https://doi.org/10.1146/annurev-pathol-012513-104706>
- Xaubet A, Ancochea J, Molina-Molina M (2017) Idiopathic pulmonary fibrosis. *Med Clin (Barc)* 148: 170–175. <https://doi.org/10.1016/j.medcli.2016.11.004>
- Zeng Z, Wang Q, Yang X, Ren Y, Jiao S, Zhu Q, Guo D, Xia K, Wang Y, Li C, Wang W (2019) Qishen granule attenuates cardiac fibrosis by regulating TGF- β /Smad3 and GSK-3 β pathway. *Phytomedicine* 62: 152949. <https://doi.org/10.1016/j.phymed.2019.152949>
- Zhang T, Wei G, Millard CJ, Fischer R, Konietzny R, Kessler BM, Schwabe JWR, Brockdorff N (2018) A variant NuRD complex containing PWWP2A/B excludes MBD2/3 to regulate transcription at active genes. *Nat Commun* 9: 3798. <https://doi.org/10.1038/s41467-018-06235-9>

The specific role of extracellular matrix metalloproteinases in the pathology and therapy of hard-to-heal wounds

Joanna B. Trojanek✉

Department of Microbiology and Clinical Immunology, The Children's Memorial Health Institute, Warsaw, Poland

Matrix metalloproteinases (MMPs) are zinc-dependent endoproteases responsible for the metabolism of extracellular matrix (ECM). MMPs can degrade the various ECM components as a variety of non-ECM molecules. Hyperactivity of MMPs and improper regulation or inhibition could lead to certain disorders, like non-healing chronic wounds. In chronic wounds, unlike in acute ones, there are always higher levels of MMPs due to the accompanying inflammation. Different proteases are responsible for this condition; nonetheless, blocking MMPs can help restore the wound's healing ability. The level of MMPs can help indicate the prognosis of chronic wounds. In some cases, the healing process is delayed by microbial wound infections. Bacterial proteases may up-regulate the levels of MMPs produced by host cells. That means that both host MMPs as proteases secreted by the infecting bacteria need to be targeted to increase the healing capacity of the wound. MMPs activity modulating treatments by superabsorbent polymer dressings can improve healing rates of chronic wounds. The main goal of this review was presentation the specific role of metalloproteinases in the pathology and therapy of hard-to-heal wounds.

Keywords: matrix metalloproteinases, healing, chronic wound, inflammation, bacterial proteases, superabsorbent polymer dressings

Received: 23 July, 2023; **revised:** 25 October, 2023; **accepted:** 27 October, 2023; **available on-line:** 03 December, 2023

✉e-mail: j.trojanek@ipczd.pl

Abbreviations: AA, acetic acid; DFUs, diabetic foot ulcers; DUs, pressure ulcers; ECM, extracellular matrix; GAG, glycosaminoglycan; HPV, Human Papillomavirus; HSV, Herpes Simplex Virus; MDROs, multidrug resistant organisms; MMPs, matrix metalloproteinases; MRSA, methicillin-resistant *S. aureus*; NOSF, Nano Oligo Saccharide Factor; ODC, octenidine dihydrochloride; ORC, oxidized regenerated cellulose; PTX, pentoxifylline; TLC, lipido-colloid technology; VLU, venous leg ulcers

INTRODUCTION

Matrix metalloproteinases (MMPs) belonging to the zinc-dependent endoproteases family are crucial molecules responsible for extracellular matrix (ECM) metabolism by the ability to degrade all kinds of extracellular matrix proteins. Besides degradation of the various ECM components like collagens, fibronectin, or elastin, MMPs can also process several non-ECM molecules, including cytokines, growth factors, their receptors, and ligands. In this way, MMPs are involved in the most physiological and pathological remodeling processes in tissues (Trojanek *et al.*, 2014; Trojanek *et al.*, 2020). The excessive production and hyperactivity of MMPs, and lack of proper regulation and inhibition could lead to certain disorders, like non-healing chronic wounds. Therefore,

this article presents how the level of MMPs can be used to indicate the prognosis of chronic wounds and how protease-modulating treatments can improve healing rates of chronic wounds with examples of specific wound dressings.

In a physiological state, most MMP expressions remain at a very low level, sometimes even close to zero. Their induction occurs in response to tissue damage, enhancing the process of extracellular remodeling. During the extracellular matrix degradation, also many growth factors are released. These growth factors can then be bound to different matrix components, thereby regulating their availability and activity in the tissues. For the proper process of wound formation, a balance between the synthesis and degradation of the extracellular matrix components is necessary. In the pathological state, the components of the ECM are accumulated. Through uncontrolled MMP expression and activation, fibrosis is formed, which may significantly delay or even entirely disturb the healing process (Lazaro *et al.*, 2016). In chronic wounds, unlike in acute ones, there are always higher levels of MMPs (especially gelatinases) due to the accompanying inflammation. It was reported that MMP-9 and MMP-8 were synthesized by inflammatory cells and presented in excess could affect the healing process (Westby *et al.*, 2020). Not only metalloproteinases were responsible for this condition (Harding *et al.*, 2018; Westby *et al.*, 2018), but blocking MMPs can help restore the wound's ability to heal, especially in combination with a good standard of care (including compression therapy, cleaning and removal of hyperkeratosis). The healing process is additionally complicated by the possibility of infection and coexisting diseases such as diabetes, cirrhosis or liver failure, renal failure, active tumor, tumor treatment, anemia, malnutrition, obesity, smoking, a prolonged hospitalization period and the advanced age of the patient (Anderson & Hamm, 2012).

WOUND HEALING STAGES

Wound healing is a physiological process after an injury to restore tissue structure and function. This process may be divided into several phases: fibrin clot formation, inflammatory response, granulation and epithelial formation, angiogenesis and fibroblast proliferation, regeneration of a functional connective tissue matrix with remodeling, and scar tissue formation (Lazarius *et al.*, 1994). The fibrin clot stores cytokines and growth factors released from injured cells and platelets during the activated coagulation cascade, initiating an inflammatory response. Incoming neutrophils secrete pro-inflammatory cytokines, activating local keratinocytes and fibroblasts. After completion of the inflammatory state, the granu-

lating tissue starts forming. Proteases are active in all phases of wound healing (homeostasis, inflammation, proliferation, and remodeling) and, therefore, could play several roles in the normal wound healing process (Velnar *et al.*, 2009; Patel *et al.*, 2016). During wound healing, MMPs participate mainly through the degradation of ECM, enabling cellular migration, facilitating the fresh epidermis formation and angiogenesis, the new extracellular matrix formation, and remodeling of wound scar tissue (Le *et al.*, 2007).

CONCISE MMPs CHARACTERISTIC

Currently, there are twenty-three variable matrix metalloproteinases in humans like MMP-1 to MMP-28 but not included four: MMP -4, -5, -6, -22 (discovered simultaneously by different research teams). Typically, the MMPs family consists of several distinct domains conserved between MMP family members. These domains are predomain, propeptide, catalytic, and hemopexin domains. The propeptide domain consists of approximately 80 aa and contains a highly conserved sequence: PRCG-VPG constituting the so-called “cysteine switch”. This regulatory element contains a conserved cysteine residue, which interacts with the zinc in the active site and prevents binding and cleavage of a substrate, keeping the enzyme in the inactive site. The catalytic domain consists of about 170 aa and contains two zinc ions (catalytic and structural) and 1-4 calcium ions Ca^{2+} . In the active center, the zinc ion is coordinated by a very conserved three-histidine sequence (for zinc chelation), creating a zinc-binding sequence HEXXHXXGXXH. A typical MMP contains a linker peptide or flexible hinge known as a hinge region of variable 75aa length and haemopexin-like-C-terminal domain (Hpx) with a sequence similar to hemopexin related with hem metabolism of approximately 200 aa. The hemopexin domain is a place of interaction between MMPs with their endogenous tissue inhibitors-TIMPs. Only two among all MMPs do not obtain this domain: MMP-7 and MMP-26 (belong to matrilysin), and MMP-12 lost it after activation. Three repeats of fibronectin type 2 in the middle of the catalytic domain enhance substrate binding by gelatinases and are the most important for effectively degrading type IV collagen, elastin and gelatin. Membrane-type MMPs (MT-MMP-1 – MT-MMP-6) contain furin cleavage sites in their propeptide domains (Fig. 1).

Based partly on the historical assessment of substrate specificity and partly on the cellular localization the MMPs family can be divided into seven groups: collagenases, gelatinases, stromelysins, matrilysins, metalloelastases, membrane-type MMPs, and other MMPs (Table 1).

MMPs IN WOUND HEALING

According to the Wound Healing Society, chronic wounds can be classified into four categories: pressure ulcers (PUs), diabetic foot ulcers (DFUs), venous leg ulcers (VLUs), and arterial insufficient ulcers (Simões *et al.*, 2018). MMP activity is strictly controlled during the post-injury processes. One example of this process disruption stuck in the inflammatory phase and thus preventing the transition to the phase of granulation tissue formation is hard-to-heal chronic wounds. In this state, there is a significant increase in the activity of MMPs, which later self-perpetuates and may increase through the secretion of cytokines. An increase in the activity was found for MMP-2, -8, -9, and -14, while a decrease

for TIMP-1 and -2, compared to the healing group. Poor healing was correlated with increased MMP-9 expression in chronic venous wound biopsy specimens and elevated levels of MMP-9/TIMP-1 in the wound exudates. However, significant differences were found between MMP-1 and other proteases. Because of heterogeneity in protease activity, MMP-1 may be associated with more healing and other proteases with less healing. A higher level of MMP-1 in healing wounds permits the proliferative phase to be completed and allows the progression of the healing process (Westby *et al.*, 2020). Limited evidence suggests correlations between elevated levels of MMPs and delayed healing in PUs (Ladwig *et al.*, 2002), in DFUs (Liu *et al.*, 2009), as well as in VLUs (Serra *et al.*, 2013). Possibly, the association of MMP level with delayed wound healing may be a general wound phenomenon; however, differences between wound types have also been observed (McCarthy & Percival, 2013; Lazaro *et al.*, 2016). The treatment strategy for such ulcerative wounds has been directed towards decreasing the concentration level of metalloproteinases and regulating their activity. The use of proper inhibitors has become one of the goals of modern wound healing therapy. MMP inhibitors, depending on the type of influence, can be divided into two types – direct or indirect. The most essential direct inhibitors are endogenous tissue MMP inhibitors – TIMPs. Four types of these multifunctional, evolutionarily stable proteins are known: TIMP-1, TIMP-2, TIMP-3, and TIMP-4, with a mass of 22-29 kD. TIMPs differ in specificity and block active MMPs by creating stable and reversible coordination bonds in a stoichiometric ratio of 1:1 or 2:2. The inhibition mechanism involves blocking the access of the substrate to the catalytic site of MMPs (Brew & Nagase, 2010). In the fluid of chronic wounds, TIMP-2 was significantly lower. Also, instead of the concentration of MMPs or TIMPs individually, the MMPs/TIMPs ratio seems to predict better wound healing (Ladwig *et al.*, 2002). Other direct MMP inhibitors include a broad spectrum of inhibitors like batimastat, marimastat, and ilomastat. Whereas tetracyclines, heparin, glycosaminoglycan (GAG)-sulodexide, pentoxifylline (PTX), reactive oxygen species, and superabsorbent polymers belong to non-direct inhibitors, they can reduce MMP expression indirectly by affecting the inflammatory cascade with immunomodulating or proteolytic actions (Krejner *et al.*, 2016).

Recently, the composite of hybrid dressings has been developed. They combine the properties of different materials (further discussed). Most of these dressings contain gel-forming superabsorbent polymers (sodium polyacrylate or sodium carboxymethylcellulose), which absorb excessive amounts of wound exudates. However, they can decrease the concentration of locally active bacterial proteases and endogenous proteolytic enzymes, including MMPs (McCarthy & Percival, 2012).

A complicated wound is a unique entity and is defined as a combination of an infection and tissue defect. Some researchers believe that every wound is contaminated regardless of the cause, location, size, and management (Velnar *et al.*, 2009).

WOUND HEALING AND INFECTION

Under normal conditions, the human body can heal wounds on its own, so maintenance of the wound in clean and moist conditions and usually used disinfectants are sufficient. However, in some cases, the healing process is delayed, or complications could happen entirely



Figure 1. Diagram of the MMPs domain structure.

Table 1. Extracellular matrix metalloproteinases.

Class	Common name	MMP number	Collagen substrate	Various substrate
Collagenases	Interstitial collagenase	MMP-1	I, II, III, VII, VIII, X	Gelatin, MMP-2,-9, proteoglycans, fibronectin, laminin, pro-TNF
	Neutrophil collagenase	MMP-8	I, II, III, V, VII, VIII, X	Gelatin, fibronectin, proteoglycans ADAMTS-1, pro-MMP-8
	Interstitial collagenase	MMP-13	I, II, III, IV, V, VII, IX, X	Gelatin, laminin, proteoglycans, fibrinogen, proMMP-9, -13
	Collagenase 4 (<i>Xenopus</i>)	MMP-18	I	Gelatin
Gelatinases	Gelatinase A	MMP-2	I, II, III, IV, V, VII, X, XI	Gelatin, fibronectin, laminin, elastin, proMMP-9, -13, IGFBPs, IL-1b, TGF-b, a1-antiprotease
	Gelatinase B	MMP-9	I, IV, V, VII, X, XI	Gelatin, elastin, laminin, fibronectin, vitronectin, CXCL5, IL-1b, TGF-b, plasminogen
Stromelysins	Stromelysin 1	MMP-3	III, IV, V, VII, IX, X, XIV	Gelatin, fibronectin, laminin, pro MMP-1, -7, -8, -9, -13, proTNFa, E-cadherin, L-selectin, tenactin
	Stromelysin 2	MMP-10	I, III, IV, V, IX, X	Gelatin, laminin, casein, MMP-1, -8, fibronectin, proteoglycans
	Stromelysin 3	MMP-11	IV	Gelatin, fibronectin, laminin
	Stromelysin 4 or RASI-1	MMP-19	native type IV	Gelatin, laminin, entactin, fibronectin, aggrecan, fibrinogen
Matrilysins	Matrilysin 1 or PUMP-1	MMP-7	I, IV	Gelatin, laminin, elastin, fibronectin, proteoglycans, proMMPs, proTNFa, E-cadherin
	Matrilysin 2 or Endometase	MMP-26	I, IV	Gelatin, laminin, elastin, fibronectin, proteoglycans, proMMPs, proTNFa, E-cadherin
Metalloelastase	Macrophage metalloelastase	MMP-12	IV	Elasin, fibronectin, gelatin, proteoglycans, plasminogen
Membrane-type MMPs	MT-MMP-1	MMP-14	I, II, III	Gelatin, fibronectin, laminin, vitronectin, proteoglycans, pro-MMP-2, -13
	MT-MMP-2	MMP-15		Fibronectin, tenascin, enactin, laminin, proMMP-2
	MT-MMP-3	MMP-16	III	Gelatin, fibronectin, vitronectin, MBP, proMMP-2
	MT-MMP-4	MMP-17		Gelatin, fibrinogen, proMMP-2
	MT-MMP-5	MMP-24		Gelatin, fibronectin, chondroitin/ dermatan proteoglycan, proMMP-2
	MT-MMP-6 or Leukolysin	MMP-25	IV	Gelatin, laminin, fibronectin, MBP, fibrinogen
Other MMPs	Enamelysin	MMP-20	XVIII	Amalogenin, ameloblastin, aggrecan, laminin, pro-MMP-20
	X-MMP <i>Xenopus</i>	MMP-21		Gelatin, aggrecan, casein
	C-MMP Chicken	MMP-22		No matrix substrate defined
	CA-MMP <i>Femalysin</i>	MMP-23		Gelatin, casein, fibronectin
Cysteine Array MMP	CA-MMP <i>Gallus</i>	MMP-27		Gelatin, casein, pro-MMP-27
	CA-MMP <i>Epilysin</i>	MMP-28		proTNFb, casein

disturbing healing. These cases include wound infections or chronic wounds. Microorganisms naturally occurring on the skin cause the most significant risk of wound infections. Among them, Gram-positive bacteria such as *Staphylococcus aureus* or *Streptococcus* spp. occur frequently

and after penetrating the wound, significantly delaying or preventing healing. Also dangerous are Gram-negative organisms, like *Escherichia coli* and *Pseudomonas aeruginosa*, as well as anaerobic bacteria – *Bacteroides* spp. and *Clostridium* spp. Wounds can also be infected with fungi

(the most common is *Candida* spp.), viruses like Human Papillomavirus (HPV) or Herpes Simplex Virus (HSV), and parasites; in each case, the wound will heal pathologically (Ding *et al.*, 2022; Diban *et al.*, 2023).

General therapy of infected wounds based on culture with antibiogram is conducted with clinically available antibiotics, including aminoglycosides, β -lactams, cephalosporins, quinolones, and tetracyclines, which interfere with different bacteria structures or metabolic pathways, and for this reason are often included in wound dressings (Simões *et al.*, 2018; Kaiser *et al.*, 2021). Unfortunately, wounds can become colonized (infection exists, but microbes do proliferate in high numbers) with multidrug-resistant pathogens termed MDROs (Multidrug-Resistant Organisms). They increase the risk of complications because antibiotics have very poor or no effect. The only method seems to be topical antiseptics, which, when used early enough, can stop spreading the infection with fewer side effects than local antibiotics. These are elementary silver, iodophors, octenidine dihydrochloride (ODC), acetic acid (AA), and plant-derived substances like Manuka honey, curcumin, essential oils and many other natural products (Chen *et al.*, 2023).

Chronic wound infections occur due to microorganisms creating biofilm, which adheres to the skin around the wound. Biofilm is a polymicrobial population less susceptible to the human immune defense system, displaying a high level of antibiotic tolerance with intense inter-bacterial communication through quorum sensing (Preda & Săndulescu, 2019; Kaiser *et al.*, 2021). Most chronic wounds are colonized with bacteria. Infections refer to the invasion of tissue by bacteria leading to a clinically evident pathogenic inflammatory response and tissue damage (Persival *et al.*, 2012; Suleman, 2016). The infections may, in some cases, e.g., with a weakened immune system, spread to the surrounding tissues (muscles, bones, joints) and even to the blood, causing systemic infections. Sepsis during chronic wound infection is an infrequent complication, but the possibility of its occurrence should be considered.

Chronic wounds are susceptible to colonization by numerous bacterial species, like *S. aureus* (93.5%), *Enterococcus faecalis* (71.1%), *P. aeruginosa* (52.2%), coagulase-negative *Staphylococci* (45.7%), *Proteus* species (43.1%), and anaerobic bacteria (39.1%). These bacterial species create a biofilm on the wound surface and may secrete bacterial proteases, essential for bacterial growth and virulence (Oldak & Trafny, 2005). Extracellular bacterial proteases can evade the host's immune response and target the immune mediators (Suleman, 2016). Moreover, proteases in wounds could originate from the host or bacteria. It was supposed that host MMPs together with bacterial proteases probably play synergistically causing tissue breakdown on the wound bed. Bacterial proteases may up-regulate the levels of MMPs produced by host cells. Many pathogenic bacteria secrete a range of proteases, of the serine, cysteine, and metallo-type that act as virulence factors. That means both host MMPs and those derived from infecting bacteria need to be targeted to improve the healing capacity of the wound (McCarthy *et al.*, 2012; McCarthy & Percival, 2013).

CHRONIC WOUND TREATMENT

The wound needs to be debrided and dressed correctly. Correct debridement means the removal of non-viable, infected, and hyperkeratotic tissue—it helps to convert a chronic wound into an acute one, which can then progress through the normal stages of healing (Lazaro *et al.*, 2016).

In 2002, a group of wound treatment experts described a simple model of chronic wound care. This model with the acronym TIME, which is described as: Tissue assessment and management, Infection/Inflammation control and management, Moisture imbalance and management, Edges of wound observation and management (Leaper *et al.*, 2012). However applying the above recommendation did not prevent some wounds from failing to heal, and additional efforts were required to resume the healing process.

SELECTED WOUND DRESSING

Wound dressings reduce excess inflammation, allowing chronic wounds to heal more readily. Non-healing wounds often become locked up in the inflammatory phase and cannot progress to produce granulating tissue. Persistent inflammation, in turn, enhances MMP activity. Therefore, one of the main goals of local treatment of wounds, regardless of their etiology, is decreasing the MMPs activity and sequestering host proteases within the wound environment (Krejner *et al.*, 2016; Westby *et al.*, 2020).

Wound dressings have progressed significantly for years, from traditional dry-type gauze or bandages to very sophisticated materials like hydrogels, foams or films. Their application's primary purpose was to maintain a sterile, hypoallergenic, moist, and thermally suitable environment to protect against bacterial infection and promote new tissue growth (angiogenesis) (Verdolino *et al.*, 2021). Some types of dressing especially deactivate elevated MMP activity. The goal was to invent a cost-reasonable dressing, which modulates inflammation and promotes healing. It could be distinguished into several kinds of dressings, which work based on the inactivation of the protease action: skin substitute dressing, collagen-based dressing, cellulose-based dressing, and synthetic dressing based on lipid-colloid technology (TLC).

The first was the skin substitute dressing named Pura-col ultraECM, a decellularised porcine mesothelium matrix. It demonstrated high angiogenic potential in vitro and MMP inhibition abilities. Simultaneously, it allowed for a high recovery of growth factor – FGF, VEGF, and TGF- β necessary for quick wound healing (Capella-Monsonis *et al.*, 2020).

The second type was a collagen-based dressing, which compiled the essential requirements for a good dressing: biocompatibility, a lack of toxicity, and a biodegradable material. It could be used for treating chronic wounds, as it demonstrated a decrease in healing times by the ability to inactivate proteases and keep moisture in the wound bed (Holmes *et al.*, 2013; Pallaske *et al.*, 2018). BIOSTEP Collagen Matrix dressing possesses type I collagen and gelatin (denatured collagen). The addition of EDTA to this type of dressing allows binding and irreversibility inactivation of both collagenase (MMP-1), like gelatinases (MMP-2; MMP-9) (Finnegan & Percival, 2015).

The next type was a cellulose-based wound dressing representing the Promogran™ Matrix family, which contained oxidized regenerated cellulose (ORC) besides collagen. This type of dressing presented both antimicrobial and anti-inflammatory properties. The studies proved that the ORC/collagen dressing and silver-ORC (Promogran Prisma™ Matrix) represent antimicrobial properties inhibiting MMP-2 and MMP-9 expressions in wound fluid, and increasing healing rates. Importantly, tEDTA demonstrates antimicrobial and antibiofilm properties, but clinical trials using a synthetic inhibitor MMP (Promogran) showed only 13% effectiveness (Cullen *et al.*, 2001; Verdolino *et al.*, 2021).

Table 2. Summary of MMPs and their role in wound healing – an overview of findings.

Main points	References
In chronic wounds, there are always higher levels of MMPs due to accompanying inflammation.	Patel <i>et al.</i> , 2016; Lazaro <i>et al.</i> , 2016; Westby <i>et al.</i> , 2018
Poor healing is correlated with increased MMP-9 expression and elevated levels of MMP-9/TIMP1 in wound secretion probes.	Ladwig <i>et al.</i> , 2002; Serra <i>et al.</i> , 2013 Westby <i>et al.</i> , 2020; Chen <i>et al.</i> , 2023
During infection, bacterial proteases may up-regulate the levels of MMPs produced by host cells.	McCarty <i>et al.</i> , 2012; Suleman <i>et al.</i> , 2016; Westby <i>et al.</i> , 2020
The treatment strategy for chronic wounds is directed towards decreasing the concentration level of MMPs and regulating their activity.	McCarty & Percival, 2013; Krejner <i>et al.</i> , 2016
The essential requirements for wound dressing were maintaining a sterile, hypoallergenic, moist, and thermally suitable environment promoting new tissue growth with antimicrobial and antibiofilm properties.	McCarty & Percival, 2013; Kaiser <i>et al.</i> , 2021
The modest wound dressing type additionally inactivated the protease action and allowed for high growth factor recovery, which was necessary for quick healing.	Meaume <i>et al.</i> , 2012; Meaume <i>et al.</i> , 2017; Sigal <i>et al.</i> , 2019; Verdolino <i>et al.</i> , 2021

Another type was the synthetic dressing Urgostart from a polyester mesh saturated with a sucrose octasulfate potassium salt (Nano Oligo Saccharide Factor – NOSF) embedded lipido-colloid matrix (Technology Lipido-Colloid, TLC). Manufacturer's patents protected NOSF and TLC compositions. Oligosaccharides (NOSF) reduce MMP levels and restore growth factor biological functions, whereas the TLC matrix creates a moist wound environment. NOSF also restores angiogenesis by migration and proliferation of endothelial cells (growth factors protection against MMPs activity). Their mechanisms of action are still unknown. NOSF probably mechanically blocks, i.e. captures and immobilizes MMP molecules, that are massively secreted during prolonged healing (causing a state of chronic inflammation) and contributes to the reduction of the proteolysis (degradation, enzymatic breakdown) of the ECM components (i.e., collagen fibers) by surrounding epithelial cells (fibroblasts and keratinocytes) and macrophages (Lazaro-Martines *et al.*, 2019). Two prospective, multicentric clinical studies named NEREIDES and CASSIOPEE were focused on patients with non-infected, moderate to strongly exudation leg ulcers of venous or mixed origin treated with a dressing and compression system for 12 weeks. Ensure the rapid transition from the debridement stage to the granulation stage, and finally to closure of the wound. Poly-absorbent fibers of the new type of dressing inhibit the proteases in excess accumulating, restore the impaired biological functions, and stimulate angiogenesis through migration and proliferation of endothelial cells (Sigal *et al.*, 2019).

Both TLC-NOSF and ORC/collagen matrix dressings improved venous leg ulcer healing (1% of the adult population in the Western world suffers from leg ulcers). Four randomized controlled trials assessing these two MMP devices were ongoing (Schultz *et al.*, 2008; Sigal *et al.*, 2019).

Urgo-Clean Ag, which combines TLC technology with silver ions, exhibits a broad spectrum of antimicrobial activity, including *S. aureus*, *P. aeruginosa*, vancomycin-resistant *Enterococci* and methicillin-resistant *S. aureus* (MRSA). Additionally, after 24 hours, according to Hieu *et al.* in 2021, UrgoClean Ag reduced the biofilm population by more than 99,99% (4,6 log reduction).

The application of TLC-NOSF technology to lipocolloid dressings (according to Explorer –NTC01717183 and Challenge clinical trials results) in the experts' opinion significantly shortens the healing time of chronically, non-infected wounds, which reduces the cost of treatment and improves the efficiency and quality of patients' life (Meaume *et al.*, 2012; Meaume *et al.*, 2017; Edmonds *et al.*, 2018).

It should be mentioned that the specific clinical study refers to optical and magnetic stimulation (COMS) therapy on wound-healing-related parameters (tissue oxygenation and water index) that were analyzed by hyperspectral imaging on 11 patients with chronic leg and foot ulcers of different etiology NCT03112395 (according to ICHGCP) (Traber *et al.*, 2023).

SUMMARY

A brief summary of the above observations on the role of MMPs in wound healing is presented in **Table 2**.

CONCLUSIONS

Generally, MMPs play a crucial role in all stages of wound healing, but it was suggested that non-healing wounds may be associated with prolonged high activity of proteases in the later stages of the wound healing process. This persistent proteolytic activity is due to damage to newly formed tissue and the degradation of growth factors necessary for healing. The primary focus in the future will be finding the selective inhibitors of distinguished members; most clinical trials on small spectrum inhibitors until now had negative results due to the widespread inhibitory effect connected with similar structures of all MMPs. It should be assumed that detailed knowledge of protease substrates, especially non-matrix molecules, could help to understand MMP's involvement in physiology and pathology and find the appropriate therapy for hard-to-heal wounds.

REFERENCES

- Anderson K, Hamm RL (2012) Factors that impair wound healing. *J Am Coll Clin Wound Spec* 4: 84–91. <https://doi.org/10.1016/j.jccw.2014.03.001>
- Brew K, Nagase H (2010) The tissue inhibitors of metalloproteinases (TIMPs) an ancient family with structural and functional diversity. Review. *Biochim Biophys Acta* 1803: 55–71. <https://doi.org/10.1016/j.bbamct.2010.01.003>
- Capella-Monsonis H, Tilbury MA, Wall JG, and Zeugolis DI (2020) Porcine mesothelium matrix as a biomaterial for wound healing applications. *Mater Today Bio* 7: 100057. <https://doi.org/10.1016/j.mtbo.2020.100057>
- Chen J, Qin S, Liu S, Zhong K, Jing Y, Wu X, Peng F, Li D, Peng C (2023) Targeting matrix metalloproteinases in diabetic wound healing. *Front Immun* 14: 1089001. <https://doi.org/10.3389/fimmu.2023.1089001>
- Cullen B, Smith R, McCulloch E, Silcock D, Morrisson L (2002) Mechanism of action of PROMOGAN, a protease modulating

- matrix, for the treatment of diabetic foot ulcers. *Wound Rep Reg* 10: 16–25. <https://doi.org/10.1046/j.1524-475x.2002.10703.x>
- Diban F, Di Lodovico S, Di Fermo P, D'Ercole S, D'Arcangelo S, Di Giulio M, Cellini L (2023) Biofilms in chronic wound infections: innovative antimicrobial approaches using the *in vitro* Lubbock chronic, wound, biofilm model. *Int J Mol Sci* 24: 1004. <https://doi.org/10.3390/ijms24021004>
- Ding X, Tang Q, Xu Z, Xu Y, Zhang H, Zheng D, Wang S, Tan Q, Maitz J, Maitz PK, Yin S, Wang Y, Chen J (2022) Challenges and innovations in treating chronic and acute wound infections: from basic science to clinical practice. *Burn and Trauma* 10: tkac014. <https://doi.org/10.1093/burnst/tkac014>
- Edmonds M, Lázaro-Martínez JL, Alfayate-García JM, Martini J, Pettit JM, Rayman G, Lobmann R, Uccioli L, Sauvadet A, Bohbot S, Kerihuel JC, Piaggese A (2018) Sucrose octasulfate dressing versus control dressing in patients with neuroischaemic diabetic foot ulcers (Explorer): an international, multicentre, double-blind, randomized, controlled trial. *Lancet Diabet Endocrinol* 6: 186–196. [https://doi.org/10.1016/S2213-8587\(17\)30438-2](https://doi.org/10.1016/S2213-8587(17)30438-2)
- Finnegan S, Percival SL (2015) EDTA: an antimicrobial and antibiofilm agent for use in wound care. *Adv Wound Care* 4: 415–421. <https://doi.org/10.1089/wound.2014.0577>
- Harding K, Armstrong DG, Barrett S, Kaufman H, Lazaro-Martinez JL, Mayer D, Moore Z, Romanelli M, Queen D, Schultz G, Serena T, Sibbald G, Snyder R, Stroh R, Vowden K, Vowden P, Zambooni P (2018) Internal consensus. The role of proteases in wound diagnostics: an expert working group review. *Wounds International*. woundchek.com/uploads/downloads/consensus_documents/Role-of-proteases-in-wound-diagnostics-International.pdf. 2018
- Hieu DV, Hung DV, Chien VH, Thiet ST, Paran B, Johnson SSB, Chalvin B, Galea E (2021) Clinical evaluation of UrgoClean Ag (poly-absorbent dressing based on technology lipido-colloid with silver ions) in the management of infected wounds in Asia. *Wounds International* 12: 54–62
- Holmes C, Wróbel J, Mac Eachern MP, Boles BR (2013) Collagen-based wound dressing for the treatment of diabetes-related foot ulcers: a systematic review. *Diabet Metabol Syndr Obes Targets Ther* 6: 17. <https://doi.org/10.2147/DMSO.S36024>
- Kaiser P, Wachter J, Windbergs M (2021) Therapy of infected wounds: overcoming clinical challenges by advanced drug delivery systems. *Drug Deliver Transl Res* 11: 1545–1567. <https://doi.org/10.1007/s13346-021-00932-7>
- Krejner A, Litwiniuk M, Grzela T (2016) Matrix metalloproteinases in the wound microenvironment: therapeutic perspectives. *Chronic Wound Care Manag Res* 3: 29–39. <https://doi.org/10.2147/CWCMR.S73819>
- Ladwig GP, Robson MC, Liu R, Kuhn MA, Muir DF, Schultz GS (2002) Ratios of activated matrix metalloproteinase-9 to tissue inhibitor of matrix metalloproteinase-1 in wound fluids are inversely correlated with healing of pressure ulcers. *Wound Rep Reg* 10: 26–37. <https://doi.org/10.1046/j.1524-475x.2002.10903.x>
- Lazarus GS, Cooper DM, Knighton DR, Percoraro RE, Rodeheaver G, Robson MC (1994) Definitions and guidelines for assessment of wounds and evaluation of healing. *Wound Rep Reg* 2: 165–170. <https://doi.org/10.1046/j.1524-475x.1994.20305.x>
- Lazaro JL, Izzo V, Meaume S, Davies AH, Lobmann R, Uccioli L (2016) Elevated levels of matrix metalloproteinases and chronic wound healing: an updated review of clinical evidence. *J Wound Care* 25: 277–287. <https://doi.org/10.12968/jowc.2016.25.5.277>
- Lázaro-Martínez JL, Edmonds M, Rayman G, Apelqvist J, VanAcker K, Hartemann A, Martini J, Lobmann R, Bohbot S, Kerihuel JC, Piaggese A (2019) Optimal wound closure of diabetic foot ulcers with early initiation of TLC-NOSF treatment: post-hoc analysis of explorer. *J Wound Care* 28: 358–367. <https://doi.org/10.12968/jowc.2019.28.6.358>
- Le NTV, Xue M, Casteinoble LA, Jackson CJ (2007) The dual personalities of matrix metalloproteinases in inflammation. *Front Biosci* 12: 1475–1487. <https://doi.org/10.2741/2161>
- Leaper DJ, Schultz G, Carville K, Fletcher J, Swanson T, Drake R (2012) Extending the TIME concept: what have we learned in the past 10 years? *Intern Wound J* 9: 1–19. <https://doi.org/10.1111/j1742-481X.2012.01097.x>
- Liu Y, Min D, Bolton T, Nubé V, Twigg SM, Yue DK, McLennan SV (2009) Increased matrix metalloproteinase-9 predicts poor wound healing in diabetic foot ulcers. *Diabet Care* 32: 117–119. <https://doi.org/10.2337/dc08-0763>
- McCarty SM, Cochrane CA, Clegg PD, Percival SL (2012) The role of endogenous and exogenous enzymes in chronic wounds: a focus on the implications of aberrant levels of both host and bacterial proteases in wound healing. *Wound Rep Reg* 20: 125–136. <https://doi.org/10.1111/j.1524-475x.2012.00763.x>
- McCarty SM, Percival SL (2013) Proteases and delayed wound healing. *Adv Wound Care* 2: 438–447. <https://doi.org/10.1089/wound.2012.0370>
- Meaume S, Truchetet F, Cambazard F (2012) A randomized, controlled, double-blind prospective trial with a Lipido-Colloid Technology-Nano-OligoSaccharide Factor wound dressing in the local management of venous leg ulcers. *Wound Rep Reg* 20: 500–511. <https://doi.org/10.1111/j.1524-475x.2012.00797.x>
- Meaume S, Domp Martin A, Lok C, Lazareth I, Signal M, Truchetet F, Sauvadet A, Bohbot S Challenge Study Group (2017) Quality of life in patients with leg ulcers: results from CHALLENGE, a double blind randomized controlled trial. *J Wound Care* 26: 368–379. <https://doi.org/10.12968/jowc.2017.26.7.368>
- Oldak E, Trafny EA (2005) Secretion of proteases by *Pseudomonas aeruginosa* biofilms exposed to ciprofloxacin. *Antimicrob Agents Chemother* 49: 3281–3288. <https://doi.org/10.1128/AAC.49.8.3281-3288.2005>
- Pallaske F, Pallaske A, Herklotz K, Boese-Landgraf J (2018) The significance of collagen dressing in wound management: a review. *J Wound Care* 27: 692–702. <https://doi.org/10.12968/jowc.2018.27.10.692>
- Patel S, Maheshwari A, Chandra A (2016) Biomarkers for wound healing and their evaluation. *J Wound Care* 25: 46–55. <https://doi.org/10.12968/jowc.2016.25.1.46>
- Percival SL, Hill KE, Williams DW, Hooper SJ, Thomas DW, Costerton JW (2012) A review of the scientific evidence for biofilms in wounds. *Wound Rep Reg* 20: 647–657. <https://doi.org/10.1111/j.1524-475x.2012.00836.x>
- Preda VG, Săndulescu O (2019) Communication is the key: biofilms, quorum sensing, formation and preventing. *Discoveries (Craiova)* 7: e100. <https://doi.org/10.15190/d.2019.13>
- Schmutz JL, Meaume S, Fays S, Ourabah Z, Guillot B, Thirion V, Collier M, Barrett S, Smith J, Bohbot S, Domp Martin A (2008) Evaluation of the nano-oligosaccharide factor lipido-colloid matrix in the local management of venous leg ulcers: results of a randomized, controlled trial. *Int Wound J* 5: 172–182. <https://doi.org/10.1111/j.1742-481X.2008.00453.x>
- Serra R, Buffone G, Falcone D, Molinari V, Scaramuzzino M, Gallelli L, de Francis S (2013) Chronic venous leg ulcers are associated with high levels of metalloproteinases-9 and neutrophil gelatinase-associated lipocalin. *Wound Rep Reg* 21: 395–401. <https://doi.org/10.1111/wrr.12035>
- Sigal ML, Addala A, Maillard H, Chahim M, Sala F, Blaise S, Dalac S, Meaume S, Bohbot S, Tumba C, Tacca O (2019) Evaluation of TLC-NOSF dressing with poly-absorbent fibres in exuding leg ulcers: two multicentric, single-arm, prospective, open-label clinical trials. *J Wound Care* 28: 164–175. <https://doi.org/10.12968/jowc.2019.28.3.164>
- Simões D, Miguel SP, Ribeiro MP, Coutinho P, Mendonça AG, Correia IJ (2018) Recent advances on antimicrobial wound dressing: A review. *Eur J Pharm Biopharm* 127: 130–141. <https://doi.org/10.1016/j.ejpb.2018.02.022>
- Suleman L (2016) Extracellular bacterial proteases in chronic wounds: a potential therapeutic target? *Adv Wound Care* 5: 455–463. <https://doi.org/10.1089/wound.2015.0673>
- Traber J, Wild T, Morotz J, Berli MC, Franco-Obregón A (2023) Concurrent optical and magnetic-stimulation-induced changes on wound healing parameters, analyzed by hyperspectral imaging: an exploratory case series. *Bioengineering* 10: 750. <https://doi.org/10.3390/bioengineering10070750>
- Trojanek JB, Cobos-Correa A, Diemer S, Kormann M, Schubert SC, Zhou-Suckow Z, Agrawal R, Duerr J, Wagner CJ, Schatterny J, Hirtz S, Sommerburg O, Hartl D, Schultz C, Mall MA (2014) Airway mucus obstruction triggers macrophage activation and matrix metalloproteinase 12-dependent emphysema. *Am J Respir Cell Mol Biol* 51: 709–720. <https://doi.org/10.1165/rcmb.2013-0407OC>
- Trojanek JB, Niemirska A, Grzywa R, Wierzbicka A, Obrycki Ł, Kulaga Z, Szalecki M, Michalkiewicz J, Litwin M (2020) Leukocyte matrix metalloproteinase and tissue inhibitor gene expression patterns in children with primary hypertension. *J Hum Hypertens* 34: 355–363. <https://doi.org/10.1038/s41371-019-0197-8>
- Velnar T, Bailey T, Smrkolj V (2009) The wound healing process: an overview of the cellular and molecular mechanisms. *J Int Med Res* 37: 1528–1542. <https://doi.org/10.1177/147323000903700531>
- Verdolino DV, Thomason HA, Fotticchia A, Cartmell S (2021) Wound dressings: curbing inflammation in chronic wound healing. Review. *Emerg Top Life Sci* 5: 523–537. <https://doi.org/10.1042/ETLS20200346>
- Westby MJ, Dumville JC, Stubbs N, Norman G, Wong JK, Cullum N, Riley RD (2018) Protease activity as a prognostic factor for wound healing in venous leg ulcers. In *Cochrane Database of Systematic Reviews* [Internet]. Cochrane Wounds Group, eds. <https://doi.wiley.com/10.1002/14651858.CD012841.pub2.2018>
- Westby MJ, Norman G, Watson REB, Cullum NA, Dumville JC (2020) Protease activity as a prognostic factor for wound healing in complex wounds. *Wound Rep Reg* 28: 631–644. <https://doi.org/10.1111/wrr.12835>

MicroRNA-1179 targets Epiregulin (EREG) regulates the proliferation and metastasis of human multiple myeloma cells

Xiao Liu, Lan Qin✉, Wei Li and Fei Fei

Department of Hematology, The Fourth Affiliated Hospital of Traditional Chinese Medicine, Xinjiang Medical University, Urumqi, Xinjiang, 830000, China

MicroRNA-1179 (miRNA-1179) is an extensively studied tumor suppressor. However, the significance of miR-1179 in multiple myeloma has not been investigated previously. So, there is a need for research to find out about the significance of miR-1179 in multiple myeloma. However, current investigations have examined the significance of miRNA-1179 in multiple myeloma for the first time by targeting epiregulin (EREG). In this study, 26 multiple myeloma specimens and 16 healthy donor specimens were examined. Multiple myeloma cell lines (U266, RPMI-8226, KMS-11, JJN-3, and IM-9) were used. In this study, expression analysis, cell viability, colony formation assay, and transwell assay were carried out by standard methods. The outcomes revealed the down-regulation of miRNA-1179 in multiple myeloma. Overexpression of miRNA-1179 promotes, while its inhibition suppresses, the survival ability and colony formation of the U266 multiple myeloma cells. Investigation of underlying mechanisms revealed apoptosis to be responsible for the tumour-suppressive effects of miRNA-1179. The proportion of apoptosis in U266 cells rose from 5.32% to 34.86% when miRNA-1179 was overexpressed. Additionally, it was discovered that miRNA-1179 directs its tumor-inhibiting activities toward EREG at the molecular level. While EREG knockdown was found to halt the proliferation of U266 cells, its overexpression could overcome the suppressive effects of miRNA-1179 on the survival ability, mobility, and invasion of the U266 cells. This research proves that miRNA-1179 can be used as a new treatment or drug for multiple myeloma.

Keywords: MicroRNA-1179, epiregulin, myeloma cells, metastasis

Received: 01 February, 2023; **revised:** 13 March, 2023; **accepted:** 03 April, 2023; **available on-line:** 17 June, 2023

✉e-mail: xj13999953719@163.com

Abbreviations: ATCC, American Type Culture Collection; EREG, Epiregulin; FBS, Foetal bovine serum; GAPDH, Glyceraldehyde 3-phosphate dehydrogenase; MM, Multiple myeloma; NPCS, normal plasma cells; S.D., Standard deviation

INTRODUCTION

Multiple myeloma is one of the deadliest disorders, with a high fatality rate. Multiple myeloma made up about 2% of all new cases of myeloma and 2.1% of deaths caused by melanoma in the United States (Pinto *et al.*, 2020). Even though research on cancer diagnosis and treatment has come a long way, multiple myeloma is still one of the hardest cancers to cure (Rajkumar & Kumar, 2020). With just over 5 years of median survival, the majority of the patients are administered four or even more different lines of therapy (Boyle *et al.*, 2021).

Researchers across the globe are looking to develop biomarkers for early diagnosis, identify therapeutic targets for efficient treatment, and identify drugs that are effective and safe.

MicroRNAs (miRNAs) have recently gained significant interest as therapeutic approaches to treat human diseases and disorders. miRNAs are non-coding RNA molecules that have the potential to control the expression of protein-coding genes. At the post-transcriptional stage, every miRNA may influence the production of multiple protein-coding genes (Tan *et al.*, 2018). Several studies on miRNAs found that the progression of many human malignancies was often associated with abnormal expression of miRNA (Ramassone *et al.*, 2018; Vannini *et al.*, 2018). For instance, miRNA-1179 has been found to post-transcriptionally suppress the expression of E2F5 to control the formation and spread of pancreatic cancer (Lin *et al.*, 2018). Song and others (Song *et al.*, 2018) observed that miRNA-1179 regulates the progression and metastasis of non-small cell lung carcinoma. Previously, several researchers investigated miR-1179 and found that it regulates chemical sensitivity in ovarian cancer cells (Zhihong *et al.*, 2020), regulates cell cycle progression in glioblastoma cells (Xu *et al.*, 2017) and the vincristine sensitivity of oral cancer cells (Gao *et al.*, 2020). But the significance of miR-1179 in multiple myeloma has not been investigated. So far, there are no reports available on this; therefore, this study intends to find out the significant influence of miR-1179 in multiple myeloma by examining the changes in epiregulin (EREG). The outcomes of this study may help us find out if miR-1179 could be a new way to treat or cure multiple myeloma.

MATERIALS AND METHODS

Study area

The present study was carried out at the Department of Hematology, The Fourth Affiliated Hospital of Traditional Chinese Medicine from March 2015 to November 2018.

Human tissues

In this study, 26 multiple myeloma specimens and 16 healthy donor specimens were collected at the The Fourth Affiliated Hospital of Traditional Chinese Medicine from March 2015 to November 2018. This research was only performed after the patients provided written permission. The research ethics committee (Reg. No. IA-CUC/EREG/2015/02) also authorised the investigation.

Cell lines

Multiple myeloma cell lines (U266, RPMI-8226, KMS-11, JJN-3, and IM-9) were obtained from the American Type Culture Collection (ATCC, USA) and grown in RPMI-1640 media (Gibco, Ireland) with 10% foetal bovine serum (FBS, Gibco, Ireland), streptomycin (100 g/mL) and 1% penicillin (100 U/mL) in ambient temperature at 37°C with 5% CO₂. Normal plasma cells (NPCs) were isolated and grown from a peripheral blood smear as described in earlier methodologies by Adham *et al.* (2020).

Cell Transfection

The miRNA-NC, miRNA-1179 mimics, siRNA-NC, siRNA-EREG, miRNA-1179 inhibitor, and inhibitor NC were constructed by the modified method of Zhihong and others (Zhihong *et al.*, 2019) as per the manufacturer's instructions (RiboBio, Invitrogen, Carlsbad, CA, USA). The appropriate concentrations of miRNA-1179 inhibitor, inhibitor NC, siRNA-NC, and siRNA-EREG were transfected into U266 cells and treated with Lipofectamine 2000 (Thermo Fisher Scientific, China) based on the kit's guidelines.

Expression analysis

Whole RNA extraction from test specimens and cell lines is performed for mRNA expression analysis by utilizing the TRIzol reagent (Invitrogen). The extracted whole RNA was subjected to RNase-free DNase treatment to eliminate the contaminated DNA. Following that, PrimeScript RT Master Mix was used to produce cDNA from the RNA (TaKaRa, Japan). Then miR-1179 expression was compared with snRNA U6, while EREG expression was compared with that Glyceraldehyde 3-phosphate dehydrogenase (GAPDH) and actin. Proteins were drawn out of cells using RIPA solution and run on an SDS-polyacrylamide gel for protein expression analysis. Then the proteins were loaded onto a polyvinylidene fluoride membrane and maintained with specific antibodies. The membrane then re-treated at room temperature with secondary antibodies and horseradish peroxidase. The proteins of concern were visualized using an increased chemiluminescence solution (Millipore).

Cell viability

In this study, the cell survival ability of treated U266 cells was examined by the MTT test. The U266 cells/well (5×10^3) were cultured for 0, 12, 24, 48, and 96 h. Thereafter, 20 μ L of MTT was added to each well, and the plates were again incubated at 37°C for 4 h. Formazan crystals were removed by DMSO. Finally, absorbance was measured by a microplate reader to evaluate cell survival ability at 490 nm.

Colony formation assay

The transfected U266 cells were inoculated in 6-well plates and grown for 2 weeks at 37°C. The grown cells were fixed with 100% methanol for 25 min. After that, 0.1% of the colonies were stained with crystal violet and counted under a microscope.

DAPI staining

Transfected U266 cells were grown in 12-well plates for 24 hours at 37°C at a concentration of 1×10^5 cells/well. Subsequently, the cells were harvested by centrifu-

gation, washed with PBS, and fixed with 70% ethanol. Finally, the U266 cells were then stained with DAPI and observed on a fluorescent microscope.

Annexin V/PI Assessment

The Annexin V/PI assay was to be employed to analyze the percentage of apoptotic U266 cells. Transfected U266 cells (1×10^6) were added into six-well plates and maintained to proliferate for 24 h. After that, the cells were harvested, and the percentage of apoptotic U266 cells was evaluated by an Annexin-VFITC apoptosis detection kit (BestBio) and a Cytomics FC500 flow cytometer using CXP software (Beckman Coulter, Fullerton, CA, USA).

Development of mutant EREG

The complementary nucleotides of miRNA-1179 were mutated using the ThermoFisher Scientific mutagenesis kit to construct the mutant EREG (EREG-MUT) by the modified method of Singh and others (Singh *et al.*, 2013)

Target identification

The fee-based online version of TargetScan (<http://www.targetscan.org/version-72/>) was employed to assess the miRNA-1179 targets. In this study, the most suitable sequence of the EREG 3'-UTR was selected for further investigation.

Luciferase assay

The 3'-UTR of EREG (EREG-WT) was cloned into the pGL3-control vector (Promega) downstream of the stop codon of firefly luciferase. Following that, cells transfected with EREG-WT or EREG-MUT were co-transfected with miRNA-1179 or miRNA-NC. The Dual-Luciferase Reporter Assay System (Promega) was employed to conduct the interaction investigation, which included 48 hours of cell culture at 37°C. Renilla luciferase was used for evaluation to normalise the luciferase.

Transwell assay

Transwell inserts with 8 μ m pore sizes that were plain and matrigel-coated were employed for migration and invasion, respectively. In 24-well plates, the transwell insert was placed, and the bottom chamber receives 500 μ L of DMEM containing 10% FBS. Transfected U266 cells were maintained in 100 μ L of DMEM in the top chamber. After 24 hours, the cells on the outer side of the membrane were scrubbed away and maintained at 37°C. The U266 cells that were adhered to the bottom side of the membrane were kept in methanol for 9 min before they were stained by using crystal violet (0.01%). Thereafter, the samples were carefully washed and cells were imaged and counted in at least five random fields under a digital microscope.

Statistical analysis

The trials were repeated in triplicate, and the outcomes were described as mean \pm standard deviation (S.D.). The GraphPad Prism 7.0 software tool was used to analyse the One-way analysis of variance (ANOVA) and Tukey's tests were carried out for multiple group comparisons. A *p*-value <0.05 was considered statistically significant.

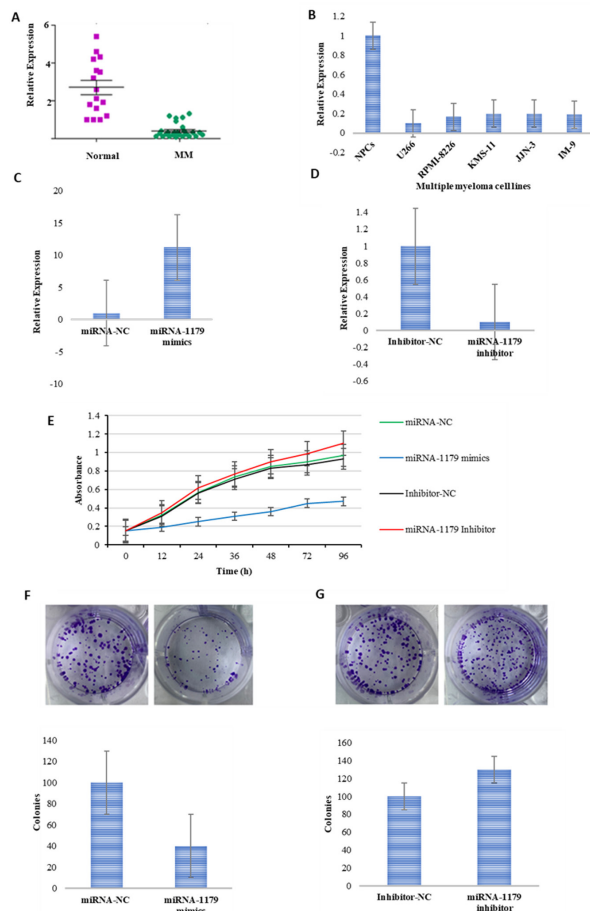


Figure 1. miRNA-1179 expression in multiple myeloma and normal tissues

(A) Relative expression between multiple myeloma and normal tissues; (B) Expression between different types of myeloma cell lines; (C) Relative expression between miRNA-1179 mimics and miRNA-NC; (D) Relative expression between miRNA-1179 inhibitor and inhibitor-NC; (E) Survival ability of the different types of myeloma cell lines; (F) Colony formation of the miRNA-1179 mimics and miRNA-NC cells; (G) Colony formation of the miRNA-1179 inhibitor and inhibitor-NC cells

RESULTS

In this investigation, the expression profile of miRNA-1179 was compared between multiple myeloma (MM) and normal cells (Fig. 1A). The relative expression profile of miRNA-1179 in multiple myeloma cells was 1.75-fold, which is considerably lower ($p < 0.05$) than the expression profile in normal tissues (5.5-fold) (Fig. 1A). The expression of miRNA-1179 was assessed in the different types of myeloma cell lines (U266; RPMI-8226; KMS-11; JJN-3; and IM-9) as well as normal plasma cells (NPCs) (Fig. 1B). When compared to NPCs, miRNA-1179 was significantly downregulated ($p < 0.05$) in all myeloma cell lines. NPCs express the highest fold (1.1-fold) compared to different types of myeloma cell lines (below 0.2-fold). Figure 1C shows that miRNA-1179 mimics expressed the highest relative expression (11.5-fold), while miRNA-NC was expressed the least (1-fold). Figure 1D depicts the highest relative expression (1-fold) by inhibitor-NC, and the miRNA-1179 inhibitor exhibits a low expression (0.1-fold). Figure 1E exhibits the cell survival ability of the cell lines. The survival ability of miRNA-1179 mimic cells was highly suppressed

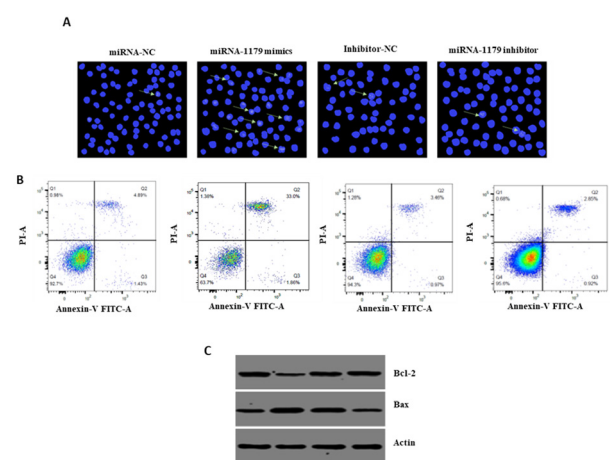


Figure 2. Alteration of the structure of the tested cells (A) Nucleus structures of the U266 cells; (B) Apoptosis of the U266 cells; (C) Expression of Bcl2, Bax, and Actin

($p < 0.05$) by miRNA-1179 overexpression, whereas the miRNA-1179 inhibitor showed a low level of suppression. Similarly, Fig. 1F expressed the colony formation potential of the miRNA-1179-overexpressing in the miRNA-NC and miRNA-1179 mimics. The miRNA-NC expressed around 100 colonies, while the miRNA-1179 mimics showed around 40 colonies. Figure 1G depicts the colony formation capability of miRNA-1179 overexpression in NC inhibitor and miRNA-1179 inhibitor cells. The inhibitor-NC expresses around 100 colonies, while the miRNA-1179 inhibitor showed around 130 colonies.

DAPI staining revealed that overexpression of miRNA-1179 altered the structure of the nucleus of the miRNA-NC, miRNA-1179 mimics, miRNA-1179 inhibitors, and inhibitor-NC cells (Fig. 2A). The miRNA-1179 inhibitor seems to not affect the nuclear morphology of cells (Fig. 2A), and annexin V/PI staining revealed that the percentage of apoptosis in cells rose from 5.32% to 34.86% when miRNA-1179 was overexpressed. However, inhibition of miRNA-1179 prevented the apoptosis of the tested cells (Fig. 2B). Similarly, the expression of Bax increased while that of Bcl-2 decreased upon miRNA-1179 overexpression. Nonetheless, inhibition of miRNA-1179 in cells exhibited opposite effects (Fig. 2C).

In the study, the target of miR-1179 was analysed and identified by online TargetScan analysis. In this EREG was selected for analysis for its potential oncogenic role in multiple myeloma, and it has not been studied as the target of miRNA-1179. TargetScan analysis showing EREG 3'-UTR sequence as the target of miR1179 (Fig. 3A). The interaction between miRNA-NC and miRNA-1179 mimics was further analyzed by the luciferase assay (Fig. 3B). The luciferase assay of miRNA-NC is high in EREG-WT, while the luciferase assay of miRNA-1179 mimics is very low. In EREG-MUT, there is little difference in luciferase activity between miRNA-NC and miRNA-1179 mimics. Moreover, significant upregulation ($p < 0.05$) of miRNA-1179 was seen in both multiple myeloma tissues compared to normal tissues (Figs 3C and 3D). Multiple myeloma tissues were expressed up to 7-fold, while normal tissues were expressed below that up to 2-fold. However, the expression of EREG was considerably suppressed in miRNA-1179 mimics upon miRNA-1179 overexpres-

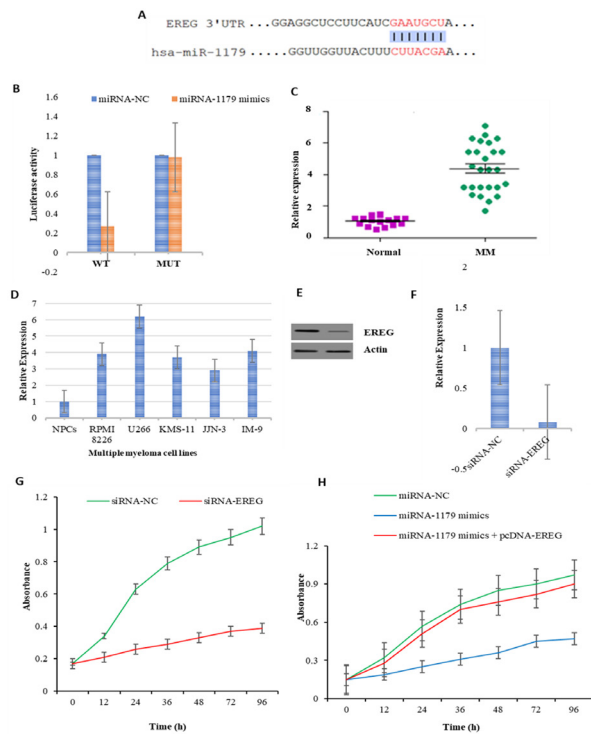


Figure 3. Expression of miRNA-1179

(A) TargetScan analysis showing EREG 3'-UTR sequence as the target of miR1179; (B) Luciferase assay between miRNA-NC and miRNA-1179 mimic; (C) Relative expression in between normal cells and multiple myeloma cells; (D) Relative expression of the different types of myeloma cell lines; (E) Expression of EREG and Actin; (F) Relative expression of the siRNA-NC and siRNA-EREG; (G) Cell Survival ability of the siRNA-NC and siRNA-EREG; (H) Cell Survival ability of the siRNA-NC, miRNA-1179 mimic and miRNA-1179 mimic + pcDNA-EREG

sion (Fig. 3E). Additionally, the knockdown of EREG inhibited the U266 cell survival ability (Fig. 3F). In this assay, siRNA-NC expressed the highest fold compared to siRNA-EREG. The survival ability of the siRNA-NC and siRNA-EREG cells was expressed in Fig. 3G. The survival ability of siRNA-EREG cells was highly suppressed ($p < 0.05$) by miRNA-1179 overexpression, whereas siRNA-NC had a low level of suppression. The survival abilities of miRNA-NC, miRNA-1179 mimics, and miRNA-1179 mimics + pcDNA-EREG were shown in Fig. 3H. This study showed that EREG overexpression eliminated the inhibitory activity of miRNA-1179 on the survival of cells (Fig. 3H).

The impact of miRNA-1179 expression on miRNA-NC, miRNA-1179 mimics, and miRNA-1179 mimics + pcDNA-EREG cell motility and invasion was examined. This study's outcomes revealed that the migration of miRNA-NC, miRNA-1179 mimics, and miRNA-1179 mimics + pcDNA-EREG were inhibited by 69%. However, EREG overexpression restored the motility potential of miRNA-1179 overexpression in the tested cells (Fig. 4A). Additionally, invasion of the tested cells was decreased by 76% compared to the control. Nevertheless, EREG inhibited the inhibitory activity of miRNA-1179 on tested cell invasion (Fig. 4B).

DISCUSSION

Multiple myeloma is one of the most devastating and incurable human malignancies and causes a large number

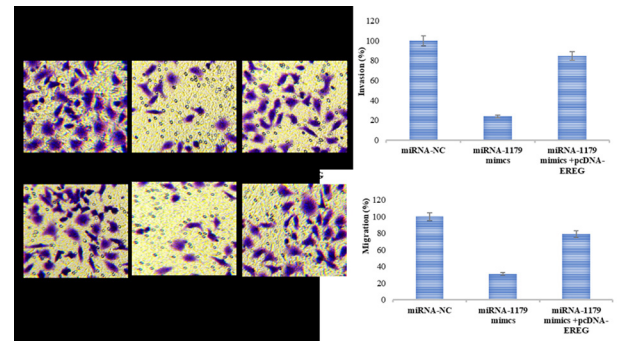


Figure 4. Motility and invasion of U266 cells by miRNA-1179 (A) Activity of miRNA-1179 on U266 cell invasion; (B) Motility potential of miRNA-1179

of human deaths (Wong *et al.*, 2020). The current work intends to explain the significance of miRNA-1179 in multiple myeloma and develop it as a therapeutic target for the disease's management. Prior research has shown that miRNA-1179 acts as a tumor inhibitor in various human malignancies. Li and Qin (Li & Qin, 2019) have shown that HMGB1 is the target of miRNA-1179, which slows down the growth of gastrointestinal cancer. Similarly, miRNA-1179 has been revealed to inhibit the formation of breast cancer cells *via* the notch signalling cascade (Li *et al.*, 2018). Consistently, the present study revealed tumour-suppressive effects of miRNA-1179 in human multiple myeloma cells and suggested that its downregulation in multiple myeloma cells might be facilitating the genesis and progression of multiple myeloma.

Cancer involves a diversity of genetic alterations resulting in the conversion of a normal cell into a malignant cell (Li *et al.*, 2018). Apoptosis eliminates the malignant cells and controls tumor progression. The suppression of apoptosis is essential in the development of human malignancies (Wanner *et al.*, 2021). The current study also found that apoptosis is responsible for the tumor-suppressing effects of miRNA-1179. This means that miRNA-1179 could be used to treat different types of myelomas. Several studies showed that miRNA-1179 can control the development of cancer by targeting a large number of genes. For example, it has been shown to target E2F5 in pancreatic cancer (Lin *et al.*, 2018), PTEN in ovarian cancer (Zhihong *et al.*, 2020), HMGB1 in gastric cancer (Li & Qin, 2019), and ZEB2 in hepatocellular carcinoma (Gao *et al.*, 2019). However, this is the first investigation to identify EREG as a target of miRNA-1179. Previously, EREG has been shown to be elevated in gastric cancer and acts as a predictor of poor prognosis (Xia *et al.*, 2019). Similarly, EREG has already been demonstrated to enhance colorectal cancer proliferation (Vychytilova-Faltejskova *et al.*, 2017). In another study, it was found that EREG makes salivary adenoid cystic carcinoma spread to the lungs (Yang *et al.*, 2017). The expression of EREG was observed to be enhanced in the current investigation. However, miRNA-1179 overexpression inhibits its expression post-transcriptionally to exert its tumor-suppressive effects in multiple myeloma, indicative of its therapeutic implications.

CONCLUSION

The current study found that miRNA-1179 was suppressed in multiple myeloma. Its overexpression suppresses the development and proliferation of human myeloma cells by inhibiting the expression of EREG.

These findings imply that miRNA-1179 might be used as a potential therapeutic agent for the therapy of multiple myeloma. Therefore, more in vivo investigation is necessary for this research area.

Declarations

Acknowledgement. The authors acknowledge the facilities provided by the superiors.

Authors Contribution. Xiao Liu and Wei Li conducted research activities and were involved in article writing. Lan Qin supervised the research activities and helped with article writing. Fei Fei helped proofread the manuscript. All authors read and approved the final version of the manuscript.

Conflicts of interest. There are no conflicts of interest.

REFERENCES

- Adham AN, Abdelfatah S, Naqishbandi AM, Mahmoud N, Efferth T (2020) Cytotoxicity of apigenin toward multiple myeloma cell lines and suppression of iNOS and COX-2 expression in STAT1-transfected HEK293 cells. *Phytomedicine* **8**: 153371. <https://doi.org/10.1016/j.phymed.2020.153371>
- Boyle EM, Deshpande S, Tytarenko R, Ashby C, Wang Y, Bauer MA, Johnson SK, Wardell CP, Thanendrarajan S, Zangari M, Facon T (2021) The molecular make up of smoldering myeloma highlights the evolutionary pathways leading to multiple myeloma. *Nat Commun* **12**: 1–13. <https://doi.org/10.1038/s41467-020-20524-2>
- Gao HB, Gao FZ, Chen XF (2019) MiRNA-1179 suppresses the metastasis of hepatocellular carcinoma by interacting with ZEB2. *Eur Rev Med Pharmacol Sci* **23**: 5149–5157. https://doi.org/10.26355/eurrev_201906_18179
- Gao Y, Xu H, Pu T (2020) MicroRNA-1179 suppresses the proliferation and enhances vincristine sensitivity of oral cancer cells via induction of apoptosis and modulation of MEK/ERK and PI3K/AKT signalling pathways. *AMB Express* **10**: 1–7. <https://doi.org/10.1186/s13568-020-01082-8>
- Li WJ, Xie XX, Bai J, Wang C, Zhao L, Jiang DQ (2018) Increased expression of miR-1179 inhibits breast cancer cell metastasis by modulating Notch signaling pathway and correlates with favorable prognosis. *Eur Rev Med Pharmacol Sci* **22**: 8374–8382. https://doi.org/10.26355/eurrev_201812_16535
- Li WJ, Xie XX, Bai J, Wang C, Zhao L, Jiang DQ (2018) Increased expression of miR-1179 inhibits breast cancer cell metastasis by modulating Notch signaling pathway and correlates with favorable prognosis. *Eur Rev Med Pharmacol Sci* **22**: 8374–8382. https://doi.org/10.26355/eurrev_201812_16535
- Li Y, Qin C (2019) MiR-1179 inhibits the proliferation of gastric cancer cells by targeting HMGB1. *Hum Cell* **32**: 352–359. <https://doi.org/10.1007/s13577-019-00244-6>
- Lin C, Hu Z, Yuan G, Su H, Zeng Y, Guo Z, Zhong F, Jiang K, He S (2018). MicroRNA-1179 inhibits the proliferation, migration and invasion of human pancreatic cancer cells by targeting E2F5. *Chem Biol Interact* **291**: 65–71. <https://doi.org/10.1016/j.cbi.2018.05.017>
- Pinto V, Bergantim R, Caires HR, Seca H, Guimarães JE, Vasconcelos MH (2020) Multiple myeloma: Available therapies and causes of drug resistance. *Cancers* **12**: 407. <https://doi.org/10.3390/cancers12020407>
- Rajkumar SV, Kumar S (2020) Multiple myeloma current treatment algorithms. *Blood Cancer J* **10**: 1–10. <https://doi.org/10.1038/s41408-020-00359-2>
- Ramassone A, Pagotto S, Veronese A, Visone R (2018) Epigenetics and microRNAs in cancer. *Int J Mol Sci* **19**: 459. <https://doi.org/10.3390/ijms19020459>
- Singh B, Bogatcheva G, Washington MK, Coffey RJ (2013) Transformation of polarized epithelial cells by apical mistrafficking of epiregulin. *Proc Natl Acad Sci U S A* **110**: 8960–8965. <https://doi.org/10.1073/pnas.1305508110>
- Song L, Dai Z, Zhang S, Zhang H, Liu C, Ma X, Liu D, Zan Y, Yin X (2018) MicroRNA-1179 suppresses cell growth and invasion by targeting sperm-associated antigen 5-mediated Akt signaling in human non-small cell lung cancer. *Biochem Biophys Res Commun* **504**: 164–170. <https://doi.org/10.1016/j.bbrc.2018.08.149>
- Tan W, Liu B, Qu S, Liang G, Luo W, Gong C (2018) MicroRNAs and cancer: Key paradigms in molecular therapy. *Oncol Lett* **15**: 2735–2742. <https://doi.org/10.3892/ol.2017.7638>
- Vannini I, Fanini F, Fabbri M (2018) Emerging roles of microRNAs in cancer. *Curr Opin Genet Dev* **48**: 128–133. <https://doi.org/10.1016/j.cde.2018.01.001>
- Vychytilova-Faltejskova P, Merhautova J, Machackova T, Gutierrez-Garcia I, Garcia-Solano J, Radova L, Brchnelova D, Slaba K, Svoboda M, Halamkova J, Demlova R, Kiss I, Vyzula R, Conesa-Zamora P, Slaby O (2017) MiR-215-5p is a tumor suppressor in colorectal cancer targeting EGFR ligand epiregulin and its transcriptional inducer HOXB9. *Oncogenesis* **6**: 399. <https://doi.org/10.1038/s41389-017-0006-6>
- Wanner E, Thoppil H, Riabowol K (2021) Senescence and apoptosis: architects of mammalian development. *Front Cell Dev Biol* **8**: 1–16. <https://doi.org/10.3389/fcell.2020.620089>
- Wong AH, Shin EM, Tergaonkar V, Chng W (2020) Targeting NF- κ B signaling for multiple myeloma. *Cancers* **12**: 2203. <https://doi.org/10.3390/cancers12082203>
- Xia Q, Zhou Y, Yong H, Wang X, Zhao W, Ding G, Zhu J, Li X, Feng Z, Wang B (2019) Elevated epiregulin expression predicts poor prognosis in gastric cancer. *Pathol Res Pract* **215**: 873–879. <https://doi.org/10.1016/j.prp.2019.01.030>
- Xu X, Cai N, Zhi T, Bao Z, Wang D, Liu Y, Jiang K, Fan L, Ji J, Liu N (2017) MicroRNA-1179 inhibits glioblastoma cell proliferation and cell cycle progression via directly targeting E2F transcription factor 5. *Am J Cancer Res* **7**: 1680–1692. PMID: 28861324
- Yang WW, Yang LQ, Zhao F, Chen CW, Xu LH, Fu J, Li SL, Ge XY (2017) Epiregulin promotes lung metastasis of salivary adenoid cystic carcinoma. *Theranostics* **7**: 3700. <https://doi.org/10.7150/thno.19712>
- Zhihong Z, Rubin C, Liping L, Anpeng M, Hui G, Yanting W, Zhenxiu S (2020) MicroRNA-1179 regulates proliferation and chemosensitivity of human ovarian cancer cells by targeting the PTEN-mediated PI3K/AKT signaling pathway. *Arch Med Sci* **16**: 907. <https://doi.org/10.5114/aoms.2019.86798>
- Zhihong Z, Rubin C, Liping L, Anpeng M, Hui G, Yanting W, Zhenxiu S (2019) MicroRNA-1179 regulates proliferation and chemosensitivity of human ovarian cancer cells by targeting the PTEN-mediated PI3K/AKT signaling pathway. *Arch Med Sci* **16**: 907–914. <https://doi.org/10.5114/aoms.2019.86798>

WIF1 was downregulated in cervical cancer due to promoter methylation

Ying Wang¹, Shifa Yuan², Jing Ma¹✉, Hong Liu³, Lizhen Huang¹, Fengzhen Zhang¹ and Xiaomei Wang⁴

¹Department of Gynecology, The Fourth Hospital of Hebei Medical University, Shijiazhuang 050011, China; ²Department of General Surgery, Hospital of Hebei Province Crop of Chinese Armed Police Force, Shijiazhuang, 050081, China; ³Department of Gynecology Oncology, The Fourth Hospital of Hebei Medical University, Shijiazhuang 050011, China; ⁴Department of Gynecology, Zhengding Maternal and Child Health Hospital, Zhengding, China

Wnt inhibitory factor 1 (WIF1) is frequently downregulated in a variety of cancer due to promoter methylation. However, the methylation status of the WIF1 promoter in cervical cancer remains unclear. This study aimed to elucidate the mechanism by which WIF1 promoter methylation contributes to cervical cancer development. The expression of WIF1 in cervical cancer tissues was examined by immunohistochemistry. The methylation status of the WIF1 promoter in cervical cancer cells was detected by methylation specific PCR. WIF1 mRNA levels and protein levels were detected by PCR and Western blot analysis. We found that WIF1 expression was low in cervical cancer tissues compared to adjacent normal cervical tissues. The WIF1 promoter was methylated in the cervical cancer SiHa cell line but not in the normal cervical epithelial cell line Ect1. Correspondingly, WIF1 mRNA levels and protein levels were significantly lower in SiHa cells than in Ect1 cells. Treatment with 5-aza-2-deoxycytidine (AZA) led to the upregulation of WIF1 mRNA and protein levels in SiHa cells, but the effects were abrogated by treatment with WIF1 siRNA. In addition, AZA treatment induced apoptosis and inhibited the invasion of SiHa cells, and the effects were abrogated by WIF1 siRNA. The protein levels of survivin, c-myc and cyclinD1 were significantly lower in SiHa cells treated with AZA, but their levels were upregulated after treatment with WIF1 siRNA. In conclusion, the methylation of the WIF1 promoter leads to the downregulation of WIF1 and the activation of Wnt/ β -catenin signaling in cervical cancer cells. WIF1 is a tumor suppressor that is inactivated in cervical cancer.

Keywords: WIF-1; Wnt/ β -Catenin; cervical cancer; methylation

Received: 01 March, 2023; **revised:** 18 April, 2023; **accepted:** 30 April, 2023; **available on-line:** 12 June, 2023

✉e-mail: shj911la@gmail.com

Acknowledgements of Financial Support: This work was supported by the Key Medical Science Research Program of Hebei Province (No. 20210605).

Abbreviations: AZA, 5-aza-2-deoxycytidine; DMSO, dimethyl sulfoxide; WIF1, Wnt inhibitory factor 1

INTRODUCTION

Cervical cancer is the second most common malignant tumor in women worldwide, and persistent infection with high-risk human papillomavirus is the main cause of cervical cancer (Halim *et al.*, 2021; Sundaram *et al.*, 2021). Although comprehensive treatment options such as surgery, radiotherapy and chemotherapy can improve

the efficacy of cervical cancer therapy, the prognosis of patients with advanced stage or relapse of cervical cancer is poor. Therefore, it is important to further investigate the mechanism of cervical cancer development to improve current treatment strategies (Gao *et al.*, 2020).

The Wnt/ β -Catenin signaling pathway is an important pathway that promotes tumorigenesis (Paul & Dey, 2008; Zhu *et al.*, 2021). Wnt inhibitory factor 1 (WIF1) gene is located at 12q14 and encodes a secreted protein that binds to Wnt and acts as a Wnt antagonist to inhibit Wnt/ β -catenin signaling (Mazieres *et al.*, 2004). *WIF1* has been shown to inhibit the proliferation of different cancer cells (Kim *et al.*, 2007; Tang *et al.*, 2009). Notably, *WIF1* is frequently downregulated in a variety of cancer due to promoter methylation, indicating that WIF1 is a tumor suppressor (Paluszczak *et al.*, 2015; Karamitrousis *et al.*, 2020; Zhang *et al.*, 2014).

DNA methylation is one important DNA epigenetic modification in eukaryotic cells. DNA methylation transferase leads to the covalency binding of methyl groups provided by S-adenosine methionine (SAM) to specific bases. Aberrant DNA methylation, especially for tumor suppressors, could silence their expression and contribute to the development and progression of cancers including cervical cancer (Lai *et al.*, 2010; Zummeren *et al.*, 2018; van Leeuwen *et al.*, 2019). Consequently, DNA methyltransferase inhibitor 5-aza-2-deoxycytidine (AZA) has been utilized to inhibit DNA methylation of tumor suppressors for cancer treatment (Donia *et al.*, 2021). However, the status of methylation of WIF1 promoter in cervical cancer remains unclear. Therefore, in this study, we aimed to detect whether the WIF1 promoter is methylated in cervical cancer and elucidate the mechanism by which WIF1 promoter methylation contributes to cervical cancer development.

MATERIALS AND METHODS

Clinical samples

The clinical samples were from 5 patients with cervical squamous cell carcinoma confirmed by pathological examinations in the Fourth Hospital of Hebei Medical University from December 2019 to June 2020. All patients signed written informed consent. This study was approved by the Ethics Committee of the Fourth Hospital of Hebei Medical University (Approval No. 2019035).

Immunohistochemistry

The streptomycin avidin-peroxidase method was used to detect the expression of WIF1 in clinical samples. The cervical cancer tissues and adjacent cervical tissues were cut into 5 μm thin sections. Antigen retrieval was performed by the incubation of the sections in 10 mM citrate buffer (pH 6.0), and the sections were heated at 100°C for 1 h to block endogenous peroxidase. Next, the sections were incubated with WIF1 antibody (Abcam, Cat# ab71204, Cambridge, MA, USA; 1:500 dilution) for 1 h at 37°C, washed with phosphate buffered saline (PBS), and then incubated with SP-9001 kit (Zhong Shan Golden Bridge, Beijing, China) to visualize the staining. PBS instead of the primary antibody was used as the negative control.

Cell culture

Human cervical cancer cell line SiHa and normal ectocervical cell line Ect1/E6E7 were purchased from American Type Culture Collection and cultured in RPMI 1640 medium containing 10% fetal bovine serum (FBS, Thermo Fisher, CA, USA). The incubator condition was 37°C with 5% CO₂. AZA was purchased from Sigma-Aldrich (St. Louis, MO, USA) and diluted in dimethyl sulfoxide (DMSO). SiHa cells were treated with 1 μM AZA or DMSO as the control for 48 h. In addition, SiHa cells were transfected with siRNA for WIF1 or scramble siRNA as control (Sangon Biotech, Shanghai, China) using Lipofectamine 3000 (Thermo Fisher, CA, USA). Cells were collected 48 h after transfection for further analysis.

Transwell invasion assay

The treated cells were added to the upper chamber of the Transwell (Corning Costar; Oneonta, USA), while the lower chamber was filled with 600 μl of RPMI 1640 medium containing 10% FBS. After incubation for 24 h, the cells were fixed with 95% methanol, stained with crystal violet for 20 min, and photographed under the microscope to count the number of invaded cells.

Flow cytometry

The apoptosis of treated cells was examined by using an Annexin V/FITC apoptosis kit (BD Biosciences, USA) following the manufacturer's protocol. The stained cells were immediately analyzed using FACS Calibur System (Becton-Dickinson). The number of positively stained cells was counted to calculate the apoptosis ratio.

Methylation-specific PCR (MSP)

Genomic DNA was extracted from SiHa and Ect1 cells using a DNeasy kit (Qiagen, Germany) following the manufacturer's protocols. Bisulfite modification of genomic DNA was performed by using a methylation kit (Zymo Research, Orange, CA, USA). MSP was performed with bisulfite-treated genomic DNA as a template and the following primers: unmethylation specific primers 5'-TTGTGGGTGTTTATTGGGT-3' (upstream) and 5'-AACAAAACC AACAAACAACA-3' (downstream); methylation specific primers 5'-TCGCGGGCGTTTATTGGGC-3' (upstream) and 5'-AACGAAACCAACAATCAACG-3' (downstream).

RT-PCR

Total RNA was extracted from cells and cDNA was synthesized from total RNA using a reverse transcrip-

tion kit. PCR was performed with cDNA as a template and the following primers: WIF1 5'-CCGAAATG-GAGGCTTTTGTA-3' (upstream) and 5'-TGGTT-GAGCAGTTTGCTTTG-3' (downstream). Glyceraldehyde-3-phosphate dehydrogenase (GAPDH) was used as an internal control to normalize WIF1 mRNA levels.

Western blot analysis

Total protein was extracted from cells using RIPA buffer and protein concentration was determined by using a bicinchoninic acid assay. Equal amounts of proteins were separated by sodium dodecyl sulfate polyacrylamide gel electrophoresis and transferred to nitrocellulose membranes (Bio-Rad). The membranes were blocked in 5% non-fat milk and then incubated with primary antibodies for WIF1 (1:800), survivin, c-myc, CyclinD1 and GAPDH (all from Abcam, Cambridge, UK). The membranes were further incubated with secondary antibodies (Abcam, Cambridge, UK), and detected by chemiluminescence. Densitometry analysis of the bands was performed using Image-J software with GAPDH as a loading control.

Statistical analysis

The data were presented as the mean \pm standard deviation (S.D.) and analyzed using SPSS statistical software (IBM Corp., Chicago, IL, USA). Comparisons between groups were performed using Student's *t*-test. The difference was considered significant for *p* < 0.05.

RESULTS

WIF1 expression was low in cervical cancer tissues

First, we compared WIF1 expression in cervical cancer tissues and adjacent normal cervical tissues by immunohistochemistry. For negative control, we could not detect WIF1 expression in normal cervical tissues because PBS was used instead of WIF1 antibody (Fig. 1A). When we used WIF1 antibody, we detected strong nuclear staining of WIF1 in normal cervical tissues (Fig. 1B). In contrast, we detected weak nuclear staining of WIF1 in cervical cancer tissues (Fig. 1C). These results indicated that WIF1 expression was low in cervical cancer.

WIF1 promoter was methylated in cervical cancer cells

To elucidate how WIF1 is downregulated in cervical cancer tissues, we used cervical cancer cell as the model. First, we detected the methylation status of the WIF1 promoter in cervical cancer cells by MSP. Compared to normal cervical epithelial cells Ect1, WIF1 promoter was methylated in cervical cancer SiHa cells (Fig. 2A). RT-PCR showed that WIF1 mRNA levels were significantly lower in SiHa cells than in Ect1 cells (Fig. 2B).

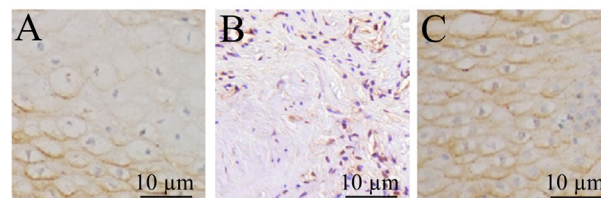


Figure 1. The expression of WIF1 in cervical cancer tissues. (A) WIF1 was barely detected in adjacent cervical tissues stained with PBS instead of WIF1 antibody as a negative control. (B) WIF1 was strongly stained in the nuclei of adjacent normal cervical cells. (C) WIF1 was weakly stained in the nuclei of cervical squamous carcinoma cells.

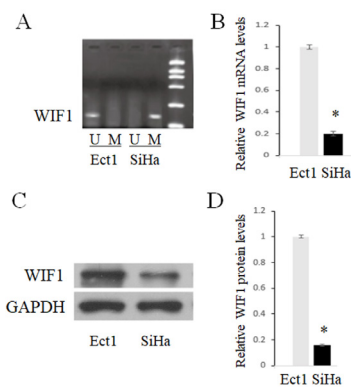


Figure 2. WIF1 promoter was methylated and WIF1 was down-regulated in cervical cancer cells.

(A) MSP analysis of WIF1 promoter in SiHa and Ect1 cells. U: un-methylated; M: methylated. (B) RT-PCR analysis of WIF1 mRNA levels in SiHa and Ect1 cells. (C) Western blot analysis of WIF1 protein levels in SiHa and Ect1 cells. GAPDH was loading control. (D) Densitometry analysis of WIF1 protein levels in SiHa and Ect1 cells. Data were expressed as the mean \pm S.D. (n=3). * P <0.05 compared to Ect1 cells.

Furthermore, we detected WIF1 protein levels in SiHa cells and Ect1 cells (Fig. 2C). The results showed that WIF1 protein levels were significantly lower in SiHa cells than in Ect1 cells (Fig. 2D). Collectively, these data indicated that WIF1 promoter was methylated and WIF1 was downregulated in cervical cancer cells.

AZA upregulated WIF1 expression in cervical cancer cells

To examine whether demethylation of the WIF1 promoter can restore WIF1 expression in cervical cancer cells, we treated SiHa cells with the demethylation agent AZA. Compared to SiHa cells treated with DMSO as control, WIF1 mRNA levels were significantly higher in SiHa cells treated with AZA. However, the upregulation of WIF1 mRNA levels by AZA was abrogated by treatment with WIF1 siRNA (Fig. 3A).

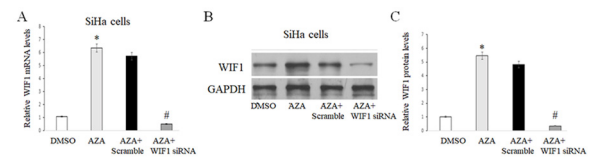


Figure 3. AZA upregulated WIF1 expression in cervical cancer cells.

(A) RT-PCR analysis of WIF1 mRNA levels in SiHa cells treated with DMSO, AZA (5-aza-2-deoxycytidine), AZA+ scramble siRNA, AZA + WIF1 siRNA. (B) Western blot analysis of WIF1 protein levels in SiHa cells treated with DMSO, AZA, AZA+ scramble siRNA, AZA + WIF1 siRNA. GAPDH was loading control. (C) Densitometry analysis of WIF1 protein levels in SiHa cells treated with DMSO, AZA, AZA+ scramble siRNA, AZA + WIF1 siRNA. Data were expressed as the mean \pm S.D. (n=3). * P <0.05 for the AZA group compared to the DMSO group. # P <0.05 for AZA + WIF1 siRNA group compared to AZA group.

Next, we examined WIF1 protein levels in SiHa cells in different treatment groups (Fig. 3B). Densitometry analysis showed that WIF1 protein levels were significantly higher in SiHa cells treated with AZA than in cells treated with DMSO as control. However, the upregulation of WIF1 protein levels by AZA was abrogated by treatment with WIF1 siRNA (Fig. 3C). These results confirmed that AZA targeted WIF1 promoter to upregulate WIF1 expression in cervical cancer cells.

AZA inhibited malignant behaviors of cervical cancer cells

To examine the effects of AZA on cervical cancer cell behaviors, we performed flow cytometry and found that AZA treatment increased the apoptosis of SiHa cells, while the effect of AZA on apoptosis was abrogated by WIF1 siRNA (Fig. 4A). Quantitative analysis showed that apoptosis percentage was significantly higher in SiHa cells treated with AZA than in cells treated with DMSO but was significantly lower in SiHa cells treated with both AZA and WIF1 siRNA than in cells treated with AZA alone (Fig. 4B).

Transwell invasion assay showed that AZA treatment inhibited the invasion of SiHa cells, while the ef-

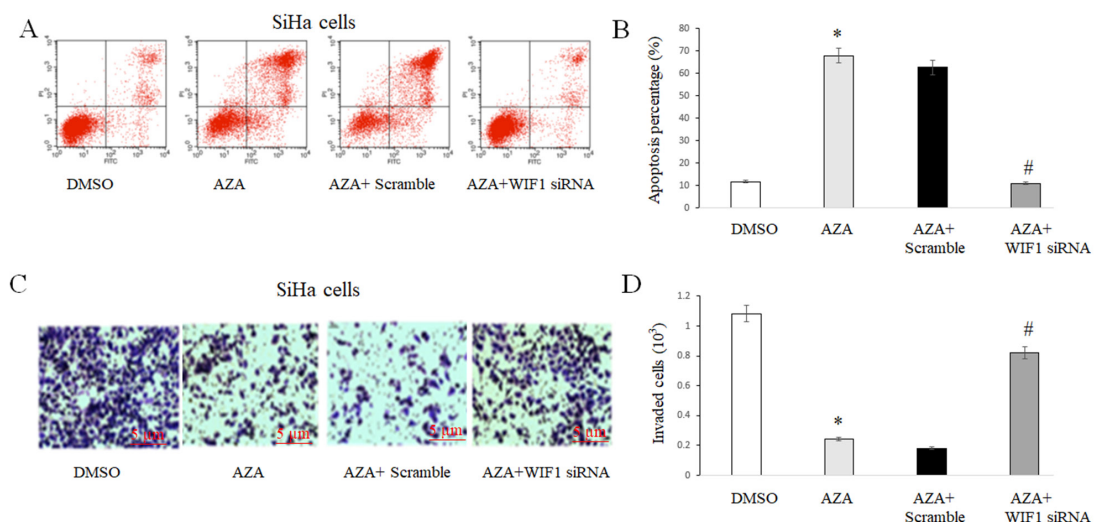


Figure 4. AZA induced the apoptosis and inhibited the invasion of cervical cancer cells.

(A) Flow cytometry analysis of apoptosis in SiHa cells treated with DMSO, AZA, AZA+ scramble siRNA, AZA + WIF1 siRNA. (B) Quantitative analysis of apoptosis percentage in SiHa cells treated with DMSO, AZA, AZA+ scramble siRNA, AZA + WIF1 siRNA. (C) Transwell invasion assay of SiHa cells treated with DMSO, AZA, AZA+ scramble siRNA, AZA + WIF1 siRNA. (D) Quantitative analysis of the number of invaded SiHa cells treated with DMSO, AZA, AZA+ scramble siRNA, AZA + WIF1 siRNA. Data were expressed as the mean \pm S.D. (n=5). * P <0.05 for the AZA group compared to the DMSO group. # P <0.05 for AZA + WIF1 siRNA group compared to AZA group.

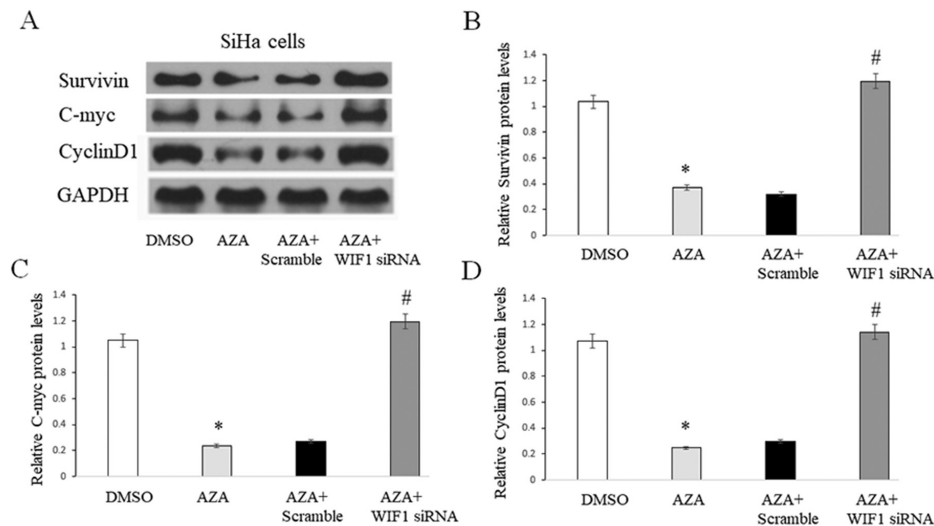


Figure 5. AZA inhibited the expression of Wnt/ β -catenin target genes in cervical cancer cells.

(A) Western blot analysis of survivin, c-myc and cyclinD1 protein levels in SiHa cells treated with DMSO, AZA, AZA+ scramble siRNA, AZA + WIF1 siRNA. GAPDH was loading control. (B) Densitometry analysis of survivin protein levels in SiHa cells treated with DMSO, AZA, AZA+ scramble siRNA, AZA + WIF1 siRNA. (C) Densitometry analysis of c-myc protein levels in SiHa cells treated with DMSO, AZA, AZA+ scramble siRNA, AZA + WIF1 siRNA. (D) Densitometry analysis of cyclinD1 protein levels in SiHa cells treated with DMSO, AZA, AZA+ scramble siRNA, AZA + WIF1 siRNA. Data were expressed as the mean \pm S.D. (n=3). * $P < 0.05$ for the AZA group compared to the DMSO group. # $P < 0.05$ for AZA + WIF1 siRNA group compared to AZA group.

fect of AZA on invasion was abrogated by WIF1 siRNA (Fig. 4C). Quantitative analysis showed that the number of invaded cells was significantly lower in SiHa cells treated with AZA than in cells treated with DMSO but was significantly higher in SiHa cells treated with both AZA and WIF1 siRNA than in cells treated with AZA alone (Fig. 4D). Taken together, these results indicated that AZA induced the apoptosis and inhibited the invasion of cervical cancer cells.

AZA inhibited the apoptosis of cervical cancer cells via the inhibition of the Wnt pathway

To investigate how AZA inhibited the apoptosis of cervical cancer cells, we detected protein levels of survivin, c-myc and cyclinD1, which are Wnt pathway target genes and regulate cell proliferation and apoptosis (Fig. 5A). Densitometry analysis showed that protein levels of survivin, c-myc and cyclinD1 were significantly lower in SiHa cells treated with AZA than in cells treated with DMSO as control. However, protein levels of survivin, c-myc and cyclinD1 were significantly higher in SiHa cells treated with both AZA and WIF1 siRNA than in cells treated with AZA alone (Fig. 5B–D).

DISCUSSION

In this study, we demonstrated that WIF1 was downregulated in cervical cancer tissues and cells due to the methylation of the WIF1 promoter. AZA abrogated the methylation of the WIF1 promoter and upregulated WIF1 expression. Consequently, AZA inhibited the invasion and induced the apoptosis of cervical cancer cells. Furthermore, AZA inhibited the expression of survivin, c-myc and cyclinD1, which may be the mechanism by which AZA inhibited apoptosis and promoted the proliferation of cervical cancer cells.

The development and progression of cervical cancer is a complex process that involves both genetic and epigenetic mechanisms (Albulescu *et al.*, 2021; Wang *et al.*,

2021). DNA methylation, especially the methylation of tumor suppressor genes, is one of the most important types of epigenetic modification that contribute to tumorigenesis (van Leeuwen *et al.*, 2019). Recent studies have shown that promoter methylation of WIF1 promoted the development of a variety of tumors (Zhang *et al.*, 2014). However, the role of WIF1 promoter methylation in cervical cancer remains unclear.

Using normal cervical epithelial cells as control, we showed that the WIF1 promoter was methylated in SiHa cervical cancer cells. Consistently, both mRNA and protein levels of WIF1 were significantly downregulated in SiHa cells compared to normal cervical epithelial cells. However, AZA treatment led to the upregulation of WIF1 at both mRNA and protein levels, and the effects of AZA on WIF1 could be abrogated by WIF1 siRNA. Taken together, these data indicate that the downregulation of WIF1 in cervical cancer cells is due to promoter methylation.

Wnt/ β -catenin signaling plays an important role in tumorigenesis. The activation of Wnt/ β -catenin signaling leads to the translocation of β -catenin from the cytoplasm into the nuclei where it interacts with transcription factor TCF/LEF to drive the transcription of downstream target genes such as survivin, c-myc and CyclinD1 (Koushyar *et al.*, 2022). Among a variety of targets of Wnt/ β -catenin signaling, survivin is a known anti-apoptosis protein that promotes cell survival. C-myc and CyclinD1 are known to promote cell proliferation and cell cycle progression. The upregulation of survivin, c-myc and CyclinD1 in SiHa cells treated by AZA may explain why the apoptosis percentage was lower in these cells compared to control cells treated with DMSO. In addition, AZA induced apoptosis of SiHa cell was abrogated by WIF1 siRNA. On the other hand, AZA inhibited the invasion of SiHa cells, and SiHa cell invasion could be restored after treatment with WIF1 siRNA. Notably, cancer cell invasion depends on the action of matrix metalloproteinases (MMPs), and MMP9 was recently identified as a target of Wnt/ β -catenin signaling

(Ingraham *et al.*, 2011; Lee *et al.*, 2014; Chen *et al.*, 2021). Cervical cancer metastasis remains a big challenge for the effective treatment of cervical cancer in the clinic (Cheng and Huang, 2021). Further studies are needed to identify target genes of Wnt/ β -catenin signaling that could be regulated by AZA, which could be novel therapeutic targets for metastatic cervical cancer.

In conclusion, this study provides evidence that the methylation of the WIF1 promoter leads to the down-regulation of WIF1 and the activation of Wnt/ β -catenin signaling in cervical cancer. AZA treatment reduced the methylation of WIF1 promoter and upregulated WIF1 expression to inhibit Wnt/ β -catenin signaling in cervical cancer cells. Consequently, AZA induced apoptosis and inhibited the invasion of cervical cancer cells, which could be rescued by WIF1 siRNA. These findings suggest that WIF1 is a tumor suppressor that is inactivated in cervical cancer, and the development of approaches to restore WIF1 expression is promising for cervical cancer treatment.

Declarations

Availability of data and material. All data and materials are included in this manuscript.

Competing interests. The authors have no conflict of interest.

Authors' contributions. YW, SY, HL, LH, FZ, and XW collected and analyzed the data, and JM designed the study and wrote the manuscript. All authors read and approved the final manuscript.

REFERENCES

- Albulescu A, Plesa A, Fudulu A, Iancu IV, Anton G, Botezatu A (2021) Epigenetic approaches for cervical neoplasia screening (Review) *Exp Ther Med* 22: 1481. <https://doi.org/10.3892/etm.2021.10916>
- Chen X, Zhang H, Li L, Chen W, Bao T, Li B (2021) miR-5100 mediates migration and invasion of melanomatous cells *in vitro* via targeting SPINK5. *J Comp Mol Sci Genet* 1: 14–23. <https://mbgm.journals.publicknowledgeproject.org/index.php/mbgm/article/view/1395>
- Cheng T, Huang S (2021) Roles of non-coding RNAs in cervical cancer metastasis. *Front Oncol* 11: 646192. <https://doi.org/10.3389/fonc.2021.646192>
- Donia T, Khedr S, Salim EI, Hessian M (2021) Trichostatin A sensitizes hepatoma cells to Taxol more than 5-Aza-dC and dexamethasone. *Drug Metab Pers Ther* 36: 299–309. <https://doi.org/10.1515/dmpt-2020-0186>
- Gao W, Ma Q, Tang C, Zhan Y, Duan Y, Ni H, Xu Y (2020) Micro-environment and related genes predict outcomes of patients with cervical cancer: evidence from TCGA and bioinformatic analysis. *BioCell* 44: 597–605. <https://doi.org/10.32604/biomed.2020.011328>
- Halim A, Mustafa WA, Khairunizam W, Rahim HA, Sakeran H (2021) Nucleus detection on pap smear images for cervical cancer diagnosis: a review analysis. *Oncology* 23: 73–88. <https://doi.org/10.32604/Oncology.2021.015154>
- Ingraham CA, Park GC, Makarenkova HP, Crossin KL (2011) Matrix metalloproteinase (MMP)-9 induced by Wnt signaling increases the proliferation and migration of embryonic neural stem cells at low O₂ levels. *J Biol Chem* 286: 17649–17657. <https://doi.org/10.1074/jbc.M111.229427>
- Karamitrousis E, Balgkouranidou I, Xenidis N, Amarantidis K, Biziota E, Koukaki T, Trypanis G, Karayiannakis A, Bolanaki H, Chatzaki E, Kolios G, Lianidou E, Lambropoulou M, Kakolyris S (2020) Association between SOX17, Wif-1 and RASSF1A promoter methylation status and response to chemotherapy in patients with metastatic gastric cancer. *Clin Chem Lab Med* 59: e73–e75. <https://doi.org/10.1515/cclm-2020-0662>
- Kim J, You L, Xu Z, Kuchenbecker K, Raz D, He B, Jablons D (2007) Wnt inhibitory factor inhibits lung cancer cell growth. *J Thorac Cardiovasc Surg* 133: 733–737. <https://doi.org/10.1016/j.jtcvs.2006.09.053>
- Koushyar S, Meniel VS, Phesse TJ, Pearson HB (2022) Exploring the Wnt pathway as a therapeutic target for prostate cancer. *Biomolecules* 12: 309. <https://doi.org/10.3390/biom12020309>
- Lai HC, Lin YW, Huang RL, Chung MT, Wang HC, Liao YP, Su PH, Liu YL, Yu MH (2010) Quantitative DNA methylation analysis detects cervical intraepithelial neoplasms type 3 and worse. *Cancer* 116: 4266–4274. <https://doi.org/10.1002/cncr.25252>
- Lee MA, Park JH, Rhyu SY, Oh ST, Kang WK, Kim HN (2014) Wnt3a expression is associated with MMP-9 expression in primary tumor and metastatic site in recurrent or stage IV colorectal cancer. *BMC Cancer* 14: 125. <https://doi.org/10.1186/1471-2407-14-125>
- Mazieres J, He B, You L, Xu Z, Lee AY, Mikami I, Reguart N, Rosell R, McCormick F, Jablons DM (2004) Wnt inhibitory factor-1 is silenced by promoter hypermethylation in human lung cancer. *Cancer Res* 64: 4717–4720. <https://doi.org/10.1158/0008-5472.CAN-04-1389>
- Paluszczak J, Sarbak J, Kostrzewska-Poczekaj M, Kiwerska K, Jarmuż-Szymczak M, Grenman R, Mielcarek-Kuchta D, Baer-Dubowska W (2015) The negative regulators of Wnt pathway-DACH1, DKK1, and WIF1 are methylated in oral and oropharyngeal cancer and WIF1 methylation predicts shorter survival. *Tumour Biol* 36: 2855–2861. <https://doi.org/10.1007/s13277-014-2913-x>
- Paul S, Dey A (2008) Wnt signaling and cancer development: therapeutic implication. *Neoplasia* 55: 165–176. PMID: 18348648
- Sundaram MK, Almutary AG, Haque S, Faheem SM, Arif Hussain A (2021) Awareness of human papilloma virus and its association with cervical cancer among female university students: a study from United Arab Emirates. *Oncology* 23: 269–277. <https://doi.org/10.32604/ONCOLOGIE.2021.016002>
- Tang Y, Simoneau AR, Liao WX, Yi G, Hope C, Liu F, Li S, Xie J, Holcombe RF, Jurnak FA, Mercola D, Hoang BH, Zi X (2009) WIF1, a Wnt pathway inhibitor, regulates SKP2 and c-myc expression leading to G1 arrest and growth inhibition of human invasive urinary bladder cancer cells. *Mol Cancer Ther* 8: 458–468. <https://doi.org/10.1158/1535-7163.MCT-08-0885>
- van Leeuwen RW, Ostrbenk A, Poljak M, van der Zee AGJ, Schuurings E, Wisman GBA (2019) DNA methylation markers as a triage test for identification of cervical lesions in a high risk human papilloma-virus positive screening cohort. *Int J Cancer* 144: 746–754. <https://doi.org/10.1002/ijc.31897>
- Wang Z, Wu R, Nie Q, Bouchonville KJ, Diasio RB, Offer SM (2021) Chromatin assembly factor 1 suppresses epigenetic reprogramming toward adaptive drug resistance. *J Natl Cancer Cent* 1: 15–22. <https://doi.org/10.1016/j.jncc.2020.12.003>
- Zhang J, Zhou B, Liu Y, Chen K, Bao P, Wang Y, Wang J, Zhou Z, Sun X, Li Y (2014) Wnt inhibitory factor-1 functions as a tumor suppressor through modulating Wnt/ β -catenin signaling in neuroblastoma. *Cancer Lett* 348: 12–19. <https://doi.org/10.1016/j.canlet.2014.02.011>
- Zhu X, Jia W, Yan Y, Huang Y, Wang B (2021) NOP14 regulates the growth, migration, and invasion of colorectal cancer cells by modulating the NRIP1/GSK-3 β / β -catenin signaling pathway. *Eur J Histochem* 65: 3246. <https://doi.org/10.4081/ejh.2021.3246>
- Zumreren MV, Kremer WW, Leeman A, Bleeker MCG, Jenkins D, Sandt MV, Doorbar J, Heideman DAM, Steenberg RDM, Snijders PJF, Kenter GG, Quint WGV, Berkhof J, Meijer CJLM (2018) HPV E4 expression and DNA hypermethylation of CADM1, MAL, and miR124-2 genes in cervical cancer and precursor lesions. *Mod Pathol* 31: 1842–1850. <https://doi.org/10.1038/s41379-018-0101-z>

MicroRNA-196-5p targets Derlin-1 to induce autophagy in human osteosarcoma cells

Zhenzhong Ji[#], Wei Chen[#], Song Wan, Yi Zhang and Junhua Xu[✉]

Department of Orthopedics, Wuhan Puren Hospital, Puren Hospital Affiliated of Wuhan University of Science and Technology, Wuhan, Hubei, 430080, China

Osteosarcoma is a highly prevalent type of primary bone tissues in children and young adolescents. Micro-RNA (miR) dysregulation has been linked to osteosarcoma tumorigenesis. The role of miR-196-5p was investigated in modulating the growth and metastatic behaviour of human osteosarcoma cells, along with exploring its mechanism of action. As shown by RT-qPCR expression analysis, osteosarcoma cell lines exhibited prominent ($P < 0.05$) transcriptional repression of miR-196-5p. The latter was thus transiently overexpressed in osteosarcoma cells, which resulted in the loss of cell viability and colony formation via induction of autophagy. The western blot analysis of the autophagy marker proteins revealed that the expression of Beclin 1 and LC3B II proteins was induced by miR-196-5p, whereas that of p62 and LC3BI was repressed. Moreover, osteosarcoma cells overexpressing miR-196-5p showed significantly ($P < 0.05$) lower migration and invasion concerning the control osteosarcoma cells. According to the results of the in-silico analysis, Derlin-1 participates in the regulation of miR-196-5p in osteosarcoma, and this prediction has been validated using a dual luciferase assay. The results indicated that miR-196-5p exerted its molecular role by targeting Derlin-1 at the post-transcriptional level. Summing up, the study revealed the modulatory potential of miR-196-5p/Derlin-1 on osteosarcoma cells and provided insights into the possible implications for the treatment and prognosis of the disease.

Keywords: metastasis, autophagy, miR-196-5p, Derlin-1, osteosarcoma

Received: 11 November, 2022; revised: 14 March, 2023; accepted: 22 March, 2023; available on-line: 23 April, 2023

✉e-mail: xujunhua879@163.com

[#]These two authors contributed equally to this work.

Abbreviations: AO, Acridine orange; DERL1, Derlin 1; DMEM, Dulbecco's Modified Eagle Medium; ER, endoplasmic reticulum; ERAD, endoplasmic reticulum-associated degradation; HCC, hepatocellular carcinoma; MUT, Mutant type; RIN, RNA integrity number; TER94, Transitional endoplasmic reticulum ATPase; TLR4, Toll-like receptor 4; UTR, untranscribed region; WT, Wild type

INTRODUCTION

Osteosarcoma is the most prevalent bone cancer, commonly affecting adolescents and young people (Ferguson & Turner, 2018; Sadykova *et al.*, 2020). This disease has been reported to exhibit a very poor prognosis, and in a considerable proportion of the diagnosed cases, it metastasizes to the pulmonary tissues (Li *et al.*, 2020). Together, these factors make osteosarcoma very lethal and therefore require the formulation of novel and efficient therapeutic measures against osteosarcoma.

Pertinently, elucidation of the tumorigenesis of osteosarcoma on a molecular basis is essential to recognise the potential prognostic and therapeutic targets against this devastating malignancy. The vast majority of localised osteosarcomas are treated with surgery, but with the introduction of multiagent chemotherapy regimens there has been an increase in survival rate to 70% in patients with osteosarcoma (Miwa *et al.*, 2019). Several patients and their families have been reported to have undergone limb salvage surgery. Most patients, more than 85%, choose to salvage a limb rather than have it amputated (Rouggraft *et al.*, 1994). It is also possible to employ radiation therapy to aid in the removal of microscopic or marginal residual tumours (DeLaney *et al.*, 2005). It has been estimated that approximately 70% of cancer patients with localized tumors will receive chemotherapy treatment (Chou *et al.*, 2005). There is a compound known as Mifamurtide, which is a liposomal TLR4 agonist that triggers macrophages and monocytes to channel the antitumor immune response against cancerous cells and inhibit malignant metastasis.

Micro-RNAs (miRs) belong to endogenous non-coding RNAs ranging in average size from 20–25 nucleotides (Donlic & Hargrove, 2018) that regulate specific protein-coding genes, mainly at the post-transcriptional level (Loukas *et al.*, 2021). These genes encode proteins that are modulated by miRs that bind to 3'-UTRs (untranscribed regions) of mRNAs post-transcriptionally via the mRNAs' 3'-UTRs (Abdalla *et al.*, 2020). The miRs displayed a vital role in human biology and physiology (Catalucci *et al.*, 2009). Interestingly, several microRNAs' deviations from the normal expression levels were linked to cancer development, among other disorders (Olson *et al.*, 2009). MiRs regulate the proliferation, cell division, apoptosis, autophagy, migratory potential, and invasiveness of human cancer cells (Gao *et al.*, 2020; Lin *et al.*, 2017; Ashrafizadeh *et al.*, 2020). Human osteosarcoma reportedly also exhibits an aberrant expression of several miRs' and regulates the growth, metastasis, and proliferation of osteosarcoma cells (Zhou *et al.*, 2018; Salah *et al.*, 2015).

Currently, miR-196-5p is known to be one of the most important functional molecules in immunity and cancer development in humans (Huang *et al.*, 2014). According to recent evidence, miR-196-5p may suppress the growth of breast cancer and melanoma (Li *et al.*, 2010; Braig *et al.*, 2010). Additionally, in several studies in human cancers like oral and colorectal cancer, miR-196-5p expression is believed to be involved in oncogenesis or tumour suppression, regulating their growth and progression (Xin *et al.*, 2019a; Stiegelbauer *et al.*, 2017; Maruyama *et al.*, 2018). Evidence suggests that the miR-196-5p gene appears to be downregulated in certain hu-

man tumours and acts as a tumour suppressor in regulating tumorigenesis (Zheng *et al.*, 2019b; Lu *et al.*, 2016). Although downregulation of miR-196-5p resulting from long noncoding RNA sponging has been shown in surface osteosarcoma, its regulatory role has not yet been reported (Chen *et al.*, 2019).

Derlin-1, one of the ATPases in the p97 complex, is believed to be involved in ER-associated degradation. The function of this enzyme is to retrotranslocate misfolded or unfolded proteins into the cytosol for degradation by proteasomes (Klopfleisch *et al.*, 2010). Many tumors have overexpressed Derlin-1, which is involved in the progression of tumors (Wang *et al.*, 2008; Dong *et al.*, 2017). There is evidence that Derlin-1 is expressed in several varieties of human carcinomas, and antibodies that target Derlin-1 have been shown to inhibit the growth of colon tumours in mice (Tan *et al.*, 2015). In a study published by Wang and others in 2008 (Wang *et al.*, 2008) it was found that Derlin-1 expression is correlated with tumor grade and lymph node metastasis in breast cancer. There is, however, little information about the biological significance of Derlin-1 in osteosarcoma cancer, and the exact relationship between microRNA196-5p, which targets Derlin-1 to induce autophagy in human osteosarcoma cells, remains unknown. Therefore, a recent study aimed to investigate the effects of miR-196-5p/Derlin-1 pathway at the molecular level involved in osteosarcoma.

MATERIALS AND METHODS

Tissues samples

Fifty five paired osteosarcoma and normal matching human tissue samples were obtained from osteosarcoma subjects during surgical resection in the Department of Orthopedics, Puren Hospital Affiliated to Wuhan University of Science and Technology, Wuhan, China. Two pathologists, blind to the study, conducted the pathological survey of the excised tissue specimens. The ethics committee of our institute approved the study (approval No. OR14PUR256/22). Liquid nitrogen was used to snap-freeze the specimens, and the latter were stored at -80°C until experimentation.

Cell lines

Three different humans (MG-63; ATCC Catalogue no.: CRL-1427), (Saos2; ATCC Catalog no.: HTB-85) and (HOS; ATCC Catalog no.: CRL-1543) osteosarcoma cell lines were obtained from the ATCC (American Type Culture Collection, USA) and the hFOB1.19 (normal osteoblast cell line; Catalog No.: CL-0353) were obtained from the Elabscience Biotechnology Inc, USA. The culturing of the cell lines was carried out using DMEM (Dulbecco's modified Eagle's medium) added with 10% FBS (fetal bovine serum), penicillin (100 U/ml) and streptomycin (10 $\mu\text{g/L}$) in an incubator (5% CO_2) at room temperature. The lowest passage numbers for the cell lines were between 3–5, respectively. Colorimetric mycoplasma detection assay using PlasmotestTM (Catalog code: rep-pt1, InvivoGen USA) for the visual, colorimetric detection of mycoplasma contamination in cell cultures was performed. A positive result indicates the presence of a cell culture contaminant. The results of our tests for mycoplasma contamination in cell cultures were negative.

Cell line transfection

As a result of comparing miR-196-5p expression levels in Saos2, MG-63, and HOS cell lines with the normal osteoblast cell line, we selected the Saos2 cell line due to their relatively significant miR-16-5p expression levels ($P < 0.01$).

After reaching 80% confluence, cells were seeded at a density of 1×10^4 cells/ cm^2 into six-well plates. We carried out transient transfection of miRNAs as previously reported (Xin *et al.*, 2019a). Twenty-four hours after seeding, transfection with miR-196-5p mimic (50 nM), miR-NC (50 nM), si-NC (50 nM), pcDNA-derlin1 (50 nM) or si-DERL1 (50 nM) was carried out using Lipofectamine 2000 (Invitrogen, CA, USA) according to the manufacturer's instructions. The presynthesised miR-196-5p mimics, miR-NC or si-NC (negative control) oligos were obtained from the Gene-Pharma Company (Suzhou, Jiangsu, China). To construct the Derlin1 expression plasmid, the mammalian overexpression vector, pcDNA3.1, was cloned with the full-length ORF of derlin1 (pcDNA-derlin1) to obtain Derlin1 whereas control vector-transfected cells were used as the negative control. As a result of using siRNA Derlin-1 sequences (Oligobio, Beijing, China) and pcDNA3.1-Derlin-1 sequences (Oligobio, Beijing, China), we were able to knock down or upregulate the expression of Derlin-1.

A Lipofectamine 2000 (5 μl) solution was placed in DMEM (250 μl) in the absence of serum and incubated for 10 minutes at 37°C . Each 5 μl of miR-196-5p mimic, miR-NC, pcDNA-derlin1, si-NC, and si-DERL1 was placed in DMEM (250 μl) in the absence of serum. Following incubation for 10 minutes, the diluted miR-196-5p mimic, miR-NC, pcDNA-derlin1, si-NC, and si-DERL1 was gently mixed with diluted Lipofectamine 2000, and then incubated at room temperature for 30 minutes. The cells were washed twice in PBS (phosphate buffered saline) after the old medium was removed from the 6-well plate. To each well containing cells and medium, 500 μl of the complexes were added before the plate was gently rocked to mix the solution. A 24-hour incubation period was conducted at 37°C in a CO_2 incubator to test for the expression of transgenes in the cells.

Extraction and quantitative RT-qPCR of RNA

Microfluidics-based Agilent Bioanalyzer (Agilent Technologies Co. Ltd., Beijing, China) classify RNA samples according to their integrity using RNA Integrity Numbers (RIN) ranging from 1 to 10. The RIN value above 8.0 indicates intact, high-quality RNA samples, the value between 5.0 and 8.0 indicates moderately degraded samples, and the value below 5.0 indicates degraded samples (Padhi *et al.*, 2018). It is typically recommended to use RNA samples that have RIN values above 5.0 in order to ensure a reliable measurement of gene expression by RT-qPCR.

Table 1. Primers used in real-time polymerase chain reaction

Primers	Sequence (5'-3')	Size (bp)
miR196-5p	5'-TAGGTAGTTTCCTGTTGTTGGG-3'	178
	5'-GCGAGCACAGAATTAATACGAC-3'	
derlin 1	5'-TCGGACATCGGAGACTGGTT-3'	186
	5'-AGCCAGTAATCAGCATGCAAA-3'	
GADPH	5'-CTTCTACAATGAGCTGCGTG-3'	156
	5'-TCATGATTGAGTCAGTCAGG-3'	

TRIzol reagent (Invitrogen; Thermo Fisher Scientific, Inc.) was used according to the manufacturer's instructions to isolate total RNA from the cells. The expression of mRNA of a cell was detected by a real-time PCR system, which used SYBR Green (Roche Diagnostics, Mannheim, Germany), with two micrograms of total RNA. The cDNA was synthesized with a Transcriptor cDNA Synthesis Kit (Thermo Fisher Scientific, Waltham, MA, USA). In order to normalize the expression of the target gene mRNA, GAPDH expression was used as an endogenous control. The inverse logarithms of the $\Delta\Delta C_t$ levels are used to calculate the relative levels of miR-196-5p. The primer sequence information is listed in Table 1. The specific method is described in the earlier study (Jhan *et al.*, 2022).

CCK-8 assays

A 96-well plate was used to plate the cells (3×10^4 cells) into each of the 96 wells after they had been transfected. After culture of cells for 0, 12, 24, 48, or 96 h at 37°C, the addition of CCK-8 reagent (10 μ l, Solarbio Life Science, Beijing, China) was transferred to each well in accordance with the manufacturer's guidelines. The incubation was extended at 37°C for 3 h, and finally, in order to measure the absorbance of the wells at 470 nm, the microplate reader (Agilent Bioscience Co. Ltd, Hangzhou China) was utilized to measure the absorbance of each well at 0 h and at intervals of 24 h until 96 h post-transfection (Xin *et al.*, 2019b).

Colony formation assay

Proliferation of cells was also determined by colony formation assays (Wang *et al.*, 2018). The transfected Saos2 cells (2.5×10^4 cells in each well) were plated in a six-well plate. During the 17 days of culture, fresh medium was changed every day during incubation and cells were incubated at room temperature after 96 hours of culture. The colonies formed were washed with PBS and paraformaldehyde (4%) fixed at 37°C for 15 min. A crystal violet stain of 0.25% was applied to the colonies at 37°C for 15 minutes. The percent colony number (for colonies with > 50 cells) was analysed by two independent researchers (blind) counted under a bright-field microscope with a low-resolution bright field microscope (Olympus, Tokyo, Japan). Image of each plate was scanned using colony counting software (ImageJ, USA)

Analysis of apoptosis in cells by flow cytometry

The FITC-Annexin V Apoptosis Detection Kit (4A Biotech, Nanjing, China) was used to measure cell apoptosis according to the instructions provided by the manufacturer (Badhai *et al.*, 2009). Briefly, 24 h after transfection with 50 nM miR-NC, miR-196-5p mimic and pcDNA-derlin1, the medium was then removed, and the cells were incubated in serum-free medium for 24 hours after removal of the medium. After digestion with trypsin, the cells were washed twice in cold phosphate buffer saline, centrifuged for five minutes at 1200 rpm, and resuspended in phosphate buffer saline (100 μ l). The cells were then resuspended in phosphate buffer saline. Incubation was carried out in the dark at room temperature in the presence of 5 μ l of FITC-labelled Annexin V and PI. We used flow cytometry to analyze apoptosis five minutes after adding 400 μ l of phosphate buffer saline. FlowJo software (Tree Star, Ashland, USA) was used to analyse the data in this study.

The Annexin V/PI assay was developed to differentiate between live and apoptotic cells, but it can also be used to differentiate between apoptotic subpopulations of cells which are in an early or late stage of apoptosis (i.e., healthy cells: (Annexin-/PI-), early apoptotic cells: Annexin V+/PI-), late apoptotic cells: (Annexin V+/PI+), necrotic/dead cells: Annexin V-/PI+). Hence, for the same miR-196-5p treated Saos2 cells, we first removed any cells having a negative value before performing further analyses. We analyzed a total of 10000 cells per measurement.

Acridine orange (AO) autophagy staining

The acidic vesicles formed during autophagy were visualized with the help of the acridine orange staining protocol (Pierzyńska-Mach *et al.*, 2014). In brief, the transfected Saos2 cancer cells were placed at 5×10^4 in each well of 12-well plate. A 24-hour culture at 37°C was carried out on the cells. After that, the cells were collected, washed with phosphate buffer saline and stained with 0.5% acridine orange (AO). We then removed the acridine orange from the cells, washed them rapidly with fresh medium, and examined them under a fluorescence microscope (Leica, Germany). The imaging conditions were AO-excitation 448 nm, emission 470–550 nm (monomers) and 580–650 nm (stacks); the scanning speed was 7000 Hz. The cover slip with the live cells were mounted on custom stainless-steel holders. The sample temperature was maintained at 37°C. ImageJ software (Rasband, WS. ImageJ) was used to perform basic image processing and analysis.

The accumulation of acridine orange in acidic autophagosomes was detected by fluorescence microscope equipped with a digital camera. The presence of cells with intense red staining indicated that autophagy occurred in these cells.

Western blot

To lyse the cells, ice-cold RIPA lysis buffer (CW-BIO, Beijing) was used after the cells were transfected for 48 hours and the total protein concentration of the transfected Saos2 cells was detected using a BCA Protein Assay Kit (Beyotime, Shanghai, China). Subsequently, 20 μ g of protein of each sample was separated by 10% SDS-PAGE gel (Bio-Rad Laboratories Co., Ltd. Shanghai, China) and then transferred onto the PVDF membranes (Millipore, USA). Primary antibodies anti-Beclin1 (Cat#11306-1-AP, Proteintech Group Inc., Rosemont, IL, USA; dilution 1:1000), anti-p62 (Cat#18420-1-AP, Proteintech Group Inc. USA; dilution 1:6000), anti-LC3BI/II (Cat# ABC929, Sigma Aldrich, USA; dilution 1:800), anti-Derlin-1 (Cat#SAB4200148, Sigma Aldrich, USA; dilution 1:2000) were added to the PVDF membrane in blocking solution (10% fat-free milk in TBST (Tris buffered saline/Tween-20), followed by washing three times with TBST and incubated for 3 h at 37°C. Next, PVDF membranes were incubated for two hours with goat anti-rabbit HRP-conjugated secondary antibodies (Proteintech Group Inc., dilution 1:7000) at room temperature. Chemiluminescent fluid (GE Healthcare Life Sciences, UK) was applied to cover the membranes after they were washed. A chemiluminescence analyzer (Biotech Co., Ltd., Beijing) was used to detect and photograph the bands. Quantity One software was used to quantify protein bands by densitometry. In order to correct for the differences in loading between the groups, the volume per group was divided by the volume of normalized β -actin for each group. A normalization pro-

cedure was then conducted to determine the differences between each group and the control group. Based on the control data, the results were presented as a percentage (Xin *et al.*, 2019a).

Assays of Migration and invasion

It was examined whether miR-196-5p mimics or miR-NC transfected into Saos2 cells could affect migrating and invading cells within the chambers using the Transwell chamber and wound healing assays, respectively. Approximately 2×10^5 transfected cells were placed in each of six wells of a six-well plate to perform the migration assay. Post 24 h cell culturing, the cell surface was scraped by a 200 μ l pipette tip. The wound was imaged with the aid of a light microscope. Upon incubation at room temperature for 24 hours, the wound was again visualised and the percent wound closure was analysed using Image J software. For the Transwell chamber invasion assay, 5×10^4 transfected cells suspended in 250 μ l of serum-free culture medium were added to the Matrigel-coated upper chamber of a 24-well Transwell plate. DMEM with 10% FBS (650 μ l) was placed in the bottom of the cell culture chamber. We fixed and stained the invaded cells in methanol with 0.2% crystal violet after 24 hours of incubation at 37°C. An inverted microscope (Olympus, Tokyo, Japan) was used to visualize the cells. Based on the number of cells counted, two independent researchers (blind) were able to calculate the percentage of cells that invaded seven random fields under the microscope (Xin *et al.*, 2019b).

miR-196-5p target analysis and dual luciferase assay

In silico analysis was conducted to predict the interaction between miR-196-5p and Derlin-1 3'-UTR using TargetScan online (http://www.targetscan.org/vert_72/). The prediction was validated using a dual luciferase assay (Promega, USA) and Microplate Luminometer (BioTek, USA). In an earlier study, the specific method was described (Jhan *et al.*, 2022). Briefly, Derlin-1 3'-UTR with wild-type miR binding site (derlin1-WT) or mutant miR binding site (Derlin-1-MUT) was first cloned in the pmir-GLO luciferase reporter vector. Next, Saos2 cells were co-transfected with 1 ng/ μ l concentrations of reporter vectors (WT or MUT) and 2.5 μ g of miR-196-5p mimics or miR-NC with the help of Lipofectamine 3000. To quantify the luciferase activity of the cells, host cells were isolated, washed, and trypsinized before being assayed with the dual luciferase assay to determine their luciferase activity 48 hours after transfection as directed by the manufacturer following the instructions.

Statistical analysis

Each experiment was presented at least three times independently in order to obtain the best results. Data were shown as means \pm S.D. GraphPad version 9.0 was run to accomplish the statistical analysis. A Student's t test was used to assess the significance of differences between the two treatment groups, assuming that the data were normally distributed. One-way ANOVA was used to compare the values of the experimental and control groups. A multiple comparison test was performed between the groups using Tukey's multiple comparison test. A *P*-value less than 0.05 was considered statistically significant.

RESULTS

miR-196-5p expression is repressed in osteosarcoma

To gain insight into the miR-196-5p expression pattern in osteosarcoma, quantitative RT-qPCR was performed. Interestingly, osteosarcoma tissue specimens displayed a remarkably lower ($P < 0.05$) miR-196-5p transcript ($P < 0.05$) compared to the normal tissues (Fig. 1A). Expression analysis was also performed from three different osteosarcoma cell lines (MG-63, Saos2, and HOS) with reference to normal osteoblast cell lines. The miR-196-5p expression was shown to be substantially ($P < 0.05$) reduced compared to that of normal cells (Fig. 1B). Additionally, miR-196-5p expression was considerably ($P < 0.01$) low in Saos2 cells compared to MG-63 and HOS cell lines. Therefore, we selected Saos2 cell lines for transfection. Thus, the results indicate that miR-196-5p is markedly reduced in osteosarcoma, suggesting its possible involvement in its growth and pro-

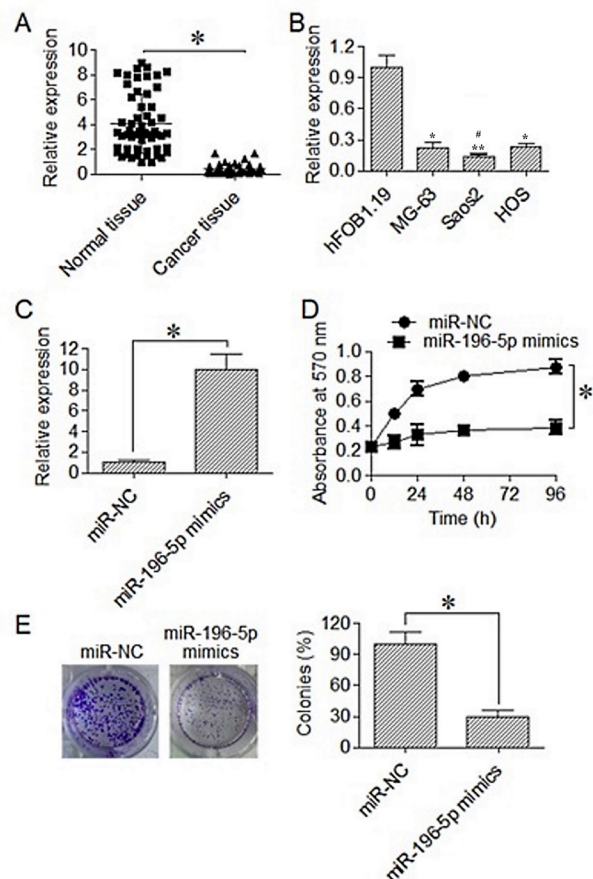


Figure 1. Over-expression of miR-196-5p in osteosarcoma cells declined their viability, *in vitro*.

(A) Relative transcript levels of miR-196-5p in osteosarcoma and normal matching human tissues. (B) Relative expression analysis of miR-196-5p from Saos2, HOS, MG-63 cell lines and with respect to hFOB1 normal osteoblast cell line. (C) qRT-PCR based confirmation of miR-196-5p over-expression in miR-196-5p mimics transfected Saos2 osteosarcoma cells with reference to respective miR-NC transfected negative control cells. (D) Viability analysis at various intervals of miR-196-5p mimics and miR-NC transfection in Saos2 cancer cells of *in vitro* culturing. (E) Colony formation assay of Saos2 cells transfected with miR-196-5p mimics or miR-NC. Each experiment was conducted using three independent biological replicates (* $P < 0.05$ vs. control group, * $P < 0.01$ vs. MG-63 and HOS cells)

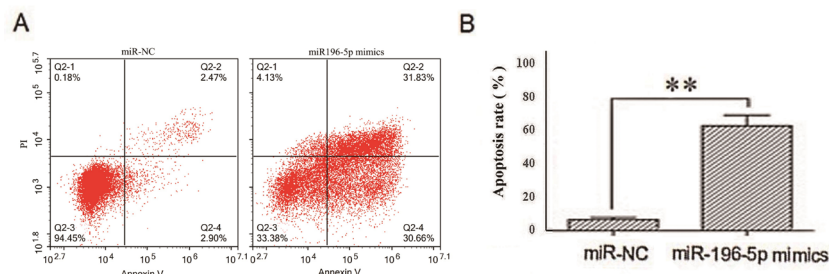


Figure 2. Effect of miR-196-5p overexpression on the rate of apoptosis.

(A) Analysis of flow cytometry results of Saos2 cells transfected with miR-196-5p mimics or miR-NC. (B) Rate of apoptosis (%) in Saos2 cells transfected with miR-196-5p mimics or miR-NC. Significant change in the percentage rate of apoptotic cells (** $P<0.01$) observed from the representative images of apoptotic cells. Cell percentages were calculated based on three independent flow cytometry experiments. Q1 represents death cells, Q2 represents the late apoptosis cells, Q3 represents the normal or live cells, Q4 represents the early apoptosis cells. The statistical result of apoptosis rate (B), which equals to the rate of late apoptosis cells (Q2) plus the rate of early apoptosis cells (Q4) plus the rate of necrotic or dead cells (Q1) respectively.

gression. The Saos2 cell line was therefore used to determine whether miR-196-5p acts in the development of osteosarcoma.

miR-196-5p inhibited osteosarcoma cell growth

To induce miR-196-5p overexpression in Saos2 cancer cells, miR-196-5p mimics were transfected into the cells. The results of RT-qPCR displayed that miR-196-5p mimics transfected Saos2 cancer cells expressed ~8-fold miR-196-5p transcript levels relative to miR-NC transfected Saos2 cells (Fig. 1C). To analyze the effect of miR-196-5p overexpression on Saos2 host cell viability, a CCK-8 assay was carried out. The findings revealed that miR-196-5p overexpressing Saos2 cells showed mark-

edly lower ($P<0.05$) *in vitro* viability ($P<0.05$) compared to negative control cells in different cultures (Fig. 1D). Again, colony formation of Saos2 cells overexpressing miR-196-5p was remarkably lower ($P<0.05$) comparatively to normal cells (Fig. 1E). Colony formation of Saos2 cancer cells overexpressing miR-196-5p was only 32% of that of control cells. As a result of these findings, it might be speculated that miR-196-5p has a growth-inhibitory function in osteosarcomas.

miR-196-5p-induced apoptosis in Saos2 cells

We evaluated the changes in apoptosis using Annexin/PI staining. The results showed that miR-196-5p transfection significantly ($P<0.01$) increased in the percentage

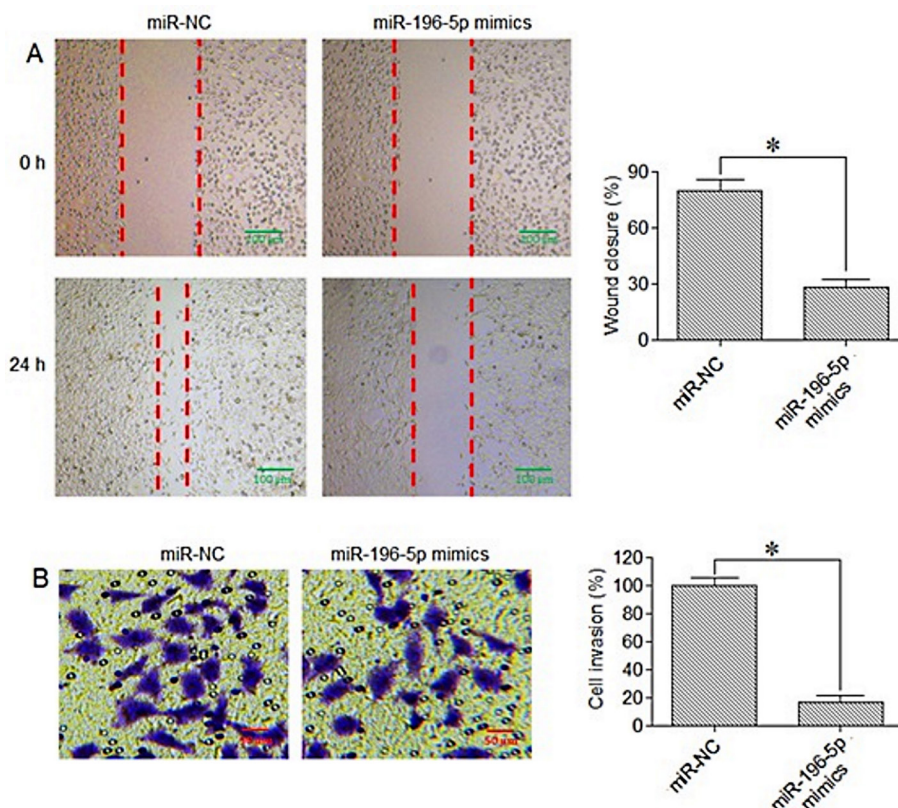


Figure 3. Osteosarcoma cells exhibited restrained motility *in vitro* by miR-196-5p up-regulation.

(A) The wound-healing assay was used to investigate the migration patterns of Saos2 osteosarcoma cells that had been overexpressed with miR-196-5p mimics or miR-NC. (B) Transwell chamber invasion assay of Saos2 osteosarcoma cells transfected with miR-196-5p mimics or miR-NC. Each experiment was conducted using three independent biological replicates (* $P<0.05$).

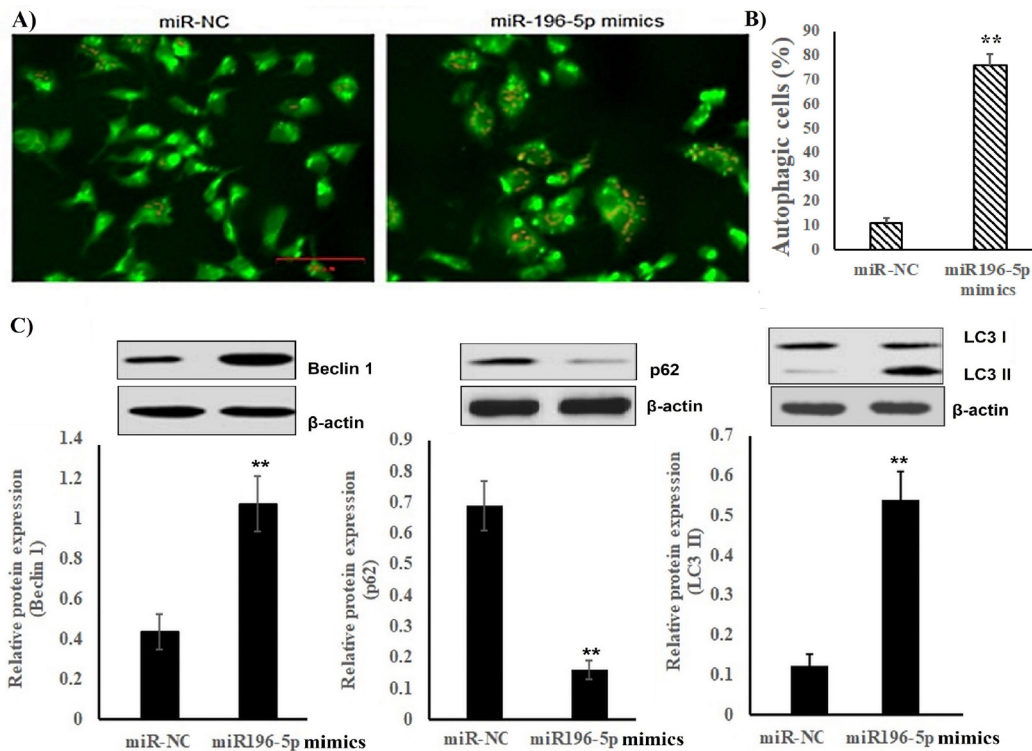


Figure 4. miR-196-5p over-expression promoted the ability of osteosarcoma cells to undergo autophagy. (A) Detection of autophagosomes by acridine orange staining in Saos2 cancer cells transfected with miR-196-5p mimics or miR-NC. (B) Quantification of autophagosomes (percent of autophagic cells) with miR-196-5p mimics or miR-NC. (C) Western blot analysis of LC3B I & II, p62 and Beclin 1 proteins from Saos2 osteosarcoma cells transfected with miR-196-5p mimics or miR-NC. The experiments were performed using three independent biological replicates.

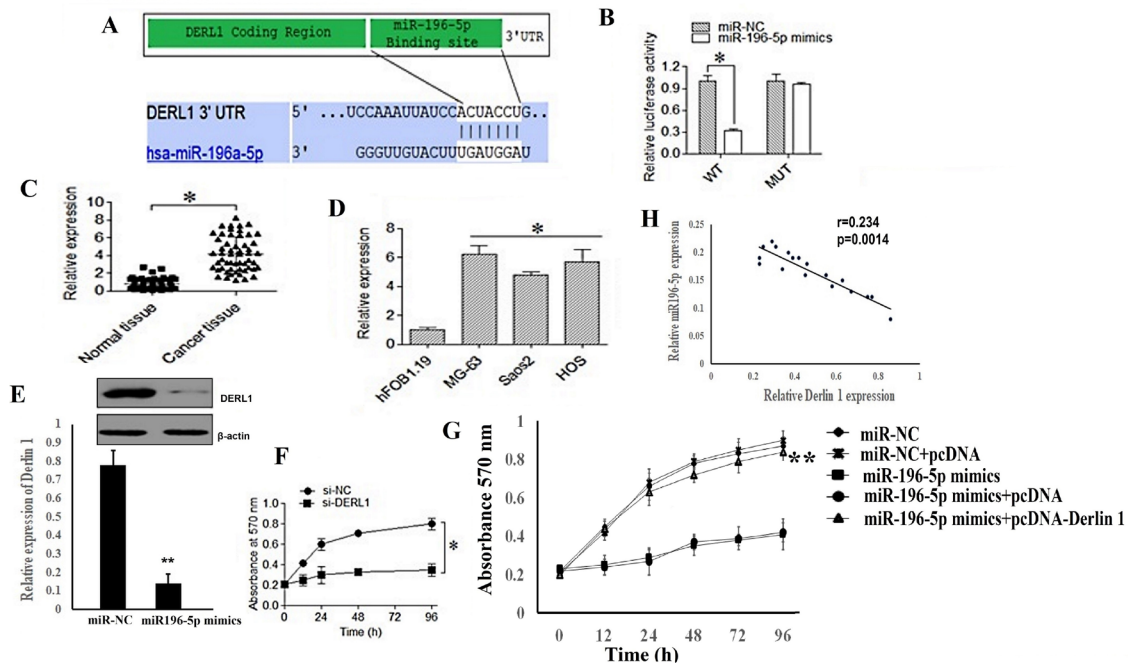


Figure 5. Derlin-1 is functionally targeted by miR-196-5p in osteosarcoma.

(A) In silico analysis of miR-196-5p with Derlin-1 3'-UTR. (B) miR-196-5p site-specific interaction with Derlin-1 3'-UTR was assessed using a dual luciferase assay. (C) qRT-PCR expression analysis of Derlin-1 from normal human and osteosarcoma cells. (D) Relative transcript levels analyses of Derlin-1 from Saos2, HOS and MG-63 cell lines relative to hFOB1 normal osteoblast cell line. (E) Western blotting of Derlin-1 miR-196-5p mimics or miR-NC expressing Saos2 cancer cells. (F) CCK-8 assay for the viability analysis of Saos2 cells transfected with si-Derlin-1 or si-NC at different intervals of *in vitro* culturing. (G) Viability analysis of Saos2 cells transfected with miR-NC, miR-NC+pcDNA, miR-196-5p mimics or miR-196-5p mimics + pcDNA or miR-196-5p mimics+pcDNA-Derlin-1 at different intervals of *in vitro* culturing. (H) A Pearson correlation analysis was performed on OS tissues to determine the correlation between miR-196-5p and Derlin-1. Each experiment was conducted using three independent biological replicates (* $P<0.05$; ** $P<0.01$).

rate of apoptosis in Saos2 cells (Fig. 2A) compared to negative control (miR-NC). These findings indicate that the miR-196-5p overexpression showed substantial increase in the rate of apoptosis in Saos2 cells (Fig. 2B). Collectively, these results suggest that miR-196-5p overexpression induces triggering cell death in Saos2 cells. In total, 9989 cells were recovered in miR-NC control group, which contained 94.45% live or normal cells (Q3), 2.9% early apoptotic cells (Q4), 2.47% late apoptotic cells (Q2) and 0.18% necrotic or dead cells (Q1). Out of 9972 total cells recovered in miR-196-5p treated Saos2 cells, 33.38% live cells (Q3), 30.66% early apoptotic cells (Q4), 31.83% late apoptotic cells (Q2) and 4.13% necrotic or dead cells (Q1).

miR-196-5p restrained migration and invasion of osteosarcoma cells

Whether miR-196-5p also regulates the migratory ability and invasiveness of osteosarcoma cells, the effect of miR-196-5p overexpression was visualized on the migration and invasion of Saos2 sarcoma cells. The results showed that Saos2 cells over-expressing miR-196-5p migrated at remarkably ($P<0.05$) reduced rates ($P<0.05$), as evidenced by the percent wound closure being markedly lower compared to control cells (Fig. 3A). Furthermore, miR-196-5p overexpression in osteosarcoma cells significantly inhibited *in vitro* invasion considerably ($P<0.05$), and it was shown that percent cell invasion was reduced to less than 20% relative to that of negative control osteosarcoma cells. Thus, the results suggest that miR-196-5p has an antitastatic regulatory role in osteosarcoma (Fig. 3B).

Osteosarcoma cells overexpressing miR-196-5p exhibited induction of autophagy

To assess whether the reduction in the replication of the Saos2 cancer cell overexpressing miR-196-5p resulted from the induction of cell autophagy, acridine orange (AO) staining was performed, followed by fluorescent microscopy. Cancer cells overexpressing miR-196-5p were shown to accumulate AO stain indicative of the possession of acidic autophagosomes (Fig. 4A). The western blot analysis of the autophagy marker proteins revealed that LC3B II and Beclin 1 expression levels were significantly elevated ($P<0.01$), whereas p62 levels were significantly decreased ($P<0.01$), indicating that miR-196-5p stimulated autophagy (Fig. 4B). Taken together, our findings demonstrated that miR-196-5p overexpression induces apoptosis through autophagy-related proteins (Beclin 1, p62, LC3B) in osteosarcoma cells.

miR-196-5p functionally targets Derlin-1 in osteosarcoma

A comprehensive *in silico* analysis of miR-196-5p was performed to predict the specific molecular target of miR-196-5p in osteosarcoma. Derlin-1 was recognized as the probable target of miR-196-5p in osteosarcoma, and this miRNA binds to a precise site within the untranslated region (3'-UTR) of Derlin-1 mRNA (Fig. 5A) corresponding to the seed region of miR-196-5p. TargetScan identified Derlin-1 as a possible target of miR-196-5p with the indicated target sites. Consequently, we assumed that miR-196-5p was regulating Derlin-1 in Saos2 cells.

Further study results revealed that overexpression of miR196-3p could significantly reduce the level of 3'-UTR activity of Derlin-1, which was in contrast to that detect-

ed for mutant Derlin-1 3'-UTR activity (Fig. 5B). Furthermore, the results of the luciferase reporter assay revealed that aberrant cells were identified, which showed that the activity of luciferase in Saos2 cells decreased significantly ($P<0.01$) only after the miR-196-5p mimics were co-transfected with luciferase plasmids containing the 3'-UTR of Derlin-1 with native binding sites. Moreover, the gene expression of Derlin-1 was shown to be considerably increased ($P<0.05$; Fig. 5C) in osteosarcoma cell lines, negatively correlating with that of miR-196-5p expression (Fig. 1A), thus substantially linked with tumor progression. A significant increase in Derlin-1 mRNA and protein levels was also observed in Saos2 cells (Fig. D, $P<0.05$). According to our findings, miR-196-5p targets Derlin-1 by direct binding to predicted sites in the 3'-UTR of Derlin-1 mRNA. The results of our luciferase reporter assay support the hypothesis that miR-196-5p targets the Derlin-1 gene. Again, the expression of the Derlin-1 protein was shown to be repressed in miR-196-5p overexpressing Saos2 cancer cells, which provides further insight into post-transcriptional down-regulation of Derlin1 by miR-196-5p in osteosarcoma (Fig. 5E).

Furthermore, it was shown that the effect of miR-196-5p on Saos2 cell migration, invasion, and proliferation was modulated by Derlin-1. The CCK-8 assay showed that Derlin-1 silencing mimicked the antiproliferative effects of miR-196-5p overexpression, suggesting that the latter could be exerting its role in osteosarcoma through post-transcriptional repression of Derlin-1 (Fig. 5F). Besides, Saos2 cancer cells over-expressing Derlin-1

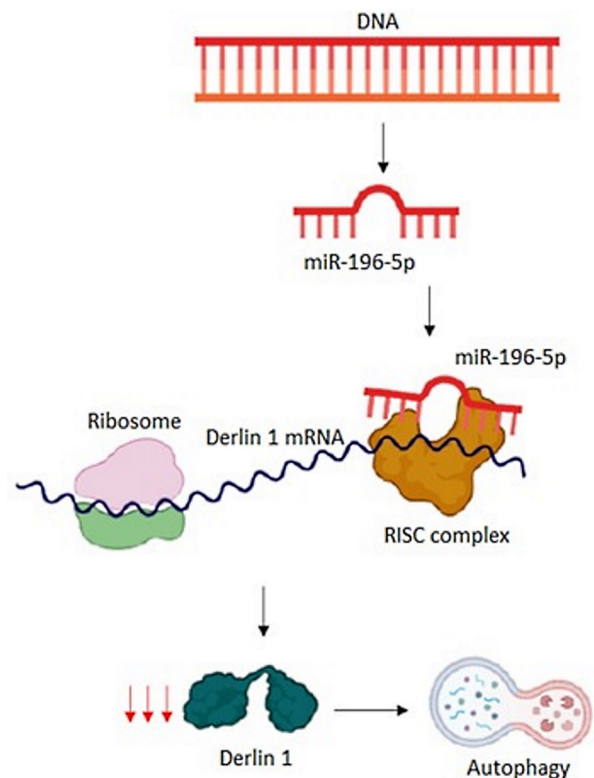


Figure 6. Model showing the molecular mechanism of miR-196-5p/derlin1 axis in osteosarcoma. miR-196-5p is synthesized and binds to the 3'-UTR of Derlin-1 through the RISC complex. This binding blocks Derlin-1 translation eventually leading to autophagy mediated inhibition of cell proliferation.

did not show proliferative decline when miR-196-5p was overexpressed (Fig. 5G). However, these findings were not noticed between the groups: miR-NC *vs.* miR-NC+pcDNA & miR-196-5p mimics *vs.* miR-196-5p mimics+pcDNA ($P>0.05$). Nevertheless, we observed significant difference in the effects of miR-196-5p overexpression suppressed by Derlin-1 between the groups ($P<0.01$): miR-196-5p mimics *vs.* miR-196-5p+pcDNA – Derlin 1 and miR-196-5p mimics+pcDNA *vs.* miR-196-5p mimics+pcDNA-Derlin 1. The results reveal that miR-196-5p targets Derlin-1 for its post-transcriptional repression to exert its functional role in osteosarcoma (Fig. 6). These findings are consistent with our earlier demonstration about the results of the luciferase reporter assay and the published results on pcDNA (Zhang *et al.*, 2021). The molecular basis of the antiproliferative effects of miR-196-5p overexpression that mediates through the decrease in the expression of Derlin-1 in Saos2 osteosarcoma cells remains unclear and needs further investigation. However, our findings confirmed that miRNA (si-Derlin-1) was silenced in Saos2 cells, thus decreasing the expression levels of Derlin-1. Based on the results of these experiments, we were able to confirm our predictions and suggest that miR-196-5p might regulate Derlin-1 to offer its antiproliferative effects. Consequently, miR-196-5p and Derlin-1 showed a significant correlation in OS tissues, demonstrating the effects of miR-196-5p on cell growth, metastasis, and apoptosis (Fig. 5H).

DISCUSSION

Numerous studies have suggested that miRs might emerge as potential molecular markers in cancer diagnosis and therapy (Iacona & Lutz, 2019). The exact mechanisms by which miRNA regulate tumorigenesis remain unclear, despite several miRNAs found to be downregulated in tissues and cells (Wang *et al.*, 2018). It is possible, however, that miR-196 suppresses tumour growth in breast cancer and melanoma (Braig *et al.*, 2010; Li *et al.*, 2010). Additionally, in several studies in human cancers like oral and colorectal cancer, miR-196-5p expression is believed to be involved in oncogenesis or tumor suppression, regulating their growth and progression (Xin *et al.*, 2019a; Stiegelbauer *et al.*, 2017; Maruyama *et al.*, 2018). Therefore, the present study was planned to show that miR-196-5p could be useful for treating osteosarcoma due to its potential efficacy. Our findings showed that miR-196-5p overexpression inhibited OS cell proliferation, colony formation, and invasion by inducing autophagy, signifying that miR-196-5p functions as a tumour suppressor of osteosarcoma progression (Fig. 1). Similar results from a study were reported, but using a different miRNA in osteosarcoma, showing that overexpression of miR-423-5p suppressed osteosarcoma invasion, colony formation, and proliferation, decreasing STMN1 expression. In osteosarcoma, miR-423-5p appears to act as a tumour suppressor gene (Wang *et al.*, 2018). Another study supporting our findings found that miR-196-5p overexpression worsened HCC (hepatocellular carcinoma) cell proliferation and metastasis *in vitro* and *in vivo* (Zheng *et al.*, 2019a). Similarly to the results of our study, recent research demonstrated that overexpression of miR-196b-5p inhibited proliferation, migration and invasion (Wharton's umbilical cord) by targeting Cdkn1b (Meyer *et al.*, 2018).

Autophagy and apoptosis are interrelated processes whose outcomes depend on both cell type and environmental factors. It has been described that autophagy can

antagonize apoptosis, but can also act as an agonist (Fan & Zong, 2012). Despite this, autophagy can induce cell death regardless of apoptosis. Consequently, we found a statistically significant difference in the percentage rate of apoptosis of Saos2 cells overexpressing miR-196-5p measured using the FITC-Annexin V Apoptosis Detection Method (Fig. 2). Therefore, we believe that miR-196-5p overexpression increases the percentage rate of apoptosis by down-regulation of Derlin-1 in Saos2 osteosarcoma cells. However, the exact molecular mechanisms underlying the cytotoxic mechanism of miR-196-5p-induced apoptosis remained unclear and warrants further investigation. However, miR-196-5p expression has been reported to be markedly reduced markedly under hypoxic conditions, and overexpression of this miRNA reversed HCC effects of hypoxia on the proliferation and invasion (hepatocellular carcinoma) (Zheng *et al.*, 2019b). Consequently, additional studies are needed to understand the molecular mechanisms of overexpression of miR-196-5p and hypoxic conditions in Saos2 cell lines.

Derlin-1 is upregulated in various human cancers, such as lung, colon, and breast cancer, and activates oncogenic pathways in the body (Dong *et al.*, 2017; Wang *et al.*, 2008; Dong *et al.*, 2013). Derlin-1 overexpression has been linked to aggressive phenotypes in breast, pancreatic, and lung cancers (Dong *et al.*, 2017). There is, however, no evidence of its involvement in human osteosarcoma. The results of our study demonstrated that osteosarcoma cells and tissues expressed low levels of miR-196-5p. Similar to our study findings, a report showed that miR-423-5p overexpression was decreased in osteosarcoma tissues and osteosarcoma (MG-63, SAOS-2, U2OS and SOSP-9607) cell lines (Wang *et al.*, 2018).

However, the effect of the overexpression of miR-196-5p targeting Derlin-1 is still unknown in osteosarcoma. Our results found that the expression of Derlin-1 was upregulated in osteosarcoma tissues and cell lines. The results of the present study revealed that Derlin-1 is a direct target gene of miR-196-5p in osteosarcoma cells. According to this report, miR-196-5p directly regulates Derlin-1 expression in Saos2 cells, and modifying Derlin-1 expression reverses miR-196-5p overexpression/inhibition of Saos2 cell proliferation and metastasis. Based on the results of this study, it appears that the miR-196-5p/Derlin-1 axis is a key pathway that regulates the progression of osteosarcomas (Zheng *et al.*, 2019a). It is in agreement with a study which demonstrated that miR-196-5p targets HMGA2 thus regulating hepatocellular carcinoma progression involving miR-196-5p/HMGA2 axis as a key pathway (Zheng *et al.*, 2019a). Additionally, a study found that miR-30b inhibited breast cancer progression and metastasis by targeting Derlin-1 *in vitro*, similar to our results.

The autophagy and apoptosis pathways are usually impaired in malignant cells, resulting in the lengthening of their survival (Jain *et al.*, 2013). Autophagy is an intrinsic process which clears off cell debris and assists in maintaining normal cell behaviour (Chua *et al.*, 2022). Our findings clearly indicated that miR-196-5p targets the expression of Derlin-1 and significantly altered the autophagy-related proteins (Beclin 1, p62, and LC3B II; Fig. 3) that demonstrate an increase of autophagosomes formation through increased levels of LC3-II, confirming the increased autophagy formation in Saos2 cells (Murugan & Amaravadi, 2016; Ji *et al.*, 2015). The results were further confirmed by the decreased expression of the autophagic flux-related protein p62 with increa-

sed autophagy (Murugan & Amaravadi, 2016). In light of these results, we hypothesized that miR196-p targets Derlin-1 to induce autophagosome formation in Saos2 cells. Our results demonstrated that the anticancer effects resulting from miR-196-5p overexpression are rising from the promotion of autophagy in osteosarcoma cells which suggests the beneficial activity of miR-196-5p against human osteosarcoma. Furthermore, our findings were supported by a study demonstrating that Derlin-1 expression was elevated in most nonsmall lung cancer cell lines, and silencing Derlin-1 mRNA suppressed autophagic flux in A549 cells that induce autophagy (Cai *et al.*, 2022). Thus, targeting autophagy will be an important consideration in developing novel strategies for cancer therapy (Fan & Zong, 2012).

In the current study, Derlin-1 was post-transcriptionally regulated (repressed) by miR-196-5p, and the former was confirmed to act as a mediator of miR-196-5p role in osteosarcoma. Down-regulation of miR-196-5p would mitigate Derlin-1 silencing at the post-transcriptional level, culminating in Derlin-1 upregulation. The latter, with its established oncogenic function, could be one of the crucial elicitors for osteosarcoma tumorigenesis. Our findings further clarified the involvement of the interactional interplay of miR-196-5p with Derlin-1 to control the progress and subsequent progression of human osteosarcoma. As a consequence, it is speculated that Derlin-1 is involved in miR-196-5p-mediated proliferation, invasion, and colony formation in osteosarcoma (Saos2) cell lines. The results of our research showed that miR-196-5p inhibited the expression of Derlin-1 in osteosarcoma, thus acting as a tumor suppressor gene. However, further studies are warranted to investigate the potential molecular mechanisms underlying its biological effects involving the miR-196-5p/Derlin-1 axis in the regulation of osteosarcoma progression.

However, it is speculated that the cause of the markedly overexpression of miR-196-5p with a decrease in Derlin-1 expression in Saos2 cells in the present study emphasises inhibition of the unfolded protein response (UPR). In addition, the removal of misfolded proteins is crucial for normal cellular functioning. Derlin-1 is a component of the p97 ATPase complex and has been shown to play a deciding role in the elimination of misfolded / unfolded proteins by regulating the ER-mediated degradation response and retrotranslocation of abnormal cellular proteins from the lumen of the endoplasmic reticulum (ER) towards the cytosol for degradation by the proteasome complex (Katiyar *et al.*, 2005).

The accumulation of misfolded proteins in the ER, a sign of disrupted ERAD (endoplasmic reticulum-associated degradation), supports the notion that Derlin-1 acts in the retro-translocation process. It is clear from the fact that loss of Derlin-1 results in lethality that ER homeostasis is crucial for the survival of animals. The results of these studies suggest that Derlin-1 and its associated retrotranslocation machinery (such as the TER94/Derlin-1 complex) are limited without ER stress. ER homeostasis is restored by synthesising additional Derlin-1 and complexing it with existing retro-translocation machinery (Liang *et al.*, 2014).

Overexpression of Derlin-1 causes increased stress in the ER, with the activation of apoptosis-triggering signals. When moderate ER stress is present, Derlin-1 levels that were induced by low levels of ER stress are likely to retrotranslocate misfolded proteins. Severe or chronic ER stress induces Derlin-1 expression, resulting in a population of Derlin-1. It is well recognised that Derlin-1 binds to retrotranslocation components to

restore homeostasis to the ER. However, an unbound Derlin-1 would lead to a worsening of ER stress, ensuring the triggering of pro-apoptotic signals (Liang *et al.*, 2014).

A cell with irreparable ER stress may exhibit a high level of unbound Derlin-1 due to the need to balance proapoptotic and cytoprotective functions during UPR induced by ER stress-induced UPR. It is possible that Derlin-1 serves as a sensor for irreparable ER stress in cells. A prolonged ER stress appears to increase the levels of unbound Derlin-1 in cells, suggesting that UPR upregulates Derlin-1 (Liang *et al.*, 2014). Although there is still a lack of knowledge about the exact mechanism by which excessive Derlin-1 induces UPR and apoptosis in cells, but we provide the evidence that comprises the effects of miR-196-5p overexpression targeting Derlin-1 involving autophagic processes. On the other hand, it is possible that there is an additional microenvironmental factor that induces cellular stress in tumor cells, such as a lack of interaction with the extracellular matrix, or diminishing contact between the cells, in addition to ER-stress (Klopfleisch *et al.*, 2010). However, further detailed molecular investigations will be needed identifying factors that interact with miR-196-5p overexpression to define the mechanism that involves Derlin-1-dependent cytotoxicity for the treatment and subsequent progression of human osteosarcoma.

LIMITATIONS OF THE STUDY

However, interpretation of the results described above should take into account some potential limitations.

First, we used a single Saos2 cell line for the functional experiments. It is because Saos2 showed a higher invasive ability employing miR-196-5p than other used cell lines (MG-63, HOS) in our preliminary study.

Second, although our data found that miR-196-5p overexpression could be beneficial in the treatment of osteosarcoma by inhibiting Derlin-1 expression through autophagic processes, but to validate the specificity of miR-196-5p, it is imperative to investigate the use of miR-196-5p inhibitors to reverse the anticancer effects of miR-196-5p/Derlin-1 axis on cell growth and osteosarcoma metastasis.

Third, our data presented and confirmed the autophagic mechanisms involved in the effects of the miR-196-5p/Derlin-1 pathways on osteosarcoma, but it is fundamental to investigate further the effects of the miR-196-5p/Derlin-1 axis using autophagic inhibitors and different cell lines.

Fourth, although our findings showed the effects of miR-196-5p overexpression on apoptosis and autophagic processes, but further studies are warranted to investigate the cell cycle proteins involved in the processes of apoptosis and autophagy.

A fifth reason is that we were only able to examine Derlin-1 and miR-196-5p expression levels in a limited number of tissue samples to compare the differences between the different tumor specimens.

The sixth aspect is that further studies are required to clarify the molecular mechanisms underlying the relationship between the miR196/Derlin-1 axis and ER stress associated with UPR.

Lastly, *in-vitro* results were not supported by *in-vivo* experiments.

CONCLUSION

The current findings revealed that miR-196-5p overexpression leads to suppression of cell migration and invasion by direct targeting of Derlin-1 in Saos2 cells. Transient overexpression of miR-196-5p in Saos2 cancer cells inhibited cell growth by inducing autophagy *in vitro*. In Saos2 cells, miR-196-5p overexpression could inversely regulate Derlin-1 expression, suggesting that miR-196-5p acts as a tumor suppressor by binding to Derlin-1. Derlin-1 showed a functional post-transcriptional modulatory effect of miR-196-5p overexpression in osteosarcoma. Thus, the findings explored the regulatory miR-196-5p/Derlin-1 axis in controlling the proliferation, movement, and invasion of osteosarcoma cells. Our findings suggested that Derlin-1 may be useful in predicting the prognosis and identifying potential therapeutic targets in osteosarcoma.

REFERENCES

- Abdalla F, Singh B, Bhat HK (2020) MicroRNAs and gene regulation in breast cancer. *J Biochem Mol Toxicol* **34**: e22567. <https://doi.org/10.1002/jbt.22567>
- Ashrafizadeh M, Najafi M, Mohammadinejad R, Farkhondeh T, Samarghandian S (2020) Flaming the fight against cancer cells: The role of microRNA-93. *Cancer Cell Int* **20**: 277. <https://doi.org/10.1186/s12935-020-01349-x>
- Badhai J, Fröjmark AS, J Davey E, Schuster J, Dahl N (2009) Ribosomal protein S19 and S24 insufficiency cause distinct cell cycle defects in Diamond-Blackfan anemia. *Biochim Biophys Acta – Molecular Basis of Disease* **1792**: 1036–1042. <https://doi.org/10.1016/j.bbdis.2009.08.002>
- Braig S, Mueller DW, Rothhammer T, Bosserhoff AK (2010) MicroRNA miR-196a is a central regulator of HOX-B7 and BMP4 expression in malignant melanoma. *Cell Mol Life Sci* **67**: 3535–3548. <https://doi.org/10.1007/s00018-010-0394-7>
- Cai Y, Xu K, Aihaiti Y, Li Z, Yuan Q, Xu J, Zheng H, Yang M, Wang B, Yang Y, Yang Y, Xu P (2022) Derlin-1, as a potential early predictive biomarker for nonresponse to infliximab treatment in rheumatoid arthritis, is related to autophagy. *Frontiers Immunol* **12**: 795912. <https://doi.org/10.3389/fimmu.2021.795912>
- Catalucci D, Gallo P, Condorelli G (2009) MicroRNAs in cardiovascular biology and heart disease. *Circ Cardiovasc Genet* **2**: 402–408. <https://doi.org/10.1161/CIRCGENETICS.109.857425>
- Chen J, Wu Z, Zhang Y (2019) LncRNA SNHG3 promotes cell growth by sponging miR-196a-5p and indicates the poor survival in osteosarcoma. *Int J Immunopathol Pharmacol* **33**: 2058738418820743. <https://doi.org/10.1177/2058738418820743>
- Chou AJ, Merola PR, Wexler LH, Gorlick RG, Vyas YM, Healey JH, LaQuaglia MP, Huvos AG, Meyers PA (2005) Treatment of osteosarcoma at first recurrence after contemporary therapy: The Memorial Sloan-Kettering Cancer Center experience. *Cancer* **104**: 2214–2221. <https://doi.org/10.1002/cncr.21417>
- Chua JP, De Calbiac H, Kabashi E, Barmada SJ (2022). Autophagy and ALS: Mechanistic insights and therapeutic implications. *Autophagy* **18**: 254–282. <https://doi.org/10.1080/15548627.2021.1926656>
- DeLaney TF, Park L, Goldberg SI, Hug EB, Liebsch NJ, Munzenrider JE, Suit HD (2005). Radiotherapy for local control of osteosarcoma. *Int J Rad Oncol Biol Phys* **61**: 492–498. <https://doi.org/10.1016/j.ijrobp.2004.05.051>
- Dong Q, Fu L, Zhao Y, Liu Y, Li Q, Qiu X, Wang E (2017). Derlin-1 is a target to improve radiotherapy effect of esophageal squamous cell carcinoma. *Oncotarget* **8**: 55135–55146. <https://doi.org/10.18632/oncotarget.19069>
- Dong Q, Wang Y, Tang Z, Fu L, Li Q, Wang E, Wang EH (2013). Derlin-1 is overexpressed in non-small cell lung cancer and promotes cancer cell invasion via EGFR-ERK-mediated up-regulation of MMP-2 and MMP-9. *Am J Pathol* **182**: 954–964. <https://doi.org/10.1016/j.ajpath.2012.11.019>
- Donlic A, Hargrove AE (2018). Targeting RNA in mammalian systems with small molecules. *Wiley Interdisciplinary Reviews, RNA* **9**: e1477. <https://doi.org/10.1002/wrna.1477>
- Fan YJ, Zong WX (2012) The cellular decision between apoptosis and autophagy. *Chinese J Cancer* **12**: 45–56. <https://doi.org/10.5732/cjc.012.10106>
- Ferguson JL, Turner SP (2018). Bone cancer: diagnosis and treatment principles. *Am Family Phys* **98**: 205–213
- Gao Y, Xu H, Pu T (2020) MicroRNA-1179 suppresses the proliferation and enhances vincristine sensitivity of oral cancer cells via induction of apoptosis and modulation of MEK/ERK and PI3K/AKT signalling pathways. *AMB Express* **10**: 149. <https://doi.org/10.1186/s13568-020-01082-8>
- Huang F, Tang J, Zhuang X, Zhuang Y, Cheng W, Chen W, Yao H, Zhang S (2014) MiR-196a promotes pancreatic cancer progression by targeting nuclear factor kappa-B-inhibitor alpha. *PLoS One* **9**: e87897. <https://doi.org/10.1371/journal.pone.0087897>
- Iacona JR, Lutz CS (2019) miR-146a-5p: Expression, regulation, and functions in cancer. *Wiley Interdisciplinary Reviews, RNA* **10**: e1533. <https://doi.org/10.1002/wrna.1533>
- Jain MV, Paczulla AM, Klonisch T, Dimba FN, Rao SB, Roberg K, Schweizer F, Lengerke C, Davoodpour P, Palicharla VR, Maddika S, Los M (2013) Interconnections between apoptotic, autophagic and necrotic pathways: Implications for cancer therapy development. *J Cell Mol Med* **17**: 12–29. <https://doi.org/10.1111/jcmm.12001>
- Jhan JH, Hsu WC, Lee YC, Li WM, Huang AM, Lin HH, Wang CS, Wu YR, Li CC, Wu WJ, Ke HL (2022) MicroRNA-375-3p suppresses upper tract urothelial carcinoma cell migration and invasion via targeting Derlin-1. *Cancers* **14**: 880. <https://doi.org/10.3390/cancers14040880>
- Ji G, Yu N, Xue X, Li Z (2015) PERK-mediated autophagy in osteosarcoma cells resists ER stress-induced cell apoptosis. *Int J Biol Sci* **11**: 803–812. <https://doi.org/10.7150/ijbs.11100>
- Katiyar S, Joshi S, Lennarz WJ (2005). The retrotranslocation protein Derlin-1 binds peptide: N-glycanase to the endoplasmic reticulum. *Mol Biol Cell* **16**: 4584–4594. <https://doi.org/10.1091/mbc.e05-04-0345>
- Klopfleisch R, Schütze M, Linzmann H, Brunnberg L, Gruber AD (2010) Increased Derlin-1 expression in metastases of canine mammary adenocarcinomas. *J Comp Pathol* **142**: 79–83. <https://doi.org/10.1016/j.jcpa.2009.06.006>
- Li Y, Li M, Wei R, Wu J (2020) Identification and functional analysis of EPOR+ tumor-associated macrophages in human osteosarcoma lung metastasis. *J Immunol Res* **32**: 9374240. <https://doi.org/10.1155/2020/9374240>
- Li Y, Zhang M, Chen H, Dong Z, Ganapathy V, Thangaraju M, Huang S (2010). Ratio of miR-196s to HOXC8 messenger RNA correlates with breast cancer cell migration and metastasis. *Cancer Res* **70**: 7894–7904. <https://doi.org/10.1158/0008-5472.CAN-10-1675>
- Liang CJ, Chang YC, Chang HC, Wang CK, Hung YC, Lin YE, Chan CC, Chen CH, Chang HY, Sang TK (2014) Derlin-1 regulates mutant VCP-linked pathogenesis and endoplasmic reticulum stress-induced apoptosis. *PLoS Genetics* **10**: e1004675. <https://doi.org/10.1371/journal.pgen.1004675>
- Lin Y, Zhao J, Wang H, Cao J, Nie Y (2017) MiR-181a modulates proliferation, migration and autophagy in AGS gastric cancer cells and downregulates MIMR3. *Mol Med Rep* **15**: 2451–2456. <https://doi.org/10.3892/mmr.2017.6289>
- Loukas I, Skamnelou M, Tsiadou S, Bournaka S, Grigoriadis S, Taraviras S, Lygerou Z, Arbi M (2021) Fine-tuning multiciliated cell differentiation at the post-transcriptional level: Contribution of miR-34/449 family members. *Biol Rev Cambridge Philosophical Soc* **96**: 2321–2332. <https://doi.org/10.1111/brv.12755>
- Lu YC, Chang JT, Chan EC, Chao YK, Yeh TS, Chen JS, Cheng AJ (2016) MiR-196, an emerging cancer biomarker for digestive tract cancers. *J Cancer* **7**: 650–655. <https://doi.org/10.7150/jca.13460>
- Maruyama T, Nishihara K, Umikawa M, Arasaki A, Nakasone T, Nimura F, Matayoshi A, Takei K, Nakachi S, Kariya KI, Yoshimi N (2018) MicroRNA-196a-5p is a potential prognostic marker of delayed lymph node metastasis in early-stage tongue squamous cell carcinoma. *Oncol Lett* **15**: 2349–2363. <https://doi.org/10.3892/ol.2017.7562>
- Meyer SE, Muench DE, Rogers AM, Newkold TJ, Orr E, O'Brien E, Perentesis JP, Doench JG, Lal A, Morris PJ, Thomas CJ, Lieberman J, McGlinn E, Aronow BJ, Salomonis N, Grimes HL (2018) MiR-196b target screen reveals mechanisms maintaining leukemia stemness with therapeutic potential. *J Exp Med* **215**: 2115–2136. <https://doi.org/10.1084/jem.20171312>
- Miwa S, Shirai T, Yamamoto N, Hayashi K, Takeuchi A, Igarashi K, Tsuchiya H (2019) Current and emerging targets in immunotherapy for osteosarcoma. *J Oncol* **23**: 7035045. <https://doi.org/10.1155/2019/7035045>
- Murugan S, Amaravadi RK (2016) Methods for studying autophagy within the tumor microenvironment. *Adv Exp Med Biol* **899**: 145–166. https://doi.org/10.1007/978-3-319-26666-4_9
- Olson P, Lu J, Zhang H, Shai A, Chun MG, Wang Y, Libutti SK, Nakamura EK, Golub TR, Hanahan D (2009) MicroRNA dynamics in the stages of tumorigenesis correlate with hallmark capabilities of cancer. *Genes Develop* **23**: 2152–2165. <https://doi.org/10.1101/gad.1820109>
- Padhi BK, Singh M, Rosales M, Pelletier G, Cakmak S (2018) A PCR-based quantitative assay for the evaluation of mRNA integrity in rat samples. *Biomol Detec Quantific* **15**: 18–23. <https://doi.org/10.1016/j.bdq.2018.02.001>

- Pierzyńska-Mach A, Janowski PA, Dobrucki JW (2014) Evaluation of acridine orange, LysoTracker Red, and quinacrine as fluorescent probes for long-term tracking of acidic vesicles: Tracking Acidic Vesicles. *Cytometry Part A* **85**: 729–737. <https://doi.org/10.1002/cyto.a.22495>
- Rouggraff BT, Simon MA, Kneisl JS, Greenberg DB, Mankin HJ (1994) Limb salvage compared with amputation for osteosarcoma of the distal end of the femur. A long-term oncological, functional, and quality-of-life study. *J Bone Joint Surg, Am Vol* **76**: 649–656. <https://doi.org/10.2106/00004623-199405000-00004>
- Sadykova LR, Ntekim AI, Muyangwa-Semenova M, Rutland CS, Jeyapalan JN, Blatt N, Rizvanov AA (2020) Epidemiology and risk factors of osteosarcoma. *Cancer Investig* **38**: 259–269. <https://doi.org/10.1080/07357907.2020.1768401>
- Salah Z, Arafah R, Maximov V, Galasso M, Khawaled S, Abou-Sharieha S, Volinia S, Jones KB, Croce CM, Aqeilan RI (2015) MiR-27a and miR-27a* contribute to metastatic properties of osteosarcoma cells. *Oncotarget* **6**: 4920–4935. <https://doi.org/10.18632/oncotarget.3025>
- Stiegelbauer V, Vychytilova-Faltejskova P, Karbiener M, Pehserl AM, Reicher A, Resel M, Heitzer E, Ivan C, Bullock M, Ling H, Deutsch A, Wulf-Goldenberg A, Adiprasito JB, Stoeger H, Haybaeck J, Svoboda M, Stotz M, Hoefler G, Slaby O, Pichler M (2017) MiR-196b-5p Regulates colorectal cancer cell migration and metastases through interaction with HOXB7 and GALNT5. *Clin Cancer Res* **23**: 5255–5266. <https://doi.org/10.1158/1078-0432.CCR-17-0023>
- Tan X, He X, Jiang Z, Wang X, Ma L, Liu L, Wang X, Fan Z, Su D (2015) Derlin-1 is overexpressed in human colon cancer and promotes cancer cell proliferation. *Mol Cell Biochem* **408**: 205–213. <https://doi.org/10.1007/s11010-015-2496-x>
- Wang J, Hua H, Ran Y, Zhang H, Liu W, Yang Z, Jiang Y (2008) Derlin-1 is overexpressed in human breast carcinoma and protects cancer cells from endoplasmic reticulum stress-induced apoptosis. *Breast Cancer Res* **10**: R7. <https://doi.org/10.1186/bcr1849>
- Wang X, Peng L, Gong X, Zhang X, Sun R, Du J (2018) MiR-423-5p inhibits osteosarcoma proliferation and invasion through directly targeting STMN1. *Cell Physiol Biochem* **50**: 2249–2259. <https://doi.org/10.1159/000495085>
- Xin H, Wang C, Liu Z (2019a) MiR-196a-5p promotes metastasis of colorectal cancer via targeting IxBa. *BMC Cancer* **19**: 30. <https://doi.org/10.1186/s12885-018-5245-1>
- Xin H, Wang C, Liu Z (2019b) MiR-196a-5p promotes metastasis of colorectal cancer via targeting IxBa. *BMC Cancer* **19**: 30. <https://doi.org/10.1186/s12885-018-5245-1>
- Zhang H, Tan M, Zhang J, Han X, Ma Y (2021) Propofol inhibits thyroid cancer cell proliferation, migration, and invasion by suppressing SHH and PI3K/AKT signaling pathways via the miR-141-3p/BRD4 axis. *J Healthcare Engin* **2**: 1–10. <https://doi.org/10.1155/2021/2704753>
- Zheng H, Bi F, Yang Y, Hong Y, Ni J, Ma L, Liu M, Hao L, Zhou W, Song L, Yan HL (2019a) Downregulation of miR-196-5p induced by hypoxia drives tumorigenesis and metastasis in hepatocellular carcinoma. *Hormones Cancer* **10**: 177–189. <https://doi.org/10.1007/s12672-019-00370-5>
- Zheng H, Bi FR, Yang Y, Hong YG, Ni JS, Ma L, Liu MH, Hao LQ, Zhou WP, Song LH, Yan HL (2019b) Downregulation of miR-196-5p induced by hypoxia drives tumorigenesis and metastasis in hepatocellular carcinoma. *Hormones Cancer* **10**: 177–189. <https://doi.org/10.1007/s12672-019-00370-5>
- Zhou G, Jiang H, Ma L (2018) MicroRNA-376a inhibits cell proliferation and invasion in osteosarcoma via directly targeting SATB1. *Mol Med Rep* **18**: 3521–3528. <https://doi.org/10.3892/mmr.2018.9344>

Wilforol A inhibits human glioma cell proliferation and deactivates the PI3K/AKT signaling pathway

Zhihan Wang, Li Ren, Hao Xu, Zilong Wei and Hongjun Zeng✉

Department of Neurosurgery, Pudong Hospital Affiliated to Fudan University, Shanghai, China

Objectives: To study the anti-proliferation activity of wilforol A against glioma cells and its possible molecular mechanisms. **Methods:** Human glioma cell lines U118 MG and A172, human tracheal epithelial cells (TECs) and astrocytes (HAs) were exposed to various concentrations of wilforol A and evaluated for viability, apoptosis, and levels of proteins using WST-8 assay, flow cytometry and Western blot analysis, respectively. **Results:** Wilforol A inhibited the growth of U118 MG and A172 cells, but not TECs and HAs, in a concentration-dependent manner and the estimated IC_{50} were 6 to 11 μ M after 4 h-exposure. Apoptosis was induced at an apoptotic rate of about 40% at 100 μ M in U118 MG and A172 cells, but the rates were less than 3% in TECs and HAs. Co-exposure to caspase inhibitor Z-VAD-fmk significantly reduced wilforol A-induced apoptosis. Wilforol A treatment also reduced the colony formation ability of U118 MG cells and triggered a significant increase in ROS production. Elevated levels of pro-apoptotic proteins p53, Bax and cleaved caspase 3 and reduced level of the anti-apoptotic protein Bcl-2 were observed in glioma cells exposed to wilforol A. The expression of PI3K and p-Akt genes in the PI3K/AKT pathways were significantly downregulated in glioma cells treated with wilforol A. **Conclusions:** Wilforol A inhibits the growth of glioma cells, reduces the levels of proteins in the PI3K/Akt signal transduction pathways and increases the levels of pro-apoptotic proteins.

Keywords: glioma; natural product; anticancer activity; apoptosis, PI3K/Akt signaling pathways

Received: 16 April, 2022; revised: 19 October, 2022; accepted: 09 January, 2023; available on-line: 16 February, 2023

✉e-mail: hongjunzeng723@yeah.net

Abbreviations: ANOVA, analysis of variance; DCFHDA, 2',7'-Dichlorofluorescein diacetate; EMEM, Eagle's minimum essential medium; EMT, epithelial-mesenchymal transition; FBS, fetal bovine serum; HAs, astrocytes; HRP, horseradish peroxidase; NR4A1, nuclear receptor subfamily 4 group A member 1; PI, propidium iodide; PVDF, polyvinylidene difluoride; RIPA, radioimmunoprecipitation assay buffer; ROS, reactive oxygen species; SEM, standard error of the mean; TECs, human tracheal epithelial cells

INTRODUCTION

Gliomas are the most common tumors with extremely broad range of clinical behaviors in the central nerve systems of children and adolescents, although the definitive cell of origin of gliomas still remains elusive (Cahill & Turcan, 2018; Sturm *et al.*, 2017). Gliomas are characterized based on histologic and molecular data into several entities including diffuse gliomas (astrocytoma, oligodendroglioma and glioblastoma) and low-grade gliomas (angiocentric glioma, pilocytic astrocytoma and sub-

ependymal giant cell astrocytoma). Genomic profiling of certain gliomas is necessary to define the histologic subtyping and proper use of prognostic and predictive biomarkers for treatment (Ferris *et al.*, 2017; Reifenberger *et al.*, 2017). Early and rational use of drugs that effectively inhibit the proliferation of glioma cells is important to obtain a good prognosis for patients (Morshed *et al.*, 2019). However, a significant portion of gliomas develop over a short period of time and progress rapidly into WHO grade III or IV high-grade gliomas. Despite all therapeutic efforts, gliomas remain largely incurable. Current treatment of gliomas relies on surgery in combination with chemotherapy and/or radiotherapy. However, many tumors show a high resistance to these interventions, and recurrences are very frequent since conventional therapies do not take into full account the unique molecular features of different subtypes of gliomas (Ghotme *et al.*, 2017). Several new therapies have been proposed to better manage the cancer, including immunotherapy that is able to penetrate the blood-brain barrier to deliver drugs to lymphatics with some promising results (Hanaci *et al.*, 2018; Xu *et al.*, 2020), use of IL15R α -IL15-armed oncolytic poxviruses in combination with adoptive T-cell therapy, rapamycin, and celecoxib (Xu *et al.*, 2020). In addition, several new strategies have been explored to treat glioma. For example, gene therapy based on lipid nanoparticles as non-viral vectors has been attempted to deliver genes across the blood-brain barrier to reach the glioma cell target (Luiz *et al.*, 2021) and ketogenic diets are suggested to induce ketosis to target the glycolytic phenotype to halt the progression of lower grade tumors to more aggressive subtypes (Poff *et al.*, 2019).

In the past decades, there have been growing interest in exploring natural medicinal plants and their bioactive molecules for potential anti-tumor activity, both *in vitro* and *in vivo* (Li *et al.*, 2019; Weng & Goel, 2022). Tripterine, also known as celastrol, is an active ingredient isolated from a vine plant *Tripterygium wilfordii*. It has been proven to have therapeutic effect on inflammatory response and tumors, including hepatoma, multiple myeloma, breast cancer, cervical cancer, prostate cancer and leukemia (Chen *et al.*, 2018b; Li *et al.*, 2021; Yang *et al.*, 2021). Using network pharmacology-based strategy, several components from *T. wilfordii* have been found to impact a number of signaling pathways, such as the Toll-like receptor signaling pathway, NF-kappa B signaling pathway and HIF-1 signaling pathway in acute myeloid leukemia (Fang *et al.*, 2020). Tripterine suppresses the malignancy of breast cancer by upregulating miR-184 (Wang, 2021) and inhibits cell proliferation by increasing the level of Bax in pancreatic cancer cells (Chen *et al.*, 2022). Studies also show that tripterine promotes autophagy and apoptosis *via* the ROS/JNK and AKT/

mTOR signaling pathways in glioma cell lines U251, U87-MG and C6 (Liu *et al.*, 2019) and blocks the PI3K/AKT/mTOR signaling pathway to suppress vasculogenic mimicry formation and angiogenesis (Zhu *et al.*, 2020). On the other hand, wilforol A, a triterpenoid and analog of celastrol from the same plant, has not been characterized for its anticancer activity.

The purpose of this study was to investigate the effect of wilforol A on proliferation of cancer cells and its possible molecular mechanisms underlying the anticancer activity using glioma cell lines U118 and A172.

MATERIALS AND METHODS

Cell lines

Two human glioma cell lines U118 MG, A172, and human tracheal epithelial cells (PCS-300-013, TECs) were purchased from American Type Collection Center (ATCC), USA, and cultured in Eagle's minimum essential medium (EMEM) containing 10% fetal bovine serum (FBS) at 37°C in 5% CO₂. Cells were digested with 0.25% trypsin for 3 min when reaching 80–90% confluence, pelleted by centrifugation at 25°C and subcultured in fresh EMEM medium with 10% FBS under the same culture conditions. Human astrocytes (HAs) were purchased from iXCells (San Diego, CA, USA) and grown in astrocyte medium (cat no. 10HU-035, iXCells) at 37°C in 5% CO₂. Adenovirus with and without the Akt gene (AD00306Z) were purchased from Creative Biogene, USA, and used to infect cells at 1×10¹⁰ PFU/ml according to the supplier's protocols to generate Akt-overexpressing cells.

Cell viability assay

The viability of cells was measured using Cell Counting Kit 8 (WST-8, Abcam, USA) based on the supplier's instructions. Wilforol A purchased from TargetMol, MA, USA, was dissolved in 1% DMSO (molecular biology grade, Sigma, USA) as stock solution. Cells were seeded in the wells of 24-well black culture plates at the density of 1×10⁴ per well in 100 µl EMEM medium and cultured at 37°C in a 5% CO₂ incubator. After incubation for 24 h, 100 µl EMEM medium containing various concentrations of wilforol A and 0.2% DMSO was added to each well and cells were cultured at 37°C in a 5% CO₂ incubator for another 4 h. EMEM medium containing 0.2% DMSO was used as control. Cells were then added with 20 µl WST-8 solution and incubated in the dark at 37°C for 2 h. The absorbance at 450 nm was measured using a plate reader. The experiments were independently repeated three times and all samples were tested in triplicate.

Soft agar assay

Soft agar assays were performed to assess the colony formation ability as described previously (Horibata *et al.*, 2015). Briefly, U118MG cells (5×10⁴ cells/ml) were suspended gently in 0.6% type VII agarose that was maintained at 42°C and prepared in EMEM medium supplemented with 10% FBS and 1% penicillin/streptomycin. The cells were poured to the bottom of 60-mm dishes to form a bottom layer over 1.2% agar. After being solidified at 25°C for 30 min, the plates were sealed and were placed into a humidified incubator for culture at 37°C. Two weeks later, the colonies were stained overnight with 200 µl of 0.1% crystal violet per

well at 37°C. The stained colonies were analyzed using a colony counter.

Flow cytometry

After exposure to wilforol A for 4 h, cells (5×10⁶) were pelleted by centrifugation at 1000 rpm at 25°C for 10 min and resuspended in 500 µl PBS. For assessment of apoptosis, the cells were washed twice with 500 µl PBS, added with 10 µl Annexin V and propidium iodide (PI) from Annexin V-DY-634 PI Apoptosis Staining/Detection Kit (Abcam) to stain the cells according to the manufacturer's instructions. For assessment of autophagy, cells were stained with autophagy probes in Autophagy Assay Red Detection Kit (cat. no. APO010B, Biorad, USA) according to the manufacturer's instructions. For determination of necrotic cells, GFP-CERTIFIED Necrosis detection kit (cat. no. ENZ5100225, Enzo Life Sciences, Thermo Fisher, USA) was used to detect necrotic cells with the FL 3 channel as instructed by the manufacturer. The stained cells were loaded and analyzed on a NovoCyte flow cytometer (Agilent, USA). The quantitation of cells was calculated by the built-in CellQuest software. To assess the effect of caspase inhibitor, 50 µM of Z-VAD-fmk (Alexis Biochemicals, San Diego, CA) was added to the culture medium. For reactive oxygen species (ROS) analysis, cells were exposed to wilforol A for 4 h and stained with DCFH-DA (cat. no. S0033S, Beyotime, Beijing, China) in serum-free medium (after 1:1000 dilution) at the final concentration of 10 µmol/L. After incubation at 37°C for 20 min, cells were washed three times with serum-free medium to remove recessive DCFH-DA and loaded to the cytometer for analysis according to the supplier's protocols. The experiments were independently repeated three times and all samples were tested in triplicate.

Western blot

After exposure to wilforol A for 4 h, cells (5×10⁶) were pelleted by centrifugation at 1000 rpm at 25°C for 10 min and were lysed in RIPA buffer (Thermo Fisher Scientific, USA) that contains protease inhibitors cocktail to minimize protein degradation. Proteins in the lysates were quantitated using BCA kit (Thermo Fisher Scientific) according to manufacturer's instructions. After denaturing by boiling at 100°C for 5 min, the proteins were loaded onto 12% polyacrylamide gels, separated by electrophoresis and transferred to PVDF membranes (Millipore, USA). The proteins of interest were detected by incubating with primary antibodies against p53 (cat. no. AF7671), Bax (cat. no. AF1270), Bcl-2 (cat. no. AF0060), cleaved caspase 3 (cat. no. AF1213), PI3K (cat. no. AF1549, specific for subunit p110α), Akt (cat. no. AF0045), p-Akt (Ser473) (cat. no. AA329), p-Akt (Thr308) (cat. no. AA331) and β-actin (cat. no. AF5001) (all from Beyotime) and secondary antibody (goat anti-human IgG H&L (HRP) (cat. no. ab97161, Abcam). The immunoreactive bands were captured using Chemi Doc XRS^{plus} chemiluminescence imaging system (Bio-Rad, USA) after visualization with a chemiluminescence kit (Thermo Fisher Scientific). The gray values of the bands on the blots were determined using Quantity One software.

Statistical analysis

All data were shown as means ± standard error of the mean (SEM) obtained from three independent experiments. Statistical comparisons among groups were

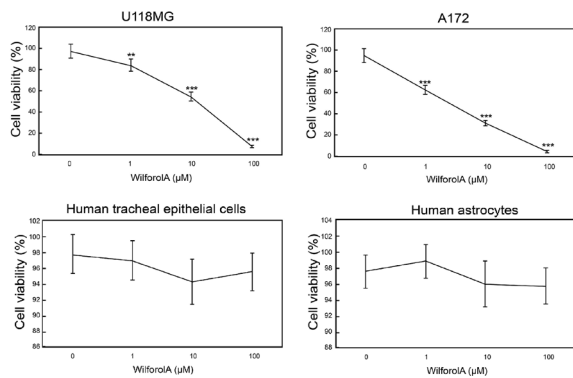


Figure 1. Viability of U118MG cells, A172 cells, tracheal epithelial cells and human astrocytes after exposure to Wilforol A for 4 h.

The viability was measured with the cell Counting Kit 8 (WST-8). 1×10^4 cells/well were seeded cultured overnight in a black wall 24-well plate. Cells were treated with diluted Wilforol A for 4 hours. The absorbance was measured at 460 nm using a plate reader. The experiments were independently repeated three times. One-way ANOVA was used to analyze the differences. ** and *** denote <0.01 , and 0.001 , respectively, compared to control.

assessed using one-way analysis of variance (ANOVA). A value of $P < 0.05$ was considered statistically significant.

RESULTS

Wilforol A reduces the viability of glioma cells

We first tested the effect of wilforol A on the viability of glioma cell lines U118 MG and A172 using WST-8 assays. After 4 h exposure to wilforol A, the viability of cells in both cell lines began to decline at $1 \mu\text{M}$ wilforol A and decreased from over 95% in controls to 8% in U118MG and 5% in A172 at $100 \mu\text{M}$ wilforol A, indicating that wilforol A is potently toxic to glioma cells and the viability reduction is concentration-dependent (Fig. 1). The IC_{50} for U118 MG and A172 were estimated to be 11 and $6 \mu\text{M}$, respectively, suggesting that A172 is more sensitive to wilforol A. Furthermore, we tested if non-glioma cells could be inhibited by wilforol A within the concentration range using TECs and HAs. No inhibition was observed up to $100 \mu\text{M}$ wilforol A (Fig. 1), suggesting that wilforol A is more toxic to glioma cells.

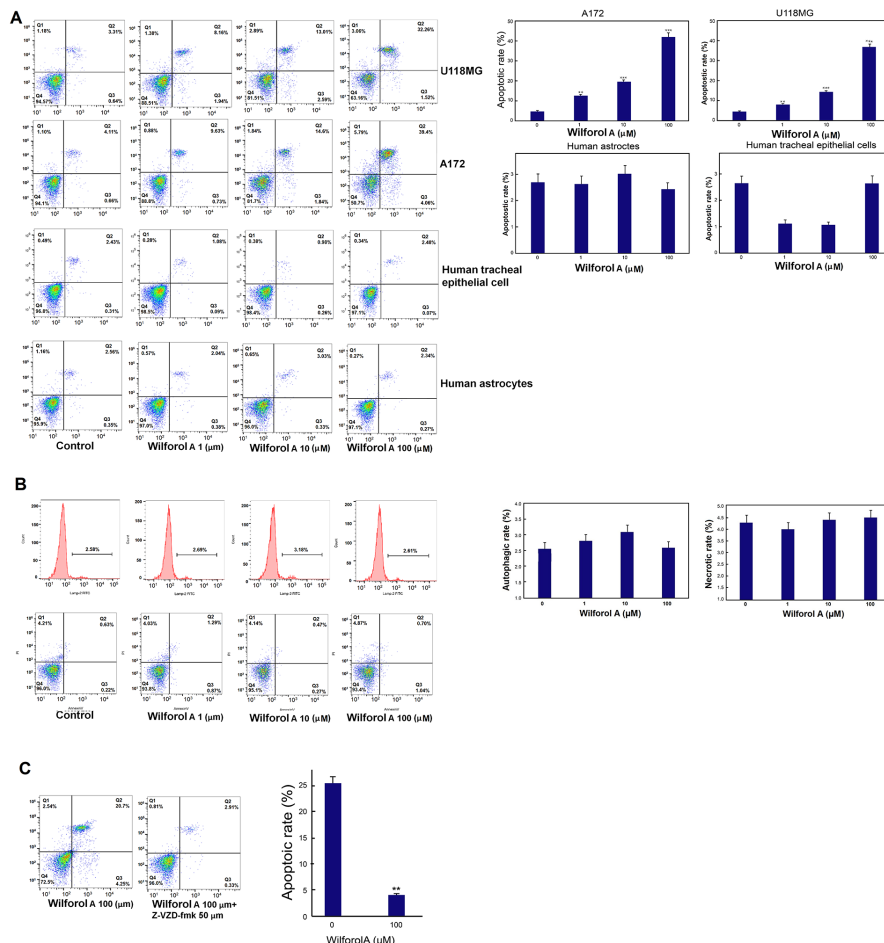


Figure 2. Apoptosis (A), autophagy and necrosis (B) of U118MG and A172 cells after exposure to wilforol A (A) and Z-VAD-fmk (C) for 4 h.

The apoptosis, autophagy and necrosis were measured with Annexin V- DY-634 PI Apoptosis Staining / Detection Kit, Autophagy Assay Red Detection Kit and GFP-CERTIFIED Necrosis detection kit. Cells (5×10^6) were seeded overnight in a black wall 24-well plate and were treated with diluted Wilforol A and $50 \mu\text{M}$ Z-VAD-fmk for 4 hours. The treated cells were stained with relevant probes and analyzed on NovoCyte flow cytometer. Left panel: representative flow cytometry results; right panel: statistical results of apoptosis. The experiments were independently repeated three times. One-way ANOVA was used to analyze the differences. ** and *** denote <0.01 , and 0.001 , respectively, compared to control.

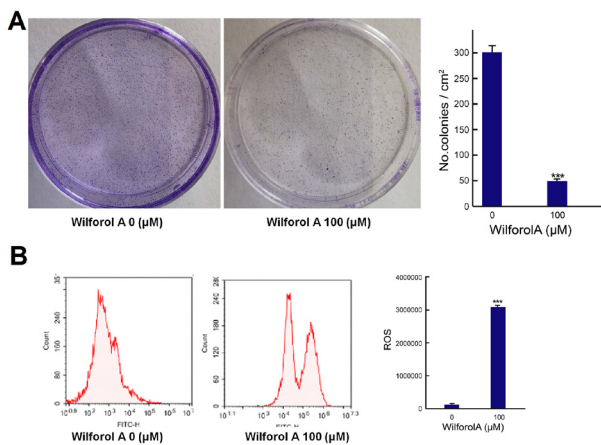


Figure 3. Colony formation and ROS production of U118MG after exposure to wilforol A for 4 h.

U118MG cells were suspended 0.6% agarose prepared in EMEM medium. The cells were poured to the bottom of 60-mm dishes and cultured at 37°C for weeks. The colonies were stained with 0.1% crystal violet and analyzed. (A) left panel: colony formation in soft-agar, right panel: number of colonies. (B) U118MG cells (5×10^5 cells/ml) were incubated with $100 \mu\text{M}$ wilforol A for 4 h and reacted with DCFH-DA in serum-free medium. After incubated at 37°C for 20 min, cells were loaded to the cytometer for analysis according to supplier's protocols. A, left panel: flow cytometry results, right panel: fluorescence density. The experiments were independently repeated three times. One-way ANOVA was used to analyze the differences. *** denotes <0.001 , compared to control.

Wilforol A increases apoptosis, but not autophagy and necrosis in glioma cells

Apoptosis is one of the most important mechanisms leading to cell death after exposure to various cytotoxic agents. We therefore analyzed the apoptosis of U118MG and A172 cells after 4 h exposure to wilforol A at different concentrations using flow cytometry. Cells with both early and later apoptosis were detected after exposure to wilforol A, although the majority was later apoptosis at all of the tested concentration levels (Fig. 2A). After exposure to $100 \mu\text{M}$ wilforol A, over 95% of apoptotic cells were later apoptotic (Fig. 2A). Analysis showed that

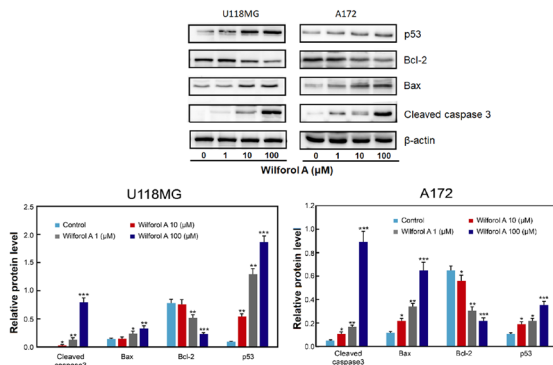


Figure 4. Expression of apoptosis-related proteins in U118MG and A172 cells after exposure to Wilforol A for 4 h.

U118MG and A172 (5×10^4) were seeded overnight in a black wall 24-well plate. Cells were treated with diluted Wilforol A for 4 hours. The treated cells were harvested, and total proteins were extract using RIPA buffer and separated on 12% SDS-PAGE. Proteins of interest were detected with relevant antibodies and visualized with a chemiluminescence kit. Upper panel: representative Western blots; lower panel: statistical results of protein expressions. The experiments were independently repeated three times. One-way ANOVA was used to analyze the differences. * ** and *** denote <0.05 , 0.01 , and 0.001 , respectively, compared to control.

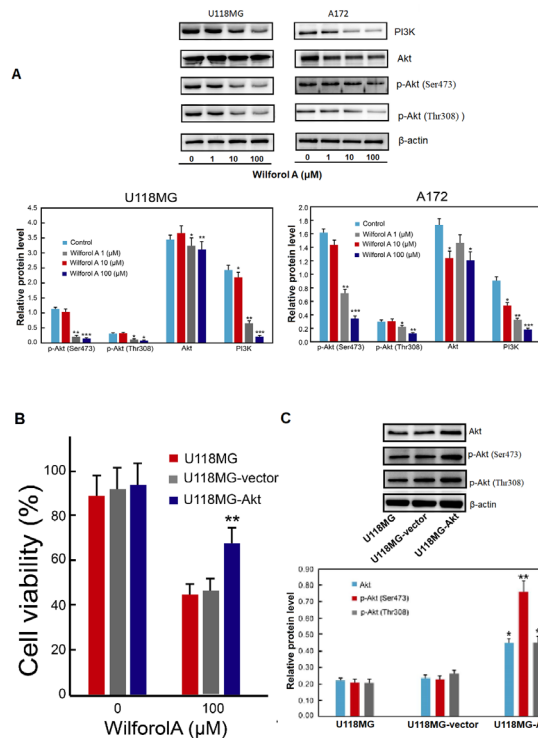


Figure 5. Levels of the PI3K/AKT signaling pathway proteins (A) in U118MG and A172 cells, viability of Akt-overexpressing U118MG cells (B) and levels of the Akt (C) after exposure to Wilforol A for 4 h.

U118MG and A172 (5×10^4), or U118MG infected with Akt over-expression vector were seeded overnight in a black wall 24-well plate. Cells were treated with diluted Wilforol A for 4 hours. The treated cells were harvested, and total proteins were extract using RIPA buffer and separated on 12% SDS-PAGE. Proteins of interest were detected with relevant antibodies and visualized with a chemiluminescence kit. The viability was measured with the cell Counting Kit 8 (WST-8). 1×10^4 cells/well were seeded cultured overnight in a black wall 24-well plate. Cells were treated with diluted Wilforol A for 4 hours. The absorbance was measured at 460 nm using a plate reader. A, Upper panel: representative Western blots; lower panel: statistical results of protein contents. B, results of viability assays; C, Upper panel: representative Western blots; lower panel: statistical results of protein levels. The experiments were independently repeated three times. One-way ANOVA was used to analyze the differences. * ** and *** denote <0.05 , 0.01 , and 0.001 , respectively, compared to control.

in both cell lines the total apoptotic rates increased from less than 5% to around 40% as the concentration of wilforol A increased from $1 \mu\text{M}$ to $100 \mu\text{M}$ (Fig. 2A). Similar to viability reduction, A172 cells had slightly more apoptotic cells than U118MG cells at the same wilforol A concentrations (Fig. 2A). On the other hand, no increase in apoptosis was observed in TECs and HAs after exposure to up to $100 \mu\text{M}$ wilforol A as compared to the controls (Fig. 2A). Autophagy and necrosis are also important pathways leading to cell death, and were assessed in U118 MG after exposure to wilforol A. The data showed that there was no significant change in autophagic and necrotic cells as compared to the unexposed cells (Fig. 2B).

To further confirm that apoptosis pathway is involved in the observed viability reduction, U118MG cells were treated with caspase inhibitor Z-VAD-fmk. The results showed that this treatment partially reduced wilforol A-induced apoptosis, suggesting that caspase is likely involved in the induced apoptosis (Fig. 2C).

Wilforol A reduces colony formation ability and triggers ROS production in glioma cells

To further assess the cytotoxicity of wilforol A to glioma cells, the colony formation ability of U118MG was assessed using soft-agar assays. The results showed that after treatment with wilforol A, the colony formation ability of U118MG was significantly reduced (Fig. 3A) and ROS production was significantly increased (Fig. 3B).

Effect of wilforol A on the level of apoptosis-related proteins

Western blot analyses showed the levels of apoptosis-related proteins p53, Bax and cleaved caspase 3 were increased, while Bcl-2 level was reduced in both cell lines after exposure to wilforol A (Fig. 4). Statistical analysis showed that the changes in the levels of these proteins were wilforol A-concentration-dependent and the greatest changes in the levels occurred at the highest wilforol A concentration (Fig. 4). While the changes in the protein levels in the two cell lines showed similar trends in response to wilforol A exposure, there were more increases in the levels of cleaved caspase 3 and higher p53 level in U118MG than in A172 cells, while Bax increased more in A172 than in U118MG cells (Fig. 4).

Effect of wilforol A on levels of PI3K/Akt signaling pathway proteins

PI3K/AKT signaling pathway plays a very important role in cancer and the epithelial-mesenchymal transition (EMT) (Xu *et al.*, 2015). Western blot analyses showed that the production of PI3K/Akt signaling pathway protein PI3K, Akt and p-Akt (both p-Akt (Ser473) and p-Akt (Thr308)) was all downregulated after U118MG and A172 cells exposure to wilforol A and the decreases were concentration-dependent, although the downregulation of Akt was not as large as other proteins and was not concentration-dependent in A172 cells (Fig. 5). To consider the contribution of Akt in wilforol A-induced cell death, U118 MG overexpressing Akt was assessed for its sensitivity to wilforol A. Compared with U118 MG and U118 MG infected with an empty vector, U118 MG overexpressing Akt had significantly higher level Akt and p-Akt (both p-Akt (Ser473) and p-Akt (Thr308)) and higher viability, suggesting the Akt pathway is at least partially involved in the wilforol A-induced cell death (Fig. 5B and C).

DISCUSSION

Wilforol A is a pentacyclic triterpenoid with the formula C₂₉H₃₈O₅ and is one of the main active ingredients extracted from the medicinal plant *T. wilfordii*. Our experimental data indicated that wilforol A is potently and preferentially toxic to glioma cells with a IC₅₀ between 6 and 11 μ M in U118MG and A172. It generates apoptosis, ROS; upregulates the production of apoptosis-related proteins and downregulates the levels of PI3K/AKT signaling pathway proteins, suggesting that more studies are warranted to investigate the anticancer activity of this compound and to explore its potential as candidate drug for cancer therapy.

Several molecules have been isolated from *T. wilfordii* that processes anticancer activity. For example, celastrol and triptolide are terpenes purified from *T. wilfordii* and have been demonstrated to be inhibitory to various cancer cells, such as promyelocytic leukemia, T cell lympho-

ma and hepatocellular carcinoma cell (Chan *et al.*, 2001; Meng *et al.*, 2011), cervical cancer cell (Kim *et al.*, 2010) and head and neck cancer cells (Cai *et al.*, 2021). However, wilforol A, which is an analog of these terpenes with structural similarity to celastrol, has not been sufficiently characterized for its activity against cancer, although it is recorded to have inhibitory activity against MIA-PaCa2 cells (hypotriploid human pancreatic cancer cells, IC₅₀=3 μ M) and A549 cells (adenocarcinomic human alveolar basal epithelial cells, IC₅₀=3 μ M) after 72 h exposure (<https://pubchem.ncbi.nlm.nih.gov/compound/Wilforol-A#section=Biological-Test-Results>). Our experimental data showed that wilforol A has a IC₅₀ of 6 to 11 μ M for glioma cell lines A172 and U118 MG after 4 h exposure, but is not inhibitory to TECs and HAs, suggesting that there are differences in the toxicity of the compound to cell lines. It is also likely that the IC₅₀ would change over the exposure time, with longer exposure generating smaller IC₅₀. Previously, it was reported that the IC₅₀ of triptolide and celastrol are 0.21 and 2.58 μ M for glioma cell line SHG44 after 48 h exposure (Zhou *et al.*, 2002). The difference in the response of cell lines to wilforol A might be attributed to their different cellular and molecular characteristics, such as cell membrane permeability and metabolic activity, because these cells were derived from different patients. After exposure to wilforol A, the colony formation ability of U118 MG was significantly reduced. Triptolide also inhibits the colony formation of breast cell lines MCF-7 and BT-20, stomach cancer cell lines MKN-45, MKN-7, and KA-TO-III, and promyelocytic leukemia cell line HL-60 (Wei & Adachi, 1991), implying that wilforol A may have anticancer activity against a broad range of cancers due to its structure similarity to celastrol and triptolide.

Several mechanisms have been proposed with regard to the inhibitory effect of these *T. wilfordii* compounds. For example, celastrol and triptolide may inhibit leukemia cell proliferation by inducing apoptosis and down-regulating NF- κ B activity and miR-16-1 (Chan *et al.*, 2001; Meng *et al.*, 2011). In cervical cancer cells caspase-dependent, mitochondria-mediated apoptosis results in loss of cell viability (Kim *et al.*, 2010) and in head and neck cancer gasdermin E-mediated pyroptosis is induced after suppressing mitochondrial hexokinase-II (Cai *et al.*, 2021). They not only directly induce apoptosis in cancer cells but also enhance apoptosis induced by tumor necrosis factor and downregulate the expression of inhibitors of apoptosis proteins (IAPs), such as IAP1 and IAP2 (Lee *et al.*, 1999). Similarly, apoptosis was observed in our experiments in both cell lines after the cells were exposed to wilforol A and increased as wilforol A concentration increases. Furthermore, exposure to caspase inhibitor Z-VAD-fmk reduced apoptosis induced by wilforol A as previously reported (Arita *et al.*, 2000; Yang *et al.*, 2003), indicating that apoptosis is likely one of the pathways leading to the inhibition of cell proliferation. Analysis showed that the pro-apoptotic proteins such as p53, Bax and cleaved caspase 3 were upregulated while the anti-apoptotic protein Bcl-2 was downregulated after wilforol A treatment. Also, these regulations are concentration-dependent and have similar trends in both cell lines, suggesting that similar apoptosis mechanisms are motivated after wilforol A treatment. Apoptosis is a very complex process in which the activation of caspase family genes plays an important role (Christgen *et al.*, 2020). Caspase 9 is a key protease in the endogenous apoptotic pathway at the top of caspase-cascade system that leads to the activation of caspase 3 to generate cleaved caspase 3, apoptosis and cell death (Nagata, 2018). How-

ever, since the apoptotic cells at the highest wilforol A concentration is about 40%, which is much less than the percentages of inviable cells determined by WST-8 assays, which were over 90%. The difference in cell death rate could be attributed to other causes of cell death, such as necrosis, pyroptosis and autophagy. In mice, celastrol acts as a nuclear receptor subfamily 4 group A member 1 (NR4A1) agonist and may induce autophagy in a Nur77-dependent manner (Hu *et al.*, 2017). However, our assessment showed that both autophagic and necrotic cells were not changed after exposure to wilforol A, suggesting that there might be other pathways of cell death that are involved in the wilforol A-induced cell injury, which needs to be identified to better understand the mechanisms underlying the anticancer activity of wilforol A (D'Arcy, 2019).

To further elucidate the mechanisms underlying the anticancer activity, we profiled the expression of proteins in the PI3K/AKT pathway, which is one of the most important signaling pathways that are crucial to many aspects of cell growth and survival (Porta *et al.*, 2014) and is often activated in various human cancers (Aoki & Fujishita, 2017), including gliomas (Li *et al.*, 2016). Akt may be activated to p-Akt by PI3K to promote or suppress a number of downstream molecules such as Bad, caspases, NF- κ B, mTOR and eNOS to play a leading role in regulating tumor development (Xia & Xu, 2015). In addition, Akt can also activate nuclear transcriptional factors NF- κ B to promote the expression of anti-apoptosis genes, such as c-Yaps and Bcl-2 that improve the survival and suppress apoptosis of tumor cells (Feng *et al.*, 2018). Furthermore, potentiated Akt and p-Akt have protective effect against cardiomyopathy (Zeng *et al.*, 2017). Our results showed that PI3K, Akt and p-Akt (phosphorylated at Ser473 or Thr308) are all downregulated in a concentration-dependent manner after the two cell lines were treated with wilforol A, although the downregulation of Akt is lower as compared to the other proteins and is not strictly concentration-dependent in A172 cells, suggesting that wilforol A might impact apoptosis in glioma cells through the PI3K/AKT signaling pathway. The reduction of total Akt might be attributed to reduced cell viability, which leads to lower metabolic activity. Furthermore, U118 MG overexpressing Akt1 was found less sensitive to wilforol A. This is consistent with previous finding that Akt overexpression decreases the chemosensitivity of gastric cancer cells to cisplatin (Zhang *et al.*, 2013), confirming that PI3K/AKT pathway is likely involved in wilforol A-induced cell death. However, a number of pathways and mechanisms might be involved in the control of viability. For instance, silencing FAM19A5 in the FAM19A5/S1PR1 signaling pathway significantly reduces the viability of mantle cell lymphoma (Wang, 2021), indirubin suppresses the viability of ovarian cancer cell through the STAT3 signaling pathway (Chen *et al.*, 2018a) and rhein induces cell death in hepaRG cells through the upregulation of proteins in the apoptotic pathways (You *et al.*, 2018). It is therefore essential to profile more signaling pathways to gain comprehensive understanding of wilforol A-induced cell death.

Although our data show that wilforol A suppresses the growth of glioma cells and induces apoptosis, it is unclear whether wilforol A exerts its biological activity from outside or inside of the cells, and if from inside of the cells, how the molecule enters the cells. Exposure of glioma cells to wilforol A generated increased ROS production, suggesting that it is likely that wilforol A exerts its biological activity from inside of the cells, because

mitochondria are major sites for ROS synthesis (Lucia *et al.*, 1997). However, more studies investigating cell membrane integrity, membrane potential changes and permeability are needed to understand the site of action of wilforol A. NR4A1 is mentioned as a target for wilforol A (<https://pubchem.ncbi.nlm.nih.gov/compound/Wilforol-A#section=Biological-Test-Results>). However, it is unclear whether the binding of wilforol A to NR4A1 results in the inhibition of cell growth. Previously, ectopic expression of NR4A1 was shown to enhance tumorigenesis by breast cancer cells (Guo *et al.*, 2021) and it may be possible that the binding of wilforol A to NR4A1 may deactivate NR4A1, resulting in reduced tumorigenesis. Furthermore, *T. wilfordii* is known to cause various adverse effects leading to leukopenia, gastrointestinal reactions, menstrual disorders and liver dysfunction when administered as crude extracts (Zhang *et al.*, 2016). However, whether purified wilforol A has adverse effects is largely unknown, and more studies are needed to further define the safety profiles and efficacy of this compound in *in vitro* and *in vivo* models.

Taken together, our experimental data have demonstrated that wilforol A has antiproliferative activity against glioma cells. It deactivates the PI3K/Akt signal transduction pathways, leading to reduced p-Akt expression and upregulated expression of pro-apoptosis genes, which might be responsible for increased apoptosis, and subsequently reduced proliferation of glioma cells.

REFERENCES

- Aoki M, Fujishita T (2017) Oncogenic roles of the PI3K/AKT/mTOR axis. *Curr Top Microbiol Immunol* **407**: 153–189. https://doi.org/10.1007/82_2017_6
- Arita K, Utsumi T, Kato A, Kanno T, Kobuchi H, Inoue B, Akiyama J, Utsumi K (2000) Mechanism of dibucaine-induced apoptosis in promyelocytic leukemia cells (HL-60). *Biochem Pharmacol* **60**: 905–915. [https://doi.org/10.1016/S0006-2952\(00\)00406-8](https://doi.org/10.1016/S0006-2952(00)00406-8)
- Cahill D, Turcan S (2018) Origin of gliomas. *Semin Neurol* **38**: 5–10. <https://doi.org/10.1055/s-0037-1620238>
- Cai J, Yi M, Tan Y, Li X, Li G, Zeng Z, Xiong W, Xiang B (2021) Natural product triptolide induces GSDME-mediated pyroptosis in head and neck cancer through suppressing mitochondrial hexokinase-IotaIota. *J Exp Clin Cancer Res* **40**: 190. <https://doi.org/10.1186/s13046-021-01995-7>
- Chan EW, Cheng SC, Sin FW, Xie Y (2001) Triptolide induced cytotoxic effects on human promyelocytic leukemia, T cell lymphoma and human hepatocellular carcinoma cell lines. *Toxicol Lett* **122**: 81–87. [https://doi.org/10.1016/S0378-4274\(01\)00353-8](https://doi.org/10.1016/S0378-4274(01)00353-8)
- Chen L, Wang J, Wu J, Zheng Q, Hu J (2018a) Indirubin suppresses ovarian cancer cell viabilities through the STAT3 signaling pathway. *Drug Des Devel Ther* **12**: 3335–3342. <https://doi.org/10.2147/DDDT.S174613>
- Chen SR, Dai Y, Zhao J, Lin L, Wang Y, Wang Y (2018b) A mechanistic overview of triptolide and celastrol, natural products from *Tripterygium wilfordii* Hook F. *Front Pharmacol* **9**: 104. <https://doi.org/10.3389/fphar.2018.00104>
- Chen XL, Geng YJ, Li F, Hu WY, Zhang RP (2022) Cytotoxic terpenoids from *Tripterygium hypoglaucaum* against human pancreatic cancer cells SW1990 by increasing the expression of Bax protein. *J Ethnopharmacol* **289**: 115010. <https://doi.org/10.1016/j.jep.2022.115010>
- Christgen S, Zheng M, Kesavardhana S, Karki R, Malireddi RKS, Banoth B, Place DE, Briard B, Sharma BR, Tuladhar S, Samir P, Burton A, Kanneganti TD (2020) Identification of the PANoptosome: A molecular platform triggering pyroptosis, apoptosis, and necroptosis (PANoptosis). *Front Cell Infect Microbiol* **10**: 237. <https://doi.org/10.3389/fcimb.2020.00237>
- D'Arcy MS (2019) Cell death: a review of the major forms of apoptosis, necrosis and autophagy. *Cell Biol Int* **43**: 582–592. <https://doi.org/10.1002/cbin.11137>
- Fang T, Liu L, Liu W (2020) Network pharmacology-based strategy for predicting therapy targets of *Tripterygium wilfordii* on acute myeloid leukemia. *Medicine (Baltimore)* **99**: e23546. <https://doi.org/10.1097/MD.00000000000023546>
- Feng H, Cheng X, Kuang J, Chen L, Yuen S, Shi M, Liang J, Shen B, Jin Z, Yan J, Qiu W (2018) Apatinib-induced protective autophagy and apoptosis through the AKT-mTOR pathway in anaplastic thy-

- roid cancer. *Cell Death Dis* 9: 1030. <https://doi.org/10.1038/s41419-018-1054-3>
- Ferris SP, Hofmann JW, Solomon DA, Perry A (2017) Characterization of gliomas: from morphology to molecules. *Virchows Arch* 471: 257–269. <https://doi.org/10.1007/s00428-017-2181-4>
- Ghotme KA, Barreto GE, Echeverria V, Gonzalez J, Bustos RH, Sanchez M, Leszek J, Yarla NS, Gomez RM, Tarasov V, Ashraf GM, Aliev G (2017) Gliomas: New perspectives in diagnosis, treatment and prognosis. *Curr Top Med Chem* 17: 1438–1447. <https://doi.org/10.2174/1568026617666170103162639>
- Guo H, Golczer G, Wittner BS, Langenbucher A, Zachariah M, Dubash TD, Hong X, Comaills V, Burr R, Ebright RY, Horwitz E, Vuille JA, Hajizadeh S, Wiley DF, Reeves BA, Zhang JM, Niederhoffer KL, Lu C, Wesley B, Ho U, Nieman LT, Toner M, Vasudevan S, Zou L, Mostoslavsky R, Maheswaran S, Lawrence MS, Haber DA (2021) NR4A1 regulates expression of immediate early genes, suppressing replication stress in cancer. *Mol Cell* 81: 4041–4058 e15. <https://doi.org/10.1016/j.molcel.2021.09.016>
- Hanaei S, Afshari K, Hirbod-Mobarakeh A, Mohajer B, Amir Dastmalchi D, Rezaei N (2018) Therapeutic efficacy of specific immunotherapy for glioma: a systematic review and meta-analysis. *Rev Neurosci* 29: 443–461. <https://doi.org/10.1515/revneuro-2017-0057>
- Horibata S, Vo T V, Subramanian V, Thompson PR, Coonrod SA (2015) Utilization of the soft agar colony formation assay to identify inhibitors of tumorigenicity in breast cancer cells. *J Vis Exp* e52727. <https://doi.org/10.3791/52727>
- Hu M, Luo Q, Alitongbieke G, Chong S, Xu C, Xie L, Chen X, Zhang D, Zhou Y, Wang Z, Ye X, Cai L, Zhang F, Chen H, Jiang F, Fang H, Yang S, Liu J, Diaz-Meco MT, Su Y, Zhou H, Moscat J, Lin X, Zhang XK (2017) Celastrol-Induced Nur77 Interaction with TRAF2 alleviates inflammation by promoting mitochondrial ubiquitination and autophagy. *Mol Cell* 66: 141–153 e6. <https://doi.org/10.1016/j.molcel.2017.03.008>
- Kim MJ, Lee TH, Kim SH, Choi YJ, Heo J, Kim YH (2010) Triptolide inactivates Akt and induces caspase-dependent death in cervical cancer cells via the mitochondrial pathway. *Int J Oncol* 37: 1177–1185. <https://doi.org/10.3892/ijo.00000769>
- Lee KY, Chang W, Qiu D, Kao PN, Rosen GD (1999) PG490 (triptolide) cooperates with tumor necrosis factor- α to induce apoptosis in tumor cells. *J Biol Chem* 274: 13451–13455. <https://doi.org/10.1074/jbc.274.19.13451>
- Li J, Wu Y, Wang D, Zou L, Fu C, Zhang J, Leung GP (2019) Oridonin synergistically enhances the anti-tumor efficacy of doxorubicin against aggressive breast cancer via pro-apoptotic and anti-angiogenic effects. *Pharmacol Res* 146: 104313. <https://doi.org/10.1016/j.phrs.2019.104313>
- Li JX, Shi JF, Wu YH, Xu HT, Fu CM, Zhang JM (2021) Mechanisms and application of triptolide against breast cancer. *Zhongguo Zhong Yao Za Zhi* 46: 3249–3256 (in Chinese). <https://doi.org/10.19540/j.cnki.cjcm.20210225.601>
- Li X, Wu C, Chen N, Gu H, Yen A, Cao L, Wang E, Wang L (2016) PI3K/Akt/mTOR signaling pathway and targeted therapy for glioblastoma. *Oncotarget* 7: 33440–33450. <https://doi.org/10.18632/oncotarget.7961>
- Liu X, Zhao P, Wang X, Wang L, Zhu Y, Song Y, Gao W (2019) Celastrol mediates autophagy and apoptosis via the ROS/JNK and Akt/mTOR signaling pathways in glioma cells. *J Exp Clin Cancer Res* 38: 184. <https://doi.org/10.1186/s13046-019-1173-4>
- Lucia MB, Rutella S, Rumi C, Ventura G, Caldarola G, Cauda R (1997) Detection of P-glycoprotein efflux activity on peripheral blood lymphocyte subsets from HIV+ patients. *Eur J Histochem* 41 (Suppl 2): 195–196
- Luiz MT, Tofani LB, Araujo VHS, di Filippo LD, Duarte JL, Marchetti JM, Chorilli M (2021) Gene therapy based on lipid nanoparticles as non-viral vectors for glioma treatment. *Curr Gene Ther* 21: 452–463. <https://doi.org/10.2174/1566523220999201230205126>
- Meng HT, Zhu L, Ni WM, You LS, Jin J, Qian WB (2011) Triptolide inhibits the proliferation of cells from lymphocytic leukemia cell lines in association with downregulation of NF- κ B activity and miR-16-1*. *Acta Pharmacol Sin* 32: 503–511. <https://doi.org/10.1038/aps.2010.237>
- Morshed RA, Young JS, Hervey-Jumper SL, Berger MS (2019) The management of low-grade gliomas in adults. *J Neurosurg Sci* 63: 450–457. <https://doi.org/10.23736/S0390-5616.19.04701-5>
- Nagata S (2018) Apoptosis and clearance of apoptotic cells. *Annu Rev Immunol* 36: 489–517. <https://doi.org/10.1146/annurev-immunol-042617-053010>
- Poff A, Koutnik AP, Egan KM, Sahebiam S, D'Agostino D, Kumar NB (2019) Targeting the Warburg effect for cancer treatment: Ketogenic diets for management of glioma. *Semin Cancer Biol* 56: 135–148. <https://doi.org/10.1016/j.semcancer.2017.12.011>
- Porta C, Paglino C, Mosca A (2014) Targeting PI3K/Akt/mTOR signaling in cancer. *Front Oncol* 4: 64. <https://doi.org/10.3389/fonc.2014.00064>
- Reifenberger G, Wirsching HG, Knobbe-Thomsen CB, Weller M (2017) Advances in the molecular genetics of gliomas – implications for classification and therapy. *Nat Rev Clin Oncol* 14: 434–452. <https://doi.org/10.1038/nrclinonc.2016.204>
- Sturm D, Pfister SM, Jones DTW (2017) Pediatric gliomas: current concepts on diagnosis, biology, and clinical management. *J Clin Oncol* 35: 2370–2377. <https://doi.org/10.1200/JCO.2017.73.0242>
- Wang J (2021) Tripterine and miR-184 show synergy to suppress breast cancer progression. *Biochem Biophys Res Commun* 561: 19–25. <https://doi.org/10.1016/j.bbrc.2021.04.108>
- Wei YS, Adachi I (1991) Inhibitory effect of triptolide on colony formation of breast and stomach cancer cell lines. *Zhongguo Yao Li Xue Bao* 12: 406–410
- Weng W, Goel A (2022) Curcumin and colorectal cancer: An update and current perspective on this natural medicine. *Semin Cancer Biol* 80: 73–86. <https://doi.org/10.1016/j.semcancer.2020.02.011>
- Xia P, Xu XY (2015) PI3K/Akt/mTOR signaling pathway in cancer stem cells: from basic research to clinical application. *Am J Cancer Res* 5: 1602–1609
- Xu S, Tang L, Li X, Fan F, Liu Z (2020) Immunotherapy for glioma: Current management and future application. *Cancer Lett* 476: 1–12. <https://doi.org/10.1016/j.canlet.2020.02.002>
- Xu W, Yang Z, Lu N (2015) A new role for the PI3K/Akt signaling pathway in the epithelial-mesenchymal transition. *Cell Adh Migr* 9: 317–324. <https://doi.org/10.1080/19336918.2015.1016686>
- Yang W, Guastella J, Huang JC, Wang Y, Zhang L, Xue D, Tran M, Woodward R, Kasibhatla S, Tseng B, Drewe J, Cai SX (2003) MX1013, a dipeptide caspase inhibitor with potent *in vivo* antiapoptotic activity. *Br J Pharmacol* 140: 402–412. <https://doi.org/10.1038/sj.bjp.0705450>
- Yang Y, Zhao M, Hu T, Su F, Qian F, Wang Z (2021) Identification of an antitumor effect of demethylzeylasteral on human gastric cancer cells. *Oncol Lett* 21: 49. <https://doi.org/10.3892/ol.2020.12310>
- You L, Dong X, Yin X, Yang C, Leng X, Wang W, Ni J (2018) Rhein induces cell death in HepaRG Cells through cell cycle arrest and apoptotic pathway. *Int J Mol Sci* 19: <https://doi.org/10.3390/ijms19041060>
- Zeng Y, Du WW, Wu Y, Yang Z, Awan FM, Li X, Yang W, Zhang C, Yang Q, Yee A, Chen Y, Yang F, Sun H, Huang R, Yee AJ, Li RK, Wu Z, Backx PH, Yang BB (2017) A circular RNA binds to and activates AKT phosphorylation and nuclear localization reducing apoptosis and enhancing cardiac repair. *Theranostics* 7: 3842–3855. <https://doi.org/10.7150/thno.19764>
- Zhang C, Sun PP, Guo HT, Liu Y, Li J, He XJ, Lu AP (2016) Safety profiles of *Tripterygium wilfordii* Hook F: A systematic review and meta-analysis. *Front Pharmacol* 7: 402. <https://doi.org/10.3389/fphar.2016.00402>
- Zhang LL, Zhang J, Shen L, Xu XM, Yu HG (2013) Overexpression of AKT decreases the chemosensitivity of gastric cancer cells to cisplatin *in vitro* and *in vivo*. *Mol Med Rep* 7: 1387–1390. <https://doi.org/10.3892/mmr.2013.1400>
- Zhou Y, Huang Y, Xu Q, Ye M, Sun C, Zhou D (2002) Several monomers from *Tripterygium wilfordii* inhibit proliferation of glioma cells *in vitro*. *Chin J Cancer* 21: 1106–1108
- Zhu Y, Liu X, Zhao P, Zhao H, Gao W, Wang L (2020) Celastrol suppresses glioma vasculogenic mimicry formation and angiogenesis by blocking the PI3K/Akt/mTOR signaling pathway. *Front Pharmacol* 11: 25. <https://doi.org/10.3389/fphar.2020.00025>

Resveratrol inhibits multiple organ injury in preeclampsia rat model

Xiao Lang^{1,2#}, Wei Liu^{1,2#}, Qinfang Chen^{1,2}, Xingyu Yang^{1,3}, Dan Chen^{1,2} and Weiwei Cheng^{1,2,3}✉

¹The International Peace Maternity and Child Health Hospital, School of Medicine, Shanghai Jiao Tong University, Shanghai, China; ²Shanghai Municipal Key Clinical Specialty, Shanghai, China; ³Shanghai Key Laboratory of Embryo Original Diseases, Shanghai, China

Objective: To investigate the effects of resveratrol on multiple organ injury and energy metabolism and its possible mechanism in preeclampsia model. **Methods:** A total of 45 clean-grade female adults Sprague Dawley (SD) rats (weight 270–320 g) were randomly divided into three groups: a control group, preeclampsia group (PE), and Preeclampsia with resveratrol treatment group (RE). Preeclampsia was induced in rats by administering 200 mg/kg/day L-NAME. Expression levels of TNF- α and IL-6 in the lungs and kidney tissues were analysed by ELISA, while the activity of superoxide dismutase (SOD) and malondialdehyde (MDA) was determined by biochemical assays. The levels of lactic acid and pyruvate were detected using biochemical assays, while the epinephrine level in the kidney and heart tissues was determined by the ELISA method. Reverse transcription polymerase chain reaction and the western blotting were used to detect the expression of pyruvate dehydrogenase kinase 4 (PDK4) in the myocardial tissues. **Results:** We found that resveratrol treatment inhibited the levels of IL-6, TNF- α , and MDA in the lungs and kidney tissues, while the SOD activity was increased. Treatment with resveratrol reduced the levels of lactic acid, pyruvate, and epinephrine in the kidney and heart tissues. Furthermore, resveratrol treatment significantly increases the expression of PDK4 myocardial tissues in RE group compared to PE group. **Conclusion:** Resveratrol may inhibit the release of tissue inflammatory factors, regulate the body's energy metabolism, and ultimately protect tissue damage caused during Preeclampsia.

Key words: preeclampsia, multiple organ injury, resveratrol, inflammatory factors, proteinuria

Received: 21 April, 2022; **revised:** 03 August, 2022; **accepted:** 21 October, 2022; **available on-line:** 03 February, 2023

✉e-mail: wwcheng29@shsmu.edu.cn

[#]These two authors contributed to this work equally

Acknowledgements of Financial Support: This study was supported by the Scientific research project plan of Shanghai Health Commission (No: 202140091), Establishment of preeclampsia-eclampsia cohort database (Clinical Research Plan of SHDC, No: SHDC2020CR6021), the interdisciplinary program of Shanghai Jiao Tong University (No: ZH2018ZDA31)

Abbreviations: COX-2, Cyclic oxygenase; HGF, Hepatocyte growth factor; ICAM-1, Intercellular Cell Adhesion Molecule; IGF-1, Insulin-like growth factor; IL, Interleukin; JNK, Jun N-terminal kinase; L-NAME, N(gamma)-nitro-L-arginine methyl ester; MAPK, Mitogen-Activated Protein Kinase; MMP, Matrix metalloproteinases; NOS, Nitric oxide synthase; PCOS, Polycystic ovarian syndrome; PDC, Pyruvate dehydrogenase complex; ROS, Reactive Oxygen Species; SBP, Systolic blood pressure; SD, Sprague Dawley; TGF- β , Transforming growth factor; TNF- α , Tumour necrosis factor

INTRODUCTION

Pregnancy is associated with many complications like polycystic ovarian syndrome (PCOS), Dysmenorrhea and Preeclampsia. Among them, Preeclampsia is a very fatal and multifactorial disorder and is strongly associated with other entities such as hypertension and proteinuria that can occur within 20 weeks of gestation (Ding *et al.*, 2017). According to the World Health Organization (WHO), only 10% of pregnant women suffer from preeclampsia but the mortality rate associated with the disease can be as high as involving one-seventh of the affected women (Say *et al.*, 2014). The pathogenesis of preeclampsia associated with pregnancy is due to limited perfusion of the placenta causing hypoxia and subsequently apoptosis. The affected placenta in turn causes an increased oxidative stress, leading to the release of the various inflammatory mediators and anti-angiogenic proteins (Roberts & Escudero, 2012). The increased blood pressure demands the need for application of anti-hypertensive drugs, namely Labetalol, Nifedipine and Hydralazine. Compared to other drugs, Nifedipine is safer due to less side effects related to the maternal or fetal development (including control of arterial pressure and maintenance of urine output) (Zuo *et al.*, 2021; Childress & Katz, 1994). Antihypertensive drugs are effective, but some adjuncts can provide additional effects. There are expectations from adjuncts to modify the destructive processes in the body. Among the adjuncts, resveratrol (potent inhibitor of the nuclear factor kappa B-NF- κ B) could prove to be an adjunct to current therapy of preeclampsia. It was found that RE has the capacity to lower the blood pressure along with several other beneficial effects related to promotion of healing and modulation of inflammatory mechanisms (Novakovic *et al.*, 2022).

The origin of resveratrol is purely natural as it is found exclusively in selected products such as red wine, grapes, peanuts, and in limited types of plants. In 1939, RE was extracted for the first time from *Veratrum grandiflorum* and was later, found in dried roots of *Polygonum cuspidatum*. Initially, resveratrol was utilized for the treatment of injuries but later used for to manage various cardiovascular diseases (Novakovic *et al.*, 2022). Resveratrol was initially used to treat injuries but later was also utilized for the management of the cardiovascular diseases (Novakovic *et al.*, 2022). Resveratrol has the capability to repress the p38-Mitogen-Activated Protein Kinase (MAPK)/NF- κ B pathway and produce several Reactive Oxygen Species (ROS) such as anti-angiogenic molecule (FMS-like tyrosine kinase 1 and sFlt-1) through which, it

mediates anti-inflammatory and anti-oxidative stress activities (Zuo *et al.*, 2021; Novakovic *et al.*, 2022).

The evidence present in the past literature shows that resveratrol can also suppress various factors such as Transforming growth factor (TGF- β), Matrix metalloproteinases (MMP), Cyclic oxygenase (COX-2), Tumour necrosis factor (TNF- α), Interleukins (IL-1 β and IL-6), and Intercellular Cell Adhesion Molecule (ICAM-1). The effects of resveratrol can be broadly classified into two major mechanisms. The first one is the p50/p65 mechanism that controls the signaling cascade IKK β /I κ B α and activator protein-1 complex of MAPK/ERK/p38/c-Jun N-terminal kinase (JNK) (Wang *et al.*, 2017). Second mechanism is the inhibition of the p65 subunit translocation but it is based on the experimental model of hepatocarcinogenesis. Basically, resveratrol leads to decrease in two processes namely – phosphorylation (both I κ B and normal) and acetylation (Chavez *et al.*, 2008). Further reduction of I κ B phosphorylation leads to variation in p65 protein levels, causing resveratrol-induced apoptosis. Resveratrol also mediate mi-RNAs by suppressing miR-21 expression and inhibition of the NF- κ B.

Studies have shown some beneficial effects of resveratrol in complicated pregnancies associated with gestational diabetes, malnutrition/obesity, any teratogen exposure or placental insufficiency (Zielinsky & Busato, 2013). It resulted in improvement of sub-optimal fetal development. Even in the treatment of polycystic ovarian syndrome, this product is providing synergistic effects with metformin through *via* SIRT1 and AMPK activation (Pan *et al.*, 2016). It is probably the inherent properties of RE (including the anti-inflammatory and anticancerous capability) which enable it to be a treatment modality for endometriosis. It was found that resveratrol has the potential to discourage the process of invasion, adhesion, and angiogenesis of endometria-related lesions, thereby, slowing the process of inflammation and oxidative stress (Vian *et al.*, 2018). Even with the involvement of eutopic endometrial stromal cells, resveratrol could definitely, cause several valuable effects by altering the gene expression and inhibiting the insulin-like growth factor (IGF-1) and hepatocyte growth factor (HGF) (Taguchi *et al.*, 2016).

The inhibitory effects of resveratrol can prove to be a useful tool for the management of cancers and chronic diseases. Like in diabetes mellitus type 1, resveratrol has been shown to attenuate testicular apoptosis while in terms of respiratory diseases, there is inhibition of LPS-induced inhibition on SIRT1 expression (Novakovic *et al.*, 2022; Pan *et al.*, 2016). In addition to them, there is repression of activation effects of LPS on MAPKs and NF- κ B activation also. Due to the inhibition of inflammatory responses leading to a complete perfusion, the healing of kidney is also promoted. Colorectal cancer is another example associated with induction of apoptosis and resveratrol provides suppression of NF- κ B activation and finally relief to the devastating condition (Chavez *et al.*, 2008). Similarly for Thyroid and breast cancer, resveratrol shows marked improvement by inhibiting the NF- κ B/p65 signaling in which levels of IL-6 and Cyclooxygenase (COX-20) are also affected. Lastly, it induces pancreatic apoptosis so it is also proven to be helpful in prevention of pancreatic cancer.

The NF- κ B plays a mighty part during the treatment of preeclampsia by exhibiting the inflammatory factors. The benefits of resveratrol along with proven clinical studies are useful in managing many clinical problems. These can range from chronic diseases like Diabetes mellitus, Respiratory diseases, Hypertension, Reproduc-

tive problems and lastly, various types of cancers. It has both modulatory and attenuated effects. No doubt we have a variety of medications for all of the above mentioned critical conditions, yet the beneficial effects of resveratrol cannot be matched easily. Hence, resveratrol can be assumed to be a good adjunct for the prevention of complications and therapies of the human diseases including preeclampsia. The present study aims to explore the possible role of resveratrol in inhibiting multiple organ injury in preeclampsia rat model.

MATERIAL AND METHODS

Animal preparation and grouping

A total of 45 healthy female adults Sprague Dawley (SD) rats (weight 270–320 g and aged 2–3 months) and were provided by the Experimental Animal Center of the Shanghai Jiao Tong University (China). The animals were maintained in fully ventilated rooms with free access to pellet diet and fresh water. The photoperiod used for keeping animals was 12 h day and 12 h night cycle. Standard institutional ethical guidelines were followed in performing various experimental procedures on the rats. The rats were divided into three groups: the control group (n=15), Preeclampsia group (PE) (n=15), and Preeclampsia with Resveratrol treatment (RE) group (n=15). The animals received humane care in compliance with the principles of laboratory animal care.

Induction of the animal model

To induce preeclampsia, nitric oxide synthase (NOS) inhibitor namely N(gamma)-nitro-L-arginine methyl ester (L-NAME) (obtained from Sigma-Aldrich) at the dose of 200 mg/kg/day was administered to the rats. Resveratrol, dissolved in distilled water were given to rats at the doses of 20 mg/kg/day orally by oral gavage for 4 weeks. Systolic blood pressure (SBP) was monitored continuously through the experimental period by using a blood pressure recorder using tail-cuff method. The protein level in urine (proteinuria) was measured by the Coomassie blue method.

After completion of experimental periods, rats were sacrificed using pentobarbital sodium anesthesia. The livers, kidneys and hearts were collected rapidly and prepared for mRNA and protein extraction.

TNF- α , IL-6, MDA, and SOD detection

In accordance with the instructions on the operating kits, enzyme-linked immunoassay (ELISA) (SOLARBIO, China) was used to detect TNF- α and IL-6 in the kidney and myocardial tissues, the xanthine oxidase method (Sun *et al.*, 1988) was used to detect the content and activity of SOD, and the thiobarbiturates method (Draper *et al.*, 1993) was used to determine the MDA content. The SOD and MDA content in the lung and kidney tissues were calculated according to the formula and Coomassie Brilliant Blue detect protein content.

Detection of lactic acid, pyruvate, and epinephrine levels

In accordance with the instructions on the operating kits, biochemical methods were used to detect lactic acid and pyruvate levels, and ELISA was used to detect epinephrine levels in the heart and kidney tissues.

Reverse transcription polymerase chain reaction (RT-PCR)

RNA from tissues were obtained using TRIzol method and then reversed to cDNA with RT Kit. Quantitative PCR was carried out using SYBRGreen (Takara) with appropriate primers designed by Primer 5.0 according to the conditions, including an initial step of 10 minute in 95°C, and then 40 cycles of amplification, which includes 10 s in 95°C, 20 s in 55°C and 25 s in 72°C. Quantification was determined by $2^{-\Delta\Delta CT}$ (Livak & Schmittgen, 2001). The internal control used was GAPDH.

Western blot

The tissue was treated with RIPA lysis buffer for the isolation of total cellular proteins. Following, the protein concentrations were determined with Bradford method. From each sample, 45 μ g of proteins were loaded and run on SDS-PAGE gels which were processed for blotting to PVDF membranes followed by exposure to primary and secondary antibodies and finally the protein bands of interest were visualized with the help of efficient chemiluminescence reagent. Primary antibodies were directed against PDK4. The GAPDH gene was used as internal control. Primary antibody treatment was followed by secondary antibody treatment overnight at 4°C. Finally, enhanced chemiluminescence (ECL) reagent was used to detect the protein signals.

Statistical analysis

Values presented in the study are the mean of three biological replicates \pm S.D., calculated from atleast three experimental replicas. ANOVA, Student's *t*-test and Duncan's test were used to estimate the significance of the statistical difference between two/among many data points. The at $p < 0.05$ was considered as statistically significant difference.

RESULTS

Resveratrol Ameliorated Hypertension and Proteinuria in Preeclampsia group (PRE)

The control group (saline) exhibited stable SBP throughout experimental period. However, in the PRE rats, we observed significantly increased SBP. Interestingly, in (RE) group, a reverse effect was observed compared to the PE group.

Furthermore, the PRE group exhibited enhanced proteinuria, a clinical marker of renal malfunction) associated with PRE compared to control group. Interestingly, in (RE) group, a reverse effect on proteinuria was observed compared to the PE group.

TNF- α and IL-6 expression level

The expression of the inflammatory factor TNF- α in the kidney and myocardial tissues was lower in the control group than in the other two groups. The TNF- α expression in the kidney and myocardial tissues in the (PE) group increased significantly and was significantly lower in the (RE) group than in the LPS group ($P < 0.05$). The concentration of IL-6 was higher in the (PE) than in the control group ($P < 0.05$), but the administration of Resveratrol downregulated IL-6 production ($P < 0.05$; see Fig. 1).

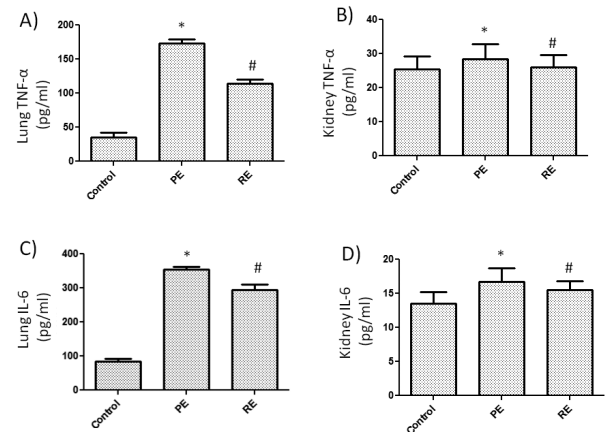


Figure 1. The expression of TNF- α and IL-6 in the lung and kidney tissues of rats.

* $P < 0.05$ for comparison with the corresponding tissue of the control group, and # $P < 0.05$ for comparison with the corresponding tissue of the preeclampsia group.

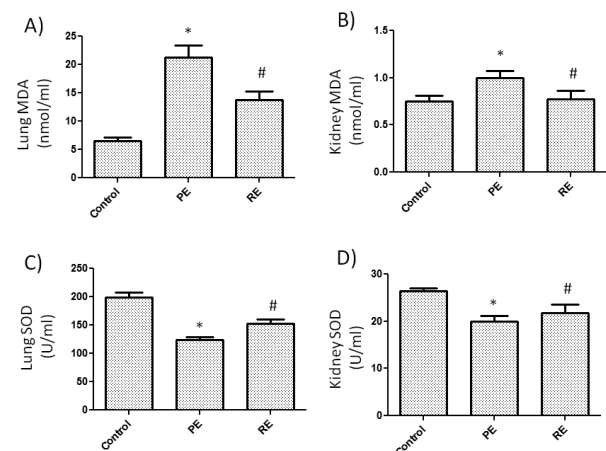


Figure 2. Malondialdehyde and superoxide dismutase levels in the lung and kidney tissues of rats.

* $P < 0.05$ for comparison with the corresponding tissue of the control group, and # $P < 0.05$ for comparison with the corresponding tissue of the preeclampsia group.

MDA and SOD levels

When compared with the control group, the MDA level was higher ($P < 0.05$), and the SOD level was significantly lower in the (PE) group ($P < 0.05$). When compared with the (PE) group, the MDA level was significantly lower ($P < 0.05$), and the SOD level was higher in the (RE) group ($P > 0.05$) (see Fig. 2).

Lactic acid, pyruvate, and epinephrine expression in the heart and kidney tissues

In order to study the effect of Resveratrol on organ metabolic damage induced by preeclampsia, the lactic acid, pyruvate, and epinephrine levels were measured in the heart and kidney tissues.

Lactic acid expression: The lactic acid level in the PE group was significantly higher than the control group ($P < 0.05$), but there was no significant difference in this level between the RE group and the control group.

Pyruvate expression: The pyruvate level in the PE group was significantly higher than the control group

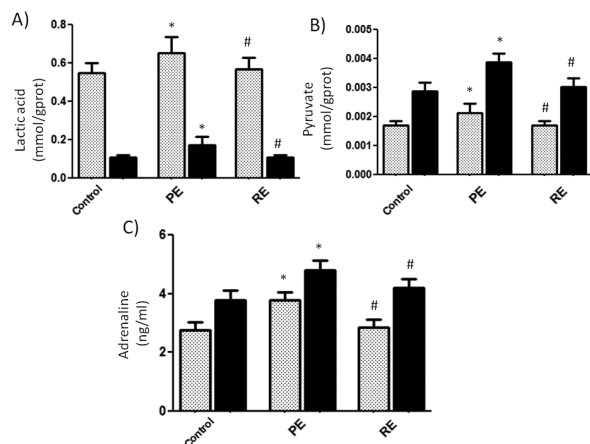


Figure 3. Lactic acid, pyruvate, and epinephrine expression in the heart and kidney tissues of rats.

* $P < 0.05$ for comparison with the corresponding tissue of the control group, and # $P < 0.05$ for comparison with the corresponding tissue of the preeclampsia group.

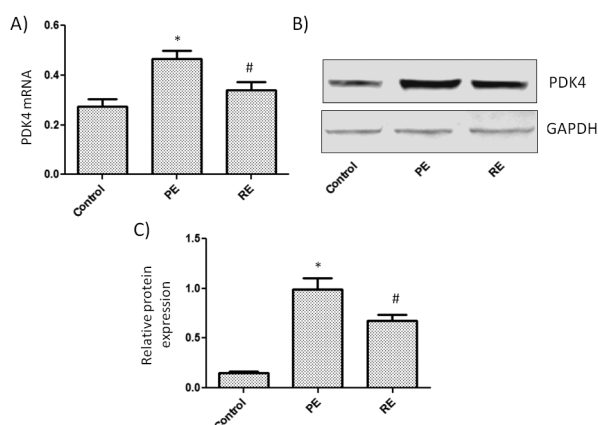


Figure 4. Pyruvate dehydrogenase kinase 4 expression in the myocardial tissue of rats.

* $P < 0.05$ for comparison with the corresponding tissue of the control group, and # $P < 0.05$ for comparison with the corresponding tissue of the preeclampsia group.

($P < 0.05$), but administration of Resveratrol downregulated the pyruvate level ($P < 0.05$).

Epinephrine expression: The epinephrine level in the PE group was significantly higher than the control group ($P < 0.05$), but administration of Resveratrol downregulated the pyruvate level ($P < 0.05$; see Fig. 3).

PDK4 expression in the heart tissue

The mRNA and protein expression levels of PDK4 were highest in the PE group compared to control. It was significantly lowered in the RE group than in the PE group ($P < 0.05$; see Fig. 4).

DISCUSSION

In the present study, the effects of Resveratrol on inflammatory cytokines and the energy metabolism disorder were evaluated in a preeclampsia rat model. We observed that Resveratrol had protective effects, as evidenced by the suppression of the expression and release of inflammatory cytokines and the regulation of energy metabolic indicators in preeclampsia rats.

Systemic inflammation plays a key role in the occurrence and development of multiple organ injury (Menden *et al.*, 2015). Endotoxin activates macrophages and monocytes, leading to an inflammatory cascade in which large quantities of inflammatory mediators, such as interleukins and TNF- α , are produced and released. Inflammatory mediators cause damage to alveolar epithelial cells, pulmonary capillary epithelial cells, and renal endothelial cells, leading to the progression of injury. Several cytokines have been implicated in the pathogenesis of preeclampsia (Conrad & Benyo, 1997). TNF- α is an important initiating factor that mediates endotoxic shock, systemic inflammatory response syndrome, and organ injury (Susantitaphong *et al.*, 2013). TNF- α damages lysosomes; causes enzymes to leak; promotes the migration of leukocytes to the site of inflammation; induces endothelial cells and macrophages to synthesize and release IL-1, IL-6, IL-8, superoxide, and lysosome; and promotes inflammation, the metabolism of arachidonic acid, the production of lipid mediators, and the formation of microthrombosis, which lead to lung and kidney damage. IL-6 is also an important inflammatory factor that is secreted in large quantities in the lungs and blood of patients with multiple organ injury. IL-6 levels in patients with multiple organ injury are significantly higher than in healthy people and can reflect the degree of lung tissue damage. IL-6 participates in the differentiation and infiltration of macrophages, which can induce the production of complement and C-reactive protein, vascular endothelial cells, and lymphocytes and participate in the acute phase response of lung and kidney injury (Hattar *et al.*, 2001). Therefore, inhibiting the production of cytokines is an effective means of treating inflammatory diseases. This study showed that during preeclampsia, a significant increase in the levels of TNF- α and IL-6 in lung and kidney tissues, and Resveratrol can reduce multiple organ dysfunction caused by preeclampsia by reducing the levels of the pro-inflammatory factors TNF- α and IL-6.

At the onset and during the development of preeclampsia, redox damage caused by oxygen free radicals is one of the important causes of multiple organ dysfunction (Gupte & Wagh, 2014). In preeclampsia, many oxygen free radicals attack the polyunsaturated fatty acids in the biofilm, triggering lipid peroxidation and forming a large quantity of the lipid peroxidation product MDA. MDA is lipid peroxide and a marker of oxidative stress and antioxidant status. MDA levels can reflect the severity of the attack of oxygen free radicals on the body. SOD is a natural scavenger of oxygen free radicals in organisms and can scavenge superoxide anions and free radicals to protect cells from damage. SOD levels can indirectly reflect the body's ability to scavenge oxygen free radicals, and maintains body's oxidation and antioxidant balance. The combined detection of SOD and MDA can accurately reflect the oxidative stress state and represent the degree of tissue damage.

This study found that when compared with the control group, MDA levels in the lung and kidney tissues of the Preeclampsia group (PR) group were significantly higher and SOD levels were significantly lower, suggesting that Preeclampsia caused oxidative stress damage to these tissues. Resveratrol can increase SOD levels and reduce MDA levels, suggesting that Resveratrol can reduce the production of oxygen free radicals, improve the body's antioxidant capacity, and inhibit the oxidative stress damage caused by Preeclampsia.

Hyperlactic acidemia is considered to be a sign of oxygen debt, systemic hypoxia, and anaerobic metabolism. Elevated lactic acid levels represent an energy metabolism disorder, and decreased levels of lactic acid signify

an improvement in tissue hypoxia and energy metabolism (Husain *et al.*, 2003). Pyruvate is the direct and sole precursor of lactic acid, the end product of glycolysis, and the starter of the tricarboxylic acid cycle. Elevated pyruvate levels may be a consequence of reduced oxygen delivery (ischemic hypoxia) and reflect mitochondrial dysfunction (Hajjej *et al.*, 2017). Both lactic acid and pyruvate are the products of glucose metabolism and abnormalities can reflect a disorder in energy metabolism.

Myocardial dysfunction is a common complication of Preeclampsia (Melchiorre *et al.*, 2012). PDK4 is a key enzyme that regulates the pyruvate dehydrogenase complex (PDC). In some cases, the overexpression of PDK4 can lead to PDC inactivation, mitochondrial dysfunction, and negative health consequences (Jeon *et al.*, 2021). Energy metabolism disorder is one of the important causes of myocardial damage in Preeclampsia (Hu *et al.*, 2022). This study found that when compared with the control group, the lactic acid and pyruvate levels and the PDK4 gene and protein expression in the myocardial tissue were significantly higher in the Preeclampsia group, which suggests that Preeclampsia leads to increased anaerobic glycolysis in the heart and kidney tissues, causes glucose metabolism disorders, and results in the accumulation of lactic acid and pyruvate, which aggravate heart and kidney dysfunction. The results demonstrated that Resveratrol downregulated the excessive expression of the PDK4 and reduced the content of lactic acid and pyruvate in the heart and kidney tissues. Therefore, Resveratrol can reduce heart and kidney dysfunction induced by preeclampsia by regulating energy metabolism.

In the present study, we deduced that Resveratrol could decrease the exaggerated inflammatory response during preeclampsia conditions. Therefore, Resveratrol may be advantageous as a potential therapeutic agent for patients with preeclampsia.

CONCLUSIONS

In summary, Resveratrol can protect against multiple organ injury caused by preeclampsia by reducing the expression of anti-inflammatory cytokines and through the anti-oxidative stress pathway. Resveratrol can also inhibit the body's stress response, improve energy metabolism, and protect the heart tissue from preeclampsia. Therefore, Resveratrol is worthy of further investigation as a potential intervention strategy for preeclampsia in preeclampsia. Further studies are required to elucidate the precise mechanism of its protective action.

Declarations

Conflict of interest. The authors declare no conflict of interest.

REFERENCES

- Chavez E, Reyes-Gordillo K, Segovia J, Shibayama M, Tsutsumi Y, Vergara P, Moreno MG, Muriel P (2008) Resveratrol prevents fibrosis, NF-kappaB activation and TGF-beta increases induced by chronic CCl4 treatment in rats. *J Appl Toxicol* **28**: 35–43. <https://doi.org/10.1002/jat.1249>
- Childress CH, Katz VL (1994) Nifedipine and its indications in obstetrics and gynecology. *Obstet Gynecol* **83**: 616–624. <https://doi.org/10.1097/00006250-199404000-00024>
- Conrad KP, Benyo DF (1997) Placental cytokines and the pathogenesis of preeclampsia. *Am J Reprod Immunol* **37**: 240–249. <https://doi.org/10.1111/j.1600-0897.1997.tb00222.x>
- Ding J, Kang Y, Fan Y, Chen Q (2017) Efficacy of resveratrol to supplement oral nifedipine treatment in pregnancy-induced preeclampsia. *Endocr Connect* **6**: 595–600. <https://doi.org/10.1530/EC-17-0130>
- Draper HH, Squires EJ, Mahmoodi H, Wu J, Agarwal S, Hadley M (1993) A comparative evaluation of thiobarbituric acid methods for the determination of malondialdehyde in biological materials. *Free Radic Biol Med* **15**: 353–363. [https://doi.org/10.1016/0891-5849\(93\)90035-s](https://doi.org/10.1016/0891-5849(93)90035-s)
- Gupte S, Wagh G (2014) Preeclampsia-eclampsia. *J Obstet Gynaecol India* **64**: 4–13. <https://doi.org/10.1007/s13224-014-0502-y>
- Hajjej Z, Meddeb B, Sellami W, Labbene I, Morelli A, Ferjani M (2017) Effects of levosimendan on cellular metabolic alterations in patients with septic shock: a randomized controlled pilot study. *Shock* **48**: 307–312. <https://doi.org/10.1097/SHK.0000000000000851>
- Hattar K, Fink L, Fietzner K, Himmel B, Grimminger F, Seeger W, Sibelius U (2001) Cell density regulates neutrophil IL-8 synthesis: role of IL-1 receptor antagonist and soluble TNF receptors. *J Immunol* **166**: 6287–6293. <https://doi.org/10.4049/jimmunol.166.10.6287>
- Hu M, Li J, Baker PN, Tong C (2022) Revisiting preeclampsia: a metabolic disorder of the placenta. *FEBS J* **289**: 336–354. <https://doi.org/10.1111/febs.15745>
- Husain FA, Martin MJ, Mullenix PS, Steele SR, Elliott DC (2003) Serum lactate and base deficit as predictors of mortality and morbidity. *Am J Surg* **185**: 485–491. [https://doi.org/10.1016/s0002-9610\(03\)00044-8](https://doi.org/10.1016/s0002-9610(03)00044-8)
- Jeon JH, Thoudam T, Choi EJ, Kim MJ, Harris RA, Lee IK (2021) Loss of metabolic flexibility as a result of overexpression of pyruvate dehydrogenase kinases in muscle, liver and the immune system: Therapeutic targets in metabolic diseases. *J Diabetes Investig* **12**: 21–31. <https://doi.org/10.1111/jdi.13345>
- Livak KJ, Schmittgen TD (2001) Analysis of relative gene expression data using real-time quantitative PCR and the 2(-Delta Delta C(T)) Method. *Methods* **25**: 402–408. <https://doi.org/10.1006/meth.2001.1262>
- Melchiorre K, Sutherland GR, Watt-Coote I, Liberati M, Thilaganathan B (2012) Severe myocardial impairment and chamber dysfunction in preterm preeclampsia. *Hypertens Pregnancy* **31**: 454–471. <https://doi.org/10.3109/10641955.2012.697951>
- Menden H, Welak S, Cossette S, Ramchandran R, Sampath V (2015) Lipopolysaccharide (LPS)-mediated angiotensin-2-dependent autocrine angiogenesis is regulated by NADPH oxidase 2 (Nox2) in human pulmonary microvascular endothelial cells. *J Biol Chem* **290**: 5449–5461. <https://doi.org/10.1074/jbc.M114.600692>
- Novakovic R, Rajkovic J, Gostimirovic M, Gojkovic-Bukarica L, Radunovic N (2022) Resveratrol and Reproductive Health. *Life (Basel)* **12**: 294. <https://doi.org/10.3390/life12020294>
- Pan W, Yu H, Huang S, Zhu P (2016) Resveratrol protects against TNF-alpha-induced injury in human umbilical endothelial cells through promoting sirtuin-1-induced repression of NF-KB and p38 MAPK. *PLoS One* **11**: e0147034. <https://doi.org/10.1371/journal.pone.0147034>
- Roberts JM, Escudero C (2012) The placenta in preeclampsia. *Pregnancy Hypertens* **2**: 72–83. <https://doi.org/10.1016/j.preghy.2012.01.001>
- Say L, Chou D, Gemmill A, Tuncalp O, Moller AB, Daniels J, Gulmezoglu AM, Temmerman M, Alkema L (2014) Global causes of maternal death: a WHO systematic analysis. *Lancet Glob Health* **2**: e323–e333. [https://doi.org/10.1016/S2214-109X\(14\)70227-X](https://doi.org/10.1016/S2214-109X(14)70227-X)
- Sun Y, Oberley LW, Li Y (1988) A simple method for clinical assay of superoxide dismutase. *Clin Chem* **34**: 497–500. PMID: 3349599
- Susantitaphong P, Perianayagam MC, Tighiouart H, Liangos O, Bonventre JV, Jaber BL (2013) Tumor necrosis factor alpha promoter polymorphism and severity of acute kidney injury. *Nephron Clin Pract* **123**: 67–73. <https://doi.org/10.1159/000351684>
- Taguchi A, Koga K, Kawana K, Makabe T, Sue F, Miyashita M, Yoshida M, Umeta Y, Izumi G, Tkamura M, Harada M, Hirata T, Hirota Y, Wada-Hiraike O, Fujii T, Osuga Y (2016) Resveratrol enhances apoptosis in endometriotic stromal cells. *Am J Reprod Immunol* **75**: 486–492. <https://doi.org/10.1111/aji.12489>
- Vian I, Zielinsky P, Zilio AM, Schaun MI, Brum C, Lampert KV, De Ávila N, Baldissera G, Klanovics TM, Zenki K, Zurita-Peralta J, Olszewski A, Piccoli A Jr, Nicoloso LH, Sulis N, Van Der Sand L, Markoski M (2018) Increase of prostaglandin E2 in the reversal of fetal ductal constriction after polyphenol restriction. *Ultrasound Obstet Gynecol* **52**: 617–622. <https://doi.org/10.1002/uog.18974>
- Wang N, Mao L, Yang L, Zou J, Liu K, Liu M, Zhang H, Xiao X, Wang K (2017) Resveratrol protects against early polymicrobial sepsis-induced acute kidney injury through inhibiting endoplasmic reticulum stress-activated NF-kappaB pathway. *Oncotarget* **8**: 36449–36461. <https://doi.org/10.18632/oncotarget.16860>
- Zielinsky P, Busato S (2013) Prenatal effects of maternal consumption of polyphenol-rich foods in late pregnancy upon fetal ductus arteriosus. *Birth Defects Res C Embryo Today* **99**: 256–274. <https://doi.org/10.1002/bdrc.21051>
- Zuo Q, Zou Y, Huang S, Wang T, Xu Y, Zhang T, Zhang M, Ge Z, Jiang Z (2021) Aspirin reduces sFlt-1-mediated apoptosis of trophoblast cells in preeclampsia. *Mol Hum Reprod* **27**: gaaa089. <https://doi.org/10.1093/molehr/gaaa089>

Lipid disorders before and after successful liver transplantation

Damian Gojowy¹, Joanna Urbaniec-Stompor¹, Joanna Adamusik¹, Gabriela Wójcik¹, Henryk Karkoszka¹, Robert Krol², Andrzej Wiecek¹ and Marcin Adamczak¹✉

¹Department of Nephrology, Transplantation and Internal Medicine, Medical University of Silesia, Katowice, Poland; ²Department of General, Vascular and Transplant Surgery, Medical University of Silesia, Katowice, Poland

Introduction: Liver transplantation (LTx) is the only successful treatment for end-stage liver disease. The results of liver transplantation depend not only on graft survival but may be also affected by superimposed cardiovascular morbidities. The aim of this retrospective study was to assess the prevalence of lipid disorders as one of the important cardiovascular risk factors in patients before and after successful LTx. **Material and Methods:** One hundred eleven patients who underwent liver transplantation because of liver cirrhosis and survived at least 2 years with functioning graft between November 2005 and May 2014 were included in this retrospective analysis. The mean age of the patients at the time of liver transplantation was 49.7 ± 12.2 years. The prevalence of dyslipidemia was assessed before and two years after liver transplantation. This was analyzed in relation to the etiology of liver disease, including alcohol toxicity, viral or autoimmune diseases. **Results:** The prevalence of hypertriglyceridemia before and after LTx was 13.5% and 40.5%, respectively ($P < 0.001$). Similarly, hypercholesterolemia was noted in 17.1% and 51.4% respectively ($P < 0.001$). The annual incidence of hypertriglyceridemia and hypercholesterolemia during the first two years after LTx was 16.2% and 20.7%, respectively. The prevalence of hypertriglyceridemia (18.5% vs 66.7%, $P < 0.001$) and hypercholesterolemia (29.6% vs 70.0%, $P = 0.002$) was significantly lower in patients with the autoimmune cause of liver cirrhosis in comparison to patients with the alcoholic liver disease. **Conclusions:** The prevalence of dyslipidemia is increased after liver transplantation. The prevalence of dyslipidemia may be related to the cause of liver injury before LTx.

Keywords: dyslipidemia, hypertriglyceridemia, hypercholesterolemia, cardiovascular risk factors, liver transplantation

Received: 17 February, 2023; **revised:** 20 November, 2023; **accepted:** 20 November, 2023; **available on-line:** 03 December, 2023

✉ e-mail: madamczak1@op.pl

Acknowledgements of Financial Support: This work was supported by the Medical University of Silesia in Katowice, Poland (PCN-1-117/N/O/K).

Abbreviations: BMI, body mass index; MELD, Model of End-Stage Liver Disease; LTx, liver transplantation

INTRODUCTION

Liver transplantation is the only successful method for the treatment of end-stage liver disease. In the last decade in Poland, about 300 patients underwent liver transplantation every year (Poltransplant, 2022). The most common indications for liver transplantation in our population included end-stage liver disease caused by infectious hepatitis, autoimmune or alcoholic liver disease.

Despite decreasing the risk of early graft failure, due to improving surgical techniques and immunosuppressive therapy, in the last three decades, long-time survival in liver transplant recipients has not substantially improved (Rana *et al.*, 2019). Therefore currently transplant community focus has shifted to maximizing long-term survival after transplantation. The results of liver transplantation not only depend on graft survival but may be affected by superimposed cardiovascular morbidities. It has been shown that cardiovascular diseases are one of the most frequent causes of premature death in patients after liver transplantation (Berenguer *et al.*, 2002; Watt *et al.*, 2010). Current immunosuppressive drugs are very effective in preventing acute rejection of transplanted organs. However, it is well-recognized that some of these drugs, like tacrolimus or steroids, result in increased rates of hypertension, diabetes, and dyslipidemia (Gojowy *et al.*, 2016). Watt *et al.*, in long-term follow-up of liver transplant recipients, have shown that some well-known cardiovascular risk factors like hypertension or diabetes mellitus may be directly or indirectly involved in premature death in patients who survive one year after liver transplantation (Watt *et al.*, 2010). According to this observation, routine screening of cardiovascular risk factors seems to be an essential component of comprehensive post-transplant care for these patients. Population studies in Poland have shown that cardiovascular risk factors are common and hypercholesterolemia is present in 61.1–64.3% of the Polish adult population (Zdrojewski *et al.*, 2013; Stepniak *et al.*, 2016; Niklas *et al.*, 2018; Rutkowski *et al.*, 2020).

The current paper presents the results of a retrospective study which aimed to assess the prevalence of lipid disorders before and after successful liver transplantation.

MATERIAL AND METHODS

This retrospective, single-center study involved 111 patients (47 female, 64 male) aged 49.7 ± 12.2 years who underwent liver transplantation because of liver cirrhosis in years 2005 to 2014 in the Department of General, Vascular and Transplant Surgery of the Medical University of Silesia in Katowice, Poland and who survived with functioning transplanted liver for at least 24 months. Patients who died or had liver re-transplantation before 24 months of observation were not included in the analysis. All transplantations were performed using cadaveric organs. After transplantation, patients were followed up in the Transplantation Outpatient Clinic of the Department of Nephrology, Transplantation and Internal Medicine Medical University of Silesia in Katowice, Poland. The median MELD score at the time of qualifica-

tion for liver transplantation was 14.0 (9.0;19.1). A retrospective analysis of the patients' medical history was performed.

In all patients, serum concentrations of total cholesterol and triglycerides, as well as doses and concentrations of immunosuppressive drugs were analyzed. Hypertriglyceridemia was diagnosed when triglycerides serum concentration was ≥ 1.7 mmol/L (150 mg/dL) or triglycerides-lowering treatment (i.e. one of the fibrates) was used. In such patients triglycerides serum concentration ≥ 1.7 mmol/L (150 mg/dL) was documented before initiation of this therapy. Hypercholesterolemia was defined as a total serum cholesterol concentration was ≥ 5.0 mmol/L (190 mg/dL) or cholesterol-lowering pharmacological treatment was used (i.e. one of statins or fibrates). In such patients, serum cholesterol concentration ≥ 5.0 mmol/L (190 mg/dL) was documented before initiation of this therapy. Because of the retrospective character of the current study due to the lack of data, the analysis of serum cholesterol fractions was not possible. Prevalence of lipid disorders was assessed a short time before liver transplantation (up to 6 months before the procedure) and two years after transplantation. Moreover, the annual incidence of these abnormalities during the first two years after liver transplantation was analyzed.

Etiology of liver disease

Thirty-seven patients had viral hepatitis as a cause of liver failure (among them, 28 patients suffered from hepatitis C, and 9 from hepatitis B infection); alcoholic liver disease was a cause of liver failure in 30 patients; autoimmune diseases in 27 patients (among them primary sclerosing cholangitis – 11 patients, autoimmune hepatitis – 9 patients, primary biliary cirrhosis – 5 patients, autoimmune hepatitis and primary sclerosing cholangitis overlapping syndrome – 2 patients) and others (17 cases).

Immunosuppressive treatment

Two years after liver transplantation, 90% of studied patients were treated with calcineurin inhibitors. Ninety-one patients (82% of all studied patients) received tacrolimus, and 9 patients (8% of all studied patients) received cyclosporine A. Eleven patients (10% of the studied patients) were treated with everolimus. Prednisone was used in 102 patients (92% of the studied patients), mainly in the dose of 5–15 mg/day. Thirty-seven patients (33% of the studied patients) were treated with mycophenolates. In three patients within 24 months after liver transplantation, the acute rejection of the transplanted liver was diagnosed only by clinical manifestation and treated with a high dose of intravenous methylprednisolone. None of these patients had a biopsy of the transplanted liver. In another two patients, it was necessary to transiently increase the prednisone dose to 60 mg/day in the early period after liver transplantation.

Statistical analysis

Statistical analysis was done using the Statistica 13.3 software (StatSoft). The Shapiro-Wilk test was used to determine the normality of distribution. Mann-Whitney U, chi-square tests, and Spearman's rank correlation were used in this study. The level of statistical significance is $\alpha=0.05$. Results were presented as a mean and standard deviation for the parametric distribution of variables and

as a median with an interquartile range for the non-parametric distribution of variables.

Ethics

Because of the retrospective character of the study, ethics committee consent was not required.

RESULTS

Hypertriglyceridemia before liver transplantation was found in 13.5% of patients. The prevalence of hypertriglyceridemia two years after liver transplantation was significantly higher – 40.5% (36.2% in females, 43.8% in males) ($P<0.001$). The annual incidence of new-onset hypertriglyceridemia in the first two years after liver transplantation was 16.2%. It has been shown a significant positive correlation between serum triglycerides concentration and the age of liver transplant recipients ($R=0.27$, $P=0.003$). Serum total cholesterol concentration was elevated above the normal range in 17% of patients before liver transplantation. After liver transplantation in 57 (51.4%) patients (51.0% of females, 51.6% of males) hypercholesterolemia was found ($P<0.001$) (Table 1). The annual incidence of new-onset hypercholesterolemia in the first two years after liver transplantation was 20.7%. It has been shown a correlation between serum total cholesterol concentration and the age of liver transplant recipients ($R=0.25$, $P=0.008$).

There was no significant correlation between MELD score before LTx and serum triglycerides and total cholesterol serum concentration before and 24 months after LTx. There were also no significant differences in MELD score before LTx between patients with and without diagnosis of any type of dyslipidemias before and 24 months after LTx.

Before LTx, none of the patients were treated with lipid-lowering therapy. Only 7 patients were treated with lipid-lowering therapy two years after LTx (3 received statins, 3 received fibrates, and one patient was treated with both drugs from the above-mentioned group of agents). Patients were not treated with other lipid-lowering drugs (i.e. ezetimibe). Hypercholesterolemia was diagnosed in three patients with normal serum total cholesterol concentration at the time of examination (i.e. 2 years after LTx) treated with lipid-lowering therapy (1 with statin and 2 with fibrates). Hypertriglyceridemia was diagnosed in one patient with normal triglycerides serum concentration at the time of examination (i.e. 2 years after LTx) treated with fenofibrate.

Immunosuppressive drugs and lipid disorders

Our study showed no significant differences in the prevalence of hypertriglyceridemia in patients treated with tacrolimus, cyclosporine A, and everolimus (40%, 33%, and 55%, respectively). There was a significant difference in the prevalence of hypercholesterolemia in patients treated with everolimus, tacrolimus and cyclosporine (91%, 45%, and 66%, respectively, $P=0.01$; everolimus vs. tacrolimus $P=0.002$). Prevalence of hypercholesterolemia and hypertriglyceridemia in patients treated and not treated with mycophenolates was 46% vs. 54% and 35% vs. 43%, respectively (differences in the above-mentioned prevalence were not significant).

There were no significant correlations between serum total cholesterol as well as triglycerides concentration and blood tacrolimus concentration (Figs 1 and 2),

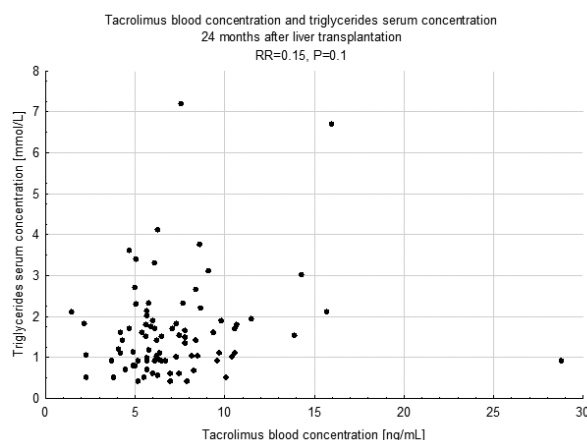


Figure 1. Tacrolimus blood concentration and triglycerides serum concentration 24 months after liver transplantation.

as well as mycophenolate and prednisone dose in liver transplant recipients.

Etiology of liver failure and lipid disorders

In an additional analysis, patients were divided into three groups - alcohol, viral and autoimmune diseases. Patients with the autoimmune disease were characterized by a significantly lower prevalence of hypercholesterolemia than patients with alcoholic disease of the native liver (29.6% *vs.* 70.0%, $P=0.002$). There was also a significantly higher prevalence of hypertriglyceridemia in patients with alcoholic liver disease than in patients with an autoimmune background (66.6% *vs.* 18.5%, $P<0.001$). The annual incidence of new-onset hypertriglyceridemia (9.3%, 13.5%, 30.0%; $P=0.001$; autoimmune *vs.* alcohol - $P=0.001$, viral *vs.* alcohol $P=0.006$) and new-onset hypercholesterolemia (13.0%, 20.3%, 28.3%; $P=0.06$; autoimmune *vs.* alcohol - $P=0.01$), were in autoimmune, viral and alcoholic liver disease, respectively (Table 2).

There was a correlation between triglycerides serum concentration and body weight as well as triglycerides serum concentration and BMI in 24 months after liver transplantation ($R=0.34$, $P<0.001$ and $R=0.32$, $P<0.001$, respectively). There was also a correlation between gain of body mass as well as gain of BMI before and 24

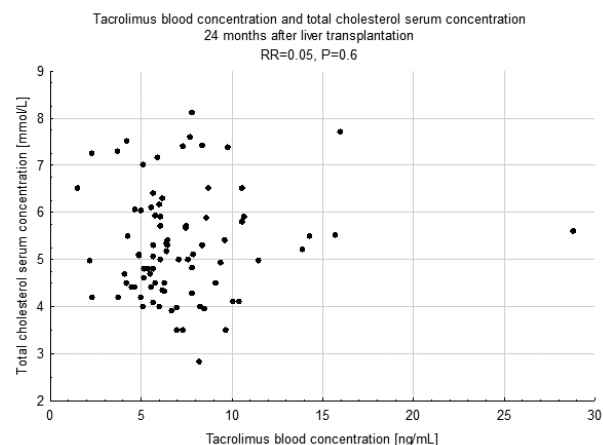


Figure 2. Tacrolimus blood concentration and total cholesterol serum concentration 24 months after liver transplantation.

months after liver transplantation and triglycerides serum concentration 24 months after LTx ($R=0.22$, $P=0.02$ and $R=0.20$, $P=0.03$, respectively). There was also a trend of correlation between total cholesterol serum concentration and body weight ($R=0.19$, $P=0.05$) and a correlation between total cholesterol serum concentration and BMI in 24 months after liver transplantation ($R=0.20$, $P=0.03$). There was also a trend of correlation between gain of body mass as well as gain of BMI before and 24 months after liver transplantation and total cholesterol serum concentration 24 months after LTx ($R=0.16$, $P=0.09$ and $R=0.17$, $P=0.08$, respectively). Patients with hypertriglyceridemia had higher BMI in comparison with patients without that disorder (28.1 ± 5.4 *vs.* 26.2 ± 4.1 kg/m²; $P=0.03$). There was no significant difference in BMI in patients with and without hypercholesterolemia (27.6 ± 5.0 *vs.* 26.3 ± 4.5 kg/m²).

DISCUSSION

The prevalence of lipid disorders increased over a 2-year survey of patients undergoing liver transplantation at our facility. According to available data prevalence of dyslipidemia in liver transplant recipients varies widely among studies, and it is present in 14–71% of patients

Table 1. Prevalence of lipid disorders before and after liver transplantation

	Before liver transplantation			After liver transplantation		
	All (n=111)	Male (n=64)	Female (n=47)	All (n=111)	Male (n=64)	Female (n=47)
Hypercholesterolemia	19 (17%)	7 (11%)	12 (25%)	55 (51%)*	33 (52%)	24 (51%)
Hypertriglyceridemia	15 (14%)	6 (9%)	9 (19%)	45 (41%)*	28 (44%)	17 (36%)

* $P<0.001$ *vs.* before liver transplantation

Table 2. Lipid disorders prevalence and etiology of liver cirrhosis

Cardiovascular risk factor (24 months after LTx)	Autoimmune (n=27)	Viral (n=37)	Alcoholic (n=30)	P-value
Hypercholesterolemia	8 (30%)	20 (54%)	21 (70%)	$P=0.05^*$ $P=0.02^+$ NS ^x
Hypertriglyceridemia	5 (19%)	15 (41%)	20 (67%)	NS [*] $P<0.001^+$ $P=0.03^x$

*autoimmune *vs.* viral; +autoimmune *vs.* alcoholic; ^xviral *vs.* alcoholic

(Clart *et al.*, 1996; Gisbert *et al.*, 1997; Kallwitz *et al.*, 2012; Niklas *et al.*, 2018). In the current study, 51.4% of patients presented hypercholesterolemia two years after liver transplantation. It is less than in the general adult Polish population (results of NATPOL 2011 61.1% and WOBASZ II – 64.3% studies) (Zdrojewski *et al.*, 2013; Rutkowski *et al.*, 2020). An opposite tendency is in the case of hypertriglyceridemia. In patients after liver transplantation hypertriglyceridemia is present in 40.5%. It is more frequent than in the general adult Polish population (21% – results of NATPOL 2011 study) (Zdrojewski *et al.*, 2013). Results of previous studies suggest that hypertriglyceridemia is even more common during the first year after liver transplantation than in long-term observation (Clark *et al.*, 1997; Gisbert *et al.*, 1997). An important risk factor for developing hypertriglyceridemia after LTx is kidney dysfunction and greater body weight gain after LTx (Gisbert *et al.*, 1997). The prevalence of studied lipid abnormalities was significantly lower before liver transplantation – hypercholesterolemia 17.1% *vs.* 51.4% and hypertriglyceridemia 13.5% *vs.* 40.5%. This might be influenced by malnutrition in patients with end-stage liver disease qualified for liver transplantation. An observational study of 165 liver transplant recipients showed that living liver donation was related to a better lipid profile (lower triglycerides and higher HDL serum concentrations) two years after transplantation (Chu *et al.*, 2017). In the current study, all transplanted livers were received from cadavers.

Dyslipidemia and immunosuppressive drugs

Dyslipidemia is a well-known complication associated with using steroids, tacrolimus, or everolimus.

Steroid therapy is a well-known risk factor for developing lipid disorders (Fatourou *et al.*, 2019). Some observational studies suggest that withdrawal of steroids in the long term after liver transplantation may decrease serum cholesterol concentration (Punch *et al.*, 1995; Stegall *et al.*, 1997; Trouillot *et al.*, 1999; Everson *et al.*, 1999).

The effect of immunosuppressive therapy with calcineurin inhibitors (cyclosporine A or tacrolimus) may also induce lipid abnormalities (Clart *et al.*, 1996; Stegall *et al.*, 1997; Fatourou *et al.*, 2019). Results of previous studies suggest that treatment with both calcineurin inhibitors predisposes to hyperglyceridemia. It has been shown that combined cyclosporine A and sirolimus therapy increase the risk of hypertriglyceridemia in liver transplant recipients (Trotter *et al.*, 2001). Canzanella *et al.* suggest that the risk of hypertriglyceridemia in patients treated with cyclosporine A is higher than in patients treated with tacrolimus [Canzanella *et al.*, 1997]. Another study by Dehghani *et al.* presents opposite findings (Dehghani *et al.*, 2007). In the observational study of 116 Spanish liver transplant recipients, Fernandez-Miranda *et al.* have shown a slight association between cyclosporine A and hypercholesterolemia in patients after LTx (odds ratio: 1.02; 95% CI: 1.00–1.03; $P=0.01$) (Fernandez-Miranda *et al.*, 2002). Because of the low number of patients treated with cyclosporine A in the current study, such an analysis was impossible to perform. Orlando *et al.*, in the interventional study of 42 liver transplant recipients with chronic toxicity of calcineurin inhibitors have shown that conversion of calcineurin inhibitors for mycophenolate leads to serum total cholesterol and triglycerides concentration reduction (Orlando *et al.*, 2007).

It has been shown that treatment with mTOR inhibitors (everolimus or sirolimus) is associated with developing hypercholesterolemia in renal transplant recipients

(Groth *et al.*, 1999). Randomized trials have shown that immunosuppressive conversion from calcineurin inhibitors to mTOR inhibitors in a short time after liver transplantation increases total cholesterol and LDL-cholesterol concentration (Masetti *et al.*, 2010; Fischer *et al.*, 2012; De Simone *et al.*, 2012; Teperman *et al.*, 2013). Only one of these trials (with modification for everolimus and low tacrolimus dose regimen) has shown an additional increase in serum triglyceride concentration and an increase in HDL-cholesterol concentration (De Simone *et al.*, 2012). Interestingly, the previously cited study has shown a hypertriglyceridemic effect of mTOR inhibitor on liver transplant recipients only in combination with cyclosporine A (Trotter *et al.*, 2001). Also, in patients long time after liver transplantation, the conversion from calcineurin inhibitor regimen to mTOR inhibitor increases the rate of hypercholesterolemia (Shenoy *et al.*, 2007; De Simone *et al.*, 2009; Abdelmalek *et al.*, 2012). The current study's results align with the above data – the prevalence of hypercholesterolemia in patients treated with everolimus is higher.

A case-control analysis of 13 liver transplant recipients who withdrew all immunosuppressive drugs long-term after liver transplantation showed lower LDL-cholesterol concentration in patients within immunosuppressive therapy than in 22 patients who stayed with immunosuppressive treatment (Duizendstra *et al.*, 2019).

García-Pajares and others (García-Pajares *et al.*, 2016) in an observational study of 204 Spanish liver transplant recipients have shown that hypertriglyceridemia in the first year after liver transplantation is an important risk factor for the development of metabolic syndrome in the next 5 years.

The current study also analyzed the impact of liver cirrhosis's etiology on dyslipidemia's prevalence. In patients with an autoimmune background of liver cirrhosis, the prevalence of hypertriglyceridemia and hypercholesterolemia was lower. This may be due to a younger age at liver failure diagnosis and a generally healthier lifestyle. Patients with an alcohol abuse history seem less likely to be on a healthy diet and their physical activity is presumably lower. This leads to an increased risk of diabetes mellitus and atherosclerosis.

In the current study, it has been shown that the prevalence of dyslipidemia increases after liver transplantation in comparison to the pre-transplant results. Moreover, hypertriglyceridemia is more frequent in a liver transplant recipient than in the general adult Polish population. Dyslipidemia is a risk factor for cardiovascular diseases, which are currently the most common causes of death in these patients (Watt *et al.*, 2010; Rana *et al.*, 2019). Available data suggest that the consequence of the increased occurrence of cardiovascular risk factors is overall survival reduction after liver transplantation (Watt *et al.*, 2010).

Treatment with hypolipidemic drugs

Patients qualified for liver transplantation mostly had end-stage liver disease, where statins were contraindicated, therefore in most patients with dyslipidemias, only diet was recommended. In the past usage of hypolipidemic drugs in our center was limited. The safety and effectiveness of statins after liver transplantation in previous years have not been well established. Nowadays there are some data suggesting the advantages of statin therapy for cardiovascular outcome and decreased risk of hepatocellular cancer recurrence after liver transplantation and us-

age of statins after LTx is more common (Becchetti *et al.*, 2022; Kim *et al.*, 2023).

Limitations

The presented study has some limitations because the retrospective nature of the study does not allow for establishing a cause-and-effect relationship between the etiology of liver failure and the incidence of dyslipidemia.

CONCLUSIONS

Our study has documented that the prevalence of dyslipidemia might increase after liver transplantation. Further research will be needed to assess if these changes result in associated cardiovascular mortality or morbidity. As these risk factors may be associated with cardiovascular disease that may limit survival, formalized efforts should be made to modify these risk factors and improve the long-term survival of patients undergoing liver transplantation. The incidence of lipid disorders in patients after LTx is related to the etiology of liver cirrhosis before liver transplantation.

REFERENCES

- Abdelmalek MF, Humar A, Stickel F, Andreone P, Pascher A, Barroso E, Neff GW, Ranjan D, Toselli LT, Gane EJ, Scarola J, Alberts RG, Maller ES, Lo CM (2012) Sirolimus Liver Conversion Trial Study Group. Sirolimus conversion regimen *versus* continued calcineurin inhibitors in liver allograft recipients: a randomized trial. *Am J Transplant* 12: 694–705. <https://doi.org/10.1111/ajt.12543>
- Becchetti C, Dirchwolf M, Schropp J, Magini G, Müllhaupt B, Immer F, Dufour JF, Banz V, Berzigotti A, Bosch J; Swiss Transplant Cohort Study (2022) Use of statins after liver transplantation is associated with improved survival: results of a nationwide study. *Aliment Pharmacol Ther* 56: 1194–1204. <https://doi.org/10.1111/apt.17192>
- Berenguer M, Prieto M, San Juan F, Rayón JM, Martínez F, Carrasco D, Moya A, Orbis F, Mir J, Berenguer J (2002) Contribution of donor age to the recent decrease in patient survival among HCV-Infected liver transplant recipients. *Hepatology* 36: 202–210. <https://doi.org/10.1053/jhep.2002.33993>
- Canzanello VJ, Schwartz L, Taler SJ, Textor SC, Wiesner RH, Porayko MK, Krom RA (1997) Evolution of cardiovascular risk after liver transplantation: a comparison of cyclosporine A and tacrolimus (FK506). *Liver Transpl Surg* 3: 1–9. <https://doi.org/10.1002/lt.500030101>
- Chu KKW, Chan SC, Sin SL, Chan ACY, Chok KSH, Cheng IKP, Lo CM (2017) Lipid profiles of donors and recipients of liver transplant: like father like son. *Hepatology Int* 11: 300–305. <https://doi.org/10.1007/s12072-017-9786-1>
- Clark W (1996) Tacrolimus: immunosuppression following liver and kidney transplant. *J Clin Pharm Ther* 21: 135–141. <https://doi.org/10.1111/j.1365-2710.1996.tb00012.x>
- De Simone P, Metselaar HJ, Fischer L, Dumortier J, Boudjema K, Hardwigen J, Rostaing L, De Carlis L, Saliba F, Nevens F (2009) Conversion from a calcineurin inhibitor to everolimus therapy in maintenance liver transplant recipients: a prospective, randomized, multicenter trial. *Liver Transpl* 15: 1262–1269. <https://doi.org/10.1002/lt.21827>
- De Simone P, Nevens F, De Carlis L, Metselaar HJ, Beckebaum S, Saliba F, Jonas S, Sudan D, Fung J, Fischer L, Duvoux C, Chavin KD, Koneru B, Huang MA, Chapman WC, Foltys D, Witte S, Jiang H, Hexham JM, Junge G; H2304 Study Group (2012) Everolimus with reduced tacrolimus improves renal function in *de novo* liver transplant recipients: a randomized controlled trial. *Am J Transplant* 12: 3008–3020. <https://doi.org/10.1111/j.1600-6143.2012.04212.x>
- Dehghani SM, Taghavi SA, Eshraghian A, Gholami S, Imanieh MH, Bordbar MR, Malek-Hosseini SA (2007) Hyperlipidemia in Iranian liver transplant recipients: prevalence and risk factors. *J Gastroenterol* 42: 769–774. <https://doi.org/10.1007/s00535-007-2092-2>
- Duizendstra AA, de Knegt RJ, Betjes MGH, Coenen S, Murad SD, de Man RA, Metselaar HJ, Sprengers D, Litjens NHR, Kwekkeboom J (2019) Immunosuppressive drug withdrawal late after liver transplantation improves the lipid profile and reduces infections. *Eur J Gastroenterol Hepatol* 31: 1444–1451. <https://doi.org/10.1097/meg.0000000000001435>
- Everson GT, Trouillot T, Wachs M, Bak T, Steinberg T, Kam I, Shrestha R, Stegall M (1999) Early steroid withdrawal in liver transplantation is safe and beneficial. *Liver Transpl Surg* 5: S48–S57. <https://doi.org/10.1053/jlts.005s00048>
- Fatourou EM, Tsochatzis EA (2019) Management of metabolic syndrome and cardiovascular risk after liver transplantation. *Lancet Gastroenterol Hepatol* 4: 731–741. [https://doi.org/10.1016/s2468-1253\(19\)30181-5](https://doi.org/10.1016/s2468-1253(19)30181-5)
- Fernández-Miranda C, Sanz M, dela Calle A, Loinaz C, Gómez R, Jiménez C, García I, Gómez de la Cámara A, Moreno E (2002) Cardiovascular risk factors in 116 patients 5 years or more after liver transplantation. *Transpl Int* 15: 556–562. <https://doi.org/10.1007/s00147-002-0464-3>
- Fischer L, Klempnauer J, Beckebaum S, Metselaar HJ, Neuhaus P, Schemmer P, Settmacher U, Heyne N, Clavien PA, Muehlbacher F, Morard I, Wolters H, Vogel W, Becker T, Sterneck M, Lehner F, Klein C, Kazemier G, Pascher A, Schmidt J, Rauchfuss F, Schnitzbauer A, Nadalin S, Hack M, Ladenburger S, Schlitt HJ (2012) A randomized, controlled study to assess the conversion from calcineurin-inhibitors to everolimus after liver transplantation – PROTECT. *Am J Transplant* 12: 1855–1865. <https://doi.org/10.1111/j.1600-6143.2012.04049.x>
- García-Pajares F, Peñas-Herrero I, Sánchez-Ocaña R, Torres-Yuste R, Cimavilla-Román M, Carbajo-López A, Almohalla-Alvarez C, Pérez-Saborido B, Muñoz-Concejo E, Gonzalez-Sagrado M, Caro-Patón A, Sánchez-Antolín G (2016) Metabolic syndrome after liver transplantation: Five-year prevalence and risk factors. *Transplant Proc* 48: 3010–3012. <https://doi.org/10.1016/j.transproceed.2016.07.038>
- Gisbert C, Prieto M, Berenguer M, Bretó M, Carrasco D, de Juan M, Mir J, Berenguer J (1997) Hyperlipidemia in liver transplant recipients: prevalence and risk factors. *Liver Transpl Surg* 3: 416–422. <https://doi.org/10.1002/lt.500030409>
- Gojowy D, Adamczak M, Dudzicz S, Gazda M, Karkoszka H, Wiecek A (2016) High frequency of arterial hypertension in patients after liver transplantation. *Transplant Proc* 48: 1721–1724. <https://doi.org/10.1016/j.transproceed.2015.11.043>
- Groth CG, Bäckman L, Morales JM, Calne R, Kreis H, Lang P, Touraine JL, Claesson K, Campistol JM, Durand D, Wrammer L, Brattström C, Charpentier B (1999) Sirolimus (rapamycin)-based therapy in human renal transplantation: similar efficacy and different toxicity compared with cyclosporine. *Sirolimus European Renal Transplant Study Group. Transplantation* 67: 1036–1042. <https://doi.org/10.1097/00007890-199904150-00017>
- Kahan BD (2000) Efficacy of sirolimus compared with azathioprine for reduction of acute renal allograft rejection: a randomised multicentre study. The Rapamune US Study Group. *Lancet* 356: 194–202. [https://doi.org/10.1016/s0140-6736\(00\)02480-6](https://doi.org/10.1016/s0140-6736(00)02480-6)
- Kallwitz ER (2012) Metabolic syndrome after liver transplantation: preventable illness or common consequence? *World J Gastroenterol* 18: 3627–3634. <https://doi.org/10.3748/wjg.v18.i28.3627>
- Kim DG, Yim SH, Min EK, Choi MC, Kim MS, Joo DJ, Lee JG (2023) Effect of statins on the recurrence of hepatocellular carcinoma after liver transplantation: An illusion revealed by exposure density sampling. *Liver Int* 43: 2017–2025. <https://doi.org/10.1111/liv.15653>
- Kniepeiss D, Iberer F, Schaffellner S, Jakoby E, Duller D, Tscheliessnigg Kh (2004) Dyslipidemia during sirolimus therapy in patients after liver transplantation. *Clin Transplant* 18: 642–646. <https://doi.org/10.1111/j.1399-0012.2004.00253.x>
- Masetti M, Montalti R, Rompianesi G, Codeluppi M, Gerring R, Romano A, Begliomini B, Di Benedetto F, Gerunda GE (2010) Early withdrawal of calcineurin inhibitors and everolimus monotherapy in *de novo* liver transplant recipients preserves renal function. *Am J Transplant* 10: 2252–2262. <https://doi.org/10.1111/j.1600-6143.2010.03128.x>
- Niklas A, Flotyńska A, Puch-Walczak A, Polakowska M, Topór-Mądry R, Polak M, Piotrowski W, Kwaśniewska M, Nadrowski P, Pająk A, Bielecki W, Kozakiewicz K, Drygas W, Zdrojewski T, Tykarski A; WOBASZ II investigators (2018) Prevalence, awareness, treatment and control of hypertension in the adult Polish population – Multi-center National Population Health Examination Surveys – WOBASZ studies. *Arch Med Sci* 14: 951–961. <https://doi.org/10.5114/aoms.2017.72423>
- Orlando G, Baiocchi L, Cardillo A, Iaria G, De Liguori Carino N, De Luca L, Ielpo B, Taricotti L, Angelico M, Tisone G (2007) Switch to 1.5 grams MMF monotherapy for CNl-related toxicity in liver transplantation is safe and improves renal function, dyslipidemia, and hypertension. *Liver Transpl* 13: 46–54. Erratum in: *Liver Transpl* 2007; 13: 778. <https://doi.org/10.1002/lt.20926>
- Poltransplant, statistics of liver transplantations from deceased donors in 2022. http://www.poltransplant.org.pl/statystyka_2022.html#gsc.tab=0 [accessed 25th November 2023].
- Punch JD, Shieck VL, Campbell DA, Bromberg JS, Turcotte JG, Merion RM (1995) Corticosteroid withdrawal after liver transplantation. *Surgery* 118: 783–788. [https://doi.org/10.1016/s0039-6060\(05\)80050-9](https://doi.org/10.1016/s0039-6060(05)80050-9)
- Rana A, Ackah RL, Webb GJ, Halazun KJ, Vierling JM, Liu H, Wu MF, Yoeli D, Kueht M, Mindikoglu AL, Sussman NI, Galván NT,

- Cotton RT, O'Mahony CA, Goss JA (2019) No gains in long-term survival after liver transplantation over the past three decades. *Ann Surg* **269**: 20–27. <https://doi.org/10.1097/sla.0000000000002650>
- Rutkowski M, Wojciechowska A, Śmigieński W, Drygas W, Piwońska A, Pająk A, Tykarski A, Kozakiewicz K, Waśniewska MK, Zdrojewski T (2020) Prevalence of diabetes and impaired fasting glucose in Poland in 2005–2014: results of the WOBASZ surveys. *Diabet Med* **37**: 1528–1535. <https://doi.org/10.1111/dme.14333>
- Shenoy S, Hardinger KL, Crippin J, Desai N, Korenblat K, Lisker-Melman M, Lowell JA, Chapman W (2007) Sirolimus conversion in liver transplant recipients with renal dysfunction: a prospective, randomized, single-center trial. *Transplantation* **83**: 1389–1392. <https://doi.org/10.1097/01.tp.0000261630.63550.41>
- Stegall MD, Everson GT, Schroter G, Karrer F, Bilir B, Sternberg T, Shrestha R, Wachs M, Kam I (1997) Prednisone withdrawal late after adult liver transplantation reduces diabetes, hypertension, and hypercholesterolemia without causing graft loss. *Hepatology* **25**: 173–177. <https://doi.org/10.1002/hep.510250132>
- Stepaniak U, Micek A, Waśkiewicz A, Bielecki W, Drygas W, Janion M, Kozakiewicz K, Niklas A, Puch-Walczak A, Pająk A (2016) Prevalence of general and abdominal obesity and overweight among adults in Poland. Results of the WOBASZ II study (2013–2014) and comparison with the WOBASZ study (2003–2005). *Pol Arch Med Wewn* **126**: 662–671. <https://doi.org/10.20452/pamw.3499>
- Teperman L, Moonka D, Sebastian A, Sher L, Marotta P, Marsh C, Koneru B, Goss J, Preston D, Roberts JP; Spare-the-Nephron Trial Liver Transplantation Study Group (2013) Calcineurin inhibitor-free mycophenolate mofetil/sirolimus maintenance in liver transplantation: the randomized spare-the-nephron trial. *Liver Transpl* **19**: 675–689. <https://doi.org/10.1002/lt.23658>
- Trotter JF, Wachs ME, Trouillot TE, Bak T, Kugelmas M, Kam I, Everson G (2001) Dyslipidemia during sirolimus therapy in liver transplant recipients occurs with concomitant cyclosporine but not tacrolimus. *Liver Transpl* **7**: 401–408. <https://doi.org/10.1053/jlts.2001.23916>
- Trouillot TE, Shrestha R, Kam I, Wachs M, Everson GT (1999) Successful withdrawal of prednisone after adult liver transplantation for autoimmune hepatitis. *Liver Transpl Surg* **5**: 375–380. <https://doi.org/10.1002/lt.500050514>
- Watt KD, Pedersen RA, Kremers WK, Heimbach JK, Charlton MR (2010) Evolution of causes and risk factors for mortality post-liver transplant: results of the NIDDK long-term follow-up study. *Am J Transplant* **10**: 1420–1427. <https://doi.org/10.1111/j.1600-6143.2010.03126.x>
- Zdrojewski T, Rutkowski M, Bandosz P, Gaciong Z, Jędrzejczyk T, Solnica B, Pencina M, Drygas W, Wojtyniak B, Grodzicki T, Piwoński J, Wyrzykowski B (2013) Prevalence and control of cardiovascular risk factors in Poland. Assumptions and objectives of the NATPOL 2011 Survey. *Kardiol Pol* **71**: 381–392. <https://doi.org/10.5603/kp.2013.0066>

Circular RNA AGFG1 motivates breast cancer cell proliferation, invasion, migration, and glycolysis by controlling microRNA-653-5p/14-3-3 protein epsilon

Liang Chen^{1#}, JinXian Qian^{1✉}, Ying Shen^{3✉} and Xiang Yu^{2#}

¹Department of Breast Surgery, The First Affiliated Hospital of Kunming Medical University, Kunming City, Yunnan Province, 650032, China;

²Emergency Trauma Surgery, First People's Hospital of Yunnan Province, Kunming City, Yunnan Province, 650034, China; ³Department of General Surgery, Yunnan New Kunhua Hospital, Anning City, Yunnan Province, 650301, China

A recent Pairwise meta-analysis confirmed that circular RNA AGFG1 (circAGFG1) is abnormally highly expressed in breast cancer (BC) and may be associated with death risk. The purpose of this study was to elucidate the biological role of circAGFG1 in BC and to explore its potential downstream molecular mechanisms. CircAGFG1, miR-653-5p and YWHAЕ expression in BC tissues and cells were analyzed by RT-qPCR or western blot. Gene expression was regulated by transfection of plasmids or oligonucleotides and the biological behaviors of BC cells were analyzed by a series of assays. The ring structure of circAGFG1 was analyzed by RNase R and actinomycin D treatment. Dual luciferase reporter assay and RNA-pull down were used to verify the targeting relationship of circAGFG1 and downstream factors. A nude mouse xenograft experiment was performed to verify the effect of circAGFG1 on cancer cells *in vivo*. The results showed that circAGFG1 and YWHAЕ were highly expressed in BC while miR-653-5p was lowly expressed. Both circAGFG1 and YWHAЕ had a targeting relationship with miR-653-5p. Knockdown of circAGFG1 inhibited BC cell proliferation, invasion, migration, and glycolysis. The inhibitory effect of circAGFG1 knockdown on BC was reversed by silencing miR-653-5p. The inhibitory effect of overexpression of miR-653-5p on malignant behaviors of BC cells was reversed by overexpression of YWHAЕ. Knockdown of circAGFG1 inhibited tumor growth *in vivo*. Taken together, these data suggest that circAGFG1 acts as a sponge for miR-653-5p to mediate YWHAЕ expression to promote the malignant behaviors of BC.

Keywords: Circular RNA AGFG1, MicroRNA-653-5p, YWHAЕ, Target binding, MDA-MB-231 cells

Received: 05 March, 2022; revised: 29 July, 2023; accepted: 16 August, 2023; available on-line: 18 October, 2023

✉ e-mail: qianjx2000@hotmail.com (JXQ); xyang56@163.com (YS)

#These authors contributed equally to this work.

INTRODUCTION

Breast cancer (BC) is a malignant tumor in the mammary gland epithelial tissue, which seriously threatens the survival and health of women worldwide (Wang *et al.*, 2021). Surgery, endocrine therapy, chemotherapy, radiotherapy and targeted therapy are applicable for BC treatment to reduce the mortality rate (Li *et al.*, 2021). However, due to high recurrence and easy metastasis, patients' prognosis is still poor, and the mortality rate is still high (Xie *et al.*, 2021). Hence, an in-depth study of

the latent molecular mechanisms of BC is crucial to provide new and effective therapeutic targets.

Circular RNAs (circRNAs) are a cluster of closed circular RNAs (Li *et al.*, 2019). A study has shown that circRNAs are available to control gene expression and the biological behavior of cancer cells (Wu *et al.*, 2019). Meanwhile, multiple circRNAs have been revealed to take part in regulating BC progression (Zhang *et al.*, 2021; Qi *et al.*, 2021; Cui *et al.*, 2021). CircAGFG1 is a novel circRNA that has been confirmed to be elevated in BC and may be implicated in the diagnosis and prognosis of BC (Ma *et al.*, 2021). However, it is unclear whether circAGFG1 affects the biological behavior of BC cells.

circRNAs can perform as competing endogenous RNAs (ceRNAs) for microRNAs (miRNAs) to control downstream targets (Chu *et al.*, 2021). In the light of the ceRNA theory, it predicted a miRNA (miR-653-5p) associated with circAGFG1. Recently, miR-653-5p has been tested to involve diversified cancers, such as non-small cell lung cancer (Han *et al.*, 2019) and gastric cancer (Li *et al.*, 2021). However, it is necessary to further elucidate other downstream target genes regulated by miR-653-5p in BC.

YWHAЕ, also known as 14-3-3ε, is a member of the YWHA protein family (Wu *et al.*, 2021). YWHAЕ which is extensively expressed in most cancers is a transcription factor (Li *et al.*, 2021). Previous studies have shown that YWHAЕ is elevated in BC and can motivate the proliferation, metastasis and chemotherapy of BC cells, and may become a latent therapeutic target for BC (Leal *et al.*, 2016; Cimino *et al.*, 2008; Park *et al.*, 2019).

This study hypothesized that circAGFG1 might indirectly regulate YWHAЕ expression by adsorbing miR-653-5p to participate in BC cell biological behaviors. Our aim was to explore the biological function of circAGFG1 in BC and to elucidate its downstream underlying mechanisms.

MATERIALS AND METHODS

Clinical tissue specimens

From January 2018 to January 2020, BC tissues and adjacent normal tissues (2–5 cm from the tumor) of 60 patients (aged 47.5±11.4 years) who underwent tumor resection at The First Affiliated Hospital of Kunming Medical University were harvested. All tissues were stored at –80°C. Approval of this study was obtained from the Ethics Committee of The First Affiliated Hos-

pital of Kunming Medical University and written informed consent was collected from all participants.

Cell culture and transfection

Normal human breast cells (MCF-10A) and human BC cell lines (MDA-MB-231, MCF-7, SK-BR-3 and MDA-MB-157) were bought from ATCC (VA, USA). The cells were cultivated in Roswell Park Memorial Institute-1640 (31800, Solarbio, China) containing 10% fetal bovine serum at 37°C, and 5% CO₂. MDA-MB-231 cells were chosen as an auxiliary study object because they had the greatest difference in expression (Yang *et al.*, 2019).

Specific short hairpin RNAs against circAGFG1, miR-653-5p mimic/inhibitor, and corresponding NCs were gained from Genescript (Shanghai, China). Lentivirus-negative vector, YWHAE and circAGFG1 lentiviral over-expression vectors were purchased from GeneCopoeia. MDA-MB-231 and MDA-MB-157 cells were transferred to a 6-well plate (1×10⁵ cells/mL) and cultured for 24 h. Cell transfection was conducted using Lipofectamine® 2000 (Invitrogen, USA) (Gong *et al.*, 2021). 48 h after transfection, the transfection efficiency was evaluated by reverse transcription-quantitative polymerase chain reaction (RT-qPCR) and Western blot.

Ribonuclease R (RNase R) and actinomycin D

To test RNase R resistance, total RNA (2 µg) from MDA-MB-231 cells was collected and incubated with 3 U/µg RNase-R (07250, Epicentre Technologies, USA) at 37°C for 30 min. Actinomycin D experiment: MDA-MB-231 cells were treated with 2 mg/mL actinomycin D (129,935, Millipore, USA) to block transcription. Then, cellular RNA was obtained to measure circAGFG1 and AGFG1 expression by RT-qPCR.

Subcellular localization analysis

Cytoplasmic and nuclear RNAs of MDA-MB-231 cells were isolated using the PARIS Kit (Invitrogen). Then, circAGFG1 in cytoplasmic RNA and nuclear RNA was checked by RT-qPCR. U6 and glyceraldehyde-3-phosphate dehydrogenase (GAPDH) were applied as nuclear and cytoplasmic controls, respectively.

RT-qPCR

Total RNA was extracted from BC tissues and cells using Trizol reagent (Invitrogen) PrimeScript RT reagent kit (Takara, Tokyo, Japan) and miRNA First Strand Synthesis kit (Takara, Japan) were employed for reverse transcription of circRNA/mRNA and miRNA, respectively. RT-qPCR was performed with SYBR Green kit (Thermo Fisher Scientific, MA, USA) and Mx3005P QPCR system (Agilent Technologies, Santa Clara, CA, USA). U6 and GAPDH were employed as internal controls for miRNA and mRNA/circRNA, respectively (Ma *et al.*, 2021). The primer sequences were manifested in Table 1. The relative expression of genes was analyzed by 2^{-ΔΔCt}.

Western blot

Total protein from cells and tissues was extracted with 500 µL radio-immunoprecipitation assay lysis buffer (Beyotime). An equal amount of protein (20 µg) was separated by 8% sodium dodecyl sulfate-polyacrylamide gel electrophoresis (Solarbio) and transferred to a polyvinylidene fluoride membrane (Invitrogen). After be-

Table 1. Primer sequence

Genes	Primer sequence (5'-3')
CircAGFG1	F: 5'-CCAGTTGTAGTCTCTCAAG-3'
	R: 5'-TCACCCTGTGTGGTGGAT-3'
miR-653-5p	F: 5'-GCCGAGGTGTTGAAACAATC-3'
	R: 5'-TGGTGTCTGGAGTTCG-3'
YWHAE	F: 5'-GGATACGCTGAGTGAAGAAAGC-3'
	R: 5'-TATTCTGCTCTTACCCTCACC-3'
U6	F: 5'-CTCGCTTCGGCAGCACA-3'
	R: 5'-AACGCTTCACGAATTTGCGT-3'
GAPDH	F: 5'-TCCCATCACCATCTTCCA-3'
	R: 5'-CATCACGCCACAGTTTCC-3'

F, forward; R, reverse

ing blocked with 5% skim milk, the membrane was incubated with primary antibodies YWHAB (8312, Cell Signaling Technology, 1:1000), glucose transporter type1 (GLUT1; ab652, 1:1000), matrix metalloproteinase-9 (MMP9; ab38898, 1:1000), B cell lymphoma 2-associated X (Bax; ab32503, 1:1000, all Abcam), and GAPDH (60004-1-Ig, 1:1000, Proteintech) overnight at 4°C. Horseradish peroxidase-conjugated goat anti-rabbit secondary antibody immunoglobulin G (1:1000, ab181236, Abcam) was added for incubation for 2 h. The signals were visualized by an enhanced chemiluminescence kit (34080, Thermo Fisher Scientific) and analyzed by ImageJ software. Three biological replicates of the experiment were performed.

Cell Counting Kit -8 (CCK-8)

MDA-MB-231 and MDA-MB-157 cells after transfection were seeded in 96-well plates (1×10⁴ cells/well). At designated time points (0, 24, 48 h), 10 µL CCK-8 reagent (Dojindo, Kumamoto, Japan) was added to each well. Optical density values at 450 nm were recorded after 2 h on a microplate reader (PerkinElmer, USA).

Colony formation assay

MDA-MB-231 and MDA-MB-157 cells after transfection were seeded in 6-well plates for 14 d, fixed in 4% paraformaldehyde (Beyotime), stained with 0.1% crystal violet (Beyotime) for 2 h, and counted.

Flow cytometry

Apoptosis rates of transfected MDA-MB-231 and MDA-MB-157 cells were analyzed by Annexin V-Fluorescein isothiocyanate (FITC) propidium iodide (PI) apoptosis kit (BD Biosciences). Briefly, cells were resuspended in 1 × binding buffer (500 µL) and mixed with 5 µL Annexin V-FITC and 5 µL PI in the dark for 15 min. Finally, the percentage of apoptotic cells was evaluated by a flow cytometer (FACS Calibur).

Transwell migration and invasion analysis

MDA-MB-231 and MDA-MB-157 cells were placed in a serum-free medium at a density of 5×10⁴ cells/well, and the medium containing 10% fetal bovine serum (Invitrogen) was added to the bottom chamber. Then after 24 h, cells were fixed with methanol for 30 min, stained with 0.1% crystal violet, and viewed in an inverted mi-

croscope (Tycom, Switzerland, magnification $\times 100$). For invasion assays, cells (1×10^6 cells/well) were placed in the upper chamber (Costar) coated with a matrix (BD Bioscience) (Wan *et al.*, 2021).

Glycolysis test

MDA-MB-231 and MDA-MB-157 cells (1×10^5 cells/well) after transfection were seeded in 12-well plates. After 48 h of transfection, glucose consumption, and lactate production, the ADP/ATP ratio were tested using a glucose detection kit (Sigma-Aldrich), a lactate detection kit (BioVision, Milpitas, CA, USA), and a carrier sensor ADP/ATP ratio detection kit (BioVision), respectively (Xie *et al.*, 2021).

The luciferase activity assay

MDA-MB-231 cells were plated on 6-well plates and then co-transfected with the luciferase reporters pRL-TK-CircAGFG1/YWHAE-WT 3-UTR or pRL-TK-CircAGFG1/YWHAE-MUT 3-UTR (Promega), and miR-653-5p mimic or mimic-NC using Lipofectamine[®]2000 (Invitrogen). After 48-h incubation, luciferase activity was measured using a dual luciferase reporter gene kit (Promega) (Wu *et al.*, 2021).

RNA-pull down assay

Biotin-labeled miR-653-5p (Bio-miR-653-5p) probe and control probe (Bio-NC) were gained from Ribobio. After transfection with Bio-NC or Bio-miR-653-5p, MDA-MB-231 cells were lysed after 48 h and incubated with Dynabeads M-280 Streptavidin (Invitrogen) at 4°C for 2 h. The RNA complexes on the beads were washed and the enrichment of circAGFG1 and YWHAE was tested by RT-qPCR.

In vivo tumor growth assay

Twelve BALB/c male nude mice (5 weeks old, body weight of 15–20 g) were purchased from Vital River

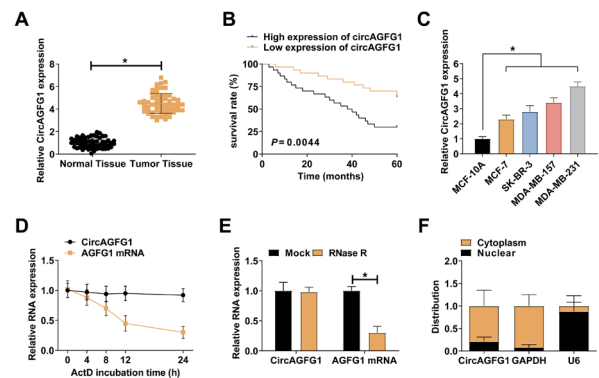


Figure 1. CircAGFG1 is elevated in BC

(A) RT-qPCR detection of circAGFG1 in normal and tumor tissues. (B) Kaplan-Meier analysis of survival prognosis of BC patients. (C) RT-qPCR detection of circAGFG1 expression in four BC cell lines (MDA-MB-231, MCF-7, SK-BR-3, and MDA-MB-157) and normal breast cell line (MCF-10A). (D/E) The ring structure of circAGFG1 was determined by RNase R and Act D methods. (F) The subcellular localization of circAGFG1 in MDA-MB-231 cells. Measurement data were clarified as mean \pm S.D. (N=3); *P<0.05.

(Beijing, China). MDA-MB-231 cells (5×10^6 cells/mouse) with or without stable knockdown of circAGFG1 were injected subcutaneously into each mouse (6 per group). Tumor volume was calculated in the light of the formula $0.5 \times \text{length} \times \text{width}^2$ and measured every 3 d. After 23 d, the mice were euthanized. Tumor tissues were excised for further analysis. This study was permitted by the Animal Research Committee of The First Affiliated Hospital of Kunming Medical University (Ding *et al.*, 2021).

Immunohistochemistry (IHC) analysis

After being fixed in 10% formalin (Beyotime), the tumor tissues were embedded in paraffin and dissected. Primary antibodies Ki67 (ab15580, 1:5000, Abcam, Cambridge, UK) and MMP9 (ab76003, 1:1000, Abcam) were

Table 2. The link of circAGFG1 and clinicopathological features of BC patients

Characteristic	Cases n=60	CircAGFG1 expression		P
		Reduction (n=30)	Elevation (n=30)	
Age (years)				
<50	27	12	15	0.512
≥ 50	33	18	15	
Tumor size				
<2cm	35	19	16	0.0357*
≥ 2 cm	25	11	14	
TNM				
I/II	29	19	10	0.0157*
II/IV	31	11	20	
Lymph node metastasis				
Negative	25	17	8	0.0076*
Positive	35	13	22	
Distant metastasis				
No	50	30	20	0.0257*
Yes	10	0	10	

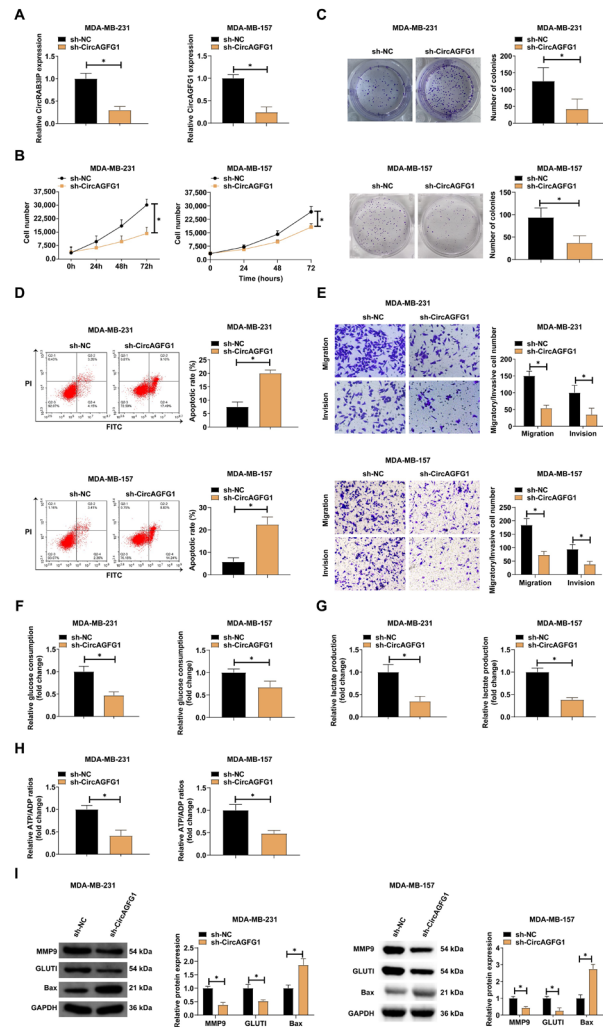


Figure 2. circAGFG1 regulates BC cell proliferation, invasion and migration, glycolysis and apoptosis. sh-circAGFG1 was transfected into MDA-MB-231 and MDA-MB-157 cells. (A) RT-qPCR detection of circAGFG1 knockdown or overexpression transfection efficiency. (B/C) Cell proliferation activity was tested by the CCK-8 method and colony formation assay. (D) Cell apoptosis detected by flow cytometry. (E) Transwell assay to measure cell migration and invasion. (F-H) glucose consumption, lactate production, and cellular ATP/ADP ratio. I. Western blot detection of GLUT1, Bax, and MMP9. Measurement data were clarified as mean \pm S.D. (N=3); * P <0.05.

incubated at 4°C overnight, followed by the secondary antibody (ab205718, 1:5000, Abcam) overnight. After treatment with 3,3'-diaminobenzidine staining (Sangon Biotech, Shanghai, China), the sections were counterstained with hematoxylin (Beyotime) and examined with a fluorescence microscope (Leica, Wetzlar, Germany).

Statistical analysis

All experiments in this study were biologically replicated at least three times. SPSS 21.0 (SPSS, Inc, Chicago, IL, USA) statistical software was applied for analysis of the data. After the Kolmogorov-Smirnov test, the data were normally distributed and expressed as mean \pm standard deviation (S.D.). The two-group comparison was done by t-test, while the multiple-group comparison was performed by one-way analysis of variance (ANOVA) and Fisher's least significant difference *t*-test (LSD-*t*). The chi-square test was used

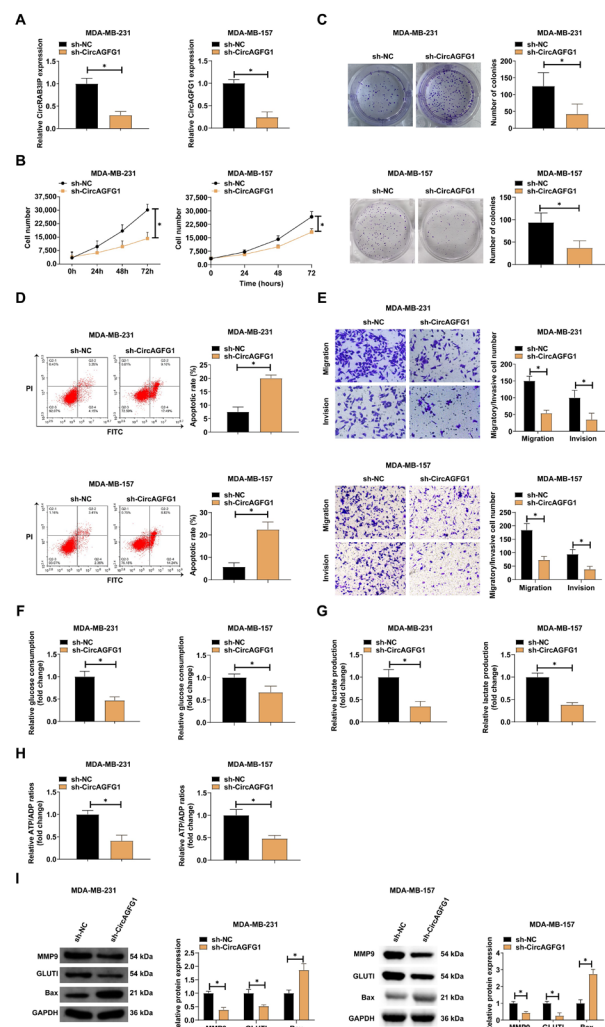


Figure 3. CircAGFG1 acts as a sponge of miR-653-5p. (A) The binding sites between circAGFG1 and miR-653-5p on the starbase. (B) RT-qPCR detection of transfection efficiency of miR-653-5p mimic. (C-D) Luciferase activity assay and RNA-pull down assay to evaluate the interaction between circAGFG1 and miR-653-5p. (E-F) RT-qPCR to examine miR-653-5p in BC tissues and cells. (G) Pearson correlation analysis to evaluate the correlation between miR-653-5p and circAGFG1. (H) RT-qPCR detection of miR-653-5p expression after transfection of sh-circAGFG1. Measurement data were clarified as mean \pm S.D. (N=3); * P <0.05.

to analyze the correlation between circAGFG1 and the clinicopathological data of patients and Kaplan-Meier analysis to examine the relationship between circAGFG1 and patients' survival P <0.05 was considered statistically significant.

RESULTS

CircAGFG1 is elevated in BC

Firstly, the circAGFG1 expression pattern in BC was detected by RT-qPCR. CircAGFG1 expression was higher in BC tissues compared with normal tissues (Fig. 1A). The link between circAGFG1 and clinicopathological characteristics of BC patients was then analyzed. The elevation of circAGFG1 was associated with tumor-node-metastasis stage, tumor size, lymph

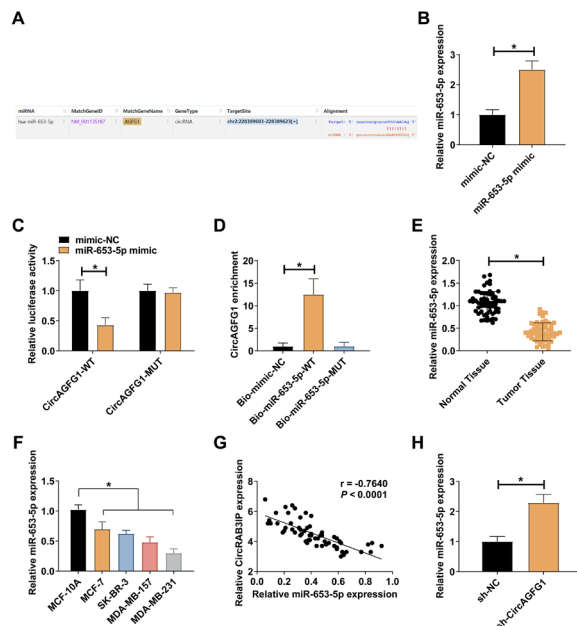


Figure 4. Repression of miR-653-5p reverses the effects of circAGFG1 knockdown on BC cells sh-circAGFG1 and miR-653-5p inhibitor were co-transfected into MDA-MB-231 and MDA-MB-157 cells. (A) The transfection efficiency of sh-circAGFG1 and miR-653-5p inhibitor detected by RT-qPCR. (B–C) Cell proliferation activity detected by the CCK-8 method and colony formation assay. (D) Apoptosis rate detected by flow cytometry. (E) Transwell detection of cell migration and invasion. (F–H) Glucose consumption, lactate production, and cellular ATP/ADP ratio. (I) Western blot detection of GLUT1, Bax, and MMP9. Measurement data were clarified as mean \pm S.D. (N=3); * P <0.05.

node metastasis and distant metastasis, but not with age (Table 2). Kaplan-Meier survival analysis clarified that the elevation of circAGFG1 was associated with worse overall survival (Fig. 1B).

CircAGFG1 expression was higher in all BC cell lines (MDA-MB-231, MCF-7, SK-BR-3, and MDA-MB-157) than in normal cells (MCF-10A) (Fig. 1C). Among them, MDA-MB-231 cells and MDA-MB-157 cells with the highest CircAGFG1 expression were selected for follow-up experiments. The circular structure of circAGFG1 was confirmed by RNase R and actinomycin D experiments, and it came out that circAGFG1 was resistant to RNase R digestion and was more stable than linear AGFG1 mRNA, and actinomycin D did not affect the stability of circAGFG1 (Fig. 1D, E). Furthermore, subcellular localization analysis clarified that circAGFG1 was majorly distributed in the cytoplasm of MDA-MB-231 cells (Fig. 1F).

The above data suggest circAGFG1 is stably elevated in BC and may take part in BC progression.

Repressing circAGFG1 restrains MDA-MB-231 cell biological behaviors and glycolysis

To figure out circAGFG1's biological function in BC, circAGFG1 was silenced in MDA-MB-231 and MDA-MB-157 cells. CircAGFG1 knockdown efficiency was shown in Fig. 2A. CCK-8 and colony formation experiments showed that the knockdown of circAGFG1 inhibited the proliferation ability of BC cells (Fig. 2B, C). Flow cytometry showed that the knockdown of circAGFG1 promoted apoptosis in cells (Fig. 2D). Transwell experiments demonstrated that the knockdown of circAGFG1 increased the migratory and invasive ability

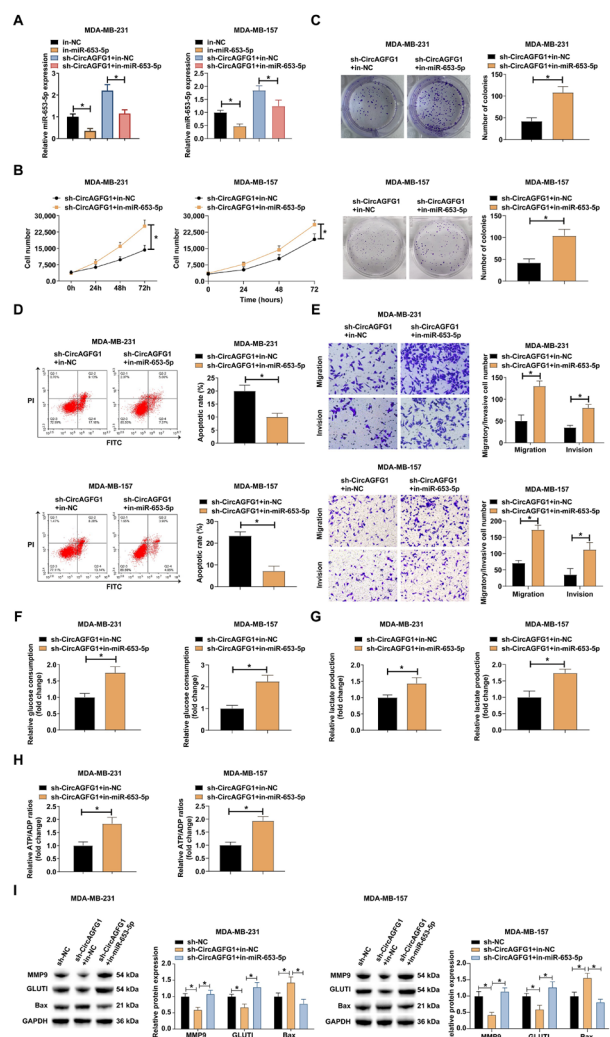


Figure 5. YWHA is a functional target of miR-653-5p in BC cells (A) Binding sites of YWHA with miR-653-5p. (B–C) The luciferase activity assay and RNA-pull down assay to evaluate the interaction between YWHA and miR-653-5p. (D–E) mRNA expression of YWHA in BC tissues and adjacent normal tissues detected by RT-qPCR and western blot. (F–G) YWHA expression in four BC cell lines (MDA-MB-231, MCF-7, SK-BR-3 and MDA-MB-157) and a normal breast cell line (MCF-10A) detected by RT-qPCR and western blot. (H–I) The correlation among YWHA, miR-653-5p, and circAGFG1 evaluated by Pearson correlation analysis. (J) Western blot detection of YWHA expression after transfection of sh-CircAGFG1 or miR-653-5p mimic. Measurement data were clarified as mean \pm S.D. (N=3); * P <0.05.

ties of cells (Fig. 2E). Most fast-growing malignant cells have active glycolysis and gain more energy through glycolysis (Zhang *et al.*, 2022). Next, the effect of circAGFG1 on glycolysis was explored. It was examined that knockdown of circAGFG1 inhibited cellular glucose consumption, lactate production and ATP/ADP ratio (Fig. 2F–H). Western blot detected that knockdown of circAGFG1 suppressed the protein expression of MMP9 and GLUT1 and promoted the protein expression of Bax (Fig. 2I). The above data indicated that knockdown of circAGFG1 refrains BC cell biological functions and glycolysis.

CircAGFG1 performs as a sponge for miR-653-5p

circAGFG1 can target miRNAs to regulate BC progression (Qi *et al.*, 2015), so a bioinformatics website

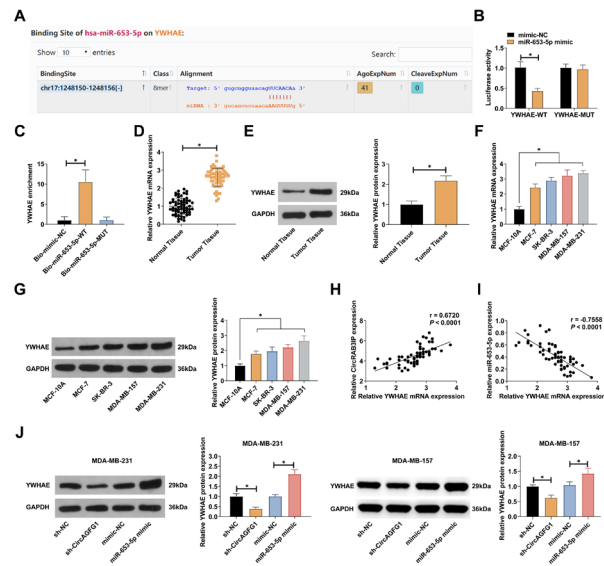


Figure 6. Elevation of miR-653-5p restrains BC cell effect via targeting YWHAE

miR-653-5p mimic and YWHAE overexpression vector were co-transfected into MDA-MB-231 and MDA-MB-157 cells. (A–B) RT-qPCR and Western blot examination of YWHAE in MDA-MB-231 cells. (C–D) Cell proliferation activity was detected by the CCK-8 method and colony formation assay. (E) Cell apoptosis rate tested by flow cytometry. (F) Transwell detection of cell migration and invasion. (G–I) Glucose consumption, lactate production, and cellular ATP/ADP ratio. (J) Western blot detection of GLUT1, Bax, and MMP9. Measurement data were clarified as mean \pm S.D. (N=3); * P <0.05.

(<https://starbase.sysu.edu.cn>) was utilized to predict the target miRNAs of circAGFG1. In Fig. 3A, miR-653-5p had a targeted binding site for circAGFG1. miR-653-5p mimic elevated miR-653-5p expression in MDA-MB-231 cells (Fig. 3B). Dual luciferase reporter gene test results showed that miR-653-5p mimic restrained the luciferase activity of circAGFG1-WT, but not that of circAGFG1-MUT (Fig. 3C). RNA-pull down assay found that miR-653-5p could specifically combine with circAGFG1 (Fig. 3D). Meanwhile, miR-653-5p expression was reduced in BC tissues and cells (Fig. 3E, F). Clinical correlation analysis found that miR-653-5p was negatively linked with circAGFG1 expression (Fig. 3G). RT-qPCR found that depression of circAGFG1 enhanced miR-653-5p expression in MDA-MB-231 cells (Fig. 3H).

All in all, miR-653-5p is regulated by circAGFG1.

Repression of miR-653-5p reverses the effects of silencing circAGFG1 on BC cells

To further study the role of CircAGFG1 in regulating the expression of miR-653-5p in BC, rescue experiments were executed. The promotion of miR-653-5p by sh-CircAGFG1 was reversed by miR-653-5p inhibitor (Fig. 4A). Colony formation and CCK-8 experiments showed that miR-653-5p inhibitor eliminated the inhibition of sh-circAGFG1 on cell proliferation (Fig. 4B, C). Flow cytometry showed that the proapoptotic effect of sh-circAGFG1 was reversed by miR-653-5p inhibitor (Fig. 4D). Transwell assay showed that sh-circAGFG1 inhibited cell invasion and migration, while miR-653-5p inhibitor prevented this change (Fig. 4E). Detection of glycolysis-related indicators showed that sh-circAGFG1 reduced glucose consumption, lactate production, and ATP/ADP ratio, but this phenomenon was reversed by miR-653-5p inhibitor (Fig. 4F–H). In addition, sh-cir-

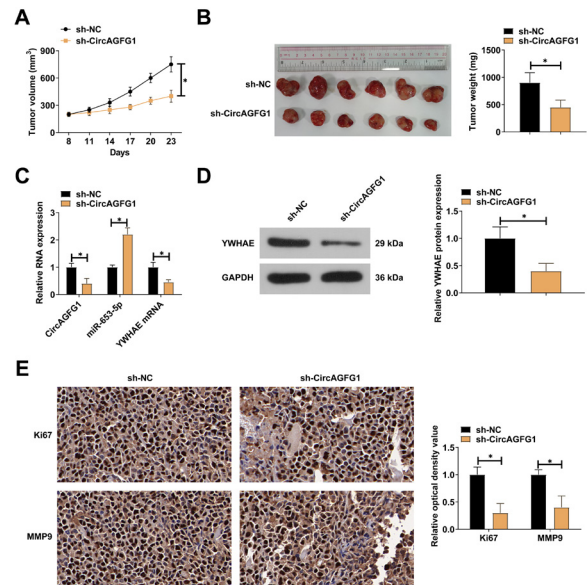


Figure 7. Deletion of circAGFG1 restrains tumorigenesis in vivo (A) Changes in tumor volume in mice. (B) The tumor weight of mice was detected after 23 days. (C) RT-qPCR to test circAGFG1 and miR-653-5p in tumor tissues. (D) Western blot to test YWHAE in tumor tissue. (E) Ki67 and MMP9 in tumor tissue detected by IHC. Measurement data were clarified as mean \pm S.D. (n=6); * P <0.05.

cAGFG1 inhibited MMP9 and GLUT1 expression and promoted Bax expression, while miR-653-5p inhibitor blocked these protein changes (Fig. 4I).

The above data suggest that circAGFG1 affects BC cell progression *via* targeting miR-653-5p.

YWHAE is a functional target of miR-653-5p in BC cells

Bioinformatics analysis on <https://starbase.sysu.edu.cn> found the multiple complementary binding sites in miR-653-5p and YWHAE (Fig. 5A). It turned out that miR-653-5p mimic effectively suppressed the luciferase activity of YWHAE-WT 3'UTR (Fig. 5B). Verified by RNA-pull down assay, YWHAE could specifically combine with miR-653-5p (Fig. 5C). The elevation of YWHAE expression was discovered in BC tissues and cells (Fig. 5D–G). Clinical correlation analysis found that YWHAE expression was positively linked with circAGFG1 expression and negatively associated with miR-653-5p expression (Fig. 5H, I). Furthermore, in MDA-MB-231 cells, down-regulation of circAGFG1 or enhancement of miR-653-5p reduced YWHAE expression (Fig. 5J).

The above data indicate that YWHAE is the downstream gene of miR-653-5p.

Elevation of miR-653-5p depresses BC cell effects *via* targeting YWHAE

For further investigating the link between miR-653-5p and YWHAE, a functional rescue experiment was performed. YWHAE expression was significantly increased after transfection of the YWHAE overexpression vector, and the inhibitory effect of miR-653-5p mimic on YWHAE was reversed by the YWHAE overexpression vector (Fig. 6A, B). CCK-8 and colony formation experiments showed that the inhibitory effect of overexpression of miR-653-5p on cell proliferation was reversed by overexpression of YWHAE (Fig. 6C, D). In addition, the promoting effect of overexpression of miR-653-5p on apoptosis was reversed by overexpression of YWHAE (Fig.

6E). Transwell experiments showed that overexpression of miR-653-5p inhibited cell invasion and migration, but overexpression of YWHAE prevented this phenomenon (Fig. 6F). Commercial kit results showed that the inhibitory effects of overexpression of miR-653-5p on cellular glucose consumption, lactate production, and ATP/ADP ratio were reversed by overexpression of YWHAE (Fig. 6G–I). Western blot showed that overexpression of miR-653-5p inhibited the expression of MMP9, GLUT1 and promoted the expression of Bax, and overexpression of YWHAE reversed the changes of these proteins (Fig. 6J).

The above data suggest that miR-653-5p affects BC cell progression by targeting YWHAE.

CircAGFG1 knockdown restrains tumor growth *in vivo*

To determine whether circAGFG1 silencing restrained tumor growth *in vivo*, sh-NC or sh-CircAGFG1-transfected MDA-MB-231 cells were implanted into nude mice. sh-CircAGFG1 reduced the tumor volume and weight of mice (Fig. 7A, B). Meanwhile, circAGFG1 knockdown suppressed circAGFG1 and YWHAE expression in tumor tissues, while elevated miR-653-5p expression (Fig. 7C, D). IHC analysis illustrated that repression of circAGFG1 repressed Ki67 and MMP9 expression in tumor tissues (Fig. 7E). All in all, it is suggested that circAGFG1 knockdown restrains BC tumor growth *in vivo*.

DISCUSSION

BC is an extremely familiar cancer worldwide and a momentous cause of death in women. Its high morbidity, high recurrence rate and unpleasing prognosis are the main reasons of patient death. Hence, in-depth studies of the molecular mechanisms of BC are urgently needed to confirm effective targets for BC therapy. With the in-depth research on regulatory mechanism in cancer, the study direction has gradually shifted from coding RNA to ncRNAs. BC development is complexly controlled by diversified ncRNAs, including circRNAs, and miRNAs (Liu *et al.*, 2021). In the research, it was discovered for the first time that circAGFG1 combined with miR-653-5p, which targeted YWHAE, thereby facilitating MDA-MB-231 cell biological behaviors and glycolysis *in vitro* and accelerating tumor growth *in vivo*.

CircAGFG1 has been confirmed to be elevated in BC and may be implicated in BC patients' diagnosis and prognosis. A study has shown that circRNAs are more stable in tissues and exosomes compared with traditional linear RNAs (He *et al.*, 2021). Likewise, in the research, circAGFG1 expression was elevated in BC, was not easily degraded by RNase R and was abundantly exhibited in the cytoplasm. In addition, this study also found that circAGFG1 elevation was associated with poor pathological features and prognosis of BC patients. CircAGFG1 expression is enhanced in various cancers like esophageal cancer (Fu *et al.*, 2021), cervical cancer, and triple-negative BC (Zhang *et al.*, 2021), and repressing its expression can restrain the malignant progression of cancer. In the research, the knockdown of circAGFG1 restrained BC cell biological behaviors and glycolysis, and depressed tumor growth *in vivo*. This suggests that circAGFG1 may offer a therapeutic target for BC. It has been reported that cells can secrete circRNAs through exosomes to regulate tumor growth and metastasis. As exemplified, in BC, has_circ_0000615 is packaged by exosomes and transported into the circulating blood (Mashouri *et al.*, 2019). Therefore, subsequent studies need to detect BC cell exosomes to detect the role of circAGFG1.

CircRNAs perform as ceRNAs to interact miRNAs. Through bioinformatics analysis, it was found that CircAGFG1 can sponge various miRNAs. Among these miRNAs, miR-653-5p was selected as circAGFG1's target in the research. Elevation of miR-653-5p restrains the proliferation and migration of melanoma (Liu *et al.*, 2020), together with the proliferation of cervical cancer cells (Wu *et al.*, 2020). MiR-653-5p's functions in BC have been initially clarified, and this miRNA is lowly expressed in BC and has anti-tumor effects. In the research, miR-653-5p expression was inhibited in BC. Furthermore, miR-653-5p inhibitor could partially suppress the effects of circAGFG1 silencing on BC cells.

YWHAE acts as a transcription factor to activate or depress the transcription of target genes. For example, targeting YWHAE to activate apoptotic signaling can suppress cutaneous squamous cell carcinoma (Holmes *et al.*, 2021). Previous studies have shown that YWHAE is elevated in BC and motivates the metastasis and chemotherapy of BC cells, and may become a latent therapeutic target for BC. However, the mechanism by which the circAGFG1/miR-653-5p/YWHAE axis affects BC has not been investigated. In the research, it was also found that YWHAE expression was elevated in BC. In addition, it was originally discovered that YWHAE was a downstream gene of miR-653-5p. Meanwhile, YWHAE can integrate multiple signaling pathways by interacting with different proteins in cancer progression (Ou *et al.*, 2021). In addition, YWHAE-NUTM2 has been reported to deregulate both v-raf-leukemia viral oncogene 1/v-Raf murine sarcoma viral oncogene homolog B and Hippo pathways, resulting in elevation of cyclin D1, which accelerates the progression of high-grade endometrial stromal sarcoma. Therefore, it was speculated that YWHAE might interact with NUTM2 protein to integrate signaling pathways, and then participate in the progression of BC, which needs to be further explored in follow-up studies.

Notably, circAGFG1 can affect MMP9, GLUT1, and Bax expression in BC cells by targeting and regulating the miR-653-5p/YWHAE axis. MMP9 can degrade matrix proteins, destroy extracellular matrix, and promote tumor cell invasion and metastasis (Augoff *et al.*, 2022). In addition, high GLUT1 expression is associated with metabolic reprogramming of tumor cells, including increased glucose uptake, lactic acid production, and acidified microenvironment (Pezzuto *et al.*, 2020). Bax activation can increase the permeability of the mitochondrial outer membrane and release apoptosis signaling molecules such as cytochrome C in mitochondria, thus inducing apoptosis (Edlich *et al.*, 2018). In this study, we speculate that circAGFG1's function in promoting BC cell invasion and migration is significantly related to the increased expression of MMP9. In addition, circAGFG1 can increase the glycolytic capacity of BC cells by promoting GLUT1 expression, which will provide powerful energy for the proliferation and metastasis of BC cells. The inhibitory effect of circAGFG1 on Bax may reduce the permeability of the mitochondrial membrane of BC cells, thereby preventing the release of apoptosis signaling molecules, which will help to reduce the apoptosis rate of cancer cells.

However, this study is limited in that the effect of circAGFG1 in multiple models of each BC subtype requires further investigation. In addition, the mechanism of YWHAE regulating BC remains to be further explored. Future multicenter trials are required to illustrate circAGFG1's function in BC.

CONCLUSION

Taken together, this study demonstrates that circAGFG1 targeted regulation of YWHAE expression *via* acting as a sponge of miR-653-5p, thereby promoting BC progression. CircAGFG1/miR-653-5p/YWHAE axis may offer as a latent therapeutic target for BC.

REFERENCES

- Augoff K, Hryniewicz-Jankowska A, Tabola R, Stach K (2022) MMP9: A tough target for targeted therapy for cancer. *Cancers (Basel)* **14**: <https://doi.org/10.3390/cancers14071847>
- Chu M, Fang Y, Jin Y (2021) CircRNAs as promising biomarker in diagnosis of breast cancer: An updated meta-analysis. *J Clin Lab Anal* **35**: e23934. <https://doi.org/10.1002/jcla.23934>
- Cimino D, Fuso L, Sfligoi C, Biglia N, Ponzone R, Maggiorotto F, Russo G, Cicatiello L, Weisz A, Taverna D, Sismonti P, De Bortoli M, De Bortoli M (2008) Identification of new genes associated with breast cancer progression by gene expression analysis of predefined sets of neoplastic tissues. *Int J Cancer* **123**: 1327–1338. <https://doi.org/10.1002/ijc.23660>
- Cui Y, Fan J, Shi W, Zhou Z (2022) Circ_0001667 knockdown blocks cancer progression and attenuates adriamycin resistance by depleting NCOA3 *via* releasing miR-4458 in breast cancer. *Drug Dev Res* **83**: 75–87. <https://doi.org/10.1002/ddr.21845>
- Ding X, Zheng J, Cao M (2021) Circ_0004771 accelerates cell carcinogenic phenotypes *via* suppressing miR-1253-mediated DDAH1 inhibition in breast cancer. *Cancer Manag Res* **13**: 1–11. <https://doi.org/10.2147/cmar.s273783>
- Edlich F (2018) BCL-2 proteins and apoptosis: Recent insights and unknowns. *Biochem Biophys Res Commun* **500**: 26–34. <https://doi.org/10.1016/j.bbrc.2017.06.190>
- Fu B, Liu W, Zhu C, Li P, Wang L, Pan L, Li K, Cai P, Meng M, Wang Y, Zhang A, Tang W, An M (2021) Circular RNA circB-CBM1 promotes breast cancer brain metastasis by modulating miR-125a/BRD4 axis. *Int J Biol Sci* **17**: 3104–3117. <https://doi.org/10.7150/ijbs.58916>
- Gong G, She J, Hu F, D, Zhen D, Zhang B (2021) Circular RNA circ_0084927 regulates proliferation, apoptosis, and invasion of breast cancer cells *via* miR-142-3p/ERC1 pathway. *Am J Transl Res* **13**: 4120–4136
- Han W, Wang L, Zhang L, Wang Y, Li Y (2019) Circular RNA circRAD23B promotes cell growth and invasion by miR-593-3p/CND2 and miR-653-5p/TIAM1 pathways in non-small cell lung cancer. *Biochem Biophys Res Commun* **510**: 462–466. <https://doi.org/10.1016/j.bbrc.2019.01.131>
- He X, Xu T, Hu W, Tan Y, Wang D, Wang Y, Zhao C, Yi Y, Xiong M, Lv W, Wu M, Li X, Wu Y, Zhang Q (2021) Circular RNAs: their role in the pathogenesis and orchestration of breast cancer. *Front Cell Dev Biol* **9**: 647736. <https://doi.org/10.3389/fcell.2021.647736>
- Holmes TR, Al Matouq J, Holmes M, Sioda N, Rudd JC, Bloom C, Nicola L, Palermo NY, Madson JG, Lovas S, Hansen LA (2021) Targeting 14-3-3 ϵ activates apoptotic signaling to prevent cutaneous squamous cell carcinoma. *Carcinogenesis* **42**: 232–242. <https://doi.org/10.1093/carcin/bgaa091>
- Leal MF, Ribeiro HF, Rey JA, Pinto GR, Smith MC, Moreira-Nunes CA, Assumpção PP, Lamarão LM, Calcagno DQ, Montenegro RC, Burbano RP (2016) YWHAE silencing induces cell proliferation, invasion and migration through the up-regulation of CDC25B and MYC in gastric cancer cells: new insights about YWHAE role in the tumor development and metastasis process. *Oncotarget* **7**: 85393–85410. <https://doi.org/10.18632/oncotarget.13381>
- Li C, Peng S, Tang C (2021) MicroRNA-4521 targets hepatoma up-regulated protein (HURP) to inhibit the malignant progression of breast cancer. *Bioengineered*. <https://doi.org/10.1080/21655979.2021.1996016>
- Li H, Jin X, Liu B, Zhang P, Chen W, Li Q (2019) CircRNA CBL11 suppresses cell proliferation by sponging miR-6778-5p in colorectal cancer. *BMC Cancer* **19**: 826. <https://doi.org/10.1186/s12885-019-6017-2>
- Li X, Wang C, Wang S, Hu Y, Jin S, Liu O, Gou R, Nie X, Liu J, Lin B (2021) YWHAE as an HE4 interacting protein can influence the malignant behaviour of ovarian cancer by regulating the PI3K/AKT and MAPK pathways. *Cancer Cell Int* **21**: 302. <https://doi.org/10.1186/s12935-021-01989-7>
- Li Z, Fan H, Chen W, Xiao J, Ma X, Ni P, Xu Z, Yang L (2021) MicroRNA-653-5p promotes gastric cancer proliferation and metastasis by targeting the SOCS6-STAT3 pathway. *Front Mol Biosci* **8**: 655580. <https://doi.org/10.3389/fmolb.2021.655580>
- Liu F, Hu L, Pei Y, Zheng K, Wang W, Li S, Qiu E, Shang G, Zhang J, Zhang X (2020) Long non-coding RNA AFAP1-AS1 accelerates the progression of melanoma by targeting miR-653-5p/RAI14 axis. *BMC Cancer* **20**: 258. <https://doi.org/10.1186/s12885-020-6665-2>
- Liu J, Peng X, Liu Y, Hao R, Zhao R, Zhang L, Zhao F, Liu Q, Liu Y, Qi Y (2021) The diagnostic value of serum exosomal hsa_circ_0000615 for breast cancer patients. *Int J Gen Med* **14**: 4545–4554. <https://doi.org/10.2147/ijgm.s319801>
- Ma X, Wang C, Chen J, Wei D, Yu F, Sun J (2021) circAGFG1 sponges miR-28-5p to promote non-small-cell lung cancer progression through modulating HIF-1 α level. *Open Med (Wars)* **16**: 703–717. <https://doi.org/10.1515/med-2021-0269>
- Ma Y, Niu X, Yan S, Liu Y, Dong R, Li Y (2021) Circular RNA profiling facilitates the diagnosis and prognostic monitoring of breast cancer: A pair-wise meta-analysis. *J Clin Lab Anal* **35**: e23575. <https://doi.org/10.1002/jcla.23575>
- Mashouri L, Yousefi H, Aref AR, Ahadi AM, Molaei F, Alahari SK (2019) Exosomes: composition, biogenesis, and mechanisms in cancer metastasis and drug resistance. *Mol Cancer* **18**: 75. <https://doi.org/10.1186/s12943-019-0991-5>
- Ou WB, Lundberg MZ, Zhu S, Bahri N, Kyriazoglou A, Xu L, Chen T, Mariño-Enríquez A, Fletcher JA (2021) YWHAE-NUTM2 oncoprotein regulates proliferation and cyclin D1 *via* RAF/MAPK and Hippo pathways. *Oncogenesis* **10**: 37. <https://doi.org/10.1038/s41389-021-00327-w>
- Park S, Han SH, Kim HG, Jeong J, Choi M, Kim HY, Kim MG, Park JK, Han JE, Cho GJ, Kim MO, Ryoo ZY, Choi SK (2019) PRPF4 is a novel therapeutic target for the treatment of breast cancer by influencing growth, migration, invasion, and apoptosis of breast cancer cells *via* p38 MAPK signaling pathway. *Mol Cell Probes* **47**: 101440. <https://doi.org/10.1016/j.mcp.2019.101440>
- Pezzuoto A, D'Ascanio M, Ricci A, Pagliuca A, Carico E (2020) Expression and role of p16 and GLUT1 in malignant diseases and lung cancer: A review. *Thorac Cancer* **11**: 3060–3070. <https://doi.org/10.1111/1759-7714.13651>
- Qi L, Sun B, Yang B, Lu S (2021) circHIPK3 (hsa_circ_0000284) Promotes proliferation, migration and invasion of breast cancer cells *via* miR-326. *Oncotargets Ther* **14**: 3671–3685. <https://doi.org/10.2147/ott.s299190>
- Qi X, Zhang DH, Wu N, Xiao JH, Wang X, Ma W (2015) ceRNA in cancer: possible functions and clinical implications. *J Med Genet* **52**: 710–718. <https://doi.org/10.1136/jmedgenet-2015-103334>
- Wan L, Han Q, Zhu B, Kong Z, Feng E (2022) Circ-TFF1 facilitates breast cancer development *via* regulation of miR-338-3p/FGFR1 axis. *Biochem Genet* **60**: 315–335. <https://doi.org/10.1007/s10528-021-10102-6>
- Wang X, Chen M, Fang L (2021) hsa_circ_0068631 promotes breast cancer progression through c-Myc by binding to EIF4A3. *Mol Ther Nucleic Acids* **26**: 122–134. <https://doi.org/10.1016/j.omtn.2021.07.003>
- Wu F, Zhou J (2019) CircAGFG1 promotes cervical cancer progression *via* miR-370-3p/RAF1 signaling. *BMC Cancer* **19**: 1067. <https://doi.org/10.1186/s12885-019-6269-x>
- Wu H, Xu J, Gong G, Zhang Y, Wu S (2021) CircARL8B contributes to the development of breast cancer *via* regulating miR-653-5p/HMGA2 axis. *Biochem Genet* **59**: 1648–1665. <https://doi.org/10.1007/s10528-021-10082-7>
- Wu N, Song H, Ren Y, Tao S, Li S (2020) DGUOK-AS1 promotes cell proliferation in cervical cancer *via* acting as a ceRNA of miR-653-5p. *Cell Biochem Funct* **38**: 870–879. <https://doi.org/10.1002/cbf.3506>
- Wu X, Ren Y, Yao R, Zhou L, Fan R (2021) Circular RNA circMMP11 contributes to lapatinib resistance of breast cancer cells by regulating the miR-153-3p/ANLN Axis. *Front Oncol* **11**: 639961. <https://doi.org/10.3389/fonc.2021.639961>
- Xie H, Wang J, Wang B (2021) Circular RNA Circ_0003221 promotes cervical cancer progression by regulating miR-758-3p/CPEB4 axis. *Cancer Manag Res* **13**: 5337–5350. <https://doi.org/10.2147/cmar.s311242>
- Xie H, Xiao R, He Y, He L, Xie C, Chen J, Hong Y (2021) MicroRNA-100 inhibits breast cancer cell proliferation, invasion and migration by targeting FOXA1. *Oncol Lett* **22**: 816. <https://doi.org/10.3892/ol.2021.13077>
- Yang YF, Lee YC, Wang YY, Wang CH, Hou MF, Yuan SF (2019) YWHAE promotes proliferation, metastasis, and chemoresistance in breast cancer cells. *Kaohsiung J Med Sci* **35**: 408–416. <https://doi.org/10.1002/kjm2.12075>
- Zhang C, Liu N (2022) Noncoding RNAs in the glycolysis of ovarian cancer. *Front Pharmacol* **13**: 855488. <https://doi.org/10.3389/fphar.2022.855488>
- Zhang D, Li C, Cheng N, Sun L, Zhou X, Pan G, Zhao J (2021) CircAGFG1 acts as a sponge of miR-4306 to stimulate esophageal cancer progression by modulating MAPRE2 expression. *Acta Histochem* **123**: 151776. <https://doi.org/10.1016/j.acthis.2021.151776>
- Zhang L, Zhang W, Zuo Z, Tang J, Song Y, Cao F, Yu X, Liu S, Cai X (2022) Circ_0008673 regulates breast cancer malignancy by miR-153-3p/CFL2 axis. *Arch Gynecol Obstet* **305**: 223–232. doi:10.1007/s00404-021-06149-w

Downregulation of circular RNA 00091761 protects against heart failure after myocardial infarction via microRNA-335-3p/ ASCL4 axis

Qian Wei^{1#}, Mengni Jiang^{2#}, Bin Tang¹, Lanlan You¹ and Lin Zhao^{1✉}

¹Department of Ultrasonics Medicine, Chengdu Medical College, Clinical Medical College and The First Affiliated Hospital of Chengdu Medical College, Sichuan 610500 China; ²Department of Cardiovascular Medicine, Chengdu Medical College, Clinical Medical College and The First Affiliated Hospital of Chengdu Medical College, Sichuan 610500 China

Our research tended to explore the biological roles and expression status of circ_00091761 in HF after MI. The hypoxia reoxygenation (H/R) injured H9c2 cells model was constructed to simulate HF after MI. The expression of circ_00091761 was examined in H/R injured H9c2 cells by qRT-PCR. Then, the effect of circ_00091761 expression on the proliferation of H/R injured H9c2 cells was evaluated by CCK-8 along with TUNEL assay. Secretion of lactate dehydrogenase (LDH), reactive oxygen species (ROS), Fe²⁺, glutathione (GSH), and malondialdehyde (MDA) was measured to evaluate cell ferroptosis of H/R injured H9c2 cells, along with protein levels of glutathione peroxidase 4 (GPX4), solute carrier family 7 member 11 (SLC7A11), and transferrin receptor protein (TFRC). Luciferase reporter as well as RNA pull-down assays revealed the binding relationship between miR-335-3p and circ_00091761 or ASCL4. Circ_00091761 was upregulated in H/R injured H9c2 cells. Knockdown of circ_00091761 promoted cell proliferation and suppressed ferroptosis of H/R injured H9c2 cells. Interestingly, circ_00091761 sponges miR-335-3p to upregulate acyl-CoA synthetase long-chain family member 4 (ACSL4) expression. miR-335-3p inhibitor attenuated the effects of circ_00091761 knockdown on cell proliferation and ferroptosis in H/R injured H9c2 cells. Additionally, upregulated ACSL4 abrogated elevated miR-335-3p-induced effects on H/R injured H9c2 cells. Circ_00091761 inhibited cell proliferation and accelerated ferroptosis of H/R injured H9c2 cells by sponging miR-335-3p to upregulated TFRC axis. Therefore, Inhibition of circ_00091761 may protect against HF after MI.

Keywords: heart failure, myocardial infarction, circ_00091761, miR-335-3p, ASCL4

Received: 23 June, 2022; **revised:** 30 December, 2022; **accepted:** 01 February, 2023; **available on-line:** 06 September, 2023

✉e-mail: drzhaolin@hotmail.com

[#]These authors contributed equally to this work and should be considered co-first authors.

Abbreviations: ACSL4, acyl-CoA synthetase long-chain family member 4; CCK-8, Cell Counting Kit-8; circRNA, circular RNA; DCFH-DA, 2',7'-Dichlorodihydrofluorescein diacetate; DMEM, dulbecco's modification of eagle's medium; ECL, enhanced chemiluminescence; Fer-1, ferrostatin-1; GPX4, glutathione peroxidase 4; GSH, glutathione; H/R, hypoxia reoxygenation; HF, heart failure; LDH, lactate dehydrogenase; MDA, malondialdehyde; MI, myocardial infarction; miRNA, micro RNA; NC, negative control; OE, overexpression; PVDF, polyvinylidene fluoride; qRT-PCR, quantitative real time polymerase chain reaction; ROS, reactive oxygen species; SD, standard deviation; SLC7A11, solute carrier family 7 member 11; TFR1, transferrin receptor protein; TUNEL, TdT-mediated dUTP nick end labeling

INTRODUCTION

Heart failure (HF) is an acute decompensation of cardiac function under various causes. The etiology and inducement of HF are complex and diverse. The necrosis of myocardial cells caused by acute ischemia and hypoxia of the coronary artery during myocardial infarction (MI) is the main cause of HF and also one of the common causes of acute decompensation of HF (Bahit *et al.*, 2018; Orrem *et al.*, 2018). HF after MI seriously endangers the life and health of patients. Early accurate judgment will greatly benefit the treatment and prognosis of the disease.

In recent years, a new type of programmed death, named ferroptosis, is found to play an essential role in diverse disorders (Xie *et al.*, 2016). Because of the dysfunction of oxidative metabolism of the cell membrane phospholipids, biofilm polyunsaturated fatty acids (PUFAs) lipid peroxidation occurs reduced glutathione (GSH) in cells will not be able to return the excess of harmful lipid hydroperoxide as harmless fatty alcohols, free iron ion mediated Fenton reaction catalyzed the accumulation of lipid free radicals within the cell leads to cell ferroptosis (Cao & Dixon, 2016). Accumulated evidence demonstrates that ferroptosis participates in HF after MI (Hu *et al.*, 2021). However, the specific mechanism needs to be further researched to clarify.

Circular RNAs (circRNAs) are a class of non-coding RNAs (ncRNAs) which can regulate the expression of several key genes by combining with microRNAs (miRNAs) or other molecules (Meng *et al.*, 2017; Ashwal-Fluss *et al.*, 2014; Zhang *et al.*, 2017). Most circRNAs show miRNA binding capabilities, and are identified as miRNA sponges and enhance downstream gene expression by sponging miRNA (Li *et al.*, 2019). Recently, researchers found the significance of circRNAs in regulating cell functions and disease processes (Meng *et al.*, 2017; Ashwal-Fluss *et al.*, 2014; Zhang *et al.*, 2017). Furthermore, growing evidence shows that circRNA has the potential to become a promising biomarker for diagnosis and therapeutic targets of HF after MI (Devaux *et al.*, 2017; Altesha *et al.*, 2019). For instance, through the ceRNA mechanism, the circHspk3 accelerates cardiac regeneration after MI via the miR-133a-CTGF axis (Si *et al.*, 2020).

CircRNA_0001654, circRNA_00091761, circRNA_0405624, and circRNA_0406698 have been identified to be obviously upregulated in MI (Zhao *et al.*, 2020), and circRNA_00091761 expressions were demonstrated to be the most significant difference in H/R injured H9c2 cells.

Therefore, this study aimed to further explore the specific mechanism of circRNA_0091761 in HF after MI *in vitro*.

MATERIALS AND METHODS

Materials

H9c2 rat cardiomyoblast cell line (American Type Culture Collection, USA). Primary antibodies and internal reference protein (Abcam Company, USA): anti-GPX4 (ab125066, 1: 1000), anti-SLC7A11 (ab175186, 1: 3000), and anti-TFR1 (ab214039, 1: 1000). anti-GAPDH (ab8245, 1: 1000). HRP labeled anti-rabbit secondary antibody (Beyotime Biotech, China). Plasmids for cell transfection (Gibco, USA): si-circ_0091761 1#, si-circ_0091761 2#, miR-335-3p mimic, miR-335-3p inhibitor, oe-AC14, and their negative controls. Polybrene and purinomycin (Sigma, USA). Lipofectamine 3000 and the reverse transcription kit (Invitrogen, USA). Fetal bovine serum (FBS; Biological Industries, USA). PrimeScript™ RT-PCR Kit (Vazyme Biotech, China). TRIzol reagent (Invitrogen, USA), Nanodrop 2000 spectrophotometer (Mettler Toledo, China). RIPA lysate (Beyotime, China). Primer sequences for circ_0091761, miR-335-3p, and all mRNAs were designed by RiboBio (Guangzhou, China). RNase R treatment (Genesee, Guangzhou, China). miRNeasy Mini Kit (QIAGEN, Dusseldorf, Germany). Actinomycin D (Merk, USA). SuperScript First-Strand Synthesis Kit (Invitrogen, USA). LDH Cytotoxicity Assay Kit (Beyotime, China). Spectrophotometer (Thermo Fisher, USA). Oxidation-sensitive fluorescent probe DCFH-DA (Sigma, USA). Iron Assay Kit (ab83366, Abcam, USA). Glutathione Assay Kit (CS0260; Sigma, USA). Malondialdehyde Kit (ab118970, Abcam, USA). Cell counting kit 8 (CCK-8; Beyotime, China). TUNEL detection kit (ab66110, Abcam, USA). Microscope (Nikon, Japan). BCA kit (Sigma, USA). PVDF membranes (Bio-Rad, USA). Dual-Luciferase Reporter Assay kit (K801-200; BioVision Tech, San Francisco, USA). Pierce™ Magnetic RNA-Protein Pull-Down Kit (Thermo Fisher, Waltham, MA, USA).

Cell culture

H9c2 cells were cultured using a DMEM medium containing 10% FBS and 1% penicillin/streptomycin, and placed in an incubator (5% CO₂, 37°C). Then, the hypoxia-reoxygenation (H/R) injured H9c2 cells model was conducted to mimic HF after MI. H9c2 cells were incubated in a hypoxic environment (95% N₂ and 5% CO₂) at 37°C for 3 h. Then, DMEM free of FBS was added to H9c2 cells in a standard incubator for 4 h.

qRT-PCR

qRT-PCR was performed to measure the mRNA levels of circRNA_0001654, circRNA_0091761, circRNA_0405624, circRNA_0406698, miR-335-3p, and ACSL4. Firstly, TRIzol was used to isolate RNA of H/R injured H9c2 cells, and RNA concentration was analyzed using a spectrophotometer. M-MLV was used to synthesize cDNA through reverse transcription. qRT-PCR was conducted with the PrimeScript™ RT-PCR Kit. GAPDH and U6 were used as reference genes. Relative gene expression was calculated through the 2^{-ΔΔCt} method.

Stability detection of circular RNA

RNase R treatment is mainly used for circRNA identification and stability detection (Xiao MS & Wilusz

JE, 2019). 5 μg total RNA extracted from H/R injured H9c2 cells were digested by RNase R enzyme. The circRNA_0091761 and the linear type mRNA levels were detected by qRT-PCR with 2 μg/mL actinomycin D for 0, 4, 8, 12, and 24 h.

Detection of lactate dehydrogenase (LDH) activity

H9c2 cells were seeded in 96-well plates and cultured in a medium containing LDH reagent for 0.5 h to measure LDH release according to the LDH kit procedure, which was provided by Nanjing Jiangcheng Bioengineering Institute (Nanjing, China).

Detection of reactive oxygen species (ROS) activity

H9c2 cells were treated with DCFH-DA (10 μmol/L) for 0.5 h at 37°C. Then, the fluorescence intensity of each group was detected under a fluorescence microscope (488 nm excitation wavelength, 525 nm emission wavelength).

Detection of Fe²⁺ content

After H9c2 cells were lysed, the Fe²⁺ level of cells in each group was detected according to the procedure of the Fe²⁺ detection kit, which was provided by Nanjing Jiangcheng Bioengineering Institute (Nanjing, China).

Detection of glutathione (GSH) content

After H9c2 cells were lysed, the GSH level of cells in each group was detected according to the procedure of the GSH Assay Kit, which was provided by Nanjing Jiangcheng Bioengineering Institute (Nanjing, China).

Detection of malondialdehyde (MDA)

After H9c2 cells were lysed, the MDA level of cells in each group was detected according to the procedure of the MDA Kit, which was provided by Nanjing Jiangcheng Bioengineering Institute (Nanjing, China).

Cell viability assay

Cell counting kit 8 (Beyotime, Shanghai, China) has been used to evaluate the cell viability of H9c2 cells of each group. Cells were collected and seeded into a 96-well plate after successful transfection. Afterwards, cell viability was detected using a microplate under the absorbance of 450 nm after a supplement of CCK-8 reagents.

TUNEL assay

H9c2 cell death was measured by a TUNEL detection kit according to the instructions of the manual (Beyotime). The H/R injured H9c2 cells were observed under a microscope.

Western blotting assay

Ferroptosis-related proteins including glutathione peroxidase 4 (GPX4), solute carrier family 7 member 11 (SLC7A11), and transferrin receptor protein (TFRC) were measured in H9c2 cells of each group. Total protein was extracted from the H9c2 cells by RIPA buffer, and determined with the BCA kit. Subsequently, proteins were isolated with 12% SDS-PAGE gel and were moved onto PVDF membranes. Then the membranes were blocked with 5% defatted milk for 2 h and then incubated with primary antibodies overnight at 4°C. Immune complexes were then incubated with secondary antibody. Finally, the ECL chemiluminescence method was used to detect the expression of each protein. All experiments were repeated three times.

Dual-luciferase reporter assay

According to the reported methods, circRNA_0091761 as well as ACSL4 recombinant pyratinase reporter plasmids containing the binding sequence of miR-335-3p and regroup plasmids containing the abrupt change of binding sequence were constructed. H9c2 cells (1×10^5 /well) seeded in a 12-well plate were transfected with 1.5 μ g recombinant luciferase reporter plasmid, 100 nmol/L miR-335-3p mimic and 10 ng PRL-TK (internal reference plasmid) for 24 h, the intensity of firefly luciferin and renal luciferin were measured.

RNA pull-down assay

500 μ g streptavidin magnetic beads combined with a 200 pmol biotin labeled miR-335-3p mimic were added to the RNA extracted from the H9c2 cells. The complexes were gently mixed at room temperature and incubated for 30 min. After eluting buffer was added, the pulled RNA complex was then collected. The circRNA_0091761 and ACSL4 level was quantitatively analyzed by qRT-PCR.

Statistical analysis

Data were analyzed with GraphPad Prism version 8.3 and presented as mean \pm SD. Student's t-test (two groups), as well as one-way ANOVA (multiple groups), were applied for difference analysis. A *P* value less than 0.05 was deemed statistically significant.

RESULTS

Circ_0091761 is highly expressed in H/R injured H9c2 cells

Expression of 4 circRNAs which have been identified to be highly expressed in MI was detected in H/R injured H9c2 cells, among which circ_0091761 was obviously highly expressed (Fig. 1A). The results of RNase R treatment indicated that the expression level of the linear group was substantially lower than that in circ_0091761 group (Fig. 1B). Meanwhile, circ_0091761 showed more stable mRNA expression compared with a linear group (Fig. 1C). The level of GSH in H/R injured and RSL3 treated H9c2 cells was notably decreased and increased in Ferrostatin-1 group; however, LDH, ROS, Fe^{2+} , as well as MDA levels were notably elevated by H/R injury and RSL3 and reduced by Ferrostatin-1 (Fig. 1D–I).

Inhibition of circ_0091761 promotes cell viability and inhibited ferroptosis of H/R injured H9c2 cells.

The expression of circ_0091761 was decreased after small interference RNA was transfected into H/R injured H9c2 cells. Circ_0091761 declined more significantly in group si-circ_0091761 1#, which was used in subsequent experiments (Fig. 2A). Knockdown of circ_0091761 notably improved cell viability (Fig. 2B), and suppressed

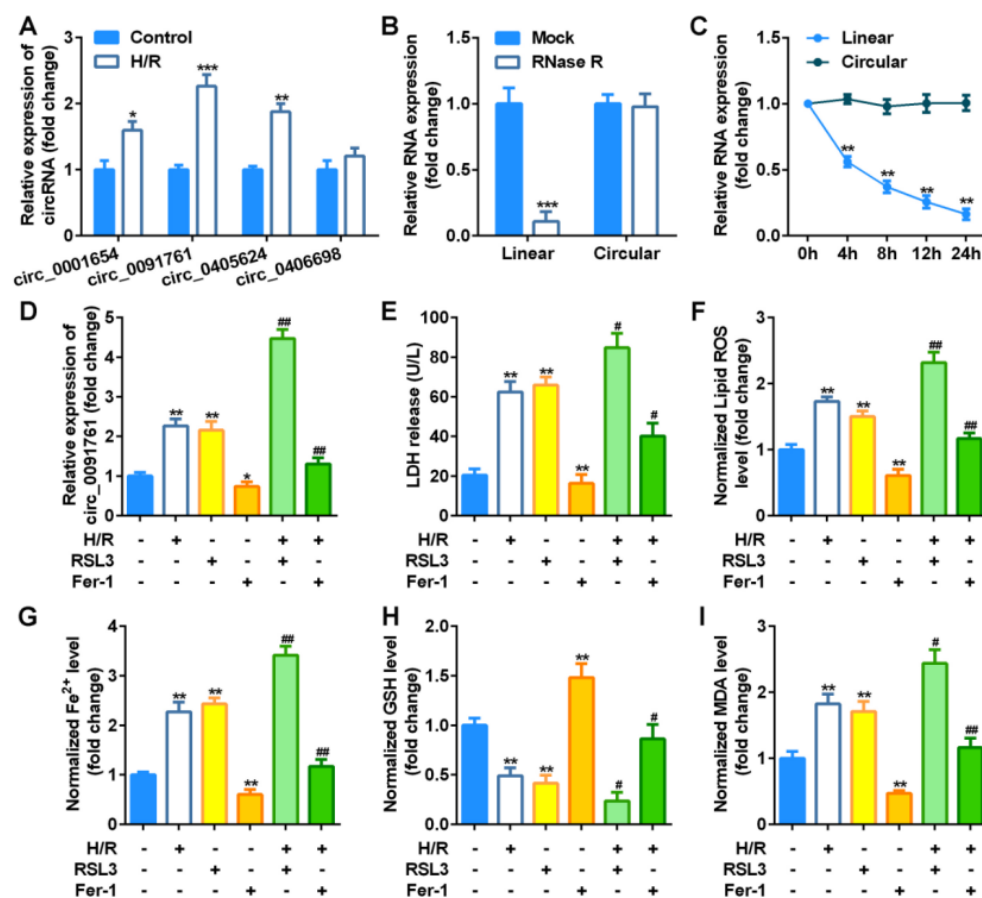


Figure 1. Expression levels of circ_0091761 in H/R injured H9c2 cells.

(A) The expression of 4 circRNAs in H/R injured H9c2 cells measured by qRT-PCR, **p*<0.05, ***p*<0.01, ****p*<0.001. (B) qRT-PCR analyses for the expression of circ_0091761 and linear one in H/R injured H9c2 cells after RNaseR treatment, ****p*<0.001. (C) qRT-PCR analyses for the expression of circ_0091761 and linear one in H/R injured H9c2 cells at the indicated time after treatment with Actinomycin D, ***p*<0.01. (D) The expression of circ_0091761 in H/R injured H9c2 cells measured by qRT-PCR, **p*<0.05, ***p*<0.01, compared with the control group; #*p*<0.01, compared with the H/R group. (E) The LDH, (F) ROS, (G) Fe^{2+} , (H) GSH, and (I) MDA levels in H/R injured and RSL3 treated H9c2 cells, ***p*<0.01, compared with the control group; #*p*<0.05, ##*p*<0.01, compared with the H/R group.

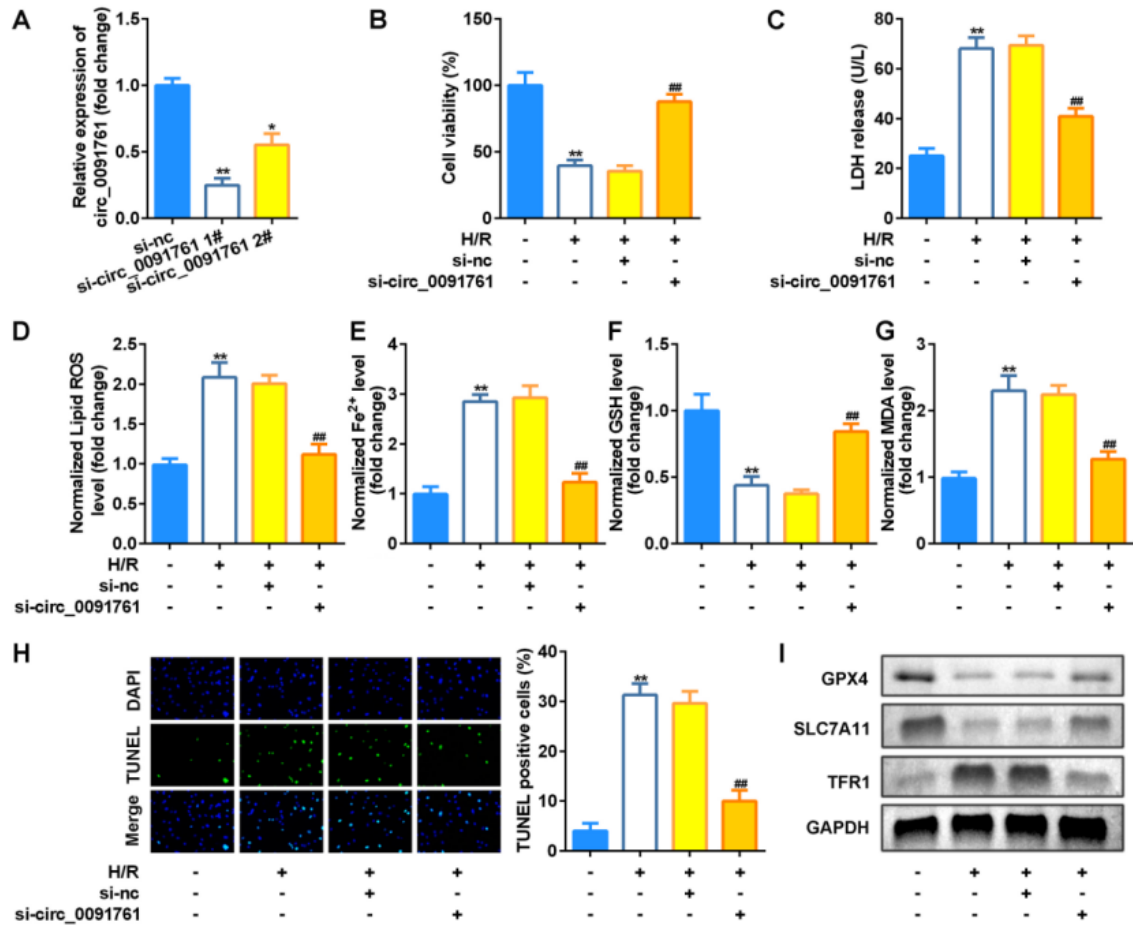


Figure 2. Inhibition of circ_0091761 promoted cell proliferation and inhibited ferroptosis of H/R injured H9c2 cells. (A) Circ_0091761 expression levels were detected by qRT-PCR in H9c2 cells after transfection, $^{*}p<0.05$, $^{**}p<0.01$, compared with the si-nc group. (B) CCK-8 assay was applied for cell viability detection, $^{*}p<0.01$, compared with the control group; $^{##}p<0.01$, compared with the H/R+ si-NC group. (C–G) Levels of LDH, ROS, Fe²⁺, GSH, and MDA in H/R injured H9c2 cells after transfection, $^{*}p<0.01$, compared with the control group; $^{##}p<0.01$, compared with the H/R+ si-NC group. (H) Images and quantized bar chart of TUNEL stained cells, $^{*}p<0.01$, compared with the control group; $^{##}p<0.01$, compared with the H/R+ si-NC group. (I) Expression of GPX4, SLC7A11, and TFR1 proteins detected by western blotting.

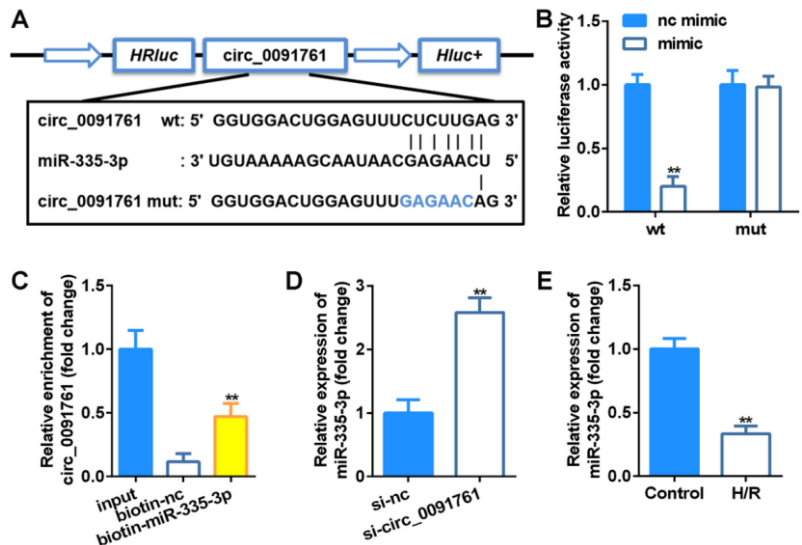


Figure 3. Circ_0091761 served as a miRNA sponge for miR-335-3p (A) The binding sites between miR-335-3p and circ_0091761. (B) Luciferase assay of H9c2 cells co-transfected with mutated miR-335-3p mimic and a luciferase vector containing circ_0091761-3'UTR-wt or mutant constructs with mutated miRNA binding sites, $^{*}p<0.01$. (C) RNA pull-down assay revealed the enrichment of circ_0091761 on biotin-miR-335-3p, $^{*}p<0.01$, compared with the biotin-NC group. (D–E) qRT-PCR analysis for the expression of miR-335-3p, $^{*}p<0.01$.

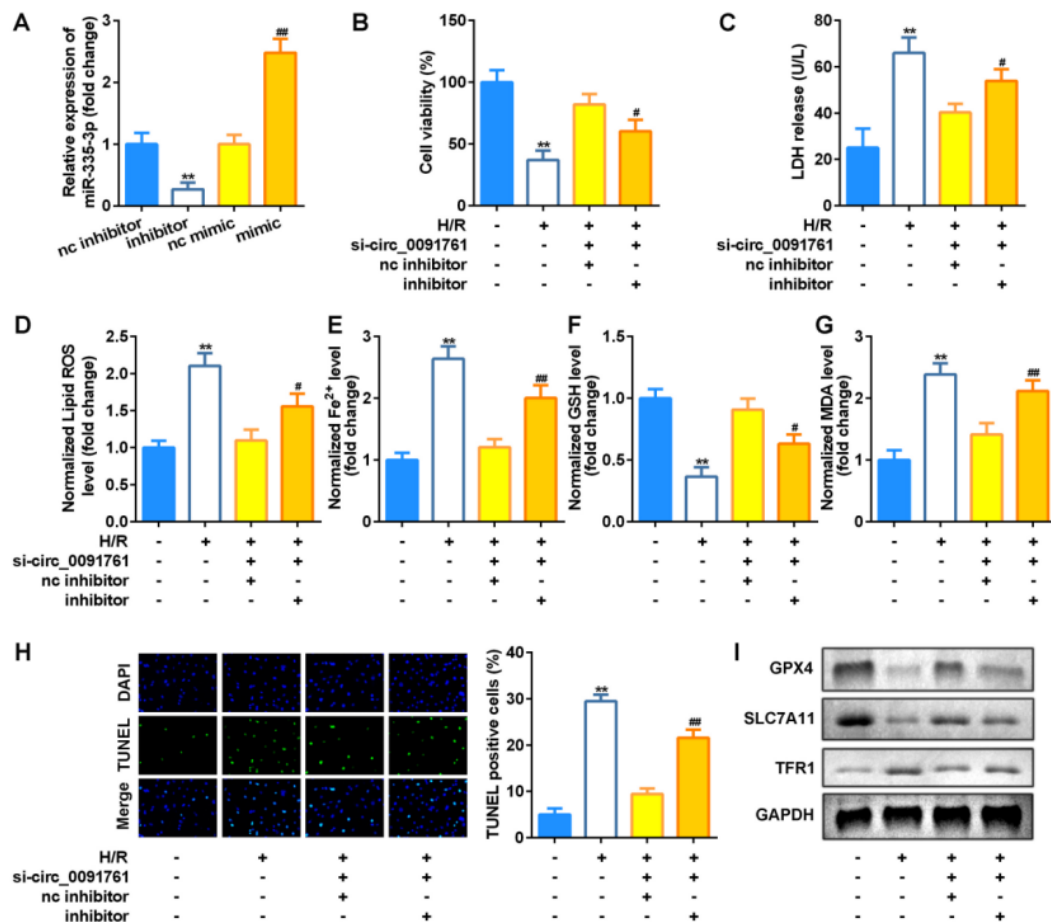


Figure 4. Suppression of miR-335-3p reversed the effects of circ_0091761 on cell proliferation and ferroptosis in H/R injured H9c2 cells.

(A) miR-335-3p expression levels were detected by qRT-PCR in H9c2 cells after transfection, $^{**}p < 0.01$, compared with the NC inhibitor group; $^{##}p < 0.01$, compared with the NC mimic group. (B) CCK-8 assay was applied for cell viability detection, $^{**}p < 0.01$, compared with the control group; $^{##}p < 0.01$, compared with the H/R+ si-circ_0091761+ NC inhibitor group. (C–G) Levels of LDH, ROS, Fe²⁺, GSH, and MDA in H/R injured H9c2 cells after transfection, $^{**}p < 0.01$, compared with the control group; $^{##}p < 0.01$, compared with the H/R+ si-circ_0091761+ NC inhibitor group. (H) Images and quantized bar chart of TUNEL stained cells, $^{**}p < 0.01$, compared with the control group; $^{##}p < 0.01$, compared with the H/R+ si-circ_0091761+ NC inhibitor group. (I) Expression of GPX4, SLC7A11, and TFR1 proteins detected by western blotting.

cell death (Fig. 2H). Simultaneously, LDH, ROS, Fe²⁺, and MDA concentrations were declined while secretion of GSH was induced after circ_0091761 was silenced (Fig. 2C–G). Furthermore, ferroptosis-related proteins were detected. H/R injury decreased the GPX4 as well as SLC7A11 expression and increased the expression of TFR1, which were reversed by si-circ_0091761 significantly (Fig. 2I).

Circ_0091761 can bind with miR-335-3p

Potential interactions between circRNAs and miRNAs were evaluated using a Circular RNA Interactome online database (<https://circinteractome.irp.nih.gov/>), and miR-335-3p was expected to bind with circ_0091761 (Fig. 3A). The luciferase activity reporter results demonstrated that luciferase-labeled miR-335-3p mimic and wild-type circ_0091761 co-transfection groups were decreased compared to that of the NC mimic (Fig. 3B). Furthermore, circ_0091761 was primarily enriched in the biotin-miR-335-3p group analyzed by RNA pull-down assay (Fig. 3C). Inhibition of circ_0091761 upregulated the expression of miR-335-3p (Fig. 3D). Furthermore, miR-335-3p was lowly expressed in H/R injured H9c2 cells (Fig. 3E).

Suppression of miR-335-3p reverses the effects of circ_0091761 on cell viability and ferroptosis in H/R injured H9c2 cells

miR-335-3p expression was downregulated by miR-335-3p inhibitor and upregulated by miR-335-3p mimic, suggesting that H/R injured H9c2 cells were successfully transfected (Fig. 4A). miR-335-3p inhibitor obviously switched the effects of si-circ_0091761 on cell proliferation (Fig. 4B) as well as cell death (Fig. 4H). Furthermore, inhibited miR-335-3p alleviated the effects of downregulated circ_0091761 on the secretion of LDH, ROS, Fe²⁺, MDA, and GSH (Fig. 4C–G) and the expression levels of GPX4, SLC7A11, and TFR1 proteins (Fig. 4I).

miR-335-3p directly targets ACSL4

TargetScan7.2 online database algorithm (http://www.targetscan.org/mmu_72/) was used to predict potential downstream targets of miR-335-3p and we identified ACSL4 as the potential candidate (Fig. 5A). Luciferase activity, as well as RNA pull-down assays further confirmed the binding relationship between miR-335-3p and ACSL4 (Fig. 5B and 5C). Furthermore, ACSL4 expression was negatively regulated by miR-335-3p (Fig. 5D).

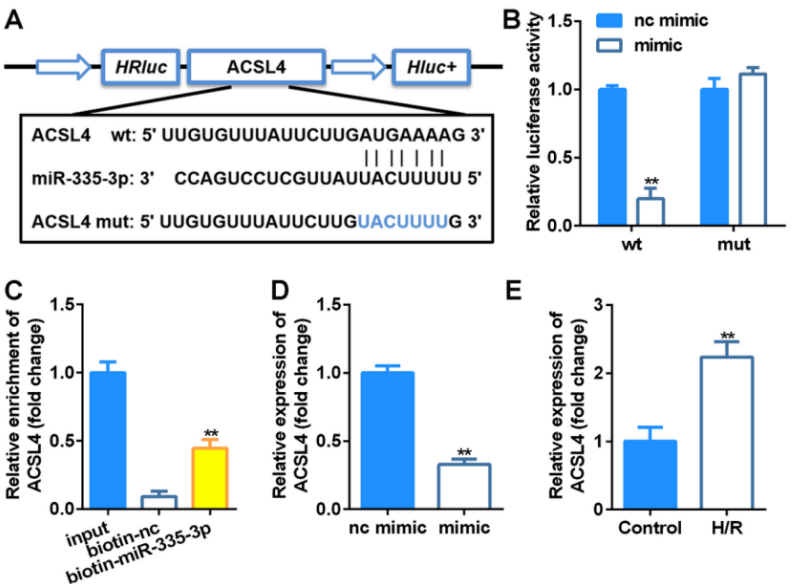


Figure 5. miR-335-3p directly targeted ACSL4. (A) Bioinformatics predicted the binding sites between miR-335-3p and ACSL4. (B) Dual-luciferase reporter assay was conducted to confirm the association between ACSL4 and miR-335-3p, $^{**}p<0.01$. (C) RNA pull-down assay revealed the enrichment of ACSL4 on biotin-miR-335-3p, $^{**}p<0.01$, compared with the biotin-NC group. (D–E) qRT-PCR analysis for the expression of ACSL4, $^{**}p<0.01$.

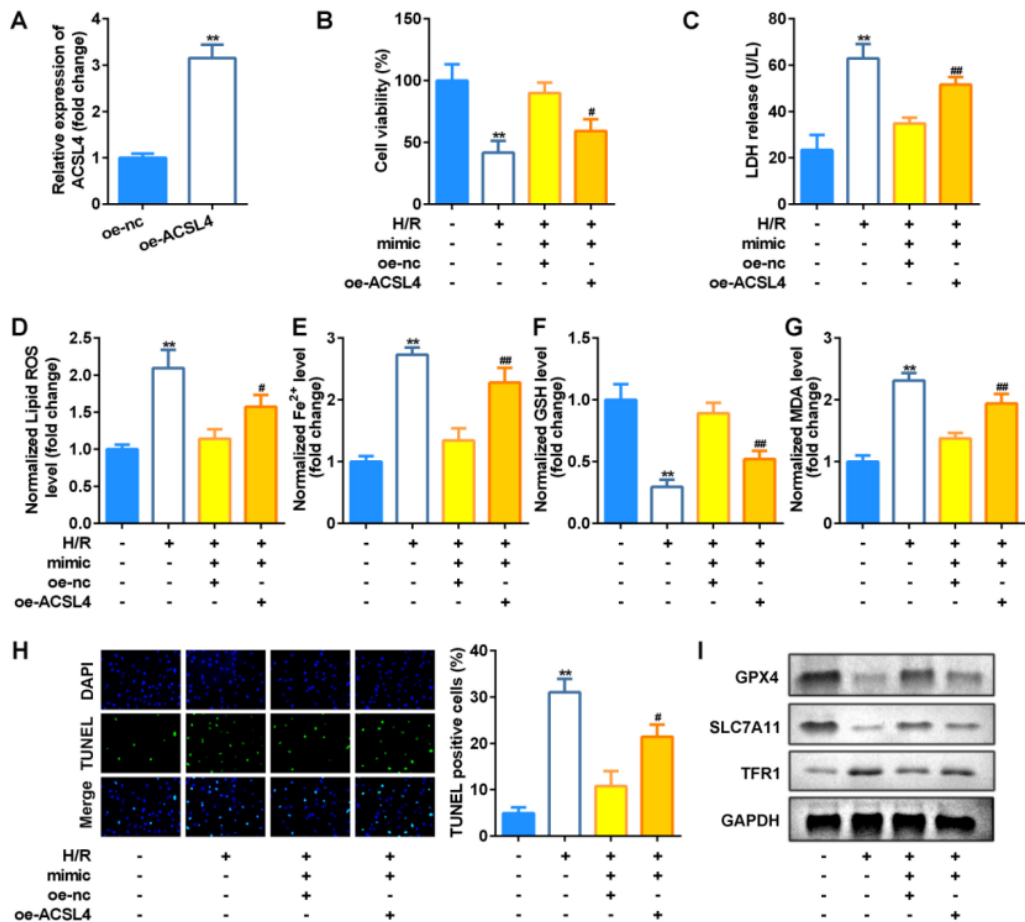


Figure 6. Overexpression of ACSL4 inhibited the effects of upregulated miR-335-3p. (A) ACSL4 expression levels were detected by qRT-PCR in H9c2 cells after transfection, $^{**}p<0.01$. (B) CCK-8 assay was applied for cell viability detection, $^{**}p<0.01$, compared with the control group; $^{*}p<0.05$, compared with the H/R+ mimic+ OE-NC group. (C–G) Levels of LDH, ROS, Fe²⁺, GSH, and MDA in H/R injured H9c2 cells after transfection, $^{**}p<0.01$, compared with the control group; $^{*}p<0.05$, $^{##}p<0.01$, compared with the H/R+ mimic+ OE-NC group. (H) Images and quantized bar chart of TUNEL stained cells, $^{**}p<0.01$, compared with the control group; $^{*}p<0.05$, compared with the H/R+ mimic+ OE-NC group. (I) Expression of GPX4, SLC7A11, and TFR1 proteins detected by western blotting.

Besides, ACSL4 was remarkably highly expressed in H/R injured H9c2 cells (Fig. 5E).

Overexpression of ACSL4 inhibits the effects of upregulated miR-335-3p

As indicated in Fig. 6A, ACSL4 was significantly highly expressed after transfection. Compared with miR-335-3p-overexpressing cells, co-transfection with miR-335-3p and ACSL4 vectors significantly suppressed cell viability (Fig. 6B) and facilitated ferroptosis (Fig. 6C–I).

DISCUSSION

HF is a common complication of MI. MI combined with HF is a clinically acute severe disease with high mortality. There is clinical value in identifying markers that can be obtained early and interpreted easily. Our study suggested that inhibition of circ_0091761 protected HF after MI by upheaving miR-335-3p to inhibit ACSL4 *in vitro*.

Accumulating studies have shown that ferroptosis plays a crucial role in the progression of cardiac dysfunction after MI (Park TJ *et al.*, 2019). In the mouse MI model, GPX4 is downregulated and heme oxygenase 1 (Hmox1) is upregulated in myocardial cells to degrade heme and release free iron, leading to mitochondrial dysfunction and ferroptosis. In addition, inhibition of GPX4 transcription in isolated H9c2 cells and neonatal mouse ventricular myocytes resulted in the accumulation of lipid hydroperoxides leading to cell ferroptosis (Park *et al.*, 2019; Li *et al.*, 2019; Fang *et al.*, 2019). These results suggest that ferroptosis is an important pathophysiological change of cardiac function injury after MI. What's more, ferroptosis participates in the occurrence and development of HF (Fang *et al.*, 2020; Vegter *et al.*, 2016). Inhibiting ferroptosis can reduce cardiomyocyte hypertrophy, improve ventricular dilation, and enhance the function of myocardial dilation and contraction (Fang *et al.*, 2020). *In vitro* cardiomyocytes pretreated with isoproterenol could inhibit the expression of GPX4 and ferritin heavy chain 1, increase the lipid hydroperoxide, and lead to ferroptosis in cardiomyocytes (Park *et al.*, 2019; Fang *et al.*, 2020). Antagonizing ferroptosis can effectively slow down the process of HF (Fang *et al.*, 2019; Friedmann *et al.*, 2014; Li *et al.*, 2020). Ferroptosis inhibitor can effectively inhibit the increase of free iron and lipid peroxidation in cardiomyocytes and reduce ferroptosis induced by isoproterenol (Fang *et al.*, 2019; Zou *et al.*, 2020).

Previous studies have shown that the Fenton reaction of ferrous iron in a labile iron pool (LIP) can produce a large number of ROS (Sui *et al.*, 2018). When the production of ROS exceeds the compensatory limit of GSH/GPX4, PUFAs containing arachidonic acid and adrenal acid are easily peroxidized and accumulated by ROS, leading to ferroptosis in cells (Yang *et al.*, 2016). In other words, GSH/GPX4 can inhibit lipid peroxidation in the cell membrane, thus inhibiting ferroptosis in cells. However, a large amount of studies have discovered new pathways that inhibit cell iron death during GSH/GPX4 inactivation. It was found that the N-terminus of Ferrastatin-1 was myristoylated to promote the recruitment of coenzyme Q10 to the cell membrane, reducing it to a reduced coenzyme, and inhibiting ferroptosis in cells (Bersuker *et al.*, 2019). The antagonistic effect of FSP1 on ferroptosis was independent of GSH/GPX4 (Doll *et al.*, 2019). In addition, the metabolites of guanosine triphosphate hydrolase 1 (GCH-1), tetrahydrobiopterin and dihydrobiopterin (BH4/BH2), can selectively inhibit

the peroxidation of membrane polyunsaturated fatty acids containing two acyl-tail, and GCH1 can promote the production of coenzyme Q10 and inhibit cell ferroptosis in collaboration with FSP1 (Kraft *et al.*, 2020). These studies also found a range of genes that suppress lipid peroxidation in the absence of GPX4, providing new directions for future research. At present, the research on the regulation factors of iron death is still insufficient and needs further exploration.

Circ_0091761 is a newfound circRNA with a sliced length of 709bp, located on the X chromosome. Zhao *et al.* collected blood samples of coronary arteries of MI patients as well as healthy controls, the intersection results of multiple bioinformatics analysis data showed that 4 dysregulated circRNAs (circRNA_0001654, circRNA_0091761, circRNA_0405624, and circRNA_0406698) may be associated with the regulation of MI process (Zhao *et al.*, 2020). In the present research, our data suggested that circRNA_0091761 was the highest expressed circRNA identified in H/R injured H9c2 cells, and was further elevated by ferroptosis inducer RSL3 whereas downregulated by ferroptosis inhibitor Ferrastatin-1, suggesting that upregulation of circ_0091761 may be associated with ferroptosis in H/R injured H9c2 cells. Subsequently, inhibition of circ_0091761 promoted cell viability and suppressed ferroptosis of H/R injured H9c2 cells, demonstrating that circ_0091761 may protect against HF after MI by suppressing ferroptosis *in vitro*, which was in line with previous studies (Fang *et al.*, 2020).

Recently, various studies have reported that miRNAs play essential roles in cardiovascular diseases (Vegter *et al.*, 2016). For instance, the downregulation of miR-221-3p and miR-222-3p promoted myocardial fibrosis of HF (Verjans *et al.*, 2018). In MI studies, miRNA-21 treatment of cardiomyocytes and endothelial cells significantly suppressed apoptosis and significantly improved cardiac function (Song *et al.*, 2019). In this study, we hypothesized that circRNA_0091761 might bind certain miRNAs to regulate HF after MI. Our data indicated that miR-335-3p has a specific binding effect with circRNA_0091761. Further functional experiments confirmed that miR-335-3p inhibitor could effectively reduce the proliferation promotion and ferroptosis inhibition effects of suppressed circRNA_0091761 on H/R injured H9c2 cells. All results confirmed that circRNA_0091761 can regulate the expression of related genes by binding miR-335-3p and play a role in inhibiting ferroptosis and thus HF progression.

ACSL4 drives ferroptosis by oxidizing cell membrane phospholipids, which have been recognized to be a typical marker of ferroptosis (Doll *et al.*, 2017; Song *et al.*, 2019). The ectonucleotide pyrophosphatase-phosphodiesterase 2 (ENPP2)/lysophosphatidic acid (LPA) protected myocardial cells from erastin induced ferroptosis by regulating the expression of GPX4, ACSL4 and Nrf2 (Bai *et al.*, 2018). Our finding demonstrated that ACSL4 was a downstream gene of miR-335-3p, and overexpression ACSL4 obviously revealed miR-335-3p mimicked induced effects on cell viability as well as ferroptosis. Thence, on the basis of these findings, we concluded that circ_0091761 promoted ferroptosis in H/R injured H9c2 cells via binding with miR-335-3p to upregulate ACSL4.

CONCLUSION

The findings of the present study indicated that circ_0091761 functioned as a ceRNA to regulate ACSL4 expression by sponging miR-335-3p to regulate HF after the MI process *in vitro*. Therefore, inhibition of

circ_0091761 may be a potential target for protection against HF after MI.

Declarations

Funding. Not applicable.

Conflict of Interests. The authors confirm that no conflicts of interest exist in this work.

Acknowledgments. Not applicable.

Ethical approval. No ethics approval was required for this study as it involved no human participants or animals.

REFERENCES

- Altesha MA, Ni T, Khan A, Liu K, Zheng X (2019) Circular RNA in cardiovascular disease. *J Cell Physiol* **234**: 5588–5600. <https://doi.org/10.1002/jcp.27384>
- Ashwal-Fluss R, Meyer M, Pamudurti NR, Ivanov A, Bartok O, Hanan M, Evantal N, Memczak S, Rajewsky N, Kadener S (2014) circRNA biogenesis competes with pre-mRNA splicing. *Mol Cell* **56**: 55–66. <https://doi.org/10.1016/j.molcel.2014.08.019>
- Bahit MC, Kochar A, Granger CB (2018) Post-myocardial infarction heart failure. *JACC Heart Fail* **6**: 179–186. <https://doi.org/10.1016/j.jchf.2017.09.015>
- Bai YT, Chang R, Wang H, Xiao FJ, Ge RL, Wang LS (2018) ENPP2 protects cardiomyocytes from erastin-induced ferroptosis. *Biochem Biophys Res Commun* **499**: 44–51. <https://doi.org/10.1016/j.bbrc.2018.03.113>
- Bersuker K, Hendricks JM, Li Z, Magtanong L, Ford B, Tang PH, Roberts MA, Tong B, Maimone TJ, Zoncu R, Bassik MC, Nomura DK, Dixon SJ, Olzmann JA (2019) The CoQ oxidoreductase FSP1 acts parallel to GPX4 to inhibit ferroptosis. *Nature* **575**: 688–692. <https://doi.org/10.1038/s41586-019-1705-2>
- Cao JY, Dixon SJ (2016) Mechanisms of ferroptosis. *Cell Mol Life Sci* **73**: 2195–209. <https://doi.org/10.1007/s00018-016-2194-1>
- Devaux Y, Creemers EE, Boon RA, Werfel S, Thum T, Engelhardt S, Dimmeler S, Squire I (2017) Cardiolinc network. Circular RNAs in heart failure. *Eur J Heart Fail* **19**: 701–709. <https://doi.org/10.1002/ehf.801>
- Doll S, Freitas FP, Shah R, Aldrovandi M, da Silva MC, Ingold I, Goya Grocin A, Xavier da Silva TN, Panzilius E, Scheel CH, Mourão A, Buday K, Sato M, Wanninger J, Vignane T, Mohana V, Rehberg M, Flatley A, Schepers A, Kurz A, White D, Sauer M, Sattler M, Tate EW, Schmitz W, Schulze A, O'Donnell V, Proneth B, Popowicz GM, Pratt DA, Angeli JPF, Conrad M (2019) FSP1 is a glutathione-independent ferroptosis suppressor. *Nature* **575**: 693–698. <https://doi.org/10.1038/s41586-019-1707-0>
- Doll S, Proneth B, Tyurina YY, Panzilius E, Kobayashi S, Ingold I, Irmeler M, Beckers J, Aichler M, Walch A, Prokisch H, Trümbach D, Mao G, Qu F, Bayir H, Füllekrug J, Scheel CH, Wurst W, Schick JA, Kagan VE, Angeli JP, Conrad M (2017) ACSL4 dictates ferroptosis sensitivity by shaping cellular lipid composition. *Nat Chem Biol* **13**: 91–98. <https://doi.org/10.1038/nchembio.2239>
- Fang X, Cai Z, Wang H, Han D, Cheng Q, Zhang P, Gao F, Yu Y, Song Z, Wu Q, An P, Huang S, Pan J, Chen HZ, Chen J, Linkermann A, Min J, Kagan VE (2020) Loss of cardiac ferritin h facilitates cardiomyopathy via SLC7A11-mediated ferroptosis. *Circ Res* **127**: 486–501. <https://doi.org/10.1161/CIRCRESAHA.120.316509>
- Fang X, Wang H, Han D, Xie E, Yang X, Wei J, Gu S, Gao F, Zhu N, Yin X, Cheng Q, Zhang P, Dai W, Chen J, Yang F, Yang HT, Linkermann A, Gu W, Min J, Wang F (2019) Ferroptosis as a target for protection against cardiomyopathy. *Proc Natl Acad Sci U S A* **116**: 2672–2680. <https://doi.org/10.1073/pnas.1821022116>
- Friedmann Angeli JP, Schneider M, Proneth B, Tyurina YY, Tyurin VA, Hammond VJ, Herbach N, Aichler M, Walch A, Eggenhofer E, Basavarajappa D, Rådmark O, Kobayashi S, Seibt T, Beck H, Neff F, Esposito I, Wanke R, Förster H, Yefremova O, Heinrichmeyer M, Bornkamm GW, Geissler EK, Thomas SB, Stockwell BR, O'Donnell VB, Kagan VE, Schick JA, Conrad M (2014) Inactivation of the ferroptosis regulator Gpx4 triggers acute renal failure in mice. *Nat Cell Biol* **16**: 1180–1191. <https://doi.org/10.1038/ncb3064>
- Hu H, Chen Y, Jing L, Zhai C, Shen L (2021) The link between ferroptosis and cardiovascular diseases: a novel target for treatment. *Front Cardiovasc Med* **8**: 710963. <https://doi.org/10.3389/fcvm.2021.710963>
- Kraft VAN, Bezjian CT, Pfeiffer S, Ringelstetter L, Müller C, Zandkarimi F, Merl-Pham J, Bao X, Anastasov N, Kössl J, Brandner S, Daniels JD, Schmitt-Kopplin P, Hauck SM, Stockwell BR, Hadian K, Schick JA (2020) GTP Cyclohydrolase 1/tetrahydrobiopterin counteract ferroptosis through lipid remodeling. *ACS Cent Sci* **6**: 41–53. <https://doi.org/10.1021/acscentsci.9b01063>
- Li M, Duan L, Li Y, Liu B (2019) Long noncoding RNA/circular noncoding RNA-miRNA-mRNA axes in cardiovascular diseases. *Life Sci* **233**: 116440. <https://doi.org/10.1016/j.lfs.2019.04.066>
- Li W, Feng G, Gauthier JM, Lokshina I, Higashikubo R, Evans S, Liu X, Hassan A, Tanaka S, Cicka M, Hsiao HM, Ruiz-Perez D, Bredemeyer A, Gross RW, Mann DL, Tyurina YY, Gelman AE, Kagan VE, Linkermann A, Lavine KJ, Kreisel D (2019) Ferroptotic cell death and TLR4/Trif signaling initiate neutrophil recruitment after heart transplantation. *J Clin Invest* **129**: 2293–2304. <https://doi.org/10.1172/JCI126428>
- Li Y, Cao Y, Xiao J, Shang J, Tan Q, Ping F, Huang W, Wu F, Zhang H, Zhang X (2020) Inhibitor of apoptosis-stimulating protein of p53 inhibits ferroptosis and alleviates intestinal ischemia/reperfusion-induced acute lung injury. *Cell Death Differ* **27**: 2635–2650. <https://doi.org/10.1038/s41418-020-0528-x>
- Meng S, Zhou H, Feng Z, Xu Z, Tang Y, Li P, Wu M (2017) CircRNA: functions and properties of a novel potential biomarker for cancer. *Mol Cancer* **16**: 94. <https://doi.org/10.1186/s12943-017-0663-2>
- Orrem HL, Nilsson PH, Pischke SE, Grindheim G, Garred P, Seljelot I, Husebye T, Aukrust P, Yndestad A, Andersen GO, Barratt-Due A, Mollnes TE (2018) Acute heart failure following myocardial infarction: complement activation correlates with the severity of heart failure in patients developing cardiogenic shock. *ESC Heart Fail* **5**: 292–301. <https://doi.org/10.1002/ehf2.12266>
- Park TJ, Park JH, Lee GS, Lee JY, Shin JH, Kim MW, Kim YS, Kim JY, Oh KJ, Han BS, Kim WK, Ahn Y, Moon JH, Song J, Bae KH, Kim DH, Lee EW, Lee SC (2019) Quantitative proteomic analyses reveal that GPX4 downregulation during myocardial infarction contributes to ferroptosis in cardiomyocytes. *Cell Death Dis* **10**: 835. <https://doi.org/10.1038/s41419-019-2061-8>
- Si X, Zheng H, Wei G, Li M, Li W, Wang H, Guo H, Sun J, Li C, Zhong S, Liao W, Liao Y, Huang S, Bin J (2020) circRNA Hspk3 induces cardiac regeneration after myocardial infarction in mice by binding to Notch1 and miR-133a. *Mol Ther Nucleic Acids* **21**: 636–655. <https://doi.org/10.1016/j.omtn.2020.06.024>
- Song Y, Zhang C, Zhang J, Jiao Z, Dong N, Wang G, Wang Z, Wang L (2019) Localized injection of miRNA-21-enriched extracellular vesicles effectively restores cardiac function after myocardial infarction. *Theranostics* **9**: 2346–2360. <https://doi.org/10.7150/thno.29945>
- Song Y, Zhang C, Zhang J, Jiao Z, Dong N, Wang G, Wang Z, Wang L (2019) Localized injection of miRNA-21-enriched extracellular vesicles effectively restores cardiac function after myocardial infarction. *Theranostics* **9**: 2346–2360. <https://doi.org/10.7150/thno.29945>
- Sui X, Zhang R, Liu S, Duan T, Zhai L, Zhang M, Han X, Xiang Y, Huang X, Lin H, Xie T (2018) RSL3 drives ferroptosis through GPX4 inactivation and ROS production in colorectal cancer. *Front Pharmacol* **9**: 1371. <https://doi.org/10.3389/fphar.2018.01371>
- Vegter EL, van der Meer P, de Windt LJ, Pinto YM, Voors AA (2016) MicroRNAs in heart failure: from biomarker to target for therapy. *Eur J Heart Fail* **18**: 457–468. <https://doi.org/10.1002/ehf.495>
- Verjans R, Peters T, Beaumont FJ, van Leeuwen R, van Herwaarden T, Verheesen W, Muntz C, Bijnen M, Henkens M, Diez J, de Windt LJ, van Nieuwenhoven FA, van Bilsen M, Goumans MJ, Heymans S, González A, Schroen B (2018) MicroRNA-221/222 family counteracts myocardial fibrosis in pressure overload-induced heart failure. *Hypertension* **71**: 280–288. <https://doi.org/10.1161/HYPERTENSIONAHA.117.10094>
- Xiao MS, Wilusz JE (2019) An improved method for circular RNA purification using RNase R that efficiently removes linear RNAs containing G-quadruplexes or structured 3' ends. *Nucleic Acids Res* **47**: 8755–8769. <https://doi.org/10.1093/nar/gkz576>
- Xie Y, Hou W, Song X, Yu Y, Huang J, Sun X, Kang R, Tang D (2016) Ferroptosis: process and function. *Cell Death Differ* **23**: 369–379. <https://doi.org/10.1038/cdd.2015.158>
- Yang WS, Kim KJ, Gaschler MM, Patel M, Shchepinov MS, Stockwell BR (2016) Peroxidation of polyunsaturated fatty acids by lipoxygenases drives ferroptosis. *Proc Natl Acad Sci U S A* **113**(34):E4966–75. <https://doi.org/10.1073/pnas.1603244113>
- Zhang Y, Liang W, Zhang P, Chen J, Qian H, Zhang X, Xu W (2017) Circular RNAs: emerging cancer biomarkers and targets. *J Exp Clin Cancer Res* **36**: 152. <https://doi.org/10.1186/s13046-017-0624-z>
- Zhao C, Liu J, Ge W, Li Z, Lv M, Feng Y, Liu X, Liu B, Zhang Y (2021) Identification of regulatory circRNAs involved in the pathogenesis of acute myocardial infarction. *Front Genet* **11**: 626492. <https://doi.org/10.3389/fgene.2020.626492>
- Zou Y, Henry WS, Ricq EL, Graham ET, Phadnis VV, Maretich P, Paradkar S, Boehnke N, Deik AA, Reinhardt F, Eaton JK, Ferguson B, Wang W, Fairman J, Keys HR, Dančik V, Clish CB, Clemmons PA, Hammond PT, Boyer LA, Weinberg RA, Schreiber SL (2020) Plasticity of ether lipids promotes ferroptosis susceptibility and evasion. *Nature* **585**: 603–608. <https://doi.org/10.1038/s41586-020-2732-8>

The role of USP1 deubiquitinase in the pathogenesis and therapy of cancer

Svitlana Antonenko¹✉, Michael Zavelevich² and Gennady Telegeev¹

¹Department of Molecular Genetics, Institute of Molecular Biology and Genetics, National Academy of Sciences of Ukraine, Kyiv, Ukraine; ²Department of Oncohematology, RE Kavetsky Institute of Experimental Pathology, Oncology and Radiobiology, National Academy of Sciences of Ukraine, Kyiv, Ukraine

Ubiquitin-specific protease 1 (USP1) is an important deubiquitinating enzyme (DUB) involved in the maintenance of genome integrity, cell cycle, and cell homeostasis. USP1 overexpression is a characteristic feature of various cancers, correlating with a poor prognosis. The review summarizes the recent knowledge in understanding the role of deubiquitinase USP1 in the stabilization of oncoproteins and tumor suppressors, as a critical event in cancer development and progression. The putative mechanisms of USP1 involvement in some prevalent human cancers are discussed. The numerous data demonstrate that inhibition of USP1 suppresses the proliferation and viability of malignant cells, sensitizes them to radiation and increases their sensitivity to various chemotherapeutic agents, which opens up new opportunities for combined therapy of malignant neoplasms.

Keywords: Deubiquitinating enzyme (DUB), USP1, cancer, targeted therapy

Received: 23 January, 2023; **revised:** 01 April, 2023; **accepted:** 03 April, 2023; **available on-line:** 12 June, 2023

✉e-mail: antonenkoimbg@gmail.com

Abbreviations: AR, androgen receptor; B-ALL, B-cell acute lymphoblastic leukemia; BC, breast cancer; BCAA, branched-chain amino acid; CML, chronic myeloid leukemia; COSMIC, catalog of somatic mutations in cancer; DUB, deubiquitinating enzyme; HCC, hepatocellular carcinoma; ID2, DNA binding 2; MINDYs, motif-interacting with ubiquitin-containing novel DUB family; MJDs, Machado-Joseph disease proteases; NES, nuclear export signal; NLSs, nuclear localization signals; NSCLC, non-small cell lung carcinoma cells; OTUs, ovarian tumor proteases; PDAC, pancreatic ductal adenocarcinoma; RPs, ribosomal proteins; ROS, reactive oxygen species; T-ALL, T-cell acute lymphoblastic leukemia; TBLR1, transducin β -like X-linked receptor 1; UAF1, USP1 cofactor-associated protein 1; USPs, ubiquitin-specific proteases; UCHs, ubiquitin carboxy-terminal hydrolases

INTRODUCTION

Deubiquitinating enzymes (DUB) are proteases that regulate ubiquitin dynamics by selectively cleaving mono- or polyubiquitin from protein substrates (Henning *et al.*, 2021; Caba *et al.*, 2022). The deubiquitination is crucial for maintaining the stability of target proteins, and in the absence of proteolytic load on proteasome it affects the activity of substrates, cellular localization, interactions with other proteins, activation or silencing of gene expression, and the functioning of signaling pathways (Snyder *et al.*, 2021; Tu *et al.* 2022; Estavoyer *et al.*, 2022 Trulsson *et al.*, 2022). More than 500 protease genes have been identified in the human genome, about 100 of which belong to DUBs (Bonacci & Emanuele, 2021). Based on the homology of the active site, DUBs

are classified into six families: ubiquitin-specific proteases (USPs), ubiquitin carboxy-terminal hydrolases (UCHs), ovarian tumor proteases (OTUs), the Machado-Joseph disease proteases (MJDs), motif-interacting with ubiquitin-containing novel DUB family (MINDYs) and JAB1/PAB1/MPN (JAMMs). The first five families (USPs, UCHs, OTUs, MJDs, MINDYs) are cysteine proteases, while the JAMMs family belongs to metalloproteases (Mullard *et al.*, 2021; Lei *et al.*, 2021a; Caba *et al.*, 2022). The largest family among DUBs is USPs. Members of the USPs family have a conserved structural organization consisting of three subdomains, namely the “thumb” and “palm” with a catalytic site between them and the “fingers” that provide interaction with ubiquitin on substrates (Fraile *et al.*, 2012; Snyder *et al.*, 2021). Sometimes USPs have additional domains, such as ubiquitin-binding zinc finger domain, ubiquitin-interacting motifs and ubiquitin-associated, etc. (Du *et al.*, 2019; Yang *et al.*, 2019).

The physiological role of DUB is to ensure the homeostasis of critical cell functions, including genome stability, gene expression, cell cycle progression, proliferation, stem cell differentiation, chromosome segregation, growth factor signaling, redox regulation, endocytosis, apoptosis, etc. Deregulation of functional activity and expression of DUB correlates with neurodegenerative and immune diseases, development and progression of cancer (Jerabkova *et al.*, 2020; Wang *et al.*, 2022; Tu *et al.*, 2022; Liu *et al.*, 2022). The growing interest in DUBs as markers of oncogenic transformation and new therapeutic targets for cancer treatment seems to be justified.

The most studied DUB to date is ubiquitin-specific protease 1 (USP1). Quite often, DUB expression is altered in many cancers (Poondla *et al.*, 2019; Lai *et al.*, 2020). Hyperexpression of USP1 is observed in glioma, osteosarcoma, leukemia, hepatocellular carcinoma, gastric cancer, breast cancer, ovarian cancer, prostate cancer, colorectal cancer, etc., being associated with low patient survival and malignant neoplasm progression (Williams *et al.*, 2011; Xu *et al.*, 2019; Ma *et al.*, 2019b; Kuang *et al.*, 2021; Liao *et al.*, 2021a; Liang *et al.*, 2022; Li *et al.*, 2021; Chen *et al.*, 2022).

Recently, many breakthroughs have been made in elucidating the role of USP1 as an important regulator of basic cellular processes including metabolism, proliferation, and apoptosis. Ensuring the balance between ubiquitination and deubiquitination, USP1 is critical for maintaining the integrity of signaling networks, the proper performance of functions controlled in a spatio-temporal mode, and the homeostasis of the cell as a whole. The impairment of this balance could be important for tumorigenesis and cancer progression (Cui *et al.*, 2020; Meng *et al.*, 2022; Sun *et al.*, 2022). USP 1

could be a valuable diagnostic marker in various types of cancer. USP1 is directly involved in tumorigenesis by regulating the stability of oncoproteins or tumor suppressors (Sonego *et al.*, 2019; Coleman *et al.*, 2022; Song *et al.*, 2022). Finally, USP1 ability to modulate the level of oncoproteins accumulating in cancer cells makes it an attractive therapeutic target for cancer treatment.

THE STRUCTURE AND FUNCTION OF USP1

USP1 belongs to the most numerous and diverse USPs of the DUB family (Cruz *et al.*, 2021). The protein was first identified in 1998 as part of the Human Genome project by a group of scientists from Japan (Fujiwara *et al.*, 1998). The USP1 gene is localized to the p31.3-p32.1 band of chromosome 1. The USP1 protein consists of 785 amino acid residues with a predicted molecular weight of 88.2 kDa. In the structure of USP1, there is a typical DUB conserved USP domain, which consists of a N-terminal Cys box motif with a C90 catalytic residue and a C-terminal His box motif with H593 and D751 catalytic residues. (Fig. 1A). It is believed that these three amino acids form the so-called catalytic triad, which actually forms the catalytic core of DUB (Yu *et al.*, 2017; Woo *et al.*, 2022). The catalytic domain of the USP1 protein is one of the largest in the USPs family due to additional insertions (Bishop *et al.*, 2016). The first additional insert L1 (within 227-433 amino acid residues) located between box 2 and 3 is able to enhance USP1

activity due to natural affinity to DNA and allosteric activation after binding of UAF1 (Dharadhar *et al.*, 2021). Within L1 there are phosphorylation sites, including the most studied S313, nuclear localization signals (NLSs) and a degradation motif (degron). A second additional L2 insert (between amino acid residues 602-744) is located between boxes 5 and 6 and includes an autocleavage site (G670-G671). The third smallest L3 insert is located between 465-483 amino acid residues. It is believed that L1 and L3 insertions together are able to cause autoinhibition that could be reversed by binding to UAF1 cofactor. Co-deletion of L1 and L3 leads to hyperactivation of USP1, while deletion of the L2 or L3 insert does not affect its enzymatic activity (Dharadhar *et al.*, 2021).

The database “Catalog of somatic mutations in cancer” (COSMIC) contains information on dozens of mutations in USP1 (Fig. 1B), among which 51% are missense substitutions, 12% are synonymous substitutions, slightly more than 7% are frameshift deletions, and 4% are nonsense substitutions. It is known that mutation of any of the C90, H593 or D751 amino acid residues significantly reduces the catalytic activity of the USP1 protein. While the functional effect of the vast majority of mutations has not been fully elucidated, about forty different mutations have been detected in various types of cancer.

For the first time, as a critical regulator of genome integrity, USP1 was described in Fanconi anemia, where its functions are realized by FANCD2 deubiquitination (Nijman *et al.*, 2005). It is believed that USP1 in complex with the cofactor UAF1 moves along the replication fork

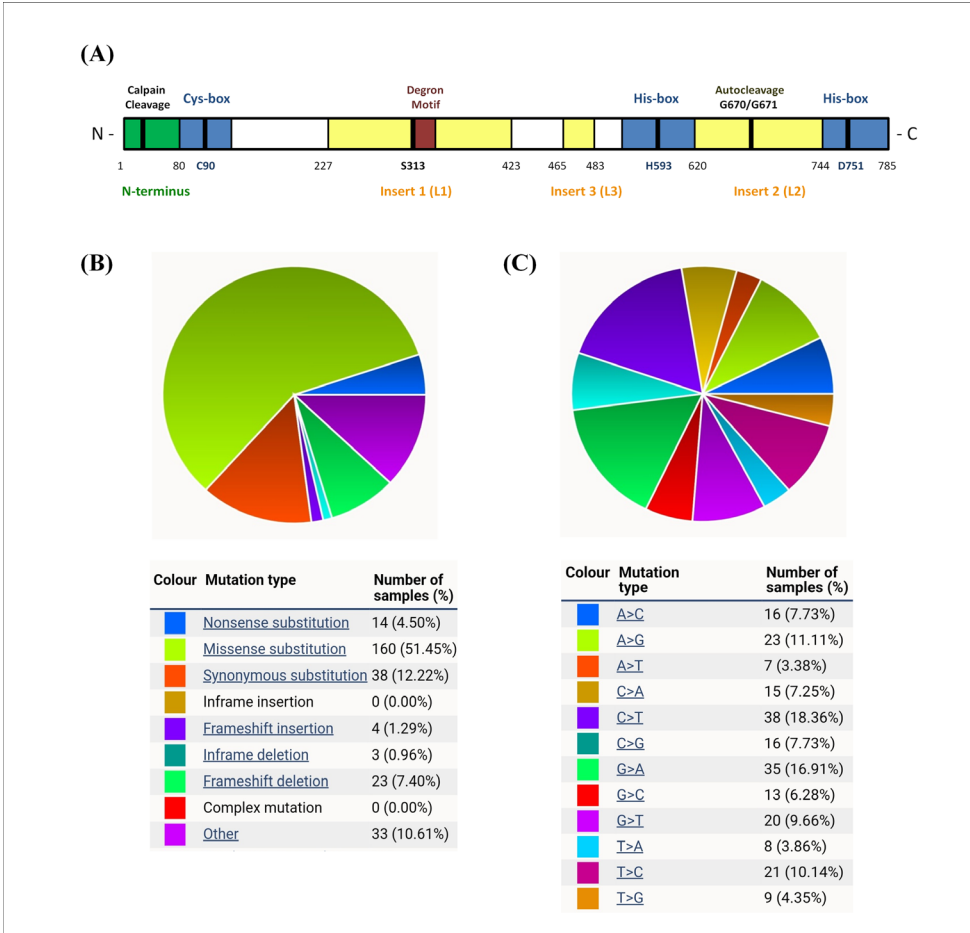


Figure 1. USP1: structure and mutations. A – USP1 domain organization. B – Distribution of different mutation types for USP1. The COSMIC database was used to analyze the mutation distribution for USP1. C – A breakdown of the observed substitution mutations in USP1.

and deubiquitinates its partner proteins (Lim *et al.*, 2018; Dharadhar *et al.*, 2021). DNA-dependent metalloprotease Spartan can cause USP1 molecule to be removed from DNA acting selectively only on catalytically active forms of USP1, while minimally affecting mutants with changes in the autocleavage domain. This defines a new role of USP1 autocleavage in its increased retention on DNA. Spartan does not specifically act on protease sequences, cleaving substrates mainly in unstructured regions near lysine, arginine, and serine residues (Coleman *et al.*, 2022). The preferential association of Spartan with ubiquitin-modified proliferating cell nuclear antigen (PCNA) protects against PCNA deubiquitylation by USP1 and facilitates the access of polymerase responsible for a translesion DNA synthesis to the replication fork (Juhasz *et al.*, 2012). These facts highlight the role of USP1 autocleavage regulation as one of the components maintaining the steady function of DNA replication machinery and genome integrity (Coleman *et al.*, 2022).

It is also known that USP1 participates in the regulation of centrosome duplication, therefore, a violation

of its activity causes the formation of an abnormal mitotic spindle, amplification of centrosomes, incorrect segregation of chromosomes, which leads to aneuploidy, instability of the genome, thus creating prerequisites for oncogenic transformation of cells (Jung *et al.*, 2016; Twest *et al.*, 2017). Today, a wide range of USP1 cellular substrates is known, the dynamic balance between the activity of DAB and ubiquitin E3 ligase underlies the modulation of protein degradation and localization, the formation of protein-protein interactions, gene expression, activation and deactivation of signaling pathways, ensures homeostasis and the performance of critical cell functions, such as metabolism, proliferation and cell differentiation, autophagy, apoptosis.

USP1/UAF1 PROTEIN COMPLEX

The catalytic activity of USP1 is dramatically increased in complex with the USP1 cofactor-associated protein 1 (UAF1), also known as protein 48, or WDR48 (Yu *et al.*,

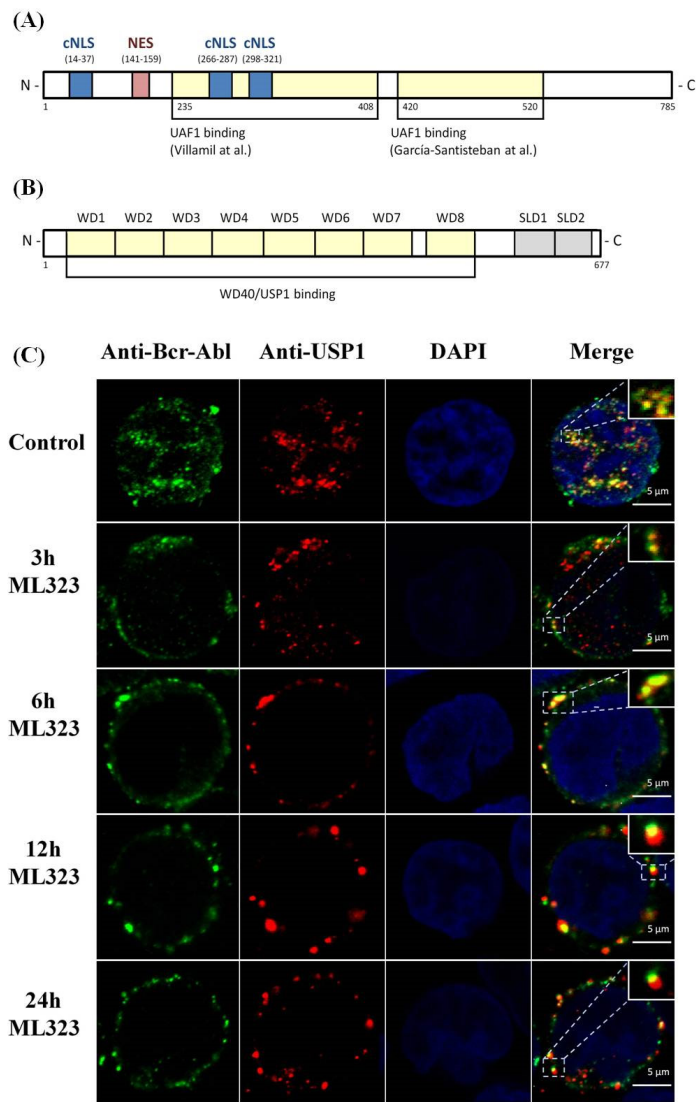


Figure 2. Localization of USP1 and the mechanism of its interaction with the UAF1 cofactor. A – schematic representation of the location of motifs in the USP1 protein, which determine its localization and interaction with the UAF1 cofactor, B – domain organization of the UAF1 cofactor, a representation of the motifs responsible for the interaction with USP1, C – USP1 is a nuclear protein that colocalizes with the Bcr-Abl oncoprotein in CML cells. In cells treated with ML323 inhibitor, which acts on the protein complex USP1/UAF1, USP1 is localized exclusively in the cytoplasm, which indicates that only its activated form enters the nucleus in a complex with a protein cofactor.

2017; Arkinson *et al.*, 2018). The UAF1 protein contains eight WD40 repeats, seven of which have a β -propeller structure, the eighth repeat belongs to the so-called auxiliary domain. WD40 repeats are localized to the N-terminal domain of UAF1, which binds to USP1 and other substrate proteins, including USP12 and USP46. Deletion of 2–4 repeats of WD40 disrupts the formation of the USP1/UAF1 protein complex, and deletion of the 8th repeat and the adjoining region causes impairment of function of the UAF1 cofactor itself, which is believed to be a consequence of disruption of its tertiary structure. At the C-terminus of UAF1, a SUMO-like domain is located with two subdomains. Deletions in the proximal part of the C-domain do not affect the formation of the USP1/UAF1 protein complex (Yang *et al.*, 2011; Goncalves *et al.*, 2017; Rennie *et al.*, 2022). Villamil *et al.* suggested that USP1 is activated by the UAF1 cofactor via modulation of the conformation of the active site of DAB, while changes due to remodeling of the ubiquitin-binding site are unlikely (Villamil *et al.*, 2012). The altered UAF1 expression has critical consequences; in particular, UAF1 deficiency causes the death of mice in the embryonic period (Arkinson *et al.*, 2018). The formation of a protein complex involves joint subcellular localization of partner proteins, however, USP1 belongs to nuclear proteins, while UAF1 is localized mainly in the cytoplasm. It is assumed that the USP1/UAF1 complex is formed in the cytoplasm and subsequently imported into the nucleus due to the NLS region of the USP1 protein (Yu *et al.*, 2017). There are contradictory data regarding the mechanisms of formation of the USP1/UAF1 protein complex. Villamil and others (Villamil *et al.*, 2012) showed that the site between 235–408 amino acid residues on the USP1 protein is responsible for cofactor binding. On the other hand, García-Santisteban and others indicated that USP1 binds to its cofactor due to the site within 420–520 amino acid residues (Fig. 2A, B) (García-Santisteban *et al.*, 2013; Yu *et al.*, 2017). Currently, it is not completely clear, which of two USP1 sites is responsible for binding to UAF1 or whether both sites are involved under different physiological conditions.

PHOSPHORYLATION OF USP1

Phosphorylation is an important post-translational modification that can stabilize proteins, increase or decrease their abundance in the cell, influence their activity, localization, interaction with other protein substrates (Wang *et al.*, 2021). Extensive phosphoproteomic studies found that the activity of the vast majority of human USPs is regulated by phosphorylation (Villamil *et al.*, 2012). Phosphorylation at the Ser313 site may be one of the ways of regulating the level of USP1 during the cell cycle, preventing its degradation during mitosis. (Cotto-Ríos *et al.*, 2011). Villamil and others (Villamil *et al.*, 2012) showed that phosphorylation of USP1 at the Ser313 site is one of the conditions for the formation of the USP1/UAF1 protein complex, while protein phosphatase treatment can lead to its inactivation. Nevertheless, Olazabal-Herrero and others (Olazabal-Herrero *et al.*, 2015) found that the mutant USP1, which is not phosphorylated at the Ser313 site, is also able to interact with UAF1. In addition, the formation of the USP1/UAF1 protein complex does not depend on the two other known sites, Ser42 and Ser67 (Villamil *et al.*, 2012). Phosphorylation of USP1 at S42 and S331 is a prerequisite for Snail interaction and deubiquitination, which promotes platinum resistance and metastatic pro-

gression in ovarian cancer. In turn, under the influence of phosphatases, the level of interaction between Snail/USP1 proteins decreases (Sonogo *et al.*, 2019). Phosphorylated forms of USP1 at tyrosine sites were detected in Bcr-Abl-positive chronic myeloid leukemia cells. USP1 is believed to be phosphorylated by interaction with the oncoprotein Bcr-Abl, which has uncontrolled tyrosine kinase activity, leading to deregulation of downstream signaling pathways and disease progression (Antonenko & Telegeev, 2020).

Taking into account the role of phosphorylation in USP1 activation, one may suggest that the inhibition of protein kinases that phosphorylate USP1 may impair its functional activity. In fact, we have observed that in CML cells treated with imatinib, the level of colocalization of USP1 and Bcr-Abl is significantly reduced, while part of the USP1 protein remains in the cytoplasm, which may indicate a lack of deubiquitinase activity (Antonenko S., unpublished data). It has been also shown that tyrosine kinase inhibitors reduce the expression of USP47 in CML cells, which can be potentially relevant to other USPs, including USP1 (Lei *et al.*, 2021b).

SUBCELLULAR LOCALIZATION OF USP1

Subcellular localization is a key for the realization of enzymatic activity by any protein, as it ensures the execution of a whole complex of intricately connected pathways and processes within and between different compartments (Garapati *et al.*, 2020). A change in subcellular localization can affect the catalytic activity of a protein, disrupt its physiological functions, protein-protein interactions, downstream signaling pathways, which creates prerequisites for the development of inflammatory and neurodegenerative diseases, malignant neoplasms (Wang & Wang, 2021; Garapati *et al.*, 2021). USP1 belongs to nuclear proteins. Three NLS sites in USP1 are responsible for its nuclear transport. The first sequence, which is between 14–37 amino acid residues, has a weak NLS and ensures uniform distribution of USP1 in the nucleus and cytoplasm. The second region of the NLS, located within 266–287 amino acid residues, ensures almost complete movement to the nucleus, the third region of the NLS within the range of 298–321 amino acid residues, provides a clear, but less marked relocation. In the physiological context, the two NLS signals (266–287), (298–321) are the main motifs of USP1 nuclear-cytoplasmic localization, while the third motif does not have a critical role. It is believed that USP1 and UAF1 form a complex in the cytoplasm, which subsequently translocates to the nucleus thanks to defined NLS (266–287), (298–321) motifs (García-Santisteban, *et al.*, 2012). The nuclear export signal (NES), located within amino acid residues 141–159 of USP1, may mediate the interaction with the export receptor CRM1, although the ultimate physiological significance of this sequence has not been established yet (Fig. 2A) (García-Santisteban *et al.*, 2013). We have demonstrated that in CML cells treated with ML323 inhibitor USP1 remains in cytoplasm suggesting that only the activated form of DUB in a complex with the UAF1 cofactor can enter the nucleus (Fig. 2C) (Antonenko & Telegeev, 2020).

DEGRADATION OF USP1

USP1 level in cells is regulated by its proteasomal degradation. The degradation motif (degron) ensures APC/CCdh1-dependent degradation of USP1 in the G1 phase

of the cell cycle (García-Santisteban *et al.*, 2013). Calpain (CAPNS1) stabilizes USP1 by activating Cdk5, which in turn inhibits cdh1 and consequent USP1 proteolysis. It is believed that the region of interaction with CAPNS1 is located at the N-terminus of the USP1 protein; mutations in this region, in particular the Leu-to-Gly substitution in amino acid 12, dramatically destabilize the DUB (Cataldo *et al.*, 2013). During mitosis, proteolytic degradation of the USP1 protein can be regulated by phosphorylation of the Ser313 site, which leads to the masking of the degradation motif and impairment of proteolysis. The USP1 level is significantly reduced in cells exposed to genotoxic agents (in particular, such as UV) due to autocleavage at the Gly670-Gly671 internal motif (Cotto-Rios *et al.*, 2011). The autocleavage of USP1 leads to the formation of two protein fragments, namely the amino-terminal USP1NT or N-terminal fragment (residues 1–671) and the shorter carboxyl-terminal USP1CT or C-terminal fragment (residues 672–785), which are subsequently subjected to proteasomal degradation (Piatkov *et al.*, 2012). It is believed that USP1 fragments may retain their enzymatic activity because they continue to form complexes with the UAF1 cofactor until their complete destruction. Destruction of the N-terminal fragment occurs at the expense of the C-terminal degron, which is recognized and eliminated by DesCEND pathway with recognition of unusual C-termini by the ubiquitin ligase CRL2. The smaller C-terminal fragment is destroyed by the Arg/N-terminal rule pathway through deamidation of its destabilizing N-terminal Gln24 residue (Piatkov *et al.*, 2012; Coleman *et al.*, 2022).

Four missense mutations G667A, L669P, K673T, A676T are known within the USP1 autocleavage site. Only the L669P mutation reduces protein cleavage, due to conformational changes of the protein impairing access to the cleavage site. USP1 autocleavage shows that the balance of USP1 autocleavage can be disrupted by a cancer-associated mutation (Olazabal-Herrero *et al.*, 2015). USP1 activity is reversibly inactivated in response to stress and the accumulation of reactive oxygen species (ROS) in the cell due to the oxidation of the catalytic cysteine (Cotto-Rios *et al.*, 2012). The mechanism of DUB inactivation involves disruption of isopeptide cleavage but without affecting affinity to ubiquitin (Lee *et al.*, 2013). Disruption of USP1 enzymatic activity as a result of ROS bursts causes accumulation of Ub-PCNA during S-phase, while the effect is negligible during G0 or G1. The accumulation of Ub-PCNA is also observed under the influence of UV irradiation, which leads to the destruction of USP1 (Cotto-Rios *et al.*, 2012; Coleman *et al.*, 2022).

USP1 IN THE DEVELOPMENT AND PROGRESSION OF CANCER

Since ubiquitination and deubiquitination are suggested to be essential regulators of basic cell functions, the impairment of the coordination in this network is inevitably associated with the characteristic features of cancer cells. In fact, a vast number of data demonstrate the altered expression of one or another DUBs in cancer. Currently, such data are available for more than 40 USPs including USP1, USP2, USP4, USP7, USP9X, USP10, USP11, USP12, USP13, USP14, USP15, USP19, USP22, USP26, USP29, USP33, USP39, USP42, USP44, USP46 and USP51. For example, USP2, USP3, USP4, USP7, USP10, USP29, and USP42 regulate the tumor suppressor protein p53. While USP7, USP10, USP29 and

USP42 stabilize the level of p53, USP2 and USP4, on the contrary, contribute to its proteasomal degradation due to the stabilization of E3 ligase. A number of DUBs (USP4, USP11, USP13, USP15, USP28, USP51) contribute to metastasis. For USP4, USP11, USP15, this is possible by altering the level of ubiquitination of the TGF β receptor, which promotes TGF β (transforming growth factor β) signaling and invasiveness of malignant cells. The functioning of DUBs is an essential component of cell cycle progression (USP1, USP2, USP3, USP7, USP17, USP22, USP39), DNA damage repair (USP1, USP3, USP4, USP7, USP9x, USP11, USP20, USP21, USP34, USP51), chromatin remodeling (USP7, USP11, USP16, USP21) (Pal *et al.*, 2014; Gorrepati *et al.*, 2018; Poondla *et al.*, 2019; Cruz *et al.*, 2021; Guo *et al.*, 2022). The list of the DUBs whose expression is deregulated in cancer is continuously expanding.

USP1 is a prime example of DUBs modulating the expression level of oncoprotein. Such an aspect is of particular interest from the point of cancer pathogenesis and antitumor therapy.

An expanding number of findings suggest the important role of USP1 in pathogenesis of various cancers via diverse mechanisms. The dynamic balance between USP1 and ubiquitin E3 ligase underlying the modulation of the activity, degradation and localization of proteins contributes to maintaining homeostasis and controlling the critical functions in cell. Overexpression of USP1 facilitates the development of metastatic phenotype as well as chemo- and radioresistance of cancer cells. Besides the expression upregulation, the fact of mutations in DUB genes demonstrated in several human cancers provides further evidence in the support of the putative involvement of these enzymes in the development and progression of various malignancies.

The USP1 activity is important for controlling expression of several proteins related to oncogenesis and cancer progression. Among them are SIK2, MMP-2, GSK-3 β , Bcl-2, Stat3, cyclin E1, Notch1, Wnt-1, and cyclin A1. Moreover, deubiquitination stabilizes the level of both oncoproteins and tumor growth suppressors such as EZH2, CHEK, TAZ, PHLPP1, Bcr-Abl, Aurora B, BCAT2, TBLR1, RPS16, c-Kit, KPNA2, KDM4A, ER α , SIX1, Snail, and ID1/ID2/ID3 impairing their intracellular balance (Table 1).

USP1 overexpression is characteristic of various types of cancer. According to GEPIA data from The Cancer Genome Atlas and the Genotype Tissue Expression databases, the highest level of USP1 expression is observed in cervical squamous cell carcinoma and endocervical adenocarcinoma, and it also significantly exceeds expression compared to normal tissue samples in breast invasive carcinoma, sarcoma, cholangiocarcinoma, colon adenocarcinoma, diffuse large B-cell lymphoma, esophageal carcinoma, glioblastoma multiforme, head and neck squamous cell carcinoma, brain lower grade glioma, rectum adenocarcinoma, thyroid carcinoma, etc. (Fig. 3). Changes in USP gene expression in cancer cells can be caused by various mechanisms, such as DNA repair defects, activation of signaling pathways, post-translational modifications, etc. A characteristic feature of increased USP1 expression for various types of cancer is a violation of cell homeostasis, proliferation, and apoptosis, which can be realized due to the stabilization of ID1, ID2, and ID3 proteins or FANCD2, as a key regulator of genome stability. siRNA knockdown or pharmacological inhibition of USP1 reduces proliferative activity and cell migration, promotes the onset of apoptosis and res-

Table 1. The putative role of USP1 in different forms of cancer.

Cancer	Known pathways affected	The role USP1 in the pathogenesis of the cancer	References
Glioma	PDGF-E2F-USP1-ID2 β-catenin-USP1-EZH2 USP1-CHEK1 USP1-ID1	Support for cell survival of the proneural subtype of glioblastoma. Promotion of tumorigenesis. Survival support. GSCs and resistance to treatment. Reduction of NgR1 promoting myelin-related infiltration	Rahme <i>et al.</i> , 2016; Ma <i>et al.</i> , 2019a; Lee <i>et al.</i> , 2016; Lee <i>et al.</i> , 2016
Osteosarcoma	USP1-ID1/ID2/ID3 USP1-TAZ	Suppression of osteoblast differentiation, increased proliferation, invasiveness, metastasis. Violation of the Hippo signaling pathway, increased proliferation and migration of malignant cells.	Williams <i>et al.</i> , 2011 Yuan <i>et al.</i> , 2022
Non-small cell lung carcinoma	USP1-PHLPP1-Akt	Disease progression. Unregulated proliferation of cancer cells.	Zhiqiang <i>et al.</i> , 2012
B-cell acute lymphoblastic leukemia	USP1-ID1 - AKT	Support for cell growth and viability. Disease progression. Suppression of cell apoptosis.	Kuang <i>et al.</i> , 2021
T-cell acute lymphoblastic leukemia	USP1-Aurora B	Promotion of chemoresistance of T-ALL cells. Promotion of cell invasion. Inhibition of glucocorticoid receptor expression and apoptosis.	Gong <i>et al.</i> , 2021
Multiple myeloma	USP1-ID-Notch-Sox2	Promotion of cell viability and resistance to bortezomib treatment. Enhances cell growth and inhibits apoptosis through the activation of caspase-3, caspase-8, and caspase-9.	Das <i>et al.</i> , 2017
Chronic myeloid leukemia	USP1-Bcr-Abl	Stabilization of the Bcr-Abl oncoprotein level in cells as one of the conditions for disease progression.	Antonenko & Telegeev, 2020
Esophageal squamous cell carcinoma	D1/CDK4/CDK6	Maintenance of esophageal cancer cell viability and colony formation. Promotion of genetic stability of cells.	Sun <i>et al.</i> , 2022
Stomach cancer	USP1-ID2	Promotes proliferation, metastasis, epithelial-mesenchymal transition of gastric cancer cells.	Li <i>et al.</i> , 2021
Pancreatic ductal adenocarcinoma	USP1-BCAT2	Promotes cell proliferation, the formation of ductal clones in pancreatic adenocarcinoma cells.	Li <i>et al.</i> , 2022b
Hepatocellular carcinoma	USP1-TBLR1 USP1-RPS16-Twist1/Snail USP1-c-Kit	Promotes the survival of circulating tumor cells, promotes metastasis. Supports cell proliferation and metastasis. Decreased overall patient survival. Resistance to treatment with lenvatinib.	Li <i>et al.</i> , 2020 Liao <i>et al.</i> , 2021b Chen <i>et al.</i> , 2022
Breast cancer	USP1-KPNA2 USP1-ERα USP1-TAZ	Correlates with a poor prognosis for patients, promotes metastatic progression of breast cancer cells. Supports breast cancer cell proliferation and invasion via estrogen signaling. Promotes the proliferation and migration of malignant cells in triple-negative breast cancer.	Ma <i>et al.</i> , 2019a Niu <i>et al.</i> , 2020 Mussell <i>et al.</i> , 2020
Prostate cancer	USP1-KDM4A-AR-c-Myc GRP75-USP1-SIX1	Promotes the proliferation and survival of prostate cancer cells. Supports the growth and proliferation of prostate cancer cells. Associated with a poor prognosis for patients. Promotes cell resistance to AR-targeted therapy.	Cui <i>et al.</i> , 2020 Liao <i>et al.</i> , 2021a, Liao <i>et al.</i> , 2022
Colorectal cancer	Upregulation of Bcl-2, Mcl1, A1, D1, E1 cyclins and DNA-repair related substrates FANCD2 and ID1	Associated with short overall patient survival. Promotes the growth and survival of colorectal cancer cells, resistance to radio- and chemotherapy.	Xu <i>et al.</i> , 2019
Ovarian cancer	ATM/ATR-USP1-Snail	Facilitates resistance to platinum treatment and promotes metastasis.	Sonogo <i>et al.</i> , 2019

toration of sensitivity to antitumor therapy (Das *et al.*, 2015; Gong *et al.*, 2021; Rennie *et al.*, 2022).

USP1-mediated stabilization of inhibitors of DNA binding and cell differentiation (ID proteins family) has been reported in many cancers (glioma, osteosarcoma, B-cell acute lymphoblastic leukemia, multiple myeloma, esophageal squamous cell carcinoma, gastric cancer, etc.). The disrupted functional activity of ID proteins is asso-

ciated with deregulation of cell proliferation, metastasis, and apoptosis impairment. Moreover, the inhibition of USP1 deubiquitination activity diminishes proliferation and colony-forming activity of cancer cells, decreases their metastatic ability and restores the sensitivity to anticancer drugs. The findings suggesting the putative role of USP1 targeting in future design of therapeutic modal-

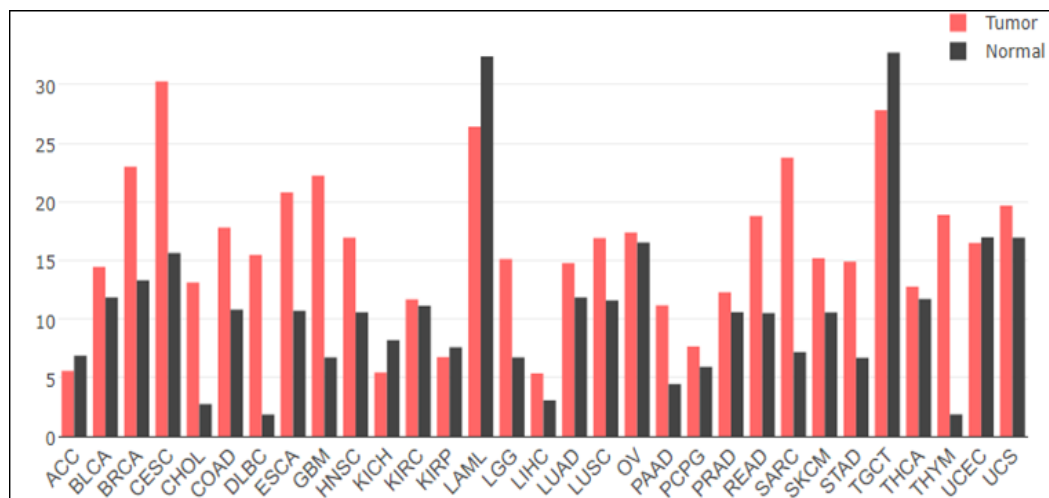


Figure 3. USP1 expression in normal samples (grey box) and tumor samples (red box) from patients with cancer compiled by GEPIA data from The Cancer Genome Atlas and the Genotype Tissue Expression databases.

ACC – adrenocortical carcinoma, BLCA – bladder urothelial carcinoma, BRCA – breast invasive carcinoma, CESC – cervical squamous cell carcinoma and endocervical adenocarcinoma, CHOL – cholangiocarcinoma, COAD – colon adenocarcinoma, DLBC – diffuse large B-cell lymphoma, ESCA – esophageal carcinoma, GBM – glioblastoma multiforme, HNSC – head and neck squamous cell carcinoma, KICH – kidney chromophobe carcinoma, KIRC – renal clear cell carcinoma, KIRP – renal papillary cell carcinoma, LAML – acute myeloid leukemia, LGG – low grade glioma, LIHC – hepatocellular carcinoma, LUAD – lung adenocarcinoma, LUSC – lung squamous cell carcinoma, MESO – mesothelioma, OV – ovarian serous cystadenocarcinoma, PAAD – pancreatic adenocarcinoma, PCPG – pheochromocytoma and paraganglioma, PRAD – prostate adenocarcinoma, READ – rectal adenocarcinoma, SARC – sarcoma, SKCM – cutaneous melanoma, STAD – stomach adenocarcinoma, TGCT – testicular germ cell tumors, THCA – thyroid carcinoma, THYM – thymoma, UCEC – uterine corpus endometrial carcinoma, UCS – uterine carcinosarcoma, UVM – uveal melanoma

ities for cancer treatment are considered below for various forms of malignancies.

USP1 in glioma

The functioning of more than 20 ubiquitin-specific proteases, including USP1, is associated with the progression of glioma. USP1 expression is upregulated in glioma, in particular in glioblastoma stem-initiating cells (CD133⁺ or CD15⁺) cells that are associated with clonogenic activity of malignant cells and radioresistance. The involvement of USP1 in glioma progression could be related to stabilization of ID1 and CHEK1 proteins, which promotes cell survival, while genetic or pharmacological inhibition of USP1 reduced tumor growth in experimental models and sensitized tumors to chemotherapeutic agents. The expression level of USP1 significantly increases upon inhibition of IRE-1 α , the most evolutionarily conserved resident protein of the endoplasmic reticulum membrane. Thus, USP1 responds to endoplasmic reticulum stress and hypoxia, potentially contributing to the regulation of cell apoptosis and proliferation (Minchenko *et al.*, 2016). A critical factor in glioma progression and recurrence is the high infiltrative capacity of glioma stem cells caused by a decrease in the level of NgR1, negatively regulated through the USP1/ID1 signaling pathway. Pharmacological inhibition of USP1 with pimozide correlates with increased NgR1 expression and decreased infiltration capacity of glioma cells (Lee *et al.*, 2016; Liang *et al.*, 2022). USP1 expression in proneural glioblastoma cells is PDGF-dependent. PDGF upregulates the expression of E2F transcription factors that directly bind to and activate USP1, which in turn stabilizes the inhibitor of DNA binding 2 (ID2). Thus, activation of the PDGF–E2F–USP1–ID2 signaling pathway is crucial for glioma cell survival and may be considered as a valuable therapeutic strategy in proneural glioblastoma (Rahme *et al.*, 2016).

USP1 in osteosarcoma

ID proteins are also involved in progression of osteosarcoma. In osteosarcoma cells, USP1 stabilizes IDs, particularly ID1, ID2, and ID3, through its deubiquitinating activity, and directly interacts with and deubiquitinates TAZ, leading to disruption of the Hippo signaling pathway. In fact, overexpression of USP1 was found in 26 out of 30 osteosarcoma samples as compared to normal bone tissues. Interestingly, USP1 stabilizes TAZ also in breast cancer, which promotes the proliferation and migration of malignant cells. Suppression of USP1 destabilizes ID proteins, disrupts osteoblast differentiation, negatively affects cell growth, colony formation, and metastasis (Williams *et al.*, 2011; Liu *et al.*, 2016; Mussell *et al.*, 2020; Yuan *et al.*, 2022).

USP1 in non-small cell lung carcinoma

In non-small cell lung carcinoma cells (NSCLC), USP1 forms a protein complex with the negative Akt regulator protein PHLPP1, deubiquitinates and stabilizes it. Knockdown of USP1 leads to rapid accumulation of ubiquitinated PHLPP1 and reduced its half-life, which is a trigger for Akt1 phosphorylation and disease progression. USP1 expression in non-small cell lung carcinoma cells is regulated by PXN and ITGB4. Current data on USP1 expression in lung cancer are somewhat controversial. Zhiqiang and others (Zhiqiang *et al.*, 2012) claim that the level of USP1 protein in non-small cell lung carcinoma is reduced, in particular in A549, H157, H2126, and H1770 cell lines, while its overexpression suppresses the growth of lung cancer cells and promotes cell death. Nevertheless, García-Santisteban and others (García-Santisteban *et al.*, 2012) demonstrated the higher USP1 mRNA levels in a panel of 20 NSCLC cell lines as well as in NSCLC tumor samples compared with normal tissue supporting the association of USP1 overexpression with NSCLC. At the same time, Chen and colleagues (Chen *et al.*, 2011) identified the USP1/UAF1

protein complex as a promising therapeutic target and talked about the feasibility of using the inhibitors, pimozide and GW7647, to reduce its activity. They found that USP1/UAF1 inhibitors sensitize cisplatin-resistant NSCLC cells to cisplatin. The therapeutic potential of using USP1/UAF1 protein complex inhibitors lies in their synergistic action with cisplatin reducing chemoresistance and inhibiting proliferation of NSCLC cells (Chen *et al.*, 2011; Mohanty *et al.*, 2020).

USP1 in B-cell acute lymphoblastic leukemia

In B-cell acute lymphoblastic leukemia (B-ALL), overexpression of USP1 promotes the progression of malignant disease through the ID1/AKT signaling pathway. Genetic and pharmacological inhibition of USP1 correlates with downregulation of ID1 and results in additional inactivation of the PI3K/AKT signaling pathway. In addition, inhibition of the deubiquitinating functions of USP1 by SJB3-019A induces G2/M cell cycle arrest in B-ALL cells (Kuang *et al.*, 2021).

USP1 in T-cell acute lymphoblastic leukemia

In T-cell acute lymphoblastic leukemia (T-ALL), high expression of USP1 is associated with the development of chemoresistance and a poor prognosis for patients. USP1 contributes to the chemoresistance of T-ALL cells by interacting with and deubiquitinating Aurora B, a key cell cycle regulator that ensures correct chromosome segregation and normal mitosis, its dysfunction is associated with tumorigenesis in many types of cancer, including solid tumors and hematological malignancies (Du *et al.*, 2021). USP1 overexpression in T-ALL cells is mediated by ALKBH5, a member of the well-conserved AlkB family of non-heme Fe(II)/ α -KG-dependent dioxygenases, which mediates the repair of N-alkylated nucleobases by oxidative demethylation and is involved in the regulation of proliferation, migration, and apoptosis. ALKBH5 reduces m6A levels and stabilizes USP1 mRNA transcript, whereas ALKBH5 inhibition significantly reduces USP1 and Aurora B levels. m6A (N6-methyladenosine) is a reversible and most common type of mRNA modification characteristic of many biological processes including tumorigenesis (Huo *et al.*, 2021). Blocking USP1 restores sensitivity of T-ALL cells to dexamethasone in vitro and in vivo, by facilitating the expression of the glucocorticoid receptor, promotes cell apoptosis and suppresses cell invasion (Gong *et al.*, 2021).

USP1 in multiple myeloma

In multiple myeloma patients, a high level of USP1 expression is an unfavorable prognostic factor associated with poor survival. Blocking the deubiquitinating activity of USP1 by SJB3-019A (a synthetic inhibitor that targets USP1 in an irreversible manner with high selectivity for other deubiquitinases) causes a series of important functional events, reducing the viability of myeloma cells, inhibiting their growth, triggering apoptosis through the activation of caspase-3, caspase-8, and caspase-9, and overcoming resistance to bortezomib, a first-in-class selective and reversible 26S proteasome inhibitor with antiproliferative and antitumor activity (Das *et al.*, 2017; Robak *et al.*, 2019).

USP1 in chronic myeloid leukemia

In chronic myeloid leukemia (CML) cells, USP1 interacts with the Bcr-Abl oncoprotein via its PH domain

with the formation of the Bcr-Abl/USP1 nuclear complex. Bcr-Abl has constitutive tyrosine kinase activity and thus uncontrollably phosphorylates its protein partners, suggesting that oncoprotein interactions may deregulate USP1 activity by overactivating the enzyme. It was established that pharmacological inhibition of the USP1/UAF1 complex by ML323 causes a decrease in the Bcr-Abl level in CML cells. It is believed that USP1 deubiquitinates Bcr-Abl, preventing its proteolysis, and leading to the Bcr-Abl accumulation (Antonenko *et al.*, 2016; Antonenko & Telegeev, 2020).

USP1 in esophageal squamous cell carcinoma

In esophageal squamous cell carcinoma cells, USP1 activity is associated with high levels of c-Myc, cyclin D1, CDK4, and CDK6 proteins, while pharmacological inhibition of USP1 by ML323 significantly affects the viability of malignant cells by blocking cell cycle traverse in G0/G1, interfering with the ability to form colonies and inducing apoptosis by p53-Noxa. Inhibition of the deubiquitinating activity of USP1 causes the accumulation of DNA damage and promotes the development of protective autophagy (Sun *et al.*, 2022).

USP1 in stomach cancer

In gastric cancer cells, USP1 stabilizes ID2 expression by its deubiquitination. Overexpression of USP1 promotes metastasis and correlates with low survival rates, while knockdown of USP1 suppresses proliferation, migration, invasion, and epithelial-mesenchymal transition of gastric cancer cells (Li *et al.*, 2021; Meng *et al.*, 2022).

USP1 in pancreatic ductal adenocarcinoma

Pancreatic ductal adenocarcinoma (PDAC) is the most common neoplastic disease of the pancreas, for the development of which BCAT2-mediated branched-chain amino acid (BCAA) catabolism is critical. A key role of USP1 in PDAC development is its ability to regulate BCAT2 levels in cells through its deubiquitinating activity. In turn, the level of USP1 increases under the influence of BCAA through the GCN2-eIF2 α signaling pathway. Inhibition of the deubiquitinating activity of USP1 reduces cell proliferation and pancreatic tumor growth in an orthotopic transplant in mice, suggesting USP1-BCAT2-BCAA signaling pathway as a potential target for PDAC therapy (Li *et al.*, 2022b).

USP1 in hepatocellular carcinoma

USP1 overexpression together with the cofactor UAF1 is a poor prognostic factor for survival of hepatocellular carcinoma (HCC) patients. A high level of USP1 promotes metastasis and survival of circulating tumor cells (CTCs) due to deubiquitination and stabilization of transducin β -like 1 X-linked receptor 1 (TBLR1), which is a critical regulator of Wnt (Li *et al.*, 2020). USP1 interacts with 37 ribosomal proteins (RPs), including RPS4X, RPS18, and RPS16, among which the USP1/RPS16 protein complex plays a key role in HCC progression. The binding of USP1 to RPS16 occurs at its C-terminal domain (401–785 aa). USP1 prevents proteasomal degradation of RPS16 by deubiquitination at the K48 site. The USP1-RPS16-Twist1/Snail signaling pathway is believed to be involved in cell proliferation and metastasis in HCC. In addition, USP1 stabilizes c-kit tyrosine kinase, which is upregulated or overexpressed in HCC. Inhibition of USP1 activity increases the sensitivity of HCC cells to lenvatinib treatment by regulating the ex-

pression of c-Kit, and also causes a decrease in the expression of PCNA, cyclin D1, cyclin E1, RPS16, Nanog, Sox2, c-Myc and is accompanied by decreased cancer stemness, including sphere formation ability. Lenvatinib is a multi-targeted tyrosine kinase inhibitor with angiogenic, antitumor, and immunomodulatory effects targeting VEGF receptors (VEGFR) and fibroblast growth factor (FGF) receptors (FGFR), platelet-derived growth factor receptor alpha (PDGFR α), KIT, and RET (Zhong *et al.*, 2021). Restoration of cell sensitivity to doxorubicin after USP1 inhibition is associated with ubiquitination of PCNA, which promotes its proteolysis. PCNA is an important factor in DNA replication and repair, chromatin remodeling, cell cycle regulation, and can be used as a marker of tumor aggressiveness (Zhao *et al.*, 2020; Liao *et al.*, 2021b; Chen *et al.*, 2022; Lu *et al.*, 2022).

USP1 in breast cancer

Elevated expression of USP1 in human breast cancer (BC) cells compared with normal breast tissue correlates with poor patient prognosis, promotes metastasis and disease progression through increased expression of a number of pro-metastatic genes, and stabilization of KPNA2 by its deubiquitination. KPNA2 is an important member of the karyopherin family, which plays a central role in nucleocytoplasmic transport and is overexpressed in malignant neoplasms. In addition, due to its deubiquitinating activity, USP1 regulates ER α and thus affects cell proliferation and invasion *via* estrogen signaling. In triple-negative BC, which is the most aggressive BC form, USP1 interacts with and deubiquitinates TAZ (WWTR1), which promotes the proliferation and migration of malignant cells. Inhibition of the USP1 functional activity causes a decrease in the level and inhibition of the activity of KPNA2, ER α , TAZ proteins, disrupts cell proliferation and migration, suppressing BC metastases and preventing the progression of the disease (Ma *et al.*, 2019a; Mussell *et al.*, 2020; Niu *et al.*, 2020).

USP1 in prostate cancer

Proliferation and survival of prostate cancer cells is regulated by the USP1/KDM4A/AR-c-Myc signaling pathway. A critical event in its activation is the increased expression of USP1, which regulates the stability of KDM4A through K48-linked deubiquitination. Inhibition of USP1 activity significantly reduces cell proliferation and enhances the response of cells to enzalutamide, a second-generation androgen receptor (AR) antagonist. However, the USP1/KDM4A/AR-c-Myc signaling pathway is not the only one involving USP1 in prostate cancer cells. USP1, through deubiquitination, stabilizes the embryonic development transcription factor SIX1 in USP1/SIX1 complex with GRP75 chaperone. High expression of SIX1 is associated with a poor prognosis for prostate cancer patients. Blocking the activity of the GRP75-USP1-SIX1 protein complex using SNS-032 inhibits the growth and proliferation of prostate cancer cells, and also restores the sensitivity of cells to AR-targeted therapy (Cui *et al.*, 2020; Liao *et al.*, 2021a; Liao *et al.*, 2022).

USP1 in colorectal cancer

A high level of USP1 expression is associated with the proliferation and survival of colorectal cancer cells and promotes resistance to radio- and chemotherapy. The properties of USP1 are realized due to its effect on the expression of anti-apoptotic proteins Bcl-2, Mcl1, cyclins A1, D1, E1 and DNA-repair related substrates FANCD2

and ID1. Knockdown of USP1 causes cell arrest in the G2/M phase and induces colorectal cancer cell death. Pharmacological inhibition of USP1 using ML323 significantly increases the sensitivity of colorectal cancer cells to DNA-targeting chemotherapy drugs, enhancing in particular, the cytotoxic effect of doxorubicin, PARP inhibitor (Olaparib), topoisomerase I and II inhibitors, and DNA-binding agent etoposide (Xu *et al.*, 2019).

USP1 in ovarian cancer

Inhibition of USP1 opens new opportunities to overcome platinum resistance in ovarian cancer. A critical event in ovarian cancer initiation is the phosphorylation of USP1 by ATM and ATR, which triggers the interaction and deubiquitination of Snail. Stabilization of Snail by USP1 correlates with the development of platinum resistance and metastasis, while knockout or pharmacological inhibition of USP1 restores platinum sensitivity (Sonego *et al.*, 2019).

USP1 INHIBITORS

The first identified inhibitors of the USP1/UAF1 protein complex were pimozide and GW7647. Pimozide belongs to the approved antipsychotic drugs, but its pharmacological properties are not limited to the neuroleptic function and it demonstrates an antitumor effect in various types of cancer, including glioma, osteosarcoma, melanoma, myeloproliferative neoplasms, lung cancer, hepatocellular carcinoma, pancreatic cancer, breast cancer, colorectal cancer, prostate cancer, ovarian cancer, etc. (Dakir *et al.*, 2018; Kim *et al.*, 2020; Cui *et al.*, 2020; Ranjan *et al.*, 2020; Vlachos *et al.*, 2021; Li *et al.*, 2022a). The ability to suppress the USP1/UAF1 protein complex is one of the key mechanisms of the effect on malignant cells. Pimozide and GW7647 belong to reversible inhibitors and are characterized by moderate PubChem promiscuity with hit rates of 9.5% and 11.4%, respectively. Both inhibitors bind outside the active site of USP1, which is thought to disrupt the protein-protein interaction between USP1 and the cofactor UAF1. Despite good cellular inhibition of the USP1/UAF1 protein complex, pimozide and GW7647 are able to show activity against unrelated targets. (USP7 for pimozide and USP2, USP7, USP12/USP46 for GW7647) (Table 2). Laboratory studies, which included kidney and liver function tests, showed non-toxicity of intraperitoneal GW6471 at a dose of 20 mg/kg for mice (Chen *et al.*, 2011; Dexheimer *et al.*, 2014; Gonçalves *et al.*, 2019; LaPlante *et al.*, 2021; Morishita *et al.*, 2022; Orozco *et al.*, 2022; Ler *et al.*, 2022). Another known USP1 inhibitor is the compound SJB2-043, which causes downregulation of ID2 and ID3 proteins, growth inhibition and apoptosis, and blocks pancreatic β -cell apoptosis by inhibiting the DNA damage response (Mistry *et al.*, 2013; Gorrepati *et al.*, 2018; Chen *et al.*, 2021). Inhibitor C527 promotes dose-dependent degradation of ID1 in osteosarcoma cells. The mechanisms of action of inhibitors SJB2-043 and C527 have currently been studied *in vitro*. Compounds flupenthixol and trifluoperazine belong to the group of antipsychotic drugs, which are widely used in medical practice for the treatment of mental disorders, in particular schizophrenia, neuroses with anxiety and fear phenomena. Flupenthixol and trifluoperazine have sufficient selectivity for human DUB, however, the mechanisms of their inhibitory effect on USP1 are currently insufficiently studied. Rottlerin is an irreversible inhibitor of USP1/UAF1 with poor selectivity for other DUBs,

Table 2. Selectivity of inhibitors to different USPs.

Compound	USPs						References
	USP1/UAF1	USP2	USP5	USP7	USP8	USP46/ UAF1	
Pimozide	+	–	–	+	–	–	Chen <i>et al.</i> , 2011; Dexheimer <i>et al.</i> , 2014
GW7647	+	+	–	+	–	+	Dexheimer <i>et al.</i> , 2014; Gonçalves <i>et al.</i> , 2019
SJB2-043	+	not tested	not tested	not tested	not tested	not tested	Mistry <i>et al.</i> , 2013
C527	+	–	+	–	–	+	Mistry <i>et al.</i> , 2013; Rennie <i>et al.</i> , 2022
Flupenthixol	+	–	–	+	+	–	Chen <i>et al.</i> , 2011
Trifluoperazine	+	–	–	+	–	–	Chen <i>et al.</i> , 2011
Rottlerin	+	+	+	+	+	+	Chen <i>et al.</i> , 2011
ML323	+	–	–	–	–	–	Dexheimer <i>et al.</i> , 2014; Rennie <i>et al.</i> , 2022
KSQ-4279	+	not tested	not tested	not tested	not tested	not tested	Shenker <i>et al.</i> , 2021

in particular it is able to bind to USP2, USP7, USP8, USP46, etc. Rottlerin is well tolerated when administered orally or intraperitoneally to mice and does not cause side effects (Chen *et al.*, 2011; Lee *et al.*, 2016; Ma *et al.*, 2018; Xia *et al.*, 2019; Chen *et al.*, 2021). ML323, the potent nanomolecular inhibitor of USP1/UAF1 complex, has excellent selective ability. The mechanism of ML323 inhibitory effect consists in replacing part of the hydrophobic core of USP1, conformational changes of the secondary structure lead to rearrangements in the active center and inhibition of USP1 activity. ML323 belongs to reversible inhibitors, being 5–10-fold more active than C527 (Dexheimer *et al.*, 2014; Rennie *et al.*, 2022). ML323 has shown good antitumor activity in various cancers, including esophageal squamous cell carcinoma, pancreatic ductal adenocarcinoma, chronic myeloid leukemia, breast cancer, colorectal cancer, etc. ML323 reduces DNA repair, increases the sensitivity of cells to cisplatin in osteosarcoma and non-small cell lung cancer. It is promising to use ML323 in combination with compounds that damage DNA, in particular cisplatin, to enhance the cytotoxicity of anticancer drugs. ML323 has low cytotoxicity *in vitro*. In mice ML323 inhibited osteosarcoma progression in the absence of significant cytotoxicity. (Dexheimer *et al.*, 2014; Yu *et al.*, 2017; Song *et al.*, 2022). In 2021, there were reports of a new compound, KSQ-4279, capable of highly selectively inhibiting the activity of USP1 and leading to the accumulation of its monoubiquitinated substrate proteins. Under *in vitro* conditions, KSQ-4279 performed well in ovarian and triple-negative breast cancer xenograft models, causing dose-dependent inhibition of tumor growth and tumor regression in models insensitive to PARP inhibitors (Shenker *et al.*, 2021). To date, in the available literature there are no reports on the study of KSQ-4279 *in vivo*.

CONCLUSIONS

In malignant cells, there are mechanisms to suppress the degradation of oncoproteins, in which DUBs play a

key role. The imbalance between ubiquitination and deubiquitination is a critical event contributing to the accumulation of oncoproteins in the cell and preventing their degradation. Plenty of current research focus on the identification of DUBs associated with different aspects of oncogenesis. Study of their cellular localization, interactions with target proteins and substrate specificity is of importance for developing selective inhibitors and implementing a new cancer treatment strategy. USP1 as an important member of the DUB family with a wide range of cellular substrates is involved in ensuring genetic stability and cell homeostasis. Deregulation of its expression and deubiquitinating activity is revealed in various malignant neoplasms. Recent studies suggest a non-genomic mechanism of protein stabilization mediated by USP1 activity allowing for controlling expression of target genes that play a key role in cancer development and progression. USP1 overexpression is a hallmark of a number of cancers including glioma, osteosarcoma, B-cell and T-cell acute lymphoblastic leukemia, hepatocellular carcinoma, gastric, breast, ovarian, prostate, and colorectal cancers, which correlates with poor survival and unfavorable prognosis. Further studies will help understand the relationship between USP1 expression profiles and cancer, opening up new possibilities for using USP1 as a tumor marker for early detection, staging, and individualized therapy of malignant neoplasms. Inhibition of USP1 *in vitro* sensitizes cancer cells to radiation and increases their sensitivity to various chemotherapeutic agents, so targeting the USP1/UAF1 complex may be of great benefit in overcoming resistance and widening the use of combination therapy for cancer. The key function of USP1 in the regulation of the substrate ubiquitination allows modulating the level of specific proteins including those contributing to the development of malignant neoplasms.

Despite tremendous progress achieved in the past decade in studying the roles of DUBs in cellular events resulting in malignant transformation, many important questions have not yet been clarified. The exact roles of

different DUBs vary in different forms of cancer and the specific substrates that are ubiquitinated. Moreover, their roles in different cells and tissues of varying histogenesis or different metabolic conditions may not be the same. One should also be aware that DUBs interact with an array of enzymes that sometimes act oppositely defining the fate of cancer cells. The increasing specificity of the substances disrupting or enhancing specific interactions of DUBs with their substrates could be promising in search of more efficient therapeutic strategies.

Although we have a long way to go before the translation of the experimental research into the clinical practice, undoubtedly, DUBs represent putative therapeutic targets for the development of a new strategy for cancer treatment by modulating the levels and the activities of oncoproteins in cancer cell.

REFERENCES

- Antonenko S, Gurianov D, Telegeev G (2016) Colocalization of USP1 and PH domain of Bcr-Abl oncoprotein in terms of chronic myeloid leukemia cell rearrangements. *Tsitol Genet* **50**: 11–15. <https://doi.org/10.3103/S0095452716050029>
- Antonenko S, Telegeev G (2020) Inhibition of USP1, a new partner of bcr-abl, results in decrease of Bcr-Abl level in k562 cells. *Expe Oncol* **42**: 109–114. <https://doi.org/10.32471/exp-oncology.2312-8852.vol-42-no-2.14533>
- Arkinson C, Chaugale V, Toth R, Walden H (2018) Specificity for deubiquitination of monoubiquitinated FANCD2 is driven by the N-terminus of USP1. *Life Sci Alliance* **1**: e201800162. <https://doi.org/10.26508/lsa.201800162>
- Bishop P, Rocca D, Henley JM (2016) Ubiquitin C-terminal hydrolase L1 (UCH-L1): structure, distribution and roles in brain function and dysfunction. *Biochem J* **473**: 2453–2462. <https://doi.org/10.1042/BCJ20160082>
- Bonacini T, Emanuele MJ (2020) Dissenting degradation: deubiquitinases in cell cycle and cancer. *Seminars Cancer Biol* **67**: 145–158. <https://doi.org/10.1016/j.semcancer.2020.03.008>
- Caba C, Mohammadzadeh A, Tong Y (2022) On the study of deubiquitinases: using the right tools for the job. *Biomolecules* **12**: 703. <https://doi.org/10.3390/biom12050703>
- Cataldo F, Peche L, Klaric E, Brancolini C, Myers M, Demarchi F, Schneider C (2013) CAPNS1 regulates USP1 stability and maintenance of genome integrity. *Mol Cell Biol* **33**: 2485–2496. <https://doi.org/10.1128/MCB.01406-12>
- Chen J, Dexheimer TS, Ai Y, Liang Q, Villamil M, Ingles J, Maloney D, Jadhav A, Simeonov A, Zhuang Z (2011) Selective and cell-active inhibitors of the USP1/UAF1 deubiquitinase complex reverse cisplatin resistance in non-small cell lung cancer cells. *Chem Biol* **18**: 1390–1400. <https://doi.org/10.1016/j.chembiol.2011.08.014>
- Chen S, Liu Y, Zhou H (2021) Advances in the development ubiquitin-specific peptidase (USP) inhibitors. *Int J Mol Sci* **22**: 4546. <https://doi.org/10.3390/ijms22094546>
- Chen Z, Ma Y, Guo Z, Song D, Chen Z, Sun M (2022) Ubiquitin-specific protease 1 acts as an oncogene and promotes lenvatinib efficacy in hepatocellular carcinoma by stabilizing c-kit. *Ann Hepatol* **27**: 100669. <https://doi.org/10.1016/j.aohep.2022.100669>
- Coleman KE, Yin Y, Lui SK, Keegan S, Fenyo D, Smith D, Rothenberg E, Huang T (2022) USP1-trapping lesions as a source of DNA replication stress and genomic instability. *Nat Commun* **13**: 1740. <https://doi.org/10.1038/s41467-022-29369-3>
- Condic M, Thiesler T, Kübler K, Staerk C, Klümper N, Ellinger J, Egger E, Kristiansen G, Mustea A, Ralsler D (2022) N6-methyladenosine (m6A) RNA modification is dysregulated in endometrial cancer. *Geburtshilfe Frauenheilkd* **82**: e57. <https://doi.org/10.1055/s-0042-1756777>
- Cotto-Rios XM, Jones MJ, Huang TT (2011) Insights into phosphorylation-dependent mechanisms regulating USP1 protein stability during the cell cycle. *Cell Cycle* **10**: 4009–4016. <https://doi.org/10.4161/cc.10.23.18501>
- Cotto-Rios XM, Békés M, Chapman J, Ueberheide B, Huang TT (2012) Deubiquitinases as a signaling target of oxidative stress. *Cell Rep* **2**: 1475–1484. <https://doi.org/10.1016/j.celrep.2012.11.011>
- Cruz L, Soares P, Correia M (2021) Ubiquitin-specific proteases: players in cancer cellular processes. *Pharmaceuticals* **14**: 848. <https://doi.org/10.3390/ph14090848>
- Cui S, Lei Z, Guan T, Fan L, Li Y, Geng X, Fu D, Jiang H, Xu S (2020) Targeting USP1-dependent KDM4A protein stability as a potential prostate cancer therapy. *Cancer Sci* **111**: 1567–1581. <https://doi.org/10.1111/cas.14375>
- Dakir EH, Pickard A, Srivastava K, Srivastava K, McCrudden C, Gross S, Lloyd S, Zhang SD, Margariti A, Morgan R, Rudland P, El-Tanani M (2018) The anti-psychotic drug pimozide is a novel chemotherapeutic for breast cancer. *Oncotarget* **9**: 34889–34910. <https://doi.org/10.18632/oncotarget.26175>
- Das DS, Das A, Ray A, Song Y, Samur M, Munshi N, Chauhan D, Anderson K (2017) Blockade of deubiquitylating enzyme USP1 inhibits DNA repair and triggers apoptosis in multiple myeloma cells. *Clin Cancer Res* **23**: 4280–4289. <https://doi.org/10.1158/1078-0432.CCR-16-2692>
- Dexheimer T, Rosenthal A, Liang Q, Liang Q, Chen J, Villamil M, Kerns E, Simeonov A, Jadhav A, Zhuang Z, Maloney D (2012) Discovery of ML323 as a novel inhibitor of the USP1/UAF1 deubiquitinase complex. In Probe Reports from the NIH Molecular Libraries Program [Internet]. Bethesda (MD): National Center for Biotechnology Information (US). [updated 2014 Sep 18].
- Dexheimer TS, Rosenthal AS, Luci DK, Liang Q, Villamil M, Chen J, Sun H, Kerns E, Simeonov A, Jadhav A, Zhuang Z, Maloney D (2014) Synthesis and structure – activity relationship studies of n-benzyl-2-phenylpyrimidin-4-amine derivatives as potent USP1/UAF1 deubiquitinase inhibitors with anticancer activity against non-small cell lung cancer. *J Med Chem* **57**: 8099–8110. <https://doi.org/10.1021/jm5010495>
- Dharadhar S, Dijk WJ, Scheffers S, Fish A, Sixma TK (2021) Insert L1 is a central hub for allosteric regulation of USP1 activity. *EMBO Rep* **22**: e51749. <https://doi.org/10.15252/embr.202051749>
- Du J, Fu L, Sui Y, Zhang L (2019) The function and regulation of OTU deubiquitinases. *Frontiers Med* **14**: 542–563. <https://doi.org/10.1007/s11684-019-0734-4>
- Du R, Huang C, Liu K, Li X, Dong Z (2021) Targeting AURKA in Cancer: molecular mechanisms and opportunities for Cancer therapy. *Mol Cancer* **20**: 5. <https://doi.org/10.1186/s12943-020-01305-3>
- Estavoyer B, Messmer C, Echbicheb M, Rudd CE, Milot E, Affar EB (2022) Mechanisms orchestrating the enzymatic activity and cellular functions of deubiquitinases. *J Biol Chem* **298**: 102198. <https://doi.org/10.1016/j.jbc.2022.102198>
- Fraile JM, Quesada V, Rodríguez D, Freije JM, López-Otín C (2012) Deubiquitinases in cancer: new functions and therapeutic options. *Oncogene* **31**: 2373–2388. <https://doi.org/10.1038/nc.2011.443>
- Fujiwara T, Saito A, Suzuki M, Shinomiya H, Suzuki T, Takahashi E, Tanigami A, Ichiyama A, Chung C, Nakamura Y, Tanaka K (1998) Identification and chromosomal assignment of USP1, a novel gene encoding a human ubiquitin-specific protease. *Genomics* **54**: 155–158. <https://doi.org/10.3390/ph14090848>
- Garapati HS, Male G, Mishra K (2020) Predicting subcellular localization of proteins using protein-protein interaction data. *Genomics* **112**: 2361–2368. <https://doi.org/10.1016/j.ygeno.2020.01.007>
- García-Santesteban I, Zorroza K, Rodríguez JA (2012) Two nuclear localization signals in USP1 mediate nuclear import of the USP1/UAF1 complex. *PLoS One* **7**: e38570. <https://doi.org/10.1371/journal.pone.0038570>
- García-Santesteban I, Peters GJ, Giovannetti E, Rodríguez J (2013) USP1 deubiquitinase: cellular functions, regulatory mechanisms and emerging potential as target in cancer therapy. *Mol Cancer* **12**: 91. <https://doi.org/10.1186/1476-4598-12-91>
- Gonçalves JM, Cordeiro MM, Rivero ER (2017) The role of the complex USP1/WDR48 in differentiation and proliferation processes in cancer stem cells. *Curr Stem Cell Res Therap* **12**: 416–422. <https://doi.org/10.2174/1574888X12666170315104013>
- Gonçalves JM, Silva CA, Rivero ER, Cordeiro MM (2019) Inhibition of cancer stem cells promoted by Pimozide. *Clin Exp Pharmacol Physiol* **46**: 116–125. <https://doi.org/10.1111/1440-1681.13049>
- Gong H, Liu L, Cui L, Ma H, Shen L (2021) ALKBH5-mediated m6A-demethylation of USP1 regulated T-cell acute lymphoblastic leukemia cell glucocorticoid resistance by Aurora B. *Mol Carcinogenesis* **60**: 644–657. <https://doi.org/10.1002/mc.23330>
- Gorrepati KD, Lupse B, Annamalai K, Yuan T, Maedler K, Ardestani A (2018) Loss of deubiquitinase USP1 blocks pancreatic β -cell apoptosis by inhibiting DNA damage response. *iScience* **1**: 72–86. <https://doi.org/10.1016/j.isci.2018.02.003>
- Guo J, Zhao J, Sun L, Yang C (2022) Role of ubiquitin specific proteases in the immune microenvironment of prostate cancer: A new direction. *Front Oncol* **12**. <https://doi.org/10.3389/fonc.2022.955718>
- Henning NJ, Boike L, Spradlin JN, Ward C, Liu G, Zhang E, Belcher B, Brittain S, Hesse M, Dovala D, McGregor L, Misolek R, Plasschaert L, Rowlands D, Wang F, Frank A, Fuller D, Estes A, Randal K, Panidapu A, McKenna J, Tallarico J, Schirle M, Nomura D (2022) Deubiquitinase-targeting chimeras for targeted protein stabilization. *Nature Chem Biol* **18**: 412–421. <https://doi.org/10.1038/s41589-022-00971-2>
- Huo FC, Zhu ZM, Pei DS (2020) N6-methyladenosine (m6A) RNA modification in human cancer. *Cell Prolif* **53**: e12921. <https://doi.org/10.1111/cpr.12921>
- Jerabkova K, Liao Y, Kleiss C, Fournane S, Durik M, Agote-Arán A, Brino L, Sedlacek R, Sumara I (2020) Deubiquitylase UCHL3 regu-

- lates bi-orientation and segregation of chromosomes during mitosis. *FASEB J* **34**: 12751–12767. <https://doi.org/10.1096/fj.202000769R>
- Jung JK, Jang SW, Kim JM (2016) A novel role for the deubiquitinase USP1 in the control of centrosome duplication. *Cell Cycle* **15**: 584–592. <https://doi.org/10.1080/15384101.2016.1138185>
- Juhász S, Balogh D, Hajdu I, Burkovics P, Villamil MA, Zhuang Z, Harácska L (2012) Characterization of human Spartan/C1orf124, an ubiquitin-PCNA interacting regulator of DNA damage tolerance. *Nucleic Acids Res* **40**: 10795–10808. <https://doi.org/10.1093/nar/gks850>
- Kim U, Kim CY, Lee JM, Ryu B, Kim J, Shin C, Park JH (2020) Pimozide inhibits the human prostate cancer cells through the generation of reactive oxygen species. *Front Pharmacol* **10**: 1517. <https://doi.org/10.3389/fphar.2019.01517>
- Kuang X, Xiong J, Lu T, Wang W, Zhang Z, Wang J (2021) Inhibition of USP1 induces apoptosis via ID1/AKT pathway in B-cell acute lymphoblastic leukemia cells. *Int J Med Sci* **18**: 245–255. <https://doi.org/10.7150/ijms.47597>
- Lai KP, Chen J, Tse WK (2020) Role of deubiquitinases in human cancers: potential targeted therapy. *Int J Mol Sci* **21**: 2548. <https://doi.org/10.3390/ijms21072548>
- LaPlante G, Zhang W (2021) Targeting the ubiquitin-proteasome system for cancer therapeutics by small-molecule inhibitors. *Cancers* **13**: 3079. <https://doi.org/10.3390/cancers13123079>
- Lee JG, Baek K, Soetandyo N, Ye Y (2013) Reversible inactivation of deubiquitinases by reactive oxygen species *in vitro* and in cells. *Nat Commun* **4**: 1568. <https://doi.org/10.1038/ncomms2532>
- Lee JK, Chang N, Yoon Y, Yang H, Cho H, Kim E, Shin Y, Kang W, Oh Y, Mun G, Joo K, Nam DH, Lee J (2016) USP1 targeting impedes GMB growth by inhibiting stem cell maintenance and radio-resistance. *Neuro-Oncol* **18**: 37–47. <https://doi.org/10.1093/neuonc/nov091>
- Lee JK, Nam DH, Lee J (2016) Repurposing antipsychotics as glioblastoma therapeutics: potentials and challenges. *Oncol Lett* **11**: 1281–1286. <https://doi.org/10.3892/ol.2016.4074>
- Lei H, Wang J, Hu J, Zhu Q, Wu Y (2021a) Deubiquitinases in hematological malignancies. *Biomarker Research* **9**: 66. <https://doi.org/10.1186/s40364-021-00320-w>
- Lei H, Xu H-Z, Shan HZ, Liu M, Lu Y, Fang ZX, Jin J, Jing B, Xiao XH, Gao SM, Gao FH, Xia L, Yang L, Liu LG, Wang WW, Liu CX, Tong Y, Wu YZ, Zheng JK, Wu YL (2021b) Targeting USP47 overcomes tyrosine kinase inhibitor resistance and eradicates leukemia stem/progenitor cells in chronic myelogenous leukemia. *Nat Commun* **12**: 51. <https://doi.org/10.1038/s41467-020-20259-0>
- Ler AA, Carty MP (2022) DNA damage tolerance pathways in human cells: a potential therapeutic target. *Front Oncol* **11**: 822500. <https://doi.org/10.3389/fonc.2021.822500>
- Li J, Qu P, Zhou XZ, Ji YX, Yuan S, Liu SP, Zhang QG (2022a) Pimozide inhibits the growth of breast cancer cells by alleviating the Warburg effect through the P53 signaling pathway. *Biomed Pharmacother* **150**: 113063. <https://doi.org/10.1016/j.biopha.2022.113063>
- Li JT, Li KY, Su Y, Shen Y, Lei MZ, Zhang F, Yin M, Chen ZJ, Wen WY, Hu WG, Su D, Qu J, Lei QY (2022b) Diet high in branched-chain amino acid promotes PDAC development by USP1-mediated BCAT2 stabilization. *Nat Sci Rev* **9**: 212. <https://doi.org/10.1093/nsr/nwab212>
- Li N, Wu L, Zuo X, Luo H, Sheng Y, Yan J (2021) USP1 promotes GC metastasis via stabilizing ID2. *Dis Markers* **2021**: 3771990. <https://doi.org/10.1155/2021/3771990>
- Li Y, Xu Y, Gao C, Sun Y, Zhou K, Wang P, Cheng J, Guo W, Ya C, Fan J, Yang X (2020) USP1 maintains the survival of liver circulating tumor cells by deubiquitinating and stabilizing TBRL1. *Front Oncol* **10**: 554809. <https://doi.org/10.3389/fonc.2020.554809>
- Liang W, Fang J, Zhou S, Hu W, Yang Z, Li Z, Dai L, Tao Y, Fu X, Wang X (2022) The role of ubiquitin-specific peptidases in glioma progression. *Biomed Pharmacother* **146**: 112585. <https://doi.org/10.1016/j.biopha.2021.112585>
- Liao Y, Liu Y, Shao Z, Xia X, Deng Y, Cai J, Yao L, He J, Yu C, Hu T, Sun W, Liu F, Tang D, Liu J, Huang H (2021a) A new role of GRP75-USP1-SIX1 protein complex in driving prostate cancer progression and castration resistance. *Oncogene* **40**: 4291–4306. <https://doi.org/10.1038/s41388-021-01851-0>
- Liao Y, Shao Z, Liu Y, Xia X, Deng Y, Yu C, Sun W, Kong W, He X, Liu F, Guo Z, Chen G, Tang D, Gan H, Liu J, Huang H (2021b) USP1-dependent RPS16 protein stability drives growth and metastasis of human hepatocellular carcinoma cells. *J Exp Clin Cancer Res* **40**: 201. <https://doi.org/10.1186/s13046-021-02008-3>
- Liao Y, Sun W, Shao Z, Liu Y, Zhong X, Deng Y, Liu F, Huang H, Liu J (2022) A SIX1 degradation inducer blocks excessive proliferation of prostate cancer. *Int J Biol Sci* **18**: 2439–2451. <https://doi.org/10.7150/ijbs.67873>
- Lim KS, Li H, Roberts EA, Gaudiano E, Clairmont C, Sambel L, Ponnienselvam K, Liu J, Yang C, Kozono D, Parmar K, Yusufzai T, Zheng N, D'Andrea A (2018) USP1 is required for replication fork protection in brca1-deficient tumors. *Mol Cell* **72**: 925–941. <https://doi.org/10.1016/j.molcel.2018.10.045>
- Liu J, Zhu H, Zhong N, Jiang Z, Xu L, Deng Y, Jiang Z, Wang H, Wang J (2016) Gene silencing of USP1 by lentivirus effectively inhibits proliferation and invasion of human osteosarcoma cells. *Int J Oncol* **49**: 2549–2557. <https://doi.org/10.3892/ijo.2016.3752>
- Liu J, Leung CT, Liang L, Wang Y, Chen J, Lai K, Tse W (2022) Deubiquitinases in cancers: aspects of proliferation, metastasis, and apoptosis. *Cancers* **14**: 3547. <https://doi.org/10.3390/cancers14143547>
- Lu Z, Zhang Z, Yang M, Xiao M (2022) Ubiquitin-specific protease 1 inhibition sensitizes hepatocellular carcinoma cells to doxorubicin by ubiquitinated proliferating cell nuclear antigen-mediated attenuation of stemness. *Anticancer Drugs* **33**: 622–631. <https://doi.org/10.1097/CAD.0000000000001311>
- Ma J, Hou Y, Xia J, Zhu X, Wang P (2018) Tumor suppressive role of rottlerin in cancer therapy. *Am J Transl Res* **10**: 3345–3356
- Ma L, Lin K, Chang G, Chen Y, Yue C, Guo Q, Zhang S, Jia Z, Tony T, Huang TT, Zhou A, Huang S (2019a) Aberrant activation of β -catenin signaling drives glioma tumorigenesis via USP1-mediated stabilization of EZH2. *Cancer Res* **79**: 72–85. <https://doi.org/10.1158/0008-5472.CAN-18-1304>
- Ma A, Tang M, Zhang L, Wang B, Yang Z, Liu Y, Xu G, Wu L, Jing T, Xu X, Yang S, Liu Y (2019b) USP1 inhibition destabilizes KPNA2 and suppresses breast cancer metastasis. *Oncogene* **38**: 2405–2419. <https://doi.org/10.1038/s41388-018-0590-8>
- Meng D, Li D (2022) Ubiquitin-specific protease 1 overexpression indicates poor prognosis and promotes proliferation, migration, and invasion of gastric cancer cells. *Tissue Cell* **74**: 101723. <https://doi.org/10.1016/j.tice.2021.101723>
- Minchenko O, Tsybalyk O, Minchenko O, Riabovol O, Halkin O, Ratushna O (2016) IRE-1 α regulates expression of ubiquitin specific peptidases during hypoxic response in U87 glioma cells. *Endoplasmic Reticulum Stress Dis* **3**: 50–62. <https://doi.org/10.1515/ersc-2016-0003>
- Mistry H, Hsieh G, Buhrlage SJ, Huang M, Park E, Cuny G, Galinsky I, Stone R, Gray N, D'Andrea A, Parmar K (2013) Small-molecule inhibitors of USP1 target ID1 degradation in leukemic cells. *Mol Cancer Ther* **12**: 2651–2662. <https://doi.org/10.1158/1535-7163.MCT-13-0103-T>
- Mohanty A, Nam A, Pozhitkov A, Yang L, Srivastava S, Nathan A, Wu X, Mambetsariev I, Nelson M, Subbalakshmi A, Guo L, Nasser M, Batra S, Orban J, Jolly M, Erminia Massarelli E, Kulkarni P, Sallgia R (2020) A non-genetic mechanism involving the integrin β 4/paxillin axis contributes to chemoresistance in lung cancer. *iScience* **23**: 101496. <https://doi.org/10.1016/j.jisci.2020.101496>
- Morishita H, Perera LM, Zhang X, Mizoi K, Ito MA, Yano K, Ogihara T (2022) P-glycoprotein-mediated pharmacokinetic interactions increase pimozide hERG channel inhibition. *J Pharm Sci* **111**: 3411–3416. <https://doi.org/10.1016/j.xphs.2022.09.025>
- Mullard M, Lavaud M, Regnier L, Tesfaye R, Ory B, Françoise Rédini F, Verrecchia F (2021) Ubiquitin-specific proteases as therapeutic targets in paediatric primary bone tumours? *Biochem Pharmacol* **194**: 114797. <https://doi.org/10.1016/j.bcp.2021.114797>
- Mussell A, Shen H, Chen Y, Mastri M, Eng K, Bshara W, Frangou C, Zhang J (2020) USP1 regulates TAZ protein stability through ubiquitin modifications in breast cancer. *Cancers* **12**: 3090. <https://doi.org/10.3390/cancers12113090>
- Nijman SM, Huang TT, Dirac AM, Brummelkamp T, Kerkhoven R, D'Andrea A, Bernards R (2005) The deubiquitinating enzyme USP1 regulates the fanconi anemia pathway. *Mol Cell* **17**: 331–339. <https://doi.org/10.1016/j.molcel.2005.01.008>
- Niu Z, Li X, Feng S, Huang Q, Zhuang T, Yan C, Qian H, Ding Y, Zhu J, Xu W (2020) The deubiquitinating enzyme USP1 modulates ER α and modulates breast cancer progression. *J Cancer* **11**: 6992–7000. <https://doi.org/10.7150/jca.50477>
- Olazabal-Herrero A, García-Santisteban I, Rodríguez J (2015) Structure-function analysis of USP1: insights into the role of Ser313 phosphorylation site and the effect of cancer-associated mutations on autocleavage. *Mol Cancer* **14**: 33. <https://doi.org/10.1186/s12943-015-0311-7>
- Orozco Morales ML, Rinaldi CA, de Jong E, Lansley S, Gummer J, Olasz B, Nambiar S, Hope D, Casey T, Lee G, Leslie C, Nealon G, Shackleford D, Powell A, Grimaldi M, Balaguer P, Zemek R, Bosco A, Piggott M, Vrielink A, Lesterhuis W (2022) PPAR α and PPAR γ activation is associated with pleural mesothelioma invasion but therapeutic inhibition is ineffective. *iScience* **25**: 103571. <https://doi.org/10.1016/j.jisci.2021.103571>
- Pal A, Donato J (2014) Ubiquitin-specific proteases as therapeutic targets for the treatment of breast cancer. *Breast Cancer Res* **16**: 416. <https://doi.org/10.1186/s13058-014-0461-3>
- Piatkov KI, Colnaghi L, Békés M, Varshavsky A, Huang TT (2012) The auto-generated fragment of the usp1 deubiquitylase is a physiological substrate of the n-end rule pathway. *Mol Cell* **48**: 926–933. <https://doi.org/10.1016/j.molcel.2012.10.012>
- Poonalia N, Chandrasekaran AP, Kim KS, Ramakrishna S (2019) Deubiquitinating enzymes as cancer biomarkers: new therapeutic

- opportunities? *BMB Rep* **52**: 181–189. <https://doi.org/10.5483/BMBRep.2019.52.3.048>
- Rahme GJ, Zhang Z, Young AL, Cheng C, Bivona E, Fiering S, Hitoshi Y, Israel M (2016) PDGF engages an E2F-USP1 signaling pathway to support id2-mediated survival of proneural glioma cells. *Cancer Res* **76**: 2964–2976. <https://doi.org/10.1158/0008-5472.CAN-15-2157>
- Ranjan A, Kaushik I, Srivastava SK (2020) Pimozide suppresses the growth of brain tumors by targeting stat3-mediated autophagy. *Cells* **9**: 2141. <https://doi.org/10.3390/cells9092141>
- Rennie ML, Arkinson C, Chaugule VK, Walden H (2022) Cryo-EM reveals a mechanism of USP1 inhibition through a cryptic binding site. *Sci Adv* **8**: eabq6353. <https://doi.org/10.1126/sciadv.abq6353>
- Robak P, Robak T (2019) Bortezomib for the treatment of hematologic malignancies: 15 years later. *Drugs R D* **19**: 73–92. <https://doi.org/10.1007/s40268-019-0269-9>
- Shenker S, Gannon H, Carlson A, Grasberger P, Sullivan P, Middleton C, Dodson A, Bullock C, McGuire M, Tobin E, Sinkevicius K, Schlabach M, Stegmeier F, Cadzow L, Wylie A (2021) Functional genomic characterization of the USP1 inhibitor KSQ-4279 reveals a distinct mechanism of action and resistance profile relative to other DDR targeting drugs. *Cancer Res* **81**: 1337. <https://doi.org/10.1158/1538-7445.AM2021-1337>
- Snyder NA, Silva GM (2021) Deubiquitinating enzymes (DUBs): regulation, homeostasis, and oxidative stress response. *J Biol Chem* **297**: 101077. <https://doi.org/10.1016/j.jbc.2021.101077>
- Sonego M, Pellarin I, Costa A, Vinciguerra GL, Coan M, Kraut A, D'Andrea S, Dall'Acqua D, Castillo-Tong DC, Califano D, Losito S, Spizzo R, Couté Y, Vecchione A, Belletti B, Schiappacassi M, Baldassarre G (2019) USP1 links platinum resistance to cancer cell dissemination by regulating Snail stability. *Sci Adv* **5**: eaav3235. <https://doi.org/10.1126/sciadv.aav3235>
- Song B, Jiang Y, Jiang Y, Lin Y, Liu J (2022) ML323 suppresses the progression of ovarian cancer via regulating USP1-mediated cell cycle. *Front Genet* **13**: 917481. <https://doi.org/10.3389/fgene.2022.917481>
- Sun Y, Sha B, Huang W, Li M, Zhao S, Zhang Y, Yan J, Li Z, Tang J, Duan P, Shi J, Li P, Hu T, Chen P (2022) ML323, a USP1 inhibitor triggers cell cycle arrest, apoptosis and autophagy in esophageal squamous cell carcinoma cells. *Apoptosis* **27**: 545–560. <https://doi.org/10.1007/s10495-022-01736-x>
- Twist S, Murphy V, Hodson C, Tan W, Swuec P, O'Rourke J (2017) Mechanism of ubiquitination and deubiquitination in the fanconi anemia pathway. *Mol Cell* **65**: 247–259. <https://doi.org/10.1016/j.molcel.2016.11.005>
- Trulsson F, Akimov V, Robu M, Overbeek N, Berrocal DA, Shah RG, Cox J, Shah GM, Blagoev B, Vertegaal AC (2022) Deubiquitinating enzymes and the proteasome regulate preferential sets of ubiquitin substrates. *Nat Commun* **13**: 2736. <https://doi.org/10.1038/s41467-022-30376-7>
- Tu R, Ma J, Zhang P, Kang Y, Xiong X, Zhu J, Li M, Zhang C (2022) The emerging role of deubiquitylating enzymes as therapeutic targets in cancer metabolism. *Cancer Cell Int* **22**: 130. <https://doi.org/10.1186/s12935-022-02524-y>
- Villamil MA, Chen J, Liang Q, Zhuang Z (2012a) A noncanonical cysteine protease USP1 is activated through active site modulation by usp1-associated factor 1. *Biochemistry* **51**: 2829–2839. <https://doi.org/10.1021/bi3000512>
- Villamil MA, Liang Q, Chen J, Choi Y, Hou S, Lee KH, Zhuang Z (2012b) Serine phosphorylation is critical for the activation of ubiquitin-specific protease 1 and its interaction with wd40-repeat protein UAF1. *Biochemistry* **51**: 9112–9123. <https://doi.org/10.1021/bi300845s>
- Vlachos N, Lampros M, Voulgaris S, Alexiou GA (2021) Repurposing antipsychotics for cancer treatment. *Biomedicines* **9**: 1785. <https://doi.org/10.3390/biomedicines9121785>
- Wang Y, Wang F (2021) Post-Translational modifications of deubiquitinating enzymes: expanding the ubiquitin code. *Front Pharmacol* **12**: 685011. <https://doi.org/10.3389/fphar.2021.685011>
- Williams SA, Maecker HL, French DM, Liu J, Gregg A, Silverstein LB, Cao TC, Carano RA, Dixit VM (2011) USP1 deubiquitinates ID proteins to preserve a mesenchymal stem cell program in osteosarcoma. *Cell* **146**: 918–930. <https://doi.org/10.1016/j.cell.2011.07.040>
- Woo SM, Kim S, Seo SU, Kim S, Park JW, Kim G, Choi YR, Hur K, Kwon TK (2022) Inhibition of USP1 enhances anticancer drugs-induced cancer cell death through downregulation of survivin and miR-216a-5p-mediated upregulation of DR5. *Cell Death Dis* **13**: 821. <https://doi.org/10.1038/s41419-022-05271-0>
- Xia Y, Jia C, Xue Q, Jiang J, Xie Y, Wang R, Ran Z, Xu F, Zhang Y, Ye T (2019) Antipsychotic drug trifluoperazine suppresses colorectal cancer by inducing G0/G1 arrest and apoptosis. *Front Pharmacol* **10**: 1029. <https://doi.org/10.3389/fphar.2019.01029>
- Xu X, Li S, Cui X, Han K, Wang J, Hou X, Cui L, He S, Xiao J, Yang Y (2019) Inhibition of ubiquitin specific protease 1 sensitizes colorectal cancer cells to dna-damaging chemotherapeutics. *Front Oncol* **9**: 1406. <https://doi.org/10.3389/fonc.2019.01406>
- Yang K, Moldovan GL, Vinciguerra P, Murai J, Takeda S, D'Andrea AD (2011) Regulation of the Fanconi anemia pathway by a SUMO-like delivery network. *Genes Develop* **25**: 1847–1858. <https://doi.org/10.1101/gad.17020911>
- Yang Y, Ding Y, Zhou C, Wen Y, Zhang N (2019) Structural and functional studies of USP20 ZnF-UBP domain by NMR. *Protein Sci* **28**: 1606–1619. <https://doi.org/10.1002/pro.3675>
- Yu Z, Song H, Jia M, Zhang J, Wang W, Li Q, Zhang L, Zhao W (2017) USP1–UAF1 deubiquitinase complex stabilizes TBK1 and enhances antiviral responses. *J Exp Med* **214**: 3553–3563. <https://doi.org/10.1084/jem.20170180>
- Yuan P, Feng Z, Huang H, Wang G, Chen Z, Xu G, Xie Z, Jie Z, Zhao X, Ma Q, Wang S, Shen Y, Yizhen Huang Y, Han Y, Ye H, Wang J, Shi P, Sun X (2022) USP1 inhibition suppresses the progression of osteosarcoma via destabilizing TAZ. *Int J Biol Sci* **18**: 3122–3136. <https://doi.org/10.7150/ijbs.65428>
- Zhao Y, Xue C, Xie Z, Ouyang X, Li L (2020) Comprehensive analysis of ubiquitin-specific protease 1 reveals its importance in hepatocellular carcinoma. *Cell Prolif* **53**: e12908. <https://doi.org/10.1111/cpr.12908>
- Zhiqiang Z, Qinghui Y, Yongqiang Z, Jian Z, Xin Z, Haiying M, Yuepeng G (2012) USP1 regulates AKT phosphorylation by modulating the stability of PHILPP1 in lung cancer cells. *J Cancer Res Clin Oncol* **138**: 1231–1238. <https://doi.org/10.1007/s00432-012-1193-3>
- Zhong L, Li Y, Xiong L, Wang W, Wu M, Yuan T, Yang W, Tian C, Miao Z, Wang T, Yang S (2021) Small molecules in targeted cancer therapy: advances, challenges, and future perspectives. *Signal Transduct Target Ther* **6**: 201. <https://doi.org/10.1038/s41392-021-00572-w>

Involvement of Rictor/mTORC2/Akt/GLUT4 pathway in the regulation of energy metabolism in the gastric smooth muscle of diabetic rats

Sun Yan^{1#}, Yu-Rong Zheng^{2#}, Zheng Jin¹, Mo-Han Zhang^{1✉} and Xiang-Shu Cui^{2✉}

¹Yanbian University College of Medicine, Yanji 133000, Jilin, China; ²Yanbian University School of Nursing, Yanji 133000, Jilin, China

Diabetes mellitus can be accompanied by a variety of complications. The purpose of the present study was to characterize the Rictor/mTOR complex 2 (mTORC2)/Akt/glucose transporter 4 (GLUT4) pathway and its effects on energy metabolism in the gastric smooth muscle of diabetic rats. Diabetes was induced in rats using streptozotocin and their phenotype was compared with untreated rats. The relationship between gastric motility and energy metabolism was analyzed by comparing the contraction and ATP metabolism of muscle strips. Western blotting was used to detect the expression of key proteins in the pathway. The diabetic rats demonstrated less frequent and less powerful gastric smooth muscle contractions. The concentrations of ADP, AMP, and ATP, and the energy charge in gastric smooth muscle changed in different periods of diabetes, and these changes were consistent with changes in mechanistic target of rapamycin (mTOR) protein content. The expression of the key intermediates in signal transduction in the Rictor/mTORC2/Akt/GLUT4 pathway also underwent significant changes. Rictor protein expression increased during the development of diabetes, but the activation of mTORC2 did not increase with the increase in Rictor expression. GLUT4 translocation is regulated by Akt and its expression change during the development of diabetes. These findings suggest that altered energy metabolism is present in gastric smooth muscle that is associated with changes in the Rictor/mTORC2/Akt/GLUT4 pathway. Rictor/mTORC2/Akt/GLUT4 pathway may be involved in the regulation of energy metabolism in the gastric smooth muscle of diabetic rats and the development of diabetic gastroparesis.

Keywords: Gastric smooth muscle; Rictor; mTORC2; Akt; Glucose uptake

Received: 10 April, 2021; revised: 25 August, 2022; accepted: 01 February, 2023; available on-line: 12 June, 2023

✉e-mail: mhzhang@ybu.edu.cn (M-HZ); xscui@ybu.edu.cn (X-SC)

[#]Sun Yan and Yu-Rong Zheng contributed equally to this work, should be considered co-first authors.

Acknowledgements of Financial Support: This work was supported by National Natural Science Foundation of China (Funder Id: 82060154, 81560142)

INTRODUCTION

Diabetic gastroparesis is a gastric motility disorder characterized by delayed gastric emptying. The underlying reduction in gastric motility is directly related to changes in energy metabolism in gastric smooth muscle cells. ATP is the universal energy currency in cells and is predominantly generated in mitochondria by the action

of ATP synthase (Kimoloi, 2018), although glucose can also be metabolized *via* the glycolytic pathway in the cytoplasm to generate a small amount of ATP.

Extensive research over the past two decades has established a central role for mechanistic target of rapamycin (mTOR) in the regulation of many fundamental cell processes, from protein synthesis to autophagy, and deregulated mTOR signaling is implicated in the progression of cancer and diabetes, as well as in the aging process (Kleinert *et al.*, 2014). Since mTOR is a protein kinase related to energy metabolism and diabetes, the putative relationship between mTOR and diabetes should be further explored. mTOR is a serine/threonine protein kinase and a member of the phosphoinositide 3-kinase (PI3K)-related kinase (PIKK) family. It forms the catalytic subunit of two structurally and functionally distinct protein complexes: mTOR complex 1 (mTORC1) and complex 2 (mTORC2) (Kleinert *et al.*, 2014; Saxton & Sabatini, 2017). Each complex has its own unique roles but they also interact with each other. mTORC1 is a major regulator of protein synthesis and cell growth, and comprises three components: mTOR, regulatory protein associated with mTOR (Raptor), and mammalian lethal with Sec13 protein 8 (GβL; mLST8) (Kimoloi 2018; Hara *et al.*, 2002). Recently, it has been shown that mTORC1 senses glucose through more than one mechanism (Kimoloi 2018; Kleinert *et al.*, 2014; Zhang *et al.*, 2017), and it also responds to intracellular and environmental stresses that are incompatible with growth, such as low ATP concentration. A reduction in cellular energy during glucose deprivation activates the stress-responsive metabolic regulator AMP-activated protein kinase (AMPK), which inhibits mTORC1 both indirectly, through the phosphorylation and activation of tuberous sclerosis complex 2 (TSC2), and directly, through the phosphorylation of Raptor (Kimoloi, 2018; Hara *et al.*, 2002; Zhang *et al.*, 2017). Most studies have pointed out that mTORC1 is involved in energy metabolism, but mTORC2 is rarely studied.

Rictor is essential for the integrity and stability of the mTORC2 complex (Kimoloi, 2018; Knudsen *et al.*, 2020). Low Rictor expression leads to lower SIN1 expression and *vice versa* (Hara *et al.*, 2002; Knudsen *et al.*, 2020). Studies have found that the deletion of Rictor gene affects the body's absorption of glucose. Diabetes mellitus is the disorder of glucose absorption and utilization. This suggests that Rictor may play a role in diabetes pathogenesis. It has been reported that alterations to the mTORC1 signaling pathway in skeletal muscle directly affects whole-body energy homeostasis (Mukaida *et al.*, 2017). mTORC2 is also a major upstream kinase for the Akt Ser473 residue (Kleinert *et al.*, 2014; Mu-

kaida *et al.*, 2017). The activation of Akt promotes glucose transporter 4 (GLUT4) translocation to the plasma membrane, which leads to increases in glucose uptake, glucose metabolism, and ATP synthesis (Mukaida *et al.*, 2017; Cosimo *et al.*, 2019; Hasannejad *et al.*, 2019). At the same time, the interaction between mTORC1 and mTORC2 may also affect the energy metabolism of the body.

Glucose is an important source of energy for muscle contraction. Furthermore, normal glucose metabolism is essential for the maintenance of good health, and abnormal glucose metabolism can lead to serious health problems, such as diabetes. Increases in glucose uptake are due to translocation of glucose transporters from intracellular storage vesicles in adipocytes and skeletal muscle cells to the plasma membrane (Khan & Kamal, 2019). GLUT4 is the principal transporter of glucose in muscle and fat cells and has a key role in the control of cellular glucose metabolism and whole-body energy homeostasis, which are strongly linked to type 2 diabetes (Zhao *et al.*, 2019).

The purpose of the present study was to characterize the Rictor/mTORC2/Akt/GLUT4 pathway and its effects on energy metabolism in the gastric smooth muscle of diabetic rats.

MATERIALS AND METHODS

Animals

Forty 8-week-old Sprague-Dawley male rats, weighing 200 ± 20 g, were housed in single cages at 20–25°C, under a 12-h light/dark cycle, and had free access to food and water. All animal experimental procedures were approved by the Ethics Committee of Yanbian University College of Medicine.

Preparation of the animal model

A 0.5% solution of streptozotocin (STZ) (Cat No. S0130, SIGMA, USA) was prepared in 0.1 mmol/L citrate buffer (pH 4.0). 40 rats were fasted for 12 hours, after which 30 of them were randomly selected, weighed, and given a single intraperitoneal injection of STZ at 65 mg/kg to induce diabetes. The remaining 10 rats were intraperitoneally injected with the same dose of citrate buffer and comprised a normal control (NC) group. One week later, glucose levels were measured in blood taken from the tail vein, and rats with glucose concentration of ≥ 16.9 mmol/L were regarded as diabetic. One diabetic rat died following the STZ injection; therefore, one rat was randomly selected from the control group and injected with STZ. Thus, 30 diabetic rats and 9 normal rats were studied. The diabetic rats were randomly allocated to 4-week (DM4w), 6-week (DM6w), and 8-week (DM8w) endpoints ($n=10$ rats per group). The NC rats were allocated to three groups, with $n=3$ rats per group, and they were sacrificed at 4, 6, and 8 weeks.

Preparation of muscle strips and measurement of spontaneous muscular contraction

The rats were euthanized at the determined time points. For each individual, the entire stomach was dissected, had its contents removed, and its muscle tissue peeled off. Gastric antrum ring muscle strips were dissected and placed vertically in oxygen-saturated Krebs's buffer (NaCl 118 mmol/L, KCl 4.75 mmol/L, CaCl_2 2.54 mmol/L, KH_2PO_4 1.2 mmol/L, MgSO_4 1.2

mmol/L, NaHCO_3 25 mmol/L, and glucose 10 mmol/L, Kernel, TianJing, China) and connected with a tension sensor and a RM-6240 multi-channel physiological signal recorder (SCCHENGYI, ChengDu, China). Before each experiment readout, a load of 1 g was applied to each muscle strip for 30 min. After the spontaneous contractions of the smooth muscle strips stabilized, the number of muscle contractions every 400 s was recorded as the frequency, and the height of the peaks was recorded as the amplitude of the muscle contractions. All experiments were repeated independently 8 times.

High-performance liquid chromatography (HPLC)

One hundred milligrams of fresh gastric antrum anular muscle were added at 10 g/mg/mL to 0.4 mol/L perchloric acid solution that had been pre-cooled to 4°C, and the muscle was homogenized in an ice-bath. The supernatant was obtained by centrifugation (10 000 rpm, 10 min) and its pH was adjusted to 6.5. Twenty microliter samples in triplicates at 4°C and at dilutions of 200, 100, 50, 20, and 10 mg/L were then subjected to HPLC to measure the concentrations of ATP, AMP, and ADP. A C18 column (4.6 mm \times 150 mm, 5 μ m; Shimadzu, Japan), a column temperature of 25°C, and a mobile phase of 100 mmol/L phosphate buffer (12 mmol/L disodium phosphate and 88 mmol/L sodium dihydrogen phosphate, pH=6.5) and methanol (99:1 volume ratio) were used. The flow rate was 1.0 mL/min and the UV detection wavelength was 254 nm. The energy charge was calculated according to the following formula: energy charge = $(\text{ATP} + 1/2\text{ADP}) / (\text{ATP} + \text{ADP} + \text{AMP})$ (Wilbring *et al.*, 2013). All experiments were repeated 8 times, independently.

Western blotting

Western blotting was used to detect protein levels of Akt, phospho-Akt Ser473, mTOR, phospho-mTOR Ser2481, and Rictor. The circular muscle of the gastric antrum was added to a precooled lysis buffer at 75–125 μ l/g, homogenized, and incubated at 4°C for 30 min. The lysates were then centrifuged at 14 000 rpm for 30 min, the supernatants were obtained, and their protein concentration was determined. Samples containing 60 μ g protein were subjected to SDS-PAGE, then electrotransferred to PVDF membranes. The membranes were then incubated with anti-Akt (1:1000, Cat No. 9272, Cell Signaling Technology®, Inc., MA, USA), phospho-Akt (1:1000, Cat No. 4060, Cell Signaling Technology®, Inc., MA, USA), mTOR (1:1000, Cat No. 2792, Cell Signaling Technology®, Inc., MA, USA), phospho-mTOR Ser 2481 (1:500, SAB4301526, Sigma, MO, USA), Rictor (1:1,000, Cat No. 2974, Cell Signaling Technology®, Inc., MA, USA), or β -actin (1:500, A5316, Sigma, MO, USA) at 4°C overnight. After washing, the membranes were incubated with secondary antibody (1:1000, Cat No. 7055, Cell Signaling Technology®, Inc., MA, USA) solution, washed, and exposed to a chromogenic agent. The expression of the proteins of interest was calculated relative to β -actin levels (A5316, Sigma, MO, USA).

Western blotting was also used to measure the relative expression of GLUT4 protein (rabbit anti-GLUT4 antibody, Cat No. ab654, Abcam, Cambridge, UK) in gastric antrum teres muscle. The tissue was lysed as described above. The supernatant (containing cytoplasmic proteins) was added to the cell membrane lysate and the samples were mixed and centrifuged. Next, the supernatant (containing cell membrane proteins) was collected and its

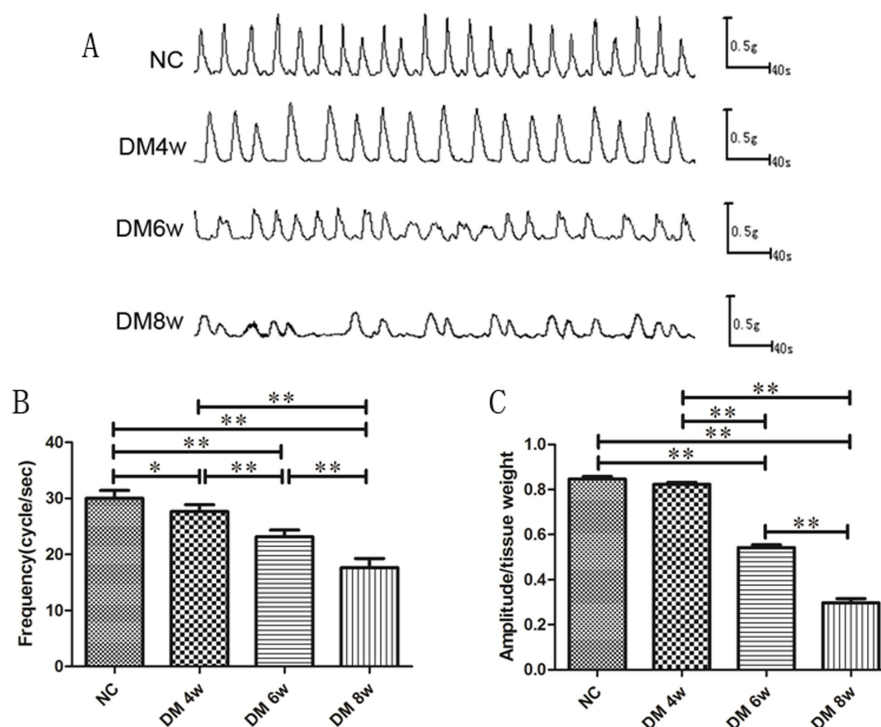


Figure 1. Amplitude of spontaneous contractions in normal gastric smooth muscle and at each time point during the progression of diabetes mellitus.

(A) Gastric smooth muscle strip motility analysis; (B) The frequency of spontaneous contraction of gastric smooth muscle. (C) The amplitude of the contractions of the gastric smooth muscle. The data are displayed as mean \pm S.D.; * P <0.05, ** P <0.01.

protein concentration was determined. Samples containing 60 μ g of protein were subjected to SDS-PAGE and electrotransfer, as described above. The membranes were incubated with the antibody against GLUT4 (1:1,000) at 4°C overnight, or with or β -actin at (temperature, time), a secondary antibody (1:1,000), and a chromogenic agent, and the expression of GLUT4 was calculated relative to that of β -actin. All experiments were repeated 8 times, independently.

Statistical analysis

Statistical analyses were performed with SPSS 19.0 software, and the figures were made with GraphPad Prism5 software (GraphPad Software, San Diego, CA). All experiments were repeated at least 8 times. The data are expressed as mean \pm standard deviation (S.D.). Differences between groups were compared using t-test and two-way analysis of variance (ANOVA). P <0.05 was considered to indicate a significant difference, P <0.01 was considered to indicate a highly significant difference.

RESULTS

Contraction frequency and amplitude in gastric smooth muscle

We evaluated the rate and amplitude of the contraction of stomach muscle strips from diabetic and normal rats (Fig. 1A). The number of muscle contractions during 400 s was recorded as the frequency and the height of each registered peak was recorded as the amplitude of muscle contraction. The frequency of spontaneous contractions of gastric smooth muscle was lower in DM4w, DM6w, and DM8w groups compared to the NC

group (P <0.05 or P <0.01). This decrease in contraction frequency corresponded to the duration of diabetes: it was the lowest in the DM8w group (P <0.01 compared to DM6w, Fig. 1B), and both in the DM6w and DM8w groups displayed lower frequency than DM4w group (both P <0.01). The amplitude of the contractions of the gastric smooth muscle was decreased in the DM6w and DM8w groups compared to the NC group (both P <0.01), and compared to the DM4w group as well (both P <0.01). The amplitude of the contractions of the gastric smooth muscle was lower in the DM8w group than that in the DM6w group (P <0.01, Fig. 1C). Thus, the motility of rat gastric smooth muscle decreased with the progression of diabetes in the rats.

The concentrations of ATP, ADP, AMP and energy charge in gastric smooth muscle

ATP is the basic molecular unit of energy in the body; therefore, the amount of ATP present in a tissue and the rate of ATP synthesis (ADP/ATP) reflect overall energy metabolism in the tissue. We measured the concentrations of ATP, ADP, and AMP in the gastric smooth muscle of rats using HPLC (Fig. 2) and found that the concentration of ATP was not affected by diabetes (P >0.05). However, ADP concentration was decreased in the DM4w group (P <0.01), and increased in the DM6w and DM8w groups (both P <0.01) as compared to NC. It was also higher in the DM6w and DM8w groups than in the DM4w group (both P <0.01), and higher in the DM8w group than in the DM6w group (P <0.01, Fig. 2A). Therefore, a trend was observed for the ATP production (ADP/ATP ratio). The ADP/ATP ratio was the lowest in the DM4w group (P <0.05 compared to the NC) and the highest in the DM8w group (P <0.01 compared to the NC). The ADP/ATP ratio was higher

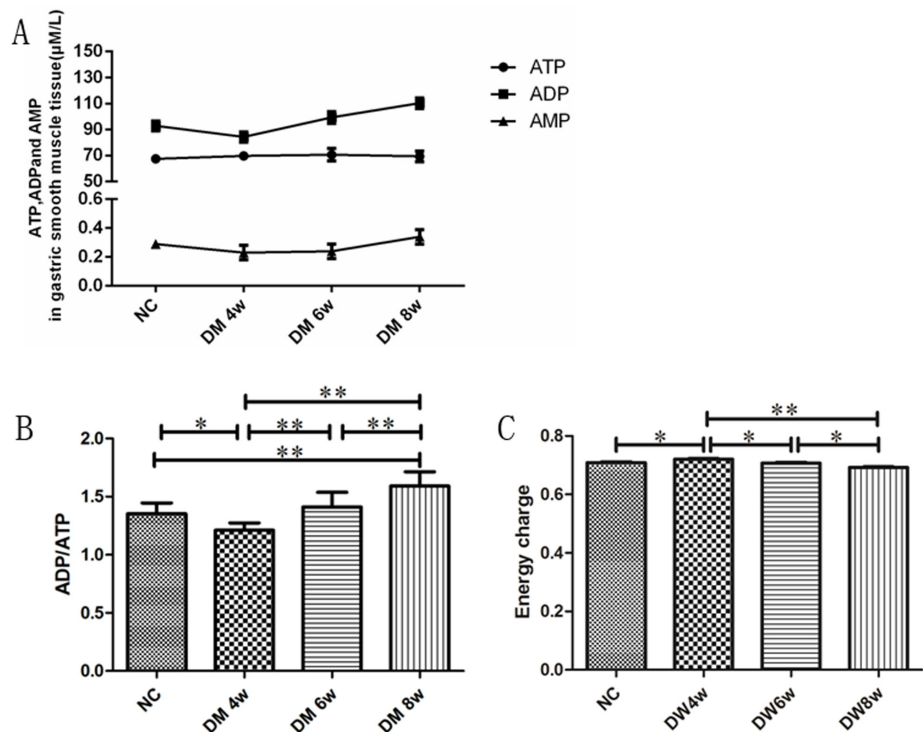


Figure 2. Concentrations of ATP, ADP, and AMP ($\mu\text{mol/L}$) in the gastric smooth muscle of diabetic rats. (A) ATP, ADP, and AMP concentrations in control and diabetic rats. (B) ADP/ATP ratio in control and diabetic rats. (C) The energy charge in control and diabetic rats. The data are displayed as mean \pm S.D.; * $P < 0.05$, ** $P < 0.01$.

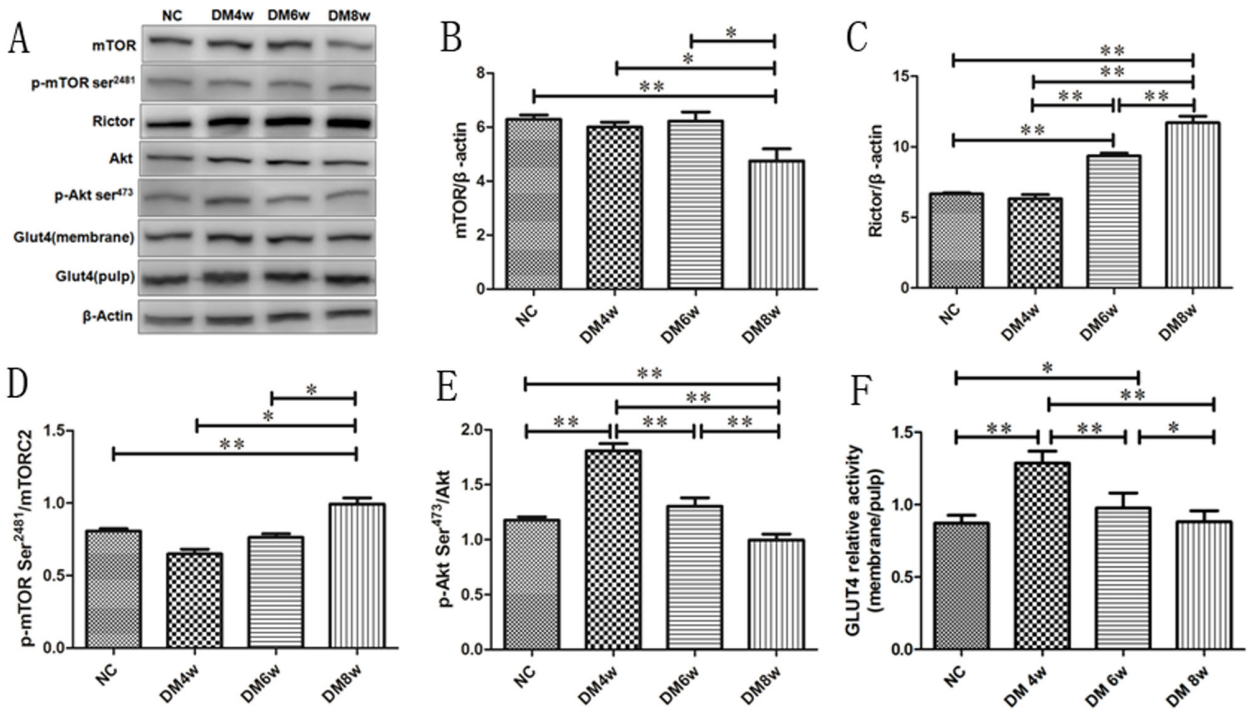


Figure 3. Protein expression of the key proteins in the Rictor/mTORC2/Akt/GLUT4 pathway in control and diabetic rats. (A) Western blot of the key proteins in the Rictor/mTORC2/Akt/GLUT4 pathway in the rat gastric smooth muscle; (B) mTOR expression in the rat gastric smooth muscle; (C) Rictor expression in the rat gastric smooth muscle; (D) p-mTOR Ser2481/mTOR ratio; (E) p-Akt Ser473/Akt ratio; (F) GLUT4 expression in the gastric smooth muscle of control and diabetic rats. The data are displayed as mean \pm S.D.; * $P < 0.05$, ** $P < 0.01$.

in the DM6w and DM8w than in DM4w (DM8w vs DM4w $P<0.01$, DM6w vs DM4w $P<0.01$), and higher in DM8w than in DM6w ($P<0.01$, Fig. 2B). The energy charge of the gastric smooth muscle was increased in DM4w as compared to NC ($P<0.05$). Conversely, the energy charge was decreased in the DM6w and DM8w compared to DM4w ($P<0.05$, $P<0.01$), and was lower in DM8w than in DM6w ($P<0.05$, Fig. 2C). These results suggested that energy metabolism disorder was present in the gastric smooth muscle of diabetic rats, leading to the impairment of the energy supply to muscle and the development of diabetic gastroparesis.

Akt, phospho-Akt Ser473, mTOR, phospho-mTOR Ser2481, GLUT4, and Rictor protein expression in gastric smooth muscle

We used Western blotting to measure the expression of the key proteins in the Rictor/mTORC2/Akt/GLUT4 pathway in the gastric smooth muscle of rats in each group (Fig. 3A). mTOR expression in the gastric smooth muscle was decreased in the DM8w group compared to NC ($P<0.01$), DM4w ($P<0.05$), and DM6w ($P<0.05$) groups (Fig. 3B). Rictor is an important component of TORC2 but does not promote the phosphorylation of mTOR at Ser2481. Rictor expression in the gastric smooth muscle was increased in the DM6w and DM8w groups compared to the NC (both $P<0.01$), and DM4w groups (both $P<0.01$). It was also higher in DM8w than in DM6w ($P<0.01$, Fig. 3C). The p-mTOR Ser²⁴⁸¹/mTOR ratio was increased in the DM8w group compared to the NC ($P<0.01$), DM4w ($P<0.05$), and DM6w ($P<0.05$) groups (Fig. 3D). The p-Akt Ser⁴⁷³/Akt ratio was increased in both DM4w and DM8w compared to NC (both $P<0.01$). Also, the p-Akt Ser⁴⁷³/Akt ratio was lower both in DM6w and DM8w than in DM4w (both $P<0.01$), and lower in DM8w than in DM6w ($P<0.01$, Fig. 3E). The gastric smooth muscle cell surface expression of GLUT4 was increased in both DM4w and DM6w groups compared to NC ($P<0.01$, $P<0.05$). It was also lower in both DM6w and DM8w than in DM4w (both $P<0.01$) and lower in DM8w than in DM6w ($P<0.05$, Fig. 3F). These results suggested that the Rictor/mTORC2/Akt/GLUT4 pathway is involved in the regulation of energy metabolism in the gastric smooth muscle, alters energy supply to muscle, which in turn participates in the development of diabetic gastroparesis.

DISCUSSION

ATP is the most direct source of body energy, and 90% of it is produced by mitochondria (Barros & Baeza-Lehnert, 2019; Marklund *et al.*, 2006; Korchazhkina *et al.*, 1999). There are two main ways to generate ATP in the body: in the anaerobic state, glucose undergoes glycolysis, during which each molecule of glucose is converted to pyruvate and two molecules of ATP are produced, whereas in the aerobic state, pyruvate is completely metabolized to generate 32 molecules of ATP per molecule of glucose. In the present study, we found that in the diabetic state, starting from the sixth week following the induction of diabetes, there was an obvious reduction in gastric motility, which corresponds to the development of diabetic gastroparesis. The ATP concentration in the muscle did not change significantly with the progression of diabetes, but we observed an upward trend for ADP and AMP and ATP generation (ADP/ATP ratio), and a downward trend for energy charge. Energy charge rep-

resents the number of high-energy phosphate groups in the total adenylate system (the total concentration of ATP+ADP+AMP), which reflects the energy status of the cell. The above results imply deterioration in the energy status of the tissue. This may reflect a reduction in the aerobic metabolism of glucose because of partial replacement by other pathways, mitochondrial damage, or other factors. Although the substrate in the muscle is sufficient to ensure the conversion of ADP, it cannot reverse the trend of reduced synthesis. The specific explanation for this requires further study.

Diabetic gastroparesis has previously been shown to develop 6 weeks after the induction of diabetes in rats and is accompanied by changes in mTOR pathway (Zhang *et al.*, 2017). mTOR is an atypical serine/threonine protein kinase that can integrate various extracellular signals, such as growth factors, nutrition, and energy status to regulate processes such as growth and the cell cycle. The mTOR complexes: mTORC1 and mTORC2 have different structures and functions, and different mTOR residues are phosphorylated in each complex (Saxton & Sabatini, 2017; Copp *et al.*, 2009; Gnocchi *et al.*, 2020). mTOR is activated by phosphorylation at multiple residues, including Ser2448 and Ser2481 (Saxton & Sabatini, 2017; Copp *et al.*, 2009; Vazquez-Martin *et al.*, 2012). Previous studies have shown that in mTORC1, mTOR is phosphorylated at Ser 2448, whereas in mTORC2, it is phosphorylated at Ser 2481 (Knudsen *et al.*, 2020; Copp *et al.*, 2009; Vazquez-Martin *et al.*, 2012). mTORC1 contains rapamycin-sensitive Raptor, MLST8 a proline-rich Akt substrate of 40 kDa, (PRAS40), and DEP domain of mTOR-interacting protein (DEP domain-containing mTOR-interacting protein, DEPTOR); whereas, mTORC2 contains Rictor and MLST8, neither of which is sensitive to rapamycin, and SAPK interacting protein 1 (SIN1) (Saxton & Sabatini, 2017). Thus, Raptor and Rictor are characteristic proteins of the mTORC1 and mTORC2, respectively. In the present study we found that Rictor protein expression increased with the progression of diabetes, but mTOR expression was decreased at 8 weeks of diabetes. The phosphorylation of mTOR-Ser²⁴⁸¹ requires intact mTORC2 (Knudsen *et al.*, 2020), as the autophosphorylation of Ser²⁴⁸¹ is proportional to the specific catalytic activity of mTORC2. By observing the changes in the p-mTOR Ser²⁴⁸¹/mTOR ratio, we found that the phosphorylation of mTOR at Ser²⁴⁸¹ decreased prior to the development of gastroparesis, but increased after the onset of this complication, indicating that there are other factors that regulate the activation of mTORC2.

Rictor participates in glucose metabolism as an upstream effector of Akt, and when Rictor or mTORC2 is absent, glucose intolerance develops. While mTORC2 activates Akt, Akt can activate mTORC1 activity via Akt-(TSC1/2)-Ras homolog (Rheb)-mTORC1, as was shown for brain tissue (Saxton & Sabatini, 2017). In another study, it was shown that the expression of Rictor in muscle cells is lower in a high-glucose environment and that the cells show lower insulin-induced glucose uptake, such that the glucose metabolism becomes disrupted (Mukaida *et al.*, 2017). A reduction in Rictor expression also affects GLUT4 translocation, resulting in a reduction in glucose transport and deleterious effects on overall glucose and energy metabolism (Mukaida *et al.*, 2017; Hasannejad *et al.*, 2019; Khan & Kamal, 2019; Zhao *et al.*, 2019). In this study, we found that the phosphorylation of Akt at Ser473 in the diabetic state gradually decreases, despite the increase in mTORC2 expression, which suggests that mTORC2 is not the dominant

regulator of Akt. GLUT4 translocation is mainly regulated by Akt, but Rictor is also required for this process. Although GLUT4 translocation is not mainly affected by mTORC2, there should be other ways to affect it.

GLUT4 translocation, and therefore glucose uptake by muscle cells, is promoted by Akt phosphorylation, but GLUT4 translocation decreases with the development of gastroparesis. In this study, the translocation of GLUT4 was found to be increased first and then decreased with disease progression. This result implies that in the diabetic state, glucose is taken up and used by cells also independently of insulin.

One of the limitations of this study is that we did not quantify the mRNA expression levels of the key proteins in the Rictor/mTORC2/Akt/GLUT4 pathway in the gastric smooth muscle of diabetic rats with RT-PCR.

CONCLUSIONS

Our findings documented that during the pathogenesis of diabetic gastroparesis, altered energy metabolism was present in the gastric smooth muscle of diabetic rats. The change in energy metabolism was associated with the changes in protein expression and phosphorylation in the Rictor/mTORC2/Akt/Glut4 pathway, suggesting that this pathway may be involved in both the regulation of energy metabolism in the gastric smooth muscle of diabetic rats and in the development of diabetic gastroparesis.

Declarations

Conflicts of Interest. The authors declare no conflict of interest.

REFERENCES

Barros LF, Baeza-Lehnert F (2019) Perfect energy stability in neurons. *Aging (Albany NY)* **11**: 6622–6623. <https://doi.org/10.18632/aging.102257>

Copp J, Manning G, Hunter T (2009) TORC-specific phosphorylation of mammalian target of rapamycin (mTOR): phospho-Ser2481 is a marker for intact mTOR signaling complex 2. *Cancer Res* **69**: 1821–1827. <https://doi.org/10.1158/0008-5472.CAN-08-3014>

Cosimo E, Tarafdar A, Moles MW, Holroyd AK, Malik N, Catherine MA, Hay J, Dunn KM, Macdonald AM, Guichard SM, O'Rourke D, Leach MT, Sansom OJ, Cosulich SC, McCaig AM, Michie AM (2019) AKT/mTORC2 inhibition activates FOXO1 function in CLL cells reducing B-Cell receptor-mediated survival. *Clin Cancer Res* **25**: 1574–1587. <https://doi.org/10.1158/1078-0432.CCR-18-2036>

Gnocchi D, Ellis ECS, Johansson H, Eriksson M, Bruscalupi G, Stefensen KR, Parini P (2020) Diiodothyronines regulate metabolic homeostasis in primary human hepatocytes by modulating mTORC1 and mTORC2 activity. *Mol Cell Endocrinol* **499**: 110604. <https://doi.org/10.1016/j.mce.2019.110604>

Hara K, Maruki Y, Long X, Yoshino K, Oshiro N, Hidayat S, Tokunaga C, Avruch J, Yonezawa K (2002) Raptor, a binding partner of target of rapamycin (TOR), mediates TOR action. *Cell* **110**: 177–189. [https://doi.org/10.1016/s0092-8674\(02\)00833-4](https://doi.org/10.1016/s0092-8674(02)00833-4)

Hasannejad M, Samsamshariat SZ, Esmaili A, Jahanian-Najafabadi A (2019) Klotho induces insulin resistance possibly through interference with GLUT4 translocation and activation of Akt, GSK3 β , and PFKf3 in 3T3-L1 adipocyte cells. *Res Pharm Sci* **14**: 369–377. <https://doi.org/10.4103/1735-5362.263627>

Khan S, Kamal MA (2019) Wogonin alleviates hyperglycemia through increased glucose entry into cells via AKT/GLUT4 pathway. *Curr Pharm Des* **25**: 2602–2606. <https://doi.org/10.2174/1381612825666190722115410>

Kleinert M, Sylow L, Fazakerley DJ, Krycer JR, Thomas KC, Oxboll AJ, Jordy AB, Jensen TE, Yang G, Schjerling P, Kiens B, James DE, Ruegg MA, Richter EA (2014) Acute mTOR inhibition induces insulin resistance and alters substrate utilization *in vivo*. *Mol Metab* **3**: 630–641. <https://doi.org/10.1016/j.molmet.2014.06.004>

Kimoloi S (2018) Modulation of the *de novo* purine nucleotide pathway as a therapeutic strategy in mitochondrial myopathy. *Pharmacol Res* **138**: 37–42. <https://doi.org/10.1016/j.phrs.2018.09.027>

Knudsen JR, Fritzen AM, James DE, Jensen TE, Kleinert M, Richter EA (2020) Growth factor-dependent and -independent activation of mTORC2. *Trends Endocrinol Metab* **31**: 13–24. <https://doi.org/10.1016/j.tem.2019.09.005>

Korchazhkina O, Wright G, Exley C (1999) No effect of aluminium upon the hydrolysis of ATP in the coronary circulation of the isolated working rat heart. *J Inorg Biochem* **76**: 121–126. [https://doi.org/10.1016/s0162-0134\(99\)00123-3](https://doi.org/10.1016/s0162-0134(99)00123-3)

Marklund N, Salci K, Ronquist G, Hillered L (2006) Energy metabolic changes in the early post-injury period following traumatic brain injury in rats. *Neurochem Res* **31**: 1085–1093. <https://doi.org/10.1007/s11064-006-9120-0>

Mukaida S, Evans BA, Bengtsson T, Hutchinson DS, Sato M (2017) Adrenoceptors promote glucose uptake into adipocytes and muscle by an insulin-independent signaling pathway involving mechanistic target of rapamycin complex 2. *Pharmacol Res* **116**: 87–92. <https://doi.org/10.1016/j.phrs.2016.12.022>

Saxton RA, Sabatini DM (2017) mTOR Signaling in growth, metabolism, and disease. *Cell* **168**: 960–976. <https://doi.org/10.1016/j.cell.2017.02.004>

Vazquez-Martin A, Sauri-Nadal T, Menendez OJ, Oliveras-Ferraro C, Cufi S, Corominas-Faja B, López-Bonet E, Menendez JA (2012) Ser2481-autophosphorylated mTOR colocalizes with chromosomal passenger proteins during mammalian cell cytokinesis. *Cell Cycle* **11**: 4211–4221. <https://doi.org/10.4161/cc.22551>

Manuel Wilbring, Annette Ebner, Katrin Schoenemann, Michael Knaut, Sems Malte Tugtekin, Birgit Zatschler, Thomas Waldow, Konstantin Alexiou, Klaus Matschke, Andreas Deussen (2013) Heparinized blood better preserves cellular energy charge and vascular functions of intraoperatively stored saphenous vein grafts in comparison to isotonic sodium-chloride-solution. *Clin Hemorheol Microcirc* **55**: 445–455. <https://doi.org/10.3233/CH-131781>

Zhang MH, Jiang JZ, Cai YL, Piao LH, Jin Z (2017) Significance of dynamic changes in gastric smooth muscle cell apoptosis, PI3K-AKT-mTOR and AMPK-mTOR signaling in a rat model of diabetic gastroparesis. *Mol Med Rep* **16**: 1530–1536. <https://doi.org/10.3892/mmr.2017.6764>

Zhao P, Tian D, Song G, Ming Q, Liu J, Shen J, Liu QH, Yang X (2019) Neferine promotes GLUT4 expression and fusion with the plasma membrane to induce glucose uptake in L6 cells. *Front Pharmacol* **10**: 999. <https://doi.org/10.3389/fphar.2019.00999>

Circular RNA-AnnexinA7 accelerates cisplatin resistance in non-small cell lung cancer *via* modulating microRNA-545-3p to mediate Cyclin D1

Jian Yao✉, Hai Yang Zhang, Shuang Gu, Jin Long Zou, Qiang Zhang and Ri Chu Qu

Department of Thoracic Surgery, Jilin Provincial People's Hospital, Changchun City, Jilin Province, 130021, China

Objective: To explore the mechanism of circular RNA (circRNA)-AnnexinA7 (ANXA7) in non-small cell lung cancer (NSCLC) cisplatin (DDP) resistance through microRNA (miR)-545-3p to target Cyclin D1 (CCND1). **Methods:** DDP-resistant and non-resistant NSCLC tissues and normal tissues were collected. DDP-resistant cells (A549/DDP and H460/DDP) were constructed. circ-ANXA7, miR-545-3p, CCND1, P-Glycoprotein, and glutathione S-transferase- π in tissues and cells were measured. Analysis of circ-ANXA7 ring structure was performed, as well as detection of circ-ANXA7 distribution in cells. Cell proliferation was detected by MTT and colony formation assay, apoptosis rate was detected by flow cytometry, and cell migration and invasion were evaluated by Transwell assay. The targeting relationship between circ-ANXA7, miR-545-3p and CCND1 was verified. Measurement of tumor volume and quality in mice was performed. **Results:** Circ-ANXA7 and CCND1 were elevated, while miR-545-3p was suppressed in DDP-resistant NSCLC tissues and cells. Circ-ANXA7 combined with miR-545-3p, which targeted CCND1 to expedite A549/DDP cell proliferation, migration, invasion, DDP resistance, but inhibited cell apoptosis. **Conclusion:** Circ-ANXA7 enhances DDP resistance in NSCLC *via* absorbing miR-545-3p to target CCND1 and might be a latent therapeutic target for NSCLC.

Keywords: Circular RNA-AnnexinA7, MicroRNA-545-3p, Cyclin D1, Target binding, A549/cisplatin cells

Received: 01 November, 2022; revised: 03 April, 2023; accepted: 11 April, 2023; available on-line: 23 May, 2023

✉e-mail: yaojian@dmu-edu.cn

Acknowledgements of Financial Support: Science and technology development project of Jilin (No. 201903031605F).

Abbreviations: ANOVA, Analysis of variance; ANXA7, AnnexinA7; CCND1, Cyclin D1; circRNAs, Circular RNAs; DDP, Cisplatin; FBS, fetal bovine serum; FITC, Fluorescein isothiocyanate; GAPDH, Glyceraldehyde-3-phosphate dehydrogenase; GST- π , Glutathione S-transferase π ; IgG, Immunoglobulin G; LC, Lung cancer; MTT, 3-(4,5-dimethylthiazol-2-yl)-2,5-diphenyltetrazolium bromide assay; MUT, Mutant type; NC, Negative control; NSCLC, Non-small cell lung cancer; P-gp, P-glycoprotein; PI, Propidium iodide; RIP, RNA immunoprecipitation; RT-qPCR, Reverse transcription quantitative polymerase chain reaction; S.D., Standard deviation; UTR, Untranslated region; WT, Wild-type

INTRODUCTION

Lung cancer (LC) is a malignant tumor with the uppermost morbidity and mortality in the world (Zhang *et al.*, 2021). Non-small cell lung cancer (NSCLC) is an extremely critical type of LC, taking up about 85% of LC cases (Xu *et al.*, 2020). Treatment strategies for NSCLC have improved recently, but the 5-year survival rate is

still greatly reduced by about 10–15% (Xu *et al.*, 2021). Cisplatin (DDP) chemotherapy is a first-line anti-cancer chemotherapy agent in NSCLC. Nevertheless, patients treated with DDP for a long time develop DDP resistance (Wu *et al.*, 2020). As reported, around 63% of NSCLC patients have DDP resistance (Ye *et al.*, 2020). Consequently, lessening DDP resistance is the crux to ameliorating NSCLC patients' outcomes. This study was to comprehend latent mechanisms in NSCLC DDP resistance and identify latent biomarkers, offering brand-new insights into NSCLC therapy.

Circular RNAs (circRNAs), a non-coding RNA with closed continuous loops, have been testified to mediate primary or antitumor responses in different cancer treatments (Fan *et al.*, 2021). Notably, numerous circRNAs exert critical roles in multiple biological processes of NSCLC. For instance, circ_PIP5K1A (Feng *et al.*, 2021), circ-RNF121 (Liu *et al.*, 2022) and circ_0076305 (Wang *et al.*, 2021) have been reported to be implicated in the cancer progression and DDP resistance of NSCLC. Circ-AnnexinA7 (ANXA7), as a member of circRNA, has been reported to expedite lung adenocarcinoma progression (Wang, 2021). In the preliminary experiment, this circRNA was aberrantly modulated in DDP-resistant NSCLC tissues. Nevertheless, the latent impact of circ-ANXA7 on DDP resistance in NSCLC is unknown.

circRNA/miRNA/mRNA regulatory network has been adopted to elucidate circRNA's mechanism in multiple biological processes (Xu *et al.*, 2020). Bioinformatics predicted that miR-545-3p was the target of circ-ANXA7. Recently, miR-545-3p has been reported to participate in NSCLC progression. For instance, blocking circ_0014130 restrains resistance and malignant behaviors of NSCLC cells *via* modulating miR-545-3p (Du *et al.*, 2021). Circ_0072083 knockdown is involved in DDP-triggered NSCLC tumor inhibition through the miR-545-3p/CBLL1 axis (Li *et al.*, 2020). Nevertheless, it has not been reported that circ-ANXA7, as a competitive endogenous RNA, combined with miR-545-3p to participate in NSCLC DDP resistance.

Cyclin D1 (CCND1), a recognized cell cycle-associated protein, exerts a crucial action in cell cycle change (Meng *et al.*, 2021). CCND1 is a critical driver of malignant transformation and is frequently elevated in NSCLC, leading to the aberrant proliferation of NSCLC cells (Liu *et al.*, 2020). Notably, modulating CCND1 can alter DDP-resistant cell malignant phenotype (Ju *et al.*, 2020). In this study, it was hypothesized that circ-ANXA7 might participate in NSCLC DDP resistance *via* miR-545-3p to modulate CCND1.

In this study, 2 DDP-resistant NSCLC cell lines (A549/DDP and H460/DDP) were constructed, and

circ-ANXA7 was confirmed to modulate DDP-resistant NSCLC cell sensitivity and behavior. Additionally, this research further elucidated the action of circ-ANXA7/miR-545-3p/CCND1 axis in DDP resistance and cancerization of NSCLC.

MATERIALS AND METHODS

Clinical tissue specimen

90 tissue samples were obtained from the School of Medicine, University of Electronic Science and Technology of China, including 30 non-tumor tissue samples from patients with pulmonary laceration repair (control) and 60 NSCLC tissue samples from NSCLC patients with radical resection. Patients with progressive disease (PD) or postoperative recurrence less than 6 months were DDP-resistant, while patients without PD and postoperative recurrence over 12 months were non-resistant. All tissue samples were placed at -80°C . Authorization of the study was performed by the Ethics Committee of the School of Medicine, University of Electronic Science and Technology of China, and written informed consent was obtained from all participants.

Cell culture and transfection

NSCLC cell lines (A549 and H460) were purchased from American Tissue Culture Collection (Manassas, VA), and human bronchial epithelioid cells (HBE-1) were from Bena Culture Collection (Beijing, China). Cells were cultured in Roswell Park Memorial Institute-1640 medium (Hyclone, Logan, UT, USA) containing 10% fetal bovine serum, 100 U/ml penicillin and 100 mg/mL streptomycin (Gibco, Carlsbad, CA). DDP-resistant cells (A549/DDP and H460/DDP) were established and grown in a complete medium replenished with DDP (1 $\mu\text{g}/\text{mL}$, Sigma-Aldrich, St. Louis, MO) to maintain resistance. All cells were cultured in 5% CO_2 at 37°C (Pang *et al.*, 2020).

sh-circ-ANXA7, miR-545-3p mimic and inhibitor, as well as corresponding negative controls (sh-NC, mimic-NC, in-NC) were designed and generated (Ribo Biotech, Guangzhou, China). CCND1 overexpression plasmid was purchased from ORIGENE, with empty plasmid as NC. When cell confluence reached 70% to 80%, A549/DDP cells were plated into 6-well plates (1×10^5 cells/mL) and cultured for 24 h. Transfection of cells was performed using Lipofectamine 3000 (Invitrogen) (Hu *et al.*, 2021). Transfection concentrations of mimic and inhibitor were 50 nM and 20 nM, respectively, and 1 μg and 2500 ng for sh-circANXA7 and CCND1 overexpressed plasmid, respectively. After 48 h, the transfection efficiency was evaluated by reverse transcription quantitative polymerase chain reaction (RT-qPCR) or Western blot.

Ribonuclease R and actinomycin D assays

RNase R assay: total RNA (2 μg) from A549 cells was incubated with 3 U/ μg RNase-R (07250, Epicentre Technologies, USA) at 37°C for 30 min. circ-ANXA7 and ANXA7 mRNA expressions were subsequently determined by RT-qPCR.

Actinomycin D test: Cells were cultured with or without 2 $\mu\text{g}/\text{mL}$ actinomycin D (Sigma, USA) and harvested at different points in time. Circ-ANXA7 and ANXA7 mRNA was determined by RT-qPCR (Wu *et al.*, 2020).

Subcellular localization analysis

Cytoplasm RNA and nuclear RNA of cells were isolated using PARIS Kit (Invitrogen). Then, the examination of circ-ANXA7 in cytoplasm RNA and nuclear RNA was implemented by RT-qPCR. U6 and glyceraldehyde-3-phosphate dehydrogenase (GAPDH) were nuclear and cytoplasmic controls, respectively.

RT-qPCR

Extraction of total RNA from NSCLC tissues and cells was done using Trizol reagent (Invitrogen). Reverse transcription of circRNA/mRNA and miRNA was performed with PrimeScript RT reagent Kit and miRNA First Strand Synthesis Kit (both Takara, Tokyo, Japan), respectively. RT-qPCR was performed with SYBR Green kit (Thermo Fisher Scientific, Waltham, MA, USA) and Mx3005P qPCR system (Agilent Technologies, Santa Clara, CA, USA). U6 and GAPDH were loading controls for miRNA and mRNA/circRNA, respectively. Primer sequences were presented in Table 1 (Song *et al.*, 2021).

Western blot

Extraction of total protein was done with 500 μL Radio-Immunoprecipitation assay lysis buffer (Beyotime, China). An equal amount of protein (20 μg) was separated by 8% sodium dodecyl sulfate-polyacrylamide gel electrophoresis (Solarbio), electroblotted onto polyvinylidene fluoride membranes (Invitrogen), and blocked with 5% skimmed milk, followed by incubation with primary antibodies CCND1 (ab134175, Abcam, 1:1000), anti-P-glycoprotein (P-gp) (ab170904, Abcam, 1:3,000), glutathione S-transferase π (GST- π) (ab233112, Abcam, 1:1,000) and GAPDH (1:7,500, ab8245) at 4°C overnight and horseradish peroxidase-conjugated goat anti-rabbit Immunoglobulin G (IgG) (1:1000, ab181236, Abcam) for 2 h. Visualization of the signal was performed with an enhanced chemiluminescence kit (34080, Thermo Fisher Scientific). Density analysis was performed with ImageJ software.

3-(4,5-dimethylthiazol-2-yl)-2,5-diphenyltetrazolium bromide (MTT) assay

A549/DDP cells (5×10^3 /well) were seeded into 96-well plates and cultured overnight. MTT reagent (beyotime) was added at different time points (0, 24, 48, 72 h) and incubated at 37°C for 4 h. Then, 150 μL Dimethyl Sulfoxide was added to each well and 10 min later, optical density at 490 nm was read with a microplate reader (PerkinElmer) (Zhu *et al.*, 2021).

Colony formation assay

A549/DDP cells (5×10^3 /well) were seeded in 12-well plates and cultured for 14 d, during which a fresh complete medium was replaced every 3 days and the wells were washed twice with PBS. Then, colonies were fixed in paraformaldehyde (4%, Beyotime), dyed with 0.1% crystal violet (Beyotime) for 2 h, and washed with ddH_2O_3 times. The number of colonies was counted under an inverted microscope (Nikon).

Flow cytometry

A549/DDP cells (1×10^5 cells/well) after DDP treatment were incubated for 48 h. Cell apoptosis was analyzed by Annexin V-fluorescein isothiocyanate (FITC)/Propidium iodide (PI) assay kit (BestBio, Shanghai, China). In brief, cells were rinsed with cold phosphate-

buffered saline (PBS) and incubated with 5 μ L Annexin V-FITC and 5 μ L PI for 20 min. Ultimately, the assessment of cell apoptosis was implemented on a flow cytometer (FACS Calibur flow cytometer) (Wei *et al.*, 2021).

Transwell migration and invasion analysis

Transwell assay evaluated A549/DDP cell invasion and migration. For migration and invasion measurements, transwell chambers were used without or with Matrigel, respectively (Corning, USA). Cells were prepared at 2×10^6 cells/mL, then 400 μ L cell suspension was inoculated into the upper chamber containing serum-free medium, and 10% FBS was added to the lower chamber. After 24 h of culture, cells in the upper layer were removed with cotton swabs, while those in the lower layer were fixed with methanol for 30 min, stained with 0.1% crystal violet, and counted in five fields under a microscope (Swiss taikang, magnification $\times 100$) (Guo *et al.*, 2022).

Luciferase activity assay

A549/DDP cells were plated on a 24-well plate. circ-ANXA7 or CCND1 3' untranslated region (UTR) (Promega) containing miR-545-3p wild-type (WT) or mutant-type (MUT) binding sites was inserted into the pmirGLO vector (Promega, Madison, WI), and circ-ANXA7/CCND1-WT 3'UTR and circ-ANXA7/CCND1-MUT 3'UTR reporter genes were named. Co-transfection of the corresponding luciferase reporter gene with miR-545-3p mimic or miR-NC was done in A549/DDP cells. After 48 h of incubation, the determination of the luciferase activity was implemented with the luciferase reporter gene kit (Promega) (Guo *et al.*, 2022).

RNA immunoprecipitation (RIP) experiment

Anti-Ago2 (ab252812) and anti-IgG (ab109489) antibodies were utilized for detection. In short, cells were lysed with a lysis buffer and then incubated with protein-g magnetic beads-conjugated anti-Ago2 or IgG at 40°C for 6 h. Microbeads were later collected, and binding RNA was extracted to examine the enrichment of circ-ANXA7 and miR-545-3p (Zhang *et al.*, 2021).

Table 1. Primer sequences

Genes	Primer sequences (5'-3')
Circ-ANXA7	F: 5'-GCTATCCCCAACAGGCTAC-3'
	R: 5'-CCTGGTGGGACTCCAAATC-3'
MiR-545-3p	F: 5'-TGCCTCAGCAACATTATTG-3'
	R: 5'-CCAGTGCAGGGTCCGAGGTATT-3'
CCND1	F: 5'-AGCTGTGCATCTACACCGAC-3'
	R: 5'-GAAATCGTGGGGTTCATTG-3'
U6	F: 5'-CTCGCTTCGGCAGCAC-3'
	R: 5'-AACGCTTCACGAATTTGCGT-3'
GAPDH	F: 5'-TCCCATCACCATCTTCCA-3'
	R: 5'-CATCACGCCACAGTTTCC-3'

Note: F, forward; R, reverse.

In vivo tumor growth test

The tumor formation experiment was conducted in BALB/c male nude mice ($n=24$, 6 weeks old, weight of 18–20 g, Huafukang, Beijing, China). A549/DDP cells transfected with sh-Circ-ANXA7, or sh-NC (1×10^7) were injected subcutaneously into the back of mice. Mice were divided into four groups: sh-NC+PBS, sh-NC+DDP, sh-circ-ANXA7+PBS, and sh-circ-ANXA7+DDP groups. DDP (5 mg/kg) or PBS was injected to measure the tumor volume once a week. After 4 weeks, transplanted tumors from euthanized mice were weighed. Animal treatments were approved by the Animal Research Committee of the School of Medicine, University of Electronic Science and Technology of China (Shao *et al.*, 2021).

Statistical analysis

Statistical software SPSS 21.0 (SPSS, Inc, Chicago, IL, USA) was utilized to analyze data. Kolmogorov-Smirnov test checked the normal distribution of data, and the results were presented as mean \pm standard deviation (S.D.). Two-group comparisons were performed using t-test. Comparisons among multiple groups were imple-

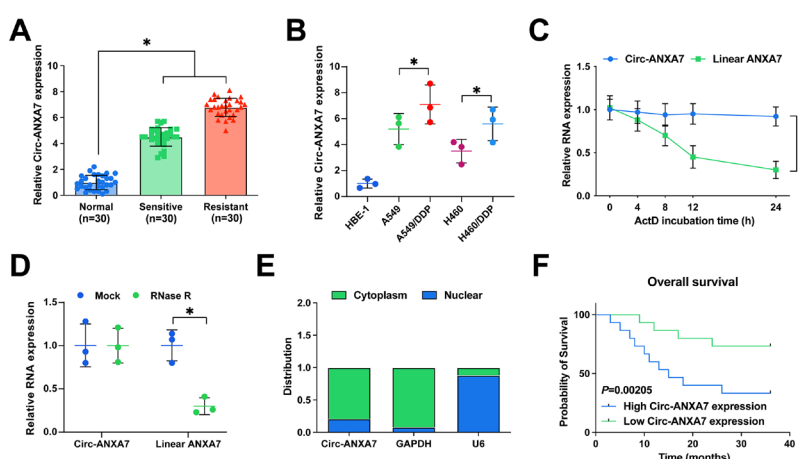


Figure 1. Circ-ANXA7 is modulated in DDP-resistant NSCLC tissues and cells

(A) RT-qPCR test of circ-ANXA7 in each tissue; (B) RT-qPCR examination of circ-ANXA7 in each cell; (C–D) RNase R and Actinomycin D determination of the stability of circ-ANXA7; (E) RT-qPCR test of the localization of circ-ANXA7 in A549/DDP cells; (F) Kaplan-Meier analysis of the survival prognosis of DDP-resistant NSCLC patients. Data were expressed as mean \pm S.D. (Number of samples = 3). * $P < 0.05$.

Table 2. Clinicopathological characteristics of non-resistant and resistant patients

Characteristic	Cases	Nonresistant cases (n=30)	Resistant cases (n=30)	P
Age (year)				
60 or less	33	17	16	0.859
More than 60	27	13	14	
Gender				
Male	35	19	16	0.554
Female	25	11	14	
Circ-ANXA7 level				
0.5 fold of control or less	27	19	8	<0.001***
More than 0.5 fold of control	33	11	22	
Tumor size				
Less than 5 cm	32	18	14	0.355
5 cm or more	28	12	16	
Distant metastasis				
No	34	18	16	0.438
Yes	26	12	14	
Depth of invasion				
N0/N1	26	18	8	0.041*
N2/N3	34	12	22	
Differentiation				
Good/Moderate	31	21	10	0.005**
Poor	29	9	20	

* $P < 0.05$. ** $P < 0.01$. *** $P < 0.001$.

mented with one-way analysis of variance (ANOVA) and pairwise comparison after ANOVA analysis was performed using Fisher's Least Significant Difference *t*-test. Enumeration data were shown as rate or percentage and analyzed by Chi-square test. * $p < 0.05$ indicates a significant difference.

RESULTS

Circ-ANXA7 expression is modulated in DDP-resistant NSCLC tissues and cells

circ-ANXA7 levels in resistant and non-resistant NSCLC tissues and normal tissues were tested by RT-qPCR. Compared with non-resistant NSCLC tissues and normal tissues, circ-ANXA7 was elevated in DDP-resistant NSCLC tissues, clarifying that circ-ANXA7 was associated with DDP resistance in NSCLC (Fig. 1A). Subsequently, analysis of the clinicopathological characteristics was implemented. Table 2 elucidated no difference in age, tumor size, gender, and metastasis between DDP-resistant patients with non-resistant patients. Nevertheless, DDP resistant patients had high levels of circ-ANXA7, deep invasion, low rate of tumor metastasis, and poor differentiation.

Likewise, in normal cells (HBE-1), NSCLC cell lines (A549 and H460) and DDP-resistant NSCLC cells (A549/DDP and H460/DDP), it was observed that circ-ANXA7 was the highest in DDP-resistant cells (Fig. 1B).

RNase R analysis and Act D analysis confirmed the circular characteristics of circ-ANXA7, showing that circ-ANXA7 was available to resist RNase R detachment, and its stability was better than linear ANXA7 mRNA (Fig. 1C–D). Additionally, circ-ANXA7 was primarily distributed in NSCLC cell cytoplasm (Fig. 1E). Kaplan-Meier analysis revealed that high circ-ANXA7 was associated with unpleasing overall survival in DDP-resistant NSCLC patients, as presented in Fig. 1F.

To sum up, circ-ANXA7 was stable and elevated in DDP-resistant NSCLC and might be implicated in NSCLC DDP resistance.

Repressive circ-ANXA7 gene is available to suppress NSCLC's progression and strengthens DDP's sensitivity

It was found that A549 cells had stronger DDP resistance (Fig. 2A) than H460 cells, and circANXA7 expression in A549 and A549/DDP cells was higher than that in H460 and H460/DDP cells (Fig. 1B), so A549/DDP cells were selected for subsequent studies. As presented in Fig. 2B, circ-ANXA7 was repressed in A549/DDP cells after transfection with sh-circ-ANXA7. Silence of circ-ANXA7 declined DDP IC₅₀ (Fig. 2C). Cell proliferation and apoptosis were subsequently examined, and it was found that circ-ANXA7 gene knockout inhibited the viability of A549/DDP cells (Fig. 2D–E), while the apoptosis rate increased significantly (Fig. 2F). In addition, Transwell analysis confirmed that circ-ANXA7 silencing effectively blocked A549/DDP cell migration

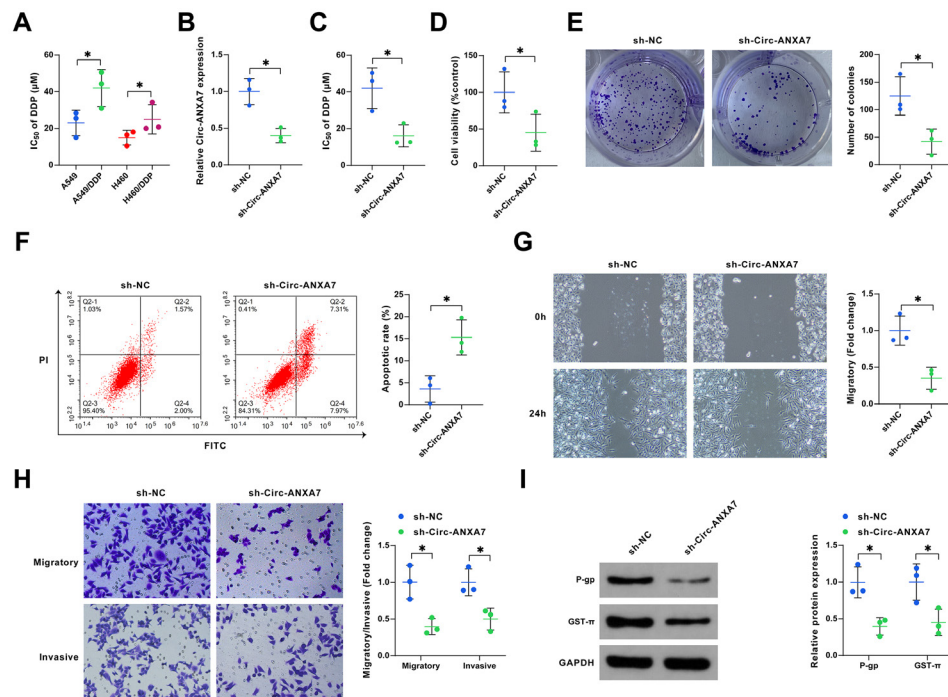


Figure 2. Repression of circ-ANXA7 restrains NSCLC progression and strengthens DDP sensitivity

(A) MTT analysis of IC₅₀; (B) RT-qPCR test of sh-circ-ANXA7 transfection efficiency; (C) MTT analysis of IC₅₀ of DDP in A549/DDP cells after transfection; (D–E) MTT and colony formation assay detection of cell proliferative activity; (F) Flow cytometry test of cell apoptosis; (G–H) Transwell assay test of cell migration and invasion; (I) Western blot detection of drug-resistance associated proteins (P-GP and GST-π). Data were expressed as mean ± S.D. (Number of samples=3). *P<0.05.

and invasion (Fig. 2G–H). Western blot analysis of drug resistance-associated proteins (P-gp and GST-π) was performed, elucidating that P-gp and GST-π in A549/DDP cells were lowered after suppressing circ-ANXA7, as presented in Fig. 2I.

In general, repressing circ-ANXA7 was available to suppress NSCLC progression and strengthened DDP sensitivity.

Circ-ANXA7 performs as a sponge for miR-545-3p

To explore the novel mechanism of circ-ANXA7 to modulate NSCLC, prediction of the target miRNA of circ-ANXA7 was performed on the bioinformatics website starBase. circ-ANXA7 and miR-545-3p had complementary fragments (Fig. 3A). MiR-545-3p in A549/DDP cells was elevated after transfecting miR-545-3p mimic (Fig. 3B). The interaction of miR-545-3p with circ-ANXA7 was verified. As presented in Fig. 3C, elevated miR-545-3p constrained the luciferase activity of circ-ANXA7-WT 3'UTR, but it did not repress that of the mutant construct. Circ-ANXA7 and miR-545-3p were abundant in Ago2 antibody-immunoprecipitated RNA complex, but not in IgG antibody-immunoprecipitated RNA complex (Fig. 3D). Additionally, miR-545-3p expression was downregulated in DDP-resistant NSCLC tissues and cells (Fig. 3E–F), and clinical correlation analysis found that miR-545-3p was negatively associated with circ-ANXA7 in DDP-resistant NSCLC tissues (Fig. 3G).

All in all, miR-545-3p could be modulated by circ-ANXA7.

Suppression of miR-545-3p turns around circ-ANXA7 knockdown's influence on NSCLC

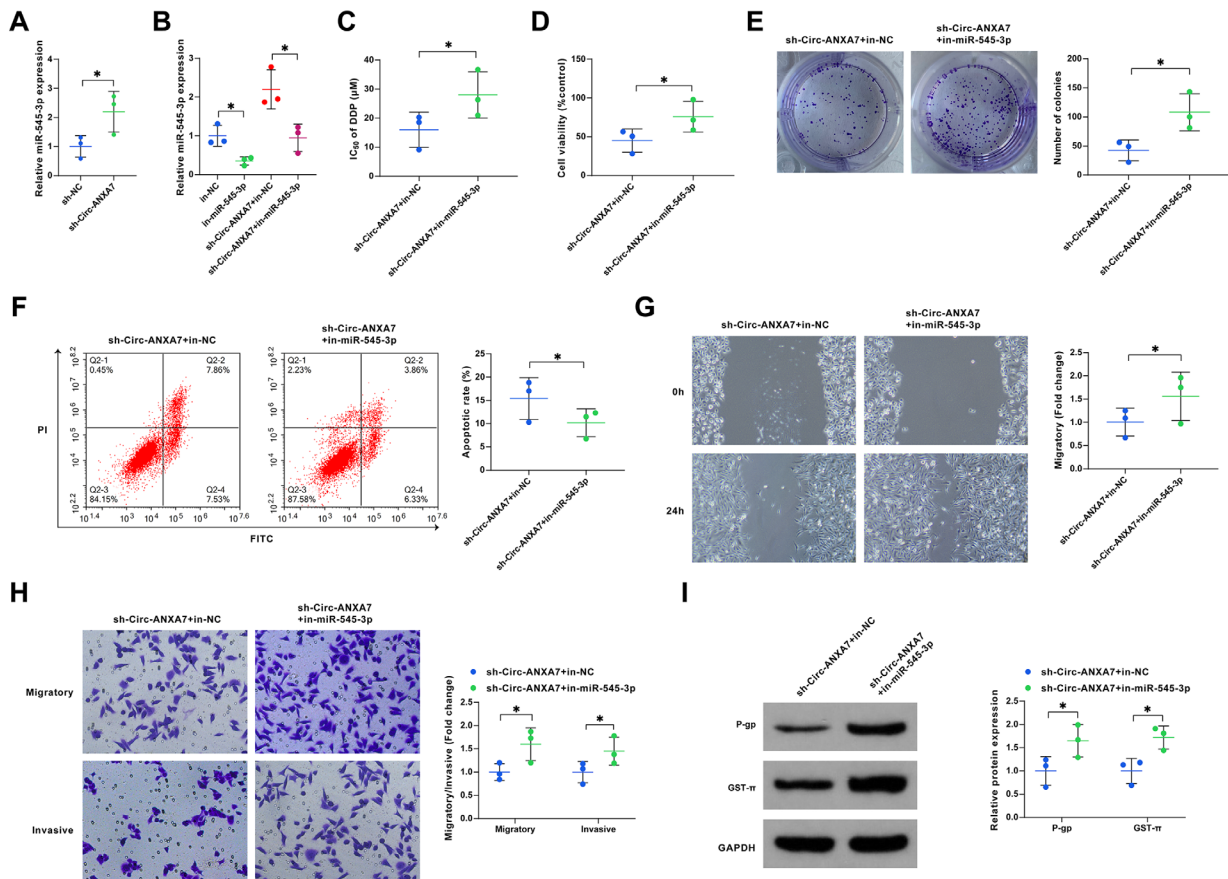
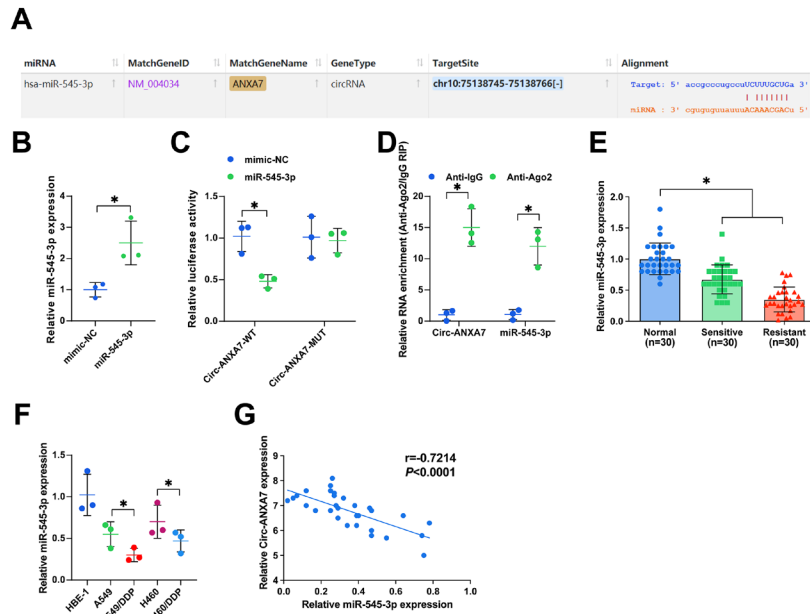
To determine the functional regulation of circ-ANXA7 and miR-545-3p, sh-circ-ANXA7 and in-miR-

545-3p were constructed, and their efficacy was explicitly verified *in vitro*. It was discovered that silence of circ-ANXA7 elevated miR-545-3p (Fig. 4A). Subsequently, sh-circ-ANXA7 in combination with in-miR-545-3p or in-NC was transfected into A549/DDP cells. As presented in Fig. 4B, transfection with in-miR-545-3p declined miR-545-3p expression. MiR-545-3p expression was suppressed after sh-circ-ANXA7 was blocked by the miR-545-3p inhibitor. Additionally, it was observed that silence of circ-ANXA7 declined DDP IC₅₀, but this effect was suppressed by in-miR-545-3p (Fig. 4C). In the meantime, inhibition of cell viability and promotion of apoptosis by circ-ANXA7 knockdown could be partially reversed by in-miR-545-3p (Fig. 4D–F). Additionally, the introduction of in-miR-545-3p was available to eliminate silenced circ-ANXA7's suppression of cell invasion and migration (Fig. 4G–H). Reduction in circ-ANXA7 led to a decrease in resistance-associated proteins, and this inhibition could be mitigated by supplementation with in-miR-545-3p (Fig. 4I).

In short, circ-ANXA7 modulated NSCLC cell progression and DDP sensitivity *via* absorbing miR-545-3p.

MiR-545-3p immediately targets CCND1

As mentioned above, it was attempted to search for miR-545-3p's direct targets. As presented in Fig. 5A, starBase predicted the common binding site of miR-545-3p and CCND1. In the meantime, miR-545-3p mimic was available to weaken the luciferase activity of CCND1-WT 3'UTR, while no distinct change was presented in the luciferase activity of CCND1-MUT 3'UTR (Fig. 5B). Additionally, circ-ANXA7 and miR-545-3p were abundant in Ago2 antibody immunoprecipitation but not in IgG antibody immunoprecipitation (Fig. 5C). Compared with non-resistant and normal tissues, CCND1 in DDP-



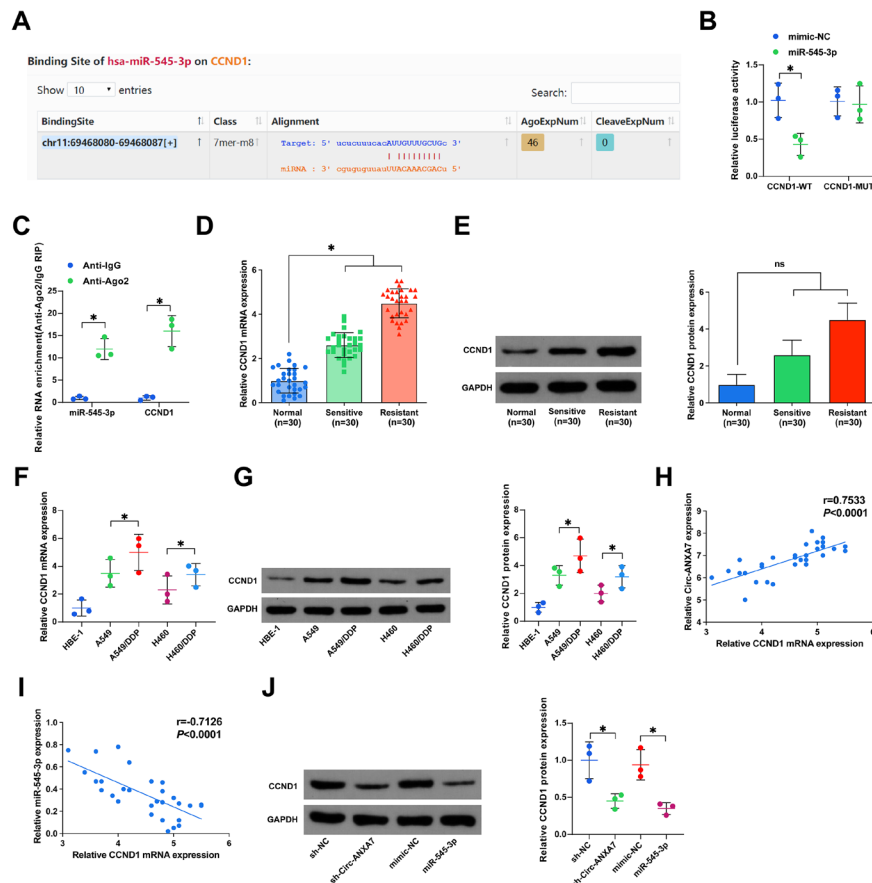


Figure 5. CCND1 is the functional target of miR-545-3p

(A) Bioinformatics sites forecast of binding sites of CCND1 with miR-545-3p; **(B–C)** Luciferase activity assay, and RIP assay evaluation of the interaction of CCND1 with miR-545-3p; **(D–G)** RT-qPCR and Western blot test of CCND1 in tissues and cells; **(H–I)** Pearson correlation analysis assessment of the association of CCND1 with miR-545-3p and circ-ANXA7. **(J)** Western blot examination of CCND1 after transfection with sh-circ-ANXA7 or miR-545-3p mimic. Data were expressed as mean \pm S.D. (Number of samples = 3). * $P < 0.05$.

resistant tissues was elevated (Fig. 5D–E). Likewise, CCND1 was also elevated in DDP-resistant NSCLC cells (Fig. 5F–G). In clinical tissues characterized by drug resistance, CCND1 was positively correlated with circ-ANXA7 expression and negatively correlated with miR-545-3p expression (Fig. 5H–I). In A549/DDP cells, downregulation of circ-ANXA7 or overexpression of miR-545-3p decreased CCND1 expression (Fig. 5J).

In brief, CCND1 was miR-545-3p's downstream gene.

Circ-ANXA7 impacts NSCLC progression and DDP resistance via miR-545-3p/CCND1 axis

Functional tests were performed considering the association of miR-545-3p with circ-ANXA7 or CCND1. CCND1 overexpression plasmid strengthened CCND1 expression in A549/DDP cells (Fig. 6A–B). Then, to explain whether CCND1 mediates the effect of circ-ANXA7 on NSCLC progression and DDP resistance, A549/DDP cells were co-transfected with sh-circ-ANXA7 and CCND1 overexpression plasmid or empty plasmid. As presented in Fig. 6A–B, sh-circ-ANXA7 restrained CCND1 expression, which was reversed after co-transfection with the CCND1 overexpression plasmid. Additionally, the upregulation of CCND1 significantly restored the inhibitory effect of circ-ANXA7 silencing on DDP IC₅₀ and cell viability in A549/DDP cells *in vitro* (Fig. 6C–E). In the meantime, downregulation of circ-ANXA7 promoted apoptosis, which was eliminated by

CCND1 overexpression plasmid (Fig. 6F). Additionally, elevating CCND1 restrained sh-circ-ANXA7-mediated repression of A549/DDP cell migration and invasion (Fig. 6G–H). Additionally, silenced circ-ANXA7-induced suppression of P-gp and GST- π was turned around by overexpressing CCND1 (Fig. 6I).

In short, circ-ANXA7 modulated NSCLC progression and DDP resistance via miR-545-3p/CCND1 axis.

Loss of circ-ANXA7 reduces tumor growth *in vivo*

After sh-circ-ANXA7 or DDP treatment, tumor volume and weight were reduced, and sh-circ-ANXA7 and DDP treatment were provided with synergistic suppression (Fig. 7A–B). By examining circ-ANXA7 levels in xenografts, sh-Circ-ANXA7 did decrease circ-ANXA7 expression and promote miR-545-3p levels in excised tumors (Fig. 7C). Additionally, loss of circ-ANXA7 repressed CCND1 expression in excised tumors (Fig. 7D–E).

All in all, loss of circ-ANXA7 interacted with DDP therapy, thereby restraining tumor growth in xenograft tumor models.

DISCUSSION

Globally, NSCLC is a deadly cancer with elevated morbidity and mortality (Cao *et al.*, 2021). DDP is the most frequently-adopted chemotherapy drug for the

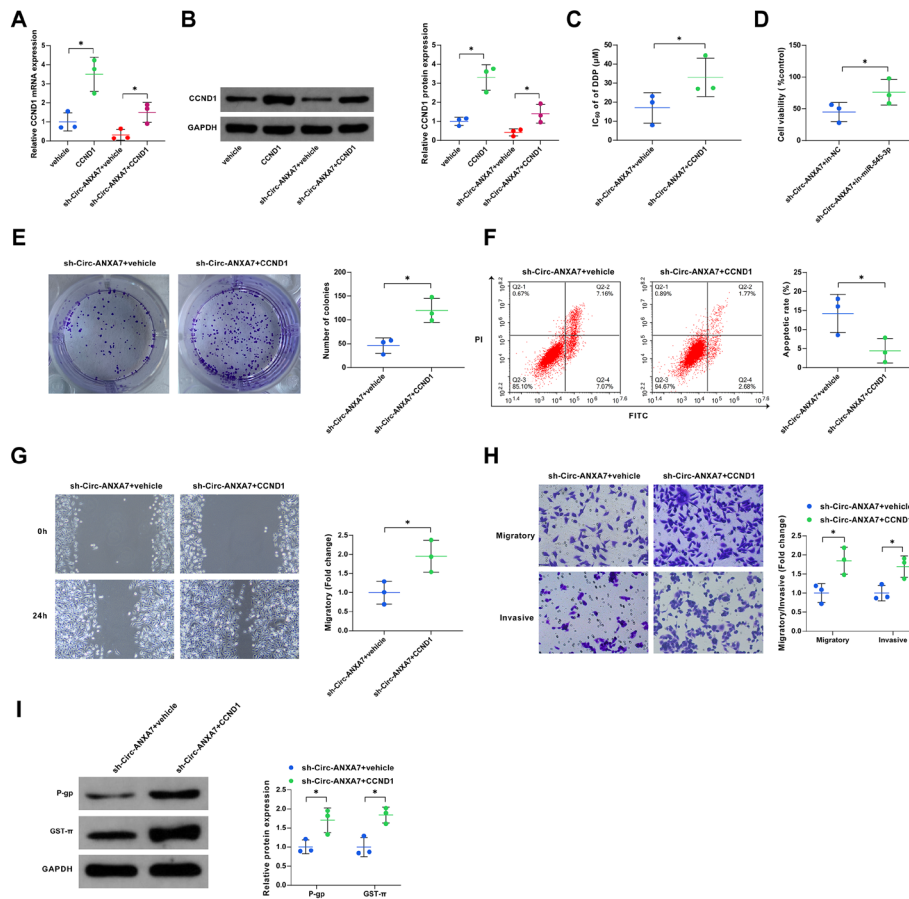


Figure 6. Circ-ANXA7 impacts NSCLC progression and DDP resistance via miR-545-3p/CCND1 axis

(A–B) RT-qPCR and Western blot examination of CCND1 in A549/DDP cells; (C) MTT analysis of IC₅₀ of DDP in A549/DDP cells; (D–E) MTT and colony formation assay detection of cell proliferative activity; (F) Flow cytometry test of cell apoptosis; (G–H) Transwell assay test of cell migration and invasion; (I) Western blot test of drug-resistance associated proteins (P-gp and GST- π). Data were expressed as mean \pm S.D. (Number of samples = 3). * P < 0.05.

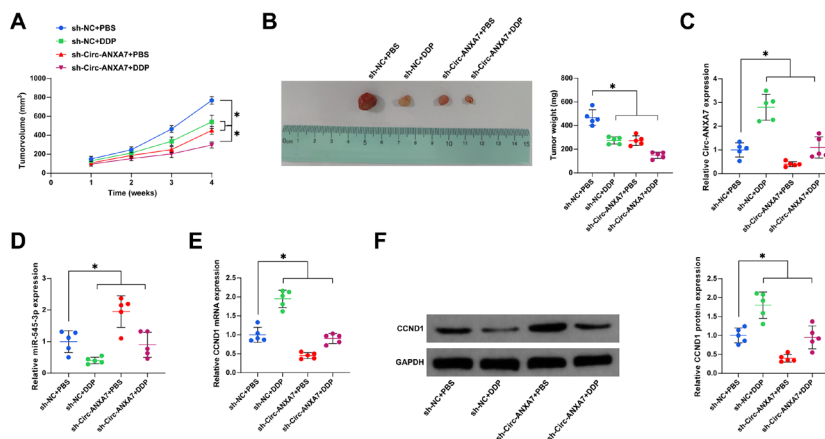


Figure 7. Loss of circ-ANXA7 lessens tumor growth in vivo

(A) Tumor volume changes of mice in each group; (B) Tumor weight of mice at 4th week; (C) Circ-ANXA7 and miR-545-3p in resected tumors; (D–E) CCND1 expression in resected tumors. Data were expressed as mean \pm S.D. (Number of samples = 3). * P < 0.05.

treatment of NSCLC (Dong *et al.*, 2019). Nevertheless, DDP resistance severely limits its clinical efficacy (Hong *et al.*, 2020). Consequently, it was crucial to suppress DDP resistance for better treatment of NSCLC patients. It is reported that aberrant circRNA impacts NSCLC cancerization and chemotherapy resistance (Zhang *et al.*, 2021). In this study, it was first discovered that repres-

sion of circ-ANXA7 suppressed NSCLC progression and strengthened DDP sensitivity. Additionally, this study first verified the regulatory network of circ-ANXA7/miR-545-3p/CCND1.

Research has shown that the covalent closed structure of circRNAs makes them more stable in eukaryotes (Fu *et al.*, 2021). Likewise, the data displayed that circ-

ANXA7 after RNase R and Actinomycin D treatment was more stable than linear ANXA7. circRNAs exert critical roles in multiple biological processes of NSCLC (Liu *et al.*, 2021). For instance, in DDP-resistant NSCLC tissues and cells, circ_PIP5K1A expression is augmented, while silencing circ_PIP5K1A is available to restrain cancer progression and strengthen DDP sensitivity (Feng *et al.*, 2021). Additionally, silencing circ_0076305 ameliorates the DDP sensitivity of NSCLC (Wang *et al.*, 2021). In other words, circRNAs modulate cancer progression and DDP resistance. This research focused on a novel circRNA (Circ-ANXA7) derived from host gene ANXA7 chr10 (75138745-75138766). Expression analysis displayed that circ-ANXA7 was elevated in DDP-resistant NSCLC tissues and cells, clarifying that circ-ANXA7 might participate in DDP resistance progression in NSCLC. As expected, it was discovered that circ-ANXA7 silencing inhibited the proliferative activity, migration, invasion, and DDP sensitivity of DDP resistant cells, but promoted apoptosis. Overall, the data have illustrated that circ-ANXA7 is a promoter of NSCLC progression and drug resistance. Nevertheless, circ-ANXA7 in patients' serum was not detected in this study. Notably, a recent report has clarified that exosomes-delivered hsa_circ_0014235 expedites DDP resistance and exacerbates NSCLC development *via* mediating miR-520a-5p/CDK4 pathway (Xu *et al.*, 2020). Consequently, it was a necessity to further examine circ-ANXA7 in NSCLC clinical serum samples in subsequent studies, which might offer novel data support for circ-ANXA7 as a promoter of NSCLC resistance.

As reported, the regulatory function of circRNA is associated with the miRNA/mRNA signaling network (Feng *et al.*, 2021). Notably, it is reported that circRNAs participate in various human cancers *via* effectively targeting miRNA to mediate gene (Liu *et al.*, 2022). For instance, silencing circ_0007385 restrains malignant behavior and DDP resistance of NSCLC cells *via* miR-519d-3p/HMGB1 axis (Ye *et al.*, 2020). Circ_0076305 modulates STAT3 and DDP resistance of NSCLC cells *via* absorbing miR-296-5p as a sponge (Dong *et al.*, 2019). Consequently, miR-545-3p was discovered to have a targeted binding site with circ-ANXA7. Foregoing studies have elucidated that miR-545-3p is silenced in NSCLC and performs as a tumor suppressor gene, restraining NSCLC progression and strengthening DDP sensitivity (Du *et al.*, 2021; Li, Liu, and Qin 2020). Likewise, in this study, it was discovered that miR-545-3p was silenced in DDP-resistant NSCLC tissues and cells and performed as a tumor suppressor gene. Additionally, it was first discovered that miR-545-3p was competitively adsorbed by circ-ANXA7, and upregulating miR-545-3p reversed the inhibitory effect of circ-ANXA7 loss on NSCLC progression and DDP resistance.

miRNAs are available to repress specific proteins after transcription *via* combining with the 3'UTR of target mRNA (Pang *et al.*, 2020). Consequently, the target genes of miR-545-3p were predicted, and CCND1 among numerous mRNAs has drawn our attention due to its relationship with DDP resistance (Zuo *et al.*, 2021). CCND1 performs as a carcinogen in NSCLC, promoting proliferation, migration, invasion, and drug resistance of NSCLC cells, and may become a potential therapeutic target for NSCLC (Huang *et al.*, 2020; Cui *et al.*, 2020; Liu *et al.*, 2020). Nevertheless, the mechanism of circ-ANXA7/miR-545-3p/CCND1 axis in NSCLC DDP resistance has not been explored. In this research, it was testified that elevated CCND1 was presented in DDP-resistant NSCLC tissues and cells. Additionally, it was

first discovered that miR-545-3p was implicated in DDP resistance in NSCLC *via* targeting CCND1.

In brief, circ-ANXA7 accelerated DDP resistance in NSCLC *via* the miR-545-3p/CCND1 axis, which might offer brand-new insights into the treatment of DDP resistance in NSCLC. Nevertheless, the potential involvement of downstream pathways was not considered in this study. In addition, future multicenter and animal studies are needed to further elucidate the role of circ-ANXA7 in DDP resistance in NSCLC.

Declarations

Data availability. The figures and tables used to support the findings of this study are included in the article.

Conflicts of interest. The authors declare that they have no conflicts of interest.

Acknowledgements. The authors would like to show sincere thanks to those techniques who have contributed to this research.

REFERENCES

- Cao F, Wu X, Shan Y, Zhang B, Wang H, Liu H, Yu H (2021) Circular RNA NEK6 contributes to the development of non-small-cell lung cancer by competitively binding with miR-382-5p to elevate BCAS2 expression at post-transcriptional level. *BMC Pulm Med* 21: 325. <https://doi.org/10.1186/s12890-021-01617-0>
- Cui D, Qian R, Li Y (2020) Circular RNA circ-CMPK1 contributes to cell proliferation of non-small cell lung cancer by elevating cyclin D1 *via* sponging miR-302e. *Mol Genet Genomic Med* 8: e999. <https://doi.org/10.1002/mgg3.999>
- Dong Y, Xu T, Zhong S, Wang B, Zhang H, Wang X, Wang P, Li G, Yang S (2019) Circ_0076305 regulates cisplatin resistance of non-small cell lung cancer *via* positively modulating STAT3 by sponging miR-296-5p. *Life Sci* 239: 116984. <https://doi.org/10.1016/j.lfs.2019.116984>
- Du D, Cao X, Duan X, Zhang X (2021) Blocking circ_0014130 suppressed drug resistance and malignant behaviors of docetaxel resistance-acquired NSCLC cells *via* regulating miR-545-3p-YAP1 axis. *Cytotechnology* 73: 571–584. <https://doi.org/10.1007/s10616-021-00478-z>
- Fan L, Li B, Li Z, Sun L (2021) Identification of autophagy related circRNA-miRNA-mRNA-subtypes network with radiotherapy responses and tumor immune microenvironment in non-small cell lung cancer. *Front Genet* 12: 730003. <https://doi.org/10.3389/fgene.2021.730003>
- Fan W, Chen L, Wu X, Zhang T (2021) Circ_0031242 Silencing mitigates the progression and drug resistance in DDP-Resistant hepatoma cells by the miR-924/POU3F2 axis. *Cancer Manag Res* 13: 743–755. <https://doi.org/10.2147/cmar.S272851>
- Feng N, Guo Z, Wu X, Tian Y, Li Y, Geng Y, Yu Y (2021) Circ_PIP5K1A regulates cisplatin resistance and malignant progression in non-small cell lung cancer cells and xenograft murine model *via* depending on miR-493-5p/ROCK1 axis. *Respir Res* 22: 248. <https://doi.org/10.1186/s12931-021-01840-7>
- Fu B, Liu W, Zhu C, Li P, Wang L, Pan L, Li K, Cai P, Meng M, Wang Y, Zhang A, Tang W, An M (2021) Circular RNA circCBM1 promotes breast cancer brain metastasis by modulating miR-125a/BRD4 axis. *Int J Biol Sci* 17: 3104–3117. <https://doi.org/10.7150/ijbs.58916>
- Guo C, Wang H, Jiang H, Qiao L, Wang X (2022) Circ_0011292 Enhances paclitaxel resistance in non-small cell lung cancer by regulating miR-379-5p/TRIM65 axis. *Cancer Biother Radiopharm* 37: 84–95. <https://doi.org/10.1089/cbr.2019.3546>
- Hong W, Xue M, Jiang J, Zhang Y, Gao X (2020) Circular RNA circ-CPA4/let-7 miRNA/PD-L1 axis regulates cell growth, stemness, drug resistance and immune evasion in non-small cell lung cancer (NSCLC). *J Exp Clin Cancer Res* 39: 149. <https://doi.org/10.1186/s13046-020-01648-1>
- Hu X, Wang P, Qu C, Zhang H, Li L (2021) Circular RNA Circ_0000677 promotes cell proliferation by regulating microRNA-106b-5p/CCND1 in non-small cell lung cancer. *Bioengineered* 12: 6229–6239. <https://doi.org/10.1080/21655979.2021.1965697>
- Huang SR, Jin SS, Xu B, Wang RP (2020) Puerarin alleviates the progression of non-small cell lung cancer by regulating the miR-342/CCND1 axis. *Neoplasma* 67: 1244–1255. https://doi.org/10.4149/neo_2020_191107N1145
- Ju ZS, Sun B, Bao D, Zhang XF (2020) Effect of lncRNA-BLACAT1 on drug resistance of non-small cell lung cancer cells in DDP chem-

- otherapy by regulating cyclin D1 expression. *Eur Rev Med Pharmacol Sci* **24**: 9465–9472. https://doi.org/10.26355/eurrev_202009_23031
- Li H, Liu F, Qin W (2020) Circ_0072083 interference enhances growth-inhibiting effects of cisplatin in non-small-cell lung cancer cells via miR-545-3p/CBLL1 axis. *Cancer Cell Int* **20**: 78. <https://doi.org/10.1186/s12935-020-1162-x>
- Liu B, Chen D, Chen S, Saber A, Haisma H (2020) Transcriptional activation of cyclin D1 via HER2/HER3 contributes to EGFR-TKI resistance in lung cancer. *Biochem Pharmacol* **178**: 114095. <https://doi.org/10.1016/j.bcp.2020.114095>
- Liu D, Li W, Zhong F, Yin J, Zhou W, Li S, Sun X, Xu J, Li G, Wen Y, Wang J, Hong M, Cheng Z, Yuan J, Dai L, Sun J, Wang J, Qiu C, Wang G, Zou C (2020) METTL7B Is required for cancer cell proliferation and tumorigenesis in non-small cell lung cancer. *Front Pharmacol* **11**: 178. <https://doi.org/10.3389/fphar.2020.00178>
- Liu Y, Li C, Liu H, Wang J (2021) Circ_0001821 knockdown suppresses growth, metastasis, and TAX resistance of non-small-cell lung cancer cells by regulating the miR-526b-5p/GRK5 axis. *Pharmacol Res Perspect* **9**: e00812. <https://doi.org/10.1002/prp2.812>
- Liu Y, Zhai R, Hu S, Liu J (2022) Circular RNA circ-RNF121 contributes to cisplatin (DDP) resistance of non-small-cell lung cancer cells by regulating the miR-646/SOX4 axis. *Anticancer Drugs* **33**: e186–e197. <https://doi.org/10.1097/cad.0000000000001184>
- Meng Y, Yang L, Wei X, Luo H, Hu Y, Tao X, He J, Zheng X, Xu Q, Luo K, Yu G, Luo Q (2021) CCT5 interacts with cyclin D1 promoting lung adenocarcinoma cell migration and invasion. *Biochem Biophys Res Commun* **567**: 222–229. <https://doi.org/10.1016/j.bbrc.2021.04.105>
- Pang J, Ye L, Zhao D, Zhao D, Chen Q (2020) Circular RNA PRMT5 confers cisplatin-resistance via miR-4458/REV3L axis in non-small-cell lung cancer. *Cell Biol Int* **44**: 2416–2426. <https://doi.org/10.1002/cbin.11449>
- Shao N, Song L, Sun X (2021) Exosomal circ_PIP5K1A regulates the progression of non-small cell lung cancer and cisplatin sensitivity by miR-101/ABCC1 axis. *Mol Cell Biochem* **476**: 2253–2267. <https://doi.org/10.1007/s11010-021-04083-8>
- Song HM, Meng D, Wang JP, Zhang XY (2021) circRNA hsa_circ_0005909 predicts poor prognosis and promotes the growth, metastasis, and drug resistance of non-small-cell lung cancer via the miRNA-338-3p/SOX4 pathway. *Dis Markers* **2021**: 8388512. <https://doi.org/10.1155/2021/8388512>
- Wang X, Wang H, Jiang H, Qiao L, Guo C (2021) Circular RNA circ_0076305 Promotes Cisplatin (DDP) Resistance of non-small cell lung cancer cells by regulating ABCC1 through miR-186-5p. *Cancer Biother Radiopharm* <https://doi.org/10.1089/cbr.2020.4153>
- Wang Y (2021) circ-ANXA7 facilitates lung adenocarcinoma progression via miR-331/LAD1 axis. *Cancer Cell Int* **21**: 85. <https://doi.org/10.1186/s12935-021-01791-5>
- Wei D, Sun L, Feng W (2021) hsa_circ_0058357 acts as a ceRNA to promote non-small cell lung cancer progression via the hsa-miR-24-3p/AVL9 axis. *Mol Med Rep* **23**. <https://doi.org/10.3892/mmr.2021.12109>
- Wu Z, Gong Q, Yu Y, Zhu J, Li W (2020) Knockdown of circ-AB-CB10 promotes sensitivity of lung cancer cells to cisplatin via miR-556-3p/AK4 axis. *BMC Pulm Med* **20**: 10. <https://doi.org/10.1186/s12890-019-1035-z>
- Xu J, Ni L, Zhao F, Dai X, Tao J, Pan J, Shi A, Shen Z, Su C, Zhang Y (2021) Overexpression of hsa_circ_0002874 promotes resistance of non-small cell lung cancer to paclitaxel by modulating miR-1273f/MDM2/p53 pathway. *Aging (Albany NY)* **13**: 5986–6009. <https://doi.org/10.18632/aging.202521>
- Xu X, Tao R, Sun L, Ji X (2020) Exosome-transferred hsa_circ_0014235 promotes DDP chemoresistance and deteriorates the development of non-small cell lung cancer by mediating the miR-520a-5p/CDK4 pathway. *Cancer Cell Int* **20**: 552. <https://doi.org/10.1186/s12935-020-01642-9>
- Ye Y, Zhao L, Li Q, Xi C, Li Y, Li Z (2020) circ_0007385 served as competing endogenous RNA for miR-519d-3p to suppress malignant behaviors and cisplatin resistance of non-small cell lung cancer cells. *Thorac Cancer* **11**: 2196–2208. <https://doi.org/10.1111/1759-7714.13527>
- Zhang W, Song C, Ren X (2021) Circ_0003998 Regulates the progression and docetaxel sensitivity of DTX-resistant non-small cell lung cancer cells by the miR-136-5p/CORO1C axis. *Technol Cancer Res Treat* **20**: 1533033821990040. <https://doi.org/10.1177/1533033821990040>
- Zhang Y, Ge P, Zhou D, Xing R, Bai L (2021) Circular RNA FOXO3 accelerates glycolysis and improves cisplatin sensitivity in lung cancer cells via the miR-543/Foxo3 axis. *Oncol Lett* **22**: 839. <https://doi.org/10.3892/ol.2021.13100>
- Zhang Y, Zeng S, Wang T (2021) Circular RNA hsa_circ_0002360 promotes non-small cell lung cancer progression through upregulating matrix metalloproteinase 16 and sponging multiple micorRNAs. *Bioengineered* **12**: 12767–12777. <https://doi.org/10.1080/21655979.2021.1999370>
- Zhu K, Zhu J, Geng J, Zhang Y, Qin Y, Wang F, Weng Y (2021) circSNX6 (hsa_circ_0031608) enhances drug resistance of non-small cell lung cancer (NSCLC) via miR-137. *Biochem Biophys Res Commun* **567**: 79–85. <https://doi.org/10.1016/j.bbrc.2021.06.032>
- Zuo Y, Zheng W, Tang Q, Liu J, Wang S, Xin C (2021) miR-576-3p overexpression enhances cisplatin sensitivity of ovarian cancer cells by dysregulating PD-L1 and cyclin D1. *Mol Med Rep* **23**. <https://doi.org/10.3892/mmr.2020.11719>

Effect of 6-hydroxydopamine increase the glutathione level in SH-SY5Y human neuroblastoma cells

Natalia Pieńkowska¹, Grzegorz Bartosz² and Izabela Sadowska-Bartosz¹✉

¹Laboratory of Analytical Biochemistry, Institute of Food Technology and Nutrition, College of Natural Sciences, University of Rzeszów, Rzeszów, Poland; ²Department of Bioenergetics, Food Analysis and Microbiology, Institute of Food Technology and Nutrition, College of Natural Sciences, University of Rzeszów, Rzeszów, Poland

Treatment of human neuroblastoma SH-SY5Y cells with a catecholaminergic neurotoxin, 6-hydroxydopamine (6-OHDA) is an acknowledged *in vitro* experimental model of Parkinson disease (PD). A decrease in the glutathione content occurs in PD. Higher concentrations of 6-OHDA lowered the glutathione level in SH-SY5Y cells, nonetheless, we and other authors found a considerable increase in these cells' glutathione content after 24 h treatment with 60 μ M 6-OHDA. A synthetic antioxidant, 4-aminotetramethylpiperidine-1-oxyl (4-AT) exerted a similar effect. The aim of the present study was to explain this surprising effect by monitoring the time course of changes in the levels of reduced (GSH) and oxidized glutathione (GSSG), total antioxidant activity (TAC) of human neuroblastoma cell SH-SY5Y extracts as well as the level of reactive oxygen species and activities of enzymes of glutathione metabolism after treatment of the cells with 60 μ M 6-OHDA and/or 4-AT for 30 min – 24 h. A transient decrease in the level of GSH and TAC of cell extracts, increase in the level of GSSG, and decrease in the activities of glutathione peroxidase, glutathione reductase, glutathione S-transferase and γ -glutamyl-cysteine ligase activities were found followed by normalization or overshoot of the GSH level, TAC and enzyme activities. Increased activity of γ -glutamyl-cysteine ligase activity starting after 4–6 h was responsible for the elevation of the level of GSH and TAC in cells treated with 6-OHDA, 4-AT, and both compounds. The 6-OHDA-induced increase in the GSH content is a result of an overcompensatory response. The antioxidant 4-AT may be useful for the induction of an increase in the level of GSH in neural cells, without the negative effect of 6-OHDA.

Key words: Parkinson disease, 6-OHDA, 4-amino-TEMPO, glutathione, γ -glutamyl-cysteine ligase, oxidative stress

Received: 18 May, 2023; **revised:** 27 May, 2023; **accepted:** 30 May, 2023; **available on-line:** 01 June, 2023

✉e-mail: isadowska@ur.edu.pl

Acknowledgements of financial support. This research was performed within the project “Nanomolecular antioxidants: biological basis of targeted therapy of neurodegenerative diseases” (number of the application 2016/22/E/NZ7/00641) financed by the National Science Centre (NCN), Poland, within the “SONATA-BIS 6” program. **Abbreviations:** ABTS; 2,2'-azino-bis(3-ethylbenzothiazoline-6-sulfonic acid radical); 4-AT, 4-amino-(2,2,6,6-tetramethylpiperidine)-1-oxyl; DHE, dihydroethidium; GCL, γ -glutamyl-cysteine ligase; GPx, glutathione peroxidase; GR, glutathione reductase; GSH, glutathione; GSSG, oxidized glutathione; GST, glutathione S-transferase; NEM, N-ethylmaleimide; OPA, ortho-phthalaldehyde; PD, Parkinson disease; 6-OHDA, 6-hydroxydopamine; PBS, phosphate-buffered saline; ROS, reactive oxygen species; TAC, total antioxidant capacity

INTRODUCTION

Glutathione (GSH) is the most abundant intracellular antioxidant playing a crucial role in the maintenance of redox homeostasis in cells, including neurons (Aoyama, 2021). A decrease in the GSH content was observed in the substantia nigra of patients with Parkinson disease (PD) and attributed mainly to its reactions with dopamine and its degradation products (Smeyne & Smeyne, 2013; Björklund *et al.*, 2021).

The treatment of human neuroblastoma SH-SY5Y cells with 6-hydroxydopamine (6-OHDA) is an acknowledged cellular model of PD (Lopes *et al.*, 2010; Tsai *et al.*, 2020; Xicoy *et al.*, 2020; Pichla *et al.*, 2020; Elyasi *et al.*, 2021; Pichla *et al.*, 2021). 6-Hydroxydopamine induces oxidative stress in the neuroblastoma cells, as demonstrated by increased levels of reactive oxygen species (ROS), decreased activity of superoxide dismutase and catalase, decreased total antioxidant capacity (TAC) as well as increased total oxidant status and heightened levels of oxidative DNA damage, lipid peroxidation, and protein carbonylation (Pichla *et al.*, 2020; Cirmi *et al.*, 2021; Lee *et al.*, 2020; Rashidi *et al.*, 2021; Sun *et al.*, 2020; Ko *et al.*, 2019; Betharia *et al.*, 2019; Hara *et al.*, 2003a; Chen *et al.*, 2022; Ferak Okay *et al.*, 2021; Ryu *et al.*, 2013; Zhang *et al.*, 2014). Although 6-OHDA is able to cause dopaminergic neurodegeneration in experimental models of PD by an oxidative stress-mediated process, the underlying molecular mechanism remains unclear. There are divergent data on the effect of 6-OHDA on the GSH level in the SH-SY5Y human neuroblastoma cell line. Sun and others (Sun *et al.*, 2020) observed about a 50% decrease in the GSH content after the treatment of SH-SY5Y cells with 80 μ M 6-OHDA for 21 h. In turn, Urano and others (Urano *et al.*, 2018) found an about 50% decrease in the GSH content after 3 h treatment of the SH-SY5Y neuroblastoma cell line with 100 μ M 6-OHDA. Ko and others (Ko *et al.*, 2019) reported an about 40% decrease in GSH content, while Jing and others (Jing *et al.*, 2016) a 30% decrease in GSH content after 24 h treatment of SH-SY5Y cells with 100 μ M 6-OHDA. SH-SY5Y cells treated with 250 μ M 6-OHDA for 24 h showed a decrease in the GSH content to about 60% (Cirmi *et al.*, 2021) and to about 20% of the control value (Rashidi *et al.*, 2021). Treatment with 500 μ M 6-OHDA for 4 h decreased the GSH level by 40% in neuroblastoma cells (Barrachina *et al.*, 2003), whereas treatment with 600 μ M 6-OHDA induced a progressive decrease of the GSH content in SH-SY5Y cells during 3 h incubation (Miyama *et al.*, 2011).

In contrast, other authors reported increases in the GSH content after treatment of SH-SY5Y cells with lower concentrations of 6-OHDA. Betharia *et al.* (2019)

observed a 6-fold increase in total glutathione after 24-h SH-SY5Y cells treatment with 40 μ M 6-OHDA. Tirmenstein and others (Tirmenstein *et al.*, 2005) found a 12-fold increase in the GSH concentration after 24 h treatment of SH-SY5Y cells with 50 μ M 6-OHDA noting no change in the GSH: GSSG ratio. We observed no change and an about 2.6-fold increase in the GSH content after 1 h and 24 h treatment of SH-SY5Y human neuroblastoma cells with 65 μ M 6-OHDA, respectively (Pichla *et al.*, 2020).

The level of glutathione seems to be critical for the survival of SH-SY5Y cells treated with 6-OHDA since a pretreatment with compounds increasing the level of glutathione ameliorated the toxicity of 6-OHDA to the cells. Pretreatment of SH-SY5Y cells with 3 H-1,2-dithiole-3-thione (Jia *et al.*, 2008), *t*-butyl hydroquinone (Hara *et al.*, 2003b), dithiolethiones (Brown *et al.*, 2014, 2016) and 3,4-dihydroxybenzalacetone (Gunjima *et al.*, 2014) protected the cells against 6-OHDA toxicity; all these compounds increased the glutathione content of the cells. Buthionine sulfoximine, an inhibitor of glutathione synthesis, prevented this effect (Gunjima *et al.*, 2014, Brown *et al.*, 2016).

The increase in the GSH content of SH-SY5Y cells induced by lower concentrations of 6-OHDA is intriguing. We decided to study the kinetics of changes in the activities of glutathione metabolism enzymes and glutathione levels in order to understand the mechanism of alterations in the GSH level evoked by 60 μ M 6-OHDA, a concentration causing 50% inhibition of cell proliferation and an over 2-fold increase in the GSH content, as found in our previous study (Pichla *et al.*, 2020). We observed previously the protection of SH-SY5Y cells by nitroxides and nitroxide-containing redox nanoparticles from oxidative stress so in this study, we checked also the effect of one of the previously employed nitroxides, 4-amino-(2,2,6,6-tetramethylpiperidine)-1-oxyl (4-amino-TEMPO, 4-AT), applied alone and in combination with 6-OHDA on the glutathione metabolism enzymes. The concentration of 4-AT of 75 μ M was employed; this concentration offered significant (ca 50%) protection against 6-OHDA (Pichla *et al.*, 2020). Not differentiated cells were used, like in the previous study (Pichla *et al.*, 2020) and in most studies on the effects of 6-OHDA on the glutathione level in SH-SY5Y cells. We examined also the dynamics of changes in the TAC of SH-SY5Y cell extracts and in the level of ROS in the treated cells.

MATERIALS AND METHODS

Materials and equipment

Human neuroblast cell line from neural tissue SH-SY5Y (CRL-2266) was obtained from the American Cell Culture Collection. This cell line was derived from a metastatic bone tumor of a 4-year-old cancer patient.

Dulbecco's Modified Eagle Medium/Nutrient Mixture F-12 without phenol red (cat. no. 21041025), Dulbecco's Phosphate Buffered Saline (DPBS) (cat. no. 14040-117), and Geltrex™ LDEV-Free Reduced Growth Factor Basement Membrane Matrix (cat. no. A1413202) were purchased from Thermo Fisher Scientific (Waltham, MA, USA). Fetal Bovine Serum (cat. no. S1813), Penicillin-Streptomycin solution (cat. no. L0022), and Trypsin-EDTA solution (10 \times) (cat. no. X0930) were obtained from Biowest (Nuaille, France). Dihydroethidium (DHE) (cat. no. 37291), 0.4% Trypan Blue solution (cat. no. T8154), 4-amino-TEMPO (4-AT; cat. no. 163945), N-

ethylmaleimide (NEM) (cat. no. E3876), dithiothreitol (DTT) (cat. no. D9760), trichloroacetic acid (TCA) (cat. no. T4885), diethylenetriaminepentaacetic acid (DTPA), ethylenediaminetetraacetic acid (EDTA) (cat. no. D1133), L-ascorbic acid (cat. no. A0278), dimethyl sulfoxide (DMSO) (cat. no. D2438), *o*-phthalaldehyde (OPA) (cat. no. P1378), 6-hydroxydopamine hydrobromide (6-OHDA) (cat. no. 162957), Triton X-100 (cat. no. X-100), monosodium phosphate (cat. nos. 567545), disodium phosphate (cat. no. 106580), 2,2'-azino-bis(3-ethylbenzothiazoline-6-sulfonic acid) (ABTS) (cat. no. 10102946001), potassium persulfate (cat. no. 216224), (\pm)-6-hydroxy-2,5,7,8-tetramethylchromane-2-carboxylic acid (Trolox; cat. no. 238813), reduced glutathione (GSH) (cat. no. G4251), oxidized glutathione (GSSG) (cat. no. G4376), NADPH (cat. no. 10107824001), 1-chloro-2,4-dinitrobenzene (CDNB) (cat. no. 237329), the Folin-Ciocalteu reagent (cat. no. F9252), sodium carbonate (cat. no. 223530), sodium hydroxide (cat. no. S5881), copper sulfate (cat. no. 209198), sodium tartrate (cat. no. 217255), bovine serum albumin (cat. no. A7030), and methanol (cat. no. 322415) were provided by Merck (Poznań, Poland). Hydrochloric acid was purchased from Chempur (Piekary Śląskie, Poland; cat. no. 115752837). Glutathione Peroxidase Assay Kit was obtained from BioAssay Systems, (Hayward, CA, USA; cat. no. EGPX-100). γ -Glutamylcysteine Ligase (GCL) Activity Assay Kit was from Solarbio Life Sciences (Beijing, China; cat. no. BC1210).

Cell culture T25 flasks (cat. no. 156367) were provided by Thermofisher Scientific (Waltham, MA, USA). Transparent 96-well Advanced TCTM culture plates (cat. no. 655980), black 96-well flat bottom μ Clear® Advanced TCTM plates (cat. no. 655986), transparent 96-well plates (cat. no. 655101), black 96-well flat bottom plates (cat. no. 655209) and 24-well cell culture transparent plates (cat. no. 662160) were obtained from Greiner Bio-One (Kremsmünster, Austria). Other sterile cell culture materials were provided by Nerbe (Winsen, Germany) or Greiner Bio-One (Kremsmünster, Austria).

4-amino-TEMPO was dissolved in PBS, filtered through a 0.22 μ m filter before each experiment, and diluted in the cell medium. 6-Hydroxydopamine hydrobromide was freshly prepared and stabilized with 0.01% L-ascorbic acid and filtered using a 0.22 μ m syringe filter for each experiment. Distilled water was purified using a Milli-Q system (Millipore, Bedford, MA, USA). Fluorometric and absorptiometric measurements were performed in a Tecan Infinite 200 PRO multimode reader or a Spark multimode microplate reader (Tecan Group Ltd., Männedorf, Switzerland). Measurements were performed in nine repetitions (GSH and GSSG content) or in triplicate (ROS level, enzyme activities). Transmission light microscope observations were done in an inverted Olympus CKX53 microscope (OLYMPUS, Tokyo, Japan).

SH-SY5Y cell culture

SH-SY5Y cells were cultured in DMEM/F12 without phenol red (Dulbecco's Modified Eagle Medium Nutrient Mixture F-12), supplemented with 10% v/v heat-inactivated fetal bovine serum (hi-FBS) and 1% v/v penicillin/streptomycin solution. Cells were maintained at 37°C under 5% carbon dioxide and 95% humidity. The medium was changed twice a week, and the cells were passaged at about 80% confluence. For all studies, cells up to 14 passages were used. The morphology was examined under an inverted microscope with phase con-

trast Zeiss Primo Vert (Oberkochen, Germany). Cell viability was estimated by the Trypan Blue exclusion test. Cells were counted using a Thoma hemocytometer (Marianfeld Superior, Lauda-Königshofen, Germany).

Cell treatment

Cells were seeded into wells of transparent 96-well plates, previously covered with 1% Geltrex™ LDEV-Free Reduced Growth Factor Basement Membrane Matrix, according to the manufacturer's protocol, at an amount of 3.5×10^4 cells/well in 100 μ L culture medium. After 48-hour incubation, the medium was gently removed and replaced with 100 μ L/well of fresh culture medium or culture medium supplemented with adequate compounds: 60 μ M 6-OHDA, 75 μ M 4-AT, or both compounds together and placed in an incubator. Alternatively, when more cells were needed, 0.5×10^6 cells were grown in T-25 flasks for 48 h and added with proportionally higher volumes of the medium. After various times (30 min, 1 h, 2 h, 4 h, 6 h, 8 h, and 24 h) the plates were withdrawn and analyses were performed immediately.

Estimation of the content of reduced and oxidized glutathione (GSH and GSSG)

The content of GSH was assayed with OPA using a slightly modified method of Senft and others (Senft *et al.*, 2000). Briefly, the medium was gently removed and cells were washed with 150 μ L/well of phosphate-buffered saline (PBS). PBS was gently removed by aspiration. Subsequently, 60 μ L/well of freshly prepared cold lysis buffer (RQB buffer: 20 mM HCl, 5% TCA, 5 mM DTPA, and 10 mM L-ascorbic acid was added; then, the plates were shaken at 900 rpm for 5 minutes, and centrifuged at 4,000 rpm (5 min, room temperature).

Cell lysates were transferred into two separate black 96-well plates ("+" NEM" and "-" NEM") with a black bottom in a volume of 25 μ L/well. Into the first plate, "+"NEM", 4 μ L/well of freshly prepared 7.5 mM NEM in ice-cold RQB buffer were added. Then, 40 μ L/well of 1 M phosphate buffer, pH 7.0, was pipetted into both plates, which were shaken for 5 minutes at 900 rpm. Then, 160 μ L/well of ice-cold 0.1 M phosphate buffer (pH 6.8) and 25 μ L/well of newly prepared 0.5% OPA in methanol were added into "+"NEM" and "-"NEM" plates. Then, the plates were shaken at 900 rpm for 30 minutes. Fluorescence was measured with a TECAN Spark® multimode plate reader at 355/430 nm. GSH concentration was obtained by subtracting the fluorescence of the plate without NEM from the fluorescence of the NEM-containing plate and the GSH content was calculated, respectively, with reference to protein content in each well.

To determine the content of GSSG, 100 μ L/well of the cell lysate was added to the "-DTT" and "+DTT" black 96-well plates followed by 4 μ L/well of freshly prepared 7.5 mM NEM and 40 μ L/well of 1 M phosphate buffer, pH 7.0. After 5-min shaking, 10 μ L of 10 mM DTT was added to the "+DTT" plate, and the plates were incubated for 60 min at room temperature with shaking. Then, 80 μ L/well of 0.2 M phosphate buffer (pH 6.8) and 25 μ L/well of newly prepared 0.5% OPA were added and the procedure was run as above. The fluorescence of "-DTT" plate was subtracted from that of the "+DTT" plate and the GSSG content was calculated, respectively, with reference to protein content in each well.

Estimation of total antioxidant capacity

The cells (5×10^5) were seeded in T25 flasks and cultured for 48 h; after this time the flask contained about 10^6 cells. Then the cells were subjected to respective treatments and after 24 h, detached by trypsinization, centrifuged (1000 rpm, 5 min) washed with PBS, centrifuged, and added with 500 μ L of ice-cold 10 mM TCA to lyse the cells and prevent oxidation of cell constituents by acidification of the mixture, and frozen at -80°C . After thawing, the lysates were centrifuged (5 min, 13,000 rpm). The total antioxidant activity of the supernatants was assayed using a modified ABTS• decolorization assay (Kut *et al.*, 2022). Briefly, stock ABTS• solution prepared by oxidation of ABTS solution with potassium persulfate was diluted so that absorbance of 200 μ in a well of a 96-well plate at 734 nm was equal to 1. To this solution, 25 μ L of the supernatants were added and a decrease of absorbance was measured after 1 min and after 30 min at room temperature and corrected for the ABTS• self-decomposition. Total antioxidant capacity was calculated using Trolox with reference to the protein content in each well.

Estimation of the level of reactive oxygen species (ROS)

Cells were seeded on black 96-well plates, cultured, and treated as described above. 100 μ L/well of freshly prepared DHE working solution in PBS was added; the final concentration of DHE was 10 μ M. The fluorescence was measured immediately at 37°C , at 405/570 nm for 30 min at 1 min intervals. The "area under the curve" (sum of the fluorescence values measured at successive times) was assumed as a measure of the level of ROS.

Estimation of glutathione peroxidase activity

The cells were grown in T25 flasks as above, and after 24 h of the treatments, were detached by trypsinization, centrifuged (1000 rpm, 5 min) washed with PBS, centrifuged, and added with 500 μ L of ice-cold 20 mM phosphate buffer, frozen and thawed. Glutathione peroxidase activity was determined in the cell lysates using the EnzyChrom Glutathione Peroxidase Assay Kit according to the manufacturer's instructions.

Estimation of glutathione reductase activity

Glutathione reductase was assayed by a modification of the method of Carlberg and Mannervik (1975). Aliquots (50 μ L) of lysates prepared as above were pipetted to wells of a transparent 96-well plate, added with 110 μ L of 0.1 M phosphate buffer, pH 7.6, 20 μ L of 1 mM NADPH and 20 μ L of 1 mM GSSG. Kinetics of absorbance decrease at 340 nm was measured in a plate reader at 37°C for 5 min. On the basis of the rate of absorbance decrease, the enzyme activity was calculated with respect to the protein content of a well.

Estimation of glutathione S-transferase activity

Glutathione S-transferase activity was assayed by a modification of the procedure proposed by Habig *et al.* (1974). Cell lysates (50 μ L) were pipetted to wells of a transparent 96-well plate and added with 130 μ L of 0.1 M phosphate buffer, pH 6.5, 10 μ L of 20 mM GSH, and 10 μ L of 20 mM CDNB in ethanol. An increase in absorbance at 340 nm was monitored for 10 min at room temperature. On the basis of the rate of absorb-

ance increase, the enzyme activity was calculated with respect to the protein content of a well.

Estimation of γ -glutamyl-cysteine ligase activity

Gamma-glutamyl-cysteine ligase activity was assayed using the γ -Glutamylcysteine Ligase (GCL) Activity Assay Kit according to the manufacturer's instructions. The cells were grown in T25 flasks, subjected to the treatments, detached by trypsinization, and washed with PBS. They were lysed by sonication (3 min on ice) as recommended in the instruction.

Protein assay

Protein content was determined according to Lowry *et al.* (Lowry *et al.*, 1951) using bovine serum albumin as a standard.

Statistical analysis

The results are expressed as a percent of values obtained for control (not treated cells) cultured in parallel for the same time. The significance of differences between the control and treated cells was estimated using the Student's "*t*" test.

RESULTS

The time course of the contents of reduced and oxidized glutathione in SH-SY5Y cells treated with 6-OHDA, the nitroxide 4-AT, and both compounds together is shown in Fig. 1. After an initial decrease in the GSH content in cells subjected to all treatments after 30 min, the GSH content increased progressively with respect to control after all treatments. This increase reached statistical significance after 6, 8, and 24 h in cells treated with 6-OHDA, and after 2, 4, 6, 8, and 24 h in cells treated with 4-AT and treated with 6-OHDA and 4-AT. Changes at the "zero time" with respect to control observed in cells treated with 6-OHDA were apparently due to the fact that the minimal manipulation of the cells till complete stopping the reactions took at least a minute; during this time, the reagents applied could react with glutathione and other cell components.

There was an initial small increase in the GSSG content of the cells treated with 6-OHDA or 4-AT after 30

min. Then the GSSG level remained constant, except for a small decrease for 4-AT-treated cells after 8 hours.

Total antioxidant capacity of cell extracts measured by the reduction of the ABTS \bullet radical after 1 min reflects mainly the content of "fast" (rapidly reacting) antioxidants while the measurement of the ABTS \bullet reduction after 30 min reflects the content of the sum of "fast" and "slow" antioxidants ("summary" TAC). The values of TAC obtained after 1 min reduction by the cell extracts were about 67% of the values of TAC obtained after 30 min; this percentage was not affected by the treatments applied. Changes in TAC of cell extracts measured after both 1 min and 30 min were similar to those of the GSH content. There was an initial (for the 0 time) decrease in the content of "fast antioxidants" for cells treated with 4-AT and after 30 min for cells treated with 6-OHDA and a decrease of the "summary TAC" at the 0 time for all types of treatment, maintained after 30 min in cells treated with 6-OHDA. After 4, 6, 8, and 24 h the content of "fast" antioxidants increased over the control levels in cells treated with 6-OHDA, 4-AT, and both compounds, reaching the highest values after 24 h for cells treated with 6-OHDA and 6-OHDA plus 4-AT. Statistically significant elevation of the "summary TAC" was observed after 6, 8 and 24 h for all types of treatment (Fig. 2).

The level of ROS was elevated in cells treated with 6-OHDA over the entire experiment, after 30 min in cells treated with 4-AT, and at the 0 time and after 30 min and 1 h in cells treated with 6-OHDA and 4-AT simultaneously. Later on, the ROS level decreased in cells treated with 4-AT after 8 and 24 h, and in cells treated with 6-OHDA and 4-AT simultaneously after 24 h (Fig. 3).

The patterns of changes in the activities of glutathione peroxidase (GPx; EC 1.11.1.9) and glutathione reductase (GR; EC 1.6.4.2) were similar. Initially, the GPx activity was decreased in cells treated with 6-OHDA after 30 min, 1 h, and 2 h, and increased over the control level for cells treated with 6-OHDA and with 6-OHDA and 4-AT simultaneously after 8 h. GR activity decreased after 30 min for all types of treatment, and after 1 h in cells treated with 6-OHDA and 6-OHDA and 4-AT simultaneously. Later on, an increase in the GR activity was noted, peaking after 6 and 8 h for types of treatment. This increase was maintained after 8 h for cells

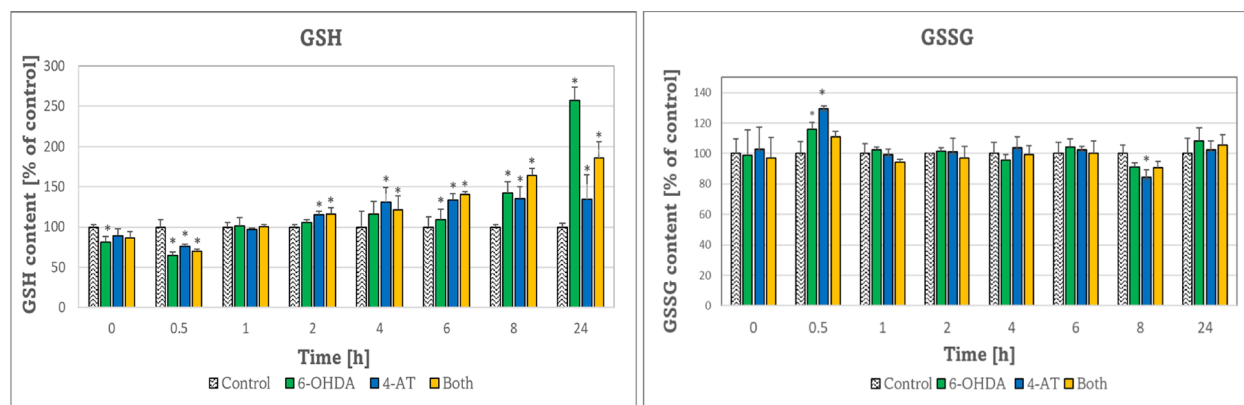


Figure 1. Time course of changes in the GSH and GSSG content of SH-SY5Y cells treated with 50 μ M 6-OHDA, 75 μ M 4-AT, and both compounds together.

* $p \leq 0.05$ vs. control (not treated) cells (Student's "*t*" test); $n=9$.

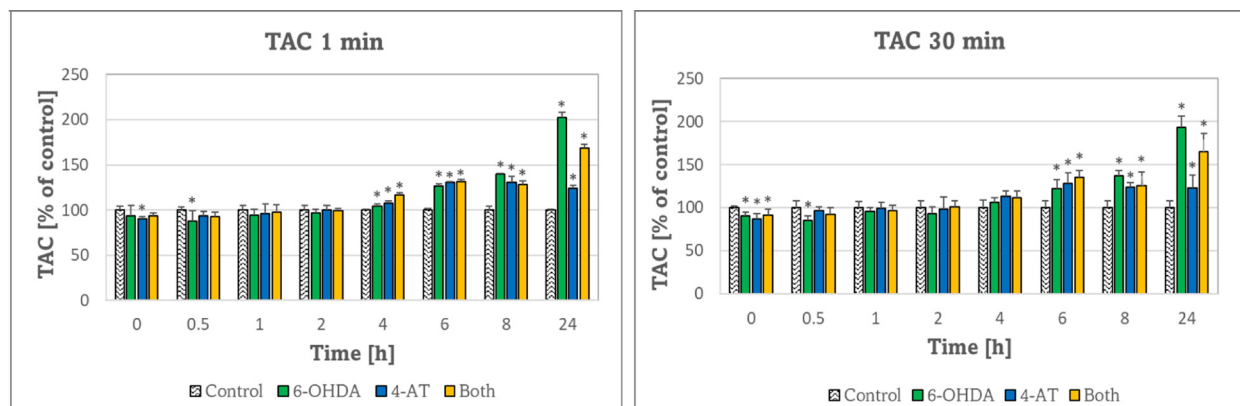


Figure 2. Time course of changes in the total antioxidant capacity of extracts of SH-SY5Y cells treated with 50 μ M 6-OHDA, 75 μ M 4-AT, and both compounds together.

* $p \leq 0.05$ vs. control (not treated) cells (Student's "t" test); $n=3$.

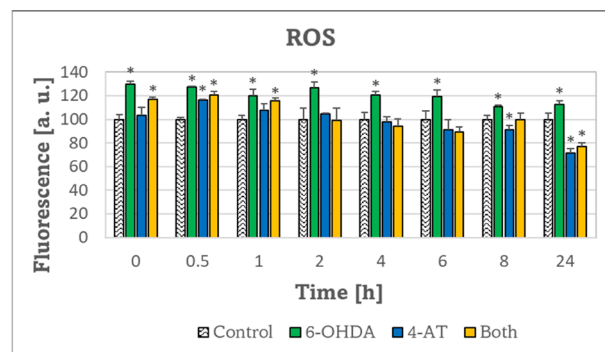


Figure 3. Time course of changes in the level of ROS in SH-SY5Y cells treated with 50 μ M 6-OHDA, 75 μ M 4-AT, and both compounds together.

* $p \leq 0.05$ vs. control (not treated) cells (Student's "t" test); $n=3$.

treated with 6-OHDA and with 4-AT, coming back to control values after 24 h (Fig. 4).

The activities of glutathione S -transferase (GST; EC 2.5.1.18) and γ -glutamyl-cysteine ligase (GCL; EC 6.3.2.2) changed in a similar way though the amplitude of changes was greater for the latter enzyme. The activity of GST was decreased after 30 min in cells treated

with 6-OHDA, after 0.5 and 1 h for cells treated with 4-AT and after 30 min, 1 h and 2 h for cells treated with 6-OHDA and 4-AT simultaneously. Then its activity was significantly increased after 8 h in cells treated with 4-AT, and after 8 and 24 h in cells treated with 6-OHDA and 4-AT simultaneously. The activity of GCL was decreased after 0.5 h and elevated after 4, 6, 8 and 24 h in cells treated with 6-OHDA, decreased after 0.5 h, and increased after 2, 4, 8 and 24 h in cells treated with 4-AT, and increased after 6, 8 and 24 h in cells treated with 6-OHDA and 4-AT simultaneously (Fig. 5).

DISCUSSION

It was speculated that supplementation with N-acetyl-cysteine to restore the level of glutathione may inhibit the progression of PD (Aaseth *et al.*, 2018; Tardiolo *et al.*, 2018). The results of animal experiments are encouraging (Tardiolo *et al.*, 2018).

A decrease in the GSH level was observed in SH-SY5Y cells treated with relatively high concentrations of 6-OHDA as a cellular model of PD. Interestingly, cell treatment with lower concentrations of 6-OHDA induced a profound increase in the cellular GSH content (Tirmenstein *et al.*, 2005; Betharia *et al.*, 2019; Pichla *et al.*, 2020). Exact comparison of data of various authors

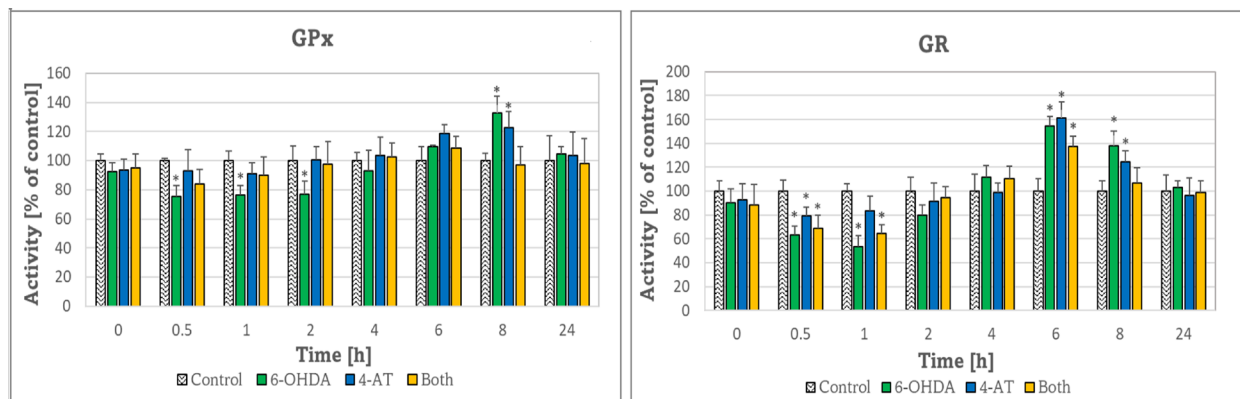


Figure 4. Time course of changes in the activities of glutathione peroxidase (GPx) and glutathione reductase (GR) in SH-SY5Y cells treated with 50 μ M 6-OHDA, 75 μ M 4-AT and both compounds together.

* $p \leq 0.05$ vs. control (not treated) cells (Student's "t" test); $n=3$.

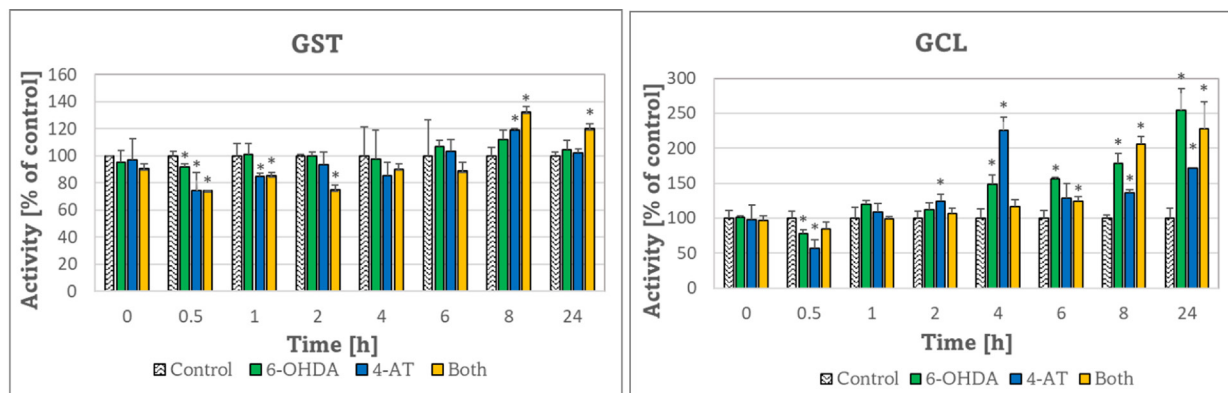


Figure 5. Time course of changes in the activities of glutathione S-transferase (GST) and γ -glutamyl-cysteine ligase (GCL) in SH-SY5Y cells treated with 50 μ M 6-OHDA, 75 μ M 4-AT and both compounds together.

* $p < 0.05$ vs. control (not treated) cells (Student's "t" test); $n = 3$.

may be not easy due to subtle differences in conditions. Inter alia, concentrations of the treating agents are usually reported while a description of exposure conditions in the mole per cell metric would be more relevant (Doskey *et al.*, 2015; Bartosz *et al.*, 2022). In any case, treatment with lower amounts of 6-OHDA induced an increase rather than a decrease in the glutathione content of SH-SY5Y cells. This phenomenon is intriguing as it may point to the ways of elevation of the glutathione content in neuronal cells subjected to oxidative stress.

Results of the present study strongly suggest that this increase in the GSH content is of adaptive nature and is preceded by a transient decrease in the GSH level in the cells shortly after the addition of 6-OHDA, 4-AT, and both compounds together. There was an initial small increase in the content of GSSG in cells treated with 6-OHDA and 4-AT alone and, with one exception, no significant changes afterward. The lack of significant changes in the GSSG level in SH-SY5Y cells challenged with a similar concentration of 6-OHDA after 4 h and 24 h was reported previously (Tirmenstein *et al.*, 2005).

The small increase in the GSSG content being a result of GSH oxidation after 30 min can contribute to but cannot account for the decrease in the GSH content occurring at this time as the GSSG constituted not more than 2% of the total glutathione content in SH-SY5Y cells. The main reason for the transient decrease in the content of GSH is most probably the formation of conjugates with products of 6-OHDA oxidation, especially *p*-quinone (Izumi *et al.*, 2005). Nitroxides are known to oxidize glutathione (Glebska *et al.*, 2003) the relatively low decrease in the GSH content and the relatively high increase of the GSSG content in cells treated with 4-AT are compatible with the assumption that in this case, GSH loss was mainly due to the GSH oxidation by 4-AT. 4-AT is a nitroxide, an antioxidant able to decompose superoxide radical anions in a pseudo-superoxide dismutase reaction and to react with other free radicals (Lewandowski & Gwozdziński, 2017; Prescott & Bottle, 2017); reactions with free radicals can contribute to the GSH loss as well. It is therefore not surprising that the loss of the GSH content observed after 30 min in cells treated with 6-OHDA and 4-AT together is not higher than those observed for cells treated with any of these agents alone and the increase of the GSSG content observed after this time is even lower than that those found after the action of the single compounds. Changes in TAC of cell extracts generally coincided with those

observed for GSH content, in agreement with the view that thiols are the main determinants of cellular TAC.

The permanent elevation of the ROS level in cells treated with 6-OHDA evidences permanent oxidative stress induced by this compound, not counteracted efficiently by increased levels of GSH and TAC. The ROS level was not increased and even decreased by 4-AT at longer incubation times. The presence of 4-AT decreased the ROS level in cells treated with 6-OHDA, evidencing the antioxidant action of this compound.

Cell treatment with 6-OHDA, 4-AT, and both compounds together brought about transient decreases of activity of all enzymes of glutathione metabolism studied, starting at 30 min of incubation and followed by a recovery or even an overshoot several hours later. The loss of enzyme activity may be due to a non-covalent inhibition and (probably mostly) to the damage to enzymatic proteins by thiol oxidation (6-OHDA, 4-AT) and reactions of free radicals and products of 6-OHDA degradation.

Of particular importance are the changes in the GCL activity since it is the rate-limiting enzyme of glutathione biosynthesis. The decrease in GCL activity coincided with the loss of GSH level, apparently evidencing the inability of the enzyme to secure the normal level of GSH consumed at this stage of incubation. The activity of the enzyme was restored relatively quickly; later on, an overshoot took place lasting until 24 h and apparently was responsible for the elevation of GSH content over the control level. It was reported previously that exposure of SH-SY5Y cells to 6-OHDA results increased the expression of the Nrf-2-dependent genes coding for the GCL modifier and catalytic subunits (Tirmenstein *et al.*, 2005). Our results demonstrate that an increase in the activity of this enzyme indeed takes place under these conditions and leads to an overcompensatory increase in the GSH content.

An increase in the expression of increased genes coding for the GCL modifier and catalytic subunits was reported in SH-SY5Y cells treated with a similar concentration of 6-OHDA (Tirmenstein *et al.*, 2005). Genes coding for other enzymes studied (GPx, GR, and GST) are also under the control of the Nrf2 transcription factor (He *et al.*, 2020), which explains the common pattern of activation of all enzymes covered by this study. Semi-quinones and quinones react with the Keap protein and activate Nrf2; such products of 6-OHDA metabolism are formed in the cells (Kang *et al.*, 2005).

4-amino-TEMPO increased the level of GSH and TAC, especially after 2-24 h (GSH content) and 4-24 h (TAC). Nitroxides can also activate Nrf2 (Greenwald *et al.*, 2014), which explains the similar pattern of enzyme activation by 6-OHDA and 4-AT. The common mechanism of Nrf2 activation may explain the lack of synergy or additivity of the response.

CONCLUSION

Elevation of the level of cellular GSH is apparently an adaptive reaction to oxidative stress imposed by 6-OHDA, occurring if the cell viability is not compromised too strongly and seems to be advantageous for the cells. Mounting of the Nrf2 response by 4-AT may be of potential therapeutic interest since in PD the level of GSH is decreased in substantia nigra and application of a nitroxide, which has beneficial antioxidant properties *per se*, might be an acceptable way in attempts to increase the level of this key cellular antioxidant.

Declarations

Conflict of interest statement. The authors declare that they have no known competing financial interests or personal relationships that could have appeared to influence the work reported in this paper.

Acknowledgements. We would like to express our special appreciation and thank M.Sc. Edyta Bieszczad-Bedrejczuk (Laboratory of Analytical Biochemistry, University of Rzeszow, Rzeszów, Poland) for the excellent technical assistance.

REFERENCES

- Aaseth J, Dusek P, Roos PM (2018) Prevention of progression in Parkinson's disease. *Biomaterials* **31**: 737–747. <https://doi.org/10.1007/s10534-018-0131-5>
- Aoyama K. (2021) Glutathione in the Brain. *Int J Mol Sci* **22**: 5010. <https://doi.org/10.3390/ijms22095010>
- Barrachina M, Domínguez I, Ambrosio S, Secades J, Lozano R, Ferrer I (2003) Neuroprotective effect of citicoline in 6-hydroxydopamine-lesioned rats and in 6-hydroxydopamine-treated SH-SY5Y human neuroblastoma cells. *J Neurol Sci* **215**: 105–110. [https://doi.org/10.1016/S0022-510X\(03\)00204-1](https://doi.org/10.1016/S0022-510X(03)00204-1)
- Bartosz G, Piękowska N, Sadowska-Bartos I (2022) Dosing metric in cellular experiments: The mol/cell metric has its limitations. *Toxicol In Vitro* **78**: 105272. <https://doi.org/10.1016/j.tiv.2021.105272>
- Betharia S, Rondón-Ortiz AN, Brown DA (2019) Disubstituted Dithiolethione ACDT Exerts Neuroprotective Effects Against 6-Hydroxydopamine-Induced Oxidative Stress in SH-SY5Y Cells. *Neurochem Res* **44**: 1878–1892 <https://doi.org/10.1007/s11064-019-02823-3>
- Bjorklund G, Peana M, Maes M, Dadar M, Severin B (2021) The glutathione system in Parkinson's disease and its progression. *Neurosci Biobehav Rev* **120**: 470–478. <https://doi.org/10.1016/j.neubiorev.2020.10.004>
- Brown DA, Betharia S, Yen JH, Kuo PC, Mistry H (2016) Further structure-activity relationships study of substituted dithiolethiones as glutathione-inducing neuroprotective agents. *Chem Cent J* **10**: 64. <https://doi.org/10.1186/s13065-016-0210-z>
- Brown DA, Betharia S, Yen JH, Tran Q, Mistry H, Smith K (2014) Synthesis and structure-activity relationships study of dithiolethiones as inducers of glutathione in the SH-SY5Y neuroblastoma cell line. *Bioorg Med Chem Lett* **24**: 5829–5831. <https://doi.org/10.1016/j.bmcl.2014.10.005>
- Carlberg I, Mannervik B (1975) Purification and characterization of the flavoenzyme glutathione reductase from rat liver. *J Biol Chem* **250**: 5475–5480. [https://doi.org/10.1016/S0021-9258\(19\)41206-4](https://doi.org/10.1016/S0021-9258(19)41206-4)
- Chen CH, Hsu PC, Hsu SW, Hong KT, Chen KY, He JL, Cho DY, Wang YC, Chang WS, Bau DT, Tsai CW (2022) Protective effects of jujubosides on 6-OHDA-induced neurotoxicity in SH-SY5Y and SK-N-SH Cells. *Molecules* **27**: 4106. <https://doi.org/10.3390/molecules27134106>
- Cirmi S, Maugeri A, Lombardo GE, Russo C, Musumeci L, Gangemi S, Calapai G, Barreca D, Navarra MA (2021) Flavonoid-rich extract of mandarin juice counteracts 6-OHDA-induced oxidative stress in SH-SY5Y cells and modulates Parkinson-related genes. *Antioxidants (Basel)* **10**: 539. <https://doi.org/10.3390/antiox10040539>
- Doskey CM, van 't Erve TJ, Wagner BA, Buettner GR (2015) Moles of a substance per cell is a highly informative dosing metric in cell culture. *PLoS One* **10**: e0132572. <https://doi.org/10.1371/journal.pone.0132572>
- Elyasi L, Jahanshahi M, Jameie SB, Hamid Abadi, HG, Nikmahzar E, Khalili M, Jameie M, Jameie M (2020) 6-OHDA mediated neurotoxicity in SH-SY5Y cellular model of Parkinson disease suppressed by pretreatment with hesperidin through activating L-type calcium channels. *J Basic Clin Physiol Pharmacol* **32**: 11–17. <https://doi.org/10.1515/jbcpp-2019-0270>
- Ferah Okkay I, Okkay U, Cicek B, Yilmaz A, Yesilyurt F, Mendil AS, Hacimuftuoglu A (2021) Neuroprotective effect of bromelain in 6-hydroxydopamine induced *in vitro* model of Parkinson's disease. *Mol Biol Rep* **48**: 7711–7717. <https://doi.org/10.1007/s11033-021-06779-y>
- Glebska J, Skolimowski J, Kudzin Z, Gwoździński K, Grzelak A, Bartosz G (2003) Pro-oxidative activity of nitroxides in their reactions with glutathione. *Free Radic Biol Med* **35**: 310–316. [https://doi.org/10.1016/S0891-5849\(03\)00306-x](https://doi.org/10.1016/S0891-5849(03)00306-x)
- Greenwald MB, Anzi S, Ben Sasson S, Bianco-Peled H, Kohen R (2014) Can nitroxides evoke the Keap1-Nrf2-ARE pathway in skin? *Free Radic Biol Med* **77**: 258–269. <https://doi.org/10.1016/j.freeradbiomed.2014.08.021>
- Gunjima K, Tomiyama R, Takakura K, Yamada T, Hashida K, Nakamura Y, Konishi T, Matsugo S, Hori O (2014) 3,4-dihydroxybenzalacetone protects against Parkinson's disease-related neurotoxin 6-OHDA through Akt/Nrf2/glutathione pathway. *J Cell Biochem* **115**: 151–160. <https://doi.org/10.1002/jcb.24643>
- Habig WH, Pabst MJ, Jakoby WB (1974) Glutathione S-transferases. The first enzymatic step in mercapturic acid formation. *J Biol Chem* **249**: 7130–7139. [https://doi.org/10.1016/S0021-9258\(19\)42083-8](https://doi.org/10.1016/S0021-9258(19)42083-8)
- Hara H, Ohta M, Ohta K, Kuno S, Adachi, T (2003a) Apomorphine attenuates 6-hydroxydopamine-induced apoptotic cell death in SH-SY5Y cells. *Redox Rep* **8**: 193–197. <https://doi.org/10.1179/135100003225002682>
- Hara H, Ohta M, Ohta K, Kuno S, Adachi T (2003b) Increase of anti-oxidative potential by tert-butylhydroquinone protects against cell death associated with 6-hydroxydopamine-induced oxidative stress in neuroblastoma SH-SY5Y cells. *Brain Res Mol Brain Res* **119**: 125–131. <https://doi.org/10.1016/j.molbrainres.2003.08.021>
- He F, Ru X, Wen T (2020) NRF2, a transcription factor for stress response and beyond. *Int J Mol Sci* **21**: 4777. <https://doi.org/10.3390/ijms21134777>
- Izumi Y, Sawada H, Sakka N, Yamamoto N, Kume T, Katsuki H, Shimohama S, Akaike A (2005) p-Quinone mediates 6-hydroxydopamine-induced dopaminergic neuronal death and ferrous iron accelerates the conversion of p-quinone into melanin extracellularly. *J Neurosci Res* **79**: 849–860. <https://doi.org/10.1002/jnr.20382>
- Jia Z, Zhu H, Misra HP, Li Y (2008) Potent induction of total cellular GSH and NQO1 as well as mitochondrial GSH by 3H-1,2-dithiole-3-thione in SH-SY5Y neuroblastoma cells and primary human neurons: protection against neurocytotoxicity elicited by dopamine, 6-hydroxydopamine, 4-hydroxy-2-nonenal, or hydrogen peroxide. *Brain Res* **1197**: 159–169. <https://doi.org/10.1016/j.brainres.2007.12.044>
- Jing X, Wei X, Ren M, Wang L, Zhang X, Lou H (2016) Neuroprotective effects of tanshinone I against 6-OHDA-induced oxidative stress in cellular and mouse model of Parkinson's disease through upregulating Nrf2. *Neurochem Res* **41**: 779–786. <https://doi.org/10.1080/10.1007/s11064-015-1751-6>
- Kang KW, Lee SJ, Kim SG (2005) Molecular mechanism of nrf2 activation by oxidative stress. *Antioxid Redox Signal* **7**: 1664–1673. <https://doi.org/10.1089/ars.2005.7.1664>
- Ko YH, Kim SK, Kwon SH, Seo JY, Lee BR, Kim YJ, Hur KH, Kim SY, Lee SY, Jang CG (2019) 7,8,4'-Trihydroxyisoflavone, a metabolized product of Daidzein, attenuates 6-hydroxydopamine-induced neurotoxicity in SH-SY5Y Cells. *Biomol Ther (Seoul)* **27**: 363–372. <https://doi.org/10.4062/biomolther.2018.211>
- Kut K, Cieniek B, Stefaniuk I, Bartosz G, Sadowska-Bartos I (2022) A modification of the ABTS• decolorization method and an insight into its mechanism. *processes* **10**: 1288. <https://doi.org/10.3390/pr10071288>
- Lee GH, Lee WJ, Hur J, Kim E, Lee HG, Seo HG (2020) Ginsenoside Re mitigates 6-hydroxydopamine-induced oxidative stress through upregulation of GPX4. *Molecules* **25**: 188. <https://doi.org/10.3390/molecules25010188>
- Lewandowski M, Gwozdziński K (2017) Nitroxides as antioxidants and anticancer drugs. *Int J Mol Sci* **18**: 2490. <https://doi.org/10.3390/ijms18112490>
- Lopes FM, Schröder R, da Frota ML Jr, Zanotto-Filho A, Müller CB, Pires AS, Meurer RT, Colpo GD, Gelain DP, Karczinski F, Moreira JC, Fernandes Mda C, Klant F (2010) Comparison between proliferative and neuron-like SH-SY5Y cells as an *in vitro* model

- for Parkinson disease studies. *Brain Res* **1337**: 85–94. <https://doi.org/10.1016/j.brainres.2010.03.102>
- Lowry OH, Rosebrough NJ, Farr AL, Randall RJ (1951) Protein measurement with the Folin phenol reagent. *J Biol Chem* **193**: 265–275. [https://doi.org/10.1016/S0021-9258\(19\)52451-6](https://doi.org/10.1016/S0021-9258(19)52451-6)
- Miyama A, Saito Y, Yamanaka K, Hayashi K, Hamakubo T, Noguchi N (2011) Oxidation of DJ-1 induced by 6-hydroxydopamine decreasing intracellular glutathione. *PLoS One* **6**: e27883. <https://doi.org/10.1371/journal.pone.0027883>
- Pichla M, Bartosz G, Stefaniuk I, Sadowska-Bartos I (2021) pH-Responsive redox nanoparticles protect SH-SY5Y cells at lowered pH in a cellular model of Parkinson's disease. *Molecules* **26**: 543. <https://doi.org/10.3390/molecules26030543>
- Pichla M, Pulaski L, Kania KD, Stefaniuk I, Cieniek B, Pieńkowska N, Bartosz G, Sadowska-Bartos I (2020) Nitroxide radical-containing redox nanoparticles protect neuroblastoma SH-SY5Y cells against 6-hydroxydopamine toxicity. *Oxid Med Cell Longev* **2020**: 9260748. <https://doi.org/10.1155/2020/9260748>
- Prescott C, Bottl SE (2017) Biological relevance of free radicals and nitroxides. *Cell Biochem Biophys* **75**: 227–240. <https://doi.org/10.1007/s12013-016-0759-0>
- Rashidi R, Ghorbani A, Rakhshandeh H, Mousavi SH (2021) Protective effect of *Artemisia absinthium* on 6-hydroxydopamine-induced toxicity in SH-SY5Y cell line. *Avicenna J Phytomed* **11**: 238–246
- Ryu J, Zhang R, Hong BH, Yang EJ, Kang KA, Choi M, Kim KC, Noh SJ, Kim HS, Lee NH, Hyun JW, Kim HS (2013) Phloroglucinol attenuates motor functional deficits in an animal model of Parkinson's disease by enhancing Nrf2 activity. *PLoS One* **8**: e71178. <https://doi.org/10.1371/journal.pone.0071178>
- Senft AP, Dalton TP, Shertzer HG (2000) Determining glutathione and glutathione disulfide using the fluorescence probe *p*-phthalaldehyde. *Anal Biochem* **80**: 80–86. <https://doi.org/10.1006/abio.2000.4498>
- Smeyne M, Smeyne RJ (2013) Glutathione metabolism and Parkinson's disease. *Free Radic Biol Med* **62**: 13–25. <https://doi.org/10.1016/j.freeradbiomed.2013.05.001>
- Sun Y, He L, Wang T, Hua W, Qin H, Wang J, Wang L, Gu W, Li T, Li N, Liu X, Chen F, Tang L (2020) Activation of p62-Keap1-Nrf2 pathway protects 6-hydroxydopamine-induced ferroptosis in dopaminergic cells. *Mol Neurobiol* **57**: 4628–4641. <https://doi.org/10.1007/s12035-020-02049-3>
- Tardiolo G, Bramanti P, Mazzon E (2018) Overview on the effects of N-acetylcysteine in neurodegenerative diseases. *Molecules* **23**: 3305. <https://doi.org/10.3390/molecules23123305>
- Tirmenstein MA, Hu CX, Scicchitano MS, Narayanan PK, McFarland DC, Thomas HC, Schwartz LW (2005) Effects of 6-hydroxydopamine on mitochondrial function and glutathione status in SH-SY5Y human neuroblastoma cells. *Toxicol In Vitro* **19**: 471–479. <https://doi.org/10.1016/j.tiv.2005.01.006>
- Tsai RT, Tsai CW, Liu SP, Gao JX, Kuo YH, Chao PM, Hung HS, Shyu WC, Lin SZ, Fu RH (2020) Maaackia ameliorates 6-hydroxydopamine and SNCA pathologies by modulating the PINK1/Parkin pathway in models of Parkinson's disease in *Caenorhabditis elegans* and the SH-SY5Y cell line. *Int J Mol Sci* **21**: 4455. <https://doi.org/10.3390/ijms21124455>
- Urano Y, Mori C, Fuji A, Konno K, Yamamoto T, Yashirogi S, Ando M, Saito Y, Noguchi N (2018) 6-Hydroxydopamine induces secretion of PARK7/DJ-1 via autophagy-based unconventional secretory pathway. *Autophagy* **14**: 1943–1958. <https://doi.org/10.1080/15548627.2018.1493043>
- Xicoy H, Brouwers JF, Kalnytska O, Wieringa B, Martens GJM (2020) Lipid analysis of the 6-hydroxydopamine-treated SH-SY5Y cell model for Parkinson's disease. *Mol Neurobiol* **57**: 848–859. <https://doi.org/10.1007/s12035-019-01733-3>
- Zhang N, Shu HY, Huang T, Zhang QL, Li D, Zhang GQ, Peng XY, Liu CF, Luo WF, Hu LF (2014) Nrf2 signaling contributes to the neuroprotective effects of urate against 6-OHDA toxicity. *PLoS One* **9**: e100286. <https://doi.org/10.1371/journal.pone.0100286>

NADPH oxidase 4 facilitates progression of chondrosarcoma via generation of reactive oxygen species

Zheng Jun✉, Wang Lei, Fang Ce, Ren Wen Tao, Meng Xiang Hui and Qing Ci Nan

Department of Orthopedics, Anhui Provincial Cancer Hospital, China

Nicotinamide adenine dinucleotide phosphate oxidase 4 (NOX4) is an enzyme that regulates reactive oxygen species (ROS) generation, and its function in the development of chondrosarcoma remains unclear. In the present study, we studied NOX4 expression in chondrosarcoma by immunochemical examination, and analyzed the role of NOX4 in viability and apoptosis of human chondrosarcoma cell line SW1353 using NOX4 siRNA or NOX4 inhibitor GKT137831. NOX4 level significantly increased in tumor compared to that in para-carcinoma sample. The levels of NOX4 were positively correlated with histological grade and Musculoskeletal Tumor Society stage of the patients. NOX4 level was significantly increased in SW1353 compared with that in chondrocytes CHON-001. Knockdown of NOX4 or inhibition of NOX4 by GKT137831 both decreased generation of ROS, and induced growth inhibition and apoptosis in SW1353, accompanied with the activation of caspases (caspase-3, caspase-8 and caspase-9), upregulation of Bax, cytochrome C (cyt-c), cleaved-PARP and down-regulation of Bcl-2. Moreover, NOX4 siRNA and GKT137831 decreased the expression of p-Akt, p-ERK and p-p65 in SW1353 cells. In an *in vivo* study, NOX4 shRNA transfected SW1353 have shown impaired growth ability compared to the SW1353 when they were injected into the nude mice. Meanwhile, GKT137831 induced growth inhibition and apoptosis in SW1353 xenograft animals, together with increased expression of Bax, cyt-c, cleaved-PARP, and decreased expression of Bcl-2, p-Akt, p-ERK and p-p65. NOX4 plays a positive role in the development of chondrosarcoma and could serve as a promising target against chondrosarcoma clinically.

Keywords: NADPH oxidase 4, chondrosarcoma, oxidative stress, reactive oxygen species, growth, apoptosis

Received: 13 December, 2022; **revised:** 09 March, 2023; **accepted:** 05 May, 2023; **available on-line:** 18 September, 2023

✉e-mail: zhengjunhefei1980@163.com

Abbreviations: DCFH-DA, 2',7'-Dichlorodihydrofluorescein diacetate; NOX4, Nicotinamide adenine dinucleotide phosphate oxidase 4; ROS, reactive oxygen species

INTRODUCTION

Chondrosarcoma is a primary bone cancer with diverse morphological features and clinical behavior. Chondrosarcoma takes up about 20% of all primary malignant tumors of the bone and may occur at any age between 10 and 80 years old (MacDonald *et al.*, 2019). Although chondrosarcomas typically arise from cartilage or cartilaginous precursors within bone, they may occasionally develop within soft tissues through-

out the body. At present, clinical treatment options (chemotherapy or radiation treatment) are labeled with poor response and unsatisfied effect, making a challenge to the management of chondrosarcomas (MacDonald *et al.*, 2019; Lee *et al.*, 2012; Gelderblom *et al.*, 2008). Due to absence of effective adjuvant therapy, mesenchymal malignancy has a poor prognosis.

Complicated biochemical processes involved in malignant tumor formation and development provide a lot of promising therapeutic targets and strategies. One of these strategies is to inhibit oxidative stress, as oxidative stress produced reactive oxygen species (ROS) is served as a stimulus for tumor angiogenesis (Klaunig, 2018; Ratliff *et al.*, 2016). Oxidative stress is the cellular state in which levels of ROS override antioxidant defense of the cell. ROS is an oxygen-based chemical intermediate with high reactivity. Under physiological condition, ROS level is tightly regulated through action of various scavenging and antioxidant systems to mediate the normal activity of cellular signaling pathways (Ratliff *et al.*, 2016). However, abnormally elevated ROS production that exceeds scavenging capacity of the antioxidant system has linked to pathobiology of many diseases. Many reports (Chen *et al.*, 2020; Chen *et al.*, 2020; Lee *et al.*, 2019) have supported that ROS play a positive role in the prevention of tumor programmed cell death and promotion of immortalization, metastasis, and other tumor features.

Nicotinamide adenine dinucleotide phosphate (NADPH) oxidase (NOX) produces superoxide anion and other ROS from molecular oxygen throughout the body. NOX transfers electrons from NADPH, they react with oxygen to form superoxide, which is usually rapidly converted to hydrogen peroxide (Ratliff *et al.*, 2016; Bedard & Krause, 2007). Therefore, NOX is a major component of oxidative stress system. At present, several members have been discovered and identified in the family of NOX, including NOX1, NOX2, NOX4, NOX5, etc. (Bedard & Krause, 2007). NOX4 is the sole NOX isoform present in human primary chondrocytes (Drevet *et al.*, 2018). Several reports confirmed the positive role of NOX4 in bone and cartilage homeostasis associated diseases (Drevet *et al.*, 2018; Wegner & Haudenschild, 2020). Moreover, NOX4 was involved in advanced glycation end-products-induced degradation of articular extracellular matrix (Lei *et al.*, 2019). However, NOX4's biological effect in the development of chondrosarcoma is still unclear. Therefore, the aim of the present study was to disclose NOX4's role in the development of chondrosarcoma, and meanwhile to evaluate effectiveness of targeted NOX4 in the prevention of chondrosarcoma.

MATERIAL AND METHODS

Clinical specimens

The present study was approved by the Ethics Committee of Anhui provincial Cancer Hospital and conducted along with the ethical standards of the Helsinki Declaration of 1975, as revised in the year 2000. A total of 40 patients with conventional chondrosarcoma were recruited into current study between 2019 and 2020 at Anhui provincial Cancer Hospital. Informed consents were obtained from all enrolled patients. None of the enrolled patients received radiotherapy or chemotherapy prior to surgery. A total of 80 samples (cancer and adjacent normal tissues) were obtained. Specimens were frozen in liquid nitrogen after resection and stored at -80°C until use.

Cells lines and culture

Human cancer cell lines

Human chondrosarcoma cell line SW1353 and chondrocytes cell line CHON-001 were obtained from the American Type Culture Collection (Manassas, VA, USA). All cells were conventionally maintained in Dulbecco's modified Eagle medium (DMEM) supplemented with 10% fetal bovine serum, 100 U/ml penicillin and 100 µg/ml streptomycin, and routinely cultured in a humidified incubator at 37°C supplemented with 5% CO₂.

Transfection of cells

siRNAs against NOX4 and control siRNA were purchased from Gene Pharma (Shanghai, China). SW1353 cells were transfected with siRNAs using Lipofectamine 2000 (Invitrogen, Carlsbad, CA, USA) according to the manufacturer's instruction. Briefly, the special NOX4 siRNA (40 nM) or non-binding control siRNA (40 nM) was transfected into SW1353 cells and cultured for 12h. After 12 h, the transfection medium was removed and 2 ml DMEM without FBS was added to recover cell growth for 24 h. The NOX4 siRNA sequences were sense 5'-CCAUGUGCCGAACACUCUUTT-3' and antisense 5'-AAGAGUGUUCGGCACAUGGTT-3' (Genepharma, Shanghai, China). Moreover, for stable transfection of shRNA *in vivo*, pGIPZ-lentiviral shRNA vectors targeting NOX4 gene and control vector were purchased from Open Biosystems (Thermo Fisher Scientific, Inc. Waltham, MA, USA), pGIPZ cloning vector contains a puromycin-resistant gene. Briefly, the nucleotide sequences were as follows: shNox4, 5'-GCATG-GTGGTGGTGCTATTCC-3'; and shNC, 5'-TTCTC-CGAACGTGTACACGT-3'. To generate lentiviral particles, HEK-293-T cells were transiently transfected with 4 mg pLKO.1 lentiviral vector (Sigma) containing shNOX4 or sh nontargeting control (Sigma) plus 4 mg of pCMVDR8.91 and 1.0 mg of pMD.2G plasmids using transfection reagent Lipofectamine 2000. SW1353 cells were transduced with lentiviral particles plus 0.4 mg/mL polybrene (Sigma) and infected overnight, and the selection of transfected cells was done by adding 0.75 mg/mL puromycin (Sigma).

Cell Viability Assay

Cell viability was analyzed using MTT assay. Briefly, 5×10³ cells of SW1353 were seeded into 96-well plates and incubated with 1 µM cisplatin (Sigma Aldrich, St. Louis, MO, USA), 5 µM N-Acetyl-L-cysteine

(NAC, Sigma Aldrich, St. Louis, MO, USA) and 1 µM GKT137831 (Med Chem Express, Shanghai, China) for 96 h. At the end of culture, DMSO was added to dissolve the formazan crystals. Absorbance was detected at a wavelength of 570 nm by a microplate reader (BioTek, Winooski, VT, USA). Percentages of cell viability (%) were determined by comparing with the untreated control.

Apoptosis assay

Cells (5×10⁴/well) were treated with NOX4 siRNA for 48 h. Quantitative assessment of apoptotic cells was assessed by Annexin V/PI dual dyeing, as reported previously (Chen *et al.*, 2020). Briefly, at the end of the study, the cells were centrifuged at 1500 rpm for 5 min, washed twice with PBS, and resuspended in 0.5 mL binding buffer containing 1 µg/mL propidium iodide (PI) and 0.025 µg/mL annexin V-FITC (BD Biosciences, CA, USA). Finally, apoptotic cells were analyzed by using FACSscan and the CellQuest program (Becton Dickinson, Lincoln Park, NJ, USA).

Measurement of caspases activities

Cells were seeded on 6-well plates (5×10⁵ cells/well) and treated with 1µM GKT137831 for 48h or transfected by siRNA NOX4 for 48h. Caspase-3, caspase-8, and caspase-9 activities were measured using commercial colorimetric assay kits (Beyotime, Haimen, China) according to the protocol provided by the manufacturer.

Measurement of intracellular ROS

Intracellular levels of ROS were determined using the fluorescent probe 2',7'-Dichlorodihydrofluorescein diacetate (DCFH-DA) (Santa Cruz Biotechnology, Santa Cruz, CA, USA). The cells were treated with NOX4 siRNA for 48 h, and then were centrifuged, suspended in PBS, and loaded with 20 µM DCFH-DA at 37°C for 30 min. Fluorescence intensity of the formed DCF was analyzed by flow cytometry (Beckman Coulter, Fullerton, CA, USA). Similarly, ROS levels in the grown tumor were measured as described previously, based on the oxidation of DCFH-DA. ROS formation was quantified from a DCF standard curve, and data are expressed as pmol DCF formed/min/mg protein.

Western blot analysis

Western blotting analysis was performed to semi-quantitatively measure targeted proteins. In brief, the cellular or tissue lysates were prepared, and protein concentrations were determined using a bicinchoninic acid assay kit (Thermo Fisher Scientific, Inc., Waltham, MA, USA). Cell lysates were separated by 10% SDS-PAGE and transferred to polyvinylidene fluoride membranes. Blots were blocked with 4% BSA for 1 h at room temperature and then incubated with antibodies against NOX4 (1:1000, Abcam, Cambridge, MA, USA), Bax (1:1000, Abcam, Cambridge, MA, USA), Bcl-2 (1:1000, Abcam, Cambridge, MA, USA), cytochrome c (cyt-c, 1:1000, Abcam, Cambridge, MA, USA), cleaved poly ADP-ribose polymerase (PARP, 1:1000, Abcam, Cambridge, MA, USA), phosphorylated Akt (p-Akt, 1:1000, Abcam, Cambridge, MA, USA), Akt (Akt, 1:1500, Abcam, Cambridge, MA, USA), p-ERK (1:1000, Abcam, Cambridge, MA, USA), ERK (1:1500, Abcam, Cambridge, MA, USA), p-p65 (1:1000, Abcam, Cambridge, MA, USA), and p65 (1:1000, Abcam, Cambridge, MA, USA). After being washed three times, the blots were incubated with peroxidase-conjugated secondary antibody for 1 h at

room temperature, and finally, the bands were visualized by enhanced chemiluminescence gel imaging system, and semi-quantitatively analyzed by Image J software.

In vivo tumor xenograft study

The present animal study was approved by animals' care and use of ethics committee of Anhui provincial Cancer Hospital and carried out in accordance with the U.K. Animals (Scientific Procedures) Act, 1986 and associated guidelines. Male BALB/c nude mice (6 weeks old) were purchased from the Beijing Vital River Laboratory Animal Technology Co., Ltd. (Beijing, China). Animals were housed in a temperature-controlled room with a 12 h light/12 h dark cycle and provided with autoclaved chow and water *ad libitum*. SW1353 cells or shRNA transfected SW1353 cells (5×10^6 cells in 100 μ l) were injected subcutaneously into the flanks of nude mice, and tumors were allowed to develop for 14 days until they reached a size of approximately 100 mm³. Animals were divided into control group, cisplatin group (5 mg/kg, intragastric administration), GKT137831 group (50 mg/kg, intragastric administration), shRNA control group and NOX4 shRNA group. The mice were treated with vehicle or medicine for 14 days. The volume of implanted tumor of mice was measured twice a week with a caliper, using the formula (width² × length)/2. At the end of the study, all mice were killed, and the tumors were surgically excised, weighed and stored for further use.

Immunohistochemistry detection

Immunohistochemical (IHC) staining of tissue sections were performed using the manufacturer's standard protocols (Beyotime, Haimen, China). Briefly, sections were deparaffinized, and hydrated in a graded alcohol series. The protein reacted with antibody of NOX4 overnight at 4°C. Finally, the slides were incubated for 5 min with chromogen 3,3'-diaminobenzidine tetrahydrochloride. The level of NOX4 was analyzed by a pathologist according to the positive staining area.

Statistical analysis

The data are represented as the mean \pm standard deviation. Statistical analysis between groups was performed using one-way analysis of variance and Dunnett's

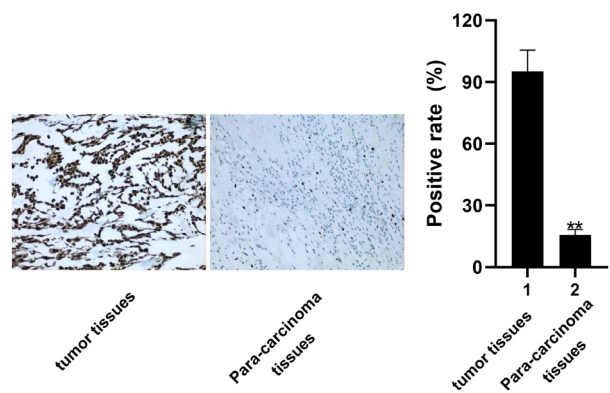


Figure 1. Representative images of NOX4 immunohistochemical staining of patients with conventional chondrosarcoma. Numerous positive cytoplasmic NOX4 staining was observed in the tumor samples, but not in the para-carcinoma samples. Results are expressed as the mean \pm S.D. ** $P < 0.01$ compared with tumor samples.

tests (SPSS15.0, SPSS Inc., Chicago, IL, USA). Differences were considered statistically significant at $P < 0.05$.

RESULTS

NOX4 overexpressed in chondrosarcoma

As shown in Table 1 and Fig. 1, 40 pairs of chondrosarcoma specimens were collected, and NOX4 expression in the tumor sites was detected and compared with that in para-carcinoma sites *via* IHC assay. The data in Fig. 1 has shown that NOX4 expression was significantly increased in the tumor tissue compared with those in the para-carcinoma ($P < 0.01$). NOX4 was lightly expressed in the cytoplasm and nuclei of para-carcinoma sample, however, high staining was observed in the cytoplasm and nuclei of most tumor samples. We analyzed clinicopathologic parameters of the patients and then divided them into two groups based on the NOX4 expression. The result is summarized in Table 1. Briefly, it was interesting to find that NOX4 levels were correlated with histological grade and MSTS stage in patients.

Table 1. Association between clinicopathologic parameters and NOX4 levels in chondrosarcoma

Characteristics	Numbers		P value
	NOX4 high	NOX4 low	
Age (years)			
> or= 40	12	11	> 0.05
<40	8	9	
Gender			
Male	9	13	> 0.05
Female	11	7	
Anatomical Location			
Limb bone	14	10	> 0.05
Axial bone	6	10	
Histological Grade			
Well/moderate	16	7	<0.01
Poor	4	13	
MSTS Stage			
IA + IB	5	14	<0.01
IIA + IIB	15	6	

$P < 0.05$ statistically significant difference; Musculoskeletal Tumor Society: MSTS

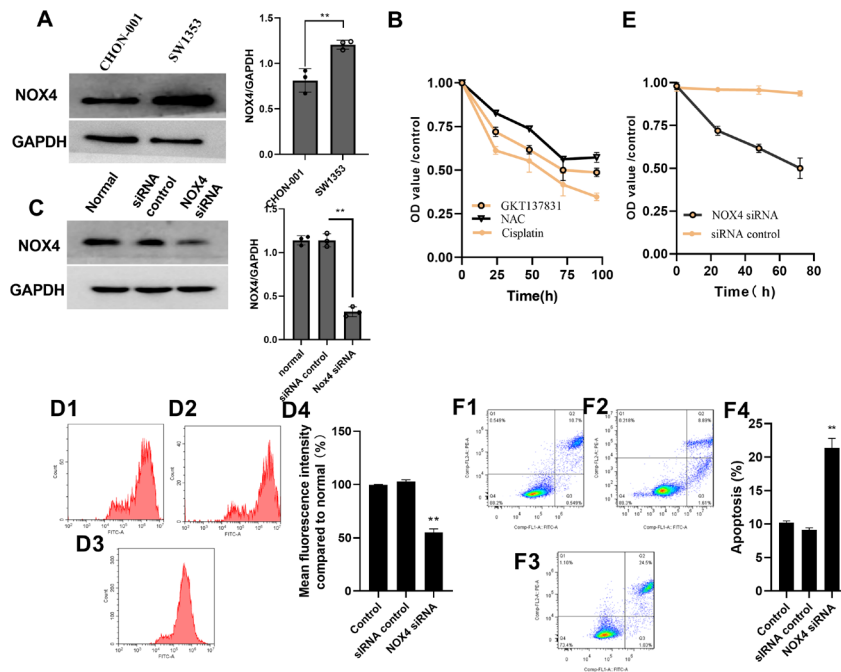


Figure 2. Depletion of NOX4 inhibits chondrosarcoma cell line SW1353 viability. (A) NOX4 levels in cell line SW1353 and chondrocytes CHON-001 were evaluated by western blotting, ** $P < 0.01$ compared with CHON-001 group; (B) SW1353 was treated with 5 μ M NAC, 1 μ M GKT137831 and 1 μ M cisplatin for 96h. The viability of cells was determined by MTT assay; (C) NOX4 was knocked down in SW1353 by siRNA interference; (D) ROS generation of SW1353 (D1), siRNA control (D2) and siRNA NOX4 (D3) was measured by FACS analysis using DCFH-DA, and results were shown in D4; (E) Viability of NOX4 silenced SW1353 was determined by MTT assay; (F) Apoptosis of NOX4 siRNA transfected cells were detected by propidium iodide/annexin V-FITC dual dying. F1: SW1353; F2: siRNA control; F3: siRNA NOX4; Results are expressed as the mean \pm S.D. ** $P < 0.01$ compared with siRNA control group.

NOX4 mediated viability and apoptosis of chondrosarcoma cell line SW1353

Expression of NOX4 was measured in chondrosarcoma cell line SW1353 and chondrocytes cell line CHON-

001. Figure 2A has shown that NOX4 expression was significantly higher in SW1353 than in CHON-001 cells. We used antioxidants NAC and NOX4 specific inhibitor GKT137831 to verify the effect of NOX4 on cell viability. The data in Fig. 2B has shown that SW1353 vi-

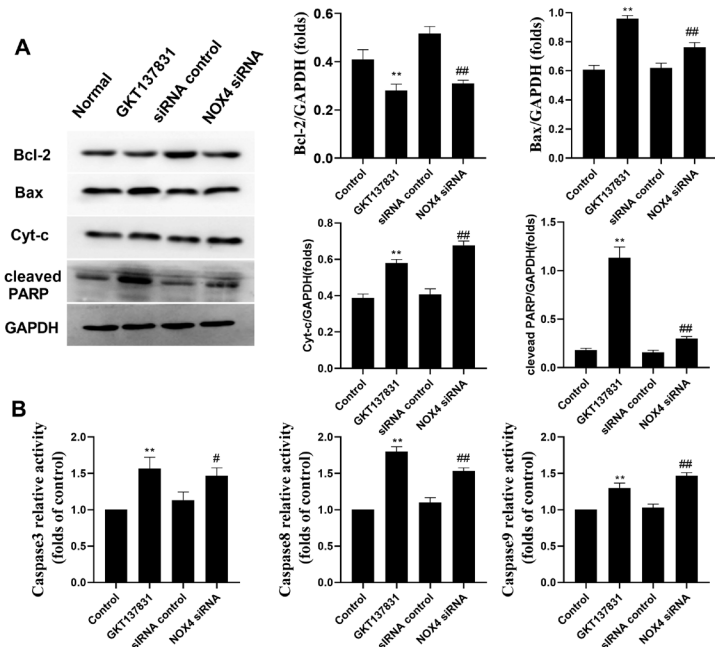


Figure 3. Depletion and inhibition of NOX4 mediates activation of Caspases and expression of apoptotic related proteins. (A) SW1353 were treated with 1 μ M GKT137831 or transfected by NOX4 siRNA for 48 h, and expression of apoptotic related proteins was evaluated by western blotting analysis; (B) caspases activities were measured by commercial kits. Results are expressed as the mean \pm S.D. ** $P < 0.01$ compared with control group; * $P < 0.05$, ## $P < 0.01$ compared with siRNA control group.

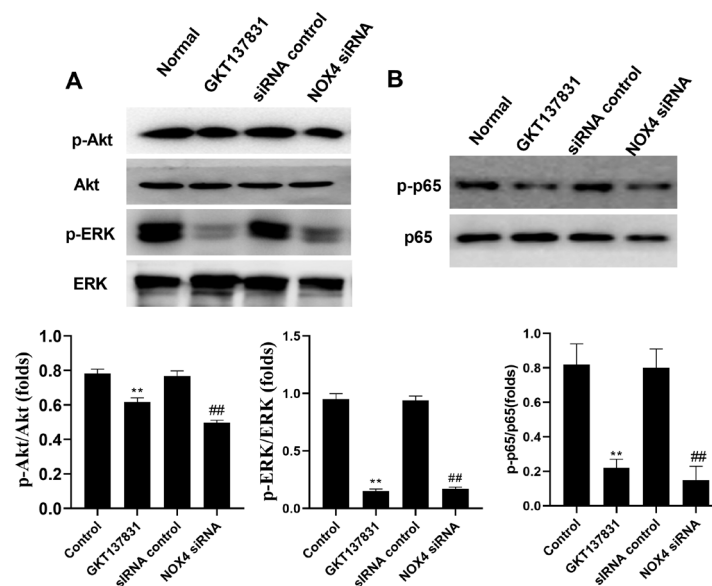


Figure 4. Depletion and inhibition of NOX4 decrease the expression of pro-survival proteins.

SW1353 was treated with 1 μ M GKT137831 or transfected by NOX4 siRNA for 48 h. Pro-survival protein p-Akt, Akt, p-ERK, ERK (A), p-p65 and p65 (B) were evaluated by western blotting analysis. Results are expressed as the mean \pm S.D. ** P <0.01 compared with control group; ## P <0.01 compared with siRNA control group.

ability was inhibited by GKT137831 as well as NAC in a time-dependent manner. To further disclose bio-function and effect of NOX4 on cells viability, NOX4 knock-down cell model was developed in SW1353, and changes in the expression of NOX4 and ROS generation were verified by western blotting and flow cytometry analysis (Fig. 2C–2D, P <0.01). As seen in Fig. 2E–2F, cell viability and apoptotic death in the NOX4 depletion group was significantly attenuated and enhanced, respectively, compared with the control group (P <0.01).

Blocked or silenced NOX4 activated apoptotic related pathway in SW1353

ROS mediates activation of apoptotic related proteins (Bedard & Krause, 2007). Therefore, we measured the change in the expression of cyt-c and Bcl-2 family proteins. As shown in Fig. 3A, NOX4 knockdown by NOX4 siRNA or functional inhibition by GKT137831 greatly increased cytosolic cyt-c, Bax and cleaved-PARP compared with that in the control group. On the other hand, treatment of the cells with GKT137831 or siRNA NOX4 decreased level of Bcl-2 (P <0.01). Moreover, we have observed NOX4 siRNA and GKT137831 greatly increased activity of caspases family members (caspase-3, caspase-8 and caspase-9) as well.

Blocked or silenced NOX4 inhibited activation of pro-survival proteins in SW1353

Pro-survival protein Akt, ERK and NF- κ B are mediated by ROS as well (Coso *et al.*, 2012). Therefore, we further measured the change in expression of p-Akt, Akt, p-ERK, ERK, p-p65 and p65 by western blot analysis. As shown in Fig. 4A, the group that received NOX4 siRNA or GKT137831 showed decreased ratios of p-Akt/Akt and p-ERK/ERK compared with control group (P <0.01). Moreover, as can be seen from the results present in Fig. 4B, p-p65/p65 was markedly decreased in cells that received NOX4 siRNA or GKT137831 (P <0.01). Therefore, it is suggested that NOX4 mediated SW1353 apoptosis may occur through the regulation of pro-survival proteins.

Blocked or silenced NOX4 effectively inhibited growth of chondrosarcoma in vivo

On the basis of NOX4 mediated pro-apoptotic effect *in vitro*, we further verified whether blocking or silencing NOX4 could possess an anti-chondrosarcoma action. As shown in Fig. 5A–B, in mice injected with NOX4 shRNA transfected cells, the tumor size and weight were significantly smaller than that of shRNA control group (P <0.01). Moreover, in the mice treated with GKT137831 or positive drug Cisplatin, the tumor size and weight were significantly smaller than that of control group as well (P <0.01). Further *ex vivo* analysis of tumors excised from mice was conducted (Fig. 5C–D), and we confirmed that NOX4 expression and ROS production were effectively reduced by treatment with NOX4 shRNA or GKT137831 (P <0.01). As seen in Fig. 6, increased expression of Cyt-c, Bax, cleaved-PARP and decreased level of Bcl-2 were shown in GKT137831/NOX4shRNA groups compared with control group (P <0.01). Moreover, we found that p-Akt/Akt, p-ERK/ERK and p-p65/p65 ratios in GKT137831/NOX4 shRNA groups were remarkably decreased compared with control group (P <0.01).

DISCUSSION

In recent years, more and more investigations focus on tumor prevention based on inhibiting oxidative stress (Klaunig, 2018). Recent investigations have implicated various NOX isoforms in pathological processes of malignant tumor. For instance, it has been reported that up-regulated NOX1 expression in gallbladder cancer associated fibroblasts predicts a poor prognosis (Wang *et al.*, 2019), and NOX2 expressed in endosomes promotes cell proliferation and prostate tumour development (Harrison *et al.*, 2018). However, little is known about the role of NOX in the development of chondrosarcoma. In previous studies (Drevet *et al.*, 2018; Wegner & Haudenschild, 2020; Lei *et al.*, 2019), it has been reported that among 7 NADPH oxidases expressed in humans, NOX4 is the sole isoform present in human primary chondro-

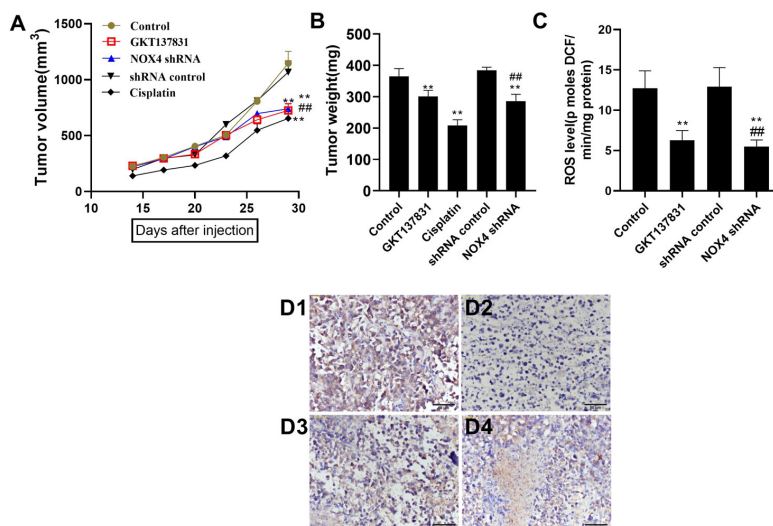


Figure 5. Depletion or inhibition of NOX4 abolishes growth of chondrosarcoma xenografts in mice.

Nude mice bearing tumor xenografts were injected intraperitoneally with vehicle or GKT137831. (A–B) Tumor volumes and weight were measured; (C) ROS levels were measured based on the oxidation of DCFH-DA to DCF in the tumor samples; (D) Immunostaining detection was used to examine NOX4, in which D1 represent control mice, D2 represent GKT137831 treated mice; D3 represent shRNA control mice and D4 represent NOX4 shRNA treated mice. Results are expressed as the mean \pm S.D. ** P <0.01 compared with control group; ## P <0.01 compared with shRNA control group.

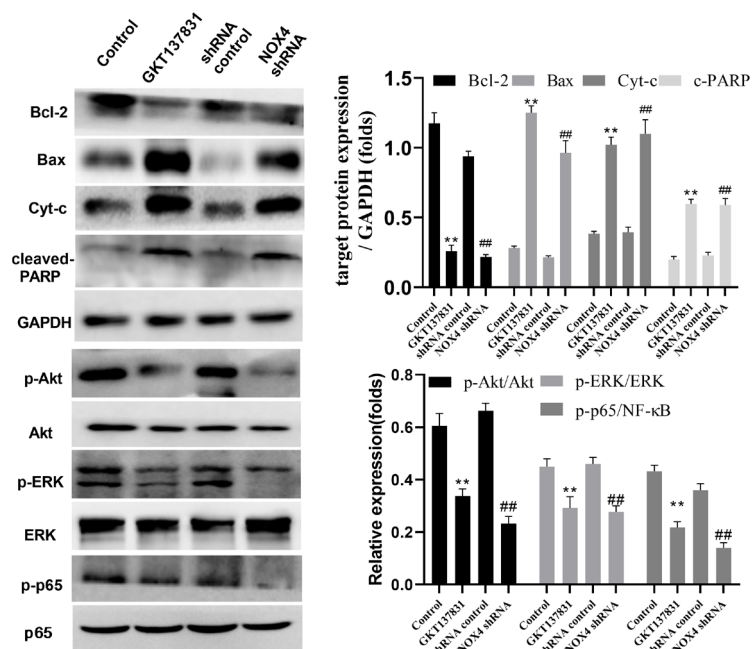


Figure 6. Depletion or inhibition of NOX4 mediates activation of apoptotic related proteins in vivo.

Protein in the tumor was examined by western blotting assay. Results are expressed as the mean \pm S.D. ** P <0.01 compared with control group; ## P <0.01 compared with shRNA control group.

cytes. Moreover, NOX4 has been involved in the degradation of articular extracellular matrix. Therefore, we suspect that NOX4 plays an important biological effect in the development of chondrosarcoma.

In the present study, we collected clinical samples from chondrosarcoma patients who received surgical operation and found that the NOX4 expression significantly increased in tumor compared with those in paracarcinoma samples. To the best of our knowledge, this was the first time to semi-quantitatively analyze NOX4 in chondrosarcoma. Further study was conducted to

investigate the effect of NOX4 inhibitor on viability of SW1353. In previous studies, diphenylene iodonium (DPI) has been extensively used to inhibit activity of NOX4 because of its powerful inhibition (Yao *et al.*, 2017; Hwang *et al.*, 2020). However, several studies (Rand & Li, 1993; Castro *et al.*, 2009) found that DPI is a non-selective NOX4 inhibitor with mild inhibition on nitric oxide synthase and xanthine oxidase. GKT137831 is a specific inhibitor of NOX4 with high selectivity. Therefore, we used GKT137831 to treat SW1353. In the current study, GKT137831 induced an inhibitory ef-

fect on viability of SW1353 in a time-dependent manner and has shown a similar effect to that of positive medicine cisplatin. Additionally, to identify the potential role of NOX4 in the viability of chondrosarcoma cells, we transfected SW1353 with NOX4 siRNA and then validated transfection efficiency by western blotting and ROS generation. Our results revealed that prevention of NOX4 induced a significant increase in the proliferation inhibition and apoptosis of the cells. More importantly, animal studies demonstrated that NOX4 knockdown or function inhibition by GKT137831 significantly impaired growth of the tumor. In line with previous reports regarding the role of NOX4 in the development of malignant tumors (Tang *et al.*, 2018; Li *et al.*, 2014), NOX4 is a promising pharmacological target for chondrosarcoma prevention.

NOX4 generated ROS has a close relationship with intrinsic apoptosis pathway (Coso *et al.*, 2012). In brief, the status of intrinsic pathway is governed by interplay between pro- and anti-apoptosis members of the Bcl-2 family, including Bcl-2 and Bax. They keep cell death in check by restraining the pro-apoptotic protein Bax, which are the final arbiters of cell death. When activated, Bax triggers mitochondrial damage, allowing release of cyt-*c* and caspases activation (Franklin *et al.*, 2011; Jendrossek *et al.*, 2012). Here, we found that NOX4 knockdown by siRNA intervene, or function inhibited by GKT137831 significantly activate mitochondrial related apoptosis pathway, which was evidenced by increased expression of Bax, cyt-*c*, decreased level of Bcl-2, and activation of caspase-3, caspase-8 and caspase-9. In agreement with these observations, we noted similar results *in vivo* as well.

Some second messengers (such as protein kinases) and the third messenger are well known downstream of ROS. The first one is Akt, and it is a serine threonine kinase that mediates various biological functions, such as cell proliferation, survival, glucose metabolism, protein synthesis, genome stability, and inhibition of apoptosis in response to different growth factors and extracellular stimuli. Akt inactivates pro-apoptotic proteins (Bcl-2 antagonist of cell death and procaspase-9) to block apoptosis (Shariati & Meric-Bernstam, 2019; Downward, 2004). The second one is ERK. RAS-RAF-MEK-ERK pathway is the most well-studied of the mitogen-activated protein kinase cascades and is critical for cell proliferation, differentiation, and survival. Activation of receptor tyrosine kinases by growth factors and extracellular signals results in sequential activation of RAS, RAF, MEK, and finally ERK, which activates numerous transcription factors and facilitates oncogenesis in the case of aberrant pathway activation (Asati *et al.*, 2016; Barbosa *et al.*, 2021). The third one is NF- κ B p65, and it is a ubiquitous transcription factor that mediates cytoplasmic/nuclear signaling pathway and regulates gene expression of various cytokines, cytokine receptors, which affected cell proliferation, differentiation, migration, and angiogenesis in tumor cells (Soleimani *et al.*, 2020). To disclose underlying mechanism involved in the NOX4 mediated apoptosis of chondrosarcoma cells, we focused on the effect of blocking NOX4 on activity of Akt, ERK as well as NF- κ B. Here, we showed that NOX4 knockdown or functional inhibition both induced decreased levels of p-Akt, p-ERK and p-p65 *in vivo* and *in vitro*. These results, together with impaired tumorigenic capacity of NOX4-silenced SW1353 in mice, suggest that NOX4 acts as a growth promoter in chondrosarcoma.

CONCLUSIONS

Our results suggest that NOX4 mediates proliferation and apoptosis of chondrosarcoma cells. Moreover, inhibition of NOX4 induced tumor growth may be via activation of intrinsic apoptosis pathway and regulation of pro-survival factors Akt, ERK and NF- κ B. NOX4 is a novel and promising target for the drug development against chondrosarcoma.

Declarations

Acknowledgements. The current study did not receive any Financial Support.

Ethical Issue. The present study was approved by the Ethics Committee of Anhui Provincial Cancer Hospital and conducted along with the ethical standards of the Helsinki Declaration of 1975, as revised in the year 2000.

Conflict of interest. The authors declare that there are no conflicts of interest.

REFERENCES

- Asati V, Mahapatra DK, Bharti SK (2016) PI3K/Akt/mTOR and Ras/Raf/MEK/ERK signaling pathways inhibitors as anticancer agents: Structural and pharmacological perspectives. *Eur J Med Chem* **109**: 314–341. <https://doi.org/10.1016/j.ejmech.2016.01.012>
- Barbosa R, Acevedo LA, Marmorstein R (2021) The MEK/ERK network as a therapeutic target in human cancer. *Mol Cancer Res* **19**: 361–374. <https://doi.org/10.1158/1541-7786.MCR-20-0687>
- Bedard K, Krause KH (2007) The NOX family of ROS-generating NADPH oxidases: physiology and pathophysiology. *Physiol Rev* **87**: 245–313. <https://doi.org/10.1152/physrev.00044.2005>
- Castro GD, Costantini MH, Castro JA (2009) Rat ventral prostate xanthine oxidase-mediated metabolism of acetaldehyde to acetyl radical. *Hum Exp Toxicol* **28**: 203–208. <https://doi.org/10.1177/0960327109105406>
- Chen X, Cao X, Xiao W, Li B, Xue Q (2020) PRDX5 as a novel binding partner in Nrf2-mediated NSCLC progression under oxidative stress. *Aging (Albany NY)* **12**: 122–137. <https://doi.org/10.18632/aging.102605>
- Chen X, Zhao Y, Luo W, Chen S, Lin F, Zhang X, Fan S, Shen X, Wang Y, Liang G (2020) Celastrol induces ROS-mediated apoptosis via directly targeting peroxiredoxin-2 in gastric cancer cells. *Theranostics* **10**: 10290–10308. <https://doi.org/10.7150/thno.46728>
- Coso S, Harrison I, Harrison CB, Vinh A, Sobey CG, Drummond GR, Williams ED, Selemidis S (2012) NADPH oxidases as regulators of tumor angiogenesis: current and emerging concepts. *Antioxid Redox Signal* **16**: 1229–1247. <https://doi.org/10.1089/ars.2011.4489>
- Downward J (2004) PI 3-kinase, Akt and cell survival. *Semin Cell Dev Biol* **15**: 177–182. <https://doi.org/10.1016/j.semcdb.2004.01.002>
- Drevet S, Gavazzi G, Grange L, Dupuy C, Lardy B (2018) Reactive oxygen species and NADPH oxidase 4 involvement in osteoarthritis. *Exp Gerontol* **111**: 107–117. <https://doi.org/10.1016/j.exger.2018.07.007>
- Franklin JL (2011) Redox regulation of the intrinsic pathway in neuronal apoptosis. *Antioxid Redox Signal* **14**: 1437–1448. <https://doi.org/10.1089/ars.2010.3596>
- Gelderblom H, Hogendoorn PC, Dijkstra SD, van Rijswijk CS, Krol AD, Taminiau AH, Bovée JV (2008) The clinical approach towards chondrosarcoma. *Oncologist* **13**: 320–329. <https://doi.org/10.1634/theoncologist.2007-0237>
- Harrison IP, Vinh A, Johnson IRD, Luong R, Drummond GR, Sobey CG, Tiganis T, Williams ED, O'Leary JJ, Brooks DA, Selemidis S (2018) NOX2 oxidase expressed in endosomes promotes cell proliferation and prostate tumour development. *Oncotarget* **9**: 35378–35393. <https://doi.org/10.18632/oncotarget.26237>
- Hwang CY, Han YH, Lee SM, Cho SM, Yu DY, Kwon KS (2020) Sestrin2 attenuates cellular senescence by inhibiting NADPH oxidase 4 expression. *Ann Geriatr Med Res* **24**: 297–304. <https://doi.org/10.4235/agmr.20.0051>
- Jendrossek V (2012) The intrinsic apoptosis pathways as a target in anticancer therapy. *Curr Pharm Biotechnol* **13**: 1426–1438. <https://doi.org/10.2174/138920112800784989>
- Klaunig JE (2018) Oxidative stress and cancer. *Curr Pharm Des* **24**: 4771–4778. <https://doi.org/10.2174/1381612825666190215121712>
- Lee D, Xu IM, Chiu DK, Leibold J, Tse AP, Bao MH, Yuen VW, Chan CY, Lai RK, Chin DW, Chan DF, Cheung TT, Chok SH, Wong CM, Lowe SW, Ng IO, Wong CC (2019) Induction of oxida-

- tive stress through inhibition of thioredoxin reductase 1 is an effective therapeutic approach for hepatocellular carcinoma. *Hepatology* **69**: 1768–1786. <https://doi.org/10.1002/hep.30467>
- Lee HP, Li TM, Tsao JY, Fong YC, Tang CH (2012) Curcumin induces cell apoptosis in human chondrosarcoma through extrinsic death receptor pathway. *Int Immunopharmacol* **13**: 163–169. <https://doi.org/10.1016/j.intimp.2012.04.002>
- Lei C, Wu S, Wen C, Li Y, Liu N, Huang J, Li L, Fu M, Liu J (2019) Zafirlukast attenuates advanced glycation end-products (AGEs)-induced degradation of articular extracellular matrix (ECM). *Int Immunopharmacol* **68**: 68–73. <https://doi.org/10.1016/j.intimp.2018.12.056>
- Li Y, Han N, Yin T, Huang L, Liu S, Liu D, Xie C, Zhang M (2014) Lentivirus-mediated Nox4 shRNA invasion and angiogenesis and enhances radiosensitivity in human glioblastoma. *Oxid Med Cell Longev* **2014**: 581732. <https://doi.org/10.1155/2014/581732>
- MacDonald IJ, Lin CY, Kuo SJ, Su CM, Tang CH (2019) An update on current and future treatment options for chondrosarcoma. *Expert Rev Anticancer Ther* **19**: 773–786. <https://doi.org/10.1080/14737140.2019.1659731>
- Rand MJ, Li CG (1993) The inhibition of nitric oxide-mediated relaxations in rat aorta and anococcygeus muscle by diphenylene iodonium. *Clin Exp Pharmacol Physiol* **20**: 141–148. <https://doi.org/10.1111/j.1440-1681.1993.tb01661.x>
- Ratcliff BB, Abdulmahdi W, Pawar R, Wolin MS (2016) Oxidant mechanisms in renal injury and disease. *Antioxid Redox Signal* **25**: 119–146. <https://doi.org/10.1089/ars.2016.6665>
- Shariati M, Meric-Bernstam F (2019) Targeting AKT for cancer therapy. *Expert Opin Investig Drugs* **28**: 977–988. <https://doi.org/10.1080/13543784.2019.1676726>
- Soleimani A, Rahmani F, Ferns GA, Ryzhikov M, Avan A, Hassanian SM (2020) Role of the NF- κ B signaling pathway in the pathogenesis of colorectal cancer. *Gene* **726**: 144132. <https://doi.org/10.1016/j.gene.2019.144132>
- Tang CT, Lin XL, Wu S, Liang Q, Yang L, Gao YJ, Ge ZZ (2018) NOX4-driven ROS formation regulates proliferation and apoptosis of gastric cancer cells through the GIL1 pathway. *Cell Signal* **46**: 52–63. <https://doi.org/10.1016/j.cellsig.2018.02.007>
- Wang FT, Hassan M, Ansari KH, Xu GL, Li XP, Fan YZ (2019) Up-regulated NOX1 expression in gallbladder cancer-associated fibroblasts predicts a poor prognosis. *Oncol Rep* **42**: 1475–1486. <https://doi.org/10.3892/or.2019.7249>
- Wegner AM, Haudenschild DR (2020) NADPH oxidases in bone and cartilage homeostasis and disease: A promising therapeutic target. *J Orthop Res* **38**: 2104–2112. <https://doi.org/10.1002/jor.24693>
- Yao M, Gao F, Wang X, Shi Y, Liu S, Duan H (2017) Nox4 is involved in high glucose-induced apoptosis in renal tubular epithelial cells via Notch pathway. *Mol Med Rep* **15**: 4319–4325. <https://doi.org/10.3892/mmr.2017.6516>



OPEN ACCESS

EDITED BY

Janka Vašková,
University of Pavol Jozef Šafárik,
Slovakia

REVIEWED BY

Beata Hukowska-Szemutowicz,
University of Szczecin, Poland
Jozef Židzik,
University of Pavol Jozef Šafárik,
Slovakia

*CORRESPONDENCE

Monika Sarnat-Kucharczyk,
✉ msarnat@sum.edu.pl

RECEIVED 25 July 2024

ACCEPTED 09 October 2024

PUBLISHED 18 October 2024






CITATION

Wilczyński T, Zalejska-Fiolka J,
Sapeta-Wieckowska S,
Sarnat-Kucharczyk M and Rokicki W
(2024) *In situ* oxidative stress in patients
with epiretinal membrane.
Acta Biochim. Pol 71:13581.
doi: 10.3389/abp.2024.13581

COPYRIGHT

© 2024 Wilczyński, Zalejska-Fiolka,
Sapeta-Wieckowska, Sarnat-
Kucharczyk and Rokicki. This is an
open-access article distributed under
the terms of the [Creative Commons
Attribution License \(CC BY\)](#). The use,
distribution or reproduction in other
forums is permitted, provided the
original author(s) and the copyright
owner(s) are credited and that the
original publication in this journal is
cited, in accordance with accepted
academic practice. No use, distribution
or reproduction is permitted which does
not comply with these terms.

In situ oxidative stress in patients with epiretinal membrane

Tomasz Wilczyński ¹, Jolanta Zalejska-Fiolka ²,
Sabina Sapeta-Wieckowska ¹,
Monika Sarnat-Kucharczyk ^{1,3*} and Wojciech Rokicki ^{1,3}

¹Department of Ophthalmology, Professor K. Gibinski University Clinical Center, Medical University of Silesia, Katowice, Poland, ²Department of Biochemistry, Faculty of Medical Sciences in Zabrze, Medical University of Silesia, Zabrze, Poland, ³Department of Ophthalmology, Faculty of Medical Sciences in Katowice, Medical University of Silesia, Katowice, Poland

Context: Oxidative stress is an important factor for vitreomacular interface disease development in a theoretical model.

Purpose: The aim of the study was to evaluate the correlation between oxidative stress in the human epiretinal membrane (ERM) and retinal morphological changes.

Material and methods: The study included patients scheduled for vitrectomy with epiretinal membrane removal. LogMAR best corrected visual acuity was assessed and optical coherence tomography was performed. Patients were divided into three groups: Type 1 – epiretinal membrane with premacular fibrosis; type 2 – epiretinal membrane with co-existing layer hole; and type 3 – ERM with co-existing full-thickness macular hole. During vitrectomy, epiretinal membranes were collected. Total oxidant status was determined by an automated colorimetric method in homogenates of epiretinal membrane.

Statistical analysis: The Mann-Whitney U test, Kruskal-Wallis test and Spearman linear correlation analysis were used. Statistical significance was set with a level of $\alpha = 0.05$.

Results: Twenty-one Caucasian women (60%) and 14 men (40%) were included in the study. The average age of participants was 74.7 years (95% CI: 71.13–75.45). The mean best corrected visual acuity LogMAR value in the group was 0.8 (95% CI: 0.9–0.7). The mean ratio of total oxidant status to protein level in the collected samples was 0.161 (95% CI: 0.08–0.23) $\mu\text{mol/mg}$ of protein. No correlation was found between total oxidant status and the degree of morphological retinal changes.

Conclusion: The study found no significant correlation between the level of oxidative stress in epiretinal membrane and retinal morphological changes.

KEYWORDS

oxidative stress, epiretinal membrane, retina, total oxidant status, macular hole

Introduction

Epiretinal membrane (ERM) is a disease occurring predominantly among patients over 50 years old. It may originate from disorders such as retinal tear, branch or central retinal vein occlusion, and diabetic retinopathy. However, it may also occur without a known reason, and then is termed idiopathic. Previously published data on ERM prevalence in ethnic and age groups vary in the range 2%–29% (Stevenson et al., 2016; Bu et al., 2014; Xiao et al., 2017).

Idiopathic ERM typically consists of a cellular part on the vitreous chamber side and a layer of extracellular matrix (Bu et al., 2014). The exact etiology of ERM is unknown. The cellular layer is mainly composed of retinal glial cells, which have probably migrated to its surface through microdamage of the internal limiting membrane, secondary to posterior vitreous detachment (PVD). Vitreous cortex hyalocytes are the second significant group of cells remaining on the internal limiting membrane (ILM) surface in the course of PVD. Moreover, the presence of macrophages and fibroblasts is found. Myofibroblasts are an important cellular ingredient, originating through the differentiation of glial cells or hyalocytes. They are responsible for formation of a significant part of the ERM extracellular matrix and in further stages for its contraction (Chen and Lee, 2008; Snead et al., 2004; Smiddy et al., 1989).

Another theory of ERM formation is the RPE cells migration through hidden breaks into the inner retina. However, there is currently no direct evidence to support this theory (Wang et al., 2015). Next possible theory suggests that other cell types, such as glial cells, may transform into RPE cells. These GFAP-positive cells could originate from hyalocytes or Müller cells (Bringmann and Wiedemann, 2009; Zhao et al., 2013).

Cellophane maculopathy is the early, asymptomatic stage of idiopathic ERM where the retinal architecture is not considerably affected. In advanced stages the growth and shrinkage of membranes result in retinal fold formation, its swelling, and retinoschisis, and can lead to the formation of holes. The condition is described as macular pucker or premacular fibrosis (Xiao et al., 2017). The coexistence of ERM and lamellar or full-thickness holes may be related to oxidative stress (Chen and Lee, 2008).

Metabolic processes allowing for the correct functioning of cells are largely based on oxidation reactions. They naturally result in the creation of the reactive oxygen species (ROS) which play a crucial role in numerous physiological processes such as the functioning of the immune system, cellular growth, proliferation, differentiation or apoptosis (Wert et al., 2018). An excess of ROS has a highly toxic impact on cells. Thus, its production is balanced predominantly by the activity of anti-oxidation mechanisms. The natural system designed to balance the toxic influence of free oxygen radicals is based on a system of a dozen enzymes. An excess of these reactive oxygen species may be reduced by two anti-oxidation systems, enzymatic and non-

enzymatic (Wert et al., 2018; Beyazyıldız et al., 2013; Erel, 2005; Altinisik et al., 2018).

Oxidative stress is an imbalance between reactive oxygen species production and their neutralization capabilities (Altinisik et al., 2018).

Rokicki et al. (2016) reported an important association between oxidative stress and glaucoma. Other studies have described the connection of oxidative stress with retinal diseases such as retinitis pigmentosa, retinal diabetes complications as well as retinal vessel diseases, e.g., central retinal vein occlusion (Erel, 2005; Martínez-Fernández de la Cámara et al., 2013; Guidry et al., 2003).

Retinal photoreceptor cells are a cellular population which is one of the most sensitive to oxidative stress in the body (Guidry et al., 2003). This particular vulnerability results from the fact that the retina is one of the most metabolically active human tissues additionally subjected to constant ultraviolet radiation exposure. As a result it produces particularly large amounts of ROS. Moreover, due to its structure and limited contact with the vascular system, the removal of free radicals is particularly ineffective. This is primarily related to the internal retinal layers where the maximization of tissue transparency takes place at the expense of vascularization. It is associated with the most intensive ROS production (Wert et al., 2018; Guidry et al., 2003). Internal layers of the retina are rich in extracellular free radicals, scavengers of vitreous cortex, and their damage may lead to the development of vitreomacular interface diseases (Kohno et al., 2009).

Total oxidant status (TOS) is one of the methods of describing the oxidative stress value, expressing the total oxidation activity of the tested material (Altinisik et al., 2018).

The objective of our research was to assess *in situ* oxidative stress in human tissues, in the direct vicinity of internal retinal layers. For the purposes of the study, it was hypothesized that the presence of lamellar and full-thickness holes is associated with greater oxidative stress than the presence of ERM itself.

Material and methods

The ethics committee of the Medical University of Silesia, Katowice (permission number: KNW/0022/KB1/85/III/18/19) approved the study protocol. The study adhered to the tenets of the Declaration of Helsinki for experiments involving human tissue samples. Written informed consent was obtained from all patients after explanation of the nature and possible consequences of the study.

Posterior vitrectomy with removal of ERM and ILM around the macula was performed in 35 eyes from 35 patients. The first collected structure during the surgery was directed for the examination, with its character determined based on interoperative dying of the retina internal limiting membrane at least twice with the MembraneBlue Dual DORC dye as ERM or ERM/ILM complex collected *en bloc*.

The criteria for inclusion in the study group were: age 65–80 years, white race, patient eligibility for ERM and/or ILM removal, informed consent to the procedure, and written consent to participate in the study.

The exclusion criteria were metabolic and inflammatory diseases in medical history, features of active inflammation measured by C-reactive protein (CRP) activity, and obesity above BMI 29.99.

Depending on the pre-surgery retinal morphology the cases were divided into three types. Type 1 – patients with diagnosed ERM presence with premacular fibrosis (PMF), type 2 – patients with ERM with co-existing lamellar hole, type 3 – patients with ERM with co-existing full-thickness macular hole.

For each patient LogMAR best corrected visual acuity (BCVA) was assessed. Optical coherence tomography (Cirrus HD-OCT 5000, Carl Zeiss Meditec, Dublin, CA) was performed to assess the morphology and describe central retina thickness parameters.

Analysis of Total Oxidant Status (TOS) was performed in ERM homogenate and was conducted using a PerkinElmer automated analyzer (PerkinElmer, Waltham, MA, United States) in according to Erel (2005). This method excludes the influence of solution dilution on the TOS value. The assay is based on the oxidation of ferrous ion to ferric ion in the presence of various oxidant species in acidic medium. The change in color of the ferric ion by xylenol orange is measured as a change in absorbance at 560 nm. The automated analyzer Perkin Elmer was calibrated with hydrogen peroxide. The TOS value was expressed in $\mu\text{mol}/\text{mg}$ of protein.

Statistical data analysis was conducted using tools available in the Statistica v. 12.0 software. Quantitative variables are presented as the mean and 95% confidence interval. Statistical significance of differences in quantitative variables between two groups was estimated based on the Mann-Whitney U test and in the case of comparison of three groups the Kruskal-Wallis test. Spearman linear correlation analysis was used for the simple analysis of correlation between quantitative variables. The interpretation of results of simple statistical significance tests of differences and correlations was conducted with the adopted significance level $\alpha = 0.05$.

Results

The examined group consisted of 21 Caucasian women (60%) and 14 men (40%). The average age of participants in the whole group was 74.7 years (95% CI: 71.13–76.45). There were no statistically significant differences between the groups of men and women. Three groups were distinguished among the patients, based on the preoperative retinal morphology in OCT. Type 1 was represented by 18 people with a mean age of 74.11 (95% CI: 69.06–77.15); type 2 included 11 people, with a mean age of 75 (95% CI: 70.09–79.9); type 3 was represented by six people, with a mean age of 74.66 (95% CI: 66.99–82.34). Age differences among the groups were not statistically significant.

TABLE 1 Total oxidant status in groups.

Disease type	Parameter	Mean	95% CI
Type 1	TOS/protein [$\mu\text{mol}/\text{mg}$]	0.12	0.03–0.20
Type 2	TOS/protein [$\mu\text{mol}/\text{mg}$]	0.15	(–0.05) –0.37
Type 3	TOS/protein [$\mu\text{mol}/\text{mg}$]	0.28	0.09–0.47

The mean postoperative BCVA LogMAR value in the entire study group was 0.8 (95% CI: 0.9–0.7). For type 1 the mean BCVA was 0.8 (95% CI: 1.0–0.6), for type 2 the mean BCVA was 0.6 (95% CI: 0.9–0.5), for type 3 the mean BCVA was 1.4 (95% CI: 1.7–1.2). A statistically significant difference was found between types 3 and 2 ($p = 0.001$) and between types 3 and 1 ($p = 0.03$).

The average ratio of total TOS to protein level in the collected sample was 0.161 (95% CI: 0.08–0.23) $\mu\text{mol}/\text{mg}$ protein. The analysis by group showed no statistically significant differences. The p -value for comparisons between the three groups was 0.3. The values of average TOS in relation to the amount of material collected, divided into groups, are presented in Table 1. There was no statistically significant relationship between the age of participants and the tested parameters ($p > 0.05$). The highest TOS value was in group 3 and was 0.28 $\mu\text{mol}/\text{mg}$ protein. The mean TOS value in patients with ERM was 0.09 (95% CI: 0.03–0.15). However, the average TOS value in people with ERM/ILM was 0.17 (95% CI: 0.06–0.28). The p -value for the correlation between ERM and the ERM/ILM complex was 0.73.

The average value of central retinal thickness (CRT) in the entire group was 410.8 μm (95% CI: 373.74–447.85). When analyzing correlations with TOS parameters, protein concentration and age, no statistically significant correlations were observed. When divided into groups according to the type of disease, there was a statistically significant difference between the CRT value in patients with type 1 (460.22 μm) and type 3 disease (304.16 μm ; $p = 0.012$). Detailed parameters in the groups are presented in Table 2.

Discussion

To the best of our knowledge this is the first study to assess the total oxidant status *in vivo* in internal retinal layers and in ERM directly associated with them. It is also the first study to determine the oxidative stress level in eyes with ERM depending on their morphology and degree of central retinal deformation estimated in the OCT examination.

The retinal membranes (pathological structure) and the internal limiting membrane (one of the layers of the retina) are the material closest to the nervous tissue of the eye that can be collected and evaluated *in vivo* in the immediate vicinity of the macula. The collection of the above membranes is part of the surgical procedure and the resulting limitation is a negligible

TABLE 2 Central retinal thickness.

Disease type	Central retinal thickness – CRT (μm)	95% CI
Type 1	460.22	415.20–505.23
Type 2	388.09	448.99–287.00
Type 3	304.16	192.86–415.47

amount of material that is obtained for testing. In our study we decided to assess the correlation between morphological changes of the retina and TOS. Previous studies demonstrated that in patients with ERM the mean central retinal thickness significantly corresponds with visual acuity. This constitutes an objective and repetitive parameter obtained in the OCT examination and is the basis of ERM severity grading systems (Stevenson et al., 2016).

We did not detect a significant relationship between the amount of oxidative stress, expressed by TOS *in situ*, and the thickness of the retina in the place where the material for testing was taken. We also found no statistically significant differences between TOS in the case of the co-occurrence of lamellar or full-thickness holes in the central retina. The determined TOS values do not show any dependence on the severity of morphological changes in the retina.

The myofibroblasts in the ERM cell layer are responsible for its tendency to contract, resulting in the formation of holes in the retina and/or its wrinkle and edema. They are derived from differentiated retinal glial cells and hyalocytes of the posterior hyaloid membrane (Kohno et al., 2009; Abrahan et al., 2009).

Abrahan et al. (2009) observed *in vitro* the effect of oxidative stress on the differentiation and proliferation of retinal microglia and Müller cells. In our *in vivo* model, we examined only one parameter of oxidative stress at the time of an already developed ERM and an advanced disease process known as macular wrinkle or PMF. The small amount of material obtained during the surgical procedure did not allow for the determination of a greater number of markers of oxidative stress with the biochemical methodology applied in this study.

The influence of oxidative stress on the function of the retina *in vivo* in an animal study was demonstrated by Berkowitz (Berkowitz et al., 2019). They found damage to the retinal light response in mice with pharmacologically induced oxidative stress, regressing with administration of antioxidants. Although the reduction of oxidative stress in the animal model led to the improvement of the functional retina, the available human studies did not confirm the effect of orally administered antioxidants on the improvement of retinal morphology parameters in optical coherent tomography (Garcia-Medina et al., 2015).

Available *in vivo* studies on humans refer to single oxidative stress marker assessment in patients with diabetic retinopathy. Collected samples of vitreous body or secondary ERM were

compared with idiopathic ERM (Augustin et al., 1995; Lu et al., 2014).

When examining TOS, we did not find any relationship between the severity of changes in OCT and the state of oxidative stress in the retina. The advantage of our study is primarily the attempt to assess the state of oxidative stress *in situ*, which does not always correspond to the systemic state (Lavi et al., 2008; Davel et al., 2012). In our opinion, it gives a more precise picture of changes induced by oxidative stress in such specific oxygen conditions as the vitreoretinal region.

Study limitations

The main limitation of the study was the lack of measurement of TOS in both the ERM and the peripheral blood. However, due to the strong blood-retina barrier, oxidative stress in the eye may not reflect oxidative stress in the whole body.

The very strong point of this study is the measurement of oxidative stress *in vivo*, i.e., in the eye tissues, precisely in the ERM, and not using *in vitro* method. This pilot study included only 35 patients. A broader study is planned, including a larger group of patients, taking into account TOS parameters in both eye tissues and peripheral blood, and assessing their relationship.

Conclusion

The degree of epiretinal membrane does not directly depend on the state of oxidative stress.

Data availability statement

The raw data supporting the conclusions of this article will be made available by the authors, without undue reservation.

Ethics statement

The studies involving humans were approved by The Medical University of Silesia ethics committee, Katowice

(permission number: KNW/0022/KB1/85/III/18/19). The studies were conducted in accordance with the local legislation and institutional requirements. The participants provided their written informed consent to participate in this study. Written informed consent was obtained from the individual(s) for the publication of any potentially identifiable images or data included in this article.

Author contributions

TW—data collection, analysis and interpretation of the examinations. JZ-F—biochemical data analysis. SS-W—manuscript preparation, ophthalmic examinations interpretation, MS-K—manuscript preparation, analysis and interpretation of results, ophthalmic examinations interpretation. WR—study conception and design, data

collection, manuscript preparation. All authors contributed to the article and approved the submitted version.

Funding

The author(s) declare that financial support was received for the research, authorship, and/or publication of this article. The manuscript was supported by a research grant from the Medical University of Silesia (Grant No. PCN-1-138/K/0/K).

Conflict of interest

The authors declare that the research was conducted in the absence of any commercial or financial relationships that could be construed as a potential conflict of interest.

References

- Abraham, C. E., Insua, M. F., Politi, L. E., German, O. L., and Rotstein, N. P. (2009). Oxidative stress promotes proliferation and dedifferentiation of retina glial cells *in vitro*. *J. Neurosci. Res.* 87, 964–977. doi:10.1002/jnr.21903
- Altinisik, M., Koytak, A., Elbay, A., Toklu, E., Sezer, T., and Kocyigit, A. (2018). Oxidant-Antioxidant balance in the aqueous humor of patients with retinal vein occlusion. *Seminars Ophthalmol.* 33, 675–682. doi:10.1080/08820538.2017.1416412
- Augustin, A. J., Spitznas, M., Koch, F., Grus, F., and Böker, T. (1995). Indicators of oxidative tissue damage and inflammatory activity in epiretinal membranes of proliferative diabetic retinopathy, proliferative vitreoretinopathy and macular pucker. *Ger. J. Ophthalmol.* 4, 47–51.
- Berkowitz, B. A., Podolsky, R. H., Lins-Childers, K. M., Li, Y., and Qian, H. (2019). Outer retinal oxidative stress measured *in vivo* using QUEEnch-assISTed (QUEST) OCT. *Investig. Ophthalmol. Vis. Sci.* 60, 1566–1570. doi:10.1167/iov.18-26164
- Bayazıldız, E., Cankaya, A. B., Ergun, E., Anayol, M. A., Ozdamar, Y., Sezer, S., et al. (2013). Changes of total antioxidant capacity and total oxidant status of aqueous humor in diabetes patients and correlations with diabetic retinopathy. *Int. J. Ophthalmol.* 6, 531–536. doi:10.3980/j.issn.2222-3959.2013.04.23
- Bringmann, A., and Wiedemann, P. (2009). Involvement of Muller glial cells in epiretinal membrane formation. *Graefes Arch. Clin. Exp. Ophthalmol.* 247, 865–883. doi:10.1007/s00417-009-1082-x
- Bu, S. C., Kuijter, R., Li, X. R., Hooymans, J. M., and Los, L. I. (2014). Idiopathic epiretinal membrane. *Retina* 34, 2317–2335. doi:10.1097/IAE.0000000000000349
- Chen, J. C., and Lee, L. R. (2008). Clinical spectrum of lamellar macular defects including pseudoholes and pseudocysts defined by optical coherence tomography. *Br. J. Ophthalmol.* 92, 1342–1346. doi:10.1136/bjo.2007.133041
- Davel, A. P., Lemos, M., Pastro, L. M., Pedro, S. C., de André, P. A., Hebeda, C., et al. (2012). Endothelial dysfunction in the pulmonary artery induced by concentrated fine particulate matter exposure is associated with local but not systemic inflammation. *Toxicology* 295, 39–46. doi:10.1016/j.tox.2012.02.004
- Erel, O. (2005). A new automated colorimetric method for measuring total oxidant status. *Clin. Biochem.* 38, 1103–1111. doi:10.1016/j.clinbiochem.2005.08.008
- García-Medina, J. J., García-Medina, M., Garrido-Fernández, P., Galván-Espinosa, J., García-Maturana, C., Zanon-Moreno, V., et al. (2015). A two-year follow-up of oral antioxidant supplementation in primary open-angle glaucoma: An open-label, randomized, controlled trial. *Acta Ophthalmol.* 93, 546–554. doi:10.1111/aos.12629
- Guidry, C., Bradley, K. M., and King, J. L. (2003). Tractional force generation by human müller cells: Growth factor responsiveness and integrin receptor involvement. *Investig. Ophthalmol. Vis. Sci.* 44, 1355–1363. doi:10.1167/iov.02-0046
- Kohno, R. I., Hata, Y., Kawahara, S., Kita, T., Arita, R., Mochizuki, Y., et al. (2009). Possible contribution of hyalocytes to idiopathic epiretinal membrane formation and its contraction. *Br. J. Ophthalmol.* 93, 1020–1026. doi:10.1136/bjo.2008.155069
- Lavi, S., Yang, E. H., Prasad, A., Mathew, V., Barsness, G. W., Rihal, C. S., et al. (2008). The interaction between coronary endothelial dysfunction, local oxidative stress, and endogenous nitric oxide in humans. *Hypertension* 51, 127–133. doi:10.1161/HYPERTENSIONAHA.107.099986
- Lu, Q., Ma, Y., Xu, Y. S., and Jiang, Y. R. (2014). Apelin in epiretinal membranes of patients with proliferative diabetic retinopathy. *Mol. Vis.* 20, 1122–1131.
- Martínez-Fernández de la Cámara, C., Salom, D., Sequeado, M. D., Hervás, D., Marín-Lambies, C., Aller, E., et al. (2013). Altered antioxidant-oxidant status in the aqueous humor and peripheral blood of patients with retinitis pigmentosa. *PLoS ONE* 8, e74223. doi:10.1371/journal.pone.0074223
- Rokicki, W., Zalejska-Fiolk, J., Pojda-Wilczek, D., Kabiesz, A., and Majewski, W. (2016). Oxidative stress in the red blood cells of patients with primary open-angle glaucoma. *Clin. Hemorheol. Microcirc.* 62, 369–378. doi:10.3233/CH-152029
- Smiddy, W. E., Maguire, A. M., Green, W. R., Michels, R. G., de la Cruz, Z., Enger, C., et al. (1989). Idiopathic epiretinal membranes. Ultrastructural characteristics and clinicopathologic correlation. *Ophthalmology* 96, 811–820. discussion 821. doi:10.1016/s0161-6420(89)32811-9
- Snead, D. R., Cullen, N., James, S., Poulson, A. V., Morris, A. H., Lukaris, A., et al. (2004). Hyperconvolution of the inner limiting membrane in vitreomaculopathies. *Graefes Arch. Clin. Exp. Ophthalmol.* 242, 853–862. doi:10.1007/s00417-004-1019-3
- Stevenson, W., Prospero Ponce, C. M., Agarwal, D. R., Gelman, R., and Christoforidis, J. B. (2016). Epiretinal membrane: Optical coherence tomography-based diagnosis and classification. *Clin. Ophthalmol.* 10, 527–534. doi:10.2147/OPTH.S97722
- Wang, L. C., Hung, K. H., Hsu, C. C., Chen, S. J., Li, W. Y., and Lin, T. C. (2015). Assessment of retinal pigment epithelial cells in epiretinal membrane formation. *J. Chin. Med. Assoc.* 78, 370–373. doi:10.1016/j.jcma.2015.01.003
- Wert, K. J., Velez, G., Cross, M. R., Wagner, B. A., Teoh-Fitzgerald, M. L., Buettner, G. R., et al. (2018). Extracellular superoxide dismutase (SOD3) regulates oxidative stress at the vitreoretinal interface. *Free Radic. Biol. Med.* 124, 408–419. doi:10.1016/j.freeradbiomed.2018.06.024
- Xiao, W., Chen, X., Yan, W., Zhu, Z., and He, M. (2017). Prevalence and risk factors of epiretinal membranes: A systematic review and meta-analysis of population-based studies. *BMJ Open* 7, e014644. doi:10.1136/bmjopen-2016-014644
- Zhao, F., Gandorfer, A., Haritoglou, C., Scheler, R., Schaumberger, M. M., Kampik, A., et al. (2013). Epiretinal cell proliferation in macular pucker and vitreomacular traction syndrome: Analysis of flat-mounted internal limiting membrane specimens. *Retina* 33, 77–88. doi:10.1097/IAE.0b013e3182602087

Osteosarcoma's genetic landscape painted by genes' mutations

Wiktoria Urban^{1#}, Dagmara Krzystańska^{1#}, Michał Piekarczyk^{2#}, Jerzy Nazar^{2#} and Anna Jankowska^{1✉}

¹Department of Cell Biology, Poznan University of Medical Sciences, Poznań, Poland; ²Department of Orthopaedics and Traumatology of Locomotor System, Heliodor Swiecicki Clinical Hospital in Poznań, Poznan University of Medical Sciences, Poznań, Poland

Purpose: Osteosarcoma (OS) is one of the most common primary bone tumors. Direct pathogenesis remains unknown, however, genes' mutations are proven to participate in the process. This study aimed to examine the most frequently mutated genes in OS to appoint candidates for the cancer markers. **Methods:** Using the COSMIC Catalogue twenty the most frequently mutated genes were selected leading to an up-to-date genetic OS landscape summary. The genes can be classified into four categories: suppressor genes (*TP53*, *RB1*, *NCOR1*, *SMAD2*, *NF1*, *TSC2*, *KMT2C*), proto-oncogenes (*GNAS*, *BRAF*, *MLLT3*), epigenetic and post-translational modification-related genes (*SMARCA4*, *ARID1A*, *ATRX*, *BCOR*, *H3F3A*) and cell growth and survival regulating genes (*EGFR*, *CAMTA1*, *LRP1B*, *PDE4DIP*, *MED12*). **Results and conclusions:** Their role in cancerogenesis was confirmed by the analysis of available articles published previously. The results of the study indicate that examination of selected genes' mutations might help to identify patients' predisposition to OS development, as well as monitor the disease progression, and establish prognosis. However, to fully understand the pathogenesis of OS further studies are required.

Keywords: osteosarcoma, genes'mutations, COSMIC catalogue, bio-markers

Received: 02 June, 2023; **revised:** 14 August, 2023; **accepted:** 14 August, 2023; **available on-line:** 17 September, 2023

✉e-mail: ajanko@ump.edu.pl

#These authors equally contributed to the work.

Abbreviations: ALP, alkaline phosphatase; ANPEP, alanyl aminopeptidase; AP-1, activator protein 1; ARID1A, AT-rich interactive domain-containing protein 1A; ATRX, alpha thalassemia/mental retardation syndrome X-linked; BCOR, BCL6 Corepressor; BRAF, serine/threonine kinase; c-Myc, cellular myelocytomatosis oncogene; CAMTA1, calmodulin binding transcription activator 1; CD133, CD133 antigen; COSMIC, Catalogue Of Somatic Mutations In Cancer; CRP, C-reactive protein; EGFR, epidermal growth factor receptor; EMT, epithelial-mesenchymal transition; FLNA, filamin A; FUCA1, alpha-L-fucosidase 1; GNAS, guanine nucleotide binding protein alpha stimulating; H3F3A, H3 histone family 3A; HER-4, human epidermal growth factor receptor 4; ICB, immune checkpoint blockade; ICIs, immune checkpoint inhibitors; KMT2C, lysine methyltransferase 2C; LAMA3, laminin subunit alpha 3; LGALS1, galectin 1; LRP1B gene, low density lipoprotein receptor-related protein 1B; MATN3, matrilin 3; MED12, mediator complex subunit 12; miRNA, microRNA; MLLT3, MLLT3 super elongation complex subunit 3; MMGL, myomegalin-like; MSCs, mesenchymal stem cells; NANOG, homeobox protein NANOG; NCOR1, nuclear receptor corepressor 1; NF1, neurofibromin 1; OS, Osteosarcoma; PDE4DIP, phosphodiesterase 4D-interacting protein; RB, retinoblastoma protein; RB1, RB transcriptional corepressor 1; SEC, super elongation complex; SGCG, sarcoglycan gamma; SMAD2, SMAD family member 2; SMARCA4, SWI/SNF-related, matrix-associated, actin-dependant regulator of chromatin, subfamily a, member 4; SOX4, SRY-box transcription factor 4; TCGA, The Cancer Genome Atlas; TICs, tumor-initiating cells; TP53, tumor protein p53; TSC, tuberous sclerosis complex; TSC2, TSC complex subunit 2; TWIST, Twist Family BHLH Transcription Factor; VEGFA, Vascular endothelial growth factor A; WNT5A, Wnt Family Member 5A

INTRODUCTION

Osteosarcoma (OS) is one of the most common primary bone tumors. It occurs intraosseous, mainly in the metaphyseal region of the long bones. OS is inflicting an accelerated osteoid matrix production, which is connected to being developed at sites where bone grows expeditiously. Current data prove that OS has two main peaks of incidence: in childhood and adolescence. OS is the third most common type of tumor affecting young people, with the highest incidents in the early twenties (Wu & Livingston, 2020; Sun *et al.*, 2020; Misaghi *et al.*, 2018; Czarnecka *et al.*, 2020).

Osteosarcoma is divided into several subtypes (Fig. 1). It can be categorized depending on the region of bone it affects (the surface and central part of the bone, and within the medulla). The staging scheme divides OS into two classes depending on the grade of the tumor (low or high), as well as the localization of the compartment (extra- or intra-compartmental). Additionally, it is classified considering the metastatic level of the tumor. The most common classification groups OS as osteoblastic, chondroblastic, fibroblastic, and small cell subtypes. Among mention above types of osteosarcoma, the most often diagnosed one is a high-grade tumor, occurring extra-cortically (Misaghi *et al.*, 2018).

Even though the exact mechanisms responsible for OS pathogenesis are not known, it is confirmed that genetics play a role in the tumor origin. The most common characteristic of OS includes genome disorganization, together with alterations of tumor suppressor and DNA repair, as well as changes in cell cycle aneuploids with chromosomal alterations (de Azevedo *et al.*, 2020).

Classification of osteosarcoma subtypes

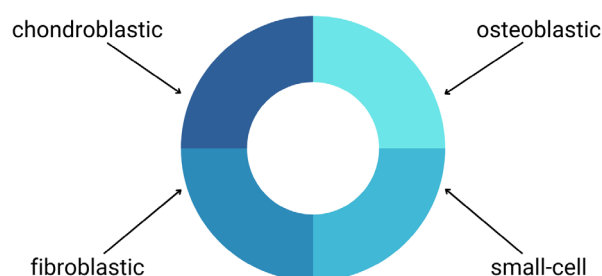


Figure 1. The most common classification of osteosarcoma subtypes, depending on the predominant type of cells affected by OS.

It was proved that OS can be developed as a consequence of alteration in tumor suppressor genes, including *TP53* and *Rb1*, during hereditary disorders such as Li-Fraumeni cancer family syndrome and retinoblastoma (Porter *et al.*, 1992; Fletcher & Unni, 2002; Misaghi *et al.*, 2018; Sun *et al.*, 2020). However, also other genes, such as transcription factors, and tumor suppressor genes, including *CAMTA1*, or *KMT2C* might participate in osteosarcoma development (He *et al.*, 2021; Chen *et al.*, 2016; Chiappetta *et al.*, 2019).

Currently, there are no laboratory tests or specific biomarkers to diagnose osteosarcoma (Misaghi *et al.*, 2018). Even though there are some molecules expressed in OS that are proposed as their potential markers. The most promising one appears to be alkaline phosphatase (ALP), which increased serum level and seems to correlate positively with tumor volume (Limahakun *et al.*, 2011). Additionally, C-reactive protein (CRP), Cathepsin D, osteocalcin, SATB2, and aspartic endoprotease can help distinguish OS (Misaghi *et al.*, 2018; Czarnecka *et al.*, 2020; Agustina *et al.*, 2018; Machado *et al.*, 2016; Tallegas *et al.*, 2022).

In addition to proteins, microRNA expression also seems to be valuable in the diagnosis of osteosarcomas. Overexpression of miR-421 and miR-191 proves to be linked with proliferation, migration, and malignant character of the tumors. Their levels in the serum of OS patients were higher compared to samples from healthy volunteers (Czarnecka *et al.*, 2020).

Moreover, the presence of tumor-initiating cells (TICs) may help in OS diagnostics. TICs expressing markers of stem cell phenotype, such as NANOG or SOX4 were observed in both primary and metastatic tumor tissue (Yan *et al.*, 2016). These proteins, together with CD133+, which is a distinctive marker of TICs observed in osteosarcoma cell lines (Czarnecka *et al.*, 2020). It has been proved that the expression of CD133 in OS patients is related to distant metastasis and poor prognosis. making this a tumor marker (Xie *et al.*, 2018).

Finally, the prevalence of mesenchymal stem cells (MSCs) connected with OS progression is proposed to be the tumor marker. Changes in the expression of c-Myc, Rb, AP-1 or TWIST were shown to contribute to the transformation of MSCs into osteosarcoma tumor cells (Yang *et al.*, 2020). Most sarcomas characterize a permanent mesenchymal state. However, their phenotype can change by factors regulating epithelial-mesenchymal transition – EMT. These factors have been shown to be highly correlated with the invasiveness and higher risk of metastasis in malignant OS (Wu *et al.*, 2019; Yu, Yustein & Xu, 2021). An EMT-related genes' panel (including *LAMA3*, *LGALS1*, *SGCG*, *VEGFA*, *WNT5A*, *MATN3*, *ANPEP*, *FUCA1*, and *FLNA*) was used as a predictive marker in a multi-cohort study of OS. The panel proved to be a reliable tool for estimating the overall survival of OS patients. Moreover, it was proposed as a selection method for patients with metastases for personalized treatment (Yiqi *et al.*, 2020).

Even though numerous studies describe molecules, whose expression may characterize osteosarcomas, all pointed proteins and/or miRNA are not specific to OS. Thus, further studies are needed to establish biomarkers helping to diagnose and treat OS.

The present study aims to provide a comprehensive, up-to-date study of genes the most frequently mutated in osteosarcoma using the COSMIC Catalogue. Such genes would become candidates for OS markers.

COSMIC, the Catalogue Of Somatic Mutations In Cancer (<https://cancer.sanger.ac.uk>) is a database providing tools to explore somatic mutations and their correlation

with human cancers. The catalogue is the collection of somatic mutations. The data used to build this catalogue derives strictly from the scientific literature. COSMIC additionally provides information about patients' genetic pre-dispositions and environmental factors participating in the process of cancerogenesis (Tate *et al.*, 2019).

MATERIALS AND METHODS

To identify the most common somatic mutations occurring in osteosarcoma patients, the COSMIC Cancer Browser tool (<https://cancer.sanger.ac.uk/cosmic/browse/tissue>) was used. The catalogue provides information about 282 osteosarcoma samples (classified into 9 histological subtypes). The biological relevance of the 20 most frequently mutated genes pointed out by the COSMIC Cancer Browser was investigated by the analysis of publications available on PubMed (<https://pubmed.ncbi.nlm.nih.gov/>). To search for the publications, specific keywords, such as: selected genes' name, osteosarcoma, cancer, and mutation were used. For each gene research was divided into two keyword panels – first: selected genes' name, cancer, mutation; second: selected genes' name, osteosarcoma, mutation.

RESULTS AND DISCUSSION

Genes the most frequently mutated in OS

The analysis of the COSMIC Catalogue provided a list of genes in which somatic mutation may participate in osteosarcoma development. Out of 18,309 entries of genes, the top 20 genes, based on the frequency of their

Table 1. The frequency of gene mutation in OS samples in the COSMIC Catalogue

Gene	Number of OS samples available in COSMIC catalogue	Number of mutated samples and % of frequency
TP53	371	91 (25%)
RB1	285	22 (8%)
ATRX	212	16 (8%)
KMT2C	215	13 (6%)
LRP1B	136	8 (6%)
CAMTA1	134	7 (5%)
NCOR1	208	9 (4%)
MLLT3	134	6 (4%)
PDE4DIP	134	6 (4%)
GNAS	352	9 (3%)
SMARCA4	211	6 (3%)
ARID1A	210	6 (3%)
H3F3A	453	11 (2%)
EGFR	280	5 (2%)
BRAF	257	6 (2%)
SMAD2	243	5 (2%)
NF1	216	5 (2%)
MED12	210	5 (2%)
TSC2	210	5 (2%)
BCOR	209	5 (2%)

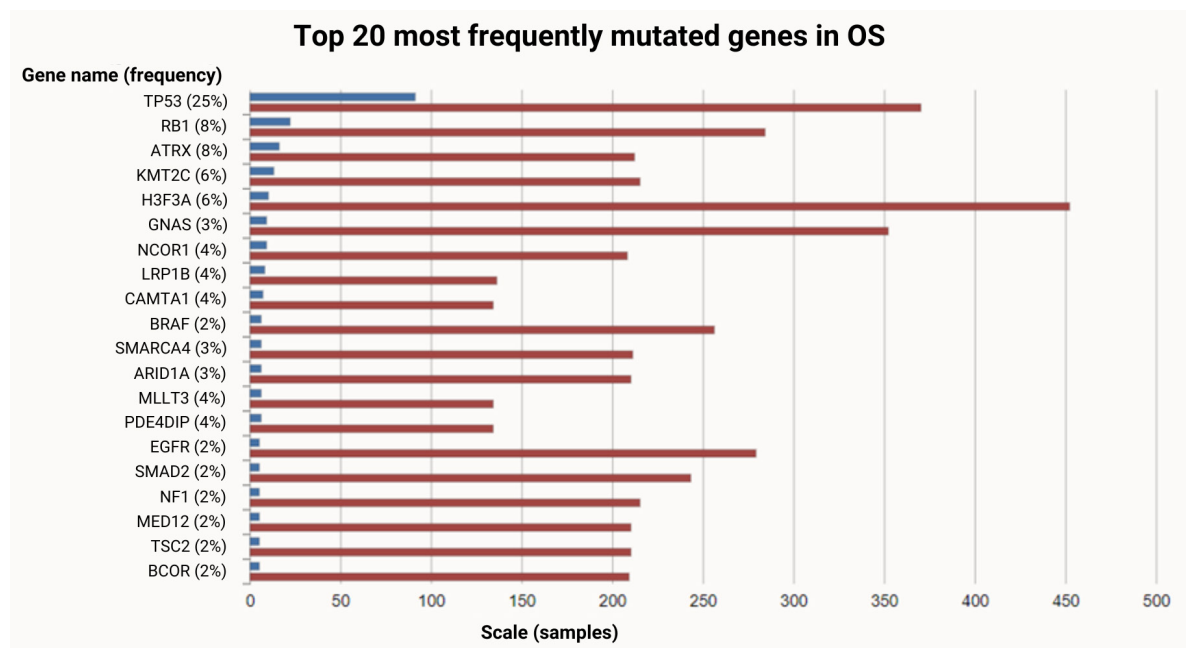


Figure 2. The top 20 most frequently mutated genes in OS according to COSMIC Catalogue

mutation were selected. They are shown in Table 1 and shown in Fig. 2.

All these genes are directly or indirectly involved in oncogenesis (Table 2). Seven out of these 20 genes – *TP53*, *RB1*, *NCOR1*, *SMAD2*, *NF1*, *TSC2*, *KMT2C* are

known to be tumor suppressor genes. Thus, their mutations lead to the expression of malfunctioning protein products and strictly correlate with tumorigenesis. The following three genes: *GNAS*, *BRAF*, and *MLLT3* are protooncogenes. Other genes – *SMARCA4*, *ARID1A*,

Table 2. Genes the most frequently mutated in osteosarcomas and their function

Gene	Function	References
TP53	tumor suppression	(Synoradzki <i>et al.</i> , 2021)
RB1	tumor suppression	(Li <i>et al.</i> , 2022)
ATRX	epigenetics and post-translational modifications	(He <i>et al.</i> , 2015)
KMT2C	tumor suppression	(Gala <i>et al.</i> , 2018; Lian <i>et al.</i> , 2022; Liu <i>et al.</i> , 2021)
LRP1B	cell growth, metabolism and survival	(Wang & Xiong, 2021)
CAMTA1	cell growth, metabolism and survival	(Lu <i>et al.</i> , 2018)
NCOR1	tumor suppression	(Tang <i>et al.</i> , 2020)
MLLT3	protooncogene	(Sun <i>et al.</i> , 2017)
PDE4DIP	cell growth, metabolism and survival	(Soejima <i>et al.</i> , 2001; Lehnart <i>et al.</i> , 2005)
GNAS	protooncogene	(Nomura <i>et al.</i> , 2014; Zaubner, Marotta & Sabbath-Solitare, 2016; Patra <i>et al.</i> , 2018; Afolabi <i>et al.</i> , 2022)
SMARCA4	epigenetics and post-translational modifications	(Xu <i>et al.</i> , 2021; Jelinic <i>et al.</i> , 2014)
ARID1A	epigenetics and post-translational modifications	(Xu <i>et al.</i> , 2019)
H3F3A	post-translational modifications of histone H3.3	(Sturm <i>et al.</i> , 2012; Park <i>et al.</i> , 2016)
EGFR	cell growth, metabolism and survival	(Wang <i>et al.</i> , 2004)
BRAF	protooncogene	(Śmiech <i>et al.</i> , 2020)
SMAD2	tumor suppression	(Piek, Heldin & Ten Dijke, 1999; Pasche, 2001)
NF1	tumor suppression	(Trovó-Marqui & Tajara, 2006)
MED12	cell growth, metabolism and survival	(Ding <i>et al.</i> , 2008)
TSC2	tumor suppression	(Inoki <i>et al.</i> , 2002)
BCOR	epigenetics and post-translational modifications	(Huynh <i>et al.</i> , 2000)

ATRX, *BCOR*, and *H3F3A* are related to the epigenetic status of gene expression or posttranslational histone modifications. Finally, *EGFR*, *CAMTA1*, *LRP1B*, *PDE4DIP*, and *MED12* are associated with cell growth, metabolism, and survival.

Molecular basis of OS

Genome destabilization, aneuploids with chromosomal changes, dysregulation of cell cycle and tumor suppressor genes, as well as a lack of DNA repair are some of the most prevalent characteristics of OS (de Azevedo *et al.*, 2020). Epigenetic changes are also recognized as risk factors for OS (Sharma, Kelly & Jones, 2009). Still, the pathogenesis of OS is complex and poorly understood. Thus, the identification of additional genes involved in oncogenesis may lead to advances in understanding OS biology, as well as shortening the time needed to establish diagnosis and introduce proper treatment.

The results of the COSMIC Catalogue analysis allowed distinguishing 20 genes the most frequently mutated in cancer. All recognized genes (Table 2) are known to be key regulators of vital cellular processes such as DNA repair, cell proliferation and differentiation. Thus, their mutations might lead to cancer development.

The most frequently mutated genes and their possible role in OS biology

Among the genes examined during the analysis of the COSMIC Catalogue, the most frequently mutated gene in OS was *TP53*. Its mutation characterized 25% of samples available in the database. *TP53* encodes the P53 protein, which is an essential transcription factor with a tumor suppressor function. It stimulates several processes that result in cell cycle arrest, DNA repair, alterations in metabolism in response to cellular stress, apoptosis, and cell senescence. Moreover, it plays an important role in ontogenesis, myogenesis, and angiogenesis (Synoradzki *et al.*, 2021). Thus, mutated *TP53* appears to be essential for cancer development and its progression. Mutations in *TP53* are known to increase protein instability, which affects clinical characteristics of osteosarcoma, such as metastatic potential, tumor type, and grade as well as its aggressiveness. According to Chen *et al.* *TP53* mutations are a reliable predictive indicator for osteosarcoma patient survival (Chen *et al.*, 2016).

Another gene commonly mutated in OS is Retinoblastoma transcriptional corepressor 1 gene – *RB1*. Its mutations were observed in 8% of samples available in the COSMIC catalogue. Between 50% and 70% of osteosarcoma cases exhibit mutations in *RB1* (Wu & Livingston, 2020). *RB1* encodes retinoblastoma protein controlling the transition from the G1 to S phase. This makes it a crucial regulator of cell cycle progression. It is suggested that during OS oncogenesis, alterations of *RB1* may correlate with *TP53* inactivation (Wu & Livingston, 2020; Li *et al.*, 2022). Indeed, using mice models it was proved that deletion of *RB1* leads to osteosarcomas development. Osteoblast development and mineralization as well as an increase in the expression of osteogenic markers were positively impacted by the gene deletion (Li *et al.*, 2022).

Yet another gene mutated in 8% of OS is *ATRX* – alpha thalassemia/mental retardation syndrome X-linked. The gene encodes the protein that plays a role in chromatin remodeling and DNA repair. Loss of *ATRX* function has been linked to the accumulation of repetitive DNA sequences and alterations in the epigenetic regulation of the gene expression, which may contribute to the

development and progression of tumor (He *et al.*, 2015). Mutations in *ATRX* have been observed in a variety of cancer types (Haase *et al.*, 2018). In osteosarcoma, *ATRX* dysfunction was linked with chromosomal instability, which contributes the tumor development. The gene's mutations were also associated with poor prognosis and resistance to chemotherapy (Masliah-Planchon *et al.*, 2018). Thus, *ATRX* is pointed out as a promising biomarker of osteosarcoma.

6% of OS samples in the COSMIC catalogue manifested mutation of the *KTM2C* gene. *KTM2C* has been shown to act as a tumor suppressor. Its expression in OS has been shown to be downregulated, like in a variety of other human cancers, including breast and prostate cancer (Gala *et al.*, 2018; Lian *et al.*, 2022; Liu *et al.*, 2021). Loss of *KTM2C* expression is associated with poor prognosis and resistance to chemotherapy (Lian *et al.*, 2022; Liu *et al.*, 2021). What is more, *KTM2C* has been shown to regulate the other tumor suppressor genes, such as *TP53* and *p16INK4a*. By removing methyl groups from histones, *KTM2C* also activates the expression of oncogenes, such as *MYC* (Liu *et al.*, 2021; Lian *et al.*, 2022; Gala *et al.*, 2018). All these data demonstrate that the *KTM2C* gene can play an important role in OS development.

6% of available OS samples of the COSMIC catalogue were mutated in the *LRP1B* gene – Low Density Lipoprotein Receptor-Related Protein 1B that encodes cell surface receptor for LDL. *LRP1B* has been previously shown to play a role in tumor growth and progression. Additionally, it regulates angiogenesis in some of the cancer types, such as non-small cell lung cancer, renal cell cancer, and neuroglioma (Wang & Xiong, 2021). The gene overexpression observed in various cancers is linked to poor prognosis and decreased patient survival (Brown *et al.*, 2021; Príncipe *et al.*, 2021; Wang & Xiong, 2021). *LRP1B* is associated with the occurrence of osteosarcoma and its overexpression correlates with poor prognosis and decreased patient survival. Therefore the gene might be one relevant factor helping in OS diagnosis (Xu *et al.*, 2021).

A significant role in tumorigenesis and tumor progression is also played by the *CAMTA1* gene encoding a transcription factor – Calmodulin Binding Transcription Activator 1 (He *et al.*, 2021). The gene down-expression correlates with chemoresistance (Pan *et al.*, 2022). It has been shown that the expression of long noncoding RNA *CAMTA1* (lncCAMTA1) in breast cancer affects cells viability and promotes their migratory state. Knock-down of lncCAMTA1 leads to cancer cell apoptosis (Lu *et al.*, 2018). *CAMTA1* mutations were observed in 5% of OS COSMIC samples. Even though there is a lack of information about the gene significance for osteosarcoma, still in Epithelioid hemangioendothelioma, that can arise from soft tissues and bones, *CAMTA1* was proposed to be an immunohistochemical marker (Anderson & Jo, 2021).

Yet another gene shown to play a role in tumor development and its progression is *NCOR1* (Nuclear Receptor Corepressor 1) gene. COSMIC catalogue analysis showed that as many as 4% of OS samples showed *NCOR1* mutation. The gene encodes a corepressor involved in the regulation of gene expression (Tang *et al.*, 2020). *NCOR1* was observed to be frequently upregulated in breast cancer, and its high expression is associated with good prognosis and better patient survival (Noblejas-López *et al.*, 2018). Interestingly, in bladder cancer, *NCOR1* strongly correlated with immunogenicity, and its mutations were shown to cause activation of anti-tumor

immunity, as well as overexpression of immune-related genes (Lin *et al.*, 2021). According to Luo *et al.* *NCOR* is widely amplified in osteosarcoma, as it might participate in tumor growth as a regulator of other gene transcription (Luo *et al.*, 2019).

Four percentage of OS samples of the COSMIC catalogue showed mutations of the *MLLT3* gene. *MLLT3* protein is part of a super elongation complex (SEC), which is needed to increase the catalytic function of RNA polymerase II (Calvanese *et al.*, 2019). The knock-out of the *MLLT3* gene can lead to decreased proliferation of osteosarcoma cell lines, associated with the JNK signaling pathway. Thus, *MLLT3* can be an oncogene candidate involved in osteosarcomas development (Sun *et al.*, 2017).

As much as 4% of samples deposited in the COSMIC catalogue were characterized by *PDE4DIP* gene mutations. Even though there is no information about the gene significance in osteosarcomas, still, *PDE4DIP* protein, also known as MMGL (myomegalin-like) protein is involved in several intracellular metabolic pathways, which may control OS biology (Soejima *et al.*, 2001; Lehnart *et al.*, 2005).

Three percentage of OS samples carried a mutation of *GNAS* (Guanine Nucleotide Binding Protein, Alpha Stimulating). The gene encodes a signaling molecule involved in many cellular processes involving cAMP signaling. It has been shown to play a role in tumorigenesis (Nomura *et al.*, 2014; Zaubner, Marotta & Sabbath-Solitare, 2016; Patra *et al.*, 2018; Afolabi *et al.*, 2022). *GNAS* mutations were observed in various cancers, such as colon, pancreas, and gastrin adenocarcinoma as well as in fibrous dysplasia, which is known to have the potential to form malignancies such as osteosarcoma (Sugiyama *et al.*, 2018).

Three percentage of samples deposited in the COSMIC catalogue manifested mutations of the *SMARCA4* gene. *SMARCA4* encodes the catalytic subunit of SWI/SNF complexes, which is associated with chromatin remodeling and making genes accessible for transcriptional factors. Unfortunately, there is a lack of information about the significance of gene alterations in osteosarcomas.

Also, the *ARID1A* gene product (AT-rich interactive domain-containing protein 1A) is a part of the SWI/SNF complex, associated with chromatin remodeling (Xu *et al.*, 2019). *ARID1A* mutations were observed in many cancers before (Jones *et al.*, 2010). Recent studies show that in osteosarcomas the expression of *ARID1A* is down-regulated compared to non-tumor tissues (Xu *et al.*, 2019). This can be correlated with the gene mutations measured in 3% of OS samples of the COSMIC catalogue.

Yet another mutated gene affecting the structure of chromatin and contributing to tumorigenesis is *H3F3A* (Sturm *et al.*, 2012; Park *et al.*, 2016). *H3F3A* overexpression has been shown to correlate with aggressive phenotype and chemoresistance leading to lower survival rates and relapse in lung cancer patients (Park *et al.*, 2016). COSMIC catalogue analysis showed that 2% of OS samples are mutated in *H3F3A*. This data finds approval in Koelsche *et al.* study showing hotspot mutations in *H3F3A* in six osteosarcoma cases analysed by the authors. Observed alternations were correlated with age and increased the incidence of osteosarcoma in patients over the age of 30 (Koelsche *et al.*, 2017).

Two percentage of the samples of the COSMIC catalogue were carrying mutations in the *BCOR* gene. *BCOR* protein is involved in the process of deacetylation of

histones and when over-expressed inhibits BCL-6 tumor suppressor (Huynh *et al.*, 2000). Mutations in *BCOR* are associated with many types of cancer, such as clear cell sarcoma of the kidney, endometrial stromal sarcoma, or small round blue cell sarcomas (Astolfi *et al.*, 2019; Ueno-Yokohata *et al.*, 2015; Marinó-Enriquez *et al.*, 2018; Sbaraglia *et al.*, 2020).

Among samples deposited in the COSMIC catalogue, approximately 2% carry mutations in the *MED12* gene. *MED12* is part of a larger, multiprotein complex that mediates polymerase II RNA during the process of transcription (Ding *et al.*, 2008). *MED12* is associated with 70% of uterine leiomyomas and fibroepithelial tumors of the breast (Croce & Chibon, 2015; Lerwill *et al.*, 2022). As for now, only two clinical case reports described *MED12* mutations in osteosarcomas. Le and others (Le *et al.*, 2021) showed that the patient with *MED12*-mutated high-grade uterine sarcoma developed osteosarcoma with the same L36R missense mutation. Another team described *MED12* mutation in osteosarcoma which further led to the development of breast malignant phyllodes tumor (Tokoyoda *et al.*, 2018). More study is needed to assess the link between *MED12* mutations and the occurrence of osteosarcoma, especially since according to The Cancer Genome Atlas (TCGA) data, mutations in *MED12* can be biomarkers helping to select patients for the therapy with immune checkpoint inhibitors (ICIs) (Zhou *et al.*, 2022).

Two percentage of OS samples from the COSMIC catalogue displayed changes in the *EGFR* gene encoding receptor for the epidermal growth factor (EGFR). The receptor is known for its crucial role in the signaling pathway responsible for cell proliferation, differentiation, and/or survival (Wang *et al.*, 2004). Mutations of *EGFR* in a variety of malignancies are well documented. Most frequent is the gene's amplification leading to EGFR overexpression increasing cellular signaling (Sigismund, Avanzato & Lanzetti, 2018; Cheng *et al.*, 2021). The gene importance for OS has been already documented. Sheng-Lin and others (Sheng-Lin *et al.*, ????) reported that high expression of EGFR together with HER-4 (human epidermal growth factor receptor 4) was associated with distant metastasis and the level of *EGFR* expression was proposed to be a potential prognostic biomarker of OS (Wang *et al.*, 2018).

Among OS samples deposited in the COSMIC catalogue, 2% manifested mutations of the *SMAD2* gene. This low number of samples can indicate that the gene mutations are not osteosarcoma specific. However, is worth mentioning that SMAD2, as a part of the TGF-beta superfamily, plays an important role in cell signaling, proliferation, and differentiation (Piek *et al.*, 1999) and may act as an oncosuppressor (Piek *et al.*, 1999; Pasche, 2001). Moreover, it has been shown that there are statistically significant changes in *SMAD2* expression in OS compared to healthy tissue. The correlation between alterations of Smad signaling, the high proliferation rate, and the invasive phenotype of osteosarcoma cells was observed in OS with Serine/threonine kinase 39 (STK39) knockdown (Won *et al.*, 2010; Yang *et al.*, 2013; Huang *et al.*, 2017).

Another gene selected during our study was the *NF1* gene. According to the data from the COSMIC catalogue 2% of OS samples were carrying the gene's mutations. The product of *NF1* is neurofibromin 1 – a cytoplasmic protein expressed in neurons, Schwann cells, and leukocytes. The protein is a part of the RAS/MAPK signaling pathway controlling cell proliferation (Huang *et al.*, 2017). It is suggested that NF1 can act also as an oncos-

uppressor. Although the *NF1* gene is associated mostly with neural malignancies, its mutations are observed in many cancers, e.g. lung cancers or melanomas (Trovó-Marqui & Tajara, 2006). Further studies are needed to prove *NF1* role in OS development.

An additional gene involved in the inhibition of cell proliferation is the tumor-suppressor gene *TSC2* (Inoki *et al.*, 2002). The gene's mutations were described in tuberous sclerosis complex (TSC) and non-small cell lung cancer. It was proved that patients with *TSC1/TSC2* loss can benefit from target therapy including treatment with immune checkpoint blockade (ICB) (Huang *et al.*, 2022). Kuroda *et al.* reported a clinical case of a young patient with tuberous sclerosis complex (TSC) who developed osteosarcoma. Analysis of the tumor sample showed additional mutations in *TP53* as well as *TSC2* genes (Kuroda *et al.*, 2021). This observation is in agreement with COSMIC catalogue data showing that approximately 2% of OS samples were characterized by mutated *TSC2*.

Two percentage of OS samples were also characterized by mutated proto-oncogene *BRAF*. *BRAF* activates signaling pathways involved in the cell cycle, including proliferation, differentiation, and cell death. The gene mutations may result in malignancies development. In fact, dysregulation of gene expression was observed in several cancers, including melanoma, colorectal cancer, and non-small cell lung cancer (Śmiech *et al.*, 2020). Pignochino *et al.* reported that in 4 of 30 osteosarcoma patients analysed in their study, *BRAF* gene mutation was confirmed (Pignochino *et al.*, 2009).

CONCLUSIONS

COSMIC catalogue analysis allows to identify genes that are the most frequently mutated in osteosarcoma. Since 20 of the selected genes have previously been shown to be involved in cancerogenesis, thus their mutation might also play a role in OS development. However, to prove their clinical significance and the possibility of using them as OS biomarkers further studies are needed. The results of such a study would help to identify patient predisposition to OS development, follow cancer progression, and establish patients' treatment and prognosis.

REFERENCES

- Afolabi HA, Salleh SM, Zakaria Z, Ch'ng ES, Mohd Nafi SN, Abdul Aziz AA Bin, Irekeola AA, Wada Y, Al-Mhanna SB (2022) A *GNAS* gene mutation's independent expression in the growth of colorectal cancer: a systematic review and meta-analysis. *Cancers (Basel)* **14**: 5480. <https://doi.org/10.3390/cancers14225480>
- Agustina H, Asyifa I, Aziz A, Hernowo BS (2018) The role of osteocalcin and alkaline phosphatase immunohistochemistry in osteosarcoma diagnosis. *Patholog. Res. Int.* **2018**: 6346409 <https://doi.org/10.1155/2018/6346409>
- Anderson WJ, Jo VY (2021) Diagnostic immunohistochemistry of soft tissue and bone tumors: An update on biomarkers that correlate with molecular alterations. *Diagnostics* **11**: 690 <https://doi.org/10.3390/diagnostics11040690>
- Astolfi A, Fiore M, Melchionda F, Indio V, Bertuccio SN, Pession A (2019) BCOR involvement in cancer. *Epigenomics* **11**: 835–855. <https://doi.org/10.2217/epi-2018-0195>
- de Azevedo JWV, de Medeiros Fernandes TAA, Fernandes JV, de Azevedo JCV, Lanza DCF, Bezerra CM, Andrade VS, de Araújo JMG, Fernandes JV (2020) Biology and pathogenesis of human osteosarcoma (Review). *Oncol. Lett.* **19**: 1099–1116. <https://doi.org/10.3892/ol.2019.11229>
- Brown LC, Tucker MD, Sedhom R, Schwartz EB, Zhu J, Kao C, Labriola MK, Gupta RT, Marin D, Wu Y, Gupta S, Zhang T, Harrison MR, George DJ, Alva A, Antonarakis ES, Armstrong AJ (2021) LRP1B mutations are associated with favorable outcomes to immune checkpoint inhibitors across multiple cancer types. *J. Immunother. Cancer* **9**: 1–10. <https://doi.org/10.1136/jitc-2020-001792>
- Calvanese V, Nguyen AT, Bolan TJ, Vavilina A, Su T, Lee LK, Wang Y, Lay FD, Magnusson M, Crooks GM, Kurdistani SK, Mikkola HKA (2019) MLLT3 governs human haematopoietic stem-cell self-renewal and engraftment. *Nature* **576**: 281–286. <https://doi.org/10.1038/s41586-019-1790-2>
- Chen Z, Guo J, Zhang K, Guo Y (2016) TP53 Mutations and survival in osteosarcoma patients: a meta-analysis of published data. *Dis. Markers* **2016** <https://doi.org/10.1155/2016/4639575>
- Cheng WL, Feng PH, Lee KY, Chen KY, Sun WL, Van Hiep N, Luo CS, Wu SM (2021) The role of EREG/EGFR pathway in tumor progression. *Int. J. Mol. Sci.* **22**: 12828. <https://doi.org/10.3390/ijms222312828>
- Chiappetta C, Carletti R, Della Rocca C, Di Cristofano C (2019) KMT2C modulates migration and invasion processes in osteosarcoma cell lines. *Pathol. Res. Pract.* **215**: 152534. <https://doi.org/10.1016/j.prp.2019.152534>
- Croce S, Chibon F (2015) MED12 and uterine smooth muscle oncogenesis: State of the art and perspectives. *Eur. J. Cancer* **51**: 1603–1610. <https://doi.org/10.1016/j.ejca.2015.04.023>
- Czarnecka AM, Synoradzki K, Firliej W, Bartnik E, Sobczuk P, Fiedorowicz M, Griep P, Rutkowski P (2020) Molecular biology of osteosarcoma. *Cancers (Basel)* **12**: 1–27. <https://doi.org/10.3390/cancers12082130>
- Ding N, Zhou H, Esteve PO, Chin HG, Kim S, Xu X, Joseph SM, Friez MJ, Schwartz CE, Pradhan S, Boyer TG (2008) Mediator links epigenetic silencing of neuronal gene expression with X-linked mental retardation. *Mol. Cell* **31**: 347–359. <https://doi.org/10.1016/j.molcel.2008.05.023>
- Fletcher CDM, Unni KK (2002) World Health Organization Classification of Tumours Pathology and Genetics of Tumours of Soft Tissue and Bone
- Gala K, Li Q, Sinha A, Razavi P, Dorso M, Sanchez-Vega F, Chung YR, Hendrickson R, Hsieh JJ, Berger M, Schultz N, Pastore A, Abdel-Wahab O, Chandraratna S (2018) KMT2C mediates the estrogen dependence of breast cancer through regulation of ER α enhancer function. *Oncogene* **37**: 4692–4710. <https://doi.org/10.1038/s41388-018-0273-5>
- Haase S, Garcia-Fabiani MB, Carney S, Altschuler D, Núñez FJ, Méndez FM, Núñez F, Lowenstein PR, Castro MG (2018) Mutant ATRX: uncovering a new therapeutic target for glioma. *Expert Opin. Ther. Targets* **22**: 599–613. <https://doi.org/10.1080/14728222.2018.1487953>
- He Q, Kim H, Huang R, Lu W, Tang M, Shi F, Yang D, Zhang X, Huang J, Liu D, Songyang Z (2015) The Daxx/Atx complex protects tandem repetitive elements during DNA hypomethylation by promoting H3K9 trimethylation. *Cell Stem Cell* **17**: 273–286. <https://doi.org/10.1016/j.stem.2015.07.022>
- He Z, Yang C, He Y, Gong B, Yin C, Feng J, Chen L, Tang J, Chen Y (2021) CAMTA1, a novel antitumor gene, regulates proliferation and the cell cycle in glioma by inhibiting AKT phosphorylation. *Cell. Signal.* **79**: 109882. <https://doi.org/https://doi.org/10.1016/j.cellsig.2020.109882>
- Huang Q, Li F, Hu H, Fang Z, Gao Z, Xia G, Ng WL, Khodadadi-Jamayran A, Chen T, Deng J, Zhang H, Almonte C, Labbe K, Han H, Geng K, Tang S, Freeman GJ, Li Y, Chen H, Wong KK (2022) Loss of TSC1/TSC2 sensitizes immune checkpoint blockade in non-small cell lung cancer. *Sci. Adv.* **8**: 1–11. <https://doi.org/10.1126/sciadv.abi9533>
- Huang T, Zhou Y, Cao Y, Tao J, Zhou ZH, Hang DH (2017) STK39, overexpressed in osteosarcoma, regulates osteosarcoma cell invasion and proliferation. *Oncol. Lett.* **14**: 4599–4604. <https://doi.org/10.3892/ol.2017.6728>
- Huynh KD, Fischle W, Verdin E, Bardwell VJ (2000) BCoR, a novel corepressor involved in BCL-6 repression. *Genes Dev.* **14**: 1810–1823.
- Inoki K, Li Y, Zhu T, Wu J, Guan KL (2002) TSC2 is phosphorylated and inhibited by Akt and suppresses mTOR signalling. *Nat. Cell Biol.* **4**: 648–657. <https://doi.org/10.1038/ncb839>
- Jelinic P, Mueller JJ, Olvera N, Dao F, Scott SN, Shah R, Gao J, Schultz N, Gonen M, Soslow RA, Berger MF, Levine DA (2014) Recurrent SMARCA4 mutations in small cell carcinoma of the ovary. *Nat. Genet.* **46**: 424–426. <https://doi.org/10.1038/ng.2922>
- Jones S, Wang T-L, Shih I-M, Mao T-L, Nakayama K, Roden R, Glas R, Slamon D, Diaz LAJ, Vogelstein B, Kinzler KW, Velculescu VE, Papadopoulos N (2010) Frequent mutations of chromatin remodeling gene ARID1A in ovarian clear cell carcinoma. *Science* **330**: 228–231. <https://doi.org/10.1126/science.1196333>
- Koelsche C, Schrimpf D, Tharun L, Roth E, Sturm D, Jones DTW, Renker E-K, Sill M, Baude A, Sahm F, Capper D, Bewerunge-Hudler M, Hartmann W, Kulozik AE, Petersen I, Flucke U, Schreuder HWB, Büttner R, Weber M-A, Schirmacher P *et al.* (2017) Histone 3.3 hotspot mutations in conventional osteosarcomas: a comprehensive clinical and molecular characterization of six H3F3A mutated cases. *Clin. Sarcoma Res.* **7**: 9 <https://doi.org/10.1186/s13569-017-0075-5>

- Kuroda K, Moriya K, Nakano T, Saito R, Sato D, Katayama S, Nii-zuma H, Watanuki M, Uematsu M, Sasahara Y, Kure S (2021) A pediatric case of osteosarcoma and tuberous sclerosis complex with a novel germline mutation in the TSC2 gene and a somatic mutation in the TP53 gene. *Pediatr. Blood Cancer* **68**: 2–3. <https://doi.org/10.1002/pbc.28960>
- Le MK, Omori M, Oishi N, Oi M, Fukasawa H, Hirata S, Kondo T (2021) High-grade uterine sarcoma with osteosarcomatous differentiation arising from a MED12-mutated leiomyoma, a case report. *Pathol. Int.* **71**: 199–203. <https://doi.org/10.1111/pin.13065>
- Lehnart SE, Wehrens XHT, Reiken S, Warriar S, Belevych AE, Harvey RD, Richter W, Jin SLC, Conti M, Marks AR (2005) Phosphodiesterase 4D deficiency in the ryanodine-receptor complex promotes heart failure and arrhythmias. *Cell* **123**: 25–35. <https://doi.org/10.1016/j.cell.2005.07.030>
- Lerwill MF, Lee AHS, Tan PH (2022) Fibroepithelial tumours of the breast-a review. *Virchows Arch.* **480**: 45–63. <https://doi.org/10.1007/s00428-021-03175-6>
- Li Y, Yang S, Liu Y, Yang S (2022) Deletion of Trp53 and Rb1 in Ctsk-expressing cells drives osteosarcoma progression by activating glucose metabolism and YAP signaling. *Med. Commun.* **3**: 1–15. <https://doi.org/10.1002/mco2.131>
- Lian J, Xu C, Chen X, Huang S, Wu D (2022) Histone methyltransferase KMT2C plays an oncogenic role in prostate cancer. *J. Cancer Res. Clin. Oncol.* **148**: 1627–1640. <https://doi.org/10.1007/s00432-022-03968-5>
- Limmahakhun S, Pothacharoen P, Theera-Umpon N, Arpornchayanon O, Leerapun T, Luevitonvechhij S, Pruksakorn D (2011) Relationships between serum biomarker levels and clinical presentation of human osteosarcomas. *Asian Pacific J. Cancer Prev.* **12**: 1717–1722
- Lin A, Qiu Z, Zhang J, Luo P (2021) Effect of NCOR1 mutations on immune microenvironment and efficacy of immune checkpoint inhibitors in patient with bladder cancer. *Front. Immunol.* **12**: 630773. <https://doi.org/10.3389/fimmu.2021.630773>
- Liu X, Qiu R, Xu M, Meng M, Zhao S, Ji J, Yang Y (2021) KMT2C is a potential biomarker of prognosis and chemotherapy sensitivity in breast cancer. *Breast Cancer Res. Treat.* **189**: 347–361. <https://doi.org/10.1007/s10549-021-06325-1>
- Lu P, Gu Y, Li L, Wang F, Yang X, Yang Y (2018) Long Noncoding RNA CAMTA1 Promotes proliferation and mobility of the human breast cancer cell line MDA-MB-231 via targeting miR-20b. *Oncol. Res.* **26**: 625–635. <https://doi.org/10.3727/096504017X14953948675395>
- Luo Z, Xiao L, Li J, Dong B, Wang C (2019) Integrative analysis reveals driver long non-coding RNAs in osteosarcoma. *Medicine (Baltimore)* **98**: e14302. <https://doi.org/10.1097/MD.00000000000014302>
- Machado I, Navarro S, Picci P, Llombart-Bosch A (2016) The utility of SATB2 immunohistochemical expression in distinguishing between osteosarcomas and their malignant bone tumor mimickers, such as Ewing sarcomas and chondrosarcomas. *Pathol. Res. Pract.* **212**: 811–816. <https://doi.org/10.1016/j.prp.2016.06.012>
- Marinó-Enríquez A, Lauria A, Przybyl J, Ng TL, Kowalewska M, Debiec-Rychter M, Ganesan R, Sumathi V, George S, Glenn McCluggage W, Nucci MR, Lee CH, Fletcher JA (2018) BCOR internal tandem duplication in high-grade uterine sarcomas. *Am. J. Surg. Pathol.* **42**: 335–341. <https://doi.org/10.1097/PAS.0000000000000993>
- Mashiah-Planchon J, Lévy D, Héron D, Giuliano F, Badens C, Fréneaux P, Galmiche L, Guinebrethier JM, Cellier C, Waterfall JJ, Ait-Raïs K, Pierron G, Glorion C, Desguerre I, Soler C, Deville A, Delattre O, Michon J, Bourdeaut F (2018) Does ATRX germline variation predispose to osteosarcoma? Three additional cases of osteosarcoma in two ATRX syndrome patients. *Eur. J. Hum. Genet.* **26**: 1217–1221. <https://doi.org/10.1038/s41431-018-0147-x>
- Misaghi A, Goldin A, Awad M, Kulidjian AA (2018) Osteosarcoma: a comprehensive review. *SICOT J.* **4** <https://doi.org/doi:10.1051/sicotj/2017028>
- Noblejas-López M del M, Morcillo-García S, Nieto-Jiménez C, Nuncia-Cantarero M, Györfy B, Galan-Moya EM, Pandiella A, Ocaña A (2018) Evaluation of transcriptionally regulated genes identifies NCOR1 in hormone receptor negative breast tumors and lung adenocarcinomas as a potential tumor suppressor gene. *PLoS One* **13**: 1–12. <https://doi.org/10.1371/journal.pone.0207776>
- Nomura R, Saito T, Mitomi H, Hidaka Y, Lee S, Watanabe S, Yao T (2014) GNAS mutation as an alternative mechanism of activation of the Wnt/ β -catenin signaling pathway in gastric adenocarcinoma of the fundic gland type. *Hum. Pathol.* **45**: 2488–2496. <https://doi.org/10.1016/j.humpath.2014.08.016>
- Pan R, Zhang Z, Jia H, Ma J, Wu C, Xue P, Cai W, Zhang X, Sun J (2022) CAMTA1-PPP3CA-NFATc4 multi-protein complex mediates the resistance of colorectal cancer to oxaliplatin. *Cell Death Discov.* **8** <https://doi.org/10.1038/s41420-022-00912-x>
- Park S-M, Choi E-Y, Bae M, Kim S, Park JB, Yoo H, Choi JK, Kim Y-J, Lee S-H, Kim I-H (2016) Histone variant H3F3A promotes lung cancer cell migration through intronic regulation. *Nat. Commun.* **7** <https://doi.org/10.1038/ncomms12914>
- Pasche B (2001) Role of transforming growth factor beta in cancer. *J. Cell. Physiol.* **186**: 153–168. [https://doi.org/10.1002/1097-4652\(200002\)186:2<153::AID-JCP1016>3.0.CO;2-J](https://doi.org/10.1002/1097-4652(200002)186:2<153::AID-JCP1016>3.0.CO;2-J)
- Patra KC, Kato Y, Mizukami Y, Widholz S, Revenco I, Grossman EA, Ji F, Sadreyev RI, Liss AS, Sreanont RA, Sakamoto K, Ryan DP, Mino M, Castillo CF, Nomura DK, Haas W, Bardeesy N (2018) Mutant GNAS drives pancreatic tumorigenesis by inducing PKA-mediated SIK suppression and reprogramming lipid metabolism. *Nat. Cell Biol.* **20**: 811–822. <https://doi.org/10.1038/s41556-018-0122-3>
- Piek E, Heldin CH, Ten Dijke P (1999) Specificity, diversity, and regulation in TGF-beta superfamily signaling. *FASEB J* **13**: 2105–2124. PMID: 10593858
- Pignochino Y, Grignani G, Cavalloni G, Motta M, Tapparo M, Bruno S, Bottoni A, Gammaitoni L, Migliardi G, Camussi G, Alberghini M, Torchio B, Ferrari S, Bussolino F, Fagioli F, Picci P, Aglietta M (2009) Sorafenib blocks tumour growth, angiogenesis and metastatic potential in preclinical models of osteosarcoma through a mechanism potentially involving the inhibition of ERK1/2, MCL-1 and ezrin pathways. *Mol. Cancer* **8**: 1–17. <https://doi.org/10.1186/1476-4598-8-118>
- Porter, DE; Holden, ST; Steel, CM; Cohen, BB; Wallace, MR; Reid R (1992) A significant proportion of patients with osteosarcoma may belong to Li-Fraumeni cancer families. *J. Bone Jt. Surg.* **74**: 883–886. <https://doi.org/10.1302/0301-620x.74b6.1447251>
- Príncipe C, Dionisio de Sousa IJ, Prazeres H, Soares P, Lima RT (2021) LRP1B: A Giant Lost in Cancer Translation. *Pharmaceuticals (Basel)* **14**: <https://doi.org/10.3390/ph14090836>
- Sbaraglia M, Righi A, Gambarotti M, Dei Tos AP (2020) Ewing sarcoma and Ewing-like tumors. *Virchows Arch.* **476**: 109–119. <https://doi.org/10.1007/s00428-019-02720-8>
- Sharma S, Kelly TK, Jones PA (2009) Epigenetics in cancer. *Carcinogenesis* **31**: 27–36. <https://doi.org/10.1093/carcin/bgp220>
- Sigismund S, Avanzato D, Lanzetti L (2018) Emerging functions of the EGFR in cancer. *Mol. Oncol.* **12**: 3–20. <https://doi.org/10.1002/1878-0261.12155>
- Śmiech M, Leszczyński P, Kono H, Wardell C, Taniguchi H (2020) Emerging BRAF mutations in cancer progression and their possible effects on transcriptional networks. *Genes (Basel)* **11**: <https://doi.org/10.3390/genes11111342>
- Soejima H, Kawamoto S, Akai J, Miyoshi O, Arai Y, Morohka T, Matsuo S, Niihara N, Kimura A, Okubo K, Mukai T (2001) Isolation of novel heart-specific genes using the BodyMap database. *Genomics* **74**: 115–120. <https://doi.org/10.1006/geno.2001.6527>
- Sturm D, Witt H, Hovestadt V, Khuong-Quang DA, Jones DT, Konermann C, Pfaff E, Tönjes M, Sill M, Bender S, Kool M, Zapatka M, Becker N, Zucknick M, Hielscher T, Liu XY, Fontebasso AM, Ryzhova M, Albrecht S, Jacob K, Wolter M, Ebinger M, Schuhmann MU, van Meter T, Frühwald MC, Hauch H, Pekrun A, Radlwimmer B, Niehues T, von Komorowski G, Dürken M, Kulozik AE, Madden J, Donson A, Foreman NK, Drissi R, Fouldi M, Scheurlen W, von Deimling A, Monoranu C, Roggendorf W, Herold-Mende C, Unterberg A, Kramm C, Felsberg J, Hartmann C, Wiestler B, Wick W, Milde T, Witt O, Lindroth AM, Schwartzentruber J, Faury D, Fleming A, Zakrzewska M, Liberski PP, Zakrzewski K, Hauser P, Garami M, Klekner A, Bognar L, Morrissy S, Cavalli F, Taylor MD, van Sluis P, Koster J, Versteeg R, Volckmann R, Mikkelsen T, Aldape K, Reifemberger G, Collins VP, Majewski J, Korshunov A, Lichter P, Plass C, Jabado N, Pfister SM (2012) Hotspot mutations in H3F3A and IDH1 define distinct epigenetic and biological subgroups of glioblastoma. *Cancer Cell* **22**: 425–437. <https://doi.org/10.1016/j.ccr.2012.08.024>
- Sugiura Y, Kanda H, Motoi N, Nomura K, Inamura K, Okada E, Matsumoto H, Shimoji T, Matsumoto S, Nakayama J, Takazawa Y, Ishikawa Y, Machinami R (2018) Osteosarcoma arising in fibrous dysplasia, confirmed by mutational analysis of GNAS gene. *Pathol. - Res. Pract.* **214**: 318–324. <https://doi.org/https://doi.org/10.1016/j.prp.2017.10.018>
- Sun J, Ren P, Ye L, Li N, Wang D (2017) MLLT3 promotes proliferation of osteosarcoma cells by regulating JNK signaling. *Int. J. Clin. Exp. Pathol.* **10**: 9444–9451
- Sun Y, Wang L, Li C, Gu R, Zang W, Song W, Xia P (2020) Construction of an integrated human osteosarcoma database, HOsDB, based on literature mining, microarray analysis, and database retrieval. *BMC Cancer* **20**: 1–9. <https://doi.org/10.1186/s12885-020-06719-2>
- Synoradzki KJ, Bartnik E, Czarnecka AM, Fiedorowicz M, Firlej W, Brodzia A, Stasinska A, Rutkowski P, Grieb P (2021) Tp53 in biology and treatment of osteosarcoma. *Cancers (Basel)*. **13**: 1–23. <https://doi.org/10.3390/cancers13174284>
- Tallegas M, Gomez-Bouchet A, Legrand M, Bouvier C, de Pinieux G (2022) Markers for bone sarcomas. In *Bone Sarcomas and Bone Metastases - From Bench to Bedside*. Heymann D eds., pp 543–577. Academic Press. <https://doi.org/https://doi.org/10.1016/B978-0-12-821666-8.00017-7>

- Tang L, Zhang L, Liu L, Dong L, Dong Y, Zhu W, Wang H (2020) NCOR1 may be a potential biomarker of a novel molecular subtype of prostate cancer. *FEBS Open Bio* **10**: 2678–2686. <https://doi.org/10.1002/2211-5463.13004>
- Tate JG, Bamford S, Jubb HC, Sondka Z, Beare DM, Bindal N, Boutselakis H, Cole CG, Creatore C, Dawson E, Fish P, Harsha B, Hathaway C, Jupp SC, Kok CY, Noble K, Ponting L, Ramshaw CC, Rye CE, Speedy HE, Stefancsik R, Thompson SL, Wang S, Ward S, Campbell PJ, Forbes SA (2019) COSMIC: The Catalogue of Somatic Mutations in Cancer. *Nucleic Acids Res.* **47**: D941–D947. <https://doi.org/10.1093/nar/gky1015>
- Tokoyoda M, Adachi S, Ishida Y, Yamazaki K (2018) Osteosarcoma mimic in the breast: A recurrent malignant phyllodes tumour harbouring MED12 and hTERT mutations. *Cytopathology* **29**: 383–385. <https://doi.org/10.1111/cyt.12544>
- Trovó-Marqui AB, Tajara EH (2006) Neurofibromin: A general outlook. *Clin. Genet.* **70**: 1–13. <https://doi.org/10.1111/j.1399-0004.2006.00639.x>
- Ueno-Yokohata H, Okita H, Nakasato K, Akimoto S, Hata JI, Koshinaga T, Fukuzawa M, Kiyokawa N (2015) Consistent in-frame internal tandem duplications of BCOR characterize clear cell sarcoma of the kidney. *Nat. Genet.* **47**: 861–863. <https://doi.org/10.1038/ng.3338>
- Wang K, Yamamoto H, Chin JR, Werb Z, Vu TH (2004) Epidermal growth factor receptor-deficient mice have delayed primary endochondral ossification because of defective osteoclast recruitment. *J. Biol. Chem.* **279**: 53848–53856. <https://doi.org/10.1074/jbc.M403114200>
- Wang M, Xiong Z (2021) The mutation and expression level of Irp1b are associated with immune infiltration and prognosis in hepatocellular carcinoma. *Int. J. Gen. Med.* **14**: 6343–6358. <https://doi.org/10.2147/IJGMS.S333390>
- Wang SL, Zhong GX, Wang XW, Yu FQ, Weng DF, Wang XX, Lin JH (2018) Prognostic significance of the expression of HER family members in primary osteosarcoma. *Oncol. Lett.* **16**: 2185–2194. <https://doi.org/10.3892/ol.2018.8931>
- Won KY, Kim YW, Park YK (2010) Expression of Smad and its signalling cascade in osteosarcoma. *Pathology* **42**: 242–247. <https://doi.org/10.3109/00313021003631288>
- Wu CC, Livingston JA (2020) Genomics and the immune landscape of osteosarcoma. *Adv. Exp. Med. Biol.* **1258**: 21–36. https://doi.org/10.1007/978-3-030-43085-6_2
- Wu F, Zhong Y, Lang XB, Tu YL, Sun SF (2019) MNX1-AS1 accelerates the epithelial-mesenchymal transition in osteosarcoma cells by activating MNX1 as a functional oncogene. *Eur. Rev. Med. Pharmacol. Sci.* **23**: 8194–8202. https://doi.org/10.26355/eurrev_201910_19126
- Xie Y, Huang J, Wu M, Zhou Y (2018) Expression of CD133 protein in osteosarcoma and its relationship with the clinicopathological features and prognosis. *J. Cancer Res. Ther.* **14**: 892–895. https://doi.org/https://doi.org/10.4103/jcrt.JCRT_461_17
- Xu L, Xie X, Shi X, Zhang P, Liu A, Wang J, Zhang B (2021) Potential application of genomic profiling for the diagnosis and treatment of patients with sarcoma. *Oncol. Lett.* **21**: 1–12. <https://doi.org/10.3892/ol.2021.12614>
- Xu N, Wang L, Sun P, Xu S, Fu S, Sun Z (2019) Low Arid1a expression correlates with poor prognosis and promotes cell proliferation and metastasis in osteosarcoma. *Pathol. Oncol. Res.* **25**: 875–881. <https://doi.org/10.1007/s12253-017-0338-8>
- Yan GN, Lv YF, Guo QN (2016) Advances in osteosarcoma stem cell research and opportunities for novel therapeutic targets. *Cancer Lett.* **370**: 268–274. <https://doi.org/10.1016/j.canlet.2015.11.003>
- Yang C, Tian Y, Zhao F, Chen Z, Su P, Li Y, Qian A (2020) Bone microenvironment and osteosarcoma metastasis. *Int. J. Mol. Sci.* **21**: 1–17. <https://doi.org/10.3390/ijms21196985>
- Yang G, Yuan J, Li K (2013) EMT transcription factors: Implication in osteosarcoma. *Med. Oncol.* **30**: 1–5. <https://doi.org/10.1007/s12032-013-0697-2>
- Yiqi Z, Ziyun L, Qin F, Xingli W, Liyu Y (2020) Identification of 9-gene epithelial-mesenchymal transition related signature of osteosarcoma by integrating multi cohorts. *Technol. Cancer Res. Treat.* **19**: 1–11. <https://doi.org/10.1177/1533033820980769>
- Yu X, Yustein JT, Xu J (2021) Research models and mesenchymal/epithelial plasticity of osteosarcoma. *Cell Biosci.* **11**: 1–12. <https://doi.org/10.1186/s13578-021-00600-w>
- Zauber P, Marotta SP, Sabbath-Solitare M (2016) GNAS gene mutation may be present only transiently during colorectal tumorigenesis. *Int. J. Mol. Epidemiol. Genet.* **7**: 24–31.
- Zhou Y, Tan Y, Zhang Q, Duan Q, Chen J (2022) MED12 mutation as a potential predictive biomarker for immune checkpoint inhibitors in pan-cancer. *Eur. J. Med. Res.* **27**: 1–5. <https://doi.org/10.1186/s40001-022-00856-z>

MiRNA-19b-3p downregulates the endothelin B receptor in gastric cancer cells to prevent angiogenesis and proliferation

Xiaodong Hu✉, Hongbing Liu and Chaoyu Li

Department of General Surgery, Medical Centre Hospital of Qionglai City, Qionglai, Sichuan, 611530, China

MiR19b-3p acts as a tumor suppressor gene in various cancers, but its function in gastric cancer is unknown. This study investigated the role of miR19b-3p in angiogenesis and the proliferation of human gastric cancer cells targeting ET_BR expression. Cell proliferation in SGC-7901 cells, cell transfection, luciferase reporter assay, detection of endothelin B receptor mRNAs by RT-qPCR, and a Western blot assay were carried out. RT-qPCR expression analysis showed a prominent ($p < 0.01$) downregulation of miR19b-3p in SGC-7901 cells, which was inversely correlated with a substantial increase ($p < 0.01$) in the endothelin B receptor (ET_BR). However, overexpression of miR19b-3p in SGC-7901 cells with its mimic ($p < 0.01$) resulted in the loss of cell viability in the MTT assay. This effect was reversed ($p < 0.01$) by the inhibitor. Western blot analysis revealed that ET_BR was significantly ($p < 0.01$) decreased by miR19b-3p overexpression compared with that of the negative control or its inhibitor. Based on bioinformatics tools and luciferase reporter assays, we found that miR19b-3p interacts with the 3'-untranslated region (3'UTR) of ET_BR. Restoring miR19b-3p overexpression with its mimic led to downregulation of ET_BR in gastric cancer cells (SGC-7901), which significantly ($p < 0.01$) decreased the expression of vascular endothelial growth factor A (VEGF-A). These findings were considerably reversed by miR19b-3p inhibitors ($p < 0.01$). The results indicated that miR19b-3p exerts its molecular action by targeting ET_BR at the post-transcriptional level by regulating angiogenesis and proliferation by overexpressing miR19b-3p as a potential treatment target for gastric cancer.

Keywords: miRNA, gastric cancer, proliferation, angiogenesis, endothelial B receptor

Received: 26 December, 2022; revised: 31 March, 2023; accepted: 05 April, 2023; available on-line: 25 May, 2023

✉e-mail: 3097317821@qq.com

Abbreviations: GC, Gastric cancer; RT-qPCR: Reverse transcriptase quantitative polymerase chain reaction; 3'-UTR, untranslated region; ETBR, Endothelin B receptor; VEGF-A, vascular endothelial growth factor A; FBS, fetal bovine serum; PVDF, polyvinylidene fluoride membrane; MTT, 3-(4,5-dimethylthiazol-2-yl)-2,5-diphenyl tetrazolium bromide; ET-1, endothelin-1; ECE-1 & -2, endothelin-converting enzymes-1 & -2; PBS, Phosphate buffer saline; RIN, RNA Integrity Numbers; NSCLC, non-small cell lung carcinoma cell line

INTRODUCTION

Cancer-related deaths from gastric cancer (GC) are among the fourth highest worldwide. The treatment strategies for GC depend on the stage of the disease. Early-stage GC can be treated with surgery, whereas advanced GC requires more aggressive treatments, such as chemotherapy and radiation therapy (Li *et al.*, 2019).

Combination treatment can be effective in treating non-metastatic stomach cancer. Gastric cancer treatment includes perioperative or postoperative chemotherapy with radiation treatment. Early-stage gastric cancers are best treated with endoscopic resection. Fluoropyrimidines, platinum, taxanes, and irinotecan are active cytotoxic agents in gastric cancer. However, combination regimens are more effective and offer improved survival rates. Immunotherapy is an emerging treatment strategy for stomach cancers. A monoclonal antibody (ramucirumab) against VEGFR-2, either alone or along with paclitaxel, decreases the risk of gastric cancer (Joshi & Badgwell, 2021). Novel therapies are required to treat gastric cancer, which can be achieved by fully understanding its pathogenesis and associated molecular changes. Many disease states, including cancer, are associated with miRNA dysregulation and serve as significant markers for early diagnosis, prognosis, and treatment. Gastric cancer may be caused by dysfunctional miRNAs that disrupt the target genes of these miRNAs. This results in the downregulation and overexpression of tumor suppressor genes and oncogenes (Choi *et al.*, 2019).

miRNAs can regulate gene and miRNA expression in gastric cancer (Alessandrini *et al.*, 2018). These miRNAs (miR-143, miR-200, and miR-145) regulate cell movement and metastasis in gastric cancer by inhibiting Myo6 expression (Lei *et al.*, 2017a) and protein translation (N-cadherin) (Yuan *et al.*, 2014). According to previous studies, gastric cancer cells exhibit abnormal miRNA expression compared to surrounding normal cells (Li *et al.*, 2019). One of the earlier reports revealed that miRNAs have the potential to control or regulate several genes, and downregulation of miRNAs is correlated with the progression and development of gastric cancer (Zhu *et al.*, 2020). A recent study suggested that miR-19b-3p/NRP1 may play a role in inhibiting the GC progression (Wei *et al.*, 2020a). Another study reported that miR-19b-3p and miR-16-5p may be able to detect and predict the progression of gastric cancer (Zhang *et al.*, 2015a).

There is growing evidence that miRNAs, such as miR-125a, miR-1, miR-125b, miR-199, and miR155 modulate ET-1 expression through the 3' untranslated region (3'UTR) (Jacobs *et al.*, 2013). The small peptide endothelin-1 (ET-1) contains 21 amino acids and plays a variety of roles that affect various tissues, cells, and organs. However, the interaction between ET-1 and miRNAs in the gastric cancer is unfamiliar. Based on its own receptors, it has been established that it can exert a wide range of biological effects. Three endothelins (ET-1, ET-2, and ET-3), two G-protein-coupled receptors (ET_AR and ET_BR), and two endothelin-converting enzymes (ECE-1 and ECE-2) encompass the ET axis (Gu *et al.*, 2019). Different types of cancers, such as lung, prostate, colorectal, liver, breast and ovarian cancers includ-

ing melanoma, have been found to express ET-1 more frequently. There is some evidence that this may contribute to the proliferation, metastasis, angiogenesis, and suppressed apoptosis of cancer cells (Kalles *et al.*, 2019). The ET_AR receptor is primarily responsible for ET-1's ability to induce cell proliferation. A reduction in ET_BR expression has been implicated in the pathogenesis of various cancers, including those of the oesophagus, nasopharynx, prostate, and ovaries (Yin *et al.*, 2020). High levels of ET-1 have been detected in the plasma of patients with gastric cancer. This suggests that ET-1 can be used as a reliable indicator for predicting disease recurrence (Aliabadi *et al.*, 2022).

Currently, it is still unknown what biological function endothelin receptor B plays in gastric cancer and the mechanisms by which miR19b-3p regulates it. Our study was conducted to demonstrate that ET_BR plays a critical function in gastric cancer progression and to identify probable target sites for miR19b-3p and their cognate interactions within the 3'UTR of ET_BR employing a bioinformatics approach. We investigated the effects of miR19b-3p and its role in both the normal gastric epithelium and human gastric cancer cells targeting the endothelin B receptor (ET_BR) to prevent angiogenesis and proliferation. There is a possibility that this could lead to a new therapeutic approach and the identification of novel targets. Therefore, it is possible to use miRNAs as therapeutic targeting agents for various types of cancer.

MATERIALS AND METHODS

Cell culture

We obtained SGC-7901 (a human gastric cell line) and GES-1 (normal Gastric epithelial cell line) from the Chinese Academy of Sciences (Shanghai, China). RPMI-1640 was used to grow cells (Corning Life Sciences, Wujiang, China) added with 10% foetal bovine serum (FBS) (Corning Life Sciences, Wujiang, China) and 1% antibiotics such as streptomycin. The cells were allowed to grow in an incubator at room temperature with CO₂ (5%). For each line, the lowest passage number was between 3–5. A total of 1×10⁵ cells were seeded in six wells of a six-well plate. The cells were then exposed to saturated humidity for 24 h. It is generally recommended that cells pass through when they reach 80–90% confluence. Immediately after the medium was removed, the cells were rinsed twice with phosphate-buffered saline (PBS), incubated for 2 min with 0.3% trypsin, and then resuspended in RPMI 1640 medium (5 ml) with 10% FBS before passing a second time. Plasmotest™ (InvivoGen, USA) was used for colorimetric detection of mycoplasma contamination in cell cultures. Positive results indicate contamination of the cell culture. We did not detect mycoplasma contamination in cell cultures.

Cell transfection

A density of 2×10⁵ cells/cm² was seeded in six-well plates once the cells reached 80% confluence. As previously reported (Xin *et al.*, 2019), miRNAs were transfected into the SGC-7901 cells. MiR19b-3p was evaluated by transfecting cells with miR19b-3p mimic (40 nM), miR19b-3p inhibitor (40 nM), mimic control (40 nM), or inhibitor control (40 nM) (Sangon, China) using HiPerFect transfection reagent from Qiagen (Hilden, Germany), according to the manufacturer's instructions. During the logarithmic growth phase, gastric cancer

cells (SGC-7901) were transfected and divided into five groups: blank group (SGC-7901 cells without transfection), miR19b-3p-NC control group (SGC-7901 cells transfected with miR19b-3p mimic control), miR19b-3p mimic group (SGC-7901 cells transfected with miR19b-3p mimic), miR19b-3p inhibitor group (SGC-7901 cells transfected with miR19b-3p inhibitor), and miR19b-3p inhibitor control group (SGC-7901 cells transfected with miR19b-3p inhibitor control). Plasmid expression vectors encoding ET_BR and the accompanying empty vector (pGEM-T) controls were purchased from Origene (Rockville, MD, USA). For transfection of expression plasmids, 2.5 µg of empty vector or plasmid DNA was diluted with HiPerFect transfection reagent and added to cells grown in 6-well plates. Transfected cells were incubated for 24–72 h at room temperature, harvested for further assays with untreated cells, and used as blanks.

HiPerFect transfection solution (5 µL) was incubated at 37°C for 15 min in DMEM (300 µL) without serum. Five microliters of miR19b-3p mimic, miR19b-3p-NC, miR19b-3p inhibitor, or miR19b-3p-NC were placed in DMEM (250 µL) without serum. After incubation for 15 min, diluted miR19b-3p mimics, miR19b-3p mimic-NC, miR19b-3p inhibitor, and miR19b-3p inhibitor-NC were gently mixed with the diluted HiPerFect transfer reagent and incubated for another 20 min at 37°C. Phosphate-buffered saline (PBS) was used to wash the cells twice after removing the medium. Complexes (500 µL) were added to each well containing the cells and medium, and the plate was gently rocked to mix the solutions. To determine whether transgenes were expressed in cells, cells were incubated in a CO₂ incubator for 24 hours at 37°C.

Cell proliferation

The proliferation of transfected SGC-7901 cells with a miR19b-3p mimic, a miR19b-3p inhibitor, or their controls was studied using the MTT assay as previously described (Mu *et al.*, 2019). After transfection for 48 h, 1×10⁵ cells were grown in 96 well plates and the assays were carried out in triplicate. MTT reagent (Thermo Fisher Scientific, Waltham, USA) at a concentration of 5 µg/ml was added to each well of 96 well plates containing cells (Thermo Fisher Scientific, Waltham, USA). After incubation for four hours, 150 µL DMSO was added after removing the MTT reagent. The optical density of each sample was determined at 490 nm after shaking each sample at room temperature using a microplate reader (Molecular Devices, USA). SGC-7901 cells were seeded in 96-well plates and incubated at room temperature with 5% CO₂ in a humidified atmosphere for two weeks to examine their morphology. After 48 h of transfection, cell morphology was observed. To measure the amount of absorbance, cells were seeded (2×10⁵ cells per well) in a 96-well plate, and the proliferative rate of the cells was assessed. The general morphology and proliferative rate of SGC-7901 cells was observed every day with the aid of an inverted microscope (Olympus, Japan). Proliferation rates were calculated by determining the percentage change in the number of viable cells in relation to the period over which they were measured.

Assay for Luciferase reporter activity

We used Target Scan Human (http://www.targetscan.org/vert_72/), an online prediction tool for miRNA targets, to determine miR19b-3p binding targets in humans. Based on the predicted results, miR19b-3p may play a role in the regulation of ET_BR expression. Human tar-

get scanning indicated a potential binding site. RT-qPCR was used to amplify the 3'-UTR of the human ET_BR. The amplified human ET_BR sequence was cloned into a pGL3 control vector containing the XbaI site. The Q5 site-specific mutagenesis kit (Q5® Site-Directed Mutagenesis Kit; catalogue no: E0554S, NE Biolabs Inc., China) was used to generate the mutated binding site of miR19b-3p in the 3'-UTR of ET_BR following the manufacturer's protocol. Prediction validation was performed using a dual-luciferase assay (Promega, USA) and a microplate luminometer (BioTek, USA). Briefly, the ET_BR 3'-UTR with wild-type (ET_BR-wt) miR binding site or mutant-type (ET_BR/mut) miR binding site was first cloned into the pmir-GLO luciferase reporter vector. According to a previous study (L. Zhang *et al.*, 2018) prior to transfection, SGC-7901 cells were maintained in nutrient-enriched medium for 24 h in a 24-well plate. Using the HiPerFect-Transfection reagent, 0.5 µg of 3'-UTR-ET_BR with reporter vectors (1 ng/µL, WT or MUT type) and 0.5 µg miR19b-3p-mimic or control were transfected into SGC-7901 cells. To quantify the luciferase activity of the cells, host cells were isolated, washed, trypsinized for 48 h after transfection, and assayed as directed by the manufacturer using a dual luciferase assay.

Detection of endothelin B receptor mRNAs by RT-q PCR

Agilent Bioanalyzers (Agilent Technologies Co. Ltd., Beijing, China) using microfluidics to classify RNA samples based on RNA Integrity Numbers (RIN) ranging from 1 to 10. According to a study (Padhi *et al.*, 2018), a RIN of more than 8.0 indicates intact and high-quality RNA samples, a RIN between 5.0 and 8.0 indicates moderately degraded samples, and a RIN of less than 5.0 indicates degraded samples. To ensure reliable measurement of gene expression by RT-qPCR, it is generally recommended that RNA samples with a RIN value above 5.0.

As previously reported (Skovsted *et al.*, 2015), the total RNAs was extracted from normal and gastric cancer cells using TRIzol reagent RNA extraction reagent was purchased from Dongsheng Biotech (Guangzhou, China). The extracted RNA was verified by agarose gel electrophoresis. Approximately five µg of RNA from both cell lines was reverse-transcribed using Moloney Murine leukemia virus reverse transcriptase (Sigma-Aldrich, Germany) and oligo (dT)18 primers in 20 µL reaction mixture. Then, the solution was made up to 50 µL with deionized water. For the PCR reaction, one µL of the solution was used as a substrate for PCR amplification. After 28 cycles, 25 µL of the solution was removed (91°C for 40 s, 57°C for 40 s, and 75°C for 50 s). Agarose gel electrophoresis was used to analyse approximately 10 µL of the solution containing the amplified products. PCR was carried out using pairs of primers specific for human GAPDH (5'-CATGTTTCGTCATGGGGTGAACCA-3' and 5'-AGTGATGGCATGGACTGTGGTCAT-3') and ET_BR (5'-ACTGGCCATTGGAGCTGAGAT-3' and

5'-CTGCATGCCACTTCTTCTCAA-3'). GAPDH was used as an endogenous control for the normalization of target gene expression. Inverse logarithms of $\Delta\Delta C_t$ values were used to calculate the relative levels of miR19b-3p. Table 1 lists the information of the primer sequence.

Western blot assay and antibodies

RIPA lysis buffer was used to collect total protein from cells. We measured the protein concentration using a BCA protein assay kit. Protein separation of proteins (30 µg) was carried out using SDS-PAGE (Bio-Rad Laboratories Co., Ltd. Shanghai, China). A polyvinylidene fluoride membrane (PVDF) was then used to transfer the proteins. A 5–6% non-fat dry milk solution was used to occlude the membranes for one hour to prevent nonspecific binding. After blocking, antibodies such as anti-ET_BR (1:200) or anti-VEGF-A (1:3000) were transferred to the membranes and allowed for incubation for 10 hours at 4°C. Subsequently, HRP-conjugated secondary antibodies (1:2500) were applied to the membranes at 37°C for 1 hour. The protein bands on the membrane bound to antibodies were detected by a chemiluminescence system (GE LAS4000 Image, Quant, CA, USA). Protein expression was analysed using ImageQuant software. The bands were detected and photographed using a chemiluminescence analyser (Biotech Co., Ltd., Beijing). Densitometry was used to quantify protein bands using Quantity One software. The difference in loading between groups was corrected by dividing the volume per individual group by the volume of normalised β -actin for each group. The differences between each group and the control group were then determined by a normalisation procedure. The results were presented as percentages based on the control data (Sun *et al.*, 2022).

Statistical analyses

A minimum of three independent analyses of each experiment were performed to achieve the most accurate results. Data were analysed using GraphPad Prism (Version 9.0) using a student's *t*-test. In this study, we used the *t*-test to determine whether there was a significant difference between two groups. The values of the experimental and control groups were compared using one-way ANOVA. Tukey's multiple comparison test was used to compare the groups. We define statistical significance as a *p*-value <0.05.

RESULTS

miR19b-3p inhibits proliferation in SGC-7901 cells

Quantitative real-time PCR findings revealed that miR19b-3p expression in SGC-7901 cells was substantially (*p*<0.01) reduced compared to GES-1 cells (Fig. 1A). To examine the role of miR19b-3p in gastric cancer, the role of miR19b-3p in SGC-7901 cells was investigated by

Table 1. List of primers used in the study

No	Primers	Sequences
1	miR19b-3p-mimic	forward: 5'-UGUGCAAUCCAUGCAAACUGA-3' and reverse, 5'-AGUUUUGCAUG GAUUUGCA-CAUU-3'
2	miR19b-3p-mimic control	forward: 5'-UUCUCCGAACGUGUCACGUTT-3', and reverse, 5'-ACGUGACACGUUCGGAGAATT-3'
3	miR19b-3p-inhibitor	forward: 5'-UCAGUUUUGCAUGGAUUUGCACA-3' and reverse, 5'-ACGAGAAGGAUGGATTUGGAU-3'
4	miR19b-3p-inhibitor control	forward: 5'-CAGUACUUUUGUGUAGUACAA-3' and reverse, 5'-ACGAUTTUAATGCCGUAAUUA-3'

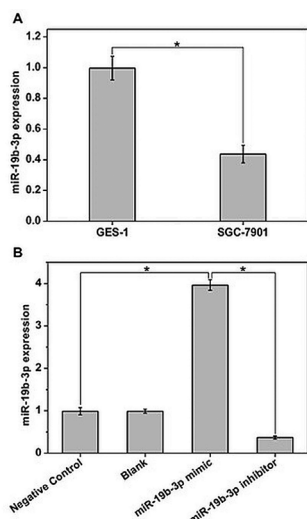


Figure 1. Downregulation of miR19b-3p in SGC-7901 cells.

(A) The miR19b-3p expression in normal gastric epithelial cells and gastric cancer cell line detected by RT-qPCR. (B) The miR19b-3p expression after transfection with negative control, blank, miR19b-3p mimic, and miR19b-3p inhibitor in SGC-7901 cells. * $p < 0.01$.

transfection with miR19b-3p-mimic, a miR19b-3p inhibitor or negative control in SGC7901 cells and transfection efficiency was measured by RT-qPCR. Figure 1B shows that miR19b-3p mimics markedly elevated miR19b-3p expression levels ($p < 0.01$) in SGC-7901 cells, while it decreased dramatically ($p < 0.01$) with the miR19b-3p inhibitor transfected into SGC-7901 cells.

The morphology of SGC-7901 cells treated with a miR19b-3p mimic or its inhibitor or NCs was examined under inverted microscopy (Fig. 2A–E). Cells in control groups (NCs) appeared round shaped and were densely packed. In the miR19b-3p mimic group, the cells showed a gradual rounding with significantly less densely

packed compared to those seen in the control groups. Furthermore, an increased number of floating cells in the miR19b-3p mimic-group indicated a decrease in cell viability. These findings indicated that SGC-7901 cells showed a significant decrease ($p < 0.01$) in their viability in the presence of a miR19b-3p mimic, but viability was significantly restored ($p < 0.01$) in response to miR19b-3p inhibitor. Cell proliferation analysis studied by the MTT assay showed the substantial ($p < 0.05$) inhibitory effects ($p < 0.05$) of miR19b-3p mimic on cell viability compared to negative controls, as shown in Fig. 2F.

The expression level of miR19b-3p was reversely correlated with the expression of the endothelin B receptor in SGC-7901 cells

To study the function of miR19b-3p in the angiogenesis of gastric cancer cells, the relationship between miR19b-3p and ET_BR was studied. The relationship between angiogenesis and endothelin receptor B is well documented. Endothelin-1 (ET-1) and its two receptors, endothelin receptor A (ET_AR) and ET_BR, are overexpressed in tumour cells. ET_BR has been reported to be a key regulator of tumour angiogenesis by being directly involved in VEGF-A expression. Changes in miR19b-3p expression levels and its effect on ET_BR expression were evaluated in SGC-7901 cells. We used Western blot to study ET_BR expression in SGC-7901 cells and GES-1 cells. According to our findings, higher ET_BR levels were found in cancerous gastric cells compared to normal cells (Fig. 3A). Based on the results, it was evident that ET_BR was negatively correlated with miR19b-3p expression, as shown in Fig. 3B ($p < 0.01$). From these results, we hypothesise that miR19b-3p might negatively regulate ET_BR expression in gastric cancer cells.

ET_BR is one of the target genes for miR19b-3p

To identify putative targets for miR19b-3p, we used an online bioinformatics tool, Target Human Scan. Figure 4A shows that ET_BR is presumed to be the target

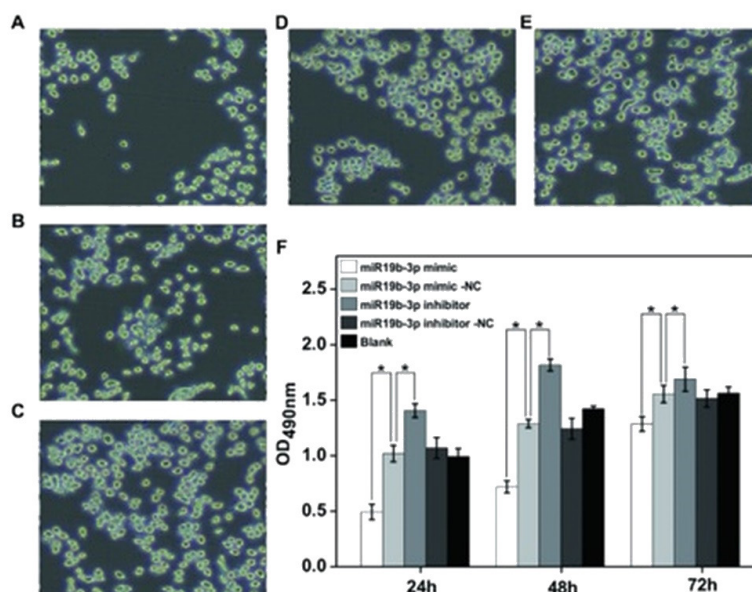


Figure 2. Transfection of miR19b-3p mimics decreases SGC-7901 cell proliferation.

(A) Observation of cell morphology under inverted microscope. The cells transfected with miR19b-3p mimic. (B) Cells transfected with miR19b-3p mimic negative control. (C) Cells transfected with miR19b-3p inhibitor. (D) Cells transfected with miR19b-3p inhibitor negative control. (E) Cells without transfection (blank). (F) Cell proliferation by MTT assay of various transfected groups at 24, 48 and 72 h. * $p < 0.01$.

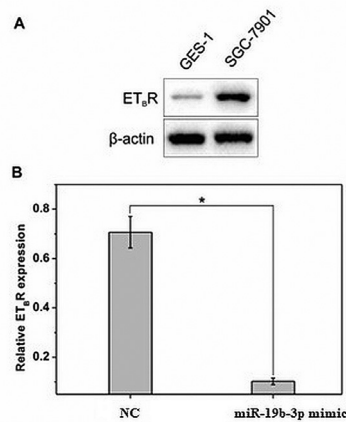


Figure 3. Enhanced expression of ETBR in human gastric cancer cells compared to normal gastric epithelial cells showing reverse correlation to miR19b-3p expression.

(A) The results from Western blot showing the relative ETBR expression. (B) Changes in the expression of ETBR after transfecting with miR19b-3p mimic or negative control into SGC-7901 cells. The data is presented from the average of three independent experiments. * $p < 0.01$.

site for miR19b-3p and the possible binding site between miR19b-3p and the predicted 3'-UTR of ET_BR. We used a luciferase reporter assay to verify whether miR19b-3p plays a role in ET_BR regulation through the binding site at the 3'-UTR of ET_BR. The predicted miR19b-3p binding site was cloned along with its wild- or mutant-type ET_BR. SGC-7901 cells were transfected with wild ET_BR or mutant ET_BR together with precursor and control. Cell luciferase transfection was performed 48 h after cell harvesting followed by total protein extraction. Figure 4B shows the significant expression of ET_BR in SGC-7901 cells compared to the reporter vector. However, a luciferase reporter assay was performed to identify aberrant cells in SGC-7901 cells. It was determined that luciferase activity decreased significantly ($p < 0.01$, Fig. 4C) when miR-19b-5p mimics were co-transfected

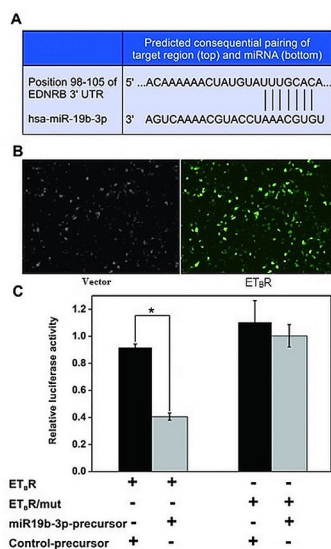


Figure 4. The ETBR is a target gene of miR19b-3p.

(A) Predicted binding site for miR19b-3p in ETBR. (B) Luciferase reporter assay for ETBR in human gastric cancer cells, SGC-7901. (C) Down-regulation of miR19b-3p precursor affect luciferase activity by ETBR 3' UTR in wild type but no effect was noticed on luciferase activity in mutant ETBR 3' UTR. The data presented is the average of three independent experiments. * $p < 0.01$.

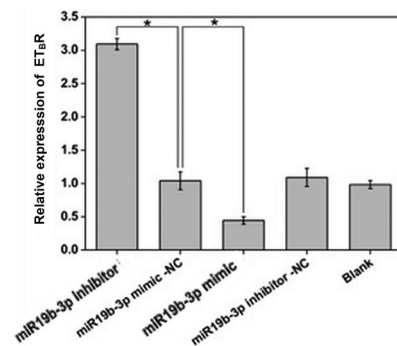


Figure 5. Effect of miR19b-3p on ETBR relative expression.

RT-qPCR results show decrease in the expression of ETBR with miR19b-3p mimic and increased expression of ETBR with miR19b-3p inhibitor when compared with miR19b-3p mimic negative control in the transfected SGC-7901 cells. * $p < 0.01$.

with luciferase plasmids containing ET_BR 3' UTRs with native binding sites. Figure 4C shows that the expression of the miR19b-3p precursor with ET_BR wild type significantly reduced luciferase activity.

Inhibition of ET_BR expression in gastric cancer cells by restoring miR19b-3p expression.

To study the role of ET_BR regulation in human gastric cancer, SGC-7901 cells were transfected with miR19b-3p mimic, miR19b-3p inhibitor, miR19b-3p mimic negative control, miR19b-3p inhibitor negative control or mock transfection. Real-time qPCR was performed to measure relative expression between the various groups of transfected cells. Figure 5 shows that ET_BR expression in the miR19b-3p mimic group was substantially decreased ($p < 0.01$) whereas the expression was significantly restored when treated with miR19b-3p inhibitor relative to the control group.

Furthermore, we studied ET_BR expression levels in SGC-7901 cells with Western blot experiments. As shown in Fig. 6, ET_BR expression was reduced in the miR-19b-3p mimic group and elevated with the miR-19b-3p inhibitor, thus restoring its expression.

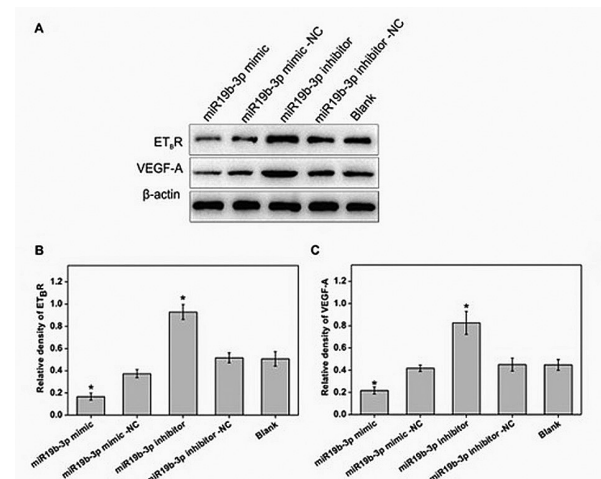


Figure 6. The miR19b-3p overexpression regulates ETBR expression in SGC-7901 cells using Western blot analysis.

(A) Western blot analysis of ETBR and VEGF-A expressions. (B) Relative densitometry analysis of ETBR analysis after transfecting with miR19b-3p mimic or inhibitor or controls or blank in SGC-7901 cells. (C) Relative densitometry analysis of VEGF-A after transfecting with miR19b-3p mimic or inhibitor or controls or blank. The data presented is an average of three independent experiments. * $p < 0.01$.

The study aims to confirm the function of ET_BR in cancer angiogenesis, and we also studied the expression level of VEGF-A along with ET_BR. The results showed that the increase in ET_BR regulation is positively correlated with VEGF-A expression. When miR19b-3p expression increased, ET_BR and VEGF-A expression levels decreased (Fig. 6, $p < 0.01$). The results showed that miR19b-3p played an active role in gastric cancer angiogenesis by regulating ET_BR expression, which is positively correlated with VEGF-A.

DISCUSSION

The miRNA has been shown to play a key role in tumour progression by regulating various genes after transcription. It is identified as a potential marker for cancer diagnosis and treatment (Blandino *et al.*, 2014). miR19b-3p has been shown in the regulation of various cancers (Jin *et al.*, 2018; Song *et al.*, 2019). Down-regulation of miR19b-3p was previously reported in patients with gastric cancer at different stages (Zhang *et al.*, 2015b). The precise role of miR19b-3p in gastric cancer and its angiogenesis remains unexplored.

The study findings showed that miR19b-3p could be involved in gastric carcinoma cells and healthy gastric epithelial cells. In this study, miR19b-3p was negatively regulated in SGC-7901 cells relative to GES-1 cells, which is consistent with previous reports (Wei *et al.*, 2020b). Our findings showed that miR19b-3p mimic transfections reduced the proliferation of SGC-7901 cells, indicating the role of miR19b-3p as a tumour suppressor by inhibiting the progression of gastric cancer cells. Similar results from a study were reported, but using a different miRNA in gastric cancer through EMT (epithelial-mesenchymal transitions) regulation, showing that miR-423-5p overexpression suppressed gastric cancer cell invasion, colony formation, and proliferation through the Smad3 pathway (Li *et al.*, 2022). Another showed that miR19b-3p negatively controlled the expression of NRP1 by targeting its 3'-UTR, thus suppressing gastric cancer cell growth, migration, and invasion (Zhang *et al.*, 2018). Previous studies have established that miR19b-3p is capable of inhibiting breast cancer cell proliferation through PI3K/Akt signaling (Jin *et al.*, 2018). Reduction in the accumulation of the non-small cell lung carcinoma (NSCLC) cell line A549 was observed when miR-19b was overexpressed (Li *et al.*, 2015). However, some findings have also been reported to contradict the idea that miR19b-3p promotes proliferation of NSCLC cells (Baumgartner *et al.*, 2018), colon cancer (Jiang *et al.*, 2017), and pancreatic cancer (Song *et al.*, 2019), which contrasts with our findings. The findings imply that miR-19b-3p plays a different role due to the untargeted effect of increased expression or cell-specific effects.

Our findings showed elevated expression of ET_BR in gastric cancer cells, SGC-7901. The similar results in the study were demonstrated the elevated levels of ET-1 and ET_BR expression in pancreatic adenocarcinoma relative to normal pancreatic samples (Cook *et al.*, 2015). To investigate the interaction of miR19b-3p, we used bioinformatic analysis to look for miR19b-3p target genes. The results showed that miR19b-3p interacts with ET_BR at its 3'UTR binding site. The luciferase reporter assay confirmed ET_BR as the target gene for miR19b-3p in human gastric cancer cells. The role of ET-1 and its receptors, ET_AR and ET_BR, in cancer angiogenesis has been investigated and reviewed (Olender *et al.*, 2016).

Tumour angiogenesis is directly promoted by ET-1 by inducing endothelial cell survival and proliferation and by upregulating ET_BR expression that causes the progression of breast cancer, and invasion and bone metastasis of triple negative breast cancer cells (Gu *et al.*, 2019). Our findings revealed that increased expression of miR19b-3p is reversely correlated with a lower expression of ET_BR, resulting in decreased angiogenesis in gastric cancer cells. When miR-19b-3p expression was restored in SGC-7901 cells, it reduced ET_BR expression and angiogenesis. Similarly, to our findings, a recent study reported that up-regulation of miR-449a-5p, miR-19b-3p, miR-223-3p, miR-511-3p, and miR-130b-3p are likely involved in flow-stimulated angiogenesis *in vivo* through modulation of the expression of the mitochondrial membrane protein SYNJ2BP, oxygenation-associated genes (HIF1A, HMOX1), cytokines (e.g., IL1A, CXCL2) as well as the embryonic transcription factor FOXC1 (Henn *et al.*, 2019).

The relationship between ET_BR expression and VEGF expression was studied by Western blotting. When miR19b-3p down-regulated ET_BR expression, VEGF expression was also reduced, leading to reduced angiogenesis in gastric cancer cells. The findings showed that angiogenesis indirectly reduced the up-regulation of VEGF by ET-1 through the down-regulation of ET_BR. Our findings are supported by the study results that demonstrate inhibited angiogenesis and permeability of blood vessels through the VEGF or VEGFR2 signalling pathway by antiangiogenic medicine (asiatic acid) significantly suppresses breast cancer growth and metastasis (Tian *et al.*, 2021). In another study, it was found that miR-638 overexpression inhibited the processes of tumour angiogenesis *in vitro* and *in vivo*, suppressing angiogenesis and tumour growth of hepatocellular carcinoma by inhibiting VEGF signaling (Cheng *et al.*, 2016). However, there are contrasting reports that ET_BR downregulation leads to upregulation of VEGF, causing an increase in angiogenesis in human melanoma cells (Carpenter *et al.*, 2003; Lahav *et al.*, 2004) and ET_BR mutant rats showed an increase in VEGF expression compared to wild-type (Li *et al.*, 2012).

Regardless of the role of ET_BR in suppressing or repressing VEGF, our results showed that regulation of ET_BR expression plays a considerable role in controlling angiogenesis in human gastric cancer cells. In our investigation, we also tried to find whether miR19b-3p expression directly affects VEGF expression without ET_BR regulation, but there was no significant effect on VEGF expression. This shows that miR19b-3p is not directly involved in the regulation of VEGF expression.

The role of miRNAs in modulating endothelin expression by binding to a 3 untranslated region was previously reported (Lei *et al.*, 2017b; Jacobs *et al.*, 2013). Several research articles have been published on the possibility of using endothelin receptors as a new approach to cancer treatment (Tocci *et al.*, 2019). However, how miRNAs interact and regulate endothelin-1 and its receptors must be clarified. Our findings suggest that miR19b-3p may be able to function as a tumour suppressor by regulation of ET_BR in human gastric cancer cells. Therefore, we propose that miR19b-3p could be used to inhibit the angiogenesis and proliferation of gastric cancer.

LIMITATIONS OF THE STUDY

Our functional experiments were conducted on a single SGC-7901 cell line. In our preliminary study, SGC-

7901 demonstrated greater proliferation ability using miR19b-3p than MKN-45 or AGS.

The *in vivo* expression of miR19b-3p and its regulation in gastric cancer remain unknown. More detailed *in vivo* studies on the role of miR19b-3p in gastric cancer should be explored.

There is a need for further studies exploring the effects of miR19b-3p on cell invasion, apoptosis and apoptotic proteins including cell cycle proteins.

CONCLUSIONS

According to our findings, reduced expression of miR19b-3p was found to be instrumental in the development and angiogenesis of cancerous cells in gastric tissues. However, overexpression of miR19b-3p could significantly inhibit ET_BR expression, leading to a reduction in angiogenesis and proliferation through the reduced expression of VEGF *in vitro*. Further studies on the role of gastric cancer will help develop potential therapies for gastric cancer.

Declarations

Authors' contributions. XH and C.L designed the study plan and performed experiments. B.X and T.W drafted the original manuscript. WG and BP were involved in the formal analysis. T.W supervised the whole study.

Financial disclosure. In the present study, no specific funding or support from any agency in the public, private, or non-profit sectors has been received for the conduct of this study.

Acknowledgements. The authors would like to thank Medical Centre Hospital of Qionglai City for providing all the facilities to conduct this study.

Conflict of interest. There is no conflict of interest to declare.

11.0 Ethics statement (including the committee approval number) for animal and human studies – Not applicable

REFERENCES

- Alessandrini L, Manchi M, De Re V, Dolcetti R, Canzonieri V (2018) Proposed molecular and mirna classification of gastric cancer. *Int J Mol Sci* 19: 1683. <https://doi.org/10.3390/ijms19061683>
- Aliabadi P, Sadri M, Siri G, Ebrahimzadeh F, Yazdani Y, Gusarov AM, Kharkouci SA, Asadi F, Adili A, Mardi A, Mohammadi H (2022) Restoration of miR-648 overcomes 5-FU-resistance through targeting ET-1 in gastric cancer cells *in-vitro*. *Pathol – Res Pract* 239: 154139. <https://doi.org/10.1016/j.prp.2022.154139>
- Baumgartner U, Berger F, Hashemi Gheini A, Burgener SS, Monastyrskaya K, Vassella E (2018) MiR-19b enhances proliferation and apoptosis resistance *via* the EGFR signaling pathway by targeting PP2A and BIM in non-small cell lung cancer. *Mol Cancer* 17: 44. <https://doi.org/10.1186/s12943-018-0781-5>
- Blandino G, Fazi F, Donzelli S, Kedmi M, Sas-Chen A, Muti P, Strano S, Yarden Y (2014) Tumor suppressor microRNAs: A novel non-coding alliance against cancer. *FEBS Lett* 588: 2639–2652. <https://doi.org/10.1016/j.febslet.2014.03.033>
- Carpenter T, Schomberg S, Steudel W, Ozimek J, Colvin K, Stenmark K, Ivy DD (2003) Endothelin B receptor deficiency predisposes to pulmonary edema formation *via* increased lung vascular endothelial cell growth factor expression. *Circ Res* 93: 456–463. <https://doi.org/10.1161/01.RES.0000090994.15442.42>
- Cheng J, Chen Y, Zhao P, Liu X, Dong J, Li J, Huang C, Wu R, Lv Y (2016) Downregulation of miRNA-638 promotes angiogenesis and growth of hepatocellular carcinoma by targeting VEGF. *Oncotarget* 7: 30702–30711. <https://doi.org/10.18632/oncotarget.8930>
- Choi RSY, Lai WYX, Lee LTC, Wong WLC, Pei XM, Tsang HF, Leung JJ, Cho WCS, Chu MKM, Wong EYL, Wong SCC (2019) Current and future molecular diagnostics of gastric cancer. *Exp Rev Mol Diag* 19: 863–874. <https://doi.org/10.1080/14737159.2019.1660645>
- Cook N, Brais R, Qian W, Chan Wah Hak C, Corrie PG (2015) Endothelin-1 and endothelin B receptor expression in pancreatic adenocarcinoma. *J Clin Pathol* 68: 309–313. <https://doi.org/10.1136/ijclinpath-2014-202521>
- Gu X, Han S, Cui M, Xue J, Ai L, Sun L, Zhu X, Wang Y, Liu C (2019) Knockdown of endothelin receptor B inhibits the progression of triple-negative breast cancer. *Ann N Y Acad Sci* 1448: 5–18. <https://doi.org/10.1111/nyas.14039>
- Henn D, Abu-Halima M, Wermke D, Falkner F, Thomas B, Köppler C, Ludwig N, Schulte M, Brockmann MA, Kim YJ, Sacks JM, Kneser U, Keller A, Meese E, Schmidt VJ (2019) MicroRNA-regulated pathways of flow-stimulated angiogenesis and vascular remodeling *in vivo*. *J Trans Med* 17: 22. <https://doi.org/10.1186/s12967-019-1767-9>
- Jacobs ME, Wingo CS, Cain BD (2013) An emerging role for microRNA in the regulation of endothelin-1. *Frontiers Physiol* 4: 22. <https://doi.org/10.3389/fphys.2013.00022>
- Jiang T, Ye L, Han Z, Liu Y, Yang Y, Peng Z, Fan J (2017) miR-19b-3p promotes colon cancer proliferation and oxaliplatin-based chemoresistance by targeting SMAD4: Validation by bioinformatics and experimental analyses. *J Exp Clin Cancer Res* 36: 131. <https://doi.org/10.1186/s13046-017-0602-5>
- Jin J, Sun Z, Yang F, Tang L, Chen W, Guan X (2018) MiR-19b-3p inhibits breast cancer cell proliferation and reverses saracatinib-resistance by regulating PI3K/Akt pathway. *Arch Biochem Biophys* 645: 54–60. <https://doi.org/10.1016/j.abb.2018.03.015>
- Joshi SS, Badgwell BD (2021) Current treatment and recent progress in gastric cancer. *Cancer J Clin* 71: 264–279. <https://doi.org/10.3322/caac.21657>
- Kalles V, Papapanagiotou I, Matiatou M, Georgiou G, Theodoropoulos C, Triantafyllou T, Zografos E, Mitrousi A, Provatopoulou X, Michalopoulos N (2019) Evaluation of plasma and tissue expression levels of Endothelins (ET-1, Big ET-1) and VEGF in lobular neoplasia of the breast. *J BUON* 24: 1913–1919. PMID: 31786855
- Lahav R, Suvà ML, Rimoldi D, Patterson PH, Stamenkovic I (2004) Endothelin receptor B inhibition triggers apoptosis and enhances angiogenesis in melanomas. *Cancer Res* 64: 8945–8953. <https://doi.org/10.1158/0008-5472.CAN-04-1510>
- Lei C, Du F, Sun L, Li T, Li T, Min Y, Nie A, Wang X, Geng L, Lu Y, Zhao X, Shi Y, Fan D (2017a) MiR-143 and miR-145 inhibit gastric cancer cell migration and metastasis by suppressing MYO6. *Cell Death Dis* 8: e3101. <https://doi.org/10.1038/cddis.2017.493>
- Lei C, Du F, Sun L, Li T, Li T, Min Y, Nie A, Wang X, Geng L, Lu Y, Zhao X, Shi Y, Fan D (2017b) MiR-143 and miR-145 inhibit gastric cancer cell migration and metastasis by suppressing MYO6. *Cell Death Dis* 8: e3101–e3101. <https://doi.org/10.1038/cddis.2017.493>
- Li D, Yang P, Li H, Cheng P, Zhang L, Wei D, Su X, Peng J, Gao H, Tan Y, Zhao Z, Li Y, Qi Z, Rui Y, Zhang T (2012) MicroRNA-1 inhibits proliferation of hepatocarcinoma cells by targeting endothelin-1. *Life Sci* 91: 440–447. <https://doi.org/10.1016/j.lfs.2012.08.015>
- Li H, Xue S, Zhang X, Li F, Bei S, Feng L (2022) CircRNA PVT1 modulated cell migration and invasion through Epithelial-Mesenchymal Transition (EMT) mediation in gastric cancer through miR-423-5p/Smad3 pathway. *Regen Therap* 21: 25–33. <https://doi.org/10.1016/j.reth.2022.02.003>
- Li J, Yang S, Yan W, Yang J, Qin YJ, Lin XL, Xie RY, Wang SC, Jin W, Gao F, Shi JW, Zhao WT, Jia JS, Shen HF, Ke JR, Liu B, Zhao YQ, Huang WH, Yao KT, Xiao D (2015) MicroRNA-19 triggers epithelial-mesenchymal transition of lung cancer cells accompanied by growth inhibition. *Lab Invest J Tech Methods Pathol* 95: 1056–1070. <https://doi.org/10.1038/labinvest.2015.76>
- Li W, Li J, Mu H, Guo M, Deng H (2019) MiR-503 suppresses cell proliferation and invasion of gastric cancer by targeting HMGA2 and inactivating WNT signaling pathway. *Cancer Cell Int* 19: 164. <https://doi.org/10.1186/s12935-019-0875-1>
- Mu J, Wang H, Wang X, Sun P (2019) Expression of miR-124 in gastric adenocarcinoma and the effect on proliferation and invasion of gastric adenocarcinoma SCG-7901 cells. *Oncol Lett* 17: 3406–3410. <https://doi.org/10.3892/ol.2019.9981>
- Olender J, Nowakowska-Zajdel E, Walkiewicz K, Muc-Wierzygón M (2016) Endothelins and carcinogenesis. *Postepy Hig Med Dosw (Online)* 70: 872–880. <https://doi.org/10.5604/17322693.1214386>
- Padhi BK, Singh M, Rosales M, Pelletier G, Cakmak S (2018) A PCR-based quantitative assay for the evaluation of mRNA integrity in rat samples. *Biomol Detect Quantifi* 15: 18–23. <https://doi.org/10.1016/j.bdq.2018.02.001>
- Skovsted GF, Kilic S, Edvinsson L (2015) Endothelin-1 and endothelin-3 regulate endothelin receptor expression in rat coronary arteries. *Basic Clin Pharm Toxicol* 117: 297–305. <https://doi.org/10.1111/bcpt.12407>
- Song M, Sun M, Xia L, Chen W, Yang C (2019) MiR-19b-3p promotes human pancreatic cancer Capan-2 cells proliferation by targeting phosphatase and tension homolog. *Ann Trans Med* 7: 236. <https://doi.org/10.21037/atm.2019.04.61>

- Sun X, Zhang H, Qin Q, Zhang X, Hou Y, Chen D, Su X, Jia M, Chen Y (2022) Inhibitors of the MAPK/ NF- κ B pathway attenuate the upregulation of the ETB receptor mediated by high glucose in vascular smooth muscle cells. *Peptides* **150**: 170732. <https://doi.org/10.1016/j.peptides.2021.170732>
- Tian M, Chen K, Huang J, Chu D, Li J, Huang K, Ma C (2021) Asiatic acid inhibits angiogenesis and vascular permeability through the VEGF/VEGFR2 signaling pathway to inhibit the growth and metastasis of breast cancer in mice. *Phytotherap Res* **35**: 6389–6400. <https://doi.org/10.1002/ptr.7292>
- Tocci P, Rosanò L, Bagnato A (2019) Targeting endothelin-1 receptor/ β -arrestin-1 axis in ovarian cancer: from basic research to a therapeutic approach. *Frontiers Endocrinol* **10**: 609. <https://doi.org/10.3389/fendo.2019.00609>
- Wei Y, Guo S, Tang J, Wen J, Wang H, Hu X, Gu Q (2020a) MicroRNA-19b-3p suppresses gastric cancer development by negatively regulating neuropilin-1. *Cancer Cell Int* **20**: 193. <https://doi.org/10.1186/s12935-020-01257-0>
- Wei Y, Guo S, Tang J, Wen J, Wang H, Hu X, Gu Q (2020b) MicroRNA-19b-3p suppresses gastric cancer development by negatively regulating neuropilin-1. *Cancer Cell Int* **20**: 193. <https://doi.org/10.1186/s12935-020-01257-0>
- Xin H, Wang C, Liu Z (2019) MiR-196a-5p promotes metastasis of colorectal cancer via targeting lxBx. *BMC Cancer* **19**: 30. <https://doi.org/10.1186/s12885-018-5245-1>
- Yin H, Wang L, Li F, Wang D, Zhang Z, Yu B, Liu Y (2020) E-T-1 promotes the growth and metastasis of esophageal squamous cell carcinoma via activating PI3K/Akt pathway. *Trans Cancer Res* **9**: 3282–3292. <https://doi.org/10.21037/tcr.2020.04.26>
- Yuan D, Xia H, Zhang Y, Chen L, Leng W, Chen T, Chen Q, Tang Q, Mo X, Liu M, Bi F (2014) P-Akt/miR-200 signaling regulates epithelial-mesenchymal transition, migration and invasion in circulating gastric tumor cells. *Int J Oncol* **45**: 2430–2438. <https://doi.org/10.3892/ijo.2014.2644>
- Zhang J, Song Y, Zhang C, Zhi X, Fu H, Ma Y, Chen Y, Pan F, Wang K, Ni J, Jin W, He X, Su H, Cui D (2015a) Circulating MiR-16-5p and MiR-19b-3p as two novel potential biomarkers to indicate progression of gastric cancer. *Theranostics* **5**: 733–745. <https://doi.org/10.7150/thno.10305>
- Zhang J, Song Y, Zhang C, Zhi X, Fu H, Ma Y, Chen Y, Pan F, Wang K, Ni J, Jin W, He X, Su H, Cui D (2015b) Circulating MiR-16-5p and MiR-19b-3p as two novel potential biomarkers to indicate progression of gastric cancer. *Theranostics* **5**: 733–745. <https://doi.org/10.7150/thno.10305>
- Zhang L, Kang W, Lu X, Ma S, Dong L, Zou B (2018) LncRNA CASC11 promoted gastric cancer cell proliferation, migration and invasion *in vitro* by regulating cell cycle pathway. *Cell Cycle* **17**: 1886–1900. <https://doi.org/10.1080/15384101.2018.1502574>
- Zhu H, Wu Y, Kang M, Zhang B (2020) MiR-877 suppresses gastric cancer progression by downregulating AQP3. *J Int Med Res* **48**: 030006052090366. <https://doi.org/10.1177/0300060520903661>

Determination of modified nucleosides in the urine of children with autism spectrum disorder

Joško Osredkar^{1,10}✉, Kristina Kumer¹, Teja Fabjan¹, Maja Jekovec Vrhovšek², Jerneja Maček², Mojca Zupan³, Barbara Bobrowska-Korczak⁴, Paulina Gałtarek^{5,6}, Angelina Rosiak^{5,6}, Joanna Giebułtowicz⁷, Geir Bjørklund⁸, Salvatore Chirumbolo⁹ and Joanna Kałużna-Czaplińska^{5,6}✉

¹Institute of Clinical Chemistry and Biochemistry, University Medical Center Ljubljana, Ljubljana, Slovenia; ²Center for Autism, Unit of Child Psychiatry, University Children's Hospital, University Medical Centre Ljubljana, Ljubljana, Slovenia; ³Blood Transfusion Centre of Slovenia, Ljubljana, Slovenia; ⁴Department of Bromatology, Faculty of Pharmacy with the Laboratory Medicine Division, Medical University of Warsaw, Warsaw, Poland; ⁵Institute of General and Ecological Chemistry, Faculty of Chemistry, Lodz University of Technology, Lodz, Poland; ⁶CONEM Poland Chemistry and Nutrition Research Group, Lodz University of Technology, Lodz, Poland; ⁷Department of Bioanalysis and Drug Analysis, Faculty of Pharmacy with the Laboratory Medicine Division, Medical University of Warsaw, Warsaw, Poland; ⁸Council for Nutritional and Environmental Medicine (CONEM), Mo i Rana, Norway; ⁹Department of Neurological and Movement Science, University of Verona, Verona, Italy; ¹⁰Faculty of Pharmacy, University of Ljubljana, Ljubljana, Slovenia

Metabolic disorders and nutritional deficiencies in ASD children may be identified by the determination of urinary-modified compounds. In this study, levels of selected seven modified compounds: O-methylguanosine, 7-methylguanosine, 1-methyladenosine, 1-methylguanine, 7-methylguanine, 3-methyladenine, and 8-hydroxy-2'-deoxyguanosine in the group of 143 ASD children and 68 neurotypical controls were analyzed. An ancillary aim was to verify if the reported levels differed depending on the pathogenetic scoring of ASD (mild deficit, moderate deficit, severe deficit). Elevated O-methylguanosine and 7-methylguanosine levels and significantly lower levels of 3-methyladenine, 1-methylguanine, 1-methyladenosine, 7-methylguanine, and 8-hydroxy-2'-deoxyguanosine were observed in ASD children compared to controls. O-methylguanosine levels were elevated in the mild and moderate groups, while the levels of 1-methylguanine, 1-methyladenosine, 7-methylguanine, and 8-hydroxy-2'-deoxyguanosine in the same groups were lower than in neurotypical controls. The reported evidence shows that modified nucleosides/bases can play a potential role in the pathophysiology of ASD and that each nucleoside/base shows a unique pattern depending on the degree of the deficit.

Keywords: autism, methylation, modified nucleosides, bases

Received: 30 November, 2022; **revised:** 30 January, 2023; **accepted:** 27 March, 2023; **available on-line:** 02 May, 2023

✉e-mail: josko.osredkar@kclj.si (JO); joanna.kaluzna-czaplińska@p.lodz.pl (JKC)

Acknowledgements of Financial Support: This research was funded by a research grant from ARRS Research Programme P3-0124, ARRS Project J3-1756, and the University Medical Centre Ljubljana Project - Number 20150085. LC-MS/MS analysis was carried out with the use of the CePT infrastructure financed by the European Union – the European Regional Development Fund within the Operational Programme “Innovative Economy” for 2007-2013.

Abbreviations: ADA, adenosine deaminase; ADSL, adenylosuccinate lyase; ANOVA, analysis of variance; ASD, autism spectrum disorder; ATP, adenosine triphosphate; AUC, area under the curve; GTP, guanosine triphosphate; HPRT, hypoxanthine-guanine phosphoribosyl transferase; LC-MS/MS, liquid chromatography coupled to mass spectrometry; NAPDD, nucleotidase-associated pervasive developmental disorder; PRPS, phosphoribosyl-pyrophosphate synthetase; ROC curves, receiver operating characteristic curves; ROS, reactive oxygen species; SAH, S-adenosylhomocysteine; SAM, S-adenosylmethionine; S.D., standard deviation

INTRODUCTION

Autism spectrum disorder (ASD) is a complex, pervasive developmental disorder with a neurological-etiopathogenetic basis, mainly occurring in childhood (Mughal & Saadabadi, 2020). It appears primarily as a qualitatively altered behaviour in social interaction, verbal and nonverbal communication. ASD covers a wide range of disorders, from mild to severe forms. “The Diagnostic and Statistical Manual of Mental Disorders, 5th Revision (DSM-5)” defines ASD as a neurodevelopmental disorder in which there are qualitative disorders in the field of social contacts, qualitative disorders in communication, which manifest themselves as stereotypical patterns of behaviour, interests, and life itself (American Psychiatric Association, 2013). ASD affects more than 1% (from 1 in 88 to 1 in 68) of children worldwide (male to female ratio of approximately 4:1) (Liu *et al.*, 2019). Generally, ASD is diagnosed based on assessing behavioural symptoms, including a questionnaire and a psychologist evaluation. Due to the early onset of symptoms (in the first two years of life) and their diversity, the diagnosis of ASD is difficult and often unreliable, especially at an earlier stage of development (Anwar *et al.*, 2018). Several studies indicate that there are metabolic disorders associated with ASD that can be assessed by identifying and determining characteristic biomarkers (Emanuele *et al.*, 2010; Kałużna-Czaplińska *et al.*, 2014; Żurawcz & Kałużna-Czaplińska, 2015; Kałużna-Czaplińska *et al.*, 2017; Kałużna-Czaplińska *et al.*, 2018; Adams *et al.*, 2019; Glin-ton & Elsea, 2019; Bitar *et al.*, 2020).

An accumulation of evidence suggests that environment-gene interactions may be critically important for the onset of ASD (Imamura *et al.*, 2020). The genetic endowment appears crucial to highlight both the etiopathogenesis and the development of ASD. However, different environmental impacts could play an important role in ASD onset and progress (Costa *et al.*, 2017; Ng *et al.*, 2017; Costa *et al.*, 2020; Ongono *et al.*, 2020; Radke *et al.*, 2020). Many pollutants are xenobiotics able to trigger the usual oxidative stress response of the individual. Under normal physiological conditions, the formation of free radicals and their neutralization is in a dynamic equilibrium. However, excessive production of reactive oxygen species and reduced antioxidant capacity, however, can lead to an imbalanced oxidative stress response, which

may contribute to the pathophysiology of ASD in predisposed individuals (Lambeth, 2007; Melnyk *et al.*, 2012; Ranjbar *et al.*, 2014; Kalużna-Czaplińska & Józwick-Pruska, 2016; Bobrowska-Korczak *et al.*, 2019; Osredkar *et al.*, 2019; Gątarek *et al.*, 2020). Nevertheless, excessive production of reactive oxygen species (ROS), particularly due to the imbalance between oxidants and antioxidants, can be toxic to neurons triggering DNA methylation (Wong *et al.*, 2019; Dreser, 2020; Sedley, 2020), which in turn means correlated damage to multiple further tissues (Ranjbar *et al.*, 2014). Several studies have suggested that redox imbalance and oxidative stress are integral parts of ASD pathophysiology (Björklund *et al.*, 2020). Early assessment and treatment of antioxidant status may result in a better prognosis as it could decrease the oxidative stress in the brain before it can induce more irreversible brain damage. However, the full comprehension of the role of ROS in ASD is still far to be elucidated. It was noted that oxidative stress can be attributable to the genotoxic effects of ROS, which can cause base modifications and genetic instability. Oxidative stress could induce an alteration in the methylation status of DNA/RNA, mainly by affecting the function and activity of the enzymes responsible for maintaining the epigenetic status, such as methyltransferases, histone methylase, and histone deacetylase. Additionally, it is worth underlining that children with autism have abnormal plasma levels of metabolites in pathways of folate-dependent methionine (transmethylation) and glutathione (transsulfuration) metabolism relative to unaffected age-matched control children (Melnyk *et al.*, 2012). Specifically, cellular methylation capacity expressed as the mean ratio of the methyl donor S-adenosylmethionine (SAM) to the methylation inhibitor, S-adenosylhomocysteine (SAM/SAH ratio), was significantly reduced in many children with autism. A decrease in the SAM/SAH ratio has been associated with the hypomethylation of DNA, RNA, proteins, phospholipids, and neurotransmitters with functional consequences in terms of gene expression, protein expression, membrane phospholipid composition, and dopamine synthesis, respectively. Based on the critical role of the redox and methylation status, it is, therefore, relevant to define biomarkers and show evidence of a functional impact on epigenetic regulation and antioxidant/detoxification capacity in children with autism. The development of tests based on ASD-specific biomarkers would certainly improve the diagnosis of ASD in children. Also, ASD-specific biomarkers may be used to evaluate treatment efficacy as a complement to current behavioral assessment (James *et al.*, 2004; Melnyk *et al.*, 2012). Recent studies show that the assessment of oxidative stress can be based on measurements of antioxidant enzymes and compounds, protein/DNA oxidation, and lipid peroxidation, such as important potential biomarkers of oxidative stress in ASD, e.g., methionine, cysteine, transferrin, 8-hydroxy-2'-deoxyguanosine, ceruloplasmin, 3-chlorotyrosine, 3-nitrotyrosine, F2-isoprostanes, and compounds in the glutathione system (Ranjbar *et al.*, 2014; Kalużna-Czaplińska *et al.*, 2017; Ginton & Elsea, 2019; Osredkar *et al.*, 2019). Measurements of reduced glutathione concentration, glutathione/glutathione disulfide ratio, or homocysteine thiolactone concentration provide information on whether patients are exposed to oxidative stress and whether their cellular antioxidant defense mechanisms work effectively (Kalużna-Czaplińska *et al.*, 2017; Gątarek *et al.*, 2020).

In the previous study (Bobrowska-Korczak *et al.*, 2019), the levels of 6 modified nucleosides/bases such as guanosine, adenosine, guanine, and adenine nucleotides

were studied. A group of 22 children with ASD and 20 neurotypical children participated in the study. The results showed significantly lower levels of 7-methylguanosine, 1-methyladenosine, 1-methylguanine, 7-methylguanine, and 3-methyladenine in the urine of children with ASD compared to neurotypical children. These preliminary results show that modified compounds suggest metabolic disorders and nutritional deficiencies in ASD children. The same nucleosides/bases in a larger group of 143 ASD children and 68 matched neurotypical controls were further analyzed to confirm these results. These 7 metabolites were selected as being considered the major physiological catabolites of human purines and pyrimidine metabolism in these subjects (Micheli *et al.*, 2011; Fumagalli *et al.*, 2017). The present study aims: (1) to determine the concentrations of O-methylguanosine, 7-methylguanosine, 1-methyladenosine, 1-methylguanine, 7-methylguanine, 8-hydroxy-2'-deoxyguanosine, and 3-methyladenine in the urine of children and adolescents with ASD in comparison to their neurotypical peers; (2) to check if the results of modified compounds differ depending on the level of autistic-mediated deficit (mild, moderate or severe). Due to the small size of the severe deficit group, these results were not further considered.

MATERIALS AND METHODS

Participants

The study group included 143 children. Sample size calculations, to reach the minimal significant sample size for two independent study groups, with anticipated incidence (endpoint) of 20% of subjects with ASD and impairments in the purine and pyrimidine metabolism, according to Gevi and coworkers (Gevi *et al.*, 2016), with statistic power=80% $\alpha=0.05$, $\beta=0.2$ gave the minimal number of 68 patients, 34 individuals with ASD and 34 neuro-typical controls. In the recruited samples, the subjects' average age was 9.5 years in the range of 2.1–18.1 years. The control group included 68 neurotypical children without any acute or chronic illness, who were, on average, 8.3 years of age in the range of 2.5–20.8 years. Children in the study group were diagnosed with ASD by an expert paediatrician or a neuropsychiatrist in collaboration with a psychologist (Supplementary Material Table S1). The diagnosis was made using a multidisciplinary approach which combined a clinical evaluation with a psychological assessment. Children were grouped according to the criteria detailed and summarized by DSM-5 (American Psychiatric Association, 2013; Kuhn *et al.*, 2018). Additional behavioural ratings were based on a standardized classification of behaviour for children with ASD developed by the local educational authority for providing additional school support (Chawla *et al.*, 2002; Vovk-Ornik, 2015; Osredkar *et al.*, 2019). Ratings were given for two separate dimensions: a) the presence of deficits in social communication and social interaction, and b) the presence of deficits in behavioural flexibility and limited interests and activities. Each child in the ASD group received a rating on each of the two dimensions on a three-point rating scale (1: mild deficit; 2: moderate deficit; 3: severe deficit). Children in the control groups received a rating of 0 for both dimensions. Children with other additional diagnoses were excluded from the study. The children with ASD were not on a gluten-free, casein-free, or sugar-free diet.

The demographic characteristics of participating children and adolescents are given in Table 1. The study

Table 1. Demographic characteristics of autism spectrum disorder (ASD) and neurotypical control group.

	ASD	Control
N	143	68
Male	88%	60%
Median Age (in years)	9.5	8.3
Age range (in years)	2.1–18.1	2.5–20.8
Deficits in social communication		
Mild	47%	/
Moderate	47%	/
Severe	6%	/
Deficits in behavioural flexibility		
Mild	48%	/
Moderate	43%	/
Severe	9%	/

protocol was approved by the National Medical Ethics Committee (0120-201/2016-2 KME 78/03/16).

Analytical Methods

Second-morning urine specimens from all participants were collected. Urine samples were aliquoted immediately after collection and frozen at temperature of -80°C until they were analyzed. Before analysis, urine was thawed and centrifugated.

Modified nucleobases and nucleosides were determined using liquid chromatography coupled to mass spectrometry (LC-MS/MS) on Agilent 1260 Infinity (Agilent Technologies, Santa Clara, CA, US) coupled to QTRAP 4000 (AB Sciex, Framingham, MA, US). The method was validated and described previously (Rackowska *et al.*, 2019). Briefly, MRM transitions, for O-methylguanosine, 1-methyladenosine, 7-methylguanosine, 7-methylguanine, 3-methyladenine, 1-methylguanine, and 8-hydroxy-2'-deoxyguanosine tubercidin (internal standard) were (m/z): 298->152 (collision energy, CE=17 V), 282->55 (CE=87 V), 298->166 (CE=19 V), 166->79 (CE=43 V), 150->123 (CE=31 V), 166->135 (CE=31 V) and 267->135 (CE=27 V), respectively. The curtain gas, ion source gas 1, ion source gas 2, and collision gas (all high-purity nitrogen) were set at 241 kPa, 207 kPa, 345 kPa, and "high" instrument units, respectively. The ion spray voltage and source temperature were fixed at 5500 V and 600°C , respectively. SeQuant® ZIC®-HILIC column (50 mm×2.1 mm; 5 μm) obtained from Merck (Darmstadt, Germany) was used for chromatography. The gradient of 20 mM ammonium acetate (eluent A) and acetonitrile with 0.2% formic acid (eluent B) presented as (%B) was as follows: 0 min, 95%; 1 min, 95%; 7 min, 50%; and 8 min, 50%. Second-morning urine was collected from all the participants, aliquoted, immediately frozen, and stored at -80°C till the analysis. On the day of the analysis, the sample was allowed to thaw. The centrifuged urine sample (5 min at $1000\times g$, 0.1 mL) was mixed with the tubercidin (0.1 mL, 1 $\mu\text{g}/\text{mL}$) and shaken for 3 min at high speed. Then, 0.6 mL of ice-cold acetonitrile was added, and the samples were vortexed for 3 min and centrifuged (5 min at $10000\times g$). Five μL of supernatant was injected into LC-MS/MS.

The analysis was performed following the Guideline on bioanalytical method validation of European Medicines Agency guidelines in its work. Thus, together with

the study samples we analyzed the blank sample (processed matrix sample without analyte and internal standard), zero sample (processed matrix with internal standard), and quality control samples (at low, medium, and high concentrations) at the level of at least 5% of the number of study samples.

The level of the modified nucleosides/bases in urine was standardized by conversion to the creatinine level.

Quantitative determination of creatinine concentration in urine was performed on a Roche Modular P analyzer (Roche Diagnostics GmbH, Mannheim, Germany).

Statistical Analysis

Statistical analysis was performed using Statistica 9.0 software (StatSoft, Poland STATISTICA, version 9.0, Quest Software, Aliso Viejo, CA, USA). The normal distribution of the data was tested using the Kolmogorov-Smirnov test. In the case of normal distribution and homogeneity of variance, a one-way ANOVA was used, while in the case of non-normal distribution, median values were calculated following the Mann-Whitney U non-parametric test. The results were considered statistically significant when $p < 0.001$. Spearman's Rank Correlation Coefficient was used to verify if the results correlate to the disorder's severity.

RESULTS

Table 1 presents the demographic characteristics of autism spectrum disorder (ASD) and neurotypical control groups showing that the samples' statistical stratification is homogeneously dispersed.

One of the study's major objectives was to examine the levels of O-methylguanosine, 7-methylguanosine, 1-methyladenosine, 1-methylguanine, 7-methylguanine, 8-hydroxy-2'-deoxyguanosine, and 3-methyladenine in the urine of children and adolescents with ASD in comparison to their neurotypical peers. The distribution of urine concentrations of a selected representative group of metabolites, referred to excreted creatinine as ng/mg and $\mu\text{g}/\text{mg}$, was not normal if one considers their own different ability in metabolizing nucleotides (intraindividual variability). Curves have skewness and kurtosis values that obliged researchers to use medians as a main comparative variable. Table 2 shows both mean \pm standard deviation (S.D.) and median with CI95 of the indicated metabolites. The major observation is that only 2 of 5 measured guanine/guanosine metabolites were higher: O-methylguanosine and 7-methylguanosine in ASD patients compared with neurotypical controls. Children with ASD have about a 20–30% reduction in metabolite excretion, whereas they exhibit a very high 7-methylguanosine excretion (>65%), a modest higher O-methylguanosine excretion (13%), and a quite unchanged (+2%) level of 8-hydroxy-2'-deoxyguanosine (Table 2).

The values in Table 2 are compared according to their medians, but further comparisons conducted by removing the highest outliers (\pm S.D.) confirmed the observed differences in excreted metabolites between ASD subjects and neurotypical controls. Due to the fact that the Bonferroni correction was applied in the multiple comparison. To determine if any of the 7 correlations is statistically significant, the p -value must be $p \leq 0.007$. Therefore, we considered the p -value ≤ 0.001 to be statistically significant. Due to the high variability in the levels of the determined compounds at this stage of the study, their usefulness as potential biomarkers in ASD cannot be clearly concluded.

Table 2. Statistical evaluations with corresponding *p* values of ASD and control group.

Name of the compound	ASD	Control		Delta % ¹	<i>p</i> ²
All results are expressed as on mg creatinine	Mean ± S.D. Median (IC95)	Mean ± S.D. Median (IC95)			
O-methylguanosine [ng/mg]	913.98±1528.08 434.11 (661.38–1166.59)	494.36±651.34 384.49 (336.70–652.02)	↑	12.90	0.0745
3-methyladenine [ng/mg]	14.09±30.50 6.33 (8.84–19.34)	14.68±17.10 9.11 (10.47–18.88)	↓	30.52	0.0015
1-methylguanine [ng/mg]	460.04±617.12 299.75 (358.02–562.05)	450.25±300.60 421.71 (377.49–523.01)	↓	28.92	0.0084
1-methyladenosine [µg/mg]	48.87±62.58 30.87 (38.53–59.22)	52.99±25.73 45.33 (46.77–59.22)	↓	31.90	<1.99×10 ⁻⁵
7-methylguanine [ng/mg]	55.23±69.55 35.93 (43.74–66.73)	53.24±24.78 45.59 (47.24–59.24)	↓	21.19	0.0002
7-methylguanosine [µg/mg]	136.67±241.70 51.96 (96.71–176.62)	75.40±104.57 44.30 (48.62–102.18)	↑	17.29	0.1035
8-hydroxy-2'-deoxyguanosine [ng/mg]	14.62±22.68 9.46 (10.57–18.67)	11.97±10.13 9.69 (9.48–14.46)	↓	2.37	0.3243

¹ calculated on medians; ² *p*-values calculated by a Mann-Whitney U test.

The differences with the *p*-value ≤ 0.001 were considered statistically significant. The Spearman's Rank Correlation Coefficient was used to verify if the results correlate to the age (Supplementary Materials Table S4 at <https://ojs.ptbioch.edu.pl/index.php/abp/>). Only O-methylguanosine concentrations (*p* < 0.001) in the control group were significantly correlated with age. No correlations between the other metabolites and age were observed. Scatterplots illustrating the relationship between the age and the concentration of metabolites (A–G) in the urine of ASD patients (Fig. S4 at <https://ojs.ptbioch.edu.pl/index.php/abp/>) and controls (Fig. S5 at <https://ojs.ptbioch.edu.pl/index.php/abp/>) were added to the Supplementary Material (<https://ojs.ptbioch.edu.pl/index.php/abp/>). In the Supplementary Material, (<https://ojs.ptbioch.edu.pl/index.php/abp/>) plots were provided to illustrate the relationship between the male-female differences in the ASD and control groups. 7-panel (A–G), 4-group scatter plot (mild, moderate, severe, and control) for each of the 7 urinary purines was presented in Fig. S1 (<https://ojs.ptbioch.edu.pl/index.php/abp/>). The relationship between the gender and the concentration of metabolites in the urine of ASD patients and the concentration of metabolites in the control group were presented in Figs S2 and S3 (<https://ojs.ptbioch.edu.pl/index.php/abp/>), and also individual differences in the levels of compounds between the groups were found in Fig. S6 (<https://ojs.ptbioch.edu.pl/index.php/abp/>).

We encountered some significant differences again when examining the relationship between different levels of severity and excreted metabolites. Table 3 shows the proportion of children by group according to the level of deficit. Groups with mild (N=70) or moderate (N=61) impairment are comparable in terms of the number of individuals classified, while the group with severe disability

(N=12) is small and thus presents a problem for us in interpreting the results. Due to the small size of the severe deficit group, only the results of the mild and moderate deficit groups were compared. Groups were comparable in age 9.4 (mild) and 9.7 (moderate), as well as the male to female ratio.

The next objective was to verify if the results correlated with the severity of the disorder. The results were checked as to whether metabolites differed depending on the deficit (mild, moderate, or severe). In Table 4, patients were divided into three groups depending on the level of deficit.

This table shows different excreted metabolites related to the level of deficit. As the group with a severe deficit is small, only the results of children from the mild and moderate groups were compared. These data need to be reappraised in the next research study. When comparing median values, taking into account the severity of the disorder (mild and moderate) compared to controls, it can be observed that the values for two compounds (O-methylguanosine and 7-methylguanosine) are similar for both the mild and moderate groups, while they are higher compared to the controls. For all other 5 compounds in the severity groups, the median values are similar but smaller compared to the control group. The Nonparametric Mann-Whitney U test was used to compare the concentration of compounds between the groups. The differences with a *p*-value lower than 0.001 were considered significant. Statistically significant differences between the mild and control groups for 1-methyladenosine (30.5 *vs* 43.51 µg/mg, *p* = 1.83 × 10⁻⁵) and 7-methylguanine (38.41 *vs* 45.11 µg/mg, *p* = 0.0009) were observed. For all other determined compounds, no statistically significant difference was found, with a *p*-value greater than 0.001. In the moderate group, a statistically significant difference in the case of 7-methylguanine (34.09 *vs* 45.11 µg/mg, *p* = 0.0007) was found. It was not statistically significantly different between the mild and moderate groups with a *p*-value greater than 0.001, while statistically significant differences between the ASD and control groups for 1-methyladenosine (*p* = 1.99 × 10⁻⁵) and 7-methylguanine (*p* = 0.0002) were observed. All results are expressed on creatinine to eliminate the impact of fluid intake.

Table 3. The proportion of patients with a mild, moderate, and severe level of deficit.

	Mild	Moderate	Severe
N	70 (49.0%)	61 (42.6%)	12 (8.4%)
Male %	63 (90%)	54 (88.5%)	9 (75%)
Median age	9.4	9.7	9.9
Age range	4.5–18.1	2.1–17.5	6.1–13.9

Table 4. The statistical distribution of excreted metabolites and severity level of deficit.

Compound	ASD			Control		
	Mild	<i>p</i>	Moderate	<i>p</i>	<i>*p</i>	Severe
	Median (range)		Median (range)			Median (range)
O-methylguanosine [ng/mg]	444.51 (44.51–12586.37)	0.0605	432.62 (80.82–3450.42)	0.2376	0.5213	447.59 (14.26–5164.59)
3-methyladenine [ng/mg]	6.66 (0.60–288.69)	0.0362	6.21 (0.39–75.42)	0.0015	0.3167	4.86 (0.38–44.94)
1-methylguanine [ng/mg]	304.04 (26.32–5830.77)	0.0148	272.64 (41.84–1588.26)	0.0317	0.8881	313.32 (14.18–1330.31)
1-methyladenosine [μg/mg]	30.50 (2.07–454.16)	1.83×10 ⁻⁵	31.82 (4.97–203.21)	0.0011	0.8917	42.12 (1.34–150.07)
7-methylguanine [μg/mg]	38.41 (3.84–568.44)	0.0009	34.09 (8.22–261.10)	0.0007	0.4287	44.30 (1.72–153.09)
7-methylguanosine [ng/mg]	59.67 (4.20–1798.71)	0.0454	44.36 (4.22–838.80)	0.5341	0.1593	92.95 (5.34–307.56)
8-hydroxy-2'-deoxyguanosine [ng/mg]	9.96 (0.85–68.23)	0.5086	8.16 (0.89–55.49)	0.1058	0.8662	15.29 (4.58–43.10)
						Median (range)

**p* Mann-Whitney U test *p*-value for the comparison of Mild and Moderate groups.

Finally, the Spearman's Rank Correlation Coefficient was used to verify if the results correlate to the severity of the disorder. The *p*-value ≤ 0.001 was considered to be statistically significant. No correlations between the severity of the disorder and the levels of metabolite concentrations were observed (Supplementary Materials Table S2 at <https://ojs.ptbioch.edu.pl/index.php/abp/>). Nonparametric correlation analysis showed a strong and moderately positive correlation between the concentrations of metabolites determined in ASD urine (Supplementary Materials Table S3 at <https://ojs.ptbioch.edu.pl/index.php/abp/>).

To accurately demonstrate the biological variation among children with ASD, appropriate graphs are included in the supplementary material (Fig. S1–S6 at <https://ojs.ptbioch.edu.pl/index.php/abp/>).

Receiver operating characteristic (ROC) curves were used to characterize the diagnostic accuracy and evaluate the predictive accuracy. To obtain a final diagnostic score, ROC curves were generated using the MetaboAnalyst 5.0 (<http://www.metaboanalyst.ca>). ROC curve showed diagnostic values for 7 urinary purine results classified as mild, moderate, or severe severity of the disorder in ASD compared to controls. The area under the curve (AUC) was used to measure the overall degree of identification power. By combining the all metabolites, the AUC of the ROC curve reached 0.856 (95% CI 0.776 to 0.937) for mild severity of the disorder, 0.838 (95% CI 0.744 to 0.927) for moderate severity of the disorder, and 0.669 (95% CI 0.391 to 0.885) for severe severity of the disorder. The results of the AUC analysis stratified by severity of the disorder were shown in Fig. S7 at <https://ojs.ptbioch.edu.pl/index.php/abp/>.

DISCUSSION

The significant difference in excreted purines (adenine and guanine) with respect to control neurotypical subjects is a clear marker of impaired ASD metabolism (Gevi *et al.*, 2016). The hypothesis based on folate defi-

ciency in individuals with ASD suggests a possible explanation for our results. Folate depletion may reduce adenosine triphosphate (ATP) and then in S-adenosylmethionine (SAM) in neurons during a rapid cellular division. If a methylation defect arises, this might be a potential, etiopathogenetic, causative factor of ASD due to the consequent depletion in purine and, therefore, in SAM biosynthesis (Geryk *et al.*, 2020). Whereas this could explain the reduction in adenine/adenosine metabolites in ASD patients, the increase in guanine/guanosine metabolites can be explained due to the increase in the ATP/GTP exchange to support the energetic demand, following ATP-SAM impairment.

In the current literature, elevated levels of modified nucleosides/bases are usually associated with ASD. The lack of conclusive evidence that ASD is only a genetic disorder suggests that epigenetic factors may impact ASD's susceptibility. Moreover, there is now compelling evidence that gene by environment interactions are important in the etiology of ASD (Gui *et al.*, 2020; López-Tobón *et al.*, 2020). However, there is a lack of knowledge of how environmental factors interact with genetic susceptibilities to confer individual risk for ASD. In normal and pathogenic brain development, a critical gene expression regulatory mechanism is DNA/RNA methylation. The pathogenesis of ASD leads to miscoded epigenetic mechanisms, cellular processes and functions, and altered expression of genes (Melnik *et al.*, 2012; Keil & Lein, 2016).

The results showed that in contrast to other urinary metabolites, lower concentrations of 3-methyladenine, 1-methylguanine, 1-methyladenosine, and 7-methylguanine in the urine of ASD were observed, confirming an abnormal purine metabolism in ASD children. Additionally, the concentration of the marker of oxidative stress, 8-hydroxy-2'-deoxyguanosine, was also lower in ASD than in controls, although not at such an exceptional level as other markers. A more complete picture can be observed when children with ASD are rated into three groups: mild, moderate, and severe. A statistically

significant difference between mild and control groups for 1-methyladenosine ($p=1.83 \times 10^{-5}$) and 7-methylguanine ($p=0.0009$) was observed. A difference between mild and control groups in the level of 8-hydroxy-2'-deoxyguanosine ($p=0.5086$) was observed, but it was not statistically significant again. In the moderate group, statistical differences in the case of only 7-methylguanine ($p=0.0007$) were found. Furthermore, other metabolites are not statistically different between the mild and moderate groups. However, the lack of statistical significance might result from the high variability in the metabolite's data distribution.

Moreover, the findings indicate that these compounds could play a potential role in the pathophysiology of ASD. Nutrient deficiencies may lead to hypomethylation, where the nutrients are the source of methyl donors. Significantly lower levels of urinary 7-methylguanosine, 1-methyladenosine, 1-methylguanine, 7-methylguanine, and 3-methyladenine were observed in the research on ASD children conducted by Bobrowska-Korczak and coworkers (Bobrowska-Korczak *et al.*, 2019). Alteration of urinary metabolites is related to a purine metabolism disorder in ASD children (Bobrowska-Korczak *et al.*, 2019). Nucleosides and deoxynucleosides are endogenous metabolites excreted from RNA turnover and DNA degradation, respectively (Patejko *et al.*, 2018). Because the concentration of RNA nucleosides exceeds DNA nucleosides in the cell by about 10 to 1, most of the measured abnormalities are reported as coming from modified mRNA, rRNA, and tRNAs. 7-methylguanosine comes from mRNA. This suggests that capped mRNAs turn over more in ASD patients than in controls. 1-methyladenosine is most commonly found in tRNA and it also is an important regulator of mRNA efficiency. Studies have shown that the up-regulated genes modified by N-6-methyladenine are mainly related to neuron differentiation, neurogenesis, and cell proliferation (Zhou *et al.*, 2020). N-6-methyladenine is the most abundant methylation modification of mRNA in eukaryotic cells, which affects every process of the RNA life cycle. Alteration in the purine metabolism was also observed in the research on ASD children conducted by Bitar and coworkers (Bitar *et al.*, 2018). They found that 5-aminoimidazole-4-carboxamide, an intermediate metabolite in purine synthesis and guanine, was altered in ASD children's urine. Accumulation of aminoimidazole carboxamide and succinyladenosine in body fluids is caused by adenylosuccinase deficiency, an inborn error of purine metabolism. This is manifested by epilepsy, developmental delay, and ASD. The deficiency may cause neurological problems like developmental delay and intellectual disability in purine nucleoside phosphorylase, which is responsible for the metabolism of purine such as guanine (Markert, 1991; Zecavati & Spence, 2009; Bitar *et al.*, 2018). Other researchers have also studied epigenetic changes in ASD (Goldani *et al.*, 2014; Tang *et al.*, 2017).

Several purine metabolism disorders are linked to ASD or behavioural features (Balasubramaniam *et al.*, 2014). Adenylosuccinate lyase (ADSL) deficiency is also an alteration of purine (adenine) metabolism and is caused by mutations in the ADSL gene. The symptoms of this deficiency are various and include delayed development of mental and movement abilities, problems with communication and social interaction, psychomotor retardation, hypotonia, and seizures. However, it is still unclear whether this alteration of pathological mechanisms results directly from the deficiency of intermediates' purines or toxicity (Spiegel *et al.*, 2006; Micheli *et al.*, 2011).

Adenosine deaminase (ADA) is one of the essential enzymes in purine catabolism, which catalyzes adenosine deamination into inosine, thus having an important role in immunological responses. Examples of ADA neurological deficiency, include hearing loss, seizures, autism-like behavior, learning disability, and attention deficit (Bottini *et al.*, 2001; Kelley & Andersson, 2014). Phosphoribosyl-pyrophosphate synthetase (PRPS) superactivity is a disorder with overproduction and accumulation of uric acid (2,6,8-trioxypurine) in blood and urine. The major manifestations of PRPS are hyperuricemia with gout, sensorineural hearing loss, mental retardation, and hypotonia. Hypoxanthine-guanine phosphoribosyl transferase (HPRT) deficiency is related to recycling the purine bases hypoxanthine and guanine to nucleotides. HPRT deficiency occurs as a full spectrum of residual enzyme activity, from mild to severe. Three major clinical features are connected with HPRT: hyperuricemia, neurologic manifestations, and behavioural disturbance (Kelley & Andersson, 2014). Nucleotidase-associated pervasive developmental disorder (NAPDD) is another kind of disorder in purine metabolism and is related to a ten-fold increase in purine and pyrimidine 5'-nucleotidase activity (Page *et al.*, 1997). There are numerous symptoms associated with this disorder. Among them are language delay, behavioural disorders, hyperactivity, attention deficit, aggressiveness, social maladjustment, epilepsy, coordination impairment, ataxic gait, and dexterity problems (Micheli *et al.*, 2011). Some of these symptoms are characteristic of ASD (Abraham *et al.*, 2019).

The research on epigenetic mechanisms connected with RNA/DNA molecules is still under-investigated. At present, there is no clear answer to whether methyl marks of RNA/DNA play any role in ASD (Abraham *et al.*, 2019).

CONCLUSIONS

The results reported in the present study show that modified metabolites can play a potential role in the pathophysiology of ASD and that each compound shows a unique pattern that depends on the degree of deficit. These results showed that in contrast to other urinary metabolites, only 2 of 5 measured guanine/guanosine metabolites were higher: O-methylguanosine and 7-methylguanosine in ASD patients compared to neurotypical controls. Moreover, lower concentrations of 3-methyladenine, 1-methylguanine, 1-methyladenosine, and 7-methylguanine in the urine of ASD children were observed, indicating abnormal purine metabolism in ASD children.

Additionally, the concentration of the oxidative stress marker, 8-hydroxy-2'-deoxyguanosine, was also lower in ASD compared to controls. A different picture is seen when we rate patients into mild and moderate deficits. A statistically significant difference between mild and control groups for 1-methyladenosine ($p=1.83 \times 10^{-5}$) and 7-methylguanine ($p=0.0009$) was observed. The levels of 3-methyladenine, 1-methylguanine, 1-methyladenosine, and 7-methylguanine in the mild and moderate groups were lower than in the control group. These findings must be further confirmed in future studies.

Declarations

Conflicts of Interest. The authors declare no conflict of interest.

Acknowledgment. The authors thank the participants for providing urine samples, Katja Stres Kavčič and

Tinkara Smeh for physiological assessments, and Vera Troha for processing the samples.

REFERENCES

- Abraham J, Szoko N, Natowicz MR (2019) Proteomic investigations of autism spectrum disorder: past findings, current challenges, and future prospects. In *Reviews on Biomarker Studies in Psychiatric and Neurodegenerative Disorders. Advances in Experimental Medicine and Biology* 1118. Guest P eds, pp 235–252. Springer, Cham. https://doi.org/10.1007/978-3-030-05542-4_12
- Adams D, Young K, Keen D (2019) Anxiety in children with autism at school: a systematic review. *Rev. J. Autism Dev. Disord.* **6**: 274–288. <https://doi.org/10.1007/s40489-019-00172-z>
- American Psychiatric Association (2013) Diagnostic and Statistical Manual of Mental Disorders, 5th edn.
- Anwar A, Abruzzo PM, Pasha S, Rajpoot K, Bolotta A, Ghezzi A, Marini M, Posar A, Visconti P, Thornalley PJ, Rabbani N (2018) Advanced glycation endproducts, dityrosine and arginine transporter dysfunction in autism – A source of biomarkers for clinical diagnosis. *Mol. Autism* **9**: 3. <https://doi.org/10.1186/s13229-017-0183-3>
- Balasubramaniam S, Duley JA, Christodoulou J (2014) Inborn errors of purine metabolism: clinical update and therapies. *J. Inher. Metab. Dis.* **37**: 669–686. <https://doi.org/10.1007/s10545-014-9731-6>
- Bitar T, Gerges P, Kassab MC, Hallit S, Mattar H, Soufia M, Andres CR, Hleihel W (2020) Factors associated with Autism Spectrum Disorder: a case-control study in the Lebanese population. *Epidemiol. Biostat. Public Health* **17**: e13218. <https://doi.org/10.2427/13218>
- Bitar T, Mavel S, Emond P, Nadal-Desbarats L, Lefèvre A, Mattar H, Soufia M, Blasco H, Vourch P, Hleihel W, Andres CR (2018) Identification of metabolic pathway disturbances using multimodal metabolomics in autistic disorders in a Middle Eastern population. *J. Pharm. Biomed. Anal.* **152**: 57–65. <https://doi.org/10.1016/j.jpba.2018.01.007>
- Bjorklund G, Meguid NA, El-Bana MA, Tinkov AA, Saad K, Dadar M, Hemimi M, Skalny A V, Hosnedlová B, Kizek R, Osredkar J, Urbina MA, Fabjan T, El-Houfey AA, Kalužna-Czaplińska J, Gatarek P, Chirumbolo S (2020) Oxidative stress in autism spectrum disorder. *Mol. Neurobiol.* **57**: 2314–2332. <https://doi.org/10.1007/s12035-019-01742-2>
- Bobrowska-Korczak B, Gatarek P, Rosiak A, Giebułtowicz J, Kalužna-Czaplińska J (2019) Reduced levels of modified nucleosides in the urine of autistic children. Preliminary studies. *Anal. Biochem.* **571**: 62–67. <https://doi.org/10.1016/j.ab.2019.02.009>
- Bottini N, De Luca D, Saccucci P, Fiumara A, Elia M, Porfrio MC, Lucarelli P, Curatolo P (2001) Autism: Evidence of association with adenosine deaminase genetic polymorphism. *Neurogenetics* **3**: 111–113. <https://doi.org/10.1007/s100480000104>
- Chawla NV, Bowyer KW, Hall LO, Kegelmeyer WP (2002) SMOTE: Synthetic minority over-sampling technique. *J. Artif. Intell. Res.* **16**: 321–357. <https://doi.org/10.48550/arXiv.1106.1813>
- Costa LG, Chang YC, Cole TB (2017) Developmental neurotoxicity of traffic-related air pollution: Focus on autism. *Curr. Environ. Health Rep.* **4**: 156–165. <https://doi.org/10.1007/s40572-017-0135-2>
- Costa LG, Cole TB, Dao K, Chang YC, Coburn J, Garrick JM (2020) Effects of air pollution on the nervous system and its possible role in neurodevelopmental and neurodegenerative disorders. *Pharmacol. Ther.* **210**: 107523. <https://doi.org/10.1016/j.pharmthera.2020.107523>
- Dresner N (2020) Early neurodevelopmental disturbances during sensitive periods of stem cell differentiation [Dissertation] Konstanz: University of Konstanz.
- Emanuele E, Orsi P, Boso M, Broglia D, Brondino N, Barale F, di Nemi SU, Politi P (2010) Low-grade endotoxemia in patients with severe autism. *Neurosci. Lett.* **471**: 162–165. <https://doi.org/10.1016/j.neulet.2010.01.033>
- Fumagalli M, Lecca D, Abbracchio MP, Ceruti S (2017) Pathophysiological role of purines and pyrimidines in neurodevelopment: Unveiling new pharmacological approaches to congenital brain diseases. *Front. Pharmacol.* **8**: 941. <https://doi.org/10.3389/fphar.2017.00941>
- Gatarek P, Józwick-Pruska J, Bjorklund G, Chirumbolo S, Kalužna-Czaplińska J (2020) Urinary carboxylic acids (UCAs) in subjects with autism spectrum disorder and their association with bacterial overgrowth. *Rev. Anal. Chem.* **39**: 78–87. <https://doi.org/10.1515/revac-2020-0109>
- Geryk J, Krsička D, Vlčková M, Havlovicová M, Macek M, Pourová RK (2020) The key role of purine metabolism in the folate-dependent phenotype of autism spectrum disorders: An *in silico* analysis. *Metabolites* **10**: 184. <https://doi.org/10.3390/metabo10050184>
- Gevi F, Zolla L, Gabriele S, Persico AM (2016) Urinary metabolomics of young Italian autistic children supports abnormal tryptophan and purine metabolism. *Mol. Autism* **7**: 47. <https://doi.org/10.1186/s13229-016-0109-5>
- Glinton KE, Elsea SH (2019) Untargeted metabolomics for autism spectrum disorders: current status and future directions. *Front. Psychiatry* **10**: 647. <https://doi.org/10.3389/fpsyt.2019.00647>
- Goldani AAS, Downs SR, Widjaja F, Lawton B, Hendren RL (2014) Biomarkers in autism. *Front. Psychiatry* **5**: 100. <https://doi.org/10.3389/fpsyt.2014.00100>
- Gui A, Jones EJH, Wong CCY, Meaburn E, Xia B, Pasco G, Lloyd-Fox S, Charman T, Bolton P, Johnson MH (2020) Leveraging epigenetics to examine differences in developmental trajectories of social attention: A proof-of-principle study of DNA methylation in infants with older siblings with autism. *Infant. Behav. Dev.* **60**: 101409. <https://doi.org/10.1016/j.infbeh.2019.101409>
- Imamura A, Morimoto Y, Ono S, Kurotaki N, Kanegae S, Yamamoto N, Kinoshita H, Tsujita T, Okazaki Y, Ozawa H (2020) Genetic and environmental factors of schizophrenia and autism spectrum disorder: insights from twin studies. *J. Neural Transm.* **127**: 1501–1515. <https://doi.org/10.1007/s00702-020-02188-w>
- James SJ, Cutler P, Melnyk S, Jernigan S, Janak L, Gaylor DW, Neubrandner JA (2004) Metabolic biomarkers of increased oxidative stress and impaired methylation capacity in children with autism. *Am. J. Clin. Nutr.* **80**: 1611–1617. <https://doi.org/10.1093/ajcn/80.6.1611>
- Kalužna-Czaplińska J, Józwick J, Żurawicz E (2014) Analytical methods used in autism spectrum disorders. *TrAC Trends Anal. Chem.* **62**: 20–27. <https://doi.org/10.1016/j.trac.2014.06.014>
- Kalužna-Czaplińska J, Józwick-Pruska J (2016) Chromatographic and mass spectrometric techniques in studies on oxidative stress in autism. *J. Chromatogr. B Anal. Technol. Biomed. Life Sci.* **1019**: 4–14. <https://doi.org/10.1016/j.jchromb.2015.12.035>
- Kalužna-Czaplińska J, Józwick-Pruska J, Chirumbolo S, Bjorklund G (2017) Tryptophan status in autism spectrum disorder and the influence of supplementation on its level. *Metab. Brain Dis.* **32**: 1585–1593. <https://doi.org/10.1007/s11011-017-0045-x>
- Kalužna-Czaplińska J, Żurawicz E, Józwick-Pruska J (2018) Focus on the Social Aspect of Autism. *J. Autism Dev. Disord.* **48**: 1861–1867. <https://doi.org/10.1007/s10803-017-3407-7>
- Keil KP, Lein PJ (2016) DNA methylation: a mechanism linking environmental chemical exposures to risk of autism spectrum disorders? *Environ. Epigenet.* **2**: dvv012. <https://doi.org/10.1093/eeep/dvv012>
- Kelley RE, Andersson HC (2014) Disorders of purines and pyrimidines. *Handb. Clin. Neurol.* **120**: 827–838. <https://doi.org/10.1016/B978-0-7020-4087-0.00055-3>
- Lambeth JD (2007) Nox enzymes, ROS, and chronic disease: An example of antagonistic pleiotropy. *Free Radic. Biol. Med.* **43**: 332–347. <https://doi.org/10.1016/j.freeradbiomed.2007.03.027>
- Liu A, Zhou W, Qu L, He F, Wang H, Wang Y, Cai C, Li X, Zhou W, Wang M (2019) Altered Urinary Amino Acids in Children With Autism Spectrum Disorders. *Front. Cell. Neurosci.* **13**: 7. <https://doi.org/10.3389/fncel.2019.00007>
- López-Tobón A, López-Tobón A, Trattaro S, Trattaro S, Testa G, Testa G (2020) The sociability spectrum: Evidence from reciprocal genetic copy number variations. *Mol. Autism* **11**: 50. <https://doi.org/10.1186/s13229-020-00347-0>
- Markert ML (1991) Purine nucleoside phosphorylase deficiency. *Immunodef. Rev.* **3**: 45–81. PMID: 1931007
- Kuhn M, Contributions from Jed Wing A, Weston S, Williams A, Keefer C, Engelhardt A, Cooper T, Mayer Z, Kenkel B, Benesty M, Lescaubeau R, Ziem A, Scrucca L, Tang Y, Candan C, Hunt T (2018) The R Core Team 2018 Package “caret”. Classification and Regression Training. <https://cran.r-project.org/web/packages/caret/caret.pdf>
- Melnik S, Fuchs GJ, Schulz E, Lopez M, Kahler SG, Fussell JJ, Belando J, Pavliv O, Rose S, Seidel L, Gaylor DW, James SJ (2012) Metabolic imbalance associated with methylation dysregulation and oxidative damage in children with autism. *J. Autism Dev. Disord.* **42**: 367–377. <https://doi.org/10.1007/s10803-011-1260-7>
- Micheli V, Camici M, G Tozzi M, I Ipata P, Sestini S, Bertelli M, Pompucci G (2011) Neurological disorders of purine and pyrimidine metabolism. *Curr. Top. Med. Chem.* **11**: 923–947. <https://doi.org/10.2174/156802611795347645>
- Mughal S, Faizy RM, Saadabadi A (2020) *Autism Spectrum Disorder (Regressive Autism, Child Disintegrative Disorder)*, StatPearls Publishing. PMID: 30247851
- Ng M, de Montigny JG, Ofner M, Do MT (2017) Environmental factors associated with autism spectrum disorder: A scoping review for the years 2003–2013. *Heal. Promot. Chronic Dis. Prev. Canada* **37**: 1–23. <https://doi.org/10.24095/hpcdp.37.1.01>
- Ongono JS, Béranger R, Baghdadi A, Mortamais M (2020) Pesticides used in Europe and autism spectrum disorder risk: can novel exposure hypotheses be formulated beyond organophosphates, organochlorines, pyrethroids and carbamates? A systematic review. *Environ. Res.* **187**: 109646. <https://doi.org/10.1016/j.envres.2020.109646>
- Osredkar J, Gosar D, Maček J, Kumer K, Fabjan T, Finderle P, Šterpin S, Zupan M, Vrhovšek MJ (2019) Urinary markers of oxidative stress in children with autism spectrum disorder (ASD). *Antioxidants* **8**: 187. <https://doi.org/10.3390/antiox8060187>

- Page T, Yu A, Fontanesi J, Nyhan WL (1997) Developmental disorder associated with increased cellular nucleotidase activity. *Proc. Natl. Acad. Sci. U. S. A.* **94**: 11601–11606. <https://doi.org/10.1073/pnas.94.21.11601>
- Patejko M, Struck-Lewicka W, Siluk D, Waszczuk-Jankowska M, Markuszewski MJ (2018) Urinary nucleosides and deoxynucleosides. *Adv. Clin. Chem.* **83**: 1–51. <https://doi.org/10.1016/bs.acc.2017.10.001>
- Račkowska E, Bobrowska-Korczak B, Giebułtowicz J (2019) Development and validation of a rapid LC–MS/MS method for determination of methylated nucleosides and nucleobases in urine. *J. Chromatogr. B Anal. Technol. Biomed. Life Sci.* **1128**: 121775. <https://doi.org/10.1016/j.jchromb.2019.121775>
- Radke EG, Braun JM, Nachman RM, Cooper GS (2020) Phthalate exposure and neurodevelopment: A systematic review and meta-analysis of human epidemiological evidence. *Environ. Int.* **137**: 105408. <https://doi.org/10.1016/j.envint.2019.105408>
- Ranjbar A, Rashedi V, Rezaei M (2014) Comparison of urinary oxidative biomarkers in Iranian children with autism. *Res. Dev. Disabil.* **35**: 2751–2755. <https://doi.org/10.1016/j.ridd.2014.07.010>
- Sedley L (2020) Advances in nutritional epigenetics – a fresh perspective for an old idea. Lessons Learned, Limitations, and Future Directions. *Epigenet. Insights* **13**: 2516865720981924. <https://doi.org/10.1177/2516865720981924>
- Spiegel EK, Colman RF, Patterson D (2006) Adenylosuccinate lyase deficiency. *Mol. Genet. Metab.* **89**: 19–31. <https://doi.org/10.1016/j.ymgme.2006.04.018>
- Tang J, Yu Y, Yang W (2017) Long noncoding RNA and its contribution to autism spectrum disorders. *CNS Neurosci. Ther.* **23**: 645–656. <https://doi.org/10.1111/cns.12710>
- Vovk-Ornik N (2015) The criteria for identifying the type and level of handicap or disorders of children with special needs. Ljubljana: ZRSŠ (in Slovenian)
- Wong CCY, Smith RG, Hannon E, Ramaswami G, Parikshak NN, As-sary E, Troakes C, Poschmann J, Schalkwyk LC, Sun W, Prabhakar S, Geschwind DH, Mill J (2019) Genome-wide DNA methylation profiling identifies convergent molecular signatures associated with idiopathic and syndromic autism in post-mortem human brain tissue. *Hum. Mol. Genet.* **28**: 2201–2211. <https://doi.org/10.1093/hmg/ddz052>
- Zecavati N, Spence SJ (2009) Neurometabolic disorders and dysfunction in autism spectrum disorders. *Curr. Neurol. Neurosci. Rep.* **9**: 129–136. <https://doi.org/10.1007/s11910-009-0021-x>
- Zhou Y, Kong Y, Fan W, Tao T, Xiao Q, Li N, Zhu X (2020) Principles of RNA methylation and their implications for biology and medicine. *Biomed. Pharmacother.* **131**: 110731. <https://doi.org/10.1016/j.biopha.2020.110731>
- Żurawicz E, Kaluźna-Czaplińska J (2015) Analysis of amino acids in autism spectrum disorders. *TrAC Trends Anal. Chem.* **73**: 91–118. <https://doi.org/10.1016/j.trac.2015.04.029>



OPEN ACCESS

EDITED BY
Jarosław Czyż,
Jagiellonian University, Poland

REVIEWED BY
Przemysław Mieszko Płonka,
Jagiellonian University, Poland

*CORRESPONDENCE
MengZhu Li,
✉ llimengzhu555@outlook.com

RECEIVED 27 November 2023

ACCEPTED 12 April 2024

PUBLISHED 15 May 2024

CITATION

Guo W and Li M (2024), Clinical efficacy of different androgen deprivation therapies for prostate cancer and evaluation based on dynamic-contrast enhanced magnetic resonance imaging. *Acta Biochim. Pol* 71:12473. doi: 10.3389/abp.2024.12473

COPYRIGHT

© 2024 Guo and Li. This is an open-access article distributed under the terms of the Creative Commons Attribution License (CC BY). The use, distribution or reproduction in other forums is permitted, provided the original author(s) and the copyright owner(s) are credited and that the original publication in this journal is cited, in accordance with accepted academic practice. No use, distribution or reproduction is permitted which does not comply with these terms.

Clinical efficacy of different androgen deprivation therapies for prostate cancer and evaluation based on dynamic-contrast enhanced magnetic resonance imaging

WenXiao Guo and MengZhu Li*

Department of Radiology, Wuhan Fourth Hospital, Wuhan, Hubei, China

Objective: To evaluate the clinical efficacy of different androgen deprivation therapies for prostate cancer (PCa) based on dynamic-contrast enhanced magnetic resonance imaging (DCE-MRI).

Methods: 104 patients with PCa were studied, all of whom were treated with androgen deprivation therapy. The patients were divided into a continuous group (continuous androgen deprivation therapy) and an intermittent group (intermittent androgen deprivation therapy) by random number table method, 52 cases/group. The therapeutic effect and DCE-MRI indices were compared and the relationship between DCE-MRI indices and clinical efficacy and the evaluation value of therapeutic efficacy were analyzed.

Results: The objective response rate (ORR) of the intermittent group was higher than that of the continuous group ($p < 0.05$), and there was no significant difference in disease control rate (DCR) between the two groups ($p > 0.05$). After treatment, volume transfer coefficient (K^{trans}), reverse transfer constant (K_{ep}), volume fraction (Ve), blood volume (BV), and blood flow (BF) in both groups were lowered, and those in the intermittent group were lower than the continuous group ($p < 0.05$). K^{trans} , K_{ep} , Ve, BF, and BV in the ORR group were lower than those in the non-ORR group ($p < 0.05$). K^{trans} , K_{ep} , Ve, BF, and BV were correlated with the therapeutic effect of PCa ($p < 0.05$). The AUC value of the combined detection of DCE-MRI indices in evaluating the therapeutic effect of PCa was greater than that of each index alone ($p < 0.05$).

Conclusion: Compared with continuous androgen deprivation therapy, intermittent androgen deprivation therapy has better clinical efficacy in the treatment of PCa, and DCE-MRI indices are related to the treatment efficacy of PCa and have an evaluation value.

KEYWORDS

prostate cancer, clinical effect, DCE-MRI, intermittent androgen deprivation therapy, continuous androgen deprivation therapy

Introduction

Prostate cancer (PCa) mainly refers to the pathological changes in the tissues around the prostate gland affected by various complex factors, resulting in the growth dysfunction or irregular growth of acinar cells and eventually inducing malignant tumors (Mori et al., 2022). Androgen deprivation therapy (ADT) is the main method to treat PCa, which can block androgens from testis and adrenal gland and has become the gold standard in the treatment of advanced PCa. However, total ADT can lead to adverse reactions in patients, such as hot flashes, gynecomastia, and osteoporosis, which significantly affect the quality of life of patients (Kishan et al., 2022). In recent years, intermittent androgen deprivation has become increasingly prominent in prolonging androgen resistance and reducing adverse reactions and has gradually attracted attention in the treatment of PCa (Denmeade et al., 2022). Currently, it is believed that the premise and basis of tumor formation are tumor neovascularization, which is an important index to evaluate tumor growth, metastasis, and malignancy degree, so the evaluation of tumor hemodynamics is extremely essential (Qu et al., 2021). Dynamic-contrast enhanced magnetic resonance imaging (DCE-MRI) calculates volume transfer coefficient (K^{trans}), reverse transfer constant (K_{ep}), and extracellular volume fraction (V_e) values through the pharmacokinetic model, which can reflect the changes of neovascularization density and blood perfusion in tumor tissues physiologically and pathologically before the changes of morphology and thereby provide quantitative data on the therapeutic effect of tumors at the molecular level (Ghoreifi et al., 2023). This study evaluated the clinical efficacy of different androgen deprivation therapies in the treatment of PCa from the perspective of DCE-MRI and provided references for the evaluation of therapeutic efficacy of this disease.

Materials and methods

Clinical data

104 patients with PCa from January 2020 to January 2023 were studied, all of whom were treated with ADT. The patients were divided into a continuous group (continuous ADT) and an intermittent group (intermittent ADT) by random number table method, 52 cases/group. Study procedures were reviewed and approved by the Ethics Committee of Wuhan Fourth Hospital (IRB number: 201912WH10; Registration number: ChiCTR1900075593; Date Granted: 2019-12), and all study subjects gave informed consent and signed written consent.

Inclusion criteria: (1) Patients confirmed as PCa by transrectal ultrasound-guided puncture and patients staged at T3~T4; (2) Patients with expected survival greater than 6 months;

(3) Patients with complete clinical data; (4) Patients with well tolerance to MRI.

Exclusion criteria: (1) Patients with poor image quality; (2) Patients with other prostate diseases; (3) Patients with other malignant tumor diseases; (4) Patients with a history of radiation therapy and endocrine therapy before enrollment; (5) Patients with a recent history of prostatic puncture (within 1 month before enrollment).

Treatment methods

Intermittent group received intermittent ADT, that is, anti-androgen combined with medical castration. All patients took 50 mg bicalutamide tablets orally once daily (CORDEN PHARMA GMBH, H20140720). Two weeks later, 3.6 mg goserelin acetate sustained-release depot (AstraZeneca UK Limited, J20100126) was injected subcutaneously into the lower abdomen. Serum prostate specific antigen (PSA), testosterone, and DCE-MRI were measured monthly during the treatment. Treatment was given every 4 weeks until PSA dropped to the lowest level (4 ng/mL), after which treatment was stopped at 3 months from PSA stabilization, entering the treatment intermission. Subsequently, serum PSA and blood testosterone levels were measured monthly, and DCE-MRI examinations were conducted to determine lesion expansion and the emergence of new metastatic lesions. If serum PSA rose again to more than 10 ng/mL or 50% of the initial diagnosis, the second cycle of treatment was required until serum PSA reduced to the lowest value. When intermittent therapy was completed, the treatment was stopped until new metastatic lesions appeared or primary lesions expanded. All patients were treated for 4–6 months and followed up for more than 6 months.

Serum PSA is a specific marker of PCa according to Prostate Cancer Diagnosis and Treatment Guidelines in 2014. PSA levels less than 4.0 ng/mL are considered normal, while PSA levels greater than 10 ng/mL are considered high-risk PCa. In this study, serum PSA and testosterone were monitored with regular follow-up, and Imaging examinations were performed to see if any new lesions had developed or if existing lesions had expanded. Medication can be stopped when serum PSA is less than 4.0 ng/mL and serum testosterone is less than 20.0 ng/dL.

The continuous group was given continuous ADT after bilateral testicle resection. Patients were given 50 mg bicalutamide orally, qd. Patients with hormone resistance received 250 mg flutamide (TASLY Diyi, H19990144) tid rather than bicalutamide tablets. Serum PSA, testosterone, and DCE-MRI examinations were monitored monthly (Yu et al., 2010; Mottet et al., 2012). Serum PSA levels must be reduced to 4 ng/mL, and serum testosterone to 20 ng/dL.

Resistance was defined as serum testosterone <50 ng/dL with a continuous PSA increase greater than 10 ng/mL 1 week apart.

DCE-MRI detection method

Siemens 1.5T MR Scanner was used for DCE-MRI examination with 8 channel array coil and Siemens Syngo.via equipment. The scanning sequence mainly included T₂WI, T₁WI, diffusion weighted imaging (DWI), and DCE-MRI. DCE-MRI sequence took FLASH 3D-VIBE, T₁WI axis position, layer thickness 3.5 mm, TR 4.2 ms, TE 1.58 ms, FOV 260 mm × 260 mm, NEX1, inverse angle 12°, voxel size 1.4 mm × 1.4 mm × 3.5 mm. Gd-diethylenetriamine pentaacetic acid (Gd-DTPA) and 20 mL normal saline were prepared according to the standard of 0.2 mmol/kg, and Gd-DTPA and 20 mL normal saline were simultaneously injected with a high-pressure syringe at 2.5 mL/s starting from the fourth stage. The scan was repeated for 36 stages, with a total scanning time of 4.1 min. 20 images were obtained in each stage, and a total of 720 original images were obtained. The original DCE-MRI images were transmitted to Siemens Syngo.via, Tissue 4d was specified as the workflow, and quantitative parameter values were obtained through motion correction, alignment, processing, and film reading. Alignment and motion correction were performed on 720 original images. In the processing program, The region of interest of the whole prostate was manually sketched through axial, coronal, and sagittal views, K^{trans}, K_{ep}, and Ve were quantified and measured twice to get an average value. The perfusion parameters blood volume (BV) and blood flow (BF) were calculated according to the first-pass effect of the drug. DCE-MRI were measured monthly during the treatment and follow-up in both the intermittent group and continuous group.

Clinical efficacy evaluation

Efficacy evaluation was conducted according to the RECIST criteria (Uemura et al., 2022). Complete response (CR): all target lesions disappeared completely except nodular diseases. These target nodules should be evaluated and reduced to normal size (short diameter <10 mm). Partial response (PR): The total diameter of all target lesions is ≥30% below baseline. Target nodules are measured by short diameter to calculate total diameter, whereas all other target lesions are measured by longest diameter. Progressive disease (PD): The minimum sum of the target lesion diameters was used as reference, and the relative increase in the diameter sum was at least 20% (if the baseline measurement was minimal, the baseline was used as reference); In addition, an absolute increase of at least 5 mm in the diameter sum must be satisfied (the presence of one or more new lesions is also considered disease progression). Stable disease (SD): The reduction of target lesions did not reach PR, and the increase did not reach PD, the minimum sum of diameters can be used as a reference. Objective response rate (ORR): the proportion of patients with a complete response or partial response to treatment. Disease control rate (DCR): the percentage of patients with advanced cancer whose therapeutic intervention has led to a complete response, partial response, or stable disease. The

comparison results are the data after the end of treatment compared with those before treatment, no data during follow-up were included.

Observation measures

(1) Clinical efficacy and DCE-MRI indicators. (2) DCE-MRI indices were compared after treatment, and the influence of DCE-MRI indices on the therapeutic effect of PCa was analyzed by logistic regression, and the evaluation value of DCE-MRI on the therapeutic effect of ADT was analyzed by operator characteristic (ROC) curve.

Statistical analysis

Statistical data were analyzed using SPSS 22.0 software, and differences in enumeration data (percentage) were compared using the χ^2 test. Measurement data were expressed by ($\bar{x} \pm s$) after normal test, and the differences were compared by *t*-test. DCE-MRI was evaluated for its efficacy in the treatment of PCa using logistic regression, and its effectiveness in ADT was evaluated using ROC curves. A statistically significant difference was indicated by $p < 0.05$.

Results

Clinical data

Clinical data from both groups were not significantly different. There was no significant difference in age, BMI, fasting blood glucose, blood lipid levels and PSA between the two groups. In addition, tumor related data, such as maximum tumor diameter, IPSS score and TNM staging, were not statistically significant ($p > 0.05$, Table 1).

Clinical effect

The ORR of the intermittent group was higher than that of the continuous group ($p < 0.05$). Although there was no significant difference in DCR between the two groups ($p > 0.05$, Table 2), compared with the continuous group, the DCR in the intermittent group still showed an upward trend.

DCE-MRI indices of patients with different therapeutic effects

As a result of treatment, K^{trans}, K_{ep}, Ve, BF, and BV decreased, and those decreased in the intermittent group significantly more

TABLE 1 Comparison of clinical data between the two groups.

Items	Continuous group (<i>n</i> = 52)	Intermittent group (<i>n</i> = 52)	χ^2/t	P
Age (years)	69.03 ± 5.37	70.15 ± 5.31	1.069	0.287
BMI (kg/m ²)	22.74 ± 2.19	22.58 ± 1.97	0.392	0.696
FPG (mmol/L)	5.26 ± 1.03	5.19 ± 1.16	0.325	0.746
TG (mmol/L)	1.47 ± 0.28	1.51 ± 0.24	0.782	0.436
TC (mmol/L)	4.53 ± 0.81	4.60 ± 0.85	0.43	0.668
PSA (μg/L)	62.76 ± 3.56	63.01 ± 3.78	0.347	0.729
Maximum tumor diameter (cm)	7.95 ± 1.16	8.05 ± 1.24	0.425	0.672
IPSS score	24.15 ± 2.09	23.98 ± 2.76	0.354	0.724
TNM staging			0.158	0.691
T3	31	29		
T4	21	23		

Notes: BMI, body mass index; FPG, fasting plasma glucose; TG, triglyceride; TC, cholesterol; PSA, prostate specific antigen; IPSS, score, International Prostatism Symptom score.

TABLE 2 Comparison of clinical efficacy between the two groups (*n*, %).

Groups	<i>n</i>	CR	PR	SD	PD	ORR	DCR
Continuous group	52	9	19	20	4	53.85	92.31
Intermittent group	52	13	25	11	3	73.08	94.23
χ^2						4.147	1.182
<i>P</i>						0.042	0.277

Notes: CR, complete response; PR, partial response; SD, standard deviation; PD, progressive disease; ORR, objective response rate; DCR, disease control rate.

than those in the continuous group ($p < 0.05$, Figure 1). These data show that the efficacy of intermittent ADT treatment is significantly higher than that of continuous ADT treatment group in terms of MRI performance. K^{trans} , K_{ep} , V_e , BF , and BV in the ORR group were lower than those in the non-ORR group ($p < 0.05$, Figure 2).

Comparison of DCE-MRI indices of the therapeutic effect of PCa in the two treatment

Logistic regression analysis showed that K^{trans} , K_{ep} , V_e , BF , and BV values were correlated with the therapeutic effect of PCa ($p < 0.05$, Table 3). These suggests that these DCE-MRI parameters can well predict the clinical treatment efficacy of PCa.

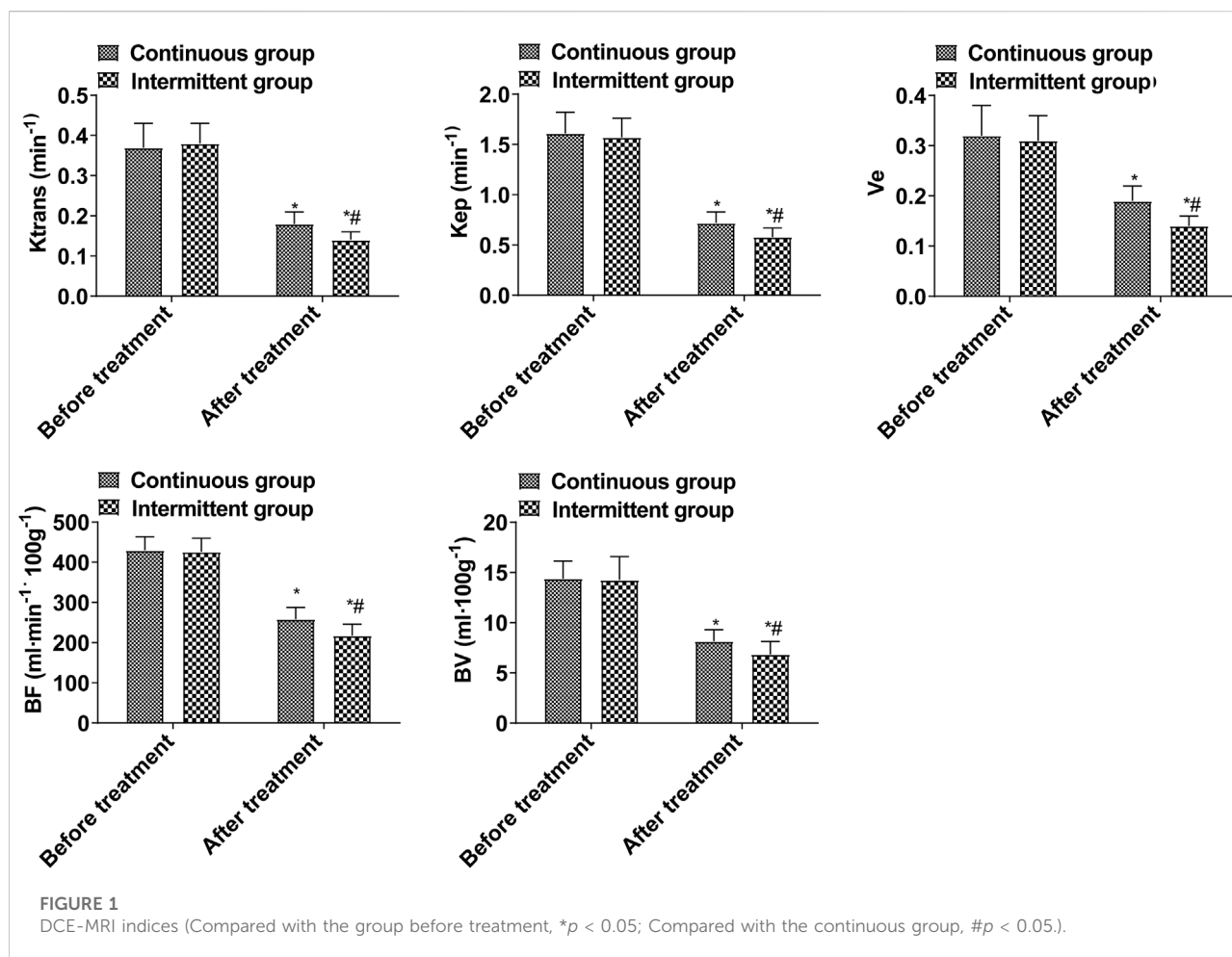
Evaluation value of DCE-MRI indices on the therapeutic effect of PCa

AUC value evaluated by the combined detection of K^{trans} , K_{ep} , V_e , BF , and BV was greater than that by each index alone ($p <$

0.05, Table 4; Figure 3). The combination of five items of DCE-MRI had the best predictive effect on PCa disease.

Discussion

PCa is a common malignant tumor of the male reproductive system. For patients with advanced PCa and those who cannot tolerate surgery, ADT is the most widely used therapeutic means at present (Cucchiara et al., 2019; Cipollari et al., 2022). ADT can inhibit the synthesis of vascular endothelial growth factor, induce endothelial cell apoptosis, inhibit the growth of androgen-dependent PCa tumors, and manage lymph node and bone metastasis (Al Salmi et al., 2020). At present, ADT is not only used for palliative treatment of advanced PCa but also adjuvant therapy before or after radical resection or radical radiotherapy to improve prognosis (Cereser et al., 2022). Continuous ADT can block androgens from testis and adrenal glands to the greatest extent, while intermittent ADT has become increasingly prominent in prolonging androgen resistance and reducing adverse reactions (Schaudinn et al., 2019; Carvajal et al., 2021). This study showed that the ORR of the intermittent



group was higher than that of the continuous group, indicating that the clinical efficacy of intermittent ADT was better than that of continuous ADT. This was mainly because intermittent ADT could not prevent the transformation of androgen-dependent tumors into non-androgen-dependent tumors, but it could delay the transformation process and thus improve the therapeutic efficacy.

ADT is mainly recommended for symptomatic patients, patients with metastatic (M1) prostate cancer, or PSA dynamics characterized by rapid PSA rise or short PSA doubling time (less than 6 months). Intermittent ADT has been used as a method of monotherapy for ADT, which limits the incidence by periodically restoring serum testosterone levels. However, the clinical efficacy of intermittent ADT and continuous ADT is still controversial (Perera et al., 2020). The best method for ADT has not been clearly established. Traditionally, ADT is administered in a continuous manner, and the castration level of testosterone is ensured by repeated injections. This scheme usually continues to be used (Ravi and Choudhury, 2023). However, continuous use of GnRH analogues for ADT treatment can lead to considerable incidence of sexual

and endocrine dysfunction and poor quality of life (QOL) outcomes. These problems led to the proposed intermittent application of ADT. The existing data of patients with locally advanced or recurrent non metastatic prostate cancer suggest that intermittent ADT treatment does not significantly affect OS outcome. Studies have shown that intermittent treatment may be the most beneficial for men with locally advanced or recurrent non metastatic prostate cancer and low baseline risk (PSA ≤ 1 ng/mL) (Bianchi et al., 2021).

ADT-treated PCa progresses to castration-resistant PCa after remission (Zhang et al., 2020). Patients may develop castration-resistant PCa within 5 years of treatment. Therefore, monitoring the efficacy of PCa after treatment is particularly considerable (Christophe et al., 2020). PSA is an index for monitoring the efficacy of PCa after radical surgery or conservative treatment. Although *post hoc* analyses of contemporary ARPI trials suggest that the depth of the initial PSA response is associated with favorable long-term outcomes. However, it could not reflect the changes of tumor morphology and microcirculation characteristics. PSA levels cannot truly reflect the histological and biological changes of tumors after endocrine therapy or

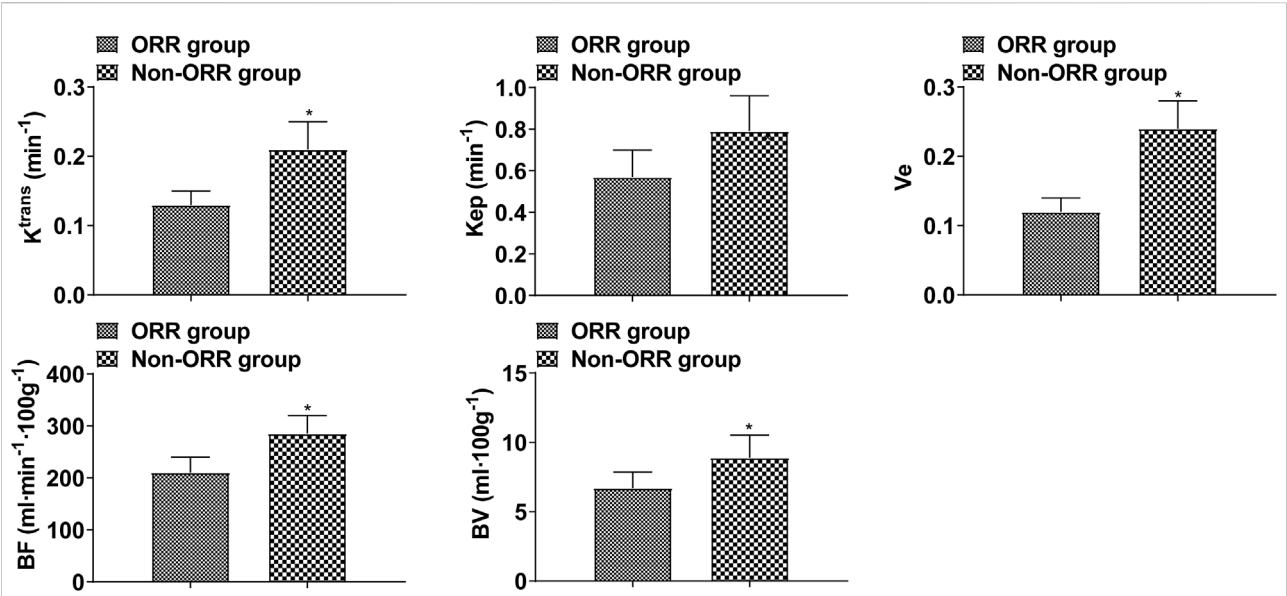


FIGURE 2
DCE-MRI indices in patients with different therapeutic effects (Compared with ORR group, * $p < 0.05$).

TABLE 3 Analysis of the influence of DCE-MRI indexes on the therapeutic effect of prostate cancer.

Indices	β	SE	wald χ^2	OR	95%CI	P
Ktrans	-5.43	1.477	13.516	0.004	<0.001-0.079	<0.001
Kep	-0.606	0.212	8.171	0.546	0.360-0.827	0.004
Ve	-3.969	1.516	6.854	0.019	0.001-0.369	0.009
BF	-0.025	0.013	3.698	0.975	0.951-1.000	0.055
BV	-0.153	0.25	0.375	0.858	0.526-1.401	0.541

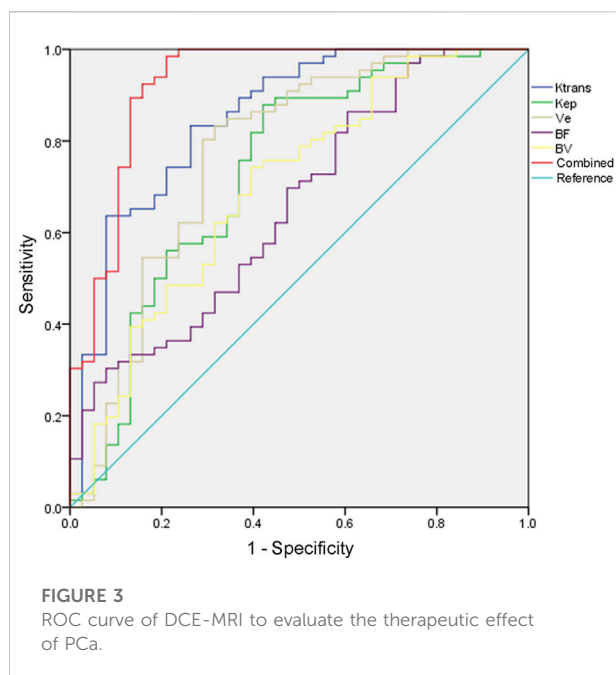
Notes: K^{trans} , volume transfer coefficient; K_{ep} , reverse transfer constant; V_e , volume fraction; BF, blood flow; BV, blood volume; CI, confidence interval.

TABLE 4 Value analysis of DCE-MRI index in evaluating the therapeutic effect of prostate cancer.

Indices	Cut-off value	AUC	SE	P	95%CI
K^{trans}	0.17 min^{-1}	0.851*	0.041	<0.001	0.771-0.931
K_{ep}	0.63 min^{-1}	0.731*	0.055	<0.001	0.622-0.839
V_e	0.19	0.770*	0.053	<0.001	0.666-0.874
BF	253.86 $\text{mL min}^{-1} \cdot 100 \text{g}^{-1}$	0.658*	0.056	0.008	0.549-0.767
BV	8.01 $\text{mL} \cdot 100\text{g}^{-1}$	0.698*	0.055	0.001	0.590-0.806
Combined	—	0.924	0.031	<0.001	0.863-0.986

Note: BV, blood volume; BF, blood flow; CI, confidence interval. Compared with combination, * $p < 0.05$.

radiation therapy, especially in cases with metastasis (Pesapane et al., 2020). ADT monitoring for PCa should therefore be applied with other indicators. Currently, it is believed that the growth and invasion of PCa depend on the tumor neovascularization. As the neovascularization wall fails to develop correctly, permeability increases, and blood is exchanged more rapidly between tumor and blood vessel, resulting in tumor invasion. MRI is the best imaging method



for PCa, among which DCE-MRI quantitative analysis has been proven to be useful for evaluating tumor hemodynamics. Based on the difference in microvascular characteristics of lesions with different properties, DCE-MRI technology uses the difference in the time and concentration of contrast agent to reach normal tissues and pathological tissues with different properties to form different intensification methods, which can evaluate blood perfusion status of different tissues, so as to achieve the purpose of lesion diagnosis (Tamada et al., 2021; Forster et al., 2022).

DCE-MRI, combined with corresponding pharmacokinetic models, can obtain parameters that reflect tissue perfusion and permeation characteristics and quantitatively analyze the physiological characteristics of pathological tissues, which can be applied not only to the clinical diagnosis but also to the evaluation of the efficacy of tumor radiotherapy and chemotherapy (Prendeville et al., 2018). The common penetration parameters of DCE-MRI are K^{trans} , V_e , and K_{ep} . K^{trans} refers to the volume transport constant of contrast agent diffused from plasma into extravascular extracellular space, reflecting the level of vascular permeability in tissues. K_{ep} is the rate constant at which contrast agent diffuses from interstitial space to reflow into blood vessels. V_e refers to the volume ratio of EES per unit tissue volume. The perfusion parameters of DCE-MRI to reflect the blood perfusion status include BF and BV. BF represents the BF velocity in the blood vessels of the interest area per unit time, and BV represents the BV, both of which mainly reflect blood perfusion and depend on the microvascular density in the tissue (Arnoldner et al., 2022; Chatterjee et al., 2022; Fan et al., 2022; Nakayama et al., 2022). This study showed that DCE-MRI indices were all decreased after ADT, and K^{trans} , K_{ep} , V_e , BF, and BV

in the ORR group were lower than those in the non-ORR group, suggesting that DCE-MRI indices may be used to evaluate the efficacy of ADT. This is mainly related to the reduction of PCa volume, gland atrophy, and fibrosis after ADT treatment (Lu et al., 2020). BF and BV of tumors after endocrine therapy are significantly reduced, and K^{trans} and K_{ep} are significantly reduced (Ikoma et al., 2020), which was consistent with the results of this study. ADT causes acinar atrophy, fibrosis, and basal cell hyperplasia in the prostate, resulting in a reduction in total glandular interstitial tissue and ultimately, total gland. In addition, after ADT, not only does vascular endothelial growth factor decrease with the decrease of androgen level, but also the BF of PCa tissues decreases, and cells show obvious apoptosis and necrosis, thus achieving anti-tumor angiogenesis, so K^{trans} , K_{ep} , and V_e values are significantly reduced after endocrine therapy (Kim et al., 2021; Ueda et al., 2022). Further analysis found that K^{trans} , K_{ep} , V_e , BF, and BV were correlated with the therapeutic effect of PCa, and the AUC value of the combined detection of all indicators to evaluate the therapeutic effect of PCa was greater than 0.9, indicating that the DCE-MRI indices were correlated with the therapeutic effect of PCa.

In summary, As compared with continuous ADT, intermittent ADT improves PCa treatment outcomes, and DCE-MRI indicators are correlated with PCa treatment outcomes.

Data availability statement

The original contributions presented in the study are included in the article/Supplementary material, further inquiries can be directed to the corresponding author.

Ethics statement

The studies involving humans were approved by the Ethics and Scientific Committees of Wuhan Fourth Hospital and performed in accordance with The Declaration of Helsinki. The studies were conducted in accordance with the local legislation and institutional requirements. The participants provided their written informed consent to participate in this study. Written informed consent was obtained from the individual(s) for the publication of any potentially identifiable images or data included in this article.

Author contributions

WG designed the research study. WG and ML performed the research. ML provided help and advice. WG and ML analyzed the data. WG wrote the manuscript. ML reviewed and edited the manuscript. All authors contributed to editorial changes in the manuscript. All authors contributed to the article and approved the submitted version.

Funding

The author(s) declare(s) that no financial support was received for the research, authorship, and/or publication of this article.

References

- Al Salmi, I., Menezes, T., El-Khodary, M., Monteiro, S., Haider, E. A., and Alabousi, A. (2020). Prospective evaluation of the value of dynamic contrast enhanced (DCE) imaging for prostate cancer detection, with pathology correlation. *Can. J. Urol.* 27 (3), 10220–10227. Epub 2020/06/17.
- Arnoldner, M. A., Polanec, S. H., Lazar, M., Noori Khadavi, S., Clauser, P., Pötsch, N., et al. (2022). Rectal preparation significantly improves prostate imaging quality: assessment of the PI-QUAL score with visual grading characteristics. *Eur. J. Radiology* 147, 110145. Epub 2022/01/11. doi:10.1016/j.ejrad.2021.110145
- Bianchi, S., Mosca, A., Dalla Volta, A., Prati, V., Ortega, C., Buttiglieri, C., et al. (2021). Maintenance versus discontinuation of androgen deprivation therapy during continuous or intermittent docetaxel administration in castration-resistant prostate cancer patients: a multicentre, randomised phase III study by the piemonte oncology network. *Eur. J. Cancer* 155, 127–135. doi:10.1016/j.ejca.2021.06.034
- Briones Carvajal, J. R., Naimi, M. F., Zhang, L., and Emmenegger, U. (2021). Real-world comparison of abiraterone (A) versus enzalutamide (E) for first-line therapy of metastatic castration-resistant prostate cancer (mCRPC). *J. Clin. Oncol.* 39 (6 Suppl. 1), 133. doi:10.1200/jco.2021.39.6_suppl.133
- Cereser, L., Giannarini, G., Bonato, F., Pizzolitto, S., Como, G., Valotto, C., et al. (2022). Comparison of multiple abbreviated multiparametric MRI-derived protocols for the detection of clinically significant prostate cancer. *Minerva Urol. Nephrol.* 74 (1), 29–37. Epub 2020/10/06. doi:10.23736/s2724-6051.20.03952-1
- Chatterjee, A., Turchan, W. T., Fan, X., Griffin, A., Yousuf, A., Karczmar, G. S., et al. (2022). Can pre-treatment quantitative multi-parametric MRI predict the outcome of radiotherapy in patients with prostate cancer? *Acad. Radiol.* 29 (7), 977–985. Epub 2021/10/15. doi:10.1016/j.acra.2021.09.012
- Christophe, C., Montagne, S., Bourrellet, S., Roupert, E., Barret, E., Rozet, F., et al. (2020). Prostate cancer local staging using biparametric MRI: Assessment and comparison with multiparametric MRI. *Eur. J. Radiology* 132, 109350. Epub 2020/10/21. doi:10.1016/j.ejrad.2020.109350
- Cipollari, S., Guarrasi, V., Pecoraro, M., Bicchetti, M., Messina, E., Farina, L., et al. (2022). Convolutional neural networks for automated classification of prostate multiparametric magnetic resonance imaging based on image quality. *J. Magnetic Reson. Imaging* 55 (2), 480–490. Epub 2021/08/11. doi:10.1002/jmri.27879
- Cucchiara, V., Yang, J. C., Liu, C., Adomat, H. H., Tomlinson Guns, E. S., Gleave, M. E., et al. (2019). GnRH antagonists have direct inhibitory effects on castration-resistant prostate cancer via intracrine androgen and AR-V7 expression. *Mol. Cancer Ther.* 18 (10), 1811–1821. Epub 2019/07/26. doi:10.1158/1535-7163.Mct-18-1337
- Denmeade, S., Antonarakis, E. S., and Markowski, M. C. (2022). Bipolar androgen therapy (bat): a patient's guide. *Prostate* 82 (7), 753–762. Epub 2022/04/01. doi:10.1002/pros.24328
- Fan, X., Chatterjee, A., Pittman, J. M., Yousuf, A., Antic, T., Karczmar, G. S., et al. (2022). Effectiveness of dynamic contrast enhanced MRI with a split dose of gadoterate meglumine for detection of prostate cancer. *Acad. Radiol.* 29 (6), 796–803. Epub 2021/09/30. doi:10.1016/j.acra.2021.07.028
- Forster, R. B., Engeland, A., Kvåle, R., Hjellevik, V., and Bjørge, T. (2022). Association between medical androgen deprivation therapy and long-term cardiovascular disease and all-cause mortality in nonmetastatic prostate cancer. *Int. J. Cancer* 151 (7), 1109–1119. Epub 2022/05/01. doi:10.1002/ijc.34058
- Ghoreifi, A., Kaneko, M., Peretsman, S., Iwata, A., Brooks, J., Shakir, A., et al. (2023). Patient-reported satisfaction and regret following focal therapy for prostate cancer: a prospective multicenter evaluation. *Eur. Urology Open Sci.* 50, 10–16. Epub 2023/04/27. doi:10.1016/j.euro.2023.02.003
- Ikoma, Y., Kishimoto, R., Tachibana, Y., Omatsu, T., Kasuya, G., Makishima, H., et al. (2020). Reference region extraction by clustering for the pharmacokinetic analysis of dynamic contrast-enhanced MRI in prostate cancer. *Magn. Reson. Imaging* 66, 185–192. Epub 2019/09/06. doi:10.1016/j.mri.2019.08.034
- Kim, H., Thomas, J. V., Nix, J. W., Gordetsky, J. B., Li, Y., and Rais-Bahrami, S. (2021). Portable perfusion phantom offers quantitative dynamic contrast-enhanced magnetic resonance imaging for accurate prostate cancer grade stratification: a pilot study. *Acad. Radiol.* 28 (3), 405–413. Epub 2020/04/01. doi:10.1016/j.acra.2020.02.027
- Kishan, A. U., Sun, Y., Hartman, H., Pisansky, T. M., Bolla, M., Neven, A., et al. (2022). Androgen deprivation therapy use and duration with definitive radiotherapy for localised

Conflict of interest

The authors declare that the research was conducted in the absence of any commercial or financial relationships that could be construed as a potential conflict of interest.

prostate cancer: An individual patient data meta-analysis. *Lancet Oncol.* 23 (2), 304–316. Epub 2022/01/21. doi:10.1016/s1470-2045(21)00705-1

Lu, Y., Ge, S., Liu, Y., and Bai, G. (2020). Withdrawn: the changes of ADC value, DCE-MRI parameters and their influence on neuropsychology in prostate cancer patients after endocrine therapy based on magnetic resonance imaging. *Neurosci. Lett.*, 135221. Epub 2020/07/03. doi:10.1016/j.neulet.2020.135221

Mori, J. O., Shafran, J. S., Stojanova, M., Katz, M. H., Gignac, G. A., Wisco, J. J., et al. (2022). Novel forms of prostate cancer chemoresistance to successful androgen deprivation therapy demand new approaches: rationale for targeting BET proteins. *Prostate* 82 (10), 1005–1015. Epub 2022/04/12. doi:10.1002/pros.24351

Mottet, N., Van Damme, J., Loulidi, S., Russel, C., Leitenberger, A., Wolff, J. M., et al. (2012). Intermittent hormonal therapy in the treatment of metastatic prostate cancer: A randomized trial. *BJU Int.* 110 (9), 1262–1269. doi:10.1111/j.1464-410X.2012.11120.x

Nakayama, H., Sekine, Y., Oka, D., Miyazawa, Y., Arai, S., Koike, H., et al. (2022). Combination therapy with novel androgen receptor antagonists and statin for castration-resistant prostate cancer. *Prostate* 82 (3), 314–322. Epub 2021/11/30. doi:10.1002/pros.24274

Perera, M., Roberts, M. J., Klotz, L., Higano, C. S., Papa, N., Sengupta, S., et al. (2020). Intermittent versus continuous androgen deprivation therapy for advanced prostate cancer. *Nat. Rev. Urol.* 17 (8), 469–481. doi:10.1038/s41585-020-0335-7

Pesapane, F., Standaert, C., De Visschere, P., and Villeirs, G. (2020). T-staging of prostate cancer: identification of useful signs to standardize detection of posterolateral extraprostatic extension on prostate MRI. *Clin. Imaging* 59 (1), 1–7. Epub 2019/11/13. doi:10.1016/j.clinimag.2019.08.007

Prendeville, S., Gertner, M., Maganti, M., Pintilie, M., Perlis, N., Toi, A., et al. (2018). Role of magnetic resonance imaging targeted biopsy in detection of prostate cancer harboring adverse pathological features of intraductal carcinoma and invasive cribriform carcinoma. *J. Urology* 200 (1), 104–113. Epub 2018/02/07. doi:10.1016/j.juro.2018.01.081

Qu, F., Gu, Y., Xue, M., He, M., Zhou, F., Wang, G., et al. (2021). Impact of therapy on cancer metabolism in high-risk localized prostate cancer treated with neoadjuvant docetaxel and androgen deprivation therapy. *Prostate* 81 (9), 560–571. Epub 2021/04/28. doi:10.1002/pros.24134

Ravi, P., and Choudhury, A. D. (2023). Defining patient benefits from high-intensity intermittent therapy for hormone-sensitive prostate cancer. *Eur. Urol. Focus* 9 (3), 419–421. doi:10.1016/j.euf.2023.01.004

Schaudinn, A., Gawlitza, J., Mucha, S., Linder, N., Franz, T., Horn, L. C., et al. (2019). Comparison of PI-RADS v1 and v2 for multiparametric MRI detection of prostate cancer with whole-mount histological workup as reference standard. *Eur. J. Radiology* 116, 180–185. Epub 2019/06/04. doi:10.1016/j.ejrad.2019.04.012

Tamada, T., Kido, A., Yamamoto, A., Takeuchi, M., Miyaji, Y., Moriya, T., et al. (2021). Comparison of biparametric and multiparametric MRI for clinically significant prostate cancer detection with PI-rads version 2.1. *J. Magnetic Reson. Imaging* 53 (1), 283–291. Epub 2020/07/03. doi:10.1002/jmri.27283

Ueda, T., Fujita, K., Nishimoto, M., Shiraishi, T., Miyashita, M., Kayukawa, N., et al. (2022). Predictive factors for the efficacy of abiraterone acetate therapy in high-risk metastatic hormone-sensitive prostate cancer patients. *World J. Urol.* 40 (12), 2939–2946. Epub 2022/11/05. doi:10.1007/s00345-022-04200-2

Uemura, H., Kobayashi, K., Yokomizo, A., Hinotsu, S., Horie, S., Kakehi, Y., et al. (2022). Health-related quality of life with enzalutamide versus flutamide in castration-resistant prostate cancer from the AFTERCAB study. *Int. J. Clin. Oncol.* 27 (10), 1632–1643. Epub 2022/08/11. doi:10.1007/s10147-022-02221-w

Yu, E. Y., Gulati, R., Telesca, D., Jiang, P., Tam, S., Russell, K. J., et al. (2010). Duration of first off-treatment interval is prognostic for time to castration resistance and death in men with biochemical relapse of prostate cancer treated on a prospective trial of intermittent androgen deprivation. *J. Clin. Oncol.* 28 (16), 2668–2673. Epub 2010 Apr 26. PMID: 20421544. doi:10.1200/JCO.2009.25.1330

Zhang, G. M., Han, Y. Q., Wei, J. W., Qi, Y. F., Gu, D. S., Lei, J., et al. (2020). Radiomics based on MRI as a biomarker to guide therapy by predicting upgrading of prostate cancer from biopsy to radical prostatectomy. *J. Magnetic Reson. Imaging* 52 (4), 1239–1248. Epub 2020/03/18. doi:10.1002/jmri.27138

Competitive binding of circCCDC6 to microRNA-128-3p activates TXNIP/NLRP3 pathway and promotes cerebral ischemia-reperfusion defects

ChongShu Wang¹, MingMing Dong², XiaoYi Zhang³, XiaoYu Wang⁴, Yan Zhao² and Yunpeng Cao¹✉

¹Department of Neurology, The Fourth People's Hospital of Shenyang, Shenyang City, Liaoning Province, 110001, China; ²Department of Neurology, The Fourth People's Hospital of Shenyang, Shenyang City, Liaoning Province, 110031, China; ³Department of Geriatric Medicine, The First Affiliated Hospital of China Medical University, Shenyang City, Liaoning Province, 110001, China; ⁴Department of Neurology, Liaoyang Central Hospital, Liaoyang City, Liaoning Province, 111010, China

Objective: Circular RNAs (circRNAs) are enriched in the brain and involved in various central nervous system diseases. The potential role of circCCDC6 in cerebral ischemia-reperfusion defects was partly elucidated in the work. **Methods:** A middle cerebral artery occlusion/reperfusion (MCAO/R) rat model and an oxygen-glucose deprivation and re-oxygenation (OGD/R)-treated SH-SY5Y cell model were constructed. CircCCDC6 expression in the two models was examined, and circCCDC6-involved mechanisms in neuronal pyroptosis and inflammation were analyzed through loss- and gain-of-function assays. **Results:** MCAO/R rat brain tissues and OGD/R-treated SH-SY5Y cells exhibited upregulated circCCDC6. Silencing circCCDC6 attenuated neuronal pyroptosis and inflammation in the brain tissue of MCAO/R rats. Overexpressing circCCDC6 or inhibiting miR-128-3p stimulated OGD/R-induced pyroptosis and inflammation in SH-SY5Y cells, while upregulating miR-128-3p attenuated OGD/R injury. CircCCDC6 silencing-induced effects on SH-SY5Y cells were antagonized by TXNIP overexpression. **Conclusion:** Mechanistically, circCCDC6 mediates miR-128-3p and activates TXNIP/NLRP3, thereby promoting OGD/R-induced neuronal pyroptosis and inflammation. CircCCDC6 may provide a new strategy for the treatment of MCAO/R.

Keywords: Cerebral ischemia-reperfusion, Circular RNA CCDC6, microRNA-128-3p, TXNIP/NLRP3, Pyroptosis, Inflammation

Received: 16 November, 2022; **revised:** 02 August, 2023; **accepted:** 10 August, 2023; **available on-line:** 07 November, 2023

✉ e-mail: chenjiajin470@hebmu-edu.cn

Abbreviations: AKT, Protein kinase B; ASC, Apoptosis-associated speck-like protein containing a CARD; BCA, Bicinchoninic acid; CIR, Cerebral ischemia-reperfusion; circCCDC6, Circular RNA Coiled-coil domain containing 6; circRNAs, Circular RNAs; DMEM, Dulbecco's modified essential medium; ELISA, Enzyme-linked immunosorbent assay; GAPDH, Glyceraldehyde-3-phosphate dehydrogenase; GSDMD, Gasdermin D; IgG, Immunoglobulin G; IL-1 β , Interleukin-1beta; Interleukin-18 (IL-18); IS, Ischemic stroke; LDH, Lactate dehydrogenase; LPS, Lipopolysaccharide; MCAO, Middle cerebral artery occlusion; miRNAs, microRNAs; MTT, 3-(4,5-dimethylthiazol-2-yl)-2,5-diphenyltetrazolium bromide; MUT, Mutant type; NF- κ B, Nuclear factor-kappaB; NLRP3, NOD-like receptor family pyrin domain containing 3; OA, Osteoarthritis; OGD/R, Oxygen-glucose deprivation/re-oxygenation; PI3K, Phosphoinositide 3-kinase; RIP, RNA immunoprecipitation assay; RIPA, Radio-Immunoprecipitation Assay; ROS, Reactive oxygen species; TGF β 2, Transforming Growth Factor-beta Receptor 2; TUNEL, Transferase-mediated deoxyuridine triphosphate-biotin nick end labeling staining; TXNIP, Thioredoxin interacting protein; WT, Wild type

INTRODUCTION

Ischemic stroke (IS) is a severe neurological response syndrome that leads to damage to neurovascular units, inflammation, and neuronal death (Zhu *et al.*, 2020). Reperfusion after cerebral ischemia often leads to a series of cellular and biochemical consequences, including the production of reactive oxygen species (ROS) and inflammatory cytokines, and brain cell damage, collectively referred to as cerebral ischemia-reperfusion (CIR) injury (Lim *et al.*, 2021), which are also key factors attributing to the poor prognosis of IS patients (Zuo *et al.*, 2018). It is unable to effectively protect the neurological function of IS patients despite great progress in the treatment options. Therefore, an urgent need for new therapeutic approaches is on the agenda to protect CIR-induced neurological deficits.

Pyroptosis is a special way of cell death, which is different from necrosis and apoptosis (Yu *et al.*, 2021). Pyroptosis plays an important role in CIR injury (Zhang *et al.*, 2022). Cerebral ischemia leads to the disruption of intracellular energy metabolism and oxidative stress, which activates the inflammatory response and intracellular inflammasome recombination (Zhang *et al.*, 2022). The inflammasome complex includes molecules such as ASC, NLRP3, and Caspase-1, which interact and activate the Caspase-1 enzyme. Activated Caspase-1 cleaves the precursor's IL-1 β and IL-18, releasing active pro-inflammatory cytokines (Wang *et al.*, 2022; Luo *et al.*, 2022). These pro-inflammatory cytokines induce inflammation in CIR injury and promote the further development of pyroptosis.

Circular RNAs (circRNAs) are highly stable covalently closed endogenous non-coding RNAs that are specifically expressed in tissues and cells (Vo *et al.*, 2019). CircRNAs are enriched in multiple organs, especially the brain, and a large body of evidence indicates that circRNAs are involved in the physiological and pathological processes of the brain, including CIR (Yang *et al.*, 2018). In addition, circRNAs exert their biological functions as molecular decoys of microRNAs (miRNAs) (Zhang *et al.*, 2020). In a circRNA expression profile after transient focal ischemia, circCCDC6 is confirmed to be upregulated in the brain of a model of middle cerebral artery occlusion (MCAO) rats (Mehta *et al.*, 2017). However, its related mechanism in CIR awaits further investigation.

MiRNAs, a group of post-transcriptional regulators of gene expression (Brennan *et al.*, 2020) are involved in the regulation of various cellular activi-

ties (Saliminejad *et al.*, 2019). miRNAs are emerging regulators of neuronal survival during CIR injury (Liu *et al.*, 2020). For instance, promoting miR-34c-5p expression is able to suppress inflammation and apoptosis, thereby preventing CIR injury (Tu *et al.*, 2021). The anti-inflammatory and anti-apoptotic properties of miR-128-3p have been accepted previously. miR-128-3p overexpression could protect against chronic constrictive injury to suppress neuroinflammation (Zhang *et al.*, 2020) and could restrain sepsis-induced apoptosis and inflammation (Yang *et al.*, 2021). However, not much was known about miR-128-3p-involved mechanism in CIR injury.

Hence, the function of circCCDC6 in neurological deficits following CIR was probed through *in vivo* and *in vitro* experiments. Speculation was put up that circCCDC6 activates TXNIP/NLRP3 inflammasome pathway by miR-128-3p to exacerbate CIR.

MATERIALS AND METHODS

MCAO/R animal model

Sixty male Sprague-Dawley rats, with a body weight of 220–280 g (Hunan SJA Laboratory Animal Co., Ltd., Changsha, China) were housed in an environment of 24–26°C with an adequate supply of water and food. The MCAO/R model was established as previously described (Yan *et al.*, 2020). Briefly, after anesthetization with 5% (v/v) isoflurane at a flow rate of 2 L/min, a monofilament nylon suture was inserted into the right common carotid artery through an incision over the head, and passed through the internal carotid artery as possible. After blocking the common carotid artery for 1 h, the suture was slowly retracted for reperfusion. Monitored by Laser Doppler flowmetry, and blood flow falling below 30% of baseline flow suggested the success of MCAO. Restoration of cerebral blood flow to >80% of baseline indicated the success of reperfusion. For the sham group, the same procedure was performed without suture insertion. After 24 h of reperfusion, neurological function was evaluated. After that, the rats were euthanized by overdosed CO₂, and 10 successfully modeled rats were selected from each group, of which the brain tissue of 5 rats was used for histopathological analysis, and that of the remaining 5 rats was for RNA or protein extraction. The success rate of modeling was 80%, and some rats died during the experiment. Authorization of animal care and methods procedures was by the Animal Ethics Committee of Dalian Municipal Central Hospital.

Lentiviral vector injection

circ shRNA-GFP (shRNA-Con) lentivirus or circCCDC6 shRNA-GFP (shRNA-circ CCDC6) lentivirus (2 µl, 1×10⁹ TU/ml) was microinjected into the left ventricle of the rat to knock down circ CCDC6 at the following coordinates: AP, −0.3 mm; lateral, 1.0 mm; and ventral, 2.2 mm. The lentiviral vector was injected 2 weeks before MCAO/R surgery. All lentiviral vectors mentioned above were purchased from GenePharma.

Neurological function scoring

Neurological function was assessed 7 d after MCAO/R surgery (Tatlisumak *et al.*, 1998). 0–no obvious defect, 1–failure to fully extend the left front paw when

stimulating tails, 2–circling to the left contralateral side when stimulating tails, 3–turning or walking left, 4–walking only when stimulating tails, 5–no response to stimuli, and unconsciousness.

Nissl staining

Brain tissues that were fixed with 4% paraformaldehyde were made into coronal fragments of 10 µm after routine paraffin embedding (Meng *et al.*, 2018). Each fragment was observed by light microscopy after staining with Nissl staining kit (Beyotime, Shanghai, China).

Immunofluorescence staining

After antigen retrieval through citrate buffer, brain slices were incubated with primary antibody GSDMD (20770-1-AP, Proteintech), followed by the addition of a secondary fluorescent antibody. Afterward, 4',6-diamidino-2-phenylindole-stained slices were observed under a fluorescence microscope (Olympus, Tokyo, Japan).

Transferase-mediated deoxyuridine triphosphate-biotin nick end labeling (TUNEL) staining

Pyroptosis was assessed using the TUNEL staining kit (Roche, Mannheim, Germany) following the protocols, and the percentage of pyroptotic cells was calculated.

Cell culture

Dulbecco's modified essential medium (DMEM, Gibco, Thermo Fisher Scientific) containing 10% fetal bovine serum (Gibco), 100 U/ml penicillin, and 100 µg/ml streptomycin was the culture system for SH-SY5Y cells (Cell Bank Type Culture Collection, Shanghai, China). For oxygen-glucose deprivation/reoxygenation (OGD/R) treatment, SH-SY5Y cells were cultured in glucose-free DMEM for 4 h in an anoxic environment (95% N₂ and 5% CO₂), and maintained in a normoxic environment with normal DMEM for 24 h (Xin *et al.*, 2017).

Cell transfection

Small interfering RNAs targeting circCCDC6 and TXNIP and negative controls (si-CCDC6, si-TXNIP, si-NC), pcDNA 3.1 overexpression vector and empty vector (pcDNA 3.1-circCCDC6, pcDNA 3.1-TXNIP, pcDNA 3.1) were purchased from Ribobio (Guangzhou, China), whereas miR-128-3p mimic/inhibitor and mimic/inhibitor NC were from Invitrogen (CA, USA). Transient transfection of SH-SY5Y cells was implemented by Lipofectamine 2000 (Invitrogen), followed by OGD/R treatment.

ELISA

Concentrations of IL-1β and IL-18 in cell supernatants or brain tissue homogenates were quantified using ELISA kits (Thermo Fisher Scientific).

Viability analysis

SH-SY5Y cells, along with MTT solution (20 µL/well, Sigma-Aldrich) were incubated for 4 h. Then, the original medium was replaced with dimethyl sulfoxide (150 µL/well), and absorbance was measured at 490 nm using a microplate reader (Bio-Rad, CA, USA).

Table 1. PCR primers

Genes	Sequences
circCCDC6	Forward: 5'-AGCCGAAGTAGAACAGCATCT-3'
	Reverse: 5'-TCTCCTTCTGCAAAGCCTGA-3'
miR-128-3p	Forward: 5'-TCACAGTGAACCGGTC-3'
	Reverse: 5'-CAGTGCCTGCTCGTGGAGT-3'
GAPDH	Forward: 5'-CTGCCAACGTGTCTAGTGGTG-3'
	Reverse: 5'-TCAGTGTAGCCAGGATGCC-3'
U6	Forward: 5'-CGAATTTGCGTGCATCCTT-3'
	Reverse: 5'-CGAATTTGCGTGCATCCTT-3'

Note: circCCDC6, circular RNA CCDC6; miR-128-3p, microRNA-128-3p; GAPDH, glyceraldehyde-3-phosphate dehydrogenase

Colorimetry

Lactate dehydrogenase (LDH) release from cell supernatants was quantified colorimetrically to determine cytotoxicity using the kit (Clontech, CA, USA).

Flow cytometry

Using the FAM FLICATM Caspase-1 kit (AbD Serotec, Oxford, UK), pyroptosis of SH-SY5Y cells was tested. SH-SY5Y cells after trypsinization were made into cell suspension for staining with 5 μ L caspase-1 FLICA and 5 μ L propidium solution, followed by analysis on a flow cytometer (BD Company, NJ, USA). Data quan-

tification was done by FlowJo software (TreeStar, CA, USA).

Quantitative PCR

From brain tissues and cells, total RNA extracts were collected *via* Trizol reagent (Invitrogen), and made into first-strand cDNA through PrimeScript RT kit (Takara, Tokyo, Japan). On the ABI7500 system, PCR was conducted by the SYBR Green method. Primers for all genes (Table 1) were from GeneCreate (Wuhan, Hubei, China). Standard controls for mRNA and miRNA were glyceraldehyde-3-phosphate dehydrogenase (GAPDH) and U6, respectively. Relative expression was calculated using the $2^{-\Delta\Delta C_t}$ method.

Immunoblotting

Total protein extracts were obtained using RIPA buffer (CST, USA), which was then quantified by BCA kit (Abbkine, USA) and separated on sodium dodecyl sulfate polyacrylamide gel electrophoresis. After that, proteins were covered with polyvinylidene fluoride membrane (Millipore, USA), followed by blockade with 5% nonfat milk and incubation with primary antibodies β -actin (sc-47778, Santa Cruz), IL-1 β (12242, CST), IL-18 (10663-1-AP, Proteintech), cleaved caspase-1 (4199, CST), TXNIP (14715, CST), NLRP3 (15101, CST), ASC (sc-514414, Santa Cruz) and the horseradish peroxidase-conjugated secondary antibody (CST). Through visualization by an enhanced chemiluminescence kit (GE Healthcare), band plots were further analyzed using ImageJ.

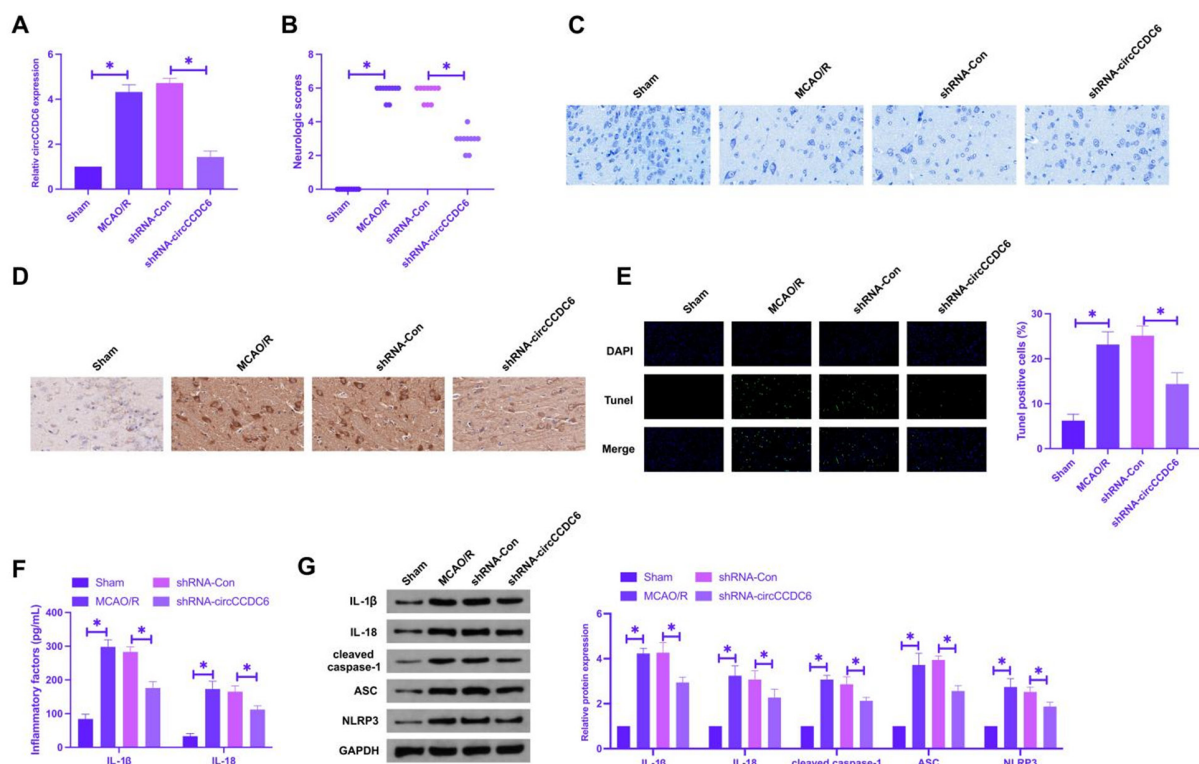


Figure 1. Effects of injection of shRNA-circCCDC6 lentiviral vector on biochemical indexes and pathological tissue damage of MCAO/R rat brain.

circCCDC6 expression in brain tissue (A), neurological function score (B), Nissl-stained cerebral cortex (C), immunofluorescence staining of GSDMD (D), TUNEL-stained brain tissue (E), IL-1 β and IL-18 contents in brain tissue (F), protein expressions of IL-1 β , IL-18, cleaved caspase-1, ASC and NLRP3 in brain tissue (G); data were reported as mean \pm S.D. (C, n=10; rest, n=5).

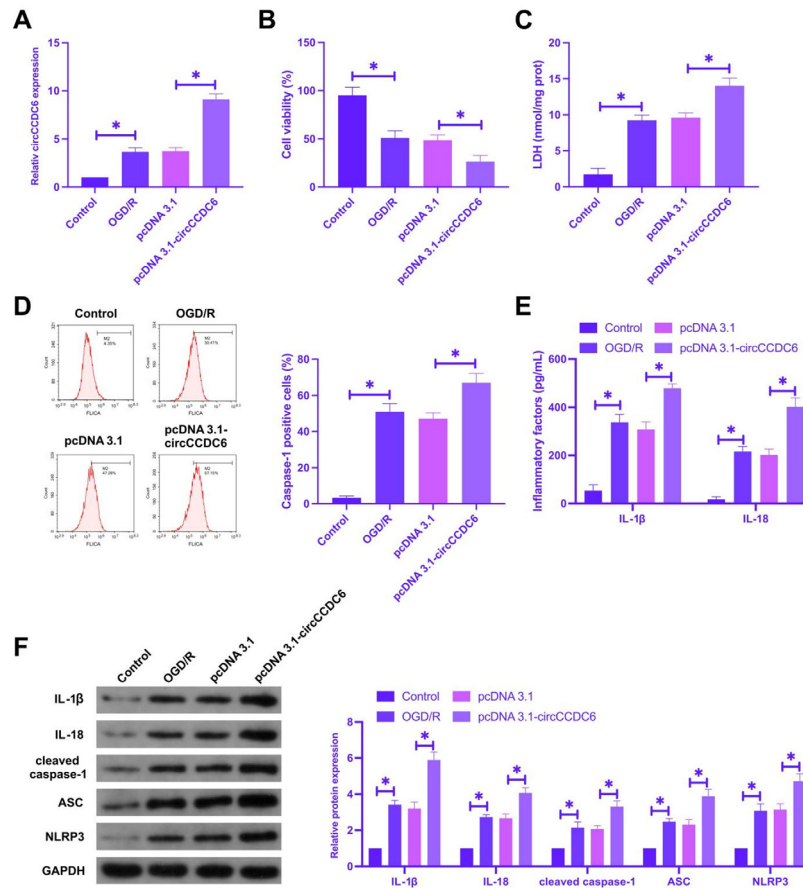


Figure 2. Effect of transfection of pcDNA 3.1-circCCDC6 on the biological behavior and biochemical indexes of OGD/R-treated SH-SY5Y cells. circCCDC6 expression (A), cell viability (B), toxicity (C), caspase-1 positive cells (D), IL-1β and IL-18 contents (E), protein expression of IL-1β, IL-18, cleaved caspase-1, ASC and NLRP3 (F); data were reported as mean ± S.D. (N=3).

Dual-luciferase reporter assay

The putative binding site of circCCDC6 or TXNIP 3'UTR was amplified by PCR and cloned into a pmirGLO vector to generate pmirGLO-circCCDC6-WT and pmirGLO-TXNIP-3'UTR WT. Mutants of circCCDC6 or TXNIP 3'UTR were created based on QuickChange Lighting Multi Site-Directed Mutagenesis Kit (Agilent Technologies, CA, USA) to produce pmirGLO-circCCDC6-Mut and pmirGLO-TXNIP-3'UTR-Mut. The generated reporter, in combination with mimic NC or miR-128-3p mimic was co-transfected into SH-SY5Y cells to determine luciferase activity 48 h later using a dual-luciferase reporter gene assay system (Promega, WI, USA).

Antibody enrichment analysis

RNA immunoprecipitation assay was performed using the Magna RNA-Binding Protein Immunoprecipitation Kit (Millipore). Cell lysates were incubated with RIP buffer containing magnetic beads conjugated to mouse IgG or human anti-Ago2 antibody. After digestion with proteinase K, the resulting immunoprecipitated RNA was purified and utilized for quantitative PCR.

Statistics

Data were presented as mean ± standard deviation (S.D.), and statistical analysis was performed using

GraphPad Prism 9.0. Unpaired Student's *t*-test was utilized for bilateral comparison whereas one-way analysis of variance for multi-data comparison. $P < 0.05$ was considered statistically significant.

RESULTS

Silencing circCCDC6 ameliorated MCAO/R-induced pyroptosis and inflammation

CircCCDC6 is abnormally expressed after MCAO/R injury. To examine the biological role of circCCDC6 in CIR-induced pyroptosis, we interfered with circCCDC6 expression in MCAO/R rats by injecting lentivirus. It was demonstrated that the promoted expression of circCCDC6 induced by MCAO/R treatment was suppressed after injection of shRNA-circCCDC6 (Fig. 1A). Assessment of neurological function presented that MCAO/R rats had severe nerve damage, which could be alleviated by knocking down circCCDC6 (Fig. 1B). Nissl staining pictured that neurons in MCAO/R rats were swollen, vacuolated in the cytoplasm, and the number of Nissl bodies was reduced, and knockdown of circCCDC6 alleviated these symptoms (Fig. 1C). During pyroptosis, GSDMD mediates the formation of membrane pores (Wang *et al.*, 2020). Here, we performed immunofluorescence staining of GSDMD and ultimately report-

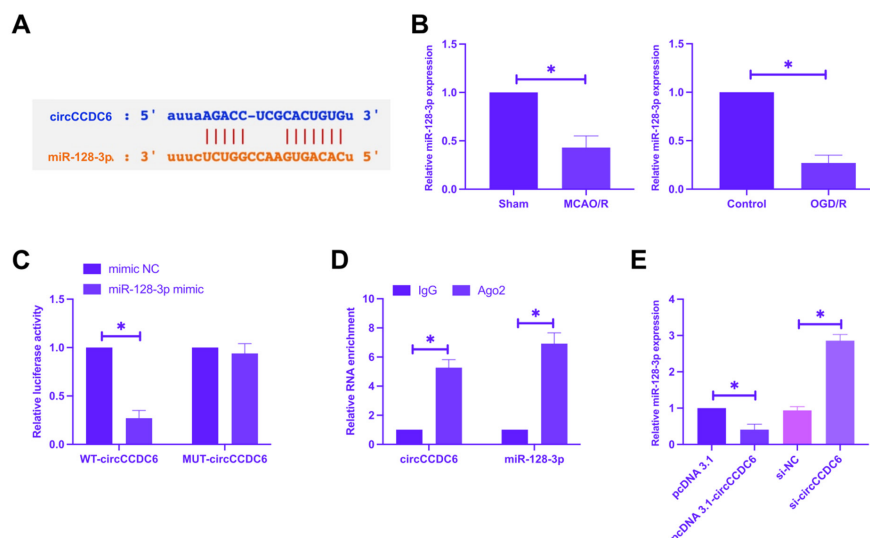


Figure 3. Binding relation of circCCDC6 and miR-128-3p.

Potential binding sites of miR-128-3p and circCCDC6 (**A**), miR-128-3p expression in *in vivo* and *in vitro* models (**B**), verification of targeting relationship between circCCDC6 and miR-128-3p (**C-D**), effects of low or overexpression of circCCDC6 on miR-128-3p expression in SH-SY5Y cells (**E**). data were reported as mean \pm S.D. (N=3).

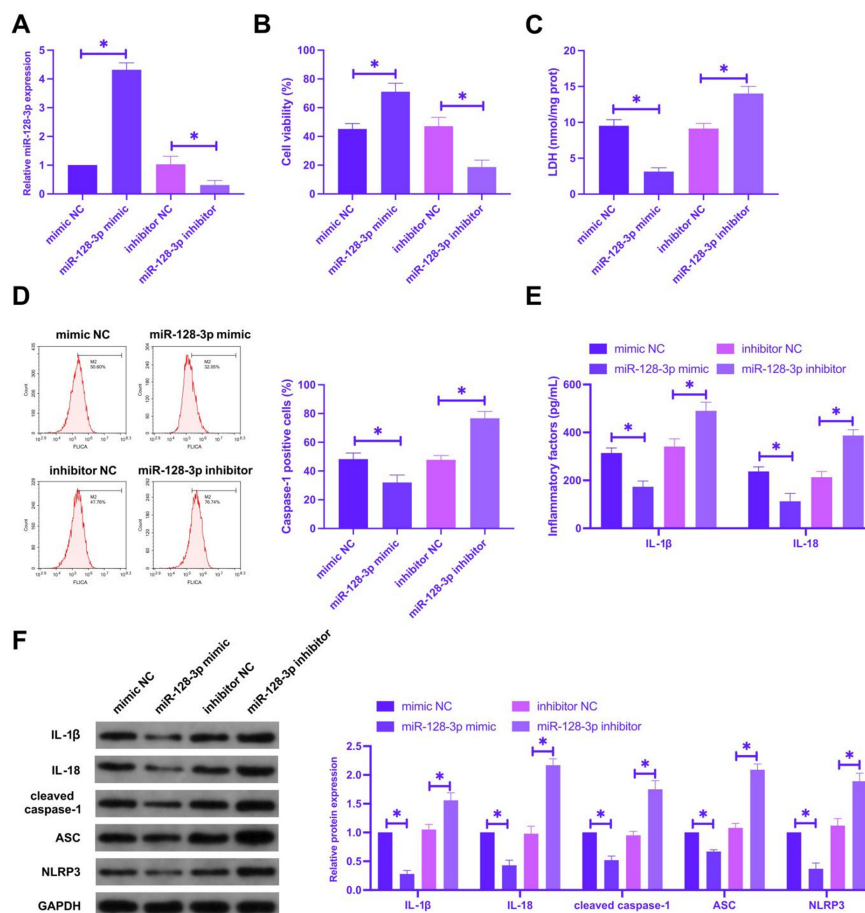


Figure 4. Effects of transfection of miR-128-3p mimic/inhibitor on the biological behavior and biochemical indexes of SH-SY5Y cells treated with OGD/R. miR-128-3p expression (**A**), cell viability (**B**), toxicity (**C**), caspase-1 positive cells (**D**), IL-1 β and IL-1 β contents (**E**), protein expression of IL-1 β , IL-18, cleaved caspase-1, ASC and NLRP3 (**F**); data were reported as mean \pm S.D. (N=3).

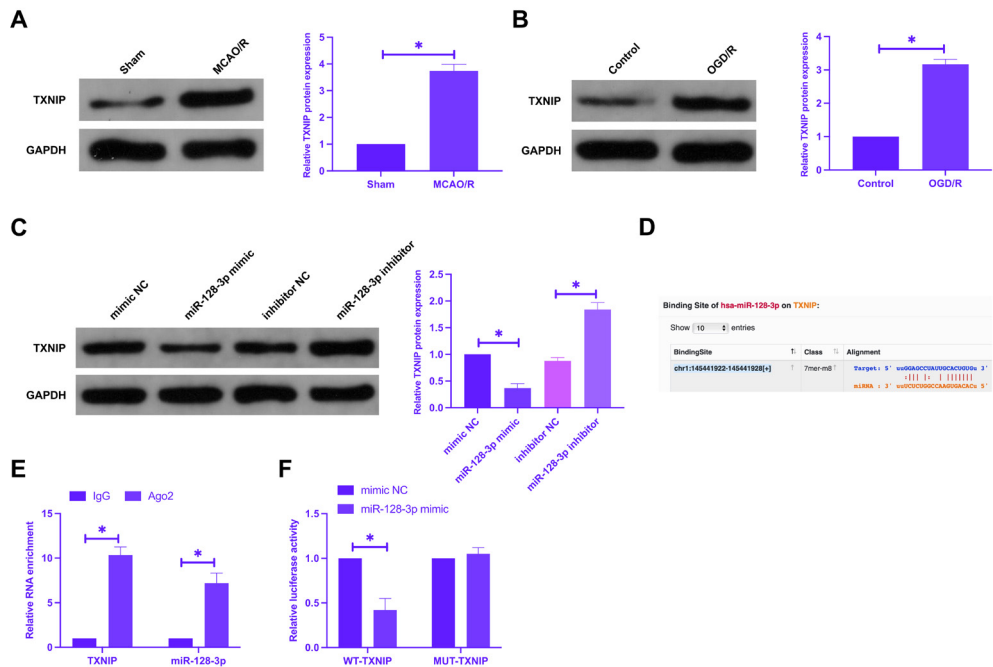


Figure 5. Targeting relation between miR-128-3p and TXNIP. TXNIP expression in *in vivo* and *in vitro* models (A–B), effect of miR-128-3p mimic/inhibitor on TXNIP protein expression in SH-SY5Y cells (C), potential binding sites of miR-128-3p and TXNIP (D), verification of the targeting relationship between miR-128-3p and TXNIP (E–F); data were reported as mean \pm S.D. (N=3).

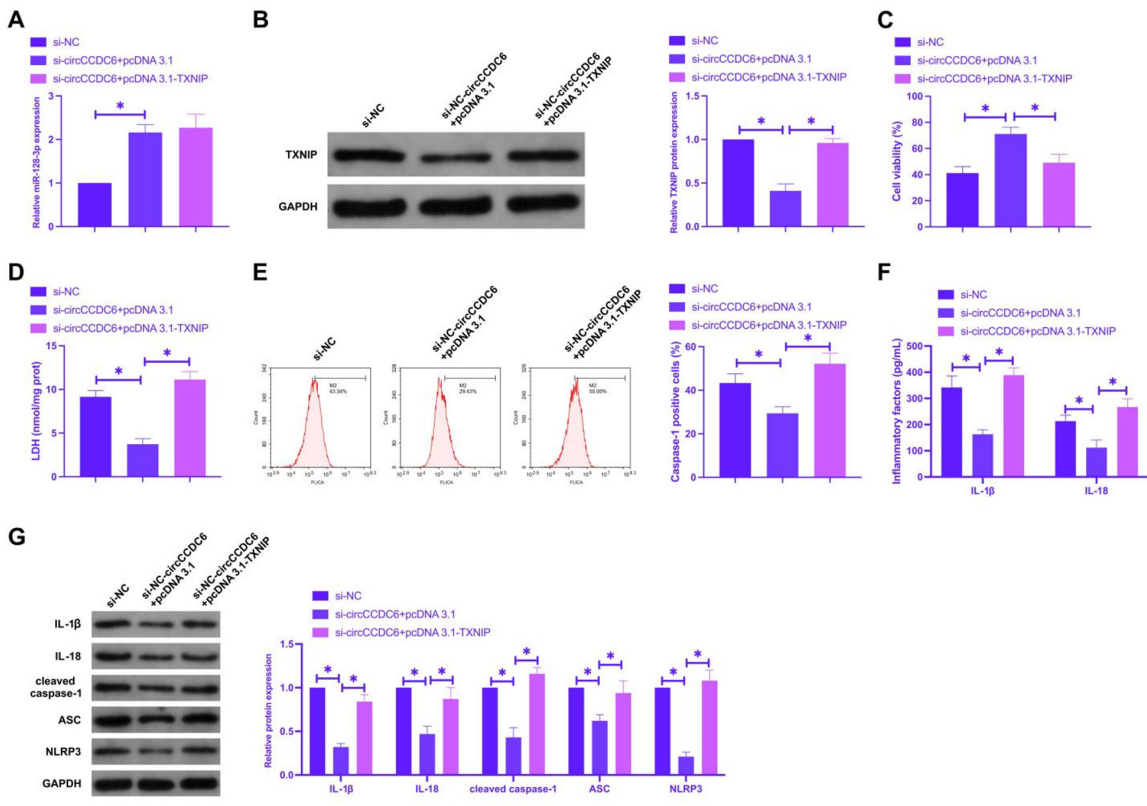


Figure 6. Effects of transfection of si-circCCDC6 and pcDNA 3.1-TXNIP on the biological behavior and biochemical indicators of OGD/R-treated SH-SY5Y cells. miR-128-3p expression (A), TXNIP protein expression (B), viability (C), toxicity (D), caspase-1 positive cells (E), contents of IL-1 β and IL-18 (F), protein expression of IL-1 β , IL-18, cleaved caspase-1, ASC and NLRP3 (G) in SH-SY5Y cells; data were reported as mean \pm S.D. (N=3).

ed that MCAO/R treatment increased the fluorescence intensity of GSDMD, but this trend was restricted in response to knockdown of circCCDC6 (Fig. 1D). Additionally, there were an increased number of TUNEL-positive cells (Fig. 1E), promoted release of IL-1 β and IL-18 (Fig. 1F), and elevated protein expression of IL-1 β , IL-18, cleaved caspase-1, ASC and NLRP3 (Fig. 1G) in the brain tissue of rats receiving MCAO/R surgery; the changes induced by MCAO/R were all reversed when circCCDC6 was knocked down (Fig. 1E). Clearly, silencing circCCDC6 ameliorated MCAO/R-induced pyroptosis and inflammation.

Overexpression of circCCDC6 aggravates OGD/R-induced neuronal pyroptosis and inflammation

Next, the molecular mechanism of circCCDC6 affecting neuronal pyroptosis and inflammation was explored through cellular experiments. It was checked that OGD/R treatment-induced elevation of circCCDC6 expression in neurons was further raised after transfection of pcDNA 3.1-circCCDC6 (Fig. 2A). Neuronal viability and toxicity were examined by MTT and colorimetry, respectively. The collected data displayed that after OGD/R treatment, neuronal viability was suppressed and LDH release was increased, and these changes were enhanced by overexpression of circCCDC6. Besides, it was further examined that OGD/R treatment induced the increase in the percentage of caspase-1 positive cells (Fig. 2D), contents of IL-1 β and IL-18 (Fig. 2E), and protein expression of IL-1 β , IL-18, cleaved caspase-1, ASC and NLRP3 in neurons (Fig. 2F); moreover, circCCDC6 upregulation further facilitated all of these alterations. Evidently, overexpression of circCCDC6 aggravates OGD/R-induced neuronal pyroptosis and inflammation.

CircCCDC6 competitively binds miR-128-3p

Next, we explored the downstream effectors bound by circCCDC6. Through the bioinformatics website <https://starbase.sysu.edu.cn/>, we predicted 20 miRNAs with potential binding sites for circCCDC6, among which miR-128-3p was particularly focused. miR-128-3p and circCCDC6 had binding sites at chr10:61564232-61564251[-] (Fig. 3A). miR-128-3p has been reported to be down-regulated in spinal cord I/R injury, and its overexpression is capable of ameliorating neuroinflammation and apoptosis (Wang *et al.*, 2020). Similar results were obtained in this study, with miR-128-3p down-regulated in both MCAO/R rats and OGD/R neurons (Fig. 3B). Dual-luciferase reporter experiments showed that co-transfection of WT-circCCDC6 with miR-128-3p mimic reduced luciferase activity (Fig. 3C), and RIP experiment further supported that circCCDC6 and miR-128-3p were increased in the Ago2 group (Fig. 3D). Subsequently, we examined that knockdown or overexpression of circCCDC6 upregulated and downregulated miR-128-3p expression, respectively. To conclude, circCCDC6 competitively binds miR-128-3p.

MiR-128-3p is involved in the process of pyroptosis and inflammation of OGD/R-conditioned neurons

Subsequently, we explored the role of miR-128-3p in OGD/R-induced neuronal pyroptosis and inflammation. Transfection of miR-128-3p mimic and inhibitor upregulated and down-regulated miR-128-3p expression in SH-SY5Y cells, respectively (Fig. 4A). Responded to miR-128-3p upregulation, neuronal viability increased

and LDH release reduced, percentage of caspase-1 positive cells, contents of IL-1 β and IL-18, and protein expressions of IL-1 β , IL-18, cleaved caspase-1, ASC and NLRP3 decreased; while knockdown of miR-128-3p had completely opposite effects (Fig. 4B–F). Anyway, miR-128-3p is involved in the regulation of neuronal pyroptosis and inflammation.

A binding of miR-128-3p TXNIP 3' UTR

TXNIP has been shown to be a pro-inflammatory factor in I/R injury (Jia *et al.*, 2020), and activation of the TXNIP/NLRP3 inflammasome pathway is a key factor in pyroptosis (Kong *et al.*, 2021). In both *in vivo* and *in vitro* models of CIR, TXNIP expression was found to be increased (Fig. 5A, B). Regarding miR-128-3p-mediated TXNIP expression change, quantitative PCR was performed to prove that transfection of miR-128-3p mimic or miR-128-3p inhibitor decreased and increased the protein level of TXNIP in neurons, respectively (Fig. 5C). Bioinformatics website searched for the complementary sequences of miR-128-3p and TXNIP 3'UTR (Fig. 5D), and their targeting relationships were subsequently by dual-luciferase reporter assays and RIP experiment (Fig. 5E, F). In short, a binding of miR-128-3p TXNIP 3' UTR is ensured.

CircCCDC6 affects neuronal pyroptosis and inflammation by regulating the miR-128-3p/TXNIP/NLRP3 pathway

Finally, rescue experiments were implemented to identify the effect of the circCCDC6/miR-128-3p/TXNIP/NLRP3 axis on OGD/R-induced neuronal pyroptosis and inflammation. It was examined that knockdown of circCCDC6 promoted miR-128-3p expression, while overexpression of TXNIP had no effect on miR-128-3p expression (Fig. 6A); circCCDC6 knockdown-induced suppression of TXNIP protein expression was reversed by overexpressing TXNIP (Fig. 6B). Functionally, circCCDC6 silencing-mediated protection against pyroptosis and inflammation was prevented when TXNIP was upregulated (Fig. 6C–G). CircCCDC6 affects neuronal pyroptosis and inflammation by regulating the miR-128-3p/TXNIP/NLRP3 pathway.

DISCUSSION

The key to the treatment of IS is blood reperfusion, but this can cause I/R injury (Wen *et al.*, 2019). Permanent damage to neurons with concomitant cell death happens in the hours following an IS (Zhang *et al.*, 2020). Acute neuroprotective agents attract much attention, however, clinical outcomes are often unsatisfactory. A genome-wide RNA sequencing report on the subcortical structure of CIR-injured rats shows that the expression of nearly 400 circRNAs is significantly altered 24 hours after tMCAO (Filippenkov *et al.*, 2021). This study reported a potential mechanism by which circCCDC6, regulates CIR injury-induced neurological deficits.

CircRNAs can interact with miRNAs, and their interaction is key in human diseases, including IS. For example, circTTC3 silencing could upregulate miR-372-3p, thereby suppressing CIR injury and neural stem cell apoptosis (Yang *et al.*, 2021). Moreover, depletion of circ_008018 in MCAO/R mice could prevent CIR damage by targeting miR-99a (Yang *et al.*, 2018). Also, in the model of MCAO/R, circHECTD1 knockdown induces neuroprotection against IS through binding to miR-133b

(Dai *et al.*, 2021). In this study, we found for the first time that circCCDC6 was upregulated in MCAO/R mouse model and OGD/R-treated neurons, and that circCCDC6 depletion alleviated MCAO/R-induced neuronal pyroptosis and inflammation, while overexpression circCCDC6 exacerbates OGD/R-induced neuronal pyroptosis and inflammation. Importantly, we investigated the possible miRNA sponge mechanism of circCCDC6 in CIR injury, paid great attention to the binding of circCCDC6 to miR-128-3p, and eventually confirmed that circCCDC6 may be involved in the pathogenesis of CIR injury by targeting miR-128-3p to promote neuronal pyroptosis and inflammation.

More attention is currently focused on the neuroinflammatory response triggered by I/R, and anti-inflammatory is likely to be a potential therapeutic strategy after IS (Wang *et al.*, 2020). miR-128-3p can exert anti-inflammatory effects by regulating gene expression and multiple signaling pathways. For example, overexpressing miR-128-3p could inhibit OA progression through PI3K/Akt/NF- κ B pathway (Chen *et al.*, 2020), and restrain apoptosis and inflammation in LPS-induced sepsis by targeting TGFBR2. In both MACO/R rats and OGD/R neurons, we examined the downregulation of miR-128-3p and validated the protective actions of overexpressed miR-128-3p on increasing neuronal viability and reducing LDH release as well as inflammatory factors. Notably, MCAO/R treatment and OGD/R treatment promoted TXNIP and NLRP3 expression, while their expression could be regulated by circCCDC6 and miR-128-3p, suggesting that the role of circCCDC6 in CIR injury may be related to TXNIP/NLRP3 axis-mediated inflammation and pyroptosis.

TXNIP/NLRP3 signaling pathway is the key to pyroptosis and is activated in a variety of inflammatory diseases. It has been documented that (Chen *et al.*, 2021) in a rat model of myocardial I/R injury, the promoted expression of TXNIP reverses the inhibition of cardiomyocyte pyroptosis by overexpression of miR-200a-3p by promoting NLRP3 expression. (Yao *et al.*, 2022) have explained that cerebral ischemia leads to the accumulation of ROS, driving TXNIP overexpression and NLRP3 activation to induce pyroptosis. Furthermore, TXNIP/NLRP3 pathway has been shown to mediate pyroptosis by activating inflammatory factors such as IL-1 β (Liu *et al.*, 2019). In CIR, we found increased expression of TXNIP and NLRP3 in animal and cell experiments, and confirmed that TXNIP was a downstream target of miR-128-3p, a result similar to the previous report (Liu *et al.*, 2021). Furthermore, rescue experiments obtained a conclusion that overexpression of TXNIP reversed the effects of silencing circCCDC6 on neuronal pyroptosis and inflammation.

However, there are some limitations as to the study design: 1, no detection of circCCDC6 expression in IS patients; 2, the correlation of circCCDC6 expression with clinicopathological features and whether it can be used as a diagnostic biomarker for IS has not yet been determined; 3, further systematic investigation of the relevant mechanism of circCCDC6 in MCAO-induced neurological deficits is required to further define the circRNA-miRNA gene network.

CONCLUSION

To sum up, circCCDC6 mediates neuronal pyroptosis and inflammation through the miR-128-3p/TXNIP/NLRP3 axis. This finding provides new insights into the

mechanism by which circCCDC6 regulates CIR injury-induced neurological deficits and provides a potential target for CIR injury therapy.

Declarations

Acknowledgments. Not applicable.

Funding. Not applicable.

Competing interests. The authors have no conflicts of interest to declare.

Availability of data and materials. The datasets used and/or analyzed during the present study are available from the corresponding author on reasonable request.

REFERENCES

- Brennan GP, Henshall DC (2020) MicroRNAs as regulators of brain function and targets for treatment of epilepsy. *Nat Rev Neurol* 16: 506–519. <https://doi.org/10.1038/s41582-020-0369-8>
- Chen S, Li B (2020) MiR-128-3p Post-transcriptionally inhibits WISP1 to suppress apoptosis and inflammation in human articular chondrocytes via the PI3K/AKT/NF- κ B signaling pathway. *Cell Transplant* 29: 963689720939131. <https://doi.org/10.1177/0963689720939131>
- Chen ZQ, Zhou Y, Chen F, Huang JW, Li HL, Li T, Li L (2021) miR-200a-3p Attenuates coronary microembolization-induced myocardial injury in rats by Inhibiting TXNIP/NLRP3-mediated cardiomyocyte pyroptosis. *Front Cardiovasc Med* 8: 693257. <https://doi.org/10.3389/fcvm.2021.693257>
- Dai Q, Ma Y, Xu Z, Zhang L, Yang H, Liu Q, Wang J (2021) Down-regulation of circular RNA HECTD1 induces neuroprotection against ischemic stroke through the microRNA-133b/TRAFF3 pathway. *Life Sci* 264: 118626. <https://doi.org/10.1016/j.lfs.2020.118626>
- Filippenkov IB, Stavchansky VV, Denisova AE, Valieva LV, Remizova JA, Mozgovoy IV, Zaytceva EI, Gubsky LV, Limborska SA, Dergunova LV (2021) Genome-wide RNA-sequencing reveals massive circular RNA expression changes of the neurotransmission genes in the rat brain after ischemia-reperfusion. *Genes (Basel)* 12. <https://doi.org/10.3390/genes12121870>
- Jia Y, Cui R, Wang C, Feng Y, Li Z, Tong Y, Qu K, Liu C, Zhang J (2020) Metformin protects against intestinal ischemia-reperfusion injury and cell pyroptosis via TXNIP-NLRP3-GSDMD pathway. *Redox Biol* 32: 101534. <https://doi.org/10.1016/j.redox.2020.101534>
- Kong L, Zhang H, Lu C, Shi K, Huang H, Zheng Y, Wang Y, Wang D, Wang H, Huang W (2021) AICAR, an AMP-activated protein kinase activator, ameliorates acute pancreatitis-associated liver injury partially through Nrf2-mediated antioxidant effects and inhibition of NLRP3 inflammasome activation. *Front Pharmacol* 12: 724514. <https://doi.org/10.3389/fphar.2021.724514>
- Lim S, Kim TJ, Kim YJ, Kim C, Ko SB, Kim BS (2021) Senolytic therapy for cerebral ischemia-reperfusion injury. *Int J Mol Sci* 22. <https://doi.org/10.3390/ijms222111967>
- Liu W, Miao Y, Zhang L, Xu X, Luan Q (2020) MiR-211 protects cerebral ischemia/reperfusion injury by inhibiting cell apoptosis. *Bio-engineered* 11: 189–200. <https://doi.org/10.1080/21655979.2020.1729322>
- Liu X, Zhang YR, Cai C, Ni XQ, Zhu Q, Ren JL, Chen Y, Zhang LS, Xue CD, Zhao J, Qi YF, Yu YR (2019) Taurine alleviates schistosoma-induced liver injury by inhibiting the TXNIP/NLRP3 inflammasome signal pathway and pyroptosis. *Infect Immun* 87. <https://doi.org/10.1128/iai.00732-19>
- Liu Y, Li YP, Xiao LM, Chen LK, Zheng SY, Zeng EM, Xu CH (2021) Extracellular vesicles derived from M2 microglia reduce ischemic brain injury through microRNA-135a-5p/TXNIP/NLRP3 axis. *Lab Invest* 101: 837–850. <https://doi.org/10.1038/s41374-021-00545-1>
- Luo L, Liu M, Fan Y, Zhang J, Liu L, Li Y, Zhang Q, Xie H, Jiang C, Wu J, Xiao X, Wu Y (2022) Intermittent theta-burst stimulation improves motor function by inhibiting neuronal pyroptosis and regulating microglial polarization via TLR4/NF- κ B/NLRP3 signaling pathway in cerebral ischemic mice. *J Neuroinflammation* 19: 141. <https://doi.org/10.1186/s12974-022-02501-2>
- Mehta SL, Pandi G, Vemuganti R (2017) Circular RNA expression profiles alter significantly in mouse brain after transient focal ischemia. *Stroke* 48: 2541–2548. <https://doi.org/10.1161/strokeaha.117.017469>
- Meng X, Xie W, Xu Q, Liang T, Xu X, Sun G, Sun X (2018) Neuroprotective effects of radix scrophulariae on cerebral ischemia and reperfusion injury via MAPK pathways. *Molecules* 23. <https://doi.org/10.3390/molecules23092401>
- Saliminejad K, Khorram Khorshid HR, Soleymani Fard S, Ghaffari SH (2019) An overview of microRNAs: Biology, functions, therapeutic

- tics, and analysis methods. *J Cell Physiol* **234**: 5451–5465. <https://doi.org/10.1002/jcp.27486>
- Tatlisumak T, Takano K, Carano RA, Miller LP, Foster AC, Fisher M (1998) Delayed treatment with an adenosine kinase inhibitor, GP683, attenuates infarct size in rats with temporary middle cerebral artery occlusion. *Stroke* **29**: 1952–1958. <https://doi.org/10.1161/01.str.29.9.1952>
- Tu Y, Hu Y (2021) MiRNA-34c-5p protects against cerebral ischemia/reperfusion injury: involvement of anti-apoptotic and anti-inflammatory activities. *Metab Brain Dis* **36**: 1341–1351. <https://doi.org/10.1007/s11011-021-00724-5>
- Vo JN, Cieslik M, Zhang Y, Shukla S, Xiao L, Zhang Y, Wu YM, Dhannasekaran SM, Engelke CG, Cao X, Robinson DR, Nesvizhskii AI, Chinnaiyan AM (2019) The landscape of circular RNA in cancer. *Cell* **176**: 869–881.e813. <https://doi.org/10.1016/j.cell.2018.12.021>
- Wang D, Chen F, Fang B, Zhang Z, Dong Y, Tong X, Ma H (2020) MiR-128-3p Alleviates spinal cord ischemia/reperfusion injury associated neuroinflammation and cellular apoptosis via SP1 suppression in rat. *Front Neurosci* **14**: 609613. <https://doi.org/10.3389/fnins.2020.609613>
- Wang K, Sun Q, Zhang X, Zeng M, Zeng H, Shi X, Li Z, Wang Y, Zhao Q, Shao F, Ding J (2020) Structural mechanism for GS-DMD targeting by autoprocessed caspases in pyroptosis. *Cell* **180**: 941–955.e920. <https://doi.org/10.1016/j.cell.2020.02.002>
- Wang L, Ren W, Wu Q, Liu T, Wei Y, Ding J, Zhou C, Xu H, Yang S (2022) NLRP3 Inflammasome activation: a therapeutic target for cerebral ischemia-reperfusion injury. *Front Mol Neurosci* **15**: 847440. <https://doi.org/10.3389/fnmol.2022.847440>
- Wang Y, Xiao G, He S, Liu X, Zhu L, Yang X, Zhang Y, Orgah J, Feng Y, Wang X, Zhang B, Zhu Y (2020) Protection against acute cerebral ischemia/reperfusion injury by QiShenYiQi via neuroinflammatory network mobilization. *Biomed Pharmacother* **125**: 109945. <https://doi.org/10.1016/j.biopha.2020.109945>
- Wen M, Jin Y, Zhang H, Sun X, Kuai Y, Tan W (2019) Proteomic analysis of rat cerebral cortex in the subacute to long-term phases of focal cerebral ischemia-reperfusion injury. *J Proteome Res* **18**: 3099–3118. <https://doi.org/10.1021/acs.jproteome.9b00220>
- Xin L, Junhua W, Long L, Jun Y and Yang X (2017) Exogenous Hydrogen Sulfide Protects SH-SY5Y Cells from OGD/R-induced Injury. *Curr Mol Med* **17**: 563–567. <https://doi.org/10.2174/1566524018666180222121643>
- Yan Q, Sun SY, Yuan S, Wang XQ, Zhang ZC (2020) Inhibition of microRNA-9-5p and microRNA-128-3p can inhibit ischemic stroke-related cell death *in vitro* and *in vivo*. *IUBMB Life* **72**: 2382–2390. <https://doi.org/10.1002/iub.2357>
- Yang B, Zang L, Cui J and Wei L (2021, Feb 12) Circular RNA TTC3 regulates cerebral ischemia-reperfusion injury and neural stem cells by miR-372-3p/TLR4 axis in cerebral infarction. *Stem Cell Res Ther* **12**: 125. <https://doi.org/10.1186/s13287-021-02187-y>
- Yang J, Chen M, Cao RY, Li Q, Zhu F (2018) The role of circular RNAs in cerebral ischemic diseases: ischemic stroke and cerebral ischemia/reperfusion injury. *Adv Exp Med Biol* **1087**: 309–325. https://doi.org/10.1007/978-981-13-1426-1_25
- Yang P, Han J, Li S, Luo S, Tu X, Ye Z (2021) miR-128-3p inhibits apoptosis and inflammation in LPS-induced sepsis by targeting TGFBR2. *Open Med (Wars)* **16**: 274–283. <https://doi.org/10.1515/med-2021-0222>
- Yang X, Ji H, Yao Y, Lai X, Jiang Y, Wu D, Cai L, Zhu W, Gu X, Hu R, Li L, Xu L, Jiang M (2018) Downregulation of circ_008018 protects against cerebral ischemia-reperfusion injury by targeting miR-99a. *Biochem Biophys Res Commun* **499**: 758–764. <https://doi.org/10.1016/j.bbrc.2018.03.218>
- Yao Y, Hu S, Zhang C, Zhou Q, Wang H, Yang Y, Liu C, Ding H (2022) Ginsenoside Rd attenuates cerebral ischemia/reperfusion injury by exerting an anti-pyrototic effect via the miR-139-5p/FoxO1/Keap1/Nrf2 axis. *Int Immunopharmacol* **105**: 108582. <https://doi.org/10.1016/j.intimp.2022.108582>
- Yu P, Zhang X, Liu N, Tang L, Peng C, Chen X (2021) Pyroptosis: mechanisms and diseases. *Signal Transduct Target Ther* **6**: 128. <https://doi.org/10.1038/s41392-021-00507-5>
- Zhang M, Lu H, Xie X, Shen H, Li X, Zhang Y, Wu J, Ni J, Li H, Chen G (2020) TMEM175 mediates Lysosomal function and participates in neuronal injury induced by cerebral ischemia-reperfusion. *Mol Brain* **13**: 113. <https://doi.org/10.1186/s13041-020-00651-z>
- Zhang Q, Jia M, Wang Y, Wang Q, Wu J (2022) Cell death mechanisms in cerebral ischemia-reperfusion injury. *Neurochem Res* **47**: 3525–3542. <https://doi.org/10.1007/s11064-022-03697-8>
- Zhang X, Zhang Y, Cai W, Liu Y, Liu H, Zhang Z, Su Z (2020) MicroRNA-128-3p Alleviates neuropathic pain through targeting ZEB1. *Neurosci Lett* **729**: 134946. <https://doi.org/10.1016/j.neulet.2020.134946>
- Zhang Y, Yao Z, Xiao Y, Zhang X, Liu J (2022) Downregulated XBP-1 rescues cerebral ischemia/reperfusion injury-induced pyroptosis via the NLRP3/Caspase-1/GSDMD axis. *Mediators Inflamm* **2022**: 8007078. <https://doi.org/10.1155/2022/8007078>
- Zhang ZH, Wang YR, Li F, Liu XL, Zhang H, Zhu ZZ, Huang H, Xu XH (2020) Circ-camk4 involved in cerebral ischemia/reperfusion induced neuronal injury. *Sci Rep* **10**: 7012. <https://doi.org/10.1038/s41598-020-63686-1>
- Zhu T, Wang L, Tian F, Zhao X, Pu XP, Sun GB, Sun XB (2020) Anti-ischemia/reperfusion injury effects of notoginsenoside R1 on small molecule metabolism in rat brain after ischemic stroke as visualized by MALDI-MS imaging. *Biomed Pharmacother* **129**: 110470. <https://doi.org/10.1016/j.biopha.2020.110470>
- Zuo G, Zhang D, Mu R, Shen H, Li X, Wang Z, Li H, Chen G (2018) Resolvin D2 protects against cerebral ischemia/reperfusion injury in rats. *Mol Brain* **11**: 9. <https://doi.org/10.1186/s13041-018-0351-1>

Pheochromocytoma and paraganglioma in children and adolescents

Teresa Stachowicz-Stencel✉, Natalia Pasikowska and Anna Synakiewicz

Department of Pediatrics, Hematology and Oncology, Medical University of Gdansk, Gdańsk, Poland

Pheochromocytoma (PPC) and paraganglioma (PGL) are the tumors that rarely occur in the pediatric population (PPGL). Both originate from chromaffin cells, pheochromocytoma is localized in the adrenal gland, whereas paragangliomas are regarded as the tumors present in other localizations, from head to the pelvis. The clinical image is characterized by the presence of the sustained hypertension, headaches, sweating, palpitations. The symptoms are caused by the catecholamine secretion or are related to tumor mass pressure on different organs. The catecholamines and their metabolites levels in urine collection or plasma are necessary for further evaluation of the diagnosis. In pediatric population the tumors occur in multiple familial syndromes such as Multiple Endocrine type 2, Neurofibromatosis type 1, Von Hippel-Lindau syndrome, Familial Paraganglioma syndrome are related to specific mutations (*SDHx*, *RET*, *VHL*, *NF1*) leading to the characteristic phenotype. The radiological and nuclear imaging are an important part of the examination. Although CT and MR are reported to have overall good sensitivity for the tumor detection, further analysis with nuclear imaging is recommended for the specified diagnosis. Right now ⁶⁸GA-DOTATATE is regarded as the tracer of choice, leading to the complex evaluation of patients with different mutations and metastatic disease. The treatment of choice is the tumor excision. Also, lately new therapeutic approaches including genetically targeted therapies are under investigation for more complex treatment of tumors with underlying genetic cause or metastatic disease. Long term follow-up after treatment to avoid recurrence or to detect it in early stadium must be performed.

Keywords: children, malignant tumors, paraganglioma, pheochromocytoma, treatment, young adults

Received: 31 July, 2023; **revised:** 31 August, 2023; **accepted:** 05 September, 2023; **available on-line:** 17 September, 2023

✉e-mail: tsten@gumed.edu.pl

Abbreviations: CT, computed tomography; F-DOPA, 6,18F-fluoro,L-3,4-dihydroxyphenylalanine; HU, Hounsfield unit; MEN 2, Multiple Endocrine; MR, magnetic resonance; Neoplasia type 2; NF 1, Neurofibromatosis Type 1; PET/CT, pet ct positron emission tomography computed tomography; PGL, paraganglioma; PPC, pheochromocytoma; PZS, Pacak Zhuang syndrome; VHL, von Hippel-Lindau

INTRODUCTION

Pheochromocytoma (PPC) and paraganglioma (PGL) are rare tumors in the pediatric population. The prevalence is 0.2–0.5 per million of children, which constitutes only for 20% of its general incidence in the population (Ardicli *et al.*, 2021; Park *et al.*, 2021). They can occur at any age, however the mean age at diagnosis is reported to be 11 years old, with male predominance (Ross *et*

al., 2000; Havekes *et al.*, 2009). Pheochromocytoma and paraganglioma are the neuroendocrine tumors originating from chromaffin cells which form the adrenal medulla. Tumors located in the adrenal medulla are regarded as pheochromocytomas. The chromaffin cells can also be present extramedullary around sympathetic and parasympathetic ganglia, resulting in the formation of paragangliomas in various localizations of the body, from head to the pelvis (Park *et al.*, 2021; Ross *et al.*, 2000). Around 33% of tumors are located in the adrenal glands, and the rest are found in the other body regions (Pamporaki C *et al.* 2017). The tumors produce and most of them (70%) release catecholamines such as epinephrine and norepinephrine and their metabolites, metanephrines and normetanephrines. Head and neck paragangliomas are mostly biochemically silent, however they can produce dopamine (Shah MH *et al.*, 2021). The catecholamine production contributes to the symptoms and clinical image of the PPGL, leading to the occurrence of hypertension, excessive sweating, palpitations, headaches and abdomen pains (Eisenhofer *et al.*, 2022). Around 0.5–1.7% of pediatric hypertension is the implication of the PPGL (Ross *et al.*, 2000; Yen & Lodish, 2021; Barontini *et al.*, 2006). 50–80% of the tumors present in the pediatric population are showing the germline mutations in the known genes, including *VHL*, *RET*, *SDHx*, *MAX*, *NF1*, *HIF2* presenting the phenotype characteristic for various familial syndromes (Park *et al.*, 2021; Shah *et al.*, 2021; De Tersant *et al.*, 2020). Due to the high incidence of the mutations in pediatric PPGL population, the tumors tend to be more aggressive and metastatic, which should lead to the complex evaluation of diagnosis, treatment and lifetime surveillance (Shah *et al.*, 2021).

CLINICAL IMAGE

The clinical image of pheochromocytoma and paraganglioma depends predominantly on the catecholamine secretion. As the tumors present in the pediatric population are highly related to the germline mutations, leading to the metastatic, multifocal and aggressive disease, the majority of the pediatric patients – 90% show the symptoms of the illness (Kuo *et al.*, 2022). The most common symptom is the sustained hypertension, which, in rare and severe cases can lead to the encephalopathy, cardiomyopathy, hypertensive crisis and cardiac failure (Edmonds *et al.*, 2011; Armstrong *et al.*, 2008). The paroxysmal hypertension is less frequent in children comparing to adults (Kuo *et al.*, 2022; Jain *et al.*, 2020; Edmonds *et al.*, 2011; Ben-Skowronek & Kozaczuk, 2015). It is reported that there is no direct correlation between the catecholamine level and the severity of hypertension (Havekes *et al.*, 2009; Bravo & Tagle, 2003). The triad of

symptoms typical for the pediatric population includes: palpitations (53%), excessive sweating and headaches (39–95%) (Jain *et al.*, 2020; Kuo *et al.*, 2022). Other frequently and less commonly occurring symptoms of the tumor presence include the disturbances in vision, diarrhea, orthostatic hypotension, nausea, flushing, pallor, behavioral and psychiatric changes. The tumor can also be found incidentally in the radiological work-up or due to the mass-related symptoms e.g. abdomen pain, back pain, loss of weight and constipation (Jain *et al.*, 2020; Edmonds *et al.*, 2011). Pheochromocytoma and Paraganglioma can be present in various familial syndrome including Von Hippel-Lindau syndrome, Multiple Endocrine Neoplasia type 2 syndrome, Neurofibromatosis type 1 syndrome and Familial Paraganglioma syndrome, so that once the syndrome is diagnosed or suspected, the patient should be under the specialist care for tumor evaluation (Edmonds *et al.*, 2011; Fargette *et al.*, 2023). The VHL syndrome is characteristic for the occurrence of various tumors, in pediatric population especially PPGLs and hemangioblastomas which can remain silent until presence of serious symptoms as a result of a tumor mass pressure on organs (Rednam *et al.*, 2017; Ben-Skowronek & Kozaczuk, 2015). In neurofibromatosis, the clinical image develops with children's age and the most common features include cafe-au-lait spots, freckles of auxiliary and inguinal regions, plexiform neurofibromas and gliomas of optic nerves, pheochromocytoma occurs rarely, nonetheless the patients should be under observation (Edmonds *et al.*, 2011; Miller *et al.*, 2019). Familial Paraganglioma syndrome is the result of the *SDHx* pathogenic variants, according to Chetty *et al.* it is reported that patients with *SDHA* pathogenic variants do not develop paragangliomas (Chetty *et al.*, 2010), however Nölting and others proves that paragangliomas can be present in this pathogenic variant (Nölting S *et al.*, 2022; Bausch B *et al.*, 2014). In *SDHB* pathogenic variants the tumors are solitary, in various localizations including abdomen, pelvis, retroperitoneum; less common in mediastinum and head/neck, and they tend to metastasize. Up to 70% of patients with *SDHB* mutations can show metastases. Most commonly metastases can be found in bones, lymph nodes, liver and lungs (Kuo *et al.*, 2022). *SDHD* and *SDHC* pathogenic variants carriers show incidence in presence of tumors in the head and neck localization, but *SDHD* pathogenic variant carriers can show multiple tumor presence, whereas *SDHC* carriers solitary tumor (Chetty *et al.*, 2010). The patients with head and neck paragangliomas are mostly asymptomatic, while tumors in other localization show typical symptoms (Işık *et al.* 2006). Multiple Endocrine Neoplasia type 2 syndrome is divided in type 2A and type 2B. Type A is associated with C-cell hyperplasia or medullary thyroid cancer, pheochromocytoma and hyperparathyroidism, while type B is associated with higher prevalence of C-cell hyperplasia or medullary thyroid cancer than type A, pheochromocytoma, mucosal neuromas and marfanoid habitus (Van Treijen *et al.*, 2022).

BIOCHEMICAL TESTING

As the pheochromocytomas and paragangliomas can secrete catecholamines and their metabolites e.g. metanephrines and normetanephrines, the laboratory 24-hours urine or plasma collection need to be undertaken to evaluate the diagnosis. Before the beginning of the laboratory tests, the patient should be prepared for the sample taking, which means going off the drugs and di-

etary products that would impact the catecholamine production or that would influence the methods of its detection. The products that must be avoided are bananas, cheese, nuts, tomatoes, alcohol, disulfiram, metronidazole, paracetamol, amoxicillin, methenamine, urapidil, L-dopa and others (Corcuff *et al.*, 2017; Shah *et al.*, 2021). As well the stress should be avoided before the sample taking and the blood tests should be undertaken while patient is laying as it is reported that sitting position can alter the level of blood metanephrines (Lenders & Eisenhofer, 2017; Seamon & Yamaguchi, 2021). It is reported that measurements taken from the plasma samples show higher sensitivity than from the urine collection (Lenders & Eisenhofer, 2017). The results of plasma level metanephrines 2 times more than the upper normal limit is considered to result in PPGL diagnosis (Lenders & Eisenhofer, 2017; Eisenhofer *et al.*, 2023). Shah MH *et al.* consider the diagnosis while the metanephrines level is 3 times upper than the cut-off value (Shah *et al.* 2021). The *SDHB* pathogenic variant carriers can show lack of elevation of catecholamines, while increased level of 3-metoxxythyramine can be useful to assess the metastatic disease (Lenders & Eisenhofer, 2017).

GENETICS

Owing to germline mutation in one of the subsequent susceptibility genes: *VHL*, *SDHx*, *RET*, and *NFI*, pediatric PPGLs are frequently found to possess a genetic cause. Genes encoding for pseudohypoxia in cluster 1 are organized to cluster 1A with TCA-cycle genes, along with the *SDHx* genes, and cluster 1B associated with hypoxia signaling, primarily *VHL* and *EPAS1*. Cluster 2 is where the other two crucial genetic causes of pediatric PPGL, *RET* and *NFI* associated with kinase signaling are located (Crona *et al.* 2017; Nölting *et al.*, 2022). Genetic abnormalities undermining PPGL are all inherited in autosomal dominant patterns, but with the risk of increased PPGL susceptibility in case of paternal inheritance as a result of pathogenic variants of *SDHD* (including *SDHAF2* and *MAX*). Nevertheless, identification of *SDHD* variants inherited from the mother is implicated for screening of the relatives and further generations. Although genealogical records of PPGL are often present in pediatric patients with PPGL, the lack of genealogical record should not restrain clinicians from referring for genetic counseling and testing, as the feasibility of de novo mutations must be contemplated. With no exception, genetic counseling and evaluation are encouraged in all patients with PPGL.

Succinate Dehydrogenase Subunit Defects (*SDHD*)

PPGLs were reported to harbor mutations in four subunits of *SDHD* and assembly factor gene *SDHAF2*. Mutations in *SDHB* on chromosome 1p36.13 were proved to be responsible for metastatic PPGL. In the study of King and others 71.9% patients who were younger than 20 years had a germline mutation in *SDHB* (King *et al.*, 2011). The risk of a metastatic disease for *SDHB* carriers with PPGL is noted about 31–70% (Rijken *et al.*, 2018). Other authors reported that 70% children with PPGL had metastases at a median age of 16. *SDHC* on chromosome 1q23.3 and *SDHA* on chromosome 5p15.33 are less common in PPGLs with a percentage of 8.3 and 1.7, respectively (Benn *et al.*, 2018). Nonetheless, the metastatic risk is higher in *SDHA* in 30–60% but in *SDHC* it is very low (Nölting *et al.*, 2022; Bausch *et al.*, 2014). *SDHC* and *SDHD* are present in

head and neck PGLs (Read *et al.*, 2021). In accordance with the international guidelines for PPGLs in asymptomatic *SDHA*, *SDHB*, *SDHC* and paternally-inherited *SDHD* variants screening should be conducted (Amar *et al.*, 2021). Pediatric patients with *SDHB* carriers screening is worth doing at the age of 6–10 years old and at 10–15 years old in cases of other mutations. The tumor size plays an essential role in the prognosis. Patients with tumor's diameter less than 5 cm developed metastases within 7 years post the primary treatment, while patients with larger tumors show metastatic spread within 2 years. (Jochmanova *et al.*, 2020). It has been reported that mutations in *SDHD* on chromosome 11q23.1 show higher penetrance than in *SDHB* and autosomal dominant inheritance pattern is modified by maternal imprinting, hence the disease is frequently inherited from the paternal allele (Bayley *et al.*, 2020).

Von Hippel-Lindau Syndrome (VHL)

VHL syndrome is a consequence of pathogenic variants in *VHL* located on chromosome 3p25.3. Owing to the loss of tumor suppressor gene function that encoded for an E3 ubiquitin ligase degrading HIF-2 α . *VHL*, a cluster 1B gene, is linked to noradrenergic biochemical phenotype. About 10–25% individuals with VHL develop PPC, with sympathetic and parasympathetic PGLs occurring less commonly, bearing metastatic risk of 5–8%. It has been proved that VHL is the cause of PGLs in children and it develops at the age of 11–12. Every fifth patients will possess *de novo* mutation. What is worth noticing is that the rate of *de novo* mutation has been found to be significantly higher in PPGL patients representing an overall rate of 60% and 50% for the pediatric group; the sample size was accredited by the researchers. (Cascion *et al.*, 2013; Rednam *et al.*, 2017). The earliest onset of PPGL occurs in patients between the age of 11–12 on average.

EPAS1 Gain-of-Function Syndrome

Pacac Zhuang syndrome (PZS) characterized by polycythemia, PPGL, and duodenal somatostatinoma is the noteworthy exception for the generally established rule of germline susceptibility; it was initially discerned in two female patients with congenital polycythemia and PGL in the adolescence. Post-zygotic somatic mutation in the gene encoding for the transcription factor HIF-2 α (the *EPAS1* gene located on chromosome 2p21) can lead to PZS which is hardly ever related to germline inheritance (Zhuang *et al.*, 2012; Lorenzo *et al.*, 2013). PGLs were occurring repeatedly in all patients and almost 30% of them had metastatic disease, which was indicated in a study of 7 patients with PZS (Darr *et al.*, 2016). Hence, those cases are a profound driving factor in favor of somatic, as well as germline, genetic testing when patient tumor tissue is inaccessible. Not only may it provide information about the etiological factors, but also it may improve omnipresent understanding of related formidable clinical characteristics and risk of “multiplicity, recurrence, and malignancy”.

Neurofibromatosis Type 1

The undermining factor of neurofibromatosis type 1 is mutation in the *NF1* gene that encodes for neurofibromin placed on chromosome 17q11.2. *NF1*, a tumor suppressor in cluster 2, inhibits the RAS-MAPK signaling pathway. National Institutes of Health established the clinical diagnostic criteria for NF1 (Gutmann *et al.*,

2017). Interestingly, up to 50% patients with NF1 arise *de novo*, which is why the absence of a family history should not preclude NF1 from the differential diagnosis in the presence of suggestive clinical findings. Pheochromocytomas occur in patients with NF1 in 0.1 to 5.7%, yet in 3.3 to 13% on autopsy (Plouin *et al.*, 2001). Kepenekian and others (Kepenekian *et al.*, 2016) identified pheochromocytoma in 7.7% adult patients with NF1 presenting no symptoms. The adrenal disease presents most commonly unilaterally (in 78–84%), with bilateral disease reported in 9.6 to 16.6% of patients with pheochromocytoma (Al-Sharefi *et al.*, 2019). Metastatic PCC was mainly noted in adults in 11.5% (Jiang *et al.*, 2020). Fortunately PPGL in children with NF1 is less frequent (1–3%) (Pamporaki *et al.*, 2017).

Multiple Endocrine Neoplasia Type 2 (MEN-2)

MEN-2A is associated with pheochromocytoma in 57% and other diseases such as medullary thyroid cancer or hyperparathyroidism. MEN-2B is only in 5% of MEN-2 and is linked to pheochromocytoma in 50% and aggressive medullary thyroid cancer, mucosal neuromas and a marfanoid habitus (Moriaitis *et al.*, 2014). The risk of metastases in pheochromocytoma is less than 5% (Nolting *et al.*, 2022).

RADIOLOGICAL AND NUCLEAR DIAGNOSTIC WORK UP

Computed Tomography (CT) and Magnetic Resonance

Although the computer tomography is an easily accessible diagnostic method, with no specific preparation needed before the examination and short time of the imaging test, it is not considered as the best diagnostic method for children's PPGL tumors detection, as it leads to the radiation absorption. In children, MR is preferred for the initial diagnostic pathway as it is a safer method. Both methods are good in imaging tumors, including incidentalomas and differentiating them between benign tumors like adenoma or PPGLs (Carrasquillo *et al.*, 2021). Adenomas on CT show the attenuation value of around 10 HU, while pheochromocytomas around 50–60 HU (Carrasquillo *et al.*, 2021; Ferrugia *et al.* 2019). The MR examination is important, as it can show the vascularization of the big tumors which is necessary to be determined before further evaluation (Ferrugia & Charalampopoulos, 2019). Nevertheless, Havekes *et al.* report that as much as MR sensitivity is high for tumor detection, its specificity for the PPGLs is not enough and further nuclear imaging is recommended (Havekes *et al.*, 2009).

Somatostatin receptor-based PET/CT

68Ga-DOTATATE (68Ga-DOTA(0)-Tyr(3)-octreotate)

A radiotracer composed of hormone peptide and 68Ga positron emitter, targeting the somatostatin receptors. It has a 68-minutes half-life period and can accumulate in every tissue providing the entire body scan. It is used in PPGL/PCC detection due to the high level of somatostatin receptors expression in PCC/PPGL (Rees *et al.*, 2023; Jaiswal *et al.*, 2021). The substance can be easily administered to the patient as no preparation is needed before the examination (unless the anesthesia in pediatric population is necessary, then 6 hours prior to examination food/fluids uptake is forbidden) (Rees *et al.*, 2023). It is used in paraganglioma diagnostic work up in

adult population as it is reported that patients with sporadic and *SDHx*-related paraganglioma indicate higher number of lesions found by Ga-DOTATATE PET CT compared to F-FDG PET CT and CECT/MRI (Jaiswal *et al.*, 2021; Jha *et al.*, 2018). Jaiswal and others reported that it has a better sensitivity for both primary and metastatic lesions, as well as for VHL-associated lesions not detected by CECT in pediatric population (Jaiswal *et al.*, 2021). Also it has a higher susceptibility for head and neck paragangliomas, which are difficult to be found as they are not biochemically active (Carrasquillo *et al.*, 2021; Yen & Lodish, 2021). 68GA-DOTATATE is a tracer of choice in any situation stated above (Janssen *et al.*, 2016).

CU-DOTATATE

Another target for somatostatin receptors, with a higher half-life period and similar sensitivity to 68GA-DOTATATE, however not yet approved in the paediatric population (Rees *et al.*, 2023; Yen & Lodish, 2021).

18FDG PET/CT (18fluorodeoxyglucose)

Before the diagnostic work up patient should not be given glucose or any fluid containing glucose intravenously for 6 hours prior to the examination, no food should be administered orally as it interferes with the radiotracer and can lead to false positive results (Rees *et al.*, 2023). The F-FDG is better in detecting metastatic PCC/PPGL than MIBG, but has a lower sensitivity than 68GA-DOTATATE, for benign tumors its sensitivity is similar/lower than MIBG (Carrasquillo *et al.*, 2021; Jaiswal *et al.*, 2021). 18FDG PET/CT has a higher detection for the tumors with *SDHx* pathogenic variant comparing to the *SDHx* negative tumors, however still lower than 68GA-DOTATATE (Carrasquillo *et al.*, 2021).

131/123 I-MIBG

A guanethidine analog, the compound is structurally similar to norepinephrine, binds with norepinephrine transporters and accumulates in adrenergic tissues (Carrasquillo *et al.*, 2021; Rufini *et al.*, 2008). Prior to the examination, the uptake of potassium iodate is mandatory for thyroid blockade, also interfering medications including anti-arrhythmics, beta-, adrenergic-, calcium-blockers, vasoconstrictors and others should be gone off before the diagnostic work up (Rees *et al.*, 2023; Jacobson & Travin, 2015). The I-MIBG has a significantly high detection rate for non metastatic PPC/PPGL, the overall rate is higher for pheochromocytoma rather than paraganglioma. The detection of tumors with *SDHx* pathogenic variant is low, in general the rate of hereditary tumors discovery is low by I-MIBG (Carrasquillo *et al.*, 2021).

F-DOPA (6-18F-fluoro-L-3,4-dihydroxyphenylalanine)

The amino acid radio tracer which was predominantly and historically used to diagnose parkinsonian's syndromes as it evaluates the dopamine synthesis (Carrasquillo *et al.*, 2021; Darcourt *et al.*, 2014). No preparation is needed before the tracer administration as no drugs have been claimed to disturb the radioimaging with F-DOPA (Carrasquillo *et al.*, 2021). The tracer has a high detection rate for benign PCC/PPGL and metastatic pheochromocytoma, though sensitivity for metastatic paraganglioma is low, 68GA-DOTATATE outperforms F-DOPA in the general detection rate of PCC/PPGL (Carrasquillo *et al.*, 2021). It is reported that

MYC-associated factor X (*MAX*) pheochromocytomas show high level of F-DOPA uptake and should be considered a tracer of choice in those particular cases (Taieb *et al.*, 2018).

TREATMENT

Before the surgery is performed the crucial role plays the cooperation of the endocrinologist, oncologist, surgeon, cardiologist and anesthesiologist. The surgical resection is the mainstay of the treatment of patient with diagnosed PPGL. The type of surgery (laparoscopy *vs* open access) depends on the individual assessment of patient including tumor localization, age of the patient and clinical stage of the disease. Before the surgery is performed the patient needs the hypertension evaluation e.g normalizing blood pressure, heart rate and preventing patient from excess of catecholamine secretion. Two-three weeks before surgery antihypertensive drug such as non-selective (phenoxybenzamine) α -antagonist should be administered, if this treatment is insufficient the calcium antagonists can be used as the additional drugs. It is important for the patient to be well hydrated. In case of tachycardia, after the α -blocker administration, the cardioselective β -blocker is recommended (Fang *et al.*, 2020). The preparation for surgery in pediatric patients takes about longer as a result of lower starting dose of medications to avoid complications and increased sympathetic activity in children than in adults (Amrishi *et al.*, 2020). Laparoscopic excision is recommended, however the surgery type depends of the anesthesiological assessment before and during surgery. Open laparotomy is reserved for the patients with huge tumors or difficult to approach paragangliomas. During surgeries there is a huge risk of hypertensive crisis, myocardial ischemia, stroke, etc. (Schutler *et al.*, 1995). Previously the mortality risk was high, nowadays it is reduced to less than 2% (Ploutin *et al.*, 2001).

It was proved that about 70–80% of patients with PPGL have a germline or somatic mutation, so genetic testing ought to be performed in each patient with that diagnosis to guide their management and improve their clinical outcome (Jiang *et al.*, 2020; Ochmanova *et al.*, 2018). According to the literature germline mutations are known in 30–35% of patients and somatic mutations were found in 50% of patients (Jhwar *et al.*, 2022). While treating patients with PPGL, the metastatic disease is still a challenge and there is no way to completely cure the disease. It is documented that about 10% to 15% of all patients with pheochromocytoma and 35–40% with paraganglioma, develop metastases (Eisenhofer *et al.*, 2012; Patel *et al.*, 2020). Metastasizing depends on the type of the pathogenic variant. In patients with *SDHB* and *SDHA*-mutant PPGL, there is a high risk of metastases, about 75% (Bechmann *et al.*, 2020; Crona *et al.*, 2019). On the other hand, cluster 2 pathogenic variants disrupt the kinase signaling pathway and lead to their overactivation (*RET*, *BRAF*, *NF1*, *HRAS*, *MAX*, *NGFR*) and are associated with low metastatic risk of 3–10% (Bechmann *et al.*, 2020; Kumar *et al.*, 2021). Cluster 3 pathogenic variants affect the Wnt signaling pathway (*MAML3*, *CSDCE1*) and are rare but very aggressive with poor prognosis. Overall 5-year mortality rates is 37% but 10-year mortality rate is 29% (Alzofin *et al.*, 2021; Nolting *et al.*, 2022).

In this situation, novel therapeutic approaches are needed (Nolting *et al.*, 2022; Nolting *et al.*, 2019). Lately a lot of genetically guided therapies were investigated and used some molecular treatment in patients with met-

astatic PPGs. (Wang *et al.*, 2022; Lee *et al.*, 2018; Mak *et al.*, 2019).

CONCLUSION

Pheochromocytoma and paraganglioma in pediatric patients are rare, but should always be considered with tumor mass detected or when typical symptoms such as hypertension, palpitations, sweating or headaches are happening. Genetic testing should be performed in every patient with this diagnosis, as it helps in the initial diagnostic pathway, targeted treatment, prognosis of the disease and follow up for early detection of recurrence of the disease. The main treatment is the radical excision of the tumor.

Patients with a hormonally active tumor are at risk of complications such as internal instabilities and pressure fluctuations. Long follow-up of a patient with PPGL is essential to avoid recurrence. It is important to monitor blood pressure and the level of catecholamines in the urine collection as well as radiological imaging tests in case of clinical symptoms or catecholamine increase. For patients with certain mutations (*SDHD* and *VHL*) where there is a risk of recurrence, there is a need for frequent and long-term monitoring.

REFERENCES

- Al-Sharefi A, Javaid U, Perros P, Ealing J, Truran P, Nag S, Kamarudin S, Abouglila K, Cains F, Lewis L, James RA (2019) Clinical presentation and outcomes of pheochromocytomas/paragangliomas in neurofibromatosis type 1. *Eur Endocrinol* 15: 95–100. <https://doi.org/10.17925/EE.2019.15.2.95>
- Alzofon N, Koc K, Panwell K, Pozdeyev N, Marshall CB, Albuja-Cruz M, Raeburn CD, Nathanson KL, Cohen DL, Wierman ME, Kiseljak-Vassiliades K, Fishbein L (2021) Mastermind Like transcriptional coactivator 3 (MAML3) drives neuroendocrine tumor progression. *Mol Cancer Res* 19: 1476–1485. <https://doi.org/10.1158/1541-7786.MCR-20-0992>
- Amar L, Pacak K, Steichen O, Akker SA, Aylwin SJB, Baudin E, Bufet A, Burnichon N, Clifton-Bligh RJ, Dahia PLM, Fassnacht M, Grossman AB, Herman P, Hicks RJ, Januszewicz A, Jimenez C, Kunst HPM, Lewis D, Mannelli M, Naruse M, Robledo M, Taieb D, Taylor DR, Timmers HJLM, Treglia G, Tufton N, Young WF, Lenders JWM, Gimenez-Roqueplo AP, Lussery-Lepoutre C (2021) International consensus on initial screening and follow-up of asymptomatic SDHx mutation carriers. *Nat Rev Endocrinol* 17: 435–444. <https://doi.org/10.1038/s41574-021-00492-3>
- Ardicli B, User IR, Ciftci AO, Akyuz C, Kutluk MT, Gonc N, Ozon ZA, Alikasifoglu A, Oguz B, Haliloglu M, Orhan D, Tanyel FC, Karnak I, Ekinici S (2021) Approach to pheochromocytoma and paraganglioma in children and adolescents: A retrospective clinical study from a tertiary care center. *J Pediatr Urol* 17: 400.e1–400.e7. <https://doi.org/10.1016/j.jpurol.2021.01.043>
- Armstrong R, Sridhar M, Greenhalgh KL, Howell L, Jones C, Landes C, McPartland JL, Moores C, Losty PD, Didi M (2008) Pheochromocytoma in children. *Arch Dis Child* 93: 899–904. <https://doi.org/10.1136/adc.2008.139121>
- Barontini M, Levin G, Sanso G (2006) Characteristics of pheochromocytoma in a 4- to 20-year-old population. *Ann N Y Acad Sci* 1073: 30–37. <https://doi.org/10.1196/annals.1353.003>
- Bausch B, Wellner U, Bausch D, Schiavi F, Barontini M, Sanso G, Walz MK, Peczkowska M, Weryha G, Dall'igna P, Cecchetto G, Bisogno G, Moeller LC, Bockenhauer D, Patocs A, Rácz K, Zabolotnyi D, Yaremchuk S, Dzivite-Krisane I, Castinetti F, Taieb D, Malinoc A, von Dobschuetz E, Roessler J, Schmid KW, Opocher G, Eng C, Neumann HP (2014) Long-term prognosis of patients with pediatric pheochromocytoma. *Endocr Relat Cancer* 21: 17–25. <https://doi.org/10.1530/ERC-13-0415>
- Bayley JP, Bausch B, Rijkman JA, van Hulstijn LT, Jansen JC, Ascher D, Pires DEV, Hes FJ, Hensen EF, Corssmit EPM, Devilee P, Neumann HPH (2020) Variant type is associated with disease characteristics in SDHB, SDHC and SDHD-linked pheochromocytoma-paraganglioma. *J Med Genet* 57: 96–103. <https://doi.org/10.1136/jmedgenet-2019-106214>
- Bechmann N, Moskopp ML, Ullrich M, Calsina B, Wallace PW, Richter S, Friedemann M, Langton K, Fliedner SMJ, Timmers HJLM, Nölting S, Beuschlein F, Fassnacht M, Prejbisz A, Pacak K, Ghayee HK, Bornstein SR, Dieterich P, Pietzsch J, Wielockx B, Robledo M, Qin N, Eisenhofer G (2020) HIF2α supports pro-metastatic behavior in pheochromocytomas/paragangliomas. *Endocr Relat Cancer* 27: 625–640. <https://doi.org/10.1530/ERC-20-0205>
- Benn DE, Zhu Y, Andrews KA, Wilding M, Duncan EL, Dwight T, Tothill RW, Burgess J, Crook A, Gill AJ, Hicks RJ, Kim E, Luxford C, Marfan H, Richardson AL, Robinson B, Schlosberg A, Sisman R, Tacon L, Trainer A, Tucker K, Maher ER, Field M, Clifton-Bligh RJ (2018) Bayesian approach to determining penetrance of pathogenic SDH variants. *J Med Genet* 55: 729–734. <https://doi.org/10.1136/jmedgenet-2018-105427>
- Ben-Skowronek I, Kozaczuk S (2015) Von Hippel-Lindau Syndrome. *Horm Res Paediatr* 84: 145–152. <https://doi.org/10.1159/000431323>
- Bravo EL, Tagle R (2003) Pheochromocytoma: state-of-the-art and future prospects. *Endocr Rev* 24: 539–553. <https://doi.org/10.1210/er.2002-0013>
- Carrasquillo JA, Chen CC, Jha A, Ling A, Lin FI, Pryma DA, Pacak K (2021) Imaging of pheochromocytoma and paraganglioma. *J Nucl Med* 62: 1033–1042. <https://doi.org/10.2967/jnumed.120.259689>
- Cascón A, Inglada-Pérez L, Comino-Méndez I, de Cubas AA, Letón R, Mora J, Marazuela M, Galofré JC, Quesada-Charneco M, Robledo M (2013) Genetics of pheochromocytoma and paraganglioma in Spanish pediatric patients. *Endocr Relat Cancer* 20: L1–L6. <https://doi.org/10.1530/ERC-12-0339>
- Chetty R (2010) Familial paraganglioma syndromes. *J Clin Pathol* 63: 488–491. <https://doi.org/10.1136/jcp.2010.076257>
- Corcuff JB, Chardon L, El Hajji Ridah I, Brossaud J (2017) Urinary sampling for 5HIAA and metanephrines determination: revisiting the recommendations. *Endocr Connect* 6: R87–R98. <https://doi.org/10.1530/EC-17-0071>
- Crona J, Lamarca A, Ghosal S, Welin S, Skogseid B, Pacak K (2019) Genotype-phenotype correlations in pheochromocytoma and paraganglioma: a systematic review and individual patient meta-analysis. *Endocr Relat Cancer* 26: 539–550. <https://doi.org/10.1530/ERC-19-0024>
- Crona J, Taieb D, Pacak K (2017) New perspectives on pheochromocytoma and paraganglioma: toward a molecular classification. *Endocr Rev* 38: 489–515. <https://doi.org/10.1210/er.2017-00062>
- Darcourt J, Schiavza A, Sapin N, Dufour M, Ouvrier MJ, Benisvy D, Fontana X, Koulibaly P (2014) 18F-FDOPA PET for the diagnosis of parkinsonian syndromes. *Q J Nucl Med Mol Imaging* 58: 355–365. PMID: 25366711
- Därr R, Nambuba J, Del Rivero J, Janssen I, Merino M, Todorovic M, Balint B, Jochmanova I, Prchal JT, Lechan RM, Tischler AS, Popovic V, Miljic D, Adams KT, Prall FR, Ling A, Golomb MR, Ferguson M, Nilubol N, Chen CC, Chew E, Taieb D, Stratakis CA, Fojo T, Yang C, Kebebew E, Zhuang Z, Pacak K (2016) Novel insights into the polycythemia-paraganglioma-somatostatinoma syndrome. *Endocr Relat Cancer* 23: 899–908. <https://doi.org/10.1530/ERC-16-0231>
- Edmonds S, Fein DM, Gurtman A (2011) Pheochromocytoma. *Pediatr Rev* 32: 308–310. <https://doi.org/10.1542/pir.32-7-308>
- Eisenhofer G, Lenders JW, Siegert G, Bornstein SR, Friberg P, Milosevic D, Mannelli M, Linehan WM, Adams K, Timmers HJ, Pacak K (2012) Plasma methoxytyramine: A novel biomarker of metastatic pheochromocytoma and paraganglioma in relation to established risk factors of tumour size, location and SDHB mutation status. *Eur J Cancer* 48: 1739–1749. <https://doi.org/10.1016/j.ejca.2011.07.016>
- Eisenhofer G, Pamporaki C, Lenders JWM (2023) Biochemical Assessment of Pheochromocytoma and Paraganglioma. *Endocr Rev* 44: 862–909. <https://doi.org/10.1210/endrev/bnad011>
- Eisenhofer G, Peitzsch M, Bechmann N, Huebner A (2022) Biochemical diagnosis of catecholamine-producing tumors of childhood: neuroblastoma, pheochromocytoma and paraganglioma. *Front Endocrinol (Lausanne)* 13: 901760. <https://doi.org/10.3389/fendo.2022.901760>
- Fang F, Ding L, He Q, Liu M (2020) Preoperative management of pheochromocytoma and paraganglioma. *Front Endocrinol (Lausanne)* 11: 586795. <https://doi.org/10.3389/fendo.2020.586795>
- Fargette C, Shulkin B, Jha A, Pacak K, Taieb D (2023) Clinical utility of nuclear imaging in the evaluation of pediatric adrenal neoplasms. *Front Oncol* 12: 1081783. <https://doi.org/10.3389/fonc.2022.1081783>
- Farrugia FA, Charalampopoulos A (2019) Pheochromocytoma. *Endocr Regul* 53: 191–212. <https://doi.org/10.2478/enr-2019-0020>
- Havekes B, Romijn JA, Eisenhofer G, Adams K, Pacak K (2009) Update on pediatric pheochromocytoma. *Pediatr Nephrol* 24: 943–950. <https://doi.org/10.1007/s00467-008-0888-9>
- İşik AC, Erem C, Imamoğlu M, Cinel A, Sari A, Maral G (2006) Familial paraganglioma. *Eur Arch Otorhinolaryngol* 263: 23–31. <https://doi.org/10.1007/s00405-004-0885-y>
- Jacobson AF, Travin MI (2015) Impact of medications on mIBG uptake, with specific attention to the heart: Comprehensive review of the literature. *J Nucl Cardiol* 22: 980–993. <https://doi.org/10.1007/s12350-015-0170-z>
- Jain A, Baracco R, Kapur G (2020a) Pheochromocytoma and paraganglioma – an update on diagnosis, evaluation, and management. *Pediatr Nephrol* 35: 581–594. <https://doi.org/10.1007/s00467-018-4181-2>

- Jaiswal SK, Sarathi V, Malhotra G, Verma P, Hira P, Badhe P, Memon SS, Barnabas R, Patil VA, Anurag, Lila R, Shah NS, Bandgar T (2021) The utility of ^{68}Ga -dotatate pet/ct in localizing primary/metastatic pheochromocytoma and paraganglioma: Asian Indian experience. *Indian J Endocrinol* **25**: 410–417. https://doi.org/10.4103/ijem.ijem_307_21
- Janßen I, Chen CC, Taieb D, Patronas NJ, Millo CM, Adams KT, Nambuba J, Herscovitch P, Sadowski SM, Fojo AT, Buchmann I, Kebebew E, Pacak K (2016) ^{68}Ga -DOTATATE PET/CT in the Localization of head and neck paragangliomas compared with other functional imaging modalities and CT/MRI. *J Nucl Med* **57**: 186–191. <https://doi.org/10.2967/jnumed.115.161018>
- Jha A, Ling A, Millo C, Gupta G, Viana B, Lin FI, Herscovitch P, Adams KT, Taieb D, Metwalli AR, Linehan WM, Brofferio A, Stratakis CA, Kebebew E, Lodish M, Civelek AC, Pacak K (2018) Superiority of ^{68}Ga -DOTATATE over ^{18}F -FDG and anatomic imaging in the detection of succinate dehydrogenase mutation (SDHx)-related pheochromocytoma and paraganglioma in the pediatric population. *Eur J Nucl Med Mol Imaging* **45**: 787–797. <https://doi.org/10.1007/s00259-017-3896-9>
- Jhawar S, Arakawa Y, Kumar S, Varghese D, Kim YS, Roper N, El-loumi F, Pommier Y, Pacak K, Del Rivero J (2022) New insights on the genetics of pheochromocytoma and paraganglioma and its clinical implications. *Cancers* **14**: 594. <https://doi.org/10.3390/cancers14030594>
- Jiang J, Zhang J, Pang Y, Bechmann N, Li M, Monteagudo M, Calsina B, Gimenez-Roqueplo AP, Nölting S, Beuschlein F, Fassnacht M, Deutschbein T, Timmers HJLM, Åkerström T, Crona J, Quinkler M, Flidner SMJ, Liu Y, Guo J, Li X, Guo W, Hou Y, Wang C, Zhang L, Xiao Q, Liu L, Gao X, Burnichon N, Robledo M, Eisenhofer G (2020) Sino-European differences in the genetic landscape and clinical presentation of pheochromocytoma and paraganglioma. *J Clin Endocrinol Metab* **105**: 3295–3307. <https://doi.org/10.1210/clinem.dgaa502>
- Jochmanova I, Abcede AMT, Guerrero RJS, Malong CLP, Wesley R, Huynh T, Gonzales MK, Wolf KJ, Jha A, Knue M, Prodanov T, Nilubol N, Mercado-Asis LB, Stratakis CA, Pacak K (2020) Clinical characteristics and outcomes of SDHB-related pheochromocytoma and paraganglioma in children and adolescents. *J Cancer Res Clin Oncol* **146**: 1051–1063. <https://doi.org/10.1007/s00432-020-03138-5>
- Képénékian L, Moggetti T, Lifante JC, Giraudet AL, Hozard C, Pinson S, Borson-Chazot F, Combemale P (2016) Interest of systematic screening of pheochromocytoma in patients with neurofibromatosis type 1. *Eur J Endocrinol* **175**: 335–344. <https://doi.org/10.1530/EJEnd-16-0233>
- King KS, Prodanov T, Kantorovich V, Fojo T, Hewitt JK, Zacharin M, Wesley R, Lodish M, Raygada M, Gimenez-Roqueplo AP, McCormack S, Eisenhofer G, Milosevic D, Kebebew E, Stratakis CA, Pacak K (2011) Metastatic pheochromocytoma/paraganglioma related to primary tumor development in childhood or adolescence: significant link to SDHB mutations. *J Clin Oncol* **29**: 4137–4142. <https://doi.org/10.1200/JCO.2011.34.6353>
- Kumar S, Lila AR, Memon SS, Sarathi V, Patil VA, Menon S, Mittal N, Prakash G, Malhotra G, Shah NS, Bandgar TR (2021) Metastatic cluster 2-related pheochromocytoma/paraganglioma: a single-center experience and systematic review. *Endocr Connect* **10**: 1463–1476. <https://doi.org/10.1530/EC-21-0455>
- Kuo, M. J. M., Nazari, M. A., Jha, A., & Pacak, K. (2022) Pediatric Metastatic Pheochromocytoma and Paraganglioma: Clinical Presentation and Diagnosis, Genetics, and Therapeutic Approaches. *Frontiers in Endocrinology*, **13**. <https://doi.org/10.3389/fendo.2022.936178>
- Lee YT, Tan YJ, Oon CE (2018) Molecular targeted therapy: Treating cancer with specificity. *Eur J Pharmacol* **834**: 188–196. <https://doi.org/10.1016/j.ejphar.2018.07.034>
- Lenders JWM, Eisenhofer G (2017) Update on modern management of pheochromocytoma and paraganglioma. *Endocrinol Metab (Seoul)* **32**: 152. <https://doi.org/10.3803/EnM.2017.32.2.152>
- Lorenzo FR, Yang C, Ng Tang Fui M, Vankayalapati H, Zhuang Z, Huynh T, Grossmann M, Pacak K, Prchal JT (2013) A novel EPAS1/HIF2A germline mutation in a congenital polycythemia with paraganglioma. *J Mol Med (Berl)* **91**: 507–512. <https://doi.org/10.1007/s00109-012-0967-z>
- Mak IYF, Hayes AR, Khoo B, Grossman A (2019) Peptide receptor radionuclide therapy as a novel treatment for metastatic and invasive pheochromocytoma and paraganglioma. *Neuroendocrinology* **109**: 287–298. <https://doi.org/10.1159/000499497>
- Miller DT, Freedenberg D, Schorry E, Ullrich NJ, Viskochil D, Korf BR; COUNCIL ON GENETICS; AMERICAN COLLEGE OF MEDICAL GENETICS AND GENOMICS (2019) Health Supervision for children with neurofibromatosis type 1. *Pediatrics* **143**: e20190660. <https://doi.org/10.1542/peds.2019-0660>
- Moraitis AG, Martucci VL, Pacak K (2014) Genetics, diagnosis, and management of medullary thyroid carcinoma and pheochromocytoma/paraganglioma. *Endocr Pract* **20**: 176–187. <https://doi.org/10.4158/EP13268.RA>
- Nölting S, Bechmann N, Taieb D, Beuschlein F, Fassnacht M, Kroiss M, Eisenhofer G, Grossman A, Pacak K (2022) Personalized management of pheochromocytoma and paraganglioma. *Endocr Rev* **43**: 199–239. <https://doi.org/10.1210/edrv/bnab019>
- Nölting S, Grossman A, Pacak K (2019) Metastatic pheochromocytoma: spinning towards more promising treatment options. *Exp Clin Endocrinol Diabetes* **127**: 117–128. <https://doi.org/10.1055/a-0715-1888>
- Pamporaki C, Hamplova B, Peitzsch M, Prejbisz A, Beuschlein F, Timmers HJLM, Fassnacht M, Klink B, Lodish M, Stratakis CA, Huebner A, Flidner S, Robledo M, Sinnott RO, Januszewicz A, Pacak K, Eisenhofer G (2017) Characteristics of pediatric vs adult pheochromocytomas and paragangliomas. *J Clin Endocrinol Metab* **102**: 1122–1132. <https://doi.org/10.1210/clinem.dgaa502>
- Park H, Kim MS, Lee J, Kim JH, Jeong BC, Lee S, Lee SK, Cho SY, Jin DK (2021) Clinical presentation and treatment outcomes of children and adolescents with pheochromocytoma and paraganglioma in a single center in Korea. *Front Endocrinol (Lausanne)* **11**: 610746. <https://doi.org/10.3389/fendo.2020.610746>
- Patel D, Phay JE, Yen TWF, Dickson PV, Wang TS, Garcia R, Yang AD, Solórzano CC, Kim LT (2020) Update on pheochromocytoma and paraganglioma from the SSO endocrine/head and neck disease-site work group. Part 1 of 2: Advances in pathogenesis and diagnosis of pheochromocytoma and paraganglioma. *Ann Surg Oncol* **27**: 1329–1337. <https://doi.org/10.1245/s10434-020-08220-3>
- Plouin PF, Duclos JM, Soppelsa F, Boulblil G, Chatellier G (2001) Factors associated with perioperative morbidity and mortality in patients with pheochromocytoma: analysis of 165 operations at a single center. *J Clin Endocrinol Metab* **86**: 1480–1486. <https://doi.org/10.1210/clinem.dgaa502>
- Quee TC, Bergeron MJ, Amsel R, Chan EC (1986) A staining method for monitoring subgingival bacteria associated with periodontal disease. *J Periodontol Res* **21**: 722–727. <https://doi.org/10.1111/j.1600-0765.1986.tb01510.x>
- Read AD, Bentley RE, Archer SL, Dunham-Snary KJ (2021) Mitochondrial iron-sulfur clusters: Structure, function, and an emerging role in vascular biology. *Redox Biol* **47**: 102164. <https://doi.org/10.1016/j.redox.2021.102164>
- Rednam SP, Erez A, Druker H, Janeway KA, Kamihara J, Kohlmann WK, Nathanson KL, States LJ, Tomlinson GE, Villani A, Voss SD, Schiffman JD, Wasserman JD (2017) Von Hippel-Lindau and hereditary pheochromocytoma/paraganglioma syndromes: clinical features, genetics, and surveillance recommendations in childhood. *Clin Cancer Res* **23**: e68–e75. <https://doi.org/10.1158/1078-0432.CCR-17-0547>
- Rees MA, Morin CE, Behr GG, Davis JC, Lai H, Morani AC, Parisi MT, Saigal G, Singh S, Yedururi S, Towbin AJ, Shulkin BL (2023) Imaging of pediatric adrenal tumors: A COG Diagnostic Imaging Committee/SPR Oncology Committee White Paper. *Pediatr Blood Cancer* **70** (Suppl 4): e2997. <https://doi.org/10.1002/pbc.29973>
- Rijken JA, Niemeijer ND, Jonker MA, Eijkelenkamp K, Jansen JC, van Berkel A, Timmers HJLM, Kunst HPM, Bisschop PHLT, Kerstens MN, Dreijerink KMA, van Dooren MF, van der Horst-Schrivers ANA, Hes FJ, Leemans CR, Corssmit EPM, Hensen EF (2018) The penetrance of paraganglioma and pheochromocytoma in SDHB germline mutation carriers. *Clin Genet* **93**: 60–66. <https://doi.org/10.1111/cge.13055>
- Ross JH (2000) Pheochromocytoma. Special considerations in children. *Urol Clin North Am* **27**: 393–402. [https://doi.org/10.1016/S0094-0143\(05\)70088-4](https://doi.org/10.1016/S0094-0143(05)70088-4)
- Rufini V, Treglia G, Perotti G, Giordano A (2013) The evolution in the use of MIBG scintigraphy in pheochromocytomas and paragangliomas. *Hormones (Athens)* **12**: 58–68. <https://doi.org/10.1007/BF03401287>
- Schüttler J, Westhofen P, Kania U, Ihmsen H, Kammerecker S, Hirner A (1995) Quantitative assessment of catecholamine secretion as a rational principle of anesthesia management in pheochromocytoma surgery. *Anesthesiol Intensivmed Notfallmed Schmerzther* **30**: 341–349 (in German). <https://doi.org/10.1055/s-2007-996507>
- Seamon ML, Yamaguchi I (2021) Hypertension in pheochromocytoma and paraganglioma: evaluation and management in pediatric patients. *Curr Hypertens Rep* **23**: 32. <https://doi.org/10.1007/s11906-021-01150-9>
- Shah MH, Goldner WS, Benson AB, Bergsland E, Blaszkowsky LS, Brock P, Chan J, Das S, Dickson PV, Fanta P, Giordano T, Halfdanarson TR, Halperin D, He J, Heaney A, Heslin MJ, Kandel F, Kardan A, Khan SA, Kuvshinov BW, Lieu C, Miller K, Pillarisetty VG, Reidy D, Salgado SA, Shaheen S, Soares HP, Soulen MC, Strosberg JR, Sussman CR, Trikalinos NA, Uboba NA, Vijayvergia N, Wong T, Lynn B, Hochstetler C (2021) Neuroendocrine and Adrenal Tumors, Version 2.2021, NCCN Clinical Practice Guidelines in Oncology. *J Natl Compr Canc Netw* **19**: 839–868. <https://doi.org/10.6004/jnccn.2021.0032>
- Taieb D, Jha A, Guerin C, Pang Y, Adams KT, Chen CC, Romanet P, Roche P, Essamet W, Ling A, Quezado MM, Castinetti F, Sebag F, Pacak K (2018) ^{18}F -FDOPA PET/CT Imaging of MAX-Re-

- lated Pheochromocytoma. *J Clin Endocrinol Metab* **103**: 1574–1582. <https://doi.org/10.1210/jc.2017-02324>
- van Treijen MJC, de Vries LH, Hertog D, Vriens MR, Verrijn Stuart AA, van Nesselrooij BPM, Valk GD (2022) *Multiple Endocrine Neoplasia Type 2*. In Feingold KR, Anawalt B, Blackman MR, Boyce A, Chrousos G, Corpas E, de Herder WW, Dhatariya K, Dungan K, Hofland J, Kalra S, Kaltsas G, Kapoor N, Koch C, Kopp P, Korbonits M, Kovacs CS, Kuohung W, Laferrère B, Levy M, McGee EA, McLachlan R, New M, Purnell J, Sahay R, Shah AS, Singer F, Sperling MA, Stratakis CA, Trencle DL, Wilson DP, eds. Endotext [Internet]. South Dartmouth (MA): MDTText.com, Inc.; 2000–. PMID: 29465928.
- Wang K, Crona J, Beuschlein F, Grossman AB, Pacak K, Nölting S (2022) Targeted therapies in pheochromocytoma and paraganglioma. *J Clin Endocrinol Metab* **107**: 2963–2972. <https://doi.org/10.1210/clinem/dgac471>
- Yen K, Lodish M (2021) Pheochromocytomas and paragangliomas. *Curr Opin Pediatr* **33**: 430–435. <https://doi.org/10.1097/MOP.0000000000001029>
- Zhuang Z, Yang C, Lorenzo F, Merino M, Fojo T, Kebebew E, Popovic V, Stratakis CA, Prchal JT, Pacak K (2012) Somatic *HIF2A* gain-of-function mutations in paraganglioma with polycythemia. *N Engl J Med* **367**: 922–930. <https://doi.org/10.1056/NEJMoa1205119>

Nephro-oncology: clinical and biochemical aspects of kidney disease and cancer

Sławomir Lizakowski¹✉, Alicja Dębska-Ślizień¹, Ilona Kurnatowska², Maciej J. Zaucha³, Marcin Matuszewski⁴, Beata Naumnik¹⁴, Marcin Adamczak⁵, Jerzy Chudek⁶, Magdalena Durlak⁷, Carla Ferrándiz-Pulido⁸, Bartosz Foronczewicz⁹, Ryszard Gellert¹⁰, Magdalena Krajewska¹¹, Michał Nowicki¹², Andrzej Więcek⁵ and Jolanta Małyszko¹³

¹Department of Nephrology, Transplantology and Internal Medicine, Medical University of Gdańsk, Gdańsk, Poland; ²Department of Internal Diseases and Transplant Nephrology, Medical University of Łódź, Łódź, Poland; ³Department of Hematology and Transplantology, Medical University of Gdańsk, Gdańsk, Poland; ⁴Department of Urology, Medical University of Gdańsk, Gdańsk, Poland; ⁵Department of Nephrology, Transplantation and Internal Medicine, Medical University of Silesia in Katowice, Katowice, Poland; ⁶Department of Internal Diseases and Oncological Chemotherapy, Faculty of Medical Sciences in Katowice, Medical University of Silesia in Katowice, Poland; ⁷Department of Transplantation Medicine, Nephrology and Internal Diseases, Medical University of Warsaw, Poland; ⁸Department of Dermatology, Hospital Universitari Vall d'Hebron, Universitat Autònoma de Barcelona, Barcelona, Spain; ⁹Department of Immunology, Transplantology and Internal Medicine, Medical University in Warsaw, Warsaw, Poland; ¹⁰Department of Nephrology and Internal Medicine, Centre of Postgraduate Medical Education, Bielanski Hospital, Warsaw, Warsaw, Poland; ¹¹Department of Nephrology and Transplantation Medicine, Wrocław Medical University, Wrocław, Poland; ¹²Department of Nephrology, Hypertension and Kidney Transplantation, Medical University of Łódź, Łódź, Poland; ¹³Department of Nephrology, Dialysis and Internal Medicine, The Medical University of Warsaw, Warsaw, Poland; ¹⁴Department of Nephrology and Transplantation with Dialysis Unit, Medical University of Białystok, Białystok, Poland

Onco-nephrology is a new field of medicine which combines many aspects of kidney injury in cancer patients and cancers in patients with kidney disease. This connection takes many forms and includes drug-induced nephrotoxicity, electrolyte disorders, numerous paraneoplastic syndromes and an increased rate cancers in dialysis and transplanted patients. The appropriate laboratory assessment of the kidney function allows to optimize chemotherapy and thus minimizes the risk of complications. This article focuses on acute kidney injury (AKI), chronic kidney disease (CKD), various electrolyte and acid-base disorders, the most common cancers after kidney transplantation and the kidney disorders associated with HSCT (hematopoietic stem cell transplantation). The possibility of the application of novel cancer therapy, such as cancer immunotherapy and proton therapy in transplant recipients was also discussed.

Key words: onco-nephrology, cancer, kidney disease, transplantation, HCT, therapy

Received: 19 December, 2022; **revised:** 22 February, 2022; **accepted:** 11 March, 2023; **available on-line:** 09 May, 2023

✉e-mail: slizak@gumed.edu.pl

*The paper is a multidisciplinary summary of the updated information provided in lectures delivered during the 2nd Scientific and Training Conference “Nephro-oncology” in Gdańsk, Poland, on October 2–3, 2020.

Abbreviations: ACKD, acquired cystic kidney disease; ADPKD, autosomal dominant polycystic kidney disease; AKD, Acute kidney disease; AKI, acute kidney injury; AML, acute myeloid leukaemia; ANP, atrial natriuretic peptide; BC, bladder cancer; BCC, basal cell carcinoma; BSA, body surface area; CKD, chronic kidney disease; CNL, calcineurin inhibitors; CTLA4, cytotoxic T-lymphocyte-associated protein 4; EFS, event-free survival; eGFR, estimated glomerular filtration rate; ESKD, end-stage kidney disease; FGFR, fibroblast growth factor -23 receptor; FSGS, focal segmental glomerulosclerosis; GvHD, graft versus host disease; HCT, hematopoietic cell transplantation; HCT-CI, specific comorbidity index; HD, hemodialysis; HSCT, hematopoietic stem cell transplantation; ICIs, immune checkpoint inhibitors; irAEs, immune-related adverse events; KDIGO, Kidney Disease Improving Global Outcomes; KTx, kidney transplantation; MCC, Merkel cell carcinoma; MDRD, Modification of Diet in Renal Disease; MM, malignant melanoma; mTOR, mammalian target of rapamycin kinase; PC, prostate cancer; PD-1, programmed cell death-1; RCC, renal cell carcinoma; RT, radiotherapy; SCC, squamous cell carcinoma; SCLC, small-cell lung cancer; SIADH,

inappropriate secretion of antidiuretic hormone; SOTR, solid organ transplant recipients; TA-TMA, transplant-associated thrombotic microangiopathy; TBI, total body irradiation; TNF, tumor necrosis factor; UTIs, Urinary tract infections; VEGF, vascular endothelial growth factor

INTRODUCTION

There are complex relationships between kidneys and cancer. Many crucial points could be underlined by factors such as acute kidney injury and chronic kidney disease in a cancer patient, the renal effects of anticancer therapy, adverse effects of the tumor itself, management of patients after nephrectomy due to kidney cancer, cancer treatment on dialysis and after kidney transplantation (KT). Another very important issue is oncological treatment in other than kidney solid organ transplant recipients (SOTR) and in hematopoietic cell transplantation (HCT).

A multidisciplinary onco-nephrology team, including not only oncologist and nephrologist, but also other health professionals is crucial to providing care to the aforementioned groups of patients (Cosmai *et al.*, 2016). This was the reason for the creation of a new field of medicine – called onco-nephrology (Bączkowska *et al.*, 2019).

In this paper, we discussed acute and chronic kidney disease in SOTRs with cancer as well as nephrotoxicity associated with existing and novel cancer therapy. We also focused on the most common cancers in SOTRs such as skin cancer and urinary tract cancer. An additional part is dedicated to kidney disease in HCT recipients.

Adequate assessment of kidney function allows for selecting the optimal anticancer therapy in terms of the type of drug and its dose (Małyszko *et al.*, 2020a). Treatment efficacy and outcomes, as well as survival, could be affected by both the overestimation and underestimation of renal function.

Patients with impaired renal function are at a higher risk of developing adverse events and toxicities to an anti-cancer drug. The use of some drugs in patients with renal failure can lead more often to myelotoxicity, hepatotoxicity, and life-threatening electrolyte disorders (e.g., cisplatin, cyclophosphamide, vinblastine, and vincristine).

An equally important issue is the use of new groups of anticancer drugs in patients with kidney damage and kidney transplanted patients (Malyszko *et al.*, 2016; Sprangers *et al.*, 2021). In recent years, novel therapies, including immunotherapy with immune checkpoint inhibitors (ICIs) and proton therapy, have revolutionized cancer treatment and are becoming a new standard of care for many tumor types. Nephrological problems more and more often also affect patients undergoing stem cell transplantation (Kępska-Dzilińska *et al.*, 2022). Kidney damage/deterioration is often found in these patients due to the extension of the eligibility criteria for this procedure and its use in older patients and/or with additional chronic diseases. Kidney injury after high-dose chemotherapy might be due to the direct effect of cytotoxic agents or indirect complications caused by cytotoxic agents such as mucositis and diarrhea, infections, or veno-occlusive disease. On the other hand, HCT is increasingly used in patients with renal failure, including end-stage renal disease undergoing dialysis due to multiple myeloma. The different HCT protocols are required in patients with normal renal function, mild impaired renal function, and dialysis-dependent patients, which is discussed in this article.

Kidney transplantation is the best method of renal replacement therapy, it prolongs the patient's life by decades but the price is much higher than in the general population - the risk of cancer. Cancer is listed as the second, after cardiovascular diseases, cause of death in patients after KT and also causes death in many other SOTRs (Serkies *et al.*, 2022). Treatment of these patients is very complex due to immunosuppression and requires the cooperation of specialists in many fields depending on the transplanted organ and type of neoplastic disease. Skin cancers are the most common tumors in SOTRs. The most prevalent are squamous cell carcinoma (SCC), basal cell carcinoma (BCC), malignant melanoma (MM), and Merkel cell carcinoma (MCC) (Mittal & Colegio, 2017). Appropriate prophylaxis allows for a considerable reduction of the risk of skin cancer, while regular dermatological examination allows for a diagnosis in the early phase of the disease and improves the prognosis. The second most common are cancers of the urinary tract, including the transplanted kidney (Bellini *et al.*, 2022). As these neoplasms occur more often in older age, their detection is growing with time, with the number of recipients followed up. In the case of urinary tract cancers, surgery is recommended. The possibilities and limitations of urological management are presented in our article.

The presented paper summarizes the key information provided in lectures delivered during the 2nd Scientific

and Training Conference “Nephro-oncology” in Gdańsk, Poland, on October 2–3, 2020. It is also updated using crucial management issues in nephrology relevant to patients with malignancy, published by KDIGO (Kidney Disease: Improving Global Outcomes) and the current status on malignancies in adult kidney transplant candidates and recipients published most recently in NDT (Porta *et al.*, 2020; Malyszko *et al.*, 2020a; Serkies *et al.*, 2022).

KIDNEY INJURY IN CANCER

Acute and chronic kidney disease definition and classification

The term Acute kidney disease (AKD) was introduced recently to incorporate both acute kidney diseases and disorders. The definition of AKD includes abnormalities of kidney function and/or structure with implications for health lasting ≤ 3 months. AKD may include AKI (acute kidney injury), but, more importantly, also other abnormalities in kidney function that are not as severe as AKI or that develop over a period of > 7 days (Table 1) (Lameire *et al.*, 2021; Levey *et al.*, 2022). The cause(s) of AKD should be sought, and classification includes functional and structural parameters. Minimal dataset for evaluation: history and examination including; past medical history, drug history (in cancer patients particularly important), infectious diseases, full physical examination including blood pressure, assessment of volume, serum creatinine and eGFR (estimated glomerular filtration rate), urea and electrolytes, full blood count, urinary dipstick (qualitative albuminuria/proteinuria), and ultrasound. Management of AKD is currently based on empirical considerations.

Kidney function assessment in oncology

It has been learnt that renal function in patients with malignancy should be estimated to profile the survival risk, assess the appropriate dose of antineoplastic drugs and define the eligibility of these patients for clinical trials with novel therapies (Porta *et al.*, 2020). The problem of drug dosing in oncology was described in detail in two recent reviews (Sprangers *et al.*, 2021; Malyszko *et al.*, 2020a). Treatment efficacy and outcomes as well as survival could be affected by both overestimation and underestimation of renal function. Overestimation of renal function may result in overdose or inappropriate choice of anticancer drugs with their serious adverse

Table 1. Functional and structural criteria for kidney diseases and disorders.

	AKI	AKD	CKD
Duration	Within 7 days	≤ 3 months	> 3 months
Functional criteria	increase Scr by $> 50\%$ within 7 days or increase Scr by > 0.3 mg/dL ($26.5 \mu\text{mol/L}$) within 2 days or oliguria for ≥ 4 hours	AKI or GFR < 60 mL/min/ 1.73m^2 or decrease GFR by $> 35\%$ vs baseline or increase Scr $> 50\%$ w vs baseline	GFR < 60 mL/min/ 1.73m^2
And/or		And/or	And/or
Structural criteria	Not defined	Markers of kidney damage (albuminuria, hematuria, or pyuria are most common)	Markers of kidney damage (albuminuria is most common)

Abbreviations: AKD, acute kidney disease; AKI, acute kidney injury; CKD, chronic kidney disease; GFR, glomerular filtration rate; Scr, serum creatinine.

events. On the other hand, underestimation of renal function may cause underdosing or exclusion/withdrawal of an anticancer agent leading to worse outcomes/subsequent treatment failure. The majority of patients with malignancies are treated with several anticancer drugs with renal clearance. Therefore, patients with impaired renal function are at higher risk for developing adverse events and toxicities to these therapeutic protocols. Recently introduced immune checkpoint inhibitors (e.g., ipilimumab, nivolumab, and pembrolizumab) may cause acute interstitial nephritis and podocytopathy. Moreover, anti-VEGF (vascular endothelial growth factor) drugs may cause microvascular injury and DITMA (drug-induced thrombotic microangiopathy) or various glomerulopathies, in particular, minimal change disease and/or collapsing-like FSGS (focal segmental glomerulosclerosis). Therefore, in patients with malignancy, an accurate assessment of kidney function i.e. GFR is critical. To date, creatinine is a nearly ideal filtration marker, despite some limitations. Therefore, several formulae assessing GFR were introduced in healthy subjects as well as in patients with chronic kidney disease, however, the use of these formulae in cancer patients is not established. Sarcopenia is a common finding in patients with advanced malignancy prior therapy, in addition, it develops or worsens during anticancer therapy in the vast majority of patients. As creatinine is produced by muscles, in patients with reduced muscle mass creatinine-based formulae are not appropriate with potentially negative consequences. Recently, Janowitz and others performed an extensive study and showed that the BSA-adjusted CKD-EPI formula appeared to be the most accurate and least biased GFR estimate of those currently used in oncology patients when compared with ^{51}Cr -EDTA (Janowitz *et al.*, 2017). Calculation of GFR based on the Janowitz formula is available online at <http://tavarelab.cruk.cam.ac.uk/JanowitzWilliamsGFR/>. It appears that the Janowitz formula is the best option for creatinine-based equations in cancer patients. In everyday clinical oncology practice, adjustment of drug dosage is generally based on eGFR. However, The US FDA promotes the usage of Cockcroft-Gault or the MDRD formulae for drug dosage prescriptions (Malyszko *et al.*, 2020a). Despite the fact, that either Janowitz or CKD-EPI formula estimates GFR more precisely, the drug manufactures still refer drug dosage to other eGFR formulae. Therefore, we need to take into account these eGFR formulae when adjusting the drug dose. Kidney function, besides changes in glomerular filtration rate/serum creatinine, also encompasses tubular dysfunction and vascular disorders, more studies including urinalysis and imaging studies such as computed tomography, magnetic resonance imaging, etc are to be considered prior to taking therapeutic decisions (Malyszko *et al.*, 2020a).

Evaluation of renal function in AKI is another challenge for nephro-oncologists, as AKI is common in cancer patients either due to malignancy or its therapy. It is of utmost importance as AKI represent a dynamic state with a fast fall in GFR whereas CKD is a relatively stable state and GFR formulae were developed in stable CKD patients. Therefore, in AKI, estimation of eGFR based on creatinine may lead to serious errors. Moreover, as kidney injury originates in tubules, significant tubulopathy may not result in significant rise in serum creatinine concentration and changes in creatinine/GFR represent relatively late changes. Taking into account these limitations, there is a search for serum and urinary markers. Several biomarkers such as neutrophil gelatinase-associated lipocalin, proinflammatory cytokines (in-

terleukin-6 and interleukin-8), kidney injury molecule-1, netrin, semaphorin, etc and some others were assessed (Malyszko *et al.*, 2020a). However, no data are available on their application in cancer patients. Serum uric acid might reflect a convenient and simple measure of kidney function. Recently, fasting urine osmolality has been proposed as a simple measure of tubular function (Malyszko *et al.*, 2020a). In the setting of known tubular damage, impaired urine concentration ability precedes a decline in GFR. Thus, fasting urine osmolality determination may be a simple and inexpensive tool to assess renal function and could be done at the bedside.

As kidney function assessment and the problem of the narrow therapeutic range of anticancer drugs is critical, we should look for the appropriate methods used to assess renal function to avoid either underdosing or overdosing leading to failure/relapse or toxicity, respectively, both resulting in worse outcomes (Sprangers *et al.*, 2021).

Acute kidney injury in patients with cancer

Acute kidney injury is diagnosed frequently in patients with cancer (Porta *et al.*, 2020). The incidence of AKI differs from 12 to more than 20% of these patients. It is significantly higher in patients with multiple myeloma (up to 50%) and those who were treated with cisplatin (20-30%) or were admitted to the Intensive Care Unit (more than 50%) (Salahudeen *et al.*, 2013). Up to 70% of all AKI develop during the first week after admission to the cancer centre. Many patient-specific (age, comorbidity especially diabetes mellitus, nephrotoxic chemotherapy, etc.) and cancer-related risk factors (neutropenia, sepsis, haematological cancers, hypercalcemia, tumour lysis syndrome, and many others) may increase the risk of AKI in patients with cancer (Rosner & Perazella, 2019). In the pathogenesis of AKI in patients with cancer several prerenal (extracellular fluid depletion, cardiac failure), intrarenal (glomerular or tubulointerstitial diseases, sepsis, thrombotic microangiopathy) or postrenal (obstructive uropathy) causes may play an important role. Many of these factors are present in patients with multiple myeloma; therefore, the incidence rate of AKI is high in these patients (Malyszko *et al.*, 2020b). Chemotherapy plays a crucial role in the pathogenesis of AKI in cancer patients, which may affect each of the nephron segments (Malyszko *et al.*, 2016). Mortality related to AKI in patients with cancer is high (25-30%) and up to 60% of these patients will develop end-stage kidney disease in the future, requiring renal replacement therapy (Salahudeen *et al.*, 2013). Therefore all prophylactic maneuvers are very essential, including magnesium supplementation and the algorithms for the prevention of AKI after CT with contrast media frequently performed in patients with cancer (Cosmai *et al.*, 2020).

Electrolyte disorders in cancer patients

Electrolyte disorders are very common conditions in cancer patients, and may significantly worsen the treatment outcome. Malignancy-specific electrolyte disorders can lead to life-threatening complications, particularly in patients with AKI. Hyponatremia, hypokalemia, hypomagnesemia, hypercalcemia and hyperphosphatemia can be disturbances directly related to the tumour or its treatment.

The Chinese population study revealed electrolytes and acid-base balance disturbances in 58% of 25,800 cancer patients (Li *et al.*, 2020). This proportion is significantly higher than in other reported patient populations,

such as elderly people (22%) or patients admitted to the emergency units (14%).

Hyponatremia

Hyponatremia is the most common electrolyte disorder in patients with cancer. The prevalence of hyponatremia ranges from approximately 4% to as high as 44% (Berardi *et al.*, 2019). The most common disturbance directly related to malignancy is the inappropriate secretion of antidiuretic hormone (SIADH) from cancer cells (paraneoplastic syndrome). It is most commonly seen in small-cell lung cancer (SCLC) and head/neck cancer because as many as 10% to 15% of patients are hyponatremic from the beginning of the disease. Additionally, up to 70% of patients have significant elevations of plasma arginine vasopressin (AVP) (Rosner & Dalkin, 2014). The drugs most often associated with SIADH are cyclophosphamide, cisplatin, vinblastine, and vincristine (Verzicco *et al.*, 2020). For many patients with malignancy-related SIADH, the hyponatremia can be refractory to therapy. Another possible mechanism of hyponatremia in SCLC is the nonphysiological release of atrial natriuretic peptide (ANP) (Berardi *et al.*, 2019). Cisplatin can cause not only SIADH but also salt-losing nephropathy.

Hypokalemia

Hypokalemia is the second most common electrolyte disorder, with a prevalence of around 15% (Li *et al.*, 2020). The reasons for hypokalemia can be related to cancer and/or the used treatment. Cancer-specific causes include tumours that secrete ectopic adrenocorticotropin hormone (ACTH) such as SCLC, carcinoids, neuroendocrine tumours, or thyroid medullary carcinoma. These tumours cause the typical symptoms of hypercortisolemia and stimulate renal potassium wasting by activating the mineralocorticoid pathway. Another cancer-specific etiology for hypokalemia is possible in M4 and M5 subtypes of acute myeloid leukaemia (AML) (Milionis *et al.*, 1999). These malignancies increase serum lysozyme and lysozymuria, which leads to tubular injury (Mason *et al.*, 1975). Hypokalemia in these patients usually occurs together with other electrolyte and acid-base disorders (hyponatremia, hypokalemia, hypophosphatemia, hypomagnesemia and metabolic acidosis).

Chemotherapeutic agents (such as cisplatin, and ifosfamide) may induce serum potassium derangements mainly by changing renal tubular transport. Platinum-derived agents can also induce hypokalemia due to renal potassium wasting secondary to hypomagnesemia. In this case, potassium supplementation may fail until hypomagnesemia has been corrected. The incidence of cisplatin-related hypokalemia is around 27%. The treatment for hypokalemia often prevents the continuation of anticancer therapy with cisplatin, ifosfamide or/and cyclophosphamide.

Calcium and phosphate disturbances

The most common and relevant mineral disturbances in malignancies include hypercalcemia and hyperphosphatemia in the tumour lysis syndrome, and calcium and phosphate disturbances associated with the use of anticancer drugs and tumor-induced osteomalacia.

The tumour lysis syndrome is a consequence of the massive and acute lysis of the cancer cells caused either by chemotherapy or, rarely, due to their spontaneous rupture (Belay *et al.*, 2017). The lysis of the cancer cells leads to the release of large amounts of ions, including potassium and phosphate, that rapidly proliferating neo-

plastic cells are rich in. Tumour lysis syndrome is mainly diagnosed in hematologic malignancies and is uncommon in solid tumours. The release of phosphate leads to secondary hypocalcemia that may cause muscle cramps and seizures. The most important measures in managing patients with a high risk of tumour lysis syndrome include intensive hydration and monitoring of the serum levels of phosphate and calcium. Only the patients with the highest risk are administered allopurinol for prophylaxis and recombinant enzyme rasburicase for the treatment (Belay *et al.*, 2017).

Many drugs used for chemotherapy may cause mineral disturbances. The pathomechanism of these disturbances may vary from the tumour cell lysis, acute tubular necrosis with a secondary tubulopathy resulting in an impaired urine electrolyte excretion, a direct interference of the drug with the tubular transport of water and electrolytes, to thrombotic microangiopathy and thrombosis (Verzicco *et al.*, 2020).

The drugs that frequently cause mineral disturbances include cisplatin and carboplatin (hypocalcemia, hypophosphatemia and hypomagnesemia), ifosfamide and bendamustine (hypophosphatemia), sorafenib, nilotinib and erlotinib (hypocalcemia), cetuximab, panitumumab and 5-fluorouracil (hypocalcemia), and anthracyclines (hypophosphatemia) (Verzicco *et al.*, 2020).

The new promising class of antineoplastic drugs includes blockers of the fibroblast growth factor-23 receptor (FGFR). These drugs directly interfere with the mechanism of renal phosphate disposal and therefore hyperphosphatemia has been a major concern in clinical trials (Mahipal *et al.*, 2020).

Tumour-induced osteomalacia is a rare paraneoplastic syndrome caused by increased production of the fibroblast growth factor-23 by tumour cells (Florenzano *et al.*, 2021). It is mainly caused by slow-growing benign mesenchymal tumours and may manifest with muscle weakness, bone pain and bone fractures. The treatment of the condition includes the surgical removal of the tumour, phosphate and vitamin D supplementation.

Other consequences of oncological therapy

Hypertension

Several classes of antineoplastic drugs have hypertensinogenic properties (angiogenesis inhibitors, 17 α -hydroxylase CYP17 inhibitor - abiraterone, aromatase inhibitors – anastrozole and letrozole and cisplatin derivatives) (Essa *et al.*, 2020). New onset hypertension or aggravation of pre-existing hypertension is predominantly found in patients treated with angiogenesis inhibitors like vascular endothelial growth factor (VEGF) inhibitors and tyrosine kinase inhibitors (Katsi *et al.*, 2019). Angiogenesis inhibitors exert their effect through inhibition of the VEGF signalling pathway. Inhibition of this pathway suppresses nitric oxide synthesis, leading to endothelial dysfunction and capillary rarefaction. VEGF signalling inhibitor-induced blood pressure increase appears to be mechanism-dependent on-target toxicity and has been suggested to be a positive biomarker of the clinical efficacy of these drugs. Results of several retrospective studies demonstrated that hypertension caused by angiogenesis inhibitors was associated with improved results of antineoplastic therapy (Liu *et al.*, 2019).

In the absence of controlled trials, hypertension in oncology patients should be managed by utilising the same treatment guidelines as for the general population (Tini *et al.*, 2019). The only specific recommendation is that

non-dihydropyridine calcium channel blockers, such as verapamil and diltiazem, should be avoided by patients treated with angiogenesis inhibitors. These antihypertensive drugs inhibit cytochrome P450 3A4, leading to the potentially high, toxic plasma concentration of angiogenesis inhibitors (Rizzoni *et al.*, 2017). It should be stressed that, in clinical practice, new onset hypertension or aggravation of pre-existing hypertension due to antineoplastic therapy, should be treated preferably by initiation or intensification of antihypertensive therapy, but not by reduction of dose or by ceasing therapy with antineoplastic agents.

Urinary tract infections

Urinary tract infections (UTIs) represent a severe complication in immunocompromised-neoplastic patients. Predisposing factors include urinary tract obstruction, catheterisation (i.e. with Foley catheter most often), percutaneous nephrostomy (PCN), hemorrhagic cystitis (after chemo- or radiotherapy), neutropenia, bone marrow transplantation, neoplasms (especially of the urinary tract) after transplantation, history of recurrent UTIs and/or kidney stones with prolonged antibiotics treatment, and autosomal dominant polycystic kidney disease (ADPKD). Enterococcus species are the leading cause of UTIs, especially in hospitalized patients, regardless of a cancer diagnosis. Despite the fact that their clinical manifestation is often mild, they can cause serious complications such as bacteraemia or endocarditis. Limited therapeutic options for UTIs due to the emergence of multidrug-resistant enterococci, particularly vancomycin-resistant *E. faecium* and *E. faecalis*, have become a global crisis over the last few years. It became a cause of higher patient mortality as well as increased worldwide healthcare costs (Giannakopoulos *et al.*, 2019). Currently, there is an overall lack of consensus about the optimal approach to catheter-associated urinary tract infections (CAUTIs). One of the strategies is an evidence-based, nurse-driven protocol for discontinuing indwelling urinary catheters (McCoy *et al.*, 2017). To reduce the high rate of recurrent infections and the potential delay of further chemotherapy, when the result of the antimicrobial susceptibility test is available and the patient is under compatible antimicrobial therapy, clinicians should proceed with an immediate Foley catheter or PCN replacement (PCN ideally within the first 4 days of the infection) (Szvalb *et al.*, 2019).

On the other hand, the link between recurrent UTIs and cancer development has been studied for many years, but the results are inconclusive so far. Several of them reported an association between chronic UTIs and prostate or bladder cancer (Giannakopoulos *et al.*; Anderson-Otunu & Akhtar, 2016). There are some prerogatives that ADPKD, besides ascending UTIs, cyst infections and haemorrhage, predispose to renal cell carcinoma, mainly in chronic dialysis patients.

Chronic kidney disease

According to registries and population studies, as many as 16–25% of cancer patients present with $\text{eGFR} < 60 \text{ mL/min}$ (de Francisco *et al.*, 2019). Considering that every fifth cancer patient developed CKD, the mutual relationship between malignancy and CKD seems obvious. It was demonstrated that in the Chinese population 32.4% of patients with newly diagnosed cancer exhibited CKD. In addition, renal function was inversely related to all-cause mortality. Moreover, eGFR below $60 \text{ mL/min/1.73m}^2$ was an independent predictor of mor-

tality relative to $\text{eGFR} \geq 60 \text{ mL/min/1.73 m}^2$, and it was dependent upon the cancer site (Yang *et al.*, 2016).

On the one hand, CKD progression and accumulation of uremic toxins cause multiple quantitative and functional changes in the immune system, resulting in reduced malignancy surveillance and aberrant responses to cancer (Corredor *et al.*, 2020). On the other hand, cancer may induce CKD in numerous, largely unknown mechanisms. Circulating factors produced by the tumour cells may be suspected. For example, IL6 and TNF concentrations were reported to be significantly higher in cervical cancer patients than in the controls (Vitkauskaitė *et al.*, 2020). Also, other tumours including lung cancer and renal cell carcinoma were found to produce excess amounts of IL6. Another factor derived from the tumour mass, and able to stimulate autoimmune reactions, is circulating free DNA (cfDNA). After release from cancer cells, the cfDNA circulates and can be detected in serum. Several types of cancer are currently diagnosed using specific cfDNA analysis. The potential of cfDNA to stimulate dendritic cells via toll-like receptor 9 could explain glomerular immune activation, inflammation and damage. Increased incidences of CKD, particularly in the elderly, are of clinical importance and relevance. Many cancer drugs are cleared primarily by the kidneys as unchanged drugs or active metabolites. Therefore, any impairment in kidney function can potentially lead to alterations in pharmacokinetics, elevated blood levels of the drugs, and the increased toxicity discussed in the first parts of the paper (Janus *et al.*, 2010).

THE MOST OFTEN CANCERS IN SOLID ORGAN TRANSPLANT RECIPIENTS

Skin cancers

Skin cancers are the most common tumours in SOTRs. The most often are squamous cell carcinoma (SCC), basal cell carcinoma (BCC), malignant melanoma (MM) and Merkel cell carcinoma (MCC) (Euvrard *et al.*, 2003; Mittal & Colegio, 2017). Common risk factors include: chronic exposure to ultraviolet (UV) radiation, HPV infection, pretransplant skin cancer, older age at transplantation, white race, male sex and immunosuppression (being those with a higher risk azathioprine and cyclosporine) (Al-Adra *et al.*, 2022). The mean interval between transplantation and skin tumour diagnosis is 3 to 5 years (Euvrard *et al.*, 2003). Skin tumours in SOTRs are also more likely to be multiple and more aggressive with a higher risk of relapse, metastasis and death due to tumour progression.

The risk of developing BCC in patients after solid organ transplantation (SOT) is about 10 times higher than in the general population (GP). BCC is the most common skin cancer in the GP, while in SOTRs the SCC/BCC ratio changes in favour of SCC. BCC may develop at the site of precancerous conditions or previously unchanged skin. BCC occurs in younger patients than in the GP and grows more often multifocally and more extensively. The prognosis for early diagnosis and appropriate treatment of BCC is good, and the risk of recurrence is 5–10% (Euvrard *et al.*, 2003).

Squamous-cell carcinoma is the most common skin cancer in SOTRs, occurring 65 to 250 times as frequently as in the GP (Euvrard *et al.*, 2003; Mittal & Colegio, 2017). The majority of cancers arise from precancerous lesions including actinic keratosis, Bowen's disease, and Queyrat erythroplasia. Patients who develop their first

focus SCC have an over 60% risk of developing more SCC in the next 5 years. According to Lindelöf *et al.*, 25% of patients with a first SCC will have a second lesion within 13 months, and 50% will have a second lesion within 3.5 years (Lindelöf *et al.*, 2000). SCC develops in younger patients and has a rapid growth rate. In 50% of cases it develops multifocally, more often presents deep tissue invasion and metastasizes (8–12%) (Liddington *et al.*, 1989; Berg *et al.*, 2002). As in the GP, recipients with a fair skin phototype and high cumulative dose of UV radiation are associated with a higher risk of SCC. The main location of the SCC is the face, backs of the hands, forearms and mucous membranes, mainly the lower lip. Tumours appearing on the skin usually are asymptomatic, but 1/3 of patients experience tenderness, pain or itching. These symptoms constitute an unfavourable prognostic factor that may indicate a perineural invasion. The risk of metastases in the course of SCC in GP is 3.6% within 3 years, whereas for immunocompromised such as SOTRs the risk reaches 7%–12%. In SOTRs SCC may cause distant metastases. Patients who suffer from metastatic SCC have a bad prognosis (3-year survival is 56%, and 5-year survival is 34%) (Haug *et al.*, 2020; Imko-Walczuk *et al.*, 2015). SOTRs have a 2 to 8-fold increased risk of developing MM in the post-transplant period (Mittal & Colegio, 2017). Melanoma in SOTRs can arise in three principal scenarios; an existing MM prior to transplantation, an MM arising *de novo* after transplantation and MM derived from an organ donor (Imko-Walczuk *et al.*, 2009; Matin *et al.*, 2008). Melanoma results from the malignant transformation of melanocytes, representing the skin tumour with the highest mortality rate. This tumour has high immunogenicity and changes its behaviour in the field of immunosuppression. The incidence of MM in SOTRs is increased to a smaller degree as compared to SCC and BCC, although its potential morbidity and mortality have to be considered in post-transplant care. In candidates for SOT with MM in medical history, such factors as: tumour stage, disease control, and the period from diagnosis to transplantation are the most relevant factors to consider. In a study conducted by Penn and others the risk of MM recurrence in SOTRs was 19% which was similar to the GP subjects, whereas mortality was 30% (50% higher than in the GP) (Penn, 1996). Waiting time for transplantation depends on the MM stage and is as follows: MM *in situ* has 100% survival therefore no waiting time is required (Imko-Walczuk *et al.*, 2015); MM of <1 mm depth and without surface ulceration (stage I) have a good prognosis (85% 5-year survival), however, due to a risk of metastasis, the waiting time should be two years; MM with a 4-mm-depth, has a high potential of metastasis, and bad prognosis (5-year survival is 45–67%), it is, therefore, necessary to postpone SOT for 5 to 10 years (Penn, 1996; Imko-Walczuk *et al.*, 2015).

The risk of MM transmission from the donor through circulating cells localized in the graft is very high. To prevent this transmission, the donor's medical history and physical examination are essential, and the history of MM in a donor candidate is an absolute exclusion criterion for donating organs (Penn, 1996). Initial treatment of melanoma appearing in the posttransplant period does not differ from the standard approach in the GP. In addition to that, reduction or change of immunosuppression is suggested to be a reasonable and effective adjuvant strategy. A balance must be struck between a strength of immunosuppression that does not favour tumour spread and that, at the same time, avoids rejection of the transplanted organ. Therapeutic management

is particularly challenging in advanced MM stages as the use of immune checkpoint inhibitors confers a high risk of organ rejection.

Merkel cell carcinoma (MCC) is a rare neuroendocrine neoplasm that typically appears in the elderly in sun-exposed areas. SOTRs have a 24-fold higher risk of MCC. This tumour presents at a younger age than in immunocompetent individuals (the mean age at diagnosis is 50 years) (Goedert, 2009). Most cases result from malignant transformation secondary to the Merkel cell polyomavirus infection, which may be relevant in SOTRs. It was confirmed that immunosuppression is an established risk factor for MCC (Hernandez *et al.*, 2022; Penn & First, 1999). Just as with other skin cancer, the highest incidence of MCC was observed in patients receiving a combined regimen of azathioprine and cyclosporine (Hernandez *et al.*, 2022). The key role of immunosuppressants on MCC development is also confirmed by the fact of temporary regression of the tumour upon reduction or withdrawal of the immunosuppressive treatment. MCC typically presents as a painless, rapidly expanding cutaneous nodule or plaque. Lesions are often erythematous or violaceous with a smooth and shiny appearance and generally arise on sun-exposed areas, notably the head and neck, and limbs (Euvrard *et al.*, 2003; Kanitakis Jean, 2009). SOTRs with MCC should be treated with similar modalities as patients without immunosuppression i.e. wide local excision, radical node dissection, radiation therapy, and chemotherapy. The prognosis is serious because 31% of patients develop tumour recurrence with a mean interval of 58 months after excision of the primary foci. Two-thirds of SOTRs MCC develop rapid lymphatic metastases to the regional lymph nodes and systemic metastases to the liver, bones, and lung with a high 1-, 3-, and 5-year mortality rate (20%, 51%, and 54%, respectively) (Greenberg & Zwald, 2011; Goedert, 2009; Lewis *et al.*, 2020).

In summary, it should be underlined that the risk of all skin cancers in SOTRs is much higher than in the GP. They appear at a younger age, the clinical course is much more serious, and they are more likely to relapse, metastasize and appear *de novo* in another location. Survival of patients is worse than in the GP.

Urinary tract cancers

The second most common cancers in SOTRs particularly in kidney transplant recipients are urinary tract cancers (Bellini *et al.*, 2022). They are common, and as these neoplasms occur more often in older age, their detection is growing with time, with the number of recipients followed-up (Karami *et al.*, 2016).

Renal cell carcinoma

The most frequent urological neoplasm encountered after kidney transplantation is renal cell carcinoma (RCC). It may appear in the native kidneys or the transplanted ones. It may arise *de novo* or be transmitted with the kidney graft and also recur after treatment of the recipient in the past (Porta *et al.*, 2020; Serkies *et al.*, 2022). The literature shows that the risk of RCC in the native kidneys of dialyzed patients due to end-stage kidney disease (ESKD) is increased by 10–15 times. The incidence grows with the dialysis time along with the development of acquired cystic kidney disease (ACKD). Some authors claim that transplantation, by improving kidney function may reduce ACKD and its oncological potential, but this effect is probably decreased by immunosuppression (Yanik *et al.*, 2016). Interestingly, the

longer the dialysis lasts the percentage of a less aggressive papillary RCC in relation to clear cell RCC grows. Nowadays, diseased kidneys are most often left in place after their failure, so the risk of RCC in them has to be addressed and they should be observed by at least an annual ultrasound (Dahle *et al.*, 2022). Nevertheless, the risk of cancer and mortality rate in patients with functioning kidneys or already on dialysis are similar. They are also better compared to the general population as RCC in ESKD tends to present lower malignant potential. It has been generally accepted that in the case of RCC in the native diseased kidneys total nephrectomy is the most appropriate strategy (Yanik *et al.*, 2016).

Noteworthy, nowadays according to Kidney Disease Improving Global Outcomes (KDIGO) in 2020, after radical removal of small <3 cm low-grade T1NOMO RCC the patient can be qualified for the KTx with no waiting period (Karami *et al.*, 2016).

Another issue is de novo cancers in the transplanted kidney. Overall, the risk of it stays within 0.2–0.7% with the observation of 5 years (Hevia *et al.*, 2019). It may be caused by a tumour transmission with unintentional kidney transplantation with an undetected small or even microscopic RCC or by the origination of the tumour in the kidney afterwards (Boissier *et al.*, 2018). It is difficult to distinguish these two scenarios with the time between KTx and diagnosis being the most logical parameter. Its incidence is lower with living donors, who are generally healthy, their kidneys are better examined, and the history of the donor and his family may be well-known, especially as we now are aware of a possible inherited RCC in 5–8%. The transmission may be higher if the donors are older than 50, which is currently accepted more freely because the RCC develop more frequently in older age (Boissier *et al.*, 2018). As far as the treatment of RCC in the graft is concerned, the European Urological Association recommends its surgical removal with the increasing role of the nephron-sparing approach as an alternative to graftectomy, which was the gold standard in the past. Tumours are usually discovered in the early stage without symptoms. The disease staging may be tricky due to the changed tissue layers after implantation (Rodríguez Faba *et al.*, 2018; Tillou *et al.*, 2012).

Nowadays, data shows that total nephrectomy should be restricted to high-grade, high-stage tumours or tumours in the irreversible dysfunctional kidney. It is also known that these high-risk RCCs have a poor prognosis, so many authors recommend biopsy before treatment method selection. Nephron-sparing procedures should be preferred if possible because they give a chance of up to 95% of 5 years survival time in T₁N₀M₀. On the other hand, graftectomy with a return to dialysis results in only 34% of 5-year survival, although the patient groups studied usually are different (Boissier *et al.*, 2018).

The nephron-sparing surgery which is limited to the tumour less than 4 cm may be challenging with more complications in about 20% of cases. The open approach is usually used, but recently robot-assisted laparoscopy has also been reported. In some series, a minimally invasive approach using Radio Frequency Ablation or Cryoablation is also described as promising in very small exophytic tumors (Dhakal *et al.*, 2017). The surgery should be used together with a modification of the immunosuppression regimen. In this case, the use of mammalian target of rapamycin (mTOR) inhibitors seems to be the most interesting drug, because of their anti-neoplastic properties (Boissier *et al.*, 2018).

There are interesting considerations about the origin of cancer occurring in the allograft kidney. We used to

assume that it arises from the donor cell. Still, some reports suggest that a significant percentage (up to 40 %) may be of recipient origin proved by DNA analysis, with some having mixed DNA being a form of chimerism. Whether it has any clinical importance for example on the choice of immunosuppression, is not known yet (Dhakal *et al.*, 2017).

Having in mind that there is a global lack of kidney donors, there has appeared to be a little controversial concept of using kidneys removed for small, low-risk RCC as a possible so-called “restored” donor of kidneys. The tumour is biopsied and removed outside the body, then prepared and implanted. The published result shows more than 90% of 5-years graft survival and a low cancer recurrence rate of about 2% (Xiao *et al.*, 2013)

Prostate cancer

Generally, the significance of prostate cancer (PC) has been growing as the population of kidney recipients gets more extensive and older. The data about the increased incidence of PC after KTx are unclear, though recent studies suggest that it is higher. However, one has also to remember that any data about this group of patients must consider the estimated life expectancy independent of malignant disease before making any therapeutic decision (Sherer *et al.*, 2017).

Especially interesting is an issue of low-risk PC, which occurs very often and often is managed by active surveillance meaning repeated exams (DRE, PSA, MRI) and biopsies and postponing of the intervention until the proven progression. In the GP it leads to sparing of the treatment in a significant part of patients. Recent studies have shown that active surveillance can be possible also in KTx candidates, where we must assume that undetected small focuses of PC already exist. The same strategy is acceptable in patients on dialysis. The survival in both groups should not differ from the GP (Stöckle *et al.*, 2018).

The situation changes if a medium-risk or a high-risk PC is diagnosed. Then active treatment ought to be implemented with radical prostatectomy being the most popular solution, as it leads to the elimination of the cancer cells, with PSA becoming a perfect cancer marker to follow-up. In KTx candidates, the 2-year waiting time after renal surgery is recommended (Bratt *et al.*, 2020a; Bratt *et al.*, 2020b).

A urologist must regard anatomical relations between the graft and the prostate when the clinically significant PC is discovered after KT. The diagnosis usually is early because the patients are closely controlled. The staging is similar to that of the GP. Surgery can be challenging and this side's lymphadenectomy has very often been skipped. Nonetheless, the results are promising with a 14-years survival time reaching 65% (Carvalho *et al.*, 2017). Modern series recommend using the robot-assisted technique for this situation with a result similar to GP.

Radiation therapy is also a feasible option with some limitations in planning to avoid ureteral stricture or post-radiation nephritis. However, there are a few papers recommending brachytherapy as the better solution (Bratt *et al.*, 2020a).

Bladder cancer

The incidence of bladder cancer (BC) in KTx is reported to be 2–4 times higher than in the GP with the age of presentation being lower and the malignant po-

tential much higher. The non-urothelial histology is also found more often. The upper urinary tract of native kidneys is also involved more frequently. Some authors suggest the BK or HPV viral infection is responsible (Leon *et al.*, 2020). The diagnosis is usually made after hematuria. The median time after KT is 4 to 5 years. The more aggressive course of the disease caused the waiting time for kidney candidates to be usually preserved with the only exception of very low-risk superficial tumours (Chadban *et al.*, 2020). The staging is based on imaging and transurethral resection with microscopic invasion analysis. The role of surgery is crucial. Superficial tumours in the bladder should be endoscopically resected with adjuvant intravesical chemotherapy. The BCG installation is viewed to be possible, but some authors underline a risk that immunosuppression can provoke Mycobacterium sepsis. In the case of upper tract involvement radical nephroureterectomy is recommended. When there is a high-risk bladder tumour most authors favour early cystectomy with some form of urinary diversion. It can be bowel neobladder or uretero-ileocectomy according to Bricker. During surgery, the lymphadenectomy can be difficult as well as anastomosing of the short transplanted ureter to the bowel without kinking. The same problem exists when a kidney is transplanted into the patient with urinary diversion due to a previous cystectomy due to bladder cancer. Then, it can be solved by implanting the kidney upside down. The treatment results of superficial bladder tumours are similar between kidney recipients and the GP with more local recurrences in the former group.

Urothelial cancer in the native kidney upper tract has a worse prognosis than matched ESKD patients, underlining the role of immunosuppression (Chadban *et al.*, 2020). Data about the results of invasive bladder cancer treatment after KTx are limited, but generally high-risk urothelial cancers have a poor prognosis even with an aggressive protocol including early cystectomy and chemotherapy.

Penile Cancer and Testicular Neoplasm

These urological malignancies are so rare that there is no robust data about their association with KTx. Penile cancer occurs in 10 per 1 million a year and testicular neoplasms in 50 per 1mln per year. Both treatments after KTx should not differ from the GP, with the need to modify immunosuppression in more advanced cases. In both, chemotherapy plays an essential role, so the renal function is important. Results of both depend strongly also on lymphadenectomy so it is vital that surgically there may be some difficulties when dealing with the patient after KTx (Besarani & Cranston, 2007).

KIDNEY IN BONE MARROW TRANSPLANTATION

Bone marrow transplantation is a common name for hematopoietic cell transplantation (HCT) in which the most important for hematopoietic system recovery are stem cells present among the CD34+ cell population. The stem cell source might be autologous or allogeneic; determining the type of HCT (autologous or allogeneic; auto-HCT, allo-HCT). These two types of transplantation have different spectra of complications. In fact, the synonym of auto-HCT is high-dose chemotherapy with the support of the hematopoietic cells; therefore, the complications including those related to kidneys are limited to high-dose chemo/radiotherapy administered as a conditioning regimen before cell infusion. In allo-

HCT, in addition to the conditioning regimen that might be myeloablative, reduced, or even non-myeloablative, two other important factors contribute to kidney injury: post-transplant immunosuppression and immune-related complications such as graft versus host disease (GvHD) or transplant-associated thrombotic microangiopathy (TA-TMA). Hence, the greatest risk of acute kidney injury (AKI) carries myeloablative allo-HCT (21–73%), followed by nonmyeloablative allo-HCT (29–56%), and then autologous HCT (10.4–19%) (Miyata *et al.*, 2022).

Chronic kidney disease is a risk factor for transplant-related complications. In the HCT-specific comorbidity index (HCT-CI) the presence either of serum creatinine concentration above 2 mg/dL (177 μ mol/L), being on dialysis or prior renal transplant increases 1-year non-relapse mortality (NRM) to 21% in allo-HCT and 3% in auto-HCT recipients, respectively. Chronic kidney disease present after HCT also indicates poor survival both after auto-HCT and allo-HCT. A recently published study on a large cohort of allo-HCT recipients showed the impact of different degrees of renal dysfunction on HCT outcomes using growing grades of renal dysfunction based on estimated glomerular filtration rate (eGFR) (<45; 45–59; 60–90; and >90 mL/min); Increased risk for NRM and the requirement for dialysis post-HCT were associated with an eGFR <60 mL/min (Gutiérrez-García *et al.*, 2020; Farhadfar *et al.*, 2021).

Kidney injury related to high-dose chemotherapy

Kidney injury after high-dose chemotherapy might be due to the direct effect of cytotoxic agents or indirect complications caused by cytotoxic agents such as mucositis and diarrhoea, infections or veno-occlusive disease. The most common cytotoxic agents used as a part of the conditioning regimen before auto- and allo-HCT are alkylating agents such as melphalan, cyclophosphamide, busulfan, carmustine, bendamustine; antimetabolites: fludarabine, and much less common cladribine and clofarabine and most recently bcl-2 inhibitors such as venetoclax. Most of the aforementioned agents do not induce nephrotoxicity directly despite some of them (e.g. busulfan, cyclophosphamide) being used in much higher doses compared to standard chemotherapy regimens. A few exceptions include bendamustine (used in the BeEAM protocol: bendamustine, etoposide, cytarabine, melphalan) that have been reported in three cases to induce nephrogenic diabetes insipidus (Desjardins *et al.*, 2022).

High-dose chemotherapy adjustment in patients with chronic kidney disease

HCT recipients suffering from CKD have a substantial risk of unintended overdosing or underdosing due to variable pharmacokinetics in this patient population. Overdosing may lead to multiorgan toxicity and/or graft failure whereas underdosing may result in graft rejection or inadequate disease control (Bodge *et al.*, 2014). Therefore, the dose adjustment of some agents used in the conditioning regimens in patients with CKD is recommended to avoid excessive toxicity, particularly to hematopoietic cells usually infused 24 hours after the end of the conditioning regimen.

The best example is melphalan commonly used as a single agent dosed on body surface area (BSA) at day-1 (200 mg/m²) of the conditioning regimen before auto-HCT for patients with multiple myeloma (MM). Patients with CKD and eGFR <50 mL/min/1.73 m² or older than 70 years with additional co-morbidities or frailty

Table 2. The different auto-HCT protocols applied in patients with: a) normal renal function, b) impaired renal function and c) patients on haemodialysis.

Autologous High-Dose Melphalan (HDM) transplant protocol			
Day	Normal Renal Function	Impaired Renal Function	Haemodialysis
-5			Admission
-4			Dialysis
-3		Admission	Melphalan 140 or 100 mg/m ² ^a
-2	Admission	*Melphalan 140 or 100 mg/m ²	Rest day: dialysis
-1	Melphalan 200 mg/m ²	Rest day	Rest day
0 ^b	Cell return 24 hrs after Melphalan infusion	Cell return 48 hrs after Melphalan infusion	Cell return 72 hrs after Melphalan infusion
			Return units and dialysis Ensure 2 hrs gap if dialysis post-re-infusion ^c
+5	GCSF	GCSF	GCSF

Abbreviations: GCSF granulocyte colony-stimulating factor. ^aPatients on dialysis require a 72-hour (hr) gap after the Melphalan infusion and prior to stem cell infusion, whereas patients with renal impairment require a 48 hr gap. ^bThe Melphalan dose can be further reduced to 100 mg/m², depending on the presence of co-existent comorbidities. ^c For patients on hemodialysis, a repeat dialysis session is scheduled after the return of the fourth stem cell unit, with a 2hr gap between the stem cell infusion and the dialysis.

usually receive a lower dose of melphalan of 100 or 140 mg/m². Recently, CKD was reported as an independent risk factor for AKI after HCT for MM, with a significantly higher mortality rate in this subgroup of patients (Andronesi *et al.*, 2019). Surprisingly some centers do not reduce melphalan dose in patients with moderate CKD since despite higher toxicity improved outcomes were reported in patients with moderate CKD receiving melphalan at a high dose of 200 mg/m² (Sweiss *et al.*, 2016). Of note, melphalan is not removed by dialysis (Bodge *et al.*, 2014).

However, recently published data on 370 MM patients who underwent the first auto-HCT without CKD or with mild, moderate, and severe CKD showed no significant difference in NRM, progression-free (PFS), or overall survival (OS) regardless of renal function. The results of this study indicate that auto-HCT is an effective and rather safe option for MM patients with CKD, including those on dialysis, allowing some of them to permanently discontinue dialysis. Specific protocols applied in this population are presented in **Table 2**.

The second most common agent used agent for HCT and the most common for allo-HCT is fludarabine (Flu). The dose of Flu is calculated using BSA. The drug is administered IV as a monophosphate prodrug (F-ara-AMP) that is converted to the circulating metabolite F-ara-A, which is mainly excreted by the kidney. Recently published data indicated a substantial variability (more than sixfold) in F-ara-A plasma exposure using standard BSA-based dosing. Extended but still retrospective analysis in 192 allo-HCT recipients showed that Flu exposure is a strong predictor of event-free survival (EFS) (events: relapse, NRM, and graft failure) with two-fold higher HR for EFS in overexposed patients. This translates to the lowest overall mortality in the optimally exposed group (31%), compared to the under- (43%) and overexposed groups (64%). This increase in overall mortality was mainly caused by infections (over- and underexposure), multiorgan failure (overexposure), and GVHD (overexposure). Of note, overall GVHD (grade 2–4 or 3–4) incidence was similar among groups with different exposures (Langenhorst *et al.*, 2019). The data presented above suggest that the current dosing method based on BSA is not optimal and should include not only weight but also kidney function based on eGFR using the

Cockcroft–Gault equation. Flu is adequately removed during dialysis, therefore, the dose should be adjusted after dialysis (van Besien *et al.*, 2012; Shadman *et al.*, 2017). Cyclophosphamide may increase myocardial toxicity in CKD patients. Pharmacokinetic studies have demonstrated decreased clearance with renal insufficiency, therefore dosage reduction in the setting of moderate to severe renal impairment should be considered. Cyclophosphamide is moderately dialyzable (20–50%); for dialysis-dependent patients, cyclophosphamide should be administered after hemodialysis (Bodge *et al.*, 2014). The cyclophosphamide doses should be reduced by 25–50% in patients with severe renal impairment (GFR <10 mL/min) and a supplemental dose after dialysis should be considered (Shadman *et al.*, 2017). Clofarabine should be avoided in adults >60 years with creatinine clearance <60 mL/min (NCCN AML guidelines), and a 50% dosage adjustment should be made for patients with eGFR 30 to 60 mL/min. Busulfan and thiopeta dosing does not require modification in patients with CKD (Bodge *et al.*, 2014).

Kidney injury in recipients of allogeneic HCT

Acute kidney injury is a common and important complication after allo-HCT since it increases the risk of both early and late NRM (Malyszko *et al.*, 2020a). The recently published meta-analysis based on reports from 1995–2019 indicates AKI occurrence in about half (55.1%) of allo-HCT recipients, with the most severe form (stage 3) in 8.3% of patients (Kanduri *et al.*, 2020). AKI leading to CKD increases mortality about three times at 1-year post-allo-HCT (HR: 3.54; *p*<0.001). In most allo-HCT recipients the development of AKI is multifactorial. Conditioning with total body irradiation (TBI) and using calcineurin inhibitors for GVHD prevention contribute to the risk of AKI development with a little lower likelihood of AKI induced by tacrolimus relative to cyclosporine (Malyszko *et al.*, 2020b). Other patient-related factors contributing to the risk of AKI after HCT include female sex, older age (>55 years), and comorbidities such as diabetes, hypertension, and pre-transplant CKD that are also associated with early mortality (Miyata *et al.*, 2022; Gutiérrez-García *et al.*, 2020). Additionally, other transplant-related complications such as veno-occlusive disease, also known as sinusoidal ob-

struction syndrome, cytomegalovirus reactivation, and bacterial infections (sepsis) increase the risk of AKI (Gutiérrez-García *et al.*, 2020). Finally, in allo-HCT recipients, acute GVHD and TA-TMA often induced by calcineurin inhibitors, especially tacrolimus, make the aetiology of AKI multifactorial and sometimes difficult to determine the leading cause. All attempts should be therefore made to decrease the risk of AKI development including a proper choice of conditioning regimen (myeloablative *versus* reduced intensity or non-myeloablative) regular blood levels measurement of calcineurin inhibitors and other nephrotoxic agents (such as vancomycin, and amikacin), proper hydration, careful dose adjustment for drug interactions – for example, reduction of 90% dose of calcineurin inhibitors in the case of concomitant anti-fungal treatment with voriconazole. Cases with hypertension, refractoriness to platelet transfusions, and increased lactate dehydrogenase activity should prompt suspicion of TA-TMA and a fast decision regarding the continuation of calcineurin inhibitors.

Hemodialyzed patient as a bone marrow transplant recipient

Almost all patients on dialysis are referred for HCT because of MM. Indeed, dialysis-dependent patients with MM should not be excluded from high-dose melphalan and auto-HCT since some of them may even recover renal function on top of other benefits related to auto-HCT. The shorter the hemodialysis period prior to transplantation, the higher the probability of renal function recovery in patients with MM. Improvement of kidney function following auto-HCT can also be observed later after transplants in patients with severe kidney failure. However, only a few cases have been reported so far who became dialysis-independent after a high-dose melphalan autograft (Waszczuk-Gajda *et al.*, 2018). Recent data suggest that auto-HCT can be performed safely in MM patients on dialysis using a specific adjustment to the routine protocol (Table 2). Prior experience including the experience of the Polish centers (24 cases) indicates higher toxicity in hemodialyzed patients compared to non-dialysis matched cases in the following endpoints: mucositis (88% *vs* 55%), infection (79% *vs* 51%), parenteral nutrition (50% *vs* 24%), diarrhea (71% *vs* 38%), prolonged duration of hospitalization (medians: 30 *vs* 21 days), the requirement for red blood cell transfusion (83% *vs* 36%) while no significant differences were found in post-transplant response (ORR; 75% *vs* 87%), 5-year PFS (36% *vs* 20%) and OS (39% *vs* 50%) (Waszczuk-Gajda *et al.*, 2018).

Research conducted by Chapchap and others indicates that HD was associated with decreased survival in allo-HSCT (Chapchap *et al.*, 2022). The HD group (34 HD cases versus 151 controls) had a higher mortality rate (HR:6.68; 95% CI: 4.1–10.9; $p < 0.001$). At the Fred Hutchinson Cancer Research Center between 1997 and 2014, only six patients on hemodialysis received allo-HCT. Recently reported the largest group of patients on dialysis at the time of alloHCT (46 patients) had a 1-year probability of OS of 20%, and NRM of 67% (Farhadfar *et al.*, 2021).

The data on patients after kidney transplantation is very limited, and in most institutions, these patients are not referred for allogeneic HCT. Even in very big transplant centres, these patients are exceptional.

CKD in patients after HCT

In most auto-HCT recipients CKD after HCT results from precedent CKD before transplant. A minor-

ity experience *de novo* CKD related to sepsis or drug toxicity. The need for hemodialysis after HCT increases late NRM. In allo-HCT recipients, renal dysfunction is a common complication. The cumulative incidence of CKD after allo-HCT varies from 13–60% in adult studies to as high as 62% in children (Chen *et al.*). Causes of CKD are multifactorial and usually overlapping. The result of an interesting paper in which 24 allo-HCT recipients underwent kidney biopsy for either proteinuria or deterioration of kidney function confirms the great diversity of putative causes of kidney damage. The most common pathological findings were GVHD ($n=8$), membranous nephropathy (MN, $n=5$), TA-TMA, ($n=4$), BK virus nephropathy ($n=2$), and single cases with ischemic nephropathy, chronic interstitial nephritis, minimal change disease (MCD), GVHD with TMA, MN with focal segmental glomerular sclerosis (FSGS), MCD with acute tubular injury, BK virus nephropathy combined with calcineurin inhibitor nephrotoxicity (Chen *et al.*, 2019). Clearly, a kidney biopsy with an expert histopathology examination might be necessary to establish the proper cause of kidney injury after allo-HCT.

NOVEL CANCER THERAPY

The use of cancer immunotherapy and proton therapy in transplant recipients (IK)

The standard of care in different cancers includes surgery, chemo- and radiotherapy. In recent years, novel therapy, including immunotherapy with immune checkpoint inhibitors (ICIs) and proton therapy, has revolutionized cancer treatment and is becoming a new standard of care for many tumour types.

ICIs in transplant patients

Mechanism of ICIs action

Cancers can weaken the immune system, and the host's immune system does not destroy cancer cells. The so-called negative regulatory components participate in this phenomenon (Szychowska, 2021). ICIs are monoclonal antibodies capable of blocking negative signals for T-cell activation or T-cell effector activity and represent an essential therapeutic option in the case of many tumours, including melanoma, non-small cell lung cancer, kidney cancer, urothelial cells cancer, Hodgkin's lymphoma, oral, throat or larynx squamous cell carcinoma etc. It seems that about 44% of newly diagnosed cancer can be qualified for ICIs (Haslam & Prasad, 2019).

The anti-CTLA4 (cytotoxic T-lymphocyte-associated protein 4) monoclonal antibody (e.g., ipilimumab or tremelimumab) binds to the CTLA4 receptor and activates a T cell (Perazella & Shirali, 2020). AntiPD-1 (nivolumab, pembrolizumab, cemiplimab) and antiPD-L1 (atezolizumab, avelumab, durvalumab) antibodies act through the activation of programmed cell death-1 (PD-1) receptors on the T cell with its ligand PD-L1 or PD-L2 (Perazella & Shirali, 2018; Perazella & Shirali, 2020).

Considering the mechanism of action of ICIs which is based on the stimulation of the immune system, their use in transplant patients may raise doubts. These drugs have the effect opposite to what is anticipated in the organs of recipients as they stimulate the immune system and, therefore, may facilitate the occurrence of acute or chronic rejection. In the group of 119 KTx recipients to whom ICIs were administered due to other tu-

mours: cutaneous melanoma, hepatocellular carcinoma and cutaneous squamous cell carcinoma, 41.2% patients experienced acute rejection, 23.5% graft failure and immune-related adverse events (irAEs) developed in 18.5%. The overall objective response rate was 34.5%, with a median duration of response of 8.0 months (Portuguese *et al.*, 2022). The symptoms of acute rejection, which is the most frequent cellular rejection, were observed on average around three weeks after ICIs administration (Portuguese *et al.*, 2022; Manohar *et al.*, 2020). Moreover, the activation of T-lymphocytes may cause adverse effects resulting from excessive immune system stimulation (immune-related adverse events, irAEs). They may affect different organs and tissues: skin, lungs, heart, digestive system, liver, endocrine glands, central and peripheral nervous system and also the kidney (Perazella & Shirali, 2020). The kidney-related adverse effect that occurs most often, is deterioration of kidney function, and another one is proteinuria, usually non-nephrotic. Pyuria and haematuria are also quite frequent (Szychowska, 2021). The distinction between irAEs and rejection may be difficult in kidney recipients due to the fact that the symptoms may be similar. The treatment of irAEs depends on symptom severity and includes drug discontinuation and steroid administration (Sise *et al.*, 2019; Brahmer *et al.*, 2018).

One problem is the implementation of treatment with ICIs to the SOTRs with tumours, but another is the lack of recommendations for immunosuppression management. There are challenges concerning the continuation of immunosuppressive treatment or its minimization. The most frequently described alteration to the immunosuppression plan is the discontinuation of calcineurin inhibitors (CNI) or conversion to mTOR inhibitors (everolimus, sirolimus), the suspension of mycophenolate mofetil/sodium as well as the use of steroids in monotherapy. The minimization of immunosuppression which is frequently recommended in SOTRs with a cancer diagnosis may be one of the causes of such a frequent rejection noted in patients treated with ICIs. As the recent analysis showed, the maintenance of treatment with tacrolimus was associated with a reduction in post-ICI rejection without compromising the effectiveness of cancer response (Portuguese *et al.*, 2022). In another study, in the group of patients who were treated with the continuous dose of <10 mg/d of prednisone, there was a higher percentage of acute rejection of the kidney graft, but anticancer effectiveness was better: in 63% of patients' disease remission or stabilization were observed. In patients who continued CNI, acute graft rejection occurred less often, but the anti-cancer therapy was also less effective (Manohar *et al.*, 2020). In the Australian, phase 1 study, 17 kidney transplant recipients with low or intermediate immunological risk with various solid tumours were treated with nivolumab and baseline immunosuppression was left unchanged. Complete responses were observed in four of 17 patients, including one patient with microsatellite instability-high colorectal cancer, and three with squamous cell carcinoma of the head and neck. Partial responses were observed in five patients (with squamous cell carcinoma of the head and neck), one with bladder cancer, and one with hepatocellular carcinoma. Only two patients developed acute rejection (T-cell mediated) with a good response to antithymocyte globulin and plasmapheresis in one case, the other patient commenced hemodialysis. There were no treatment-related deaths or treatment-related serious adverse events. The most common adverse events were decreased lymphocyte count, fever or infection, decreased haemoglobin, and increased

creatinine in three patients. Based on their observations, the authors concluded that maintaining baseline immunosuppression before treatment with ICIs in kidney transplant recipients might not affect expected efficacy and might reduce the risk of allograft rejection mediated by immune checkpoint inhibitors (Carroll *et al.*, 2022). In the management of acute graft rejection during oncologic ICIs therapy, it is considered reasonable to discontinue ICIs and use steroid pulse therapy (Venkatachalam *et al.*, 2020; Perazella & Shirali, 2020). As shown in Carroll RP *et al.* study the antithymocyte globulin and plasmapheresis may also be a treatment option (Carroll *et al.*, 2022).

Some observations indicated that complications occur more often in patients treated with the anti-PD-1 group. The PD-1/PD-L1 pathway plays a significant role in the preservation of immunotolerance. PD-L1 present in the epithelium of renal tubules represses cytokines' production by T-lymphocytes, regulating T-lymphocytes' activation and anergy, and providing the immune balance. In view of the foregoing, blocking the PD-1: PD-L1 pathway may increase the risk of transplant rejection (Perazella & Shirali, 2020; Perazella & Shirali, 2018; Kumar *et al.*, 2020).

In conclusion, ICIs are a feasible option for transplant recipients with advanced malignancies but doctors and patients should be aware of the increased risk of acute rejection. Close monitoring and tailoring of immunosuppression are critical. Maintaining an appropriate balance between immunosuppressive treatment, the preservation of the graft function and anti-cancer management requires collaboration between oncologists and transplant physicians as well as the patients and their families.

Radiotherapy and proton therapy in transplant recipients

The kidneys are the dose-limiting organs for radiotherapy (RT) in case of gastrointestinal and gynecologic cancers, lymphomas and sarcomas of the upper abdomen as well as during total body irradiation (TBI). The cause of RT-induced kidney injury is poorly understood but the incidence of this complication largely depends on the use of whole-volume or partial-volume RT to one or both kidneys (Dawson *et al.*, 2010).

Even if short-term kidney function is preserved, radiation-induced kidney injury is subclinical and frequently presents during the subacute (3–18 months) and chronic (>18 months) periods and may have a negative consequence on patients' health in the future (Dawson *et al.*, 2010).

The KTx patients requiring RT treatment find themselves in a special situation: they have one kidney often with initial kidney impairment; moreover, the presence of a transplanted kidney in the pelvis can be a therapeutic challenge in patients who require pelvis radiation as management. The inferior border of KTx located at the iliac fossa usually lies at the bottom of S2 or S3. Therefore, radiotherapy that includes pelvic lymph nodes will need further evaluation to determine the benefits and the risks. Treatment of pelvic tumours with definitive or neoadjuvant radiotherapy usually includes iliac lymph nodes in the nodal target volume. This nodal target is also included in some cases of adjuvant radiotherapy. The location of the graft in relation to radiation therapy fields increases the risk of damage to the transplanted organ. In the presence of a transplanted kidney, the dose required for the region at risk must be balanced against the potential risk of graft injury (Detti *et al.*, 2011). Furthermore, during RT, the increased risk of urethral/ureteral stricture KTx dysfunction should be taken into consideration.

In proton therapy (PT) due to a phenomenon known as the Bragg peak, protons deposit their maximum energy at a specific depth with no exit. This allows for the delivery of a high therapeutic dose of radiation to tumours in challenging anatomic locations, close to critical organs and within damaged organs with a reduced risk of late toxicities in the surrounding tissues and a lower incidence of secondary malignancies (LaRiviere *et al.*, 2019). PT is being investigated as an alternative to intensity-modulated radiation therapy because of its potential to minimize radiation exposure to the transplanted kidney and other organs at risk. Dosimetric studies have demonstrated that PT improves organ-at-risk sparing compared with intensity-modulated radiation therapy, and it does not sacrifice the coverage of the target. There are only some papers based on clinical cases describing the utility of PT in KTx recipients, mainly as a treatment in the case of pelvic tumours (Buchberger *et al.*, 2019; Ilciana *et al.*, 2020). Given the relative radiosensitivity of native kidneys, the tissue-sparing effects of proton therapy are of utmost importance in the treatment of patients with pelvic kidneys and pelvic malignancies.

SUMMARY

To identify key management issues in nephrology relevant to patients with malignancy, the panel of multidisciplinary specialists organized the conference on Nephro-oncology in Gdańsk (October 2020). The conference participants emphasized the importance of collaboration among nephrology, haematology/oncology, dermatology, urology and transplant specialists to improve medical care for cancer and kidney disease patients. The four main parts of the paper present the most current diagnostic and therapeutic approaches to cancer and kidney disease patients. This study is based on the authors' expertise and the most recently published relevant literature with their participation.

REFERENCES

Al-Adra D, Al-Qaoud T, Fowler K, Wong G (2022) *De Novo* malignancies after kidney transplantation. *Clin J Am Soc Nephrol* **17**: 434–443. <https://doi.org/10.2215/CJN.14570920>

Anderson-Otunu O, Akhtar S (2016) Chronic infections of the urinary tract and bladder cancer risk: a systematic review. *Asian Pac J Cancer Prev* **17**: 3805–3807

Androne AG, Tanase AD, Sorohan BM, Craciun OG, Stefan L, Vardy Z, Lipan L, Obrisa B, Truica A, Ismail G (2019) Incidence and risk factors for acute kidney injury following autologous stem cell transplantation for multiple myeloma. *Cancer Med* **8**: 3278–3285. <https://doi.org/10.1002/cam4.2187>

Bączkowska T, Bissler JJ, Błańska-Przerwa K, Borawski J, Chudek J, Ciechanowski K, Czarkowska-Pączek B, Dębska-Słizień A, Domański M, Durlak M, Gellert R, Gozdowska J, Goździk M, Imko-Walczyk B, Janiszewski J, Januszko-Giergielewicz B, Jeśkiewicz M, Jóźwiak S, Kadylak D, Klinger M, Kosieradzki M, Kotulska K, Kozak Ł, Król E, Krzanowska K, Kurnatowska I, Labij-Reduta B, Lichodziejewska-Niemierko M, Lizakowski S, Malyszko J, Matuszewski M, Mazurkiewicz J, Melań-Mucha G, Myślak M, Naumnik B, Nowicki M, Oko A, Pączek Ł, Perkowska-Ptasńska A, Piątek M, Piecha G, Radzikowska E, Renke M, Rutkowska B, Sawosz M, Skutecki R, Słowińska M, Sosńska-Mielcarek K, Szafran-Dobrowolska J, Szolkowska M, Szczepulska-Wójcik E, Szurawska E, Tarasiewicz A, Wągrowa-Danilewicz M, Wołowicz D, Woźniak J, Zawiasa-Bryszewska A (2019) Problems of nephrooncology. Proceedings from the 1st Scientific and Training Conference Nephrooncology 5–6 October 2018, Gdańsk, Poland. *Pol Arch Intern Med* **129**: 1–74. <https://doi.org/10.20452/pamw.14821>

Belay Y, Yirdaw K, Enawgaw B (2017) Tumor lysis syndrome in patients with hematological malignancies. *J Oncol* **2017**: 1–9. <https://doi.org/10.1155/2017/9684909>

Bellini MI, Nozdrin M, Pengel L, Knight S, Papalois V (2022) How good is a living donor? Systematic review and meta-analysis of the

effect of donor demographics on post kidney transplant outcomes. *J Nephrol* **35**: 807–820. <https://doi.org/10.1007/s40620-021-01231-7>

Berardi R, Torniai M, Lenci E, Pecci F, Morgese F, Rinaldi S (2019) Electrolyte disorders in cancer patients: a systematic review. *J Cancer Metastasis Treat* **2019**. <https://doi.org/10.20517/2394-4722.2019.008>

Berg A, Mauro P, Borensztein E (2002) An Evaluation of monetary regime options for Latin America. *IMF Working Papers* **02**: 1. <https://doi.org/10.5089/9781451874853.001>

Besarani D, Cranston D (2007) Urological malignancy after renal transplantation. *BJU Int* **100**: 502–505. <https://doi.org/10.1111/j.1464-410X.2007.07049.x>

van Besien K, Schouten V, Parsad S, Smith S, Odenike O, Artz AS (2012) Allogeneic stem cell transplant in renal failure: Engraftment and prolonged survival, but high incidence of neurologic toxicity. *Leuk Lymphoma* **53**: 158–159. <https://doi.org/10.3109/10428194.2011.604756>

Bodge MN, Reddy S, Thompson MS, Savani BN (2014) Preparative regimen dosing for hematopoietic stem cell transplantation in patients with chronic kidney disease: analysis of the literature and recommendations. *Biol Blood Marrow Transplant* **20**: 908–919. <https://doi.org/10.1016/j.bbmt.2014.02.013>

Boissier R, Hevia V, Bruins HM, Budde K, Figueiredo A, Lledó-García E, Olsburgh J, Regele H, Taylor CF, Zakri RH, Yuan CY, Breda A (2018) The risk of tumour recurrence in patients undergoing renal transplantation for end-stage renal disease after previous treatment for a urological cancer: a systematic review. *Eur Urol* **73**: 94–108. <https://doi.org/10.1016/j.eururo.2017.07.017>

Brahmer JR, Lacchetti C, Schneider BJ, Atkins MB, Brassil KJ, Caterino JM, Chau I, Ernstoff MS, Gardner JM, Ginex P, Hallmeyer S, Holter Chakrabarty J, Leigh NB, Mammen JS, McDermott DF, Naing A, Nastoupil LJ, Phillips T, Porter LD, Puzanov I, Reichner CA, Santomasso BD, Seigel C, Spira A, Suarez-Almazor ME, Wang Y, Weber JS, Wolchok JD, Thompson JA (2018) Management of immune-related adverse events in patients treated with immune checkpoint inhibitor therapy: American society of clinical oncology clinical practice guideline. *J Clin Oncol* **36**: 1714–1768. <https://doi.org/10.1200/JCO.2017.77.6385>

Bratt O, Drevin L, Prütz KG, Carlsson S, Wennberg L, Stattin P (2020a) Prostate cancer in kidney transplant recipients – a nationwide register study. *BJU Int* **125**: 679–685. <https://doi.org/10.1111/bju.15002>

Bratt O, Drevin L, Prütz KG, Carlsson S, Wennberg L, Stattin P (2020b) Prostate cancer in kidney transplant recipients – a nationwide register study. *BJU Int* **125**: 679–685. <https://doi.org/10.1111/bju.15002>

Buchberger D, Kreinbrink P, Kharofa J (2019) Proton therapy in the treatment of anal cancer in pelvic kidney transplant recipients: a case series. *Int J Part Ther* **6**: 28–34. <https://doi.org/10.14338/ijpt-19-00067.1>

Carroll RP, Boyer M, Gebiski V, Hockley B, Johnston JK, Kireta S, Tan H, Taylor A, Wyburn K, Zalchley JR (2022) Immune checkpoint inhibitors in kidney transplant recipients: a multicentre, single-arm, phase 1 study. *Lancet Oncol* **23**: 1078–1086. [https://doi.org/10.1016/S1470-2045\(22\)00368-0](https://doi.org/10.1016/S1470-2045(22)00368-0)

Carvalho JA, Nunes P, Dinis PJ, Antunes H, Parada B, Marconi L, Moreira P, Roseiro A, Bastos C, Rolo F, Dias V, Figueiredo A (2017) Prostate cancer in renal transplant recipients: diagnosis and treatment. *Transplant Proc* **49**: 809–812. <https://doi.org/10.1016/j.transproceed.2017.03.006>

Chadban SJ, Ahn C, Axelrod DA, Foster BJ, Kasiske BL, Kher V, Kumar D, Oberbauer R, Pascual J, Pilmore HL, Rodrigue JR, Segev DL, Sheerin NS, Tincam KJ, Wong G, Knoll GA (2020) KDIGO clinical practice guideline on the evaluation and management of candidates for kidney transplantation. *Transplantation* **104**: S11–S103. <https://doi.org/10.1097/TP.00000000000003136>

Chapchapp EC, Doherty MP, Kerbauy LN, Belucci TR, Santos FP de S, Ribeiro AAF, Hamerschlag N (2022) Need for hemodialysis in patients undergoing hematopoietic stem cell transplantation: risk factors and survival in a retrospective cohort. *Hematol Transfus Cell Ther* <https://doi.org/10.1016/j.htct.2022.04.005>

Chen F, Wu D, Wang R, Huang X, Li X, Huang CH (2019) Histopathology of chronic kidney disease after allogeneic hematopoietic cell transplantation: a multi-center observational study of kidney biopsies. *Blood* **134**: 5696–5696. <https://doi.org/10.1182/blood-2019-128121>

Corredor Z, da Silva Filho MI, Rodríguez-Ribera L, Catalano C, Hemminki K, Coll E, Silva I, Diaz JM, Ballarín JA, Henández A, Först A, Marcos R, Pastor S (2020) Loci associated with genomic damage levels in chronic kidney disease patients and controls. *Mutation Res/Genet Toxicol Environ Mutagen* **852**: 503167. <https://doi.org/10.1016/j.mrgentox.2020.503167>

Cosmai L, Porta C, Gallieni M, Perazella MA (2016) Onco-nephrology: a decalogue. *Nephrol Dial Transplant* **31**: 515–519. <https://doi.org/10.1093/NDT/GFV320>

Cosmai L, Porta C, Privitera C, Gesualdo L, Procopio G, Gori S, Laghi A (2020) Acute kidney injury from contrast-enhanced CT

- procedures in patients with cancer: white paper to highlight its clinical relevance and discuss applicable preventive strategies. *ESMO Open* 5: e000618. <https://doi.org/10.1136/esmoopen-2019-000618>
- Dahlé DO, Skauby M, Langberg CW, Brabrand K, Wessel N, Midtvedt K (2022) Renal cell carcinoma and kidney transplantation: a narrative review. *Transplantation* 106: E52–E63. <https://doi.org/10.1097/TP.0000000000003762>
- Dawson LA, Kavanagh BD, Paulino AC, Das SK, Miften M, Li XA, Pan C, ten Haken RK, Schultheiss TE (2010) Radiation-associated kidney injury. *Int J Radiat Oncol Biol Phys* 76: (3 Suppl): S108–S115. <https://doi.org/10.1016/j.ijrobp.2009.02.089>
- Desjardins A, Le-Nguyen V, Turgeon-Mallete L, Vo C, Boudreault JS, Rioux JP, Feng X, Veilleux A (2022) Bendamustine-induced nephrogenic diabetes insipidus – A case report. *J Oncol Pharm Practice* 28: 205–210. <https://doi.org/10.1177/10781552211013878>
- Deti B, Scoccianti S, Franceschini D, Villari D, Greto D, Cipressi S, Sardaro A, Zanassi M, Cai T, Biti G (2011) Adjuvant radiotherapy for a prostate cancer after renal transplantation and review of the literature. *Jpn J Clin Oncol* 41: 1282–1286. <https://doi.org/10.1093/jjco/hyr133>
- Dhakal P, Giri S, Siwakoti K, Rayamajhi S, Bhatt VR (2017) Renal cancer in recipients of kidney transplant. *Rare Tumors* 9: 9–13. <https://doi.org/10.4081/rt.2017.6550>
- Essa H, Dobson R, Wright D, Lip GYH (2020) Hypertension management in cardio-oncology. *J Hum Hypertens* 34: 673–681. <https://doi.org/10.1038/s41371-020-0391-8>
- Euvrard S, Kanitakis J, Claudy A (2003) Skin cancers after organ transplantation. *N Engl J Med* 348: 1681–1691. <https://doi.org/10.1056/NEJMRA022137>
- Farhadfar N, Dias A, Wang T, Fretham C, Chhabra S, Murthy HS, Broglie L, D'Souza A, Gadalla SM, Gale RP, Hashmi S, Al-Homsi AS, Hildebrandt GC, Hematti P, Rizzieri D, Chee L, Lazarus HM, Bredeson C, Jaimes EA, Beitinjaneh A, Bashay A, Prestidge T, Krem MM, Marks DI, Benoit S, Yared JA, Nishihori T, Olson RF, Freytes CO, Stadtmayer E, Savani BN, Sorror ML, Ganguly S, Wingard JR, Pasquini M (2021) Impact of pretransplantation renal dysfunction on outcomes after allogeneic hematopoietic cell transplantation. *Transplant Cell Ther* 27: 410–422. <https://doi.org/10.1016/j.jctc.2021.02.030>
- Florenzano P, Hartley IR, Jimenez M, Roszko K, Gafni RI, Collins MT (2021) Tumor-induced osteomalacia. *Calcif Tissue Int* 108: 128–142. <https://doi.org/10.1007/s00223-020-00691-6>
- de Francisco ALM, Macía M, Alonso F, García P, Gutierrez E, Quintana LF, Quiroga B, Torregrosa I (2019) Onco-Nephrology: Cancer, chemotherapy and kidney. *Nefrología (English edn)* 39: 473–481. <https://doi.org/10.1016/j.nefro.2018.10.016>
- Giannakopoulos X, Sakkas H, Ragos V, Tsiambas E, Bozidis P, M Evangelou A, Papadopoulou C, Petrogianopoulos L, Sofikitis N (2019) Impact of enterococcal urinary tract infections in immunocompromised – neoplastic patients. *J BUON* 24: 1768–1775. PMID: 31786836
- Goedert JJ (2009) Merkel cell carcinoma: recent progress and current priorities on etiology, pathogenesis, and clinical management. *J Clin Oncol* 27: 4021. <https://doi.org/10.1200/JCO.2009.22.6605>
- Greenberg JN, Zwald FO (2011) Management of skin cancer in solid-organ transplant recipients: a multidisciplinary approach. *Dermatol Clin* 29: 231–241. <https://doi.org/10.1016/j.DET.2011.02.004>
- Gutiérrez-García G, Villarreal J, Garrote M, Rovira M, Blasco M, Suárez-Lledó M, Rodríguez-Lobato LG, Charry P, Rosiñol L, Marín P, Pedraza A, Solano MT, Ramos C, de Llobet N, Lozano M, Cid J, Martínez C, Poch E, Carreras E, Urbano-Ispizua Á, Fernández-Avilés F, Pereira A, Quintana LF (2020) Impact of severe acute kidney injury and chronic kidney disease on allogeneic hematopoietic cell transplant recipients: a retrospective single center analysis. *Bone Marrow Transplant* 55: 1264–1271. <https://doi.org/10.1038/s41409-020-0843-3>
- Haslam A, Prasad V (2019) Estimation of the percentage of us patients with cancer who are eligible for and respond to checkpoint inhibitor immunotherapy drugs. *JAMA Netw Open* 2: <https://doi.org/10.1001/jamanetworkopen.2019.2535>
- Haug K, Breuninger H, Metzler G, Eigentler T, Eichner M, Häfner HM, Schnabl SM (2020) Prognostic impact of perineural invasion in cutaneous squamous cell carcinoma: results of a prospective study of 1,399 tumors. *J Invest Dermatol* 140: 1968–1975. <https://doi.org/10.1016/j.jid.2020.01.035>
- Hernandez LE, Mohsin N, Yaghi M, Frech FS, Dreyfuss I, Nouri K (2022) Merkel cell carcinoma: An updated review of pathogenesis, diagnosis, and treatment options. *Dermatol Ther* 35: e15292. <https://doi.org/10.1111/DTH.15292>
- Hevia V, Hassan Zakri R, Fraser Taylor C, Bruins HM, Boissier R, Lledo E, Regele H, Budde K, Figueiredo A, Breda A, Yuan CY, Olsburgh J (2019) Effectiveness and harms of using kidneys with small renal tumors from deceased or living donors as a source of renal transplantation: a systematic review. *Eur Urol Focus* 5: 508–517. <https://doi.org/10.1016/j.euf.2018.01.018>
- Ileana PÁS, Rubi RP, Javier LRF, Sagrario MGM del, Haydeé FBC (2020) Pelvic radiation therapy with volumetric modulated arc therapy and intensity-modulated radiotherapy after renal transplant: A report of 3 cases. *Rep Pract Oncol Radiother* 25: 548–555. <https://doi.org/10.1016/j.rpor.2020.04.003>
- Imko-Walczuk B, Turner R, Wojnarowska F (2009) Malignant melanoma. *Cancer Treat Res* 146: 311–322. https://doi.org/10.1007/978-0-387-78574-5_25
- Imko-Walczuk B, Kielbowicz M, Dębska-Ślizień A, Rutkowski B (2015) Skin cancers as contraindication to organ transplantation. *Transplant Proc* 47: 1547–1552. <https://doi.org/10.1016/j.TRANSPROCEED.2015.03.047>
- Janowitz T, Williams EH, Marshall A, Ainsworth N, Thomas PB, Sammut SJ, Shepherd S, White J, Mark PB, Lynch AG, Jodrell DI, Tavaré S, Earl H (2017) New model for estimating glomerular filtration rate in patients with cancer. *J Clin Oncol* 35: 2798–2805. <https://doi.org/10.1200/JCO.2017.72.7578>
- Janus N, Launay-vacher V, Byloos E, Machiels J-P, Duck L, Kerger J, Wynendaele W, Canon J-L, Lybaert W, Nortier J, Deray G, Wildiers H (2010) Cancer and renal insufficiency results of the BIRMA study. *Br J Cancer* 103: 1815–1821. <https://doi.org/10.1038/sj.bjc.6605979>
- Kanduri SR, Cheungpasitporn W, Thongprayoon C, Bathini T, Kovvuru K, Garla V, Medaura J, Vaitla P, Kashani KB (2020) Incidence and mortality of acute kidney injury in patients undergoing hematopoietic stem cell transplantation: A systematic review and meta-analysis. *QJM* 113: 621–632. <https://doi.org/10.1093/qjmed/hcaa072>
- Kanitakis Jean (2009) Merkel cell carcinoma. In *Skin Cancer After Kidney Transplantation*. Rosen T. Steven ed, pp 239–241. New York: Springer Science
- Karami S, Yanik EL, Moore LE, Pfeiffer RM, Copeland G, Gonsalves L, Hernandez BY, Lynch CF, Pawlish K, Engels EA (2016) Risk of renal cell carcinoma among kidney transplant recipients in the United States. *Am J Transplant* 16: 3479–3489. <https://doi.org/10.1111/ajt.13862>
- Katsi V, Magkas N, Georgiopoulos G, Athanasiadi E, Virdis A, Masi S, Kliridis P, Hatziyanni A, Tsioufis C, Tousoulis D (2019) Arterial hypertension in patients under antineoplastic therapy. *J Hypertens* 37: 884–901. <https://doi.org/10.1097/HJH.0000000000002006>
- Kępska-Dziłińska M, Zhymla A, Malyszko J (2022) Kidney damage in patients after allogeneic stem cell transplantation. *Wiad Lek* 75: 877–880. <https://doi.org/10.36740/WLEK202204123>
- Kumar V, Shinagare AB, Rennke HG, Ghai S, Lorch JH, Ott PA, Rahma OE (2020) The safety and efficacy of checkpoint inhibitors in transplant recipients: A case series and systematic review of literature. *Oncologist* 25: 505–514. <https://doi.org/10.1634/theoncologist.2019-0659>
- Lameire NH, Levin A, Kellum JA, Cheung M, Jadoul M, Winkelmayer WC, Stevens PE; Conference Participants (2021) Harmonizing acute and chronic kidney disease definition and classification: report of a Kidney Disease: Improving Global Outcomes (KDIGO) Consensus Conference. *Kidney Int* 100: 516–526. <https://doi.org/10.1016/j.kint.2021.06.028>
- Langenhorst JB, Dorlo TPC, van Maarseveen EM, Nierkens S, Kuball J, Boelens JJ, van Kesteren C, Huitema ADR (2019) Population pharmacokinetics of fludarabine in children and adults during conditioning prior to allogeneic hematopoietic cell transplantation. *Clin Pharmacokinet* 58: 627–637. <https://doi.org/10.1007/s40262-018-0715-9>
- LaRivière MJ, Santos PMG, Hill-Kayser CE, Metz JM (2019) Proton therapy. *Hematol Oncol Clin North Am* 33: 989–1009. <https://doi.org/10.1016/j.hoc.2019.08.006>
- Leon G, Szabla N, Boissier R, Gigante M, Caillet K, Verhoest G, Tillou X (2020) Kidney graft urothelial carcinoma: results from a multicentric retrospective national study. *Urology* 135: 101–105. <https://doi.org/10.1016/j.urology.2019.09.015>
- Levey AS, Grams ME, Inker LA (2022) Uses of GFR and albuminuria level in acute and chronic kidney disease. *New Eng J Med* 386: 2120–2128. <https://doi.org/10.1056/nejma2201153>
- Lewis CW, Qazi J, Hippe DS, Lachance K, Thomas H, Cook MM, Juhlin I, Singh N, Thuesmann Z, Takagishi SR, McEvoy A, Doolittle-Amieva C, Bhatia S, Paulson KG, O'Malley RB, Wang CL, Nghiem P (2020) Patterns of distant metastases in 215 Merkel cell carcinoma patients: Implications for prognosis and surveillance. *Cancer Med* 9: 1374–1382. <https://doi.org/10.1002/cam4.2781>
- Li Y, Chen X, Shen Z, Wang Y, Hu J, Xu J, Shen B, Ding X (2020) Electrolyte and acid-base disorders in cancer patients and its impact on clinical outcomes: evidence from a real-world study in China. *Ren Fail* 42: 234–243. <https://doi.org/10.1080/0886022X.2020.1735417>
- Liddington M, Richardson AJ, Higgins RM, Endre ZH, Venning VA, Murie JA, Morris PJ (1989) Skin cancer in renal transplant recipients. *Br J Surg* 76: 1002–1005. <https://doi.org/10.1002/BJS.1800761005>
- Lindelöf B, Sigurgeirsson B, Gäbel H, Stern RS (2000) Incidence of skin cancer in 5356 patients following organ transplantation.

- Brit J Dermatol* **143**: 513–519. <https://doi.org/10.1111/J.1365-2133.2000.03703.X>
- Liu Y, Zhou L, Chen Y, Liao B, Ye D, Wang K, Li H (2019) Hypertension as a prognostic factor in metastatic renal cell carcinoma treated with tyrosine kinase inhibitors: a systematic review and meta-analysis. *BMC Urol* **19**: 49. <https://doi.org/10.1186/s12894-019-0481-5>
- Mahipal A, Tella SH, Kommalapati A, Yu J, Kim R (2020) Prevention and treatment of FGFR inhibitor-associated toxicities. *Crit Rev Oncol Hematol* **155**: 103091. <https://doi.org/10.1016/j.critrevonc.2020.103091>
- Malyszko J, Kozłowska K, Kozłowski L, Malyszko J (2016) Nephrotoxicity of anticancer treatment. *Nephrol Dial Transplant* **32**: 924–936. <https://doi.org/10.1093/ndt/gfw338>
- Malyszko J, Bamias A, Danesh FR, Dębska-Ślizię A, Gallieni M, Gertz MA, Kielstein JT, Tesarova P, Wong G, Cheung M, Wheeler DC, Winkelmayer WC, Porta C; Conference Participants (2020a) KDIGO Controversies Conference on onco-nephrology: kidney disease in hematological malignancies and the burden of cancer after kidney transplantation. *Kidney Int* **98**: 1407–1418. <https://doi.org/10.1016/j.kint.2020.07.012>
- Malyszko J, Lee MW, Capasso G, Kulicki P, Matuszkiewicz-Rowinska J, Ronco P, Stevens P, Tesarova P, Viggiano D, Capasso A (2020a) How to assess kidney function in oncology patients. *Kidney Int* **97**: 894–903. <https://doi.org/10.1016/j.kint.2019.12.023>
- Malyszko J, Tesarova P, Capasso G, Capasso A (2020b) The link between kidney disease and cancer: complications and treatment. *Lancet* **396**: 277–287. [https://doi.org/10.1016/S0140-6736\(20\)30540-7](https://doi.org/10.1016/S0140-6736(20)30540-7)
- Malyszko J, Bamias A, Danesh FR, Dębska-Ślizię A, Gallieni M, Gertz MA, Kielstein JT, Tesarova P, Wong G, Cheung M, Wheeler DC, Winkelmayer WC, Porta C; Conference Participants (2020b) KDIGO Controversies Conference on onco-nephrology: kidney disease in hematological malignancies and the burden of cancer after kidney transplantation. *Kidney Int* **98**: 1407–1418. Elsevier B.V. <https://doi.org/10.1016/j.kint.2020.07.012>
- Manohar S, Thongprayoon C, Cheungpasitporn W, Markovic SN, Herrmann SM (2020) Systematic review of the safety of immune checkpoint inhibitors among kidney transplant patients. *Kidney Int Rep* **5**: 149–158. <https://doi.org/10.1016/j.ekir.2019.11.015>
- Mason DY, Howes DT, Taylor CR, Ross BD (1975) Effect of human lysozyme (muramidase) on potassium handling by the perfused rat kidney: A mechanism for renal damage in human monocytic leukemia. *J Clin Pathol* **28**: 722–727. <https://doi.org/10.1136/jcp.28.9.722>
- Matin RN, Mesher D, Proby CM, McGregor JM, Bouwes Bavinck JN, del Marmol V, Euvrard S, Ferrandiz C, Geusau A, Hackenthal M, Ho WL, Hofbauer GF, Imko-Walczuk B, Kanitakis J, Lally A, Lear JT, Lebbe C, Murphy GM, Piaserico S, Seckin D, Stockfleth E, Ulrich C, Wojnarowska FT, Lin HY, Balch C, Harwood CA; Skin Care in Organ Transplant Patients, Europe (SCOPE) group (2008) Melanoma in organ transplant recipients: clinicopathological features and outcome in 100 cases. *Am J Transplant* **8**: 1891–1900. <https://doi.org/10.1111/j.1600-6143.2008.02326.x>
- McCoy C, Paredes M, Allen S, Blackey J, Nielsen C, Paluzzi A, Jonas B, Radovich P (2017) Catheter-associated urinary tract infections: implementing a protocol to decrease incidence in oncology populations. *Clin J Oncol Nurs* <https://doi.org/10.1188/17.CJON.460-465>
- Milionis HJ, Bourant CL, Siamopoulos KC, Elisaf MS (1999) Acid-base and electrolyte abnormalities in patients with acute leukemia. *Am J Hematol* **62**: 201–207. [https://doi.org/10.1002/\(SICI\)1096-8652\(199912\)62:4<201::AID-AJH1>3.0.CO;2-I](https://doi.org/10.1002/(SICI)1096-8652(199912)62:4<201::AID-AJH1>3.0.CO;2-I)
- Mittal A, Colegio OR (2017) Skin cancers in organ transplant recipients. *Am J Transplant* **17**: 2509–2530. <https://doi.org/10.1111/AJT.14382>
- Miyata M, Ichikawa K, Matsuki E, Watanabe M, Peltier D, Toubai T (2022) Recent advances of acute kidney injury in hematopoietic cell transplantation. *Front Immunol* **12**: <https://doi.org/10.3389/fimmu.2021.779881>
- Penn I (1996) Malignant melanoma in organ allograft recipients. *Transplantation* **61**: 274–278. <https://doi.org/10.1097/00007890-199601270-00019>
- Penn I, First MR (1999) Merkel's cell carcinoma in organ recipients: Report of 41 cases. *Transplantation* **68**: 1717–1721. <https://doi.org/10.1097/00007890-199912150-00015>
- Perazella MA, Shirali AC (2018) Nephrotoxicity of Cancer Immunotherapies: Past, Present and Future. *J Am Soc Nephrol* **29**: 2039–2052. <https://doi.org/10.1681/ASN.2018050488>
- Perazella MA, Shirali AC (2020) Immune checkpoint inhibitor nephrotoxicity: what do we know and what should we do? *Kidney Int* **97**: 62–74. <https://doi.org/10.1016/j.kint.2019.07.022>
- Porta C, Bamias A, Danesh FR, Dębska-Ślizię A, Gallieni M, Gertz MA, Kielstein JT, Tesarova P, Wong G, Cheung M, Wheeler DC, Winkelmayer WC, Malyszko J; Conference Participants (2020) KDIGO Controversies Conference on onco-nephrology: understanding kidney impairment and solid-organ malignancies, and managing kidney cancer. *Kidney Int* **98**: 1108–1119. <https://doi.org/10.1016/j.kint.2020.06.046>
- Portuguese AJ, Tykodi SS, Blosser CD, Gooley TA, Thompson JA, Hall ET (2022) Immune checkpoint inhibitor use in solid organ transplant recipients: a systematic review. *JNCCN Journal of the National Comprehensive Cancer Network* **20**: 406–416. <https://doi.org/10.6004/jnccn.2022.7009>
- Rizzoni D, de Ciuceis C, Porteri E, Agabiti-Rosei C, Agabiti-Rosei E (2017) Use of antihypertensive drugs in neoplastic patients. *High Blood Press Cardiovasc Prevent* **24**: 127–132. <https://doi.org/10.1007/s40292-017-0198-z>
- Rodríguez Faba O, Boissier R, Budde K, Figueiredo A, Taylor CF, Hevia V, Lledó García E, Regele H, Zakri RH, Olsburgh J, Breda A (2018) European Association of Urology Guidelines on Renal Transplantation: Update 2018. *Eur Urol Focus* **4**: 208–215. <https://doi.org/10.1016/j.euf.2018.07.014>
- Rosner MH, Dalkin AC (2014) Electrolyte disorders associated with cancer. *Adv Chronic Kidney Dis* **21**: 7–17. <https://doi.org/10.1053/j.ackd.2013.05.005>
- Rosner MH, Perazella MA (2019) Acute kidney injury in the patient with cancer. *Kidney Res Clin Pract* **38**: 295–308. <https://doi.org/10.23876/j.krcp.19.042>
- Salahudeen AK, Doshi SM, Pawar T, Nowshad G, Lahoti A, Shah P (2013) Incidence rate, clinical correlates, and outcomes of AKI in patients admitted to a comprehensive cancer center. *Clin J Am Soc Nephrol* **8**: 347–354. <https://doi.org/10.2215/CJN.03530412>
- Serkies K, Dębska-Ślizię A, Kowalczyk A, Lizakowski S, Malyszko J (2022) Malignancies in adult kidney transplant candidates and recipients: current status. *Nephrol Dial Transplant* <https://doi.org/10.1093/ndt/gfac239>
- Shadman B, Hingorani S, Lanum SA, Pagel JM, Storb R, Maloney DG, Sandmaier BM (2017) Allogeneic hematopoietic cell transplant for patients with end stage renal disease requiring dialysis—a single institution experience. *Leuk Lymphoma* **58**: 740–742. <https://doi.org/10.1080/10428194.2016.1211280>
- Sherer BA, Warrior K, Godlewski K, Hertl M, Olaitan O, Nehra A, Deane LA (2017) Prostate cancer in renal transplant recipients. *International Braz J Urol* **43**: 1021–1032. <https://doi.org/10.1590/S1677-5538.IBJU.2016.0510>
- Sise ME, Seethapathy H, Reynolds KL (2019) Diagnosis and management of immune checkpoint inhibitor-associated renal toxicity: Illustrative case and review. *Oncologist* **24**: 735–742. <https://doi.org/10.1634/theoncologist.2018-0764>
- Sprangers B, Sandhu G, Rosner MH, Tesarova P, Stadler WM, Malyszko J (2021) Drug dosing in cancer patients with decreased kidney function: A practical approach. *Cancer Treat Rev* **93**: 102139. <https://doi.org/10.1016/j.ctrv.2020.102139>
- Stöckle M, Junker K, Fornara P (2018) Low-risk prostate cancer prior to or after kidney transplantation. *Eur Urol Focus* **4**: 148–152. <https://doi.org/10.1016/j.euf.2018.07.003>
- Sweiss K, Patel S, Culos K, Oh A, Rondelli D, Patel P (2016) Melfalan 200 mg/m² in patients with renal impairment is associated with increased short-term toxicity but improved response and longer treatment-free survival. *Bone Marrow Transplant* **51**: 1337–1341. <https://doi.org/10.1038/bmt.2016.136>
- Szvalb AD, el Haddad H, Rolston KV, Sabir SH, Jiang Y, Raad II, Viola GM (2019) Risk factors for recurrent percutaneous nephrostomy catheter-related infections. *Infection* **47**: 239–245. <https://doi.org/10.1007/s15010-018-1245-y>
- Szychowska K KI (2021) Nephrotoxicity of immune checkpoint inhibitors in immunotherapy of oncologic patients. *Renal Dis Transplant Forum* **14**: 1–6
- Tillou X, Doerfler A, Collon S, Kleinclauss F, Patard JJ, Badet L, Barrou B, Audet M, Bensadoun H, Berthoux E, Bigot P, Boutin JM, Bouzuenda Y, Chambade D, Codas R, Dantal J, Deturmeny J, Devonne M, Dugardin F, Ferrière JM, Erauso A, Feuillu B, Gigante M, Guy L, Karam G, Lebrete T, Neuzillet Y, Legendre C, Perez T, Rerolle JP, Salomon L, Sallusto F, Sénéchal C, Terrier N, Thuret R, Verhoest G, Petit J (2012) De novo kidney graft tumors: Results from a multicentric retrospective national study. *Am J Transplant* **12**: 3308–3315. <https://doi.org/10.1111/j.1600-6143.2012.04248.x>
- Tini G, Sarocchi M, Tocci G, Arboscio E, Ghigliotti G, Novo G, Brunelli C, Lenihan D, Volpe M, Spallarossa P (2019) Arterial hypertension in cancer: The elephant in the room. *Int J Cardiol* **281**: 133–139. <https://doi.org/10.1016/j.ijcard.2019.01.082>
- Venkatachalam K, Malone AF, Heady B, Santos RD, Alhamad T (2020) Poor outcomes with the use of checkpoint inhibitors in kidney transplant recipients. *Transplantation* **104**: 1041–1047. <https://doi.org/10.1097/TP.0000000000002914>
- Verziceo I, Regolisti G, Quaini F, Bocchi P, Brusasco I, Ferrari M, Passeri G, Cannone V, Coghi P, Fiaccadori E, Vignali A, Volpi R, Cabassi A (2020) Electrolyte disorders induced by antineoplastic drugs. *Front Oncol* **10**: <https://doi.org/10.3389/fonc.2020.00779>
- Vitkauskaitė A, Urbonienė D, Celiesiute J, Jariene K, Skrodeniene E, Nadisauskienė RJ, Vaitkiene D (2020) Circulating inflammatory markers in cervical cancer patients and healthy controls. *J Immunotoxicol* **17**: 105–109. <https://doi.org/10.1080/1547691X.2020.1755397>

- Waszczuk-Gajda A, Lewandowski Z, Drozd-Sokołowska J, Boguradzki P, Dybko J, Wróbel T, Basak GW, Jurczyszyn A, Mądry K, Snarski E, Frączak E, Charliński G, Feliksbro-Bratosiewicz M, Król M, Matuszkiewicz-Rowińska J, Klinger M, Krajewska M, Augustyniak-Bartosik H, Kościelska M, Rusicka P, Dwilewicz-Trojaczek J, Wiktor Jędrzejczak W (2018) Autologous peripheral blood stem cell transplantation in dialysis-dependent multiple myeloma patients – DAUTOS Study of the Polish Myeloma Study Group. *Eur J Haematol* **101**: 475–485. <https://doi.org/10.1111/ejh.13101>
- Xiao D, Craig JC, Chapman JR, Dominguez-Gil B, Tong A, Wong G (2013) Donor cancer transmission in kidney transplantation: A systematic review. *Am J Transplant* **13**: 2645–2652. <https://doi.org/10.1111/ajt.12430>
- Yang Y, Li H, Zhou Q, Peng Z, An X, Li W, Xiong L, Yu X, Jiang W, Mao H (2016) Renal function and all-cause mortality risk among cancer patients. *Medicine* **95**: e3728. <https://doi.org/10.1097/MD.0000000000003728>
- Yanik EL, Clarke CA, Snyder JJ, Pfeiffer RM, Engels EA (2016) Variation in cancer incidence among patients with esrd during kidney function and nonfunction intervals. *J Am Soc Nephrol* **27**: 1495–1504. <https://doi.org/10.1681/ASN.2015040373>

Knockdown of CD44 inhibits proliferation, migration, and invasiveness in hepatocellular carcinoma cells by modulating CXCR4/Wnt/ β -Catenin Axis

Xiaojing Song^{1✉}, Fanghui Ding¹, Wei Luo¹, Juan Tao², Kaili Yang², Qiaoping Li² and Zhitao Zhang²

¹Department of General Surgery, The First Hospital of Lanzhou University, Lanzhou, Gansu, 730000, China; ²The First School of Clinical Medicine, Lanzhou University, Lanzhou, Gansu, 730000, China

Hepatocellular carcinoma (HCC) has high mortality and incidence worldwide. The molecular mechanism associated with HCC is largely unexplored. Objective: To investigate the impact of CD44 knock-down on the proliferation, migration, and invasiveness in HCC cells. **Methods:** Colony formation and MTT assay were used to observe cellular proliferation and viability. In addition, cellular invasion and migration were studied by Transwell and wound healing assays respectively. Finally, western blotting was utilized to check the protein expression levels. **Results:** The cellular proliferation, invasion and metastasis in Huh7 cells were inhibited after the silencing of CD44. Furthermore, expression levels of MMP-2, MMP-9, CXCR4, GSK-3 β and β -catenin was significantly decreased. However, opposite results were demonstrated when CD44 was overexpressed. **Conclusions:** Interference with the expression of CD44 significantly inhibits the invasion and metastasis in the HCC cell line, Huh7. Furthermore, CD44 was found to regulate the expression of MMP-2, MMP-9, CXCL12, CXCR4 and Wnt/ β -catenin signal pathway.

Key words: CD44, Hepatocellular carcinoma, invasion, metastasis, Wnt/ β -catenin

Received: 11 April, 2022; revised: 31 July, 2022; accepted: 15 August, 2022; available on-line: 03 February, 2022

✉e-mail: songxiaojing4227@126.com

Acknowledgements of Financial Support: This study was supported by Lanzhou science and technology development guiding plan project (No: 2019-ZD-35), and the fund of the first hospital of Lanzhou University (No: ldyyn2018-58)

Abbreviations: CSCs, Cancer stem cells; DMSO, Dimethyl sulfoxide; ECM, extracellular matrix; EMT, epithelial-mesenchymal transition; EpCAM, epithelial adhesion molecule; HCC, hepatocellular carcinoma; MMPs, matrix metalloproteinases; MTT, (3-[4,5-dimethylthiazol-2-yl]-2,5 diphenyl tetrazolium bromide); PVDF, polyvinylidene fluoride

INTRODUCTION

In the primary liver cancer class, HCC is the first one in frequency and accounts for 80–90% of all malignant tumors (Davis *et al.*, 2008; Ghouri *et al.*, 2017). Worldwide, HCC has emerged as a major health issue increasing continuously due to its association with viruses like hepatitis B and C (El-Serag, 2012). The world trends are unevenly distributed, finding the highest incidence in eastern Asia (McGlynn *et al.*, 2015). Incidence ratio of HCC varies among sex, and the reasons for such is still unknown (Wilson and Buetow, 2020). Concerning age distribution, it also varies depending on the geographic

situation (Sung *et al.*, 2021). HCC is mostly found in the late stage when radiotherapy, chemotherapy and other treatments are ineffective. However, surgery in the early stage is currently the most effective treatment. Consequently, it has become one of the research focuses on exploring the detailed mechanism of metastasis and malignancy to explore novel treatment options for HCC.

The CD44 antigen, as an important epigenomic regulator, is involved in tumor development (Luo & Tan, 2016; Asai *et al.*, 2019). Numerous studies have confirmed that CD44 can be used as a molecular marker for different cancer (Malhotra *et al.*, 2010; Moldovan *et al.*, 2017). Zhang and colleagues demonstrated that CD44 could promote HCC progression by up-regulating YAP (Zhang *et al.*, 2021). Shah and colleagues found that interfering with CD44 could lead to the death of ovarian cancer cells (Shah *et al.*, 2013). It has been found that up-regulation of CD44 can promote metastasis and poor prognosis of Hepatocellular carcinoma, however, the mechanism by which CD44 regulates HCC is unclear (Asai *et al.*, 2019). Epithelial to mesenchymal transition (EMT) in cancer cells results in the acquisition of stem cell-like characteristics and increased CD44 expression (Mani *et al.*, 2008). Because of the clinicopathological effects that CD44 and its isoforms have on carcinogenesis, CD44 may one day serve as a molecular target for cancer treatment (Li *et al.*, 2014). Additionally, the demonstrated function of CD44 in preserving stemness and the ability of cancer stem cells to regenerate tumors after treatment raises the possibility that CD44 may play a significant prognostic marker. Clinical research on treatment plans that concentrate on CD44 or lessen CD44 expression is ongoing (Matzke-Ogi *et al.*, 2016; Todaro *et al.*, 2014). These methods include ectodomain mimics, aptamers, tumor-delivery shRNAs, and CD44 neutralizing antibodies (Orian-Rousseau and Ponta, 2015; Iida *et al.*, 2014). Consequently, it is crucial to further clarify the functional roles of CD44 as a focus of research.

Growing data indicates that cancer stem cells (CSCs) are responsible for the recurrence and metastasis of many malignancies (Vlashi *et al.*, 2011; Gao *et al.*, 2013). CSCs are essential for starting and maintaining tumour phenotypes because they can self-renewal and differentiation, which other cancer cells (non-CSCs) lack (Ayob & Ramasamy, 2018). The presence of CSCs in numerous malignancies, including those of the brain, breast, lung, colon, and liver, has been demonstrated utilizing particular CSC markers (Yang *et al.*, 2020). Epithelial adhesion molecule (EpCAM), CD13, CD44, and/or CD133 are among the markers that liver CSCs display and studies

have shown that the expression of these molecules on HCC cells is associated with a poor prognosis (Yamashita *et al.*, 2009; Zhu *et al.*, 2010). Although traditional therapies could eradicate non-CSCs, it is claimed that surviving CSCs eventually induce tumour recurrence and metastasis because they exhibit the characteristics of tumorigenicity and resistance to conventional chemotherapy and radiotherapy (Cross & Laidler, 1990; Gao *et al.*, 2013). Therefore, eliminating CSCs is crucial for fully curing cancer.

Tumor invasion and metastasis is a complex biological process (Nguyen *et al.*, 2009a). Gene regulation is crucial in different processes, like unlimited growth potential, epithelial-mesenchymal transition (EMT), and apoptosis avoidance (Perlikos *et al.*, 2013). Wnt signaling is an essential pathway affecting tumor cells' cellular migration and invasion ability. The Wnt/ β -catenin signaling system is a conserved signalling axis involved various physiological processes, including tissue homeostasis, migration, invasion, differentiation, proliferation, and apoptosis (Salik *et al.*, 2020). There is mounting evidence that certain solid tumors and hematological malignancies were aided in their development and progression by deregulation of the Wnt/ β -catenin cascade (Gajos-Michniewicz & Czyz, 2020). Early events in carcinogenesis are brought on by aberrant regulation of the transcription factor β -catenin, a crucial part of the Wnt signaling pathway, in the Wnt/ β -catenin pathway (Zhang *et al.*, 2020). GSK3 β and CK1a, two enzymes in the degradation complex, facilitate the phosphorylation of β -catenin, boosting its ubiquitination and subsequent proteasomal destruction (Wiese *et al.*, 2018). When β -catenin is accumulated at a certain amount, it gets translocated to nucleus, and binds to the target transcription factor to form a transcriptional complex. This complex subsequently activates its downstream target genes matrix metalloproteinases (MMPs), p21, and C-myc (Wiese *et al.*, 2018; Tai *et al.*, 2015). MMPs are a group of proteolytic enzymes which are highly homologous and zinc-dependent. The extracellular matrix (ECM) holds cells together and is essential for cell survival, motility, differentiation, and proliferation. The ECM components that serve as the physical impediments to cell migration must be locally broken down for a tumour cell to spread from the main tumour to other organs. Matrix metalloproteinases (MMPs) are the primary enzymes responsible for the breakdown of the ECM (Conlon & Murray, 2019).

Chemokine (CXCL12) and its receptor (CXCR4) have emerged as key factors in the development of tumors and their metastasis. CXCL12 has been reported to induce signaling *via* AKT and ERK pathways and thereby induce cancerous growth (Scotton *et al.*, 2002). In breast cancer, CXCL12 expression has been linked with pathological features and clinical outcomes (Kang *et al.*, 2005). The expression levels of CXCL12 have been reported on the higher side in different human cancers, including HCC (Sakai *et al.*, 2012) (Ghanem *et al.*, 2014; Teng *et al.*, 2016). The essential role of CXCL12 is yet to be fully explored in most cancers. The involvement of the CXCL12/CXCR4 axis in tumor progression, survival, metastasis and angiogenesis is well known. The current investigation aims to study the effect of CD44 on proliferation, migration, and invasiveness in HCC cells for CXCL12/CXCR4/Wnt/ β -Catenin Axis.

MATERIALS AND METHODS

Cell culture and cell transfection

The human hepatocellular carcinoma (HCC) cell line, Huh7 was purchased from ATCC. Huh7 were grown in DMEM containing 10% FBS (Sigma). The medium was put in a saturated humidity incubator at 37°C with 5% CO₂. siRNA (Si-CD44) was obtained from Ruibo Biotechnology Co., Ltd (Guangzhou, China). Over-expressing plasmid pcDNA3.1-CD44 (CD44) along with control vector (Vector) was purchased from General Biol (Anhui, China). Huh7 cells were grown in 6-well plates and divided into six groups, namely: blank group (Blank), Si-CD44 group, Si-NC, CD44 and Vector. Lipofectamine was used for the transfection of different vectors into the cells.

MTT assay

Cell viability in each group was observed MTT assay (Gibco, USA). Huh7 cells were grown into 96-well plates (6×10³ cells/well) for 48 h. It was followed by transfection studies using siRNAs (Si-CD44 and si-NC) and vectors (empty vector and vector-CD44) in the Huh7 cells, using lipofectamine and in accordance with the manufacturer's protocol. The efficacy of transfection was checked by western blotting. After incubation, the medium was removed from the wells, followed by the addition of 20 μ L MTT reagent (5 mg/mL; Gibco, USA) to each well. At the end of the experiment, MTT (Sigma) stock solution of 5 mg/mL concentration and volume 100 μ L was supplemented to cells with 4 h of incubation. The formazan crystals then produced are dissolved with DMSO, and thereafter, absorbance was measured at 540nm using a microplate reader. Each experiment for individual drug concentrations and controls was performed thrice.

Colony formation assay

Cell viability was observed via colony formation assay. Cells were rinsed twice with PBS. Afterward, individual cell in each group was obtained with 0.25% trypsin and then inoculated into culture dishes for one hour. Serially dilute the samples to obtain 100 cells in a 10 mL culture medium. At last, the cells were inoculated into other culture dishes for 10–14 days, followed by an observation of the cell colony formation under a microscope.

Transwell assay

The anti-invasive and anti-migratory effects of each group were monitored *via* transwell chambers assay. The upper chambers of the transwell were loaded with 600 μ L of DMEM medium and 3×10⁴ Huh7 cells (transfected or un-transfected) each well. In the transwell's lower chambers, only cultural medium of 800 μ L with FBS 10% was filled. Cells in each group were cultured in upper chambers for 24 h at 37°C. Then clean off the non-migrated cells and the migrated cells were processed routinely by 10 minutes of fixation with formalin 4%. Afterward staining was accomplished with crystal violet (0.1%) for 12 minutes, followed by photographing the randomly selected 5 fields using microscopy with 100× magnification. Finally, the invasion was determined, except transwell chambers were coated with Matrigel.

Table 1. Primer sequences

Gene	Forward primer	Reverse primer
CD44	5'-ACTTGGAGGCCTTGGCTAAC-3'	5'-GACAGACAGACTGCGACCTG-3'
GAPDH	5'-TGTGTCCGTCGTGGATCTGA-3'	5'-TTGCTGTTGAAGTCGAGGAG-3'

Wound healing assay

Huh7 cells were cultured in 12-well plate overnight for wound healing assay purposes. With the help of a 10 μ l tip, a scratch was created on the monolayer cells. After scratching, cells were washed with culture media to remove floating cells. Cells were kept untreated or either transfected with different vectors. The transfection of siRNAs (Si-CD44 and si-NC) and vectors (empty vector and vectore-CD44) was performed in the Huh7 cells, using lipofectamine and according to the manufacturer's protocol. The efficacy of transfection was checked by western blotting. Images of fresh scratch were captured immediately with the help of a digital camera. After treatment completion, cells were washed thrice with culture media and followed by capturing pictures of the scratch. The scratch area was determined using Image-Pro software. Cell migration was determined by calculating the scratch closure.

RT-qPCR assay

RNA from Huh7 cells was obtained using TRIzol method and then reversed to cDNA with RT Kit. Quantitative PCR was carried out using SYBRGreen (Takara) with appropriate primers designed by Primer 5.0 (Table 1) according to the conditions, including an initial step of 10 minute in 95°C, and then 40 cycles of amplification, which includes 10 s in 95°C, 20 s in 58°C and 25 s in 72°C. Quantification was determined by $2^{-\Delta\Delta CT}$ (26). The internal control used was GAPDH.

Western Blot

Total cellular protein from each group was extracted, followed by protein concentration determination using a BCA protein quantification kit (Pierce, 23225). From each sample, 45 μ g of proteins were loaded and run on SDS-PAGE gels, which were processed for blotting to PVDF membranes. Blocking PVDF membrane with 5% non-fat dry milk was done at room temperature for 2 h. It was followed by overnight incubation with primary antibodies like anti-MMP-9 (abcam, ab58803, 1:1000) anti-MMP-2 (Santa Cruz, sc-13594, 1:800), anti- β -catenin (Sigma Aldrich, C7207, 1:1000), anti-GSK-3 β (Santa Cruz, sc-81462, 1:1000), anti-CXCR4 (abcam, ab124824, 1:800) and anti-GAPDH (Cell Signaling Technology, 5174, 1:1000). Next day, after washing with PBS thrice, membranes were incubated with HRP-linked secondary antibodies (Cell Signaling Technology, 7074 and 7076, 1:3000) for 90 minutes at room temperature. Finally, ECL chromogenic substrate was added for color reaction.

Statistical analysis

The experimental data were expressed as mean \pm standard deviation (S.D.), and SPSS 21.0 software was utilized for statistical analysis. In addition, *t*-test and ANOVA were used for comparison between groups. Each experiment was repeated thrice. *P*<0.05 was considered that the results were statistically significant.

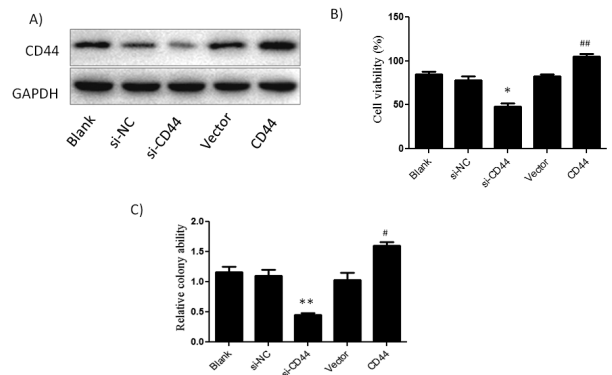


Figure 1. Transfection efficacy (A) and Effect of CD44 expressions on proliferation and cell viability of Huh7 cells (B, C). Cell viability of Huh7 cells was detected by MTT while as Cell viability was detected by colony formation assay. **P*<0.05 and ***P*<0.01 vs. si-NC group; **P*<0.05 and ***P*<0.01: vs. Vector group.

RESULTS**Inhibition of CD44 inhibits proliferation and cell viability**

Knockdown of CD44 can inhibit its expression in Huh7 cells, while overexpression can reverse the result (Fig. 1A). The results of immunoblotting showed that CD44 is expressed in Huh7 cells. The expression level of CD44 significantly decreased in the Si-CD44 group compared to the Si-NC group. However, the expression level of CD44 increased significantly in the CD44 group compared to the vector group.

MTT assay showed that the proliferation ability of Huh7 cells were significantly reduced in the si-CD44 group compared to the si-NC group (Fig. 1B). On the contrary, the proliferation ability of Huh7 cells increased significantly in the CD44 group compared to the vector group. Furthermore, knockout of CD44 significantly in-

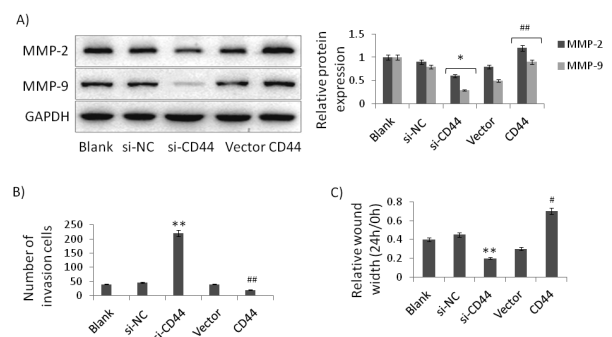


Figure 2. Effect of CD44 expression on invasion and metastasis of hepatocellular carcinoma cells.

(A) The expression of MMP-2 and MMP-9 in Huh7 cells detected by western blot. (B) Effect of CD44 expression on invasive ability of Huh7 cells detected by Transwell assay. (C) Effect of CD44 expression on migration ability of Huh7 cells detected by wound healing assay. **P*<0.05 and ***P*<0.01 vs. si-NC group; **P*<0.05 and ***P*<0.01: vs. Vector group.

hibited cell viability of Huh7 cells, while overexpression of CD44 significantly motivates it (Fig. 1C). The results showed that CD44 was involved in the proliferation and cell viability of hepatocellular carcinoma cells.

Inhibition of CD44 can inhibit invasion and metastasis

Further, we studied the role of CD44 on cellular invasion and metastasis in Huh7 cells. Transwell and wound healing assay were used to evaluate the invasive and migration ability of Huh7 cells. The results (Fig. 2A–B) suggested that the invasion and metastasis of Huh7 cells decreased significantly after silencing CD44 compared to si-NC group. Instead, cellular invasion and metastasis were significantly increased after overexpressing CD44 compared to the vector group ($P < 0.05$). To investigate the possible mechanism through which CD44 regulates functional changes in Huh7 cells, MMP-2 and MMP-9 expressions were examined (Fig. 2C). The expression level of MMP-2 and MMP-9 was significantly increased after CD44 silencing and a reverse trend was observed after overexpressing CD44.

Inhibition of CD44 can inhibit the expression levels of CXCR4/CXCL12 proteins

The effect of CD44 expression on CXCR4 proteins associated with induction of cancer growth was detected. Western blot indicated (Fig. 3) that the expression levels of CXCR4 were significantly decreased in the si-CD44 group, and opposite results were observed in the CD44 group compared to the control group. These results confirmed that the activation of CXCR4 signal pathway was inhibited after silencing CD44.

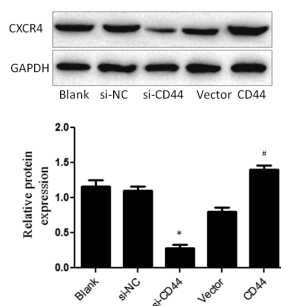


Figure 3. Effect of CD44 expression on the expression levels of CXCR4.

The expression of CXCR4 in Huh7 cells was detected by western blot. * $P < 0.05$ vs. si-NC group; * $P < 0.05$: vs. Vector group.

Inhibition of CD44 inhibits the expression levels of Wnt/ β -catenin signal proteins

The expression of β -catenin decreased significantly in the si-CD44 group compared to the si-NC group. On the other hand, GSK-3 β expression increased significantly in the si-CD44 group compared to the si-NC group (Fig. 4). Thus confirming an association between Wnt/ β -catenin pathway activation and CD44.

DISCUSSION

Wnt signal is divided into the typical Wnt pathway and two atypical Wnt pathways (Reya & Clevers, 2005). The typical Wnt signal pathway is currently the most widely studied in clinical practice. Studies have demonstrated that nearly 50% of currently known tumors show an association with abnormal Wnt/ β -catenin signal path-

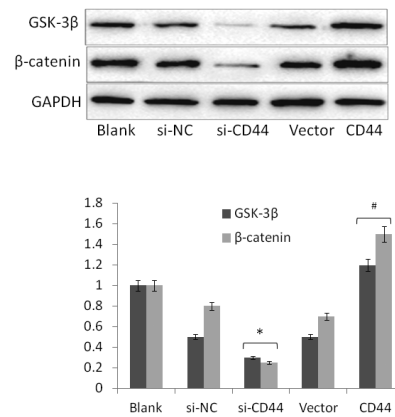


Figure 4. Effect of CD44 expression on Wnt/ β -catenin signal pathway.

The expression of GSK-3 β and β -catenin in Huh7 cells was detected by western blot. * $P < 0.05$ vs. si-NC group; * $P < 0.05$: vs. Vector group.

ways, such as intestinal cancer (Barker *et al.*, 2009), breast cancer (Shackleton *et al.*, 2006; Teissedre *et al.*, 2009), etc. Abnormal expression of proteins such as GSK-3 β (Cho *et al.*, 2010), β -catenin (Clements *et al.*, 2002), and MMPs (Conlon & Murray, 2019) in the pathway triggers sustained cell proliferation, ultimately leading to cancer (MacDonald *et al.*, 2009). Meanwhile, it performs a crucial role in cellular invasion and metastasis (Nguyen *et al.*, 2009b; Stein *et al.*, 2006). Therefore, the present study investigated whether CD44 could mediate invasion and metastasis in HCC cells by regulating the Wnt/ β -catenin signal pathway.

In the present study, cellular proliferation and invasion (Huh7 cells) reduced after silencing of CD44. However, the proliferative and invasive capacity of cells increased after overexpressing CD44 and thus confirmed that CD44 is involved in the progression of HCC. In addition, protein levels of MMP-2, MMP-9, and β -catenin were decreased; the expression of GSK-3 β was increased after CD44 silencing in Huh7 cells. However, the opposite results were presented after over-expression of CD44. These findings suggest that down-regulation of CD44 inhibits the Wnt/ β -catenin signal pathway and gradually inhibit invasion and metastasis of Huh7 cells.

The activated Wnt pathway stimulates CXCL12 release, a key paracrine molecule that controls different biological processes like cellular activation and migration, influences inflammation, and angiogenesis (Giordano *et al.*, 2019; Meng *et al.*, 2018). The earlier connection between CXCL12 expression and the Wnt/ β -catenin pathway has been reported in fibrosis, particularly in liver fibrosis (Akcora *et al.*, 2018). But no study involving CD44/CXCL12/Wnt/ β -Catenin Axis has been reported to date. To support our current findings, additional in vivo research is necessary. Additionally, this study was conducted using a hepatocellular carcinoma cell line, which does not reflect a real-world scenario. However, this study offered the first proof-of-concept data indicating CD44/Wnt/CXCL12 signaling axis in hepatocellular carcinoma cells.

CONCLUSION

In summary, by silencing CD44 expression, invasion and metastasis of HCC cells could be inhibited. This result could possibly be obtained by mediating the Wnt/ β -

catenin signal pathway. This provides the more comprehensive role of CD44 as a therapeutic target in patients with HCC.

Declarations

Author Contributions. XS, FD and WL contributed to the study conception and design. Data collection and analysis were performed by JT and KY, while analysis and interpretation of the results were performed by QL and ZZ. The manuscript was written by XS, FD, WL, JT, KY, QL and ZZ read, interpreted and revised the manuscript critically for important intellectual content. All authors approved the final manuscript.

Conflict of interest. No conflict of interest is associated with this work.

Acknowledgements. Declared none

REFERENCES

- Akcora BO, Storm G, Bansal R (2018) Inhibition of canonical WNT signaling pathway by beta-catenin/CBP inhibitor ICG-001 ameliorates liver fibrosis *in vivo* through suppression of stromal CXCL12. *Biochim Biophys Acta Mol Basis Dis* **1864**: 804–818. <https://doi.org/10.1016/j.bbdis.2017.12.001>
- Asai R, Tsuchiya H, Amisaki M, Makimoto K, Takenaga A, Sakabe T, Hoi S, Koyama S, Shiota, G (2019) CD44 standard isoform is involved in maintenance of cancer stem cells of a hepatocellular carcinoma cell line. *Cancer Med* **8**: 773–782. <https://doi.org/10.1002/cam4.1968>
- Ayob AZ, Ramasamy TS (2018) Cancer stem cells as key drivers of tumour progression. *J Biomed Sci* **25**: 20. <https://doi.org/10.1186/s12929-018-0426-4>
- Barker N, Ridgway RA, van Es JH, van de Wetering M, Begthel H, van den Born M, Danenberg E, Clarke AR, Sansom OJ, Clevers H (2009) Crypt stem cells as the cells-of-origin of intestinal cancer. *Nature* **457**: 608–611. <https://doi.org/10.1038/nature07602>
- Cho YJ, Kim JH, Yoon J, Cho SJ, Ko YS, Park JW, Lee HS, Lee HE, Kim WH, Lee BL (2010) Constitutive activation of glycogen synthase kinase-3beta correlates with better prognosis and cyclin-dependent kinase inhibitors in human gastric cancer. *BMC Gastroenterol* **10**: 91. <https://doi.org/10.1186/1471-230X-10-91>
- Clements WM, Wang J, Sarnaik A, Kim OJ, MacDonald J, Fenoglio-Preiser C, Groden J, Lowy AM (2002) beta-Catenin mutation is a frequent cause of Wnt pathway activation in gastric cancer. *Cancer Res* **62**: 3503–3506. PMID: 12067995
- Conlon GA, Murray GI (2019) Recent advances in understanding the roles of matrix metalloproteinases in tumour invasion and metastasis. *J Pathol* **247**: 629–640. <https://doi.org/10.1002/path.5225>
- Cross SS, Laidler P (1990) Computer-assisted learning in morbid anatomy. A stimulation of autopsy procedures and death certification. *Med Sci Law* **30**: 115–118. <https://doi.org/10.1177/002580249003000206>
- Davis GL, Dempster J, Meler JD, Orr DW, Walberg MW, Brown B, Berger BD, O'Connor JK, Goldstein RM (2008) Hepatocellular carcinoma: management of an increasingly common problem. *Proceedings* **21**: 266–280. <https://doi.org/10.1080/08998280.2008.11928410>
- El-Serag HB (2012) Epidemiology of viral hepatitis and hepatocellular carcinoma. *Gastroenterology* **142**: 1264–1273 e1261. <https://doi.org/10.1053/j.gastro.2011.12.061>
- Gajos-Michniewicz A, Czyz M (2020) WNT Signaling in Melanoma. *Int J Mol Sci* **21**: 4852. <https://doi.org/10.3390/ijms21144852>
- Gao W, Chen L, Ma Z, Du Z, Zhao Z, Hu Z, Li Q (2013) Isolation and phenotypic characterization of colorectal cancer stem cells with organ-specific metastatic potential. *Gastroenterology* **145**: 636–646 e635. <https://doi.org/10.1053/j.gastro.2013.05.049>
- Ghanem I, Riveiro ME, Paradis V, Faivre S, de Parga PM, Raymond E (2014) Insights on the CXCL12-CXCR4 axis in hepatocellular carcinoma carcinogenesis. *Am J Transl Res* **6**: 340–352. PMID: 25075251
- Ghouri YA, Mian I, Rowe JH (2017) Review of hepatocellular carcinoma: Epidemiology, etiology, and carcinogenesis. *J Carcinog* **16**: 1. https://doi.org/10.4103/jcar.JCar_9_16
- Giordano FA, Link B, Glas M, Herrlinger U, Wenz F, Umansky V, Brown JM, Herskind C (2019) Targeting the post-irradiation tumor microenvironment in glioblastoma *via* inhibition of CXCL12. *Cancers* **11**: 272. <https://doi.org/10.3390/cancers11030272>
- Iida J, Clancy R, Dorchak J, Somiari RI, Somiari S, Cutler ML, Mural RJ, Shriver CD (2014) DNA aptamers against exon v10 of CD44 inhibit breast cancer cell migration. *PLoS One* **9**: e88712. <https://doi.org/10.1371/journal.pone.0088712>
- Kang H, Watkins G, Parr C, Douglas-Jones A, Mansel RE, Jiang WG (2005) Stromal cell derived factor-1: its influence on invasiveness and migration of breast cancer cells *in vitro*, and its association with prognosis and survival in human breast cancer. *Breast Cancer Res* **7**: R402–R410. <https://doi.org/10.1186/bcr1022>
- Li L, Hao X, Qin J, Tang W, He F, Smith A, Zhang M, Simeone DM, Qiao XT, Chen ZN, Lawrence TS, Xu L (2014). Antibody against CD44s inhibits pancreatic tumor initiation and postradiation recurrence in mice. *Gastroenterology* **146**: 1108–1118. <https://doi.org/10.1053/j.gastro.2013.12.035>
- Luo Y, Tan Y (2016) Prognostic value of CD44 expression in patients with hepatocellular carcinoma: meta-analysis. *Cancer Cell Int* **16**: 47. <https://doi.org/10.1186/s12935-016-0325-2>
- MacDonald BT, Tamai K, He X (2009) Wnt/beta-catenin signaling: components, mechanisms, and diseases. *Dev Cell* **17**: 9–26. <https://doi.org/10.1016/j.devcel.2009.06.016>
- Malhotra GK, Zhao X, Band H, Band V (2010) Histological, molecular and functional subtypes of breast cancers. *Cancer Biol Ther* **10**: 955–960. <https://doi.org/10.4161/cbt.10.10.13879>
- Mani SA, Guo W, Liao MJ, Eaton EN, Ayyanan A, Zhou AY, Brooks M, Reinhard F, Zhang CC, Shipitsin M, Campbell LL, Polyak K, Briskin C, Yang J, Weinberg RA (2008) The epithelial-mesenchymal transition generates cells with properties of stem cells. *Cell* **133**: 704–715. <https://doi.org/10.1016/j.cell.2008.03.027>
- Matzke-Ogi A, Jannasch K, Shatirishvili M, Fuchs B, Chiblak S, Morton J, Tawak B, Lindner T, Sansom O, Alves F, Warth A, Schwager C, Mier W, Kleeff J, Ponta H, Abdollahi A, Orian-Rousseau V (2016) Inhibition of tumor growth and metastasis in pancreatic cancer models by interference with CD44v6 signaling. *Gastroenterology* **150**: 513–525, e510. <https://doi.org/10.1053/j.gastro.2015.10.020>
- McGlynn KA, Petrick JL, London WT (2015) Global epidemiology of hepatocellular carcinoma: an emphasis on demography and regional variability. *Clin Liver Dis* **19**: 223–238. <https://doi.org/10.1016/j.cld.2015.01.001>
- Meng W, Xue S, Chen Y (2018) The role of CXCL12 in tumor microenvironment. *Gene* **641**: 105–110. <https://doi.org/10.1016/j.gene.2017.10.015>
- Moldovan IM, Susman S, Pirlog R, Jianu EM, Leucuta DC, Melincovici CS, Crisan D, Florian IS (2017) Molecular markers in the diagnosis of invasive pituitary adenomas – an immunohistochemistry study. *Rom J Morphol Embryol* **58**: 1357–1364. PMID: 29556628
- Nguyen DX, Bos PD, Massague J (2009a) Metastasis: from dissemination to organ-specific colonization. *Nat Rev Cancer* **9**: 274–284. <https://doi.org/10.1038/nrc2622>
- Nguyen DX, Chiang AC, Zhang XH, Kim JY, Kris MG, Ladanyi M, Gerald WL, Massague J (2009b) WNT/TCF signaling through LEF1 and HOXB9 mediates lung adenocarcinoma metastasis. *Cell* **138**: 51–62. <https://doi.org/10.1016/j.cell.2009.04.030>
- Orian-Rousseau V, Ponta H (2015) Perspectives of CD44 targeting therapies. *Arch Toxicol* **89**: 3–14. <https://doi.org/10.1007/s00204-014-1424-2>
- Perlikos F, Harrington KJ, Syrigos KN (2013) Key molecular mechanisms in lung cancer invasion and metastasis: a comprehensive review. *Crit Rev Oncol Hematol* **87**: 1–11. <https://doi.org/10.1016/j.critrevonc.2012.12.007>
- Reya T, Clevers H (2005). Wnt signalling in stem cells and cancer. *Nature* **434**: 843–850. <https://doi.org/10.1038/nature03319>
- Sakai N, Yoshidome H, Shida T, Kimura F, Shimizu H, Ohtsuka M, Takeuchi D, Sakakibara M, Miyazaki M (2012) CXCR4/CXCL12 expression profile is associated with tumor microenvironment and clinical outcome of liver metastases of colorectal cancer. *Clin Exp Metastasis* **29**: 101–110. <https://doi.org/10.1007/s10585-011-9433-5>
- Salik B, Yi H, Hassan N, Santiapillai N, Vick B, Connerty P, Duly A, Trahair T, Woo AJ, Beck D, Liu T, Spiekermann K, Jeremias I, Wang J, Kavallaris M, Haber M, Norris MD, Liebermann DA, D'Andrea RJ, Murriel C, Wang JY (2020) Targeting RSP03-LGR4 signaling for leukemia stem cell eradication in acute myeloid leukemia. *Cancer Cell* **38**: 263–278, e266. <https://doi.org/10.1016/j.cccell.2020.05.014>
- Scotton CJ, Wilson JL, Scott K, Stamp G, Wilbanks GD, Fricker S, Bridger G, Balkwill FR (2002) Multiple actions of the chemokine CXCL12 on epithelial tumor cells in human ovarian cancer. *Cancer Res* **62**: 5930–5938. PMID: 12384559
- Shackleton M, Vaillant F, Simpson KJ, Sting J, Smyth GK, Asselin-Labat ML, Wu L, Lindeman GJ, Visvader JE (2006) Generation of a functional mammary gland from a single stem cell. *Nature* **439**: 84–88. <https://doi.org/10.1038/nature04372>
- Shah V, Taratula O, Garbuzenko OB, Taratula OR, Rodriguez-Rodriguez I, Minko T (2013) Targeted nanomedicine for suppression of CD44 and simultaneous cell death induction in ovarian cancer: an optimal delivery of siRNA and anticancer drug. *Clin Cancer Res* **19**: 6193–6204. <https://doi.org/10.1158/1078-0432.CCR-13-1536>
- Stein U, Arlt F, Walther W, Smith J, Waldman T, Harris ED, Mertins SD, Heizmann CW, Allard D, Birchmeier W, et al (2006) The metastasis-associated gene S100A4 is a novel target of beta-catenin/T-cell factor signaling in colon cancer. *Gastroenterology* **131**: 1486–1500. <https://doi.org/10.1053/j.gastro.2006.08.041>

- Sung H, Ferlay J, Siegel RL, Laversanne M, Soerjomataram I, Jemal A, Bray F (2021) Global Cancer Statistics 2020: GLOBOCAN Estimates of incidence and mortality worldwide for 36 cancers in 185 countries. *CA Cancer J Clin* **71**: 209–249. <https://doi.org/10.3322/caac.21660>
- Tai D, Wells K, Arcaroli J, Vanderbilt C, Aisner DL, Messersmith WA, Lieu CH (2015) Targeting the WNT signaling pathway in cancer therapeutics. *Oncologist* **20**: 1189–1198. <https://doi.org/10.1634/theoncologist.2015-0057>
- Teissedre B, Pinderhughes A, Incassati A, Hatsell SJ, Hiremath M, Cowin P (2009) MMTV-Wnt1 and -DeltaN89beta-catenin induce canonical signaling in distinct progenitors and differentially activate Hedgehog signaling within mammary tumors. *PLoS One* **4**: e4537. <https://doi.org/10.1371/journal.pone.0004537>
- Teng F, Tian WY, Wang YM, Zhang YF, Guo F, Zhao J, Gao C, Xue FX (2016) Cancer-associated fibroblasts promote the progression of endometrial cancer via the SDF-1/CXCR4 axis. *J Hematol Oncol* **9**: 8. <https://doi.org/10.1186/s13045-015-0231-4>
- Todaro M, Gaggianesi M, Catalano V, Benfante A, Iovino F, Bifoni M, Apuzzo T, Sperduti I, Volpe S, Cocorullo G, Gulotta G, Dieli F, De Maria R, Stassi G (2014) CD44v6 is a marker of constitutive and reprogrammed cancer stem cells driving colon cancer metastasis. *Cell Stem Cell* **14**: 342–356. <https://doi.org/10.1016/j.stem.2014.01.009>
- Vlashi E, Lagadec C, Vergnes L, Matsutani T, Masui K, Poulou M, Popescu R, Della Donna L, Evers P, Dekmezian C, Reue K, Christofk H, Mischel PS, Pajonk F (2011) Metabolic state of glioma stem cells and nontumorigenic cells. *Proc Natl Acad Sci U S A* **108**: 16062–16067. <https://doi.org/10.1073/pnas.1106704108>
- Wiese KE, Nusse R, van Amerongen R (2018) Wnt signalling: conquering complexity. *Development* **145**: dev165902. <https://doi.org/10.1242/dev.165902>
- Wilson MA, Buetow KH (2020) Novel mechanisms of cancer emerge when accounting for sex as a biological variable. *Cancer Res* **80**: 27–29. <https://doi.org/10.1158/0008-5472.CAN-19-2634>
- Yamashita T, Ji J, Budhu A, Forgues M, Yang W, Wang HY, Jia H, Ye Q, Qin LX, Wauthier E, Reid LM, Minato H, Honda M, Kaneko S, Tang ZY, Wang XW (2009) EpCAM-positive hepatocellular carcinoma cells are tumor-initiating cells with stem/progenitor cell features. *Gastroenterology* **136**: 1012–1024. <https://doi.org/10.1053/j.gastro.2008.12.004>
- Yang L, Shi P, Zhao G, Xu J, Peng W, Zhang J, Zhang G, Wang X, Dong Z, Chen F, Cui H (2020) Targeting cancer stem cell pathways for cancer therapy. *Signal Transduct Target Ther* **5**: 8. <https://doi.org/10.1038/s41392-020-0110-5>
- Zhang J, He X, Wan Y, Zhang H, Tang T, Zhang M, Yu S, Zhao W, Chen L (2021) CD44 promotes hepatocellular carcinoma progression via upregulation of YAP. *Exp Hematol Oncol* **10**: 54. <https://doi.org/10.1186/s40164-021-00247-w>
- Zhang X, Wang L, Qu Y (2020) Targeting the beta-catenin signaling for cancer therapy. *Pharmacol Res* **160**: 104794. <https://doi.org/10.1016/j.phrs.2020.104794>
- Zhu Z, Hao X, Yan M, Yao M, Ge C, Gu J, Li J (2010) Cancer stem/progenitor cells are highly enriched in CD133+CD44+ population in hepatocellular carcinoma. *Int J Cancer* **126**: 2067–2078. <https://doi.org/10.1002/ijc.24868>

MicroRNA-411-3p motivates methotrexate's cellular uptake and cytotoxicity *via* targeting Yin-yang 1 in leukemia cells

HuiJing Sun^{1#}, ShuGuang Zhou^{1#}, ZhouSheng Yang¹, MingYu Meng¹, Yan Dai², XinYe Li² and XiaoYu Chen^{1✉}

¹Department of Pharmacy, The People's Hospital of Guangxi Zhuang Autonomous Region, Nanning City, Guangxi Zhuang Autonomous Region, 530021, China; ²Department of Paediatrics, The People's Hospital of Guangxi Zhuang Autonomous Region, Nanning City, Guangxi Zhuang Autonomous Region, 530021, China

This study aimed to figure out how microRNA (miR)-411-3p's impacts on methotrexate (MTX)'s cellular uptake and cytotoxicity in acute lymphoblastic leukaemia (ALL) CEM-C1 cells by targeting Yin-yang 1 (YY1). miR-411-3p and YY1 were detected by RT-qPCR or Western blot. Intracellular MTX concentration was measured by enzyme-linked immunosorbent assay. Cell viability and apoptosis were evaluated by CCK-8, clonal formation assay, and flow cytometry. Verification of miR-411-3p and YY1's targeting link was manifested. It came out that miR-411-3p mimic or si-YY1 elevated intracellular MTX, MTX-induced cytotoxicity and apoptosis rate in CEM-C1. However, the inverse results were noticed in cells introduced with miR-411-3p inhibitor or oe-YY1. Meanwhile, it was found that cell relative luciferase activity was reduced after co-transfection of miR-411-3p mimic with YY1-WT, indicating that miR-411-3p targeted YY1. Elevation of YY1 could turn around elevating miR-411-3p's impacts on MTX's cellular uptake and cytotoxicity in CEM-C1 cells. These findings convey that miR-411-3p motivated MTX's cellular uptake and cytotoxic impacts via targeting YY1 in leukemia cells. This study is helpful for learning about the mechanisms underlying MTX responses in ALL patients.

Keywords: MicroRNA-411-3p, Yin-yang 1, methotrexate, acute lymphoblastic leukemia

Received: 01 March, 2023; **revised:** 19 December, 2022; **accepted:** 18 April, 2023; **available on-line:** 19 September, 2023

✉e-mail: cxiaoouchina@hotmail.com

[#]These authors contributed equally to this work.

Acknowledgements of Financial Support: Guangxi Zhuang Autonomous Region Self-funded by Health Commission of Guangxi Zhuang Autonomous Region, (No. Z20190278).

Abbreviations: ALL, Acute lymphoblastic leukaemia; MTX, methotrexate; YY1, Yin-yang 1

INTRODUCTION

Acute lymphoblastic leukaemia (ALL) is an extremely common malignant tumor, which frequently shows up in children, taking up about 80% of ALL cases, and occasionally takes place in adults (Liang *et al.*, 2021). ALL is featured by malignant transformation and proliferation of T- or B-cell progenitors which invade blood, bone marrow, and extramedullary sites, thereby preventing normal blood cell production (Ranjbar *et al.*, 2019). Methotrexate (MTX) is a chemotherapeutic drug for ALL and has been applied to cure leukemia and lymphoma patients (Woźniak *et al.*, 2021). Al-

though most patients are available to achieve long-term disease-free survival *via* standardized treatments, including MTX, some ALL treatments for children are still ineffective, and drug resistance is a vital reason for this phenomenon (Jaramillo *et al.*, 2019). Therefore, discovering approaches to suppress chemotherapy resistance in ALL patients is crucial for ALL cure.

MTX is a folate antagonist, whose action is extremely complicated, involving some transporters determining intracellular drug levels and active MTX polyglutamate and some metabolic enzymes (Gervasini *et al.*, 2017). MTX enters cells by passive diffusion via the solute carrier 19A1 transporter (RFC1) (Ando *et al.*, 2013), while the drug is pumped out by some membrane efflux transporters of the ATP-binding cassette family (Aberuyi *et al.*, 2021). MTX is converted into active polyglutamate form (MTX polyglutamate, MTXPG) by folate polyglutamate synthase intracellularly (De Beaumais *et al.*, 2012). MTX and MTXPG inhibit thymidine synthesis by targeting dihydrofolate reductase and thymidine synthase (Rushworth *et al.*, 2015), thereby impairing DNA and RNA synthesis and leading to cell death (Oosterom *et al.*, 2018). In conclusion, the accumulation of MTX and its active metabolite methotrexate polyglutamate (MTXPG) in all cells is an important determinant of its anti-leukemia effect (Panetta *et al.*, 2010).

MicroRNAs (miRNAs), a cluster of endogenous single-stranded non-coding RNAs, modulate gene expression (Lin *et al.*, 2021). Much evidence illustrates that miRNAs participate in almost all biological processes, including drug resistance (Xian *et al.*, 2019; Naghizadeh *et al.*, 2020; Wei *et al.*, 2021). Genetic variation in MTX transporter genes has been reported to be implicated in toxicity, and these transporters are controlled by miRNAs (Iparraguirre *et al.*, 2016). Wang SM (Wang *et al.*, 2017). confirm that two miRNA-binding site polymorphisms (rs3737966 G>A and rs35134728 DEL/TTC) in the 3'-UTR of 5,10-methylenetetrahydrofolate reductase were linked with serum MTX concentrations. Xu Wen (Xu *et al.*, 2018). discovered that miR-29 family restrained MTX resistance but motivated apoptosis by targeting COL3A1 and MCL1 in osteosarcoma. MiR-411-3p, a newly studied miRNA, has been discovered to be aberrantly expressed in some human cancers (Huang *et al.*, 2021; Wang *et al.*, 2019; Wang *et al.*, 2020). However, no studies have been conducted to clarify its role in MTX resistance. In the research, the main focus was on miR-411-3p's function in controlling Yin-yang 1 (YY1) and its impact on ALL CEM-C1 cell uptake and MTX cytotoxicity.

MATERIALS AND METHODS

Cell culture

Growth of human ALL CEM-C1 cells was in Roswell Park Memorial Institute – 1640 medium replenished with 10% fetal bovine serum (Gibco, Grand Island, NY, USA), 100 U/ml penicillin, and 100 U/ml streptomycin (Beyotime Biotechnology, Shanghai, China). CEM-C1 cells were purchased from the Cell Bank of the Chinese Academy of Sciences (Shanghai, China).

Cell transfection

Synthesis of miR-411-3p mimic/inhibitor, mimic/inhibitor negative control (NC), si-YY1/-NC, and oe-YY1/-NC was done by Invitrogen. Oligonucleotides or plasmids (8 µmol/ml) were transfected into CEM-C1 cells based on Lipofectamine 2000 reagent (Invitrogen; Thermo Fisher Scientific). After transfection, cells were treated with different concentrations of MTX (10, 20 and 40 ng/ml).

Intracellular MTX Concentration Determination

Cells were dispersed in 96-well plates at 5.0×10^5 cells per well prior to transfection and MTX treatment. Quantification of intracellular MTX was done using human methotrexate, MTX ELISA kit (HB1386-Hu, Shanghai Hengyuan Biotechnology Co., LTD). Absorbance at 450 nm was recorded on a microplate reader (ELX800, BioTek Instruments, Inc.) and MTX concentrations were calculated.

Cell proliferation assay

Cell proliferation assays were conducted using the Cell Counting Kit-8 (CCK-8; Beyotime Institute of Biotechnology, Inc.). CEM-C1 cells were combined with CCK-8 solution (10 µL) in each well. Next, 4-h cell incubation was conducted, followed by measurement of optical density (OD) value at 450 nm on a microplate reader (ELX800, BioTek Instruments, Inc.). Proliferation rate: $\{[(OD_{\text{control}} - OD_{\text{blank}}) - (OD_{\text{treated}} - OD_{\text{blank}})] / (OD_{\text{control}} - OD_{\text{blank}})\} \times 100\%$.

Colony formation assay

Treatment of transfected CEM-C1 cells was done with different concentrations of MTX (10, 20 and 40 ng/ml). The cells were then transferred to a 6-well plate (1×10^3 cells/well) and supplemented with RPMI-1640 medium containing 10% fetal bovine serum at 37°C. After 14 days, the cells were fixed with formaldehyde and stained with 0.1% crystal violet solution (Sigma Aldrich) at 25°C for 15 min and counted under a CKX41 microscope (Olympus).

Apoptosis assay

Annexin V-fluorescein isothiocyanate Apoptosis Detection Kit (BD, USA) was applied to detect apoptosis. In brief, cells were stained with 10 µL Annexin V and 5 µL propidium iodide for 15 min. Then, quantitative analysis was performed using BD FACSCalibur™ (BD, USA).

Reverse transcription quantitative polymerase chain reaction (RT-qPCR)

Total RNA's extraction was conducted using the miRNeasy extraction kit (Qiagen, Valencia, CA, USA).

MiR-411-3p's quantification was conducted using the Hairpin-it miRNA qPCR quantification kit (GenePharma, Shanghai, China) with U6 as a loading control. Detection of YY1 was implemented using Power SYBR Green PCR Master Mix (Applied Biosystems) with glyc-

Table 1. RT-qPCR primers

Genes	Primer sequence (5'-3')
MiR-411-3p	F: CCGAGTATGTAACACGGTC
	R: TATGTAACACGGTCCACTAAC
YY1	F: AAAACGACACCAACTGGTTCATAC
	R: AAGTCCAGTGAAAAGCGTTTCC
Bcl-2	F: ATCCAGGACAACGGAGGCTG
	R: CAGATAGGCACCCAGGGTGA
Bax	F: GATCGAGCAGGGCGAATG
	R: CATCTCAGCTGCCACTCG
U6	F: CTCGCTTCGGCAGCACA
	R: AACGCTTCACGAATTGCGT
GAPDH	F: CACCCACTCCTCCACCTTG
	R: CCACCACCCTGTTGCTGTAG

eraldehyde-3-phosphate dehydrogenase (GAPDH) as internal control, and all PCR reactions were conducted on a 7500 Fast Real-Time PCR Systems (Applied Biosystems, CA, USA). All primer sequences were manifested in Table 1. Calculation of miR-411-3p or YY1 was implemented using the $2^{-\Delta\Delta CT}$ method (Wu *et al.*, 2020).

Western blot

Isolation of total protein was done using mammalian protein extraction reagents (Thermo Fisher Scientific, Inc.) and 1% protease inhibitor cocktail (Merck KGaA, Darmstadt, Germany). The Bicinchoninic acid assay method (Thermo Fisher Scientific, Inc.) was applied for determining the protein concentration. 10 µg protein separated by 1% sodium dodecyl sulfate-polyacrylamide gel electrophoresis was electro-blotted onto polyvinylidene fluoride membranes (Millipore, Bedford, MA, USA), followed by blocking with 7% skim milk and incubation with primary antibody and horseradish peroxidase-conjugated secondary antibody (ab6721; 1: 2000; Abcam). Primary antibodies applied in this study included: YY1 (sc-7341; 1: 1000; Santa Cruz Biotechnology) and GAPDH (ab8245; 1: 1000; Abcam). Detection of proteins was done by enhanced chemiluminescence (Thermo Fisher Scientific, Inc.) (Liu *et al.*, 2019).

The luciferase activity assay

Construction of the luciferase reporter gene plasmids (Promega, USA) covering the 3'-UTR of YY1 with forecast miR-411-3p target sites (Wild-type) or the mutated sites of 3'-UTR of YY1 (Mutant) was implemented. Transient co-transfection of CEM-C1 cells was then done with reporters and miR-411-3p mimic or mimic NC. Detection of Firefly and renilla luciferase activities was conducted using a dual-luciferase reporter assay system (Promega) (Liu *et al.*, 2020).

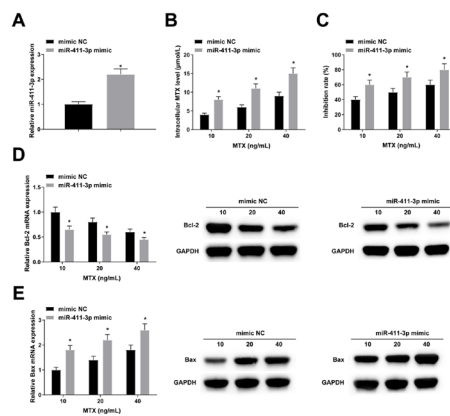


Figure 1. Elevating miR-411-3p motivates MTX's cellular uptake and cytotoxic influences.

(A) RT-qPCR detection of miR-411-3p; (B) ELISA detection of intracellular MTX concentration; (C) CCK-8 detection of cell viability; (D/E) RT-qPCR and Western blot detection of Bcl-2 and Bax; the values were clarified as mean \pm S.D. (N=3); *vs. the mimic NC, $P < 0.05$.

2RNA immunoprecipitation (RIP)

Cell lysates were collected. Incubation of the supernatant from cell lysates was implemented with human anti-Ago2 antibody (SCBT, Santa Cruz, CA, USA) or mouse Immunoglobulin G (SCBT, Santa Cruz). Detachment of proteins was done using Proteinase K buffer and the quantitative real time PCR examined co-precipitated RNAs.

2Statistical analysis

Data were presented as mean \pm standard deviation (S.D.) unless otherwise noted. Two groups' comparisons were implemented using the unpaired two-tailed Student's *t*-test. Application of Graphpad Prism software version 4.0 was for all statistical analyses. $P < 0.05$ emphasized obvious statistical meaning.

RESULTS

Elevating miR-411-3p motivates MTX's cellular uptake and cytotoxic influences

CEM/C1 cells were transfected with miR-411-3p mimic or mimic NC. miR-411-3p was elevated after transfection of miR-411-3p mimic (Fig. 1A). CEM/C1 cells were treated with disparate concentrations of MTX (10, 20 and 40 ng/ml). Detection of the intracellular MTX concentration was conducted, and the results displayed that the intracellular MTX was elevated in CEM/C1 cells introduced with miR-411-3p mimic (Fig. 1B). The cell growth was tested. The results illustrated that after incubation with different concentrations of MTX, elevating miR-411-3p resulted in a clear augmentation in the repression rate of CEM/C1 cells (Fig. 1C) and a memorable decline in the number of colonies (Fig. 2A). Considering that apoptosis is a mechanism by which MTX exerts its antitumor effect, the latent function of miR-411-3p in MTX-induced apoptosis in CEM/C1 cells was then figured out. It turned out that the apoptosis index of CEM/C1 cells in the miR-411-3p mimic introduced with different concentrations of MTX was elevated at all MTX concentrations (Fig. 2B). Moreover, after incubation with different concentrations of MTX,

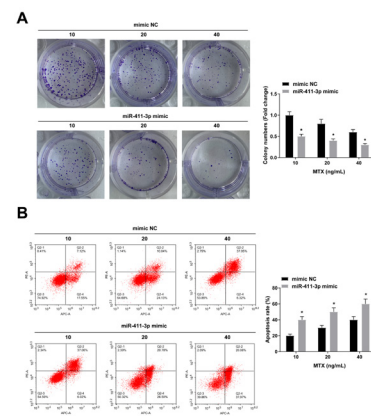


Figure 2. Elevating miR-411-3p motivates MTX's cellular uptake and cytotoxic influences.

(A) Clone formation assay detection of cell proliferation; (B) Flow cytometry detection of cell apoptosis; The data in the figures were all measurement data, and the values were clarified as mean \pm S.D. (N=3); *vs. the mimic NC, $P < 0.05$.

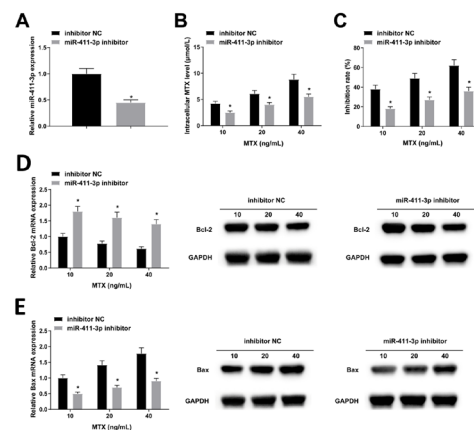


Figure 3. Depressing miR-411-3p restrains the cellular uptake and cytotoxic effects of MTX.

(A) RT-qPCR detection of miR-411-3p; (B) ELISA detection of intracellular MTX concentration; (C) CCK-8 detection of cell viability; (D/E) RT-qPCR and Western blot detection of Bcl-2 and Bax; the values were clarified as mean \pm S.D. (N=3); *vs. the inhibitor NC, $P < 0.05$.

enhancing miR-411-3p could restrain Bcl-2 but accelerate Bax (Fig. 1D-E). These results suggest that elevating miR-411-3p restrains CEM/C1 cell growth by motivating MTX's cellular uptake and cytotoxic influences.

Depressing miR-411-3p restrains MTX's cellular uptake and cytotoxic influences

To further testify miR-411-3p's function, miR-411-3p inhibitor or inhibitor NC was transfected into CEM/C1 cells, and the successful transfection was verified (Fig. 3A). It turned out that intracellular MTX was clearly reduced in CEM/C1 cells introduced with miR-411-3p inhibitor (Fig. 3B). It came out after incubation with different concentrations of MTX, that depressing miR-411-3p resulted in a clear decline of the repression rate of CEM/C1 cells (Fig. 3C) and a distinct elevation in the number of colonies (Fig. 4A). Meanwhile, CEM/C1 cells' apoptosis index after depressing miR-411-3p was declined at all MTX concentrations (Fig. 4B). Moreover, after incubation with different concentrations of MTX, depressing miR-411-3p could motivate Bcl-2 but restrain Bax (Fig. 3D/E). Taken together, repressing miR-411-3p

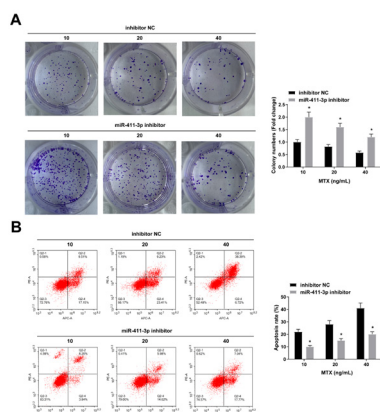


Figure 4. Depressing miR-411-3p restrains the cellular uptake and cytotoxic effects of MTX.

(A) Clone formation assay detection of cell proliferation; (B) Flow cytometry detection of cell apoptosis; the values were clarified as mean \pm S.D. (N=3); *vs. the inhibitor NC, $P<0.05$.

motivates CEM/C1 cell growth by refraining MTX's cellular uptake and cytotoxic influences.

MiR-411-3p targets YY1

For further understand miR-411-3p's possible downstream mechanism, Starbase database was applied to forecast that miR-411-3p had a binding site with YY1 (Fig. 5A). YY1 was clearly reduced after elevating miR-411-3p, while depressive miR-411-3p could motivate YY1 (Fig. 5B). Then for further verification of their targeting link, the luciferase activity assay was conducted. Results illustrating co-transfection of YY1-WT with miR-411-3p mimic showed a clear decrease in cell luciferase activity (Fig. 5C). Moreover, miR-411-3p and YY1 were apparently abundant in Ago2 immuno-precipitates (Fig. 5D). These results clarify that miR-411-3p targets YY1.

Depressing YY1 motivates MTX's cellular uptake and cytotoxic influences

To figure out YY1's impact on MTX's cellular uptake and cytotoxicity in CEM/C1 cells, si-YY1/NC was

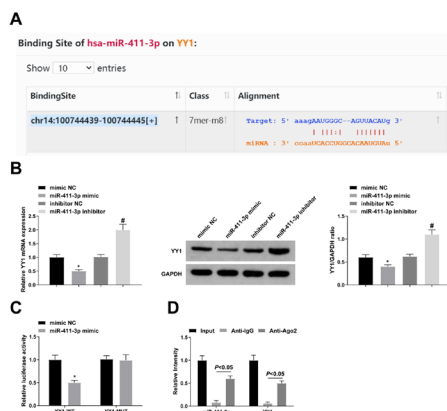


Figure 5. MiR-411-3p negatively modulates YY1.

(A) The binding site of miR-411-3p and YY1 predicted by Starbase database; (B) RT-qPCR and Western blot detection of YY1; (C) The targeting link between miR-411-3p and YY1 verified by the luciferase activity assay; (D) RIP experiment verification of the targeting link between miR-411-3p and YY1; the values were clarified as mean \pm S.D. (N=3); *vs. the mimic NC, $P<0.05$; *vs. the inhibitor NC, $P<0.05$.

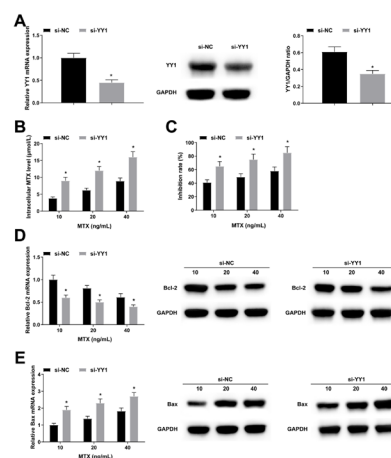


Figure 6. Depressing YY1 motivates the cellular uptake and cytotoxic effects of MTX.

(A) RT-qPCR and Western blot detection of YY1; (B) ELISA detection of intracellular MTX concentration; (C) CCK-8 detection of cell viability; (D/E) RT-qPCR and Western blot detection of Bcl-2 and Bax; the values were clarified as mean \pm S.D. (N=3); *vs. the si-NC, $P<0.05$.

transfected into CEM/C1 cells (Fig. 6A). It turned out that intracellular MTX was clearly elevated in CEM/C1 cells transfected with si-YY1 (Fig. 6B). It came out that after incubation with different concentrations of MTX, repressing YY1 resulted in a clear elevation in the inhibition rate of CEM/C1 cells (Fig. 6C) and a distinct decline in the number of colonies (Fig. 7A). It turned out that the apoptosis index of CEM/C1 cells in the si-YY1 treated with different concentrations of MTX was elevated at all MTX concentrations (Fig. 7B). Moreover, after incubation with different concentrations of MTX, depressing YY1 could restrain Bcl-2 but motivate Bax (Fig. 6D/E). The above results illustrate that repressive YY1 can accelerate MTX's cellular uptake and cytotoxicity, thereby refraining CEM/C1 cell growth.

Enhancing YY1 restrains MTX's cellular uptake and cytotoxic influences

To further testify YY1's role, it was transfected oe-YY1/NC into CEM/C1 cells and successful transfection was verified (Fig. 8A). It turned out that intracellular

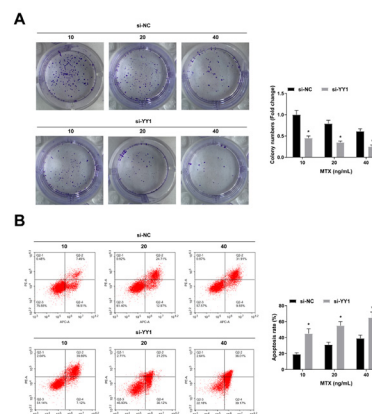


Figure 7. Depressing YY1 motivates the cellular uptake and cytotoxic effects of MTX.

(A) Clone formation assay detection of cell proliferation; (B) Flow cytometry detection of cell apoptosis; the values were clarified as mean \pm S.D. (N=3); *vs. the si-NC, $P<0.05$.

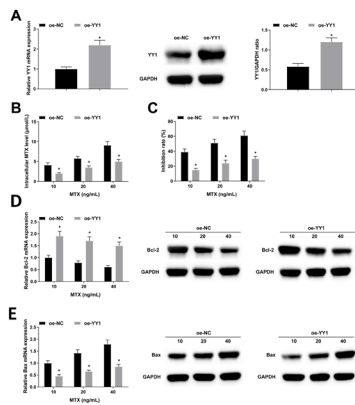


Figure 8. Enhancing YY1 restrains the cellular uptake and cytotoxic effects of MTX.

(A) RT-qPCR and Western blot detection of YY1; (B) ELISA detection of intracellular MTX concentration; (C) CCK-8 detection of cell viability; (D/E) RT-qPCR and Western blot detection of Bcl-2 and Bax; the values were clarified as mean \pm S.D. (N=3); *vs. the oe-NC, $P < 0.05$.

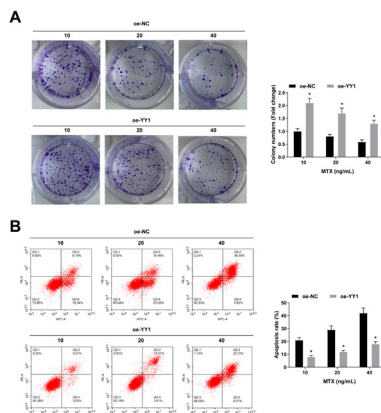


Figure 9. Enhancing YY1 restrains the cellular uptake and cytotoxic effects of MTX.

(A) Clone formation assay detection of cell proliferation; (B) Flow cytometry detection of cell apoptosis; The data in the figures were all measurement data, and the values were clarified as mean \pm S.D. (N=3); *vs. the oe-NC, $P < 0.05$.

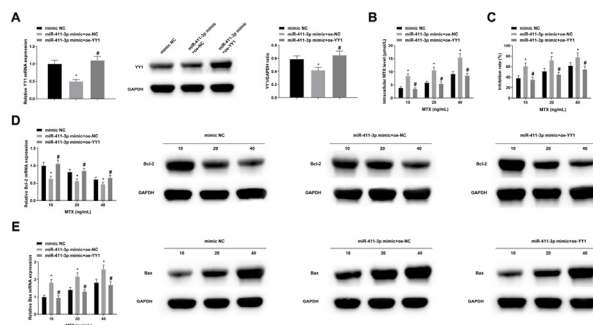


Figure 10. Elevation of YY1 could turn around elevating miR-411-3p's impacts on MTX cellular uptake and cytotoxicity in CEM-C1 cells.

(A) RT-qPCR and Western blot verification of successful transfection; (B) ELISA detection of intracellular MTX concentration; (C) CCK-8 detection of cell viability; (D/E) RT-qPCR and Western blot detection of apoptosis-linked genes (Bcl-2 and Bax); The data in the figures were all measurement data, and the values were clarified as mean \pm S.D. (N=3); *vs. the mimic NC group, $P < 0.05$; #vs. the miR-411-3p mimic+oe-NC, $P < 0.05$.

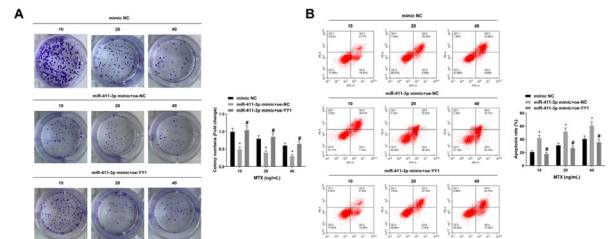


Figure 11. Elevation of YY1 could turn around elevating miR-411-3p's impacts on MTX cellular uptake and cytotoxicity in CEM-C1 cells.

(A) Clone formation assay detection of cell proliferation; (B) Flow cytometry detection of cell apoptosis; The data in the figures were all measurement data, and the values were clarified as mean \pm S.D. (N=3); *vs. the mimic NC group, $P < 0.05$, #vs. the miR-411-3p mimic+oe-NC, $P < 0.05$.

MTX was clearly declined in CEM/C1 cells transfected with oe-YY1 (Fig. 8B). It came out that after incubation with different concentrations of MTX, strengthening YY1 resulted in a clear decline in the repression rate of CEM/C1 cells (Fig. 8C) and a distinct elevation in the number of colonies (Fig. 9A). It turned out that the apoptosis index of CEM/C1 cells in the si-YY1 treated with different concentrations of MTX was declined at all MTX concentrations (Fig. 9B). Moreover, after incubation with different concentrations of MTX, depressing YY1 could motivate Bcl-2 but restrain Bax (Fig. 8DE). Overall, elevating YY1 can restrain MTX's cellular uptake and cytotoxicity, thereby motivating CEM/C1 cell growth.

Elevating YY1 turns around enhance miR-411-3p's impacts on MTX's cellular uptake and cytotoxicity in CEM-C1 cells

To further explore miR-411-3p/YY1 axis' impacts on MTX's cellular uptake and cytotoxicity in CEM/C1 cells, it was transfected with mimic NC-miR-411-3p mimic+oe-YY1 or miR-411-3p mimic+oe-NC into CEM/C1 cells, and the successful transfection was verified (Fig. 10A). All results clarify that elevation of YY1 can turn around elevating miR-411-3p's impacts on MTX cellular uptake and cytotoxicity in CEM-C1 cells (Fig. 10B-E, Fig. 11A/B).

DISCUSSION

MTX is a chemotherapeutic drug for ALL's, which majorly exerts its therapeutic impact in ALL by impairing the synthesis of DNA in cells. The ability of leukemic blasts to uptake MTX and MTX-polyglutamate has been reported to be vital for the survival of children with ALL. However, MTX has a narrow therapeutic range, its pharmacokinetics and therapeutic response display great variability in ALL's, and it exhibits serious toxicity in plentiful patients, often resulting in an interruption or discontinuation of chemotherapy (Hu *et al.*, 2019). Recent studies have exhibited that miRNAs are implicated in the concentration of MTX in the blood of ALL patients (Wang *et al.*, 2014), suggesting that miRNAs are likely to participate in controlling the uptake of MTX by ALL cells. This research illustrated originally that elevation of miR-411-3p could motivate MTX's cellular uptake and cytotoxicity in CEM/C1 cells, and restrain cell growth, whereas repressing miR-411-3p did the opposite. Meanwhile, it was also testified that miR-411-3p functioned by targeting YY1.

Multiple studies have clarified that miR-411-3p takes part in various human diseases. For example, miR-411-3p was reduced in the tumor tissues of patients with multiple myeloma, and mediated lncRNA ANRIL dysregulation through hypoxia-inducible factor 1 α to suppress the malignant proliferation and tumor growth of multiple myeloma stem cell-like properties (Wang *et al.*, 2020). (Fu *et al.*, 2020) testified that miR-411-3p was reduced in oral squamous cell carcinoma cells, and elevating miR-411-3p restrained cell growth by targeting NFAT5. miR-411-3p mitigated silica-induced pulmonary fibrosis (Gao *et al.*, 2020). Meanwhile, miR-411-3p was linked with the improved overall survival in lung cancer patients treated with nivolumab (Halvorsen *et al.*, 2018). However, miR-411-3p's impacts on the efficacy of MTX treatment in ALL patients are uncertain. In this research, elevation of miR-411-3p memorably enhanced MTX concentration, cell repression rate and apoptosis index, reduced colony number and suppressed Bcl-2 but motivated Bax in CEM/C1 cells treated with disparate concentrations of MTX, whereas depressing miR-411-3p had the exact opposite effect. These results conveyed that miR-411-3p could control MTX sensitivity in CEM/C1 cells.

YY1 is an extensively expressed multifunctional transcription factor affiliated with the GLI-Krüppel class of zinc finger proteins (Zhang *et al.*, 2021), which takes on momentous roles in diversified biological processes and is linked with tumorigenesis (Li *et al.*, 2020). discovered that YY1-mediated elevation of lncRNA MCM3AP-AS1 motivated lung cancer angiogenesis and progression (Chen *et al.*, 2019). confirmed that YY1 targeted tubulin polymerization-promoting protein and restrained pancreatic cancer migration, invasion, and angiogenesis through p38/MAPK and PI3K/AKT pathways (Li *et al.*, 2021). verified that YY1-induced elevation of lncRNA SNHG5 motivated angiogenesis in AML through the miR-26b/CTGF/VEGFA axis. Recently (Antonio-Andres *et al.*, 2021). confirmed that YY1 was elevated in peripheral blood leukemia cells of children with ALL with Pro-B and T phenotypes, and its elevation is clearly linked with poor survival. Meanwhile, YY1 has also been shown to be linked with drug resistance to multiple leukemia chemotherapeutics. For example (Zhang *et al.*, 2021). demonstrated that in chronic myeloid leukemia, KDM6A motivated imatinib resistance through YY1-mediated transcriptional elevation of TRKA. The present study discovered that repressing YY1 motivated MTX's cellular uptake and cytotoxic impacts, but repressed CEM/C1 cell growth, while enhancing YY1 turned around strengthening miR-411-3p's impacts on MTX cell uptake and cytotoxicity in CEM-C1 cells, and enhanced CEM/C1 cell growth.

However, this research still has several limitations. First, animal experiments were not performed to clarify miR-411-3p's impacts on MTX sensitivity. Secondly, it only figured out the regulatory effect of miR-411-3p on MTX sensitivity in a single ALL cell line (CEM/C1 cells) and not in other leukemia cell lines. Finally, further exploration of the downstream mechanisms of YY1 was not conducted. It is hoped that in future studies, the regulatory mechanism of miR-411-3p in leukemia MTX resistance can be further improved.

CONCLUSION

In short, this research demonstrated that miR-411-3p motivated MTX's cellular uptake and cytotoxic influences by targeting YY1 in ALL cells. The findings not

only offer new insights into the mechanisms of variable MTX responses noticed in ALL patients, but also new references for addressing MTX chemotherapy resistance in ALL patients.

Declarations

Acknowledgments. Not applicable.

Availability of data and materials. The data are available from the corresponding author upon request.

Competing interests. The authors have no conflicts of interest to declare.

REFERENCES

- Aberuyi N, Rahgozar S, Pourabutaleb E, Ghaedi K (2021) Selective dysregulation of ABC transporters in methotrexate-resistant leukemia T-cells can confer cross-resistance to cytarabine, vincristine and dexamethasone, but not doxorubicin. *Curr Res Transl Med* **69**: 103269. <https://doi.org/10.1016/j.retram.2020.09.003>
- Ando Y, Shimada H, Matsumoto N, Hirota T, Oribe M, Otsuka E, Ishii K, Morimoto T, Ohashi K, Ieiri I (2013) Role of methotrexate polyglutamation and reduced folate carrier 1 (RFC1) gene polymorphisms in clinical assessment indexes. *Drug Metab Pharmacokinet* **28**: 442–445. <https://doi.org/10.2133/dmpk.dmpk-12-rg-128>
- Antonio-Andres G, Jiménez-Hernández E, Estrada-Abreo LA, Garfías-Gómez Y, Patino-Lopez G, Juárez-Mendez S, Huerta-Yepez S (2021) Expression of YY1 in pro-B and T phenotypes correlation with poor survival in pediatric acute lymphoblastic leukemia. *Pediatr Hematol Oncol* **38**: 456–470. <https://doi.org/10.1080/08880018.2020.1871139>
- Chen Q, Yang C, Chen L, Zhang JJ, Ge WL, Yuan H, Meng LD, Huang XM, Shen P, Miao Y, Jiang KR (2019) YY1 targets tubulin polymerisation-promoting protein to inhibit migration, invasion and angiogenesis in pancreatic cancer via p38/MAPK and PI3K/AKT pathways. *Br J Cancer* **121**: 912–921. <https://doi.org/10.1038/s41416-019-0604-5>
- de Beaumais TA, Jacqz-Aigrain E (2012) Intracellular disposition of methotrexate in acute lymphoblastic leukemia in children. *Curr Drug Metab* **13**: 822–834. <https://doi.org/10.2174/138920012800840400>
- Fu SW, Zhang Y, Li S, Shi ZY, Zhao J, He QL (2020) lncRNA TTN-AS1 promotes the progression of oral squamous cell carcinoma via miR-411-3p/NFAT5 axis. *Cancer Cell Int* **20**: 415. <https://doi.org/10.1186/s12935-020-01378-6>
- Gao X, Xu H, Xu D, Li S, Wei Z, Li S, Cai W, Mao N, Jin F, Li Y, Li T, Yi X, Liu H, Yang F (2020) MiR-411-3p alleviates Silica-induced pulmonary fibrosis by regulating Smurf2/TGF- β signaling. *Exp Cell Res* **388**: 111878. <https://doi.org/10.1016/j.yexcr.2020.111878>
- Gervasini G, de Murillo SG, Jiménez M, de la Maya MD, Vagace JM (2017) Effect of polymorphisms in transporter genes on dosing, efficacy and toxicity of maintenance therapy in children with acute lymphoblastic leukemia. *Gene* **628**: 72–77. <https://doi.org/10.1016/j.gene.2017.07.025>
- Halvorsen AR, Sandhu V, Sprauten M, Flote VG, Kure EH, Brustugun OT, Helland A (2018) Circulating microRNAs associated with prolonged overall survival in lung cancer patients treated with nivolumab. *Acta Oncol* **57**: 1225–1231. <https://doi.org/10.1080/0284186x.2018.1465585>
- Hu YH, Zhou L, Wang SS, Jing X, Guo HL, Sun F, Zhang Y, Chen F, Xu J, Ji X (2019) Methotrexate disposition in pediatric patients with acute lymphoblastic leukemia: what have we learnt from the genetic variants of drug transporters. *Curr Pharm Des* **25**: 627–634. <https://doi.org/10.2174/1381612825666190329141003>
- Huang T, Chen Y, Zeng Y, Xu C, Huang J, Hu W, Chen X, Fu H (2021) Long non-coding RNA PSMA3-AS1 promotes glioma progression through modulating the miR-411-3p/HOXA10 pathway. *BMC Cancer* **21**: 844. <https://doi.org/10.1186/s12885-021-08465-5>
- Iparraguirre L, Gutierrez-Camino A, Umeriz M, Martín-Guerrero I, Astigarraga I, Navajas A, Sastre A, García de Andoin N, García-Orad A (2016) MiR-pharmacogenetics of methotrexate in childhood B-cell acute lymphoblastic leukemia. *Pharmacogenet Genomics* **26**: 517–525. <https://doi.org/10.1097/fpc.0000000000000245>
- Jaramillo AC, Cloos J, Lemos C, Stam RW, Kaspers GJL, Jansen G, Peters GJ (2019) *Ex vivo* resistance in childhood acute lymphoblastic leukemia: Correlations between BCRP, MRP1, MRP4 and MRP5 ABC transporter expression and intracellular methotrexate polyglutamate accumulation. *Leuk Res* **79**: 45–51. <https://doi.org/10.1016/j.leukres.2019.02.008>
- Li X, Yu M, Yang C (2020) YY1-mediated overexpression of long noncoding RNA MCM3AP-AS1 accelerates angiogenesis and progression in lung cancer by targeting miR-340-5p/KPNA4 axis. *J Cell Biochem* **121**: 2258–2267. <https://doi.org/10.1002/jcb.29448>

- Li ZJ, Cheng J, Song Y, Li HH, Zheng JF (2021) LncRNA SNHG5 upregulation induced by YY1 contributes to angiogenesis *via* miR-26b/CTGF/VEGFA axis in acute myelogenous leukemia. *Lab Invest* **101**: 341–352. <https://doi.org/10.1038/s41374-020-00519-9>
- Liang C, Li Y, Wang LN, Zhang XL, Luo JS, Peng CJ, Tang WY, Huang LB, Tang YL, Luo XQ (2021) Up-regulated miR-155 is associated with poor prognosis in childhood acute lymphoblastic leukemia and promotes cell proliferation targeting ZNF238. *Hematology* **26**: 16–25. <https://doi.org/10.1080/16078454.2020.1860187>
- Lin C, Chen D, Xiao T, Lin D, Lin L, Zhu H, Xu J, Huang W, Yang T (2021) DNA methylation-mediated silencing of microRNA-204 enhances T cell acute lymphoblastic leukemia by up-regulating MMP-2 and MMP-9 *via* NF- κ B. *J Cell Mol Med* **25**: 2365–2376. <https://doi.org/10.1111/jcmm.15896>
- Liu H, Ni Z, Shi L, Ma L, Zhao J (2019) MiR-486-5p inhibits the proliferation of leukemia cells and induces apoptosis through targeting FOXO1. *Mol Cell Probes* **44**: 37–43. <https://doi.org/10.1016/j.mcp.2019.02.001>
- Liu J, Chen Z, Cui Y, Wei H, Zhu Z, Mao F, Wang Y, Liu Y (2020) Berberine promotes XIAP-mediated cells apoptosis by upregulation of miR-24-3p in acute lymphoblastic leukemia. *Ageing (Albany NY)* **12**: 3298–3311. <https://doi.org/10.18632/ageing.102813>
- Naghizadeh S, Mohammadi A, Duijf PHG, Baradaran B, Safarzadeh E, Cho WC, Mansoori B (2020) The role of miR-34 in cancer drug resistance. *J Cell Physiol* **235**: 6424–6440. <https://doi.org/10.1002/jcp.29640>
- Oosterom N, Berrevoets M, den Hoed MAH, Zolk O, Hoerning S, Pluijm SMF, Pieters R, de Jonge R, Tissing WJE, van den Heuvel-Eibrink MM, Heil SG (2018) The role of genetic polymorphisms in the thymidylate synthase (TYMS) gene in methotrexate-induced oral mucositis in children with acute lymphoblastic leukemia. *Pharmacogenet Genomics* **28**: 223–229. <https://doi.org/10.1097/fpc.0000000000000352>
- Panetta JC, Sparreboom A, Pui CH, Relling MV, Evans WE (2010) Modeling mechanisms of *in vivo* variability in methotrexate accumulation and folate pathway inhibition in acute lymphoblastic leukemia cells. *PLoS Comput Biol* **6**: e1001019. <https://doi.org/10.1371/journal.pcbi.1001019>
- Ranjbar R, Karimian A, Aghaie Fard A, Tourani M, Majidinia M, Jaddi-Niaragh F, Yousefi B (2019) The importance of miRNAs and epigenetics in acute lymphoblastic leukemia prognosis. *J Cell Physiol* **234**: 3216–3230. <https://doi.org/10.1002/jcp.26510>
- Rushworth D, Mathews A, Alpert A, Cooper LJ (2015) Dihydrofolate reductase and thymidylate synthase transgenes resistant to methotrexate interact to permit novel transgene regulation. *J Biol Chem* **290**: 22970–22976. <https://doi.org/10.1074/jbc.C115.671123>
- Wang LS, Li L, Li L, Chu S, Shiang KD, Li M, Sun HY, Xu J, Xiao FJ, Sun G, Rossi JJ, Ho Y, Bhatia R (2015) MicroRNA-486 regulates normal erythropoiesis and enhances growth and modulates drug response in CML progenitors. *Blood* **125**: 1302–1313. <https://doi.org/10.1182/blood-2014-06-581926>
- Wang M, Zhao HY, Zhang JL, Wan DM, Li YM, Jiang ZX (2020) Dysregulation of LncRNA ANRIL mediated by miR-411-3p inhibits the malignant proliferation and tumor stem cell like property of multiple myeloma *via* hypoxia-inducible factor 1 α . *Exp Cell Res* **396**: 112280. <https://doi.org/10.1016/j.yexcr.2020.112280>
- Wang SM, Sun LL, Zeng WX, Wu WS, Zhang GL (2014) Effects of a microRNA binding site polymorphism in SLC19A1 on methotrexate concentrations in Chinese children with acute lymphoblastic leukemia. *Med Oncol* **31**: 62. <https://doi.org/10.1007/s12032-014-0062-0>
- Wang SM, Zeng WX, Wu WS, Sun LL, Yan D (2017) Association between MTHFR microRNA binding site polymorphisms and methotrexate concentrations in Chinese pediatric patients with acute lymphoblastic leukemia. *J Gene Med* **19**: 353–359. <https://doi.org/10.1002/jgm.2990>
- Wang Y, Huang Y, Liu H, Su D, Luo F, Zhou F (2019) Long non-coding RNA CDKN2B-AS1 interacts with miR-411-3p to regulate ovarian cancer *in vitro* and *in vivo* through HIF-1 α /VEGF/P38 pathway. *Biochem Biophys Res Commun* **514**: 44–50. <https://doi.org/10.1016/j.bbrc.2019.03.141>
- Wei J, Lu Y, Wang R, Xu X, Liu Q, He S, Pan H, Liu X, Yuan B, Ding Y, Zhang J (2021) MicroRNA-375: potential cancer suppressor and therapeutic drug. *Biosci Rep* **41**. <https://doi.org/10.1042/bsr20211494>
- Woźniak M, Makuch S, Pastuch-Gawolek G, Wiśniewski J, Szeja W, Nowak M, Krawczyk M, Agrawal S (2021) The effect of a new glucose-methotrexate conjugate on acute lymphoblastic leukemia and non-hodgkin's lymphoma cell lines. *Molecules* **26**. <https://doi.org/10.3390/molecules26092547>
- Wu F, Yin C, Qi J, Duan D, Jiang X, Yu J, Luo Z (2020) miR-362-5p promotes cell proliferation and cell cycle progression by targeting GAS7 in acute myeloid leukemia. *Hum Cell* **33**: 405–415. <https://doi.org/10.1007/s13577-019-00319-4>
- Xian D, Zhao Y (2019) LncRNA KCNQ1OT1 enhanced the methotrexate resistance of colorectal cancer cells by regulating miR-760/PPP1R1B *via* the cAMP signalling pathway. *J Cell Mol Med* **23**: 3808–3823. <https://doi.org/10.1111/jcmm.14071>
- Xu W, Li Z, Zhu X, Xu R, Xu Y (2018) miR-29 Family inhibits resistance to methotrexate and promotes cell apoptosis by targeting COL3A1 and MCL1 in osteosarcoma. *Med Sci Monit* **24**: 8812–8821. <https://doi.org/10.12659/msm.911972>
- Zhang C, Shen L, Zhu Y, Xu R, Deng Z, Liu X, Ding Y, Wang C, Shi Y, Bei L, Wei D, Thorne RF, Zhang XD, Yu L, Chen S (2021) KDM6A promotes imatinib resistance through YY1-mediated transcriptional upregulation of TRKA independently of its demethylase activity in chronic myelogenous leukemia. *Theranostics* **11**: 2691–2705. <https://doi.org/10.7150/thno.50571>
- Zhang L, Zou L, Sun P (2021) Relationship between miR-378c and YY1 expression in patients with gastric cancer and the clinicopathological features. *Cell Mol Biol Lett* **26**: 12. <https://doi.org/10.1186/s11658-021-00256-x>

Molecular and biochemical mechanisms of diabetic encephalopathy

Igor Belenichev¹, Olena Aliyeva²✉, Olena Popazova³ and Nina Bukhtiyarova⁴

¹Department of Pharmacology and Medical Formulation with Course of Normal Physiology, Zaporizhzhia State Medical and Pharmaceutical University, Zaporizhzhia, Ukraine; ²Department of Medical Biology, Parasitology and Genetics, Zaporizhzhia State Medical and Pharmaceutical University, Zaporizhzhia, Ukraine; ³Department of Histology, Cytology and Embryology, Zaporizhzhia State Medical and Pharmaceutical University, Zaporizhzhia, Ukraine; ⁴Department of Clinical Laboratory Diagnostics, Zaporizhzhia State Medical and Pharmaceutical University, Zaporizhzhia, Ukraine

Diabetes mellitus is one of the important independent risk factors for the development of neurological disorders such as ischemic stroke, transient ischemic attacks, vascular dementia and neurodegenerative processes. Hyperglycemia plays a crucial role as a trigger in the pathogenesis of these disorders. In this review, we summarize the existing data on the molecular mechanisms of diabetic encephalopathy development, consider the features of oxidative and nitrosative stresses, changes in the thiol-disulfide system, as well as mitochondrial and endothelial dysfunction in diabetes. We focus on the role of HSP 70 in cellular responses in diabetic encephalopathy. HSP70 protein is an important component of the endogenous system of neuroprotection. It acts as an intracellular chaperone, providing the folding, retention, and transport of synthesized proteins, as well as their degradation under both normoxic and stress-induced denaturation conditions. HSP70 can be considered a molecular marker and a promising therapeutic target in the treatment of diabetes mellitus.

Keywords: diabetes mellitus, diabetic encephalopathy, thiol-disulfide system, mitochondrial dysfunction, HSP70, HIF-1α

Received: 31 July, 2023; **revised:** 13 October, 2023; **accepted:** 13 October, 2023; **available on-line:** 22 November, 2023

✉ e-mail: aliyeva1eg@gmail.com

Abbreviations: AMPA, α-amino-3-hydroxy-5-methyl-4-isoxazolepropionic acid; BDNF, brain-derived neurotrophic factor; DE, diabetic encephalopathy; DM, diabetes mellitus; eNOS, endothelial nitric oxide synthase; GABA, Gamma-aminobutyric acid; GLUT4, glucose transporter type 4; GR, glutathione reductase; GSH, reduced glutathione; GSSG, glutathione disulphide; GST, glutathione S-transferase; HIF-1, hypoxia-inducible Factor 1; HSP70, 70 kilodalton heat shock protein; IGF, insulin-like growth factor; IL-1β, interleukin-1β; IL-6, interleukin 6; iNOS, inducible nitric oxide synthase; IRAK-1, interleukin-1 receptor-associated kinase; JNK, N-terminal kinase; MD, mitochondrial dysfunction; NMDA, N-methyl-D-aspartate; ROS, reactive oxygen species; TLR, toll-like receptors; TNF-α, tumour necrosis factor α

INTRODUCTION

Diabetes mellitus (DM) is recognized by numerous studies as an independent risk factor for ischemic stroke, transient ischemic attacks and vascular dementia (Tun *et al.*, 2017; Maida *et al.*, 2022). In some cases, it can be associated not only with cerebral vascular disease but also with neurodegenerative processes, in particular Alzheimer's disease. At the same time, diabetic neuropathy is the most common complication of diabetes mellitus and the leading factor among the causes of reduced quality of life in patients with diabetes (Feldman *et al.*, 2019;

Aleidan *et al.*, 2020). One of the most difficult parts of diabetes mellitus treatment is the correction of its late neurological complications. Diabetic lesions of the nervous system inevitably occur even against the background of many years of compensation for the disease, achieved through the use of modern effective and affordable antidiabetic drugs. For example, diabetes increases the risk of acute cerebrovascular events 6 times, with a nearly three-fold increase in mortality from them (Maida *et al.*, 2022; Ergul *et al.*, 2012). The development of cerebral circulatory disorders in such patients is severe, and carbohydrate metabolism disorders are associated with high mortality and disability (Lin *et al.*, 2020; Hill-Briggs *et al.*, 2021). Chronic lesions of the brain in diabetes are called diabetic encephalopathy, which leads to a decrease in cognitive and mental functions, loss of performance and quality of life in this category of patients. The discovery of new mechanisms of many cerebrovascular diseases, in particular, disturbances of the functional state of the endothelium, inflammation of the vascular wall, and programmed cell death, has opened up opportunities for the development of effective pathogenetic correction measures. In the pathogenesis of diabetic encephalopathy, the trigger link is hyperglycemia (Shi *et al.*, 2016). An important mechanism of vascular complications against the background of hyperglycemia is the activation of the polyol pathway of glucose oxidation under the influence of the enzyme aldose reductase. As a result, glucose is converted into sorbitol under the influence of aldose reductase, which leads to depletion of NADPH and, subsequently, to depletion of the glutathione link of the thiol-disulfide system, reduction of endothelial NO synthase expression, necessary for NO synthesis. A special role in the formation of vascular complications in DM belongs to the activation of protein kinase C, and subsequently to the increase in the concentration of endothelin-1 and the production of growth factors: vascular endothelial growth factor VEGF, epidermal growth factor EGF and transformed growth factor TGF-β. Also, hyperglycemia leads to increased incorporation of glucose into the hexose substitutable pathway, resulting in increased transcription of inflammatory cytokine genes and hyperproduction of reactive oxygen species and NO. Currently, oxidative and nitrosative stress are considered a universal mechanism of development of all complications in DM, including neurodegeneration and endothelial dysfunction (Tota *et al.*, 2021; Pitocco *et al.*, 2013). Recently, experimental studies have discovered a new mechanism that explains many aspects of endothelial dysfunction and neurodegradation in DM (Sivitz &

Yorek, 2010; Teodoro *et al.*, 2019; Cheng *et al.*, 2020). This is mitochondrial dysfunction, which is one of the causes of the increase in oxidative stress. Endogenous mechanisms, limiting the harmful effects of cytotoxic derivatives of NO, are provided by the thiol-disulfide system, the derivatives of which have transport properties with respect to NO, thus increasing its bioavailability. In addition, many thiols (glutathione, cysteine, methionine) can significantly limit the cytotoxicity of nitrosative stress, increasing the chance of cell survival (Kükürt *et al.*, 2021; Ren *et al.*, 2017; Aoyama, 2021). A significant role in the mechanisms of endogenous cyto- and neuroprotection is attributed to the proteins shaperones (HSP) especially, with mM 70 kDa (Belenichev *et al.*, 2023; Zhang *et al.*, 2022). However, their involvement in the molecular and biochemical mechanisms of the damage cascade mechanism in DM has not been fully identified; experimental data are scarce and sometimes contradictory. All this has prompted us to analyze and systematize world achievements in this direction, taking into account our modest results as well.

DIABETIC ENCEPHALOPATHY

The term “diabetic encephalopathy” (DE) was proposed by R. de Jong in 1950 and represents a persistent cerebral pathology resulting from the effects of acute, subacute and chronic vascular disorders, which are clinically manifested as neurosis-like and psychosis-like defects, organic, mild to moderate cognitive deficit (De-jong, 1950). It has been established that the most significant pathogenic factors initiating the development of DE are the duration of the disease, degree of DM, level of glycosylated hemoglobin, diastolic BP and total cholesterol (Li *et al.*, 2023; Wang *et al.*, 2020). In clinical observations and experimental equivalents of diabetes in animals, the duration of DM is associated with pathological changes in the CNS, characterized by cognitive and emotional deficits, which can be considered a factor in the development of dementia, as well as the risk of vascular brain complications (Feldman *et al.*, 2019; Aleidan *et al.*, 2020; Ergul *et al.*, 2012; Li *et al.*, 2023). A probable correlation between DM and cognitive function was established as early as 1922 (Miles & Root, 1922). Over the past 20 years, a number of studies evaluating the relationship between type 2 diabetes and cognitive function have been completed (Moheet *et al.*, 2015; Alkethiri *et al.*, 2021; Antal *et al.*, 2022; Kinattungal *et al.*, 2023). In DM, memory and attention are the most frequently impaired cognitive functions. Hypoglycemic conditions have a pronounced effect on the development of mnemonic disorders. In some cases, the development of dementia is possible. Under the term dementia, we understand a diffuse disorder of mental functions as a result of organic brain damage, manifested by primary disorders of thinking and memory, as well as secondary emotional and behavioral disorders. A diagnosis of dementia can be made when impairments of memory and other cognitive functions are pronounced to an extent that significantly interferes with the performance of professional and social activities in previous amounts and quality (Hugo & Ganguli, 2014). In its development, DE passes through several stages of its formation, which fully depend on the age of the disease: subclinical (coinciding with the debut of DM), clinical (corresponding to the age of the disease – from 2 to 5 years), subcompensation (over 5 years), severe (10–15 years) and decompensation (with the age

of the disease over 20 years) (Cheon & Song, 2021; Popruga *et al.*, 2021). The clinical picture of DE is characterized by a typical triad of symptoms: headaches, dizziness, and memory impairment, which in general unite DE with other types of encephalopathies. However, DE has its own specific features: progressive cognitive decline, which is sometimes referred to as cognitive aging, and sometimes is considered as a pre-stage of Alzheimer’s disease (Jayaraj *et al.*, 2020; Falvo *et al.*, 2023). Moreover, it has been established that the leading domains of cognitive impairment in type 2 DM patients are a decrease in short-term verbal memory and attention, correlating with atrophic changes in the cerebral cortex, which appear already in the early stages of diabetes and are not associated with vascular factors (Moheet *et al.*, 2015; Antal *et al.*, 2022). In addition, the clinical course of DE is characterized by frequent episodes of acute impairment of cerebral circulation, transient ischemic attacks and cerebral strokes. In particular, cerebral strokes are 6 times more frequently registered in DM patients (Maida *et al.*, 2022; Ergul *et al.*, 2012). Furthermore, chronic cerebral circulatory disorders are observed to a greater extent in patients with diabetes, leading to chronic cerebrovascular insufficiency syndrome, and the mechanisms of progressive memory decline are associated with chronic hypoxia, cerebral tissue ischemia, and neurometabolic disorders (Ergul *et al.*, 2012; Pitocco *et al.*, 2013). The concept of “brain insulin resistance”, according to which insulin receptors exist in the limbic system along with neurotransmitter receptors, is of certain interest. Their role in the mechanisms of synaptic plasticity in the hippocampus has now been established. In particular, it has been shown that insulin rapidly mobilizes functional GABA-A receptors on postsynaptic membranes of hippocampal neurons and improves synaptic transmission. In addition, a regulatory role of insulin in the functioning of AMPA and NMDA receptors of hippocampal neuronal membranes has been established (Spinelli *et al.*, 2019). Insulin can act as a mediator by accelerating the synthesis and synaptic trafficking of acetylcholine, dopamine, and other mediators. With time there is a depletion of insulin receptors in the CNS and a weakening of the function of other neurotransmitter systems, which to some extent explains the processes of cognitive aging (Kleinridders *et al.*, 2014). In addition, it has been experimentally established that insulin also has a neuroprotective effect under conditions of oxidative stress or DM (Soto *et al.*, 2019). Pathomorphological studies have determined a decrease in the expression of insulin and insulin-like growth factor-1 (IGF) in the hippocampus, cerebellum, pons, and basal ganglia, as well as neuronal losses in the hippocampus and frontal neocortex (Jafferli *et al.*, 2000). In the brain, insulin and IGF-1 mediate numerous effects, including glucose utilization and energy metabolism, oxidative stress, genetic regulation of other neurotrophic factors and their receptors, cholinergic gene expression and tau-protein phosphorylation, and formation regulation. They also exhibit anti-inflammatory and anti-apoptotic effects (Dandona *et al.*, 2007). Decrease of insulin regulation inhibits early response genes c-fos and c-jun with subsequent expression of IGF1 and IGF2, nerve growth factor, neurotrophin-3 and their receptors (Griffiths *et al.*, 1998; Zhang & Li, 2017). Also, insulin and IGF provide neurotrophic support in the hippocampus. It is known that diabetic neurovascular pathology is a metabolic disorder whose pathogenesis is based on the lack of insulin requirement for glucose to enter both nerve

tissue and the vascular wall. Hyperglycemia contributes to a significant (up to fourfold) increase in neuronal glucose levels with subsequent disruption of intracellular glucose metabolism and neuronal damage (Barrett *et al.*, 2017). This results in the development of secondary processes in the form of oxidative stress and protein glycosylation. At the same time, it was found that insulin activates the movement of GLUT4 to the plasma membrane in hippocampal neurons by mechanisms similar to those observed in peripheral tissues. It is considered that due to this, hippocampal neurons can significantly increase glucose utilization during neuronal activity growth (Cisternas *et al.*, 2019). But it was found that elevated plasma glucose levels of up to 6.1 mmol/L were associated with greater atrophy of structures associated with aging and neurodegeneration processes, in particular, the hippocampus and amygdala. This indicates the relevance of glycemic control and correction in the subclinical course of DM or its absence. Disregarding the interdependence and similarity of pathogenesis, damages to the neuronal and vascular systems are fundamentally different, including the therapeutic approaches. Studies have established the role of hippocampal dysfunction in diabetes mellitus and its role in the development of DE (Spinelli *et al.*, 2019). In particular, it was electrophysiologically discovered that behavioral and mnemonic deviations in diabetic animals are associated with a deficit of long-term potentiality in the CA1 area of the hippocampus (Kumar, 2011). This factor, which reflects the synaptic plasticity of the hippocampus, was prevented by insulin therapy, while interventional treatment to normalize hyperglycemia had only a partial effect on long-term potentiality (Ho *et al.*, 2013). The role of hyperglycemia in the activation of damage mechanisms and activation of apoptosis in the rat hippocampus has also been established (Chen *et al.*, 2019). Induction of apoptosis in the hippocampus may be associated with an increase in the Bax/Bcl-2 and Bax/Bcl-xl ratio as well as caspase-3 activity (Liu *et al.*, 2013). It was experimentally determined that streptozotocin-induced diabetes led to cholinergic receptor dysfunction and reduced the neuroprotective activity of the GABAergic system in the hippocampus, indicating a high vulnerability of neurons of this brain formation and a relationship between the development of cognitive impairment and deficit (Sherin *et al.*, 2012).

Processes of systemic neuronal inflammation in the CNS also correlate with manifestations of cognitive deficits and are associated with increased levels of inflammatory cytokines (IL-1 β , TNF- α and IL-6) against a decrease in BDNF in the hippocampus (Fourrier *et al.*, 2019; Dugue *et al.*, 2017). Long-term hyperglycemia leads to the activation of cyclooxygenase-2 expression that in turn results in the increase in biosynthesis of prostaglandin E₂, which inhibits glucose-stimulated insulin secretion that disturbs cell tolerance to glucose and plays a significant role in the pathogenesis of DM. It has been experimentally established that streptozotocin-induced diabetes leads to an increase in the immunoreactivity of the inducible form of cyclooxygenase-2 (Cox-2) in the dentate gyrus and CA3-zone of the hippocampus and can thereby influence the synaptic plasticity processes in this structure (Nam *et al.*, 2011).

In general, such disorders can be the cause of rapid development of neurodegenerative changes in DM. The leading role in the pathogenesis of these complications belongs to the negative impact of oxidative stress on the function of the cells of the central nervous system,

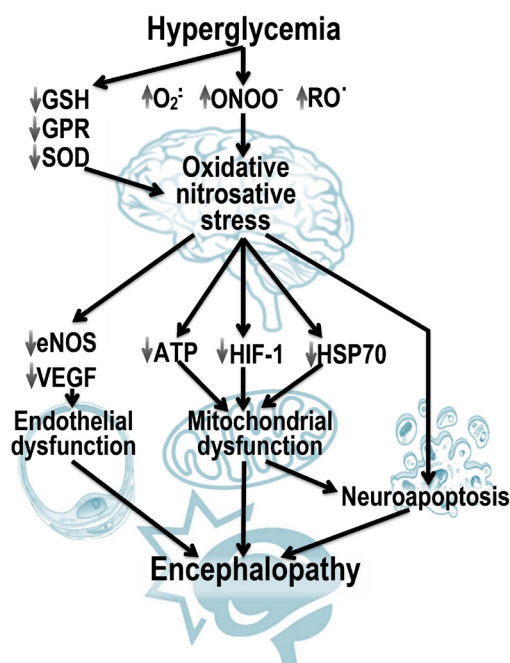


Figure 1. Molecular and biochemical cascade of links of diabetic encephalopathy pathogenesis.

and in particular the hippocampus, provided both high intracellular glucose levels and impaired microcirculation (Kükürt *et al.*, 2021; Li *et al.*, 2023). (Fig. 1).

OXIDATIVE STRESS

The main source of free-radical oxidation processes in DM is a state of chronic hyperglycemia. The development of neuronal dysfunction and the appearance of signs of cognitive deficit are based on disorders of carbohydrate metabolism, which lead to self-oxidation of glucose, to activation of the polyol (sorbitol) and hexoamine pathways of glucose metabolism with intracellular accumulation of their reaction end products, to an increase in intracellular glutathione and ascorbate redox systems, as well as disorders of the metabolism of NO and prostaglandins, non-enzymatic glycosylation of proteins and formation of glycosylation end products with the subsequent development of neuroinflammatory processes and cytotoxic edema of neuronal tissue (Kükürt *et al.*, 2021; Belenichev, 2013). Hypoxia observed in DM is an additional factor contributing to the increased formation of reactive oxidants. The accumulation of peroxidation products under conditions of hyperglycemia leads to the interaction of glucose with amino groups of proteins, increasing their glycosylation and oxidation (auto-oxidative oxidation). Non-enzymatic glycosylation of antioxidant defense enzymes leads to a decrease in their activity and even complete inactivation (Belenichev *et al.*, 2015). The greatest number of free radicals in the organism refers to combinations of reactive oxygen with a very short lifetime: the superoxide oxygen radical anion ($O_2^{\cdot-}$) and alkoxy radical (RO^{\cdot}) – 10^{-6} s, hydroxyl radical (OH^{\cdot}) – 10^{-9} s, peroxy radical (ROO^{\cdot}) – 10^{-12} s (Collin, 2019; Edge & Truscott, 2021).

NITROXIDERGIC SYSTEM AND NITROSATIVE STRESS

The unique chemical nature and large number of intracellular targets for NO and its physiologically active oxidative-redox forms leave open the question of the way and the specificity in which the damaging effect of nitric oxide is mediated in the neuron under ischemic conditions. Numerous studies have shown the direct involvement of NO in the process of neuronal destruction in ischemia, arterial hypertension, and DM. A slight increase in NO concentration activates the synthesis of chaperone proteins and NO-dependent activation of HSP70 may constitute an important endogenous cellular defense mechanism. However, iNOS hyperexpression is suppressed by HSP70 by reducing the activation of the iNOS transcription factor (NF- κ B), which leads to the limitation of nitrosative stress and neuroapoptosis (Belenichev *et al.*, 2015). Now, there is an active study of NO targets and whether NO is sufficiently cytotoxic, or whether its derivatives are more active (Aquilano *et al.*, 2011; Liu *et al.*, 2019). Studies in recent years have established that NO, and especially the products of its conversion, such as peroxynitrite (ONOO⁻), nitrosonium ion (NO⁺), nitroxyl (NO⁻) and diazotrioxide (N₂O₃), are major factors in the realization of nitrosative stress, which results in direct interaction of NO with metals (hem iron of hemoglobin, myoglobin, iron-containing enzymes, as well as non-heme iron of iron-sulfur proteins and DNA, copper and zinc of active enzyme centers), and indirect interaction of NO⁺ (S-, N-, O-nitrosation) with thiol, phenolic, hydroxyl and amino groups of proteins and DNA. Such interaction leads to receptor desensitization, inhibition of mitochondrial enzyme activity and fragmentation of nucleic acids (Belenichev *et al.*, 2015; Liu *et al.*, 2019).

GLUTATHIONE LINK OF THE THIOL-DISULFIDE SYSTEM

Hyperglycemia promotes the activation of the sorbitol pathway of glucose metabolism, which, together with activation of NADPH oxidase, leads to depletion of the NADPH cytosolic level and, consequently, of the reduced glutathione (GSH) level (Yan, 2018). (Fig. 2). A decrease in GSH levels below normal values can serve as an indicator of impaired cellular redox status and changes in the redox-dependent regulation of genes. The consequence of this disturbance is a significant change in the mechanism of cellular redox-dependent signaling, controlled both non-enzymatically and enzymatically with the participation of glutathione transferase and glutaredoxin isoforms (Luo *et al.*, 2016; Ohiagu *et al.*, 2021). It is known that GSH is a neurotransmitter and neuromodulator (in micromolar concentrations it is an agonist of glutamate receptors; in millimolar concentrations, it modulates the SH groups of NMDA receptors). Oxidized forms of glutathione in concentrations above 200 μ M decrease the expression of early response genes, and in concentrations of 5 mM or more, it activates p53-dependent apoptosis and reduces HSP levels (Belenichev *et al.*, 2020). GSH, competitively binding to nitric oxide, forms a complex in the form of S-nitrosoglutathione, which forms a depot of endogenous NO (further NO release is catalyzed by the thioredoxin system). Also, the release of NO from S-nitrosoglutathione occurs with glutamyltranspeptidase to form S-nitrosocysteinylglycine as a producer of NO. Cystine, which is

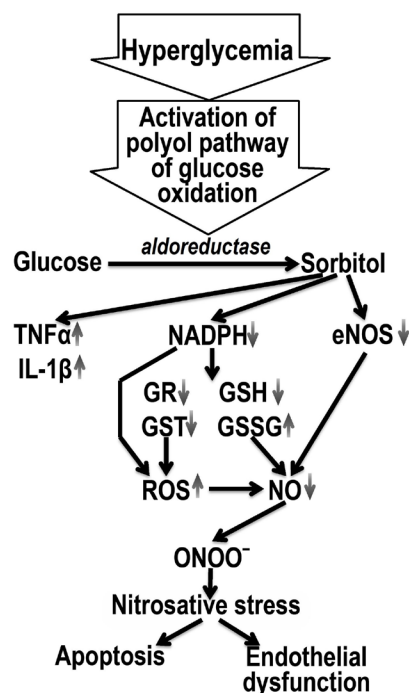


Figure 2. Disturbance in the coupling of NO/SH system in diabetes mellitus and nitrosative stress activation.

reduced to cysteine, takes part in the transport of S-nitrosoglutathione. These reactions are controlled by glutathione reductase and glutathione transferase. Nitrosative stress results in oxidative modification of low molecular weight thiols, formation of homocysteine and its cytotoxic derivatives which enhance thiol oxidation (Ren *et al.*, 2017; Aoyama, 2021; Belenichev *et al.*, 2015). It should be noted that the increased intracellular levels of cytotoxic forms of NO and decreased levels of reduced glutathione may be associated with deprivation of the heat shock protein (HSP70) level (Belenichev *et al.*, 2020). The action of NO formed with the participation of mtNOS results in the opening of mitochondrial pores and the release of pro-apoptotic proteins into the cytosol. The opening of the pores is due to oxidation or nitrosylation of the thiol groups of the cysteine-dependent portion of the mitochondrial inner membrane protein (ATP/ADP-antiporter), and this converts it into a permeable nonspecific pore channel (Pavlov *et al.*, 2017). The interaction of NO with members of the Bcl-2 superfamily is also reflected in the fact that the action of nitric oxide in the cell decreases significantly the level of intracellular Bcl-2 protein, possibly through caspase-induced splitting or p53-dependent inhibition of its expression (Shamas-Din *et al.*, 2013; Fricker *et al.*, 2018; Török *et al.*, 2002). The proapoptotic effect of nitric oxide is also expressed in its induced increase in the expression of apoptogenic Bax proteins. GSH and its precursor N-acetylcysteine can modulate NF- κ B, inhibit IL-1 β expression, and exhibit anti-inflammatory effects (Belenichev *et al.*, 2020; Pavlov *et al.*, 2017). It is known that increased production of TNF- α , IL-1 β , IL-6, and iNOS occurs against a background of GSH deficiency (Skelly *et al.*, 2013).

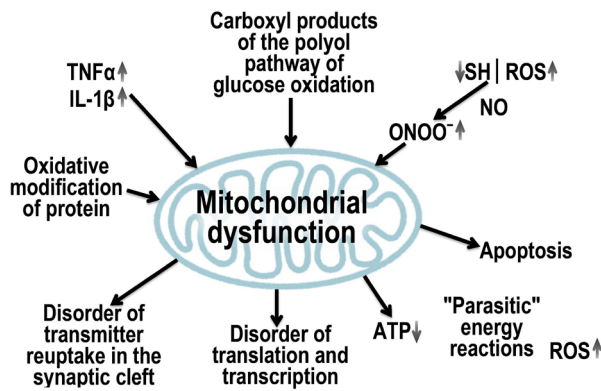


Figure 3. Formation of mitochondrial dysfunction in diabetes mellitus and its consequences.

MITOCHONDRIAL DYSFUNCTION

Mitochondrial dysfunction (MD) has no etiological and nosological specificity and is a typical pathological process. However, it leads to disruption of mediator reuptake (noradrenaline, dopamine, serotonin), ion transport, impulse generation and conduction, protein synthesis, processes of transcription and translation, and activation of “parasitic” energy-producing reactions, resulting in significant energy expenditure in the neuronal cell. The role of MD in the development of various pathological conditions, including neurodegenerative ones, has also been confirmed in DM (Norat *et al.*, 2020; Wang *et al.*, 2020; Pessoa & Duarte, 2023).

It was experimentally determined that diabetes mellitus leads to a significant decrease in the membrane potential of rat brain mitochondria. These changes were accompanied by a decrease in the ATP content and ATP/ADP ratio in brain synaptosomes, which indicates diabetes-induced disorders in the functioning of the electron-transport chain and energy coupling of the electron transfer process with ATP synthesis (Belenichev *et al.*, 2015; Pinti *et al.*, 2019; Singh *et al.*, 2021).

In conditions of hypoperfusion of brain tissues, compensatory mechanisms are depleted and energy deficiency develops, which leads to an increase in Ca^{2+} levels in the cell cytoplasm because energy-dependent pumps that “load” Ca^{2+} into the cisterns of the endoplasmic reticulum or “unload” it from the cell are blocked. These processes activate Ca^{2+} -dependent phospholipases. One of the defense mechanisms preventing the accumulation of calcium ions in the cytoplasm is their capture by mitochondria. However, it increases their metabolic activity aimed at maintaining intramitochondrial charge and proton pumping. This is accompanied by an increase in ATP expenditure. In general, a vicious circle occurs when oxygen deficiency disrupts energy exchange and stimulates the formation of ROS damaging mitochondrial and lysosome membranes, which can lead to mitochondrial dysfunction. In turn, mitochondrial dysfunction leads to the initiation of apoptosis and irreversible damage and death of the neuron (Norat *et al.*, 2020). In addition, the key enzyme of the Krebs cycle, aconitate hydratase (aconitase), is highly sensitive to the effects of oxidative and nitrosative stress (Pessoa & Duarte, 2023). In DM its activity is significantly reduced, and this leads to impaired mitochondrial glucose oxidation, and ATP deficiency (Sivitz & Yorek, 2010; Kuretu, 2023) (Fig. 3).

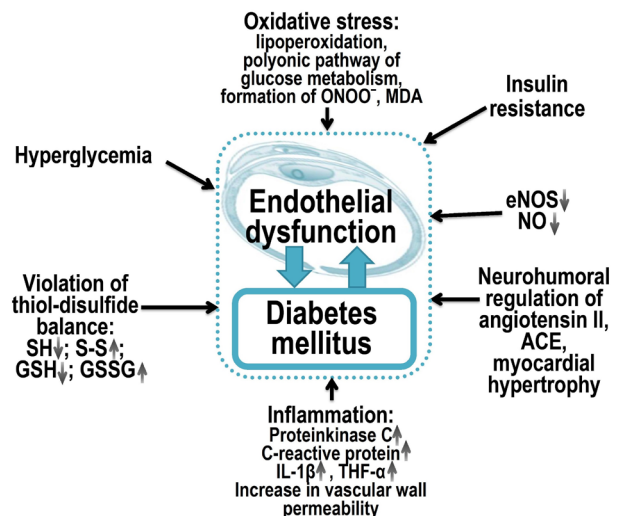


Figure 4. Pathogenesis of endothelial dysfunction in diabetes mellitus.

ENDOTHELIAL DYSFUNCTION

Hyperglycemia is a trigger in the pathogenesis of diabetic encephalopathy. As a result of protein kinase C activation, there is an increase in the concentration of endothelin-1 and production of growth factors: vascular endothelial growth factor VEGF, epidermal growth factor EGF and transformed growth factor TGF- β (Ergul, 2011; Heydarpour *et al.*, 2020; Wu & Derynck, 2009; Chen *et al.*, 2020). Also in hyperglycemia, there is an increased incorporation of glucose into the hexose-substituted pathway, resulting in increased transcription of inflammatory cytokine genes, which also contributes to the formation of vascular inflammation and proatherogenic state (Shi *et al.*, 2016; Wang *et al.*, 2020). Currently, oxidative stress is considered the main universal mechanism of development of all complications in DM, in particular, as a result of endothelial dysfunction. Moreover, hyperglycemia-induced oxidative stress triggers damage reactions to protein structures of ion channels and receptors, as well as activation and phosphorylation of cytosolic phospholipase A2 (cPLA2) with increased formation of arachidonate and prostaglandin E2, which leads to changes in vascular permeability (Wang & Hsiao, 2020; Sun *et al.*, 2021). As a result of oxidative stress, DNA damage occurs, an obligatory stimulus for the activation of the nuclease enzyme poly(ADP-ribose) polymerase, which depletes the intracellular concentration of NAD^+ , reducing the level of glycolysis, slowing electron transport and ATP formation, blocking glyceraldehyde-3-phosphate activity, which leads to endothelial dysfunction and development of diabetic complications (Liu *et al.*, 2017; Pacher & Szabó, 2005) (Fig. 4).

HEAT SHOCK PROTEINS

Clinical studies of HSP70 levels in diabetes are limited. It is known that patients with DM1 had elevated blood levels of HSP72, which decreased significantly after treatment (Ludwig *et al.*, 2014). However, another case-control study reported reduced serum HSP70 levels in type 1 diabetic patients with and without microvascular complications (Atalay *et al.*, 2004). Increased

serum HSP70 levels were also found in patients with type 2 DM not treated with insulin (Nakhjavani *et al.*, 2010). A decrease in iHSP70 expression and an increase in eHSP70 expression are found in patients with obesity and metabolic diseases, including DM2. HSF-1, which is one of the HSP72 transcription factors, is also repressed in subjects with DM2 (Seibert *et al.*, 2022). HSF-1 expression in skeletal muscle was found to be five times lower in obese and DM2 patients than in a control obese group.

The family of heat shock proteins HSPs (Heat shock proteins) is considered to be one of the most studied cytoprotective factors (Kim *et al.*, 2020; Deka & Saha, 2018; Belenichev *et al.*, 2022). There is a class of proteins (chaperones) whose main function is to restore the correct tertiary structure of damaged proteins, as well as to form and dissociate protein complexes. Many chaperones are heat shock proteins, that is, proteins whose expression is initiated in response to increased temperature or other cellular stresses (Belenichev, 2013; Ortan *et al.*, 2018). HSPs act as intracellular chaperones that maintain cell proteostasis in normal and under various stress conditions (hyperthermia, hypoxia, oxidative stress, radiation, etc.).

The most interesting is the HSP70 protein as an important component of the system of endogenous cyto- and neuroprotection, which, first of all, performs the function of intracellular chaperones and provides the processes of folding, holding and transport of synthesized proteins, as well as their degradation, both in normoxia and under stress-induced denaturation (Turturici *et al.*, 2011). It is known that the heat shock protein family 70 includes: inducible/stress-inducible block HSP72/HSP70i, constitutive/physiological protein HSP73/HSC70, constitutive glucose-regulating mitochondrial protein GRP75, constitutive heme oxygenase-1 (HO⁻¹) participates in bilirubin metabolism (Belenichev *et al.*, 2023). The constitutive form of HSP70 is still present in all subcellular compartments and participates in the functioning of cell life support systems in normoxia. On the contrary, the inducible form of HSP70 appears in cells in response to stress, including ischemic stroke (Turturici *et al.*, 2011). In response to stress, ischemia, hypoxia, etc., a sharp increase in the level of HSP70 is registered, and its highest concentration is observed in vital parts of cells: nuclear, perinuclear space, mitochondria, endoplasmic reticulum, which indicates the importance of chaperone70 in protecting cells from death. As nuclear pre-ribosomes resume functioning, the concentration of HSP70 in the nucleus decreases and increases in the cell cytoplasm. Thus, the level of HSP70 can be considered as a marker of cellular and tissue damage. Hyperproduction of HSP70 in cells inhibits the development of autophagy as an alternative, more “radical” mechanism of cellular stress response (Belenichev, 2013; Ortan *et al.*, 2018). Recent studies have established a direct cytoprotective effect of HSP70, which is realized by regulating the processes of apoptosis and cell necrosis. HSP70 inhibits mitochondrial and cytoplasmic pathways of apoptosis. Thus, HSP70 inhibits the transition of procaspase 9 into active caspase 9 and disrupts apoptosome formation in the cytoplasm of cells. Against the background of HSP70 hyperexpression the level of anti-apoptotic protein Bcl-2 increases, which prevents the release of cytochrome c from mitochondria and translocation of apoptosis-inducing factor (AIF) into the nucleus preventing cell apoptosis. HSP70 protein inhibits

TNF α -induced apoptosis and also effectively inhibits the development of Fas- and TRAIL- (TNF-related apoptosis-inducing ligand) mediated apoptosis in different cell types. Accumulation of HSP70 in cells increases their resistance to staurosporine, and doxorubicin, known as apoptosis inducers (Naka *et al.*, 2014). Ubiquitination of the insulin-like growth factor-1 receptor is inhibited by HSP10 and HSP60 which results in insulin-like growth factor-1 receptor signaling in cardiac muscle in streptozotacin-induced DM (Shan *et al.*, 2003). It is known that ischemia and hyperglycemia lead to the development of local inflammation. In this situation, HSP70 blocks the activation of the inflammatory transcription factor NF- κ B and inhibits its cytokine-mediated translocation to the nucleus (Belenichev, 2013). HSP70 inhibits the production of proinflammatory cytokines (TNF- α , IL-6), inhibits the activity of matrix metalloproteinases (MMPs) and inducible nitric oxide synthase (iNOS) in models of ischemia *in vitro* and *in vivo* (Belenichev *et al.*, 2015). It was found that HSP70 in astrocyte culture under ischemia inhibits proapoptotic Jun N-terminal kinases (JNK) and p38 mitogen activating protein kinase (MAPK), disrupting the apoptosis signaling pathway (Giffard *et al.*, 2008). The studies demonstrated a direct relationship between HSP70 and TNF α expression levels, iNOS in microglia, and MMP-9 in astrocytes. When IL-1b interacts with receptors, the nuclear transcription factors AP-1 and NF- κ B are activated, which alters the behavior of target cells and leads to the development of an acute cellular response, to the expression of other pro-inflammatory factors, to the stimulation of iNOS and cytotoxic NO produced by astrocytes, to an increase in mitochondrial pore permeability and to the initiation of neuroapoptosis. The IL-1b signaling pathway that enhances mechanisms of delayed neuronal death may be regulated by HSP70 (Kim *et al.*, 2020). An increase in HSP70 concentration within the physiological norm leads to an increase in IL-1 β to levels necessary for its participation in cyto- and neuroprotection; while HSP70 deficiency can lead to a significant increase in IL-1. Overexpression of HSP70 attenuates IL-1 β expression by inhibiting the C/EBP β and C/EBP δ transcription factors (Senf *et al.*, 2008). HSP70 can prevent the production of inflammatory cytokines by inhibiting NF- κ B-dependent transcription (Lyu *et al.*, 2020; Ferat-Orsorio *et al.*, 2014). Many studies investigating the mechanisms of endogenous neuroprotection in ischemia show that the glutathione link of the thiol-disulfide system is reactivated against the background of an increase in the level of HSP70, and the introduction of exogenous HSP70 leads to an increase in the functional activity of the glutathione system (Belenichev *et al.*, 2020). HSP70 proteins mobilize antioxidant resources in neurons by increasing the level of both cytosolic and mitochondrial pools of reduced glutathione (Belenichev, 2013; Belenichev *et al.*, 2015; Zhang *et al.*, 2022). The data on the role of HSP in the stabilization of hypoxia-inducible factor (HIF-1a), which in conditions of ischemia is responsible for providing proliferation, apoptosis, angiogenesis, stabilization of protein molecules under oxidative stress, have recently emerged (Belenichev *et al.*, 2023). Under hypoxia conditions, HSP 70 is displaced from the complex with HIF-1a, thus, during 20–30 min of hypoxia, protecting the factor structure from targeted proteolysis. It is likely that HSP 70 is able to increase the lifetime of factor HIF-1a under pre- and post-hypoxia conditions and

is required for cells to respond appropriately to oxygen deprivation under ischemic conditions (Kim *et al.*, 2020). HIF-1 α determines the ability to activate the compensatory energy shunt and HSP 70 determines the ability of its long-term function. This statement is supported by the works of other researchers. It was found that one of the chaperones, the HSP 90 protein, is able to bind to the PAS domain of B-factor and stabilize it. Another cellular chaperone, HSP 70, recognizes a different structural motif of the HIF-1 α molecule, the so-called oxygen-dependent degradation (ODD) domain (Dery *et al.*, 2005). It should be noted that the role of these inter-protein interactions is unclear; it is assumed that they are required for the stabilization of HIF-1 α under normoxia conditions. Under hypoxia conditions, at least one of the chaperones (HSP 70) is displaced from the complex with HIF-1 α by the ARNT protein, which protects the factor structure from targeted proteolysis during 20–30 min of hypoxia. Thus, HSP 70 is able to increase the lifetime of the HIF-1 α factor under pre- and post-hypoxia conditions and is required for cells for an appropriate response to oxygen deprivation (Belenichev *et al.*, 2022; Belenichev *et al.*, 2023; Kim *et al.*, 2019).

Under DM, HSP levels are higher in some tissues and lower in other tissues. Defects in response to heat shock are seen in diabetic wounds. Both chaperones play important roles in cardiac defense. HSP60 expression is impaired in the heart of diabetic animals and this may contribute to diabetic cardiomyopathy (Atalay *et al.*, 2004). Also, expression of HSP72 is suppressed in streptozotacin-induced DM. A decrease of HSP70 was found in the mitochondria and cytosol of neurons in the CA1 hippocampus and sensorimotor cortex of rats with streptozotacin-induced DM (Chen *et al.*, 2013)15. Lower levels of HSP70 expression have been reported in insulin-sensitive tissues such as muscle and heart. There is evidence of decreased HSP70 protein levels in exercising diabetic animals with increased mRNA expression. Insulin resistance may contribute to a decrease in HSP70 levels in the heart and brain. It is hypothesized that increased expression of HSP70 in the brain is found in insulin sensitivity, in the brain as well as in peripheral tissues (Moin *et al.*, 2021).

HSP70 demonstrates diverse mechanisms of action on the development of inflammation and insulin resistance. Extracellular eHSP70 plays a role as a ligand for TLR2 and TLR4 in surrounding cells, which activates JNK *via* MEKK4/7 and suppresses NF- κ B through IRAK4 activation (Mulyani *et al.*, 2020; Zhang *et al.*, 2013). eHSP70 also regulates the expression of eNOS, iNOS and other cytokines such as TNF α and IL1 β (Belenichev *et al.*, 2023; Kim *et al.*, 2020; Deka & Saha, 2018; Giffard *et al.*, 2008). Activation of JNK leads to increased inflammation, triggers insulin resistance mechanisms and enhances the formation of mitochondrial dysfunction. In contrast, intracellular iHSP70 inhibits JNK activation and suppresses pathological mechanisms associated with its activation such as inflammation, insulin resistance, mitochondrial dysfunction, and ROS production (Bironaite *et al.*, 2012; Nagai & Kaji, 2023). The effect of HSP70 action depends on the iHSP70/eHSP70 ratio. A higher level of iHSP70 compared to eHSP70 leads to a decrease in inflammation processes (Krause *et al.*, 2015; Oliveira *et al.*, 2022; Seibert *et al.*, 2022; Alemi *et al.*, 2019).

LABORATORY DIAGNOSTICS

As a molecular marker in DM, it is necessary to determine the iHSP70/eHSP70 ratio in patients' serum or lymphocytes instead of total HSP70, which leads to a departure from the real picture of the pathological process. In healthy people, it is about 1 (Krause *et al.*, 2015; Seibert *et al.*, 2022). An [eHSP70]/[iHSP70] ratio of more than 5 indicates a significant pathological process – inflammation, insulin resistance, and endothelial dysfunction in DM (Mulyani *et al.*, 2020). The lower the ratio or the dynamics are more negative, the better the outcome of the disease.

PERSPECTIVES ON THE DEVELOPMENT OF PHARMACEUTICAL PRODUCTS

Such a role of chaperone proteins in cellular responses in pathological conditions raises the question of developing new drugs capable of providing modulation/protection of the genes encoding the synthesis of HSP 70 and HIF-1 α proteins. Strategies aimed at modulating HSP70 in DM (prolonged exercise, pharmacological modulation of HSP70) require adherence to and maintenance of iHSP70 expression, thus preventing progression toward more severe DM and allowing restoration of insulin sensitivity. Thus, HSP70 is attractive as a therapeutic target in the treatment of DM.

Declarations

Author contributions. IB designed the research. IB and OA wrote the original manuscript. OP and NB performed the literature search and revised the manuscript. All authors contributed to the article and approved the submitted version.

Conflict of interest. The authors declare that the research was conducted in the absence of any commercial or financial relationships that could be construed a potential conflict of interest.

REFERENCES

- Aleidan FAS, Ahmad BA, Alotaibi FA, Aleesa DH, Alhefthi NA, Badri M, Abdel Gader AG (2020) Prevalence and risk factors for diabetic peripheral neuropathy among saudi hospitalized diabetic patients: a nested case-control study. *Int J Gen Med* 13: 881–889. <https://doi.org/10.2147/IJGM.S273807>
- Alemi H, Khaloo P, Rabizadeh S, Mansournia MA, Mirmiranpour H, Salehi SS, Esteghamati A, Nakhjavani M (2019) Association of extracellular heat shock protein 70 and insulin resistance in type 2 diabetes; independent of obesity and C-reactive protein. *Cell Stress Chaperones* 24: 69–75. <https://doi.org/10.1007/s12192-018-0942-x>
- Alkethiri K, Almrtroudi T, Jurays AB, Abanumay F, Aldammas M, AlKhodheer M, Iqbal M, Habib SS, Bashir S (2021) The relationship between type 2 diabetes mellitus with cognitive functions. *Heliyon* 7: e06358. <https://doi.org/10.1016/j.heliyon.2021.e06358>
- Antal B, McMahon LP, Sultan SF, Lithen A, Wexler DJ, Dickerson B, Ratai EM, Mujica-Parodi LR (2022) Type 2 diabetes mellitus accelerates brain aging and cognitive decline: Complementary findings from UK Biobank and meta-analyses. *Elife* 11: e73138. <https://doi.org/10.7554/eLife.73138>
- Aoyama K (2021) Glutathione in the brain. *Int J Mol Sci* 22: 5010. <https://doi.org/10.3390/ijms22095010>
- Aquilano K, Baldelli S, Cardaci S, Rotilio G, Ciriolo MR (2011) Nitric oxide is the primary mediator of cytotoxicity induced by GSH depletion in neuronal cells. *J Cell Sci* 124: 1043–1054. <https://doi.org/10.1242/jcs.077149>
- Atalay M, Oksala NK, Laaksonen DE, Khanna S, Nakao C, Lappalainen J, Roy S, Hänninen O, Sen CK (2004) Exercise training modulates heat shock protein response in diabetic rats. *J Appl Physiol* 97: 605–11. <https://doi.org/10.1152/japplphysiol.01183.2003>
- Belenichev IF, Aliyeva OG, Popazova OO, Bukhtiyarova NV (2023) Involvement of heat shock proteins HSP70 in the mechanisms

- of endogenous neuroprotection: the prospect of using HSP70 modulators. *Front Cell Neurosci* **17**: 1131683. <https://doi.org/10.3389/fncel.2023.1131683>
- Belenichev I F (2013) The Role of heat shock proteins in realization of molecular biochemical mechanisms of neuroprotection. *Pharm Drug Toxicol* **36**: 72–80
- Belenichev IF, Aliyeva EG, Popazova OO (2022) Experimental substantiation of new target links in complex therapy of prenatal CNS damage. pharmacological modulation of HSP70-dependent mechanisms of endogenous neuroprotection. *Neurotherapeutics* **19**: 1414–1431. <https://doi.org/10.1007/s13311-022-01298-5>
- Belenichev IF, Cherniy VI, Nagornaya EA, Pavlov SV, Cherniy TV (2015) *Neuroprotection and neuroplasticity*. Logos, Kyiv
- Belenichev IF, Chekman IS, Nagornaya EA, Gorbacheva SV, Gorchakova NA, Bukhtiyarova NV, Reznichenko NU, Feroz S (2020) *Thiol-disulfide System: Role in Endogenous Cyto- and Organoprotection, Pathways of Pharmacological Modulation*. Yuston Publishing House, Kyiv
- Bironaite D, Pivoriunas A, Venalis A (2012) Upregulation of iHsp70 by mild heat shock protects rabbit myogenic stem cells: involvement of JNK signalling and c-Jun. *Cell Biol Int* **36**: 1089–1096. <https://doi.org/10.1042/CBI20120143>
- Chen HY, Ho YJ, Chou HC, Liao EC, Tsai YT, Wei YS, Lin LH, Lin MW, Wang YS, Ko ML, Chan HL (2020) The role of transforming growth factor-beta in retinal ganglion cells with hyperglycemia and oxidative stress. *Int J Mol Sci* **21**: 6482. <https://doi.org/10.3390/ijms21186482>
- Chen YW, Hsieh PL, Chen YC, Hung CH, Cheng JT (2013) Physical exercise induces excess hsp72 expression and delays the development of hyperalgesia and allodynia in painful diabetic neuropathy rats. *Anesth Analg* **116**: 482–490. <https://doi.org/10.1213/ANE.0b013e318274e4a0>
- Chen Z, Guo H, Lu Z, Sun K, Jin Q (2019) Hyperglycemia aggravates spinal cord injury through endoplasmic reticulum stress mediated neuronal apoptosis, gliosis and activation. *Biomed Pharmacother* **112**: 108672. <https://doi.org/10.1016/j.biopha.2019.108672>
- Cheng H, Gang X, Liu Y, Wang G, Zhao X, Wang G (2020) Mitochondrial dysfunction plays a key role in the development of neurodegenerative diseases in diabetes. *Am J Physiol Endocrinol Metab* **318**: E750–E764. <https://doi.org/10.1152/ajpendo.00179.2019>
- Cheon SY, Song J (2021) The association between hepatic encephalopathy and diabetic encephalopathy: the brain-liver Axis. *Int J Mol Sci* **22**: 463. <https://doi.org/10.3390/ijms22010463>
- Cisternas P, Martinez M, Ahima RS, William Wong G, Inestrosa NC (2019) Modulation of glucose metabolism in hippocampal neurons by adiponectin and resistin. *Mol Neurobiol* **56**: 3024–3037. <https://doi.org/10.1007/s12035-018-1271-x>
- Collin F (2019) Chemical basis of reactive oxygen species reactivity and involvement in neurodegenerative diseases. *Int J Mol Sci* **20**: 2407. <https://doi.org/10.3390/ijms20102407>
- Dandona P, Chaudhuri A, Mohanty P, Ghanim H (2007) Anti-inflammatory effects of insulin. *Curr Opin Clin Nutr Metab Care* **10**: 511–517. <https://doi.org/10.1097/mco.0b013e3181e38774>
- Dejong RN (1950) The nervous system complications of diabetes mellitus, with special reference to cerebrovascular changes. *J Nerv Ment Dis* **111**: 181–206. <http://dx.doi.org/10.1097/00005053-195011130-00001>
- Deka K, Saha S (2018) Regulation of Mammalian HSP70 Expression and Stress Response. In *Regulation of heat shock protein responses. Heat shock proteins*, Asea A, Kaur P eds, vol 13, pp 3–25. Cham, Springer. https://doi.org/10.1007/978-3-319-74715-6_1
- Dery MA, Michaud MD, Richard DE (2005). Hypoxia-inducible factor 1: Regulation by hypoxic and non-hypoxic activators. *Int J Biochem Cell Biol* **37**: 535–540. <https://doi.org/10.1016/j.biocel.2004.08.012>
- Dugue R, Nath M, Dugue A, Barone FC (2017) Roles of pro- and anti-inflammatory cytokines in traumatic brain injury and acute ischemic stroke. In *Mechanisms of Neuroinflammation*, Chapter 9, Abreu GEA eds. IntechOpen. <https://doi.org/10.5772/intechopen.70099>
- Edge R, Truscott TG (2021) The reactive oxygen species singlet oxygen, hydroxy radicals, and the superoxide radical anion - examples of their roles in biology and medicine. *Oxygen* **1**: 77–95. <https://doi.org/10.3390/oxygen1020009>
- Ergul A, Kelly-Cobbs A, Abdalla M, Fagan SC (2012). Cerebrovascular complications of diabetes: focus on stroke. *Endocr Metab Immune Disord Drug Targets* **12**: 148–158. <https://doi.org/10.2174/187153012800493477>
- Ergul A (2011) Endothelin-1 and diabetic complications: focus on the vasculature. *Pharmacol Res* **63**: 477–482. <https://doi.org/10.1016/j.phrs.2011.01.012>
- Barrett EJ, Liu Z, Khamaisi M, King GL, Klein R, Klein BEK, Hughes TM, Craft S, Freedman BI, Bowden DW, Vinik AI, Casellini CM (2017) Diabetic microvascular disease: an endocrine society scientific statement. *J Clin Endocrinol Metab* **102**: 4343–4410. <https://doi.org/10.1210/clinem.2017.01922>
- Falvo E, Giatti S, Diviccaro S, Cioffi L, Herian M, Brivio P, Calabrese F, Caruso D, Melcangi RC (2023) Diabetic encephalopathy in a preclinical experimental model of type 1 diabetes mellitus: observations in adult female rat. *Int J Mol Sci* **24**: 1196. <https://doi.org/10.3390/ijms24021196>
- Feldman EL, Callaghan BC, Pop-Busui R, Zochodne DW, Wright DE, Bennett DL, Bril V, Russell JW, Viswanathan V (2019) Diabetic neuropathy. *Nat Rev Dis Primers* **5**: 42. <https://doi.org/10.1038/s41572-019-0097-9>
- Hill-Briggs F, Adler NE, Berkowitz SA, Chin MH, Gary-Webb TL, Navas-Acien A, Thornton PL, Haire-Joshu D (2020) Social determinants of health and diabetes: a scientific review. *Diabetes Care* **44**: 258–279. <https://doi.org/10.2337/dci20-0053>
- Ferat-Osorio E, Sánchez-Anaya A, Gutiérrez-Mendoza M, Boscó-Gárate I, Wong-Baeza I, Pastelin-Palacios R, Pedraza-Alva G, Bonifaz LC, Cortés-Reynosa P, Pérez-Salazar E, Arriaga-Pizano L, López-Macías C, Rosenstein Y, Isibasi A (2014) Heat shock protein 70 down-regulates the production of toll-like receptor-induced pro-inflammatory cytokines by a heat shock factor-1/constitutive heat shock element-binding factor-dependent mechanism. *J Inflamm* **11**: 19. <https://doi.org/10.1186/1476-9255-11-19>
- Fourrier C, Singhal G, Baune B (2019) Neuroinflammation and cognition across psychiatric conditions. *CNS Spectrums* **24**: 4–15. <https://doi.org/10.1017/S1092852918001499>
- Fricker M, Tolkovsky AM, Borutaite V, Coleman M, Brown GC (2018) Neuronal cell death. *Physiol Rev* **98**: 813–880. <https://doi.org/10.1152/physrev.00011.2017>
- Giffard RG, Han RQ, Emery JF, Duan M, Pittet JF (2008) Regulation of apoptotic and inflammatory cell signaling in cerebral ischemia: the complex roles of heat shock protein 70. *Anesthesiology* **109**: 339–448. <https://doi.org/10.1097/ALN.0b013e31817f4ce0>
- Griffiths MR, Black EJ, Culbert AA, Dickens M, Shaw PE, Gillespie DA, Tavaré JM (1998) Insulin-stimulated expression of c-fos, fra1 and c-jun accompanies the activation of the activator protein-1 (AP-1) transcriptional complex. *Biochem J* **335**: 19–26. <https://doi.org/10.1042/bj3350019>
- Heydarpour F, Sajadimajd S, Mirzarazi E, Haratipour P, Joshi T, Farzaci MH, Khan H, Echeverría J (2020) Involvement of TGF-β and autophagy pathways in pathogenesis of diabetes: a comprehensive review on biological and pharmacological insights. *Front Pharmacol* **11**: 498758. <https://doi.org/10.3389/fphar.2020.498758>
- Ho N, Sommers MS, Lucki I (2013) Effects of diabetes on hippocampal neurogenesis: links to cognition and depression. *Neurosci Biobehav Rev* **37**: 1346–1362. <https://doi.org/10.1016/j.neubiorev.2013.03.010>
- Hugo J, Ganguli M (2014) Dementia and cognitive impairment: epidemiology, diagnosis, and treatment. *Clin Geriatr Med* **30**: 421–442. <https://doi.org/10.1016/j.cger.2014.04.001>
- Jafferali S, Dumont Y, Sotty F, Robitaille Y, Quirion R, Kar S (2000) Insulin-like growth factor-I and its receptor in the frontal cortex, hippocampus, and cerebellum of normal human and Alzheimer disease brains. *Synapse* **38**: 450–459. [https://doi.org/10.1002/1098-2396\(20001215\)38:4<450::AID-SYN10>3.0.CO;2-J](https://doi.org/10.1002/1098-2396(20001215)38:4<450::AID-SYN10>3.0.CO;2-J)
- Jayaraj RL, Azimullah S, Beiram R (2020) Diabetes as a risk factor for Alzheimer's disease in the Middle East and its shared pathological mediators. *Saudi J Biol Sci* **27**: 736–750. <https://doi.org/10.1016/j.sjbs.2019.12.028>
- Kim JY, Barua S, Huang MY, Park J, Yenari MA, Lee JE (2020) Heat Shock Protein 70 (HSP70) induction: chaperonotherapy for neuroprotection after brain injury. *Cells* **9**: 2020. <https://doi.org/10.3390/cells9092020>
- Kim JY, Huang M, Lee JE, Yenari MA (2019) Role of Heat Shock Proteins (HSP) in neuroprotection for ischemic stroke. In *Heat Shock Proteins in Neuroscience. Heat Shock Proteins*, Vol 20, Asea A, Kaur P eds, Cham, Springer. https://doi.org/10.1007/978-3-030-24285-5_6
- Kinattungal N, Mehdi S, Undela K, Wani SUD, Almuqbil M, Alshehri S, Shakeel F, Imam MT, Manjula SN (2023) Prevalence of cognitive decline in type 2 diabetes mellitus patients: a real-world cross-sectional study in Mysuru, India. *J Pers Med* **13**: 524. <https://doi.org/10.3390/jpm13030524>
- Kleinridders A, Ferris HA, Cai W, Kahn CR (2014) Insulin action in brain regulates systemic metabolism and brain function. *Diabetes* **63**: 2232–2243. <https://doi.org/10.2337/db14-0568>
- Krause M, Heck TG, Bittencourt A, Scomazzon SP, Newsholme P, Curi R, Homem de Bittencourt PI Jr (2015) The chaperone balance hypothesis: the importance of the extracellular to intracellular HSP70 ratio to inflammation-driven type 2 diabetes, the effect of exercise, and the implications for clinical management. *Mediators Inflamm* **2015**: 249205. <https://doi.org/10.1155/2015/249205>
- Kükürt A, Gelen V, Başer Ö, Deveci H, Karapehlivan M (2021) *Thiols: Role in Oxidative Stress-Related Disorders*. IntechOpen. <https://doi.org/10.5772/intechopen.96682>
- Kumar A (2011) Long-term potentiation at CA3-CA1 hippocampal synapses with special emphasis on aging, disease, and stress. *Front Aging Neurosci* **3**: 7. <https://doi.org/10.3389/fnagi.2011.00007>
- Kureti A, Arinew C, Mothibe M, Ngubane P, Khathi A, Sibiya N (2023) Drug-induced mitochondrial toxicity: Risks of developing glucose handling impairments. *Front Endocrinol* **14**: 1123928. <https://doi.org/10.3389/fendo.2023.1123928>

- Li Y, Liu Y, Liu S, Gao M, Wang W, Chen K, Huang L, Liu Y (2023) Diabetic vascular diseases: molecular mechanisms and therapeutic strategies. *Signal Transduct Target Ther* 8: 152. <https://doi.org/10.1038/s41392-023-01400-z>
- Lin X, Xu Y, Pan X, Xu J, Ding Y, Sun X, Song X, Ren Y, Shan PF (2020) Global, regional, and national burden and trend of diabetes in 195 countries and territories: an analysis from 1990 to 2025. *Sci Rep* 10: 14790. <https://doi.org/10.1038/s41598-020-71908-9>
- Liu C, Liang MC, Soong TW (2019) Nitric oxide, iron and neurodegeneration. *Front Neurosci* 13: 114. <https://doi.org/10.3389/fnins.2019.00114>
- Liu G, Wang T, Wang T, Song J, Zhou Z (2013) Effects of apoptosis-related proteins caspase-3, Bax and Bcl-2 on cerebral ischemia rats. *Biomed Rep* 1: 861–867. <https://doi.org/10.3892/br.2013.153>
- Liu C, Vyas A, Kassab MA, Singh AK, Yu X (2017) The role of poly ADP-ribosylation in the first wave of DNA damage response. *Nucleic Acids Res* 45: 8129–8141. <https://doi.org/10.1093/nar/gkx565>
- Ludwig MS, Minguetti-Camara VC, Heck TG, Scomazzon SP, Nunes PR, Bazotte RB, Homem de Bittencourt PIJ (2014) Short-term but not long-term hypoglycaemia enhances plasma levels and hepatic expression of HSP72 in insulin-treated rats: an effect associated with increased IL-6 levels but not with IL-10 or TNF- α . *Mol Cell Biochem* 397: 97–107. <https://doi.org/10.1007/s11010-014-2176-2>
- Lyu Q, Wawrzyniuk M, Rutten VPMG, van Eden W, Sijs AJAM, Broere F (2020) Hsp70 and NF- κ B mediated control of innate inflammatory responses in a canine macrophage cell line. *Int J Mol Sci* 21: 4664. <https://doi.org/10.3390/ijms211846464>
- Maida CD, Daidone M, Pacinella G, Norrito RL, Pinto A, Tuttolomondo A (2022) Diabetes and ischemic stroke: an old and new relationship: an overview of the close interaction between these diseases. *Int J Mol Sci* 23: 2397. <https://doi.org/10.3390/ijms23042397>
- Miles WR, Root HF (1922) Psychologic tests applied to diabetic patients. *Arch Intern Med* 30: 767–777. <https://doi.org/10.1001/archinte.1922.00110120086003>
- Moheet A, Mangia S, Seaquist ER (2015) Impact of diabetes on cognitive function and brain structure. *Ann N Y Acad Sci* 1353: 60–71. <https://doi.org/10.1111/nyas.12807>
- Moin ASM, Nandakumar M, Diane A, Dehbi M and Butler AE (2021) The role of heat shock proteins in type 1 diabetes. *Front Immunol* 11: 612584. <https://doi.org/10.3389/fimmu.2020.612584>
- Mulyani WRW, Sanjiwani MID, Sandra, Prabawa IPY, Lestari AAW, Wihandani DM, Suastika K, Saraswati MR, Bhargah A, Manuaba IBAP (2020) Chaperone-based therapeutic target innovation: Heat Shock Protein 70 (HSP70) for type 2 diabetes mellitus. *Diabetes Metab Syndr Obes* 13: 559–568. <https://doi.org/10.2147/DMSO.S232133>
- Nagai M, Kaji H (2023) Thermal effect on heat shock protein 70 family to prevent atherosclerotic cardiovascular disease. *Biomolecules* 13: 867. <https://doi.org/10.3390/biom13050867>
- Naka K K, Veziraki P, Kalaitzakis A, Zerikiotis S, Michalis L, Angelidis C (2014) Hsp70 regulates the doxorubicin-mediated heart failure in Hsp70-transgenic mice. *Cell Stress Chaperones* 19: 853–864. <https://doi.org/10.1007/s12192-014-0509-4>
- Nakhjavani M, Morteza A, Khajehali L, Esteghamati A, Khalilzadeh O, Asgarani F, Outeiro TF (2010) Increased serum HSP70 levels are associated with the duration of diabetes. *Cell Stress Chaperones* 15: 959–964. <https://doi.org/10.1007/s12192-010-0204-z>
- Nam SM, Yi SS, Yoo KY, Park OK, Yan B, Song W, Won MH, Yoon YS, Seong JK (2011) Differential effects of treadmill exercise on cyclooxygenase-2 in the rat hippocampus at early and chronic stages of diabetes. *Lab Anim Res* 27: 189–195. <https://doi.org/10.5625/lar.2011.27.3.189>
- Norat P, Soldozy S, Sokolowski JD, Gorick CM, Kumar JS, Chae Y, Yağmurlu K, Prada F, Walker M, Levitt MR, Price RJ, Tvrdik P, Kalani MYS (2020) Mitochondrial dysfunction in neurological disorders: Exploring mitochondrial transplantation. *NPJ Regen Med* 5: 22. <https://doi.org/10.1038/s41536-020-00107-x>
- Ohiagu F, Chikezie P, Chikezie C (2021) Pathophysiology of diabetes mellitus complications: Metabolic events and control. *Biomed Res Ther* 8: 4243–4257. <https://doi.org/10.15419/bmrat.v8i3.663>
- Oliveira AA, Priviero F, Webb RC, Nunes KP (2022) Increased eHSP70-to-iHSP70 ratio disrupts vascular responses to calcium and activates the TLR4-MD2 complex in type 1 diabetes. *Life Sci* 310: 121079. <https://doi.org/10.1016/j.lfs.2022.121079>
- Ortan P, Akan OY, Hosgorler F (2018) Heat Shock Protein70 in Neurological Disease. In *HSP70 in Human Diseases and Disorders*. Heat Shock Proteins, Vol 14, pp 57–69, Asea A, Kaur P eds. Cham, Springer. https://doi.org/10.1007/978-3-319-89551-2_3
- Pacher P, Szabó C (2005) Role of poly(ADP-ribose) polymerase-1 activation in the pathogenesis of diabetic complications: endothelial dysfunction, as a common underlying theme. *Antioxid Redox Signal* 7: 1568–1580. <https://doi.org/10.1089/ars.2005.7.1568>
- Pavlov SV, Belenichev IF, Nikitchenko YV, Gorbachova SV (2017) Molecular bio-chemical mechanisms of HSP 70-mediated cytoprotection in pathologies of ischemic origin. *Bull Probl Biol Med* 1: 61–67
- Pessoa J, Duarte AI (2023) Overcoming mitochondrial dysfunction in neurodegenerative diseases. *Neural Reg Res* 18: 1486–1488. <https://doi.org/10.4103/1673-5374.360279>
- Pinti MV, Fink GK, Hathaway QA, Durr AJ, Kunovac A, Hollander JM (2019) Mitochondrial dysfunction in type 2 diabetes mellitus: an organ-based analysis. *Am J Phys-Endocr Metab* 316: E268–E285. <https://doi.org/10.1152/ajpendo.00314.2018>
- Pitocco D, Tesaro M, Alessandro R, Ghirlanda G, Cardillo C (2013) Oxidative stress in diabetes: implications for vascular and other complications. *Int J Mol Sci* 14: 21525–21550. <https://doi.org/10.3390/ijms141121525>
- Popruha A, Mykhaylychenko T, Samarchenko L, Bobyrova L (2021) Mathematical model of diabetic encephalopathy in diagnosis of complicated forms of diabetes mellitus. *Int J Endocr (Ukr)* 13: 420–423. <https://doi.org/10.22141/2224-0721.13.6.2017.112882>
- Ren X, Zou L, Zhang X, Branco V, Wang J, Carvalho C, Holmgren A, Lu J (2017) Redox signaling mediated by thioredoxin and glutathione systems in the central nervous system. *Antioxid Redox Signal* 27: 989–1010. <http://doi.org/10.1089/ars.2016.6925>
- Seibert P, Anklam CFV, Costa-Beber LC, Sulzbacher LM, Sulzbacher MM, Sangiovo AMB, Dos Santos FK, Goettems-Fiorin PB, Heck TG, Frizzo MN, Ludwig MS (2022) Increased eHSP70-to-iHSP70 ratio in prediabetic and diabetic postmenopausal women: a biomarker of cardiometabolic risk. *Cell Stress Chaperones* 27: 523–534. <https://doi.org/10.1007/s12192-022-01288-8>
- Senf SM, Dodd SL, McClung JM, Judge AR (2008) Hsp70 overexpression inhibits NF- κ B and Foxo3a transcriptional activities and prevents skeletal muscle atrophy. *FASEB J* 22: 3836–3845. doi: 10.1096/fj.08-110163
- Shamas-Din A, Kale J, Leber B, Andrews DW (2013) Mechanisms of action of Bcl-2 family proteins. *Cold Spring Harb Perspect Biol* 5: a008714. <https://doi.org/10.1101/cshperspect.a008714>
- Shan YX, Yang TL, Mestrl R, Wang PH (2003) Hsp10 and Hsp60 suppress ubiquitination of insulin-like growth factor-1 receptor and augment insulin-like growth factor-1 receptor signaling in cardiac muscle: implications on decreased myocardial protection in diabetic cardiomyopathy. *J Biol Chem* 278: 45492–45498. <https://doi.org/10.1074/jbc.M304498200>
- Sherin A, Anu J, Peeyush KT, Smijin S, Anitha M, Roshni BT, Paulose CS (2012) Cholinergic and GABAergic receptor functional deficit in the hippocampus of insulin-induced hypoglycemic and streptozotocin-induced diabetic rats. *Neuroscience* 202: 69–76. <https://doi.org/10.1016/j.neuroscience.2011.11.058>
- Shi J, Dong B, Mao Y, Guan W, Cao J, Zhu R, Wang S (2016) Review: Traumatic brain injury and hyperglycemia, a potentially modifiable risk factor. *Oncotarget* 7: 71052–71061. <https://doi.org/10.18632/oncotarget.11958>
- Singh R, Mohapatra L, Tripathi, AS (2021) Targeting mitochondrial biogenesis: a potential approach for preventing and controlling diabetes. *Futur J Pharm Sci* 7: 212. <https://doi.org/10.1186/s43094-021-00360-x>
- Sivitz WI, Yorek MA (2010) Mitochondrial dysfunction in diabetes: from molecular mechanisms to functional significance and therapeutic opportunities. *Antioxid Redox Signal* 12: 537–577. <https://doi.org/10.1089/ars.2009.2531>
- Skelly DT, Hennessy E, Dansereau M-A, Cunningham C (2013) A systematic analysis of the peripheral and CNS effects of systemic LPS, IL-1 β , TNF- α and IL-6 challenges in C57BL/6 mice. *PLoS ONE* 8. <https://doi.org/10.1371/journal.pone.0064482>
- Soto M, Cai W, Konishi M, Kahn CR (2019) Insulin signaling in the hippocampus and amygdala regulates metabolism and neurobehavior. *Proc Natl Acad Sci USA* 116: 6379–6384. <https://doi.org/10.1073/pnas.1817391116>
- Spinelli M, Fusco S, Grassi C (2019) Brain insulin resistance and hippocampal plasticity: mechanisms and biomarkers of cognitive decline. *Front Neurosci* 13: 788. <https://doi.org/10.3389/fnins.2019.00788>
- Sun GY, Geng X, Teng T, Yang B, Appenteng MK, Greenleaf CM, Lee JC (2021) Dynamic role of phospholipids A2 in health and diseases in the central nervous system. *Cells* 10: 2963. <https://doi.org/10.3390/cells10112963>
- Teodoro JS, Nunes S, Rolo AP, Reis F, Palmeira CM (2019) Therapeutic options targeting oxidative stress, mitochondrial dysfunction and inflammation to hinder the progression of vascular complications of diabetes. *Front Physiol* 9: 1857. <https://doi.org/10.3389/fphys.2018.01857>
- Török NJ, Higuchi H, Bronk S, Gores GJ (2002) Nitric oxide inhibits apoptosis downstream of cytochrome c release by nitrosylating caspase 9. *Cancer Res* 62: 1648–1653
- Tota L, Matejko B, Morawska-Tota M, Pilch W, Mrozińska S, Palka T, Klupa T and Malecki MT (2021) Changes in oxidative and

- nitrosative stress indicators and vascular endothelial growth factor after maximum-intensity exercise assessing aerobic capacity in males with type 1 diabetes mellitus. *Front Physiol* **12**: 672403. <https://doi.org/10.3389/fphys.2021.672403>
- Tun NN, Arunagirinathan G, Munshi SK, Pappachan JM (2017) Diabetes mellitus and stroke: A clinical update. *World J Diabetes* **8**: 235–248. <https://doi.org/10.4239/wjd.v8.i6.235>
- Turturici G, Sconzo G, Geraci F (2011) Hsp70 and its molecular role in nervous system diseases. *Biochem Res Int* **2011**: 618127. <https://doi.org/10.1155/2011/618127>
- Wang C, Li J, Zhao S, Huang L (2020) Diabetic encephalopathy causes the imbalance of neural activities between hippocampal glutamatergic neurons and GABAergic neurons in mice. *Brain Res* **1742**: 146863. <https://doi.org/10.1016/j.brainres.2020.146863>
- Wang MH, Hsiao G, Al-Shabrawey M (2020) Eicosanoids and oxidative stress in diabetic retinopathy. *Antioxidants (Basel)* **9**: 520. <https://doi.org/10.3390/antiox9060520>
- Wang W, Zhao F, Ma X, Perry G, Zhu X (2020) Mitochondria dysfunction in the pathogenesis of Alzheimer's disease: recent advances. *Mol Neurodegener* **15**: 30. <https://doi.org/10.1186/s13024-020-00376-6>
- Wu L, Derynck R (2009) Essential role of TGF-beta signaling in glucose-induced cell hypertrophy. *Dev Cell* **17**: 35–48. <https://doi.org/10.1016/j.devcel.2009.05.010>
- Luo X, Wu J, Jing S, Yan LJ (2016) Hyperglycemic stress and carbon stress in diabetic glucotoxicity. *Aging Dis* **7**: 90–110. <https://doi.org/10.14336/AD.2015.0702>
- Yan LJ (2018) Redox imbalance stress in diabetes mellitus: Role of the polyol pathway. *Animal Model Exp Med* **1**: 7–13. <https://doi.org/10.1002/ame2.12001>
- Zhang Y, Zhang X, Shan P, Hunt CR, Pandita TK, Lee PJ (2013) A protective Hsp70-TLR4 pathway in lethal oxidant lung injury. *J Immunol* **191**: 1393–403. <https://doi.org/10.4049/jimmunol.1300052>
- Zhang Y, Li H (2017) Reprogramming interferon regulatory factor signaling in cardiometabolic diseases. *Physiology* **32**: 210–223. <https://doi.org/10.1152/physiol.00038.2016>
- Zhang H, Gong W, Wu S, Perrett S (2022) HSP70 in Redox homeostasis. *Cells* **11**: 829. <https://doi.org/10.3390/cells11050829>

Silencing lncRNA EZR-AS1 induces apoptosis and attenuates the malignant properties of lung adenocarcinoma cells

Xianjing Yu¹, Lixue Wu¹, Zhongcui Lu¹, Junli Zhang² and Yunfeng Zhou³✉

¹Department of Pathology, West China School of Public Health and West China Forth Hospital, Sichuan University, Chengdu, China; ²Department of Pathology, The First Affiliated Hospital of Chengdu Medical College, Chengdu, China; ³Department of Cardiothoracic Surgery, West China School of Public Health and West China Forth Hospital, Sichuan University, Chengdu, China

Adenocarcinoma is one of the major subtypes of lung cancer. This study aimed to investigate the effect of silencing long non-coding RNA (lncRNA) EZR-AS1 on the biological behaviors of lung adenocarcinoma (ADC) cells. EZR-AS1 expression levels in lung ADC tissues and cells, as well as in adjacent non-cancerous tissues, were determined using quantitative reverse transcription polymerase chain reaction (qRT-PCR). EZR-AS1 was knocked down in two lung ADC cell lines using small interfering RNA specific for EZR-AS1 (siEZR-AS1). Proliferation, migration, and apoptosis of EZR-AS1-knockdown cells were assessed using the CCK-8 viability assay, flow cytometry, or wound healing experiments. The levels of proteins related to migration pathways were evaluated using western blotting analysis. EZR-AS1 contents were significantly higher in lung ADC tissues and cells than in the levels in the non-cancerous tissues and cells ($p < 0.01$). Transfection of ADC cell lines H1437 and H1975 significantly downregulated EZR-AS1 levels in both cell lines. Cytotoxicity assays revealed that the viability of EZR-AS1-knockdown cells significantly decreased over culture time, and a significant level of apoptosis was induced ($p < 0.01$). Wounding healing experiments revealed that EZR-AS1-knockdown significantly reduced the migration rate of both cell lines ($p < 0.01$). Furthermore, proteins related to migration pathways such as vimentin, MMP2, and MMP9 were significantly downregulated, whereas the E-cadherin level was significantly increased after EZR-AS1 knockdown. Our work demonstrated that EZR-AS1 is associated with ADC progression, and silencing this gene inhibits proliferation and reduces migration of ADC cells *in vitro*. The altered expression of metastasis-related genes was likely responsible for the reduced migration ability after EZR-AS1 knockdown.

Keywords: lung cancer; long non-coding RNA; cell viability; migration; apoptosis

Received: 26 March, 2023; revised: 02 August, 2023; accepted: 22 August, 2023; available on-line: 18 September, 2023

✉e-mail: c11231354@163.com

Abbreviations: lncRNA, lncRNA long non-coding RNA; ADC, adenocarcinoma; qRT-PCR, quantitative reverse transcription polymerase chain reaction; SCLC, small cell lung cancer; HOTAIR, HOX transcript antisense RNA; cSCC, cutaneous squamous cell carcinoma; ESCC, esophageal squamous cell carcinoma; FBS, fetal bovine serum; TBS, tris buffered saline; HRP, horseradish peroxidase; RIPA, radioimmunoprecipitation assay; SDS-PAGE, polyacrylamide gel electrophoresis; PVDF, polyvinylidene fluoride; ANOVA, analysis of variance; HCC, hepatocellular carcinoma; MEtT, mesenchymal to epithelial reverting transition; IF, intermediate filament; URI, unconventional prefoldin RPB5 interactor; CRC, colorectal cancer; MMP, matrix metalloproteinase; ECM, the extracellular matrix

INTRODUCTION

With the increasing number of cancer patients worldwide in recent years, the total prevalence and mortality rate of lung cancer have always been among the highest, particularly in China (Bade & Dela Cruz, 2020; Bai *et al.*, 2018; Cao & Chen, 2019). Annually, there are about 1.8 million new cases of lung cancer and nearly 1.6 million people die because of lung cancer. Studies show that the five-year survival rate of patients is 4–17% (Klimaszewska-Wisniewska *et al.*, 2018; Musika *et al.*, 2021). Histologically, lung cancer is divided into four types including small-cell lung cancer (SCLC), squamous cell carcinoma, adenocarcinoma (ADC), and large-cell carcinoma (Densisenko *et al.*, 2018). ADC accounts for the highest proportion of lung cancers and is responsible for up to 40% of all lung cancers in China (Wu *et al.*, 2021). However, the specific mechanisms of the occurrence, development, and metastasis of ADC are still largely unclear, and elucidation of these mechanisms will be of great significance in the management of the disease.

Long non-coding RNAs (lncRNAs) are endogenous RNAs that have more than 200 nucleotides in length but do not encode proteins (Saigoh *et al.*, 1998). They play various roles in numerous biological activities and processes, including epigenetic regulation, DNA methylation, histone modification, cell cycle regulation, post-transcriptional and post-translational regulation of DNA expression, and histone modification (Hosseini *et al.*, 2017). lncRNAs have been demonstrated to participate in the occurrence, proliferation, invasion, metastasis and prognosis of many tumors, including lung cancer. For example, the level of lncRNA DANCR is elevated in tissues isolated from high-grade lung cancer and DANCR knockdown reduces the progression of lung cancer in a xenograft mouse model (Figg *et al.*, 1978); HOTAIR level is upregulated in lung cancer and the level is correlated with the degree of metastasis and outcome with poor prognosis (Loewen *et al.*, 2014); and lncRNA ezrin antisense RNA 1 (EZR-AS1) is highly expressed in various cancers such as cutaneous squamous cell carcinoma (cSCC), colon cancer, breast cancer, and esophageal squamous cell carcinoma (ESCC) compared with non-cancer tissues (Bai *et al.*, 2018; Ghaffari *et al.*, 2019; Lu *et al.*, 2021; Xie *et al.*, 2011).

EZR-AS1, 362 bp in length, is an endogenous lncRNA transcribed from the antisense strand of the EZR gene that is located on chromosome 6q25.3 (Liu *et al.*, 2019). As a cytoskeletal-membrane linker protein, *ezrin* is highly expressed in lymph node metastases but not in matched primary tumors, and downregulating *ezrin* with a small-molecule compound could impede the migration

ability of cancer cells (Ghaffari *et al.*, 2019). Knockdown of EZR-AS1 results in reduced proliferation ability of breast cancer cells *in vitro* and arrests the cell cycle by inactivating the Wnt/ β -catenin pathway (Bai *et al.*, 2018). In ESCC, high EZR expression was found to be the cause of poor overall survival and is considered a new molecular marker to predict the prognosis of ESCC patients (Xie *et al.*, 2011). However, the role of EZR-AS1 in ADC remains to be elucidated.

In the present work, the effect of silencing lncRNA EZR-AS1 on the growth, migration, and apoptosis of lung ADC cells was investigated in an attempt to explore the therapeutic option of ADC by lncRNA.

MATERIALS AND METHODS

Reagents and instruments

Fetal bovine serum (FBS; Cat. no. 26140079) was purchased from Sigma-Aldrich-Aldrich (USA). The RPMI-1640 medium (cat. no. 11875119), Tris-buffered saline (TBS; cat. no. BP2471100), BCA protein assay kit (cat. no. 712853), and Annexin V-FITC kit (cat. no. 331200) was obtained from Thermo Fisher Scientific (USA). The BeyoRT III cDNA Synthesis Kit (with gDNA EZeracer) (cat. no. D7180M), Trizol total RNA extraction reagent (cat. no. R0016), and BeyoFast SYBR Green qPCR Mix (cat. no. D7260), and Lipofectamine 6000 transfection reagent (cat. no. C0526), cell counting kit-8 (cat. no. C0037), and RNase A (Cat. no. ST579) and E-cadherin (cat. no. AF0138; dilution 1:1500) and vimentin (cat. no. AF0318; dilution, 1:1000), MMP9 (cat. no. AF7935, dilution 1:1500), MMP2 (cat. no. AF1420, dilution 1:1500), and GAPDH (cat. no. AF2819, dilution 1:1200), goat horseradish peroxidase (HRP)-conjugated anti-rabbit IgG (cat. no. A0208, dilution 1:2000) and a chemiluminescent kit (cat. no. GS009) was purchased from Beyotime (Shanghai, China). A microplate reader (GloMax® Discover) was purchased from Promega (USA). Flow cytometry (FACS LSR) data were obtained from BD Biosciences (USA). An inverted light microscope (IX73P2F) was obtained from Olympus (Tokyo, Japan). A Real-time PCR Detection System (CFX96) was obtained from Bio-Rad, Hercules, CA, USA.

Cell culture

The human lung adenocarcinoma cell line H1437 (cat. no. CRL-5872), H1975 cells (cat. no. CRL-5908), lung epithelial cell line HBE3-KT (cat. no. CRL-4051) and NL20 (cat. no. CRL-2503) were obtained from ATCC, Manassas, VA, USA. The cells were grown in RPMI-1640 medium added with 10% FBS, penicillin (100 U/ml), and mycomycin (100 μ g/ml) in a humidified incubator with 5% CO₂ at 37°C. The medium was changed every 2–3 days when the cell culture reached the logarithmic phase.

Clinical specimens

Clinical specimens (lung ADC samples and matched paracancerous tissues) were isolated from 50 patients who underwent surgical treatment at The First Affiliated Hospital of Chengdu Medical College in Chengdu, China, between July 2017 and January 2019. All ADC were primary, and the patients had not received any radiotherapy or chemotherapy prior to surgery. This study was approved by the Ethics Committee of Sichuan Uni-

versity (approval no. SU3312D). Informed consent was secured from each patient.

Quantitative reverse transcription polymerase chain reaction (RT-qPCR)

Total RNA was prepared from tissues and cells using TRIzol reagent based on the manufacturer's protocols. RNA (1 μ g) was reversely transcribed into cDNA using the BeyoRT III cDNA synthesis kit and the resultant cDNA was used as a template for RT-qPCR assays with primers designed using Primer Premier 5 (<https://www.bioprocesonline.com/doc/primer-premier-5-design-program-0001>). RT-qPCR was carried out on CFX96 Real-time PCR System using BeyoFast SYBR Green qPCR mix based on the manufacturer's instructions, with the cycling parameters: pre-denaturing at 95°C for 3 min, followed by 40 cycles of denaturing at 95°C for 10 s, annealing for 30 s with a final extension at 72°C for 30 s. The GAPDH gene was employed as the endogenous expression reference. The expression level relative to GAPDH was determined using the 2^{- $\Delta\Delta C_t$} method as outlined described (Livak & Schmittgen, 2001). The primers used for EZR-AS1 were forward: 5'-CCCTCTCCAATGAAGCCTCTC-3' and reverse: 5'-ACCGAAAATGCCGAAACCAG-3'; and for GAPDH forward: 5'-GTCTCCTCTGACTTCAACAGCG-3' and reverse, 5'-ACCACCCTGTTGCTGTAGCCAA-3'.

Transfection

Cells were cultured to 70–80% confluency and divided into aliquots for transfection using Lipofectamine 6000 transfection reagent, based on the manufacturer's instructions. The cells were either non-transfected (non-transfected, control), transfected with 0.5 μ g siNC (siNC, scrambled control), siEZR-AS1 or pEZR-AS1 (positive control). siRNA (5'-AAA UAA UAC UAC AAU UAA A-3') was synthesized by Wigen Biomedicine (Shanghai, China). After transfection, cells were grown in 96 well plates containing RPMI-1640 medium at 37°C for 48 h and then used for subsequent experiments.

Cell viability assay

The viability of treated cells was determined using a CCK-8 cell counting kit based on the manufacturer's protocols. Briefly, cells were inoculated into the wells of 96-well plates at a density of 5 \times 10⁴ cells/well and grown in RPMI-1640 medium at 37°C in 5% CO₂. At predetermined time points, 20 μ l CCK-8 solution was dropped to the wells and the cells were incubated at 37°C with 5% CO₂ for 4 h. After the incubation, optical density (OD) of the plates was determined at 460 nm using a microplate reader. All assays were performed in triplicates. Cell viability was calculated as follows: OD_{sample}/OD_{control} \times 100%.

Apoptosis analysis

The apoptosis of treated cells was assessed using the ApoDETECT Annexin V-FITC kit based on the manufacturer's protocols. Briefly, after transfection, the cells were inoculated into the wells of 6-well plates at 5 \times 10⁴ cells/well containing RPMI-1640 medium. The cells were cultured at 37°C in 5% CO₂ to a confluence between 50 and 70%, harvested after centrifugation at 750 \times g at 25°C for 10 min, washed with 1 ml PBS three times, and digested with RNase A (100 μ g/ml) at 37°C for 20 min. The digested cells were resuspended in pre-chilled binding buffer in an ice bath, and stained with Annexin

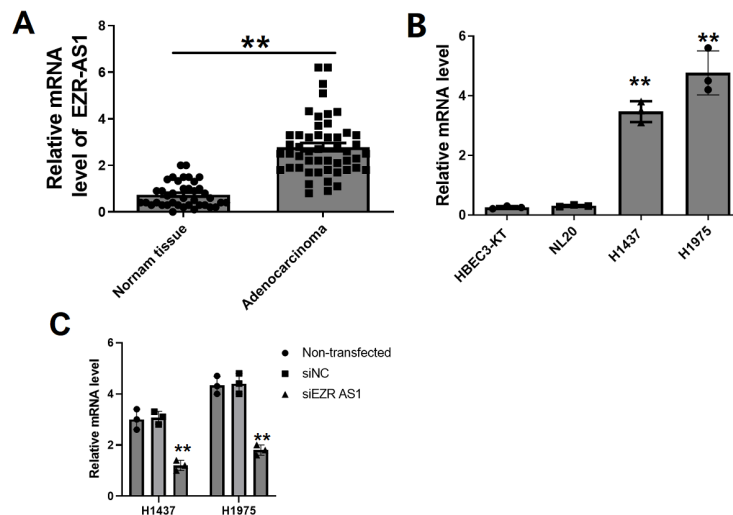


Figure 1. Determination of expression level of long non-coding RNA EZR-AS1 (ezrin antisense RNA 1) in lung ADC tissues and cells by RT-qPCR.

(A) EZR-AS1 levels in lung ADC and healthy tissues. (B) EZR-AS1 levels in lung ADC cell lines (H1437 and H1975) and non-cancer lines (HBEC3-KT and NL20). (C) EZR-AS1 levels in ADC cell lines H1437 and H1975 transfected with siEZR-AS1 (si, small interfering RNA), siNC (NC, negative control). All assays were repeated three times. **denotes $p < 0.01$ compared to si-NC or non-transfected cells using one-way ANOVA.

V-FITC (3 μ l) and PI-PE (7 μ l) in the dark at 25°C for 10 min. After the staining, the cells were loaded onto a FACS LSR flow cytometer for analysis with built-in software. All assays were carried out in triplicates.

Wound healing assay

To assess the migration ability, cells were cultured on slides in the wells of 6-well plate containing RPMI-1640 medium with 10% FBS at 37°C. At 100% confluence, a scratch was created on the monolayer with the tip of a 10 μ l pipette as previously described (Justus *et al.*, 2014). Serum-free RPMI-1640 medium was added and cell migration was recorded at 0 and 48 h with an inverted light microscope (at 100 \times magnification) and cell migration distances were calculated using Image-Pro Plus software obtained from Media Cybernetics, Inc. USA.

Western blot analysis

To assess the levels of specific proteins, treated cells were collected after centrifugation at 500 g at 25°C for 10 min, rinsed twice with pre-chilled PBS, and lysed in the radioimmunoprecipitation assay (RIPA) buffer. The total levels of protein in the lysates were determined using a BCA protein assay kit following the supplier's instructions. After boiling at 100°C for 5 min, 60 μ g denatured proteins were loaded to the gels and separated by 12% polyacrylamide gel electrophoresis (SDS-PAGE). The separated proteins on the gels were blot-transferred to polyvinylidene fluoride (PVDF) membranes, then blocked by gentle shaking in 5% non-fat milk solution in 1 \times TBS containing 0.1% Tween 20 (TBST) for 4 h at 25°C. After blocking, the membrane filters were incubated with antibodies to E-cadherin, vimentin, MMP9, MMP2, and GAPDH (served as internal control) at 4°C overnight, rinsed three times at room temperature with TBS buffer, reacted with goat HRP-conjugated anti-rabbit IgG at 25°C for 2 h. Immunoreactive bands on the blots were developed using a chemiluminescent kit in the dark following the manufacturer's protocols. The gray values of the reactive bands were determined using Quantity One software.

Statistical analysis

Data are shown as the means \pm standard error derived from three independent experiments. One-way ANOVA with post-hoc Tukey's honest significant difference test was applied to compare the means among the groups. A value of $p < 0.05$ was considered to be statistically significant.

RESULTS

EZR-AS1 level is highly elevated in lung ADC tissues and cells

We first determined the level of EZR-AS1 mRNA in lung ADC tissues and cells as well as in non-cancerous tissues and cells. RT-qPCR analysis showed that EZR-AS1 were significantly upregulated in ADC tissues in comparison with the adjacent healthy tissues obtained from patients undergoing surgical resection ($p < 0.01$; Fig. 1A). Furthermore, EZR-AS1 mRNA levels in ADC cell lines H1437 and H1975 were significantly elevated compared to those in the non-cancer cell lines HBEC3-KT and NL20 ($p < 0.01$; Fig. 1B).

EZR-AS1 knockdown reduces the viability of ADC cells

We then tested whether silencing EZR-AS1 inhibits the growth of ADC cells. H1437 and H1975 cells were transfected with siEZR-AS1 using Lipofectamine-mediated transfection. RT-qPCR analysis showed that siEZR-AS1 transfection resulted in significantly reduced EZR-AS1 levels in both cell lines compared with the controls (non-transfected cells or cells transfected with siNC) ($p < 0.01$; Fig. 1C). The cell counting assay showed that the viability of H1437 and H1975 cells decreased over time compared to the controls ($p < 0.01$; Fig. 2A). After 72 h of culture, the viability of H1437 and H1975 cells was less than 10%, while that of controls (non-transfected cells or cells transfected with siNC) was over 90% ($p < 0.01$; Fig. 2A). Flow cytometry study revealed a significant increase in apoptosis after the cells were

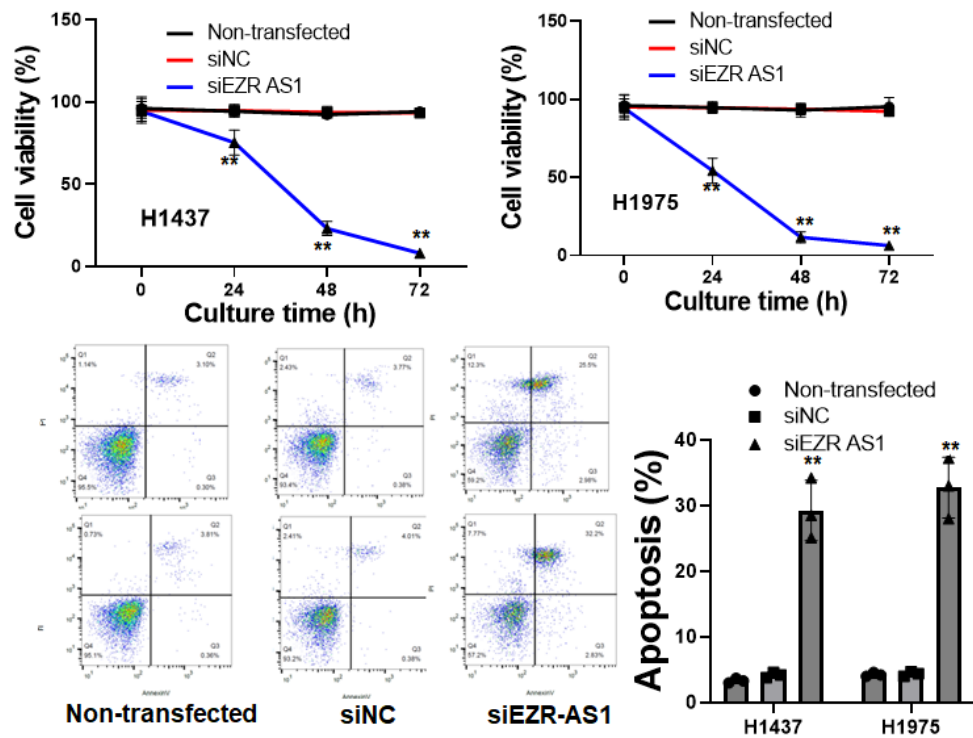


Figure 2. Cell viability and apoptosis of lung ADC cells after transfection with siEZR-AS1. (A) Cell viability was assessed using the CCK-8 assay at different culture times in lung ADC cell lines H1437 and H1975; (B) apoptosis by flow cytometry 48 h after transfection with siEZR-AS1 in lung ADC cell lines H1437 and H1975. Right panel: flow cytometry, left panel: statistical analysis of flow cytometry data. (si, small interfering RNA), siNC (NC, negative control). All assays were repeated three times. **denotes $p < 0.01$ compared to si-NC or non-transfected cells using one-way ANOVA.

transfected with siEZR-AS1 in both cell lines at 48 h after transfection compared with the controls ($p < 0.01$; Fig. 2B).

EZR-AS1 knockdown suppresses the migration of ADC cells

To evaluate the functions of EZR-AS1 in lung ADC progression, cell migration assays based on wound-healing experiments were performed. The results showed that cell migration rates were significantly reduced af-

ter H1437 and H1975 cells were transfected with siEZR-AS1 compared to the controls ($p < 0.01$; Fig. 3).

EZR-AS1 knockdown alters the levels of metastasis-related proteins

Since the migration rate of lung ADC cells was reduced after EZR-AS1 knockdown, the levels of a few selected genes that are related to invasion and metastasis pathways were analyzed. Western blotting was used to measure the protein levels of E-cadherin, vimentin, MMP2, and MMP9 in cells after EZR-AS1 knockdown.

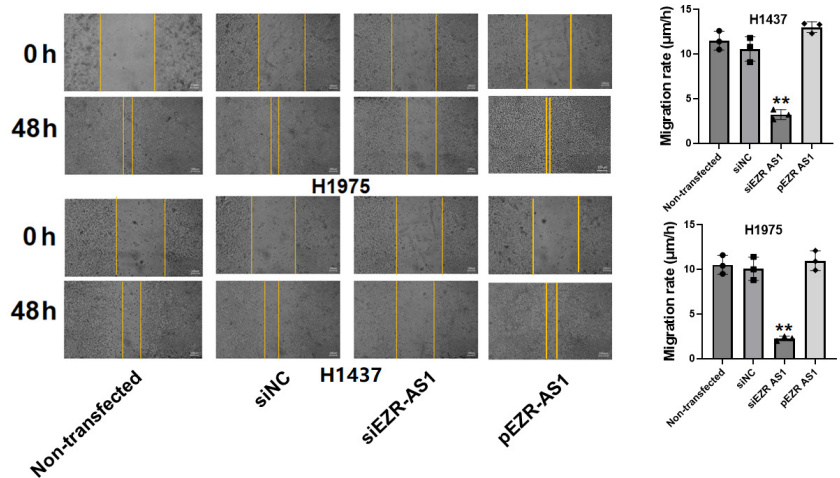


Figure 3. Migration of lung ADC cell lines H1437 and H1975 after transfected with siEZR-AS1. (A) cell migrations in wound healing experiment and (B) statistical analysis of migration rate. Scale bar, 100 μm . (si, small interfering RNA), siNC (NC, negative control) and pEZR-AS1 (positive control). All assays were repeated three times. **denotes $p < 0.01$ compared to si-NC or non-transfected cells using one-way ANOVA.

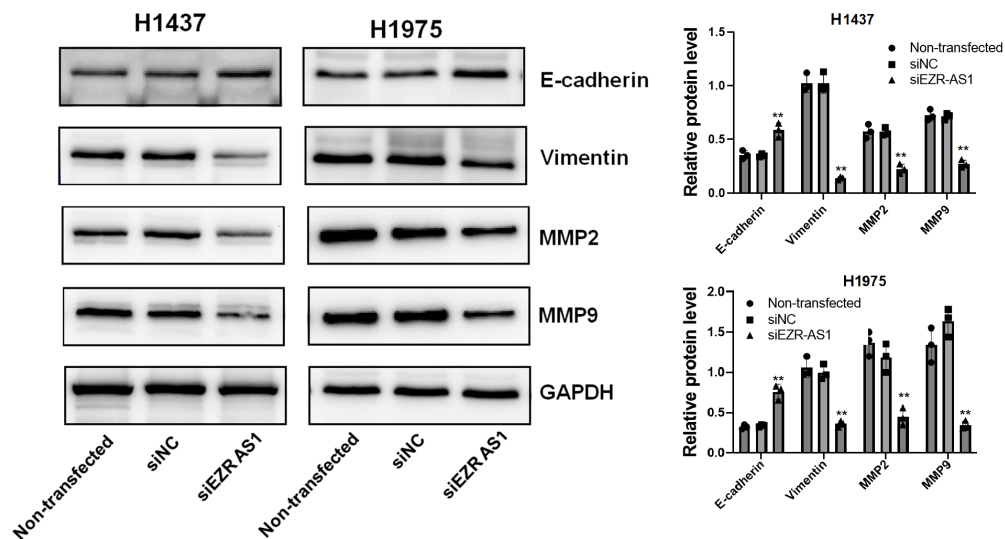


Figure 4. Level of metastasis-related proteins in lung ADC cell lines H1437 and H1975 after transfected with siEZR-AS1.

Right panel: typical Western blots, **left panel:** statistical analysis of relative protein content. All assays were repeated three times. **denotes $p < 0.01$ compared to si-NC or non-transfected cells using one-way ANOVA.

The band imaging showed that the levels of these proteins were all significantly downregulated, except for E-cadherin, which was significantly upregulated compared to the controls ($p < 0.01$; Fig. 4).

DISCUSSION

EZR-AS1 is implicated in disease progression in various cancers, such as cSCC, ESCC, breast cancer, and colorectal cancer (Bai *et al.*, 2018; Liu *et al.*, 2019; Lu *et al.*, 2021; Peng *et al.*, 2017), its biological role of EZR-AS1 in lung ADC is largely unknown. In the present study, it was found that EZR-AS1 levels were significantly elevated in lung ADC tissues and cells compared to those in non-cancerous tissues and cells. After transfection with siEZR-AS1 specifically targeting EZR-AS1, EZR-AS1 levels in the lung ADC cell lines H1437 and H1975 were significantly downregulated compared to the controls. After EZR-AS1 knockdown, the viability and migration rates of H1437 and H1975 cells were remarkably reduced, while apoptosis was significantly increased. EZR-AS1 knockdown also leads to the altered expression of migration-related genes, thus reducing the migration ability of lung ADC cells and affecting ADC progression.

Previously, it was found that silencing EZR-AS1 inhibits TGF- β -mediated signaling, leading to reduced growth and EMT of colorectal cancer cells (Liu *et al.*, 2019), and EZR-AS1 knockdown significantly reduced phosphorylated (p)-PI3K/PI3K and p-AKT/AKT levels in cSCC, leading to reduced cell viability and migration ability (Lu *et al.*, 2021). Furthermore, silencing EZR-AS1 significantly suppressed the migration, tumorigenicity, and metastatic lymph nodes of ESCC cells in mice (Zhang *et al.*, 2018). In the present experiments, we first profiled the level of EZR-AS1 mRNA in lung ADC and revealed that EZR-AS1 was higher in both ADC tissues from patients and cells established from ADC patients than in non-cancer tissues and cells. This is consistent with previous findings in cSCC, ESCC, breast cancer, and colorectal cancer (Bai *et al.*, 2018; Liu *et al.*, 2019; Lu *et al.*, 2021; Peng *et al.*, 2017), further confirming that EZR-AS1 is deregulated in cancer cells and involved in cancer progression.

To evaluate the effect of EZR-AS1 knockdown on the malignant behavior of ADC cancer cells, we transfected two ADC cell lines with siRNA specific for EZR-AS1 using Lipofectamine-mediated transfection. RT-qPCR analysis revealed that in siEZR-AS1-transfected cells, EZR-AS1 mRNA levels were significantly lower than those in the controls (both non-transfected cells and siNC-transfected cells), demonstrating that siEZR-AS1 is effective in specifically knocking down EZR-AS1. Subsequent analysis revealed that ADC cell viability was significantly reduced following EZR-AS1 silencing, suggesting that EZR-AS1 is likely essential for the occurrence and development of ADC. lncRNAs have been shown to play various roles in cancer occurrence, development, growth, invasion, migration, and prognosis (Bhan *et al.*, 2017; Peng *et al.*, 2017). They can either promote or inhibit the proliferation and metastasis of cancer cells, and knockdown of lncRNAs often results in suppression of cancer cell proliferation (Kong *et al.*, 2019; Zhen *et al.*, 2018). Apoptosis is an important process that regulates tumorigenesis and cancer development (Wong, 2011). Increased apoptosis is often associated with reduced proliferation and viability of cancer cells (Kou *et al.*, 2020). For example, lncRNA NEAT1 knockdown inhibits cell proliferation and increases caspase 3 activity and apoptosis in hepatocellular carcinoma (HCC) cells (Kou *et al.*, 2020), and downregulation of lncRNA MAGI2-AS3 inhibits proliferation and triggers apoptosis in prostate cancer by acting as a microRNA-424-5p sponge (Wei *et al.*, 2022). Previously, downregulation of EZR-AS1 was found to increase apoptosis in breast cancer cells by modulating the Wnt/ β -catenin pathway (Bai *et al.*, 2018) and in colorectal cancer cells by inhibiting transforming growth factor- β signaling (Liu *et al.*, 2019). These findings were consistent with our data. Apoptosis is also associated with the expression of specific proteins such as Bax, Bcl2, and cleaved-caspase3. In EZR-AS1 knockdown cSCC cells, Bax was significantly upregulated and Bcl-2 was significantly reduced, suggesting that EZR-AS1 likely functions as an oncogene that contributes to the malignancy of lung cancer (Lu *et al.*, 2021).

Several mechanisms have been reported in EZR-AS1 knockdown-induced loss of cell viability. Lu *et al.* found that the inhibition of the PI3K/AKT signaling path-

way was associated with EZR-AS1-knockdown-induced reduction in cell viability and increase in apoptosis in SCC13 and SCL-1 colon cancer cells (Lu *et al.*, 2021). Using LncTar, a software for predicting lncRNA-RNA interactions by means of free energy minimization, they found that focal adhesion kinase (FAK) is a target of EZR-AS1, and FAK is a crucial regulator in PI3K/AKT signaling pathway and its expression was suppressed after EZR-AS1-knockdown. This might be the reason that the PI3K/AKT signaling pathway is deactivated after EZR-AS1-knockdown. This signaling pathway plays a critical role in cell survival and in protecting cancer cells from apoptosis (Xu & Zhang, 2021). In breast cancer, EZR-AS1 protected β -catenin from degradation and EZR-AS1 knockdown inactivated the Wnt/ β -catenin pathway (Bai *et al.*, 2018). Since cyclin D1 and c-Myc are target genes of β -catenin, EZR-AS1 knockdown would downregulate the expression of cyclin D1 and c-Myc leading to reduced cell viability and migration (Sarooha *et al.*, 2022). Needless to say, more experiments such as ribonucleoprotein Immunoprecipitation (RIP) and chromatin immunoprecipitation (ChIP) may be carried out to further confirm and elucidate the mechanisms associated with the biological functions of EZR-AS1-knockdown.

Metastasis and treatment resistance are the main reasons for clinical recurrence and poor prognosis in patients with ADC. Several genes, such as RHOB and MMPs, and signaling pathways, such as the TGF- β /Smad signaling pathway, have been identified as metastatic effectors in ADC. Wound-healing experiments showed that after EZR-AS1 downregulation, the migration rate of ADC cells was significantly reduced, suggesting that silencing EZR-AS1 may regulate the expression of metastasis-related genes such as MMP2 and MMP9, as reported previously (Lu *et al.*, 2021). To confirm this is true for lung ADC cells, we also examined the levels of several metastasis-related proteins such as E-cadherin, vimentin, MMP2, and MMP9, in the cells after EZR-AS1 knockdown. E-cadherin is important for maintaining cell integrity, and reduced E-cadherin expression can lead to EMT events (Guilford, 1999; Wells *et al.*, 2008). Our analysis demonstrated that E-cadherin level was upregulated in EZR-AS1 knockdown-cells with reduced migration ability. It is possible that the increased E-cadherin may result in mesenchymal to epithelial reverting transitions (MERIT) (Chao *et al.*, 2010). When E-cadherin is upregulated in bladder cancer cells, growth and metastasis are inhibited as a result of deactivation of the β -catenin/TCF target genes (Li *et al.*, 2018). As such, the upregulation of E-cadherin has been explored as a therapeutic option in cancer treatment (Howard *et al.*, 2008).

In addition, vimentin expression was downregulated following EZR-AS1 knockdown. Vimentin codes for one of the 71 human intermediate filament (IF) proteins that are required for the migration of cancer cells that have undergone EMT. Vimentin can integrate the mechanical input and signals from the surrounding environment to promote cell migration and various other signaling pathways, such as the AKT pathway, also participate in regulating the migration of cancer cells through vimentin (Sim *et al.*, 2021). The gene is highly expressed in various epithelial cancers, including prostate, gastrointestinal, and cervical cancers (Lin *et al.*, 2017; Satelli & Li, 2011). Overexpression and silencing of vimentin by manipulation of URI (unconventional prefoldin RPB5 interactor) expression increases or decreases the migration and invasion ability of cervical cancer cells, respectively and vimentin knockdown by vimentin small hairpin RNA de-

creases colorectal cancer (CRC) cell migration (Wang *et al.*, 2021).

Matrix metalloproteinases (MMPs) are prominent proteinases associated with tumorigenesis. They regulate signaling pathways that are responsible for cell growth, inflammation, and angiogenesis in a non-proteolytic manner and are involved in EMT, a crucial step in the invasion and migration of tumor cells, because they decompose and modify the extracellular matrix (ECM) and cell-to-ECM and cell-to-cell interface contacts, facilitating the detachment and separation of epithelial cells from the surrounding tissue (Radisky & Radisky, 2010). MMP2 and MMP9 are particularly potent in digesting the components that make up the basement membrane, such as laminin and collagen IV, or interstitial collagen fragments, resulting in cancer metastasis (Barillari, 2020; Cui *et al.*, 2017; Vandooren *et al.*, 2013). Our study showed that EZR-AS1 knockdown reduced MMP2 and MMP9 expression, which could be partially responsible for the reduced cell migration ability observed in siEZR-AS1-transfected ADC cell lines.

CONCLUSION

Taken together, our results demonstrated that EZR-AS1 is highly expressed in both lung ADC tissues and cells. Knockdown of EZR-AS1 with siRNA led to reduced cell viability, increased apoptosis, and reduced migration ability compared with the control. Alterations in the levels of metastasis-related proteins such as E-cadherin, vimentin, MMP2, and MMP9 likely contribute to the reduced migration ability after EZR-AS1 knockdown. Since silencing of EZR-AS1 results in reduced ADC viability, this strategy should be explored in animal models to confirm the therapeutic effect for potential application in human ADC therapy.

Declarations

Ethics approval: The Ethics Committee of Sichuan University approved this study (Approval no. SU3312D).

Funding: No specific funding.

Availability of data and material: The data and materials are available upon request from the corresponding author.

Competing interests: none.

Authors' contributions: XY, LW, and YZ: project conceptualization, investigation, and data analysis. XY, LW, ZL, and JZ: Data collection, analysis, and methodology development. XY, LW, ZL, and JZ: Investigation and methodology development. All the authors have written, read and approved the final version of the manuscript.

Acknowledgement: Not applicable.

REFERENCES

- Bade BC, Dela Cruz CS (2020) Lung Cancer 2020: Epidemiology, etiology, and prevention. *Clin Chest Med* 41: 1–24. <https://doi.org/10.1016/j.ccm.2019.10.001>
- Bai Y, Zhou X, Huang L, Wan Y, Li X, Wang Y (2018) Long non-coding RNA EZR-AS1 promotes tumor growth and metastasis by modulating Wnt/beta-catenin pathway in breast cancer. *Exp Ther Med* 16: 2235–2242. <https://doi.org/10.3892/etm.2018.6461>
- Barillari G (2020) The impact of matrix metalloproteinase-9 on the sequential steps of the metastatic process. *Int J Mol Sci* 21. <https://doi.org/10.3390/ijms21124526>
- Bhan A, Soleimani M, Mandal SS (2017) Long noncoding RNA and cancer: a new paradigm. *Cancer Res* 77: 3965–3981. <https://doi.org/10.1158/0008-5472.CAN-16-2634>

- Caio M, Chen W (2019) Epidemiology of lung cancer in China. *Thorac Cancer* **10**: 3–7. <https://doi.org/10.1111/1759-7714.12916>
- Chao YL, Shepard CR, Wells A (2010) Breast carcinoma cells re-express E-cadherin during mesenchymal to epithelial reverting transition. *Mol Cancer* **9**: 179. <https://doi.org/10.1186/1476-4598-9-179>
- Cui N, Hu M, Khalil RA (2017) Biochemical and biological attributes of matrix metalloproteinases. *Prog Mol Biol Transl Sci* **147**: 1–73. <https://doi.org/10.1016/bs.pmbts.2017.02.005>
- Denisenko TV, Budkevich IN, Zhivotovsky B (2018) Cell death-based treatment of lung adenocarcinoma. *Cell Death Dis* **9**: 117. <https://doi.org/10.1038/s41419-017-0063-y>
- Figg DM, Bratt HJ, VanVliet PD, Dean RE (1978) Thyroid cancer: diagnosis and management based on a review of 142 cases. *Am J Surg* **135**: 671–674. [https://doi.org/10.1016/0002-9610\(78\)90133-2](https://doi.org/10.1016/0002-9610(78)90133-2)
- Ghaffari A, Hoskin V, Turashvili G, Varma S, Mewburn J, Mullins J, Greer PA, Kiefer F, Day AG, Madarnas Y, SenGupta S, Elliott BE (2019) Intravital imaging reveals systemic ezrin inhibition impedes cancer cell migration and lymph node metastasis in breast cancer. *Breast Cancer Res* **21**: 12. <https://doi.org/10.1186/s13058-018-1079-7>
- Guilford P (1999) E-cadherin downregulation in cancer: fuel on the fire? *Mol Med Today* **5**: 172–177. [https://doi.org/10.1016/s1357-4310\(99\)01461-6](https://doi.org/10.1016/s1357-4310(99)01461-6)
- Hosseini ES, Meryet-Figuere M, Sabzalipoor H, Kashani HH, Nikzad H, Asemi Z (2017) Dysregulated expression of long noncoding RNAs in gynecologic cancers. *Mol Cancer* **16**: 107. <https://doi.org/10.1186/s12943-017-0671-2>
- Howard EW, Camm KD, Wong YC, Wang XH (2008) E-cadherin up-regulation as a therapeutic goal in cancer treatment. *Mini Rev Med Chem* **8**: 496–518. <https://doi.org/10.2174/138955708784223521>
- Justus CR, Leffler N, Ruiz-Echevarria M, Yang LV (2014) In vitro cell migration and invasion assays. *J Vis Exp* **88**: 51046. <https://doi.org/10.3791/51046>
- Klimaszewska-Wisniewska A, Halas-Wisniewska M, Grzanka A, Grzanka D (2018) Evaluation of anti-metastatic potential of the combination of fisetin with paclitaxel on A549 non-small cell lung cancer cells. *Int J Mol Sci* **19**. <https://doi.org/10.3390/ijms19030661>
- Kong X, Duan Y, Sang Y, Li Y, Zhang H, Liang Y, Liu Y, Zhang N, Yang Q (2019) lncRNA-CDC6 promotes breast cancer progression and function as ceRNA to target CDC6 by sponging microRNA-215. *J Cell Physiol* **234**: 9105–9117. <https://doi.org/10.1002/jcp.27587>
- Kou JT, Ma J, Zhu JQ, Xu WL, Liu Z, Zhang XX, Xu JM, Li H, Li XL, He Q (2020) lncRNA NEAT1 regulates proliferation, apoptosis and invasion of liver cancer. *Eur Rev Med Pharmacol Sci* **24**: 4152–4160. https://doi.org/10.26355/eurrev_202004_20995
- Li C, Liu J, Zhang Q, Cui K, Ge Q, Wang C, Chen Z (2018) Up-regulation of Ecadherin expression mediated by a novel dsRNA suppresses the growth and metastasis of bladder cancer cells by inhibiting beta-catenin/TCF target genes. *Int J Oncol* **52**: 1815–1826. <https://doi.org/10.3892/ijo.2018.4346>
- Lin J, Lu J, Wang C, Xue X (2017) The prognostic values of the expression of Vimentin, TP53, and Podoplanin in patients with cervical cancer. *Cancer Cell Int* **17**: 80. <https://doi.org/10.1186/s12935-017-0450-6>
- Liu Z, Wang N, Wang F, Zhang S, Ding J (2019) Silencing of lncRNA EZR-AS1 inhibits proliferation, invasion, and migration of colorectal cancer cells through blocking transforming growth factor beta signaling. *Biosci Rep* **39**. <https://doi.org/10.1042/BSR20191199>
- Livak KJ, Schmittgen TD (2001) Analysis of relative gene expression data using real-time quantitative PCR and the 2(-Delta Delta C(T)) Method. *Methods* **25**: 402–408. <https://doi.org/10.1006/meth.2001.1262>
- Loewen G, Jayawickramarajah J, Zhuo Y, Shan B (2014) Functions of lncRNA HOTAIR in lung cancer. *J Hematol Oncol* **7**: 90. <https://doi.org/10.1186/s13045-014-0090-4>
- Lu D, Sun L, Li Z, Mu Z (2021) lncRNA EZR-AS1 knockdown represses proliferation, migration and invasion of cSCC via the PI3K/AKT signaling pathway. *Mol Med Rep* **23**. <https://doi.org/10.3892/mmr.2020.11714>
- Musika W, Kamsa-Ard S, Jirapornkul C, Santong C, Phunmanee A (2021) Lung cancer survival with current therapies and new targeted treatments: a comprehensive update from the srinagarind hospital-based cancer registry from (2013 to 2017). *Asian Pac J Cancer Prev* **22**: 2501–2507. <https://doi.org/10.31557/APJCP.2021.22.8.2501>
- Peng WX, Koirala P, Mo YY (2017) lncRNA-mediated regulation of cell signaling in cancer. *Oncogene* **36**: 5661–5667. <https://doi.org/10.1038/onc.2017.184>
- Radisky ES, Radisky DC (2010) Matrix metalloproteinase-induced epithelial-mesenchymal transition in breast cancer. *J Mammary Gland Biol Neoplasia* **15**: 201–212. <https://doi.org/10.1007/s10911-010-9177-x>
- Saigoh K, Matsui K, Takahashi K, Nishikawa T, Wada K (1998) The stereo-specific effect of D-serine ethylester and the D-cycloserine in ataxic mutant mice. *Brain Res* **808**: 42–47. [https://doi.org/10.1016/s0006-8993\(98\)00810-5](https://doi.org/10.1016/s0006-8993(98)00810-5)
- Saroja HS, Kumar Guddeti R, Jacob JP, Kumar Pulukuri K, Karyala P, Pakala SB (2022) MORC2/beta-catenin signaling axis promotes proliferation and migration of breast cancer cells. *Med Oncol* **39**: 135. <https://doi.org/10.1007/s12032-022-01728-6>
- Satelli A, Li S (2011) Vimentin in cancer and its potential as a molecular target for cancer therapy. *Cell Mol Life Sci* **68**: 3033–3046. <https://doi.org/10.1007/s00018-011-0735-1>
- Sim HJ, Song MS, Lee SY (2021) Kv3 channels contribute to cancer cell migration via vimentin regulation. *Biochem Biophys Res Commun* **551**: 140–147. <https://doi.org/10.1016/j.bbrc.2021.03.019>
- Vandooren J, Van den Steen PE, Opdenakker G (2013) Biochemistry and molecular biology of gelatinase B or matrix metalloproteinase-9 (MMP-9): the next decade. *Crit Rev Biochem Mol Biol* **48**: 222–272. <https://doi.org/10.3109/10409238.2013.770819>
- Wang Q, Zhu G, Lin C, Lin P, Chen H, He R, Huang Y, Yang S, Ye J (2021) Vimentin affects colorectal cancer proliferation, invasion, and migration via regulated by activator protein 1. *J Cell Physiol* **236**: 7591–7604. <https://doi.org/10.1002/jcp.30402>
- Wei X, Hou Y, Zhang Y, Zhang H, Sun Z, Meng X, Wang Z (2022) Long non-coding RNA MAG12-AS3 inactivates STAT3 pathway to inhibit prostate cancer cell proliferation via acting as a microRNA-424-5p sponge. *J Cancer* **13**: 343–353. <https://doi.org/10.7150/jca.60749>
- Wells A, Yates C, Shepard CR (2008) E-cadherin as an indicator of mesenchymal to epithelial reverting transitions during the metastatic seeding of disseminated carcinomas. *Clin Exp Metastasis* **25**: 621–628. <https://doi.org/10.1007/s10585-008-9167-1>
- Wong RS (2011) Apoptosis in cancer: from pathogenesis to treatment. *J Exp Clin Cancer Res* **30**: 87. <https://doi.org/10.1186/1756-9966-30-87>
- Wu F, Wang L, Zhou C (2021) Lung cancer in China: current and prospect. *Curr Opin Oncol* **33**: 40–46. <https://doi.org/10.1097/CCO.0000000000000703>
- Xie JJ, Xu LY, Wu ZY, Zhao Q, Xu XE, Wu JY, Huang Q, Li EM (2011) Prognostic implication of ezrin expression in esophageal squamous cell carcinoma. *J Surg Oncol* **104**: 538–543. <https://doi.org/10.1002/jso.21909>
- Xu J, Zhang W (2021) EZR promotes pancreatic cancer proliferation and metastasis by activating FAK/AKT signaling pathway. *Cancer Cell Int* **21**: 521. <https://doi.org/10.1186/s12935-021-02222-1>
- Zhang XD, Huang GW, Xie YH, He JZ, Guo JC, Xu XE, Liao LD, Xie YM, Song YM, Li EM, Xu LY (2018) The interaction of lncRNA EZR-AS1 with SMYD3 maintains overexpression of EZR in ESCC cells. *Nucleic Acids Res* **46**: 1793–1809. <https://doi.org/10.1093/nar/gkx1259>
- Zhen Q, Gao LN, Wang RF, Chu WW, Zhang YX, Zhao XJ, Lv BL, Liu JB (2018) lncRNA DANCER Promotes Lung Cancer by Sequestering miR-216a. *Cancer Control* **25**: 1073274818769849. <https://doi.org/10.1177/1073274818769849>

Could the lake ecosystems influence the pathogenicity of the SARS-CoV-2 in the air?

Janusz Boratynski✉

Ludwik Hirsfeld Institute of Immunology and Experimental Therapy, Polish Academy of Sciences, Laboratory of Biomedical Chemistry "Neolek", 53-114 Wrocław, Poland

During the first 200 days of the Covid-19 pandemic in Poland, lower morbidity and mortality due to SARS-CoV-2 infection were recorded in three regions covered by many small and large lakes (West Pomerania 5.8 deaths/100 000 population, Warmian & Masurian 7.6 deaths/100 000 population, Lubusz 7.3 deaths/100 000 population, compared to Poland average of 16.0 deaths/100 000 population). Moreover, in Mecklenburg (Germany), bordering West Pomerania, only 23 deaths (1.4 deaths/100 000 population) were reported during the same period (Germany 10 649 deaths, 12.6 deaths/100 000 population). This unexpected and intriguing observation would not have been noticed if SARS-CoV-2 vaccinations were available at that time. The hypothesis presented here assumes the biosynthesis of biologically active substances by phytoplankton, zooplankton or fungi and transfer of these lectin-like substances to the atmosphere, where they could cause agglutination and/or inactivation of pathogens through supramolecular interactions with viral oligosaccharides. According to the presented reasoning, the low mortality rate due to SARS-CoV-2 infection in Southeast Asian countries (Vietnam, Bangladesh, Thailand) could be explained by the influence of monsoons and flooded rice fields on microbiological processes in the environment. Considering the universality of the hypothesis, it is important whether the pathogenic nano- or micro particles are decorated by oligosaccharides (as in case of the African swine fever virus, ASFV). On the other hand, the interaction of influenza hemagglutinins with sialic acid derivatives biosynthesized in the environment during the warm season may be linked to seasonal fluctuations in the number of infections. The presented hypothesis may be an incentive to study unknown active substances in the environment by interdisciplinary teams of chemists, physicians, biologists, and climatologists.

Keywords: COVID-19, SARS-CoV-2, phytoplankton, atmosphere, lectin, lake

Received: 11 October, 2022, revised: 07 December, 2022, accepted: 19 January, 2023, available on-line: 03 March, 2023

✉e-mail: janusz.boratynski@hirsfeld.pl

Abbreviations: LU, Lubusz region, W&M, Warmian and Masurian region, WP, West Pomerania region, PL, Poland, *Infections per 100 000 inhabitants, **deaths per 100 000 inhabitants.

INTRODUCTION

The global COVID-19 pandemic has led to an unprecedented mobilization of the scientific community. This defence is taking place on multiple fronts, similar

to military operations, and the ongoing battle constantly brings new strategies into play. Pioneering research on transfection of conglomerates of mRNA and cationic lipids initiated by Robert Malone in 1987 (Malone *et al.*, 1989) and the intuition, perseverance, and efforts of Katalin Karikó (Karikó *et al.*, 2008), Uğur Şahin and Collaborators ushered perspectives for RNA vaccines (Niknam *et al.*, 2022; Dolgin, 2021; Yin *et al.*, 2022). In 2020 Food and Drug Administration office (USA) issued an emergency use authorization for RNA vaccines to the Pfizer–BioNTech and Moderna companies.

Independently, the effectiveness of many substances, ranging from low-molecular compounds to proteins, including antibodies and plasma of convalescent plasma therapy, has been tested. The first large-scale use of the convalescent plasma therapy was to stop the rinderpest epidemic in Poland in 1921 (Orzechowska *et al.*, 2018). For therapeutic use in humans, plasma is sterilized with oxidants that modify methionine and tryptophan residues. This may result in the weakening of the effector activities of antibodies, including their interaction with the Fc receptor and complement activation (Mo *et al.*, 2016). Therefore, it may be necessary to move away from routine sterilization technologies and reassess the effectiveness of improved plasma preparations (Li *et al.*, 2020; Pan *et al.*, 2022). **Figure 1** illustrates the participation of the environment (bodies of water, atmosphere, pollens) that may modulate the activity of SARS-CoV-2 virus (Kisajno Lake, Warmian & Masurian Region, Poland) © Worldisbeautiful.eu



Figure 1. Illustration of the main assumptions of the hypothesis: Lake Kisajno (W&M) represents the place of biosynthesis of active substances.

Plant pollens indicate the role of various substances that affect the activity of the SARS-CoV-2 (Picture: Kisajno Lake, Warmian & Masurian Region, Poland). © Worldisbeautiful.eu

MATERIALS, OBSERVATIONS, AND DISCUSSION

The hypothesis of influence of aquatic plankton and fungi on airborne pathogen agglutination/inactivation (referred to hereafter as “the hypothesis”) is based on official reports, perceptiveness, and reflection. Although some conclusions may seem controversial, in the Author’s view, they should inspire further investigations. Analyses of the course of the pandemic were prepared by Michał Rogalski (Report based on data from the Ministry of Health, Rogalski, 2022). During the initial stages of the pandemic, significantly fewer infections and deaths were recorded in three regions of Poland (LU, W&M, WP) as compared to the rest of Poland.

Figure 2 illustrates the epidemiological situation in Poland during the first 200 days of the COVID-19 pandemic. The curves are a collection of 2281 independent points, each of which represents one human tragedy. The chart is therefore a tribute to those who died during the global COVID-19 pandemic around the world.

Two events may be important for the hypothesis construction:

- 1. Despite the enormous effort of science the introduction of vaccination was not immediate and did not obscure the observation of the first period of pandemic progression,
- 2. The winter of 2019/20, preceding the pandemic in Poland, was mild and the lakes in question did not freeze. The liquid water, in which the microorganisms lived, was constantly in contact with the air, and the transport of biomass could happen all the time. Therefore, the alleged “antiviral substances of lake origin” could protect the inhabitants of the land of the lakes.

Statistical significance of the difference between mortality curves for lake districts and the rest of Poland was calculated in GraphPad Prism using Akaike’s (Bozdogan, 2000) Information Criterion. Differentiation between the curves for each data set is >99.99%. (Poland lake districts – blue line: $Y=0.0072x-0.1999$. $R^2=0.943$, the rest of Poland – red line: $Y=0.0355x-0.3074$. $R^2=0.9772$) indicating a limited progression of the disease in areas covered with lakes

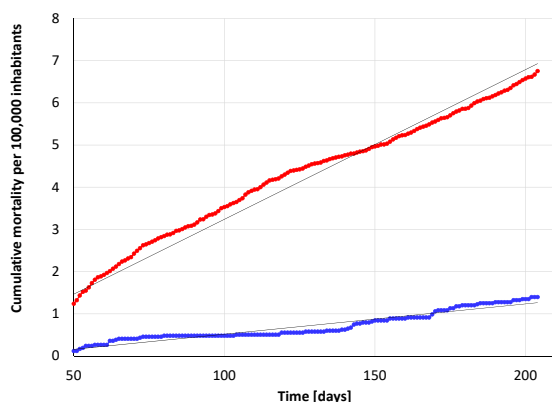


Figure 2. Cumulative mortality per 100 000 population during the first 200 days of the COVID-19 pandemic in Poland (from March 2020 to 19 September 2020). Blue line: deaths per 100 000 inhabitants in “lake-rich regions”: LU+W&M+WP, red line: deaths per 100 000 inhabitants in the rest of Poland (source data: Rogalski, 2022). Statistical significance (different curves for all data set >99.99%), was calculated using GraphPad Prism, Akaike’s Information Criterion (Bozdogan, 2000).

(LU+W&M+WP) compared to the rest of Poland. However, after 200 days of the pandemic, significant perturbations appeared. After this period, both insolation and temperature decreased, which affected the biological life in the lakes (Edwards *et al.*, 2016).

The further course of the pandemic is shown in the Fig. 3A and 3B and Table 1. Figures 3A and 3B show the ratio of the officially recorded data of SARS-CoV-2 infections or deaths in Poland to the numbers of infections in lake-covered regions for the first year of the pandemic. The ratio of (LU+W&M+WP)/PL shows differences in the dynamics of the pandemic in lake districts compared to the rest of Poland. The intersection of the blue and red curves coincides with the onset of temperatures at which the lakes reach their freezing point. The data may suggest the possibility of a protective role of lakes during the COVID-19 pandemic. Paradoxically, the protective role of lakes presumably delayed the induction of herd immunity, contributing to an increase in infections and deaths in the cold period while the lakes froze (winter 2020/21).

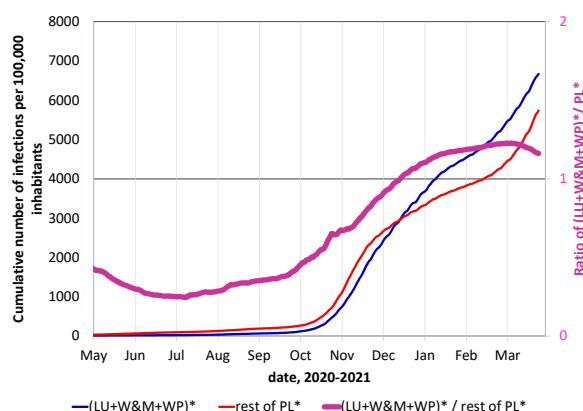


Figure 3A. Coronavirus infections/100 000 population in (LU+W&M+WP) (blue) and in the rest of Poland [PL- (LU+W&M+WP)] (red). The bold purple line shows the ratio between cases per 100 000 population in the (LU+W&M+WP) and the cases in the rest of Poland (May 2020/March 2021). It should be added that the official reports on the number of SARS-CoV-2 infections in Poland can be considered as estimates (data for May 2020–March 2021).

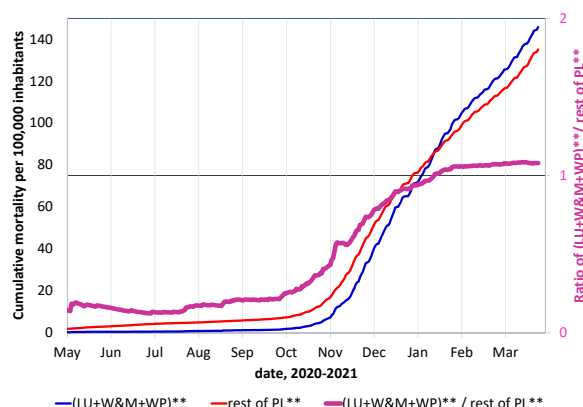


Figure 3B. Cumulative coronavirus deaths/100 000 population in the lake-rich regions (LU+W&M+WP), (blue) and in the rest of Poland [PL- (LU+W&M+WP)] (red). The bold purple line depicts the ratio between mortality in the (LU+W&M+WP) regions and the rest of Poland (data for May 2020–March 2021).

Table 1. Cumulative COVID-19 cases and deaths in Poland's lake-rich regions between May 1, 2020, and April 1, 2021.

LU, Lubusz region; W&M, Warmian and Masurian region; WP, West Pomeranian region; PL***, Poland excluding the three lake-rich regions (LU+W&M+WP). Table presents the total number of COVID-19 cases and deaths since the beginning of the pandemic (Rogalski, 2022).

Region	Date	Infections/100 000 population	Number of infections	Deaths/100 000 population	Number of deaths
LU	1 May 2020	8.6	87	0	0
W&M		10.5	148	0.07	1
WP		23.7	401	0.59	10
PL ***		36.3	12469	1.84	632
LU	1 Jun 2020	11.7	118	0	0
W&M		12.7	179	0.07	1
WP		31.7	536	1.12	19
PL ***		62.9	24159	3.04	1054
LU	1 Jul 2020	15.0	151	0	0
W&M		17.8	250	0.07	1
WP		36.1	611	1.30	22
PL ***		94.1	32293	4.28	1470
LU	1 Aug 2020	40.6	410	0.99	10
W&M		26.7	379	0.14	2
WP		43.8	741	1.36	23
PL ***		135.1	46348	4.92	1686
LU	1 Sep 2020	69.9	706	1.39	14
W&M		63.5	902	0.64	9
WP		67.8	1132	1.59	27
PL ***		190.2	65252	5.85	2008
LU	1 Oct 2020	105	1046	1.88	19
W&M		124	1745	1.20	17
WP		110	1869	2.15	36
PL ***		258.9	88821	7.20	2470
LU	1 Nov 2020	724	7310	7.20	72
W&M		654	9292	7.55	106
WP		679	11478	5.79	98
PL ***		1025	351813	16.0	5507
LU	1 Dec 2020	2188	22097	36.8	372
W&M		2330	32702	40.2	565
WP		2269	38460	35.0	497
PL ***		2574	882979	47.1	16154
LU	1 Jan 2021	3114	31457	67.7	684
W&M		3805	54032	84.1	1195
WP		3758	62762	62.3	1041
PL ***		3293	1129575	75.9	26031
LU	1 Feb 2021	3690	37273	95.0	960
W&M		4738	67289	119.5	1679
WP		4732	75903	90.7	1536
PL ***		3787	1299088	96.3	33034
LU	1 March 2021	5478	43945	116.4	1176
W&M		5985	82089	140	1988
WP		5314	87416	114	1901
PL ***		4260	1461250	115	39521

LU	1 April 2021	6137	61983	146	1472
W&M		7678	109032	172	2442
WP		6480	108216	130	2172
PL***		5917	2029658	138	47503

The impact of the inland water ecosystems and climate in neighbouring and distant countries on the COVID-19 pandemic

To further evaluate this hypothesis, the epidemiology of COVID-19, as of October 2020, was analysed in countries neighbouring Poland and having similar climate and inland water reservoirs. The observed mortality per 100 000 population in the five chosen regions was as follows: Lithuania, 4.0**, Latvia, 2.5**, Estonia, 5.3**, Finland, 6.2** (Worldometer COVID-19, 2023), Kaliningrad Oblast, 9.7**, while in the reference regions it reached 21.6** in Europe and 17.5** in Russia (Development of Number of Coronavirus, Russia, 2022). Due to the impact of soil and lakes acidification, Sweden was excluded from the present considerations (Almer & Dickson, 2021). As shown in Fig. 4 during the first period of the pandemic, each of the five analysed regions reported low mortality rates from COVID-19. For example, in Mecklenburg-Vorpommern, a German land bordering Western Pomerania and rich in lakes, only 23 (1.43**) deaths were recorded until November 1, 2020, while, at the same time, the mortality rate for the entire Germany amounted to 10 649 (12.8**) deaths. Also

later, the pandemic situation in Mecklenburg (62.5**) remained more favourable than in the rest of Germany where it amounted to 101.6** (83292) deaths (2 May 2021). (Development of number of Coronavirus cases: Mecklenburg-Vorpommern, Germany, 2022)

In addition, the progression of the pandemic was analysed in three Asian countries: India, Bangladesh (Beany *et al.*, 2021), and Iran. These countries differ in climate and population density, which amounts to 460, 1260 and 52 inhabitants/km², respectively. The official COVID mortality data for the period from the beginning of the pandemic to November 14, 2022 are as follows: India 37.7**, Bangladesh 17.5**, and Iran 168.2** (Worldometer COVID-19 Coronavirus Pandemic, 2023). These numbers, opposite to expected in terms of the relationship between population density and mortality due to COVID-19, prompt discussion. Two of the distinguishing features of these countries, apart from population density, are climate and rainfall. Bangladesh has tropical-monsoon warm climate, India is a hot tropical country, and Iran is mainly arid and semiarid. In the context of the presented hypothesis, the spread and growth of phytoplankton, zooplankton and fungi in rice-growing areas cannot be overlooked (Nam *et al.*, 2022, Anyanwu *et al.*, 2001). For example, in Bangladesh, rice fields cover over 7% of the country's land area. Other global rice producers also show low mortality due to COVID-19 (for example: Thailand – 47.4**, Vietnam – 43.6** (December 2022).

Moreover, in the light of this hypothesis, the microbiological status of the warm seas of Southeast Asia should also be considered (Cochran *et al.*, 2017; Gao *et al.*, 2021).

Therefore, it would be interesting to study and compare the antiviral properties of substances produced and released into the atmosphere by phytoplankton, zooplankton, and fungi in various climatic zones in Central Europe, Southeast Asia, Canada, etc.

Transfer of lake biomass into the atmosphere.

The aquatic environment is in constant equilibrium with the atmosphere. I assume that phytoplankton, under the influence of wind and waves, is blown off the surface of lakes or thrown out onto the coastline of small and large lakes to undergo biodegradation, biotransformation, drying, etc., and is disseminated by wind in the local atmosphere. In the case of the Great Lakes in the USA, biological matter from the lakes was found about 25 km from the coastline (May *et al.*, 2018). Moreover, gas bubbles from the depths of the lakes transfer biological matter to the surface of water. These bubbles burst upon reaching the air/water boundary, transferring biomass into the atmosphere (Blanchard & Syzdek, 1970, Cochran *et al.*, 2017, Kim *et al.*, 2020). This can be compared to the behaviour of bubbles on the surface of carbonated beverages. A pioneering study on the transfer of biological matter (*B. fluorescens liquefaciens* and *B. fluorescens putidus*) from water reservoirs to the atmosphere was conducted in 1887 by Odo Bujwid (Bujwid, 1887).

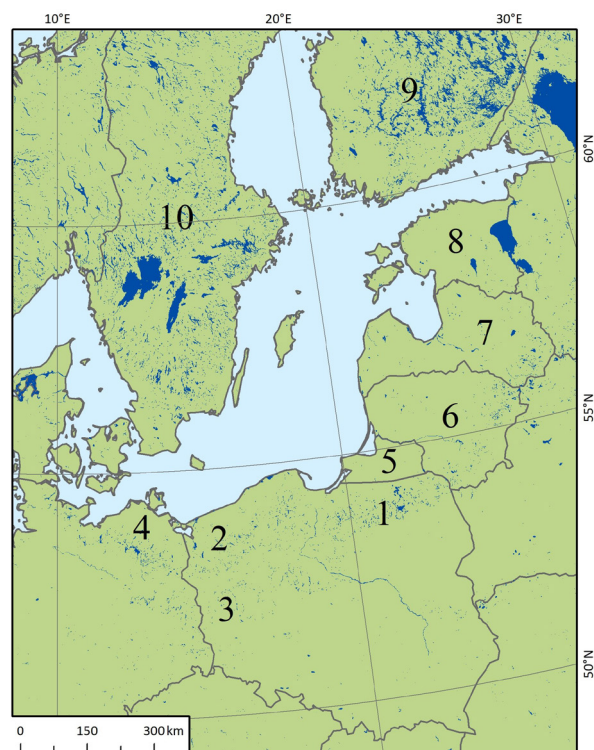


Figure 4. Map of the selected fragment of Central Europe: (1) W&M – Warmian & Masurian (Poland), (2) WP – West Pomerania (Poland), (3) LU – Lubusz (Poland), (4) Mecklenburg (Germany), (5) Kaliningradskaja Oblast (Russia), (6) Lithuania, (7) Latvia, (8) Estonia, (9) Finland, (10) Sweden.

The map was made using ArcGIS 10.7.1 software and the geographical data were taken from WWF and Eurostat databases (<https://www.worldwildlife.org/pages/global-lakes-and-wetlands-database>, <https://ec.europa.eu/eurostat/web/gisco/geodata>).

The interaction of gas bubbles with the matter present in aqueous environment is a multifaceted process widely used in flotation technology (Krasowska, *et al.*, 2019). The surroundings of the lakes are sometimes accompanied by a subtle odor, which can result from biological life in the lakes. Phytoplankton content in Polish lakes fluctuates qualitatively and quantitatively from year to year and month to month (Napiórkowska-Krzebietke & Hutorowicz, 2006).

Cyanobacteria (blue-green algae), a constituent of phytoplankton, produce chemically diverse antiviral compounds such as lectins, cyclic peptides, lipopeptides, fatty acids, alkaloids, and saccharides (Codd *et al.*, 2016, Mazur-Marzec *et al.*, 2021, Sami *et al.*, 2020, Singh *et al.*, 2017). Aggregates of blue-green algae in water often display compact, strong, spongy structures resulting from specific and nonspecific interactions with a variety of macro- and nanomolecules.

For a long time, it was believed that lectins play a role in the plant world only. The overthrow of this dogma in 1975 opened new perspectives in science, medicine, and technology. The antiviral activity of lectins against SARS-CoV-2 has been investigated, but all studies have been conducted in an aquatic environment (Wang *et al.*, 2021, Gupta & Gupta, 2022, Nabi-Afjadi *et al.*, 2022, Stravalaci *et al.*, 2022, Simplicien *et al.*, 2022). The virus, being molecularly dispersed in air (Greenhalgh *et al.*, 2021, Nissen *et al.*, 2020), could interact with water (moisture) and/or with organic and inorganic pollutants (Yang & Marr, 2020, Domingo & Rovira, 2020, Ishmatov, 2022, Damialis *et al.*, 2021, Rzymński *et al.*, 2022).

From the perspective of the presented consideration, the key point would be to investigate the interaction between viral oligosaccharides (Zhang *et al.*, 2021, Banerjee & Mukhopadhyay, 2016) and macro- and nanoparticles of lake origin in the air. A resulting hybrid nanoparticle, similar in architecture to a conjugate vaccine, could not only interact with the virus itself but could also activate the immune system.

The aim of this hypothesis is to explain the reasons for the lower COVID-19 infection and death rates in the lake-rich regions. Three regions of Poland (LU, W&M, WP) have a large number of lakes (covering 4.4% of the total region area) and low population density (70/km² *versus* 120/km² for the entire Poland). In Poland, the average population density relies on the number of cities rather than the uniform dispersion of the population. Moreover, the official population density reports do not include mass tourism to these lake areas. Despite many analyses, the search for consensus linking population density with pandemic progression is still ongoing (Moosa & Khatatbeh, 2021).

CONCLUSIONS

The hypothesis presented herein raises the following questions:

- How would the transfer of biological matter from the lakes to the atmosphere take place?
- How can the substances from phytoplankton potentially neutralize the SARS-CoV-2 virus?
- What is the epidemiological situation in Poland and its neighbouring lake-rich countries?
- What could be the practical consequences of the existence of antiviral bio-aerosols?

It should be added that the official reports on the number of SARS-CoV-2 infections in Poland can be considered as estimates. The observed fluctuations in the

number of infections may be due to the seasonal presence of biological substances released into the environment. For example, it was shown that the presence of pollen in the air correlates with increased COVID-19 morbidity (Damialis *et al.*, 2021).

The type of chemical supramolecular bonds between a virus and a carrier (hydrogen bonds, van der Waals forces, ion-ion, and π -cation interactions) may be crucial for its biological activity. Hypothetically, interactions of pathogens with airborne contaminants could contribute to viral infectivity in two different ways. If, as a result of the interaction, the virulence factors are not blocked, the pathogen's activity may increase (Damialis *et al.*, 2021) in a mechanism of avidity. Conversely, if the molecules critical for viral infectivity are blocked, pathogenicity may be reduced.

The moderate sensitivity and selectivity of the interactions between lectins and sugars (Sharon & Lis, 2001) enables for the potential application of this mechanism to a broad range of viruses. If the mutations do not significantly alter the glycosylation of viral envelope, these "airborne lectins" could neutralize also the new strains (Markov *et al.*, 2022, Barre *et al.*, 2022). Interactions of pathogen's sugars with lectins in aerosols could contribute to local inactivation of the dispersed viruses. As an example, assuming this line of thinking is correct, the inactivation of the ASF virus could be a result of an interaction of its glycolipids (Del Val & Vinuela, 1986) or saccharides (Zhu, 2022) with molecularly dispersed lectins from selected legume seeds.

From a practical point of view, spraying of the nano-components present in phytoplankton in the air in populated areas (city centres, transportation vehicles, etc.) could entrap viral particles *via* lectin-virus interactions and lower the transmission rate at low cost and low risk. Hybrid nanoparticles (lectin-agglutinated viruses) suspended in the still air would sediment faster than virus particles alone, according to Stokes's law (though air turbulences would interfere with the sedimentation process) (Adamczyk, 2006). Agglutination and/or aggregation of viruses may affect their biological activity and modify their physico-chemical properties (Gerba & Betancourt, 2017, Del Val & Vinuela, 1986, Szermer-Olechnik *et al.*, 2017).

The interpretation of the reasoning presented in the hypothesis goes beyond the environment of water bodies and includes the air temperatures.

This is prompted by the report on the course of the COVID-19 pandemic in 2020–2023 (Fig. 5).

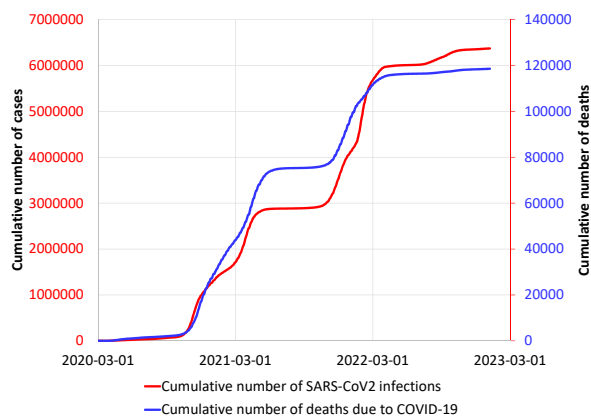


Figure 5. Infectivity and mortality during the COVID-19 pandemic in Poland (2020–2023). Based on Worldometer COVID-19 Coronavirus Pandemic (2023).

Table 2. Infectivity and mortality during the COVID-19 pandemic in Poland in arbitrarily designated cold and warm periods of the year.

Period of year	Date	Average number of infections/day	Average number of deaths/day
Warm	01/05–01/10 2020	534	12.3
Cold	01/11–01/03 2020/21	10800	316.6
Warm	01/05–01/10 2021	724	64.6
Cold	01/11–01/03 2021/22	21550	290
Warm	01/05–01/10 2022	1750	10.3
Cold	01/11–01/03 2022/23	676	6.4

Data source: Worldometer COVID-19 Coronavirus Pandemic (2023).

Comparing the infection rates in warm and cold seasons, it can be observed that low disease propagation was found in the warm periods and conversely, high incidence occurred in cold periods. The seasons of the year are arbitrarily determined (cold period: 1st Nov/1st March, warm period: 1st May/1st Oct). The reduced mortality observed at the end of 2022 may be due to the changes in the profile of viruses circulating in the environment.

Table 2 presents the influence of the seasons on the progression of the COVID-19 pandemic in Poland. According to the main idea of the hypothesis, this phenomenon could be explained by the release into the atmosphere of biologically active substances related to vegetation, agriculture, and putrefactive processes of decay, especially during warm periods (Górska *et al.*, 2022).

A similar correlation applies to the widely studied influenza. Viral hemagglutinins which are an integral part of viruses play a key role in the pathogenesis of infection through interactions with sialic acid terminated glycans.

One may ask why the number of flu cases decreases in the warm season. According to the hypothesis, one of the reasons that can be considered is the release of sialic acid derivatives into the atmosphere. Numerous bacteria species biosynthesize sialic acid polymers (González-Clemente *et al.*, 1989) and fungi produce a variety of the derivatives of sialic acid (Alviano *et al.*, 1999). These substances released into the atmosphere could agglutinate and/or neutralize influenza viruses.

Addressing these complex problems highlighted by the hypothesis presented here, would require interdisciplinary efforts in medicine, biology, chemistry, climatology, and biophysics. The first step could be the attempt at isolation of the alleged active substances from the atmosphere using electroseparators dedicated for biological components (Maineli *et al.*, 2002). Another approach could be used to pass air through the filters containing immobilized oligosaccharides to specifically adsorb the sought-after biomolecules. The task of isolating the active substance from the air could prove similar in scale to the challenge of obtaining 8 mg erythropoietin from 2550 litres of urine (Miyake *et al.*, 1987) (the value of the erythropoietin market in 2021 was USD 8.8 billion). The observation would not have been made if it had not been for two facts. Until January 2021, the progression of the pandemic was not hindered by vaccination programs as the introduction of vaccines followed the observed phenomena. Moreover, the winter of 2019/2020 was exceptionally warm and Polish lakes did not freeze for the first time in many years, enabling the “biology and biochemistry in water” to interact with the air constantly.

Appendix (Dec. 2022).

COVID-19 deaths/100 000 inhabitants: Poland 314** (LU 332**, WP 278**, W&M 326**), Finland 140**, Latvia 331**, Lithuania 355**, Estonia 213**, Germany 190**, Mecklenburg 162.5**, Canada 126** (more than 9% of Canada is covered by lakes), USA 332**, all countries 85.6** (Worldometer COVID-19 Coronavirus Pandemic, 2023).

Declarations

Acknowledgements of Financial Support. This research did not receive any specific grant from funding agencies in the public, commercial, or non-profit sectors. It was funded by the statutory budget of the Hirsfeld Institute of Immunology and Experimental Therapy, Polish Academy of Sciences.

Acknowledgements. The author would like to thank for valuable help (in alphabetical order): Dr. Jarosław Ciekot, Prof. Anna Dunin-Dudkowska, Prof. Marek Drab, Dr. Krzysztof Fink, Dr. Magdalena Kotowska, MSc. Adam Kowalski, Prof. Hubert Krotkiewski, Dr. Joanna Kuldo, Dr. Maciej Litwin, Prof. Hanna Mazur-Marzec, Mr. Marcin Rogalski, MSc. Wojciech Rybka, Dr. Grzegorz Skibiński, Dr. Maria Wysocka, Prof. Maria Zembala and Prof. Tomasz Żal.

Conflict of interest. The author declares no conflicts of interest.

REFERENCES

- Adamczyk Z (2006) *Particles at interfaces: interactions, deposition, structure*. Chapter 4 “Transfer of Particles to Interfaces – Linear Problems”. Adamczyk Z, ed, 1st edn, 9: 375–565. Amsterdam, Boston: Elsevier/Academic Press, 012370541X, eBook ISBN: 9780080464954
- Almer B, Dickson W (2021). The discovery and early study of acidification of lakes in Sweden: This article belongs to Ambio’s 50th Anniversary Collection. Theme: Acidification. *Ambio* 50: 266–268. <https://doi.org/10.1007/s13280-020-01439-0>
- Alviano CS, Travassos LR, Schauer R (1999) Sialic acids in fungi: a minireview. *Glycoconj J* 16: 545–554. <https://doi.org/10.1023/a:1007078106280>
- Anyanwu IN, Ezema CA, Ebi SE, Nwajiuba CA, Nworie O, Anorue CO (2021) Seasonal variation in water quality. Plankton diversity and microbial load of tropical freshwater lakes in Nigeria. *Afr J Aquat Sci* 46: 3. <https://doi.org/10.2989/16085914.2021.1931000>
- Barre A, Van Damme EJM, Klonjowski B, Simplicien M, Sudor J, Benoist H, Rouge P (2022) Legume lectins with different specificities as potential glycan probes for pathogenic enveloped viruses. *Cells* 11: 339. <https://doi.org/10.3390/cells11030339>
- Banerjee N, Mukhopadhyay S (2016) Viral glycoproteins: biological role and application in diagnosis Virus disease. *Virusdisease* 27: 1–11. <https://doi.org/10.1007/s13337-015-0293-5>
- Beany T, Clarke J, Jain V (2021) Measuring the toll of the COVID-19 pandemic in rural Bangladesh. *JAMA Netw* 4: e2133167. <https://doi.org/10.1001/jamanetworkopen.2021.33167>

- Blanchard DC, Syzdek L (1970) Mechanism for the water-to-air transfer and concentration of bacteria. *Science* **170**: 626–662. <https://doi.org/10.1126/science.170.3958.626>
- Bozdoğan H (2000) Akaike's Information criterion and recent developments in information complexity. *J Math Psychol* **44**: 62–91. <https://doi.org/10.1006/jmps.1999.1277>
- Bujwid O (1887) Bacteria found in hail lumps. *Wszczęświat (Universe)* **50**: 793–794
- Cochran RE, Laskina O, Trueblood JV, Estill AD, Morris HS, Jayarathne T, Sultana CM, Lee C, Lin P, Laskin J, Laskin A, Dowling JA, Qin Z, Cappa CD, Bertram TH, Tivanski AV, Stone EA, Prather KA, Grassian VH (2017) Molecular diversity of sea spray aerosol particles: impact of ocean biology on particle composition and hygroscopicity. *Chem* **2**: 655–667. <https://doi.org/10.1016/j.chempr.2017.03.007>
- Codd GA, Meriluoto J, Metcalf JS (2016) Cyanobacteria: Cyanotoxins, their human impact, and risk management. In *Handbook of Cyanobacterial Monitoring and Cytotoxic Analysis*. Meriluoto J, Spoof L, Codd GA eds. <https://doi.org/10.1002/9781119068761.ch1>
- Damialis A, Gilles S, Sofiev M, Sofieva V, Kolek F, Bayr D, Plaza MP, Leier-Wirtz V, Kaschuba S, Ziska LH, Bielory L, Makra L, Del Mar Trigo M (2021) Higher airborne pollen concentrations correlated with increased SARS-CoV-2 infection rates, as evidenced from 31 countries across the globe. *Proc Natl Acad Sci U S A* **118**: e2019034118. <https://doi.org/10.1073/pnas.2019034118>
- Del Val M, Vinuela E (1986) Glycosylated components of African swine fever virus particles. *Virology* **15**: 39–49. [https://doi.org/10.1016/0042-6822\(86\)90369-7](https://doi.org/10.1016/0042-6822(86)90369-7)
- Development of number of Coronavirus cases: Mecklenburg-Vorpommern, Germany (2022) <https://coronalevel.com/Germany/Mecklenburg-Vorpommern> (Date accessed, July 04, 2022)
- Development of number of Coronavirus, Russia (2022) (Kaliningrad Oblast). https://coronalevel.com/Russia/Kaliningrad_Oblast/ (Date accessed, August 19, 2022)
- Dolgin E (2021) The tangled history of mRNA vaccines. *Nature* **597**: 318–324. <https://doi.org/10.1038/d41586-021-02483-w>
- Domingo JL, Rovira J (2020) Effects of air pollutants on the transmission and severity of respiratory viral infections. *Environ Res* **187**: 109650. <https://doi.org/10.1016/j.envres.2020.109650>
- Edwards KF, Thomas MK, Klausmeier CA, Litchman E (2016) Phytoplankton growth and the interaction of light and temperature: A synthesis at the species and community level. *Limnol Oceanogr* **61**: 1232–1244. <https://doi.org/10.1002/lno.10282>
- Gao P, Du G, Zhao D, Wei Q, Zhang X, Qu L, Gong X (2021) Influences of seasonal monsoons on the taxonomic composition and diversity of bacterial community in Eastern Tropical Indian Ocean. *Front Microbiol* **11**: 615221. <https://doi.org/10.3389/fmicb.2020.615221>
- Gerba CP, Betancourt WQ (2017) Viral aggregation: Impact on virus behaviour in the Environment. *Environ Sci Technol* **51**: 7318–7325. <https://doi.org/10.1021/acs.est.6b05835>
- González-Clemente C, Luengo JM, Rodríguez-Aparicio LB, Reglero A (1989) Regulation of colominic acid biosynthesis by temperature: role of cytidine 5'-monophosphate N-acetylneuraminic acid synthetase. *FEBS Letters* **250**: 429–432. [https://doi.org/10.1016/0014-5793\(89\)80770-7](https://doi.org/10.1016/0014-5793(89)80770-7)
- Górska K, Lis S, Gawor W, Karuga F, Romaszko K, Brzeźniańska-Lasota E (2022) Culturable filamentous fungi in the air of recreational areas and their relationship with bacteria and air pollutants during winter. *Atmosphere* **13**: 207. <https://doi.org/10.3390/atmos13020207>
- Greenhalgh T, Jimene JL, Prather KA (2021) Ten scientific reasons in support of airborne transmission of SARS CoV-2. *Lancet* **397**: 1603–1605. [https://doi.org/10.1016/S0140-6736\(21\)00869-2](https://doi.org/10.1016/S0140-6736(21)00869-2)
- Gupta A, Gupta GS (2021) Status of mannose-binding lectin (MBL) and complement system in COVID-19 patients and therapeutic applications of antiviral plant MBLs. *Mol Cell Biochem* **476**: 2917–2942. <https://doi.org/10.1007/s11010-021-04107-3>
- Ishmatov A (2022) SARS-CoV-2 is transmitted by particulate air pollution: Misinterpretations of statistical data, skewed citation practices, and misuse of specific terminology spreading the misconception. *Environ Res* **204** (Pt B): 112116. <https://doi.org/10.1016/j.envres.2021.112116>
- Karikó K, Muramatsu H, Welsh FA, Ludwig J, Kato H, Akira S, Weissman D (2008) Incorporation of pseudouridine into mRNA yields superior nonimmunogenic vector with increased translational capacity and biological stability. *Mol Ther* **16**: 1833–1840. <https://doi.org/10.1038/mt.2008.200>
- Kim J, Lee S, Joong YS (2020) Schlieren imaging for the visualization of particles entrapped in bubble films. *J Colloid Interface Sci* **570**: 3958. <https://doi.org/10.1016/j.jcis.2020.02.085>
- Krasowska M, Malysa K, Beattie DA (2019) Recent advances in studies of bubble-solid interactions and wetting film stability. *Curr Opin Colloid Interface Sci* **44**: 48–58. <https://doi.org/10.1016/j.cocis.2019.09.002>
- Li L, Zhang W, Hu Y, Tong X, Zheng S, Yang J, Kong Y, Ren L, Wei Q, Mei H, Hu C, Tao C, Yang R, Wang J, Yu Y, Guo Y, Wu X, Xu Z, Zeng L, Xiong N, Chen L, Wang J, Man N, Liu Y, Xu H, Deng E, Zhang X, Li C, Wang C, Su S, Zhang L, Wang J, Wu Y, Liu Z (2020) Effect of convalescent plasma therapy on time to clinical improvement in patients with severe and life-threatening COVID-19: A randomized clinical trial. *JAMA* **324**: 460–470. <https://doi.org/10.1001/jama.2020.10044>
- Mainelis G, Willeke K, Adhikari A, Reponen T, Grinshpun SA (2002) Design and collection efficiency of a new electrostatic precipitator for bio-aerosol collection. *Aerosol Sci Technol* **36**: 1073–1085. <https://doi.org/10.1080/02786820290092212>
- Malone RW, Felonger PL, Verma IM (1989) Cationic liposome-mediated RNA transfection. *Proc Natl Acad Sci* **86**: 6077–6081. <https://doi.org/10.1073/pnas.86.16.6077>
- Markov PV, Katzourakis A, Stilianakis NI (2022) Antigenic evolution will lead to new SARS-CoV-2 variants with unpredictable severity. *Nat Rev Microbiol* **20**: 251–252. <https://doi.org/10.1038/s41579-022-00722-z>
- May NW, Gunsh MJ, Bondy AL, Kirpes R, Bertman S, Swarup C, Laskin A, Hopke PK, Ault A, Pratt KA (2018) Unexpected contributions of sea spray and lake spray aerosol to inland particulate matter. *Environ Sci Technol Lett* **5**: 405–412. <https://doi.org/10.1021/acs.estlett.8b00254>
- Mazur-Marzec H, Ceglowska M, Konkel R, Pyrc K (2021) Antiviral Cyanometabolites – A review. *Biomolecules* **11**: 474. <https://doi.org/10.3390/biom11030474>
- Miyake T, Kung CK, Goldwasser E (1987) Purification of human erythropoietin. *J Biol Chem* **262**: 5558–5564. [https://doi.org/10.1016/S0021-9258\(19\)63387-9](https://doi.org/10.1016/S0021-9258(19)63387-9)
- Mo J, Yan Q, So CK, Soden T, Lewis MJ, Hu P (2016) Understanding the impact of methionine oxidation on the biological functions of IgG1 antibodies using hydrogen/deuterium exchange mass spectrometry. *Anal Chem* **88**: 9495–9502. <https://doi.org/10.1021/acs.analchem.6b01958>
- Moosa IA, Khatatbeh IN (2021) The density paradox: Are densely populated regions more vulnerable to Covid-19? *Int J Health Plann Management* **36**: 1575–1588. <https://doi.org/10.1002/hpm.3189>
- Nabi-Afjadi M, Heydari M, Zalpoor H, Arman I, Sadoughi A, Sahami P, Aghazadeh S (2022) Lectins and lectinobodies: potential promising antiviral agents. *Cell Mol Biol Lett* **13**: 37. <https://doi.org/10.1186/s11658-022-00338-4>
- Nam NDG, Gao NT, Nguyen MN, Downes NK, Ngan NVC, Anh LHH, Trung NH (2022) The diversity of phytoplankton in a combined rice-shrimp farming system in the coastal area of the Vietnamese Mekong Delta. *Water* **14**: 487. <https://doi.org/10.3390/w14030487>
- Niknam Z, Jafari A, Golchin A, Pouya FD, Nemati M, Rezaei-Tavirani M, Rasmi Y (2022) Potential therapeutic options for COVID-19: an update on current evidence. *Eur J Med Res* **27**: 6. <https://doi.org/10.1186/s40001-021-00626-3>
- Nissen K, Krambrich J, Akaberi D, Hoffman T, Ling J, Lundkvist A, Svensson L, Salaneck E (2020) Long-distance airborne dispersal of SARS-CoV-2 in COVID-19 wards. *Sci Rep* **10**: 19589. <https://doi.org/10.1038/s41598-020-76442-2>
- Orzechowska B, Bezpalko L, Lis M, Boratynski J (2018) Eradication of Rinderpest from Poland in 1921–1922. *Postep Hig Med Dosw* **72**: 966–974. <https://doi.org/10.5604/01.3001.0012.7305>
- Pan C, Chen H, Xie J, Huang Y, Yang Y, B Du, Qiu H (2022) The efficiency of convalescent plasma therapy in the management of critically ill patients infected with COVID-19: A matched cohort study. *Front Med (Lausanne)* **9**: 822821. <https://doi.org/10.3389/fmed.2022.822821>
- Napiórkowska-Krzebietke A, Hutorowicz A (2006) Long-term changes of phytoplankton in Lake Niegocin, in the Masurian Lake Region, Poland. *Oceanol Hydrobiol Stud* **35**: 209–226
- Rogalski M (2022). Civic project – COVID-19 in Poland <https://docs.google.com/spreadsheets/d/1ierEhD6gcq51HAm433knjVvwey4ZE5DCnu1bW7PRG3E/edit#gid=1309014089> (Date accessed March 12, 2022)
- Rzymyski P, Poniedziałek B, Rosińska J, Ciechanowski P, Peregrym M, Pokorska-Spiwak M, Talarek E, Zalewska I, Franczak-Chmura M, Pilarczyk M, Figlerowicz M, Kucharek I, Flisiak R (2022) Air pollution might affect the clinical course of COVID-19 in pediatric patients. *Ecotoxicol Environ Saf* **239**: 113651. <https://doi.org/10.1016/j.ecoenv.2022.113651>
- Sami N, Ahmad R, Fatima T (2021) Exploring algae and cyanobacteria as a promising natural source of antiviral drug against SARS-CoV-2. *Biomed J* **44**: 54–62. <https://doi.org/10.1016/j.bj.2020.11.014>
- Sharon N, Lis H (2001) The structural basis for carbohydrate recognition by lectins. *Adv Exp Med Biol* **491**: 1–16. https://doi.org/10.1007/978-1-4615-1267-7_1
- Singh RS, Walia AK, Khattar JS, Singh DP, Kennedy JF (2017) Cyanobacterial lectins characteristics and their role as antiviral agents. *Int J Biol Macromol* **102**: 475–496. <https://doi.org/10.1016/j.ijbiomac.2017.04.041>

- Simplicien M, Péro P, Sudor J, Barre A, Benoist H, Van Damme EJM, Rougé P (2022) Plant lectins as versatile tools to fight coronavirus outbreaks. *Glikoconjugate J* **40**: 109–118. <https://doi.org/10.1007/s10719-022-10094-4>
- Stravalaci M, Pagani I, Paraboschi EM, Pedotti M, Doni A, Scavello F, Mapelli SN, Sironi M, Perucchini C, Varani L, Matkovic M, Cavalli A, Cesana D, Gallina P, Pedemonte N, Capurro V, Clementi N, Mancini N, Invernizzi P, Bayarri-Olmos R, Garred P, Rappuoli R, Duga S, Bottazzi B, Ugucioni M, Asselta R, Vicenzi E, Mantovani A, Garlanda C (2022) Recognition and inhibition of SARS-CoV-2 by humoral innate immunity pattern recognition molecules. *Nat Immunol* **23**: 275–286. <https://doi.org/10.1038/s41590-021-01114-w>
- Szermier-Olearnik B, Drab M, Makosa M, Zembala M, Barbasz J, Dąbrowska K, Boratyński J (2017) Aggregation/dispersion transitions of T4 phage triggered by environmental ion availability. *J Nanobiotechnol* **24** 32. <https://doi.org/10.1186/s12951-017-0266-5>
- Wang W, Li Q, Wu J, Hu Y, Wu G, Yu C, Xu K, Liu X, Wang Q, Huang W, Wang L, Wang Y (2021) Lentil lectin derived from *Lens culinaris* exhibit broad antiviral activities against SARS-CoV-2 variants. *Emerg Microbes Infect* **110**: 1519–1529. <https://doi.org/10.1080/22221751.2021.1957720>
- Worldometer COVID-19 Coronavirus Pandemic (2023) <https://www.worldometers.info/coronavirus> (Date accessed March 2, 2023)
- Yang W, Marr LC (2012) Mechanisms by which ambient humidity may affect viruses in aerosols. *Appl Environ Microbiol* **78**: 6781–6788. <https://doi.org/10.1128/AEM.01658-12>
- Yin J, Li C, Ye C, Ruan Z, Liang Y, Li Y, Wu J, Luo Z (2022) Advances in the development of therapeutic strategies against COVID-19 and perspectives in the drug design for emerging SARS-CoV-2 variants. *Comput Struct Biotechnol J* **20**: 824–837. <https://doi.org/10.1016/j.csbj.2022.01.026>
- Zhang S, Go EP, Ding H, Anang S, Kappes JC, Desaire H, Sodroski J (2021) Analysis of glycosylation and disulfide bonding of wild-type SARS-CoV-2 spike glycoprotein. *J Virol* **96**: 3 e01626-21. <https://doi.org/10.1128/jvi.01626-21>
- Zhu JJ (2022) African swine fever vaccinology: The biological challenges from immunological perspectives. *Viruses* **14**: 9. <https://doi.org/10.3390/v14092021>

Assessing the pharmacological and biochemical effects of *Salvia hispanica* (Chia seed) against oxidized *Helianthus annuus* (sunflower) oil in selected animals

Tariq Aziz¹✉, Fawad Ihsan², Ayaz Ali Khan²✉, Shafiq ur Rahman³, Ghazala Yasmin Zamani⁴, Metab Alharbi⁵, Abdulrahman Alshammari⁵ and Abdullah F. Alasmari⁵

¹Department of Agriculture, University of Ioannina, Arta 47100, Ioannina, Greece; ²Department of Biotechnology, University of Malakand, Chakdara, 18800, Pakistan; ³Department of Environmental Sciences, Shaheed Benazir Bhutto University, Sheringal Dir upper, Pakistan; ⁴Department of Biotechnology, Bacha Khan University, Charsadda, Pakistan; ⁵Department of Pharmacology and Toxicology, College of Pharmacy, King Saud University, P.O. Box 2455, Riyadh 11451, Saudi Arabia

Oil oxidation is important in terms of taste, nutritive component quality and toxic effect of the oil. In this study, the oxidized sunflower oil was used along with chia seed in rabbits for the determination of its effects on various hematological and serum biochemical parameters as well as on liver histopathology. Three rabbits were fed with oxidized oil (obtained by heating) at the dose rate of 2 ml/kg body weight by mixing it with green fodder. The other rabbit groups were fed with Chia seed at dose rate of 1, 2 and 3 g/kg along with oxidized sunflower oil. Chia seed was fed alone to three rabbits at the dose rate of 2 g/kg body weight. All rabbits were fed regularly for twenty-one days. For the determination of hematological and biochemical parameters, whole blood and serum samples were collected on different days during feeding period. For histopathology, liver samples were used. Significant changes ($p < 0.05$) were noted in the hematology and biochemical indices in the rabbits that were fed with oxidized sunflower oil alone, and along with different doses of Chia seed. In a dose-dependent manner, all these parameters were significantly improved ($p < 0.05$), when the amount of Chia seed was increased. The biochemical and hematological indices were in normal range in the group fed only with Chia seed. In oxidized oil fed group, liver histopathological analysis showed that cholestasis was present at both sides (bile pigment secretion) and zone 3 necrosis with mild inflammatory cells. Mild vacuolization of hepatocytes was also observed. In Chia seed fed group, hepatocyte vacuolization and mild necrosis was noted. It was concluded that oxidized sunflower oil alters the biochemical and hematological parameters and causes liver abnormalities. Chia seeds act as an antioxidant and retrieve those alterations.

Keywords: Chia seed, hematological parameters, oxidized sunflower oil, rabbits

Received: 17 January, 2023; **revised:** 09 February, 2023; **accepted:** 17 February, 2023; **available on-line:** 27 February, 2023

✉e-mail: iwocdk@gmail.com (TA), ayazkhan@uom.edu.pk (AAK)

Acknowledgments of Financial Support: The authors greatly acknowledge and express their gratitude to the Researchers Supporting Project number (RSP2023R462), King Saud University, Riyadh, Saudi Arabia

[†]Equal contribution

Abbreviations: ALT, alanine transaminase; B, basophils; C, total cholesterol; E, eosinophils; H, hemoglobin; HDL, high density lipoproteins; L, lymphocytes; LDL, low density lipoproteins; M, monocytes; N, neutrophils; P, platelets; S, blood glucose; TG, triglycerides; WBCs, white blood cells

INTRODUCTION

Vegetable oils and fats are important constituents of foods and are essential components of our daily diet (Brahmi *et al.*, 2020). Vegetable oils are obtained by mechanical expelling or solvent extraction of oleaginous seeds (soybeans, rapeseed, sunflower, etc.) or oleaginous fruit like palm and olive (Vidrih *et al.*, 2010). Vegetable oils generally contain triglycerides (about 98 g/100 g) (Qian *et al.*, 2020). Triglyceride is formed from a reaction between glycerol and fatty acids and other substances in a small proportion (Gnanaprakasam *et al.*, 2021). Some of them such as diglycerides, vitamins, phytosterols, tocopherols and polyphenols have important health benefits in humans (Gharby *et al.*, 2021; Chew *et al.*, 2016), and therefore, they should not be removed during processing. Other compounds known for their negative effect on the quality and stability of oils include free fatty acids, unsaponifiable matters, waxes, pigments, solid impurities (mainly fibers), oxidation products (peroxides, aldehydes, ketones, alcohols, and oxidized fatty acids) (Gharby *et al.*, 2016; Aliyar-Zanjani *et al.*, 2019; Said *et al.*, 2022). Several plants contain different chemicals which can be used for treatment of various diseases if they are consumed entirely or in parts with lower cost and less side effects (Sana *et al.*, 2022; Bisht *et al.*, 2021). Sunflower oil is one of the most widely grown essential oils in the world. The total world's oilseed production is forecasted at nearly 647 million tons (United States Department of Agriculture Foreign Agricultural Service Oilseeds: World Markets and Trade. 2022). In 1998, the world's seed oil was about 28.5 million tons and, as a vegetable oil, only soybean (*Glycine max*) and *Brassica* species (*Brassica napus* and *Brassica campestris*) produced more oil (Flagella *et al.*, 2002). Sunflower (*Helianthus annuus*) is used in food, for oil, as a dye, for medicinal purposes, and as an ornamental plant species. Sunflower oil has been used since ancient times as a food and as a medicinal plant to cure many ailments. From a dietary point of view, a diet enriched in monounsaturated fatty acids has been recommended to reduce cholesterol in blood plasma (Dimitrijevic and Horn 2018). Sunflower is often used to produce oils from seeds but is also used as a protein source for human consumption as well as food (Choe and Min 2006). Oil oxidation is important in terms of palatability, nutritional quality and acidity of edible oils. Various chemical compounds, autoxidation and photosensitized oxidation are responsible for the degra-

dation of edible oils during production and storage with respect to oxygen (Khan *et al.*, 2022; Knez *et al.*, 2019).

Salvia hispanica, also called Chia, is an annual herbaceous plant native to southern Mexico and northern Guatemala. It belongs to *Lamiales*, family *Labiatae*, subfamily *Nepetoideae*, and genus *Salvia* (Segura-Campos *et al.*, 2014). The *Salvia* genus comprises of about 900 species, which have been extensively distributed for thousands of years in many regions of the world, including South Africa, North, Central and South America, and Southeast Asia (Grancieri *et al.*, 2019; Ullah *et al.*, 2016; Campos *et al.*, 2016; Das *et al.*, 2018; Mohd Ali *et al.*, 2012).

Many studies have reported that Chia today is grown not only in Mexico and Guatemala, but also in Australia, Bolivia, Columbia, Peru, Argentina, America, and Europe. Today, Mexico is known as the largest producer of Chia in the world (Silva *et al.*, 2016). Chia is the dietary seed of *Salvia hispanica*, a flowering plant, known for its antioxidants that is often used in food production (Coorey *et al.* 2016). Recently, Chia seeds have been given more consideration and have become one of the most popular foods in the world based on their medicinal values and nutritional properties (Ullah *et al.*, 2016; Das *et al.*, 2018; Mohd Ali *et al.*, 2012; Silva *et al.*, 2016). Coorey *et al.* (2016) demonstrated that Chia is an excellent food ingredient as it contains a huge amount of α -linolenic acid and is easily added to commercial foods. In addition to that it has also been reported that Chia seeds contain high percentage of fatty acids, which make it crucial for health, antioxidant, and antimicrobial property (Ullah *et al.*, 2016; Mohd Ali *et al.*, 2012; Ixtaina *et al.*, 2008; Reyes *et al.*, 2008). Furthermore, several other studies (Grancieri *et al.*, 2019; Silva *et al.*, 2016; Ixtaina *et al.*, 2008; Reyes *et al.*, 2008; Ayerza *et al.*, 2016; Muñoz *et al.*, 2012) demonstrated that the Chia is an oil seed composed of fats, carbohydrates, dietary fiber, proteins, vitamins (A, B, K, E, D), minerals and antioxidants and its benefits of using as a nutritional supplement are numerous, such as supporting digestive system, helping the intestinal mucosa, stronger bones, reducing the risk of constipation, irritable bowel disease, heart diseases, diabetes, and many more (Silva *et al.*, 2016; Correy *et al.*, 2016; Ixtaina *et al.*, 2008; Reyes *et al.*, 2008; Ayerza *et al.*, 2016; Muñoz *et al.*, 2012; de Falco *et al.*, 2018). In the region of Malakand, Khyber Pakhtunkhwa, Pakistan, different food items are fried and cooked using either ghee or oils. Persistent heating causes ghee and oil oxidation, hence, making it toxic. Therefore, the present study was aimed to check the toxic effects of oxidized sunflower (*Helianthus annuus*) oil on hematological and biochemical parameters in rabbits. As Chia seeds (*Salvia hispanica*) are sources of one of the potent antioxidants, they were used to check its curing potential against the toxic effects of oxidized sunflower (*Helianthus annuus*) oil.

MATERIALS AND METHODS

Materials

Sunflower oil was purchased from local market of Matta, Swat, Khyber Pakhtunkhwa, Pakistan. The sunflower oil was selected based on its high linoleic acid and oleic acid content. Chia seeds and rabbits ($n=60$) were purchased in the local market of Chakdara, Lower Dir, Khyber Pakhtunkhwa. EDTA containing tubes and gel

tubes were purchased from the local market for whole blood collection and serum isolation. Formaldehyde and chloroform were provided by organic chemistry laboratory, Department of Chemistry, University of Malakand.

Thermal oxidation of oil

Sunflower oil samples were subjected to a five-hour long regular heating on hot plates at 100°C. These samples were then kept at -20°C to prevent them from further chemical changes.

Experimental animal clustering and feeding

Rabbits were reared in Bio-park of University of Malakand. Food and water were freely available to all the animals. They had an average weight of 1200 grams at the start of the experiment, and among the 60 rabbits, 21 individuals were selected for the experiment based on body weight and health status. The study was started after the approval of the ethical committee, Department of Biotechnology, University of Malakand. Rabbits were divided into seven groups, each having three rabbits ($n=3$). Groups were labelled as NC, NO, OO, C, CO1, CO2 and CO3 representing negative control, normal sunflower oil, oxidized oil, Chia seed only, Chia seed with oxidized oil (low dose), Chia seed with oxidized oil (medium dose) and Chia seed with oxidized oil (high dose), respectively. The negative control group was fed with green fodder and water. NO was fed with normal sunflower oil at a dose of 2 ml/kg with fodder and water. Group OO was fed with oxidized sunflower oil at a dose of 2 ml/kg. Group C was given Chia seed at a dose of 2 g/kg. Group CO1 was fed with Chia seed at a dose of 1g/kg and oxidized sunflower oil at a dose of 2 ml/kg. Group CO2 was fed with Chia seed at a dose of 2 g/kg and oxidized sunflower oil at a dose of 2 ml/kg. Group CO3 was fed with Chia seed at a dose of 3 g/kg and oxidized sunflower oil at a dose of 2 ml/kg. The feeding was continued for 21 consecutive days and blood samples were collected at day 0, 11 and 21 for hematological parameters and serum biochemical parameters.

Hematological and serum biochemical parameters

The whole blood was used for the analyses of hemoglobin (Hb), platelets (P), white blood cells (WBCs), neutrophils (N), lymphocytes (L), monocytes (M), eosinophils (E) and basophils (B) count by using a fully automated blood hematology analyzer (ERBA – XL 1000). About 5 ml of blood was collected and transferred to gel tubes to isolate serum. The serum was used for the analyses of total triglyceride (TG), total cholesterol (C), blood glucose (S), alanine transferase (ALT), creatinine, urea, high density (HDL) and low density lipoproteins (LDL) level.

Histopathological examination of liver

At the end of the experiment, rabbits were slaughtered according to the method described by Hussain and others (Hussain *et al.*, 2022) and their liver was isolated and preserved in formalin buffer (10%). Tissues sectioning were made, stained and histopathologically examined as described by Khan and others (Khan *et al.*, 2022). Prepared slides were observed under the light microscope, model no. M 7000 D (SWIFT, Japan) and images were taken by a digital camera coupled with a microscope with a resolution of 2.4 Mpixel.

Table 1. Effect of oxidized sunflower oil and Chia seed on different hematological parameters in rabbits on different days.

Gro-ups	Hemoglobin (gm/dl)			Platelets ($\times 10^9/L$)			Neutrophils (%)			Lymphocytes (%)			Monocytes (%)			Eosinophils (%)		
	Day 0	Day 11	Day 21	Day 0	Day 11	Day 21	Day 0	Day 11	Day 21	Day 0	Day 11	Day 21	Day 0	Day 11	Day 21	Day 0	Day 11	Day 21
NC	8.37 \pm 0.35 \pm a	11.2 \pm 2.00a	12.2 \pm 1.6a	5.5 $\times 105 \pm$ 300a	5.8 $\times 105 \pm$ 200a	3.8 $\times 10^5 \pm$ 200a	42.3 \pm 2.52a	53.0 \pm 2.00a	40.0 \pm 2.00a	42.0 \pm 2.00a	50.7 \pm 2.52a	55.0 \pm 2.0a	1.67 \pm 0.57a	1.00 \pm 1.00a	2.33 \pm 1.3a	1.00 \pm 1.00a	3.00 \pm 2.00a	3.00 \pm 2.0a
NO	7.47 \pm 0.45a	12.0 \pm 2.15a	14.3 \pm 1.8a	5.5 $\times 105 \pm$ 251a	5.0 $\times 105 \pm$ 200b	3.9 $\times 10^5 \pm$ 251b	42.7 \pm 2.52a	67.0 \pm 2.00b	42.7 \pm 2.52a	41.7 \pm 2.52a	34.0 \pm 2.00b	52.0 \pm 2.00a	2.00 \pm 1.00a	1.00 \pm 1.00a	3.67 \pm 1.53a	2.00 \pm 1.00a	2.33 \pm 1.53a	2.67 \pm 1.53a
OO	9.33 \pm 0.35b	11.3 \pm 2.15a	13.4 \pm 2.1a	5.5 $\times 105 \pm$ 251a	2.7 $\times 105 \pm$ 200c	3.0 $\times 10^5 \pm$ 251c	41.3 \pm 2.52a	42.3 \pm 2.52c	22.7 \pm 2.2b	43.0 \pm 2.00a	59.0 \pm 2.00c	78.0 \pm 2.0b	1.00 \pm 1.00a	2.00 \pm 1.00a	2.33 \pm 1.5a	1.00 \pm 1.00a	3.00 \pm 2.00a	3.00 \pm 2.0a
C	10.7 \pm 0.20c	13.2 \pm 2.15a	13.7 \pm 2.4a	5.4 $\times 105 \pm$ 300b	3.8 $\times 105 \pm$ 251d	3.5 $\times 10^5 \pm$ 200d	45.0 \pm 2.00a	98.0 \pm 2.00d	32.0 \pm 2.00b	45.0 \pm 2.00a	1.00 \pm 1.00d	67.0 \pm 2.00c	2.00 \pm 1.00a	2.00 \pm 1.00a	2.33 \pm 1.53a	1.33 \pm 0.57a	1.33 \pm 1.53a	4.00 \pm 2.65a
CO1	7.40 \pm 0.40a	12.4 \pm 1.90a	12.4 \pm 1.5a	5.6 $\times 105 \pm$ 200a	4.2 $\times 105 \pm$ 200e	2.8 $\times 10^5 \pm$ 305e	47.7 \pm 2.52a	97.3 \pm 2.52d	26.0 \pm 2.0b	42.0 \pm 2.00a	1.00 \pm 1.00d	65.7 \pm 2.2c	2.00 \pm 1.00a	1.33 \pm 0.577a	4.00 \pm 2.0a	1.00 \pm 1.00a	2.33 \pm 1.53a	4.00 \pm 2.0a
CO2	11.3 \pm 0.25c	10.6 \pm 1.80a	12.4 \pm 2.1a	5.5 $\times 105 \pm$ 251a	5.7 $\times 105 \pm$ 200f	4.0 $\times 10^5 \pm$ 251f	48.7 \pm 3.06a	83.0 \pm 2.00e	29.0 \pm 2.0b	43.7 \pm 2.52a	18.0 \pm 2.00e	68.0 \pm 2.0c	1.00 \pm 1.00a	2.00 \pm 1.00a	2.33 \pm 1.5a	1.33 \pm 0.57a	3.00 \pm 2.00a	2.67 \pm 1.3a
CO3	12.3 \pm 0.30d	12.5 \pm 2.00a	11.5 \pm 1.8a	5.5 $\times 105 \pm$ 300a	2.5 $\times 105 \pm$ 200g	2.0 $\times 10^5 \pm$ 200g	47.7 \pm 8.50a	66.7 \pm 2.52b	31.3 \pm 2.52b	41.0 \pm 2.00a	31.7 \pm 1.53b	68.3 \pm 2.52c	2.00 \pm 1.00a	2.67 \pm 1.53a	3.33 \pm 1.53a	1.00 \pm 1.00a	2.00 \pm 2.00a	3.33 \pm 1.53a

Same letters in a row show no significant difference ($p < 0.05$), while diverse letters in the same row indicate for a significant difference ($p < 0.05$). NO-normal Oil, OO – oxidized oil, C – Chia Seed, CO1– Chia seed at a dose of 1 g/kg along with 2 ml of oil, CO2 – Chia seed at a dose of 2 g/kg along with 2 ml of oil, CO3 – Chia seed at a dose of 3 g/kg along with 2 ml of oil

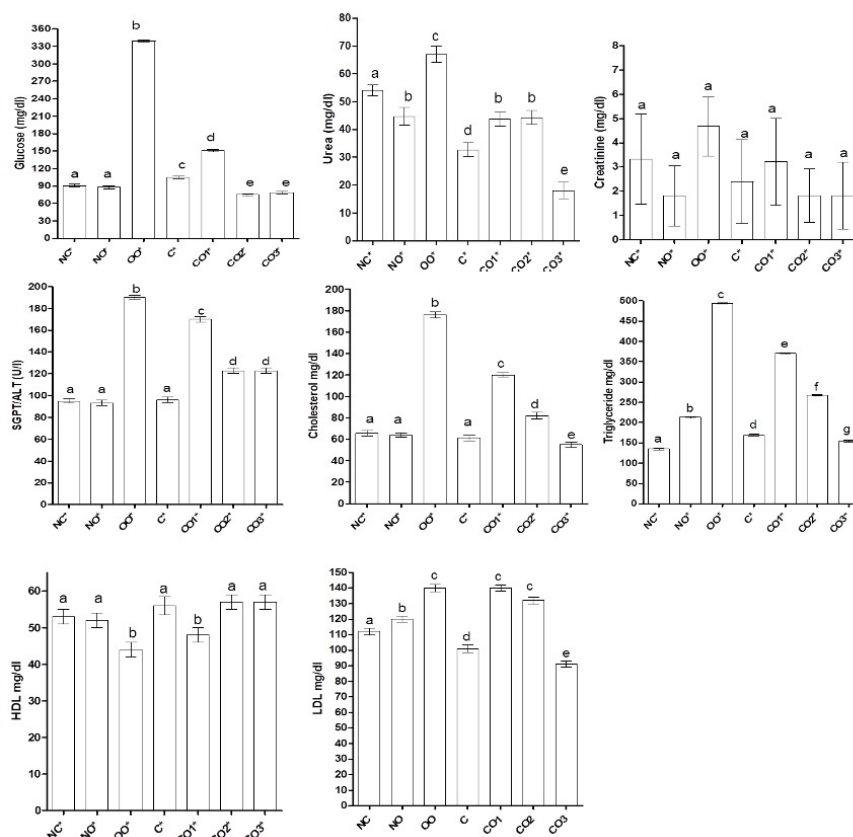


Figure 1. Effects of oxidized sunflower oil and Chia seed on different biochemical parameters in rabbits.

Statistical analysis

Data were analyzed by one way analysis of variance (ANOVA) and Tukey test using online statistical software, prism demo version 05 (www.graphpad.com). Data were presented as mean from triplicate results ($n=3$) with standard deviation. The mean and standard deviation were sorted out for each parameter.

RESULTS

Effects on hematological parameters

Results showed no significant effect ($p<0.05$) on the Hb level; however, the platelet count remarkably decreased in all groups after the 21st day. The platelet count was the lowest in the CO3 group. Similarly, no significant change was observed for neutrophils and lymphocyte count. The monocyte count doubled in both CO2 and CO3 groups. The eosinophile number increased in all groups, but such increase was not remarkably high. The results from all measurements (day 0, 11th and 21st day) were combined in Table 1. Different biochemical parameters of the rabbits were shown in Fig. 1.

Effects on biochemical parameters

The glucose level was significantly ($p<0.05$) high in the oxidized oil (OO) group; however, groups C and CO1 also reflected substantial elevated sugar level. The urea level remained the same in all groups except for CO3 that showed a significant decrease at 21st day. The SGPT/ALT level were significantly ($p<0.05$) increased in all groups, especially among OO, C, CO1, CO2, and

CO3 variants. After the 21st day, the cholesterol levels in NC, NO and CO2 groups remained almost like day 0 values. However, in the OO group, the cholesterol level was high, and the result was the opposite in the C group, wherein cholesterol levels decreased. In CO1 variant, the total cholesterol level significantly ($p<0.05$) increased, as compared to CO3, where the cholesterol level decreased on the 21st day. The triglyceride values were significantly ($p<0.05$) elevated in all groups, but they were remarkably high in OO, CO1, and CO2 variants. The HDL levels in all groups showed no significant change. The LDL levels increased in all groups except CO3 wherein, a significant decrease was noted; pertinent to mention, the OO group showed the most negatively correlated LDL values. The results of biochemical parameters on days 0, 11 and 21 were combined in Table 2.

Histopathological pattern

At the end of the experiment, the rabbits were slaughtered, and liver samples were collected for the histopathological analysis. Liver slides were studied under 10X and 40X magnitude for detailed histopathological changes. Results have been presented in Fig 2. Liver histopathology of control variant showed that endothelial linings of central veins had normal morphology, and no evidence of pericentral fibrosis was noted. Kupffer cells were non-reactive. The orientation of the hepatic cord was very good. Hepatic portal veins and arteries showed a normal structure (Fig 2A). On the contrary, in the oxidized oil fed group, cholestasis was present on both sides (bile pigment secretion). Zone 3 necrosis with mild inflammatory cells was noted. Mild hepatocytic vacuolization was also observed (Fig 2B). However, in the normal oil fed group, there was mild zone 2 necro-

Table 2. Effect of oxidized sunflower oil and Chia seed on different biochemical parameters in rabbits on different days.

Groups	Glucose level mg/dl			Urea level mg/dl			creatinine level (mg/dl)			SGPT/ALT level (U/l)			Cholesterol level (mg/dl)			Triglyceride level (mg/dl)			HDL level (mg/dl)			LDL level (mg/dl)		
	Day 0	Day 11	Day 21	Day 0	Day 11	Day 21	Day 0	Day 11	Day 21	Day 0	Day 11	Day 21	Day 0	Day 11	Day 21	Day 0	Day 11	Day 21	Day 0	Day 11	Day 21	Day 0	Day 11	Day 21
NC	77.0 ± 2.0a	63.0 ± 2.00a	90.7 ± 2.52a	35.0 ± 2.0a	33.0 ± 2.00a	54.0 ± 2.00a	0.60 ± 0.2a	1.21 ± 0.20a	3.33 ± 1.86a	34.3 ± 2.5a	40.3 ± 2.52a	95.0 ± 2.00a	67.0 ± 2.0a	125 ± 2.08a	65.7 ± 2.52a	120 ± 2.00a	145 ± 2.00a	135 ± 2.00a	54.7 ± 3.0a	39.0 ± 2.00a	53.0 ± 2.00a	97 ± 2.00a	97.0 ± 2.00a	112 ± 2.00a
NO	77.0 ± 2.00a	85.7 ± 1.53b	87.7 ± 2.52a	33.7 ± 2.08a	23.3 ± 2.52b	44.7 ± 3.21b	0.833 ± 0.15a	0.700 ± 0.20a	1.81 ± 1.24a	34.0 ± 2.00a	71.0 ± 2.00b	93.3 ± 2.52a	65.0 ± 2.00a	121 ± 2.00a	64.0 ± 2.00a	125 ± 2.52a	233 ± 2.00b	213 ± 2.52b	60.3 ± 2.52b	43.0 ± 2.00a	52.0 ± 2.00a	85 ± 1.00b	37.0 ± 2.00b	120 ± 2.00a
OO	82.7 ± 2.52b	94.7 ± 2.52c	339 ± 2.00b	36.3 ± 2.52a	35.0 ± 2.00a	67.0 ± 3.00c	0.833 ± 0.20a	0.86 ± 0.15a	4.67 ± 1.22a	39.3 ± 2.52b	100 ± 2.52c	190 ± 2.00b	73.7 ± 2.52b	170 ± 2.00b	176 ± 3.06b	126 ± 2.52a	410 ± 2.00c	494 ± 2.00c	64.7 ± 0.58b	38.3 ± 2.52a	44.0 ± 2.00b	80.3 ± 1.53b	51.7 ± 2.52c	140 ± 2.52b
C	85.7 ± 1.53b	90.7 ± 2.52c	105 ± 2.08c	38.0 ± 2.00a	23.3 ± 1.53b	32.7 ± 2.52d	1.03 ± 0.252a	0.83 ± 0.15a	2.40 ± 1.73a	38.7 ± 2.52b	94.7 ± 2.52c	96.3 ± 2.52a	75.0 ± 2.00b	111 ± 2.52c	61.3 ± 2.52a	131 ± 2.00b	113 ± 2.00d	169 ± 2.00d	75.0 ± 1.00c	41.0 ± 2.00a	56.3 ± 2.52a	95.3 ± 1.53a	49.3 ± 2.52d	101 ± 2.52c
CO1	73.0 ± 2.00a	82.3 ± 2.52b	151 ± 2.00d	28.7 ± 2.52a	35.3 ± 2.52a	43.7 ± 2.52b	0.967 ± 0.30a	0.73 ± 0.25a	3.22 ± 1.79a	41.3 ± 2.08b	81.7 ± 2.52d	170 ± 2.52c	71.7 ± 2.52b	148 ± 2.65	120 ± 2.00c	132 ± 3.51b	554 ± 2.00e	370 ± 2.00e	48.0 ± 2.00d	39.0 ± 2.00a	48.0 ± 2.00b	103 ± 1.53c	51.0 ± 2.00c	140 ± 2.00b
CO2	93.7 ± 2.52c	101 ± 2.08d	75.0 ± 2.00e	33.0 ± 2.00a	41.0 ± 2.00c	44.3 ± 2.52b	1.33 ± 0.35b	0.83 ± 0.25a	1.82 ± 1.11a	32.7 ± 2.52a	54.3 ± 1.15e	123 ± 2.52d	79.0 ± 1.73b	111 ± 2.52c	82 ± 3.06d	136 ± 2.52b	136 ± 2.00f	267 ± 2.00f	63.0 ± 1.00b	40.3 ± 2.52a	57.0 ± 2.00a	108 ± 1.53c	48.3 ± 2.52d	132 ± 2.00d
CO3	94.7 ± 2.52c	143 ± 3.06e	79.0 ± 2.00e	35.3 ± 2.08a	38.0 ± 2.65d	18.0 ± 3.00e	1.23 ± 0.30a	0.94 ± 0.26a	1.81 ± 1.38a	38.0 ± 2.00b	83.7 ± 1.53d	123 ± 2.52d	77.0 ± 2.00b	123 ± 2.00a	55 ± 2.52e	135 ± 2.52b	111 ± 2.00d	154 ± 2.52g	61.0 ± 2.00b	38.0 ± 2.00a	57.0 ± 2.00a	110 ± 2.52d	95.0 ± 2.00a	91 ± 2.00c

Same letters in a row show no significant difference ($p < 0.05$) while diverse letters in the same row indicate for a significant difference ($p < 0.05$). NO-normal oil, OO – oxidized oil, CO1 – Chia Seed, CO1 – Chia seed at a dose of 1 g/kg along with 2 ml of oil, CO2 – Chia seed at a dose of 2 g/kg along with 2 ml of oil, CO3 – Chia seed at a dose of 3 g/kg along with 2 ml of oil

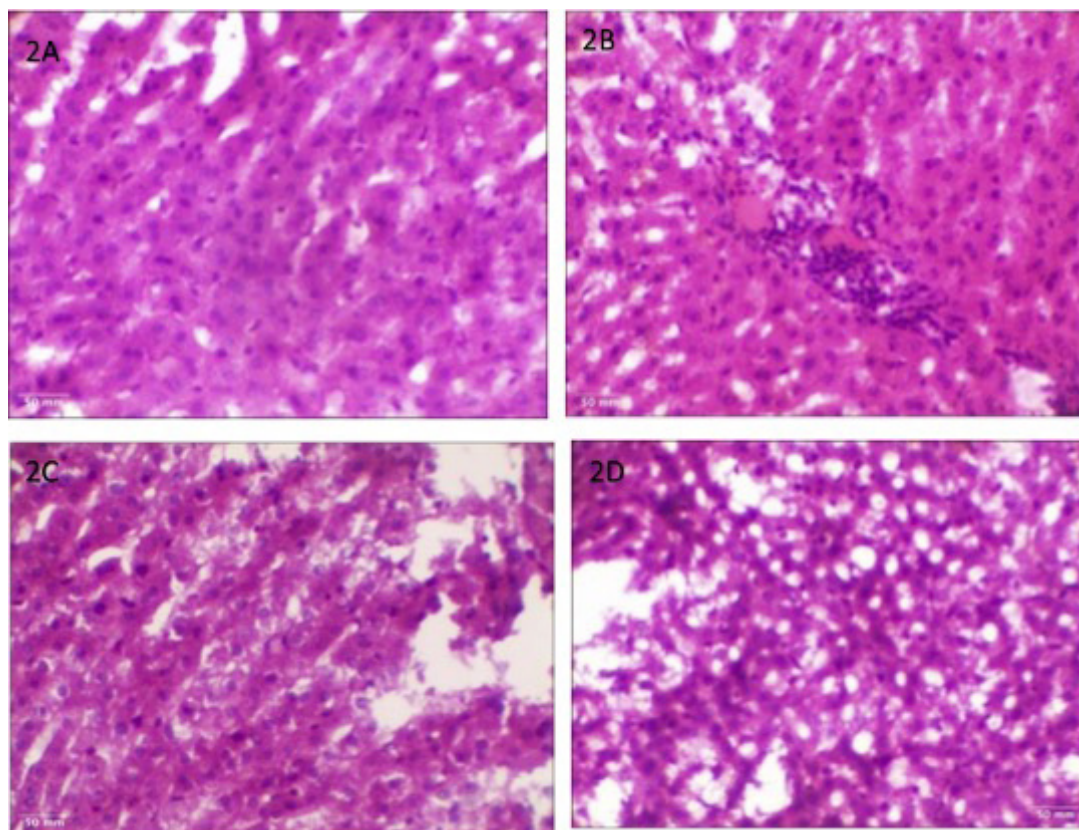


Figure 2. Histopathology of the normal rabbit liver (2A), oxidized oil-fed rabbits (2B), normal oil (2C) and Chia seed-fed rabbits (2D).

sis especially central vein inflammation and fatty changes (Fig 2C). In Chia seed fed group, there was hepatocyte vacuolization and visible signs of mild necrosis (Fig 2D).

DISCUSSION

It is common practice to repeatedly heat vegetable oils at high temperatures during cooking. Oils are heated during food preparation or deep frying. The present study aimed to sort out the effect of Chia seed against oxidized sunflower oil in rabbits. In our findings, lymphocyte count was significantly increased, while there was a low number of platelets, neutrophils, and monocytes after feeding with oxidized oil as compared to control. The results for these parameters were similar to control ones when fed with Chia seeds. Similar to our results, fresh palm oil was fed to rats, and it was observed that heated oil decreased PCV, Hb level, RBCs and increased WBCs (Mesembe *et al.*, 2004). Similarly, oxidized olive oil significantly altered hematological parameters in rats (Khan *et al.*, 2017). No effects of repeatedly heating cooking oil were observed on hematological parameters after its administration to Wistar rats (Shue *et al.*, 1968; Perumalla *et al.*, 2016), which is not in accordance with our findings. In our study, we heated the sunflower oil for 5 hours at 100°C which may have led to the accumulation of free radicals and altered the hematological parameters. The consumption of Chia has shown good digestibility, hypoglycemic effects, improved lipid and glycemic profiles, and reduced fat deposition in the animal liver.

There was a statistically significant increase in creatinine and urea level in rabbits that were fed with oxidized sunflower oil, and the Chia seed reduced their levels to

normal. The co-administration of oxidized oil and Chia seed decreased the creatinine and urea level in a dose-dependent manner. Much of the toxicity of severely heated food oils has been associated with a non-urea-adducting fatty acid (urea filtrate) fraction (Shue *et al.*, 1968; Billek *et al.*, 2000). Certain fractions of the heated oils, the total polar materials cause growth retardation, increased liver and kidney weights and disorders of the enzyme system, but only if fed in high doses (Billek *et al.*, 2000; Ani *et al.*, 2015).

The significant increase in serum creatinine concentration in the group fed with thermo-oxidized palm oil may be suggestive of possible renal system damage. Creatinine levels in plasma are usually measured to determine acute or chronic renal insufficiency. They are usually raised in renal disease (Ani *et al.*, 2015; Toscano *et al.*, 2014). Chia seeds contain high fiber and linolenic fatty acid which may reduce the creatinine level of the rabbits. *Salvia hispanica* controls blood pressure (BP) and its associated cardiometabolic factors. Also, Chia flour could reduce ambulatory and clinical BP in both treated and untreated hypertensive individuals (Toscano *et al.*, 2014; Al-Othman *et al.*, 2006).

For rabbits fed with un-oxidized sunflower oil, the ALT level was normal. Oxidized sunflower oil increased ALT level in rabbits. In the group which was fed with Chia seeds, ALT level was in normal range. Oxidized oil promotes serum ALT level significantly (Khan *et al.*, 2017; Al-Othman *et al.*, 2006; Zeb *et al.*, 2019), leading to hepatotoxicity. Unoxidized oil is beneficial for liver as it has oleuropein that protects hepatocytes from damage. It had been observed that oxidative stress induced by rancid oils leads to liver injury, which caused an increase in the ALT level (Zeb *et al.*, 2019; Aguilera *et al.*, 2002). In

our study, unoxidized oil had no effect on cholesterol level, while oxidized sunflower oil elevated the cholesterol level in rabbits. Chia seeds had a positive effect on lowering blood cholesterol level. Similar to our results, blood cholesterol levels were increased by oxidized olive oil in rats (Khan *et al.*, 2017; Kritchevsky *et al.*, 2000) and by oxidized sunflower in rabbits (Khan *et al.*, 2022). The Chia seed significantly decreased serum cholesterol level when compared to oxidized and un-oxidized sunflower oil treatments. Oxidized sunflower oil elevates the blood cholesterol level, while chia seed decreases its level. After absorption, it increases serum cholesterol level and may lead to atherosclerosis (Lou *et al.*, 2012).

The oxidized sunflower oil fed group significantly increased the triglyceride level of rabbits, while Chia seed decreased the triglyceride level in rabbits. Thermally oxidized oils keep users at risk to arteriosclerosis and cardiovascular diseases due to the depletion of phenolic as well as antioxidants in its constituents. A significant ($p < 0.05$) increase in the triglyceride level was observed when rabbits were fed with the oxidized olive oil (Khan *et al.*, 2017), oxidized sunflower oil (Zeb *et al.*, 2017) and mustard oil (Carmena *et al.*, 1996). The HDL concentration after feeding with oxidized sunflower oil was significantly decreased, whereas LDL values were increased as compared to normal group. Chia seed significantly increased HDL and decreased LDL level in rabbits. It has been suggested that HDL cholesterol and its constituents is increased after feeding sunflower oil, which helps in prevention of heart diseases (Lou *et al.*, 2012; Carmena *et al.*, 1996; Quiles *et al.*, 1998). A significantly higher LDL susceptibility to oxidation was observed after sunflower oil intake in comparison with virgin olive oil, despite an increase in LDL α -tocopherol concentration in sunflower oil group (Aguilera *et al.*, 2004). Histological studies revealed that un-oxidized sunflower oil caused no significant effect on the liver morphology and functions. Oxidized sunflower oil caused necrosis in centrilobular regions. It has also been reported that thermally oxidized ground nut oil leads to some liver diseases (Aguilera *et al.*, 2004; Jimoh *et al.*, 2004; Abdel Raouf *et al.*, 2012). On the other hand, Chia seed caused no significant changes, as hepatocyte vacuolization and mild necrosis were present in the liver.

CONCLUSIONS

In comparison to unoxidized oil, it has been determined that oxidized sunflower oil significantly affects hematological and biochemical parameters of serum and alters liver histological pattern in rabbits. Chia seed on the other hand, minimizes harmful effects of oxidized oil and display antioxidant potential.

Declarations

Author contribution. Conceptualization, T.A and A.A.K.; Original draft, G.Y.Z, S.R and F.I ; Methodology, M.A and F.I.; Data curation: M.A and A.A.S.; Writing- review & editing, A.A.K, and T.A.; Visualization, T.A.; Resources, M.A.; Project administration, T.A and A.A.K ; Funding acquisition, T.A.; Validation, F.A ; Investigation, S.R and A.A.K ; Formal analysis, T.A and S.R.; Supervision, T.A and A.A.K

Funding: This research work received no external funding.

Conflicts of Interest: The authors declare no conflict of interest.

REFERENCES

- Abdel-Raouf N, Al-Homaidan AA, Ibraheem IB (2012) Microalgae and wastewater treatment. *Saudi J Biol Sci* **19**: 257–275. <https://doi.org/10.1016/j.sjbs.2012.04.005>
- Al-Othman AM, Ahmad F, Al-Orf S, Al-Murshed KS, Arif Z (2006) Effect of dietary supplementation of *Ellataria cardamomum* and *Nigella sativa* on the toxicity of rancid corn oil in rats. *Int J Pharmacol* **2**: 60–65. <https://doi.org/10.3923/ijp.2006.60.65>
- Aguilera CM, Mesa MD, Ramirez-Tortosa MC, Nestares MT, Ros E, Gil A (2004) Sunflower oil does not protect against LDL oxidation as virgin olive oil does in patients with peripheral vascular disease. *Clin Nutr* **23**: 673–681. <http://doi.org/10.1016/j.clnu.2003.11.005>
- Aguilera CM, Ramirez-Tortosa MC, Mesa MD, Ramirez-Tortosa CL, Gil A (2002) Sunflower, virgin-olive and fish oils differentially affect the progression of aortic lesions in rabbits with experimental atherosclerosis. *Atherosclerosis* **162**: 335–344. [http://doi.org/10.1016/s0021-9150\(01\)00737-7](http://doi.org/10.1016/s0021-9150(01)00737-7)
- Aliyar-Zanjani N, Piravi-Vanak N, Ghavami Z (2019) Study on the effect of activated carbon with bleaching earth on the reduction of polycyclic aromatic hydrocarbons (PAHs) in bleached soybean oil. *Grasas y Aceites* **70**: 304. <https://doi.org/10.3989/gya.0577181>
- Ani EJ, Victor U, Nna VU, Owu DU, EE (2015) Effect of chronic consumption of two forms of palm oil diet on serum electrolytes, creatinine, and urea in rabbits. *J Appl Pharma Sci* **5**: 115–119. <https://doi.org/10.7324/JAPS.2015.50619>
- Ayerza R (2016) Crop year effects on seed yields, growing cycle length, and chemical composition of chia (*Salvia hispanica* L.) growing in Ecuador and Bolivia. *Emir J Food Agric* **28**: 196–200. <https://doi.org/10.9755/ejfa.2015-05-323>
- Billek G (2000) Health aspects of thermoxidized oils and fats. *Eur J Lipid Sci Tech* **102.8/9**: 587–593. [https://doi.org/10.1002/1438-9312\(200009\)102:8/9<587::AID-EJLT587>3.0.CO;2-9](https://doi.org/10.1002/1438-9312(200009)102:8/9<587::AID-EJLT587>3.0.CO;2-9)
- Bisht A, Jain S, Misra A, Dwivedi J, Paliwal S, Sharma S (2021) *Cedrus deodara* (Roxb. ex D. Don) G. Don: A review of traditional use, phytochemical composition and pharmacology. *J Ethnopharmacol* **279**: 114361. <https://doi.org/10.1016/j.jep.2021.114361>
- Brahmi F, Haddad S, Bouamara K, Yalaoui-Guellal D, Prost-Camus E, Pais de Barros JP, Prost M, Atanasov AG, Madani K, Boulekbache-Makhlouf L, Lizard G (2020) Comparison of chemical composition and biological activities of Algerian seed oils of *Pistacia lentiscus* L., *Opuntia ficus indica* (L.) mill. and *Argania spinosa* L. skeys. *Industrial Crops and Products* **151**: 112456. <https://doi.org/10.1016/j.indcrop.2020.112456>
- Campos BE, Dias Ruivo T, da Silva Scapim MR, Madrona GS, de C Bergamasco R (2016) Optimization of the mucilage extraction process from chia seeds and application in ice cream as a stabilizer and emulsifier. *LWT – Food Sci Technol* **65**: 874–883. <https://doi.org/10.1016/j.lwt.2015.09.021>
- Carmena R, Ascaso JF, Camejo G, Varela G, Hurt-Camejo E, Ordovas JM, Martinez-Valls J, Bergstöm M, Wallin B (1996) Effect of olive and sunflower oils on low density lipoprotein level, composition, size, oxidation and interaction with arterial proteoglycans. *Atherosclerosis* **125**: 243–255. [https://doi.org/10.1016/0021-9150\(96\)05882-0](https://doi.org/10.1016/0021-9150(96)05882-0)
- Chew SC, Tan CP, Long K, Nyam K-L (2016) Effect of chemical refining on the quality of kenaf (*Hibiscus cannabinus*) seed oil. *Industrial Crops and Products* **89**: 59–655. <https://doi.org/10.1016/j.indcrop.2016.05.002>
- Choe E, Min DB (2006) Mechanisms, and factors for edible oil oxidation. *Compr Rev Food Sci Food Saf* **5**: 169–186. <https://doi.org/10.1111/j.1541-4337.2006.00009.x>
- Coorey R, Tjoe A, Jayasena V (2014) Gelling properties of chia seed and flour. *J Food Sci* **79**: E859–E866. <https://doi.org/10.1111/1750-3841.12444>
- Das A (2018) Advances in chia seed research. *Adv Biotechnol Microbiol* **5**: 5–7. <https://doi.org/10.19080/AIBM.2017.05.555662>
- Dimitrijevic A, Horn R (2018) Sunflower hybrid breeding: from markers to genomic selection. *Front Plant Sci* **8**: 2238. <https://doi.org/10.3389/fpls.2017.02238>
- de Falco B, Fiore A, Rossi R, Amato M, Lanzotti V (2018) Metabolomics driven analysis by UAE-GC-MS and antioxidant activity of chia (*Salvia hispanica* L.) commercial and mutant seeds. *Food Chem* **254**: 137–143. <https://doi.org/10.1016/j.foodchem.2018.01.189>
- Flagella Z, Rotunno T, Tarantino E, Di Caterina R, De Caro A (2002) Changes in seed yield and oil fatty acid composition of high oleic sunflower (*Helianthus annuus* L.) hybrids in relation to the sowing date and the water regime. *Eur J Agron* **17**: 221–230. [https://doi.org/10.1016/S1161-0301\(02\)00012-6](https://doi.org/10.1016/S1161-0301(02)00012-6)
- Gharby S, Harhar H, Mamouni R, Matthaus B, Ait Addi EH, Charrouf Z (2016) Chemical characterization and kinetic parameter determination under rancimat test conditions of four monovarietal virgin olive oils grown in Morocco. *OCL* **23**: A401. <https://doi.org/10.1051/ocl/2016014>
- Gharby S, Guillaume D, Elibrahimi M, Charrouf Z (2021) Physico-chemical properties and sensory analysis of deodorized argan

- oil. *ACS Food Sci Technol* **1**: 275–281. <https://doi.org/10.1021/acsfoodscitech.0c00107>
- Gharby S, Charrouf Z (2022) Argan oil: Chemical composition, extraction process, and quality control. *Front Nutr* **8**: 804587. <https://doi.org/10.3389/fnut.2021.804587>
- Gnanaprakasam A, Sivakumar VM, Surendhar A, Irumarimurugan M, Kannadasan T (2021) Recent strategy of biodiesel production from waste cooking oil and process influencing parameters: a review. *J Energy* **2013**: Article ID 926392. <https://doi.org/10.1155/2013/926392>
- Grancieri M, Martino HSD, Gonzalez de Mejia E (2019) Chia seed (*Salvia hispanica* L.) as a source of proteins and bioactive peptides with health benefits: a review. *Compr Rev Food Sci Food Saf* **18**: 480–499. <https://doi.org/10.1111/1541-4337>
- Hussain A, Khan AA, Ali M, Iqbal J, Iqbal Z, Ullah Q, Zamani GY, Shahzad M, Aziz T (2022) *In-vitro* and *In-vivo* Assessment of toxic effects of *Parthenium hysterophorus* leaves extract. *J Chil Chem Soc* **67**: 5484–5489. <http://doi.org/10.4067/S0717-97072022000205484>
- Ixtaina VY, Nolasco SM, Tomás MC (2008) Physical properties of chia (*Salvia hispanica* L.) seeds. *Ind Crops Prod* **28**: 286–293. <https://doi.org/10.1016/j.indcrop.2008.03.009>
- Jimoh FO, Odutuga AA (2004) Histological changes of selected rat tissues following the ingestion of thermally oxidized groundnut oil. *Biokemistri* **16**: 1–10
- Khan AA, Zeb A, Sherazi ST (2017) Thermally oxidized olive oil produces biochemical, physiological effects and fatty liver in rats. *Chiang Mai J Sci* **44**: 847–857. <https://www.thaiscience.info/journals/Article/CMJS/10985831.pdf>
- Khan S, Khan AA, Zamani GY, Ihsan F (2022) The effects of *Camellia sinensis* (Green Tea) against oxidized *Helianthus annuus* (Sunflower) oil in rabbits. *Bioscience Res* **19**: 844–852
- Knez Hrnčić M, Ivanovski M, Cör D, Knez Ž (2019) Chia seeds (*Salvia hispanica* L.): An overview-phytochemical profile, isolation methods, and application. *Molecules* **25**:11. <https://doi.org/10.3390/molecules25010011>
- Kritchevsky D, Tepper SA, Chen SC, Meijer GW, Krauss RM (2000) Cholesterol vehicle in experimental atherosclerosis. 23. Effects of specific synthetic triglycerides. *Lipids* **35**: 621–625. <https://doi.org/10.1007/s11745-000-0565-3>
- Lou Bonafonte JM, Fitó M, Covas MI, Farràs M, Osada J (2012) HDL-related mechanisms of olive oil protection in cardiovascular disease. *Curr Vasc Pharmacol* **10**: 392–409. <https://doi.org/10.2174/157016112800812827>
- Mesembe OE, Ibanga I, Osim EE (2004) The effects of fresh and thermoxidized palm oil diets on some haematological indices in the rat. *Nigerian J Physiol Sci* **19**. <https://doi.org/10.4314/njps.v19i1.32641>
- Mohd Ali N, Yeap SK, Ho WY, Beh BK, Tan SW, Tan SG (2012) The promising future of chia, *Salvia hispanica* L. *J Biomed Biotechnol* **1**–9. <https://doi.org/10.1155/2012/171956>
- Muñoz LA, Cobos A, Diaz O, Aguilera JM (2012) Chia seeds: Microstructure, mucilage extraction and hydration. *J Food Eng* **108**: 216–224. <https://doi.org/10.1016/j.jfoodeng.2011.06.037>
- Quiles JL, Aguilera C, Mesa MD, Ramírez-Tortosa MC, Baró L, Gil A (1998) An ethanolic-aqueous extract of *Curcuma longa*. decreases the susceptibility of liver microsomes and mitochondria to lipid peroxidation in atherosclerotic rabbits. *Biofactors* **8**: 51–57. <https://doi.org/10.1002/biof.5520080110>
- Reyes-Caudillo E, Tecante A, Valdivia-López MA (2008) Dietary fiber content and antioxidant activity of phenolic compounds present in Mexican chia (*Salvia hispanica* L.) seeds. *Food Chem* **107**: 656–663. <https://doi.org/10.1016/j.foodchem.2007.08.062>
- Sana, Ur Rahman S, Zahid M, Khan AA, Aziz T, Iqbal Z, Ali W, Khan FF, Jamil S, Shahzad M, Alharbi M, Alshammari A (2022) Hepato-protective effects of walnut oil and *Caralluma tuberculata* against paracetamol in experimentally induced liver toxicity in mice. *Acta Biochim Pol* **69**: 871–878. https://doi.org/10.18388/abp.2020_6387
- Segura-Campos MR, Ciau-Solis N, Rosado-Rubio G, Chel-Guerrero L, Betancur-Ancona D (2014) Chemical and functional properties of chia seed (*Salvia hispanica* L.) gum. *Int J Food Sci* **2014**: 241053. <https://doi.org/10.1155/2014/241053>
- Shue GM, Douglass CD, Firestone D, Friedman L, Sage JS (1968) Acute physiological effects of feeding rats non-urea-adducting fatty acids (urea-filtrate). *J Nutr* **94**: 171–177. <https://doi.org/10.1093/jn/94.2.171>
- Silva C, Garcia VAS, Zanette CM (2016) Chia (*Salvia hispanica* L.) oil extraction using different organic solvents: Oil yield, fatty acids profile and technological analysis of defatted meal. *Int Food Res J* **23**: 998–1004. [http://www.ifrj.upm.edu.my/23%20\(03\)%202016/\(13\).pdf](http://www.ifrj.upm.edu.my/23%20(03)%202016/(13).pdf)
- Toscano LT, da Silva CS, Toscano LT, de Almeida AE, Santos Ada C, Silva AS (2014) Chia flour supplementation reduces blood pressure in hypertensive subjects. *Plant Foods Hum Nutr* **69**: 392–398. <https://doi.org/10.1007/s11130-014-0452-7>
- Ullah R, Nadeem M, Khalique A, Imran M, Mehmood S, Javid A, Hussain J (2016) Nutritional, and therapeutic perspectives of Chia (*Salvia hispanica* L.): a review. *J Food Sci Technol* **53**: 1750–1758. <https://doi.org/10.1007/s13197-015-1967-0>
- United States Department of Agriculture Foreign Agricultural Service Oilseeds: World Markets and Trade. 2022. <https://apps.fas.usda.gov/psdonline/circulars/oilseeds.pdf>
- Vidrih R, Vidaković S, Abramović H (2010) Biochemical parameters, and oxidative resistance to thermal treatment of refined and unrefined vegetable edible oils. *Czech J Food Sci* **28**: 376–384. <https://www.agriculturejournals.cz/pdfs/cjf/2010/05/04.pdf>
- Qian Y, Rudzińska M, Grygier A, Przybylski R (2020) Determination of triacylglycerols by HTGC-FID as a sensitive tool for the identification of rapeseed and olive oil adulteration. *Molecules* **25**: 3881. <https://doi.org/10.3390/molecules25173881>
- Zeb A, Khan AA (2019) Improvement of serum biochemical parameters and hematological indices through α -Tocopherol administration in dietary oxidized olive oil induced toxicity in rats. *Front in Nutr* **5**: 137. <https://doi.org/10.3389/fnut.2018.00137>
- Zeb A, Rahman SU (2017) Protective effects of dietary glycine and glutamic acid toward the toxic effects of oxidized mustard oil in rabbits. *Food Funct* **8**: 429–436. <https://doi.org/10.1039/c6fo01329e>

Characterization and gastroprotective effects of *Rosa brunonii* Lindl. fruit on gastric mucosal injury in experimental rats – A preliminary study

Ejaz Ahmad¹✉, Muhammad Jahangir¹, Zahid Mahmood Akhtar², Tariq Aziz³✉, Metab Alharbi⁴, Abdulrahman Alsahammari⁴, Abdullah F. Alasmari⁴ and Nadeem Irfan Bukhari⁵

¹Department of Chemistry, GC University Lahore, Pakistan; ²Department of Pathology, Gujranwala Medical College, Gujranwala, Pakistan; ³Department of Agriculture, University of Ioannina, 47100 Arta, Greece; ⁴Department of Pharmacology and Toxicology, College of Pharmacy, King Saud University, P.O. Box 2455, Riyadh 11451, Saudi Arabia; ⁵University College of Pharmacy, University of the Punjab, Lahore, Pakistan

Gastric ulcer is the most prevalent disorder affecting a large population. *Rosa brunonii* Lindl. fruit (RBF) has traditionally been used to treat stomach pains. Therefore, the current work aimed to isolate, characterize, and investigate the gastro-protective effect of *Rosa brunonii* Lindl. fruit chloroform extract (RBFCE) against ethanol-induced gastric ulcers in rats. Quercetin 3-O-glucoside (QUE-G) was isolated and characterized by modern spectroscopic techniques. RBFCE was orally administered at 250 mg/kg, 500 mg/kg, and 750 mg/kg doses for ten days. Gastric ulcer was induced by a single dose of absolute ethanol (5 ml/kg) on the last day of the study. Histological changes were calculated, along with ulcer inhibition and the ulcer index (UI). Gastric juice volume, pH, acidity, mucus content, and protein content were evaluated to understand the mechanism underlying its gastroprotective effect. Omeprazole (OMP) was used as the positive control. RBFCE at a dose of 750 mg/kg significantly ($p < 0.01$) reduced the UI (3.54) and increased the protection rate (67.63%) compared to the negative (ulcer) control group. Treatment with RBFCE in a dose-dependent manner increased the gastric pH, mucus content, and total protein while decreasing gastric juice volume and total acidity. Histopathological studies showed severe gastric mucosal injury and edema in ulcer control animals compared to extract-treated groups. This study demonstrated that oral administration of RBFCE possesses a significant gastroprotective effect due to its anti-secretory and cytoprotective mechanisms. Our findings support the traditional use of RBF to treat the gastric ulcer.

Keywords: gastroprotective, *Rosa brunonii* Lindl. fruit, ulcer, quercetin 3-O-glucoside

Received: 02 April, 2023; **revised:** 21 April, 2023; **accepted:** 05 May, 2023; **available on-line:** 18 August, 2023

✉e-mail: iwockd@gmail.com (TA); ejaz_ravian@yahoo.com (EA)

Acknowledgements of Financial Support: The authors greatly acknowledge and express their gratitude to the Researchers Supporting Project number (RSP2023R462), King Saud University, Riyadh, Saudi Arabia.

Abbreviations: NSAIDs, non-steroidal anti-inflammatory drugs; OMP, Omeprazole; RBFCE, *Rosa brunonii* Lindl. fruit chloroform extract; QUE-G, Quercetin 3-O-glucoside; UI, ulcer index

INTRODUCTION

Gastric ulcer is one of the common digestive disorders affecting 10% of world population. It is a complex and multifactorial disease, characterized by pathological lesion

in digestive tract, gastrointestinal bleeding, perforations and erosions of gastric mucosa (Saranya *et al.*, 2011). It occurs as a result of imbalance between invasive and defensive factors. Stress, smoking, alcohol consumption, nutritional deficiencies, infection by *Helicobacter pylori* (Yu *et al.*, 2022) and use of non-steroidal anti-inflammatory drugs (NSAIDs) cause imbalance in the gastric acid, pepsin, mucus secretion, prostaglandins and sulfhydryl compounds (Zakaria *et al.*, 2016b). The imbalanced secretions cause mucosal damage, which can lead to perforations and bleeding if not treated properly (Yuan *et al.*, 2006; Balan *et al.*, 2014; Kangwan *et al.*, 2014; Khoder *et al.*, 2016; Kim *et al.*, 2019). Conventional pharmacotherapeutic treatments for gastric ulcers include acid suppressants, that may have certain side effects like impotence, osteoporotic bone fracture, gynecomastia and iron deficiencies (Baiubon *et al.*, 2016; Zakaria *et al.*, 2016b; Yu *et al.*, 2017). Furthermore, the symptoms of gastric ulcers may usually reoccur on discontinuation of antiulcer therapy (Kangwan *et al.*, 2014). Consequently, antiulcer remedies with minimal side effects are required for possibility of their long use (Kang *et al.*, 2009). Mucosal protective agents can be a good alternative as they are considered to have relatively low side effects (Shim *et al.*, 2017). Beside use of synthetic drugs to cure gastric ulcers, people also rely on phytomedicines as an alternative therapeutic source which being natural are considered without side effects (Rozza *et al.*, 2012; Chatterjee *et al.*, 2014).

Rosa brunonii Lindl., also called “Himalayan musk rose,” is a member of the *Rosaceae* family and found in the western Himalayas. Locals use the plant’s roots, known as “*Rajatarini*,” to cure inflammation in the eyes. Plant flowers are used to produce gulkand, a sweet preserve used as a laxative and a remedy for stomach aches. Literature reported substantial in-vitro antioxidant activity of crude extract from *Rosa brunonii* Lindl. flowers (Ahmad *et al.*, 2020). Some of the compounds such as quercetin-3-O-rhamnoside, astragalin and tiliroside were isolated from RBF such as quercetin-3-O-rhamnoside, astragalin with strong antioxidant properties (Ishaque *et al.*, 2017) which increased the medicinal value of RBF. RBFCE possess significant hepatoprotective potential against Rifampicin/Isoniazid induced toxicity in rats. It possess various classes of phytochemicals including cardiac glycosides, flavonoids, steroids, phenolic compounds, terpenoids, anthraquinones and proteins (Ahmad *et al.*, 2020).

Rosa brunonii Lindl. is of particular interest due to its widespread use in folklore medicine and the presence of

highly antioxidant bioactive secondary metabolites. Furthermore, no reports showing gastroprotective effects of RBFCE were found in the literature, which encouraged us to appraise the possible anti-ulcer potential of the plant (Aziz *et al.*, 2023; Saleem *et al.*, 2023, Sana *et al.*, 2022). Given the preceding, the current study sought to isolate and characterize bioactive metabolites from RBFCE and investigate its potential gastroprotective effects in ethanol-induced gastric ulcers in rats. The medium polar chloroform fraction was selected for the study due to the ease of separating bioactive secondary metabolites for further trials.

MATERIALS AND METHODS

Collection of plant material

Fruits and leaves of *Rosa brunonii* Lindl. were collected from Murree, Punjab Pakistan, identified at Department of Botany, GC University, Lahore (Pakistan) under voucher specimen number, GC.Herb.Bot.3314 for future reference.

Chemicals and Reagents

Omeprazole (Dr. Reddy Pharma, India) and carboxymethylcellulose (CMC) (India) were kindly provided by Next Pharmaceuticals (Pvt) Ltd. Pakistan. Silica gel (Merck), Bovine serum albumin (BSA) and Alcian blue dye 8GX were obtained from BioShop (Canada) and Uni-chem (China). Ethanol, methanol, hexane, dimethyl sulphoxide, chloroform (CHCl_3) and ethyl acetate were obtained from Sigma Aldrich Chemicals (Germany) and of analytical grade.

Preparation of extract

The fruits of *Rosa brunonii* Lindl. were washed with distilled water, shade-dried, and crushed using a mechanical grinder. Extraction was carried out by reported maceration method with slight modifications (Sambandam *et al.*, 2016). Finely ground powdered material (500 g) was dipped into 5 L of CHCl_3 . The extract was filtered, and the solvent was evaporated using a rotary evaporator. The resulting semisolid residue was weighed and kept at -4°C in an airtight container for later use. The semisolid residue was fractionated using a solvent extraction technique that began with hexane and progressed through chloroform, ethyl acetate, and methanol. The chloroform fraction was dried, examined, and evaluated for anti-ulcer activity.

Isolation and characterization of compound

Isolation was carried out by using conventionally reported isolation method with slight modifications (Ahmadu *et al.*, 2007). Silica gel (60 mesh) was added in hexane to form slurry and loaded into the column. The column was packed carefully by minimizing the bubble interruption. Sample of RBFCE weighing about 187 g was loaded onto the column packed with silica gel. Separation was started with non-polar solvent, hexane as an eluent. Polarity of the eluent was raised by mixing 10% CHCl_3 at one time and up to 100% CHCl_3 . In order to further raise the polarity of the eluent, 10% ethyl acetate was added at each step. Thin layer chromatography (TLC) was continuously carried out after every 10% rise in polarity of eluent. Fractions showing same Rf values were combined and at the end (1-6), (11-16) and (19-25) fractions were obtained.

On the basis of TLC, fractions (19-25) were loaded onto the Sephadex LH-20 column and eluted with ethyl acetate and polarity was increased by adding 25% CH_3OH at each step. At 100% CH_3OH as an eluent, polarity was further raised by adding 1.0% water in the eluent. At polarity of 97.0% CH_3OH and 3.0% water, the pure compound was eluted and showed single spot on TLC plate under UV light at mobile phase ratio of ethyl acetate, methanol and water (10:5:3) and (7:5:3). The isolated compound was weighed using calibrated Sartorius TE214S weighing balance. Melting point of compound was determined using Melting point apparatus (SMP-10), FTIR of the compound was performed on IR Prestige-21, NMR spectra was obtained on NMR, Bruker (500 MHz) and mass was determined by LC-MS/MS (Agilent).

Experimental animals

The experiment was carried out on healthy adult Wistar albino rats of either sex (172–204 g) obtained from a local animal house facility and acclimatized for 1 week under standard environmental conditions with free access to food and water ad libitum. The study was carried out according to the protocols approved by the Animal Ethical Committee of the University of Punjab, College of Pharmacy. The animals were divided into different groups, detailed in the proceeding text.

Acute toxicity study

The acute toxicity of RBFCE was studied to determine the safe dose of the extract. Rats were divided into three groups ($n=6$ in each) and given a vehicle (CMC, 5 ml/kg), a low dose (1000 mg/kg), a medium dose (2500 mg/kg), and a high dose (5000 mg/kg) of RBFCE. Before dosing, rats were deprived of food for 24 h with free access to water. Food was also withheld for another 4 hours after dosing. Animals were monitored for morbidity and mortality for 4 hours and then daily for 14 days.

Determination of gastroprotective effect

The gastroprotective effect of RBFCE was studied in an ethanol-induced gastric ulcer rat model, which was deprived of water just 2 h before starting the experimental procedure. The animals were randomly divided into six groups ($n=6$) and treated for 14 days with extract and drug as follows:

Normal control group: Animals received drinking water to show the normal gastric parameters.

Negative control group: Animals were given vehicle solution 5 ml/kg 0.5% CMC. (Hariprasath *et al.*, 2012; Rahim *et al.*, 2014). This group was only included to check the effect of CMC on gastric parameters.

Positive control group: Animals were given OMP (20 mg/kg p.o, OD) for 14 consecutive days (Al-Wajeeh *et al.*, 2016).

Low dose RBFCE group: Animals were given RBFCE (250 mg/kg/p.o, OD) for 14 consecutive days.

Medium dose RBFCE group: Animals were given RBFCE (500 mg/kg/p.o, OD) for 14 consecutive days.

High dose RBFCE group: Animals were given RBFCE (750 mg/kg/p.o, OD) for 14 consecutive days.

All therapies were given through intragastric gavage. After 30 min of above mentioned treatments, 10% ethanol solution was given orally to all animals on the first day of the trial, with the exception of the normal control group. From second day of trial, animals in all other

groups received 30% (v/v) ethanol orally for 14 days, except normal control group.

Sample collection and processing

On the 14th day, all animals were anesthetized with an overdose of xylazine and ketamine and sacrificed after 1 h of ethanol administration (Ketuly *et al.*, 2013). After cutting stomach tissues along the larger curvature, gastric contents were collected in glass tubes. Gastric mucosa was inspected after stomach tissues were cleaned with ice-cold normal saline (Das *et al.*, 2012). The number of lesions, their details, and their scores was all recorded. Stomach tissues were then fixed in 10% formalin solution to evaluate histopathological parameters (Qaiser *et al.*, 2018).

Macroscopic and microscopic evaluation

The excised stomach tissues were observed under magnifying glass and dissecting microscope to count lesions present on inner side of the stomachs (Dashputre *et al.*, 2011; Qaiser *et al.*, 2018).

Ulcer scoring

Ulcer scoring was carried out as follows on the basis of their intensity (Raju *et al.*, 2009).

0	No ulcer
0.5	reddish mucosa
1	red spots
1.5	hemorrhagic streaks
2	profound ulcers
3	punctures/perforations

Ulcer index

Ulcer index was calculated using the formula (Ahmad *et al.*, 2015; Gul *et al.*, 2015).

$$\text{Ulcer Index} = [\text{UN} + \text{US} + \text{UP}] \times 10^{-1}$$

Where UN=average number of ulcers per animal, US=average of severity score, and UP=percentage of animals with ulcer.

Percentage protection

The percentage protection by RBFCE was calculated by the following formula and compared with negative control group (Raju *et al.*, 2009).

$$\% \text{ age protection} =$$

$$\frac{[\text{Ulcer index of ethanol treated group}] - [\text{Ulcer index of treated group}]}{[\text{Ulcer index of ethanol treated group}]} \times 100$$

Estimation of gastric content volume, pH and total acidity

Following the stomach opening, the entire gastric contents were put into the test tubes and centrifuged for 10 minutes at 1000 rpm. The volume and pH of the supernatant were determined using a 5 mL burette and a pH metre (Thermo Orion thermoscientific 3-star). The supernatant (1 ml) was titrated against freshly prepared 0.1N NaOH using phenolphthalein as an indicator (Shukla *et al.*, 2017). Correction factor of 0.1 N NaOH was also calculated.

$$\text{Total activity} =$$

$$\frac{[\text{Volume of NaOH used}] \times [\text{Normality of NaOH used}] \times 100}{n.1}$$

Results were expressed in terms of the clinical units (mEq/L).

Gastric mucous content determination

Estimation of gastric mucous content was carried out by using standard curve of alcian blue according to the reported protocol (Hajrezaie *et al.*, 2015).

Protein content determination

Protein content was assessed by using standard curve of bovine albumin solution (BSA standard curve) (Markwell *et al.*, 1981).

Histopathological investigations of gastric ulcer

The separated stomachs were sliced along the larger curvature and rinsed in ice-cold normal saline. The stomach tissues were partially preserved in a 10% formalin solution and further processed by embedding them in paraffin wax. For histological investigation, 3–5 mm thick slices were cut and stained with hematoxylin and eosin (Hajrezaie *et al.*, 2015). The sections were photographed after being evaluated under a light microscope for histological changes such as ulceration, decongestion, necrosis, congestion, and erosions on an arbitrary scale (Bancroft *et al.*, 2013).

Statistical analysis

Data was articulated as the mean \pm S.E.M., where applicable. Data for gastric content volume, pH, total acidity, percentage protection and protein content were analyzed using one-way analysis of variance (ANOVA). Tukey's post hoc multiple comparison test was applied for determination of statistical difference among all groups. $p < 0.05$ considered significant. Graph Pad Prism® (Version 8.0.1 (244) for Windows) was used for statistical calculations and plotting graphs.

RESULTS

Acute oral toxicity

During the observation period, no behavioral changes or signs of toxicity were observed in any of the treated rats. During the 14-day observation period following oral administration of all three doses of RBFCE, none of the rats died.

Characterization of isolated compound

Characterization of the isolated compound was carried out by spectral studies such as IR, NMR, and mass spectroscopy and melting range. The observed data was examined and compared with the published data for pos-

Table 1. Physical characteristics of the isolated compound.

Source	<i>Rosa brunonii</i> Lindl. Fruit
state	Yellowish powder
yield	34 mg
molecular weight	464.3
molecular formula	C ₂₁ H ₂₀ O ₁₂
melting range	233–237

Table 2. ^{13}C and ^1H NMR data of isolated compound

C.No	Multiplicity	^{13}C -NMR (δ)		^1H -NMR (δ)	
		Experimental	Reported (Kuruüzüm-Uz <i>et al.</i> , 2013)	Experimental	Reported (Kuruüzüm-Uz <i>et al.</i> , 2013)
O					
C-2	C	157.61	157.30		
C-3	C	134.22	134.50		
C-4	C	178.08	178.30		
C-5	C	161.63	161.90		
C-6	CH	98.49	98.90	6.21, d ($J=2.0$ Hz)	6.18 d ($J=2.0$ Hz)
C-7	C	164.63	165.30		
C-8	CH	93.31	93.60	6.40, d ($J=2.0$ Hz)	6.37 d ($J=2.0$ Hz)
C-9	C	157.06	157.80		
C-10	C	104.28	104.40		
C-1'	C	121.79	121.90		
C-2'	CH	114.60	114.80	7.73, d ($J=2.5$ Hz)	7.70, d ($J=2.0$ Hz)
C-3'	C	144.50	144.70		
C-4'	C	148.44	148.70		
C-5'	CH	116.16	116.40	6.89, d ($J=8.6$ Hz)	6.86, d ($J=8.4$ Hz)
C-6'	CH	121.67	122.00	7.61, dd ($J=8.5, 2.5$ Hz)	7.58, dd ($J=8.4, 2.0$ Hz)
C-1''	CH	102.93	103.20	5.26, d ($J=7.5$ Hz)	5.22, d ($J=7.6$ Hz)
C-2''	CH	74.33	74.60	3.37, t ($J=9.5$ Hz)	†
C-3''	CH	76.98	77.00	3.73, dd ($J=2.5, 12.0$ Hz)	†
C-4''	CH	69.81	70.10	3.59, dd ($J=5.5, 12$ Hz)	†
C-5''	CH	76.71	77.20	3.25, m	†
C-6''	CH ₂	61.15	61.40	3.51, m	†

sible flavonoid glycoside and found matched with QUE-G. The observations regarding compound under study are as follows in Table 1.

The proton NMR showed peaks in aromatic region and the presence of a sugar moiety. The splitting of aromatic proton exhibited two distinct coupling patterns, one was meta coupling ($J=2.0$ Hz) and the other 1,4,5 coupling pattern. As hydroxyl was normally appeared at carbon number 5 in flavonoid that normally hydrogen bonded with carbonyl, therefore meta coupling could be suggested in A ring and 3,4-disubstituted pattern in B ring of flavonoid that was also matched with the published data (Table 2). Anomeric proton appeared at δ 5.2 ppm as doublet and six other protons from 3.60 to 3.25 δ ppm due to possible sugar moiety. The experimental data was matched with the NMR data of QUE-G according to literature.

IR spectrum confirms the characteristic of flavonol system. Peaks at wave numbers 3214 cm^{-1} indicates OH-stretching and at 1671 cm^{-1} confirms presence of $\text{C}=\text{O}$ group. Similarly, the molecular formula of isolated compound was determined as $\text{C}_{21}\text{H}_{20}\text{O}_{12}$ by NMR and mass spectrum. The molecular weight (464.30 g/mol) of the isolated compound also confirms the isolated compound as QUE-G (Fig. 1). Melting range of the isolated

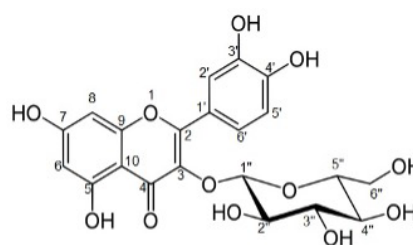


Figure 1. Structure of quercetin-3-O-glucoside.

compound ($233\text{--}237^\circ\text{C}$) confirms that compound under study is QUE-G as it has melting point 236°C .

Macroscopic evaluation of stomach tissue treated with RBFCE

Macroscopic evaluation of control animals showed the normal mucosa without any signs of erosion/ulceration. Gross appearance of ulcer control tissue exhibited various notable lesions and signs of ulcerations. No remarkable signs of ulcerations were observed in the positive control group. On the other hand, macroscopic evaluation of low dose RBFCE treated group showed marked degree of erosion as compared to medium and high

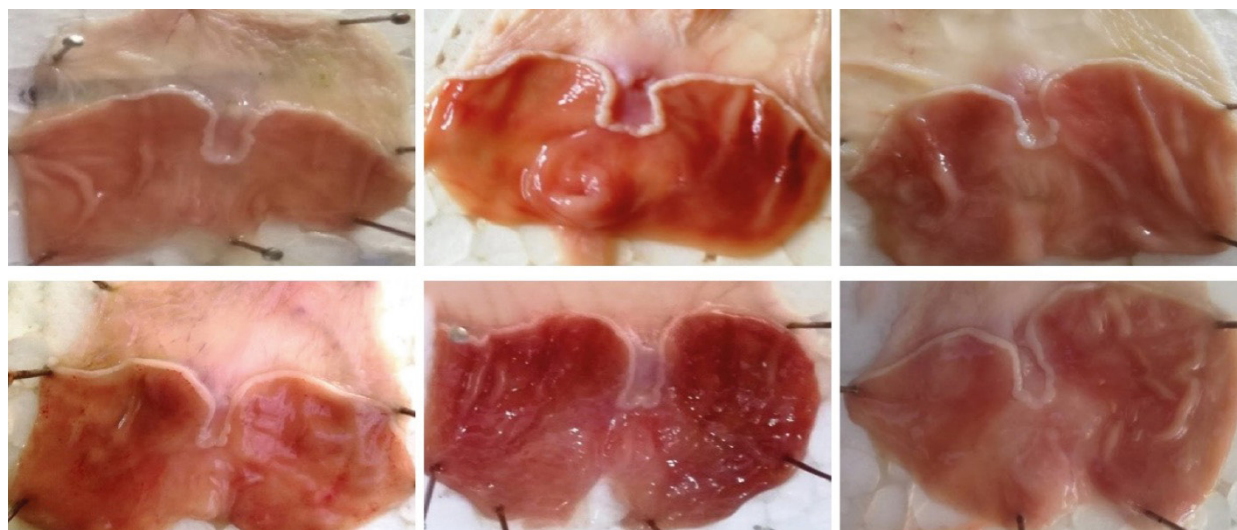


Figure 2. Macroscopic examination of:

(a) Normal rats (b) Rats pre-treated with CMC (negative control group) showing severe mucosal injuries (c) OMP 20 mg/kg (positive control) showing normal looking mucosa (d) RBFCE 250 mg/kg treated group indicates surface erosions (e) RBFCE 500 mg/kg treated group indicates relatively protected mucosal surface with only focal erosion (f) RBFCE 750 mg/kg treated group indicates no injuries to gastric mucosa.

Table 3. Title!

Group	Mean \pm S.E.M.				
	Ulcer no	Ulcer Score	Ulcer Incidence (%)	Ulcer index	Ulcer Inhibition (%)
Normal Control	0	0	0	0	0
Negative control	4.5 \pm 0.67 ***	4.92 \pm 0.46***	100	10.94	0
Positive control	0.67 \pm 0.42	1.17 \pm 0.74	33.33	3.52	68.20
Low dose RBFCE	3.33 \pm 0.30	3.60 \pm 1.00	82.00	8.90	18.72
Medium dose RBFCE	*3.00 \pm 0.40	*2.70 \pm 0.90	68.00	7.40	32.67
High dose RBFCE	**2.20 \pm 0.60	**1.92 \pm 0.70	56.00	6.00	45.10

The results are expressed in the form of mean \pm S.E.M. Significant at $p < 0.05^*$, 0.01^{**} and 0.001^{***} , ns=not significant compared to negative control.

Table 4. Effect of RBFCE on gastric juice parameters

Sr. No.	Group Name	Gastric volume (mL)	Gastric pH	Total acidity (mEq/L)
1	Normal control	1.33 \pm 0.25	4.03 \pm 0.18	27.5 \pm 3.45
2	Negative control	3.97 \pm 0.49***	2.9 \pm 0.26	89.83 \pm 3.0***
3	Positive control	1.4 \pm 0.26	6.48 \pm 0.18	37.5 \pm 3.80
4	Low dose RBFCE	**2.53 \pm 0.30	*3.22 \pm 0.34	***67.66 \pm 7.80
5	Medium dose RBFCE	***2.30 \pm 0.29	**3.60 \pm 0.40	***58.60 \pm 5.10
6	High dose RBFCE	***1.95 \pm 0.50	***4.40 \pm 0.30	***52.00 \pm 6.00

dose treated groups. Gross appearance of gastric mucosa showed milder injuries in low dose extract treated group compared to medium and high dose and negative control groups as shown in Fig. 2.

Effect of RBFCE on ulcer score, ulcer index and percentage protection

Ethanol administration significantly ($p < 0.001$) increased the ulcer score (Mean=4.91 \pm 1.11) and ulcer index (Mean=10.94) in negative control group compared to the normal animals (0 ± 0.00). Low dose of RBFCE decreased ($p > 0.05$) the ulcer score to

–26.80% (Mean=3.60 \pm 1.00), ulcer index to –18.72% (Mean=8.90) and increased the percentage protection by 18.72% compared to the negative control group. Likewise, oral administration of medium dose of RBFCE reduced ($p < 0.05$) the ulcer score to –45.80% (Mean=2.70 \pm 0.90), ulcer index to –32.70% (Mean=7.40) and increased the percentage protection by 32.67% compared to the negative control group. Moreover, high dose of RBFCE reduced ($p < 0.01$) the ulcer score to –61.0% (Mean=1.92 \pm 0.70), ulcer index to –45.10% (Mean=6.00) and increased the percentage

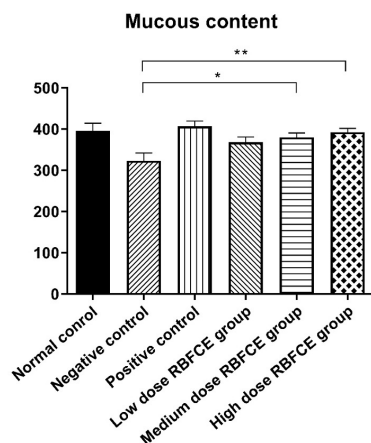


Figure 3. Mucous content of normal, negative control, positive control, low dose RBFCE, medium dose RBFCE and high dose RBFCE groups. The results of low, medium and high dose RBFCE groups were compared with negative control group.

protection by 45.10 % compared to the negative control group (Table 3).

Effect of RBFCE on Gastric content volume, acidity, pH

Ethanol administration significantly ($p < 0.001$) increased the gastric content volume and acidity ($p < 0.001$) by 197.5% (Mean = 3.96 ± 1.19) and 226.70% (Mean = 89.83 ± 7.35) while decreased the pH -28.10% (Mean = 2.90 ± 0.64), respectively compared to the normal group. Low dose of RBFCE reduced ($p < 0.05$) the gastric content volume to -36.13% (Mean = 2.53 ± 0.30), acidity ($p < 0.05$) to -24.70% (Mean = 67.66 ± 7.80) and increased the pH ($p < 0.05$) by 10.92% (Mean = 3.22 ± 0.34) compared to the negative control group. Likewise, medium dose of RBFCE reduced ($p < 0.01$) the gastric content volume to -42.90% (Mean = 2.30 ± 0.29), acidity ($p < 0.01$) to -34.70% (Mean = 58.60 ± 5.10) and increased the pH by 23.0% (Mean = 3.60 ± 0.40), compared to the negative control animals. High dose of RBFCE reduced ($p < 0.01$) the gastric content volume to -50.84% (Mean = 1.95 ± 0.50), acidity ($p < 0.01$) to -42.10% (Mean = 52.00 ± 6.00) and increased the pH by ($p < 0.01$) 50.60% (Mean = 4.40 ± 0.30) in comparison with negative control group (Table 4).

Effect of RBFCE on mucous and protein content

Ethanol administration to negative control group significantly decreased the mucous and protein content ($p < 0.05$) by -18.32% (Mean = 323.33 ± 45.46) and protein by -47.94% (Mean = 36.24 ± 5.57) ($p < 0.01$), respectively, compared to the normal group as shown in Fig. 1 and 2, respectively. Oral treatment of low dose of RBFCE increased ($p < 0.05$) the mucous content by 9.28% (Mean = 368.17 ± 12.27), and protein content 10.82% (Mean = 45.50 ± 2.03) compared to the negative control group. Likewise, oral administration of medium dose of RBFCE increased the mucous content ($p < 0.05$) 18.60% (Mean = 380.16 ± 10.12) and protein content by 29.70% (Mean = 53.17 ± 2.04) ($p < 0.01$), compared to the negative control group. Oral treatment of high dose of RBFCE increased the mucous content (Fig. 3) ($p < 0.05$) by 21.40% (Mean = 392.66 ± 9.01) and protein content by 56.92% (Mean = 56.87 ± 2.41) ($p < 0.001$) compared to the negative control group as shown in Figs. 4 and 5.

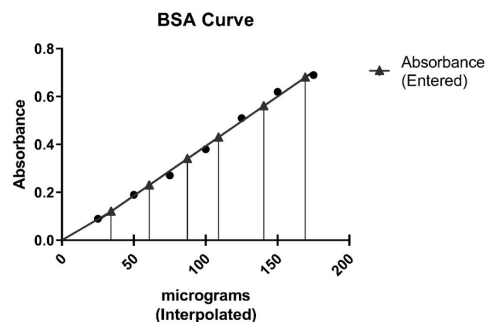


Figure 4. BSA standard curve

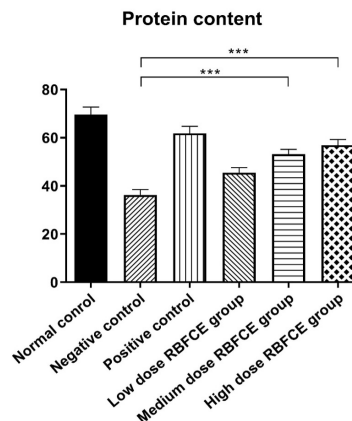


Figure 5. The protein content of normal, negative control, positive control, low dose RBFCE, medium dose RBFCE and high dose RBFCE groups. The low, medium and high dose RBFCE groups were compared with negative control group.

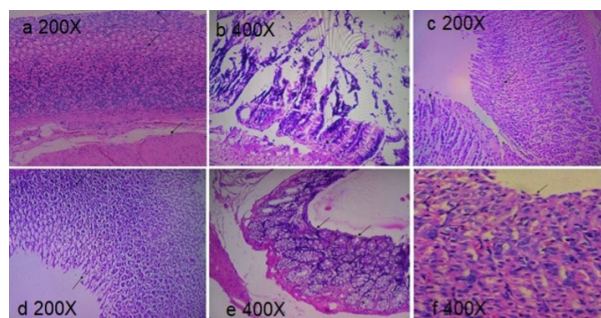


Figure 6. Histopathological evaluation of stomach tissues of : (a) normal rats (b) Rats pretreated with CMC (negative control group) (c) OMP 20 mg/kg (positive control group) (d) RBFCE 250 mg/kg treated group (e) RBFCE 500 mg/kg treated group (f) RBFCE 750 mg/kg treated group. Histopathological images (a), (c) and (d) were magnified at 200X. However, images (b), (e) and (f) were magnified at 400X.

Effect of RBFCE on histopathology of stomach tissue

Histological evaluation of gastric tissue of normal control rats showed the normal looking mucosa without any surface erosion/ulceration. Submucosa and muscularis propria were unremarkable. Rats of negative control group (CMC pre-treated) showed marked degree of mucosal surface ulceration and inflammation. Metaplastic change was also present. On the other hand, animals of positive control group showed only focal erosion. However, no mucosal or submucosal inflammation was seen. Animals of low dose RBFCE (250 mg/kg) treated group

reflected mucosa with focal erosion and inflammation. The histopathological investigations of medium dose RBFCE treated group (500 mg/kg) showed normal surface epithelium having only focal erosion without inflammatory changes. The high dose RBFCE group (750 mg/kg) showed normal looking mucosal epithelium without surface erosion/ulceration and inflammation (Fig. 6).

DISCUSSION

The present study investigated the acute oral toxicity and gastroprotective effect of RBFCE on ethanol-induced gastric ulcer model and its possible mechanism. Characterization of isolated compound, QUE-G confirms the presence of flavonoid class of compound. Flavonoids are safe and effective therapeutic agents for the treatment of gastrointestinal diseases. Previously, QUE-G has been isolated from *Azadirachta indica* (Tatke *et al.*, 2014), *Prangos ferulaceae* (Razavi *et al.*, 2009), *Manibot glaziovii* (Hakim *et al.*, 2020), and *Byrsocarpus Coccineus* etc. (Ahmadu *et al.*, 2007). However, this compound was the first report from RBF. QUE, a naturally occurring bioflavonoid is commonly found as QUE-G in herbs, fruits, and vegetables. Presence of glucose moiety makes QUE more stable compared to aglycone form. Only, a very small quantity of naturally occurring QUE lacks a glycoside chain. Bioavailability of QUE-G is much better than aglycone form (without glycoside chain) (Kaşıkçı *et al.*, 2016), which is commonly available form of QUE as a supplement. It is a globally recognized safe complementary or alternative medicine used for different various comorbidities including heart (Patel *et al.*, 2018), liver (Li *et al.*, 2018), and stomach (Ekström *et al.*, 2011). It also possess anticancer (Vafadar *et al.*, 2020) and neuroprotective potential (Khan *et al.*, 2018; Salehi *et al.*, 2020). QUE inhibits several cytochrome P450 isoenzymes, i.e., CYP3A4, CYP2C8 CYP2C9 and CYP1A2 (Umathe *et al.*, 2008; Samala *et al.*, 2016) and considered to be involved in herb-drug interactions (HDIs). Therapeutic profile of glucoside form is identical to that of aglycone form. QUE also possess significant antiulcer and gastroprotective activity due to its antioxidant, anti-secretory, antihistaminic and proton pump inhibiting properties (de Lira Mota *et al.*, 2009). QUE-G possesses cardiovascular benefits (Terao, 2023).

The toxicity study demonstrated that rats treated with RBFCE did not show any sign of toxicity or mortality and LD50 value was found above 5000 gm/kg. All the three orally administered once daily doses of RBFCE (250, 500, 750 mg/kg) to rats for 10 days for gastroprotective activity, were safe. OMP, a widely used proton pump inhibitor for the treatment of gastric ulcers, was used as positive control, in line with the literature (Nordin *et al.*, 2014). After one hour on last (14th) day of treatment, single dose (5 ml/kg) of absolute ethanol was orally administered to animals. Ethanol is most widely used in experimental models to assess the gastroprotective activity in rats (Sidahmed *et al.*, 2015). It rapidly penetrates into the gastric mucosa, increases mucosal absorptivity (Sidahmed *et al.*, 2013) and releases vasoactive mediators (histamine, leukotrienes C4 and endothelin-1). The vasoactive mediators cause blood flow stasis in circulation of mucous membrane and increasing lesions in mucosa. In addition, ethanol also reduced the mucus production, gastric mucosal blood flow, bicarbonate secretion, prostaglandin production, tissue levels of DNA, RNA and proteins, which leads to tissue injury. Formation of superoxide and reactive oxygen species

generates oxidative stress which, in turn results rupturing of the blood vessels that contributes to the hemorrhage, tissue necrosis and disrupting the protective mucosal layer (Fahmy *et al.*, 2015). In the present study, oral administration of ethanol to rats produced hemorrhagic red streaks of various sizes on the gastric mucosa of the control group. RBFCE pre-treated groups (250, 500, 750 mg/kg) showed protected gastric mucosa and significantly reduced the rate of ethanol-induced damage to the gastric mucosa, compared to the negative control group. RBFCE showed gastroprotective effect in dose dependent manner, comparable to the OMP group (Table 1). Pretreatment with RBFCE significantly reduced UI, maximum being seen at 750 mg/kg, similar to that of the OMP.

Any agent that reduces the gastric acid secretion or increases the mucous secretion is an effective gastroprotective agent (Oliveira *et al.*, 2014). Gastric secretions in rats were studied because they may contribute to RBFCE's gastroprotective action. The ulcer control group had a lower pH, a higher volume of gastric juice, and total acidity. Pre-treatment with either OMP or different doses of RBFCE significantly decreased gastric juice volume and total acidity, coupled with a significant increase in gastric pH when compared to the ulcer control group. Oral administration of RBFCE for 10 days strengthened the gastrointestinal system in such a way that gastric volume and the total acidity was significantly reduced in the treated rats with a corresponding increase in pH compared to the negative control group. A decrease in gastric juice volume could be due to less acid production, as evidenced by the pH and total acidity of the gastric juice. These findings indicated presence of therapeutically active compounds in RBFCE that reduced the acidity of gastric acid secretions, which was increased by ethanol administration. Therefore, anti-secretory effect RBFCE could be a possible mechanism of gastroprotection. The gastric epithelium, which is surrounded by a continuous mucous layer, acts as the first line of mucosal defense against luminal acid by acting as a barrier against luminal pepsin to protect the underlying mucosa from proteolytic digestion. Mucus comprises mucin-type glycoproteins detectable by amount of *alcian blue* binding (Zakaria *et al.*, 2016a). Microscopic evaluation revealed the comprehensive damage to gastric mucosa in ulcer control group (Fig. 2). Animals treated with RBFCE showed protection to gastric mucosa with significant reduction in inflammation in dose dependent manner. The daily RBFCE treatment for 10 days found to amplify the amount of gastric mucous as compared to the vehicle. Increased mucous content may be liable to gastric cytoprotection. Therefore, it may be another possible mechanism of gastroprotective effect of RBFCE.

Stomach from normal control animals in histopathological examination showed normal-looking mucosal surface which indicates absence of any signs of ulceration in normal control group. The presence of focal mucosal inflammation and metaplastic changes in stomach of negative control animals indicates development of ulceration. Gastric metaplastic cells may transform into precancerous cells which increase the risk of gastric cancer if untreated. While the positive control group revealed mucosa and part of submucosa with only focal erosion, but no mucosal or submucosal inflammation was observable. Stomach section from low dose (250 mg/kg) RBFCE treated animals showed mucosa with focal erosion and mild chronic inflammation while the medium dose RBFCE treated group (500 mg/kg) exhibited normal surface epithelium with mild degree of erosion. Rest of the

mucosa was normal looking without evidence of inflammation. On the other hand, high dose RBFCE treated animals (750 mg/kg) revealed normal looking mucosal epithelium without surface erosion/ulceration, metaplastic and inflammatory changes which indicates protective potential of RBFCE at medium and high doses. A high dose of RBFCE could significantly reduce gastric lesions and histological damage in a dose-dependent manner comparable to OMP. The present findings supported the ethnopharmacological use of RBF and highlighted its potential to be used as herbal gastroprotective medicine. Some of the limitations of the research work include (1) study was performed in rats but not in humans (2) only preliminary data was collected (3) study was performed on extract, not on isolated compound.

CONCLUSIONS

RBFCE showed a significant gastroprotective effect against ethanol-induced gastric ulcer, as reflected by a decreased gastric juice volume and acidity, parallel to an increased gastric mucus secretion. The above activity could be attributed to QUE-G, major bioactive flavonoid isolated from RBFCE in this study. These findings deliver considerable evidence in favor of the folk use of RBF in the treatment of gastric disorders.

Declarations

Author Contributions: Conceptualization, E.A, M.J, Z.M.A, N.I.B and T.A.; methodology, E.A, M.J, Z.M.A, N.I.B and T.A.; software, T.A.; validation, A.A.S.; formal analysis, T.A.; investigation, E.A, M.J, Z.M.A, N.I.B and T.A.; resources, M.A and A.A.S.; data curation, T.A.; writing—original draft preparation, T.A and E.A; writing—review and editing, T.A and A.F.A; visualization, A.A.S; supervision, T.A and B.I.; project administration, A.A.S and M.A ; funding acquisition, T.A

Funding: This research work received no external funding.

Data Availability statement: We have presented all our data in the form of figs. and tables. The datasets supporting the conclusions of this article are presented in the paper. The *Rosa brunonii* Lindl. fruits were collected from Murree, Punjab, Pakistan and identified by an expert taxonomist at Department of Botany, GC University, Lahore, Pakistan. A voucher specimen (GC. Herb.Bot.3315) was deposited in the Herbarium of GC University, Lahore, Pakistan for future reference.

Compliance with Ethical Standards: All the animal studies were carried out according to internationally accepted protocols, which were approved by the institutional animal ethical committee College of Pharmacy, University of Punjab (AEC/PUCP/1077) dated 03–05–2018.

Conflicts of Interest: The authors declare no conflict of interest.

REFERENCES

- Ahmad E, Jahangir M, Akhtar ZM, Ishtiaq S, Mukhtar H, Haidar HMF, Bukhari NI (2020) *Rosa brunonii* Lindl fruit as a new protective agent evaluated against Rif/INH induced toxicity in rats. *Pak J Pharm Sci*. <http://dx.doi.org/10.123456789/13305>
- Ahmad MF, Ahmad SM, Keservani RK, Pradhan A (2015) Anti-ulcer activity of tuber extracts of *Solanum tuberosum* (Solanaceae) in rats. *Acta Facultatis Pharm Univ Comenianae* 62: 32–37. <https://doi.org/10.1515/afpuc-2015-0029>
- Ahmadu A, Hassan H, Abubakar M, Akpulu I (2007) Flavonoid glycosides from *Byrsocarpus coccineus* leaves. *Schum and Thonn (Connaraceae)*. *Afr J Traditional, Complem Alter Med* 4: 257–260. <https://doi.org/10.4314/ajtcam.v4i3.31215>
- Aziz T, Fawad I, Khan AA, Shafiq UR, Ghazala YZ, Metab A, Abdulrahman A, Abdullah FA (2023) Assessing the pharmacological and biochemical effects of *Salvia hispanica* (Chia seed) against oxidized *Helianthus annuus* (sunflower) oil in selected animals. *Acta Biochim Pol* 67: 1–8. <https://doi.org/10.18388/abp.2020.6621>
- Al-Wajeeh NS, Hajerezaie M, Noor SM, Halabi MF, Al-Henhena N, Azizan AHS, Kamran S, Hassandarvish P, Shwter AN, Ali HM (2016) The gastro protective effects of *Cibotium barometz* hair on ethanol-induced gastric ulcer in Sprague-Dawley rats. *BMC Vet Res* 13: 27. <https://doi.org/10.1186/s12917-017-0949-z>
- Baiboun P, Kunanusorn P, Khonsung P, Chiranthanut N, Panthong A, Rujjanawate C (2016) Gastroprotective activity of the rhizome ethanol extract of *Zingiber simaoense* YY Qian in rats. *J Ethnopharmacol* 194: 571–576. <https://doi.org/10.1016/j.jep.2016.10.049>
- Balan T, Mohd. Sani MH, Suppaiah V, Mohtarrudin N, Suhaili Z, Ahmad Z, Zakaria ZA (2014) Antiulcer activity of *Muntingia calabura* leaves involves the modulation of endogenous nitric oxide and non-protein sulfhydryl compounds. *Pharm Biol* 52: 410–418. <https://doi.org/10.3109/13880209.2013.839713>
- Bancroft J, Christopher L (2013) The hematoxylin and eosin, connective and mesenchymal tissues with their stains. In *Theory & Practice of Histological Techniques*, Suvarna SK, Layton C, Bancroft JD, Eds, 7th Edn, Churchill Livingstone of El Sevier, Philadelphia, Ch. 10 and 11, pp 172–214. <https://doi.org/10.1016/B978-0-7020-4226-3.00010-X>
- Chatterjee A, Bandyopadhyay SK (2014) Herbal remedy: An alternate therapy of nonsteroidal anti-inflammatory drug induced gastric ulcer healing. *Ulcers* 2014. <https://doi.org/10.1155/2014/361586>
- Das AK, Bigoniya P, Verma NK, Rana A (2012) Gastroprotective effect of *Achyranthes aspera* Linn. leaf on rats. *Asian Pacific J Trop Med* 5: 197–201. [https://doi.org/10.1016/s1995-7645\(12\)60024-8](https://doi.org/10.1016/s1995-7645(12)60024-8)
- Dashputre N, Naikwade N (2011) Evaluation of anti-ulcer activity of methanolic extract of *Abutilon indicum* Linn leaves in experimental rats. *Int J Pharm Sci Res* 3: 97–100. <https://ijpsdr.com/index.php/ijpsdr/article/view/175>
- de Lira Mota KS, Dias GEN, Pinto MEF, Luiz-Ferreira Â, Monteiro Souza-Brito AR, Hiruma-Lima CA, Barbosa-Filho JM, Batista LM (2019) Flavonoids with gastroprotective activity. *Molecules* 14: 979–1012. <https://doi.org/10.3390/molecules14030979>
- Ekström A, Serafini M, Nyren O, Wolk A, Bosetti C, Bellocchio R (2011) Dietary quercetin intake and risk of gastric cancer: results from a population-based study in Sweden. *Ann Oncol* 22: 438–443. <https://doi.org/10.3390/molecules14030979>
- Deshpande S, Shah G, Parmar N (2003) Antiulcer activity of *Tephrosia purpurea* in rats. *Indian J Pharmacol* 35: 168–172.
- Ekström A, Serafini M, Nyren O, Wolk A, Bosetti C, Bellocchio R (2011) Dietary quercetin intake and risk of gastric cancer: results from a population-based study in Sweden. *Ann Oncol* 22: 438–443. <https://doi.org/10.1093/annonc/mdq390>
- Fahmy HA, Ismail AF (2015) Gastroprotective effect of kefir on ulcer induced in irradiated rats. *J Photochem Photobiol B: Biol* 144: 85–93. <https://doi.org/10.1016/j.jphotobiol.2015.02.009>
- Gul H, Abbas K, Qadir MI (2015) Gastro-protective effect of ethanol extract of *Mentha longifolia* in alcohol- and aspirin-induced gastric ulcer models. *Bangladesh J Pharmacol* 10: 241–245. <https://doi.org/10.3329/bjp.v10i1.21689>
- Hajerezaie M, Salehen N, Karimian H, Zahedifard M, Shams K, Al-Batran R, Majid NA, Khalifa SA, Ali HM, El-Seedi H (2015) Biochanin A gastroprotective effects in ethanol-induced gastric mucosal ulceration in rats. *PLOS One* 10: e0121529. <https://doi.org/10.1371/journal.pone.0121529>
- Hakim A, Loka IN, Hajar S, Junaidi E (2020) Isolation and confirmation of quercetin-3-o-glycosides from rubber cassava leaves. *Nat Res* 11: 420–425. <https://doi.org/10.4236/nr.2020.119024>
- Hariprasath L, Raman J, Nanjian R (2012) Gastroprotective effect of *Senecio candicans* DC on experimental ulcer models. *J Ethnopharmacol* 140: 145–150. <https://doi.org/10.1016/j.jep.2012.01.002>
- Ishaque M, BiBi Y, Valant-Vetschera KM, Schinnerl J, Bachner M (2017) Fruits of *Rosa brunonii* – A source of antioxidant phenolic compounds. *Nat Product Commun* 12. <http://dx.doi.org/10.1177/1934578X1701201106>
- Kang JM, Kim N, Kim B, Kim J-H, Lee B-Y, Park JH, Lee MK, Lee HS, Jang I-J, Kim JS (2009) Gastroprotective action of cochinchina momordica seed extract is mediated by activation of CGRP and inhibition of cPLA 2/5-LOX pathway. *Digestive Dis Sci* 54: 2549. <https://doi.org/10.1007/s10620-008-0671-6>
- Kangwan N, Park J-M, Kim E-H, Hahn KB (2014) Quality of healing of gastric ulcers: natural products beyond acid suppression. *World J Gastrointest Pathophysiol* 5: 40. <https://doi.org/10.4291%2Fwjg.v5.i1.40>
- Kaşıkçı MB, Bağdathoğlu N (2016) Bioavailability of quercetin. *Curr Res Nutr Food Sci J* 4: 146–151. <http://dx.doi.org/10.12944/CRNFSJ.4.Special-Issue-October.20>

- Ketuly KA, Hadi AHA, Golbabapour S, Hajrezaie M, Hassandarvish P, Ali HM, Majid NA, Abdulla MA (2013) Acute toxicity and gastroprotection studies with a newly synthesized steroid. *Plos One* **8**: e59296. <https://doi.org/10.1371/journal.pone.0059296>
- Khan A, Ali T, Rehman SU, Khan MS, Alam SI, Ikram M, Muhammad T, Saeed K, Badshah H, Kim MO (2018) Neuroprotective effect of quercetin against the detrimental effects of LPS in the adult mouse brain. *Front Pharmacol* **9**: 1383. <https://doi.org/10.3389/fphar.2018.01383>
- Khoder G, Al-Menhali AA, Al-Yassir F, Karam SM (2016) Potential role of probiotics in the management of gastric ulcer. *Exp Therap Med* **12**: 3–17. <https://doi.org/10.3892/etm.2016.3293>
- Kim Y-S, Park HJ, Kim H, Song J, Lee D (2019) Gastroprotective effects of paeonia extract mixture HT074 against experimental gastric ulcers in rats. *Evidence-Based Comp Alter Med* **2019**. <https://doi.org/10.1155/2019/3546258>
- Kuruüzüm-Uz A, Güvenalp Z, Kazaz C, Demirezer LÖ (2013) Phenolic compounds from the roots of *Anchusa azurea* var. *azurea*. *Turkish J Pharm Sci* **10**: 177–184
- Li X, Jin Q, Yao Q, Xu B, Li L, Zhang S, Tu C (2018) The flavonoid quercetin ameliorates liver inflammation and fibrosis by regulating hepatic macrophages activation and polarization in mice. *Front Pharmacol* **9**: 72. <https://doi.org/10.3389/fphar.2018.00072>
- Markwell MAK, Haas SM, Tolbert N, Bieber L (1981). Protein determination in membrane and lipoprotein samples: Manual and automated procedures. *Methods Enzymol* **72**: 296–303. [https://doi.org/10.1016/s0076-6879\(81\)72018-4](https://doi.org/10.1016/s0076-6879(81)72018-4)
- Nordin N, Salama SM, Golbabapour S, Hajrezaie M, Hassandarvish P, Kamalidehghan B, Majid NA, Hashim NM, Omar H, Fadaenasab M (2014) Anti-ulcerogenic effect of methanolic extracts from *Eniosanthellum pulchrum* (King) Heusden against ethanol-induced acute gastric lesion in animal models. *PLOS One* **9**: e111925. <https://doi.org/10.1371/journal.pone.0111925>
- Oliveira FdA, Andrade LN, De Sousa ÉBV, De Sousa DP (2014) Anti-ulcer activity of essential oil constituents. *Molecules* **19**: 5717–5747. <https://doi.org/10.3390/m19055717>
- Patel RV, Mistry BM, Shinde SK, Syed R, Singh V, Shin H-S (2018) Therapeutic potential of quercetin as a cardiovascular agent. *Eur J Med Chem* **155**: 889–904. <https://doi.org/10.1016/j.ejmech.2018.06.053>
- Qaiser J, Sidra A, Fayyaz A (2018) Chemically-induced peptic ulcer: gastroprotective effects of peach fruit. *Curr Trends Gastroenterol Hepatol* **1**. <http://dx.doi.org/10.32474/CTGH.2018.01.000107>
- Rahim NA, Hassandarvish P, Golbabapour S, Ismail S, Tayyab S, Abdulla MA (2014) Gastroprotective effect of ethanolic extract of *Curcuma xanthorrhiza* leaf against ethanol-induced gastric mucosal lesions in Sprague-Dawley rats. *BioMed Res Int* **2014**. <https://doi.org/10.1155/2014/416409>
- Raju D, Ilango K, Chitra V, Ashish K (2009) Evaluation of Anti-ulcer activity of methanolic extract of *Terminalia chebula* fruits in experimental rats. *J Pharm Sci Res* **1**: 101
- Razavi SM, Zahri S, Zarrini G, Nazemiyeh H, Mohammadi S (2009) Biological activity of quercetin-3-O-glucoside, a known plant flavonoid. *Russ J Bioorg Chem* **35**: 376–378. <https://doi.org/10.1134/s1068162009030133>
- Rozza A, Hiruma-Lima CA, Tanimoto A, Pellizzon C (2012) Morphologic and pharmacological investigations in the epicatechin gastroprotective effect. *Evidence-Based Comp Alter Med* **2012**. <https://doi.org/10.1155/2012/708156>
- Saleem K, Aziz T, Ali Khan A, Muhammad A, Ur Rahman S, Alharbi M, Alshammari A, F Alasmari A (2023) Evaluating the *in-vivo* effects of olive oil, soya bean oil, and vitamins against oxidized ghee toxicity. *Acta Biochim Pol* **70**: 10. https://doi.org/10.18388/abp.2020_6549
- Salehi B, Machin L, Monzote L, Sharifi-Rad J, Ezzat SM, Salem MA, Merghany RM, El Mahdy NM, Kılıç CS, Sytar O (2020) Therapeutic potential of quercetin: New insights and perspectives for human health. *ACS Omega* **5**: 11849–11872. <https://doi.org/10.1021/acsomega.0c01818>
- Samala S, Veeresham C (2016) Pharmacokinetic and pharmacodynamic interaction of boswellic acids and andrographolide with glyburide in diabetic rats: including its PK/PD modeling. *Phytotherap Res* **30**: 496–502. <https://doi.org/10.1002/ptr.5556>
- Sambandam B, Thiyagarajan D, Ayyaswamy A, Raman P (2016) Extraction and isolation of flavonoid quercetin from the leaves of *Trigonella foenum-graecum* and their anti-oxidant activity. *Int J Pharm Pharm Sci* **8**: 120–124. <https://journals.innovareacademics.in/index.php/ijpps/article/view/10943>
- Sana, Ur Rahman S, Zahid M, Khan AA, Aziz T, Iqbal Z, Ali W, Khan FF, Jamil S, Shahzad M, Alharbi M, Alshammari A (2022). Hepatoprotective effects of walnut oil and *Caralluma tuberculata* against paracetamol in experimentally induced liver toxicity in mice. *Acta Biochim Pol* **68**: 1–8. https://doi.org/10.18388/abp.2020_6387
- Saranya P, Geetha A, Selvamathy SN (2011) A biochemical study on the gastroprotective effect of andrographolide in rats induced with gastric ulcer. *Indian J Pharm Sci* **73**: 550. <https://doi.org/10.4103/0250-474X.99012>
- Shim YK, Kim N (2017) The effect of H2 receptor antagonist in acid inhibition and its clinical efficacy. *Korean J Gastroenterol* **70**: 4–12. <https://doi.org/10.4166/kjg.2017.70.1.4>
- Shukla P, Porwal A, Roy S, Chaturvedi S, Tripathi S, Arya N (2017) Preliminary study on antiulcer effect of agomelatine and its potentiation with pyridoxine. *Int J Basic Clin Pharmacol* **6**: 2566. <https://doi.org/10.18203/2319-2003.ijbcp20174655>
- Sidahmed HMA, Azizan AHS, Mohan S, Abdulla MA, Abdelwahab SI, Taha MME, Hadi AHA, Ketuly KA, Hashim NM, Loke MF (2013) Gastroprotective effect of desmosmodin C isolated from *Mitrella kentii* against ethanol-induced gastric mucosal hemorrhage in rats: possible involvement of glutathione, heat-shock protein-70, sulfhydryl compounds, nitric oxide, and anti-*Helicobacter pylori* activity. *BMC Compl Alter Med* **13**: 1–15. <https://doi.org/10.1177/1535370215600099>
- Sidahmed HMA, Hashim NM, Abdulla MA, Ali HM, Mohan S, Abdelwahab SI, Taha MME, Fai LM, Vadivelu J (2015) Antisecretory, gastroprotective, antioxidant and anti-helicobacter pylori activity of zerumbone from *Zingiber Zerumbet* (L.) Smith. *PLoS One* **10**: e0121060. <https://doi.org/10.1371/journal.pone.0121060>
- Tatke P, Desai S, Gabhe S (2014) Isolation of quercetin-3-O-β-D-glucoside from *Azadirachta indica*. *Am J Phytomed Clin Therap* **2**: 870–876
- Terao J (2023) Potential role of quercetin glycosides as anti-atherosclerotic food-derived factors for human health. *Antioxidants* **12**: 258. <https://doi.org/10.3390/antiox12020258>
- Umathe SN, Dixit PV, Bansod KU, Wanjari MM (2008) Quercetin pretreatment increases the bioavailability of pioglitazone in rats: involvement of CYP3A inhibition. *Biochem Pharmacol* **75**: 1670–1676. <https://doi.org/10.1016/j.bcp.2008.01.010>
- Vafadar A, Shabaninejad Z, Movahedpour A, Fallahi F, Taghavi-pour M, Ghasemi Y, Akbari M, Shafee A, Hajighadimi S, Moradizarmehri S (2020) Quercetin and cancer: new insights into its therapeutic effects on ovarian cancer cells. *Cell Biosci* **10**: 1–17. <https://doi.org/10.1186/s13578-020-00397-0>
- Yu C, Qiu J, Xiong M, Ou C, Zeng M, Song H (2022) Trends in *Helicobacter pylori*-related gastric ulcer research from 2012 to 2022: A bibliometric and visual analysis. *Front Med* **9**. <https://doi.org/10.3389/fmed.2022.1027534>
- Yu L-Y, Sun L-N, Zhang X-H, Li Y-Q, Yu L, Meng L, Zhang H-W, Wang Y-Q (2017) A review of the novel application and potential adverse effects of proton pump inhibitors. *Adv Therap* **34**: 1070–1086. <https://doi.org/10.1007/s12325-017-0532-9>
- Yuan Y, Padol IT, Hunt RH (2006) Peptic ulcer disease today. *Nat Clin Practice Gastroenterol Hepatol* **3**: 80–89. <https://doi.org/10.1038/nccpgasthep0393>
- Zakaria ZA, Balan T, Azemi AK, Omar MH, Mohtarrudin N, Ahmad Z, Abdullah MNH, Desa MNM, Teh LK, Salleh MZ (2016a) Mechanism (s) of action underlying the gastroprotective effect of ethyl acetate fraction obtained from the crude methanolic leaves extract of *Muntingia calabura*. *BMC Compl Alter Med* **16**: 78. <https://doi.org/10.3390/ph15040427>
- Zakaria ZA, Zainol ASN, Sahmat A, Salleh NI, Hizami A, Mahmood ND, Nasir N, Mamat SS, Kamisan FH, Mohtarrudin N (2016b) Gastroprotective activity of chloroform extract of *Muntingia calabura* and *Melastoma malabathricum* leaves. *Pharm Biol* **54**: 812–826. <https://doi.org/10.3109/13880209.2015.1085580>

Molecular cloning of glutathione reductase from *Oryza sativa*, demonstrating its peroxisomal localization and upregulation by abiotic stresses

Pamela Chanda Roy and Gopal Chowdhary✉

Plant Molecular Biology Laboratory, School of Biotechnology, KIIT, Bhubaneswar-751024, Odisha, India

Abiotic stress is a major constraint on crop productivity and in the agricultural field, multiple abiotic stresses act synchronously leading to substantial damage to plants. A common after-effect of abiotic stress-induced damage in plants is an increased concentration of reactive oxygen species (ROS) leading to oxidative damage. Glutathione reductase (GR) plays a significant role in curtailing ROS. Apart from the GR enzyme, the peroxisome as an organelle also plays a significant role in ROS homeostasis. Here, we report a peroxisome localized GR, whose expression was found to be upregulated by various abiotic stresses. The *in silico* analysis also revealed that the peroxisomal localization of GR could be a common phenomenon in angiosperms, suggesting that it could be a suitable candidate against abiotic stress combinations.

Keywords: glutathione reductase, abiotic stress, stress combination, peroxisome, PTS

Received: 26 July, 2022; revised: 01 December, 2022; accepted: 05 December, 2022; available on-line: 08 January, 2023

✉e-mail: gkchowdhary@kiitbiotech.ac.in

Acknowledgments of Financial Support: The financial support from the Science and Engineering and Research Board (SERB), Govt of India, and KIIT University is acknowledged.

Abbreviations: At, *Arabidopsis thaliana*; BLAST, basic local alignment search tool; CaMV, cauliflower mosaic virus; CT, cycle threshold; EYFP, enhanced yellow fluorescent protein; GR, Glutathione reductase; HT, high temperature; LT, low temperature; PCR, polymerase chain reaction; NCBI, National Center for Biotechnology Information; Os, *Oryza sativa*; PEX, Peroxin; PTS, peroxisomal targeting signal; ROS, reactive oxygen species; TAIR, The Arabidopsis Information Resource

INTRODUCTION

Abiotic stress is one of the significant factors which limits the yield of crops. Due to the untimely onset of abiotic stress conditions, crops worth millions of dollars are lost annually worldwide (Wang *et al.*, 2003; Wania *et al.*, 2016). Abiotic stress leads to a series of detrimental activities in the plant, which cause either partial or complete loss of yield (Yousuf *et al.*, 2012; Harshavardhan *et al.*, 2017). One such after-effect is an increase in the cellular concentration of reactive oxygen species (ROS), which has been observed as a common phenomenon in the case of all types of abiotic stresses. Uncontrolled increase and accumulation of ROS can lead to oxidative damage to the cell, such as oxidation of nucleic acids, protein denaturation, breakdown of cell and organelle membrane, lipid peroxidation, and carbohydrate oxidation (Scandalios, 1993; Noctor & Foyer, 1998). This imbalance in the redox state of the cell is dangerous and could be lethal if left unchecked. ROS also plays a sig-

nificant role in regulating the response of plants, against environmental stimuli by a redox-dependent reprogramming of signalling pathways (Harshavardhan *et al.*, 2017), thereby making ROS not only an oxidative deterrent but also a signalling molecule (Mittler *et al.*, 2004; Miller *et al.*, 2010). Hence, a delicate balance between ROS production and scavenging needs to be maintained, making ROS homeostasis very crucial. To defend themselves from this abiotic stress-induced oxidative damage, plants have developed various mechanisms. One such mechanism is the glutathione reductase (GR) mediated ascorbate-glutathione pathway, also known as the Foyer-Halliwell-Asada pathway (Asada, 2006; Foyer & Noctor, 2011). In plant cells, GR activity has primarily been found in the chloroplast (70–80%) with a minor presence in mitochondria and cytosol (Edwards *et al.*, 1990; Creissen *et al.*, 1994). However, with recent development in molecular and proteomic techniques, the peroxisomal localization of *Arabidopsis thaliana* GR has also been demonstrated (Kataya & Reumann, 2010). Also, it is pertinent to mention that the peroxisomes in association with chloroplast and mitochondria are primarily responsible for cellular ROS homeostasis (Foyer & Noctor, 2003; Habib *et al.*, 2016; Dietz *et al.*, 2016; Huang *et al.*, 2016). The significant role of peroxisomes in ROS scavenging and abiotic stress tolerance makes a peroxisome-localized GR of special significance.

Peroxisomes are small, single membrane-bound organelles whose proteome is encoded by nuclear genes, synthesized on cytosolic ribosomes, and imported in a signal-dependent manner (Hu *et al.*, 2012; Emmanouilidis *et al.*, 2016). Depending upon the protein location, peroxisomal proteins could be divided into two broad categories- peroxisomal membrane and matrix proteins, both of which are imported in entirely different manners. GR happens to be a peroxisomal matrix protein (Kataya & Reumann, 2010). The peroxisomal matrix proteins are largely imported either by peroxisomal targeting signal (PTS) type one or PTS type two (Gould *et al.*, 1987; Swinkels *et al.*, 1991). The bulk of the matrix proteins is imported by PTS type 1 while a comparatively smaller number of matrix proteins are imported by PTS type 2 (Brocard & Hartig, 2006; Lazarow, 2006). After being synthesized on cytosolic ribosomes, PTS1 and PTS2 containing proteins are recognized by their respective cytosolic receptors, PEX (peroxin) 5 and PEX7 respectively, which ultimately bring them to peroxisome with the help of other PEX proteins (Kunze, 2019; Kim & Hettema, 2015; Kunze *et al.*, 2011; Kiel *et al.*, 2009; Niederhoff *et al.*, 2005; Reumann, 2004; Bottger *et al.*, 2000; Lametschwandtner *et al.*, 1998; Albertini *et al.*, 1997). The PTS1 is located at the C-terminus of protein and

is primarily represented by the last three amino acids, however, the upstream residues also play a significant role in PEX5 binding (Neuberger *et al.*, 2003; Brocard & Hartig, 2006; Lingner *et al.*, 2011; Lametschwandtner *et al.*, 1998; Reumann, 2004; Fodor *et al.*, 2012; 2015), while the PTS2 is located at N-terminus, represented by a nonapeptide (Petriv *et al.*, 2004; Lazarow, 2006). It has also been observed that depending upon the composition of amino acids present at the C-terminus, the PTS1 shows a varying degree of efficiency in peroxisome targeting (Gatto *et al.*, 2000; Stanley *et al.*, 2006) and this has led to the classification of PTS1 into a canonical and noncanonical type (Skoulding *et al.*, 2015). The canonical ones lead to efficient and strong targeting while the non-canonical ones are comparatively less efficient and lead to weak targeting of the protein to the peroxisome. The strong and weak efficiencies have been explained based on the time required for the fluorescent detection of the peroxisome targeting under *in vitro* conditions (Skoulding *et al.*, 2015; Chowdhary *et al.*, 2012).

In this work, we reported the peroxisome localization of GR and its involvement in abiotic stress tolerance in the monocot model plant *Oryza sativa* (rice) which is a crop of global significance and is responsible for feeding more than half of the world's population, especially in Asian, African continents, and other third world nations.

MATERIALS AND METHODS

Data retrieval for *in silico* work

The protein sequences of *A. thaliana* and *O. sativa* GR were retrieved from The Arabidopsis Information Resource (TAIR, Tanya *et al.*, 2015, <https://www.arabidopsis.org/>) and the rice genome annotation database (Kawahara *et al.*, 2013, <http://rice.uga.edu/>) respectively. For multiple sequence alignment, CLUSTAL W 2.1 program (Larkin *et al.*, 2007) was used at pir.georgetown.edu (Cathy *et al.*, 2003). The OsGR was used as a query in protein BLAST at NCBI and 80 GR orthologs were obtained.

Plant material and growth condition

For all experiments, *O. sativa* IR 64 (Indica rice) variety was used. This is an abiotic stress-sensitive variety. The seeds were obtained from National Rice Research Institute, Cuttack, India. The seeds were sterilized with 70% ethanol for 2 min followed by rinsing with distilled water three times each for 2 min. The sterilized seeds were kept in germination paper pre-wet with distilled water, which was incubated in dark for 24 h followed by shifting to the plant growth room maintained at $28 \pm 2^\circ\text{C}$, 60% humidity, and a light/dark cycle of 16/8 h. For all experimentation, 11 days old seedlings were used. The abiotic stresses were induced by treatment with 200 mM sodium chloride (saline stress), $4 \pm 2^\circ\text{C}$ (cold stress), and $45 \pm 2^\circ\text{C}$ (heat stress) for 2 h. The untreated seedlings served as a control and were used for the calculation of the relative transcript level of OsGR.

RNA extraction and cloning of OsGR

For RNA extraction, 100 mg of seedling was used and crushed in liquid nitrogen followed by extraction using RNeasy plant mini kit (Qiagen) as per the manufacturer's protocol, with the modification of inclusion of in-column DNase digestion step (RNase free DNase set, Qiagen). The extracted RNA was checked for its quan-

tity and quality using a microvolume spectrophotometer (ThermoFisher Scientific) and agarose gel electrophoresis.

The extracted RNA was converted to cDNA using Revert Aid First Strand cDNA Synthesis Kit (ThermoFisher Scientific) as per the manufacturer's manual. The obtained cDNA was used for polymerase chain reaction (PCR) amplification using the primers: Forward AATTGCGGCCGCGATGGCTAGGAAGATGCTCAAG, Reverse TATGTCTAGAGCTACAAGTTTGTCTTTGGCTTGATGATGG, using HiFidelity polymerase (Qiagen), with PCR cycle of denaturation 94°C for 20 s, annealing 60°C for 30 s and extension 72°C for 90 s. The obtained PCR product was checked for amplification using agarose gel electrophoresis followed by digestion using NotI and XbaI restriction enzymes. The digested product was resolved in an agarose gel followed by gel purification using the GenJET gel extraction kit (ThermoFisher Scientific). The digested product was cloned into the pCAT plant expression vector, as an enhanced yellow fluorescent protein (EYFP) fusion product under the control of a double 35 S cauliflower mosaic virus (CaMV) promoter (Fulda *et al.*, 2002). The insert was verified using automated DNA sequencing.

Subcellular localization of OsGR

For subcellular localization studies, the biolistic bombardment method was used, in which onion epidermal cells were transformed with plasmid constructs coated on gold particles, which were further examined under a fluorescent microscope after an appropriate incubation time. Under standard conditions, the transformed onion epidermal cells are examined after 18–24 h post-transformation. However, it has also been observed that the sensitivity of detection of the reporter protein in peroxisome increases after an extended incubation time at reduced temperature (Lingner *et al.*, 2011; Chowdhary *et al.*, 2012).

The gene of interest (OsGR) was cloned as an EYFP fusion product and as a peroxisomal marker, Ds-Red-SKL was used (Matre *et al.*, 2009). In the case of single transformation experiments pCAT plasmid containing EYFP-OsGR was coated with gold particles, while in the case of double transformation experiments pCAT plasmid containing EYFP-OsGR and peroxisomal marker (Ds-Red-SKL) together were coated with gold particles and bombarded to onion epidermal cells (Ma *et al.*, 2006). The onion slices were placed on wet blotting paper in Petri dishes and stored at room temperature in the dark followed by analysis using fluorescent microscopy or after additional incubation at 10°C for 1 to 6 d. Image capture and analysis were done as explained in Chowdhary *et al.*, (2012).

Expression analysis by real-time PCR

The expression analysis of peroxisomal GR was carried out by real-time PCR technique using SYBR green chemistry. For this, the total RNA was extracted from stress-treated and control (untreated) plants as explained above, its concentration was determined, equalized, and converted to cDNA using high-capacity cDNA reverse transcription kit (ThermoFisher Scientific) as per the manufacturer's manual. Total RNA, 1 μg , was converted to cDNA, which was diluted and further used for quantitative real-time PCR using SYBR green chemistry. Real-time PCR was performed using QuantiNova 2X PCR master mix containing SYBR green dye with ROX as passive reference dye (Qiagen) in QuantStudio 5 (ThermoFisher Scientific) real-time PCR



Figure 1. Multiple sequence alignment of GRs from *Arabidopsis thaliana* and *Oryza sativa*.

GR sequences were obtained from the database and aligned using CLUSTAL W 2.1. "*" represents the same amino acids, "-" represents the similar amino acids present in both the sequences. The red rectangle highlights the PT51 tripeptide with seven upstream residues. The figure at the bottom shows the diagrammatic representation of the interaction of PEX5 with the C-terminus end of GR. The solid black and blue rectangle represents the OsGR and PEX5, respectively.

machine. The conditions for real-time PCR were as follows: initial denaturation at 95°C for 2 min, followed by 40 cycles of 95°C for 15 s, 60°C for 60 s, and 72°C for 60 s. To obtain the melting curve a program of 95°C for 15 s and 60°C for 1 min was followed. All qPCR analyses were performed in three biological replicates. *O. sativa* actin was used as an endogenous control for the normalization of the transcript. The relative transcript level or "fold change" (degree of change in expression between the treated sample and untreated sample) was calculated by the $\Delta\Delta CT$ method using the formula, relative transcript level/fold change = $2^{-\Delta\Delta CT}$, where $\Delta\Delta CT = \Delta CT_{\text{test sample}} - \Delta CT_{\text{calibrator sample}}$ ($\Delta CT_{\text{test sample}} = CT_{\text{test}} - CT_{\text{reference}}$, $\Delta CT_{\text{calibrator}} = CT_{\text{calibrator}} - CT_{\text{reference}}$; test sample = stress treated sample, calibrator = untreated sample, reference = endogenous control) (Livak & Schmittgen, 2001). The data provided represents an average of three biological replicates of independent samples and the values depicted represent mean \pm standard deviation. The primer used for expression analysis were, OsGR Forward primer – CGACCTTTGACAGCACTGTTGG, reverse primer – TGGTCAAGGTC-CGCATTGTCAC, OsActin forward primers – CAGCCACACTGTCCCATCTA, Reverse primer – AGCAAG-GTCGAGACGAAGGA.

RESULTS

Bioinformatics analysis of OsGR

The protein sequence of *A. thaliana* and *O. sativa* GR were aligned using CLUSTAL W 2.1 and the alignment revealed the significant conservation among both sequences (Fig. 1). The peroxisome targeting of *A. thaliana*

GR is dependent on the PTS type 1, which is localized at the C-terminus of the protein. In the case of AtGR the PTS1 is represented by TNL> (Kataya & Reumann, 2010), the symbol ">" represents the end of the polypeptide. The presence of the same tripeptide in *O. sativa* GR provided a hint for peroxisomal localization of OsGR via PTS1 (Fig. 1). Hence, OsGR was fused at the C-terminus of the EYFP, so that the targeting signal is freely available for the cytosolic receptor, PEX5 binding followed by peroxisome targeting (Fig. 1).

Molecular cloning and subcellular localization of OsGR

The cDNA of the *O. sativa* was used as a template for PCR-based cloning of GR. The primer sequences and PCR cycle are explained in the materials and method section. The PCR amplified product was found to be of 1500 bp and was cloned in the pCAT vector under the control of a double 35 S CaMV promoter. The gene was cloned as a C-terminal fusion of enhanced yellow fluorescent protein (EYFP, Fig. 1). The sequence of the cloned gene was verified using automated DNA sequencing. No mutations were detected.

Onion epidermal cells transformed with EYFP, which served as a negative control showed uniform cytosolic fluorescence (Fig. 2A). The OsGR, which was expressed as a fusion protein with EYFP, showed green cytosolic fluorescence after 24 h of incubation (Fig. 2B1), however the same was observed in small punctuate structures after an extended time of incubation (Fig. 2B2). The identity of fluorescing punctuate structures was confirmed by double transformation experiments co-expressing peroxisomal marker DsRed-SKL. The double transformation experiments demonstrated the overlapping of both green and red fluorescence from

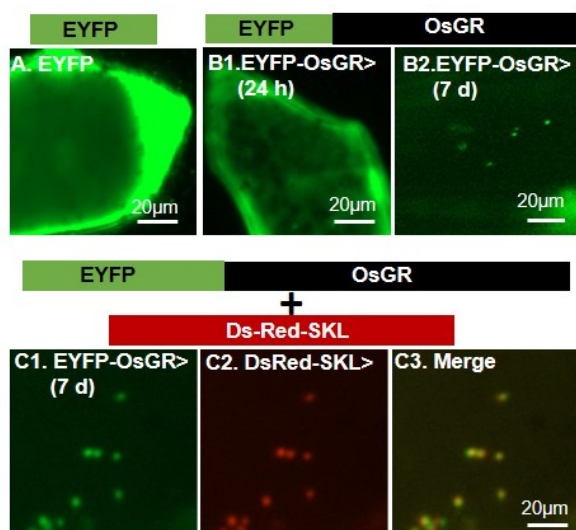


Figure 2. Experimental validation of peroxisome localization of *Oryza sativa* GR by *in vitro* subcellular targeting.

The OsGR was cloned in the pCAT plant transient vector under the control of a double 35 S CaMV promoter. The plasmids were coated with gold particles and bombarded biolistically to onion epidermal cells. The onion epidermal cells were incubated in dark for 24 h at room temperature or low temperature for an extended time period (24 h RT plus 6 d cold ca. 10°C) followed by analysis using fluorescent microscopy. EYFP alone was included as negative control (A). 24 h p.t., EYFP fluorescence was detected in cytosol only (B1), while after extended incubation the EYFP fluorescence was detected in punctuate structures (B2). The identity of the dot-like punctuate structure was confirmed by double transformation experiments, where peroxisomes were labelled with Ds-Red-SKL. The green (C1) and red fluorescence (C2) from EYFP and Ds-Red-SKL> respectively merged to show yellow fluorescence (C3) confirming the punctuate structure to be peroxisomes. The green rectangle bar fused to black depicts the diagrammatic representation of OsGR fused at the C-terminus of EYFP, while the red rectangular bar represents the Ds-RED-SKL>. The upper and bottom halves of the image show the single and double transformation experiments respectively.

EYFP and peroxisomal marker respectively, (Fig. 2C), confirming the identity of the punctuate fluorescing organelle to be peroxisome. Since fluorescence could not be detected in peroxisome 24 h post-transformation and it took an extended time of incubation for the fluorescence to be detected in peroxisome it was presumed that the GR is targeted to peroxisome with lesser efficiency and hence the PTS1 present in GR was termed as weak or non-canonical PTS1.

Expression analysis of OsGR

For OsGR gene expression analysis, the abiotic stress-treated seedlings were used for RNA extraction, followed by cDNA synthesis and real-time PCR. The untreated seedlings were used as a control. The expression data were represented as relative transcript level or “fold change” which essentially means the change in the degree of expression between the treated sample and untreated samples. The details are explained in the materials and method section. Expression analysis was performed with respect to heat, cold, and salinity (sodium chloride) stresses. All the treatments were provided for 2 h. In the case of heat stress, the change in the transcript accumulation was observed to a tune of 3.1-fold (Fig. 3), meaning that GR gene transcripts accumulated 3.1 times more in the heat stress as compared to untreated samples. This was followed by cold and saline stress with transcript level accumulation of about 3.7 and 10.4-fold respectively (Fig. 3). This demonstrated that the expression of peroxisomal

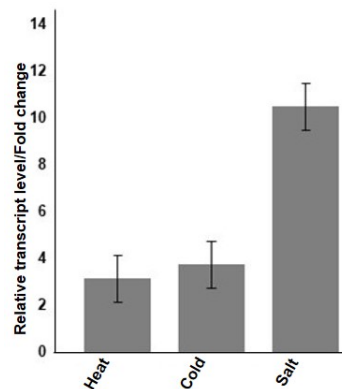


Figure 3. Expression analysis of OsGR.

The expression analysis was performed using the RNA isolated from *Oryza sativa* seedlings after the treatments. RNA extraction was done by RNeasy plant mini kit, (Qiagen) followed by cDNA synthesis (High-Capacity cDNA Reverse Transcription Kit, ThermoFisher Scientific). The cDNA obtained was used for expression analysis by real-time PCR using SYBR green chemistry. OsActin was used as endogenous control. The assays were repeated with a minimum of three replicates and $\Delta\Delta CT$ values were calculated, relative transcript level (fold change) was determined, and the graph was plotted. The x and y-axis show the various abiotic stress treatments and fold change, respectively. The data represent three biological replicates and error bars have been shown.

localized GR in *O. sativa* upregulated in the presence of heat, cold, and salinity stress conditions.

DISCUSSION

Abiotic stress is the major bottleneck in the sustainability of the global agricultural system. The harmful effect of abiotic stress is further compounded when more than one abiotic stress factor negatively affects the plant in synchrony, which is more often the case in field conditions. This phenomenon has been termed stress combinations (Zandalinas *et al.* 2020; 2021) or stress matrix (Mittler, 2006). This necessitates the development of crop varieties that would be tolerant to multiple abiotic stresses. Hence, candidate genes are required which would be effective against most if not all the abiotic stresses. Since the production of ROS is a common factor among all abiotic stresses, we intend to investigate the problem of abiotic stress combinations from the perspective of ROS homeostasis.

Since, peroxisomes play a significant role in cellular ROS homeostasis, a peroxisome-localized candidate participating in ROS homeostasis would be of greater significance. Using *in vitro* subcellular localization techniques, we reported a GR isoform from *Oryza sativa* to be localized in peroxisomes. Previously, Kataya & Reumann, (2010) have reported the localization of *A. thaliana* GR in peroxisomes. The peroxisome targeting of GR is mediated *via* a non-canonical type of PTS1. The PTS1 tripeptide of GR is represented by TNL> in both *A. thaliana* (Kataya & Reumann, 2010) and *O. sativa*. In the case of non-canonical PTS1, the seven upstream residues also play a significant role in binding with the cytosolic receptor PEX5 (Fodor *et al.*, 2012; Brocard & Hartig, 2006; Lingner *et al.*, 2011), which is represented by SPSSKPKTNL> and AHKPKPKTNL> (underlined residues PTS1 tripeptide, others, seven upstream residues) in the case of *O. sativa* and *A. thaliana* respectively. Being a non-canonical type of PTS1, the targeting is not very efficient and requires an extended incubation time for the fluorescence to be detected in the peroxisome (Lingner *et al.*, 2011; Chowdhary *et al.*, 2012). To further understand the peroxisome targeting signal of GRs in angiosperms we

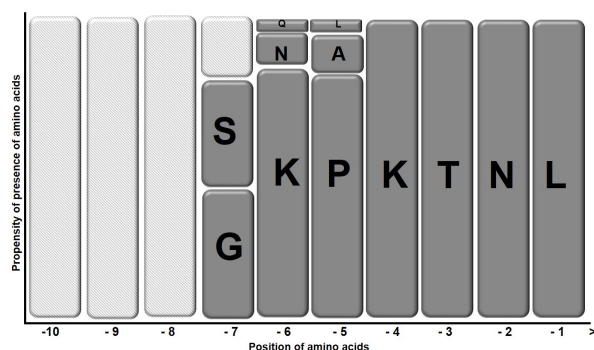


Figure 4. Graphical representation of PTS1 domain present in GR of various angiosperm plants.

The 80 numbers of GR sequences from various dicot and monocot plant species were obtained from NCBI. The sequences were aligned using CLUSTAL W 2.1 (Supplementary Fig. 1 at <https://ojs.ptbioch.edu.pl/index.php/abp/>). From the multiple sequence alignment, the consensus amino acids were derived. The y-axis shows the propensity of the presence of specific amino acid at a specific position while the x-axis represents the position of amino acids in the C-terminus of the respective protein. ">" denotes the end of the polypeptide chain. Each square represents one amino acid. The bigger the size of the squares, the higher the propensity of amino acids to remain present at that specific position. The empty squares represent the high variability.

obtained GR protein sequences from 80 plant species, and the last ten amino acids were aligned by multiple sequence alignment (Supplementary Fig. 1 at <https://ojs.ptbioch.edu.pl/index.php/abp/>). The alignment revealed that all the sequences were terminating with TNL> suggesting that the presence of a peroxisomal GR could be a common feature among angiosperms. At the -4 position, all the 80 GR orthologs have lysine while at the -5 position 73 sequences have proline except six sequences, one each from *Elaeis guineensis*, *Gossypium hirsutum*, *Gossypium Raimondi*, *Amborella trichopoda*, *Cinnamomum micranthum*, and *Phoenix dactylifera* have alanine and one sequence namely *Brachypodium distachyon* had leucine. At the -6 position, 75 sequences had lysine while asparagine was present at four places (one sequence each from *Citrus clementina*, *Olea europaea* and two sequences from *Citrus sinensis*) and glutamine was present at one place (*Phoenix dactylifera*). The most favourable amino acid at the -7 position is glycine which is present in 35 sequences followed by serine present in 29 sequences. At -8, -9 and -10 positions variability increases. The analysis curtailed here reveals that the consensus PTS1 sequence for peroxisomal GRs present in the angiosperms would be [G/S/T/N/A/V] [L/N/Q] [P/A/L] [K] [I] [N] [L]> at -7, -6, -5, -4, -3, -2 and -1> positions, respectively. Figure 4 demonstrates the diagrammatic representation of the propensity of specific amino acids to remain present at specific positions.

Further, the expression pattern of peroxisomal GR was investigated under various abiotic stress conditions. It was found to be upregulated upon heat, cold, and salinity stress in increasing order. GR expression has been reported to get affected due to stress conditions in various plant species, however, all previous reports are of either chloroplastic or cytosolic variants. Salinity and drought stress-dependent upregulation of GR has been demonstrated in *Cicer arietinum* and *O. sativa* respectively (Yousuf *et al.*, 2012). A positive correlation between tolerance to low temperature (LT)-induced photoinhibition and high GR activities has been observed in *O. sativa* (Guo *et al.*, 2006; Huang & Guo, 2005), *C. sativus* (Hu *et al.*, 2008), (Xu *et al.*, 2008), *Glycine max* (Sun *et al.*, 2011), *Cucumis melo* (Fogelman *et al.*, 2011) and *Citrullus lanatus*

(Gill *et al.*, 2013). Increased GR activity has been widely observed in plant species like *T. aestivum* (Hasanuzzaman *et al.*, 2012), *Z. mays* (Kumar *et al.*, 2012), *Cucumis sativus* (Dai *et al.*, 2012), *N. tabacum* (Tan *et al.*, 2011) and *Phaseolus aureus* (Kumar *et al.*, 2011) under high temperature (HT) stress. Thus, the upregulation in the expression of GR is postulated to play an important role in plant protection against various forms of abiotic stresses (Trivedi *et al.*, 2013; Gullner *et al.*, 2001; Reisinger *et al.*, 2008).

The overexpression of enzymes of the ascorbate-glutathione (AsA-GSH) pathway has been demonstrated to confer abiotic stress tolerance in plants by reducing the stress-induced cellular reactive oxygen species (ROS). The work has been critically reviewed by Hasanuzzaman *et al.*, (2019). It has been observed that in *Vigna radiata* (Nahar *et al.*, 2016) and *Solanum lycopersicum* (Sabeha *et al.*, 2022), the upregulation of AsA-GSH cycle components leads to saline stress and heavy metal (mercury) stress tolerance, respectively. The overexpression of AsA-GSH enzymes from *Pennisetum glaucoma* in *S. lycopersicum* has been reported to be responsible for the reduced accumulation of malondialdehyde and H_2O_2 (Raja *et al.*, 2022). The impairment of AsA-GSH cycle enzymes has been demonstrated to increase saline stress sensitivity in *A. thaliana* (Huang *et al.*, 2005). Further, the overexpression of *Malpighia glabra* monodehydroascorbate reductase (MDHAR) leads to saline stress tolerance in *Nicotiana tabacum* (Eltelieb *et al.*, 2012). The transgenic *O. sativa* plants overexpressing MDHAR from *Acanthus ebracteatus* were found to demonstrate enhanced saline tolerance (Sultana *et al.*, 2012). The overexpression of MDHAR and dehydroascorbate reductase (DHAR) in *N. tabacum* (Eltayeb *et al.*, 2007) and *A. thaliana* (Ushimaru *et al.*, 2006) have been demonstrated to increase saline stress tolerance. The overexpression of APX has been demonstrated to reduce the toxic effects of stress-induced H_2O_2 and enhance salinity tolerance in *N. tabacum* (Badawi *et al.*, 2004). Similarly, the overexpression of APX in *N. tabacum* has been demonstrated to relieve it from high and low-temperature stress (Yabuta *et al.*, 2002).

It has also been suggested that different GR isoforms can be stimulated by varied environmental signals and can have different functional manifestations in the response to stress in plants (Stevens *et al.*, 1997). This further supports our analysis that a peroxisomal localized GR could have a more pronounced effect in imparting ROS scavenging properties to plants and hence providing better abiotic stress tolerance. It is also pertinent to mention here that ample literature is available about chloroplastic and cytosolic forms while no work has yet been reported on peroxisomal GR. This would be the first report of a full-length GR to be localized in peroxisome from a monocot plant and its involvement in abiotic stress tolerance. Since both peroxisome and GR are the key entities in cellular ROS homeostasis, a peroxisome localized GR would be of much significance in contributing to the abiotic stress tolerance in plants. The *in silico* analysis also revealed that the peroxisomal localization of GR could be a universal feature among angiosperms. Further, we also reported that the GR was induced by multiple abiotic stress conditions, suggesting that this could also be effective in providing stress tolerance under stress combination or stress matrix situations as well, however, further studies need to be done in this regard.

CONCLUSION

In the nutshell, we reported a peroxisome localized GR from the monocot model plant *Oryza sativa*. The *in silico*

analysis also revealed that the peroxisomal localization of GR could be a common feature amongst angiosperms. The peroxisome localized GR was also found to be induced by multiple abiotic stress conditions. The role of GR in ROS homeostasis combined with its peroxisome localization and induction by multiple abiotic stress conditions suggests that it could be a prime candidate for the development of tolerance against abiotic stress combinations.

Declarations

Conflict of interests. The authors confirm that there are no conflicts of interest.

REFERENCES

- Albertini M, Rehling P, Erdmann R, Girzalsky W, Kiel JA, Veenhuis M, Kunau WH (1997) Pex14p, a peroxisomal membrane protein binding both receptors of the two PTS-dependent import pathways. *Cell* **89**: 83–92. [https://doi.org/10.1016/s0092-8674\(00\)80185-3](https://doi.org/10.1016/s0092-8674(00)80185-3)
- Asada K (2006) Production and scavenging of reactive oxygen species in chloroplasts and their functions. *Plant Physiol* **141**: 391–396. <https://doi.org/10.1104/pp.106.082040>
- Badawi GH, Kawano N, Yamauchi Y, Shimada E, Sasaki R, Kubo A, Tanaka K (2004) Over-expression of ascorbate peroxidase in tobacco chloroplasts enhances the tolerance to salt stress and water deficit. *Physiol Plant* **121**: 231–238. <https://doi.org/10.1111/j.0031-9317.2004.00308.x>
- Botter G, Barnett P, Klein AJ, Kragt A, Tabak HF, Distel B (2000) Saccharomyces cerevisiae PTS1 receptor Pex5p interacts with the SH3 domain of the peroxisomal membrane protein Pex13p in an unconventional, non-PXXP-related manner. *Mol Biol Cell* **11**: 3963–3976. <https://doi.org/10.1091/mbc.11.11.3963>
- Brocard C, Hartig A (2006) Peroxisome targeting signal 1: Is it really a simple tripeptide? *Biochim Biophys Acta - Mol Cell Res* **1763**: 1565–1573. <https://doi.org/10.1016/j.bbamcr.2006.08.022>
- Cathy HW, Lai-Su LY, Hongzhan H, Leslie A, Jorge CA, Yongxing C, Zhang-Zhi H, Robert SZ, Panagiotis K, Baris ES, Vinayaka CR, Jian Z, Winona CB (2003) The Protein Information Resource. *Nucleic Acids Res* **31**: 345–347. <https://doi.org/10.1093/nar/gkg040>
- Chowdhary G, Kataya ARA, Lingner T, Reumann S (2012) Non-canonical peroxisome targeting signals: identification of novel PTS1 tripeptides and characterization of enhancer elements by computational permutation analysis. *BMC Plant Biol* **12**: 142. <https://doi.org/10.1186/1471-2229-12-142>
- Creissen GP, Broadbent P, Kular B, Reynolds H, Wellburn AR, Mullineaux PM (1994) Manipulation of glutathione reductase in transgenic plants: implications for plant responses to environmental stress. *Proc R Soc Edinb* **102B**: 167–175. <https://doi.org/10.1017/S0269727000014081>
- Dai AH, Nie YX, Yu B, Li Q, Lu LY, Bai JG (2012) Cinnamic acid pre-treatment enhances heat tolerance of cucumber leaves through modulating antioxidant enzyme activity. *Environ Exp Bot* **79**: 1–10. <https://doi.org/10.1016/j.envexpbot.2012.01.003>
- Dietz KJ, Turkan I, Krieger-Liszka A (2016) Redox and reactive oxygen species-dependent signaling into and out of the photosynthesizing chloroplast. *Plant Physiol* **171**: 1541–1550. <https://doi.org/10.1104/pp.16.00375>
- Edwards EA, Rawsthorne S, Mullineaux PM (1990) Subcellular distribution of multiple forms of glutathione reductase in leaves of pea (*Pisum sativum* L.). *Planta* **180**: 278–284. <https://doi.org/10.1007/BF00194008>
- Eltayeb AE, Kawano N, Badawi GH, Kaminaka H, Sanekata T, Shibahara T, Inanaga S, Tanaka K (2007) Overexpression of monodehydroascorbate reductase in transgenic tobacco confers enhanced tolerance to ozone, salt and polyethylene glycol stresses. *Planta* **225**: 1255–1264. <https://doi.org/10.1007/s00425-006-0417-7>
- Eltelb HA, Fujikawa Y, Esaka M (2012) Overexpression of the acerola (*Malpighia glabra*) monodehydroascorbate reductase gene in transgenic tobacco plants results in increased ascorbate levels and enhanced tolerance to salt stress. *S Afr J Bot* **78**: 295–301. <https://doi.org/10.1016/j.sajb.2011.08.005>
- Emmanouilidis L, Gopalswamy M, Passon DM, Wilmanns M, Sattler M (2016) Structural biology of the import pathways of peroxisomal matrix proteins. *Biochim Biophys Acta - Mol Cell Res* **1863**: 804–813. <https://doi.org/10.1016/j.bbamcr.2015.09.034>
- Fodor K, Wolf J, Reglinski K, Passon DM, Lou Y, Schliebs W, Erdmann R, Wilmanns M (2015). Ligand-induced compaction of the PEX5 receptor-binding cavity impacts protein import efficiency into peroxisomes. *Traffic* **16**: 85–98. <https://doi.org/10.1111/tra.12238>
- Fodor K, Wolf J, Erdmann R, Schliebs W, Wilmanns M (2012) Molecular requirements for peroxisomal targeting of alanine-glyoxylate aminotransferase as an essential determinant in primary hyperoxaluria type 1. *PLoS Biol* **10**: e1001309. [doi:10.1371/journal.pbio.1001309](https://doi.org/10.1371/journal.pbio.1001309)
- Fogelman E, Kaplan A, Tanami Z, Ginzberg I (2011) Antioxidative activity associated with chilling injury tolerance of muskmelon (*Cucumis melo* L.) rind. *Sci Hortic* **128**: 267–273. <https://doi.org/10.1016/j.scienta.2011.01.034>
- Foyer CH, Noctor G (2003) Redox sensing and signalling associated with reactive oxygen in chloroplasts, peroxisomes and mitochondria. *Physiol Plant* **119**: 355–364. <https://doi.org/10.1034/j.1399-3054.2003.00223.x>
- Foyer CH, Noctor G (2011) Ascorbate and glutathione: the heart of the redox hub. *Plant Physiol* **155**: 2–18. <https://doi.org/10.1104/pp.110.167569>
- Fulda M, Shockey J, Werber M, Wolter FP, Heinz E (2002) Two long-chain acyl-CoA synthetases from Arabidopsis thaliana involved in peroxisomal fatty acid beta-oxidation. *Plant J* **32**: 93–103. <https://doi.org/10.1046/j.1365-3113X.2002.01405.x>
- Gatto G, Geisbrecht B, Gould S, Berg J (2000) Peroxisomal targeting signal-1 recognition by the TPR domains of human PEX5. *Nat Struct Mol Biol* **7**: 1091–1095. <https://doi.org/10.1038/81930>
- Gill SS, Anjum NA, Hasanuzzaman M, Gill R, Trivedi DK, Ahmad I, Pereira E, Tuteja N (2013) Glutathione and glutathione reductase: a boon in disguise for plant abiotic stress defense operations. *Plant Physiol Biochem* **70**: 204–212. <https://doi.org/10.1016/j.plaphy.2013.05.032>
- Gould SG, Keller GA, Subramani S (1987) Identification of a peroxisomal targeting signal at the carboxy terminus of firefly luciferase. *J Cell Biol* **105**: 2923–2931. <https://doi.org/10.1083/jcb.105.6.2923>
- Gullner G, Kömives T, Rennenberg H (2001) Enhanced tolerance of transgenic poplar plants overexpressing g-glutamyl cysteine synthetase towards chloroacetanilide herbicides. *J Exp Bot* **52**: 971–979. <https://doi.org/10.1093/jxbbot/52.358.971>
- Guo Z, Ou W, Lu S, Zhong Q (2006) Differential responses of anti-oxidative system to chilling and drought in four rice cultivars differing in sensitivity. *Plant Physiol Biochem* **44**: 828–836. <https://doi.org/10.1016/j.plaphy.2006.10.024>
- Habib SH, Kausar H, Saud HM (2016) Plant growth-promoting rhizobacteria enhance salinity stress tolerance in okra through ROS-scavenging enzymes. *BioMed Res Int* **6284547**. <https://doi.org/10.1155/2016/6284547>
- Hasanuzzaman M, Bhuyan MHM, Borhannuddin A, Taufika I, Parvin K, Nahar K, Mahmud JA, Fujita M (2019) Regulation of ascorbate-glutathione pathway in mitigating oxidative damage in plants under abiotic stress. *Antioxidants* **8**: 384. <https://doi.org/10.3390/antiox809384>
- Harshvardhan VT, Wu TM, Hong CY (2017) Glutathione reductase and abiotic stress tolerance in plants, pp 265–286. Springer International Publishing AG. https://doi.org/10.1007/978-3-319-66682-2_12
- Hasanuzzaman M, Nahar K, Alam MM, Fujita M (2012) Exogenous nitric oxide alleviates high temperature induced oxidative stress in wheat (*Triticum aestivum*) seedlings by modulating the antioxidant defense and glyoxalase system. *Aust J Crop Sci* **6**: 1314–1323. <https://search.informit.org/doi/10.3316/informit.732190847330318>
- Hu J, Baker A, Bartel B, Linka N, Mullen RT, Reumann S, Zolman BK (2012) Plant Peroxisomes: Biogenesis and Function. *The Plant Cell Preview* **24**: 2279–2303. <https://doi.org/10.1105/tpc.112.096586>
- Hu W, Song X, Shi K, Xia X, Zhou Y, Yu J (2008) Changes in electron transport, superoxide dismutase and ascorbate peroxidase isoenzymes in chloroplasts and mitochondria of cucumber leaves as influenced by chilling. *Photosynthetica* **46**: 581–588. <https://doi.org/10.1007/s11099-008-0098-5>
- Huang C, He W, Guo J, Chang X, Su P, Zhang L (2005) Increased sensitivity to salt stress in an ascorbate-deficient Arabidopsis mutant. *J Exp Bot* **56**: 3041–3049. <https://doi.org/10.1093/jxb/eri301>
- Huang M, Guo Z (2005) Responses of antioxidant system to chilling stress in two rice cultivars differing in sensitivity. *Biol Plant* **49**: 81–84. <https://doi.org/10.1007/s00000-005-1084-3>
- Huang S, Van Aken O, Schwarzlander M, Belt K, Millar AH (2016) The roles of mitochondrial reactive oxygen species in cellular signaling and stress response in plants. *Plant Physiol* **171**: 1551–1559. <https://doi.org/10.1104/pp.16.00166>
- Kataya AR, Reumann S (2010) Arabidopsis glutathione reductase 1 is dually targeted to peroxisomes and the cytosol. *Plant Signal Behav* **5**: 171–175. <https://doi.org/10.4161/psb.5.2.10527>
- Kawahara Y, de la Bastide M, Hamilton JP, Kanamori H, McCombie WR, Ouyang S, Schwartz DC, Tanaka T, Wu J, Zhou S, Childs KL, Davidson RM, Lin H, Quesada-Ocampo L, Vaillancourt B, Sakai H, Lee SS, Kim J, Numa H, Itoh T, Buell CR, Matsumoto T (2013) Improvement of the *Oryza sativa* Nipponbare reference genome using next generation sequence and optical map data. *Rice* **6**: 4. <https://doi.org/10.1186/1939-8433-6-4>
- Kiel JA, van den Berg MA, Fusetti F, Poolman B, Bovenberg R, Veenhuis M, van der Klei IJ (2009) Matching the proteome to the genome: the microbody of penicillin-producing *Penicillium chrysogenum*

- num cells. *Funct Integr Genomics* 9: 167–184. <https://doi.org/10.1007/s10142-009-0110-6>
- Kim PK, Hettema EH (2015) Multiple pathways for protein transport to peroxisomes. *J Mol Biol* 427: 1176–1190. <https://doi.org/10.1016/j.jmb.2015.02.005>
- Kumar S, Gupta D, Nayyar H (2012) Comparative response of maize and rice genotypes to heat stress: status of oxidative stress and antioxidants. *Acta Physiol Plant* 34: 75–86. <https://doi.org/10.1007/s11738-011-0806-9>
- Kumar S, Kaur R, Kaur N, Bhandhari K, Kaushal N, Gupta K, Bains T, Nayyar H (2011) Heat-stress induced inhibition in growth and chlorosis in mung bean (*Phaseolus aureus* Roxb.) is partly mitigated by ascorbic acid application and is related to reduction in oxidative stress. *Acta Physiol Plant* 33: 2091–2101. <https://doi.org/10.1007/s11738-011-0748-2>
- Kunze M (2019) The type-2 peroxisomal targeting signal. *Biochim. Biophys. Acta Mol Cell Res* 1867: 118609. <https://doi.org/10.1016/j.bbamcr.2019.118609>
- Kunze M, Neuberger G, Maurer-Stroh S, Ma J, Eck T, Braverman N, Schmid JA, Eisenhaber F, Berger J (2011) Structural requirements for interaction of peroxisomal targeting signal 2 and its receptor PEX7. *J Biol Chem* 286: 45048–45062. <https://doi.org/10.1074/jbc.M111.301853>
- Lametschwandtner G, Brocard C, Fransen M, Van Veldhoven P, Berger J, Hartig A (1998) The difference in recognition of terminal tripeptides as peroxisomal targeting signal I between yeast and human is due to different affinities of their receptor Pex5p to the cognate signal and to residues adjacent to it. *J Biol Chem* 273: 33635–33643. <https://doi.org/10.1074/jbc.273.50.33635>
- Larkin MA, Blackshields G, Brown NP, Chenna R, McGettigan PA, McWilliam H, Valentin F, Wallace IM, Wilm A, Lopez R, Thompson JD, Gibson TJ, Higgins DG (2007) Clustal W and Clustal X version 2.0. *Bioinformatics* 23: 2947–2948. <https://doi.org/10.1093/bioinformatics/btm404>
- Lazarow PB (2006) The import receptor Pex7p and the PTS2 targeting sequence. *Biochim Biophys Acta - Mol Cell Res* 1763: 1599–1604. <https://doi.org/10.1016/j.bbamcr.2006.05.001>
- Lingner T, Kataya AR, Antonicelli GE, Benichou A, Nilssen K, Chen XY, Siemsen T, Morgenstern B, Meinicke P, Reumann S (2011) Identification of novel plant peroxisomal targeting signals by a combination of machine learning methods and *in vivo* subcellular targeting analyses. *Plant Cell* 23: 1556–1572. <https://doi.org/10.1105/tpc.111.084095>
- Livak KJ, Schmittgen TD (2001) Analysis of relative gene expression data using Real-Time quantitative PCR and the 2⁻(Delta Delta C(T)) method. *Methods* 25: 402–408. <https://doi.org/10.1006/meth.2001.1262>
- Ma C, Haslbeck M, Babujee L, Jahn O, Reumann S (2006) Identification and characterization of a stress-inducible and a constitutive small heat-shock protein targeted to the matrix of plant peroxisomes. *Plant Physiol* 141: 47–60. <https://doi.org/10.1104/pp.105.073841>
- Matre P, Meyer C, Lillo C (2009) Diversity in subcellular targeting of the PP2A B'eta subfamily members. *Planta* 230: 935–945. <https://doi.org/10.1007/s00425-009-0998-z>
- Miller G, Suzuki N, Ciftci-Yilmaz S, Mittler R (2010) Reactive oxygen species homeostasis and signalling during drought and salinity stresses. *Plant Cell Environ* 33: 453–467. <https://doi.org/10.1111/j.1365-3040.2009.02041.x>
- Mittler R (2006) Abiotic stress, the field environment and stress combination. *Trends Plant Sci* 11: 15–19. <https://doi.org/10.1016/j.tplants.2005.11.002>
- Mittler R, Vanderauwera S, Gollery M, Van Breusegem F (2004) Reactive oxygen gene network of plants. *Trend Plant Sci* 9: 490–498. <https://doi.org/10.1016/j.tplants.2004.08.009>
- Nahar K, Rahman M, Hasanuzzaman M, Alam MM, Rahman A, Suzuki T, Fujita M (2016) Physiological and biochemical mechanisms of spermine-induced cadmium stress tolerance in mung bean (*Vigna radiata* L.) seedlings. *Environ Sci Pollut Res Int* 21: 21206–21218. <https://doi.org/10.1007/s11356-016-7295-8>
- Neuberger G, Maurer-Stroh S, Eisenhaber B, Hartig A, Eisenhaber F (2003) Prediction of peroxisomal targeting signal 1 containing proteins from amino acid sequence. *J Mol Biol* 328: 581–592. [https://doi.org/10.1016/S0022-2836\(03\)00319-X](https://doi.org/10.1016/S0022-2836(03)00319-X)
- Niederhoffer K, Meindl-Beinker NM, Kerssen D, Perband U, Schäfer A, Schliebs W, Kunau W (2005) Yeast Pex14p possesses two functionally distinct Pex5p and one Pex7p binding sites. *J Biol Chem* 280: 35571–35578. <https://doi.org/10.1074/jbc.M502460200>
- Noctor G, Foyer CH (1998) Ascorbate and Glutathione: Keeping Active Oxygen Under Control. *Annu Rev Plant Physiol Plant Mol Biol* 49: 249–279. <https://doi.org/10.1146/annurev.arplant.49.1.249>
- Petriv OI, Tang L, Titorenko VI, Rachubinski RA (2004) A new definition for the consensus sequence of the peroxisome targeting signal type 2. *J Mol Biol* 341: 119–134. <https://doi.org/10.1016/j.jmb.2004.05.064>
- Raja V, Wani UM, Wani ZA, Jan N, Kottakota C, Reddy M, Kaul T, John R (2022) Pyramiding ascorbate–glutathione pathway in *Lycopersicon esculentum* confers tolerance to drought and salinity stress. *Plant Cell Rep* 41: 619–637. <https://doi.org/10.1007/s00299-021-02764-8>
- Reisinger S, Schiavon M, Terry N, Smits EAP (2008) Heavy metal tolerance and accumulation in Indian mustard (*Brassica juncea* L.) expressing bacterial g-glutamylcysteine synthetase or glutathione synthetase. *Int J Phytorem* 10: 440–454. <https://doi.org/10.1080/15226510802100630>
- Reumann S (2004) Specification of the peroxisome targeting signals type 1 and type 2 of plant peroxisomes by bioinformatics analyses. *Plant Physiol* 135: 783–800. <https://doi.org/10.1104/pp.103.035584>
- Sabeeha B, Nelofer J, Umer MW, Vaseem R, Rifat J (2022) Co-over expression of Ascorbate Glutathione pathway enzymes improve mercury tolerance in tomato. *Plant Physiol Biochem* 186: 170–181. <https://doi.org/10.1016/j.plaphy.2022.07.015>
- Scandalios JG (1993) Oxygen stress and superoxide dismutases. *Plant Physiol* 101: 7–12. <https://doi.org/10.1104/pp.101.1.7>
- Skoulding NS, Chowdhary G, Deus MJ, Baker A, Reumann S, Wariner SL (2015) Experimental validation of plant peroxisomal targeting prediction algorithms by systematic comparison of *in vivo* import efficiency and *in vitro* PTS1 binding affinity. *J Mol Biol* 427: 1085–1101. <https://doi.org/10.1016/j.jmb.2014.12.003>
- Stanley WA, Filipp FV, Kursula P, Schiller N, Erdmann R, Schliebs W, Sattler M, Wilmanns M (2006) Recognition of a functional peroxisome type 1 target by the dynamic import receptor pex5p. *Mol Cell* 24: 653–663. <https://doi.org/10.1016/j.molcel.2006.10.024>
- Stevens RG, Creissen GP, Mullineaux PM (1997) Cloning and characterization of a cytosolic glutathione reductase cDNA from pea (*Pisum sativum* L.) and its expression in response to stress. *Plant Mol Biol* 35: 641–654. <https://doi.org/10.1023/A:1005858120232>
- Sultana S, Khew CY, Morshed MM, Namasivayam P, Napis S, Ho CL (2012) Over-expression of monodehydroascorbate reductase from a mangrove plant (*AeMDHAR*) confers salt tolerance on rice. *J Plant Physiol* 169: 311–318. <https://doi.org/10.1016/j.jplph.2011.09.004>
- Sun H, Li L, Wang X, Wu S, Wang X (2011) Ascorbate-glutathione cycle of mitochondria in osmoprimed soybean cotyledons in response to imbibitional chilling injury. *J Plant Physiol* 168: 226–232. <https://doi.org/10.1016/j.jplph.2010.07.017>
- Swinkels BW, Gould SJ, Bodnar AG, Rachubinski RA, Subramani S (1991) A novel, cleavable peroxisomal targeting signal at the amino-terminus of the rat 3-ketoacyl-CoA thiolase. *EMBO J* 10: 3255–3262. <https://doi.org/10.1002/j.1460-2075.1991.tb04889.x>
- Tan W, Brestic M, Olsovska K, Yang X (2011) Photosynthesis is improved by exogenous calcium in heat-stressed tobacco plants. *J Plant Physiol* 168: 2063–2071. <https://doi.org/10.1016/j.jplph.2011.06.009>
- Tanya ZB, Leonore R, Donghui L, Yarik M, Robert M, Emily S, Eva H (2015) The Arabidopsis Information Resource: Making and mining the “gold standard” annotated reference plant genome. *Genes* 53: 474–485. <https://doi.org/10.1002/dvg.22877>
- Trivedi D, Gill SS, Yadav S, Tuteja S (2013) Genome-wide analysis of glutathione reductase (GR) genes from rice and Arabidopsis. *Plant Signal Behav* 8: 0e1. <https://doi.org/10.4161/psb.23021>
- Ushimaru T, Nakagawa T, Fujioka Y, Daicho K, Naito M, Yamauchi Y, Nonaka H, Amako K, Yamawaki K, Murata N (2006) Transgenic Arabidopsis plants expressing the rice dehydroascorbate reductase gene are resistant to salt stress. *J Plant Physiol* 163: 1179–1184. <https://doi.org/10.1016/j.jplph.2005.10.002>
- Wang W, Vinocur B, Altman A (2003) Plant responses to drought, salinity and extreme temperatures: towards genetic engineering for stress tolerance. *Planta* 218: 1–14. <https://doi.org/10.1007/s00425-003-1105-5>
- Wania SH, Kumar V, Shriram V, Sah SK (2016) Phytohormones and their metabolic engineering for abiotic stress tolerance in crop plants. *Crop J* 4: 162–176. <https://doi.org/10.1016/j.cj.2016.01.010>
- Xu PL, Guo YK, Bai JG, Shang L, Wang XJ (2008) Effects of long-term chilling on ultrastructure and antioxidant activity in leaves of two cucumber cultivars under low light. *Physiol Plant* 132: 467–478. <https://doi.org/10.1111/j.1399-3054.2007.01036.x>
- Yabuta Y, Motoki T, Yoshimura K, Takeda T, Ishikawa T, Shigeoka S (2002) Thylakoid membrane-bound ascorbate peroxidase is a limiting factor of antioxidative systems under photo-oxidative stress. *Plant J* 32: 915–925. <https://doi.org/10.1046/j.1365-3113x.2002.01476.x>
- Yousuf PY, Hakeem KUR, Chandna R, Ahmad P (2012) *Role of Glutathione Reductase in Plant Abiotic Stress*, pp 149–158. Springer Science. https://doi.org/10.1007/978-1-4614-0634-1_8
- Zandalinas SI, Fritsch FB, Mittler R (2020) Signal transduction networks during stress combination. *J Exp Bot* 71: 1734–1741. <https://doi.org/10.1093/jxb/erz486>
- Zandalinas SI, Soham S, Felix BF, Rajeev KA, Rachel N, Ron M (2021) The impact of multifactorial stress combination on plant growth and survival. *New Phytol* 230: 1034–1048. <https://doi.org/10.1111/nph.17232>

Evaluating the influence of *Aloe barbadensis* extracts on edema induced changes in C-reactive protein and interleukin-6 in albino rats through *in vivo* and *in silico* approaches

Benish Rauf¹, Sobia Alyas¹, Nureen Zahra¹, Sohail Ahmad², Abid Sarwar³, Najeeb Ullah³, Tariq Aziz⁴✉, Metab Alharbi⁵, Abdulrahman Alsahammari⁵ and Abdullah F. Alasmari⁵

¹Institute of Molecular Biology and Biotechnology (IMBB), The University of Lahore, Lahore 54000, Punjab, Pakistan; ²Department of Poultry Production, Faculty of Animal Production and Technology, University of Veterinary and Animal Sciences, Lahore, Pakistan; ³Food and Biotechnology Research Center PCSIR Complex Lahore 54590 Punjab, Pakistan; ⁴Department of Agriculture University of Ioannina Arta 47100 Greece; ⁵Department of Pharmacology and Toxicology, College of Pharmacy, King Saud University, P.O. Box 2455, Riyadh 11451, Saudi Arabia

The current study investigated the *in-vivo* and *in-silico* anti-inflammatory effect of *Aloe barbadensis* in edema induced rat and its blood biomarkers. 60 albino rats (160-200 g) were divided into 4 groups. The 1st group (control) comprised of 6 rats that were treated with saline. The 2nd group (standard) comprised of 6 rats that were treated with diclofenac. The 3rd and 4th experimental groups consisted of 48 rats, treated with *A. barbadensis* gel ethanolic and aqueous extracts respectively at doses of 50, 100, 200 and 400 mg/kg. According to paw sizes, groups III and IV showed 51% and 46% inhibition respectively at the 5th hour, as compared to group II with 61% inhibition. Correlation was negative between biomarkers in group III, while, positive in group IV. Blood samples were collected; C-reactive protein and interleukin-6 were measured using commercially available ELISA kits. Similarly, biomarkers showed significant effect in dose-dependent manner. In molecular docking, for CRP both ligands aloe emodin and emodin showed -7.5 kcal/mol binding energy as compared to diclofenac with -7.0 kcal/mol. For IL-1beta, both ligands showed -4.7 kcal/mol binding energy as compared to diclofenac -4.4 kcal/mol. Hence, we concluded that *A. barbadensis* extracts can be used as an effective drug for managing inflammation.

Keywords: *A. barbadensis*, albino rats, carrageenan, inflammation, biomarkers, computational analysis

Received: 03 March, 2023; **revised:** 21 April, 2023; **accepted:** 07 June, 2023; **available on-line:** 17 June, 2023

✉e-mail: iwockd@gmail.com

Abbreviations: CRP, C-reactive protein; IL-6, Interleukin-6; NSAIDs, Non-Steroidal Anti-Inflammatory Drugs; TNF- α , Tumor necrosis factor alpha

INTRODUCTION

Inflammation is an immunological reaction of vascular tissues to detrimental stimuli like foreign organisms and allergens (Riddle *et al.*, 2022) It involves an intricate array that modulates enzyme activation, mediator discharge, tissue damage and repair. Carrageenan is a phlogistic intermediary causing edema in pathophysiological reactions (Rahmawati *et al.*, 2022) Macrophage releases IL-6, in addition to resident cells into circulation at the site of infection. IL-6 stimulates the production of CRP in the liver. IL-1 β and TNF- α also triggers IL-6. Increas-

ing CRP levels causes a discharge of TNF- α , IL-1 β and IL-6 leading to an inflammation cascade (Mahnashi *et al.*, 2021) Many NSAIDs or SAIDs encompass an edge to manage diseases but often pose serious health issues, so there should be remedies with natural origins with fewer adverse effects (Grzybowski *et al.*, 2018)

The traditional medical system is an ancient health-care system dating back to 5000 years and includes many indigenous practices including Ayurveda, Siddha, and Unani (Maurya *et al.*, 2022) Research on remedial plants has been intended to authenticate its traditional exploitations in the management of different kinds of ailments through the inflection of molecular and biochemical pathways (Zhang *et al.*, 2019) According to the World Health Organization, 80% of the world's inhabitants use phytotherapeutic drugs to meet their basic health and 11% of essential therapeutic drugs are of plant origin (Annad *et al.*, 2019) Asphodelaceae family includes the largest genus "Alloeh," and 548 accepted species possessing potential biological activities. Among them, *Aloe barbadensis* possesses a legendary medicinal reputation. It is a multifunctional xerophytic medicinal plant having 75 bioactive compounds (Leitgeb *et al.*, 2018) The gel is transparent mucilaginous jelly present in parenchyma cells. It has the ability to penetrate the deepest body tissues and ensures good health. *A. barbadensis* has effective anti-inflammatory activity through the inflection of molecular and biochemical pathways (Alven *et al.*, 2021)

A. barbadensis is cultivated worldwide and broadly dispersed in arid regions. It grows in an extensive variety of habitats. PH ranges from 7.0 to 8.5 and the required temperature ranges from 4°C to 21°C. Fully drained grimy topsoil is considered to be ideal for the nurture of the Aloe plant. The Egyptians called it the "Plant of immortality" due to its ability to colonize and ameliorate severe conditions in completely denuded or less vegetated landscapes (Salehi *et al.*, 2018) *A. barbadensis* has abundant therapeutic applications like anti-inflammatory, anti-diabetic, antioxidant, antiseptic, anticancer, immunomodulatory, antipyretic and analgesic activity (Majumder *et al.*, 2019) These properties have been credited to a range (100) of secondary metabolites called phytochemicals present in them. The outer green epidermis consists of mostly glycosides, pre-anthraquinones and anthraquinones. Acemannan and phenolic compounds are the main component of the outer pulp. Salicylic acid, proteins, vitamins, minerals, and enzymes are present in the inner leaf pulp (Wu *et al.*, 2022)

A. barbadensis reduces the leukocyte adhesion and pro-inflammatory cytokines like IL- β , interleukin 17, TNF- α and interleukins by inhibiting cyclooxygenase pathway and lessens prostaglandin E2 production via arachidonic acid (Gupta *et al.*, 2020) Increasing CRP levels causes the discharge of TNF- α , IL-1 β and IL-6. Whilst, promoting edema, CRP has some anti-inflammatory effects by stimulating the discharge of anti-edemic mediators such as IL-1ra and IL-10 (Del Giudice *et al.*, 2018) Bioinformatics is a promising field based on the application of computational techniques to resolve biological problems. It is an effective approach that provides favors such as ligand-receptor binding affinity, time organization and drug-drug interactions. Hence, it aids researchers to design the latest drugs for disease management. Anti-edematous effect of *A. barbadensis* and the molecular docking of some of its constituents by inflammatory proteins identified its potential inhibitors (Dali *et al.*, 2019) The current study is designed to investigate the effect of *A. barbadensis* in the induced inflammatory rat model and its blood biomarkers with molecular docking assay.

MATERIALS AND METHODS

Sample collection and preparation of *A. barbadensis* gel extract

Fresh leaves of *A. barbadensis* were collected as a sample from the University of the Punjab, Lahore and were identified by the staff members of the botany department. After the identification, the leaves were washed with water. Lower 1 inch of leaf base and spines around the leaf were removed using a clean knife. Aloe gel was collected, dried, weighed and mixed with distilled water and 70% ethanol (semi-polar solvent) Bottles were placed at room temperature for 15 days. Extracts were filtered by Whatman no.1 paper and filtrate was permitted to peter out in rotary and glass Petri plates for 1 week as shown in Fig. 1A. When dried, the extract was scratched, measured and stored in labelled Eppendorf for further use (Abubakar *et al.*, 2020).

Experimental rats

Albino rats of either sex weighing (160–200 g) were purchased from the University of Lahore and kept in polypropylene cages in the animal house of (UOL) Before experimental work, rats were kept in fasting condition. After that, they were given distilled water and balanced feed (Alyas *et al.*, 2020)

Drugs used in the experiment.

A. barbadensis gel ethanolic and aqueous extracts were prepared at concentrations of 50, 100, 200 and 400 mg/kg. Diclofenac, normal saline was given at 10 ml/kg and 100 mg/kg respectively. Carrageenan for inducing inflammation was given at 100 mg/kg.

Procedure

Carrageenan-induced paw edema.

1% carrageenan of 100 mg/kg was injected into all rat groups in the left hind paw in the sub-planter region for inducing edema. Paw sizes were taken with a Vernier caliper before and after the injection of carrageenan (Ou *et al.*, 2019)

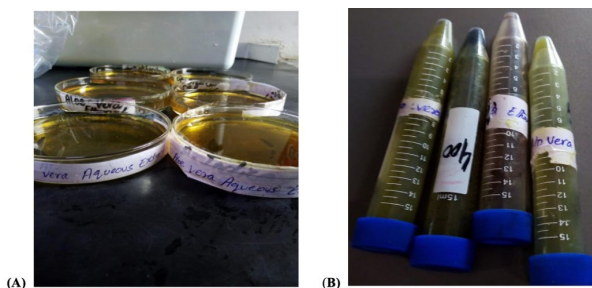


Figure 1. (A) Filtrate of plant extract in glass Petri plates to dry at room temperature. (B) Prepared *A. barbadensis* gel extracts at 4 different concentrations of 50, 100, 200 and 400.

Grouping and treatment schedule

In group I (control) rats were injected with normal saline 10 ml/ kg in the sub-planter region of the hind paw. Paw size was measured with a Vernier calliper. At first, paw size increased due to edema but after 4or 5 hours it begins to decrease and normalized after 18 hours.

In group II (standard) rats were injected with diclofenac 100 mg/kg in sub-planter region of the hind paw. Paw size was measured with a Vernier calliper. At first paw, size was increased due to edema but after injecting diclofenac, it has begun to decrease and got normalized after 3 hours.

In group III and IV *A. barbadensis* gel extracts at doses of 50, 100,200 and 400 mg/kg, were injected Fig. 2A. Paw size was measured with a Vernier calliper. The Formula for calculating the anti-inflammatory activity is given below (Choudhury *et al.*, 2016)

$$\% \text{ inhibition} = \frac{\text{control mean} - \text{treated mean}}{\text{control mean}} \times 100$$

Collection of blood samples and assessment of inflammatory biomarkers

At the end of the experiment blood samples were collected via cardiac puncture in EDTA tubes exclusive of anticoagulant, Fig. 2B, left for 10 minutes. Tubes were centrifuged at 4000 r/min for 10 minutes and obtained serum was put at -20°C for further treatment (Sakr *et al.*, 2019) Different values of edema biomarkers like C-reactive protein and interleukin-6 were examined using commercially available ELISA kits (DiaMetra, Italy) Different concentrations of inflammatory biomarkers were evaluated at different concentrations of dose. Protocols of the above-mentioned parameters are attached in annexure-I and annexure-II.

Anti-inflammatory activity model

Inflammation in the albino rats' paw was caused by the carrageenan and reduced by the diclofenac and ethanolic leaf extracts of *C. paradisi* (50, 100, 200 and 400 mg/kg)

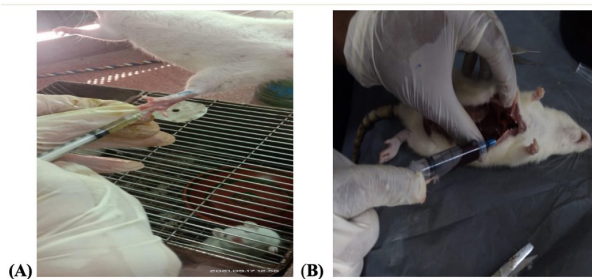


Figure 2. (A) Rats were injected with *A. barbadensis* gel extract in the sub-planter region of the left hind paw. (B) Blood samples collection by cardiac puncture for blood biomarker.

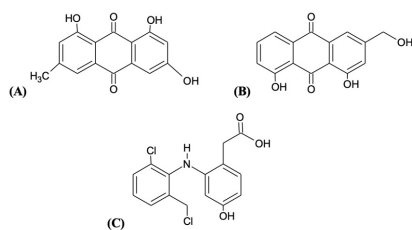


Figure 3. 3D structure of ligand molecules.

(A) Emodin and (B) Aloe-emodin are chemical compounds of aloe gel, selected as ligand molecules to target inflammatory proteins. (C) Diclofenac is a standard drug to target edema proteins.

A total of 36 albino rats were equally divided into three groups (control, standard, and experimental). In the control group, rats were treated with normal saline. In the standard group, rats were treated with diclofenac (100 mg/kg), and in the experimental group, rats were treated with the *C. paradisi* leaf aqueous extract. First, the size of the hind paw of rats was measured, followed by injecting the carrageenan doses (50, 100, 200, and 400 mg/kg) into the hind paw at the sub-planter region. The carrageenan doses start producing inflammation in the rat's hind paws. After 3 hours of carrageenan injection, the doses of *C. paradisi* leaf extract and diclofenac (12.5, 25, 50, and 100 mg/kg) were injected into the hind paw, and the paw size was measured at the time interval of 1, 2, and 3 h.

Anti-pyretic Activity Model

Pyrexia is induced in antipyretic activity in albino rats by normal saline and yeast and then treated with leaf ethanolic extracts of *C. paradisi* (50, 100, 200 and 400 mg/kg) for reducing fever. The rats in this model were also divided according to the anti-inflammatory activity model. In the control group, rats were treated with normal saline (2 ml/kg) below the nape of the neck, and in the standard group, rats were treated with normal saline + brewer's yeast. In the experimental group, rats were treated with doses of ethanolic leaf extracts of *C. paradisi*. After injecting yeast, fever developed after 21 hours, and the highest temperature, 101.81 Fahrenheit was measured.

In silico anti-inflammatory activity of *A. barbadensis*

To begin with *in silico* analysis, different computational tools including chemskekch, chimera, pymol, pyrx, depth

residue and discovery studio were used in support of the anti-inflammatory effect of *A. barbadensis*.

Selection and preparation of ligands

Aloe emodin and emodin are chemical compounds of the anthraquinone family present in the Aloe gel, which possesses an anti-inflammatory role. Therefore, analysis was done targeting these intermediates using as it may control the undue inflammation and consequently prevents acute inflammatory infections. Three ligand molecules emodin, aloe emodin and diclofenac were selected for molecular docking studies. ChemSketch was assessed for the 3D structure of ligand molecules as shown in Fig. 3A, B, C.

Protein preparation and prediction of the active site

CRP and IL-1 β were selected for *in silico* studies as target proteins. The 3D structures of CRP and IL-1 β were occupied from Swiss prot, subsequent to open in Chimera. Out of four, one chain of IL-1 β was selected. All unnecessary ions and metals were removed. The geometry of all hetero groups was assured and the structure of the protein was saved as a PDB file. The active sites of CRP and IL-1 β were found in depth residue.

Protein-ligand docking

To identify the potential anti-inflammatory drug or ligand molecule for a particular protein, PyRx was used for virtual screening. In this procedure, both target proteins CRP and IL-1b and ligand molecules were opted from pdb files; fasten to the binding pocket of the receptor protein. Following to docking run, results were estimated on the strength of bond interaction, binding site energy and ligand-molecule interface. Discovery studio was used to fashion complexes of proteins-ligand molecules and 3D structure of complex for high-quality observation respectively. The Chimera tool was operated to generate the 3D structure of the complex for high-quality observation.

Emodin, aloe-emodin and diclofenac have molecular formulas $C_{15}H_{10}O_5$, $C_{15}H_{10}O_5$ and $C_{14}H_{11}Cl_2NO_2$ with PubChem ID 3220, 10207 and 3033 respectively.

Statistical analysis

The data were subjected to homogeneity of variance to check normality and preceded to one-way ANOVA

Table 1. % age inhibition of paw size in group III (*A. barbadensis* gel ethanolic extracts) in dose-dependent manner exhibiting significant $p < 0.05$ decrease at 5th hour (mean \pm S.D. 30.83 \pm 0.60) with 51% inhibition p -value < 0.0001 . While no such effect was demonstrated in group I (control) (mean \pm S.D. 62.33 \pm 1.67).

Treatment	Reaction Time with mean \pm S.D. (% inhibition) per hour				
	1-hour	2-hour	3-hour	4-hour	5-hour
Group I	45.17 \pm 1.66	47.83 \pm 2.29	55.67 \pm 2.58	64.17 \pm 1.66	62.33 \pm 1.67
Group II	33.17 \pm 1.19 (48%)	34.33 \pm 0.80 (46%)	33.50 \pm 2.03 (52%)	29.50 \pm 1.06 (54%)	25.00 \pm 0.73 (61%)
Dose 50 mg/kg	39.50 \pm 0.76 (17%)	40.17 \pm 1.08 (27%)	40.33 \pm 1.20 (29%)	37.00 \pm 0.58 (21%)	36.00 \pm 0.52 (23%)
Dose 100 mg/kg	37.50 \pm 0.76 (18%)	38.00 \pm 0.58 (21%)	39.00 \pm 1.00 (30%)	35.50 \pm 0.56 (44%)	34.50 \pm 0.43 (45%)
Dose 200 mg/kg	34.00 \pm 0.58 (47%)	38.83 \pm 0.60 (39%)	41.00 \pm 1.29 (36%)	36.17 \pm 1.62 (43%)	32.67 \pm 0.33 (49%)
Dose 400 mg/kg	33.17 \pm 0.60 (46%)	35.50 \pm 0.76 (43%)	38.50 \pm 1.02 (38%)	32.50 \pm 0.43 (49%)	30.83 \pm 0.60 (51%)
p -value	< 0.0001	< 0.0001	< 0.0001	< 0.0001	< 0.0001

Superscripts on different means within the column differ significantly at $p \leq 0.05$.

Table 2. % age inhibition of paw size in group IV (*A. barbadensis* gel aqueous extracts) in dose-dependent manner demonstrating significant $p \leq 0.05$ decrease at 5th hour (mean \pm S.D. 34.50 ± 0.56) with 46% inhibition p -value < 0.0001 . While, no such surge was shown in group I (control) (mean \pm S.D. 62.33 ± 1.67).

Treatment	Reaction Time with mean \pm S.D (% inhibition) per hour				
	1-hour	2-hour	3-hour	4-hour	5-hour
Group I	45.17 ^{ab} \pm 1.66	47.83 ^a \pm 2.29	55.67 ^a \pm 2.58	64.17 ^a \pm 1.66	62.33 ^a \pm 1.67
Group II	33.17 ^d \pm 1.19 (48%)	34.33 ^c \pm 0.80 (46%)	33.50 ^c \pm 2.03 (52%)	29.50 ^e \pm 1.06 (54%)	25.00 ^f \pm 0.73 (61%)
Dose 50 mg/kg	48.00 ^a \pm 0.73 (12%)	50.33 ^a \pm 0.80 (19%)	51.17 ^a \pm 1.54 (20%)	45.83 ^b \pm 1.11 (27%)	45.50 ^b \pm 0.43 (29%)
Dose 100 mg/kg	45.00 ^{ab} \pm 0.58 (18%)	47.67 ^a \pm 0.67 (14.5%)	46.17 ^b \pm 1.35 (28%)	43.17 ^{bc} \pm 0.83 (33%)	41.17 ^c \pm 0.60 (36%)
Dose 200 mg/kg	42.33 ^{bc} \pm 0.88 (34%)	44.17 ^b \pm 0.91 (31%)	45.17 ^b \pm 1.01 (29%)	40.50 ^c \pm 0.76 (36%)	38.17 ^d \pm 0.60 (41%)
Dose 400 mg/kg	39.50 ^c \pm 0.76 (38%)	41.67 ^b \pm 0.76 (35%)	41.67 ^b \pm 1.05 (35%)	35.33 ^d \pm 1.02 (45%)	34.50 ^e \pm 0.56 (46%)

Superscripts on different means within the column differ significantly at $p < 0.05$.

using PROC GLM in SAS software (version 9.1) Duncan's multiple range test, Pearson correlation method and Dunnett's t -test were used considering $p \leq 0.05$.

RESULTS

In this study, the anti-edematous effect of *A. barbadensis* gel ethanolic and aqueous extracts at different concentrations (50, 100, 200 and 400 mg/kg) was observed against rat models of acute edema. The results showed a significant difference between the groups of rats treated with the extracts and the control group.

Effect of *A. barbadensis* on paw sizes in rat

All groups showed a significant increase in paw edema volume injected with 1% carrageenan. Group I showed the most pronounced increase in paw volume (45.17 ± 1.66 , 47.83 ± 2.29 , 55.67 ± 2.58 , 64.17 ± 1.66 and 62.33 ± 1.67) after 1 to 5 hours of injection. While, group III and IV treated with *A. barbadensis* gel extracts at different concentrations (50, 100, 200 and 400 mg/kg) reduced paw edema at 1 to 5 hours as compared to group I. showed an improvement in the edema volume as compared to group I. The improvement was more pronounced at the 5th hour in a dose-dependent manner with PI 23, 45, 49 and 51% closer to diclofenac treated group 61% as shown in Table 1. Group IV treated with *A. barbadensis* gel aqueous extracts showed

($p < 0.05$) % inhibition activity 29, 36, 41 and 46 % closer to group III. *A. barbadensis* gel ethanolic extract (group III) showed the most pronounced effect as compared to *A. barbadensis* gel aqueous extracts (group IV) as shown in Table 2.

Effect of *A. barbadensis* on immunological and biochemical parameter

Carrageenan is an intermediary of edema cascade. C-reactive protein is produced in the liver by IL-6 and is involved in edema and innate immune reactions. In response to inflammation, IL-6 is triggered by macrophages and neutrophils into the bloodstream and increases CRP and IL-6 levels in the blood. Hence, both CRP and IL-6 are broadly recognized as edema biomarkers. To additionally expose the means of the action of *A. barbadensis* gel extracts, the immunological and biochemical parameters in inflammation and pro-inflammatory cytokines like CRP and IL-6 were analyzed by ELISA method. *A. barbadensis* gel extracts significantly ($p \leq 0.05$) reduced the elevated levels of CRP and IL-6 in blood. CRP biomarker values significantly differ in group III (4.75 ± 0.02) and IV (6.94 ± 0.04) as compared to group I (control) with elevated levels of CRP (9.48 ± 0.22) IL-6 values also differ significantly ($p \leq 0.05$) at different doses in extract-treated groups III (13.48 ± 0.02) and IV (14.23 ± 0.03) as compared to group I control (17.21 ± 0.10) as shown in Table 3.

Table 3. Effect of *A. barbadensis* gel extracts on biomarkers CRP (ng/ml) and IL-6 (pg/ml) in group III and IV representing significant p -value < 0.0001 reduction in edema as compared to group I (control).

Treatment	CRP(ng/ml)		IL-6(pg/ml)	
	Group III	Group IV	Group III	Group IV
Group I	9.48 ^a \pm 0.22	9.48 ^a \pm 0.22	17.21 ^a \pm 0.10	17.21 ^a \pm 0.10
Group II	2.48 ^e \pm 0.08	2.48 ^e \pm 0.08	10.42 ^e \pm 0.04	10.42 ^e \pm 0.04
Dose 50 mg/kg	5.28 ^b \pm 0.01	7.76 ^b \pm 0.08	14.08 ^b \pm 0.05	14.92 ^b \pm 0.06
Dose 100 mg/kg	5.17 ^{bc} \pm 0.01	7.55 ^{bc} \pm 0.03	13.80 ^c \pm 0.03	14.60 ^c \pm 0.02
Dose 200 mg/kg	4.93 ^{cd} \pm 0.04	7.39 ^c \pm 0.03	13.58 ^d \pm 0.02	14.43 ^d \pm 0.03
Dose 400 mg/kg	4.75 ^d \pm 0.02	6.94 ^d \pm 0.04	13.48 ^d \pm 0.02	14.23 ^e \pm 0.03
p -value	< 0.0001	< 0.0001	< 0.0001	< 0.0001

Superscripts on different means within the column differ significantly at $p < 0.05$.

Table 4. Comparisons of CRP biomarker means through Dunnett's *t*-test

Group III (Ethanollic extracts)				
Treatment comparison	Difference between means	Simultaneous 95% confidence limits		Significance
Dose 50 vs group I	-4.1967	-4.5680	-3.8253	***
Dose 100 vs group I	-4.3050	-4.6763	-3.9337	***
Dose 200 vs group I	-4.5483	-4.9197	-4.1770	***
Dose 400 vs group I	-4.7300	-5.1013	-4.3587	***
Dose 50 vs group II	2.79833	2.64663	2.95004	***
Dose 100 vs group II	2.69000	2.53829	2.84171	***
Dose 200 group II	2.44667	2.29496	2.59837	***
Dose 400 vs group II	2.26500	2.11329	2.41671	***
Group IV (Aqueous extracts)				
Dose 50 vs group I	-1.7183	-2.1149	-1.3218	***
Dose 100 vs group I	-1.9233	-2.3199	-1.5268	***
Dose 200 vs group I	-2.0900	-2.4866	-1.6934	***
Dose 400 vs group I	-2.5367	-2.9332	-2.10401	***
Dose 50 vs group II	5.27667	5.06355	5.48979	***
Dose 100 vs group II	5.07167	4.85855	5.28479	***
Dose 200 group II	4.90500	4.69188	5.11812	***
Dose 400 vs group II	4.45833	4.24521	4.67145	***

In a comparison of the experimental group IV with the control and standard group, our results showed a significant difference where, *** $p < 0.001$.

The most significant ($p \leq 0.05$) effect of both extracts was observed at a dose of 400 mg/kg closer to group II (standard) treated with diclofenac drug (2.48 ± 0.08) in a dose-dependent manner, where p -value < 0.0001 .

Comparison study of biomarker CRP

By comparing CRP biomarker in group III and IV doses *vs* group I and II, there is a significant $p < 0.001$ mean difference between treated groups at different doses. Group III was treated with a dose of 400 mg/kg *vs* control and standard group has a mean difference of -4.7300 and 2.26500 respectively. Group IV was treated with a dose of 400mg/kg *vs* control and standard group has a mean difference of -2.5367 and 4.45833 respectively as shown in Table 4.

Comparison study of biomarker IL-6

By comparing IL-6 biomarker at different doses, group III treated with a dose of 400 mg/kg *vs* control and standard has a mean difference of -3.73167 and 3.05667, respectively. Group IV treated with a dose of 400 mg/kg *vs* control and standard group has a mean difference of -3.19264 and 3.80333, respectively as shown in Table 5.

Correlation study

The study of correlations is fundamental to the comprehension of biological methods. Correlation analysis is abundantly used to interpret, quantify, and visualize the association between measured values.

According to Pearson's correlation, there was a strong positive correlation (0.19) between biomarker CRP and IL-6 ($p < 0.05$) in the control group. While, it was negative (-0.18) in the standard group and all doses of 50, 100, 200 and 400 mg/kg as highly strong negative correlation (-0.71), weak negative (-0.07), strong negative cor-

relations (-0.27) and (-0.29) correspondingly. In group IV there was a strong negative correlation at higher doses of 200 and 400mg/k (-0.69) and (-0.06) respectively.

A positive correlation was observed between the IL-6 marker and paw size where the correlation was significant at ($p < 0.05$) A strongly positive association was evident with increasing dose rate at 100, 200 and 400 mg/kg i.e. 0.18, 0.58 and 0.89 in group III and 0.2, 0.21 and 0.74 in group IV correspondingly.

Based on the results, CRP marker and paw sizes depicted a negative correlation of -0.37 in both the control group and the standard group. At the 4th hour, there was a positive correlation at a dose of 50 and 100 mg/kg as (0.22) and (0.4) However, the correlation was weakly negative at a dose of 200 and strongly negative at 400 mg/kg i.e. -0.06 and -0.51 correspondingly. At the end of the 4th hour, there was a negative correlation between the biomarker IL-6 and paw sizes ($p < 0.05$) in the experimental group IV at doses 50, 100 and 200 as (-0.9), (-0.36) and (-0.05), respectively as shown in Table 6.

In-silico analysis

In-silico analysis examined the potential of *A. barbadensis* to target cytokine IL-1b and CRP. The molecular binding energy of ligands against CRP scored -7.5Kcal/mol for aloe emodin and emodin and -7.0 Kcal/mol for diclofenac. IL-1b has -4.7Kcal/mol energy for aloe emodin and emodin and -4.4 Kcal/mol for diclofenac. While aloe emodin exhibited the highest score among the three as shown in Fig. 4.

Protein structure analysis and binding pocket with ligands

IL-1b has one chain, and CRP has five chains. All ligand molecules and proteins were adjusted in the grid box.

Table 5. Comparisons of IL-6 biomarker means through Dunnett's *t*-test

Group III (Ethanol extracts)				
Treatment comparison	Difference between means	Simultaneous 95% confidence limits		Significance
Dose 50 vs group I	-3.13667	-3.33813	-2.93521	***
Dose 100 vs group I	-3.41000	-3.61146	-3.20854	***
Dose 200 vs group I	-3.63167	-3.83313	-3.43021	***
Dose 400 vs group I	-3.73167	-3.93313	-3.53021	***
Dose 50 vs group II	3.65167	3.51733	3.78601	***
Dose 100 vs group II	3.37833	3.24399	3.51267	***
Dose 200 group II	3.15667	3.02233	3.29101	***
Dose 400 vs group II	3.05667	2.92233	3.19101	***
Group IV (Aqueous extracts)				
Dose 50 vs group I	-2.28833	-2.49598	-2.08069	***
Dose 100 vs group I	-2.61500	-2.82264	-2.40736	***
Dose 200 vs group I	-2.78000	-2.98764	-2.57236	***
Dose 400 vs group I	-3.19264	-2.98500	-2.77736	***
Dose 50 vs group II	4.50000	4.35519	4.64481	***
Dose 100 vs group II	4.17333	4.02852	4.31814	***
Dose 200 group II	4.00833	3.86352	4.15314	***
Dose 400 vs group II	3.80333	3.65852	3.94814	***

Table 6. Correlation between Paw sizes, CRP and IL-6

Treatment	CRP and IL-6		IL-6 and paw sizes		CRP and Paw sizes	
	Group III	Group IV	Group III	Group IV	Group III	Group IV
Control	0.19	0.19	0.34	0.33	-0.37	0.04
Standard	-0.18	-0.18	0.06	0.06	-0.37	-0.37
Dose 50 mg/kg	-0.71	0.09	-0.33	0.12	0.22	-0.9
Dose 100 mg/kg	-0.07	0.45	0.18	0.2	0.4	-0.36
Dose 200 mg/kg	-0.27	-0.69	0.58	0.21	-0.06	-0.05
Dose 400 mg/kg	-0.29	-0.06	0.89	0.74	-0.51	0.04

¹Correlation was significant at $p \leq 0.05$.

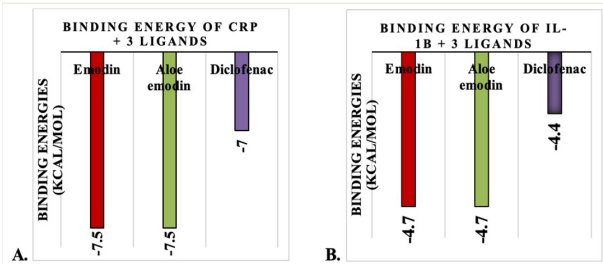


Figure 4. Graphical representation of binding energy of (A) CRP and (B) IL-6 with 3 ligand molecules: Emodin; red, Aloe-emodin; green and diclofenac; purple.

Docking analysis with hydrogen bonds and binding energies

CRP and IL-1beta with ligand molecules interaction. CRP is represented by silver color, the binding pocket: golden color, ligand molecules aloe emodin: green, emodin: reddish brown and diclofenac purple as shown in Fig. 5. Diclofenac with CRP has 2 hydrogen bonds at TRP-204 (2.86 Å) and ARG-205 (2.14 Å) It has 2 hydrophobic bonds at PHE-197 (4.71 Å) and

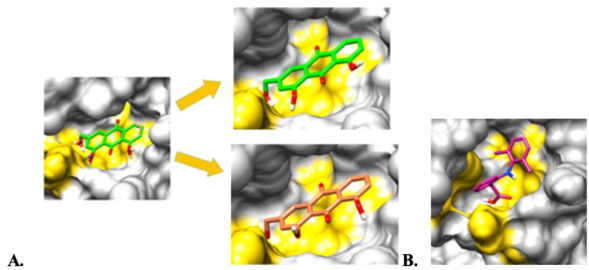


Figure 5. C-reactive protein and ligand molecules (A) emodin and aloe emodin (B) diclofenac.

ASP-175 (3.56 Å) Emodin with CRP has 1 hydrogen bond at ASN-203(1.90 Å) and 2 hydrophobic interactions at TRP-204(4.04 Å) and ASP-175(5.20 Å) Aloe-emodin with CRP has 1 hydrogen bond at ARG (2.90 Å) and 2 hydrophobic interactions at ASP-175(3.77Å) and TRP-205 (5.24 Å) as shown in Fig. 6.

IL-1β is represented by grey color, the binding pocket: golden and ligand molecules aloe emodin: green, emodin: red and diclofenac purple as shown in Fig. 6. Di-

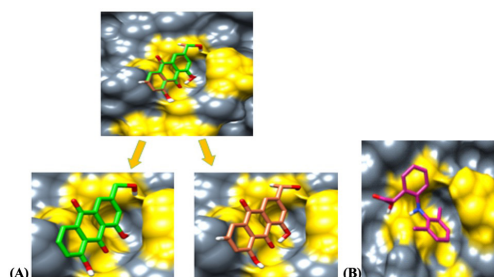


Figure 6. Interlukin-1 β and ligand molecules (A) emodin and aloe emodin (B) diclofenac

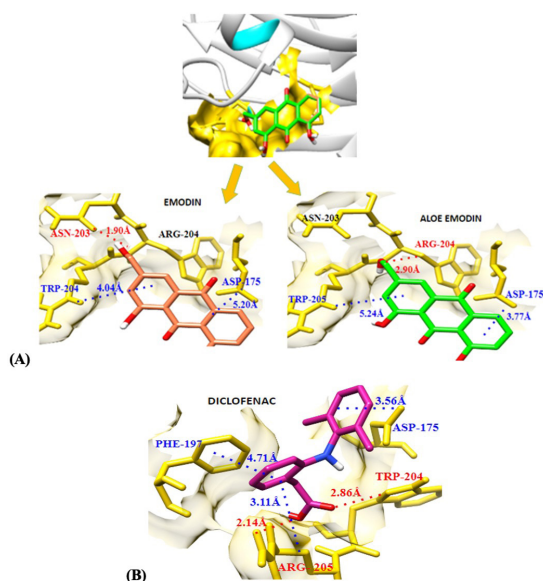


Figure 7. Binding affinities of CRP with ligand molecules (A) emodin and aloe emodin (B) diclofenac. The dotted red lines represent the hydrogen bonds. While dotted blue lines represent hydrophobic interactions.

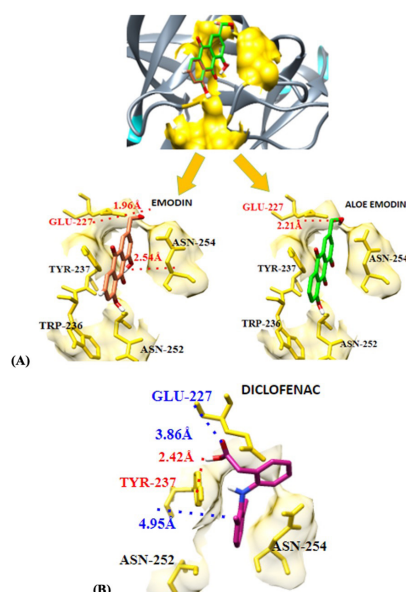


Figure 8. Binding affinities of IL-1 β with ligand molecules (A) emodin and aloe emodin (B) diclofenac. The dotted red lines represent the hydrogen bonds. While dotted blue lines represents hydrophobic interactions.

clofenac with IL-1 β has 1 hydrogen bond at TYR-237 (2.42 Å) and 2 hydrophobic bonds at GLU-227 (3.86 Å) and TYR-237 (4.95 Å) Emodin with IL-1 β has 2 hydrogen bonds at GLU-227 (1.96 Å) and ASN-254 (2.54 Å) Aloe-emodin with IL-1 β has 1 hydrogen bond at GLU-227 (2.21 Å) shown in Fig. 7.

DISCUSSION

The present study was evaluated to assess the medicinal capacity of *A. barbadensis* against induced inflammation in rat paw. Plant-derived remedies exhibit high medicinal properties when extracted *via* organic solvents. Previous studies reported carrageenan for its biphasic outcomes triggered by the production of endogenous mediators in addition to the discharge of serotonin and histamine in the earliest hour compelling vasodilatory cores, following period is mediated by the discharge of prostaglandins, free radicals, interferons, interleukins, tumor necrosis factor, lysozyme and bradykinin in the progression of inflammation from two to six hours post carrageenan injection. Major cells of the immune system are concerned in these processes including mast cells, basophils, and neutrophils. This time is insightful to evaluate the anti-edematous effect of natural and clinically efficient drugs. These natural antioxidants have the ability to detoxify and neutralize free radicals to protect against oxidative stress-induced cellular injuries (Jyothi *et al.*, 2022; Rosales *et al.*, 2020)

In our study, inflammation was significantly ($p < 0.05$) reduced in groups III and IV in dose-dependent manner. A higher dose of 400 mg/kg showed 51% and 46% inhibition of paw edema effective as imitating the action of the drug diclofenac with 61% inhibition. High concentration of anthraquinones, like aloe-emodin, carboxylic acid and polysaccharides in aloe-gel may trigger an immune response, while lower dose do not persuade such an effect. Results of another study were concurrent with our findings (Gupta *et al.*, 2020; Pradhan *et al.*, 2021)

Previous studies have shown that edema may be clarified by reducing cyclooxygenase and PGE2 levels from arachidonic acid. Presence of phytoconstituents, phenolic compounds, flavonoids like quercetin and salicylic acid, choline, vitamins, folic acid, B1, B2, B6, C, β -carotene and α -tocopherol in aqueous extract of *A. barbadensis* gel may be accountable for anti-inflammatory activity in sub-acute edema model. The results of another study were concurrent with our findings (Gul *et al.*, 2023; Naureen *et al.*, 2023; Naveed *et al.*, 2022b; Jhundoo *et al.*, 2020) CRP is an acute phase protein and IL-6 is a reliable biomarker (cell signaling agent) which amplifies at the inflammation site. The previous studies reported CRP as a key role in inflammatory courses and host retorts to infections together with the complement pathway, nitric oxide (NO) release, apoptosis, phagocytosis, and the assembly of cytokines, predominantly tumor necrosis factor- α and interleukin-6. Group I demonstrated a noteworthy elevation in serum levels of CRP and IL-6 post-carrageenan injection. In a similar trend, others reported remarkable elevation in serum levels of IL-6 and CRP in rats subsequent to 4 hours post carrageenan injection (Acharya *et al.*, 2019)

A higher dose of extract (400 mg/kg) has exposed an enhanced inhibitory effect in IL-6 than the lower dose (50mg/kg) in groups III and IV. For CRP, it demonstrated inhibition of increased serum cytokines and proteins in dose-dependent manner. The use of *A. barbadensis* in some inflammatory cascades confirmed the occur-

rence of active biochemical compounds and minerals and gallic acid related to these edema inhibition activities (Asci *et al.*, 2017). The correlation was positive between biomarkers CRP and IL-6 in group IV in our findings. Similarly, other reports are in concurrence with our data set showing that classic and trans-pathways together take part in the inflammatory bout, although, both pathways are diverse. Through classic signaling in the liver, IL-6 up-regulates the production of CRP, with lipolysis. IL-6 correlates well with the severity of other inflammatory processes interceding the edema reaction (Vreugdenhil *et al.*, 2018).

Molecular docking is a new strategy to analyze binding energy or interaction. Results evidenced that phytoconstituents emodin and aloe-emodin showed interaction with active sites of protein concerned with inflammation and have utmost inhibitory potential against CRP and IL-1 β and could be practiced in the treatment of edema disorders. The binding interaction of the phytoconstituents of *A. barbadensis* and standard drug diclofenac against edema cytokines like IL-1 β and protein CRP exhibited maximum affinity -7.5 by aloe emodin, diclofenac with -7.0 Kcal/mol and emodin with -4.5 Kcal/mol binding score. Aloe-emodin demonstrated the utmost part for inhibiting edema, which are in accordance with our findings (Syed *et al.*, 2023; Sana *et al.*, 2023; Khushnuma *et al.*, 2023; Aziz *et al.*, 2023; Ahmad *et al.*, 2023; Naureen *et al.*, 2023; Kaloni *et al.*, 2019; Modak *et al.*, 2021; Saleem *et al.*, 2023; Naveed *et al.*, 2022a).

CONCLUSIONS

Use of SAID and NSAIDS possibly helpful in disease management but their adverse impacts pretence health problems. Therefore, therapies with safe natural sources are mandatory. Our study concluded that potentially bioactive phytochemicals in *A. barbadensis* detoxify and counteract free radicals to reduce edema. Hence, our study supports the traditional use of *A. barbadensis* gel extract as an effective and safe drug against inflammation.

Declarations

Ethical Approval. Ethical approval for this research work was granted by the Institute of Molecular Biology and Biotechnology of the University of Lahore. Animal maintenance and experimental protocols were carried out in accordance with guidelines approved by the Care Committee of Animal House at the University of Lahore.

Conflict of Interest. The authors declare that the research was conducted in the absence of any commercial or financial relationships that could be construed as a potential conflict of interest. No conflict of interest. All the authors declare no conflict of interest.

Author Contributions. Conceptualization, B.R., S.I., S.A. and B.Z.; methodology, T.A.; software, B.R., S.I., S.A. and B.Z.; validation, M.A., and T.A.; formal analysis, A.A.S.; investigation, M.A.; resources, T.A.; data curation, A.S.; writing – original draft preparation, A.S. and N.U.; writing – review and editing, M.A. and A.A.S.; visualization, N.U. supervision, T.A.; project administration, M.A., A.F.A. and A.A.S.; funding acquisition, T.A.

Funding. No external funding was received.

Acknowledgments. The authors greatly acknowledge and express their gratitude to the Researchers Supporting Project number (RSP2023R462), King Saud University, Riyadh, Saudi Arabia.

REFERENCES

- Abubakar AR, Haque M (2020) Preparation of medicinal plants: Basic extraction and fractionation procedures for experimental purposes. *J Pharm Bioallied Sci* 12: 1. https://doi.org/10.4103/jpbs.JPBS_175_19
- Acharya P, Talahalli RR (2019) Aging and hyperglycemia intensify dyslipidemia-induced oxidative stress and inflammation in rats: assessment of restorative potentials of ALA and EPA+ DHA. *Inflammation* 42: 946–952. <https://doi.org/10.1007/s10753-018-0949-6>
- Ahmad B, Muhammad AY, Maria H, Khan AA, Aziz T, Alharbi M, Alsahammari A, Alasmari AF (2023) Curative effects of *Dianthus orientalis* against paracetamol triggered oxidative stress, hepatic and renal injuries in rabbit as an experimental model. *Separations* 10: 182. <https://doi.org/10.3390/separations10030182>
- Alven S, Khwaza V, Oyediji OO, Aderibigbe BA (2021) Polymer-based scaffolds Loaded with aloe vera extract for the treatment of wounds. *Pharmaceutics* 13: 961. <https://doi.org/10.3390/pharmaceutics13070961>
- Alyas S, Zahra N, Zahid N, Nisar A, Ahmad MI (2020) Anti-inflammatory, antipyretic and analgesic activities of ethanol extract of *Eugenia jambolana* lam. *Int J Biosci* 16: 506–511. <http://dx.doi.org/10.12692/ijb/16.3.493-498>
- Anand U, Jacobo-Herrera N, Altemimi A, Lakhssassi N (2019) A comprehensive review on medicinal plants as antimicrobial therapeutics: potential avenues of biocompatible drug discovery. *Metabolites* 9: 258. <https://doi.org/10.3390/metabo9110258>
- Asci H, Ozmen O, Ellidag HY, Aydin B, Bas E, Yilmaz N (2017) The impact of gallic acid on the methotrexate-induced kidney damage in rats. *J Food Drug Anal* 25: 890–897. <https://doi.org/10.1016/j.jfda.2017.05.001>
- Aziz T, Fawad I, Ayaz AK, Shafiq UR, Ghazala YZ, Metab A, Abdulrahman A, Abdullah FA (2023) Assessing the pharmacological and biochemical effects of *Sabia hispanica* (Chia seed) against oxidized *Helianthus annuus* (sunflower) oil in selected animals. *Acta Biochim Pol* 70: 211–218. https://doi.org/10.18388/abp.2020_6621
- Choudhury D, Roy D (2016) Evaluation of anti-inflammatory effect of aqueous extract of Aloe vera in albino rats. *Int J Basic Clin Pharmacol* 5: 2488–2495. <https://doi.org/10.18203/2319-2003.ijbcp20164110>
- Dali Y, Abbasi SM, Khan SA, Larra SA, Rasool R, Ain QT, Jafar TH (2019) Computational drug design and exploration of potent phytochemicals against cancer through in silico approaches. *Biomedical Lett* 5: 21–26
- Del Giudice M, Gangestad SW (2018) Rethinking IL-6 and CRP: Why they are more than inflammatory biomarkers, and why it matters. *Brain Behav Immun* 70: 61–75. <https://doi.org/10.1016/j.bbi.2018.02.013>
- Grzybowski A, Kanclerz P (2018) The role of steroids and NSAIDs in prevention and treatment of postsurgical cystoid macular edema. *Curr Pharm Design* 24: 4896–4902. <https://doi.org/10.2174/1381612825666190206104524>
- Gul R, Rahmatullah Q, Ali H, Bashir A, Ayaz AK, Aziz T, Metab A, Abdulrahman A, Alasmari A (2023) Phytochemical, antimicrobial, radical scavenging and in-vitro biological activities of *Teucrium stockianum* leaves. *J Chil Chem Soc* 68: 5748–5754. <https://www.jccchems.com/index.php/JCCHEMS/article/view/2295/582>
- Gupta VK, Kumar A, Pereira MD, Siddiqi NJ, Sharma B (2020) Anti-inflammatory and antioxidative potential of Aloe vera on the carap and malathion mediated toxicity in Wistar rats. *Int J Environ Res Public Health* 17: 5177. <https://doi.org/10.3390/ijerph17145177>
- Jhundoo HD, Siefen T, Liang A, Schmidt C, Lokhnauth J, Béduneau A, Pellequer Y, Larsen CC, Lamprecht A (2020) Anti-inflammatory activity of chitosan and 5-amino salicylic acid combinations in experimental colitis. *Pharmaceutics* 12: 1038. <https://doi.org/10.3390/pharmaceutics12111038>
- Jyothi VG, Pawar J, Fernandes V, Kumar R, Singh C, Singh SB, Madan J, Khatri DK (2022) Film forming topical dermal spray of meloxicam attenuated pain and inflammation in carrageenan-induced paw oedema in Sprague Dawley rats. *J Drug Deliver Sci Technol* 70: 103195. <https://doi.org/10.1016/j.jddst.2022.103195>
- Kaloni D, Tiwari A, Biswas S (2019) Aloe vera as an antagonist for TNF- α : In-silico study. *Pharmacology* 4
- Khushnuma S, Tariq A, Ayaz AK, Ali M, Shafiq UR, Metab A, Abdulrahman A, Abdullah FA (2023) Evaluating the in-vivo effects of olive oil, soya bean oil, and vitamins against oxidized ghee toxicity. *Acta Biochim Pol* Epub: No 6549. https://doi.org/10.18388/abp.2020_6549
- Khushnuma S, Tariq A, Ayaz AK, Ali M, Shafiq UR, Metab A, Abdulrahman A, Abdullah FA (2023) Evaluating the in-vivo effects of olive oil, soya bean oil, and vitamins against oxidized ghee toxicity. *Acta Biochim Pol* 6549. https://doi.org/10.18388/abp.2020_6549
- Leitgeb M, Kupnik K, Knez Ž, Primožič M (2021) Enzymatic and antimicrobial activity of biologically active samples from *Aloe arborescens* and *Aloe barbadensis*. *Biology* 10: 765. <https://doi.org/10.3390/biology10080765>
- Mahnashi MH, Jabbar Z, Irfan HM, Asim MH, Akram M, Saif A, Alshahrani MA, Alshehri MA, Asiri SA (2021) Venlafaxine dem-

- onstrated anti-arthritis activity possibly through down regulation of TNF- α , IL-6, IL-1 β , and COX-2. *Inflammopharmacology* **29**: 1413–1425. <https://doi.org/10.1007/s10787-021-00849-0>
- Majumder R, Das CK, Mandal M (2019) Lead bioactive compounds of *Aloe vera* as potential anticancer agent. *Pharmacol Res* **148**: 104416. <https://doi.org/10.1016/j.phrs.2019.104416>
- Maurya VK, Kumar S, Bhatt ML, Saxena SK (2022) Antiviral activity of traditional medicinal plants from Ayurveda against SARS-CoV-2 infection. *J Biomol Struct Dynamics* **40**: 1719–1735. <https://doi.org/10.1080/07391102.2020.1832577>
- Modak D, Paul S, Sarkar S, Thakur S, Bhattacharjee S (2021) Validating potent anti-inflammatory and anti-rheumatoid properties of *Drynaria quercifolia* rhizome methanolic extract through *in vitro*, *in vivo*, *in silico* and GC-MS-based profiling. *BMC Comp Med Therap* **21**: 1–20. <https://doi.org/10.1186/s12906-021-03265-7>
- Naureen Z, Tahira F, Muhammad H, Basit Z, Abid S, Tariq A, Metab A, Abdulrahman A, Abdullah FA (2023) *In-vivo* and *in-silico* analysis of anti-inflammatory, analgesic, and anti pyretic activities of *Citrus paradisi* leaf extract. *J Chil Chem Soc* **68**: 5813–5821. <https://www.jcchems.com/index.php/JCCEMS/article/view/2306/590>
- Naveed M, Batool H, Rehman SU, Javed A, Makhdoom SI, Aziz T, Mohamed AA, Sameeh MY, Alruways MW, Dabool AS, Alruways MW, Almalki AA, Alamri AS, Alhomrani M (2022) Characterization and evaluation of the antioxidant, antidiabetic, anti-inflammatory, and cytotoxic activities of silver nanoparticles synthesized using *Brachycton populneus* leaf extract. *Processes* **10**: 1521. <https://doi.org/10.3390/pr10081521>
- Naveed M, Bukhari B, Aziz T, Zaib S, Mansoor MA, Khan AA, Shahzad M, Dabool AS, Alruways MW, Almalki AA, Alamri AS, Alhomrani M (2022) Green synthesis of silver nanoparticles using the plant extract of *Acer oblongifolium* and study of its antibacterial and antiproliferative activity *via* mathematical approaches. *Molecules* **27**: 4226. <https://doi.org/10.3390/molecules27134226>
- Ou Z, Zhao J, Zhu L, Huang L, Ma Y, Ma C, Luo C, Zhu Z, Yuan Z, Wu J, Li R (2019) Anti-inflammatory effect and potential mechanism of betulinic acid on λ -carrageenan-induced paw edema in mice. *Biomed Pharmacother* **118**: 109347. <http://doi.org/10.1016/j.biopha.2019.109347>
- Pradhan R, Singh S (2021) Antiarthritic activity of aqueous extract of *Aloe vera* in Freund's complete adjuvant-induced arthritis model in Wistar albino rats. *Natl J Physiol Pharm Pharmacol* **11**: 1399–1405. <https://doi.org/10.5455/njppp.2021.11.10368202123102021>
- Rahmawati L, Park SH, Kim DS, Lee HP, Aziz N, Lee CY, Kim SA, Jang SG, Kim DS, Cho JY (2022) Anti-inflammatory activities of the ethanol extract of *Prasiola japonica*, an edible freshwater green alga, and its various solvent fractions in lps-induced macrophages and carrageenan-induced paw edema *via* the ap-1 pathway. *Molecules* **27**: 194. <https://doi.org/10.3390/molecules27010194>
- Riddle RB, Jennbacken K, Hansson KM, Harper MT (2022) Endothelial inflammation and neutrophil transmigration are modulated by extracellular matrix composition in an inflammation-on-a-chip model. *Sci Rep* **12**: 6855. <https://doi.org/10.1038/s41598-022-10849-x>
- Rosales C (2020) Neutrophils at the crossroads of innate and adaptive immunity. *J Leucocyte Biol* **108**: 377–396. <https://doi.org/10.1002/JLB.4MIR0220-574RR>
- Sakr HF, Abbas AM, Khalil K, Shata AM (2019) Modulatory effect of concomitant administration of sitagliptin and vitamin E on inflammatory biomarkers in rats fed with high fat diet: role of adiponectin. *J Physiol Pharmacol* **70**: 955–967. <https://doi.org/10.26402/jpp.2019.6.13>
- Saleem A, Afzal M, Naveed M, Makhdoom SI, Mazhar M, Aziz T, Khan AA, Kamal Z, Shahzad M, Alharbi M, Alshammari A (2022) HPLC, FTIR and GC-MS analyses of *Thymus vulgaris* phytochemicals executing *in vitro* and *in vivo* biological activities and effects on COX-1, COX-2 and gastric cancer genes computationally. *Molecules* **27**: 8512. <https://doi.org/10.3390/molecules27238512>
- Salehi B, Albayrak S, Antolak H, Kregiel D, Pawlikowska E, Sharifirad M, Uprety Y, Tsouh Fokou PV, Yousef Z, Amiruddin Zakaria Z, Varoni EM (2018) *Aloe* genus plants: from farm to food applications and phytopharmacotherapy. *Int J Mol Sci* **19**: 2843. <https://doi.org/10.3390/ijms19092843>
- Sana, Shafiq UR, Muhammad Z, Ayaz AK, Tariq A, Zafar I, Waqar A, Muhammad S, Metab A, Abdulrahman A (2022) Hepatoprotective effects of walnut oil and *Caralluma tuberculata* in experimentally induced liver toxicity in selected animals. *Acta Biochim Pol* **69**: 871–878. https://doi.org/10.18388/abp.2020_6387
- Syed WAS, Muhammad SA, Mujaddad UR, Azam H, Abid S, Aziz T, Metab A, Abdulrahman A, Abdullah FA (2023) *In-vitro* evaluation of phytochemicals, heavy metals and antimicrobial activities of leaf, stem and roots extracts of *Caliba palustris* var. alba *J Chil Chem Soc* **68**: 5807–5812. <https://www.jcchems.com/index.php/JCCEMS/article/view/2306/590>
- Vreugdenhil B, van der Velden WJ, Feuth T, Kox M, Pickkers P, van de Veerdonk FL, Blijlevens NM, Brüggemann RJ (2018) Moderate correlation between systemic IL-6 responses and CRP with trough concentrations of voriconazole. *Brit J Clin Pharmacol* **84**: 1980–1988. <https://doi.org/10.1111/bcp.13627>
- Wu Y, Li K, Zeng M, Qiao B, Zhou B (2022) Serum metabolomics analysis of the anti-inflammatory effects of gallic acid on rats with acute inflammation. *Front Pharmacol* **992**. <https://doi.org/10.3389/fphar.2022.830439>
- Zhang R, Zhu X, Bai H, Ning K (2019) Network pharmacology databases for traditional Chinese medicine: review and assessment. *Front Pharmacol* **10**: 123. <https://doi.org/10.3389/fphar.2019.00123>

Evaluating the *in-vivo* effects of olive oil, soya bean oil, and vitamins against oxidized ghee toxicity

Khushnuma Saleema^{1†}, Tariq Aziz^{2†✉}, Ayaz Ali Khan^{3✉}, Ali Muhammad¹, Shafiq ur Rahman⁴, Metab Alharbi⁵, Abdulrahman Alshammari⁵ and Abdullah F. Alasmari⁵

¹Department of Zoology, Islamia College University, Peshawar, 25120, Pakistan; ²Department of Agriculture, University of Ioannina Arta 47100, Greece; ³Department of Biotechnology, University of Malakand, Chakdara, 18800, Pakistan; ⁴Department of Environmental Science, Shaheed Benazir Bhutto University, Sheringal Dir Upper, Pakistan; ⁵Department of Pharmacology and Toxicology, College of Pharmacy, King Saud University, P.O. Box 2455, Riyadh 11451, Saudi Arabia

The aim of this study was to examine the protective role of various lipids (olive and soya oil) and vitamin (E and C) against the toxicity of thermally oxidized ghee in rabbits. Vanaspati ghee was thermally oxidized on a hot plate at 100°C for ten consecutive hours, and the oxidized ghee was stored in a refrigerator at –20°C until administration. Thirty male rabbits were purchased as experimental animals at a local market and were divided into ten corresponding groups of three based on their body weight. The blood samples of 5 ml were collected on day 0, 7, and 14 of the experiment for the analysis of hematological and biochemical serum parameters. We observed that oxidized ghee significantly elevated ALT level by affecting liver hepatocytes. Furthermore, vitamin E rapidly decreased the ALT levels compared to vitamin C and other oils. The oxidized ghee caused a significant increase in cholesterol compared to the other groups. Vitamin E and C showed the best antioxidant activity and decreased cholesterol levels to normal. Histopathological examinations of the normal rabbits' liver sections revealed no significant histological abnormality. The liver of the rabbits fed with oxidized ghee had an intact lobular architecture but the portal tracts showed inflammation and mild fibrosis, the bile ducts showed proliferation, and the hepatocytes showed feathery degeneration. In the liver sections from the groups fed with oxidized ghee and different doses of olive oil inflammation in portal tracts and large vacuoles in the hepatocytes were observed. The group fed with oxidized ghee and vitamin E had intact lobular architecture with no significant histological abnormality in portal tracts but fatty changes were present in the hepatocytes. These findings support the antioxidant activity of vitamins C and E as they reduced liver infection caused by oxidized ghee. It was concluded that oxidized ghee was highly toxic and not safe for consumption. The present study indicated that soya bean oil and vitamin E were more effective in protecting against the toxicity of thermally oxidized ghee than olive oil and vitamin C.

Keywords: olive oil, soybean oil, vanaspati ghee, hepatotoxicity, ALT, AST

Received: 10 November, 2022; **revised:** 03 February, 2023; **accepted:** 26 February, 2023; **available on-line:** 10 May, 2023

✉e-mail: iwockd@gmail.com (TA); ayazkhan@uom.edu.pk (AAK)

Acknowledgments of Financial Support: The authors greatly acknowledge and express their gratitude to the Researchers Supporting Project number (RSP2023R462), King Saud University, Riyadh, Saudi Arabia

Abbreviations: ALT, alanine transaminase; HDL, high density lipoproteins; LDL, low density lipoprotein; TG, Triglycerides

INTRODUCTION

Vegetable oils and fats make up a significant portion of our daily diet. Lipids comprise triglycerides, cholesterol, and antioxidants, among others, and when subjected to cooking or heating can convert into oxidized compounds like hydroperoxides, epoxides, and hydroxides (Fatiha *et al.*, 2020; Zeb & Khan, 2019; Kamal *et al.*, 2003). The three above types of oxidized compounds produced during heating usually convert into other compounds; however, the hydroperoxides convert into a variety of oxidized products that have been documented to be toxic for humans; and some of them are deemed to contribute to liver cancer (Zeb & Mehmood., 2012). Lipids, react with reactive oxygen species in a process is known as lipid peroxidation, which proceeds by a free radical chain reaction mechanism enhancing the production of free radicals (Gutteridge 1995; Halliwell & Gutteridge 1990). Free radicals significantly contribute to developing diseases like diabetes, atherosclerosis, cancer, chronic inflammatory disorders, and neurodegenerative diseases (Mobin, 2012). Free radicals are usually neutralized by enzymes (superoxide dismutase, catalase, and glutathione peroxidase) and antioxidants (vitamin E, vitamin C, carotenes, flavonoids, glutathione, uric acid, and taurine) (Jadhav & Priyanka, 2016). The benefits of olive oil for human health have been well reported and documented in the literature. Olive oil comprises monounsaturated fatty acids, like oleic acid, vitamin E, and polyphenols, which have beneficial effects on cardiac health (Nocella *et al.*, 2018). Particular attention has been given to VOO (virgin olive oil) because it contains antioxidants such as lipophilic and hydrophilic phenols (Kiritsakis *et al.*, 2020). Olive oil also contains 3,4-dihydroxy phenyl ethanol, an antioxidant with antithrombotic action (Paiva *et al.*, 2017). Vitamins E and C are known antioxidants that prevent the harmful effect of free radicals (Chan & Alvin, 1993). The co-loading of antioxidant vitamins E and C in olive oil emulsions has shown to be effective in maintaining the peroxide values (Cuomo *et al.*, 2020). Soybean oil is the leading edible vegetable oil in the world and is usually consumed in partially hydrogenated forms (Cinelli *et al.*, 2020). It contains many aromatic compounds, such as eugenol, which have antioxidant properties; it is worth mentioning that this oil is also one of the richest sources of vitamin E (Applewhite, 1981; Lee & Shibamoto, 2000). Commonly known as hydrogenated vegetable oils, Vanaspati ghee and banaspati ghee are high in trans fats, are hazardous to health, contributing to diseases like cardiovas-

cular diseases, obesity, and cancer (Rusin & Krawczyk, 2011). Ghee, when heated up to 120°C, becomes oxidized and hazardous for health, and is known as thermally oxidized ghee (Iqbal, 2014). It has been reported that thermally oxidized ghee causes *in vivo* toxicity by increasing hydroperoxide production and decreasing the radical scavenging assay (RSA) value. Oxidized ghee's toxicity increases with the oxidation time, leading to hypertriglyceridemia, and increase in total cholesterol and LDL-cholesterol level (Zeb & Mehmood, 2012). As ghee is used to fry and cook food in our society, and persistently heated for a long time, hence, ghee oxidation occurs and its oxidative products, toxic to humans, accumulate in food. Therefore, in this study we describe the toxic effects of the heated ghee on a number of hematological and biochemical parameters and liver histology in rabbits. Moreover, a number of antioxidant oils and vitamins were used along with oxidized ghee to determine their effect against the ill effects of thermally oxidized ghee.

MATERIALS AND METHODS

Materials:

The Vanaspati ghee used in this research was from Halal Associated Industries Limited. The olive oil was packed and exported by Aceites Borges Pont, S.A.U, marketed in Pakistan by Zaitoon Pakistan (Pvt) Ltd, Islamabad, Pakistan. The soya bean oil utilized in this experiment was from Agro Processors and Atmospheric Gasses Pvt Ltd. The vitamin E: DL-alpha tocopherol acetate was from Merck Pharmaceuticals (Private Limited, 200 mg), and the Vitamin C was from Abbot Laboratories (Pak, 500 mg).

Thermal oxidation of ghee:

Vanaspati ghee was thermally oxidized on a hot plate at 100°C for ten consecutive hours, and oxidized ghee was stored in the refrigerator at -20°C until administration.

Experimental animals

Approval of the study was granted by Advanced Studies and Research Board and Ethical committee of Islamia College University, Peshawar, Pakistan. Rabbits were purchased from the dealers in Chakdara city and kept in the Bio-Park for two weeks. Green fodder and water were provided *ad libitum*. The experiments were conducted in the Biotechnology Department, University of Malakand, Chakdara, Dir (Lower), Khyber Pakhtunkhwa, Pakistan.

Experimental groups

After acclimatization, thirty rabbits were divided into ten replicate groups based on their body weight. Each group comprised three male rabbits. Group A (NC) served as negative control and was fed a regular diet. Group B (OG) was provided with oxidized ghee at the dose rate of 2 g per a kg of body weight. Group C was fed with oxidized ghee at the dose rate of 2 g/kg, and 1 g/kg of olive oil as an antioxidant. Group D was fed with oxidized ghee at 2 g/kg and an extra virgin olive oil at a dose rate of 2 g/kg body weight. Group E was fed with oxidized ghee at 2 g/kg, and 1 g/kg of soya bean oil. Group F was fed with oxidized ghee at 2 g/kg, and

2 g/kg of soya-bean oil. Group G was fed with oxidized ghee at 2 g/kg, and vitamin E at 100 mg/kg. Group H was fed with oxidized ghee at 2 g/kg and vitamin E at 200 mg/kg. Group I was fed with oxidized ghee at 2 g/kg, and vitamin C was given as an antioxidant at 100 mg/kg. Group J was fed with oxidized ghee at 2 g/kg with vitamin C as an antioxidant at 200 mg/kg.

Blood collection

The 5 ml blood samples were collected on experimental day, 0, 7, and 14, to analyze hematological and biochemical parameters of the serum. Strict aseptic conditions were applied during the blood sampling.

Hematological parameters

Three milliliters of the whole blood samples were transferred to heparinized tubes. A fully automated blood hematology analyzer (SYS MIX, Japan) was used to measure total red blood cells number, hemoglobin concentration, hematocrit value, mean corpuscular cell volume, mean corpuscular hemoglobin, mean corpuscular hemoglobin concentration, total leukocyte count, and neutrophils, eosinophils, lymphocytes, and platelets count.

Analysis of the biochemical parameters

Biochemical parameters of the serum were analyzed using total cholesterol and triglycerides test kits (Merck, Germany) and human HDL-c, LDL-c, ALT, and glucose assay kits (HUMAN Diagnostics, Germany).

Histopathology

The rabbits were sacrificed at the end of the experiment, and their livers were dissected and stored in a formalin solution as previously described in Ayaz and others (Ayaz *et al.*, 2017). Each animal's liver was washed in normal saline solution and cut into slices. The slices were embedded in paraffin after dehydration with 100% ethanol and fixation with 10% formalin. The slices were then cut into 4 to 5 micrometers thick sections and stained with hematoxylin-eosin (HE, M 7000 D, SWIFT, Japan). A light microscope was used to examine the sections, while a 1.3 MP digital camera placed atop the microscope was used to capture images.

Statistical Analysis

All the experimental points consisted of 3 different samples. Data were analyzed by one-way analysis of variance (ANOVA) using GraphPad Prism version 5.

RESULTS

Analysis of blood biochemical parameters

After 7 days of the experiment, rabbit blood samples were collected, and serum was isolated from the samples for biochemical measurements.

It was observed that oxidized ghee significantly elevated the ALT level, suggesting affecting liver hepatocytes. Vitamin E decreased ALT level to the greatest extent, as compared to vitamin C and other oils that were fed.

The oxidized ghee diet caused significant raise in cholesterol levels that was mitigated with vitamins C and E, olive oil and soybean oil. The groups fed with vitamin E and C showed the greatest improvement of cholesterol

Table 1. Biochemical parameters in the studied groups of rabbits measured on day 7 and day 14 of the treatment.

Groups	ALT (IU/L)	Cholesterol (mg/dl)			TG (mg/dl)			HDL (mg/dl)			LDL (mg/dl)			Glucose (mg/dl)		
		Day 14	Day 7	Day 14	Day 7	Day 14	Day 7	Day 14	Day 7	Day 14	Day 7	Day 14	Day 7	Day 14	Day 7	Day 14
NC*	62±0.26a	62±1.0a	67±0.2 a	70±1.1a	60±2.1a	63±1.5a	48±1.8a	47±1.0a	21±1.8a	2 ±1.5a	113±1.0a	112±2.1a	113±1.0a	112±2.1a	113±1.0a	112±2.1a
OG*2 g gm/kg	118±0.15b	148±1.5b	121±0.26b	130±2.0b	112±1.6b	121±2.0b	30±1b	26±2.0b	92±1.5b	104±2.1b	124±2.1b	95±1.0b	124±2.1b	95±1.0b	124±2.1b	95±1.0b
OO 1 gm/kg	83±0.26c	81±2.1c	109±0.30c	111±2.1c	107±2.0b	103±2.2c	35±0.68b	37±2.0c	74±1.4c	78±1.4c	75±1.0c	61±2.2c	75±1.0c	61±2.2c	75±1.0c	61±2.2c
OO 2 gm/kg	80±0.25d	74±1.6d	115±0.15d	116±1.5d	104±3.0b	99±2.2d	40±c	42±1.6a	76±1.5d	76±1.5c	80±2.0c	71±1.3d	80±2.0c	71±1.3d	80±2.0c	71±1.3d
SO1 2 gm/kg	85±0.15e	80±2.5e	92±0.26e	100±1.7e	104±2.5b	100±2.2d	40±1c	42±1.8a	50±2.5e	49±1.6d	80±2.5c	66±2.1d	80±2.5c	66±2.1d	80±2.5c	66±2.1d
SO 2 gm/kg	75±0.25f	72±1.8d	89±0.31f	85±2.2f	85±2.1c	79±1.7e	42±2c	43±2.1a	47±1.6e	40±2.4e	105±1.5d	77±2.1e	105±1.5d	77±2.1e	105±1.5d	77±2.1e
Vitamin E 100 mg/kg	55±0.21g	53±1.5f	75±0.27g	69±1.1a	97±2.1d	93±1.8f	30±2.3b	31±1.9d	48±2e	38±0.85d	83±3.5c	94±1.3b	83±3.5c	94±1.3b	83±3.5c	94±1.3b
Vitamin E 200 mg/kg	51±0.31h	56±1.8f	71±0.30h	68±2.1a	89±1.0e	83±1.5e	32±1.3b	35±2.0c	40±2.0f	33±1.0f	88±2.1e	103±2.5f	88±2.1e	103±2.5f	88±2.1e	103±2.5f
Vitamin C 100 mg/kg	84±0.15i	86±1.0g	81±0.31i	76±2.0g	93±2.5d	88±1.5f	34±1.5b	36±1.5c	48±2.0e	47±1.0d	76±3.2c	85±2.0g	48±2.0e	76±3.2c	76±3.2c	85±2.0g
Vitamin C 200 mg/kg	73±0.35j	70±2.0d	76±0.3j	71±1.0a	75±2.0e	70±1.5g	37±2b	40±2.1c	39±1.0f	3 ±2.0f	102±1.0f	105±2.0f	39±1.0f	102±1.0f	102±1.0f	105±2.0f

OO, olive oil; SO, soya bean oil; NC, normal control; OG, oxidized ghee

level parameters, that were close to normal. A significant decrease in cholesterol level was observed also in the groups that were fed with olive oil and soya bean oil, but it still remained above the normal range.

As shown in Table 1, oxidized ghee significantly elevated the level of triglycerides in serum. Vitamin E and C significantly decreased the triglycerides' level increased by oxidized ghee. At day 14, no significant difference ($P<0.05$) was observed between the mean values of triglycerides' levels in soya bean oil (2 g/kg) and vitamin E 200 g/kg fed groups. There was also no significant difference ($P<0.05$) between vitamin E (100 mg/kg) and vitamin C (100 mg/kg) fed groups. The triglycerides' levels differed significantly ($P<0.05$) between the remaining experimental groups. Olive oil lowered the triglycerides' level, but to a smaller extent than other antioxidants tested.

Oxidized ghee significantly lowered HDL serum levels. Soya bean oil and olive oil counteracted this effect, increasing HDL level close to normal. Vitamin E and C also increased HDL level but still it was below normal. There was significant difference in HDL serum level among all the groups except vitamin E and C groups. Figure 1 demonstrates that oxidized ghee significantly increased LDL level. There was a significant decrease in LDL level in the groups that were fed with soya bean oil, vitamin E and C but still it was above the normal range. Olive oil also lowered LDL level, but its effect was weaker than other antioxidants.

Statistical significance of the comparison between the means in a row is denoted with letters: the same letter shows no significant difference between the means, while different letters represent a significant difference ($P<0.05$).

Effects on hematological parameters

Whole blood samples were analyzed for complete hematology for each of the groups. As shown in Table 2; at day 14, the groups fed with soya bean oil and vitamin E had increased TRBC, Hb, PCV, and MCH level compared to the ghee fed group. Vitamins E and C showed better antioxidant activity as compared to other oils in reference to MCHC. Oxidized ghee significantly elevated TLC and decreased neutrophil number whereas olive and soya bean oils counteracted this effect on neutrophils. In addition, soya bean oil significantly decreased lymphocytes count increased by the oxidized ghee. Soya bean oil and vitamin C significantly increased platelets count lowered by the oxidized ghee.

Liver histopathology

Histopathological examination of the rabbits' liver sections are demonstrated in Fig. 2. Hepatocytes of the Group A (normal control) revealed no significant histological abnormality (Fig. 2A–2B). Liver sections from the Groups B and C showed intact lobular architecture but the portal tracts showed inflammation and mild fibrosis. The bile ducts showed increased proliferation and the hepatocytes displayed feathery degeneration. (Fig. 2C–2D and 2E–2F). In the liver sections from Groups D to G; the portal tracts showed inflammation; and large vacuoles were present in the hepatocytes (Fig. 2G–2H to 2M–2N). The liver sections of rabbits in groups H and I showed intact lobular architecture with no significant histological abnormality in portal tracts but fatty changes in hepatocytes were present (Fig. 2O–2P and 2Q–2R). Liver sections of rabbits in Group J showed abnormalities similar to the rest of the non-normal control groups,

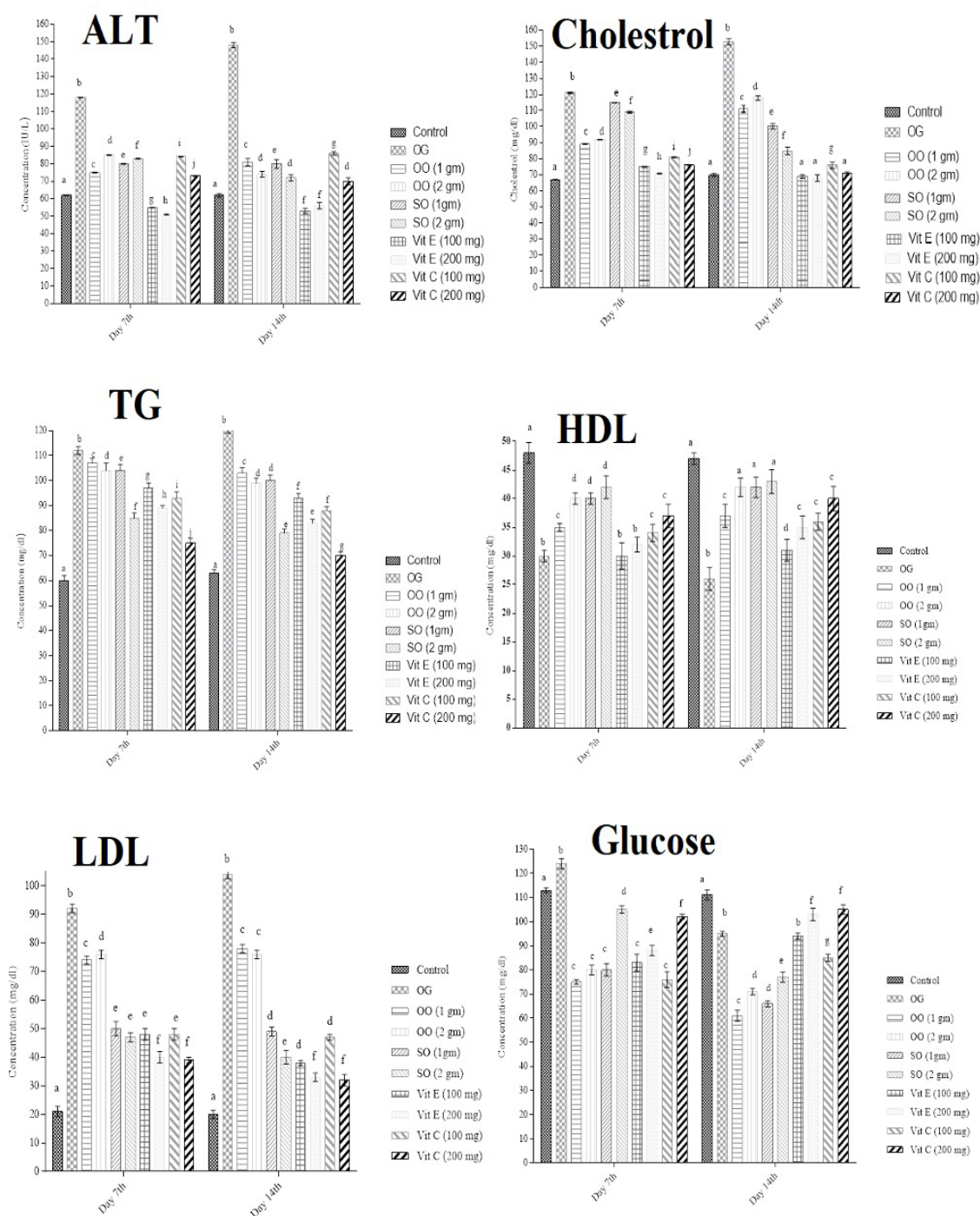


Figure 1. Hematological and biochemical parameters in the studied groups of rabbits at different timepoints.

Significant difference ($P < 0.05$) in glucose levels at day 14 was observed among all the groups, however, glucose levels were all in normal reference range in each group.

namely, sinusoidal dilation due to fats (Fig. 2S–2T). These findings revealed that vitamin E had superior antioxidant activity among the tested antioxidants because it effectively decreased liver inflammation caused by oxidized ghee.

Statistical significance of the comparison between the means in a row is denoted with letters: the same letter shows no significant difference between the means, while different letters represent a significant difference ($P < 0.05$).

DISCUSSION

This study showed that feeding rabbits with oxidized ghee at 2 g per kg body weight resulted in elevated ALT, triglycerides, total cholesterol and LDL levels, and overall decrease in HDL levels. Although this intervention decreased blood glucose levels, they remained in the reference range. These results corroborate similar recent study, where high triglycerides, cholesterol and LDL levels as well as low glucose level were observed in mice fed with heated ghee. Also, HDL level was low in ani-

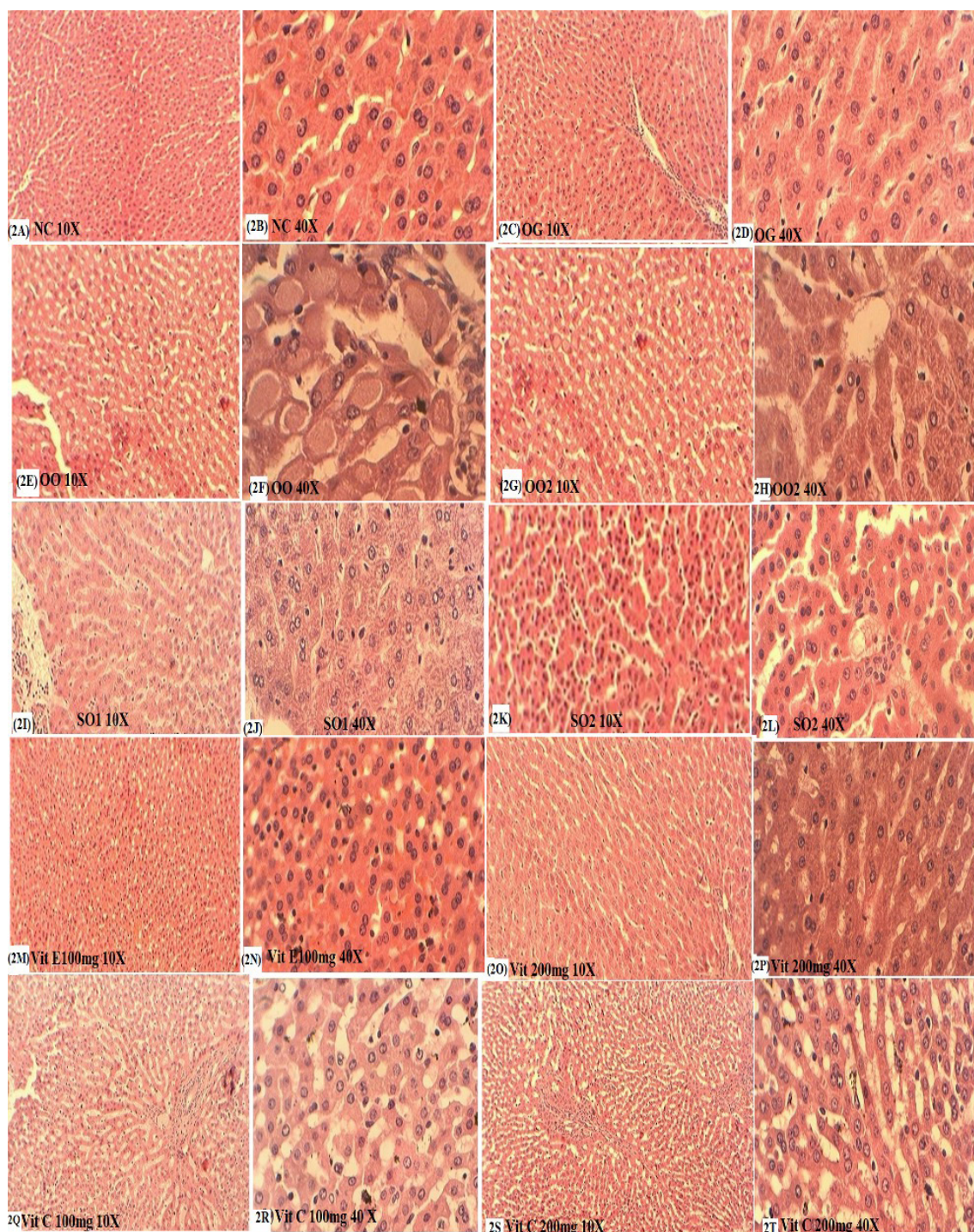


Figure 2. Histopathology of the rabbit liver samples

mals that were fed with thermally oxidized oils (Zahid *et al.*, 2022; Hina *et al.*, 2022; Sana *et al.*, 2022; Chinu & Rajamohan., 2011). Another study conducted in 2015 supports the findings of this study, i.e., high level of ALT, total cholesterol, triglycerol and LDL, as well as low glucose were observed in rabbits fed with oxidized corn oil (Aziz *et al.*, 2023; Uddin *et al.*, 2015). In the current paper, a decrease in TRBC, Hb, PCV, MCH, MCHC, neutrophils was observed in the rabbits fed with oxidized ghee. The platelets count was low but still in the normal range. Conversely, total leucocytes and lymphocytes numbers were increased above norm. When oxidized

ghee was fed to animals, it led to harmful effects on the blood cells (Sana *et al.*, 2022; Zeb & Ullah, 2015). Uddin and his coworkers (Uddin *et al.*, 2015) observed a decrease in TRB, hemoglobin, HCT, and an increase in WBC count in rabbits fed with oxidized corn oil. In the present study, it was observed that oxidized ghee was hepatotoxic and had adverse effect on liver histopathology. The liver tissue showed intact lobular architecture but the portal tracts showed inflammation and mild fibrosis, as well as accumulation of fat deposition in portal tract. The bile ducts showed signs of proliferation. The hepatocyte showed feathery degeneration. Similar results

Table 2. Hematology of different rabbits groups at 7th and 14th day.

Groups	RBC* (x 10 ⁶ /μl)		Hb* (%)		PCV* (%)		MCH* (pg)		MCHC* (gm/dl)		TLC* (103/ μl)		N* (%)		L* (%)		PLT%	
	Day 7	Day 14	Day 7	Day 14	Day 7	Day 14	Day 7	Day 14	Day 7	Day 14	Day 7	Day 14	Day 7	Day 14	Day 7	Day 14	Day 7	Day 14
NC*	5.7±0.1a	5.6±0.21a	11± 0.3a	12±0.2a	42±0.2a	44±2.5a	20.1±0.2a	21±1.5a	31.7±0.7a	33±1.5a	13.8±0.15a	13.8±0.32a	65.0±0.2a	65±2.1a	31.0±0.25a	34± 3.0a	530±1.5a	535±1.0a
OG*2 2gm/kg	4.1±0.15b	4.0±0.15	8.37±0.2b	8.1±0.2b	24±0.2b	23±2.0b	11±0.20b	10±2.0b	20±0.20b	19±1.5b	14.3±0.20a	14.3±0.15b	80.1± 0.2b	30±2.5b	17.0±0.20b	67±2.5b	345±1b	330±2.0b
OO 1 gm/kg	4.6±0.15c	4.3±0.31	9.17±0.15b	9.0±0.1c	29±0.15c	27±2.0b	15±0.20c	14±2.1b	25.0±0.15c	22±2.1b	15.1±0.15b	15±0.25c	76.0±0.15c	43±1.5c	21.1±0.20c	56±2.5c	435±1.5c	429±1.5c
OO 2 gm/kg	4.33±0.15c	4.4±0.25	8.5±0.1b	8.5±0.1b	26±0.15d	25±1.0b	13.0±0.20d	11±2.5b	23.1±0.21d	22±2.1b	14.4±0.20a	15±0.15c	77.1±0.2d	45±1.5d	20.0±0.20d	52±2.1c	402±2.1d	400±1.5d
SO1 2 gm/kg	4.30±0.20c	4.5±0.10	8.7±0.2b	8.8±0.2c	26.0±0.2d	27±1.5b	13.1±0.21d	13±1.5a	23.0±0.25d	24±1.5b	13.4±0.25 a	14±0.25a	78±0.153e	56±2.0e	19.0±0.157e	42±2.1a	397±2.0e	386±1.5e
SO 2 gm/kg	5.57±0.15a	5.7±0.21a	10.9±0.21a	11±0.1d	42.1±0.21a	41±2.0a	20.0±0.25a	19±2.0	31.0±0.15a	30±1.6a	11.4±0.15c	12±0.15d	61±0.25f	58±2.5e	36.0±0.153f	40±3.5a	521±1f	516±1.5f
Vitamin E 100 mg/kg	4.57±0.15c	4.6±0.17	9.7±0.25b	9.9±0.1c	31±0.42e	33±1.5c	16.0±0.20e	19±2.5a	27.0±0.20e	28±2.5a	13.4±0.252a	14±0.21a	73.1±0.208g	34±2.6b	24.1±0.208g	63±2.5b	467±1.5g	450±2.0g
Vitamin E 200 mg/kg	5.10±0.20a	5.2±0.20a	10.4±0.2c	11±0.1d	40±0.40f	41±1.5a	19.1±0.21f	20±2.5a	29.0±0.20f	29±2.0a	15.2±0.1a	15±0.20c	68±0.20h	31±2.0b	29.0±0.153h	69±2.5c	496±1.5h	491±2.1h
Vitamin C 100 mg/kg	4.9±0.15c	4.9±0.25	8.1±0.2b	9.6±0.2c	22±0.25g	39±1.5a	11.0±0.20b	14±2.0c	18.1±0.21g	24±2.0b	10.1±0.1b	10±2.0d	82.1±0.208i	33±2.0b	15.0±0.15i	63±2.5b	317 ± 1.5i	515±2.5i
Vitamin C 200 mg/kg	5.1±0.20a	5.1±0.15	8.67±0.25b	9.00±0.1c	26±0.20d	43±2.1a	13.1±0.21d	17±2.1a	21.0±0.25h	29±2.0a	15.1±0.25a	15±0.21c	78.1±0.2e	34±2.5b	19.1±0.20e	62±2.5c	394±2e	403±2.5d

OO, olive oil; SO, soya bean oil; NC, normal control; OG, oxidized ghee

were reported by Rahman and his team (Rahman *et al.*, 2012), in Long Evans rats, which showed scattered hepatocellular necrosis and degeneration of hepatocytes when fed with ghee (Zeb & Ullah, 2015; Rehman *et al.*, 2012).

The effect of olive oil and its high polyphenol contents have been studied before and the results support the present study's findings, i.e., increased HDL levels, decreased cholesterol, TG, and LDL levels in oxidized ghee fed rabbits (Covas *et al.*, 2006). However, our study's results are a little different from one of the earliest papers published in 1996 that stated that olive oil protects low-density lipoprotein from oxidative activities (Jassim *et al.*, 2010). It has also been observed that feeding of olive oil along with mercuric chloride gradually normalized serum ALT level (Wiserman *et al.*, 1996; Youcef *et al.*, 2014). Administration of olive oil appeared to decrease Hb concentration, WBC, platelet, and lymphocyte numbers in the treated rats, however, the difference was statistically significant only in the case of the platelet count (Nandakumaran *et al.*, 2014).

In the present study, rabbits fed with olive oil along with oxidized ghee had intact lobular architecture of the liver but their portal tracts showed inflammation and their hepatocytes contained large vacuoles. Szende and colleagues observed that olive oil reduced hepatotoxicity of oral carbon tetrachloride (CCl₄) (Szende *et al.*, 1994). Olive oil partially protected the liver from mercuric chloride (HgCl₂) induced damage. A prominent recovery in the form of normal hepatocytes and greatly reduced centrilobular necrosis were observed. Pronounced sinusoid with granular hepato-cytoplasm were also present (Nandakumaran *et al.*, 2014). Similar results were reported by another study in rats, in which the ingestion of olive oil protected the liver from ethanol-induced oxidative damage by affecting the cellular redox potential (Kasdal-lah *et al.*, 2008).

A significant mitigating effect against ghee-induced hepatotoxicity was observed for soya bean oil. This effect was dose dependent. One study showed that feeding rats with non-oxidized soya bean oil alone induced significant and dose-dependent alteration in biochemical and hematological parameters (Robaina *et al.*, 1995; Salahuddin *et al.*, 2013). Another study conducted using soybean oil showed that animals fed with the oil had changes in the liver, including distinct enlargement of central veins and erythrocyte accumulation, enlargement and congestion of sinusoids (Salahuddin *et al.*, 2013).

In the present study, we observed a protective role of vitamin E against the oxidized ghee-induced toxicity. Rabbits fed with oxidized ghee and vitamin E at 100 mg/kg or 200 mg/kg had decreased ALT, triglycerides, total cholesterol, and LDL levels, and increased HDL level in the direction of norm but still outside of the reference range. Similar results have previously been reported in case of mice fed with high fat diet and high-fat and high-cholesterol diet by increasing serum total triglycerides, cholesterol, and altered alanine aminotransferase, aspartate aminotransferase, and alkaline phosphatase (Liang *et al.*, 2021). It was also observed that vitamin E increased TRBC, Hb, PCV, MCH, MCHC, and neutrophil counts, and decreased TLC and lymphocyte count, but not to such an extent that these indicators were within the normal range. Amer and his research team also support these results showing that vitamin E and C reduce oxidative damage to RBC and platelets (Amer *et al.*, 1991).

In our study, the protective effect of vitamin E against oxidized ghee induced toxicity was also observed in the liver histopathology. An intact lobular architec-

ture with no significant histological abnormality in portal tracts was observed, however mild inflammation and mild fibrosis were detected in the portal tracts. These results are in agreement with the results of earlier studies which showed that vitamins E and C significantly improved liver fibrosis (Amer *et al.*, 2006). Also, vitamin C, when fed along with sodium fluoride (NaF) partially protected the liver from NaF toxicity (Stawiarska *et al.*, 2012). Uboh and his colleagues in 2012 demonstrated that in a model of gasoline vapor-induced liver injury in rats, vitamin E and C had protective effect on liver histopathology. The hepatoprotective effect was significantly higher in case of vitamin E than vitamin C (Uboh *et al.*, 2009). These findings support the results obtained in our study. In the previous studies, oxidized ghee caused inflammation and degeneration of hepatocytes (Zeb & Uddin 2017b), which is in concordance with our results. Also, both, enlargement of hepatic capillaries and severe liver necrosis were observed in the previous studies (Jimoh *et al.*, 2004). In our histopathological findings, we observed a protective role of olive oil, soybean oil, and vitamins E and C against the oxidized ghee effects, and only mild liver inflammation and fibrosis (groups that received antioxidants together with the oxidized ghee) were observed in oxidized ghee fed animals co-fed with these antioxidants.

CONCLUSIONS

The experiment presented here was designed to examine a protective role of various lipids (olive and soya oil) and vitamins (E and C) against thermally oxidized ghee toxicity in rabbits. Oxidized ghee diet altered the hematological and biochemical parameters and induced abnormalities in liver histopathology in rabbits. Soya bean oil and vitamin E were the most effective against the toxic effects of thermally oxidized ghee as compared to olive oil and Vitamin C. It is recommended that ghee can be substituted with soya bean oil. Further studies can be conducted to identify the oxidative products accumulated in oxidized ghee and test other antioxidants' potential against the toxic effects of the oxidized ghee.

Declarations

Conflict of interest: All the authors declare no conflict of interest.

REFERENCES

- Amer J, Ghoti H, Rachmilewitz E, Koren A, Levin C, Fibach E (2006) Red blood cells, platelets and polymorphonuclear neutrophils of patients with sickle cell disease exhibit oxidative stress that can be ameliorated by antioxidants. *Br J Hematol* **132**: 108–113. <https://doi.org/10.1111/j.1365-1412.2005.05834.x>
- Applewhite TH (1981) Nutritional effects of hydrogenated soya oil. *J American Oil Chem Soc* **58**: 260–269. <https://doi.org/10.1007/BF02582353>
- Aziz T, Ihsan F, Ali Khan A, Ur Rahman S, Zamani GY, Alharbi M, Alshammari A, Alasmari AF (2023) Assessing the pharmacological and biochemical effects of *Salvia hispanica* (Chia seed) against oxidized *Helianthus annuus* (sunflower) oil in selected animals. *Acta Biochim Pol* **27**. <https://doi.org/10.18388/abp.2020.6621>
- Szende B, Timár F, Hargitai B (1994) Olive oil decreases liver damage in rats caused by carbon tetrachloride (CCl₄) *Exp Tox Pharmacol* **46**: 355–359. [https://doi.org/10.1016/S0940-2993\(11\)80116-8](https://doi.org/10.1016/S0940-2993(11)80116-8)
- Brahmi F, Haddad S, Bouamara K, Yalaoui-Guellal D, Prost-Camus E, de Barros JP, Prost M, Atanasov AG, Madani K, Boulekbache-Makhlouf L, Lizard G (2020) Comparison of chemical composition and biological activities of Algerian seed oils of *Pistacia lentiscus* L., *Opuntia ficus indica* (L.) mill. and *Argania spinosa* L. skeys. *Industrial Crops Products* **151**: 112456. <https://doi.org/10.1016/j.indcrop.2020.112456>
- Chan, AC (1993) Partners in defense, vitamin E and vitamin C. *Canadian J Physiol Pharmacol* **71**: 725–731. <https://doi.org/10.1139/y93-109>
- Chinu C, Rajamohan T (2011) Repeatedly heated cooking oils alter platelet functions in cholesterol fed Sprague Dawley rats. *Int J Biolog Med Res* **2**: 991–997
- Covas MI, Nyyssönen K, Poulsen HE, Kaikkonen J, Zunft HJ, Kiesewetter H, Gaddi A, de la Torre R, Mursu J, Bäumlér H, Nascetti S, Salonen JT, Fitó M, Virtanen J, Marrugat J (2006) The effect of polyphenols in olive oil on heart disease risk factors: a randomized trial. *Ann Int Med* **145**: 333–341. <https://doi.org/10.7326/0003-4819-145-5-200609050-00006>
- Cuomo F, Cinelli G, Chirascu C, Marconi E, Lopez F (2020) Antioxidant effect of vitamins in olive oil emulsion. *colloids and interfaces*. **4**: 23. <https://doi.org/10.3390/colloids4020023>
- Friday, EU, Effiong, PE, Akpan, HD, Usho, IF (2012) Hepatoprotective effect of vitamins C and E against gasoline vapor-induced liver injury in male rats. *Turkish J Bio* **36**: 217–223. <https://doi.org/10.3906/biy-1004-111>
- Gutteridge JM (1995) Lipid peroxidation and antioxidants as biomarkers of tissue damage. *Clin Chem* **41**: 1819–1828
- Halliwell, B, Gutteridge JM (1990) Role of free radicals and catalytic metal ions in human disease: an overview. *Methods Enzymol* **186**: 1–85. [https://doi.org/10.1016/0076-6879\(90\)86093-b](https://doi.org/10.1016/0076-6879(90)86093-b)
- Iqbal MP (2014) Trans fatty acids – A risk factor for cardiovascular disease. *Pak J Med Sci* **30**: 194–197. <https://doi.org/10.12669/pjms.301.4525>
- Priyanka JM (2016) Ayurvedic perspective on oxidative stress management: *The Science of Free Radical Biology and Disease*. Armstrong D, Stratton RD eds, pp 483–492. <https://doi.org/10.1002/9781118832431.ch29>
- Jassim RA, Mihele D, Dogaru E (2010) Study regarding the influence of *Vitis vinifera* fruit (Muscat of Hamburg species) on some biochemical parameters. *FARMACIA* **58**: 332–340
- Kamal Eldin A, Mäkinen M, Lampi AM (2003) The challenging contribution of hydroperoxides to the lipid oxidation mechanism. Lipid oxidation pathways. *Swedish Univ Agri Sci* 1–36, Uppsala, Sweden
- Kasdallah-Grissa A, Nakbi A, Koubaa N, El-Fazaâ S, Gharbi N, Kamoun A, Hammami M (2008) Dietary virgin olive oil protects against lipid peroxidation and improves antioxidant status in the liver of rats chronically exposed to ethanol. *Nutr Res* **28**: 472–479. <https://doi.org/10.1016/j.nutres.2008.03.014>
- Khan AA, Zeb A, Shirazi STH (2017) Thermally oxidized olive oil produces biochemical, physiological effects and fatty liver in rats. *Chiang Mai J Sci* **44**: 847–857
- Kiritsakis, AK, Tsitsipis, CK (2020) A review of the evolution in the research of antioxidants in olives and olive oil during the last four decades. *J Food Bioactive* **11**. <https://doi.org/10.31665/JFB.2020.11236>
- Kosif, R, Yilmaz, F, Evrendilek, GA, Diramal, M (2010) Histopathological effects of Aloe barbadensis and soybean oil on rat liver. *Int J Morphol* **28**: 1101–1106. <http://dx.doi.org/10.4067/S0717-95022010000400019>
- Kumar MV, Sambaiah K, Lokesh BR (2000) Hypocholesterolemic effect of anhydrous milk fat ghee is mediated by increasing the secretion of biliary lipids. *J Nutrit Biochem* **11**: 69–75. [https://doi.org/10.1016/S0955-2863\(99\)00072-8](https://doi.org/10.1016/S0955-2863(99)00072-8)
- Lee KG, Shibamoto T (2000) Antioxidant properties of aroma compounds isolated from soybeans and mung beans. *J Agric Food Chem* **48**: 4290–4293. <https://doi.org/10.1021/jf000442u>
- Liang H, Jiang F, Cheng R, Luo Y, Wang J, Luo Z, Li M, Shen X, He F (2021) A high-fat diet and high-fat and high-cholesterol diet may affect glucose and lipid metabolism differentially through gut microbiota in mice. *Exp Anim* **70**: 73–83. <https://doi.org/10.1538/expanim.20-0094>
- Mobin J (2012) *Role of Reactive Oxygen Species in Normal Postnatal Lung Growth*. MSc. Thesis, University of Toronto (Canada) <https://hdl.handle.net/1807/33251>
- Moorkath N, Al-Sannan B, Al-Dossary M, Al-Shammari M (2014) Effect of olive oil administration on some hematologic and metabolic parameters in female rats. *Int J Pure Appl Biosci* **2**: 93–99
- Necib Y, Bahi A, Zerizer S, Abdennour C, Boulakoud MS (2014) Protective effect of virgin olive oil (*Olea europaea* L.) against oxidative damage induced by mercuric chloride in rat Albino Wistar. *J Stress Physiol Biochem* **10**: 45–58
- Nocella C, Cammisotto V, Fianchini L, D'Amico A, Novo M, Castellani V, Stefanini L, Violi F, Carnevale R (2018) Extra virgin olive oil and cardiovascular diseases: benefits for human health. *endocrine, metabolic. Immune Disorders Drug Targets* **18**: 4–13. <https://doi.org/10.2174/1871530317666171114121533>
- Rahman MA, Jahan M, Karmaker S, Islam MK (2012) Effects of different fatty acid supplementation on body weight and hematobiochemical parameters in rat. *Int J Nat Sci* **2**: 21–25. <https://doi.org/10.3329/ijns.v2i1.10879>
- Robaina L, Izquierdo MS, Moyano FJ, Socorro J, Vergara JM, Montero D, Fernández-Palacios H (1995) Soybean and lupin seed meals as

- protein sources in diets for gilthead seabream (*Sparus aurata*): nutritional and histological implications. *Aquaculture* **130**: 219–233.
- Rusin, A, Krawczyk, Z (2011) Genistein derivatization from a dietary supplement to a pharmaceutical agent. In *Soybean and Health*, pp 253–282. <https://doi.org/10.5772/18733>
- Salahuddin, M, Sarker, M, Ahmad, N, Miah, MA (2013) Effects of varying concentration of soybean oils on hemato-biochemical profile in mice. *Bangladesh J Anim Sci* **42**: 148–151. <https://doi.org/10.3329/bjas.v42i2.18502>
- Sana, Ur Rahman S, Zahid M, Khan AA, Aziz T, Iqbal Z, Ali W, Khan FF, Jamil S, Shahzad M, Alharbi M, Alshammari A (2022) Hepatoprotective effects of walnut oil and *Caralluma tuberculata* against paracetamol in experimentally induced liver toxicity in mice. *Acta Biochim Pol* **69**: 871–878. https://doi.org/10.18388/abp.2020_6387
- Stawiarska-Pięta B, Bielec B, Birkner K, Birkner E (2012) The influence of vitamin E and methionine on the activity of enzymes and the morphological picture of liver of rats intoxicated with sodium fluoride. *Food Chem Toxicol* **50**: 972–978. <https://doi.org/10.1016/j.fct.2012.01.014>
- Uddin, MS, Sarker, MZI, Ferdosh, S, Akanda, MJH, Easmin, MS, Bt Shamsudin, SH, Yunus, KB (2015) Phytosterols and their extraction from various plant matrices using supercritical carbon dioxide: a review. *J Sci Food Agric* **95**: 1385–1394. <https://doi.org/10.1002/jsfa.6833>
- Uboh FE, Ekaideem IS, Ebong PE, Umoh IB (2009) The hepatoprotective effect of vitamin A against gasoline vapor toxicity in rats. *Gastroenterol Res* **2**: 162–167. <https://doi.org/10.4021/gr2009.06.1297>
- Wiseman, SA, Mathot JN, de Fouw NJ, Tijburg LB (1996) Dietary non-tocopherol antioxidants present in extra virgin olive oil increase the resistance of low-density lipoproteins to oxidation in rabbits. *Atherosclerosis* **120**: 15–23. [https://doi.org/10.1016/0021-9150\(95\)05656-4](https://doi.org/10.1016/0021-9150(95)05656-4)
- Wójcicki J, Rózewicka L, Barcew-Wiszniewska B, Samochowiec L, Juźwiak S, Kadłubowska D, Tustanowski S, Juzyszyn Z (1991) Effect of selenium and vitamin E on the development of experimental atherosclerosis in rabbits. *Atherosclerosis* **87**: 9–16. [https://doi.org/10.1016/0021-9150\(91\)90227-t](https://doi.org/10.1016/0021-9150(91)90227-t)
- Necib Y, Bahi A, Zerizer S, Abdenmour C, Boulakoud MS (2014) Protective effect of virgin olive oil (*Olea europaea* L.) against oxidative damage induced by mercuric chloride in rat Albinos Wistar. *J Stress Physiol Biochem* **10**: 45–58. <https://citeseerx.ist.psu.edu/document?repid=rep1&type=pdf&doi=de85afd8e76571d60913553a40eed96f51b82dcf>
- Zahid H, Shahab M, Ur Rahman S, Iqbal Z, Khan AA, Aziz T, Ali W, Zamani GY, Ahmad S, Shahzad M, Alharbi M, Alshammari A (2022) Assessing the effect of walnut (*Juglans regia*) and olive (*Olea europaea*) oil against the bacterial strains found in Gut Microbiome. *Progr Nutr* **27**: 1–13. <https://doi.org/10.23751/pn.v24i3.13311>
- Zeb A, Khan AA (2019) Improvement of serum biochemical parameters and hematological indices through α -Tocopherol administration in dietary oxidized olive oil induced toxicity in rats. *Front Nut* **5**: 137. <https://doi.org/10.3389/fnut.2018.00137>
- Zeb A, Mehmood A (2012) Effects of oxidized vanaspati ghee on the serum lipids profile and radical scavenging activity of the *in vitro* lipids of liver, brain and muscles. *Türk Biyokimya Dergisi/Turkish J Biochem* **37**: 417–423. <https://doi.org/10.5505/tjb.2012.63325>
- Zeb A, Uddin I (2017) The coadministration of unoxidized and oxidized desi ghee ameliorates the toxic effects of thermally oxidized ghee in rabbits. *J Nutr Met* **2017**: 4078360. <https://doi.org/10.1155/2017/4078360>
- Zeb A, Ullah S (2015) Sea buckthorn seed oil protects against the oxidative stress produced by thermally oxidized lipids. *Food Chem* **186**: 6–12. <https://doi.org/10.1016/j.foodchem.2015.03.053>
- Zalejska-Fiolka J, Kasperczyk A, Kasperczyk S, Stawiarska-Pięta B, Fiolka R, Birkner E (2012) Influence of non-oxidised and oxidised rapeseed oil consumption on liver metabolism pathways and non-alcoholic steatohepatitis development in rabbits. *Bull Vet Inst Pulawy* **56**: 255–259. <https://doi.org/10.2478/v10213-012-0045-x>

Acta Biochimica Polonica (ABP) is a multidisciplinary Open Access journal that publishes premier research in the field of biochemistry

ABP is the official journal of Polskie Towarzystwo Biochemiczne (Polish Biochemical Society). The journal welcomes research contributions in the various domains of biochemistry, which bridge the gap between scientific discovery and clinical application.

Discover more of our Special Issues

See more →

Find out more

Polish Biochemical Society
Acta Biochimica Polonica
Frontiers Partnerships

Contact

abp@frontierspartnerships.org

